ASM HANDBOOK

VOLUME 9

Metallography and Microstructures 2004

ASM INTERNATIONAL®
The Materials Information Company

Publication Information and Contributors

Introduction

Metallography and Microstructures was published in 2004 as Volume 9 of the *ASM Handbook*. The Volume was prepared under the direction of the ASM Handbook Committee.

Volume Editors

The Volume Editor was George F. Vander Voort.

Authors and Contributors

Brent L. Adams, Brigham Young University
Debbie Aliya, Aliya Analytical, Inc.
David Alman, Albany Research Center, U.S. Dept. of Energy
Roland Aubin, Amsco Cast Products (Canada) Inc.
Steven Axdal, Seagate Technology Inc.
William Baldwin, ChevronTexaco
Bruce Bardes, Cincinnati Metallurgical Consultants LLC
Bob Barth, Olin Brass
Kurt W. Batson, The Boeing Company
Peter Bauer, Leica Microsystems
Arlan O. Benscoter, Lehigh University
Michael Blum, Materials Technology Associates Inc.
Richard Bodnar, International Steel Group, Inc.
Rodney R. Boyer, The Boeing Company
Bruce L. Bramfitt, International Steel Group, Inc.
Amarjit S. Brar, Seagate Technology Inc.
Robert D. Briggs, The Boeing Company
Thomas Calahan, Carl Zeiss, Inc.
Veronika Carle, Max-Planck Institut für Metallforschung
R.N. Caron, Olin Brass
Lichun Leigh Chen, Engineered Materials Solutions
Richard C. Compton, Zimmer, Inc.
Lesley Cornish, MINTEK
W. Raymond Cribb, Brush Wellman Inc.
Paul Crook, Haynes International
Paul E. Danielson, Albany Research Center, U.S. Dept. of Energy
Joseph R. Davis, Davis & Associates
M. Dayananda, Purdue University
Ryan M. Deacon, Lehigh University
Raymond L. Decker, Thixomat, Inc.
Robert T. DeHoff, University of Florida
Omer Dogan, Albany Research Center, U.S. Dept. of Energy
Roger Doherty, Drexel University
Charles W. Domby, The Boeing Company
Timothy Eck, Alcoa Mill Products
Mario Epler, Lehigh University
Craig Eucken, Wah Chang
H.E. Exner, Darmstadt University of Technology

Henry E. Fairman, Cincinnati Metallurgical Consultants LLC
David P. Field, Washington State University
Luther M. Gammon, The Boeing Company
Frank C. Gift, Jr., Lehigh University
Arun Gokhale, Georgia Institute of Technology
Peter J. Goodhew, University of Liverpool
Martha Goodway, Smithsonian Institution
Stewart Grice, Hoover & Strong Inc.
Amitava Guha
Larry Hanke, Materials Evaluation & Engineering Inc.
Niels Hansen, Risø National Laboratory
John C. Harkness, Brush Wellman Inc.
Craig S. Hartley, Air Force Office of Scientific Research
Jeffrey A. Hawk, Albany Research Center, U.S. Dept. of Energy
Dennis W. Hetzner, The Timken Company
Michael J. Hoffmann, Universität Karlsruhe
Frauke Hogue, Hogue Metallography
Michael Holt, Frog, Switch and Manufacturing Company
Dennis D. Huffman, The Timken Company (retired)
Darcy Hughes, Sandia National Laboratories
Gene Ice, Oak Ridge National Laboratory
Kent L. Johnson, Engineering Systems Inc.
John Jorstad, J.L.J. Technologies, Inc.
Ann Kelly, Los Alamos National Laboratory
Dwaine L. Klarstrom, Haynes International
Jacek Komenda, Swedish Institute for Metals Research
Paul Kovach, Stress Engineering Services, Inc
Milo Kral, University of Canterbury (Australia)
George Krauss, Colorado School of Mines
Krzysztof J. Kurzydłowki, Warsaw University of Technology
Selcuk Kuyucak, CANMET
Samuel J. Lawrence, International Steel Group, Inc.
Todd A. Leonhardt, Rhenium Alloys Inc.
Heiner Lichtenberger, Williams Advanced Materials Inc.
Huimin Liu, Ford Motor Company
Gabriel M. Lucas, Buehler Ltd.
Elena P. Manilova, Polzunov Central Boiler and Turbine Institute (Russia)
William L. Mankins, Metallurgical Services, Inc.
Arnold R. Marder, Lehigh University
Dana J. Medlin, Zimmer, Inc.
M.K. Miller, Oak Ridge National Laboratory
John E. Morral, The Ohio State University
Yellapu V. Murty, CMI, Inc.
Brian Newbury, Lehigh University
Rick Noecker, Lehigh University
Michael Notis, Lehigh University
James J. Oakes, Metalworking Products
Sidnei Paciornik, DCMM PUC-Rio
John M. Packard, The Boeing Company
Toby V. Padfield, ZF Sachs Automotive of America
Shane Para, Lehigh University
Leander F. Pease, III, Powder-Tech Associates, Inc.
Matthew J. Perricone, Lehigh University
Samuel M. Purdy

Janina M. Radzikowska, The Foundry Research Institute (Kraków)
Brian Ralph, Brunel University
Jonathan Regina, Lehigh University
Maria Richert, University of Mining & Metallurgy (Kraków)
R.O. Rosenberg, Naval Research Laboratory
Roxana Ruxanda, The University of Alabama
A.T. Santhanam, Kennametal Inc.
John P. Sauer, Sauer Engineering
Ute Schäfer, Max-Planck Institut für Metallforschung
Shahram Shebany, Pacific Metallurgical Company
Robert C. Solbach
Karl P. Staudhammer, Los Alamos National Laboratory
Doru M. Stefanescu, The University of Alabama
Jeff Stewart, Stern Leach Company
Rainer Süss, MINTEK
Richard C. Sutherlin, Wah Chang
Janusz Szala, Silesian University of Technology
Jerzy A. Szpunar, McGill University
Ulrike Täffner, Max-Planck Institut für Metallforschung
Keith Taylor, International Steel Group Inc.
Stefanie Taylor, MINTEK
Derek E. Tyler, Olin Metals Research Laboratory
M.D. Uchic, Air Force Research Laboratory
Elma van der Lingen, MINTEK
George Vander Voort, Buehler Ltd.
Edward J. Vinarcik, Robert Bosch Corporation
Fran Warmuth, Wyman-Gordon Forgings
Małgorzata Warmuzek, Foundry Research Institute (Poland)
Michael L. Wayman, University of Alberta
S. Weinbruch, Darmstadt University of Technology
Matthew A. Willard, Naval Research Laboratory
Richard D. Wilson, Albany Research Center, U.S. Department of Energy
Leczek D. Wojnar, Krakow University of Technology
J. Wu, Deloro Stellite Group Limited

Foreword

ASM International is pleased to publish a new edition of *Metallography and Microstructures,* Volume 9 of the *ASM Handbook* series. Metallography is a longstanding core interest of ASM International members, and this new Volume 9 reflects the continuing importance of metallography in metallurgical analyses for production quality control, research, engineering, and educational training. Since the 1985 edition of Volume 9, substantial changes have occurred in automation, equipment, preparation methodology, alloys, manufacturing technologies, and digital imaging. The new Volume 9 addresses these and other developments, as described in the Preface.

We commend the Volume Editor, George Vander Voort, for his vision and direction in revising *Metallography and Microstructures*. His familiarity with past and present volumes of the Handbook series has been instrumental in this project. His worldwide acquaintances with members of the metallographic community also have made this Volume an international effort with important contributions from authors around the world. Moreover, many thanks are extended to the devoted volunteers and ASM members, who have contributed their time and expertise as authors and reviewers. This Volume would not have been possible without their commitment. The sharing of their knowledge and experience is the basis for ASM International as their professional society.

Robert C. Tucker, Jr., President, ASM International
Stanley C. Theobald, Managing Director, ASM International

Preface

This new edition of *Metallography and Microstructures,* Volume 9 of the *ASM Handbook* series, is quite different from the 1985 edition in several ways. One difference is that the citations of micrographs are integrated within the textual discussions on the metallography and microstructures of materials. This is distinctly different from the previous edition, in which the end of each article contained an atlas of many micrographs without citation in text. The atlas method in the previous edition was effective at that time, as micrograph collections are useful in making visual comparisons for different materials conditions and/or specimen preparation techniques. However, with the development of electronic publication, a new approach is possible, where a large collection of micrographs can be stored and searched electronically. This is the underlying concept of the newly released Micrograph Center as part of the ASM International Materials Information Online. This electronic archive provides a collection of the previously published micrograph atlases in the 8th and the 9th Editions *Metals Handbook.* As such, one objective of the new Volume 9 is to complement more closely the electronic archive of the Micrograph Center by moving away from an atlas format and by focusing more on representative micrographs that are visual tools in assisting experienced and new practitioners in the preparation and interpretation of micrographs.

The new Volume 9 also places more emphasis on the underlying physical metallurgy of alloys, as an important part in the interpretation and understanding of microstructural development. In this regard, formation of phase constituents is described in more detail in terms of the general concepts in physical metallurgy and key compositional categories of important alloy systems. Some coverage on phase diagrams is included, although binary phase diagrams are not collected to the same extent as in the 8th Edition *Metals Handbook,* Volume 8, *Metallography, Structures, and Phases Diagrams* (1973). This is because binary phase diagrams are covered extensively in other publications such as *ASM Handbook,* Volume 3, *Alloy Phase Diagrams,* and the *Desk Handbook: Phase Diagrams for Binary Alloys,* ASM International, 2000. In this volume, the key emphasis is on the concepts for using phase diagrams as a tool in metallographic interpretation and on the presentation of important binary-phase regions or the quasi-binary and pseudo-binary diagrams of key compositional components.

The new Volume 9 edition also provides important updates and new information reflecting the substantial changes in automation, equipment, consumable products, and preparation methodology, as well as new metals, alloys, and manufacturing technologies that have emerged since 1985. Expanded and new coverage includes:

- New articles on field metallography, digital imaging, and quantitative image analysis, quantitative metallography, and color metallography
- All-new articles on the metallography and microstructural interpretation of cast irons, coated steel, carbon and low-alloy steels, aluminum alloys, precious-metal alloys, titanium alloys, ceramics, and thermal spray coatings
- Substantially revised articles on metallography and microstructural interpretation of tool steels, stainless steels, copper alloys, P/M alloys, and cemented carbides
- New micrographs throughout
- More integrated in-text citation of micrograph images with respect to discussions on preparation techniques and alloy metallurgy
- Updated coverage on specimen-preparation techniques for both manual methods and semi-automatic machines
- Practical coverage on sectioning and specimen extraction
- Laboratory safety guide
- New expanded color section

The titles of new articles on metallurgical topics include:

- Metallography: An Introduction
- Physical Metallurgy Concepts in Interpretation of Microstructure
- Fundamentals of Solidification
- Solidification Structures of Steels and Cast Iron
- Solidification Structures of Aluminum Alloys

- Solidification Structures of Titanium Alloys
- Inter-Diffusion Structures
- Plastic Deformation Structures
- Textured Structures

Titles of all-new articles on metallography include:

- Metallographic Sectioning and Specimen Extraction
- Light and Electron Microscopy
- Digital Imaging
- Quantitative Image Analysis
- Quantitative Characterization and Representation of Global Microstructural Geometry
- Three-Dimensional Microscopy
- Metallography of Archaeological Alloys
- Field Metallography Techniques
- Color Metallography
- Laboratory Safety in Metallography

In addition, this edition of Volume 9 has all-new articles on the metallography and microstructures of the following materials:

- Cast Iron
- Carbon and Low-Alloy Steels
- Aluminum and Its Alloys
- Cobalt and Its Alloys
- Precious Metals and Their Alloys
- Titanium and Its Alloys
- Biomedical Orthopedic Alloys
- Semisolid Formed Alloys
- Thermal Spray Coatings
- Ceramics

With this extensive revision of Volume 9, *Metallography and Microstructures* continues to be a comprehensive and indispensable reference work for anyone who specifies, performs, monitors, evaluates, or uses metallurgical analyses for production quality control, research, or educational training.
George Vander Voort, Buehler Ltd., Volume Editor
Steven Lampman, ASM International, Staff Editor

Officers and Trustees of ASM International (2003–2004)

Officers

Robert C. Tucker, Jr., President and Trustee
The Tucker Group LLC
Andrew R. Nicoll, Sulzer Metco (U.S.) Inc.
Vice President and Trustee
Donald R. Muzyka, Immediate Past President and Trustee
Special Metals Corporation (retired)
Paul L. Huber, Treasurer
Seco/Warwick Corporation
Stanley C. Theobald, Secretary and Managing Director
ASM International

Trustees

Reza Abbaschian, University of Florida
Rodney R. Boyer, Boeing Commercial Airplane Group
Dianne Chong, The Boeing Company
Roger J. Fabian, Bodycote Thermal Processing
William E. Frazier, Naval Air Systems Command
Richard L. Kennedy, Allvac
Richard D. Sisson, Jr., Worcester Polytechnic Institute
George F. Vander Voort, Buehler Ltd.
Lawrence C. Wagner, Texas Instruments

Members of the ASM Handbook Committee (2003–2004)

Henry E. Fairman, (Chair 2002–; Member 1993–)
Cincinnati Metallurgical Consultants
Jeffrey A. Hawk, (Vice Chair 2002–; Member 1997–)
U.S. Department of Energy
David E. Alman (2002–)
U.S. Department of Energy
Bruce P. Bardes (1993–)
Cincinnati Metallurgical Consultants
Lichun Leigh Chen (2002–)
Engineered Materials Solutions
Craig V. Darragh (1989–)
The Timken Company
Larry D. Hanke (1994–)
Materials Evaluation and Engineering Inc.
Michael A. Hollis (2003–)
Delphi Corporation
Dennis D. Huffman (1982–)
The Timken Company (retired)
Dwight Janoff (1995–)
FMC Corporation
Kent L. Johnson (1999–)
Engineering Systems Inc.
Paul J. Kovach (1995–)
Stress Engineering Services Inc.
Donald R. Lesuer (1999–)
Lawrence Livermore National Laboratory
Huimin Liu (1999–)
Ford Motor Company
Alan T. Male (2003–)
University of Kentucky
William L. Mankins (1989–)
Metallurgical Services Inc.
Srikanth Raghunathan (1999–)
Nanomat Inc.
Karl P. Staudhammer (1997–)
Los Alamos National Laboratory
Kenneth B. Tator (1991–)
KTA-Tator Inc.
George F. Vander Voort (1997–)
Buehler Ltd.

Previous Chairs of the ASM Handbook Committee

R.J. Austin, (1992–1994) (Member 1984–)
L.B. Case, (1931–1933) (Member 1927–1933)
T.D. Cooper, (1984–1986) (Member 1981–1986)
C.V. Darragh, (1999–2002) (Member 1989–)
E.O. Dixon, (1952–1954) (Member 1947–1955)
R.L. Dowdell, (1938–1939) (Member 1935–1939)
M.M. Gauthier, (1997–1998) (Member 1990–)
J.P. Gill, (1937) (Member 1934–1937)
J.D. Graham, (1966–1968) (Member 1961–1970)
J.F. Harper, (1923–1926) (Member 1923–1926)
C.H. Herty, Jr., (1934–1936) (Member 1930–1936)
D.D. Huffman, (1986–1990) (Member 1982–)
J.B. Johnson, (1948–1951) (Member 1944–1951)
L.J. Korb, (1983) (Member 1978–1983)
R.W.E. Leiter, (1962–1963) (Member 1955–1958, 1960–1964)
G.V. Luerssen, (1943–1947) (Member 1942–1947)
G.N. Maniar, (1979–1980) (Member 1974–1980)
W.L. Mankins, (1994–1997) (Member 1989–)
J.L. McCall, (1982) (Member 1977–1982)
W.J. Merten, (1927–1930) (Member 1923–1933)
D.L. Olson, (1990–1992) (Member 1982–1988, 1989–1992)
N.E. Promisel, (1955–1961) (Member 1954–1963)
G.J. Shubat, (1973–1975) (Member 1966–1975)
W.A. Stadtler, (1969–1972) (Member 1962–1972)
R. Ward, (1976–1978) (Member 1972–1978)
M.G.H. Wells, (1981) (Member 1976–1981)
D.J. Wright, (1964–1965) (Member 1959–1967)

Staff

ASM International staff who contributed to the development of the Volume included Steven R. Lampman, Project Editor; Bonnie R. Sanders, Manager of Production; Gayle J. Anton, Editorial Assistant; Carol Polakowski, Production Supervisor; Jill Kinson, Production Editor; Kathryn Muldoon, Production Assistant; Scott D. Henry, Senior Manager, Product and Service Development ; and William W. Scott, Jr., Director of Technical Publications

Preparation of Online Volume

ASM Handbook, Volume 9, *Metallography and Microstructure*, was converted to electronic files in 2004. The conversion was based on the First printing (2003). No substantive changes were made to the content of the Volume, but some minor corrections and clarifications were made as needed. ASM International staff who oversaw the conversion of the Volume to electronic files were Sally Fahrenholz-Mann and Sue Hess. The electronic version was prepared under the direction of Stanley Theobald, Managing Director.

Copyright Information

Copyright © 2004
by
ASM International®
All rights reserved
No part of this book may be reproduced, stored in a retrieval system, or transmitted, in any form or by any means, electronic, mechanical, photocopying, recording, or otherwise, without the written permission of the copyright owner.
First printing, December 2004

This book is a collective effort involving hundreds of technical specialists. It brings together a wealth of information from worldwide sources to help scientists, engineers, and technicians solve current and long-range problems.

Great care is taken in the compilation and production of this Volume, but it should be made clear that NO WARRANTIES, EXPRESS OR IMPLIED, INCLUDING, WITHOUT LIMITATION, WARRANTIES OF MERCHANTABILITY OR FITNESS FOR A PARTICULAR PURPOSE, ARE GIVEN IN CONNECTION WITH THIS PUBLICATION. Although this information is believed to be accurate by ASM, ASM cannot guarantee that favorable results will be obtained from the use of this publication alone. This publication is intended for use by persons having technical skill, at their sole discretion and risk. Since the conditions of product or material use are outside of ASM's control, ASM assumes no liability or obligation in connection with any use of this information. No claim of any kind, whether as to products or information in this publication, and whether or not based on negligence, shall be greater in amount than the purchase price of this product or publication in respect of which damages are claimed. THE REMEDY HEREBY PROVIDED SHALL BE THE EXCLUSIVE AND SOLE REMEDY OF BUYER, AND IN NO EVENT SHALL EITHER PARTY BE LIABLE FOR SPECIAL, INDIRECT OR CONSEQUENTIAL DAMAGES WHETHER OR NOT CAUSED BY OR RESULTING FROM THE NEGLIGENCE OF SUCH PARTY. As with any material, evaluation of the material under end-use conditions prior to specification is essential. Therefore, specific testing under actual conditions is recommended.

Nothing contained in this book shall be construed as a grant of any right of manufacture, sale, use, or reproduction, in connection with any method, process, apparatus, product, composition, or system, whether or not covered by letters patent, copyright, or trademark, and nothing contained in this book shall be construed as a defense against any alleged infringement of letters patent, copyright, or trademark, or as a defense against liability for such infringement.

Comments, criticisms, and suggestions are invited, and should be forwarded to ASM International.

Library of Congress Cataloging-in-Publication Data
ASM International
ASM Handbook
Includes bibliographical references and indexes
Contents: v.1. Properties and selection—irons, steels, and high-performance alloys—v.2. Properties and selection—nonferrous alloys and special-purpose materials—[etc.]—v.21. Composites
1. Metals—Handbooks, manuals, etc. 2. Metal-work—Handbooks, manuals, etc. I. ASM International. Handbook Committee. II. Metals Handbook.
TA459.M43 1990 620.1′6 90-115
SAN: 204-7586
ISBN: 0-87170-706-3
ASM International®
Materials Park, OH 44073-0002
www.asminternational.org
Printed in the United States of America

Multiple copy reprints of individual articles are available from Technical Department, ASM International.

Metallography: An Introduction, *Metallography and Microstructures,* Vol 9, *ASM Handbook,* ASM International, 2004, p. 3–20

Metallography: An Introduction

Introduction

METALLOGRAPHY is the scientific discipline of examining and determining the constitution and the underlying structure of (or spatial relationships between) the constituents in metals, alloys and materials (sometimes called materialography). The examination of structure may be done over a wide range of length scales or magnification levels, ranging from a visual or low-magnification (~20×) examination to magnifications over 1,000,000× with electron microscopes. Metallography may also include the examination of crystal structure by techniques such as x-ray diffraction. However, the most familiar tool of metallography is the light microscope, with magnifications ranging from ~50 to 1000× and the ability to resolve microstructural features of ~0.2 μm or larger.

The other major examination tool in metallography is the scanning electron microscope (SEM). Compared to the light microscope, the SEM expands the resolution range by more than two orders of magnitude to approximately 4 nm in routine instruments, with ultimate values below 1 nm. Useful magnification covers the range from the stereomicroscope, the entire range of the light microscope, to much of the range of the transmission electron microscope (TEM) for possible viewing from 1,000× to >100,000×. The SEM also provides a greater depth of field than the light microscope, with depth of focus ranging from 1 μm at 10,000× to 2 mm at 10×, which is larger by more than two orders of magnitude compared to the light microscope (Table 1). This higher depth of field allows better discernment of topology features during a microscopic investigation, such as the examination of fracture surface during failure analysis. The depth of field of an SEM also may be a factor of choice over light macroscopy, when very rough surfaces are being examined on a macroscopic level. For additional information on the comparative capabilities of light and electron microscopy, see the article "Light and Electron Microscopy" in this Volume.

Table 1 Depth of field of typical light microscope objectives

Final magnification, diameters	Objective		Area of field[(a)], μm	Depth of field, μm
	Magnification, diameters	**Numerical aperture**		
100	5.6	0.20[(b)]	1000	20
250	8.0	0.40[(b)]	400	3
500	21.0	0.65[(b)]	200	1
750	41.0	0.85[(b)]	135	0.4
1000	58.0	0.95[(b)]	100	0.1
	50.0	1.0[(c)]	100	0.6
1500	75.0	1.4[(c)]	65	0.2

(a) For a final projected image 10 cm (4 in.) in diameter.
(b) Dry objective.
(c) Oil-immersion objective

However, even with the advent of electron microscopy, the light microscope is still the first and most important examination device in metallography. Sometimes the contrast in a microstructure is inadequate with a SEM under 500×, while it is highly visible with a basic light microscope and a properly prepared sample. Indeed, light microscopy is the historical and practical cornerstone of metallography, as described in the next section "The Origins of Metallography," which summarizes the basic discovery by Sorby demonstrating the importance of specimen preparation when examining metals with a light microscope. Contrast between microstructural constituents in light microscopy is very dependent on specimen preparation. Light microscopes also have

various types of special illumination modes that can increase the information gained from the image (see the article “Light Microscopy” in this Volume). For example, polarized-light illumination can improve phase contrast, and the differential interference contrast (DIC) method can be used to identify topological height differences on a sample surface that are smaller than 0.2 μm.

The objective of these tools is to accurately reveal material structure at the surface of a sample and/or from a cross-section specimen. Examination may be at the macroscopic, mesoscopic, and/or microscopic levels. For example, cross sections cut from a component or sample may be macroscopically examined by light illumination in order to reveal various important macrostructural features (on the order of 1 mm to 1 m) such as:

- Flow lines in wrought products
- Solidification structures in cast products
- Weld characteristics, including depth of penetration, fusion-zone size and number of passes, size of heat-affected zone, and type and density of weld imperfections
- General size and distribution of large inclusions and stringers
- Fabrication imperfections, such as laps, cold welds, folds, and seams, in wrought products
- Gas and shrinkage porosity in cast products
- Depth and uniformity of a hardened layer in a case-hardened product

Macroscopic examination of a component surface is also essential in evaluating the condition of a material or the cause of failure. This may include:

- Characterization of the macrostructural features of a fracture surfaces to identify fracture initiation site and changes in crack-propagation process
- Estimations of surface roughness, grinding patterns, and honing angles
- Evaluation of coating integrity and uniformity
- Determination of extent and location of wear
- Estimation of plastic deformation associated with various mechanical processes
- Determination of the extent and form of corrosive attack; readily distinguishable types of attack include pitting, uniform, crevice, and erosion corrosion
- Evaluation of tendency for oxidation
- Association of failure with welds, solders, and other processing operations

This listing of macrostructural features in the characterization of metals, though incomplete, represents the wide variety of features that can be evaluated by light macroscopy.

Mesoscale structure is on the order of 1 mm to 100 μm. It includes microstructural features at the grain level, without resolving the intricacies of the grain structure. For example, uniformity of case depth is an example of a mesoscale feature. Solidification structures at the mesoscale level include features such as cell sizes (eutectic cell), dendrites and arms, grain type (columnar or equiaxed), the type and concentration of chemical microsegregation, and the amount of microshrinkage, porosity, and inclusions. The term “mesoscale” is a relatively new term, introduced in part to more accurately distinguish between different scales.

Microstructure is the classic term used in metallography to describe features observed under a microscope in the scale range of 1000–0.1 μm. The importance of microstructure to the properties of metals and alloys has long been recognized. Grain size, twins, and the size, shape, and distribution of second-phase particles are important in determining the behavior of most metals and alloys. These microstructural features are within the fundamental resolution limits of light of 0.2 μm (or greater). Then, if necessary, the examination may move to higher levels of magnifications with a scanning electron microscope, or a transmission electron microscope (TEM). For example, dislocations, numerous types of second-phase particles, spinodal and ordered structures, and many aspects of martensitic structures are too small for resolution by light microscopy. Therefore, metallographic observation of these very fine structural features is generally restricted to electron microscopy. The scale hierarchy of microstructural features is described in more detail in the article “Introduction to Structures in Metals.”

Metallography: An Introduction, *Metallography and Microstructures,* Vol 9, *ASM Handbook,* ASM International, 2004, p. 3–20

The Origins of Metallography

The critical factor in the light microscopy of metals is the surface preparation of the specimen. This is the basic insight discovered by the father of metallography, Henry Clifton Sorby (Fig. 1), who was the first person to examine correctly polished and chemically etched metal samples under the microscope in 1863 (Ref 1). This application of microscopy is more than two centuries later than the biological microscope, because the microscopy of metals requires careful preparation of the surface. Unlike biological samples, metals are opaque and thus require reflected light microscopy (where the impinging light for viewing is reflected off the specimen surface). In contrast, biological samples are transparent and thus can be examined by transmitted light (transmission microscopy). Sorby understood the need for proper surface preparation when examining metals by reflected-light microscopy. Prior to Sorby, samples were only "distorted fractures and brutally burnished or abraded surfaces" (Ref 2). He advised that "(the final) polish must not be one which gives bright reflection but one which may show all the irregularities of the material and is as far removed as possible from a burnished surface" (Ref 3).

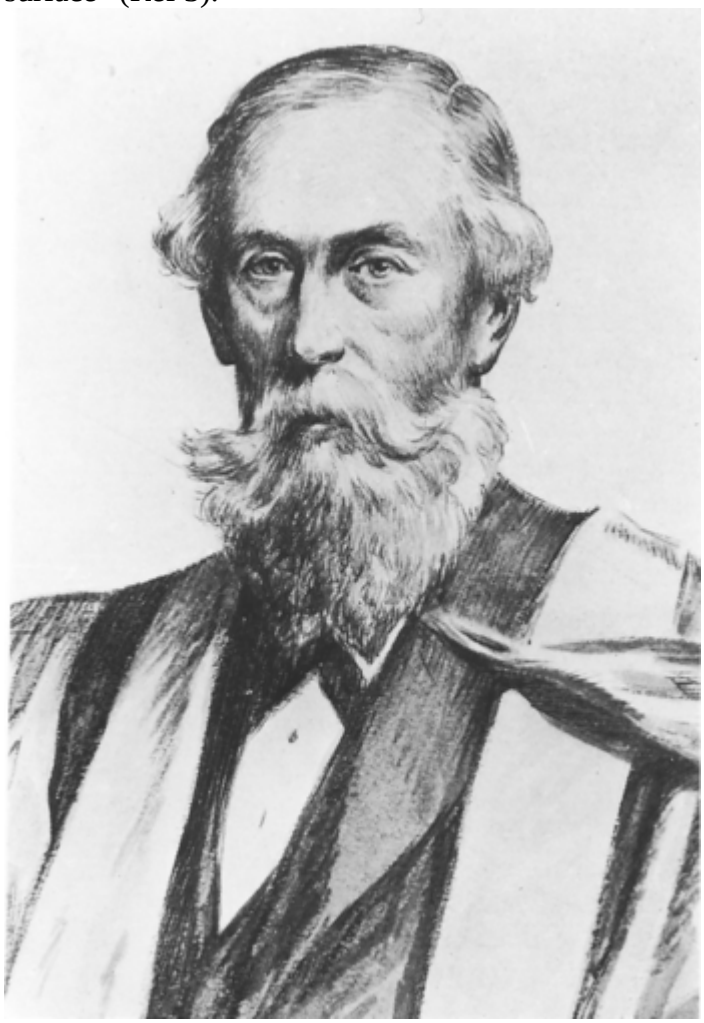

Fig. 1 Henry Clifton Sorby (1826–1908), geologist, petrographer, mineralogist, and founder of metallography. Source: Ref 6

The other piece of the metallographic puzzle is the art of etching. An extremely smooth surface appears nearly featureless when examined by reflected-light microscopy, because the light reflects uniformly from the surface

and appears as a uniform contrast by human eye. Thus, techniques are needed to enhance contrast differences between the different phases of constituents. These methods include etching, thin-film formation, or special illumination modes with light microscopes (see the article “Contrast Enhancement and Etching” in this Volume). Of these, chemical recipes for etching the surface are the oldest of the various contrasting techniques. Etching even precedes Sorby by at least four centuries, as in the case of macroetching techniques to reveal the damask patterns of swords and various pieces of armor. Macroetching was also used to reveal the structure of polished meteorites, such as the famous Widmanstätten structure discovered by count Alos von Widmanstätten, a geologist and museum curator in Vienna, and his coworker Carl von Schreibers in 1808. They etched various meteorites to show the outstanding crystalline patterns in the Elbogen iron meteorite that fell in 1751. An excellent example of their work is shown in Fig. 2 (from Ref 4).

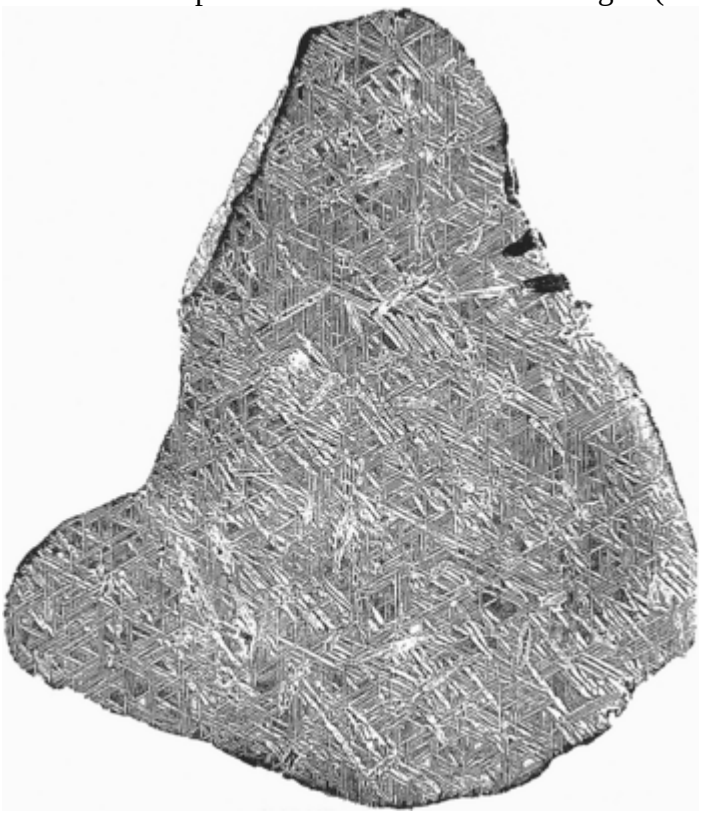

Fig. 2 Macrograph of the Elbogen iron meteorite prepared in 1808 by Widmanstätten and Schreibers using heavy etching in nitric acid. After rinsing in water and drying, printer's ink was rolled on the etched surface, and the sample was pressed onto a piece of paper. Source: Ref 4

Widmanstätten and Schreibers etched specimens that could be viewed with the naked eye, but Sorby was the first to etch specimens and observe the true microstructure with a microscope. Sorby first cut and polished his specimens to remove all “traces of roughness.” After polishing, he used extremely dilute nitric acid to etch his specimens. He actually followed the progress of etching in order not to overetch the specimen. The critical factor in this procedure was Sorby's laborious preparation of specimens carried out by hand. The polished surfaces were etched in dilute nitric and were undoubtedly of a considerably higher standard than those of his contemporaries, such as Wedding and Martins in Germany (Ref 5), who were also attempting to reveal the microstructures of steels.

Sorby may not have realized the exact reasons for the success of his preparation methods, but more importantly, all of the structures reported by Sorby are still accepted as being correct structures. On 28 July 1863, Sorby recorded in his diary that he had “discovered” the structure of an iron. It was not until 1886 and 1887, however, that his results were recorded in a journal with a wide readership (Ref 1, 3). By careful observation he identified major microstructural constituents of ferrous materials (the constituents now known as graphite, cementite, pearlite,* austenite, and the phosphide eutectic). He recognized that iron was composed of a number of crystal grains, and he also realized that iron underwent an allotropic change on heating. As noted by Samuels (Ref 6), these are awesome achievements considering that he started from scratch and that they were achieved after such a short period of investigation.

From this beginning, the importance of specimen preparation remains central today. Many deficiencies arise when the preparation methods are neglected. False structures (or artifacts) can arise from the preparation in many ways. In particular, Jose Ramon Vilella (Fig. 3) was the first to realize that artifacts were sometimes being observed due to the presence of a layer of “distorted or disturbed” metal formed during the early stages of surface preparation and not during polishing itself (Ref 7). He demonstrated that the true microstructure was seen only when the disturbed layer was removed, and he devised a method (alternate etching and polishing) of doing this (Fig. 4) (Ref 7).



Fig. 3 Jose Ramon Vilella (1897–1971), distinguished metallographer who understood the need to faithfully prepare representative surfaces in metallographic examinations. Source: Ref 6

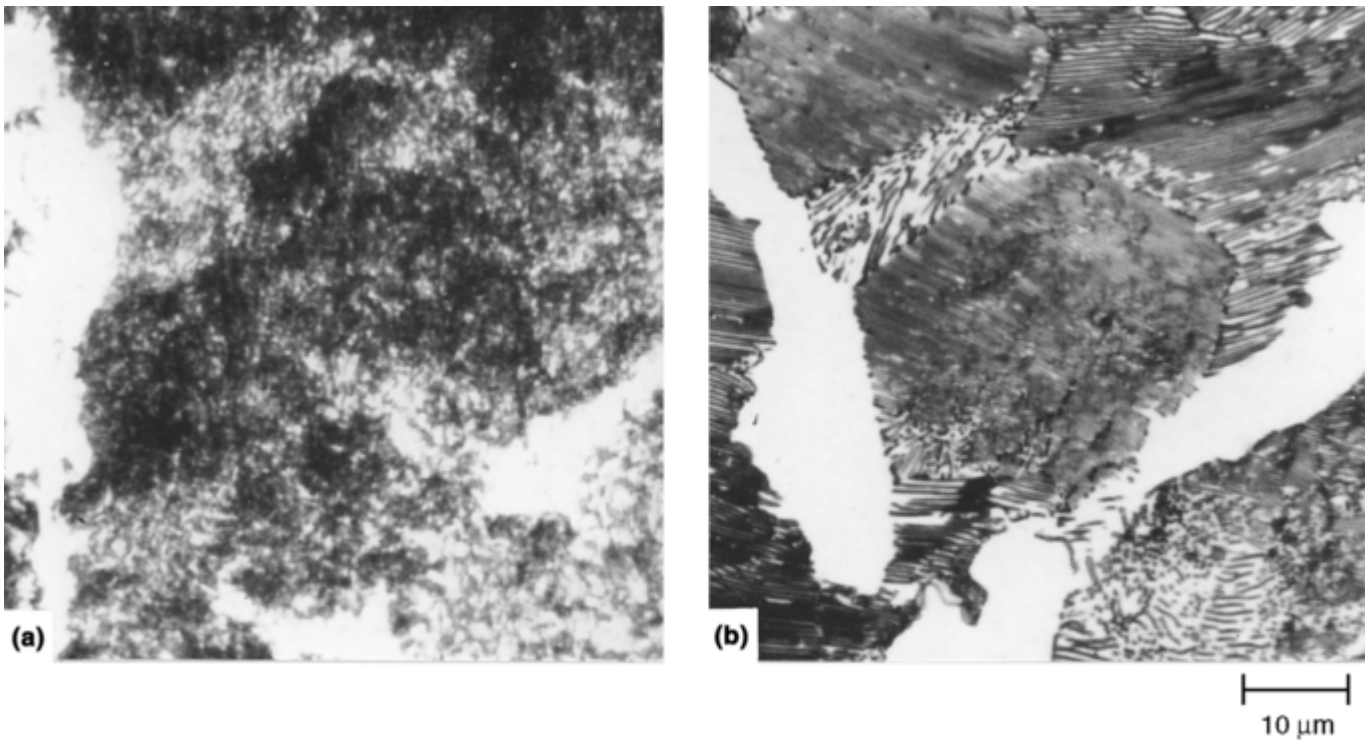

Fig. 4 An example used by Vilella to illustrate the effect of disturbed metal on the appearance of pearlite. (a) Polished surface covered by a layer of disturbed metal; structures such as this were called sorbite or troostite-sorbite by some early investigators. (b) Same field after removing the layer of disturbed metal by alternate polishing and etching; true structure of lamellar pearlite. Etched in picral reagent. 1000×. Source: Ref 7

Vilella's seminal work established the need for preparation procedures beyond just the production of reflecting surfaces. Successful metallography imposes the following requirements on the final preparation of the specimen surface (Ref 6):

- Surface layers that might obscure structural features must not be present.
- False structures that might be detected during a subsequent examination must not have been introduced.
- All desired fields of view must be coplanar within the depth-of-field limits of the system to be employed for examination.
- The surface must be adequately free from stains and other accidental blemishes.

With these basic objectives in mind, then the next question is determining the most effective mechanical, chemical, and/or physical methods of specimen preparation for the appropriate microscopic tool. These methods are described in more detail in the Section “Metallographic Techniques” of this Volume.

After a micrograph from a properly prepared specimen is obtained and recorded, the next challenge is to interpret, understand, and use the information contained on the recorded image. Interpretation of microstructural features requires an understanding of crystal structure, kinetics, and the metallurgical mechanisms of solidification, deformation, and phase transformations. These topics, as they relate to structure, are introduced in more detail in the series of articles in the next Section “Metallurgy and Microstructure.” Interpretation of micrographs also requires an understanding of how specimen preparation and microscopic techniques affect the appearance of particular phases in a given material. Thus, the cataloging of micrographs (in print and/or electronic form) can be useful when comparing the effects of material variations and changes in specimen preparation.

Footnote

* At the end of the 19th century, very fine pearlite unresolved in the light microscopes was referred to as “sorbite” in honor of Sorby. However, because it is not a new constituent, the term “sorbite” did not survive.

The term “pearlite” survives to this day and is actually connected to Sorby, because he described the “pearly constituent,” i.e., pearlite, as having a “mother of pearl” appearance.

References cited in this section

1. H.C. Sorby, in *How to Work with the Microscope,* London, 1867
2. C.S. Smith, *A History of Metallography,* University of Chicago Press, 1960
3. H.C. Sorby, *J. Iron Steel Inst.,* Vol 28, 1886, p 140
4. B.L. Bramfitt and A.O. Benscoter, *Metallographer's Guide: Practices and Procedures for Irons and Steels,* ASM International, 2002, p 88
5. H. Wedding, *J. Iron Steel Inst.,* Vol 27, 1885, p 187
6. L.E. Samuels, *Metallographic Polishing by Mechanical Means,* 4th ed., ASM International, 2003, p 6
7. J.R. Vilella, *Metallographic Techniques for Steels,* American Society for Metals, 1938

Metallography: An Introduction, *Metallography and Microstructures,* Vol 9, *ASM Handbook*, ASM International, 2004, p. 3–20

Macroanalysis (Adapted from Ref 8)

Macrostructural characterization of metals and alloys is the detailed evaluation of large-scale inhomogeneities in composition, morphology, and/or density. These inhomogeneities may develop during such procedures as casting, extrusion, forging, rolling, and welding or during service. Macroscale examination of surfaces is also essential in the failure analysis of fractured, corroded, and/or worn parts. Microscopic evaluation clearly is a significant step in any failure examination, but it should not replace characterization by macroscopy. These two types of metallography are complementary, but examination during failure analysis should always begin at low magnification and work upward. A frequent mistake in failure analysis is to neglect examination of the broken pieces at low magnifications. Too frequently, the component is sectioned immediately.

Examination techniques other than metallography may also be more effective during macroscale examination. For example, Fig. 5 shows spider cracks in the center of a copper specimen. This specimen was sectioned, ground, and polished, but not etched. Chemical etching and subsequent evaluation of the macrostructure may fail to reveal this type of structural imperfection (Fig. 5b). The cracks shown in Fig. 5(a) were revealed by applying a dye penetrant to the polished specimen. The dye was drawn into the cracks by capillary action, and the surface was then wiped clean. The specimen was then placed under a light that caused the dye to fluoresce, and the cracks became readily observable. Dye-penetrant techniques are excellent for examination of cracklike macrostructural imperfections in metals. However, grains and other microstructural features are visible only after etching, which frequently obscures the presence of the cracks. Therefore, different metallographic techniques are necessary to reveal various macrostructural elements.

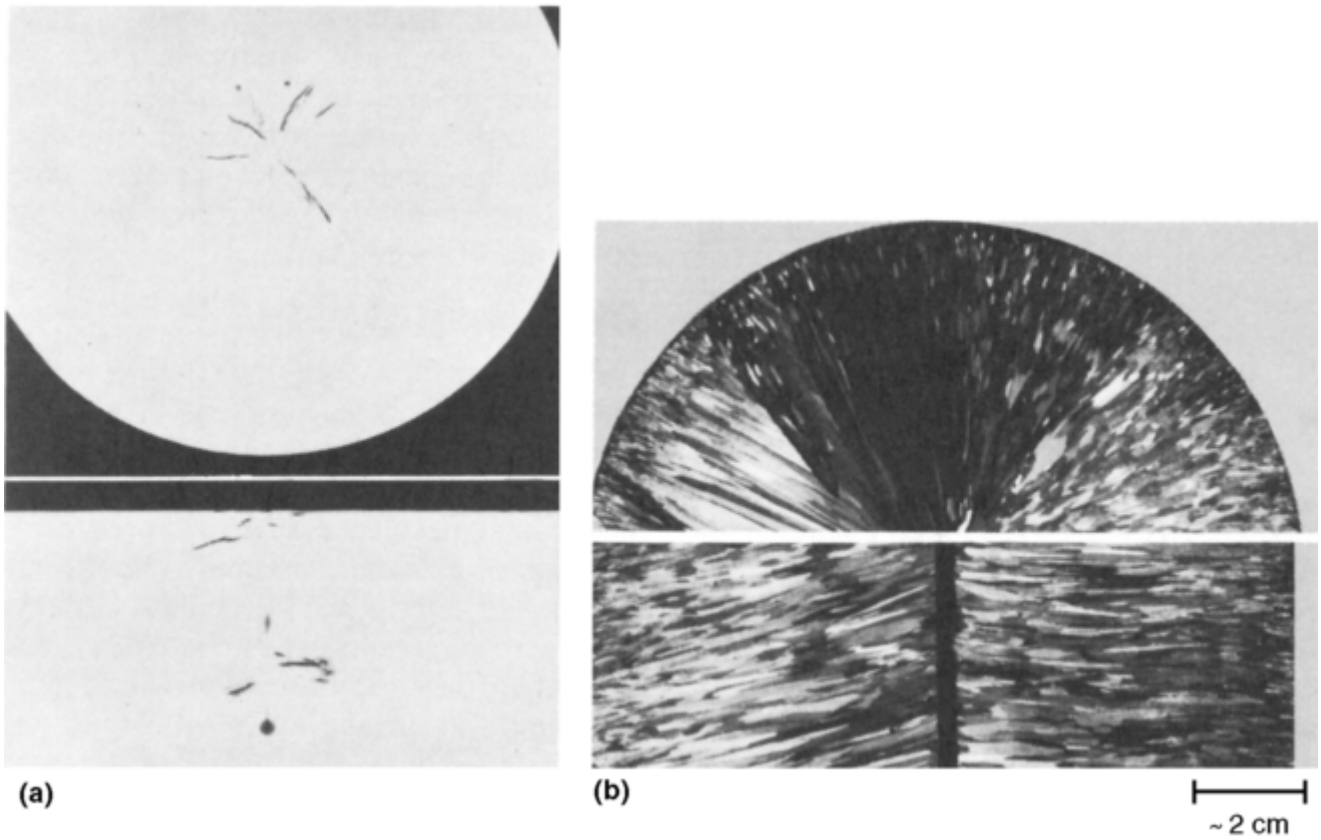

Fig. 5 Macrostructure of a continuous-cast copper ingot. (a) Spider cracks revealed using dye-penetrant inspection. Transverse section at top; longitudinal section at bottom. (b) Same ingot, etched using Waterbury's reagent. Cracks are not revealed. Both approximately 0.5×. Source: Ref 8

Macroscopy of Sections

Preparation of a metallographic section for examination requires careful selection of the area to be characterized (see the article “Metallographic Sectioning and Specimen Extraction” in this Volume). This area must be chosen to represent the unique features of a specific zone of interest or the general features of a part or component selected for process characterization or quality assurance. The selected region of the specimen must then be removed from the component using techniques that do not damage or distort the features of interest. The section of interest is then prepared metallographically, and the prepared section is characterized using macroscopic examination.

Macroscopic examination generally does not require the extreme surface smoothness needed for microscopic examinations. Such surface preparation techniques as etching are frequently prolonged such that surface features are greatly enhanced; therefore, quantitative measurements should not be conducted on macroetched samples. Heavy etching accentuates any microstructural inhomogeneity (Fig. 6). The flow lines show the direction of metal flow during processing and frequently represent paths for easy fracture. Figure 7 shows the use of similar macroscopic techniques to illustrate the depth of case hardening in a tool steel. Figure 8 is a weld macrograph that shows the different etching characteristics of the fusion zone and heat-affected zone (HAZ) of a weld. The 2% nital etchant used to reveal the weld macrostructure is much less aggressive than the 50% hydrochloric acid etchants used on the specimens shown in Fig. 6 and 7 and reveals finer structural detail but requires a polished specimen.

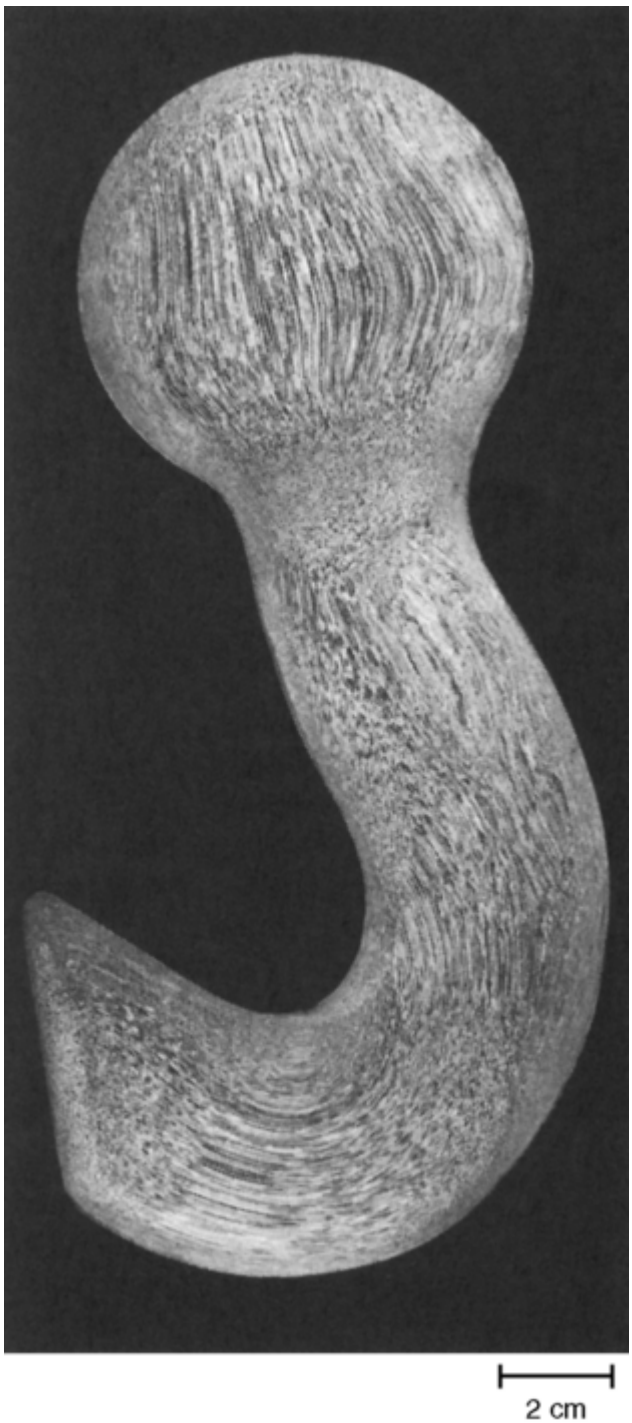

Fig. 6 Flow lines in a forged 4140 steel hook. Specimen was etched using 50% HCl. 0.5×. Source: Ref 8

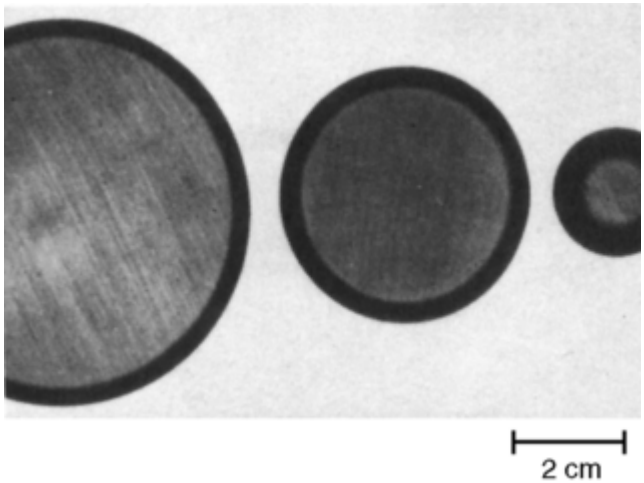

Fig. 7 Case-hardened layer in W1 tool steel. Specimens were austenitized at 800 °C (1475 °F), brine quenched, and tempered 2 h at 150 °C (300 °F). Black rings are hardened zones. Etched using 50% hot HCl. Approximately 0.5×. Source: Ref 8

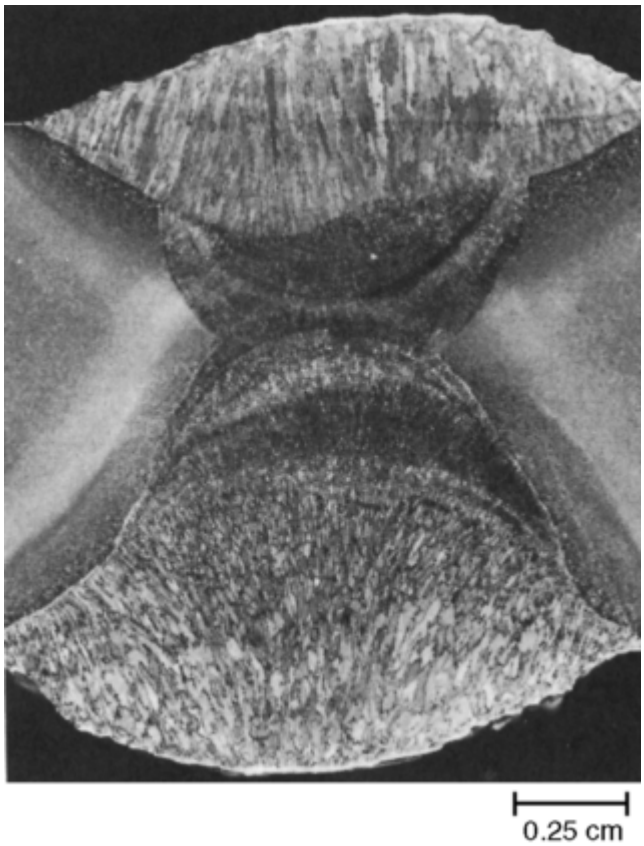

Fig. 8 Section through an arc butt weld joining two 13 mm (0.5 in.) thick ASTM A517, grade J, steel plates. Etched using 2% nital. 4×. Source: Ref 8

In castings, macroscopy is used to establish the outer chill zone depth, shape, and size of the columnar or dendritic grains perpendicular to the mold wall, and size of the central equiaxed zone (Fig. 9). For example, Fig. 10 shows the macrostructure of a small, relatively pure aluminum ingot exhibiting typical cast grain structure. To obtain the macrograph, the aluminum ingot was sectioned, then ground and polished to produce a flat reflective surface. The polished section was then etched by immersion in a solution that attacked the various grain orientations at different rates. The structural elements visible in this macrograph are grains. The small grains near the bottom of the ingot appear relatively equiaxed. This region of small equiaxed grains is the chill zone. Macroscopy of cast structures is also used to reveal imperfections such as shrinkage, gas, porosity, and center cracks.

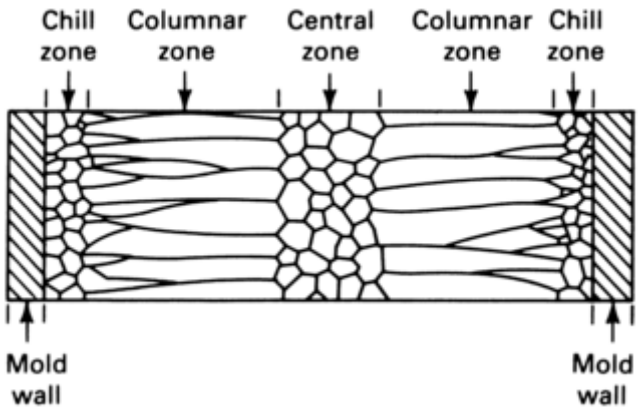

Fig. 9 Sketch of grains in a typical cast ingot

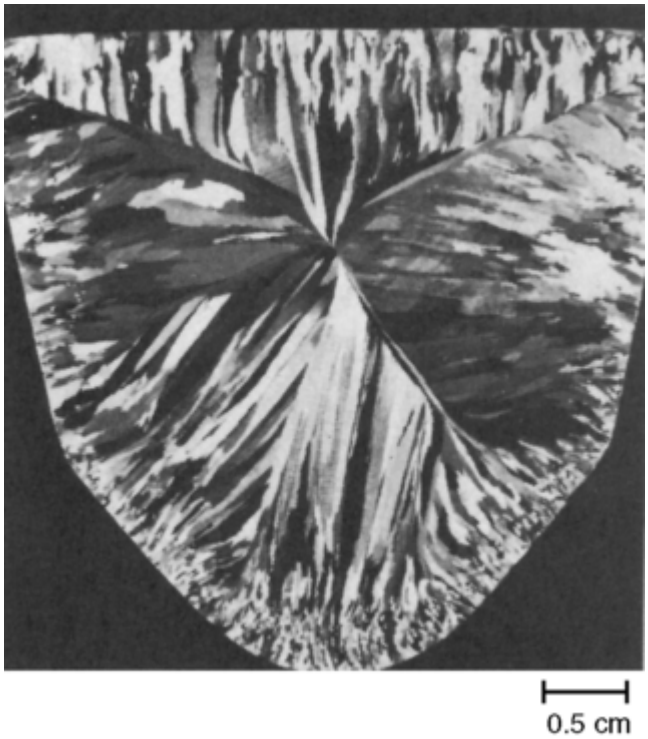

Fig. 10 Macrostructure of as-cast aluminum ingot. Transverse section shows outer chill zone and columnar grains that have grown perpendicularly to the mold faces. Etched using Tucker's reagent. 1.5×. Source: Ref 8

Macroscopy of Fracture Surfaces (Adapted from Ref 9)

Both the macroscale and microscale appearances of fracture-surface features can tell a story of how and sometimes why fracture occurred. Features often associated with the fracture surface at the macroscale and microscale are shown in Table 2 and 3. Examination of the information in these tables shows that the fracture features provide information about (Ref 9):

- The crack-initiation site and crack-propagation direction
- The mechanism of cracking and the path of fracture
- The load conditions (monotonic or cyclic)
- The environment
- Geometric constraints that influenced crack initiation and/or crack propagation
- Fabrication imperfections that influenced crack initiation and/or crack propagation

Table 2 Macroscale fractographic features

Mark/Indication	Implication
Visible distortion	Plastic deformation exceeded yield strength and may indicate instability (necking, buckling) or post-failure damage
Visible nicks and gouges	Possible crack initiation site
Fracture surface orientation relative to component geometry and loading conditions	• Helps separate loading modes I, II, III • Identifies macroscale ductile and brittle fracture.
Both flat fracture and shear lips present on fracture surface	• Crack propagation direction parallel to shear lips • Mixed-mode fracture (incomplete constraint)
Tightly closed crack on surface	• Possible cyclic loading • Possible processing imperfection, e.g., from shot peening,

	quench cracks
Radial marks and chevrons (V-shape)	• Point toward crack initiation site • Show crack propagation direction
Crack arrest lines (monotonic loading) (U-shape)	• Lines point in direction of crack propagation • Indicate incomplete constraint
Crack arrest lines (cyclic loading) (beach marks, conchoidal marks)	• Indicates cyclic loading • Propagation from center of radius of curvature • Curvature may reverse on cylindrical sections as crack propagates
Ratchet marks	• More likely in cyclic loading • Indicates initiation site(s)
Adjacent surface and or fracture surface discoloration	• May indicate corrosive environment • May indicate elevated temperature
Oxidized fingernail on fracture surface	Possible crack initiation site
Fracture surface reflectivity	• *Matte:* ductile fracture or cyclic loading • *Shiny:* cleavage likely • Faceted (“bumpy”) and shiny; intergranular fracture in large grain size
Fracture surface roughness	• Increase in surface roughness in direction of crack growth (may be affected in bending by compressive stressed region when crack moves into this region) • Smooth region plus rough region in direction of growth—cyclic loading • Rough matte fractures are ductile • May indicate transition from fatigue crack growth to overload
Rubbing (general)	• May indicate vibration • May show final direction of separation • Swirl pattern indicates torsion
Rubbing (localized)	• May indicate crack closure in cyclic loading • May obliterate beach marks
Deformed draw marks, rolling scratches	If twisted, indicates torsion loading
Machining marks (normal to axis of component)	Not distorted in torsion loading
Variable roughness of fracture edge	In brittle bending, rough side is tension side

Source: Ref 9

Table 3 Microscale fractography features

Mark/Indication	Implication
Dimpled fracture surface	Ductile overload fracture at this location
Faceted fracture surface	• Brittle cleavage fracture • Possible SCC fracture • May be low ΔK fatigue
Intergranular with smooth grain boundaries	• Likely either improper thermal processing or environmental assisted fracture (high temperature, corrosive environment) • Less common is low ΔK fatigue
Intergranular with dimpled grain boundaries	• "Decohesive" rupture—fracture at high fraction of melting point • Possible improper processing creating denuded zone adjacent to grain boundary
River pattern or fan pattern	Cleavage fracture; crack runs "down" river; fan rays point to initiation site within a grain.
Tongues	Twinning deformation during rapid crack propagation
Flutes on transgranular fracture surface	• Indicates corrsive environment and ductile fracture • Crack propagates parallel to flutes.
Striated or ridged fracture	• Cyclic loading fatigue striations; Constant spacing, constant stress amplitude; variable spacing, variable stress amplitude or block loading • Striated surface caused by second phases in microstructure.
Grooves or flutes	• SCC • Transgranular fracture
Artifacts (mud cracks)	Dried liquid on surface. May indicate incomplete cleaning of surface. If in the as-received condition, may indicate fluids from service and may indicate SCC conditions. Material should be analyzed.
Artifacts (tire tracks)	• Common in cyclic loading • Due to entrapped particulate matter

Source: Ref 9

It should also be clear that not all features created by a given cause for failure are necessarily present on a given fracture surface. For example, beach marks (at low magnification) and striations (at higher magnification) are well-known features of fatigue cracks, but are not always present or visible. In addition, not all fracture mechanisms have unique appearances. For example, intergranular fracture can be caused by a number of mechanisms.

It is also important to understand that the fracture surface only provides evidence of the crack-propagation process; it does not reveal evidence of events prior to nucleation and growth. Examination beyond the fracture surface also provides information. For example, visual inspection of a fractured component may indicate events prior to fracture initiation, such as a shape change indicating prior deformation. Metallographic examination of material removed far from the fracture surface also can provide information regarding the penultimate microstructure, including the presence of cold work (slip, bent annealing twins, deformation bands, and/or grain shape change), evidence of rapid loading and/or low-temperature service (deformation twins), and so forth. This also is very necessary to the failure investigation.

Macroscopic features typically help identify the fracture-initiation site and crack-propagation direction. The orientation of the fracture surface, the location of crack-initiation site(s), and the crack-propagation direction should correlate with the internal state of stress created by the external loads and component geometry. When the failed component is in multiple pieces, and chevrons are visible on the fracture surface, analysis of crack branching (crack bifurcation) (Fig. 11) (Ref 10) can be used to locate the crack-initiation site. Fracture initiates

in the region where local stress (as determined by the external loading conditions, part geometry, and/or macroscopic and microscopic regions of stress concentration) exceeds the local strength of the material. Thus, variations in material strength and microscale discontinuities (such as an inclusion or forging seam) must be considered in conjunction with variations in localized stress that is determined by applied loads and macroscopic stress concentrations (such as a geometric notch or other change in cross section).

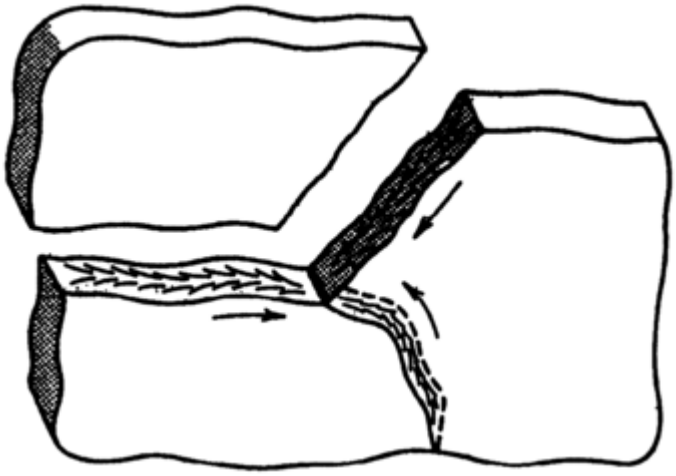

Fig. 11 Component that has fractured in multiple pieces. If chevrons are visible on the fracture surface, the sequence of crack formation can be used to obtain the crack formation of sequence and the location of the initiation site. Source: Ref 10

The fracture surface orientation relative to the component geometry may also exclude some loading conditions (axial, bending, torsion, monotonic versus cyclic) as causative factors. For example, crack initiation is not expected along the centerline of a component loaded in bending or torsion, even if a significant material imperfection is present at that location because no normal stress acts at the centerline. (There is a shear stress at this location in bending, but in a homogeneous material, it is too small to initiate fracture. That might not be the case for a laminated structure loaded in bending.)

Likewise, the profile of a fracture surface relative to loading direction can indicate the mode of fracture by elastic (plane-strain) conditions or elastic-plastic (plane-stress) conditions. Plane-strain (or mode I) fracture is characterized by a flat surface perpendicular to the applied load. Plane-stress (mode II) fracture occurs when shear strain becomes the operative mode of deformation and fracture (as maximum stresses occur along the shear plane from the basic principles of continuum mechanics). In plane-stress cracking, the fracture profile is characterized by shear lips, which are at about a 45° oblique angle to the maximum stress direction (although this angle may vary depending on material condition and loading condition). In general, these variations in fracture profiles are related to fracture toughness, which depends on section thickness (B) and the size (a) of a preexisting discontinuity such as a notch. This is shown in Fig. 12. Crack-tip radius also influences fracture behavior.

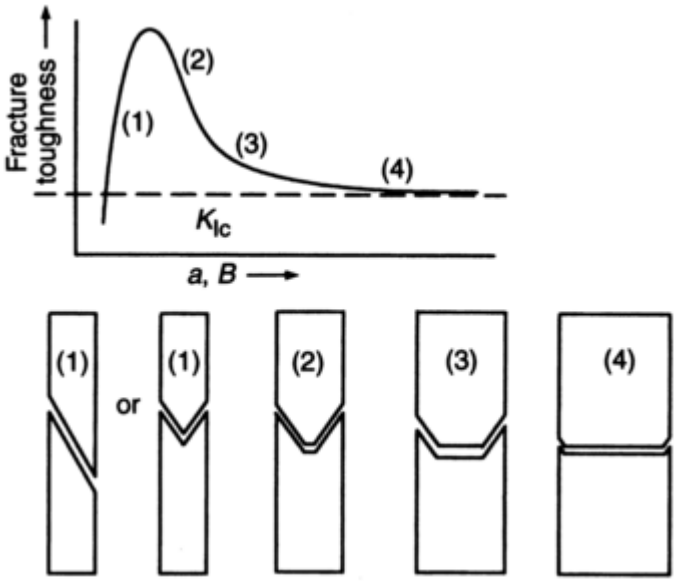

Fig. 12 Variation in fracture toughness and macroscale features of fracture surfaces for an inherently ductile material. As section thickness (*B*) or preexisting crack length (*a*) increases, plane-strain conditions develop first along the centerline and result in a flat fracture surface. With further increases in section thickness or crack size, the flat region spreads to the outside of the specimen, decreasing the widths of the shear lips. When the minimum value of plane-strain toughness (K_{Ic}) is reached, the shear lips have very small width. Source: Ref 9

Surface roughness and optical reflectivity also provide qualitative clues to events associated with crack propagation. For example, a dull/matte surface indicates microscale ductile fracture, while a shiny, highly reflective surface indicates brittle cracking by cleavage or intergranular fracture. In addition, when intergranular fracture occurs in coarse-grained materials, individual equiaxed grains have a distinctive rock-candy appearance that may be visible with a hand lens. In terms of documenting surface conditions, one major problem with optical (light) macroscopic or microscopic examination of fracture surfaces is its inability to obtain favorable focus over the entire surface if the magnification exceeds 5 to 10×. Therefore, SEM also has become a standard metallographic tool in failure analysis.

Surface roughness provides clues as to whether the material is high strength (smoother) or low strength (rougher) and whether fracture occurred as a result of cyclic loading. The surfaces from fatigue crack growth are typically smoother than monotonic overload fracture areas. The monotonic overload fracture of a high-strength quenched-and-tempered steel is significantly smoother overall than is the overload fracture of a pearlitic steel or annealed copper. Also, fracture surface roughness increases as a crack propagates so the roughest area on the fracture surface is usually the last to fail. Fracture surface roughness and the likelihood of crack bifurcation also increase with magnitude of the applied load and depend on the toughness of the material. Brittle failures often contain multiple cracks and separated pieces, while ductile overload failures often progress as single cracks, without many separated pieces or substantial crack branching at the fracture location.

Under the right conditions, fracture surfaces may also have radial marks and chevrons, which are macroscopic surface features that indicate the region of crack initiation and propagation direction. They are common and dominant macroscopic features of the fracture of wrought metallic materials, but are often absent or poorly defined in castings. The “V” of a chevron points back to the initiation site, and a sequence of “V”s across the fracture surface indicates the crack-propagation direction. The appearance of chevrons or radial marks near the crack origin depends in part on whether the crack-growth velocity at the surface is greater or less than that below the surface. If crack-growth velocity is at a maximum at the surface, radial marks have a fan-shaped appearance (Fig. 13). If crack-growth rate is greatest below the surface, the result is chevron patterns (Fig. 14).

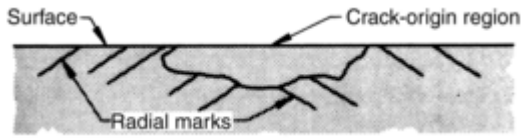

Fig. 13 Radial marks typical of crack propagation that is fastest at the surface (if propagation is uninfluenced by the configuration of part or specimen)

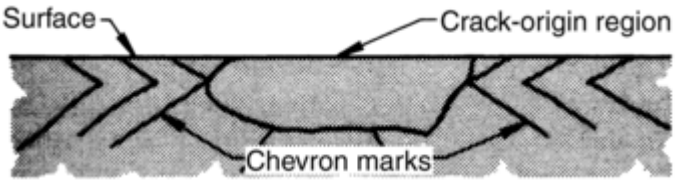

Fig. 14 Chevron patterns typical when crack propagation is fastest below the surface. It is also observed in fracture of parts having a thickness much smaller than the length or width (see middle illustration in Fig. 15).

In rectangular sections, specimen dimensions can affect the appearance of radial markings and chevron patterns. For example, the macroscale fracture appearances of unnotched sections are shown in Fig. 15 for sections with various width-to-thickness(*w*/*t*) ratios. The *w*/*t* ratio influences the ability of the sample to maintain a unidirectional state of stress during tension. In a thick section (top), strain in the width direction is constrained and thus tends to a condition of plane-strain (mode I) fracture. In this case, a large portion of the fracture surface comprises radial markings or chevron patterns indicative of rapid, unstable cracking. At higher *w*/*t* ratios, the radial zone is suppressed in favor of a larger shear-lip zone. In very thin sections (bottom), plane-stress conditions apply, and the fracture surface is composed almost entirely of a shear lip outside the fibrous zone of crack initiation. Figure 16 shows radial marks and chevrons when fracture initiates from surface notches.

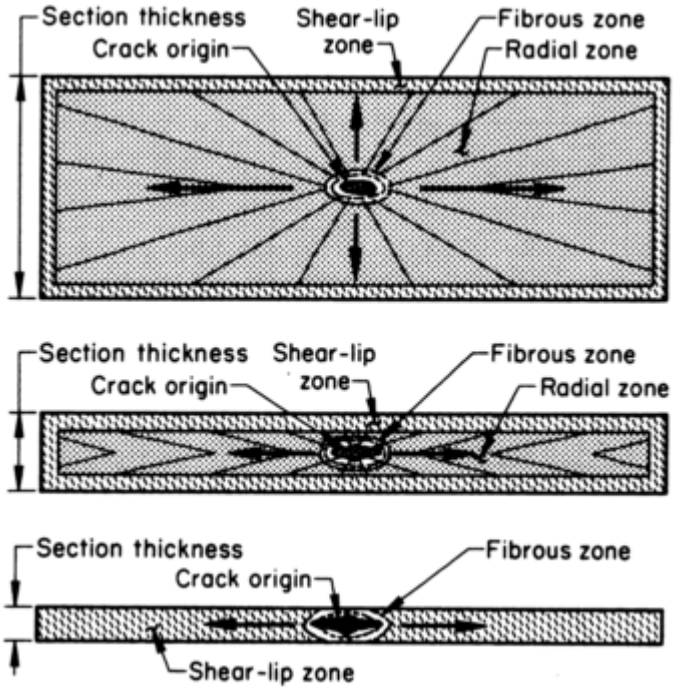

Fig. 15 Typical fracture appearances for unnotched prismatic tension-test sections. Source: Ref 9

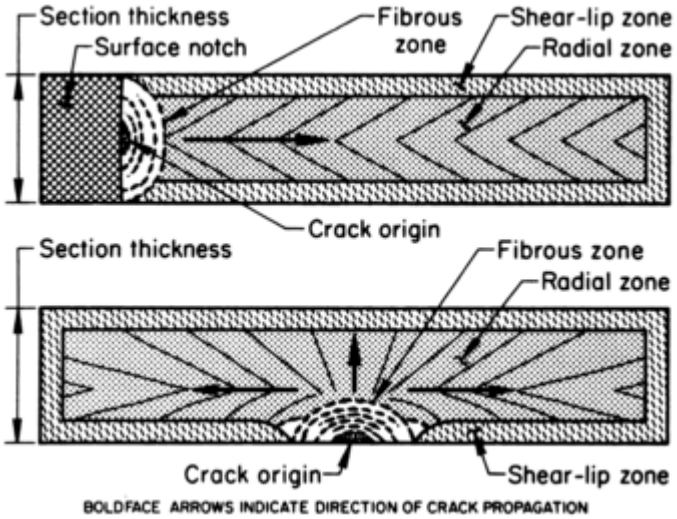

Fig. 16 Typical fracture appearances for edge- and side-notched rectangular tension-test sections. Note the shear lips when the fracture approaches the edge of the specimen. Source: Ref 9

If conditions are right, the radial patterns associated with rapid or unstable crack propagation can also occur in a cylindrical section. This radial pattern, sometimes called a radial shear, star, or rosette, is perpendicular to the crack front and, as such, may be considered to be the round-sample equivalent of the radial markings or chevron patterns that appear on sheet or plate samples, as previously described. The radial marks, or radial shear marks, are visually distinct from the fibrous region, as shown in Fig. 17 for an unnotched SAE 4150 steel specimens with different strengths. Figure 17(a) shows a clear boundary between the fibrous central region and the large ridge pattern of the radial marks. Figure 17(b) shows shallower radial marks and a slightly larger fibrous zone from a heat treatment that results in more ductility. Figure 17(c) shows very weak or shallow radial marks that develop further from the center.

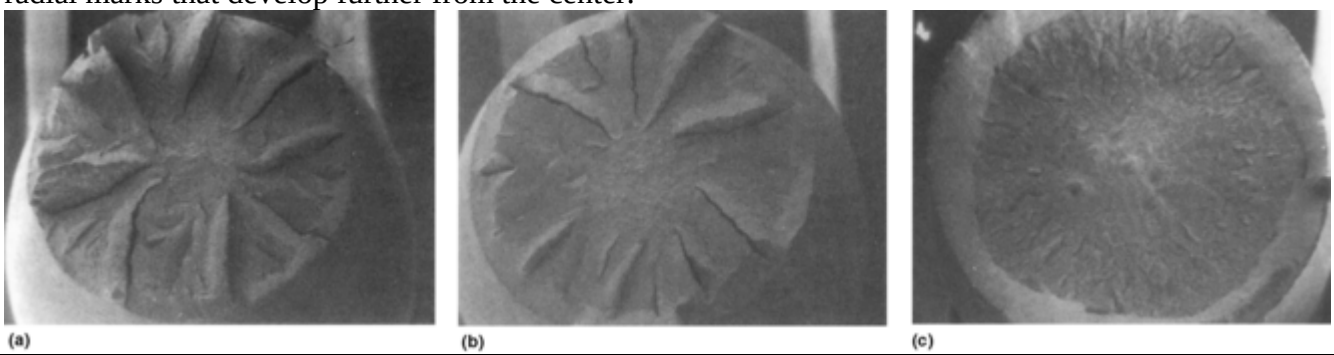

Specimen	Hardness, HV	Yield strength		Ultimate tensile strength		Reduction of area, %	Charpy V-notch impact energy		Fibrous zone as percentage of total area
		MPa	**ksi**	**MPa**	**ksi**		**J**	**ft · lbf**	
(a)	285	0.73	0.106	0.83	0.120	66	163	120	~25
(b)	258	0.65	0.094	0.79	0.115	67	174	128	~31
(c)	301	0.81	0.117	0.97	0.141	49	27	20	~44

Fig. 17 Radial marks on tensile test specimen of Society of Automotive Engineers (SAE) 4150 steel isothermally transformed to bainite, quenched to room temperature, and then tempered. (a) Lower bainite, isothermally transformed at 300 °C (570 °F) for 1 h, tempered at 600 °C (1110 °F) for 48 h. (b) Lower bainite, isothermally transformed at 375 °C (705 °F) for 1 h, tempered at 600 °C (1110 °F) for 48 h. (c) Upper bainite, isothermally transformed at 450 °C (840 °F) for 24 h, as-quenched. Source: David Johnson, Master's thesis, University of Tennessee

Radial marks on the fracture surface of an unnotched cylindrical tension-test specimen (Fig. 18) point to the center, which has a fibrous appearance that is associated with ductile crack initiation and growth by microvoid

coalescence. However, if the specimen is notched (Fig. 18b), then crack initiation may begin at several locations along the circumference near the root of the notch, where stress concentration occurs. The region of crack initiation may still have a fibrous appearance indicative of microvoid coalescence (MVC) near the root of the notch, but the region of final, fast fracture is in the center and roughly perpendicular to the applied load. Thus, even though the radial markings may appear to point to the center, the surface conditions indicate that the central region is the area of final fracture, not crack initiation. In effect, the notch size is sufficient to cause plane-strain fracture, as evidenced by the lack of shear lips.

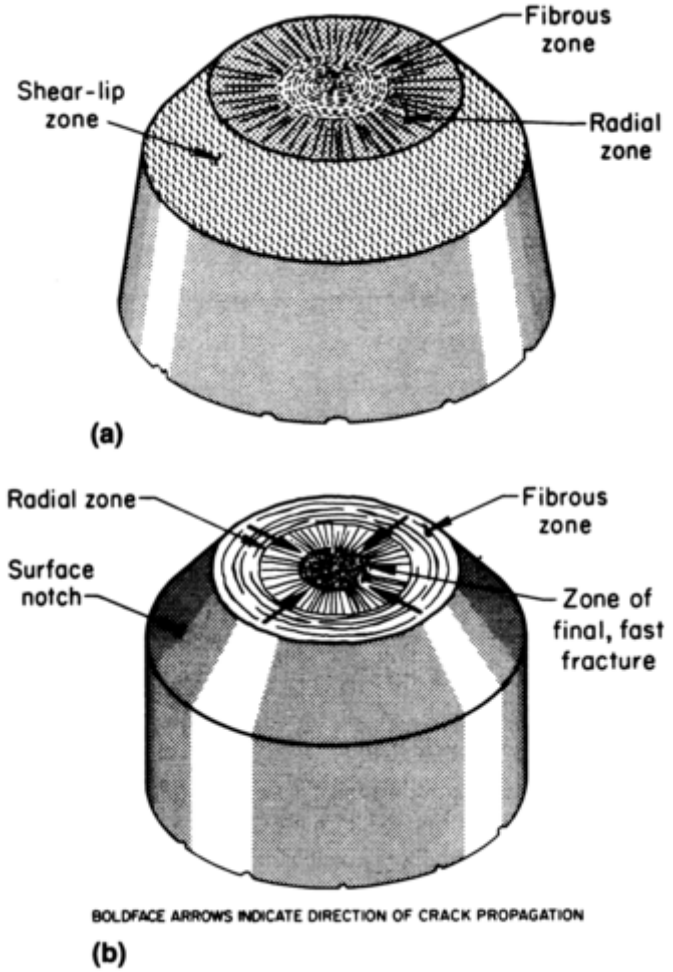

Fig. 18 Fracture surface regions in cylindrical tension-test specimens. (a) Surface from cone portion of fractured unnotched tensile specimen. (b) Surface of fractured notched specimen. Unlike the fracture surface for an unnotched specimen, the fracture surface for the notched specimen (b) does not have shear lips, because the fracture initiates near the root of the notch (and completely around the specimens in this idealized case without additional stress raisers). Source: Ref 9

Macroscopic Appearance of Ductile Fractures. As noted in Table 2, ductile fractures are typically characterized by evidence of plastic deformation, such as necking of a tension-test specimen. Ductile fractures often progress as single cracks, without many separated pieces or substantial crack branching at the fracture location. The region of a crack-initiation typically has a dull fibrous appearance that is indicative of cracking by MVC. The crack profiles adjacent to the fracture are consistent with tearing. The fracture surface may have radial markings, chevrons, and/or shear lips depending on the specimen geometry and material condition, as previously noted.

An example of mixed-mode (mode I and II) fracture is the classic cup-and-cone appearance from ductile fractures of unnotched cylindrical tension-test specimen (Fig. 18a). In this case, the fracture originates near the specimen center, where hydrostatic stresses develop during the onset of necking and where microvoids develop and grow. Multiple cracks join and spread outward along the plane normal to loading axis, as representative of mode I (plane-strain) crack propagation. When cracks reach a region near the outer surface, the mode of fracture changes to mode II (plane-stress) condition, where shear strain becomes the operative mode of deformation. Thus, even though the overall applied stress is still a tensile load, deformation makes a transition

to the shear plane in the outer regions of the specimen and thus results in the 45° shear lips that are indicative of a mode II fracture. Alternatively, the fracture mode may be entirely plane strain when a sufficiently large crack or notch is introduced (Fig. 18b).

Macroscopic Appearances of Brittle Fractures. Brittle overload failures, in contrast to ductile overload failures, are characterized by little or no macroscopic plastic deformation. Brittle fracture initiates and propagates more readily than ductile fracture or so-called "subcritical" crack-propagation processes such as fatigue or stress-corrosion cracking. Because brittle fractures are characterized by relatively rapid crack growth, the cracking process is sometimes referred to as being "unstable" or "critical" because the crack propagation leads quickly to final fracture.

The macroscopic behavior is essentially elastic up to the point of failure. The energy of the failure is principally absorbed by the creation of new surfaces, that is, cracks. For this reason, brittle failures often contain multiple cracks and separated pieces, which are less common in ductile overload failures. Brittle fracture mechanisms may exhibit chevron or herringbone patterns that indicate the fracture origin and direction of rapid fracture. Chevrons occur mainly in structural steels and rail (web) steel or relatively ductile low-strength alloys. Chevrons are dependent on strength, ductility, and section thickness, and are not normally seen in high strength alloys.

Herringbone patterns are unique microscopic features of brittle fractures (Ref 9). Ductile cracking, which occurs by microvoid coalescence, does not result in a herringbone pattern. On a microscopic scale, the features and mechanisms of fracture may have components of ductile or brittle crack propagation, but the macroscopic process of fracture is characterized by little or no work being expended from deformation.

Macroscopic Appearances of Fatigue Fractures (Adapted from Ref 11). Examination of a fatigue fracture usually begins with unaided visual observation, often followed by viewing with a hand lens or stereomicroscope. Macroscopic examination of fracture surfaces can be performed on-site (when the broken part is accessible), requires little or no preparation of the specimen, and uses minimal and relatively simple equipment. It does not destroy the specimen or alter fracture surfaces. Macroscopic examination is particularly useful in correlating fracture surface characteristics with part size and shape and with loading conditions.

Fatigue origins are frequently located most readily by viewing the fracture surface at low magnifications (up to 30 to 50×). For example, Fig. 19 shows a fracture of a steel housing tube. The initiation region is observable in the macrograph, as shown by the arrow. The position of the crack front at various times during the failure process is also visible as the so-called beach marks that are initially fairly concentric to the origin.

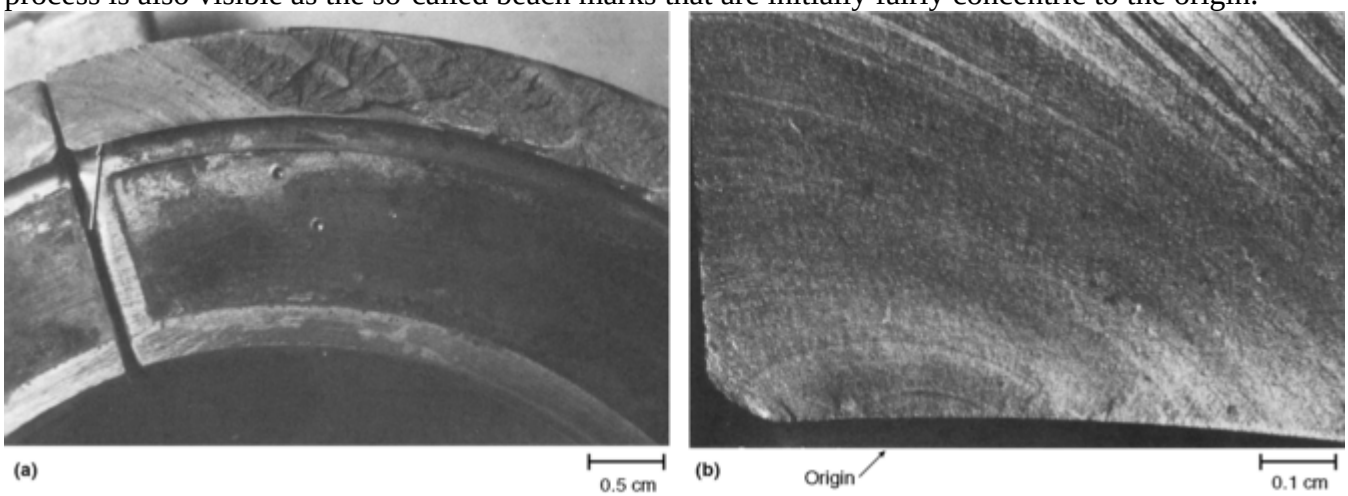

Fig. 19 Fractographs of a typical fatigue crack in a clamp. (a) The fatigue crack origin is marked by the arrow. The crack propagated to the right by continuous fatigue cracking (light) region, then continued alternately by rapid tearing and slow fatigue cracking. 2×. (b) Higher-magnification view of the region near the arrow in (a). 10×. Source: Ref 8

Macroscopically, fatigue fracture ordinarily has a brittle appearance and lacks the gross plastic deformation (e.g., necking) characteristic of ductile tensile overload fracture. In contrast with ductile overload fracture, which generally has more-or-less shear lip (slant 45° fracture) along free surfaces, propagating fatigue fractures typically intersect free surfaces at right angles (Fig. 20). This provides a tool for helping to identify fatigue locations. In common with other progressive fracture modes, such as stress-corrosion cracking, field fatigue

fractures are frequently decorated by more-or-less curved marks that delineate the position of the crack front at a particular point in time. These marks are commonly called beach marks and are also known as clamshell marks or arrest marks.

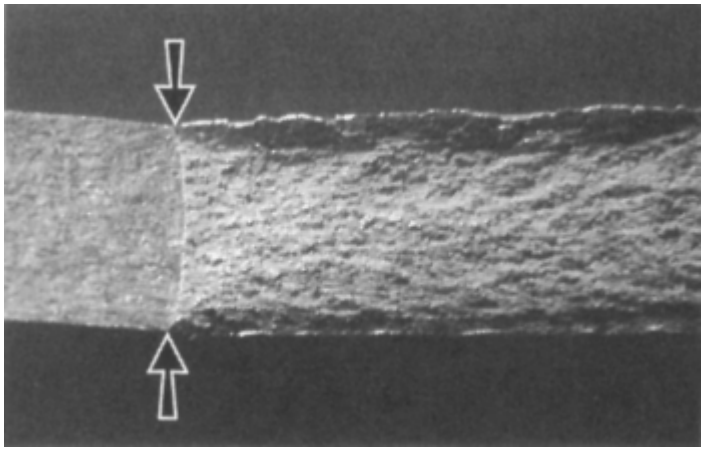

Fig. 20 Aluminum alloy fracture mechanics test specimen, 6.3 mm (0.25 in.) thick. Fatigue crack at left of arrows is flat and perpendicular to side surfaces (note absence of beach marks in this laboratory fatigue fracture). Overload fracture to right of arrows has 45° shear lips extending upward at the top side of the sample and downward at the bottom side. Source: Ref 11

Beach marks are produced by a change in crack-growth conditions, such as a change in environment or stress level or a pause in stress cycling (interruption in service). Thus, beach marks are not always present on the surface of a fatigue fracture. For example, beach marks are not found in laboratory tests conducted under uniform loading and environmental conditions (e.g., Fig. 20). Moreover, the presence of beach marks also is not conclusive evidence of fatigue fracture. Beach marks may also appear when fracture is from stress-corrosion cracking Fig. 21 (Ref 12).

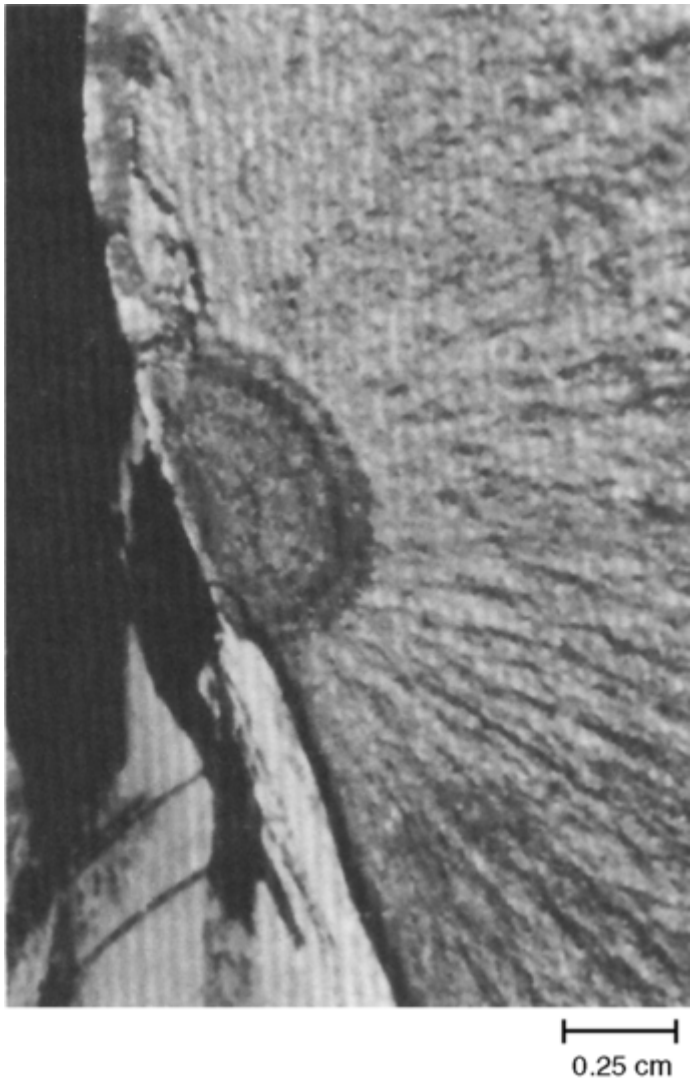

Fig. 21 Beach marks on a 4340 steel part caused by stress-corrosion cracking. Tensile strength of the steel was approximately 1780 to 1900 MPa (260 to 280 ksi). The beach marks are a result of differences in the rate of penetration of corrosion on the surface. They are in no way related to fatigue marks. 4×

References cited in this section

8. M.R. Louthan, Jr., Optical Metallography, *Materials Characterization,* Vol 10, *ASM Handbook,* American Society for Metals, 1986, p 299–308

9. W.T. Becker, Fracture Appearance and Mechanisms of Deformation and Fracture, *Failure Analysis and Prevention,* Vol 11, *ASM Handbook,* ASM International, 2002, p 559–586

10. R.W. Hertzberg, *Deformation and Fracture Mechanics of Engineering Materials,* 4th ed., John Wiley, 1996

11. R.A. Lund and S. Sheybany, Fatigue Fracture Appearances, *Failure Analysis and Prevention,* Vol 11, *ASM Handbook,* ASM International, 2002, p 627–640

12. Fatigue Failures, *Failure Analysis and Prevention,* Vol 11, *ASM Handbook,* ASM International, 2002, p 708

Metallography: An Introduction, *Metallography and Microstructures,* Vol 9, *ASM Handbook*, ASM International, 2004, p. 3–20

Microscopic Examination

The importance of microstructure to the properties of metals and alloys has long been recognized. Grain size, twins, and the size, shape, and distribution of second-phase particles are important in determining the behavior of most structural metals. Therefore, characterization of microstructures by light microscopy is essential. Process-control parameters are established to provide specific grain sizes. The number, size, and distribution of second-phase particles, such as inclusions, are frequently specified, and quantitative metallographic procedures have been developed to describe microstructure.

This section on microanalysis focuses mainly on the method of light microscopy with some discussion of SEM in fractography. As previously noted, the upper limit of useful magnification in a light microscope is approximately 1500×, and the fundamental limitations of light optic systems limit resolution to features that are ~0.2 μm or larger. Light microscopy, then, is used primarily to examine grain structures and the morphology of large second-phase particles. However, many other microstructural features that are too small to be observed using light microscopy also can influence the properties of metals and alloys. Dislocations, numerous types of second-phase particles, spinodal and ordered structures, and many aspects of martensitic structures can be categorized as too small for light microscopy. These features require examination by electron microscopy, which are discussed elsewhere (see the articles “Scanning Electron Microscopy” in this Volume and “Analytical Transmission Electron Microscopy” in *Materials Characterization*, Volume 10 of *ASM Handbook*). Microscopy is also essential in the analysis of failures due to fracture, wear, and/or corrosion. These topics and the use of light and electron microscopy in failure analysis are discussed in more detail in *Failure Analysis and Prevention,* Volume 11 of *ASM Handbook.* However, the section “Microfractography” in this article briefly compares the application of light and electron microscopy in fractographic analysis. Another important technique in microanalysis is replica metallography, where specimens are replicas taken in situ from components in the field. There are two types of replicas: surface replicas and extraction replicas. Surface replicas provide an image of the surface topography of a specimen, while extraction replicas lift particles from the specimen. The application of replica metallography is discussed in more detail in the article “Field Metallography Techniques” in this Volume.

Microstructure

Optical (light) characterization of the microstructures of metals and alloys involves the identification and measurement of phases, precipitates, and constituents, and the determination of the size and shape of the grains, the extent of twinning, and some of the characteristics of grain boundaries and other observable defects. Solidification, solid-state transformation, deformation, and annealing microstructures are the four basic types in metals and alloys. Each of these has distinct characteristics, as described below. Anisotropy of grain orientation is also important when characterizing the microstructure of a material.

Anisotropy. Microstructural features exist in three dimensions, while metallographic observation typically represents only two dimensions. Therefore, effective microscopy frequently requires microstructural observations in two or more directions. For example, Fig. 22 and 23 illustrate the value of viewing the microstructure in several directions. Figure 22 shows an annealed microstructure exhibiting similar grain shapes in all three views. Grain size is characterized by placing a line of known length (or preferably a circle of known circumference) on the magnified image of the microstructure and counting the number of intersections between the line and grain boundaries in the microstructure. The number of grain boundary intersections, *P*, can be converted to a measure of grain size, *l*, using:

$$l = \frac{L}{PM} \qquad \text{(Eq 1)}$$

where *M* is the magnification of the image observed, *L* is the length of line on the image, and grain size (*l*) is the mean lineal intercept length (per ASTM E112). The microstructure of the annealed alloy (Fig. 22) is isotropic, while the grains are elongated in the rolling direction and flattened in the transverse directions when alloy is in the cold-rolled condition. This anisotropic grain structure also renders anisotropic mechanical properties. Physical properties may also be anisotropic, especially in single-phase alloys due to texture. Thus, anisotropic materials may require selection, preparation, and viewing of specimens from different orientations. This is discussed further in the article "Metallographic Sectioning and Specimen Extraction" in this Volume. Modern techniques also include methods of three-dimensional representation (see the article "Three-Dimensional Microscopy" in this Volume).



Fig. 22 Copper alloy 26000 (cartridge brass, 70%) sheet, hot rolled to a thickness of 10 mm (0.4 in.), annealed, cold rolled to a thickness of 6 mm (0.230 in.), and annealed to a grain size of 0.120 mm (0.005 in.). At this reduction, grains are basically equiaxed. Compare with Fig. 23. Diagram in lower left of each micrograph indicates orientation of the view relative to the rolling plane of the sheet. Etched using NH_4OH plus H_2O_2. 75×. Source: Ref 8



Fig. 23 Same alloy and processing as in Fig. 22, but reduced 50% by cold rolling from 6 mm (0.239 in.) to 3 mm (0.120 in). Grains are elongated in the rolling direction. Diagrams indicate same orientation of view as in Fig. 22. Etched using NH_4OH plus H_2O_2. 75×. Source: Ref 8

Solidification Structures. The most commonly observed solidification structure is dendritic (Fig. 24). A dendritic structure usually exhibits compositional variations, with the primary, secondary, and tertiary dendrite arms containing less alloying or impurity elements than interdendritic regions. Because of such compositional changes (termed "*coring*"), the rate of etching at interdendritic regions differs from that at dendrite arms. If the alloying element or impurity content is high, interdendritic regions may develop a two-phase structure. Because dendrite arm spacing tends to decrease with increasing cooling rates, the properties of as-cast metals depend on the solidification rates.

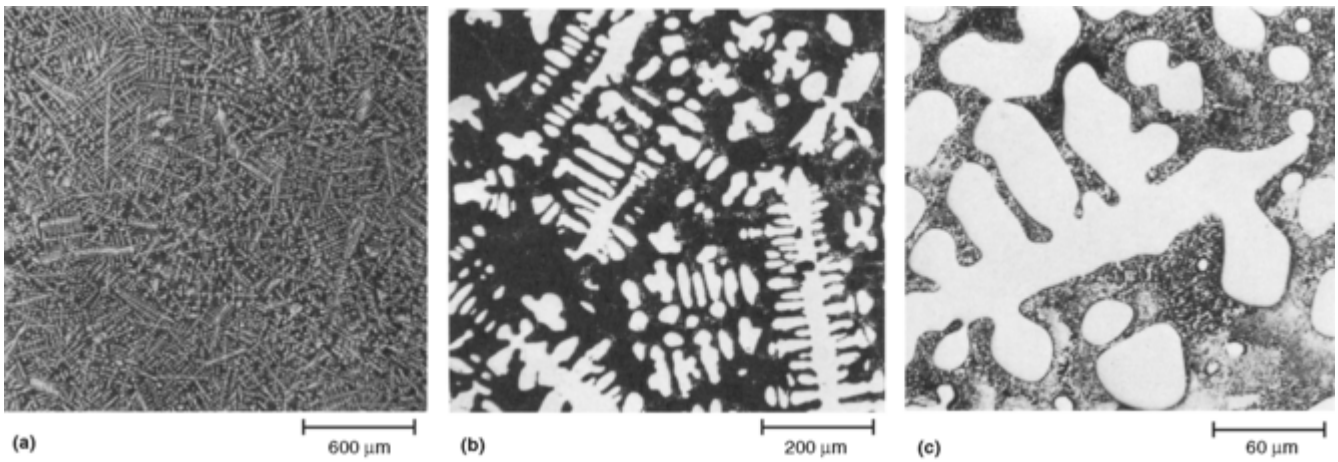

Fig. 24 Dendritic solidification structure in a Ni-5Ce (at.%) alloy. Nickel dendrites (light in b and c) are surrounded by a matrix of nickel-cerium eutectic. (a) 25×. (b) 75×. (c) 250×. Source: Ref 8

Most metals shrink during solidification. Therefore, the liquid trapped between dendrite arms during solidification is frequently insufficient to fill the space between the arms when solidification is complete. This inability to fill the remaining space leads to shrinkage voids, which can be observed microscopically. Voids are generally easier to observe on as-polished specimens than on polished and etched ones. Figure 25(a) shows a typical example of shrinkage voids.

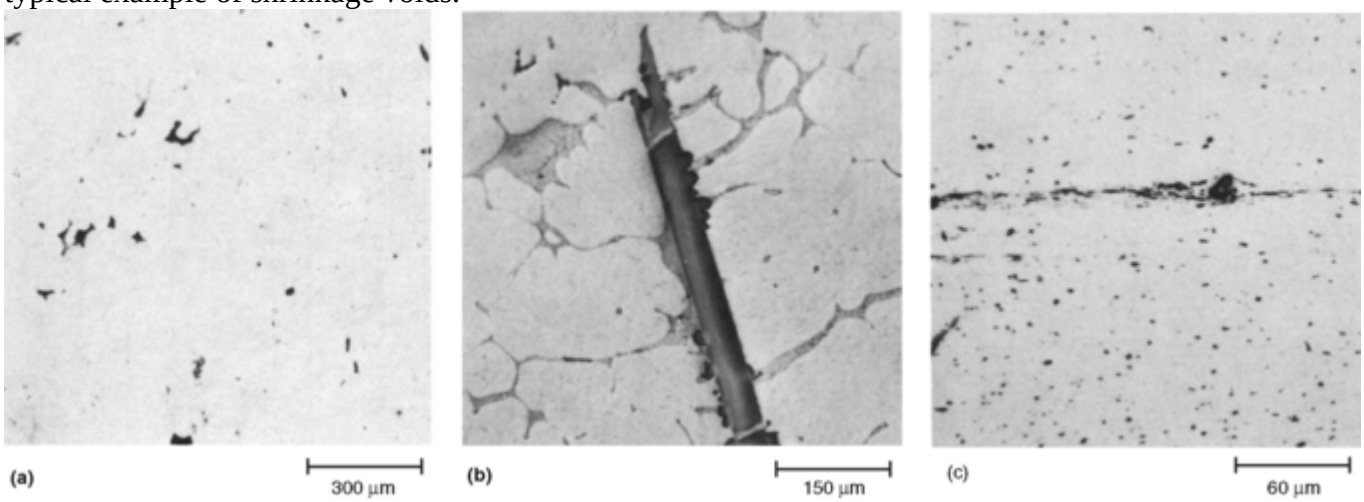

Fig. 25 Typical imperfections observable using optical microscopy. (a) Shrinkage porosity in an aluminum alloy 5052 ingot. Note angularity. 50×. (b) Coarse primary $CrAl_7$ crystal in aluminum alloy 7075 ingot. 100×. (c) Oxide stringer inclusion in a rolled aluminum alloy 1100 sheet. 250×. All as-polished. Source: Ref 8

Discontinuities. Various materials discontinuities, such as inclusions and stringers (Fig. 25b and c) can also be observed microscopically in as-polished specimens. Such imperfections as those shown in Fig. 25 can serve as failure-initiation sites in metals and alloys; therefore, characterization of their size, shape, and distribution is necessary to establish material properties and engineering reliability. Quality-assurance programs frequently require controlling imperfections to regulate their type, number, size, and shape in a particular manner. For example, a component having a stringer distribution such as that shown in Fig. 25(c) would have better ductility if specimens or components were tested with the major stresses parallel to the stringer than if specimens were oriented with the major stresses perpendicular to the stringer.

Transformation structures often consist of two phases. In such structures, the major phase is typically termed the matrix, or base structure, and the minor phase is termed the second phase. The size, shape, and distribution of second-phase particles are important in determining the properties of metals and alloys. Characterization of second-phase morphology can sometimes be accomplished using optical metallography. However, the second phase is sometimes so small that the resolution necessary to characterize the phase morphology exceeds the limits of the light microscope. In these cases, SEM may be used, or transmission electron microscopy may be

needed. Age-hardenable or precipitation-hardened metals and alloys generally must be characterized using electron microscopy.

High-temperature phase transformations frequently nucleate at grain boundaries. The grain-boundary structures can be discrete or continuous. Continuous grain-boundary constituents (Fig. 26) provide easy fracture paths when the grain-boundary phase is less ductile than the matrix phase. For the material shown in Fig. 26, the expected failure would be fracture along the grain-boundary carbides. Heterogeneous precipitation at grain-boundary regions is typically based on the classic mechanism of precipitate nucleation and growth, where the initial nucleus starts at critical size to allow reduction in the interfacial surface energy between the precipitate and parent phases (see the article “Structures by Precipitation from Solid Solution” in this Volume). The transformation processes may also be continuous (e.g., see the article “Spinodal Transformation Structures” in this Volume).

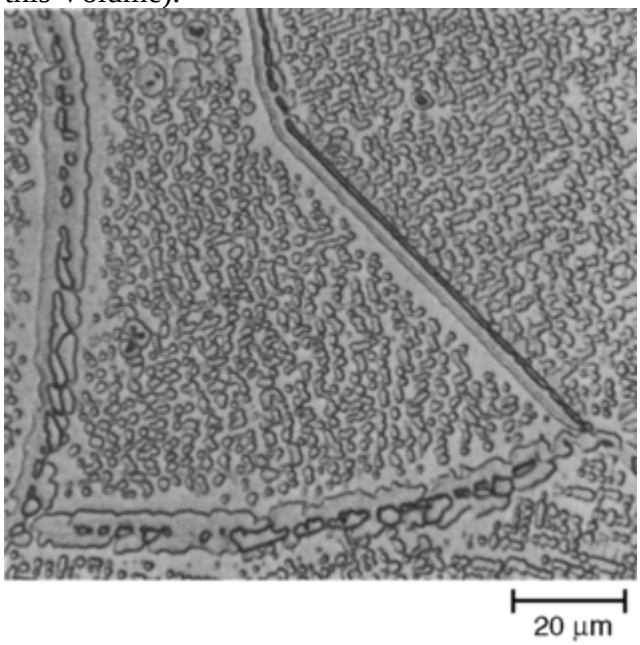

Fig. 26 Continuous grain-boundary precipitate in U-700 nickel-base heat-resistant alloy. Etched using HCl, ethanol, and H_2O_2. 500×. Source: Ref 8

Deformation Structures. The microscopic details of deformation structures typically cannot be fully established using light metallography. Deformation changes the number and arrangement of dislocations (crystal defects) in the metal on an atomic scale. This dislocation substructure is best characterized using TEM. Light-microscope metallography can be used to supplement TEM through characterization of the grain size and anisotropy in grain shape and distribution. Microstructural changes due to annealing can be studied using TEM or light microscopy. The most important structural changes that occur during annealing are recovery, recrystallization, and grain growth.

Recovery is the rearrangement and annihilation of imperfections (primarily vacancies and interstitials) within each grain of a cold-worked polycrystalline component. Because recovery deals mainly with point defects, any microstructural observations of it are difficult, and light microscopy cannot be used because of its limited resolution.

Recrystallization is the formation of new strain-free grains within the previously cold-worked (strained) grains. The initial stages of recrystallization occur on such a fine scale that TEM is necessary; however, light-microscope metallography can be readily used to study most of the recrystallization. The size of the recrystallized grains depends on the amount of cold working of the specimen before the recrystallization anneal. The greater the amount of cold work, the finer the recrystallized grain size (Fig. 27). Because grain boundaries are a crystalline defect, continued annealing will cause this array of grains to be unstable, and grain growth will take place. Grain growth in a recrystallized specimen decreases the grain-boundary surface area to specimen volume ratio because the average grain size increases as grain growth takes place. The rate of grain growth depends on temperature and time.

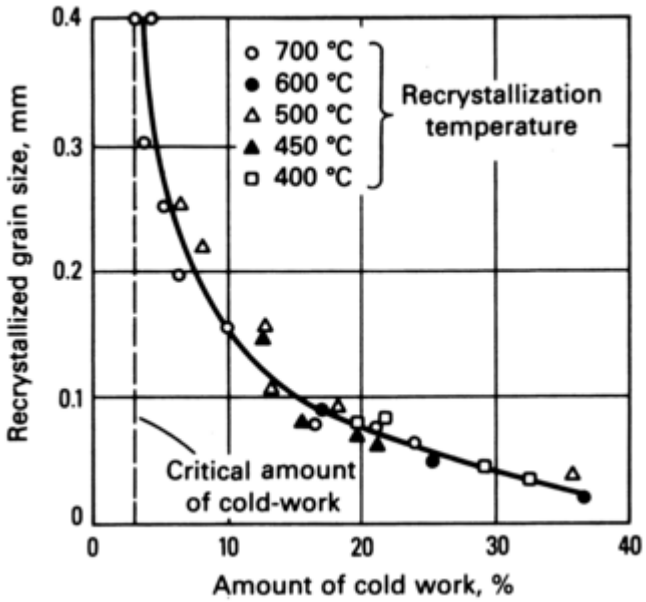

Fig. 27 The effect of prior cold work on recrystallized grain size. Source: Ref 8

Microfractography (Adapted from Ref 13)

Microscopic examination of the fracture surface is best accomplished by use of the scanning electron microscope (SEM) and in some cases by examination of replicas with the transmission electron microscope (TEM). The SEM images in Fig. 28 show the distinctive microscopic features of the three basics types of overload fracture: transgranular brittle fracture (cleavage), transgranular ductile fracture (microvoid coalescence), and brittle fracture by intergranular separation. The SEM provides good depth of focus to observe topological features of the fracture surface. Modern SEM instruments also typically have x-ray spectroscopic attachments that allow elemental analysis of constituents on (or near) the specimen surface. This can be very helpful in failure analysis.

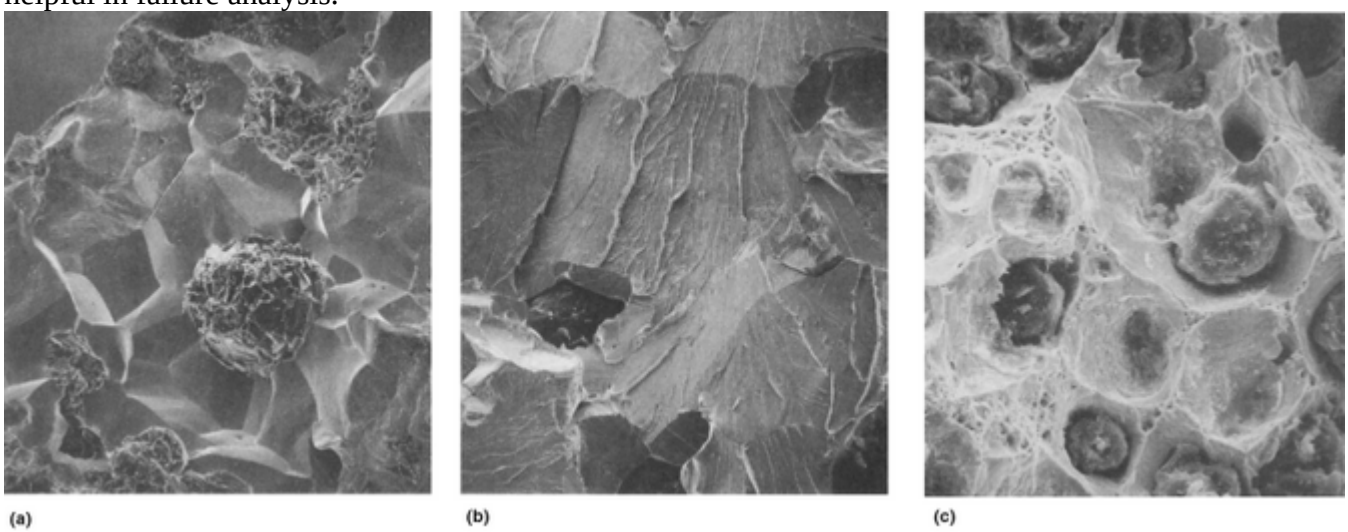

Fig. 28 Scanning electron micrograph images of the basic types of overload fracture. (a) Intergranular fracture in ion-nitrided layer of ductile iron (ASTM 80-55-06). (b) Transgranular fracture by cleavage in ductile iron (ASTM 80-55-06). (c) Ductile fracture with equiaxed dimples from microvoid coalescence around graphite nodules in a ductile iron (ASTM 65-40-10). Picture widths are approximately 0.2 mm (0.008 in.) from original magnifications of 500×. Courtesy of Mohan Chaudhari, Columbus Metallurgical Services

However, lack of access to a SEM or TEM should not be viewed as a crippling obstacle to performing failure analysis, because such work was done successfully prior to the development of these instruments. In many studies, such equipment is not needed, while in other cases, they are very important tools. In most cases,

electron microscopy and light microscopy should be considered complementary tools. Microstructural examination can be performed with the SEM over the same magnification range as the light microscope (LM), but examination with the latter is more efficient. Contrast mechanisms for viewing microstructures are different for LM and SEM. Many microstructures, for example, tempered martensite, exhibit poor contrast in the SEM and are best viewed by light microscopy.

When atomic number contrast or topographic contrast is strong, the SEM provides good structural images, particularly above 500× (Ref 14). Again, because of the limitations and advantages of each instrument, they are complementary rather than competitive tools. All studies of microstructures and fractures should begin at the lowest magnification level, the unaided human eye, and progress upward, first using the stereomicroscope for fractures and the LM for fracture path and microstructural studies, before using electron metallographic equipment.

Microfractography is a relatively new field; its roots can be traced to the light optical fractographs published by Zapffe and coworkers (Ref 15) beginning in the early 1940s, although a few studies of historical value predated their efforts. Zapffe's work, however, was almost exclusively confined to observation of cleavage facets on rather brittle, coarse-grained specimens. The technique, basically an interesting academic exercise, did stimulate interest in fracture examination as part of failure analysis. However, the depth-of-field limitation of the light microscope has restricted its use for such work. Aside from the published light optical fractographs made by Zapffe (see Ref 16 for a review of many of these), very few optical fractographs of metallic materials have been published by others. Microfractography gained momentum with the development of TEM replication methods and became commonplace after the commercial introduction of the SEM in approximately 1965.

A flat, brittle fracture can be examined with the light microscope by orienting the fracture perpendicularly to the optical axis. It is best to start with a low-power objective; long-working-distance types are preferred. Focusing reveals the limitations of the method, because only part of the fracture is in focus at any setting. Thus, photographs* reveal only a portion of the fracture in focus, depending on the coarseness and orientation of the fracture facets. Figure 29 shows an example of a brittle fracture in a low-carbon steel examined in this manner. Figure 29 also shows a LM image of the fracture profile, a LM image of a replica of the fracture, SEM images of the fracture and a replica of the fracture, and a TEM replica of the fracture. Although Zapffe used bright-field illumination for this work, dark-field illumination often produces superior results. Figure 30 illustrates the use of bright-field and dark-field illumination for viewing a brittle fracture in an Fe-Cr-Al alloy, plus a SEM fractograph of the same area. Dark-field illumination is better at collecting the light scattered from the fracture features; glare is reduced, and image contrast is improved. Examination of fracture replicas with the light microscope (Ref 16, 17, 18) can extend the use of the method only to a limited extent, because the replica collapses slightly, producing less depth of field. Also, with a replica, the risk of damaging the objective is eliminated.

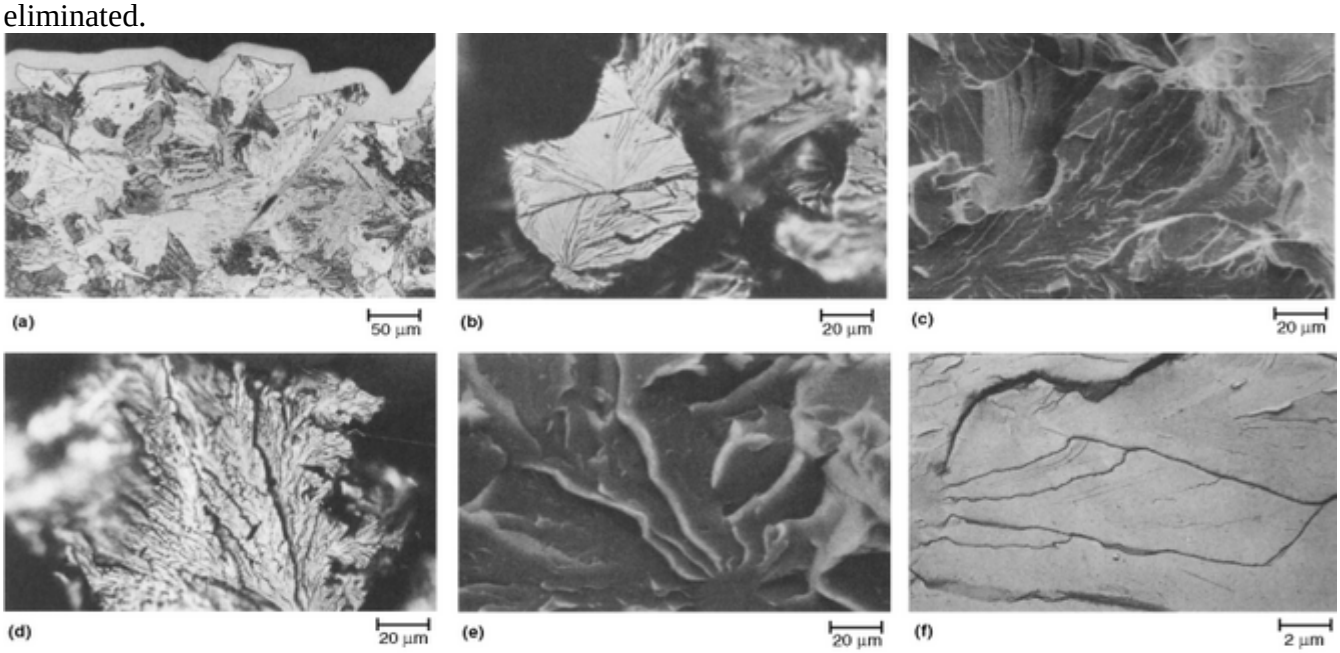

Fig. 29 Cleavage fracture in a quenched-and-tempered low-carbon steel examined using three direct methods and three replication methods. (a) Light microscopy (LM) cross section (nickel plated). Etched

with Vilella's reagent. (b) LM fractograph (direct). (c) Scanning electron microscopy (SEM) fractograph (direct). (d) LM replica. (e) SEM replica. (f) Transmission electron microscopy replica. Source: Ref 13

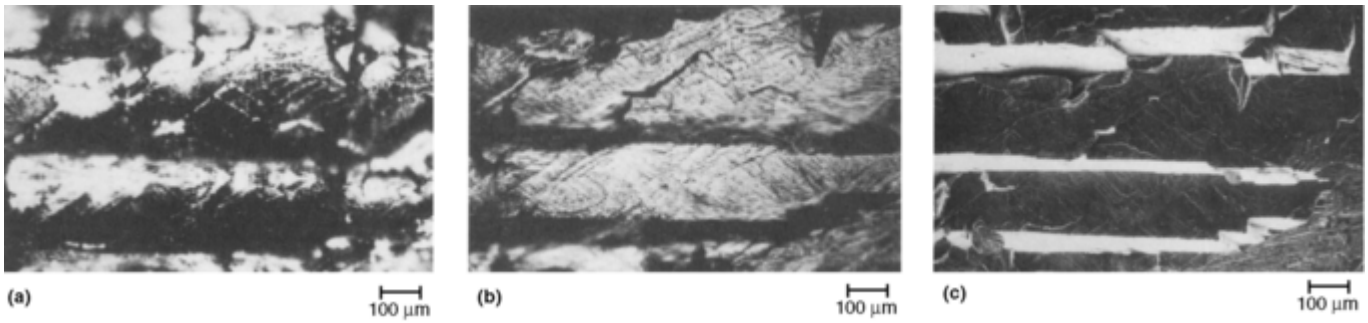

Fig. 30 Light microscope fractographs taken with (a) bright-field and (b) dark-field illumination compared to (c) a scanning-electron secondary-electron image fractograph of the same area. Sample is Fe-Al-Cr alloy. Source: Ref 13

Considerable information concerning the fracture mode and the relationship of the microstructure to the fracture path can be obtained by LM examination of the profile of partially fractured (Ref 19, 20, 21) or completely fractured (Ref 22, 23, 24, 25, 26) polished metallographic specimens. Such examinations have been conducted for many years, long before the development of electron metallographic techniques, and continue to be used because of the value of the method. If the fracture has progressed to complete rupture, so that only one side of the fracture is to be examined, it may be best to nickel plate the fracture to enhance edge retention. This is not required if the crack has not separated the component into two pieces, or if a secondary crack is to be examined. Examination of the crack path using cross sections is also very useful for study of fractures due to environmental problems. Figure 31 shows a stress-corrosion crack in a partially broken sample of solution-annealed AISI 304 stainless steel tested in boiling (151 °C, or 304 °F) magnesium chloride. The crack path is predominantly intergranular, but considerable transgranular fracture is also present. The SEM fractograph of the specimen clearly reveals the intergranular nature of the crack.

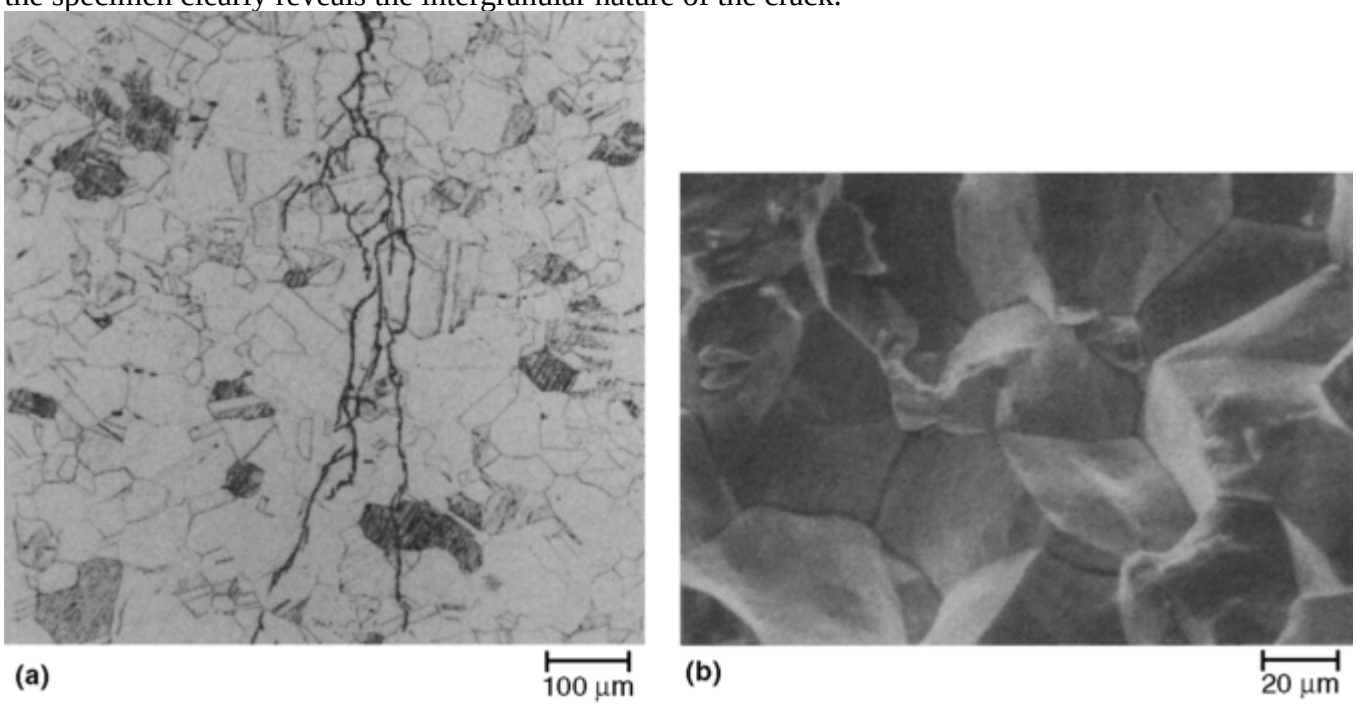

Fig. 31 Light micrograph of a cross section of (a) partially broken specimen and (b) a scanning electron fractograph of a completely broken specimen of solution-annealed AISI 304 stainless steel after stress-corrosion crack testing in boiling (151 °C, or 304 °F) magnesium chloride. Source: Ref 13

Fracture profile examination is also very useful in the study of failures due to liquid metal embrittlement (LME). Figure 32 shows the microstructure adjacent to a LME crack in a eutectoid steel where liquid copper

has penetrated the grain boundaries at 1100 °C (2012 °F) while the sample was austenitic and under an applied tensile load. Light microscope examination reveals a discontinuous film of copper in the prior-austenite grain boundaries and an intergranular fracture path. Scanning electron microscope examination of the fracture also reveals the intergranular nature of the crack path.

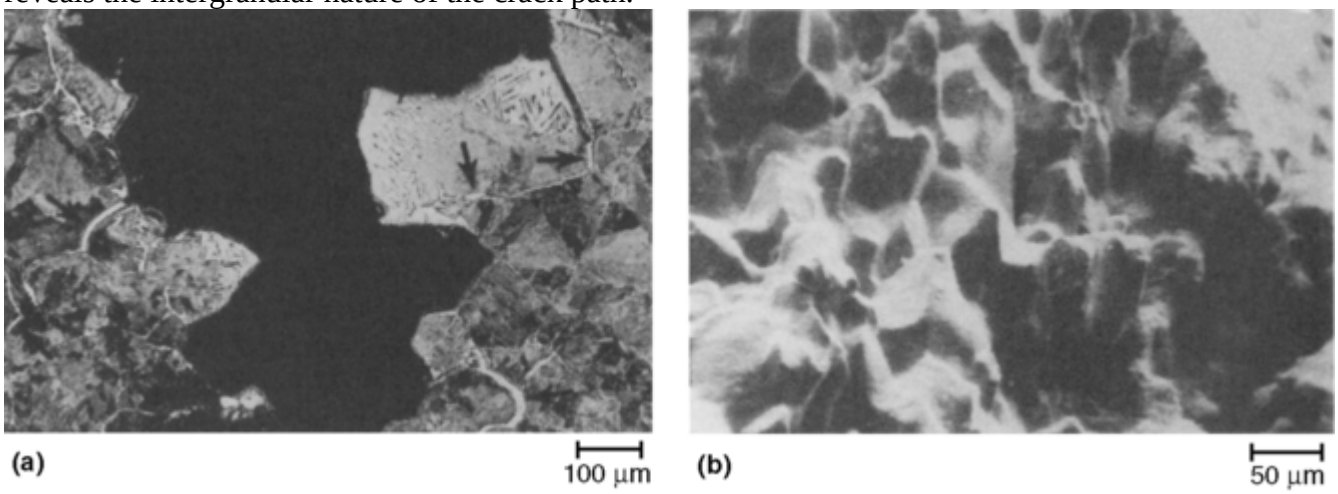

Fig. 32 Light micrograph of (a) partially broken eutectoid carbon steel specimen embrittled by liquid copper at 1100 °C (2012 °F) (arrows point to grain-boundary copper penetration) and (b) scanning electron fractograph of the completely broken specimen. Source: Ref 13

Surface detail can also be studied by LM using taper sections (Ref 27, 28, 29). This method has been used to study wear phenomena, surface coatings, fatigue damage, and other fine surface detail. In this method, the surface is sectioned at a slight angle to the surface. Polishing on this plane produces a magnified view of the structure in the vertical direction. The degree of magnification is defined by the cosecant of the sectioning angle; an angle of 5° 43′ produces a tenfold magnification.

Finally, considerable progress has been made in applying the principles of quantitative metallography to the study of fractures (Ref 25, 26, 30, 31, 32, 33, 34). Much of this work has used measurements made on polished sections taken parallel to the crack-growth direction ("vertical sections"). This work provides new insight into fracture processes and should be useful in failure analysis, although its application to date has been limited mainly to research studies.

Footnote

* With digital imaging, portions of the fracture surface can be focused, and then all images combined to form one large image in focus.

References cited in this section

8. M.R. Louthan, Jr., Optical Metallography, *Materials Characterization,* Vol 10, *ASM Handbook,* American Society for Metals, 1986, p 299–308

13. G.F. Vander Voort, Metallographic Techniques in Failure Analysis, *Failure Analysis and Prevention,* Vol 11, *ASM Handbook,* ASM International, 2002, p 498–510

14. G.F. Vander Voort, The SEM as a Metallographic Tool, *Applied Metallography,* Van Nostrand Reinhold Co., 1986, p 139–170

15. C.A. Zapffe and M. Clogg, *Trans. ASM,* Vol 34, 1945, p 71–107

16. K. Kornfeld, *Met. Prog.,* Vol 77, Jan 1960, p 131–132

17. P.J.E. Forsyth and D.A. Ryder, *Metallurgia,* March 1961, p 117–124

18. K.R.L. Thompson and A.J. Sedriks, *J. Aust. Inst. Met.,* Vol 9, Nov 1964, p 269–271

19. H.C. Rogers, *Trans. AIME,* Vol 218, June 1960, p 498–506

20. C. Laird and G.C. Smith, *Philos. Mag.,* Vol 7, 1962, p 847–857

21. R.H. Van Stone and T.B. Box, "Use of Fractography and Sectioning Techniques to Study Fracture Mechanisms," STP 600, *Annual Book of ASTM Standards,* ASTM, 1976, p 5–29

22. W. Staehle et al., *Corrosion,* Vol 15, July 1959, p 51–59 (373t–381t)

23. D. Eylon and W.R. Kerr, "Fractographic and Metallographic Morphology of Fatigue Initiation Sites," STP 645, *Annual Book of ASTM Standards,* ASTM, 1978, p 235–248

24. W.R. Kerr et al., *Metall. Trans.,* Vol 7A, Sept 1976, p 1477–1480

25. W.T. Shieh, *Metall. Trans.,* Vol 5, May 1974, p 1069–1085

26. J.R. Pickens and J. Gurland, Metallographic Characterization of Fracture Surface Profiles on Sectioning Planes, *Proc. Fourth International Congress for Stereology,* NBS Spec. Publ. 431, 1976, p 269–272

27. E. Rabinowicz, *Met. Ind.,* Vol 76, 3 Feb 1950, p 83–86

28. L.E. Samuels, *Metallurgia,* Vol 51, March 1955, p 161–162

29. M.H. Hurdus, "Taper Sectioning of Tubular Specimens and Its Application to Corrosion Oxide Film Examination," Report AERE-R9704, U.K. Atomic Energy Authority, Harwell, Oct 1980

30. S.M. El-Soudani, *Metallography,* Vol 11, July 1978, p 247–336

31. E.E. Underwood and E.A. Starke, Jr., "Quantitative Stereological Methods for Analyzing Important Features in Fatigue of Metals and Alloys," STP 675, *Annual Book of ASTM Standards,* ASTM, 1979, p 633–682

32. E.E. Underwood and S.B. Chakrabortty, "Quantitative Fractography of a Fatigued Ti-28V Alloy," STP 733, *Annual Book of ASTM Standards,* ASTM, 1981, p 337–354

33. M. Coster and J.L. Chermant, *Int. Met. Rev.,* Vol 28, 1983, p 228–250

34. E.E. Underwood, Quantitative Fractography, *Applied Metallography,* Van Nostrand Reinhold, 1986, p 101–122

Metallography: An Introduction, *Metallography and Microstructures,* Vol 9, *ASM Handbook,* ASM International, 2004, p. 3–20

Image Analysis (Adapted from Ref 37)

Metallography involves various methods to compare and quantify microstructural patterns, spatial relationships, and shapes and to derive numerical data from micrographs. Some examples of image analysis include:

- Quantitative determination of grain size, grain shape, grain-boundary area per unit volume, and so on, in single-phase metals and ceramics
- Quantitative determination of second-phase volume fractions, sizes, interfacial areas per unit volume, spacings, and so on, in multiphase metals and ceramics
- Quantitative determination of particle size distributions in powders

Historically, most microstructural ratings, particularly in quality-control studies and for specification compliance, have been performed using simple chart comparison ratings for features such as grain-size measurements (e.g., ASTM E 112) and inclusion ratings (e.g., ASTM E 45). In recent years, however, increased use has been made of manual and automated stereological relationships to describe microstructural characteristics. Stereological methods are described in more detail in the article "Quantitative Characterization and Representation of Global Microstructural Geometry" in this Volume.

The tedious nature of manual methods of such measurements has spurred development of automated procedures. Although microstructural patterns, spatial relationships, and shapes are relatively easy to recognize in an image, reliable numerical data, such as counts, are far more difficult to obtain manually. Therefore, automation addresses a long-recognized need in microstructural analysis for more precise data for quality-control and structure-property studies. The first approach was simply to develop devices to facilitate manual data collection. These methods reduce the influence of operator fatigue, which affects the accuracy and reproducibility of manual measurements.

More recently, various semiautomatic and fully automatic devices have been developed that permit more rapid data collection, analysis, and formatting. The continued improvements in the speed and memory of affordable computers also have greatly aided the development of these tools. The initial development of these devices concentrated on hardware-centered systems, but has since evolved to software-centered systems using faster, inexpensive computers with more memory. Thus, better-quality data can be obtained from analyzing a larger sample area and/or more samples. This allows better statistical accuracy and more meaningful results from image analysis. In addition, image analyzers can perform several measurements on a field within milliseconds, providing a more complete description of the microstructure. Finally, automation can be introduced in stage movement, focusing, data analysis, and formatting. Image analyzers are available at various levels of sophistication and cost, but all use electronic data processing for image detection and measurement of stereological and nonstereological parameters.

However, not all structures lend themselves to accurate automatic detection; the structure must exhibit adequate contrast to allow the analyzer to distinguish its various components. For low-contrast samples, semiautomatic analyzers may provide more reliable feature discrimination at the loss of some measurement speed. Sample preparation procedures used for qualitative assessment or manual measurements also may be unsuitable for image analysis. Therefore, much more care must be exercised in sample preparation. The ability to prepare the sample properly is often the most critical and most difficult factor in image analysis.

Obtaining maximum value from image analysis usually necessitates knowledge of sample preparation, stereology, machine operation, statistics, and computer programming. Image analysis consists of sample selection and preparation, image preprocessing, measurement, and data analysis and output. Each step must be controlled properly to obtain accurate, reproducible results. Sample selection must be systematic and well planned to ensure that the samples analyzed are representative. Image preprocessing refers to the manipulation of the detected image to improve the accuracy of measurements, for example, separating adjoining particles

before counting, or to facilitate desired measurements, as in the fusing of aligned inclusion stringers for a length measurement.

Errors can arise in image analysis measurements from such sources as the representativeness of the sample, quality of sample preparation, operator bias in setting controls, and instrument errors. Errors can also result when assumptions upon which stereological formulas are based are invalid. A typical example of such a problem is the mathematical procedure for determining the number of grains per unit volume, N_V, based on planar grain-size measurements and grain-shape assumptions. The further the grains differ from the assumed shape, the greater the error in estimating N_V.

When a relatively small polished area of one or more samples is used to determine some quantity for a relatively large mass of material, errors also occur if sampling is inadequate or does not represent the mass. This problem is common in analyzing inclusions in a heat of steel. Because the quantity of inclusions is relatively or extremely low, and the inclusion distribution is not homogeneous, some degree of uncertainty is associated with such measurements. This error can be minimized by using a systematic sampling plan and by increasing the number of samples and area measured. In practice, compromise is necessary between the amount of time available for such measurements and the desired accuracy.

Effect of Magnification. The selected magnification influences the measurement value and the statistics of the measurement. Numerous cases have been documented in which the measured values were altered significantly as the magnification was changed. Examples of this problem have been summarized (Ref 35).

Choice of magnification is basically a compromise. Small features require a relatively high magnification for accurate measurements, particularly for size, shape, or perimeter measurements. However, the field area decreases with increasing magnification. Increasing the magnification improves resolution, but the area measured, if the number of fields is limited, may not be representative. For example, if there is a low volume fraction of inclusions that are not uniformly distributed, a substantial area must be examined to obtain a workable estimate of the volume fraction. For such a sample, field-to-field volume fraction variation increases as the magnification increases and thus results in a larger standard deviation. One method of assessing this is to examine the range of volume fraction measurements as a function of the number of fields for each magnification.

The magnification effect has been observed in many studies involving various materials, measurements, and measuring devices. The problem is not simply one of poor technique. Two basic types of magnification-affected data can be found in the literature. The first involves counting type data in which the count increases rapidly with initial increases in magnification, then levels off at high magnifications. The second involves spacing measurements in which there is an initial rapid drop in the spacing measurements with an increase in magnification, followed by a leveling off with further increases in magnification. Both situations arise from the observer's seeing more at the higher magnifications (Ref 35).

A somewhat different magnification problem may also be encountered in performing fully automated measurements. To illustrate this problem, a medium-carbon hot-rolled steel containing ferrite and pearlite was analyzed for the volume fraction of ferrite using 8, 16, 32, 50, 80, and 160× objectives. The sample was etched using picral. At low magnifications, the volume fraction of proeutectoid ferrite could be measured with favorable accuracy. However, as the magnification was increased, the structure of the pearlite became resolvable, and ferrite within the pearlite constituent was also detected. Thus, with increasing magnification and resolution, the volume fraction of ferrite increased. Figure 33 shows the measurement results as a function of the magnification and number of fields measured. The best determination of the volume fraction of proeutectoid ferrite was obtained using the 16× objective. This is not obvious from the data, but can be discerned while viewing the detection.

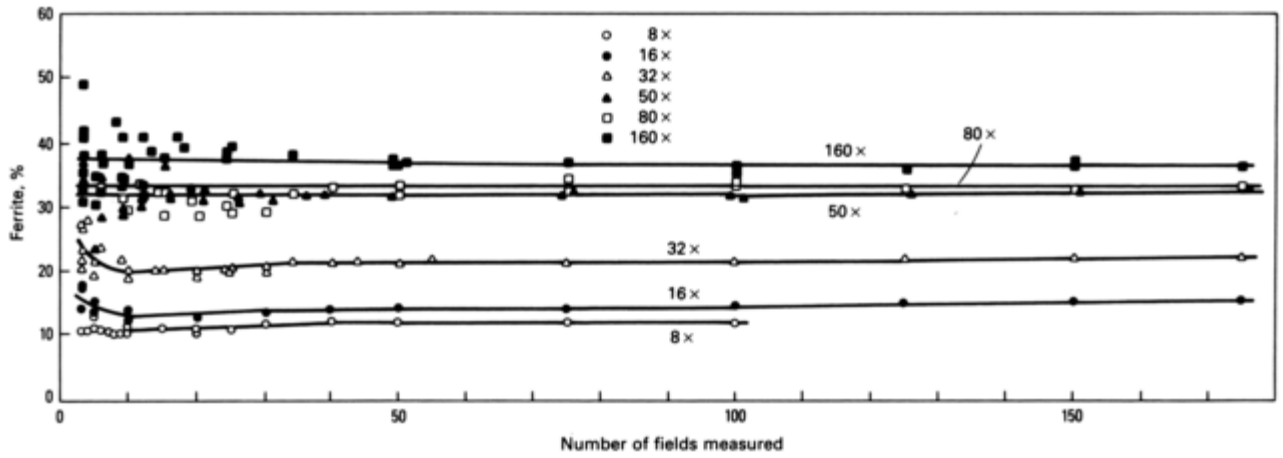

Fig. 33 Volume fraction of ferrite as a function of number of fields measured and magnification. At high magnifications, equiaxed ferrite within the coarse pearlite were detected. Source: Ref 37

From a statistical viewpoint, lower magnifications enable measurement of large areas, lessening the influence of sample heterogeneity. As magnification increases, greater field-to-field measurement variations are encountered. The choice of magnification influences the number of fields to be measured. As magnification increases, more fields are required to obtain a certain degree of accuracy. Automatic stage movement and automatic focusing facilitate increasing the number of fields. Automatic stage movement ensures selection of fields without introducing operator bias. Automatic focusing should not be taken for granted. At higher magnifications, the potential for improper focusing increases. For volume-fraction measurements, as the volume fraction decreases, more fields must be measured to obtain the desired degree of accuracy. This problem becomes particularly acute when measuring volume fractions less than 0.01 (1%).

A serious problem is encountered when the feature to be measured exhibits a rather wide range of sizes or a bimodal size distribution. The larger particles are best measured at relatively low magnifications, but the smaller particles must be measured at a higher magnification. At a high magnification, the guard-frame procedure must be used, or any large feature not within the measurement area will be truncated and undersized. Two magnifications have been used for such measurements, and the analyses have been combined; however, this is a difficult procedure.

Sample preparation also influences measurement accuracy significantly. Samples must be polished with minimum relief, the desired constituents must be retained, and polishing artifacts must be controlled. Because sample volume can be high, automatic polishing equipment is generally necessary to provide the required sample throughput and quality. Etching techniques used for qualitative structure assessment and manual measurements are frequently inadequate for image analysis. Instead, selective etching or staining techniques usually must be used. Color (tint) etching is extremely useful because of its high selectivity and near absence of etch relief.

Electrolytic etching techniques are also valuable. The optimal procedure darkens either the phase of interest or all other phases, distinguishing the constituents clearly by gray levels. In many studies, proper sample selection and careful polishing and etching are the most critical factors in obtaining favorable results. This is especially important in grain-size measurements, in which all the grain boundaries must be revealed clearly.

Gray-Level Thresholding (Ref 36, 37). Many experiments have demonstrated that the setting of the detector threshold for feature discrimination is a significant source of instrument error (Ref 38). Machine problems may also influence measurement accuracy. Noise or random variations of current or voltage may also introduce errors. Noise problems become important when measuring features with low contrast.

As previously noted, the quality and integrity of the specimens that are to be evaluated are probably the most critical factors in image analysis. No system can compensate for poorly prepared specimens. While current systems can perform gray image transformations at very rapid rates relative to systems manufactured in the 1970s and 1980s, gray image processing should be used as a last resort for metallographic specimens. Different etches and filters (other than the standard green filter used in metallography) should be evaluated prior to using gray image transformations. To obtain meaningful results, the best possible procedures for polishing and etching the specimens to be observed must be used. Factors such as inclusion pullout, comet tails, or poor or

variable contrast caused by improper etching cannot be eliminated by the image analysis system. There is no substitute for properly prepared metallographic specimens.

One of the most common hardware variables that can affect system performance is the illumination system of a light microscope. Proper alignment of the microscope lamp and correct adjustment are of paramount importance for optimal performance of the image analysis system. The alignment, resolution, and response of the CCD camera used to convert the image into an electrical signal can have a large influence on performance. After properly aligning the microscope, some minor variations in the gray level of a blank image might be observed. Because neither the CCD camera nor the lenses in the microscope are perfect, some slight variations in the gray image can occur. The shading corrector observes each pixel in a blank field of view and changes its gray level to produce a uniform white background. This correction factor is then applied to every image to correct for minor problems in the system. If a large degree of correction is required, this may indicate that the microscope is seriously misaligned, or the CCD camera has deteriorated from use.

Once these concerns have been properly rationalized, the next major variable to consider is how to select the gray level of the objects to be characterized as described further in Ref 36. For optimal detection accuracy, the sample features of interest must be treated to have as narrow a contrast (gray-level) range as possible (Ref 37). The light source in the microscope must then be aligned for even illumination. Most image analyzers provide shading correction to even out variations across the screen. The gray-level range of the image from the darkest black to the lightest white feature is usually segmented into 256 increments. As an example of gray-level feature detection, five iron-carbon alloys with carbon contents of 0.003 and approximately 0.2, 0.4, 0.6, and 0.8% were prepared metallographically and etched using picral. The microstructures consisted of varying amounts of ferrite and pearlite. The samples were scanned in 1% increments from black to whiter.

Figure 34 (Ref 37) shows the area percent in the detected field area at each 1% portion in the gray-level scan for these alloys. The 0.003% C alloy, consisting almost entirely of ferrite, exhibits the highest ferrite peak, with maximum detection at approximately 81% on the threshold device. As the carbon content increased to 0.6%, the size of the ferrite peak decreased, and the peak position increased slightly. For the 0.8% C alloy (all pearlite), no image was detectable above 76%. This suggests that the pearlite constituent is generally detected between approximately 16 and 76%, and the ferrite constituent is detected between approximately 76 and 91 to 99%, depending on the alloy. Figure 35 shows the same data plotted as a cumulative percentage of area fraction.

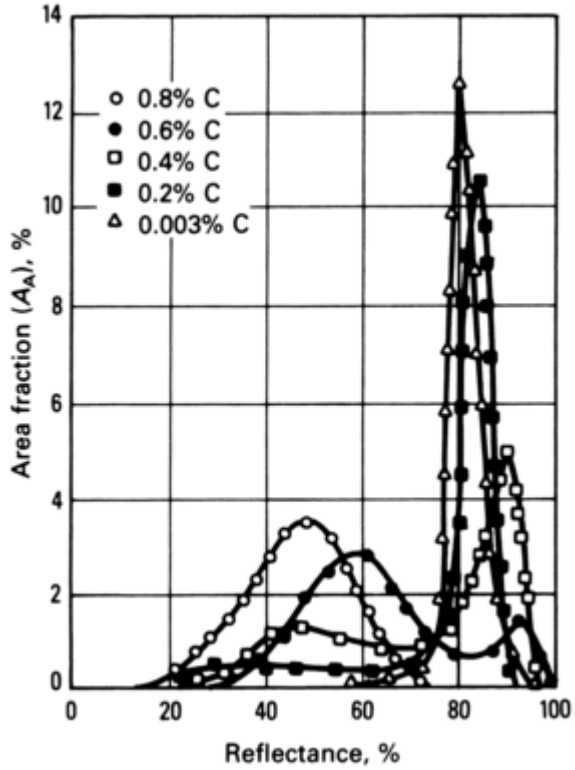

Fig. 34 Plot of the detected area fraction in 1% increments from black to white for five iron-carbon alloys. Microstructures consisted of varying amounts of ferrite and pearlite, ranging from the 0.003% C alloy (almost all ferrite) to the 0.8% C alloy (all pearlite). Source: Ref 37

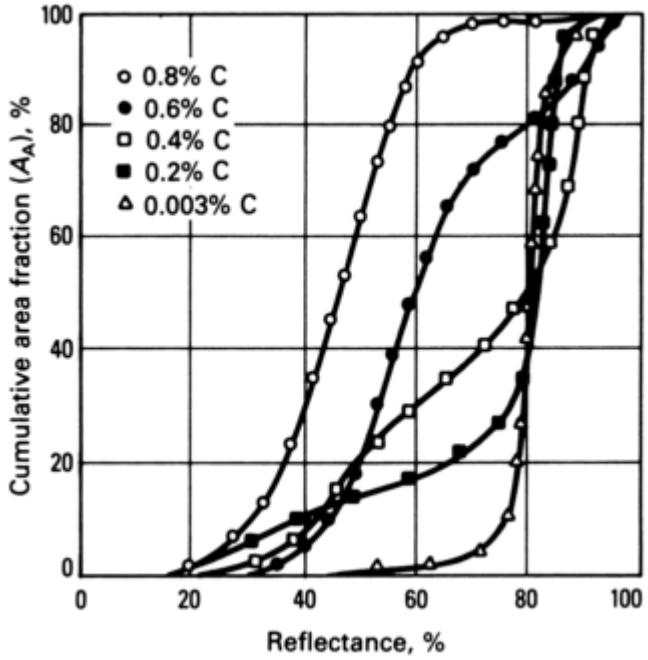

Fig. 35 Plot of cumulative detected area fraction in 1% increments from black to white for the five iron-carbon alloys in Fig. 34. Source: Ref 37

Setting the threshold to detect only gray levels within specific ranges enables selective detection of constituents. For example, Fig. 36 shows the microstructure of AISI type 416 stainless steel etched using Vilella's reagent. This is a resulfurized grade that has been heat treated to form tempered martensite but also contains δ-ferrite stringers. Figure 36(a) shows the live microscope image before phase detection. In Fig. 36(b), the threshold has been set to detect only the pale gray sulfides that appear white on the screen. Detection setting can be aided by alternating between the live image and the detected image (flicker mode) while observing the size correlation between these two images. If the gray-level ranges of two constituents overlap, detected (white) points will be visible in the undesired phase as the threshold setting is changed. If the degree of overlap is excessive, an alternate preparation procedure is required. In nearly all inclusion studies, the sample is examined unetched because detection of the inclusions is more reliable. Figure 36(c) shows detection of the martensite; Fig. 36(d) detection of the δ-ferrite. The optimal procedure for δ-ferrite detection is to etch the sample electrolytically using 20% aqueous NaOH, which colors only the δ-ferrite.

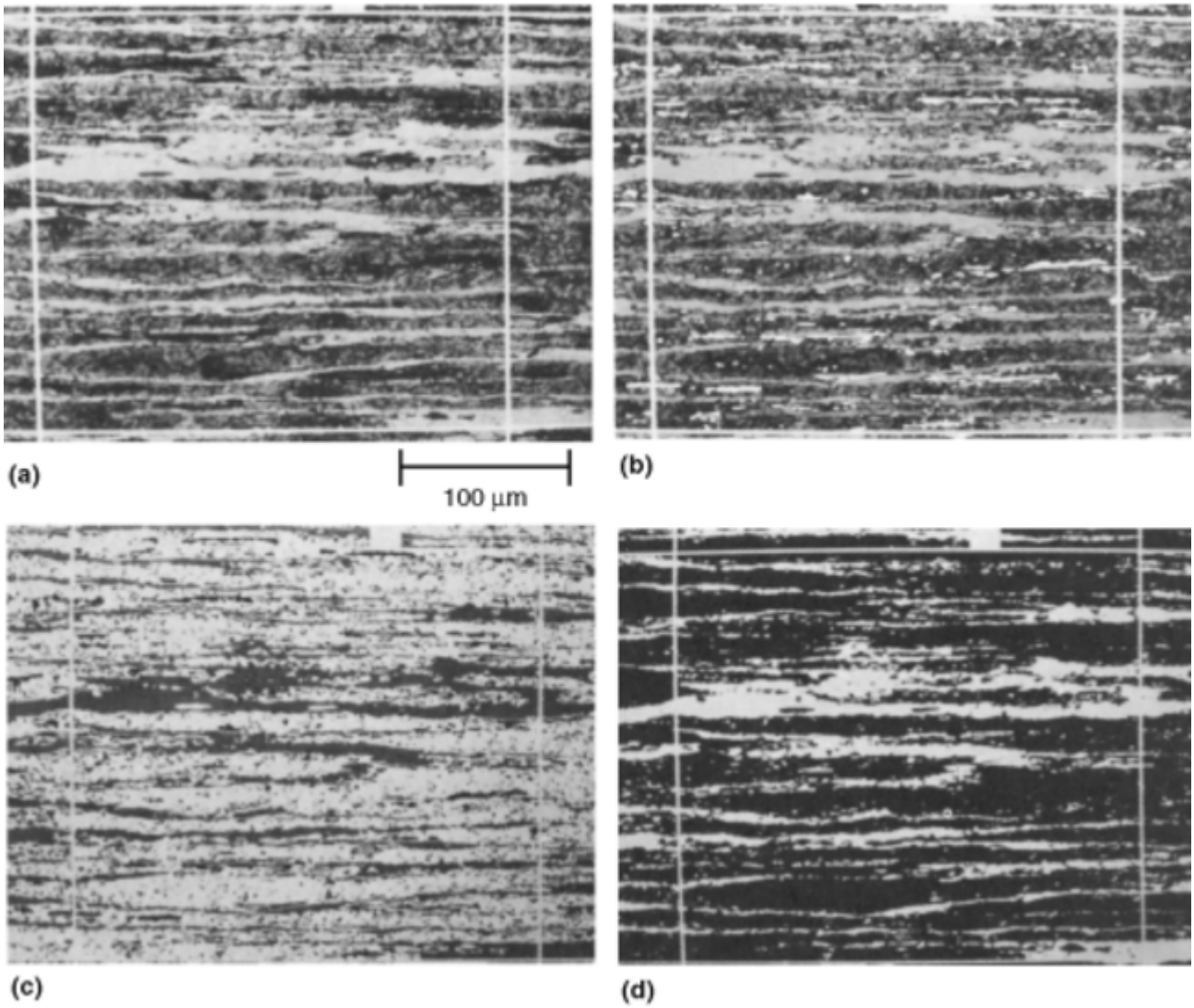

Fig. 36 Examples of preferential detection in an AISI 416 stainless steel sample. (a) Live image. (b) Preferential detection of manganese sulfides (white). (c) Preferential detection of tempered martensite (white). (d) Preferential detection of δ-ferrite (white). Sample etched using Vilella's reagent. 175×. Source: Ref 37

In attempting to detect all three constituents in this manner, it may be difficult, if not impossible, to have the three volume-fraction measurements add up to 100% on every measurement field. This example illustrates the ability to separate a complex image by thresholding. The preferred procedure would be to measure the sulfides in the as-polished condition, etch electrolytically and measure the amount of δ-ferrite, then determine the amount of martensite (major constituent) by difference.

Figure 37 illustrates the degree of error that can be encountered when thresholding is incorrect. Figure 37(a) shows the live image of a ferrite-pearlite sample etched using picral. Picral is far more accurate for such measurements because it does not etch the ferrite grain boundaries, which would be detected with the pearlite, and it produces more uniform darkening of the pearlite than nital. Figure 37(b) shows an underdetected image containing 28.1% pearlite. Some of the pearlite patches contain undetected regions. Figure 37(c) illustrates a correctly detected field with 34.05% pearlite. Figure 37(d) shows excessive detection, in which the features are enlarged and the volume fraction of pearlite is 42.3%.

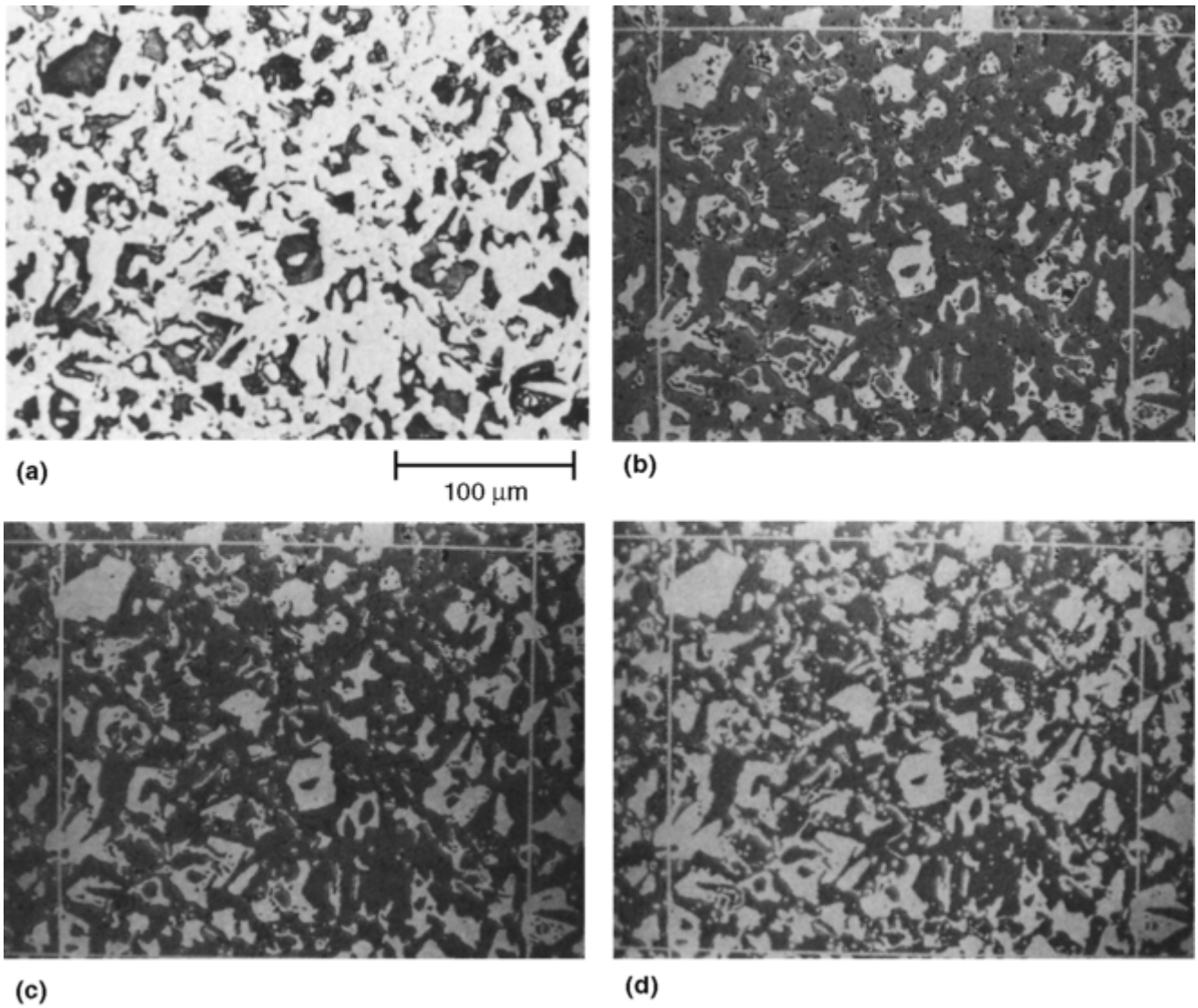

Fig. 37 Example of the influence of detection setting on the area fraction (A_A) of pearlite detected in a low-carbon steel. (a) Live image showing ferrite and pearlite. (b) Pearlite underdetected (A_A = 28.1%). (c) Pearlite detected correctly (A_A = 34.05%). (d) Pearlite overdetected (A_A = 42.3%). Sample etched using 4% picral. 180×. Source: Ref 37

The above examples illustrate field measurements; that is, all the features are measured simultaneously. Image analyzers also can perform feature-specific measurements; that is, each distinct feature in the field is measured individually. This technique is highly useful for particle sizing or shape measurements. When such capability is available, features with the same gray level can be further discriminated by differences in size or shape. For example, the various graphite shapes of a cast iron sample can be sorted by size or shape, then measured.

Most image analyzers can perform measurements over the full screen (blank frame) or within a smaller frame. In Fig. 36 and 37, the central screen area within the vertical and horizontal lines is the live-frame region, which is generally used when feature-specific measurements are conducted. Particles that intersect the live frame can be deleted from the detected region to prevent particle measurement errors. The region between the edge of the screen and the live frame is the guard region.

Image analyzers can store several images in memory and use these images variously to enhance feature selection. The ability to erode or dilate features and compare these images to the original image can be useful in separating contiguous particles or fusing stringered features. Image analysis is much more precise than manual techniques for the counting of particles, but adjoining particles are difficult to handle without these special image-editing procedures. Accurate counting is also influenced by the shape of a particle and the counting procedure used. Spherical particles are easiest to count. More complex shapes require selection of the proper counting technique to obtain accurate counts.

Measurements are performed based on the number and distribution of detected picture points relative to the scan line and the total number of picture points. For example, the area fraction is simply the ratio of the number of detected picture points to the total number of picture points in the measurement field; that is, the detected area divided by the measurement area. Therefore, the true size of the measurement field must be determined accurately using a stage micrometer for each magnification to operate in the calibrated mode. Other measurements are more complex. For example, to count the number of detected particles in an image field of known size, that is, to obtain N_A, the number of particles per unit area, the image analyzer must first determine what portions of the detected image are discrete particles. A particle is any detected feature completely surrounded by undetected picture points. After this discrimination, the particles are counted, and the number is divided by the measurement area.

Sizing can be performed in several ways. The simplest procedure for determining the average particle area, A_{avg}, is to divide the area fraction by the number of particles per unit area, that is, A_A/N_A. This is the most direct procedure using field measurements. Feature-specific measurements provide several possible procedures. One is to measure the area of each feature and determine the average area of all the measured particles. Another involves measuring the area of each particle and computing the equivalent diameter based on some assumption about their shape. The projected height of the particles, the maximum and minimum length and thickness, and so on, could also be measured.

References cited in this section

35. E.E. Underwood, "Practical Solutions to Stereological Problems," STP 839, *Annual Book of ASTM Standards,* ASTM, 1984, p 160–179

36. D.W. Hetzner, Applications, Chapter 8 in *Practical Guide to Image Analysis,* ASM International, p 203–256

37. G.F. Vander Voort, Image Analysis, *Materials Characterization,* Volume 10, *ASM Handbook,* American Society for Metals, 1986, p 309–322

38. C. Fisher, The Quantimet: Setting the Threshold and the Correction of Off-Set Threshold Error, *Pract. Metallogr.,* Vol 6, Nov 1969, p 659–672

Metallography: An Introduction, *Metallography and Microstructures,* Vol 9, *ASM Handbook,* ASM International, 2004, p. 3–20

Metallography: An Introduction

Acknowledgment

This article contains excepts and adapted text from the following sources:

- W.T. Becker, Fracture Appearance and Mechanisms of Deformation and Fracture, *Failure Analysis and Prevention,* Volume 11, *ASM Handbook,* 2002, p 559–586
- B.L Bramfitt and A.O. Benscoter, *Metallographer's Guide: Practices and Procedures for Irons and Steels,* ASM International, 2002, p 88
- D.W. Hetzner, Applications, Chapter 8 in *Practical Guide to Image Analysis,* ASM International, 2000, p 203–256
- M.R. Louthan, Jr., Optical Metallography, *Materials Characterization,* Volume 10, *ASM Handbook,* American Society for Metals, 1986, p 299–308

- R.A. Lund and S. Sheybany, Fatigue Fracture Appearances, *Failure Analysis and Prevention,* Volume 11, *ASM Handbook,* 2002, p 627–640
- L.E. Samuels, *Metallographic Polishing by Mechanical Methods,* 4th ed., ASM International, 2003, p 6
- G.F. Vander Voort, Image Analysis, *Materials Characterization,* Volume 10, *ASM Handbook,* American Society for Metals, 1986, p 309–322
- G.F. Vander Voort, Metallographic Techniques in Failure Analysis, *Failure Analysis and Prevention,* Volume 11, *ASM Handbook,* ASM International, 2002, p 498–510

Metallography: An Introduction, *Metallography and Microstructures,* Vol 9, *ASM Handbook*, ASM International, 2004, p. 3–20

References

1. H.C. Sorby, in *How to Work with the Microscope,* London, 1867
2. C.S. Smith, *A History of Metallography,* University of Chicago Press, 1960
3. H.C. Sorby, *J. Iron Steel Inst.,* Vol 28, 1886, p 140
4. B.L. Bramfitt and A.O. Benscoter, *Metallographer's Guide: Practices and Procedures for Irons and Steels,* ASM International, 2002, p 88
5. H. Wedding, *J. Iron Steel Inst.,* Vol 27, 1885, p 187
6. L.E. Samuels, *Metallographic Polishing by Mechanical Means,* 4th ed., ASM International, 2003, p 6
7. J.R. Vilella, *Metallographic Techniques for Steels,* American Society for Metals, 1938
8. M.R. Louthan, Jr., Optical Metallography, *Materials Characterization,* Vol 10, *ASM Handbook,* American Society for Metals, 1986, p 299–308
9. W.T. Becker, Fracture Appearance and Mechanisms of Deformation and Fracture, *Failure Analysis and Prevention,* Vol 11, *ASM Handbook,* ASM International, 2002, p 559–586
10. R.W. Hertzberg, *Deformation and Fracture Mechanics of Engineering Materials,* 4th ed., John Wiley, 1996
11. R.A. Lund and S. Sheybany, Fatigue Fracture Appearances, *Failure Analysis and Prevention,* Vol 11, *ASM Handbook,* ASM International, 2002, p 627–640
12. Fatigue Failures, *Failure Analysis and Prevention,* Vol 11, *ASM Handbook,* ASM International, 2002, p 708
13. G.F. Vander Voort, Metallographic Techniques in Failure Analysis, *Failure Analysis and Prevention,* Vol 11, *ASM Handbook,* ASM International, 2002, p 498–510
14. G.F. Vander Voort, The SEM as a Metallographic Tool, *Applied Metallography,* Van Nostrand Reinhold Co., 1986, p 139–170

15. C.A. Zapffe and M. Clogg, *Trans. ASM,* Vol 34, 1945, p 71–107

16. K. Kornfeld, *Met. Prog.,* Vol 77, Jan 1960, p 131–132

17. P.J.E. Forsyth and D.A. Ryder, *Metallurgia,* March 1961, p 117–124

18. K.R.L. Thompson and A.J. Sedriks, *J. Aust. Inst. Met.,* Vol 9, Nov 1964, p 269–271

19. H.C. Rogers, *Trans. AIME,* Vol 218, June 1960, p 498–506

20. C. Laird and G.C. Smith, *Philos. Mag.,* Vol 7, 1962, p 847–857

21. R.H. Van Stone and T.B. Box, "Use of Fractography and Sectioning Techniques to Study Fracture Mechanisms," STP 600, *Annual Book of ASTM Standards,* ASTM, 1976, p 5–29

22. W. Staehle et al., *Corrosion,* Vol 15, July 1959, p 51–59 (373t–381t)

23. D. Eylon and W.R. Kerr, "Fractographic and Metallographic Morphology of Fatigue Initiation Sites," STP 645, *Annual Book of ASTM Standards,* ASTM, 1978, p 235–248

24. W.R. Kerr et al., *Metall. Trans.,* Vol 7A, Sept 1976, p 1477–1480

25. W.T. Shieh, *Metall. Trans.,* Vol 5, May 1974, p 1069–1085

26. J.R. Pickens and J. Gurland, Metallographic Characterization of Fracture Surface Profiles on Sectioning Planes, *Proc. Fourth International Congress for Stereology,* NBS Spec. Publ. 431, 1976, p 269–272

27. E. Rabinowicz, *Met. Ind.,* Vol 76, 3 Feb 1950, p 83–86

28. L.E. Samuels, *Metallurgia,* Vol 51, March 1955, p 161–162

29. M.H. Hurdus, "Taper Sectioning of Tubular Specimens and Its Application to Corrosion Oxide Film Examination," Report AERE-R9704, U.K. Atomic Energy Authority, Harwell, Oct 1980

30. S.M. El-Soudani, *Metallography,* Vol 11, July 1978, p 247–336

31. E.E. Underwood and E.A. Starke, Jr., "Quantitative Stereological Methods for Analyzing Important Features in Fatigue of Metals and Alloys," STP 675, *Annual Book of ASTM Standards,* ASTM, 1979, p 633–682

32. E.E. Underwood and S.B. Chakrabortty, "Quantitative Fractography of a Fatigued Ti-28V Alloy," STP 733, *Annual Book of ASTM Standards,* ASTM, 1981, p 337–354

33. M. Coster and J.L. Chermant, *Int. Met. Rev.,* Vol 28, 1983, p 228–250

34. E.E. Underwood, Quantitative Fractography, *Applied Metallography,* Van Nostrand Reinhold, 1986, p 101–122

35. E.E. Underwood, "Practical Solutions to Stereological Problems," STP 839, *Annual Book of ASTM Standards,* ASTM, 1984, p 160–179

36. D.W. Hetzner, Applications, Chapter 8 in *Practical Guide to Image Analysis,* ASM International, p 203–256

37. G.F. Vander Voort, Image Analysis, *Materials Characterization,* Volume 10, *ASM Handbook,* American Society for Metals, 1986, p 309–322

38. C. Fisher, The Quantimet: Setting the Threshold and the Correction of Off-Set Threshold Error, *Pract. Metallogr.,* Vol 6, Nov 1969, p 659–672

Introduction to Structures in Metals, *Metallography and Microstructures,* Vol 9, *ASM Handbook,* ASM International, 2004, p. 23–28

Introduction to Structures in Metals

Introduction

FOR MORE THAN A CENTURY, dating back to the pioneering contributions of Henry Clifton Sorby, metallurgists have not been satisfied merely to describe their metallographic observations, but have striven to explain them and to understand their implications (Ref 1, 2, 3, 4). In addition, new techniques of structural investigation have yielded new observations and posed new problems. The quest for meaningful and precise explanations of metallurgical structures has been the primary driving force in the development of the science of physical metallurgy (Ref 5, 6, 7, 8), which is a very broad topic that includes the structure of metals.

The general structural features of metals are introduced in this article, while more details on the physical metallurgy of metal structure are given in the other articles in this Section. The purpose of the articles in this Section is to assist in the interpretation of microstructure. Such interpretation requires an understanding of crystal structure, physical metallurgy, and the processes by which various structures are formed. Therefore, articles are organized accordingly, beginning with crystal structure and general alloying, and followed by the major processes that produce characteristic structures. A special article describes textures that can result from several of these processes.

This article provides background, general references, and some connections among the subject matter explored more fully in the specialized articles. This article also treats important topics, such as grain structure and substructure, that are not covered systematically and comprehensively in the other articles. Finally, it introduces the scale of structural features and the concept of hierarchical relations among them.

References cited in this section

1. R.F. Mehl, *A Brief History of the Science of Metals,* American Institute of Mining and Metallurgical Engineers, 1948

2. C.S. Smith, *A History of Metallography,* University of Chicago Press, 1960

3. C.S. Smith, Ed., *Sorby Centennial Symposium on the History of Metallurgy,* Gordon and Breach, 1965

4. R.F. Mehl and R.W. Cahn, The Historical Development of Physical Metallurgy, *Physical Metallurgy,* Part I, 3rd ed., R.W. Cahn and R. Haasen, Ed., North-Holland, 1983, p 1–35

5. R.W. Cahn and P. Haasen, Ed., *Physical Metallurgy,* Parts I and II, 3rd ed., North-Holland, 1983

6. A.G. Guy and J.J. Hren, *Elements of Physical Metallurgy,* 3rd ed., Addison-Wesley, 1974

7. W.F. Smith, *Structures and Properties of Engineering Alloys,* McGraw-Hill, 1981

8. R.E. Smallman, *Modern Physical Metallurgy,* 4th ed., Butterworths, 1985

Introduction to Structures in Metals, *Metallography and Microstructures*, Vol 9, *ASM Handbook*, ASM International, 2004, p. 23–28

General Features of Structure

The term structure, as used here, refers primarily to the study of those microstructural features that can be investigated using optical (light) and electron microscopy (Ref 9, 10, 11, 12, 13, 14, 15, 16, 17). The results of investigations using other techniques, such as x-ray diffraction, are included when pertinent (Ref 18, 19). Macrostructural features, which can be observed with little or no magnification, are also considered. The principles applicable to various types of structures are illustrated by micrographs in other articles. Several works that treat the interpretation of microstructures systematically are cited in Ref 9, 10, 11, 12, 13.

Size Scales and Hierarchical Structures. The structure of metals comprises features of various magnitudes. The size scales of structural features of metals extend from the atomic level, ~0.1 nm (~1 Å) to the size of entire metallic objects, ~1 m (~$3\frac{1}{4}$ ft). This range spans 10 orders of magnitude. The techniques for observing structural features requires adequate resolving powers, and Fig. 1 shows the sizes of some common structural features of metals and various techniques for their observation with limits of resolution.

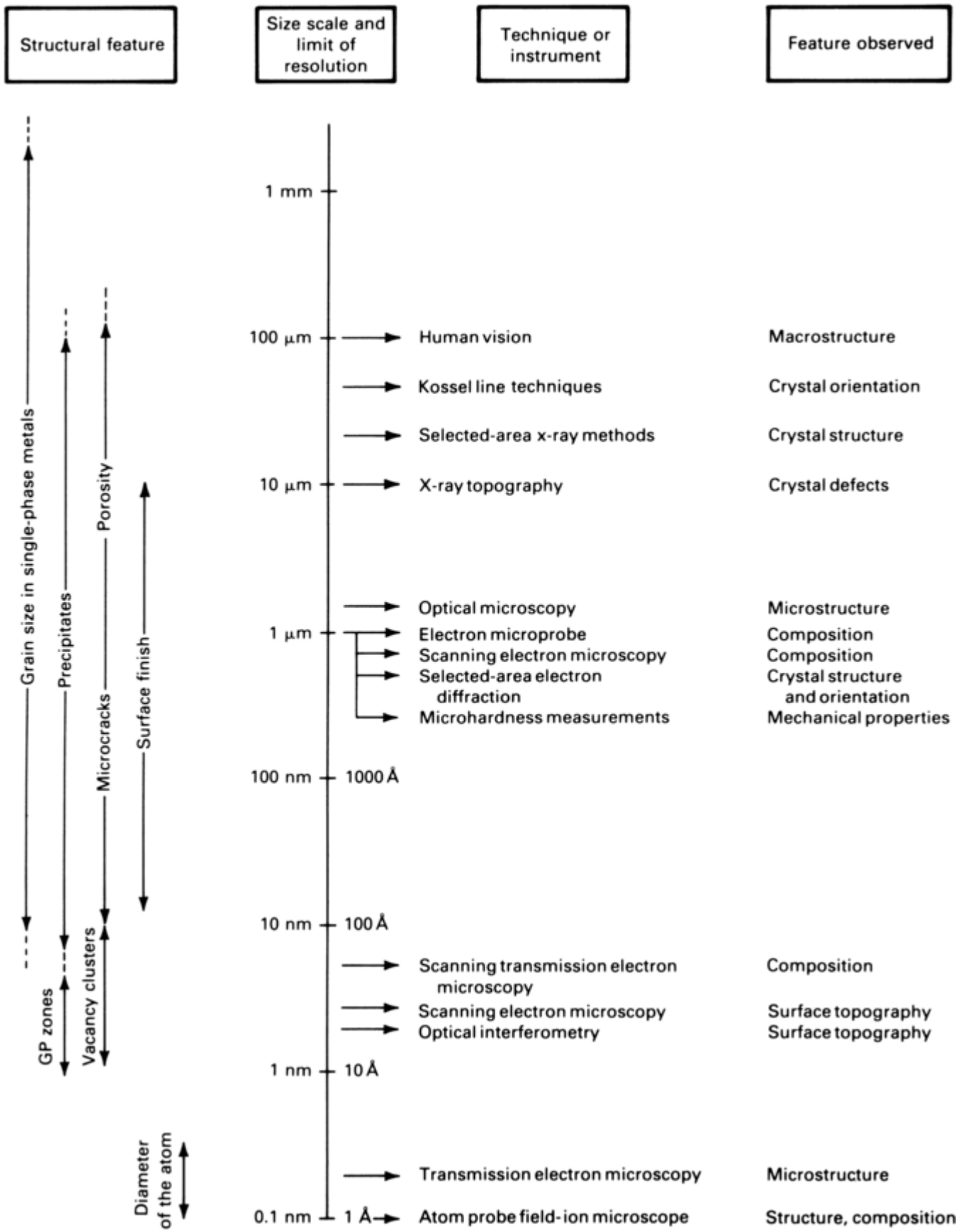

Fig. 1 Size scale relating structural features of metals to techniques of observation (after Ref 20)

Frequently, several structural features on different levels in a given metallic system are of interest. For example, a polycrystalline single-phase metal has a grain structure, and within each grain a substructure may be present, or, in a polycrystalline long-range ordered binary alloy, a substructure of antiphase boundaries may exist within each grain. In a forging, the macroscopic flow lines may coexist with a structure of matrix grains in which

precipitates are dispersed. These examples of structural features that coexist at different levels are typical hierarchical structures.
The major structural features, listed generally in increasing size, are:

- *Atomic and electronic structures,* which are below the resolving power of light and electron microscopy and are covered in texts on general physics and in specialized presentations (Ref 21, 22, 23)
- *Crystal structure:* perfect crystals and crystal imperfections (such as dislocations, dislocation dipoles, dislocation networks, dislocation loops, and stacking faults)
- *Substructure:* subgrains, other cellular structures
- *Microstructure:* grains of single-phase metals and alloys, shapes and sizes of microconstituents, and their arrangement/morphology in multiphase systems
- *Textured structure,* when the crystal lattices of grains in a polycrystalline material are arranged in a correlated or organized manner from a preferred orientation of the grains
- *Structural features from composition effects* on phase relations and from compositional variations such as microsegregation in solidified metals, and solute-enriched regions in or near grain boundaries or other regions of crystal imperfections (Ref 24)
- *Structural gradients* such as grain-size gradients within a plate product, composition gradients in case-hardened steel, reinforcing phases in composites (Ref 25)
- *Porosity and voids,* which are structural features that are characterized by a large range of sizes
- *Macrostructural features,* including various macroscopic inhomogeneities that develop solidification and deformation, as discussed later in this article

Other special features of metal structure include:

- *Twins,* which occur within grains, are special imperfections that may originate during growth processes, for example, the annealing of cold-worked metal, or during deformation.
- *Antiphase domain boundaries* occur in solid solutions with long-range order, reducing the perfection of the order.
- *Ferromagnetic domains* are characteristic of ferromagnetic materials. Unlike typical metallurgical processes, a change in ferromagnetic domain structure requires a variation in magnetic field. Antiferromagnets also have domain structures.

References cited in this section

9. A. Tomer, *Structure of Metals through Optical Microscopy,* ASM International, 1991

10. R.H. Greaves and H. Wrighton, *Practical Microscopical Metallography,* 4th ed., Chapman & Hall, 1957

11. H. Gleiter, Microstructure, *Physical Metallurgy,* Part I, 3rd ed., R.W. Cahn and P. Haasen, Ed., North-Holland, 1983, p 650–712

12. G.F. Vander Voort, *Metallography: Principles and Practice,* McGraw-Hill, 1984, reprinted by ASM International, 1999

13. W. Rostoker and J.R. Dvorak, *Interpretation of Metallographic Structures,* 2nd ed., Academic Press, 1977

14. J.W. Edington, *Practical Electron Microscopy in Materials Science,* Van Nostrand Reinhold, 1976

15. P.J. Goodhew, *Electron Microscopy and Analysis,* Wykeham Publications, 1975

16. M.H. Loretto and R.E. Smallman, *Defect Analysis in Electron Microscopy,* Chapman & Hall—Halsted/Wiley, 1975

17. G. Thomas and M.J. Goringe, *Transmission Electron Microscopy of Materials,* John Wiley & Sons, 1979

18. C.S. Barrett and T.B. Massalski, *Structure of Metals,* 3rd ed., Pergamon Press, 1980

19. B.D. Cullity, *Elements of X-ray Diffraction,* 2nd ed., Addison-Wesley, 1978

20. S.M. Allen and M.B. Bever, Structure of Materials, *Encyclopedia of Materials Science and Engineering,* MIT Press, 1986

21. H.W. King, Structure of the Pure Metals, *Physical Metallurgy,* Part I, 3rd ed., R.W. Cahn and P. Haasen, Ed., North-Holland, 1983, p 37–79

22. D.G. Pettifor, Electron Theory of Metals, *Physical Metallurgy,* Part I, 3rd ed., R.W. Cahn and P. Haasen, Ed., North-Holland, 1983, p 73–152

23. W.A. Harrison, *Electronic Structure and the Properties of Solids,* Freeman, 1980

24. R.W. Balluffi, Grain Boundary Structure and Segregation, *Interfacial Segregation,* W.C. Johnson and J.M. Blakely, Ed., American Society for Metals, 1979, p 193–236

25. M.B. Bever and P.E. Duwez, Gradients in Composite Materials, *Mater. Sci. Eng.,* Vol 10, 1972, p 1–8

Introduction to Structures in Metals, *Metallography and Microstructures,* Vol 9, *ASM Handbook,* ASM International, 2004, p. 23–28

Origins of Structures

At the atomic structure level, individual atoms exhibit differences in the number of electrons in the various electron shells. This results in different types of bonding and bond strength, such as the relatively strong covalent and ionic bonds, the intermediate metallic bonds, or the weak van der Waals bonds. The bonds between atoms also may occur in specific directions and periodic spatial orientations. The formation of crystal lattices occurs as a result of bonding between atoms. Strong bonding forces between atoms cause atoms to pack efficiently (high packing densities). These arrangements exhibit planes of high atomic density, which contain close-packed directions.

In most metals, the metallic bonds between atoms typically result in a crystalline structure, although amorphous or random spatial arrangement of atoms can be achieved in metallic materials (see the article “Metallic Glasses” in *Properties and Selection: Nonferrous Alloys and Special-Purpose Materials,* Volume 2, *ASM Handbook,* 1990). Most engineering alloys are polycrystalline materials with crystal types that are face-centered cubic (fcc), body-centered cubic (bcc), or hexagonal close-packed (hcp) structures. Crystal structures often found in metallic phases are described in the article “Crystal Structure” in this Section, and some texts apply the fundamentals of crystallography to metals (Ref 26, 27). *Crystal imperfections* include point defects, such as impurity atoms, vacancies and vacancy aggregates, and interstitial atoms; line defects (dislocations); and area defects, for example, stacking faults, twin interfaces, subboundaries, and grain boundaries. They are described in specialized texts on the theory of dislocations and other crystal imperfections (Ref 28, 29, 30). Electron microscopy is capable of resolving various crystal defects such as dislocations, dislocation dipoles, dislocation networks, and dislocation loops.

The characteristic structures of metals and alloys are produced by (1) transformations in which one or more parent phases are converted into one or more new phases, (2) deformation processes, (3) thermal processes, (4) thermomechanical processes, or (5) diffusion processes that do not result in a transformation, such as sintering. A typical deformation process is cold working. Examples of thermal processes are the annealing of a cold-worked metal and the homogenization of an alloy with microsegregation. The principles underlying and governing these processes are the subject of physical metallurgy (see Ref 5, 6, 7, 8, 31, 32, 33).

The production of typical structures involves transformations and processes such as solidification and solid-state transformation. The most important mechanisms of solid-state transformation are diffusion, nucleation, and growth; more complex mechanisms operate in martensitic and bainitic transformations.

Basic deformation mechanisms include slip, twinning, and grain-boundary sliding. Annealing processes leading to recovery, recrystallization, and grain growth proceed by the mechanisms of polygonization, nucleation and growth, and grain-boundary migration, respectively.

Processes developed in recent years, such as rapid solidification, mechanical alloying, ion implantation, deformation of superplastic alloys, and laser annealing, have introduced new structural morphologies. For example, rapid solidification can result in structures without dendritic or cellular microsegregation. In addition, rapid-solidification techniques, such as melt spinning and splat cooling, can produce metallic glasses, that is, amorphous (noncrystalline) metals.

References cited in this section

5. R.W. Cahn and P. Haasen, Ed., *Physical Metallurgy,* Parts I and II, 3rd ed., North-Holland, 1983

6. A.G. Guy and J.J. Hren, *Elements of Physical Metallurgy,* 3rd ed., Addison-Wesley, 1974

7. W.F. Smith, *Structures and Properties of Engineering Alloys,* McGraw-Hill, 1981

8. R.E. Smallman, *Modern Physical Metallurgy,* 4th ed., Butterworths, 1985

26. A. Kelly and G.W. Groves, *Crystallography and Crystal Defects,* Addison-Wesley, 1970

27. E. Prince, *Mathematical Techniques in Crystallography and Materials Science,* Springer-Verlag, 1982

28. H.G. van Bueren, *Imperfections in Crystals,* North-Holland, 1960

29. J.P. Hirth and J. Lothe, *Theory of Dislocations,* 2nd ed., John Wiley & Sons, 1982

30. D. Hull, *Introduction to Dislocations,* 3rd ed., Pergamon Press, 1975

31. J.W. Christian, *The Theory of Transformations in Metals and Alloys,* Pergamon Press, 1965; 2nd ed., Part I, Pergamon Press, 1975

32. D.A. Porter and K.E. Easterling, *Phase Transformations in Metals and Alloys,* Van Nostrand Reinhold, 1981

33. R.W.K. Honeycombe, *The Plastic Deformation of Metals,* 2nd ed., St. Martin's Press, 1982

Introduction to Structures in Metals, *Metallography and Microstructures*, Vol 9, *ASM Handbook*, ASM International, 2004, p. 23–28

Single-Phase Microstructures

The major types of microstructures—solidification structures, solid-state transformation structures, and deformation and annealing structures—are shown in Fig. 2, 3, and 4. The characteristic structural features of single-phase metals and alloys, such as grain structure and substructure, are discussed below. Some of the features of single-phase metals are also found in multiphase structures (Ref 34, 35).

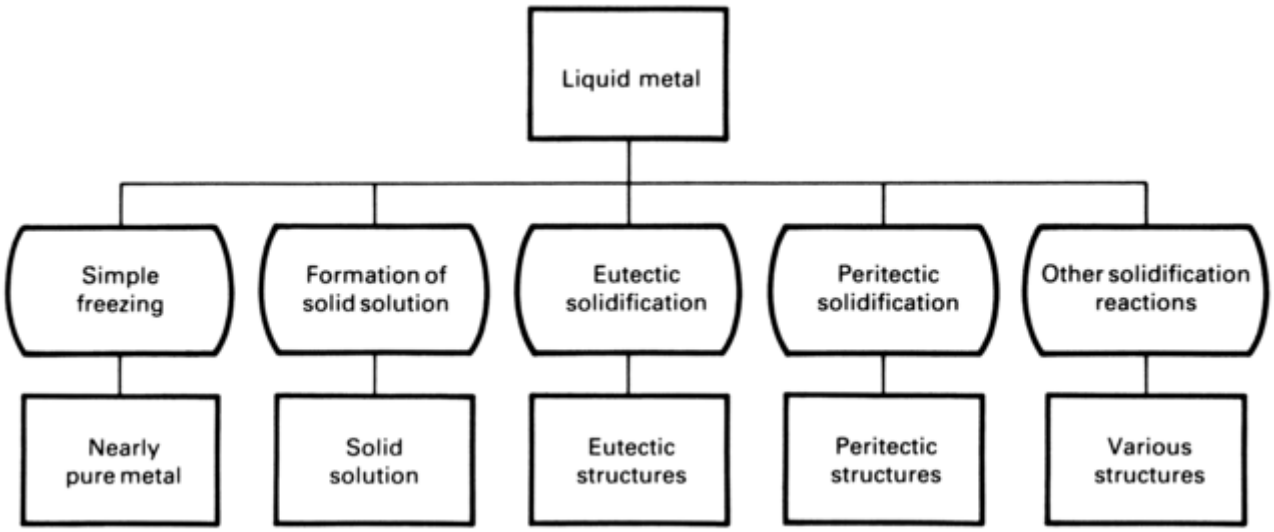

Fig. 2 An outline of solidification structures

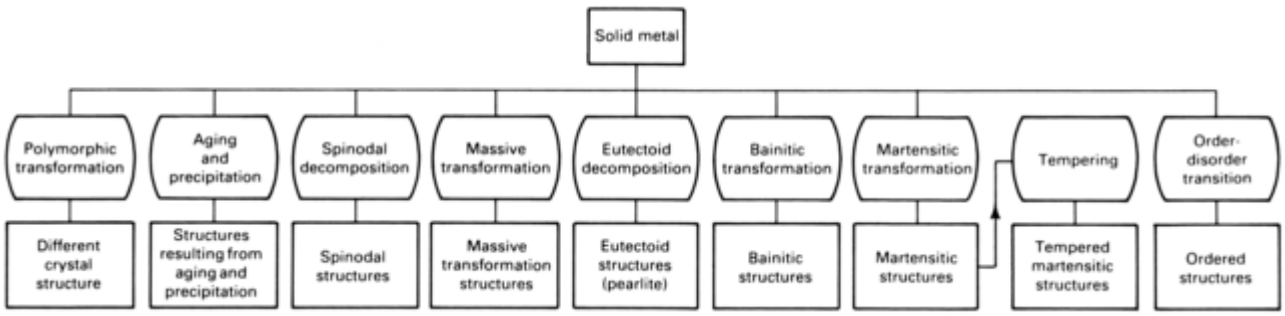

Fig. 3 An outline of solid-state transformation structures

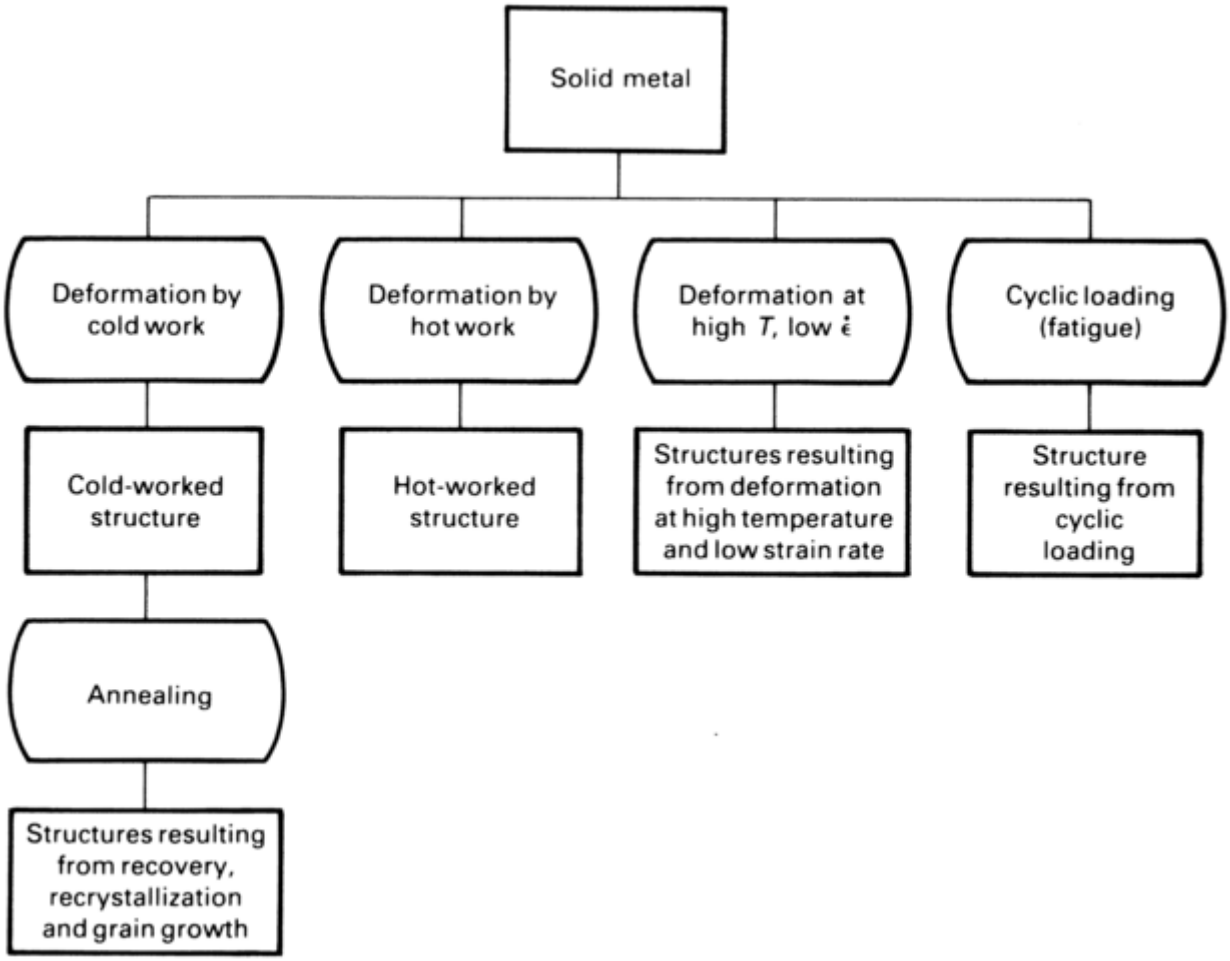

Fig. 4 An outline of deformation and annealing structures

Grain Structure. Grains are small crystals (crystallites) that form a three-dimensional aggregate; they are normally viewed in sections, which by their nature are limited to two dimensions. The main characteristics of a grain structure are grain size, grain shape, and grain-shape anisotropy.

Types of Grain Structure. Typical grain structures include impingement structure, columnar structure, equiaxed grain structure, mature grain structure, deformed grain structure, inhibited recrystallization structure, and duplex grain structure.

Impingement structure forms when grains grow until they meet or impinge, producing characteristic ragged interfaces. This type of structure is rarely observed, because the interfaces usually are smoothed while the specimen remains at elevated temperature. Impingement grains have been observed after secondary recrystallization (Ref 36).

Columnar structure forms by unidirectional growth processes, especially during solidification, and by a growth process involving diffusion accompanied by a solid-state transformation. A columnar structure is typical of ingot castings.

Equiaxed grain structure may form by several processes, such as solidification and recrystallization after or during deformation processes.

Mature grain structure forms when the interfaces—for example, those resulting from impingement—adjust themselves under capillary driving forces.

Deformed grain structure is the product of cold working. In such cases, the grain shapes are anisotropic. Deformed grain structure also occurs from hot working and is an important feature during controlled rolling of some high-strength low-alloy (HSLA) steels. In conventional controlled rolling of HSLA steels, austenite is conditioned into a “pancake” shape that promotes transformation into fine-grain ferrite.

Inhibited recrystallization structure forms when second-phase particles arranged in a nonrandom pattern inhibit the motion of grain boundaries and impose their nonrandom pattern on the resulting recrystallized structure (see Fig. 5b).

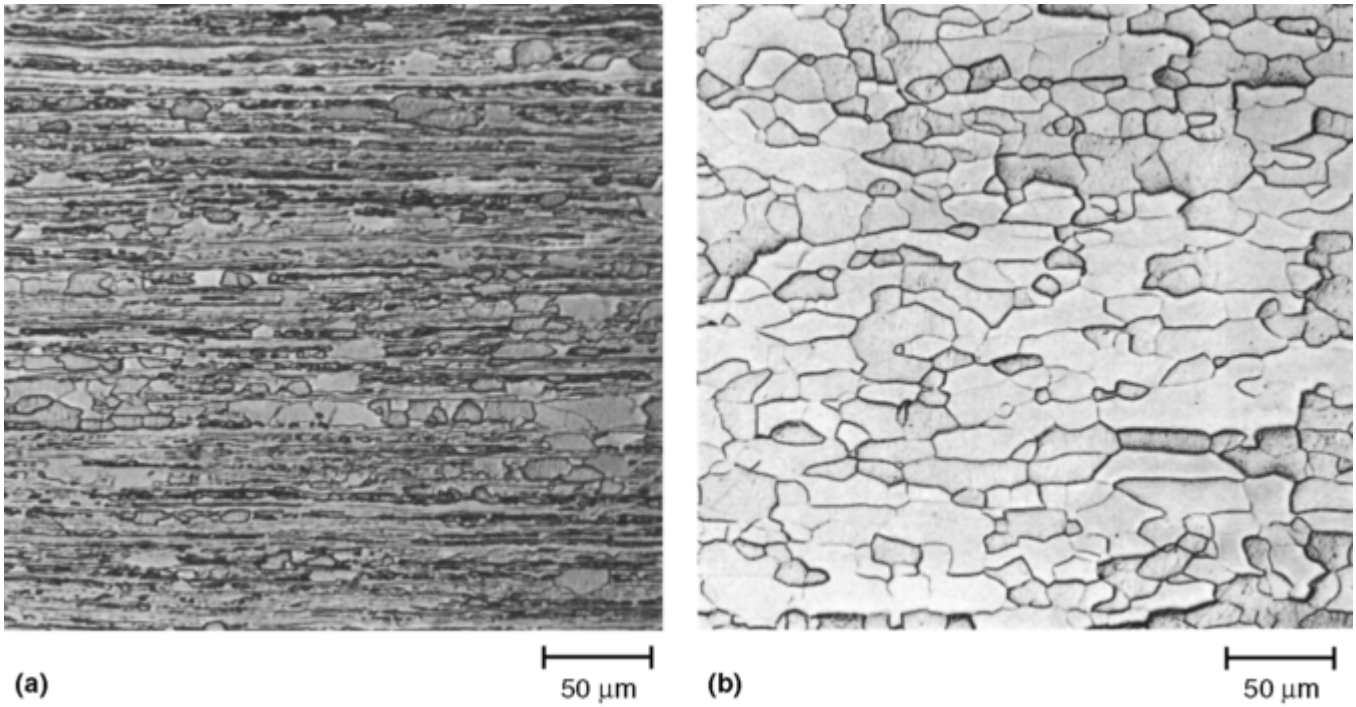

Fig. 5 Partly recrystallized (a) and completely recrystallized (b) commercially pure molybdenum rolled to 1.0 mm (0.040 in.) thick sheet. (a) Longitudinal section of partly recrystallized structure after anneal at 900 °C (1650 °F) for 1 h. (b) Completely recrystallized after a 15 min anneal at 1350 °C (2460 °F) with structure indicative of inhibited recrystallization. No voids are visible. Murakami's reagent (mod). 200×

Duplex grain structure consists of discrete regions of larger and smaller grain sizes, that is, a bimodal distribution of grain sizes (see Fig. 6b). This structure is not related to microduplex alloys, which have characteristic duplex structures involving composition of two coexisting microconstituents rather than grain size (see the section “Multiphase Microstructures” below).

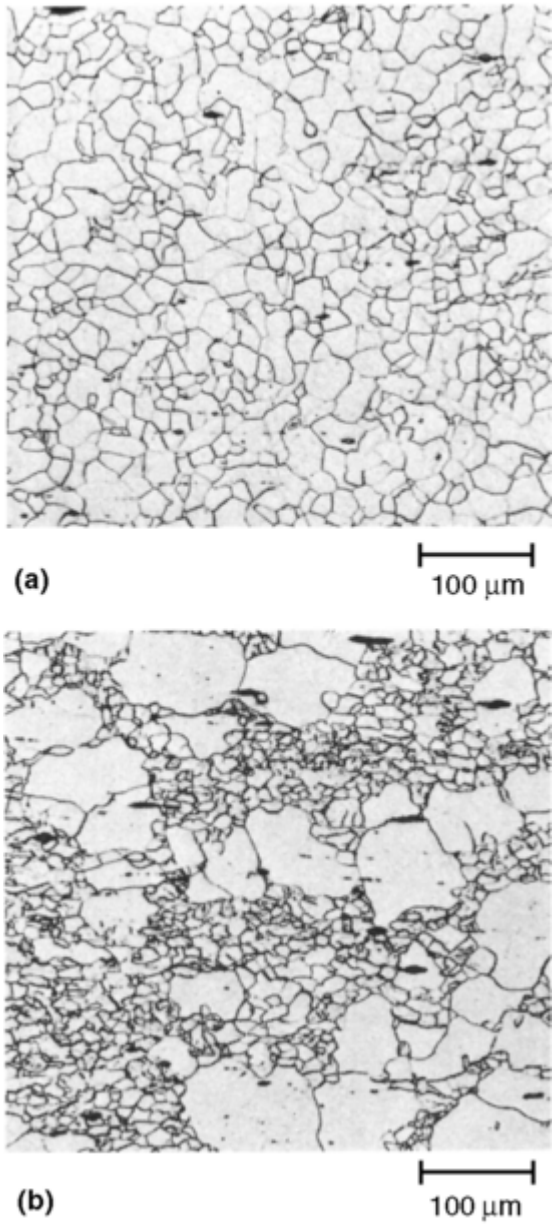

Fig. 6 Examples of ferrite grains in rolled rimmed steel (0.013% C) (a) finish rolled at 940 °C (1720 °F) and coiled at 725 °C (1340 °F). The relatively fine ferrite grain is unusual for a steel rolled at a temperature this high. (b) Finish rolled at 845 °C (1550 °F) and coiled at 695 °C (1280 °F). At this rolling temperature, low carbon content contributed to development of a duplex ferrite grain. Nital. 100×

Three-Dimensional Grain Structure. Grain structures exist in three dimensions. In a typical structure, two grains are separated by an interface; three interfaces join along a line or edge, and four edges join at a point or junction. Six interfaces and four grains join at a junction in addition to the four edges. Junctions of four grain edges are the basic units of a mature grain structure; these junctions can be connected in innumerable ways without structural symmetry or exact repetition of detail (Ref 36, 37).

The major factors controlling grain structure are the requirement of space filling and the tendency toward minimum interfacial energy. Space filling implies that adjoining grains interact to determine each other's shapes. The problem of filling space with regular geometrical bodies has been studied for many years, beginning with Lord Kelvin in 1887 (Ref 36, 37). These studies have contributed to the understanding of grain structure, although actual grains may have irregular shapes.

The tendency toward minimum interfacial energy operates by reducing the grain-boundary area as much as possible or, when applicable, by rotating the grain boundary into low-energy orientations. The reduced grain-boundary area is an essential characteristic of mature grain structures.

Topological relations for three-dimensional grain structures, such as the average number of sides of a grain face, have been analyzed. The relations applicable to metal grains resemble those for certain nonmetallic materials, such as biological cell structures and foam structures (Ref 36, 37, 38).

Crystallography of Grain Boundaries. Various models have been proposed for the grain-boundary region, ranging from simple models for low-angle tilt boundaries to complicated transition regions in high-angle boundaries (Ref 39). Coincidence and twin boundaries are discussed in the article "Solidification Structures of Pure Metals" in this Section.

Two-Dimensional Grain Structure. Sectioning of a three-dimensional grain structure presents the grain structure in only two dimensions for observation. In a typical grain structure, the following simple relations between the three-dimensional and the two-dimensional structures can be established:

- A volume—three-dimensional cell or spatial grain—becomes an area, that is, a two-dimensional cell or planar grain.
- An interface in a three-dimensional structure becomes a line or a grain boundary in a two-dimensional structure.
- An edge becomes a point.
- A corner or junction (zero-dimensional cell) has an infinitesimal probability of being intersected by the plane of observation.
- The true dihedral angle becomes an apparent dihedral angle, as discussed below.

In the transition from a three- to a two-dimensional grain structure, another basic relation is that a structure consisting of uniformly sized three-dimensional, or spatial, grains becomes a two-dimensional structure in which the planar grains are not of uniform size. This is because a random plane cuts grains at random positions, ranging from a corner to the largest cross section. However, the resulting two-dimensional distribution of a grain structure of uniform three-dimensional grain size has definite statistical regularity. In general, the true three-dimensional grain size is more nearly uniform than the apparent two-dimensional grain size. The problems of grain-size measurement, grain shape, and grain-size statistics are covered in texts on quantitative metallography such as Ref 40, 41, 42 (see also the article "Quantitative Characterization and Representation of Global Microstructural Geometry" in this Volume).

The topological relations of grains in two dimensions (planar grains) have been observed, demonstrating that the average planar grain in a mature structure is a hexagon. Consequently, a seven-sided grain in a microsection must be balanced by a five-sided grain, a nine-sided grain by a three-sided grain, or by three five-sided grains, and so on. In addition, correct sampling for polygon distribution ensures better sampling for size (see Ref 36, 37, 38).

Grain Shape. Quantitative description of grain shape in three dimensions (Ref 41) may be approximated by a sphere when the average shape of grains are equiaxed. Similarly, nonequiaxed grains may be represented by ellipsoids. When viewed in two dimensions, nonequiaxed grains have extended shapes.

Dihedral Angles. In three dimensions, the true dihedral angle is the angle between two faces of a grain measured in a plane normal to the edge at which the faces intersect. In any actual section, the faces are intersected by planes oriented randomly at all angles. Therefore, the apparent angle in two dimensions generally differs from the true angle in three dimensions. Stated differently, the apparent or observed angle is the angle between the traces of grain faces in the plane of a random section. The angles in a two-dimensional section are statistically random in the absence of any orientation effect or preselection.

Quantitative relations exist between the true angle in three dimensions and the apparent angle observed in two dimensions. If the true angle is 120°, as in a mature grain structure, the probability of finding an angle within 5° of the true angle is greater than the probability of finding an angle in any other 10° range (Ref 43). In fact, four angles out of five are expected to be within 25° of the true angle. However, in actual grain structures, the true angles and, to a greater extent, the observed angles will have a distribution range.

In two-phase structures, the true dihedral angles may differ from 120° even if the structure is equilibrated. The extent to which the true angles differ depends on the relative interfacial tensions between grains of the two phases present. It has been suggested that the true angle can be found by matching calculated and observed frequency plots. The most probable angle is in every instance the true dihedral angle (Ref 44).

A simpler procedure for finding the true angle uses a cumulative distribution curve. The median angle differs only slightly, and correctably, from the true angle. In addition, fewer measurements—perhaps 25 instead of

several hundred—are sufficient (Ref 45). Errors in measurement have been systematically analyzed, and dihedral angles with nonunique values have been considered (Ref 46).

References cited in this section

34. R.D. Doherty, Stability of Grain Structure in Metals, *J. Mater. Educ.,* Vol 6, 1984, p 845

35. A.P. Sutton, Grain Boundary Structure, *Int. Met. Rev.,* Vol 29, 1984, p 377

36. C.S. Smith, Some Elementary Principles of Polycrystalline Microstructure, *Met. Rev.,* Vol 9, 1964, p 1–62

37. C.S. Smith, Grain Shapes and Other Metallurgical Applications of Topology, in *Metal Interfaces,* American Society for Metals, 1952, p 65–133

38. C.S. Smith, Microstructure, *Trans. ASM,* Vol 45, 1953, p 533–575

39. R.W. Balluffi, Ed., *Grain Boundary Structure and Kinetics,* American Society for Metals, 1979

40. G.F. Vander Voort, Examination of Some Grain Size Measurement Problems, *Metallography: Past, Present, and Future,* STP 1165, Vander Voort, Warmuth, Purdy, and Szirmae, Ed., ASTM 1993, p 266–294

41. L. Karlsson and A.M. Gokhale, Stereological Estimation of Mean Linear Intercept Length in Metallography Using Vertical Sections and Trisector, *J. Microsc.,* Vol 186, 1997, p 143–152

42. B.R. Morris, A.M. Gokhale, and G.F. Vander Voort, Estimation of Grain Size in Anisotropic Materials, *Metall. Mater. Trans.,* Vol 29A, 1998, p 237–244

43. D. Harker and E.R. Parker, Grain Shape and Grain Growth, *Trans. ASM,* Vol 34, 1945, p 156–195

44. C.S. Smith, Grains, Phases and Interfaces: An Interpretation of Microstructure, *Trans. AIME,* Vol 175, 1948, p 15

45. O.K. Riegger and L.H. Van Vlack, Dihedral Angle Measurement, *Trans. Met. Soc. AIME,* Vol 218, 1960, p 933–935

46. C.A. Stickels and E.E. Hucke, Measurement of Dihedral Angles, *Trans. Met. Soc. AIME,* Vol 230, 1964, p 795–801

Introduction to Structures in Metals, *Metallography and Microstructures,* Vol 9, *ASM Handbook*, ASM International, 2004, p. 23–28

Substructure

Crystal imperfections of all kinds, including subboundaries, may occur in single crystals and within the grains of polycrystalline metals. In the broadest sense, substructure comprises all imperfections within the grains of a polycrystalline metal or a single crystal. In the conventional sense, substructure refers to the subgrains formed

by subboundaries (low-angle boundaries). This structure is revealed at intermediate magnifications; crystal imperfections, such as dislocations and stacking faults, can be revealed individually only at much higher magnifications.
Examples of special kinds of substructure are:

- *Lineage structure,* mosaics originating by solidification
- *Veining* originating by transformation of fcc iron to bcc iron
- *The cellular structure* resulting from cold work
- *Impurity substructure* involving solute atmospheres associated with dislocations
- *Dislocation networks* originating by solidification, cold work, or fatigue (cyclic loading)
- *Polygonized structure* resulting from cold work followed by annealing
- *Imperfections* resulting from quenching or radiation damage

Subgrains and cellular structures are formed by subboundaries (low-angle boundaries). The simplest of these boundaries consists of periodically spaced dislocations. In more complex instances, particularly in structures resulting from deformation, dislocation tangles can form cellular structures.
The subgrains that constitute substructure in the conventional sense have a large range of possible sizes. The angular misorientations resulting from subboundaries range from a fraction of 1° to well over 1°.

Introduction to Structures in Metals, *Metallography and Microstructures,* Vol 9, *ASM Handbook,* ASM International, 2004, p. 23–28

Multiphase Microstructures

Although many industrial alloys are single-phase materials—for example, cartridge brass, silicon steel, and austenitic stainless steels—multiphase alloys are more often encountered. The shapes, sizes, and configuration of two or more microconstituents in a multiphase system produce a variety of typical microstructures, depending on the nature of phase transformations during heating, cooling, or solidification (see the article "Physical Metallurgy Concepts in Interpretation of Microstructures" in this Volume). For example, most ferrous metals as well as many nonferrous alloys, especially the age-hardening and precipitation-hardening alloys, consist of more than one phase.
The characteristic multiphase structures can be related to their modes of origin (see Fig. 2 and 3). The major types of multiphase structures are discussed below.
Structures in which both phases form entirely distinct grains have been called aggregated two-phase structures or random duplex aggregates. They develop most clearly in alloys in which both phases are present in approximately equal volume fractions (Ref 47). In microduplex alloys, the two phases are distributed uniformly such that the boundaries are predominantly interphase interfaces. This structure is usually fine scale and resistant to microstructural coarsening.
Structures in which each phase is closely interconnected can result from spinodal decomposition (see the article "Spinodal Transformation Structures" in this Volume). The scale of these spinodal structures is very small. They are characterized principally by their high degree of connectivity and often by crystallographic alignment of the phases (Ref 48).
Structures consisting of one continuous phase and isolated particles of a second phase (the matrix-plus-dispersed-phase structure) are the most varied of the multiphase structures. Among their characteristic variables are the relative volumes of the two phases, the size of the particles of the dispersed phase, the interparticle distance, the shape of the dispersed particles, and any special orientation of the dispersed particles with respect to each other and the matrix. Some of these variables are interdependent; all of them can be measured. Examples of the matrix-plus-dispersed-phase structure are rod-shaped particles embedded in a matrix and cellular precipitates. Another important example is the type of dual-phase HSLA sheet steels characterized by a

microstructure consisting of about 20% hard martensite particles dispersed in a soft ductile ferrite matrix (Fig. 7). The term dual phase refers to ferrite and martensite as the two dominant phases, although small amounts of other phases, such as bainite, pearlite, or retained austenite, may also be present (Ref 49).

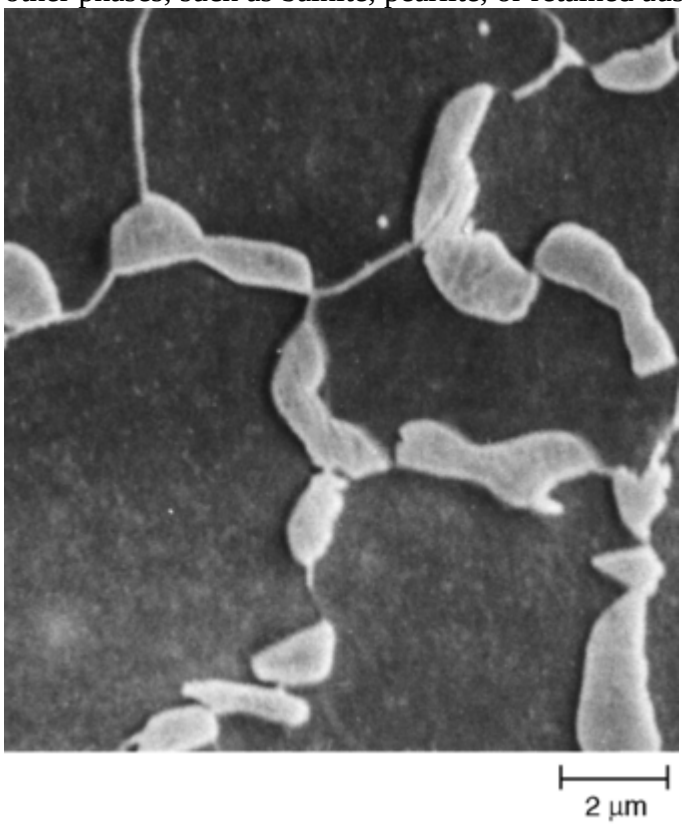

Fig. 7 Ferrite-martensite microstructure of a dual-phase steel (0.06% C, 1.5% Mn; water quenched from 760 °C, or 1400 °F). Source: Ref 49

Structures in which the two phases are arranged in alternate layers or lamellas form as eutectics, as pearlites in steels, and as pearlites in nonferrous eutectoid alloys. Their characteristic variable is the interlamellar spacing or thickness of the lamellas.

A second phase can be distributed along the grain boundaries of a matrix phase, as in copper that is contaminated by bismuth. Particles of a dispersed phase can also be located at other preferential sites, such as at slip planes after cold work followed by a precipitation process.

Crystallography of Interphase Interfaces. The two phases that meet at an interface may differ in lattice constants, lattice type, and orientation. These differences result in a mismatch or disregistry at the interface.

This mismatch can be accommodated in one of the following three ways (Ref 39, 50): (1) A coherent interface exists when, in two adjoining structures, corresponding rows and planes of lattice points are continuous across the interface. However, the rows and planes may change direction, resembling a coherent twin boundary. Fully coherent interfaces between crystals of appreciable size are rare. However, in limited areas, elastic straining can make it possible for coherency to exist. The particles of transformation products with such coherency generally are too small to be observed using optical microscopy. (2) At a semicoherent interface, the two lattices are elastically strained into coherence over limited areas; they accumulate misfit that is corrected periodically by discontinuities (dislocations). In other words, regions of forced elastic coherence alternate with regions of misfit. (3) At an incoherent interface, the two lattices are discontinuous. It was thought that such an interface could be explained in terms of dislocations compensating for the mismatch; however, such explanations have no physical significance, and the dislocation model of incoherent interfaces retains little interest.

References cited in this section

39. R.W. Balluffi, Ed., *Grain Boundary Structure and Kinetics,* American Society for Metals, 1979

47. R.W. Cahn, Metal Systems, *Composite Materials,* L. Holliday, Ed., Elsevier, 1966, p 65–90

48. J.W. Cahn, A Model for Connectivity in Multiphase Structures, *Acta Metall.,* Vol 14, 1966, p 477–480

49. G.R. Speich, Dual-Phase Steels, *Properties and Selection: Irons, Steels, and High-Performance Alloys,* Vol 1, *ASM Handbook,* 1990, p 424

50. G.B. Olson and M. Cohen, Interphase Boundaries and the Concept of Coherency, *Acta Metall.,* Vol 27, 1979, p 1907–1918

Introduction to Structures in Metals, *Metallography and Microstructures,* Vol 9, *ASM Handbook,* ASM International, 2004, p. 23–28

Macrostructure

The macrostructure of metals and alloys consists of inhomogeneities on a fairly large scale. For example, gradients in a macrostructure exist on a much larger scale than that of the constituents of the microstructure. A macrostructure may also comprise other inhomogeneities, such as blowholes or porosity in cast or weld metal and flow lines in forgings. Flow lines in forgings may be caused by elongated inclusions or by inhomogeneities in grain-shape alignment. Other examples of macrostructures are presented in the articles in this Volume dealing with metallographic procedures and representative microstructures of specific metals and alloys.

Introduction to Structures in Metals, *Metallography and Microstructures,* Vol 9, *ASM Handbook,* ASM International, 2004, p. 23–28

Introduction to Structures in Metals

Acknowledgment

This article is adapted from Michael B. Bever, Introduction (to Structures), *Metallography and Microstructures,* Vol 9, *ASM Handbook,* 1985, p 601 to 606.

Introduction to Structures in Metals, *Metallography and Microstructures,* Vol 9, *ASM Handbook,* ASM International, 2004, p. 23–28

Introduction to Structures in Metals

References

1. R.F. Mehl, *A Brief History of the Science of Metals,* American Institute of Mining and Metallurgical Engineers, 1948

2. C.S. Smith, *A History of Metallography,* University of Chicago Press, 1960

3. C.S. Smith, Ed., *Sorby Centennial Symposium on the History of Metallurgy,* Gordon and Breach, 1965

4. R.F. Mehl and R.W. Cahn, The Historical Development of Physical Metallurgy, *Physical Metallurgy,* Part I, 3rd ed., R.W. Cahn and R. Haasen, Ed., North-Holland, 1983, p 1–35

5. R.W. Cahn and P. Haasen, Ed., *Physical Metallurgy,* Parts I and II, 3rd ed., North-Holland, 1983

6. A.G. Guy and J.J. Hren, *Elements of Physical Metallurgy,* 3rd ed., Addison-Wesley, 1974

7. W.F. Smith, *Structures and Properties of Engineering Alloys,* McGraw-Hill, 1981

8. R.E. Smallman, *Modern Physical Metallurgy,* 4th ed., Butterworths, 1985

9. A. Tomer, *Structure of Metals through Optical Microscopy,* ASM International, 1991

10. R.H. Greaves and H. Wrighton, *Practical Microscopical Metallography,* 4th ed., Chapman & Hall, 1957

11. H. Gleiter, Microstructure, *Physical Metallurgy,* Part I, 3rd ed., R.W. Cahn and P. Haasen, Ed., North-Holland, 1983, p 650–712

12. G.F. Vander Voort, *Metallography: Principles and Practice,* McGraw-Hill, 1984, reprinted by ASM International, 1999

13. W. Rostoker and J.R. Dvorak, *Interpretation of Metallographic Structures,* 2nd ed., Academic Press, 1977

14. J.W. Edington, *Practical Electron Microscopy in Materials Science,* Van Nostrand Reinhold, 1976

15. P.J. Goodhew, *Electron Microscopy and Analysis,* Wykeham Publications, 1975

16. M.H. Loretto and R.E. Smallman, *Defect Analysis in Electron Microscopy,* Chapman & Hall—Halsted/Wiley, 1975

17. G. Thomas and M.J. Goringe, *Transmission Electron Microscopy of Materials,* John Wiley & Sons, 1979

18. C.S. Barrett and T.B. Massalski, *Structure of Metals,* 3rd ed., Pergamon Press, 1980

19. B.D. Cullity, *Elements of X-ray Diffraction,* 2nd ed., Addison-Wesley, 1978

20. S.M. Allen and M.B. Bever, Structure of Materials, *Encyclopedia of Materials Science and Engineering,* MIT Press, 1986

21. H.W. King, Structure of the Pure Metals, *Physical Metallurgy,* Part I, 3rd ed., R.W. Cahn and P. Haasen, Ed., North-Holland, 1983, p 37–79

22. D.G. Pettifor, Electron Theory of Metals, *Physical Metallurgy,* Part I, 3rd ed., R.W. Cahn and P. Haasen, Ed., North-Holland, 1983, p 73–152

23. W.A. Harrison, *Electronic Structure and the Properties of Solids,* Freeman, 1980

24. R.W. Balluffi, Grain Boundary Structure and Segregation, *Interfacial Segregation,* W.C. Johnson and J.M. Blakely, Ed., American Society for Metals, 1979, p 193–236

25. M.B. Bever and P.E. Duwez, Gradients in Composite Materials, *Mater. Sci. Eng.,* Vol 10, 1972, p 1–8

26. A. Kelly and G.W. Groves, *Crystallography and Crystal Defects,* Addison-Wesley, 1970

27. E. Prince, *Mathematical Techniques in Crystallography and Materials Science,* Springer-Verlag, 1982

28. H.G. van Bueren, *Imperfections in Crystals,* North-Holland, 1960

29. J.P. Hirth and J. Lothe, *Theory of Dislocations,* 2nd ed., John Wiley & Sons, 1982

30. D. Hull, *Introduction to Dislocations,* 3rd ed., Pergamon Press, 1975

31. J.W. Christian, *The Theory of Transformations in Metals and Alloys*, Pergamon Press, 1965; 2nd ed., Part I, Pergamon Press, 1975

32. D.A. Porter and K.E. Easterling, *Phase Transformations in Metals and Alloys,* Van Nostrand Reinhold, 1981

33. R.W.K. Honeycombe, *The Plastic Deformation of Metals,* 2nd ed., St. Martin's Press, 1982

34. R.D. Doherty, Stability of Grain Structure in Metals, *J. Mater. Educ.,* Vol 6, 1984, p 845

35. A.P. Sutton, Grain Boundary Structure, *Int. Met. Rev.,* Vol 29, 1984, p 377

36. C.S. Smith, Some Elementary Principles of Polycrystalline Microstructure, *Met. Rev.,* Vol 9, 1964, p 1–62

37. C.S. Smith, Grain Shapes and Other Metallurgical Applications of Topology, in *Metal Interfaces,* American Society for Metals, 1952, p 65–133

38. C.S. Smith, Microstructure, *Trans. ASM,* Vol 45, 1953, p 533–575

39. R.W. Balluffi, Ed., *Grain Boundary Structure and Kinetics,* American Society for Metals, 1979

40. G.F. Vander Voort, Examination of Some Grain Size Measurement Problems, *Metallography: Past, Present, and Future,* STP 1165, Vander Voort, Warmuth, Purdy, and Szirmae, Ed., ASTM 1993, p 266–294

41. L. Karlsson and A.M. Gokhale, Stereological Estimation of Mean Linear Intercept Length in Metallography Using Vertical Sections and Trisector, *J. Microsc.,* Vol 186, 1997, p 143–152

42. B.R. Morris, A.M. Gokhale, and G.F. Vander Voort, Estimation of Grain Size in Anisotropic Materials, *Metall. Mater. Trans.,* Vol 29A, 1998, p 237–244

43. D. Harker and E.R. Parker, Grain Shape and Grain Growth, *Trans. ASM,* Vol 34, 1945, p 156–195

44. C.S. Smith, Grains, Phases and Interfaces: An Interpretation of Microstructure, *Trans. AIME,* Vol 175, 1948, p 15

45. O.K. Riegger and L.H. Van Vlack, Dihedral Angle Measurement, *Trans. Met. Soc. AIME,* Vol 218, 1960, p 933–935

46. C.A. Stickels and E.E. Hucke, Measurement of Dihedral Angles, *Trans. Met. Soc. AIME,* Vol 230, 1964, p 795–801

47. R.W. Cahn, Metal Systems, *Composite Materials,* L. Holliday, Ed., Elsevier, 1966, p 65–90

48. J.W. Cahn, A Model for Connectivity in Multiphase Structures, *Acta Metall.,* Vol 14, 1966, p 477–480

49. G.R. Speich, Dual-Phase Steels, *Properties and Selection: Irons, Steels, and High-Performance Alloys,* Vol 1, *ASM Handbook,* 1990, p 424

50. G.B. Olson and M. Cohen, Interphase Boundaries and the Concept of Coherency, *Acta Metall.,* Vol 27, 1979, p 1907–1918

Crystal Structure, *Metallography and Microstructures,* Vol 9, *ASM Handbook,* ASM International, 2004, p. 29–43

Crystal Structure*

Introduction

THE CRYSTAL STRUCTURES presented in this article are those that have been widely studied and are of most importance to metallurgists. More complete coverage is given in the references listed at the end of this article.

Footnote

* Reprinted from C.S. Barrett, Crystal Structure of Metals, *Metallography and Microstructures,* Vol 9, *Metals Handbook,* 9th ed., American Society for Metals, 1985, p 706–719. The structure-type nomenclature used in this article was supplied by W.B. Pearson, Department of Physics, University of Waterloo.

Crystal Structure, *Metallography and Microstructures,* Vol 9, *ASM Handbook,* ASM International, 2004, p. 29–43

Crystallographic Terms and Concepts

The terms and concepts defined and explained in this section are basic to an understanding of the descriptions and illustrations of crystal structures presented in the next section of this article.

Crystal structure is the arrangement of atoms in the interior of a crystal. A fundamental unit of the arrangement repeats itself at regular intervals in three dimensions throughout the interior of the crystal.

A unit cell is a parallelepiped whose edges form the axes of a crystal. A unit cell is the smallest pattern of atomic arrangement. A crystal consists of unit cells stacked tightly together, each identical in size, shape, and orientation with all others. The choice of the boundaries of a unit cell is somewhat arbitrary, being conditioned by symmetry considerations and by convenience.

Crystal Systems. Crystallography uses seven different systems of axes, each with a specified equality or inequality to others of axial lengths and interaxial angles. These are the basis of the following crystal systems—

triclinic (anorthic), monoclinic, orthorhombic, tetragonal, hexagonal, rhombohedral (trigonal), and cubic—employed in the classification of crystals.

The edge lengths *a*, *b*, and *c* (along the corresponding crystal axes) of unit cells are expressed in angstroms (1 Å = 0.1 nm, or 10^{-10} m). Faces of unit cells are identified by the capital letter *A*, *B*, or *C*, when the faces contain axes *b* and *c*, *c* and *a*, or *a* and *b*, respectively.

Angles between the axes are expressed in degrees, with the angle in the *A* face denoted α, the angle in the *B* face β, and the angle in the *C* face γ. Table 1 shows the relationships of the edge lengths along the crystal axes, and of the interaxial angles, for each of the seven crystal systems. The edge lengths and angles are sometimes referred to as the lattice parameters, lattice spacings, or lattice constants for a unit cell.

Table 1 Relationships of edge lengths and of interaxial angles for the seven crystal systems

Crystal system	Edge lengths	Interaxial angles	Examples
Triclinic (anorthic)	$a \neq b \neq c$	$\alpha \neq \beta \neq \gamma \neq 90°$	HgK
Monoclinic	$a \neq b \neq c$	$\alpha = \gamma = 90° \neq \beta$	β-S; $CoSb_2$
Orthorhombic	$a \neq b \neq c$	$\alpha = \beta = \gamma = 90°$	α-S; Ga; Fe_3C (cementite)
Tetragonal	$a = b \neq c$	$\alpha = \beta = \gamma = 90°$	β-Sn (white); TiO_2
Hexagonal	$a = b \neq c$	$\alpha = \beta = 90°; \gamma = 120°$	Zn; Cd; NiAs
Rhombohedral[(a)]	$a = b = c$	$\alpha = \beta = \gamma \neq 90°$	As; Sb; Bi; calcite
Cubic	$a = b = c$	$\alpha = \beta = \gamma = 90°$	Cu; Ag; Au; Fe; NaCl

(a) Rhombohedral crystals (sometimes called trigonal) can also be described by using hexagonal axes (rhombohedral-hexagonal).

A lattice (space lattice or Bravais lattice) is a regular, periodic array of points (lattice points) in space, at each of which is located the same kind of atom or a group of atoms of identical composition, arrangement, and orientation in a perfect crystal (at least, on a time-average basis).

There are five (actually, four plus rhombohedral) basic arrangements for lattice points within a unit cell, and each is identified by a Hermann-Mauguin letter symbol in a space-lattice notation. These letter symbols and the arrangements they identify are *P*, for primitive (simple), with lattice points only at cell corners; *C*, for base-face centered (end-centered), with lattice points centered on the *C* faces or ends of the crystal; *F*, for all-face centered, with lattice points centered on all faces; and *I*, for innercentered, with lattice points at the center of volume of the unit cell (body-centered). The rhombohedral cell, also primitive, has *R* as its symbol.

The face having the base-face centered lattice point may be designated the *C* face, because the choice of axes is arbitrary and does not alter the atom positions in the space lattice. Rhombohedral crystals can be considered as having either a rhombohedral cell or a primitive hexagonal cell.

The aforementioned letter symbols and definitions apply only to basic arrangement of atoms and do not limit the number of atoms in a unit cell. Atoms may be found at each corner of a base-centered, face-centered, or inner-centered cell and, in some crystals, also at other positions on the cell faces or within the cell.

There are 14 kinds of space lattices, derived from all the combinations of equality and inequality of lengths of axes and interaxial angles. They are listed in Table 2, along with Hermann-Mauguin and Pearson symbols. The Pearson symbols (Ref 1) consist of Hermann-Mauguin space-lattice letters preceded by *a*, *m*, *o*, *t*, *h*, and *c* to denote, respectively, six crystal systems: triclinic (anorthic), monoclinic, orthorhombic, tetragonal, hexagonal, and cubic.

Table 2 The 14 space (Bravais) lattices and their Hermann-Mauguin and Pearson symbols

System	Space lattice	Hermann-Mauguin symbol	Pearson symbol
Triclinic (anorthic)	Primitive	*P*	*aP*
Monoclinic	Primitive	*P*	*mP*
	Base-centered[(a)]	*C*	*mC*
Orthorhombic	Primitive	*P*	*oP*
	Base-centered[(a)]	*C*	*oC*
	Face-centered	*F*	*oF*
	Body-centered	*I*	*oI*

Tetragonal	Primitive	*P*	*tP*
	Body-centered	*I*	*tI*
Hexagonal	Primitive	*R*[(b)]	*hP*
Rhombohedral	Primitive	*R*	*hR*
Cubic	Primitive	*P*	*cP*
	Face-centered	*F*	*cF*
	Body-centered	*I*	*cI*

(a) The face that has a lattice point at its center may be chosen as the *c* face (the *xy* plane), denoted by the symbol *C*, or as the *a* or *b* face, denoted by *A* or *B*, because the choice of axes is arbitrary and does not alter the actual translations of the lattice.

(b) The symbol *C* may be used for hexagonal crystals, because hexagonal crystals may be regarded as base-centered orthorhombic.

Structure symbols are arbitrary symbols that designate the type of crystal structure. The Strukturbericht symbols (Ref 2) were widely used in the past and are still used today, but this system of naming structure types has been overwhelmed by the number and complexity of types that are now recognized. Furthermore, the final publication of Strukturbericht was in 1939.

Today, the accepted system of naming the types of crystal structures that metals and alloys adopt is to select arbitrarily the formula of a phase with the structure type (that is, a prototype) followed by its Pearson symbol. When the seven crystal systems are considered together with the five space lattices, the combinations listed in Table 2 are obtained. These 14 combinations form the basis of the system of ***Pearson symbols*** developed by William B. Pearson, which are widely used to identify crystal types. As can be seen in Table 2, the Pearson symbol uses a small letter to identify the crystal system and a capital letter to identify the space lattice. To these is added a number equal to the number of atoms in the unit cell conventionally selected for the particular crystal type. For example, the nickel-arsenide structure is referred to as the NiAs *hP*4 type (meaning hexagonal, primitive, 4 atoms per unit cell) and rock salt as the NaCl *cF*8 type.

The arbitrariness in the system does not appear to be a problem, because norms become established by common usage. Therefore, the ordered AuCu structure should properly be described as AuCu *tP*2, according to the smallest primitive cell, but due to association of the structure with ordering from a face-centered cubic solid solution (*cF*4), it is typically referred to as AuCu *cF*4. When determining the number of atoms in the unit cell, it should be remembered that each atom that is shared with an adjacent cell (or cells) must be counted as only a fraction of an atom. The Pearson symbols for some simple metal crystals are shown in Fig. 1.

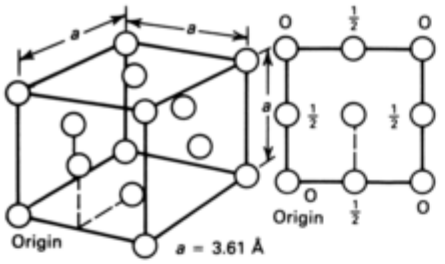

a = 3.61 Å

Face-centered cubic: *Fm*3*m*

Cu *cF*4

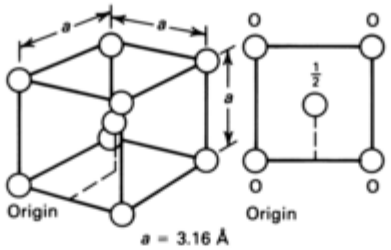

a = 3.16 Å

Body-centered cubic: *Im*3*m*

W *cI*2

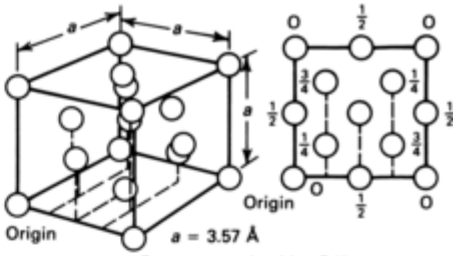

a = 3.57 Å

Face-centered cubic: *Fd*3*m*

C *cF*8 (diamond)

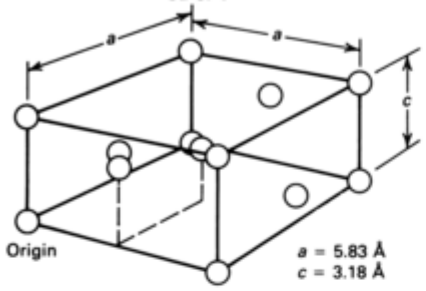

a = 5.83 Å

c = 3.18 Å

Body-centered tetragonal: $I4_1/amd$

Sn *tI*4 (white)

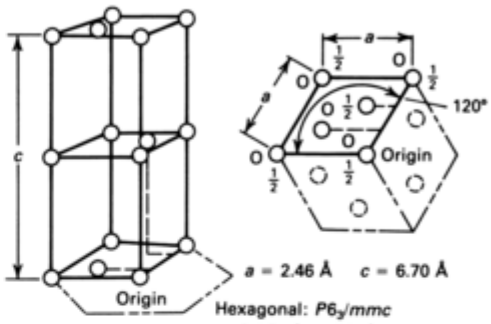

a = 2.46 Å c = 6.70 Å

Hexagonal: $P6_3/mmc$

C *hP*4 (graphite)

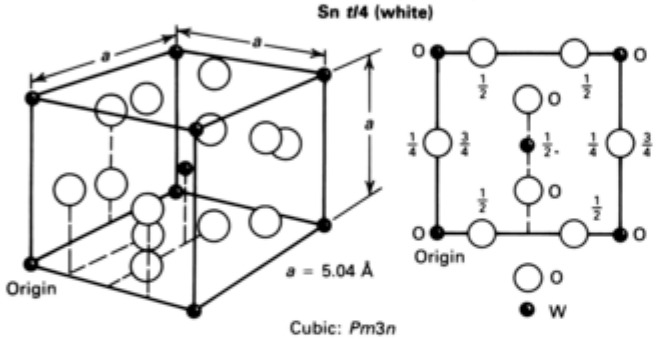

Cubic: *Pm*3*n*

W_3O *cP*8

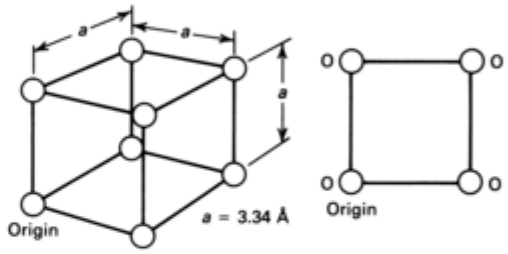

a = 3.34 Å

Primitive cubic: *Pm*3*m*

Po *cP*1

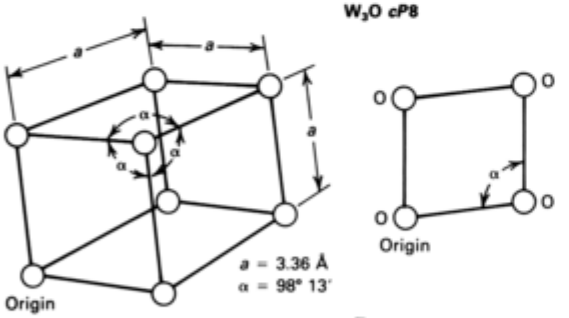

a = 3.36 Å

α = 98° 13′

Rhombohedral: $R\bar{3}m$

Hg *hR*1

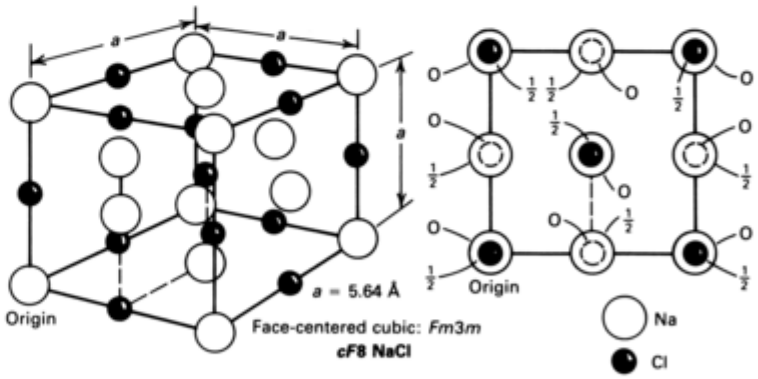

a = 5.64 Å

Face-centered cubic: *Fm*3*m*

***cF*8 NaCl**

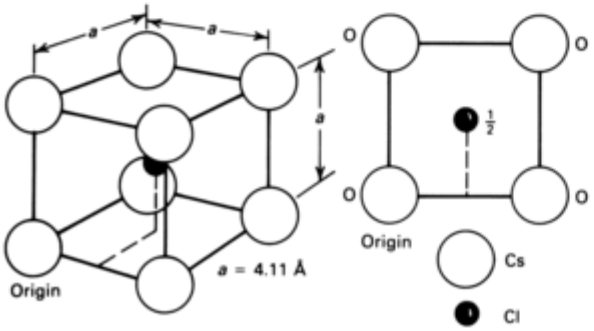

a = 4.11 Å

Cubic: *Pm*3*m*

CsCl *cP*2

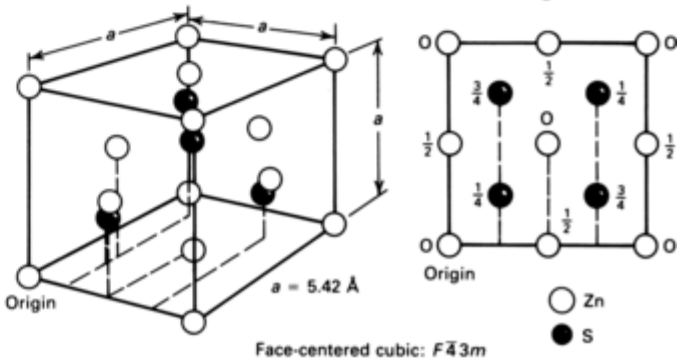

a = 5.42 Å

Face-centered cubic: $F\bar{4}3m$

ZnS *cF*8 (sphalerite)

(continued)

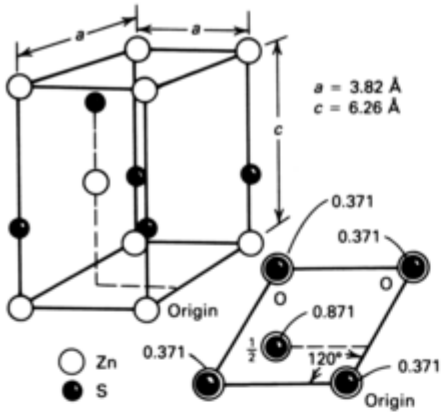

Hexagonal: $P6_3mc$

ZnS *hP*4 (wurtzite)

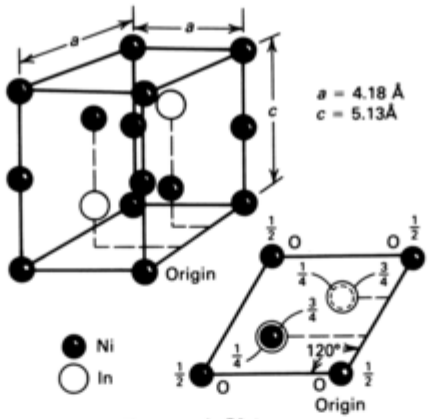

Hexagonal: $P6_3/mmc$

$InNi_2$ *hP*6

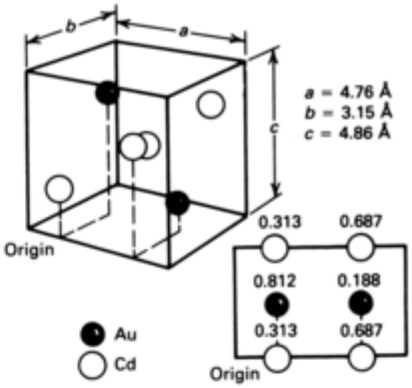

Orthorhombic: *Pmma*

AuCd *oP*4

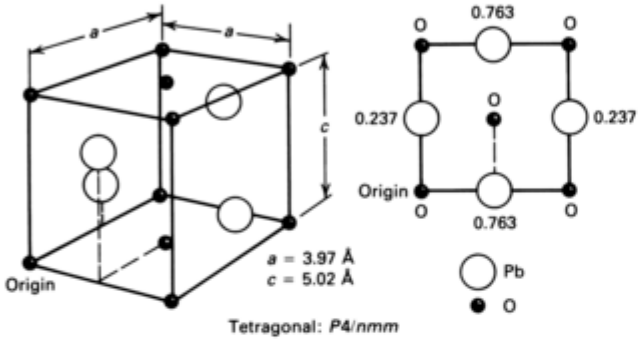

Tetragonal: $P4/nmm$

PbO *tP*4

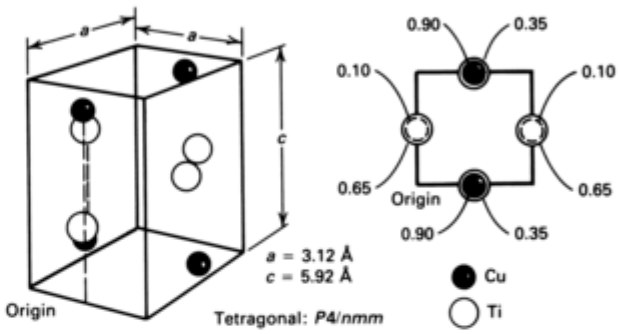

Tetragonal: $P4/nmm$

γ CuTi *tP*4

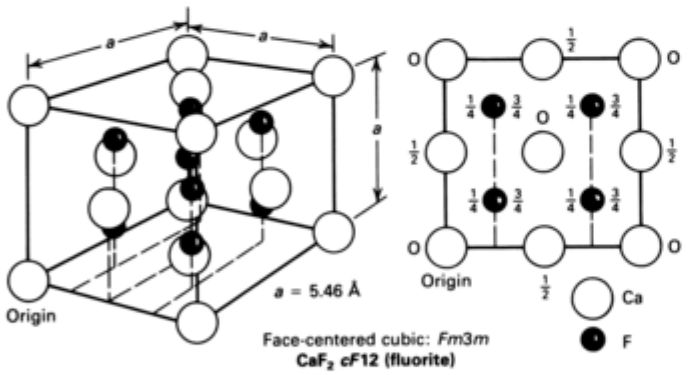

Face-centered cubic: $Fm3m$

CaF_2 *cF*12 (fluorite)

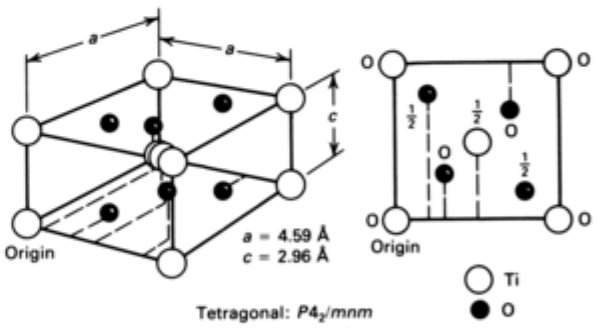

Tetragonal: $P4_2/mnm$

TiO_2 *tP*6 (rutile)

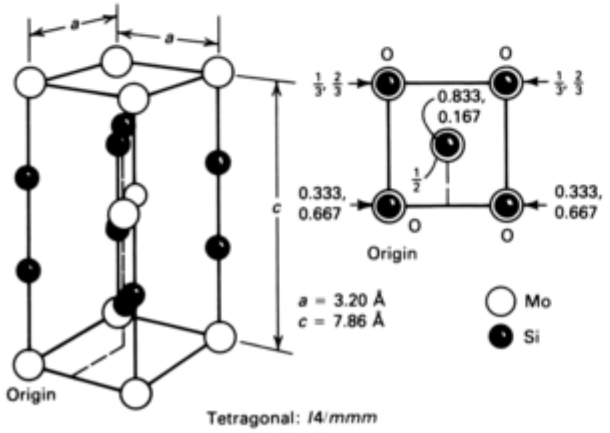

Tetragonal: $I4/mmm$

$MoSi_2$ *tI*6

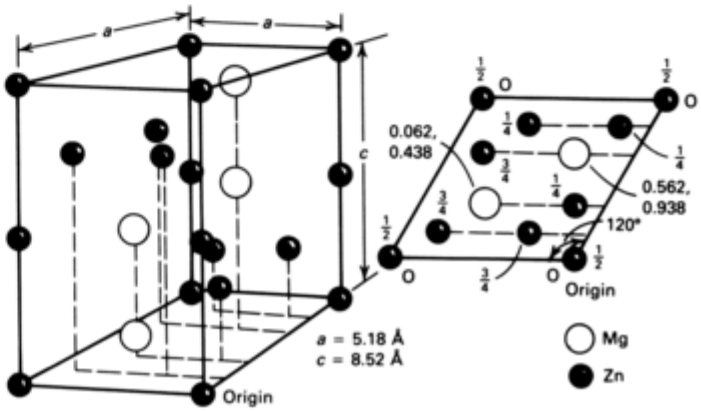

Hexagonal: $P6_3/mmc$

$MgZn_2$ *hP*12

(continued)

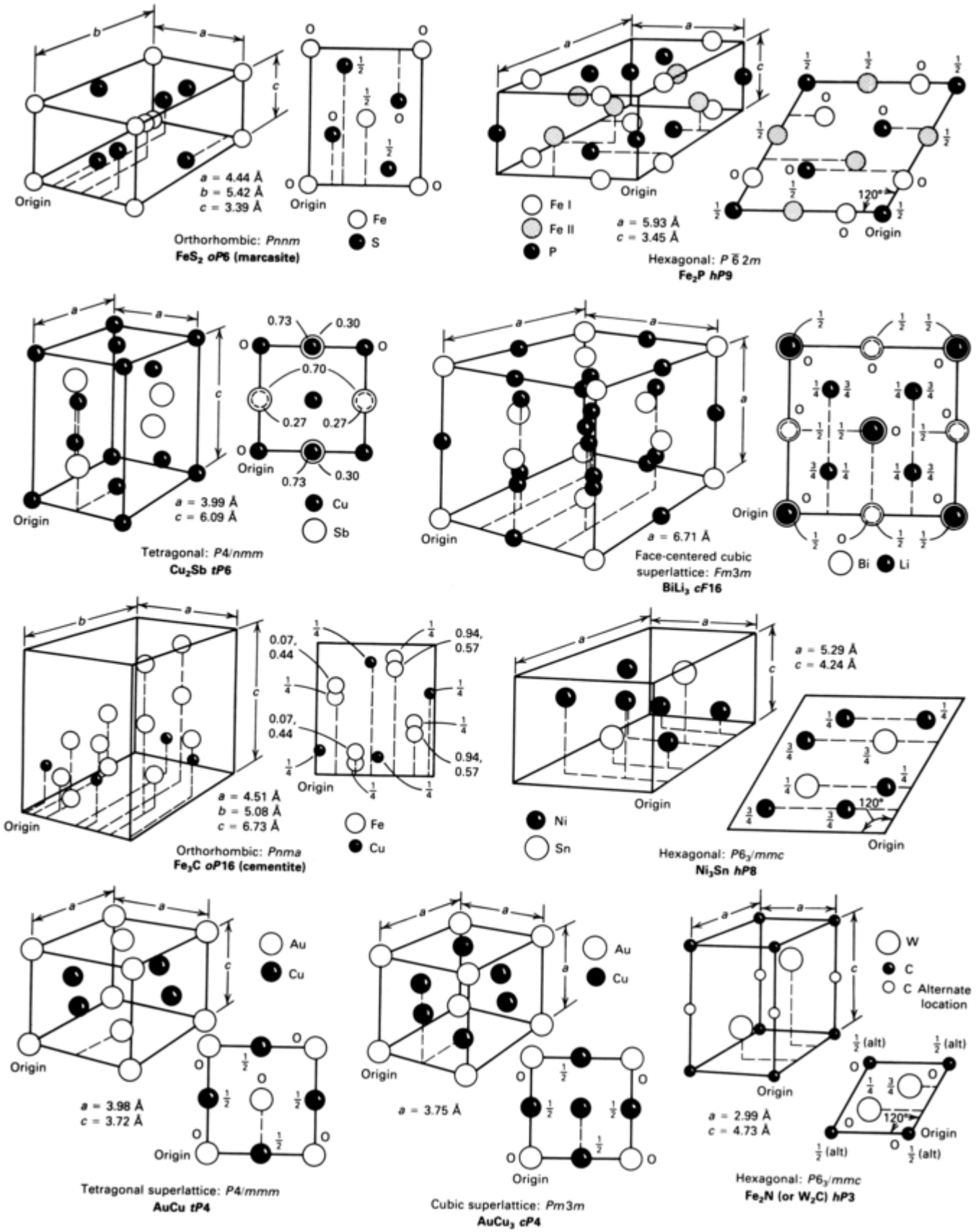

Fig. 1 Atom positions, prototypes, structure symbols, space-group notations, and lattice parameters for some of the simple metallic crystals

The advantage of this way of naming structure types is that it is open ended, that is, not limited in use by future discoveries of new crystal-structure types. Secondly, compared to using only a formula name, it is crystallographically informative due to the addition of the Pearson symbol and thus amenable to classification. Therefore, on discovering a new intermetallic phase and establishing for it preliminary crystallographic

information (the space lattice and the number of atoms in the unit cell), a table of known structure types, classified by Pearson symbols can be consulted to determine what already characterized types may resemble the newly discovered phase. For convenience, Table 3 lists Strukturbericht structure symbols, prototype names, and the corresponding Pearson symbols.

Table 3 Conversion of Strukturbericht to Pearson symbol

Strukturbericht designation	Structure prototype	Pearson symbol
***A*1**	Cu	*cF*4
***A*2**	W	*cI*2
***A*3**	Mg	*hP*2
***A*4**	C	*cF*8
***A*5**	Sn	*tF*4
***A*6**	In	*tI*2
***A*7**	As	*hR*2
***A*8**	Se	*hP*3
***A*10**	Hg	*hR*1
***A*11**	Ga	*oC*8
***A*12**	α-Mn	*cI*58
***A*13**	β-Mn	*cP*20
***A*15**	W_3O	*cP*8
***A*20**	α-U	*oC*4
***B*1**	NaCl	*cF*8
***B*2**	CsCl	*cP*2
***B*3**	ZnS	*cF*8
***B*4**	ZnS	*hP*4
***B*8$_1$**	AsNi	*hP*4
***B*8$_2$**	$InNi_2$	*hP*6
***B*9**	HgS	*hP*6
***B*10**	PbO	*tP*4
***B*11**	γ-CuTi	*tP*4
***B*13**	α-NiS	*hR*6
***B*16**	GeS	*oP*8
***B*17**	PtS	*tP*4
***B*18**	CuS	*hP*12
***B*19**	β′-AuCd	*oP*4
***B*20**	FeSi	*cP*8
***B*27**	BFe	*oP*8
***B*31**	MnP	*oP*8
***B*32**	NaTl	*cF*16
***B*34**	PdS	*tP*16
***B*35**	CoSn	*hP*6
***B*37**	SeTl	*tI*16
***B*$_e$**	CdSb	*oP*16
***B*$_f$(*B*33)**	ξ-CrB	*oC*8
***B*$_g$**	BMo	*tI*16
***B*$_h$**	WC	*hP*2
***B*$_i$**	γ′-CMo (AsTi)	*hP*8
***C*1**	CaF_2	*cF*12
***C*1$_b$**	AgAsMg	*cF*12
***C*2**	FeS_2	*cP*12
***C*3**	Cu_2O	*cP*6

Strukturbericht designation	Structure prototype	Pearson symbol
***C*4**	TiO_2	*tP*6
***C*6**	CdI_2	*hP*3
***C*7**	MoS_2	*hP*6
***C*11$_a$**	CaC_2	*tI*6
***C*11$_b$**	$MoSi_2$	*tI*6
***C*12**	$CaSi_2$	*hR*6
***C*14**	$MgZn_2$	*hP*12
***C*15**	Cu_2Mg	*cF*24
***C*15$_b$**	$AuBe_5$	*cF*24
***C*16**	Al_2Cu	*tI*12
***C*18**	FeS_2	*oP*6
***C*19**	$CdCl_2$	*hR*3
***C*22**	Fe_2P	*hP*9
***C*23**	$PbCl_2$	*oP*12
***C*32**	AlB_2	*hP*3
***C*33**	Bi_2STe_2	*hR*5
***C*34**	$AuTe_2$	*mC*6
***C*36**	$MgNi_2$	*hP*24
***C*38**	Cu_2Sb	*tP*6
***C*40**	$CrSi_2$	*hP*9
***C*44**	GeS_2	*oF*72
***C*46**	$AuTe_2$	*oP*24
***C*49**	Si_2Zr	*oC*12
***C*54**	Si_2Ti	*oF*24
***C*$_c$**	Si_2Th	*tI*12
***C*$_e$**	$CoGe_2$	*oC*23
***D*0$_2$**	As_3Co	*cI*32
***D*0$_3$**	BiF_3	*cF*16
***D*0$_9$**	O_3Re	*cP*4
***D*0$_{11}$**	Fe_3C	*oP*16
***D*0$_{18}$**	$AsNa_3$	*hP*8
***D*0$_{19}$**	Ni_2Sn	*hP*8
***D*0$_{20}$**	Al_3Ni	*oP*16
***D*0$_{21}$**	Cu_3P	*hP*24
***D*0$_{22}$**	Al_3Ti	*tI*8
***D*0$_{23}$**	Al_3Zr	*tI*16
***D*0$_{24}$**	Ni_3Ti	*hP*16
***D*0$_c$**	SiU_3	*tI*16
***D*0$_e$**	Ni_3P	*tI*32
***D*1$_3$**	Al_4Ba	*tI*10
***D*1$_a$**	$MoNi_4$	*tI*10
***D*1$_b$**	Al_4U	*oI*20
***D*1$_c$**	$PtSn_4$	*oC*20
***D*1$_e$**	B_4Th	*tP*20
***D*1$_f$**	BMn_4	*oF*40
***D*2$_1$**	B_6Ca	*cP*7
***D*2$_3$**	$NaZn_{13}$	*cF*112
***D*2$_b$**	$Mn_{12}Th$	*tI*26
***D*2$_c$**	MnU_6	*tI*28
***D*2$_d$**	$CaCu_5$	*hP*6

Strukturbericht designation	Structure prototype	Pearson symbol
***D*2$_f$**	UB_{12}	*cF*52
***D*2$_h$**	Al_6Mn	*oC*28
***D*5$_1$**	α-Al_2O_3	*hR*10
***D*5$_2$**	La_2O_3	*hP*5
***D*5$_3$**	Mn_2O_3	*cI*80
***D*5$_8$**	S_3Sb_2	*oP*20
***D*5$_9$**	P_2Zn_3	*tP*40
***D*5$_{10}$**	Cr_3C_2	*oP*20
***D*5$_{13}$**	Al_3Ni_2	*hP*5
***D*5$_a$**	Si_2U_3	*tP*10
***D*5$_c$**	C_3Pu_2	*cI*40
***D*7$_1$**	Al_4C_3	*hR*7
***D*7$_3$**	P_4Th_3	*cI*28
***D*7$_b$**	Ta_3B_4	*oI*14
***D*8$_1$**	Fe_3Zn_{10}	*cI*52
***D*8$_2$**	Cu_3Zn_8	*cI*52
***D*8$_3$**	Al_4Cu_9	*cP*52
***D*8$_4$**	$Cr_{23}C_6$	*cF*116
***D*8$_5$**	Fe_7W_6	*hR*13
***D*8$_6$**	$Cu_{15}Si_4$	*cI*76
***D*8$_8$**	Mn_5Si_3	*hP*16
***D*8$_9$**	Co_9S_8	*cF*68
***D*8$_{10}$**	Al_8Cr_5	*hR*26
***D*8$_{11}$**	Al_5Co_2	*hP*28
***D*8$_a$**	$Mn_{23}Th_6$	*cF*116
***D*8$_b$**	σ-phase (CrFe)	*tP*30
***D*8$_f$**	Ge_7Ir_3	*cI*40
***D*8$_i$**	B_5Mo_2	*hR*7
***D*8$_h$**	B_5W_2	*hP*14
***D*8$_l$**	Cr_5B_3	*tI*32
***D*8$_m$**	Si_3W_5	*tI*32
***D*10$_1$**	Cr_7C_3	*hP*80
***D*10$_2$**	Fe_3Th_7	*hP*20
***E*0$_1$**	ClFPb	*tP*6
***E*1$_1$**	$CuFeS_2$	*tI*16
***E*2$_1$**	CaO_3Ti	*cP*5
***E*3**	Al_2CdS_4	*tI*14
***E*9$_3$**	Fe_3W_3C	*cF*112
***E*9$_a$**	Al_7Cu_2Fe	*tP*40
***E*9$_b$**	$AlLi_3N_2$	*cI*96
***F*0$_1$**	NiSSb	*cP*12
***F*5$_1$**	$CrNaS_2$	*hR*4
***H*1$_1$**	$Al_2M_gO_4$	*cF*56
***H*2$_4$**	Cu_3S_4V	*cP*8
***L*1$_0$**	AuCuI	*tP*4
***L*1$_2$**	$AuCu_3$	*cP*4
***L*2$_1$**	$AlCu_2Mn$	*cF*16
***L′*2$_b$**	H_2Th	*tI*6
***L′*3**	Fe_2N	*hP*3
***L*6$_0$**	$CuTi_3$	*tP*4

Source: Ref 3

Space-group notation is a symbolic description of the space lattice and the symmetry of a crystal. The notation for a space group consists of the symbol for a space lattice followed by letters and numbers describing the symmetry of the crystal. These symmetry designations are not discussed here but are described in various textbooks and are tabulated in the *International Tables for Crystallography* (Ref 4).

Structure Prototype. To assist in classification and identification, each structure type has been given the name of a representative substance (an element or phase) having that structure. Unit cells with the same structure type generally do not have dimensions identical to the prototype or to each other, because different materials with the same type of atomic arrangement have atoms that differ in size, causing the lengths of the *a*, *b*, and *c* edges to differ. Similarly, the atom-position coordinates *x*, *y*, and *z* vary among different materials.

Atom Positions. The position of an atom, or the lattice point, in a unit cell is expressed by three coordinates (Ref 5)—the three distances parallel to the *a*, *b*, and *c* axes, respectively, from the origin at one corner of the cell to the atom in question. These distances are expressed in fractions of the edge lengths *a*, *b*, and *c*, respectively, rather than in angstroms. Therefore, $\frac{1}{2}$,0,0 is the midpoint of the *a* edge, $\frac{1}{2},\frac{1}{2}$,0 is at the center of the *C* face, and $\frac{1}{2},\frac{1}{2},\frac{1}{2}$ is at the center of the volume of the unit cell. The letters *x*, *y*, and *z* are used for the coordinates that are not convenient fractions or that differ in different phases.

A primitive (simple) unit cell has lattice points at its corners only, that is; at 0,0,0. A body-centered unit cell has lattice points at the corners (at 0,0,0) and also at the center of volume (at $\frac{1}{2},\frac{1}{2},\frac{1}{2}$). A face-centered unit cell has lattice points at the corners and at the center of all six faces. The lattice points are at 0,0,0; 0,$\frac{1}{2},\frac{1}{2}$; $\frac{1}{2},\frac{1}{2}$,0; and $\frac{1}{2}$,0,$\frac{1}{2}$. A negative value for a coordinate is indicated by placing a bar over the letter—for example, $\bar{x}$.

Point Groups. A structure described by a specific space lattice (for example, *cP*) may not have any atoms lying at the (space) lattice points; instead, groups of atoms with specific so-called point symmetries may be clustered identically about each of the space-lattice points. Nevertheless, the same space-lattice symmetry (*cP*) still pertains to the crystal structure. Thus, for example, in the close-packed hexagonal structure Mg *hP*2, the primitive space-lattice points are vacant, and the two magnesium atoms are located within the unit cell at $\frac{1}{3}$, $\frac{2}{3}$ and $\frac{1}{4}$, and at $\frac{2}{3}$, $\frac{1}{3}$, $\frac{3}{4}$. The structure type *hP*1, where only the primitive hexagonal space-lattice points are occupied, does not exist.

Alternatively, the space-lattice points may be occupied by atoms, and, in addition, there may be groups of other atoms with various point-group symmetries surrounding the atoms on the space-lattice points, as in the CaF_2 *cF*12 structure, where calcium occupies the face-centered cubic space-lattice sites; the fluorine atoms surround these sites.

Equivalent Positions. In each unit cell, there are positions that are equivalent because of crystal symmetry. This is often true of atoms at special positions (such as $\frac{1}{2}$,0,0) and also of atoms at *x*, *y*, and *z*, where the coordinates may have specific values. At each point of a set of equivalent positions in a unit cell, the same kind of atom will be found (if the crystal is perfect), and all of the cells will be identical. The coordinates listed for each kind of atom in the descriptions of crystal structure in Table 4 are thus coordinates of sets of equivalent positions.

Table 4 Crystal structures of the elements

Element	Phase[(a)]	Structure type	Ref[(b)]
Ac (actinium)	…	Cu *cF*4	1
Ag (silver)	…	Cu *cF*4	1
Al (aluminum)	…	Cu *cF*4	1
Am (americium)	α (RT)	La *hP*4	7
	β (HT)	Cu *cF*4	1
Ar (argon)	…	Cu *cF*4	7
As (arsenic)	α	As *hR*2	1
	β	P *oC*8	1
At (astatine)	…	…	…

Element	Phase[a]	Structure type	Ref [b]
Au (gold)	…	Cu *cF*4	1
B (boron)	α	B *hR*12	7
	β	B *hR*105	8
	γ	B *tP*190	7
Ba (barium)	…	W *cI*2	1
	Ba II (62 kbar; RT)	Mg *hP*2	1
Be (beryllium)	α	Mg *hP*2	1
	β (HT)	W *cI*2	1
Bi (bismuth)	α (RT)	As *hR*2	1
	HP phases uncertain	…	8
Bk (berkelium)	α (RT)	La *hP*4	9
	β (HT)	Cu *cF*4	9
C (carbon)	Graphite	C *hP*4	7
	Rhombohedral graphite	C *hR*2	8
	Diamond	C *cF*8	1
	Hexagonal diamond	C *hP*4	8
Ca (calcium)	α (RT)	Cu *cF*4	1
	β (HT)	W *cI*2	1
Cd (cadmium)	…	Mg *hP*2	1
	Cd II (HP: above about 100 kbar)	La *hP*4(?)	10, 11
Ce (cerium)	α (RT)	Cu *cF*4	7
	β (<250 K)	La *hP*4	7
	γ (<110 K)	Cu *CF*4	7
	δ (HT)	W *cI*2	7
Cm (curium)	α (LT)	La *hP*4	12
	β (HT?)	Cu *cF*4	12
Co (cobalt)	α	Mg *hP*2	1
	β	Cu *cF*4	1
Cr (chromium)	…	W *cI*2	1
Cs (cesium)	…	W *cI*2	1
Cu (copper)	…	Cu *cF*4	1
Dy (dysprosium)	α (RT)	Mg *hP*2	1
	β (HT)	W *cI*2	1
	γ (<86 K)	Tb *oC* 4	1, 7
	δ (at 75 kbar and RT)	Sm *hR*3	8
Er (erbium)	α (RT)	Mg *hP*2	1
Es (einsteinium)	…	…	…
Eu (europium)	…	W *cI*2	1
F (fluorine)	α (<45.6 K)	Monoclinic	13
	β (>45.6 K)	Cubic	13
Fe (iron)	α (RT)	W *cI*2	1
	β (910–1390 °C, or 1670–2535 °F)	Cu *cF*4	1, 8
	δ (>1390 °C, or 2535 °F)	W *cI*2	1, 8
	Fe II ($\gtrsim$130 kbar)	Mg *hP*2	1
Fm (fermium)	…	…	…
Fr (francium)	…	…	…
Ga (gallium)	α (RT)	Ga *oC*8	1
	β (metastable, but stable above about 15 kbar at 0 °C, or 32	Ga *mC*4	1

Element	Phase[a]	Structure type	Ref [b]
	°F)		
	(metastable or stable above 30 kbar at 50–70 °C, or 120–160 °F)	Ga *oC*40	1
Gd (gadolinium)	α (RT)	Mg *hP*2	1
	β (HT)	W *cI*2	1
	Gd II (formed at 400 °C, or 750 °F, and 40 kbar, retained at normal T and P)	Sm *hR*3	1
Ge (germanium)	RT	C *cF*8	1
	Ge II (RT; 120 kbar)	SN *tI*4	1
	Ge III (formed above 120 kbar, retained when pressure removed)	Ge *tP*2	1
H (hydrogen)	α	Mg *hP*2(?)	7
	β	fcc	7
He (helium)	α	Mg *hP*2	7
	β	Cu *cF*4	7
	γ	W *cI*2	7
Hf (hafnium)	α (RT)	Mg *hP*2	1
	β (HT)	W *cI*2	1
Hg (mercury)	Below RT	Hg *hR*1	1
	Hg II (formed at HP, retained at 77 K when pressure removed)	Pa *tI*2	1
Ho (holmium)	α (RT)	Mg *hP*2	1
	Ho II (>75 kbar at RT)	Sm *hR*3	8
In (indium)	…	In *tF*4	1
Ir (iridium)	…	Cu *cF*4	1
K (potassium)	…	W *cI*2	1
Kr (krypton)	…	Cu *cF*4	7
La (lanthanum)	α (RT)	La *hP*4	1
	β (RT)	Cu *cF*4	1
	γ (HT)	W *cI*2	1
Li (lithium)	α (RT)	W *cI*2	7
	β (LT: 78 K)	Mg *hP*2	7
	γ (LT; strain induced at 20 K)	Cu *cF*4	1
Lr (lawrencium)	…	…	…
Lu (lutetium)	α (RT)	Mg *hP*2	1
Md (mendelevium)	…	…	…
Mg (magnesium)	…	Mg *hP*2	1
Mn (manganese)	α (RT)	Mn *cI* 58	1
	β (HT: >727 °C, or 1341 °F)	Mn *cP*20	1, 8
	γ (HT: >1095 °C, or 2003 °F)	Cu *cF*4	1, 8
	δ (HT: >1133 °C, or 2071 °F)	W *cI*2	1, 8
Mo (molybdenum)	…	W *cI*2	1
N (nitrogen)	α	Cubic	7
	γ (HP)	Tetragonal	14
	β	Hexagonal	7
Na (sodium)	α (RT)	W *cI*2	1
	β (LT)	Mg *hP*2	1
Nb (niobium)	…	W *cI*2	1
Nd (neodymium)	α (RT)	La *hP*4	1

Element	Phase[a]	Structure type	Ref [b]
	β (HT)	W *cI*2	1
	Nd II (RT; 50 kbar)	Cu *cF*4	8
Ne (neon)	…	Cu *cF*4	7
Ni (nickel)	…	Cu *cF*4	1
No (nobelium)	…	…	…
Np (neptunium)	α (RT)	Np *oP*8	1
	β (HT: >280 °C, or 535 °F)	Np *tP*4	1, 8
	γ (HT: >577 °C, or 1071 °F)	W *cI* 2	1, 8
O (oxygen)	α	Monoclinic	5
	β	Hexagonal	7
	γ	Cubic	7
Os (osmium)	…	Mg *hP*2	1
P (phosphorus)	White	Cubic	1, 7
	Black	P *oC*8	1, 7
	Red	P *c*-66	1, 7
	Hittorf's	P *mP*84	8
	P II (RT; 50–83 kbar)	As *hR*2	1
	P III (RT; 120 kbar)	Po *cP*1	1
Pa (protactinium)	…	Pa *tI*2	1
Pb (lead)	RT	Cu *cF*4	1
	Pb II (RT; 130 kbar)	Mg *hP*2	8
Pd (palladium)	…	Cu *cF*4	1
Pm (promethium)	α (RT)	La *hP*4	16
	β (HT)	W *cI*2	…
Po (polonium)	α (10 °C, or 50 °F)	Po *cP*1	1
	β (75 °C, or 167 °F)	Hg *hR*1	1
Pr (praseodymium)	α (RT)	La *hP*4	1
	β (HT)	W *cI*2	1
	Pr II (RT; 40 kbar)	Cu *cF*4	1
Pt (platinum)	…	Cu *cF*4	1
Pu (plutonium)	α (RT)	Pu *mP*16	7, 8
	β (>122 °C, or 252 °F)	Pu *mI*32	7, 8
	γ (>206 °C, or 403 °F)	Pu *oF*8	7, 8
	δ (>319 °C, or 606 °F)	Cu *cF*4	7, 8
	δ′ (>451 °C, or 844 °F)	In *tF*4	7, 8
	ε (>476 °C, or 889 °F)	W *cI*2	7, 8
Ra (radium)	…	W *cI*2	17
Rb (rubidium)	…	W *cI*2	1
Re (rhenium)	…	Mg *hP*2	1
Rh (rhodium)	…	Cu *cF*4	1
Rn (radon)	…	…	…
Ru (ruthenium)	…	Mg *hP*2	1
S (sulfur)	α (RT)	S *oF*128	7
	β (RT)	S *mP*48	7
	γ (RT)	S *hR*6	7
Sb (antimony)	α (RT)	As *hR*2	1
	Sb II (RT; 50–70 kbar)	Po *cP*1	1
	Sb III (RT; 90 kbar)	Mg *hP*2	1
Sc (scandium)	α (RT)	Mg *hP*2	1

Element	Phase[a]	Structure type	Ref[b]
	β (HT)	W *cI*2	1
Se (selenium)	α (RT)	Se(1) *mP*32	1
	β (RT)	Se(2) *mP*32	1
	γ (RT)	Se *hP*3	1
Si (silicon)	…	C *cF*8	1
	Si II (RT; 195 kbar)	Sn *tI*4	1
	Si III (110–160 kbar; retained when pressure removed)	Si *cI*16	1
Sm (samarium)	α (RT)	Sm *hR*3	1
	β (HT)	W *cI*2	7
	Sm II (300 °C, or 572 °F; 40 kbar)	La *hP*4	8
Sn (tin)	α (gray; LT)	C *cF*8	1
	β (white)	Sn *tI*4	1
	Sn II (314 °C, or 597 °F; 39 kbar)	Pa *tI*2	1
	Sn III (RT; 110 kbar)	Cubic (?)	1
Sr (strontium)	α (RT)	Cu *cF*4	7
	β (HT)	W *cI*2	7
	Sr II (RT; 35 kbar)	W *cI*2	1
Ta (tantalum)	…	W *cI*2	1
Tb (terbium)	α (RT)	Mg *hP*2	1
	β (HT)	W *cI*2	1
Tb (terbium)	γ (<220 K)	Tb *oC*4	1
	δ (60 kbar at RT)	Sm *hR*3	8
Tc (technetium)	…	Mg *hP*2	1, 8
Te (tellurium)	…	Se *hP*3	1
	Te II (>15 kbar)	As *hR*2(?)	1
	Te II (>70 kbar)	Hg *hR*1	8
Th (thorium)	α (RT)	Cu *cF*4	1
	β (HT)	W *cI*2	1
Ti (titanium)	α (RT)	Mg *hP*2	1
	β (HT)	W *cI*2	1
	Ti II (HP; retained when pressure removed)	Ti *hP*3 (ω phase)	1
Tl (thallium)	α (RT)	Mg *hP*2	1
	β (HT)	W *cI*2	1
	γ (HP: >40 kbar)	Cu *cF*4(?)	8
Tm (thulium)	α (RT)	Mg *hP*2	1
U (uranium)	α (RT)	U *oC*4	1
	β (HT: 720 °C, or 1328 °F)	CrFe *tP*30 (σ phase)	1
	γ (HT: 805 °C, or 1481 °F)	W *cI*2	1
V (vanadium)	…	W *cI*2	1
W (tungsten)	…	W *cI*2	1
Xe (xenon)	…	Cu *cF*4	7
Y (yttrium)	α (RT)	Mg *hP*2	7
	β (HT)	W *cI*2	7
Yb (ytterbium)	α (RT)	Cu *cF*4	7
	β (HT; also at RT and 40 kbar)	W *cI*2	7
	γ (LT: <270 K)	Mg *hP*2	8
Zn (zinc)	…	Mg *hP*2	1
	Zn II (HP: above about 40 kbar)	La *hP*4(?)	10, 11

Element	Phase[a]	Structure type	Ref [b]
Zr (zirconium)	α (RT)	Mg *hP*2	1
	β (HT)	W *cI*2	1
	Zr II (HP; retained when pressure removed)	Ti *hP*3	1

Note: 1 kbar = 100 MPa.

(a) RT, room temperature; HT, high temperature; LT, low temperature; HP, high pressure; phases formed under high-pressure conditions are designated by roman numerals—e.g., Ge II, Ge III.

(b) See also table of "Crystal Structures and Lattice Parameters of Allotropes of the Metallic Elements," in Volume 1, Ref 6.

The more complete tables, such as those in the *International Tables for Crystallography* (Ref 4), show clearly the number of equivalent points belonging to each set (the multiplicity of the set) and therefore the number of atoms that could be located at the equivalent points of each set in a crystal. To save space in tabulating all these sets of equivalent points in Ref 4, the coordinates of certain special points are given at the top of the list and these coordinates must be added to each of the coordinates listed below them.

As an example, for arsenic, *hR*2, in the cell based on hexagonal axes, the equivalent points are (0,0,0; $\frac{1}{3},\frac{2}{3},\frac{2}{3}$; $\frac{2}{3},\frac{1}{3},\frac{1}{3}$) with coordinates 0,0,*z*; 0,0,$\overline{z}$ to be added. The full list for the six atoms in the unit cell, obtained by addition of coordinates, is thus 0,0,*z*; $\frac{1}{3},\frac{2}{3},\frac{2}{3} + z$; $\frac{2}{3},\frac{1}{3},\frac{1}{3} + z$; 0,0,$\overline{z}$; $\frac{1}{3},\frac{2}{3},\frac{2}{3} - z$; $\frac{2}{3},\frac{1}{3},\frac{1}{3} - z$.

Effect of Alloy Composition. Structures are described by giving a prototype structure, as if they were compounds of unvarying stoichiometric composition; in general, composition can vary and unit cell edges vary in length somewhat without changing the type of structure. Interaxial angles other than 90° or 120° may also change slightly.

The special atom-coordinate values, such as 0, $\frac{1}{8}$, $\frac{1}{4}$, $\frac{1}{2}$, and $\frac{1}{3}$, often do not change, but *x*, *y*, and *z* values, which are variable, generally change with composition across a single-phase region of a phase diagram.

Disordered versus Ordered Superstructures. Solid solutions may have more than one kind of atom at a set of equivalent positions. In an alloy of A and B atoms, the probability of finding an A atom (or a B atom) at a given atomic position is a function of the alloy composition and, in simple alloys, is equal to the atomic percentage of A atoms (or B atoms) in the alloy. If occupation of the individual sites by A or B atoms is random, or nearly so, the solid solution is said to be disordered; if A atoms occupy one set of positions and B atoms the other set, the solution is said to be ordered. A solid solution is most likely to be disordered at high temperatures.

At lower temperatures, the tendency for A atoms to locate at some positions and B atoms at others may overcome the randomizing action of thermal agitation and produce partial or complete order. When this occurs, the unit cell may be larger than that for the disordered state (usually, with one, two, or all three edges doubling in length), the number of atoms per unit cell is proportionately larger, and the crystal is said to be an ordered superstructure or superlattice.

Alternatively, the ordering of atoms that have previously been randomly distributed in a solid solution may occur with a lowering of the crystal symmetry of the structure but without multiplication of the length of any of the unit-cell edges. An example of this is β brass, which has a disordered body-centered cubic structure (W *cI*2) at high temperatures and is designated β Cu-Zn but which on cooling acquires an ordered (CsCl *cP*2) structure designated β′ Cu-Zn, in which copper atoms are chiefly at positions 0,0,0, and zinc atoms are chiefly at positions $\frac{1}{2},\frac{1}{2},\frac{1}{2}$ or conversely.

Number of Atoms per Cell: Calculated Density. Calculation of the number of atoms in a unit cell requires inspecting the cell to determine those atoms that are shared by other unit cells, the number of cells that share each of these atoms, and those atoms that are entirely within the cell. The atoms at each of the eight corners of a unit cell are shared by the eight cells that share that corner and thus count as only one atom per cell ($\frac{1}{8} \times 8$). In a face-centered cell (such as that of Cu *cF*4), there is, in addition, an atom in each of the six faces; each of these atoms is shared by two cells, and therefore, an atom in a face counts as one half an atom per cell. With six faces, there are three ($\frac{1}{2} \times 6$) atoms per cell in the faces; therefore, a face-centered cell has a total of four atoms. In a body-centered cell (such as that of W *cI*2), there is one atom at the corners plus one atom in the center of the volume, totaling two atoms per body-centered cell. The calculated density, ρ, of a crystal is given by ρ =

$n\bar{A}/VN$, where n is the total number of atoms in the unit cell, $\bar{A}$ is their mean atomic weight (calculated with atomic percentages), V is the volume of the unit cell, and N is Avogadro's number (6.022×10^{23}).

Miller Indices for Planes and Direction. Miller indices used for designating planes within a crystal are based on the intercepts of the plane with the crystal axes. If the unit-cell edges are of lengths *a*, *b*, and *c* and if a plane intersects these edges at *a*/*h*, *b*/*k*, and *c*/*l*, the fractional intercepts are 1/*h*, 1/*k*, and 1/*l*. The reciprocals of these fractional intercepts, when reduced to the smallest common denominator, are the Miller indices of the plane. They are written in parentheses—for example, (*hkl*). A negative intercept is indicated using an overbar; for example, ($hk\bar{l}$) indicates a negative intercept along the *c* axis. Integers enclosed by braces designate all the equivalent nonparallel planes of a crystal; for example, the entire set of cube faces of a cubic crystal is designated {100}.

In Miller indices specifying directions in a crystal, the notation [*uvw*] is used to indicate the direction of a line from the origin to a point whose coordinates are *u*, *v*, and *w*. It is customary to use square brackets, to avoid fractional coordinates, and to use the smallest integers that will locate a point on the line. Negative indices are indicated using overbars. Because of symmetry, various directions in a crystal are equivalent. A full set of equivalent directions (directions of a form) is enclosed by carets, as in $\langle uvw \rangle$. For additional information, see Ref 18, Ref 19, Ref 20.

Miller-Bravais indices, instead of Miller indices, are used for hexagonal crystals. These crystals have three equal axes in the basal plane of the unit cell: a_1, a_2, and a_3. If the fractional intercepts on these three axes are 1/*h*, 1/*k*, and $1/\bar{\imath}$ and the intercept on the *c* axis is 1/*l*, the Miller-Bravais indices of the plane are ($hk\bar{\imath}l$).

Crystal Zone and Zone Axes. A crystal zone is that set of nonparallel faces that intersect each other in a series of parallel straight lines. Crystal faces belonging to a zone lie parallel to a line that is called the zone axis and that defines a specific direction in the crystal. A line passing through the lattice point defined as the origin (0,0,0) and through a neighboring lattice point whose coordinates are *u*, *v*, and *w* in terms of the axial lengths *a*, *b*, and *c*, respectively, defines the direction of the zone axis or line and is designated by the indices [*uvw*]. Two intersecting zone axes define a plane and thus a possible crystal face or face of a unit cell.

References cited in this section

1. W.B. Pearson, *A Handbook of Lattice Spacings and Structures of Metals and Alloys,* Pergamon Press, Vol 1, 1958; Vol 2, 1967

2. *Strukturbericht,* Akademische Verlagsgesellschaft m.b.H., Leipzig, Germany, 1913–1939; continued as *Structure Reports,* International Union of Crystallography, 1940 to the present

3. C.R. Hubbard and L.D. Calvert, *Bulletin of Alloy Phase Diagrams,* Vol 2, 1981, p 153–156

4. T. Hahn, Ed., *International Tables for Crystallography,* Vol A, International Union of Crystallography, D. Reidel Publishing, 1983

5. R.W.G. Wyckoff, *Crystal Structures,* Interscience, Vol 1, 1963; Vol 2, 1964; Vol 3, 1965

6. T.B. Massalski, Ed., *Binary Alloy Phase Diagrams,* 2nd. ed., ASM International, 1990, p T9

7. R. Hultgren et al., *Selected Values of the Thermodynamic Properties of the Elements.* American Society for Metals, 1973

8. J. Donohue, *The Structures of the Elements.* Wiley-Interscience, 1974

9. J.R. Peterson, J.A. Fahey, and R.D. Baybarz, *J. Inorg. Nucl. Chem.,* Vol 33, 1971, p 3345–3351

10. R.W. Lynch and H.G. Drickamer, *J. Phys. Chem. Solids,* Vol 26, 1965, p 63

11. E.A. Perez-Albuerne et al., *Phys. Rev.,* Vol 142, 1966, p 392

12. P.K. Smith, W.H. Hale, and M.C. Thompson, *J. Chem. Phys.,* Vol 50, 1969, p 5066–5076

13. L. Pauling et al., *J. Solid State Chem.,* Vol Z, 1970, p 225

14. A.F. Schach and R.L. Mills, *J. Chem. Phys.,* Vol 1 (No. 52), 1970, p 6000

16. P.G. Pallmer and T.D. Chikalla, *J. Less-Common Metals,* Vol 24, 1971, p 233–236

17. F. Weigel and A. Trinkl, *Radiochim Acta,* Vol 10, 1967, p 78–82

18. C.S. Barrett and T.B. Massalski, *Structure of Metals,* 3rd ed., Pergamon Press, 1980

19. A.G. Guy, *Elements of Physical Metallurgy,* Addison-Wesley, 1959

20. L.H. Van Vlack, *Elements of Materials Science,* Addison-Wesley, 1964

Crystal Structure, *Metallography and Microstructures,* Vol 9, *ASM Handbook,* ASM International, 2004, p. 29–43

Metallurgically Important Crystal Types

Table 4 gives the crystal structures of the elements. These are described by the Pearson symbols for crystal system (*c*, *h*, *o*, *t*, *m* or *a*), space lattice (*P*, *F*, *I*, *C* or *R*; see Table 2), and the total number of atoms per unit cell, and by the prototype structure.

Table 5 describes the crystal structures of selected phases of special interest to metallurgists. This table also uses Pearson symbols for crystal system, space lattice, and the total number of atoms per unit cell. The prototype formula name, as well as the space group, is given. The last column gives atom positions (for the simpler structures) in the prototype structure; interaxial angles are mentioned only when they differ from 90° (or 120° in hexagonal crystals). Several of the listed phases have the same prototype.

Table 5 Assorted structure types of metallurgical interest arranged according to Pearson symbol

Pearson symbol	Prototype	Space group	Unit-cell description[(a)]
***cP*1**	α-Po	*Pm*3*m*	One atom per cell, at 0,0,0. For α-Po, *a* = 3.34 Å. See Fig. 1. **Examples:** Ag-Te (metastable), Au-Te (metastable), α-Po, Sb II (high pressure)
***cP*2**	CsCl	*Pm*3*m*	One cesium atom at 0,0,0, and one chlorine atom at $\frac{1}{2},\frac{1}{2},\frac{1}{2}$. For CsCl, *a* = 4.11 Å. See Fig. 1. **Examples:** AgCd, CoTi, CsCl, FeAl, FeCo, FeTi, FeV, β NiAl, β NiGa, δ NiIn, NiTi, β′ Cu-Zn
***cP*4**	$AuCu_3$	*Pm*3*m*	One gold atom at 0,0,0; three copper atoms at $0,\frac{1}{2},\frac{1}{2}$; $\frac{1}{2},0,\frac{1}{2}$; and $\frac{1}{2},\frac{1}{2},0$. For $AuCu_3$, *a* = 3.74 Å. See Fig. 1. **Examples:** α′ $AlNi_3$, $AlZr_3$, Au_3Cu, $AuCu_3$, I, $CoPt_3$, Cr_3Pt, Fe_3Ga, $FePd_3$, Ni_3Fe, Ni_3Mn, Sn_3U
***cP*5**	$CaTiO_3$	*Pm*3*m*	Perovskite. One calcium atom at 0,0,0; one titanium atom at $\frac{1}{2},\frac{1}{2},\frac{1}{2}$; three oxygen atoms at $0,\frac{1}{2},\frac{1}{2}$; $\frac{1}{2},0,\frac{1}{2}$; and $\frac{1}{2},\frac{1}{2},0$. **Examples:** $AlCFe_3$, $AlCMn_3$, $AlCTi_3$, $CaTiO_3$, Fe_3C_xIn, Fe_3NNi, Fe_3NPd, Fe_3NSn

***cP*7**	B_6Ca	*Pm*3*m*	One calcium atom at 0,0,0; six boron atoms at $x,\frac{1}{2},\frac{1}{2}$; $\frac{1}{2},x,\frac{1}{2}$; $\frac{1}{2},\frac{1}{2},x$; $\overline{x},\frac{1}{2},\frac{1}{2}$; $\frac{1}{2},\overline{x},\frac{1}{2}$; $\frac{1}{2},\frac{1}{2},\overline{x}$ with x = 0.207. For B_6Ca, a = 4.15 Å. **Examples:** B_6Ba, B_6Gd, B_6Sc, B_6Th, B_6Yb
***cP*8**	FeSi	$P2_13$	Four iron atoms at x,x,x; $\frac{1}{2}+x,\frac{1}{2}-x,;\overline{x}$; $\overline{x},\frac{1}{2}+x,\frac{1}{2}-x$; and $\frac{1}{2}-x,\overline{x},\frac{1}{2}+x$ (with x = 0.137); four silicon atoms at x,x,x; $\frac{1}{2}+x,\frac{1}{2}-x,\overline{x}$; $\overline{x},\frac{1}{2}+x,\frac{1}{2}-x$; and $\frac{1}{2}-x,\overline{x}\ \frac{1}{2}+x$, (with x = 0.842). For FeSi a = 4.49 Å. **Examples:** CoSi, FeSi, MnSi
	W_3O or Cr_3Si	*Pm*3*n*	Atom I, two at 0,0,0; and $\frac{1}{2},\frac{1}{2},\frac{1}{2}$; atom II, six at $\frac{1}{4},0,\frac{1}{2}$; $\frac{1}{2},\frac{1}{4},0$; $0,\frac{1}{2},\frac{1}{4}$; $\frac{3}{4},0,\frac{1}{2}$; $\frac{1}{2},\frac{3}{4},0$; and $0,\frac{1}{2},\frac{3}{4}$. For W_3O, a = 5.04 Å. See Fig. 1. The prototype structure originally was attributed to β-W. This has since been shown to be the oxide, W_3O, having random distribution of atoms. **Examples:** AlV_3, $AuTi_3$, CoV_3, Cr_3O, Cr_3Si, Mo_3O, V_3Si, W_3O, W_3Si
***cP*12**	NiSSb	$P2_13$	For NiSSb, α = 5.88 Å. **Examples:** AsPdSe. BiPtTe, IrSbSe, RhSSb
	FeS_2	*Pa*3	Pyrite. Four iron atoms at 0,0,0; $0,\frac{1}{2},\frac{1}{2}$; $\frac{1}{2},0,\frac{1}{2}$; and $\frac{1}{2},\frac{1}{2},0$; eight sulfur atoms at x,x,x; $\frac{1}{2}+x,\frac{1}{2}-x,\overline{x}$; $\overline{x},\frac{1}{2}+x,\frac{1}{2}-x$; $\frac{1}{2}-x,\overline{x},\frac{1}{2}+x$; $\overline{x},\overline{x},\overline{x}$; $\frac{1}{2}-x,\frac{1}{2}+x,x$; $x,\frac{1}{2}-x,\frac{1}{2}+x$; and $\frac{1}{2}+x,x,\frac{1}{2}-x$. For FeS_2 (pyrite), x = 0.386 and a = 5.42 Å. **Examples:** CoPS, CoS_2, $CoSe_2$, FeS_2 (pyrite), MnS_2, $MnTe_2$, NiS_{2+x}, $NiSe_2$
***cP*20**	β-Mn	$P4_132$	For β-Mn, a = 6.13 Å. **Examples:** Ag_3Al, Au_9Nb_{11}, T C-Cr-Fe-W, γ Cu_3Si
***cP*36**	$BaHg_{11}$	*Pm*3*m*	For $BaHg_{11}$, a = 9.59 Å. **Examples:** $Cd_{11}Ce$, $Hg_{11}K$, $Hg_{11}Sr$
***cP*52**	Al_4Cu_9	$P\overline{4}3m$	γ brass. For Al_4Cu_9, a = 8.70 Å. **Example:** Ga_4Cu_9
***cF*4**	Cu	*Fm*3*m*	Four atoms at 0,0,0; $\frac{1}{2},0,\frac{1}{2}$; $0,\frac{1}{2},\frac{1}{2}$; and $\frac{1}{2},\frac{1}{2},0$. For Cu, a = 3.61 Å. See Fig. 1. **Examples:** Ag, Al, Au, α-Ca, α-Ce, β-Co, Cu, γ-Fe, Ir, Ni, Pb, Pd, Pt, Rh, α-Sr, α-Th
***cF*8**	ZnS	$F\overline{4}3m$	Sphalerite. Four zinc atoms at 0,0,0; $0,\frac{1}{2},\frac{1}{2}$; $\frac{1}{2},0,\frac{1}{2}$; and $\frac{1}{2},\frac{1}{2},0$; four sulfur atoms at $\frac{1}{4},\frac{1}{4},\frac{1}{4}$; $\frac{1}{4},\frac{3}{4},\frac{3}{4}$; $\frac{3}{4},\frac{1}{4},\frac{3}{4}$; and $\frac{3}{4},\frac{3}{4},\frac{1}{4}$. For ZnS (sphalerite), a = 5.42 Å. See Fig. 1. **Examples:** CdS, CdSe, CdTe, $CuFeS_2$ (high temperature), GaP, GaSb, InAs, InP, InSb, β MnS, β SiC, ZnO, ZnS (sphalerite), ZnSe
***cF*8**	NaCl, rocksalt	*Fm*3*m*	Four sodium atoms at 0,0,0; $0,\frac{1}{2},\frac{1}{2}$; $\frac{1}{2},0,\frac{1}{2}$; and $\frac{1}{2},\frac{1}{2},0$; four chlorine atoms at $\frac{1}{2},\frac{1}{2},\frac{1}{2}$; $\frac{1}{2},0,0$; $0,\frac{1}{2},0$; and $0,0,\frac{1}{2}$. For NaCl, a = 5.64 Å. See Fig. 1. **Examples:** BaS, CdO, CdS, CrN, HfC, HfN, NaCl, NiO (high temperature), PbS, PbSe, TiO, UC, UO, UP, US, VO, ZrO
	C	*Fd*3*m*	Diamond. Eight atoms per cell, at 0,0,0; $0,\frac{1}{2},\frac{1}{2}$; $\frac{1}{2},0,\frac{1}{2}$; $\frac{1}{2},\frac{1}{2},0$; $\frac{1}{4},\frac{1}{4},\frac{1}{4}$; $\frac{1}{4},\frac{3}{4},\frac{3}{4}$; $\frac{3}{4},\frac{1}{4},\frac{3}{4}$; and $\frac{3}{4},\frac{3}{4},\frac{1}{4}$. For C (diamond), a = 3.57 Å. See Fig. 1. **Examples:** C (diamond), Ge, Si, α-Sn
***cF*12**	AgAsMg	$F\overline{4}3m$	Ternary version of fluorite. For AgAsMg, a = 6.25 Å. **Examples:** AlBBe, CdCuSb, CuMnSb, NiSbV
	CaF_2	*Fm*3*m*	Fluorite. Four calcium atoms at 0,0,0; $0,\frac{1}{2},\frac{1}{2}$; $\frac{1}{2},0,\frac{1}{2}$; and $\frac{1}{2},\frac{1}{2},0$; eight fluorine atoms at $\frac{1}{4},\frac{1}{4},\frac{1}{4}$; $\frac{1}{4},\frac{3}{4},\frac{3}{4}$; $\frac{3}{4},\frac{1}{4},\frac{3}{4}$; $\frac{3}{4},\frac{3}{4},\frac{1}{4}$; $\frac{3}{4},\frac{3}{4},\frac{3}{4}$; $\frac{3}{4},\frac{1}{4},\frac{1}{4}$; $\frac{1}{4},\frac{3}{4},\frac{1}{4}$; and $\frac{1}{4},\frac{1}{4},\frac{3}{4}$. For CaF_2, a = 5.46 Å. See Fig. 1. **Examples:** Be_2B, Be_2C, CaF_2, $CoSi_2$, rare-earth hydrides, K_2O, K_2S, Mg_2Pb, Mg_2Si, ξ $NiSi_2$, UN_2, UO_2
***cF*16**	$AlCu_2Mn$	*Fm*3*m*	Heusler alloy. For $AlCu_2Mn$, a = 5.95 Å. **Examples:** $AgAuCd_2$,

			$AlNi_2Ta$, Co_2GaTi, CsK_2Sb
	BiF_3 or $BiLi_3$	*Fm*3*m*	Four bismuth atoms at 0,0,0; $0,\frac{1}{2},\frac{1}{2}$; $\frac{1}{2},0,\frac{1}{2}$; and $\frac{1}{2},\frac{1}{2},0$; 12 fluorine (or lithium) atoms at $\frac{1}{2},\frac{1}{2},\frac{1}{2}$; $\frac{1}{2},0,0$; $0,\frac{1}{2},0$; $0,0,\frac{1}{2}$; $\frac{1}{4},\frac{1}{4},\frac{1}{4}$; $\frac{1}{4},\frac{3}{4},\frac{3}{4}$; $\frac{3}{4},\frac{1}{4},\frac{3}{4}$; $\frac{3}{4},\frac{3}{4},\frac{1}{4}$; $\frac{3}{4},\frac{3}{4},\frac{3}{4}$; $\frac{3}{4},\frac{1}{4},\frac{1}{4}$; $\frac{1}{4},\frac{3}{4},\frac{1}{4}$; and $\frac{1}{4},\frac{1}{4},\frac{3}{4}$. For $BiLi_3$, *a* = 6.71 Å. See Fig. 1. **Examples:** BiF_3, $BiLi_3$, Fe_3Al, γ Cu_3Sn (high temperature), α Fe_3Si, Mn_3Si, Ni_3Sn (high temperature)
	NaTl	*Fd*3*m*	For NaTl, *a* = 7.49 Å. **Examples:** AlLi, CdLi, GaLi, InNa, LiZn
***cF*24**	$AuBe_5$	$F\bar{4}3m$ or *F*23	For $AuBe_5$, *a* = 6.1 Å. **Examples:** Au_5Ca, Be_5Pd, $HfNi_5$, Ni_5U
	Cu_2Mg	*Fd*3*m*	Eight magnesium atoms at 0,0,0; $0,\frac{1}{2},\frac{1}{2}$; $\frac{1}{2},0,\frac{1}{2}$; $\frac{1}{2},\frac{1}{2},0$; $\frac{1}{4},\frac{1}{4},\frac{1}{4}$; $\frac{1}{4},\frac{3}{4},\frac{3}{4}$; $\frac{3}{4},\frac{1}{4},\frac{3}{4}$; and $\frac{3}{4},\frac{3}{4},\frac{1}{4}$; 16 copper atoms at $\frac{5}{8},\frac{5}{8},\frac{5}{8}$; $\frac{5}{8},\frac{1}{8},\frac{1}{8}$; $\frac{1}{8},\frac{5}{8},\frac{1}{8}$; $\frac{1}{8},\frac{1}{8},\frac{5}{8}$; $\frac{5}{8},\frac{7}{8},\frac{7}{8}$; $\frac{5}{8},\frac{3}{8},\frac{3}{8}$; $\frac{1}{8},\frac{7}{8},\frac{3}{8}$; $\frac{1}{8},\frac{3}{8},\frac{7}{8}$; $\frac{7}{8},\frac{5}{8},\frac{7}{8}$; $\frac{7}{8},\frac{1}{8},\frac{3}{8}$; $\frac{3}{8},\frac{5}{8},\frac{3}{8}$; $\frac{3}{8},\frac{1}{8},\frac{7}{8}$; $\frac{7}{8},\frac{7}{8},\frac{5}{8}$; $\frac{7}{8},\frac{3}{8},\frac{1}{8}$; $\frac{3}{8},\frac{7}{8},\frac{1}{8}$; and $\frac{3}{8},\frac{3}{8},\frac{5}{8}$. For Cu_2Mg, *a* = 7.05 Å. **Examples:** Al_2Ca, Al_2U, CdCuZn, Co_2U, Co_2Zr, Cr_2Ti, Cu_2Mg, FeNiTa, Fe_2U, Fe_2Zr, MgNiZn, α $TiCo_2$, ZrW_2
***cF*52**	UB_{12}	*Fm*3*m*	For UB_{12}, *a* = 7.48 Å. **Examples:** DyB12, ScB_{12}, ZrB_{12}
***cF*56**	Al_2MgO_4	*Fd*3*m*	Spinel. **Examples:** Al_2CrS_4, Al_2MgO_4, Co_2NiS_4, Co_3O_4, Co_3S_4, CuS_4Ti_2, $FeNi_2S_4$, Fe_3O_4, Fe_3S_4 (greigite), Ni_3S_4 (low temperature)
***cF*112**	$NaZn_{13}$	*Fm*3*c*	For $NaZn_{13}$, *a* = 12.28 Å. **Examples:** $AmBe_{13}$, $Be_{13}Ho$, $Be_{13}Zr$, $Cd_{13}Cs$, KZn_{13}
	Fe_3W_3C	*Fd*3*m*	η-carbide. For Fe_3W_3C, *a* = 11.06 Å. **Examples:** $CoNb_2$ (C, N, O)$_x$, Co_2Mo_4C, Cr_3Nb_3C, η Fe_2Nb_3, Fe_3Mo_3C, Fe_3Mo_3N, Fe_3W_3C, Mn_3Mo_3C, Mo_3Ni_3C, $NiTi_2$, Ni_3W_3C
***cF*116**	$Cr_{23}C_6$	*Fm*3*m*	For $Cr_{23}C_6$, *a* = 10.66 Å. **Examples:** $Mn_{23}C_6$, $Fe_{21}Mo_2C_6$
	$Mn_{23}Th_6$ ($Cu_{16}Mg_6Si_7$)	*Fm*3*m*	For $Mn_{23}Th_6$, *a* = 12.52 Å. **Examples:** Dy_6Mn_{23}, $Mg_{23}Sr_6$, $Co_{16}Hf_6Si_7$, $Mn_6Ni_{16}Si_7$
***cI*2**	W	*Im*3*m*	Two atoms at 0,0,0 and $\frac{1}{2},\frac{1}{2},\frac{1}{2}$. For W, *a* = 3.16 Å. See Fig. 1 **Examples:** Ba, Nb, Cr, Cs, β Cu-Zn (high temperature), α-Fe, δ-Fe, K, β-Li, Mo, β-Na, Rb, Ta, V, W
Pearson symbol	Prototype	Space group	Unit-cell description[(a)]
***cI*26**	$Al_{12}W$	*Im*3	For $Al_{12}W$, *a* = 7.58 Å. **Examples:** $Al_{12}Mo$, $Al_{12}Re$, $Al_{12}Tc$
***cI*28**	P_4Th_3	$I\bar{4}3d$	For P_4Th_3, *a* = 8.62 Å. **Examples:** As_4Th_3, $BaLa_2S_4$, Bi_4U_3, Gd_2Se_4Sr, Se_4U_3
***cI*32**	As_3Co	*Im*3	For As_3Co, *a* = 8.20 Å. **Examples:** As_3Ir, $CoSb_3$, IrP_3, $RhSb_3$
***cI*40**	C_3Pu_2	$I\bar{4}3d$	For C_3Pu_2, *a* = 8.13 Å. **Examples:** C_3Ce_2, C_3Pr_2, C_3U_2
***cI*52**	Cu_5Zn_8	$I\bar{4}3m$	γ brass. For Cu_5Zn_8, *a* = 8.86 Å. **Examples:** Ag_5Cd_8, Ag_5Zn_8, Al_8V_5, Cd_8Cu_5
***cI*58**	α-Mn	$I\bar{4}3m$	α-Mn appears to be an ordered array of two or three physically distinguishable types of manganese atoms located on four crystallographically different sets of positions, which have an ordered array of atoms in the chi-phase structure ($Fe_{36}Cr_{12}Mo_{12}$ and $Al_{12}Mg_{17}$). For α-Mn, *a* = 8.91 Å. Other closely related structures are the μ-, *P*-, *R*-, and δ-phases (see Ref 5, Ref 17, Ref 18). **Examples:** γ $Al_{12}Mg_{17}$, χ $Co_5Cr_3Si_2$, $CrMn_2$, $Fe_{36}Cr_{12}Mo_{12}$, $Fe_5Si_2V_3$, α-Mn
***cI*80**	β Mn_2O_3	*Ia*3	Type C. For Mn_2O_3, *a* = 9.41 Å. **Examples:** Am_2O_3, Be_3P_2, Cd_3N_2, N_2Zn_3, O_3Y_2
***hP*2**	WC	$P\bar{6}m2$	One tungsten atom at 0,0,0; one carbon atom at $\frac{1}{3},\frac{2}{3},\frac{1}{2}$ or at $\frac{2}{3},\frac{1}{3},\frac{1}{2}$. For WC, *a* = 2.91 Å and *c* = 2.84 Å. **Examples:** γ MoC, TiS, WC, WN, Zr_3S_2

	Mg	$P6_3/mmc$	Hexagonal close-packed. Atoms at $\frac{1}{3},\frac{2}{3},\frac{1}{4}$; $\frac{2}{3},\frac{1}{3},\frac{3}{4}$. These are the positions of the In atoms of the Ni_2In structure shown in Fig. 1 For Mg, a = 3.21 Å, c = 5.20 Å. **Examples:** α-Be, Cd, α-Co, Mg, α-Ti, Zn, α-Zr
***hP*3**	CdI_2	$P\bar{3}m1$	One cadmium atom at 0,0,0; two iodine atoms at $\frac{1}{3},\frac{2}{3},z$; $\frac{2}{3},\frac{1}{3},\bar{z}$, with $z = \frac{1}{4}$. For SnS_2, a = 3.65 Å, c = 5.88 Å. **Examples:** HfS_2, $PdTe_2$, S_2Ta, Se_2V, Te_2Zr
	Fe_2N or W_2C	$P6_3/mmc$	Two iron atoms at $\frac{1}{3},\frac{2}{3},\frac{1}{4}$ and $\frac{2}{3},\frac{1}{3},\frac{3}{4}$; one nitrogen atom at 0,0,0 or 0,0,$\frac{1}{2}$. See Fig. 1 **Examples:** Fe_2N, ζ Mn_2N, β Ta_2C, $Ta_{\sim 2}N$, V_2C, W_2C
	Se	$P3_121$ or $P3_221$	Three atoms at x,0,$\frac{1}{3}$; 0,x,$\frac{2}{3}$; and $\bar{x},\bar{x}$,0 (or at x,0,$\frac{2}{3}$; 0,x,$\frac{1}{3}$; and $\bar{x},\bar{x}$,0). For Se, a = 4.36 Å, c = 4.96 Å and x = 0.217. **Examples:** γ-Se
	AlB_2	$P6/mmm$	One aluminum atom at 0,0,0; two boron atoms at $\frac{1}{3},\frac{2}{3},\frac{1}{2}$; $\frac{2}{3},\frac{1}{3},\frac{1}{2}$. For AlB_2, a = 3.01 Å, c = 3.25 Å. **Examples:** Al_2Th, B_2Lu, B_2Mg, Ga_2Ho, Hg_2U, $PuZr_2$
***hP*4**	AsNi	$P6_3/mmc$	Two nickel atoms at 0,0,0 and 0,0,$\frac{1}{2}$; two arsenic atoms at $\frac{1}{3},\frac{2}{3},\frac{1}{4}$ and $\frac{2}{3},\frac{1}{3},\frac{3}{4}$. For AsNi, a = 3.62 Å, c = 5.03 Å. **Examples:** CoSb, CoSe, CoTe, CrH, CrSe, α″ FeS, MnSb, NiAs, NiSb, NiTe, TiS, VS, VSb
	C	$P6_3/mmc$	Graphite. Two carbon(1) atoms at 0,0,$\frac{1}{4}$; 0,0,$\frac{3}{4}$. Two carbon(2) atoms at $\frac{2}{3},\frac{1}{3},\frac{1}{4}$; $\frac{1}{3},\frac{2}{3},\frac{3}{4}$. For hexagonal graphite, a = 2.46 Å, c = 6.71 Å. See Fig. 1
	La	$P6_3mmc$	Two lanthanum(1) atoms at 0,0,0; 0,0,$\frac{1}{2}$; two lanthanum(2) at $\frac{1}{3},\frac{2}{3},\frac{1}{4}$; $\frac{2}{3},\frac{1}{3},\frac{3}{4}$. For La, a = 3.77 Å, c = 12.16 Å. **Examples:** Am, α-Nd, α-Pr, α-Pm
***hP*4**	ZnS	$P6_3mc$	Würtzite. Two zinc atoms at $\frac{1}{3},\frac{2}{3},z$ and $\frac{2}{3},\frac{1}{3},\frac{1}{2}+z$ (with z = 0); two sulfur atoms at $\frac{1}{3},\frac{2}{3},z$ and $\frac{2}{3},\frac{1}{3},\frac{1}{2}+z$ (with z = 0.371). For ZnS (würtzite), a = 3.82 Å and c = 6.26 Å. See Fig. 1 **Examples:** AlN, BeO, CdS, CdSe, CuH, InN, InSb, γ MnS, ZnO, ZnS (würtzite), ZnSe
***hP*5**	Al_3Ni_2	$P\bar{3}m1$	One aluminum(1) atom at 0,0,0; two aluminum(2) at $\frac{1}{3},\frac{2}{3},z$; $\frac{2}{3},\frac{1}{3},z$; with z = 0.648. Two nickel atoms as Al(2) with z = 0.149. For Al_3Ni_2, a = 4.04 Å, c = 4.90 Å. **Examples:** Al_3Pd_2, Al_3Ru_2, Ga_3Ni_2, In_3Pt_2
	La_2O_3	$P\bar{3}m1$	Type A. One oxygen(1) atom at 0,0,0; two oxygen(2) atoms at positions of Al(2) in Al_3Ni_2 *hP*5, with z = 0.63, La similarly with z = 0.235. For La_2O_3, a = 3.94 Å, c = 6.13 Å. **Examples:** Ce_2O_3, N_3Th_2, N_3U_2, O_3Pu_2
***hP*6**	$CaCu_5$	$P6/mmm$	One calcium atom at 0,0,0; two copper(1) atoms at $\frac{1}{3},\frac{2}{3},0$; $\frac{2}{3},\frac{1}{3},0$; three copper(2) at $\frac{1}{2},0,\frac{1}{2}$; $0,\frac{1}{2},\frac{1}{2}$; $\frac{1}{2},\frac{1}{2},\frac{1}{2}$. For $CaCu_5$, a = 5.1 Å, c = 4.1 Å. **Examples:** Ag_5Ba, Be_5Sc, $CeNi_5$, Cu_5Y, $LaNi_5$, Pt_5Sr
	CoSn	$P6/mmm$	For CoSn, a = 5.28 Å, c = 4.26 Å. **Examples:** FeGe, FeSn, InNi, PtTl
	$CaIn_2$	$P6_3/mmc$	Two calcium atoms at 0,0,$\frac{1}{4}$; 0,0,$\frac{3}{4}$; four indium atoms at $\frac{1}{3},\frac{2}{3},z$; $\frac{2}{3},\frac{1}{3},\frac{1}{2}+z$; $\frac{2}{3},\frac{1}{3},\bar{z}$; $\frac{1}{3},\frac{2}{3},\frac{1}{2}-z$; with z = 0.455. For $CaIn_2$, a = 4.90 Å, c = 7.75 Å. **Examples:** $EuIn_2$, Ga_2Y, In_2Sr, $SrTl_2$
	$InNi_2$	$P6_3/mmc$	Two nickel atoms at 0,0,0 and 0,0,$\frac{1}{2}$; two nickel atoms at $\frac{1}{3},\frac{2}{3},\frac{3}{4}$ and $\frac{2}{3},\frac{1}{3},\frac{1}{4}$; two indium atoms at $\frac{1}{3},\frac{2}{3},\frac{1}{4}$ and $\frac{2}{3},\frac{1}{3},\frac{3}{4}$. For $InNi_2$, a = 4.18 Å and c = 5.13 Å. See Fig. 1 **Examples:** $AlZr_2$, CoNiSn, Cu_2In, In_2Bi, Ni_2In, $Ni_{1.4}Sn$, Ti_2Sn
***hP*8**	*H*-$AlCCr_2$	$P6_3/mmc$	Two aluminum atoms at $\frac{1}{3},\frac{2}{3},\frac{3}{4}$; $\frac{2}{3},\frac{1}{3},\frac{1}{4}$; two carbon atoms at 0,0,0; 0,0,$\frac{1}{2}$; four chromium atoms at $\frac{1}{3},\frac{2}{3},\bar{z}$; $\frac{2}{3},\frac{1}{3},\bar{z}$; $\frac{2}{3},\frac{1}{3},\frac{1}{2}+z$; $\frac{1}{3},\frac{2}{3},\frac{1}{2}-z$; with z = 0.086.

			For $AlCCr_2$, a = 2.86 Å, c = 12.82 Å. **Examples:** $AlCNb_2$, $CCdTi_2$, $CGeV_2$, $InNTi_2$
	$AsNa_3$	$P6_3/mmc$	For $AsNa_3$, a = 8.8 Å, c = 9.0 Å. **Examples:** $AuMg_3$, K_3P, Li_3Sb, Mg_3Pt
***hP*8**	Ni_3Sn	$P6_3/mmc$	Two tin atoms at $\frac{1}{3},\frac{2}{3},\frac{1}{4}$ and $\frac{2}{3},\frac{1}{3},\frac{3}{4}$; six nickel atoms at $x,2x,\frac{1}{4}$; $2\bar{x},\bar{x},\frac{1}{4}$; $x,\bar{x},\frac{1}{4}$; $\bar{x},2\bar{x},\frac{3}{4}$; $2x,x,\frac{3}{4}$; and $\bar{x},x,\frac{3}{4}$ (with x = 0.833). For Ni_3Sn, a = 5.29 Å and c = 4.24 Å. See Fig. 1 **Examples:** $AlTi_{2–3}$, Cd_3Mg, $CdMg_3$, Co_3Mo, Co_3W, β″ Fe_3Sn, γ Ni_3In, Ni_3Sn, Ti_4Pb
***hP*9**	Fe_2P	$P\bar{6}2m$	Three iron atoms at x,0,0; 0,x,0 and $\bar{x},\bar{x},0$ (with x = 0.256); three iron atoms at $x,0,\frac{1}{2}$; $0,x,\frac{1}{2}$; and $\bar{x},\bar{x},\frac{1}{2}$ (with x = 0.594); three phosphorus atoms at $0,0,\frac{1}{2}$; $\frac{1}{3},\frac{2}{3},0$; and $\frac{2}{3},\frac{1}{3},0$. For Fe_2P, a = 5.93 Å and c = 3.45 Å. See Fig. 1 **Examples:** Fe_2P, Mn_2P, Ni_2P, Pt_2Si (high temperature)
***hP*12**	$MgZn_2$	$P6_3/mmc$	Four magnesium atoms at $\frac{1}{3},\frac{2}{3},z$; $\frac{2}{3},\frac{1}{3},\bar{z}$; $\frac{2}{3},\frac{1}{3},\frac{1}{2}+z$; and $\frac{1}{3},\frac{2}{3},\frac{1}{2}-z$ (with z = 0.062); two zinc atoms at 0,0,0 and $0,0,\frac{1}{2}$; six zinc atoms at $x,2x,\frac{1}{4}$; $2\bar{x},\bar{x},\frac{1}{4}$; $x,x,\frac{1}{4}$; $\bar{x},2\bar{x},\frac{3}{4}$; $2x,x,\frac{3}{4}$; and $\bar{x},x,\frac{3}{4}$ (with x = 0.83). For $MgZn_2$, a = 5.18 Å and c = 8.52 Å. See Fig. 1 **Examples:** Al_2Zr, Be_2Mo, $CaCd_2$, $CaMg_2$, $CdCu_2$, Fe_2Mo, FeSiW, Fe_2Ta, Fe_2Ti, Fe_2W, $MgZn_2$, $TiZn_2$
Pearson symbol	Prototype	Space group	Unit-cell description[(a)]
***hP*16**	Mn_5Si_3	$P6_3/mcm$	For Mn_5Si_3, a = 6.91 Å, c = 4.81 Å. **Examples:** Al_3Zr_5, Dy_5Ge_3, Ga_3Y_5, P_3Ti_5, Sn_3Zr_5
	Ni_3Ti	$P6_3/mmc$	Four titanium atoms at 0,0,0; $0,0,\frac{1}{2}$; $\frac{1}{3},\frac{2}{3},\frac{1}{4}$; and $\frac{2}{3},\frac{1}{3},\frac{3}{4}$; 12 nickel atoms at $\frac{1}{2},0,0$; $0,\frac{1}{2},0$; $\frac{1}{2},\frac{1}{2},0$; $\frac{1}{2},0,\frac{1}{2}$; $0,\frac{1}{2},\frac{1}{2}$; $\frac{1}{2},\frac{1}{2},\frac{1}{2}$; $x,2x,\frac{1}{4}$; $2\bar{x},\bar{x},\frac{1}{4}$; $\bar{x},\bar{x},\frac{1}{4}$; $\bar{x},2\bar{x},\frac{3}{4}$; $2x,x,\frac{3}{4}$; and $\bar{x},x,\frac{3}{4}$ (with x = 0.833). For Ni_3Ti, a = 2.55 Å and c = 8.31 Å. **Examples:** Co_3Ti, Ni_3Ti, Pd_3Zr
***hP*20**	Fe_3Th_7	$P6_3/mc$	For Fe_3Th_7, a = 9.85 Å, c = 6.15 Å. **Examples:** B_3Re_7, C_3Fe_7, Co_3Th_7, Ru_3Th_7
***hP*24**	HoH_3	$P\bar{3}c1$	For HoH_3, a = 6.31 Å, c = 6.56 Å. **Examples:** DyH_3, LuH_3, YH_3
	$MgNi_2$	$P6_3/mmc$	For $MgNi_2$, a = 4.82 Å, c = 15.80 Å. **Examples:** $CdCu_2$, Cr_2Hf, Fe_2Sc, $NbZn_2$
***hR*1**	Hg	$R\bar{3}m$	One atom per cell, at 0,0,0. For Hg, a = 3.005 Å and α = 70° 32′. A hexagonal cell, where a = 3.47 Å and c = 6.74 Å, has three atoms per cell, at 0,0,0; $\frac{1}{3},\frac{2}{3},\frac{2}{3}$; and $\frac{2}{3},\frac{1}{3},\frac{1}{3}$. **Example:** Hg
***hR*2**	As	$R\bar{3}m$	In the cell based on hexagonal axes, there are six atoms, at 0,0,z; $\frac{1}{3},\frac{2}{3},\frac{2}{3}+z$; $\frac{2}{3},\frac{1}{3},\frac{1}{3}+z$; 0,0,$\bar{z}$; $\frac{1}{3},\frac{2}{3},\frac{2}{3}-z$; and $\frac{2}{3},\frac{1}{3},\frac{1}{3}-z$; where z = 0.226, a = 3.76 Å and c = 10.55 Å for α-As. The cell based on rhombohedral axes contains two atoms, at x,x,x and $\bar{x},\bar{x},\bar{x}$; where x = 0.276, a = 4.13 Å and α = 54° 8′ for α-As. **Examples:** α-As, Bi, Sb
***hR*3**	Sm	$R\bar{3}m$	In a cell based on a hexagonal axis, there are nine atoms per cell, at 0,0,0; $\frac{1}{3},\frac{2}{3},\frac{2}{3}$; $\frac{2}{3},\frac{1}{3},\frac{1}{3}$; 0,0,$z$; 0,0,$\bar{z}$; $\frac{1}{3},\frac{2}{3},\frac{2}{3}+z$; $\frac{1}{3},\frac{2}{3},\frac{2}{3}-z$; $\frac{2}{3},\frac{1}{3},\frac{1}{3}+z$; and $\frac{2}{3},\frac{1}{3},\frac{1}{3}-z$. For α-Sm, a = 3.621 Å, c = 26.25 Å and $z=\frac{2}{9}$. The cell based on rhombohedral axes contains three atoms per cell, at 0,0,0; x,x,x; and $\bar{x},\bar{x},\bar{x}$; with a = 9.00 Å, α = 23° 19′ and $x=\frac{2}{9}$. **Examples:** α-Sm, Ce-Y, δ Nd-Tm, δ Pr-Y
***hR*5**	Bi_2STe_2	$R\bar{3}m$	One sulfur atom at 0,0,0; two bismuth atoms at x,x,x; $\bar{x},\bar{x},\bar{x}$ with x = 0.392. Tellurium atoms similarly with x = 0.788. For Bi_2STe_2, a = 10.33 Å, α = 24° 10′. **Examples:** Bi_2Se_3 Bi_2SeTe_2, Sb_2Te_3

***hR*10**	α Al_2O_3	$R\bar{3}c$	Ten atoms per unit rhombohedral cell or 30 atoms per unit hexagonal cell. There are also other structures of Al_2O_3 (alumina). **Examples:** α Al_2O_3, α Fe_2O_3, Rh_2O_3, Ti_2O_3, V_2O_3 (high temperature)
***hR*13**	Fe_7W_6	$R\bar{3}m$	μ-phase. For Fe_7W_6, a = 9.04 Å, α = 30° 30′. **Examples:** Co_7Mo_6, Fe_7Mo_6, $(Fe,Si)_7Re_6$
***hR*19**	Th_2Zn_{17}	$R\bar{3}m$	For Th_2Zn_{17} in the hexagonal cell containing 57 atoms, a = 9.03 Å, c = 13.20 Å. **Examples:** Ba_2Mg_{17}, Ce_2Fe_{17}, U_2Zn_{17}
***hR*26**	Al_8Cr_5	*R*3*m*	Rhombohedrally distorted γ brass: **Examples:** Fe-Ga, Ga-Mn
***hR*53**	*R* Co-Cr-Mo	$R\bar{3}$	*R*-phase. For *R* Co-Cr-Mo, a = 9.01 Å, α = 74° 27′. See α-Mn *cI*58 type, above; and Ref 17, Ref 18, Ref 19. **Examples:** *R*-(Co-Cr-Mo), $Co_3Cr_3Si_2$, *R*-(Co-Mn-,Mo), *R*-$Fe_{52}Mn_{16}Mo_{32}$, Fe_2SiV_2, $Mn_{78}Mo_3Si_{19}$, Mn_6Si, Ni_3SrV_6
***tP*4 (*tP*2)**	AuCu	*P*4/*mmm*	Two gold atoms at 0,0,0 and $\frac{1}{2},\frac{1}{2},0$; two copper atoms at $0,\frac{1}{2},\frac{1}{2}$ and $\frac{1}{2},0,\frac{1}{2}$. For AuCu, a = 3.97 Å, c = 3.67 Å. A smaller cell can also be taken with $a/\sqrt{2}$ and Au and Cu atoms at 0,0,0 and $\frac{1}{2},\frac{1}{2},\frac{1}{2}$, respectively. See Fig. 1 **Examples:** AgTi, AlTi, AuCu I, θ CdPt, FePd, γ″ FePt, θ MnNi, NiPt
	$CuTi_3$	*P*4/*mmm*	One copper atom at 0,0,0; one titanium(1) atom at $\frac{1}{2},\frac{1}{2},0$; two titanium(2) atoms at $0,\frac{1}{2},\frac{1}{2}$; $\frac{1}{2},0,\frac{1}{2}$. For $CuTi_3$, a = 4.16 Å, c = 3.59 Å. **Examples:** $AgZr_3$, $BaBi_3$, $DyIn_3$, Pc_3T1
	γ CuTi	*P*4/*nmm*	Two copper atoms at $0,\frac{1}{2},z$ and $\frac{1}{2},0,\bar{z}$ (with z = 0.10); two titanium atoms at $0,\frac{1}{2},z$ and $\frac{1}{2},0,\bar{z}$ (with z = 0.65). For γ CuTi, a = 3.12 Å and c = 5.92 Å. See Fig. 1 **Examples:** AgZr, AuTi (low temperature), γ CuTi
	PbO	*P*4/*nmm*	Two oxygen atoms at 0,0,0 and $\frac{1}{2},\frac{1}{2},0$; two lead atoms at $0,\frac{1}{2},z$ and $\frac{1}{2},0,\bar{z}$ (with z = 0.237). For PbO, a = 3.97 Å, c = 5.02 Å. See Fig. 1 **Examples:** FeS, β $FeTe_{0.9}$, PbO, SnO
***tP*6**	Cu_2Sb (GeSeZr)	*P*4/*nmm*	Two copper atoms at 0,0,0; $\frac{1}{2},\frac{1}{2},0$; two at $0,\frac{1}{2},z$ and $\frac{1}{2},0,\bar{z}$ (with z = 0.27); two antimony atoms at $0,\frac{1}{2},z$ and $\frac{1}{2},0,\bar{z}$ (with z = 0.70). Thus, ordered ternary phases also take the structure. For Cu_2Sb, a = 3.99 Å and c = 6.09 Å. See Fig. 1 **Examples:** $AlNaSi_4$, $AsCr_2$, $AsMn_2$, Bi_2U, Cu_2Sb, Mn_2Sb, Pu_2U, Sb_2U
	TiO_2	*P*4$_2$/*mnm*	Rutile. Two titanium atoms at 0,0,0 and $\frac{1}{2},\frac{1}{2},\frac{1}{2}$; four oxygen atoms at $x,x,0$; $\bar{x},\bar{x},0$; $\frac{1}{2}+x,\frac{1}{2}-x,\frac{1}{2}$; and $\frac{1}{2}-x,\frac{1}{2}+x,\frac{1}{2}$. For TiO_2, x = 0.3056, a = 4.59 Å and c = 2.96 Å. See Fig. 1 **Examples:** CrO_2, β MnO_2, PbO_2, SnO_2, TaO_2, TeO_2, TiO_2 (rutile), VO_2 (high temperature), WO_2
***tP*10**	Si_2U_3	*P*4/*mbm*	For Si_2U_3, a = 7.33 Å, c = 3.90 Å. **Examples:** Al_2Th_3, B_2V_3, Be_2Ta_3, Ga_2Ta_3, Si_2Zr_3
***tP*16**	$CoGa_3$	$P\bar{4}n2$	For $CoGa_3$, a = 6.26 Å, c = 6.48 Å. **Examples:** $FeGa_3$, Ga_3Os, In_3Ir, In_3Rh
***tP*20**	B_4Th	*P*4/*mbm*	For B_4Th, a = 7.26 Å, c = 4.11 Å. **Examples:** B_4Ce, B_4Ho, B_4Pu, B_4U, B_4Y
***tP*30**	CrFe (α-phase)	*P*4$_2$/*mnm*	This is a complex structure formed by transition-metal alloys in which the metal atoms occupy five independent site-sets. For CrFe, a = 8.80 Å, c = 4.54 Å. **Examples:** $AlNb_2$, CoCr, Co_2Mo_3, Cr_2Os, Cr_2Ru, FeMo, FeV, $MoTc_3$, Ni_2V_3, Re_3Ta_2
***tI*2**	In	*I*4/*mmm*	Two atoms per cell, at 0,0,0 and $\frac{1}{2},\frac{1}{2},\frac{1}{2}$. It is conventional also to use the cell that has four atoms, at 0,0,0; $0,\frac{1}{2},\frac{1}{2}$; $\frac{1}{2},0,\frac{1}{2}$; and $\frac{1}{2},\frac{1}{2},0$. For In, $a = b$ = 4.60 Å and c = 4.95 Å. At room temperature, the unit cell resembles that of Cu, which is shown in Fig. 1 **Examples:** δ $GaNi_2$, In, $InPd_3$
	Pa	*I*4/*mmm*	Atom positions as for In *tI*2, but $c/a < 1$. For Pa, a = 3.93 Å, c = 3.24 Å

tI*4-*x	Fe-C	*I*4/*mmm*	Martensite. In the unit cell there are iron atoms at 0,0,0 and $\frac{1}{2},\frac{1}{2},\frac{1}{2}$; the carbon atoms are random, at $\frac{1}{2},\frac{1}{2}$,0 and/or 0,0,$\frac{1}{2}$, to provide two iron atoms and up to 0.12 carbon atoms per cell. **Examples:** Fe-C martensite, α′ Fe-N martensite
Pearson symbol	Prototype	Space group	Unit-cell description[(a)]
***tI*4**	Sn	$I4_1/amd$	White Sn. Four atoms per cell, at 0,0,0; $\frac{1}{2},\frac{1}{2},\frac{1}{2}$; 0,$\frac{1}{2},\frac{1}{4}$; and $\frac{1}{2}$,0,$\frac{3}{4}$. For β-Sn, *a* = 5.83 Å and *c* = 3.18 Å. See Fig. 1 **Examples:** AlSb II (high pressure). InSb II (high pressure), β-Sn (white)
***tI*6**	CaC_2	*I*4/*mmm*	Two calcium atoms at 0,0,0; $\frac{1}{2},\frac{1}{2},\frac{1}{2}$. Four carbon atoms at 0,0,*z*; 0,0,$\overline{z}$; $\frac{1}{2},\frac{1}{2}$ + *z*; $\frac{1}{2},\frac{1}{2},\frac{1}{2}$ − *z* with *z* = 0.407, form dumbbells along [001]. For CaC_2, *a* = 3.88 Å, *c* = 6.37 Å. **Examples:** BaC_2, ErC_2, NDC_2, UC_2, SrO_2
	$MoSi_2$	*I*4/*mmm*	Two molybdenum atoms at 0,0,0 and $\frac{1}{2},\frac{1}{2},\frac{1}{2}$; four silicon atoms at 0,0,*z*; 0,0,$\overline{z}$; $\frac{1}{2},\frac{1}{2},\frac{1}{2}$ + *z*; and $\frac{1}{2},\frac{1}{2},\frac{1}{2}$ − *z* (with *z* = 0.333). For $MoSi_2$, *a* = 3.20 Å and *c* = 7.85 Å. See Fig. 1 **Examples:** $AgZr_2$, $AlCr_2$, Au_2Be, Au_2Mn, $CuTi_2$, Hg_2Mg, $MoSi_2$, Ni_2Ta, Si_2W
***tI*8**	Al_3Ti	*I*4/*mmm*	Two titanium atoms at 0,0,0; $\frac{1}{2},\frac{1}{2},\frac{1}{2}$. Two aluminum(1) atoms at 0,0,$\frac{1}{2}$; $\frac{1}{2}$,$\frac{1}{2}$,0. Four aluminum(2) atoms at 0,$\frac{1}{2},\frac{1}{4}$; $\frac{1}{2}$,0,$\frac{1}{4}$; $\frac{1}{2}$,0,$\frac{3}{4}$; 0,$\frac{1}{2},\frac{3}{4}$. For Al_3Ti, *a* = 3.85 Å, *c* = 8.60 Å. **Examples:** Al_3Nb, Ga_3Ti, Ni_3Ta, Pd_3V, Pt_3V
***tI*10**	$MoNi_4$	*I*4/*m*	For $MoNi_4$, *a* = 5.73 Å, *c* = 3.57 Å. **Examples:** Au_4Cr, Au_4Ti, Ni_4W
***tI*10**	Al_4Ba (Cu_2Si_2Th)	*I*4/*mmm*	Two barium atoms at 0,0,0; $\frac{1}{2},\frac{1}{2},\frac{1}{2}$. Four aluminum(1) atoms at 0,$\frac{1}{2},\frac{1}{4}$; $\frac{1}{2}$,0,$\frac{1}{4}$; $\frac{1}{2}$,0,$\frac{3}{4}$; 0,$\frac{1}{2},\frac{3}{4}$. Four aluminum(2) atoms at 0,0,*z*; 0,0,$\overline{z}$; $\frac{1}{2},\frac{1}{2},\frac{1}{2}$ + *z*; $\frac{1}{2}$,$\frac{1}{2}$,$\frac{1}{2}$ − *z*, with *z* = 0.380. The three atom sites allow the formation of ordered ternary phases. For Al_4Ba, *a* = 4.57 Å, *c* = 11.25 Å. **Examples:** $BaGa_4$, $ThZn_4$, B_2Co_2Nd, Au_2GdSi_2. N.B. There are more recognized phases with this structure type than with any other structure of metallurgical interest.
***tI*12**	Al_2Cu	*I*4/*mcm*	Four copper atoms at 0,0,$\frac{1}{4}$; $\frac{1}{2},\frac{1}{2},\frac{3}{4}$; 0,0,$\frac{3}{4}$; and $\frac{1}{2},\frac{1}{2},\frac{1}{4}$; eight aluminum atoms at *x*,$\frac{1}{2}$ + *x*,0; $\overline{x}$,$\frac{1}{2}$ − *x*,0; $\frac{1}{2}$+ *x*,$\overline{x}$,0; $\frac{1}{2}$− *x*,*x*,0; $\frac{1}{2}$+ *x*,*x*,$\frac{1}{2}$; $\frac{1}{2}$− *x*,$\overline{x}$,$\frac{1}{2}$; *x*,$\frac{1}{2}$ − *x*,$\frac{1}{2}$; and $\overline{x}$,$\frac{1}{2}$ + *x*,$\frac{1}{2}$ (with *x* = 0.158). For Al_2Cu, *a* = 6.07 Å and *c* = 4.87 Å. **Examples:** Co_2B, Cr_2B, θ $CuAl_2$, Fe_2B, $FeSn_2$, Mo_2B, Ni_2B, W_2B
	Si_2Th	$I4_1/amd$	For Si_2Th, *a* = 4.14 Å, *c* = 14.38 Å. **Examples:** $CeGe_2$, $DySi_{1.4}$, Ga_2Th, $LaSi_2$
***tI*16**	$CuFeS_2$	$I\bar{4}2d$	Chalcopyrite. For $CuFeS_2$, *a* = 5.25 Å, *c* = 10.32 Å. **Examples:** $AgAlS_2$, $AlCuSe_2$, GeP_2Zn, CuS_2Tl
	Al_3Zr	*I*4/*mmm*	For Al_3Zr, *a* = 4.01 Å, *c* = 17.32 Å. **Examples:** Al_3Hf, Ga_3Zr
	SiU_3	*I*4/*mcm*	For SiU_3, *a* = 6.03Å, = 8.70 Å. **Examples:** Ir_3Si, Pt_3Si
	SeTl	*I*4/*mcm*	For SeTl, *a* = 8.04 Å, *c* = 7.01 Å. **Examples:** InTe, STl
***tI*18**	Te_4Ti_5	*I*4/*m*	For Te_4Ti_5, *a* = 10.16 Å, *c* = 3.77 Å. **Examples:** Nb_5Sb_4, Nb_5Te_4, Sb_4Ta_5
***tI*26**	$Mn_{12}Th$	*I*4/*mmm*	For $Mn_{12}Th$, *a* = 8.74 Å, *c* = 4.95 Å. **Examples:** $AgBe_{12}$, Al_8CeMn_4, $Mg_{12}Nd$, $Mn_{12}Y$
***tI*28**	MnU_6	*I*4/*mcm*	For MnU_6, *a* = 10.29 Å, *c* = 5.24 Å. **Examples:** CoU_6, $FePu_6$, NiU_6
***tI*32**	Ni_3P	$I\bar{4}$	For Ni_3P, *a* = 8.95 Å, *c* = 4.39 Å. **Examples:** Cr_3P, Fe_3P, Mo_3P

	B_3Cr_5	*I*4/*mcm*	For B_3Cr_5, *a* = 5.46 Å, *c* = 10.64 Å. **Examples:** Ag_3Ca_5, B_2Co_5P, Ba_5Pb_3, Si_3Ta_5
	Si_3W_5	*I*4/*mcm*	For Si_3W_5, *a* = 9.61 Å, *c* = 4.96 Å. **Examples:** $CeCo_3Pu_4$, Cr_5Ge_3, Ga_3Ti_5, Re_5Si_3
***tI*48**	$BaCd_{11}$	$I4_1/amd$	For $BaCd_{11}$, *a* = 12.02 Å, *c* = 7.74 Å. **Examples:** $Cd_{11}Eu$, $LaZn_{11}$, $PrZn_{11}$
***tI*64**	NaPb	$I4_1/acd$	For NaPb, *a* = 10.58 Å, *c* = 17.75 Å. **Examples:** CsPb, KSn, PbRb, RbSn
***oP*4**	AuCd	*Pmma*	Two gold atoms at $\frac{1}{4},\frac{1}{2},z$ and $\frac{3}{4},\frac{1}{2},\overline{z}$ (with *z* = 0.812); two cadmium atoms at $\frac{1}{4},0,z$ and $\frac{3}{4},0,\overline{z}$ (with *z* = 0.313). For β′ AuCd, *a* = 4.76 Å, *b* = 3.15 Å and *c* = 4.86 Å. See Fig. 1 **Examples:** β″ AgCd, β′ AuCd, CdMg, IrMo, IrW
***oP*6**	FeS_2	*Pnnm*	Marcasite. Two iron atoms at $0,0,0$ and $\frac{1}{2},\frac{1}{2},\frac{1}{2}$; four sulfur atoms at $x,y,0$; $\overline{x},\overline{y},0$; $\frac{1}{2}+x,\frac{1}{2}-y,\frac{1}{2}$; and $\frac{1}{2}-x,\frac{1}{2}+y,\frac{1}{2}$ (with *x* = 0.200 and *y* = 0.378). For FeS_2 (marcasite), *a* = 4.44 Å, *b* = 5.42 Å and *c* = 3.39 Å. See Fig. 1 **Examples:** γ $CrSb_2$, FeP_2, FeS_2 (marcasite), $FeSe_2$, $FeTe_2$, $NiSb_2$
***oP*8**	β Cu_3Ti	*Pmmn*	For Cu_3Ti, *a* = 5.16 Å, *b* = 4.35 Å, *c* = 4.53 Å. **Examples:** Au_3Hf, $MoNi_3$, Ni_3Sb, Pt_3Ta
	FeB	*Pnma*	For FeB, *a* = 5.51 Å, *b* = 2.95 Å, *c* = 4.06 Å. **Examples:** CoB, MnB, DyNi, LuPt, SiTi
	GeS	*Pnma*	For GeS, *a* = 10.44 Å, *b* = 3.65 Å, *c* = 4.30 Å. **Examples:** GeSe, PbSe II, SnS, SnTe II
	MnP	*Pnma*	Four manganese atoms at $x,\frac{1}{4},z$; $\overline{x},\frac{3}{4},\overline{z}$; $\frac{1}{2}-x,\frac{3}{4},\frac{1}{2}+z$ and $\frac{1}{2}+x,\frac{1}{4},\frac{1}{2}-z$ (with *x* = 0.20 and *z* = 0.005); four phosphorus atoms at $x,\frac{1}{4},z$; $\overline{x},\frac{3}{4},\overline{z}$; $\frac{1}{2}-x,\frac{3}{4},\frac{1}{2}+z$; and $\frac{1}{2}+x,\frac{1}{4},\frac{1}{2}-z$ (with *x* = 0.57 and *z* = 0.19). For MnP, *a* = 5.26 Å, *b* = 3.17 Å, *c* = 5.92 Å. **Examples:** CoP, CrP, FeP, MnP, WP
***oP*12**	$PbCl_2$ (NiSiTi)	*Pnma*	The atoms occupy three independent site-sets, so that ordered ternary phases occur with this structure. For $AlPd_2$, *a* = 5.41 Å, *b* = 4.06 Å, *c* = 7.77 Å. **Examples:** $AlPd_2$, As_2Zr, CoMnSi, CoGeV, NiSiZr
***oP*16**	AlEr	*Pmma*	For AlEr, *a* = 5.57 Å, *b* = 5.80 Å, *c* = 11.27 Å. **Examples:** AlDy, AlHo, AlTb
	Ge_3Rh_5	*Pbam*	For Ge_3Rh_5, *a* = 5.42 Å, *b* = 10.32 Å, *c* = 3.96 Å. **Examples:** Al_3Pd_5, Ge_3Rh_5, In_3Pd_5, Rh_5Si_3
	Fe_3C	*Pnma*	Cementite. For Fe_3C, *a* = 5.09 Å, *b* = 6.74 Å, *c* = 4.52 Å. **Examples:** Co_3B, Co_3C, Ni_3C, Pd_3P
***oP*20**	Sb_2S_3	*Pbnm*	For Sb_2S_3, *a* = 11.25 Å, *b* = 11.33 Å, *c* = 3.84 Å. **Examples:** Bi_2S_3, Dy_2Se_3, Np_2S_3, U_2Se_3
***oP*56**	*P*-$Cr_{18}Mo_{42}Ni_{40}$	*Pbnm*	*P*-phase. For $Cr_{18}Mo_{42}Ni_{40}$, *a* = 9.07 Å, *b* = 16.98 Å, *c* = 4.75 Å. See α-Mn *cI*58 type, above, and Ref 17, Ref 18, Ref 19. **Examples:** *P*-$Cr_{18}Mo_{42}Ni_{40}$, *P*-(Mo-Fe-Ni), *P*-(Mo-Mn-Co)
***oC*4**	α-U	*Cmcm*	Four atoms at $0,y,\frac{1}{4}$; $0,\overline{y},\frac{3}{4}$; $\frac{1}{2},\frac{1}{2}+y,\frac{1}{4}$; and $\frac{1}{2},\frac{1}{2}-y,\frac{3}{4}$. For α-U, *a* = 2.85 Å, *b* = 5.87 Å, *c* = 4.95 Å, and *y* = 0.1024
***oC*8**	CrB	*Cmcm*	Four chromium atoms at $0,y,\frac{1}{4}$; $0,\overline{y},\frac{3}{4}$; $\frac{1}{2},\frac{1}{2}+y,\frac{1}{4}$; $\frac{1}{2},\frac{1}{2}-y,\frac{3}{4}$; with *y* = 0.146. Four boron atoms at similar positions with *y* = 0.440. For CrB, *a* = 2.97 Å, *b* = 7.86 Å, *c* = 2.93 Å. **Examples:** AgCa, NiB, CeNi, HfNi, NdRh, RuTh
	Ga	*Cmca*	Eight atoms at $0,y,z$; $0,\overline{y},\overline{z}$; $\frac{1}{2},y,\frac{1}{2}-z$; $\frac{1}{2},\overline{y},\frac{1}{2}+z$; $\frac{1}{2},\frac{1}{2}+y,z$; $\frac{1}{2},\frac{1}{2}-y,\overline{z}$;

			$0,\frac{1}{2}+y,\frac{1}{2}-z$; and $0,\frac{1}{2}-y,\frac{1}{2}+z$. For Ga, *a* = 2.90 Å, *b* = 8.13 Å, *c* = 3.17 Å, *y* = 0.1549, and *z* = 0.081
Pearson symbol	Prototype	Space group	Unit-cell description[(a)]
***oC*12**	Si_2Zr	*Cmcm*	All atoms at the same sites as for BCr *oC*8 with Zr: *y* = 0.102; Si(1): *y* = 0.752; Si(2): *y* = 0.447. For Si_2Zr, *a* = 3.72 Å, *b* = 14.68 Å, *c* = 3.68 Å. **Examples:** Ge_2Hf, Ge_2U, Si_2Ti
***oC*28**	Al_6Mn	*Cmcm*	For Al_6Mn, *a* = 7.55 Å, *b* = 6.50 Å, *c* = 8.87 Å. **Examples:** Al_6Fe, Al_6Re, Al_6Tc
***oF*24**	Si_2Ti	*Fddd*	For Si_2Ti, *a* = 8.25 Å, *b* = 4.78 Å, *c* = 8.54 Å. **Examples:** Al_2Ru, Ga_2Ru, Ge_2Ti, Sn_2Zr
***oI*6**	$MoPt_2$	*Immm*	Two molybdenum atoms at $0,0,0$; $\frac{1}{2},\frac{1}{2},\frac{1}{2}$. Four platinum atoms at $0,y,0$; $0,\overline{y},0$; $\frac{1}{2},\frac{1}{2}+y,\frac{1}{2}$; $\frac{1}{2},\frac{1}{2}-y,\frac{1}{2}$, with *y* = 0.353. For $MoPt_2$, *a* = 2.75 Å, *b* = 8.24 Å, *c* = 3.92 Å. **Examples:** $NbPd_2$, Ni_2V, Pd_2V, Pt_2V
***oI*12**	$CeCu_2$	*Imma*	For $CeCu_2$, *a* = 4.43 Å, *b* = 7.06 Å, *c* = 7.48 Å. **Examples:** Ag_2Ca, Cu_2Dy, Cu_2Pr, Hg_2K, $SrZn_2$
	$GdSi_2$ ($GdSi_{1.4}$)	*Imma*	Atoms at $0,\frac{1}{4},z$; $0,\frac{3}{4},\overline{z}$; $\frac{1}{2},\frac{3}{4},\frac{1}{2}+z$; $\frac{1}{2},\frac{1}{4},\frac{1}{2}-z$ with Gd: *z* = 0.375; Si(1): *z* = 0.786; Si(2): *z* = 0.964. For $GdSi_{14}$, *a* = 4.09 Å, *b* = 4.01 Å, *c* = 13.44 Å. **Examples:** $CeGe_2$, $DySi_{1.4}$, $HoSi_2$, $PrSi_{1.4}$
***oI*14**	B_4Ta_3	*Immm*	For B_4Ta_3, *a* = 3.28 Å, *b* = 13.38 Å, *c* = 3.13 Å. **Examples:** B_4Cr_3, B_4Cr_2Ni, B_4Mn_3, B_4V_3
***oI*20**	Al_4U	*Imma*	For Al_4U, *a* = 4.41 Å, *b* = 6.27 Å, *c* = 13.71 Å. **Examples:** Al_4Np, Al_4Pu
***mP*8**	Se_3Zr	$P2_1/m$	For Se_3Zr, *a* = 5.4 Å, *b* = 3.78 Å, *c* = 9.45 Å, β = 97.6°. **Examples:** HfS_3, $HfSe_3$, TiS_3
***mP*12**	$CoSb_2$	$P2_1/c$	For $CoSb_2$, *a* = 6.52 Å, *b* = 6.38 Å, *c* = 6.55 Å. β = 118.2°. As the atoms occupy three different site-sets, ordered ternary phases with the structure occur. **Examples:** As_2Co, As_2Ir, IrP_2, $RhSb_2$, $AS_{1.1}FeS_{0.9}$, AsOsS, AsOsTe, RuSbTe
***mP*16**	AsLi	$P2_1/c$	For AsLi, *a* = 5.79 Å, *b* = 5.24 Å, *c* = 10.70 Å, β = 117.4° **Examples:** KSb, NaSb
***mC*12**	As_2Nb	*C*2	For As_2Nb, *a* = 9.36 Å, *b* = 3.38 Å, *c* = 7.79 Å, β = 119.5°. **Examples:** As_2Mo, $NbSb_2$, Sb_2Ta
***mC*14**	Cr_3S_4	*C*2/*m*	For Cr_3S_4, *a* = 12.6 Å, *b* = 3.43 Å, *c* = 5.96 Å, β = 116.7°. **Examples:** Cr_3Se_4, Fe_3,Se_4, $CoCr_2Se_4$
***mC*28**	$CoZn_{13}$	*C*2/*m*	For $CoZn_{13}$, *a* = 13.31 Å, *b* = 7.54 Å, *c* = 4.99 Å, β = 126.8°.**Examples:** $CrZn_{13}$, $FeZn_{13}$
	Mn_5C_2	*C*2/*c*	For Mn_5C_2, *a* = 5.09 Å, *b* = 4.57 Å, *c* = 11.66 Å, β = 97.7°. **Examples:** Pd_5B_2, Fe_5C_2
***aP*8**	HgK	$P\overline{1}$	For HgK, *a* = 6.59 Å, *b* = 6.76 Å, *c* = 7.06 Å, α = 106°, β = 102°, γ = 93°
***aP*12**	$ReSe_2$	$P\overline{1}$	For $ReSe_2$, *a* = 6.73 Å, *b* = 6.61 Å, *c* = 6.72 Å, α = 119°, β = 92°, γ = 105°

(a) For lattice parameters of prototypes and examples, see also Ref 21

Figure 1 illustrates many of the crystals described in this article; the illustrations include perspective drawings of unit cells and projections onto cell faces. Small circles indicate the position of atom centers, without implying that the atoms are as small and as widely separated as the circles. Included in Fig. 1 are views in which the atoms are projected onto the (001) face of the unit cell, the face containing the origin and the axes *a* and *b*. The circles represent atom positions; the numbers adjacent to the circles indicate the distance from the atom to that face in terms of fractions (or decimal equivalents of fractions) of the length of the unit-cell edge extending up from that face. The edge lengths and interaxial angles shown are those that apply to the structure prototype. Cell dimensions for other element or alloy phases with the same structure prototype vary according to phase and composition, as discussed in the section “Effect of Alloy Composition” in this article.

Long-Period Superlattices. Some alloys in the ordered state have periodic structures with unit cells many times larger than in the disordered state; the long period may be along one axis, as in Fig. 2, along two axes, as in Fig. 3, or along three axes. The superperiods, which have different values in different alloy systems and which differ with composition, are known to depend on the average number of valence electrons per atom. Figure 2 shows an AuCu II structure with a one-dimensional long-range superlattice, with antiphase boundaries at intervals of five unit cells of the disordered state. It is orthorhombic when ordered and face-centered cubic when disordered. Figure 3 shows a two-dimensional long-period superlattice as in certain AB_3 alloys (Cu-Pd, Au-Zn, Au-Mn), with antiphase boundaries spaced at intervals M_1 and M_2 and unit cell dimensions ***a***, ***b***, and ***c*** in the ordered state. This superlattice is orthorhombic when ordered and face-centered cubic when disordered.

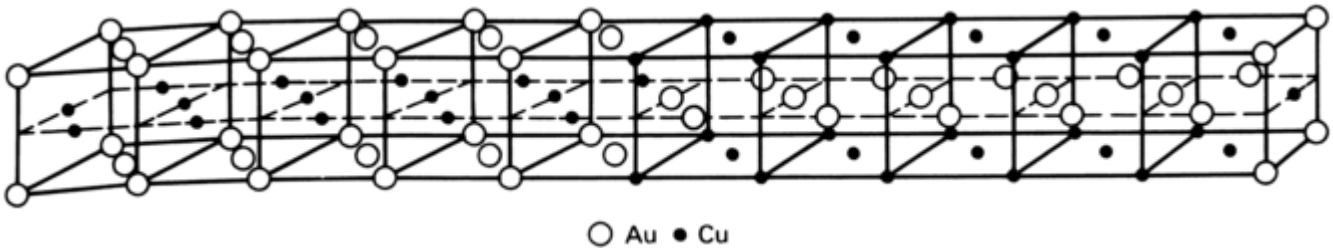

Fig. 2 AuCu II structure: a one-dimensional, long-period superlattice, with antiphase boundaries at intervals of five unit cells of the disordered state

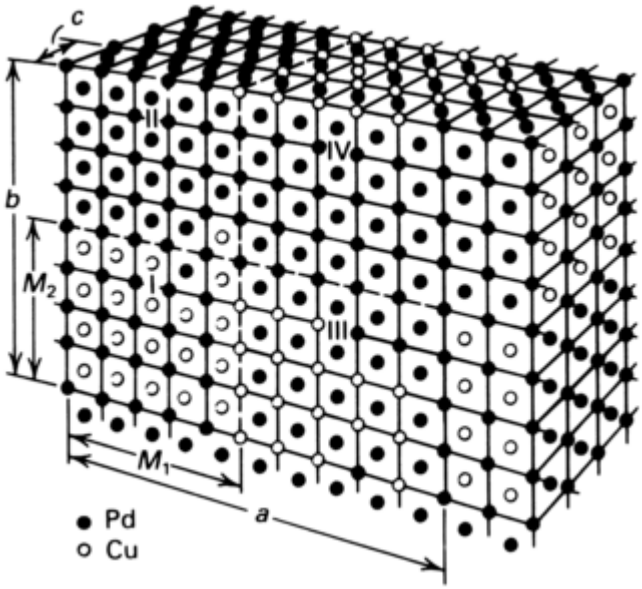

Fig. 3 Two-dimensional, long-period superlattice (as in Cu-Pd), with antiphase boundaries spaced at intervals M_1 and M_2 and unit-cell dimensions *a*, *b*, and *c* in the ordered state. The palladium atom has different positions in the small cubes in domains I, II, III, and IV.

References cited in this section

5. R.W.G. Wyckoff, *Crystal Structures,* Interscience, Vol 1, 1963; Vol 2, 1964; Vol 3, 1965

17. F. Weigel and A. Trinkl, *Radiochim Acta,* Vol 10, 1967, p 78–82

18. C.S. Barrett and T.B. Massalski, *Structure of Metals,* 3rd ed., Pergamon Press, 1980

19. A.G. Guy, *Elements of Physical Metallurgy,* Addison-Wesley, 1959

21. P. Villars, Ed., *Pearson's Handbook Desk Edition,* Vol 1 and 2, ASM International, 1997

Crystal Structure, *Metallography and Microstructures,* Vol 9, *ASM Handbook,* ASM International, 2004, p. 29–43

Crystal Defects

Crystal defects are important features in all real crystals. Some of the most significant defects are described in the following paragraphs. Additional information on defects, slip, twinning, and cleavage can be found in Ref 17, Ref 18, Ref 19.

Point defects include vacant atom positions that are occupied in perfect crystals. These vacancies increase in number as temperature is increased, and, by jumping about from one lattice site to another, they cause diffusion.

Interstitial atoms are those located between the atoms of the normal, perfect-crystal array; therefore, the carbon atoms in body-centered cubic ferrite are interstitials in that they fit between the iron atoms of its body-centered cubic structure, which is similar to the W *cI*2 type illustrated in Fig. 1. Substitutional atoms are those located at atom positions normally occupied by the atoms of the host crystal, and thus "substitute" for host atoms. There are also many close pairs and clusters of point defects, such as divacancies, trivacancies, and interstitial-vacancy pairs.

Line Defects. Dislocations are line defects that exist in nearly all real crystals. An edge dislocation, which is the edge of an incomplete plane of atoms within a crystal, is represented in cross section in Fig. 4. In this illustration, the incomplete plane extends partway through the crystal from the top down, and the edge dislocation (indicated by the standard symbol ⊥) is its lower edge.

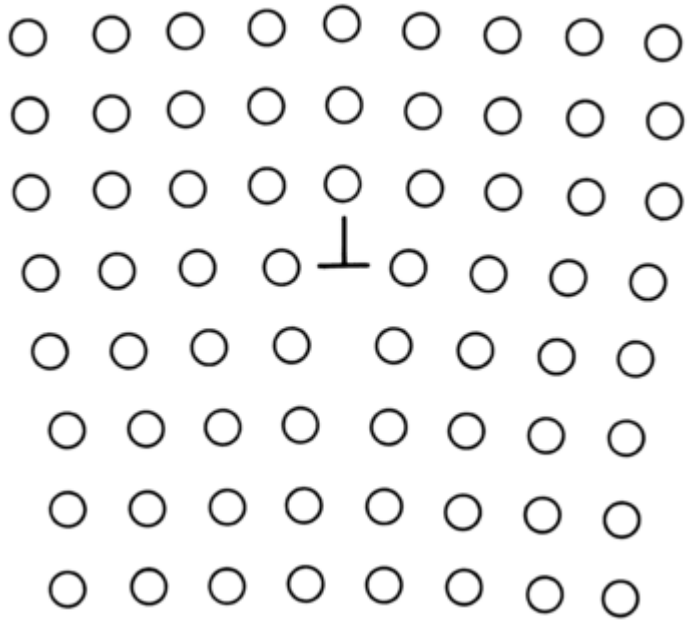

Fig. 4 Schematic representation of a section through an edge dislocation, which is perpendicular to the plane of the illustration and is indicated by the symbol ⊥

If forces, as indicated by the arrows in Fig. 5, are applied to a crystal, such as the perfect crystal shown in Fig. 5(a), one part of the crystal will slip. The edge of the slipped region, shown as a dashed line in Fig. 5(b), is a dislocation. The portion of this line at the left near the front of the crystal and perpendicular to the arrows, in Fig. 5(b), is an edge dislocation, because the displacement involved is perpendicular to the dislocation.

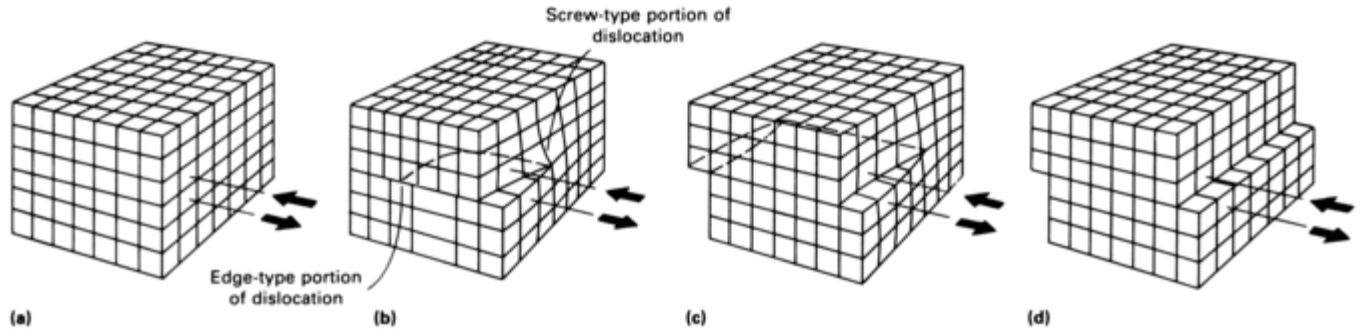

Fig. 5 Schematic representation of four stages of slip deformation by formation and movement of a dislocation (dashed line) through a crystal. (a) Crystal before displacement. (b) Crystal after some displacement. (c) Complete displacement across part of crystal. (d) Complete displacement across entire crystal

The slip deformation in Fig. 5(b) has also formed another type of dislocation. The part of the slipped region near the right side, where the displacement is parallel to the dislocation, is termed a screw dislocation. In this part, the crystal no longer is made of parallel planes of atoms, but instead consists of a single plane in the form of a helical ramp (screw).

As the slipped region spread across the slip plane, the edge-type portion of the dislocation moved out of the crystal, leaving the screw-type portion still embedded, as shown in Fig. 5(c). When all of the dislocation finally emerged from the crystal, the crystal was again perfect but with the upper part displaced one unit from the lower part, as shown in Fig. 5(d). Therefore, Fig. 5 illustrates the mechanism of plastic flow by the slip process, which is actually produced by dislocation movement.

The displacement that occurs when a dislocation passes a point is described by a vector, known as the Burgers vector. The fundamental characteristics of a dislocation are the direction of the vector with respect to the dislocation line, and the length of the vector with respect to the identity distance in the direction of the vector. The perfection of a crystal lattice is restored after the passage of a dislocation, as indicated in Fig. 5(d), provided that no additional defects are generated in the process.

Each dislocation in a crystal is the source of local stresses. The nature of these microstresses is indicated by the arrows in Fig. 6, which represent (qualitatively) the stresses acting on small volumes at different positions around the dislocation at the lower edge of the incomplete plane of atoms. Interstitial atoms usually cluster in regions where tensile strains and stresses make more room for them, as in the lower central part of Fig. 6.

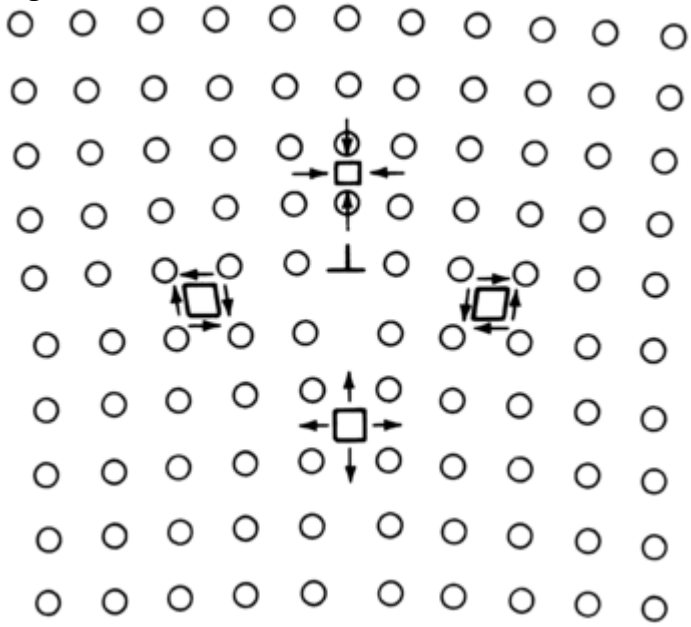

Fig. 6 Schematic representation of a crystal containing an edge dislocation, indicating qualitatively the stresses (shown by direction of arrows) at four positions around the dislocation

In addition to the large-angle boundaries that separate crystal grains, which have different lattice orientations, the individual grains are separated by small-angle boundaries (subboundaries) into subgrains that differ very little in orientation. These sub-boundaries may be considered as arrays of dislocations; tilt boundaries are arrays of edge dislocations, and twist boundaries are arrays of screw dislocations. A tilt boundary is represented in Fig. 7 by the series of edge dislocations in a vertical row. Compared with large-angle boundaries, small-angle boundaries are less severe defects, obstruct plastic flow less, and are less effective as regions for chemical attack and segregation of alloying constituents. In general, mixed types of grain-boundary defects are common. All grain boundaries are sinks into which vacancies and dislocations can disappear and may also serve as sources of these defects; they are important factors in creep deformation.

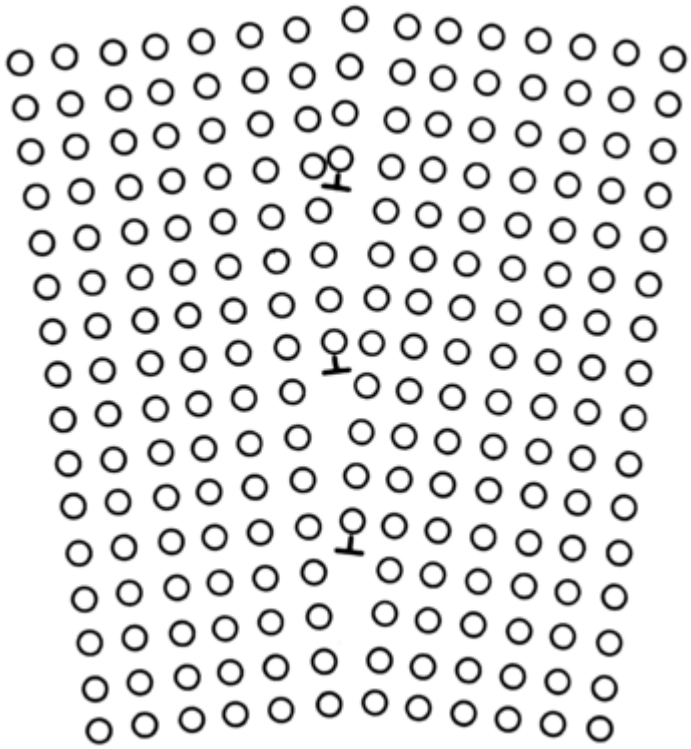

Fig. 7 Small-angle boundary (subboundary) of the tilt type, which consists of a vertical array of edge dislocations

Stacking faults are two-dimensional defects that are planes where there is an error in the normal sequence of stacking of atom layers. Stacking faults may be formed during the growth of a crystal. They may also result from motion of partial dislocations. Unlike a full dislocation, which produces a displacement of a full distance between the lattice points, a partial dislocation produces a movement that is less than a full distance.

Twins are portions of a crystal that have certain specific orientations with respect to each other. The twin relationship may be such that the lattice of one part is the mirror image of that of the other, or one part may be related to the other by a rotation about a specific crystallographic axis. Growth twins may occur frequently during crystallization from the liquid or the vapor state by growth during annealing (by recrystallization or by grain-growth processes) or by the movement between different solid phases, such as during phase transformation. Plastic deformation by shear may produce deformation (mechanical) twins. Twin boundaries generally are very flat, appearing as straight lines in micrographs, and are two-dimensional defects of lower energy than large-angle grain boundaries. Twin boundaries, therefore, are less effective as sources, and sinks, of other defects and are less active in deformation and corrosion than are ordinary grain boundaries. Textbooks and reference books, such as Ref 17, Ref 18, Ref 19 list the indices of twinning planes (shear planes) and the directions of shear that occur when deformation twins are formed.

References cited in this section

17. F. Weigel and A. Trinkl, *Radiochim Acta,* Vol 10, 1967, p 78–82

18. C.S. Barrett and T.B. Massalski, *Structure of Metals,* 3rd ed., Pergamon Press, 1980

19. A.G. Guy, *Elements of Physical Metallurgy,* Addison-Wesley, 1959

Crystal Structure, *Metallography and Microstructures,* Vol 9, *ASM Handbook,* ASM International, 2004, p. 29–43

References

1. W.B. Pearson, *A Handbook of Lattice Spacings and Structures of Metals and Alloys,* Pergamon Press, Vol 1, 1958; Vol 2, 1967

2. *Strukturbericht,* Akademische Verlagsgesellschaft m.b.H., Leipzig, Germany, 1913–1939; continued as *Structure Reports,* International Union of Crystallography, 1940 to the present

3. C.R. Hubbard and L.D. Calvert, *Bulletin of Alloy Phase Diagrams,* Vol 2, 1981, p 153–156

4. T. Hahn, Ed., *International Tables for Crystallography,* Vol A, International Union of Crystallography, D. Reidel Publishing, 1983

5. R.W.G. Wyckoff, *Crystal Structures,* Interscience, Vol 1, 1963; Vol 2, 1964; Vol 3, 1965

6. T.B. Massalski, Ed., *Binary Alloy Phase Diagrams,* 2nd. ed., ASM International, 1990, p T9

7. R. Hultgren et al., *Selected Values of the Thermodynamic Properties of the Elements.* American Society for Metals, 1973

8. J. Donohue, *The Structures of the Elements.* Wiley-Interscience, 1974

9. J.R. Peterson, J.A. Fahey, and R.D. Baybarz, *J. Inorg. Nucl. Chem.,* Vol 33, 1971, p 3345–3351

10. R.W. Lynch and H.G. Drickamer, *J. Phys. Chem. Solids,* Vol 26, 1965, p 63

11. E.A. Perez-Albuerne et al., *Phys. Rev.,* Vol 142, 1966, p 392

12. P.K. Smith, W.H. Hale, and M.C. Thompson, *J. Chem. Phys.,* Vol 50, 1969, p 5066–5076

13. L. Pauling et al., *J. Solid State Chem.,* Vol Z, 1970, p 225

14. A.F. Schach and R.L. Mills, *J. Chem. Phys.,* Vol 1 (No. 52), 1970, p 6000

15. C.S. Barrett and L. Meyer, *Phys. Rev.,* Vol 160, 1967, p 694

16. P.G. Pallmer and T.D. Chikalla, *J. Less-Common Metals,* Vol 24, 1971, p 233–236

17. F. Weigel and A. Trinkl, *Radiochim Acta,* Vol 10, 1967, p 78–82

18. C.S. Barrett and T.B. Massalski, *Structure of Metals,* 3rd ed., Pergamon Press, 1980

19. A.G. Guy, *Elements of Physical Metallurgy,* Addison-Wesley, 1959

20. L.H. Van Vlack, *Elements of Materials Science,* Addison-Wesley, 1964

21. P. Villars, Ed., *Pearson's Handbook Desk Edition,* Vol 1 and 2, ASM International, 1997

Crystal Structure, *Metallography and Microstructures,* Vol 9, *ASM Handbook,* ASM International, 2004, p. 29–43

Selected References

- E.A. Brandes and G.B. Brook, Ed., *Smithells Metals Reference Book,* 7th ed., Butterworth-Heinemann, 1992
- J.D.H. Donnay, *Crystal Data,* American Crystallographic Assn., 1963
- T.B. Massalski, *Binary Alloy Phase Diagrams,* Vol 1–3, 2nd Edition, ASM International, 1990
- H. Okamoto, *Desk Handbook: Phase Diagrams for Binary Alloys,* ASM International, 2000
- "Powder Diffraction Data File," International Center for Diffraction Data, Swarthmore, PA
- P. Villars, A. Prince, and H. Okamoto, Ed., *Handbook of Ternary Alloy Phase Diagrams,* 10 volumes, ASM International, 1995
- J.H. Westbrook and R.L. Fleischer, Ed., *Intermetallic Compounds,* Vol 1, *Crystal Structures of Intermetallic Compounds,* John Wiley & Sons, 2000

D. Aliya and S. Lampman, Physical Metallurgy Concepts in Interpretation of Microstructures, *Metallography and Microstructures,* Vol 9, *ASM Handbook,* ASM International, 2004, p. 44–70

Physical Metallurgy Concepts in Interpretation of Microstructures

Debbie Aliya, Aliya Analytical, Inc.; Steve Lampman, ASM International

---

Introduction

THE INTERPRETATION OF MICROSTRUCTURES is as much a cornerstone of metallography as proper specimen preparation. Like specimen preparation, the interpretation of microstructures is a mixture of art, experience, and science. The art of interpretation relies on experience and the large body of recorded images captured and interpreted by many metallographers over the years. However, it is clearly impossible to become an expert on every possible microstructure of every possible alloy. Using existing micrographs as a tool in interpretation requires an understanding of alloy and process conditions, which may not be available for exactly the same conditions as the specimen of interest. Therefore, it is necessary to have a basic understanding of physical metallurgy.

This article is intended to serve two main purposes. The first is to provide a conceptual framework of the physical metallurgy principles required for interpretation of microstructures. While a single article can not replace semesters of college-level study of physical metallurgy, the intent here is to give an introduction to the major aspects of physical metallurgy that allow an understanding of how microstructures are developed and

changed due to the variations of processing history. Metallographic novices are encouraged to read the section "Transformation Diagrams" to understand theory explained in the section "Nonequilibrium Phase Nucleation and Growth" in this article. More advanced material is also included here on phase transformations in steels, still the most common of all commercial metal alloys. It is hoped that both the beginner and the more advanced practitioner of metallography should be able to advance their ability to interpret microstructures after reading this article.

The main concepts that a study of physical metallurgy provides include phase transformations, such as solidification and solid-state transformations such as the eutectoid and the martensitic types; the role of diffusion rate in promoting different microstructures in different temperature ranges; the nature of equilibrium driving forces in promoting different microstructures in different alloys; the role of kinetics in promoting particular microstructures in a given alloy system; the effects of deformation on the microstructure; and, very importantly, the effects of the microstructural features on the properties or characteristics of the material. In addition, an understanding of physical metallurgy should allow the metallographer to understand the importance of the location or position of the cross section used to evaluate the microstructure. The nested levels of features made visible by lower and higher magnifications require an understanding of the effects of the processing conditions on the expected microstructure. In addition, the experienced and knowledgeable metallographer takes care to understand the limitations of his or her technology. This article contains a section on this subject.

The most common types of features in the microstructures in metallic materials are the boundaries between crystalline grains and/or the boundaries between different solid phases in multiphase alloys. The vast majority of commercial metals and alloys are polycrystalline materials, which means that the material consists of many individual crystalline grains with an intergranular region known as the grain-boundary region. Different grain sizes and shapes may have significant effects on the behavior of the material, and so metallography can be a useful tool in defining relationships between the microstructure of a material and its macroscopic properties.

Second-phase boundaries also exist in many alloys (either intentionally from alloying or from impurities). Second phases are precipitates that form when a solute (i.e., alloying element or impurities) exceeds its solubility limit in a base metal (or so-called solvent). For example, cementite (Fe_3C) is a second-phase constituent in carbon steel. Second-phase constituents form because, at some point, the lattice of the host metal cannot accommodate any more atoms of the alloying element. When an alloy element is below its solubility limits, it is completely "dissolved" in the host metal and thus forms a solid solution. In contrast, if the concentration of an alloying element exceeds its solubility limit, a new phase forms with a different crystal structure that is more able to cope with the additional alloying atoms that cannot be accommodated by the lattice of the host. These new phases are described by equilibrium phase diagrams, which are briefly described in this article.

It is also important to understand that the morphology of second phases can vary significantly. For example, cementite in steel can have different morphologies, ranging from a spheroidized shape to a fine, alternating platelet morphology known as pearlite. Pearlite is a two-phase structure of cementite (Fe_3C) and ferrite with a distinctive appearance of alternating thin and thick platelets, often in a swirling pattern. This distinctive morphology is a type of eutectoid structure (as briefly described in the section "The Iron-Carbon Eutectoid" in this article and in the separate article "Invariant Transformation Structures" in this Volume). The key point is that equilibrium phase diagrams are important in identifying phase constituents in alloys, but that phase diagrams do not provide the complete story in terms of phase morphology. Additional concepts in physical metallurgy are also needed to understand the variation in size, shape, and distribution of grains and second-phase particles in alloys.

This article introduces some basic physical-metallurgy concepts that may be useful for understanding and interpreting variations in metallographic features and how processing affects microstructure. Concepts are presented at an introductory level, with an emphasis on their concrete connection with microstructural features. In addition, this article also introduces some basic concepts in structure-property relationships. One significant reason for metallographic examination is to gain information about the expected behavior of the material. Sometimes, valid predictions about the mechanical, physical, or chemical properties of a material can be made by looking at the patterns revealed by metallography. Microstructures have been studied and classified for many different alloy systems for many years; sometimes, the patterns have been correlated with mechanical, corrosion, electrical resistivity, and other properties.

D. Aliya and S. Lampman, Physical Metallurgy Concepts in Interpretation of Microstructures, *Metallography and Microstructures*, Vol 9, *ASM Handbook*, ASM International, 2004, p. 44–70

Physical Metallurgy Concepts in Interpretation of Microstructures

Debbie Aliya, Aliya Analytical, Inc.; Steve Lampman, ASM International

Structure and Properties

The heart of metallurgical engineering is to manipulate the size, shape, and distribution of the crystalline grains and second-phase particles in metallic materials to create materials with specific desired characteristics. Sometimes, even the orientation of the crystalline grains are controlled to provide texture (see the article "Textured Structures" in this Volume). Most alloys are polycrystalline materials, and so grain structure is a key feature that can be examined and evaluated by metallographic techniques. Second-phase particles may be beneficial or detrimental, depending on their size, shape, and distribution. Metallography also can sometimes shed light on the composition of the material, although some alloys and process conditions are more revealing than others in this aspect. For example, annealed carbon steels can be easily grouped into low-, medium-, or high-carbon families by estimating the amount of pearlite present in comparison to the amount of ferrite or cementite present outside of the pearlite colonies. On the other hand, most annealed 300-series stainless steels will look quite similar, as long as they are fully annealed. Most microstructure differences in such stainless steels are more readily linked with process history than they are to differences in composition.

There are deviations from the above correlations. For example, there are cases when the same process operation is believed to have occurred, but the expected structure is not produced. Another example is when the same structure is observed, but the mechanical properties are not what would be expected. It is in this effort to understand deviations from expectations, it is most useful to go beyond the pattern-matching level of metallographic analysis and to learn how changes in processing details may affect structure. Likewise, structural features may look very similar or even nominally identical yet produce very different hardness or strength values, crack resistance, or ductility.

Grain Size and Growth. In polycrystalline materials, fine grains and finely divided phase regions are typically the preferred microstructure (at least for good strength and ductility in room-temperature structural applications). Typically, the grain boundaries are stronger than individual grains in a properly processed material. The grain boundaries are disruptions between the crystal lattice of individual grains, and this disruption can provide a source of strengthening (below creep temperatures) by pinning the movement of dislocations. Thus, a finer-grain alloy imparts more grain-boundary regions for improved strength.

However, the grain boundaries are also a region with many irregularly placed atoms, dislocations, and voids. This relative atomic disarray of the grain boundaries, as compared to the more regular atomic arrangement of the grain interiors, provides an easy path for diffusion-related alterations. Grain boundaries are thus the preferential region for congregation and segregation of many types of impurities. Weakening or embrittlement can also occur by preferential phase precipitation or absorption of environmental species (such as hydrogen or oxygen) in the grain boundaries. In addition, the grain-boundary regions are also weakened by high temperature, whereby the predominant fracture path becomes intergranular. Thus, a reasonably coarse grain structure may be desirable for high-temperature applications, while fine grains and finely divided phase regions would be preferred for most room- and low-temperature applications.

The size, distribution, and growth of grains and second-phase particles depend on many factors. Because grain boundaries are disordered regions, atoms may move from the grain boundary to an adjoining crystal or vice versa. If these processes occur repeatedly in one direction, then the grain boundary moves, and one crystal grows at the expense of the other. Grain-boundary energy is like surface energy—it tends to minimize itself. Thus, grains tend to grow to reduce the surface energy of the crystal. Surface energy of a boundary (in concept) can be related to the radius of curvature of a boundary; grain boundaries that are sharply bent tend to straighten out, and small grains adjacent to large grains tend to move into the larger grains. This process also is enhanced at high temperature (because, by definition, temperature is a measure of the average kinetic energy of atoms/molecules in an ensemble). Thus, migration (diffusion) of atoms between boundaries increases at higher

temperatures. Conversely, migration of grain boundaries and grain growth may be impeded by second-phase particles. Solutes may also retard grain growth, depending on how much the lattice structure of the host metal is distorted by the solute.

The boundaries in a polycrystalline material require energy to maintain. The fact that they are present affects how much internal energy is retained when the materials cool after either intentional or unintentional heating events. If there are many tiny regions of each type of phase, there is more boundary area than if there are few large regions of each type of phase. Materials with finely divided regions of different phases and/or fine grains are in a higher energy state than material with large phase regions or large grains. When fine grains and finely divided phase regions are preferred, the major factor that keeps the materials in a finely divided state is that, even though it takes energy to maintain the boundaries, it may also take even more energy (at least momentarily) to eliminate or minimize the boundaries. As long as that extra energy is not available, the material will maintain its high-energy boundaries.

Thus, high-temperature excursions, either very high for even a short time or a lower temperature for a more extended time, have a tendency to cause grain coarsening, coalescence of small second-phase particles, and/or the addition of atoms to larger particles. How fast and how easily this happens depends on how frequently the atoms in the small particles, through random diffusion of single atoms, end up attaching themselves to the larger particles. The number of atoms that are allowed to leave their home-phase particles (or grains, in the case of grain-boundary area reduction) at any time is controlled mainly by the temperature. The rate at which the atoms from the second-phase particles are able to travel through the matrix phase (diffusion rate) is also mainly controlled by the temperature. Solute solubility in solid materials also generally increases with temperature.

Processing Effects on Grain Structure. Metallography can provide information about the processing history of a material based on its grain structure. Some grain structures appear relatively equiaxed in cross section. In some cases, this may be due to a processing history where a material section was essentially exposed to the same thermal and/or thermomechanical conditions in every direction. Such structures often exist in the core of castings. The surfaces of as-cast materials often show grains that are elongated in one direction, due to different rates of heat extraction in different directions. Weld fusion zones also often show such directionality (Fig. 1a).

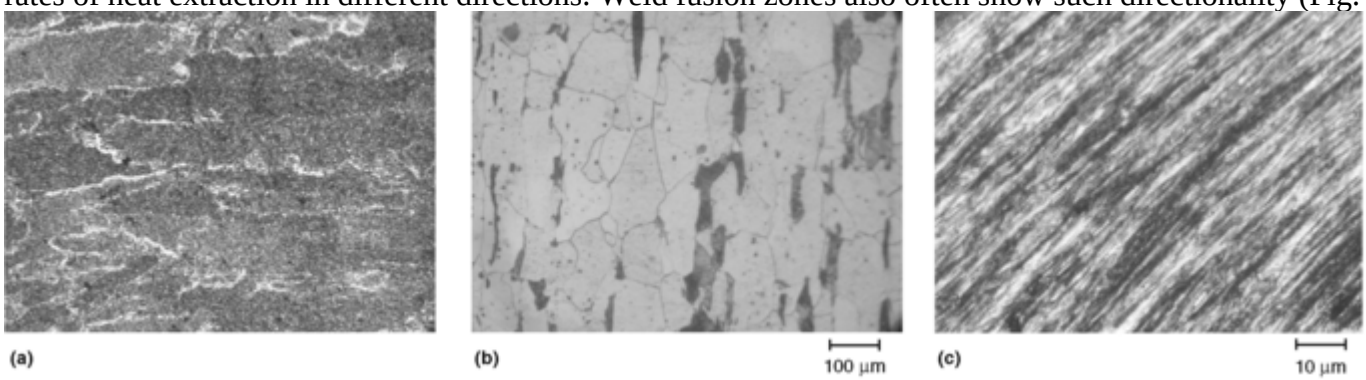

Fig. 1 Directionality in microstructure. (a) From directional heat flow during welding. 5% nital etch. (b) From deformation and subsequent annealing. 5% nital etch. Original magnification 100×. (c) From deformation in a heavily drawn steel wire. 5% nital etch. Original magnification 1000×

Elongated grains are also produced when metals are deformed by rolling. In hot rolling operations, the deformed grains recrystallize into new, smaller grains as the rolling proceeds. The new recrystallized grains typically have an equiaxed structure. In cold rolling, however, the deformed grains do not have enough energy to recrystallize. The typical microstructure after cold rolling is thus elongated grains that are flattened in the same direction of rolling (Fig. 1b). In some cases, very heavily worked metals can have a grain size and shape that is impossible to measure. The microstructure appears fibrous, as seen in the small-diameter steel wire shown in Figure 1(c).

In a cross section produced with cold rolling as its final step, the aspect ratio (defined as the average ratio of grain dimensions in the long and short dimensions) will generally be similar everywhere. Subsequent annealing often produces an equiaxed microstructure. However, looks can be deceiving, because crystals may have a preferred orientation (or texture) made visible only with x-ray diffraction techniques. Sometimes, aspect ratios other than 1 persist through recrystallization during an annealing cycle.

Even more complex patterns are often found in extrusions, where some portions of the extruded cross section may be much more heavily deformed than others. Because there is a minimum amount of energy required for recrystallization, it follows that the more heavily deformed portions of the extrusion may recrystallize, while the grains in the less heavily deformed portions may retain an elongated shape. Sometimes, the characteristics of the surface layers are different from the underlying material, due to frictional interaction with the extrusion dies. Often, the surface layers may have enough stored energy to recrystallize, while the underlying material retains a high aspect ratio.

Limitations of Metallography to Predict Properties. Even though metallography is useful in many circumstances, its limitations also must be appreciated in order to minimize errors in interpretation. There are many changes in properties that are not predictable using metallography. For example, the microstructure of steel suffering from hydrogen embrittlement generally looks exactly the same as it did before being exposed to the hydrogen, which, in some cases, can reduce the tensile strength by as much as 90% of the expected value. A normalized steel at the lower end of the range of medium-carbon steels may appear very similar to an annealed higher-carbon steel. Without doing extensive and careful quantitative analysis of the volume fractions of ferrite and cementite, it may be impossible to visually distinguish a normalized AISI 1030 steel from an annealed AISI 1045 steel, yet these two materials may behave differently.

The microstructural features affecting the strength characteristics of many precipitation-hardening alloys also are too small to be visible in a light microscope. Thus, metallography generally will not be helpful in determining whether the precipitation-hardening process was properly performed. Nonetheless, it may still be worthwhile to perform a metallographic examination, because information about other parts of the processing sequence may shed light on the situation.

Another limitation to the usefulness of metallography in predicting behavior is that some properties are a result of the atomic structure or the crystal structure, both much finer-scale features than could ever be seen in an optical microscope. Figure 2 (Ref 1) shows a striking hexagonal spiral microstructure. Clearly, the crystal structure of the individual phases is influencing the appearance of the microstructure in this case. Still other properties are a result of the distribution of the orientation of the crystals within the material. For example, the preferred orientation of the crystal texture produced in many low-carbon steels by controlled hot and warm rolling practices cannot readily be made visible by metallographic methods, because the shape of the grains often remains equiaxed. X-ray diffraction can demonstrate this level of structure that lies beyond light microscopy.

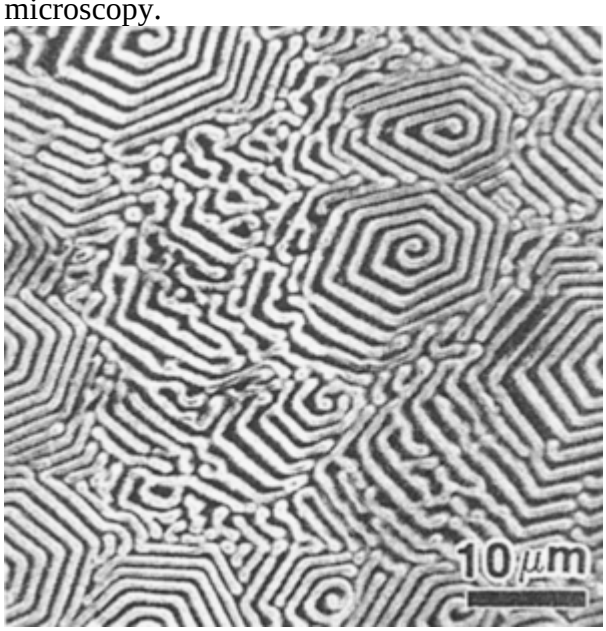

Fig. 2 Spiral morphology of Zn-$MgZn_2$ eutectic in a zinc-magnesium binary alloy. This striking hexagonal eutectic microstructure is partially a result of the crystal structure of the individual phases. The crystal structure does not often reveal its characteristics in such a direct way in the microstructure. Dark-field illumination. Source: Ref 1

Metallographic examination can also be assisted by the use of electron microscopy, which provides higher resolution than light (optical) microscopes. For example, pearlite is often unresolved when examined under a

light microscope, appearing as a more or less uniform or slightly mottled gray phase (Fig. 3a). The experienced ferrous metallographer would immediately know that this is ferrite (light) and pearlite (dark). However, the appearance of pearlite, on this scale, does not have the distinctive features (lamellar morphology) of a eutectoid structure. In this case, the lamellar structure is too fine for resolution with light microscopy, although it could be revealed with the higher resolution of a scanning electron microscope as is the case for the specimen shown in Fig. 3(b).

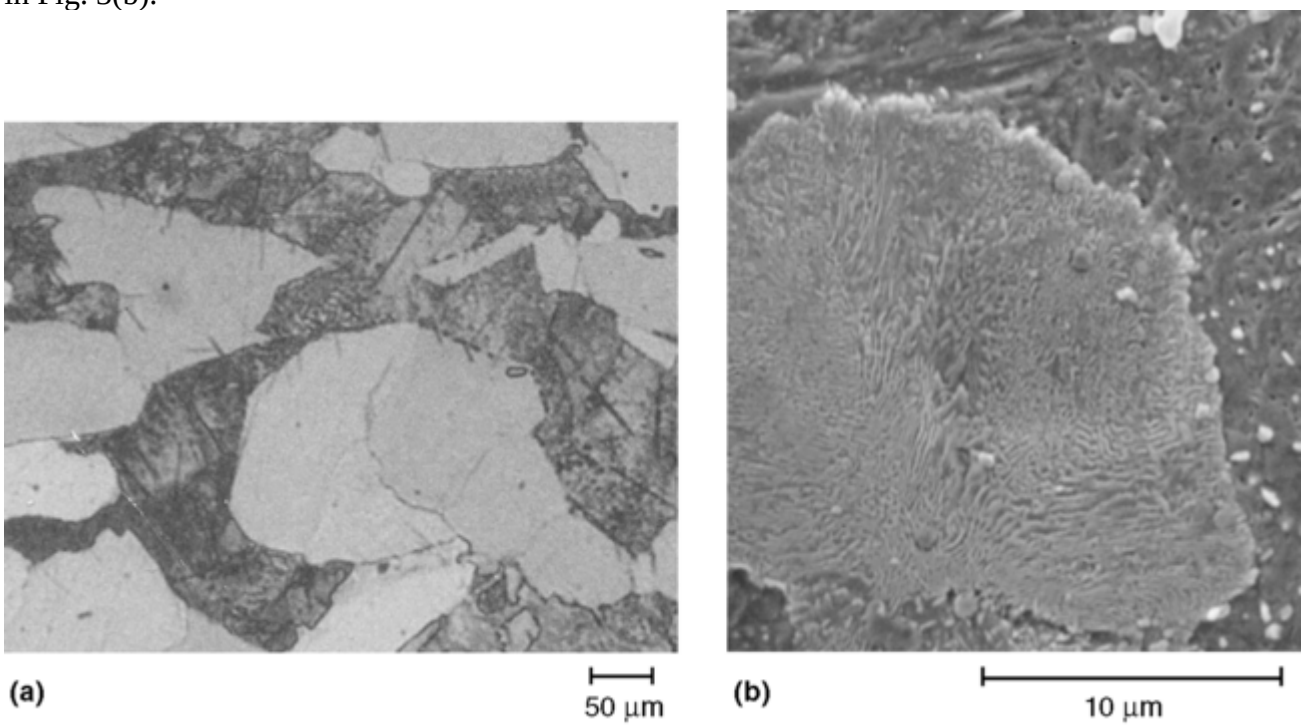

Fig. 3 Appearance of pearlitic microstructure. (a) Unresolved lamellar structure of pearlite (dark) in hot-rolled low-carbon steel viewed at 300×. 5% nital etch. The light-etching phase is ferrite, and there are a few stray chunky carbides (cementite) in the ferrite grains. (b) Alternating lamellae of pearlite, surrounded by martensite, revealed by scanning electron microscopy. Original magnification 3000×

Another limitation of using metallographic data to predict behavior is that the data, by its nature, are two-dimensional representations of a three-dimensional material. Even if multiple sections are prepared in multiple directions, one can only see two dimensions at a time. Any mathematical method intended to provide three-dimensional data from multiple two-dimensional images or measurements made on two-dimensional images will have assumptions embedded that may or may not be accurate in a given case.

One of the biggest limitations of metallography in general is the specimen size. Because the characteristics displayed by the material are a result of “nested” levels of structures, from atomic- to macroscale levels, it can be easy to miss a characteristic of interest in any particular situation. Getting an accurate representation of composition gradients from the outer layers to the core of a casting will generally require a different specimen from that required to document the grain size or the distribution and shape of second-phase particles created after the same casting is heat treated. Note also that the distribution and shape of the second-phase particles created during the heat treating may well vary from location to location as a result of the composition gradients created during the solidification process, as well as the local thermomechanical history.

The standard method of evaluation of nonmetallic inclusions in steel is made at 100×. Examining a piece of AISI 52100 steel for evidence of complete solution of carbides prior to hardening will, in many cases, require examination at 1000×. Both excessive nonmetallic inclusions at the wrong location and improper heat treatments can have a devastating effect on the durability of the final product. It is important to recognize the way that different levels of features, sometimes only visible at different magnifications or with different specimen preparation techniques, interact with each other to create the actual characteristics one observes.

The metallographer who is trying to interpret features of a microstructure from a component returned from service has a much more challenging task than someone who is simply checking today's production to see if it looks the same as yesterday's production. The changes in the microstructure occur as a result of process history. The atoms in the material do not care if the heat came from a heat treating furnace, a mechanic's blow torch, or

normal service heat. The details of exposures to time at temperature are generally impossible to determine in a completely independent manner from the microstructure alone.

Reference cited in this section

1. A. Tomer, Phase Diagrams, Classical Metallography and Advanced Techniques, *Computer-Aided Microscopy and Metallography,* Vol 18, *Microstructural Science Series,* T. Place et al., Ed., ASM International, 1990, p 188

D. Aliya and S. Lampman, Physical Metallurgy Concepts in Interpretation of Microstructures, *Metallography and Microstructures,* Vol 9, *ASM Handbook,* ASM International, 2004, p. 44–70

Physical Metallurgy Concepts in Interpretation of Microstructures

Debbie Aliya, Aliya Analytical, Inc.; Steve Lampman, ASM International

---

Equilibrium Phase Diagrams

For purposes of conceptual introduction, equilibrium phase diagrams of binary (two-element) alloys are the easiest way to begin a discussion on physical metallurgy. Equilibrium phase diagrams provide useful information in interpretation of microstructures, and an understanding of equilibrium phase diagrams also is needed to properly understand isothermal transformation curves and continuous cooling transformation curves that are plotted on time-temperature (isothermal) transformation diagrams (see the section “Transformation Diagrams” in this article).

A phase is simply defined by the type of atomic bonding and arrangement of elements in a material. In pure metals, for example, the phases may be solid, liquid, or gas (depending on the conditions of pressure or temperature). Alloys (which, by definition, contain two or more elements) also have solid, liquid, and gas phases, but solid alloys may also contain phases with different crystal structures (depending on the temperature and the concentration of alloying elements). These various phases are described in binary equilibrium diagrams. As noted, second phases are precipitates that form when a solute (i.e., alloying element or impurities) exceeds its solubility limit in a base metal (or so-called solvent). For example, cementite (Fe_3C) is a second-phase constituent in carbon steel. The presence of second phases is shown on equilibrium phase diagrams, as described in more detail in Ref 2 for binary alloys and Ref 3 for binary and selected ternary alloys.

The formation of phases in alloys is influenced by temperature and alloy concentration. For example, Fig. 4 (Ref 2) shows a simplified phase diagram for a hypothetical binary system with two elements, A and B. This particular type of phase diagram is that of an isomorphous system, in that elements A and B are somewhat similar to each other in terms of crystal structure, atomic size, and lattice parameters. In this case, due to their similarity of crystal structure, the solid crystalline structures of elements A and B can adequately fit with each other over the entire composition range ($0\% < B < 100\%$). Thus, the solid forms of elements A and B combine to form a solid solution (α), where all atoms are accommodated within a single crystal structure.

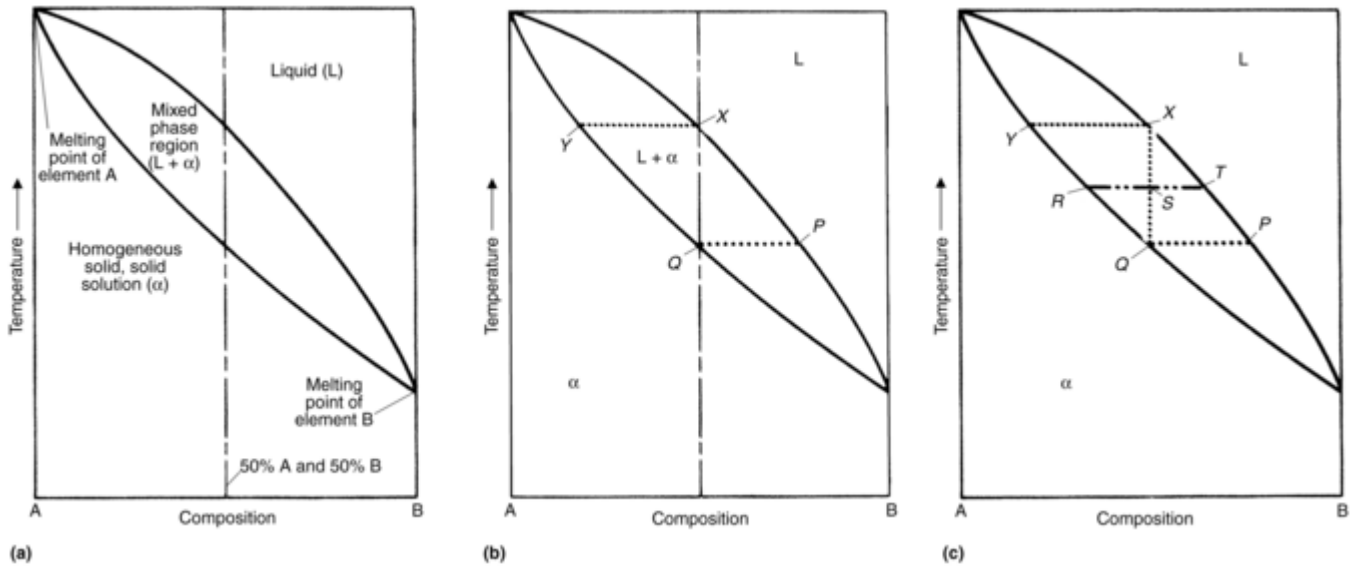

Fig. 4 Freezing curve of an idealized solid-solution alloy in a binary isomorphous system. (a) The solid-solution phase (α) is a homogeneous solid at all compositions in this idealized isomorphous system. (b) When the alloy solidifies under equilibrium conditions, phase compositions can be determined from points on the liquidus and solidus for a given alloy composition (A-B). Point *X* and *Y* are compositions of the liquid and solid phases, respectively, when alloy A-B starts to freeze. Points *Q* and *P* are compositions of the final solid and liquid phases, respectively, when the last parts of alloy A-B completely solidify after slow (equilibrium) cooling. (c) The lever rule can be used to determine phase compositions and volume fractions at intermediate points along the solidus and liquidus lines when alloy A-B freezes under equilibrium conditions. See text in the section "Isomorphous Alloy Systems" in this article.

Most alloys, however, do not have such simple phase systems. Typically, alloy elements have significant differences in their atomic size and crystal structure, and so the mismatch may force the formation of a new crystal phase that more easily accommodates alloying elements in solid form. For example, the difference in atomic weights of iron and carbon is part of the reason for formation of additional new phases and/or constituents (i.e., new crystal structures) in the iron-rich side of the well-known iron-carbon phase diagram. This can be appreciated by considering iron-carbon alloy composition in terms of both weight percent and atomic percent, as described subsequently.

Alloy composition on phase diagrams can be plotted in terms of weight percent or atomic percent (i.e., the number of atoms of each element). The general relation to find weight percent A from a composition given in atomic percent is:

$$\text{wt\% A} = 100\left[\frac{(\text{at.\% A})(\text{atomic weight A})}{(\text{at.\% A})(\text{atomic weight A})+(\text{at.\% B})(\text{atomic weight B})}\right]$$

Thus, in the simplified situation of alloying at 50 at.% (both A and B have equal number of atoms), then:

$$\text{wt\% A}\,(\text{at 50 at.\%}) = 100\left[\frac{(\text{atomic weight A})}{(\text{atomic weight A})+(\text{atomic weight B})}\right]$$

This calculation is instructive in thinking about the differences in atomic weight of alloying elements and the extent of mismatch that may require formation of new phases to accommodate alloy concentrations. For example, the equivalent atomic concentration for a steel with approximately 7 wt% C would be approximately 25 at.% C in iron, given the lower atomic weight of carbon relative to iron. This helps illustrate the difficulty of achieving a complete iron-carbon solid solution in terms of being able to substitute carbon for iron atoms in the crystalline lattice.

This section briefly describes how to use equilibrium binary phase diagrams as a tool in the interpretation of microstructures. It is also important to emphasize that equilibrium phase diagrams identify phase changes under

conditions of very slow changes in temperature. In practical situations, where heating and cooling occur more rapidly, the atoms do not have enough time to get into the equilibrium positions, and the reactions may start or end at temperatures different from those shown on the equilibrium phase diagrams. In these practical circumstances, the actual temperature at which the phase transformation occurs will depend on both the rate and direction of temperature change.

Phase changes may also involve the release or absorption of heat. In melting, for example, heat is absorbed. This type of phase change is said to be an endothermic reaction (where "endo" means within in Greek). Endothermic changes require energy to be added to the system and thus will not generally happen when the material is in an unstressed condition at a low temperature. In contrast, exothermic reactions involve the release of energy (or heat) to the environment. For example, solidification is an exothermic reaction, where heat is given off by the metal.

Exothermic reactions release energy to the outside environment and thus create a lower energy state for the material. Materials generally prefer to be in a lower energy state, so exothermic reactions can take place spontaneously and will whenever the material is given the chance to do so. In general, hot environments promote endothermic reactions, while cold environments (relative to the specific temperature range of the phase change reaction of the alloy in question) promote exothermic reactions.

In some cases, exothermic transformations are delayed, and the material may be in what is called a metastable condition. While exothermic reactions are theoretically capable of happening spontaneously, some small amount of energy is often required to initiate the transformation. For example, carbon steel typically contains cementite (Fe_3C), which is a phase that can have different morphologies ranging from a spheroidized condition or a fine, alternating platelet morphology in pearlite. The spheroidized condition is a more stable condition thermodynamically, but without thermal activation, the process of change may be sluggish. This is why pearlite stays as pearlite at room temperature, rather than changing to a spheroidized condition. In fact, the true equilibrium form of carbon in an iron-carbon alloy is graphite, not cementite. However, the time required for transformation is so long that the iron-cementite structure is considered to be quasi-equilibrium.

Isomorphous Alloy Systems

As described in the simplified system of Fig. 4(a), an isomorphous binary alloy system is when the two elements (A and B) are somewhat similar to each other in terms of crystal structure, atomic size, and lattice parameters. This allows formation of a single solid-solution phase (α), where the crystal structures of elements A and B adequately fit with each other. In addition, there is a mixed-phase region (L + α), or so-called "mushy" zone, in the region between the liquid phase (L) and the solid-solution phase (α). Unlike the pure form of elements A and B (which have singular points of melting, as indicated in Fig. 4a), the A-B alloy compositions melt/solidify over a range of temperature. The upper curve, called the liquidus, gives the lowest temperature at which any given composition can be found in an entirely molten state. The lower curve, called the solidus, gives the highest temperature when all atoms of a given composition can be found in an entirely solid state. For a simple isomorphous phase diagram such as this, a straight line between the melting points of the two pure elements is roughly the actual center of the freezing range.

During solidification, the actual concentration of newly formed solid and the remaining liquid portion can be easily determined from the phase diagram, if the solidification proceeds with equilibrium slowness. For example, Fig. 4(b) shows compositions at the initiation of solidification (point *X*) and the completion of solidification (point *Q*) for an alloy of given bulk composition (say, equal amounts, 50% of elements A and B). When solidification starts, the liquid phase has a bulk composition of 50% A and 50% B, as indicated by point *X*. When the first atoms begin to group together as solid crystals on cooling, the overall (bulk) composition is similar to the liquidus composition, while the composition of the tiny amount of just-formed solid is very different. In this case, the composition for the first appearance of solid phase corresponds to point *Y* in Fig. 4(b), if the solidification proceeds with equilibrium slowness. Then, if the temperature slowly cools to complete solidification at point *Q*, the overall composition is similar to that of the solid (point *Q*), while the small amount of remaining liquid has a very different composition. The small amount of last remaining liquid phase has a composition identified by point *P* in Fig. 4(b).

In an isomorphous system, the element with the higher melting point preferentially begins to form into solid. For example, the copper-nickel phase diagram is an isomorphous system (Fig. 5a), as far as the initial

solidification goes. In this system, nickel, with a higher melting point (1455 °C, or 2651 °F) versus that of copper (1086 °C, or 1987 °F), solidifies preferentially no matter what the composition of the alloy.

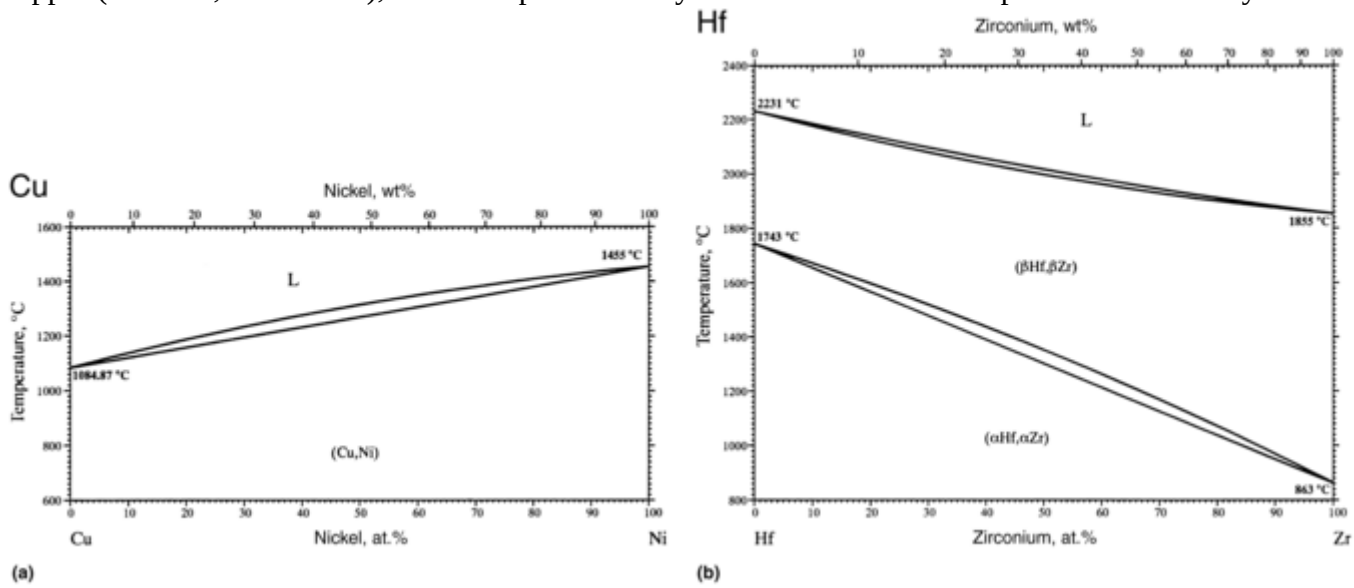

Fig. 5 Examples of isomorphous elements with homogenous solid solution over the range of compositions. (a) Solidification region of copper-nickel phase diagram. (b) Hafnium-zirconium phase diagram with an isomorphism during solidification (L → β) and a solid-state isomorphism (β → α). Source: Ref 2, Ref 3

The lever rule (Fig. 4c) also allows easy calculation of theoretical compositions and amounts of phase constituents (in this case, L and α) for any given temperature between the start of solidification (point *X*) and the completion of solidification (point *Q*). At the intermediate temperature in Fig. 4(c), composition of the solid phases is determined by point *R*, while liquid phase composition is determined by point *T*. The volume fraction of the solid phase is determined by the length ratio of lines *ST*/*RT*, and the volume fraction of the liquid phase is determined by the length ratio of lines *RS*/*RT*. It is easy to check the calculations by ensuring that there is more than 50% liquid when the temperature is near the liquidus point.

Some binary alloy systems having simple isomorphous phase diagrams include silver/gold, bismuth/antimony, silver/palladium, and germanium/silicon. Hafnium/zirconium has an interesting variation of the isomorphous solidification transformation, which is mirrored in a second solid-to-solid-phase isomorphous transformation at a lower temperature range (Fig. 5b). In this isomorphous variant, all compositions are capable of existing in either the alpha or the beta form.

Eutectic Alloy Systems

Most alloy systems do not have such simple phase diagrams as a completely isomorphous system (Fig. 4). For example, one common type of binary phase diagram is a eutectic system, where the term *eutectic* is taken from the Greek for easy melting. Figure 6 shows a generic eutectic phase diagram. Eutectic systems form when alloying additions cause a lowering of the liquidus lines from both melting points of the two pure elements. At some composition, there is a minimum melting point, where the mixed solid-liquid phases (L + α and L + β) vanish. This is the eutectic point (e), which defines an alloy composition that has the lowest melting point of the A-B system, hence the name eutectic. The eutectic composition also solidifies completely at a single temperature and thus is also referred to as an invariant point.

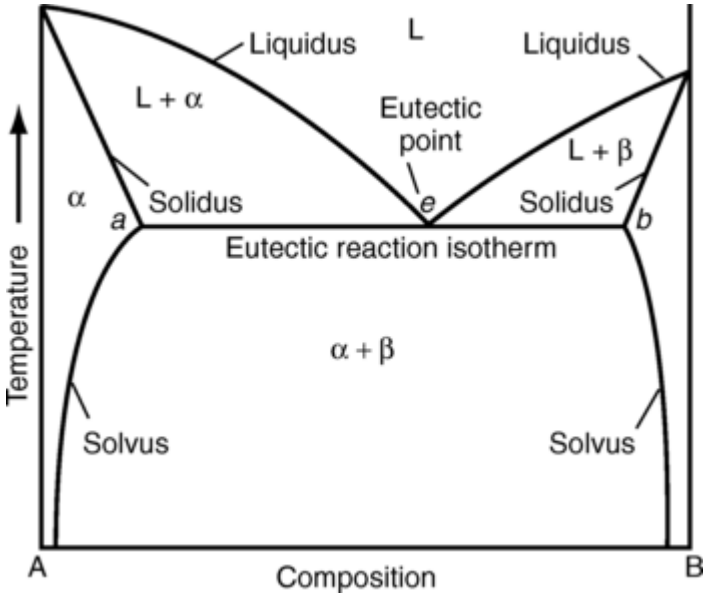

Fig. 6 General schematic of a eutectic phase system, where a minimum melting point occurs at a specific (invariant) composition and temperature defined by the eutectic point (e). The maximum solid solubility of element B is defined by point *a* on the A-rich side of the diagram, and the maximum solid solubility of element A in the lattice of element B is defined by point *b*. The methods of determining the equilibrium temperature ranges for solidification, fractions of phases, and compositions of phases are all similar to those illustrated for the isomorphous systems. The first element to solidify during the onset of freezing depends on the composition. See text.

Because eutectic alloys have a single melting/solidification point, eutectic compositions include important types of commercial alloys. Traditional lead-tin solder alloys are based on a eutectic system (Fig. 7). Lead-antimony, aluminum-germanium, and silver-copper all have simple eutectic phase diagrams. Casting alloys are often based on eutectic compositions for various reasons, including the minimization of both energy input and coring, or alloy segregation (see the section “Coring” in this article). For example, the iron-carbon system has a eutectic at composition of 4.3 wt% C, which is the basis of cast irons. Many other binary systems have phase diagrams where the eutectic theme may be repeated several times within the range of compositions.

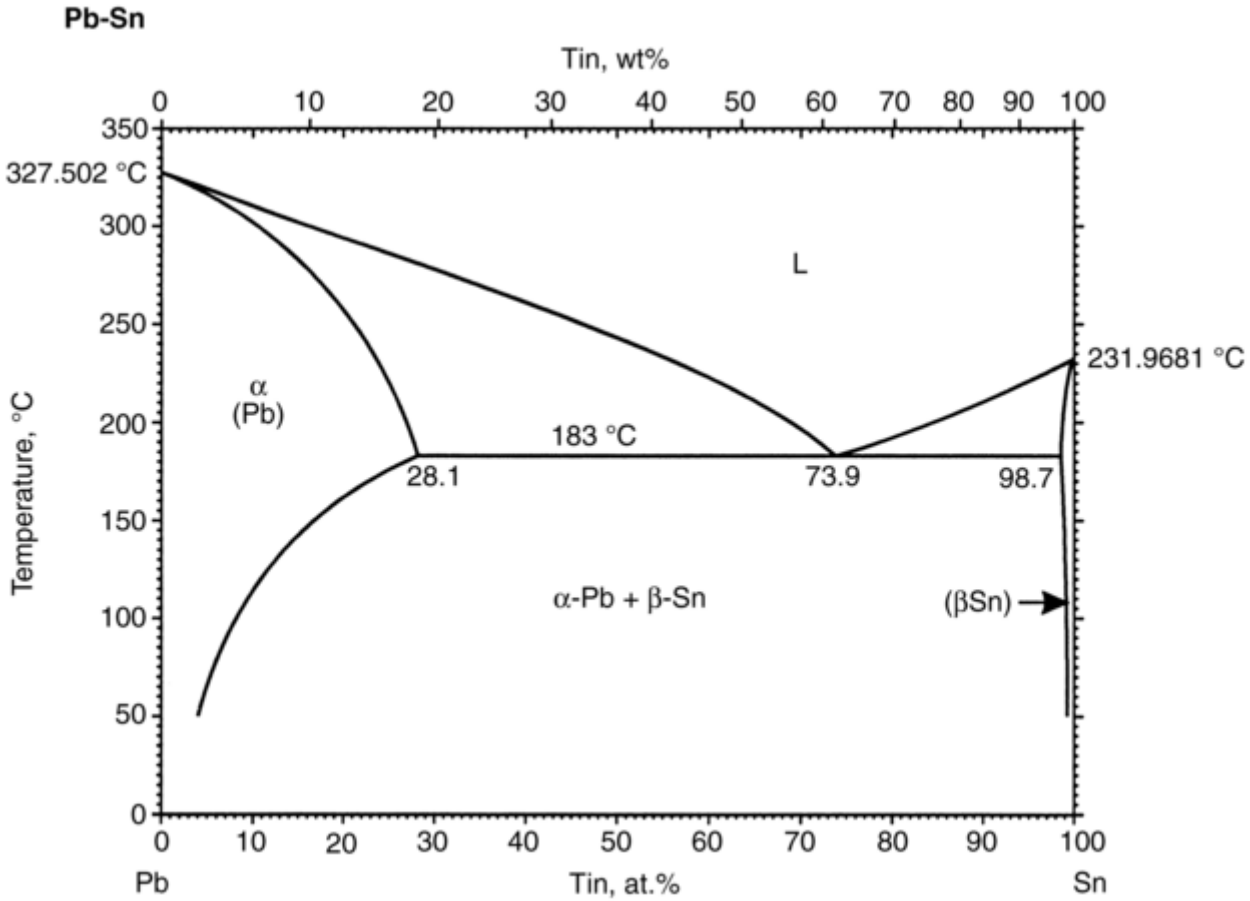

Fig. 7 Classic example of eutectic system in lead-tin alloys. Diagram contains the more scientifically useful atomic %. Weight % is shown at the top. Source: Ref 2, Ref 3

Solidification of Eutectics. In contrast to an isomorphous system, the element to solidify first in a eutectic system depends on the composition of the alloy. For example, the lead-tin system (Fig. 7) has a eutectic composition at 61.9 wt% Sn, with a eutectic temperature of 183 °C (361 °F). At the eutectic point, both elements in the liquid-phase alloy transform to a solid phase with two distinct phases (α-Pb and β-Sn). At other compositions, the element that forms first as an enriched solid is determined by the nearness of the particular composition to each side of the eutectic point. For example, in a 75% Sn, 25% Pb alloy, the lower-melting-point tin (232 °C, or 450 °F) will be enriched first in the solid-state form. From the tin side of the diagram, the tin-rich phase solidifies first, while initial solidification of a lead-rich phase is preferred on the lead side of the diagram. The important concept to grasp is that there is segregation of atomic species during solidification. This means that there will be some differences in composition on the microscopic scale from one location to another. This inhomogeneity can significantly affect the final properties of the component.

At all noneutectic compositions, the composition of the solid and liquid phases and the amounts of solid and liquid phases at any partially solidified material may be calculated in the same way as those of the isomorphous system. Likewise, if the temperature is close to the liquidus temperature, there will be mostly liquid present, and the composition of the liquid will be near the overall bulk composition of the alloy. If the temperature is near the solidus temperature, there will be mostly solid material, and the composition of the solid will be near the overall composition. The difference is that the liquid composition remaining just prior to solidification will not be the lower-melting-point element, as is the case in the isomorphous diagrams, but the eutectic composition itself.

Eutectic Microstructures. Isomorphous systems are characterized by a solid with a single-phase structure, while eutectic systems have a two-phase solid (the α + β region in Fig. 6), where α and β are solid phases with different crystal structures. Each of the elements has its own preferred crystal structure, which can accommodate the presence of some of the other atom types. The solid form of eutectic alloys contains two separate and distinct solid phases, which generally can be readily viewed using metallographic techniques (see also the article “Fundamentals of Solidification” in this Volume).

When a eutectic composition solidifies, both the α and β solid phases must deposit on the grain nuclei until all of the liquid is converted to solid. This simultaneous deposition results in microstructures made up of distinctively shaped particles of one phase in a matrix of the other phase, or alternate layers of the two phases. Examples of characteristic eutectic microstructures include spheroidal, nodular, or globular; acicular (needles) or rod; and lamellar (platelets, Chinese script or dendritic, or filigreed). Each eutectic alloy has its own characteristic microstructure when slowly cooled (Fig. 8). More rapid cooling, however, can affect the microstructure obtained (Fig. 9). Care must be taken in characterizing eutectic structures, because elongated particles can appear nodular, and flat platelets can appear elongated or needlelike when viewed in cross section.

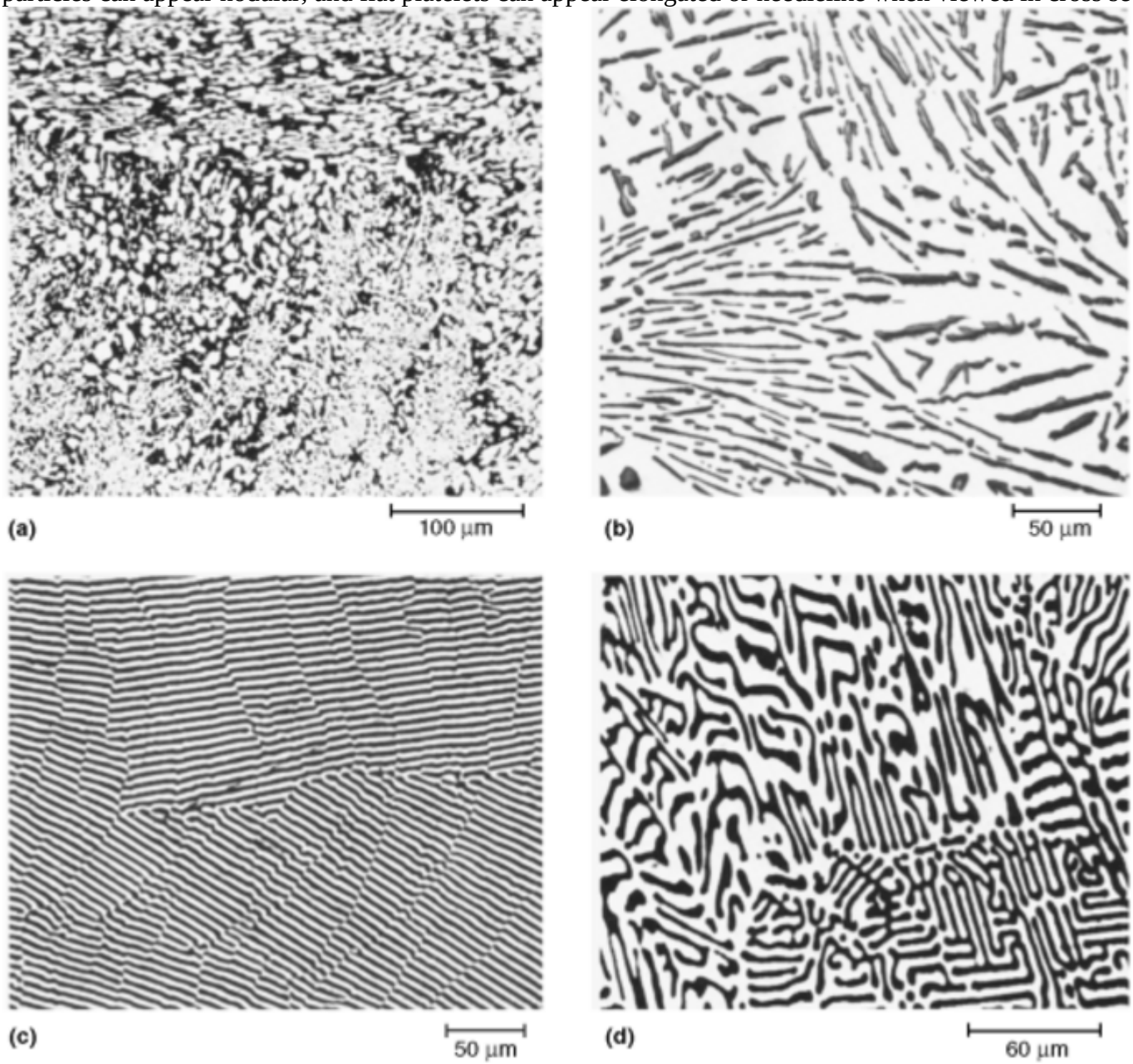

Fig. 8 Examples of characteristic eutectic microstructures in slowly cooled alloys. (a) 50Sn-50In alloy showing globules of tin-rich intermetallic phase (light) in a matrix of dark indium-rich intermetallic phase. Original magnification 150×. (b) Al-13Si alloy showing an acicular structure consisting of short, angular particles of silicon (dark) in a matrix of aluminum. Original magnification 200×. (c) Al-33Cu alloy showing a lamellar structure consisting of dark platelets of $CuAl_2$ and light platelets of aluminum solid solution. Original magnification 180×. (d) Mg-37Sn alloy showing a lamellar structure consisting of Mg_2Sn "Chinese script" (dark) in a matrix of magnesium solid solution. Original magnification 250×. Source: Ref 2, Ref 3

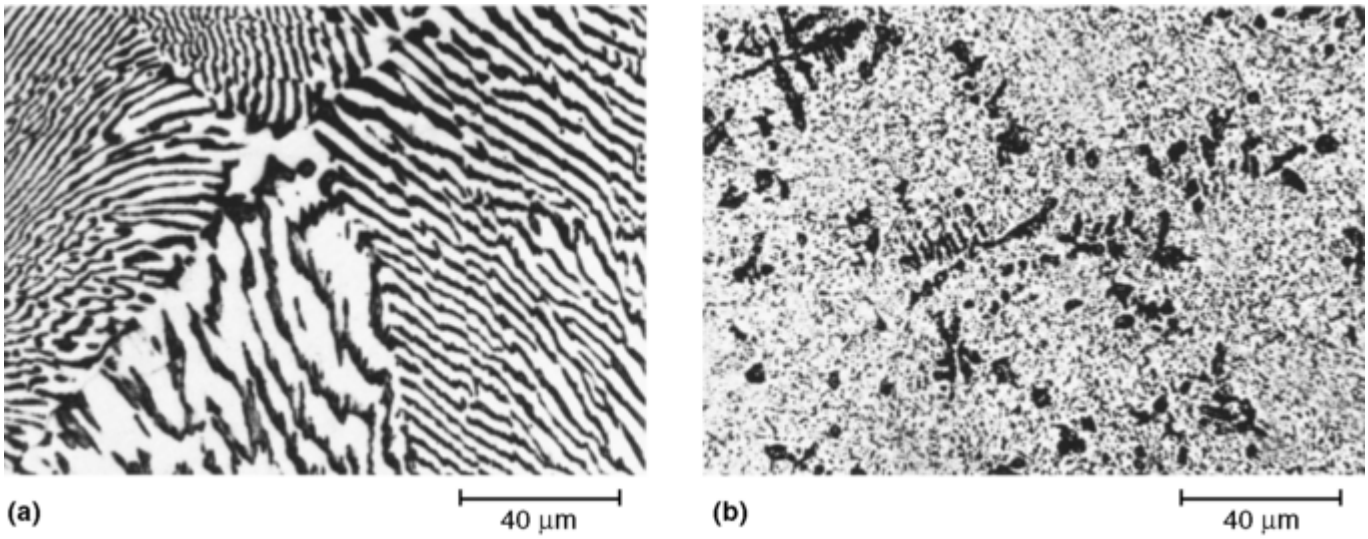

Fig. 9 Effect of cooling rate on the microstructure of Sn-37Pb alloy (eutectic soft solder). (a) Slowly cooled sample shows a lamellar structure consisting of dark platelets of lead-rich solid solution and light platelets of tin. (b) More rapidly cooled sample shows globules of lead-rich solid solution, some of which exhibit a slightly dendritic structure, in a matrix of tin. Both original magnification 375×. Source: Ref 2, Ref 3

If the alloy composition is different from the eutectic composition, then solidification begins before the eutectic temperature is reached. If the alloy composition is hypoeutectic (i.e., concentration of element B in Fig. 6 is less than the eutectic composition), some dendrites of α will form in the liquid before the remaining liquid solidifies at the eutectic temperature. If the alloy is hypereutectic (element B is higher than the eutectic), the first (primary) material to solidify will be dendrites of β. The microstructure produced by slow cooling of a hypoeutectic and hypereutectic alloy will consist of relatively large particles of primary constituent, consisting of the phase that begins to freeze first, surrounded by relatively fine eutectic structure. In many instances, the shape of the particles will show a relationship to their dendritic origin (Fig. 10a). In other instances, the initial dendrites will have filled out somewhat into idiomorphic particles (particles having their own characteristic shape) that reflect the crystal structure of the phase (Fig. 10b).

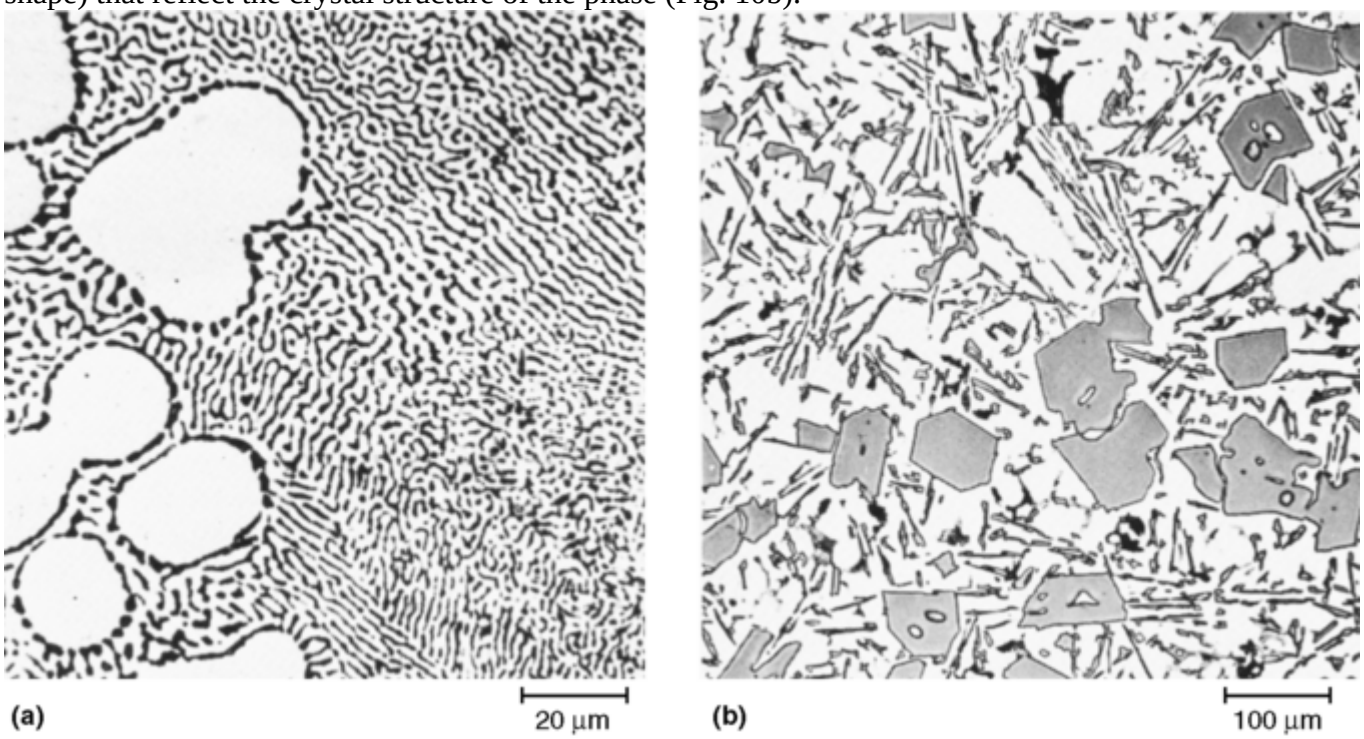

Fig. 10 Examples of primary particle shape. (a) Sn-30Pb hypoeutectic alloy showing dendritic particles of tin-rich solid solution in a matrix of tin-lead eutectic. Original magnification 500×. (b) Al-19Si

hypereutectic alloy, phosphorus-modified, showing idiomorphic particles of silicon in a matrix of aluminum-silicon eutectic. Original magnification 100×. Source: Ref 2, Ref 3

As stated earlier, cooling at a rate that does not allow sufficient time to reach equilibrium conditions will affect the resulting microstructure. For example, it is possible for an alloy in a eutectic system to obtain some eutectic structure in an alloy outside the normal composition range for such a structure. For example, solidification of alloy X in Fig. 11 begins at starting point (S_X) on the solidus curve. If alloy X is cooled slowly, the phase change from liquid to solid follows the solidus curve until it reaches the final point of solidification (point S_1), with the final liquid-phase composition of L_1. However, if the alloy is rapidly cooled from point S to a metastable point, shown as S* in Fig. 11, the last liquid to solidify will have the eutectic composition L_e rather than L_1. In this case, the solid will have some eutectic structure in the microstructure.

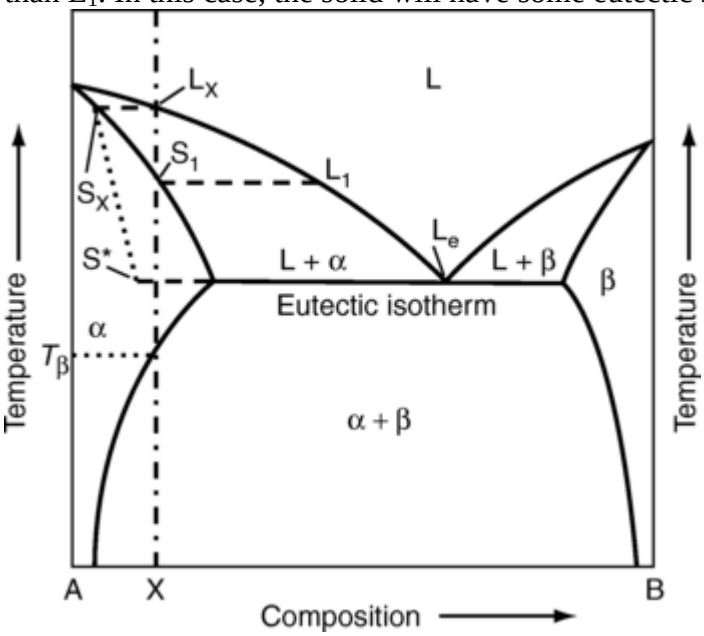

Fig. 11 Schematic binary phase diagram illustrating the effect of cooling rate on an alloy lying outside the equilibrium eutectic transformation line. Rapid solidification from S_x to a metastable position (S*) can result in some eutectic structure being formed, because the last liquid to solidify will have the eutectic composition L_e rather than L_1. Homogenization at temperatures in the single-phase field will eliminate the eutectic structure. The β phase will precipitate out of solid solution when the composition alloy X is slowly cooled below T_β.

Peritectic Alloy Systems

Another important type of solidification structure is that due to peritectic systems. In cooling through the peritectic transformation, a two-phase region, composed of a liquid and a solid, transforms to a new solid phase. The commercially important iron-carbon system has a peritectic transformation at 0.16 wt% C and 1493 °C (2719 °F). At this temperature, the mostly δ-phase iron material, containing 0.09% C, and a small remaining trace of liquid iron, containing 0.58% C, combine to form γ-phase iron (the top of the austenite “diamond”), with 0.16% C. More information on peritectic structures is contained in the articles “Invariant Transformation Structures” and “Fundamentals of Solidification” in this Volume. As in the isomorphous and the eutectic systems, cooling at faster than equilibrium conditions will produce microstructures with segregated (cored) compositions. This is discussed in the section “Coring” in this article.

Ternary Phase Diagrams

Of course, almost all alloys are not simple binary systems. Additional elements (added intentionally as alloys or as impurities) exist in alloys or commercially pure metals. Sometimes, these constituents interact in important ways and thus require phase diagrams with more than two compositional elements. As such, much research has

been done to determine the phase boundaries in many ternary alloy systems, which are plotted in graphical form as a three-sided prism.

However, because the third dimension of a ternary phase diagram is difficult to represent on a flat page, various approaches have been taken in order to get around the complexity of representing an entire ternary phase diagram in a single plot. For example, one approach is to plot triangular "slices" showing the phases present for all compositions at a particular temperature. Rectangular or vertical slices may also be plotted from various sections of ternary systems to allow a simplified two-dimensional plot.

A useful type of ternary section is known as a pseudobinary diagram, which is developed from ternary systems by holding one composition constant. This is not a true binary system, hence the name pseudobinary. Another type of ternary section is known as a quasi-binary section, which is derived from a section that cuts through a corner of the ternary and a melting point of a compound on the opposite side of the ternary diagram. Unlike pseudobinary diagrams, quasi-binary diagrams can be read like a true binary diagram, hence the name quasi.

Alternatively, projections, similar to those used to turn the shapes of continents on the earth into a flat map, are used to show the temperature boundaries of a particular situation, such as the temperature of solidification for all possible compositions. In this case, instead of having phase boundaries specifically marked, the liquidus temperature is indicated for each possible composition. For example, the liquidus projection of the Cr-Fe-Ni system may be of interest to welding engineers trying to understand the microstructure and behavior of a stainless steel weld.

References cited in this section

2. H. Okamato, *Desk Handbook: Phase Diagrams for Binary Alloys,* ASM International, 2000

3. *Alloy Phase Diagrams,* Vol 3, *ASM Handbook,* ASM International, 1992

D. Aliya and S. Lampman, Physical Metallurgy Concepts in Interpretation of Microstructures, *Metallography and Microstructures,* Vol 9, *ASM Handbook,* ASM International, 2004, p. 44–70

Physical Metallurgy Concepts in Interpretation of Microstructures

Debbie Aliya, Aliya Analytical, Inc.; Steve Lampman, ASM International

---

Nonequilibrium Phase Nucleation and Growth

Most phase changes of interest to physical metallurgists occur by melting, solidification, or solid-state transformations. This section focuses on the latter two processes and how the mechanisms of phase nucleation and growth influence the morphology, size, and distribution of grains and second phases. Segregation of elements and phase formation, as briefly discussed in the section "Equilibrium Phase Diagrams" in this article, is also described further in this section for solidification processes and solid-state transformations.

There are many factors that affect the distribution, size, and shape of microstructural features, so care must be exercised when interpreting microstructures from different materials, lots, or producers. Higher temperatures enhance diffusion and thus tend to produce coarser structures due to the elimination of higher energy boundaries in the microstructure. However, other factors may impede growth and affect the driving force for boundary elimination. Even very high-energy boundaries may be relatively stable, if the solubility of the second-phase particle atoms in the matrix is very low. In this case, it will be difficult for the atoms in the small second-phase particles to travel through the matrix.

Solidification and solid-state transformations must take place in an orderly manner. One atom at a time is added to the initially tiny solid nucleus of the new phase. This growth of the new phase depends on the temperature (i.e., the average kinetic energy of the atoms/molecules in an ensemble). At high temperatures, the atoms are more mobile, and thus growth rates of newly formed phases are higher when temperature is increased.

However, the formation of the initial nuclei also depends on temperature in an opposite way (at least for nucleation caused from the cooling of a high-temperature phase). For example, the high-temperature austenite phase (γ) in steel undergoes a phase change when it is cooled below the eutectoid isothermal (A_1) of austenite (see the section “The Iron-Carbon Eutectoid” in this article). If the transformation occurs at a temperature just below the A_1 temperature, the nucleation rate of new-phase particles would be slower than in the case of transformation at a temperature further below the A_1 isotherm. This is just the opposite of temperature effects on the growth rates, which are low at lower temperatures. These competing kinetics of phase nucleation and growth give rise to the classic C-type curve of isothermal transformation curves (as described in more detail in the section “Transformation Diagrams” in this article).

The effects of nucleation rates and growth rates may also be complex in alloy systems where one phase transforms into two new phases, as in the case of eutectic solidification or solid-state transformation of a eutectoid such as pearlite (as briefly described in the section “Isothermal Transformation Curves” in this article). Complex kinetic effects can also occur in the reverse (although less common) instance, when two solid phases transform to one solid phase. In addition to general coarse or fine microstructures, the shapes of the single-phase constituents within multiphase alloys or two-phase mixed structures can be quite complex and varied. For example, the variations of ferrite-cementite morphologies in carbon steels are described in more detail in the section “Proeutectoid and Pearlite Structures in Steel” in this article.

In general, the processes of phase nucleation and growth can be classified as either homogeneous or heterogeneous. Most transformations are of the heterogeneous type, where initiation of the transformation requires a critical nuclei size for further growth of a new phase. The critical nuclei size for growth is based on the competition between bulk energy and surface energy. When a new phase or grouping of atoms begins to form, sufficient bulk size must be obtained in order to grow. This represents the classic model of nucleation and growth in solid-state transformations. In heterogeneous transformations, growth of a new phase begins at preferential sites such as crystal imperfections. Preferential nucleation occurs at crystal imperfections (such as grain boundaries, grain corners, vacancies, or dislocations) because the nucleation of the new phase acts to eliminate the high-energy surface of the imperfection.

The initial nucleation process is fundamentally a fluctuation phenomenon, and the rate of heterogeneous nucleation thus is influenced by the density of preferred sites, the work required to form a critical nucleus, and the rate of atomic migration. In solids, the nucleation barrier controlling the formation of a second phase depends on the interfacial energy and strain energy of the critical nucleus. The nucleus shape is influenced by these factors and the crystallographic relationship between the new phase and its parent phase (e.g., see the article “Structures by Precipitation from Solid Solution” in this Volume).

The three basic types of heterogeneous transformations are (Fig. 12):

- Solidification (where growth is controlled by heat transport)
- Thermally activated solid-state growth (diffusive reconstruction)
- Athermal (displacive) solid-state transformation

These three types of heterogeneous phase growth are described in the sections “Solidification” and “Solid-State Phase Transformations” in this article. However, solid-state homogeneous transformations are also an important mechanism of phase growth.

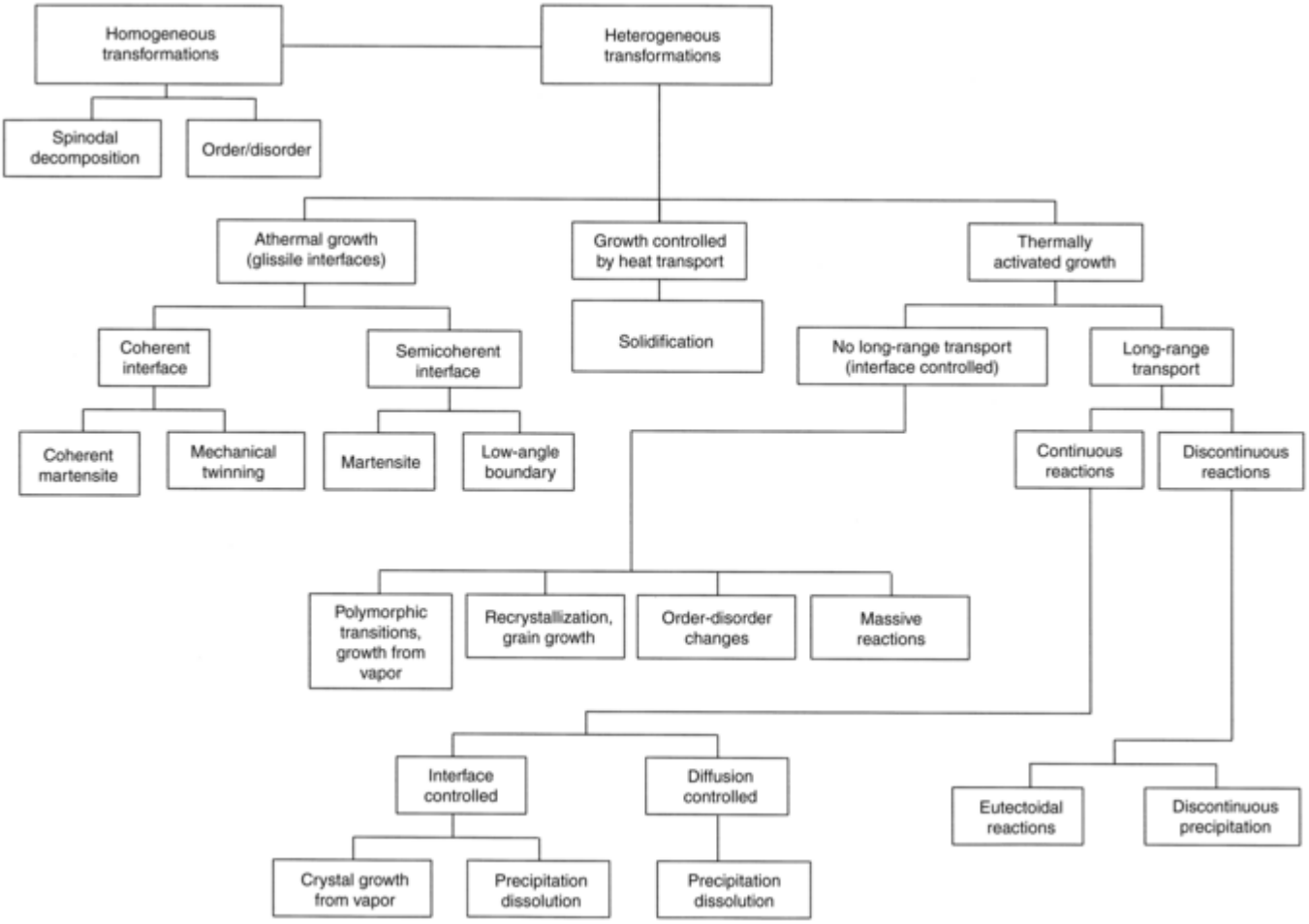

Fig. 12 Classification of transformations by growth processes

Homogeneous Transformation. Unlike the classical model of nucleation and growth, homogeneous transformations in solids do not involve initiation of a critical nucleus size for bulk growth of the new phase. The classic example of a homogeneous transformation is spinodal decomposition, where diffusional clustering or spontaneous unmixing occurs homogeneously throughout the alloy via the gradual buildup of enriched-solute regions (see the article “Spinodal Transformation Structures” in this Volume). Spinodal decomposition is not really defined by a phase boundary but is rather derived from a difference in thermodynamic stability for the kinetic process that governs the initial stages of phase separation. However, because the process occurs homogeneously throughout the material, a two-phase modulated structure can be produced.

Guinier-Preston Zones. The formation of Guinier-Preston (GP) zones is another example of a homogeneous transformation. Guinier-Preston zones are coherent, solute-rich regions that are not phases in the classic sense, because there is no discernible phase boundary between the solute and the host. Rather, the solute atoms fit within the lattice of the host with only some strain to accommodate the slight difference in both lattice parameters of the host phase and the solute (as shown schematically in Fig. 13). The GP zones are small in size (on the order of 1 to 5 nm in size) and can form homogeneously throughout the host lattice. They are also a coherent structure, because continuity is maintained between the host lattice and the solute-rich regions.

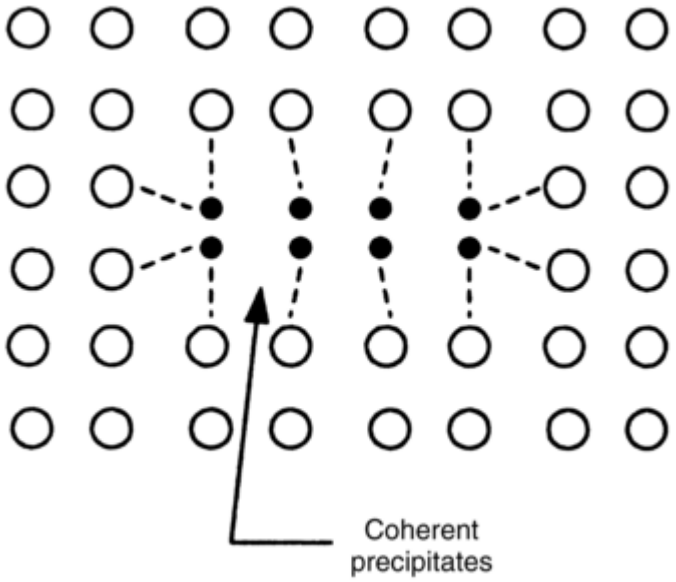

Fig. 13 Schematic of coherent structure of solute-rich precipitates region that causes lattice strain (indicated schematically by dashed lines)

Guinier-Preston zones are metastable, and further aging causes the GP zones to decompose into more stable forms. During aging, the initially coherent precipitate also will tend to lose coherency as it grows beyond a critical size by nucleating misfit dislocations at the interface or by attracting matrix dislocations. However, because GP zones can form homogeneously throughout the material, effective precipitation hardening can be achieved from the more stable precipitates that occur from aging the GP zones (see the article "Structures by Precipitation from Solid Solution" in this Volume).

Aluminum-copper alloys are the classic example of precipitation hardening from GP zones (see the article "Metallographic Techniques for Aluminum and Its Alloys" in this Volume). The solute-rich transition region in precipitation-hardening phase aluminum-copper alloys forms with a crystalline orientation defined from the initial supersaturated solid solution. For example, in the aluminum-copper system, the segregating copper atoms collect on the {100} crystal planes, forming a coherent structure with the matrix.

D. Aliya and S. Lampman, Physical Metallurgy Concepts in Interpretation of Microstructures, *Metallography and Microstructures,* Vol 9, *ASM Handbook*, ASM International, 2004, p. 44–70

Physical Metallurgy Concepts in Interpretation of Microstructures

Debbie Aliya, Aliya Analytical, Inc.; Steve Lampman, ASM International

---

Solidification

The change from a solid to liquid or a liquid to solid state is a commonly recognized phase change. During solidification, atoms arrange themselves into a crystalline structure. This means that in order to solidify, the atoms must be added to a growing crystal one by one in the next available position. This takes time. In addition, the crystalline structure of metals in the solid state has an important influence in the characteristics of solidification. In most common alloys, microstructure is affected by the element that solidifies first from the melt, as described in more detail in the preceding section, "Equilibrium Phase Diagrams," for isomorphous and eutectic alloy systems.

In terms of initial nucleation during solidification of an alloy, tiny groups of atoms begin to solidify into a crystalline form. These groups of atoms, or nuclei, may grow or redissolve, depending on the kinetic (or thermal) conditions of the solidification process. For example, if the surrounding liquid is just below the

liquidus of the alloy (or the melting point in a pure metal), the so-called driving force for nucleation is low. In this condition, many nuclei may redissolve into the liquid phase. However, some remaining nuclei also may easily grow because of the high diffusion rate associated with the high temperature near the melting point (or near the top of the melting range of an alloy).

Thus, very slowly cooled metals will tend to have coarse microstructures, because the solid crystal phase forms at a temperature near the top of the melting range, where nucleation of many particles is difficult, but growth of nucleated particles is easy because diffusion is enhanced at higher temperatures. In contrast, quick cooling tends to produce relatively fine grains, because the atoms quickly solidify with less diffusion-activated growth of the grains. Likewise, the size and general coarseness of second-phase particles in a microstructure are determined by how far the temperature is above or below the critical temperature of phase formation. Some nuclei also may form as a separate liquid within the matrix or main liquid phase. Sulfur and some oxygen-containing compounds often separate out in a liquid condition from the surrounding iron-base liquid in molten steel. When the steel cools, these separate high-sulfur areas become embedded as distinct solid particles in the solid steel.

Because most real castings are not solidified in an equilibrium manner, deviations from the temperatures predicted by the phase diagrams for the upper and lower ends of the freezing range may be expected. The general trend is that faster cooling will depress the temperature range. Phase diagrams also can be used to illustrate how and why one of the common microstructural features of coring is created in commercially produced castings.

Coring is a microlevel segregation of alloying elements that occurs during solidification of many commercial castings. The origin of coring can be understood by referring back to the phase diagram of a simple isomorphous system (Fig. 4). The atoms already present in the solid state must mix with the new atoms just solidified. This mixing is very slow in the solid state, because it depends on multiple-step diffusion of single atoms. If there is not enough time for the composition to homogenize before new layers are added, there will be a difference in composition between the first portions of the material to solidify and the last portions to do so. In the case of the solidification isomorphism of the hafnium-zirconium system, very little segregation due to coring is possible, because the liquidus and solidus are close together (Fig. 5b)

Figure 14(a) shows a heavily banded medium-carbon steel microstructure from an initially heavily microsegregated, or cored, as-cast structure. The medium-carbon steel was produced by a continuous casting process, with higher manganese in the pearlitic regions. This segregation of the manganese tends to persist through austenitizing in subsequent transformation of the austenite, where martensite forms in the regions previously occupied by pearlite, while bainite or pearlite form where the ferrite was. While carbon segregation is relatively easy to overcome, due to the small size of the carbon atoms, alloy segregation is difficult or practically impossible to overcome. This shows that cored structures, once created, can be very persistent, even after many thermal cycles and deformation. Figure 14(b) shows an aluminum casting with a noticeably different composition (as revealed by the response to the etchant) in the (dark) centers of the dendrites and the lighter outer areas.

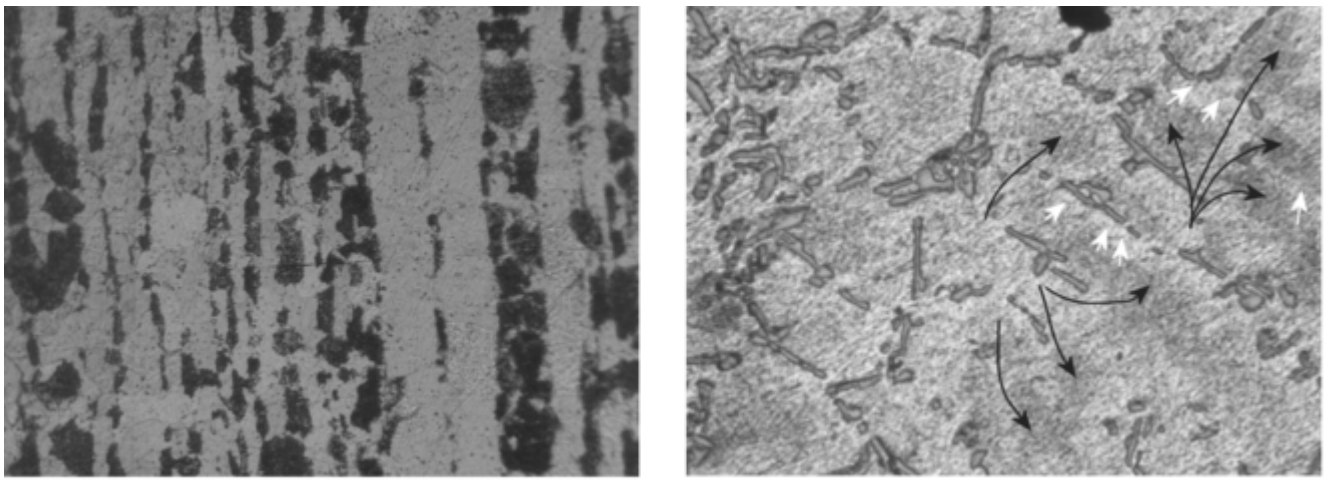

Fig. 14 Examples of microstructure with alloy microsegregation from coring. (a) Heavily banded medium-carbon steel microstructure that was produced by a continuous casting process with alternating

layers of ferrite (light) and pearlite (dark). The initial as-cast structure was heavily cored (microsegregated), with higher manganese in the pearlitic regions indicated by energy-dispersive spectroscopy microchemical analysis. 5% nital etch. (b) Coring during solidification in the as-cast microstructure of an aluminum alloy revealed by differences in etching due to compositional differences. The dark arrows show the central (core) portions of the primary dendrites, while the light arrows show the last part of the material to solidify. Keller's reagent

Although coring may not be a concern at the eutectic concentration, because solidification occurs at one single temperature at the eutectic, any deviation from the eutectic can create the possibility of coring. Sometimes, deviations from the eutectic composition are not obvious by viewing a microstructure. Fast cooling near eutectic compositions may also result in microstructures that appear to be eutectic, but only careful quantitative evaluation may reveal that the percentages of each of the two solid phases are not equal to those predicted for the eutectic composition.

Liquation. Because the lowest freezing material in a cored microstructure is segregated to the edges of the solidifying crystals (the grain boundaries), this material can remelt when the alloy sample is heated to temperatures below the equilibrium solidus line. If grain-boundary melting (called liquation, or, less correctly "burning") occurs while the sample also is under stress, such as during hot forming, the liquefied grain boundaries will rupture, and the sample will lose its ductility and be characterized as a hot short.

D. Aliya and S. Lampman, Physical Metallurgy Concepts in Interpretation of Microstructures, *Metallography and Microstructures,* Vol 9, *ASM Handbook*, ASM International, 2004, p. 44–70

Physical Metallurgy Concepts in Interpretation of Microstructures

Debbie Aliya, Aliya Analytical, Inc.; Steve Lampman, ASM International

---

Solid-State Phase Transformations

Segregation of elements and phase formation can also take place in the solid-state condition. Solid-state transformations may be grasped somewhat less intuitively than melting and crystallization, but the same basic concept applies. Atoms are responding to thermal conditions. In general, there are two basic types of solid-state transformation:

- Isothermal transformations are produced by diffusion-controlled (thermally activated) growth mechanisms that occur over time on a prolonged basis.
- Athermal transformations occur from temperature changes that result in shear displacement of atomic positions. Athermal transformations are referred to as a "diffusionless" process, because it requires a rapid change in temperature rather than random atomic movement over a prolonged period of time.

Both isothermal and athermal transformations involve some changes of atomic neighbors, and the ease with which the atoms can change neighbors (so-called kinetic effects) affect the shape of the phases. Even the so-called diffusionless mechanism of athermal transformations takes time and thus involves kinetic factors in the atomic rearrangement of a phase transformation.

Isothermal Growth

Isothermal transformations occur by phase growth that is activated by the thermal (kinetic) energy of the atoms in an ensemble. Agitated atoms migrate from boundaries by diffusion, and thus growth occurs as more stable phases accumulate by combination with other atoms. These types of growth processes are thus referred to as isothermal transformations, because thermally activated growth can occur at constant (isothermal) temperature.

In an isothermal transformation, diffusion of atoms in the solid state may cause the formation of distinct chemical constituents in an alloy. These chemical constituents, or phases, can be identified and documented with the aid of equilibrium diagrams. Unfortunately, the same mixture of specific phases can be found in several different types of arrangements or microstructures. Segregation of elements can also take place in solid-state transformations. Because segregation, by its nature, involves motion of atoms, the speed with which the atoms can change neighbors (diffuse) is an important factor that affects the shapes of the new phase areas. Thus, while understanding phase diagrams is an essential part of understanding microstructural development, phase diagrams cannot predict all the morphological characteristics of phase growth.
Isothermal transformations can be grouped into the following two categories of phase growth (Fig. 12):

- Interface-controlled reactions
- Discontinuous or continuous reaction with long-range transport

Interface-controlled reactions include changes such as grain growth and recrystallization, as briefly described in a previous section, “Grain Size and Growth,” in this article. Another example of an interface-controlled transformation would be massive reactions (see the article “Massive Transformation Structures” in this Volume).
Transformations by long-range transport include discontinuous reactions and continuous reactions. The main distinction here is one of moving reaction fronts. Discontinuous reactions under isothermal conditions involve phase separation with moving reaction boundaries, as indicated in the classification of Fig. 15 (Ref 4). When the process of phase separation involves a migrating reaction front, the change in composition and orientation is discontinuous and occurs from various reaction mechanisms, such as discontinuous precipitation, discontinuous coarsening, and diffusion-induced recrystallization/grain-boundary migration. These discontinuous mechanisms may compete with each other and with other processes, such as continuous precipitation.

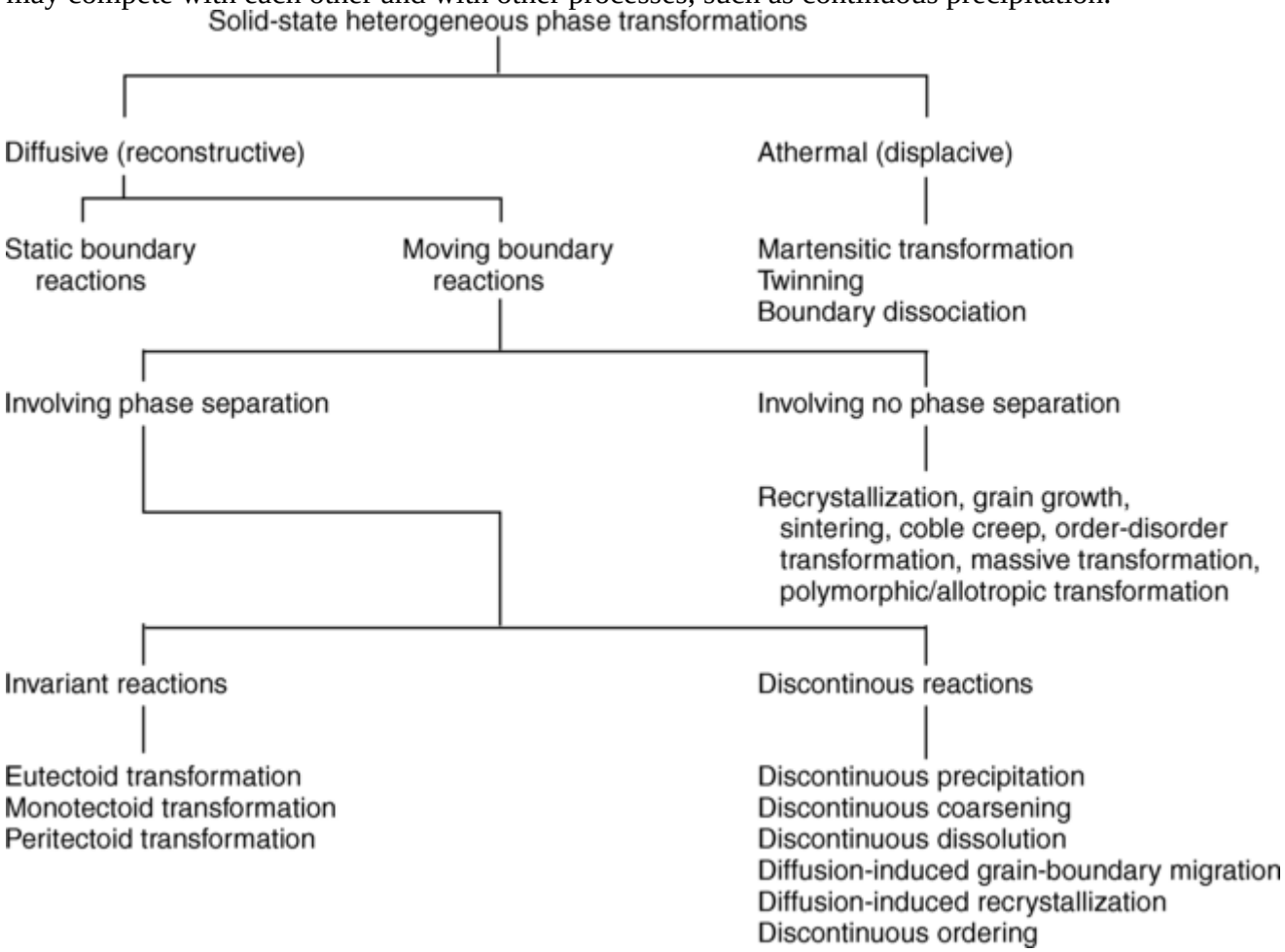

Fig. 15 General classification of solid-state heterogeneous phase transitions Source: Ref 4

In terms of phase separation with moving reaction boundaries, there are two basic types of phase-separation reactions (Fig. 15):

- Invariant reactions
- Discontinuous reactions

These two types of reactions both produce a new two-phase structure from an initial single-phase matrix (or parent). However, the important difference is the crystal structure of the matrix after transformation (phase separation) of the single-phase parent. In discontinuous precipitation, a new second phase is produced, but the matrix after the reaction has the same crystal structure as the initial parent phase. In contrast, invariant transformations produce two new phases that both have distinct crystal structures from that of the original parent phase. Because two new phases are produced during invariant transformations, the resulting microstructures can be quite varied in terms of morphology. Discontinuous solid-state precipitation can be quite varied (see the article “Structures by Precipitation from Solid Solution” in this Volume).

The Iron-Carbon Eutectoid. The classic example of a solid-state invariant transformation is the iron-carbon eutectoid (Fig. 16). Like a eutectic transformation during solidification, the eutectoid decomposition of ferrous austenite ($\gamma \rightarrow \alpha + Fe_3C$) produces a distinctive microstructure (pearlite) with alternate layers or platelets of the two new phases. However, even though eutectoid and eutectic reactions are both invariant transformations, diffusion in solids during a eutectoid reaction is much lower than in liquids. Therefore, in practical situations nonequilibrium transformation may be even more important in the eutectoid solid-state reactions than in the liquid-solid eutectic reaction.

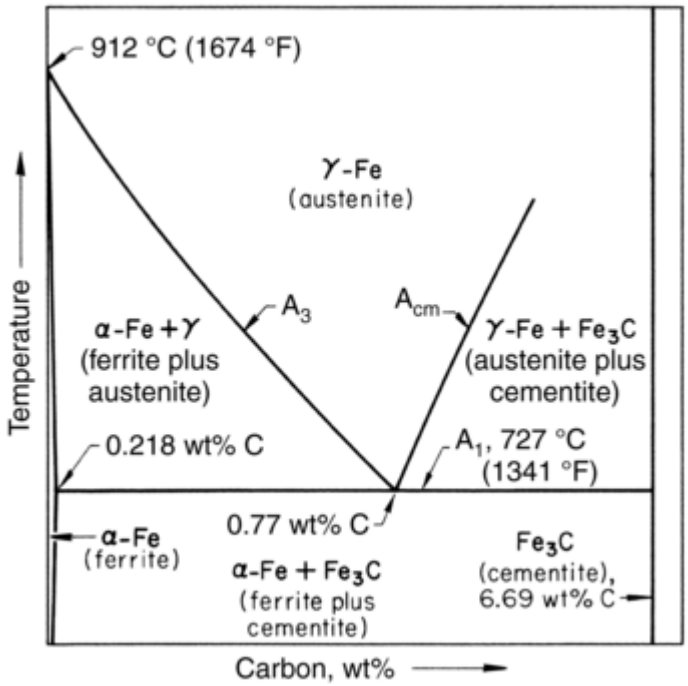

Fig. 16 The Fe-Fe_3C eutectoid region of the iron-carbon phase diagram

The morphologies of pearlite, and its occurrence or distribution in a microstructure, can be quite varied, depending on the composition and heat treatment of steel. Therefore, the best place to begin is with the simple situation of a eutectoid steel (carbon content of ~0.8 wt%) that undergoes slow cooling through the eutectoid isotherm of 727 °C (1341 °F). In this classic case, the austenite phase transforms into the expected form of pearlite with a lamellar structure consisting of alternate platelets (Fig. 17). The alternating platelet structure of pearlite means that each carbon atom has a shorter distance to travel than it would if it had to end up in dispersed spheroids, which would otherwise be the preferred shape (based on energy minimization).

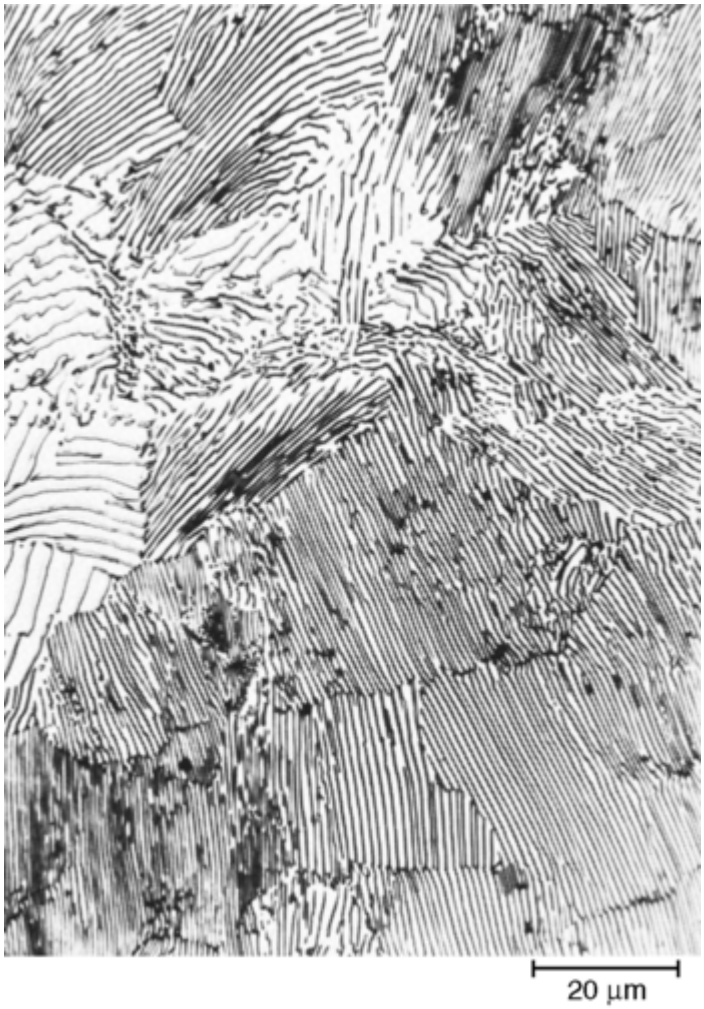

Fig. 17 Classic lamellar appearance of pearlite in a eutectoid steel (~0.8% C) after slow cooling (2.5 °C/min, or 4.5 °F/min) from austenite. Picral etch. Original magnification 650×. Source: Ref 5

The appearance of the pearlite in Fig. 17 is very similar to a lamellar eutectic structure. However, the approximation of equilibrium conditions with slow cooling is not typical of heating and cooling rates in general. In practice, there is a departure from the lamellarity of pearlite in steels, depending on composition, transformation temperature, and cooling rates. This complexity is due to the fact that eutectoid structures, such as pearlite, describe a two-phase structure that can have a spectrum of morphologies. The same applies to bainite, which also is a eutectoid product with some athermal (shear-controlled) component in the transformation process (see the section "Bainite" in this article). Thus, eutectoid structures are two-phase mixtures that involve more diverse variations in their description than for single-phase constituents (e.g., austenite, ferrite, cementite, carbides, graphite, and, to a limited extent, martensite) that can be described unambiguously (Table 1).

Table 1 Metallurgical phases and microconstituents in steel

Phase (microconstituent)	Crystal structure of phases[(a)]	Characteristics
Ferrite (α-iron)	bcc	Relatively soft low-temperature phase; stable equilibrium phase
δ-ferrite (δ-iron)	bcc	Isomorphous with α-iron; high-temperature phase; stable equilibrium phase
Austenite (γ-iron)	fcc	Relatively soft medium-temperature phase; stable equilibrium phase
Cementite (Fe_3C)	Complex orthorhombic	Hard metastable phase
Graphite	Hexagonal	Stable equilibrium phase

Pearlite		Metastable microconstituent; lamellar mixture of ferrite and cementite
Martensite	bct (supersaturated solution of carbon in ferrite)	Hard metastable phase; lath morphology when <0.6 wt% C; plate morphology when >1.0 wt% C and mixture of those in between
Bainite	…	Hard metastable microconstituent; nonlamellar mixture of ferrite and cementite on an extremely fine scale; upper bainite formed at higher temperatures has a feathery appearance; lower bainite formed at lower temperatures has an acicular appearance. The hardness of bainite increases with decreasing temperature of formation.

(a) bcc, body-centered cubic; fcc, face-centered cubic; bct, body-centered tetragonal

Proeutectoid and Pearlite Structures in Steel. The term *proeutectoid* refers to the microconstituents that form before the eutectoid isothermal is reached during cooling (that is, proeutectoid constituents are analogous to the so-called primary phase constituents in eutectic solidification).

A simplified schematic of the general process is illustrated in Fig. 18 (Ref 6). For example, in hypoeutectoid carbon steels (<0.8 wt% C), the proeutectoid phase is low-carbon α ferrite that forms along prior-austenite grain boundaries (Fig. 18a). In the center of the grains, pearlite colonies then form, with various orientations, during the eutectoid part of the transformation. Conversely, the proeutectoid phase in hypereutectoid steel (>0.8 wt% C) is cementite (Fe_3C), which also tends to form along prior-austenite grain boundaries. In terms of morphology, the microstructure of hypo- and hypereutectic steels may, in principle, have similar morphologies, as shown schematically in Fig. 18. The distinction between the ferrite carbide phases (illustrated by shading) is revealed differently in light-microscope metallography and electron microscopy (Fig. 19). Other contrast techniques, such as color metallography, also can distinguish ferrite from the carbide phase.

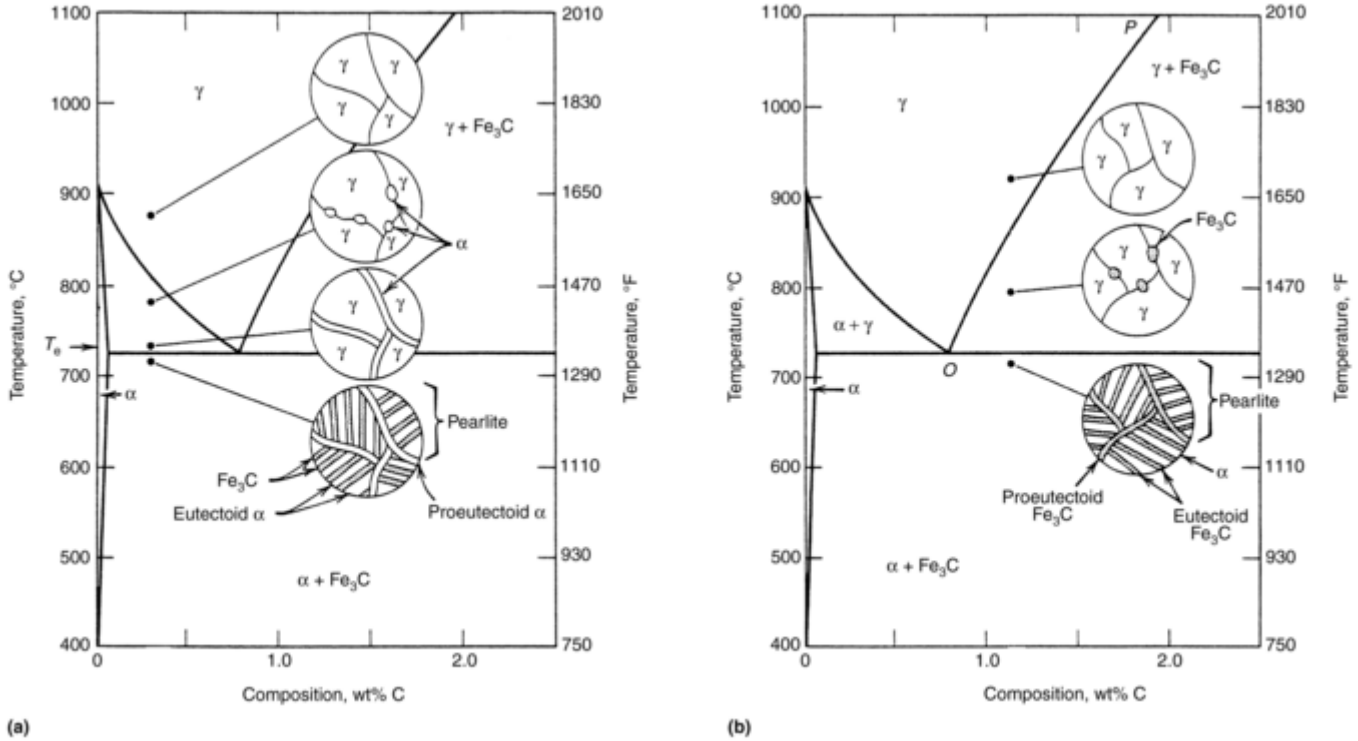

Fig. 18 Schematic of proeutectoid and eutectoid (pearlite) formation from austenite transformation in slowly cooled steels. (a) Hypoeutectoid steels. (b) Hypereutectoid steels

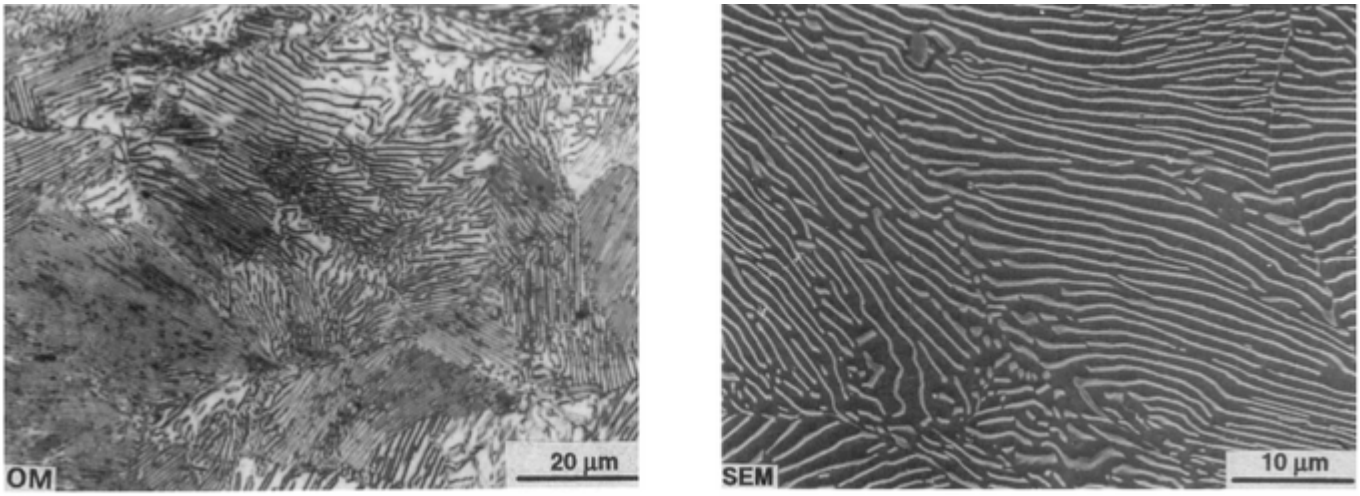

Fig. 19 Different appearance of ferrite and cementite (Fe_3C) constituents of pearlite when examined by optical (light) and scanning electron microscopes (SEMs). A polished specimen is chemically etched such that the Fe_3C platelets stand out in relief. (a) In optical microscopy at low magnification, the cementite platelets appear as dark lines. (b) When viewed at high magnification with a SEM, the carbide phase appears white. Source: Ref 6

Formation of Pearlite in Eutectoid Steels. Before discussing the formation of the proeutectoid phase and the eutectoid (pearlite) in steels with hypo- and hypereutectoid compositions, it is useful to describe the rates of pearlite nucleation and growth in eutectoid steel (~0.8 wt% C). The rates of phase nucleation and growth can be understood with the aid of isothermal transformation (IT) curves plotted on time-temperature transformation (TTT) diagrams (see also the section “Transformation Diagrams” in this article). The isothermal TTT of eutectoid steel is shown in Fig. 20 (Ref 7). At high temperature just below the eutectoid isothermal (A_1), pearlite nucleates at a slow rate but grows easily at a high temperature. Thus, large pearlite colonies form.

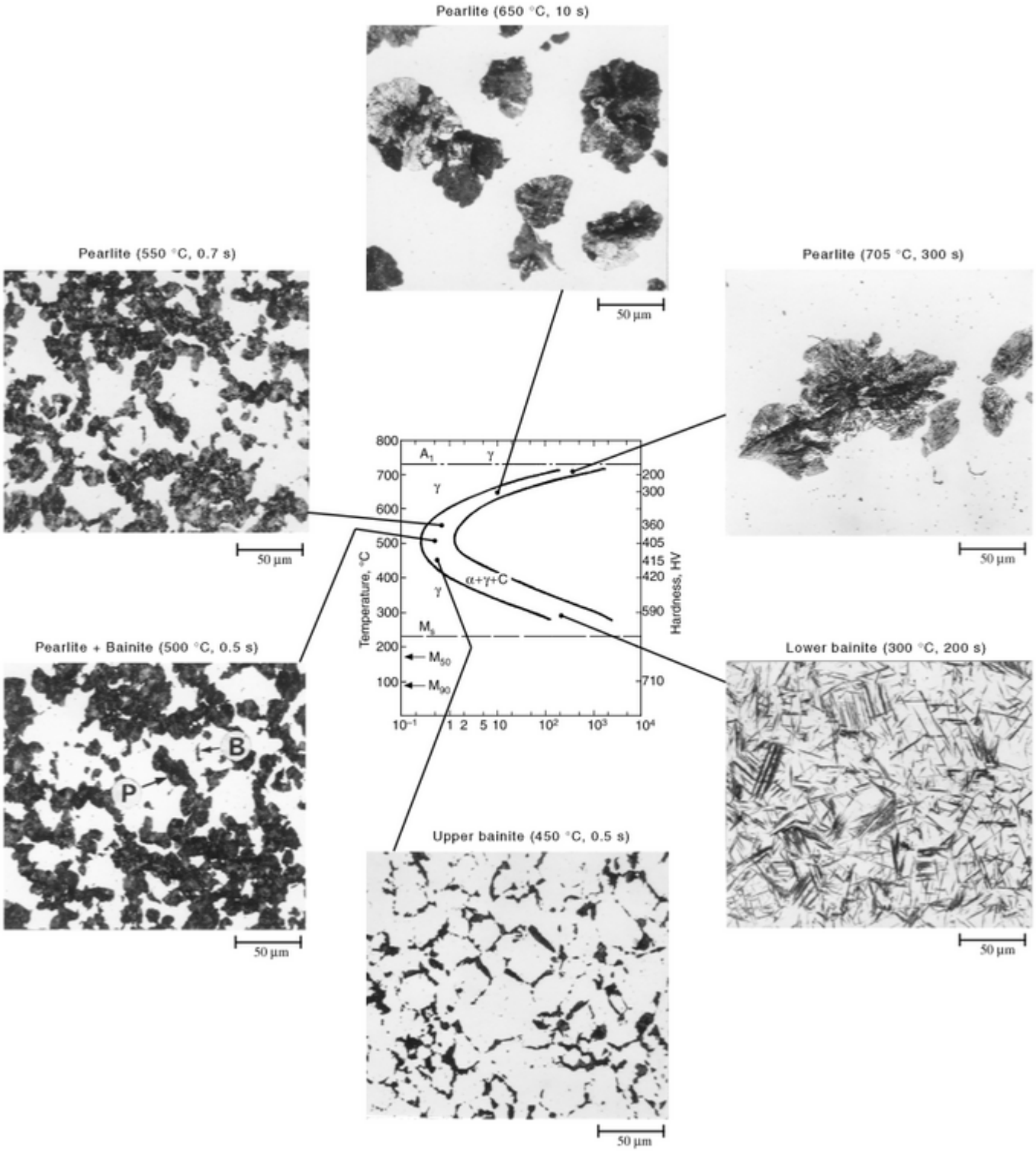

Fig. 20 Isothermal transformation (IT) diagram for a eutectoid composition (~0.8% C) of carbon steel (0.81C-0.07Si-0.65Mn, wt%). The IT curves show the time for the start and finish of austenite (γ) transformation into a two-phase structure consisting of ferrite (α) and the cementite carbide (c). Formation of the pearlite morphology, consisting of alternating plate crystals of ferrite and Fe_3C, is dominant at the higher transformation temperatures. The nucleation rates of pearlite are low at temperatures near A_1, but nuclei growth is enhanced by diffusion of constituents at the higher temperature. At low temperatures (below the nose of the C-shaped boundary), the bainite eutectoid product becomes more prevalent. Micrographs are from specimens that were austenitized at 860 °C (1580 °F), with isothermal exposures as indicated for each. Specimens were quenched to make martensite (white) of the material remaining as austenite at the end of the specified time. All picral etch and original magnification 250×. Adapted from Ref 7

The classic C-shape of the IT curve illustrates the combined effect of nucleation rates and growth rates. As temperature is lowered toward the nose of the IT curve, growth rates decrease, but nucleation rates increase. Near the nose of the IT curve, the amount of transformation is maximum due to higher nucleation rates and moderate growth. In this case, the colonies of pearlite are smaller but more numerous than that from transformation at a higher temperature. In these small pearlite colonies, it may be difficult to resolve the very fine internal lamellar structure with a light microscope. In this case, electron microscopy would be required to resolve the pearlite structure. At temperatures below the IT nose, growth of pearlite is reduced substantially.

There also is some presence of upper bainite from transformations near the nose region of the IT curve. Like the pearlite, in this case the bainite is a eutectoid product from the diffusion-controlled decomposition of austenite into a two-phase structure with ferrite and cementite. However, bainite is distinct from pearlite, because the more rapid quench from austenite also causes some athermal transformation due to continuous cooling. Finally, at low transformation temperatures closer to the martensite start temperature, the transformation product is that of lower bainite (see the section “Bainite” in this article).

Hypoeutectoid Carbon Steels. The morphologies of the ferrite-cementite mixtures can be quite varied in hypoeutectic steels. Sometimes, the eutectoid product (pearlite) is regularly lamellar, while other parts may only be slightly lamellar. The morphology of the proeutectoid phase (i.e., ferrite) in hypoeutectic steels also can be quite varied.

Typically, the proeutectoid phase nucleates along the prior-austenite grain boundaries and then grows into the interior of the austenite grain. As the austenite transforms to the ferrite (with less capacity than austenite to dissolve carbon), the excess carbon in the remaining austenite is available for eventual formation of cementite carbide or pearlite. The nucleation of pearlite starts at the interface between the ferrite and austenite, at which point the growth of the proeutectoid ferrite stops. The volume fraction of proeutectoid ferrite decreases as the transformation temperature is lowered below A_1 and is 0 near the nose of the IT curve. This is shown in the isothermal TTT curve of Fig. 21 for 0.55% hypoeutectoid steel.

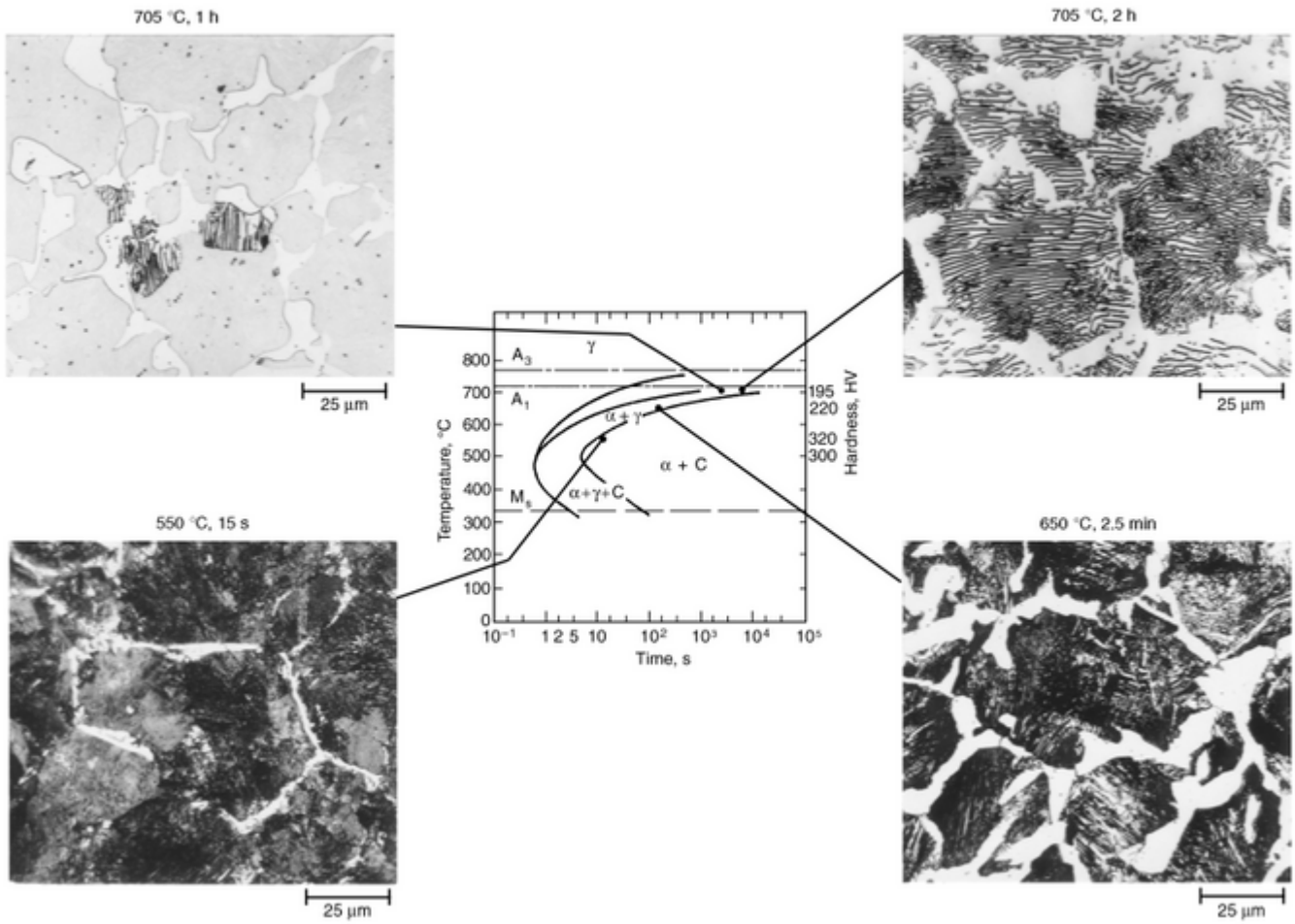

Fig. 21 Isothermal transformation (IT) diagram of a hypoeutectoid carbon steel (0.55C-0.08Si-0.60Mn, wt%). Proeutectoid ferrite forms first, starting below the critical temperature of γ-to-α transformation (A_3). The transformation region of proeutectoid ferrite (α + γ) ceases near the nose of the IT curve, at

which point pearlite formation begins. Micrographs are from specimens that were austenitized at 860 °C (1580 °F), with isothermal exposures as indicated for each. All picral etch and original magnification 500×. Adapted from Ref 7

The dominant morphologies of ferrite and cementite from isothermal transformation fall roughly within the composition temperature regions shown in Fig. 22. As described by Samuels (Ref 7), these shapes are part of a general classification developed by Dubé (Fig. 23). For hypoeutectoid steels, Samuels (Ref 7) notes the following on proeutectoid morphology:

- Massed areas of ferrite usually are present only after complete transformation at high temperatures, because growing ferrite grains tend to obscure the morphology in the early stages of proeutectoid growth.
- An acicular grain shape may appear in massed ferrite when the ferrite has grown with a Widmanstätten morphology.
- Grain-boundary allotriomorphs tend to form when the composition is near the eutectoid, because so little proeutectoid ferrite forms that there is little opportunity for Widmanstätten plates to develop.
- Widmanstätten morphologies of proeutectoid ferrite are observed after complete transformation over only a limited range of carbon contents and transformation temperatures, which are wider in coarse-grained steels (Fig. 22).

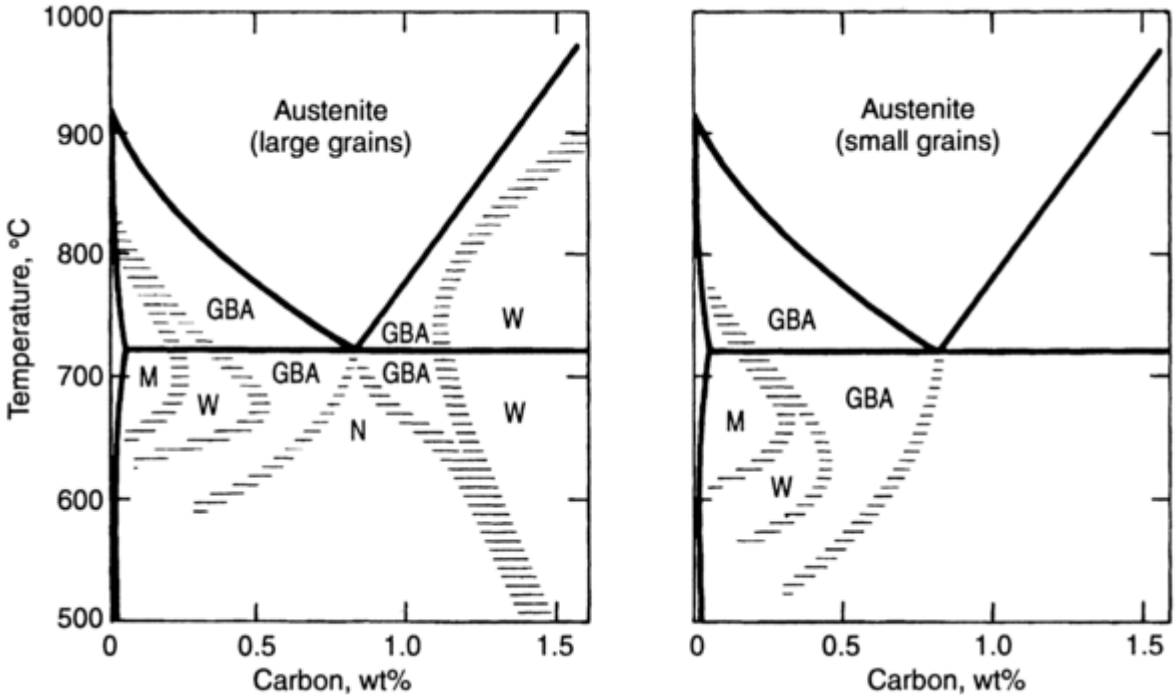

Fig. 22 Temperature-composition regions indicating the morphological tendencies of proeutectoid ferrite and cementite from isothermal decomposition of large-grain (ASTM 0 to 1) and small-grain (ASTM 7 to 8) austenite. See also Fig. 23 for descriptions of GBA, grain-boundary allotriomorphs; W, Widmanstätten sideplates and/or intergranular plates; and M, massed ferrite. The region N indicates little or no presence of proeutectoid ferrite or cementite from the decomposition of large-grained austenite with near-eutectoid compositions. Adapted from Ref 8 and Ref 9 and reprinted from Ref 7

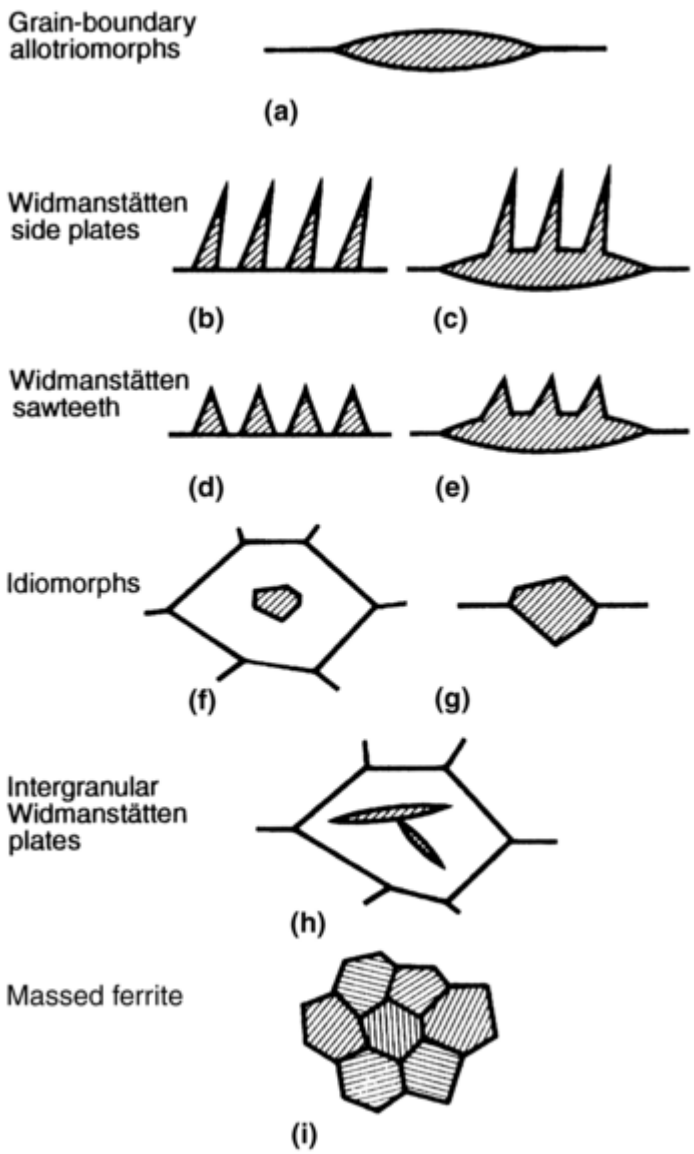

Fig. 23 The Dubé classification (Ref 8) of ferrite morphologies. (a) Grain-boundary allotriomorphs grow preferentially and more or less smoothly along grain boundaries, with little thickening. (b) Primary Widmanstätten sideplates grow from boundaries and have plate-shaped crystals (needle-shaped sections) that grow into the grains. (c) Secondary Widmanstätten sideplates grow from the crystal of the same phase with another morphology, usually grain-boundary allotriomorphs. (d) Primary Widmanstätten sawteeth grow from grain boundaries with a triangular appearance in section. (e) Secondary Widmanstätten sawteeth grow the crystal of the same phase with another morphology. (f) Idiomorphs that are equiaxed but faceted ferrite form almost entirely in the interior of parent austenite grains. (g) Grain-boundary idiomorphs are not normally observed in steels. (h) Intergranular Widmanstätten plates in parent grain of austenite. (i) Massed ferrite, also referred to as massive ferrite, for large areas with no obvious morphology other than a bulky, roughly equiaxed structure. Adapted from Ref 7

On slow cooling or at high temperatures, eutectoid pearlite formation occurs when the remaining austenite is of the eutectoid composition (0.77 wt% C). However, when isothermal transformation occurs at lower temperatures, the amount of proeutectoid ferrite is reduced (Fig. 21), and thus, less excess carbon after ferrite formation goes into the remaining austenite. In this case, the remaining austenite may not be sufficiently enriched with additional carbon to reach the eutectoid composition for pearlite formation. Therefore, the morphology of pearlite in hypoeutectic steels may be more variable or uneven with respect to its classic morphology. For example, Fig. 24 shows pearlite in a 0.6% C steel. Only some regions have the lamellar appearance, while short plates or globular particles of cementite appear in other regions.

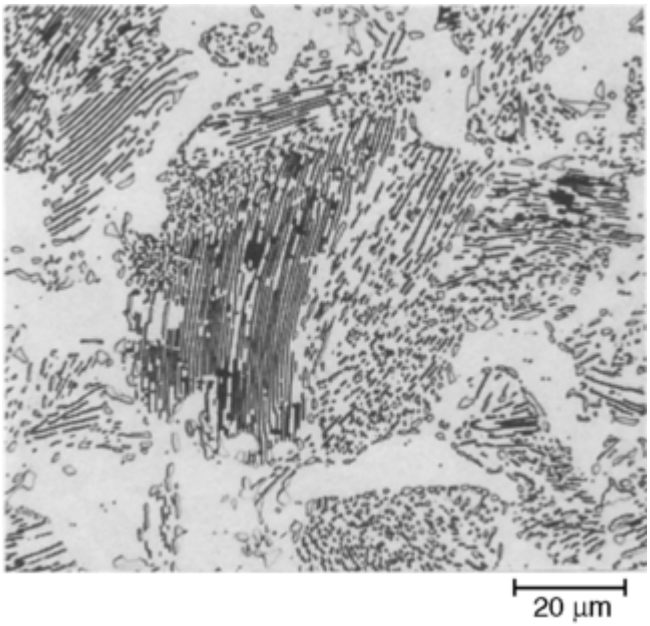

Fig. 24 Pearlite with lamellar appearance in only some regions, with short plates or globular particles of cementite in other regions. 0.6% C steel (0.61C-0.08Si-0.60Mn) austenitized at 860 °C (1580 °F) and isothermally transformed at 705 °C (1300 °F) for 17 h. 185 HV. Picral etch. Original magnification 500×. Source: Ref 7

Pearlite degeneracy in hypoeutectoid steels depends on various factors, as described by Samuels (Ref 7). In general, the most marked tendency for development of degenerate pearlite is in low-carbon steels with low manganese contents that have been transformed at temperatures close to A_1 after having been austenitized to produce a small grain size (Ref 7). The effect of transformation temperature on degeneracy is shown in Fig. 25. The effect of austenite grain size on pearlite morphology is shown in Fig. 26.

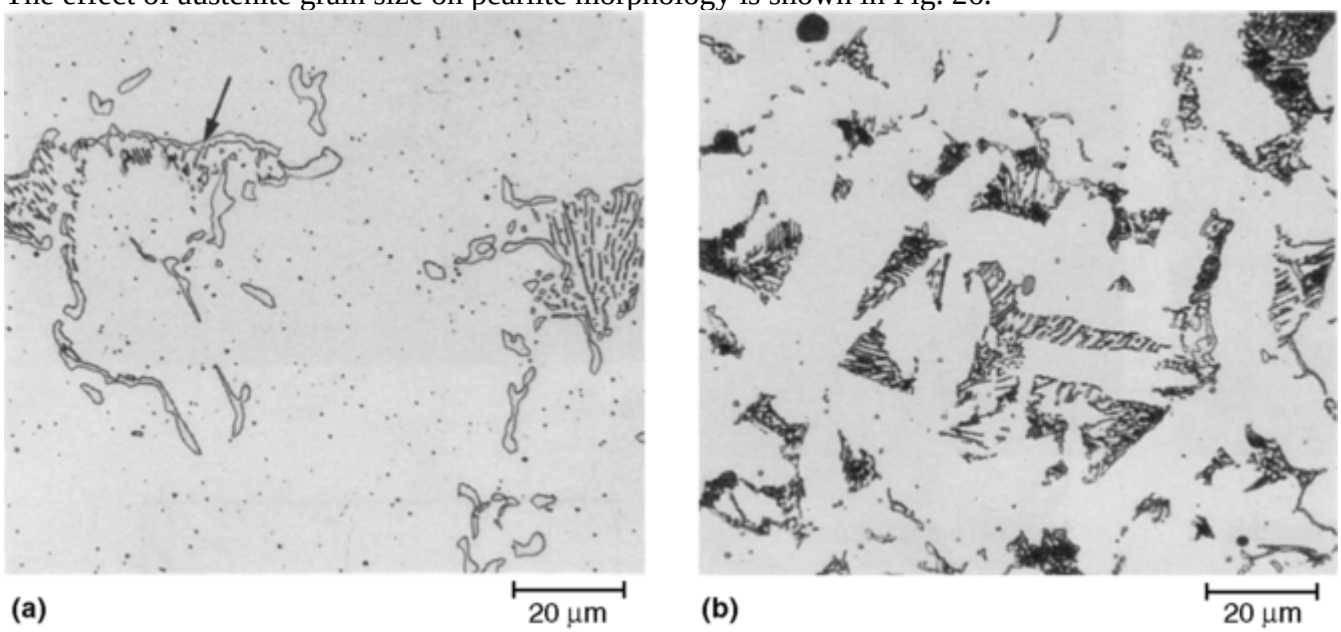

Fig. 25 Effect of transformation temperature on extent of degenerate (nonlamellar) pearlite in a 0.25% C hypoeutectoid steel (0.23C-0.06Si-0.52Mn, wt%). (a) A structure with prominent nonlamellar features is observed in the steel austenitized at 900 °C (1650 °F) and isothermally transformed at 705 °C (1300 °F) for 16 h. Cementite is present as thick films that occasionally have an embryonic lamellar grouping of cementite (indicated by arrow). (b) Pearlite with a more regular lamellar appears in the steel (austenitized at 925 °C, or 1700 °F) after isothermal transformation at 675 °C (1250 °F). Both are 180 HV, picral etch, and original magnification 500×. Source: Ref 7

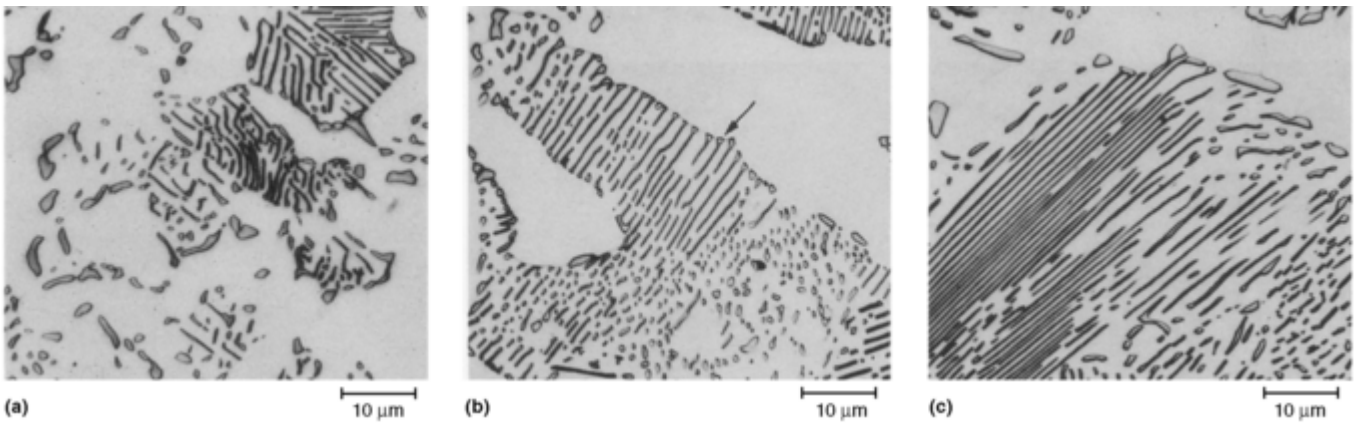

Fig. 26 Effect of austenite grain size on pearlite in 0.4% C aluminum deoxidized steel (0.4C-0.19Si-0.73Mn, wt%) after austenitization and isothermal transformation at 695 °C (1280 °F). (a) Austenitized at 840 °C (1550 °F) ASTM grain No. 7. (b) Austenitized at 950 °C (1740 °F), ASTM grain size No. 5. (c) Austenitized at 1090 °C (2000 °F), ASTM grain size No. 3. Higher austenitizing temperatures result in a larger grain size of austenite, and the extent of pearlite degeneracy is reduced. The dog-bone terminations (see arrow in b) are thought to be indicative of an early stage of degeneracy. All 150 HV, picral etch, and original magnification 1000×. Source: Ref 7

Hypereutectoid Carbon Steels. The proeutectoid phase in hypereutectic carbon steel is cementite, which forms along the austenite grain boundaries (Fig. 18b). The proeutectoid cementite can form with a number of morphologies that are similar to those for proeutectoid ferrite (Fig. 23). Isothermal kinetics of a relatively high-carbon composition (1.2% C) are summarized in Fig. 27. Hypereutectic steels are typically heat treated below the A_1 temperature in order to spheroidize the brittle cementite phase. In terms of pearlite formation from austenite, markedly degenerate forms of pearlite do not develop in hypereutectoid steels, because the carbon content of the transforming austenite would remain high at the lower isothermal transformation temperatures (where a smaller volume fraction of proeutectoid Fe_3C means that carbon would remain in the austenite). As shown by the IT curve of Fig. 27, the proeutectoid formation of cementite ceases near the nose of the curve.

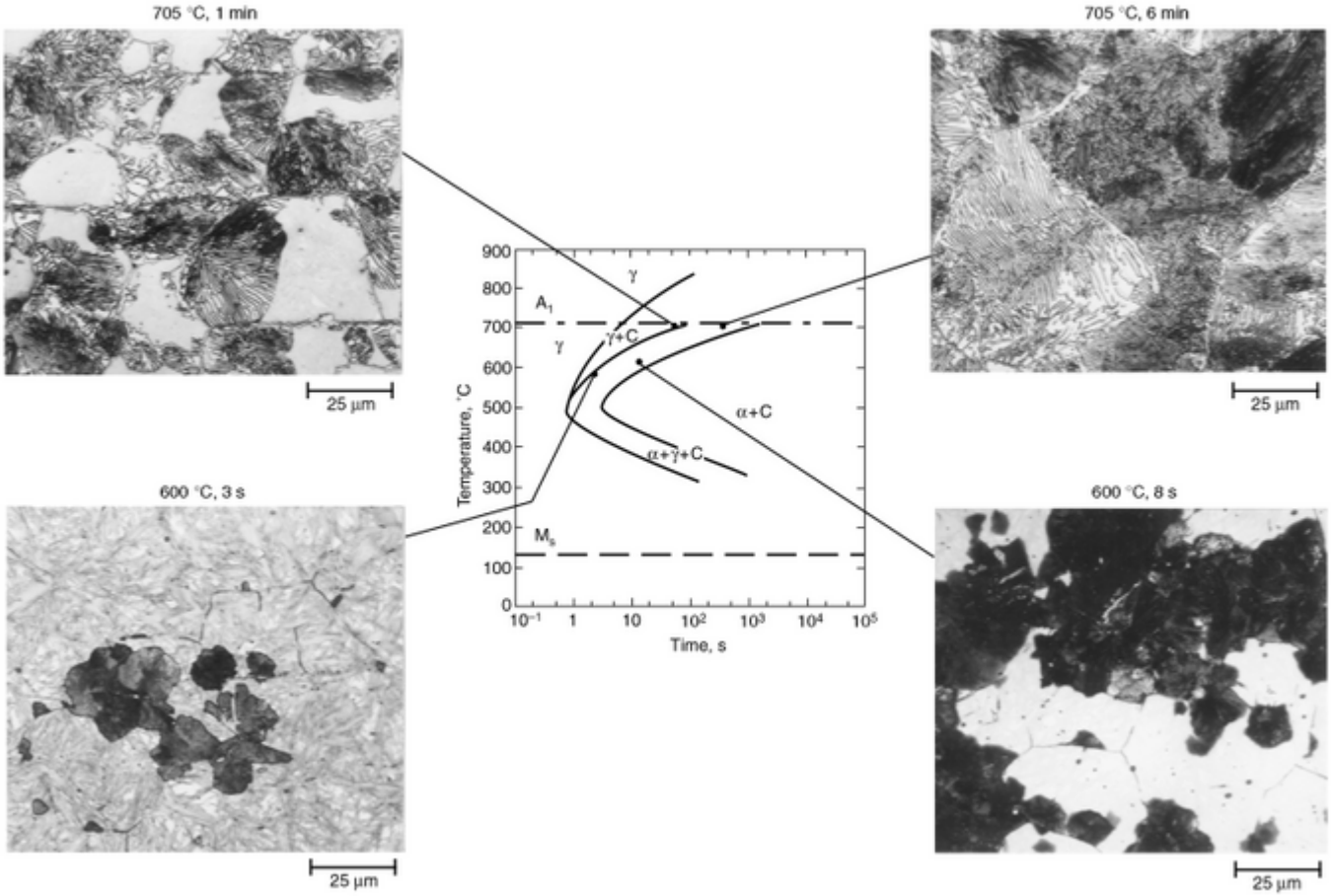

Fig. 27 Isothermal transformation (IT) diagram for a hypereutectoid carbon steel with a composition of 1.2 wt% C (1.18C-0.19Si-0.25Mn, wt%). Proeutectoid cementite (c) forms first, starting below A_1. This transformation region (γ + c) for proeutectoid cementite ceases near the nose of the IT curve, at which point pearlite formation (γ + α + c) begins. Micrographs are from specimens that were austenitized at 960 °C (1760 °F), with isothermal exposures as indicated for each. All picral etch and original magnification 500×. Adapted from Ref 7

Precipitation from Solid Solution. When the solvus line in a phase diagram has a significant slope (rather than being nearly vertical), solid-state precipitation of a two-phase solid (α + β) can be developed by heat treatment (as in a general eutectic system, Fig. 6). Fast cooling from the single-phase α field can create a metastable state known as a supersaturated solid solution, where the atoms of the alloying element are trapped in the single-phase structure of the host, even at low temperatures. This kind of heat treatment is referred to as solution annealing. After the material has been solution treated in this manner, the second phase is allowed to form during aging of the material, often at room temperature or some moderately elevated temperature. For example, any temperature below T_β for alloy X in Fig. 11 would cause precipitation of β phase from a supersaturated α solid solution.

Solid state precipitation provides an important basis of strengthening known as precipitation hardening, as discussed in more detail in the article “Structures by Precipitation from Solid Solution” in this Volume. Often, solution-treated and aged materials have superior mechanical properties to those of equilibrium or near-equilibrium eutectic microstructures, because the second-phase particles tend to be much smaller, have a rounded shape, and are more uniformly distributed throughout the grains rather than being concentrated in the eutectic constituent in the grain boundaries. This more uniform composition, which tends to minimize cracking tendency, may also have a profound effect on the corrosion behavior of the alloy. The classic system of precipitation hardening is that of the aluminum-copper system, as described in more detail in the article “Metallographic Techniques for Aluminum and Its Alloys” in this Volume.

Coherent Precipitation from Solid Solution. Precipitation of new phases typically occurs at crystalline discontinuities such as grain boundaries. However, another important type of isothermal transformation is coherent precipitation, where the new phase maintains continuity with the crystal lattice of the matrix. Guinier-Preston (GP) zones are an example of a coherent structure, although GP zones are not strictly a new phase (as previously mentioned in the section “Homogeneous Transformation” in this article). Examples of coherent precipitates include the γ′(Ni_3[Al,Ti]) and the closely related γ″(Ni_3Nb) intermetallic phases in precipitation-hardening phases in nickel alloys. These nickel precipitates are based on the intermetallic compound Ni_3Al, which has a face-centered cubic L12 ordered crystal structure with a lattice parameter differing from the nickel austenite (γ) matrix by ≤1%. This small misfit allows the homogeneous nucleation and growth of rather stable arrays of coherent precipitates (Fig. 28).

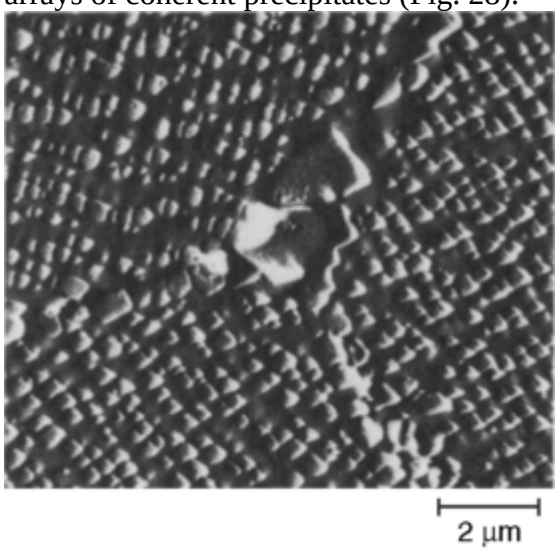

Fig. 28 Replica electron micrograph of the nickel alloy Udimet 700 (Ni-15Cr-17Co-5Mo-3.5Ti-4A1-0.06C) in the solution-annealed and aged condition, showing precipitation of carbide at grain boundaries and arrays of γ′ within grains of the γ solid-solution matrix. Original magnification 4500×

Athermal Transformations

An athermal transformation, by definition, is one that depends on a rate of change in temperature. If cooling (or perhaps heating in some materials) is done quickly enough, structural rearrangement of atoms can occur by shear displacement over a small distance, on the order of approximately an interatomic spacing (Ref 10). This shear movement of atoms and phase growth occurs rapidly (e.g., on the order of the speed of sound for martensite formation in steel). It is not an instantaneous transformation, but it is quicker and distinct from the random-walk process of diffusion in isothermal transformations. Athermal transformations are more regimented than the random diffusion of individual atoms, and so some refer to isothermal transformation as "civilian" and athermal transformation as "military" (Ref 10).

The other key difference is that athermal transformations produce metastable states that do not appear on equilibrium phase diagrams. In steel, for example, martensite is essentially an interstitial, supersaturated (i.e., metastable) solid solution of iron and carbon. Martensite has a unique crystal (phase) structure, but it cannot be obtained by the arbitrarily slow approach to equilibrium by diffusion. Thus, athermal transformations are also referred to as diffusionless.

Martensite in Steel. Martensite is a single-phase metastable state that occurs in both ferrous and nonferrous alloys (see the article "Martensitic Structures" in this Volume). In steel, martensite is a body-centered tetragonal (bct) structure that occurs when steel is cooled rapidly from the austenite (γ) phase. When steel is cooled slowly from austenite, it changes into ferrite, which is a more compact body-centered cubic crystal form. At faster cooling rates, however, the formation of ferrite is suppressed, and martensite forms. This mechanism involves shear displacement of iron atoms on {111} planes. The result is a bct crystal structure that is even less densely packed than the face-centered cubic structure of austenite. Hence, the martensitic transformation results in a volumetric expansion and a hardening of steel.

The extent of martensitic transformation depends on temperature, and it only occurs within a range of temperature defined by a martensite start (M_s) and martensite finish (M_f) temperature. Above the M_s temperature, martensite does not form, even at high cooling rates. The transformation occurs when the steel (cooled at sufficiently high rates) is at temperatures between M_s and M_f. The transformation then ceases when the steel falls below the M_f temperature. Some remaining austenite may still be present when the transformation stops. This remaining austenite is referred to as retained austenite.

It is also important to note that the M_s and M_f temperatures do not have hysteresis (time lag) like the critical temperatures of diffusion-type transformations. That is, the martensitic transformation starts and finishes at the M_s and M_f temperatures, respectively, just so long as the cooling rate is sufficiently high to allow martensitic transformation. The M_s and M_f temperatures depend on the carbon content of steel. When carbon is increased, carbide formation (Fe_3C) becomes more dominant (under either isothermal or athermal conditions), and thus, the M_s and M_f temperatures are lowered (see the section "Ferrous Martensitic Structures" in the article "Martensitic Structures" in this Volume).

The morphology of martensite also depends on carbon content (Fig. 29). If the carbon content is below 0.6 wt%, the resulting structure is referred to as lath martensite (Fig. 29a), which consists of martensite needles with different but well-defined orientations. When carbon content is above 1.0 wt%, plate martensite grows across the complete austenite grain. Some untransformed austenite (retained austenite) always remains between the plates. There are also martensite needles extending from the plates (Fig. 29b). Because the growth is rapid and regimented, these needles occur with a specific orientation (~57°) relative to the plates crossing the complete grains. With carbon contents between 0.6 and 1.0 wt%, the martensite is a mixture of lath and plate morphologies (Fig. 29c).

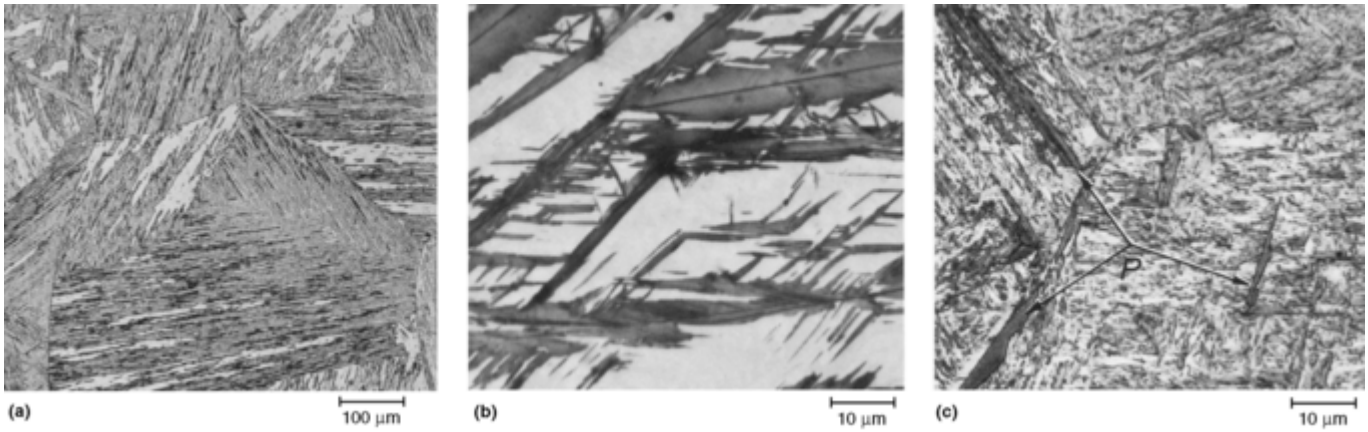

Fig. 29 Light micrographs of morphologies of martensite. (a) Lath martensite in low-carbon steel (0.03C-2.0Mn, wt%) at original magnification 100×. (b) Plate martensite in matrix of retained austenite in a high-carbon (1.2 wt% C) steel at 1000×. (c) Mixed morphology of lath martensite with some plate martensite (P) in a medium-carbon (0.57 wt% C) steel at original magnification 1000×. All 2% nital etch

Because martensite is metastable, decomposition into more stable constituents can occur by diffusion. In steels, the metastable state of martensite will remain indefinitely at room temperature but will decompose into ferrite and cementite at high temperatures. This tempering results in carbide phase (cementite) that has a shape very much different from that of cementite in pearlite. In tempered martensite, the carbide consists of small, chunky particles rather than platelets (Fig. 30). These finely divided particles of cementite in tempered martensite provide strengthening and some degree of freedom for ductile deformation. As the types of carbides present in the steel change during tempering, the overall density of the steel also changes.

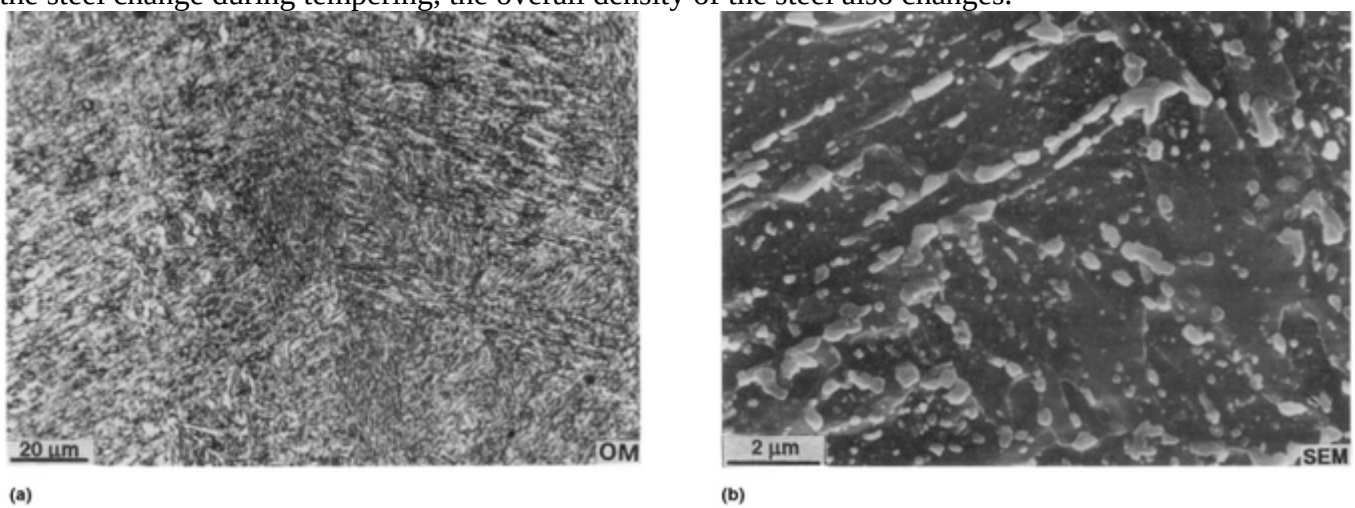

Fig. 30 Microstructures typical of tempered martensite. (a) In optical (light) microscopy, the dark regions are caused by scattering of light from carbide clusters that stand in relief above the etched ferrite. (b) In scanning electron microscopy examination, the carbides are resolved and are the light particles. Source: Ref 6

Retained Austenite. Solid-state phase changes are associated with changes in crystal structure that are often associated with significant changes in density. Some of these density changes have significant effects on microstructure. One of the common density-related effects in alloy and high-carbon steels is that of retained austenite after cooling. Retained austenite is a result of the fact that, like water changing to ice, steel expands when it transforms from austenite to martensite. The austenite starts transforming to martensite when it reaches the M_s temperature and continues to transform until the M_f temperature is reached. When the transformation ceases, some remaining austenite may still be present.

When retained austenite is present, it usually presents as small island grains surrounded by martensite (Fig. 31). Because martensite expands when it is formed, the remaining austenite is effectively pressurized from all sides. This makes it more difficult for it to expand, which it needs to do in order to transform itself into martensite.

Note that because elastic deformation results in a volume expansion (Poisson's ratio of 0.3), impact-related stresses or other service-loading conditions, as well as low-temperature exposure, can allow retained austenite to transform to martensite in service. Unless the service temperature is somewhat elevated, the new martensite will remain in an essentially untempered condition.

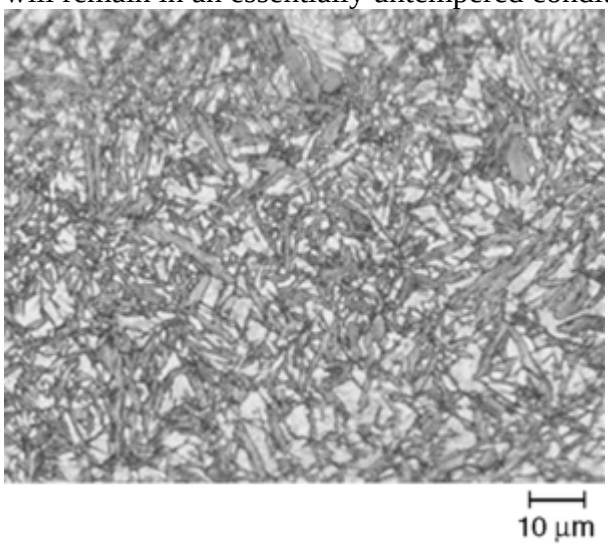

Fig. 31 Microstructure with retained austenite (light-etching phase here) with its distinctive sharp corners. 5% nital etch. Original magnification 1000×

Bainite

Bainite is a eutectoid type structure that forms from a combination of athermal (shear) transformation and diffusion-controlled growth. Like pearlite, the particular nonequilibrium cooling conditions in question can create noneutectoid bainite. Thus, bainitic transformations require some combination of continuous cooling (at intermediate cooling rates) and some time at temperature. For example, bainitic transformation can occur when steel is quenched to and held at a temperature between approximately 300 to 550 °C (570 to 1020 °F).

In some respects, bainite in steel is a cross between pearlite and tempered martensite. Like pearlite, bainite is a two-phase structure that contains ferrite-cementite regions from the eutectoid decomposition of austenite. However, the carbide particles in bainite are small and chunky (as in tempered martensite), rather than the cementite platelets of pearlite. The two-phase structure of bainite may appear similar to martensitic plates in light microscopy, while the small and chunky carbide particles are more apparent at higher magnification (Fig. 32).

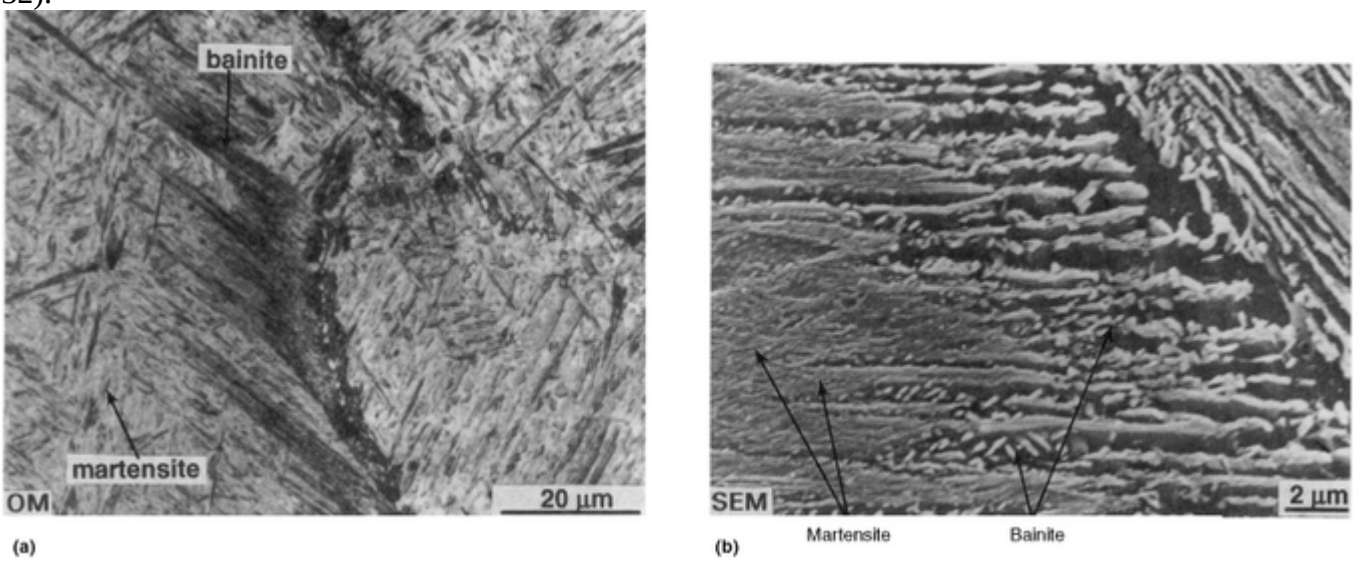

Fig. 32 Bainite in oil-quenched 0.47 wt% C steel. (a) Light micrograph. (b) Better resolution of carbide morphology in scanning electron microscopy image, where rodlike carbides appear white in a ferrite background. Source: Ref 6

Bainite has two distinct forms that nucleate and grow by different mechanisms. The first is upper bainite that nucleates and grows at high transformation temperatures (near or in the lower-temperature region of pearlite formation). The second type is lower bainite that forms at lower transformation temperatures (closer to the M_s temperature). In carbon steels, the transition temperature from upper-bainite formation to lower-bainite formation depends on composition in a complex way for carbon steels (Ref 7).

Upper bainite in hypoeutectoid steels forms as stacks or parallel laths or needles of ferrite. Nucleation of ferrite typically starts at the grain boundaries of austenite, and cementite grows as elongated particles that are generally oriented parallel to the direction of growth of the ferrite laths (Fig. 33) (Ref 11). The cementite forms near the ferrite, because the nucleation ability of the ferrite in this temperature range is much greater than the diffusion of excess carbon near the newly formed ferrite.

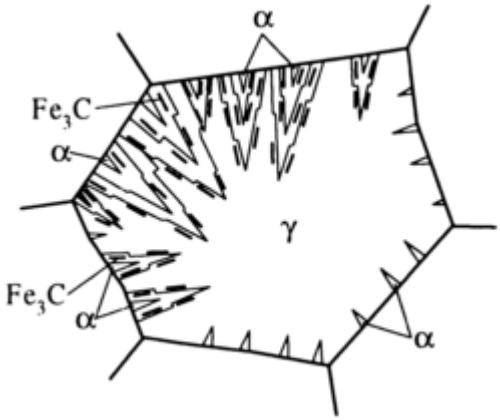

Fig. 33 Schematic of mechanism in the formation of upper bainite. Source: Ref 11

The interparticle spacing of cementite particles in upper bainite is determined primarily by the size of the ferrite laths, and this spacing is generally quite large relative to the lamellar spacing of pearlite. Thus, upper bainite etches more lightly than pearlite and may be relatively easy to distinguish from pearlite by light microscopy (Fig. 34). The appearance of upper bainite also varies gradually with the transformation temperature. Lowering of the transformation temperature promotes more ferrite plates in close proximity to each other and increases the extent of cementite precipitation (Fig. 35).

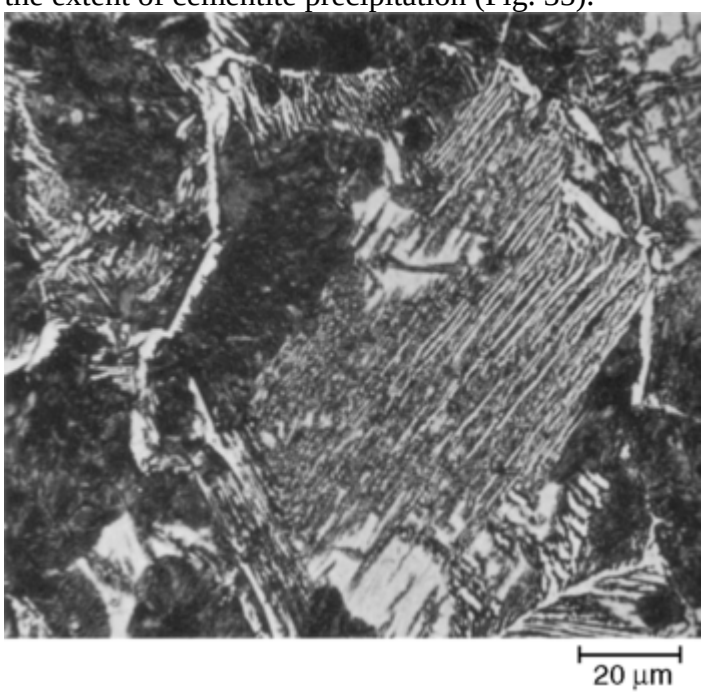

Fig. 34 Lighter etch of upper bainite as compared to pearlite (dark areas). Acicular structure is upper bainite in a pearlitic matrix. 1045 steel, 50 mm (2 in.) bar stock, austenitized at 843 °C (1550 °F) for 2 h, oil quenched 15 s, air cooled 5 min, and oil quenched to room temperature. 4% picral etch. Original magnification 500×

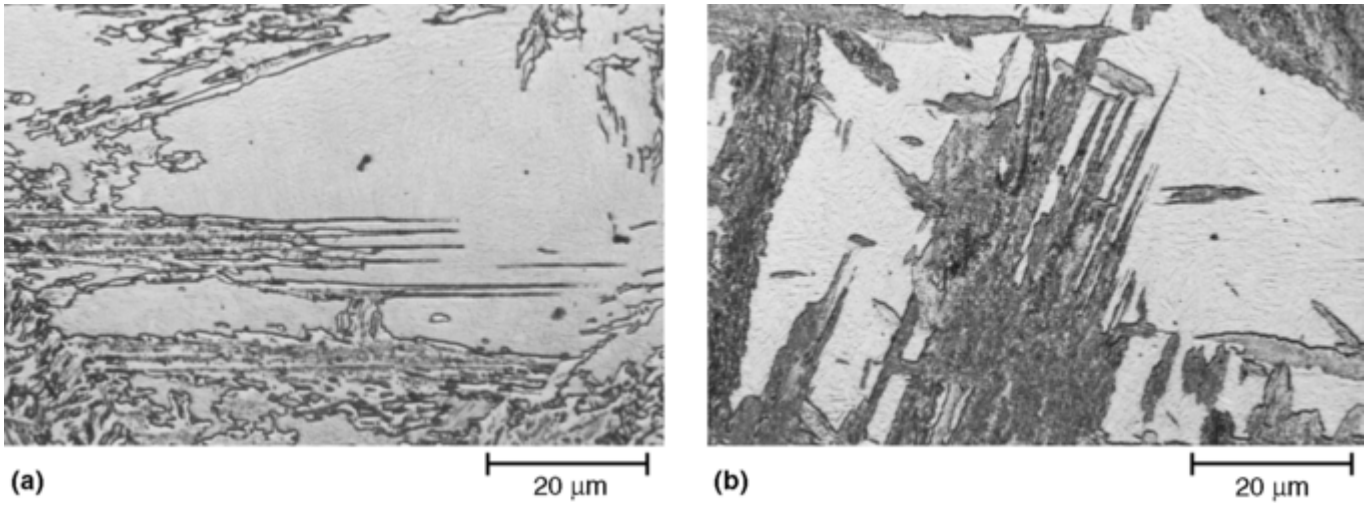

Fig. 35 Effect of isothermal transformation temperature on appearance of upper bainite in two specimens of 4360 steel. (a) Structure from isothermal transformation at 495 °C (923 °F). (b) Transformation at a lower temperature of 410 °C (770 °F) resulted in more precipitation of cementite and thus a darker etch response. Both picral etch and original magnification 750×

Upper bainite in carbon steel becomes progressively coarser and more feathery with decreased carbon content, and particles of cementite can be resolved when carbon content is less than approximately 0.25%. Along with pearlite, substantial volume fractions of bainite form when the austenite of low-carbon steels transforms at approximately 500 °C (930 °F).

Lower Bainite. Bainite that forms at temperatures below approximately 350 or 400 °C (660 or 750 °F) is referred to as lower bainite. It is significantly different from upper bainite in terms of the kinetics and the carbide phase. At the lower transformation temperatures (closer to the M_s temperatures), the ferrite tends to form martensite needles with a distinctly more lenticular shape, as compared to upper bainite (Fig. 36). Lower bainite also consists of a carbide that is crystallographically distinct from that of cementite. The carbide in lower bainite is the so-called epsilon carbide ($Fe_{2.4}C$) or Hägg's carbide, named after its discoverer.

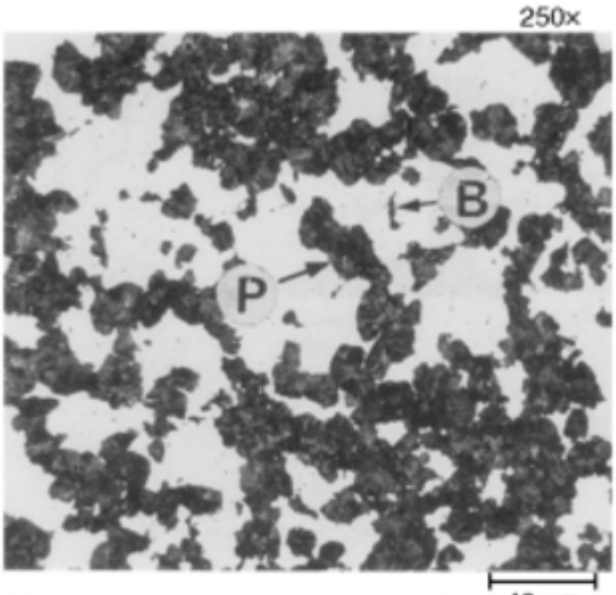

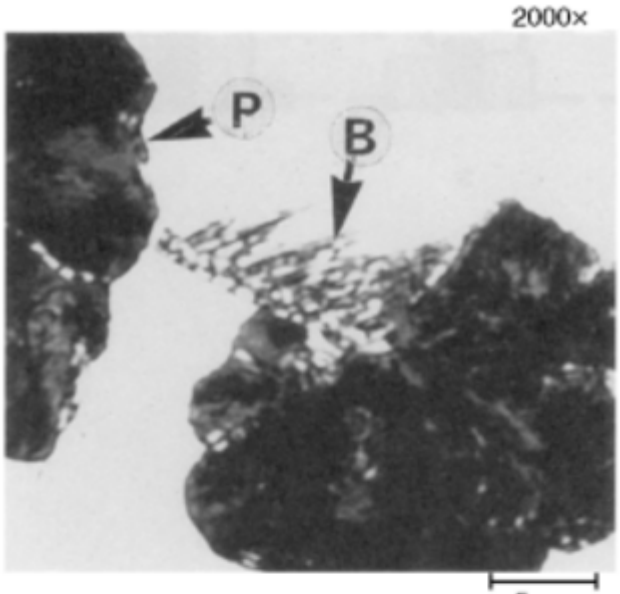

(a) Pearlite and bainite (500 °C, 0.5 s)

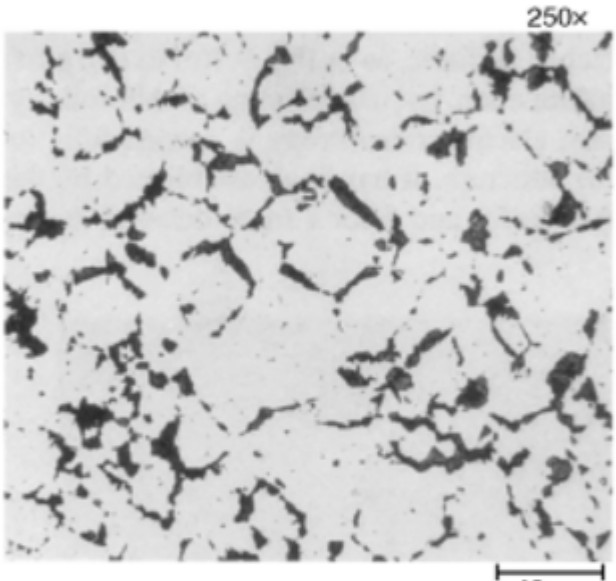

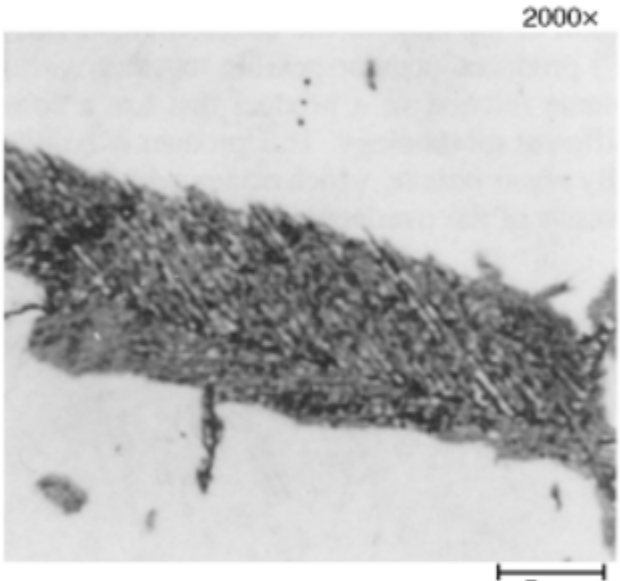

(b) Upper bainite (450 °C, 0.5 s)

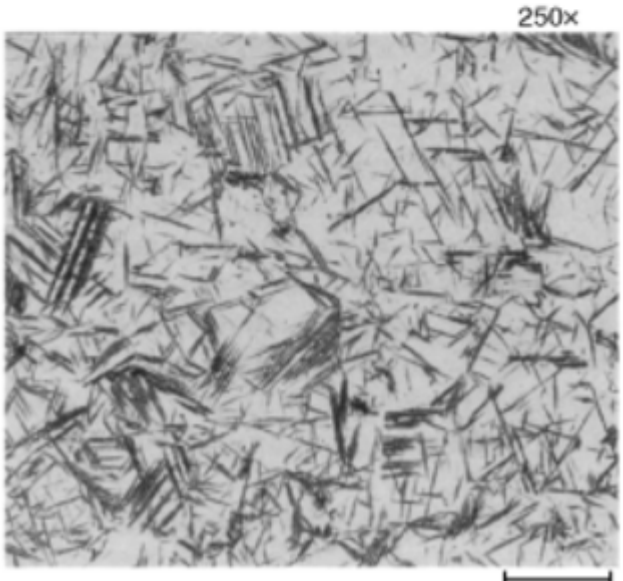

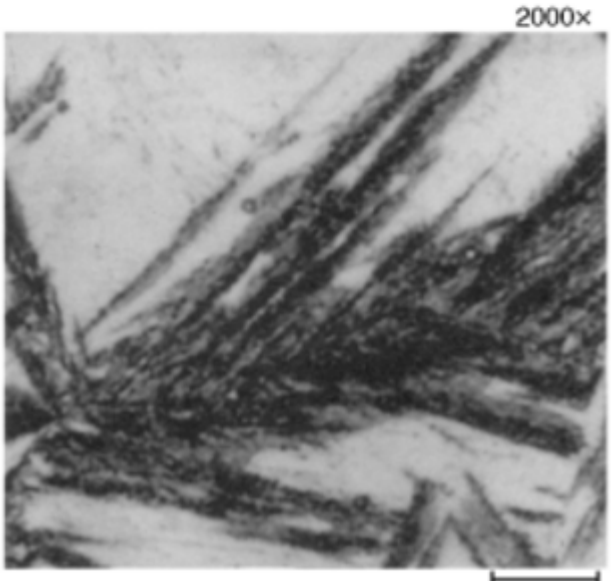

(c) Lower bainite (300 °C, 200 s)

Fig. 36 Appearance of upper bainite (a and b) and lower bainite (c) in eutectoid steel (0.8% C) at original magnification 250× (left) and 2000× (right). (a) The structure is pearlite with some upper bainite after isothermal exposure at 500 °C (930 °F) for 0.5 s. (b) Upper bainite is dominant after transformation at 450 °C (840 °F) for 0.5 s. Magnification of 2000× reveals a feathery appearance of upper bainite. (c) Lower bainite is dominant after isothermal transformation at 300 °C (570 °F) for 200 s. Lower bainite has a more acicular shape that is revealed at original magnification 250× (left) and 2000× (right). Same specimens as in Fig. 20. Composition: 0.81C-0.07Si-0.65Mn, wt%. Austenitized at 860 °C (1580 °F), followed by isothermal transformation as indicated. All picral etch. Adapted from Ref 7

Diffusion plays a role in tempering the needles of lower bainite, and the appearance of lower bainite is very similar to tempered martensite. It is very difficult to distinguish between lower bainite and tempered martensite by light microscopy. However, electron microscopy can show lower bainite with ferrite plates that contain internal carbide particles with a specific orientation (Fig. 37). This is in sharp contrast to carbides with two or more orientations in tempered martensite. Also, lower bainite does not exhibit transformation twins that characterize martensite in high-carbon steels.

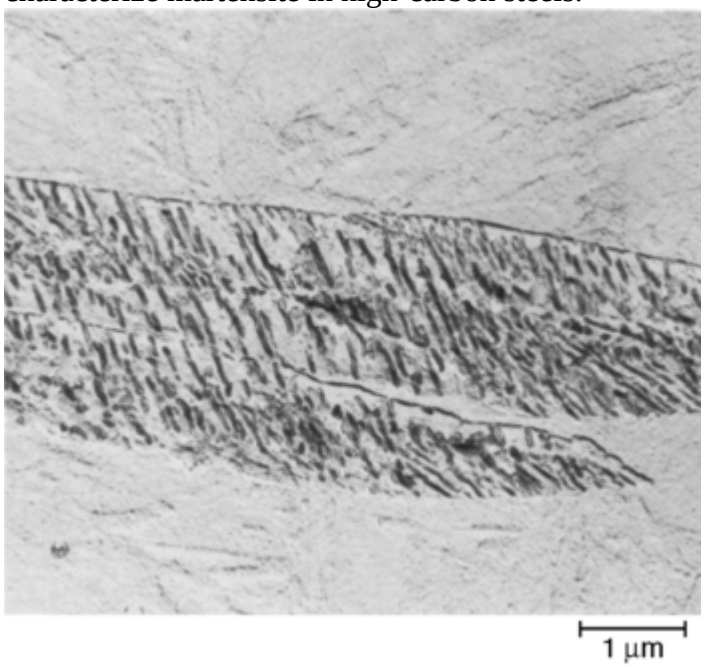

Fig. 37 Replica electron micrograph of lower bainite with carbide particles aligned at 60°. Light area is martensite. 4250 steel bar austenitized at 843 °C (1550 °F), quenched to 343 °C (650 °F), held 12 min for partial isothermal transformation, and water quenched. Nital etch. Original magnification 11,000×

References cited in this section

4. I. Manna, S.K. Pabi, J.M. Manero, and W. Gust, Discontinuous Reactions in Solids, *Int. Mater. Rev.*, Vol 46 (No. 2), 2001, pp 53–91

5. *Metallography, Structures and Phase Diagrams,* Vol 8, *Metals Handbook,* 8th ed., American Society for Metals, 1973

6. C. Brooks, *Principles of the Heat Treatment of Plain Carbon and Low-Alloy Steels,* ASM International, 1996

7. L.E. Samuels, Chapter 9: Transformation of Austenite, *Light Microscopy of Carbon Steels,* ASM International, 1999

8. R.F. Mehl and A. Dubé, *Phase Transformations in Steels,* R. Smoluchowski, Ed., Wiley, 1951

9. H.I. Aaronson, *Decomposition of Austenite by Diffusion Processes,* V.F. Zackay and H.I. Aaronson, Ed., Wiley, 1962, p 387

10. D. Porter and K.E. Easterling, Diffusionless Transformations, *Phase Transformations in Metals and Alloys,* 2nd ed., Chapman & Hall, 1992, p 382

11. M. Tisza, *Physical Metallurgy for Engineers,* ASM International and Freund Publishing House, Ltd., 2001, p 251

D. Aliya and S. Lampman, Physical Metallurgy Concepts in Interpretation of Microstructures, *Metallography and Microstructures,* Vol 9, *ASM Handbook,* ASM International, 2004, p. 44–70

Physical Metallurgy Concepts in Interpretation of Microstructures

Debbie Aliya, Aliya Analytical, Inc.; Steve Lampman, ASM International

---

Transformation Kinetics

Phase transformations involve the rearrangement of atoms into new crystal structures, and the overall rate of change involves the combined processes of nucleation and growth of the new phase. This is illustrated in the series of IT curves for eutectoid, hypoeutectoid, and hypereutectoid steels (Fig. 20, Fig. 20, and Fig. 27). The nucleation rate of a new phase is slow when isothermal transformation occurs slightly below the A_1 eutectoid isothermal, but the few nuclei can easily grow at high temperatures due to the thermal (kinetic) energy of the phase constituents. When the isothermal transformation occurs at a temperature closer to the nose of the C-shaped curve, nucleation rates are higher, and the temperature is high enough for sufficient diffusion rates and growth. Thus, the kinetics of transformation reach a peak at some point, as represented by the nose of the IT curve plotted on a TTT diagram. This underscores the importance of kinetics and how quickly a metastable or quasi-stable state approaches a more stable condition. For example, even though cementite (Fe_3C) can be considered to be a quasi-stable phase in steel at room temperature, the carbon transforms into the more stable form of graphite at high temperatures. Transformation kinetics is thus a function of both time and temperature.

The two-phase morphology of pearlite is another example related to a combination of kinetics and thermodynamics. At slow (near-equilibrium) cooling, the eutectoid decomposition of austenite drives the near-simultaneous formation of both ferrite and the cementite carbide (Fe_3C). The two phases thus form in the shape of closely spaced platelets that is distinctive of pearlite. However, this two-phase structure is not the most thermodynamically stable morphology of cementite and ferrite. Over time, the cementite platelets tend to transform into spheroidal carbides, given enough time at temperature. Short times at a high temperature, or longer time at a moderate temperature, allow diffusion of the carbides, which then combine to form a more thermodynamically stable condition of larger particles with a spheroidal shape. For example, Fig. 38 is spheroidized cementite in a hypoeutectic steel that was heated after cold rolling of a prior-ferrite-pearlite microstructure.



Fig. 38 Spheroidized cementite in a hypereutectoid steel that was heated after cold rolling of a prior-ferrite-pearlite microstructure. During plastic deformation, dislocations broke up the cementite lamellae in the pearlite, and subsequent heating allowed the material to minimize its energy state by rounding off the broken-up cementite lamellae. Original magnification 1000×

The approach to the thermodynamic ideal of equilibrium can be very slow, because the mechanism of stable growth is based on the random-walk motion of individual atoms. In contrast, the formation of metastable solid requires an athermal process of continuous cooling. If the cooling rate is high enough, the atoms do not have enough time to diffuse and form into a more stable phase. This is the case in solution heat treatment, where precipitates are dissolved at high temperature, followed by a rapid quench to prevent reprecipitation by diffusion. This creates a metastable supersaturated solid solution. It is also possible to produce a supersaturated solid solution with a phase (crystal) structure that is distinct. This is the case of martensite formation when iron-carbon austenite is quickly cooled. Thus, in addition to temperature, continuous cooling transformation (CCT) curves are used to identify cooling conditions that allow either athermal or isothermal transformation (Fig. 39) (Ref 12).

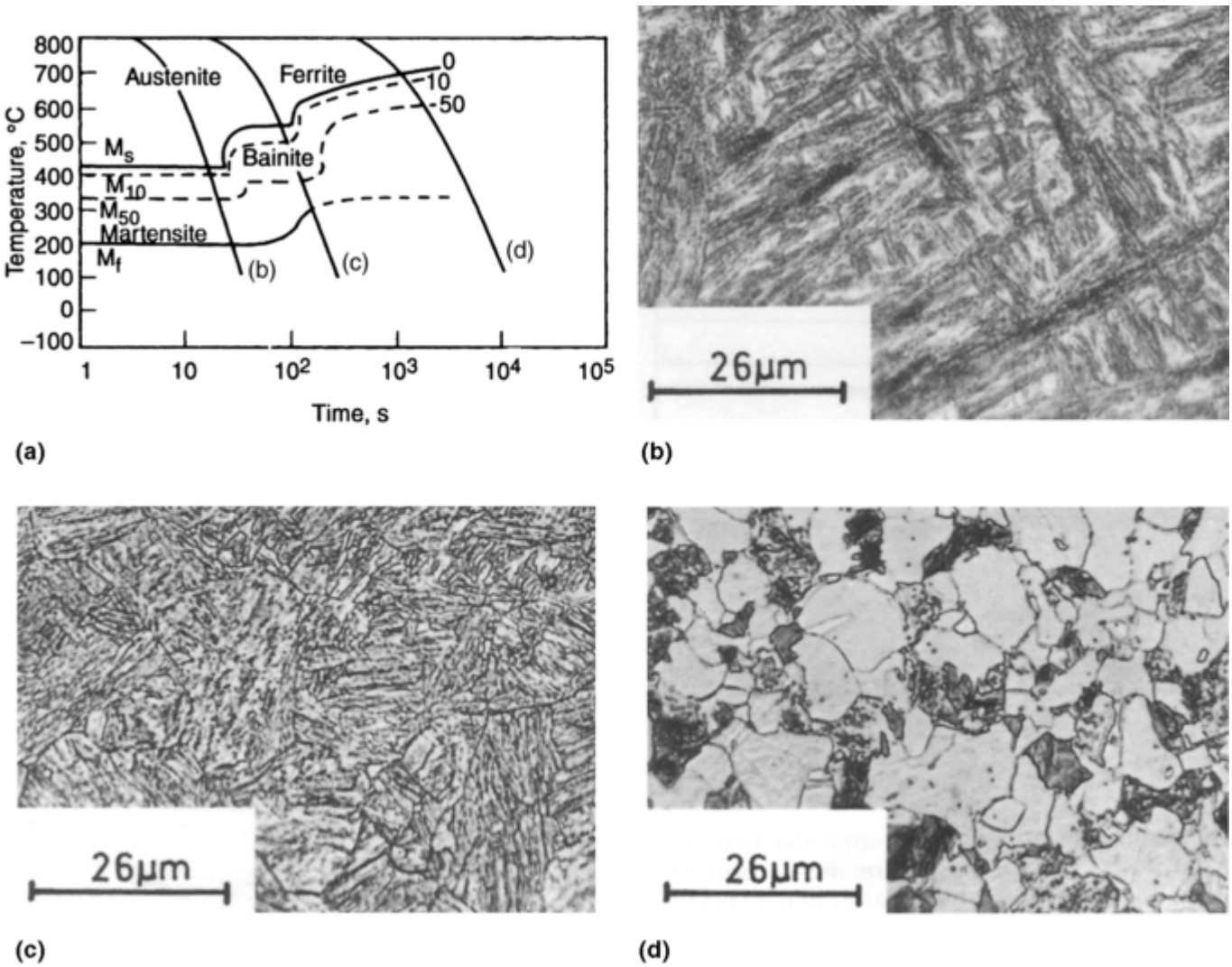

Fig. 39 Continuous cooling transformation (CCT) curves and representative microstructures of a 0.16%C-3%Ni steel. (a) CCT diagram. (b) Martensite structure after fast cooling from 920 to 200 °C (1690 to 390 °F) in 30 s. (c) Bainite structure after intermediate cooling from 920 to 250 °C (1690 to 480 °F) in 200 s. (d) Ferrite-pearlite structure after slow cooling from 920 to 250 °C (1690 to 480 °F) in 10,000 s. Source: Ref 12

Transformation Diagrams

This section briefly describes IT and CCT diagrams. These tools are useful in determining conditions for proper heat treatment (solid-state transformation) of metals and alloys, and basic trends in microstructure formation are relatively easy to predict with CCT and IT diagrams. It must also be noted that IT and CCT conditions of metastable states are time-dependent and thus involve dynamic factors for mass and heat transport. Thus, grain size is a factor that influences the extent and/or speed of both athermal transformations and the isothermal decomposition of metastable states. For example, steel hardenability is influenced by grain size (in addition to a host of other dynamic factors beyond the scope of this article). Similarly, IT curves are also influenced by grain size.

Thermal conductivity is another important factor that affects the heating and cooling rates. Obviously, the surface of a component cools down and heats up more quickly than the inside. This may give more time for grain growth at the surface, for example. If this happens, it can have additional effects on the microstructure of quenched steels, because the grain size is such an important factor in determining the hardenability. Even in induction heating, where the heating cycle does not entirely depend on conductivity, the microstructure of the layers underlying those affected by the electrical field will be influenced by the conductivity.

Another situation where the thermal conductivity strongly influences microstructures is in welding. The heat-affected zones of aluminum alloys, for example, are very large compared to ferrous alloys, because the thermal

conductivity of aluminum is so high. Heat-affected zones can be very complex, with many distinct areas depending on whether the particular band of material was only heated enough to age or temper slightly, or whether the particular band of material was heated to a high temperature where it was partly or completely homogenized. Other bands of material heated to temperature ranges where other metallurgical effects may occur include those experiencing grain growth, precipitation hardening, or other transformations.

Thus, it should be starting to be clear that accurate quantitative prediction of microstructures, even in cases where it appears that data are relatively readily available, is quite complicated. For that reason, atlases and databases of microstructures of actual components are very useful. In many practical cases, most people will end up using their experience to determine whether the microstructure "looks normal." Manufacturers or designers of components of any but the simplest shapes may find it very useful to actually analyze the microstructures present at high-stress positions on their heat treated prototype components. This will provide a record of the actual microstructure for comparison in case of subsequent manufacturing or service problems.

Time-temperature transformation diagrams contain curves that identify regions of phase change from either isothermal or athermal conditions. In the cases of isothermal transformation, the IT curves plot boundaries of when an isothermal transformation starts, stops, or reaches a transformation product of a measurable volume fraction or property value. The other type of curve on a TTT plot is a CCT diagram that plots transformation according to temperature and cooling-rate curves. Reference 13, 14, 15, and 16 contain collections of TTT diagrams. Reference 17 is a program that calculates transformation curves of steel based on composition.

Isothermal Transformation Curves. An IT curve is a map of sorts, which plots the occurrence of microstructural phases as a function of time and a given temperature. Sometimes, hardness or other mechanical property data may be plotted on the graph instead of or in addition to microstructural features, as shown in Fig. 40 for 1080 carbon steel. Typically, IT curves are developed by heat treating many small specimens and then examining the microstructure of each specimen under a microscope. An alternative method involves using a single specimen and a dilatometer, which measures volumetric changes associated with new phase (crystal) formation.

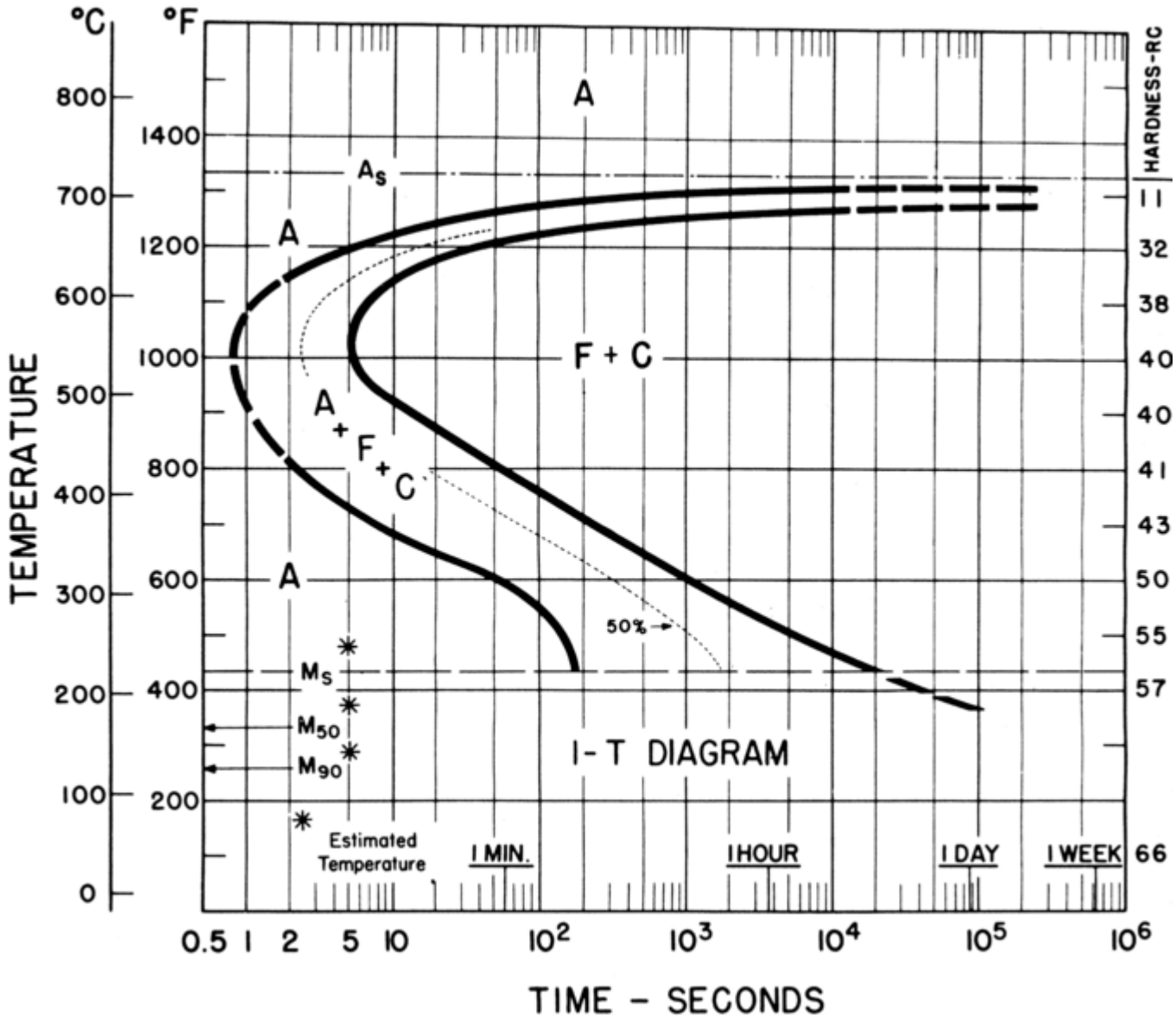

Fig. 40 Isothermal transformation diagram of 1080 steel (0.79 wt% C, 0.76 wt% Mn). Austenitized at 900 °C (1650 °F); ASTM grain size No. 6. Source: Ref 18

In principle, IT curves can plot either the phase formation or phase decomposition from cooling or heating. In the case of microstructure formation by cooling from austenite in steels, the IT curve is usually produced by solution treating (austenitizing) small samples of steel at the appropriate temperature for the alloy, quickly transferring samples to a lead or salt bath, holding for selected periods of time, and water quenching. This is repeated for many exposure times at different temperatures. The microstructure of each sample after quenching is examined to determine the point in time when the transformation to ferrite, pearlite, or bainite began and the rate at which the transformation progressed with increasing isothermal holding time. The start of transformation in IT curves is usually defined as the time required to produce 0.1% transformation at the specified holding temperature.

Conversely, an IT diagram for austenite formation can be plotted in terms of heating from an original ferritic-pearlitic microstructure or tempered martensite. In this case, it is important that the heating rate to the hold temperature be very high if a true isothermal diagram is to be obtained. It is also important to emphasize that the original microstructure plays a great role in the IT response of a material. For example, a finely distributed structure such as tempered martensite is more rapidly transformed to austenite than, for example, a ferritic-pearlitic structure. Likewise, carbide-forming alloying elements such as chromium in alloy steels would affect the IT response. The importance of the starting structure also applies to transformation of single-phase austenite during cooling, because grain size can affect the rates of transformation.

In the IT diagram for AISI 1080 steel (Fig. 40), note that the austenitization temperature prior to each quench event is given along with the grain size. Also note that the diagram does not distinguish between pearlite and bainite. Both are listed simply as “ferrite + carbide.” The experienced ferrous metallurgist may presume that the upper portions of this ferrite + carbide region are probably pearlite, while the lower portions are probably bainite. Martensite is distinguished from the high-temperature transformation products and austenite shown on the upper part of the diagram.

Transformation of metastable phases can also be plotted on IT diagrams for structure-dependent properties. For example, Fig. 41 (Ref 13) shows yield strength of a precipitation-hardening aluminum alloy, where the time and temperature of aging influences the extent of precipitation and thus strength. Figure 42 (Ref 13) shows the result of a metallographic study of microstructure on isothermally aged test coupons made from previously solution-treated (homogenized) aluminum alloy, as a function of time at temperature. Note that there is no explicit information on the size of the S-phase particles; only the total volume fraction is indicated. Because the actual mechanical (and other) properties of the material are highly dependent on the particle size, this information is somewhat limited in use. However, it does provide a starting point.

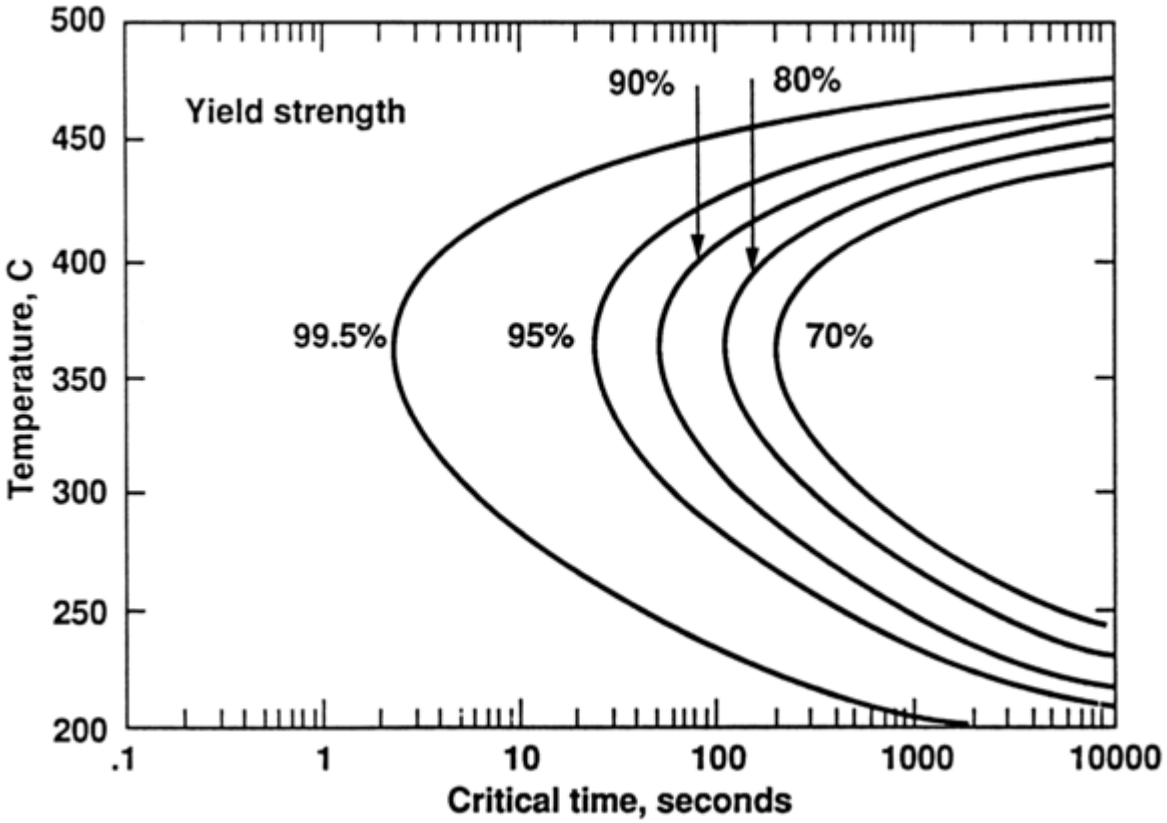

Fig. 41 Isothermal transformation diagram with C-shaped precipitation-hardening response of an aluminum-lithium alloy (Al-2.7%Cu-1.6%Li). Source: Ref 13

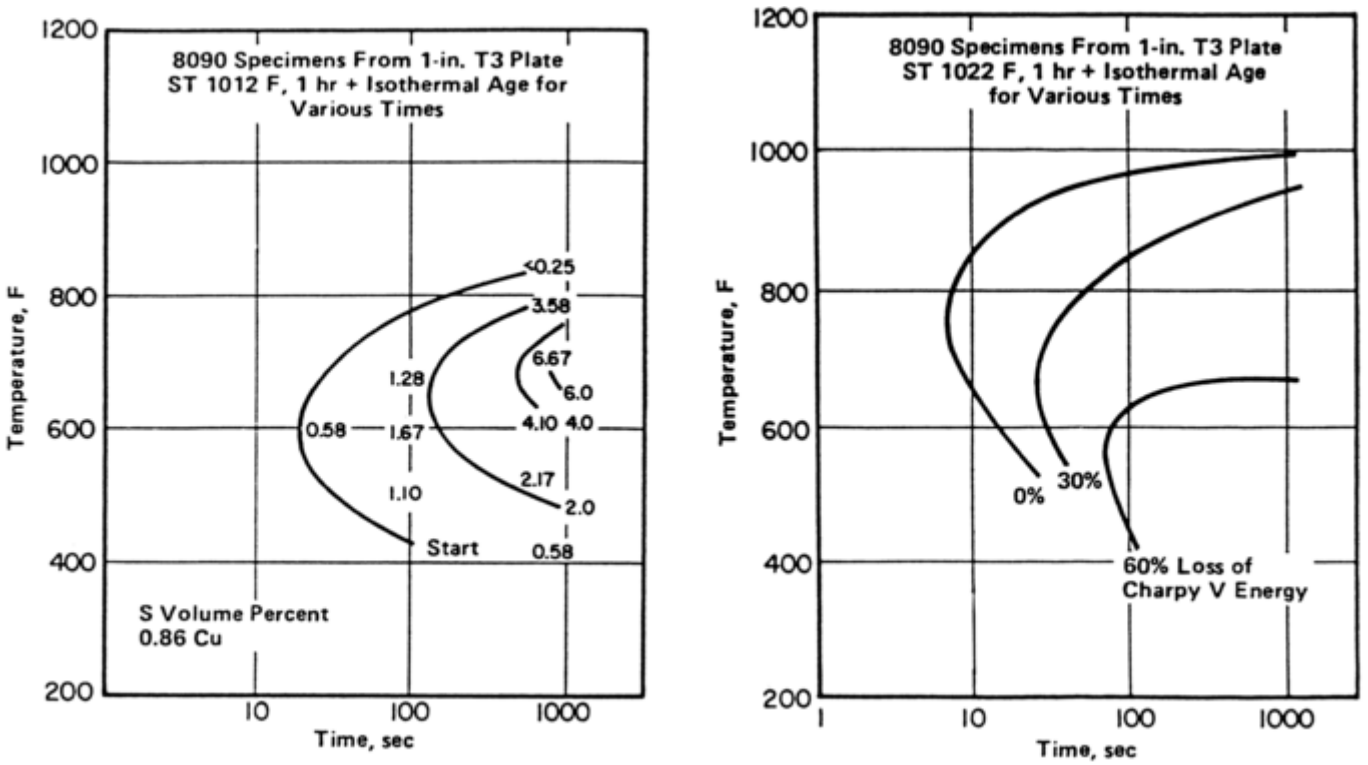

Fig. 42 Time-temperature diagram of precipitation responses of an aluminum-lithium alloy (alloy 8090) for volume formation of the S phase (Al_2CuMg). This practical isothermal transformation curve is based on a real commercial-sized component that has been exposed to aging temperatures to precipitate the second-phase particles. Source: Ref 13

Continuous Cooling Transformation Diagrams. In most practical situations, temperature changes during either cooling or heating. For this reason, continuous heating transformation (CHT) and continuous cooling transformation (CCT) diagrams are useful. Continuous cooling transformation diagrams are more common than CHT diagrams, but like IT diagrams for heating, CHT diagrams can be useful. For example, CHT diagrams are useful in predicting the effect of short-time austenitization that occurs in induction and laser hardening. One typical question is how high the maximum surface temperature should be in order to achieve complete austenitization for a given heating rate. Too high a temperature may cause unwanted austenite grain growth, which produces a more brittle martensitic microstructure.

In continuous cooling experiments, actual cooling rates can be determined by drilling holes in large pieces to different depths. Larger testpieces are used to obtain a continuous cooling process instead of an isothermal quench. Thermocouples can then be inserted into the holes, so that the thermal history of each layer could be determined from a single heat treating event. Much of this data was collected in the middle of the 20th century. Today, mathematical models based on theoretical thermal conductivity as a function of temperature and theoretical heat extraction rates in different quench media are often used instead of actual temperature monitoring.

Regardless of how the data on cooling rates are obtained, CCT diagrams are made more useful when cooling rates are defined in terms of position in a simple standardized test configuration. For example, one approach is to plot continuous cooling curves based on natural cooling rates (according to Newton's law of cooling) in terms of distance from the end of the Jominy end-quench specimen for steel hardenability (Fig. 43, Ref 19). In this simplified approach, it is possible to indicate how the interior of a large part would respond to cooling. Of course, this is only an approximate measure of actual circumstances, because cooling from the surface is influenced by many factors. Computer programs also exist that allow heat extraction rates to be calculated as a function of position in a complex part. From this data, the microstructure, and possibly mechanical properties, may be estimated at different locations within the part.

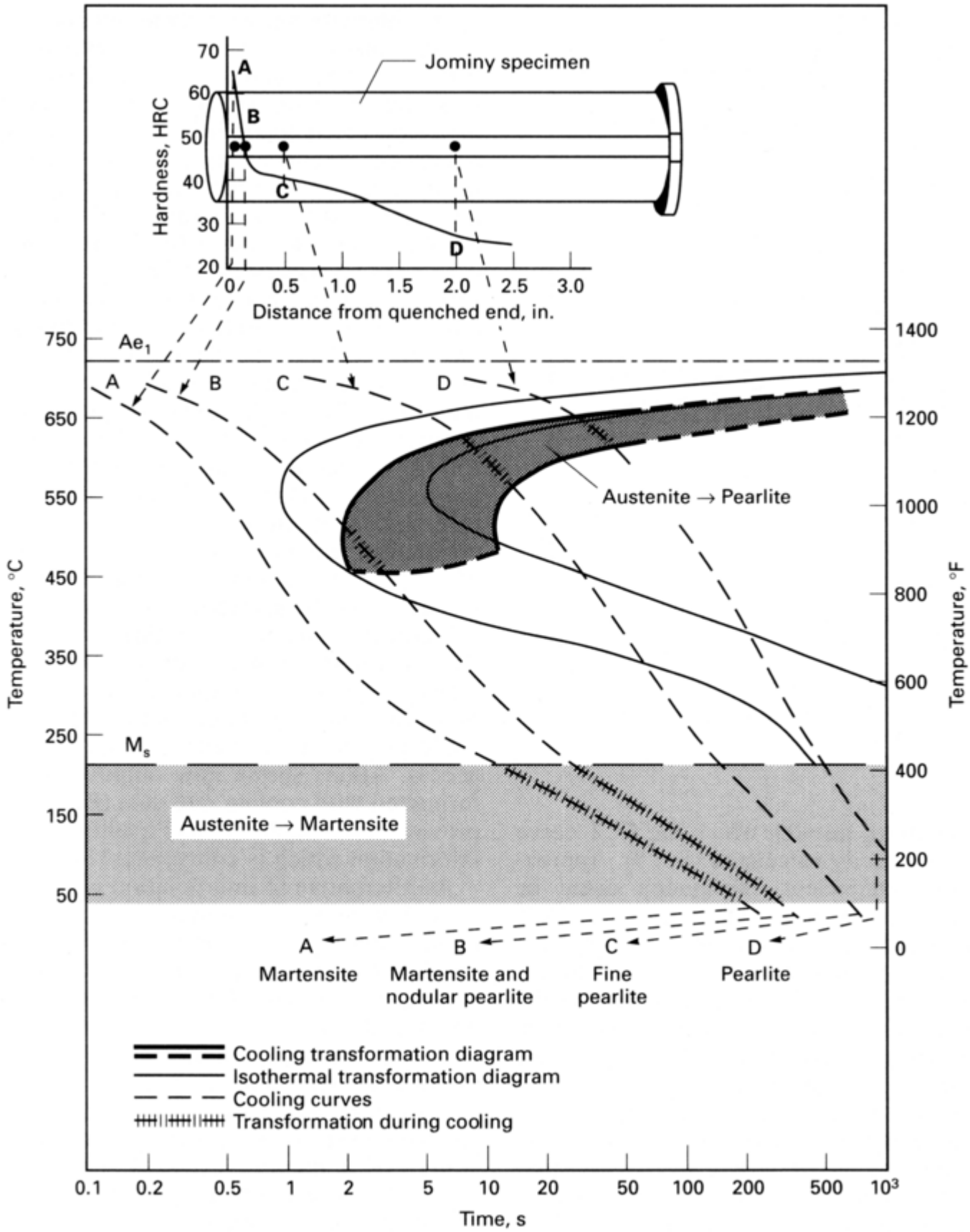

Fig. 43 Relationship of continuous cooling transformation (CCT) (heavy lines) and isothermal transformation (IT) (light lines) diagrams of eutectoid (0.8 wt% C) steel. See also Fig. 1 for IT diagram of eutectoid steel. Four cooling rates from different positions on a Jominy end-quench specimen are superimposed on the CCT diagram. Source: Ref 19

Various other approaches have been made to present cooling curves in convenient graphical form for prediction of steel transformations (Ref 14, Ref 20). The approach developed by Atkins (Ref 14) involves the plotting of experimental cooling curves for round bars of various diameters at fractional radii 0.5 and 0.8 from the center during cooling in water, oil, and air. The cooling curves were used in dilatometer measurements to get the transformation temperatures, and the resulting microstructures and hardnesses were also noted.

A diagram of this type is shown in Fig. 44. In this form of data compilation, various bar diameters are shown along the bottom axis, with approximate cooling rates indicated for various types of quenchants. These graphs are read along vertical lines from the top of the graph toward the bottom and show the beginning and ending core temperatures of the transformation process. From the diagram, one can correlate that a specimen 10 mm (0.4 in.) in diameter being cooled in air corresponds to a bar somewhat less than 100 mm (4 in.) in diameter being cooled in oil. Shown in the upper part of the figure are the amount and type of microstructure. Hardness after hardening and tempering at various temperatures is also plotted in the diagrams of Ref 14, which are reproduced in Ref 15 and 16.

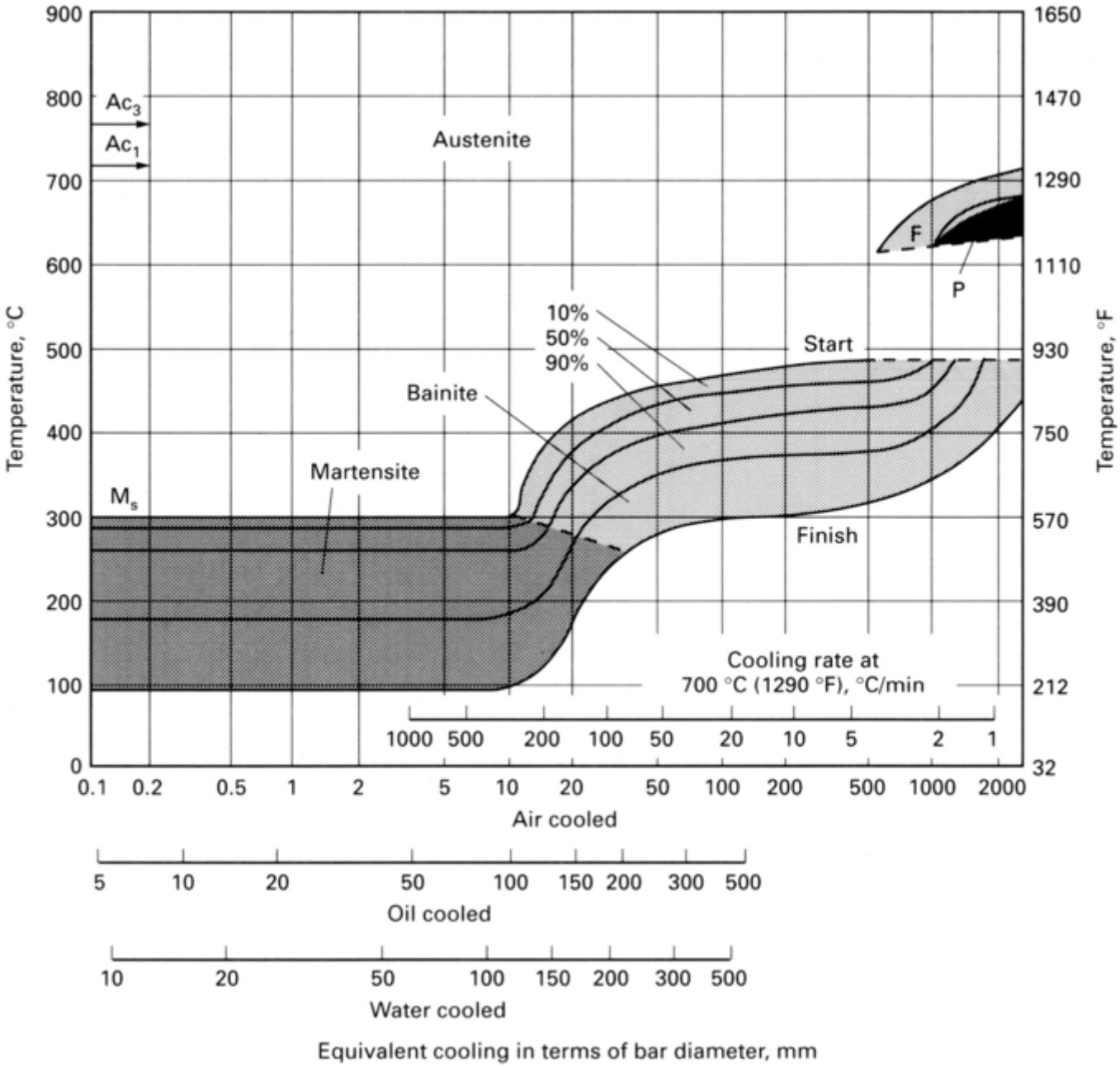

Fig. 44 Continuous cooling transformation diagram for an alloy steel with 0.40% C, 1.50% Ni, 1.20% Cr, and 0.30% Mo, plotted as a function of bar diameter. Steel was austenitized at 850 °C (1560 °F); previous treatment: rolling, then softening at 650 °C (1200 °F). Source: Ref 14

Diagrams like that in Fig. 44 are read along vertical lines from the top of the graph toward the bottom. They show the beginning and end core temperatures of the transformation process. For example, the center of a 20 mm (0.78 in.) diameter bar that is air cooled would start to transform to bainite when the core reached a little more than 400 °C (750 °F). The bainite transformation would cease when the core temperature reaches approximately 275 °C (525 °F), and approximately 90% of the transformation product would be bainite. The remaining 10% would be martensite. This graph also indicates regions of high-temperature transformation of the core into ferrite (F) and pearlite (P) when large-diameter bars are air cooled. Obviously, the surface microstructure may be somewhat different. For cooling rates shown toward the left side of the graph, the microstructure of the entire cross section may be expected to be fully martensitic. Estimation of surface and intermediate position microstructures can be made by estimating the equivalent diameter size where the core would have the same cooling rate. British Standard 5046 gives a method for calculating equivalent diameters.

Cooling curves have limitations. One is that the predictions will be incorrect if the material is not completely in the phase noted prior to cooling. For example, Fig. 45 shows a piece of medium-carbon steel cooled at a moderate rate, and the phases present are (proeutectoid) ferrite (in the grain boundaries) and what appears to be mainly pearlite with some additional ferrite in the grain interiors. Figure 46 also shows a mixture of ferrite, fine pearlite, and bainite. The ferrite here, though, has a different shape. Ferrite does not form in this shape on cooling. This example indicates why familiarity with microstructures is so important in order to be able to properly interpret their meaning. The ferrite in Fig. 46 must have been left in the microstructure because it never dissolved prior to quenching. Obviously, the percentages of ferrite predicted by the cooling curve will not agree with this material, even if the exact cooling rate was known, because the material did not start from 100% austenite and likely did not start from the temperature indicated for the grade of steel in question. It is important to remember that the data shown on both isothermal and continuous cooling curves are obtained by experiment. If the precooling microstructure of the component in question is not the same as those of the specimens used to obtain the data, the resulting microstructures will also differ.

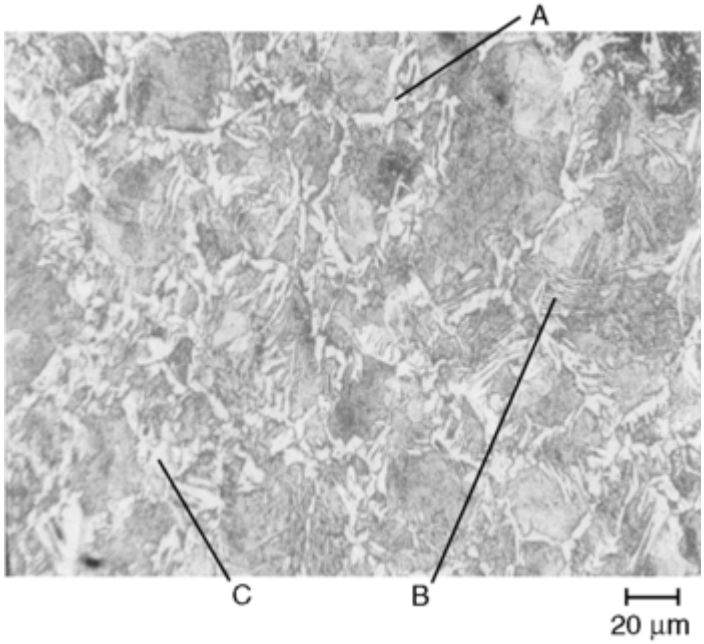

Fig. 45 Typical shapes of proeutectoid ferrite (the light-etching phase) in the grain boundaries (A), protruding into the grain interiors as needlelike (acicular) features (B), and chunky form at triple points (C). 5% nital etch. Original magnification 500×

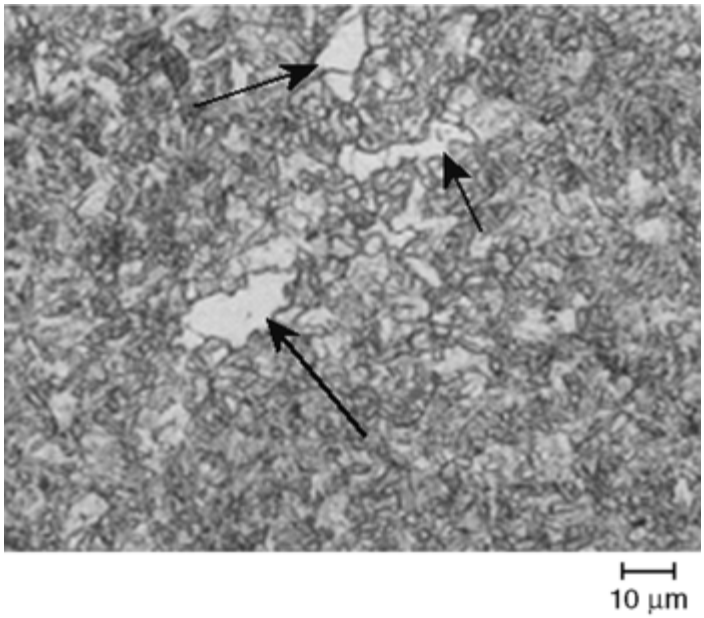

Fig. 46 Irregularly shaped ferrite grains (arrows) that did not dissolve into the austenite before it was quenched to the martensite form. 5% nital etch. Original magnification 1000×

References cited in this section

12. G. Parrish, *Carburizing: Microstructures and Properties,* ASM International, 1999, p 137

13. *Atlas of Time-Temperature Diagrams for Nonferrous Alloys,* ASM International, 1991, p 28, 31

14. M. Atkins, *Atlas of Continuous Transformation Diagrams for Engineering Steels,* British Steel Corporation, Sheffield, 1977, and American Society for Metals, 1980

15. G.F. Vander Voort, Ed., *Atlas of Time-Temperature Diagrams for Irons and Steels,* ASM International, 1991

16. *Heat Treater's Guide: Practices and Procedures for Irons and Steels,* 2nd ed., H. Chandler, Ed., ASM International, 1995

17. P. Tarin and J. Perez, SteCal 3.0, ASM International, 2004

18. *Isothermal Transformation and Cooling Transformation Diagrams,* American Society for Metals, 1977, p 28

19. G. Krauss, *Steels: Heat Treatment and Processing Principles,* ASM International, 1990, p 94

20. K.-E. Thelning, *Steel and Its Heat Treatment,* 2nd ed., Butterworths, 1984

D. Aliya and S. Lampman, Physical Metallurgy Concepts in Interpretation of Microstructures, *Metallography and Microstructures,* Vol 9, *ASM Handbook,* ASM International, 2004, p. 44–70

Debbie Aliya, Aliya Analytical, Inc.; Steve Lampman, ASM International

Acknowledgments

Thanks to W.T. Becker, H.E. Fairman, and Brett Miller for their comments and suggestions on the first draft of this article. Significant portions of this article were also adapted from the text by Leonard Samuels (Ref 7).

Reference cited in this section

7. L.E. Samuels, Chapter 9: Transformation of Austenite, *Light Microscopy of Carbon Steels,* ASM International, 1999

D. Aliya and S. Lampman, Physical Metallurgy Concepts in Interpretation of Microstructures, *Metallography and Microstructures,* Vol 9, *ASM Handbook,* ASM International, 2004, p. 44–70

Physical Metallurgy Concepts in Interpretation of Microstructures

Debbie Aliya, Aliya Analytical, Inc.; Steve Lampman, ASM International

References

1. A. Tomer, Phase Diagrams, Classical Metallography and Advanced Techniques, *Computer-Aided Microscopy and Metallography,* Vol 18, *Microstructural Science Series,* T. Place et al., Ed., ASM International, 1990, p 188

2. H. Okamato, *Desk Handbook: Phase Diagrams for Binary Alloys,* ASM International, 2000

3. *Alloy Phase Diagrams,* Vol 3, *ASM Handbook,* ASM International, 1992

4. I. Manna, S.K. Pabi, J.M. Manero, and W. Gust, Discontinuous Reactions in Solids, *Int. Mater. Rev.,* Vol 46 (No. 2), 2001, pp 53–91

5. *Metallography, Structures and Phase Diagrams,* Vol 8, *Metals Handbook,* 8th ed., American Society for Metals, 1973

6. C. Brooks, *Principles of the Heat Treatment of Plain Carbon and Low-Alloy Steels,* ASM International, 1996

7. L.E. Samuels, Chapter 9: Transformation of Austenite, *Light Microscopy of Carbon Steels,* ASM International, 1999

8. R.F. Mehl and A. Dubé, *Phase Transformations in Steels,* R. Smoluchowski, Ed., Wiley, 1951

9. H.I. Aaronson, *Decomposition of Austenite by Diffusion Processes,* V.F. Zackay and H.I. Aaronson, Ed., Wiley, 1962, p 387

10. D. Porter and K.E. Easterling, Diffusionless Transformations, *Phase Transformations in Metals and Alloys,* 2nd ed., Chapman & Hall, 1992, p 382

11. M. Tisza, *Physical Metallurgy for Engineers,* ASM International and Freund Publishing House, Ltd., 2001, p 251

12. G. Parrish, *Carburizing: Microstructures and Properties,* ASM International, 1999, p 137

13. *Atlas of Time-Temperature Diagrams for Nonferrous Alloys,* ASM International, 1991, p 28, 31

14. M. Atkins, *Atlas of Continuous Transformation Diagrams for Engineering Steels,* British Steel Corporation, Sheffield, 1977, and American Society for Metals, 1980

15. G.F. Vander Voort, Ed., *Atlas of Time-Temperature Diagrams for Irons and Steels,* ASM International, 1991

16. *Heat Treater's Guide: Practices and Procedures for Irons and Steels,* 2nd ed., H. Chandler, Ed., ASM International, 1995

17. P. Tarin and J. Perez, SteCal 3.0, ASM International, 2004

18. *Isothermal Transformation and Cooling Transformation Diagrams,* American Society for Metals, 1977, p 28

19. G. Krauss, *Steels: Heat Treatment and Processing Principles,* ASM International, 1990, p 94

20. K.-E. Thelning, *Steel and Its Heat Treatment,* 2nd ed., Butterworths, 1984

D.M. Stefanescu and R. Ruxanda, Fundamentals of Solidification, *Metallography and Microstructures,* Vol 9, *ASM Handbook* , ASM International, 2004, p. 71–92

Fundamentals of Solidification

Doru M. Stefanescu and Roxana Ruxanda, The University of Alabama

Introduction

SOLIDIFICATION PROCESSING is one of the oldest manufacturing processes as it is the principal component of metal casting processing. While solidification science evolved from the need to better understand and further develop casting processes, in 2004 solidification science is at the base of many new developments that fall out of the realm of traditional metal casting.

Solidification is, strictly speaking, the transformation of liquid matter into solid matter. The microstructure that results from solidification may be the final one, in which case it directly affects the mechanical properties of the product. In other cases, heat treatment or other processes may be used after solidification to further modify the solidification microstructure. However, the outcome of this additional processing will be greatly affected by the solidification microstructure.

D.M. Stefanescu and R. Ruxanda, Fundamentals of Solidification, *Metallography and Microstructures,* Vol 9, *ASM Handbook* , ASM International, 2004, p. 71–92

Fundamentals of Solidification

Doru M. Stefanescu and Roxana Ruxanda, The University of Alabama

Length Scale of Solidification Structures

The effect of solidification on the morphology of the matrix can be deconstructed at four different length scales (Ref 1) (Fig. 1):

- *The macroscale (macrostructure)* is of the order of 10^{-3} to 1 m. Elements of the macroscale include shrinkage cavity, macrosegregation, cracks, surface roughness (finish), and casting dimensions. A typical example of a solidification macrostructure is given in Fig. 2. Columnar grains growing inward into the casting are seen.
- *The mesoscale* is of the order of 10^{-4} m. It allows description of the microstructure features at the grain level, without resolving the intricacies of the grain structure. As seen in Fig. 1, the solid/liquid (S/L) interface is not sharp. Three regions can be observed: liquid, mushy (containing both liquid and solid grains), and solid. Mechanical properties are affected by the solidification structure at the mesoscale level, which is described by features such as grain size and type (columnar or equiaxed), the type and concentration of chemical microsegregation, and the amount of microshrinkage, porosity, and inclusions. The term “mesoscale” has been introduced in solidification science to more accurately describe the results of computer models. An example of a solidification mesoscale structure is given in Fig. 3.
- *The microscale (microstructure)* is of the order of 10^{-6} to 10^{-5} m. The microscale describes the complex morphology of the solidification grain. In a sound casting, mechanical properties depend on the solidification structure at the microscale level. To evaluate the influence of solidification on the properties of the castings, it is necessary to know the as-cast grain morphology (i.e., size and type,

columnar or equiaxed) and the length scale of the microstructure (interphase spacing, e.g., dendrite arm spacing and eutectic lamellar spacing). The term microstructure is the classic term used in metallography to describe features observed under the microscope, as seen in the electron micrograph from Fig. 4, which shows the etched surface of a pure aluminum sample (99.99 % Al). Etching removed the layers of atoms, one after the other, preferentially from crystallographic planes parallel to the faces of the elementary cube (Ref 2).

- *The nanoscale (atomic scale)* is of the order of 10^{-9} m (nanometers) and describes the atomic morphology of the S/L interface. At this scale, nucleation and growth kinetics of solidification are discussed in terms of the transfer of individual atoms from the liquid to the solid state. Features such as dislocations and individual atoms are observed with electronic microscopes. An example of dislocations seen at nanoscale magnification is given in Fig. 5.

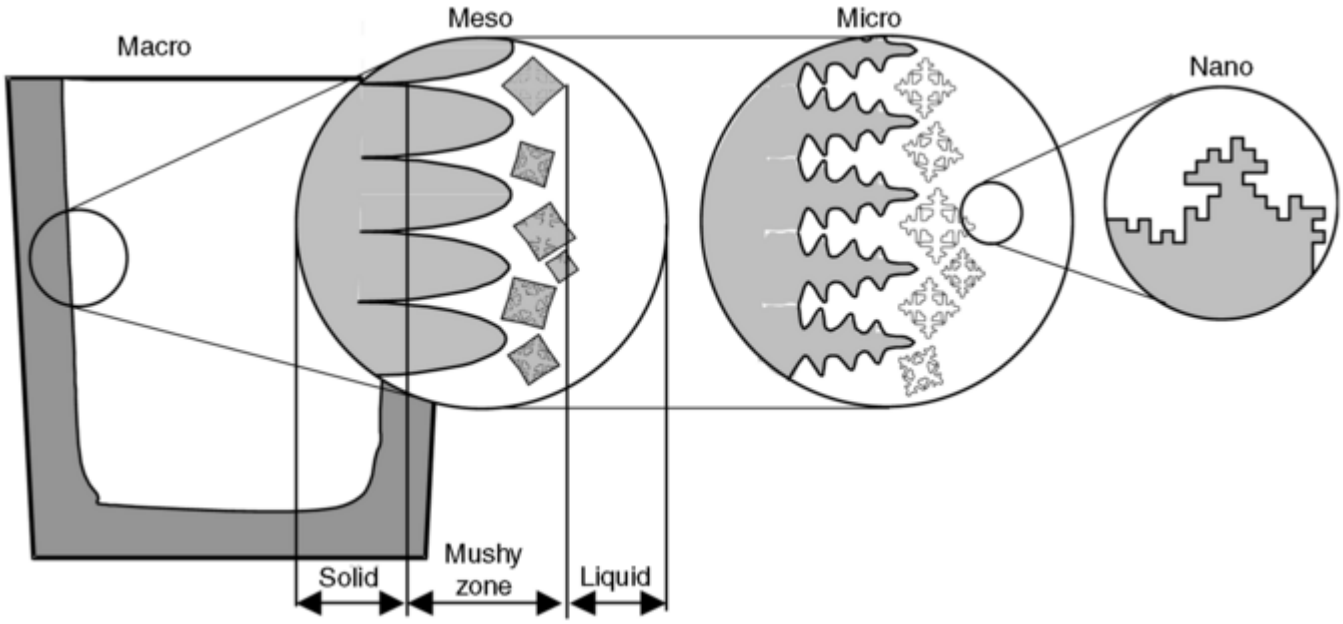

Fig. 1 Solidification length scale. Source: Ref 1

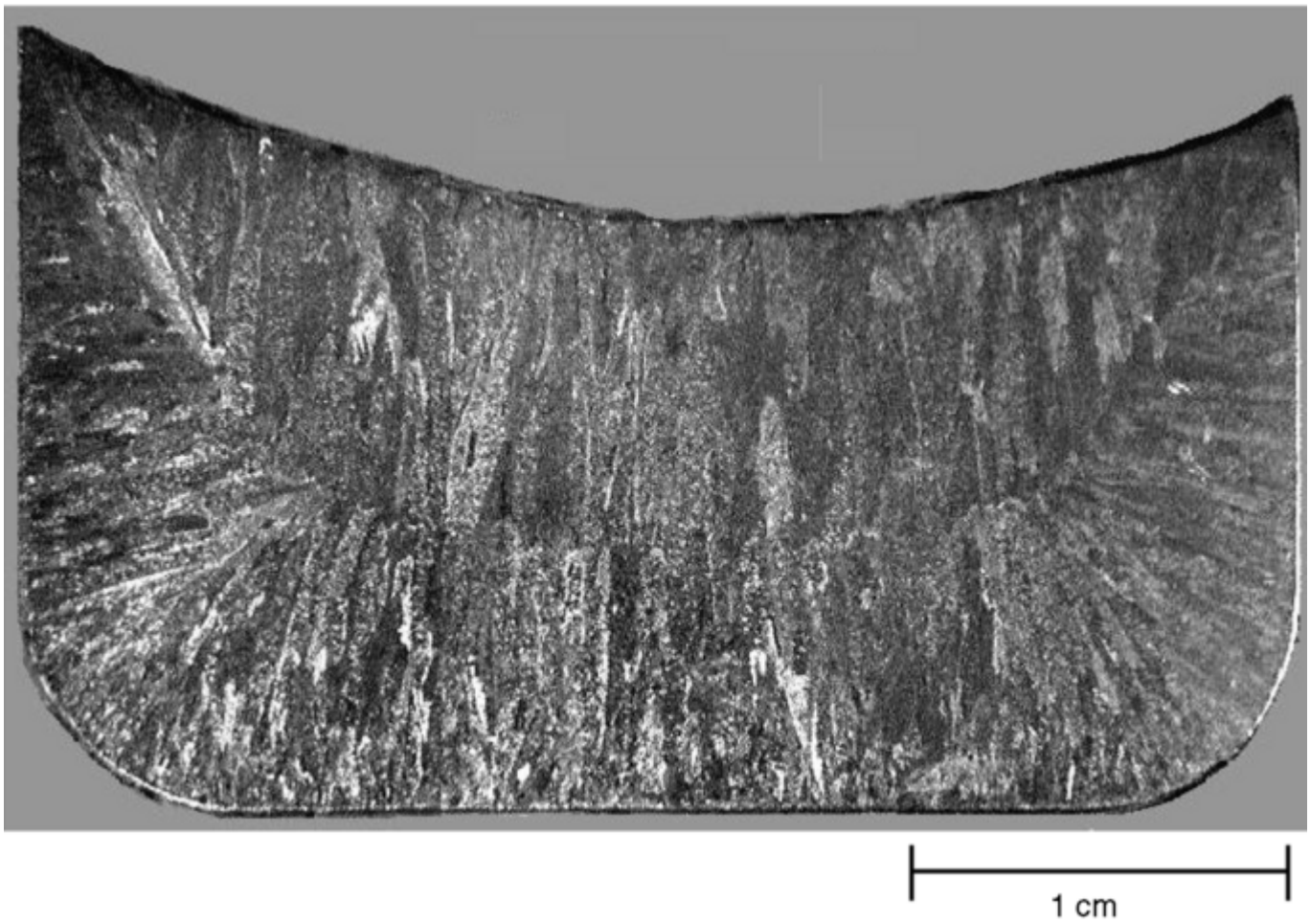

Fig. 2 Macrostructure of a cast Ti-6Al-4V alloy specimen. Etchant: Keller's reagent

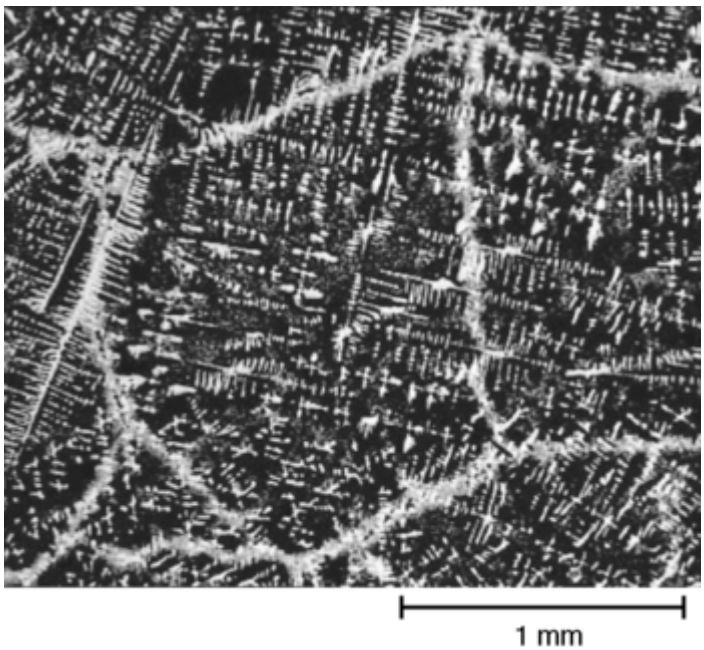

Fig. 3 Cast aluminum-silicon alloy. Etchant: 60% HCl, 30% HNO_3, 5%HF, 5%H_2O

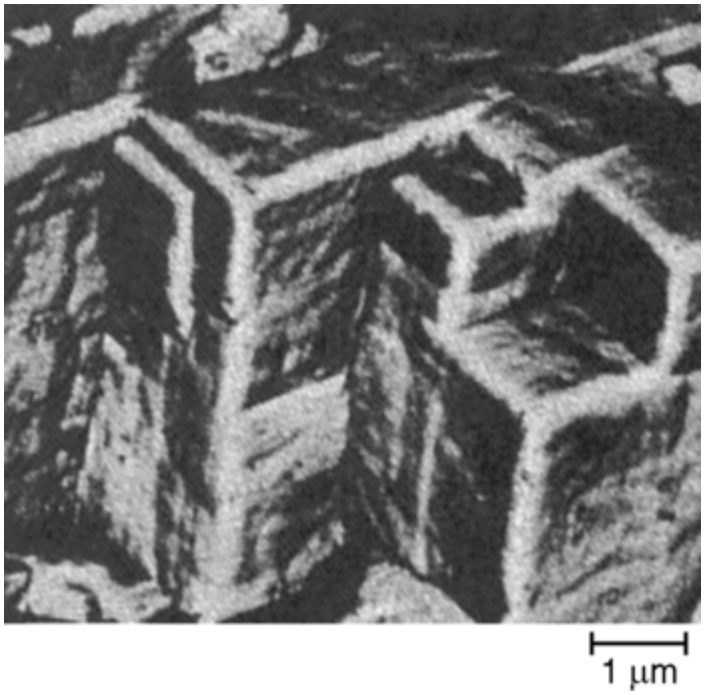

Fig. 4 Microstructure (electron micrograph) of a preferentially etched surface of a pure aluminum sample (99.99% Al). Etchant not reported. Source: Ref 2

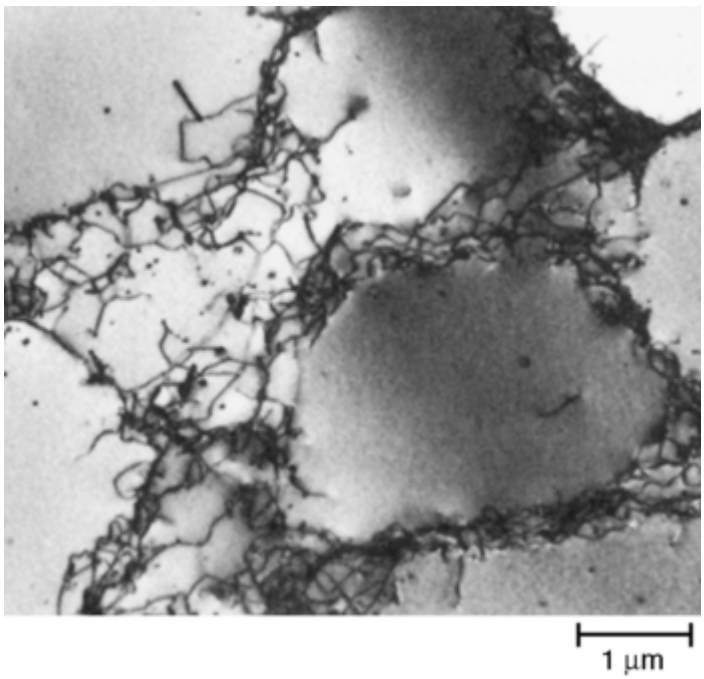

Fig. 5 Cellular dislocation arrangement in direct chill cast 99.0% Al. Dislocation lines in the as-cast structure. Transmission electron micrograph. 10,000×. Source: Ref 2

As is discussed in some detail in the following sections, two basic phenomena must take place in the liquid for solidification to occur: undercooling and nucleation. If these conditions are met, the nuclei can grow into the new solid grains.

References cited in this section

1. D.M. Stefanescu, *Science and Engineering of Casting Solidification,* Kluwer Academic, 2002

2. D.G. Altenpohl, *Aluminum: Technology, Applications, and Environment. A Profile of a Modern Metal. Aluminum from Within—the Sixth Edition,* The Aluminum Association and the Minerals, Metals, and Materials Society, 1999

D.M. Stefanescu and R. Ruxanda, Fundamentals of Solidification, *Metallography and Microstructures,* Vol 9, *ASM Handbook* , ASM International, 2004, p. 71–92

Fundamentals of Solidification

Doru M. Stefanescu and Roxana Ruxanda, The University of Alabama

Undercooling

Global equilibrium phase diagrams are frequently used to understand alloy behavior when the alloy is cooled from the liquid state to room temperature. Global equilibrium requires uniform chemical potentials and temperature across the system. Under such conditions, no changes occur with time. When global equilibrium exists, the fraction of phases can be calculated with the lever rule, and the phase diagram gives the uniform composition of the liquid and solid phases. Such conditions exist only when the solidification velocity is much smaller than the diffusion velocity. Uniform chemical potentials and temperature may truly appear only when solidification takes place over geological times.

Solidification as encountered in common processes does not occur at equilibrium, since during solidification of most castings, both temperature and composition gradients exist across the casting. Elementary thermodynamics demonstrates that a liquid cannot solidify unless some undercooling below the equilibrium (melting) temperature, T_e, occurs. Five types of solidification undercooling have been identified: kinetic undercooling, thermal undercooling, constitutional (solutal) undercooling, curvature undercooling, and pressure undercooling.

Nevertheless, in most cases, the overall solidification kinetics can be described with sufficient accuracy by using the local equilibrium condition, that is, by using the mass, energy, and species transport equations to express the temperature and composition variation within each phase and by using equilibrium phase diagrams to evaluate the temperature and composition of phase boundaries, such as the S/L interface (corrections must be made for interface curvature). Most phase transformations, with the exception of massive (partitionless) and martensitic transformations can be described with the local equilibrium condition. When the stable phase cannot nucleate or grow sufficiently fast (e.g., gray-to-white transition in cast iron), metastable local equilibrium can occur. For both stable and metastable local equilibrium, the chemical potentials of the components across the interface must be equal for the liquid and for the solid.

However, at large undercooling the solidification velocity exceeds the diffusive speed of solute atoms in the liquid phase (rapid solidification). The solute is trapped into the solid at levels exceeding the equilibrium solubility. Typically, for solute trapping the solidification velocity must exceed 5 m/s.

Kinetic Undercooling. When a number of simplifying assumptions are introduced (pure metal, constant pressure, no thermal gradient in the liquid, and flat S/L interface—that is, the radius of curvature of the interface is $r = \infty$), the only undercooling driving the S/L interface is the kinetic undercooling. It is a nanoscale length effect, resulting from the net difference in atoms transported from L to S and from S to L. Typically for metals, the kinetic undercooling is very small, of the order of 0.01 to 0.05 K.

When the simplifying assumptions are relaxed to reflect typical solidification scenarios, upon the solidification of a discrete volume of liquid the free energy of the liquid-solid system will increase by (Ref 1):

$$\Delta F_v = \Delta G_T + \Delta G_c + \Delta G_r + \Delta F_P \qquad \text{(Eq 1)}$$

where F and G are the Helmholtz and Gibbs free energy, respectively. The four right-hand terms are the change in free energy because of temperature, composition, curvature, and pressure variation, respectively. Solidification cannot occur unless each of these energies is balanced by a corresponding undercooling of the system, as discussed in this section.

Thermal Undercooling. If nucleation does not occur, a pure metal can undercool under the equilibrium temperature because of heat extraction. The liquid is said to be thermally undercooled by a quantity:

$$\Delta T_T = T_e - T^* \quad \text{(Eq 2)}$$

where ΔT_T is the thermal undercooling, T_e is the equilibrium (melting) temperature of the flat interface, and T^* is the interface temperature.

Constitutional (Solutal) Undercooling. During alloy solidification, solute is rejected by the solid. This can be understood from the phase diagram in Fig. 6. For a given temperature, T^*, the composition of the solid, C_S, is smaller than that of the liquid, C_L, in equilibrium with the solid. The ratio $k = C_S/C_L$ is called the partition coefficient. For the case in the figure (where the equilibrium temperatures decrease with increased alloy composition) $k < 1$. The slope of the liquidus line is $m_L = dT_L/dC_L$, where T_L is the liquidus temperature.

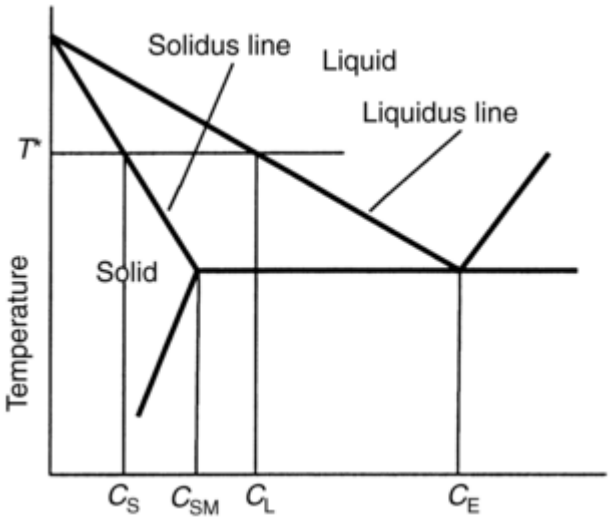

Fig. 6 Left corner of a phase diagram. C_E, eutectic composition; C_L, composition of liquid; C_S, composition of solid; C_{SM}, maximum solubility in solid; T^*, interface temperature; T_L, liquidus temperature; T_S, solidus temperature

Because of solute rejection, a boundary layer, richer in solute than the bulk liquid, is formed at the S/L interface. A direct consequence of this phenomenon is that the liquidus temperature is lower next to the interface than away from it (Fig. 7). The heat flow from the liquid to the solid imposes a thermal gradient, G_T, which dictates the local temperature in the melt. If the thermal gradient is lower than the liquidus gradient, G_L (the tangent to T_L at the S/L interface), which is the case shown in Fig. 7, the temperature in the boundary layer will be lower than the equilibrium liquidus temperature. Thus, a constitutionally undercooled region will result. The size of the local constitutional (solutal) undercooling can be calculated as a function of the local composition as:

$$\Delta T_c = T_L - T^* = -m_L\left(C_L^* - C_0\right) \quad \text{(Eq 3)}$$

where ΔT_c is the constitutional undercooling, C_L^* is the composition of the liquid, C_0 is the bulk composition of the alloy at the beginning of solidification, and the other terms are as previously defined.

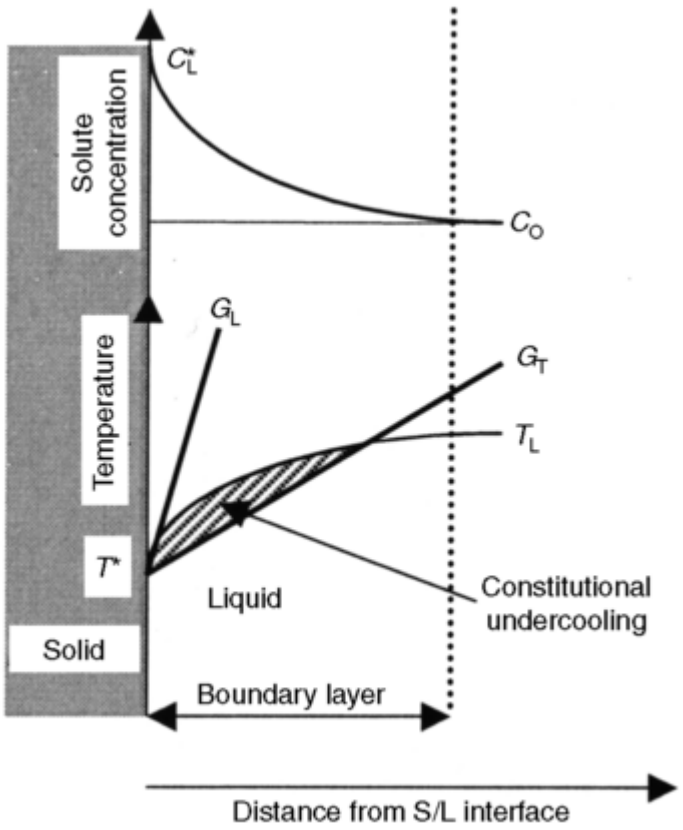

Fig. 7 Formation of a constitutionally undercooled region (dashed area) in the liquid next to the solid/liquid interface because of the lower liquidus temperature produced by the higher solute content. C_L*, composition of the liquid; C_o, bulk composition of the alloy at the beginning of solidification; G_L, liquidus (solutal) temperature gradient; G_T, thermal gradient in the liquid; T_L, liquidus temperature

Curvature Undercooling. When a discrete liquid volume becomes solid, the newly formed S/L interface produces an increase in the energy of the system through the interface energy associated with it. For solidification to continue, additional undercooling is required. This undercooling is called the curvature undercooling. Since a smaller radius (higher curvature) of the solid results in a higher surface-to-volume ratio, higher curvature is associated with higher undercooling. Thus:

$$\Delta T_r = T_e - T_e^r = \frac{\gamma}{\Delta S_f} K = \Gamma K \qquad \text{(Eq 4)}$$

where ΔT_r is the curvature undercooling, T_e^r is the equilibrium temperature for a sphere of radius r, γ is the S/L interface energy, ΔS_f is the entropy of fusion, $K = 1/r$ is the curvature, and Γ is the Gibbs-Thomson coefficient.

Pressure Undercooling. An increase in the pressure applied to the liquid, ΔP, will cause an increased undercooling of the liquid, called pressure undercooling, ΔT_P. It can be calculated as:

$$\Delta T_P = \frac{\Delta P \Delta v}{\Delta S_f} \qquad \text{(Eq 5)}$$

where Δv is the change in volume. For metals the pressure undercooling is rather small, of the order of 10^{-2} K/atm. Therefore, typical pressure changes for usual processes have little influence on the melting temperature and the pressure undercooling is negligible.

Undercooling is a basic condition required for solidification. However, for solidification to occur nuclei must form in the liquid.

Reference cited in this section

1. D.M. Stefanescu, *Science and Engineering of Casting Solidification,* Kluwer Academic, 2002

D.M. Stefanescu and R. Ruxanda, Fundamentals of Solidification, *Metallography and Microstructures,* Vol 9, *ASM Handbook* , ASM International, 2004, p. 71–92

Fundamentals of Solidification

Doru M. Stefanescu and Roxana Ruxanda, The University of Alabama

Nucleation

It is convenient to classify the types of nuclei available in the melt as resulting from homogeneous nucleation, heterogeneous nucleation, and dynamic nucleation (Ref 1).

Homogeneous nucleation, which implies that growth is initiated on substrates having the same chemistry as the solid, is not common in casting alloys.

Heterogeneous nucleation is based on the assumption that the development of the grain structure occurs upon a family of substrates of chemistry different than that of the solid. Heterogeneous nucleation occurs when substrate particles are deliberately introduced into a melt to promote equiaxed grain formation. This is common practice in liquid processing of metallic alloys.

Dynamic nucleation occurs because of the action of convective currents within the melt. The initial chilling action of the mold may induce local solid grain formation. These grains are then carried into the bulk by fluid flow and survive and grow in the undercooled liquid. This is called the big bang mechanism. Experimental evidence for this mechanism is provided in Fig. 8, which shows the results of experiments with a steel net inserted in the middle of a crucible where an Al-2%Cu alloy was allowed to solidify (Ref 3). In the lower part, only columnar grains are formed. In the upper part, a large number of small equiaxed grains are seen in the vicinity of the sieve. It is argued that these grains have originated at the mold wall, then have been carried by convection currents in the middle of the ingot, and have been prevented from sinking by the sieve.

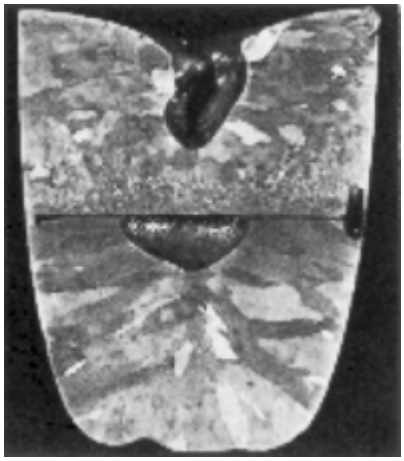

Fig. 8 Equiaxed grain accumulation on a steel sieve inserted in a solidifying Al-2%Cu alloy. Source: Ref 3

Another possible mechanism for dynamic nucleation is the fragmentation of existing crystals through ripening and local remelting of columnar dendrites. The detached dendrite arms are carried to the center of the mold by convection currents (Fig. 9) (Ref 4). If the center of the mold is undercooled, these crystals act as nuclei for equiaxed grains.

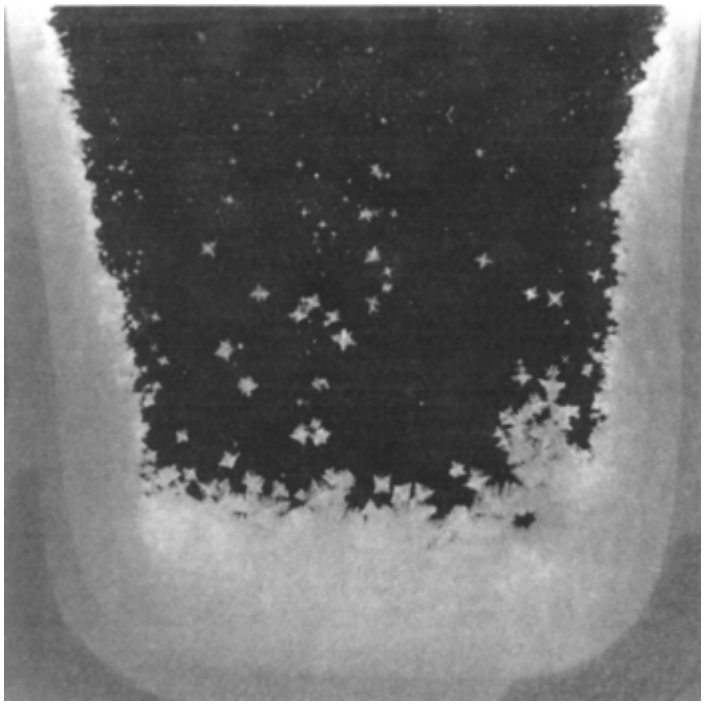

Fig. 9 Broken dendrite branches transported in the center of the ingot by liquid convection in an ammonium-chloride/water system. Source: Ref 4

The number of grains identified by metallographic techniques at the end of solidification is not necessarily equal to the number of initial nuclei. Some nuclei may redissolve because of insufficient undercooling, while others may grow and coalesce, thus decreasing the final number of grains. As demonstrated through liquid quenching experiments on gray cast iron (Ref 5), the final eutectic volumetric grain density was found to be as much as 27% less than the maximum number of grains developed during solidification (Fig. 10).

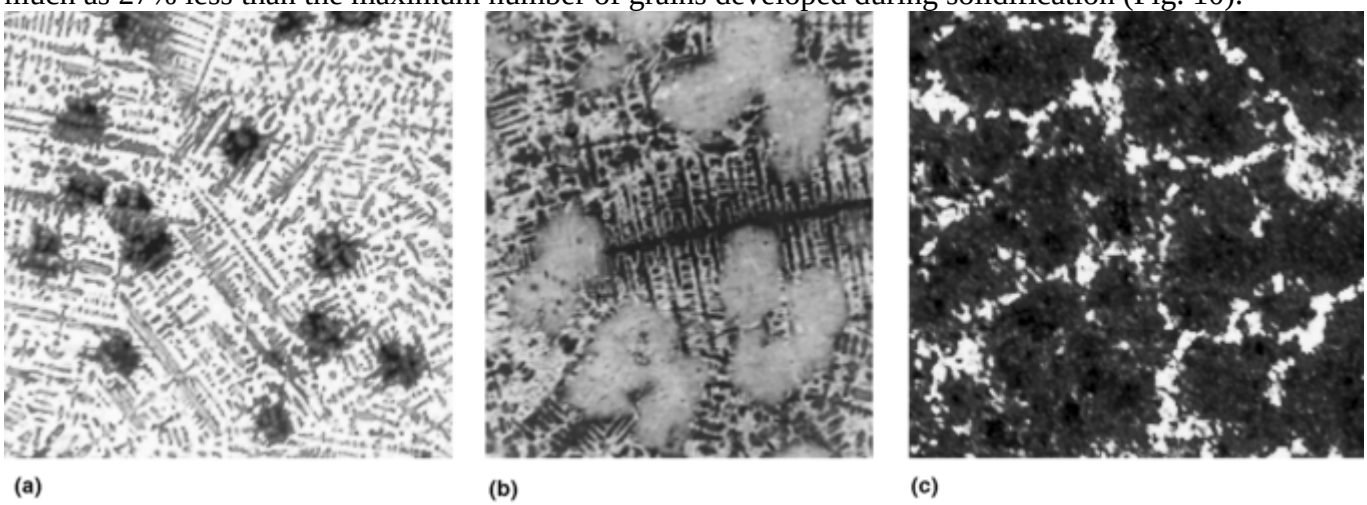

Fig. 10 Nucleation and coalescence of eutectic grains in cast iron. (a) Early solidification. (b) Late solidification. (c) After solidification at room temperature. Source: Ref 5

References cited in this section

1. D.M. Stefanescu, *Science and Engineering of Casting Solidification,* Kluwer Academic, 2002

3. A. Ohno, *Solidification. The Separation Theory and Its Practical Applications,* Springer-Verlag, Berlin, 1987

4. R. Trivedi and W. Kurz, Solidification of Single-Phase Alloys, *Casting,* Vol 15, *ASM Handbook,* D.M. Stefanescu, Ed., ASM International, 1988, p 114

5. M. Schenck, referred to in *Solidification. The Separation Theory and Its Practical Applications,* Springer-Verlag, Berlin, 1987

D.M. Stefanescu and R. Ruxanda, Fundamentals of Solidification, *Metallography and Microstructures,* Vol 9, *ASM Handbook* , ASM International, 2004, p. 71–92

Fundamentals of Solidification

Doru M. Stefanescu and Roxana Ruxanda, The University of Alabama

Growth and Interface Stability

The thermal and compositional fields at the S/L interface determine the morphology of the interface. During growth, local perturbations (instabilities) will form at the S/L interface. If the perturbations cannot survive, the interface remains planar (Fig. 11a). If on the contrary they become stable, they will continue to develop and different interface morphologies can result (Fig. 11b–d). In pure metals, the only source of growing interface instabilities is the thermal field (thermal undercooling). In alloys, both thermal and solutal instabilities may grow, as a result of thermal and solutal undercooling.

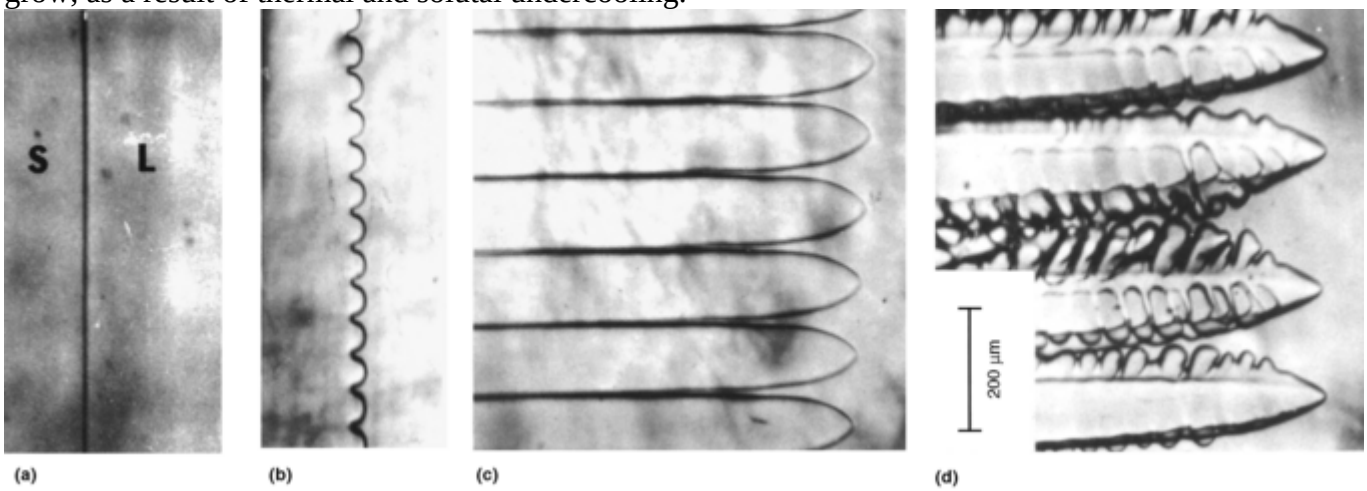

Fig. 11 The change of the morphology of the solid/liquid interface as a function of growth velocity (*V*) in a transparent organic system (pivalic acid, 0.076% ethanol) directionally solidified under a thermal gradient of 2.98 K/mm. (a) Planar interface, *V* = 0.2 μm/s. (b) Cellular interface, *V* = 1.0 μm/s. (c) Cellular interface, *V* = 3.0 μm/s. (d) Dendritic interface, *V* = 7.0 μm/s. Source: Ref 4

When the thermal gradient in the liquid at the S/L interface is less than the liquidus temperature gradient—that is, $G_T < G_L$ (see Fig. 7)—the liquid at the interface (T^*) is at a lower temperature than its liquidus (T_L). This liquid is constitutionally undercooled. Instabilities growing in this region will become stable, because they will find themselves at a temperature lower than their equilibrium temperature. They will continue to grow. On the contrary, if $G_T > G_L$, the interface will remain planar (Fig. 11a).

For small constitutional undercooling, the instabilities will only grow in the solidification direction (the *x*-direction), and a cellular interface will result (Fig. 11b and c). This is shown in Fig. 12. The planar-to-cellular transition occurs at a gradient $G_{p/c}$. As the constitutional undercooling increases because of the lower thermal gradient, the spacing between the cells increases, and constitutional undercooling may also occur perpendicular to the growth direction (in the *y*-direction). Instabilities will develop on the sides of the cells, resulting in the formation of dendrites (Fig. 11d). This is the cellular-to-dendrite transition. It takes place at a temperature gradient $G_{c/d}$. Both cellular and dendritic growth occurring from the wall in the direction opposite to the heat transport can be described as columnar growth.

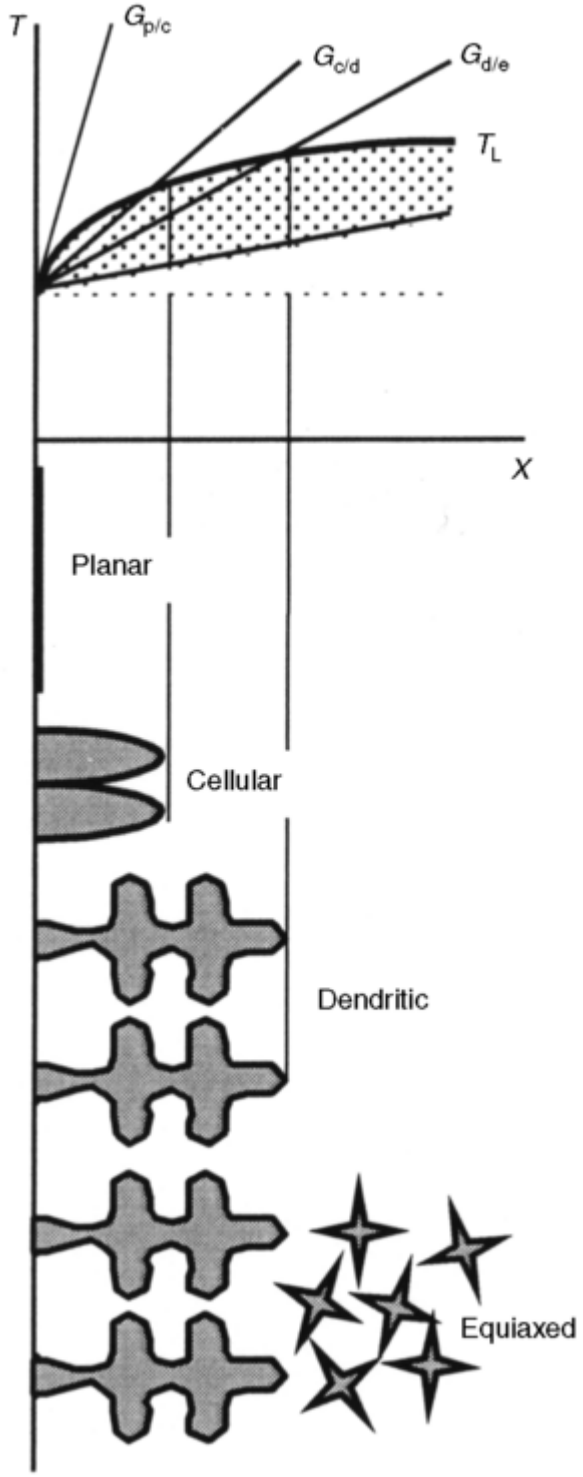

Fig. 12 Correlation between the thermal gradient at the interface and the interface morphology. Source: Ref 1

If constitutional undercooling is greater, equiaxed grains can be nucleated in the liquid away from the interface. The dendritic-to-equiaxed transition occurs at $G_{d/e}$. If the thermal gradient is almost flat—that is, $G_T = 0$—the driving force for the columnar front will be extremely small. A complete equiaxed structure is expected.

All the transitions described in the previous paragraph are controlled by the initial composition of the alloy, by the solidification velocity (V), and by the thermal gradient. The planar-to-cellular transition during steady-state solidification is governed by the criterion for the onset of constitutional undercooling given by:

$$\frac{G_T}{V} < -\frac{m_L C_0 (1-k)}{k D_L} = \frac{\Delta T_0}{D_L} \qquad \text{(Eq 6)}$$

where k is the partition coefficient, D_L is the liquid diffusivity, and ΔT_0 is the temperature difference between the equilibrium liquidus and solidus of the alloy of composition C_0. If solidification is not at steady state, ΔT_0 is substituted with the undercooling ΔT at which solidification occurs.

References cited in this section

1. D.M. Stefanescu, *Science and Engineering of Casting Solidification,* Kluwer Academic, 2002

4. R. Trivedi and W. Kurz, Solidification of Single-Phase Alloys, *Casting,* Vol 15, *ASM Handbook,* D.M. Stefanescu, Ed., ASM International, 1988, p 114

D.M. Stefanescu and R. Ruxanda, Fundamentals of Solidification, *Metallography and Microstructures,* Vol 9, *ASM Handbook* , ASM International, 2004, p. 71–92

Fundamentals of Solidification

Doru M. Stefanescu and Roxana Ruxanda, The University of Alabama

---

Basic Solidification Structures of Pure Metals

Pure metals can solidify with planar interfaces (single crystals or polycrystals with columnar front) or with equiaxed structure. To obtain single crystals the following methods are used (Ref 1): normal freezing (the boat method or the Bridgman method), crystal pulling (Czochralski), or zone melting and zone freezing (with crucible or crucibles). High-temperature gradients and low-solidification velocities are required to obtain a planar interface.

When casting a pure metal in a mold, the initial shape and size of the grains are determined by nucleation and growth during solidification, but they may be altered significantly by grain growth after solidification. Two solidification cases may be considered: starting with a melt having low superheating or with a melt having high superheating.

When the metal is poured at low superheat, nucleation will occur on the cold mold wall. A thin region of small equiaxed dendrites will be produced in the undercooled zone adjacent to the wall. Then, a thermal gradient from the melt to the mold will be established and solidification will proceed inward from the mold wall with an isothermal front. The grains will elongate in the direction of heat flow, resulting in a columnar polycrystalline grain structure. As growth proceeds, some crystal orientations will tend to persist at the expense of others, resulting in a preferred orientation texture.

For a high superheat, the mold walls may be heated above the melting point during pouring. Then, as undercooling occurs, nucleation may start in the bulk liquid producing equiaxed dendritic grains. Finer equiaxed grains can be produced by promoting heterogeneous nucleation through the addition of nucleating agents.

Single Crystals. Most metal single crystals have dislocation densities of about 10^6 to 10^7 per square centimeter. These dislocations result from stresses induced during growth by thermal, mechanical, and composition gradients, as well as from entrapped particles. In addition, vacancies can condense to form small dislocation loops subsequent to growth (Ref 6).

Dislocations present in a metal crystal often polygonize into subboundaries during growth. These subboundaries produce subgrains during solidification. The subboundaries are elongated in the direction of the growth and can be irregular if the material is pure, or are regular and straight in a very dilute alloy in which cellular growth has occurred (see Fig. 1 and 2 in the article “Solidification Structures of Pure Metals” in this Volume). Subboundaries also are formed where the liquid between two slightly misoriented dendrite arms solidifies (Ref 2). Dislocations in subboundaries can be resolved by careful etching. Dislocations produced by precipitation and condensation of vacancies during cooling usually are in the form of small loops.

Equiaxed Microstructures. After nucleation, each equiaxed dendrite will grow independently until it comes in contact with and impinges on adjacent growing dendrites. At this stage dendrite coherency has been reached, and the initial shape of the grains is formed. When all the interdendritic liquid has been solidified, the solidification grain boundaries are established. These boundaries will move during subsequent cooling in solid state when grain growth occurs to minimize free energy.

Although the grain boundaries in high-purity metals are very mobile, they may be slowed down or pinned by small concentrations of impurities. If the initial grain size was large, grain growth is less likely, but there will usually be some adjustment of the grain boundaries to lower energy configurations.

The energy of a grain boundary increases with the orientation mismatch between the grains, as shown in Fig. 13. Small-angle boundaries (up to 10°), consisting of dislocation arrays, have much lower energies than large-angle boundaries. The dislocation arrays in tilt and twist boundaries are illustrated in Fig. 11 and 12 in the article “Solidification Structures of Pure Metals” in this Volume.

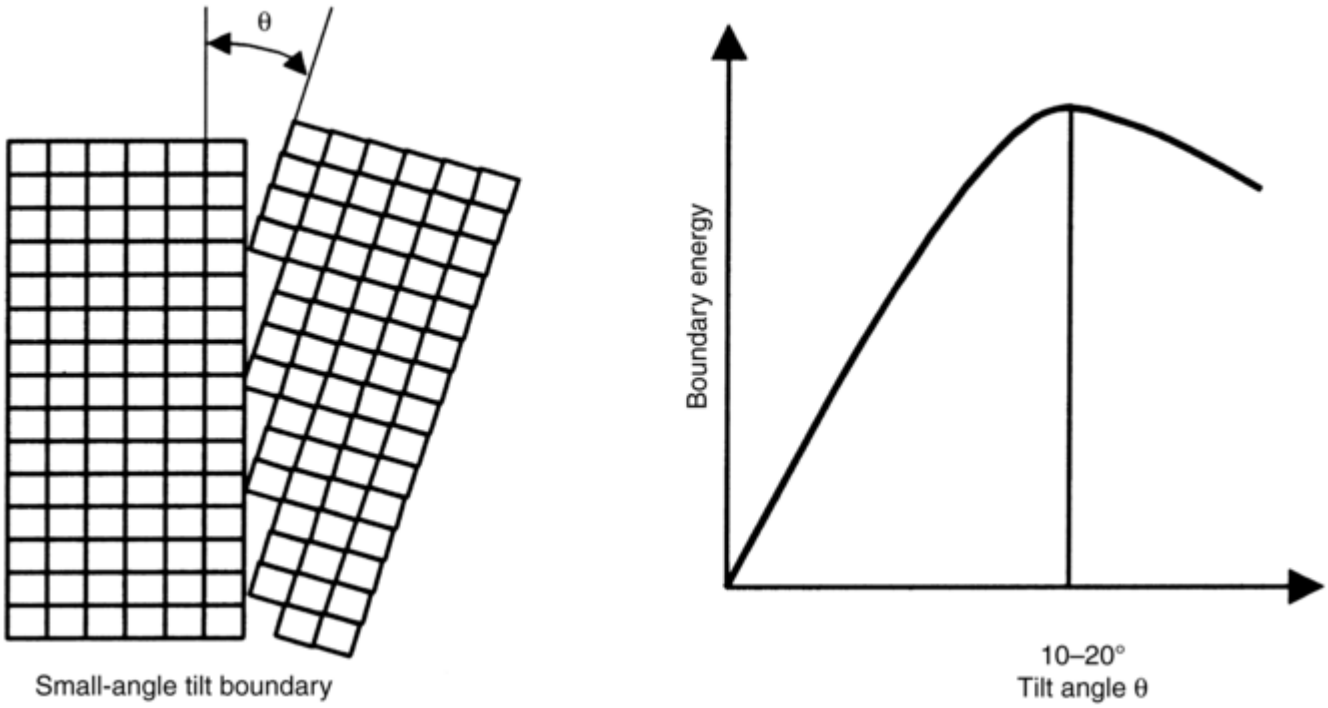

Fig. 13 Definition of orientation mismatch between grains and variation of energy associated with the boundary as a function of the tilt angle

Most boundaries between grains will be large-angle boundaries and will have more than 10° misorientation. Except twin or coincidence boundaries, these boundaries have roughly the same energy, so when equilibrated at the junction of three grains they form 120° angles with each other, as shown in Fig. 14. In Fig. 15, the junction of a small-angle boundary (low energy) with two large-angle boundaries (high energy) is shown. The ratios of the boundary energies can be calculated from the angles.

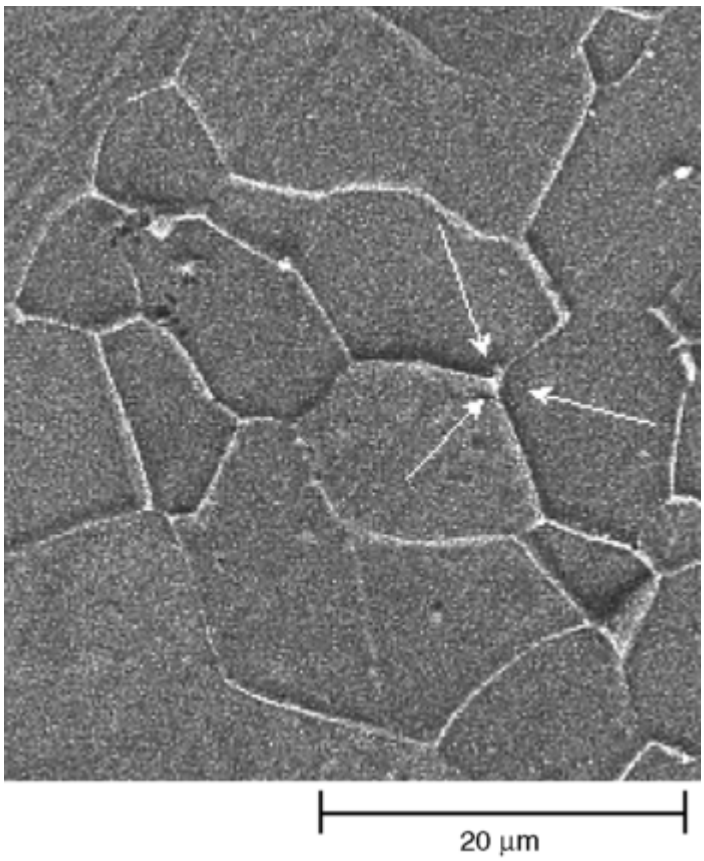

Fig. 14 Secondary electron micrograph of grain boundaries in polycrystalline iron. Angles at the indicated triple junction of the grain boundaries: 105°, 125°, and 130°

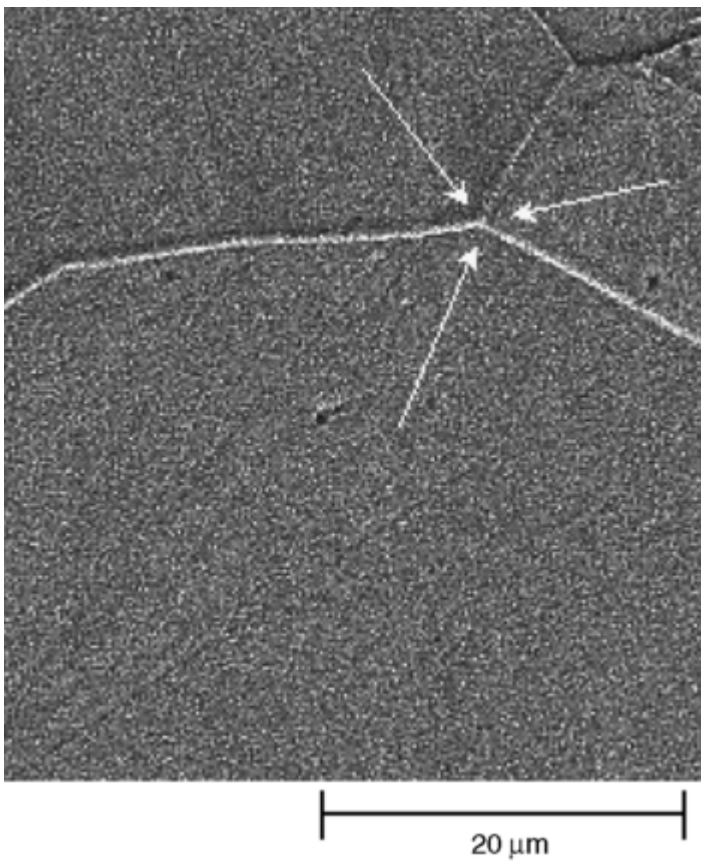

Fig. 15 Secondary electron micrograph of low-energy and high-energy grain boundaries in polycrystalline iron. Angles at the indicated triple junction of the grain boundaries: 92°, 125°, and 145° (junction at arrow).

Coincidence boundaries usually have lower energies than those of large-angle boundaries. A boundary that separates twins (two crystals oriented in a special crystallographic arrangement in which they are related by mirror symmetry) has low energy if it is coherent, that is, if it lies in the mirror plane. Twin boundaries can be produced during crystal growth or annealing. Small-angle boundaries and individual dislocations are usually present within the grains of a polycrystal, just as in a single crystal (Ref 6).

References cited in this section

1. D.M. Stefanescu, *Science and Engineering of Casting Solidification,* Kluwer Academic, 2002

2. D.G. Altenpohl, *Aluminum: Technology, Applications, and Environment. A Profile of a Modern Metal. Aluminum from Within—the Sixth Edition,* The Aluminum Association and the Minerals, Metals, and Materials Society, 1999

6. K.A. Jackson, Solidification Structures of Pure Metals, *Metallography and Microstructures,* Vol 9, *ASM Handbook,* ASM International, 1985, p 607

D.M. Stefanescu and R. Ruxanda, Fundamentals of Solidification, *Metallography and Microstructures,* Vol 9, *ASM Handbook* , ASM International, 2004, p. 71–92

Fundamentals of Solidification

Doru M. Stefanescu and Roxana Ruxanda, The University of Alabama

---

Solidification Structures of Solid Solutions

Alloys consist of a base metal, such as iron, aluminum, copper, or nickel, to which other elements (solutes) are added to yield desired properties. The simplest liquid-to-solid transformation (solidification) occurs when the liquid solution transforms into a solid solution (Fig. 16a). However, for many alloys solidification may be completed by some other process, such as a eutectic (Fig. 16b), peritectic (Fig. 16c), or monotectic reaction (Fig. 16d). The details of the solidification of the solid solution are important in determining the final microstructure and thus the properties.

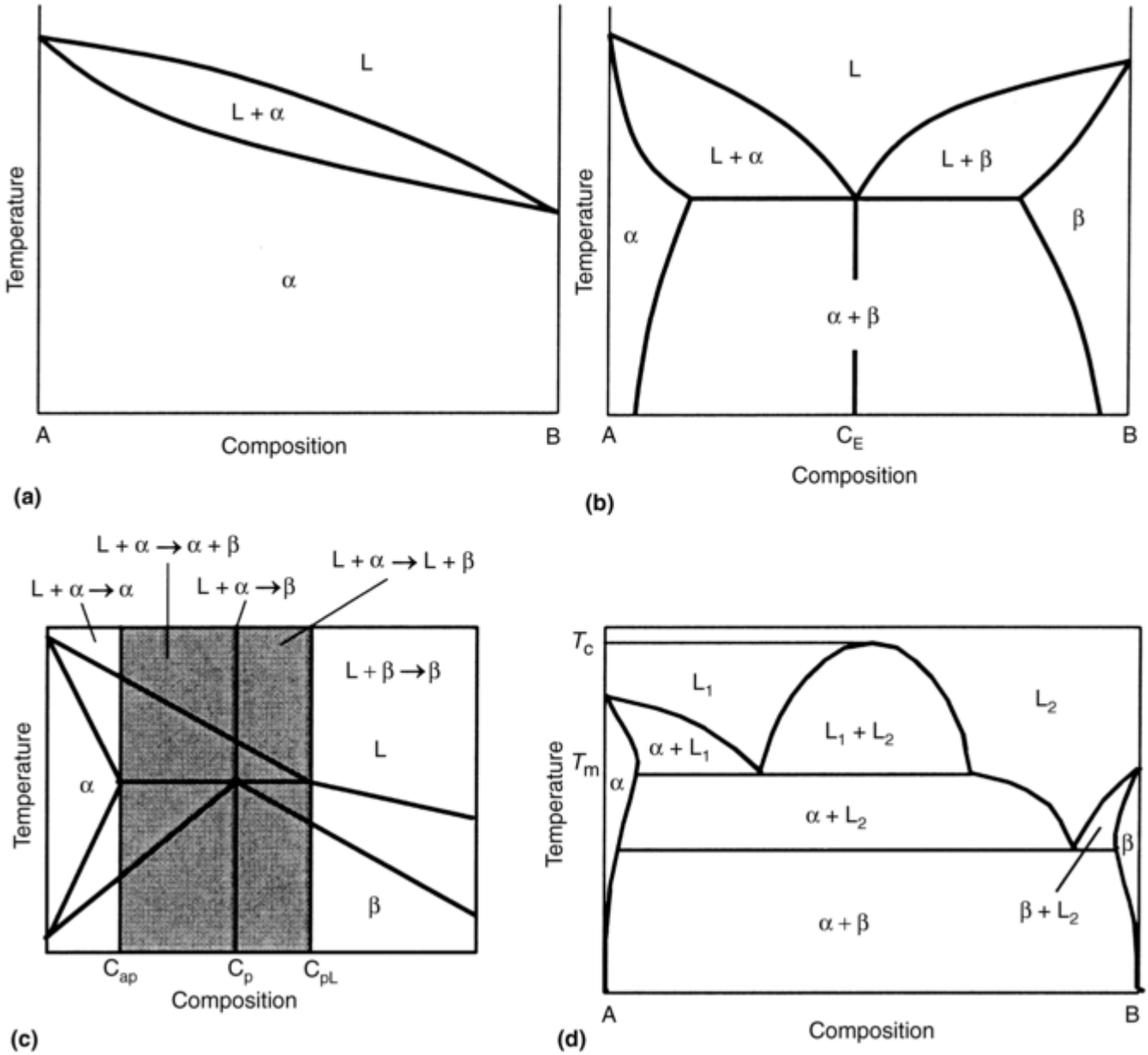

Fig. 16 Binary phase diagrams. L, L_1, and L_2 are liquid solutions. α and β are solid solutions. (a) Complete solid solubility. (b) Partial solid solubility with eutectic reaction. (c) Partial solid solubility with peritectic reaction. (d) Partial solid solubility with monotectic reaction

As shown in Fig. 6, the liquid has a different composition (C_L) than the solid (C_S) from which it is forming (in the figure $C_L > C_S$). Consequences of this phenomenon are the occurrence of constitutional undercooling and segregation.

Constitutional undercooling is instrumental in destabilizing the S/L interface and promoting interface morphologies different than planar. As inferred by Eq 6, there is a critical solute content (C_0) of the alloy for a given G_T/V ratio combination, at which the interface becomes unstable. This can be presented graphically as shown in Fig. 17, where the line for Eq 6 indicates the planar-to-cellular transition. As the G_T/V ratio continues to decreases (or C_0 to increase), the S/L interface becomes increasingly unstable with successive formation of a columnar dendritic and then equiaxed dendritic structure.

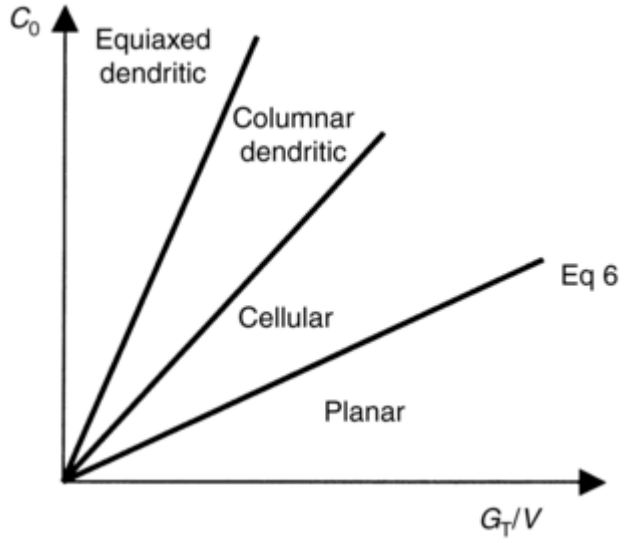

Fig. 17 Transition to different interface morphologies as a function of the temperature-gradient/solidification-velocity ratio (G_T/V) and solute concentration (C_0)

The formation of the equiaxed dendritic structure requires bulk nucleation. In the absence of bulk nucleation, the columnar front will continue to grow, or, alternatively, at high undercoolings amorphous solidification may occur (i.e., solidification without crystallization, also termed glass formation).

Planar Interfaces. Planar growth of alloys can usually be achieved only in crystal growth furnaces at high-temperature gradients and low solidification velocities. For example, for planar solidification of an alloy with ΔT = 5 K and G_T = 100 K/cm, the maximum allowable solidification velocity calculated with Eq 6 is 2 μm/s. Figure 18 shows a dilute tin-cadmium alloy solidified at high-temperature gradient and low-solidification speed to achieve planar growth (Ref 7). Planar growth of doped semiconductors constitutes the basis of an entire industry. However, most metallurgical alloys solidify with nonplanar interfaces.

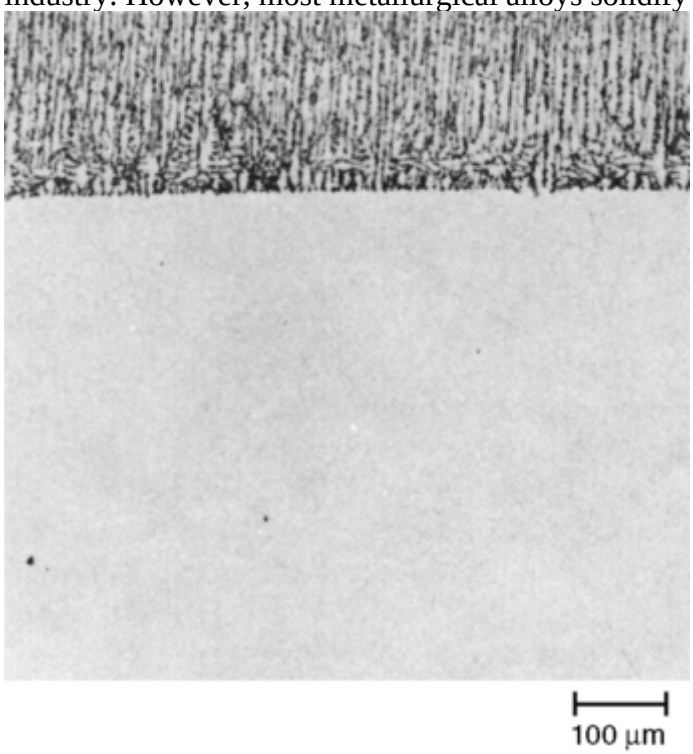

Fig. 18 Directionally solidified Sn-0.6Cd alloy. Section parallel to the growth direction shows a quenched planar solid/liquid interface. G = 320 K/cm, V = 0.85 μm/s, ΔT = 5.7 K. Etchant: 5 mL HNO_3, 95 mL lactic acid. Magnification: 80×. Courtesy of C. Brady. Source: Ref 7

Cellular Structures. When constitutional undercooling occurs, the S/L interface morphology becomes cellular or dendritic. For conditions of growth where the G_T/V ratio is only slightly smaller than the ratio $\Delta T/D_L$, the interface is cellular, as shown in Fig. 11(c) for a transparent organic "alloy" that solidifies like a metallic alloy. For conditions of growth where the ratio G_T/V is much smaller than the ratio $\Delta T/D_L$, the interface becomes columnar dendritic, as shown in Fig. 11(d). The regions between the cells and dendrites, which are still liquid in the micrographs, are enriched in solute and produce microsegregation at the end of solidification.

Cellular structures are most often observed in dilute alloys where ΔT is small. Cellular structures can take on three characteristic morphologies when viewed in a metallographic section transverse to the growth direction: nodes (Fig. 19a), elongated cells (Fig. 19b), and hexagonal cells (Fig. 19c). The hexagonal cellular structure is observed much more frequently than the node or elongated cell structures (Ref 7).

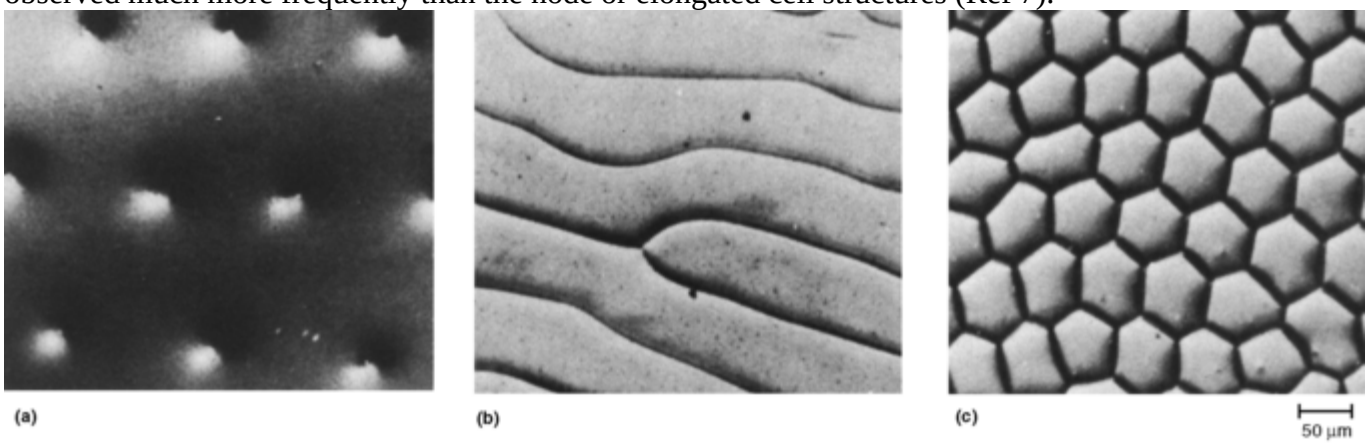

Fig. 19 Sn-0.05Pb alloy; liquid decanted to reveal structures of solid/liquid interfaces. (a) Oblique illumination reveals nodes at the solid/liquid interface. (b) Elongated cells at the solid/liquid interface under bright-field illumination. (c) Fully developed hexagonal cells at the solid/liquid interface (bright-field illumination). Unpolished, unetched. Magnification: 150×. Source: Ref 7

Dendritic Structures. The dendritic morphology is the most commonly observed solidification structure. Because dendrites are complex, three-dimensional structures, plane-section micrographs must be interpreted carefully. Figure 20 shows the structure of cobalt dendrites when the material surrounding the dendrites has been removed by selective deep etching. Figure 21 shows the same structure observed in a plane section. Parts of a single dendrite often appear disconnected when viewed in a plane section. The high degree of segregation present in this structure is revealed by the elemental mapping of cobalt and copper, as shown in Fig. 22.

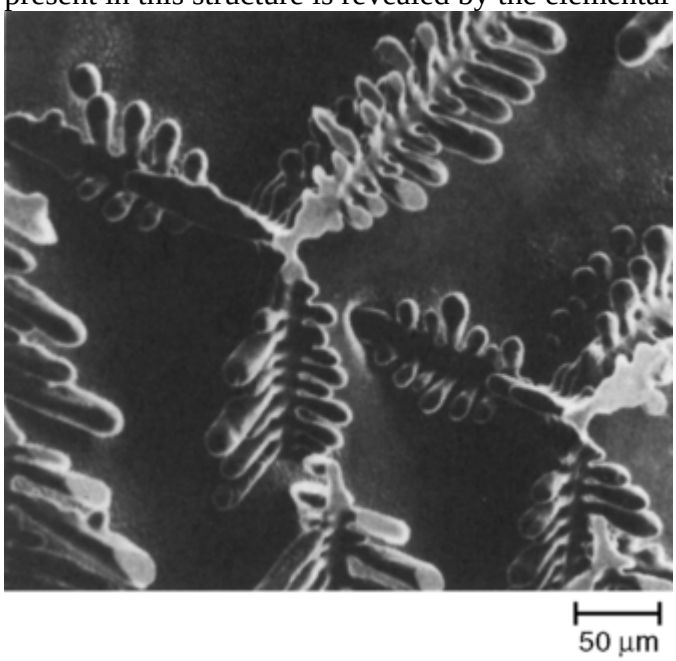

Fig. 20 Secondary electron micrograph of Cu-10Co (at.%) alloy casting. Etchant not reported. Magnification: 150×. Source: Ref 7

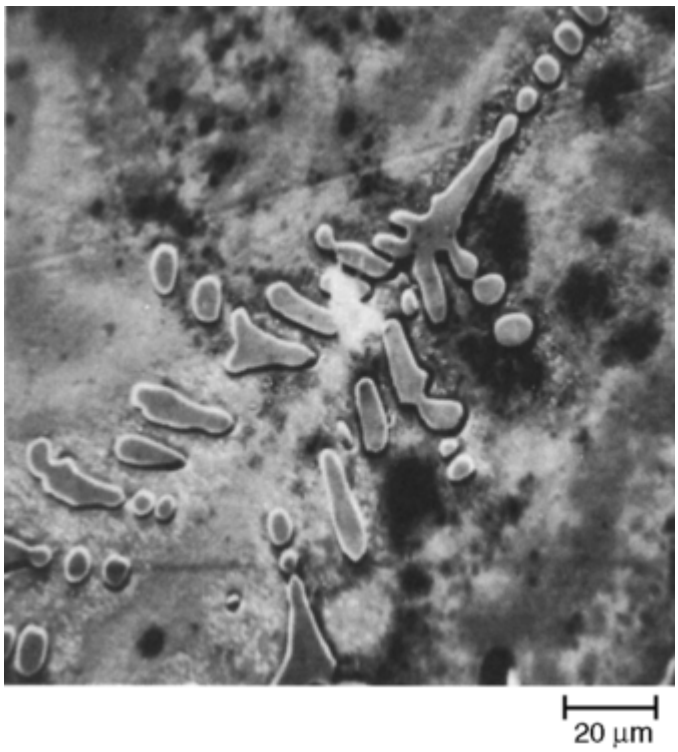

Fig. 21 Secondary electron micrograph of Cu-10Co (at.%) alloy casting. As-polished. Magnification: 400×. Source: Ref 7

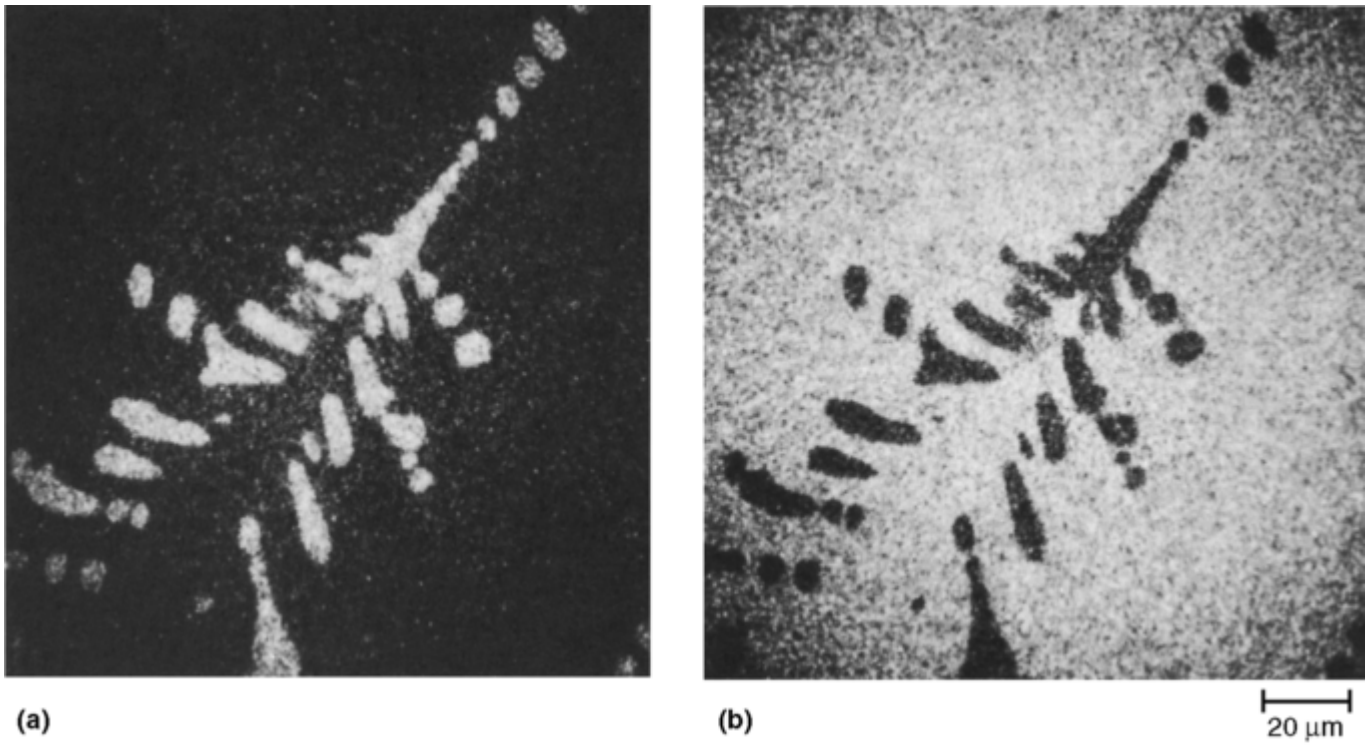

Fig. 22 Compositional map of the area shown in Fig. 21. (a) Bright cobalt-rich dendrite image formed by Co-Kα wavelength x-rays emission. Magnification: 400×. Source: Ref 7

Effect of Crystallographic Orientation. Dendrites are single grains that have preferred growth directions. The morphology of a columnar dendrite is influenced by the orientation of the grain with respect to that of heat extraction, as shown in Fig. 23, where the heat-extraction direction is upward (Ref 8).

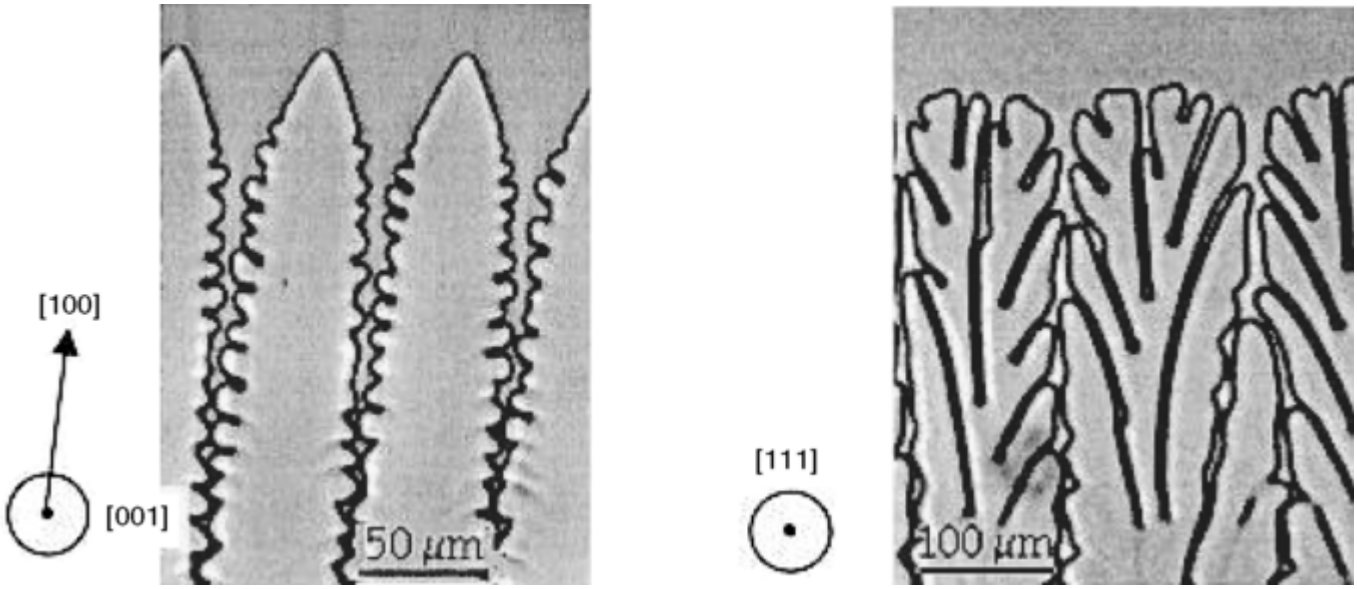

Fig. 23 Effect of crystalline anisotropy on interface shape in directional growth (growth velocity of 35 μm/s) of directional-solidification growth patterns in thin films of the CBr4–8 mol % C_2Cl_6 alloy). Source: Ref 8

Influence of the Type of Phase Diagram. The nature of the material as represented by the type of phase diagram will also influence the dendritic structures. If the phase diagram shows complete solid solubility (Fig. 16a), the structure will be single phase, containing only dendrites. If the phase diagram contains a eutectic (Fig. 16b), the interdendritic regions will be composed of the two-phase eutectic. Figure 24 presents a low-magnification microstructure of a Ni-25Cu (at.%) alloy. The microstructure appears to be fully dendritic. However, at higher magnification a large volume fraction of interdendritic eutectic is apparent (Fig. 25). For alloys where primary solidification is followed by a peritectic reaction, the microstructure depends strongly on solid diffusion rates. When this diffusion is slow, the dendrites are coated by the peritectic phase.

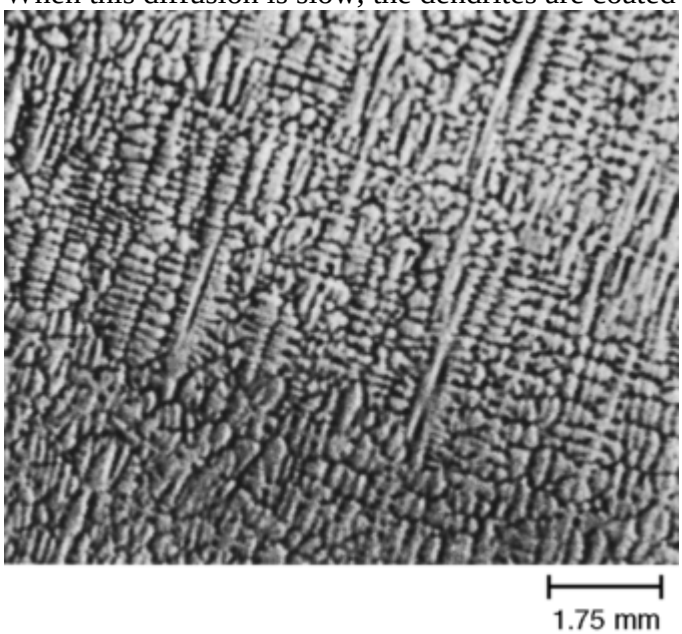

Fig. 24 Ni-25Cu (at.%) alloy. Etchant: 70 mL HNO_3 and 30 mL H_2O. Magnification: 10×. Source: Ref 7

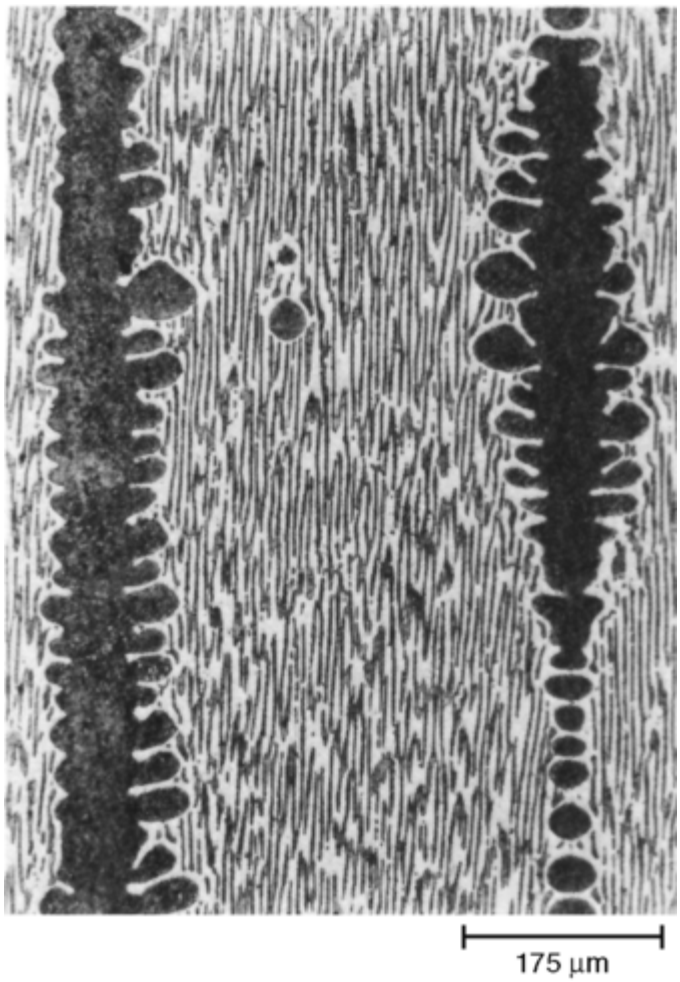

Fig. 25 12 Ni-25Cu (at.%) alloy. Etchant: 70 mL HNO_3 and 30 mL H_2O. Magnification: 175×. Courtesy of C. Brady. Source: Ref 7

Effect of Constitutional Undercooling. As shown in Fig. 17, as the amount of solute increases, or as the G_T/V ratio decreases, a cellular-to-dendritic solidification occurs. This is because the constitutional undercooling is large. An example of the cellular-to-dendritic transition produced by higher solidification velocity is presented in Fig. 26 (Ref 9).

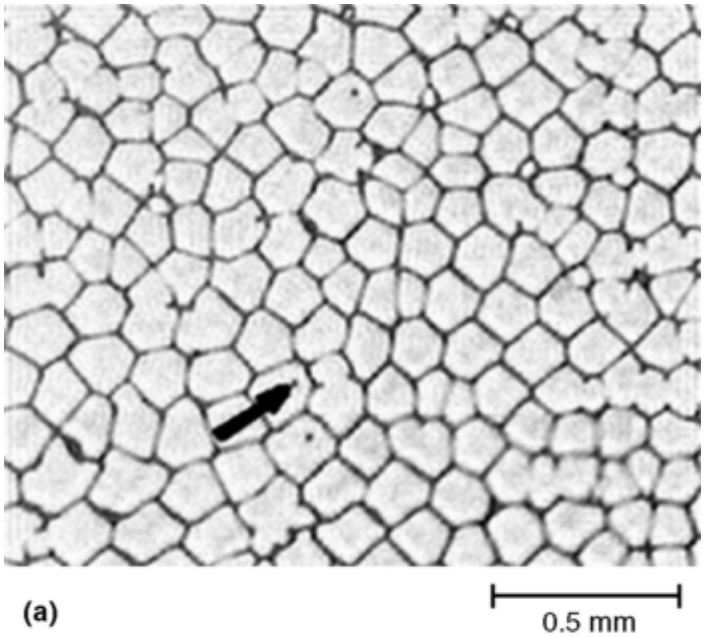

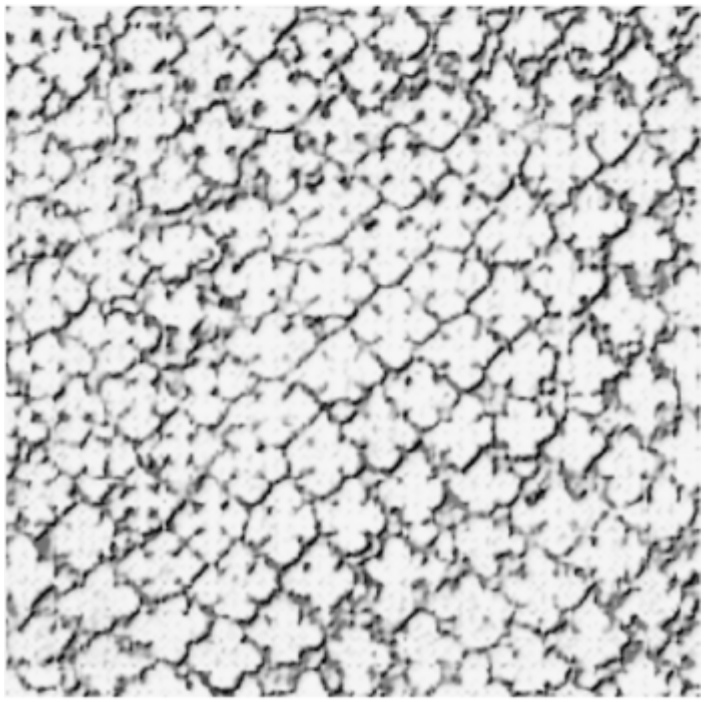

Fig. 26 Transverse microstructures of Pb-2.2Sb (wt%) alloy single-crystal samples grown along [100] at *GT* = 164 K/cm. Etchant: 60 mL acetic acid and 40 mL hydrogen peroxide (30%). (a) Deep cells grown at 2.5 μm/s. Arrow indicates tip splitting. (b) Completely dendritic structure. Dendrites grown at 10 μm/s (same scale). Adapted from Ref 9

Figure 12 indicates that for rather steep thermal gradients, columnar dendrites will form, while for shallow gradients, equiaxed dendrite will solidify. This is illustrated in Fig. 27, which shows the computer-processed images of a titanium alloy ingot. A columnar-to-equiaxed transition is also shown.

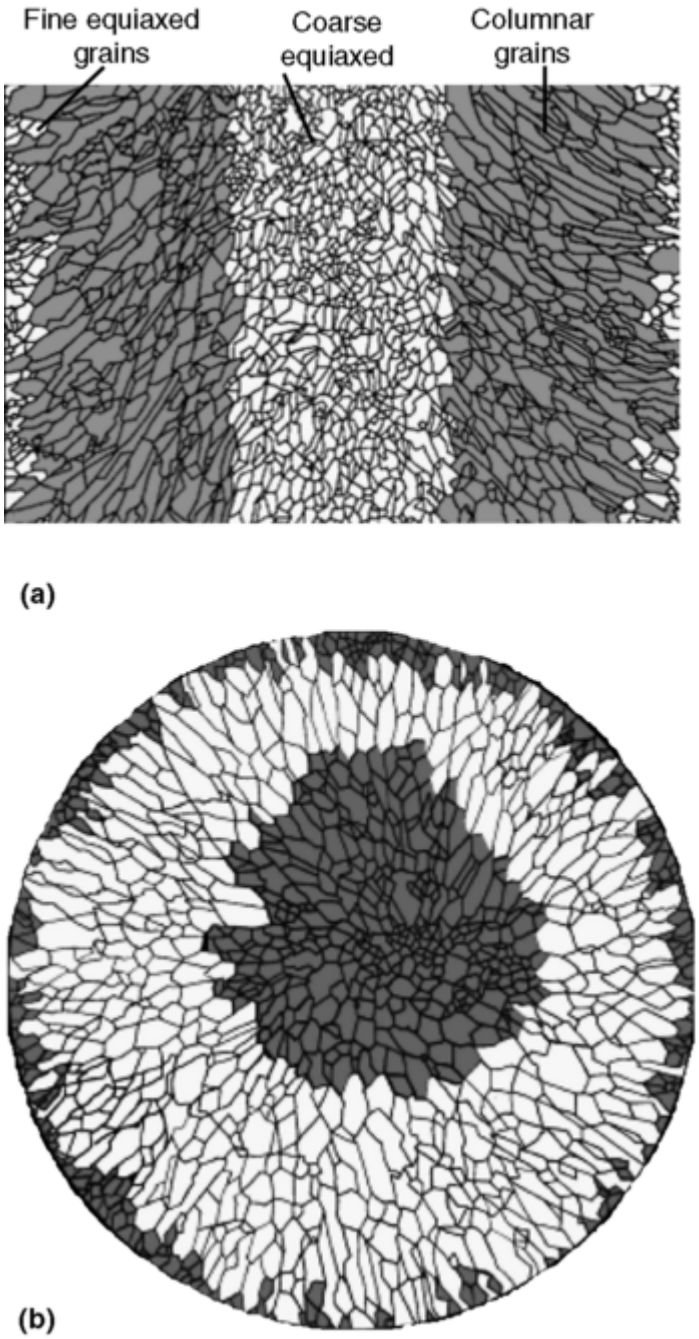

Fig. 27 Computer processed image of the macrostructure of a Ti-6Al-4V ingot. (a) Longitudinal section with coarse equiaxed grains in the center (light), columnar grains (gray), and fine equiaxed grains on the surface. (b) Cross section with reverse coloration

Effect of Solidification Velocity. As emphasized previously, solidification velocity is, together with the temperature gradient, the most important variable affecting microstructure transitions. As shown in Fig. 28, the change in solidification velocity may determine a planar S/L interface to become cellular and then dendritic (Ref 10). In addition, the morphology of the equiaxed dendrites (branching and tip radius) depends significantly on the cooling rate and/or undercooling. The effect of solidification velocity over a wide range of velocities can be understood from Fig. 29. At very small velocities the dendrite tip radius is very large, even infinity, in which case a planar interface is obtained. As the velocity increases, the radius decreases and the morphology changes from planar to globular/cellular, then to regular equiaxed dendritic. Further increase in solidification velocity in the range of rapid solidification determines a transition from fully branched to globular/cellular dendrites, and finally again to planar interface (absolute stability). A typical example illustrating the influence of cooling rate on the morphology of equiaxed dendrites of an Al-7Si alloy is given in Fig. 30 (Ref 11).

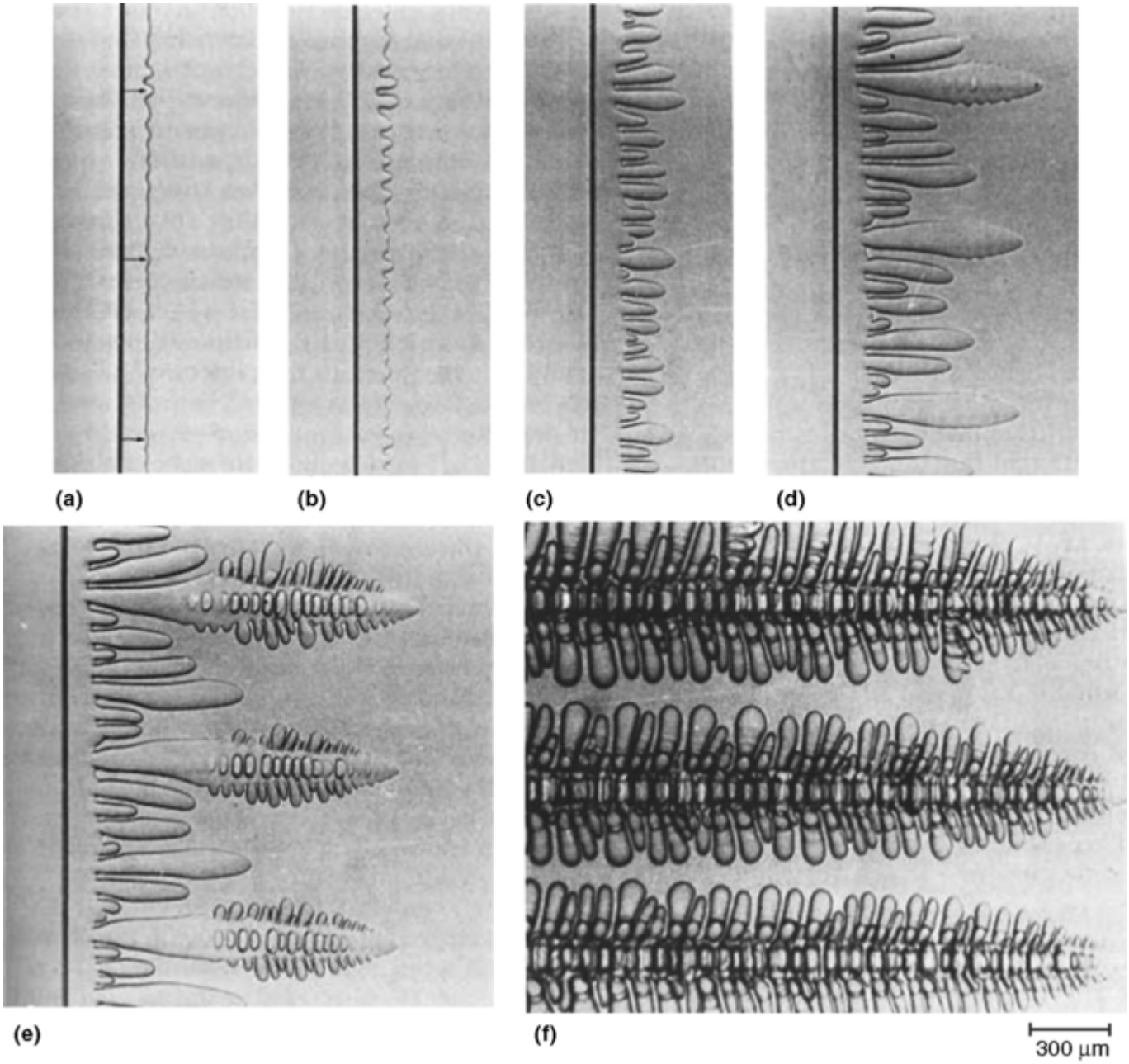

Fig. 28 Change in interface morphology of a succinonitrile-4% acetone solution when increasing the solidification velocity from 0 to 3.4 μm/s at a temperature gradient of 6.7 K/mm. (a) 50 s. (b) 55 s. (c) 65 s. (d) 80 s. (e) 135 s. (f) 740 s. Magnification: 30×. Source: Ref 10

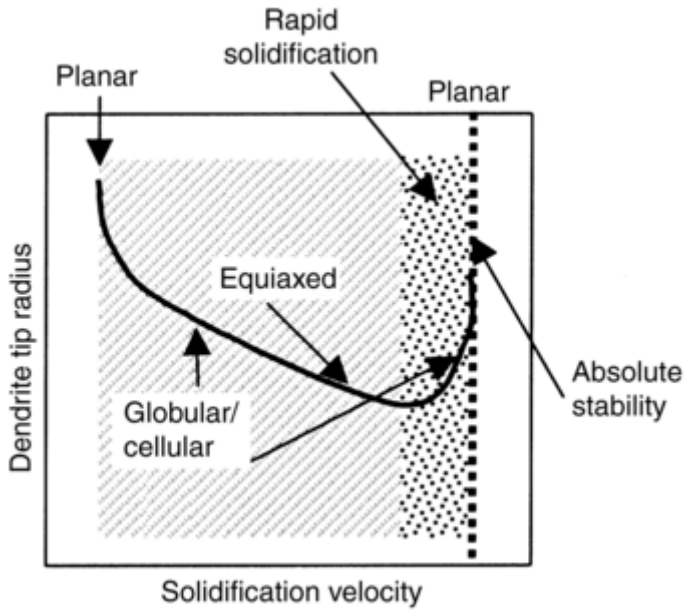

Fig. 29 Correlation between solidification velocity and dendrite tip radius

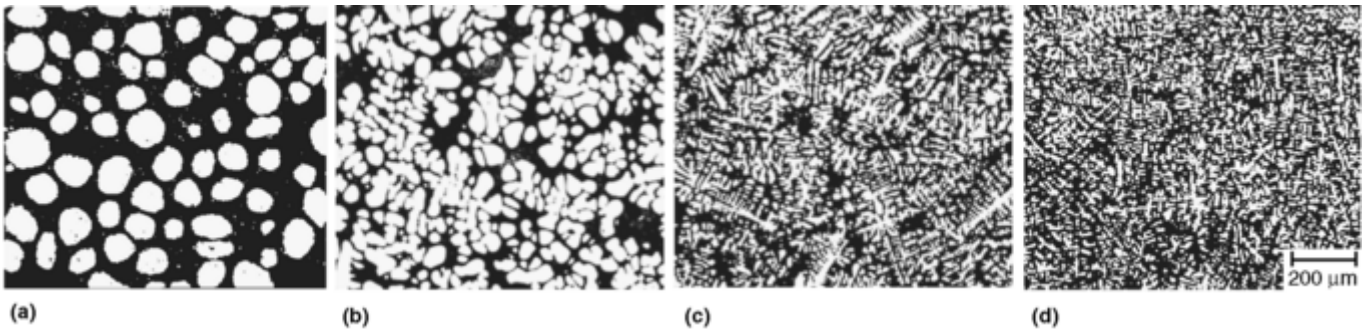

Fig. 30 The microstructures of an Al-7Si alloy at various cooling rates. (a) 0.3 °C/s. (b) 3 °C/s. (c) 10 °C/s. (d) 30 °C/s. Source: Ref 11

The solidification time scale also influences the secondary dendrite arm spacing (SDAS). The SDAS is the distance between adjacent branches growing from the main dendritic arm. It is directly related to certain mechanical properties. It is generally accepted that the SDAS is a function of the local solidification time, t_f, described by:

$$SDAS = \mu_0 \cdot t_f^{1/3} \quad \text{(Eq 7)}$$

where μ_0 is a material-specific constant (coarsening constant). Extensive experimental data on secondary arm spacing have also been reported to fit a SDAS-cooling rate equation (Ref 12):

$$SDAS = \mu_1 \cdot (\dot{T})^{-0.34\pm0.02} \quad \text{(Eq 8)}$$

where μ_1 is a material specific constant, and $\dot{T}$ is the cooling rate.

Solute Redistribution and Microsegregation in Dendritic Solidification. Rejection of solute from the solid during solidification that is responsible for the formation of the solutal boundary layer (see Fig. 7) produces compositional nonuniformity across the dendrite during solidification called microsegregation. To understand the mechanism of formation of microsegregation, consider the volume element extending from the axis of the dendrite arm to the edge of the final dendrite (at the end of solidification) shown in Fig. 31. The thick line in the lower part of the figure represents the composition change in the solid during solidification. At the beginning of solidification when there is no solid formed, the fraction solid is $f_S = 0$. The first solid to form will have the composition $kC_0 < C_0$. Assuming no diffusion in solid and liquid of uniform composition, the composition of the solid will continue to increase as solidification progresses. It will soon be higher than C_0, and then it will reach the maximum solubility in solid, C_{SM}, and then the eutectic composition, C_E, according to the phase diagram in Fig. 6. The liquid still available will now solidify as eutectic. The composition of the solid (the thick

line in Fig. 31) as well as the amount of eutectic at the end of solidification, f_E, can be calculated with the Gulliver-Scheil equation:

$$C_S = kC_0(1 - f_S)^{k-1} \quad \text{(Eq 9)}$$

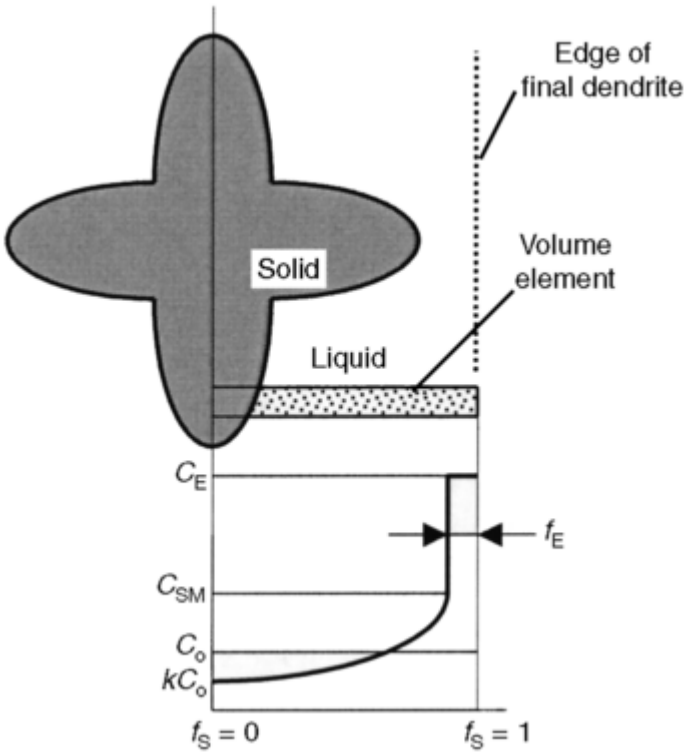

Fig. 31 Model of microsegregation occurring in the arm of a growing dendrite. C_E, eutectic composition; C_{SM}, maximum solubility in solid; f_s, solid fraction; f_E, amount of eutectic critical; C_0, initial composition of the alloy (bulk composition) at the beginning of solidification; k, partition coefficient; kC_o, composition of the first amount of solid to form

Using this approach, it can be calculated that for a 4.5%Cu-Al alloy the first solid to form (the centers of dendrites) will have a composition of 0.77% Cu and that the composition will increase to C_{SM} = 5.65% Cu when f_S = 0.91. The remaining fraction of the alloy (1 - 0.91 = 0.09) solidifies as an interdendritic eutectic with an average composition of 33% Cu. The predictions of the Gulliver-Scheil equation should be used carefully. Generally, the equation tends to underestimate slightly the composition at the center of a dendrite and to overestimate the volume fraction of eutectic (for $k < 1$). Also, if extensive fluid flow exists through the dendritic or "mushy" zone, the average composition of the solidified castings may be significantly altered in regions that are large compared to the dendrite scale. This is called macrosegregation. Details regarding this subject and the field of solidification can be found in Ref 1.

Rapid Solidification. The microstructural length scale of solidified alloys generally decreases as the rate of heat extraction (cooling rate) increases. The term rapid solidification is normally applied to casting processes in which the liquid cooling rate exceeds 100 K/s (Ref 7). This definition is rather vague because different alloys respond very differently to high rates of cooling. Also, some microstructures observed in rapidly solidified alloys can be achieved by slow cooling when large liquid undercooling is achieved prior to nucleation (Ref 13).

Techniques usually used to produce rapidly solidified alloys are melt spinning, planar flow casting, or melt extraction, which produce thin (~25 to 100 μm) ribbon, tape, sheet, or fiber; atomization, which produces powder (~10 to 200 μm); and surface melting and resolidification, which produce thin surface layers. These methods may be considered casting techniques where at least one physical dimension of the final product is small. Consolidation is used to yield large products from rapidly solidified alloys. This consolidation often alters the solidification microstructure in final products. However, as with ordinary castings, many features of the solidification structure can remain in the final product (Ref 7).

The effect of high cooling rates on the dendrite morphology can be understood from Fig. 29. It is seen that as the cooling rate increases in the rapid-solidification range, the tip radius increases. This also means that branching decreases and the equiaxed dendrite will become globular/cellular. Typical examples of the evolution

of the microstructure as a function of the solidification velocity are given in Fig. 32. Figure 32(a) shows a transverse section of a fine cellular structure of the silver-rich phase in Ag-15%Cu alloy (Ref 14). In this figure, most of the intercellular regions are filled with the copper-rich phase, not the eutectic of silver and copper as the Gulliver-Scheil equation would predict. Figure 32(b) shows a longitudinal view of a cellular solidification structure. In Fig. 32(c), the alloy has solidified with a planar interface to produce a microsegregation-free alloy. The fine particles are the result of a solid-state precipitation.

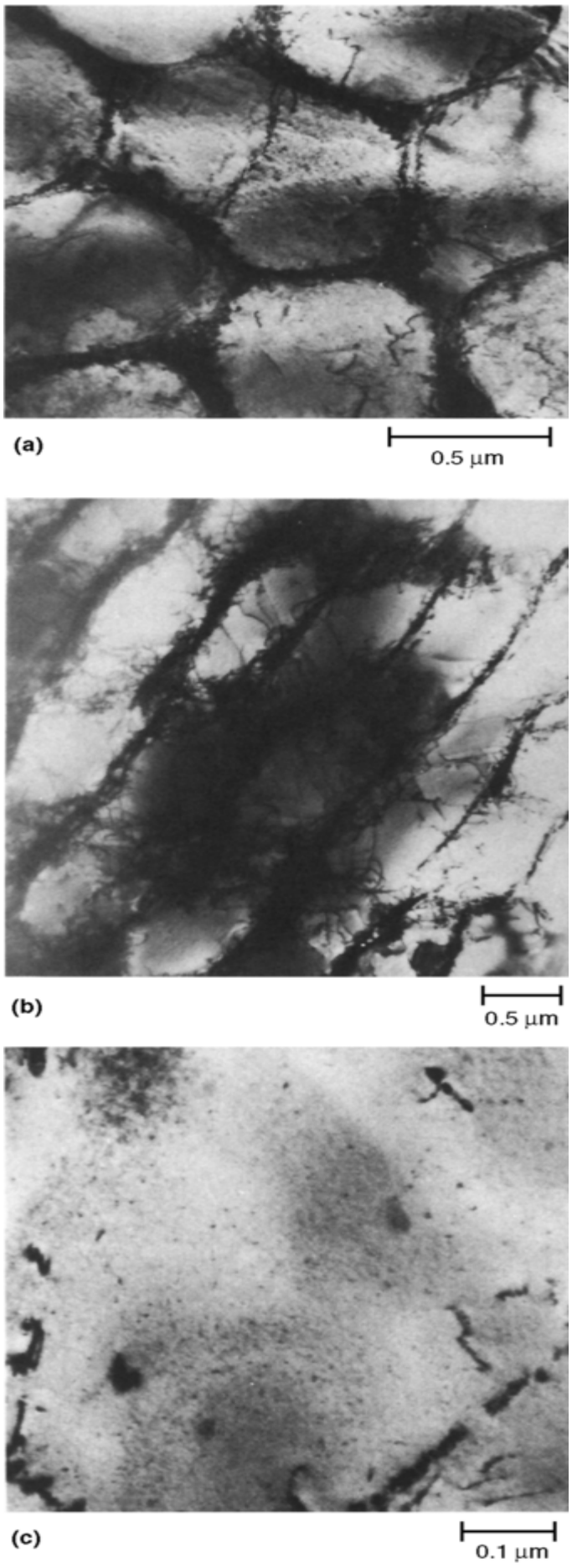

Fig. 32 Microstructures of silver-copper alloys electron beam melted and resolidified at different velocities. (a) Ag-15Cu alloy resolidified at 0.025 m/s (1 in./s). Globular microsegregation pattern.

Magnification: 32,000×. (b) Ag-15Cu alloy resolidified at 0.3 m/s (12 in./s). Cellular microsegregation pattern revealed by dislocation networks along cell walls. Magnification: 18,000×. (c) Ag-15Cu alloy resolidified at approximately 0.6 m/s (24 in./s). The cellular structure is absent, and the solid produced is uniform in composition except for fine copper precipitates formed during solid-state cooling. Magnification: 87,000×. Thin-foil transmission electron micrograph prepared by ion milling. Source: Ref 14

A common occurrence in some rapidly solidified alloys is a change in the identity of the primary solidification phase from that observed for slow solidification (Ref 7). Many examples are found in hypereutectic aluminum alloys containing transition elements such as iron, manganese, or chromium. If the alloy is hypereutectic, slowly cooled castings will contain intermetallics such as Al_3Fe or Al_6Mn as the primary (or first) phase to solidify. However, under rapid-solidification conditions the primary phase in these alloys is the aluminum solid solution, usually found in a cellular structure with an intermetallic in the intercellular regions. Figure 33 and Figure 34 show globular/cellular structures of the α-aluminum solid solution in hypereutectic aluminum-manganese alloys (Ref 15). This transition from an intermetallic to an aluminum solid solution as the primary phase can be understood by a careful examination of the kinetics of the competitive nucleation and growth of the intermetallic and α-aluminum solid solution (Ref 16).

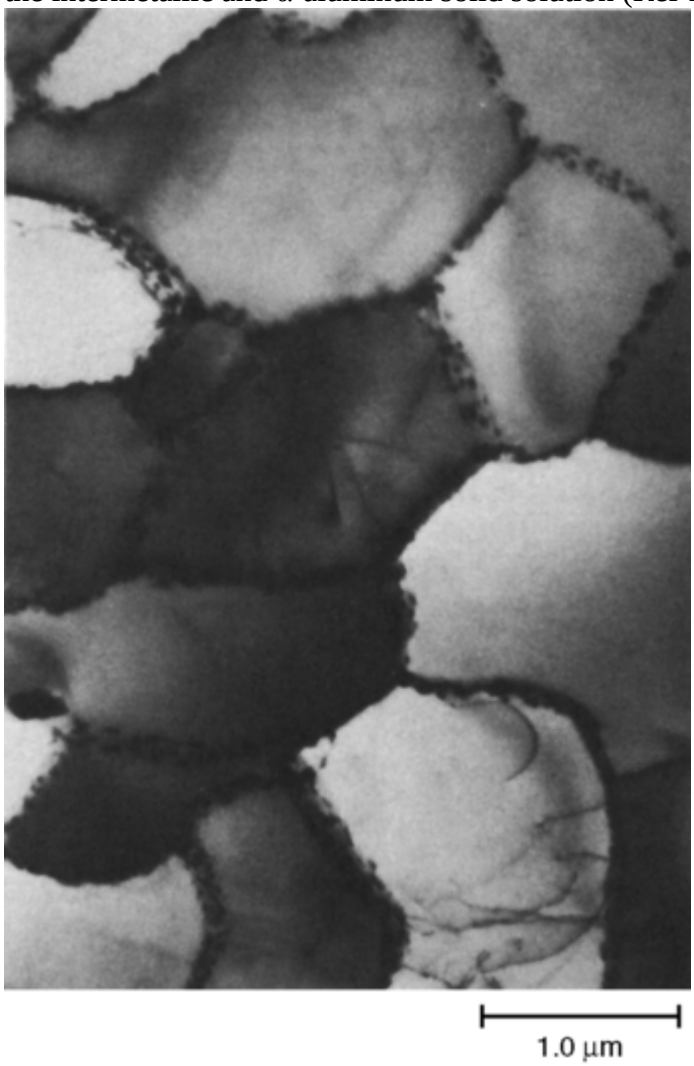

Fig. 33 Globular structure of α-aluminum in a melt-spun Al-12%Mn alloy. Small particles of a different phase decorate the cell walls. Thin-foil transmission electron micrograph (TEM). Electropolished at -30 °C (-20 °F) in 950 mL methanol, 50 mL $HClO_4$, and 15 mL HNO_3. Magnification: 16,000×. Source: Ref 15



Fig. 34 Elongated cellular structure in a melt-spun Al-15%Mn alloy. The contrast between some cells indicates crystallographic misorientation (subgrains). Thin-foil transmission electron micrograph. Electropolished at -30 °C (-22 °F) in 950 mL methanol, 50 mL $HClO_4$, and 15 mL HNO_3. Magnification: 13,000×. Source: Ref 15

In some cases, an intermetallic that is not given on the equilibrium phase diagram may compete with α-aluminum. In aluminum-iron alloys, a metastable phase, Al_6Fe, rather than the stable phase, Al_3Fe, can form under some rapid-solidification conditions. This situation is analogous to the appearance of cementite rather than graphite in some cast irons. The use of metastable phase diagrams to assist in the interpretation of rapidly solidified microstructures is described in Ref 17. As explained in the section "Undercooling" in this article, other rapidly solidified alloys have microsegregation-free structures formed by a liquid-solid transformation similar to a massive solid-solid transformation (partitionless or diffusionless transformation). The liquid transforms to solid without a change in composition. The ratio of the solid composition at the interface to the liquid composition is $C_S/C_L = 1$, rather than the equilibrium partition coefficient. Velocities required to produce partitionless solidification must exceed 5 m/s (40 to 400 in./s). The phase diagrams obviously do not apply in this situation.

Figure 35 and 36 show optical and transmission electron micrographs, respectively, of a single-phase microsegregation-free solid solution of a silver-copper alloy of eutectic composition (28% Cu) that was formed by partitionless solidification (Ref 18). The alloy is not only free of microsegregation, but also has a solid solubility of copper in silver far in excess of the equilibrium solubility limit (~9% Cu).

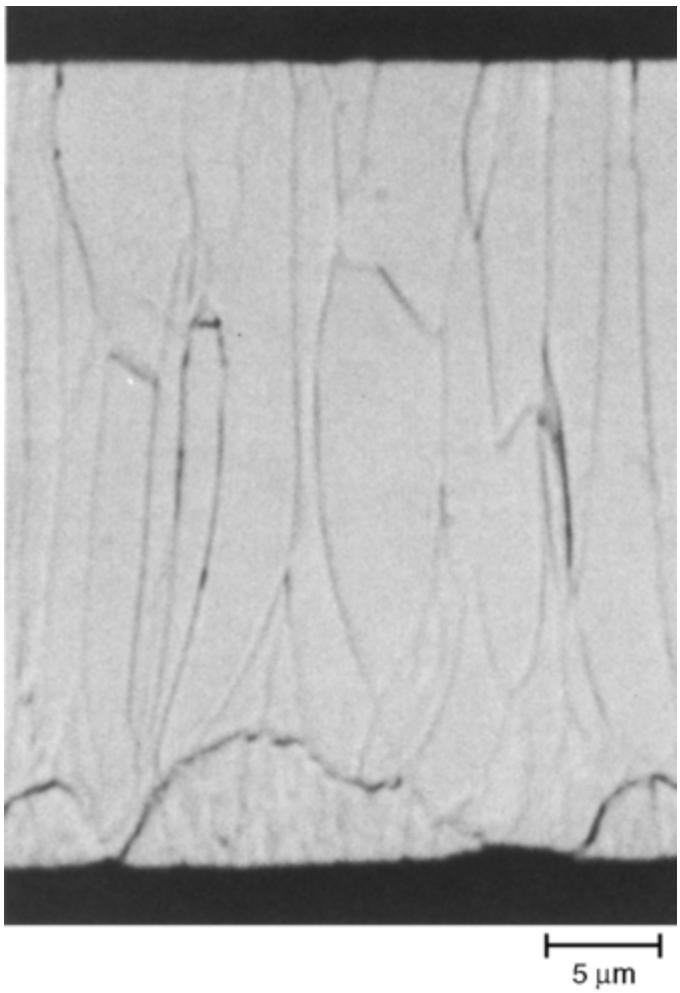

Fig. 35 Columnar grains of single-phase solid solution of melt-spun Ag-28%Cu alloy (eutectic composition). Section of full ribbon cross section. Chill (wheel) side is at bottom. Etched with: 20 mL NH_4OH, 10 mL 3% H_2O_2, 10 mL H_2O (used fresh). Magnification: 2000×. Source: Ref 18

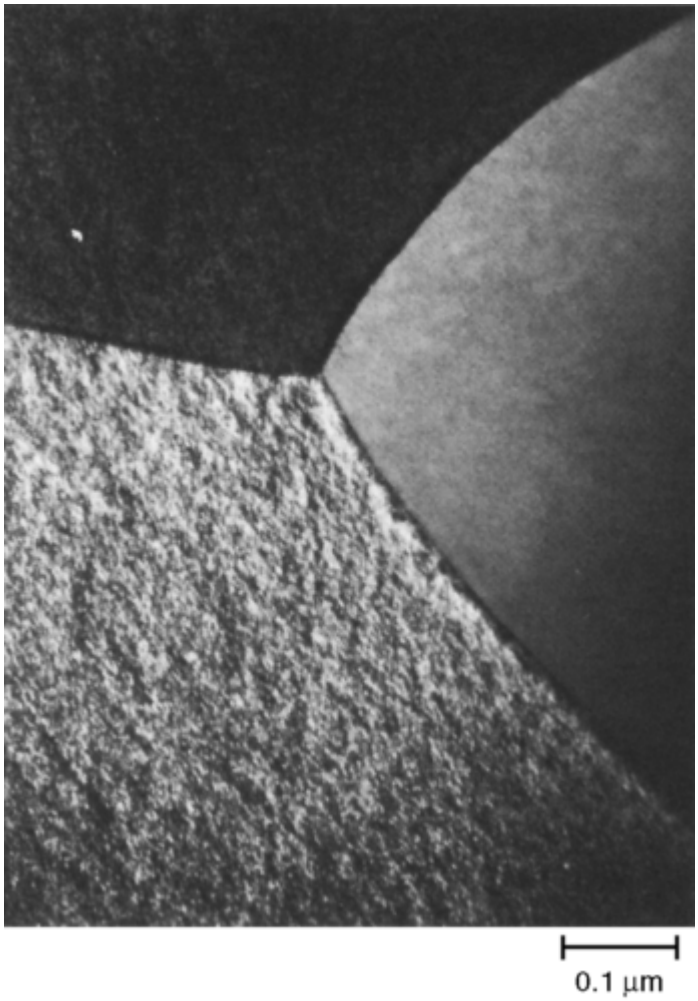

Fig. 36 Same alloy as in Fig. 35. Three grains observed in the thin foil parallel to the chill surface prepared by ion milling Transmission electron micrograph. Magnification: 100,000×. Courtesy of D. Shechtman. Source: Ref 7

Rapidly solidified alloy powders exhibit a broad spectrum of solidification structures, depending on alloy composition and solidification conditions. Figure 37 shows single powder particles of stainless steel with dendritic or cellular structure (Ref 19). The size of the particles is less than 25 μm. Different degrees of undercooling prior to nucleation for particles of almost the same size determine the type of structure. The dendritic structure radiates from a point on the surface where nucleation has occurred. The scale of the structure is relatively uniform across the powder particle.

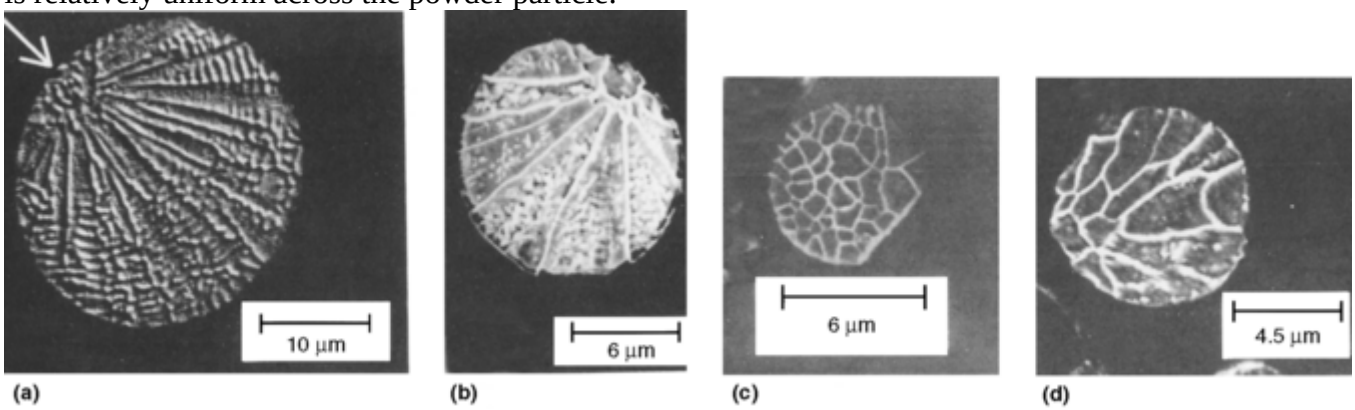

Fig. 37 Scanning electron micrographs of atomized droplets of martensitic stainless steel. (a) and (b) Dendritic structures. (c) and (d) Cellular structures. Source: Ref 19

Other rapidly solidified powders often show significant microstructural variations across individual powder particles. Initial growth of the solid may occur very rapidly in a partitionless manner. The interface velocity decreases as the S/L interface crosses the particle, because of the release of the latent heat of fusion and warming of the powder particle, and the solidification front becomes cellular. Figure 38 shows a two-zone microstructure observed in a larger diameter (~10 mm) hypereutectic Al-8%Fe powder particle. A thin foil was prepared by electropolishing a 3 mm (0.12 in.) diam green powder compact (Ref 20). In this alloy, the zone to the left where nucleation occurs contains a very fine cellular structure, and the zone to the right contains a coarse cellular structure of α-aluminum with Al_6Fe between the cells resulting in the decrease on interface velocity because of recalescence. Larger powder particles of the alloy frequently do not undercool significantly before the start of solidification and contain Al_3Fe as the primary phase.

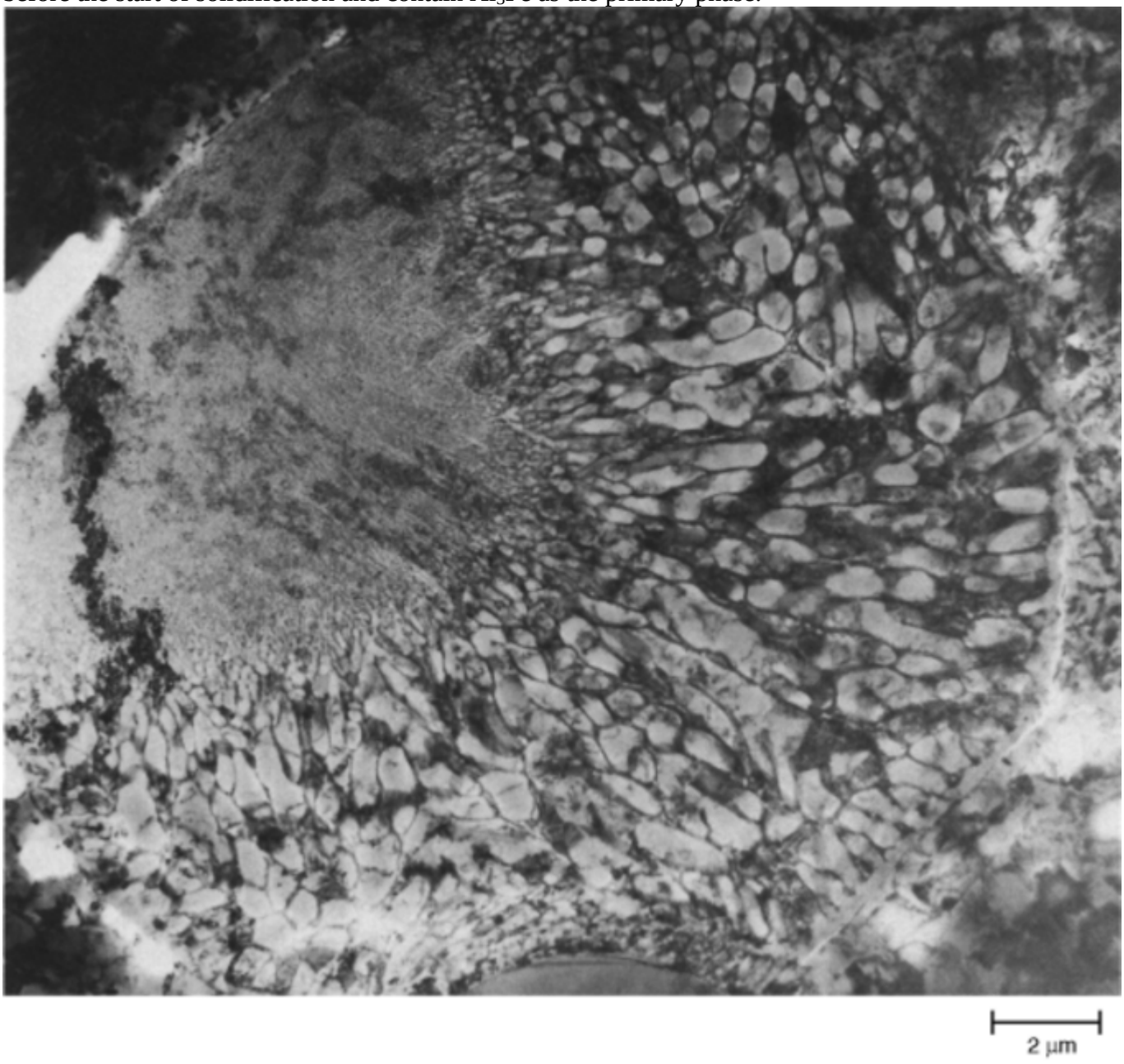

Fig. 38 Thin-foil transmission electron micrograph of vacuum-atomized Al-8Fe powder. The green powder compact was electropolished at -30 °C (-22 °F) in 950 mL methanol, 50 mL $HClO_4$, and 15 mL HNO_3. Magnification: 6300×. Courtesy of W.J. Boettinger, L. Bendersky, and J.G. Early. Source: Ref 7

References cited in this section

1. D.M. Stefanescu, *Science and Engineering of Casting Solidification,* Kluwer Academic, 2002

7. W.J. Boettinger, *Metall. Mater. Trans.*, Vol 5, 1974, p 2026

8. S. Akamatsu, G. Faivre, and Th. Ihle, *Phys. Rev.*, Vol E 51, 1995, p 4751–4773

9. S.N. Tewari, Y.-H. Weng, G.L. Ding, and R. Trivedi, *Metall. Mater. Trans. A*, Vol 33A, 2002, p 1229–1243

10. R. Trivedi and K. Somboonsuk, *Mater. Sci. Eng.*, Vol 65, 1984, p 65–74

11. C.P. Hong and M.F. Zhu, *The Science of Casting and Solidification*, D.M. Stefanescu, R. Ruxanda, M. Tierean, and C. Serban, Ed., Editura Lux Libris, Brasov, Romania, 2001, p 110s–118s

12. D. Bouchard and J.S. Kirkaldy, *Metall. Mater. Trans. B*, Vol 28B, 1997, p 651

13. J.H. Perepezko and J.J. Paike, *Rapidly Solidified Amorphous and Crystalline Alloys*, B.H. Kear, B.C. Giessen, and M. Cohen, Ed., North Holland, 1982, p 49

14. W.J. Boettinger, D. Shechtman, R.J. Schaefer, and F.S. Biancaniello, *Metall. Trans. A*, Vol 15, 1984, p 55

15. D. Shechtman, R.J. Schaefer, and F.S. Biancaniello, *Metall. Trans. A*, Vol 15, 1984, p 1987

16. I.R. Hughes and H. Jones, *J. Mater. Sci.*, Vol 11, 1976, p 1781

17. J.H. Perepezko and W.J. Boettinger, *Mater. Res. Soc. Symp. Proc.*, Vol 19, 1983, p 223

18. W.J. Boettinger, *Rapidly Solidified Amorphous and Crystalline Alloys*, B.H. Kear, B.C. Giessen, and M. Cohen, Ed., North Holland, 1982, p 15

19. N.H. Pryds and A.S. Pedersen, *Metall. Mater. Trans. A*, Vol 33A, 2002, p 3755–3761

20. D. Shechtman and E. Gutmanas, *Prakt. Metallogr.*, Vol 18, 1981, p 587

D.M. Stefanescu and R. Ruxanda, Fundamentals of Solidification, *Metallography and Microstructures*, Vol 9, *ASM Handbook* , ASM International, 2004, p. 71–92

Fundamentals of Solidification

Doru M. Stefanescu and Roxana Ruxanda, The University of Alabama

Solidification Structures of Eutectics

Eutectics are alloys that have a fixed composition in terms of species A and B and solidify as two-phase solids (α + β). The phase diagram in Fig. 16(b) shows a binary eutectic invariant point at temperature T_E and composition C_E. At this point, two solid phases, α and β, solidify simultaneously from the liquid, L. The eutectic reaction can be written as: L → α + β. As many as four phases have been observed to grow simultaneously from the melt. However, most technologically useful eutectic alloys consist of two phases. The particular morphology of the eutectic is a function of processing conditions and of the nature of the two phases.
Classification of Eutectics. Many eutectic classifications have been proposed, based on different criteria. A first classification of eutectics based on their growth mechanism is:

- *Cooperative growth:* The two phases of the eutectic grow together as a diffusion couple.
- *Divorced growth:* The two phases of the eutectic grow separately; there is no direct exchange of solute between the two solid phases and no trijunction.

Cooperative eutectics can be further classified based on the ratio between the fractions of the two phases of the eutectic, f_α and f_β, and on the morphology of the S/L interface (Ref 21) as shown in Fig. 39. The nondimensional entropy of fusion, $\Delta S_f/R$, where R is the gas constant, is used to distinguish between faceted and nonfaceted morphologies.

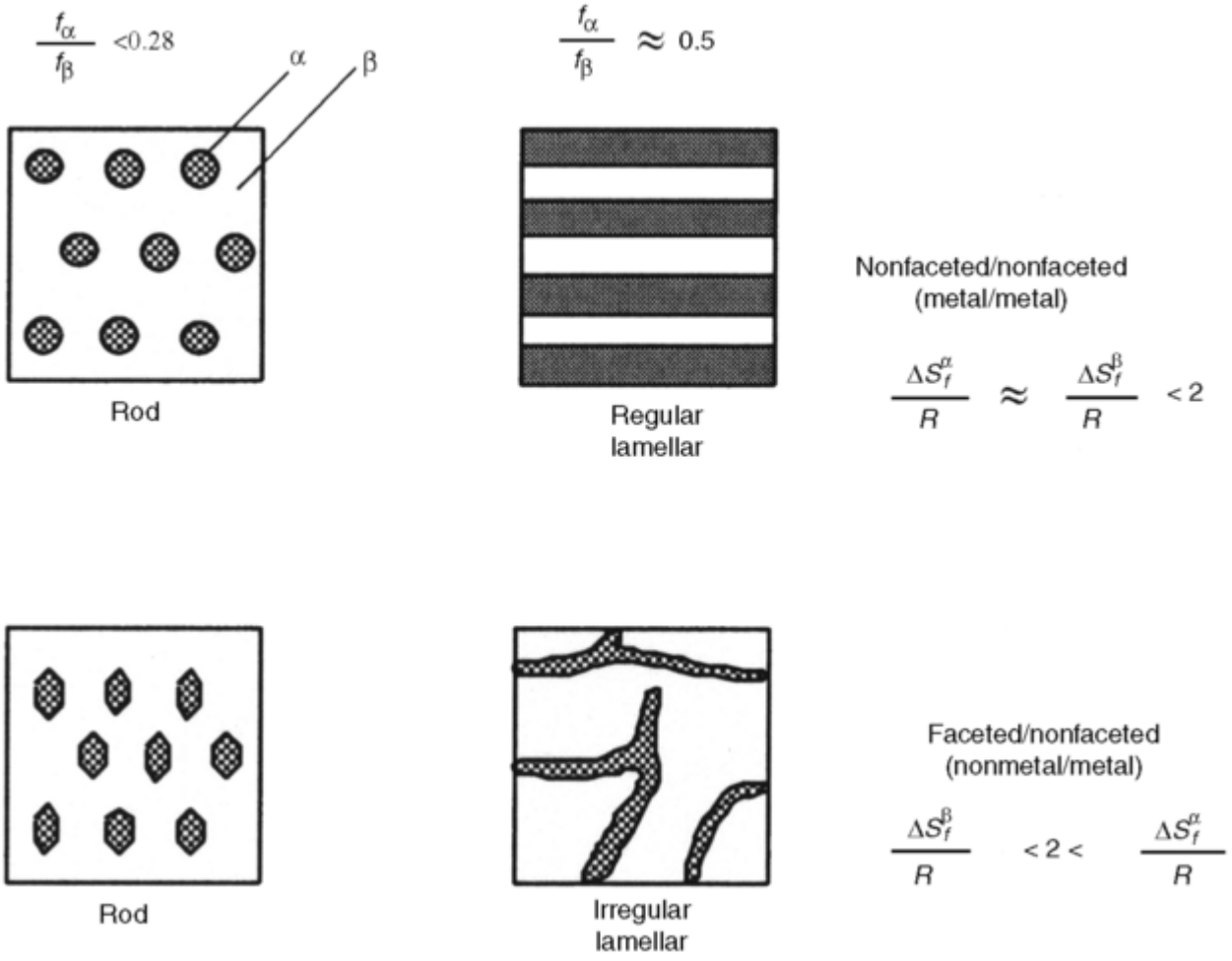

Fig. 39 Types of cooperative eutectics. Source: Ref 21

Alloys such as Pb-Sn and Al-Al_2Cu (Fig. 40a) (Ref 22), where there are approximately equal volume fractions of nonfaceted phases, solidify as regular, lamellar eutectics. If one of the phases is nonfaceted the morphology becomes irregular, because the faceted phase grows preferentially in a direction determined by specific atomic planes. Also, one solid phase projects into the liquid far in advance of the other solid phase. A typical example is the Mg-Mg_2Sn eutectic shown in Fig. 40(b) (Ref 22).

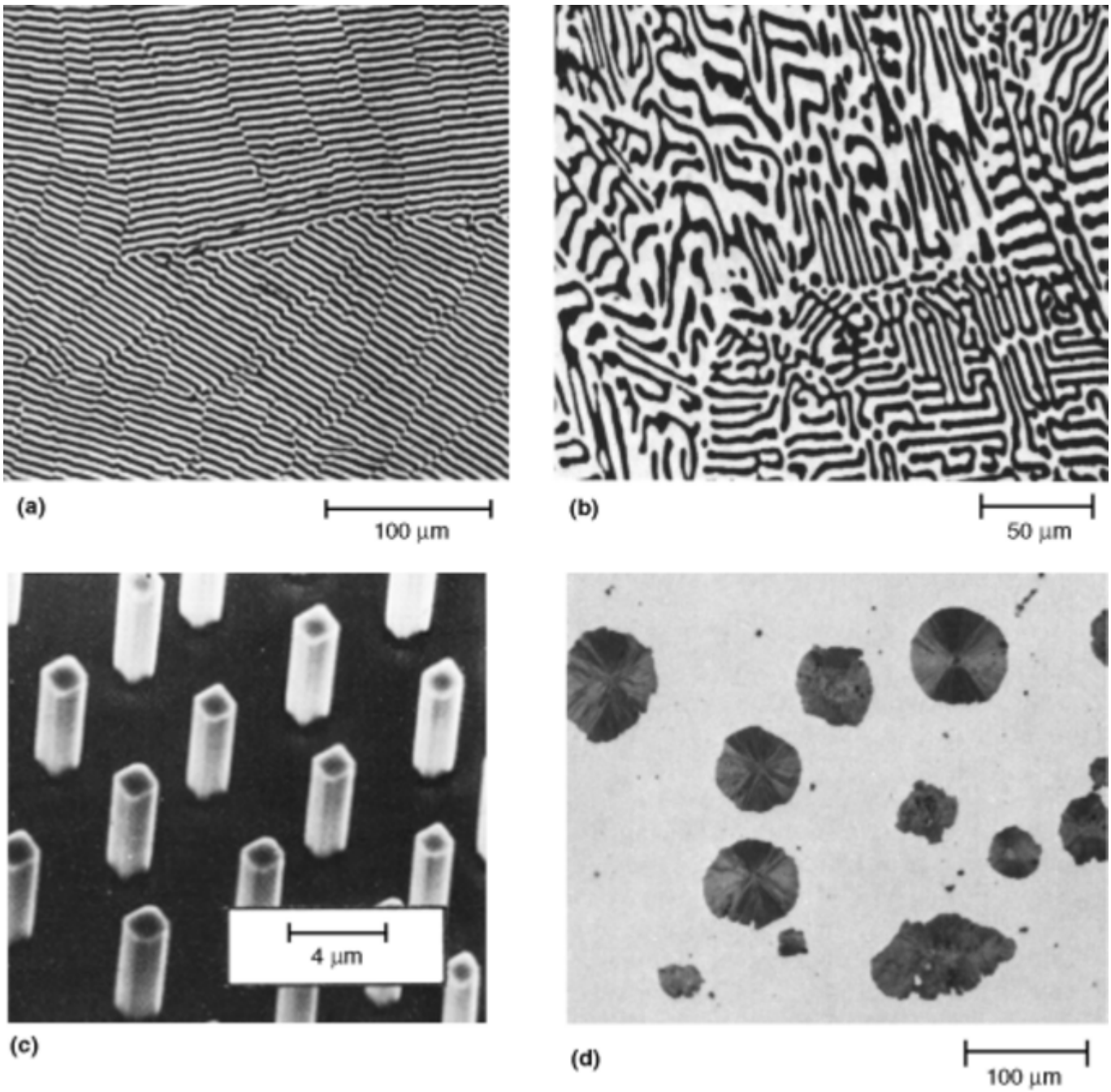

Fig. 40 Eutectic microstructures. (a) Regular nonfaceted/nonfaceted eutectic (Al-Al_2Cu). (b) Irregular faceted/nonfaceted eutectic (Mg-Mg_2Sn). The dark phase is the faceted Mg_2Sn. Ref 22. (c) Rod faceted/nonfaceted eutectic (Ni-NbC). Ref 23. (d) Divorced eutectic (Fe-spheroidal graphite)

When the volume fraction of one phase is significantly lower than that of the other (typically <0.28), a fibrous structure will result (for example, the Ni-NbC eutectic (Ref 23) shown in Fig. 40c). This is a result of the tendency of the system to minimize its interfacial energy by selecting the morphology that is associated with the smallest interfacial area. Fibers have smaller interfacial area than lamellae. However, when the minor phase is faceted, a lamellar structure may form even at a very low volume fraction, because specific planes may have the lowest interfacial energy. The minor phase will then grow such as to expose these planes even when lamellae rather than fibers are formed. The two commercially most significant eutectics, aluminum-silicon and iron-graphite fall into this category. Note that in the iron-graphite eutectic, the fraction graphite is $f_{Gr} = 0.07$. The iron-graphite eutectic can be either cooperative, irregular, as is the case for lamellar graphite cast iron, or divorced, as for spheroidal graphite cast iron (Fig. 40d) (Ref 22). In this last case, at the beginning of solidification the two phases, graphite and austenite dendrites, grow independently from the liquid without establishing a diffusion couple.

Operating Compositional Range. From the eutectic phase diagram it appears that a eutectic structure can be obtained only when the composition is exactly eutectic. Nevertheless, both experiments and theory show that, depending on the growth conditions, eutectic microstructures can be obtained at off-eutectic compositions. Such conditions include a sufficiently steep gradient or slow solidification velocity during directional solidification. This is possible because the eutectic grows faster than the dendrites, since diffusion-coupled growth is much faster than isolated dendritic growth. Accordingly, even in off-eutectic compositions, the eutectic may outgrow the individual dendrites, resulting in a purely eutectic microstructure. On the other hand, at high growth velocities, dendrites can be found in alloys of eutectic compositions.

An analysis of the possible solidification microstructure of a binary alloy can be made based on the growth velocities of the competing phases (Ref 1). On the phase diagram in Fig. 41(a), the three shaded regions extending under the eutectic invariant form a coupled zone. This is a solidification velocity dependent composition region in which the eutectic grows more rapidly, or at a lower undercooling, than the α or β dendrites. For regular eutectics the coupled zone is symmetric. Note that the widening of the coupled zone near the eutectic temperature is observed only in directional solidification (DS), where the thermal gradient is positive.

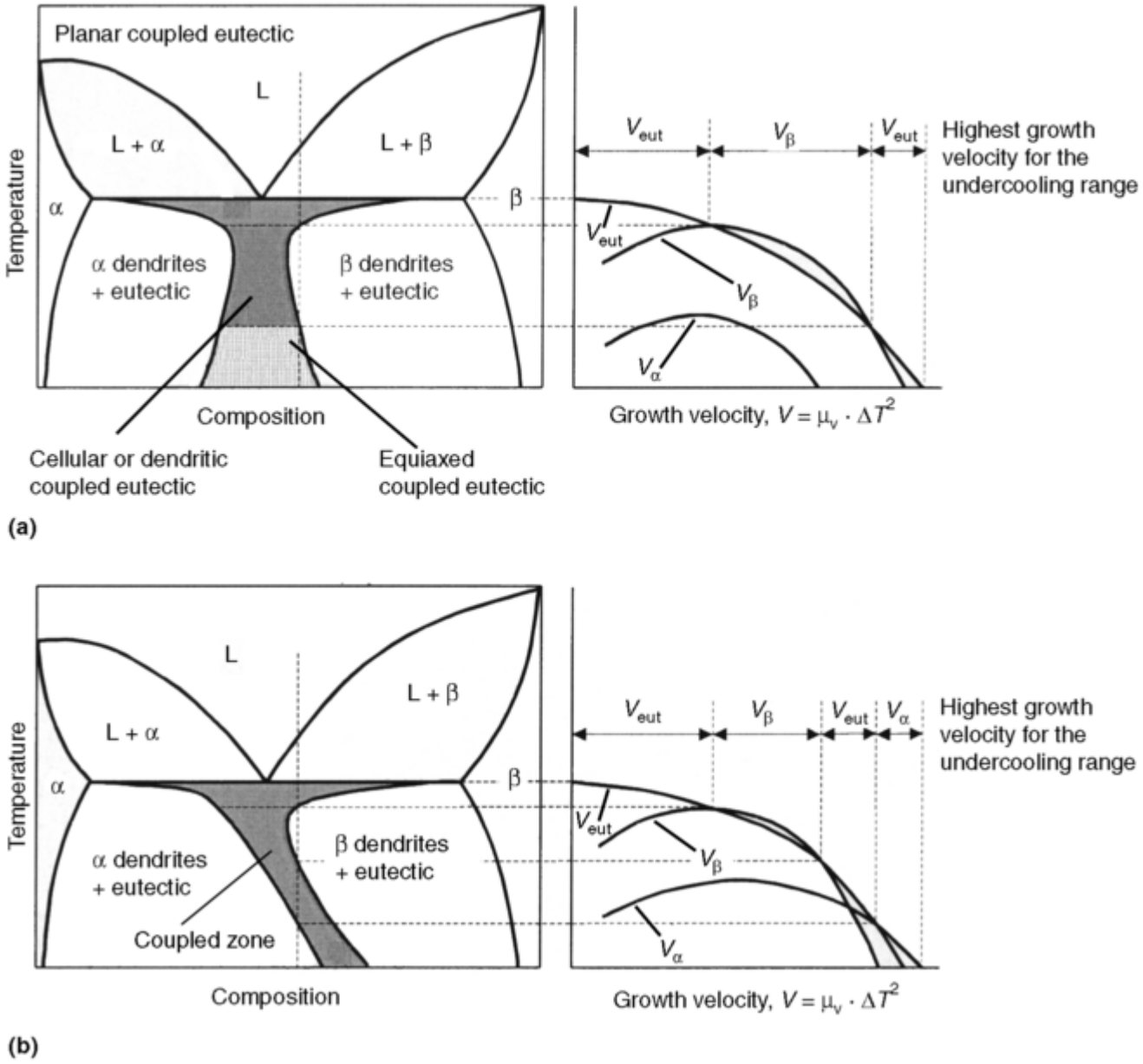

Fig. 41 Coupled eutectic zones. (a) Symmetric coupled zone (regular eutectics. (b) Asymmetric coupled zone (irregular eutectics). Source: Ref 1

For small undercooling the S/L interface is planar (see Fig. 42). As shown on the right side of Fig. 41(a), even for a hypereutectic alloy solidifying at small undercooling, the eutectic has the highest growth velocity and a planar, coupled eutectic is produced. At higher undercooling, the β phase will have higher growth velocity, and a eutectic-dendritic structure will result. At even higher undercooling, the eutectic velocity will again become the highest. However, because of the undercooling, a planar structure is not possible, and equiaxed coupled growth will result. If one of the eutectic phases is faceted, the growth of this phase and consequently that of the eutectic is slowed down. Dendrites of the other phase may grow faster at a given undercooling than the eutectic, even for the eutectic composition. Consequently, purely eutectic microstructures can be obtained only at hypereutectic compositions. This is exemplified in Fig. 41(b), for the case of faceted β phase. An asymmetric coupled zone results.

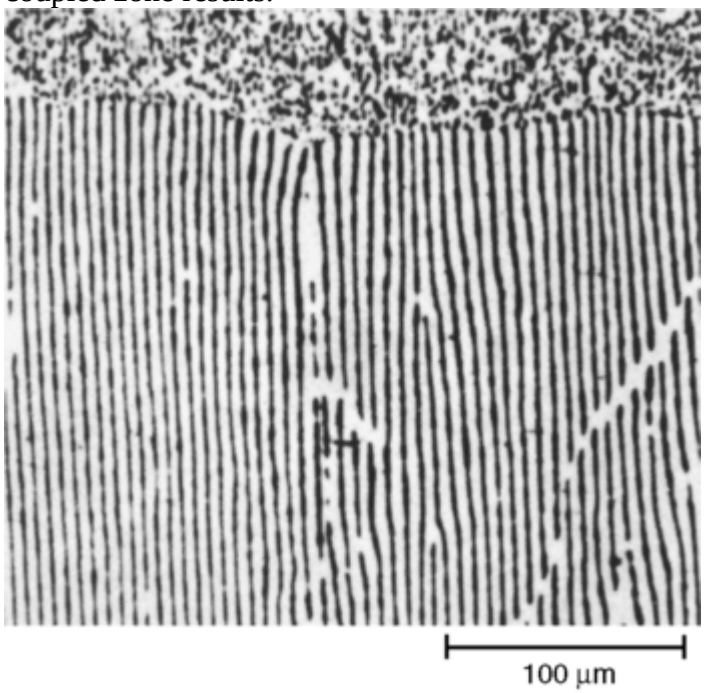

Fig. 42 Regular cadmium-tin eutectic in a casting directionally solidified from bottom to top, then rapidly cooled to preserve the shape of the solid/liquid interface. Section parallel to solidification direction. Etchant: aqueous solution of $FeCl_3$. Magnification: 210×. Source: Ref 24

From Fig. 41(a) it can be noted that as the undercooling increases, the microstructure of the eutectic changes from planar to cellular, dendritic, and then equiaxed. When the alloy solidifies with a cellular rather than a planar interface, eutectic colonies are formed. Figure 43 illustrates the effect of increased solidification velocity (higher undercooling) on the eutectic morphology (Ref 25). Alternating light regions of (Cr,Mo) plates, and dark regions of NiAl plates are seen at both growth speeds. As the solidification velocity increases, the microstructure changes from planar to fanlike arrangement colonies.

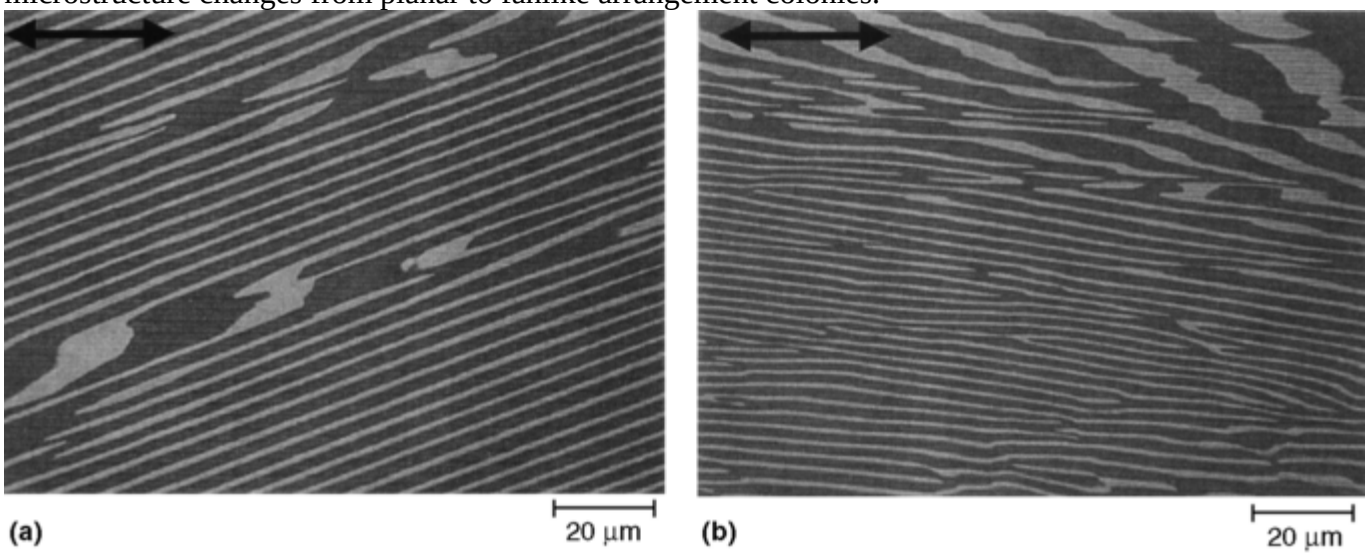

Fig. 43 Microstructure of directionally solidified Ni-33Al-31Cr-3Mo rods. The arrows indicate growth directions (longitudinal section). (a) 12.7 mm/h. (b) 25.4 mm/h. Etchant not reported. Source: Ref 25

A section normal to the direction of solidification of a colony structure is presented in Fig. 44. Note the honeycomb pattern of the colonies (Ref 24). Dark and light layers in each colony are Mg_2Al_3 phase and Al, respectively. Colony structures are observed also in non-DS specimens (Fig. 45). The section shows both the honeycomb pattern (where the metallographic plane was normal to the direction of solidification) and the fanlike arrangement (where the metallographic plane was parallel to the direction of solidification).

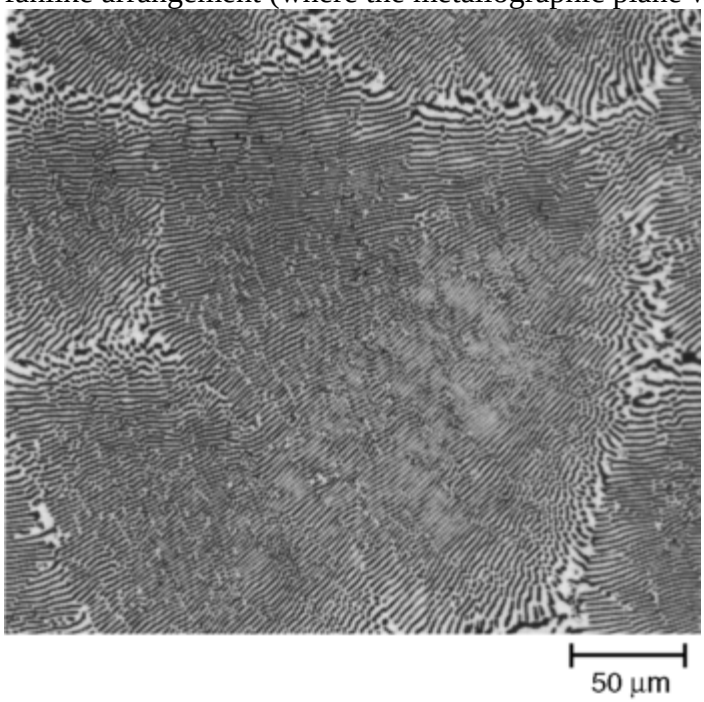

Fig. 44 Colony structure of a directionally solidified lamellar eutectic. Etchant not reported. Magnification: 200×. Source: Ref 24

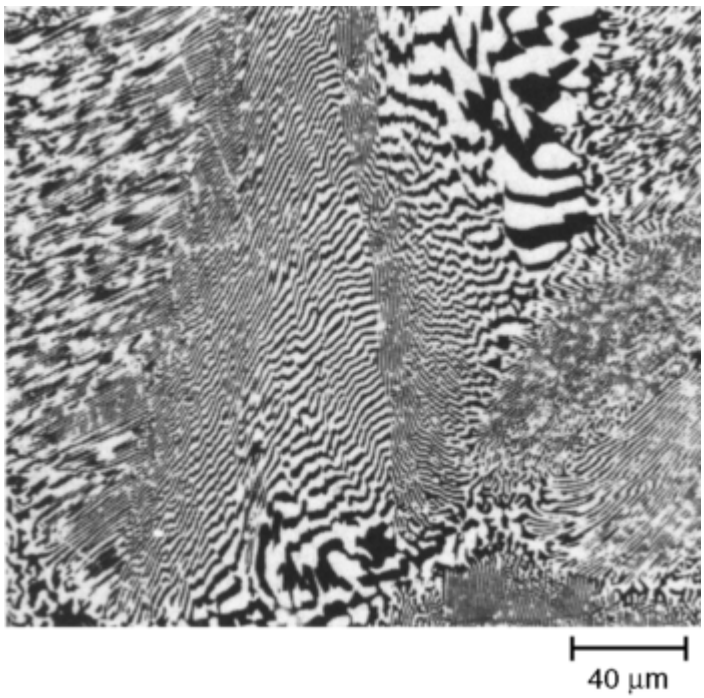

Fig. 45 Colony structure of a non-directionally solidified $CuAl_2$-Al lamellar eutectic. As-polished. Magnification: 250×. Source: Ref 24

If the undercooling is high, equiaxed eutectic grains may form even during directional solidification. A typical example is given in Fig. 10(c) for a gray cast iron. The boundaries of the grains are outlined because of the segregation of phosphorus and the formation of a low-melting-point phosphide eutectic.

Grain boundaries are not easily observable in eutectics solidifying with a planar interface. For example, the right side of Fig. 40a has the appearance of a specimen containing two grains: the lamellae in one grain are at an angle of about 40° to the lamellae in the other grain. At the left of the micrograph, however, the two grains merge into one. In other eutectics, particularly those in which the volume fraction of one phase is $f \approx 0.01$ to 0.02, grains of the predominant phase will be visible.

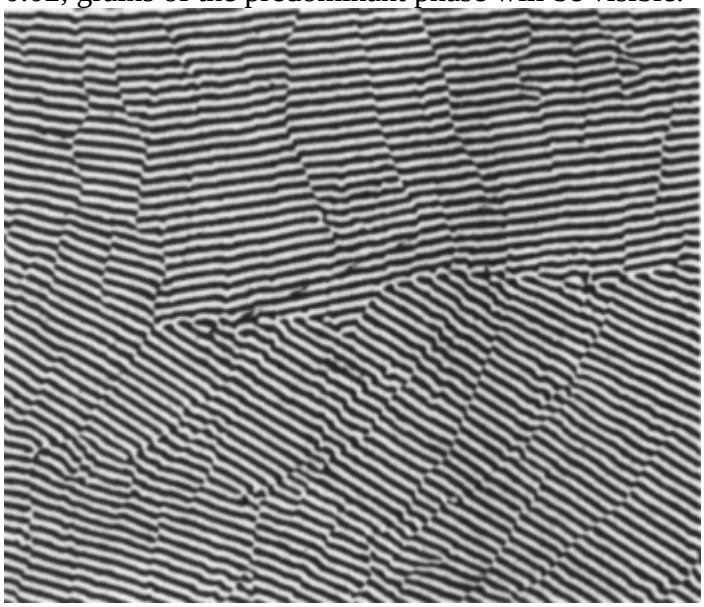

Fig. 46 Directionally solidified $CuAl_2$-Al lamellar eutectic. As-polished. Magnification: 180×. Source: Ref 24

Coupled two-phase eutectic structures also can be produced whose amounts and individual phase chemistries can be varied by solidification of compositions that lay on or near eutectic troughs in the liquidus surface of ternary alloys (see Fig. 47) (Ref 26).

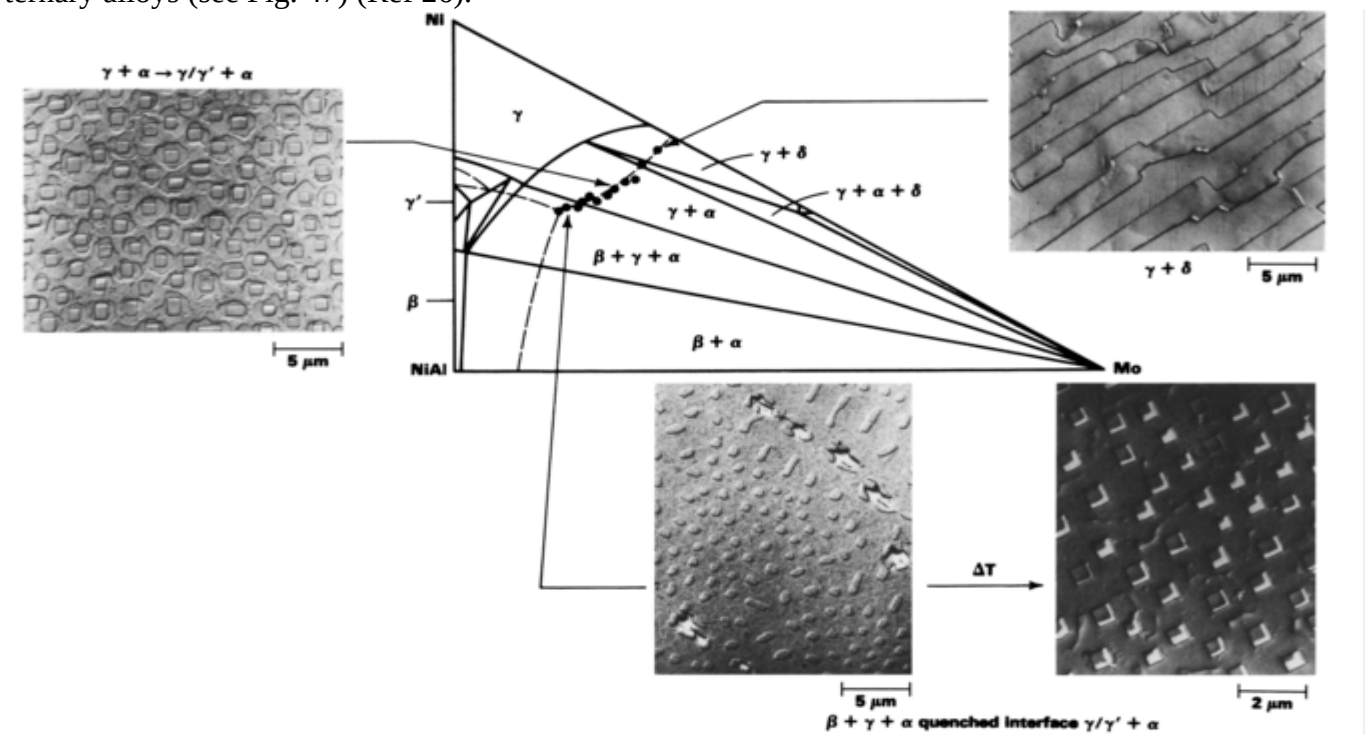

Fig. 47 Monovariant liquidus troughs (dashed lines) on a Ni-Al-Mo isothermal section at 1300 °C (2370 °F) with varying "eutecticlike" structure produced by compositional adjustment. Source: Ref 26

Caution must be exercised during metallographic analysis of eutectic microstructures. Serial sectioning, phase-extraction techniques, and examination of two sections meeting at a common edge have revealed that the microstructures of most eutectics cannot be considered aggregates of many simply shaped, discrete particles of one phase embedded in a matrix of the other phase or phases. Rather, if the three-dimensional shapes of all phases are examined, the apparently individual particles of each phase are typically found interconnected in a topologically complex arrangement. Additional examples are provided for specific alloys.

Length Scale of Eutectics. The length scale of the eutectic strongly affects the mechanical and physical properties of the eutectic aggregate. For cooperative eutectics, the length scale is given by the lamellar spacing (interlamellar or interfiber) spacing, which is affected by solidification velocity, thermal gradients, undercooling, atomic bonding, relative amounts, crystallographic factors, interfacial energies, impurity content, and alloy composition. The lamellar spacing, λ, and the solidification velocity are related by the simple equation $\lambda^2 V$ = constant. The effect of solidification velocity is illustrated in Fig. 48. It is seen that the spacing of irregular eutectics is significantly larger than that of regular eutectics.

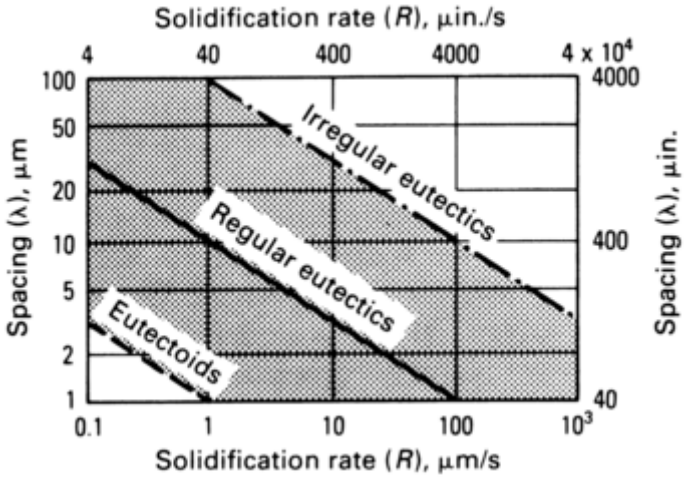

Fig. 48 Comparison of the λ - V correlation for eutectics and eutectoids. Source: Ref 1, Ref 24

The adjustment in the eutectic spacing during growth occurs through faults. Two types of faults are shown in Fig. 49. Figure 49(a) shows a no-net fault in which the number of lamellae on both sides of the fault is the same. Figure 49(b) shows a net fault in which one side of the fault has one more lamellae than the other side. This fault is analogous to an extended dislocation in that the number of lamellae above and below the fault differ by one (Ref 27).

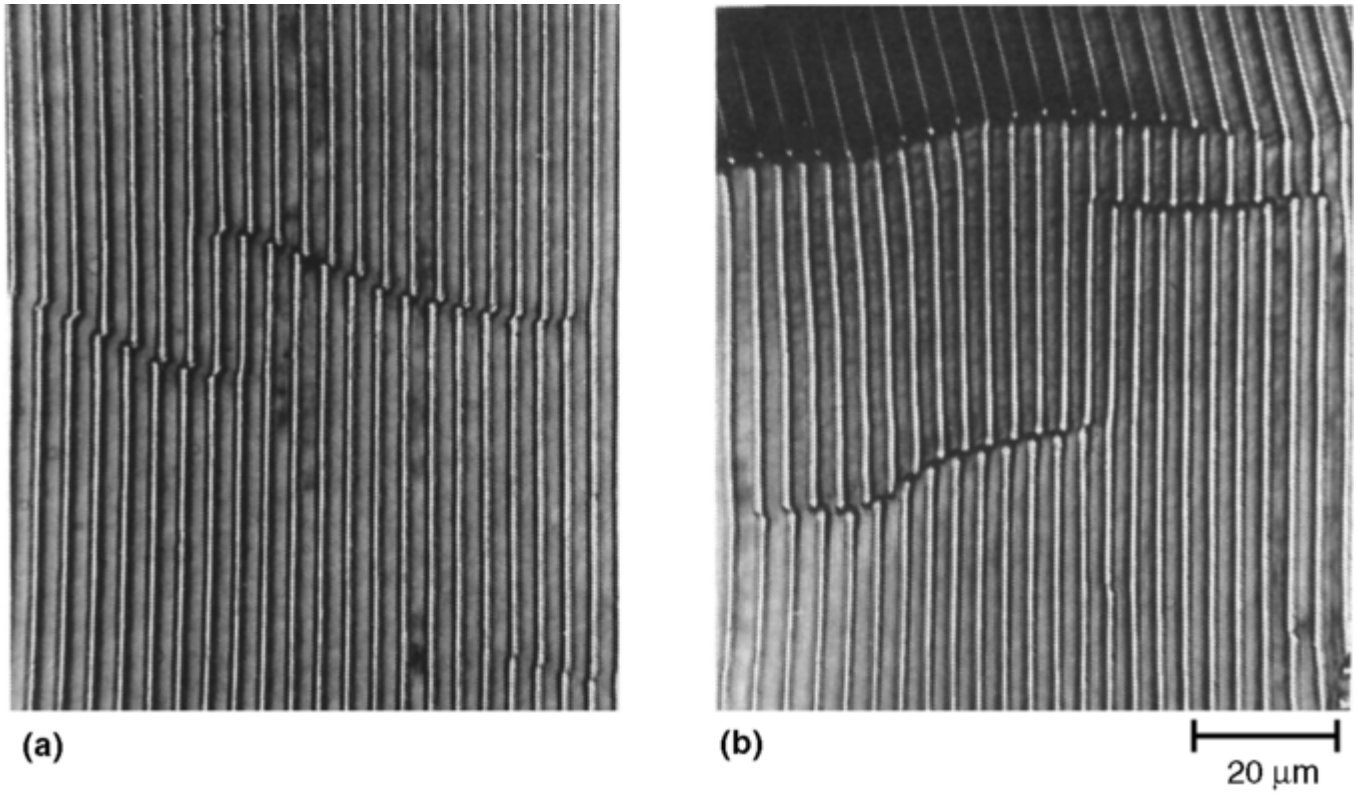

Fig. 49 Cross sections (a) and (b) of a directionally solidified lead-cadmium eutectic showing the presence of faults in the lamellae. Etchant not reported. Source: Ref 27

For equiaxed eutectics, the length scale may include grain size in addition to lamellar spacing. Metallographic identification of the grain size is alloy specific.

References cited in this section

1. D.M. Stefanescu, *Science and Engineering of Casting Solidification,* Kluwer Academic, 2002

21. W. Kurz and D.J. Fisher, *Fundamentals of Solidification,* 3rd ed., Trans Tech Publications, Switzerland, 1989

22. P. Magnin and W. Kurz, Solidification of Eutectics, *Casting,* Vol 15, *ASM Handbook,* D.M. Stefanescu, Ed., ASM International, 1988, p 119

23. M. McLean, *Directionally Solidified Materials for High Temperature Service,* The Metals Society, London, 1983

24. S.V. Raj, I.E. Locci, J.A. Salem, and R.J. Pawlik, *Metall. Mater. Trans. A,* Vol 33A, 2002, p 597–612

25. F.D. Lemkey and R.W. Kraft, Solidification Structures of Eutectic Alloys, *Metallography and Microstructures,* Vol 9, *ASM Handbook,* 1985, p 618–622

26. M.G. Day and A. Hellawell, *Proc. R. Soc.,* Vol A305, 1968, p 479–491

27. R. Trivedi, J.T. Mason, J.D. Verhoeven, and W. Kurz, *Metall. Mater. Trans. A,* Vol 22A, 1991, p 2523–2533

D.M. Stefanescu and R. Ruxanda, Fundamentals of Solidification, *Metallography and Microstructures,* Vol 9, *ASM Handbook* , ASM International, 2004, p. 71–92

Fundamentals of Solidification

Doru M. Stefanescu and Roxana Ruxanda, The University of Alabama

Solidification Structures of Peritectics

Peritectic solidification is very common in the solidification of metallic alloys. Many technically important alloy systems such as steels, copper alloys, rare-earth permanent magnets, and high T_C superconductors (T_C is the temperature above which superconductive behavior is lost) display peritectic reactions in the regions of their phase diagrams where phase and microstructure selection play an important role for the processing and the properties of the material. Basically, the peritectic solidification means that at the peritectic temperature T_P, a solid phase β of peritectic composition C_P solidifies from a mixture of liquid L and solid phase α. The peritectic solidification can be written as: L + α → β. A phase diagram with peritectic solidification is presented in Fig. 16(c). The different reactions occurring along the solidus lines, corresponding to various compositions (white and gray regions) are also shown.

Two different mechanisms are involved in peritectic solidification, namely peritectic reaction and peritectic transformation. These mechanisms are shown in Fig. 50. In a peritectic reaction, all three phases (α, β, and liquid) are in contact with each other. In the peritectic transformation, the liquid and the primary α phase are isolated by the β phase. The transformation takes place by long-range diffusion through the secondary β phase. A variety of microstructures can result from peritectic solidification, mostly depending on the G_T/V ratio and nucleation conditions. The possible structures include cellular, plane-front, bands, eutecticlike structures.

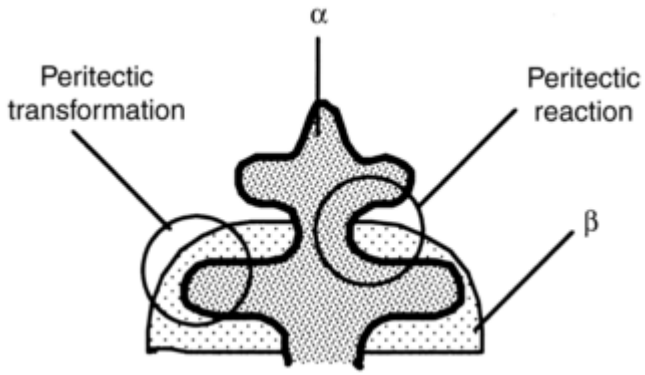

Fig. 50 Mechanisms of peritectic solidification. Source: Ref 1

Examples of such microstructures are given in Fig. 51, Fig. 52, Fig. 53, Fig. 54. The pictures have been obtained by in situ dynamic observation of the progress of peritectic reactions and transformations of iron-carbon alloys made with a combination of a confocal scanning laser microscope and an infrared image furnace (Ref 28).

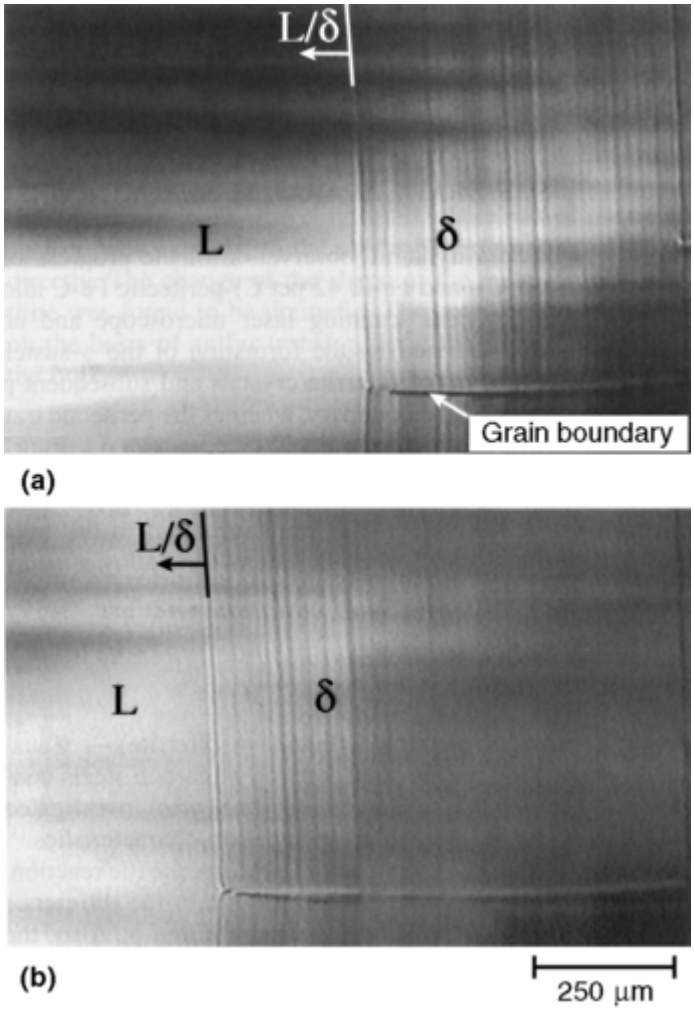

Fig. 51 Planar growth of δ crystals in Fe-0.14C alloy melt (*GT* = 22 K/mm, *V* = 4.3 μm/s), same scale. (a) At 0 s. (b) At 60 s. Source: Ref 28

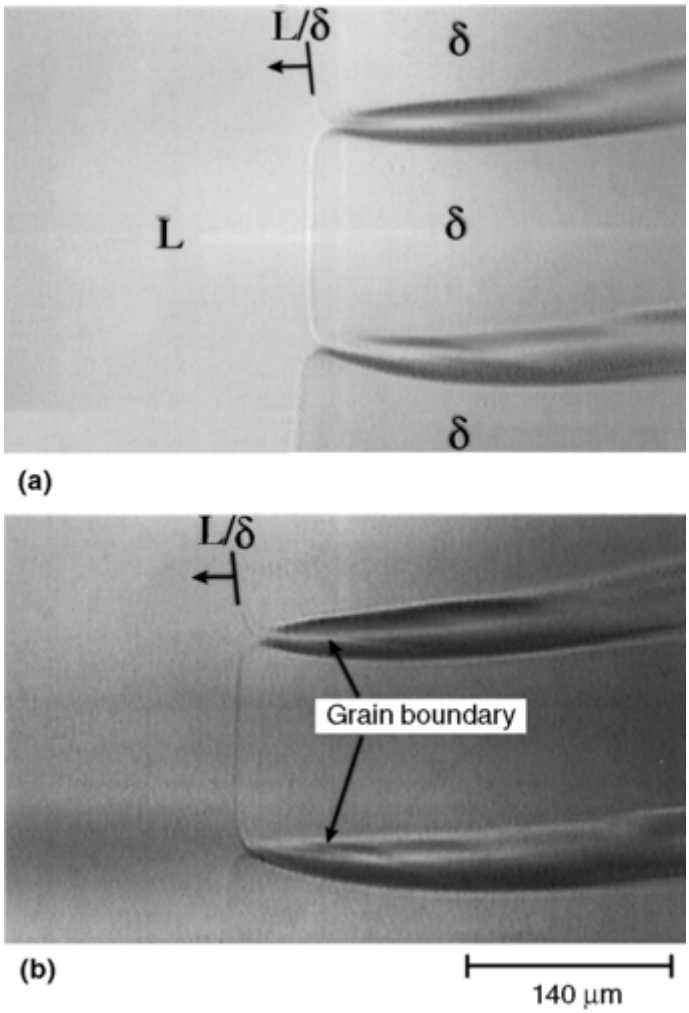

Fig. 52 Cellular growth of δ crystals in Fe-0.14% C alloy melt (*GT* = 4.3 K/mm, *V* = 2.5 μm/s). (a) At 0 s. (b) At 20 s. Source: Ref 28

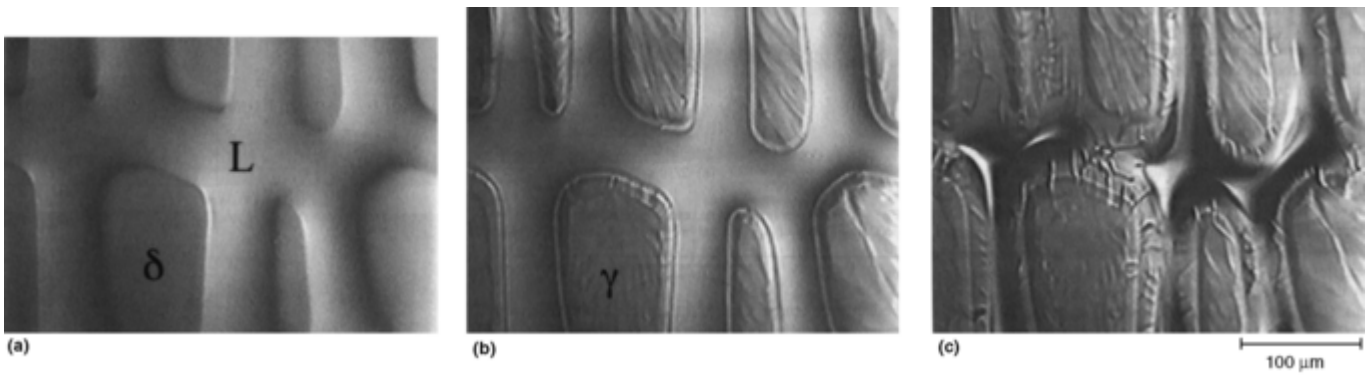

Fig. 53 Peritectic reaction and transformation of Fe-0.14C alloy during solidification and at 1768 K (*GT* = 4.3 K/mm, cooling rate = 20 K/min). (a) 0 s. (b) $\frac{1}{30}$s. (c) 2 s. Source: Ref 28

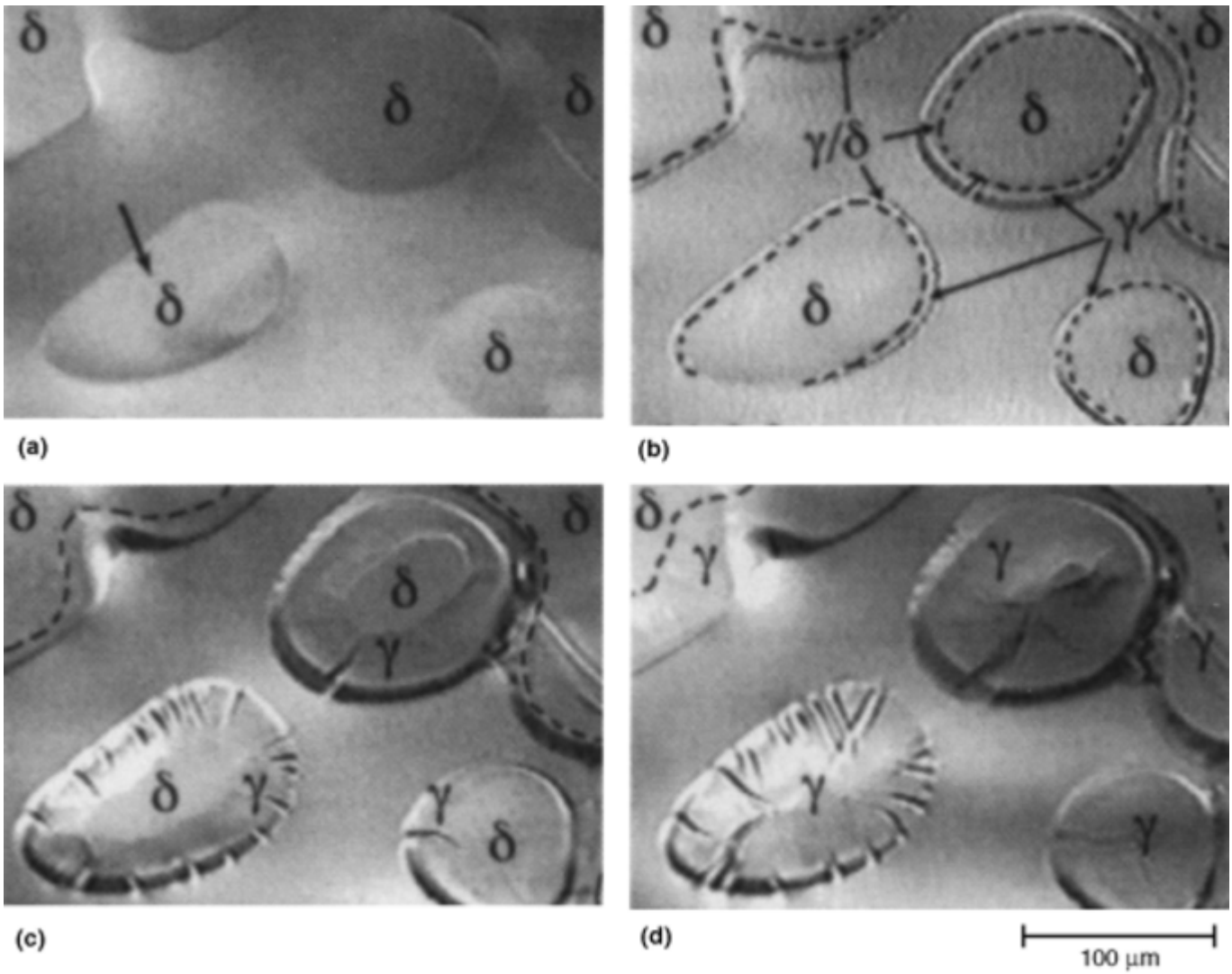

Fig. 54 Peritectic reaction and transformation of Fe-0.42C alloy during isothermal holding at 1765 K (same scale). (a) 0 s. (b) 0.2 s. (c) 3 s. (d) 7 s. Source: Ref 28

Simultaneous growth of two phases in the form of oriented fibers and lamellae has been observed in some peritectic alloys when the composition was on the tie-line of the two solid phases and the *GT*/*V* ratio was close to the limit of constitutional undercooling for the stable phase having the smaller distribution coefficient (Ref 29). Figure 55 shows such a structure for an iron-nickel alloy.

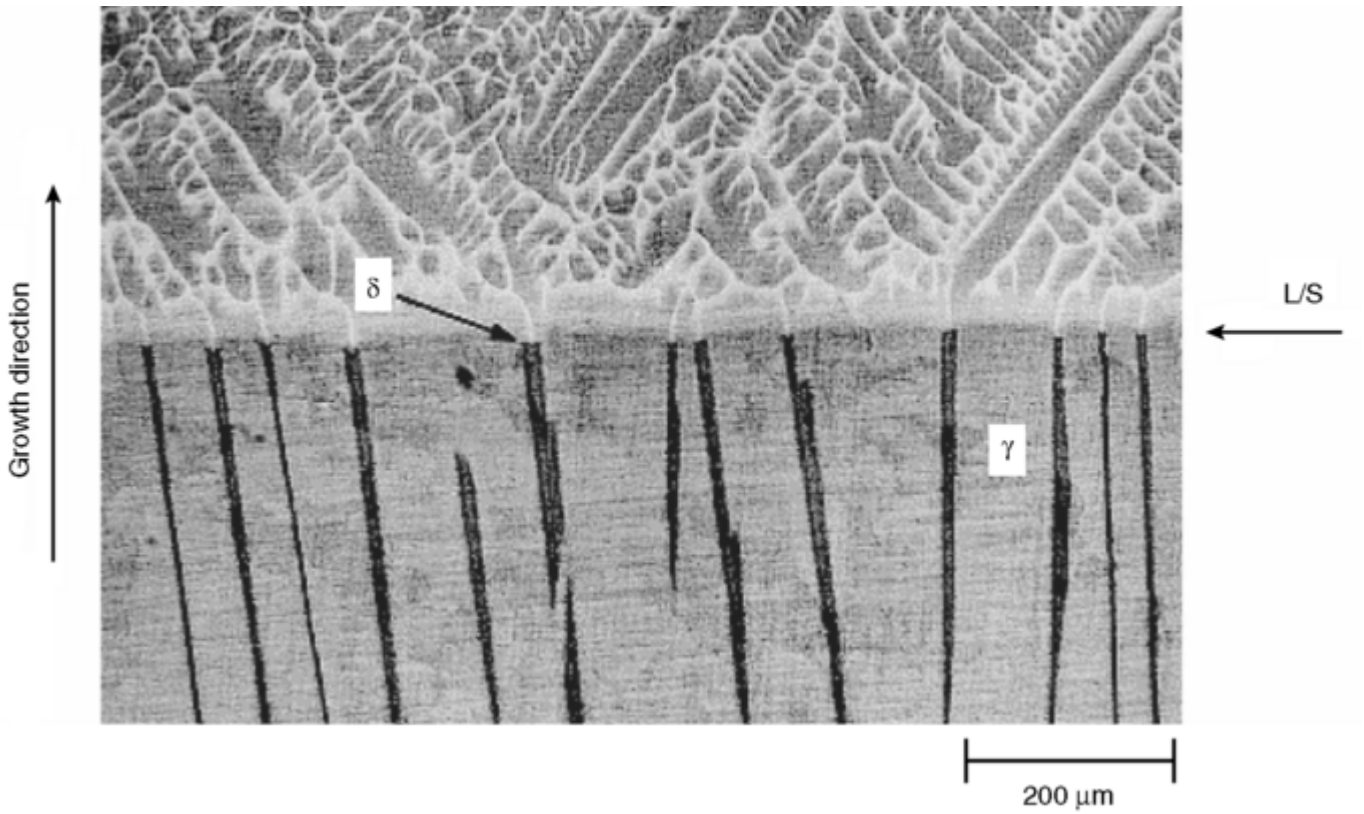

Fig. 55 Quenched solid/liquid interface of simultaneous two-phase growth in peritectic iron-nickel alloy. Source: Ref 29

Banded structures have been observed in peritectic alloys at low growth rates. An example is provided in Fig. 56 for lead-bismuth alloys (Ref 30). The formation of bands is explained by nucleation and growth of the second phase during the initial transient of planar growth of the primary phase and vice versa. This occurs because the liquid at and ahead of the growing interface is constitutionally undercooled with respect to the other phase. As the second phase nucleates and grows ahead of the primary phase, the former phase cannot reach the steady state. Similarly, the primary phase nucleates again during the transient growth regime of the second phase, preventing it from reaching the steady state. Consequently, a cycle is set up leading to the layered microstructure (Ref 31).

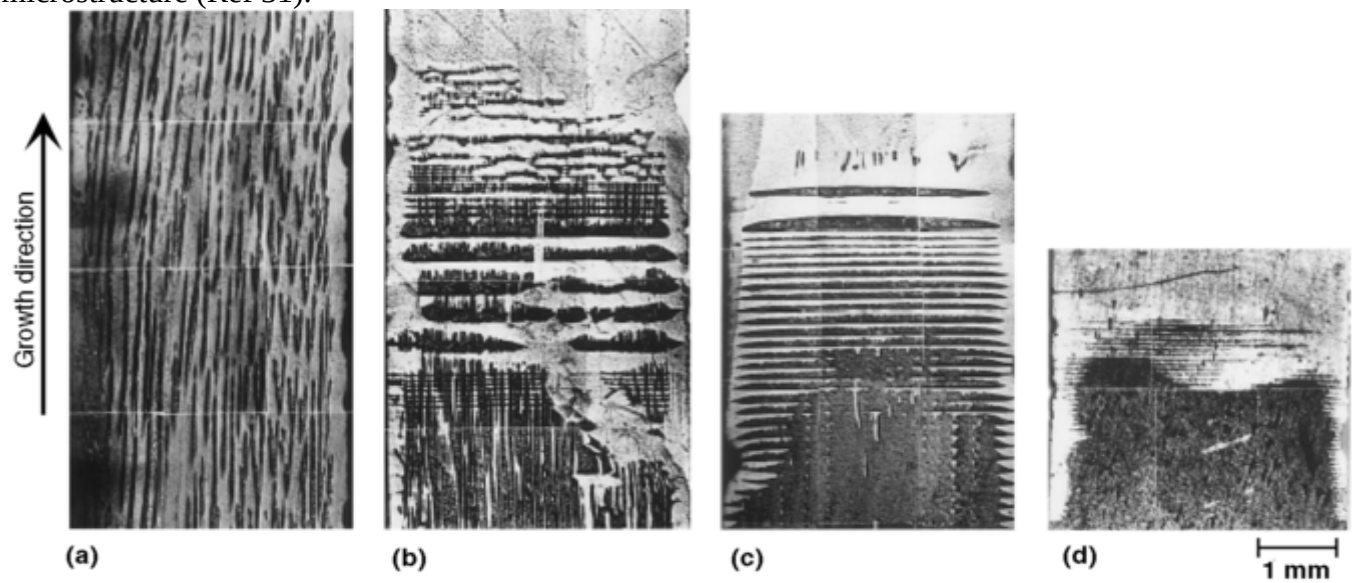

Fig. 56 Cross sections of directionally solidified Pb-33Bi (at.%) alloys (100 mm in initial melt length) at $GT = 2.7 \times 10^4$ K/m. (a) $V = 1.4$ μm/s. (b) $V = 0.83$ μm/s. (c) $V = 0.56$ μm/s. The black region is the α phase, and the white one is the β phase. Source: Ref 30

Many researchers have attempted to produce microstructure selection diagrams for peritectics in an attempt to clarify phase and microstructure selection. Taking into account nucleation and growth of the phases, Hunziker et al. (Ref 32) have proposed a criterion to determine the phase as a function of alloy composition and growth conditions. A microstructure selection diagram for peritectic alloys close to the limit of constitutional undercooling was developed (see Fig. 57). The lines 1 through 7 on the diagram were calculated. It is seen that the diagram allows prediction of planar front, cellular, dendritic, and band solidification.

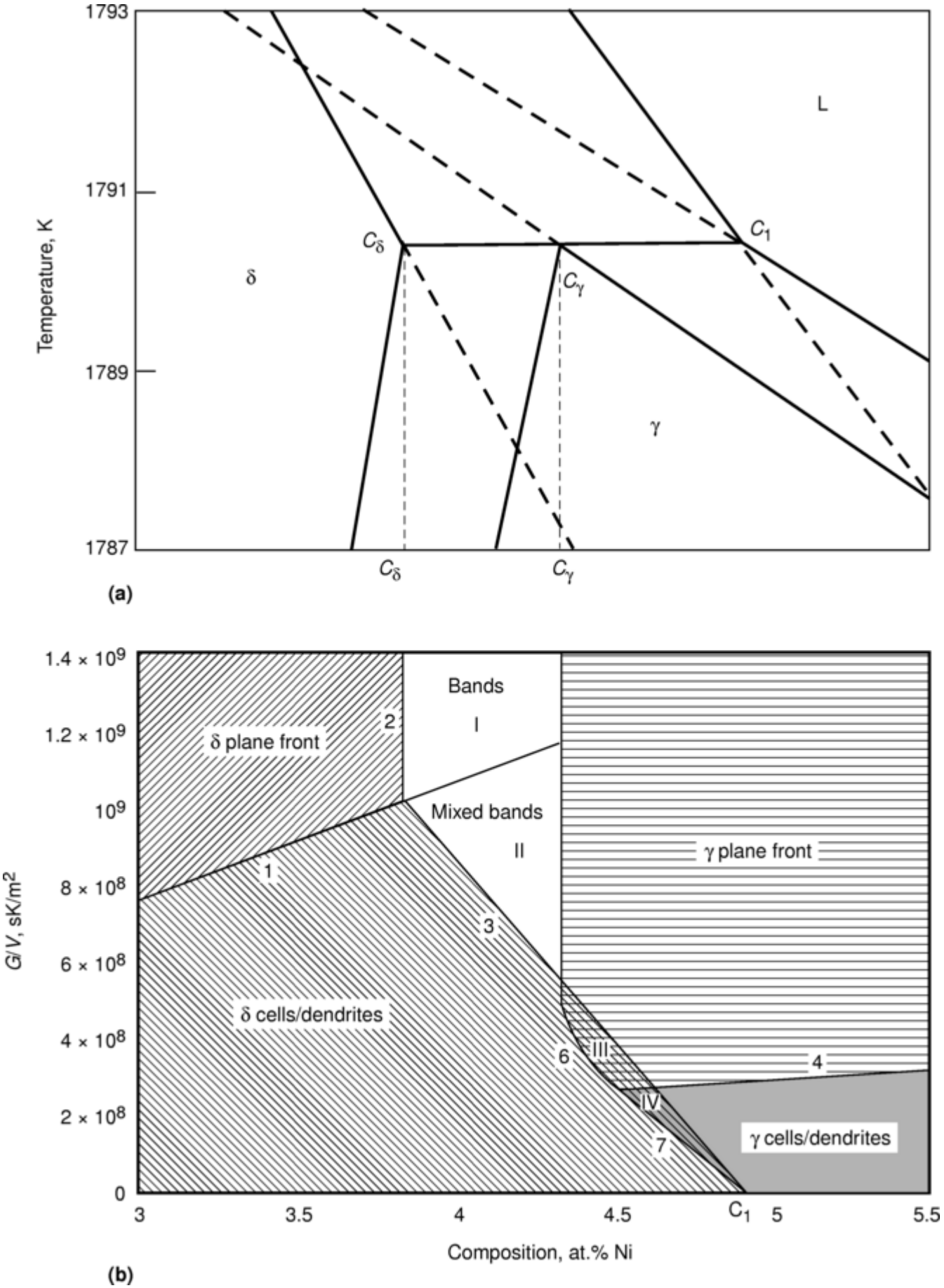

Fig. 57 Microstructural selection diagram. (a) Iron-nickel phase diagram in the vicinity of the peritectic plateau. (b) Predicted phase/microstructure selection map assuming negligible nucleation undercooling for both δ and γ phases. The calculated lines are numbered 1 through 7. Source: Ref 32

Fluid flow can further complicate the possible microstructures. Up to five different structures have been identified, as summarized in Fig. 58, where the solidification direction is upward (Ref 33).

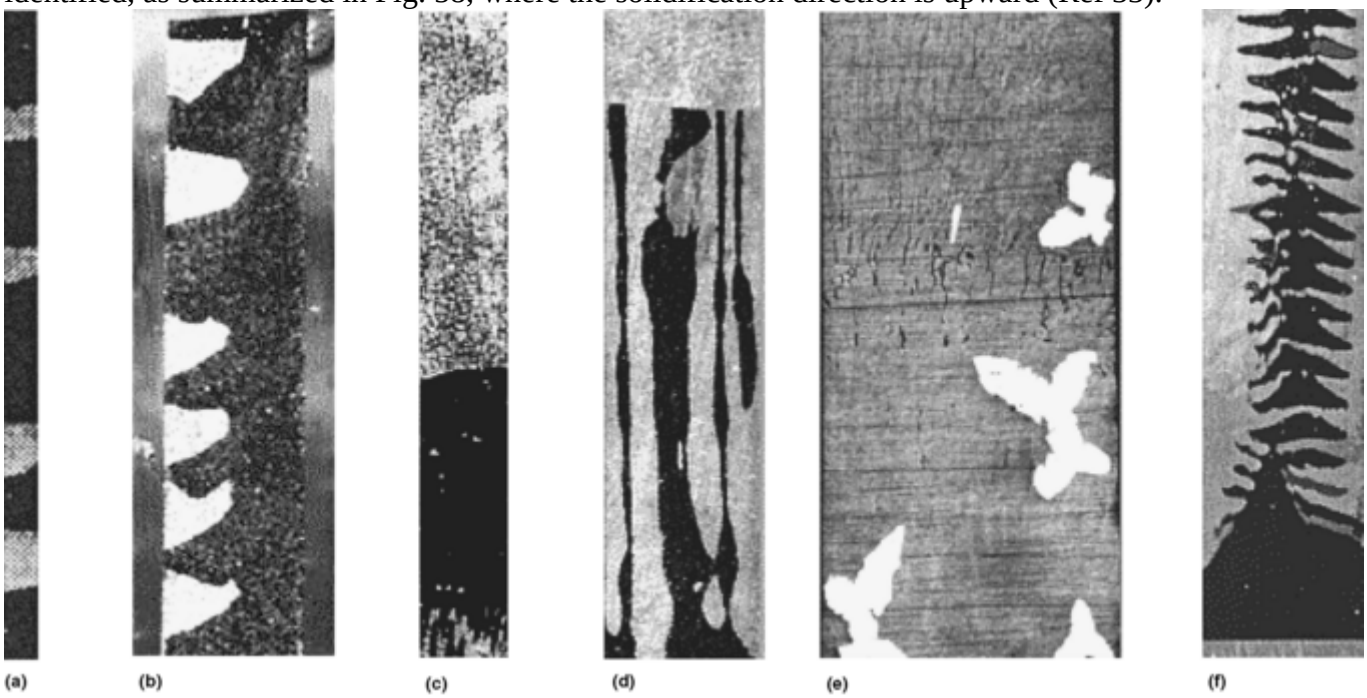

Fig. 58 Fluid-flow controlled microstructures in peritectic alloys. Solidification direction is upward. (a) Discrete bands of the two phases. (b) Partial bands or islands of one phase in the matrix of the other phase. (c) Single primary to peritectic phase transition. (d) Simultaneous growth of the two phases with a planar solid/liquid interface. (e) Dispersed phases due to nucleation ahead of the interface. (f) Oscillating continuous treelike structures of the primary phase surrounded by peritectic. Source: Ref 33

References cited in this section

1. D.M. Stefanescu, *Science and Engineering of Casting Solidification,* Kluwer Academic, 2002

28. H. Shibata, Y. Arai, and T. Emi, *Metall. Mater. Trans. B,* Vol 31B, 2000, p 981–991

29. M. Vandyoussefi, H.W. Kerr, and W. Kurz, *Acta Mater.,* Vol 48, 2000, p 2297–2306

30. K. Tokieda, H. Yasuda, and I. Ohnaka, *Mater. Sci. Eng.,* Vol A262, 1999, p 238–245

31. R. Trivedi, *Metall. Trans. A,* Vol 26A, 1995, p 1583

32. O. Hunziker, M. Vandyoussefi, and W. Kurz, *Acta Mater.,* Vol 46 (No. 18), 1998, p 6325–6336

33. R. Trivedi, A. Karma, T.S. Lo, P. Mazumder, M. Plapp, and J.S. Park, *1998 Zermatt Workshop on "Solidification Microstructures,"* M. Rappaz and R. Trivedi, Ed., CD. Swiss Federal Institute of Technology, Lausanne, Switzerland, 1998

D.M. Stefanescu and R. Ruxanda, Fundamentals of Solidification, *Metallography and Microstructures,* Vol 9, *ASM Handbook* , ASM International, 2004, p. 71–92

Doru M. Stefanescu and Roxana Ruxanda, The University of Alabama

Solidification Structures of Monotectics

Monotectic solidification occurs in alloys where the liquid separates into two distinct liquid phases of different composition during cooling. These alloys have limited commercial applications. However, one could mention lead-containing copper alloys and the possible fabrication of thin microfilters has been proposed as possible application.

A dome-shaped region within which the two liquids mix and coexist is seen on the phase diagram (Fig. 16d). The maximum temperature of this dome, T_c, is called the critical (or consolute) temperature. At the monotectic temperature, T_m, the following monotectic reaction occurs:

$$L_1 = \alpha + L_2 \quad \text{(Eq 10)}$$

Monotectic alloys can be classified based on the difference T_c - T_m as high-dome alloys (high T_c - T_m of hundreds of °C) and low-dome alloys (low T_c - T_m of tens of °C). They can also be classified based on the T_m/T_c ratio. High-dome alloys have $T_m/T_c < 0.9$, while low-dome alloys have $T_m/T_c > 0.9$.

The morphology of the microstructure produced during directional solidification is a function of the density difference between the two liquids, and of the wetting between L_2 and α. As theorized by Cahn (Ref 34), for low-dome alloys the phases α and L_2 are separated by L_1 as shown in Fig. 59. At low growth rate, L_2 particles are pushed by the S/L interface (Fig. 59a). If the solidification velocity increases above a critical velocity, V_{cr}, L_2 is incorporated with formation of an irregular fibrous composite (Fig. 59b). A detailed discussion on particle engulfment and pushing by solidifying interfaces is given in Ref 1. This mechanism has been observed experimentally.

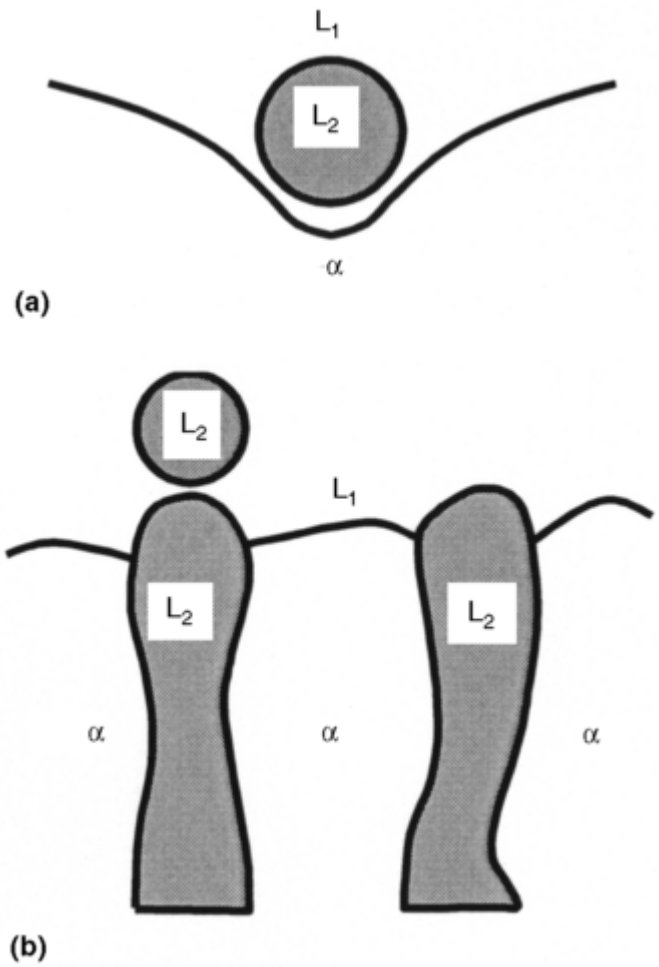

Fig. 59 Monotectic solidification for low-dome alloys. (a) Low growth velocity. (b) High growth velocity. Source: Ref 1

Figure 60 shows fibrous growth in the succinonitrile-20% ethanol system when the velocity is above the critical velocity for particle engulfment (Ref 35). Similar microstructures were observed in metallic system such as Cu-60%Pb and Bi-50%Ga alloy as shown in Fig. 61 for a copper-lead alloy (Ref 36). Note that the velocity in this last microstructure is very high.

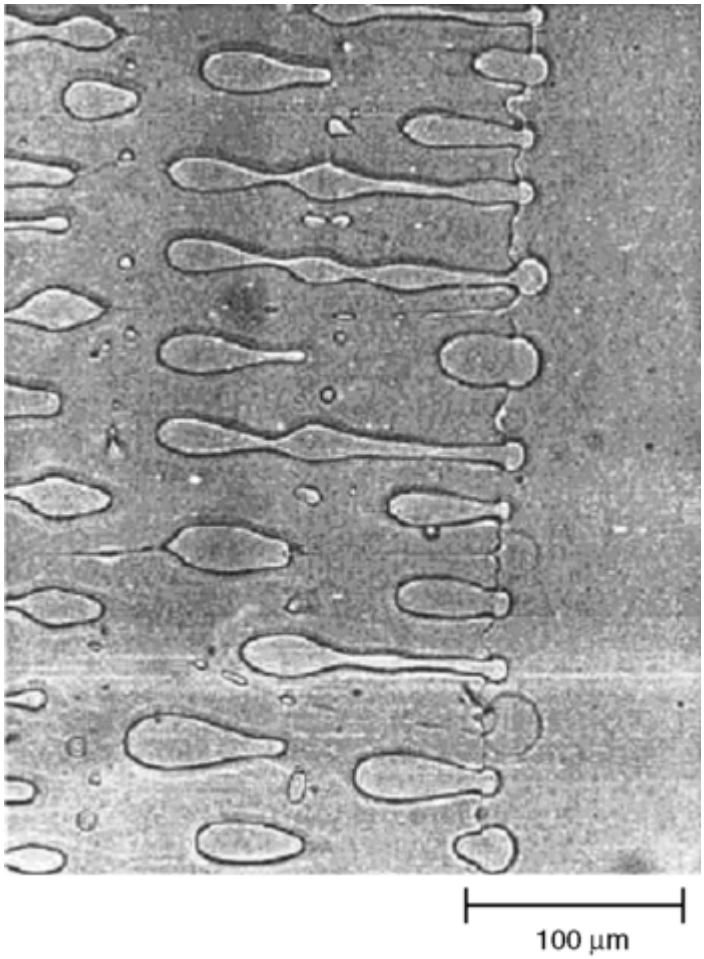

Fig. 60 Growth front in succinonitrile-20 wt% ethanol, showing incorporation of ethanol droplets. *V* = 0.27 μm/s, *G* = 4.8 K/mm. Source: Ref 35

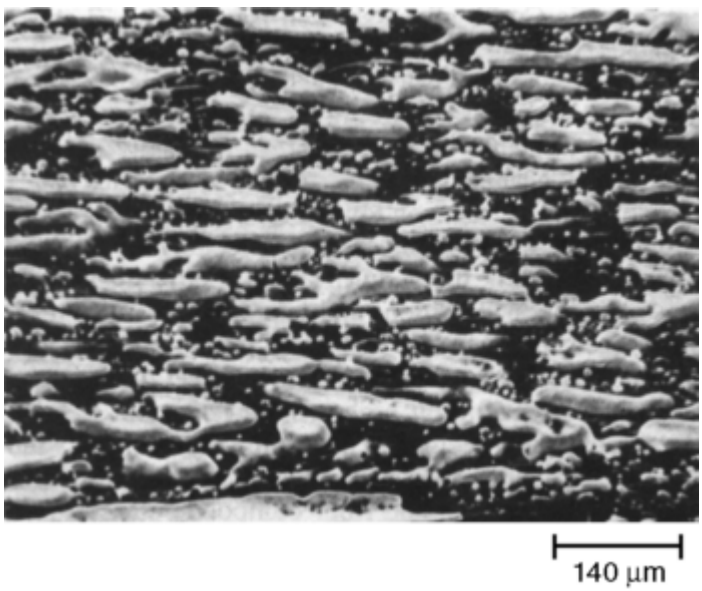

Fig. 61 Microstructure of a Cu-70Pb alloy solidified at *V* = 778 μm/s and *G* = 12 K/mm. Solidification direction right-to-left. Source: Ref 36

The range of existence of the fibrous composite is limited by the constitutional undercooling on one side and by the critical velocity of pushing-to-engulfment transition (V_{cr}) on the other (Fig. 62). When the solidification velocity is smaller than V_{cr} a banded structure may result. An example of such a structure is provided in Fig. 63 (Ref 37). It is suggested the L_2 phase, which precipitates at the solid/liquid interface, piles up and covers the

S/L interface. This produces a lead-rich layer and increases the undercooling of the L_1/L_2 interface with respect to the monotectic temperature. Then, nucleation of the αCu phase occurs on the lead-rich layer. The temperature at the growth front is also returned to the monotectic temperature. The repetition of this process will result in the banded structure. This process is shown in Fig. 64. It should be noted that some fibrous structure might form even in the case of banding as seen in Fig. 65.

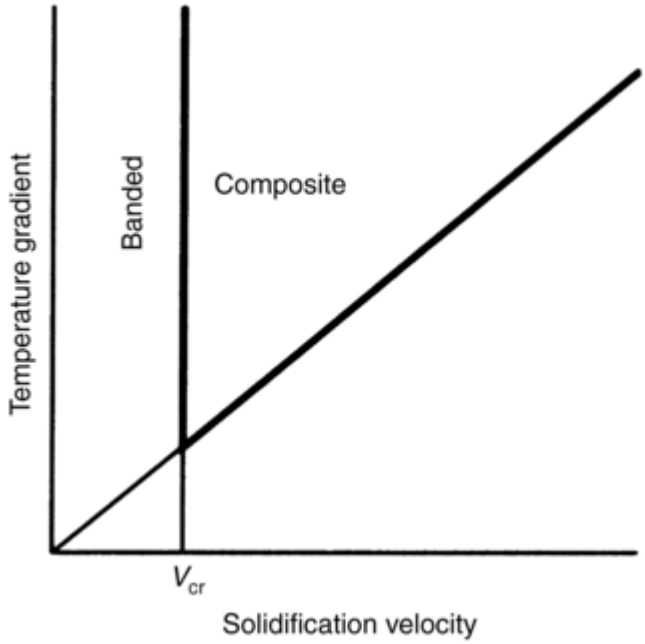

Fig. 62 Restriction on composite growth imposed by the critical velocity for the pushing engulfment transition and by constitutional undercooling. Source: Ref 1

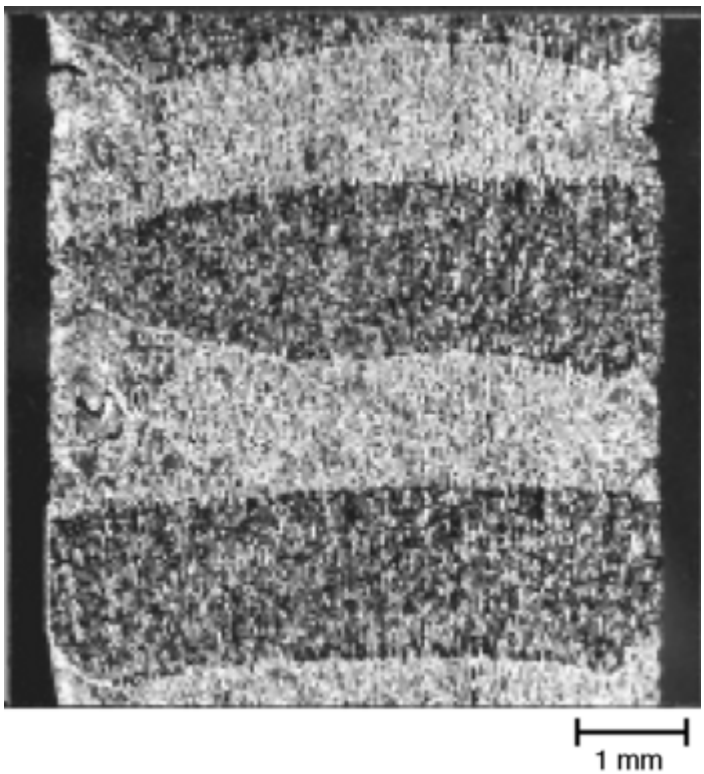

Fig. 63 Microstructure of upward directional solidification of a Cu-37.7Pb alloy in longitudinal section. *V* = 4.4 μm/s. Source: Ref 37

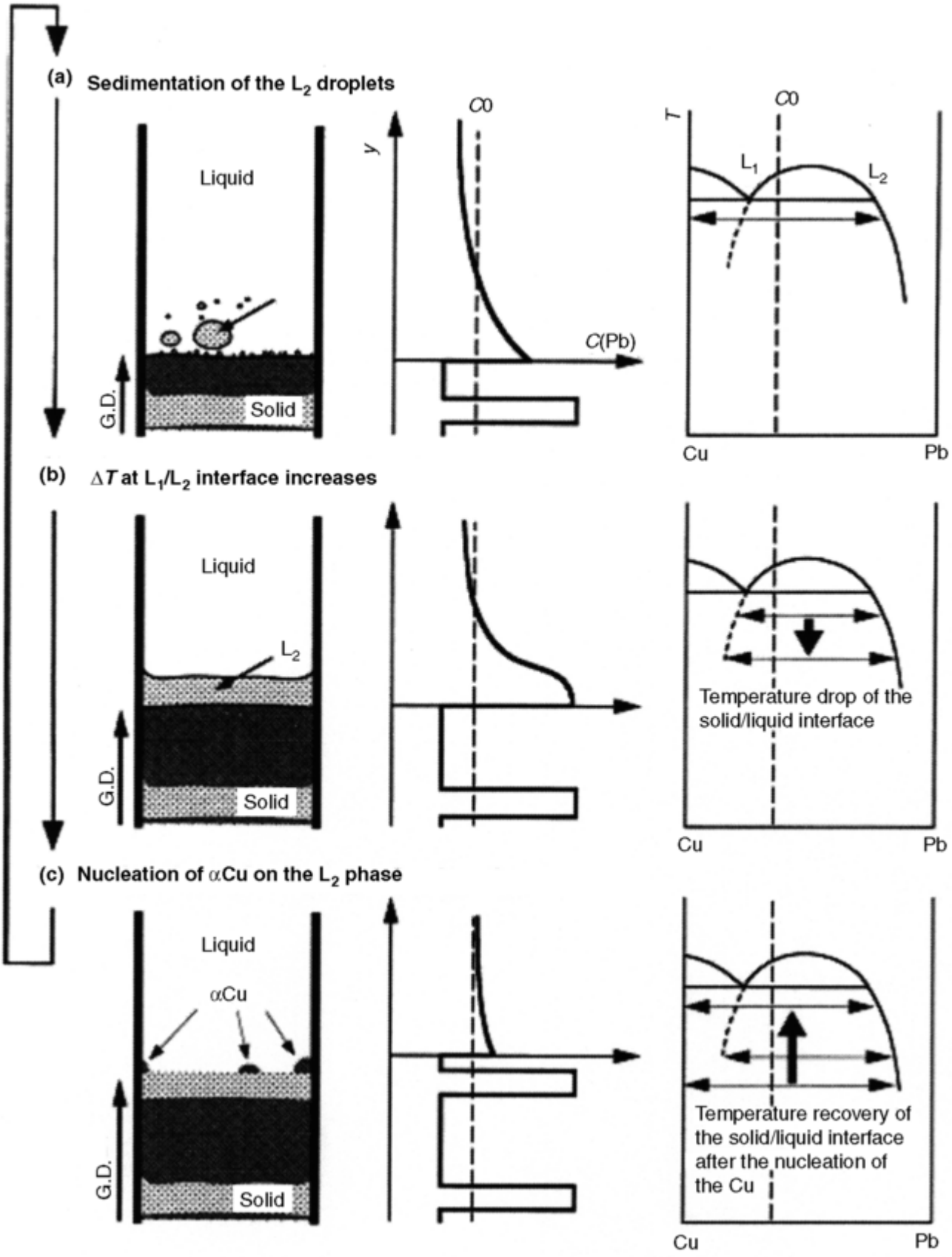

Fig. 64 Forming mechanism of the banded structure of copper-lead alloy in upward directional solidification. Source: Ref 37

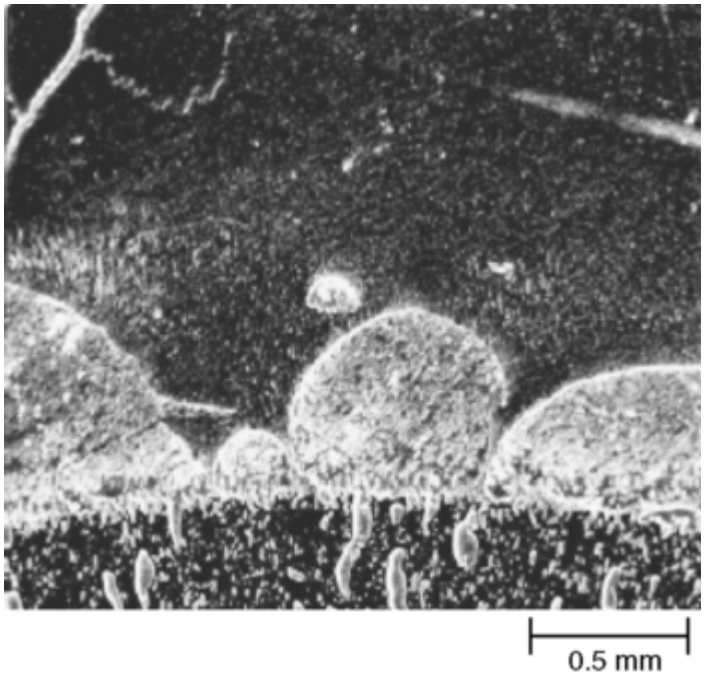

Fig. 65 The solid/liquid interface covered with coalesced L_2 phase. Cu-35.4Pb alloy, upward directional solidification, V = 2.2 μm/s. Source: Ref 37

For high-dome alloys, the lowest energy exists when an α/L_2 interface exists. Consequently, α and L_2 will grow together (L_2 wets α), resulting in a regular (uniform) fibrous composite. The $\lambda^2 \cdot V$ relationship is about two orders of magnitude larger for irregular than for regular monotectic composites (with the exception of the aluminum-bismuth alloy) and about one order of magnitude higher for regular monotectic composites than for regular eutectics. The differences come from the controlling mechanism. For irregular fibrous eutectics, the controlling mechanism is the pushing-engulfment transition, which is a function of solidification velocity and surface energy. For regular fibrous monotectics, the spacing is controlled by surface energy. For eutectics, the spacing is controlled by diffusion (Ref 1).

References cited in this section

1. D.M. Stefanescu, *Science and Engineering of Casting Solidification,* Kluwer Academic, 2002

34. J.W. Cahn, *Metall. Trans.,* Vol 10A, 1979, p 119–121

35. R.N. Grugel, T.A. Lagrasso, and A. Hellawell, *Metall. Trans. A,* Vol 15A, 1984, p 1003–1010

36. B.K. Dhindaw, D.M. Stefanescu, A.K. Singh, and P.A. Curreri, *Metall. Trans. A,* Vol 19A, 1988, p 2839

37. I. Aoi, M. Ishino, M. Yoshida, H. Fukunaga, and H. Nakae, *J. Cryst. Growth,* Vol 222, 2001, p 806–815

D.M. Stefanescu and R. Ruxanda, Fundamentals of Solidification, *Metallography and Microstructures,* Vol 9, *ASM Handbook* , ASM International, 2004, p. 71–92

Fundamentals of Solidification

Doru M. Stefanescu and Roxana Ruxanda, The University of Alabama

References

1. D.M. Stefanescu, *Science and Engineering of Casting Solidification,* Kluwer Academic, 2002

2. D.G. Altenpohl, *Aluminum: Technology, Applications, and Environment. A Profile of a Modern Metal. Aluminum from Within—the Sixth Edition,* The Aluminum Association and the Minerals, Metals, and Materials Society, 1999

3. A. Ohno, *Solidification. The Separation Theory and Its Practical Applications,* Springer-Verlag, Berlin, 1987

4. R. Trivedi and W. Kurz, Solidification of Single-Phase Alloys, *Casting,* Vol 15, *ASM Handbook,* D.M. Stefanescu, Ed., ASM International, 1988, p 114

5. M. Schenck, referred to in *Solidification. The Separation Theory and Its Practical Applications,* Springer-Verlag, Berlin, 1987

6. K.A. Jackson, Solidification Structures of Pure Metals, *Metallography and Microstructures,* Vol 9, *ASM Handbook,* ASM International, 1985, p 607

7. W.J. Boettinger, *Metall. Mater. Trans.,* Vol 5, 1974, p 2026

8. S. Akamatsu, G. Faivre, and Th. Ihle, *Phys. Rev.,* Vol E 51, 1995, p 4751–4773

9. S.N. Tewari, Y.-H. Weng, G.L. Ding, and R. Trivedi, *Metall. Mater. Trans. A,* Vol 33A, 2002, p 1229–1243

10. R. Trivedi and K. Somboonsuk, *Mater. Sci. Eng.,* Vol 65, 1984, p 65–74

11. C.P. Hong and M.F. Zhu, *The Science of Casting and Solidification,* D.M. Stefanescu, R. Ruxanda, M. Tierean, and C. Serban, Ed., Editura Lux Libris, Brasov, Romania, 2001, p 110s–118s

12. D. Bouchard and J.S. Kirkaldy, *Metall. Mater. Trans. B,* Vol 28B, 1997, p 651

13. J.H. Perepezko and J.J. Paike, *Rapidly Solidified Amorphous and Crystalline Alloys,* B.H. Kear, B.C. Giessen, and M. Cohen, Ed., North Holland, 1982, p 49

14. W.J. Boettinger, D. Shechtman, R.J. Schaefer, and F.S. Biancaniello, *Metall. Trans. A,* Vol 15, 1984, p 55

15. D. Shechtman, R.J. Schaefer, and F.S. Biancaniello, *Metall. Trans. A,* Vol 15, 1984, p 1987

16. I.R. Hughes and H. Jones, *J. Mater. Sci.,* Vol 11, 1976, p 1781

17. J.H. Perepezko and W.J. Boettinger, *Mater. Res. Soc. Symp. Proc.,* Vol 19, 1983, p 223

18. W.J. Boettinger, *Rapidly Solidified Amorphous and Crystalline Alloys,* B.H. Kear, B.C. Giessen, and M. Cohen, Ed., North Holland, 1982, p 15

19. N.H. Pryds and A.S. Pedersen, *Metall. Mater. Trans. A,* Vol 33A, 2002, p 3755–3761

20. D. Shechtman and E. Gutmanas, *Prakt. Metallogr.,* Vol 18, 1981, p 587

21. W. Kurz and D.J. Fisher, *Fundamentals of Solidification,* 3rd ed., Trans Tech Publications, Switzerland, 1989

22. P. Magnin and W. Kurz, Solidification of Eutectics, *Casting,* Vol 15, *ASM Handbook,* D.M. Stefanescu, Ed., ASM International, 1988, p 119

23. M. McLean, *Directionally Solidified Materials for High Temperature Service,* The Metals Society, London, 1983

24. S.V. Raj, I.E. Locci, J.A. Salem, and R.J. Pawlik, *Metall. Mater. Trans. A,* Vol 33A, 2002, p 597–612

25. F.D. Lemkey and R.W. Kraft, Solidification Structures of Eutectic Alloys, *Metallography and Microstructures,* Vol 9, *ASM Handbook,* 1985, p 618–622

26. M.G. Day and A. Hellawell, *Proc. R. Soc.,* Vol A305, 1968, p 479–491

27. R. Trivedi, J.T. Mason, J.D. Verhoeven, and W. Kurz, *Metall. Mater. Trans. A,* Vol 22A, 1991, p 2523–2533

28. H. Shibata, Y. Arai, and T. Emi, *Metall. Mater. Trans. B,* Vol 31B, 2000, p 981–991

29. M. Vandyoussefi, H.W. Kerr, and W. Kurz, *Acta Mater.,* Vol 48, 2000, p 2297–2306

30. K. Tokieda, H. Yasuda, and I. Ohnaka, *Mater. Sci. Eng.,* Vol A262, 1999, p 238–245

31. R. Trivedi, *Metall. Trans. A,* Vol 26A, 1995, p 1583

32. O. Hunziker, M. Vandyoussefi, and W. Kurz, *Acta Mater.,* Vol 46 (No. 18), 1998, p 6325–6336

33. R. Trivedi, A. Karma, T.S. Lo, P. Mazumder, M. Plapp, and J.S. Park, *1998 Zermatt Workshop on "Solidification Microstructures,"* M. Rappaz and R. Trivedi, Ed., CD. Swiss Federal Institute of Technology, Lausanne, Switzerland, 1998

34. J.W. Cahn, *Metall. Trans.,* Vol 10A, 1979, p 119–121

35. R.N. Grugel, T.A. Lagrasso, and A. Hellawell, *Metall. Trans. A,* Vol 15A, 1984, p 1003–1010

36. B.K. Dhindaw, D.M. Stefanescu, A.K. Singh, and P.A. Curreri, *Metall. Trans. A,* Vol 19A, 1988, p 2839

37. I. Aoi, M. Ishino, M. Yoshida, H. Fukunaga, and H. Nakae, *J. Cryst. Growth,* Vol 222, 2001, p 806–815

Solidification Structures of Pure Metals, *Metallography and Microstructures,* Vol 9, *ASM Handbook,* ASM International, 2004, p. 93–96

Solidification Structures of Pure Metals

Introduction

PURE METALS normally solidify into polycrystalline masses, but it is relatively easy to produce single crystals by directional solidification from the melt. The three common ways of growing single crystals are the Bridgman method, in which a mold is lowered out of a vertical tubular furnace; the Chalmers method, in which a boat is passed through a horizontal tubular furnace; and the Czochralski method, in which a crystal is pulled from a crucible containing the melt. Much effort has been directed toward obtaining high-purity starting materials (often by zone refining) and toward maintaining purity during crystal growth. Metal single crystals have been prepared with very low dislocation densities, but because pure metal crystals are very soft, this requires great care to reduce thermal and mechanical stresses during growth and subsequent handling. Most metal single crystals have dislocation densities of about 10^6 to 10^7 per square centimeter. These dislocations result from stresses induced during growth by thermal, mechanical, and composition gradients, as well as from entrapped particles. In addition, vacancies can condense to form small dislocation loops subsequent to growth.

Dislocations present in a metal crystal often polygonize into subboundaries during growth. These subboundaries, which frequently intersect the growth front, are propagated by the growth process and result in subgrains that are elongated in the direction of the growth. Subboundaries originating in this way are irregular (Fig. 1) if the material is pure, but are regular and straight (Fig. 2) in a very dilute alloy in which cellular growth has occurred. Subboundaries also are formed where the liquid between two slightly misoriented dendrite arms freezes.

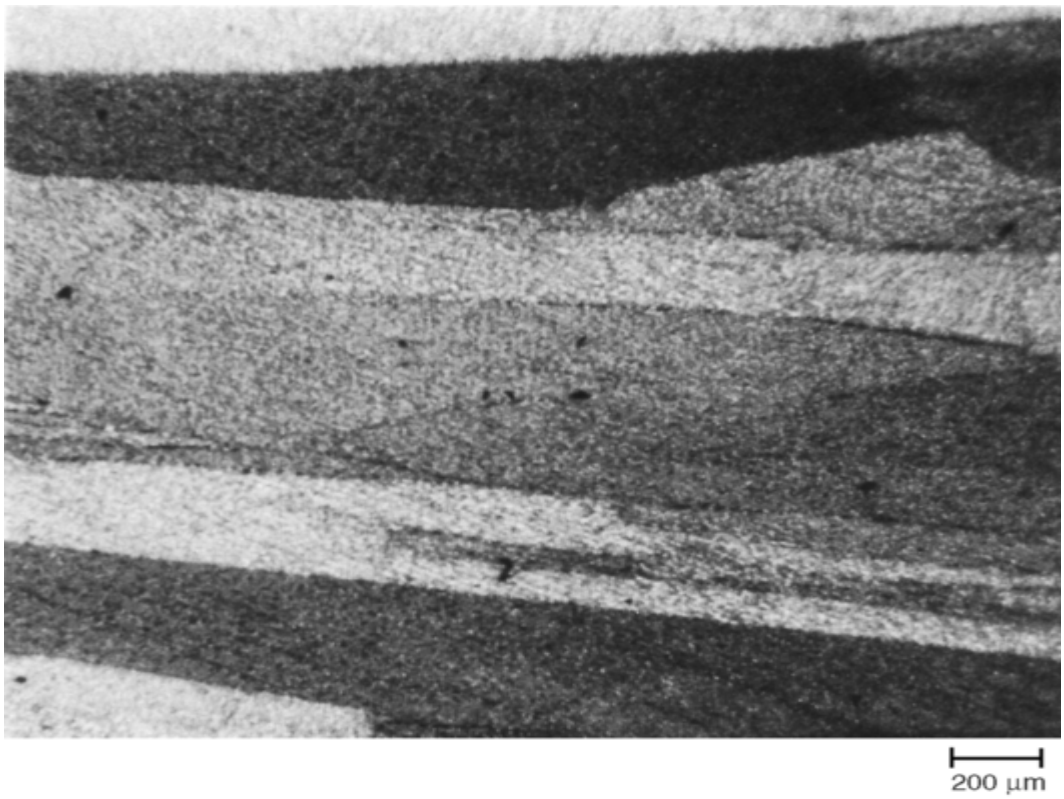

Fig. 1 Irregular subboundaries in high-purity tin grown without cells. Subboundaries similar to these form in many high-purity metals during solidification. Compare with the structure shown in Fig. 2 10% $FeCl_3$ + 2% HCl, in H_2O. 40×

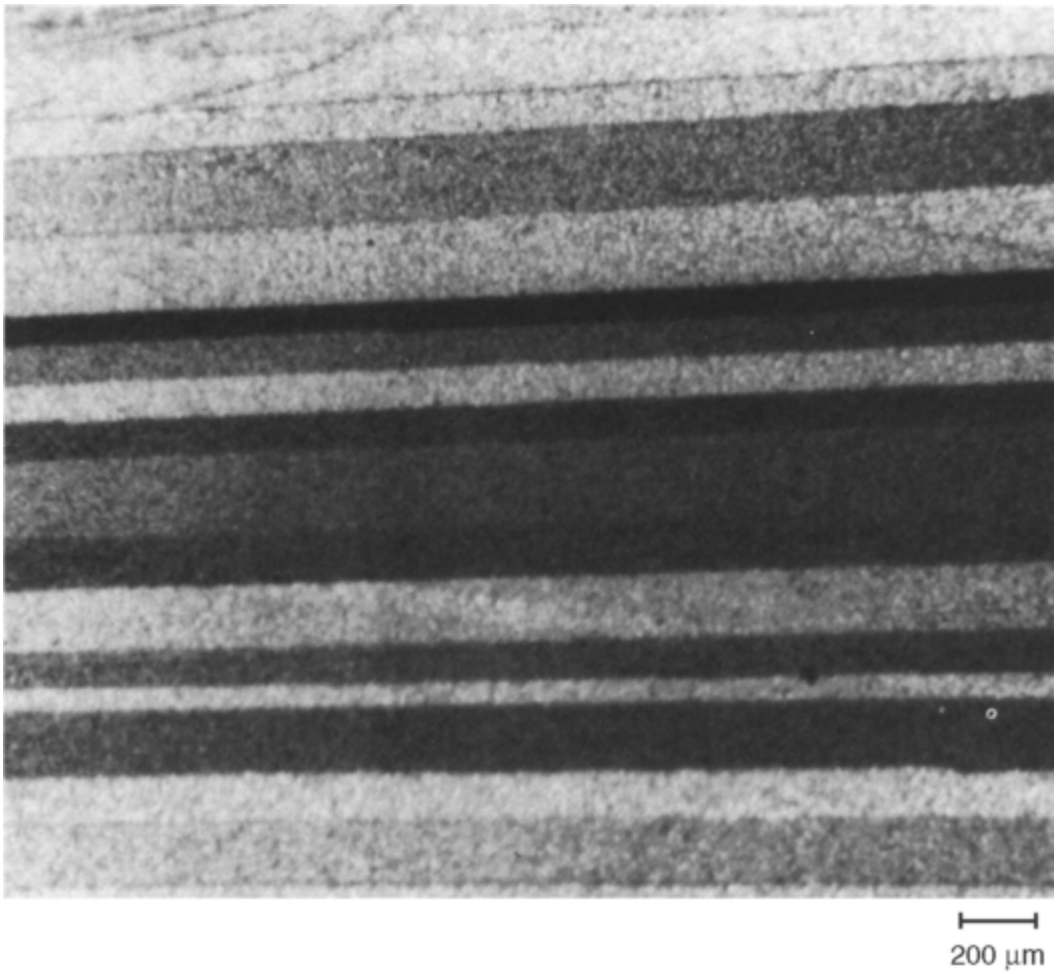

Fig. 2 Regular subboundaries in tin of lower purity than that in Fig. 1 grown with cells. Cellular growth, resulting from the presence of minute amounts of impurity, makes the subboundaries straight during solidification. 10% $FeCl_3$ + 2% HCl, in H_2O. 35×

Dislocations in subboundaries can be resolved by careful metallography; an example is shown in Fig. 3. A specimen etched to reveal the subboundaries and dislocations is depicted in Fig. 4. The number of dislocations in the subboundaries often approximately equals the number of isolated dislocations in the subgrains.

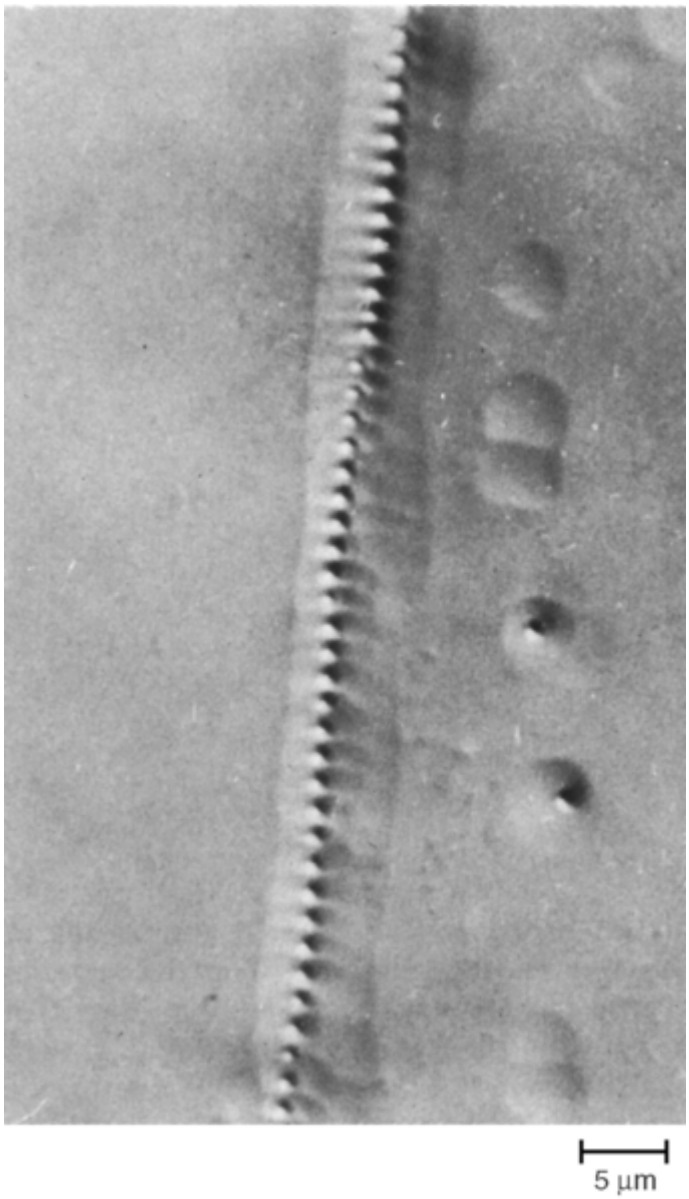

Fig. 3 Individual dislocations (revealed by careful etching) that comprise a subboundary in germanium. HNO_3-acetic-HF-bromine. 1500×. Courtesy of W.G. Pfann

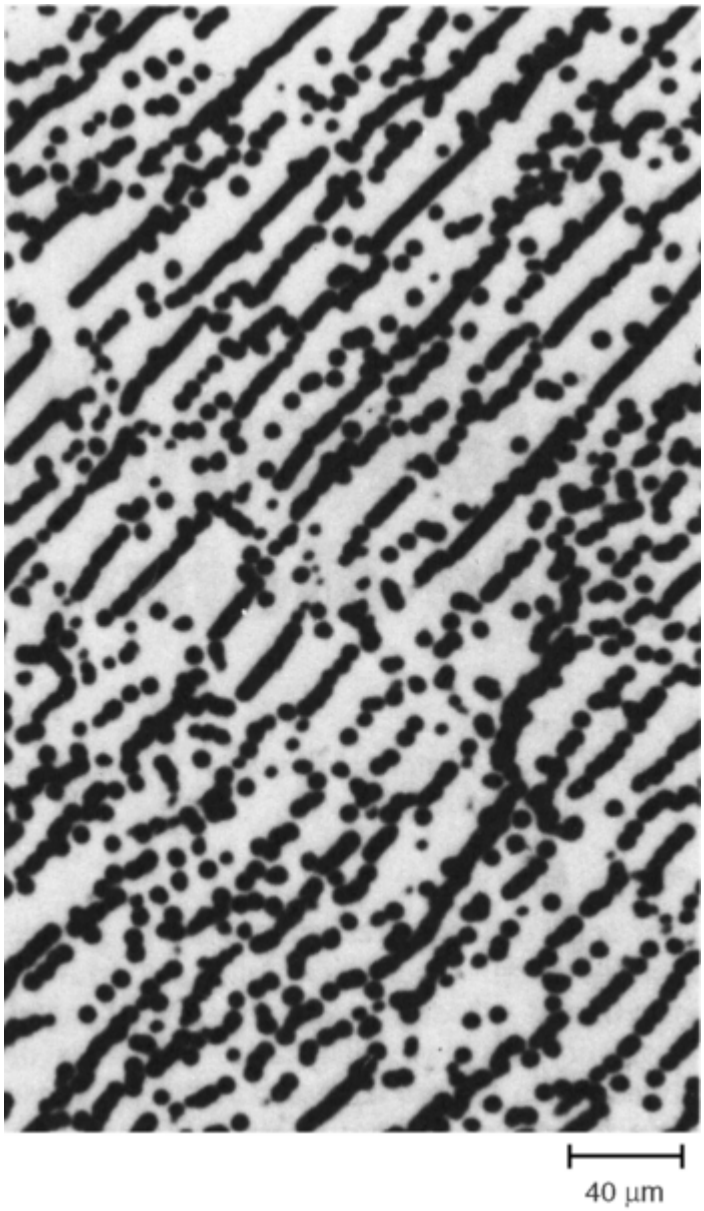

Fig. 4 Dislocations and subboundaries produced by polygonization in germanium annealed after deformation. HNO_3-acetic-HF-bromine. 250×. Courtesy of J.R. Patel

Dislocations produced by thermal or mechanical stresses at low temperature often line up on the traces of slip planes, as shown in Fig. 5. Dislocations produced by precipitation and condensation of vacancies during cooling usually are in the form of small loops (Fig. 6). These vacancies can also form other clusters, such as stacking-fault tetrahedra.

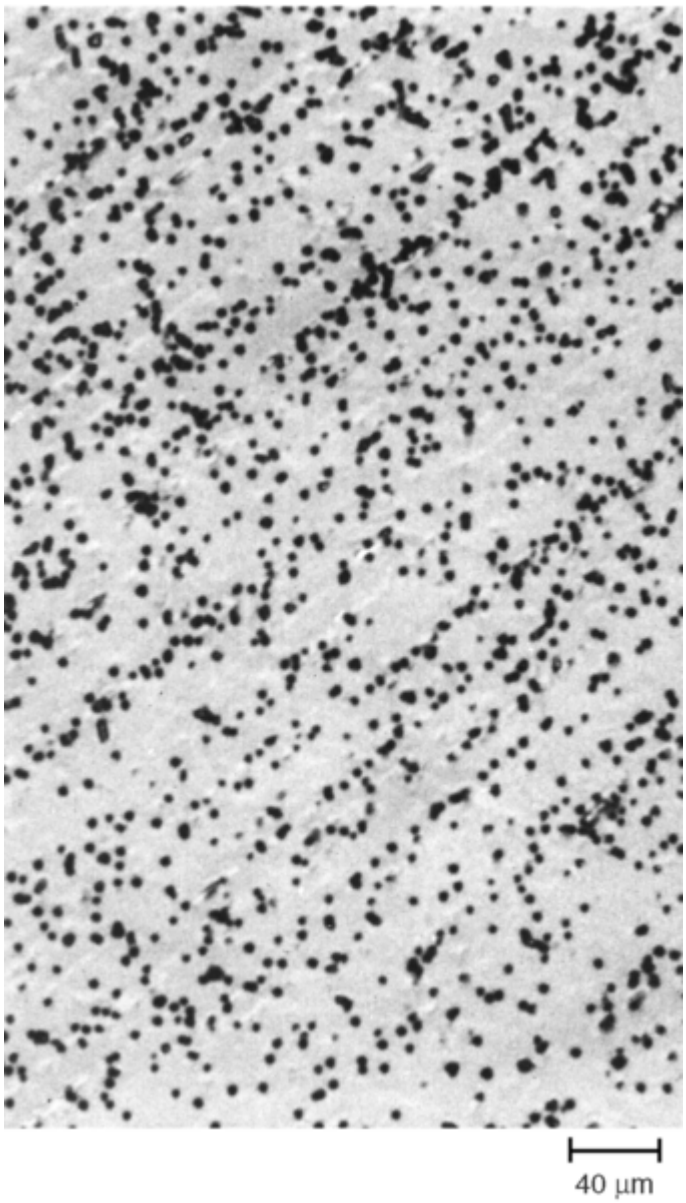

Fig. 5 Dislocations aligned on traces of slip planes in germanium deformed at low temperature. HNO_3-acetic-HF-bromine. 200×. Courtesy of J.R. Patel

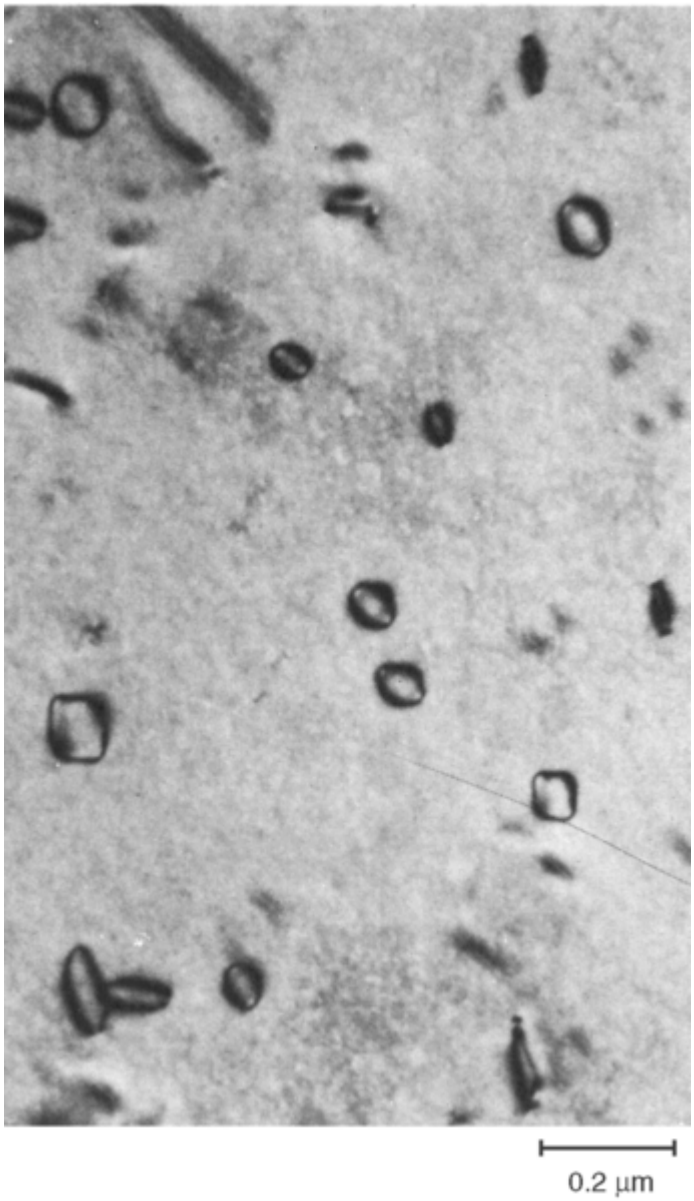

Fig. 6 Dislocation loops produced by vacancy precipitation in germanium. Thin-foil electron micrograph. 60,000×. Courtesy of D.M. Maher

Solidification Structures of Pure Metals, *Metallography and Microstructures*, Vol 9, *ASM Handbook*, ASM International, 2004, p. 93–96

Polycrystalline Metals

The shape and size of the grains in a polycrystalline specimen of a pure metal are determined initially by nucleation and growth during solidification and ultimately by grain growth after solidification. Castings are usually made by pouring hot liquid into a cold mold. The solidification process depends on the degree of superheat—that is, the degree to which the pouring temperature exceeds the melting point—and on the shape and properties of the mold. For a small superheat, crystals will nucleate on the cold mold wall, and

solidification will proceed inward from the mold wall. For a large superheat, the surface of the mold may be heated above the melting point during pouring so that nucleation occurs in the bulk of the liquid.

Nucleating agents added to the melt will promote nucleation at many sites to produce a fine grain structure. If the mold shape is intricate, it may be necessary to pour the liquid metal at a high temperature to prevent blockage of some of the channels by freezing before the mold has been filled. Proper filling of the mold also depends on its design and material. Mold design affords control of the size and shape of grains in various parts of a casting.

The initial grain structure of a casting is determined by the distribution of nucleation sites and by the subsequent growth that proceeds from these sites. If nucleation occurs in the bulk of the melt, then it must have been supercooled (that is, at a temperature below its melting point); therefore, the initial growth is likely to be dendritic. The dendrites from one nucleus grow out until they impinge upon dendrites growing from adjacent nuclei (Fig. 7). This process defines the initial shape of the grains, as shown in Fig. 8. The dendrites continue to grow and thicken until the temperature is raised to the melting point by the heat of fusion, which is released by the freezing process. The interdendritic liquid, not frozen at this point, can freeze only as heat is extracted from the sample.

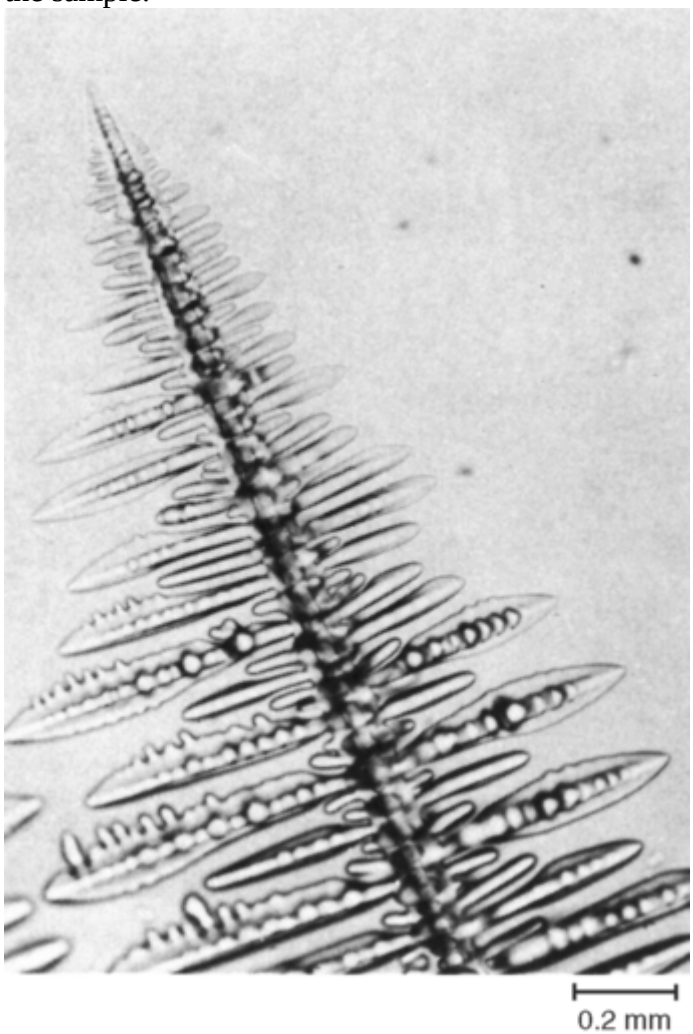

Fig. 7 Dendrites in cyclohexanol, an organic compound that crystallizes like a metal. 45×

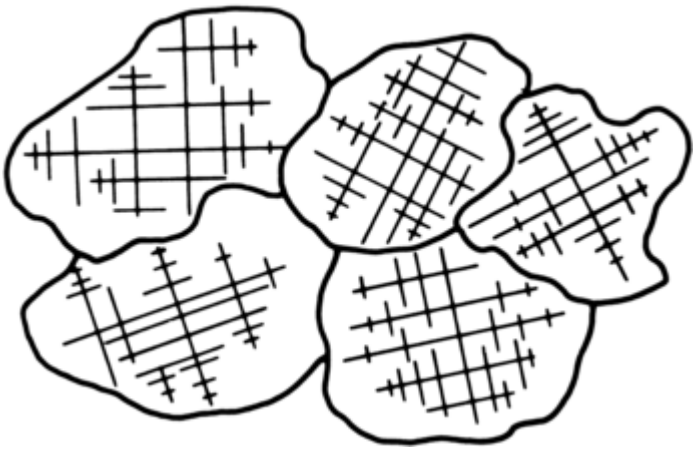

Fig. 8 Coarse, equiaxed grains produced by dendritic growth in an undercooled melt of pure metal

Nucleation can occur on the cold walls of the mold without most of the liquid being undercooled. In this case, there may be a short zone of dendritic growth, but only in a layer near the cold mold wall where the melt is undercooled. Depending on the thermal conditions, the melting point isotherm will be established somewhere between the hot melt and the cold wall. The solidification of the casting will then proceed inward, with a more or less uniform isothermal front. The grains that nucleated on the mold wall will elongate in the direction of heat flow, as shown in Fig. 9, resulting in a columnar grain structure. As growth proceeds, some crystal orientations will tend to persist at the expense of others, resulting in a preferred orientation texture.

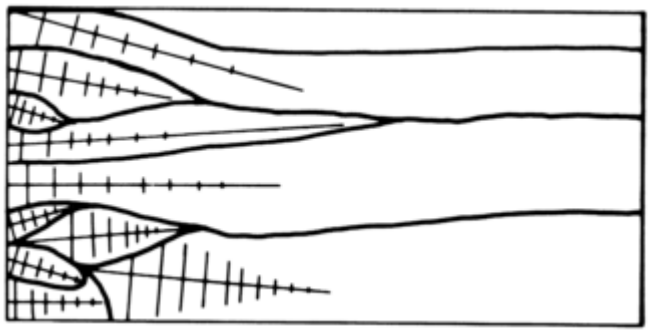

Fig. 9 Elongated grains and preferred orientation produced by directional solidification

Dendritic growth occurs in a pure material only if the melt is undercooled. This is because dendritic growth results from instability of the solid/liquid interface due to a diffusion process, which for a pure material can only be thermal diffusion. In an alloy, interface instabilities from chemical diffusion often result in dendritic growth.

Although the grain boundaries in high-purity metals are very mobile, they may be slowed down or pinned by small concentrations of impurities. If the initial grain size was large, grain growth is less likely, but there will usually be some adjustment of the grain boundaries to lower energy configurations.

Solidification Structures of Pure Metals, *Metallography and Microstructures,* Vol 9, *ASM Handbook,* ASM International, 2004, p. 93–96

Grain Boundaries

The energy of a single grain boundary as a function of the angle of misorientation is shown in Fig. 10. Small-angle boundaries, consisting of dislocation arrays, have much lower energies than large-angle boundaries. The dislocation arrays in tilt and twist boundaries are shown in Fig. 11 and 12, respectively.

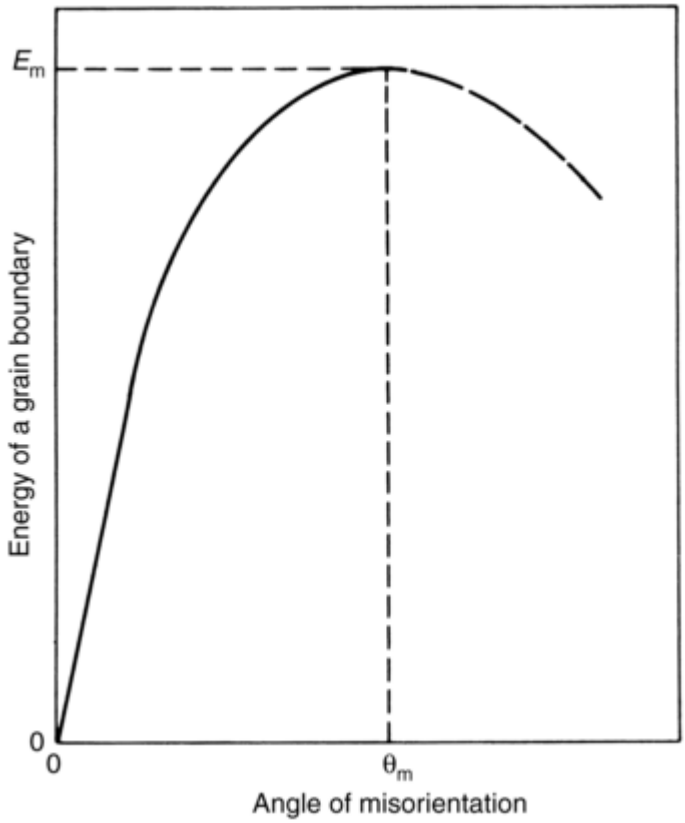

Fig. 10 Calculated energy of the boundary between two grains as a function of the angle of misorientation between the crystal lattices of the grain. The energy becomes maximum (E_m) at angle θ_m.



Fig. 11 Dislocations in a small-angle tilt boundary in gold. Thin-foil transmission electron micrograph. See also Fig. 10 24,000×. Courtesy of R.W. Balluffi



Fig. 12 Dislocations in a small-angle twist boundary in gold. Thin-foil transmission electron micrograph. See also Fig. 10 Courtesy of R.W. Balluffi

Large-angle boundaries contain regions of good fit and of bad fit. Low-energy, small-angle boundaries usually represent less than 10° to 15° of misorientation. This range is a small fraction of the total range of possible misorientations. Therefore, most random boundaries, formed by the growing together of two grains will be large-angle boundaries—that is, will have more than 10° misorientation. All large-angle boundaries except twin or coincidence boundaries have roughly the same energy and so form 120° angles with each other when equilibrated at the junction of three grains, as shown in Fig. 13 (coincidence boundaries have some lattice sites common to both crystals). In Fig. 14, the junction of a small-angle boundary with two large-angle boundaries is shown. The ratios of the boundary energies can be calculated from the angles.

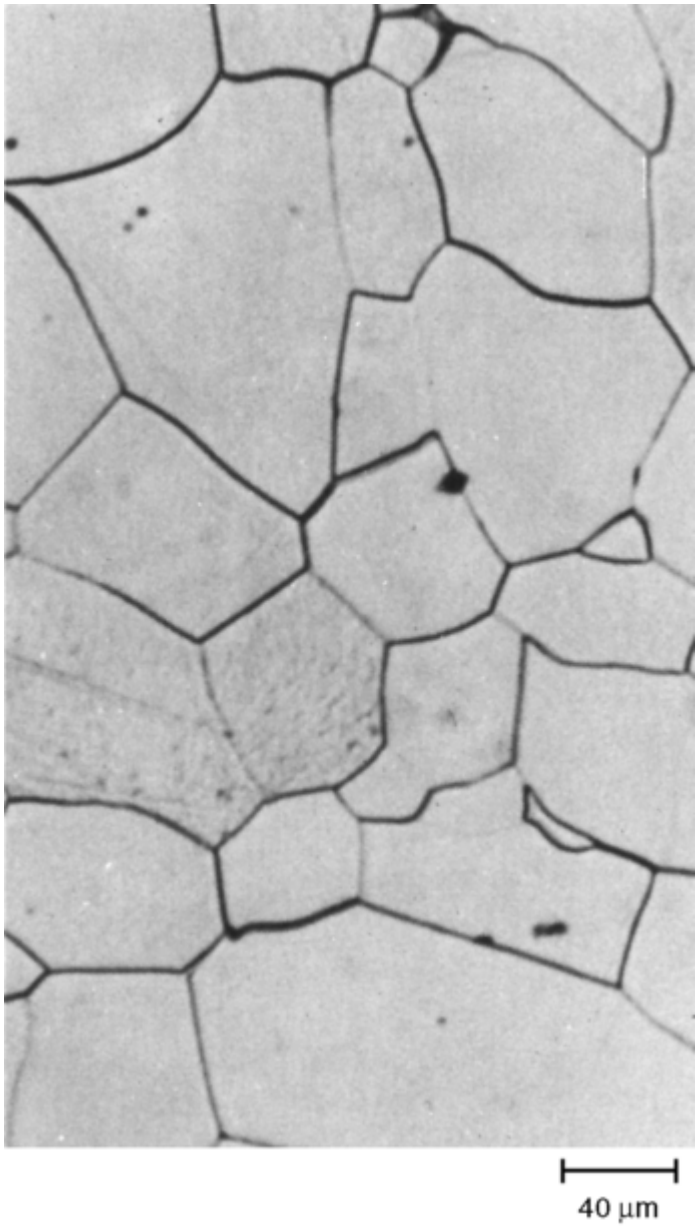

Fig. 13 Grain boundaries in polycrystalline iron. Most of the triple junctions of the grain boundaries form 120° angles. 5% nital. 250×

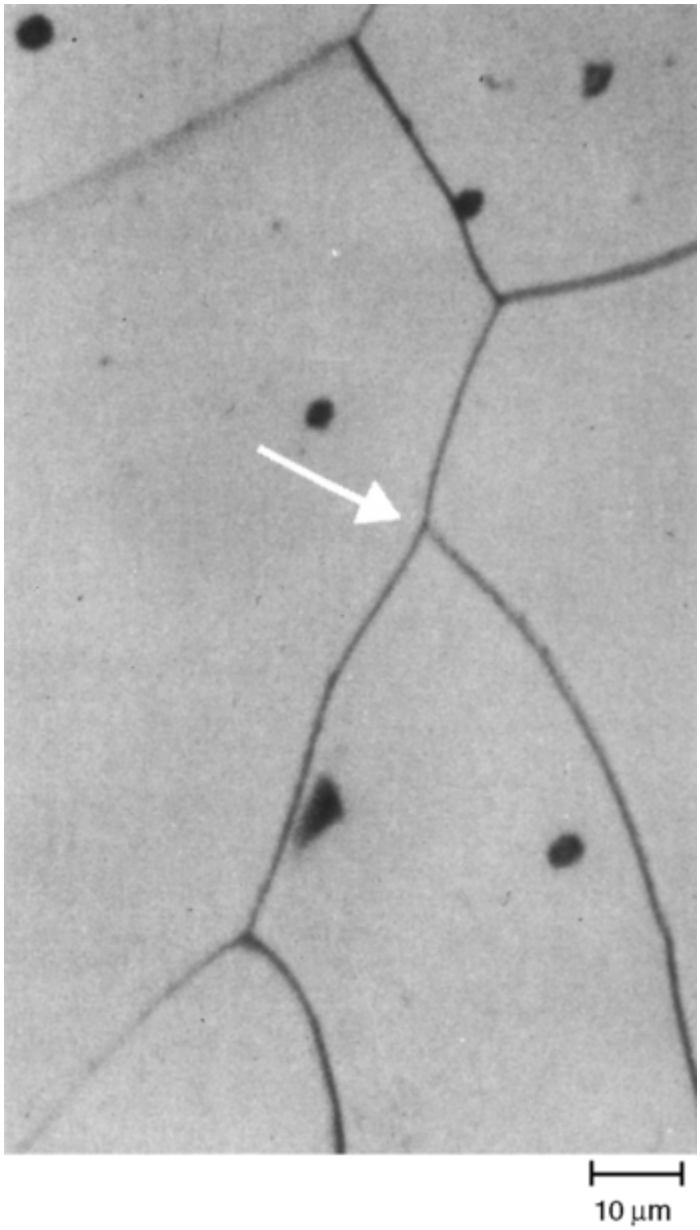

Fig. 14 Junction (at arrow) of low-energy grain boundary with high-energy grain boundary in polycrystalline iron. 5% nital. 800×

Coincidence boundaries usually have lower energies than those of large-angle grain boundaries. A boundary that separates twins (two crystals oriented in a special crystallographic arrangement in which they are related by mirror symmetry) has low energy if it is coherent; that is, if it lies in the mirror plane. Twin boundaries can be produced during crystal growth or annealing. Small-angle boundaries and individual dislocations are usually present within the grains of a polycrystal, just as in a single crystal.

Solidification Structures of Pure Metals, *Metallography and Microstructures,* Vol 9, *ASM Handbook,* ASM International, 2004, p. 93–96

Acknowledgment

Adapted from K.A. Jackson, Solidification Structures of Pure Metals, *Metallography and Microstructures,* Vol 9, 9th edition, *ASM Handbook,* American Society for Metals, 1985, p 607–610.

Solidification Structures of Pure Metals, *Metallography and Microstructures,* Vol 9, *ASM Handbook,* ASM International, 2004, p. 93–96

Solidification Structures of Pure Metals

Selected References

- B. Cantor and K. O'Reilly. *Solidification and Casting,* Institute of Physics, 2002
- B. Chalmers, *Principles of Solidification,* John Wiley & Sons, 1964
- G.J. Davies, *Solidification and Casting,* John Wiley & Sons, 1973
- R. Elliott, *Eutectic Solidification Processing: Glassy and Crystalline Alloys,* Butterworths, 1983
- J. Friedel, *Dislocations,* Pergamon Press, 1964
- A.G. Guy, *Introduction to Materials Science,* Techbooks, 1991
- *Interfaces Conference,* R.C. Gifkins, Ed., Butterworths, 1969
- *Solidification,* papers from the 1969 seminar, American Society for Metals, 1971

D.M. Stefanescu and R. Ruxanda, Solidification Structures of Steels and Cast Irons, *Metallography and Microstructures,* Vol 9, *ASM Handbook,* ASM International, 2004, p. 97–106

Solidification Structures of Steels and Cast Irons

Doru M. Stefanescu and Roxana Ruxanda, The University of Alabama

Introduction

THE FERROUS METALS are the most significant class of commercial alloys. This article describes the solidification structures of plain carbon steel, low-alloy steel, and cast iron; some high-alloy steels are addressed as well.

D.M. Stefanescu and R. Ruxanda, Solidification Structures of Steels and Cast Irons, *Metallography and Microstructures,* Vol 9, *ASM Handbook,* ASM International, 2004, p. 97–106

Solidification Structures of Steels and Cast Irons

Doru M. Stefanescu and Roxana Ruxanda, The University of Alabama

Steel

Plain carbon (unalloyed) steel is an alloy whose equilibrium phase diagram (the iron-carbon diagram) exhibits partial solid solubility with a peritectic reaction (see Fig. 1c in the article “Fundamentals of Solidification” in this Volume). Consequently, the solidification microstructure of plain carbon and low-alloy steels is made of equiaxed or columnar dendrites regardless of casting conditions and deoxidation practice.

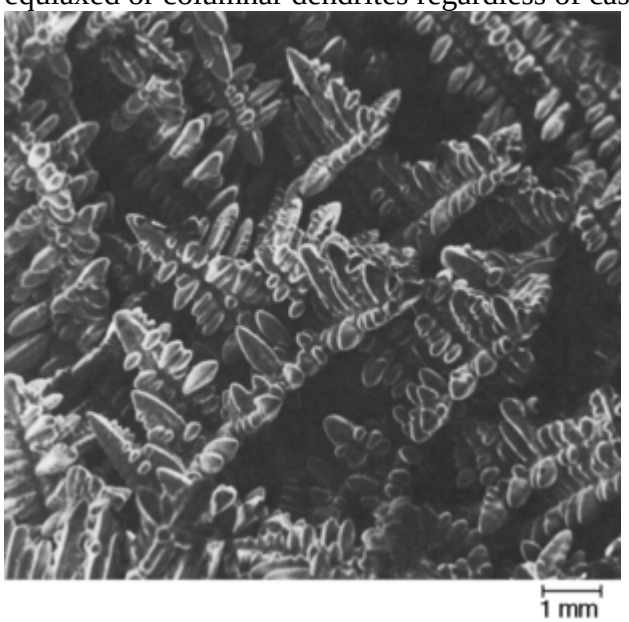

Fig. 1 Scanning electron micrograph of the center of an as-cast low-carbon steel ingot showing dendrite spikes (primary arms) and secondary arms. Unetched. Original magnification 10×. Courtesy of B.L. Bramfitt and J.R. Kilpatrick

Macrostructure

Metallographic Techniques. Sometimes the macrostructure can be observed in shrinkage cavities, which behave similarly to interrupted solidification experiments. The typical dendritic structure of steel revealed by such a technique is presented in Fig. 1 (Ref 1). The as-cast grain structure of steel can often be observed using classic metallographic etching because ferrite forms at the austenite grain boundaries during solid-state transformation (Fig. 2) (Ref 2).

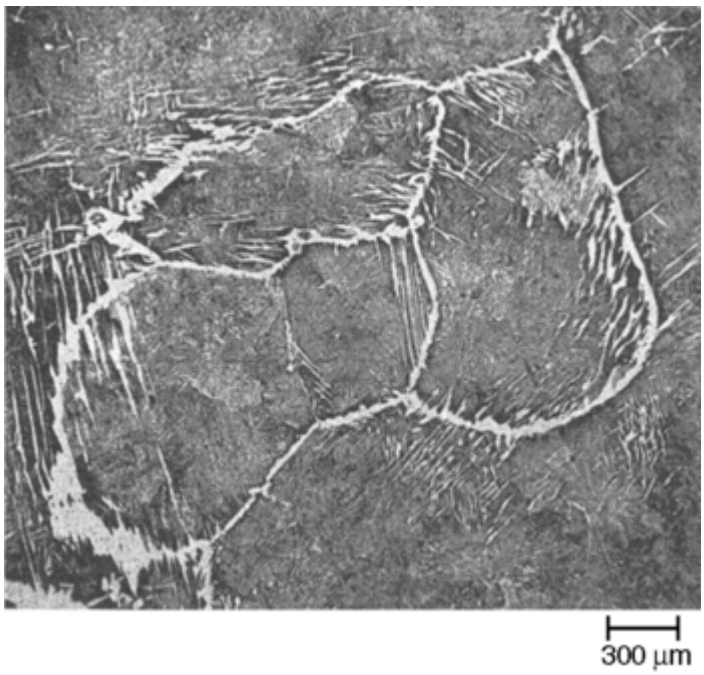

Fig. 2 Austenite grains (transformed to pearlite) outlined by ferrite network in the as-cast structure. 40×. Source: Ref 2

In most cases, more sophisticated metallographic techniques must be employed. Most of these techniques consist of outlining the microsegregation patterns. During solidification, carbon, sulfur, and most alloying elements are rejected from the iron-rich solidifying dendrites. Figure 3 shows the macrostructure of carbon steel where the areas of high carbon concentration have been etched. Note the outlines of the original columnar dendrites (light), which are oriented normal to the chill surface (left edge of macrograph). The vertical white line near the chill surface resulted from a disruption in solidification (Ref 1).

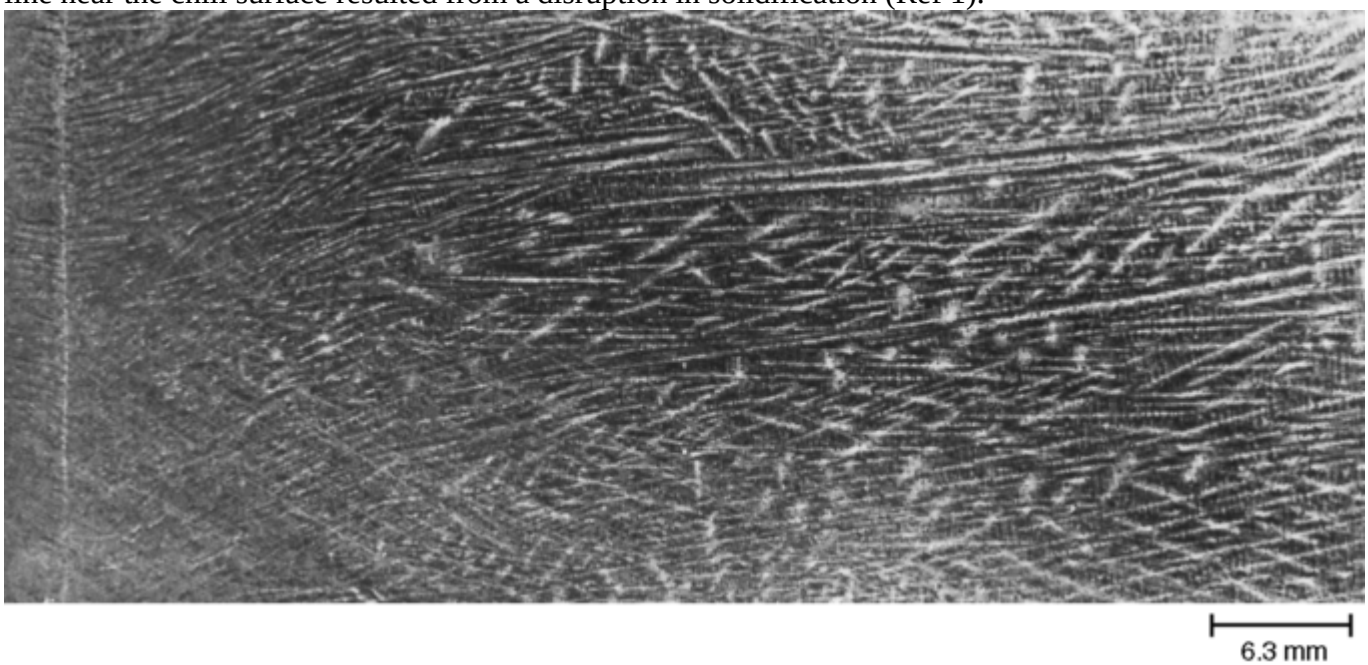

Fig. 3 Macrostructure of UNS G10170 steel, as strand cast. Compare with Fig. 4. 10% HNO_3 in H_2O. 4.75×. Courtesy of J.R. Kilpatrick

Another common technique consists of etching the sulfur-rich areas in the solidified steel. A typical sulfur print is shown in Fig. 4. It shows the outlines of the original columnar dendrites (light), which are oriented normal to the chill surface (left edge). Short-time annealing at temperatures high enough to austenitize a specimen produces a microstructure free of nonequilibrium constituents (in particular, bainite, martensite, and the

massive and Widmanstätten ferrite) that obscure the original dendritic structure. The original columnar dendrites (light) that are partially obscured by the presence of nonequilibrium constituents (Fig. 5a) become clearly visible after a short heat treatment that eliminated the nonequilibrium constituents (Fig. 5b).

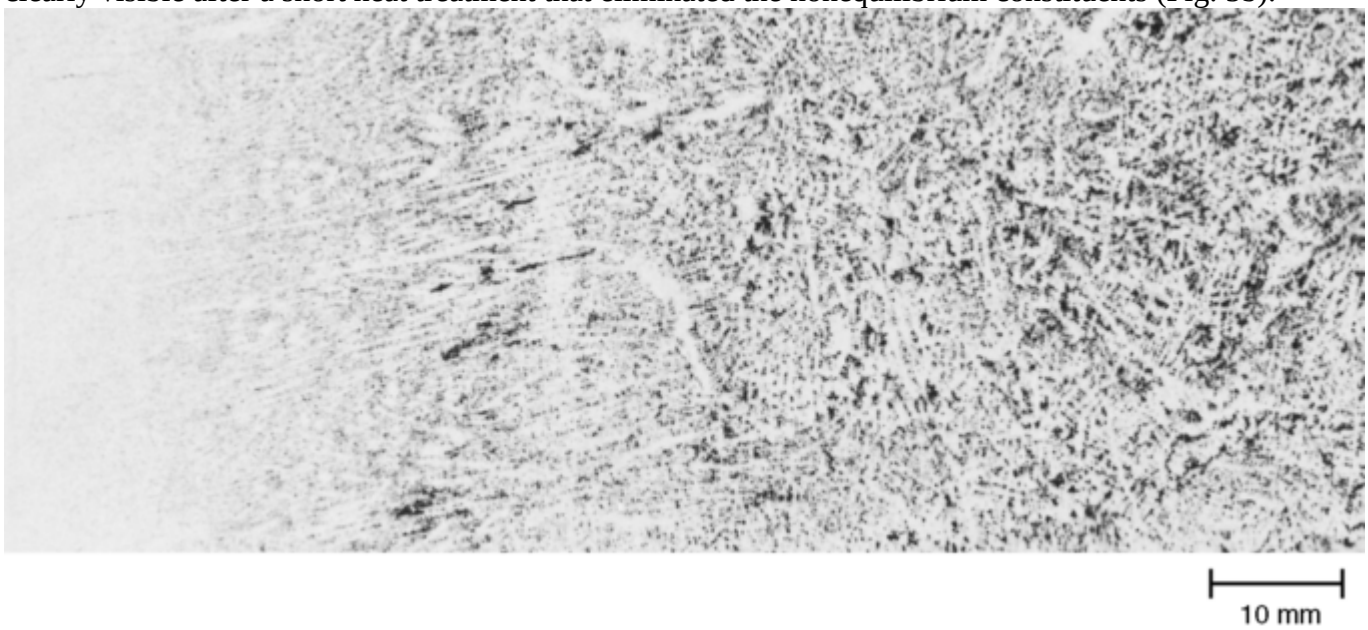

Fig. 4 Sulfur print of UNS G10170 steel, as strand cast, Compare with Fig. 3. As-polished. 1.25×. Courtesy of J.R. Kilpatrick

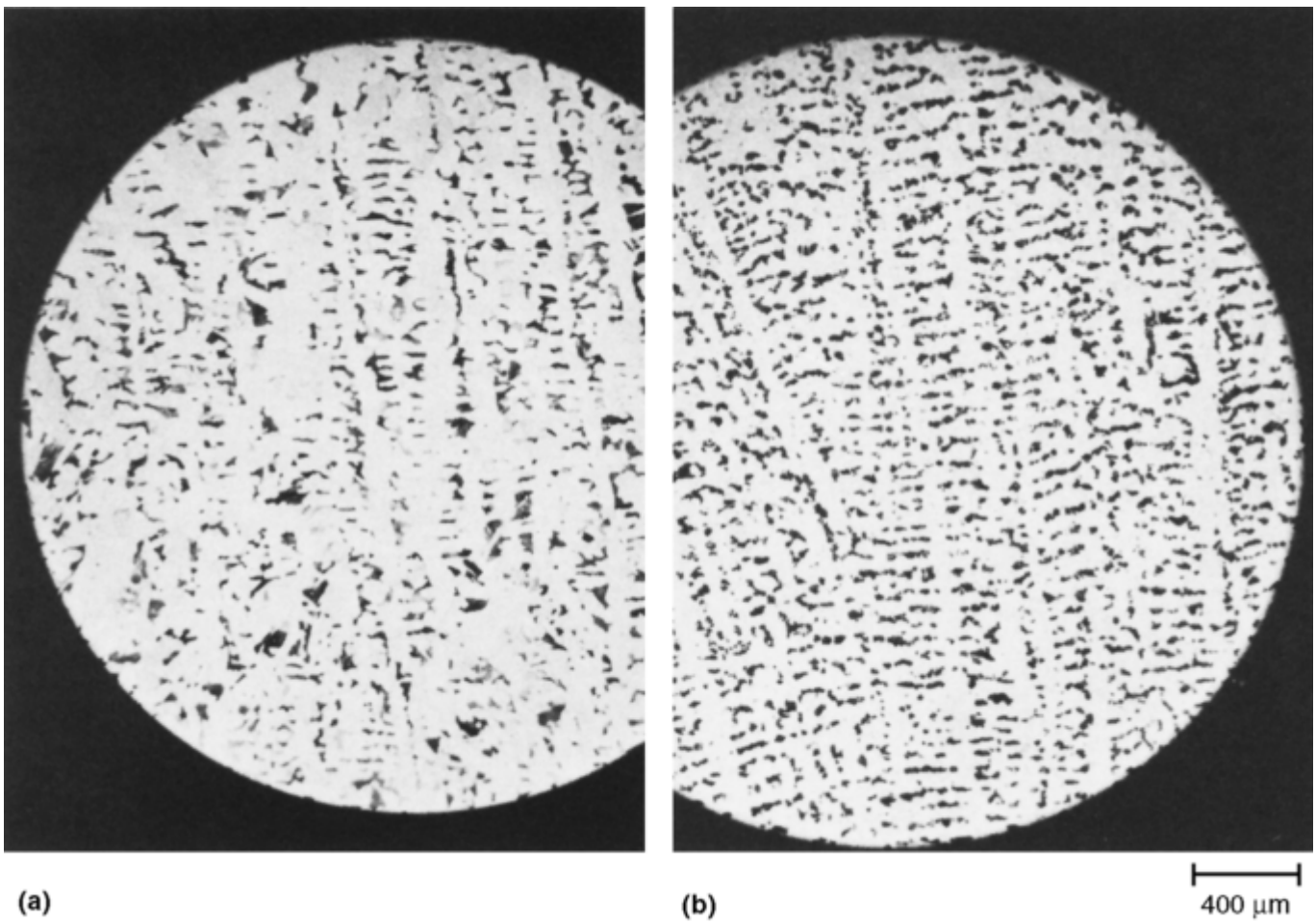

Fig. 5 Macrostructures of a strand-cast UNS G10170 steel. (a) As cast, the original columnar dendrites (light) are partially obscured by nonequilibrium components. (b) Brief annealing at austenitizing

temperature eliminates the nonequilibrium components. Etchant: picral. 25×. Courtesy of J.R. Kilpatrick

Thermal etching can be also used to outline the solidification grain size of steel, as shown in Fig. 6 (Ref 3). However, this technique must be used with care since excessive holding at high temperature will modify the grain structure through recrystallization. Specimens of solidified steel less than 0.05 mm (0.002 in.) thick can be x-rayed. Differences in x-ray absorption caused by variations in composition produce a radiograph, which can be magnified for examination. This technique can be extended to stereomicroradiography, which yields a three-dimensional view of a solidified structure (Ref 1).

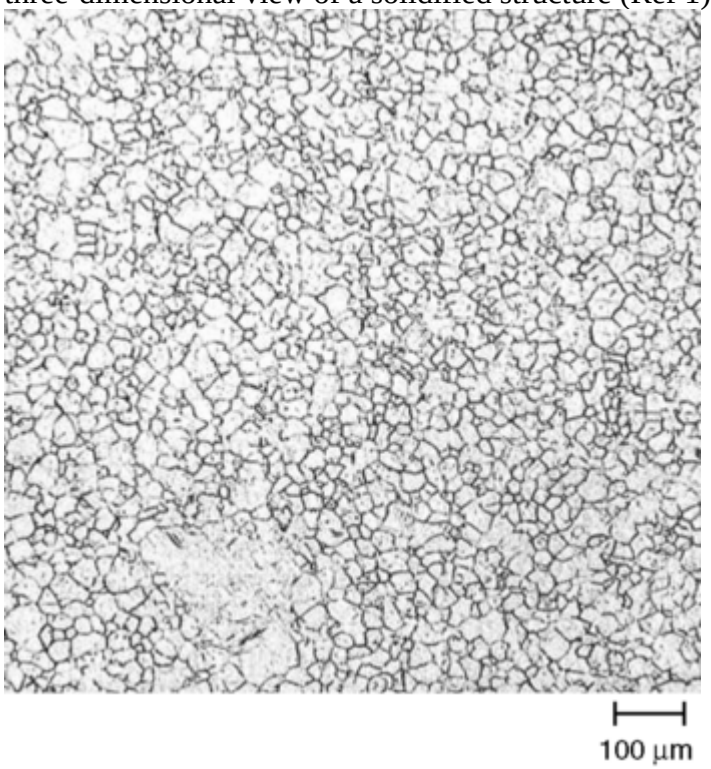

Fig. 6 Primary austenite grain structure of a fine-grained UNS G86200 steel thermally etched 2 h at 925 °C (1700 °F). 100×. Courtesy of D.L. Albright. Source: Ref 3

More recently, electron backscatter diffraction (EBSD) was used to evaluate the effect of casting conditions on the grain size of strip-cast steel (Ref 4). As shown in Fig. 7, a ridged substrate produced a higher density of randomly oriented grains at the chill surface, as compared with a smooth substrate.

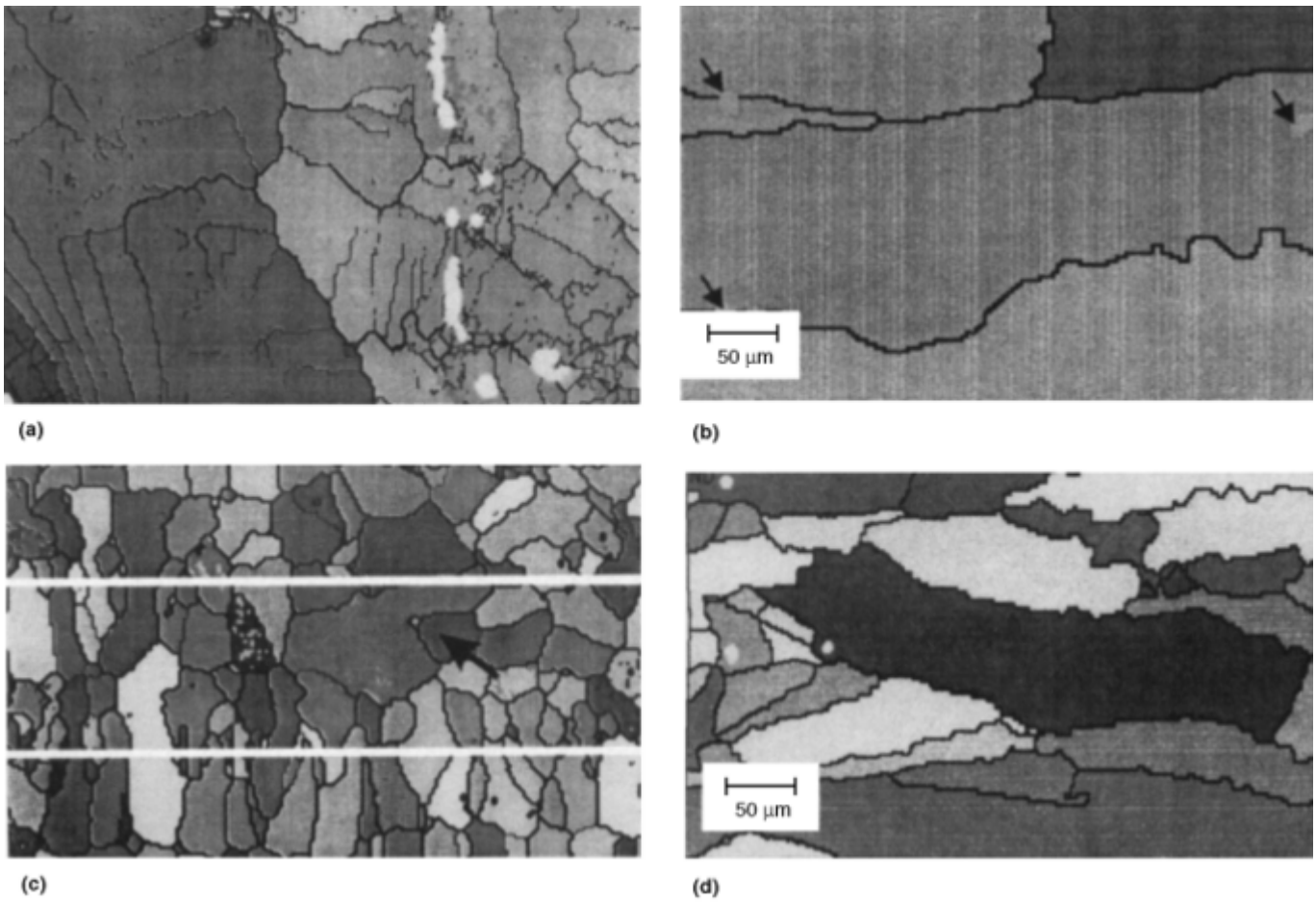

Fig. 7 Electron backscattered diffraction orientation micrographs of UNS S30400 stainless steel strip. (a) As-solidified surface cast on a smooth substrate. (b) Through-thickness structure of (a). (c) As-solidified surface cast on a ridged substrate. (d) Through-thickness structure of (c). Source: Ref 4

Major defects such as subsurface blowholes that may form in continuous-cast steel because of excess carbon, oxygen, nitrogen, and hydrogen can be seen directly by sectioning the ingot. An example is provided in Fig. 8 (Ref 5).

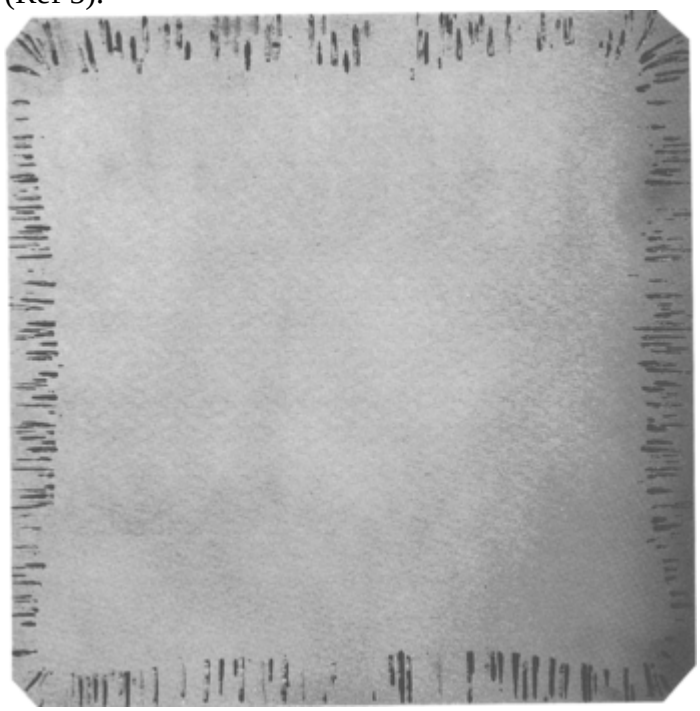

Fig. 8 Section of a continuous cast 260 mm (10 in.) bloom showing subsurface holes. Source: Ref 5

Columnar-to-Equiaxed (CET) Transition. The macrostructure of a solidified steel ingot, casting, or strand-cast slab or bloom consists of columnar or equiaxed grains or a mixture of both, depending on solidification conditions. In most applications, either a columnar or an equiaxed structure is desired for the casting. If, because of lack of adequate process control, a sudden columnar-to-equiaxed transition occurs in these castings, they will be rejected for having an unacceptable structure. As carbon steel solidifies with a peritectic transformation, the primary grain structure of steel is hard to outline metallographically because of the recrystallization occurring during cooling after solidification.

Microstructure

The solidification and as-cast microstructure of steel is a function of chemical composition and cooling rate. For plain carbon and low-alloy steels the solidification structure consists of austenite grains. However, during cooling to room temperature after solidification a peritectic and then a solid-state transformation occur that almost entirely conceal the original as-cast structure. The sequence of a peritectic transformation in a high-alloy steel is presented in Fig. 9 (Ref 6). For carbon steel, the austenite transforms into ferrite and pearlite if the composition is hypoeutectoid and into cementite and pearlite for hypereutectoid steel. Depending on cooling rate and composition, low-alloy steels can have various microstructures consisting of different forms and combinations of pearlite, bainite, martensite, cementite, and ferrite. High-alloy steels may have an austenitic structure even after cooling to room temperature. An example is shown in Fig. 10, for austenitic 18Ni-26Cr steel. Austenite grains surrounded by eutectic carbides are seen (Ref 7).

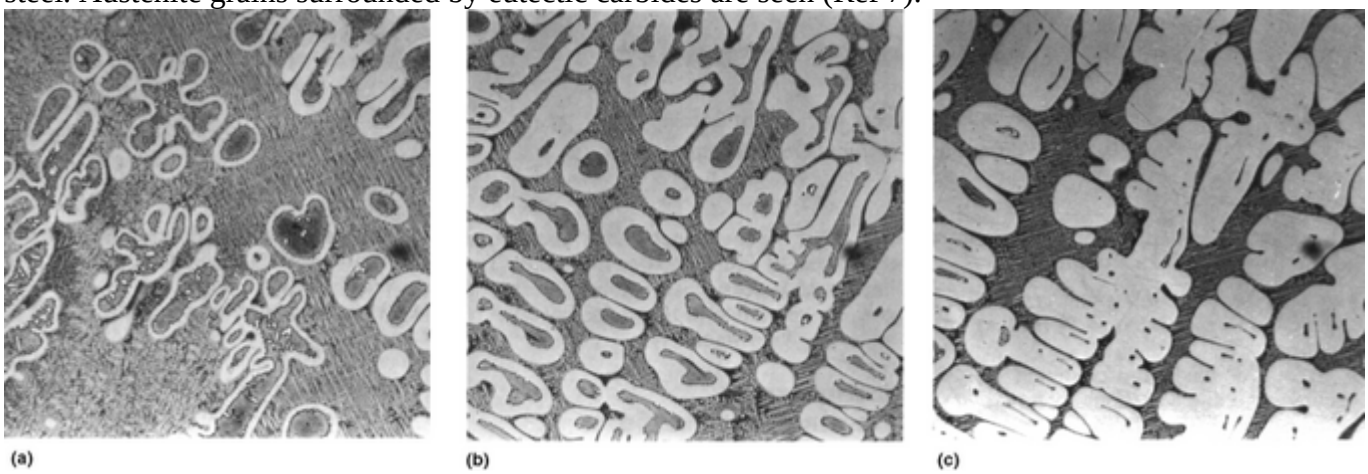

Fig. 9 Three stages of peritectic reaction in a directionally solidified high-speed steel. (a) First-stage structure. Dark gray is austenite; white is ferrite. The mottled structure is quenched liquid. (b) Subsequent peritectic transformation of (a). (c) Further peritectic transformation of (b). Dark gray in the middle of the white ferrite is newly formed liquid. Source: Ref 6

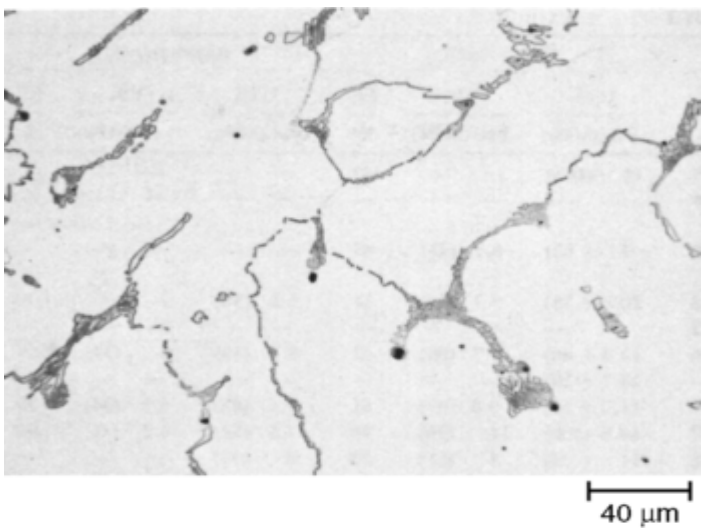

Fig. 10 The as-cast microstructure of HK-40 (J94214) steel. 250×. Source: Ref 7

Dendrite Arm Spacing. Once the dendritic structure is revealed, quantitative determinations, such as measurements of primary and secondary dendrite arm spacing (SDAS), can be made. As discussed in the article "Fundamentals of Solidification" in this Volume, the SDAS depends on the cooling rate and on the local solidification time. As shown in Fig. 11, as the cooling rate increases the average SDAS decreases (Ref 8).

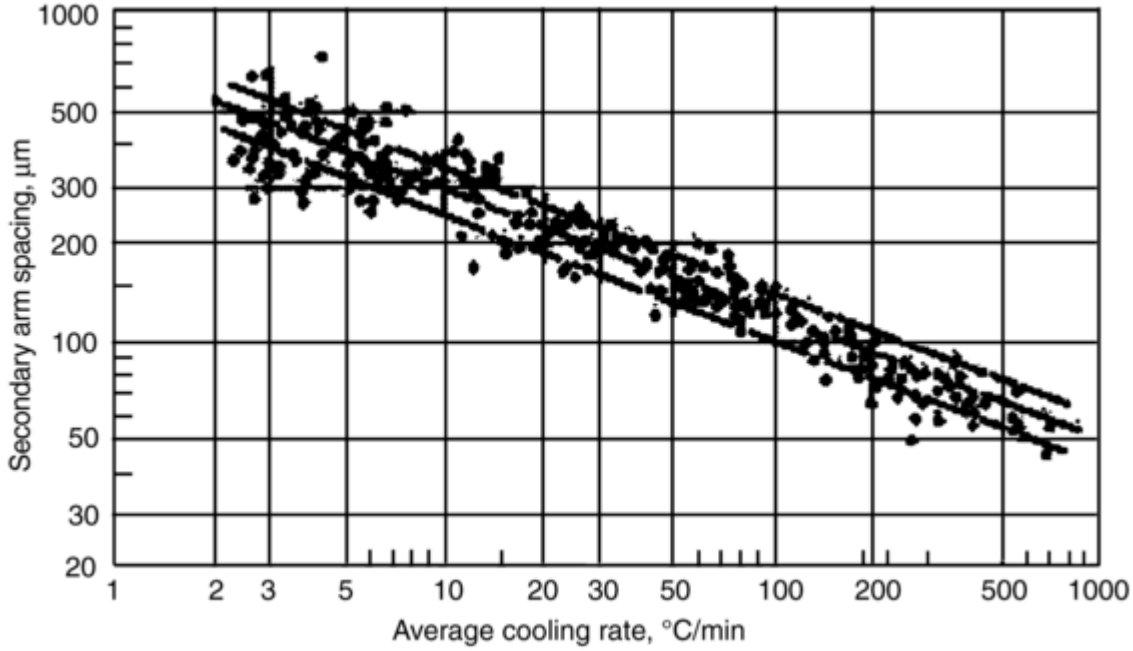

Fig. 11 Influence of cooling rate on the secondary dendrite arm spacing of commercial steels containing 0.1 to 0.9%. Source: Ref 8

Nonmetallic Inclusions. Most nonmetallic inclusions are not affected by homogenization and therefore remain unchanged during phase transformations, thus retaining their original position and shape in the solidified ingot. A notable exception is the manganese sulfides. Some nonmetallic inclusions form in the liquid before solidification, others, during solidification. Aluminates and silicates generally form before solidification, but sulfides form during solidification. Manganese sulfide inclusions frequently form in interdendritic regions and primary grain boundaries, where the last of the liquid freezes (Ref 1). Examples of manganese sulfide inclusions distributed along the boundaries of the solidified grains are shown in Fig. 12. These inclusions represent type II sulfides, which are commonly found in aluminum-killed steel ingots and castings (Ref 9). In contrast, Fig. 13 illustrates how the inclusions formed from a higher-melting-point compound, in this instance a silicate, are distributed as clusters in isolated regions in the cast product (Ref 1).

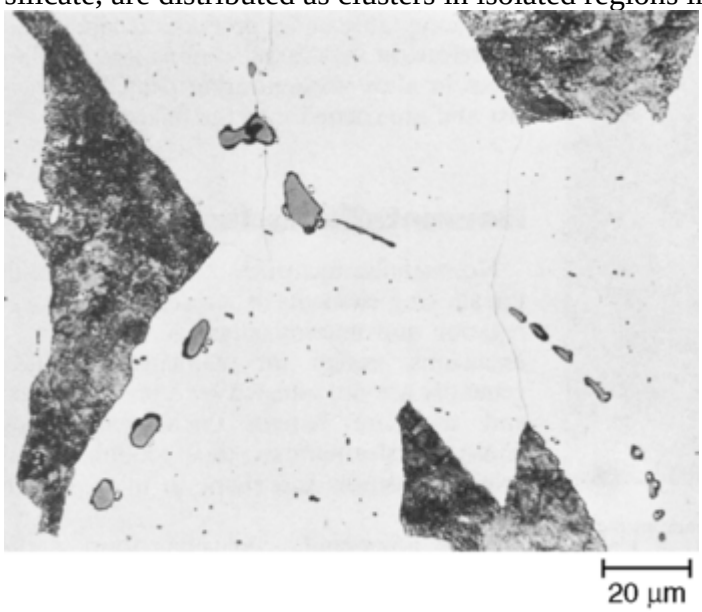

Fig. 12 Manganese sulfide inclusions in steel. MnS inclusions (rounded gray particles) at grain boundaries of strand cast UNS G10170 steel that contains pearlite (mottled gray) in a matrix of ferrite (light). Etchant: picral. 500×. Courtesy of J.R. Kilpatrick.

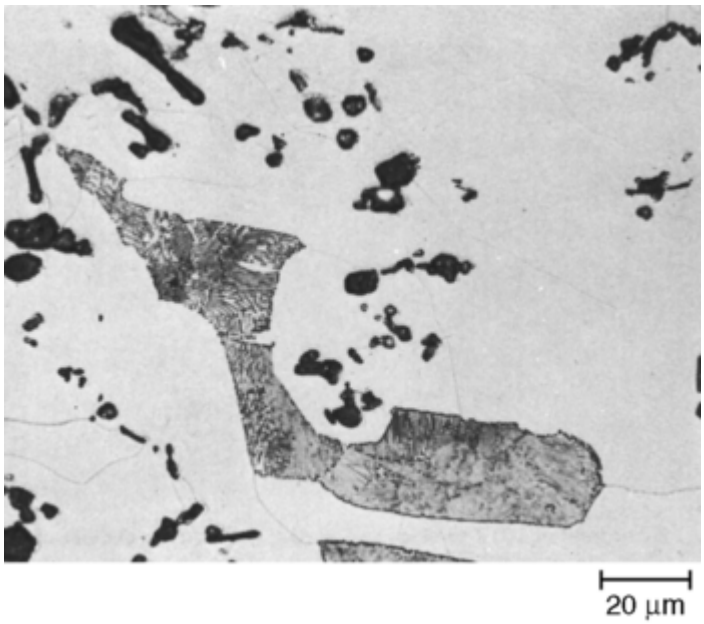

Fig. 13 Silicate inclusions (dark gray particles) randomly distributed in the ferrite matrix (light) of strand cast UNS G10170 steel that also contains pearlite (medium gray). Etchant: picral. 500×. Courtesy of J.R. Kilpatrick

Lanthanides are added to liquid steel before solidification to change sulfide inclusion morphology and composition (Ref 10). The lanthanide sulfides are less ductile during hot rolling than manganese sulfide and remain globular in the final product, providing more isotropic properties. Recent technology involves injecting calcium into liquid steel to reduce sulfur levels and change inclusion morphology and composition. Figure 14 shows a typical calcium-containing inclusion, where calcium sulfide forms a shell around a core of calcium aluminate (Ref 1).

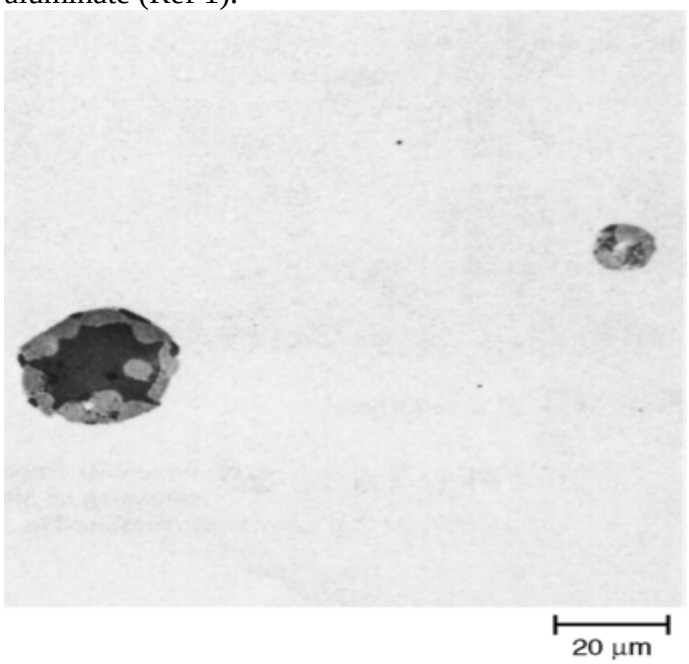

Fig. 14 Low-carbon steel showing inclusions of calcium sulfide outer rim (light gray) and calcium aluminate core (dark gray). The matrix is pearlite and ferrite. As-polished. 500×. Courtesy of B.L. Bramfitt and J.R. Kilpatrick

References cited in this section

1. B.L. Bramfitt, Solidification Structures of Steel, *Metallography and Microstructures,* Vol 9, *ASM Handbook,* ASM International, 1985, p 623–628

2. C.W. Briggs, *The Metallurgy of Steel Castings,* McGraw-Hill, 1946, 634 pages

3. *Transformation and Hardenability in Steels,* Climax Molybdenum Co. of Michigan, 1967, p 14

4. A. Hunter and M. Ferry, *Metall. Mater. Trans. A,* Vol 33A, 2002, p 3747–3754

5. E.T. Turkdogan, *Fundamentals of Steelmaking,* The Institute of Materials, London, 1996, 331 pages

6. H. Fredriksson, Solidification of Peritectics (in Solidification of Growth), *Casting,* Vol 15, *ASM Handbook,* D.M. Stefanescu, Ed., ASM International, 1988, p 129

7. P.F. Wieser, Ed., *Steel Castings Handbook,* 5th ed., Steel Founders' Society of America, 1980 p 19-6

8. A. Suzuki, T. Suzuki, Y. Nagaoka, and Y. Iawata, *Nippon Kingaku Gakkai Shuho,* Vol 32, 1968

9. C.E. Sims, *Trans. Met. Soc. AIME,* Vol 215, 1959, p 367–393

10. W.G. Wilson and A. McLean, *Desulfurization of Iron and Steel and Sulfide Shape Control,* Iron and Steel Society of AIME, 1980

D.M. Stefanescu and R. Ruxanda, Solidification Structures of Steels and Cast Irons, *Metallography and Microstructures,* Vol 9, *ASM Handbook,* ASM International, 2004, p. 97–106

Solidification Structures of Steels and Cast Irons

Doru M. Stefanescu and Roxana Ruxanda, The University of Alabama

---

Cast Iron

Cast iron is one of the most complex, if not the most complex, alloy used in industry, primarily because it can solidify with formation of either a stable (austenite-graphite) or a metastable (austenite-Fe_3C) eutectic. The iron solidifying with an austenite-graphite eutectic has a gray fracture, while the one solidifying with austenite-Fe_3C eutectic exhibits a white fracture. Sometimes a mixed structure gray + white, termed mottled, may occur. Cast iron is a multicomponent alloy, with the main elements being iron, carbon, and silicon. The carbon equivalent (CE $\simeq$% C + 0.31% Si) and the cooling rate are the main variables, dictating whether solidification will produce gray or white iron, with higher carbon equivalent and lower cooling rate favoring gray solidification. Other elements such as sulfur, magnesium, or cerium can significantly alter the morphology of the gray eutectic changing graphite shape from lamellar (flake, FG), to compacted (CG), or spheroidal (SG).

Macrostructure

Eutectic Grains. The macrostructure of gray iron can be visualized by using selective etching to outline the phosphide eutectic, which is the last to solidify, and therefore delineates the grain boundaries. An example is provided in Fig. 15 (Ref 11). The eutectic grains are termed “eutectic cells” in common foundry practice language.

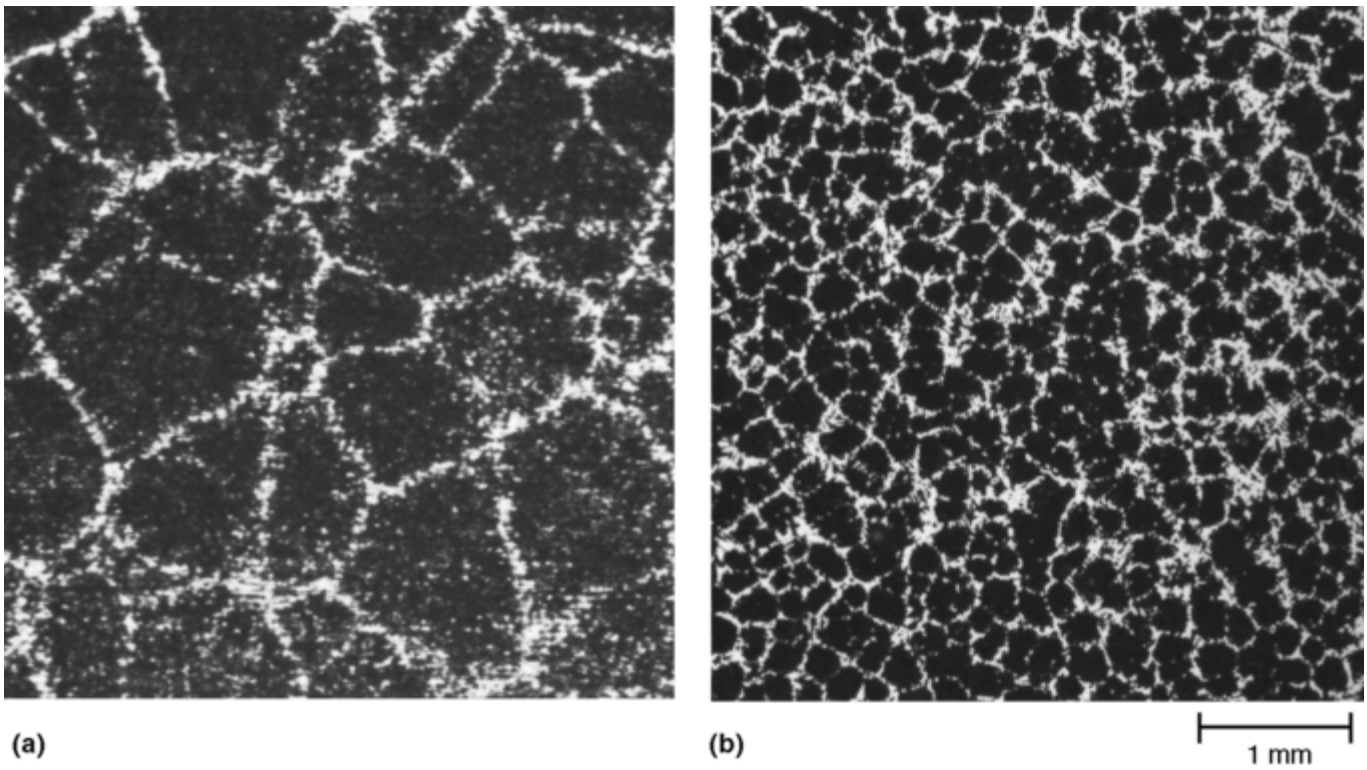

Fig. 15 Eutectic grain structure in flake graphite cast iron. Etching in Stead's reagent for 2.5 h (a) reveals coarse grains, for 1.5 h (b) shows fine grains. Magnification: 14×. Source: Ref 11

The length scale (size) of the eutectic grains depends on cooling rate and inoculation, with higher cooling rate and inoculation promoting a higher number of grains. The eutectic grains are smaller on the corners of the disk brake rotor shown in Fig. 16, because the cooling rate is higher at the edges of the casting (Ref 12).

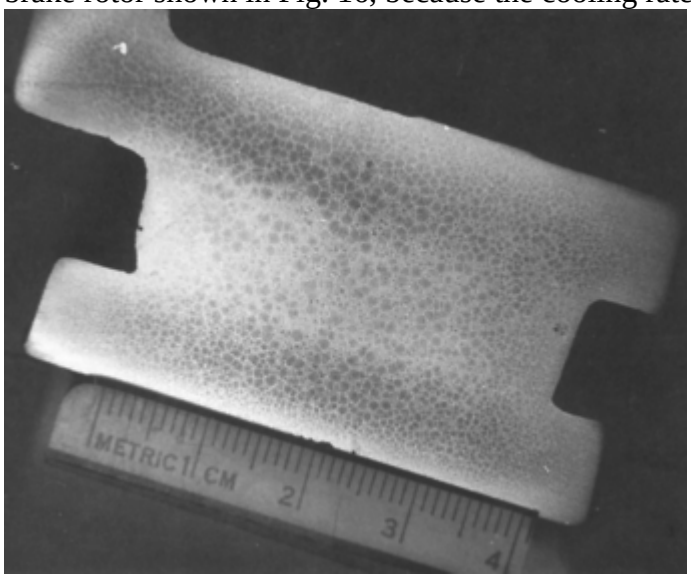

Fig. 16 Eutectic grains in inoculated flake graphite iron (class 30). Etchant: Stead's reagent. Courtesy of K. Mikkola, Michigan Technological University

Austenite Grains. Another macroetching technique proposed recently (Ref 13) allows visualization of the austenite dendrite grains. It consists in austempering the iron after solidification, without cooling to room temperature (direct austempering after solidification, or DAAS). A typical example of FG iron macrostructure revealed by this technique is shown in Fig. 17 (Ref 14). As the carbon equivalent increases, the macrostructure changes from columnar, to columnar-equiaxed, and then to mostly equiaxed.

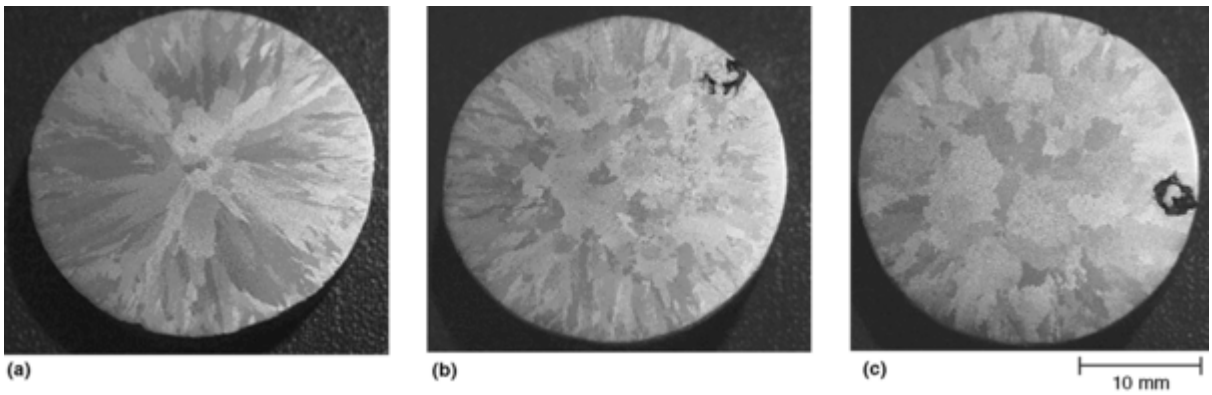

Fig. 17 Macrostructure of 30 mm (1.2 in.) diam bars. (a) Hypoeutectic, carbon equivalent = 3.94. (b) Eutectic, carbon equivalent = 4.27. (c) Hypereutectic, carbon equivalent = 4.64. Etchant: direct austempering after solidification plus picral 5%. Source: Ref 14

Similar macrostructures are found for SG iron when austenite dendrites are revealed by the DAAS technique. In the example provided in Fig. 18, a columnar structure is seen toward the outside of the cylindrical sample and an equiaxed structure in the middle.

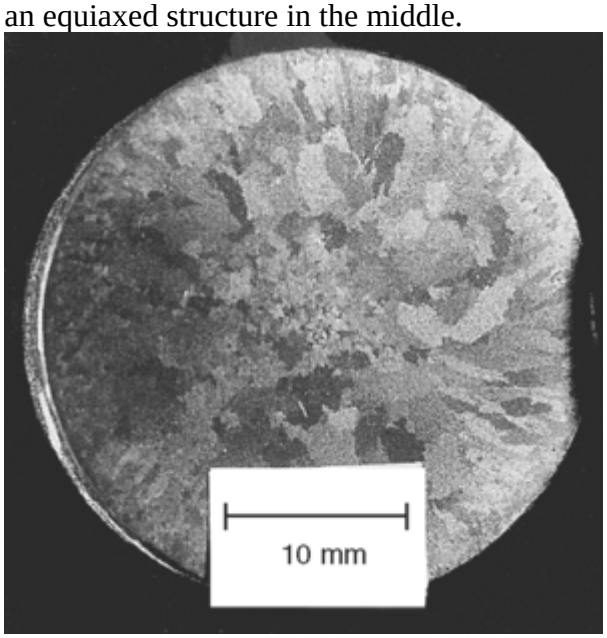

Fig. 18 Macrostructure of a spheroidal graphite iron etched by direct austempering after solidification. Source: Ref 13

Microstructure

The structural gray-to-white transition (GWT) in cast iron is the result of growth and nucleation competition between the stable (gray) and metastable (white) eutectics. Both nucleation and growth are affected by cooling rate. High carbon equivalent and low cooling rate favor solidification of gray iron. Opposite conditions promote white iron. Details on the mechanism of the GWT and its computer modeling can be found in Ref 15.

A convenient way to demonstrate the GWT on metallographic samples is by using wedge test samples (Fig. 19). These samples have an increased cooling rate from the base to the tip and can exhibit all the typical microstructures of cast iron, from gray, to mottled, to white, depending on processing variables.

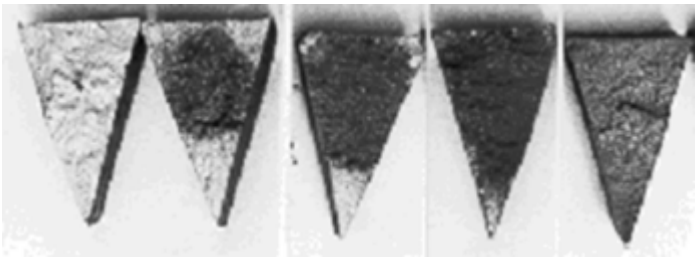

Fig. 19 Fractured wedge-test samples showing from left to right evolution from white, to mottled, to gray structure

Gray Iron (Austenite-Graphite Eutectic). Composition and cooling rate also affect the graphite shape in gray iron. If directional solidification is conducted, the cooling rate can be further divided in two independent variables, solidification velocity (V) and temperature gradient (G_T). Then, the basic processing variables affecting the morphology of the eutectic are the G_T/V ratio and composition. It is possible to obtain a variety of graphite and matrix structures in cast iron when varying G_T/V and/or the level of impurities, such as magnesium, cerium, or sulfur. The complete structural transition from metastable to stable, and for different graphite morphologies, has been documented (Ref 16) for cast irons of hypoeutectic composition, as a function of growth velocity, temperature gradients at the solid/liquid (S/L) interface, and cerium concentration (Fig. 20). It was found that while the GWT transition depends mostly on the G_T/V ratio, the transition between different graphite shapes (lamellar to compacted to spheroidal) depends mostly on the cerium concentration (Ref 15). Typical examples of graphite morphologies resulting from solidification are presented in Fig. 21 and 22. Irregular graphite shapes may result by degeneration of SG. Chunky graphite forms by extensive branching of graphite spheroids (Ref 17, 18). Typical chunky graphite morphology is shown in Fig. 23. While chunky graphite is highly interconnected and does not consist of broken pieces of graphite spheroids, some branches can be disturbed and fractured by the thermally induced turbulence of the melt during solidification. The tendency for formation of chunky graphite can be decreased by lowering the carbon equivalent and the silicon content and by increasing the cooling rate when possible.

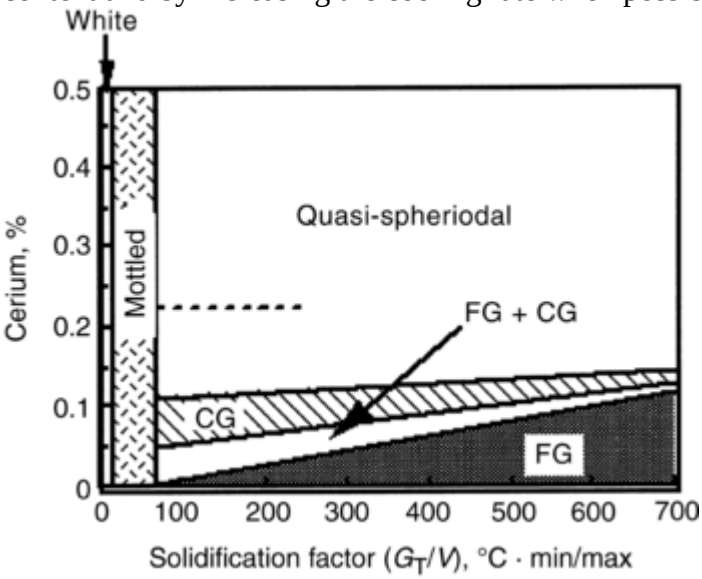

Fig. 20 Influence of temperature gradient over solidification factor (G_T/V) ratios and %Ce on structural transitions in cast irons with the same carbon equivalent. FG, flake graphite; CG, compacted graphite; SG, spheroidal graphite. Source: Ref 16

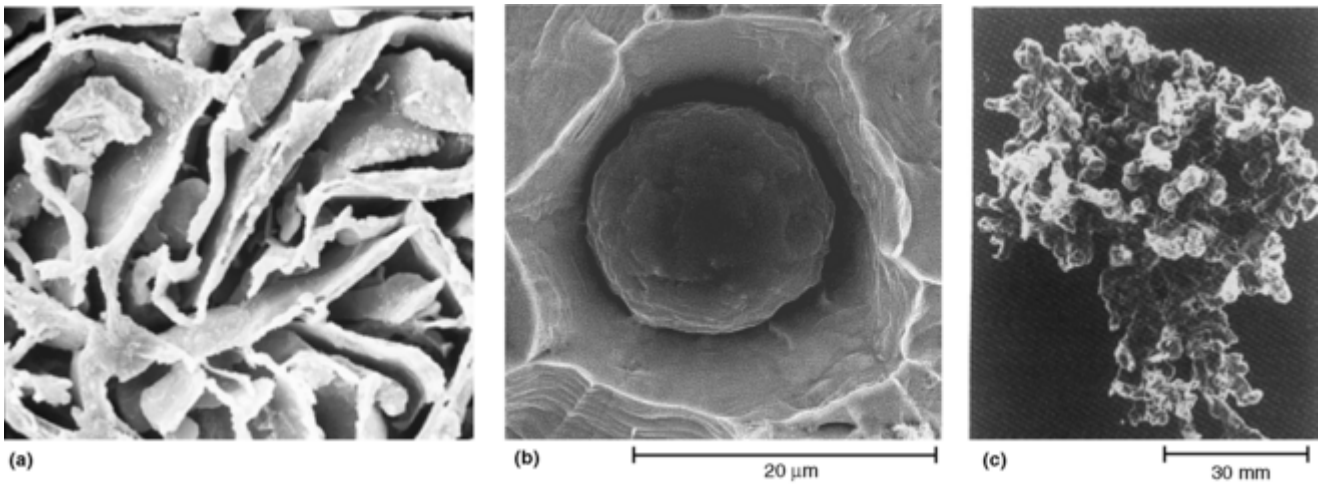

Fig. 21 Basic graphite shapes in commercial cast iron obtained by deep etching (a) and (b) or extraction through matrix dissolution (c). Source: Ref 15

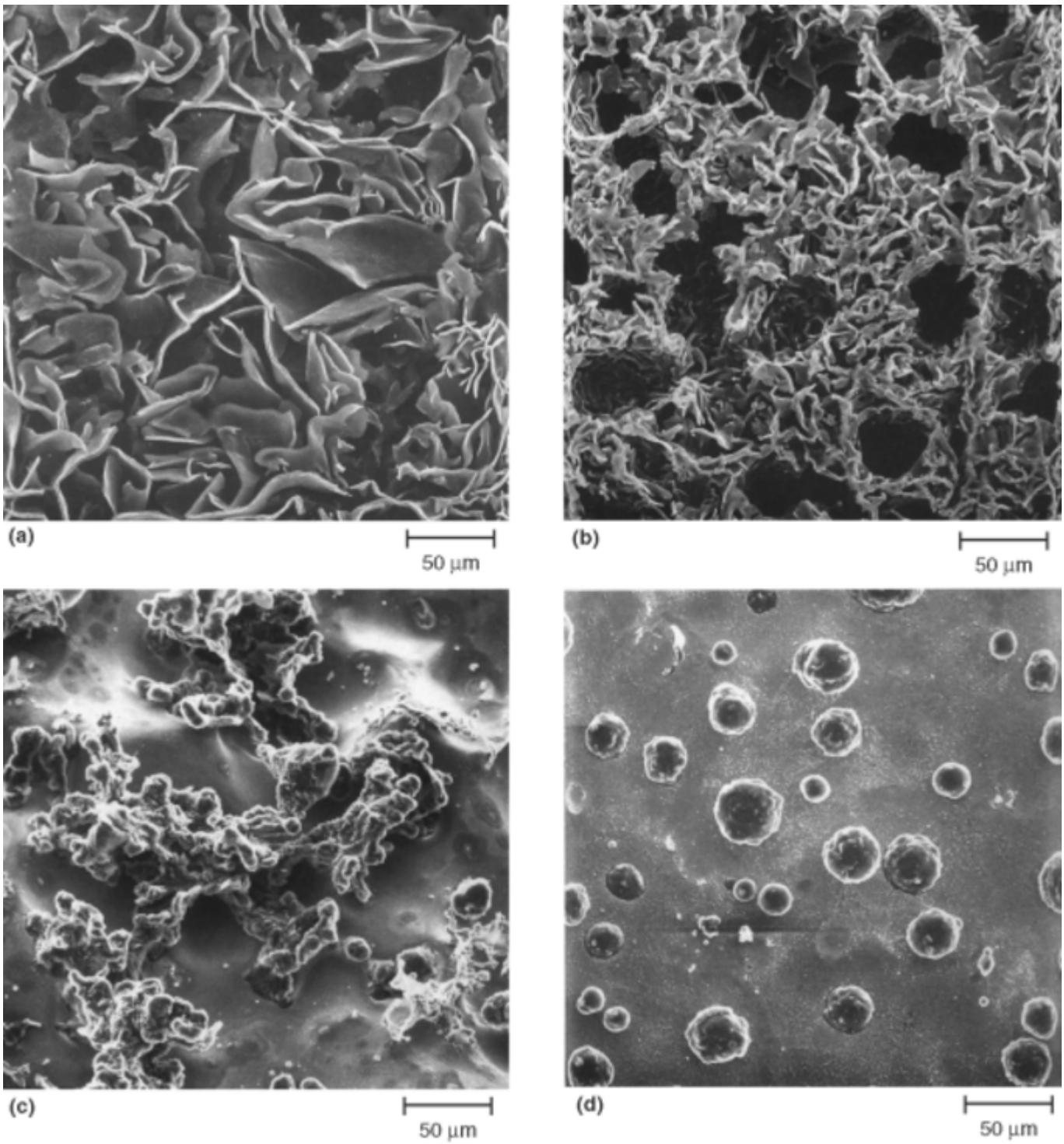

Fig. 22 Scanning electron micrographs of deep etched gray cast irons. (a) Type A graphite skeletons after etching. (b) Type D graphite skeletons after etching. (c) Vermicular graphite skeletons after etching. (d) Spheroidal (nodular) graphite skeletons after etching. All etched in 80% hydrogen peroxide, 15% distilled water, and the remainder hydrofluoric acid. Magnification: all at 300×. Courtesy of B. Boardman, Deere and Company, Technical Center

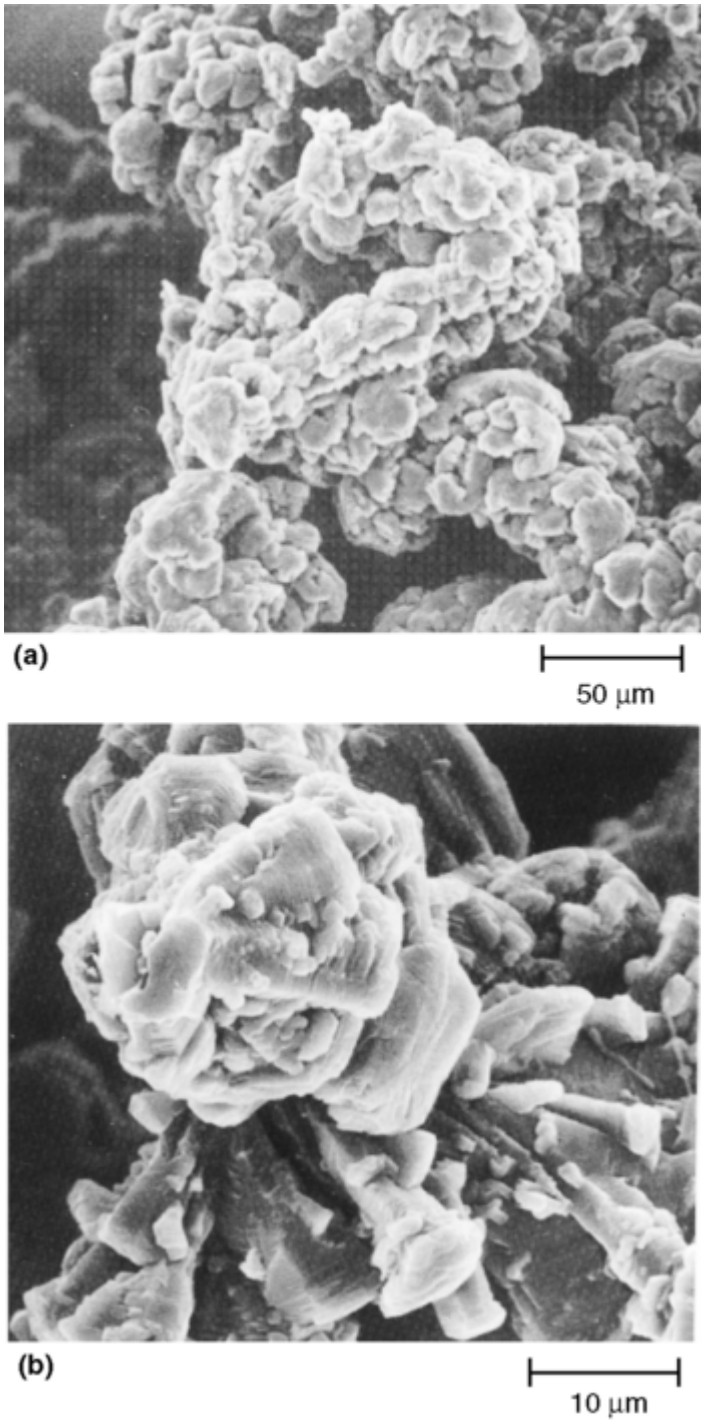

Fig. 23 Chunky graphite extracted from the matrix at two different magnifications.

The length scale of the flake graphite (the interlamellar spacing) is a function of cooling rate and composition. At high cooling rates, low CE, or low sulfur, the spacing decreases and graphite shape changes from lamellar type A (Fig. 22a) to type D (Fig. 22b) (see "Classification and Basic Metallurgy of Cast Iron," *Properties and Selection: Irons, Steels, and High-Performance Alloys*, Volume 1 of the *ASM Handbook* (1990)). The holes in Fig. 22(b) are the spaces occupied by the austenite dendrites prior to deep etching.

A more detailed analysis of the influence of sulfur and cerium on the interface morphology of iron-carbon alloys solidifying with austenite-graphite eutectic is presented in Fig. 24 (Ref 19). It is clearly seen that as the cooling rate increases the lamellar spacing decreases, and the graphite changes from type A to type D. The same trend is obtained when decreasing the sulfur content from 0.012 to 0.003%. It is also noticed that at low cooling rates, for the low-sulfur (0.003%) and cerium-containing irons, the graphite tip is completely covered by austenite during its growth into the liquid. For samples containing more than 0.006% S, the graphite tip protrudes into the melt.

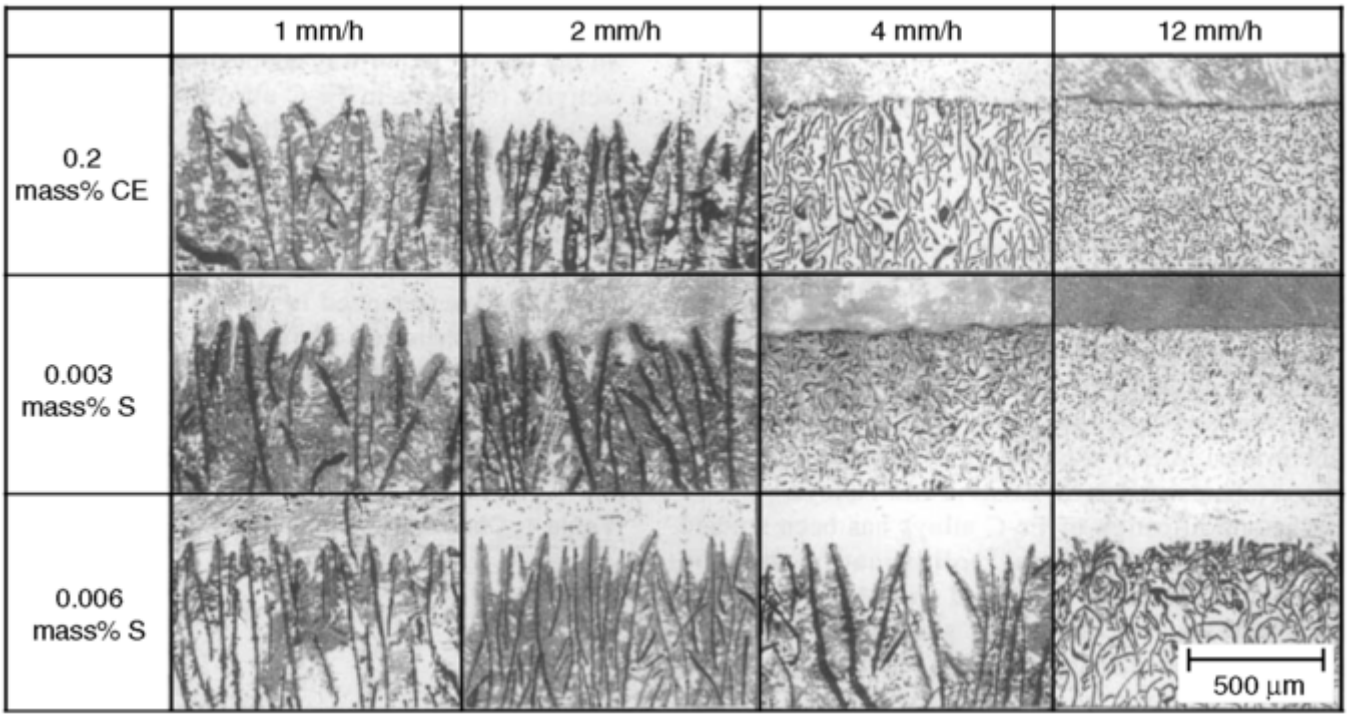

Fig. 24 Influence of sulfur and cerium (given as mass%) on the interface morphology of directionally solidified iron-carbon alloys with carbon content of 4.15–4.45% and silicon content less than 0.017%. Solidification direction upward. Source: Ref 19

Further insight in the solidification of gray iron can be gained from Fig. 25, which shows the interface morphology of directionally solidified irons containing various amounts of magnesium and processed at different solidification velocities (Ref 20). The flake graphite iron exhibits a planar S/L interface with the graphite the leading phase (Fig. 25a). As the solidification velocity is increased to 5 μm/s and some magnesium is added, the interface morphology changes to cellular and the graphite shape to compacted (Fig. 25b). Higher magnesium addition results in further interface destabilization. The austenite grows as dendrites, and the graphite becomes spheroidal (Fig. 25c).

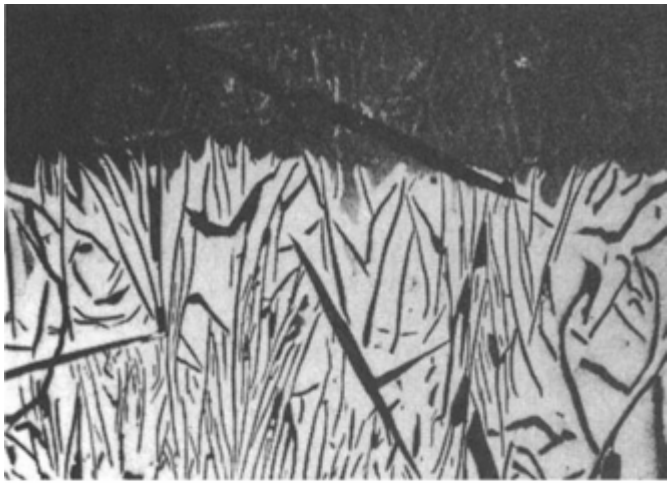

(a)

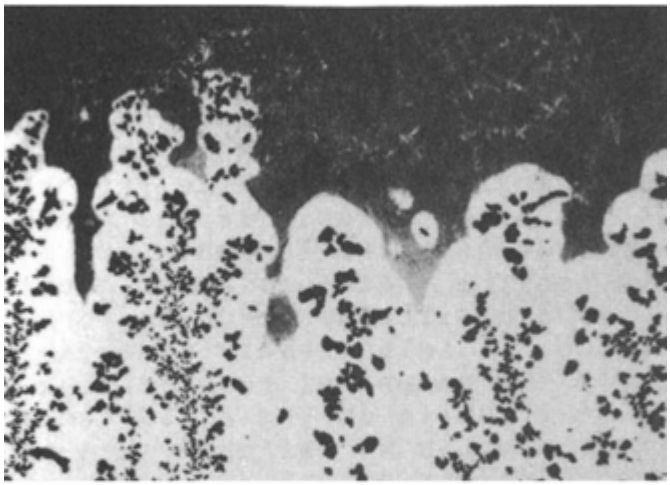

(b)

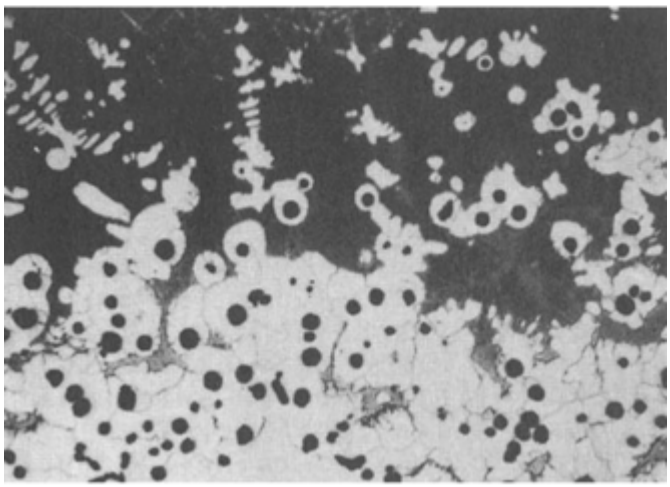

(c)

Fig. 25 Interface morphology of directionally solidified cast irons. (a) Planar (flake graphite iron). (b) Cellular (compacted graphite iron). (c) Dendritic (spheroidal graphite iron). Source: Ref 20

The sequence of changes in the eutectic morphology of directionally solidified cast iron as a function of solute content is summarized in Fig. 26. As the ratio between the temperature gradient at the S/L interface and the growth velocity, G_T/V, decreases, or the composition C_o (of, e.g., magnesium or cerium) increases, the S/L interface changes from planar, to cellular, and then to equiaxed, while graphite remains basically flake (lamellar). Cooperative growth of austenite and graphite occurs. Further change of G_T/V or of C_o brings about formation of an irregular interface, with austenite dendrites protruding in the liquid. Graphite becomes compacted and then spheroidal. Eutectic growth is divorced.

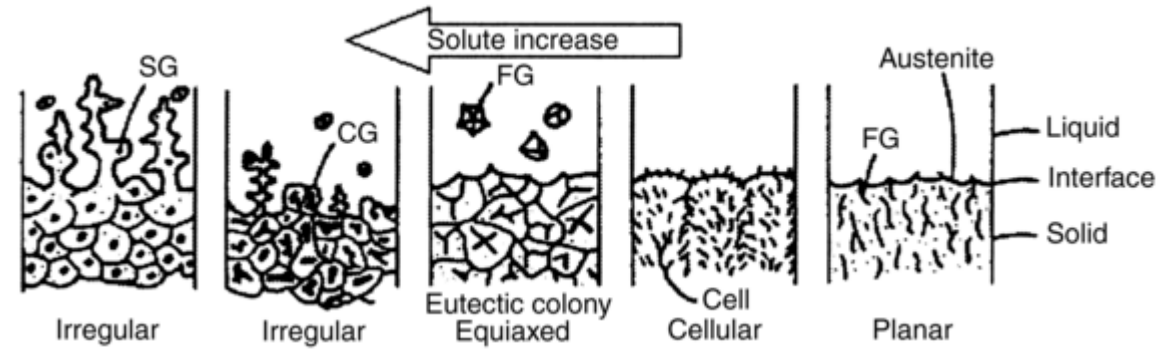

Fig. 26 Structural transitions in directionally solidified cast iron. Source: Ref 15

Primary austenite dendrites play a significant role in the eutectic solidification of SG iron. This contention is supported by microstructures found in the microshrinkage of thin SG iron plates (Ref 21) presented in Fig. 27. Microshrinkage can be rationalized as interrupted solidification. Two types of dendrites exhibiting nonsimilar morphologies can be identified: primary austenite dendrites and eutectic SG aggregates. The morphology of the primary austenite dendrites is typical for dendrites in metallic alloys. They exhibit clear primary and secondary arms (Fig. 27a). The eutectic SG aggregates (Fig. 27b) are thick and rounded, suggesting a cauliflower shape. While displaying branching, there is no clear distinction between primary and secondary arms. It appears that the SG eutectic grains are made of many graphite nodules surrounded by quasi-spherical austenite envelopes belonging to initial austenite dendrites. Thus, the eutectic grain is hard to define metallographically in SG iron. It appears that the main solidification unit is the primary austenite dendrite within which graphite nodules grow through a eutectic reaction. This model for the solidification of SG iron was proposed as early as 1985 by Rickert and Engler (Ref 22) and then further confirmed by other authors (Ref 14, 23, and 24). It is represented in Fig. 28.

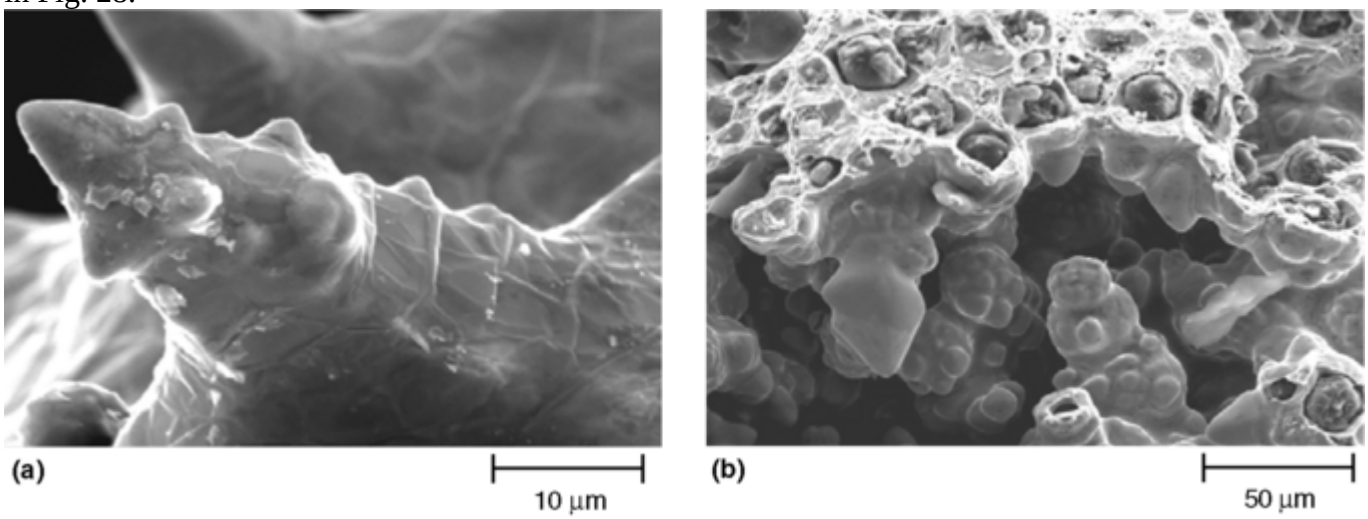

Fig. 27 Microstructures of spheroidal graphite iron found in the same microshrinkage cavity from a spheroidal graphite iron plate. (a) Austenite dendrites. (b) Eutectic (spheroidal graphite) aggregates. Source: Ref 21

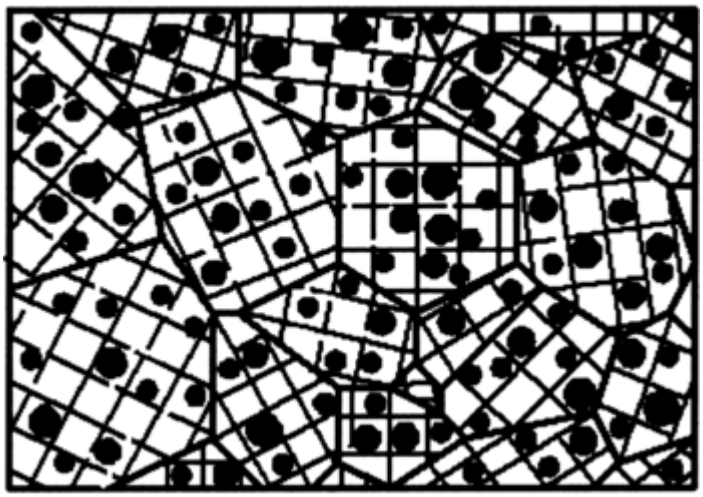

Fig. 28 Mechanism of solidification of spheroidal graphite iron showing primary dendrite grains and graphite nodules growing from the eutectic intradendritic liquid

White Iron (Austenite-Iron Carbide Eutectic). The as-cast microstructure of white iron typically consists of austenite dendrites and austenite—iron carbide eutectic (ledeburite). Hypereutectic irons will also exhibit primary iron carbides. The microstructure of the white eutectic consists of iron carbide plates or rods in an austenitic matrix that becomes pearlite at room temperature (Fig. 29) (Ref 25). Growth of ledeburite starts with the development of a cementite plate on which an austenite dendrite nucleates and grows. This destabilizes the Fe_3C that then grows through the austenite. As a result, two types of eutectic structure develop, a lamellar eutectic with Fe_3C the leading phase in the edgewise direction, and a rodlike eutectic in the sidewise direction (Fig. 30) (Ref 26). Under specific directional solidification conditions ledeburite behaves like a regular eutectic (Ref 27), as shown in Fig. 31(a); however, proper care must be exercised during metallographic preparation if the correct lamellar spacing is to be determined. The two specimens in Fig. 31 have the same spacing, but the sectioning of the metallographic sample is not perpendicular to the solidification direction for the sample in Fig. 31(b).

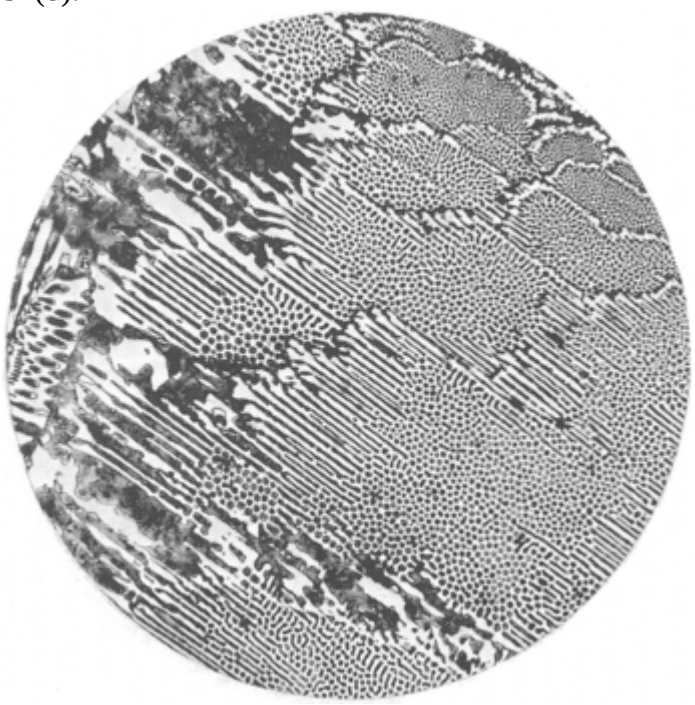

Fig. 29 Microstructure of the iron-iron carbide eutectic (ledeburite). Source: Ref 25

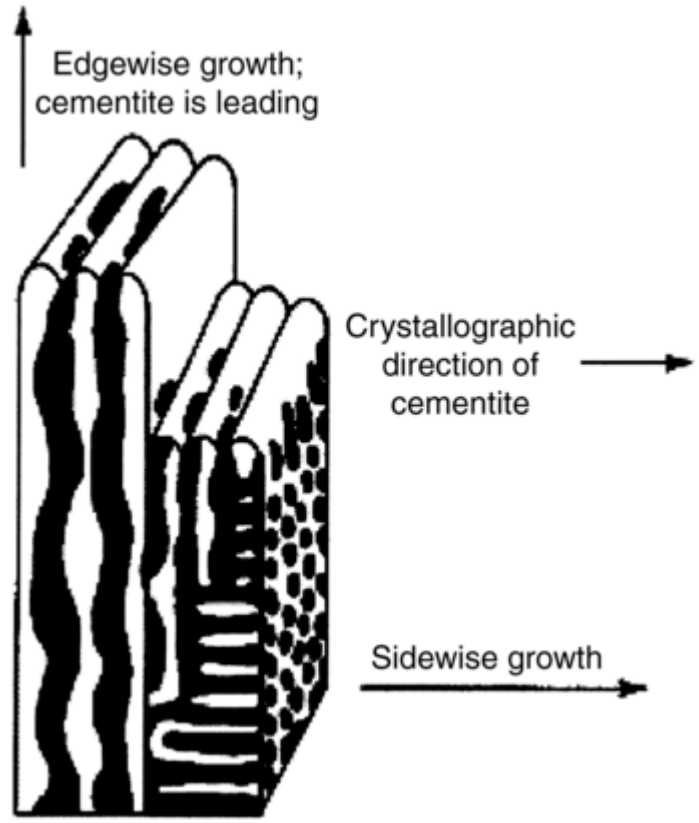

Fig. 30 Growth of the ledeburite eutectic. Source: Ref 26

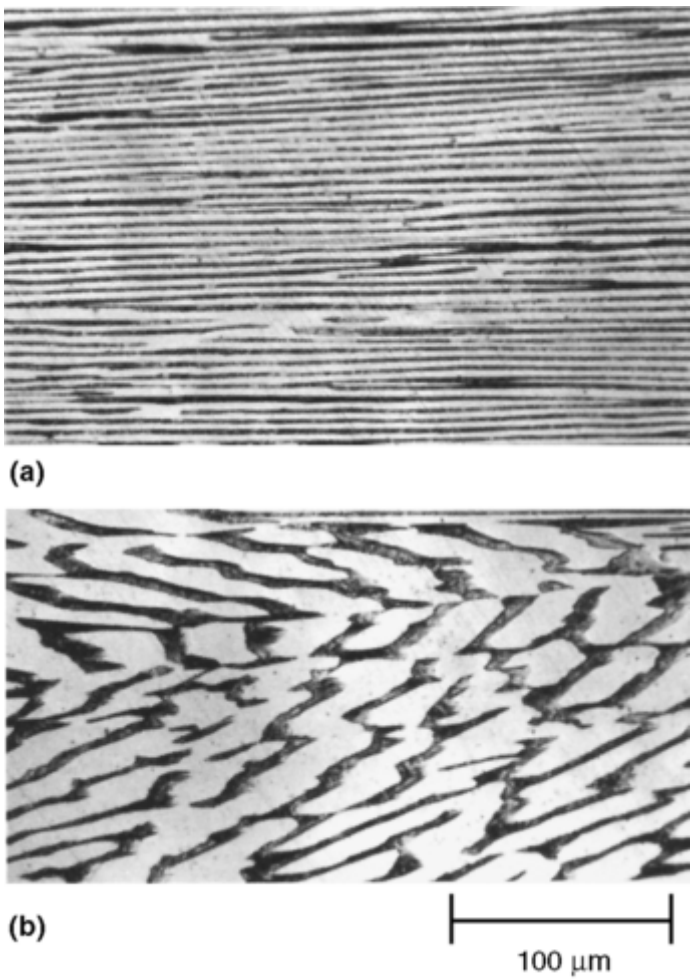

Fig. 31 Longitudinal section of directionally solidified white cast iron. (a) Section cut perpendicular to solidification direction. (b) Section made nonperpendicular. Etched with nital. Source: Ref 27

It was suggested (Ref 28) that, as the cooling rate increases, the lamellar part of the original parallelepipedic eutectic grain becomes larger at the expense of the rod eutectic (Fig. 32a), the grain starts bending inward (Fig. 32b), and eventually a spherulitic eutectic grain results (Fig. 32c).

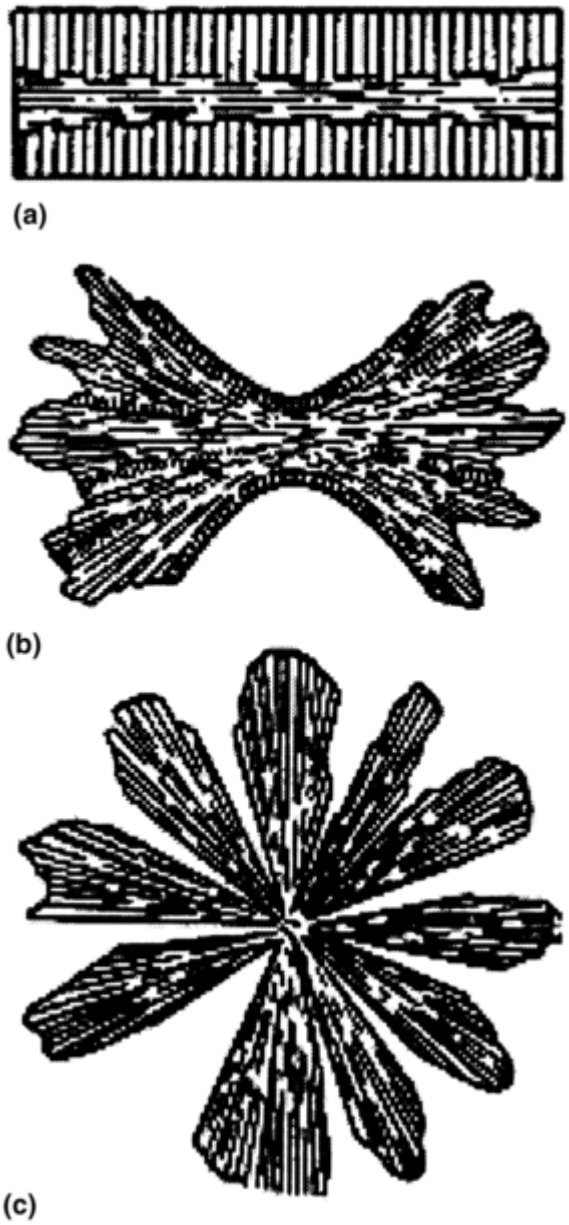

Fig. 32 Change in the morphology of the austenite-Fe_3C eutectic grain at increasing cooling rate. (a) to (c) proposed in Ref 28

Unalloyed white irons do not have significant practical applications. On the contrary, medium- and high-alloyed irons are used extensively for their abrasion resistance. The alloying elements change the composition and morphology of the carbides, as well as the microstructure of the matrix. For example, irons having relatively high carbon, 3 to 5% Ni, and 1.4 to 4% Cr solidify with a martensitic matrix (Fig. 33a). Chromium promotes white solidification with a continuous network of alloyed iron carbides, $(Fe,Cr)_3C$. When the chromium content is increased to 7 to 11%, the composition and morphology of the carbides changes to discontinuous Cr_7C_3 eutectic carbides (Fig. 33b) (Ref 29).

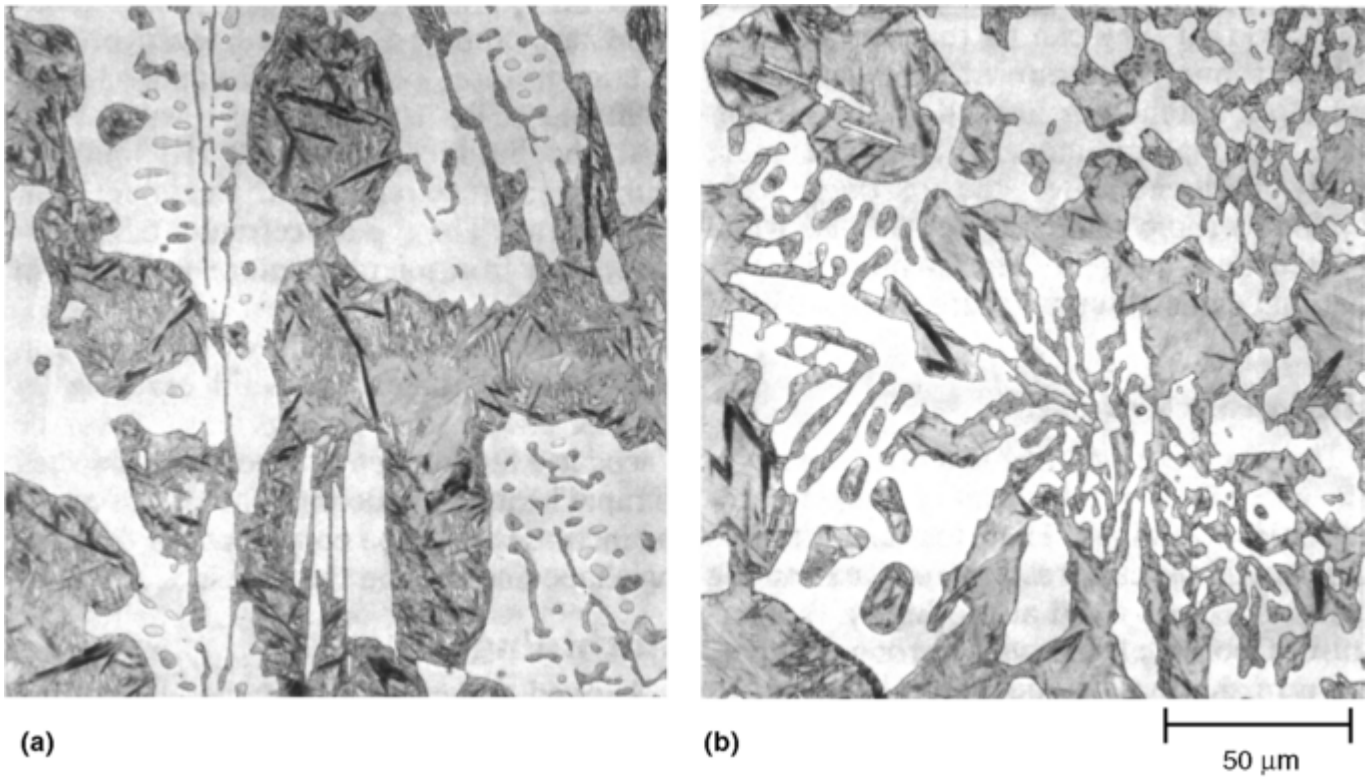

Fig. 33 Microstructures of nickel-chromium abrasion-resistant white irons. (a) With 1.4–4% Cr, martensitic matrix forms. (b) With 7–11% Cr, discontinuous eutectic carbides form. Magnification: 340×. Source: Ref 29

The amount of Cr_7C_3 carbides can be increased by increasing the amount of chromium to 15 to 25%. Examples of microstructures of high-chromium irons are provided in Fig. 34. As the carbon content increases, the amount of carbides increases. At low carbon, the carbides form a continuous network around the austenite dendrites. When the carbon content exceeds the eutectic carbon content, large hexagonal carbide rods precipitate from the melt as primary phases.

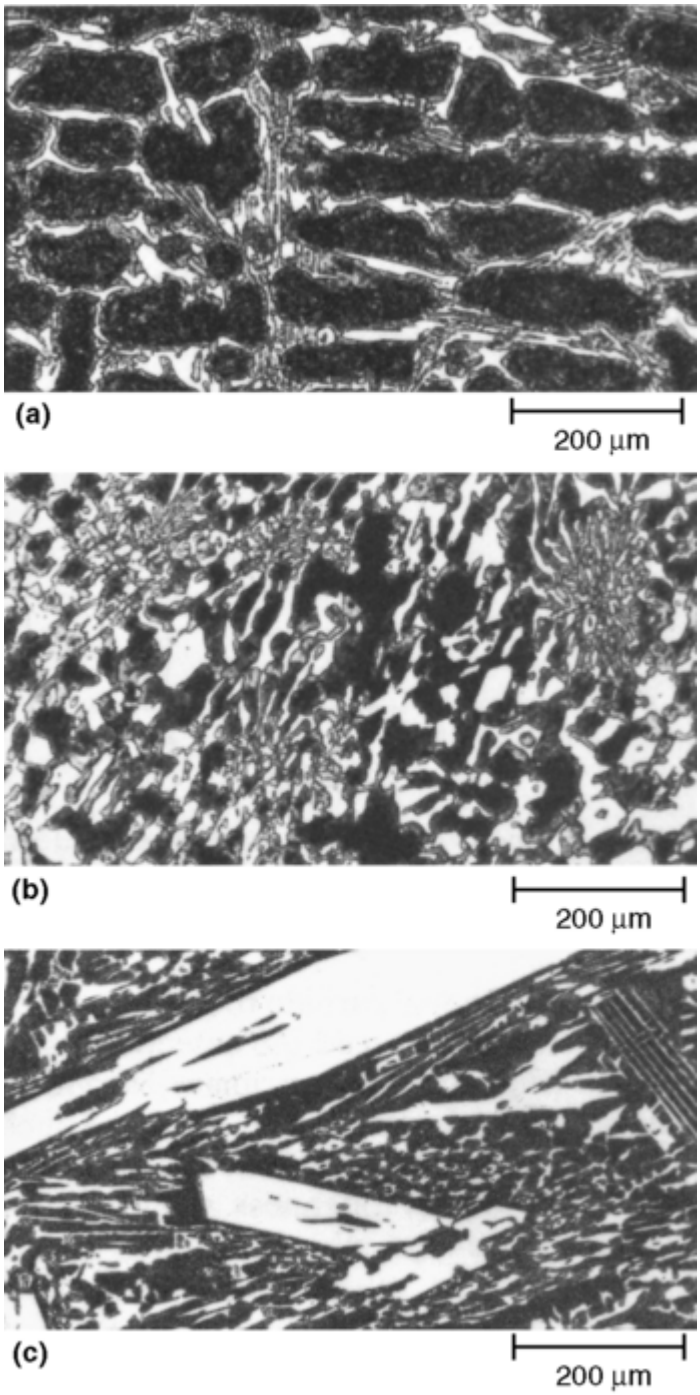

Fig. 34 Microstructures of high-chromium (15–25% Cr) white irons. Carbon content increases from (a) to (c). Magnification: 75×. Source: Ref 29

References cited in this section

11. J.C. Moore, *Metallography, Structures and Phase Diagrams,* Vol 8, 8th ed., *Metals Handbook,* American Society for Metals, 1973, p 93

12. *ASM Specialty Handbook: Cast Irons,* ASM International, 1996

13. R.E. Boeri and J.A. Sikora, *Int. J. Cast Met. Res.,* Vol 13 (No. 5), 2001, p 307–313

14. G.L. Rivera, R.E. Boeri, and J.A. Sikora, submitted to *Scr. Mater.*

15. D.M. Stefanescu, *Science and Engineering of Casting Solidification,* Kluwer Academic, 2002

16. D.K. Bandyopadhyay, D.M. Stefanescu, I. Minkoff, and S.K. Biswal, *Physical Metallurgy of Cast Iron IV,* G. Ohira, T. Kusakawa, and E. Niyama, Ed., Materials Research Society, 1989, p 27

17. P.C. Liu, C.L. Liu, D.H. Wu, and C.R. Loper, *AFS Trans.,* Vol 91, 1983, p 119–136

18. H. Itofuji and H. Uchikawa, *AFS Trans.,* Vol 98, 1990, p 429–448

19. H. Nakae and H. Shin, *Int. J. Cast Met. Res.,* Vol 11, 1999, p 345–349

20. B.C. Liu and Y.X. Li, *Physical Metallurgy of Cast Iron IV,* G. Ohira, T. Kusakawa, and E. Niyama, Ed., Materials Research Society, 1990, p 35–42

21. R. Ruxanda, L. Beltran-Sanchez, J. Massone, and D.M. Stefanescu, *Proc. Cast Iron Division,* AFS 105th Casting Congress, American Foundry Society, 2001, p 37

22. A. Rickert and S. Engler, *The Physical Metallurgy of Cast Iron,* H. Fredriksson and M. Hillert, Ed., Proc. Materials Research Society, North Holland, Vol 34, 1985, p 165

23. D.M. Stefanescu, Cast Iron (in Solidification of Eutectic Alloys), *Casting,* Vol 15, *ASM Handbook,* D.M. Stefanescu, Ed., ASM International, 1988, p 168–181

24. D.K. Bandyopadhyay and D.M. Stefanescu, *Physical Metallurgy of Cast Iron IV,* G. Ohira, T. Kusakawa, and E. Niyama, Ed., Materials Research Society, 1989, p 15–26

25. H.E. McGannon, Ed., *The Making, Shaping and Treating of Steel,* 9th ed., United States Steel, 1971, p 1079

26. M. Hillert and H. Steinhauser, *Jernkontorets Ann.,* Vol 144, 1960 p 520

27. P. Magnin and W. Kurz, Solidification of Eutectics (in Fundamentals of Growth), *Casting,* Vol 15, *ASM Handbook,* D.M. Stefanescu, Ed., ASM International, 1988, p 119

28. K.P. Bunin, I.N. Malinotchka, and I.N. Taran, *Osnovi Metallographyia Tchuguna,* Metallurghyia, Moscow, 1969

29. R.B. Gundlach, High-Alloy White Irons, *Casting,* Vol 15, *ASM Handbook,* D.M. Stefanescu, Ed., ASM International, 1988, p 678–685

D.M. Stefanescu and R. Ruxanda, Solidification Structures of Steels and Cast Irons, *Metallography and Microstructures,* Vol 9, *ASM Handbook,* ASM International, 2004, p. 97–106

Solidification Structures of Steels and Cast Irons

Doru M. Stefanescu and Roxana Ruxanda, The University of Alabama

---

References

1. B.L. Bramfitt, Solidification Structures of Steel, *Metallography and Microstructures,* Vol 9, *ASM Handbook,* ASM International, 1985, p 623–628

2. C.W. Briggs, *The Metallurgy of Steel Castings,* McGraw-Hill, 1946, 634 pages

3. *Transformation and Hardenability in Steels,* Climax Molybdenum Co. of Michigan, 1967, p 14

4. A. Hunter and M. Ferry, *Metall. Mater. Trans. A,* Vol 33A, 2002, p 3747–3754

5. E.T. Turkdogan, *Fundamentals of Steelmaking,* The Institute of Materials, London, 1996, 331 pages

6. H. Fredriksson, Solidification of Peritectics (in Solidification of Growth), *Casting,* Vol 15, *ASM Handbook,* D.M. Stefanescu, Ed., ASM International, 1988, p 129

7. P.F. Wieser, Ed., *Steel Castings Handbook,* 5th ed., Steel Founders' Society of America, 1980 p 19-6

8. A. Suzuki, T. Suzuki, Y. Nagaoka, and Y. Iawata, *Nippon Kingaku Gakkai Shuho,* Vol 32, 1968

9. C.E. Sims, *Trans. Met. Soc. AIME,* Vol 215, 1959, p 367–393

10. W.G. Wilson and A. McLean, *Desulfurization of Iron and Steel and Sulfide Shape Control,* Iron and Steel Society of AIME, 1980

11. J.C. Moore, *Metallography, Structures and Phase Diagrams,* Vol 8, 8th ed., *Metals Handbook,* American Society for Metals, 1973, p 93

12. *ASM Specialty Handbook: Cast Irons,* ASM International, 1996

13. R.E. Boeri and J.A. Sikora, *Int. J. Cast Met. Res.,* Vol 13 (No. 5), 2001, p 307–313

14. G.L. Rivera, R.E. Boeri, and J.A. Sikora, submitted to *Scr. Mater.*

15. D.M. Stefanescu, *Science and Engineering of Casting Solidification,* Kluwer Academic, 2002

16. D.K. Bandyopadhyay, D.M. Stefanescu, I. Minkoff, and S.K. Biswal, *Physical Metallurgy of Cast Iron IV,* G. Ohira, T. Kusakawa, and E. Niyama, Ed., Materials Research Society, 1989, p 27

17. P.C. Liu, C.L. Liu, D.H. Wu, and C.R. Loper, *AFS Trans.,* Vol 91, 1983, p 119–136

18. H. Itofuji and H. Uchikawa, *AFS Trans.,* Vol 98, 1990, p 429–448

19. H. Nakae and H. Shin, *Int. J. Cast Met. Res.,* Vol 11, 1999, p 345–349

20. B.C. Liu and Y.X. Li, *Physical Metallurgy of Cast Iron IV,* G. Ohira, T. Kusakawa, and E. Niyama, Ed., Materials Research Society, 1990, p 35–42

21. R. Ruxanda, L. Beltran-Sanchez, J. Massone, and D.M. Stefanescu, *Proc. Cast Iron Division,* AFS 105th Casting Congress, American Foundry Society, 2001, p 37

22. A. Rickert and S. Engler, *The Physical Metallurgy of Cast Iron,* H. Fredriksson and M. Hillert, Ed., Proc. Materials Research Society, North Holland, Vol 34, 1985, p 165

23. D.M. Stefanescu, Cast Iron (in Solidification of Eutectic Alloys), *Casting,* Vol 15, *ASM Handbook,* D.M. Stefanescu, Ed., ASM International, 1988, p 168–181

24. D.K. Bandyopadhyay and D.M. Stefanescu, *Physical Metallurgy of Cast Iron IV,* G. Ohira, T. Kusakawa, and E. Niyama, Ed., Materials Research Society, 1989, p 15–26

25. H.E. McGannon, Ed., *The Making, Shaping and Treating of Steel,* 9th ed., United States Steel, 1971, p 1079

26. M. Hillert and H. Steinhauser, *Jernkontorets Ann.*, Vol 144, 1960 p 520

27. P. Magnin and W. Kurz, Solidification of Eutectics (in Fundamentals of Growth), *Casting,* Vol 15, *ASM Handbook,* D.M. Stefanescu, Ed., ASM International, 1988, p 119

28. K.P. Bunin, I.N. Malinotchka, and I.N. Taran, *Osnovi Metallographyia Tchuguna,* Metallurghyia, Moscow, 1969

29. R.B. Gundlach, High-Alloy White Irons, *Casting,* Vol 15, *ASM Handbook,* D.M. Stefanescu, Ed., ASM International, 1988, p 678–685

D.M. Stefanescu and R. Ruxanda, Solidification Structures of Aluminum Alloys, *Metallography and Microstructures,* Vol 9, *ASM Handbook,* ASM International, 2004, p. 107–115

Solidification Structures of Aluminum Alloys

Doru M. Stefanescu and Roxana Ruxanda, The University of Alabama

Introduction

ALUMINUM-BASE ALLOYS constitute a group of cast materials second only to ferrous castings in tonnage. Aluminum alloys have gained increasing markets in the automotive and aircraft industry. New alloys are still under development, since there are still wide possibilities of improving their properties by using simple, affordable techniques, such as alloying and heat treating. A wide range of materials can be added to aluminum (Ref 1): zinc, magnesium, copper, silicon, iron, lithium, manganese, nickel, silver, tin, and titanium. The solid solubility of these elements in aluminum varies considerably. Some elements are used as solid-solution strengtheners, others form desirable intermetallic compounds. The most common alloy systems are aluminum-silicon, aluminum-copper, and aluminum-magnesium. Some typical solidification microstructures for these alloying systems are given in the following sections.

Reference cited in this section

1. I.J. Polmear, *Light Metals,* E. Arnold Publishers, London, 1981

D.M. Stefanescu and R. Ruxanda, Solidification Structures of Aluminum Alloys, *Metallography and Microstructures,* Vol 9, *ASM Handbook,* ASM International, 2004, p. 107–115

Solidification Structures of Aluminum Alloys

>Doru M. Stefanescu and Roxana Ruxanda, The University of Alabama

Basic Microstructures of Aluminum-Base Alloys

Aluminum-Silicon Alloys. The equilibrium phase diagram of the binary aluminum-silicon system is similar to that in Fig. 1(b) of the article “Fundamentals of Solidification” in this Volume, representing partial solid solubility with a eutectic reaction. The eutectic invariant is at 11.7% Si and 577 °C (1070 °F). Typical examples of hypoeutectic, eutectic, and hypereutectic aluminum-silicon commercial alloys are given in Fig. 1 (Ref 2).

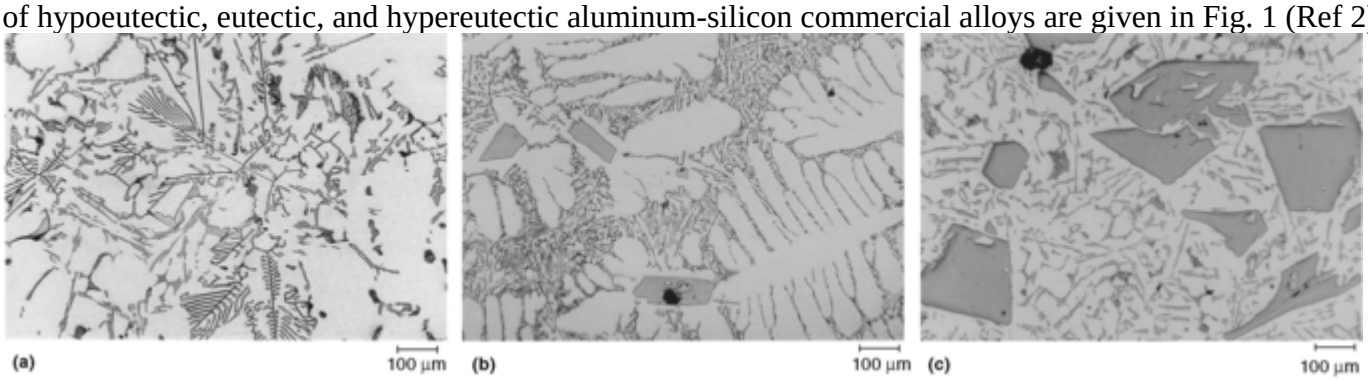

Fig. 1 Typical microstructures of hypoeutectic, eutectic, and hypereutectic aluminum-silicon commercial alloys. (a) Hypoeutectic aluminum-silicon alloy (Al-5.7Si, alloy type A319). Fan-shaped Al_{51}-$(MnFe)_3$-Si_2 phase growing in competition with the α-aluminum phase, silicon crystals, Al_2Cu, and areas with complex eutectics. Etchant: 0.5% HF. Original magnification 110×. (b) Eutectic aluminum-silicon alloy (Al-11.9Si, alloy type A339). α-aluminum dendrites, primary silicon particles, and areas with complex eutectics. Etchant: 0.5% HF. Original magnification 110×. (c) Hypereutectic aluminum-silicon alloy (Al-15Si, alloy type A390). Large primary silicon particles, eutectic silicon crystals, and Al_2Cu phase in a matrix of α-aluminum phase. Etchant: 0.5% HF. Original magnification 110×. Source: Ref 2

Binary eutectic or hypoeutectic aluminum-silicon alloys are characterized by good castability and corrosion resistance. However, the aluminum-silicon alloys are seldom binary. Strengthening of aluminum-silicon alloys is achieved by adding small amounts of other elements, such as copper, magnesium, or iron. Higher iron contents can promote the formation of brittle plates of AlFeSi or other complex intermetallics in the presence of manganese. This may have a negative influence on the mechanical properties.

Aluminum-Copper Alloys. The equilibrium diagram of the binary aluminum-copper system is given in Fig. 2. These alloys are typical solid-solution alloys generally containing 4 to 6% Cu and some magnesium. After a solution treatment, $CuAl_2$ particles precipitate from the quenched alloy, as seen in Fig. 2. The level of impurities can affect both the macrostructure and microstructure. This is demonstrated in Fig. 3 and Fig. 4 for a nominal Al-4.5Cu-0.25Mg alloy with a small amount of silver (0.7%) and titanium, respectively. Titanium addition considerably decreases the grain size.

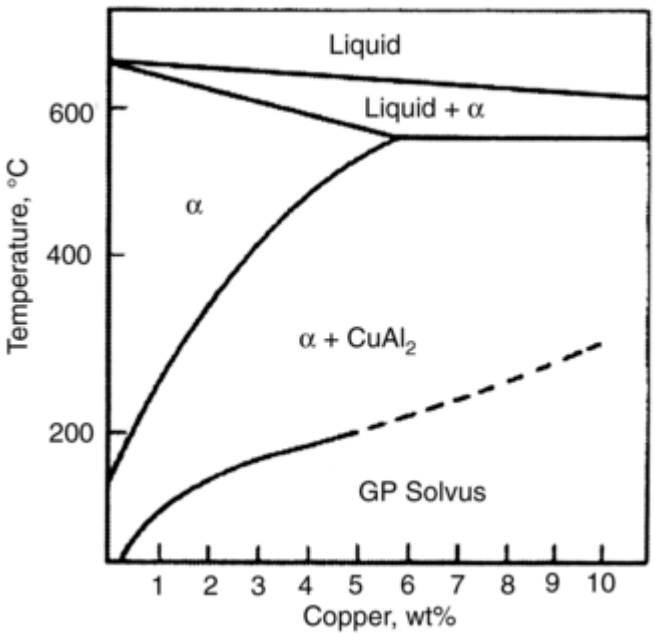

Fig. 2 A portion of aluminum-copper equilibrium diagram

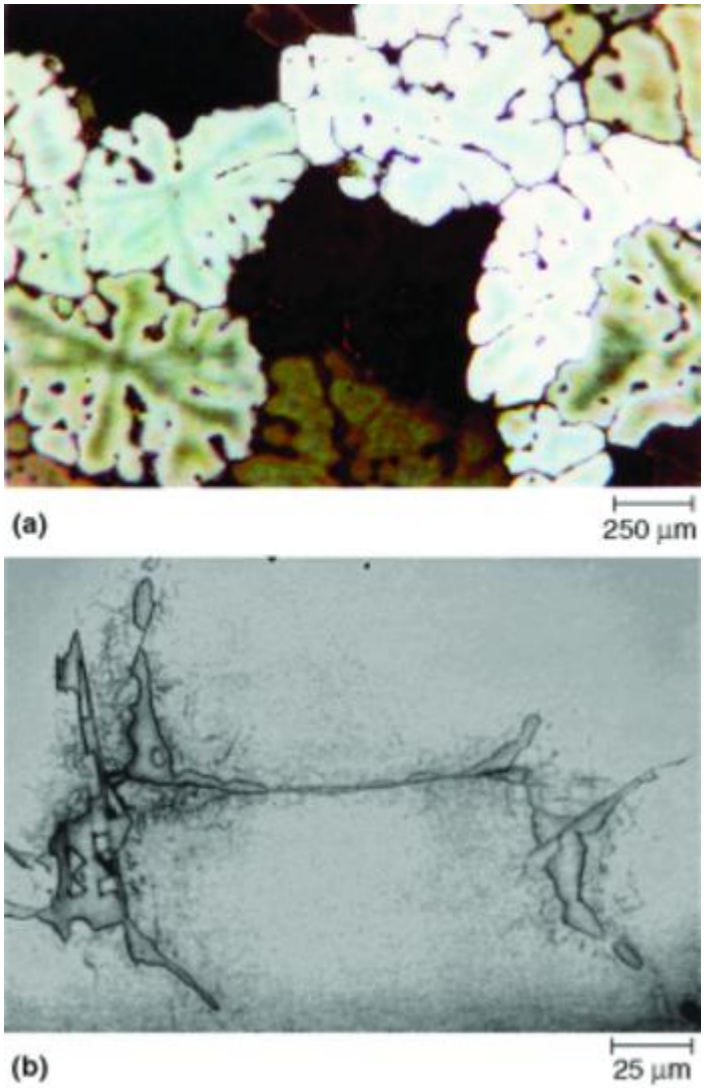

Fig. 3 Micrograph of aluminum-copper alloy with a small amount of silver, having a low level of impurities (alloy 201 with 4.10% Cu). (a) Macrostructure showing grains and dendrites. Etched with 1 mL HBF_4, 1 mL HF, 24 mL C_2H_5OH, and 74 mL H_2O electrolyte. 56×. Observed under polarized light illumination.

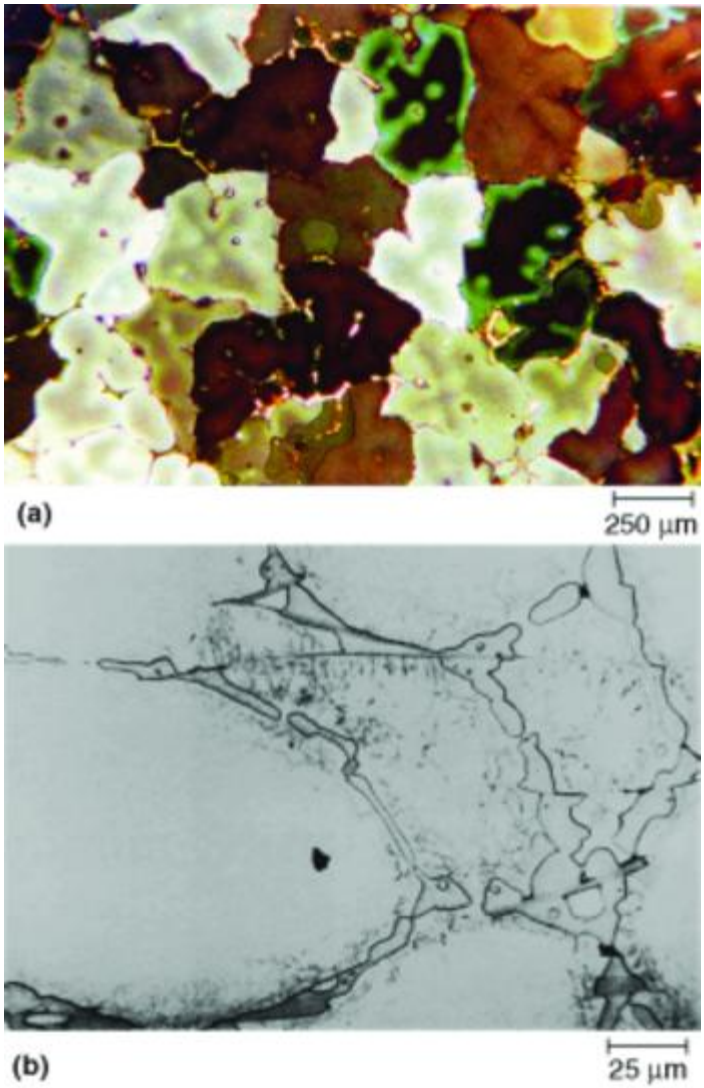

Fig. 4 Micrograph of aluminum-copper alloy with a small amount of titanium, having a higher level of impurities (alloy A206 with 4.36% Cu). (a) Macrostructure showing grains and dendrites. Etched with 1 mL HBF_4, 1 mL HF, 24 mL C_2H_5OH, and 74 mL H_2O electrolyte. 56×. Observed under polarized light illumination.

Aluminum-Magnesium Alloys. The corner of the phase diagram of practical interest is similar to that of aluminum-copper alloys, with the maximum solubility of magnesium in aluminum at 17.4% Al. Some typical examples of aluminum-magnesium commercial alloys are given in Fig. 5.

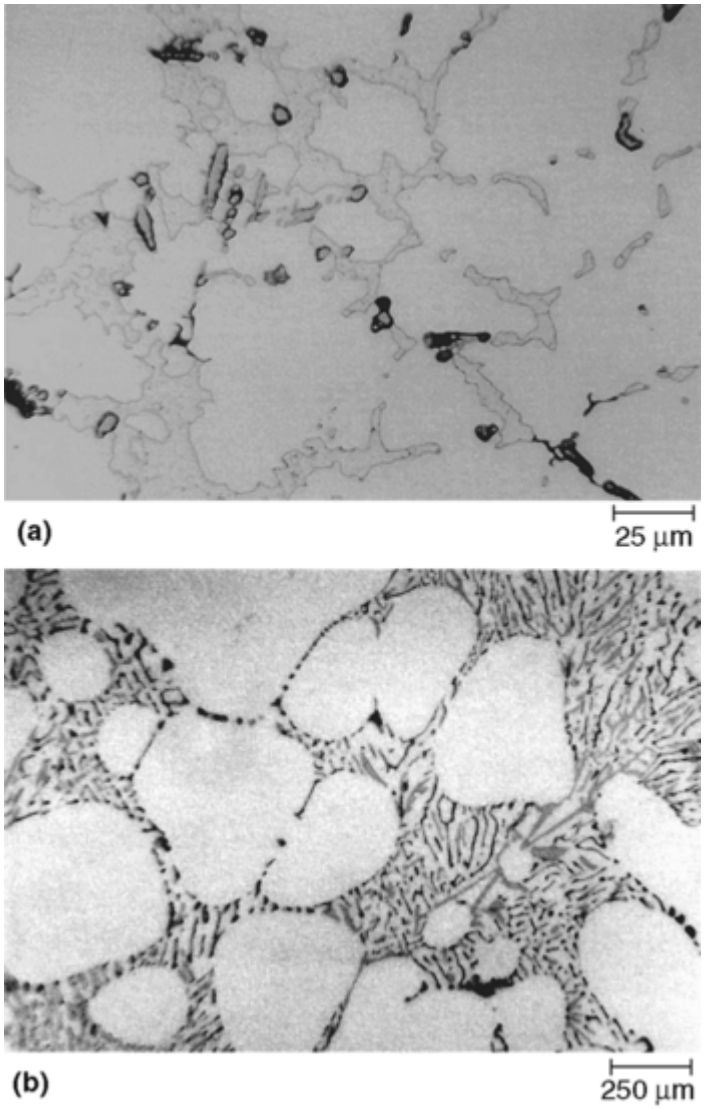

Fig. 5 Typical examples of aluminum-magnesium commercial alloys. (a) Microstructure showing Al_3Fe (gray) and Mg_2Si (black) in α-aluminum solid-solution matrix (alloy type A518 with 7.6% Mg). Etchant: 0.5% HF. Original magnification 560×. (b) Microstructure showing ternary eutectic and α-aluminum solid-solution dendrites matrix (alloy type A512 with 4Mg-1.8Si). Etchant: 0.5% HF. Original magnification 560×. Source: Ref 2

Other Multicomponent Aluminum Alloys. Investigations of higher-order multicomponent alloys solidification are rather limited. Sophisticated methods are used to identify phases and their orientation. An example of the microstructure of the Al 7050 alloy containing 11 elements is given in Fig. 6 (Ref 3). The dark areas are α-aluminum phase and the bright areas are quaternary sigma (σ) phase $(Al,Cu,Zn)_2Mg$, ternary *S* phase (Al_2MgCu), or/and binary θ phase (Al_2Cu). These phases were identified using optical metallography, scanning electron microscopy (SEM), x-ray map, and electron probe microanalysis (EPMA) techniques. The dendrite arms are separated by sigma, *S*, θ, and/or eutecticlike network, or in touch with each other. The primary stem in Fig. 6 is located at the junction of two secondary arms. The slightly darker gray scales at the center of the dendrites show lower solute contents in the α phase, indicating the main growth directions of the dendrite arms. Small, isolated intradendritic droplets are also visible especially near the primary stem and the root of the tertiary arms.

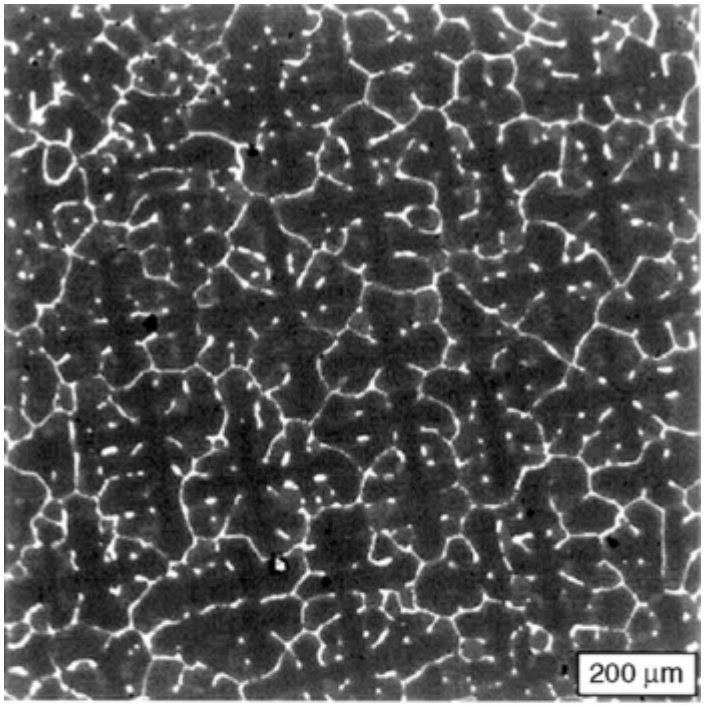

(a)

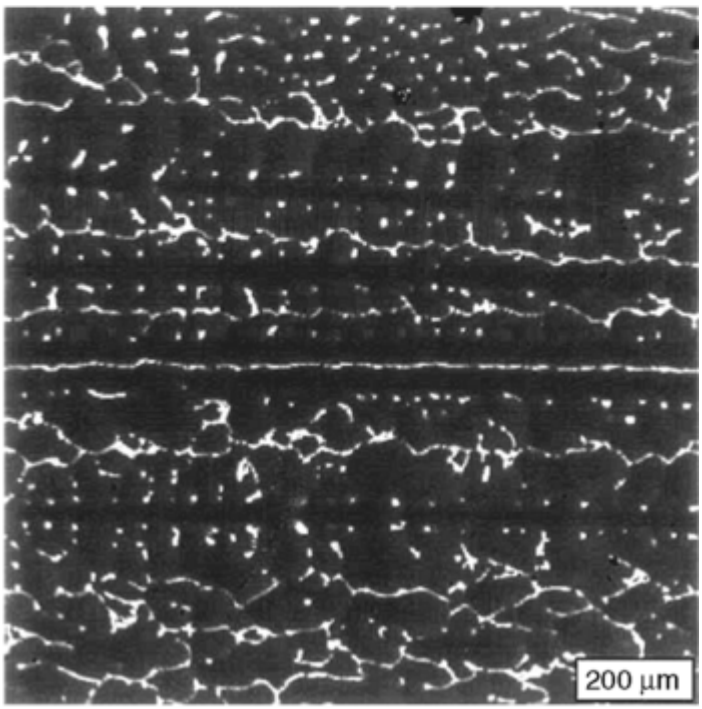

(b)

Fig. 6 Microstructure in cross and longitudinal sections of DS Al 7050 alloy cooled at 0.45 °C/s (0.8 °F/s) (BSE images). The actual bulk composition: 2.60% Cu, 2.37% Mg, 6.56% Zn, 0.03% Cr, 0.09% Fe, 0.05% Mn, 0.01% Ni, 0.06% Si, 0.018% Ti, 0.10% Zr, balance aluminum. Source: Ref 3

References cited in this section

2. L. Bäckerud, G.C. Chai, and J. Tamminen, *Solidification Characteristics of Aluminum Alloys*, Vol 2, AFS/Skanaluminum, 1990

3. F. Xie, X. Yan, L. Ding, F. Zhang, S. Chen, M.G. Chu, and Y.A. Chang, *Mater. Sci. Eng. A*, Vol A00, 2003, p 1–10 (in press)

D.M. Stefanescu and R. Ruxanda, Solidification Structures of Aluminum Alloys, *Metallography and Microstructures,* Vol 9, *ASM Handbook*, ASM International, 2004, p. 107–115

Solidification Structures of Aluminum Alloys

>Doru M. Stefanescu and Roxana Ruxanda, The University of Alabama

Grain Structure

Grain size is a readily observed feature of aluminum alloy ingots and castings. For solid-solution type alloys, mechanical properties are highly dependent on the primary grain size. A uniform, fine grain size is sought in most instances to obtain optimal properties in the wrought product. Accordingly, for solid-solution type alloys the size of the primary grains resulting from solidification is reduced by the use of grain refinement.

The properties of cast alloys containing large amounts of eutectic, such as the aluminum-silicon alloys, depend more on the eutectic morphology and the dendrite arm spacing than on the grain size. Therefore, the modification of the brittle silicon phase from the eutectic is primarily used when processing aluminum-silicon alloys.

The primary solidification grains in aluminum alloys ingots have a very pronounced columnar structure, directed from the mold interface toward the core (Ref 4). If little turbulence and steep temperature gradient exist during solidification, the entire structure will remain columnar (Fig. 7). However, in normal conditions, some arms of the floating dendrites can be detached by the convective motion of the melt, thus determining the formation of an equiaxed structure in the middle of the ingot (Fig. 8).

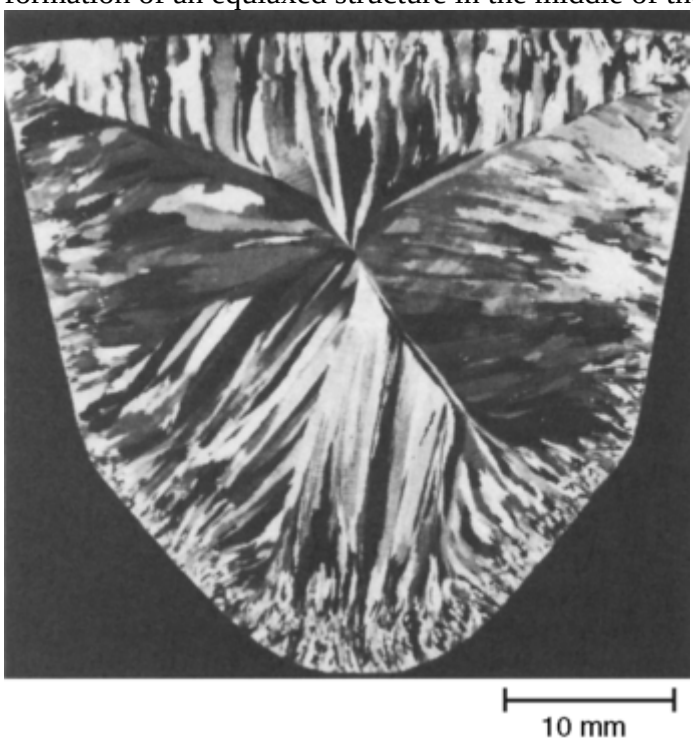

Fig. 7 Cross section through an alloy 1100 ingot cast by the Properzi (wheel-and-belt) method showing columnar grains growing perpendicularly to the faces of the mold. Tucker's reagent. Original magnification 1.5×. Source: Ref 4

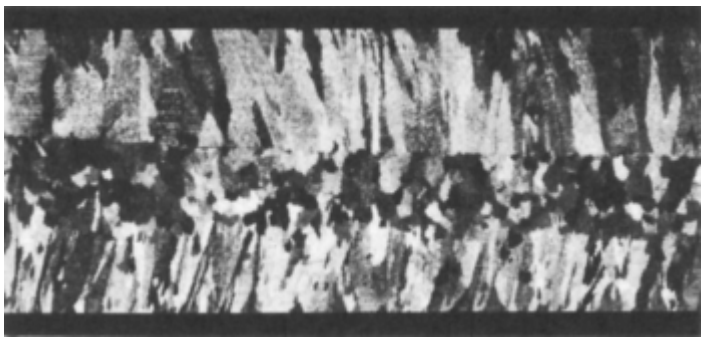

Fig. 8 Longitudinal section through 25 mm (1 in.) thick slab of alloy 1100 cast by the Hazelett (two-belt) method. Tucker's reagent. Actual size. Source: Ref 4

Grain size may be controlled by such mechanical methods as vibration, stirring, and control of metal flow, which provide nuclei by detachment of dendrite arms (Ref 5). Grain-refining additions may also be used to change the structure from coarse and nonuniform (Fig. 9a) to a fine, uniform one (Fig. 9b). The grain-refining inoculants commonly used in the aluminum industry are master alloys containing titanium or titanium plus boron (Ref 6, 7, 8, and 9).

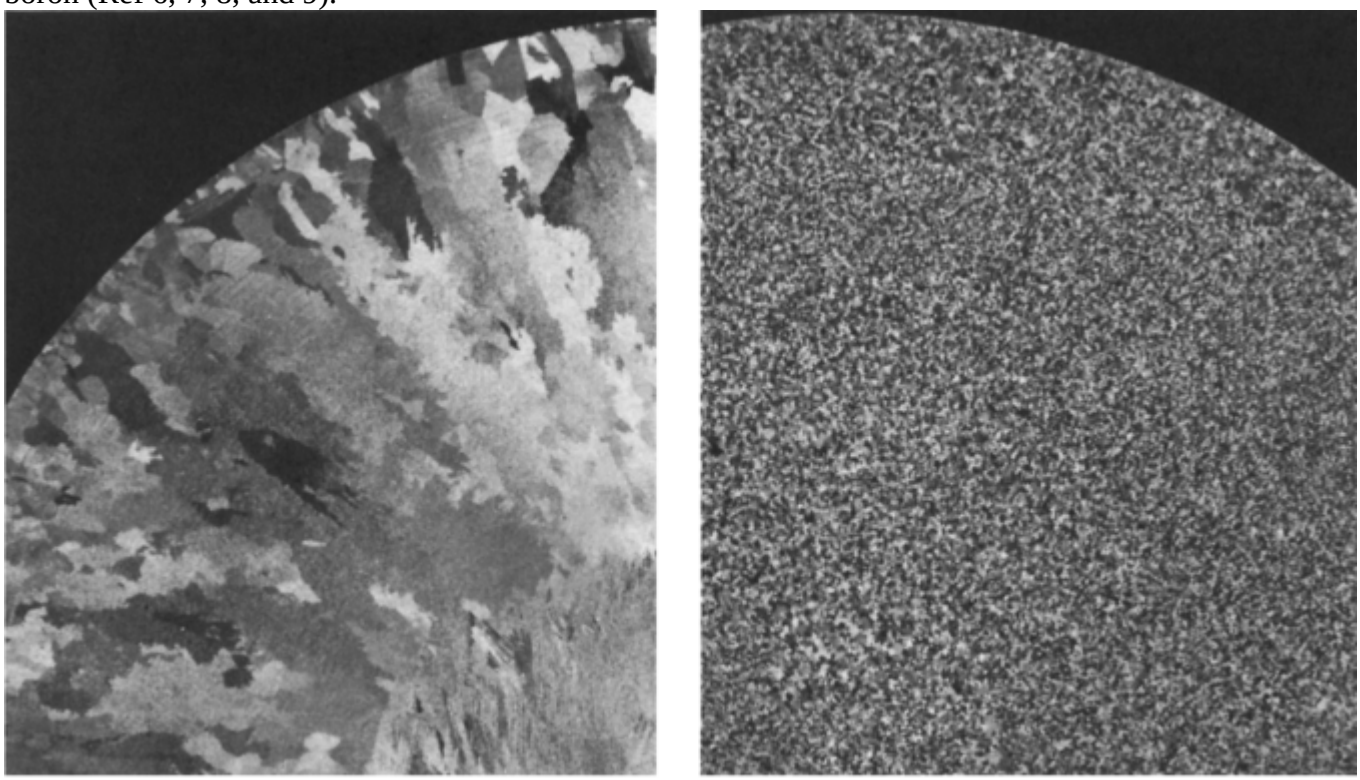

Fig. 9 Cross section of a 150 mm (6 in.) diam ingot of alloy 6063 direct-chill semicontinuous cast. (a) Without grain refiner. (b) With grain refiner. Tucker's reagent. Actual size. Source: Ref 4

The aluminum alloy ingots cast without grain refiner often exhibit a fan-shaped columnar structure, referred to as “feather crystals” (Ref 4). This structure, illustrated in Fig. 10, may be found in low- and high-solute alloys. It is most likely to develop when there is a steep thermal gradient ahead of the solidifying interface (Ref 5) or an inadequate addition of grain refiner (Ref 10). At higher magnification, the feather crystals consist of twinned columnar grains (Fig. 11).

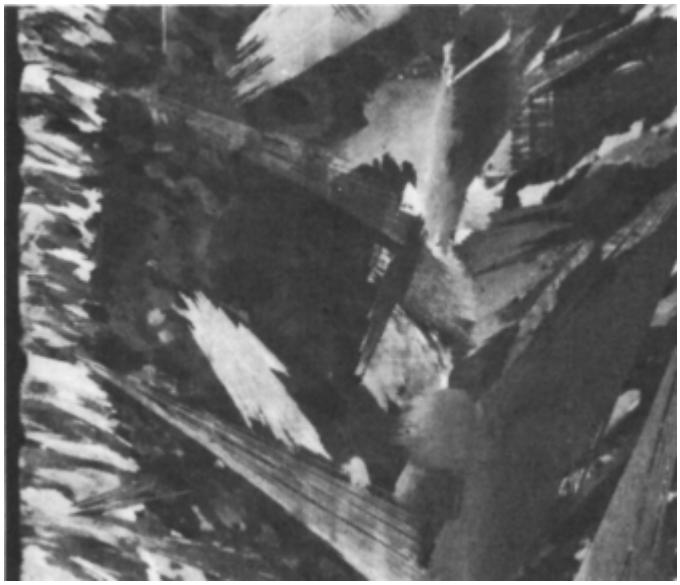

Fig. 10 Longitudinal section through a 75 mm (3 in.) diam alloy 1100 ingot, direct-chill cast without grain refiner. Center of section contains fan-shaped zones of feather crystals. Tucker's reagent. Actual size. Source: Ref 4

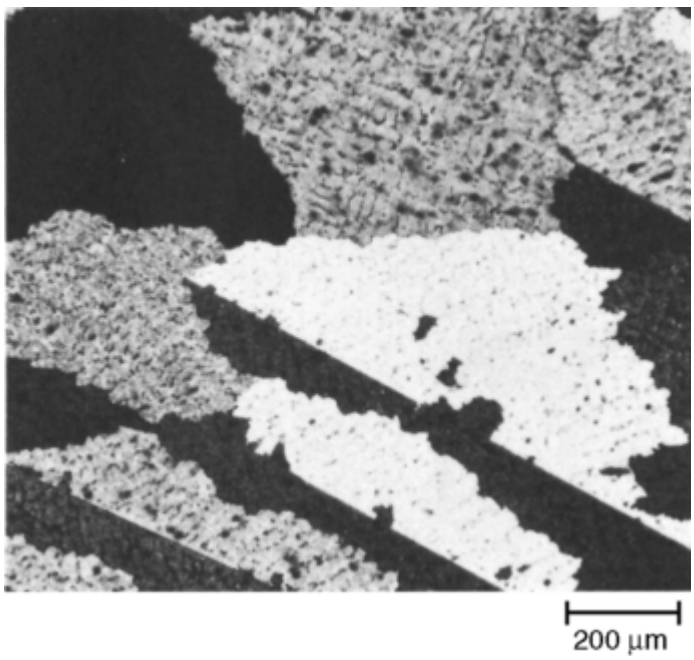

Fig. 11 Feather crystals in an alloy 3003 ingot cast by the direct-chill semicontinuous process. Growth twins in the crystals. Polarized light. Barker's reagent. Original magnification 50×. Source: Ref 4

In contrast to aluminum ingot alloys, the foundry eutectic alloys exhibit a very regular, mostly equiaxed structure, as shown in Fig. 12. If properly etched, aluminum-silicon eutectic alloys reveal both the equiaxed grains and the dendrites within each grain. Different etching techniques (Ref 11) can be used to outline the grains, as shown in Fig. 13 and 14.

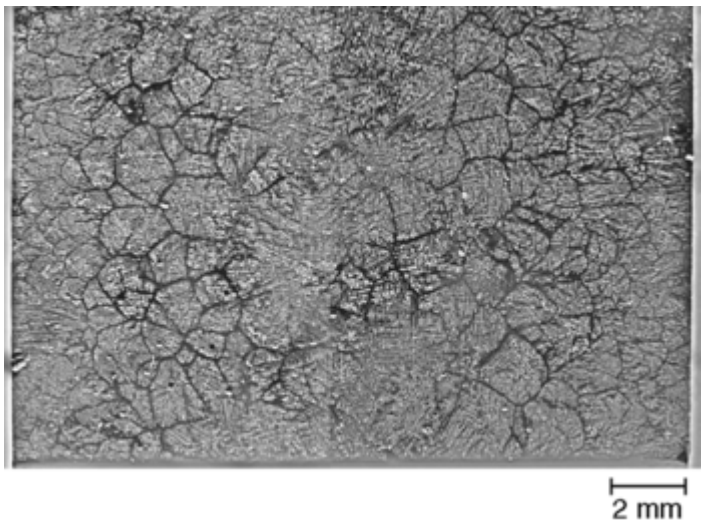

Fig. 12 Macrostructure of an Al-12.7Si alloy showing equiaxed grains and dendrites. Etchant: modified Poulton reagent (60% HCl, 30% HNO_3, 5% HF, 5% H_2O). Original magnification 5×

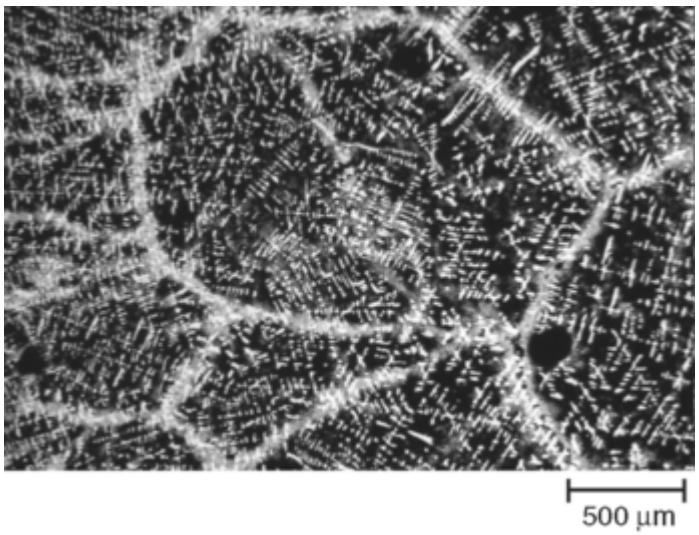

Fig. 13 Outlining of grains using chemical etching. Etchant: modified Poulton reagent (60% HCl, 30% HNO_3 5% HF, 5% H_2O)

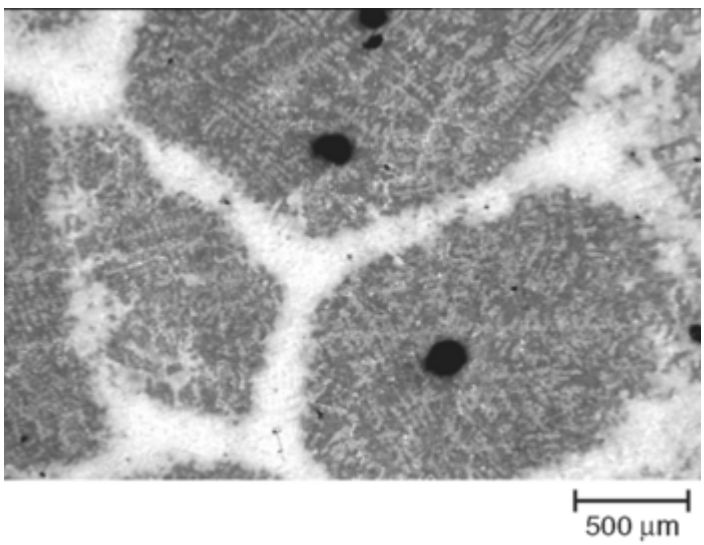

Fig. 14 Outlining of grains using thermal etching. Samples held for 1 h at 590 °C (1095 °F), then quenched in cold water and dried

References cited in this section

4. D.A. Granger, Solidification Structures of Aluminum Alloy Ingots, *Metallography and Microstructures,* Vol 9, *ASM Handbook,* ASM International, 1985, p 629–636

5. R.E. Spear, R.T. Craig, and C.R. Howle, *J. Met.,* Vol 23 (No. 10), 1971, p 42–45

6. A. Cibula, *J. Inst. Met.,* Vol 80, 1951, p 1–16

7. L. Bäckerud, *Jernkontorets Ann.,* Vol 155, 1971, p 422–424

8. L. Bäckerud, *Light Met. Age,* Oct 1983, p 6–12

9. L.F. Mondolfo, *Light Metals,* Metallurgical Society of AIME, 1972, p 405–426

10. D.A. Granger and J. Liu, *J. Met.,* Vol 35 (No. 6), 1983, p 54–59

11. C. Degand, D.M. Stefanescu, and G. Laslaz, *Solidification Science and Processing,* I. Ohnaka and D.M. Stefanescu, Ed., 1996, p 55–63

D.M. Stefanescu and R. Ruxanda, Solidification Structures of Aluminum Alloys, *Metallography and Microstructures,* Vol 9, *ASM Handbook,* ASM International, 2004, p. 107–115

Solidification Structures of Aluminum Alloys

>Doru M. Stefanescu and Roxana Ruxanda, The University of Alabama

---

Eutectic Microstructure of Aluminum-Silicon Alloys

The microstructure of the eutectic or near-eutectic alloys consists of acicular or lamellar eutectic silicon (faceted crystals) dispersed throughout the aluminum matrix. Examples are given in Fig. 15 and 16. The addition of various modifiers (sodium, calcium, strontium) in small amounts changes the morphology of the eutectic phase from acicular to fibrous (nonfaceted), as shown in Fig. 17 and 18.

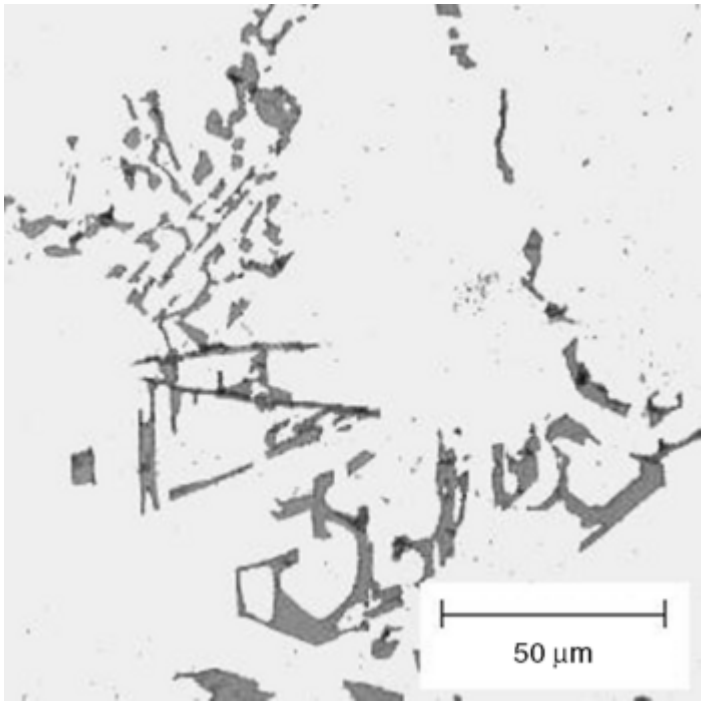

Fig. 15 Eutectic silicon crystals with acicular morphology in an unmodified sample of alloy A365. Etchant: Keller's reagent



Fig. 16 Silicon crystals with flakelike morphology in an unmodified sample of alloy A365. Scanning electron micrograph after deep etching. Original magnification 1000×. Source: Ref 2

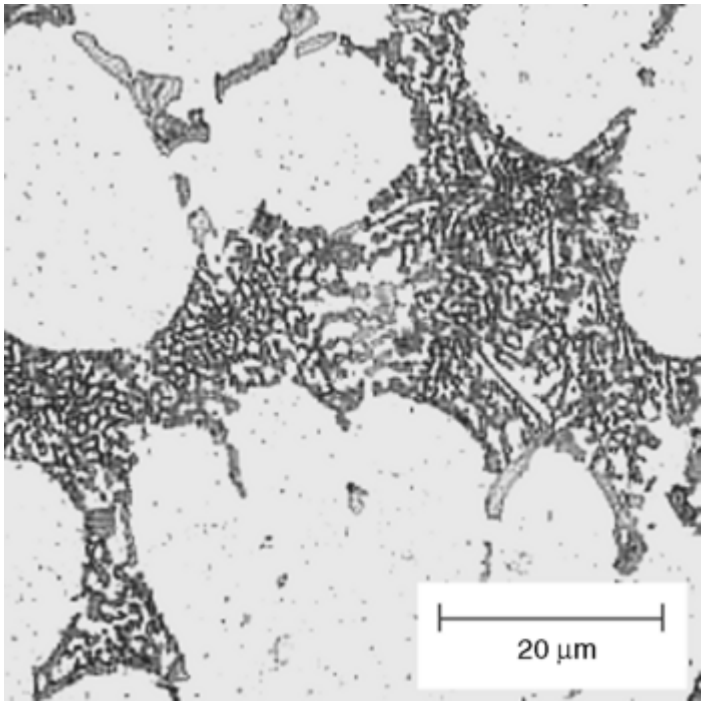

Fig. 17 Eutectic silicon crystals with fibrous morphology in a modified sample of alloy A365. Etchant: Keller's reagent

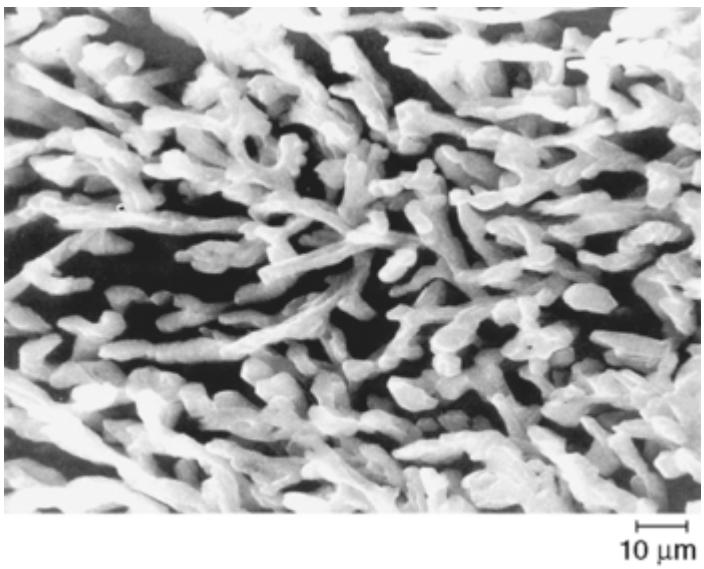

Fig. 18 Silicon crystals with seaweedlike morphology in a modified sample of alloy A365. Scanning electron microscopy image after deep etching. Original magnification 1000×. Source: Ref 2

In unmodified faceted silicon crystals, growth is favored in certain crystallographic directions. Some twin planes that form “re-entrant edges” are particularly effective in promoting growth (see Fig. 19) (Ref 2). Some theories explain the morphological change by the disturbances in the growth step of the silicon crystals induced by the adsorption of the modifying elements, which causes frequent twinning to occur (see Fig. 20) (Ref 12). Examples of the effect of modification on the microstructure of some alloys are given in Fig. 21 (Ref 13, 14).

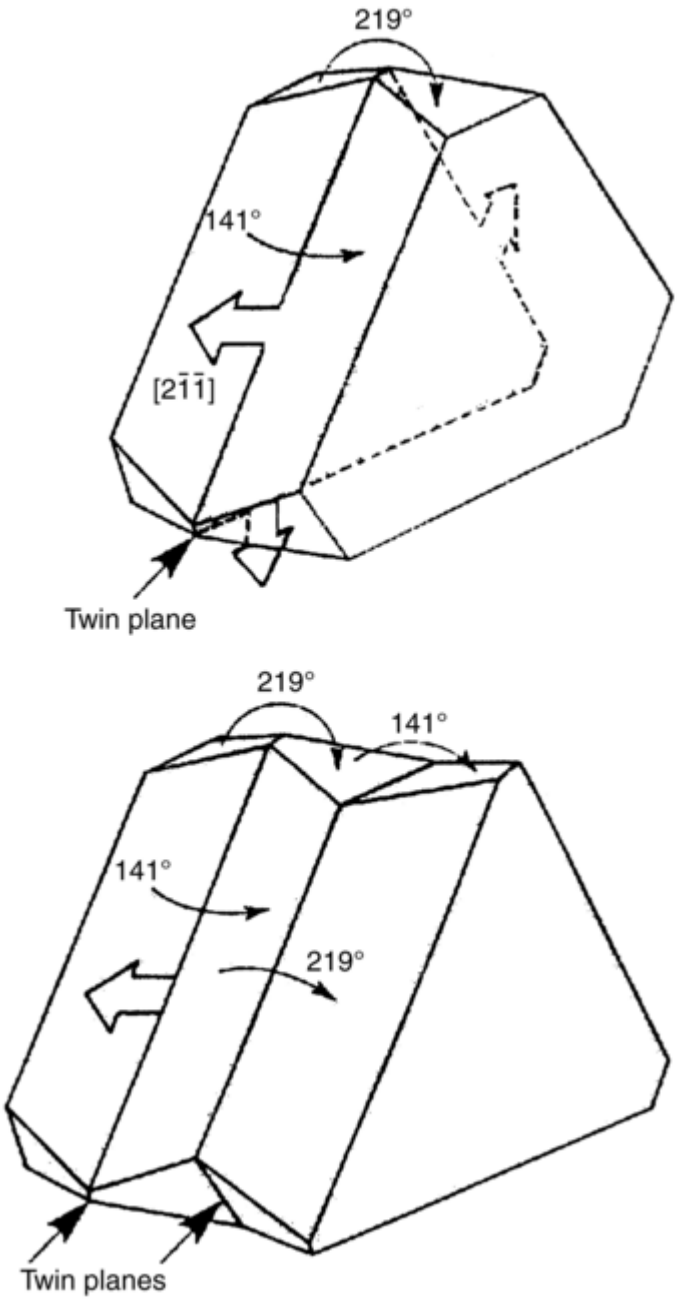

Fig. 19 Location of twin planes and re-entrant edge in a silicon crystal. Source: Ref 2

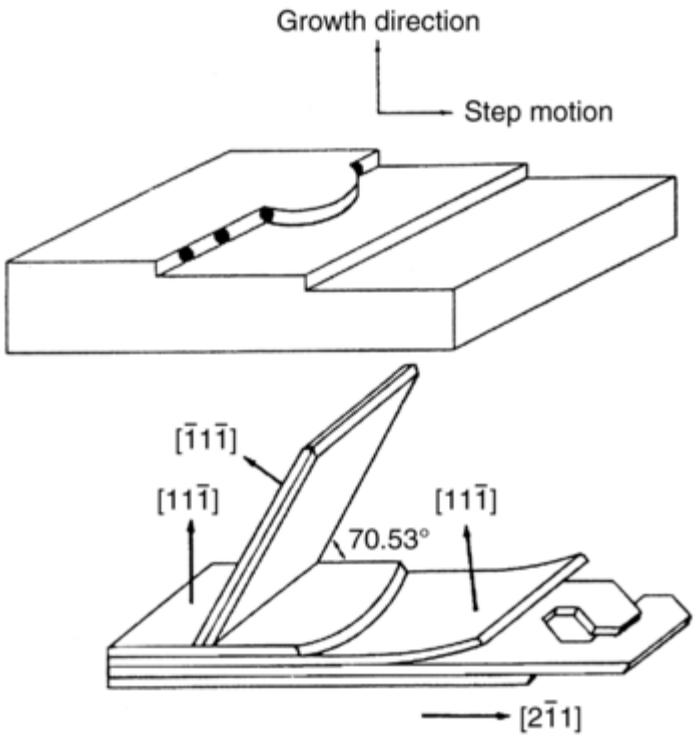

Fig. 20 Adsorption of impurity atoms on growth steps of a silicon crystal causing twinning. Source: Ref 12

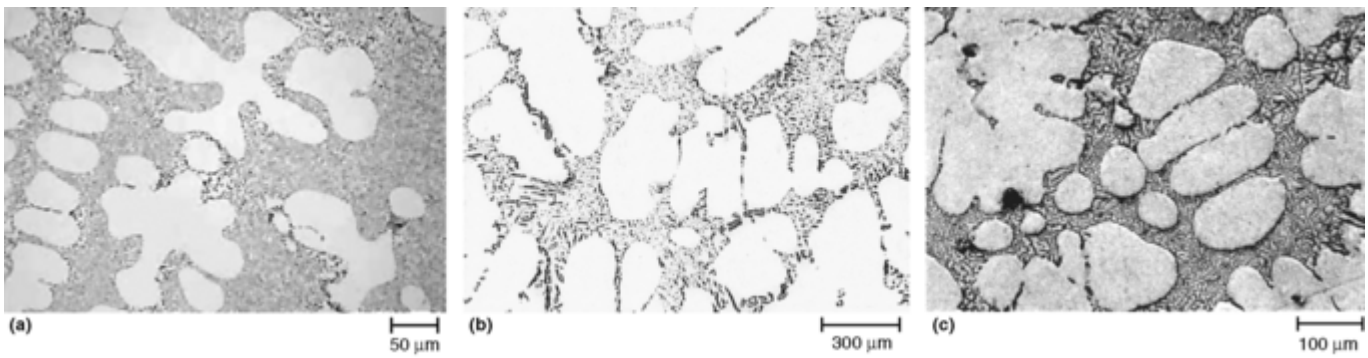

Fig. 21 Modified as-cast microstructures of aluminum alloys. (a) Al-10Si, strontium-modified eutectic. Source: Ref 13. (b) Alloy A356.0, strontium-modified eutectic. Source: Ref 14. (c) Alloy A356.0, sodium-modified eutectic. Original magnification 100×. Source: Ref 14

New methods of investigation, capable of determining the grain orientation, have emerged. The microstructure of the eutectic growth interface was investigated with electron backscattering diffraction (EBSD) in directionally solidified Al-7Si and A356 alloys, unmodified and strontium modified (Ref 15). An example of an EBSD map in relationship with the microstructure is given in Fig. 22. Colors indicate different crystallographic orientations on the EBSD map. Nonindexed points are black. The relationship between the crystallographic orientation parallel to the sample surface normal and the colors in the EBSD maps is given at the right. It was demonstrated that the eutectic aluminum has mainly the same crystallographic orientation as the dendrites in the unmodified alloys and the strontium-modified Al-7Si alloy. A planar eutectic growth front was observed in the Al-7Si alloy alloys; a more complex eutectic grain structure was found in the strontium-modified A356 alloy.

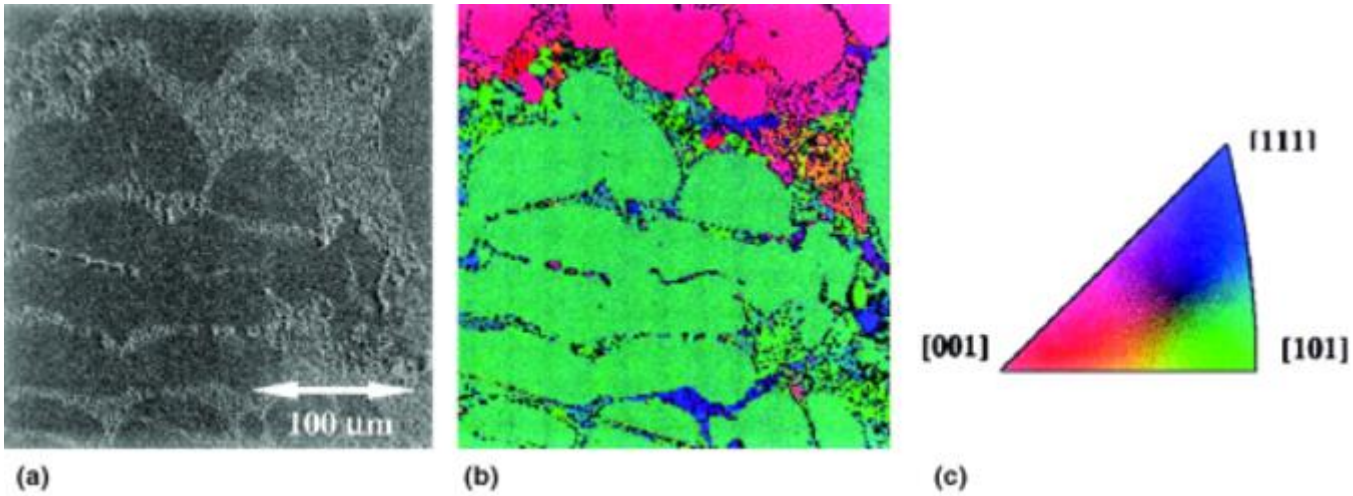

Fig. 22 Aluminum alloy A356.0 near-quenched eutectic growth interface. (a) Secondary electron black-and-white image (b) Electron backscattering diffraction map. (c) Indicates the crystallographic orientation. Source: K. Nogita and A.K. Dahle, *Scr. Mater.*, Vol 48, 2003, p 307–313

References cited in this section

2. L. Bäckerud, G.C. Chai, and J. Tamminen, *Solidification Characteristics of Aluminum Alloys,* Vol 2, AFS/Skanaluminum, 1990

12. S.-Z. Lu and A. Hellawell, *Met. Trans. A,* Vol 18A, Oct 1987, p 1721–1733

13. K. Nogita and A.K. Dahle, *Scr. Mater.,* Vol 48, 2003, p 307–313

14. J.E. Gruzleski and B.M. Closset, *The Treatment of Liquid Aluminum-Silicon Alloys,* AFS, 1990

15. G. Heiberg, K. Nogita, A.K. Dahle, and L. Arnberg, *Acta Mater.,* Vol 50, 2002, p 2537–2546

D.M. Stefanescu and R. Ruxanda, Solidification Structures of Aluminum Alloys, *Metallography and Microstructures,* Vol 9, *ASM Handbook,* ASM International, 2004, p. 107–115

Solidification Structures of Aluminum Alloys

>Doru M. Stefanescu and Roxana Ruxanda, The University of Alabama

---

Dendritic Microstructure

An example of a microstructure containing typical aluminum dendrites is shown in Fig. 23. The dendrites, revealed by deep etching the microstructure with modified Poulton reagent, were enhanced using specialized image analysis software. The three-dimensional shape of the dendrites can be observed in the microshrinkage cavities of the fractured specimen, as shown in Fig. 24.

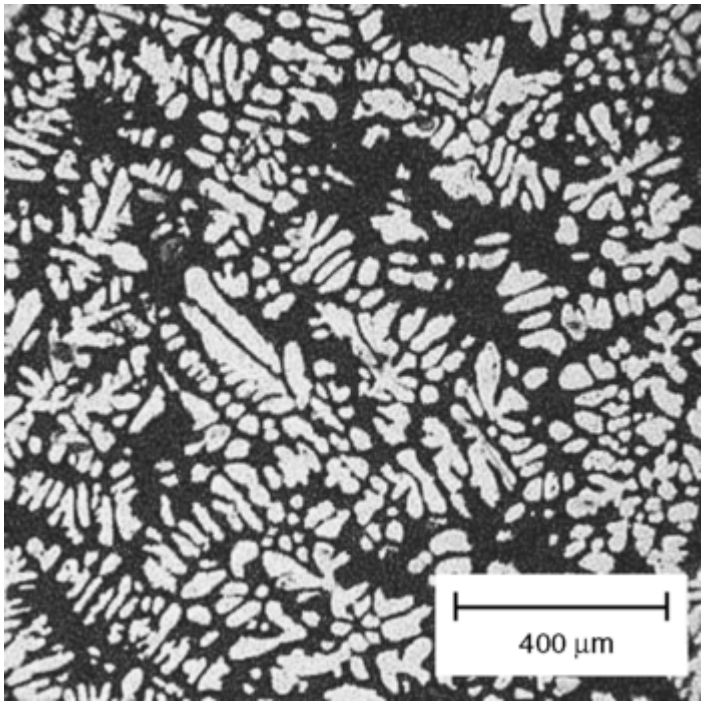

Fig. 23 Typical dendrites in an A356 alloy in a computer-processed image. Etchant: modified Poulton reagent (60% HCl, 30% HNO_3, 5% HF, 5% H_2O)

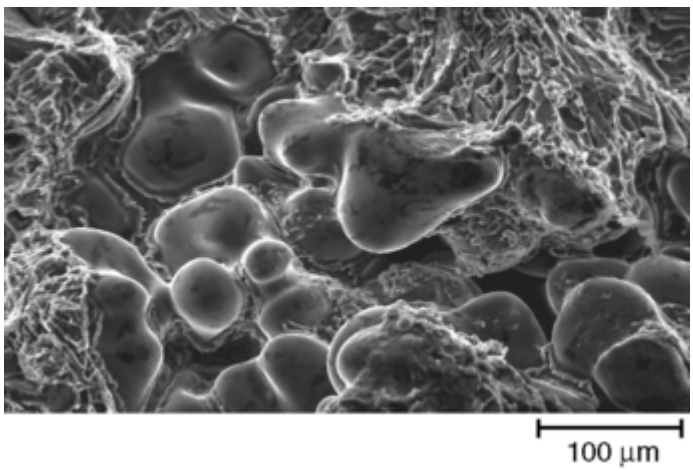

Fig. 24 Scanning electron micrography image of aluminum dendrites in the fractured surface of a tensile test bar of an A356.0 alloy

Recently, time-resolved direct-beam x-ray imaging with intense, coherent, and monochromatic third-generation synchrotron radiation and high-resolution fast-readout detector systems have been used for in situ studies of dendritic growth processes in aluminum-copper alloys (Ref 16). Two frames from a movie produced with this technique are shown in Fig. 25. Two grains nucleated through the detachment mechanism are shown: one in the center of the figures and one on the right (marked with arrow). The images are taken 34 s apart, and growth of the new crystals is clearly evident.

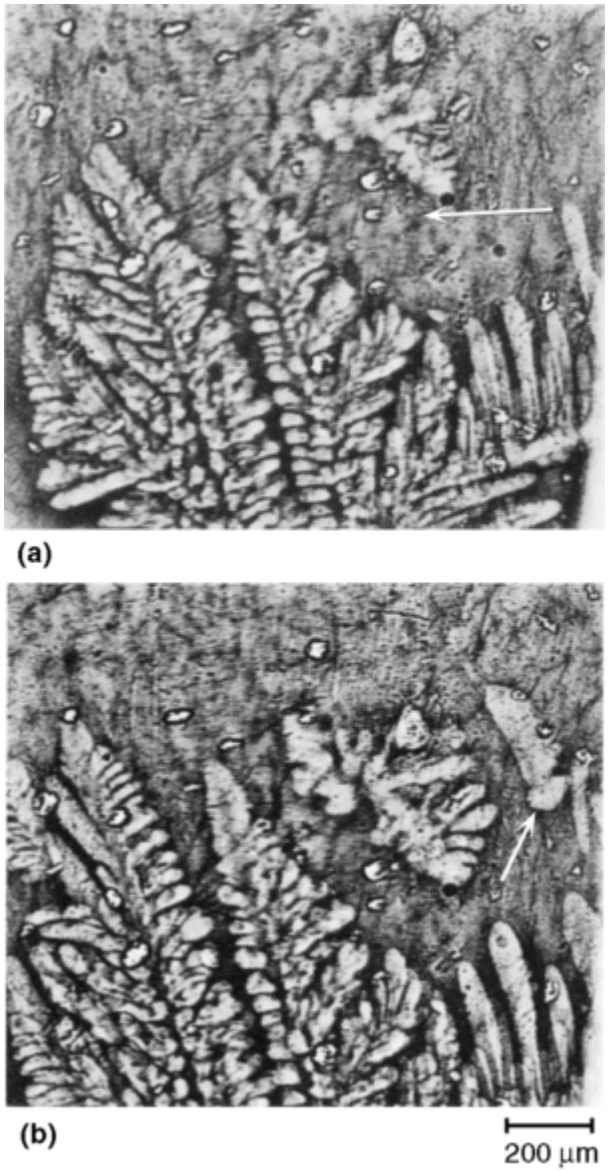

Fig. 25 Dendritic growth and grain multiplication in Al-20Cu alloy. Image (b) was taken 34 s after image (a). Arrow indicates grains nucleated by detachment. Source: Ref 16

The secondary dendrite arm spacing (SDAS) depends on the local solidification time and cooling rate as discussed in the article "Fundamentals of Solidification" in this Volume. For Al-4.5Cu alloys, the experimental data (Ref 17) in Fig. 26 can be fitted to Eq 7 in that article when the coarsening constant is 10^{-6} m/s^2. The influence of cooling rate on SDAS is illustrated in Fig. 27.

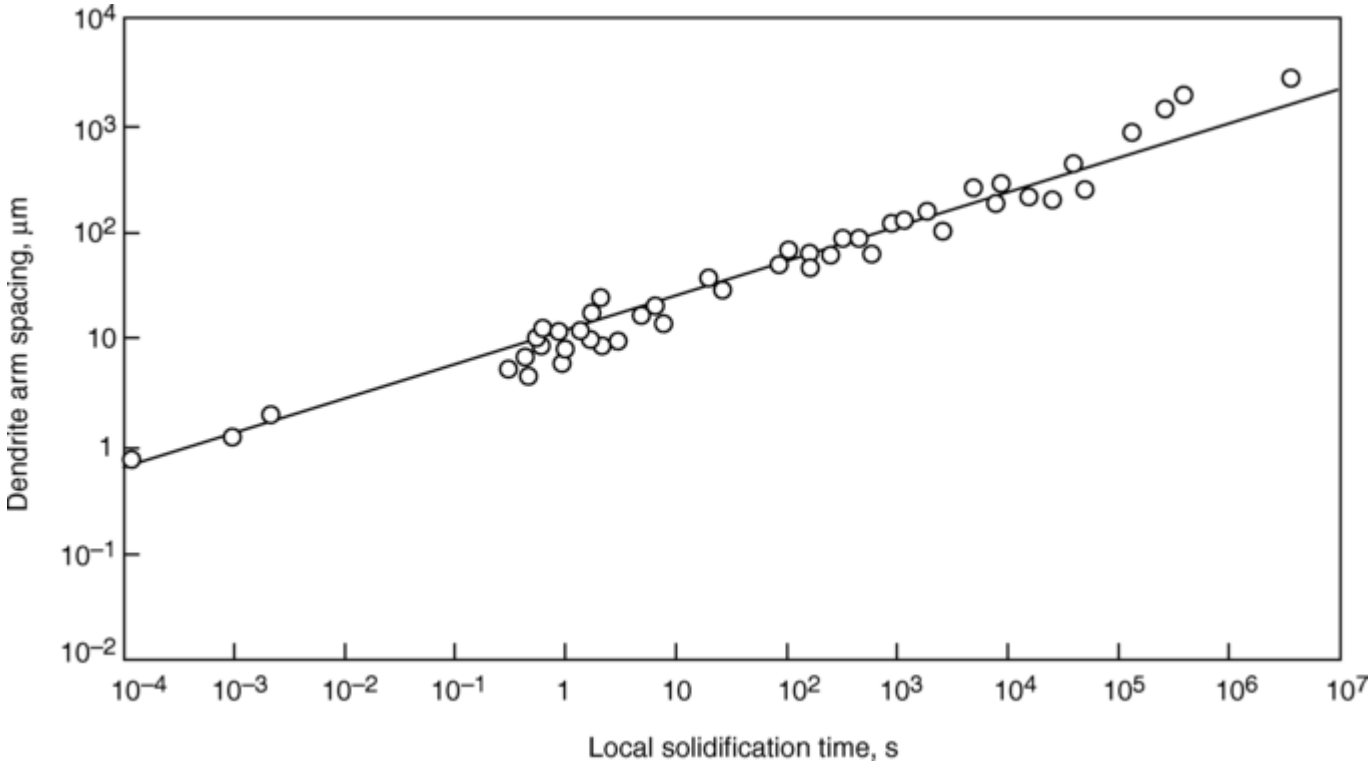

Fig. 26 Relation between secondary dendrite arm spacing and solidification time for Al-4.5Cu alloys. Data from 10 investigators. Source: Ref 17

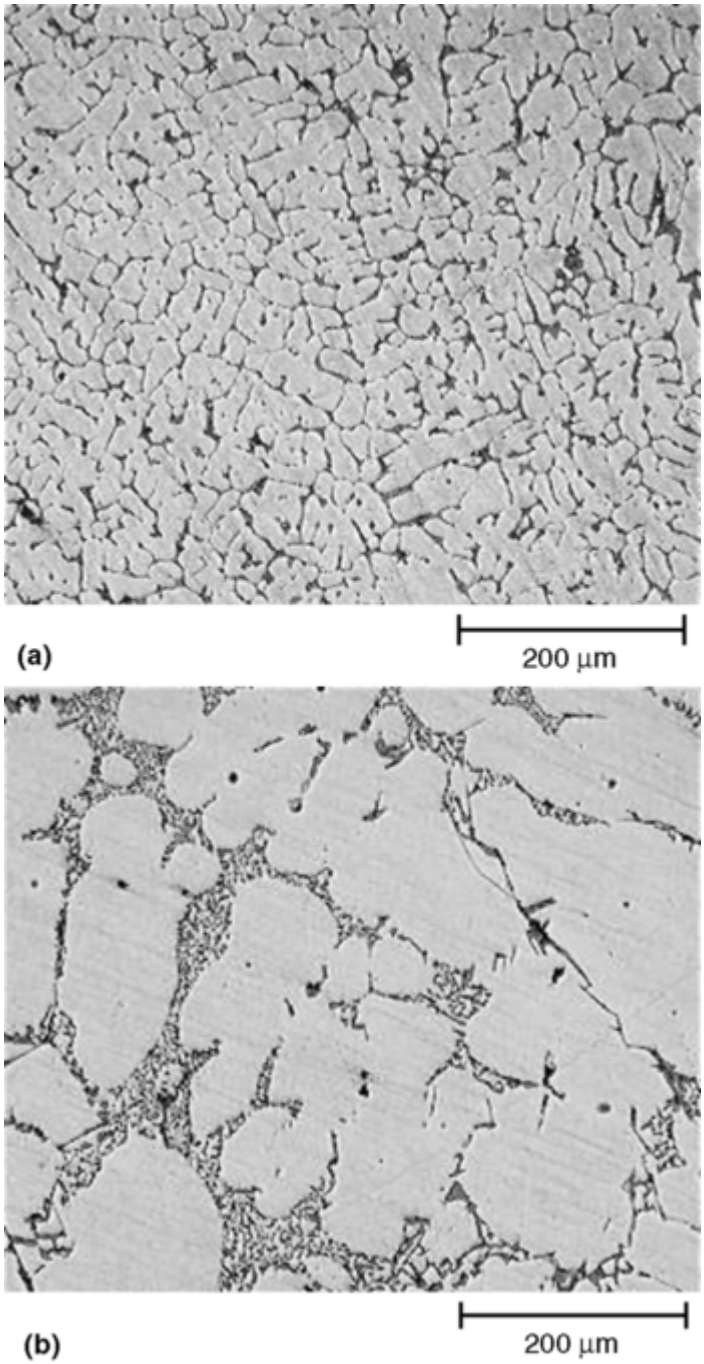

Fig. 27 Microstructures of A356 alloy solidified at different cooling rates. (a) Cast in metallic mold (high cooling rate), fine dendrites and network of interdendritic eutectic form. (b) Cast in green sand mold (low cooling rate), coarse dendrites and discontinuous network of interdendritic eutectic result. Etchant: Keller's reagent

The influence of solute content is less well defined (Ref 4). In general, up to eutectic compositions, the effect of increasing solute content at a constant cooling rate is to decrease the dendrite arm spacing (Fig. 28) (Ref 18).

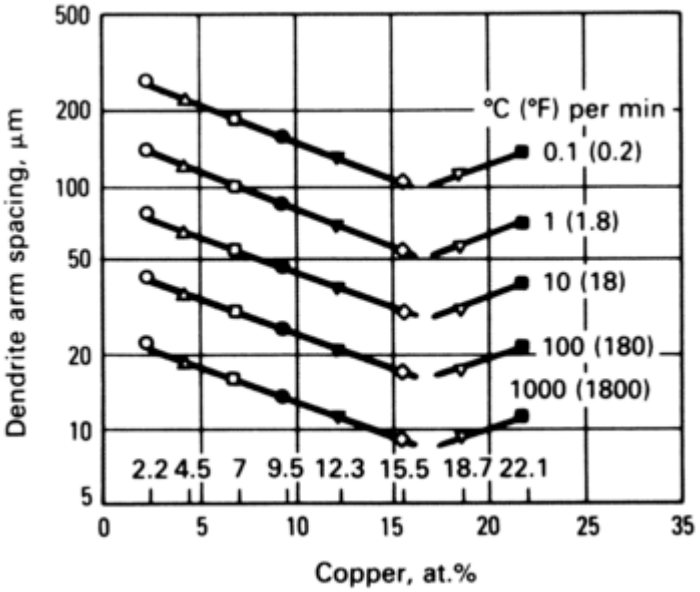

Fig. 28 Effect of copper content on secondary arm spacing in eight aluminum alloys, plotted for five cooling rates. Source: Ref 18

For Al-Cu-Si alloys the change in the copper content of the alloy has greater effect on the SDAS than silicon, when silicon content is greater than 0.5%; otherwise the silicon has greater effect. The combined influence of local solidification time, t_f, cooling rate at the liquidus temperature, $\dot{T}_L$, copper composition, C_{Cu}, and silicon composition, C_{Si}, on the SDAS can be calculated with (Ref 19):

$$SDAS = 34.9 \cdot C_{Cu}^{-0.333} \cdot C_{Si}^{-0.145} \cdot t_f^{0.208}$$

$$SDAS = 77.09 \cdot C_{Cu}^{-0.1989} \cdot C_{Si}^{-0.078} \cdot \dot{T}_L^{-0.252}$$

For Al-Mg-Si alloys, changing the magnesium content of the alloy has a greater effect on the SDAS than changing the silicon content, for silicon content greater than 0.5%. The combined influence of local solidification time, cooling rate at the liquidus temperature, magnesium composition, C_{Mg}, and silicon composition, C_{Si}, on the SDAS can be calculated with (Ref 20):

$$SDAS = 14.15 \cdot C_{Mg}^{-0.108} \cdot C_{Si}^{-0.125} \cdot t_f^{0.302}$$

$$SDAS = 65.21 \cdot C_{Mg}^{-0.235} \cdot C_{Si}^{-0.104} \cdot \dot{T}_L^{-0.22}$$

References cited in this section

4. D.A. Granger, Solidification Structures of Aluminum Alloy Ingots, *Metallography and Microstructures,* Vol 9, *ASM Handbook,* ASM International, 1985, p 629–636

16. R. Mathiesen, L. Arnberg, K. Ramsoskar, T. Weitkamp, C. Rau, and A. Snigirev, *Metall. Mater. Trans. B,* Vol 33B, 2002, p 613–623

17. M.C. Flemings, T.Z. Kattamis, and B.P. Bardes, *AFS Trans.,* Vol 99, 1991, p 501

18. J.A. Horwath and L.F. Mondolfo, *Acta Metall.,* Vol 10, 1962, p 1037–1042

19. V. Ronto and A. Roosz, *Int. J. Cast Met. Res.,* Vol 13, 2001, p 337–342

20. V. Ronto and A. Roosz, *Int. J. Cast Met. Res.,* Vol 14, 2001, p 131–135

D.M. Stefanescu and R. Ruxanda, Solidification Structures of Aluminum Alloys, *Metallography and Microstructures,* Vol 9, *ASM Handbook*, ASM International, 2004, p. 107–115

Solidification Structures of Aluminum Alloys

>Doru M. Stefanescu and Roxana Ruxanda, The University of Alabama

Microsegregation

Most of the major alloying additions in aluminum are less soluble in the solid phase than in the liquid phase (equilibrium partition ratio, $k < 1$). Moreover, for most solutes, aluminum exhibits a relatively low terminal solid solubility; therefore, second-phase constituents are invariably present in cast structures. For these reasons, the dendrites, which are the first portions of a cast structure to solidify, are low in solute content and are surrounded by interdendritic networks of one or more second-phase constituents. The size and distribution of the constituents depend on such factors as solute concentration, dendrite arm spacing, and grain size. The solute distribution characteristic of cast alloys may be described with reasonable accuracy by the Scheil equation (see Eq 3 in the article "Fundamentals of Solidification" in this Volume). Examples of elemental microsegregation are shown in Fig. 29 for the case of silicon microsegregation between the α-aluminum dendrites of solid solution and the eutectic in an Al-12.7Si cast sample, and in Fig. 30 for the case of copper and magnesium microsegregation in a 2124 direct-chill cast ingot. Microsegregation can be decreased by a homogenization treatment.

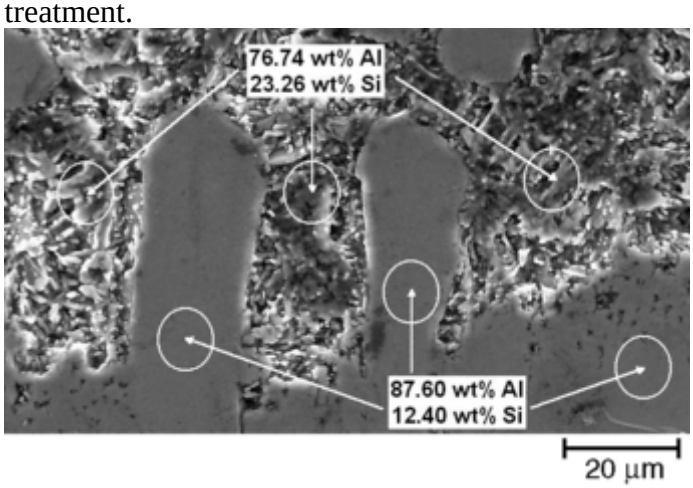

Fig. 29 Secondary electron microscopy image of dendrites and eutectic from an Al-12.7Si cast specimen. Silicon microsegregation between the dendrites of solid solution and eutectic revealed by electron probe microanalysis

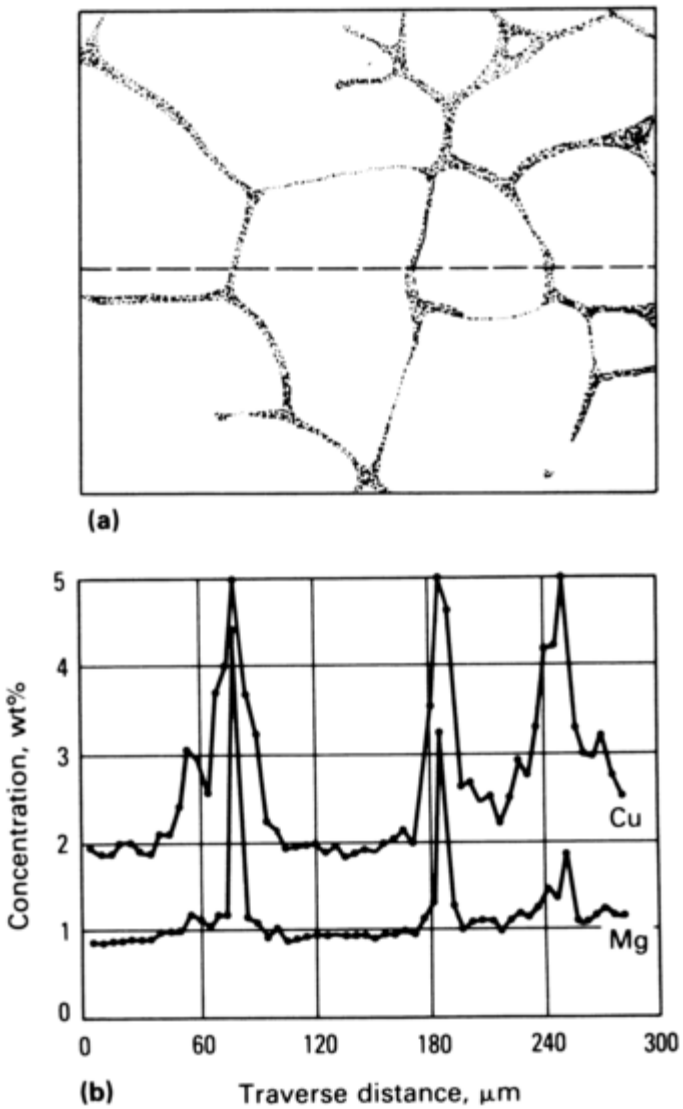

Fig. 30 Microstructure at a midthickness location. Direct-chill semicontinuous cast 610 × 1372 mm (24 × 54 in.) 2124 alloy ingot. Etchant: (a) 0.5% HF. (b) Copper and magnesium microsegregation (revealed by electron probe microanalysis) across the dendrites. Source: Ref 4

Reference cited in this section

4. D.A. Granger, Solidification Structures of Aluminum Alloy Ingots, *Metallography and Microstructures,* Vol 9, *ASM Handbook,* ASM International, 1985, p 629–636

D.M. Stefanescu and R. Ruxanda, Solidification Structures of Aluminum Alloys, *Metallography and Microstructures,* Vol 9, *ASM Handbook,* ASM International, 2004, p. 107–115

Solidification Structures of Aluminum Alloys

>Doru M. Stefanescu and Roxana Ruxanda, The University of Alabama

---

Macrosegregation

The chemical composition of large, commercial-size ingots can vary significantly from point to point through the ingot thickness, which is usually greater than 406 mm (16 in.) (see Fig. 31). This type of segregation, referred to as "macrosegregation," is only slightly affected by homogenization. In general, macrosegregation can be reduced in direct-chill ingot casting by decreasing ingot thickness, lowering the casting speed, and maximizing molten metal superheat (Ref 4). Macrosegregation is less of a problem in shaped castings. The mechanisms of formation of macrosegregation are discussed in detail in Ref 21.

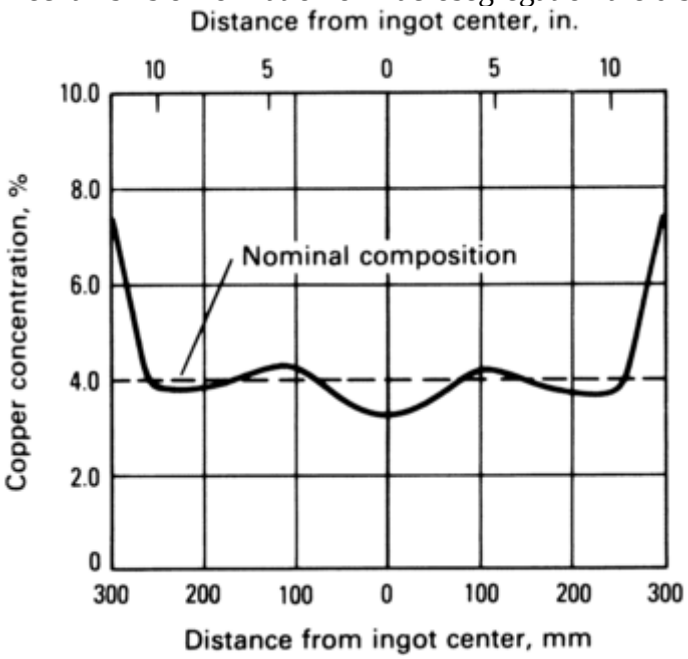

Fig. 31 Variation in copper concentration across a 600 mm (24 in.) thick direct-chill semicontinuous cast ingot of 2124 alloy. Source: Ref 4

References cited in this section

4. D.A. Granger, Solidification Structures of Aluminum Alloy Ingots, *Metallography and Microstructures,* Vol 9, *ASM Handbook,* ASM International, 1985, p 629–636

21. D.M. Stefanescu, *Science and Engineering of Casting Solidification,* Kluwer Academic, 2000

D.M. Stefanescu and R. Ruxanda, Solidification Structures of Aluminum Alloys, *Metallography and Microstructures,* Vol 9, *ASM Handbook*, ASM International, 2004, p. 107–115

Solidification Structures of Aluminum Alloys

>Doru M. Stefanescu and Roxana Ruxanda, The University of Alabama

---

Defects

Macroporosity and Microshrinkage. Gas evolution during solidification is responsible for at least two casting defects: macroporosity and microshrinkage (also called "microporosity" in the literature). While both defects have a significant influence on mechanical properties (ductility, fatigue), their mechanism of formation is quite different. Macroporosity results when gas is rejected from the liquid and is entrapped in the solidifying metals as spherical gas defects of millimeter size. Microshrinkage occurs when liquid metal cannot reach interdendritic areas during casting solidification. It is caused by a combination of shrinkage and gas evolution, being the

standard foundry defect for mushy-freezing alloys, such as aluminum alloys, steel, superalloys, brass, bronze, and cast iron. Microshrinkage voids are of the order of 10 to 100 μm (Ref 21).

The size and shape of the pore is determined by the amount of gas rejected by the melt. If this amount is large, spherical pores will form and continue to grow through diffusion before dendrite coherency is reached (Fig. 32). Their size can be of the order of tenths of mm to mm. This defect is called gas porosity. At lower amounts of gas rejected by the melt, pores form in the later stages of solidification, after dendrite coherency. The concomitant development of shrinkage cavities nucleated by these pores results in microshrinkage. The appearance of microshrinkage is not spherical, but follows the dendrite shape (Ref 22, 23) as seen in Fig. 33(a) and (b). If the melt is very well degassed, the gas bubbles form at the very end of solidification between the eutectic grains (Fig. 33c).

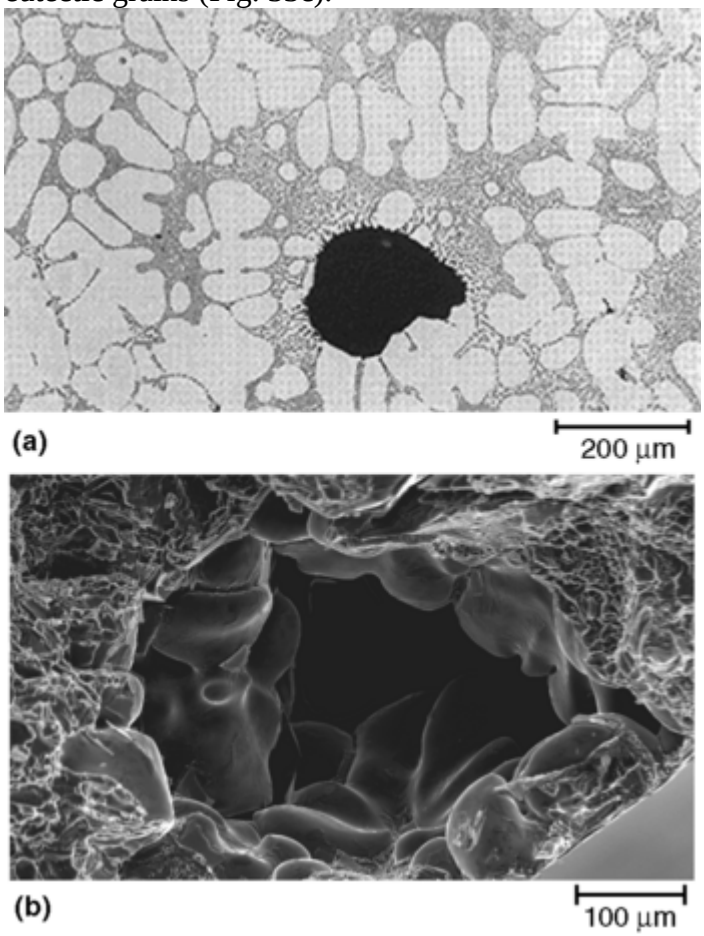

Fig. 32 Pores formed by gas evolution in the casting. (a) Light micrograph of a pore in aluminum-silicon alloy. Etchant: 0.5% HF. Source: Ref 22. (b) Scanning electron microscopy image of pore in unmodified aluminum-silicon alloy. Source: Ref 23

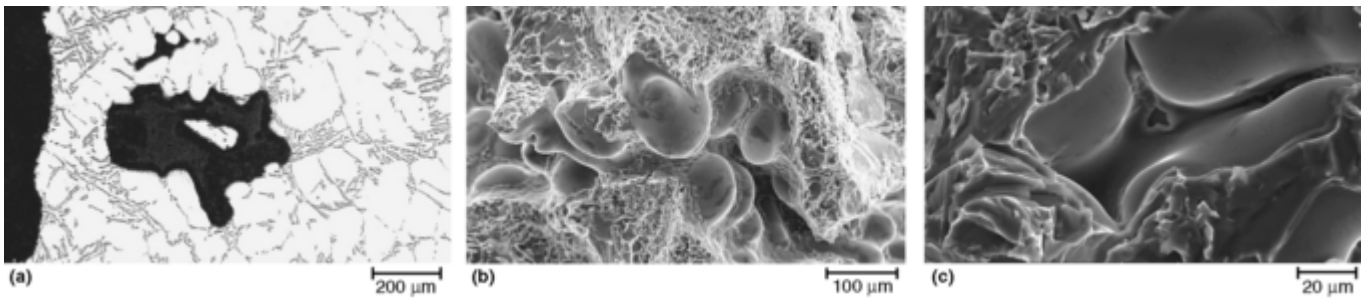

Fig. 33 Microshrinkage in aluminum alloys. (a) Light micrograph of interdendritic microshrinkage in aluminum-silicon alloy. Etchant: 0.5% HF. (b) Scanning electron microscopy image of interdendritic microshrinkage in aluminum-silicon alloy. Source: Ref 23. (c) Scanning electron microscopy image of microshrinkage between the eutectic grains in aluminum-silicon alloy. Source: Ref 23

The amount of microshrinkage seems to depend directly on the amount of hydrogen dissolved in the melt. Unless the gas content of the liquid is reduced below the solid solubility of the gas prior to solidification, the gas will precipitate when the last liquid to freeze (usually the eutectic) solidifies.

Modification of aluminum-silicon alloys with sodium or strontium increases the volume fraction of microshrinkage (Ref 24). This has been explained through a number of hypotheses such as decreased liquid surface tension because of modification, change in the dendrite morphology, increased number of inclusions, and obstruction of the liquid flow. Experimental evidence demonstrates that a high level of impurities in the melt is associated with a high microporosity.

Surface Defects. A surface layer containing an undesirable concentration of alloying elements and associated coarse particles is often found in direct-chill semicontinuous cast aluminum alloy ingots (Ref 4). A typical example in an alloy 7075 ingot is shown in Fig. 34. The constituents segregated near the surface are mainly Al-$MgZn_2$, iron-containing phases, and $MgSi_2$. In alloys with a large mushy zone, such as alloy 7075, exudations may occur on the surface. A similar surface defect, associated with dilute alloys, is the presence of bleed bands (Ref 25) (see Fig. 35). Both defects are caused by reheating the solidified shell of the casting when it separates from the mold wall, briefly ceasing heat removal (Ref 4).

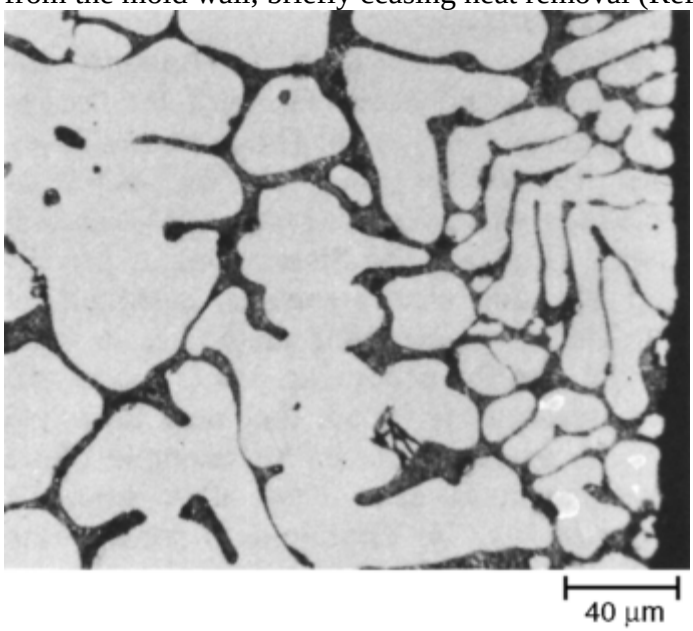

Fig. 34 Section through an alloy 7075 ingot (edge at right), direct-chill semicontinuous cast. Etchant: dilute Keller's reagent. Original magnification 250×. Source: Ref 4

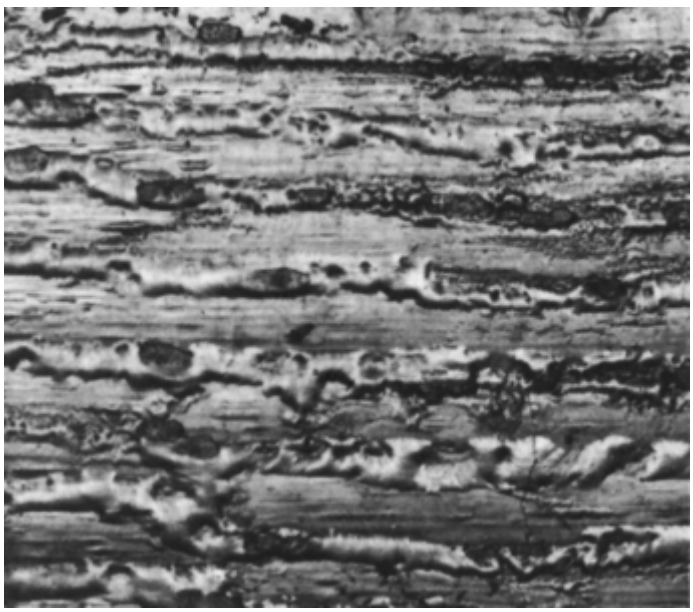

Fig. 35 Bleed bands normal to the casting direction on the surface of a direct-chill semicontinuous cast ingot of alloy 3003. Unpolished. One-fourth actual size. Source: Ref 25

The surfaces of aluminum alloy ingots are often “scalped” to remove segregated or nonuniform surface layers, which vary in thickness and may extend 20 mm (0.75 in.) below the chilled surface (Ref 26). The contrast between the coarse structure of the surface layer and the fine subsurface structure of an alloy 2024 ingot is shown in Fig. 36.

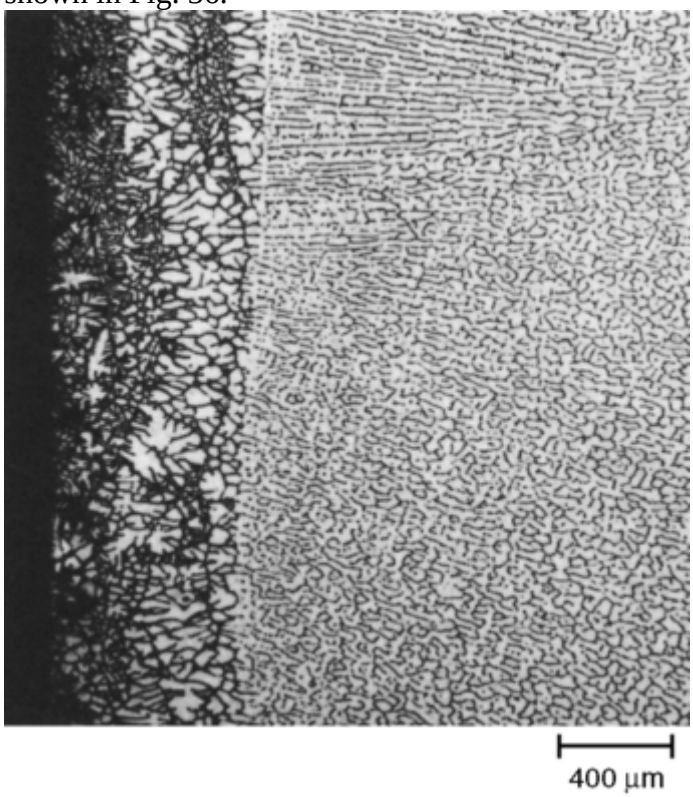

Fig. 36 Section through a 305 mm (12 in.) diam alloy 2024 ingot, direct-chill semicontinuous cast. Coarse dendrites and copper and magnesium constituents agglomeration in the surface layer. As-polished. Original magnification 25×. Source: Ref 4

Hot tearing is the result of tensile stresses building up in the mushy zone at the end of solidification. The mass deficit in the last volume to solidify produces voids in the interdendritic liquid as the dendrites are pulled apart when fluid flow cannot compensate for shrinkage. This defect is most common in dilute alloys.

The hot crack surface is very smooth, with small undulations corresponding to secondary dendrite arms (Fig. 37). This seems to indicate that hot cracking occurred while the grain boundary was covered by a thin liquid film. At many locations, spikes such as those shown in Fig. 37(a) can be observed on both sides of the hot cracked surface. They seem to have formed by elongation of a liquid region with simultaneous oxide formation at the surface, but without appreciable deformation. In a few cases, spikes such as that observed in Fig. 37(b) are seen. They exhibit a torn surface indicating that they have probably been formed by deformation and necking of a solid bridge extending across the grain boundary (Ref 27).

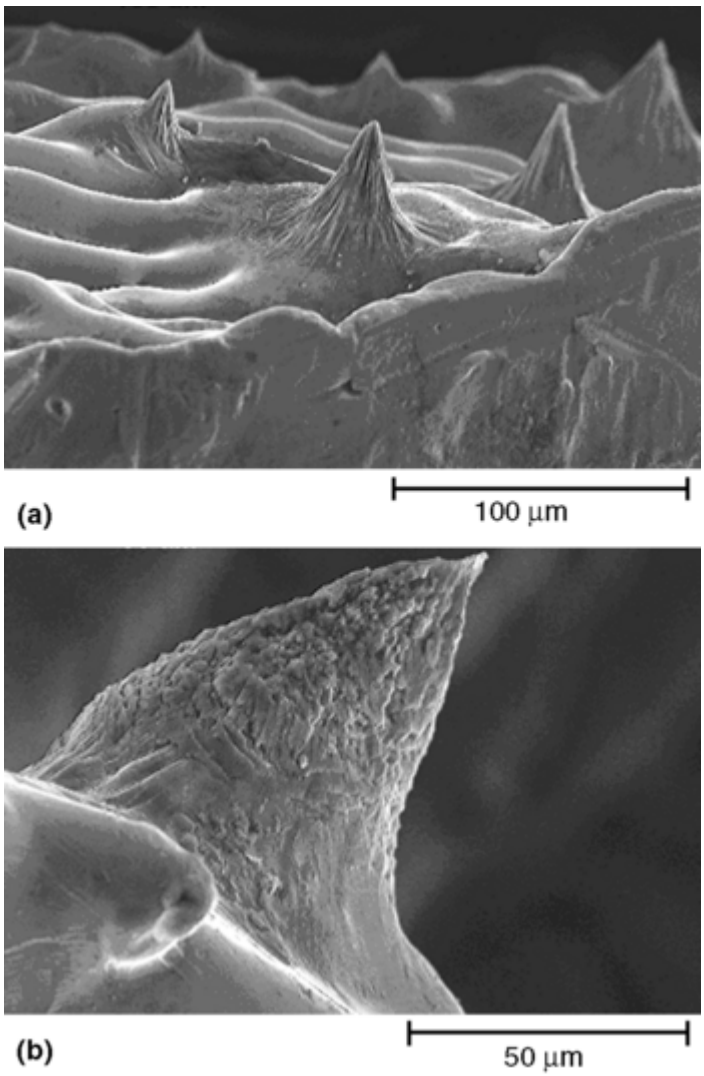

Fig. 37 Scanning electron microscopy observation of Al-3Cu. (a) Spike probably formed by the last solidification of interdendritic liquid. (b) Deformed spike probably formed by necking of a solid bridge. Source: Ref 27

Columnar structures are particularly prone to hot tearing, which may occur at the intersection of two columnar fronts, because of the mass deficit in the last region to solidify, and because of a buildup of internal tension stresses during final cooling of ingots. An example of center cracking in an alloy 1100 ingot is shown in Fig. 38. Center cracks (at arrow) resulted from excessively steep temperature gradients.

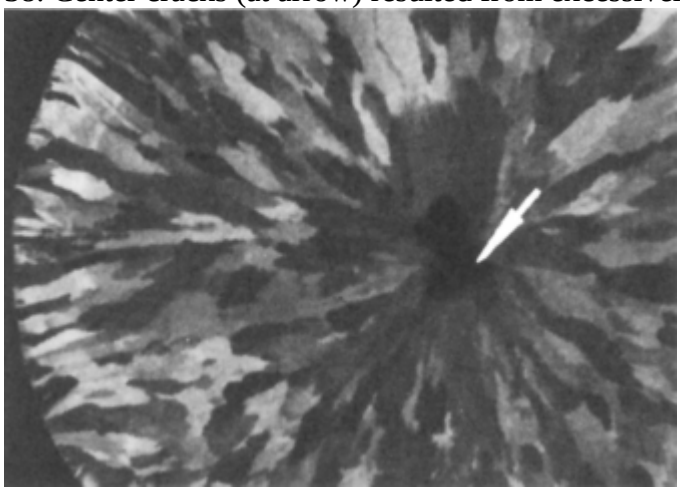

Fig. 38 Cross section through a 75 mm (3 in.) diam alloy 1100 ingot, direct-chill cast. Center cracks at arrow. Etchant: Tucker's reagent. Actual size. Source: Ref 4

Inclusions and Oxide Films. According to recent research (Ref 28), liquid metals cannot nucleate such defects as pores and cracks by heterogeneous nucleation. The melt surface is usually covered with a film, usually an oxide film. The entrainment of this surface film during pouring leads to many defects on which pores and cracks can grow. The defects include bubbles and their associated bubble trails of various kinds, and folded films (bifilms) that act as cracks and as substrates for the precipitation of many phases. Most failure mechanisms of cast products appear to be associated with bifilms, particularly those introduced during mold filling. This seems to be particularly true for hot tearing, which appears to be eliminated in even the most susceptible alloys simply by reduced surface turbulence during mold filling.

The entrainment mechanism is a simple folding-in action, thus folding the surface oxide dry side to dry side, and entraining a thin layer of adsorbed air between the films (see Fig. 39) forming a bifilm. Since there is practically no bonding across the air layer bounded by these dry interfaces, the defect acts as a crack in the liquid (Ref 28). The bifilms can be extremely thin: the oxides may be only 20 nm thick. If the air layer has a similar thickness the total thickness may be only 60 nm, although total thickness in the range 1 to 10 μm is common. However, the area of the defect can be large. In aluminum castings 10 mm square is common, but 10 to 1000 μm is probably more usual. Their volume density (number per mL) can range from 1 to 1000 or more.

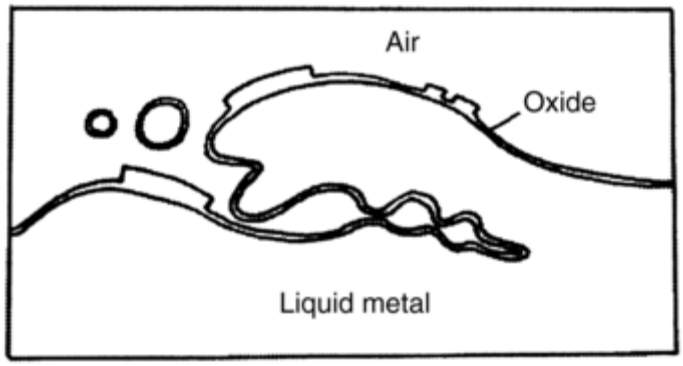

Fig. 39 Surface turbulence, acting to fold in a bifilm and bubbles. Source: Ref 28

Other inclusions may be present in the solidifying aluminum casting (Fig. 40). Hard inclusions may perforate the oxide films and initiate fracture (Fig. 41).

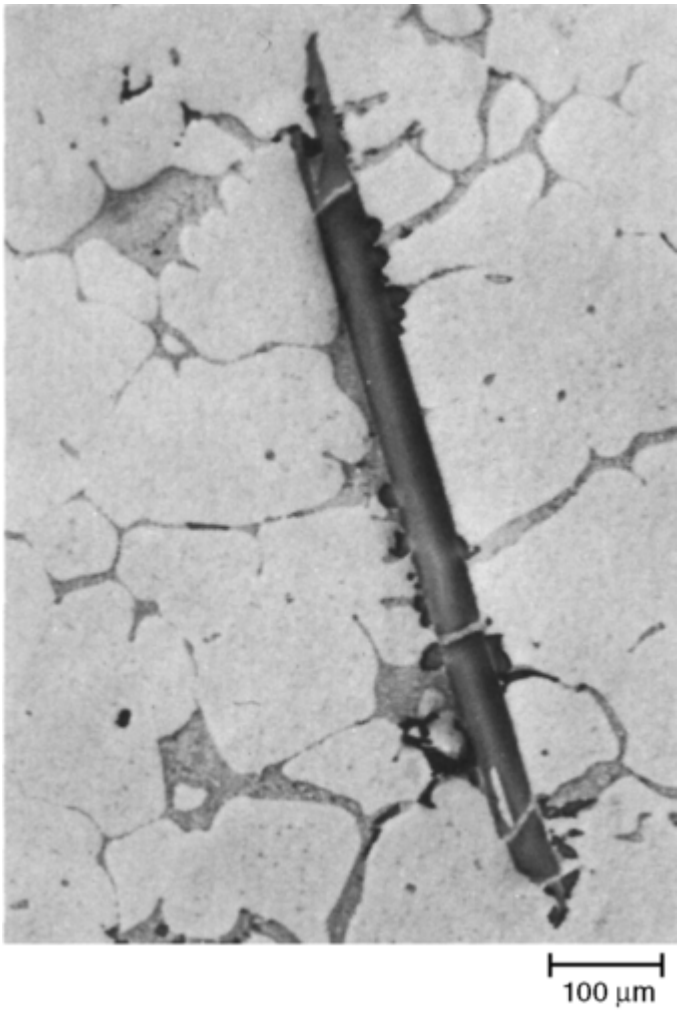

Fig. 40 Coarse primary crystal of CrAl7 in an alloy 7075 ingot. As-polished. Original magnification 100×. Source: Ref 4

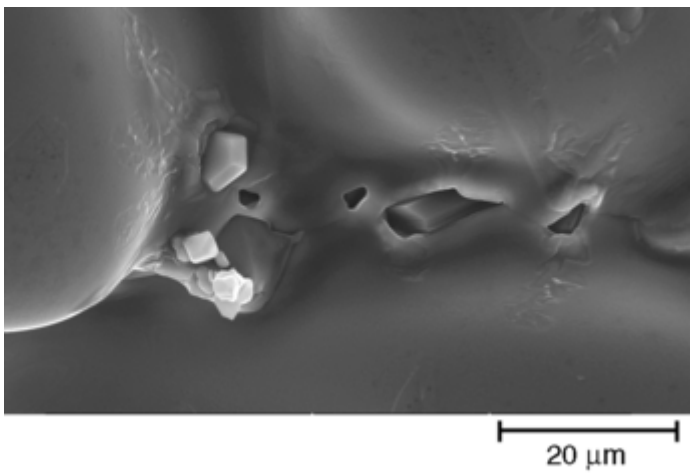

Fig. 41 Scanning electron microscopy image of oxide inclusions in aluminum cast samples (fractured surface)

References cited in this section

4. D.A. Granger, Solidification Structures of Aluminum Alloy Ingots, *Metallography and Microstructures,* Vol 9, *ASM Handbook,* ASM International, 1985, p 629–636

21. D.M. Stefanescu, *Science and Engineering of Casting Solidification,* Kluwer Academic, 2000

22. R. Fuoco, H. Goldenstein, and J.E. Gruzleski, *AFS Trans.,* Vol 101, 1994, p 297

23. T.S. Piwonka, *Proc. Merton C. Flemings Symposium on Solidification and Materials Processing,* R. Abbaschian, H. Brody, and A. Mortensen, Ed., TMS, 2000, p 363

24. D. Argo and J. Gruzleski, *AFS Trans.,* Vol 96, 1988, p 65

25. D.L.W. Collins, *Metallurgia,* Vol 76, Oct 1967, p 137–144

26. G. Siebel, D. Altenpohl, and M.H. Cohen, *Z. Metallkde.,* Vol 44, 1953, p 173–183

27. M. Rappaz, J.M. Drezet, P.D. Grasso, and A. Jacot, *Modeling of Casting, Welding and Advanced Solidification Processes,* D.M. Stefanescu, J. Warren, M. Jolly, and M. Krane, Ed., TMS, 2003, p 53–60

28. J. Campbell, *Modeling of Casting, Welding and Advanced Solidification Processes,* D.M. Stefanescu, J. Warren, M. Jolly, and M. Krane, Ed., TMS, 2003, p 209–218

D.M. Stefanescu and R. Ruxanda, Solidification Structures of Aluminum Alloys, *Metallography and Microstructures,* Vol 9, *ASM Handbook,* ASM International, 2004, p. 107–115

Solidification Structures of Aluminum Alloys

>Doru M. Stefanescu and Roxana Ruxanda, The University of Alabama

---

References

1. I.J. Polmear, *Light Metals,* E. Arnold Publishers, London, 1981

2. L. Bäckerud, G.C. Chai, and J. Tamminen, *Solidification Characteristics of Aluminum Alloys,* Vol 2, AFS/Skanaluminum, 1990

3. F. Xie, X. Yan, L. Ding, F. Zhang, S. Chen, M.G. Chu, and Y.A. Chang, *Mater. Sci. Eng. A,* Vol A00, 2003, p 1–10 (in press)

4. D.A. Granger, Solidification Structures of Aluminum Alloy Ingots, *Metallography and Microstructures,* Vol 9, *ASM Handbook,* ASM International, 1985, p 629–636

5. R.E. Spear, R.T. Craig, and C.R. Howle, *J. Met.,* Vol 23 (No. 10), 1971, p 42–45

6. A. Cibula, *J. Inst. Met.,* Vol 80, 1951, p 1–16

7. L. Bäckerud, *Jernkontorets Ann.,* Vol 155, 1971, p 422–424

8. L. Bäckerud, *Light Met. Age,* Oct 1983, p 6–12

9. L.F. Mondolfo, *Light Metals,* Metallurgical Society of AIME, 1972, p 405–426

10. D.A. Granger and J. Liu, *J. Met.,* Vol 35 (No. 6), 1983, p 54–59

11. C. Degand, D.M. Stefanescu, and G. Laslaz, *Solidification Science and Processing,* I. Ohnaka and D.M. Stefanescu, Ed., 1996, p 55–63

12. S.-Z. Lu and A. Hellawell, *Met. Trans. A,* Vol 18A, Oct 1987, p 1721–1733

13. K. Nogita and A.K. Dahle, *Scr. Mater.,* Vol 48, 2003, p 307–313

14. J.E. Gruzleski and B.M. Closset, *The Treatment of Liquid Aluminum-Silicon Alloys,* AFS, 1990

15. G. Heiberg, K. Nogita, A.K. Dahle, and L. Arnberg, *Acta Mater.,* Vol 50, 2002, p 2537–2546

16. R. Mathiesen, L. Arnberg, K. Ramsoskar, T. Weitkamp, C. Rau, and A. Snigirev, *Metall. Mater. Trans. B,* Vol 33B, 2002, p 613–623

17. M.C. Flemings, T.Z. Kattamis, and B.P. Bardes, *AFS Trans.,* Vol 99, 1991, p 501

18. J.A. Horwath and L.F. Mondolfo, *Acta Metall.,* Vol 10, 1962, p 1037–1042

19. V. Ronto and A. Roosz, *Int. J. Cast Met. Res.,* Vol 13, 2001, p 337–342

20. V. Ronto and A. Roosz, *Int. J. Cast Met. Res.,* Vol 14, 2001, p 131–135

21. D.M. Stefanescu, *Science and Engineering of Casting Solidification,* Kluwer Academic, 2000

22. R. Fuoco, H. Goldenstein, and J.E. Gruzleski, *AFS Trans.,* Vol 101, 1994, p 297

23. T.S. Piwonka, *Proc. Merton C. Flemings Symposium on Solidification and Materials Processing,* R. Abbaschian, H. Brody, and A. Mortensen, Ed., TMS, 2000, p 363

24. D. Argo and J. Gruzleski, *AFS Trans.,* Vol 96, 1988, p 65

25. D.L.W. Collins, *Metallurgia,* Vol 76, Oct 1967, p 137–144

26. G. Siebel, D. Altenpohl, and M.H. Cohen, *Z. Metallkde.,* Vol 44, 1953, p 173–183

27. M. Rappaz, J.M. Drezet, P.D. Grasso, and A. Jacot, *Modeling of Casting, Welding and Advanced Solidification Processes,* D.M. Stefanescu, J. Warren, M. Jolly, and M. Krane, Ed., TMS, 2003, p 53–60

28. J. Campbell, *Modeling of Casting, Welding and Advanced Solidification Processes,* D.M. Stefanescu, J. Warren, M. Jolly, and M. Krane, Ed., TMS, 2003, p 209–218

D.M. Stefanescu and R. Ruxanda, Solidification Structures of Titanium Alloys, *Metallography and Microstructures,* Vol 9, *ASM Handbook,* ASM International, 2004, p. 116–126

Solidification Structures of Titanium Alloys

Doru M. Stefanescu and Roxana Ruxanda, University of Alabama

Introduction

MOST TITANIUM ALLOYS, 80 to 90% of the alloy produced, is used for critical frame and engine components in the aerospace industries (Ref 1). Recently, the importance of these alloys as corrosion-resistant materials has been appreciated by the chemical industry as well as by the medical profession, which uses titanium alloy prostheses for implanting in the human body.

Titanium has a number of features that distinguish it from the other light metals (Ref 1, 2). At 882 °C (1620 °F), titanium undergoes an allotropic transformation from a low-temperature, hexagonal close-packed structure (hcp) (α) to a body-centered cubic (β) phase that remains stable up to the melting point. This transformation offers the possibility of using heat treatment. Titanium is a transition metal with an incomplete *d* shell in its electronic structure, which enables it to form solid solutions with most substitutional elements having a size factor within ±20%. Alloying of titanium is dominated by the ability of elements to stabilize either the α or the β phases. This behavior, in turn, is related to the number of bonding electrons, that is, the group number of the element concerned. Alloying elements with electron/atom ratios of less than 4 stabilize the α phase, elements with a ratio of 4 are neutral, and elements with ratios greater than 4 are β stabilizing. Titanium and its alloys react with several interstitial elements including oxygen, nitrogen, and hydrogen gases. Such reactions may occur at temperatures well below the respective melting points.

References cited in this section

1. E.W. Collings, *The Physical Metallurgy of Titanium Alloys,* American Society for Metals, 1984
2. I.J. Polmear, *Light Alloys—Metallurgy of the Light Metals,* American Society for Metals, 1982

D.M. Stefanescu and R. Ruxanda, Solidification Structures of Titanium Alloys, *Metallography and Microstructures,* Vol 9, *ASM Handbook,* ASM International, 2004, p. 116–126

Solidification Structures of Titanium Alloys

Doru M. Stefanescu and Roxana Ruxanda, University of Alabama

Classification of Titanium Alloys

The titanium-rich sections of pseudobinary systems enable them to be classified into three simple types, as shown in Fig. 1. Elements that dissolve preferentially in the α phase expand this field (α stabilizers), thereby raising the α/β transus (Fig. 1a). Elements that depress the α/β transus and stabilize the β phase (β stabilizers) may be classified in two groups: β isomorphous type that form binary systems (Fig. 1b) and those that favor formation of a β eutectoid (Fig. 1c). However, the eutectoid reactions in a number of alloys are very sluggish so that, in practice, the alloys tend to behave as if this reaction did not occur. It is customary to classify titanium alloys into three main groups designated α, α + β, and β. Typical microstructures of α, α + β, and β titanium

alloys are shown in Fig. 2. The only commonly used fully α alloys are the several grades of commercial pure titanium, which are in effect titanium-oxygen alloys, titanium-copper alloys, and the ternary composition Ti-Al-Sn. Most α-β alloys contain elements to stabilize and strengthen the α phase, together with 4 to 6% of β-stabilizing elements, which allow substantial amounts of this phase to be retained after quenching from the β or α + β phase fields. These alloys may contain between 10 and 50% β phase at room temperature (Ref 1). The α-β alloys have the greatest commercial importance with one composition, Ti-6Al-4V (IMI 318), making up more than half the sales of titanium alloys both in Europe and the United States. A typical cast Ti-6Al-4V microstructure is shown in Fig. 3.

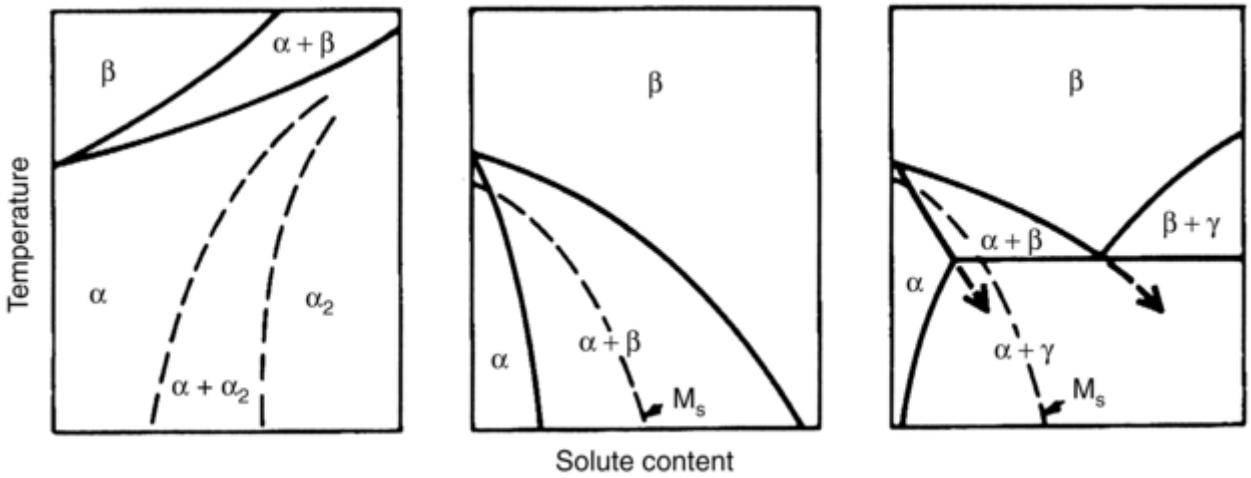

Fig. 1 Basic types of phase diagrams for titanium alloys. (a) Solute is Al, O, N, C, or Ga. The dotted phase boundaries refer specifically to the titanium-aluminum system. (b) Solute is Mo, V, V, or Ta. The dotted line shows the martensite start (M_s) temperatures. (c) Solute is Cu, Mn, Cr, Fe, Ni, Co, or H. The dotted line shows the martensite start (M_s) temperatures. Source: Ref 2

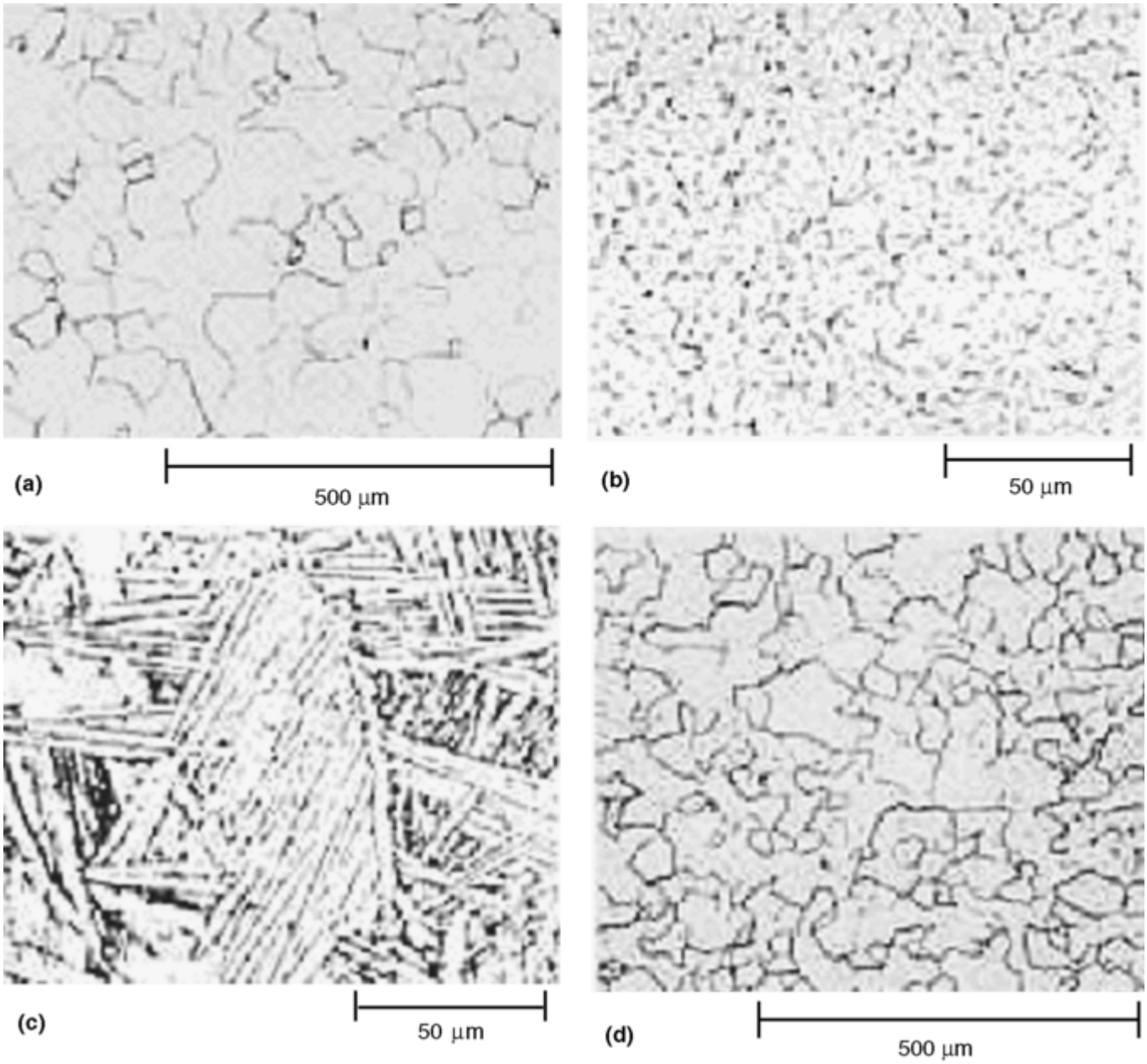

Fig. 2 Typical microstructures of α, α + β, and β titanium alloys. (a) Equiaxed α in unalloyed titanium after 1 h at 700 °C (1290 °F). (b) Equiaxed α + β. (c) Acicular α + β in Ti-6Al-4V. (d) Equiaxed β in Ti-13V-11Cr-3Al. Source: Ref 1

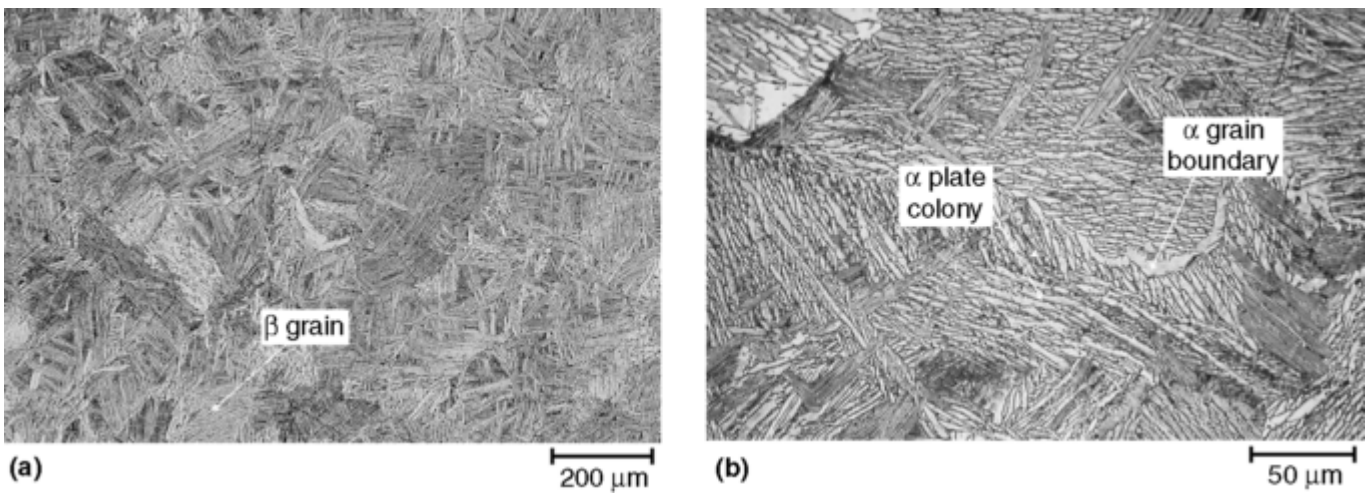

Fig. 3 Microstructures of as-cast Ti-6Al-4V. (a) With β grains. (b) With α grain and grain boundary. Etchant: 10 mL HF, 5 mL HNO_3, 85 mL H_2O

The β grain size, typically ranging from 0.5 to 5 mm (0.02 to 0.2 in.), develops during cooling through the β phase field, with slow cooling rates resulting in larger β grains (Ref 3). Alpha plates develop along the boundaries of the β grains during cooling through the α + β phase region. Finally, α plate colonies form within the β grains when cooling below the β transus temperature. When the cooling is slow, as in castings, these plates are arranged in colonies or packets, which are similarly aligned and have a common crystallographic orientation.

The α plate thickness range is 1 to 3 μm (0.04 to 0.12 mils), and the colony size range is typically 50 to 500 μm (0.2 to 20 mils) (Ref 3). As a general rule, slower cooling through the α + β phase region leads to larger colonies and thicker α plates. For this reason, slowly solidified thicker casting sections exhibit larger β grains, thicker α plates, and larger α plate colonies. In certain conditions, Ti-6Al-4V slowly cooled from β phase forms a “basketweave” structure of Widmanstätten α plates in the β matrix, as shown in Fig. 3. In more rapidly cooled samples, Ti-6Al-4V microstructure still retains the primary α dendrites (high-temperature phase), as shown in Fig. 4.

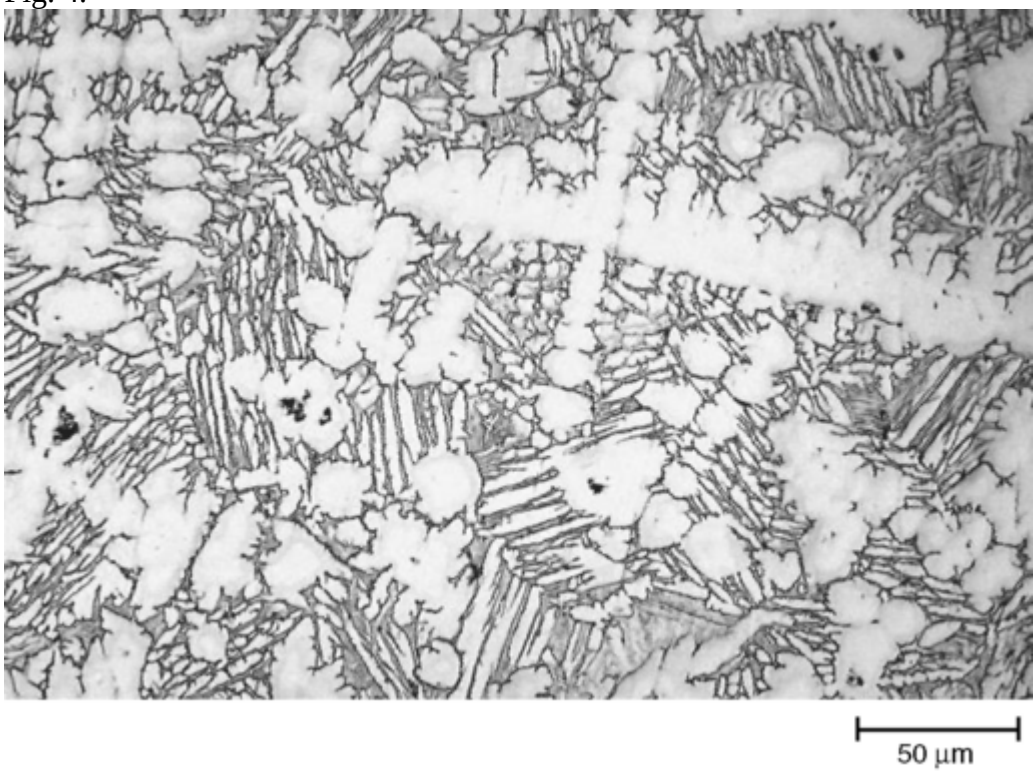

Fig. 4 Arc-melted microstructure of Ti-6Al-4V. Etchant: 10 mL HF, 5 mL HNO_3, 85 mL H_2O

The two common types of pores found in ferrous or aluminum castings, gas and microshrinkage, are also found in titanium castings. The microshrinkage cavity is placed along the grain boundary, as observed in Fig. 5.

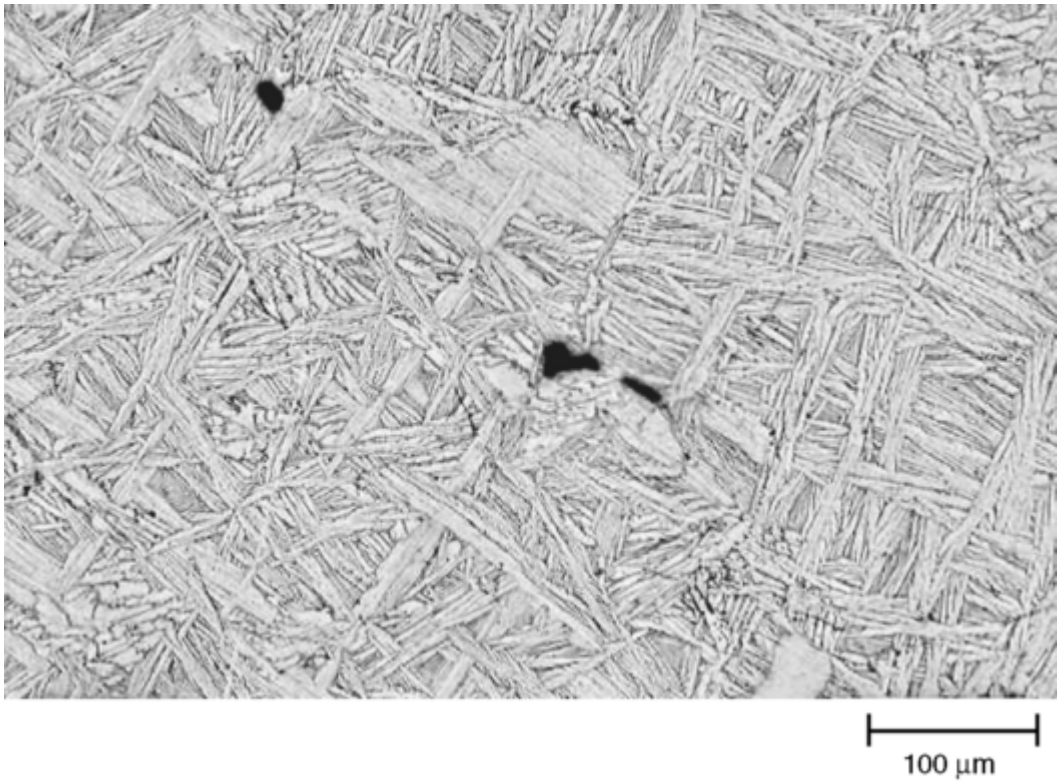

Fig. 5 Ti-6Al-4V slowly cooled from β phase. Basketweave structure of Widmanstätten α plates in a β matrix. Etchant: 10 mL HF, 5 mL HNO_3, 85 mL H_2O

The first alloy to be used commercially was the composition Ti-13V-11Cr-3Al with tensile strength as high as 1300 MPa (190 ksi). Another relatively early β alloy was the medium-strength Ti-15Mo with application in the chemical industry. More recently, other β alloys have been developed with higher levels of strengthening: Ti-8Mo-8V-2Fe-3Al, Ti-15V-3Sn-3Cr-3Al, and Ti-11.5Mo-6Zr-4.5Sn.
An example of a metastable β phase microstructure, achieved by beam welding of Ti-24Al-17Nb alloy, is given in Fig. 6. Another example, of equiaxed β phase microstructure, is given in Fig. 2(d).

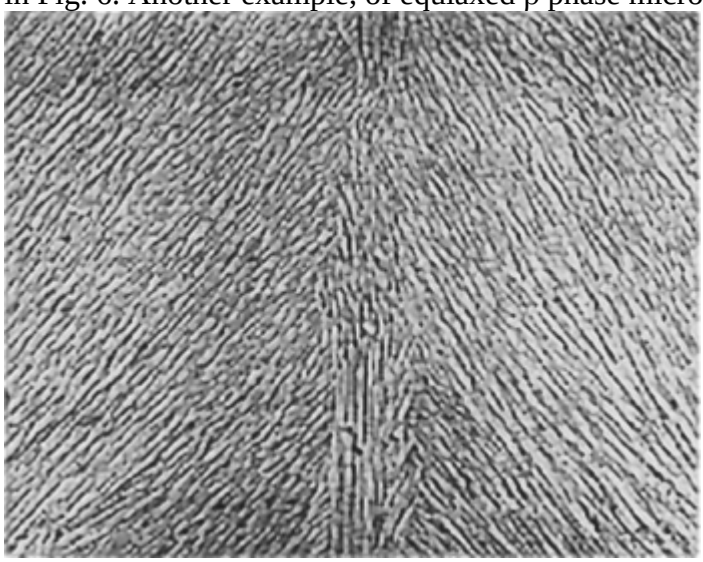

Fig. 6 Scanning electron micrograph of the beam-welding joint of a Ti-24Al-17Nb alloy, showing metastable (ordered) β phase microstructure (*B*2). Source: Ref 4

The development of heat-resistant titanium-base alloys and their classification into several microstructure categories is based on their strengthening mechanisms (Ref 5):

- Class 1: simple multicomponent α phase solid solutions

- Class 2: simple $\alpha + \alpha_2$ two-phase systems
- Class 3: simple $\alpha + \alpha_2 + \beta$ + silicide systems
- Class 4: complex $\alpha + \alpha_2 + \beta$ + intermetallic-compound systems
- Class 5: α_2 systems
- Class 6: α_2 + intermetallic-compound systems
- Class 7: β systems (stable at all temperatures)
- Class 8: β + intermetallic-compound systems

Strengthening mechanisms include: ordinary solid-solution strengthening, solid-solution strengthening augmented by short-range-order effects, solid-solution strengthening augmented by hcp ordered particle (α_2) effects, and solid-solution strengthening plus α_2 strengthening plus silicide or other intermetallic-compound precipitation within the β components of $\alpha + \beta$ alloys (Ref 1).

In this respect, lightweight titanium-aluminum intermetallic alloys have been extensively studied as potential high-temperature materials for structural applications (Ref 6, 7, 8, and 9) in the gas turbine industry, aeroengines and automotive engines (Ref 8, 9, 10, 11, and 12), turbochargers of diesel engines (Ref 12, 13, 14, and 15), and so forth. These ordered titanium-aluminum-base intermetallic alloys represent the most effective microstructure category, since they offer a good combination of low density (about 4 g/cm^3) and useful mechanical properties (ultimate strength up to 1000 MPa, or 145 ksi, high stiffness) at temperatures higher than those possible in conventional titanium alloys (700 °C, or 1300 °F). However, the ductility and fracture toughness (Ref 16) of the conventional titanium-aluminum intermetallic alloys has room for improvement by means of alloying, rapid solidification, and heat treatment, or microstructure control and design (Ref 8, 17).

References cited in this section

1. E.W. Collings, *The Physical Metallurgy of Titanium Alloys,* American Society for Metals, 1984

2. I.J. Polmear, *Light Alloys—Metallurgy of the Light Metals,* American Society for Metals, 1982

3. D. Eylon and F.H. Froes, *Titanium Net Shape Technologies,* F.H. Froes and D. Eylon, Ed., AIME, 1984

4. A.P. Wu, G.S. Zou, J.L. Ren, H.J. Zhang, G.Q. Wang, X. Liu, and M.R. Xie, Microstructures and Mechanical Properties of Ti-24Al-17Nb (at.%) Laser Beam Welding Joints, *Intermetallics,* Vol 10, 2002, p 647s–652s

5. M. Hoch, N.C. Birla, S.A. Cole, and H.L. Gegel, Tech. Report AFML-TR-73-297, Air Force Materials Laboratory, Dec 1973

6. T. Kawabata, T. Kanai, and O. Izumi, *Acta Metall. Mater.,* Vol 33, 1985, p 1355

7. M. Yamaguchi and H. Inui, *Structural Intermetallics,* R. Darolia, J.J. Lewandowski, C.T. Liu, P.L. Martin, D.B. Miracle, and M.V. Nathal, Ed., TMS, 1995, p 127

8. Y.-W. Kim, *JOM,* Vol 46, 1994, p 30

9. F. Appel and R. Wagner, *Mater. Sci. Eng.,* Vol R22, 1998, p 187

10. Y.-W. Kim and D.M. Dimiduk, *JOM,* Vol 43 (No. 8), 1991, p 40

11. Y.-W. Kim and D.M. Dimiduk, *Structural Intermetallics,* M.V. Nathal, R. Darolia, C.T. Liu, P.L. Martin, D.B. Miracle, R. Wagner, and M. Yamaguchi, Ed., TMS, 1997, p 531

12. M. Yamaguchi, H, Inui, and K. Ito, *Acta Mater.,* Vol 48, 2000, p 307

13. D.M. Dimiduk, *Mater. Sci. Eng.,* Vol A263, 1999, p 281

14. M. Nazmy, M. Staubli, G. Onofrio, and V. Lupinc, *Scr. Mater.,* Vol 45, 2001, p 787

15. E. Evangelista, W.J. Zhang, L. Francesconi, and M. Nazmy, *Scr. Metall. Mater.,* Vol 33, 1995, p 467

16. Y.W. Kim, *JOM,* Vol 24, July 1989

17. S.L. Semiatin, *Proc. Gamma Titanium Aluminides,* Y.W. Kim et al., Ed., TMS, 1993, p 509

D.M. Stefanescu and R. Ruxanda, Solidification Structures of Titanium Alloys, *Metallography and Microstructures,* Vol 9, *ASM Handbook,* ASM International, 2004, p. 116–126

Solidification Structures of Titanium Alloys

Doru M. Stefanescu and Roxana Ruxanda, University of Alabama

Phase Transformation in Titanium-Aluminum-Base Alloys

The properties of the titanium-aluminum-base alloys are predominantly affected by their microstructure. As observed from Fig. 7, the microstructure can be divided into fully lamellar grains (alternating γ and α_2 plates), duplex grains (lamellar γ/α_2 and γ grains) and equiaxed γ grains. Representative micrographs for primary α and primary β microstructures are shown in Fig. 8(a) and (b).

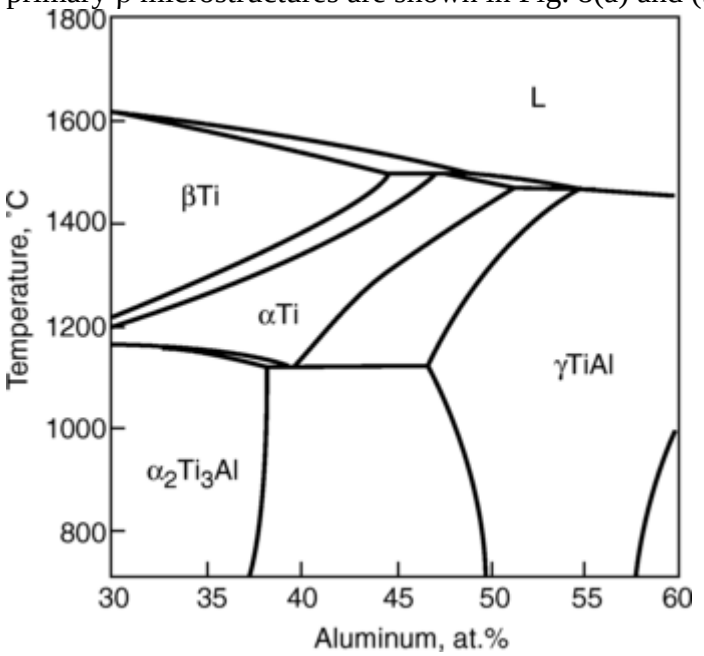

Fig. 7 The central portion of calculated phase diagram in the titanium-aluminum binary system. Source: Ref 18

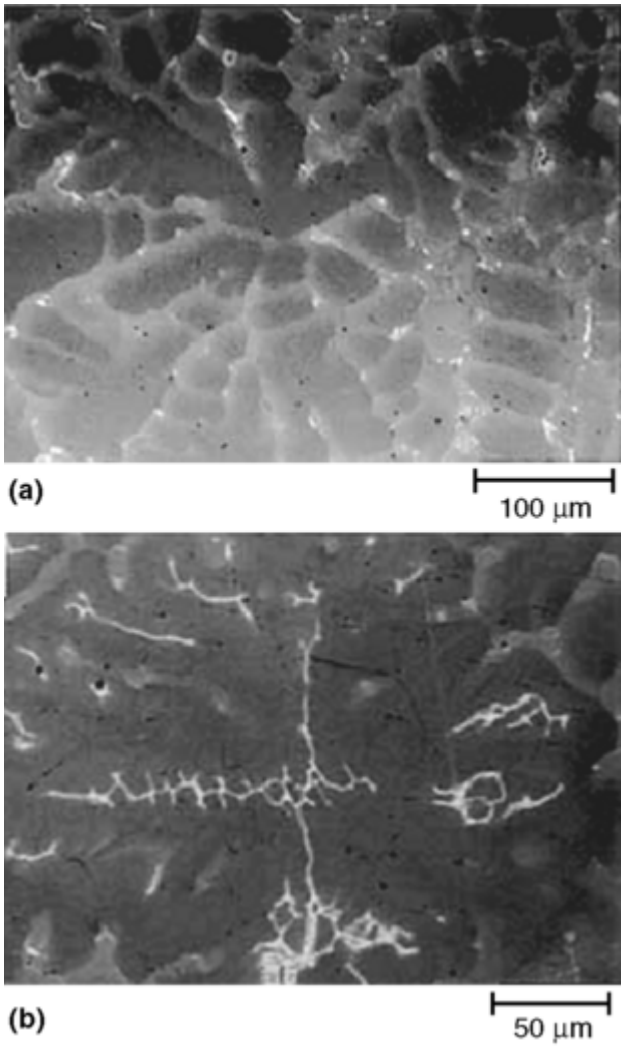

Fig. 8 Representative microstructures of titanium-aluminum alloys. (a) Primary α (Ti-51Al-2Re). (b) Primary β (Ti-50.5Al-2Re). Source: Ref 19

The fully lamellar microstructure (Fig. 9) offers higher strength, creep resistance, and fatigue and fracture toughness than the duplex microstructure, but generally has lower ductility (Ref 8, 22, and 23). Aluminum is the most influential element to the alloy strength. It acts by lowering the volume fraction of the hard phase α_2 in the $\alpha_2 + \gamma$ two-phase alloys; hence the alloy strength (Ref 24). Elements such as niobium, tungsten, tantalum, and hafnium can influence the kinetics of phase transformation and greatly improve the oxidation and creep resistance (Ref 20). Such elements, especially niobium, have been added frequently to titanium-aluminum-base alloys.

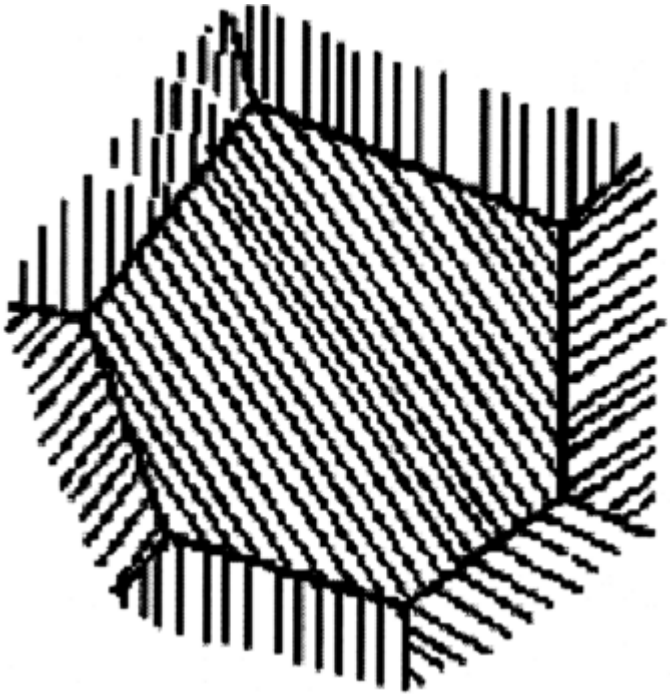

Fig. 9 Fully lamellar microstructure in titanium-aluminum-base alloy consisting of equiaxed polycrystalline grains and lamellae within the grains. The lamellar structure is composed of a few α_2 plates interspersed between many γ plates. Source: Ref 20, 21

References cited in this section

8. Y.-W. Kim, *JOM,* Vol 46, 1994, p 30

18. U.R. Kattner, J.-C. Lin, and Y.A. Chang, *Metall. Trans. A,* Vol 23A, 1992, p 2081

19. S. Muto, T. Yamanaka, D.R. Johnson, H. Inui, and M. Yamaguchi, *Mater. Sci. Eng. A,* Vol A329–331, 2002, p 424s–429s

20. S.C. Huang, *Structural Intermetallics,* R. Darolia, J.J. Lewandowski, C.T. Liu, P.L. Martin, D.B. Miracle, and M.V. Nathal, TMS, 1993, p 299

21. L. Yongchang, *Mater. Lett.,* Vol 57, 2003, p 2262s–2266s

22. D.M. Dimiduk, *Gamma Titanium Aluminides,* Y.-W. Kim, R. Wagner, and M. Yamaguchi, Ed., TMS, 1995, p 3

23. C.T. Liu and P.J. Maziasz, *Intermetallics,* Vol 6,1998, p 653

24. D. Hu, *Intermetallics,* Vol 9, 2001, p 1037s–1043s

D.M. Stefanescu and R. Ruxanda, Solidification Structures of Titanium Alloys, *Metallography and Microstructures*, Vol 9, *ASM Handbook*, ASM International, 2004, p. 116–126

Solidification Structures of Titanium Alloys

Doru M. Stefanescu and Roxana Ruxanda, University of Alabama

Solidification Structures of Titanium-Aluminum-Base Alloys

The solidification structure has rarely been subject to a detailed study except one report on the primary solidification region of α phase (Ref 25). The solidification structures are dendritic at all aluminum contents. However, as shown in Fig. 10, the symmetry of the dendrites vary from four-fold symmetry for the alloys with less than about 49 at.% Al (Fig. 10a), to six-fold symmetry for the alloys with 49 to 50 at.% Al contents (Fig. 10b), and to four-fold symmetry again for the alloys containing more than about 55 at.% Al (Fig. 10c). This indicates that the primary solidification path shifts from L → β to L → α and L → γ phase with increasing aluminum content (Ref 26). These observations are in agreement with the previous observations of the dendritic morphology in shrinkage cavities (Ref 25) and in ingots (Ref 27). The faceted dendrite exhibiting a four-fold symmetry shown in Fig. 10(c) is a commonly observed solidification structure in covalently bonded semiconductor materials, such as germanium (Ref 26).

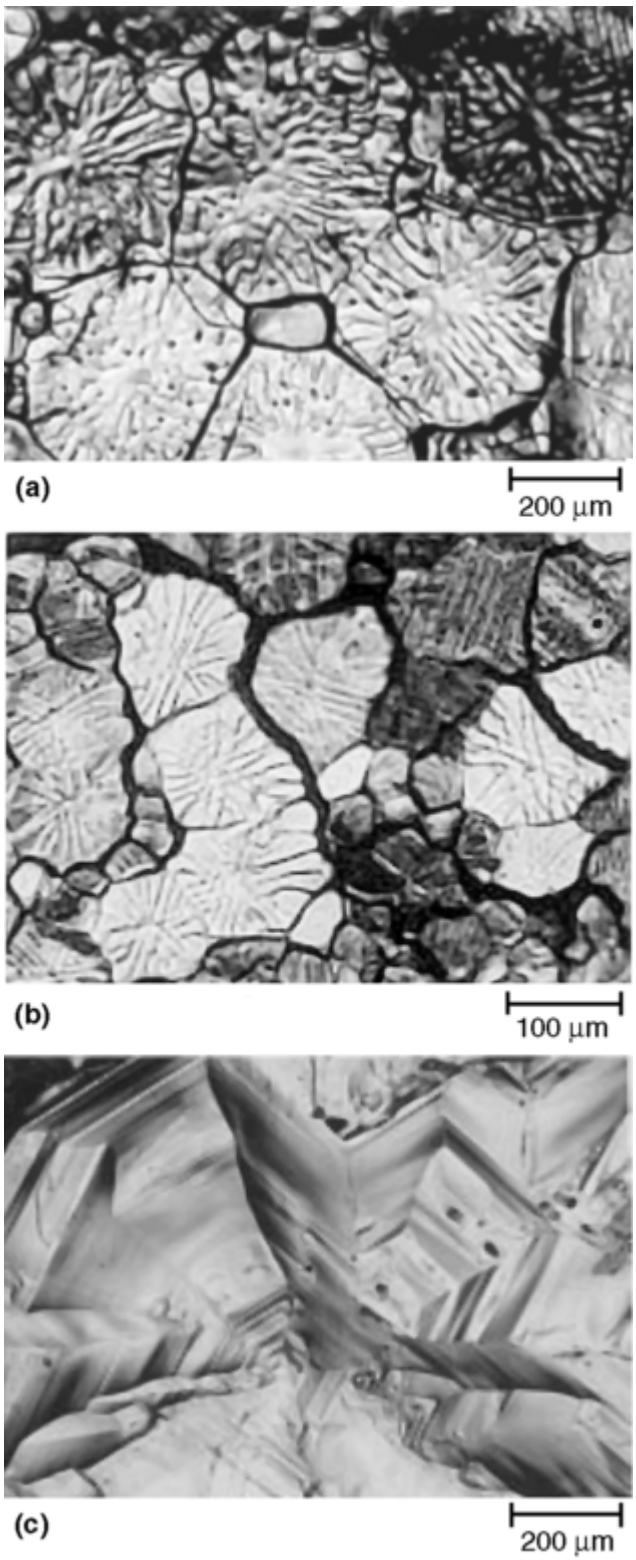

Fig. 10 Various dendritic structures formed on the surface of the ingot. (a) Ti-35Al (at.%). (b) Ti-51Al (at.%). (c) Ti-55Al (at.%). Source: Ref 26

The grain size of dendritic structure varied also with the aluminum content. A minimum size occurs at about 47 at.% Al, which is close to the peritectic composition of α phase. The dendritic arm spacing (DAS) tends to vary in a nearly proportional manner to the dendrite grain size. The DAS at the top surface of ingot was approximately one-tenth of the dendrite grain sizes in a composition range from 48 to 58 at.% Al (Ref 26).

References cited in this section

25. C. McCullough, J.J. Valencia, C.G. Levi, and M. Mehrabian, *Acta Metall.,* Vol 37, 1989, p 1321

26. J.Y. Jung, J.K. Park, and C.H. Chun, *Intermetallics,* Vol 7, 1999, p 1033s–1041s

27. S.C. Huang and P.A. Siemers, *Metall. Trans.,* Vol 20A, 1989, p 1899

D.M. Stefanescu and R. Ruxanda, Solidification Structures of Titanium Alloys, *Metallography and Microstructures,* Vol 9, *ASM Handbook,* ASM International, 2004, p. 116–126

Solidification Structures of Titanium Alloys

Doru M. Stefanescu and Roxana Ruxanda, University of Alabama

Peritectic Reactions of α_p and γ_p Phases

Two peritectic reactions take place in the TiAl system, as shown in Fig. 7, forming either peritectic α_p phase (Fig. 11) or peritectic γ_p phase (Fig. 12). The two peritectic compositions of α_p and γ_p were measured to be about 47 and 54 at.% Al, respectively. The peritectic reaction of the α_p phase occurs at dendrite edges of the primary β phase. The α_p peritectic region is difficult to distinguish in the microstructure, since during cooling through the α + γ two-phase field both β dendrite core and α_p dendrite edge transform into a lamellar structure of alternating α_2 and γ plates. However, the peritectic region can be identified by its lamellar spacing, which is coarser than the core. The spacing increases significantly with the aluminum content. The finest spacing is at about 44 at.% Al (Ref 28) and the coarser at about 47 at.%, the composition of peritectic α_p (Ref 18, 25, and 29). The individual lamellae are not easily recognizable at dendrite core in light microscopy, due to the high fineness of lamellar spacing at this region.

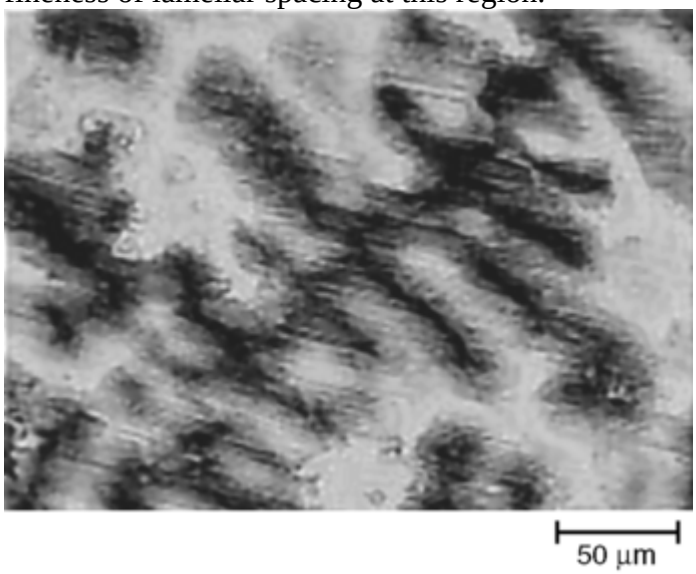

Fig. 11 Light micrograph illustrating the peritectic reaction for α_p in a Ti-48Al alloy. Source: Ref 26

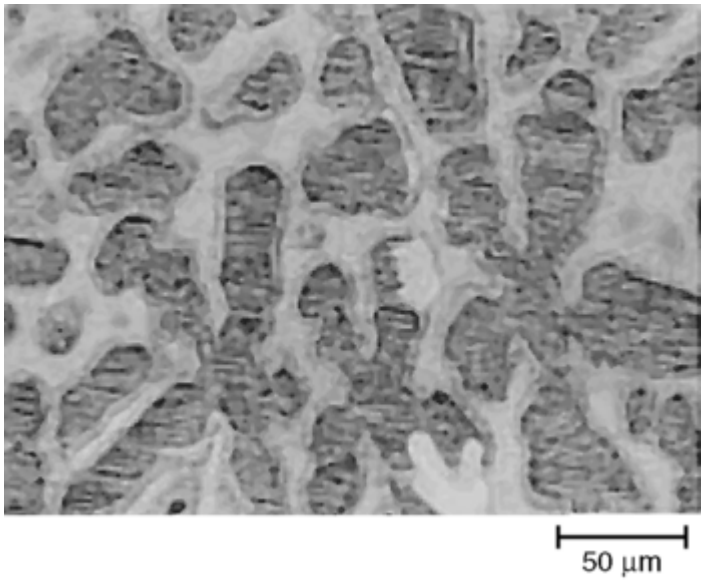

Fig. 12 Transmission electron micrograph illustrating the peritectic reaction for γ_p in a Ti-52Al alloy. Source: Ref 26

On the other hand, the γ_p peritectic region is easily recognizable (Fig. 12). In this case, although the dendrite core of primary α phase will again transform into a lamellar structure of alternating α_2 and γ plates, the γ_p at the dendrite edge will remain as a single phase down to the room temperature, since it will not go through solid-state transformation. The peritectic γ_p region at the dendrite edge is delineated by a contour from the interdendritic γ region, supposedly from impurity segregation (Ref 26).

The presence of peritectic γ phase at an interdendritic region of primary α phase is mainly responsible for the development of near γ or duplex microstructures. The composition of the dendrite edge where peritectic reaction has occurred is about 54 at.% Al. However, careful examination of Fig. 12 shows that the dendrite core of primary α phase is not always transforming into lamellar structure, but rather into γ phase by massive transformation (Ref 26).

References cited in this section

18. U.R. Kattner, J.-C. Lin, and Y.A. Chang, *Metall. Trans. A,* Vol 23A, 1992, p 2081

25. C. McCullough, J.J. Valencia, C.G. Levi, and M. Mehrabian, *Acta Metall.,* Vol 37, 1989, p 1321

26. J.Y. Jung, J.K. Park, and C.H. Chun, *Intermetallics,* Vol 7, 1999, p 1033s–1041s

28. Y. Yamabe, N. Honjo, and M. Kikuchi, *Proc. International Symp. Intermetallic Compounds—Structure and Mechanical Properties,* O. Izumi, Ed., Japan Institute of Metals, 1991, p 821

29. J.C. Mishurda and J.H. Perepezko, *Microstructure/Property Relationships in Titanium Aluminides and Alloys,* Y.-W. Kim and R.R. Boyer, Ed., 1991, p 3

D.M. Stefanescu and R. Ruxanda, Solidification Structures of Titanium Alloys, *Metallography and Microstructures,* Vol 9, *ASM Handbook*, ASM International, 2004, p. 116–126

Solidification Structures of Titanium Alloys

Doru M. Stefanescu and Roxana Ruxanda, University of Alabama

Directional Solidification

To improve the strength and ductility of titanium-aluminum alloys, the lamellar microstructure must be aligned parallel to the growth direction. This can be achieved through directional solidification (DS). To achieve the required lamellar orientation, the orientation of the high-temperature α phase must first be controlled. One approach is by seeding the α phase in the alloys where: (a) the α phase is the primary solidification phase, (b) nucleation of the primary β phase can be suppressed, and (c) α phase is the interdendritic phase and β phase is the primary solidification phase (Ref 30). Another approach is without seeding, by controlling the solidification path of alloys through appropriate alloying (Ref 31).

Seeding was used to produce ingots consisting of only a single lamellar grain (Ref 32) named polysynthetically twinned (PST) crystals by analogy with the phenomenon "polysynthetic twinning" observed in mineral crystals (Ref 33). Using the PST crystals, the lamellar structure exhibits significant anisotropy in strength and ductility. These mechanical properties strongly depend on the lamellar orientation, the best balance being obtained when the lamellar boundaries are parallel to the loading axis (Ref 32, 34, 35, 36, 37, 38, and 39). In this case, tensile yield strength greater than 400 MPa (60 ksi) and tensile elongation greater than 10% are usually obtained.

The lamellar γ/α_2 microstructure is formed in the solid state, not during the solidification, following the Blackburn phase orientation relationship (Ref 40): (0001) α|| (111)γ and $\langle 11\bar{2}0\rangle$ α|| $\langle 110\rangle$ γ. Therefore, to control the lamellar microstructure, the high-temperature α phase must be stable from melting to room temperature (Ref 41), and its orientation must be controlled. This can be achieved by using a seed of Ti-43Al-3Si (Ref 42, 43), because at this composition the original orientation of the lamellar structure can be maintained after heating to and cooling from the α single-phase region.

Using the seeding technique, single-crystal (PST)-like structures with each columnar grain having the same orientation (Fig. 13) have been produced (Ref 44) from various alloys in the Ti-Al-Si, Ti-Al-Nb-Si, and Ti-Al systems including Ti-47Al and Ti-46.5Al-3Nb-0.5Si alloys (Ref 43, 45). Figure 14 shows a microstructure taken from a Ti-47Al ingot directionally solidified with a Ti-43Al-3Si seed at 40 mm/h (1.6 in./h). The small variation in lamellar microstructure may be caused by bending of the dendrite arms during solidification.

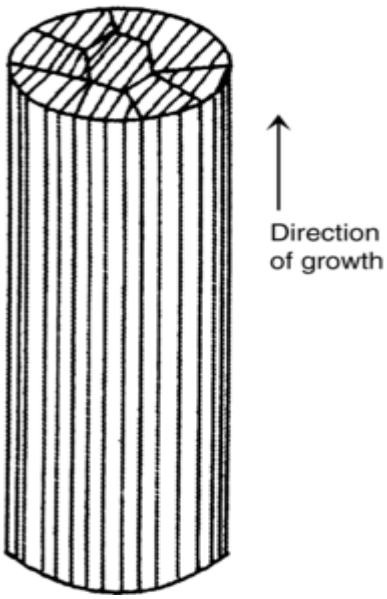

Fig. 13 Directionally solidified titanium-aluminum ingot with one lamellar orientation of the columnar grains. Source: Ref 44

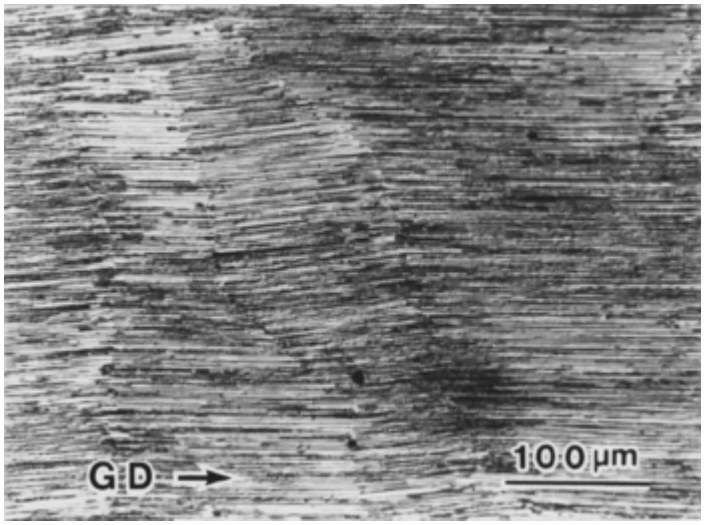

Fig. 14 Microstructure showing variation in orientation of lamellar microstructure for a Ti-47Al ingot with a Ti-43Al-3Si seed directionally solidified at 40 mm/h (1.6 in./h). GD, growth direction. Source: Ref 44

Also, DS Ti-43Al-3Si ingots having columnar grains rotated with respect to the longitudinal axis, as well as having the lamellar microstructure parallel to the axis (Fig. 15), were produced using Ti-43Al-3Si as polycrystalline seed material (Ref 46). Close examination of the part between the transition point and the seed in DS ingot is shown in Fig. 16. The aligned lamellar microstructure parallel to growth direction indicates that the seeding from the polycrystalline seeds was successful. Figure 17 shows Ti_5Si_3 morphology in two different cross sections of a DS ingot. The Ti_5Si_3 results from eutectic reaction, and thus its morphology represents the contour of interdendritic arms. The scriptlike shape was dominant in the off-aligned part (Fig. 17a), corresponding to the contour of secondary dendrite arms, while the blocky shape was dominant in the well-aligned part (Fig. 17b), implying no secondary dendrite arm (Ref 46).

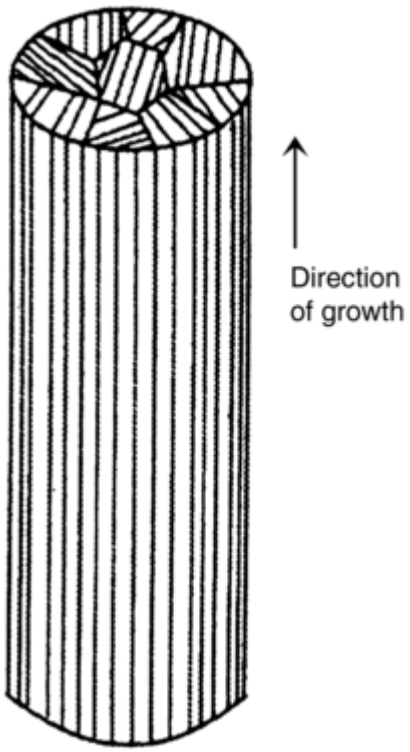

Fig. 15 Directionally solidified titanium-aluminum ingots with rotation of each columnar grain. Source: Ref 44

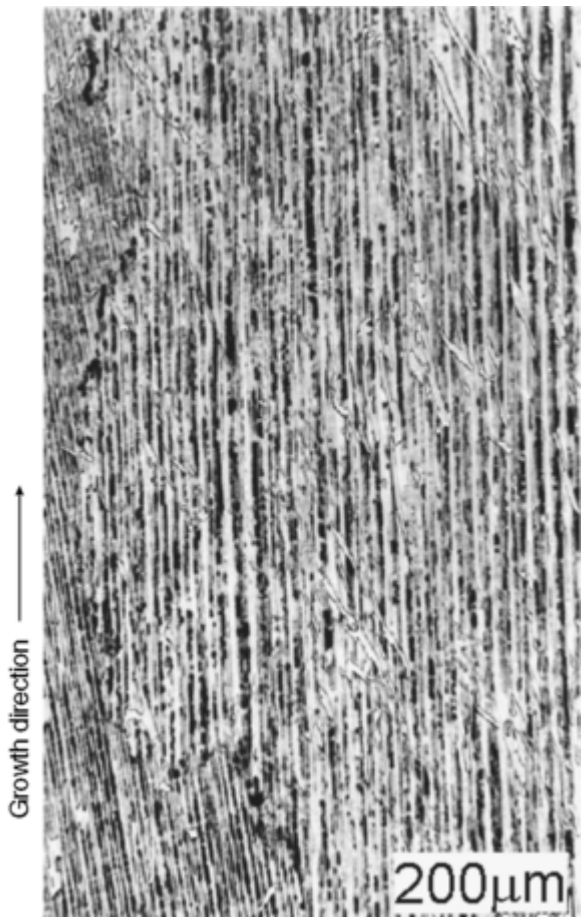

Fig. 16 Lamellar microstructure of the well-aligned part in directionally solidified ingot grown at 5 mm/h (0.2 in./h). Source: Ref 46

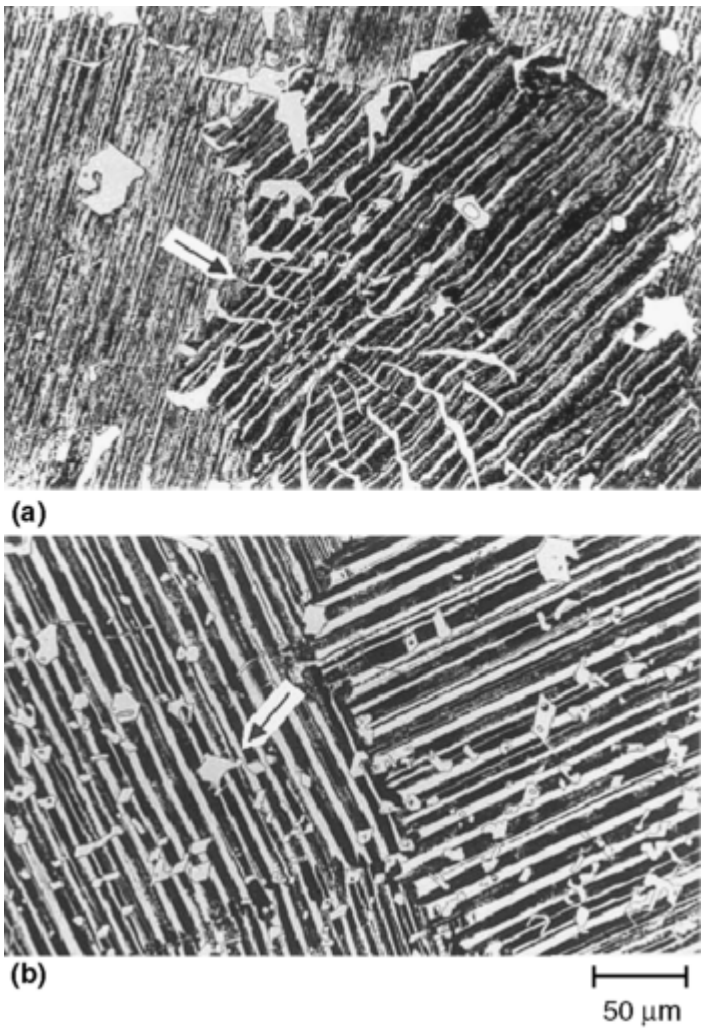

Fig. 17 Ti_5Si_3 morphology in (a) off-aligned part and (b) well-aligned part of the directionally solidified ingot grown at 5 mm/h (0.2 in./h). Growth direction is normal to the paper plane. Source: Ref 46

Aligning the lamellar structure of DS ingots by the seeding technique is successful even for binary titanium-aluminum alloys where β is the primary phase, in the composition range of 46 to 48% Al. After the β dendrite forms as the primary phase, the α_p can grow on an α crystal seed, keeping the orientation of the α crystal seed of Ti-43Al-3Si, as shown in Fig. 18. Examples of scanning electron microscopy microstructures of successfully produced DS quaternary ingots are shown in Fig. 19 for Ti-46Al-0.5Si with additions of rhenium, tungsten, and molybdenum (Ref 19). No silicide particles are visible for any of these quaternary alloys. The volume fraction of α_2 lamellae seems to increase in the alloying order of Re < Mo < W, while the lamellar spacing seems to have an opposite trend and to increase in the order of W < Mo < Re.

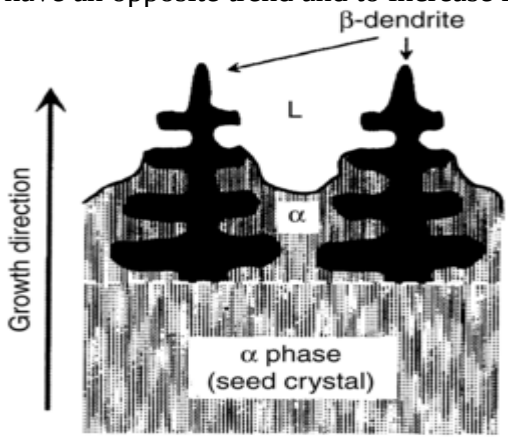

Fig. 18 Possible growth morphology consisting of β dendrites and the associated peritectic α_p phase. Source: Ref 19

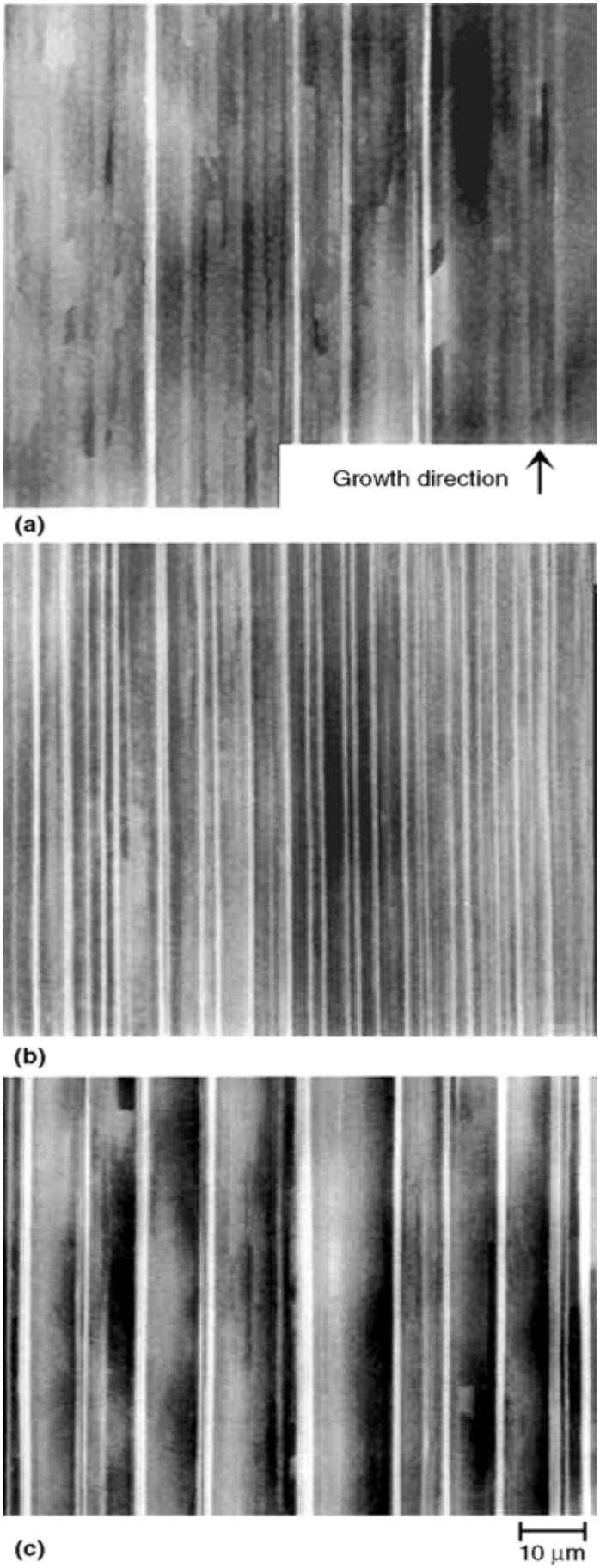

Fig. 19 Scanning electron micrographs of successfully produced directionally solidified ingots. (a) Ti-46Al-0.5Si-0.5Re. (b) Ti-46Al-0.5Si-0.5W. (c) Ti-46Al-0.5Si-0.5Mo. Source: Ref 19

Controlling the solidification path is the other approach to obtaining aligned lamellar orientation. The requirement for controlling the solidification path is the full transformation L → β (Fig. 7) (Ref 47). Once a fully β structure is obtained, the lamellar growth direction could be controlled (Ref 47, 48, 49). The β structure can be achieved by either modifying the composition or the growth rate, as shown in Fig. 20 and Fig. 21 (Ref 41). By increasing the aluminum content with only 4% (from 44 to 48% Al), the lamellar direction of the binary TiAl alloys has changed from 45° (Fig. 20a) to almost normal to the growth direction (Fig. 20b). Similar results were described in Ref 49. In the case of the ternary Ti-Al-*X* alloys (where *X* is a β-stabilizer, Ref 50, element such as molybdenum, niobium, or chromium), the lamellar direction changed from 0 to 45° to the growth direction for a growth rate of 90 mm/h (3.5 in./h) (Fig. 21a) to normal to the growth direction (Fig. 21b) for a growth rate four times higher (360 mm/h, or 14 in./h). This occurred because the L + β → β transus line was shifted toward lower aluminum content. Therefore, to effectively control the lamellar direction, the growth rate should be kept as low as possible.

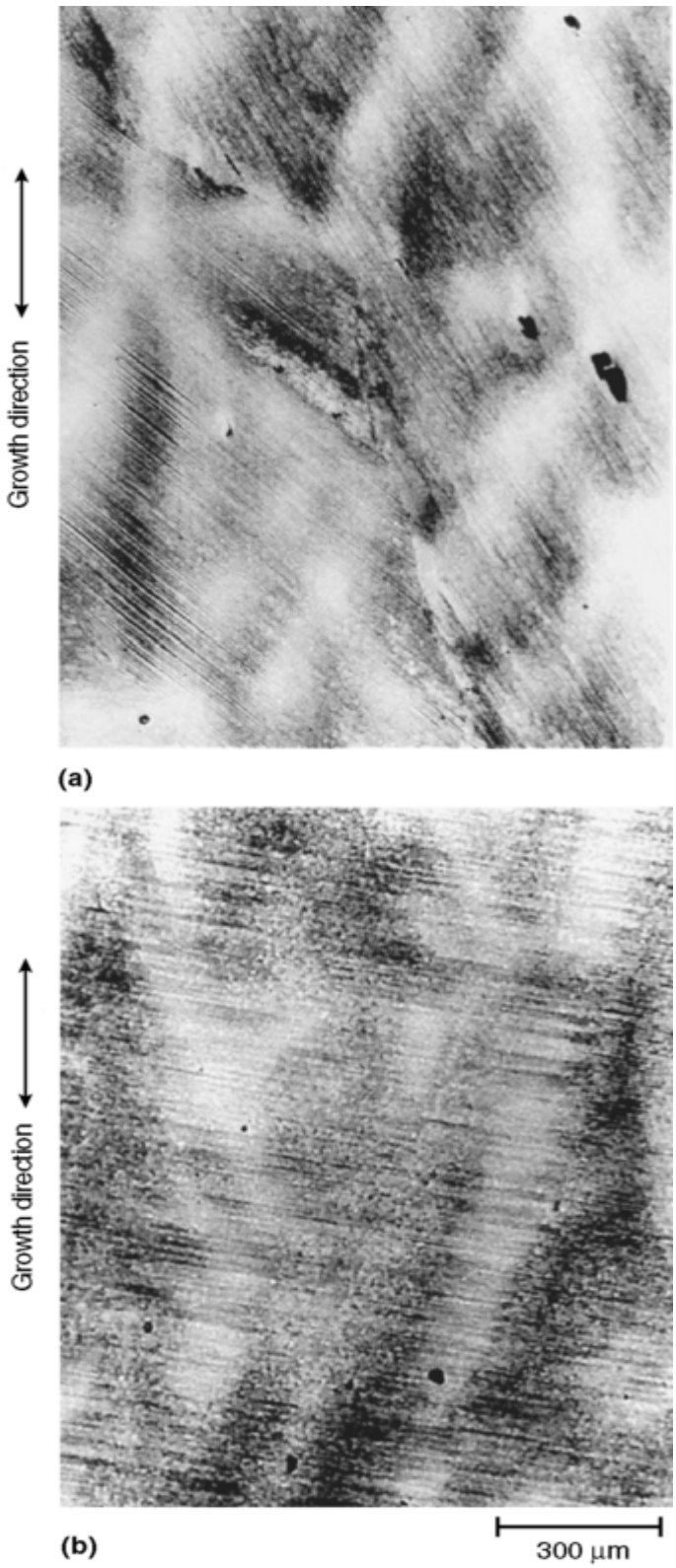

Fig. 20 Longitudinal sections in two titanium-aluminum alloys at a growth rate of 90 mm/h (3.5 in/h). GD, growth direction. (a) Ti-44Al (at.%), note lamellar direction approximately 45° to GD. (b) Ti-48Al (at.%), note lamellar direction normal to GD. Source: Ref 41

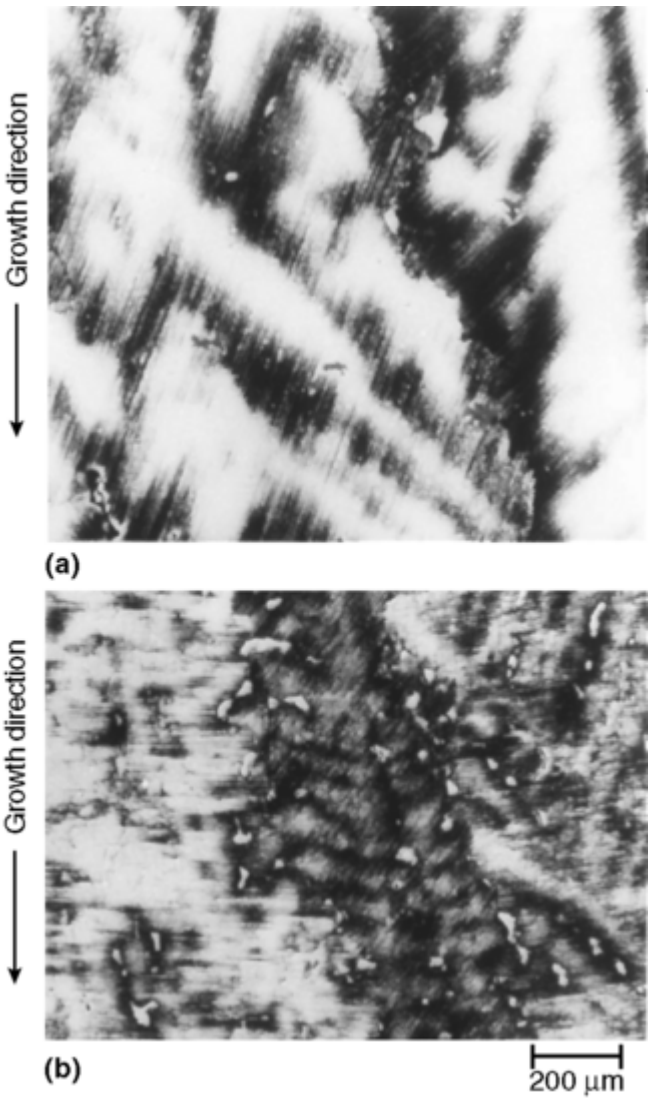

Fig. 21 Micrographs of the directionally solidified Ti-47.5Al-2.5Mo (at.%) alloy at growth rate of (a) 90 mm/h (3.5 in/h) and (b) 360 mm/h (14 in./h). GD, growth direction. Source: Ref 41

References cited in this section

19. S. Muto, T. Yamanaka, D.R. Johnson, H. Inui, and M. Yamaguchi, *Mater. Sci. Eng. A,* Vol A329–331, 2002, p 424s–429s

30. M. Yamaguchi, D.R. Johnson, H.N. Lee, and H. Inui, Directional Solidification of TiAl-Base Alloys, *Intermetallics,* Vol 8, 2000, p 511s–517s

31. D.R. Johnson, K. Chihara, H. Inui, and M. Yamaguchi, *Acta Mater.,* Vol 46, 1998, p 6529

32. T. Fujiwara, A. Nakamura, M. Hosomi, S.R. Nishitani, Y. Shirai, and M. Yamaguchi, *Philos. Mag.,* Vol 61A, 1990, p 591

33. C. Barrett and T.B. Massalski, *Structure of Metals,* 3rd rev. ed., Pergammon Press, p 406

34. H. Inui, A. Nakamura, M.H. Oh, and M. Yamaguchi, *Acta Mater.,* Vol 40, 1992, p 3059

35. M. Yamaguchi, H. Inui, S. Yokoshima, K. Kishida, and D.R. Johnson, *Mater. Sci. Eng. A,* Vol A213, 1996, p 25

36. W.R. Chen, J. Triantafillou, J. Beddoes, and L. Zhao, *Intermetallics,* Vol 7, 1999, p 171

37. Y.H. Lu, Y.G. Zhang, L.J. Qiao, Y.B. Wang, C.Q. Chen, and W.Y. Chu, *Mater. Sci. Eng., A,* Vol A289, 2000, p 91

38. K. Kishida, D.R. Johnson, Y. Masuda, H. Umeda, H. Inui, and M. Yamaguchi, *Intermetallics,* Vol 6, 1998, p 679

39. K. Kishida, H. Inui, and M. Yamaguchi, *Intermetallics,* Vol 7, 1999, p 1131

40. M.J. Blackburn, *The Science, Technology and Application of Titanium,* R.I. Jaffee and N.E. Promisel, Pergamon Press, 1970, p 633

41. M.C. Kim, M.H. Oh, J.H. Lee, H. Inui, M. Yamaguchi, and D.M. Wee, *Mater. Sci. Eng. A,* Vol 239–240, 1997, p 570s–576s

42. D.R. Johnson, Y. Masuda, H. Inui, and M. Yamaguchi, *Acta Mater.,* Vol 45, 1997, p 2523

43. D.R. Johnson, Y. Masuda, Y. Shimada, H. Inui, and M. Yamaguchi, *Structural Intermetallics,* M.V. Nathal, R. Darolia, C.T. Liu, P.L. Martin, D.B. Miracle, R. Wagner, and M. Yamaguchi, Ed., TMS, 1997, p 287

44. D.R. Johnson, H. Inui, and M. Yamaguchi, *Acta Mater.,* Vol 44, 1996, p 2523

45. D.R. Johnson, Y. Masuda, H. Inui, and M. Yamaguchi, *Mater. Sci. Eng., A,* Vol A 239–240, 1997, p 577s–583s

46. S.E. Kim, Y.T. Lee, M.H. Oh, H. Inui, and M. Yamaguchi, *Intermetallics,* Vol 8, 2000, p 399s–405s

47. M.C. Kim, M.H. Oh, J.H. Lee, and D.M. Wee, *J. Korean Inst. Met. Mater.,* Vol 35, 1997, p 31

48. M.C. Kim, M.H. Oh, D.M. Wee, H. Inui, and M. Yamaguchi, *Mater. Trans. Jpn. Inst. Met.,* Vol 37, 1996, p 1197

49. Y. Shimada, H. Inui, and M. Yamaguchi, *Proc. Fifth Symp. High-Performance Materials for Severe Environments, RIMCOF and JITA,* Japan, 1994, p 23

50. H. Nakamura, M. Takeyama, L. Wei, Y. Yamabe, and M. Kikuchi, *Proc. Third Japanese International SAMPE Symposium,* 7–10 Dec 1993, p 1353

D.M. Stefanescu and R. Ruxanda, Solidification Structures of Titanium Alloys, *Metallography and Microstructures,* Vol 9, *ASM Handbook*, ASM International, 2004, p. 116–126

Solidification Structures of Titanium Alloys

Doru M. Stefanescu and Roxana Ruxanda, University of Alabama

Grain Refinement

In cast titanium-aluminum alloys with fully lamellar microstructures the lamellar colony size is of the order of 1000 μm (40 mils), which leads to a low room-temperature ductility, typically 0.3%. It has been shown that refinement improves the ductility to a level of above 1% at room temperature and reasonable room-temperature ductility in the as-cast condition, where the lamellar colonies are randomly oriented, unlike the columnar structure in non-grain-refined alloys (Ref 10, 24).

The β grains can be refined by using inoculants in a similar manner as for aluminum and superalloys. Such inoculants may include boron or carbon, or combinations of these with alloying elements. For example, the β grain size of Ti-6Al-4V could be reduced from 1 to 0.3 mm (0.04 to 0.01 in.) by adding Ti-5C (wt%) inoculants (Ref 51). A 0.8 vol% TiB_2 addition to a Ti-(45–47)Al-2Mn-2Nb alloy decreased the as-cast grain size to 50 to 100 μm (2 to 4 mils) (Ref 52).

The critical level of boron is composition dependent (Ref 53, 54, and 55), with higher levels required for alloys that contain strong boride formers, such as tantalum. A minimum amount of boron, typically 0.5 at.%, is required. Below this level, little or no impact on the grain size is obtained (Ref 53, 54, and 56). However, because the solubility of boron in titanium-aluminum is very low, boride particles are invariably observed, even at 0.1% B where grain refinement does not occur (Ref 56). However, incorporating titanium borides into titanium-aluminum-base alloys may be helpful to some extent, since it prevents excessive alpha grain growth in ulterior heat treatments, by pinning the grain boundaries (Ref 57).

The effect of boron addition on the microstructure of the Ti-44Al-8Nb alloy is exemplified in Fig. 22, 23, and 24. The as-cast microstructure of the boron-free Ti-44Al-8Nb alloy is coarse grained with average grain sizes of 500 to 1500 μm (20 to 60 mils) (Fig. 22) exhibiting significant dendritic segregation with average dendrite arm spacing of 50 to 100 μm (2 to 4 mils).

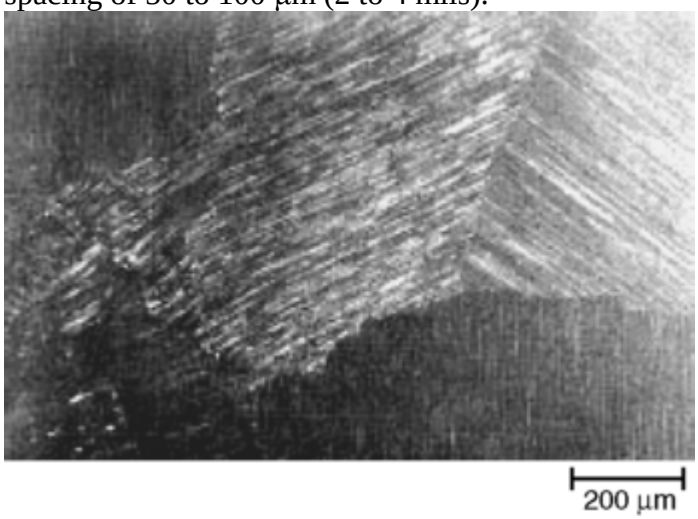

Fig. 22 Light micrograph of the Ti-Al-8Nb alloy showing coarse-grained as-cast structure. Source: Ref 55

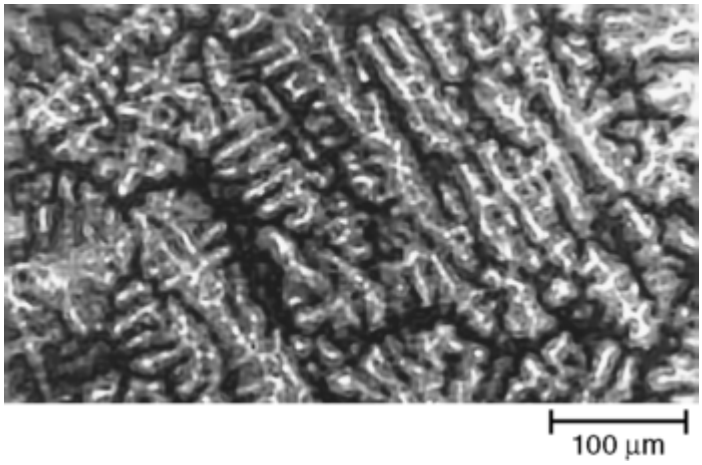

Fig. 23 Backscattered electron image of the Ti-Al-8Nb-0.3B alloy showing coarse grain structure. Source: Ref 55

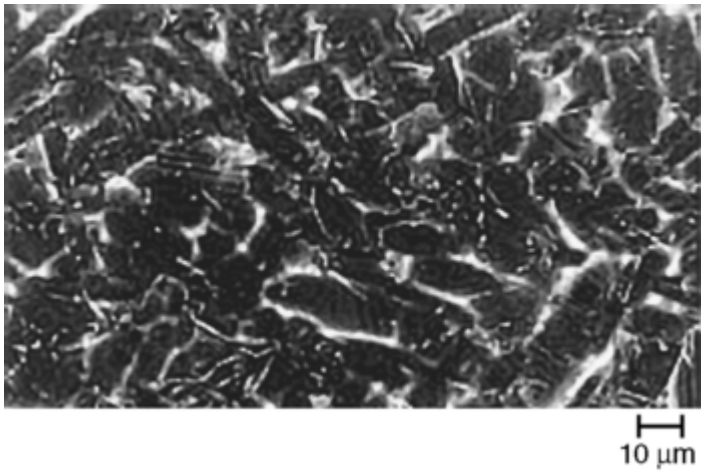

Fig. 24 Backscattered electron image showing refined as-cast structure in the Ti-Al-8Nb-1B alloy. Source: Ref 55

Adding 0.3% B to the 8Nb alloy did not change significantly the coarse as-cast structure with an average dendrite arm spacing of 20 to 50 μm (0.8 to 2 mils) (Fig. 23). Further, 1% B addition produced grain refinement to an average grain size of 30 to 70 μm (1.2 to 2.7 mils) (Fig. 24). The dendritic segregation became less evident, although more contrast due to the rejection of β stabilizers into grain boundaries during the $\beta \rightarrow \alpha$ transformation was observed.

The combined effects of boron and alloying elements on grain refinement are shown in Fig. 25. At 1% B, the as-cast microstructure is all grain refined, composed of randomly oriented lamellar colonies. However, increasing the amount of alloying elements increases the grain size. Fine dispersed titanium boride particles, which cannot be resolved in the light micrographs, were evenly distributed throughout the samples.

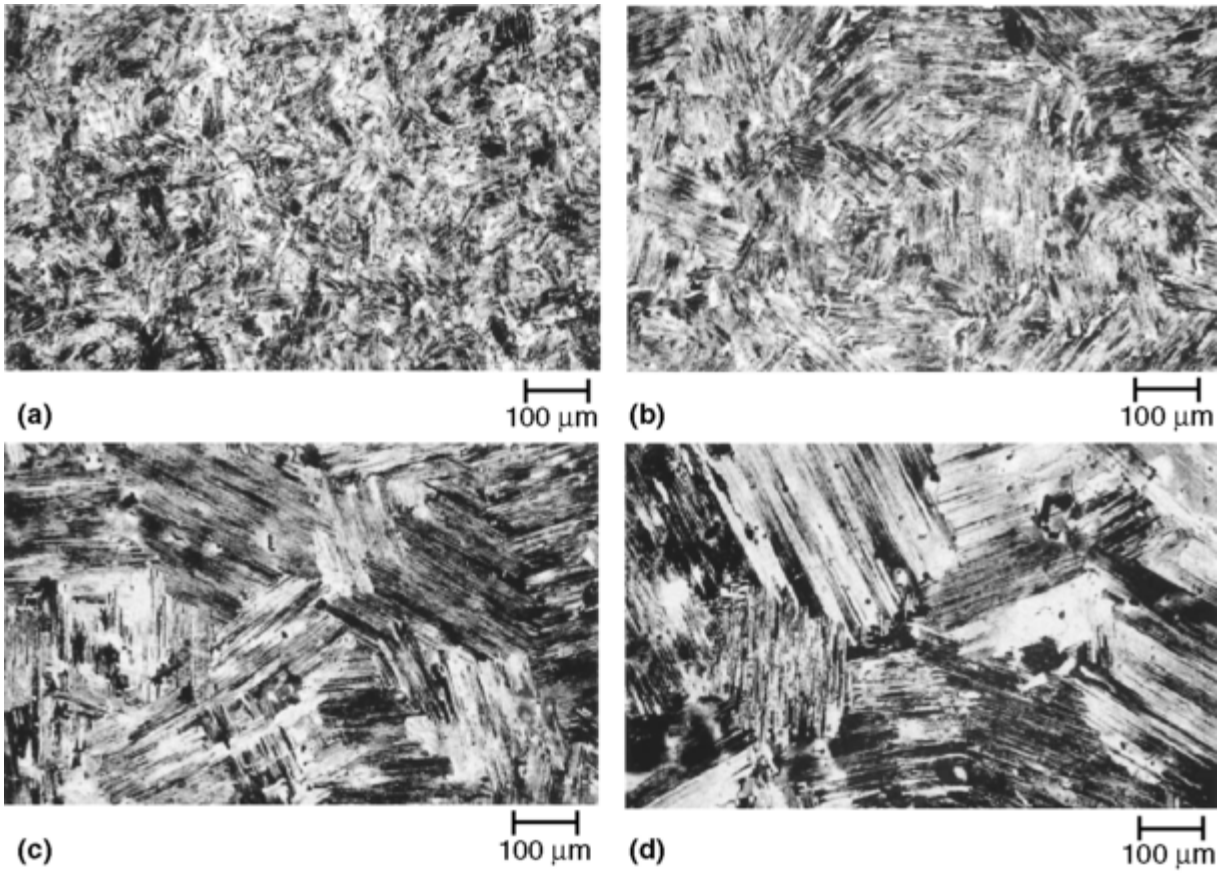

Fig. 25 Light micrographs of as-cast Ti-Al-B alloys. Alloys in (a) to (c) are in ingot form and that in (d) is in button form. (a) Grain-refined Ti-44Al-8Nb-1B. (b) Ti-46Al-8Nb-1B. (c) Ti-48Al-2Cr-2Nb-1B. (d) Ti-50Al-2Cr-2Nb-1B. (b) to (d) As the amount of alloying elements is increased the grain size increases. Source: Ref 24

Refractory elements such as tungsten, tantalum, and niobium (niobium concentration can be as high as 10 at.%, Ref 58) have strong effects on the structure and morphology of the titanium boride in cast titanium-aluminum alloys. The as-cast microstructure of Ti-46Al-8Nb-1B alloy produced by investment casting shown in Fig. 26 is fully lamellar with titanium boride precipitates distributed throughout the sample (Ref 57). These very large titanium boride ribbons enriched with niobium are suspected to cause low ductility and premature failure. The size and density of titanium borides are affected by the solidification condition. Fast cooling during solidification can suppress their formation (Ref 57).

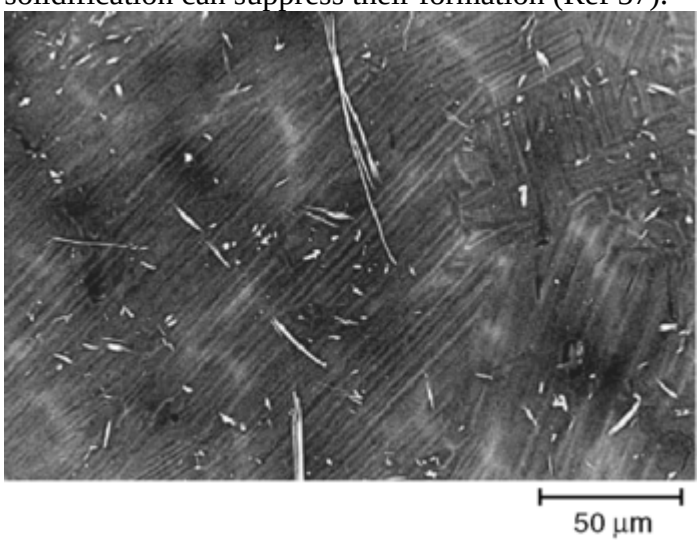

Fig. 26 Scanning electron microscope backscattered electron images of investment cast Ti-46Al-8Nb-1B test bars with 30 mm (1.18 in.) diam. Source: Ref 57

References cited in this section

10. Y.-W. Kim and D.M. Dimiduk, *JOM,* Vol 43 (No. 8), 1991, p 40

24. D. Hu, *Intermetallics,* Vol 9, 2001, p 1037s–1043s

51. F.A. Crossley, U.S. Patent No. 4,420,460, Dec 1983

52. V. Recina and D. Nilson, *Gamma Titanium Aluminides,* Y.-W. Kim, D.M. Dimiduk, and M.H. Loretto, 1999, TMS, 1999, p 447

53. L. Christodoulou, *International Workshop on Gamma Alloys, The Univ. of Birmingham,* 1–3 May 1996

54. D.E. Larson, *MRS Symp. Proc.,* Vol 194, 1990, p 285s–292s

55. T.T. Cheng, *Intermetallics,* Vol 8, 2000, p 29s–37s

56. A.B. Godfrey, Ph.D. thesis, The University of Birmingham, 1996

57. D. Hu, J.F. Mei, M. Wickins, and R.A. Harding, *Scr. Mater.,* Vol 47, 2002, p 273s–278s

58. F. Appel, U. Lorenz, J.D.H. Paul, and M. Oehring, *Gamma Titanium Aluminides,* Y.-W. Kim, D.M. Dimiduk, and M.H. Loretto, Ed., TMS, 1999, p 381

D.M. Stefanescu and R. Ruxanda, Solidification Structures of Titanium Alloys, *Metallography and Microstructures,* Vol 9, *ASM Handbook,* ASM International, 2004, p. 116–126

Solidification Structures of Titanium Alloys

Doru M. Stefanescu and Roxana Ruxanda, University of Alabama

Microstructures Produced through Various Near-Net Shape Manufacturing Processes

Although titanium alloys have an excellent combination of low density, high corrosion, and fracture resistance, high cost restricts their application. In addition, the high reactivity of molten titanium for oxygen, nitrogen, and hydrogen presents a great challenge in melting and molding of titanium castings.

The most common melting process is the consumable-electrode arc melting. Figure 27 shows a typical microstructure of the arc-melted Ti-Al-Cr-Nb alloy. It is composed of $\alpha_2 + \gamma$ lamellae and the retained high-temperature phase α. The arc-melted microstructure of Ti-Al-Re-Si alloys (Fig. 28) consisted of primary β dendrites outlined by the *B*2 phase, with eutectic silicide particles in the interdendritic spaces. Large γ-α_2 lamellar colonies are also visible. The range of molding materials available for titanium casting is limited because of the reactivity of titanium. Rammed graphite molds (Ref 60) are commonly used to produce relatively large components for industrial applications, and sand molds coated with zirconium oxide (Ref 61) are used to produce lower-cost components primarily aimed at marine and chemical applications. The sand castings have very limited α case depth (Fig. 29), but with an inferior surface finish compared to the castings produced in rammed graphite molds.

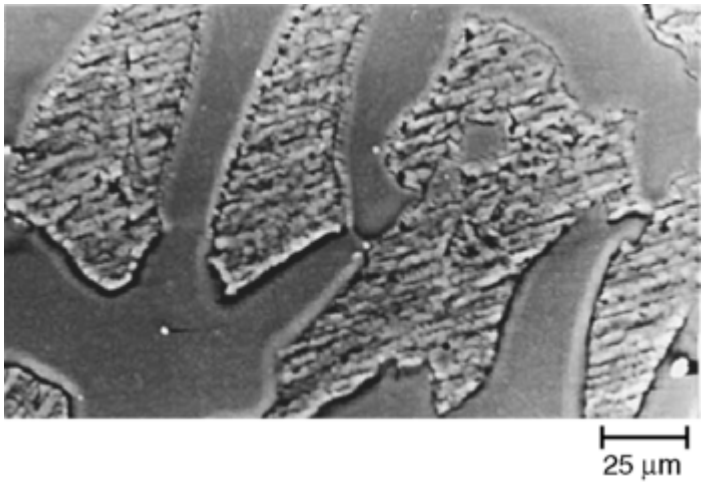

Fig. 27 Typical microstructure of arc-melted Ti-45Al-2Cr-2Nb alloy. Source: Ref 21

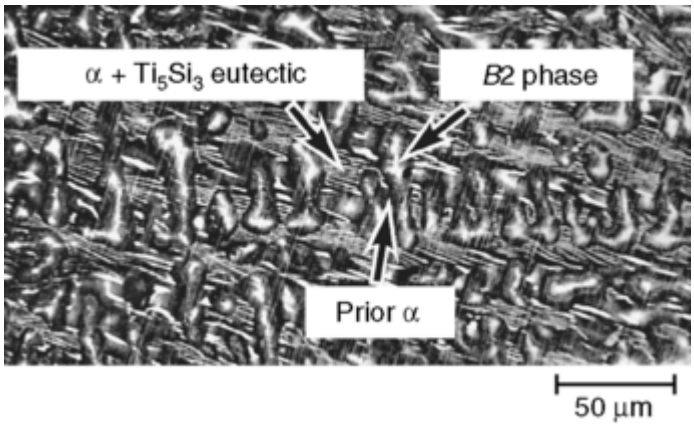

Fig. 28 Typical microstructure of arc-melted Ti-43.5Al-3Si-0.5Re alloy (scanning electron micrograph, backscattered electron image). Source: Ref 59

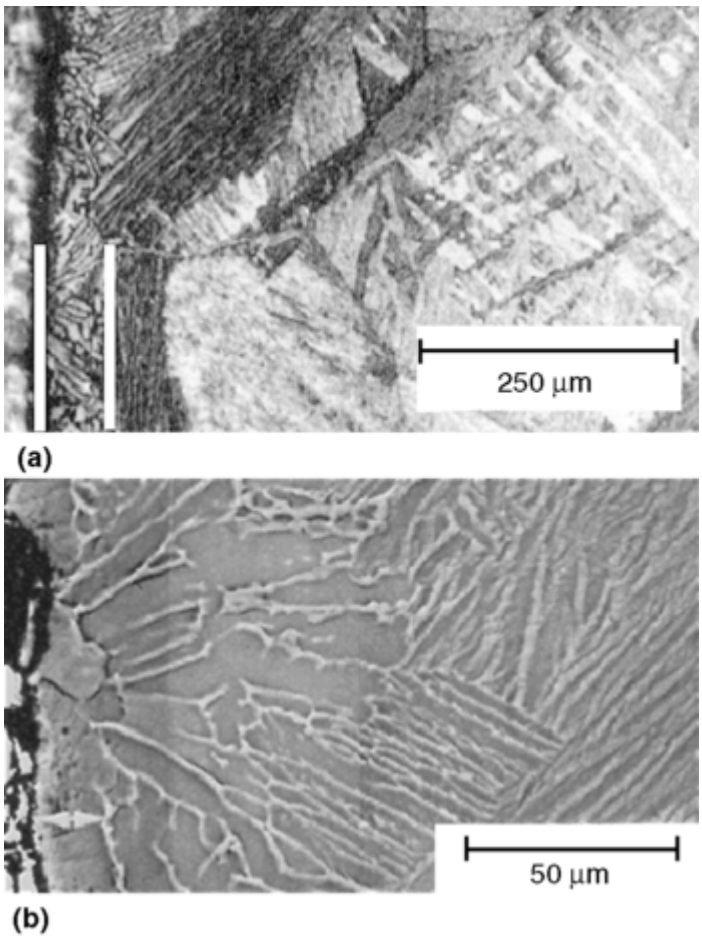

Fig. 29 Alpha case. (a) Alpha layer (within the parallel vertical lines) developed at the surface of a sand casting. (b) Detail. Source: Ref 62

The metal-mold casting method is frequently used for the casting of aluminum alloys, but has only recently been applied for titanium alloys (Ref 63). Advantages over investment casting include the elimination of processing steps, reduction of α-case thickness, elimination of ceramic inclusions, and refinement of the as-cast microstructure. In the metal-mold casting microstructure of Ti-6Al-4V, the grain morphologies vary from equiaxed in castings and prototype-production castings (slow withdrawal rates) to columnar in DS castings (fast withdrawal rate), as shown in Fig. 30. The grain size increases with increasing section size and decreasing cooling rate (Ref 64). In general, the cylindrical castings consisted primarily of α colonies, the prototype-production castings consisted of a mixture of α colonies and Widmanstätten α, and the float zone DS castings consisted almost entirely of Widmanstätten α. It is clear that a range of grain sizes and transformed β microstructures can be found in metal-mold-cast Ti-6Al-4V, but columnar grain morphologies are not likely to be found in production castings. Metal-mold Ti-6Al-4V castings tend to have prior β grains with equiaxed morphology.

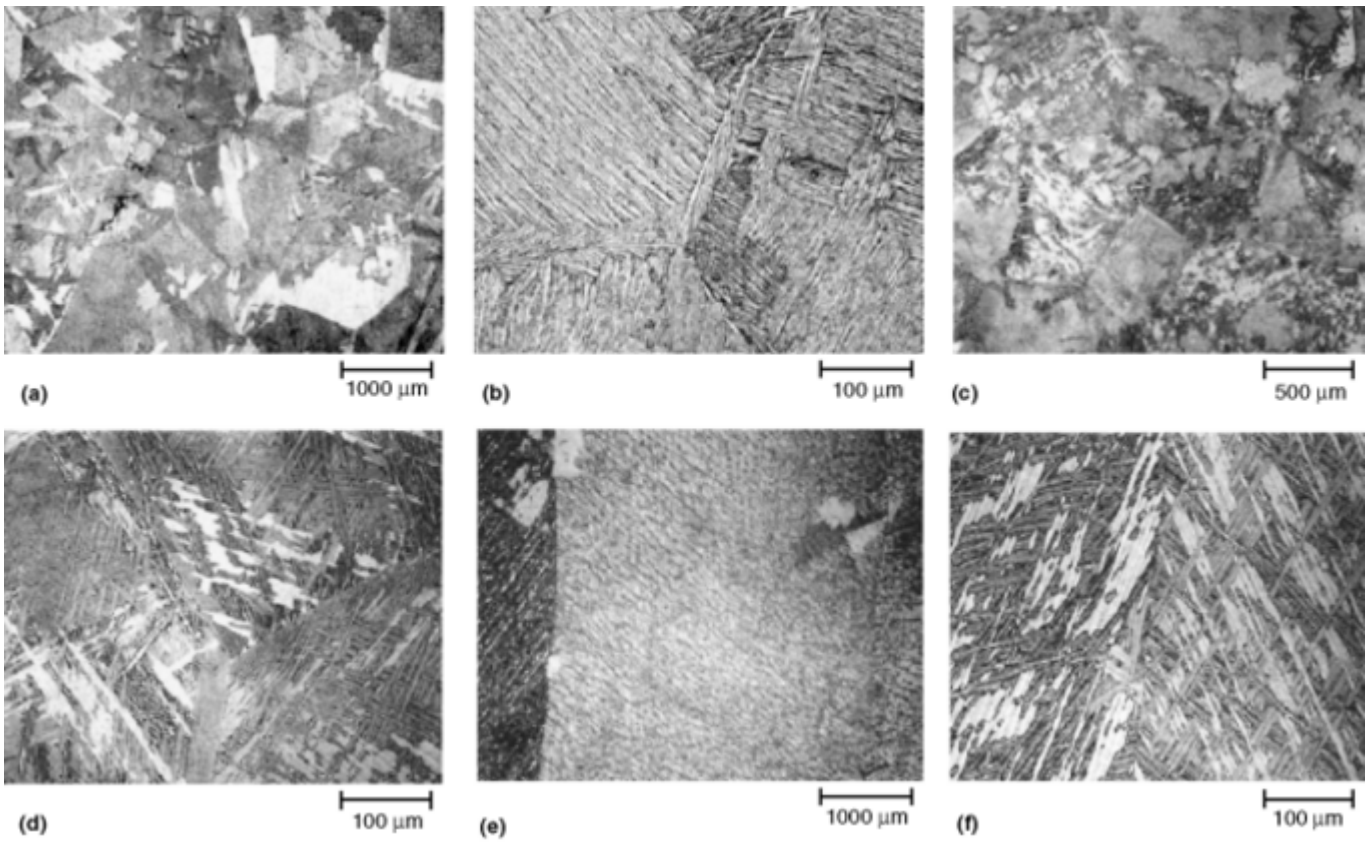

Fig. 30 Ti-6Al-4V cast products. (a), (c), and (e) show macrostructures. (b), (d), and (e) show microstructures. (a) and (b) are cylindrical casting. (c) and (d) are the spindle of an airfoil-shaped prototype production casting. (e) and (f) are the float zone directional solidification bar casting, rate 444 mm/s (17.5 in./s). Source: Ref 54

Investment casting provides very good dimensional control and is suitable for production of both small and large high-quality aerospace airframe and engine components. However, long-term interactions between the melt and ceramic mold due to low growth rates can result in contamination of the melt by ceramic inclusions (Ref 65).

A typical microstructure of the Ti-Al-Nb alloys cast in ceramic molds coated with yttria refined with boron is presented in Fig. 26. Microstructures of Ti-Al-W-Si DS ingots cast in alumina molds are presented in Fig. 31 and 32. The microstructure contains a small volume fraction of elongated *B*2 particles (ordered β phase) formed at the columnar grain boundaries and in the interdendritic region. Fine *B*2 and Ti_5Si_3 precipitates are formed at the lamellar interfaces and along the grains boundaries (Ref 67, 68, and 69). The shape of the dendrites and the orientation of the secondary dendrite arms in longitudinal section (60° with respect to the dendrite trunk) indicate that the α phase with hexagonal crystal structure is the primary phase.

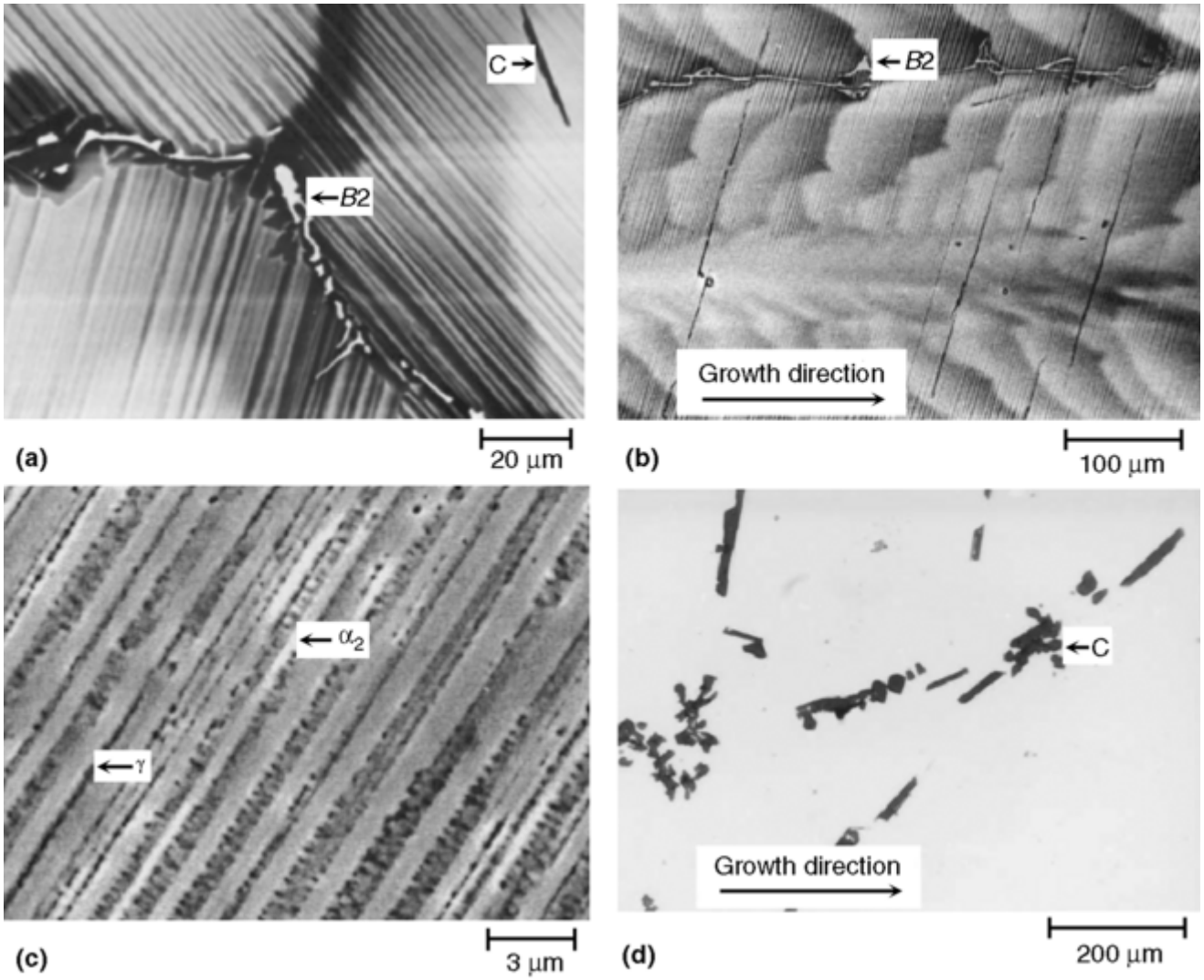

Fig. 31 Micrographs of a Ti-46Al-2W-0.5Si directionally solidified ingot solidified at 2.78 μm/s (0.11 mils/s) in an alumina mold. (a) Cross section and (b) longitudinal section show *B*2 particles (ordered β phase). (c) Detail with fine precipitates. (d) Morphology of Al_2O_3 particles (C) formed by reaction of melt with ceramic mold, also seen in (a). Source: Ref 66

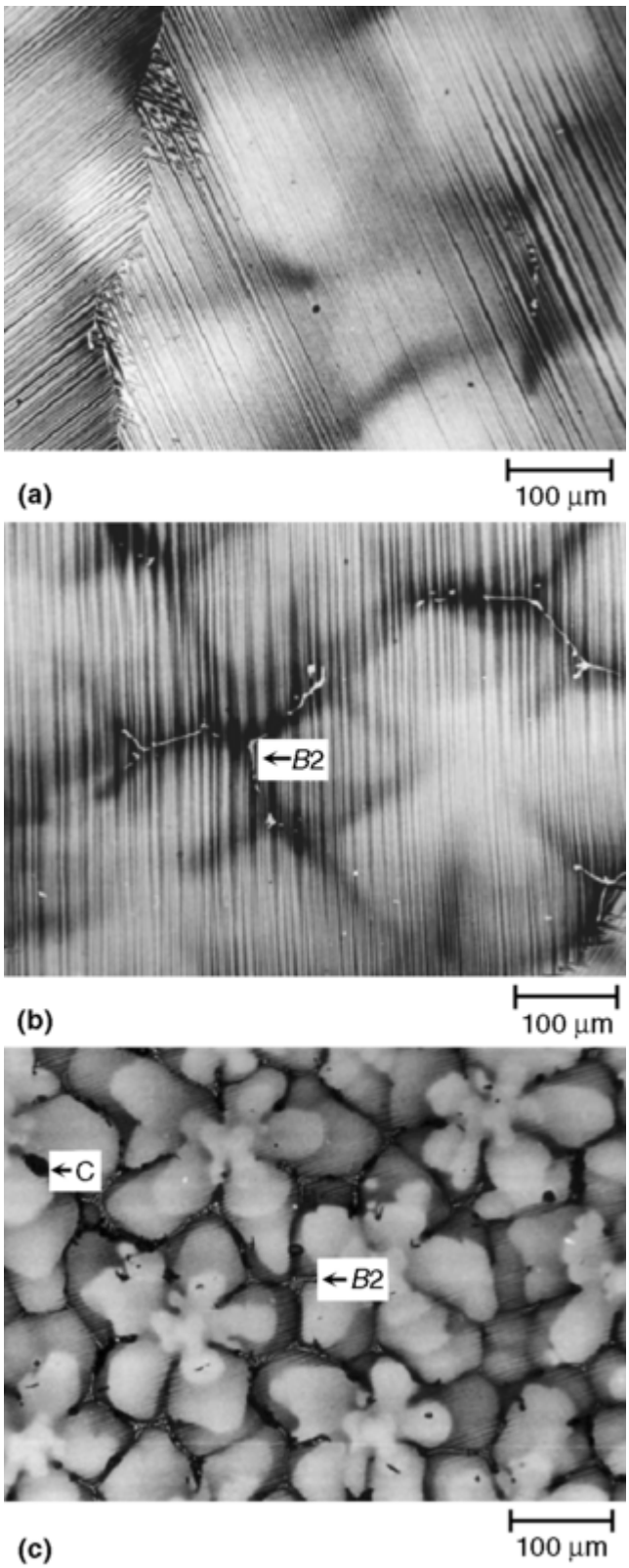

Fig. 32 Backscattered scanning electron micrographs showing the morphology of cells and dendrites within the cross section of the columnar grains in Ti-46Al-2W-0.5Si directionally solidified ingots cast in alumina molds. *B*2 particles (ordered β phase). Ceramic Al_2O_3 particle (C). The effect of solidification velocity (*V*) is shown. (a) $V = 2.78 \times 10^{-6}$ m/s. (b) $V = 1.39 \times 10^{-5}$ m/s. (c) $V = 1.18 \times 10^{-4}$ m/s. Source: Ref 66

The regular well-aligned α_2 (Ti_3Al) and β (Ti-Al) lamellar microstructure is shown in Fig. 31(c) at higher magnification. The DS ingots contain three types of Al_2O_3 particles: equiaxed, lath-shaped, and clusters of particles formed due to the reaction between the alumina mold and the melt, as seen in Fig. 31(d). Detailed microstructure analysis of the Al_2O_3 particles is published elsewhere (Ref 65).

The number of columnar grains depends on the solidification velocity and position, decreasing with increasing velocity and with increasing distance from the seed to the upper part of the ingots (Ref 66). Figure 32 illustrates the effect of the solidification velocity on the structure of the Ti-Al-W-Si alloy directionally solidified in alumina molds at a constant temperature gradient of $G_L = 14 \times 10^3$ °C/m. The microstructure varies from cellular (Fig. 32a) to regular dendritic structure (Fig. 32b and c).

Direct-laser fabrication is a solid-free-form-fabrication method that can be used to manufacture solid metallic components directly from computer-aided design files (Ref 70, 71). During direct-laser fabrication, powder is fed into a melt pool that is produced by a sharply focused laser beam. Parts are built layer-by-layer by rastering the laser and powder source across the substrate. Hence, solidification occurs rapidly in small, localized volumes, resulting in fine microstructures. Macrostructures of direct-laser deposits of Ti-6Al-4V in longitudinal sections are shown in Fig. 33(a) and (b), for low-power (neodymium:yttrium-aluminum garnet, or Nd:YAG) and high-power (CO_2) laser systems. Direct-laser-fabricated Ti-6Al-4V tends to have columnar morphology. The columnar grains are wavy in the Nd:YAG system deposits and, much different, perpendicular to the substrate in the CO_2 system deposits. The overall direction of growth of the columnar grains was likely a result of the effect of laser travel on the direction of heat removal. In the Nd:YAG system deposits, the heat flow direction was affected by the laser movement, while in the CO_2 system deposits it was not. The grain size in direct-laser-fabricated Ti-6Al-4V is strongly affected by incident energy. It can vary from 120 μm (5 mils) in the low-power systems to 750 μm (30 mils) in the high-power ones (see Fig. 33a and b).

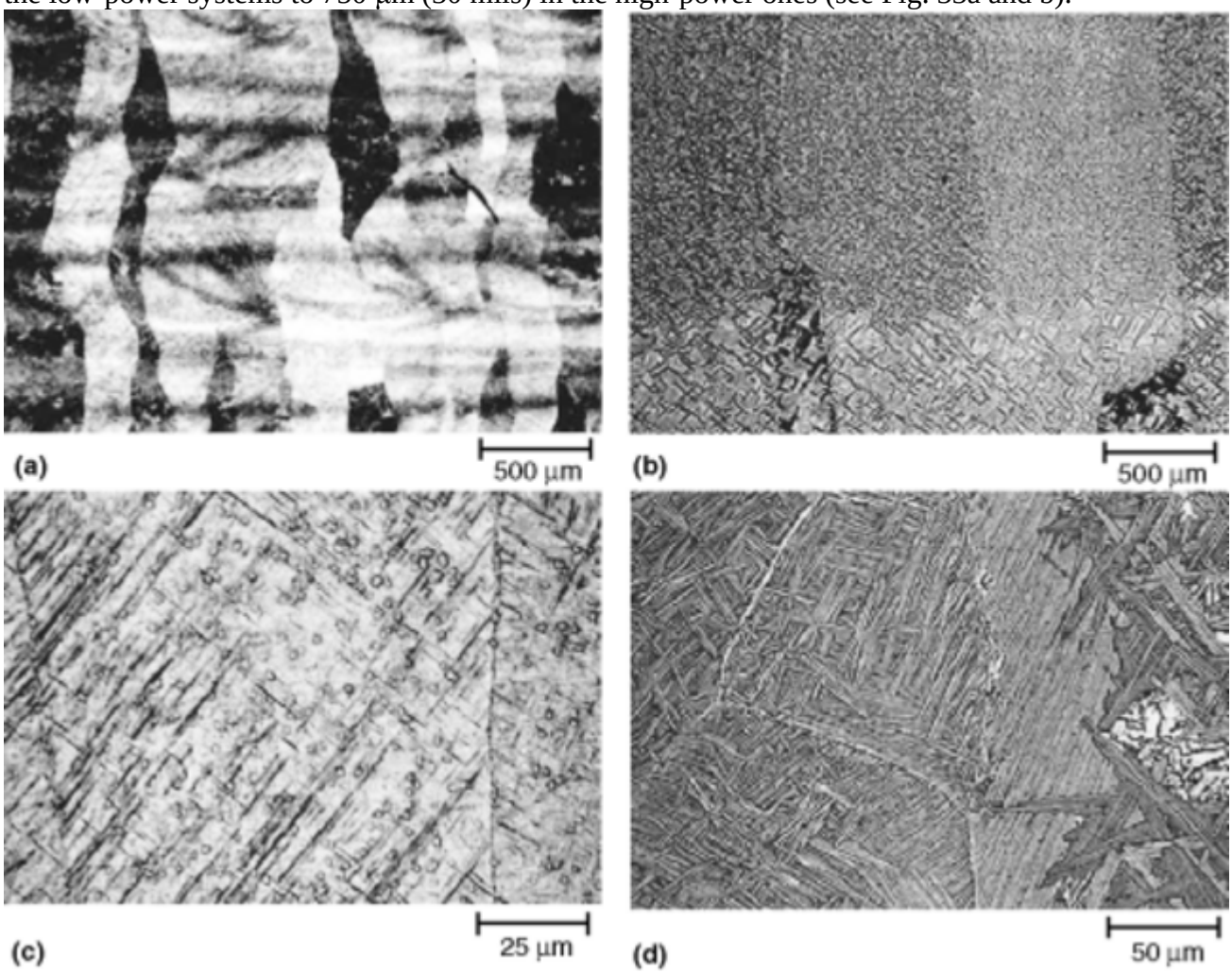

Fig. 33 Laser deposited Ti-6Al-4V. (a) and (b) Macrostructures. (c) and (d) Microstructures. Low-power laser (neodymium:yttrium-aluminum-garnet, or Nd:YAG) used for (a) and (c) and high-power laser (CO_2) used for (b) and (d). Source: Ref 64

The macroscopic "banding" formed in both cases (Fig. 33a and b) is due to a sudden change in the number of equiaxed α particles in the microstructure of the Nd:YAG specimens and to the coarseness of the Widmanstätten structure in the CO_2 specimens. Apparently, this banding was caused by the reheating of the previously deposited material that occurred during the subsequent deposition passes. In essence, a new heat-

affected zone formed locally in the deposit every time the laser passed, thereby resulting in the observed macrostructure and in the microstructure changes (Ref 64).

The microstructures of the deposits from the Nd:YAG system (Fig. 33c) were fine Widmanstätten with very small equiaxed α particles distributed both within the grains and along the grain boundaries, indicating that the cooling rate after solidification was very high. The microstructures of the CO_2 deposits were much coarser (Fig. 33d). The internal grain structure was primarily Widmanstätten in nature with occasional small α colonies along the grain boundaries. In addition, a layer of grain-boundary α was found along some of the grain boundaries in the CO_2 deposits, indicating a somewhat slower cooling rate (Ref 64).

References cited in this section

21. L. Yongchang, *Mater. Lett.,* Vol 57, 2003, p 2262s–2266s

54. D.E. Larson, *MRS Symp. Proc.,* Vol 194, 1990, p 285s–292s

59. T. Yamanaka, D.R. Johnson, H. Inui, and M. Yamaguchi, *Intermetallics,* Vol 7, 1999, p 779s–784s

60. S.L. Ausmus and R.A. Beahl, U.S. Bureau of Mines, Report 6509, 1944

61. R.K. Koch and J.M. Burrus, U.S. Bureau of Mines, Report 8587, 1981

62. W.E. Boettinger, M.E. Williams, S.R. Coriell, U.R. Kattner, and B.A. Mueller, *Metall. Mater. Trans. B,* Vol 31B, Dec 2000, p 1421

63. G.N. Colvin, *Proc. Titanium'95, Institute of Materials,* P.A. Blenkinsop, W.J. Evans, and H.N. Flower, Ed., London, 1996, p 691s–701s

64. P.A. Kobryn and S.L. Semiatin, *J. Mater. Process. Technol.,* Vol 135, 2003, p 330s–339s

65. J. Lapin and L. Ondrúš, *Kovové Mater.,* Vol 40, 2002, p 161

66. J. Lapin, L. Ondrus, and M. Nazmy, *Intermetallics,* Vol 10, 2002, p 1019s–1031s

67. W.M. Yin, V. Lupinc, and L. Battezzati, *Mater. Sci. Eng. A,* Vol 239–240, 1997, p 713

68. R. Yu, L.L. He, Z.X. Jin, J.T. Guo, H.Q. Ye, and V. Lupinc, *Scr. Mater.,* Vol 44, 2001, p 911

69. R. Yu, L.L. He, J.T. Guo, H.Q. Ye, and V. Lupinc, *Acta Mater.,* Vol 48, 2000, p 3701

70. J.T. Schriempf, E.J. Whitney, P.A. Blomquist, and F.G. Arcella, *Advances in Powder Metallurgy and Particulate Materials,* Vol 3, Metal Powder Industries Federation, 1997, p 21–51

71. D.M. Keicher, W.D. Miller, J.E. Smugeresky, and J.A. Romero, *Hard Coatings Based on Borides, Carbides and Nitrides: Synthesis, Characterization and Applications,* Y.W. Chung, R.W.J. Chia, and A. Kumar, Ed., TMS, 1998, p 369s–377s

D.M. Stefanescu and R. Ruxanda, Solidification Structures of Titanium Alloys, *Metallography and Microstructures,* Vol 9, *ASM Handbook,* ASM International, 2004, p. 116–126

Doru M. Stefanescu and Roxana Ruxanda, University of Alabama

References

1. E.W. Collings, *The Physical Metallurgy of Titanium Alloys,* American Society for Metals, 1984
2. I.J. Polmear, *Light Alloys—Metallurgy of the Light Metals,* American Society for Metals, 1982
3. D. Eylon and F.H. Froes, *Titanium Net Shape Technologies,* F.H. Froes and D. Eylon, Ed., AIME, 1984
4. A.P. Wu, G.S. Zou, J.L. Ren, H.J. Zhang, G.Q. Wang, X. Liu, and M.R. Xie, Microstructures and Mechanical Properties of Ti-24Al-17Nb (at.%) Laser Beam Welding Joints, *Intermetallics,* Vol 10, 2002, p 647s–652s
5. M. Hoch, N.C. Birla, S.A. Cole, and H.L. Gegel, Tech. Report AFML-TR-73-297, Air Force Materials Laboratory, Dec 1973
6. T. Kawabata, T. Kanai, and O. Izumi, *Acta Metall. Mater.,* Vol 33, 1985, p 1355
7. M. Yamaguchi and H. Inui, *Structural Intermetallics,* R. Darolia, J.J. Lewandowski, C.T. Liu, P.L. Martin, D.B. Miracle, and M.V. Nathal, Ed., TMS, 1995, p 127
8. Y.-W. Kim, *JOM,* Vol 46, 1994, p 30
9. F. Appel and R. Wagner, *Mater. Sci. Eng.,* Vol R22, 1998, p 187
10. Y.-W. Kim and D.M. Dimiduk, *JOM,* Vol 43 (No. 8), 1991, p 40
11. Y.-W. Kim and D.M. Dimiduk, *Structural Intermetallics,* M.V. Nathal, R. Darolia, C.T. Liu, P.L. Martin, D.B. Miracle, R. Wagner, and M. Yamaguchi, Ed., TMS, 1997, p 531
12. M. Yamaguchi, H, Inui, and K. Ito, *Acta Mater.,* Vol 48, 2000, p 307
13. D.M. Dimiduk, *Mater. Sci. Eng.,* Vol A263, 1999, p 281
14. M. Nazmy, M. Staubli, G. Onofrio, and V. Lupinc, *Scr. Mater.,* Vol 45, 2001, p 787
15. E. Evangelista, W.J. Zhang, L. Francesconi, and M. Nazmy, *Scr. Metall. Mater.,* Vol 33, 1995, p 467
16. Y.W. Kim, *JOM,* Vol 24, July 1989
17. S.L. Semiatin, *Proc. Gamma Titanium Aluminides,* Y.W. Kim et al., Ed., TMS, 1993, p 509
18. U.R. Kattner, J.-C. Lin, and Y.A. Chang, *Metall. Trans. A,* Vol 23A, 1992, p 2081
19. S. Muto, T. Yamanaka, D.R. Johnson, H. Inui, and M. Yamaguchi, *Mater. Sci. Eng. A,* Vol A329–331, 2002, p 424s–429s

20. S.C. Huang, *Structural Intermetallics,* R. Darolia, J.J. Lewandowski, C.T. Liu, P.L. Martin, D.B. Miracle, and M.V. Nathal, TMS, 1993, p 299

21. L. Yongchang, *Mater. Lett.,* Vol 57, 2003, p 2262s–2266s

22. D.M. Dimiduk, *Gamma Titanium Aluminides,* Y.-W. Kim, R. Wagner, and M. Yamaguchi, Ed., TMS, 1995, p 3

23. C.T. Liu and P.J. Maziasz, *Intermetallics,* Vol 6,1998, p 653

24. D. Hu, *Intermetallics,* Vol 9, 2001, p 1037s–1043s

25. C. McCullough, J.J. Valencia, C.G. Levi, and M. Mehrabian, *Acta Metall.,* Vol 37, 1989, p 1321

26. J.Y. Jung, J.K. Park, and C.H. Chun, *Intermetallics,* Vol 7, 1999, p 1033s–1041s

27. S.C. Huang and P.A. Siemers, *Metall. Trans.,* Vol 20A, 1989, p 1899

28. Y. Yamabe, N. Honjo, and M. Kikuchi, *Proc. International Symp. Intermetallic Compounds—Structure and Mechanical Properties,* O. Izumi, Ed., Japan Institute of Metals, 1991, p 821

29. J.C. Mishurda and J.H. Perepezko, *Microstructure/Property Relationships in Titanium Aluminides and Alloys,* Y.-W. Kim and R.R. Boyer, Ed., 1991, p 3

30. M. Yamaguchi, D.R. Johnson, H.N. Lee, and H. Inui, Directional Solidification of TiAl-Base Alloys, *Intermetallics,* Vol 8, 2000, p 511s–517s

31. D.R. Johnson, K. Chihara, H. Inui, and M. Yamaguchi, *Acta Mater.,* Vol 46, 1998, p 6529

32. T. Fujiwara, A. Nakamura, M. Hosomi, S.R. Nishitani, Y. Shirai, and M. Yamaguchi, *Philos. Mag.,* Vol 61A, 1990, p 591

33. C. Barrett and T.B. Massalski, *Structure of Metals,* 3rd rev. ed., Pergammon Press, p 406

34. H. Inui, A. Nakamura, M.H. Oh, and M. Yamaguchi, *Acta Mater.,* Vol 40, 1992, p 3059

35. M. Yamaguchi, H. Inui, S. Yokoshima, K. Kishida, and D.R. Johnson, *Mater. Sci. Eng. A,* Vol A213, 1996, p 25

36. W.R. Chen, J. Triantafillou, J. Beddoes, and L. Zhao, *Intermetallics,* Vol 7, 1999, p 171

37. Y.H. Lu, Y.G. Zhang, L.J. Qiao, Y.B. Wang, C.Q. Chen, and W.Y. Chu, *Mater. Sci. Eng., A,* Vol A289, 2000, p 91

38. K. Kishida, D.R. Johnson, Y. Masuda, H. Umeda, H. Inui, and M. Yamaguchi, *Intermetallics,* Vol 6, 1998, p 679

39. K. Kishida, H. Inui, and M. Yamaguchi, *Intermetallics,* Vol 7, 1999, p 1131

40. M.J. Blackburn, *The Science, Technology and Application of Titanium,* R.I. Jaffee and N.E. Promisel, Pergamon Press, 1970, p 633

41. M.C. Kim, M.H. Oh, J.H. Lee, H. Inui, M. Yamaguchi, and D.M. Wee, *Mater. Sci. Eng. A,* Vol 239–240, 1997, p 570s–576s

42. D.R. Johnson, Y. Masuda, H. Inui, and M. Yamaguchi, *Acta Mater.,* Vol 45, 1997, p 2523

43. D.R. Johnson, Y. Masuda, Y. Shimada, H. Inui, and M. Yamaguchi, *Structural Intermetallics,* M.V. Nathal, R. Darolia, C.T. Liu, P.L. Martin, D.B. Miracle, R. Wagner, and M. Yamaguchi, Ed., TMS, 1997, p 287

44. D.R. Johnson, H. Inui, and M. Yamaguchi, *Acta Mater.,* Vol 44, 1996, p 2523

45. D.R. Johnson, Y. Masuda, H. Inui, and M. Yamaguchi, *Mater. Sci. Eng., A,* Vol A 239–240, 1997, p 577s–583s

46. S.E. Kim, Y.T. Lee, M.H. Oh, H. Inui, and M. Yamaguchi, *Intermetallics,* Vol 8, 2000, p 399s–405s

47. M.C. Kim, M.H. Oh, J.H. Lee, and D.M. Wee, *J. Korean Inst. Met. Mater.,* Vol 35, 1997, p 31

48. M.C. Kim, M.H. Oh, D.M. Wee, H. Inui, and M. Yamaguchi, *Mater. Trans. Jpn. Inst. Met.,* Vol 37, 1996, p 1197

49. Y. Shimada, H. Inui, and M. Yamaguchi, *Proc. Fifth Symp. High-Performance Materials for Severe Environments, RIMCOF and JITA,* Japan, 1994, p 23

50. H. Nakamura, M. Takeyama, L. Wei, Y. Yamabe, and M. Kikuchi, *Proc. Third Japanese International SAMPE Symposium,* 7–10 Dec 1993, p 1353

51. F.A. Crossley, U.S. Patent No. 4,420,460, Dec 1983

52. V. Recina and D. Nilson, *Gamma Titanium Aluminides,* Y.-W. Kim, D.M. Dimiduk, and M.H. Loretto, 1999, TMS, 1999, p 447

53. L. Christodoulou, *International Workshop on Gamma Alloys, The Univ. of Birmingham,* 1–3 May 1996

54. D.E. Larson, *MRS Symp. Proc.,* Vol 194, 1990, p 285s–292s

55. T.T. Cheng, *Intermetallics,* Vol 8, 2000, p 29s–37s

56. A.B. Godfrey, Ph.D. thesis, The University of Birmingham, 1996

57. D. Hu, J.F. Mei, M. Wickins, and R.A. Harding, *Scr. Mater.,* Vol 47, 2002, p 273s–278s

58. F. Appel, U. Lorenz, J.D.H. Paul, and M. Oehring, *Gamma Titanium Aluminides,* Y.-W. Kim, D.M. Dimiduk, and M.H. Loretto, Ed., TMS, 1999, p 381

59. T. Yamanaka, D.R. Johnson, H. Inui, and M. Yamaguchi, *Intermetallics,* Vol 7, 1999, p 779s–784s

60. S.L. Ausmus and R.A. Beahl, U.S. Bureau of Mines, Report 6509, 1944

61. R.K. Koch and J.M. Burrus, U.S. Bureau of Mines, Report 8587, 1981

62. W.E. Boettinger, M.E. Williams, S.R. Coriell, U.R. Kattner, and B.A. Mueller, *Metall. Mater. Trans. B,* Vol 31B, Dec 2000, p 1421

63. G.N. Colvin, *Proc. Titanium'95, Institute of Materials,* P.A. Blenkinsop, W.J. Evans, and H.N. Flower, Ed., London, 1996, p 691s–701s

64. P.A. Kobryn and S.L. Semiatin, *J. Mater. Process. Technol.,* Vol 135, 2003, p 330s–339s

65. J. Lapin and L. Ondrúš, *Kovové Mater.,* Vol 40, 2002, p 161

66. J. Lapin, L. Ondrus, and M. Nazmy, *Intermetallics,* Vol 10, 2002, p 1019s–1031s

67. W.M. Yin, V. Lupinc, and L. Battezzati, *Mater. Sci. Eng. A,* Vol 239–240, 1997, p 713

68. R. Yu, L.L. He, Z.X. Jin, J.T. Guo, H.Q. Ye, and V. Lupinc, *Scr. Mater.,* Vol 44, 2001, p 911

69. R. Yu, L.L. He, J.T. Guo, H.Q. Ye, and V. Lupinc, *Acta Mater.,* Vol 48, 2000, p 3701

70. J.T. Schriempf, E.J. Whitney, P.A. Blomquist, and F.G. Arcella, *Advances in Powder Metallurgy and Particulate Materials,* Vol 3, Metal Powder Industries Federation, 1997, p 21–51

71. D.M. Keicher, W.D. Miller, J.E. Smugeresky, and J.A. Romero, *Hard Coatings Based on Borides, Carbides and Nitrides: Synthesis, Characterization and Applications,* Y.W. Chung, R.W.J. Chia, and A. Kumar, Ed., TMS, 1998, p 369s–377s

---

D.M. Stefanescu and R. Ruxanda, Computer Modeling of Solidification Microstructures, *Metallography and Microstructures,* Vol 9, *ASM Handbook,* ASM International, 2004, p. 127–131

Computer Modeling of Solidification Microstructures

Doru M. Stefanescu and Roxana Ruxanda, The University of Alabama

---

Introduction

A WIDELY HELD TENET of science states that the only true knowledge is that which is expressed in mathematical form. Computational modeling, which has enabled extensive use of mathematics for complicated problems, has brought engineering disciplines that have long suffered from excessive empiricism into the realm of sciences. Solidification science is a prime example. Once computers developed into the basic tool for solving the mathematics of solidification, it became possible to address the issues of solid/liquid (S/L) interface dynamics at the microlevel. The visualization of the length scale of the microstructure through computer graphical output became possible.

Based on the mathematics used to describe the physics, solidification models can be classified as deterministic or probabilistic (Fig. 1). The final product of the computation can be (Ref 1):

- Dendrite tip radius
- Solidification velocity
- Final number (size) of eutectic or dendritic grains in a volume element without graphical output (volume averaged) or with graphical output (grain envelope)
- Dendrite morphology
- Eutectic morphology

Microstructure maps for grain length scale, fraction of phases, or even microstructure transitions (columnar-to-equiaxed, stable-to-metastable) can be predicted.

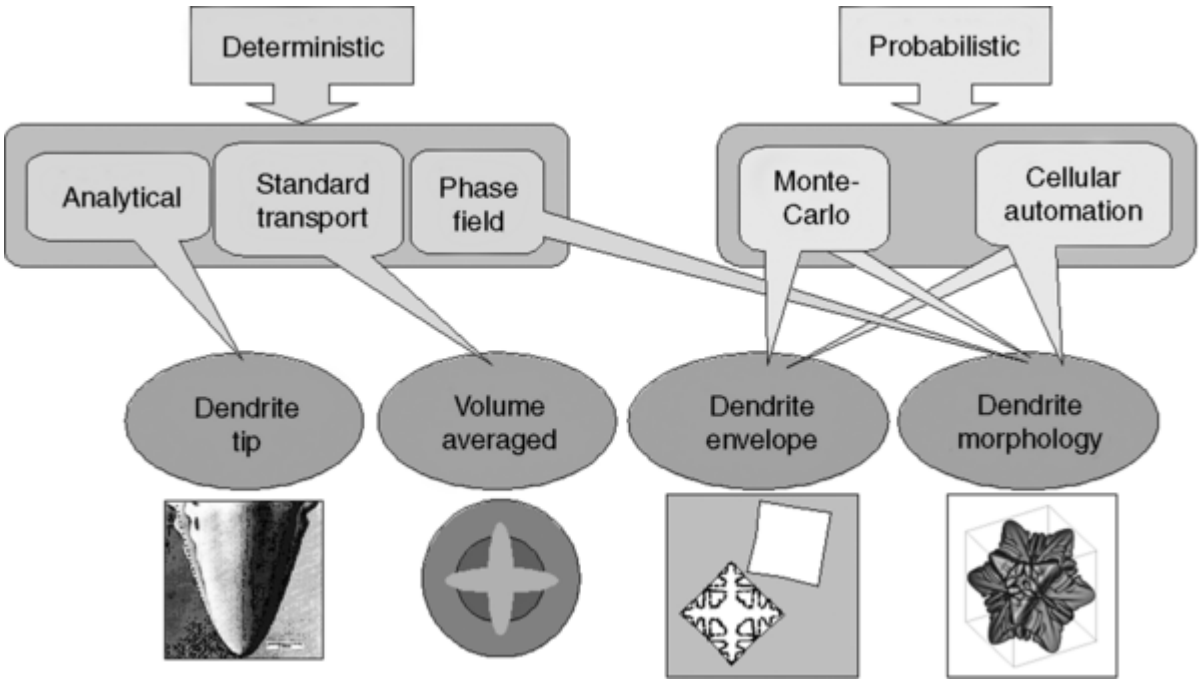

Fig. 1 Classification of computational models for microstructure evolution based on mathematical method and calculation outcome. Source: Ref 1

A detailed description of the mathematics of these models is beyond the scope of this text. The interested reader is referred to specialized books such as Ref 2. Analytical theories that deal only with dendrite tips and cannot address the overall grain morphology are not discussed any further in this article. This article presents only the general capabilities of the various models that can generate microstructure maps and thus transform the computer into a dynamic microscope. Illustrative examples are presented.

References cited in this section

1. D.M. Stefanescu, *Proc. Seventh Asian Foundry Congress,* Y.N. Pan et al., Ed., The Chinese Foundrymen's Association, Taipei, Taiwan, 2001, p 13–24

2. D.M. Stefanescu, *Science and Engineering of Casting Solidification,* Kluwer Academic, 2000

D.M. Stefanescu and R. Ruxanda, Computer Modeling of Solidification Microstructures, *Metallography and Microstructures,* Vol 9, *ASM Handbook*, ASM International, 2004, p. 127–131

Computer Modeling of Solidification Microstructures

Doru M. Stefanescu and Roxana Ruxanda, The University of Alabama

---

Standard Transport Models

Standard transport models can predict the length scale of the grains without visualization of the grain envelope. They solve the transport equations over a computational volume and output the average properties of the volume, for example, average grain size. Special techniques can be used in conjunction with deterministic standard transport models to generate microstructure maps for grain size. An example is provided in Fig. 2, where the upper part of the figure shows computational modeling results, and the lower part presents the optical metallographic microstructure (Ref 3). The number of eutectic grains increases from right to left, as the cross

section of the square specimen decreases (from 45 to 15 mm), and the cooling rate increases. The simulated grains were obtained by three-dimensional Johnson-Mehl tessellations.

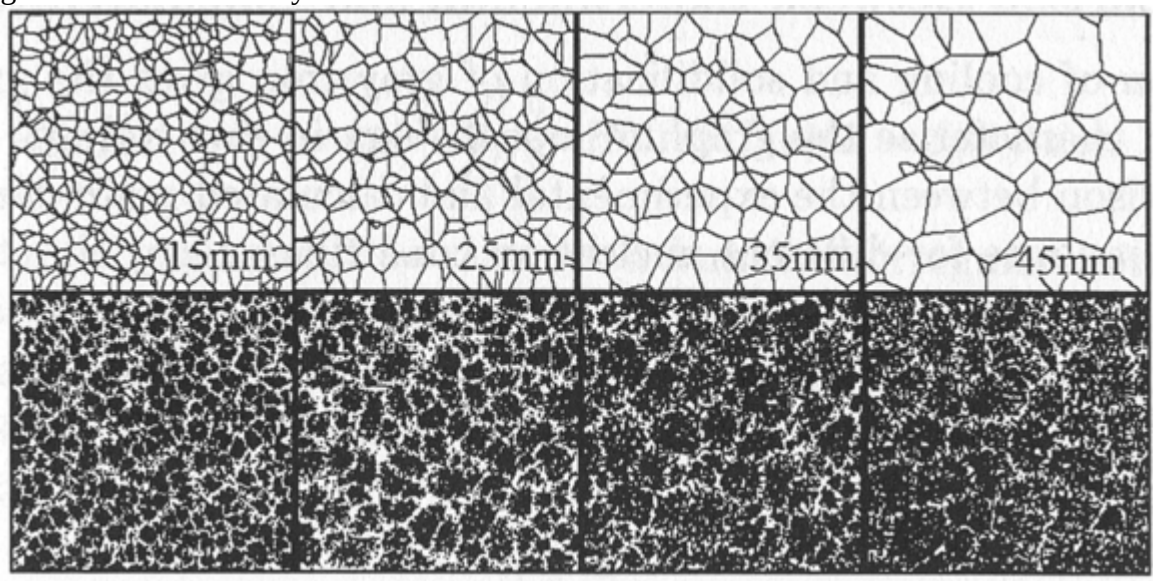

Fig. 2 Comparison between experimental (bottom) and simulated (top) gray iron grain structure at various cooling rates. Cooling rates decrease left to right. Source: Ref 3

Reference cited in this section

3. B. Leube, L. Arnberg, and R. Mai, *Modeling of Casting, Welding and Advanced Solidification Processes VIII*, B.G. Thomas and C. Beckerman, Ed., TMS, 1998, p 463

D.M. Stefanescu and R. Ruxanda, Computer Modeling of Solidification Microstructures, *Metallography and Microstructures,* Vol 9, *ASM Handbook*, ASM International, 2004, p. 127–131

Computer Modeling of Solidification Microstructures

Doru M. Stefanescu and Roxana Ruxanda, The University of Alabama

---

Phase-Field Models

A fundamental deterministic approach, the phase-field method, has been applied to modeling of dendrite growth (Ref 4, 5, 6, 7, 8). It overcomes the problems associated with interface tracking by using a thermodynamic formulation, which allows the diffusion problem to be solved over the entire calculation domain without having to consider the individual phases separately.

The liquid-to-solid transition is described by an order parameter called the phase field. The phase-field parameter has a constant value within each phase (typically 1 for the solid and 0 for the liquid) and varies smoothly across a thin interface of finite width (diffuse interface). The position of the interface is determined from the solution of the phase-field and temperature equations. Typical examples of the computation output are given in Fig. 3 for dendritic solidification and in Fig. 4 for eutectic solidification (Ref 9, 10). While phase-field models are fundamental in nature, they are not yet fully quantitative (Ref 11).

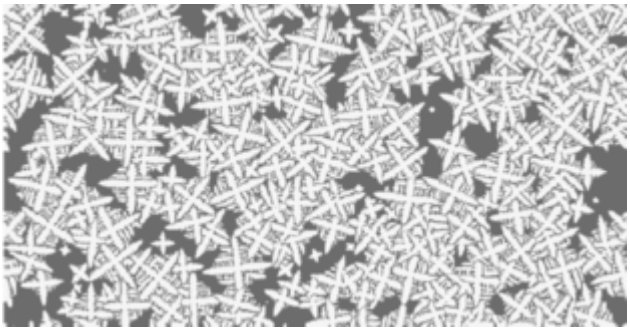

Fig. 3 Phase-field simulation of dendrite growth. Source: Ref 9

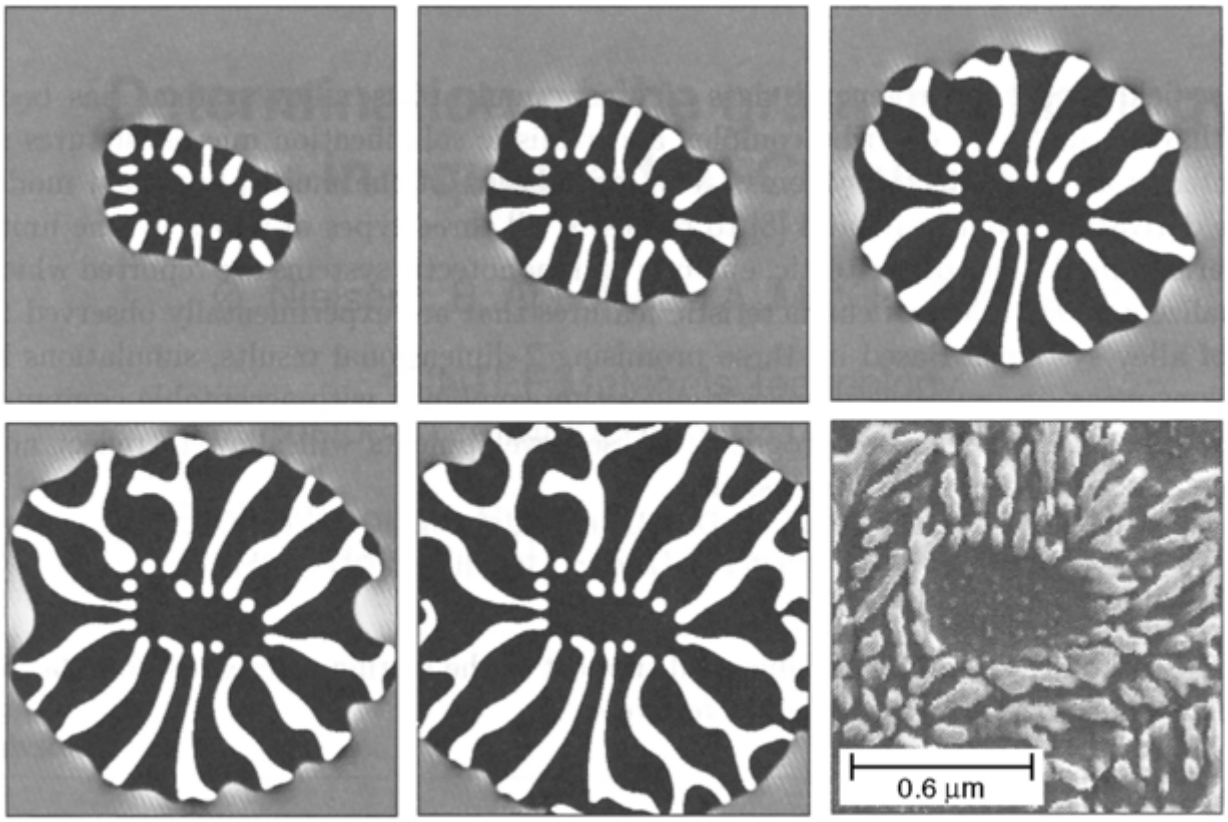

Fig. 4 Phase-field simulation of a eutectic aluminum-silicon grain in comparison with an experimental photograph. Source: Ref 10

References cited in this section

4. S. Kobayashi, *Pattern Formation in Complex Dissipative Systems*, S. Kai, Ed., World Science, Singapore, 1992, p 121

5. A.A. Wheeler, W.J. Boettinger, and G.B. McFadden, *Phys. Rev. A*, Vol 45, 1992, p 7424

6. J.A. Warren and W.J. Boettinger, *Acta Metall. Mater.*, Vol 43, 1995, p 689

7. J.A. Warren, R. Kobayashi, and W.C. Carter, *Modeling of Casting, Welding and Advanced Solidification Processes IX*, P.R. Sahm, P.N. Hansen, and J.G. Conley, Ed., Shaker Verlag, Aachen, Germany, 2000, p CII

8. C. Beckermann, X. Tong, and A. Karma, *The Science of Casting and Solidification*, D.M. Stefanescu, R. Ruxanda, M. Tierean, and C. Serban, Ed., Lux Libris, Brasov, Romania, 2001, p 100

9. J.A. Warren, I. Loginova, L. Granasy, T. Borzsonyi, T. Pusztai, *Modeling of Casting, Welding and Advanced Solidification Processes X*, D.M. Stefanescu, et al., Ed., TMS, 2003, p 45–52

10. B. Nestler and A.A. Wheeler, *Modeling of Casting, Welding and Advanced Solidification Processes IX*, P.R. Sahm, P.N. Hansen, and J.G. Conley, Ed., Shaker Verlag, Aachen, 2000, p 505

11. A. Karma, *Modeling of Casting, Welding and Advanced Solidification Processes X*, D.M. Stefanescu et al. Ed., TMS, 2003, p 3

D.M. Stefanescu and R. Ruxanda, Computer Modeling of Solidification Microstructures, *Metallography and Microstructures,* Vol 9, *ASM Handbook*, ASM International, 2004, p. 127–131

Computer Modeling of Solidification Microstructures

Doru M. Stefanescu and Roxana Ruxanda, The University of Alabama

---

Monte Carlo (MC) Models

The MC technique is based on the minimization of the interface energy of a grain assembly. The microstructure is first mapped on a discrete lattice. Each lattice site is assigned a grain index, an integer from 1 to some number, that indicates the local crystallographic orientation. Lattice sites having the same grain index value belong to the same grain. A grain-boundary segment lies between two sites of unlike orientation. The initial distribution of orientations is chosen at random and the system evolves to reduce the number of nearest-neighbor pairs of unlike crystallographic orientation. This is equivalent to minimizing the interfacial energy.
When coupled with heat and solute transport equations, the MC method can generate spectacular images. Some typical computational results of such a mesoscale model are presented in Fig. 5. A clear transition from columnar to equiaxed solidification is seen when the superheating temperature, and therefore the undercooling, is increased (Ref 12). Such a model presents considerable engineering interest.

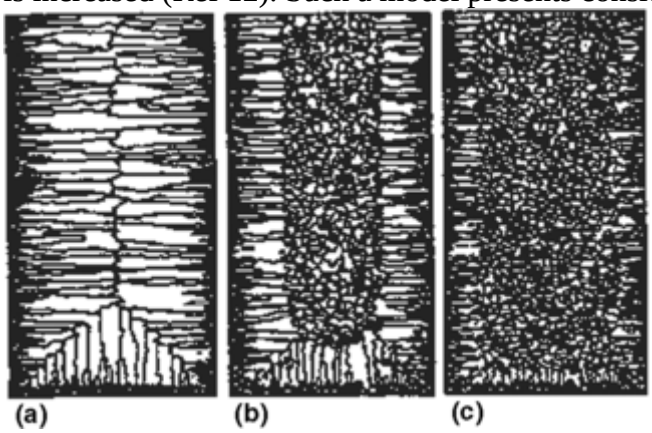

Fig. 5 Computer modeled structural regions in castings. Superheating temperatures: (a) 50 °C (122 °F), (b) 80 °C (176 °F), (c) 150 °C (302 °F). Source: Ref 12

Reference cited in this section

12. P. Zhu and R.W. Smith, *Acta Metall. Mater.*, Vol 40, 1992, p 683 and 3369

D.M. Stefanescu and R. Ruxanda, Computer Modeling of Solidification Microstructures, *Metallography and Microstructures,* Vol 9, *ASM Handbook*, ASM International, 2004, p. 127–131

Computer Modeling of Solidification Microstructures

Doru M. Stefanescu and Roxana Ruxanda, The University of Alabama

Cellular Automaton (CA) Models

The CA technique, originally developed by Hesselbarth and Göbel (Ref 13), is based on the division of the simulation domain into cells, which contain all the necessary information to represent the process to be modeled. Each cell is assigned information regarding the state (such as solid, liquid, interface, and grain orientation) and the value of the calculated fields (such as temperature, composition, and solid fraction). The fields of the cells are calculated by analytical or numerical solutions of the transport and transformation equations. The change of the cell states is calculated through transition rules, which can be analytical or probabilistic.

Cellular automaton growth models coupled with finite-element heat-flow models have been used to generate mesoscale images of grain-envelope evolution during solidification. In some models dendritic tip growth law is used, and growth velocity is then averaged for a given microvolume element. Thus, the final product of the simulation is dendritic grains, not dendritic crystals. In this respect, the method relies heavily on averaged quantities, just as continuum deterministic models do, but can display grain boundaries on the computer screen. These models can predict the columnar-to-equiaxed transition (CET) in the presence of fluid flow, which is of paramount importance if realistic microstructures are to be predicted. As shown in Fig. 6(a), without convection the calculated grain structure is fully equiaxed (Ref 14). It does not reproduce the sedimentation cone and the columnar grain structure observed experimentally. When fluid flow is included (Fig. 6(b), a clear CET and grain sedimentation at the bottom of the ingot are shown.

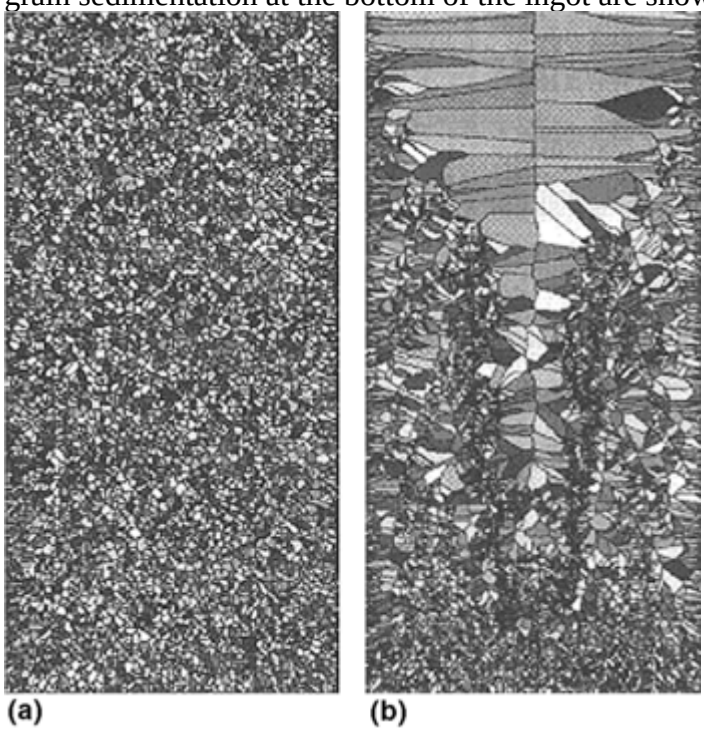

Fig. 6 Simulation of columnar-to-equiaxed transition in a conventionally cast Al-7Si alloy. (a) Calculation with no fluid flow. (b) Calculation that includes fluid flow. Source: Ref 14

Qualitative comparisons with experiments have been presented as shown in Fig. 7 for conventional casting and in Fig. 8 for rapid solidification (Ref 15, 16). Note the corner effect and grain selection at the mold surface on

Fig. 7(a) and (b). As the bulk nucleation undercooling decreases, a CET is observed in Fig. 7(b), and then a fully equiaxed structure in Fig. 7(c).

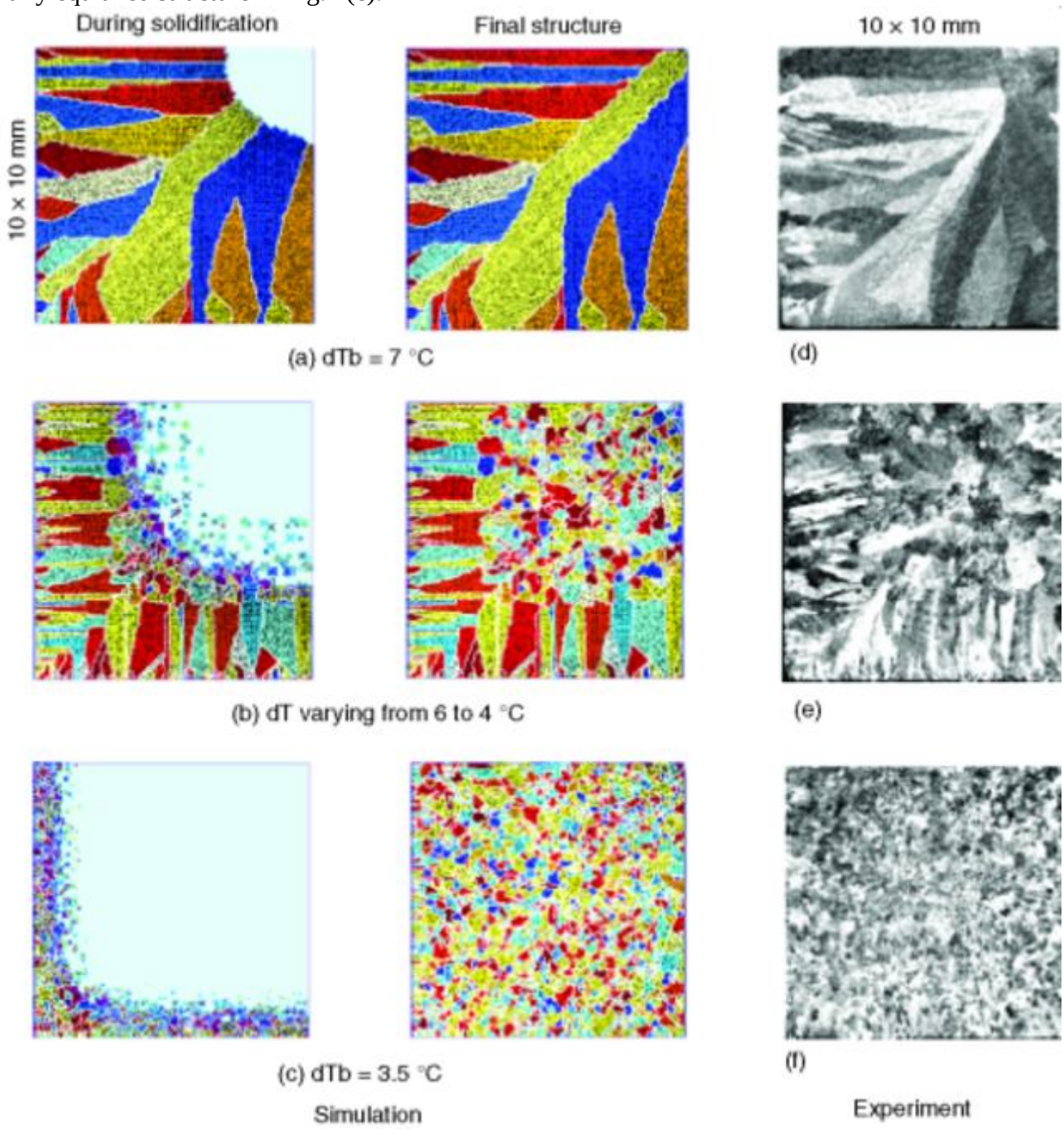

Fig. 7 Simulated and experimental grain size and orientation in Al-2.5Cu (wt%) alloys at various bulk nucleation undercoolings (ΔT_b). Source: C.P. Hong and M.F. Zhu, in *The Science of Casting and Solidification*, D.M. Stefanescu, R. Ruxanda, M. Tierean, and C. Serban, Ed., Lux Libris, Brasov, Romania, 2001, p 110–118

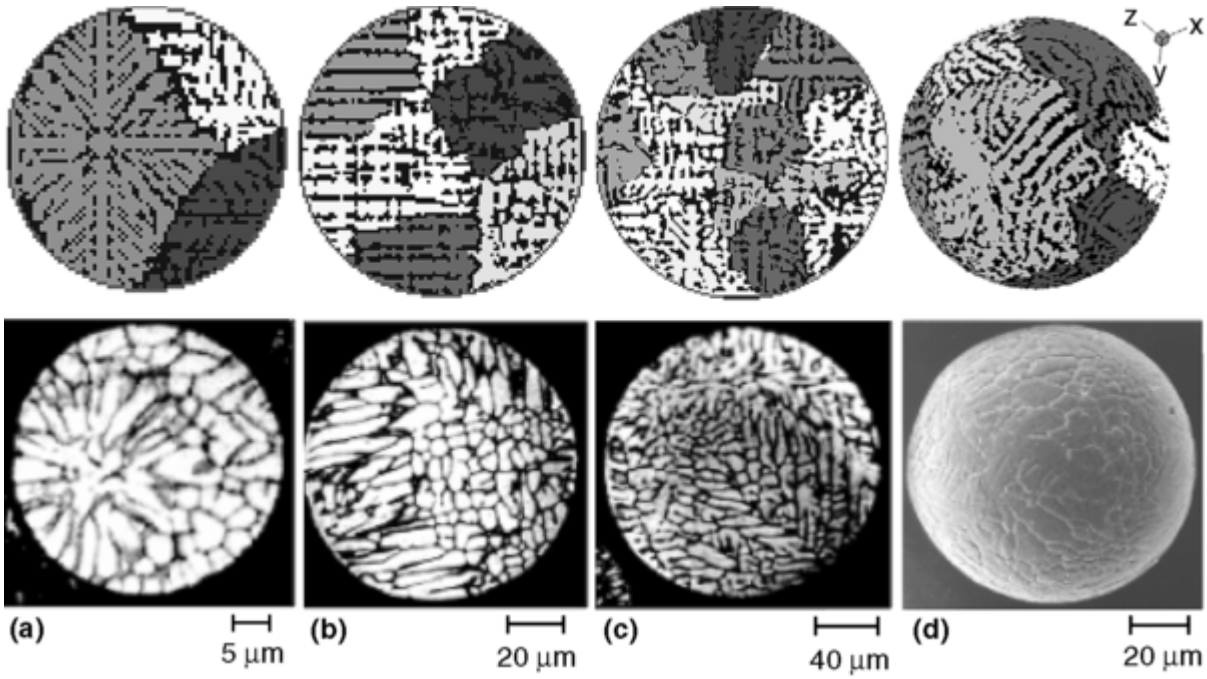

Fig. 8 Simulated (upper row) and experimental (lower row) microstructures of atomized Al-10Cu (mass%) droplets with various droplet diameters: (a) 40 μm, (b) 100 μm, (c) 200 μm, and (d) 100 μm. Here (a), (b), and (c) indicate the microstructures shown in two-dimensional cross section and three-dimensional view of a droplet. Source: Ref 16

Cellular automaton models have also been used to describe the solidification of spheroidal graphite iron. In one model (Ref 17), after reaching the nucleation or transformation temperature, the cells in the domain are allowed to change the value of their indexes. This is done according to the deterministic rules for equiaxed dendrite austenite grains and for equiaxed eutectic grains. The growth of the eutectic grains is triggered only after an austenite dendrite touches a graphite nucleus. The nucleus transforms into a graphite nodule developing an austenite shell that is considered an integral part of the original dendritic grain. The model is able to draw a realistic representation of the grain structure during the solidification of spheroidal graphite iron, as shown in Fig. 9. Similar models have been extended to describe dendrite and eutectic morphology. Figure 10 presents the simulated dendrite morphology of an Al-2Cu (mass%) alloy solidified from a melt undercooled with 6.5 K in a melt flowing at 0.1 m/s from left to right. It can be seen that the dendrite arms in the upstream direction grow faster, while the growth of the dendrite in the downstream direction is much delayed. This is indeed a demonstration of the transformation of the computer into a dynamic microscope.

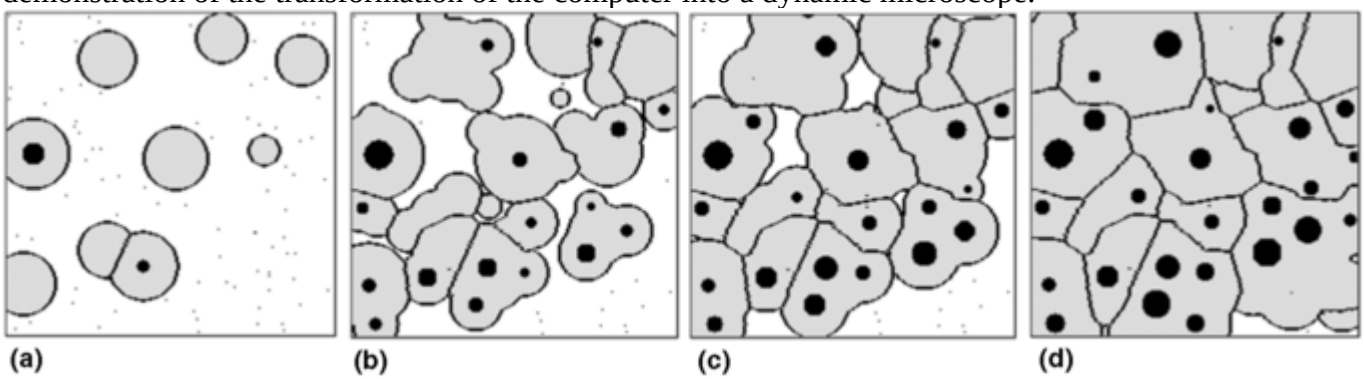

Fig. 9 Model output of microstructure evolution of eutectic spheroidal graphite iron during solidification. (a) Solidification fraction (f_s) = 0.24. (b) f_s = 0.55. (c) f_s = 0.72. (d) f_s = 0.99. Length of each square = 200 μm. Source: Ref 17

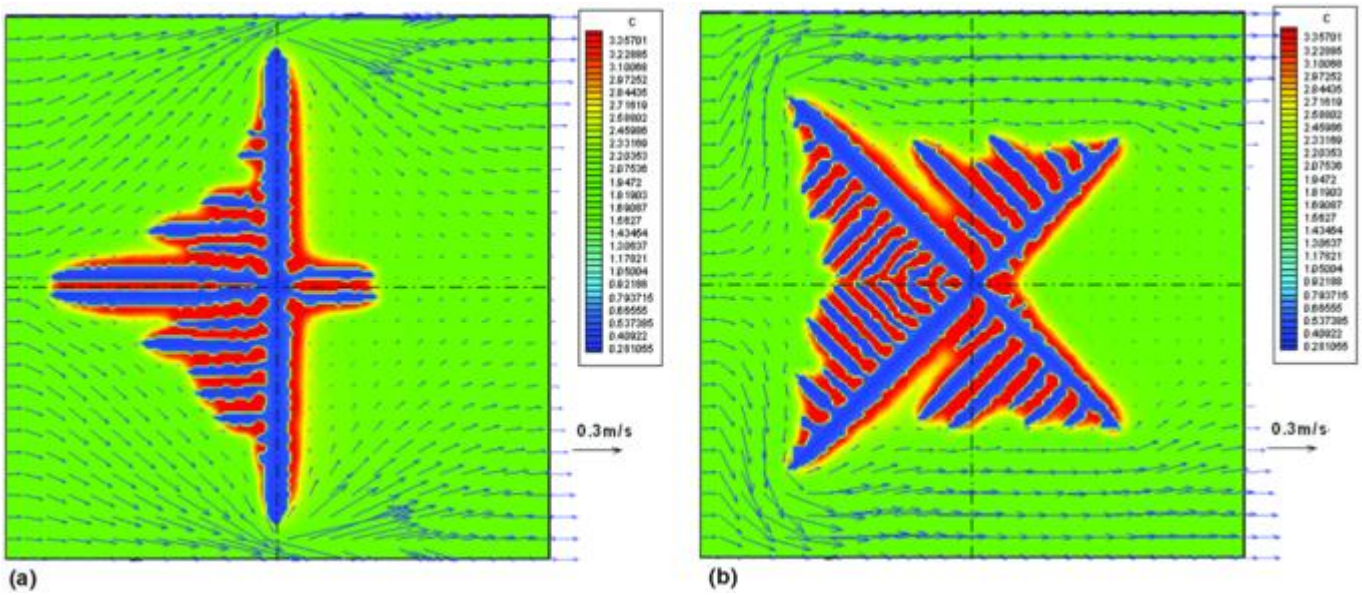

Fig. 10 Simulated dendritic growth morphology and concentration profiles of an Al-2Cu (wt%) alloy with melt convection for different crystallographic orientations. (a) 0°. (b) 45°. Source: C.P. Hong and M.F. Zhu, in *Modeling of Casting, Welding and Advanced Solidification Processes X*, D.M. Stefanescu et al., Ed., TMS, 2003, p 63–74

Figure 11 compares the calculated and experimental microstructure of an Al-7Si (mass%) alloy (Ref 18). The white phase is the primary α′-phase dendrites, while the dark phase is the eutectic. Because of the simplifying assumptions introduced in these models, in particular the use of analytical tip velocity models for dendrite growth, these models are not quantitative. A more fundamental approach (Ref 20) includes time-dependent calculations for temperature distribution, solute redistribution in the liquid and solid phases, curvature, and growth anisotropy. Solidification velocity is calculated from the transport equations and not with analytical models. Such an approach can perform not only mesoscale calculations (grain envelope), but also microscale calculations (grain morphology). In the examples provided in Fig. 12, two-dimensional calculations at the dendrite tip length scale were performed to simulate the evolution of columnar and equiaxed dendritic morphologies including the occurrence of the CET (Ref 21). Note that all dendrites are oriented in the *x-y* direction to avoid the complications resulting from mesh anisotropy.

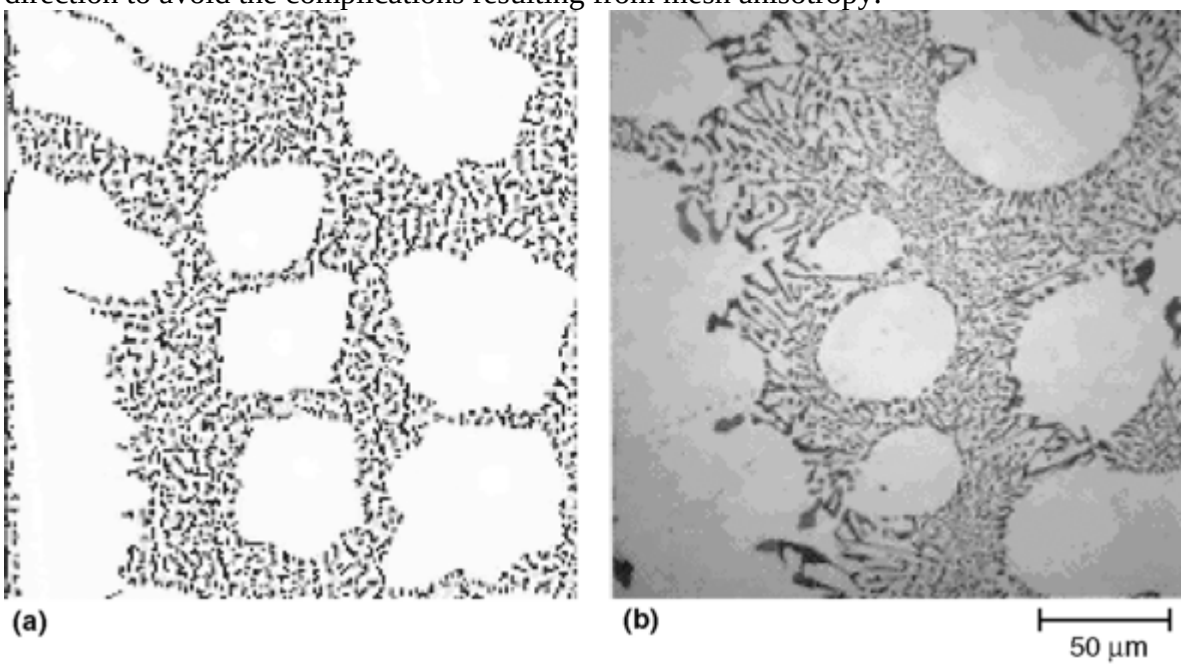

Fig. 11 Microstructures of an Al-7Si (mass%) alloy. (a) Simulation (Ref 18) and (b) experiment (Ref 19)

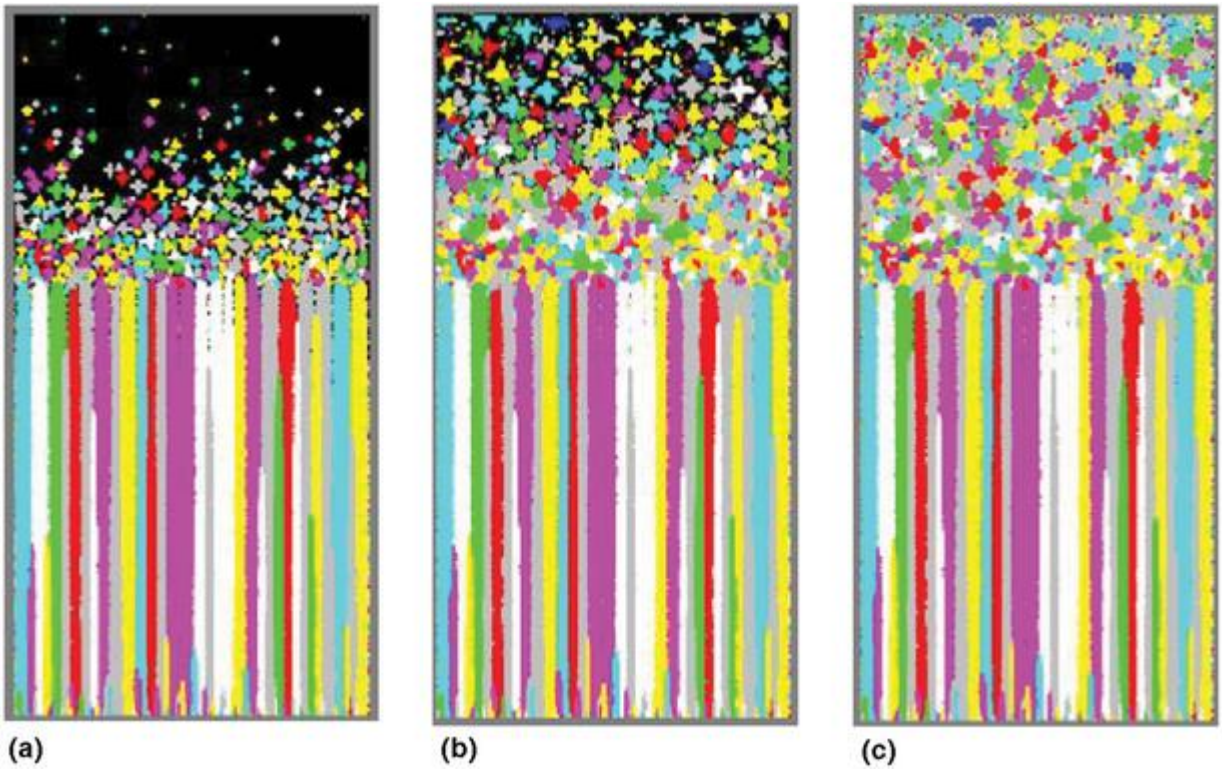

Fig. 12 Simulated microstructure. (a) Columnar cellular dendritic morphology. (b) Equiaxed dendritic morphology. (c) Columnar-to-equiaxed transition formation in unidirectional solidification of IN 718-5, a nickel-base superalloy with 5 wt% Nb. Source: Ref 21

The problem of mesh anisotropy was recently solved. A model with quantitative predictive capabilities valid for any grain orientation was proposed (Ref 22). An example of the computer output of this model is presented in Fig. 13. The dendrites grow following their crystallographic orientation more or less homogeneously at the beginning of the solidification process. Halfway through solidification, because of the interaction of the solutal fields, the morphology and growth rate of individual dendrites is significantly modified. Some of the dendrites develop secondary branching, while in others it is suppressed. Some others grow almost as globular dendrites due to their location relative to other dendrites and the crystallographic orientation. For more information on modeling, see "Modeling of Microstructural Evolution," in *Casting*, Volume 15 of *ASM Handbook* (1998).

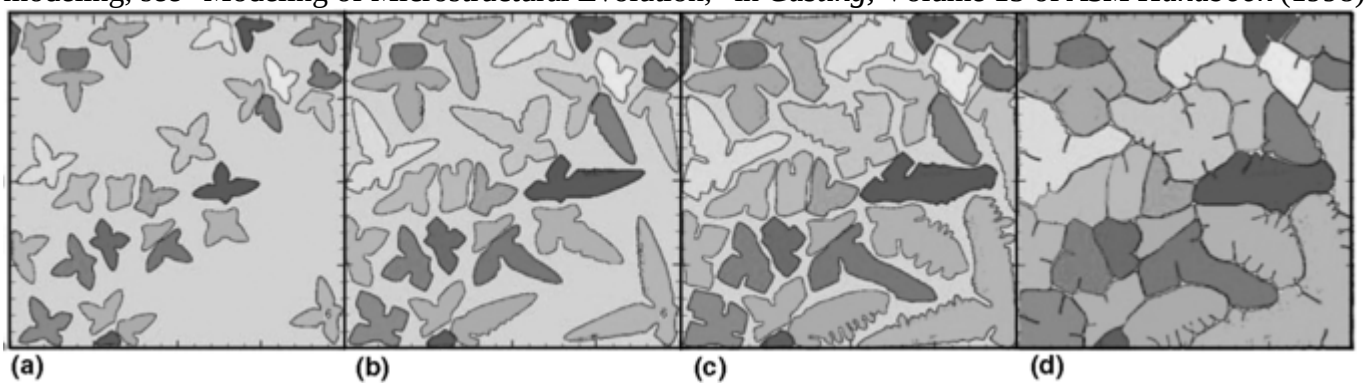

Fig. 13 Simulation of equiaxed solidification of Al-4Cu (wt%) alloy showing grain-boundary formation. Lapse time: (a) 0.04 s, (b) 0.08 s, (c) 0.16 s, (d) 0.2 s. Source: Ref 22

References cited in this section

13. H.W. Hesselbarth and I.R. Göbel, *Acta Metall.*, Vol 39, 1991, p 2135

14. C.A. Gandin, T. Jalanti, and M. Rappaz, *Modeling of Casting, Welding and Advanced Solidification Processes—VIII*, B.G. Thomas and C. Beckermann, Ed., TMS, 1998, p 363

15. C.P. Hong and M.F. Zhu, *The Science of Casting and Solidification,* D.M. Stefanescu, R. Ruxanda, M. Tierean, and C. Serban Ed., Lux Libris, Brasov, Romania, 2001, p 110–118

16. C.P. Hong and M.F. Zhu, *Modeling of Casting, Welding and Advanced Solidification Processes X,* D.M. Stefanescu et al., Ed., TMS, 2003, p 63–74

17. R. Ruxanda, L. Beltran-Sanchez, J. Massone, and D.M. Stefanescu, *Proc. Cast Iron Division,* AFS 105th Casting Congress (Dallas, TX), 2001, p 37

18. M.F. Zhu and C.P. Hong, *Modeling of Casting, Welding and Advanced Solidification Processes X,* D.M. Stefanescu et al., Ed., TMS, 2003, p 91–98

19. A.K. Dahle, K. Nogita, J.W. Zindel, S.D. Mcdonald, and L.M. Hogan, *Metall. Mater. Trans. A,* Vol 32A, 2001, p 949–960

20. U. Dilthey, V. Pavlik, and T. Reichel, *Mathematical Modelling of Weld Phenomena,* H. Cerjak, Ed., The Inst. of Materials, London, 1997, p 85

21. L. Nastac, *Acta Metall. Mater.,* Vol 47 (No. 17), 1999, p 4253

22. L. Beltran-Sanchez and D.M. Stefanescu, *Modeling of Casting, Welding and Advanced Solidification Processes X,* D.M. Stefanescu et al., Ed., TMS, 2003, p 75–82

D.M. Stefanescu and R. Ruxanda, Computer Modeling of Solidification Microstructures, *Metallography and Microstructures,* Vol 9, *ASM Handbook,* ASM International, 2004, p. 127–131

Computer Modeling of Solidification Microstructures

Doru M. Stefanescu and Roxana Ruxanda, The University of Alabama

---

References

1. D.M. Stefanescu, *Proc. Seventh Asian Foundry Congress,* Y.N. Pan et al., Ed., The Chinese Foundrymen's Association, Taipei, Taiwan, 2001, p 13–24

2. D.M. Stefanescu, *Science and Engineering of Casting Solidification,* Kluwer Academic, 2000

3. B. Leube, L. Arnberg, and R. Mai, *Modeling of Casting, Welding and Advanced Solidification Processes VIII,* B.G. Thomas and C. Beckerman, Ed., TMS, 1998, p 463

4. S. Kobayashi, *Pattern Formation in Complex Dissipative Systems,* S. Kai, Ed., World Science, Singapore, 1992, p 121

5. A.A. Wheeler, W.J. Boettinger, and G.B. McFadden, *Phys. Rev. A,* Vol 45, 1992, p 7424

6. J.A. Warren and W.J. Boettinger, *Acta Metall. Mater.,* Vol 43, 1995, p 689

7. J.A. Warren, R. Kobayashi, and W.C. Carter, *Modeling of Casting, Welding and Advanced Solidification Processes IX,* P.R. Sahm, P.N. Hansen, and J.G. Conley, Ed., Shaker Verlag, Aachen, Germany, 2000, p CII

8. C. Beckermann, X. Tong, and A. Karma, *The Science of Casting and Solidification,* D.M. Stefanescu, R. Ruxanda, M. Tierean, and C. Serban, Ed., Lux Libris, Brasov, Romania, 2001, p 100

9. J.A. Warren, I. Loginova, L. Granasy, T. Borzsonyi, T. Pusztai, *Modeling of Casting, Welding and Advanced Solidification Processes X,* D.M. Stefanescu, et al., Ed., TMS, 2003, p 45–52

10. B. Nestler and A.A. Wheeler, *Modeling of Casting, Welding and Advanced Solidification Processes IX,* P.R. Sahm, P.N. Hansen, and J.G. Conley, Ed., Shaker Verlag, Aachen, 2000, p 505

11. A. Karma, *Modeling of Casting, Welding and Advanced Solidification Processes X,* D.M. Stefanescu et al. Ed., TMS, 2003, p 3

12. P. Zhu and R.W. Smith, *Acta Metall. Mater.,* Vol 40, 1992, p 683 and 3369

13. H.W. Hesselbarth and I.R. Göbel, *Acta Metall.,* Vol 39, 1991, p 2135

14. C.A. Gandin, T. Jalanti, and M. Rappaz, *Modeling of Casting, Welding and Advanced Solidification Processes—VIII,* B.G. Thomas and C. Beckermann, Ed., TMS, 1998, p 363

15. C.P. Hong and M.F. Zhu, *The Science of Casting and Solidification,* D.M. Stefanescu, R. Ruxanda, M. Tierean, and C. Serban Ed., Lux Libris, Brasov, Romania, 2001, p 110–118

16. C.P. Hong and M.F. Zhu, *Modeling of Casting, Welding and Advanced Solidification Processes X,* D.M. Stefanescu et al., Ed., TMS, 2003, p 63–74

17. R. Ruxanda, L. Beltran-Sanchez, J. Massone, and D.M. Stefanescu, *Proc. Cast Iron Division,* AFS 105th Casting Congress (Dallas, TX), 2001, p 37

18. M.F. Zhu and C.P. Hong, *Modeling of Casting, Welding and Advanced Solidification Processes X,* D.M. Stefanescu et al., Ed., TMS, 2003, p 91–98

19. A.K. Dahle, K. Nogita, J.W. Zindel, S.D. Mcdonald, and L.M. Hogan, *Metall. Mater. Trans. A,* Vol 32A, 2001, p 949–960

20. U. Dilthey, V. Pavlik, and T. Reichel, *Mathematical Modelling of Weld Phenomena,* H. Cerjak, Ed., The Inst. of Materials, London, 1997, p 85

21. L. Nastac, *Acta Metall. Mater.,* Vol 47 (No. 17), 1999, p 4253

22. L. Beltran-Sanchez and D.M. Stefanescu, *Modeling of Casting, Welding and Advanced Solidification Processes X,* D.M. Stefanescu et al., Ed., TMS, 2003, p 75–82

A.R. Marder, Introduction to Transformation Structures, *Metallography and Microstructures*, Vol 9, *ASM Handbook*, ASM International, 2004, p. 132–133

Introduction to Transformation Structures

Arnold R. Marder, Department of Materials Science and Engineering, Lehigh University

Introduction

SOLID-STATE TRANSFORMATION structures are produced from one or more parent phases, usually on cooling, and the product structure can consist of one or more phases in a particular morphology. The morphology is one way of characterizing the phase transformation. Although, in some cases, the phases may be the same (e.g., ferrite and carbide in the ferrous system), the morphology distinguishes the transformation microstructure (e.g., pearlite, bainite, or tempered martensite in the ferrous system). The most important mechanisms involved in developing these microstructures are diffusion, nucleation, and growth. However, not all transformations rely on diffusion (e.g., martensite), and not every transformation includes nucleation and growth (e.g., spinodal decomposition). To further complicate the classification of the transformations, crystallography influences most transformations (e.g., pearlite, bainite, martensite, and precipitation).

Christian (Ref 1) has classified solid-state transformations according to their growth processes. Figure 1 is a modification of Christian's classification. Also included in this modified chart are homogeneous transformations (e.g., spinodal and ordering reactions) and the addition of the massive transformation under interface controlled—no long-range transport. Specific morphological structures from solid-state transformations are covered in subsequent articles on:

- Precipitation structures
- Spinodal decomposition
- Ordered structures
- Eutectoid structures
- Massive transformation
- Martensitic structures (ferrous, non-ferrous, shape memory)
- Bainitic structures

Although the peritectic transformation involves some solid-state interactions, it is essentially a solidification process and is discussed in the previous section “Solidification Structures.”

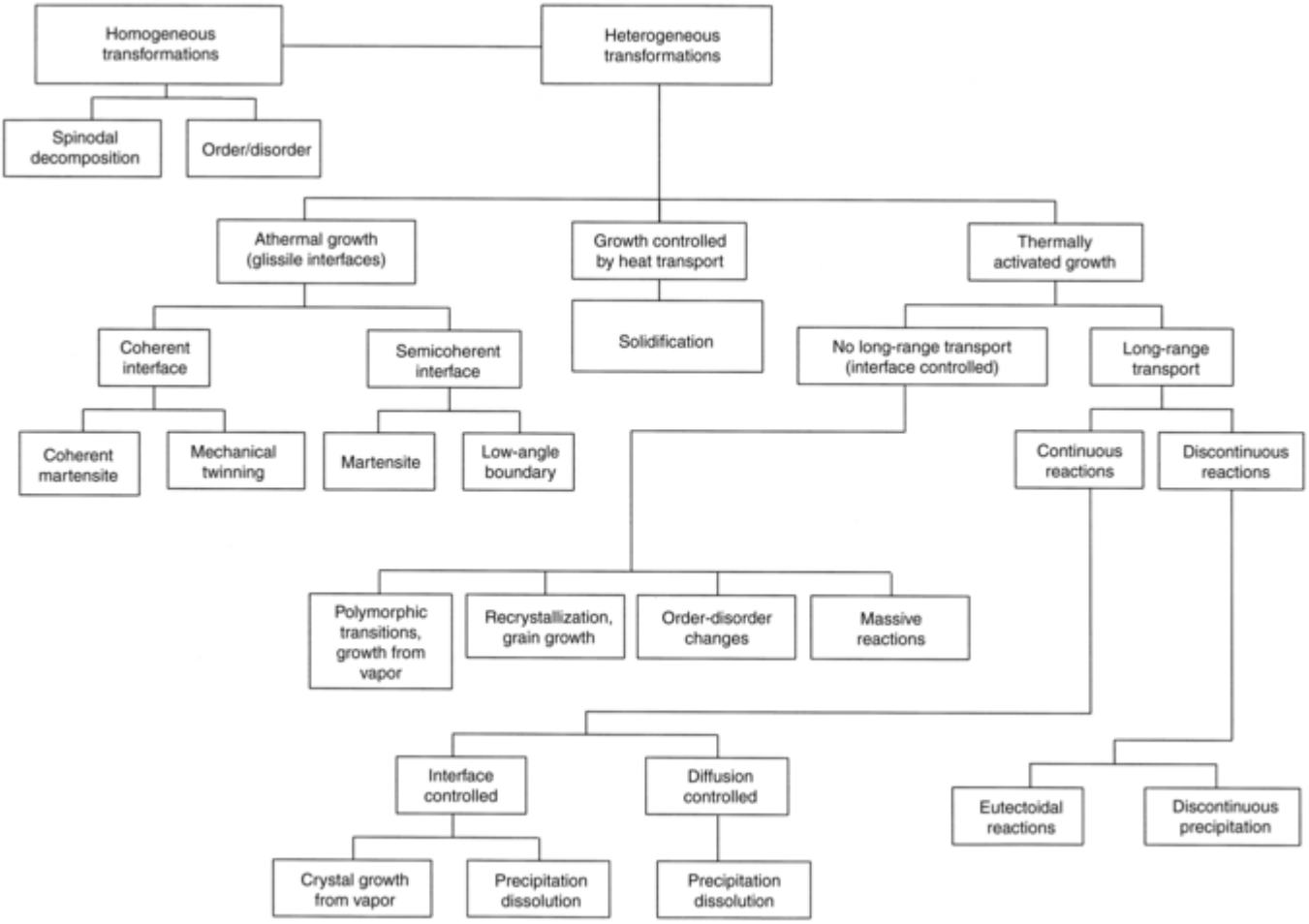

Fig. 1 Classification of transformations by growth processes. Adapted from Ref 1

Reference cited in this section

1. J.W. Christian, *The Theory of Transformations in Metals and Alloys,* Pergamon Press, Oxford, 1965, p 9

A.R. Marder, Introduction to Transformation Structures, *Metallography and Microstructures*, Vol 9, *ASM Handbook*, ASM International, 2004, p. 132–133

Introduction to Transformation Structures

Arnold R. Marder, Department of Materials Science and Engineering, Lehigh University

---

Multiphase Microstructures

Morphology, that is, the size, shape, and distribution of the phases present in the microstructure, is one way of characterizing the microstructure. Although some industrial alloys make use of single-phase structures—for example, austenitic stainless steel or cartridge brass—most alloys consist of multiphase microstructures. Ferrous alloys are obvious examples, as are precipitation-hardened nonferrous alloy systems. However, even single-phase metastable structures, particularly martensitic structures, have distinct morphologies that depend on composition. Other than macrostructure, which details large-scale inhomogeneities, the morphology of most solid-state reactions is discussed in terms of microstructure, substructure, and crystallography. The major types of microstructure morphologies are:

- *Structures in which both phases form entirely distinct grains* have been called aggregated two-phase structures or random duplex aggregates. They develop most clearly in alloys in which both phases are in equal volume fractions. In microduplex alloys, the two phases are distributed uniformly, such that the boundaries are predominantly interphase interfaces. This structure is usually fine scale and resistant to microstructural coarsening.
- *Structures in which each phase is closely interconnected* can result from spinodal decomposition. These spinodal structures are on the nanometer scale. They are characterized by their high degree of connectivity and often by crystallographic alignment of the phases.
- *Structures consisting of dispersed phases within a continuous phase matrix* are the most varied of the multiphase structures. Among their characteristic variables are the relative volumes of the two phases, the size of the particles of the dispersed phase, the interparticle spacing, the shape of the dispersed phase, and any special orientation of the dispersed particles with respect to each other and the matrix. Some of these variables are interdependent, and all of them can be quantified. Precipitation systems in which variably sized and shaped particles are embedded in a matrix are typical examples.
- *Structures in which the two phases are arranged in alternate layers,* such as two distinct phase lamellae found in pearlitic ferrous or nonferrous eutectoid alloys, have as their characteristic variables the interlamellar spacing and the thickness of the lamellae.
- *Structures in which the second phase forms at preferential sites,* such as at grain boundaries, twin boundaries, or at slip planes after cold work, are also a major type of morphology.

The preceding list is adapted from Ref 2; see also the article “Introduction to Structures in Metals” in this Volume.

Reference cited in this section

2. M. Bever, Introduction, *Metallography and Microstructures,* Vol 9, *ASM Handbook,* 1985, p 602

A.R. Marder, Introduction to Transformation Structures, *Metallography and Microstructures*, Vol 9, *ASM Handbook*, ASM International, 2004, p. 132–133

Introduction to Transformation Structures

Arnold R. Marder, Department of Materials Science and Engineering, Lehigh University

---

Substructures

In the broadest sense, substructures comprise all imperfections within the grains of polycrystalline metals or even single-phase alloys. Conventionally, substructure refers to subboundaries (low-angle boundaries), crystal imperfections (dislocations and stacking faults), and substructure impurity (solute distribution in the matrix). In all cases, the substructure is usually on the nanoscale level and includes:

- Polygonized structures resulting from cold work followed by annealing
- Dislocation networks resulting from cold work or shear-type (martensite) transformations
- Solute atmospheres associated with dislocations
- Nonequilibrium chemical distribution resulting from high-velocity kinetics such as quenching
- Imperfections resulting from quenching or radiation that produce dislocations or vacancies

A.R. Marder, Introduction to Transformation Structures, *Metallography and Microstructures*, Vol 9, *ASM Handbook*, ASM International, 2004, p. 132–133

Introduction to Transformation Structures

Arnold R. Marder, Department of Materials Science and Engineering, Lehigh University

Crystallography

The two phases that meet at an interface may differ in lattice constants, lattice type, and orientation. These differences result in a mismatch or disregistry at the interphase interface. Also, the crystallographic relationship between the parent and product phases is characteristic of specific orientations. These include:

- Atomic mismatch can result in coherent, semicoherent, and incoherent interfaces often found in precipitation-hardened systems.
- Orientation relationships can characterize specific transformations, such as martensite or pearlite.

All of these various morphological features, along with substructure and crystallography, are used to characterize a particular solid-state transformation. In conjunction with various mechanical properties, the characteristic structure-property relationships can be determined and used to improve the properties of the alloy or to contribute to the development of new alloys.

A.R. Marder, Introduction to Transformation Structures, *Metallography and Microstructures*, Vol 9, *ASM Handbook*, ASM International, 2004, p. 132–133

Introduction to Transformation Structures

Arnold R. Marder, Department of Materials Science and Engineering, Lehigh University

References

1. J.W. Christian, *The Theory of Transformations in Metals and Alloys,* Pergamon Press, Oxford, 1965, p 9

2. M. Bever, Introduction, *Metallography and Microstructures,* Vol 9, *ASM Handbook,* 1985, p 602

M. Epler, Structures by Precipitation from Solid Solution, *Metallography and Microstructures,* Vol 9, *ASM Handbook,* ASM International, 2004, p. 134–139

Structures by Precipitation from Solid Solution

Mario Epler, Lehigh University

Introduction

PRECIPITATION REACTIONS are of great importance in engineering alloys. This general phenomenon occurs in many different alloy systems when one phase (for example γ in steel) transforms into a mixed-phase system (such as $\gamma + \alpha$ in steel) as a result of cooling from high temperatures. The solid-state reaction results in a phase mixture of matrix phase and precipitates that nucleate and coarsen. The matrix may share a similar crystal structure to the parent phase, but has a different composition and often a dissimilar lattice parameter, while the precipitated phase may differ in crystal structure, composition, lattice parameter, and degree of long-range order (Ref 1). The resultant properties of the alloy after precipitation are a direct result of the type, size, shape, and distribution of the precipitated phase.

Phase diagram configurations that give rise to precipitation reactions are shown in Fig. 1. The reaction occurs when the initial phase composition (e.g., α_0, β_0, or I_0) transforms into a two-phase product that includes a new phase, or precipitate. The precipitate phase may differ in crystal structure, composition, and/or degree of long-range order from that of the initial single-phase (parent) phase and the resultant product matrix. The matrix retains the same crystal structure as the initial one-phase parent but with a different equilibrium composition (α, β, or I) and usually a different lattice parameter than the parent phase. This general type of phase change is different from reactions at the invariant points of phase transformation (e.g., a eutectic or peritectic), where any change in temperature or composition results in complete transformation of the parent into a matrix with a different crystal structure. Structures from invariant reactions are discussed in the article “Invariant Transformation Structures” in this Volume.

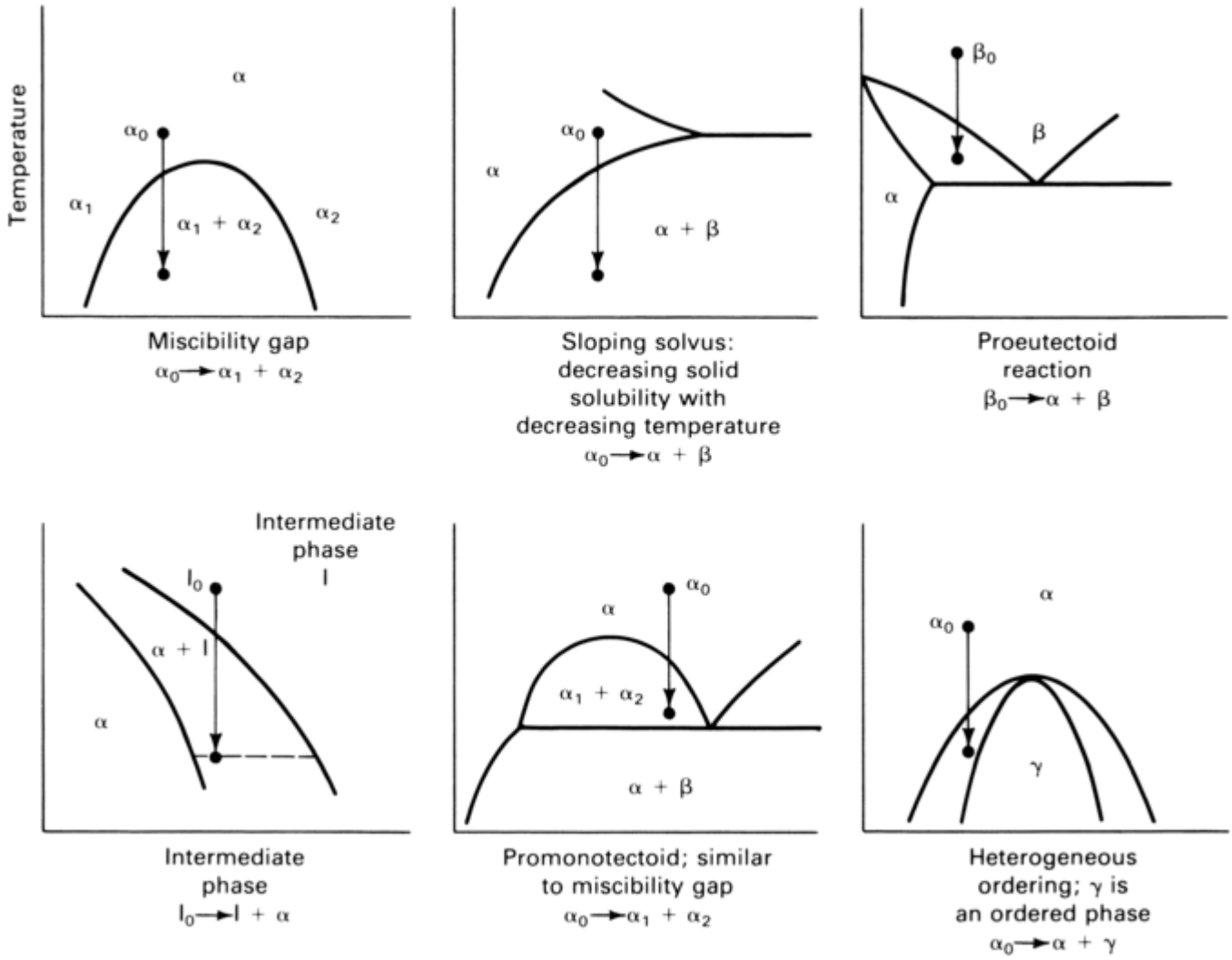

Fig. 1 Equilibrium phase diagrams illustrating various conditions for precipitation of a second phase. In all cases, the matrix of the two-phase product has the same crystal structure as the initial one-phase parent, but with a different equilibrium composition (α, β, or I). Source: Ref 1

The length scale of precipitate structures can be quite varied. For example, iron-nickel meteorites that undergo very slow cooling can have macroscopic-scale Widmanstätten structures (see the article "Metallography: An Introduction" in this Volume), while micron-scale precipitate structures occur in moderately to rapidly cooled medium-carbon steel. Precipitation also provides the basis of the strengthening mechanism in age-hardening alloys, where small-scale precipitates (on the order of tens of nanometers) are achieved by carefully controlled heat treatment or thermomechanical processing. Age hardening, which is a controlled precipitation reaction, provides enhanced mechanical properties to commercial alloys. Precipitation reactions are carefully controlled through thermomechanical treatments from supersaturated solid solutions resulting in enhanced strengthening. Precipitation reactions not only provide strengthening, but also wear, creep, and fatigue resistance to alloys.

Age hardening is an important strengthening mechanism, first discovered by Alfred Wilm in the early 1900s from the age hardening of aluminum-copper alloys. It remains an important strengthening mechanism for modern aluminum-copper alloys (as described in more detail in the article "Metallographic Techniques for Aluminum and Its Alloys" in this Volume) and many other types of commercial alloys. The typical heat treatment of an age-hardening alloy consists of (Ref 2):

1. Solution treating (solutionizing) that results in a homogenous supersaturated solid solution
2. Quenching to a temperature in the two-phase region (generally room temperature) to retain a supersaturated solid solution
3. Aging at an elevated temperature to control the precipitation of the second phase from the solid solution

In addition, thermomechanical processing, which involves cold working the as-quenched alloy before aging, is sometimes used. The deformation can affect the subsequent precipitation reaction kinetics and modify the resultant properties through dislocation generation and the influence of strain hardening. Quenching directly to the aging temperature also can influence the kinetics and reaction path in the decomposition of the supersaturated parent phase.

References cited in this section

1. W.A. Soffa, Structures Resulting from Precipitation from Solid Solution, *Metallography and Microstructures,* Vol 9, *ASM Handbook,* ASM International, 1985, p 646–650

2. D.A. Porter and K.E. Easterling, *Phase Transformations in Metals and Alloys,* 2nd ed., Chapman and Hall, 1996, p 514

M. Epler, Structures by Precipitation from Solid Solution, *Metallography and Microstructures,* Vol 9, *ASM Handbook*, ASM International, 2004, p. 134–139

Structures by Precipitation from Solid Solution

Mario Epler, Lehigh University

Nucleation and Growth

Nucleation, growth, and coarsening are important in determining the resultant microstructure of the precipitates and associated mechanical properties. During nucleation, not only is the type of precipitate that forms important, but also the distribution of the precipitates. Distribution of precipitates influences mechanical strength by affecting dislocation motion.

Nucleation can occur either homogenously (uniformly and nonpreferentially) or heterogeneously (preferentially) at specific sites such as grain boundaries or dislocations. Most precipitates involve or require the presence of preferential sites for heterogeneous nucleation, but Guinier-Preston (GP) zones and other fully coherent precipitates (such as Ni_3Al in nickel-base superalloys) nucleate homogeneously. Coherent precipitation occurs when continuity is maintained between the crystal lattice of the precipitate and the lattice of the matrix.

Typical heterogeneous nucleation sites include crystal defects such as grain boundaries, grain corners, vacancies, or dislocations. Heterogeneous nucleation occurs because the elimination of defects and high-energy surfaces (by the nucleation of a new phase) acts to reduce the overall free energy of the system. The rate of heterogeneous nucleation thus is influenced by the density of these irregularities. The free-energy relationships associated with homogenous and heterogeneous nucleation can be described as (Ref 2):

$$\Delta G_{\text{hom}} = -V\left(\Delta G_{\text{v}} - \Delta G_{\text{s}}\right) + A\gamma$$

$$\Delta G_{\text{het}} = -V\left(\Delta G_{\text{v}} - \Delta G_{\text{s}}\right) + A\gamma - \Delta G_{\text{d}}$$

where:

- ΔG_{hom} is the total free-energy change for homogeneous nucleation.
- ΔG_{het} is the total free-energy change for heterogeneous nucleation.
- V is the volume of transformed phase.
- ΔG_{v} is the volume free energy of transformed phase.
- ΔG_{s} is the volume misfit strain energy of transformed phase.
- $A\gamma$ is the surface area and surface energy term of transformed phase, assuming isotropic.
- ΔG_{d} is the free energy resulting from destruction of defect.

Additionally, typical values for surface energy are summarized in Table 1, and various interfaces are shown in Fig. 2. Faceted interfaces often are coherent, while nonfaceted interfaces are semicoherent or incoherent. As long as there is a sufficient density of heterogeneous nucleation sites, homogeneous nucleation will not be favored. Table 2 lists some selected precipitation reactions in different alloys and the crystallographic relations between the parent and precipitated phases.

Table 1 Surface energies for different types of interfaces

Type of interface	Surface energy
Coherent	$\gamma_{coherent} = \gamma_{chemical} \leq 200$ mJ/m^2
Semicoherent	$\gamma_{semicoherent} = \gamma_{chemical} + \gamma_{structural} \approx 200$ to 500 mJ/m^2
Incoherent	$\gamma_{coherent} \approx 500$ to 1000 mJ/m^2

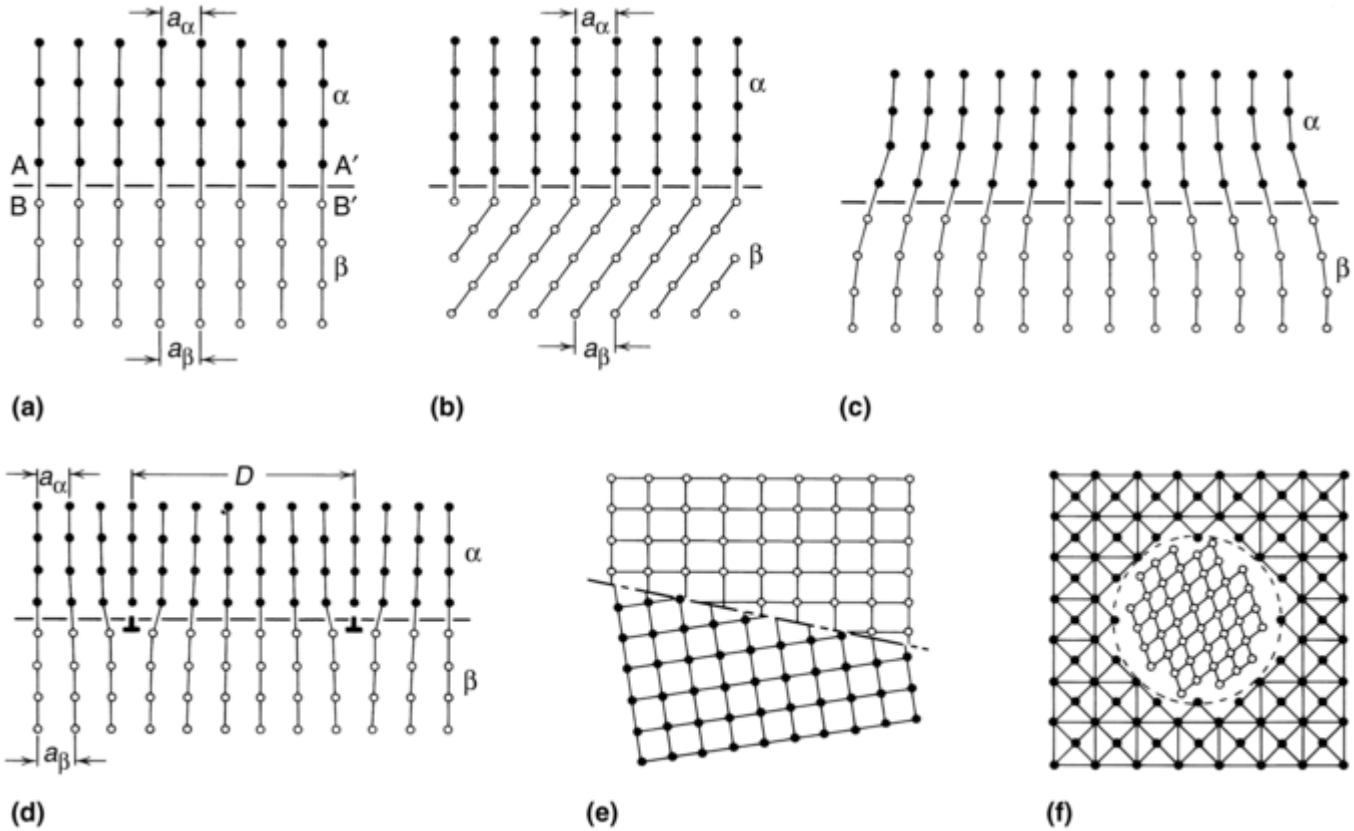

Fig. 2 Different types of interfaces. (a) and (b) Fully coherent. (c) and (d) Semicoherent showing lattice strain and the presence of dislocations. (e) and (f) Incoherent. Source: Ref 1

Table 2 Crystallographic relations between precipitate and parent phases in selected alloy systems

Alloy system	Parent phase and lattice[(a)]	Precipitate phase and lattice[(a)]	Crystallographic relations (precipitate phase described first)
Ag-Al	Al solid solution; fcc	γ (Ag_2Al); hcp	(0001) ‖ (111), $[11\bar{2}0]$ ‖ $[1\bar{1}0]$
	Al solid solution; fcc	γ′ (transitional); hcp	(0001) ‖ (111), $[11\bar{2}0]$ ‖ $[1\bar{1}0]$
Ag-Cu	Ag solid solution; fcc	Cu solid solution; fcc	Plates ‖ {100}; all directions ‖
	Cu solid solution; fcc	Ag solid solution; fcc	Plates ‖ {111} or {100}; all directions ‖
Ag-Zn	β (βAgZn); bcc	Ag solid solution; fcc	(111) ‖ (110), $[1\bar{1}0]$ ‖ $[1\bar{1}1]$
	β (βAgZn); bcc	γ (γAg_5Zn_8); bcc	(100) ‖ (100), [010] ‖ [010]

Al-Cu	Al solid solution; fcc	θ ($CuAl_2$); bct	Plates ‖ (100); (100) ‖ (100), [011] ‖ [120]
	Al solid solution; fcc	θ′ (transitional); tet	(001) ‖ (100), [010] ‖ [011]
Al-Mg	Al solid solution; fcc	β (β-Al_3Mg_2); fcc	Plates first ‖ {110}; later probably ‖ {120}
Al-Mg-Si	Al solid solution; fcc	Mg_2Si; fcc	Plates ‖ {100}
Al-Zn	Al solid solution; fcc	Nearly pure Zn; hcp	Plates ‖ {111}; (0001) ‖ {111}, $[11\bar{2}0]$ ‖ ⟨110⟩
Au-Cu [(b)]	Au-Cu solid solution; fcc	α_1(AuCu I); ord fct	(100) ‖ (100), [010] ‖ [010]
Be-Cu	Cu solid solution; fcc	γ_2 (γBeCu); ord bcc	G-P zones ‖ {100}; later γ_2 with [100] ‖ [100], [010] ‖ [011]
0.4C-Fe	Austenite (γFe); fcc	Ferrite (αFe) (proeutectoid); bcc	(110) ‖ (111), $[1\bar{1}1]$ ‖ $[1\bar{1}0]$
0.8C-Fe	Austenite (γFe); fcc	Ferrite in pearlite; bcc	(011) ‖ (001), $[\bar{1}00]$ ‖ [100], $[0\bar{1}1]$ ‖ [010]
	Austenite (γFe); fcc	Ferrite in upper bainite; bcc	(110) ‖ (111), $[1\bar{1}0]$ ‖ $[\bar{2}11]$
		Ferrite in lower bainite; bcc	(110) ‖ (111), $[1\bar{1}1]$ ‖ $[1\bar{1}0]$
1.3C-Fe	Austenite (γFe); fcc	Cementite (Fe_3C); ortho	Plates not ‖ (111); (001) Fe_3C ‖ to plane of plate
Co-Cu	Cu solid solution; fcc	αCo solid solution; fcc	Plates ‖ {100}; lattice orientation same as parent matrix
Co-Pt[(b)]	Pt-Co solid solution; fcc	α″ (CoPt); ord fct	Plates ‖ {100}; all directions ‖
Cu-Fe	Cu solid solution; fcc	γFe (transitional); fcc	Cubes {100}; lattice orientation same as parent matrix
		αFe; bcc	Plates ‖ {111}; lattice orientation random
Cu-Si	Cu solid solution; fcc	β (ζ Cu-Si); hcp	Plates ‖ {111}; (0001) ‖ (111), $[11\bar{2}0]$ ‖ $[1\bar{1}0]$
Cu-Sn	β phase; bcc	Cu solid solution; fcc	(111) ‖ (110), $[1\bar{1}0]$ ‖ $[\bar{1}11]$
Cu-Zn	β (CuZn); bcc	Cu solid solution; fcc	(111) ‖ (110), $[1\bar{1}0]$ ‖ $[\bar{1}11]$; variable habit; plates or needles ‖ [556]
	β (CuZn); bcc	γ (γCu_5Zn_8); ord bcc	(100) ‖ (100), [010] ‖ [010]
	ε (εCu-Zn); hcp	Zn solid solution; hcp	$(10\bar{1}4)$ ‖ $(10\bar{1}4)$, $[11\bar{2}0]$ ‖ $[11\bar{2}0]$
Fe-N	Ferrite (αFe); bcc	γ_1 (Fe_4N); fcc	(112) ‖ (210)
Fe-P	Ferrite (αFe); bcc	δ (Fe_3P); bct	Plates ‖ (21,1,4)
Pb-Sb	Pb solid solution; fcc	Sb solid solution; rhom	(001) ‖ (111), [100] ‖ $[1\bar{1}0]$

(a) bcc, body-centered cubic; bct, body-centered tetragonal; fcc, face-centered cubic; hcp, hexagonal close-packed; ord bcc, ordered body-centered cubic; ord fct, ordered face-centered tetragonal; ortho, orthorhombic; rhom, rhombohedral; tet, tetragonal.

(b) Ordering transformation. Source: Ref 1

A coherent interface (Fig. 2a and b) is characterized by atomic matching at the boundary and a continuity of lattice planes, although a small mismatch between the crystal lattices can lead to coherency strains (Fig. 2c). Coherent interfaces have a relatively low interfacial energy that typically ranges from 50 to 200 ergs/cm^2 (0.05 to 0.2 J/m^2).

An incoherent interface (Fig. 2e and f) is an interphase boundary that results when the matrix and precipitate have very different crystal structures and little or no atomic matching can occur across the interface. The

boundary is essentially a high-angle grain boundary characterized by a relatively high interfacial surface energy (~500 to 1000 ergs/cm^2, or 0.5 to 1.0 J/m^2).

Semicoherent interfaces (Fig. 2d) represent an intermediate case in which it becomes energetically favorable to partially relax the coherency strains, which would develop if perfect matching occurred across the boundary by introducing an array of misfit dislocations. These interfaces, which are characterized by regions of good fit punctuated by dislocations that accommodate some of the disregistry, have interfacial surface energies from 200 to 500 ergs/cm^2 (0.2 to 0.5 J/m^2).

Dislocations act as nucleation sites only for semicoherent precipitates (Ref 2). Figure 3 (Ref 3) shows precipitates forming at dislocations. The formation of semicoherent precipitates usually results in the generation of dislocations as a result of the lattice mismatch. The generation of a dislocation maintains coherency by relaxing the strains that develop because of the difference in the lattice parameter at the interface. Vacancies play several roles in the nucleation of precipitates. Vacancies allow for appreciable diffusion at temperatures where diffusion is not expected. They also act to relieve local strain allowing for the nucleation coherent precipitates. Vacancy concentration is dependent on temperature, so it is essential for high quenching rates to not only maintain a supersaturated solid solution but to retain significant numbers of vacancies.

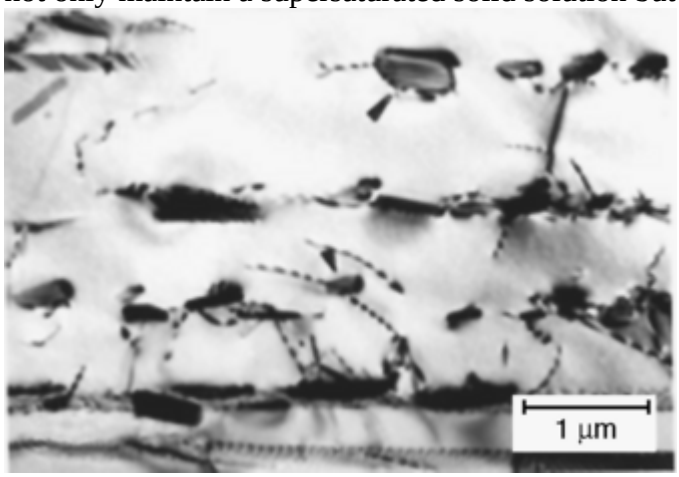

Fig. 3 Transmission electron microscopy bright field micrograph showing Ti_5Si_3 precipitates at dislocations in a $Ti_{52}Al_{48}$-3Si2Cr alloy. Source: Ref 6

Accompanying the precipitation sequence is the change in the chemistry of the matrix phase. As more and larger precipitates form, the solute is depleted in the matrix. Areas where no precipitates form are termed precipitate-free zones (PFZs) or denuded areas. These typically occur around grain boundaries or second-phase particles where the solute is trapped (Fig. 4) or regions where there are insufficient vacancies to nucleate precipitates.

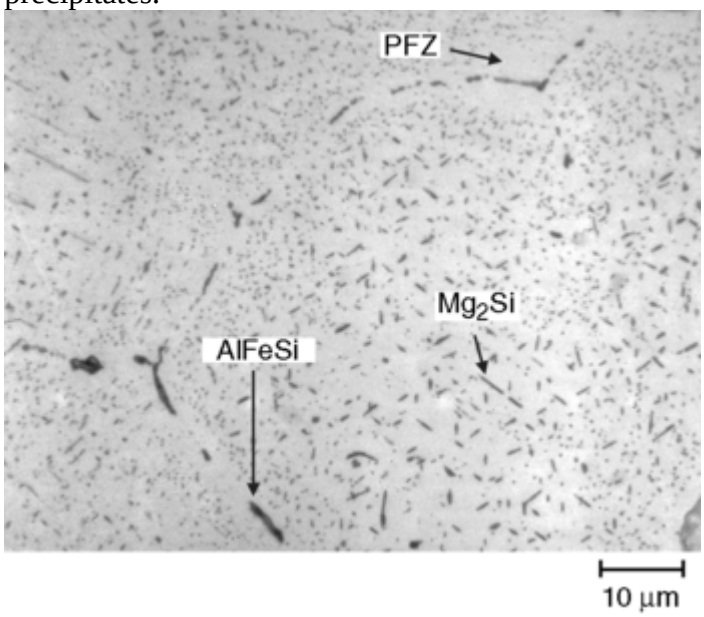

Fig. 4 Micrograph of cast and homogenized 6061 aluminum alloy, showing the precipitate-free zone (PFZ) (lack of Mg_2Si precipitates) at grain boundary. The PFZ was created by the lack of silicon, which is wrapped up in the AlFeSi precipitates at the grain boundary. Source: Ref 4

Coarsening of the particles occurs because the microstructure of a two-phase alloy is not stable unless the interfacial energy is at a minimum. A lower density of larger particles has less total interfacial energy than a high density of small particles, which provides the driving force for particle coarsening. Particle coarsening is driven by diffusion of solute atoms; thus, the rate of coarsening increases with temperature. In some cases, coarsening rates are determined by interface control.

Ostwald ripening is the mechanism where the smaller precipitates dissolve and the solute is redistributed to the larger stable precipitates. The higher solubility of the smaller particles in the matrix is termed the capillary effect and can be seen on a free-energy diagram (Fig. 5a). Smaller particles have a higher free energy due to increased pressure because of high surface curvature. The point of common tangent (Fig. 5a) therefore occurs at a higher solute concentration.

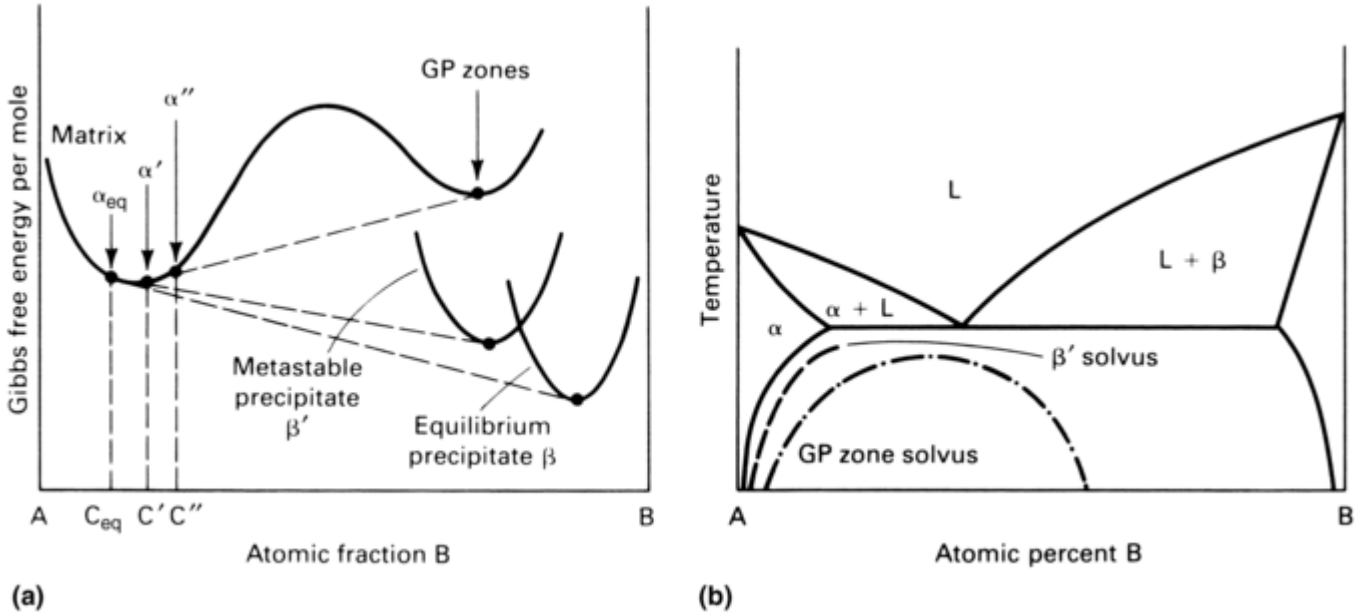

Fig. 5 Gibbs free-energy composition diagram (a) and locus of solvus curves (b) of metastable and stable equilibrium phases in a precipitation sequence. (a) The points of common tangency show the relationship between compositions of the matrix phase (C″, C′, and C_{eq}) and the various forms of precipitate phases at a given temperature. From this common tangent construction, it can be see that for the small Guinier-Preston zones, there is a higher solubility in the matrix. (b) Hypothetical phase diagram showing the locus of metastable and stable solvus curves. Source: Ref 1

Growth of precipitates occurs by either movement of the incoherent interfaces or a ledge mechanism where coherency is maintained while thickening due to diffusion (Ref 1, 2). Reversion occurs when an alloy containing GP zones or intermediate semicoherent phase is heated above their respective solvus temperatures and they redissolve into the matrix.

References cited in this section

1. W.A. Soffa, Structures Resulting from Precipitation from Solid Solution, *Metallography and Microstructures,* Vol 9, *ASM Handbook,* ASM International, 1985, p 646–650

2. D.A. Porter and K.E. Easterling, *Phase Transformations in Metals and Alloys,* 2nd ed., Chapman and Hall, 1996, p 514

3. F.-S. Sun and F.H. Sam Froes, Precipitation of Ti_5Si_3 Phase in TiAl Alloys, *Mater. Sci. Eng. A,* Vol 328 (No. 1–2), 2002, p 113–121

4. W.H. Van Geertruyden, W.Z. Misiolek, G.G. Lea, and R.M. Kelly, Thermal Cycle Simulation of 6xxx Aluminum Alloy Extrusion, *Proc. Seventh International Extrusion Technology Seminar* (Chicago, IL) Aluminum Extruders Council, 2000

6. S. Celotto and T.J. Bastow, Study of Precipitation in Aged Binary Mg-Al and Ternary Mg-Al-Zn Alloys Using ^{72}AlNMR Spectroscopy, *Acta Mater.*, Vol 49, 2001, p 41–51

M. Epler, Structures by Precipitation from Solid Solution, *Metallography and Microstructures,* Vol 9, *ASM Handbook*, ASM International, 2004, p. 134–139

Structures by Precipitation from Solid Solution

Mario Epler, Lehigh University

Precipitation Modes

General or continuous precipitation refers to the uniform appearance of second-phase particles throughout the grains of the matrix. General precipitation does not imply homogeneous nucleation, rather, the nonlocalized precipitation of the second phase. Discontinuous precipitation can occur at regions such as grain boundaries, or cellular precipitation where precipitation begins at grain boundary allotriomorphs but does not continue through the entire grain. Figure 4 and 6 show general precipitation in aluminum alloys. Figure 7 (Ref 6) shows a contrast between discontinuous and continuous precipitation in AZ91, a Mg-Al-Zn alloy.

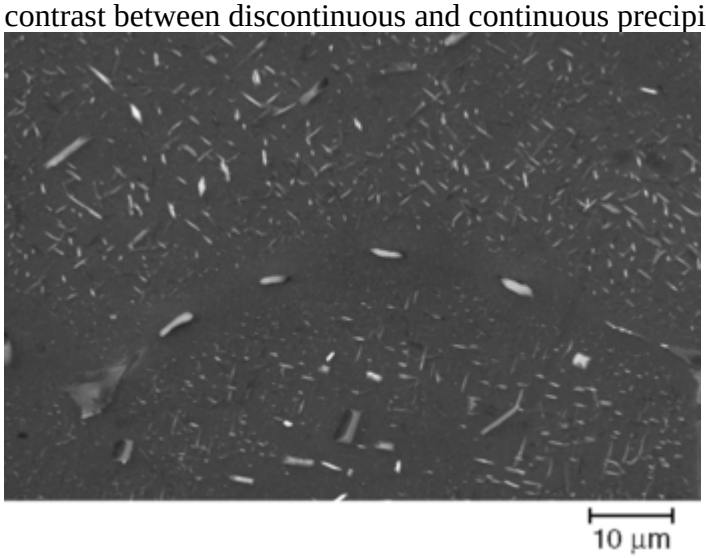

Fig. 6 Scanning electron micrograph of continuous precipitation in 6061 aluminum alloy, where the smaller precipitates are Mg_2Si, and the larger particles are AlFeSi intermetallics at the grain boundary. Note the precipitate-free zone near the AlFeSi intermetallics. Source: Ref 5

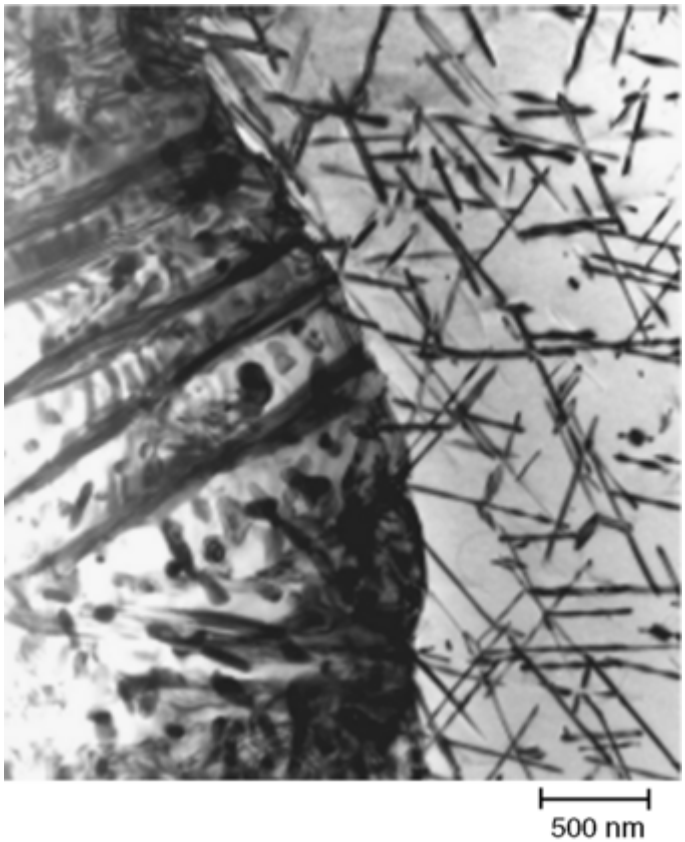

Fig. 7 Transmission electron micrograph showing a region of discontinuous (left) and continuous (right) precipitation in a specimen of AZ91 aged at 200 °C (390 °F) for 4 h. Source: Ref 6

Widmanstätten Structures. The continuous precipitation of plate or lathlike structures is referred to as Widmanstätten morphology. This distinctive plate or lathlike morphology is characterized by the presence of both high- and low-angle boundaries. Widmanstätten morphologies form in many alloy systems. This is illustrated in Fig. 8 (Ref 7), a Ti-6Al-4V alloy. As evident by the microstructure, there are specific orientation relations between the precipitate habit plane and matrix (Ref 1, 2). The long broad faces of the precipitates are the coherent, low-energy interfaces (Ref 1, 2). During growth, small ledges form on these faces, allowing for diffusional thickening while maintaining coherency. Typically, this morphology forms during low cooling rates, but the Widmanstätten morphology can occur if a sufficient driving force for growth is provided by either a fast cooling rate or large undercooling (Ref 8). As Ref 8 describes,

The development of the side plate morphology normally starts from a grain boundary allotriomorph (as in the case of steels) and growth occurs into the grain. As cooling rates increase, the diffusion of atoms to the high-angle boundaries (where no special orientation exists between austenite and ferrite) is slow, but if diffusion distances are minimized by phase morphology and growth occurs in preferred crystallographic directions, growth rates can be increased.

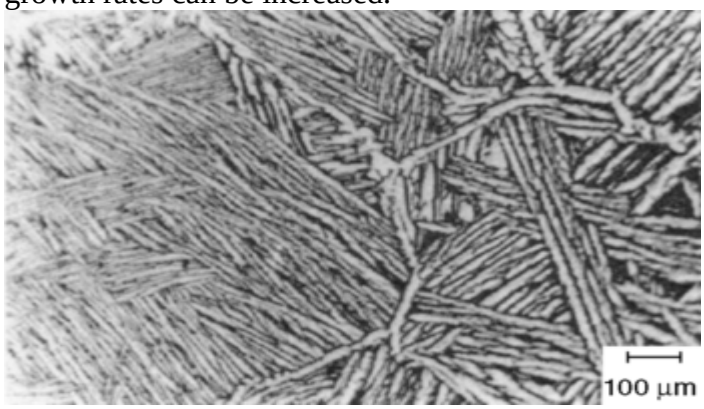

Fig. 8 Widmanstätten structure in Ti-6Al-4V alloy cooled at 3.40 °C/s (6.12 °F/s). Source: Ref 7

Cellular or Discontinuous Precipitation. Grain-boundary precipitation may result in cellular or discontinuous precipitation (DP). Figure 9 (Ref 9) and 10 show examples of the alternating lamellar structure that is common to many cellular precipitation transformations. During discontinuous precipitation, the second phase nucleates at the grain boundary, which then moves with the advancing precipitation reaction. It typically starts at a high-angle incoherent boundary, which is the most likely point to support the process of heterogeneous nucleation and boundary migration. Misfit or atomic mismatch strain are factors, although neither misfit nor atomic mismatch strain appear to be necessary conditions in several instances (e.g., Al-Li, Ni-Al, Ni-Ti, Al-Ag, and Cu-Co) (Ref 11, 12). The general conditions and criteria of DP are not completely understood due to the complex interrelationships among boundary structure, energy, mobility, and diffusivity.

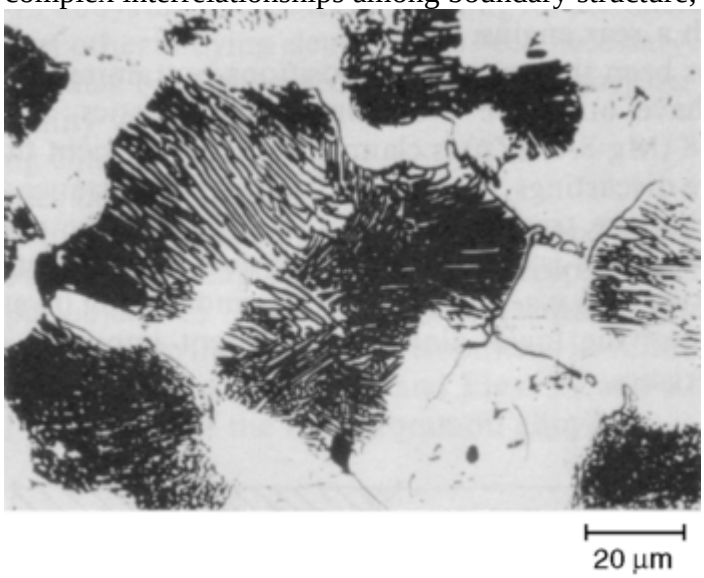

Fig. 9 Discontinuous precipitation of β phase ($Mg_{17}Al_{12}$) in cast AZ80 zirconium-free magnesium casting alloy. Source: Ref 9

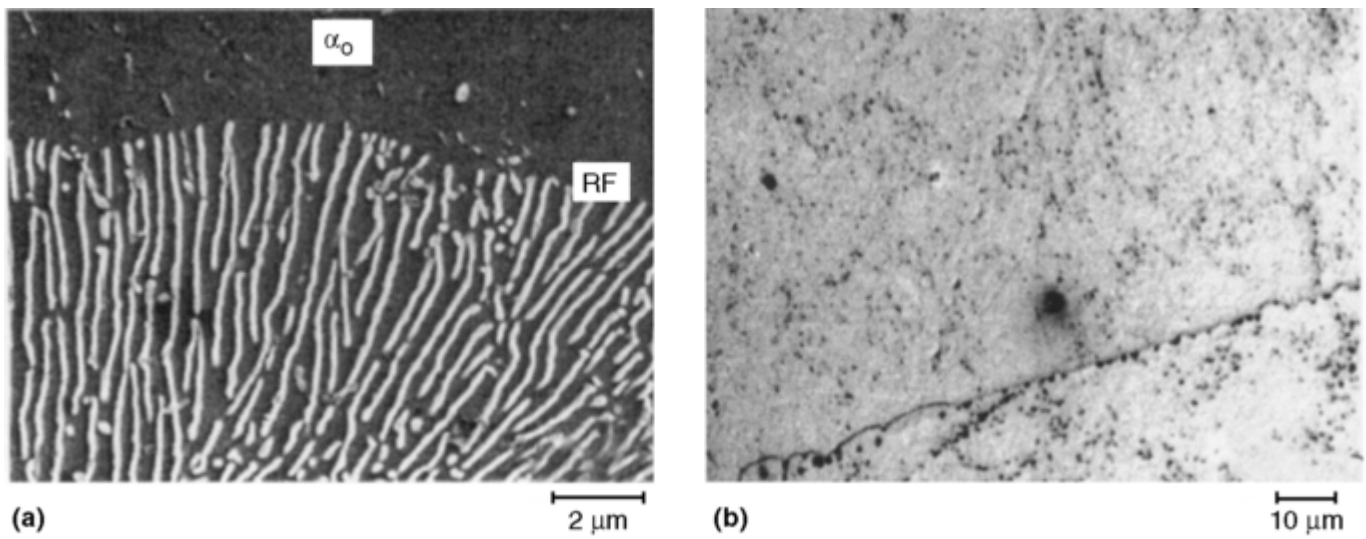

Fig. 10 Discontinuous precipitation (DP). (a) Scanning electron micrograph of lamellar structure within a DP cell Mg-10Al (wt%) annealed at 500 K for 40 min. RF, reaction front; α_0, supersaturated solid solution. (b) Light optical micrograph of early stage of the DP reaction in Mg-10Al (wt%) annealed at 500 K for 20 min. The bowing out of the grain boundary between two allotriomorphs is clearly seen. Source: Ref 10

Following nucleation, the grain boundary moves with the advancing precipitation reaction. This is illustrated in Fig. 10(b), where the grain boundary is seen bowing out at the beginning of the reaction (Ref 9). Morphologically, it resembles eutectoid decomposition (see the article “Invariant Transformation Structures” in this Volume). Discontinuous precipitation results in reaction products that are often lamellar, fibrous, or

rodlike, but rarely globular (Ref 11). Discontinuous precipitation is also often referred to as a cellular, grain-boundary, recrystallization, or autocatalytic reaction (Ref 13).

Lamellar spacing of the precipitates is dependent on aging temperature, with wider spacing occurring higher temperatures. Free energy is limited for creating of interfaces due to the lower driving force (at higher temperature). It is termed discontinuous because the matrix composition changes discontinuously as the cell advances. Cellular precipitation is also observed in Fig. 11, clearly showing the relationship between the cells and the grain boundaries.

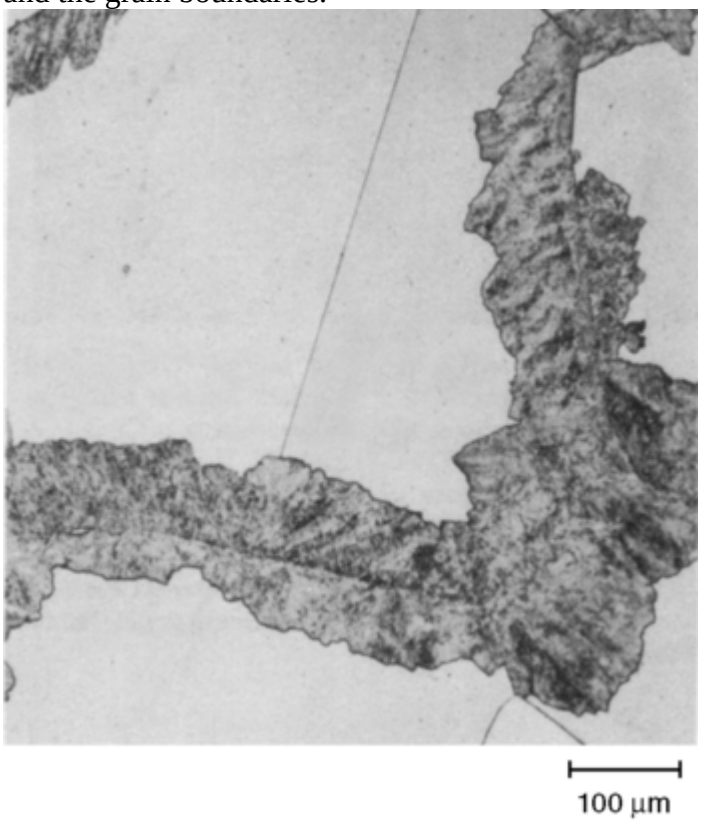

Fig. 11 Cellular colonies growing out from grain boundaries in Au-30Ni alloy aged 50 min at 425 °C (795 °F). Etchant: 50 mL 5% ammonium persulfate and 50 mL 5% potassium cyanide. 100×. Courtesy of R.D. Buchheit. Source: Ref 1

References cited in this section

1. W.A. Soffa, Structures Resulting from Precipitation from Solid Solution, *Metallography and Microstructures,* Vol 9, *ASM Handbook,* ASM International, 1985, p 646–650

2. D.A. Porter and K.E. Easterling, *Phase Transformations in Metals and Alloys,* 2nd ed., Chapman and Hall, 1996, p 514

5. S.R. Claves, D.L. Elias, and W.Z. Misiolek, Analysis of the Intermetallic Phase Transformation Occurring During Homogenization of 6xxx Aluminum Alloys, *Proc. International Conference of Aluminium Alloys 8,* Trans Tech Publications, Cambridge, U.K., 2002

6. S. Celotto and T.J. Bastow, Study of Precipitation in Aged Binary Mg-Al and Ternary Mg-Al-Zn Alloys Using ^{72}AlNMR Spectroscopy, *Acta Mater.,* Vol 49, 2001, p 41–51

7. F.J. Gil, M.P. Ginebra, J.M. Manero, and J.A. Planell, Formation of Widmanstätten Structure: Effects of Grain Size and Cooling Rate on the Widmanstätten Morphologies and on the Mechanical Properties in Ti6Al4V Alloy, *J. Alloy. Compd.,* Vol 329 (No. 1–2), 2001, p 142–152

8. A. Tomer, *Structure of Metals through Optical Microscopy,* ASM International, 1991, p 113–114

9. I.J. Polmear, *Light Alloys—Metallurgy of the Light Metals,* 3rd ed., Arnold, 1995

10. D. Bradai, P. Zieba, E. Bischoff, and W. Gust, Correlation between Grain Boundary Misorientation and the Discontinuous Precipitation Reaction in Mg-10 wt.% Al Alloy, *Mater. Chem. Phys.,* Vol 78 (No. 1), 2003, p 222–226

11. I. Manna, S.K. Pabi, and W Gust, Discontinuous Reactions in Solids, *Int. Mater. Rev.,* Vol 46 (No. 2), 2001, p 53–91

12. M. Shaarbaf and R.A. Fournelle, *Mater. Sci. Eng. A,* Vol 102, 1988, p 271–279

13. D.B. William and E.P Butler, Grain Boundary Discontinuous Precipitation Reactions, *Int. Met. Rev.,* Vol 26 (No. 3), 1981, p 153–183

M. Epler, Structures by Precipitation from Solid Solution, *Metallography and Microstructures,* Vol 9, *ASM Handbook,* ASM International, 2004, p. 134–139

Structures by Precipitation from Solid Solution

Mario Epler, Lehigh University

Precipitation Sequences

In many precipitation systems and in virtually all effective commercial age-hardening alloys, the supersaturated matrix transforms along a multistage reaction path, producing one or more metastable transition precipitates before the appearance of the equilibrium phase. The approach to equilibrium is controlled by the activation (nucleation) barriers separating the initial state from the states of lower free energy. The transition precipitates are often crystallographically similar to the matrix, allowing the formation of a low-energy coherent interface during the nucleation process.

Often the precipitation sequence begins with the nucleation of small, fully coherent phases known as Guinier and Preston zones (discovered independently by Guinier and Preston from x-ray diffraction studies). Guinier-Preston (GP) zones are solute-rich clusters resulting from phase separation or precipitation within a metastable miscibility gap in the alloy system. They may form by homogeneous nucleation and grow at small undercoolings or by spinodal decomposition at large undercoolings or supersaturations (see the article “Spinodal Transformation Structures” in this Volume).

The GP zones are the first to nucleate because of their small size and coherency with the matrix. The interfacial energy term is extremely low, providing a low barrier to nucleation, although the driving force for nucleation may not be as high as for the final phase to form. The GP zones typically take the shape of small spherical particles or disk-shaped particles (Fig. 12) that are about two atomic layers thick and several nanometers in diameter aligned perpendicular to the elastically soft direction in the matrix material crystal structure (Ref 2). The GP precipitates generally grow into more stable transition phases and eventually an equilibrium phase.

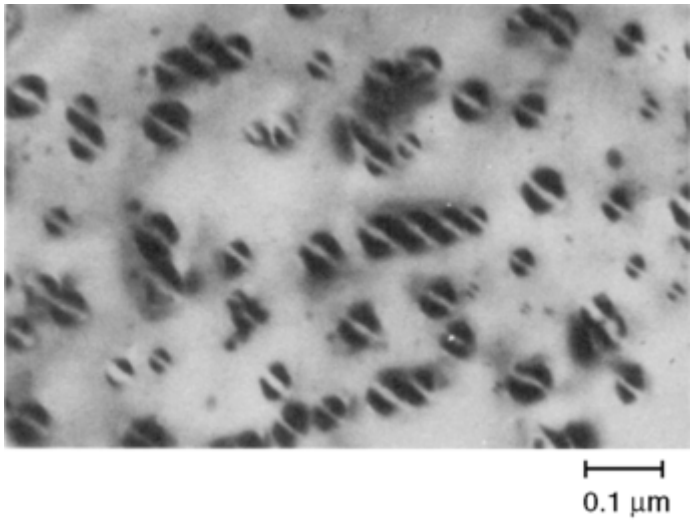

Fig. 12 Coherent transition precipitates revealed by strain contrast (dark-field) in transmission electron microscopy. The specimen is a Cu-3.1Co alloy aged 24 h at 650 °C (1200 °F). The precipitate is a metastable face-centered cubic (fcc) phase of virtually pure cobalt in the fcc matrix. The particles are essentially spherical, and the "lobe" contrast is characteristic of an embedded "misfitting sphere." This strain contrast reveals the particles indirectly through their coherency strain fields. Original magnification 70,000×. Courtesy of V.A. Phillips

The phases that nucleate and grow from the GP zones are termed "transition phases." They have an intermediate crystal structure between the matrix and equilibrium phase. This minimizes the strain contribution to energy between the precipitate and the matrix, making it more favorable in the nucleation sequence than the equilibrium phases, which is incompatible with the matrix and has high interfacial energy. A typical reaction sequence for aluminum-copper systems is shown in Fig. 13 can be written as:

$$\alpha_0 \rightarrow \alpha_1 + \text{GPZ} \rightarrow \alpha_2 + \theta'' \rightarrow \alpha_3 + \theta' \rightarrow \alpha_{eq} + \theta$$

where θ' and θ'' are transition precipitates and θ is the equilibrium precipitate. Composition of each phase and the matrix can be determined by the common tangent method applied to Fig. 14(a). As each new precipitate forms, the matrix (α) becomes more and more depleted in copper. The GP zones and θ'' precipitates are resolved in transmission electron microscopy (TEM) because of the lattice coherency strains. Each step results in the previously precipitated phase being replaced with the new, more stable phase. Figure 14(b) outlines the step reductions in total free energy for reactions in the precipitation sequence. The size of the step reduction is the activation energy for a transformation.

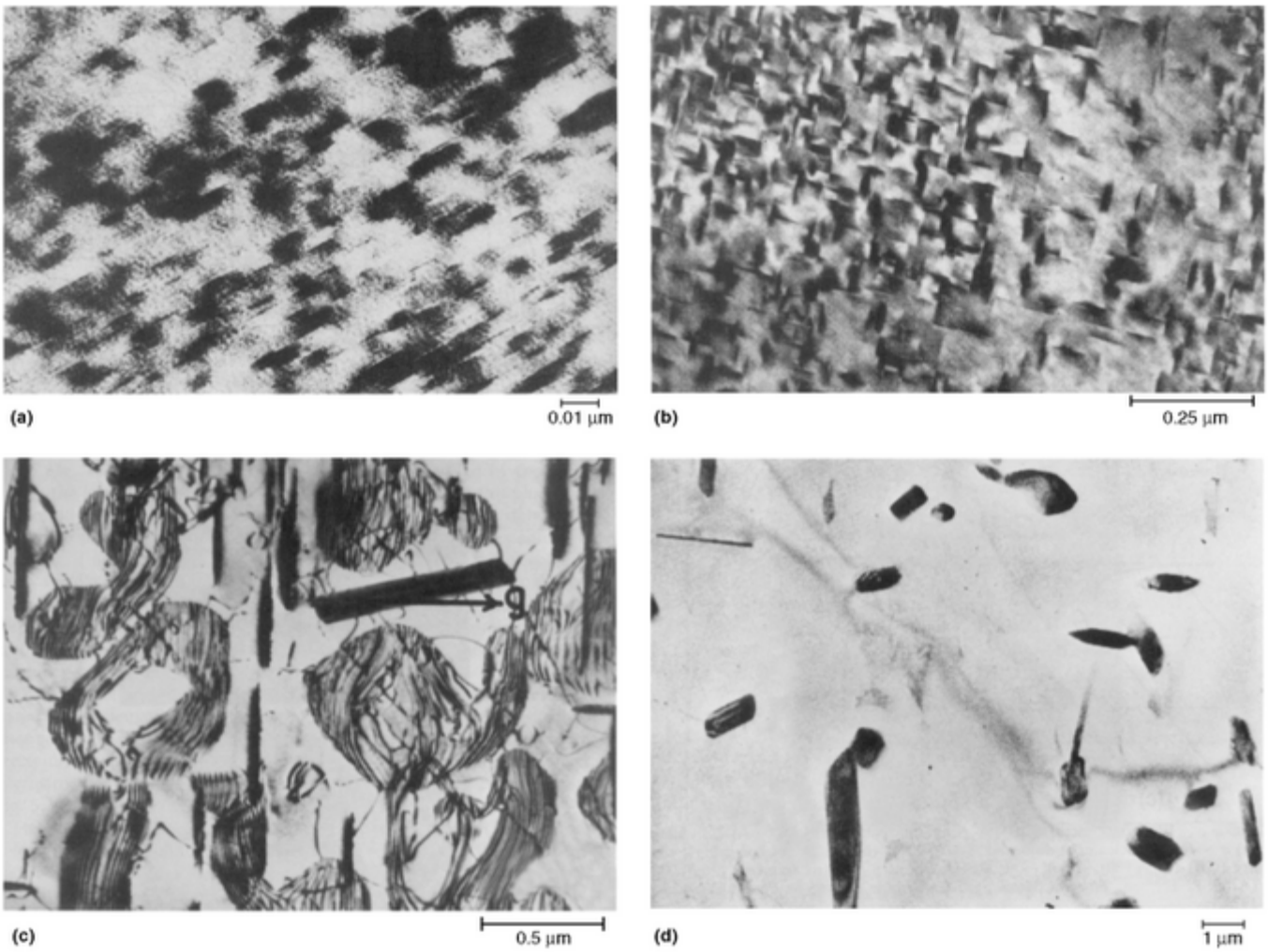

Fig. 13 Transmission electron micrographs of precipitation sequence in aluminum-copper alloys. (a) Guinier-Preston zones at 720,000×. (b) θ″ at 63,000×. (c) θ′ at 18,000×. (d) θ at 8000×. Source: Ref 2

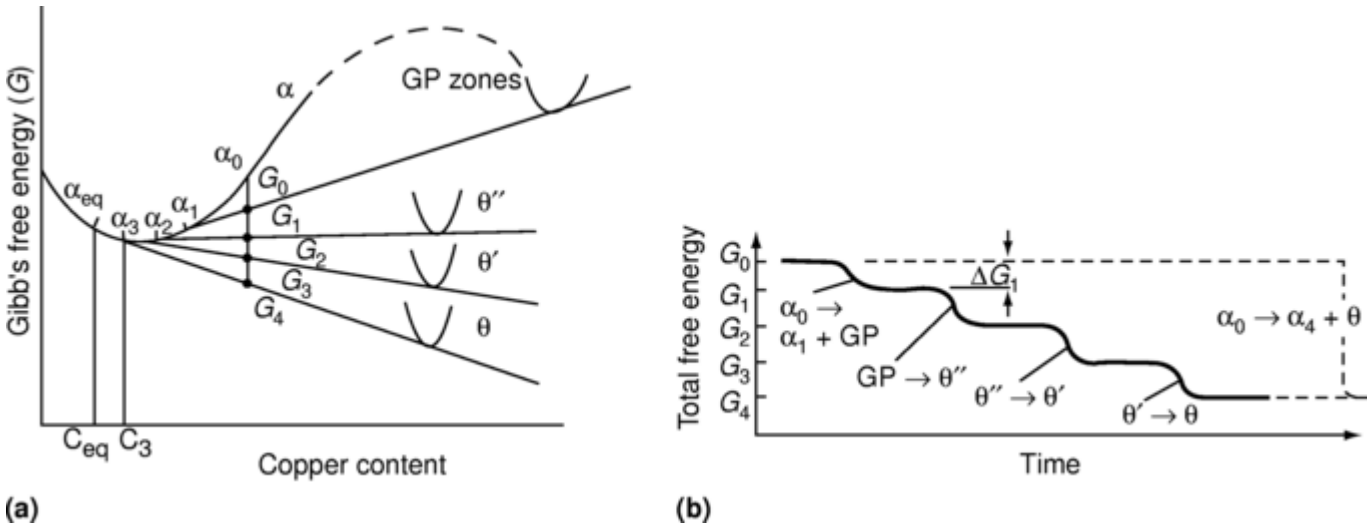

Fig. 14 Free-energy plots of precipitation sequence in aluminum-copper alloys. (a) Free-energy curve with common-tangent points for phase compositions in the matrix. (b) Step reductions in the free energy as the transformation proceeds. C_{eq} and C_3, copper content of α_{eq} and α_3 phases; ΔG_1, activation energy for $\alpha_0 \rightarrow \alpha_1$ + GP. GP, Guinier-Preston. Source: Ref 4

To maximize strengthening, aging is typically carried out to the precipitation between θ″ and θ′, because spacing and lattice strain are ideal to hinder dislocation motion. Reactions carried out beyond maximum

strengthening are termed overaged, because the beneficial effects of precipitation strengthening are lost as the precipitates grow larger in size and spacing.

References cited in this section

2. D.A. Porter and K.E. Easterling, *Phase Transformations in Metals and Alloys,* 2nd ed., Chapman and Hall, 1996, p 514

4. W.H. Van Geertruyden, W.Z. Misiolek, G.G. Lea, and R.M. Kelly, Thermal Cycle Simulation of 6xxx Aluminum Alloy Extrusion, *Proc. Seventh International Extrusion Technology Seminar* (Chicago, IL) Aluminum Extruders Council, 2000

M. Epler, Structures by Precipitation from Solid Solution, *Metallography and Microstructures,* Vol 9, *ASM Handbook,* ASM International, 2004, p. 134–139

Structures by Precipitation from Solid Solution

Mario Epler, Lehigh University

Acknowledgment

Portions of this article are adapted from the article by W.A. Soffa, "Structures Resulting from Precipitation from Solid Solution," in *Metallography and Microstructures,* Volume 9, *ASM Handbook,* 1985, pages 646–650 (Ref 1).

Reference cited in this section

1. W.A. Soffa, Structures Resulting from Precipitation from Solid Solution, *Metallography and Microstructures,* Vol 9, *ASM Handbook,* ASM International, 1985, p 646–650

M. Epler, Structures by Precipitation from Solid Solution, *Metallography and Microstructures,* Vol 9, *ASM Handbook,* ASM International, 2004, p. 134–139

Structures by Precipitation from Solid Solution

Mario Epler, Lehigh University

References

1. W.A. Soffa, Structures Resulting from Precipitation from Solid Solution, *Metallography and Microstructures,* Vol 9, *ASM Handbook,* ASM International, 1985, p 646–650

2. D.A. Porter and K.E. Easterling, *Phase Transformations in Metals and Alloys,* 2nd ed., Chapman and Hall, 1996, p 514

3. F.-S. Sun and F.H. Sam Froes, Precipitation of Ti_5Si_3 Phase in TiAl Alloys, *Mater. Sci. Eng. A,* Vol 328 (No. 1–2), 2002, p 113–121

4. W.H. Van Geertruyden, W.Z. Misiolek, G.G. Lea, and R.M. Kelly, Thermal Cycle Simulation of 6xxx Aluminum Alloy Extrusion, *Proc. Seventh International Extrusion Technology Seminar* (Chicago, IL) Aluminum Extruders Council, 2000

5. S.R. Claves, D.L. Elias, and W.Z. Misiolek, Analysis of the Intermetallic Phase Transformation Occurring During Homogenization of 6xxx Aluminum Alloys, *Proc. International Conference of Aluminium Alloys 8,* Trans Tech Publications, Cambridge, U.K., 2002

6. S. Celotto and T.J. Bastow, Study of Precipitation in Aged Binary Mg-Al and Ternary Mg-Al-Zn Alloys Using ^{72}AlNMR Spectroscopy, *Acta Mater.,* Vol 49, 2001, p 41–51

7. F.J. Gil, M.P. Ginebra, J.M. Manero, and J.A. Planell, Formation of Widmanstätten Structure: Effects of Grain Size and Cooling Rate on the Widmanstätten Morphologies and on the Mechanical Properties in Ti6Al4V Alloy, *J. Alloy. Compd.,* Vol 329 (No. 1–2), 2001, p 142–152

8. A. Tomer, *Structure of Metals through Optical Microscopy,* ASM International, 1991, p 113–114

9. I.J. Polmear, *Light Alloys—Metallurgy of the Light Metals,* 3rd ed., Arnold, 1995

10. D. Bradai, P. Zieba, E. Bischoff, and W. Gust, Correlation between Grain Boundary Misorientation and the Discontinuous Precipitation Reaction in Mg-10 wt.% Al Alloy, *Mater. Chem. Phys.,* Vol 78 (No. 1), 2003, p 222–226

11. I. Manna, S.K. Pabi, and W Gust, Discontinuous Reactions in Solids, *Int. Mater. Rev.,* Vol 46 (No. 2), 2001, p 53–91

12. M. Shaarbaf and R.A. Fournelle, *Mater. Sci. Eng. A,* Vol 102, 1988, p 271–279

13. D.B. William and E.P Butler, Grain Boundary Discontinuous Precipitation Reactions, *Int. Met. Rev.,* Vol 26 (No. 3), 1981, p 153–183

S. Para, Spinodal Transformation Structures, *Metallography and Microstructures,*Vol 9, *ASM Handbook*, ASM International, 2004, p. 140–143

Spinodal Transformation Structures

Shane Para, Lehigh University

Introduction

SPINODAL TRANSFORMATION is a phase-separation reaction that occurs from kinetic behavior first described by Gibbs in his treatment of the thermodynamic stability of undercooled or supersaturated phases. It is does not involve a nucleation step, which is the mechanism of classical nucleation and growth (Fig. 1a) of precipitates from a metastable solid solution. Instead, spinodal reactions involve spontaneous unmixing or diffusional clustering of atoms, where a two-phase structure forms by spontaneous growth from small composition fluctuations (Fig. 1b). The result is homogenous decomposition of a supersaturated single phase into two phases that have essentially the same crystal structure (but different composition) as the parent phase. Spinodal structures are characterized by what has been described as a woven or "tweedy" structure (Ref 3). The precipitation occurs in preferential crystallographic directions, providing an obvious geometric pattern in two or three directions.

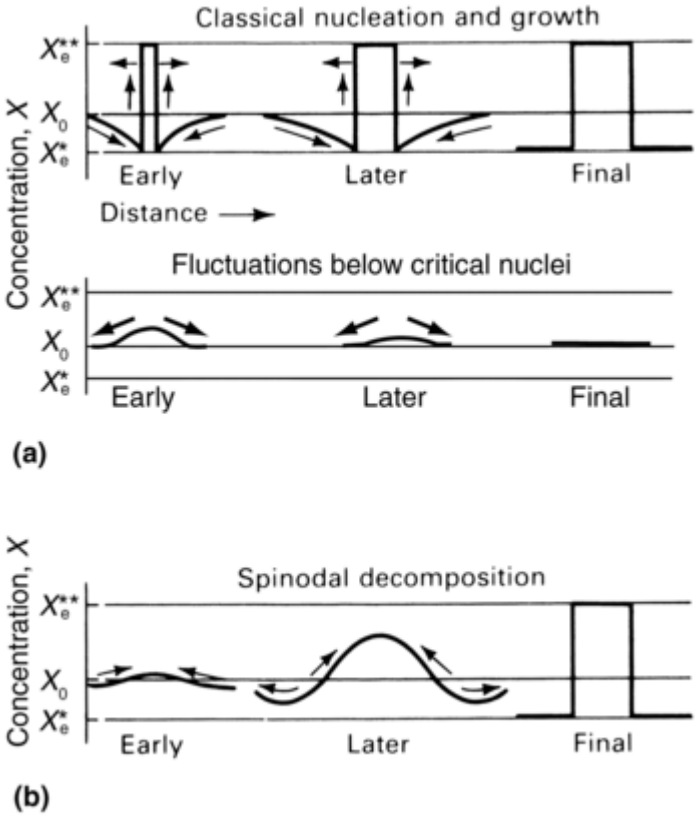

Fig. 1 Two sequences for the formation of a two-phase mixture by diffusion processes. (a) Classical nucleation and growth. (b) Spinodal decomposition. Source: Adapted from Ref 1, 2

The underlying theory of spinodal decomposition is only briefly described in this article. Readers are referred to Ref 1, which is the classic review of spinodal decomposition by Cahn. It provides basic insights on the process and how it can be understood using the concept of the gradient energy. The concept of gradient energy (which is the energy associated with a diffuse interface) in spinodal decomposition plays an equivalent role to interfacial energy in nucleation and growth reactions for setting the length scale and driving coarsening. When

a composition fluctuation has a large characteristic length, growth (or amplification) of the fluctuation is sluggish because the diffusion distances are very long. When the composition fluctuation has a very short wavelength, growth of the fluctuation is suppressed by the so-called energy gradient or surface energy of the diffuse or incipient interfaces that form during phase separation. Therefore, the microstructure that develops during spinodal decomposition has a characteristic periodicity that is typically 2.5 to 10 nm (25 to 100 Å) in metallic systems.

The spinodal mechanism provides an important mode of transformation, producing uniform, fine-scale, two-phase mixtures that can enhance the physical and mechanical properties of commercial alloys. Spinodal decomposition has been particularly useful in the production of permanent magnet materials, because the morphologies favor high coercivities. The structure can be optimized by thermomechanical processing, step aging, and magnetic aging. Continuous phase separation or spinodal decomposition appears to be important in the classic Alnicos and Cu-Ni-Fe alloys, as well as in the newly developed Fe-Cr-Co materials. Spinodal decomposition provides a practical method of producing nanophase materials that can have enhanced mechanical and physical properties.

References cited in this section

1. J.W. Cahn, *Trans. Met. Soc., AIME,* Vol 242, 1968, p 166

2. A.K. Jena and M.C. Chaturvedi, Spinodal Decomposition, *Phase Transformations in Materials,* Prentice Hall, 1992, p 373–399

3. K.B. Rundman, Spinodal Structures, *Metallography, Structures, and Phase Diagrams,* Vol 8, 8th ed., *Metals Handbook,* American Society for Metals, 1973, p 184

S. Para, Spinodal Transformation Structures, *Metallography and Microstructures,*Vol 9, *ASM Handbook*, ASM International, 2004, p. 140–143

Spinodal Transformation Structures

Shane Para, Lehigh University

Theory of Spinodal Decomposition

A simple binary phase diagram with a region of spinodal decomposition is shown in Fig. 2(a) with a corresponding free-energy curve (Fig. 2b). If a composition X_0 is heated above the critical temperature (T_c), the binary system is in the region of full solid solubility with a single-phase field (α_0) at temperature T_0. When the temperature goes below the critical temperature, a miscibility gap exists where a single-phase homogenous microstructure is no longer stable and a two-phase ($\alpha_1 + \alpha_2$) structure forms. The phase boundary on the phase diagram at temperature T' is given by the locus of points of common tangency for the two equilibrium compositions (X_e^* and X_e^{**}) on the free-energy curve (Fig. 2b) for temperature T'.

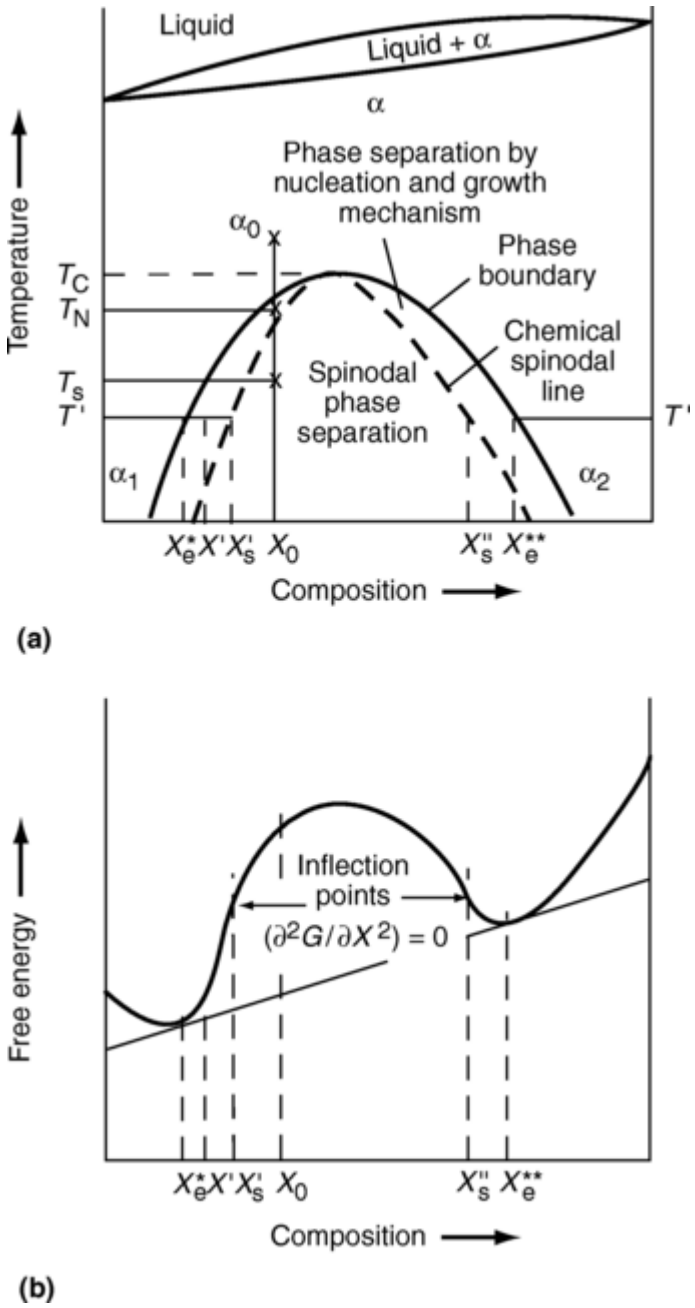

Fig. 2 Regions of spinodal decomposition and classical nucleation and growth of precipitates. (a) Phase diagram with a miscibility gap. (b) Variation in free energy with composition for the system shown in (a) at temperature *T′*. Source: Ref 2

When composition X_0 is at temperature T_N in a metastable (nonequilibrium) condition, the state is one of small undercooling or low supersaturation. The metastable state moves toward equilibrium by forming a second phase, but because this supersaturated condition is low (or not far from the equilibrium condition), the appearance of a second phase requires relatively large localized composition fluctuations. This is the classical nucleation process, when initiation requires a "critical nuclei" size for further growth of the new phase.

In contrast, if the α_0 solid-solution composition X_0 is at a lower temperature (e.g., T_s), then the supersaturated condition is higher, and initiation of two-phase growth may occur from smaller composition fluctuations. In particular, the area of spinodal decomposition defines a region of phase separation, where a particular kinetic process causes phase formation from very small composition fluctuations. It is not a new phase region, but rather a region with a difference in thermodynamic stability defined by the inflection points ($\partial^2 G/\partial X^2 = 0$) of free energy (Fig. 2b). The kinetics and reaction rate of spinodal decomposition are controlled by the rate of atomic migration and diffusion distances, which depend on the scale of decomposition (undercooling).

The kinetic process of spinodal decomposition is illustrated in Fig. 1(b), where a small fluctuation in composition becomes amplified by uphill diffusion (depicted by arrows). The reason for the uphill diffusion can

be understood when considering that the direction of atomic migration is governed by the gradient of chemical potential, not by the concentration gradient as stated by Fick's first law. Atomic migration will occur from the region of high chemical potential to the region of low chemical potential. As shown in Fig. 3, the chemical potential inside the spinodal (inflection points of the free-energy curve) decreases as the composition increases, illustrating that the atomic species inside the chemical spinodal will migrate from low concentration to high concentration. Regions surrounding the amplified composition fluctuations will become depleted as solute diffuses up the concentration gradient. These locally depleted regions will then give rise to additional amplified regions adjacent to the locally depleted region (Fig. 1b).

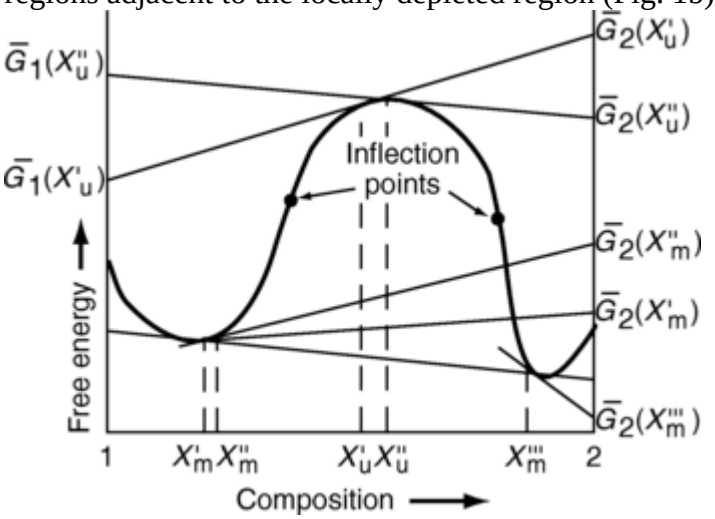

Fig. 3 Free-energy curve illustrating change in chemical potential with composition. Source: Ref 2

In the region of classical nucleation and growth, decomposition into a two-phase mixture can only occur when nucleation is allowed to begin at critical nuclei size. In this two-phase region above the “chemical spinodal” line, small composition fluctuations decay by the more common process of downhill diffusion (Fig. 1a). The downhill diffusion can be understood by considering Fig. 3 and noting that outside of the spinodal, chemical potential decreases as composition decreases. Thus, diffusion in this region involves atomic migration from areas of high concentration to low concentration, and any small composition fluctuation decays.

Because solid-state spinodal decomposition results in two phases with the same crystal structure, the lattice must remain continuous. If the atomic radii of the species present in a spinodal structure vary appreciably, then coherency strains will be present. If the strain induced in the lattice is significant, the system can be stabilized against decomposition (Ref 4). This stabilization results in a displacement of the spinodal curve and the miscibility gap below the chemical spinodal, thus defining the coherent spinodal and the coherent miscibility gap (see Fig. 4).

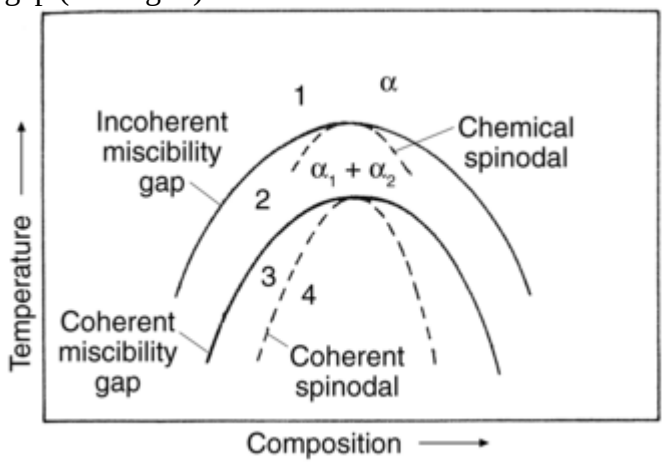

Fig. 4 Miscibility gap. Region 1: homogenous α is stable. Region 2: homogenous α is metastable, only incoherent phases can nucleate. Region 3: homogeneous α metastable, coherent phases can nucleate. Region 4: homogeneous α unstable, spinodal decomposition occurs. Source: Ref 4

The wavelength (λ) of the composition fluctuations (Δ*C*) can be understood by considering the expression for the composition wave that was derived considering the diffusion equation and gradient energy (Ref 1) (energy associated with diffuse interfaces):

$$\Delta C = C_0 \exp\left(R(\beta)t\right)$$

$$\beta = \frac{2\pi}{\lambda}$$

The amplification factor, $R(\beta)$, tends to be a maximum at intermediate wavelengths. At large wavelengths of composition fluctuation, diffusion distances are very long and slow growth results. At very short wavelengths of composition fluctuation, a gradient energy or surface energy associated with diffuse interfaces will dominate and suppress the amplification of the composition variation

Phase separated or spinodal structures cause diffraction effects called “satellites” or “sidebands” where the fundamental reflections are flanked by secondary intensity maxima (Fig. 5). The diffuse scattering that causes the satellites is a result of the periodic variation in lattice parameter and/or scattering factor. In reciprocal space, the distance between the fundamental reflection and the secondary maxima are inversely related to the wavelength of the composition waves in the solid. The kinetics of a spinodal reaction can be quantitatively studied using small-angle x-ray and neutron scattering, by monitoring the change in intensity distribution around the direct beam.

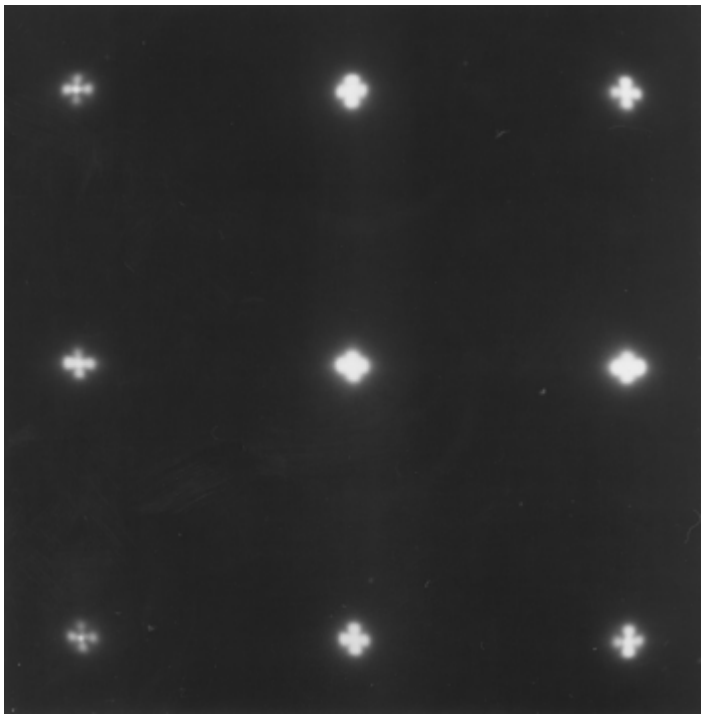

Fig. 5 Selected area diffraction pattern of Cu-15Ni-8Sn alloy showing satellites from structure modulation. Source: Ref 5

References cited in this section

1. J.W. Cahn, *Trans. Met. Soc., AIME,* Vol 242, 1968, p 166

2. A.K. Jena and M.C. Chaturvedi, Spinodal Decomposition, *Phase Transformations in Materials,* Prentice Hall, 1992, p 373–399

4. D.A. Porter and K.E. Easterling, *Phase Transformations in Metals and Alloys,* 2nd ed., Chapman and Hall, 1997

5. D.W. Zeng, C.S. Xie, and K.C. Yung, Mesostructured Composite Coatings on SAE 1045 Carbon Steel Synthesized in situ by Laser Surface Alloying, *Mater. Lett.,* Vol 6, 2002, p 680–684

S. Para, Spinodal Transformation Structures, *Metallography and Microstructures,*Vol 9, *ASM Handbook*, ASM International, 2004, p. 140–143

Spinodal Transformation Structures

Shane Para, Lehigh University

Microstructure

Spinodal structures, which are typically on the order of 2.5 to 10 nm, are too small for optical (light) microscopy. They are characterized by transmission electron microscopy (TEM) with typical images having a modulated homogenous appearance (Fig. 6). Spinodal structures are also characterized by small-angle x-ray scattering (see the article “Small-Angle X-Ray and Neutron Scattering” in *Materials Characterization,* Volume 10, *ASM Handbook,* 1986).

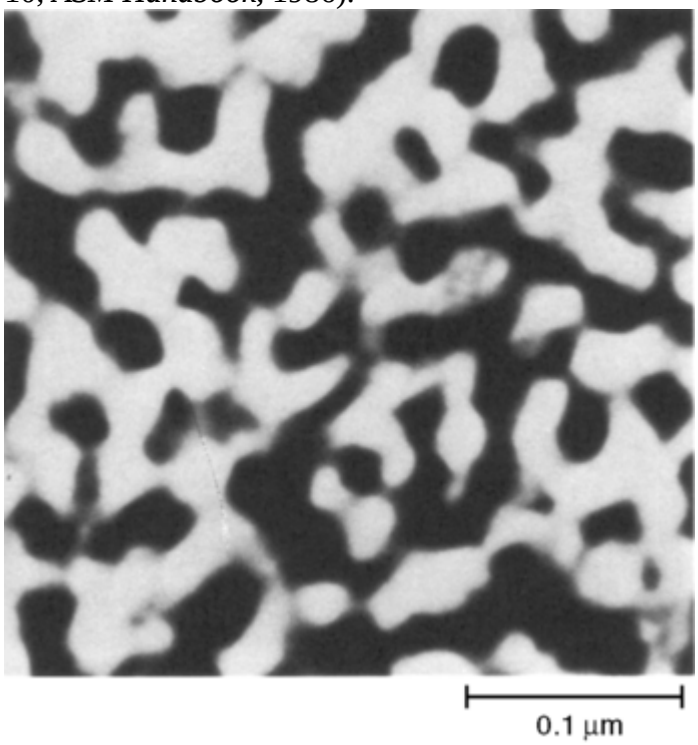

Fig. 6 Transmission electron micrograph of isotropic spinodal structure developed in Fe-28.5Cr-10.6Co (wt%) alloy aged 4 h at 600 °C (1110 °F). Contrast derives mainly from structure-factor differences. 225,000×. Courtesy of A. Zeltser

When a material is elastically isotropic or if only small misfit strains exist, the spinodal structures will be isotropic, similar to the structure found in phase-separated polymers, glasses, and liquids. Figure 7 shows a spinodal-type structure from an iron-copper alloy (Ref 5). The two phases both have different compositions and crystal structures. As the crystal structures are different, decomposition could only have occurred in the liquid phase prior to solidification. Materials that are elastically anisotropic form spinodal structures that are developed preferentially along elastically soft directions. Figure 8 illustrates calculated two-dimensional (2-D) and three-dimensional (3-D) time developments for the structure for an iron-molybdenum alloy (Ref 6). Because the iron-molybdenum system has a large lattice mismatch, the molybdenum-rich zones are aligned along the elastically soft 〈100〉 directions. Figure 9 and 10 show spinodally decomposed structures from a Fe-25Be (at.%) system and are typical microstructures that form in an elastically anisotropic system. It is obvious from Fig. 8 and 9 that the modulations in the spinodal structure coarsen as aging time increases. As spinodal decomposition occurs homogeneously throughout the microstructure by a structure-insensitive phase

separation, spinodal structures are usually uniform throughout the grains up to the grain boundary as shown in Fig. 11.

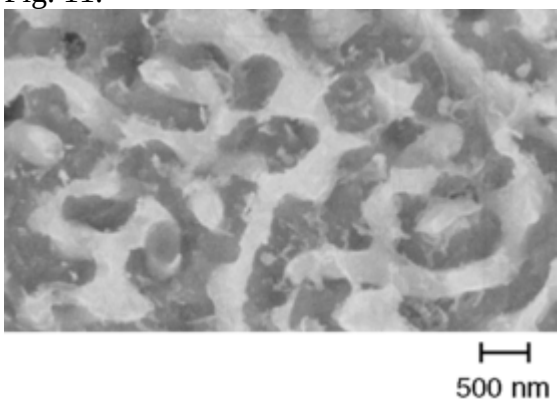

Fig. 7 Backscatter scanning electron micrograph of an iron-copper alloy that was rapidly solidified after undergoing liquid-phase spinodal decomposition. Source: Ref 5

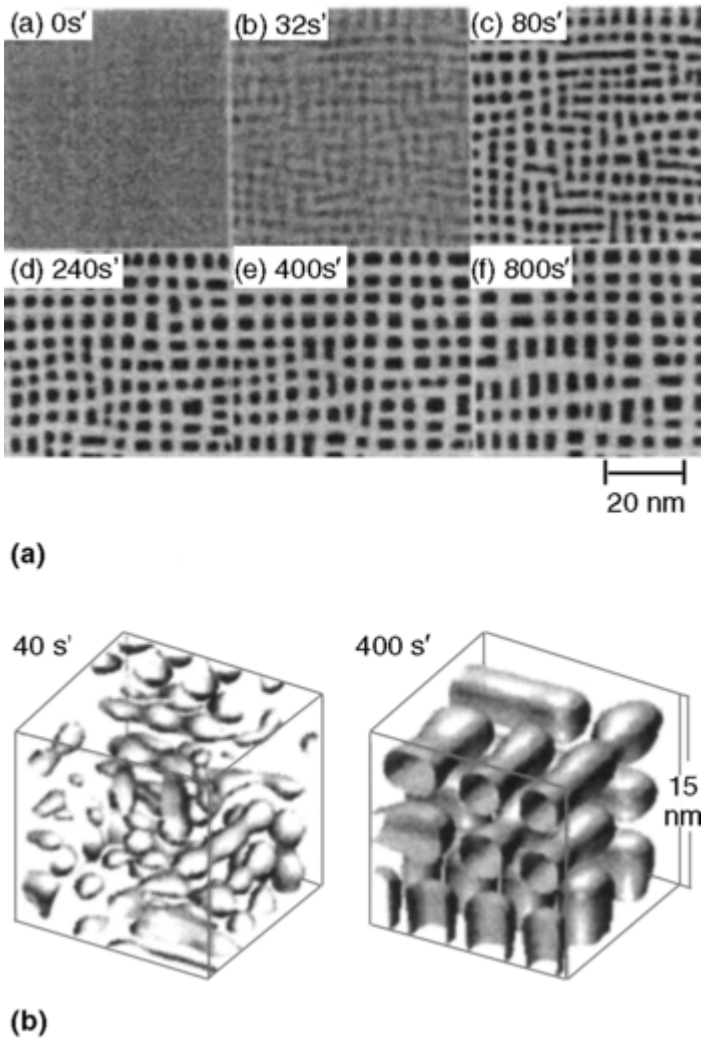

Fig. 8 Phase decomposition for the Fe-30Mo (at.%). (a) Two-dimensional time development. (b) Three-dimensional simulation. Source: Ref 6

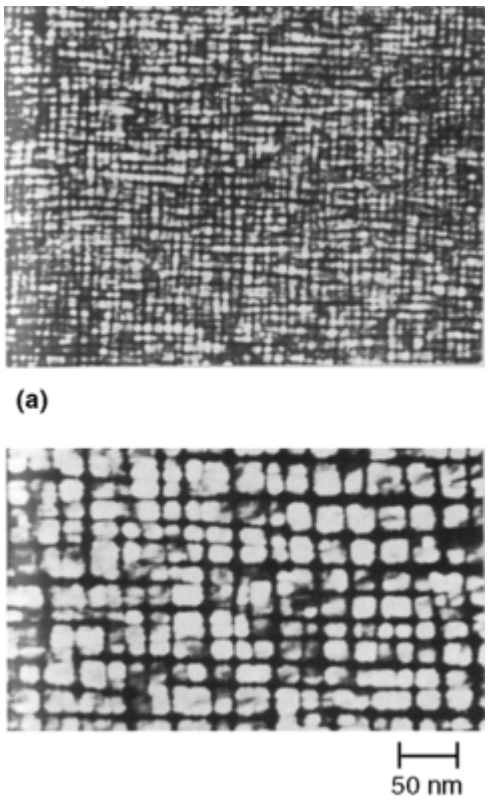

Fig. 9 Dark-field transmission electron micrograph of Fe-25Be (at.%) aged at 400 °C (750 °F) for 0.3 h (a) and 2 h (b). Source: Ref 7

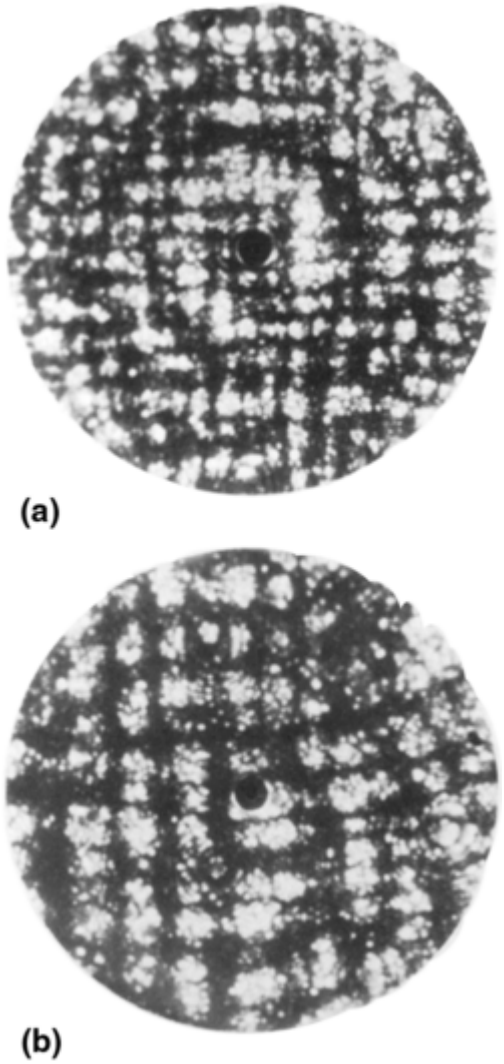

Fig. 10 Field-ion micrographs of the Fe-25Be (at.%) alloy aged at 400 °C (750 °F) for 0.3 h (a) and 2 h (b). Source: Ref 7

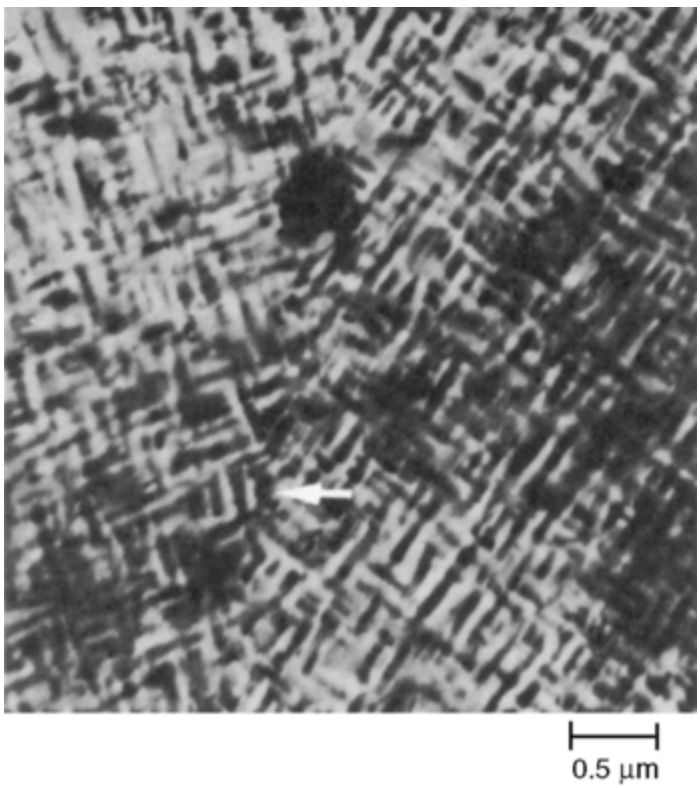

Fig. 11 Transmission electron micrograph of spinodal microstructure developed in a 66.3Cu-30Ni-2.8Cr (wt%) alloy during slow cooling from 950 °C (1740 °F). The microstructure is homogeneous up to the grain boundary indicated by the arrow. 35,000×. Courtesy of F.A. Badia. Source: Ref 8

References cited in this section

5. D.W. Zeng, C.S. Xie, and K.C. Yung, Mesostructured Composite Coatings on SAE 1045 Carbon Steel Synthesized in situ by Laser Surface Alloying, *Mater. Lett.,* Vol 6, 2002, p 680–684

6. T. Miyazaki, T. Koyama, and T. Kozakai, Computer Simulations of the Phase Transformation in Real Alloy Systems Based on the Phase Field Model, *Mater. Sci. Eng.*, Vol A312, 2001, p 38–49

7. M.G. Burke and M.K. Miller, A Combined TEM/APFIM Approach to the Study of Phase Transformations: Phase Identification in the Fe-Be System, *Ultramicroscopy,* Vol 30 (No. 1–2), 1989, p 199–209

8. D.E. Lauglin and W.A. Soffa, Spinodal Structures, *Metallography and Microstructures,* Vol 9, *ASM Handbook,* ASM International, 1985, p 652–654

S. Para, Spinodal Transformation Structures, *Metallography and Microstructures,*Vol 9, *ASM Handbook*, ASM International, 2004, p. 140–143

Spinodal Transformation Structures

Shane Para, Lehigh University

References

1. J.W. Cahn, *Trans. Met. Soc., AIME,* Vol 242, 1968, p 166

2. A.K. Jena and M.C. Chaturvedi, Spinodal Decomposition, *Phase Transformations in Materials,* Prentice Hall, 1992, p 373–399

3. K.B. Rundman, Spinodal Structures, *Metallography, Structures, and Phase Diagrams,* Vol 8, 8th ed., *Metals Handbook,* American Society for Metals, 1973, p 184

4. D.A. Porter and K.E. Easterling, *Phase Transformations in Metals and Alloys,* 2nd ed., Chapman and Hall, 1997

5. D.W. Zeng, C.S. Xie, and K.C. Yung, Mesostructured Composite Coatings on SAE 1045 Carbon Steel Synthesized in situ by Laser Surface Alloying, *Mater. Lett.,* Vol 6, 2002, p 680–684

6. T. Miyazaki, T. Koyama, and T. Kozakai, Computer Simulations of the Phase Transformation in Real Alloy Systems Based on the Phase Field Model, *Mater. Sci. Eng.*, Vol A312, 2001, p 38–49

7. M.G. Burke and M.K. Miller, A Combined TEM/APFIM Approach to the Study of Phase Transformations: Phase Identification in the Fe-Be System, *Ultramicroscopy,* Vol 30 (No. 1–2), 1989, p 199–209

8. D.E. Lauglin and W.A. Soffa, Spinodal Structures, *Metallography and Microstructures,* Vol 9, *ASM Handbook,* ASM International, 1985, p 652–654

J. Regina, Ordered Structures, *Metallography and Microstructures*, Vol 9, *ASM Handbook*, ASM International, 2004, p. 144–147

Ordered Structures

Jonathan Regina, Lehigh University

Introduction

AN ORDER-DISORDER transformation typically occurs on cooling from a disordered solid solution to an ordered phase. During this phase transformation, there is a rearrangement of atoms from random site locations in the disordered solution to specific lattice sites in the ordered structure. When atoms periodically arrange themselves into a specific ordered array, they make up what is commonly referred to as a superlattice. Although many alloy systems may contain ordered phases, only select superlattices are discussed in this article. Four common superlattice structures and ordered phases that atomically arrange into the corresponding superlattice are listed in Table 1 (Ref 1). As noted in the table, the superlattice types can be referred to by Strukturbericht symbols ($L1_0$, $L1_2$, B2, and $D0_3$) or by the prototype phase (CuAu I, Cu_3Au, FeAl, Fe_3Al) (Ref 2, 3). More detail about the select superlattice structures is provided in this article.

Table 1 Selected superlattice structures and alloy phases that order according to each superlattice

Strukturbericht symbol	Prototype phase	Base lattice type	Phases
$L1_0$	CuAu I	Face-centered cubic	AgTi, AlTi, CoPt, CrPd, CuAu, Cu_3Pd, FePd, FePt, HgPd, HgPt, HgTi, HgZr, InMg, MgTl, MnNi, Mn_2Pd_3, MnPt, NiPt, PbZn, PtZn
$L1_2$	Cu_3Au	Face-centered cubic	$AgPt_3$, Ag_3Pt, $AlCo_3$, $AlNi_3$, $AlZr_3$, $AuCu_3$ I, Au_3Pt, $CaPb_3$, $CaSn_3$, $CdPt_3$, $CePb_3$, $CeSn_3$, $CoPt_3$, Cr_2Pt, CuPd, Cu_3Au, Cu_3Pt, $FeNi_3$, $FePt_3$, Fe_3Pt, $GeNi_3$, $HgTi_3$, $InMg_3$, $LaPb_3$, $LaSn_3$, $MnNi_3$, $MnPt_3$, Mn_3Pt, $NaPb_3$, Ni_3Pt, $PbPd_3$, $PbPt_3$, Pt_3Sn, Pt_3Ti, Pt_3Zn, $TiZn_3$
B2	FeAl	Body-centered cubic	AgCd, AgCe, AgLa, AgLi, AgMg, AlCo, $AlCu_2Zn$, AuCd, AuMg, AuMn, AuZn, BeCo, BeCu, BeNi, CdCe, CeHg, CeMg, CeZn, CoFe, CoTi, CsCl, CuPd, CuZn, $CuZn_3$, FeAl, FeTi, $HgLi_2Tl$, HgMn, InNi, LaMg, LiPb, LiTl, MgPr, MgSr, MgTl, MnPt, NiAl, NiTi, RuTa, TiZn
$D0_3$	Fe_3Al	Simple cubic	$BiLi_3$, $CeMg_3$, Cu_3Sb, Fe_3Al, Fe_3Si, Mg_3Pr

(a) Source: Ref 1. For information on other superlattice structures, see Ref 2 and 3.

References cited in this section

1. A. Taylor and B.J. Kagle, *Crystallographic Data on Metal and Alloy Structures,* Dover, 1963

2. A.K. Jena and M.C. Chaturvedi, *Phase Transformations in Materials*, Prentice Hall Inc., 1992

3. F. Ducastelle, *Order and Phase Stability in Alloys*, Elsevier Science Publishing, 1991

J. Regina, Ordered Structures, *Metallography and Microstructures*, Vol 9, *ASM Handbook*, ASM International, 2004, p. 144–147

Ordered Structures

Jonathan Regina, Lehigh University

Antiphase Boundaries

Most alloys that form an ordered structure are disordered at higher temperature, which means that atoms are randomly located on lattice sites. On cooling, small ordered areas will nucleate within the disordered phase and begin to grow into ordered domains. These ordered domains can also form by a continuous ordering mechanism, where local atomic rearrangements occur homogeneously throughout the disordered phase, creating ordered domains. As the temperature is decreased further, the ordered domains will grow until they impinge on or intersect each other and form antiphase boundaries (APBs). Antiphase boundaries are boundaries between two ordered domains where the periodicity of the ordered structure in one domain is out of step with the other. This can be seen in Fig. 1, which is a schematic representing the phase transformation from a disordered structure at elevated temperature to the ordered structure, with APBs located where the domains intersect. The APBs are typically well defined within the structure and can be seen fairly easily using thin-film transmission electron microscopy (TEM) (Ref 4).

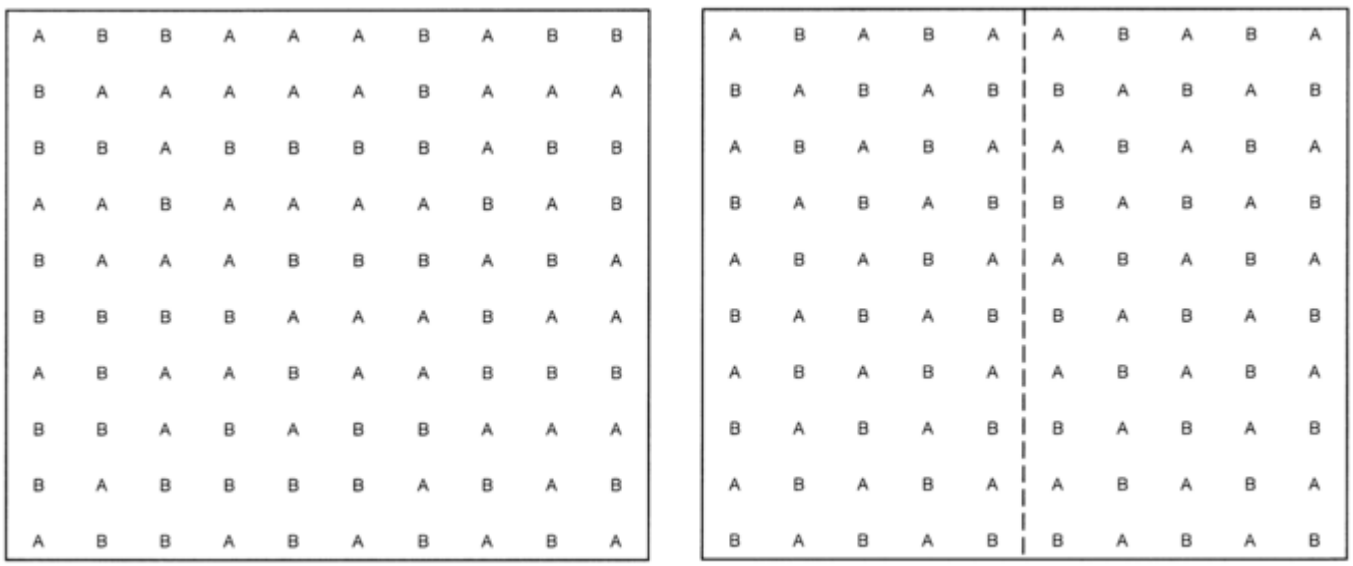

Fig. 1 Schematic representation of (a) a disordered solution and (b) an ordered structure with an antiphase boundary (dashed line) located where the atomic sequence is out of step

Reference cited in this section

4. D.B. Williams and C.B. Carter, *Transmission Electron Microscopy—A Textbook for Materials Science*, Plenum Press, 1996

J. Regina, Ordered Structures, *Metallography and Microstructures*, Vol 9, *ASM Handbook*, ASM International, 2004, p. 144–147

Ordered Structures

Jonathan Regina, Lehigh University

Long-Range and Short-Range Order

A perfectly ordered structure is one that has the periodic arrangements of atoms throughout the entire crystal, without the presence of any defects. Practically, defects that disrupt the atomic sequence are typically found within the crystal lattice. For example, if an aluminum atom replaced an iron atom in the ordered FeAl phase, the structure would be less than perfect. A parameter (*S*) was therefore established to quantify the degree of long-range order within a crystal (Ref 2). For binary alloys (alloy A-B), if A atoms occupy the α-sublattice, and B atoms occupy the β-sublattice:

$$S = \frac{f_A(\alpha) - f_A}{1 - f_A} \qquad \text{(Eq 1)}$$

where f_A is the fraction of all A atoms in the alloy, and $f_A(\alpha)$ is the fraction of A atoms that lie on the α-sublattice (Ref 2). The term $f_A(\alpha)$ can also be described as the probability that an A atom occupies an α site. It can be seen from this equation that the degree of long-range order can be quantified, where a completely disordered solution is present when $S = 0$, and a perfectly ordered structure is present when $S = 1$.

Long-range order is used to describe the degree of ordering throughout an entire crystal. There is also a degree of ordering, known as short-range ordering, that is associated with a single atom and its nearest neighbors. In a crystal lattice, each atom has first- and second-order nearest neighbors. In an A-B alloy with a random arrangement of atoms (disordered solution), each A atom should have an average number of B nearest neighbors. In an ordered structure, the number of B nearest neighbors surrounding the A atom should increase. The amount of segregation of B atoms around a single A atom is considered the degree of short-range ordering (σ). The degree of short-range order can be described quantitatively as (Ref 2):

$$\sigma = \frac{q - q_r}{q_m - q_r} \qquad \text{(Eq 2)}$$

where q is the total number of A-B pairs, q_r is the average number of A-B pairs in a disordered solution (randomly arranged), and q_m is the maximum number of A-B pairs that are possible (Ref 2). As was the case with the long-range order parameter, when the degree of short-range order is 0 ($\sigma = 0$), a disordered alloy is present, and when $\sigma = 1$, the alloy is completely ordered.

Reference cited in this section

2. A.K. Jena and M.C. Chaturvedi, *Phase Transformations in Materials*, Prentice Hall Inc., 1992

J. Regina, Ordered Structures, *Metallography and Microstructures*, Vol 9, *ASM Handbook*, ASM International, 2004, p. 144–147

Jonathan Regina, Lehigh University

$L1_0$ Superlattice (CuAu I Structure)

At elevated temperatures, the CuAu alloy is a disordered solution with a face-centered cubic lattice, where copper and gold atoms are randomly located at the face and corner sites (Fig. 2a). When the CuAu alloy is cooled and transforms to the ordered CuAu I structure, the gold atoms remain at the top and bottom faces and at the unit cell corners, while copper atoms are located at the side face sites, causing a slight change in the lattice parameter (Fig. 2b). It can be seen that the resultant superlattice is comprised of a layer of copper atoms located between two layers of gold atoms. The only other type of domain that can be present in the CuAu I phase is when a layer of gold atoms is located between two layers of copper atoms.

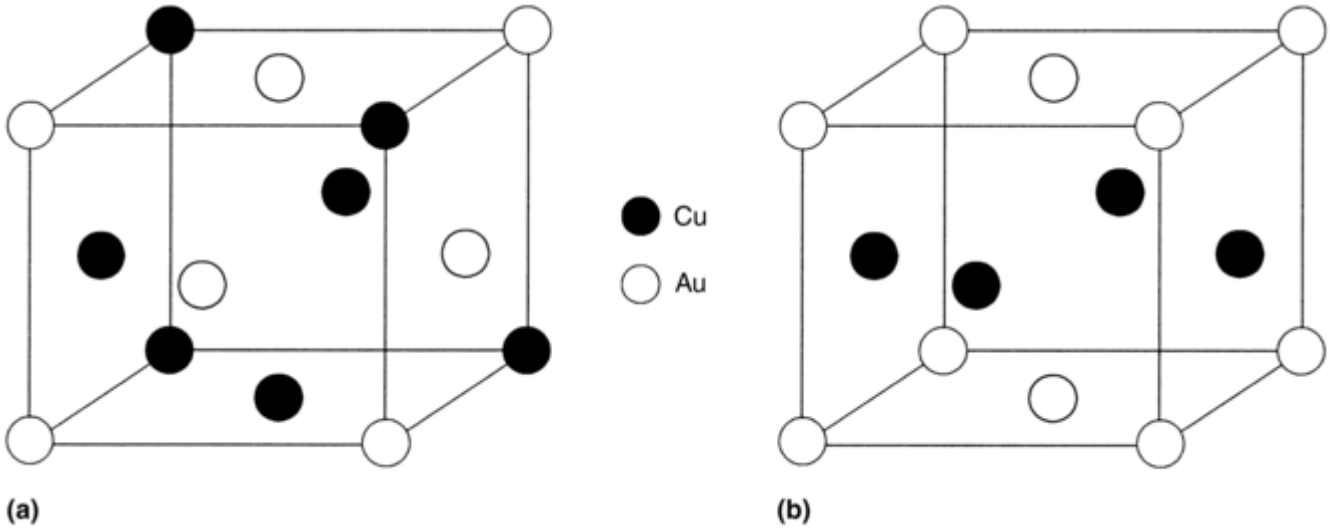

Fig. 2 Unit cells of (a) the disordered CuAu face-centered cubic solution at elevated temperatures and (b) the ordered CuAu I structure representing the $L1_0$ superlattice

J. Regina, Ordered Structures, *Metallography and Microstructures*, Vol 9, *ASM Handbook*, ASM International, 2004, p. 144–147

Ordered Structures

Jonathan Regina, Lehigh University

$L1_2$ Superlattice (Cu_3Au Structure)

The Cu_3Au phase has the same disordered structure as the CuAu phase at high temperatures, with the exception that the gold atoms have a 25% probability of sitting on a lattice site, rather than a 50% probability for the CuAu alloy. On cooling to the ordered Cu_3Au structure, gold atoms relocate to the corner positions, while the copper atoms arrange on the faces (Fig. 3a). Three other atomic arrangements are possible for the ordered Cu_3Au structure and are similar in appearance (Fig. 3b–d). These arrangements have copper atoms at the corner

sites and at two pairs of faces, while the gold atoms are located at the remaining pair of faces. (Note that the unit cell still contains three copper atoms and one gold atom, regardless of the atomic locations.) Because there are four possible ordered configurations for the Cu_3Au alloy, neighboring domains can be out of step in four possible ways and will lead to APBs that intersect each other to form sharp boundaries (Fig. 4) (Ref 5, 6).

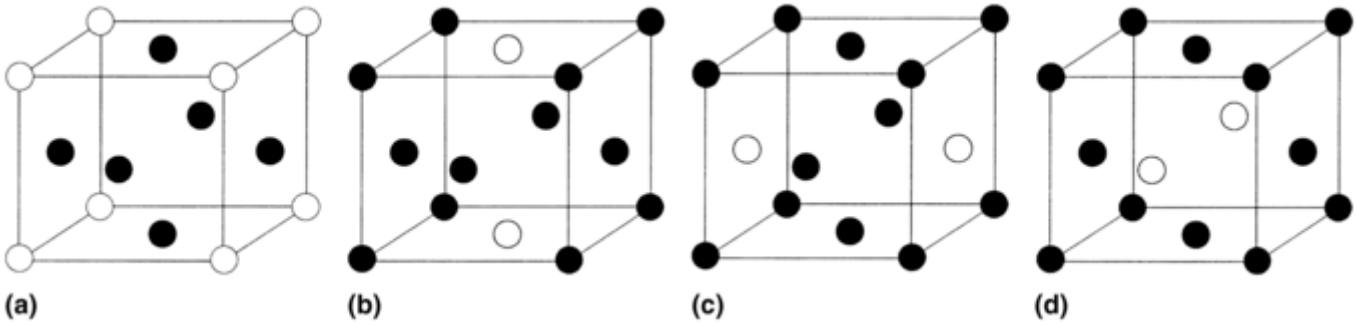

Fig. 3 Unit cells of Cu_3Au representing the four domain types found in the $L1_2$ superlattice: where the gold atoms (white) sit (a) at the corners and (b–d) at the face sites

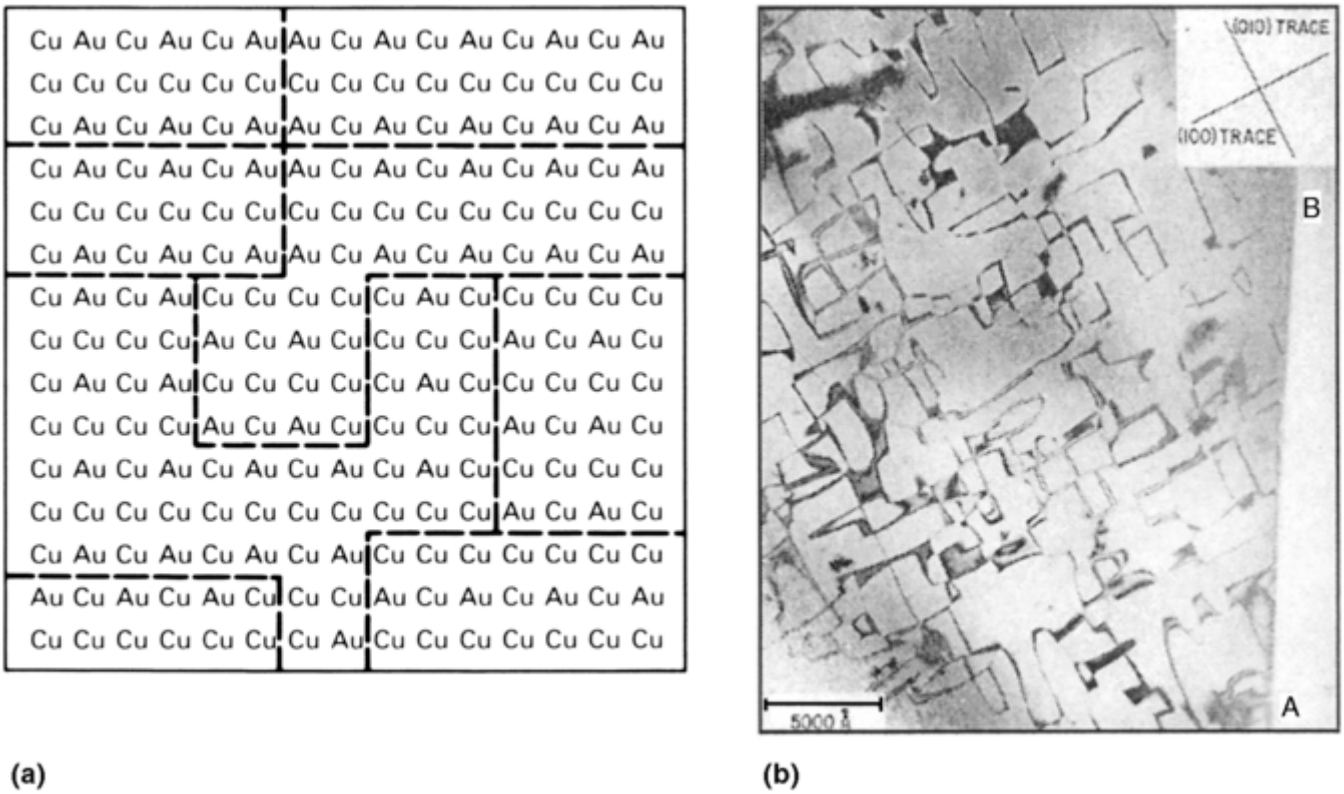

Fig. 4 Schematic diagram (a) showing the atomic configuration in Cu_3Au that results in the formation of straight antiphase boundaries, which can be seen (b) using transmission electron microscopy. Source: Ref 5, 6

References cited in this section

5. M.J. Marcinkowski, in *Electron Microscopy and Strength of Crystals*, G. Thomas and J. Washburn, Ed., Interscience, 1963

6. M.J. Marcinkowski and L. Zwell, Transmission Electron Microscopy Study of the Off-Stoichiometric Cu_3Au Superlattices, *Acta Metall.*, Vol 11, 1963, p 373–390

J. Regina, Ordered Structures, *Metallography and Microstructures*, Vol 9, *ASM Handbook*, ASM International, 2004, p. 144–147

Ordered Structures

Jonathan Regina, Lehigh University

B2 Superlattice (FeAl Structure)

Alloys that transform to a B2 superlattice on cooling typically transform from a disordered body-centered cubic (bcc) solution, where atoms are randomly located at either the center position or at the corners. One alloy that undergoes this type of phase transformation is FeAl. At high temperatures, the FeAl alloy starts as a disordered bcc lattice, where either atom has a 50% probability of lying on the body-centered site or at the corners. Once the transformation is complete, there are two possible types of ordered domains: where the aluminum atoms sit at the center positions, and the iron atoms are at the corners; or where the aluminum atoms are at the corners, and the iron atoms are at the center sites (Fig. 5). It can be seen from Fig. 6 that distinct APBs can be resolved using TEM and that these curved APBs differ from the straight APBs that were present in the ordered Cu_3Au structure (Ref 7).

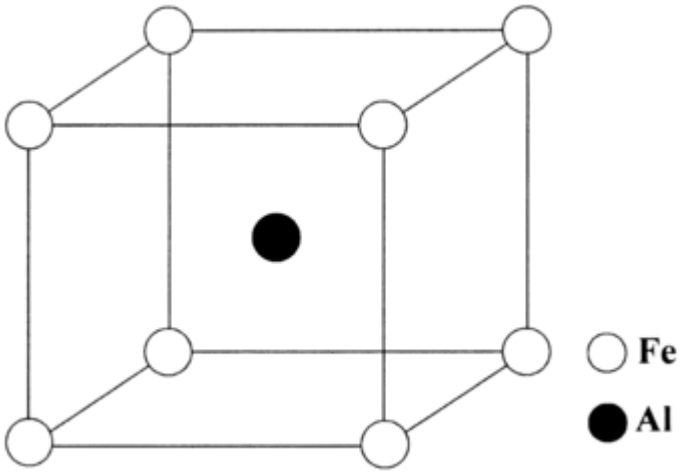

Fig. 5 Unit cell for one type of domain found in the ordered FeAl phase representing the B2 superlattice (switch atoms for other domain)

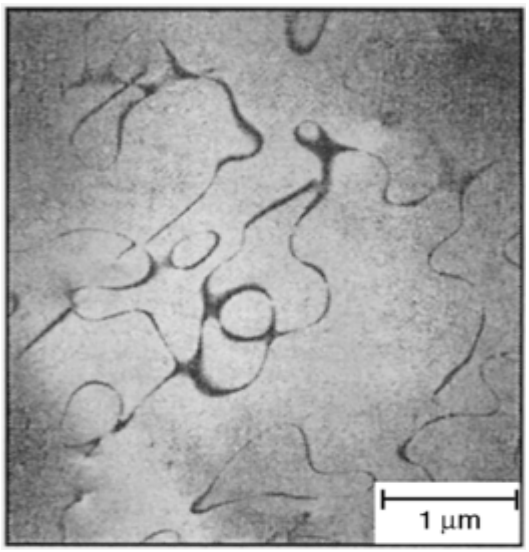

Fig. 6 Antiphase boundaries found in the ordered FeAl phase. Source: Ref 7

Reference cited in this section

7. G. Frommeyer et. al., Investigations of Phase Transformations and B2-$D0_3$ Superlattices in Ordered Iron Aluminum Alloys by FIM-Atom Probe and TEM, *Scripta Metall.,* Vol 24, 1990, p 51–56

J. Regina, Ordered Structures, *Metallography and Microstructures*, Vol 9, *ASM Handbook*, ASM International, 2004, p. 144–147

Jonathan Regina, Lehigh University

$D0_3$ Superlattice (Fe_3Al Structure)

One of the most common alloys to transform into the $D0_3$ superlattice is Fe_3Al. The $D0_3$ superlattice is based on a bcc structure, which can be considered as two interpenetrating simple cubic sublattices. The corners of the bcc unit cell are taken to be one simple cubic sublattice, and the body-centered atoms make up the other. The $D0_3$ superlattice is present when half of the lattice sites on one of the simple cubic sublattices are occupied by a specific atom (such as aluminum in Fe_3Al). This can be seen in Fig. 7, which shows the ordered Fe_3Al structure. The transformation to Fe_3Al occurs differently from most other order-disorder transformations, because the ordered FeAl phase will typically transform from the disordered solution first, and then FeAl will undergo a transformation to Fe_3Al. This unique transformation results in two distinct types of APBs in the structure: one from FeAl (wrong first-nearest neighbors) and the other from Fe_3Al (wrong second-nearest neighbors) (Ref 8). It can be seen from Fig. 8 that the small-scale APBs associated with Fe_3Al are curved and terminate at the APBs associated with FeAl.

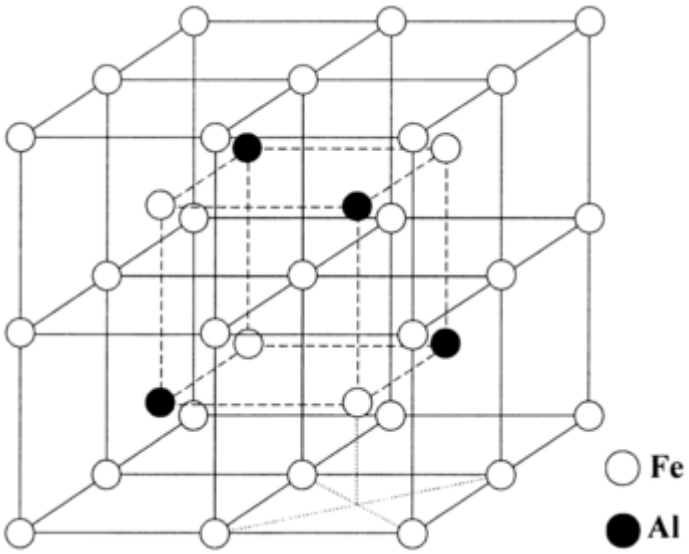

Fig. 7 Unit cell for the ordered Fe_3Al phase demonstrating the $D0_3$ superlattice

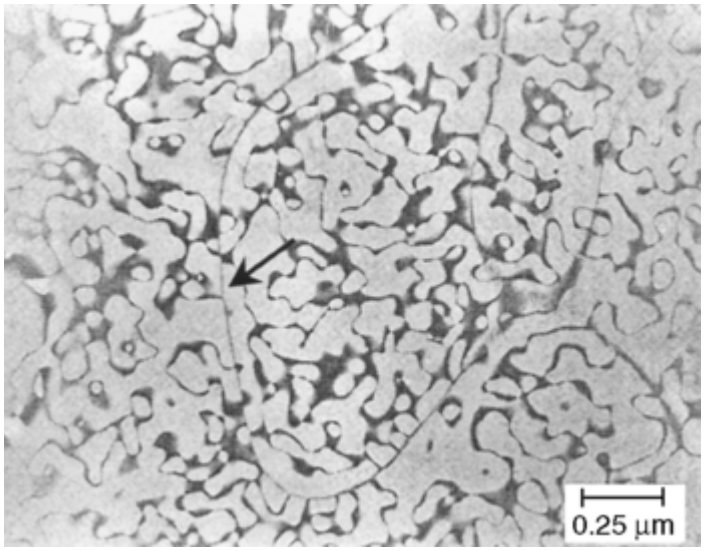

Fig. 8 Two types of antiphase boundaries (APBs) found in the ordered Fe_3Al phase: the large, curved APB from the formation of FeAl (arrow) and the small APBs within the large FeAl domains from the transformation to Fe_3Al. Source: Ref 8

Reference cited in this section

8. N.S. Stoloff and V.K. Sikka, Ed., *Physical Metallurgy and Processing of Intermetallic Compounds,* Chapman & Hall, 1996

J. Regina, Ordered Structures, *Metallography and Microstructures*, Vol 9, *ASM Handbook*, ASM International, 2004, p. 144–147

Ordered Structures

Jonathan Regina, Lehigh University

Dislocation-Generated Antiphase Boundaries

Although APBs were previously defined as the boundary between two ordered domains where the domain atomic sequence is out of step, APBs can also be generated by dislocation motion. In an ordered structure, a defect in the atomic arrangement caused by the presence of a dislocation can cause the atomic sequence to be out of step and thus generate an APB (lower section of Fig. 9). The amount of dislocation-generated APBs can be minimized if dislocation pairs (for example, two edge dislocations) align such that the dislocation-generated APB is terminated at the other edge dislocation (upper section of Fig. 9) (Ref 9). These APBs that are present between two dislocations are known as superlattice dislocations. Superlattice dislocations reduce the number of incorrect atomic bonds caused by APBs and therefore reduce the overall energy of the structure. Dislocation-generated APBs can be investigated by TEM (Ref 10), and Fig. 10 is an example of ordered Fe_3Al structure showing APBs generated by the presence of dislocations.

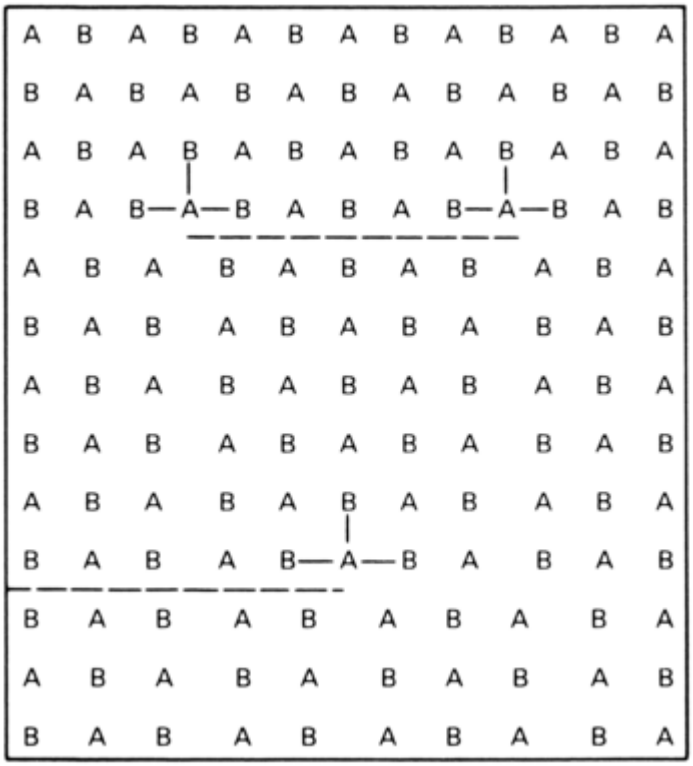

Fig. 9 Schematic representation of dislocation-generated antiphase boundaries (APBs). The lower APB is generated by one edge dislocation, while the upper APB is terminated between a pair of edge dislocations, creating a superlattice dislocation. Source: Ref 9

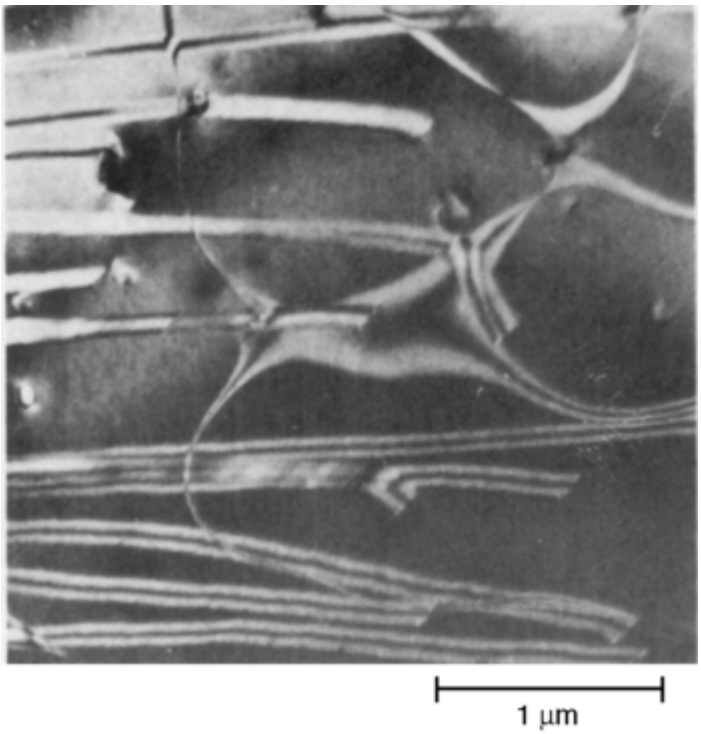

Fig. 10 Dislocation-generated antiphase domain boundaries in ordered Fe_3Al. Thin-foil electron micrograph. 20,000×. Source: Ref 9

References cited in this section

9. M.J. Marcinkowski, Ordered Structures, *Metallography and Microstructures,* Vol 9, *Metals Handbook,* 9th ed., American Society for Metals, 1985, p 681–683

10. A. Brinck et. al., Dislocation Processes in Fe_3Al Investigated by Transmission Electron, Scanning Force and Optical Microscopy, *Mater. Sci. Eng. A,* Vol 258, 1998, p 32–36

J. Regina, Ordered Structures, *Metallography and Microstructures,* Vol 9, *ASM Handbook,* ASM International, 2004, p. 144–147

Ordered Structures

Jonathan Regina, Lehigh University

References

1. A. Taylor and B.J. Kagle, *Crystallographic Data on Metal and Alloy Structures,* Dover, 1963

2. A.K. Jena and M.C. Chaturvedi, *Phase Transformations in Materials,* Prentice Hall Inc., 1992

3. F. Ducastelle, *Order and Phase Stability in Alloys,* Elsevier Science Publishing, 1991

4. D.B. Williams and C.B. Carter, *Transmission Electron Microscopy—A Textbook for Materials Science,* Plenum Press, 1996

5. M.J. Marcinkowski, in *Electron Microscopy and Strength of Crystals,* G. Thomas and J. Washburn, Ed., Interscience, 1963

6. M.J. Marcinkowski and L. Zwell, Transmission Electron Microscopy Study of the Off-Stoichiometric Cu_3Au Superlattices, *Acta Metall.,* Vol 11, 1963, p 373–390

7. G. Frommeyer et. al., Investigations of Phase Transformations and B2-$D0_3$ Superlattices in Ordered Iron Aluminum Alloys by FIM-Atom Probe and TEM, *Scripta Metall.,* Vol 24, 1990, p 51–56

8. N.S. Stoloff and V.K. Sikka, Ed., *Physical Metallurgy and Processing of Intermetallic Compounds,* Chapman & Hall, 1996

9. M.J. Marcinkowski, Ordered Structures, *Metallography and Microstructures,* Vol 9, *Metals Handbook,* 9th ed., American Society for Metals, 1985, p 681–683

10. A. Brinck et. al., Dislocation Processes in Fe_3Al Investigated by Transmission Electron, Scanning Force and Optical Microscopy, *Mater. Sci. Eng. A,* Vol 258, 1998, p 32–36

M.J. Perricone, Massive Transformation Structures, *Metallography and Microstructures,* Vol 9, *ASM Handbook,* ASM International, 2004, p. 148–151

Massive Transformation Structures

M.J. Perricone, Lehigh University

Introduction

MASSIVE TRANSFORMATIONS involve a transition in crystal structure and are characterized by the chemical invariance between parent and product phases. These transformations can occur both on heating and cooling, although the mechanism requires rapid heating and cooling rates; as such, the ability of atoms to diffuse the long distances typical of diffusion-controlled transformations is impaired. The concomitant short-range atomic mobility during the transformation maintains the bulk chemical composition of product and parent. However, unlike the cooperative growth observed in shear transformations (martensite), massive phenomena proceed by the random transfer of atoms across the interface between parent and product phases. Furthermore, while surface upheaval is commonly observed during massive transformations due to the mechanical deformation caused by volumetric differences between parent and product, no evidence has been presented in the literature of the invariant plane-strain surface relief characteristic of shear transformations.

Massive transformations are thermally activated phenomena and exhibit nucleation and growth characteristics. The kinetics of the transformation is primarily controlled by the interface between parent and product phases, which is generally considered incoherent (Ref 1). The growth of the massive phase therefore occurs by the displacement of these high-energy incoherent interfaces across the microstructure, often at velocities exceeding 1 cm/s (0.4 in./s). The incoherent nature of the advancing interface results in the unique morphology of massively transformed phases, often characterized by irregularly shaped boundaries, giving the massive grains a "patchy" appearance. Unlike martensitic transformations that occur with similar rapidity, no definitive orientation relationship between parent and product phase at the migrating interface has been established, although some controversy still surrounds this issue.

Massive transformations occur in a wide array of materials, both in pure metals and in alloys. A short list of model binary systems is shown in Table 1, although it should be noted that this list is not meant to be exhaustive, because several other binary and higher-order systems exhibit massive transformations (Ref 2).

Table 1 Typical massive transformations

Alloy system or metal	Amount of solute at which transformation occurs[a], at.%	Temperature during quenching at which transformation occurs[a]		Change in crystal structure[b]
		°C	°F	
Silver-aluminum	23–28	600	1110	bcc → hcp
Silver-cadmium	41–42	300–450	570–840	bcc → fcc
	50	300	570	bcc → hcp
Silver-zinc	37–40	250–350	480–660	bcc → fcc
Copper-aluminum	19	550	1020	bcc → fcc
Copper-zinc	37–38	400–500	750–930	bcc → fcc
Copper-gallium	21–27	580	1075	bcc $\rightleftarrows$ hcp
	20	600	1110	bcc → fcc
Iron	…	700	1290	fcc → bcc
Iron-cobalt	0–25	650–800	1200–1470	fcc → bcc
Iron-chromium	0–10	600–800	1110–1470	fcc → bcc

Iron-nickel	0–6	500–700	930–1290	fcc → bcc
Plutonium-zirconium	5–45	450	840	bcc → fcc

(a) Values listed are approximate.
(b) bcc, body-centered cubic; fcc, face-centered cubic; hcp, hexagonal close-packed

References cited in this section

1. T.B. Massalski, Distinguishing Features of Massive Transformations, *Metall. Trans. A,* Vol 15, 1984, p 421–425

2. T.B. Massalski, Massive Transformation Structures, *Metallography and Microstructures,* Vol 9, *Metals Handbook,* 9th ed., American Society for Metals, 1985, p 655–657

M.J. Perricone, Massive Transformation Structures, *Metallography and Microstructures,* Vol 9, *ASM Handbook,* ASM International, 2004, p. 148–151

Massive Transformation Structures

M.J. Perricone, Lehigh University

Pure Metals and Congruent Points

Diffusion-controlled phase changes in pure metals that can exist in more than one allotropic form can often be considered massive transformations, because all phase changes in pure materials are composition invariant by definition. Figure 1 depicts massively transformed pure iron (Ref 3) and illustrates two important characteristics of massive transformations: the irregular massive body-centered cubic (bcc)-α phase boundaries stand out in stark contrast to the faceted face-centered cubic (fcc)-γ (parent) grain boundaries, and growth of massive bcc-α phase continues unabated across parent grain boundaries. Cooling rate was found to strongly influence the transformation mechanism (Fig. 2) in pure iron (Ref 4), such that the massive transformation dominates at intermediate cooling rates before martensitic kinetics control behavior at cooling rates above 35,000 °C/s (63,000 °F/s). Similar “plateau” behavior is expected in binary systems (although under less extreme cooling rates) where two-phase fields touch at a congruent point (shown schematically in Fig. 3a). Massive transformations can occur more easily under these conditions than in a two-phase region where more interference exists from competing transformations that require long-range diffusion and solute redistribution.

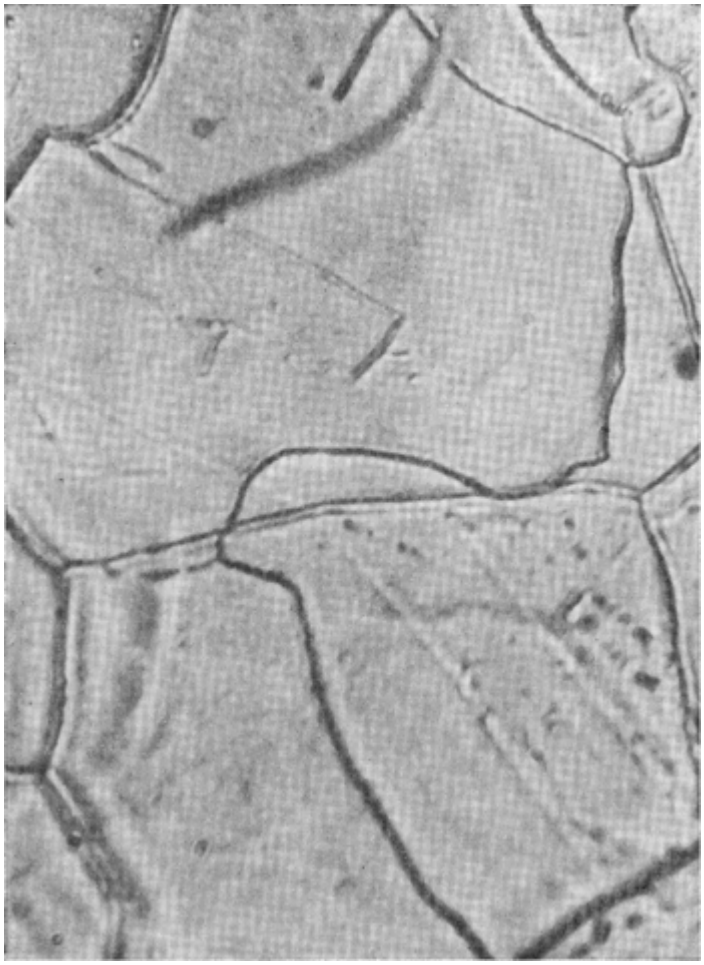

Fig. 1 Growth of massive ferrite in pure iron, illustrating the crossing of prior-γ/γ grain boundaries outlined by surface grooving. Reprinted with permission from Ref 3

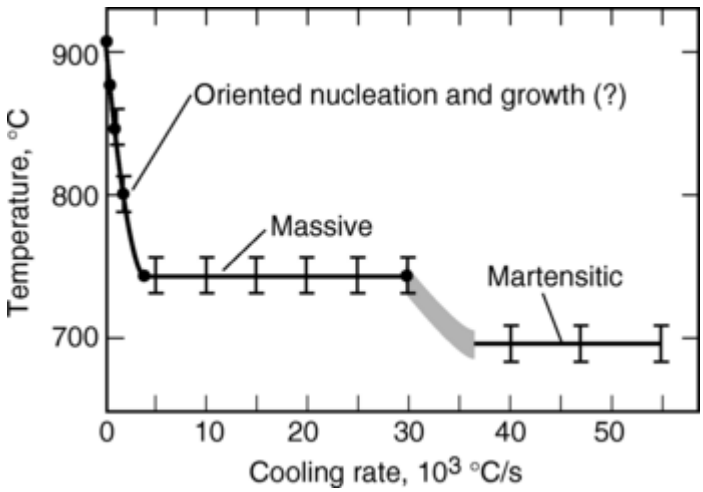

Fig. 2 The two-plateau behavior of the transformation temperature as a function of the cooling rate in pure iron. The upper plateau corresponds to the γ-to-massive-α and the lower plateau to the γ-to-martensitic-α transformation. Source: Ref 4

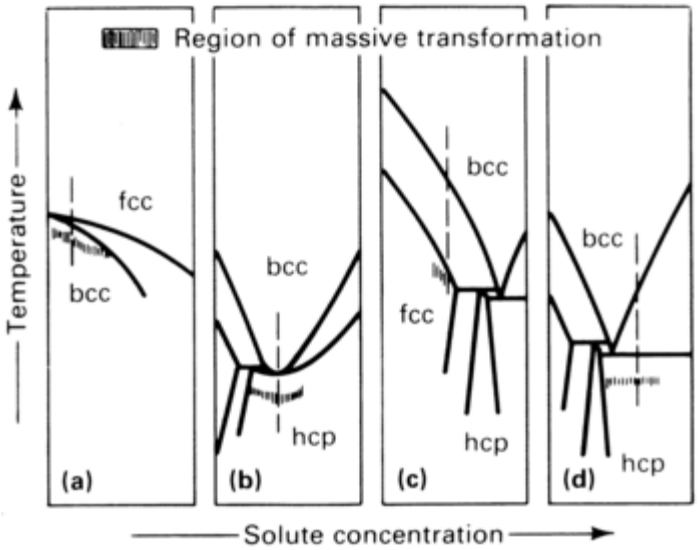

Fig. 3 Schematic phase diagrams for (a) pure metal and (b to d) three types of alloys that may undergo massive transformations. Critical compositions are indicated by the dashed vertical lines. bcc, body-centered cubic; fcc, face-centered cubic; hcp, hexagonal close-packed. Source Ref 2

References cited in this section

2. T.B. Massalski, Massive Transformation Structures, *Metallography and Microstructures,* Vol 9, *Metals Handbook,* 9th ed., American Society for Metals, 1985, p 655–657

3. W.S. Owen and E.A. Wilson, *Physical Properties of Martensite and Bainite,* Vol 93, Iron and Steel Institute, 1965, p 53

4. T.B. Massalski, Massive Transformations, *Phase Transformations,* American Society for Metals, 1970, p 433–486

M.J. Perricone, Massive Transformation Structures, *Metallography and Microstructures,* Vol 9, *ASM Handbook,* ASM International, 2004, p. 148–151

Massive Transformation Structures

M.J. Perricone, Lehigh University

Two-Phase Regions

Most massive transformations are the result of the decomposition of a high-temperature phase that has been quenched into a two-phase region of a phase diagram, as illustrated in Fig. 3(b) and (c) (e.g., β-brass) (Ref 2). However, a number of competing transformation mechanisms may occur on cooling into the two-phase region, for example, growth of equilibrium phase from parent-phase grain boundaries in the Widmanstätten morphology, equilibrium decomposition into two separate phases via precipitation, bainite transformation, and martensite transformation that occurs at very high quench rates at lower temperatures. Consequently, the partial transformation of the parent phase via these competing mechanisms is entirely possible and, in many cases, likely. In some materials, partial massive α transformation of the parent β phase may result in the retention of the high-temperature β phase at lower temperatures, as shown in Fig. 4 for a copper-zinc alloy (Ref 4).

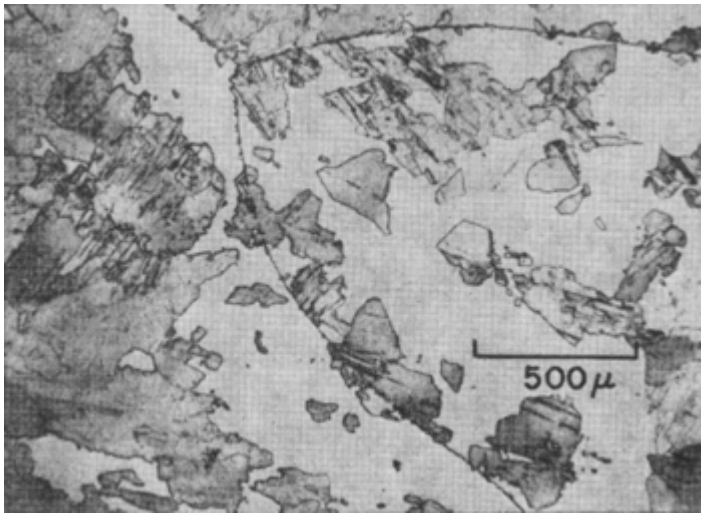

Fig. 4 Microstructure of a partially transformed Cu-37.8 at.% Zn alloy. The massive ζ phase can be seen both at the parent grain boundaries and inside the β grains. Source: Ref 4

References cited in this section

2. T.B. Massalski, Massive Transformation Structures, *Metallography and Microstructures,* Vol 9, *Metals Handbook,* 9th ed., American Society for Metals, 1985, p 655–657

4. T.B. Massalski, Massive Transformations, *Phase Transformations,* American Society for Metals, 1970, p 433–486

M.J. Perricone, Massive Transformation Structures, *Metallography and Microstructures,* Vol 9, *ASM Handbook*, ASM International, 2004, p. 148–151

Massive Transformation Structures

M.J. Perricone, Lehigh University

Nucleation and Growth Kinetics

In order for the massive transformation to occur, the material must be quenched below a critical temperature, known as T_0 and defined as the temperature at which the free energy of the product phase (to be formed massively) is equal to that of the parent phase for a given composition. The locus of such temperatures can be found as a function of composition in the two-phase regions of binary phase diagrams. Yet, while the thermodynamics of the massive transformations only require quenching to a temperature below T_0, in practice, most alloys require quenching into the single-phase region before the driving force required for massive nucleation is achieved. However, a critical limit below T_0 has recently been proposed (Ref 5) for iron-nickel in the α + γ region of the system, as shown in Fig. 5, illustrating the presence of a critical driving force required for massive transformation.

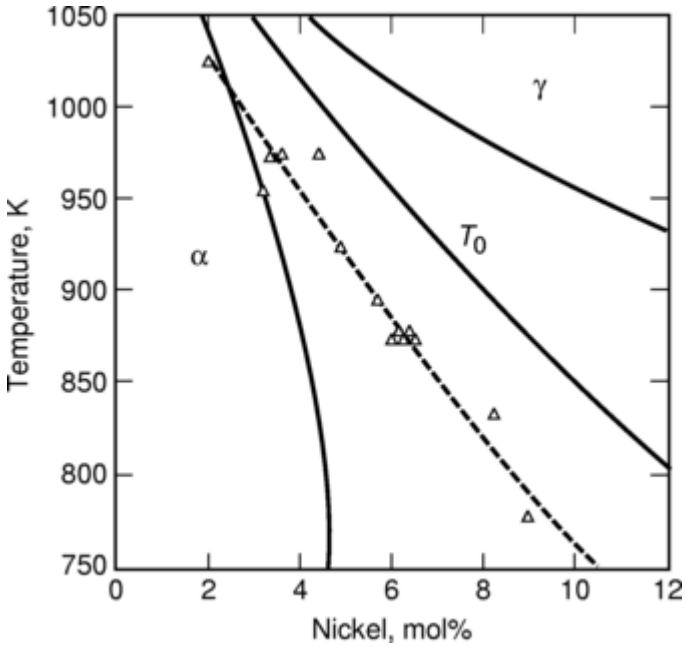

Fig. 5 Limit of massive growth of ferrite in the iron-nickel system according to experimental data (triangles and dashed line), compared with calculated phase boundaries and the T_0 line, which is the locus of points where the Gibbs free energy of α equals γ. Source: Ref 5

It is generally accepted that the nucleation process controls the rate of the massive transformation (Ref 6); once nucleation begins, the transformation moves to completion very quickly at rates ranging anywhere from 0.1 to 20 mm/s (0.004 to 0.8 in./s). The parent-phase grain boundaries serve as preferable nucleation sites, where nucleated massive grains have an orientation relationship with one parent grain (making this coherent interface relatively immobile) and grow into the neighboring one, with which no orientation relationship exists. Massive growth therefore occurs by the displacement of the mobile incoherent massive/parent-phase boundary, which is unimpeded by the presence of parent-phase grain boundaries, shown in Fig. 6 for the γ-to-α reaction in an iron-copper alloy (Ref 7). This observed phenomenon reemphasizes the lack of a simple orientation relationship at the moving interface between the massive and parent phases during transformation. As such, the resulting morphology may share qualitative similarities to a just-recrystallized microstructure.

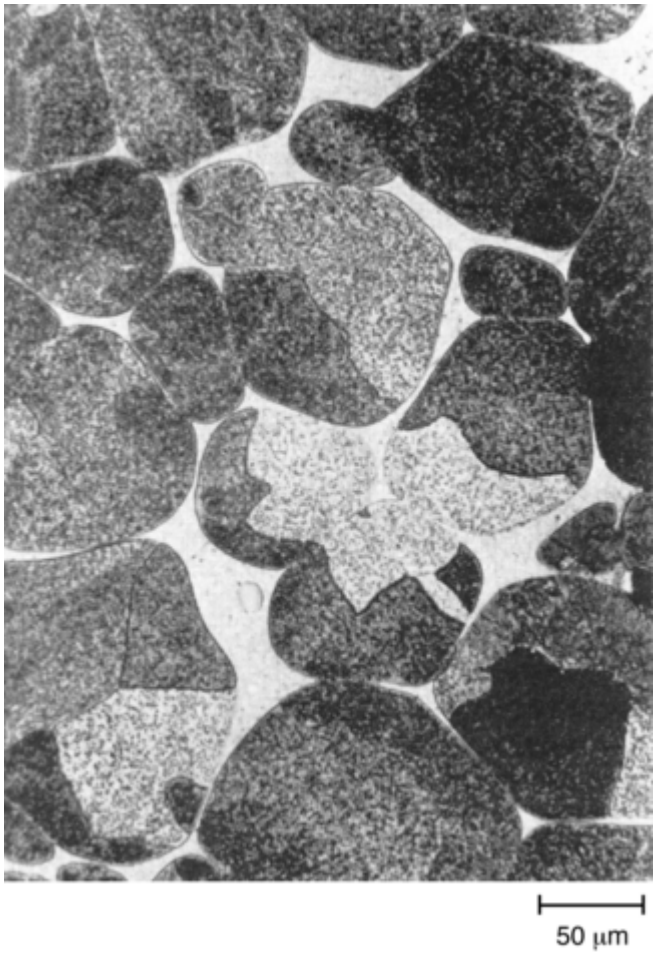

Fig. 6 Microstructure of Fe-20 wt% Cu alloy sintered at 1150 °C (2100 °F) for 12 h and then isothermally held for 48 h at 810 °C (1490 °F) before being cooled to room temperature. The light phase is the massively transformed phase. Note the growth across parent grain boundaries. Reprinted with permission from Ref 7

References cited in this section

5. A. Borgenstam and M. Hillert, Massive Transformation in the Fe-Ni System, *Acta Mater.,* Vol 48, 2000, p 2765–2775

6. M.R. Plichta, W.A.T. Clark, and H.I. Aaronson, The Nucleation Kinetics, Crystallography, and Mechanism of the Massive Transformation, *Metall. Trans. A,* Vol 15, 1984, p 427–435

7. N.M. Hwang and D.Y. Yoon, Massive Transformation in an Fe-Cu Alloy, *J. Mater. Sci.,* Vol 32, 1997, p 4847–4855

M.J. Perricone, Massive Transformation Structures, *Metallography and Microstructures,* Vol 9, *ASM Handbook,* ASM International, 2004, p. 148–151

Massive Transformation Structures

M.J. Perricone, Lehigh University

Feathery Structures

Another unique massive morphology results from duplex massive $\beta \rightarrow \alpha_m/\zeta_m$ transformations common in copper-gallium and silver-cadmium alloys. The feathery structure depicted in Fig. 7(a) for copper-gallium is the result of the formation of duplex fcc/hexagonal close-packed (hcp) massive grains, each of which is associated with a twin on the hcp {1011} family of planes. This transformation product morphology consists of the growth of alternating slabs of massive fcc and hcp parallel to their respective basal plane, with varying thickness and length, oriented on either side of the twin (Fig. 7b) (Ref 8). While not a lamellar structure in the conventional sense that is used to describe eutectic morphologies (e.g., pearlite in iron-carbon), the presence of extensive slip during transformation and the thin alternating layers of fcc and hcp phases causes surface striations that can be observed on a polished surface on etching. The low dislocation density in this massive feathery structure (Fig. 7c) further eliminates the presence of any shear component during this transformation, because dense clusters of tangled dislocations would be observed in the case of martensite.

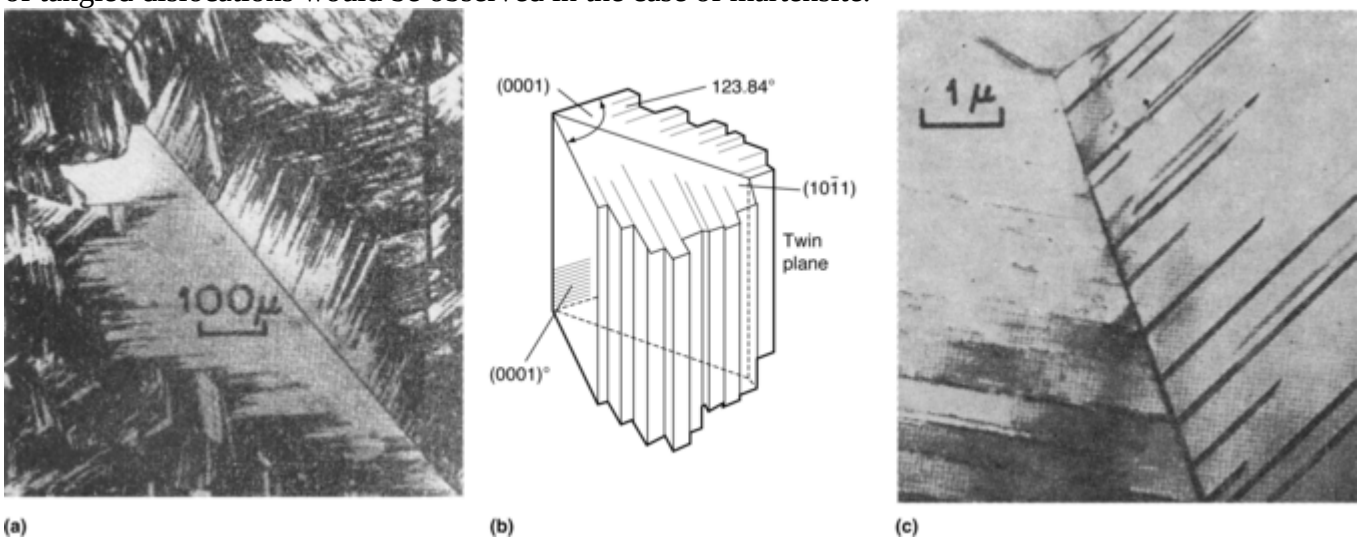

Fig. 7 Examples of feathery morphology. (a) A typical micrograph of a feathered unit showing the long {1011} midrib of twin and serrated boundaries. (b) Schematic drawing of feathered structure in three dimensions. (c) Electron transmission micrograph of a portion on the {P1011} twin plane showing massive α lamellae. Reprinted with permission from Ref 8

Reference cited in this section

8. G.A. Sargent, L. Delaey, and T.B. Massalski, *Acta Metall.,* Vol 16, 1968, p 723

M.J. Perricone, Massive Transformation Structures, *Metallography and Microstructures,* Vol 9, *ASM Handbook,* ASM International, 2004, p. 148–151

Massive Transformation Structures

M.J. Perricone, Lehigh University

Single-Crystal Growth

The large driving force required for the formation of a massive nucleus allows massive growth to continue unabated across parent grain boundaries. If controlled by the movement of a temperature gradient through the specimen, this phenomenon can be used to grow single crystals by controlling the growth of a single massive grain such that it consumes all of the prior-parent grains. Figure 8 depicts the development of a single crystal produced by the growth of a massive grain in a silver-aluminum alloy (Ref 9).

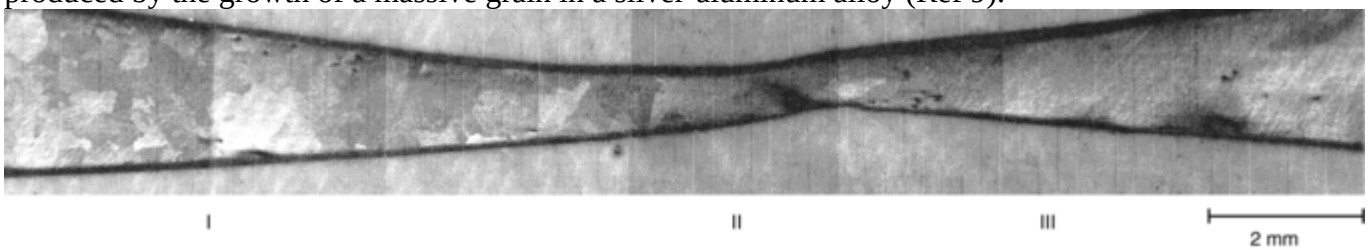

Fig. 8 Partial single crystal (region III) of a Ag-24.5 at.% Al alloy produced during the controlled β → massive ζ under directional cooling from polycrystalline region I. The constricted region of the specimen (region II) allowed for the selection of a single massive ζ grain to grow and consume the remaining parent phase in region III. Source: Ref 2, 9

References cited in this section

2. T.B. Massalski, Massive Transformation Structures, *Metallography and Microstructures,* Vol 9, *Metals Handbook,* 9th ed., American Society for Metals, 1985, p 655–657

9. J.H. Perepezko, Growth Kinetics and Mechanism of the Massive Transformation, *Metall. Trans. A,* Vol 15, 1984, p 437–447

M.J. Perricone, Massive Transformation Structures, *Metallography and Microstructures,* Vol 9, *ASM Handbook,* ASM International, 2004, p. 148–151

Massive Transformation Structures

M.J. Perricone, Lehigh University

Recent Developments

While detailed crystallographic orientation relationship studies and theoretical calculations strongly suggest that some form of rational orientation relationship is required at the nucleation stage of the massive reaction to reduce the activation energy, the existence of an orientation relationship between parent and product phases at the advancing interface continues to be a source of technical contention. A recent symposium convened on the mechanism of the massive transformation, sponsored by TMS/ASM International, re-examined this issue and highlighted many of the research efforts to understand the exact nature of the massive transformation. The interfacial structure of the advancing transformation front continues to garner a great deal of attention, as does

the critical limit at which the massive transformation can proceed without interference from competing mechanisms. For example, a critical transformation velocity (Ref 10) has been identified for iron-nickel and iron-chromium, below which massive transformations cannot occur. Figure 9 tracks the transition from coarse cellular to fine cellular to massive growth with increasing solid-state transformation velocity. Identification of massive transformations that occur in technologically significant materials (Fig. 10) continues to be a source of technical interest as well (Ref 11).

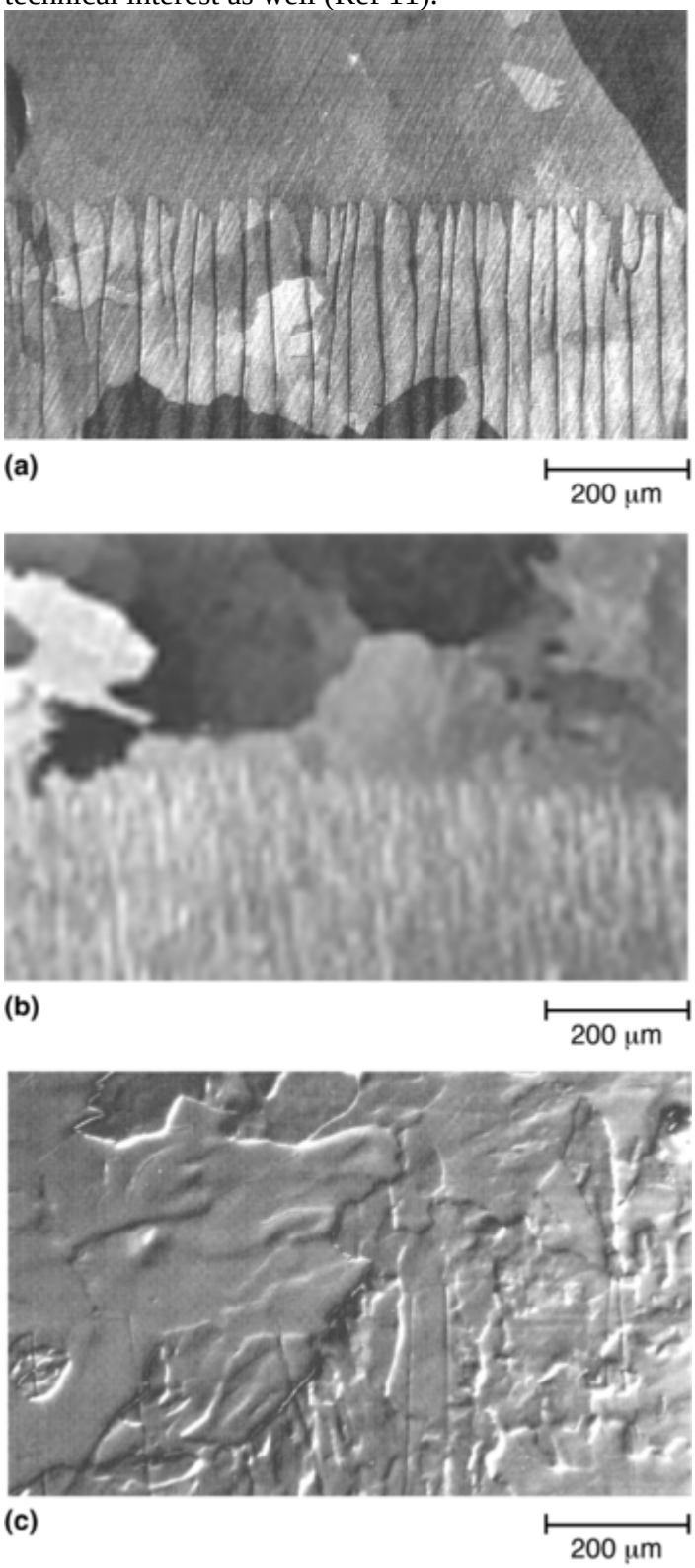

Fig. 9 Ferrite-(body-centered cubic)-to-austenite-(face-centered cubic) transformation in Fe-3.1 wt% Ni with (a) coarse cellular growth at 5 μm/s, (b) fine cellular growth at 15 μm/s, and (c) massive growth at 30 μm/s. Source: Ref 10

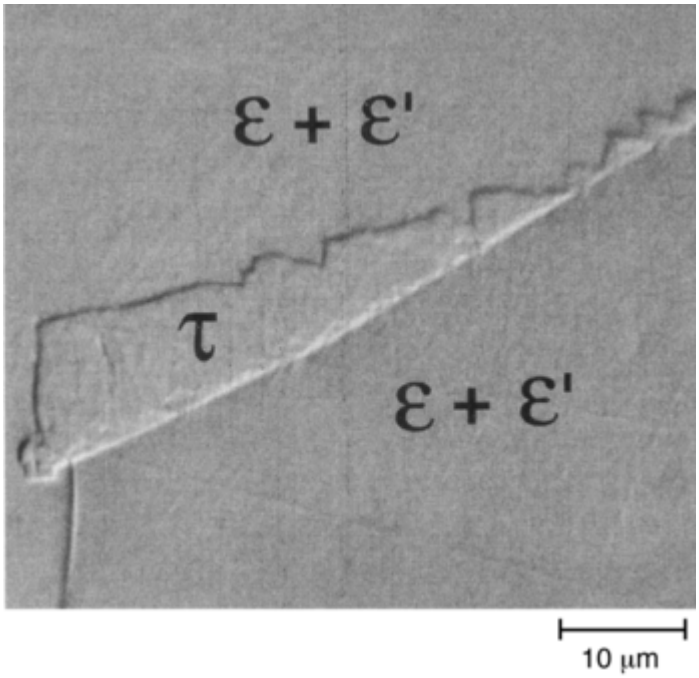

Fig. 10 Optical micrograph of a Mn-Al-C alloy showing the massive formation of the magnetic τ-MnAl phase at grain boundaries of the parent phase. Source: Ref 11

References cited in this section

10. M. Lima and W. Kurz, Massive Transformation and Absolute Stability, *Metall. Mater. Trans. A,* Vol 33, 2002, p 2337–2345

11. C. Yanar, J.M.K. Wiezorek, V. Radmilovic, and W.A. Soffa, Massive Transformation and the Formation of the Ferromagnetic L10 Phase in Manganese-Aluminum-Based Alloys, *Metall. Mater. Trans. A,* Vol 33, 2002, p 2413–2423

M.J. Perricone, Massive Transformation Structures, *Metallography and Microstructures,* Vol 9, *ASM Handbook,* ASM International, 2004, p. 148–151

Massive Transformation Structures

M.J. Perricone, Lehigh University

References

1. T.B. Massalski, Distinguishing Features of Massive Transformations, *Metall. Trans. A,* Vol 15, 1984, p 421–425

2. T.B. Massalski, Massive Transformation Structures, *Metallography and Microstructures,* Vol 9, *Metals Handbook,* 9th ed., American Society for Metals, 1985, p 655–657

3. W.S. Owen and E.A. Wilson, *Physical Properties of Martensite and Bainite,* Vol 93, Iron and Steel Institute, 1965, p 53

4. T.B. Massalski, Massive Transformations, *Phase Transformations,* American Society for Metals, 1970, p 433–486

5. A. Borgenstam and M. Hillert, Massive Transformation in the Fe-Ni System, *Acta Mater.,* Vol 48, 2000, p 2765–2775

6. M.R. Plichta, W.A.T. Clark, and H.I. Aaronson, The Nucleation Kinetics, Crystallography, and Mechanism of the Massive Transformation, *Metall. Trans. A,* Vol 15, 1984, p 427–435

7. N.M. Hwang and D.Y. Yoon, Massive Transformation in an Fe-Cu Alloy, *J. Mater. Sci.,* Vol 32, 1997, p 4847–4855

8. G.A. Sargent, L. Delaey, and T.B. Massalski, *Acta Metall.,* Vol 16, 1968, p 723

9. J.H. Perepezko, Growth Kinetics and Mechanism of the Massive Transformation, *Metall. Trans. A,* Vol 15, 1984, p 437–447

10. M. Lima and W. Kurz, Massive Transformation and Absolute Stability, *Metall. Mater. Trans. A,* Vol 33, 2002, p 2337–2345

11. C. Yanar, J.M.K. Wiezorek, V. Radmilovic, and W.A. Soffa, Massive Transformation and the Formation of the Ferromagnetic L10 Phase in Manganese-Aluminum-Based Alloys, *Metall. Mater. Trans. A,* Vol 33, 2002, p 2413–2423

Invariant Transformation Structures, *Metallography and Microstructures,* Vol 9, *ASM Handbook,* ASM International, 2004, p. 152–164

Invariant Transformation Structures

Introduction

INVARIANT TRANSFORMATIONS are isothermal reversible reactions that occur at an invariant point on the phase diagram of an alloy, where the initial (parent) phase may be either a liquid or a crystalline solid. When the parent phase is liquid, invariant transformations are classified as follows:

- *Eutectic transformation* (Fig. 1a): An isothermal reversible reaction when a liquid solution of two or more elements is converted into two or more intimately mixed solids upon cooling. The number of solids formed equals the number of components in the system.
- *Peritectic transformation* (Fig. 1b): An isothermal reversible reaction when a liquid phase reacts with a solid phase to produce another solid phase
- *Monotectic transformation* (Fig. 1c): An isothermal reversible reaction when a binary-alloy liquid phase decomposes into a second liquid and a solid. A monotectic reaction differs from a eutectic reaction in that only one of the two products of the reaction is below the freezing range.

These three invariant transformations from a liquid state are described in more detail in the article “Fundamentals of Solidification” in this Volume.

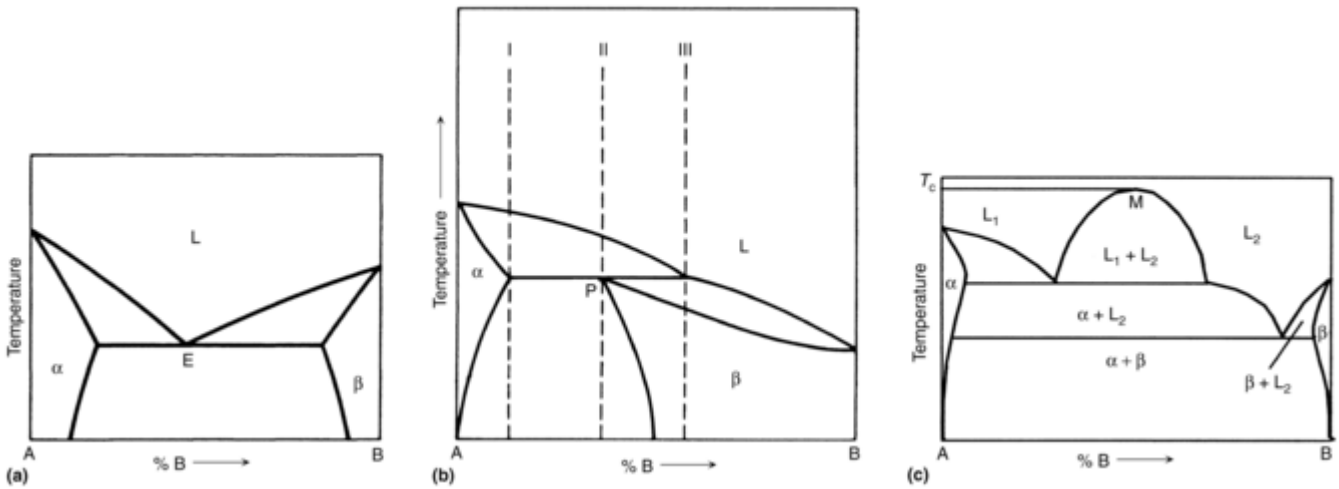

Fig. 1 Schematic binary phase diagrams of solidification from liquid (L) to solid solutions (α or β). (a) With eutectic reaction with invariant point, *E*. (b) With peritectic reaction with invariant point, *P*, where alloys between II and III first solidify to α crystals and then transform to stable β crystals. Alloys between I and II also solidify to α crystals, but they are partially transformed to β crystals later. (c) With monotectic reaction at invariant point, *M*, where liquid 1 (L_1) transforms to another liquid (L_2) and solid solution (α)

Invariant transformations may also occur from a solid-state parent phase. Solid-state invariant reactions are a category of heterogeneous phase transformations that involve moving reaction boundaries and phase separation. Invariant transformations differ from precipitation reactions in that all reaction products from an invariant transformation have a different crystal structure than that of the parent phase. In contrast, solid-state transformation from a discontinuous precipitation (Ref 1) involves the generation of new second phase within a matrix that has the same crystal structure as the parent phase (see also the article "Structures by Precipitation from Solid Solution" in this Volume).

As in the case of invariant reactions during solidification, solid-state transformations from invariant reactions are of three types:

- *Eutectoid transformation,* where a solid solution converts into two or more intimately mixed solids with different crystal structures than that of the parent phase. The number of solid phases formed equals the number of components in the system.
- *Peritectoid transformation,* where two solid phases of a binary alloy transforms into one phase ($\alpha + \beta \rightarrow \gamma$) upon cooling. Peritectoid reactions are similar to peritectic reactions, except that one of the initial phases is liquid in a peritectic reaction. As in all invariant reactions, peritectoid reactions are reversible; that is, the $\alpha + \beta$ are recovered upon heating the reaction product, γ.
- *Monotectoid transformations,* where cooling or heating of a solid solution completely converts it into a solid solution with a different crystal structure (Fig. 2). A monotectoid reaction differs from a eutectoid reaction in that only one reaction phase is produced.

Structures from monotectoid reactions are not discussed further in this article, as the reaction is not prevalent in commercial alloys, and because the microstructural features from monotectoid reactions are not as varied or complex as those from eutectoid or peritectoid decomposition. This article focuses primarily on structures from eutectoid transformations with emphasis on the classic iron-carbon system of steel. The classic Fe-C eutectoid of carbon steel is also described in more detail in the article "Physical Metallurgy Concepts in Interpretation of Microstructures" in this Volume.

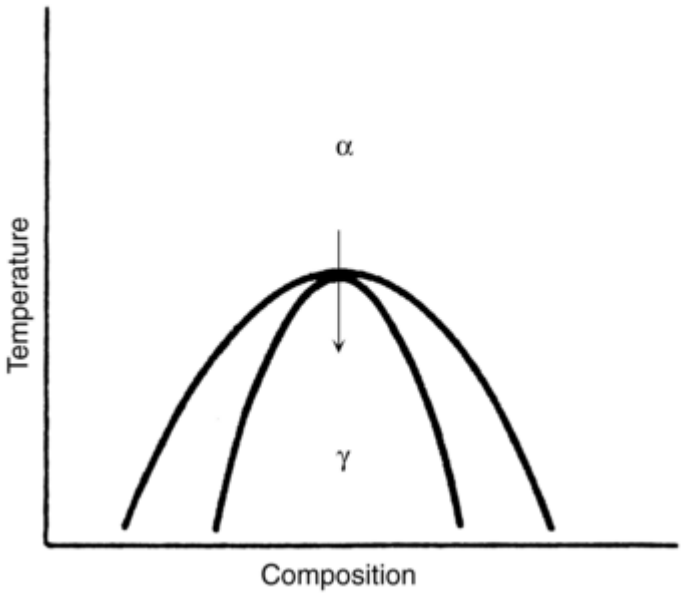

Fig. 2 Schematic phase diagram of a monotectoid reaction.

Peritectic and peritectoid phase equilibria also are very common in several binary systems. However, structures from peritectoid reactions are not as widely addressed as those of peritectic reactions. Therefore, this article only briefly reviews structures from peritectoid reactions. More emphasis is placed on peritectic reactions, which are important in the formation of solidification structures. Even though peritectic reactions involve a liquid phase, there is a solid-state reaction that occurs in the presence of the liquid phase. In this general sense, peritectic reactions are partially a solid-state reaction, where a liquid phase reacts with at least one solid phase to form one new solid phase. Thus, the term peritectic in the general context of heterogeneous equilibria may refer to all reactions in which two or more phases (gas, liquid, solid) react at a defined temperature, T_p, to form a new phase that is stable below T_p (Ref 2).

References cited in this section

1. I. Manna, S.K. Pabi, J.M. Manero, and W. Gust, Discontinuous Reactions in Solids, *Int. Mater. Rev.*, Vol 46 (No. 2), 2001, p 53–91

2. H.E. Exner and G. Petzow, Peritectic Structures, *Metallography and Microstructure,* Vol 9, *ASM Handbook,* American Society for Metals, 1985, p 675–680

Invariant Transformation Structures, *Metallography and Microstructures,* Vol 9, *ASM Handbook*, ASM International, 2004, p. 152–164

Eutectoid Structures

Brian Newbury, Lehigh University

The eutectoid reaction is defined as a single parent phase decomposing into two different product phases via a diffusional mechanism. The most famous eutectoid reaction is that in the iron-carbon system, the lamellar pearlite microstructure as seen in Fig. 3. In this structure the parent phase, austenite, decomposes into

alternating layers of ferrite and cementite. It should be noted that pearlite is not the only morphology of eutectoid decomposition, as seen in the time-temperature-transformation (TTT) diagram illustrated in Fig. 4. The upper C-curve represents pearlite formation, while the lower indicates bainite formation. There is also a region of mixed morphology where the two curves overlap in which both pearlite and bainite occur simultaneously. However, in this article only pearlite is discussed. It is important to stress that this reaction is not limited to the iron-carbon system, but examples are drawn from this system due to its industrial importance.

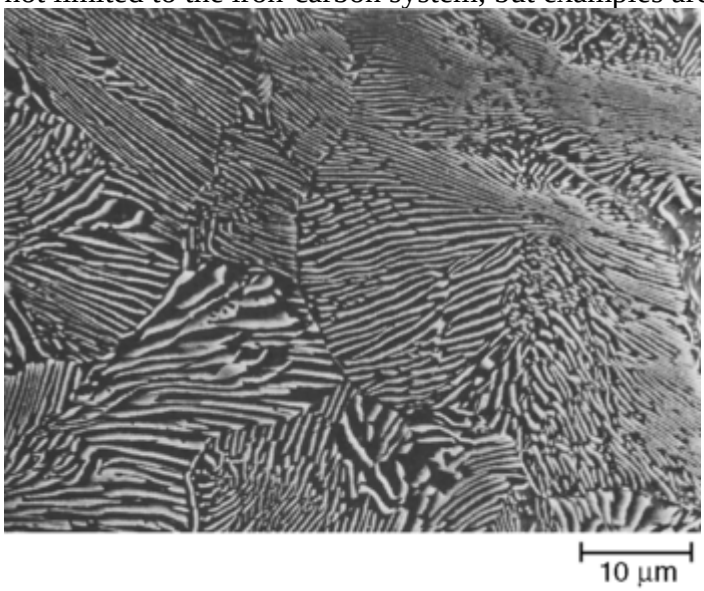

Fig. 3 Pearlite microstructure in crucible steel ingot. Source: Ref 3

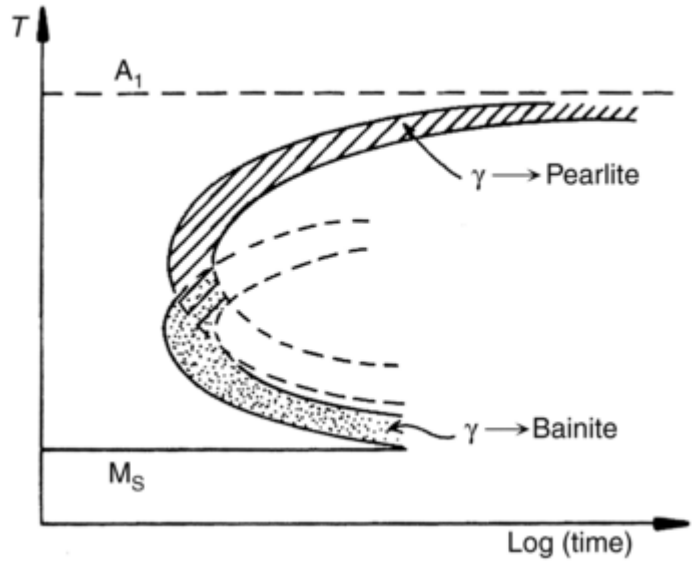

Fig. 4 Time-temperature-transformation diagram showing austenite decomposition into pearlite and bainite. Source: Ref 4, p 333

Figure 5 illustrates the morphology of a pearlite nodule. Pearlite nodules nucleate at prior austenite grain boundaries and triple points to minimize the free energy needed for the transformation. Each nodule contains subunits (colonies) of cementite and ferrite lamellae; each colony has a specific orientation relation with the parent austenite grain as is discussed later.

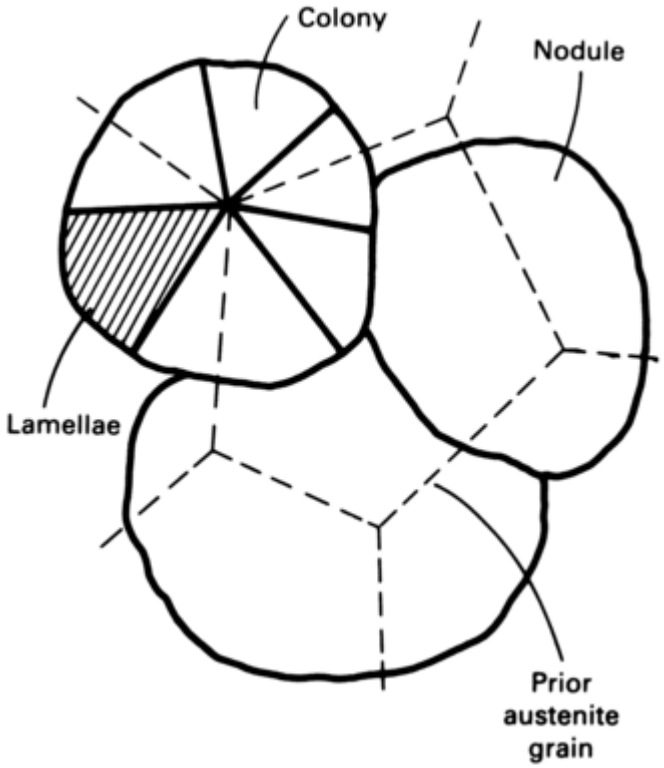

Fig. 5 Relationship of pearlite lamellae, colonies, and nodules to prior-austenite grains. Source: Ref 5

References cited in this section

3. .M.L. Wayman and G. Juleff, *Hist. Metall.,* Vol 33 (No. 1), 1999, p 26–42

4. .D.A. Porter and K.E. Easterling, *Phase Transformations in Metals and Alloys,* 2nd ed., Chapman and Hall, London, 1992

5. A.R. Marder, in *Phase Transformations in Ferrous Alloys,* A.R. Marder and J.I. Goldstein, Ed., TMS/AIME, 1984, p 201–236

Invariant Transformation Structures, *Metallography and Microstructures,* Vol 9, *ASM Handbook,* ASM International, 2004, p. 152–164

Pearlite Colony Orientation and Nucleation

Pearlite nucleation occurs when either ferrite or cementite nucleates on a heterogeneity in the parent structure: austenite (or parent phase) grain boundaries, triple points, and so forth. The selection of which phase nucleates is determined by the orientation and local composition (Ref 4, p 333). For the case of cementite, which is orthorhombic, the relationship between the newly formed cementite and the parent austenite is:

$$(100)_c \parallel (1\bar{1}1)_\gamma, (0\bar{1}0)_c \parallel (110)_\gamma, (001)_c \parallel (\bar{1}12)_\gamma$$

This creates a low-mobility semicoherent interface with the grain γ_1 (with which the orientation relation was developed) and a high-mobility incoherent interface with austenite grain γ_2 in Fig. 6(a). Thus, the newly formed pearlite colony grows by the high-mobility incoherent interface expanding into the austenite grain with which

the pearlite does not have an orientation relationship (Ref 4, p 329). The nucleation of this cementite creates a "carbon-free" region around it promoting the nucleation of ferrite on both sides of the cementite. The interface between the newly formed cementite and ferrite is semicoherent as well, which promotes lamellae lengthening through the higher-mobility incoherent interface between the lamellae and the parent austenite, rather than lamellae spacing coarsening. This causes the colony shape to become radial from the point of original nucleation as existing lamellae lengthen into the austenite and new lamellae nucleate at the edges (see Fig. 6b, 6c, and Fig. 7) (Ref 4, page 328–329). Figure 8 and Figure 9 illustrate this semicoherent interface in a commercial steel. Thus, the pearlite colony grows by the incoherent interface expanding into grain γ_2 as seen in Fig. 6(a) part (4). Shiflet has shown through high-resolution microscopy that this growth occurs by a ledge-growth mechanism, as shown in Fig. 10. This cooperative nucleation and growth is key to the development of the pearlite morphology (Ref 9). Zhou and Shiflet have shown this cooperative growth is dependent on both diffusion of carbon (as mentioned previously) as well as structural sharing of growth ledges between the cementite and ferrite as seen in Fig. 11.

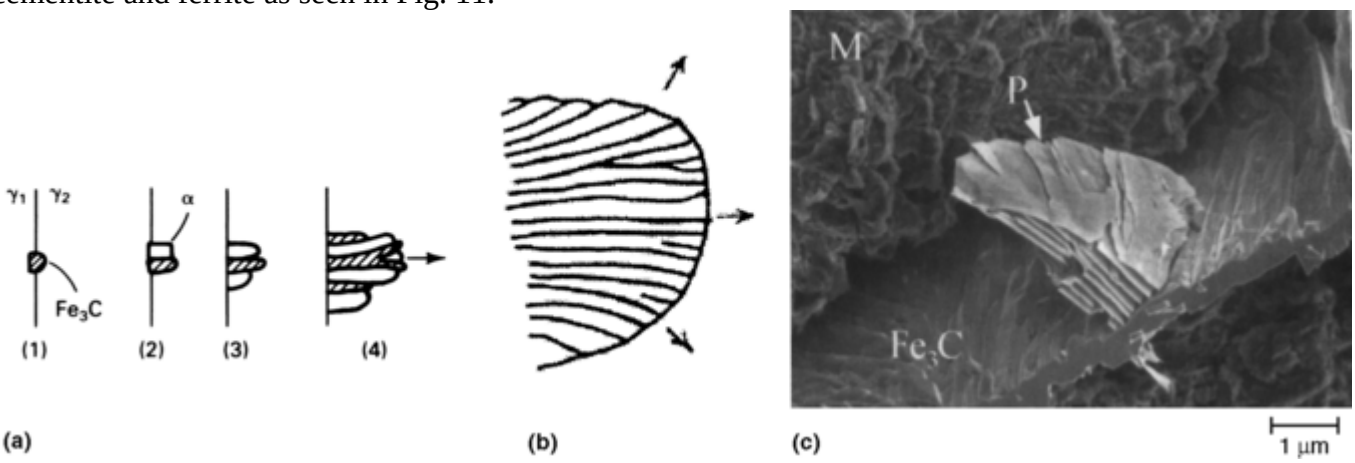

Fig. 6 (a) Pearlite nucleation. (b) Colony growth. (c) Deep-etched steel sample showing pearlite colony growth off of proeutectoid cementite plate. Source: (a) and (b) from Ref 4, p 331, (c) from Ref 6

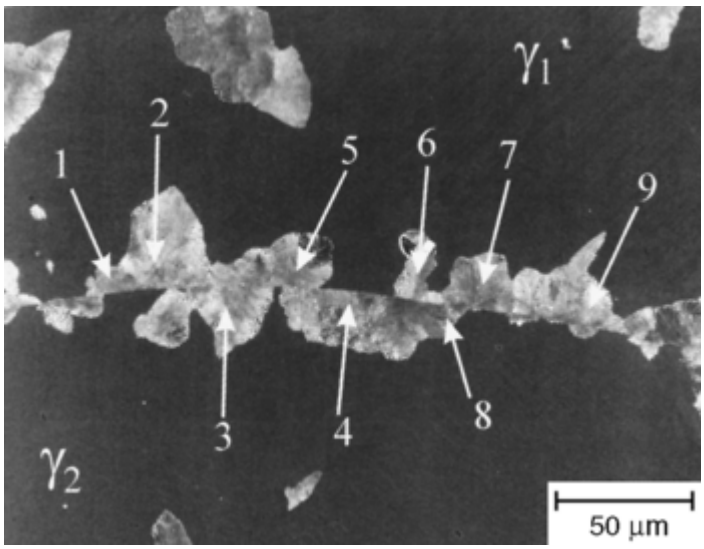

Fig. 7 Growth of intergranular pearlite nodules (numbered light regions) into the (dark) austenite matrix. Source: Ref 7. Reprinted with permission

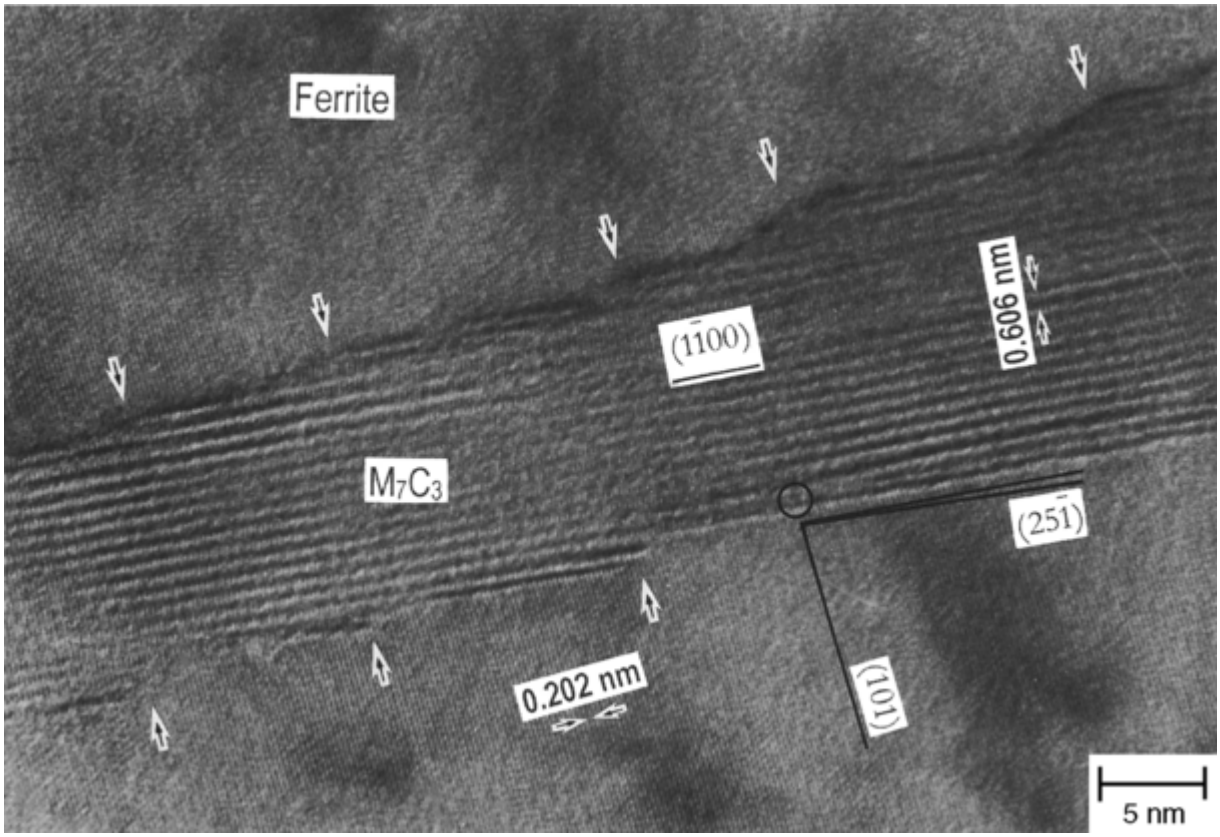

Fig. 8 High-resolution electron micrograph of two ferrite regions split by a carbon rich M_7C_3 lamellae in a Fe-8.2Cr-0.92C alloy. Source: Ref 8. Reprinted with permission

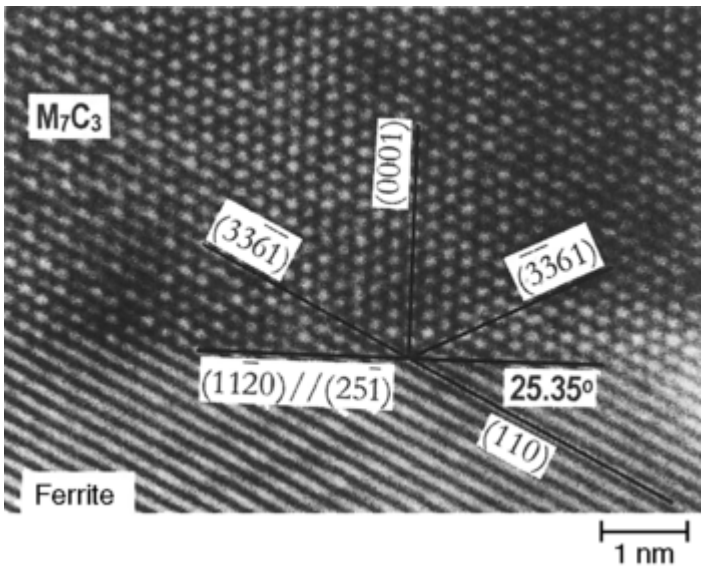

Fig. 9 Interface between M_7C_3 and ferrite seen in Fig. 6. The interface is semicoherent, pinning any movement. Source: Ref 8. Reprinted with permission

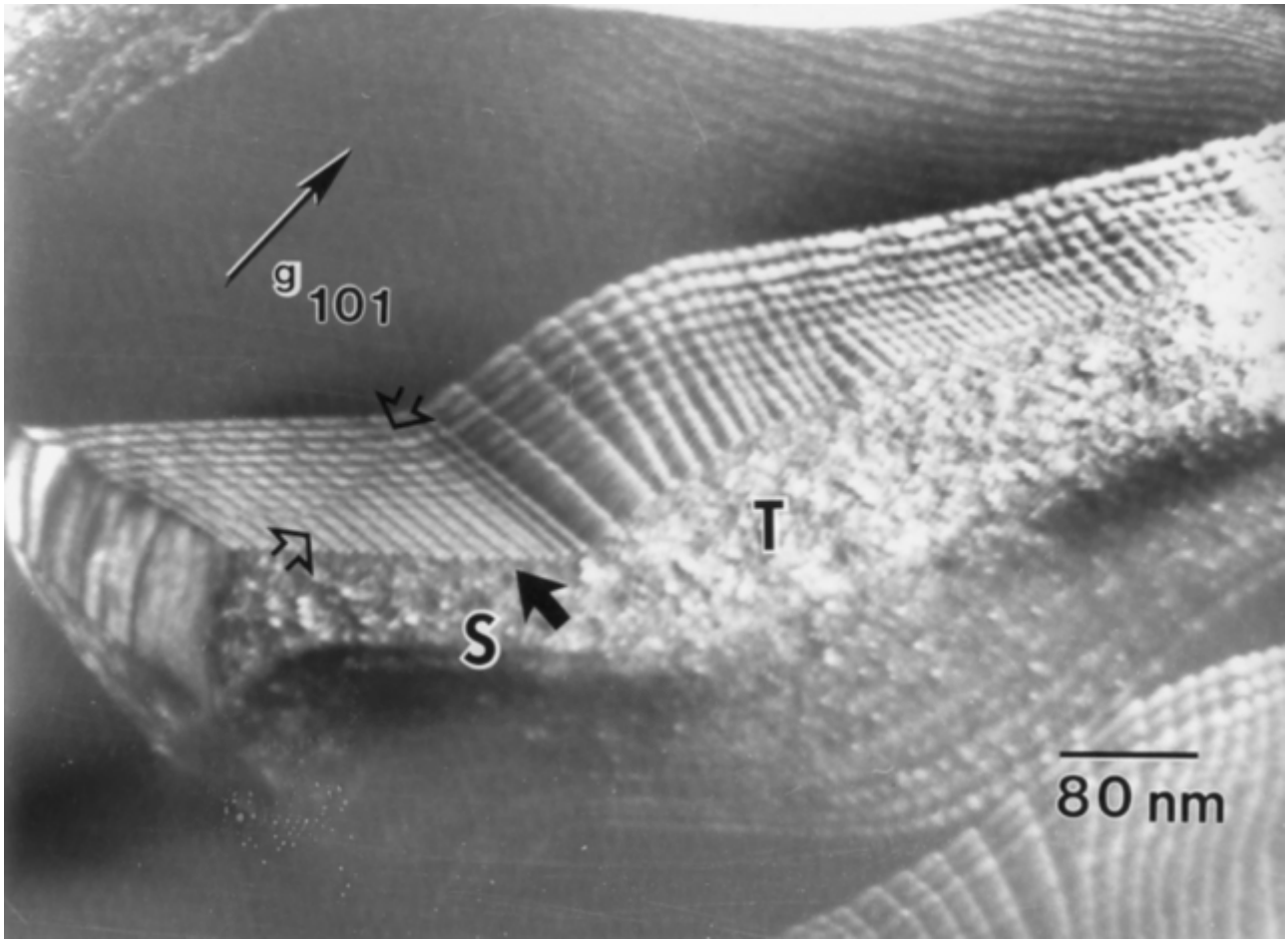

Fig. 10 Dark-field ferrite growth front illustrating ledge growth. Courtesy of G. Shiflet

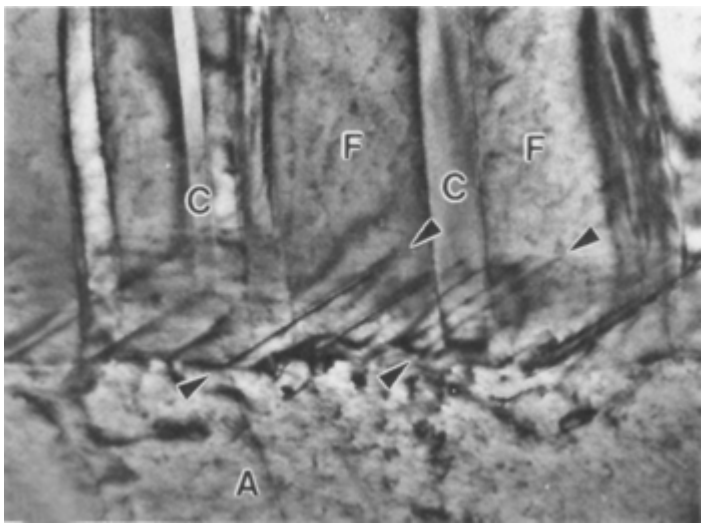

Fig. 11 Growth front of pearlite indicating that ledges span both cementite (C) and ferrite (F) as they grow into the austenite (A). Source: Ref 10

If the ferrite nucleates first, it forms an orientation relation with γ_1 that is close to the Kurdjumov-Sachs relation (Ref 9, p 592, Ref 11):

$$\{110\}_f \parallel \{111\}_\gamma \ \langle 1\bar{1}1\rangle_f \parallel \langle 1\bar{1}0\rangle_\gamma$$

Carbon is rejected into the austenite, promoting the nucleation of cementite. The pearlite colony grows into the austenite grain with which it does not have the orientation relationship (due to the relative ease of moving the high-energy incoherent interface).

References cited in this section

4. .D.A. Porter and K.E. Easterling, *Phase Transformations in Metals and Alloys,* 2nd ed., Chapman and Hall, London, 1992

6. M.A. Mangan and G.J. Shiflet, *Metall. Mater. Trans. A,* Vol 30A (No. 11), 1999, p 2767–2781

7. Z. Guo, T. Furuhara, and T. Maki, *Scr. Mater.,* Vol 45, 2001, p 525–532

8. D.V. Shtansky, K. Nakai, and Y. Ohmori, *Acta Mater.,* Vol 47 (No. 4), 1999, p 1105–1115

9. R.E. Reed-Hill and R. Abbaschian, *Physical Metallurgy Principles,* 3rd edition PWS-Kent Publishing Co., 1992 p 599

10. D.S. Zhou and G.J. Shiflet, *Metall. Trans. A,* Vol 22A (No. 6), 1991 p 1349–1365

11. J.M. Rigsbee and H.I. Aaronson, *Acta Metall.,* Vol 27, 1979, p 351–376

Invariant Transformation Structures, *Metallography and Microstructures,* Vol 9, *ASM Handbook,* ASM International, 2004, p. 152–164

Nucleation of Pearlite on Proeutectoid Ferrite or Cementite

Compositions below 0.77 wt% C in iron-carbon systems will nucleate proeutectoid ferrite before reaching the eutectoid temperature and formation of pearlite. This ferrite nucleates at the grain boundaries to reduce energy and follows the Kurdjumov-Sachs relationship stated previously. A pearlite colony will then grow from the proeutectoid ferrite once the eutectoid temperature has been reached.

For compositions above the eutectoid point, proeutectoid cementite nucleates at the grain boundaries. This tends to form as a layer with the Bagaryatski orientation relationship with the γ_1 austenite grain ($[100]_c \parallel [0\bar{1}1]_\gamma$, $[010]_c \parallel [1\bar{1}\bar{1}]_\gamma$, $(001)_c \parallel (211)_\gamma$) (Ref 12). A pearlite colony will then grow from the proeutectoid cementite once the eutectoid temperature has been reached, as seen in Fig. 12. In this case it is seen that pearlite nucleation is not limited predominantly to the grain boundaries as shown in Fig. 7.

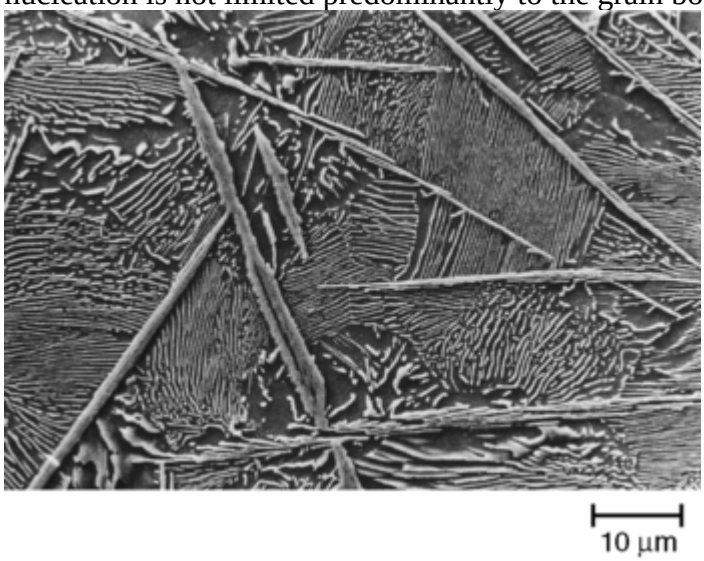

Fig. 12 Pearlitic microstructure with Widmanstätten cementite plates acting as nucleation sites. Source: Ref 10

Pearlite Lamellar Spacing. The lamellar spacing of the pearlite structure gives indication of the transformation temperature. As the transformation temperature decreases, the diffusivity of carbon in austenite decreases, which acts to limit the interlamellar spacing (Ref 13). Marder and Bramfitt have shown the variation of pearlite spacing versus transformation temperature for steel as seen in Fig. 13.

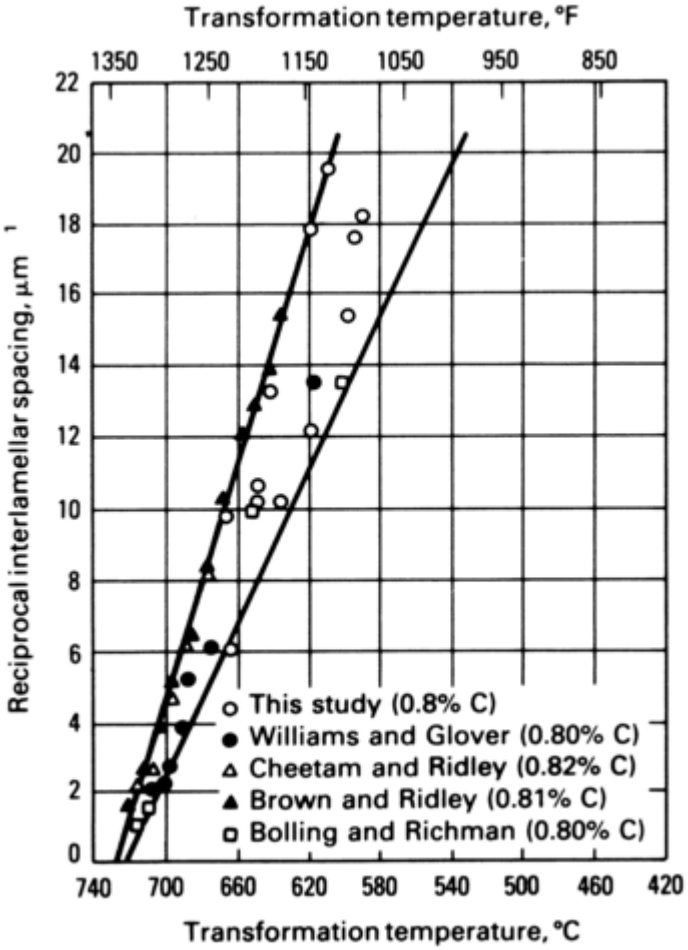

Fig. 13 Pearlite interlamellar spacing versus transformation temperature. Source: Ref 14

References cited in this section

10. D.S. Zhou and G.J. Shiflet, *Metall. Trans. A,* Vol 22A (No. 6), 1991 p 1349–1365

12. R.J. Dippenaar and R.W.K. Honeycombe, *Proc. R. Soc. (London) A,* Vol 333, 1973, p 455

13. C. Zener, *Trans. AIME,* Vol 167, 1946, p 550–595

14. A.R. Marder and B.L. Bramfitt, *Metall. Trans. A,* Vol 6, 1975, p 2009–2014

Pearlite Growth

The growth rate of pearlite is best represented by the Johnson-Mehl-Avrami equation:

$$f = 1 - \exp(-kt^n) \quad \text{(Eq 1)}$$

where f is fraction transformed, k accounts for the growth and nucleation rates, t is time, and n is the Avrami exponent (Ref 20). The exponent n varies from 1 to 4, where 1 represents a needle-shaped precipitate and 4 represents a spherical precipitate. The k factor can be rewritten as:

$$k = k_0 \exp\left[\frac{-Q}{RT}\right] \quad \text{(Eq 2)}$$

where k_0 is a constant, Q is the activation energy, R is the universal gas constant, and T is the temperature. Thus, it can be seen that the growth rate is very dependent on temperature, particle shape, and time. Figure 14 illustrates this with a TTT diagram showing the time for transformation at two different temperatures. It is seen that the fraction transformed curve is sigmoidal. The initial rate is slow due to relatively few nodules existing. The rate increases with the nucleation rate until nodule impingement, when the transformation rate slows to completion (Ref 4, p 288). Figure 14(a) shows the C-curve nature of the TTT diagram, which shows that transformation times are slow at both temperatures close to (small undercooling) and far from (large undercooling) the reaction temperature. This can be explained by the small amount of driving force for nucleation at small undercoolings and very slow diffusion rates at large undercoolings (Ref 4, p 290). The intermediate temperatures (approximately temperature T_2 in Fig. 14a), corresponding to the "nose" of the C curve, provide an optimal combination of nucleation driving force and diffusion rates for the fastest transformation rate.

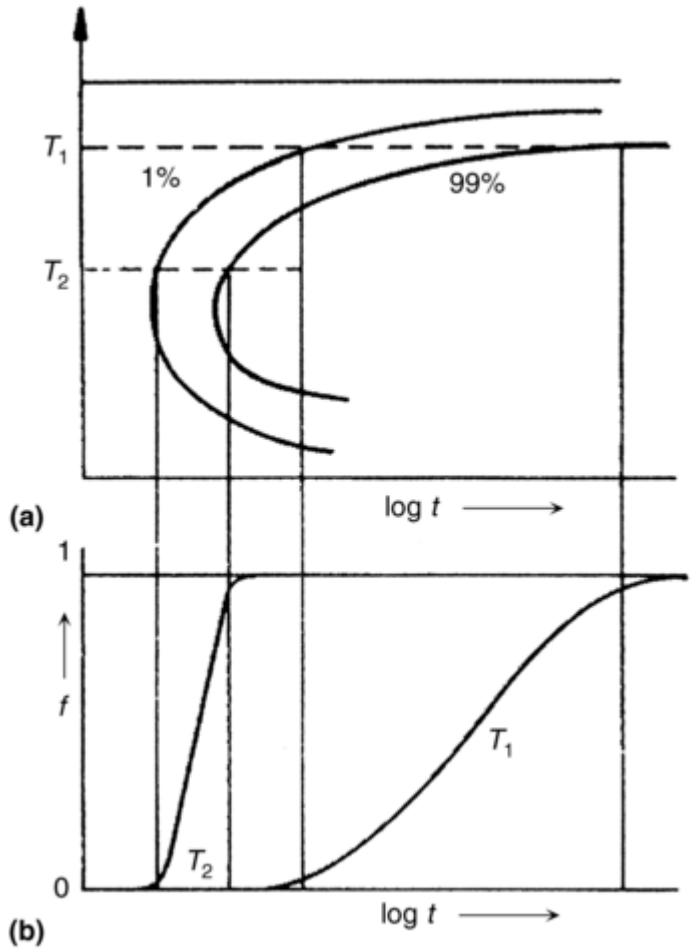

Fig. 14 (a) Time-temperature-transformation diagram indicating two temperatures for (b) indicating time required for transformation as a function of temperature. Source: Ref 4, p 288

References cited in this section

4. .D.A. Porter and K.E. Easterling, *Phase Transformations in Metals and Alloys,* 2nd ed., Chapman and Hall, London, 1992

20. F.A. Shunk, in *Constitution of Binary Alloys,* McGraw-Hill, 1969

Invariant Transformation Structures, *Metallography and Microstructures,* Vol 9, *ASM Handbook,* ASM International, 2004, p. 152–164

Alloy Effects

The addition of substitutional alloying elements causes the eutectoid composition and temperature to shift in the iron-carbon system. Figure 15 and 16 illustrate the effect of various substitutional alloy elements on the eutectoid transformation temperature and effective carbon content, respectively. Since the formation of pearlite is heavily dependent on long-range diffusion, the addition of these substitutional alloy elements will have a significant effect on the reaction kinetics as well. Addition of substitutional elements will decrease the diffusion rate and slow down the reaction kinetics, an effect known as partitioning and solute drag. Much like carbon, these substitutional alloying elements prefer to partition into either the ferrite or cementite lamellae of the pearlite. Since the rate of pearlite formation depends heavily on diffusion, the substitutional alloy elements control the rate of transformation due to substitutional diffusion being much slower than interstitial carbon diffusion. This effect is known as solute drag and can be seen by the shifting of the TTT diagram to the right, indicating increased time of reaction. Figure 17 shows the effect of alloying elements and their distribution in the pearlitic microstructure, while Fig. 18 portrays their effect on reaction time as evidenced by increasing reaction times in the TTT diagram.

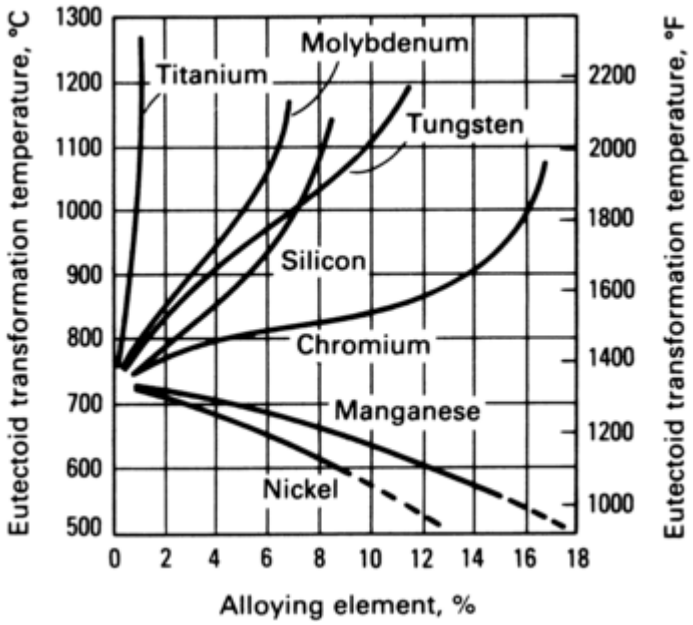

Fig. 15 Effect of alloying element on eutectoid temperature. Source: Ref 15

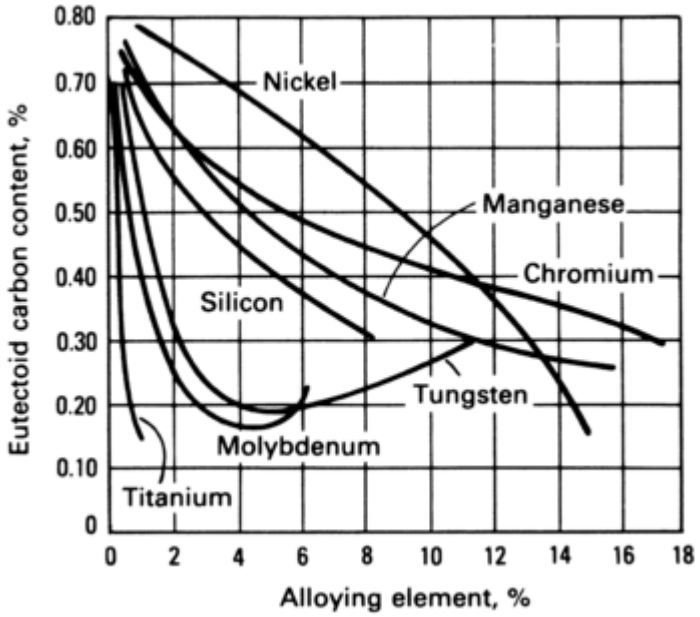

Fig. 16 Effect of alloying elements on effective carbon content. Source: Ref 15

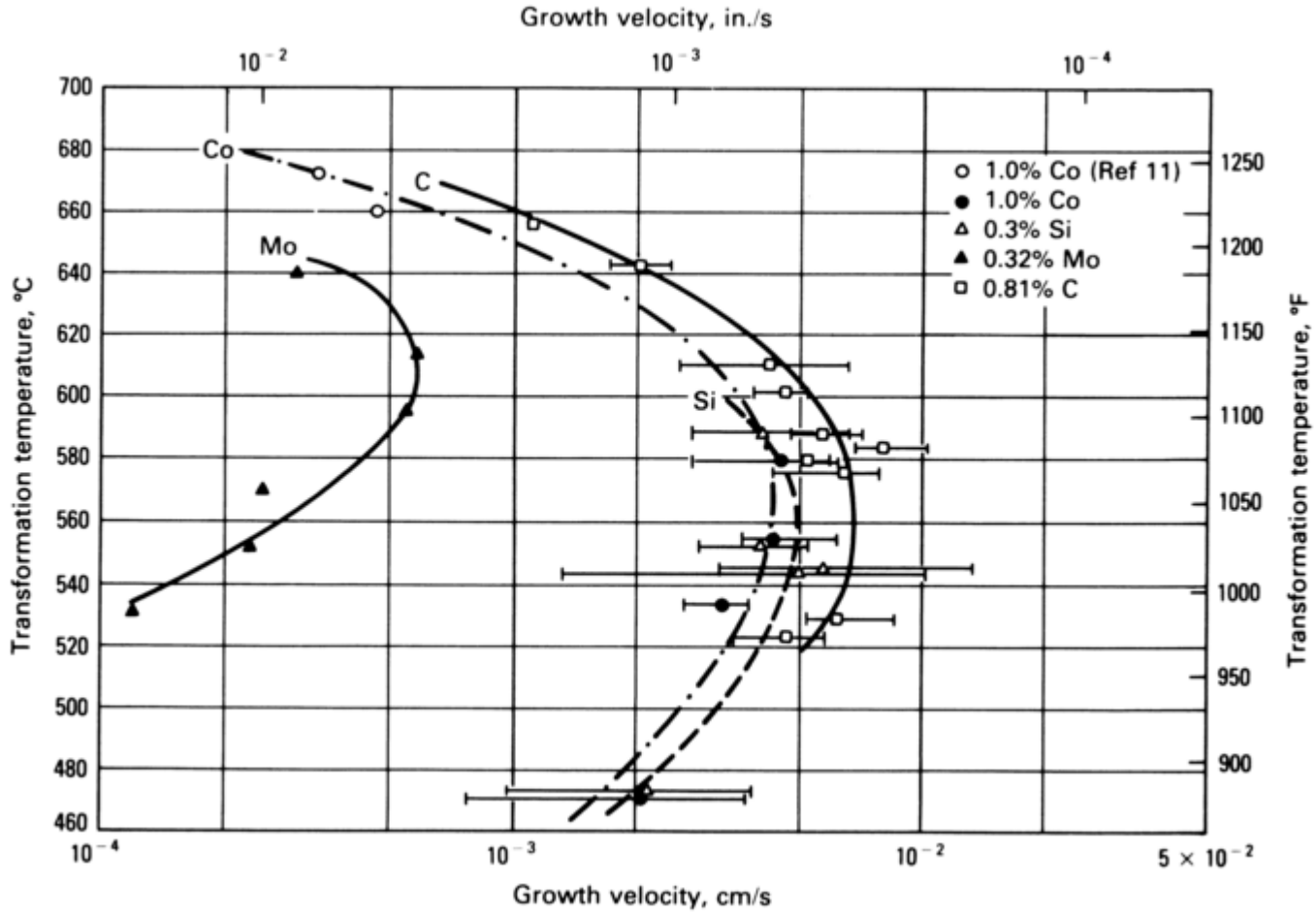

Fig. 17 The partitioning effect of substitutional alloying elements chromium, manganese, and silicon in pearlitic steel. Source: Ref 16

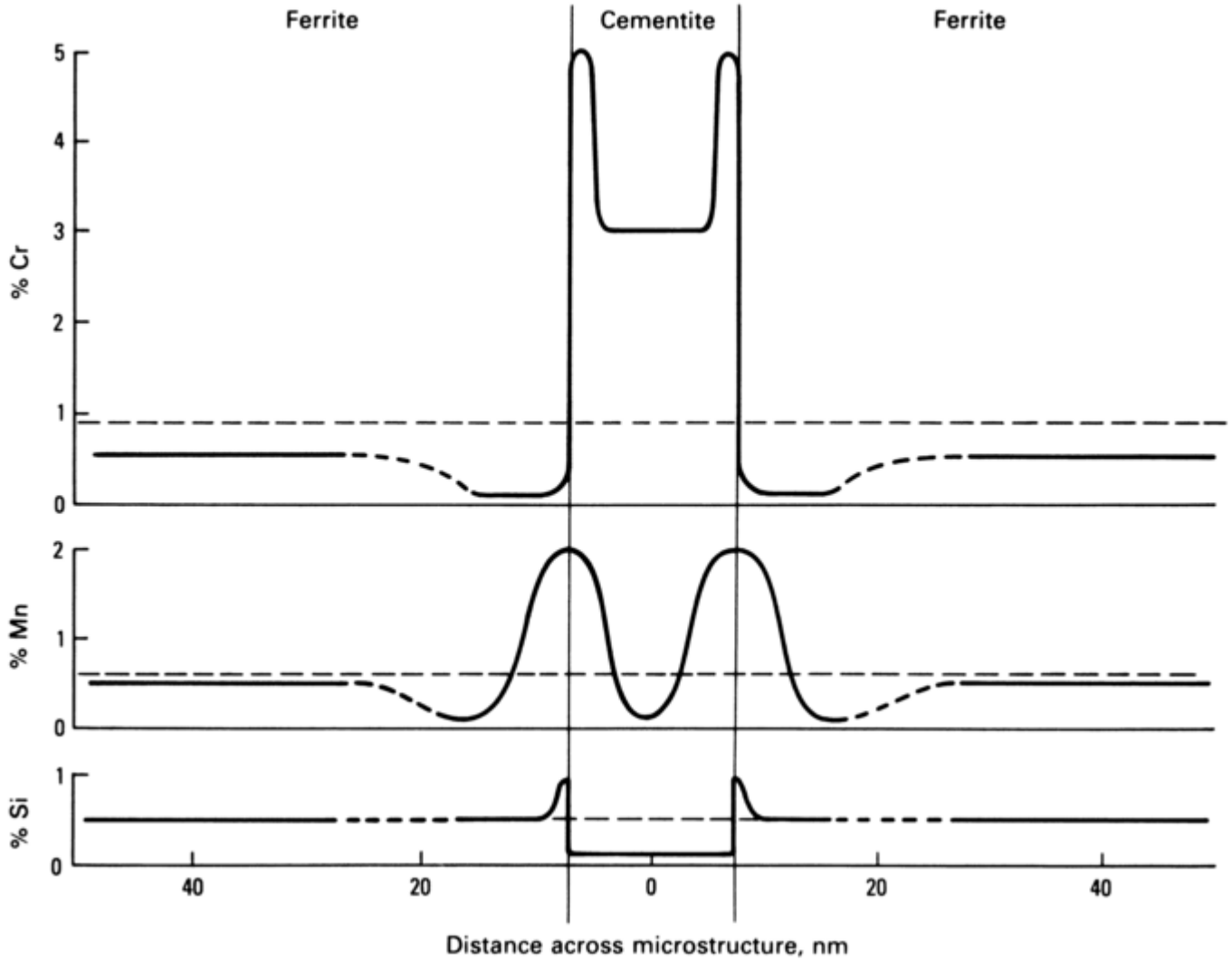

Fig. 18 Pearlite growth rate in Fe-C-X alloys as a function of temperature. Source: Ref 17

References cited in this section

15. E.C. Bain and H.W. Paxton, *Alloying Elements in Steel,* American Society for Metals, 1962, p 112

16. P.R. Williams, M.K. Miller, P.A. Beavan, and G.D.W. Smith, in *Phase Transformations,* Vol 2, The Institution of Metallurgists, London, 1979, p 11.98–11.100

17. A.R. Marder and B.L. Bramfitt, *Metall. Trans. A,* Vol 7, 1976, p 902–906

Invariant Transformation Structures, *Metallography and Microstructures,* Vol 9, *ASM Handbook,* ASM International, 2004, p. 152–164

Peritectic and Peritectoid Structures

As previously noted, the term peritectic in the science of heterogeneous equilibria may be used to define all reactions in which two or more phases (gas, liquid, solid) react at a defined temperature, T_p, to form a new phase that is stable below T_p. Usually, the term peritectic refers to reactions in which a liquid phase reacts with at least one solid phase to form one new solid phase. This reaction can be written as α + liquid → β. Furthermore, the term peritectoid denotes the special case of an equilibrium phase in which two or more solid phases (which are stable above the temperature T_p) react at T_p to form a new solid phase. This reaction can be written as α + β → γ. The phases formed during a peritectic or peritectoid reaction are a solid solution of one of the components, an allotropic phase of one of the components, or an intermetallic base. Schematics of peritectic phase diagrams are shown in Fig. 19.

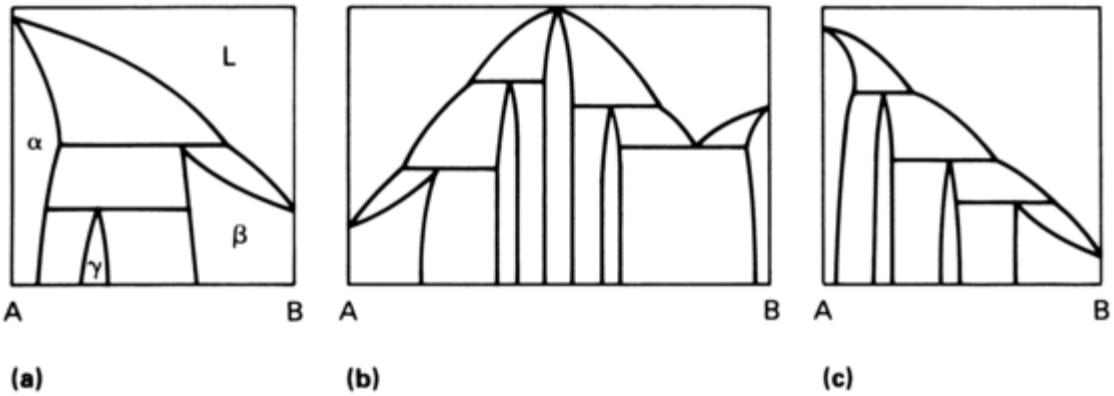

Fig. 19 Typical peritectic phase diagrams. (a) Peritectic reaction α + liquid → β and peritectoid reaction α + β → γ. (b) Peritectic formation of intermetallic phases from a high-melting intermetallic. (c) Peritectic cascade between high- and low-melting components. Source: Ref 2

Peritectic and peritectoid phase equilibria are very common in binary phase diagrams. More than 1000 reactions of this type have been registered in metallic systems, according to standard reference books on the contribution of binary alloys (Ref 18, 19, 20). In the majority of the 800 established phase diagrams involving peritectic phase equilibria, a congruently melting intermetallic or a high-melting component reacts with a melt and forms a new intermetallic phase. Published work on peritectic and peritectoid reactions in multiphase systems is less extensive, although this article does briefly describe some peritectic reactions in multicomponent systems.

References cited in this section

2. H.E. Exner and G. Petzow, Peritectic Structures, *Metallography and Microstructure,* Vol 9, *ASM Handbook,* American Society for Metals, 1985, p 675–680

18. M. Hansen and K. Anderko, in *Constitution of Binary Alloys,* McGraw-Hill, 1965

19. R.P. Elliott, in *Constitution of Binary Alloys,* McGraw-Hill, 1969

20. F.A. Shunk, in *Constitution of Binary Alloys,* McGraw-Hill, 1969

Invariant Transformation Structures, *Metallography and Microstructures,* Vol 9, *ASM Handbook,* ASM International, 2004, p. 152–164

Peritectoid Structures*

Peritectoid transformations are similar to peritectic transformations, except that the initial phases are both solid. An example of a peritectoid transformation is provided by the formation of the intermetallic compound U_3Si in uranium-silicon alloys (Ref 21). The relevant phase diagram is shown in Fig. 20. Casting uranium at the proper concentration of silicon (3.78%) results in a mixture of uranium and U_3Si_2. Morphologically, U_3Si_2 grains appear in a eutectic matrix, which is itself a mixture of uranium and U_3Si (Fig. 21). By means of thermal treatment below 930 °C (1700 °F), U_3Si grains grow at the boundary between the U_3Si_2 and the uranium phases. The reaction can be written:

$$U_3Si_2 + 3U \rightarrow 2U_3Si \qquad \text{(Eq 3)}$$

This reaction is very slow, but when allowed to go to completion, all the material transforms to U_3Si (Fig. 22). The microstructure of the U_3Si phase consists mainly of transformation twins (see Fig. 23). In Fig. 22, twins are not visible in the U_3Si phase due to a difference in the etching procedures.

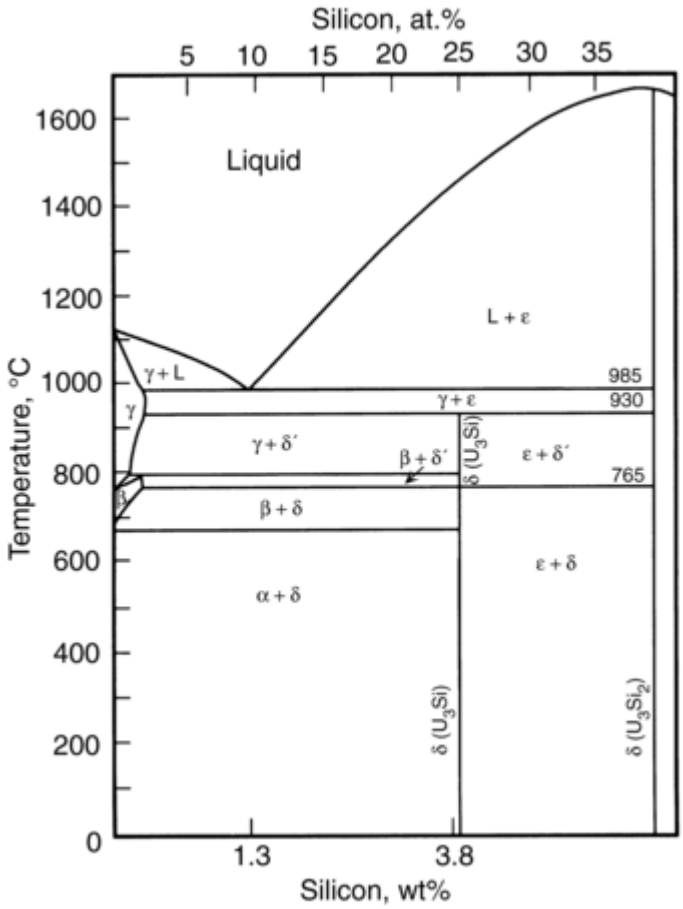

Fig. 20 Portion of the uranium-silicon phase diagram. Source: Ref 21

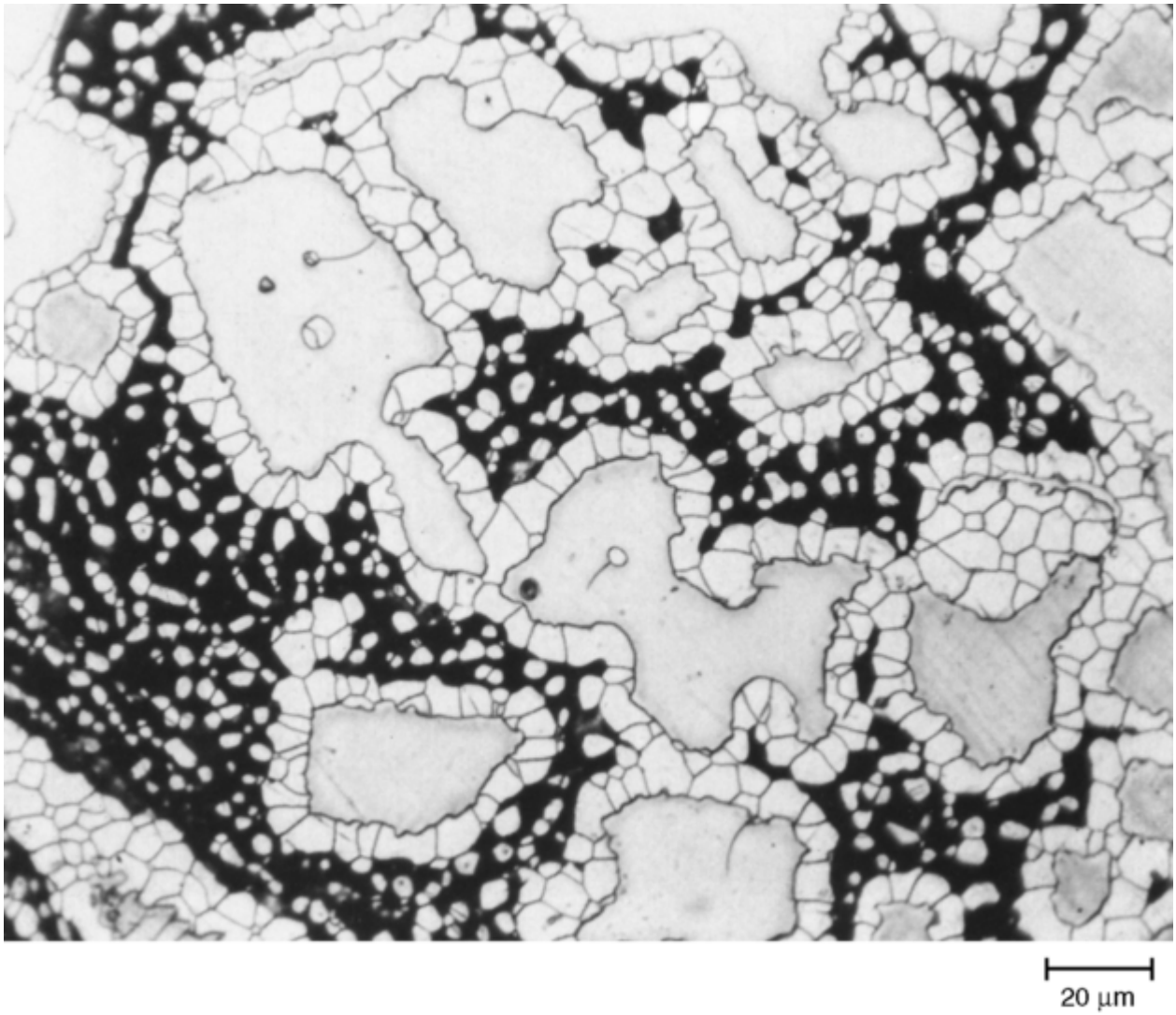

Fig. 21 Casting of a uranium-silicon alloy that contains 3.8% Si. Grains of U_3Si_2 are surrounded by grains of U_3Si on a background of a eutectic matrix that is a mixture of uranium and U_3Si. 500×. See also Fig. 23 in this article. Source: Ref 21

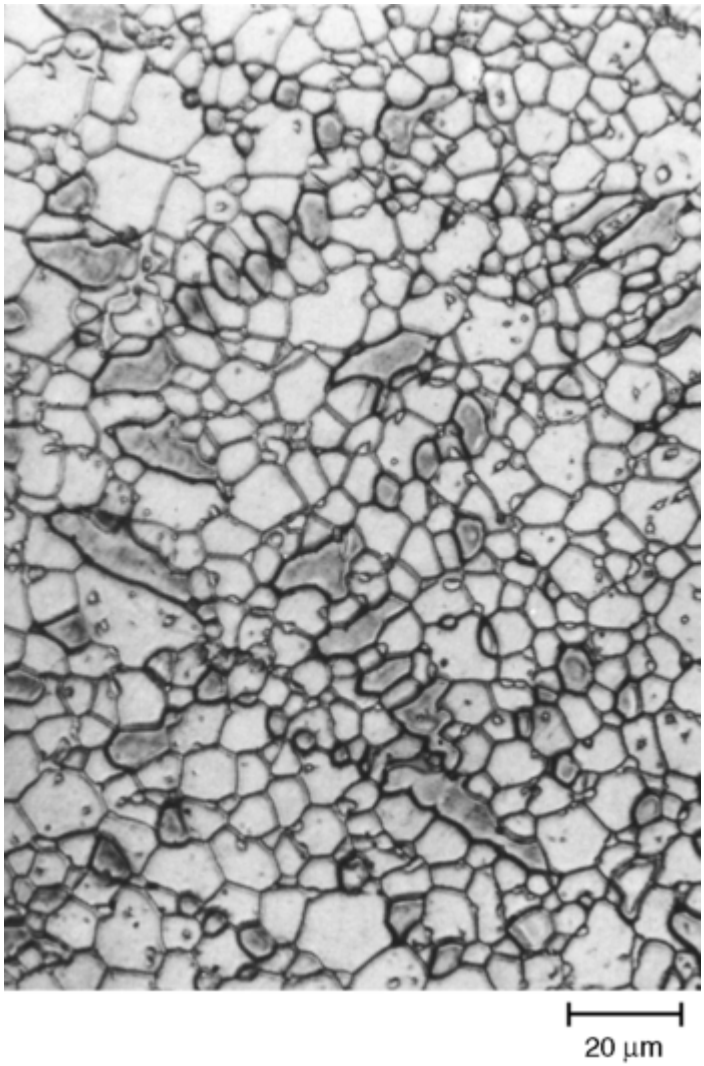

Fig. 22 Same uranium-silicon alloy as Fig. 21, but the casting has been thermally treated at 900 °C (1650 °F) for several hours. Structure is U_3Si, within which are contained the remnants of U_3Si_2. 500×

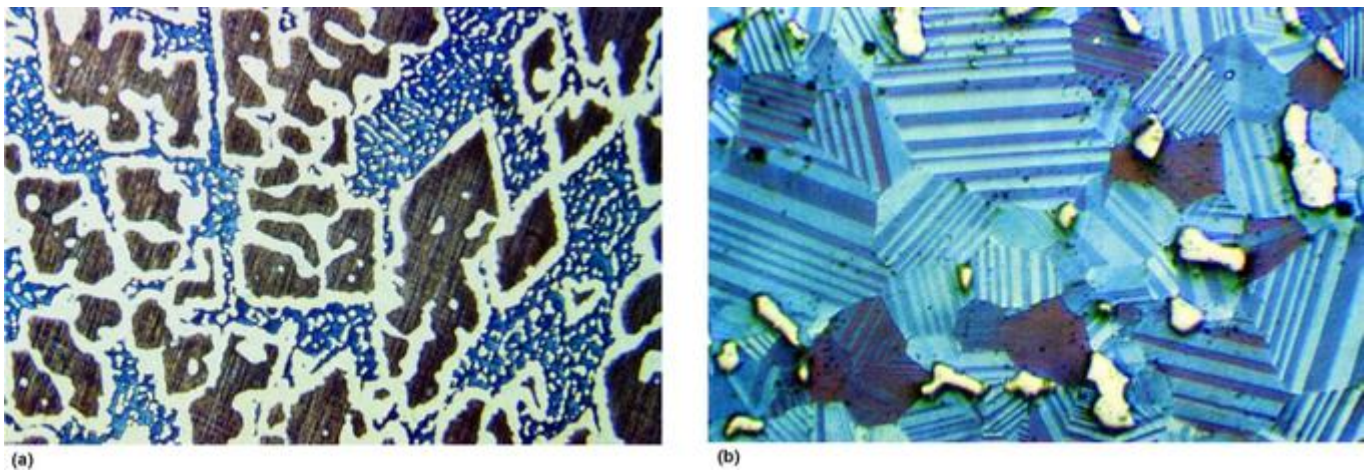

Fig. 23 Structure in U-3.8%Si alloy. (a) As-cast structure with U_3Si_2 (brown) surrounded by a rim of U_3Si (white) in a matrix of U-U_3Si eutectic. (b) Same casting as shown in (a) but after heating for three days at 870 °C (1600 °F). U_3Si twinned martensite is colored; untransformed U_3Si remains uncolored. Source: A. Tomer, *Structure of Metals through Optical Microscopy,* ASM International, 1991

Footnote

* Adapted from text in "Peritectoid Transformations" by A. Tomer, *Structure of Metals Through Optical Microscopy,* ASM International, 1991

Reference cited in this section

21. A. Tomer, Peritectoid Transformations, *Structure of Metals Through Optical Microscopy,* ASM International, 1991

Invariant Transformation Structures, *Metallography and Microstructures,* Vol 9, *ASM Handbook,* ASM International, 2004, p. 152–164

Peritectic Structures**

Up to time of publication, controlled peritectic reactions and transformations have been rarely (if ever) used to optimize the microstructure of engineering materials. Usually, peritectic structures are avoided due to their deteriorating effect on material properties. Nonetheless, a thorough understanding of peritectic reactions and transformations is required for a concise interpretation of microstructures. In addition, some technical importance may be attributed to the possibility of producing metallic alloys with aligned fibers or plates (Ref 22, 23, 24, 25) and of achieving grain refinement by means of peritectic decay of primary crystals (Ref 26, 27).
The peritectic transformation also often does not go to completion. The propensity for final solidification microstructures of peritectic alloys to be far from equilibrium is another factor limiting their widespread commercial use. St. John and Hogan (Ref 28) have examined the completion of the peritectic transformation and have ascertained that the degree of completion may be approximated based on certain characteristics of the phase diagram. From their own work on the aluminum-titanium system and the work of Titchener and Spittle (Ref 29), they describe three classes of peritectic phase diagram based on the shape of the peritectic (β) solid-solution region. These three types of diagrams are shown in Fig. 24 (Ref 30).

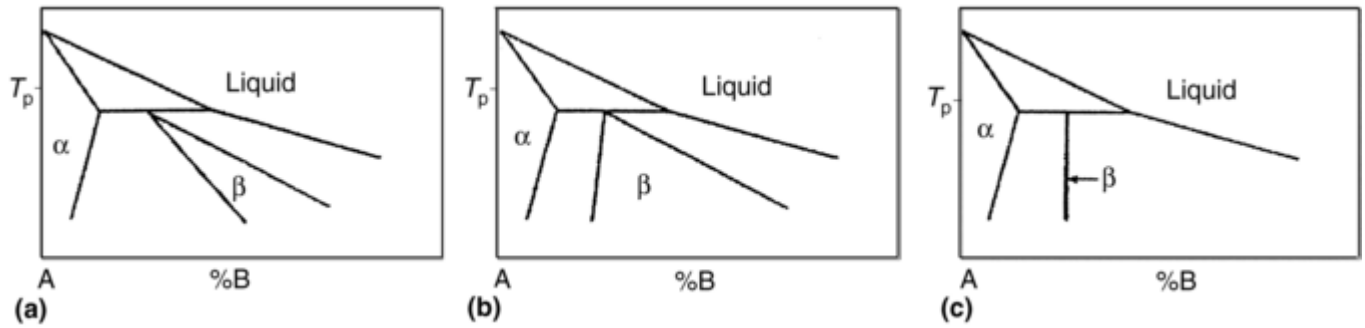

Fig. 24 Types of peritectic systems. (a) Type A system where the β/α + β solvus and the β solidus have slopes of the same sign. (b) Type B system where the slopes have opposite signs. (c) Type C system where the β phase has a limited composition. Source: Ref 2

Mechanisms of Peritectic Formation

Peritectic reactions or transformations are very common in the solidification of metals. Many interesting alloys undergo these types of reactions—for example, iron-carbon and iron-nickel-base alloys as well as copper-tin and copper-zinc alloys. The formation of peritectic structures can occur by at least three mechanisms:

- *Peritectic reaction,* where all three phases (α, β, and liquid) are in contact with each other

- *Peritectic transformation,* where the liquid and the α solid-solution phase are isolated by the β phase. The transformation takes place by long-range diffusion through the secondary β phase.
- *Direct precipitation of β from the melt,* when there is enough undercoating below the peritectic temperature (T_p) occurs. Direct precipitation of β from the melt can occur when a peritectic reaction or peritectic transformation is sluggish, as is often the case.

Peritectic reactions can proceed only as long as α and liquid are in contact. The β-phase solid nucleates at the α/liquid interface and readily forms a layer isolating α from the liquid. This mechanism occurs from short-range diffusion, as shown in Fig. 25(a). In contrast, the term peritectic transformation is used to describe a mechanism of long-range diffusion, where A atoms and B atoms migrate through the α layer to then form the β-phase solid at the α/β and the β/liquid interfaces, respectively (Fig. 25b). The terms peritectic reaction and peritectic transformation, as introduced by Kerr (Ref 32), are generally accepted in literature.

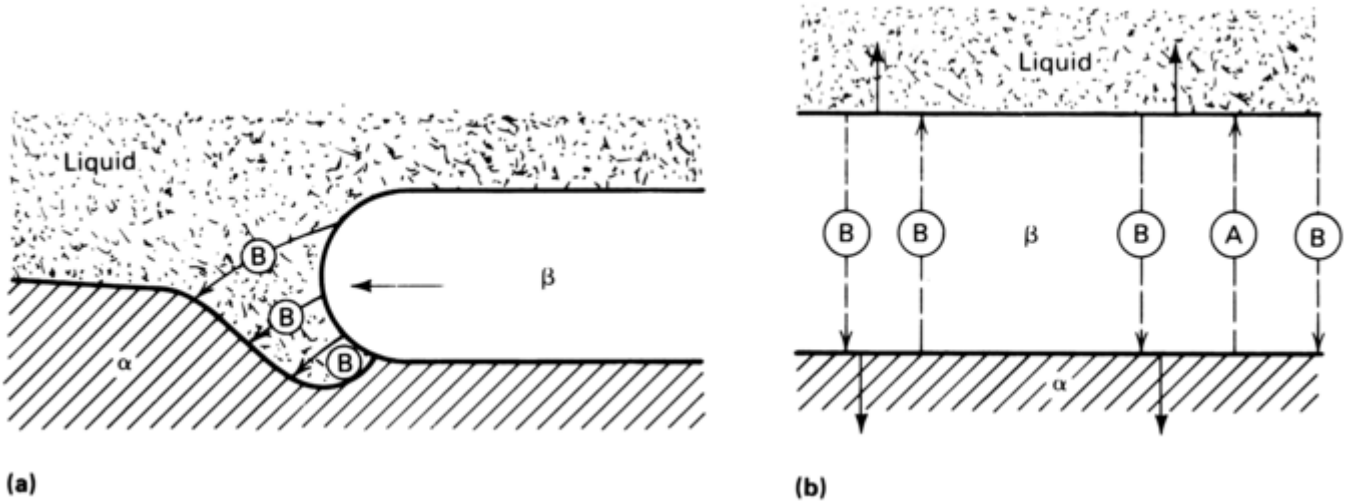

Fig. 25 Mechanisms of peritectic reaction and transformation. (a) Lateral growth of a β layer along the α/liquid interface during peritectic reaction by liquid diffusion. (b) Thickening of a β layer by solid-state diffusion during peritectic transformation. The solid arrows indicate growth direction of β; dashed arrows show the diffusion direction of the atomic species. (Ref 31)

From the final microstructure, it is not apparent by which mechanism β has formed. In any case, all three of the mechanisms require some undercooling, because the driving force is zero at the peritectic temperature. The time dependence is pronounced for the peritectic transformation. Therefore, the amount of β phase formed will depend on the cooling rate or on holding time if isothermal conditions are established.

Localized nucleation of β and shape changes of β by solution reprecipitation, which is driven by surface energy through diffusion in the liquid, also influence the microstructure of peritectic alloys. Typical and specific microstructures are discussed in the following sections. For demonstration purposes, results are included from experimental alloys that were cooled rapidly from above the liquidus to a temperature above the peritectic equilibrium temperature T_p, held for some time to achieve large homogeneous primary α crystals, then cooled to a temperature below T_p and held for extended times, inducing the formation of β by peritectic reaction and transformation, rather than by direct precipitation from the melt.

This section briefly describes the mechanisms and resultant structures of peritectic formation. Additional information on the kinetics of peritectic formation is also provided in Ref 33. Quantitative expressions for describing peritectic reactions and transformations during continuous cooling are also reviewed in Ref 34.

Nucleation-Controlled Peritectic Structures. The classical description of peritectic reactions postulates heterogeneous nucleation of β at the α/liquid interface at the peritectic equilibrium temperature T_p (Ref 26). Undercoolings of up to 4% of T_p are required for the systems investigated (Ref 35). If nucleation is limited to a few locations and lateral growth of the β nuclei does not readily occur, no continuous layer of the peritectic phase is formed, as in nickel-zinc (Ref 36) and aluminum-uranium (Ref 37) systems. Typical microstructures are shown in Fig. 26 and 27. Small crystals of the peritectic phase nucleate at the interface and grow into the primary crystals. After extended annealing below T_p, the reaction goes to completion (see Fig. 28 and 29). The

original shape of the primary crystals is lost by decay into individual β crystals that coarsen by Ostwald ripening during further annealing.

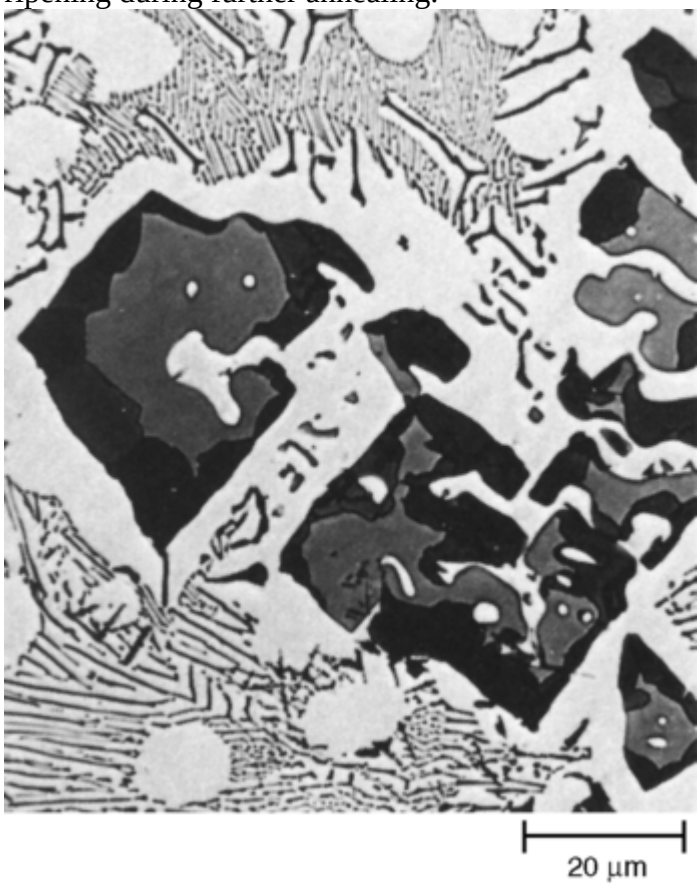

Fig. 26 Primary UAl_3 (gray) partially surrounded by peritectically formed UAl_4 (dark) in an Al-6U alloy that was cooled slowly from above liquidus to 760 °C (1400 °F) and held 10 min, then cooled to 670 °C (1240 °F) and held 15 min (peritectic temperature: 732 °C, or 1350 °F). The matrix is aluminum (white) with UAl_4 (dark) eutectic. This UAl_3 + Al → UAl_4 reaction leads to unfavorable rolling behavior. Electrolytically polished, etched in 50% HNO_3. 700×. Source: Ref 2

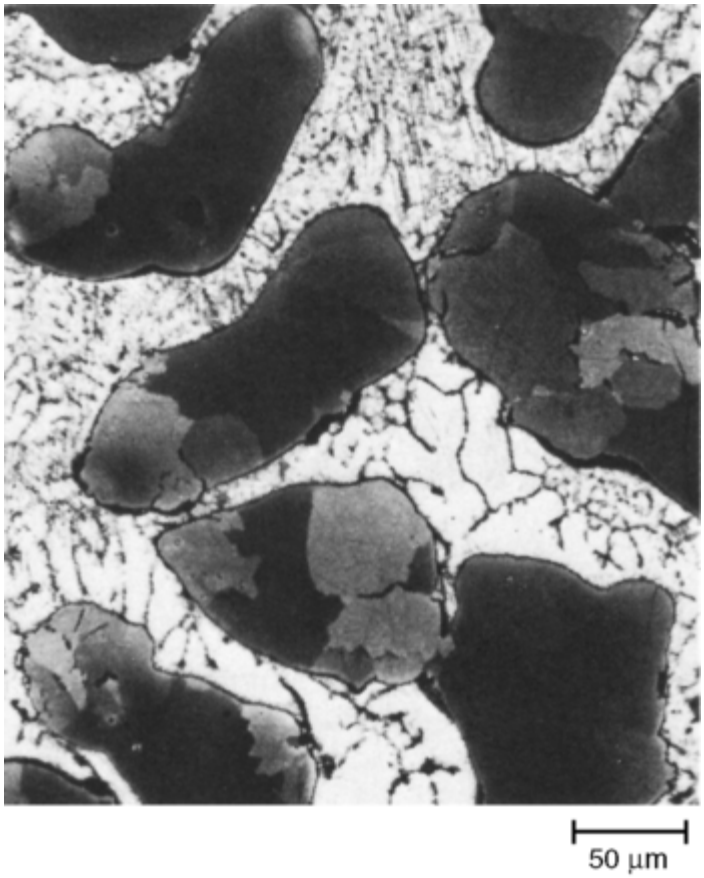

Fig. 27 Local peritectic formation in a Zn-7Ni alloy that was cooled from above liquidus to 600 °C (1110 °F) and held 24 h, then cooled to 460 °C (860 °F) and held 15 min (peritectic temperature: 490 °C, or 914 °F). The primary $NiZn_3$ is dark, the peritectic δ phase is gray, and the matrix is zinc (white) with dark cell boundaries (δ/zinc eutectic). Mechanically polished, etched with CrO_3, contrasted with reactively sputtered interference layer. 200×. Source: Ref 2

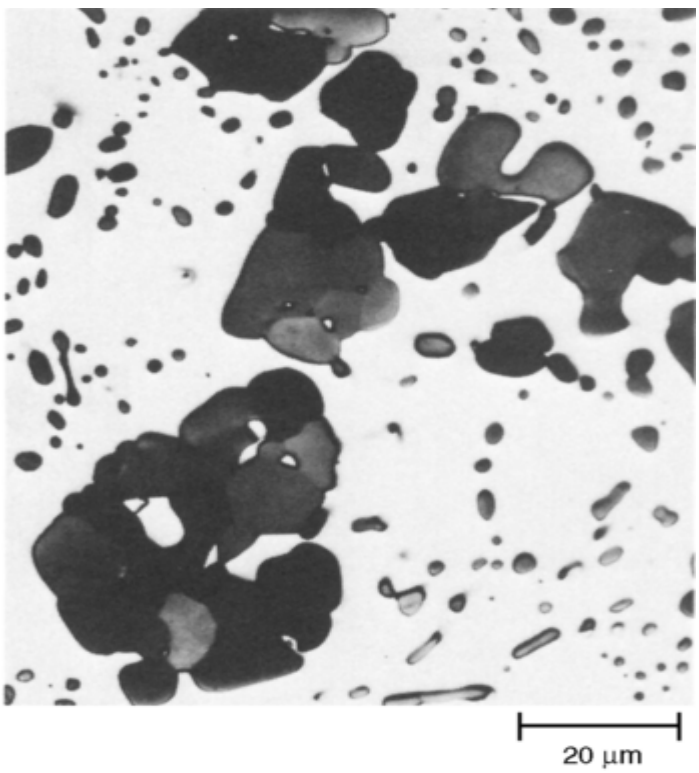

Fig. 28 Peritectically formed UAl_4 in an Al-6U alloy that was cooled from above liquidus to 760 °C (1400 °F) and held 10 min, then cooled to 600 °C (1110 °F) and held 7 days (peritectic temperature: 732 °C, or

1350 °F; eutectic temperature: 640 °C, or 1184 °F). Note the rounded crystals and the necking between crystals of different orientation. The matrix is aluminum (white) with coarsened eutectic UAl_4 (dark). Electrolytically polished, etched in 50% HNO_3. 700×. Source: Ref 2

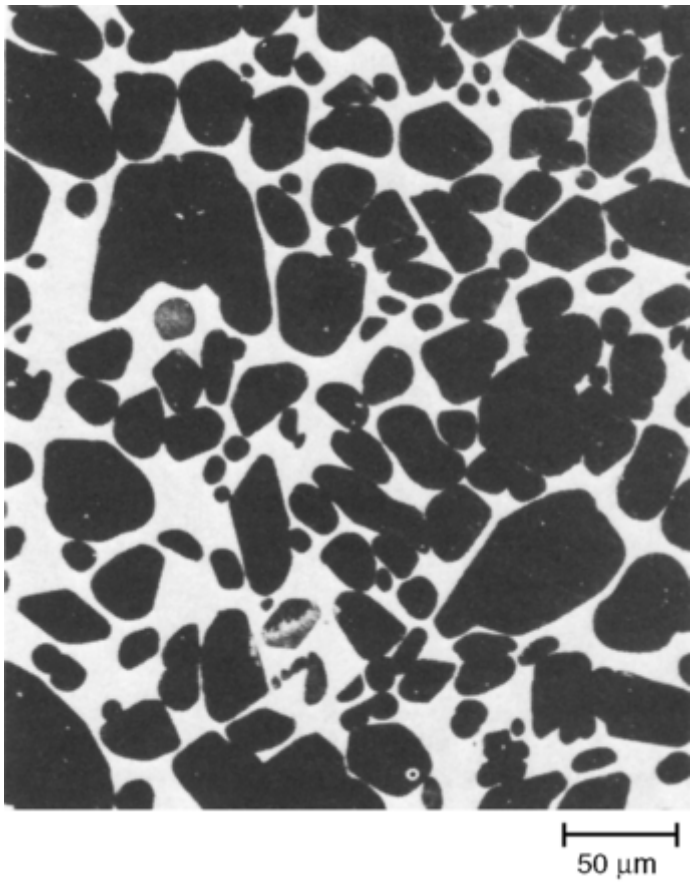

Fig. 29 Completely transformed Zn-7Ni alloy that was cooled from above liquidus to 600 °C (1110 °F) and held 24 h, then cooled to 475 °C (885 °F) and held 3 h (peritectic temperature: 490 °C, or 914 °F). Note the small crystallite size of the peritectic δ phase compared to the large primary crystals in Fig. 27. The matrix is zinc (white). Mechanically polished, contrasted with reactively sputtered interference layer. 200×. Source: Ref 2

The peritectic reaction in the aluminum-uranium system was of special interest in the production of fuel elements for early nuclear reactors. The reaction UAl_3 + Al (liquid or solid) → UAl_4 is sluggish. In Fig. 26, this reaction could not be completely suppressed during the cooling cycles used, resulting in unfavorable rolling behavior. Additions of silicon or zirconium stabilize UAl_3, extending the UAl_3-Al equilibrium region below room temperature (Ref 38).

Peritectic Reactions. Depending on surface tension conditions, two different types of the peritectic reactions can occur (Ref 33):

- Nucleation and growth of the β crystals in the liquid without contact with the α crystals
- Nucleation and growth of the β crystals in contact with the primary α phase

In the first case, the secondary phase is nucleated in the liquid and does not contact the primary phase. This is because of the surface tension conditions. Following nucleation, the secondary phase grows freely in the liquid. At the same time, the primary phase will dissolve. The secondary phase will not develop a morphology similar to a precipitated primary phase. This type of peritectic reaction has been observed for the reaction γ + L → β in the aluminum-manganese system (Ref 34). There has also been a tendency for the secondary phase to grow around the primary phase at increasing cooling rates. Similar reactions have been observed in nickel-zinc (Ref 37) and aluminum-uranium (Ref 35) systems. In the second type of reaction, which is the most common,

nucleation of the secondary β phase occurs at the interface between the primary α phase and the liquid. A lateral growth of the β phase around the α phase then takes place.

In an ideal peritectic reaction, undercooling is rather low (up to a few degrees Kelvin), and a plateau is observed in the cooling curve, as in the aluminum-titanium system (Ref 32). Envelopes of the peritectic phase around the primary phase form by direct reaction in some systems—copper-tin and silver-tin, for example—through interrupted directional solidification experiments (Ref 34). Figure 30 and 31 depict microstructures of Cu-20Sn and Cu-70Sn alloys that demonstrate the onset of the peritectic reactions α + liquid → β and ε + liquid → η, respectively. Figure 32 shows, at a higher magnification, the homogeneous thickness of the β layer around the α dendrites. The peritectic reaction can proceed very rapidly by liquid diffusion over a very short distance in the lateral direction, as shown in Fig. 25(a). The thickness of the layers has been calculated with fairly good agreement to experimental results for copper-tin and silver-tin alloys on the basis of maximum growth rate or minimum undercooling from the laws derived for solidification at low undercoolings (Ref 34). The thickness depends to some extent on the cooling rate, but more strongly on the interfacial energies, σ, with σ (liquid/β) + σ (α/β) - σ (liquid/α) as the determining factor.

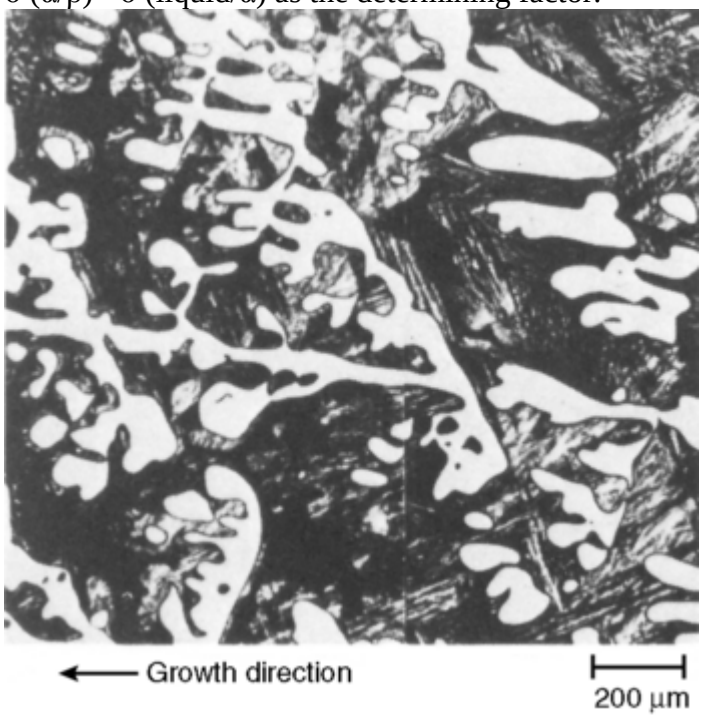

Fig. 30 Start of the peritectic reaction in a directionally solidified Cu-20Sn alloy. Primary α dendrites (white) are covered by peritectically formed β layer (gray) shortly after the temperature reaches T_p. Matrix (dark) is a mixture of tin-rich phases. Mechanically polished, etched in HNO_3. 40×. Source: Ref 34

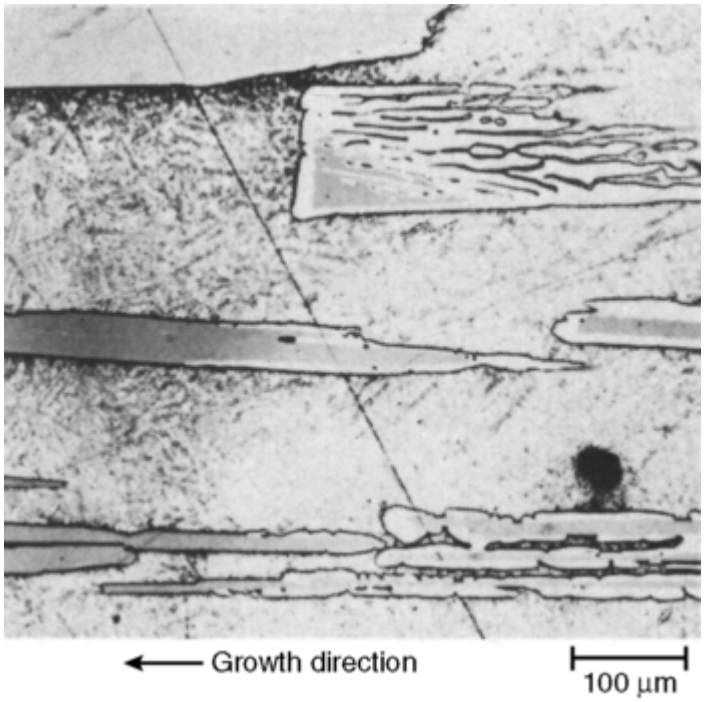

Fig. 31 Start of the peritectic reaction in a directionally solidified Cu-70Sn alloy. The primary ε phase (dark) is covered by the peritectically formed η layer (white), which thickens with increasing undercooling below T_p. The matrix is the Sn-η eutectic. Mechanically polished, etched in HNO_3. 100×. Source: Ref 34

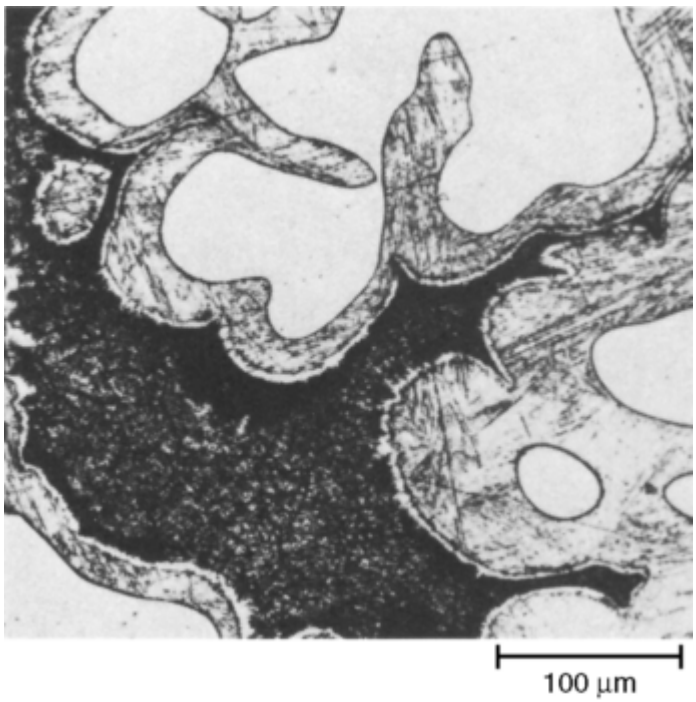

Fig. 32 Start of the peritectic transformation in the same directionally solidified Cu-20Sn alloy shown in Fig. 30, but at higher magnification. Note the homogeneous thickness of the β layers (gray) around the primary α (white). The matrix (dark) is a mixture of tin-rich phases. Mechanically polished, etched in HNO_3. 160×. Source: Ref 34

Peritectic Transformations. The precipitation of β directly from the liquid and the solid depends on the shape of the phase diagram and the cooling rate. After isolation of primary α from the liquid by the β layer, the direct peritectic reaction can no longer take place. The diffusion process through the β layer depends on the diffusion

rate, the shape of the phase diagram, and the cooling rate. The thickness of the β layer will also normally increase during subsequent cooling. There are three reasons for this:

- Diffusion through the β layer
- Precipitation of β directly from the liquid
- Precipitation of β directly from the α phase

The thickness of the β phase envelope surrounding the α phase is determined by the peritectic reaction followed by an increase in thickness due to a precipitation directly from the liquid.
The rate of the peritectic transformation is influenced by the diffusion rate and the extension of the β phase region in the phase diagram. If the diffusion rate is small, the peritectic transformation will be negligible compared to the peritectic reaction. During continuous cooling, this diffusional growth is affected by precipitation from the liquid and from the primary α or by dissolution of β, according to the slopes of the solubility limits in the phase diagram. Under simplifying conditions, the growth rates have been calculated numerically and found to be in reasonable agreement with the experimental findings in the copper-tin and silver-tin systems (Ref 34).
The kinetics of peritectic transformations can more easily be studied under isothermal conditions. Then, β is formed exclusively by diffusion of the two atomic species in the β layer at the α/β and the β/liquid interfaces. The kinetics of peritectic transformations under isothermal conditions are described in more detail in Ref 31, 33, and Ref 39.
Figure 33, 34, and 35 show typical microstructures from peritectic transformations. Similar results have been obtained in the copper-tin system for the transformation ε + liquid → η (Ref 40) and for peritectic transformations in the cobalt-tin, gold-bismuth, and chromium-antimony systems (Ref 37). In contrast, two maxima of the thickness of the peritectically formed $CuCd_3$ were observed in the copper-cadmium system, as shown in Fig. 36. The first maximum is attributed to the contribution of grain-boundary diffusion (Ref 26, 37), which is small for the faceted, large grains formed at high temperatures (Fig. 37) and large for the fine-grained, smooth layer formed below the eutectic temperature (Fig. 38).

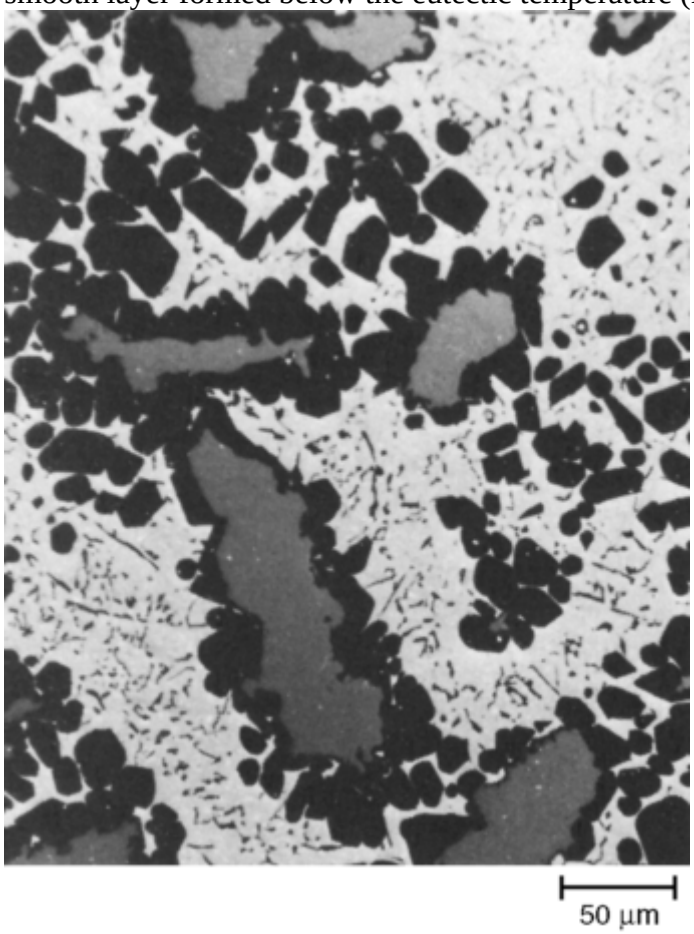

Fig. 33 Peritectic transformation of an Sb-14Ni alloy that was slowly cooled to 650 °C (1200 °F) and held 1 h, then cooled to 615 °C (1140 °F) and held 10 min (peritectic temperature: 626 °C, or 1159 °F). An irregular layer of $NiSb_2$ crystals (dark) is formed around the coarse primary NiSb crystals. The matrix is the coarsened $NiSb_2$-Sb eutectic. Mechanically polished, contrasted by a reactively sputtered interference layer. 200×. Source: Ref 2

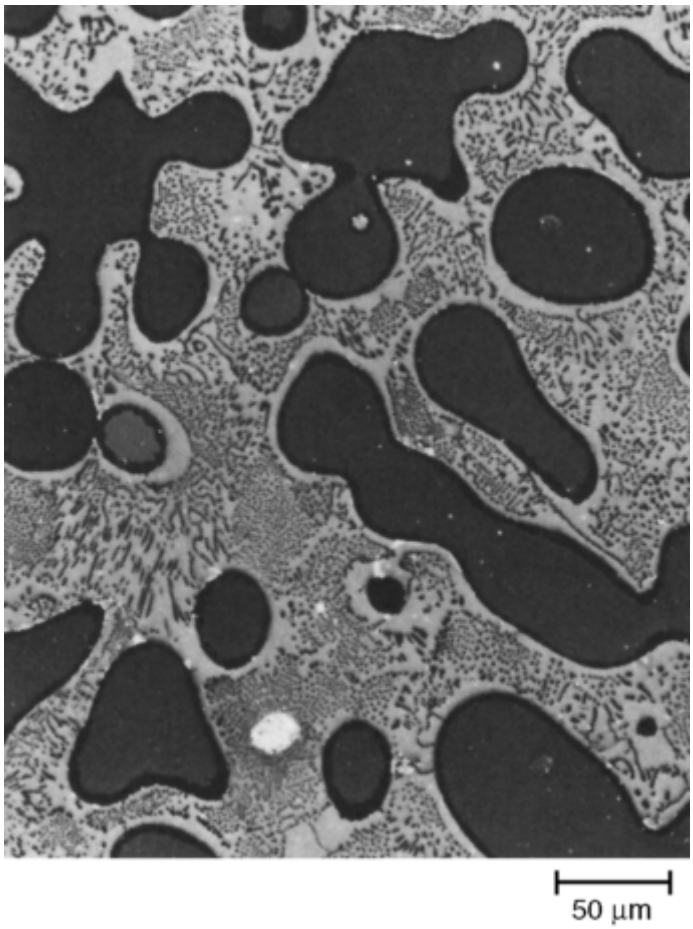

Fig. 34 Transformation of an Sb-14Ni alloy below the eutectic temperature. The alloy was slowly cooled to 650 °C (1200 °F) and held 1 h, then cooled to 500 °C (930 °F) and held 10 min (peritectic temperature: 626 °C, or 1159 °F; eutectic temperature: 612 °C, or 1134 °F). Note the layer of fine $NiSb_2$ crystals (dark) on the single crystals of NiSb (gray). The matrix is slightly coarsened $NiSb_2$-Sb eutectic. Mechanically polished, reactively sputtered. 200×. Source: Ref 2

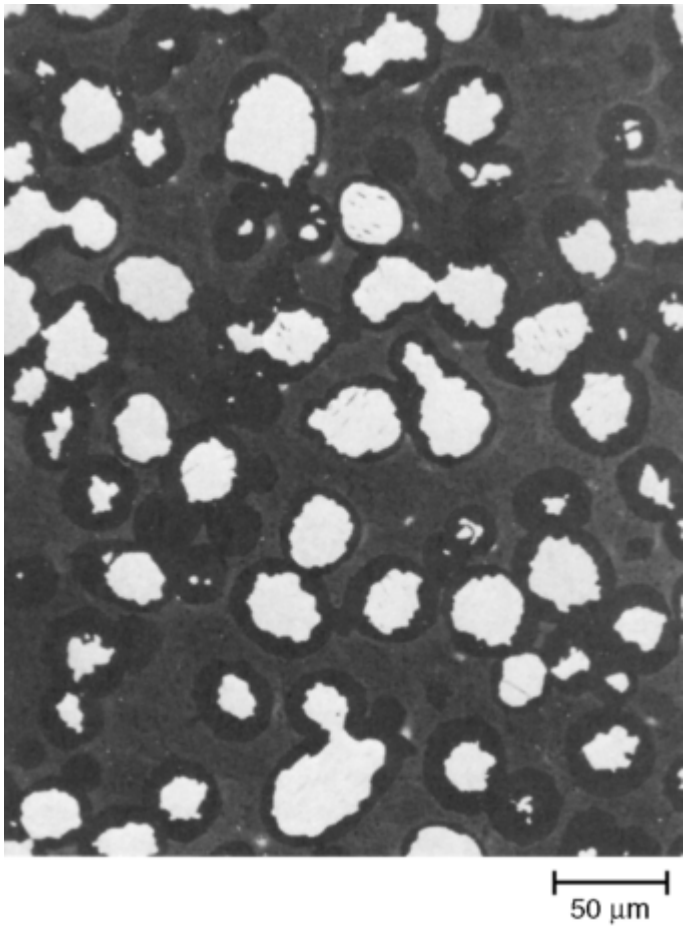

Fig. 35 Same antimony-nickel alloy as shown in Fig. 34, but held 4 h at 500 °C (930 °F). Note the rather smooth outer interface and the wavy inner interface of coarse-grained $NiSb_2$ layer, which, depending on the ratio of interfacial and grain boundary energies, form after extended isothermal annealing times at low temperatures. Mechanically polished, contrasted by a reactively sputtered interference layer. 200×. Source: Ref 2

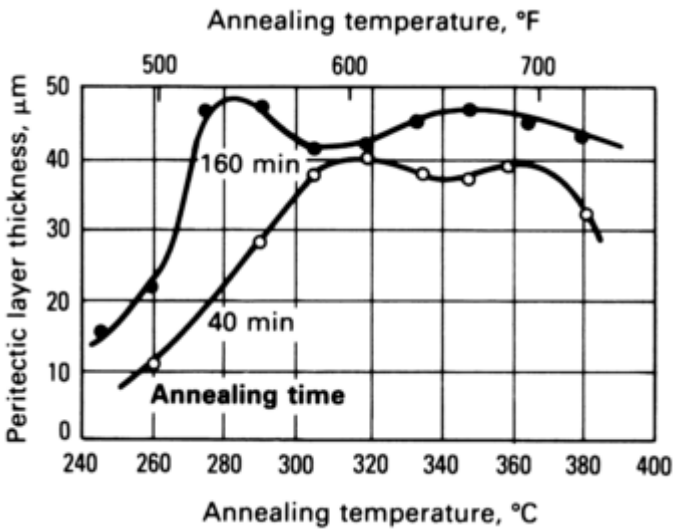

Fig. 36 Temperature dependence of the peritectic transformation Cu_5Cd_8 + liquid → $CuCd_3$ in a Cd-10Cu alloy at 40 and 160 min isothermal annealing. Source: Ref 37

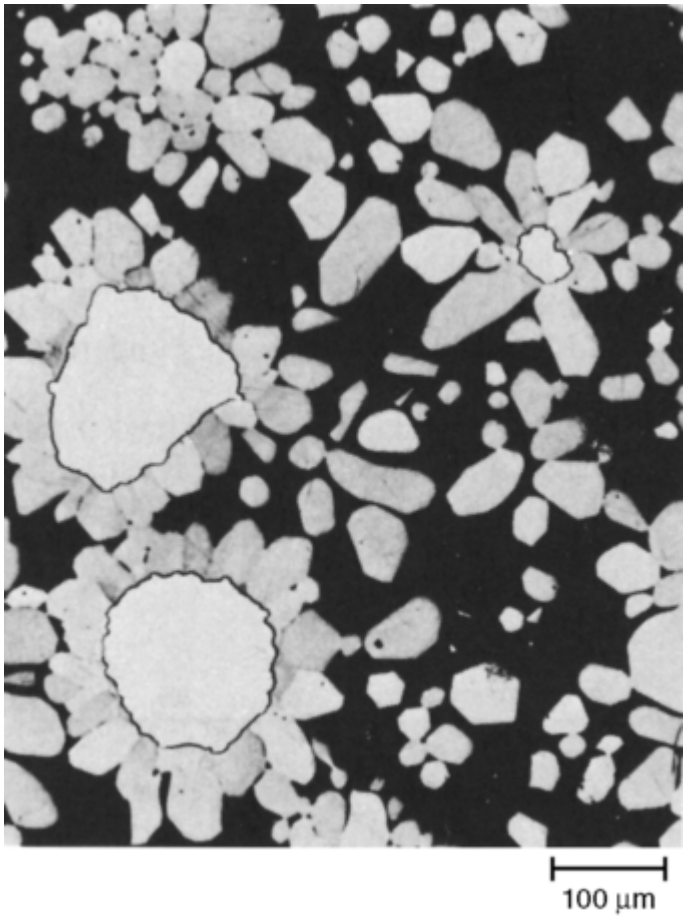

Fig. 37 Microstructure of a Cd-10Cu alloy that was cooled to 410 °C (770 °F) and held 20 h, then cooled to 305 °C (580 °F) and held 160 min (peritectic temperature: 397 °C, or 747 °F). Note the faceted coarse crystals of the peritectically formed $CuCd_3$ envelopes (gray). The primary Cu_5Cd_8 crystals are white; the dark matrix is cadmium. Mechanically polished, etched in HNO_3. 100×. Source: Ref 2

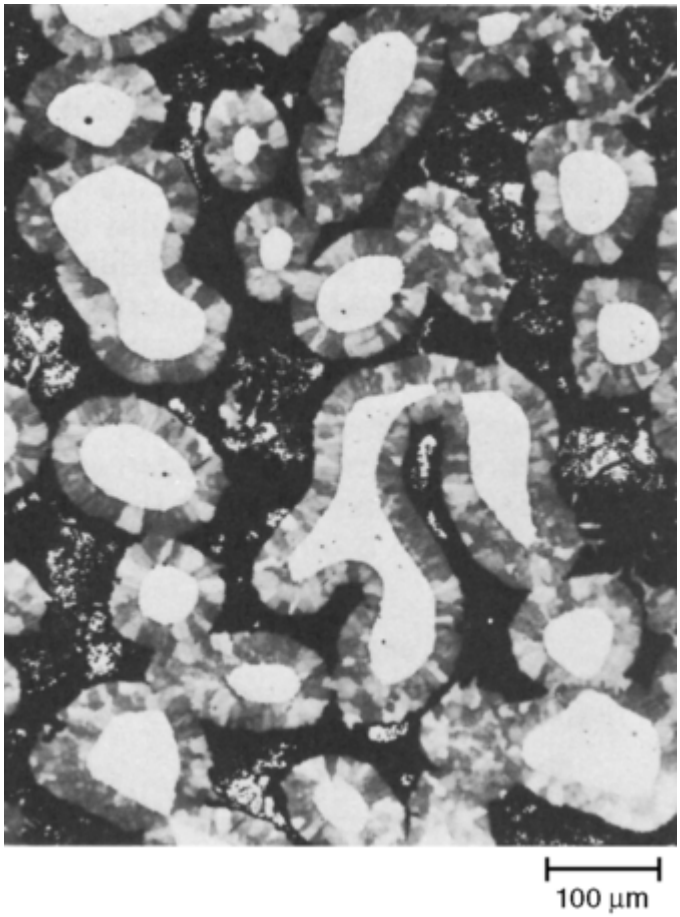

Fig. 38 Same as Fig. 37, except alloy was cooled to 410 °C (770 °F) and held 20 h, then cooled to 275 °C (525 °F) and held 160 min (peritectic temperature: 397 °C, or 747 °F; eutectic temperature: 314 °C, or 597 °F). Note large number of grain boundaries in the peritectic $CuCd_3$ phase (gray) and its smooth interfaces with the primary Cu_5Cd_8 crystals (white) and the matrix Cd (dark). 100×. Source: Ref 2

Peritectic Cascades

In many systems, one peritectic reaction at a high temperature is followed by one or more peritectic reactions at lower temperatures. If the diffusion rate is low in the initially formed peritectic layer, a second peritectic layer can be formed when the second peritectic temperature is reached. This type of series of peritectic reactions, referred to as a cascade, has been studied in Ref 37. The individual thicknesses depend on the growth rate and the rate of consumption by other growing phases, that is, on the diffusivities and the molar volumes of the individual phases (Ref 41).

For example, the binary tin-antimony systems exhibit a peritectic cascade. In this case, it is possible to get layers of each phase around the initial pro-peritectic phase as shown in Fig. 39. Another example is the tin-cobalt alloy system with a microstructure shown in Fig. 40. The cascade in the phase diagram for this alloy includes a peritectic and a peritectoid transformation. As shown in a detailed study of the zirconium-aluminum system (Ref 42), peritectoid reactions and transformations follow the same principles as the peritectic ones. The theoretical analysis is confirmed by experimental results of the reaction $Zr + Zr_2Al \rightarrow Zr_3Al$, with a parabolic growth dependence and a maximum growth rate approximately 100 K below the peritectoid temperature.

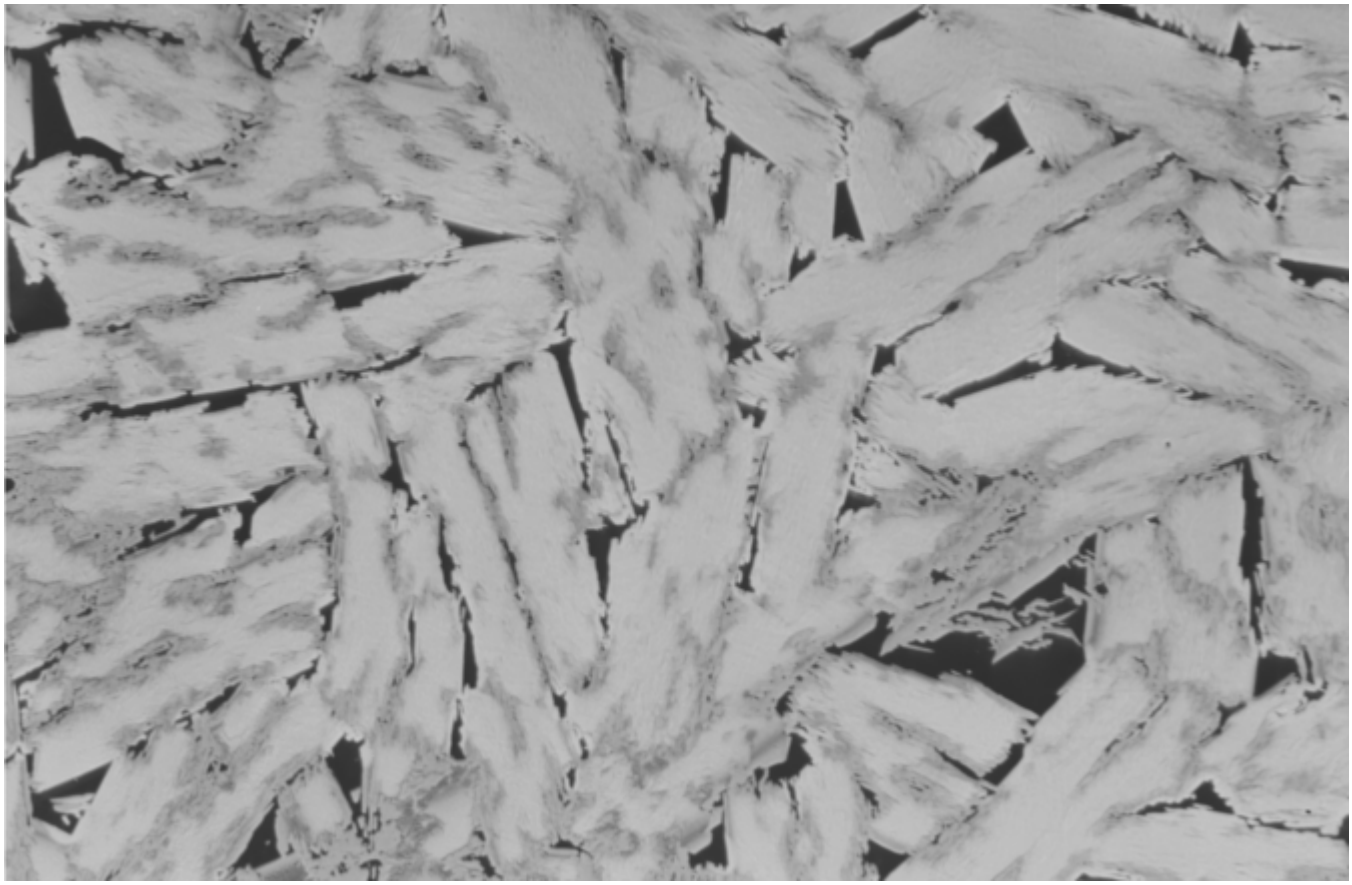

Fig. 39 Microstructure of a Sn-50wt%Sb alloy The primary β phase is light surrounded by a dark gray structure that was originally Sb_2Sn_3 but has decomposed to β + Sn. Magnification 50×. Courtesy of Daniel Lewis

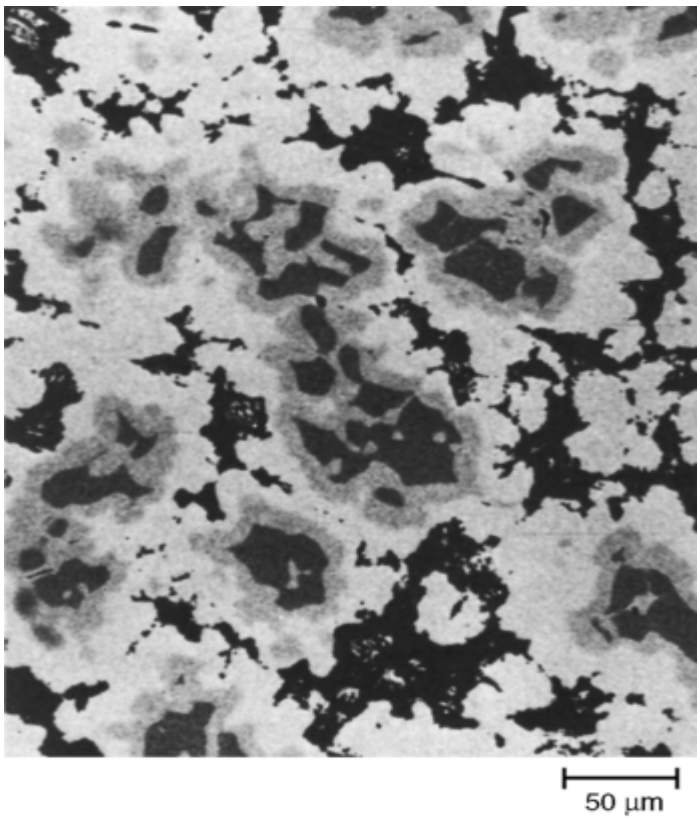

Fig. 40 Microstructure of a Sn-17Co alloy that was cooled to 1000 °C (1830 °F) and held 2 h, then cooled to 225 °C (435 °F) and held 22 h. The primary γ phase has completely transformed and dissolved into

relatively small CoSn crystals (compare with Fig. 42) that form the dark centers surrounded peritectically by $CoSn_2$ layers (gray), followed by a peritectoid envelope of the $CoSn_3$ phase that was not included in the phase diagram in Ref 18, but only found during a study of the peritectic transformation of CoSn (Ref 35). The temperatures of peritectic formation of CoSn and $CoSn_2$ are approximately 910 and 540 °C (1670 and 1005 °F), respectively; $CoSn_3$ forms peritectoidally at approximately 235 °C (455 °F). Scanning electron micrograph (backscattered electron image). 200×

Peritectic Microstructures

Smooth peritectic envelopes, according to the classical description of peritectic structures, usually develop only by a peritectic reaction or transformation during continuous cooling (see Fig. 30, 31, and 32 or by isothermal peritectic transformations at a temperature where no liquid phase exists, that is, below the eutectic temperature (see Fig. 34 and 38). After extended isothermal annealing times at low temperatures, the peritectic envelope becomes coarse grained, and wavy interfaces develop, depending on the ratio of interfacial and grain boundary energies. A typical example is shown in Fig. 35.

In the normal temperature range of peritectic transformations, a liquid phase exists that allows rapid adjustment of the interface to minimal interfacial energies. As shown in Fig. 33 and 37, the interface between the two solid phases is again moderately structured, but the liquid/solid interface is highly irregular. Faceting of the grains in the envelope is often observed. Figure 41 shows highly faceted envelopes in a bismuth-gold alloy; Fig. 42 shows separation of peritectic crystals from the primary phase by the melt in a tin-cobalt alloy. Two highly faceted peritectic envelopes are shown in Fig. 43.

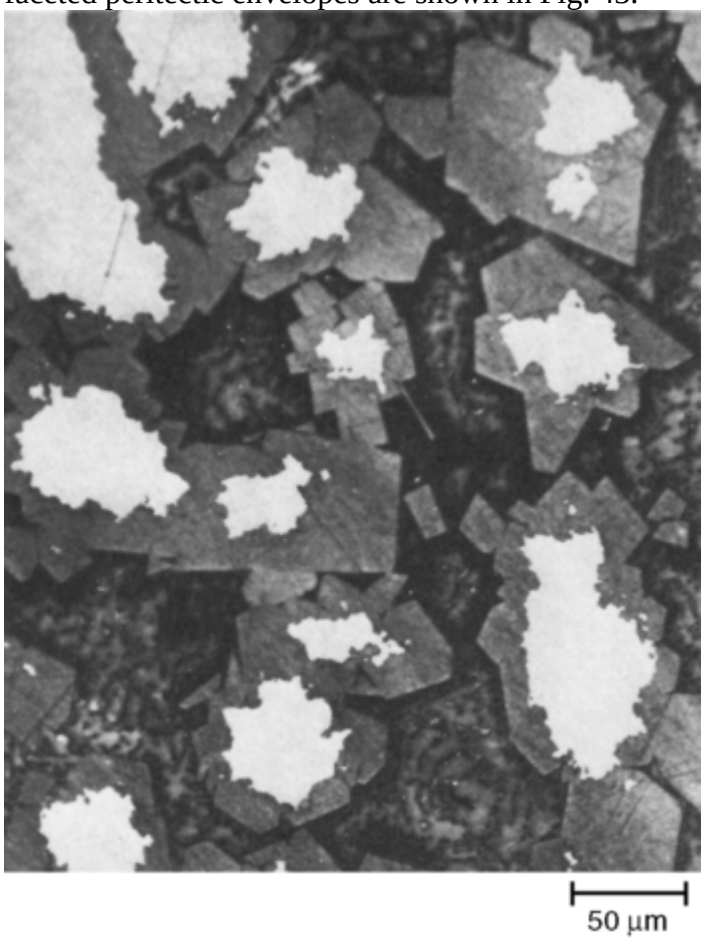

Fig. 41 Peritectic envelope in a Bi-40Au alloy that was cooled to 450 °C (840 °F) and held 5 h, then cooled to 300 °C (570 °F) and held 2 h (peritectic temperature: 373 °C, or 703 °F). The morphology is entirely determined by the anisotropy of the interfacial energy of the face-centered cubic Au_2Bi crystals (gray). The primary crystals are gold (white); the matrix is the Au_2Bi-Bi eutectic. Mechanically polished, contrasted by reactively sputtered interference layer. 200×. Source: Ref 2

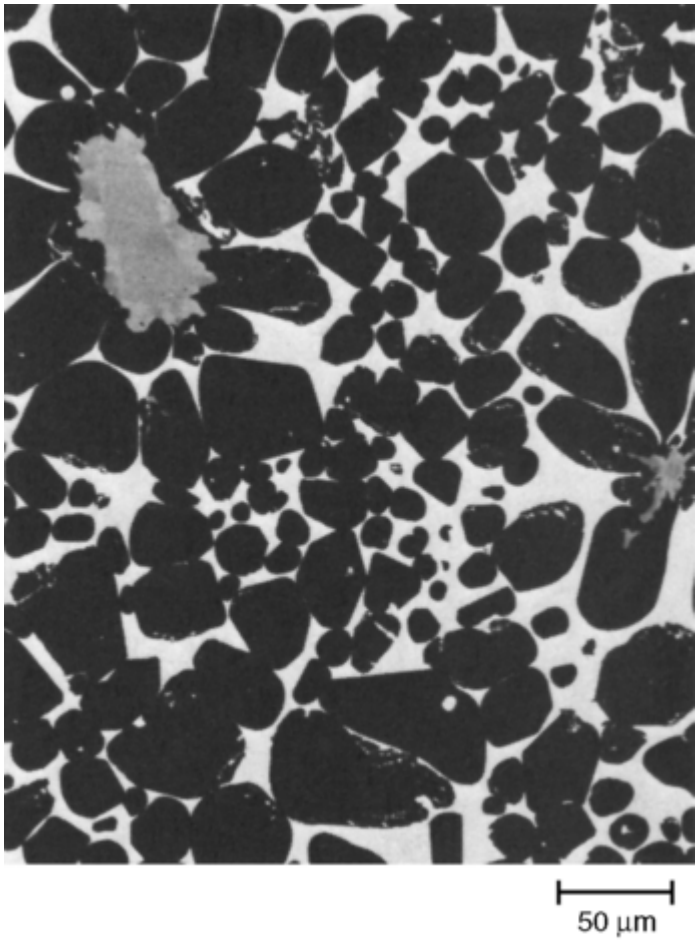

Fig. 42 Microstructure of a Sn-17Co alloy that was cooled to 1000 °C (1830 °F) and held 2 h, then cooled to 570 °C (1060 °F) and held 3 h (peritectic temperature: 935 °C, or 1715 °F). The primary γ phase (gray) has transformed nearly completely. The peritectic CoSn crystals (dark) have elongated shapes when still connected to the peritectic envelope and are separated by long channels of the liquid. Most of the peritectically formed crystals are completely isolated from the primary phase by the melt and are slightly faceted or rounded. Mechanically polished, contrasted by reactively sputtered interference layer. 200×. Source: Ref 2

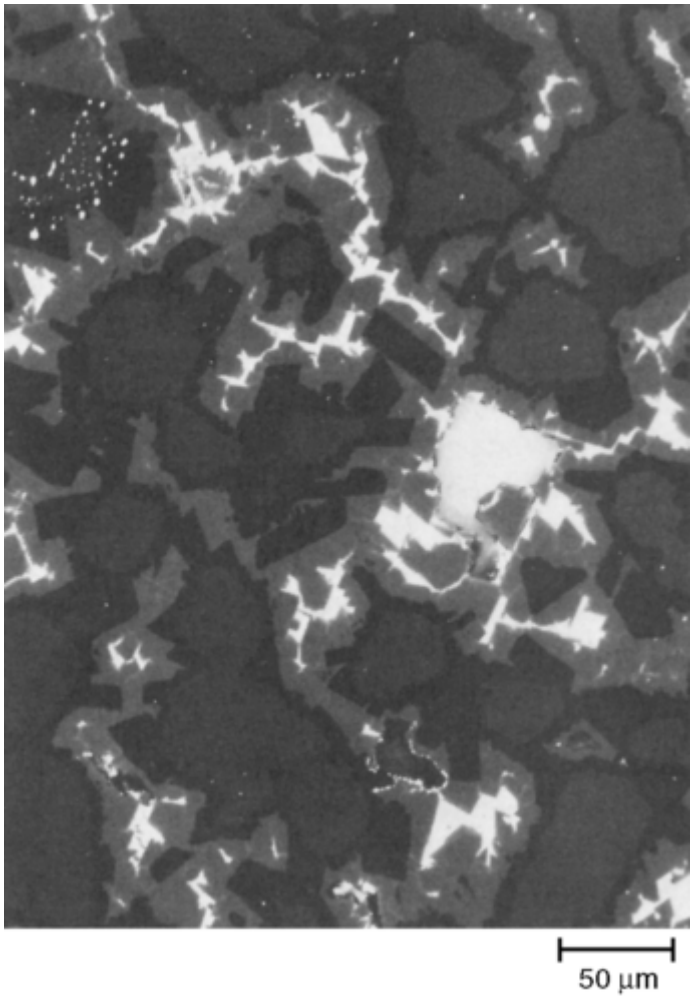

Fig. 43 Microstructure with two peritectic envelopes in a Cd-25Ni alloy that was cooled to 730 °C (1345 °F) and held 24 h, cooled to 550 °C (1020 °F) and held 40 min, then cooled to 480 °C (895 °F) and held 10 min (peritectic temperatures: Ni + liquid → β at 695 °C, or 1283 °F; β + liquid → γ_1 at 510 °C, or 950 °F; γ_1 + liquid → γ at 490 °C, or 914 °F). Coarse nickel crystals (dark gray) with a faceted inner envelope of β (black) and a faceted outer γ envelope (gray). The matrix (white) is cadmium. γ_1 has not formed during this heat treatment. Mechanically polished, contrasted by reactively sputtered interference layer. 200×. Source: Ref 2

By applying a large temperature gradient during directional solidification of a two-phase tin-cadmium alloy, it was speculated (Ref 22) that a planar solidification front with coupled (eutecticlike) precipitation of two solid phases involved in a peritectic transformation could be achieved to produce aligned microstructures. Although aligned microstructures were produced (Ref 22, 23), experimental results showed that coupled growth did not occur, and alternating bands of α (the high-temperature phase) and β (the low-temperature phase) were observed (Ref 22, 23, 24, 25), a result that was explained by kinetic analysis (Ref 22) and later by thermodynamic analysis (Ref 31).

Peritectic Structures in Iron-Base Alloys. From a technical viewpoint, the peritectic formation of austenite (γ) from primary ferrite (δ) is the most important peritectic reaction. Thermal analysis indicates that the reaction δ + liquid → γ proceeds to a great extent during continuous cooling (Ref 43), and δ-ferrite usually disappears completely upon cooling into the austenite region if not stabilized by alloying additions. Phase diagrams of iron with an austenite stabilizing element (carbon, nitrogen, nickel, manganese, and so on) always show a peritectic reaction. In most steels, austenite and ferrite stabilizing elements are present, as in stainless and high-speed steels for which peritectic formation of γ has been studied in detail (Ref 44, 45, 46). Quantitative treatments of the kinetics and the mechanisms of the transition from peritectic to eutectic solidification by the addition of ferrite stabilizers are now available. Detailed descriptions of the very complex solidification processes and microstructures in commercial high-speed steels with a thorough discussion of the peritectic transformation of δ ferrite to austenite (γ) have been given.

Figure 44 shows a directionally solidified high-speed steel with peritectic γ envelopes around the highly branched δ dendrites. Depicted in Fig. 45 is the varying thickness of the layers on the front and the back of the secondary dendrite arms. This is attributed to the wandering of the arms toward the tip of the dendrite, that is, in the solidification direction, during directional solidification due to temperature gradient zone melting (Ref 46). Under some cooling conditions, the layers appear to be partially missing on the back. This and other mechanisms related to the peritectic transformation complicate the interpretation of the microstructures found in high-speed steels and their weldments.

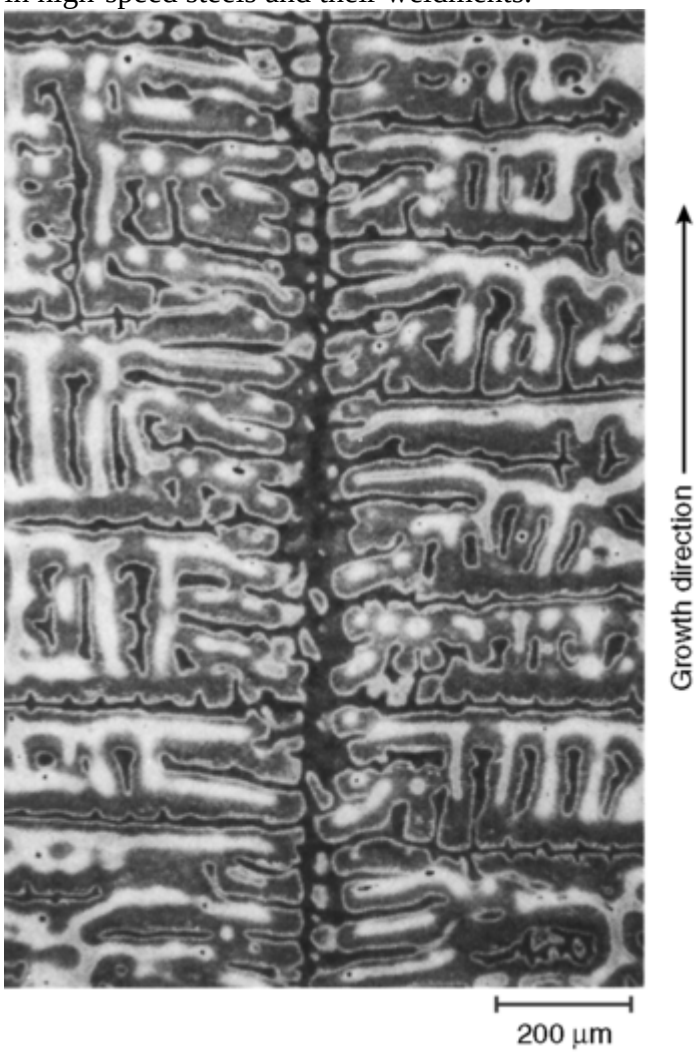

Fig. 44 Longitudinal section through directionally solidified high-speed steel (AISI T1) that was cooled at 0.23 K/s from above liquidus. The peritectic envelopes of austenite (gray) around the highly branched dendrites of δ-ferrite (discontinuously transformed to austenite and carbide, dark) are clearly distinguishable. The matrix is fine ledeburite (white). Mechanically polished, Oberhoffer's etchant (1 g $CuCl_2$, 30 g $FeCl_3$, 0.5 g $SnCl_2$, 500 mL alcohol, 42 mL HCl, and 500 mL H_2O). 60×. Source: Ref 46



Fig. 45 Longitudinal section through directionally solidified high-speed steel (AISI M2 with 1.12% C and 1% Nb) that was cooled at 0.1 K/s to approximately 1320 °C (2410 °F), that is, 20 K below the onset of the peritectic transformation. Note the thicker layers of peritectic austenite on the front faces of the secondary dendrites compared to the back. Mechanically polished, Oberhoffer's etchant. 100×. Source: Ref 2

Multicomponent Systems (Ref 33). Alloys often consist of more than two alloying elements. However, very little information is given in the literature about the peritectic reaction in multicomponent alloys. Recent investigations of iron-base alloys have shown that peritectic reactions are very common in stainless steels (Ref 44, 47). The peritectic reaction in these alloys gives the same type of distribution as that shown in Fig. 46. In stainless steels, the peritectic reaction will transfer to a eutectic reaction if the chromium content is increased to 20% or more. This transition is also influenced by the molybdenum content, as shown in Fig. 47.

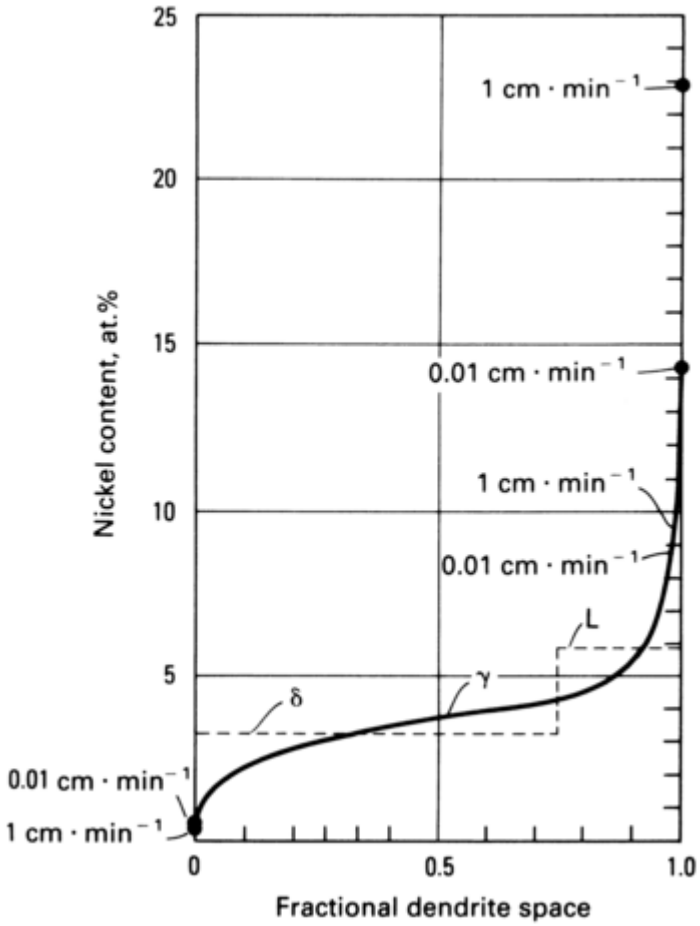

Fig. 46 Nickel distribution after peritectic reaction in a steel containing 4 wt% Ni. The temperature gradient was 60 K/cm. Calculations were made at different solidification rates. The dotted line shows the nickel distribution at the start of the peritectic reaction. δ is primary ferrite; γ is austenite. Source: Ref 47

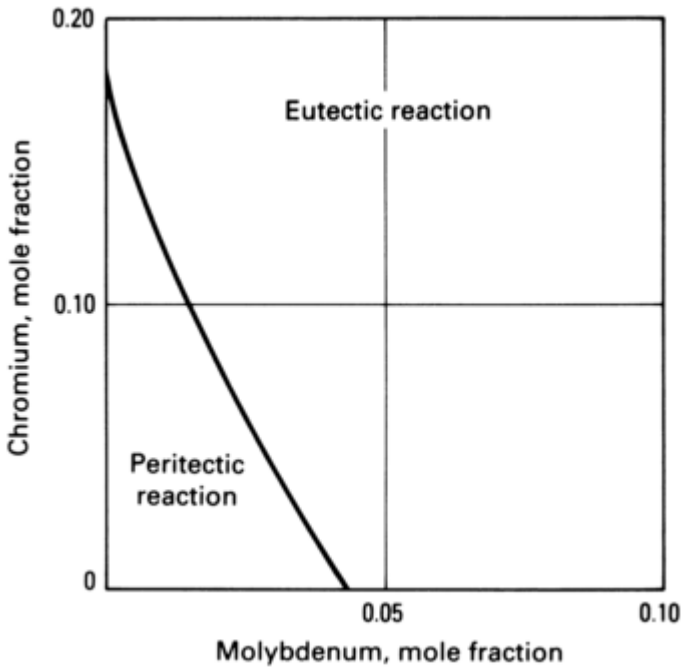

Fig. 47 The transition from a peritectic to a eutectic reaction as a function of chromium and molybdenum content in a stainless steel containing 11.9% Ni. Source: Ref 33

Both chromium and nickel are substitutionally dissolved elements. Iron-base alloys often consist of carbon with some other elements. Carbon is interstitially dissolved and has a very high diffusion rate. The other alloying elements are primarily substitutionally dissolved with very low diffusion rates. This gives rise to transformations that are determined by the movement of the substitutional elements, and carbon is distributed according to equilibrium conditions. As a result, a normal peritectic transformation does not occur. To fulfill the criterion that carbon should follow the equilibrium conditions, liquid must be formed at the border between ferrite and austenite. This reaction is shown in Fig. 48. This type of reaction has been both experimentally and theoretically analyzed in Ref 44.

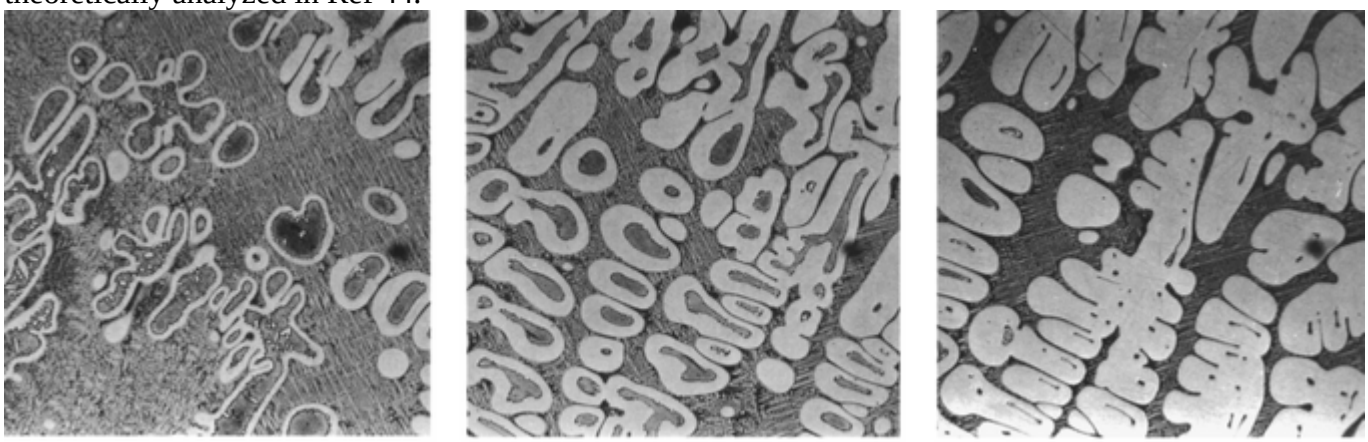

Fig. 48 Three stages of a peritectic reaction in a unidirectionally solidified high-speed steel. (a) First-stage structure. Dark gray is austenite; white is ferrite. The mottled structure is quenched liquid. (b) Subsequent peritectic transformation of (a). (c) Further peritectic transformation of (a) and (b). Dark gray in the middle of the white ferrite is newly formed liquid. Source: Ref 44

Footnote

* By H.E. Exner, G. Petzow, H. Fredriksson, and S. Lampman

References cited in this section

2. H.E. Exner and G. Petzow, Peritectic Structures, *Metallography and Microstructure,* Vol 9, *ASM Handbook,* American Society for Metals, 1985, p 675–680

18. M. Hansen and K. Anderko, in *Constitution of Binary Alloys,* McGraw-Hill, 1965

22. W.J. Boettinger, The Structure of Directionally Solidified Two-Phase Sn-Cd Peritectic Alloys, *Metall. Trans. A,* Vol 5, 1974, p 2023–2031

23. H.D. Brody and S.A. David, Controlled Solidification of Peritectic Alloys, in *Solidification and Castings of Metals,* The Metals Society, London, 1979, p 144–151

24. A.P. Tichener and J.A. Spille, The Microstructure of Directionally Solidified Alloys That Undergo a Peritectic Transformation, *Acta Metall.,* Vol 23, 1975, p 497–502

25. A. Ostrowski and E.W. Langer, Unidirectional Solidification of Peritectic Alloy, in *Solidification and Castings of Metals,* The Metals Society, London, 1979, p 139–143

26. J.A. Sartell and D.J. Mack, The Mechanism of Peritectic Reactions, *J. Inst. Met.,* Vol 93, 1964, p 19–24

27. I. Maxwell and A. Hellawell, An Analysis of the Peritectic Reaction with Particular Reference to Al-Ti Alloys, *Acta Metall.,* Vol 23, 1975, p 901–909

28. D.H. St. John and L.M. Hogan, *Acta Metall.,* Vol 35, 1987, p 171–174

29. A.P. Titchener and J.A. Spittle, *Met. Sci.,* Vol 8, 1974, p 112–116

30. J.W. Rutter et al., *Mater. Sci. Technol.,* Vol 14, 1998, p 182–186

31. M. Hillert, Keynote Address: Eutectic and Peritectic Solidification, in *Solidification and Castings of Metals,* The Metals Society, London, 1979, p 81–87

32. H.W. Kerr, J. Cisse, and G.F. Bolling, On Equilibrium and Non-Equilibrium Peritectic Transformation, *Acta Metall.,* Vol 22, 1974, p 677

33. H. Fredriksson, Solidification of Peritectics, *Casting,* Vol 15, *ASM Handbook,* ASM International, 1988, p 125–129

34. H. Frederiksson and T. Nylén, Mechanism of Peritectic Reactions and Transformations, *Met. Sci.,* Vol 16, 1982, p 283–294

35. P.G. Boswell, G.A. Chadwick, R. Elliott, and F.R. Sale, Nucleation in Peritectic Systems, in *Solidification and Castings of Metals,* The Metals Society, London, 1979, p 175–178

36. S. Uchida, "Systematik und Kinetik peritektischer Umwandlungen," Ph.D. thesis, Technical University, Stuttgart, 1980

37. G. Petzow and H.E. Exner, Zur Kenntnis peritektischer Unwandlungen, *Radex-Rundsch.,* Issue 3/4, 1967, p 534–539

38. H.E. Exner and G. Petzow, Untersuchungen zur Stabilisierung von UAl_3 in Aluminiumreichen Kernbrennstoffen, *Metall.,* Vol 23, 1969, p 220–225

39. D.H. St. John and L.M. Hogan, The Peritectic Transformation, *Acta Metall.,* Vol 25, 1977, p 77–81

40. H. Baudisch, "Mechanismus und Kinetik der peritektischer Umwandlung im System Kupfer-Zinn," Master's thesis, Technical University, Stuttgart, 1968

41. S.R. Shatynski, J.P. Hirth, and R.A. Rapp, A Theory of Multiphase Binary Diffusion, *Acta Metall.,* Vol 24, 1976, p 1071–1078

42. E.M. Schulson and D.B. Graham, The Peritectoid Transformation of Ordered Zr_3Al, *Acta Metall.,* Vol 24, 1976, p 615–625

43. M.C. Flemings, Peritectic Solidification in Polyphase Alloys: Castings and Ingots, in *Solidification Processing,* McGraw Hill, 1974, p 177–180

44. H. Frederiksson, The Mechanism of the Peritectic Reaction in Iron-Base Alloys, *Met. Sci.,* Vol 10, 1976, p 77–86

45. H. Frederiksson, Transition from Peritectic to Eutectic Reaction in Iron Base Alloys, in *Solidification and Castings of Metals,* The Metals Society, London, 1979, p 131–136

46. R. Riedl, "Erstarrungsverlauf von Schnellarbeitsstrahlen," Ph.D. thesis, University of Leoben, Austria, 1984

47. H. Fredriksson, The Solidification Sequence in an 18–8 Stainless Steel, *Metall. Trans.,* Vol 3, 1972, p 2989–2997

Invariant Transformation Structures, *Metallography and Microstructures,* Vol 9, *ASM Handbook,* ASM International, 2004, p. 152–164

References

1. I. Manna, S.K. Pabi, J.M. Manero, and W. Gust, Discontinuous Reactions in Solids, *Int. Mater. Rev.,* Vol 46 (No. 2), 2001, p 53–91

2. H.E. Exner and G. Petzow, Peritectic Structures, *Metallography and Microstructure,* Vol 9, *ASM Handbook,* American Society for Metals, 1985, p 675–680

3. .M.L. Wayman and G. Juleff, *Hist. Metall.,* Vol 33 (No. 1), 1999, p 26–42

4. .D.A. Porter and K.E. Easterling, *Phase Transformations in Metals and Alloys,* 2nd ed., Chapman and Hall, London, 1992

5. A.R. Marder, in *Phase Transformations in Ferrous Alloys,* A.R. Marder and J.I. Goldstein, Ed., TMS/AIME, 1984, p 201–236

6. M.A. Mangan and G.J. Shiflet, *Metall. Mater. Trans. A,* Vol 30A (No. 11), 1999, p 2767–2781

7. Z. Guo, T. Furuhara, and T. Maki, *Scr. Mater.,* Vol 45, 2001, p 525–532

8. D.V. Shtansky, K. Nakai, and Y. Ohmori, *Acta Mater.,* Vol 47 (No. 4), 1999, p 1105–1115

9. R.E. Reed-Hill and R. Abbaschian, *Physical Metallurgy Principles,* 3rd edition PWS-Kent Publishing Co., 1992 p 599

10. D.S. Zhou and G.J. Shiflet, *Metall. Trans. A,* Vol 22A (No. 6), 1991 p 1349–1365

11. J.M. Rigsbee and H.I. Aaronson, *Acta Metall.,* Vol 27, 1979, p 351–376

12. R.J. Dippenaar and R.W.K. Honeycombe, *Proc. R. Soc. (London) A,* Vol 333, 1973, p 455

13. C. Zener, *Trans. AIME,* Vol 167, 1946, p 550–595

14. A.R. Marder and B.L. Bramfitt, *Metall. Trans. A,* Vol 6, 1975, p 2009–2014

15. E.C. Bain and H.W. Paxton, *Alloying Elements in Steel,* American Society for Metals, 1962, p 112

16. P.R. Williams, M.K. Miller, P.A. Beavan, and G.D.W. Smith, in *Phase Transformations,* Vol 2, The Institution of Metallurgists, London, 1979, p 11.98–11.100

17. A.R. Marder and B.L. Bramfitt, *Metall. Trans. A,* Vol 7, 1976, p 902–906

18. M. Hansen and K. Anderko, in *Constitution of Binary Alloys,* McGraw-Hill, 1965

19. R.P. Elliott, in *Constitution of Binary Alloys,* McGraw-Hill, 1969

20. F.A. Shunk, in *Constitution of Binary Alloys,* McGraw-Hill, 1969

21. A. Tomer, Peritectoid Transformations, *Structure of Metals Through Optical Microscopy,* ASM International, 1991

22. W.J. Boettinger, The Structure of Directionally Solidified Two-Phase Sn-Cd Peritectic Alloys, *Metall. Trans. A,* Vol 5, 1974, p 2023–2031

23. H.D. Brody and S.A. David, Controlled Solidification of Peritectic Alloys, in *Solidification and Castings of Metals,* The Metals Society, London, 1979, p 144–151

24. A.P. Tichener and J.A. Spille, The Microstructure of Directionally Solidified Alloys That Undergo a Peritectic Transformation, *Acta Metall.,* Vol 23, 1975, p 497–502

25. A. Ostrowski and E.W. Langer, Unidirectional Solidification of Peritectic Alloy, in *Solidification and Castings of Metals,* The Metals Society, London, 1979, p 139–143

26. J.A. Sartell and D.J. Mack, The Mechanism of Peritectic Reactions, *J. Inst. Met.,* Vol 93, 1964, p 19–24

27. I. Maxwell and A. Hellawell, An Analysis of the Peritectic Reaction with Particular Reference to Al-Ti Alloys, *Acta Metall.,* Vol 23, 1975, p 901–909

28. D.H. St. John and L.M. Hogan, *Acta Metall.,* Vol 35, 1987, p 171–174

29. A.P. Titchener and J.A. Spittle, *Met. Sci.,* Vol 8, 1974, p 112–116

30. J.W. Rutter et al., *Mater. Sci. Technol.,* Vol 14, 1998, p 182–186

31. M. Hillert, Keynote Address: Eutectic and Peritectic Solidification, in *Solidification and Castings of Metals,* The Metals Society, London, 1979, p 81–87

32. H.W. Kerr, J. Cisse, and G.F. Bolling, On Equilibrium and Non-Equilibrium Peritectic Transformation, *Acta Metall.,* Vol 22, 1974, p 677

33. H. Fredriksson, Solidification of Peritectics, *Casting,* Vol 15, *ASM Handbook,* ASM International, 1988, p 125–129

34. H. Frederiksson and T. Nylén, Mechanism of Peritectic Reactions and Transformations, *Met. Sci.,* Vol 16, 1982, p 283–294

35. P.G. Boswell, G.A. Chadwick, R. Elliott, and F.R. Sale, Nucleation in Peritectic Systems, in *Solidification and Castings of Metals,* The Metals Society, London, 1979, p 175–178

36. S. Uchida, "Systematik und Kinetik peritektischer Umwandlungen," Ph.D. thesis, Technical University, Stuttgart, 1980

37. G. Petzow and H.E. Exner, Zur Kenntnis peritektischer Unwandlungen, *Radex-Rundsch.,* Issue 3/4, 1967, p 534–539

38. H.E. Exner and G. Petzow, Untersuchungen zur Stabilisierung von UAl_3 in Aluminiumreichen Kernbrennstoffen, *Metall.,* Vol 23, 1969, p 220–225

39. D.H. St. John and L.M. Hogan, The Peritectic Transformation, *Acta Metall.,* Vol 25, 1977, p 77–81

40. H. Baudisch, "Mechanismus und Kinetik der peritektischer Umwandlung im System Kupfer-Zinn," Master's thesis, Technical University, Stuttgart, 1968

41. S.R. Shatynski, J.P. Hirth, and R.A. Rapp, A Theory of Multiphase Binary Diffusion, *Acta Metall.,* Vol 24, 1976, p 1071–1078

42. E.M. Schulson and D.B. Graham, The Peritectoid Transformation of Ordered Zr_3Al, *Acta Metall.,* Vol 24, 1976, p 615–625

43. M.C. Flemings, Peritectic Solidification in Polyphase Alloys: Castings and Ingots, in *Solidification Processing,* McGraw Hill, 1974, p 177–180

44. H. Frederiksson, The Mechanism of the Peritectic Reaction in Iron-Base Alloys, *Met. Sci.,* Vol 10, 1976, p 77–86

45. H. Frederiksson, Transition from Peritectic to Eutectic Reaction in Iron Base Alloys, in *Solidification and Castings of Metals,* The Metals Society, London, 1979, p 131–136

46. R. Riedl, "Erstarrungsverlauf von Schnellarbeitsstrahlen," Ph.D. thesis, University of Leoben, Austria, 1984

47. H. Fredriksson, The Solidification Sequence in an 18–8 Stainless Steel, *Metall. Trans.,* Vol 3, 1972, p 2989–2997

Martensitic Structures, *Metallography and Microstructures,* Vol 9, *ASM Handbook*, ASM International, 2004, p. 165–178

Martensitic Structures

Introduction

MARTENSITE is a metastable structure that forms during athermal (nonisothermal) conditions. Unlike isothermal decomposition of phase constituents (which approach equilibrium conditions by diffusion-controlled mechanisms), martensite does not appear on equilibrium phase diagrams. The mechanism of martensitic transformation is a diffusionless process, where rapid changes in temperature cause shear displacement of atoms and individual atomic movements of less than one interatomic spacing. The transformation also depends on the temperature: martensite begins to form at a martensite start (M_s) temperature, and additional transformation ceases when the material reaches a martensite finish (M_f) temperature. The M_s and M_f temperatures depend on the alloying of the metal.

In general, martensitic transformation can occur in many types of metallic and non-metallic crystals, minerals, and compounds (Ref 1), if the cooling or heating rate is sufficiently rapid. The most common example is martensite in steel, when the more densely packed austenite (face-centered cubic, or fcc) phase transforms to the less densely packed crystal structures of either body-centered cubic (bcc) ferrite or body-centered tetragonal (bct) martensite (Fig. 1). When steel is slowly cooled from the austenite phase, the crystal structure (size)

transforms to the less densely packed ferrite phase. At faster cooling rates, the formation of ferrite is suppressed, while formation of martensite is enhanced by the shear displacement of iron atoms into an interstitial, supersaturated solid solution of iron and carbon. This metastable state has bct structure, which is even less densely packed than austenite. This results in lattice distortion (which provides strength/hardness by impeding dislocation movements) and a volumetric expansion at the M_s temperature (Fig. 2). During cooling, when the steel reaches the M_f temperature, the martensitic transformation ceases and any remaining γ is referred to as retained austenite.

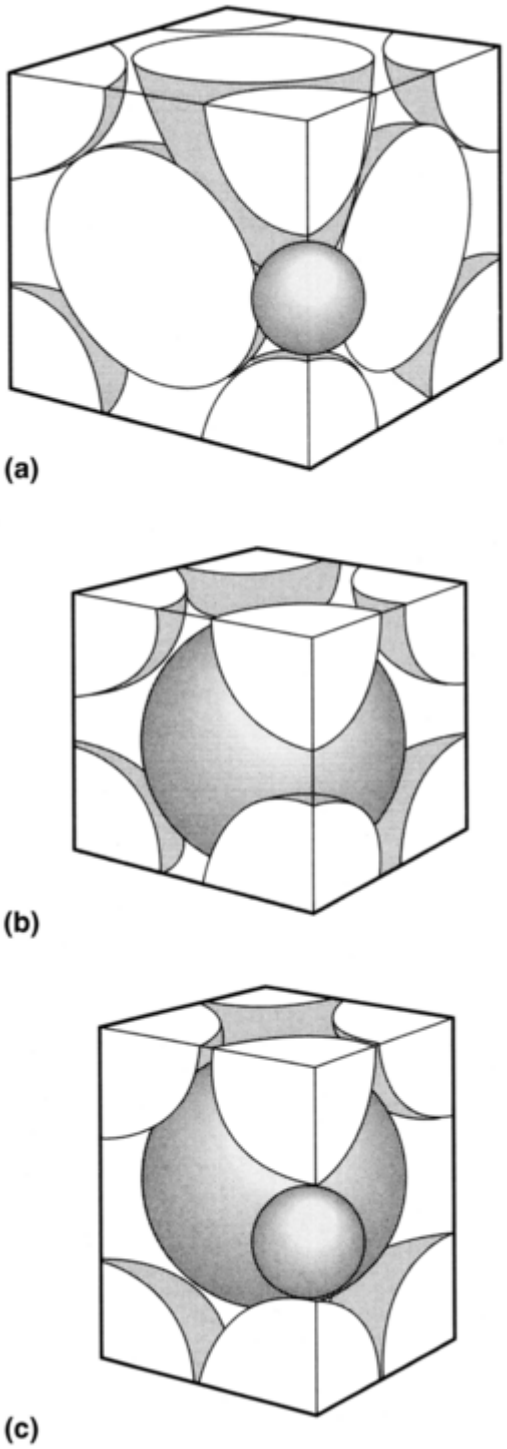

Fig. 1 Crystal structures. (a) Austenite (fcc). (b) Ferrite (bcc). (c) Martensite (bct)

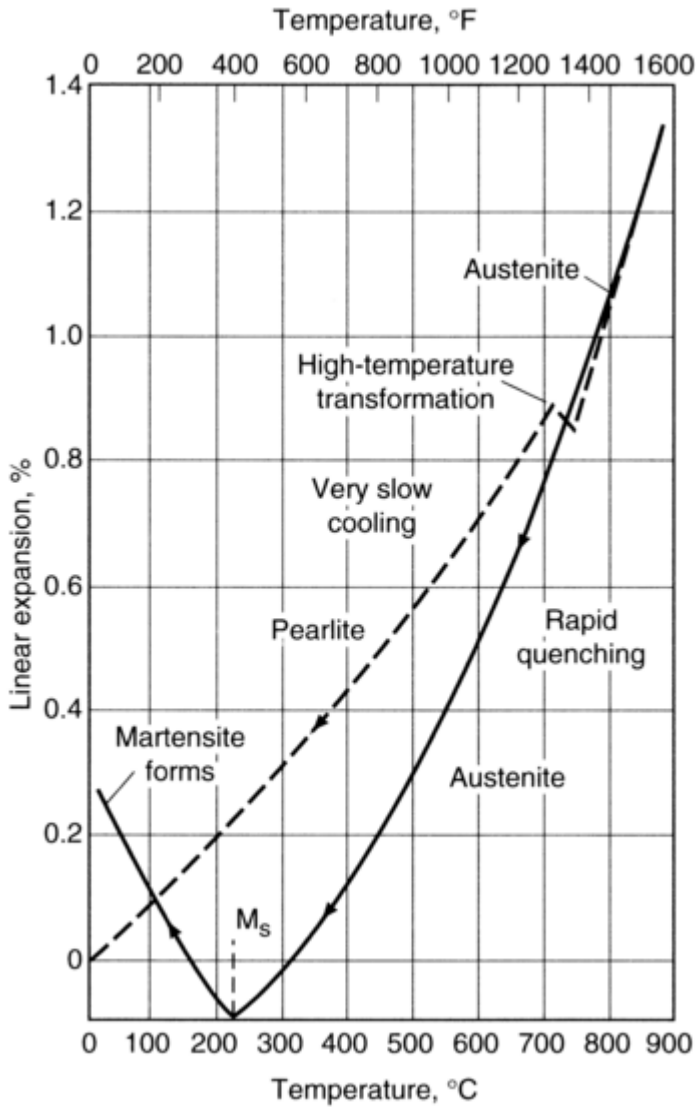

Fig. 2 Steel expansion and contraction on heating and cooling

This article briefly describes martensitic structures in ferrous alloys, nonferrous alloys, and shape-memory alloys. The detailed physical metallurgy of martensitic transformations is covered in any number of texts on physical metallurgy such as Ref 1 or more advanced treatments such as Ref 2.

References cited in this section

1. D.A. Porter and K.E. Easterling, Chapter 6, Diffusionless Transformations, *Phase Transformations in Metals and Alloys*, 2nd ed., Chapman & Hall, 1992

2. G.B. Olson and W.S. Owen, Ed., *Martensite: A Tribute to Morris Cohen*, ASM International, 1992

Martensitic Structures, *Metallography and Microstructures,* Vol 9, *ASM Handbook*, ASM International, 2004, p. 165–178

Ferrous Martensite

Ryan M. Deacon, Lehigh University

In ferrous alloy systems, martensite is the name given to the phase that forms upon rapid quenching of the austenite phase. The martensitic transformation is diffusionless, in contrast to other transformations in ferrous systems, such as the formation of pearlite from austenite. A shear mechanism controls this transformation, wherein a large number of atoms move cooperatively and almost at the same time, as opposed to the atom-by-atom movement that occurs in diffusional transformations. This shear action produces two important characteristics of the martensite transformation: orientation relationships between parent and product phases and surface tilting around the martensite crystal. Due to the absence of diffusion in the transformation, the composition of the parent austenite and product martensite are the same. Additionally, the martensite transformation is athermal—no thermal activation energy is associated with the transformation (Ref 3).

A diagram of a martensite crystal in an austenite matrix is shown in Fig. 3. The direction of the shear motion is indicated by the arrows on either side of the plate. One side of the plate is shifted or displaced above the original surface, while the other side is displaced below the surface. This shear causes the original surface to be rotated with respect to the original plane of the parent phase, creating the surface tilting. It is also important to note the regions of plastic deformation in the parent phase surrounding the martensite plate. Nucleation and growth of the martensite plate will impose strains on the surrounding phase, and when the strain limit of the surrounding material is reached, continued transformation can only be accomplished through the nucleation of new martensite crystals (Ref 3).

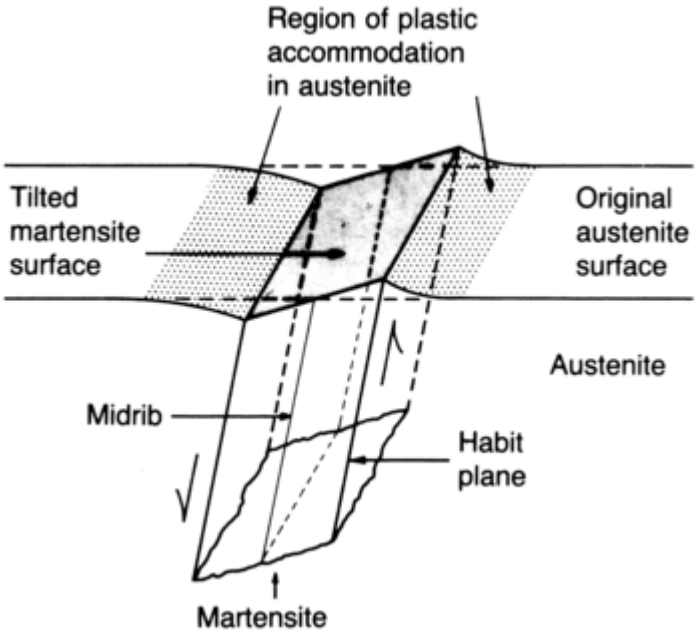

Fig. 3 Diagram of martensite crystal, showing shear and surface tilting. Source: Ref 3

Two important features of the martensite crystal, the habit plane and midrib, are also shown in Fig. 3. The habit plane is the planar interface between the martensite plate and the parent phase. The martensite crystals form on the habit plane, which varies with alloy composition. The midrib is taken to be the starting plane of the growth of the martensite crystal (Ref 3).

Reference cited in this section

3. G. Krauss, *Principles of Heat Treatment of Steel*, American Society for Metals, 1985

Martensitic Structures, *Metallography and Microstructures*, Vol 9, *ASM Handbook*, ASM International, 2004, p. 165–178

Crystallographic Theory

The crystallographic theory of the martensite transformation is useful in explaining the fine structure that develops in martensite crystals. For most steels, the parent phase is austenite, with a face-centered cubic (fcc) crystal structure. The martensitic product phase may be either body-centered cubic (bcc), body-centered tetragonal (bct), or hexagonal close packed (hcp), depending on the alloy system.

The shear mechanism in the martensite transformation produces a surface rotation, as shown in Fig. 3. During the martensite transformation, there must also be a change in crystal structure, from fcc to bct, for example. The shear that produces the surface tilting cannot also generate the lattice deformation required to change the crystal structure. Therefore, two separate shear deformations occur in the martensite transformation: a macroscopic deformation that causes the surface rotation and tilting and a second deformation that changes the structure, but not the macroscopic shape (Ref 4).

These deformations are shown in Fig. 4. Part (a) shows the perfect crystal lattice prior to transformation. The first deformation (b) creates the product phase lattice, but simultaneously causes the martensite crystal to be rotated *away* from the habit plane. By definition, a habit plane must be unrotated and undistorted. A second deformation, therefore, is required to keep the habit plane undistorted and constrained to the parent phase. Figure 4(c) and (d) show how this deformation can occur by slip or twinning, respectively (Ref 3).

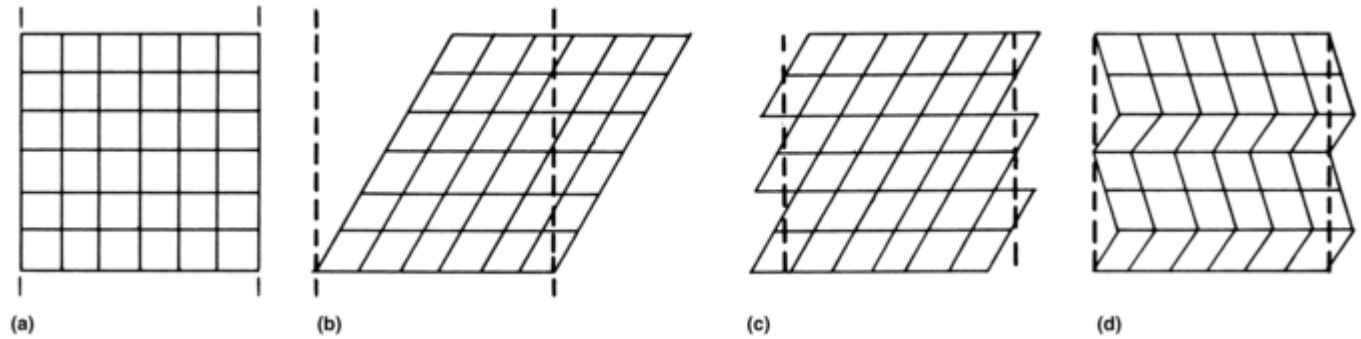

Fig. 4 Diagram illustrating both deformations required for formation of martensite phase. (a) Parent crystal structure. (b) Lattice deformation caused by change in lattice type. (c) Slip type and (d) Twin type deformation required to keep habit plane undistorted. Source: Ref 3

References cited in this section

3. G. Krauss, *Principles of Heat Treatment of Steel*, American Society for Metals, 1985

4. G. Kostorz, *Phase Transformations in Materials*, Wiley-VCH, Weinheim, Germany, 2001

Orientation Relationships and Habit Plane

The crystallography of the martensite transformation is determined by the habit plane and orientation relationships between the parent phase and the product martensite. The habit plane for martensite varies with alloy composition, though all martensite crystals in a specific alloy will be a variant of the same habit plane. The {101} and {011} planes are two examples of the variants of the {110} plane. Low-carbon steels have a {557} habit plane, which is similar to a {111} plane. Steels with a high amount of carbon have habit planes of {259} or {225}.

An orientation relationship (OR) is a parallelism that exists between planes in the parent phase and planes in the product phase. Orientation relationships can be difficult to determine in some alloys, and they are not always exact; however, they are an important artifact of the transition from the lattice of the parent phase (A) to the lattice of the product phase (M). In high-carbon steels, the Kurdjumov-Sacks relationship states the following for high-carbon steels with a $\{225\}_M$ or $\{557\}_M$ habit plane:

$$\{111\}_A \parallel \{101\}_M$$
$$\langle 110\rangle_A \parallel \langle 111\rangle_M$$

The Greninger-Troiano orientation relationship (also attributed to Nishiyama) defines the following for martensites with a $\{259\}_M$ habit plane:

$$\{111\}_A \parallel \{011\}_M$$
$$\langle 112\rangle_A \parallel \langle 011\rangle_A$$

The orientation relationship and the habit plane are the two factors that relate the transformed martensite to the parent phase. The orientation relationships are required if the transformation is to occur by shear rather than diffusion. The habit plane determines where in the parent grain the martensite will form, which will in turn affect the mechanical properties of the alloy (Ref 3).

Reference cited in this section

3. G. Krauss, *Principles of Heat Treatment of Steel,* American Society for Metals, 1985

Martensitic Structures, *Metallography and Microstructures,* Vol 9, *ASM Handbook*, ASM International, 2004, p. 165–178

Martensitic Structures

Morphology

Two different morphologies are observed in ferrous martensite microstructures: plate martensite and lath martensite, as shown in Fig. 5 (Ref 5). Plate martensite, as the name indicates, forms as lenticular (lens-shaped) crystals and is sometimes referred to as acicular (meaning needlelike) martensite or high-alloy martensite. Figure 6, 7, 8, and 9 are examples of plate martensites formed in various iron alloys. A characteristic of plate

martensite is the zigzag pattern of smaller plates, which formed later in the transformation, bounded by adjacent larger plates that formed in the beginning of the transformation. In Fig. 9, the intersection of two martensite plates is shown; the midrib in both plates is plainly visible. The substructure of plate martensite consists of transformation twins, as a result of the shear mechanism that occurred during the transformation. Figure 10 shows this substructure in a Fe-Ni-C plate martensite.

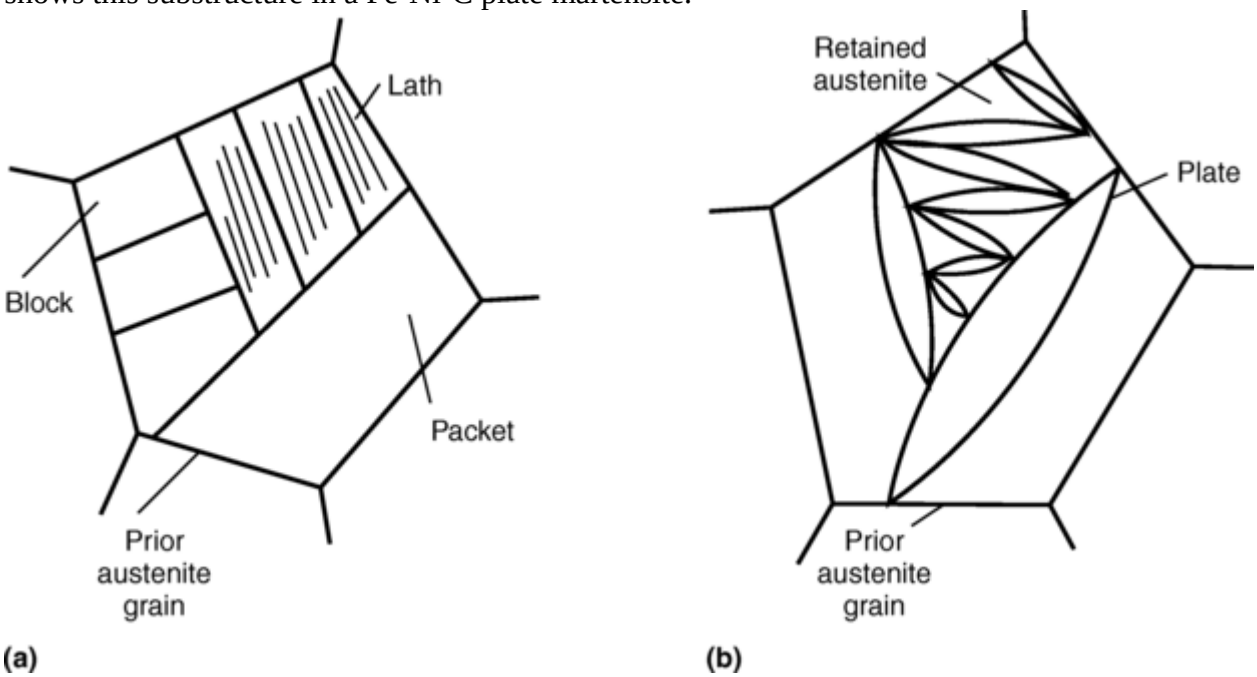

Fig. 5 Martensites. (a) Lath. (b) Plate. Source: Ref 5

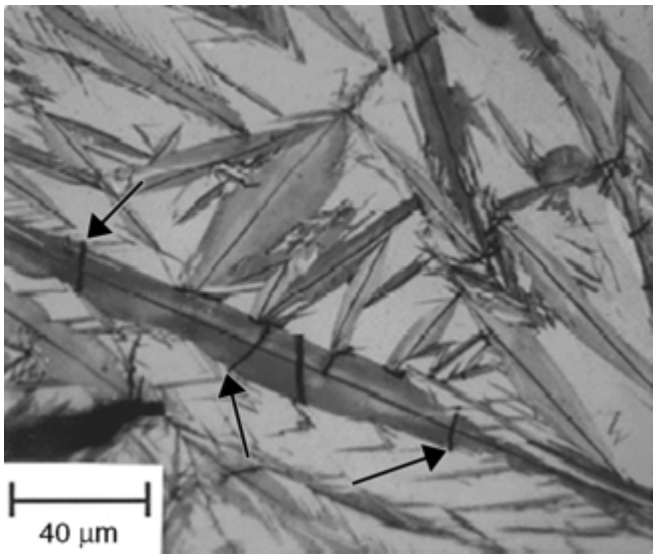

Fig. 6 Plate martensite formed in an Fe-1.86C alloy. Arrows indicate microcracks. Source: Ref 6. Reprinted with permission

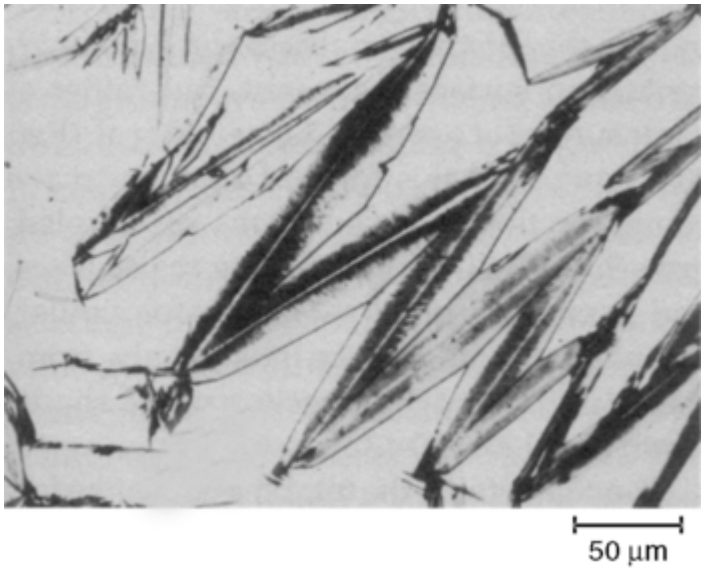

Fig. 7 Micrograph of plate martensite in an Fe-30Ni-0.38C alloy. Source: Ref 2

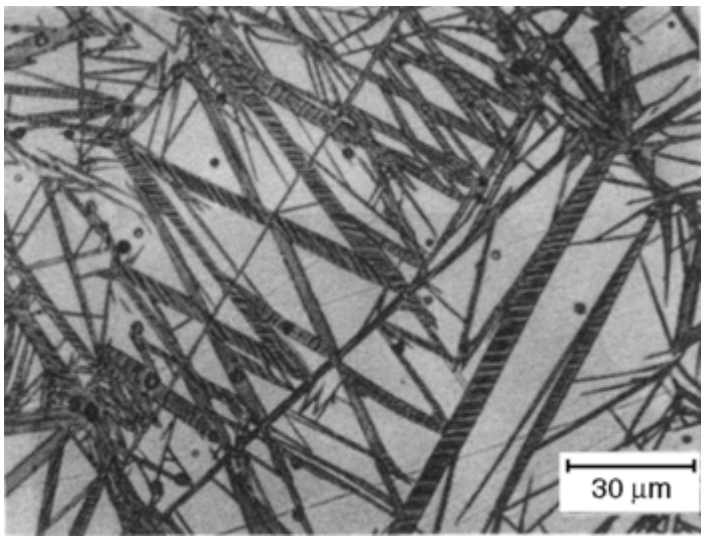

Fig. 8 Micrograph of plate martensite in an Fe-20Ni-1.2C alloy after cooling at 4 K. Source: Ref 7

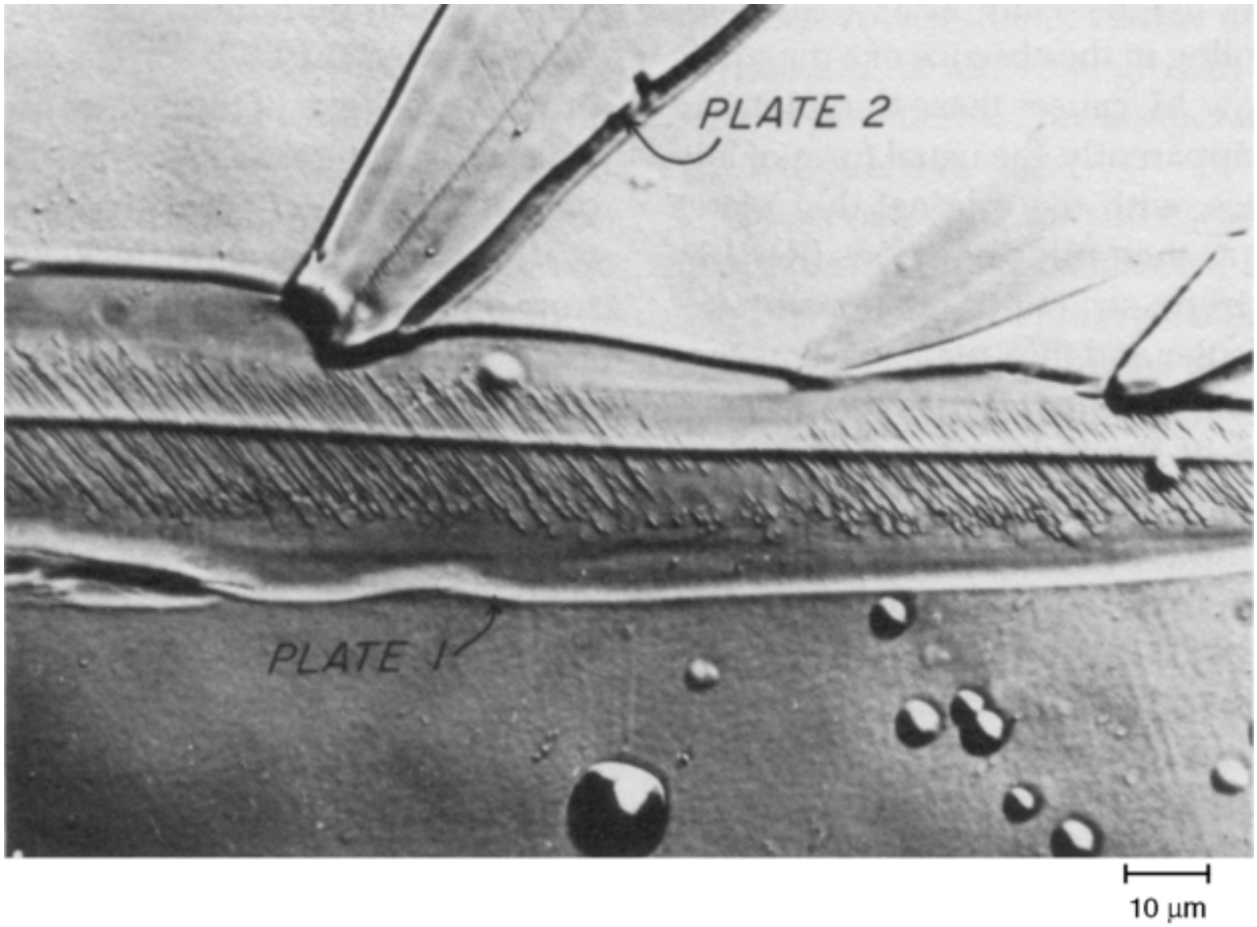

Fig. 9 Micrograph of Fe-32Ni martensite plates. Note the presence of midrib in both plates. Plate 1 shows fine structure consisting of twins. Source: Ref 2

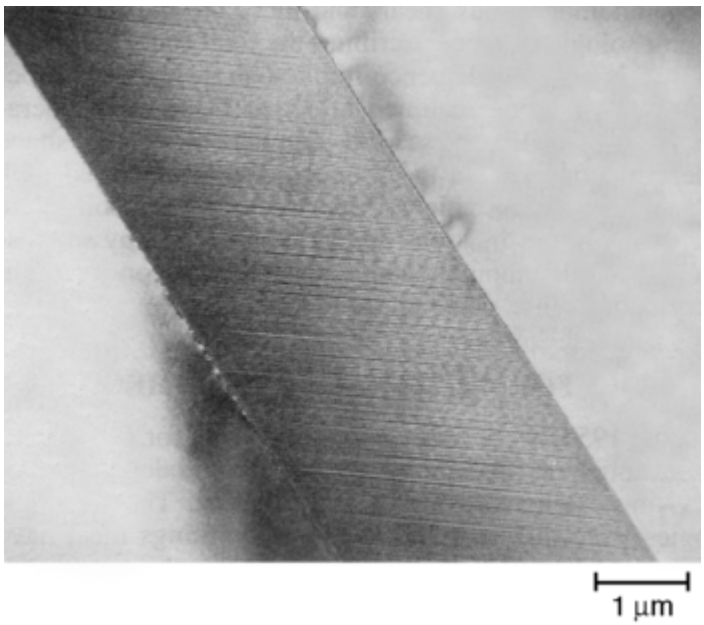

Fig. 10 Transmission electron micrograph showing internally twinned martensite plate in a matrix of retained austenite in an Fe-Ni-C alloy. The fine twins in the martensite are transformation twins. Source: Ref 8

An important feature of plate martensite is the presence of microcracks (see Fig. 6). These cracks occur when adjacent martensite crystals impinge on each other. Due to the shear-type mechanism, the transformation velocity of martensite can approach 10^6 mm/s, and thus growing martensite plates can achieve a significant

amount of momentum. Impacts between moving plates create these microcracks. The regions in between the martensite plates in these micrographs are leftover parent phase that did not transform to martensite, called retained austenite. Retained austenite between martensite plates is easily resolvable by the light optical microscope.

The other major martensite morphology is lath martensite, sometimes referred to as packet martensite. The structure of most hardened steels is lath martensite. Figure 11 is a micrograph of lath martensite in Fe-0.2C alloy. The dashed lines trace out prior austenite grain boundaries and the dark regions labeled A, B, and C are martensite laths. The term lath refers to the fine structure of the martensite crystal. The cross section of a lath is perpendicular with the larger side being on average 0.2 μm and the length being many, many microns. Laths tend to align themselves into groups with the same orientation; these groups are termed packets. This packet configuration is illustrated in the micrograph of a low-carbon iron alloy in Fig. 12. Adjacent packets are separated by high angle boundaries. Within a single packet, different blocks of laths with the same orientation may be found. Thus, the structure of lath martensite (Fig. 5a), starting at the finest scale, can be summarized as: individual laths within a block within a packet within a prior austenite grain (Ref 5).

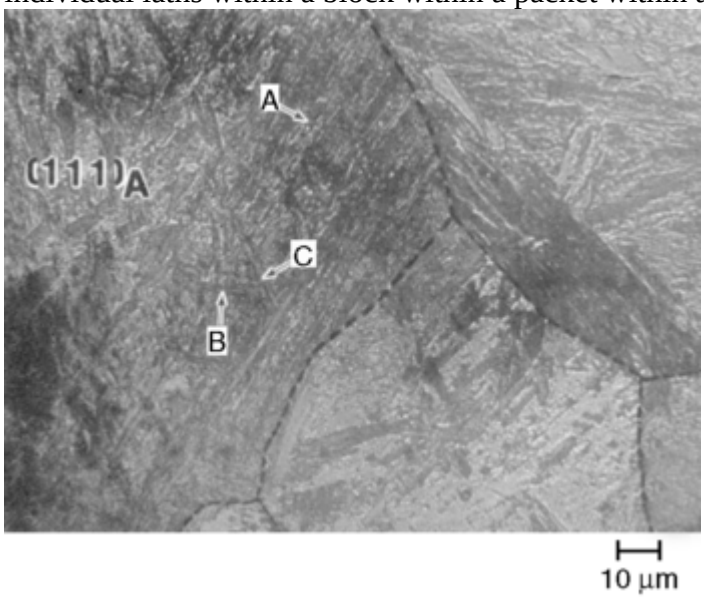

Fig. 11 Optical micrograph showing martensite laths in Fe-0.2%C alloy. Source: Ref 9

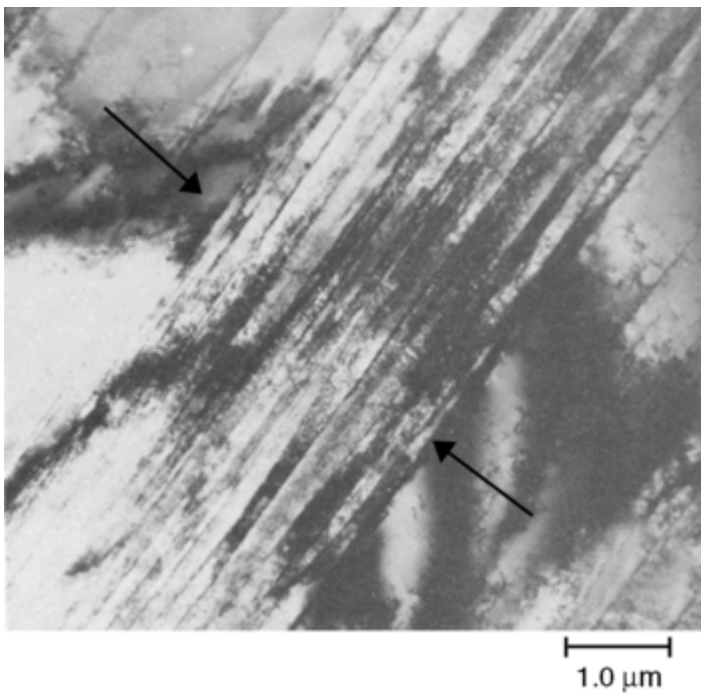

Fig. 12 Transmission electron micrograph showing a packet of martensite laths (between arrows) formed in an Fe-21Ni-4Mn alloy. Source: Ref 10. Reprinted with permission

Two individual laths in an iron-nickel alloy are shown in Fig. 13. This figure illustrates the high aspect ratio of laths. In addition to the different shape, the scale of the lath martensite structure also distinguishes it from plate martensite. Lath martensite is much finer than plate martensite, and transmission electron microscopy (TEM) is often necessary to resolve the laths. The substructure of lath martensite consists of a network of dislocations (see Fig. 14), a result of the shear processes during transformation. As with plate martensite, retained austenite can be present in lath martensite, both in between packets and between individual laths (Fig. 15). The top micrograph shows three separate packets, labeled A_1, B, and C, in one austenite grain. The region between these packets is retained austenite. The lower image in Fig. 15 is a high-magnification micrograph that resolves individual laths, labeled C, with retained austenite between them. Retained austenite between laths is also evident in Fig. 16, a TEM micrograph of four laths, labeled A, B, C, and D, in both bright-field and dark-field imaging modes. Due to the difference in martensite morphology scale, the quantity of retained austenite in lath martensite is significantly less than that for plate martensite (Ref 6).

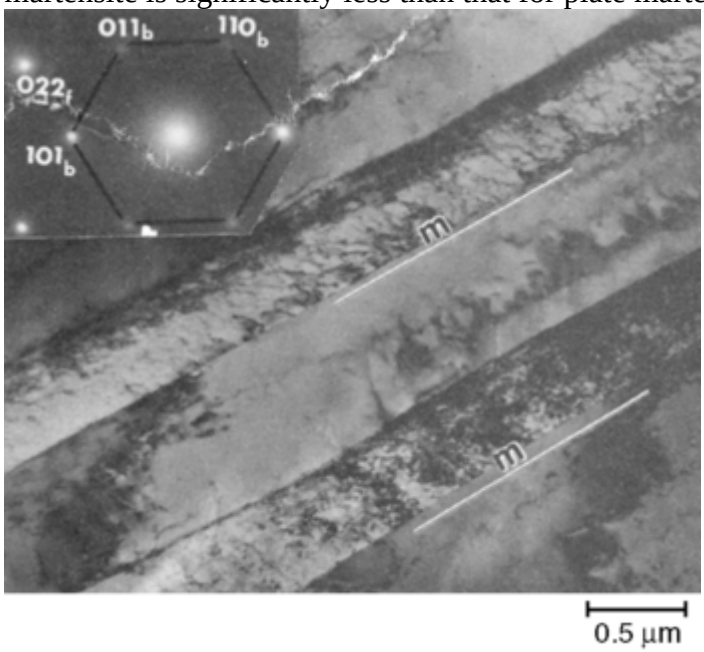

Fig. 13 Transmission electron micrograph showing two martensite laths with habit plane in "edge-on" orientation. Fe-21Ni-4Mn alloy. Source: Ref 10. Reprinted with permission

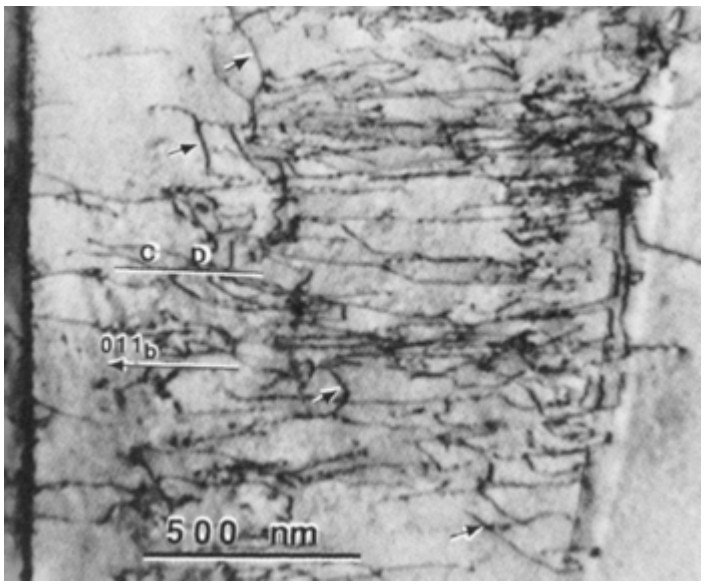

Fig. 14 Bright-field image of martensite dislocations obtained using the $(001)_b$ reflection. Source: Ref 11. Reprinted with permission

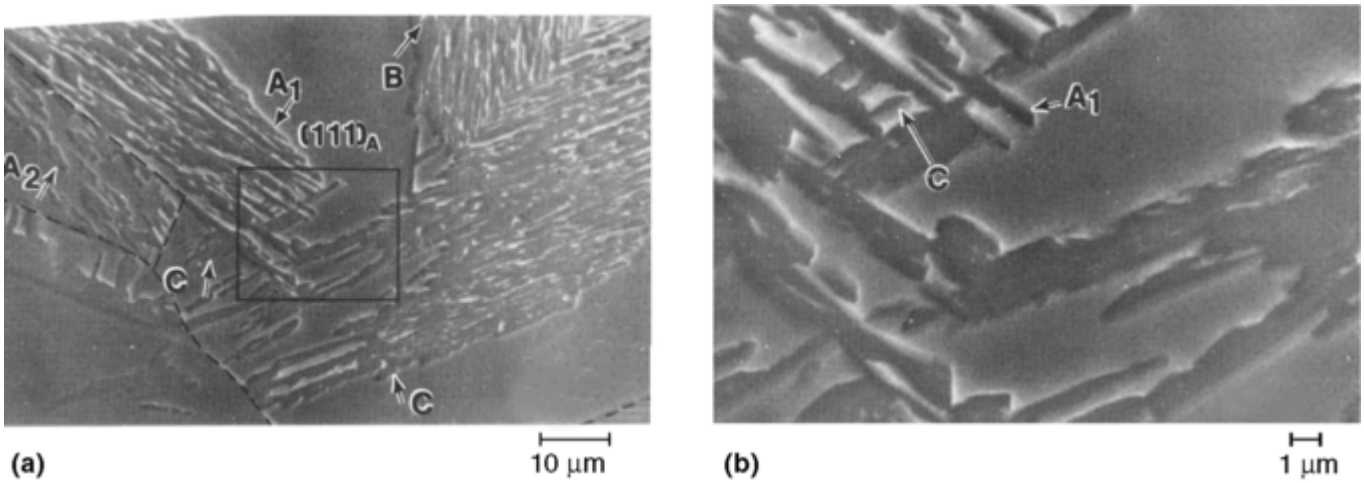

Fig. 15 Scanning electron micrograph showing distribution of martensite laths after removal of a 380 μm layer from the original specimen. (b) High-magnification micrograph of the framed region shown in (a). Source: Ref 12

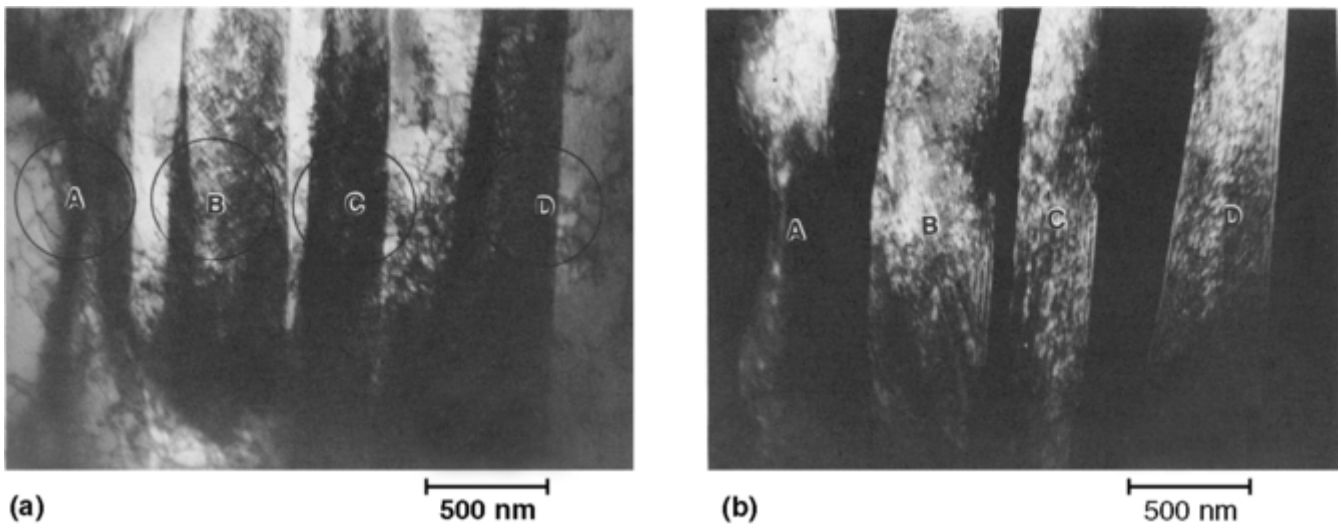

Fig. 16 (a) Bright-field transmission electron microscopy image showing four adjacent martensite laths (labeled A, B, C, D) in a matrix of austenite. (b) Dark-field image formed using the $(200)_b$ reflection. Source: Ref 11. Reprinted with permission

Most low-carbon steels form lath martensite, while higher-carbon steels form plate martensite. Figure 17 shows which martensite morphology exists for a wide range of carbon contents. Note that it is also possible to obtain microstructures with a mixture of both plate and lath martensites.

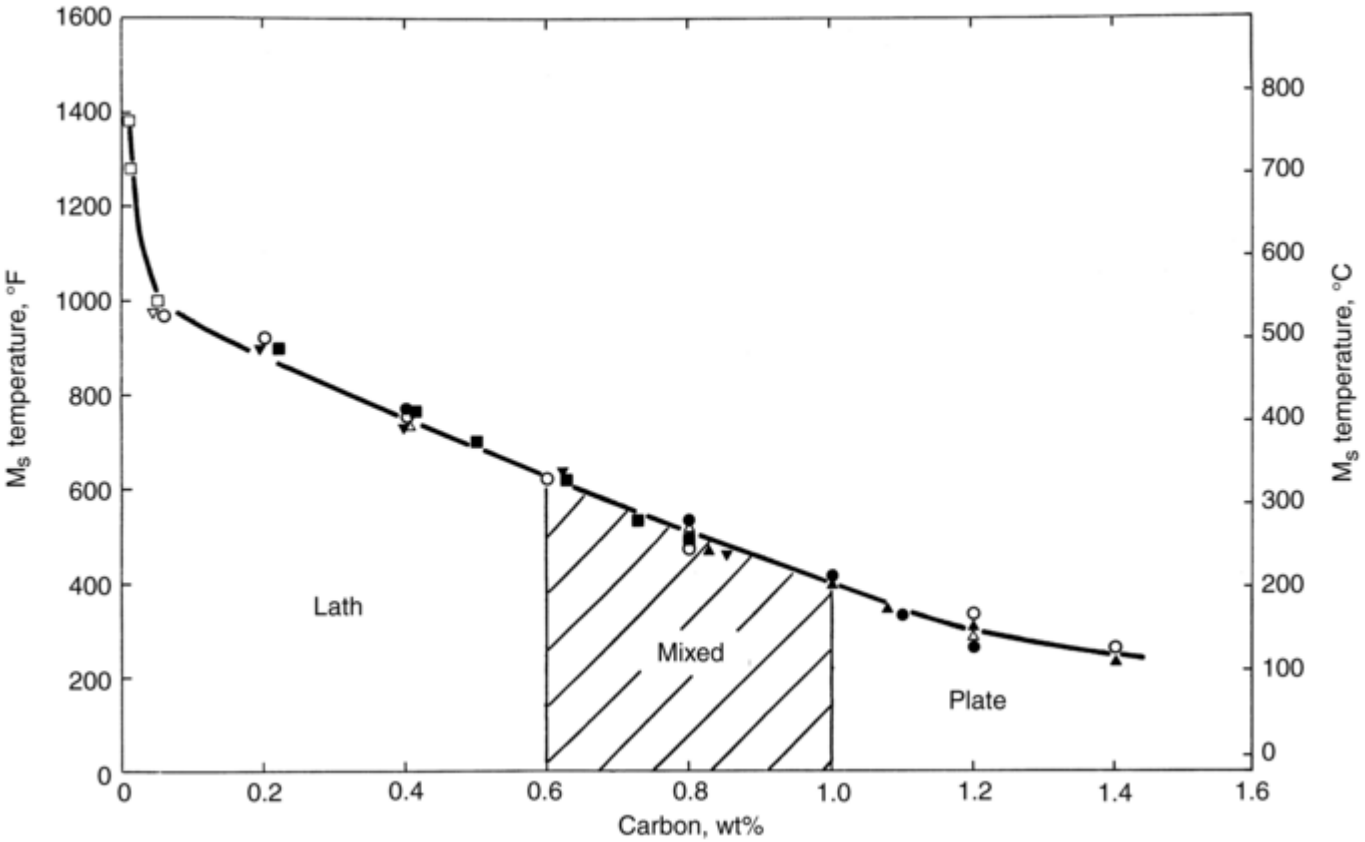

Fig. 17 Martensite transformation start temperatures versus carbon content. The range of compositions in which the various types of martensite exist is also shown (Ref 3). Data are from eight different investigators (see Ref 13).

References cited in this section

2. G.B. Olson and W.S. Owen, Ed., *Martensite: A Tribute to Morris Cohen,* ASM International, 1992

3. G. Krauss, *Principles of Heat Treatment of Steel,* American Society for Metals, 1985

5. A.R. Marder, Structure-Property Relationships in Ferrous Transformation Products, *Phase Transformation of Ferrous Alloys,* Proc. Int. Conf., TMS 1984, P11–41

6. G. Krauss, Martensite in Steel: Strength and Structure, *Mater. Sci. Eng. A,* Vol 273–275, 1999, p 40–57

7. Z.L. Xie, H. Hanninen, and J. Pietikainen, Substructures of Thin-Plate Martensite Formed under Applied Plane Stress at 4 K, *Scr. Met. Mater.,* Vol 28, 1993, p 1423–1428

8. C.M. Wayman, The Phenomenological Theory of Martensite Crystallography: Interrelationships, *Met. Mater. Trans. A, Phys. Metal. Mater. Sci.,* Vol 25A, 1994, p 1787–1795

9. B.P.J. Sandvik and C.M. Wayman, Characteristics of Lath Martensite. Part I. Crystallographic and Substructural Features, *Met. Mater. Trans. A, Phys. Metal. Mater. Sci.,* Vol 14, 1983, p 809–822

10. K. Wakasa and C.M. Wayman, Crystallography and Morphology of Ferrous Lath Martensite, *Metallography,* Vol 14, 1981, p 49–60

11. D.Z. Yang and C.M. Wayman, Slow Growth of Isothermal Lath Martensite in an Fe-21Ni-4Mn Alloy, *Acta Metall.,* Vol 32, 1984, p 949–954

12. K. Wakasa and C.M. Wayman, The Morphology and Crystallography of Ferrous Lath Martensite. Studies of Iron-20% Nickel-5% Manganese. I. Optical Microscopy, *Acta Metall.*, Vol 29, 1981, p 973–990

13. A.R. Marder and G. Krauss, The Morphology of Martensite in Iron-Carbon Alloys, *Trans. ASM*, Vol 60, 1967, p 651–660

Martensitic Structures, *Metallography and Microstructures*, Vol 9, *ASM Handbook*, ASM International, 2004, p. 165–178

Transformation Temperatures

In each alloy system, the martensite transformation occurs begins and ends between two specific temperatures: the martensite start (M_s) temperature and the martensite finish (M_f) temperature. The start temperature is an indication of the thermodynamic driving force required to begin the transformation. It has been shown (Ref 13) for iron-carbon martensites, the M_s temperature varies with carbon content (Fig. 17). The M_s temperatures for most iron-carbon alloys range from 500 to 200 °C (930 to 390 °F). The variation in M_s temperature with carbon content is easily explained by considering the strain carbon atoms induce in the lattice when in solid solution with iron. The additional strain created by the presence of carbon atoms increases the shear resistance of the austenite, which will require a larger driving force, in the form of a higher undercooling, to initiate the martensite transformation. Carbon is not the only element that affects the martensite transformation temperature. Most alloying elements, such as manganese, chromium, and nickel, lower the M_s temperatures (Ref 3). Various investigations into this phenomenon have produced equations that can be used to predict the effect of composition on the M_s temperature, such as the following, determined by Andrews (Ref 14):

$$M_s\,(°C) = 512 - 453C - 16.9Ni + 15Cr - 9.5Mo + 217(C)^2 - 71.5(C)(Mn) - 67.6(C)(Cr)$$

The martensite start temperature is also affected by mechanical deformation. Deforming the parent phase will lower the M_s temperature (termed M_d to indicate the presence of deformation). Additionally, the transformation from austenite to martensite can be accomplished solely by deformation, without a quenching process. Two different types of this deformation-induced martensite have been observed: stress assisted and strain induced (Ref 15). Stress-assisted martensite is produced when an applied stress provides the reduction in driving force for the reaction to occur. The resulting microstructure is typically a plate martensite. Strain-induced martensite occurs when an applied strain produces a plastic deformation to accomplish the transformation. This type of deformation-induced martensite usually results in a lath microstructure for ferrous systems (Ref 15).

The martensite finish temperature, M_f, is the temperature at which the transformation ceases. This does not indicate that the microstructure is 100% martensite, only that the martensitic transformation no longer occurs. A considerable amount of retained austenite may be present, as discussed previously. For some alloys, the M_f temperature is below room temperature, which can lead to a significant amount of retained austenite. Due to the athermal nature of the martensitic transformation, the amount of martensite formed depends not on the length of time the alloy is held below the transformation temperature, but rather what temperature it is cooled to.

It is also important to note that iron-carbon and iron-nitrogen martensites are unique in that they may decompose easily by precipitation, due to the high diffusivity of the interstitial carbon and nitrogen atoms (Ref 16). Conversely, substitutional martensites, such as iron-nickel, are much more stable and are able to be converted back to austenite by a separate shear mechanism.

References cited in this section

3. G. Krauss, *Principles of Heat Treatment of Steel,* American Society for Metals, 1985

13. A.R. Marder and G. Krauss, The Morphology of Martensite in Iron-Carbon Alloys, *Trans. ASM,* Vol 60, 1967, p 651–660

14. K. Andrews, Empirical Formulae for the Calculation of Some Transformation Temperatures, *J. Iron Steel Inst.,* Vol 203, 1965, p 721–727

15. V. Shrinivas, S.K. Varma, and L.E. Murr, Deformation-Induced Martensitic Characteristics of 304 and 316 Stainless Steels During Room-Temperature Rolling, *Met. Mater. Trans. A, Phys. Metal. Mater. Sci.,* Vol 26A, 1995, p 661–671

16. E.R. Petty, *Martensite: Fundamentals and Technology,* Longman Group Ltd., London, 1970

Martensitic Structures, *Metallography and Microstructures,* Vol 9, *ASM Handbook*, ASM International, 2004, p. 165–178

Tempering of Martensite

The martensitic structure that forms upon rapid quenching of austenite in iron-carbon alloys is inherently brittle due to the large amount of lattice strain from supersaturation of carbon atoms, segregation of impurity atoms to grain boundaries, and residual stresses from the quench. This brittleness imparts high hardness to the steel, but also results in low ductility and toughness. To regain ductility, the martensite may be tempered, which involves heating the steel to a temperature below the A_1 temperature (eutectoid temperature) and holding for varying amounts of time (Ref 3). Tempering will make the steel more ductile, but will also decrease the strength or hardness (Fig. 18).

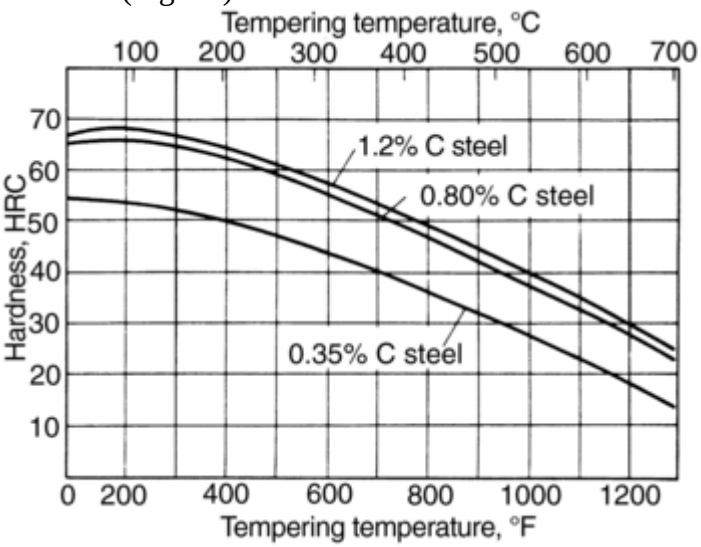

Fig. 18 Influence of increasing temperature (1 h) on decreasing the hardness of quenched carbon steels. Source: Ref 17

The as-quenched structure of iron-carbon martensite is very unstable. Factors that contribute to this instability include supersaturation of the interstitial lattice sites with carbon atoms, strain energy from the fine structure (twins or dislocations), large amounts of interfacial energy from the laths or plates, and the presence of retained

austenite (Ref 3). Upon reheating the as-quenched steel, the martensite will transform from the bct structure to a mixture of bcc iron (ferrite) and carbide (Fe_3C) precipitates. A typical tempered microstructure is shown in Fig. 19 for an Fe-0.2C alloy. Both the ferrite and the carbide will coarsen with increasing time and temperature, the driving force being the reduction of interfacial energy between the precipitates and the ferrite matrix (Ref 18).

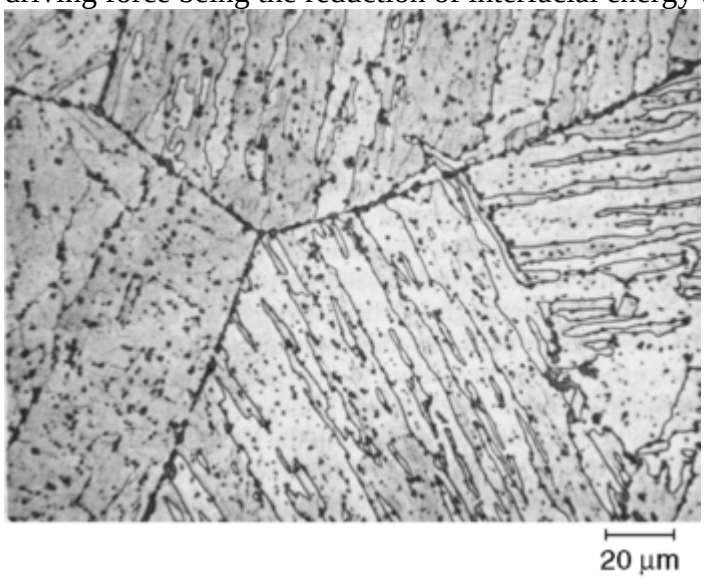

Fig. 19 Microstructure of lath martensite in an Fe-0.2C alloy after tempering at 700 °C (1290 °F) for 2 h. Nital etch. Magnification: 500×. Source: Ref 3

Early work on tempering of ferrous martensite outlined three distinct stages in the tempering process as shown in Table 1. More recent research has been published that identifies the structural changes that occur during tempering (Table 2). The temperature ranges are approximate and are usually based on 1 h treatment times (Ref 5).

Table 1 Stages of the tempering process

Stage	Description	Temperature	
		°C	**°F**
I	Formation of a transition carbide (epsilon or eta) and the lowering of the carbon content of the matrix martensite to about 0.25% C	100–250	210–480
II	Transformation of retained austenite to ferrite and cementite	200–300	390–570
III	Replacement of the transition carbide and low-carbon martensite by cementite and ferrite	250–350	480–660

Source: Ref 3

Table 2 Tempering reactions in steel

Temperature		Reaction and symbol (if designated)	Comments
°C	**°F**		
-40 to 100	-40 to 210	Clustering of two to four carbon atoms on octahedral sites of martensite; segregation of carbon atoms to dislocation boundaries	Clustering is associated with diffuse spikes around fundamental diffraction spots of martensite.
20–100	70–210	Modulated clusters of carbon atoms on (102) martensite planes (A2)	Identified by satellite spots around electron diffraction spots of martensite
60–80	140–180	Long period ordered phase with ordered carbon atoms arranged (A3)	Identified by superstructure spots in electron diffraction patterns
100–200	210–390	Precipitation of transition carbide as aligned 2 nm diam particles (T1)	Recent work identifies carbides as eta (orthorhombic, Fe_2C); earlier studies identified

			the carbides as epsilon (hexagonal, $Fe_{24}C$).
200–350	390–660	Transformation of retained austenite to ferrite and cementite (T2)	Associated with tempered martensite embrittlement in low- and medium-carbon steels
250–700	480–1290	Formation of ferrite and cementite; eventual development of well-spheroidized carbides in a matrix of equiaxed ferrite grains (T3)	This stage now appears to be initiated by chi-carbide formation in high-carbon Fe-C alloys.
500–700	930–1290	Formation of alloy carbides in Cr-, Mo-, V-, and W-containing steels. The mix and composition of the carbides may change significantly with time (T4).	The alloy carbides produce secondary hardening and pronounced retardation of softening during tempering or long-time service exposure around 500 °C (930 °F).
350–550	660–1020	Segregation and cosegregation of impurity and substitutional alloying elements	Responsible for temper embrittlement

Source: Ref 5

The fundamental mechanism responsible for tempering is a thermally activated process; both time and temperature are important variables in the tempering process. A tempering parameter is often used to describe the interaction between time and temperature: $T(20 + \log t) \times 10^{-3}$ where T is temperature in Kelvin and t is time in hours (Ref 3). The tempering parameter makes it possible to create different time and temperature combinations to achieve a certain tempered structure.

The tempering time and temperature for a martensitic steel must be chosen carefully in order to obtain the required combination of strength and ductility. Overtempering may result in a loss of strength to such a degree that the component is no longer useful for the intended application. The amount of softening that occurs with tempering can be altered with the addition of alloy elements. Softening occurs by the diffusion-controlled coarsening of cementite. Strong carbide formers, such as chromium, molybdenum, and vanadium, will reduce the rate of coarsening and thus minimize the amount of softening. Additionally, at higher tempering temperatures, these elements may themselves form carbides, leading to an increase in overall hardness; this is termed secondary hardening (Ref 3).

Different morphologies of tempered martensite will form depending on the heat treatment and the original martensite microstructure. It has been observed that packets of aligned laths in low-carbon martensites will transform into large, acicular grains, as shown in Fig. 20(a) to (c). In higher-carbon plate martensites, large martensite plates transform to equiaxed grains upon tempering (Fig. 21a to c). Additionally, these figures show how the carbides form on the grain boundaries and how both the ferrite grains and the carbides coarsen (Ref 18). When tempering procedures are not carefully chosen, spheroidization can occur, wherein the Fe_3C coalesces to form spheroid particles. The microstructures in Fig. 20(d) and Fig. 21(d) are both spheroidized.

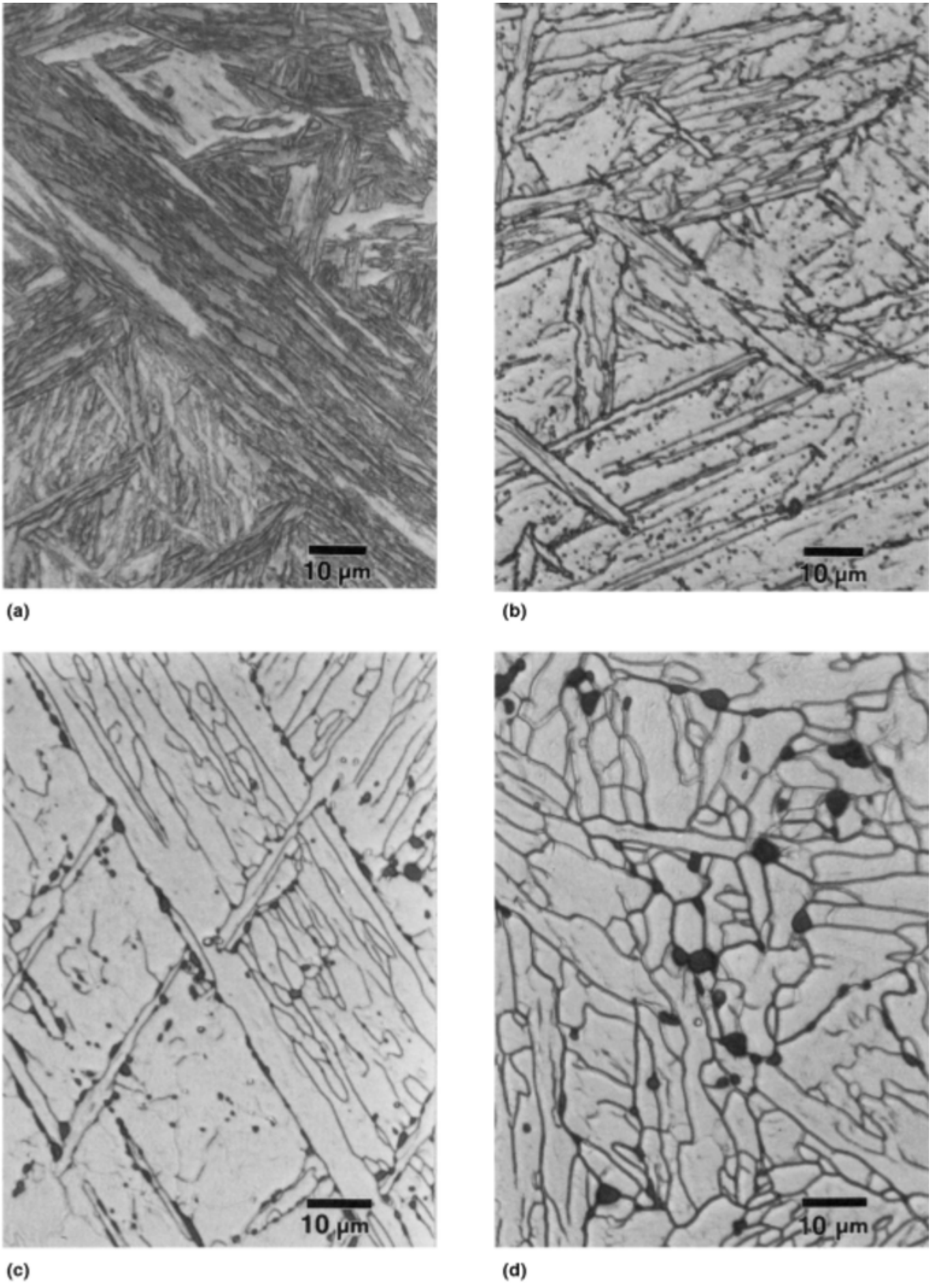

Fig. 20 Fe-0.2C alloy in the (a) water-quenched condition, followed by tempering at 690 °C (1275 °F) for (b) 1.5×10^3 s, (c) 1.03×10^4 s, and (d) 6.05×10^5 s. Source Ref 18. Reprinted with permission

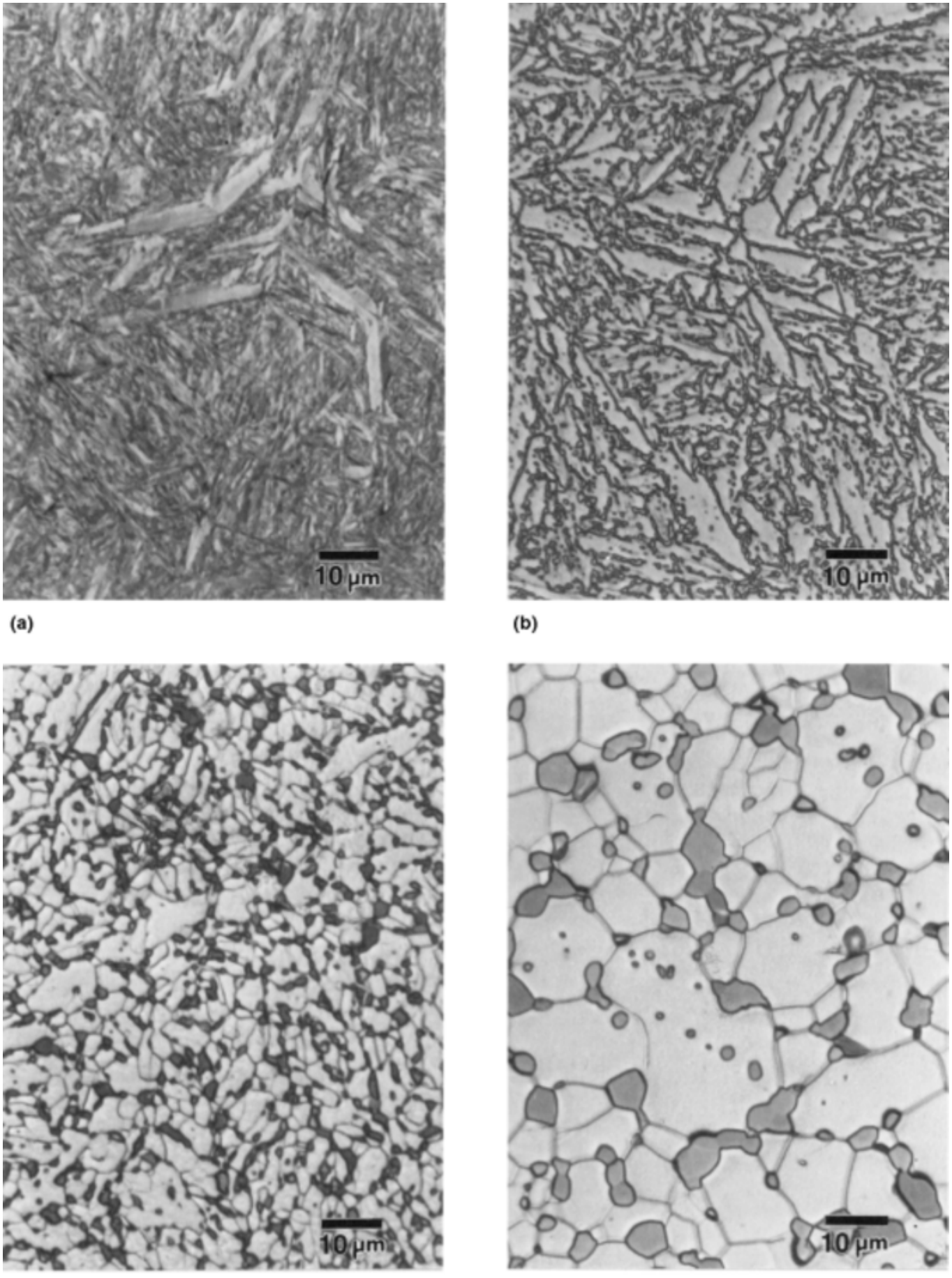

Fig. 21 Fe-1.2C alloy in the (a) water-quenched condition, followed by tempering at 690° C (1275 °F) for (b) 1.5×10^3 s, (c) 1.03×10^4 s, and (d) 6.05×10^5 s. Source Ref 18. Reprinted with permission

The change in morphology of tempered martensite, as shown in Fig. 20 and Fig. 21, provides an explanation for the change in mechanical properties of martensite from the as-quenched to the as-tempered form. As-quenched martensite has a very high density of dislocations, leading to high hardness and high work hardenability due to dislocation tangles. Tempering martensite causes the carbides to coarsen, increasing their average size while simultaneously decreasing their total population. Dislocation interactions with carbides is thus reduced significantly upon tempering, and work hardenability is reduced. This effect is depicted in Fig. 22, which shows true-stress/true-strain curves for an as-quenched and a tempered lath martensite. The work-hardening rate, indicated by the slope of the stress-strain curve, is much higher for the as-quenched steel than for the tempered steel.

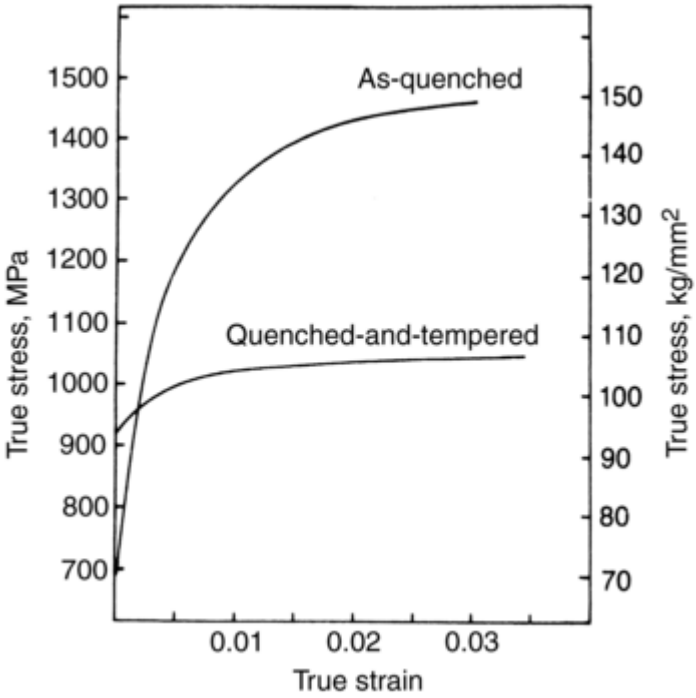

Fig. 22 True-stress/true-strain curves for Fe-0.2C as-quenched and quenched-and-tempered lath martensite with packet size of 8.2 µm. Source: Ref 3

References cited in this section

3. G. Krauss, *Principles of Heat Treatment of Steel,* American Society for Metals, 1985

5. A.R. Marder, Structure-Property Relationships in Ferrous Transformation Products, *Phase Transformation of Ferrous Alloys,* Proc. Int. Conf., TMS 1984, P11–41

17. A.K. Sinha, *Ferrous Physical Metallurgy,* Butterworth Publishers, 1989

18. B.A. Lindsley and A.R. Marder, The Morphology and Coarsening Kinetics of Spheroidized Fe-C Binary Alloys, *Acta Mater.,* Vol 46, 1997, p 341–351

Martensitic Structures, *Metallography and Microstructures,* Vol 9, *ASM Handbook*, ASM International, 2004, p. 165–178

Nonferrous Martensite

Frank C. Gift, Jr., Lehigh University

Formation of the martensite structure in nonferrous systems occurs by the same diffusionless displacive transformation mechanisms described for ferrous systems. Macroscopic deformation resulting from martensitic transformations will result in upheaval on the surface of polished specimens, as shown in Fig. 23 and 24. If there are no obstructions from a diffusion-controlled transformation (as there are for iron-carbon alloys), the martensitic surface relief formed upon cooling can be removed by heating to temperatures above the start temperature of the parent phase. The transformation hysteresis is thus defined by the difference between the forward and reverse transformation temperatures. Reversibility of the transformation is typical of nonferrous systems that undergo the martensitic transformation.

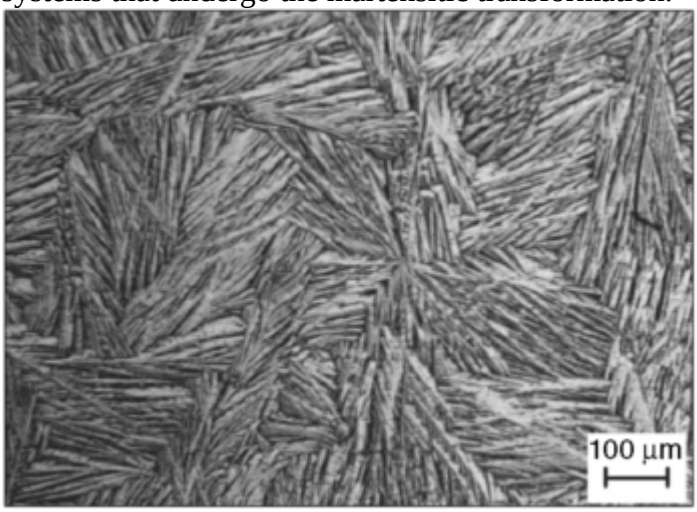

Fig. 23 Relief effects observable on a polished surface of Ni-50.3Ti-2W are characteristic of the martensitic transformation; water quenched from 550 °C (1020 °F). Source: Ref 19. Reprinted with permission

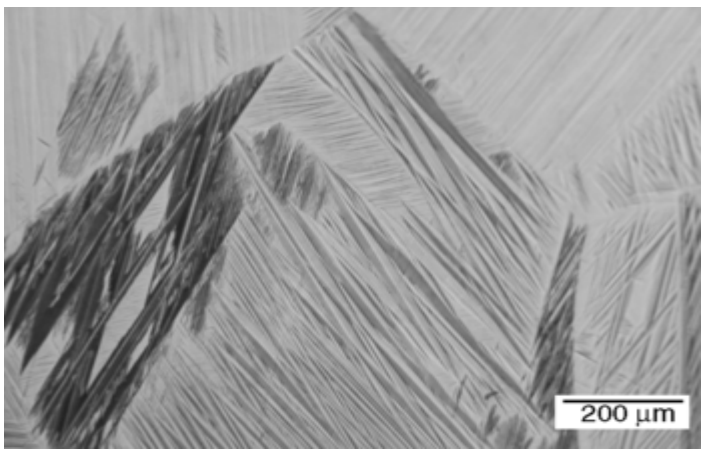

Fig. 24 Surface relief observed in martensite transformation in Cu-26.7Zn-4Al (M_s approx 20 °C (70 °F), solution heated at 900 °C (1650 °F), quenched in an ice bath, brought to room temperature, then quenched to liquid N_2 temperatures. Courtesy of F. Gift and B. Newbury

Nonferrous martensitic transformations exhibit a characteristic platelike microstructure (in most cases), such that one dimension of the martensite region is much smaller than the other two. Viewed in cross section on a scale observable in light optical microscopy (LOM), these plates have a needle shape that can traverse entire grains or form various internal arrangements within grains (see Fig. 25 and 26). Macroscopic shape changes associated with the martensitic transformation from parent to product phase, a result of the Bain strain and lattice-invariant deformation, induce stress in the surrounding matrix. Lenticular-shaped martensite plates are often observed, believed to form due to an increasing elastic stress surrounding the plate during formation (Ref 21). The lenticular plate shapes, and martensite plate groupings in various orientations (variants), have been found to reduce the constraining elastic stress through accommodation of the macroscopic shape changes (see Fig. 27).

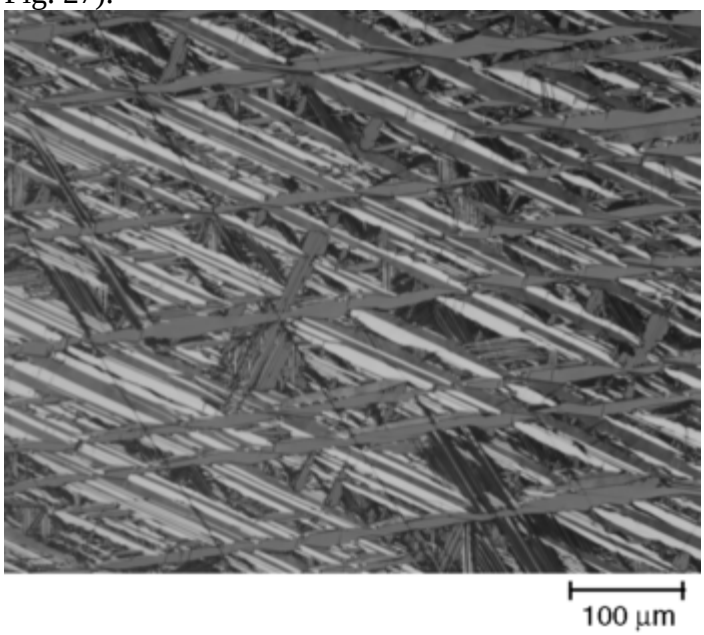

Fig. 25 This is an image of martensite, running from bottom right to top left, in aluminum bronze, Cu-11.8Al, heated to 900 °C (1650 °F), held 1 h, water quenched. It is in polarized light, as-polished, at 200× as a 4 × 5 inch print. Courtesy of G. Vander Voort

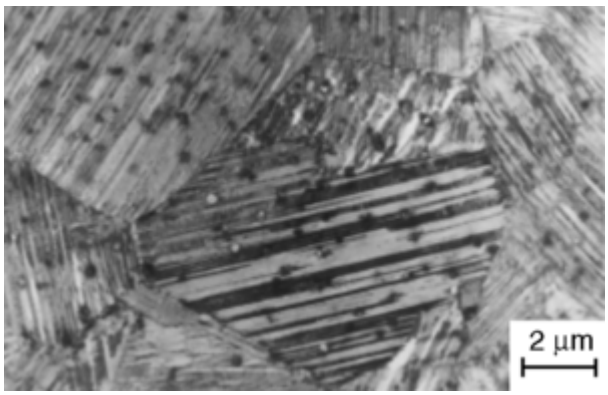

Fig. 26 Transmission electron microscopy image of martensite present in Cu-11.4Al-5Mn-2.5Ni-0.4Ti (wt%), melt spun at a wheel speed of 6.5 m/s. Precipitates of Cu_2AlTi are visible, dispersed evenly across the different grains. Source: Ref 20. Reprinted with permission

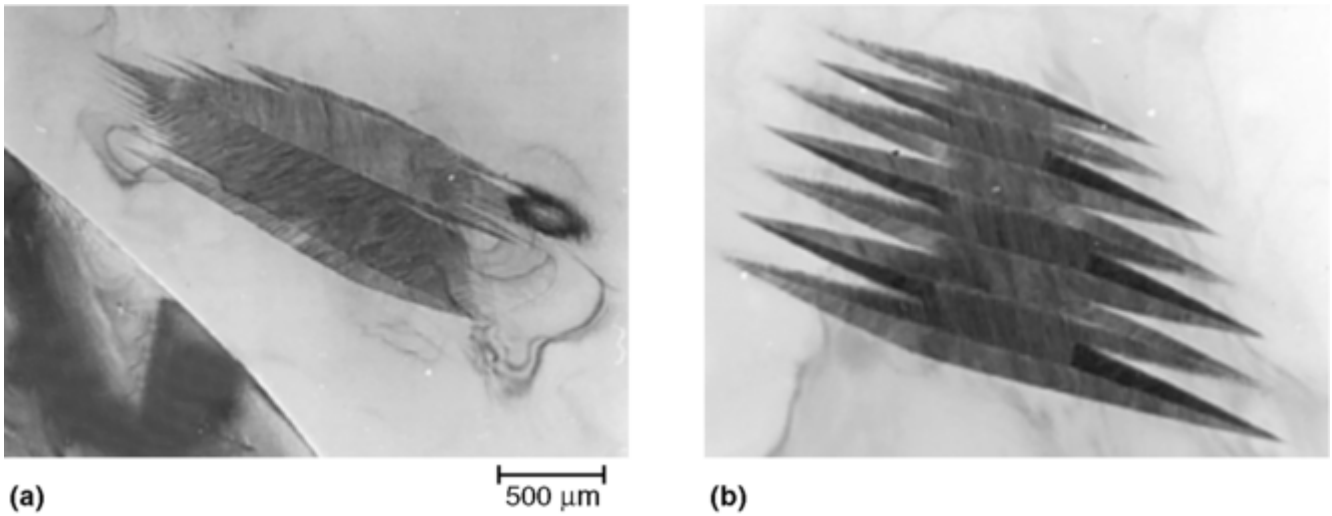

Fig. 27 Transmission electron microscopy images of splat-cooled Ni-37.5Al (at.%) showing accommodating martensite groupings. Source: Ref 22. Reprinted with permission

Historically, martensitic transformations in metal alloys (specifically steel) have been studied most frequently, but recent attention has also been applied to ceramic, mineral, and organic systems that develop martensite structures. Table 3 lists different material systems that undergo martensitic transformations, along with specific alloys or compounds and the general changes in crystal structure for such systems.

Table 3 Nonferrous martensite transformations for selected systems

Material systems	General parent crystal structure	General martensite crystal structure
Metals		
Ag alloys (Ag-Cd, Ag-Ge, Ag-Zn)	bcc	3R, 9R, 2H
Au alloys (Au-Cd, Au-Cu-Zn, Au-Zn)	bcc	3R, 9R, 2H
Co alloys (Co, Co-Be, Co-Ni)	fcc	hcp
Cu alloys (Cu-Al, Cu-Al-Ni, Cu-Sn, Cu-Zn)	bcc	3R, 9R, 2H
In alloys (In-Tl, In-Cd)	fcc	fct
Li alloys (Li, Li-Mg)	bcc	hcp
Ni alloys (Ni-Al, Ni-Ti)	bcc	3R, 9R, 2H
Mn alloys (Mn-Cu, Mn-Ni)	fcc	fct
Ti alloys (Ti, Ti-Cu, Ti-Mn, Ti-Mo, Ti-V)	bcc	hcp
Zr alloys (Zr, Zr-Mo, Zr-Nb)	bcc	hcp
Ceramics		
Dicalcium silicate (Ca_2SiO_3)	Monoclinic	Orthorhombic
Lanthanide sesquioxide (Ln_2O_3)	Monoclinic	Cubic
Lead titanate ($PbTiO_3$)	Cubic	Tetragonal
Potassium niobate ($KNbO_3$)	Tetragonal	Orthorhombic
Zirconia (ZrO_2)	Tetragonal	Monoclinic
Other		
Ammonium halides (NH_4X)	NaCl structure	CsCl structure
Enstatite ($MgSiO_3$)	Orthorhombic	Monoclinic
Nitrates ($AgNO_3$, KNO_3)	Orthorhombic	Rhombohedral
Quartz (SiO_2)	Trigonal	Hexagonal
Sulfides (MnS)	Zinc-blende	NaCl structure

Table compiled from data found in: Tables 9-3, 9-4, and 9-8 in Ref 4; Table I.1 in Ref 23; Appendix, chapter 10 in Ref 24; Tables 2.4–2.8 in Ref 25; Table 1 in Ref 26; and Table 13 in Ref 27

References cited in this section

4. G. Kostorz, *Phase Transformations in Materials,* Wiley-VCH, Weinheim, Germany, 2001

19. H. Scherngell and A.C. Kneissl, *Acta Mater.,* Vol 50, 2002, p 328

20. J. Dutkiewicz, T. Czeppe, and J. Morgiel, *Mater. Sci. Eng.,* Vol A273–275, 1999, p 706

21. L. Delaey, Diffusionless Transformations, chapter 9, *Phase Transformations in Materials,* G. Kostorz, Ed., Wiley-VCH, Weinheim, Germany, 2001

22. D. Schryvers and D. Holland-Moritz, *Mater. Sci. Eng.,* Vol A273–275, 1999, p 699

23. H. Funakubo, *Shape Memory Alloys,* Gordon and Breach Science Publishers, 1987, p 7, 18

24. A.K. Jena and M.C. Chaturvedi, *Phase Transformations in Materials,* Prentice-Hall, 1992, p 428–429

25. Z. Nishiyama, chapter 2, *Martensitic Transformation,* Academic Press, 1978

26. W.M. Kriven, *J. Phys. IV,* Vol 5 (No. C8), 1995, p 101–110

27. P.M. Kelly and L.R.F. Rose, *Prog. Mater. Sci.,* Vol 47, 2001, p 550–551

Martensitic Structures, *Metallography and Microstructures,* Vol 9, *ASM Handbook,* ASM International, 2004, p. 165–178

Metallic Systems

Nonferrous martensite in metal alloys has been studied extensively. In metallic systems, nonferrous martensite generally occurs in substitutionally alloyed systems that demonstrate small transformation strains and a small transformation hysteresis. The macroscopic deformation from the resultant transformation from one crystal structure to another can be observed from the surface relief and in the plate morphology that the martensite phase usually assumes. Substructure of the martensite plates can be characterized with the use of TEM. Stacking faults, twins, and dislocations are commonly observed within martensite plates. Twinning deformation or slip along the shear planes can accommodate structural transformations that would otherwise result in a significant shape change. Their presence and frequency within the martensite phase is dependent on the alloy system and composition.

Martensitic transformations in metallic systems can be grouped into three categories. Allotropic transformations of the solvent atom to create the martensite product comprise the first category. Martensitic transformations in cobalt, titanium, zirconium, hafnium, and lithium alloys belong to this group. Cobalt and alloys undergo the fcc to hcp (ε) martensitic transformation by shifting every other (111) plane by (a/6)[$11\bar{2}$] partial dislocations (Ref 25). This operation changes the stacking sequence from fcc to bcc, creating the following orientation relationships—$(111)_{fcc} \parallel (0001)_{hcp}$ and $[11\bar{2}]_{fcc} \parallel [1\bar{1}00]_{hcp}$ (Ref 24). Cobalt and cobalt-nickel alloys can therefore have a high measure of stacking faults within the martensite plates. Titanium, zirconium, hafnium, and lithium alloys generally transform from bcc (β-phase) to hcp structures, although fcc and orthorhombic martensite structures have been reported in some titanium and zirconium alloys (Ref 28). The bcc transformation to hcp in zirconium has the $(1\bar{1}2)_{bcc} \parallel (1\bar{1}00)_{hcp}$ and $[\bar{1}11]_{bcc} \parallel [11\bar{2}0]_{hcp}$ orientation

relationships (Ref 24, 28). Lath morphologies have been observed in some of the titanium and zirconium alloys as well. Twins are commonly found in the plate martensite form of these alloys (see Fig. 28), while stacking faults are commonly observed in lath martensite (see Fig. 29).

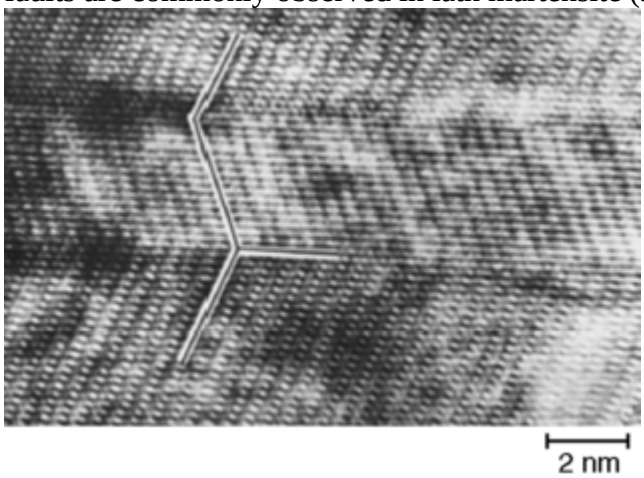

Fig. 28 High-resolution transmission electron microscopy image of a ($11\bar{1}$) twin boundary in 8% deformed Ti-44.7Ni-9Nb (at.%). Source: Ref 29. Reprinted with permission

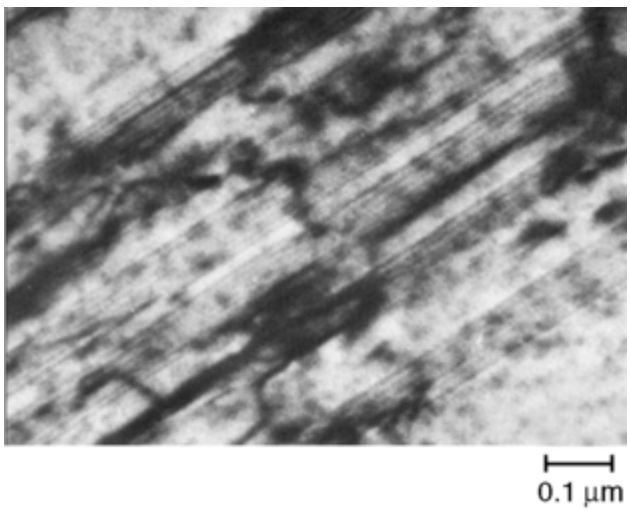

Fig. 29 Transmission electron micrograph of stacking faults, running diagonally across the image, along (0001) planes in a titanium martensite crystal. Source: Ref 25. Reprinted with permission

Copper, gold, and silver alloys belong to the β-phase Hume-Rothery alloy group, whose parent phase is a bcc structure. Nickel alloys such as nickel-aluminum and nickel-titanium (~50 to 50 ratio) are also part of this alloy group, with a bcc parent phase. Since the transformations are diffusionless and lattice correspondence is maintained, order or disorder present in the parent phase is transferred to the martensite phase (Ref 2, 30). Often a superlattice structure is present that is then conveyed to the martensite product. Ordered or disordered, the martensite phase produced is usually of the 3R, 9R, or 2H type (Ref 23). Shear along the $(011)_{bcc}$ planes in different directions and sequences creates the variations in martensite phase produced (Ref 31). These alloys all belong to the second category marking a weak first-order transformation with an intermediate stability of the martensite phase at temperatures above the M_s temperature. Alloys used in shape memory applications (discussed in another section) are found in this category.

The third category of martensitic transformations belongs to second-order transformations (very weak first order) that have a larger mechanical instability of the martensite phase. First-order phase transformations are those phase transformations for which the first derivative of Gibbs free energy with respect to temperature and pressure are discontinuous at the equilibrium transformation temperature. Second-order phase transformations have continuous first derivatives, but have discontinuous second derivatives of Gibbs free energy with respect to temperature and pressure. The fcc to face-centered tetragonal (fct) martensitic transformation of manganese and indium alloys fall into this category.

References cited in this section

2. G.B. Olson and W.S. Owen, Ed., *Martensite: A Tribute to Morris Cohen,* ASM International, 1992

23. H. Funakubo, *Shape Memory Alloys,* Gordon and Breach Science Publishers, 1987, p 7, 18

24. A.K. Jena and M.C. Chaturvedi, *Phase Transformations in Materials,* Prentice-Hall, 1992, p 428–429

25. Z. Nishiyama, chapter 2, *Martensitic Transformation,* Academic Press, 1978

28. F.E. Fujita, chapter 6, *Physics of New Materials,* 2nd ed., Springer-Verlag, 1998

29. Y.F. Zheng, L.C. Zhao, and H.Q. Ye, *Mater. Sci. Eng.,* Vol A273–275, 1999, p 272

30. A.L. Roytburd, *Mater. Sci. Eng.,* Vol A273–275, 1999, p 2

31. A.V. Srinivasan and D.M. McFarland, *Smart Structures,* Cambridge University Press, 2001, p 31

Martensitic Structures, *Metallography and Microstructures,* Vol 9, *ASM Handbook*, ASM International, 2004, p. 165–178

Ceramic Systems

Displacive polymorphic transformations occur in ceramic systems that can be regarded as martensitic transformations. The transformations are diffusionless, involving the reorientation (without breaking) of atomic bonds that leads to a macroscopic shape change of the transformed phase. Examples include the cubic-to-tetragonal transformation of lead titanate and the tetragonal-to-monoclinic transformation of zirconia (see Fig. 30).

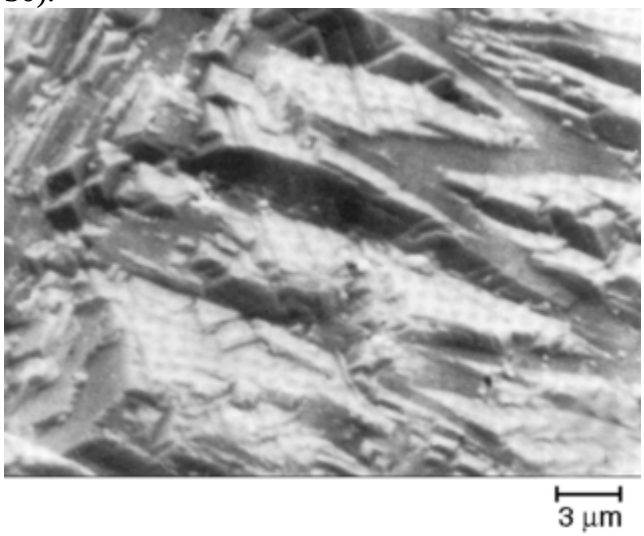

Fig. 30 Scanning electron microscopy image of surface relief created by the martensitic transformation in a single crystal of ZrO_2. Source: Ref 32. Reprinted with permission

Ceramic systems are intrinsically brittle and the martensite transformation proved to be problematic (especially in monocrystalline materials) due to unintended crack formation as a result of the volume expansion of the martensite phase. This destructive phenomenon in some material systems (such as silica) has been utilized in recent years and has been the subject of much research, in the development of other tougher ceramic materials. Stress-induced transformations within the region of tensile stresses at advancing crack tips have successfully been employed to counter these stresses and retard crack propagation (Ref 33). Much of the current literature has focused on martensite in ceramic systems in the context of the transformation-toughening mechanism.

Application of the phenomenological theory of martensite transformations to partially stabilized zirconia (PSZ) has led to the determination of the habit plane, orientation relationship, and shape strain for this system (Ref 27). Experimental observations of this system are supported by the phenomenological theory, allowing it to be used for fundamental understanding of transformation toughening and its governing factors. A positive volume change, shear-dominated strain with accommodating variants, and the ability to transform martensitically under suitable stress conditions are the characteristics of an archetype ceramic system that would be capable of transformation toughening.

Zirconia systems exhibit all of these characteristics, which is why it has been considered the prototypical system for transformation studies and applications. Pure zirconium dioxide will not be capable of transformation toughening, since the tetragonal phase needs to be stabilized until the stress needed to induce the transformation is created by the propagating crack. Additions of calcium oxide, magnesium oxide, and yttrium oxide can stabilize tetragonal precipitates of zirconia in a cubic zirconia matrix, with a suitable processing treatment (Ref 33). These compounds are PSZ (Fig. 31). Larger additions of yttrium oxide or of cerium oxide can be used to stabilize almost an entire tetragonal matrix. Such systems are called tetragonal zirconia polycrystal (PZT). Zirconia particles can also be added to the matrix of other ceramics to provide the same type of transformation toughening as the PSZ materials. Aluminum oxide with zirconia particles in the matrix is one such example.

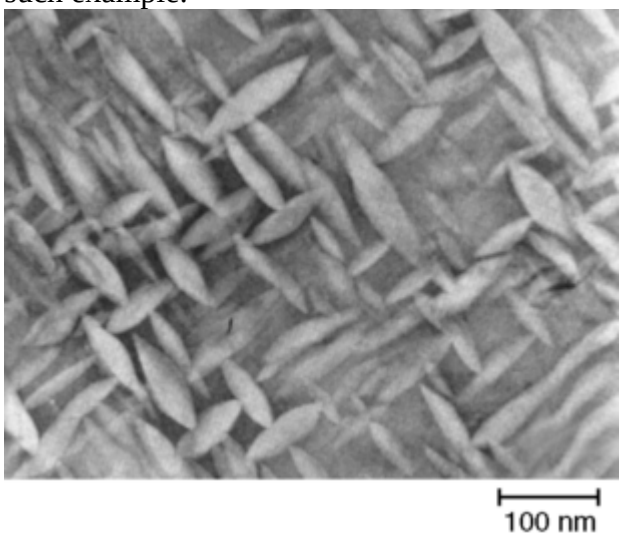

Fig. 31 Transmission electron microscopy image of tetragonal precipitates in a cubic matrix in transformation-toughened MgO-PSZ. Source: Ref 27. Reprinted with permission

Ceramic systems other than zirconia show martensitic transformations. Dicalcium silicate, lead titanate, potassium niobate, hafnium dioxide, and silicon dioxide are some examples of such systems (Ref 27, 34) (Fig. 32). The monoclinic-to-orthorhombic transformation in dicalcium silicate and the monoclinic-to-cubic transformation in the lanthanide sesquioxides show potential for use as transformation-toughening systems (Ref 27).

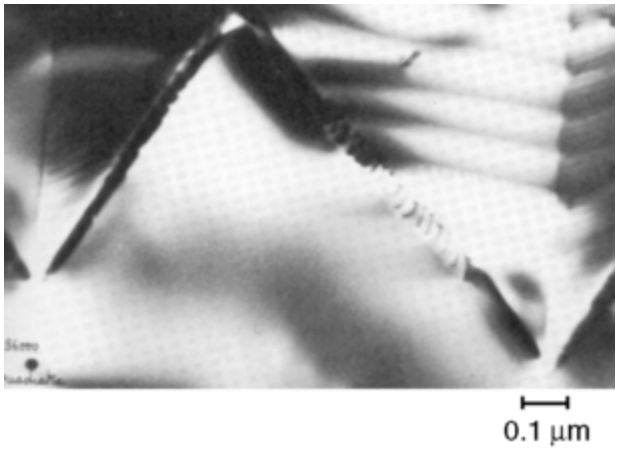

Fig. 32 Transmission electron microscopy image of HfO_2 taken at high temperature showing the coexistence of the martensitic phase—monoclinic (top), and the tetragonal phase at the bottom. Source: Ref 35. Reprinted with permission

References cited in this section

27. P.M. Kelly and L.R.F. Rose, *Prog. Mater. Sci.*, Vol 47, 2001, p 550–551

32. E.C. Subbarao, *Adv. Ceram.*, Vol 3, 1981, p 18

33. D.W. Richerson, *Modern Ceramic Engineering*, 2nd ed., Marcel Dekker, 1992 p 745

34. P.M. Kelly, *Mater. Sci. Forum*, Vol 56–58, 1990, p 335–346

35. C.M. Wayman, *Adv. Ceram.*, Vol 3, 1981, p 81

Martensitic Structures, *Metallography and Microstructures*, Vol 9, *ASM Handbook*, ASM International, 2004, p. 165–178

Other Systems

Minerals, inorganic, and organic compounds have demonstrated the ability to transform martensitically. These systems do not have commercial applications like the shape memory alloys and transformation-toughened ceramics, so less information on these systems is currently available. Nitrate salts, ammonium halides, and sulfides can undergo martensitic transformations. Minerals such enstatite, wollastonite, and the natural forms of silica (such as quartz or cristobalite) also have documented martensite transformations (Ref 26). Biological systems also have elements that are characterized by martensitic transformations, specifically the protein crystals in certain bacteria and viruses (Ref 36). The contraction of the protein crystals is utilized in the life functions of these biological systems, and the transformation mechanism has been shown to adhere to the detailed definitions of the martensitic transformation.

References cited in this section

26. W.M. Kriven, *J. Phys. IV*, Vol 5 (No. C8), 1995, p 101–110

36. G.B. Olson, *Mater. Sci. Eng.*, Vol A273–275, 1999, p 19

Martensitic Structures, *Metallography and Microstructures*, Vol 9, *ASM Handbook*, ASM International, 2004, p. 165–178

Shape Memory Materials

Rick Noecker, Lehigh University

The shape memory effect occurs when material shape is deformed at a low temperature in a martensitic state and regains its shape when heated to a higher temperature and transformed to the parent phase. This is the result of a thermoelastic martensitic transformation. The martensitic transformation in shape memory alloys is cooperative, nondiffusional, and results in a microscopic surface relief as seen in Fig. 33 (Ref 37).

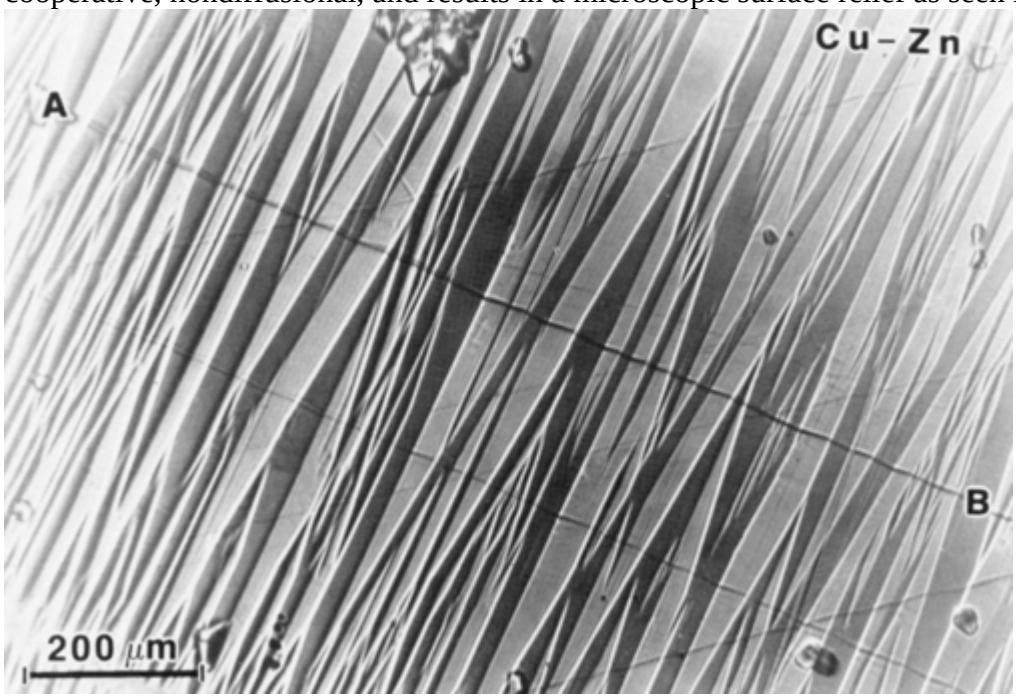

Fig. 33 Surface relief due to thermoelastic martensite transformation in a copper-zinc shape memory alloy. Source: Ref 37. Reprinted with permission

There are several characteristics of shape memory alloys (SMA) that make them unique from other alloys exhibiting martensitic transformations. First, the vast majority of shape memory alloys used in engineering applications have an ordered structure, which enhances the crystallographic reversibility by minimizing the number of crystallographic paths to the parent phase while making deformation by slip a less favorable mechanism (Ref 38). Second, the martensite forms in a self-accommodating fashion by the formation of twins. This is seen in Fig. 33 where a scratch is locally displaced and recovered by each relief. Third, the martensite formed is thermoelastic, crystallographically reversible, and consists of a highly mobile twin interface. Thermoelastic martensite exhibits a small temperature hysteresis upon transformation as seen in Fig. 34 (Ref 38).

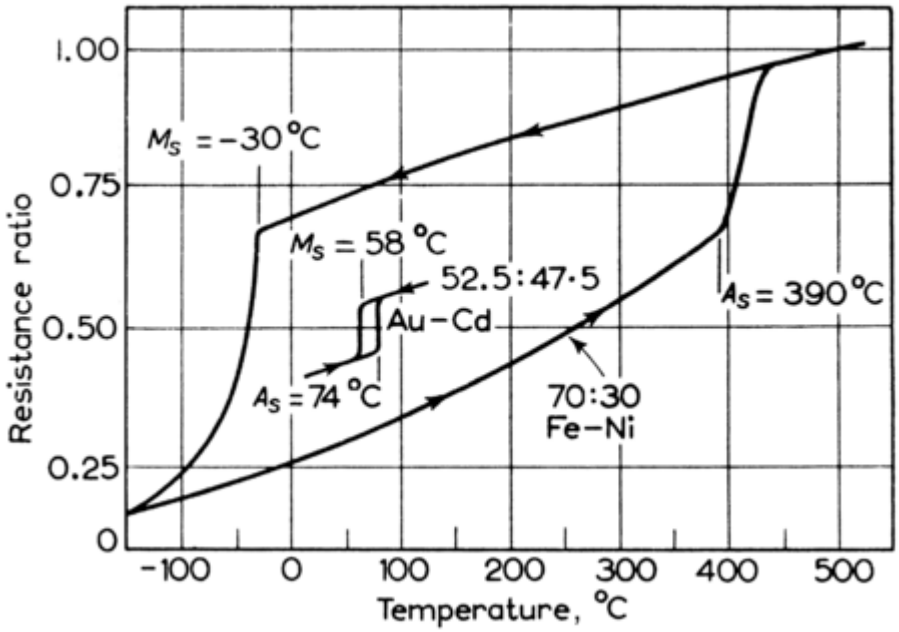

Fig. 34 Temperature hysteresis of thermoelastic martensite transformation in gold-cadmium and nonthermoelastic iron-nickel. Source: Ref 38. Reprinted with permission

In Fig. 34, Fe-30Ni (wt%) exhibits a large hysteresis of approximately 400 K, characteristic of a nonthermoelastic martensite transformation, whereas the hysteresis of Au-47.5Cd (at.%), a thermoelastic martensite, is only 15 K (Ref 38). The hysteresis is defined by measuring the change in a physical property (e.g., resistance) versus temperature. There are four temperatures that define the hysteresis, M_s and M_f, the martensite start and finish temperature upon cooling, respectively, and A_s and A_r, the austenite (or parent) start and finish temperature upon heating, respectively (Ref 39). Most thermoelastic martensite transformations, and thereby almost all shape memory alloys, exhibit a hysteresis of approximately 20 K (Ref 37).

As can be seen in Fig. 34, thermoelastic martensite and crystallographic reversibility are conjugate. A decrease in temperature between M_s and M_f results in slight growth of martensite plates, which defines thermoelastic martensite (Ref 37), whereas an incremental increase in temperature results in the reversal of the martensite transformation by formation of parent phase between A_s and A_f, which defines crystallographic reversibility (Ref 37). The relationship between parent and martensite phases can be seen in Fig. 35, in which γ_1' martensite in Cu-14.2Al-4.2Ni (wt%) is seen adjacent to the untransformed parent phase (Ref 38).

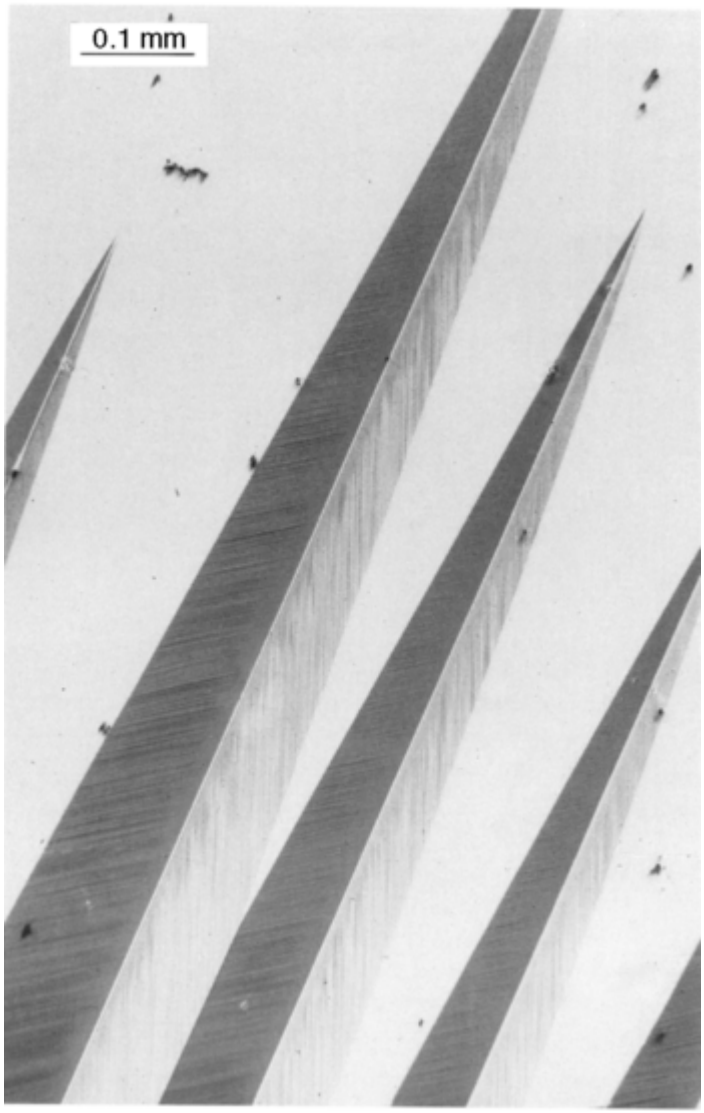

Fig. 35 γ_1' martensite adjacent to untransformed parent phase in Cu-Al-Ni. Source: Ref 38. Reprinted with permission

In one-way shape memory, the "remembered" shape is that of the material in the parent phase (Ref 38). For a complete shape memory effect, both the transformation must be crystallographically reversible and the deformation must proceed solely by twin boundary movement (Ref 38). Table 4 (Ref 38) is a list of SMAs that exhibit perfect shape memory effect.

Table 4 Alloys that exhibit perfect shape memory effect

Alloy	Composition, at.%	Structure change	Temperature hysteresis, K	Ordering
Ag-Cd	44–49 Cd	B2 to 2H	~15	Ordered
Au-Cd	46.5–48.0 Cd	B2 to 2H	~15	Ordered
	49–50 Cd	B2 to trigonal	~2	Ordered
Cu-Zn	38.5–41.5 Zn	B2-M (modified) 9R	~10	Ordered
Cu-Zn-X (X = Si, Sn, Al, Ga)	A few at.%	B2 to M9R	~10	Ordered
Cu-Al-Ni	28–29 Al, 3.0–4.5 Ni	$D0_3$ to 2H	~35	Ordered
Cu-Sn	~15 Sn	$D0_3$ to 2H, 18R	…	Ordered
Cu-Au-Zn	23–28 Au, 45–47	Heusler to 18R	~6	Ordered

	Zn			
Ni-Al	36–38 Al	B2 to 3R, 7R	~10	Ordered
Ti-Ni	49–51 Ni	B2 to monoclinic	~30	Ordered
		B2 to R-phase (monoclinic)	~2	Ordered
Ti-Ni-Cu	8–20 Cu	B2 to orthorhombic (monoclinic)	4–12	Ordered
Ti-Pd-Ni[(a)]	0–40 Ni	B2 to orthorhombic	30–50	Ordered
In-Tl	18–23 Tl	fcc to fct	~4	Disordered
In-Cd	4–5 Cd	fcc to fct	~3	Disordered
Mn-Cd	5–35 Cd	fcc to fct	…	Disordered

(a) Ti-Pd-Ni alloys with high Pd content do not exhibit good shape memory effect unless specially thermomechanically treated. Source: Ref 38

In general, lattice invariant shear (LIS) in the martensite transformation can occur by either slip and/or twinning. As seen in Fig. 36, both mechanisms produce a localized crystallographic shape change; however, the LIS in most SMAs is twinning (Ref 38). Twinning is key in reducing the strain formed by the formation of martensite, which is necessary for the further nucleation and growth during the martensite transformation (Ref 38). Because the parent phase has greater symmetry than the martensite product phase, several crystallographic variants, or domains, can form from the same parent material (Ref 39). In general, when an SMA is cooled below M_f, a single crystal will produce 24 crystallographically equivalent habit plane variants (HPVs) as predicted by the phenomenological theory of martensite crystallography (Ref 23). Martensite formed by a twin invariant plane strain will produce HPVs that consist of two martensite regions that are twin related with a specific crystallographic lattice correspondence to the parent lattice. These regions are known as correspondence variants (Ref 23).

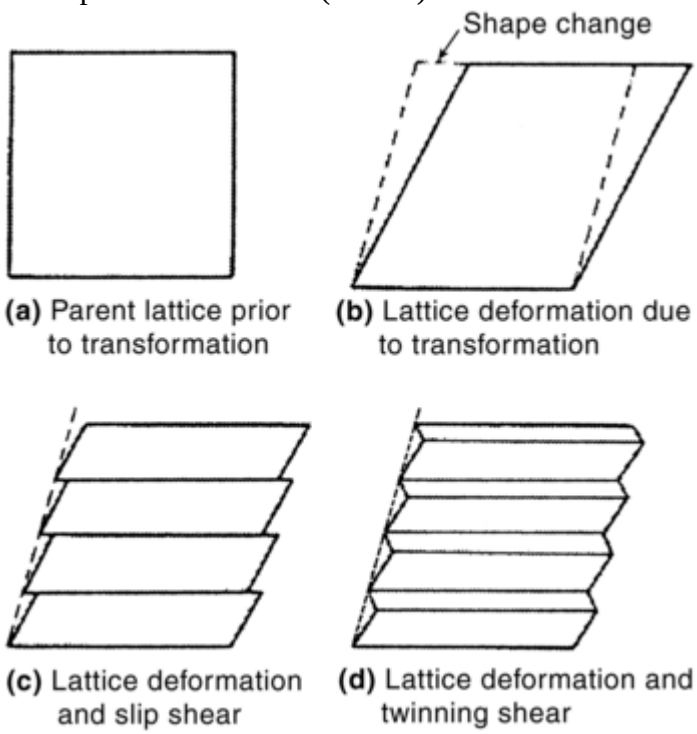

Fig. 36 Martensite shear mechanisms. (a) Parent lattice prior to transformation. (b) Lattice deformation due to transformation. (c) Lattice deformation and slip shear. (d) Lattice deformation and twinning shear. Source: Ref 23. Reprinted with permission

Figure 37(a) is an scanning electron micrograph of B2-7R(14M) martensite transformation in a Ni-37Al (at.%) SMA (Ref 40). Trace analysis identified the presence of four HPVs, each being twin related to the others (Ref 40). There are three types of twinned interfaces in this micrograph, identified by 1, 2, and 3 in Fig. 37(b) (Ref 40). Types I and II both have a spearlike interface with a long boundary and are formed between A-C or B-D and A-B or C-D variant pairs, respectively, which are shown in Fig. 37(c) (Ref 40). Type III twinned interfaces

produce a two-pronged forklike morphology with a short interface boundary and is formed between variant pairs A-D or B-C (Ref 40).

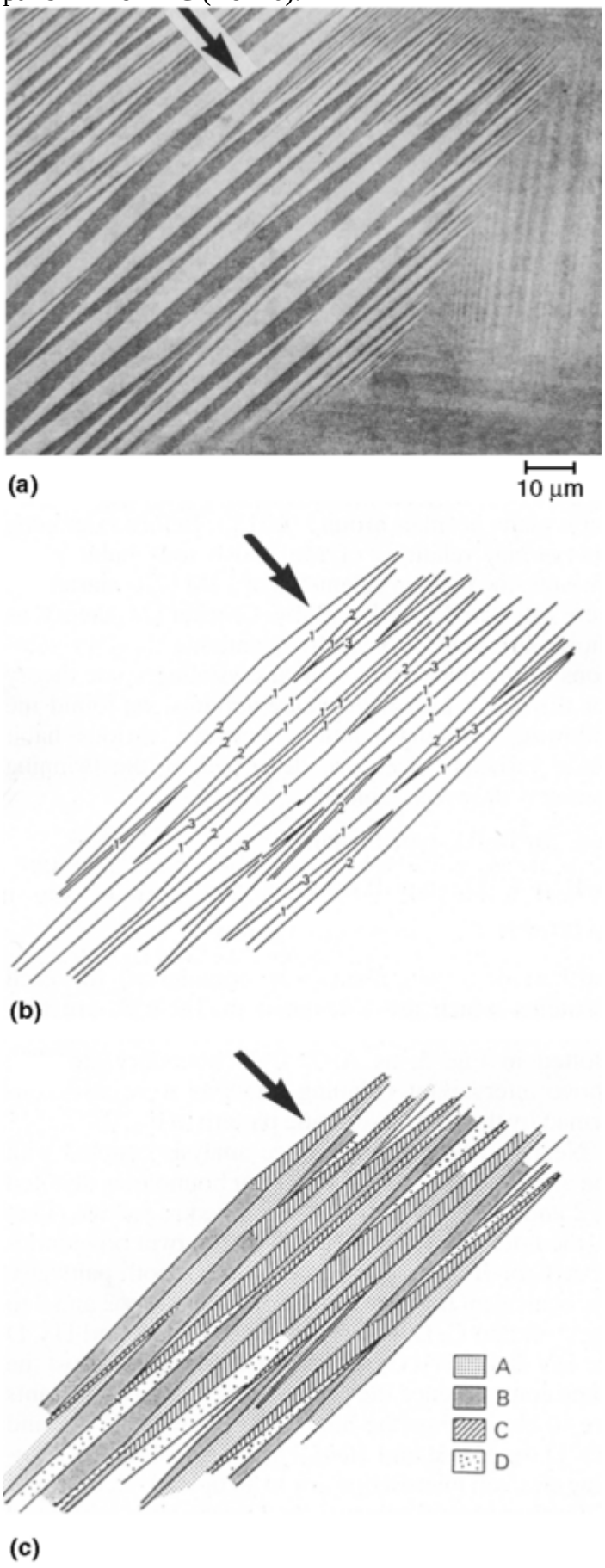

Fig. 37 (a) Scanning electron micrograph of B2-7R(14M) martensite transformation in nickel-aluminum. (b) Twin boundary types. (c) Twin variants. Source: Ref 40. Reprinted with permission

The three modes of twinning seen in Fig. 37 can be explained with the aid of Fig. 38, which graphically displays the four twinning elements K_1, K_2, η_1, and η_2 (Ref 41). K_1 and η_1 are the invariant plane of shear and shear direction respectively. K_2 is the undistorted, or conjugate plane and η_2 is the conjugate shear direction formed by the intersection of the plane of shear, P, with K_2 (Ref 41). Type I is defined by twinned crystals related by mirror symmetry with respect to the K_1 plane (Ref 38). Type II twins are defined by a rotation of π around the η_1 axis. Type III, otherwise known as compound or mixed-mode twinning, is a combination of types I and II (Ref 38). The relationship of the twin boundaries in Fig. 37 is shown in Fig. 39 (Ref 40), in which four adjacent parallelograms are twin related (Ref 38).

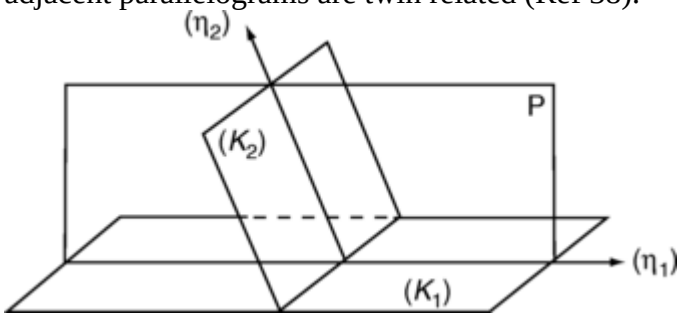

Fig. 38 Four twinning elements: K_1 and K_2 planes, η_1 and η_2 directions, which are all contained in P, the shear plane. Source: Ref 41. Reprinted with permission

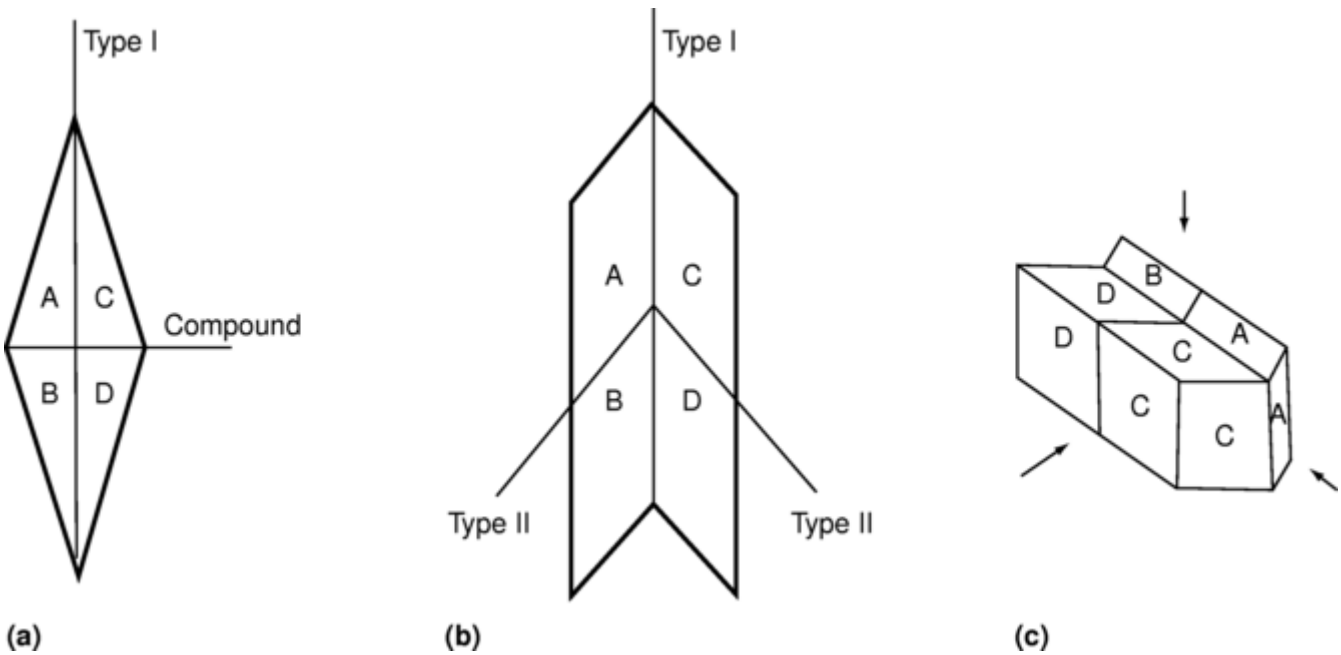

Fig. 39 Twin boundary morphology that results in self-accommodation. (a) Diamond (b) Parallelogram in two dimensions. (c) Parallelogram in three dimensions. Source: Ref 40. Reprinted with permission

This twinned relationship between adjacent martensite variants in SMA results in self-accommodation and reduction of elastic strains inherent in the martensite transformation (Ref 39). Figure 40 and Figure 41 are micrographs that show self-accommodation of martensite variants in the R-phase of Ti-48.2Ni-1.5Fe (at.%) and B19 martensite in Ti-40.5Ni-10Cu (at.%) SMAs, respectively (Ref 38). Self-accommodation occurs by grouping together equal proportions of martensite variants (Ref 37). The macroscopic result of this variant grouping is seen in Fig. 33, where a scratch that runs across several variants is locally deviated, then reversed, resulting in no net change of shape or direction (Ref 37).

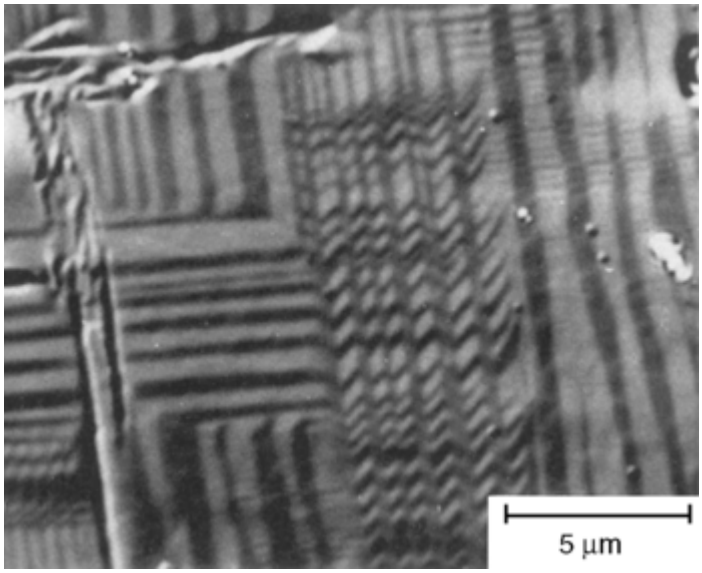

Fig. 40 Self-accommodation of R-phase in Ti-Ni-Fe. Source: Ref 38. Reprinted with permission

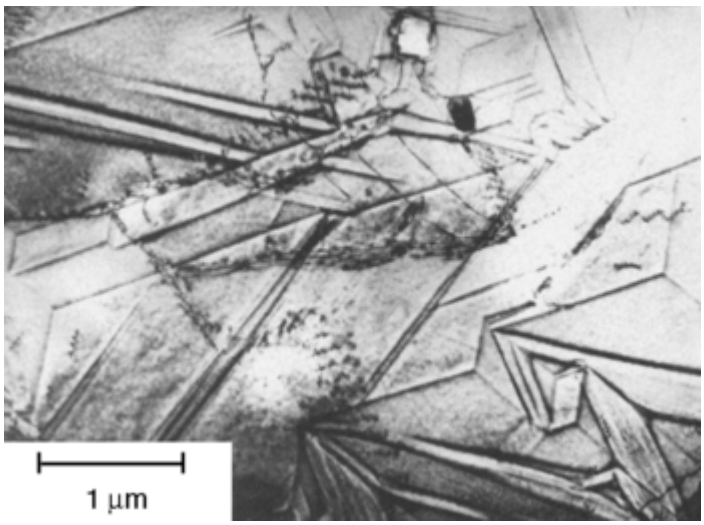

Fig. 41 Self-accommodation of B19 martensite in Ti-Ni-Cu. Source: Ref 38. Reprinted with permission

In SMAs, strains are accommodated in the martensitic state by coalescence of corresponding variants (Ref 23). When stress is applied at temperatures below M_f, variant coalescence will take place until the entire specimen consists of a single variant. This variant is dominant because it produces the greatest elongation for any applied stress (Ref 23). This is seen in Fig. 42 where 18R martensite in a Cu-20.4Zn-12.5Ga (at.%) SMA is subject to an applied stress that produces variant coalescence by the movement of twin boundaries until the entire crystal consists of variant 1′ (Ref 42).

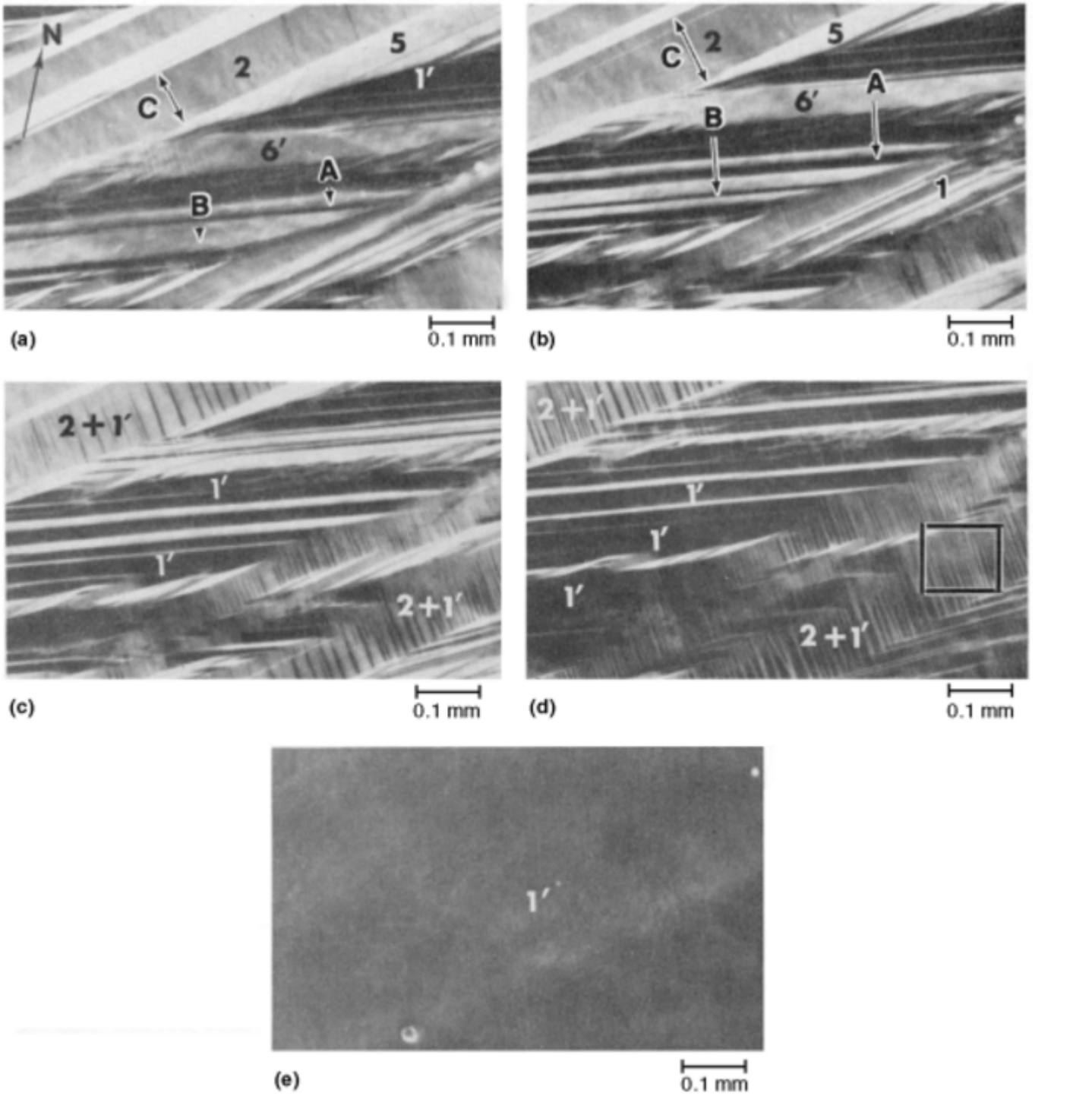

Fig. 42 Variant coalescence of 18R martensite in Cu-Zn-Ga under applied stress. Source: Ref 42. Reprinted with permission

Variant coalescence is the crystallographic cause of the shape memory effect. All strain results solely in the movement of twin boundaries between variants will be recovered upon the reverse transformation to the parent phase at temperatures greater than A_f.

Heavy or repeated deformation in the martensitic state produces dislocations and defects that stabilize certain variants (Ref 38). If these defects remain after the sample is heated above A_f, they will result in the nucleation and growth of preferred variants upon cooling below M_f (Ref 37). This occurs because martensite nucleation is very sensitive to stress fields caused by lattice defects and/or precipitates (Ref 39).

The preferential formation of certain variants during the martensite transformation is the mechanism that results in two-way shape memory effect (TWSME). An SMA exhibits TWSME when it is deformed into an initial shape at temperatures below M_f, reheated above A_f regaining the shape of the parent phase, then subsequently cooled below M_f, reforming the initial shape (Ref 37). Two-way shape memory effect is made possible by

training a one-way SMA by use of repeated (often >6) thermomechanical treatments in which each cycle consists of the sample being cooled below M_f, deformed, and subsequently reheated above A_f (Ref 37). Each cycle induces lattice defects and microstresses resulting in the shape of both the parent and martensite phases to be remembered (Ref 37).

Figure 43 is a light optical micrograph of a Cu-39.8Zn (wt%) SMA that has undergone a thermomechanical treatment (Ref 37). Figure 43(a) shows the alloy before the treatment, where the four martensite variants (A, B, C, and D) are present in equal proportions. The sample was subsequently deformed below M_f, heated above A_f while under constraint, then cooled below M_f (Ref 37). Figure 43(b) is the same region of the specimen shown in Fig. 43(a) (Ref 37). Note that variant D becomes dominant in this thermomechanical treatment (Ref 37).

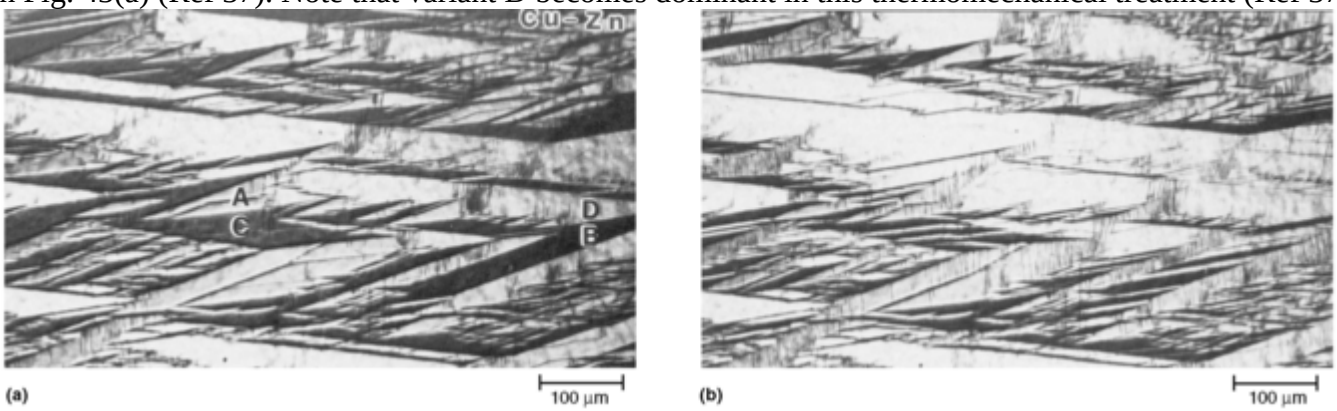

Fig. 43 (a) Copper-zinc shape memory alloy showing equal proportions of variants A, B, C, and D. (b) Variant D becomes dominant after thermomechanical training. Source: Ref 37. Reprinted with permission

References cited in this section

23. H. Funakubo, *Shape Memory Alloys,* Gordon and Breach Science Publishers, 1987, p 7, 18

37. C.M. Wayman, Shape Memory Alloys, *MRS Bull.,* Vol 18, 1993 p 49–56

38. K. Otsuka and C.M. Wayman, *Shape Memory Materials,* Cambridge University Press, Cambridge, 1998

39. K. Otsuka and T. Kakeshita, Science and Technology of Shape-Memory Alloys: New Developments, *MRS Bull.,* Vol 27, 2002 p 91–98

40. Y. Murakami, et al. Self-Accommodation and Morphology of 14M (7R) Martensites in an Ni-37.0at%Al Alloy, *Mater. Sci. Eng. A,* Vol 189, 1994 p 191–199

41. J.W. Christian and S. Mahajan, Deformation Twinning, *Prog. Mater. Sci.,* Vol 39, 1995 p 1–157

42. T. Saburi et al., The Shape Memory Mechanism in 18R Martensitic Alloys, *Acta Metall.,* Vol 28, 1980 p 15–32

References

1. D.A. Porter and K.E. Easterling, Chapter 6, Diffusionless Transformations, *Phase Transformations in Metals and Alloys*, 2nd ed., Chapman & Hall, 1992

2. G.B. Olson and W.S. Owen, Ed., *Martensite: A Tribute to Morris Cohen*, ASM International, 1992

3. G. Krauss, *Principles of Heat Treatment of Steel*, American Society for Metals, 1985

4. G. Kostorz, *Phase Transformations in Materials*, Wiley-VCH, Weinheim, Germany, 2001

5. A.R. Marder, Structure-Property Relationships in Ferrous Transformation Products, *Phase Transformation of Ferrous Alloys*, Proc. Int. Conf., TMS 1984, P11–41

6. G. Krauss, Martensite in Steel: Strength and Structure, *Mater. Sci. Eng. A*, Vol 273–275, 1999, p 40–57

7. Z.L. Xie, H. Hanninen, and J. Pietikainen, Substructures of Thin-Plate Martensite Formed under Applied Plane Stress at 4 K, *Scr. Met. Mater.*, Vol 28, 1993, p 1423–1428

8. C.M. Wayman, The Phenomenological Theory of Martensite Crystallography: Interrelationships, *Met. Mater. Trans. A, Phys. Metal. Mater. Sci.*, Vol 25A, 1994, p 1787–1795

9. B.P.J. Sandvik and C.M. Wayman, Characteristics of Lath Martensite. Part I. Crystallographic and Substructural Features, *Met. Mater. Trans. A, Phys. Metal. Mater. Sci.*, Vol 14, 1983, p 809–822

10. K. Wakasa and C.M. Wayman, Crystallography and Morphology of Ferrous Lath Martensite, *Metallography*, Vol 14, 1981, p 49–60

11. D.Z. Yang and C.M. Wayman, Slow Growth of Isothermal Lath Martensite in an Fe-21Ni-4Mn Alloy, *Acta Metall.*, Vol 32, 1984, p 949–954

12. K. Wakasa and C.M. Wayman, The Morphology and Crystallography of Ferrous Lath Martensite. Studies of Iron-20% Nickel-5% Manganese. I. Optical Microscopy, *Acta Metall.*, Vol 29, 1981, p 973–990

13. A.R. Marder and G. Krauss, The Morphology of Martensite in Iron-Carbon Alloys, *Trans. ASM*, Vol 60, 1967, p 651–660

14. K. Andrews, Empirical Formulae for the Calculation of Some Transformation Temperatures, *J. Iron Steel Inst.*, Vol 203, 1965, p 721–727

15. V. Shrinivas, S.K. Varma, and L.E. Murr, Deformation-Induced Martensitic Characteristics of 304 and 316 Stainless Steels During Room-Temperature Rolling, *Met. Mater. Trans. A, Phys. Metal. Mater. Sci.*, Vol 26A, 1995, p 661–671

16. E.R. Petty, *Martensite: Fundamentals and Technology*, Longman Group Ltd., London, 1970

17. A.K. Sinha, *Ferrous Physical Metallurgy,* Butterworth Publishers, 1989

18. B.A. Lindsley and A.R. Marder, The Morphology and Coarsening Kinetics of Spheroidized Fe-C Binary Alloys, *Acta Mater.,* Vol 46, 1997, p 341–351

19. H. Scherngell and A.C. Kneissl, *Acta Mater.,* Vol 50, 2002, p 328

20. J. Dutkiewicz, T. Czeppe, and J. Morgiel, *Mater. Sci. Eng.,* Vol A273–275, 1999, p 706

21. L. Delaey, Diffusionless Transformations, chapter 9, *Phase Transformations in Materials,* G. Kostorz, Ed., Wiley-VCH, Weinheim, Germany, 2001

22. D. Schryvers and D. Holland-Moritz, *Mater. Sci. Eng.,* Vol A273–275, 1999, p 699

23. H. Funakubo, *Shape Memory Alloys,* Gordon and Breach Science Publishers, 1987, p 7, 18

24. A.K. Jena and M.C. Chaturvedi, *Phase Transformations in Materials,* Prentice-Hall, 1992, p 428–429

25. Z. Nishiyama, chapter 2, *Martensitic Transformation,* Academic Press, 1978

26. W.M. Kriven, *J. Phys. IV,* Vol 5 (No. C8), 1995, p 101–110

27. P.M. Kelly and L.R.F. Rose, *Prog. Mater. Sci.,* Vol 47, 2001, p 550–551

28. F.E. Fujita, chapter 6, *Physics of New Materials,* 2nd ed., Springer-Verlag, 1998

29. Y.F. Zheng, L.C. Zhao, and H.Q. Ye, *Mater. Sci. Eng.,* Vol A273–275, 1999, p 272

30. A.L. Roytburd, *Mater. Sci. Eng.,* Vol A273–275, 1999, p 2

31. A.V. Srinivasan and D.M. McFarland, *Smart Structures,* Cambridge University Press, 2001, p 31

32. E.C. Subbarao, *Adv. Ceram.,* Vol 3, 1981, p 18

33. D.W. Richerson, *Modern Ceramic Engineering,* 2nd ed., Marcel Dekker, 1992 p 745

34. P.M. Kelly, *Mater. Sci. Forum,* Vol 56–58, 1990, p 335–346

35. C.M. Wayman, *Adv. Ceram.,* Vol 3, 1981, p 81

36. G.B. Olson, *Mater. Sci. Eng.,* Vol A273–275, 1999, p 19

37. C.M. Wayman, Shape Memory Alloys, *MRS Bull.,* Vol 18, 1993 p 49–56

38. K. Otsuka and C.M. Wayman, *Shape Memory Materials,* Cambridge University Press, Cambridge, 1998

39. K. Otsuka and T. Kakeshita, Science and Technology of Shape-Memory Alloys: New Developments, *MRS Bull.,* Vol 27, 2002 p 91–98

40. Y. Murakami, et al. Self-Accommodation and Morphology of 14M (7R) Martensites in an Ni-37.0at%Al Alloy, *Mater. Sci. Eng. A,* Vol 189, 1994 p 191–199

41. J.W. Christian and S. Mahajan, Deformation Twinning, *Prog. Mater. Sci.,* Vol 39, 1995 p 1–157

42. T. Saburi et al., The Shape Memory Mechanism in 18R Martensitic Alloys, *Acta Metall.,* Vol 28, 1980 p 15–32

M.J. Perricone, Bainitic Structures, *Metallography and Microstructures*, Vol 9, *ASM Handbook*, ASM International, 2004, p. 179–185

Bainitic Structures

Matthew J. Perricone, Lehigh University

Introduction

BAINITE describes the resultant microstructure in steels of the decomposition of austenite (γ) into ferrite (α) and cementite (Fe_3C) in the temperature range above the martensitic transformation and below that for pearlite. Significant overlap between the bainite and pearlite transformation temperature ranges is often observed in plain carbon steels (Fig. 1a) (Ref 1). However, in many alloy steel systems, the separation between pearlite and bainite temperature ranges is distinct, resulting in the formation of a bay between the two transformation curves on a time-temperature-transformation curve, as shown in Fig. 1(b) (Ref 1). The bainite transformation occurs below a well-defined bainite start temperature, and the fraction transformed increases with decreasing temperature. During isothermal transformation, the amount of bainite transformed increases as a sigmoidal function of time, asymptotically approaching a limit that does not change with prolonged heat treatment even though a significant amount of austenite is still present. This incomplete-reaction phenomenon is so called due to the fact that transformation ceases before the austenite achieves its equilibrium composition. The transformation temperature also has distinct ramifications on the properties of the product microstructure (Ref 2), as shown in Fig. 2 (Ref 3).

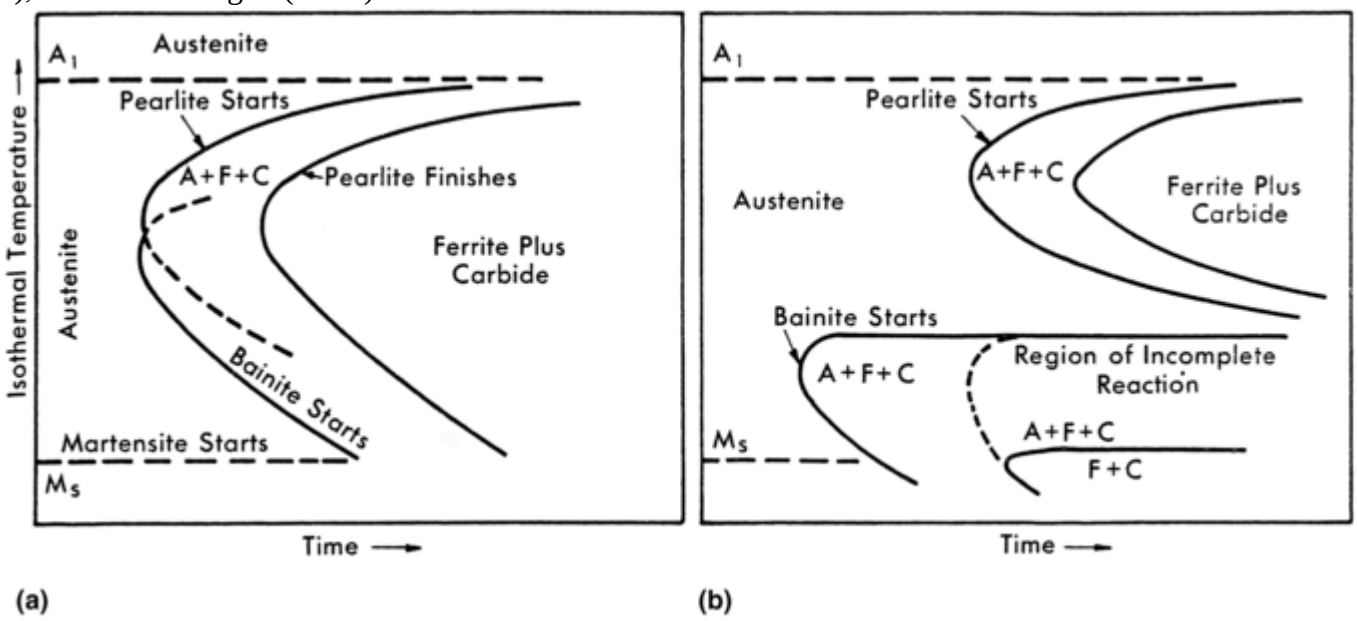

Fig. 1 Time-temperature-transformation diagrams in which (a) the pearlite and bainite regions extensively overlap, and (b) the pearlite and bainite regions are well separated in the temperature ranges in which they occur. Source: Ref 1

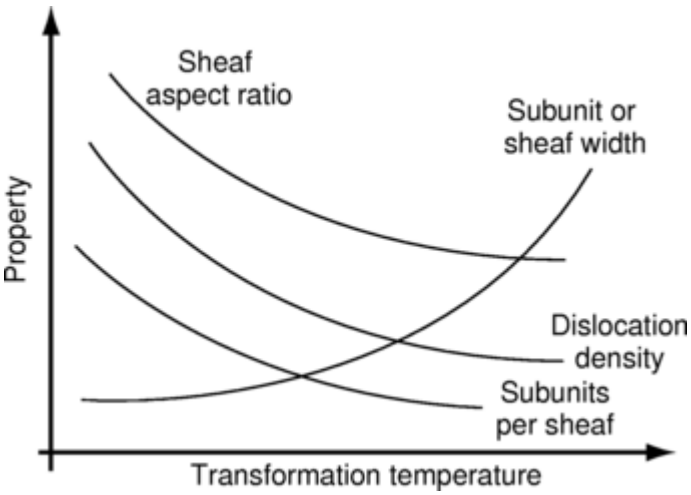

Fig. 2 Qualitative trends in microstructures as a function of transformation temperature. Source: Ref 3

The classic morphology of ferrous bainite consists of a nonlamellar aggregate of lath- or plate-shaped ferrite grains with carbides precipitated within the ferrite grains or in the interlath regions. However, in some steels (e.g., high silicon content), the carbide precipitation can be suppressed completely, resulting in a lathlike ferritic structure with the transformation morphology and kinetics identical to the formation of upper bainite (Ref 4). This same phenomenon is also observed in nonferrous alloys, either as a nonlamellar aggregate or with only one lathlike product transforming from the parent, although some controversy exists as to the classification of these transformations as bainitic.

Bainite is often grouped into two broad categories, upper and lower bainite, depending on the temperature range in which the transformation occurs. At high temperatures, the carbon-supersaturated plate of bainitic ferrite rejects carbon into the surrounding austenite via diffusion, leaving upper bainitic ferrite free of internal carbides. Thus, the increased carbon content of the austenite creates a driving force for cementite precipitation in the interlath regions of the microstructure. At low temperatures, carbon diffusion out of bainitic ferrite is slower and incomplete, leading to the precipitation of carbides in both the interlath region and the ferrite lath interior. This growth process is explained schematically in Fig. 3 (Ref 5).

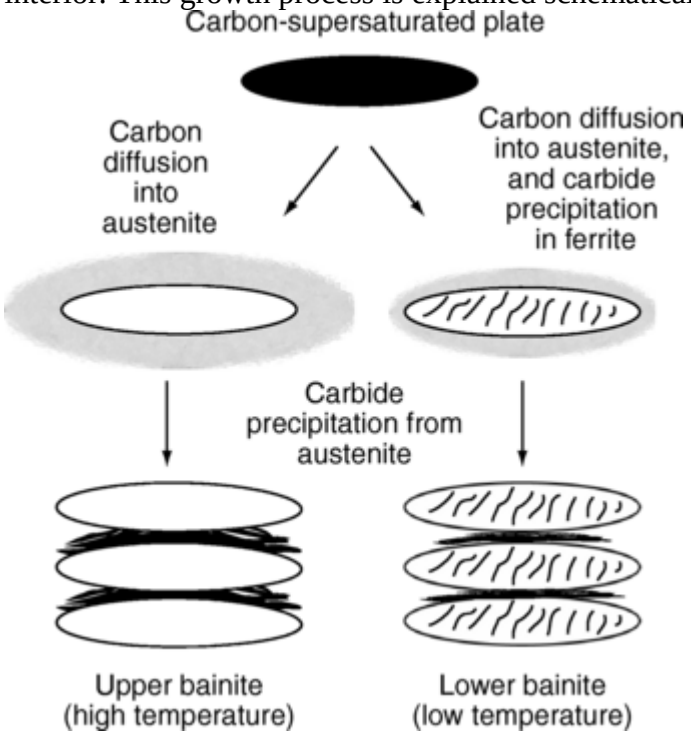

Fig. 3 An illustration of the growth of bainite and the development of upper or lower bainite morphologies. Source: Ref 5

References cited in this section

1. R.F. Hehemann and A.R. Troiano, *Met. Prog.,* Vol 70, 1956, p 97

2. H.K.D.H. Bhadeshia, Bainitic Ferrite, *Bainite in Steels,* 2nd ed., Institute of Materials, London, 2001, p 19–61

3. L.C. Chang and H.K.D.H. Bhadeshia, Metallographic Observations of Bainite Transformation Mechanism, *Mater. Sci. Technol.,* Vol 11, 1995, p 105–108

4. D.V. Edmonds, Bainitic Structures, *Metallography and Microstructures,* 9th ed., American Society for Metals, 1985, p 662–667

5. H.K.D.H. Bhadeshia, The Bainite Transformation: Unresolved Issues, *Mater. Sci. Eng. A,* Vol 273–275, 1999, p 58–66

M.J. Perricone, Bainitic Structures, *Metallography and Microstructures,* Vol 9, *ASM Handbook,* ASM International, 2004, p. 179–185

Bainitic Structures

Matthew J. Perricone, Lehigh University

Upper Bainite

This classic bainite morphology (Fig. 4) (Ref 2) occurs at higher temperatures in the bainite transformation range and consists of fine plates of ferrite (also called subunits, shown in Fig. 5) (Ref 6) that grow in clusters called sheaves. Plates in each sheaf are separated by low-angle boundaries or cementite particles (Fig. 6) (Ref 2). These ferritic structures are parallel to each other and have identical crystallographic orientation, each with a well-defined crystallographic habit plane. The crystal orientation of ferrite and the parent austenite is close to the Kurdjumov-Sachs (Ref 7) and Nishiyama-Wassermann (Ref 8, 9) orientation relationships (Table 1), although some rotation exists such that the habit planes of ferrite are irrational, similar to martensite transformation (Ref 2). The cementite particles exhibit a Pitsch (Ref 10) orientation relationship with the austenite from which they precipitate (Ref 2, 4). The addition of alloying elements, such as silicon or aluminum, can retard or completely suppress the nucleation of cementite, resulting in the stabilization of carbon-enriched austenite (Ref 11) surrounding the transformed plates of bainitic ferrite, as shown in Fig. 7 (Ref 11).

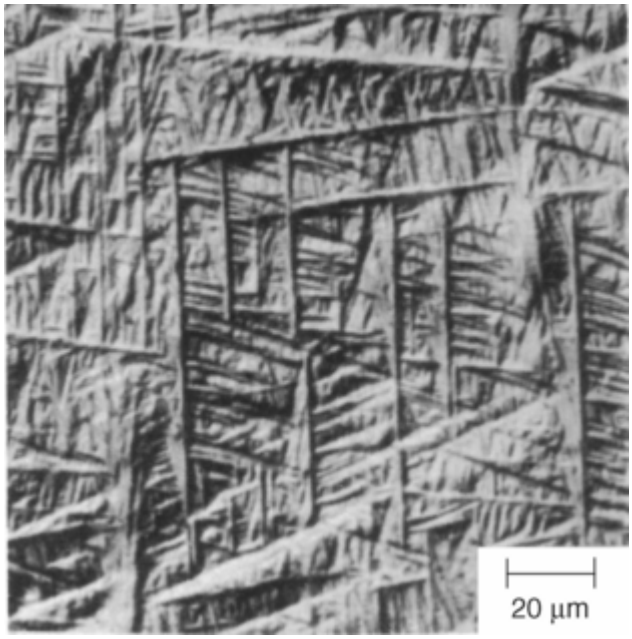

Fig. 4 Nomarski differential interference contrast micrograph showing the general surface displacements due to upper bainite. Source: Ref 2

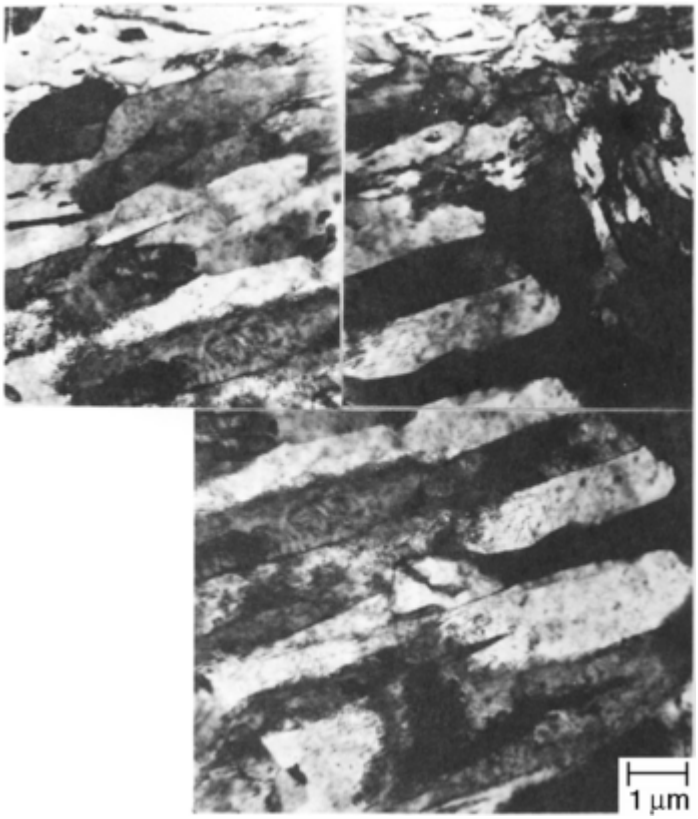

Fig. 5 Thin-foil transmission electron micrograph illustrating the substructure of upper bainite plates in a 2340 steel, austenitized at 1095 °C (2000 °F) and isothermally transformed at 540 °C (1000 °F) for 15 h. Source: Ref 6

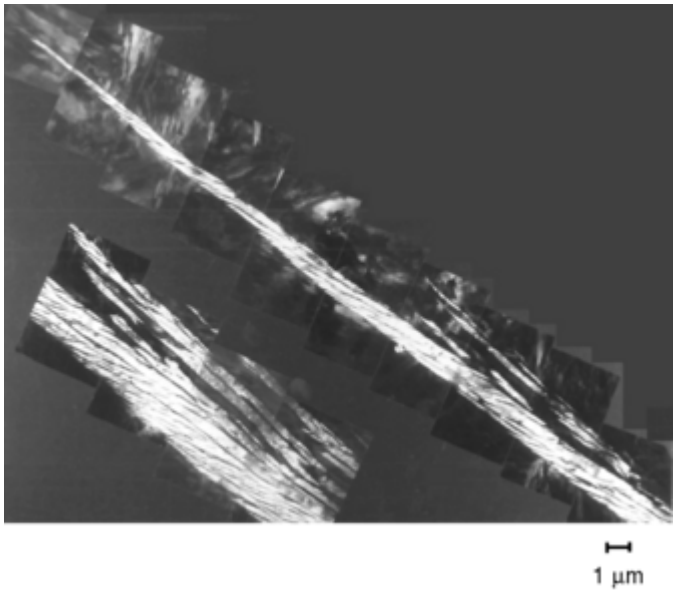

Fig. 6 Transmission electron micrograph of a sheaf of upper bainite in a partially transformed Fe-0.43C-2Si-3Mn wt% alloy. Source: Ref 2

Table 1 Orientation relationships for bainitic structures

Kurdjumov-Sachs (Ref 7)
$(011)_\alpha \| (111)_\gamma$ $[11\bar{1}]_\alpha \| [10\bar{1}]_\gamma$
Nishiyama-Wassermann (Ref 8, 9)
$(011)_\alpha \| (111)_\gamma$ $[0\bar{1}1]_\alpha \| [\bar{1}\bar{1}2]_\gamma$
Bagaryatski (Ref 21)
$(001)_\theta \| (211)_\alpha$ $[100]_\theta \| [0\bar{1}1]_\alpha$
Isaichev (Ref 22)
$(010)_\theta \| (\bar{1}11)_\alpha$ $[103]_\theta \| [101]_\alpha$
Pitsch (Ref 10)
$(010)_\theta \| (110)_\gamma$ $[001]_\theta \| [\bar{2}25]_\gamma$
Jack (Ref 27)
$(0001)_\varepsilon \| (011)_\alpha$ $[10\bar{1}1]_\varepsilon \| [101]_\alpha$

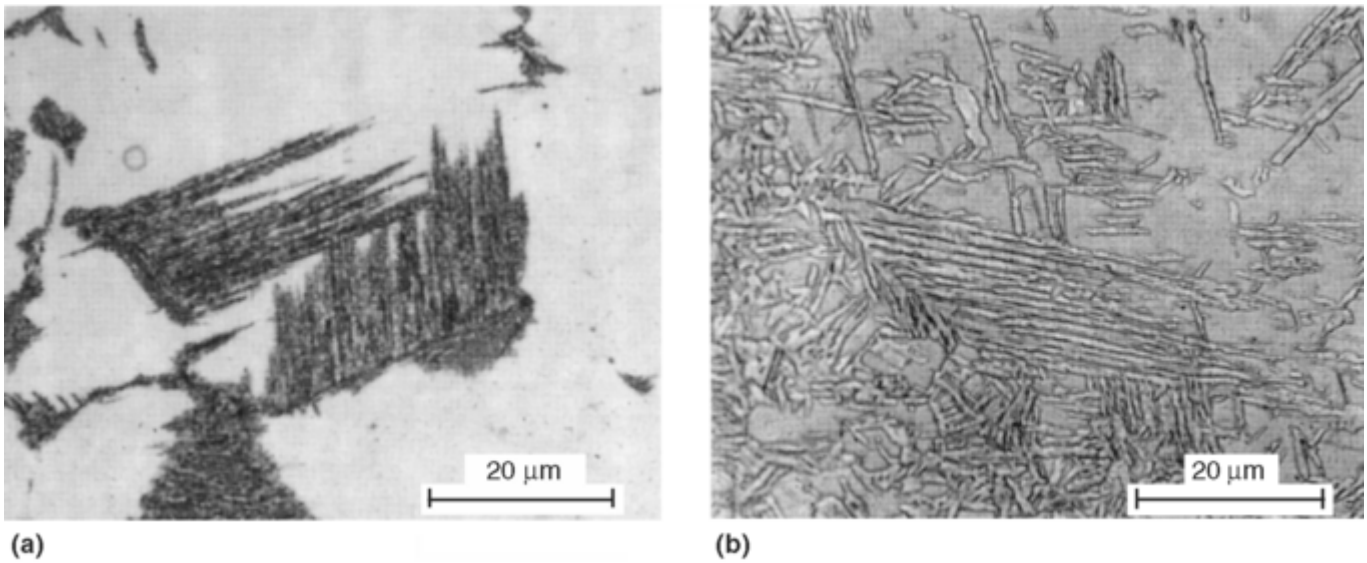

Fig. 7 Optical micrographs of the microstructures produced at 400 °C (750 °F) (a) Bainite with cementite in Fe-0.478C-4.87Ni wt% alloy. (b) Bainite without cementite in Fe-0.485C-4.82Ni-1.55Si wt% alloy. Source: Ref 11

Bainite nucleates on parent austenite grain boundaries (Fig. 8) (Ref 12), and its growth is completely contained within the parent austenite grain; that is, the orientation relationship of bainitic ferrite and austenite at the advancing interface prevents growth across γ grain boundaries (Ref 12) (Fig. 9). The reduced strength of austenite at the elevated transformation temperature range of upper bainite and the shape change associated with the bainite transformation cause deformation of the parent austenite matrix, resulting in the buildup of dislocations at the γ/α interface (Fig. 10) (Ref 13). The tangles of dislocations at the interface produce a work-hardening effect, reducing interface mobility and halting the growth process, thereby limiting the size of each platelet within the sheaf.

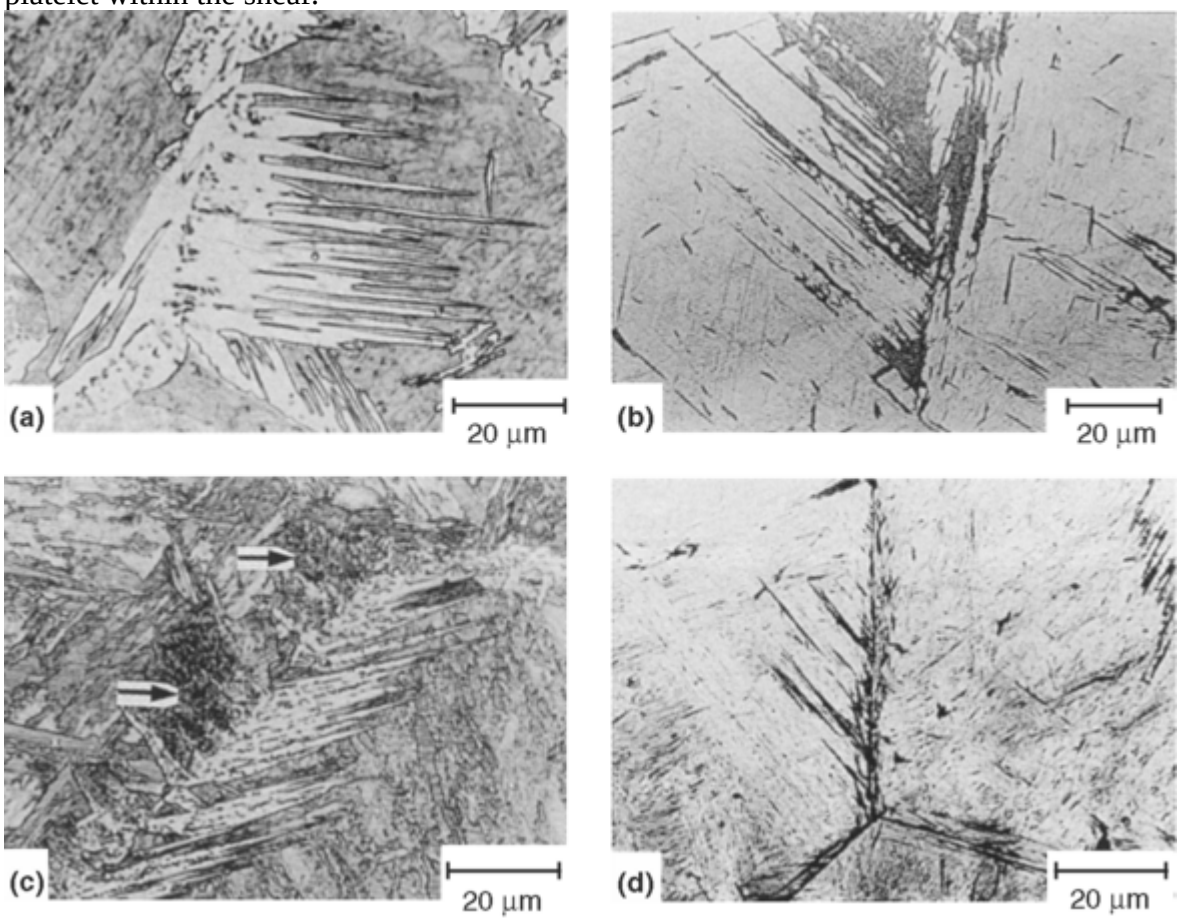

Fig. 8 Optical micrographs of (a) the structure formed by transformation at 773 K for 3 min in Fe-0.21C-8.81Ni wt% alloy, (b) typical upper bainite formed by the decomposition at 723 K for 3 min, (c) the upper bainite laths formed at 623 K for 10 min, and (d) the bainitic structure formed by the isothermal decomposition at 493 K for 150 min in Fe-0.41C-8.74Ni wt% alloy. Source: Ref 12

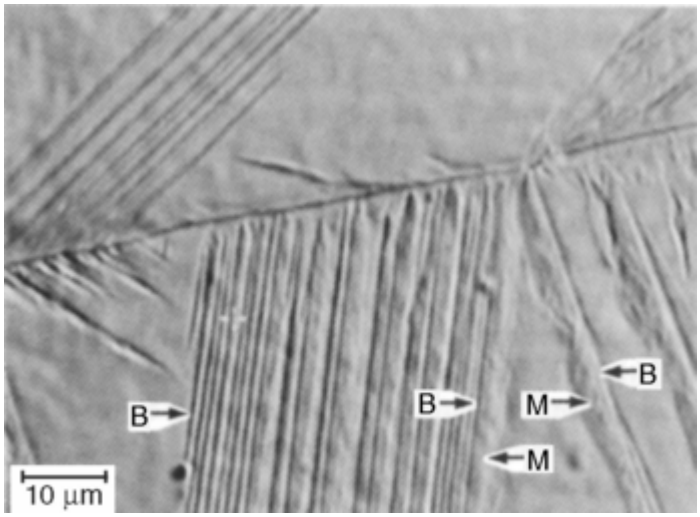

Fig. 9 Surface reliefs due to bainite (B) and martensite (M) formation. Note the abrupt halt in growth of both martensite and bainite upon impingement of growth interface and parent γ phase boundary. Source: Ref 12

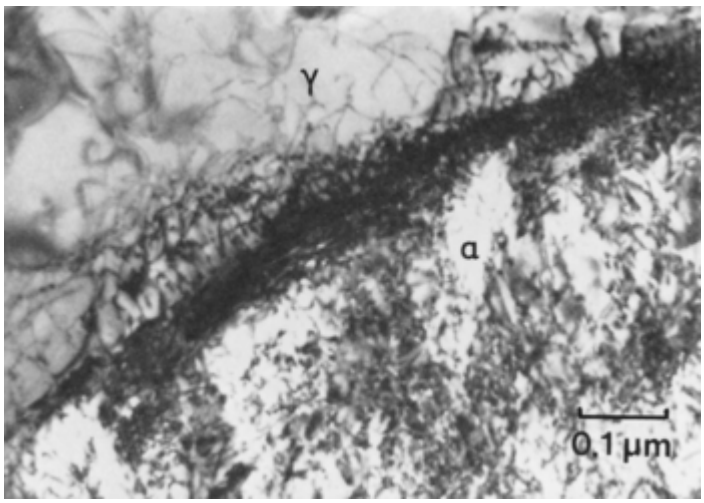

Fig. 10 Intense dislocation entanglement both at, and in the vicinity of, the bainite/austenite transformation front. Source: Ref 13

References cited in this section

2. H.K.D.H. Bhadeshia, Bainitic Ferrite, *Bainite in Steels*, 2nd ed., Institute of Materials, London, 2001, p 19–61

4. D.V. Edmonds, Bainitic Structures, *Metallography and Microstructures*, 9th ed., American Society for Metals, 1985, p 662–667

6. J.M. Oblak and R.F. Hehemann, *Transformation and Hardenability in Steels*, Climax Molybdenum Co., 1967

7. G. Kurdjumov and G. Sachs, *Z. Physik*, Vol 64, 1930, p 325–343

8. Z. Nishiyama, *Sci. Rep. Tôhoku Univ.,* Vol 23, 1934, p 637–664

9. G. Wassermann, *Arch. Eisenhüttenwes,* Vol 6, 1933, p 347–351

10. W. Pitsch, *Acta Metall.,* Vol 10, 1962, p 897–900

11. D. Quidort and Y. Brechet, Isothermal Growth Kinetics of Bainite in 0.5% C Steels, *Acta Metall.,* Vol 49, 2001, p 4161–4170

12. Y. Ohmori, Y.-C. Jung, K. Nakai, and H. Shioiri, Bainite Transformation and the Diffusional Migration of Bainite/Austenite Broad Interfaces in Fe-9%Ni-C Alloys, *Acta Metall.,* Vol 49, 2001, p 3149–3162

13. H.K.D.H. Bhadeshia and D.V. Edmonds, *Metall. Trans. A,* Vol 10, 1979, p 895–907

21. Y.A. Bagaryatski, *Dokl. Akad. Nauk SSSR,* Vol 73, 1950, p 1161–1164

22. I.V. Isaichev, *Zh. Tekh. Fiz.,* Vol 17, 1947, p 835–838

27. K.H. Jack, *J. Iron Steel Inst.,* Vol 169, 1951, p 26–36

M.J. Perricone, Bainitic Structures, *Metallography and Microstructures,* Vol 9, *ASM Handbook,* ASM International, 2004, p. 179–185

Bainitic Structures

Matthew J. Perricone, Lehigh University

Surface Relief

The bainite transformation is accompanied by a change in crystal structure from austenite (γ) to ferrite (α), a phase that has a larger molar volume than austenite and therefore requires a concomitant shape change, as shown in Fig. 11 (Ref 2). The completion of the bainite reaction, like all austenite-to-ferrite phase transformations, can therefore be tracked using dilatometry to measure material expansion, as illustrated in Fig. 12 (Ref 14). These dilatometric data provide no direct information about the actual transformation mechanism, but the generation of surface relief on a prepolished surface (Fig. 13, 14) (Ref 15, 16) can be observed due to the significant shear component required to achieve this shape change. However, it should be noted that the specifics of the mechanism of transformation (displacive versus diffusion-controlled) has been hotly contested for decades (Ref 17, 18, 19, 20).

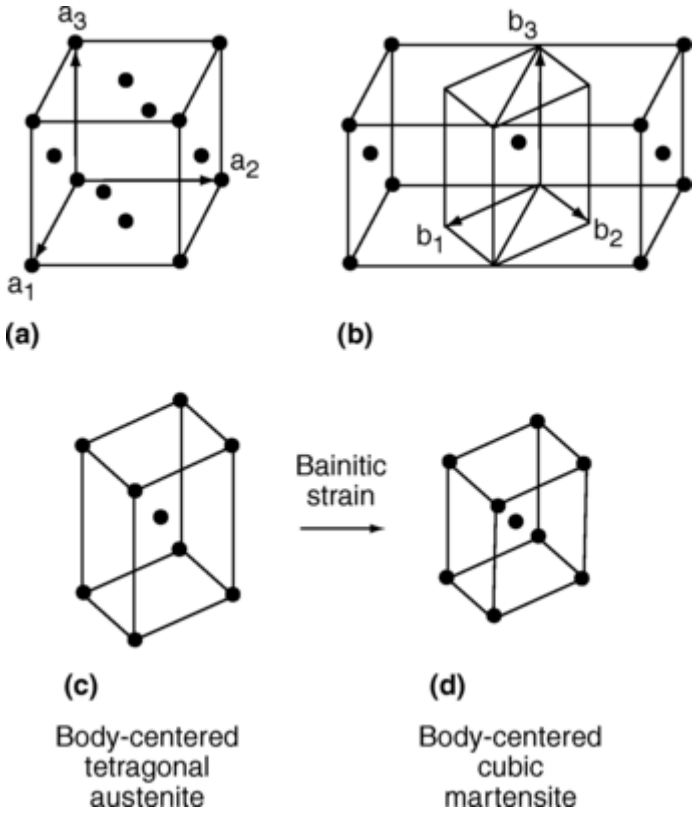

Fig. 11 Change in crystal structure due to bainitic transformation. (a) Conventional face-centered cubic (fcc) unit cell of austenite with basis vectors a_1, a_2, and a_3. (b) Relation between the fcc and the body-centered tetragonal cell (b_1, b_2, b_3) or austenite. (c,d) Bainitic strain deforming the austenite lattice (c) into a body-centered cubic martensite lattice (d). Source: Ref 2

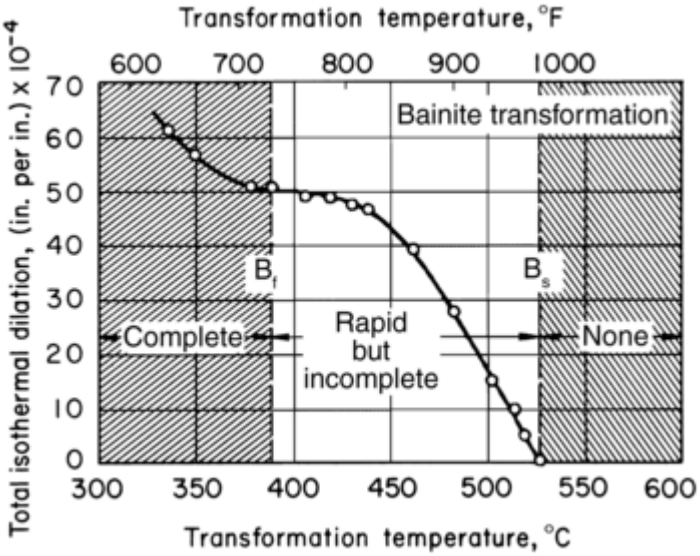

Fig. 12 Total dilation (proportional to the degree of reaction) versus transformation temperature during isothermal formation of bainite in 4340 steel. B_f, bainite finish temperature; B_s, bainite start temperature. Source: Ref 14

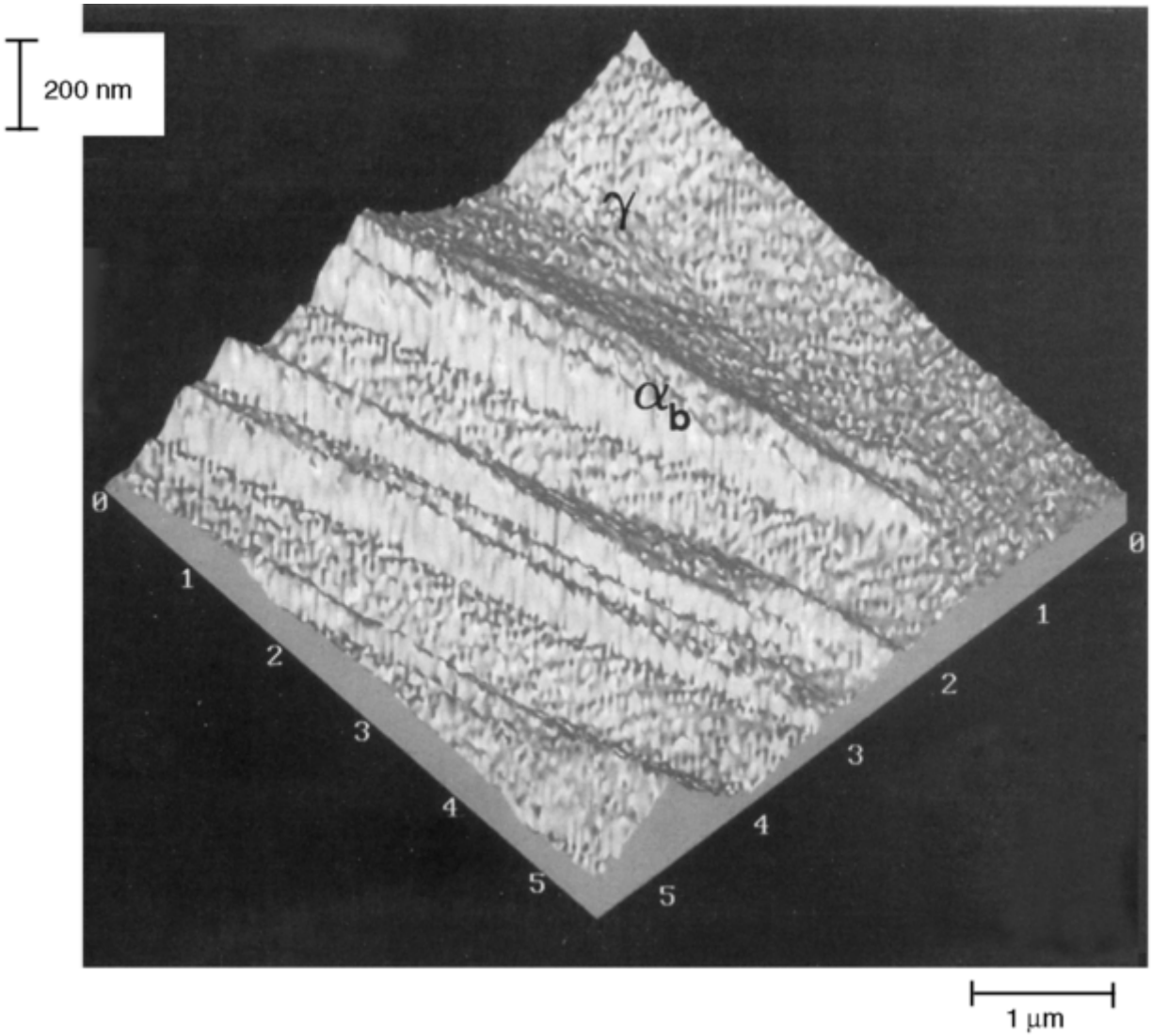

Fig. 13 High-resolution atomic-force microscope plots of the displacements caused by the formation of a single subunit of bainite. Surface was flat before transformation. Source: Ref 15

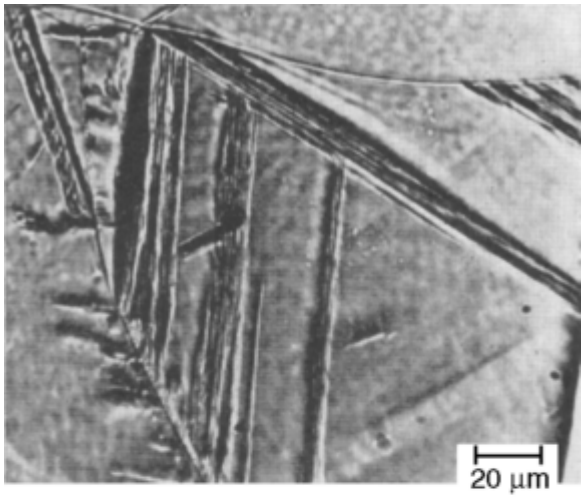

(a)



(b)

Fig. 14 Surface relief due to bainitic transformation. (a) Light micrograph showing upper bainite transformation product. (b) Accompanying interference micrograph

References cited in this section

2. H.K.D.H. Bhadeshia, Bainitic Ferrite, *Bainite in Steels*, 2nd ed., Institute of Materials, London, 2001, p 19–61

14. R.F. Hehemann, Ferrous and Non-Ferrous Bainitic Structures, *Metallography, Structures, and Phase Diagrams,* 8th ed., American Society for Metals, 1973, p 194–196

15. H.K.D.H. Bhadeshia and E. Swallow, High Resolution Observations of Displacements Caused by Bainitic Transformation, *Mater. Sci. Technol.,* Vol 12, 1996, p 121–125

16. The Bainite Transformation, *Phase Transformations,* American Society for Metals, 1970

17. H.K.D.H. Bhadeshia, A Rationalization of Shear Transformations in Steels, *Acta Metall.,* Vol 29, 1981, p 1117–1130

18. H.K.D.H. Bhadeshia and J.W. Christian, Bainite in Steels, *Metall. Trans. A,* Vol 21, 1990, p 767–797

19. H.I. Aaronson, W.T. Reynolds, Jr., G.J. Shiflet, and G. Spanos, Bainite Viewed Three Different Ways, *Metall. Trans. A,* Vol 21, 1990, p 1343–1380

20. H.I. Aaronson, T. Furuhara, J.M. Rigsbee, W.T. Reynolds, Jr., and J.M. Howe, Crystallographic and Mechanistic Aspects of Growth by Shear and by Diffusional Processes, *Metall. Trans. A*, Vol 21, 1990, p 2369–2409

M.J. Perricone, Bainitic Structures, *Metallography and Microstructures*, Vol 9, *ASM Handbook*, ASM International, 2004, p. 179–185

Bainitic Structures

Matthew J. Perricone, Lehigh University

Lower Bainite

Lower bainite (Fig. 15, 16) (Ref 2, 14) differs from upper bainite in that cementite precipitation occurs not only in the carbon-rich austenite in the interlath regions but also within the plates of ferrite, as shown in Fig. 17 (Ref 16). The cementite that precipitates at the ferrite grain interiors exhibits the orientation relationship observed in tempered martensite, termed the Bagaryatski (Ref 21) or Isaichev (Ref 22) orientation relationship (Table 1) (Ref 23, Ref 24, 25, 26). Both ε-carbide and cementite are observed to precipitate within lower bainite, with ε-carbides adopting an orientation relationship close to that proposed by Jack (Ref 27). These lathlike carbides frequently adopt a unique variant within a ferrite grain, usually oriented at a characteristic 60° angle to the long axis of the bainitic ferrite plate (Fig. 18) (Ref 13), much different than tempered martensites, in which more than one variant is always observed (Ref 4). Research (Ref 28) has shown that lower bainite may even evolve in alloy steels into an inhomogeneous structure that exhibits a midrib of thin plate martensite, as shown in Fig. 19 (Ref 28).

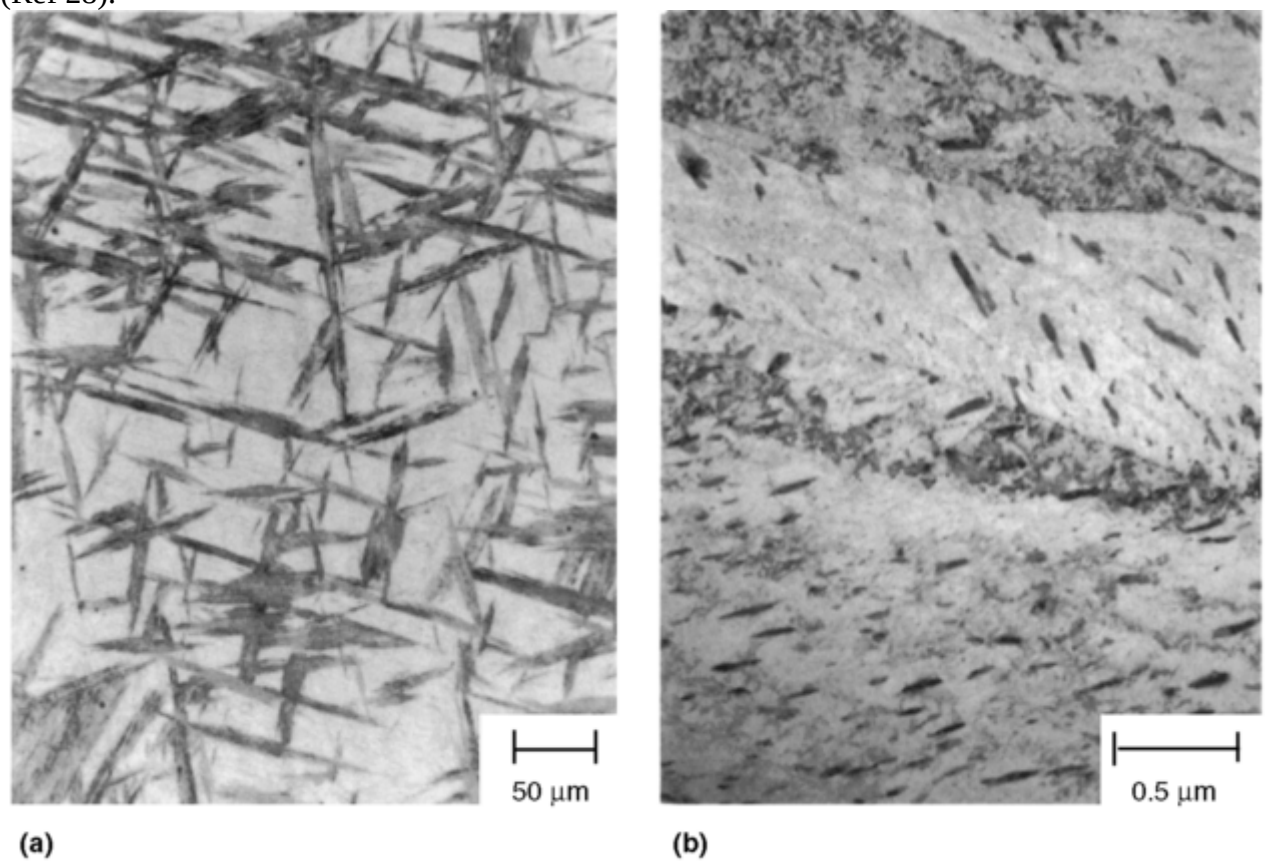

Fig. 15 Lower bainite. (a) Light micrograph illustrating sheaves of lower bainite in a partially transformed (668 K) Fe-0.3C-4Cr wt% alloy. The light matrix phase is martensite. (b) Corresponding transmission electron micrograph illustrating subunits of lower bainite. Source: Ref 2

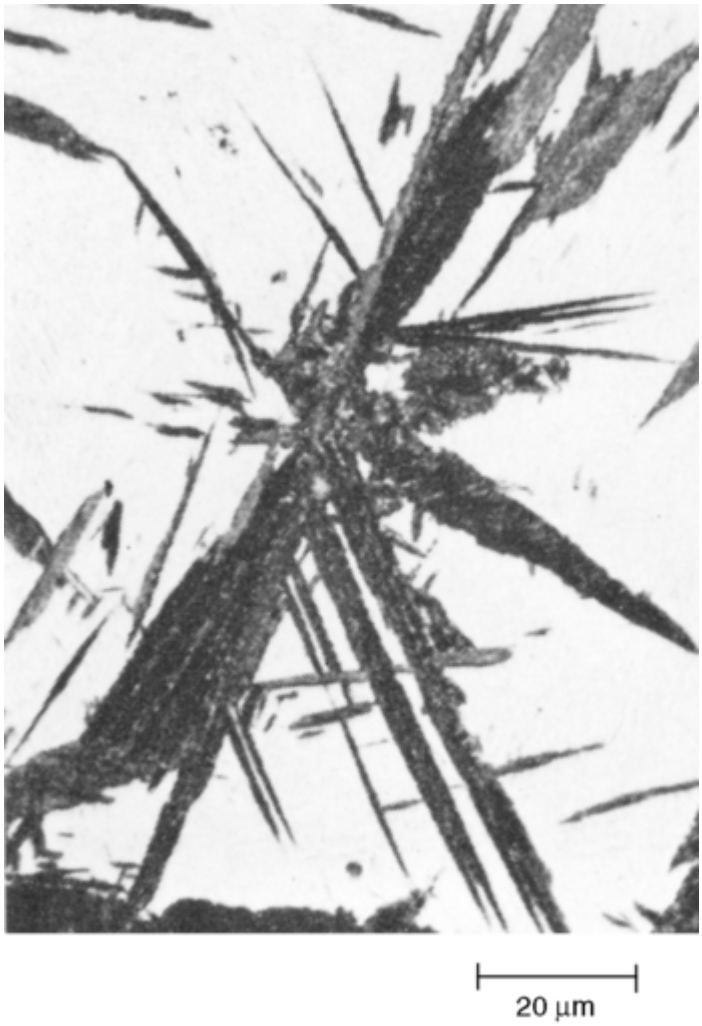

Fig. 16 Lower bainite in a 4360 steel specimen, austenitized, isothermally transformed at 300 °C (570 °F), and quenched. The matrix is untempered martensite. Picral etch. 500×. Source: Ref 14

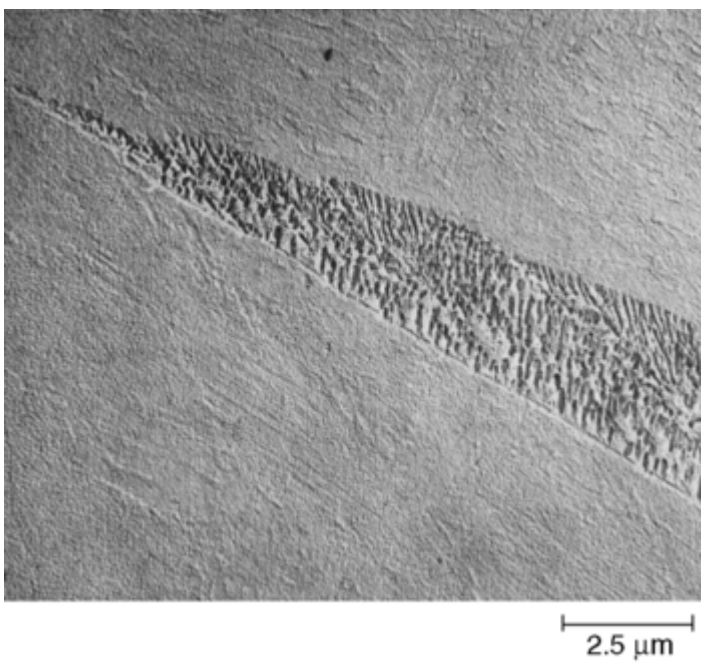

Fig. 17 Lower bainite formed at 345 °C (650 °F) in 4360 steel. 8000×. Source: Ref 16

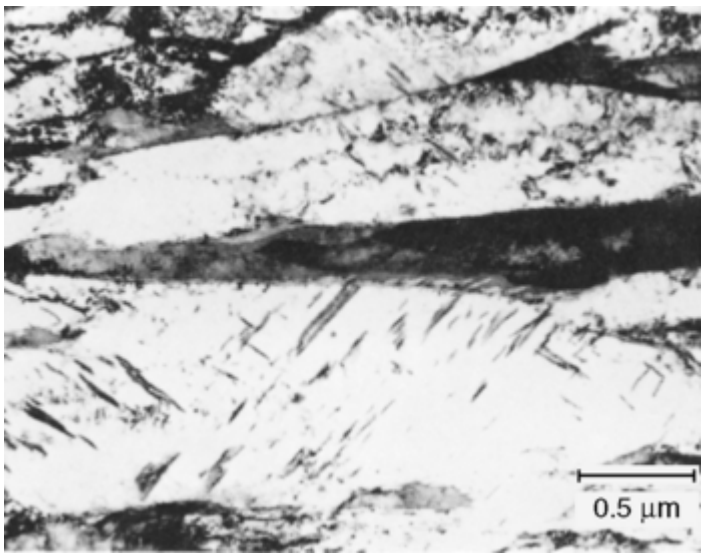

Fig. 18 Transmission electron micrograph of lower bainite showing the precipitation of several variants of carbide particles within the plate of bainitic ferrite. Source: Ref 13

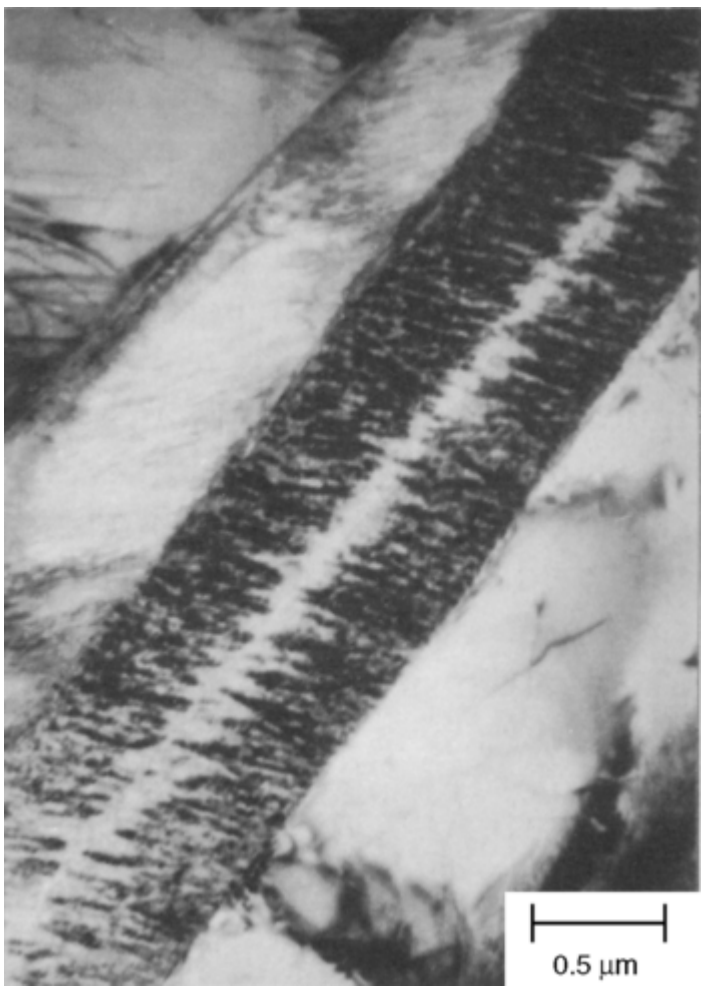

Fig. 19 Transmission electron micrograph of the midrib associated with lower bainite in plain carbon steels. Source: Ref 28

References cited in this section

2. H.K.D.H. Bhadeshia, Bainitic Ferrite, *Bainite in Steels*, 2nd ed., Institute of Materials, London, 2001, p 19–61

4. D.V. Edmonds, Bainitic Structures, *Metallography and Microstructures,* 9th ed., American Society for Metals, 1985, p 662–667

13. H.K.D.H. Bhadeshia and D.V. Edmonds, *Metall. Trans. A,* Vol 10, 1979, p 895–907

14. R.F. Hehemann, Ferrous and Non-Ferrous Bainitic Structures, *Metallography, Structures, and Phase Diagrams,* 8th ed., American Society for Metals, 1973, p 194–196

16. The Bainite Transformation, *Phase Transformations,* American Society for Metals, 1970

21. Y.A. Bagaryatski, *Dokl. Akad. Nauk SSSR,* Vol 73, 1950, p 1161–1164

22. I.V. Isaichev, *Zh. Tekh. Fiz.,* Vol 17, 1947, p 835–838

23. F.B. Pickering, The Structure and Properties of Bainite in Steels, *Transformation and Hardenability in Steels,* Climax Molybdenum Co., 1967, p 109–129

24. Y. Ohmori, The Crystallography of the Lower Bainite Transformation in a Plain Carbon Steel, *Trans. Iron Steel Inst. Jpn.,* Vol 11, 1971, p 95–101

25. D.N. Shackleton and P.M. Kelly, The Crystallography of Cementite Precipitation in the Bainite Transformation, *Acta Metall.,* Vol 15, 1967, p 979–992

26. D.-H. Huang and G. Thomas, Metallography of Bainitic Transformation in Silicon Containing Steels, *Metall. Trans. A,* Vol 8, 1977, p 1661–1674

27. K.H. Jack, *J. Iron Steel Inst.,* Vol 169, 1951, p 26–36

28. H. Okamoto and M. Oka, Lower Bainite with Midrib in Hypereutectoid Steels, *Metall. Trans. A,* Vol 17, 1986, p 1113–1120

M.J. Perricone, Bainitic Structures, *Metallography and Microstructures*, Vol 9, *ASM Handbook*, ASM International, 2004, p. 179–185

Bainitic Structures

Matthew J. Perricone, Lehigh University

Inverse Bainite

While most research attention is paid to hypoeutectoid steels, bainitic structures can also be formed in hypereutectoid steel compositions. In these cases, the carbide phase nucleates first, resulting in a different microstructural appearance (Ref 23) than normally observed (Ref 29, 30). The initial cementite precipitates as a lath or plate but is quickly engulfed by a sheath of ferrite, as shown in Fig. 20(a) (Ref 30). This formation causes the decomposition of adjacent austenite into larger ferrite laths that grow and coarsen by a more classical bainite reaction (Fig. 20b) (Ref 30). The greater volume fraction and higher growth velocity of ferrite regions ensures that the volume fraction of inverse bainite will be relatively small; consequently, a large portion of the normal bainitic structure nucleates independently of the formation of inverse bainitic structures (Ref 4).

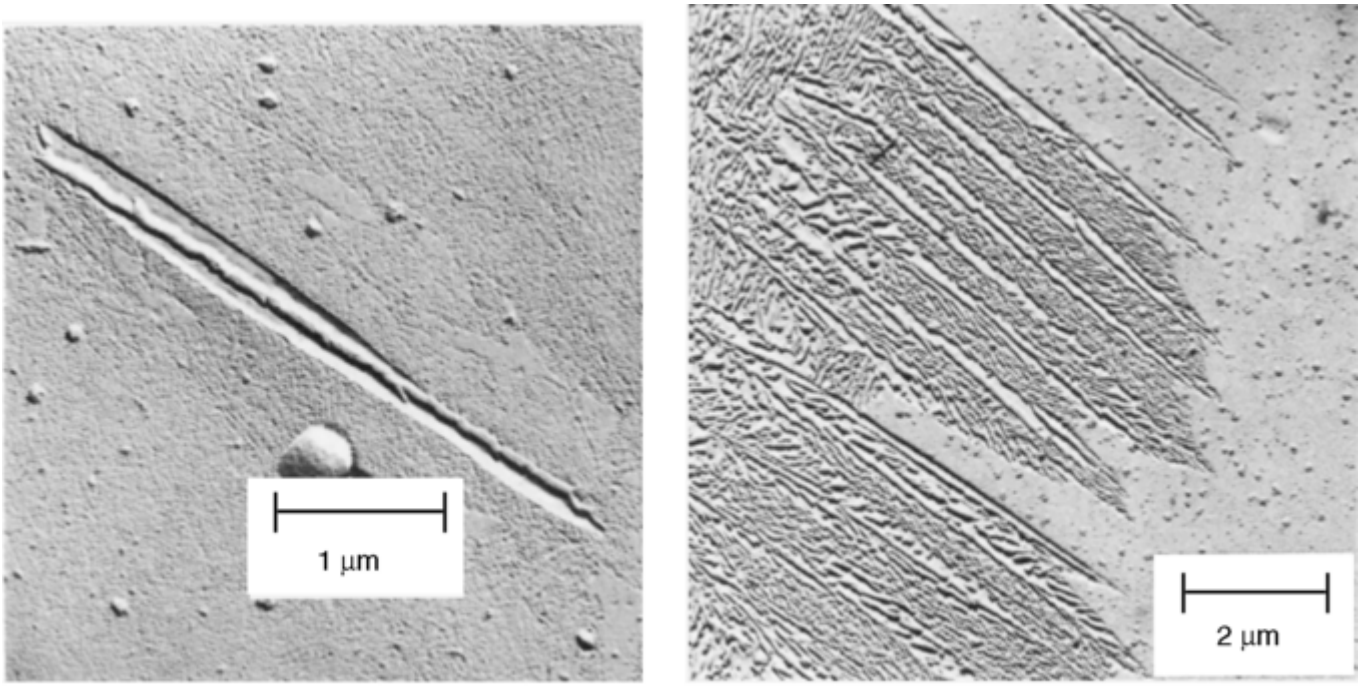

Fig. 20 Replica electron micrograph (a) showing the microstructural unit of inverse bainite comprised of a single cementite plate sheathed with ferrite in an Fe-1.34C alloy, austenitized at 1200 °C (2200 °F) for 15 min and isothermally transformed at 600 °C (1100 °F) for 2 s, and (b) showing the evolution of a normally bainitic structure from initially formed units of inverse bainite, austenitized at 1200 °C (2200 °F) for 15 min and isothermally transformed at 550 °C (1020 °F) for 7 s. Source: Ref 30

References cited in this section

4. D.V. Edmonds, Bainitic Structures, *Metallography and Microstructures,* 9th ed., American Society for Metals, 1985, p 662–667

23. F.B. Pickering, The Structure and Properties of Bainite in Steels, *Transformation and Hardenability in Steels,* Climax Molybdenum Co., 1967, p 109–129

29. M. Hillert, The Role of Interfacial Energy During Solid-State Phase Transformations, *Jernkontorets Ann.,* Vol 141, 1957, p 757–789

30. K.R. Kinsman and H.I. Aaronson, The Inverse Bainite Reaction in Hypereutectoid Fe-C Alloys, *Metall. Trans. A,* Vol 1, 1970, p 1485–1488

M.J. Perricone, Bainitic Structures, *Metallography and Microstructures,* Vol 9, *ASM Handbook,* ASM International, 2004, p. 179–185

Matthew J. Perricone, Lehigh University

Granular Bainite

This form of bainite is only observed in low- or medium-carbon steels and is associated with continuous cooling processes rather than isothermal treatments (Ref 31). Because the transformation occurs gradually during cooling, the sheaves of bainite are coarse, giving the resultant microstructure a blocky or granular appearance, as shown in Fig. 21 (Ref 31). Carbides are characteristically absent from this bainite morphology, because the carbon partitioned from the bainitic ferrite stabilizes the residual austenite; this typically results in bainite, retained austenite, and martensite being present in the microstructure (Ref 4).

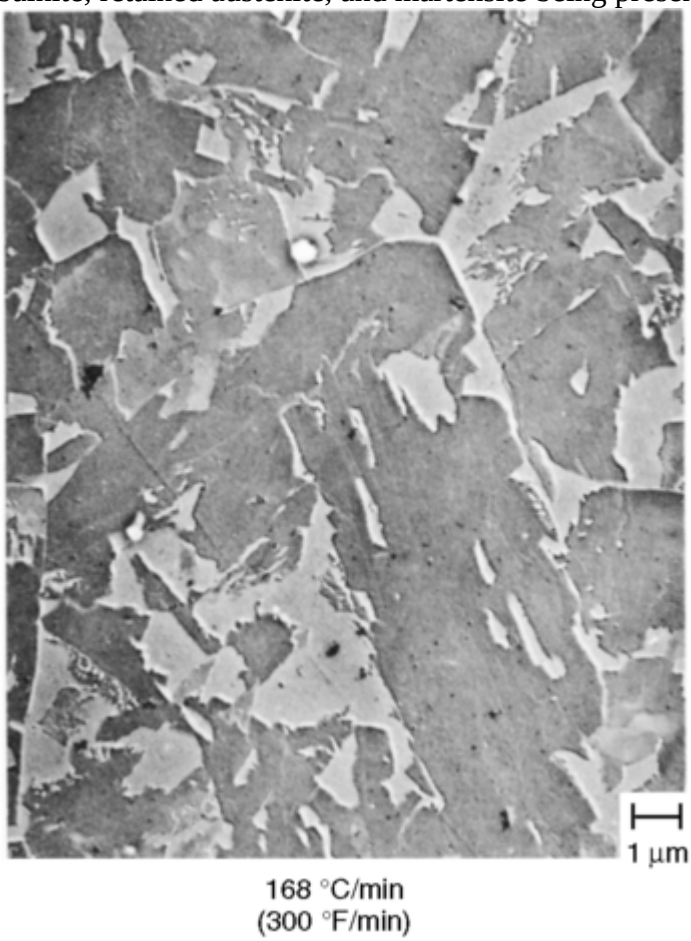

Fig. 21 Replica electron micrograph of mixed microstructure (granular bainite, austenite, and martensite), with the parent austenite boundaries delineated by irregularly shaped particles. Source: Ref 31

References cited in this section

4. D.V. Edmonds, Bainitic Structures, *Metallography and Microstructures,* 9th ed., American Society for Metals, 1985, p 662–667

31. L.J. Habrakan and M. Economopoulos, Bainitic Microstructures in Low-Carbon Alloy Steels and Their Mechanical Properties, *Transformation and Hardenability in Steels,* Climax Molybdenum Co., 1967, p 69–107

M.J. Perricone, Bainitic Structures, *Metallography and Microstructures,* Vol 9, *ASM Handbook,* ASM International, 2004, p. 179–185

Bainitic Structures

Matthew J. Perricone, Lehigh University

Columnar Bainite

This bainite morphology consists of nonacicular ferritic grains containing cementite precipitates formed in the bainitic temperature range at very high pressures (Ref 4). This microstructure is most often observed in medium- and high-carbon steels (Fig. 22) (Ref 32).

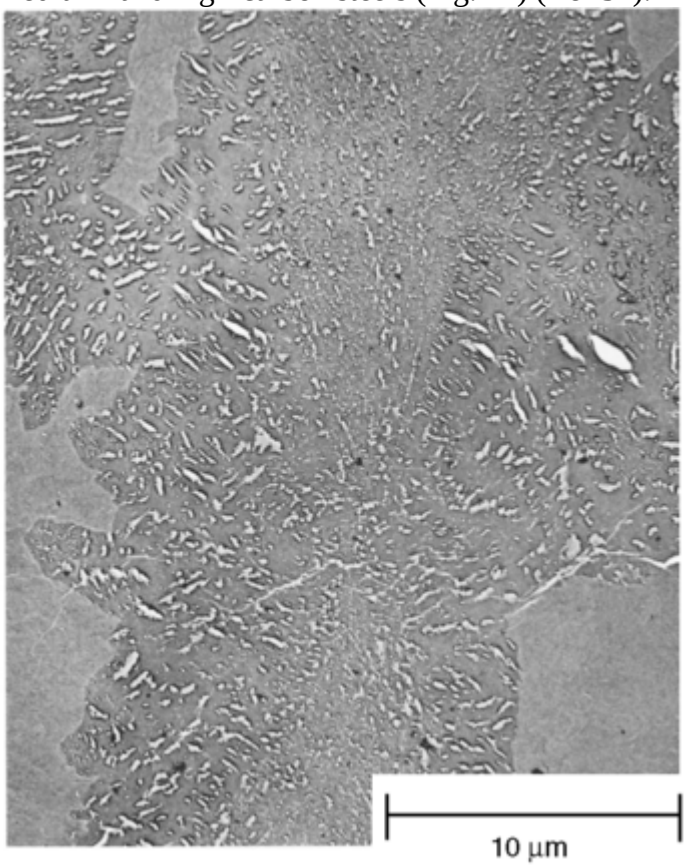

Fig. 22 Replica electron micrograph of blocky, or columnar-shaped, regions generally nucleated at grain boundaries that contain a coarse dispersion of carbides in a steel, austenitized and isothermally transformed at 290 °C (550 °F) under a pressure of 2400 MPa (24 kbar). Source: Ref 32

References cited in this section

4. D.V. Edmonds, Bainitic Structures, *Metallography and Microstructures,* 9th ed., American Society for Metals, 1985, p 662–667

32. T.G. Nilan, Austenite Decomposition at High Pressure, *Transformation and Hardenability in Steels*, Climax Molybdenum Co., 1967, p 57–66

M.J. Perricone, Bainitic Structures, *Metallography and Microstructures*, Vol 9, *ASM Handbook*, ASM International, 2004, p. 179–185

Bainitic Structures

Matthew J. Perricone, Lehigh University

Bainite in Nonferrous Systems

Several nonferrous alloy systems exhibit bainitelike transformations in a temperature range between high-temperature discontinuous reactions and low-temperature martensitic transformations. For example, the nonlamellar aggregate structures of transformation product and interlath and internal precipitation of second-phase particles have been observed in copper-base alloys (copper-aluminum, copper-tin, copper-zinc, etc.) and titanium-base alloys (uranium-titanium, titanium-nickel, etc.), as shown in Fig. 23 (Ref 33) and Fig. 24 (Ref 34), respectively.

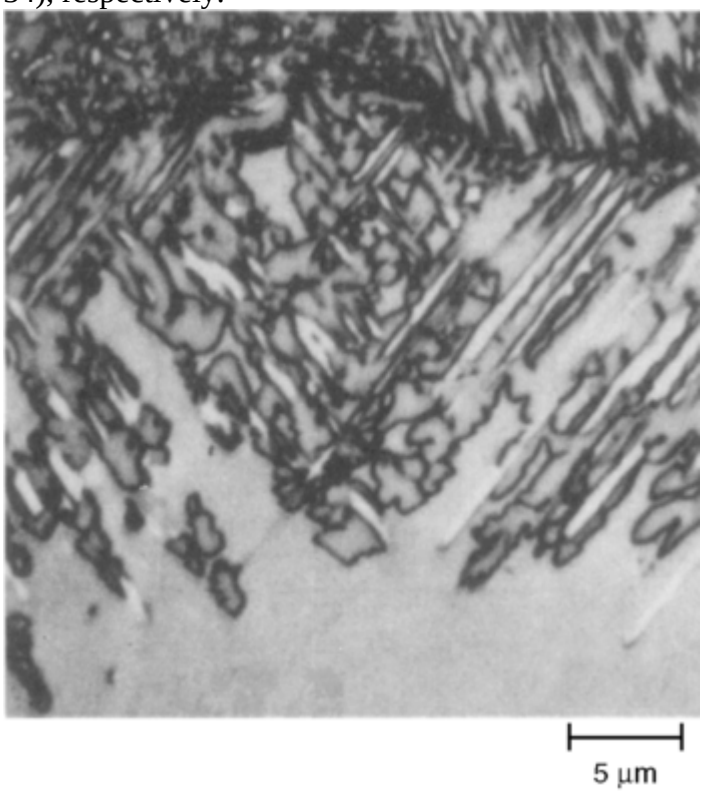

Fig. 23 Laths of a phase with interlath precipitation in a Cu-27.0Sn alloy, solution treated and isothermally transformed at 500 °C (930 °F) for 1 min. No etchant given. Source: Ref 33

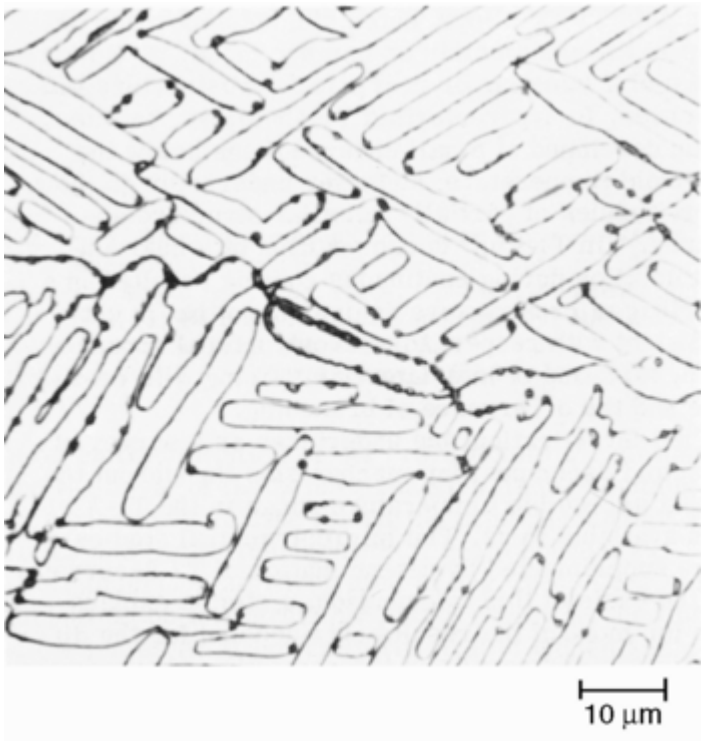

Fig. 24 Plates of a phase in α matrix of retained β phase with Ti_2Ni precipitation at the plate boundaries in a Ti-4Ni alloy, solution treated at 1000 °C (1800 °F) for 20 min and isothermally transformed at 750 °C (1400 °F) for 1 h. 95% H_2O, 4% HNO_3, 1% HF. 1000×. Source: Ref 34

References cited in this section

33. C.W. Spencer and D.J. Mack, Eutectoid Transformations in Non-Ferrous and Ferrous Alloy Systems, *Decomposition of Austenite by Diffusional Processes,* V.F. Zackay and H.I. Aaronson, Ed., Interscience, 1962, p 549–603

34. G.W. Franti, J.C. Williams, and H.I. Aaronson, A Survey of Eutectoid Decomposition in Ten Ti-X Systems, *Metall. Trans. A,* Vol 9, 1978, p 1641–1649

M.J. Perricone, Bainitic Structures, *Metallography and Microstructures,* Vol 9, *ASM Handbook,* ASM International, 2004, p. 179–185

Bainitic Structures

Matthew J. Perricone, Lehigh University

Recent Developments

A recent forum (Ref 35, 36, 37, 38, 39, 40, 41, 42, 43, 44, 45, 46) addressed the pressing controversial issues still surrounding the operating mechanism of the bainite transformation. At the center of the controversy is the role of diffusive and displacive phenomena in the nucleation and growth of bainitic ferrite from the parent austenite. The juncture of the bainite transformation in which elemental partitioning occurs continues to be a source of debate (Ref 35, 36, 37, 38), as does the generation of surface relief during the bainite transformation and its implications about the mechanism of growth (Ref 39, 40, 41, 42). The properties of the advancing γ/α transformation interface is a continual point of contention among researchers (Ref 43, 44, 45), and a consensus

has yet to be reached about the definitive crystallographic orientation relationships between parent and product phases in the bainite transformation (Ref 46).

References cited in this section

35. M. Enomoto, Partition of Carbon and Alloying Elements during the Growth of Ferrous Bainite, *Scr. Mater.,* Vol 47, 2002, p 149

36. D. Quidort and Y. Brechet, The Role of Carbon on the Kinetics of Bainite Transformation in Steels, *Scr. Mater.,* Vol 47, 2002, p 151–156

37. G.J. Shiflet and R.E. Hackenberg, Partitioning and the Growth of Bainite, *Scr. Mater.,* Vol 47, 2002, p 163–167

38. S. van der Zwaag and J. Wang, A Discussion on the Atomic Mechanism of the Bainitic Reaction in TRIP Steels, *Scr. Mater.,* Vol 47, 2002, p 169–173

39. H.I. Aaronson, G. Spanos, and W.T. Reynolds, Jr., A Progress Report on the Definitions of Bainite, *Scr. Mater.,* Vol 47, 2002, p 139–144

40. H.-S. Fang, J.-B. Yang, Z.-G. Yang, and B.-Z. Bai, The Mechanism of Bainite Transformation in Steels, *Scr. Mater.,* Vol 47, 2002, p 157–162

41. M. Hillert, Paradigm Shift for Bainite, *Scr. Mater.,* Vol 47, 2002, p 175–180

42. H.I. Aaronson, J.M. Rigsbee, B.C. Muddle, and J.F. Nie, Aspects of the Surface Relief Definition of Bainite, *Scr. Mater.,* Vol 47, 2002, p 207–212

43. G.R. Purdy, Bainite: Defect Signatures, *Scr. Mater.,* Vol 47, 2002, p 181–185

44. B.C. Muddle and J.F. Nie, Formation of Bainite as a Diffusional-Displacive Phase Transformation, *Scr. Mater.,* Vol 47, 2002, p 187–192

45. T. Moritani, N. Miyajima, T. Furuhara, and T. Maki, Comparison of Interphase Boundary Structure between Bainite and Martensite in Steel, *Scr. Mater.,* Vol 47, 2002, p 193–199

46. Y. Ohmori, Crystallographic Aspects of Bainite Transformation in Steels, *Scr. Mater.,* Vol 47, 2002, p 201–206

M.J. Perricone, Bainitic Structures, *Metallography and Microstructures,* Vol 9, *ASM Handbook,* ASM International, 2004, p. 179–185

Bainitic Structures

Matthew J. Perricone, Lehigh University

References

1. R.F. Hehemann and A.R. Troiano, *Met. Prog.,* Vol 70, 1956, p 97

2. H.K.D.H. Bhadeshia, Bainitic Ferrite, *Bainite in Steels,* 2nd ed., Institute of Materials, London, 2001, p 19–61

3. L.C. Chang and H.K.D.H. Bhadeshia, Metallographic Observations of Bainite Transformation Mechanism, *Mater. Sci. Technol.,* Vol 11, 1995, p 105–108

4. D.V. Edmonds, Bainitic Structures, *Metallography and Microstructures,* 9th ed., American Society for Metals, 1985, p 662–667

5. H.K.D.H. Bhadeshia, The Bainite Transformation: Unresolved Issues, *Mater. Sci. Eng. A,* Vol 273–275, 1999, p 58–66

6. J.M. Oblak and R.F. Hehemann, *Transformation and Hardenability in Steels,* Climax Molybdenum Co., 1967

7. G. Kurdjumov and G. Sachs, *Z. Physik,* Vol 64, 1930, p 325–343

8. Z. Nishiyama, *Sci. Rep. Tôhoku Univ.,* Vol 23, 1934, p 637–664

9. G. Wassermann, *Arch. Eisenhüttenwes,* Vol 6, 1933, p 347–351

10. W. Pitsch, *Acta Metall.,* Vol 10, 1962, p 897–900

11. D. Quidort and Y. Brechet, Isothermal Growth Kinetics of Bainite in 0.5% C Steels, *Acta Metall.,* Vol 49, 2001, p 4161–4170

12. Y. Ohmori, Y.-C. Jung, K. Nakai, and H. Shioiri, Bainite Transformation and the Diffusional Migration of Bainite/Austenite Broad Interfaces in Fe-9%Ni-C Alloys, *Acta Metall.,* Vol 49, 2001, p 3149–3162

13. H.K.D.H. Bhadeshia and D.V. Edmonds, *Metall. Trans. A,* Vol 10, 1979, p 895–907

14. R.F. Hehemann, Ferrous and Non-Ferrous Bainitic Structures, *Metallography, Structures, and Phase Diagrams,* 8th ed., American Society for Metals, 1973, p 194–196

15. H.K.D.H. Bhadeshia and E. Swallow, High Resolution Observations of Displacements Caused by Bainitic Transformation, *Mater. Sci. Technol.,* Vol 12, 1996, p 121–125

16. The Bainite Transformation, *Phase Transformations,* American Society for Metals, 1970

17. H.K.D.H. Bhadeshia, A Rationalization of Shear Transformations in Steels, *Acta Metall.,* Vol 29, 1981, p 1117–1130

18. H.K.D.H. Bhadeshia and J.W. Christian, Bainite in Steels, *Metall. Trans. A,* Vol 21, 1990, p 767–797

19. H.I. Aaronson, W.T. Reynolds, Jr., G.J. Shiflet, and G. Spanos, Bainite Viewed Three Different Ways, *Metall. Trans. A,* Vol 21, 1990, p 1343–1380

20. H.I. Aaronson, T. Furuhara, J.M. Rigsbee, W.T. Reynolds, Jr., and J.M. Howe, Crystallographic and Mechanistic Aspects of Growth by Shear and by Diffusional Processes, *Metall. Trans. A,* Vol 21, 1990, p 2369–2409

21. Y.A. Bagaryatski, *Dokl. Akad. Nauk SSSR,* Vol 73, 1950, p 1161–1164

22. I.V. Isaichev, *Zh. Tekh. Fiz.,* Vol 17, 1947, p 835–838

23. F.B. Pickering, The Structure and Properties of Bainite in Steels, *Transformation and Hardenability in Steels,* Climax Molybdenum Co., 1967, p 109–129

24. Y. Ohmori, The Crystallography of the Lower Bainite Transformation in a Plain Carbon Steel, *Trans. Iron Steel Inst. Jpn.,* Vol 11, 1971, p 95–101

25. D.N. Shackleton and P.M. Kelly, The Crystallography of Cementite Precipitation in the Bainite Transformation, *Acta Metall.,* Vol 15, 1967, p 979–992

26. D.-H. Huang and G. Thomas, Metallography of Bainitic Transformation in Silicon Containing Steels, *Metall. Trans. A,* Vol 8, 1977, p 1661–1674

27. K.H. Jack, *J. Iron Steel Inst.,* Vol 169, 1951, p 26–36

28. H. Okamoto and M. Oka, Lower Bainite with Midrib in Hypereutectoid Steels, *Metall. Trans. A,* Vol 17, 1986, p 1113–1120

29. M. Hillert, The Role of Interfacial Energy During Solid-State Phase Transformations, *Jernkontorets Ann.,* Vol 141, 1957, p 757–789

30. K.R. Kinsman and H.I. Aaronson, The Inverse Bainite Reaction in Hypereutectoid Fe-C Alloys, *Metall. Trans. A,* Vol 1, 1970, p 1485–1488

31. L.J. Habrakan and M. Economopoulos, Bainitic Microstructures in Low-Carbon Alloy Steels and Their Mechanical Properties, *Transformation and Hardenability in Steels,* Climax Molybdenum Co., 1967, p 69–107

32. T.G. Nilan, Austenite Decomposition at High Pressure, *Transformation and Hardenability in Steels,* Climax Molybdenum Co., 1967, p 57–66

33. C.W. Spencer and D.J. Mack, Eutectoid Transformations in Non-Ferrous and Ferrous Alloy Systems, *Decomposition of Austenite by Diffusional Processes,* V.F. Zackay and H.I. Aaronson, Ed., Interscience, 1962, p 549–603

34. G.W. Franti, J.C. Williams, and H.I. Aaronson, A Survey of Eutectoid Decomposition in Ten Ti-X Systems, *Metall. Trans. A,* Vol 9, 1978, p 1641–1649

35. M. Enomoto, Partition of Carbon and Alloying Elements during the Growth of Ferrous Bainite, *Scr. Mater.,* Vol 47, 2002, p 149

36. D. Quidort and Y. Brechet, The Role of Carbon on the Kinetics of Bainite Transformation in Steels, *Scr. Mater.,* Vol 47, 2002, p 151–156

37. G.J. Shiflet and R.E. Hackenberg, Partitioning and the Growth of Bainite, *Scr. Mater.,* Vol 47, 2002, p 163–167

38. S. van der Zwaag and J. Wang, A Discussion on the Atomic Mechanism of the Bainitic Reaction in TRIP Steels, *Scr. Mater.,* Vol 47, 2002, p 169–173

39. H.I. Aaronson, G. Spanos, and W.T. Reynolds, Jr., A Progress Report on the Definitions of Bainite, *Scr. Mater.,* Vol 47, 2002, p 139–144

40. H.-S. Fang, J.-B. Yang, Z.-G. Yang, and B.-Z. Bai, The Mechanism of Bainite Transformation in Steels, *Scr. Mater.,* Vol 47, 2002, p 157–162

41. M. Hillert, Paradigm Shift for Bainite, *Scr. Mater.,* Vol 47, 2002, p 175–180

42. H.I. Aaronson, J.M. Rigsbee, B.C. Muddle, and J.F. Nie, Aspects of the Surface Relief Definition of Bainite, *Scr. Mater.,* Vol 47, 2002, p 207–212

43. G.R. Purdy, Bainite: Defect Signatures, *Scr. Mater.,* Vol 47, 2002, p 181–185

44. B.C. Muddle and J.F. Nie, Formation of Bainite as a Diffusional-Displacive Phase Transformation, *Scr. Mater.,* Vol 47, 2002, p 187–192

45. T. Moritani, N. Miyajima, T. Furuhara, and T. Maki, Comparison of Interphase Boundary Structure between Bainite and Martensite in Steel, *Scr. Mater.,* Vol 47, 2002, p 193–199

46. Y. Ohmori, Crystallographic Aspects of Bainite Transformation in Steels, *Scr. Mater.,* Vol 47, 2002, p 201–206

J.E. Morral and M.A. Dayananda, Interdiffusion Structures, *Metallography and Microstructures,* Vol 9, *ASM Handbook*, ASM International, 2004, p. 186–191

Interdiffusion Structures

J.E. Morral, The Ohio State University; M.A. Dayananda, Purdue University

---

Introduction

INTERDIFFUSION occurs when two dissimilar materials are in intimate contact and are at a high enough temperature for significant atom movement. Atoms of the two materials can then intermix and react to change composition and form new phases. The resulting change in microstructure may affect properties and therein lies the importance of interdiffusion.

Interdiffusion plays a role in a number of technologies including heat treatment, coatings, joining, composite materials, powder processing, electronic materials, and oxidation prevention, especially when materials are exposed to elevated temperatures for extended periods of time. The time can be short, on the order of seconds or minutes, when operating near the melting point. The time can be much longer when operating below half the absolute melting temperature, with comparable changes requiring years or decades to occur.

This article outlines the principles used in analyzing interdiffusion microstructures and gives examples of microstructures that have resulted from either processing or service life. These examples are helpful in distinguishing between representative microstructures and artifact-ridden microstructures that are introduced by metallographic preparation or by changes that occurred upon cooling the samples to room temperature.

J.E. Morral and M.A. Dayananda, Interdiffusion Structures, *Metallography and Microstructures,* Vol 9, *ASM Handbook,* ASM International, 2004, p. 186–191

Interdiffusion Structures

J.E. Morral, The Ohio State University; M.A. Dayananda, Purdue University

Analysis of Interdiffusion Microstructures

Interdiffusion microstructures appear as a region on either side of the original interface of contact between two materials. During isothermal heat treatment, the width of the diffusion-affected zone often increases proportionally to the square root of time, at least initially. Microstructures that form under these conditions lend themselves to a straightforward analysis and are discussed in this article. However, microstructures that are not formed isothermally, or when the temperature is below half the absolute melting temperature, tend to be more complex and are difficult to interpret without the help of computer simulations. These are not discussed further. Therefore, the main focus here is on analyzing microstructures that form isothermally and follow square root of time kinetics, because it provides a basis from which more complex microstructures can be interpreted.

Although interdiffusion regions tend to be one-dimensional, expanding in width away from the original interface, the interface itself may be curved. For example, the surface of a turbine blade in contact with a coating is curved. However, there are cases when the microstructure is two- or three-dimensional. One example is precipitation along grain boundaries caused by short-circuit diffusion in the grain boundary. Such precipitation can be found well ahead of the bulk interdiffusion region.

Identification of Interdiffusion Layers and Boundaries. One-dimensional interdiffusion microstructures form in layers. The layers may be single phase or multiphase (i.e., one phase or a mixture of two or more phases). The boundaries between the layers are identified on a micrograph by an abrupt change in the volume fraction of phases present.

When analyzing a micrograph, one begins by identifying the layers and the phases present in them. Also, the location of the initial interface between the alloys in contact should be identified. The initial interface can be identified by knowing the initial dimensions of the materials or by clues in the microstructure that are discussed below. Identifying the location of the initial interface helps to establish the direction in which boundaries between layers are moving. In general, boundaries move away from the initial interface until a free surface or other interdiffusion microstructure is encountered. As discussed below, the direction of boundary movement can influence the microstructure and thereby help in identifying microstructural artifacts.

Shorthand Notation for Layers and Boundaries. When discussing interdiffusion microstructures in the literature, it is instructive to first indicate the microstructures of the initial materials that were in contact. This can be done in a compact form as explained in this section (Ref 1). First, the phases present in the starting materials are listed with a forward slash separating the two layers. For example, the initial microstructure of an MCrAlY coating on a nickel-base superalloy might be written as:

$$\gamma + \beta/\gamma + \gamma' \quad \text{(Eq 1)}$$

in which the MCrAlY coating is a mixture of gamma and beta phases, while the superalloy is a mixture of gamma and gamma prime phases. The interdiffusion microstructure is represented in a similar way, except now the intermediate layers that form on heating are inserted between the initial alloys with a carat between each layer indicating the direction of boundary movement. For example the listing:

$$\gamma + \beta < \gamma > \gamma + \gamma' \quad \text{(Eq 2)}$$

would correspond to a microstructure in which a gamma-phase layer formed at the initial interface between the coating and superalloy and grew into both starting materials. In this case, it can be deduced that the initial interface must be in the single-phase gamma region.

Another microstructure that forms in such systems is given by:

$$\gamma + \beta/\gamma + \beta > \gamma + \gamma' \quad \text{(Eq 3)}$$

in which the gamma-plus-beta layer grows into the superalloy. As seen in Fig. 1, there is a sharp change in the volume fraction and size of the beta phase at one point in the microstructure (Ref 2). Theoretical studies (Ref 3) and computer simulations (Ref 4) have shown that this is an expected feature when a multiphase region straddles the initial interface. A vertical line (|) is used to mark this boundary in the shorthand notation, because it is virtually stationary except for a small, often undetectable, shift caused by the Kirkendall effect (Ref 5). This boundary is a valuable feature because it marks the approximate location of the initial interface. All other boundaries should move away from it as long as the width of the interdiffusion zone expands proportional to the square root of time.

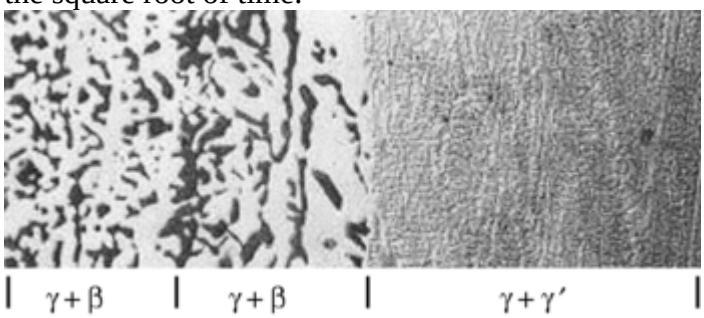

Fig. 1 An interdiffusion microstructure in a Ni-Cr-Al diffusion couple made by bonding a γ + β alloy (left) to a γ + γ′ alloy (right) (Ref 2). The microstructure can be expressed in shorthand as γ + β | γ + β > γ + γ′.

Classification of Boundaries. Boundaries between layers can be classified according to the number of phases that change on crossing the boundary (Ref 1). For example, the stationary boundary in Eq 3 indicated by a vertical slash (|) is a type 0 boundary because there are no (zero) changes in phase when crossing it. The other boundary in Eq 3 is a type 2 boundary because two phases change on crossing the boundary: moving from left to right the β phase is lost while the γ′ is formed. Four types of boundaries found in microstructures and their characteristics are listed in the Table 1. Although other types of boundary may be found, they normally suggest metallographic artifacts or a microstructure that did not form isothermally with square root of time kinetics.

Table 1 Interdiffusion microstructure boundaries

Type	Examples	Comments
Type 0	γ + β | γ + β	The same phases are present on either side of the boundary. Only the volume fraction differs.
	γ + β + α | γ + β + α	Only occurs when there is a multiphase region at the initial interface.
		Identifies the approximate location of the initial interface between alloys.
Type 1(a)	γ + β < γ	One change in phase.
	γ + β + α < γ + α	The changed phase dissolves at the boundary.
		There is a discontinuous change in volume fraction at the boundary.
Type 1(b)	γ + β > γ	One change in phase.
	γ + α + β > γ + α	The changed phase grows at the boundary.
		The volume fraction goes continuously to zero as the boundary is approached.
Type 2	γ > β	Two changes in phase, one phase is gained and one phase is lost on crossing the boundary.
	γ + α > β + α	The volume fracture changes discontinuously on crossing the boundary.
Type 3	γ + α > β	Three changes in phase, one is gained and two are lost or one is lost and two are

	gained when crossing the boundary.
$\gamma + \alpha + \delta < \beta + \delta$	The volume fraction changes discontinuously on crossing the boundary. Normally only seen when there is a single-phase region with a limited solubility range.

Identifying the types of boundaries in an interdiffusion microstructure is a quick check of whether or not the microstructure is representative of an isothermal treatment. The four types listed previously are the only ones expected, regardless of the number of components in the alloys and regardless of the numbers or types of phases in the initial materials. As noted in Table 1, it is only types 0, 1, and 2 that are normally seen unless there is an intermetallic phase or compound present, in which case type 3 can occur.

Interdiffusion Microstructure Maps. When interdiffusion microstructures are used in alloy design, it is helpful to create an interdiffusion microstructure map (IMM) (Ref 6). The map assumes that the composition of one interdiffusing material is constant while the composition of the other is varied. The map plots the microstructure, expressed in shorthand notation, as a function of the composition variation. Accordingly, boundary lines on the map correspond to changes in the shorthand notation. Figure 2 gives an IMM that was prepared for interdiffusion microstructures of MCrAlY coatings on superalloys. The map illustrates that in this case five different microstructures can form within a small range of coating compositions.

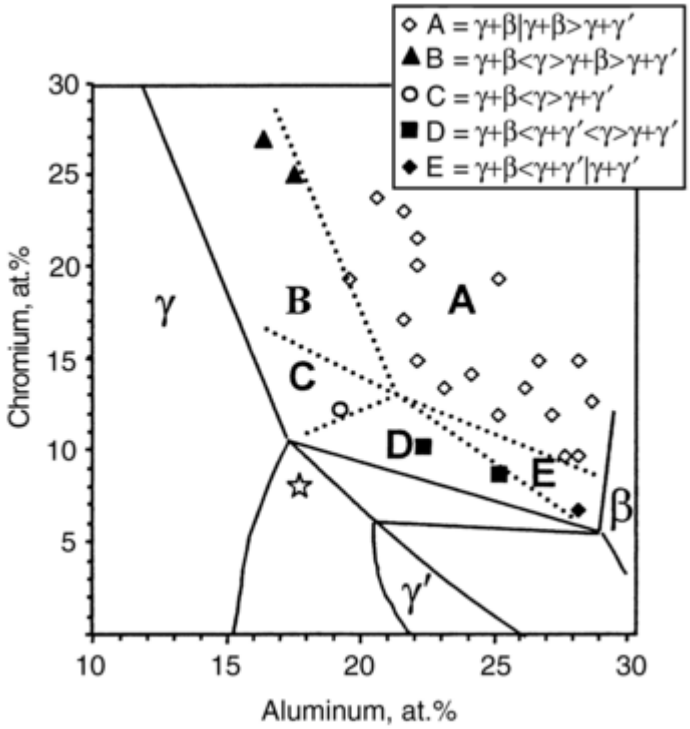

Fig. 2 Example of an interdiffusion microstructure map prepared for Ni-Cr-Al, gamma-plus-beta coatings on a superalloy annealed at 1200 °C (2190 °F). The initial γ + γ′ composition is noted by a star. Source: Ref 6

The examples that follow describe interdiffusion microstructures found in various research and industrial systems. Here, microstructures are analyzed by identifying layers, phases in layers, and, when enough information is given, the initial interface. Then the microstructure can be expressed using the shorthand notation described in this section.

References cited in this section

1. J.E. Morral, C. Jin, A. Engström, and J. Ågren, *Scr. Mater.*, Vol 34, 1996, p 1661–1666

2. X. Qiao, M.S. thesis, University of Connecticut, 1998

3. W.D. Hopfe and J.E. Morral, *Acta Metall. Mater.*, Vol 42, 1994, p 3887–3894

4. A. Engstrom, J.E. Morral, and J. Ågren, *Acta Mater.*, Vol 45, 1997, p 1189–1199

5. K. Wu, Y. Wang, and J.E. Morral, A Phase Field Study of Microstructural Changes Due to the Kirkendall Effect in Two-Phase Diffusion Couples, *Acta Mater.*, Vol 49, 2001, p 3401–3408

6. F. Meisenkothen and J.E. Morral, On the Existence of 5-Line Nodes on Interdiffusion Microstructure Maps, *Scr. Mater.*, Vol 43, 2000, p 361–364

J.E. Morral and M.A. Dayananda, Interdiffusion Structures, *Metallography and Microstructures*, Vol 9, *ASM Handbook*, ASM International, 2004, p. 186–191

Interdiffusion Structures

J.E. Morral, The Ohio State University; M.A. Dayananda, Purdue University

---

Examples of Interdiffusion Microstructures

Binary Systems

During isothermal annealing of binary systems, one normally expects planar interfaces between single-phase layers. An example is given in Fig. 3, where a planar boundary developed in a copper-zinc diffusion couple annealed at 775 °C (1425 °F) (Ref 7).

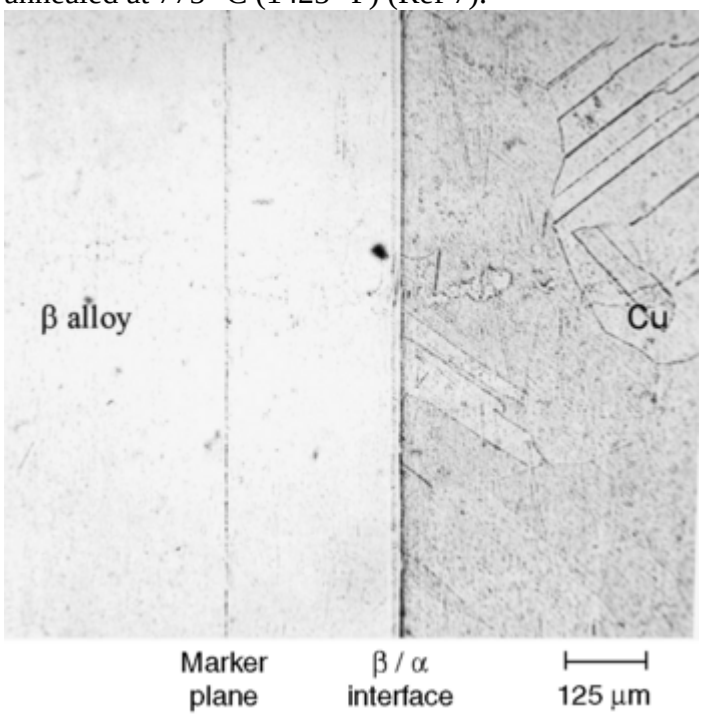

Fig. 3 A β(50Cu + 50Zn)/α(100Cu) binary diffusion couple annealed at 775 °C (1425 °F) for 2 h (Ref 7) illustrating a planar, type 2 boundary. Etched with potassium dichromate solution. The microstructure can be expressed in shorthand as β > α.

There are exceptions, one being the case when an initial alloy is multiphase. Another apparent exception is given in Fig. 4, a micrograph of a Mo/$MoSi_2$ diffusion couple (Ref 8) annealed at 1500 °C (2730 °F) for 6 h.

Here, nonplanar interfaces between phases can be seen, associated with the formation of Mo_5Si_3 and Mo_3Si (also cracks that formed on cooling can be seen). In cases when nonplanar boundaries form in binary systems, one may suspect nonisothermal conditions, for example, slow cooling after heat treatment or temperature variations in the sample during heat treatment. However, in this example, the authors thought that diffusional anisotropy was the cause.

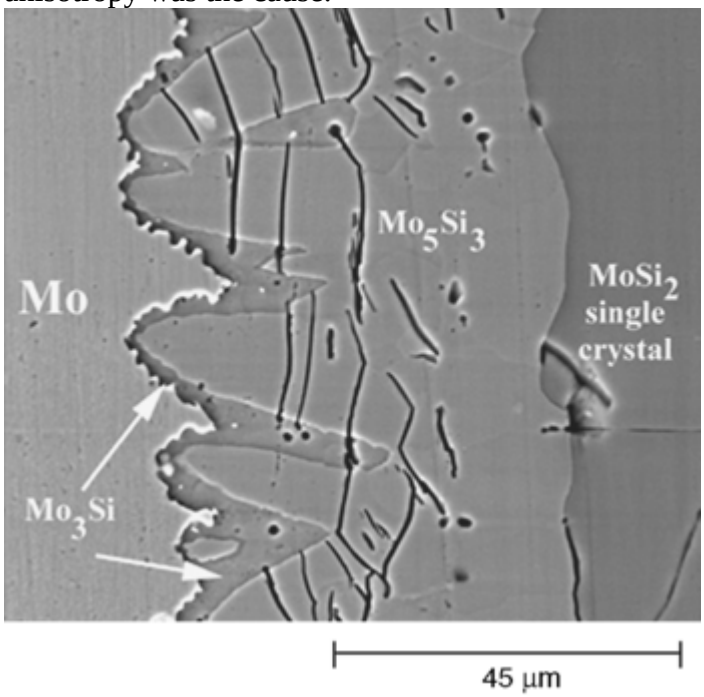

Fig. 4 A secondary-electron image of the interdiffusion zone in a Mo/$MoSi_2$ diffusion couple annealed at 1500 °C (2730 °F) for 6 h (Ref 8). Here multiphase layers can be seen, which are unexpected for binary systems.

At low temperatures one can observe microstructures with multiphase layers in binary systems, too. Figure 5 is a scanning electron micrograph (SEM) of a nickel/tin diffusion couple that was annealed at 100 °C (212 °F) for 480 h while undergoing an electric current of 4×10^3 A/cm^2 (Ref 9). To clearly observe the microstructure of the interface, tin was partially removed by using an etching solution of 2% HCl + 5% HNO_3 + 93% CH_3OH. The two-phase layer of Sn + $NiSn_3$ would not have been expected at higher temperatures where samples tend to be in local equilibrium (i.e., the phases correspond to what the phase diagram would predict for the local composition of the alloy).

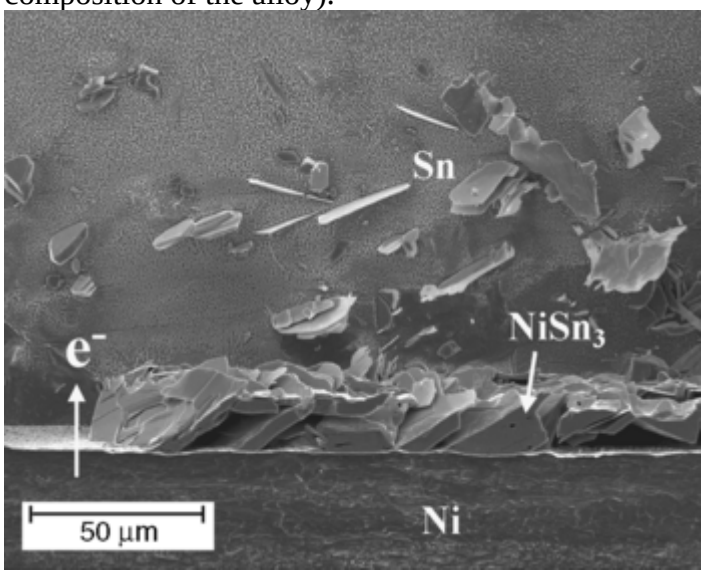

Fig. 5 Scanning electron micrographs of nickel/tin diffusion couples annealed at 100 °C (212 °F) for 480 h under an applied electric current of 4×10^3 A/cm^2 (Ref 9). Tin was partly removed by heavy etching

with a solution of 2% HCl + 5% HNO_3 + 93% CH_3OH. As in Fig. 4, there is a multiphase layer in this binary system.

Copper Base Systems

Cu-Ni-Zn Diffusion Couples. A wide variety of interdiffusion microstructures were reported for Cu-Ni-Zn diffusion couples heated at 775 °C (1425 °F) (Ref 10, 11, 12, 13, 14, 15). A few are presented here. All were prepared with an etching solution of 2 g $K_2Cr_2O_7$, 8 mL H_2SO_4, 4 mL saturated NaCl solution, and 100 mL H_2O.

A number of couples were studied that had initial alloys that were single phase. Many of these formed single-phase layers, as found in binary systems. Others formed two-phase layers, depending on the initial single-phase alloys. Figure 6, one example in which a two-phase layer formed, illustrates the difference between a type 1(a) and a type 1(b) boundary. The type 1(a) boundary is between the alpha layer and the alpha-plus-beta layer. Here there is a discontinuous change in alpha phase on crossing the 1(a) boundary as the beta phase dissolves. However, at the type 1(b) boundary, between the alpha-plus-beta and beta regions, the volume fraction of alpha goes continuously to zero as the boundary is approached where the alpha phase begins its growth. In this way, one is able to deduce that the shorthand notation for this microstructure must be $\beta < \alpha + \beta < \alpha$.



Fig. 6 A β (31.5Cu-22Ni-46.5Zn)/α (100Cu) diffusion couple annealed at 775 °C (1425 °F) for 48 h (Ref 10). Potassium dichromate etch. The microstructure can be expressed in shorthand notation as β < α + β < α.

Figure 7 is an example in which a two-phase layer formed in a couple made from two different single-phase, alpha alloys (Ref 14, 15). There is an abrupt change in the amount of alpha phase in the two-phase region, indicating that a type 0 boundary (near the initial interface) was there. Both the microstructure and consideration of the diffusion path suggest that there is a thin single-phase beta layer as well. Accordingly, the microstructure in shorthand notation is $\alpha < \beta < \alpha + \beta \mid \alpha + \beta > \alpha$..



Fig. 7 Development of a two-phase region in a Cu-Ni-Zn couple made from two single-phase α alloys and annealed at 775 °C (1425 °F) for 8 h (Ref 14, Ref 15). Potassium dichromate etch. The microstructure in shorthand notation is α < β < α + β | α + β > α.

Figure 8 came from a diffusion couple with initial alloys each containing two phases, alpha plus beta. As a result of interdiffusion, demixing occurred (Ref 14, 15) resulting in single-phase layers of both alpha and beta. When single-phase layers with planar boundaries form in the vicinity of the initial interface, it is not possible to determine with certainty the direction in which the boundaries move. However, the width of alpha phase region and the Kirkendall porosity (which is normally near the initial interface) suggest that the initial interface is in the alpha α + β < β < α > α + $\tilde{\beta}$.

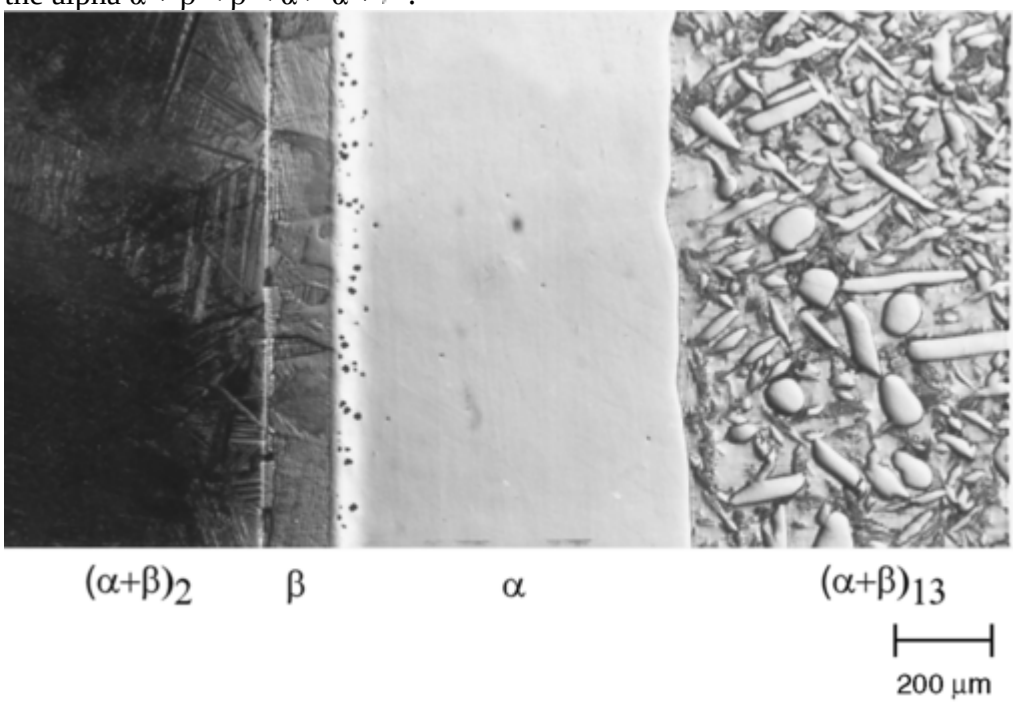

Fig. 8 A Cu-Ni-Zn, α + β/α + β diffusion couple annealed at 775 °C (1425 °F) for 8 h illustrating the phenomenon of demixing of phases (Ref 14, Ref 15). Potassium dichromate etch. The initial interface position is not known, but a likely microstructure is α + β < β < α > α + β.

Nickel-Base Systems

René/Inconel Diffusion Couples. A series of diffusion couples that combined René and Inconel alloys were prepared by hot isostatic pressing at 1150 °C (2100 °F) for 4 h, followed by diffusion annealing at 1150 °C (2100 °F) for 1000 h (Ref 16). Optical micrographs show the gamma matrix as gray, the gamma prime precipitates as white, and MC carbides as black.

Figure 9, an IN-100/IN-718 diffusion couple, and Fig. 10, a René 95/IN-718 diffusion couple, are interesting because both microstructures can be characterized by $\gamma + \gamma' + MC < \gamma + MC < \gamma > \gamma + MC$, even though their alloys and microstructural morphologies are somewhat different. Figure 11 is a René 88/IN-100 diffusion couple with a microstructure characterized by $\gamma + MC \mid \gamma + MC > \gamma + \gamma'$. Although a sharp change in the amount of MC carbide is not apparent at the initial couple interface, one can assume that a change is there because the initial interface, and therefore a Type 0 boundary, cuts through the $\gamma + MC$ region. Also, the microstructure illustrates a type 2 boundary when three, instead of just two, phases are involved. As mentioned previously, two changes in phase is the maximum number normally seen on crossing a boundary in an interdiffusion microstructure, regardless of the number of components or number of phases present.

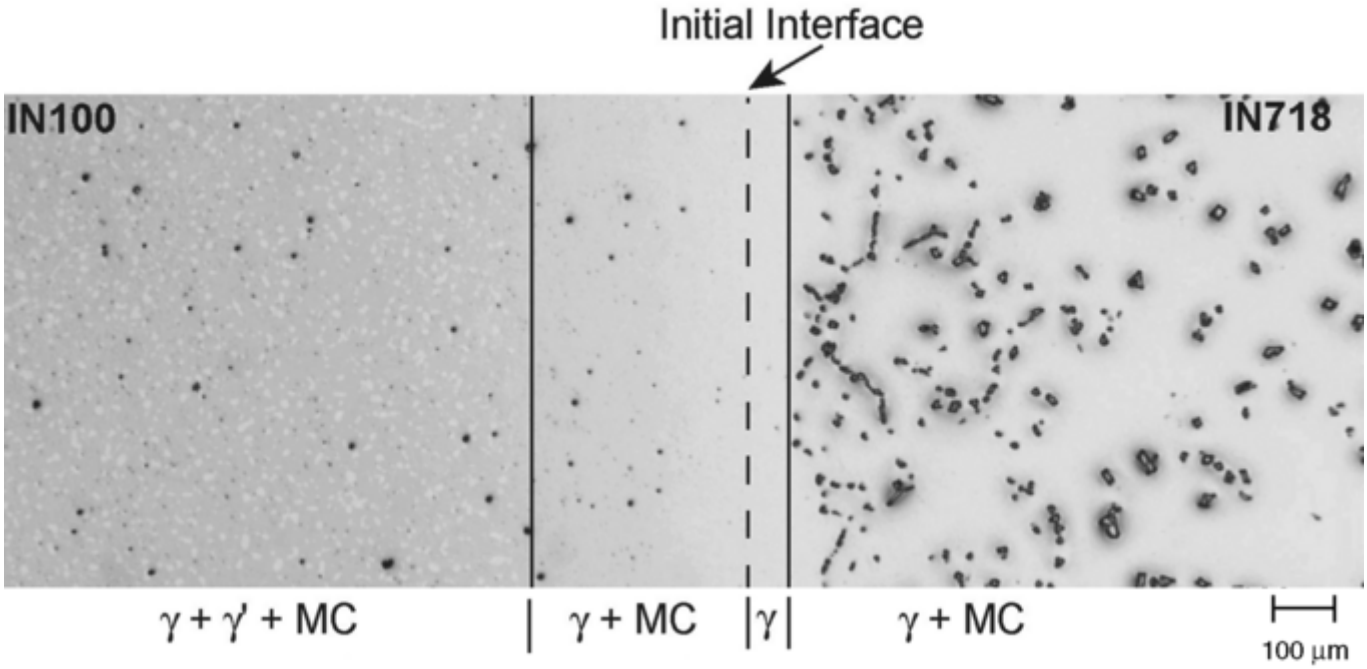

Fig. 9 An IN-100/IN-718 diffusion couple prepared by hot isostatic pressing at 1150 °C (2100 °F) for 4 h, followed by diffusion annealing at 1150 °C (2100 °F) for 1000 h (Ref 16). Optical micrographs show the gamma matrix as gray, the gamma prime precipitates as white, and MC carbides as black. Shorthand notation for the microstructure is $\gamma + \gamma' MC < \gamma + MC < \gamma > \gamma + MC$.

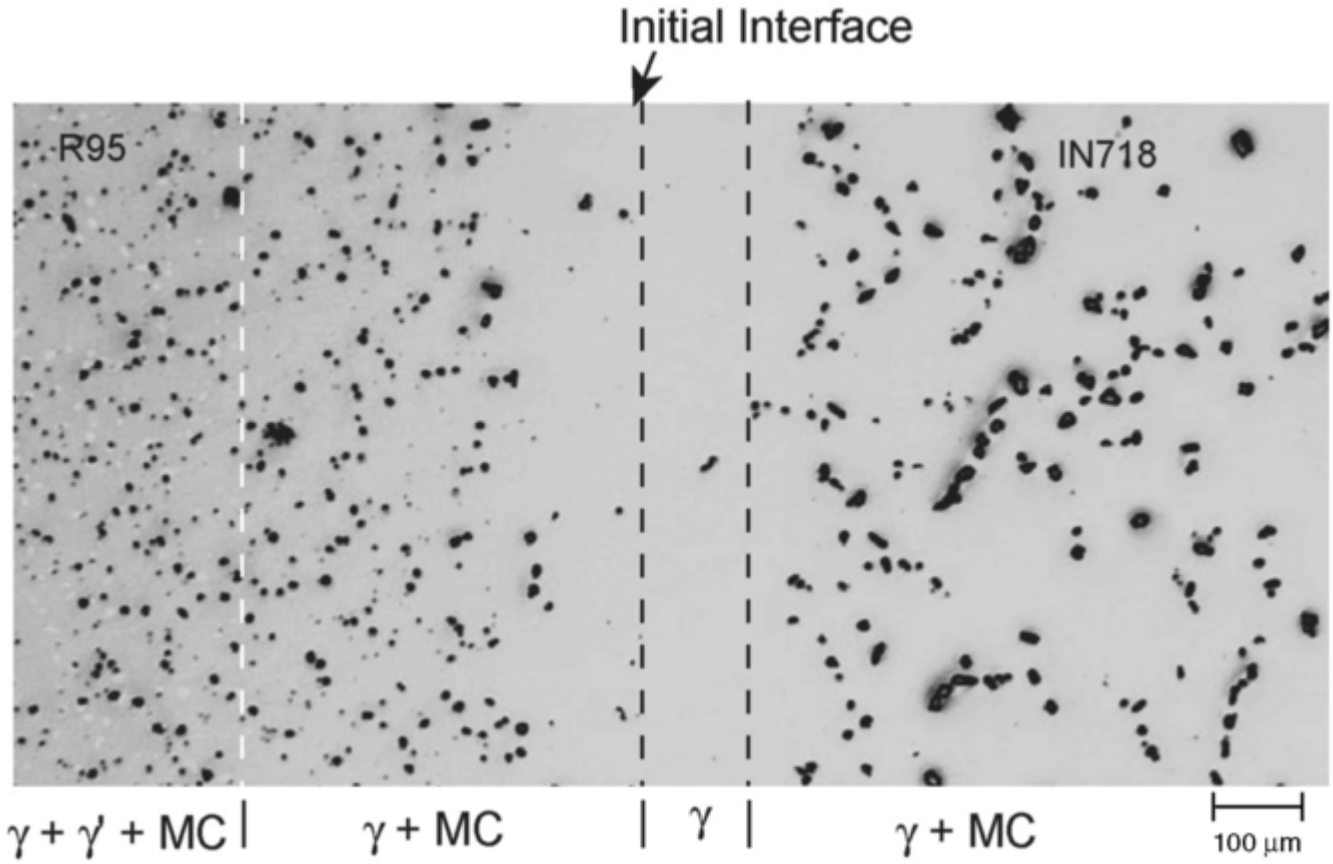

Fig. 10 A René 95/IN-718 diffusion couple prepared by hot isostatic pressing at 1150 °C (2100 °F) for 4 h, followed by diffusion annealing at 1150 °C (2100 °F) for 1000 h (Ref 16). Optical micrographs show the gamma matrix as gray, the gamma prime precipitates as white, and MC carbides as black. Shorthand notation for the microstructure is γ + γ′ + MC < γ + MC < γ > γ + MC.

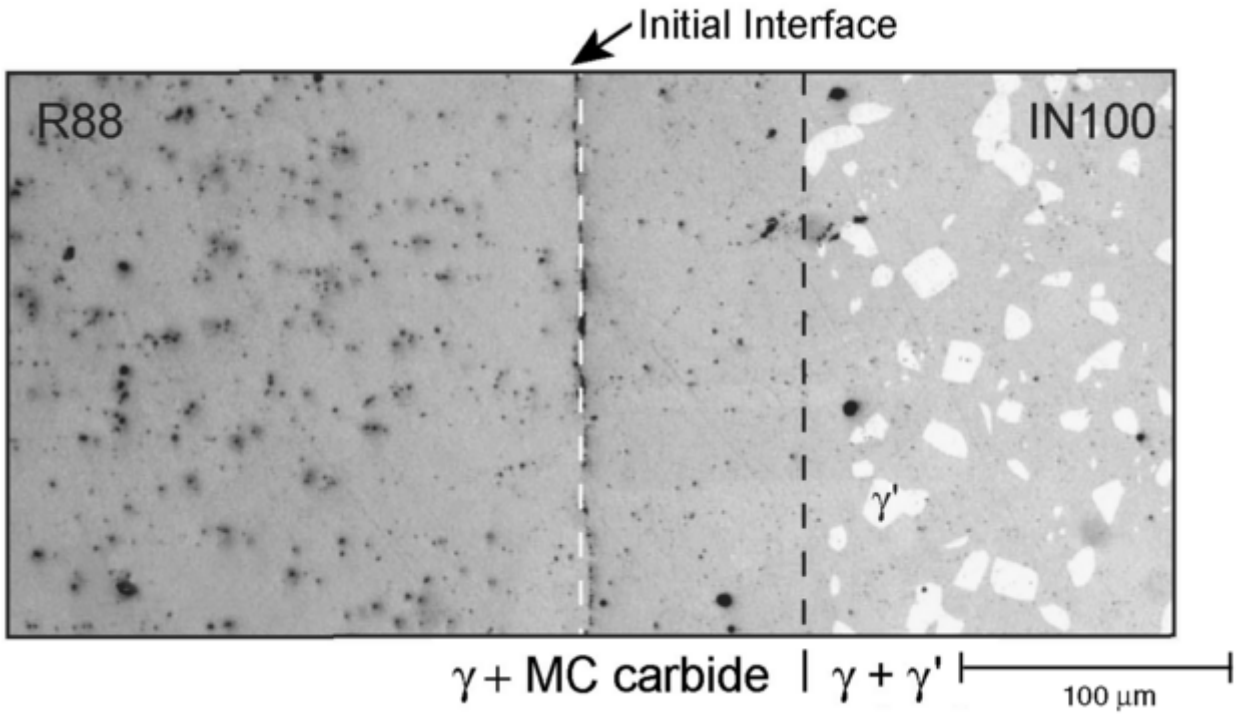

Fig. 11 A René 88/IN-100 diffusion couple prepared by hot isostatic pressing at 1150 °C (2100 °F) for 4 h, followed by diffusion annealing at 1150 °C (2100 °F) for 1000 h (Ref 16). Optical micrographs show the gamma matrix as gray, the gamma prime precipitates as white, and MC carbides as black. Shorthand for the microstructure is γ + MC | γ + MC > γ + γ′.

NiCoCrAlYRe Coating/IN-738. Figure 12 and 13 show interdiffusion microstructures of NiCoCrAlYRe coatings on IN-738 turbine blades after annealing at 1050 °C (1920 °F) for 1300 h and at 940 °C (1725 °F) for 9720 h, respectively (Ref 17). Despite the apparent complexity of these microstructures, one can see that it is still possible to divide them into layers. Figure 12 contains all type 1 boundaries, as indicated by the shorthand notation, $\gamma + \beta + \alpha < \gamma + \alpha < \gamma > \gamma + \gamma'$, in which case there is one change in phase on crossing each boundary. Figure 13 is more complex, with a microstructure characterized by:

$$\gamma+\beta+\alpha+\sigma<\gamma+\beta+\sigma<\gamma+\gamma'+\alpha\,|\,\gamma+\gamma'+\alpha>\gamma'$$
$$+\alpha>\gamma+\gamma'+\alpha>\gamma+\gamma'$$

In this case there is a type 3 boundary given by $\gamma + \beta + \sigma < \gamma + \gamma' + \alpha$. Although not impossible, one can argue it is unlikely based on phase diagram topology (Ref 1). One reason could be that the structure is not yet in local equilibrium (i.e., the microstructure has not fully changed to one characteristic of 940 °C, or 1725 °F).

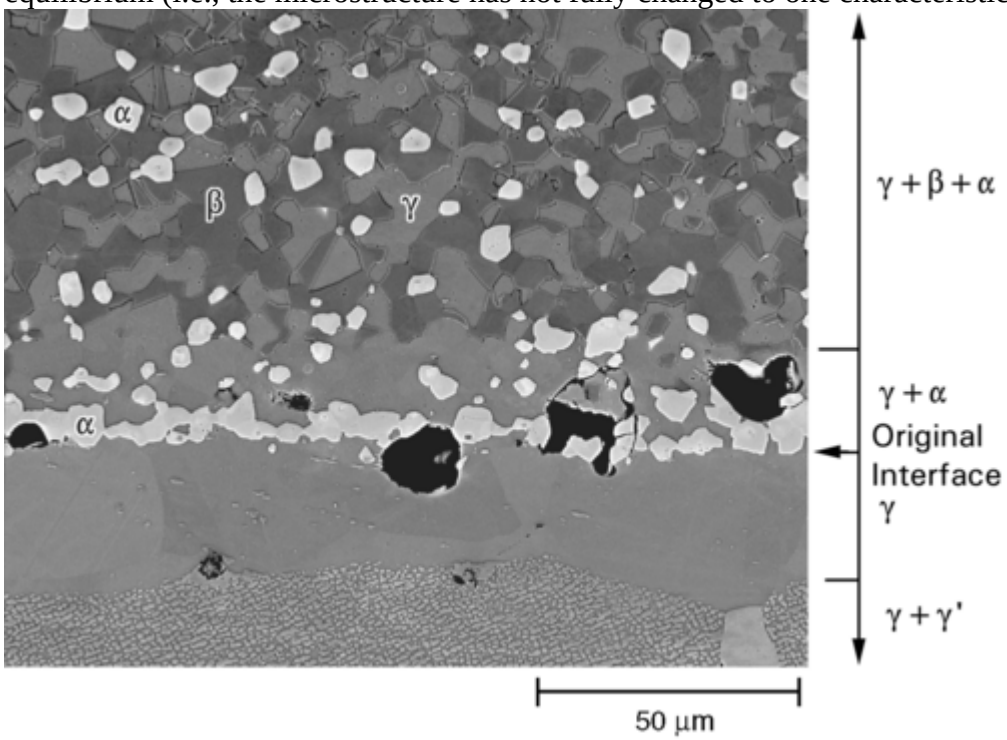

Fig. 12 Backscattered electron image of a 200 μm NiCoCrAlYRe coating on an IN-738 turbine blade after annealing at 1050 °C (1920 °F) for 1300 h (Ref 17). Etched in 1% chromic acid solution at 5 Vdc. Shorthand for the microstructure is $\gamma + \beta + \alpha < \gamma + \alpha < \gamma > \gamma + \gamma'$.

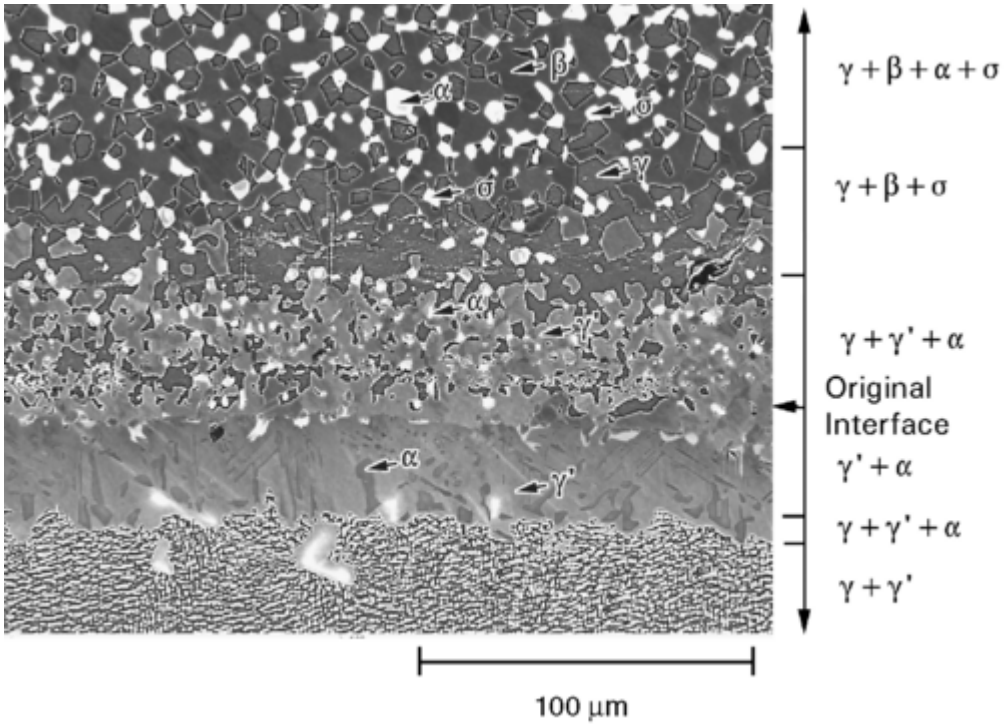

Fig. 13 Backscattered electron image of a 200 μm NiCoCrAlYRe coating on an IN-738 turbine blade after annealing at 940 °C (1725 °F) for 9720 h (Ref 17). Etched in 1% chromic acid solution at 5 Vdc. Shorthand for the microstructure is γ + β + α + σ < γ + β + σ < γ + γ′ + α | γ + γ′ + α > γ′ + α > γ + γ′.

Silicide-Forming Systems

Interdiffusion microstructures that form when materials are in contact with silicon are of considerable interest to the electronics industry. On occasion, complex and unexpected microstructures form in such systems as shown in the following. Figure 14 gives the microstructure a Si/50Co + 50Ni diffusion couple heated at 800 °C (1470 °F) for 400 h (Ref 18). Although this microstructure is complex, it conforms to what has been described already in that all boundaries are type 0, 1, or 2. The type 0 boundary in the microstructure appears to be midway between the starting phases. It follows that the microstructure can be characterized by:

$$\mathrm{Si} < \mathrm{NiSi_2} < \mathrm{NiSi} < \mathrm{Co(Ni)} < \mathrm{CoSi(Ni)}$$
$$+ \mathrm{(Co_xNi_{1-x})_2\,Si} \,|\, \mathrm{CoSi(Ni)} + \mathrm{(Co_xNi_{1-x})_2\,Si}$$
$$> \mathrm{(Co_xNi_{1-x})_2\,Si} > \mathrm{Ni_5Si_2(Co)} > \mathrm{Co_{50}Ni_{50}}$$

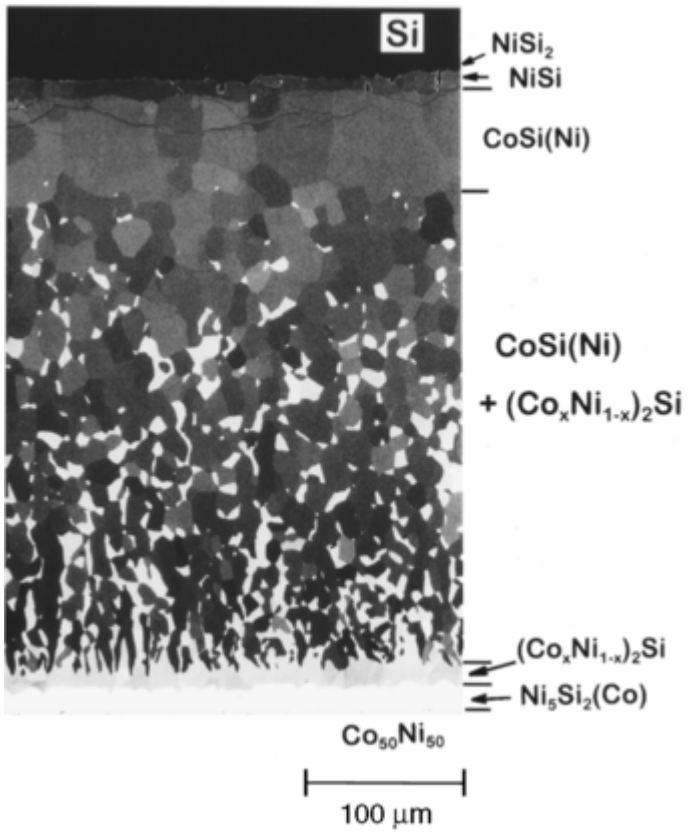

Fig. 14 Backscattered electron image of a Si/50Co + 50Ni diffusion couple heated at 800 °C (1470 °F) for 400 h (Ref 18). Shorthand for the microstructure is Si < $NiSi_2$ < NiSi < Co(Ni) < CoSi(Ni) + $(Co_xNi_{1-x})_2Si$ | CoSi(Ni) + $(Co_xNi_{1-x})_2Si$ > $(Co_xNi_{1-x})_2Si$ > $Ni_5Si_2(Co)$ > $Co_{50}Ni_{50}$.

Figure 15 gives an example of an unusual, patterned structure that forms occasionally in ternary and higher-order systems (Ref 19). Figure 15 shows a Pt/SiC couple after annealing at 700 °C (1290 °F) for 25 h. Similar microstructures have also been seen in Zn/Co_2Si, Zn/Fe_sSi, and Mg/$Ni_{50}Co_{20}Fe_{30}$ diffusion couples. If viewed as containing a two-phase layer of Pt_7Si_3 + C, then one writes the microstructure as Pt < Pt_3Si < Pt_7Si_3 + C > SiC. However, this is curious because it contains two of the rare type 3 boundaries and no type 0 boundary at the initial interface. In fact, it is not an ordinary microstructure. Research suggests that the patterned structure is formed by the Kirkendall effect breaking apart one of the phases (Ref 19), just as it has been observed to do to inert markers.

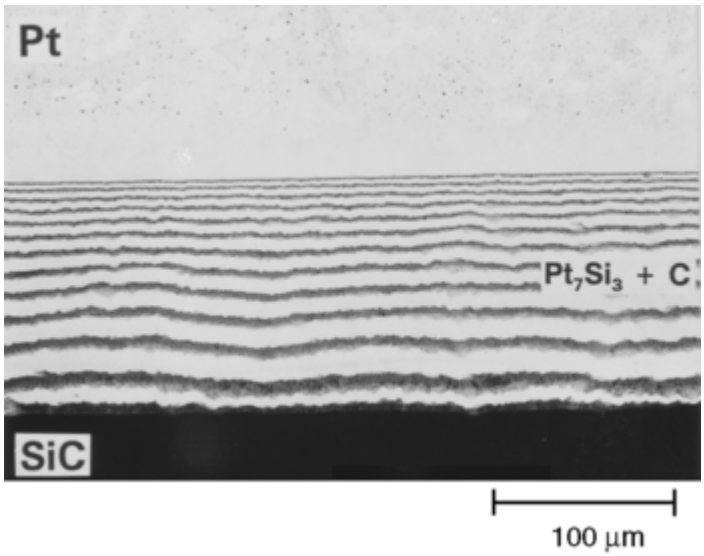

Fig. 15 Backscattered electron image of a Pt/SiC couple after annealing at 700 °C (1290 °F) for 25 h (Ref 19). The patterned structure of alternating layers of Pt_7Si_3 and carbon is unusual and thought to be caused by the Kirkendall effect.

References cited in this section

1. J.E. Morral, C. Jin, A. Engström, and J. Ågren, *Scr. Mater.,* Vol 34, 1996, p 1661–1666

7. D.A. De Leo and M.A. Dayanada, unpublished research, 1970

8. P.C. Tortorici and M.A. Dayananda, *Mater. Sci. Eng.,* Vol A261, 1999, p 64–77

9. C.-M. Chen and S.-W. Chen, *J. Mater. Res.,* Vol 18 (No. 6), 2003, p 1293–1296

10. C.W. Taylor Jr., M.A. Dayananda, and R.E. Grace, *Metall. Trans.,* Vol 1, 1970, p 127–131

11. R.D. Sisson and M.A. Dayananda, *Metall. Trans.,* Vol 3, 1972, p 647–652

12. D.E. Coates and J.S. Kirkaldy, *Metall. Trans.,* Vol 2, 1971, p 3467–3477

13. L.E. Wirtz and M.A. Dayananda, *Metall. Trans. A,* Vol 8A, 1977, p 567–575

14. M.A. Dayananda and C.L. Liu, *Proc. Int. Symposium on Fundamentals and Applications of Ternary Diffusion,* G.R. Purdy, Ed., CIM, Hamilton, Ontario, Canada, 1990, p 91–100

15. M.A. Dayananda, *Defect Diffusion Forum,* Vol 83, 1992, p 73–86

16. C.E. Campbell, J.C. Zhao, and M. Henry, *J. Phase Equilibria Diffusion,* Vol 25, 2004

17. K.A. Ellison, private communication, 2004

18. J.A. van Beek, P.J.T.L. Oberndorff, A.A. Kodentsov, and F.J.J. van Loo, *J. Alloy. Compd.,* Vol 297, 2000, p 137–143

19. A.A. Kodentsov, M.R. Rijnders, and F.J.J. van Loo, *Acta Mater.,* Vol 46, 1998, p 6521–6528

J.E. Morral and M.A. Dayananda, Interdiffusion Structures, *Metallography and Microstructures,* Vol 9, *ASM Handbook,* ASM International, 2004, p. 186–191

Interdiffusion Structures

J.E. Morral, The Ohio State University; M.A. Dayananda, Purdue University

---

Conclusions

The purpose of this article is to explain how interdiffusion microstructures can be analyzed and to give examples that show that these methods apply to a wide variety of materials. The analysis can be helpful in classifying microstructures and understanding how they change with alloy composition, especially when the thermal history is known. Also, they help in identifying microstructural artifacts caused by polishing and in recognizing errors in reported heat treating schedules.

J.E. Morral and M.A. Dayananda, Interdiffusion Structures, *Metallography and Microstructures,* Vol 9, *ASM Handbook,* ASM International, 2004, p. 186–191

Acknowledgment

The authors are grateful to F. Meisenkothen from the Wright Patterson Air Force Materials Laboratory for reviewing a draft of the manuscript and to the following people for providing micrographs: S.W. Chen from the National Tsing Hua University in Taiwan, K.A. Ellison from BWD Turbine Engines, J.C. Zhao from the G.E. R&D Laboratory, C.E. Campbell from NIST, and A.A. Kodentsov from the Eindhoven University of Technology. Also, J.E. Morral and M.A. Dayananda are grateful to the National Science Foundation for the support of interdiffusion studies under their respective grants, DMR-0139705 and DMR-0304777.

J.E. Morral and M.A. Dayananda, Interdiffusion Structures, *Metallography and Microstructures,* Vol 9, *ASM Handbook,* ASM International, 2004, p. 186–191

Interdiffusion Structures

J.E. Morral, The Ohio State University; M.A. Dayananda, Purdue University

References

1. J.E. Morral, C. Jin, A. Engström, and J. Ågren, *Scr. Mater.,* Vol 34, 1996, p 1661–1666
2. X. Qiao, M.S. thesis, University of Connecticut, 1998
3. W.D. Hopfe and J.E. Morral, *Acta Metall. Mater.,* Vol 42, 1994, p 3887–3894
4. A. Engstrom, J.E. Morral, and J. Ågren, *Acta Mater.,* Vol 45, 1997, p 1189–1199
5. K. Wu, Y. Wang, and J.E. Morral, A Phase Field Study of Microstructural Changes Due to the Kirkendall Effect in Two-Phase Diffusion Couples, *Acta Mater.,* Vol 49, 2001, p 3401–3408
6. F. Meisenkothen and J.E. Morral, On the Existence of 5-Line Nodes on Interdiffusion Microstructure Maps, *Scr. Mater.,* Vol 43, 2000, p 361–364
7. D.A. De Leo and M.A. Dayanada, unpublished research, 1970
8. P.C. Tortorici and M.A. Dayananda, *Mater. Sci. Eng.,* Vol A261, 1999, p 64–77
9. C.-M. Chen and S.-W. Chen, *J. Mater. Res.,* Vol 18 (No. 6), 2003, p 1293–1296
10. C.W. Taylor Jr., M.A. Dayananda, and R.E. Grace, *Metall. Trans.,* Vol 1, 1970, p 127–131
11. R.D. Sisson and M.A. Dayananda, *Metall. Trans.,* Vol 3, 1972, p 647–652

12. D.E. Coates and J.S. Kirkaldy, *Metall. Trans.,* Vol 2, 1971, p 3467–3477

13. L.E. Wirtz and M.A. Dayananda, *Metall. Trans. A,* Vol 8A, 1977, p 567–575

14. M.A. Dayananda and C.L. Liu, *Proc. Int. Symposium on Fundamentals and Applications of Ternary Diffusion,* G.R. Purdy, Ed., CIM, Hamilton, Ontario, Canada, 1990, p 91–100

15. M.A. Dayananda, *Defect Diffusion Forum,* Vol 83, 1992, p 73–86

16. C.E. Campbell, J.C. Zhao, and M. Henry, *J. Phase Equilibria Diffusion,* Vol 25, 2004

17. K.A. Ellison, private communication, 2004

18. J.A. van Beek, P.J.T.L. Oberndorff, A.A. Kodentsov, and F.J.J. van Loo, *J. Alloy. Compd.,* Vol 297, 2000, p 137–143

19. A.A. Kodentsov, M.R. Rijnders, and F.J.J. van Loo, *Acta Mater.,* Vol 46, 1998, p 6521–6528

D.A. Hughes and N. Hansen, Plastic Deformation Structures, *Metallography and Microstructures,* Vol 9, *ASM Handbook,* ASM International, 2004, p. 192–206

Plastic Deformation Structures

Darcy A. Hughes, Sandia National Laboratories; Niels Hansen, Risø National Laboratory

Introduction

DEFORMATION MICROSTRUCTURES have been investigated since the invention of metallurgical light microscopy more than 100 years ago (Fig. 1a, Ref 1). Advances in understanding microstructures thereafter have been closely related to the development of new microscopy techniques in which transmission electron microscopy (TEM) has been the central technique in the last 50 years (Fig. 1b, Ref 2). Three notable trends in microscopy are: (a) the ever-increasing resolution in the images so that smaller and smaller features such as dislocations and atomic arrangements can be identified and associated with larger scale structures; (b) the ability to see through opaque metals, for example, x-rays and TEM, so that the projection of the internal structures may be viewed rather than just the surface, and microstructure parameters may be defined based on the observations; and (c) development of automatic and semiautomatic techniques in the TEM and scanning electron microscope (SEM) as well as three dimensional x-ray diffraction that now enable the quantitative and statistical measurement of microstructure parameters. The driving force for these investigations has been the need for technological improvements combined with scientific interest, since microstructure and crystallographic texture are the key material features used in the continuous endeavor to relate the processing of a metal with its final properties.

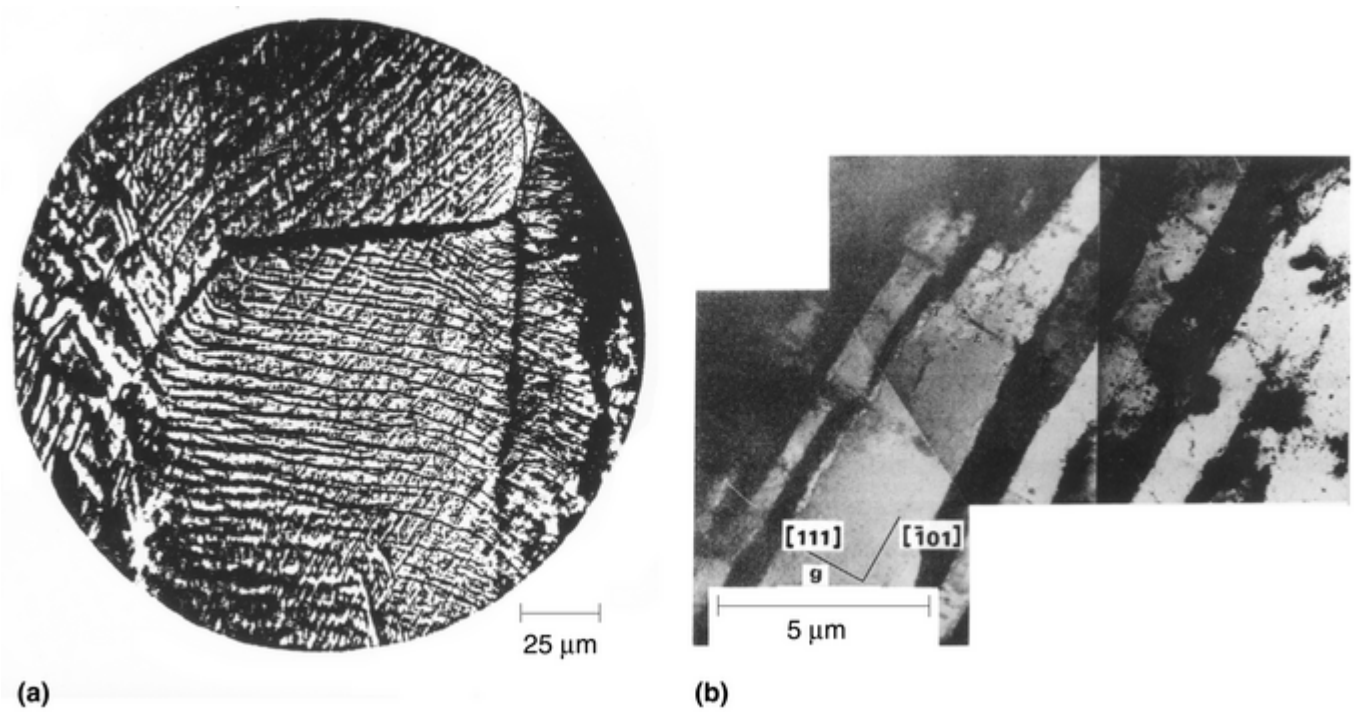

Fig. 1 (a) Optical micrograph of a slip-line pattern in polycrystalline iron from the late 19th century. Source: Ref 1. (b) Transmission electron micrograph of planar dislocation boundaries the "carpet structure" in a copper single-crystal middle of the 20th century. Source: Ref 2

For example, consider the complementary pairing of older and newer techniques to assess the same component on different levels (Fig. 2). Optical microscopy and macroetching are used to view the macroscale grain flow, size, and pattern in an austenitic stainless steel forging (Fig. 2a). Traditional grain and flow patterns remain in use today to assess die and forge process design, validate computer process models, as well as for quality control of the homogeneity of the forging deformation. On a more fundamental level, TEM (Fig. 2b) reveals the underlying arrangement of dislocations; that is, the ubiquitous crystalline line defect whose motion or slip along particular crystal planes provides a primary mechanism for the plastic deformation of metals. The trapped dislocations induce significant changes in mechanical properties such as strength as well as stored energy that depend on their number and arrangement. Semiautomatic measurement of this arrangement in the TEM, for example, Fig. 2(c), yields parameters that quantitatively describe the structure. Ideally, fundamental knowledge of the structure evolution can be used to construct predictive, quantitative theories of plastic flow.

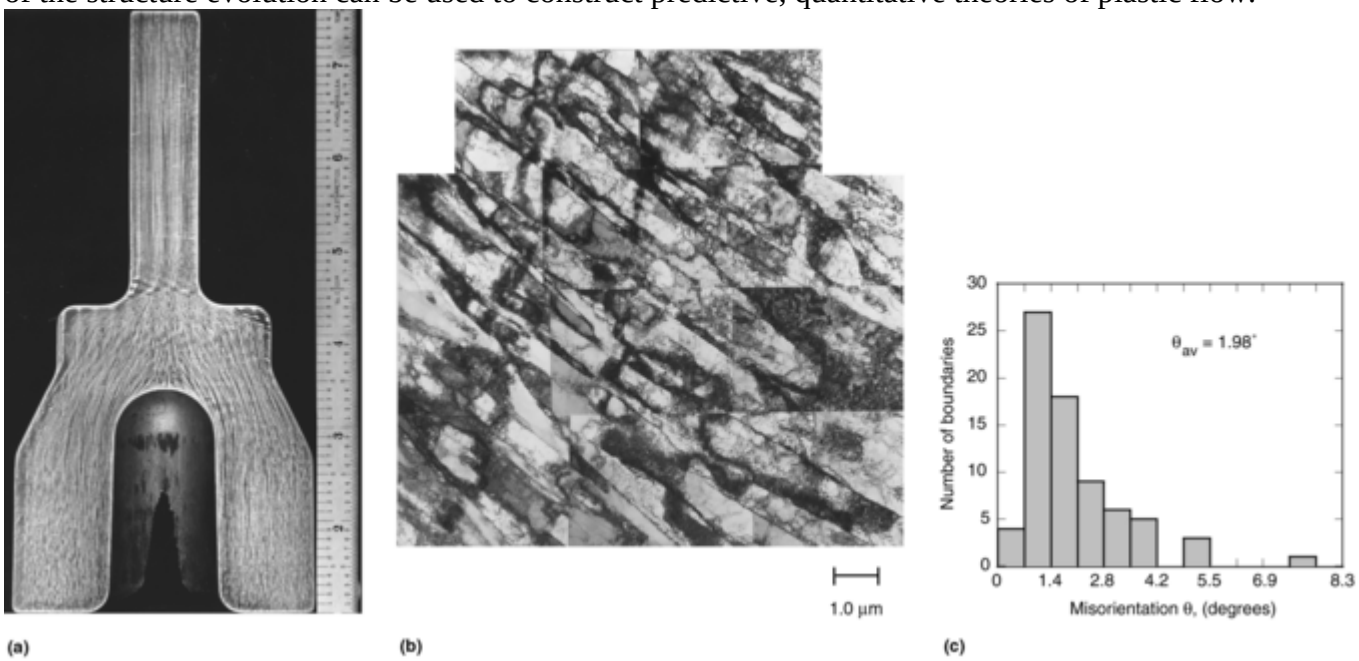

Fig. 2 (a) Flow lines in a 304L stainless steel high-temperature forging revealed by a macroetch and optical microscopy. (b) Microstructure of long dislocation boundaries in 304L stainless steel revealed by transmission electron microscope (TEM) following a moderate deformation, equivalent von Mises strain (ε_{vM}) ≈ 0.2 to 0.3, in a hammer forging, with a displacement rate 24–30 m/s and starting temperature of 1144 K. (c) Histograms showing the distribution of misorientation angles across the dislocation boundaries (GNBs) in the forging of (b) as measured in the TEM.

Many journal articles have reviewed the field of deformation microstructures (Ref 3, 4, 5, 6). This article is an overview emphasizing the following aspects in detail: (a) microstructural evolution, (b) dislocation boundaries, and (c) macroscopic properties. The microstructure and local crystallography are discussed with emphasis on the behavior of metals and single-phase alloys processed under conditions where the plastic deformation predominately takes place by dislocation slip. Monotonic deformation modes are examined including laboratory testing (i.e., compression, tension, and torsion) and metal processing techniques (rolling and extrusion).

References cited in this section

1. J.W. Ewing and W. Rosenhain, *Philos. Trans. R. Soc., London A,* Vol A193, 1899, p 353–375

2. J.W. Steeds, Dislocation Arrangement in Copper Single Crystals as a Function of Strain, *Proc. R. Soc. A,* Vol 292, 1966, p 343–373

3. J. Gil-Sevillano, P. van-Houtte, and E. Aernoudt, Large Strain Work Hardening and Textures, *Prog. Mater. Sci.,* Vol 25, 1980, p 69–412

4. S.S. Hecker and M.G. Stout, Strain Hardening of Heavily Cold Worked Metals, *Deformation Processing and Structure,* G. Krauss, Ed., ASM, 1982, p 1–46

5. M.F. Ashby, C.M. Sellars, et al., Deformation Processing of Metals, *Philos. Trans. R. Soc., London A,* Vol 357, 1999, p 1441–1729

6. N. Hansen, New Discoveries in Deformed Metals, *Metall. Mater. Trans. A,* Vol 32A, 2001, p 2917–2935

D.A. Hughes and N. Hansen, Plastic Deformation Structures, *Metallography and Microstructures,* Vol 9, *ASM Handbook,* ASM International, 2004, p. 192–206

Plastic Deformation Structures

Darcy A. Hughes, Sandia National Laboratories; Niels Hansen, Risø National Laboratory

---

Microstructural Evolution by Grain Subdivision

Fundamental Processes. During plastic deformation, a small fraction of the mechanical energy is stored in the metal, mostly in the form of dislocations. These dislocations are not randomly distributed. Commonly during straining, dislocations organize themselves into mosaic patterns in response to both their own self-stresses and the applied stress. The “mosaic,” clearly visible in Fig. 3, is composed of dislocations that are arranged in nearly two-dimensional boundaries surrounding regions that have relatively few dislocations. The regions of crystal on either side of a dislocation boundary are slightly rotated with respect to one another, with the rotation depending on the dislocation content of the boundary. The resulting angle of rotation is called the boundary

misorientation angle. A high-resolution TEM micrograph (Fig. 4) illustrates this crystal rotation on the atomic scale. The mosaic, or microstructural pattern, subdivides original grains during deformation (Fig. 5).

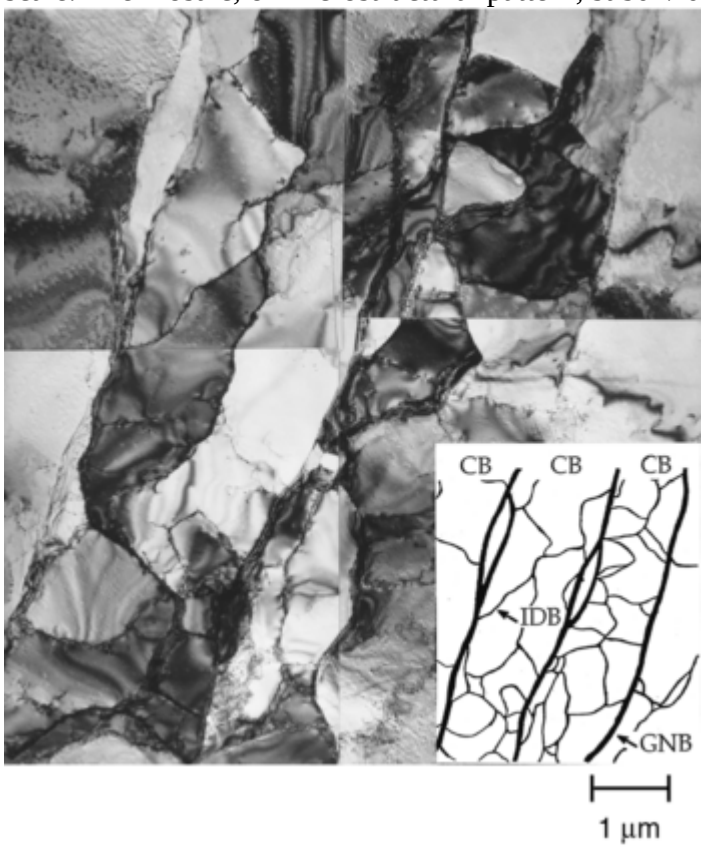

Fig. 3 Transmission electron micrograph of an Al (99.99%) single crystal following compression to a strain of ε = 0.6, showing a cell block structure (CB). Compression plane section. Source: Ref 7

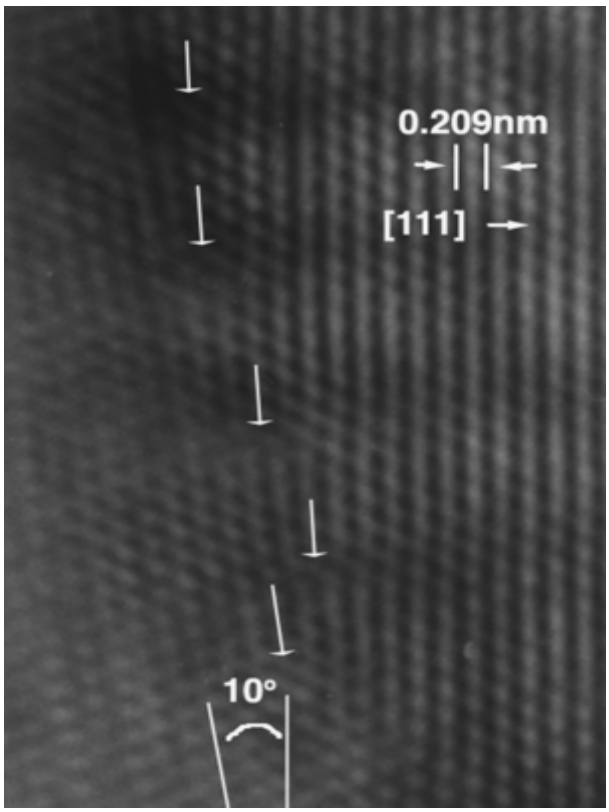

Fig. 4 High-resolution transmission electron micrograph of a dislocation tilt boundary with a [110] beam direction. A row of 60° dislocations, viewed end on with an average spacing of 1.2 nm, is organized into a

medium-angle (10°) two-dimensional tilt boundary. The inclination of the (111) crystal planes on either side of the boundary reflects this 10° misorientation.

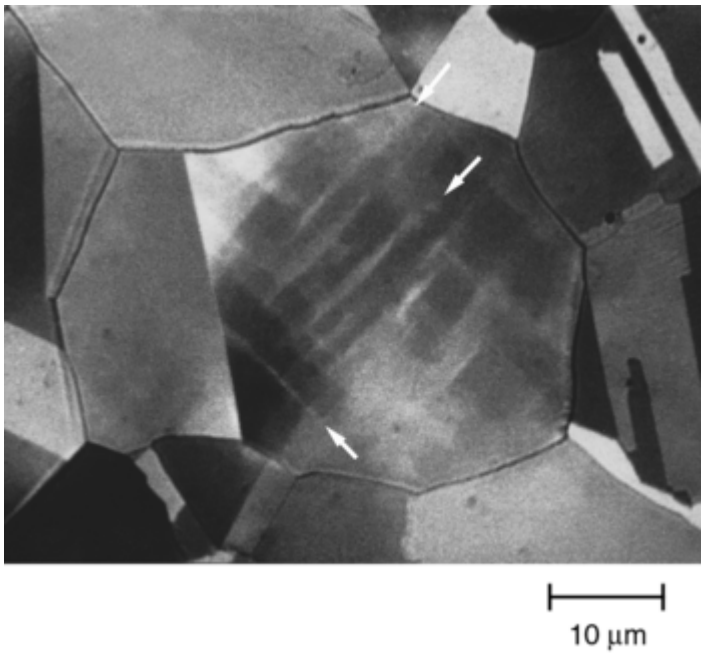

Fig. 5 Strips of light-dark contrast across the central grain (see arrows) of this channeling contrast scanning electron micrograph shows grain subdivision in rolled copper deformed to a 5% cold reduction (cr). Viewing section is the longitudinal side plane with the rolling direction vertical.

The pattern of grain subdivision by deformation-induced dislocation boundaries is governed by the motion of individual dislocations and their interactions as a whole with the large population of dislocations produced during straining. Of special importance is the ability of dislocations to move on more than one slip plane, or climb perpendicular to that plane. Dislocation motion in three dimensions is known to be a necessary component of boundary formation along more than one plane (Ref 8).

Several key factors make large differences in the motion of individual dislocations and in macroscopic mechanical properties: stacking fault energy (SFE), friction stress, the presence of solute atoms, short-range ordering of solutes, temperature, strain rate, monotonic deformation mode/slip pattern, and amount of strain:

- Stacking fault energy modifies the ability of a dislocation to glide onto an intersecting slip plane, that is, to cross slip. Three-dimensional mobility increases with increasing SFE.
- Friction stress or Peierls-Nabarro force is the lattice resistance to dislocation slip. This stress is small in face-centered-cubic (fcc) metals and larger in body-centered-cubic (bcc) metals.
- Solute atoms and impurity atoms interact strongly with gliding dislocations, thereby increasing the friction stress. Even small concentrations of solute atoms may have large effects on strength.
- Short-range ordering of solutes strongly favors true planar glide of metals, since dislocations will have a high preference for following each other on exactly the same slip plane in which the previous slip has destroyed the short-range ordering.
- Temperature and strain rate change the average velocity of thermally activated glide of dislocations past obstacles by cross slip to overcome the friction stress and also the rate of dislocation climb processes. Dislocation climb will provide additional short-range three-dimensional mobility of dislocations for deformation temperatures above one-half of the melting temperature, T_m.
- Deformation mode and grain orientation determine slip system activity and hence the Burgers vector population of dislocations. The slip pattern is thus determined by the degree of activation of the different slip systems. There are 12 slip systems in fcc metals defined by the {111} slip planes and ⟨110⟩ slip directions and 12 in bcc metals defined by {110} slip planes and ⟨111⟩ slip directions (not including the negative sense). Additionally, bcc metals may slip on 12{112}⟨111⟩ systems and/or 24 {321}⟨111⟩ systems, that is, “pencil glide.” Different slip systems are required to make the

macroscopic shape change in uniaxial tension compared to that of the plane strain constraint conditions of rolling.
- Strain changes the evolutionary stage of the microstructure as well as the crystal orientation with respect to the deformation axes (texture).

The way in which the aforementioned factors combine together, to either promote three-dimensional dislocation mobility or to significantly hinder it, is a strong predictor of the microstructural evolution. Thus, the fundamental aspect of three-dimensional dislocation mobility provides a basis for the classification of similar microstructures for a broad range of materials and conditions.

Similarity is qualitatively understood by considering that the applied stress together with the kinematics of slip (i.e., the way in which dislocations are able to move) place a strong bias on the flux of dislocations. Additionally, the self-stresses of dislocations create a large driving force to create stress-screened dislocation arrangements, thereby lowering their energy per unit line length. Structures that have the lowest energy per line length among all the configurations accessible to the dislocations as constrained by the above factors have been dubbed low-energy dislocation structures (LEDS) (Ref 8).

Grain Subdivision with Easy Three-Dimensional Mobility of Dislocations. Given the conditions of quasi-static strain rates on the order of 10^{-5} to 10^{2} s^{-1} that largely preclude dislocation climb and under conditions that do not cause dynamic recrystallization, materials exhibiting three-dimensional mobility of dislocations by cross slip and a common microstructure are represented by:

- Case 1: fcc metals with medium to high SFE at low to medium homologous temperatures, roughly <0.4 to 0.8 T_m
- Case 2: bcc metals deformed beyond yield at temperatures above ~0.05 T_m, where the friction stress is less significant
- Case 3: low SFE fcc metals when the deformation temperature is raised from roughly 0.3 to 0.8 T_m, thereby enhancing the thermal activation to overcome cross slip barriers
- Case 4: fcc and bcc alloys when the deformation temperature is raised from roughly 0.4 to 0.8 T_m, thereby enhancing the thermal activation to overcome the friction stress provided by solutes

The cell block (Ref 9) is the basic microstructural unit that forms and evolves during deformation for these materials and conditions. (A glossary of microstructural nomenclature is provided in Table 1.) Figure 6(a) illustrates the cell block structure marked, CB1, CB2, CB3, and so forth, with both a TEM micrograph and tracing. The elongated cell blocks are delineated by long, nearly planar boundaries that lie on special planes. These boundaries viewed edge on, have their traces marked A, B, C, and so forth, together with their misorientations in Fig. 6(a) and by black lines in Fig. 6(b). These long boundaries enclose blocks of approximately equiaxed cells whose cell boundaries are marked a, b, c, and so forth in Fig. 6(a) and are gray in Fig. 6(b).

Table 1 Glossary of structural features and nomenclature

Term	Definition
Bamboo incidental dislocation boundary (IDB)	An incidental dislocation boundary observed at large strain that is connected to geometrically necessary boundaries on two edges. It separates two nearly empty volumes that are rotated from each other
Cell	A roughly equiaxed volume in which the dislocation density is well below the average and that is rigidly rotated from its neighboring volumes
Cell block (CB)	A contiguous group of cells in which the same set of glide systems operates
Cell boundaries	Low-angle dislocation boundaries that surround the cells and are classified as incidental dislocation boundaries
Dense dislocation wall (DDW)	A single, nearly planar deformation induced boundary, classified as a geometrically necessary boundary, enclosing a cell block at small to intermediate strains
Geometrically necessary boundary (GNB)	Boundaries whose angular misorientations are controlled by the difference in glide-induced lattice rotations in the adjoining volumes

Incidental dislocation boundary (IDB)	A dislocation boundary formed by the mutual and statistical trapping of glide dislocations and supplemented by forest dislocations
Lamellar boundary (LB)	A single, nearly planar boundary, classified as a GNB, enclosing a narrow cell block at large strains
Microband (MB)	Platelike region formed by two closely spaced DDWs and defining the edge of a cell block
S-band	A coarse slip band that intersects parallel groups of dense DDWs, MBs, or LBs creating a string of S-shaped perturbations in those boundaries. The length of an S-band is generally shorter than a grain diameter.
Shear band	A region of intense local shear that spans several grains
Subgrains (SG)	Nearly empty volumes surrounded by higher angle boundaries that fill spaces external to the cell blocks
Taylor lattice (TL)	More or less uniform distribution of dislocations composed of one or more sets of parallel dislocations of alternating sign preferentially in edge orientation

Expanded definitions of some of these terms are found in Ref 9 and 10.

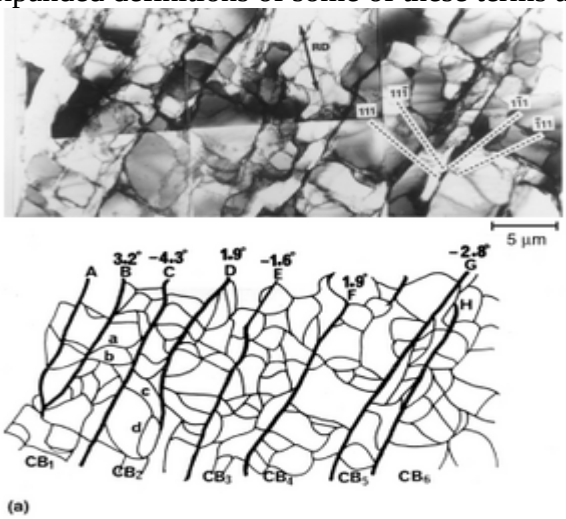

(a)

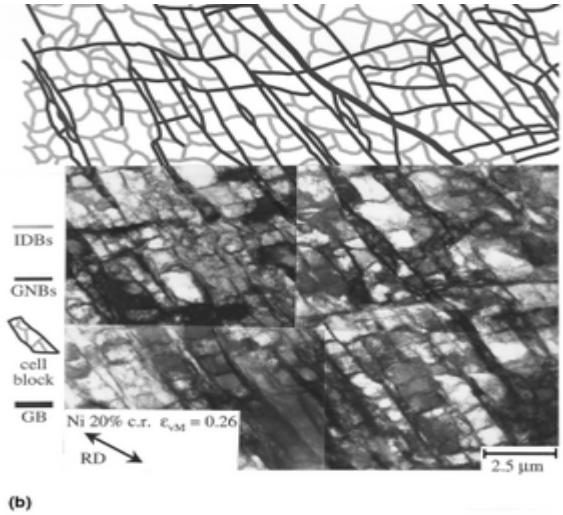

(b)

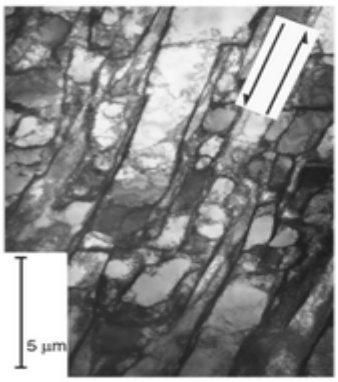

(c)

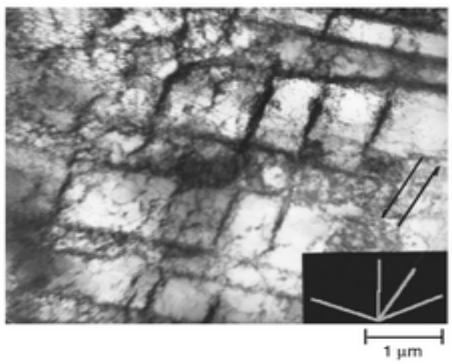

(d)

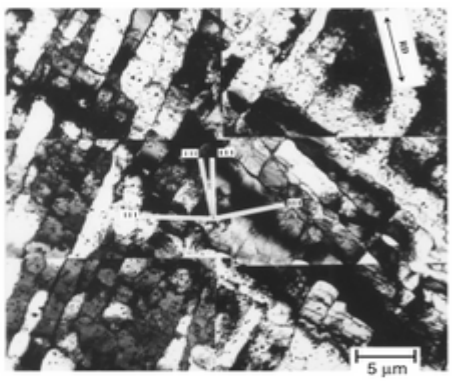

(e)

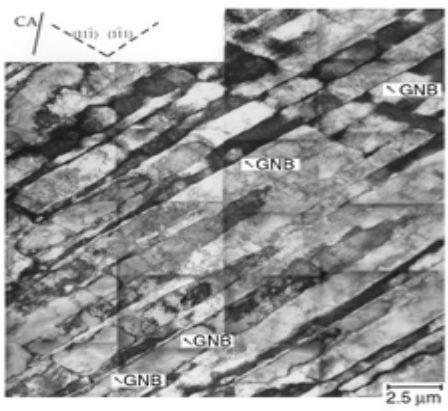

(f)

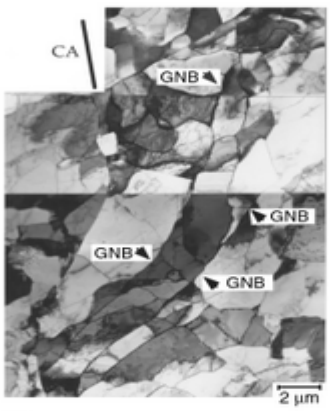

(g)

Fig. 6 Typical cell block dislocation structures composed of long geometrically necessary boundaries (GNBs) (i.e., dense dislocation walls, or DDWs, and microbands, or MBs) and incidental dislocation boundaries (IDBs) observed by TEM following low to medium deformation. (a) Aluminum (99.996%) following 10% cold reduction (cr) (equivalent von Mises strain, ε_{vM} = 0.12) (293 K). Traces of {111} are dashed lines. Source: Ref 11. (b) Nickel (99.99%) following a 20% cr (ε_{vM} = 0.26) (293 K). At the top of figure is a tracing of the underlying and adjacent micrograph. Long GNBs are nearly parallel to the main {111} slip plane. A grain boundary (GB) runs diagonally. Source: Ref 12. (c) Nickel (99.99%) deformed by torsion at 296 K and a strain rate of 10^{-4} s^{-1}, ε_{vM} = 0.35. Source: Ref 13. (d) Ni + 60 wt% Co deformed by torsion at 296 K and a strain rate of 10^{-4} s^{-1}, ε_{vM} = 0.35. Intersecting GNBs are nearly parallel to the {111} slip planes marked by white lines. Source: Ref 13. (e) Alloy AA3104 (Al-1Mg-1Mn) deformed by the plane strain compression at 783 K (~0.8 T_m) and a strain rate of 5 s^{-1} to ε_{vM} = 0.15. Source: Ref 6. (f) 304L stainless steel following compression to ε_{vM} = 0.2. Source: Ref 14. (g) 304L stainless steel following compression to ε_{vM} = 0.26 at 1273 K. Source: Ref 14

The two types of boundaries are formed by different mechanisms and have consequently been classified as geometrically necessary boundaries (GNBs) for the former and incidental dislocation boundaries (IDBs) for the latter (Ref 10). Cell boundaries have been termed “incidental dislocation boundaries,” because they are assumed to form by mutual and statistical trapping of glide dislocations. The long, nearly planar boundaries have been termed “geometrically necessary boundaries” because they are assumed to form by a different slip activity on each side of the boundary. The different slip activity may have its cause in the operation in neighboring regions of different sets of slip systems or a different partition of the total shear among a common set of slip systems.

Transmission electron microscopy viewing sections throughout Fig. 6, 7, 8, 10, 11, 12, 13, 21, 22, and 23 are as follows: for rolling or plane strain compression, the longitudinal section containing both the normal and rolling (marked RD) or extension directions; for thin-walled tube torsion, the radial plane containing the shear (marked by double arrows) and axial directions; for compression, the section parallel to the compression axes (marked CA); and for tension, the section containing the tensile axes.

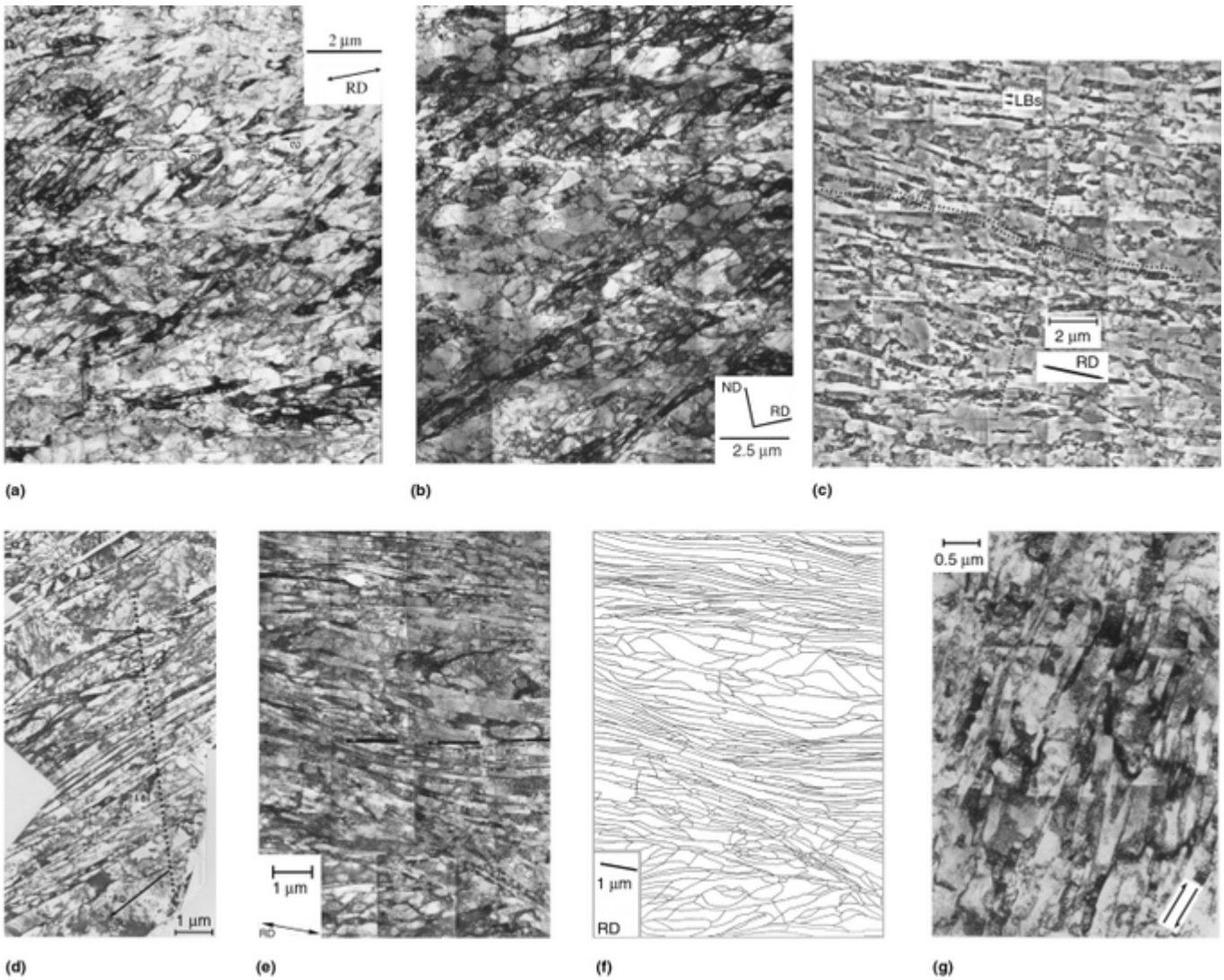

Fig. 7 Dislocation microstructures typical for large strain deformation with very long and well-developed geometrically necessary boundaries (GNBs) nearly parallel to the rolling direction with short bamboo incidental dislocation boundaries (IDBs) bridging between them observed by transmission electron microscopy. (a) Rolled nickel (99.99%) following 90% cold reduction (cr) (ε_{vM} = 2.7). Source: Ref 15. (b) Rolled interstitial-free (IF) iron (99.99%) following 90% cr (ε_{vM} = 2.7). (c) Rolled aluminum (99.8%) following 90% cr (ε_{vM} = 2.7). (d) Cross-rolled tantalum (99.99%) following 90% cr (ε_{vM} = 2.7). (e) Rolled nickel (99.99%) following 98% cr (ε_{vM} = 4.5) (Ref 16). (f) Large-scale tracing of the GNBs in the micrograph shown in Fig. (e). Note the average GNB spacing of 130 nm includes a range of boundary spacings from very fine, ~10 nm, to submicrometer, ~500 nm. The IDBs are not shown. (g) Ni + 60 wt% Co deformed by torsion at 296 K and a strain rate of 10^{-4} s^{-1}, ε_{vM} = 2.2. Source: Ref 13

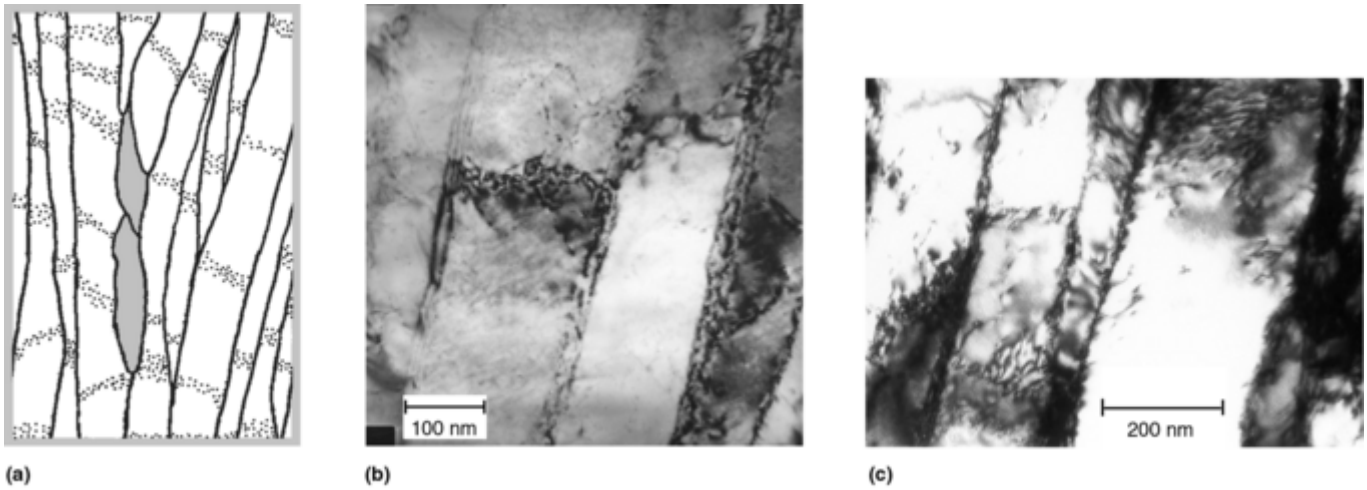

Fig. 8 Bamboo incidental dislocation boundaries spanning lamellar boundaries (LBs) shown in a tracing (a) of microstructure in nickel following 90% cold reduction (cr) (ε_{vM} = 2.7) that includes the geometrically necessary boundaries (solid lines) and bamboo incidental dislocation boundaries (IDBs) (stippled boundaries) as well as some shaded subgrains. The cell blocks contain IDBs, whereas the subgrains have none (Ref 15); micrographs for nickel 90% cr (b) (Ref 17) and iron 90% cr (c). Courtesy of X. Huang, Risø National Laboratory

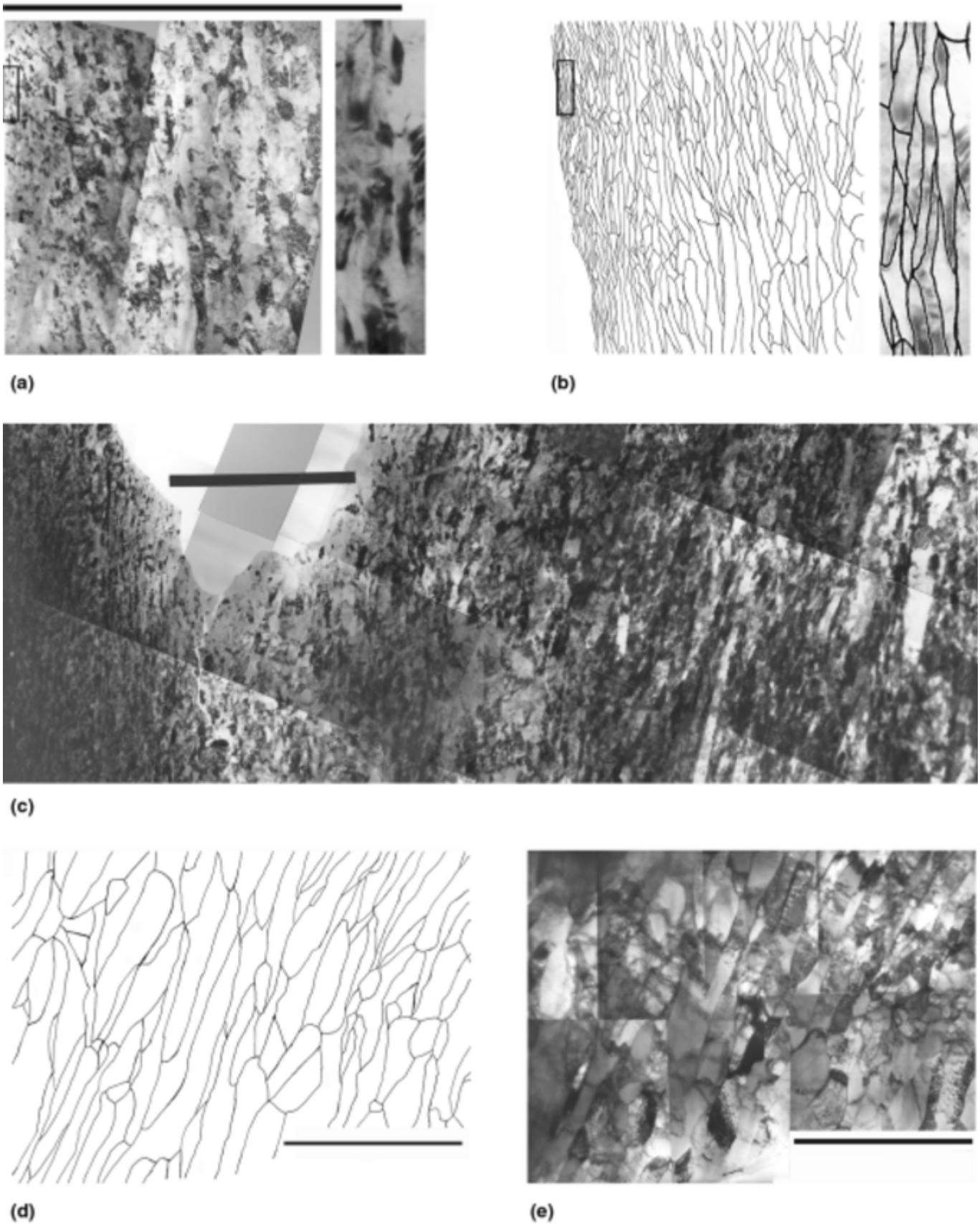

Fig. 9 Graded nanostructures produced by friction deformation as viewed in cross section by transmission electron microscopy (TEM). (a) micrograph and (b) tracing of extended boundaries in copper following 127 mm of sliding under a 12 MPa applied normal pressure; the left side is coincident with and parallel to the surface. (c) Following 127 mm of sliding with 22 MPa normal pressure; the surface is coincident and parallel to the left side. (The pale gray region underneath the scale marker is the hole produced when making the electron transparent TEM foil.) (d) Tracing and (e) Micrograph of

sample in (a), but at 20 μm below the surface. Scale markers are 2 μm long. Note the cutout box shown at higher magnification in (a) and (b) is 80 nm long. Source: Ref 24

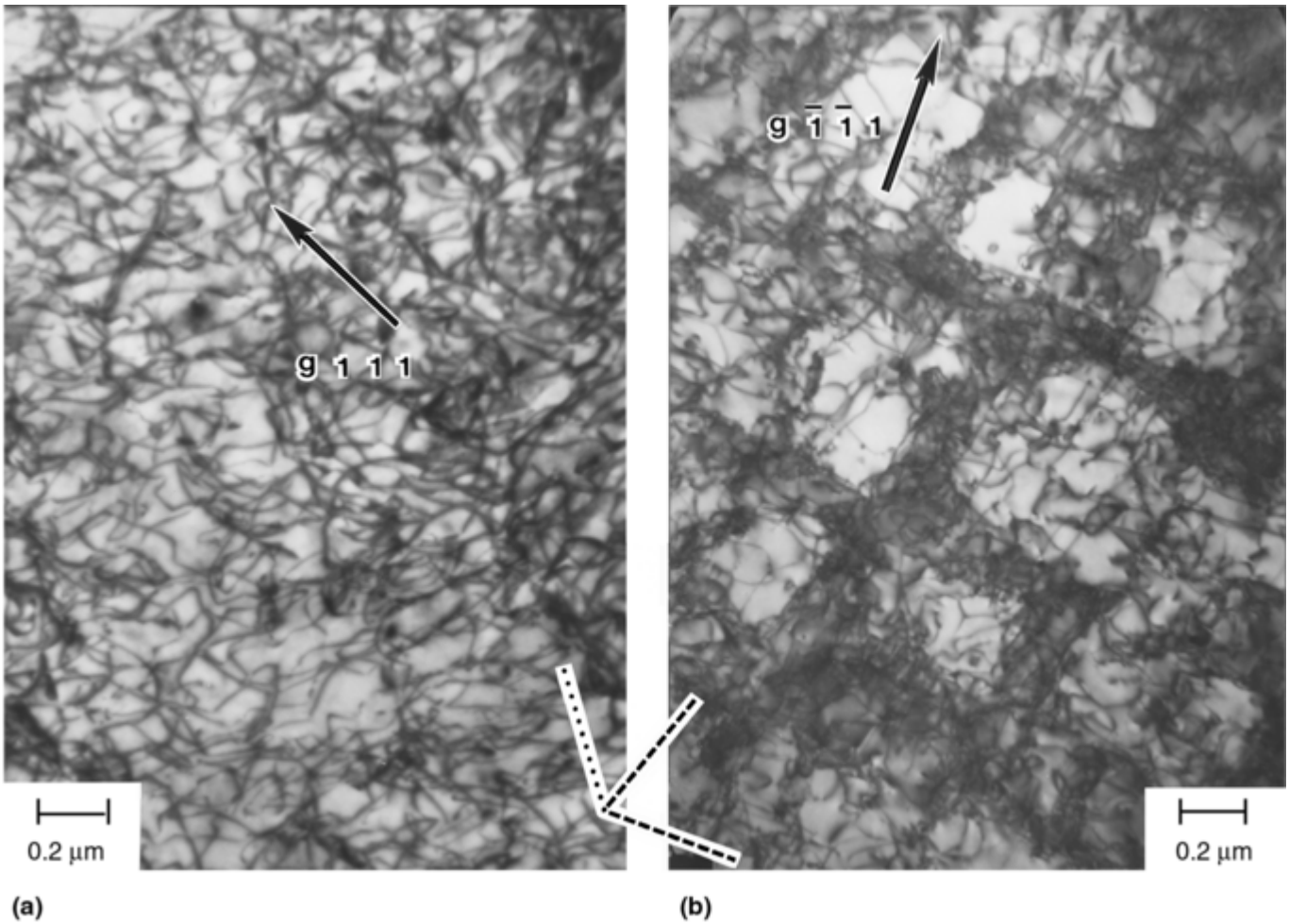

Fig. 10 Multi-Burgers vector Taylor lattice in Al-5%Mg following 30% cold reduction (cr) (ε_{vM} = 0.41). One reflecting vector (a) suggests random dislocations, while the second (b) reveals an organization along {111} slip planes whose traces are noted by dashed and dotted lines. Source: Ref 25

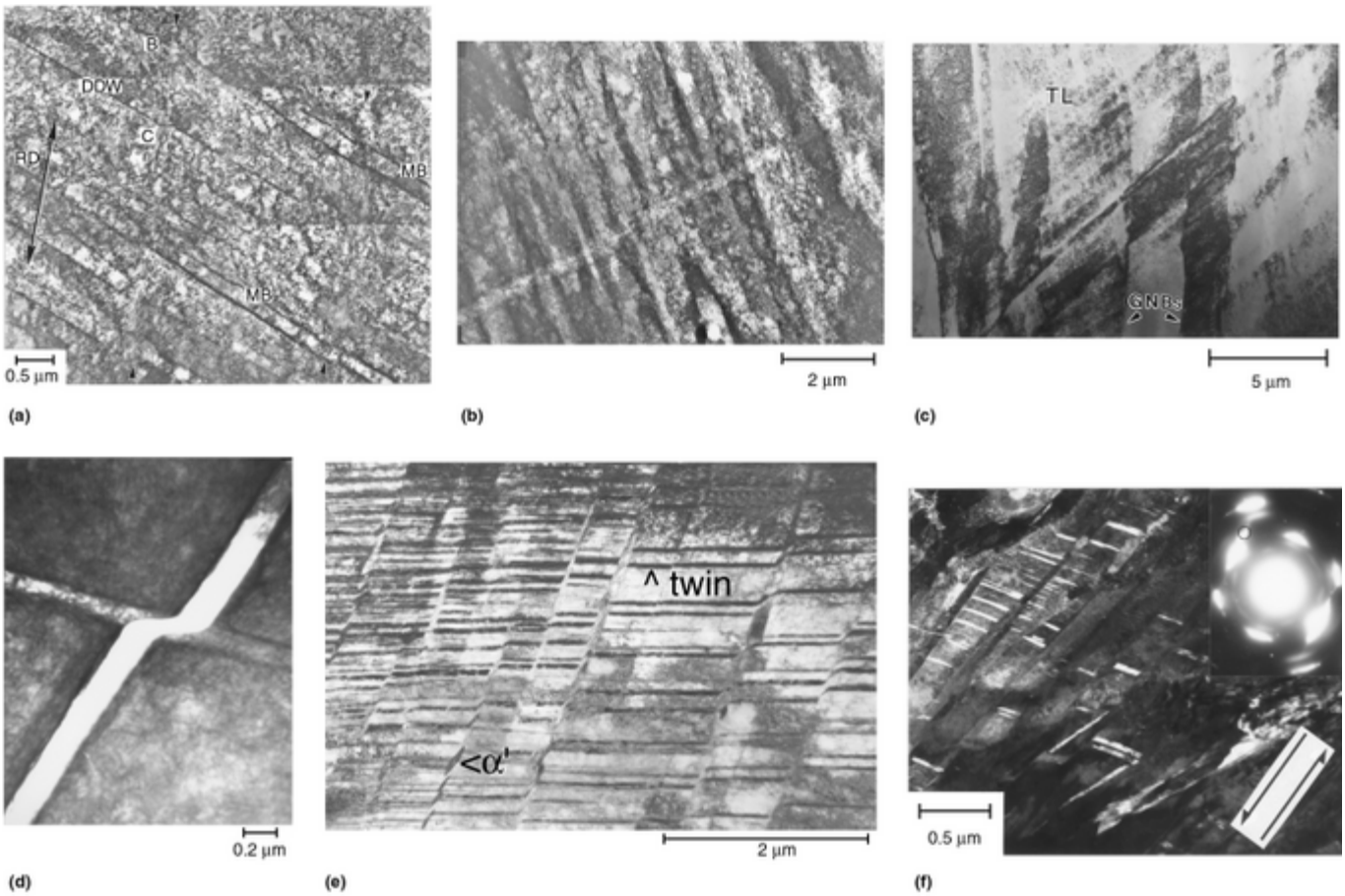

Fig. 11 Taylor lattice (TL) blocks with geometrically necessary boundaries (GNBs) (i.e., microbands, or MBs, and dense dislocation walls, or DDWs) forming at small to medium strains. (a) Ta-10wt%W following 20% cold reduction (cr) (ε_{vM} = 0.26) two vertical bands of coarse slip are indicated by arrows, and at B and C. (b) 304L stainless steel following compression (ε_{vM} = 0.3) at 293 K. (c) Al + 5 wt% Mg following warm rolling 30% (ε_{vM} = 0.41) with a preheat to 623 K. (d) Al + 5 wt% Mg following 30% cr (ε_{vM} = 0.41) showing the localized shear across the diagonal "white" MB caused by the intersection of a second-generation MB (horizontal). Source: Ref 25. (e) 304L stainless steel compressed, ε_{vM} = 0.5, at 293 K in which intersecting deformation twins, and ε and α deformation-induced martensite occur within the TL block structure. Source: Ref 14. (f) Dark field image of "white" deformation twins (TW) between lamellar boundaries (LBs) in Ni + 60 wt% Co deformed by torsion at 296 K and a strain rate of 10^{-4} s^{-1}, ε_{vM} = 2.1. Source: Ref 13

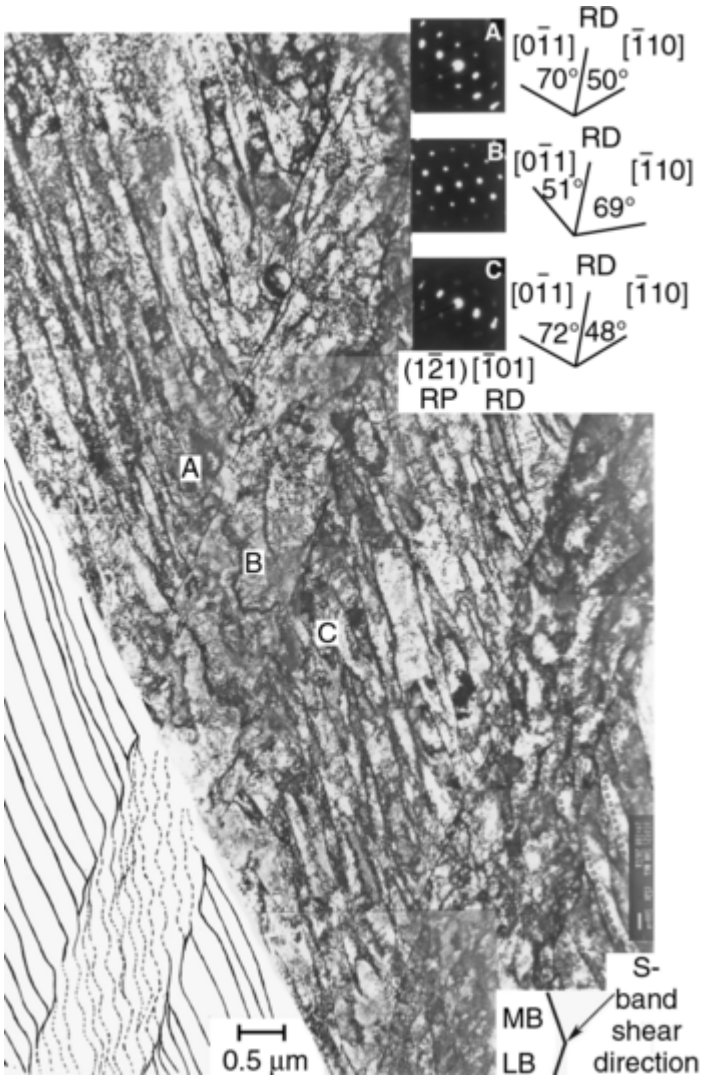

Fig. 12 Transition to large strain microstructure in rolled Ta + 10% W at ε_{vM} = 0.8 showing coarse slip in S-bands intersecting long dense dislocation walls (geometrically necessary boundaries) and creating high-angle lamellar boundaries of 20° among regions A, B, and C.

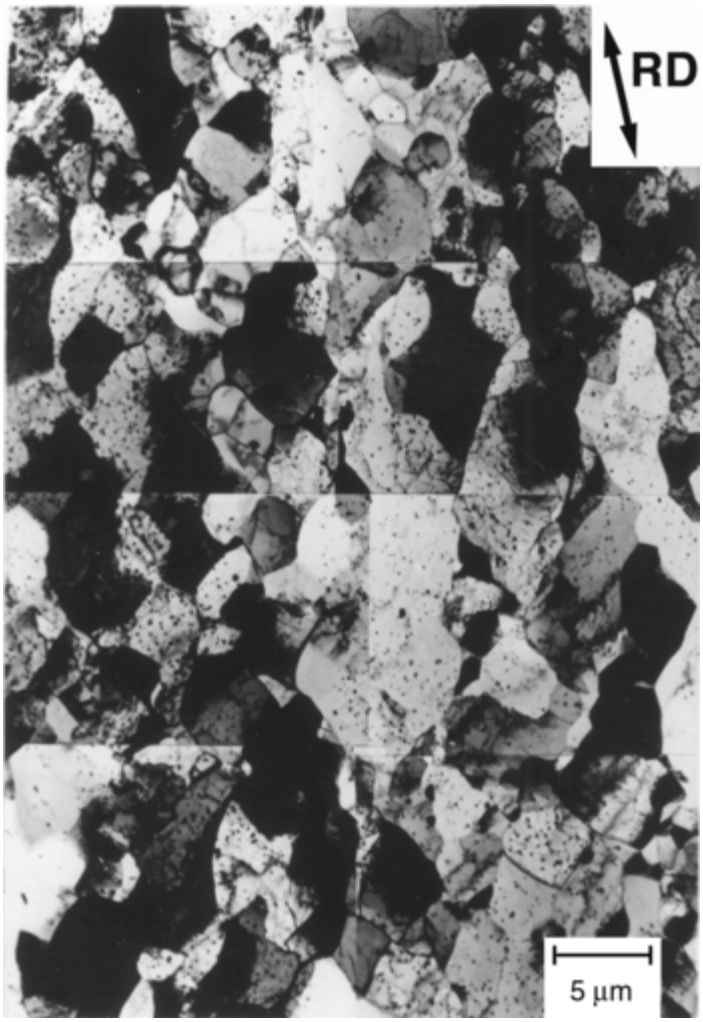

Fig. 13 Equiaxed microstructure at elevated temperatures and large strain in AA3104 deformed by the plane strain compression at 783 K (~0.8 T_m) and a strain rate of 5 s^{-1} to ε_{vM} = 1.5. Source: Ref 6

Transmission electron micrographs illustrating the universality of this common duplex boundary structure are shown for six representative metals and alloys deformed to small and medium strains, that is, a von Mises strain, ε_{Vm} = 0.05 to 0.8, in Fig. 6(a) to (g). Specific conditions are listed in the caption and include compression, plane strain compression, rolling, and torsion. Within this common structure some details may vary, since there is a range of possibilities for three-dimensional dislocation movement and interactions that satisfy a minimum requirement that three-dimensional cells form.

Visually, the morphology of the two types of boundaries is distinct. The IDBs or cell boundaries appear short, rounded, or more randomly inclined. The width of the IDBs varies from narrow and sharp in high SFE metals (Fig. 6a) to wider and loosely knit in alloys (Fig. 6d and f). The GNBs are extended flat and sheetlike, lying on special planes related to the slip system activity, for example, near a highly active {111} slip plane in fcc metals (Fig. 6b, d, and f) at small to medium strains. In different grains or under different conditions, one set of parallel GNBs may exist (Fig. 6a, c, and g) or more than one family of parallel GNBs may intersect each other (Fig. 6b, d, e, and f). While many GNBs and cell blocks divide a grain at low and intermediate temperatures, at the highest temperature only a few GNBs may subdivide a grain and also have a less regular and more undulating morphology (Fig. 6g). At this evolutionary stage of small to medium strains, their morphological appearance has also led to a description of these GNBs as dense dislocation walls (DDWs) or as microbands (MBs) when the single walls are closely paired.

The strain evolution of the microstructure is characterized by both the continuous refinement of the cell block size and an increase in the misorientation angle with increasing strain. Additionally, there is a transition in the plane or inclination of a cell block at medium strain, so that at large strain the cell block is aligned in a shape homologous with the imposed deformation. At large strain, the shape of cell blocks is planar for rolling, compression, torsion, and simple shear, whereas it is cylindrical in drawn and extruded samples. More specifically in rolling, the GNBs (DDWs/MBs) forming cell blocks that are macroscopically inclined to the

rolling plane ~40° are transformed with increasing strain from ε_{Vm} = 0.8 to 1.2 (50 to 80% cold reduction, or cr) to flat cell blocks almost parallel to the rolling plane. This transition has been related to the occurrences of localized glide (Fig. 7a and b) in S-bands.

The large strain cell blocks are composed of lamellar boundaries sandwiching a single row of cells (Fig. 7). The tracing and higher magnification in Fig. 8 clearly illustrates that IDBs and GNBs persist as the width between the lamellar GNBs decreases at very large strain. Figure 7(a) to (h) illustrate these structures for several materials and conditions at ε_{Vm} = 1 to 6 with the smallest average cell block size ranging from 300 to 100 nm. See also Ref 18, 19, 20.

Cell block structures persist over an extremely wide strain range and have been explored below a strain, ε_{vM}, of about 6 in rolling, which corresponds to a thickness reduction of about 99.5% (Ref 15, 21). The continuous structural refinement observed has led to investigations of the structural evolution of ultrahigh strains with the aim of producing nanostructured materials with an expected large strength. Processes have been developed to produce almost unlimited monotonic strain including: accumulative roll bonding (Ref 22) and high-pressure torsion (23). Microstructural observations following those processes confirm that structural refinement follows an increase in strain, and at very high strains, boundary spacings of the order of 200 and 100 nm were observed in copper and in nickel, respectively (Ref 23). High-energy ball-milled powders exhibit even finer spacings, although the strain is not monotonic.

In an alternative process, nanostructured copper was produced by deformation under large sliding loads. In the near-surface layers, ~10 nm scale microstructures form that coarsen with increasing depth from the surface (Ref 24). Cross sections of these samples show finely spaced and roughly planar boundaries parallel to the surface. Just below the surface a distribution of boundary spacings is observed from 3 to 30 nm with an average of 12 nm. Figure 9 shows this graded structure at low and high magnifications.

Structures with Restricted Three-Dimensional Mobility of Dislocations. When the deformation conditions do not provide enough thermal activation to overcome slip barriers, <0.2 to 0.5 T_m and under quasi-static strain rates from 10^{-5} to 10^{2} s^{-1}, materials that have low three-dimensional dislocation mobility are represented by:

- Case 5: low SFE fcc metals and alloys with a small friction stress
- Case 6: fcc and bcc alloys with a high friction stress
- Case 7: alloys with short-range ordering

When dislocations cannot readily move in three dimensions, dislocation cells are not formed and grain subdivision is modified. Sufficient mobility is available, however, to form planar boundaries; parallel families of GNBs are observed frequently on planes either near or related to major slip planes. In between the GNBs, dislocations are arranged in more uniform space-filling arrays called Taylor lattices (TL) (Ref 8, 25). These distributed dislocations are statistically trapped like the dislocations in cell boundaries and lower their energy somewhat from a random distribution by organizing into a multi-Burgers vector Taylor lattice. This organized arrangement is shown in Fig. 10(a) and (b), in which an apparently random array of dislocations (Fig. 10a) is tilted (Fig. 10b) to reveal an organization about the {111} slip planes. The dislocations statistically trapped in a TL are thus mechanistically equivalent to the statistical trapped dislocations in IDBs. Grain subdivision in these materials thus consists of planar GNBs surrounding a TL block instead of a cell block. Figure 11 provides examples of TL blocks for different materials and conditions at small to intermediate strain.

Depending on the degree of the increased friction stress by alloying, some variation or continuous range of structures may occur within these blocks, and between or adjacent to GNBs. With an increase in mobility, structures within the TL block change from evenly distributed dislocations in TLs (Fig. 10, 11c and d), to TL with more clustering of the dislocations (Fig. 11b), to very diffuse and wide IDBs (Fig. 11a and Fig. 6d), and finally to cells as described in the preceding section (e.g., Fig. 6). Note that the diffuse IDBs/cells in Fig. 6(d) represent an ambiguous case in which a medium-low dislocation mobility in three dimensions due to a low SFE (case 5) places this material as an intermediate between the cell block and TL block conditions. At the other extreme, very large restrictions of the mobility may result in deformation-induced twinning (Fig. 11e and f) and/or phase changes within the TL blocks (Fig. 11e). See also Ref 26 and 27.

The TLs evolve at medium to large strains toward cells (IDBs) as the number of dislocations with additional Burgers vectors increases between the GNBs (Fig. 12). With increasing strain analogous to cell blocks, the GNBs in TL/cell blocks change their inclination at large strains to be homologous to the imposed deformation,

for example, nearly parallel to the rolling plane (Fig. 12) or shear plane (Fig. 11f). This transition is also assisted by localized shear (Fig. 12).

Enhanced Three-Dimensional Dislocation Mobility. During deformation at elevated temperatures, roughly above 0.5 T_m, a gradual structural change from elongated cell blocks to more equiaxed subgrains (Fig. 13) may occur at medium to large strains for both metals and alloys. At these temperatures, while the thermal activation is high, the time at temperature/strain rates, though important, nevertheless does not allow for long-range climb of dislocations. Rather this morphological change to equiaxed subgrains is supposed to be assisted by other factors: (a) vacancies produced during deformation that increase with increasing temperature, (b) an increased mobility of dislocation boundaries as their misorientation angle increases with increasing strain, and (c) a decrease in the energy of the structure as the boundary energy per unit volume is reduced in parallel with the evolution of the equiaxed structures.

Once these equiaxed structures form at elevated temperature, the boundary spacing and area per unit volume, S_v reaches a saturation level instead of continuing to refine with increasing strain. In contrast, the subgrain-boundary misorientation angle continues to increase with strain, analogous to the lamellar boundaries formed at lower temperatures. See also Ref 28.

The formation of equiaxed subgrains and a saturation of size scale at lower temperatures requires conditions not covered herein, including nonmonotonic or cyclic deformations and strain path changes, for example, equal channel angular extrusion (ECA) (Ref 29) or cyclic compression (30), or by adding hard particles and fibers to the metal (Ref 31). Both of these conditions highly activate a large number of slip systems.

Localized Effects. In addition to the microstructural pattern shown in Fig. 6 and 7, other structural features have been observed occasionally, for example, narrow zones near some grain boundaries and triple junctions where the microstructural evolution apparently is affected by grain interaction (Ref 32). The microstructural evolution may also change locally as a result of localized shearing on a microscale and on a macroscale (Ref 15, 16).

Macroscopic Subdivision. The grain subdivision described previously covers length scales defined by the size of cells, cell blocks, and Taylor lattice blocks. Subdivision on the scale of a grain, encompassing many cell blocks, however, has also been observed in coarse-grained polycrystals and in single crystals (Ref 33, 34, 35, 36, 37, 38, 39). By this macroscopic subdivision, crystals or grains develop structures composed of well-defined wide deformation bands (or matrix bands) separated by more narrow regions, termed transition bands that are characterized by relatively large cumulative misorientation across. However, these macroscopic bands are also subdivided by cell blocks (Ref 39). Detailed studies of this macroscopic subdivision have shown that it is directly related to the external load condition, which, for example, in rolled samples may introduce a location-dependent shear strain (Ref 40, 41). Macroscopic breakup is suggested to be the way in which such a strain can be accommodated.

References cited in this section

6. N. Hansen, New Discoveries in Deformed Metals, *Metall. Mater. Trans. A,* Vol 32A, 2001, p 2917–2935

7. D.A. Hughes, D.C. Chrzan, Q. Liu, and N. Hansen, Scaling of Misorientation Angle Distributions, *Phys. Rev. Lett.,* Vol 81, 1998, p 4664–4667

8. D. Kuhlmann-Wilsdorf, Theory of Plastic Deformation: Properties of Low Energy Dislocation Structures, *Mater. Sci Eng.,* Vol A113, 1989, p 1–41

9. B. Bay, N. Hansen, D.A. Hughes, and D. Kuhlmann-Wilsdorf, Evolution of fcc Deformation Structures in Polyslip, *Acta Metall. Mater.,* Vol 40, 1992, p 205–219

10. D. Kuhlmann-Wilsdorf and N. Hansen, Geometrically Necessary, Incidental and Subgrain Boundaries, *Scr. Metall. Mater.,* Vol 25, 1991, p 1557–1562

11. Q. Liu and N. Hansen, Geometrically Necessary Boundaries and Incidental Dislocation Boundaries Formed During Cold Deformation, *Scr. Metall. Mater.,* Vol 32, 1995, p 1289

12. D.A. Hughes, Microstructure Evolution, Slip Patterns and Flow Stress, *Mater. Sci. Eng.,* Vol 319–321, 2001, p 46–54

13. D.A. Hughes, R. Lebensohn, H.R. Wenk, and A. Kumar, Stacking Fault Energy and Microstructure Effects on Torsion Texture Evolution, *Proc. R. Soc. (London) A,* Vol 456, 2000, p 921–953

14. D.A. Hughes and N. Hansen, Deformation Structures Developing at Fine Scales, *Philos. Mag.,* Vol 83, 2003, p 3871–3893

15. D.A. Hughes and N. Hansen, Microstructure and Strength of Nickel at Large Strains, *Acta Mater.,* Vol 48, 2000, p 2985–3004

16. D.A. Hughes and N. Hansen, Microstructural Evolution in Nickel During Rolling to Large Strains, *Metall. Trans. A,* Vol 24A, 1993, p 2021–2037

17. A. Godfrey and D.A. Hughes, Determination of Boundary Area and Spacing in Prismatic Structures with Applications to Dislocation Boundaries, *Mater. Charac.,* Vol 48, 2002, p 89

18. G. Langford and M. Cohen, Strain Hardening of Iron by Severe Plastic Deformation, *Trans. Am. Soc. Met.,* Vol 62, 1969, p 623–638

19. G. Langford and M. Cohen, Microstructural Analysis by High-Voltage Electron Diffraction of Severely Drawn Iron Wires, *Metall. Trans.,* Vol 6A, 1975, p 901–910

20. J.D. Embury and R.M. Fisher, Structure and Properties of Drawn Pearlite, *Acta Metall.,* Vol 14, 1966, p. 147

21. Q. Liu, X. Huang, N. Hansen, and D.J. Lloyd, Microstructure and Strength of Commercial Purity Aluminium (AA1200) Cold-Rolled to Large Strains, *Acta Mater.,* Vol 50, 2002, p 3798–3802

22. Y. Saito, H. Utsunomiya, N. Tsuji, and T. Sakai, Novel Ultrahigh Straining Process for Bulk Metals—Development of the Accumulative Roll Bonding (ARB) Process, *Acta Mater.,* Vol 47, 1999, p 579–583

23. R.Z. Valiev, R.K. Islamgaliev, and I.V. Aleksandrov, Bulk Nanostructured Materials from Severe Plastic Deformation, *Prog. Mater. Sci.,* Vol 45, 2000, p 103–189

24. D.A. Hughes and N. Hansen, Graded Nanostructures Produced by Sliding and Exhibiting Universal Behavior, *Phys. Rev. Lett.,* Vol 87 (No. 13), 2001, p 135503

25. D.A. Hughes, Microstructural Evolution in a Non-Cell Forming Metal: Al-Mg, *Acta Metall. Mater.,* Vol 41, 1993, p 1421–1430

26. R. Neuhaus and C. Schwink, On the Flow Stress of [100]- and [111]-Oriented Cu-Mn Single Crystals: A Transmission Electron Microscopy Study, *Philos. Mag.,* Vol 65, 1992, p 1463–1484

27. B.J. Duggan, M. Hatherly, W.B. Hutchinson, and P.T. Wakefield, Deformation Structures and Textures in Cold-Rolled 70:30 Brass, *Met. Sci.,* Vol 12, 1978, p 343–351

28. J.K. Solberg, H.J. McQueen, N. Ryum, and E. Nes, Influence of Ultra-High Strains at Elevated Temperature on the Microstructure of Aluminum, Part I, *Philos. Mag.,* Vol 60A, 1989, p 447–471

29. V.M. Segal, Materials Processing by Simple Shear, *Mater. Sci. Eng.,* Vol A197, 1995, p 157–164

30. P.E. Armstrong, J.E. Hockett, and O.D. Sherby, Large Strain Multidirectional Deformation of 1100 Aluminum at 300 K, *J. Mech. Phys. Solids*, Vol 30, 1982, p 37–58

31. C.Y. Barlow, Y.L. Liu, and N. Hansen, Fine Scale Structures from Deformation of Aluminium Containing Alumina Particles, *Acta Mater.*, Vol 50, 2002, p 171–182

32. V. Randle, N. Hansen, and D. Juul-Jensen, The Deformation Behaviour of Grain Boundary Regions in Polycrystalline Aluminium, *Philos. Mag.*, Vol 73, 1996, p 265–282

33. C.S. Barrett and L.H. Levenson, The Structure of Aluminum after Compression, *Trans. AIME*, Vol 137, 1940, p 112–127

34. J.L. Walter and E.F. Koch, Electron Microscope Study of the Structure of Cold-Rolled and Annealed (100)[001] Crystals of High-Purity Silicon-Iron, *Acta Metall.*, Vol 10, 1962, p 1059–1075

35. H. Hu, Annealing of Silicon-Iron Single Crystals, *Recovery and Recrystallization*, L. Himmel, Ed., AIME, Interscience, 1963, p 311–378

36. B.C. Wonsiewicz and G.Y. Chin, Inhomogeneity of Plastic Flow in Constrained Deformation, *Metall. Trans.*, Vol 1, 1970, p 57–61

37. I.L. Dillamore and H. Katoh, The Mechanisms of Recrystallization in Cubic Metals with Particular Reference to their Orientation Dependence, *Met. Sci.*, Vol 8, 1974, p 73–83

38. D. Kuhlmann-Wilsdorf, Overview No. 131 "Regular" Deformation Bands (DBs) and the LEDS Hypothesis, *Acta Mater.*, Vol 47, 1999, p 1697–1712

39. J.A. Wert, X. Huang, et al., *Proc. 20th Risø Int. Symposium on Materials Science*, J. Bilde-Sørensen, J.V. Carstensen, et al., Ed., Risø National Laboratory, 1999, p 529–534

40. C.S. Lee, B.J. Duggan, and R.E. Smallman, A Theory of Deformation Banding in Cold Rolling, *Acta Metall. Mater.*, Vol 41, 1993, p 2265–2270

41. Q. Liu and N. Hansen, Macroscopic and Microscopic Subdivision of a Cold-Rolled Aluminum Single Crystal of Cubic Orientation, *Proc. R. Soc. (London)*, Vol 454, 1998, p 2555–2591

D.A. Hughes and N. Hansen, Plastic Deformation Structures, *Metallography and Microstructures*, Vol 9, *ASM Handbook*, ASM International, 2004, p. 192–206

Plastic Deformation Structures

Darcy A. Hughes, Sandia National Laboratories; Niels Hansen, Risø National Laboratory

---

Microstructure Parameters: Quantitative and Theoretical Analysis

The previous section provided visual descriptions of the three different microstructural types: cell blocks, TL blocks, and equiaxed subgrains as well as guidelines to predict their occurrence. If these structures are to be further used to predict mechanical properties and recrystallization behavior, then it is important to define relevant microstructural parameters, measure them accurately, and identify microstructural relationships that are invariant and/or scale during straining.

Parameter Definition and Measurement. The regular and continuous evolution of grain subdivision with increasing stress and strain can be quantitatively described by the following microstructural parameters: boundary type, that is, IDB or GNB, crystal orientation with respect to the deformation axes, boundary plane, spacing, misorientation angle, and width (Fig. 14). Depending on the objective of the research, the relevant parameters must be selected.

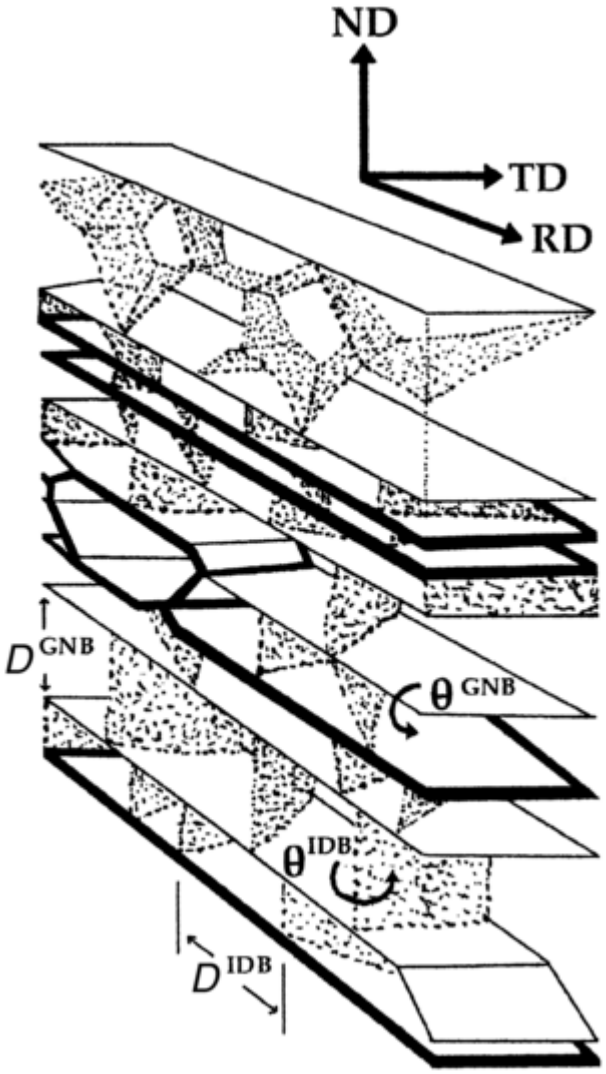

Fig. 14 Parameters in a large strain dislocation structure containing sheets of extended lamellar boundaries (LBs) with stippled low-angle (bamboo) incidental dislocation boundaries (IDBs) bridging between them. High-angle LBs are represented by heavy line weight and medium-angle LBs by medium line weight. Intercept spacings D^{GNB} of LBs and D^{IDB} of cell boundaries are defined. Source: Ref 15

Modern microscopic techniques provide new opportunities to measure these parameters and to obtain mathematical representations of their distribution(s) for a given condition. Several factors are important in measuring the structures described in the following paragraphs.

Transmission electron microscopy sample preparation must provide large, thin areas for viewing a number of grains in the same sample, that is, 50,000 to 10,000 μm^2 so that both fine details and their distribution over large areas can be observed. For metals, large areas may be obtained by electropolishing using a window technique combined with twin-jet polishing described in Ref 42. Ion milling at very low angle ~3.5°, and voltage, ~3.5, may be used for special cases, such as the friction sample cross sections, that cannot be thinned by other processes. Unfortunately, metals and alloys are very susceptible to ion beam damage that increases with ion beam energy/voltage and increasing beam angle. Note that regular ion milling introduces large numbers of dislocation loops that may obscure the original dislocation structure. Damage can be especially severe in metals and alloys when thinned to electron transparency with the very new and popular technique of focused ion beam (FIB) milling. Focused ion beam milling introduces not only dislocations loops, but also large

structural changes including recrystallization, especially in deformed structures. The FIB can be very useful, however, as a tool to precisely locate and cut thicker sections that are then thinned by a different process.

The most important viewing plane for clearly observing and measuring deformation microstructures is the section that contains both the directions of the largest imposed strain or displacement and the largest imposed stress (Ref 43). This section includes, for example, the longitudinal side plane containing both the rolling and normal directions in rolling, the plane with the tensile or compression axis in uniaxial deformation, and the plane containing both the axial direction and the shear direction in torsion. In many cases, this section becomes very thin especially at large strain, so that sample preparation is difficult: electropolished flat wires of ~0.2 mm in width! Other sections will also be needed to a lesser degree to confirm correct stereological procedures.

Stereological procedures of the three-dimensional microstructures must be utilized so that the measurements of size scale and size distributions are made correctly and accurately. Stereological relationships between the measurement and the actual parameter include those developed more generally (Ref 44), for example, the spacing of lamellar structures used here for planar GNBs, as well as ones specifically based on the TEM technique and the deformation structures observed (Ref 17, 45). Deriving distribution functions for spacings from measurements of irregular structures is especially difficult, although work is continuing. The interested reader is referred to these publications for more details. Measurements of dislocation boundary spacing in the TEM are at present done by hand, but can be facilitated by digital images. Imaging in the TEM is by electron diffraction contrast, which, while clearly showing dislocation boundaries and structures to the eye, also overlays very complex contrast patterns that strongly interfere with automatic image recognition.

Crystal orientation and misorientation analysis is facilitated by several automatic and semiautomatic methods developed mainly based on neutron, electron, and x-ray diffraction. Crystal orientations may be measured in a highly automated way in the SEM (Ref 46, 47), but this measurement is done blind to the underlying structures and at a moderate angular resolution. For measuring deformation structures composed of boundaries, the misorientation across an individual boundary is an important parameter. Thus, the orientation must be measured locally on either side of the boundary. Importantly, for further analysis, misorientation measurements are collected and separated according to boundary type (e.g., GNB or IDB), and complete distributions of the angles are necessary. This procedure is possible in the TEM using a semiautomatic technique that measures the Kikuchi diffraction pattern in the TEM to obtain the crystallite orientation (Ref 48). The misorientation across a dislocation boundary is then calculated from the two crystal orientations and characterized by an angle/axis pair.

Evolution of Misorientation Angles and Boundary Spacing. Many observations have shown that the boundary spacing decreases and the boundary misorientation angle increases with increasing stress and strain. Formerly, these changes were analyzed based on the assumption that the deformation was subdivided only by cell boundaries; that is, only two parameters, an average spacing and an average angle, were measured.

The clear morphological difference, which exists between the IDBs and the GNBs, suggests that different underlying mechanisms determine their evolution. This suggestion is supported by experimental observations showing that the increase in misorientation angles and decrease in boundary spacing with increasing strain is significantly different for IDBs and GNBs (Fig. 15). This evolutionary trend can continue to large strain without saturation.

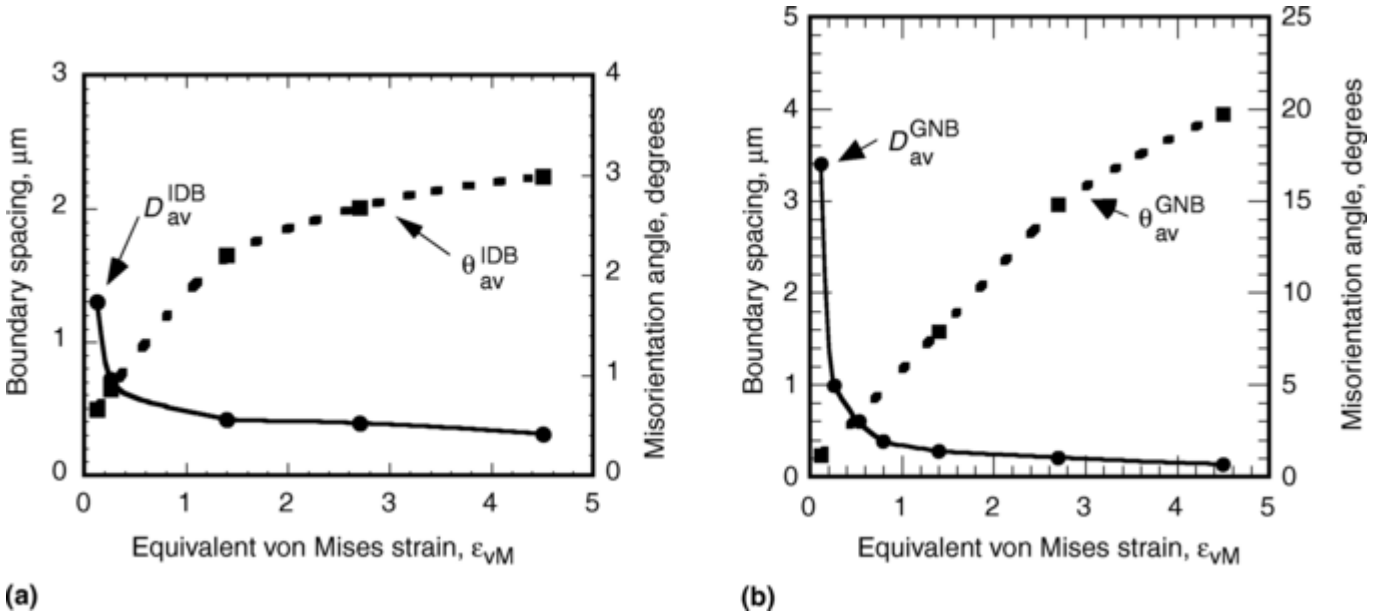

Fig. 15 The boundary spacing and misorientation angle for (a) incidental dislocation boundaries (IDBs) and (b) geometrically necessary boundaries (GNBs), respectively, as a function of strain in cold-rolled nickel (99.99%). Source: Ref 15

This trend is revealed more clearly in Fig. 16 for different materials and monotonic deformation processes, in which a power-law relationship is found between the strain and the dislocation boundary area per unit volume (S_v) of GNBs. The evolution of the misorientation angle, illustrated Fig. 17, also yields a power-law relationship between misorientation angle and strain for both IDBs and GNBs, however, with a significantly different exponent for each.

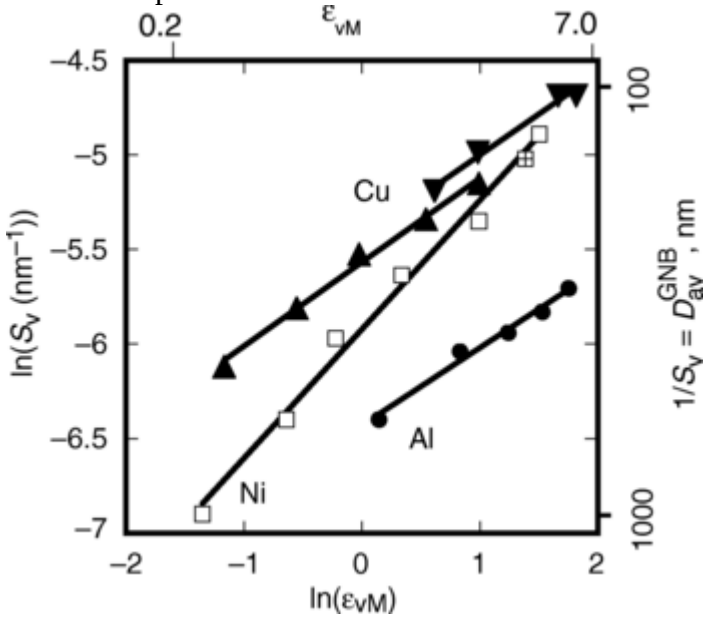

Fig. 16 Power-law relationship between boundary area per unit volume, $S_v = 1/D_{av}^{GNB}$ and strain. Data include rolled aluminum (solid circles) (Ref 21), rolled nickel (open squares) (Ref 15), and torsion-deformed nickel (square with cross), rolled copper (down solid triangles) (Ref 49), and torsion-deformed copper (up solid triangles) (Ref 50). ε_{vM}, equivalent von Mises strain

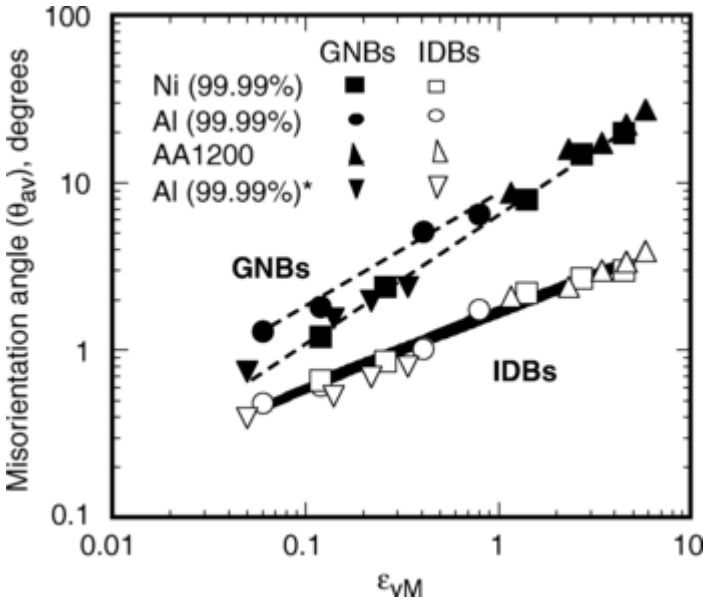

Fig. 17 Power-law relationship between misorientation angle versus strain for both geometrically necessary boundaries (GNBs) (filled symbols) and incidental dislocation boundaries (IDBs) (open symbols) for three different cold-rolled metals and one tension-deformed (down triangle); data from Ref 11, Ref 51, Ref 15, and 21, respectively. ε_{vM}, equivalent von Mises strain

The classification of two types of dislocation boundaries formed by different processes has led to a theoretical analysis of the evolution of the misorientation angles across boundaries by considering stochastic and deterministic processes acting separately or in combination. Thus, cell boundaries or IDBs are proposed to form by statistical fluctuations, whereas GNBs form by a joint operation of statistical fluctuations, activation imbalances of the slip, and formation of misfit dislocations. These calculations show a much more rapid increase in misorientation angle with increasing strain when the formation is deterministic compared to simply a stochastic formation (Ref 52). This trend agrees with the experimental measurement of misorientation angles as a function strain for IDBs and GNBs.

Scaling and Invariant Relationships. Modern microscopic techniques provide new opportunities to measure parameters and to obtain mathematical representations of the distribution(s). In general, when distributions are obtained for a given state they do not coincide. Using these distributions in a deformation or recrystallization model would require that the distribution be measured at a set of strains, necessitating an enormous experimental effort. In contrast, if one could find some organizing principle such that the distributions at different strains can be related to each other simply, the required experimental effort would be decreased markedly.

A scaling hypothesis provides the desired organizing principle. More importantly, scaling was introduced (Ref 7) to analyze structural parameters, notably misorientation angles across boundaries and the spacing between boundaries (Ref 45) on the assumption that similar underlying mechanisms control the formation of deformation microstructures. Such mechanisms are predominately dislocation glide mechanisms involving multiple slip and storage processes for glide dislocations in low-energy dislocation boundaries, that is, IDBs and GNBs.

Considering the scaling analysis, it was found that distributions at a given state depend on strain, but that the distributions can be represented by a strain-independent distribution, using as the scaling parameter, either the average misorientation angle or the average spacing at each strain, respectively, for the misorientation angle and boundary spacing distributions (Ref 7, 45). Figure 18 shows for the misorientation angles of IDBs that the scaled distribution is independent of material type, plastic strain, temperature, and deformation conditions.

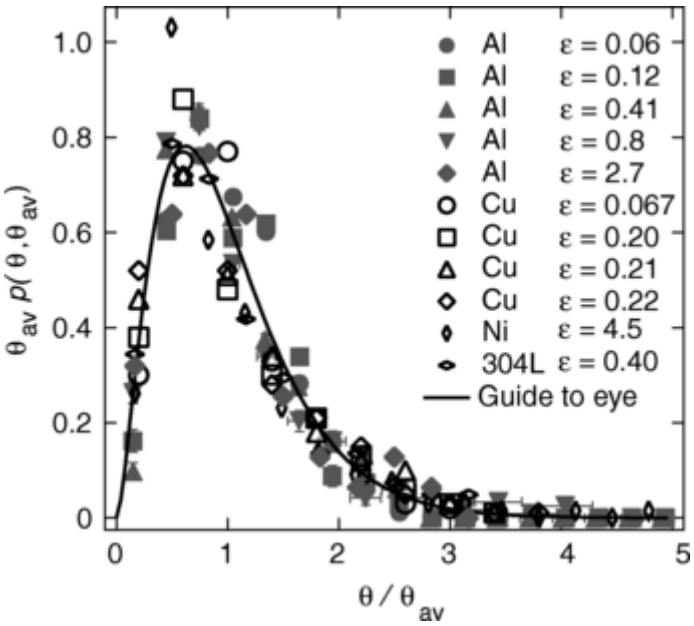

Fig. 18 The probability density functions of the incidental dislocation boundaries (IDBs) misorientation angles normalized by the average misorientation angle, for cold-rolled aluminum and nickel plus compression-deformed copper. Copper data from Ref 53 and AISI 304L data from Ref 7

In Figure 19, the misorientation angles of GNBs are scaled at small to intermediate strains. Remarkably, the data from the forging case illustrated in Fig. 2 also scales with the same distribution. The observation of scaling of the misorientation angle distributions is underpinned by a theoretical analysis in Ref 55 by considering boundary formation with the assumption of interactions with one, two, or three sets of dislocations.

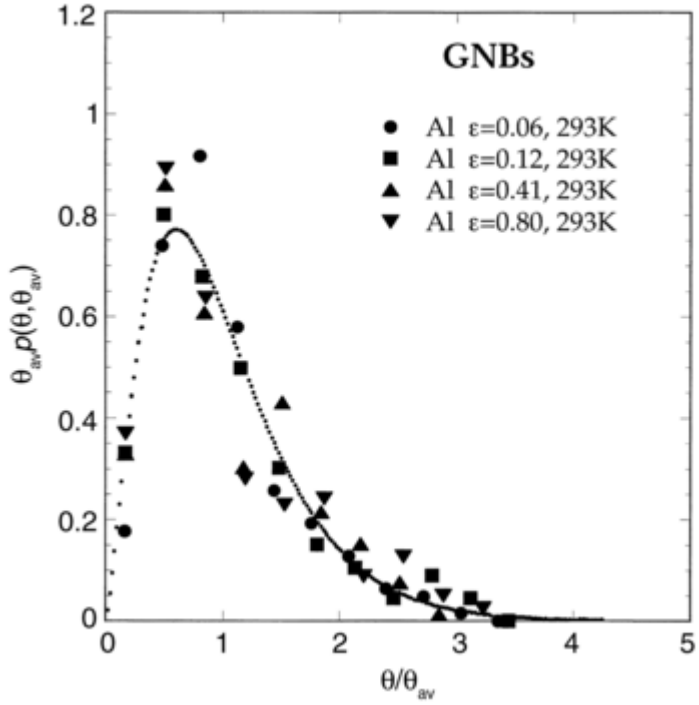

Fig. 19 The probability density functions of the geometrically necessary boundaries (GNBs) misorientation angles normalized by the average misorientation angle, for strains from 5–50% cold reduction (cr) or equivalent von Mises strain ε_{vM} = 0.06 to 0.80 in aluminum (Ref 54)

Another example of scaling is given in Fig. 20, showing that probability distributions of GNB spacings, D^{GNB}, collapse into one function when scaled by each average D_{av}^{GNB}, for a wide variety of conditions. This universal behavior is further supported by a recent analysis, which shows that scaling of the boundary spacing can be extended to also cover nanoscale structures present in friction layers (Ref 24). However, in this case scaling is

not yet underpinned by theoretical analysis. An analysis is currently underway that considers criteria for the creation of new GNBs based on slip-pattern changes and large scale coordinated or collective events involving large numbers of dislocations. The biased flux of dislocations making the slip pattern contributes both to the dislocation content and the selection of boundary plane.

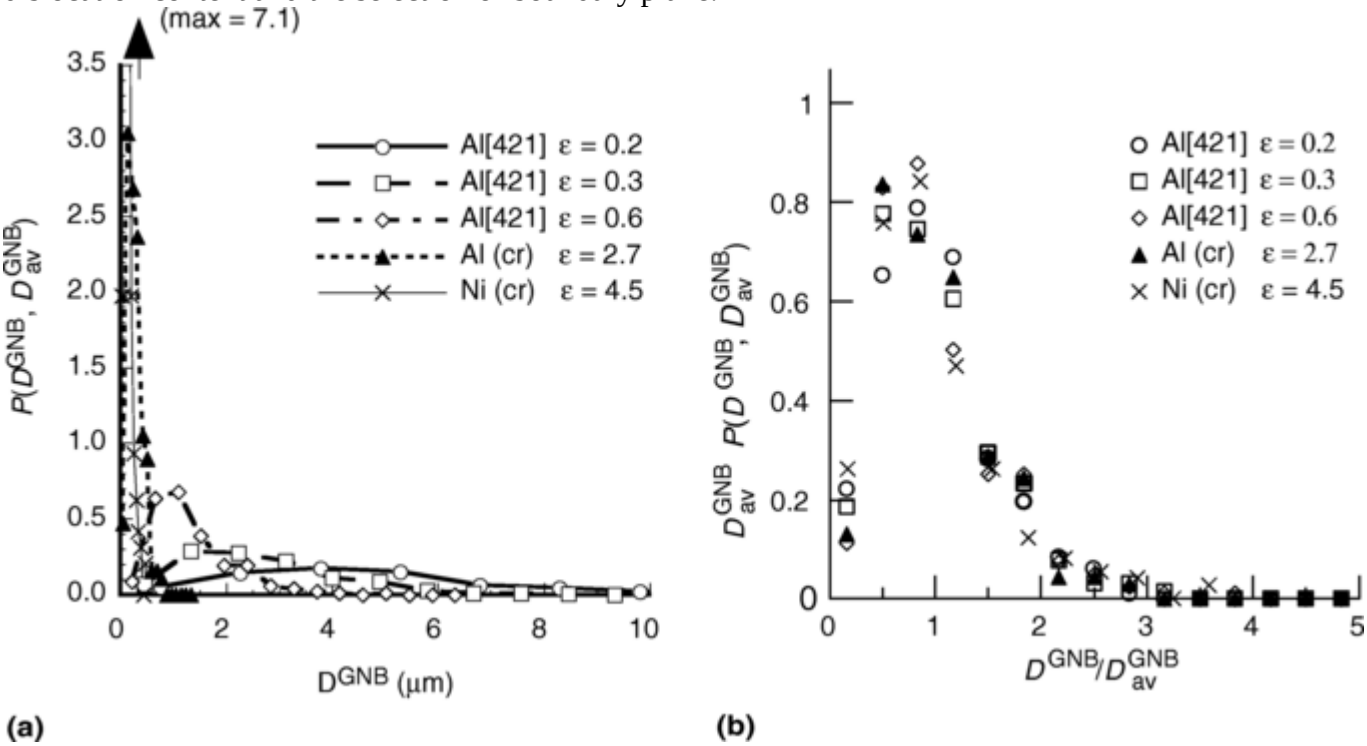

Fig. 20 Geometrically necessary boundary (GNB) spacing measurements from highly cold-rolled (cr) polycrystalline samples of aluminum (ε_{vM} = 2.7) and nickel (ε_{vM} = 4.5) compared to data from the [421] single-crystal samples compressed to strains of ε_{vM} = 0.2, 0.3, and 0.6. (a) Probability density distributions. (b) Probability density distributions normalized by their averages collapse into a single function for a wide range of conditions and average spacing. Source: Ref 45

The scaling hypothesis applies to both GNBs and IDBs when they are analyzed separately, but not when all boundaries are grouped together. The analyses of both the angle/strain dependency and scaling laws show that IDBs and GNBs develop along different evolutionary paths. In addition, GNBs and IDBs have distinctly different morphologies. Therefore, these boundaries should be measured and analyzed separately as microstructural parameters used in microstructure-property relationships.

High-Angle GNBs and Texture Components. At very large strains, the average misorientation angle across all the boundaries can reach values above 15°. This is shown in Fig. 21 for the change in misorientation angle measured across the lamellar boundaries in a direction perpendicular to the rolling plane. Figure 21 also shows the crystallographic orientation of the cell blocks given as the typical rolling texture components copper, sulfur, brass, and cube. This is an example of the pronounced grain subdivision that takes place during plastic deformation. It is not an entire grain that rotates into a new position as the deformation texture evolves. Individual parts of a grain can rotate toward different orientations, and the mutually misoriented cell blocks comprise the (macroscopic) texture components.

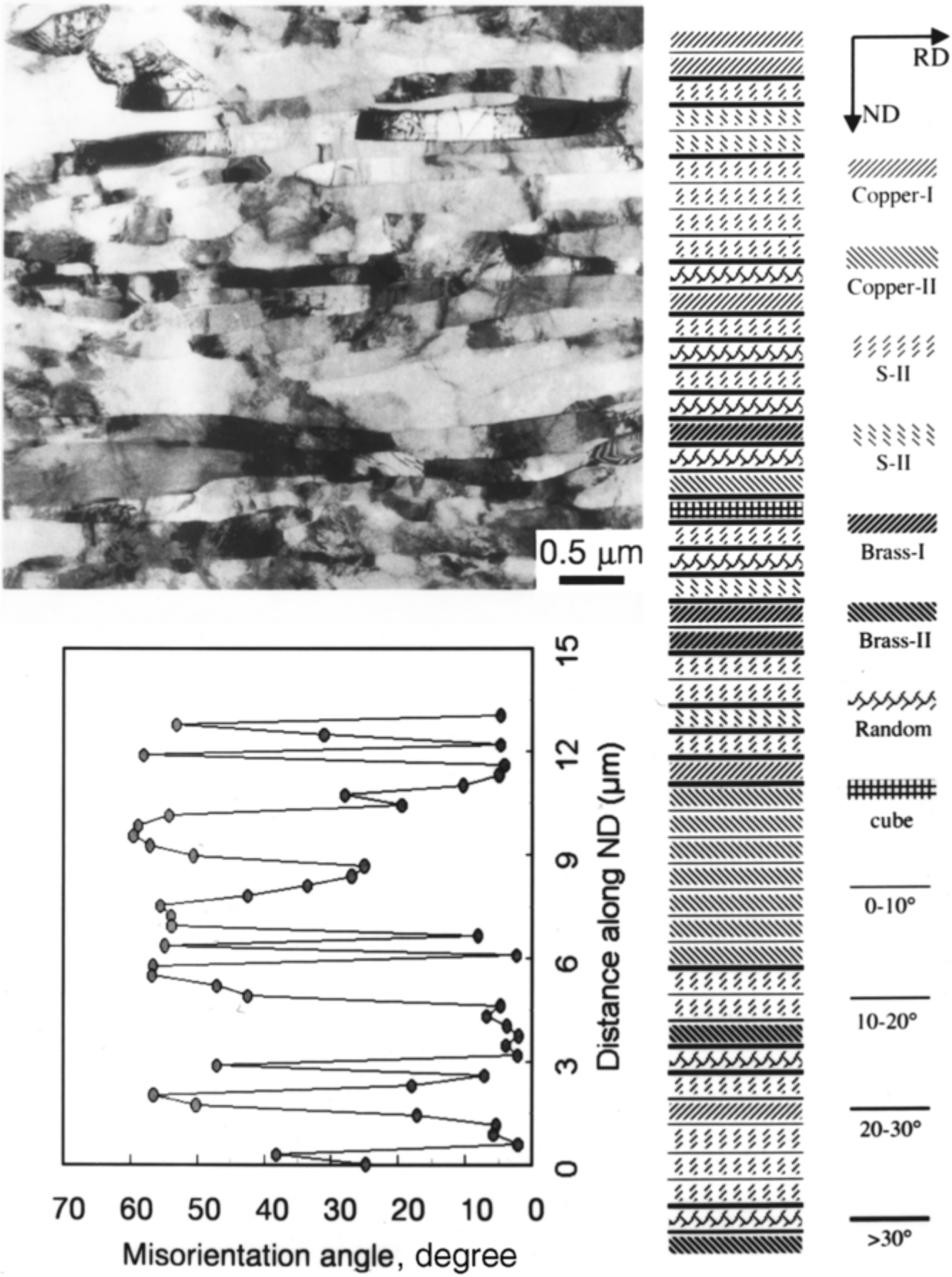

Fig. 21 Commercial purity aluminum cold rolled to ε_{vM} = 5.8. The lamellar boundaries (LBs) nearly parallel to the rolling plane have medium to high boundary angles and separate, different rolling texture components. Source: Ref 21

Low-Energy Dislocation Structures. The assumption of the elastic distortion being restricted to a region close to the boundary, that is, an absence of long-range stresses, leads to Frank's formula (Ref 56) for the relationship between the dislocation content of a boundary and its angle axis pair. (**R**/θ):

$$\mathbf{B} = (\mathbf{r} \times \mathbf{R})2 \sin (\theta/2)$$

where the vector, **r**, represents an arbitrary straight line lying in the plane of the boundary, which contains the dislocation network, and **B** is the sum of the Burgers vectors of all the dislocations intersected by **r**. This equation is the basis of a boundary analysis of which examples are given subsequently.

The assumption of low-energy structures also leads to the Read-Shockley formulation (Ref 57) of the relationship between elastic energy per unit area of boundary (E_a) and the misorientation angle (θ):

$$E_a = \gamma_{gb}(\theta_{av}/\theta_{max})(1 - \ln (\theta_{av}/\theta_{max}))$$

where γ_{gb} is the energy of a high-angle grain boundary; and θ_{av} is the average angle of misorientation of dislocation boundaries with an angle less than θ_{max}, which is of the order 15°. This equation relates the stored-energy characteristics of a deformation microstructure to its recrystallization behavior.

In the analysis of deformation microstructures, LEDS theory gives principles and guidelines, but it does not allow the prediction of specific dislocation arrangements (Ref 8). This lack of predictive capability occurs because of the immense number of dislocation configurations that can be constructed from any given dislocation population when the number of Burgers vectors within the structure is three or more. Supplementary principles, therefore, may be sought and kinematics are considered below.

Slip Pattern. A GNB can be characterized by its boundary plane. This plane can be analyzed in two different coordinate systems with respect to the sample, namely (a) the macroscopic system defined by the deformation axes and (b) the crystal axes. The former provides a macroscopic description, with the advantage of obtaining the simple approximation that boundaries in all grains lie on similar macroscopic planes, for example, inclined 40° to the rolling plane at small to medium rolling reductions, whereas the latter, more precise definition has the advantage of providing a means to find correlations between the boundary planes and grain orientations, that is, active slip systems.

A correlation between microstructure and slip pattern is generally reflected in the behavior of single and polycrystals, where a clear relationship between grain orientation and deformation microstructure has been observed. Examples are cold-rolled aluminum (Ref 58), iron (Ref 35), and tantalum (Ref 59); and tensile-strained aluminum and copper (Ref 51, 60). Figure 22 shows the result of a microstructural examination of 82 grains in tensile-strained aluminum (99.996%) having an original grain size of about 300 μm (Ref 51). A TEM investigation led to the identification of three typical structures: type I with GNBs near to an active slip plane, type II with cell structure, and type III with GNBs far from any one slip plane, but still related to a group of slip planes. The structural classification was related to the grain orientation by plotting the grain tensile axes in an inverse pole (Fig. 22). This figure shows a clear correlation with grains in the middle of the triangle developing type I structures, grains near the (100) corner developing type II, and grains near the (111) corner developing type III microstructures (Ref 51, 61). A similar result was obtained for copper. The structural characterization was carried out at different tensile strains in the range 0.05 to 0.34, but no effect of strain on the grouping in Fig. 22 was observed.

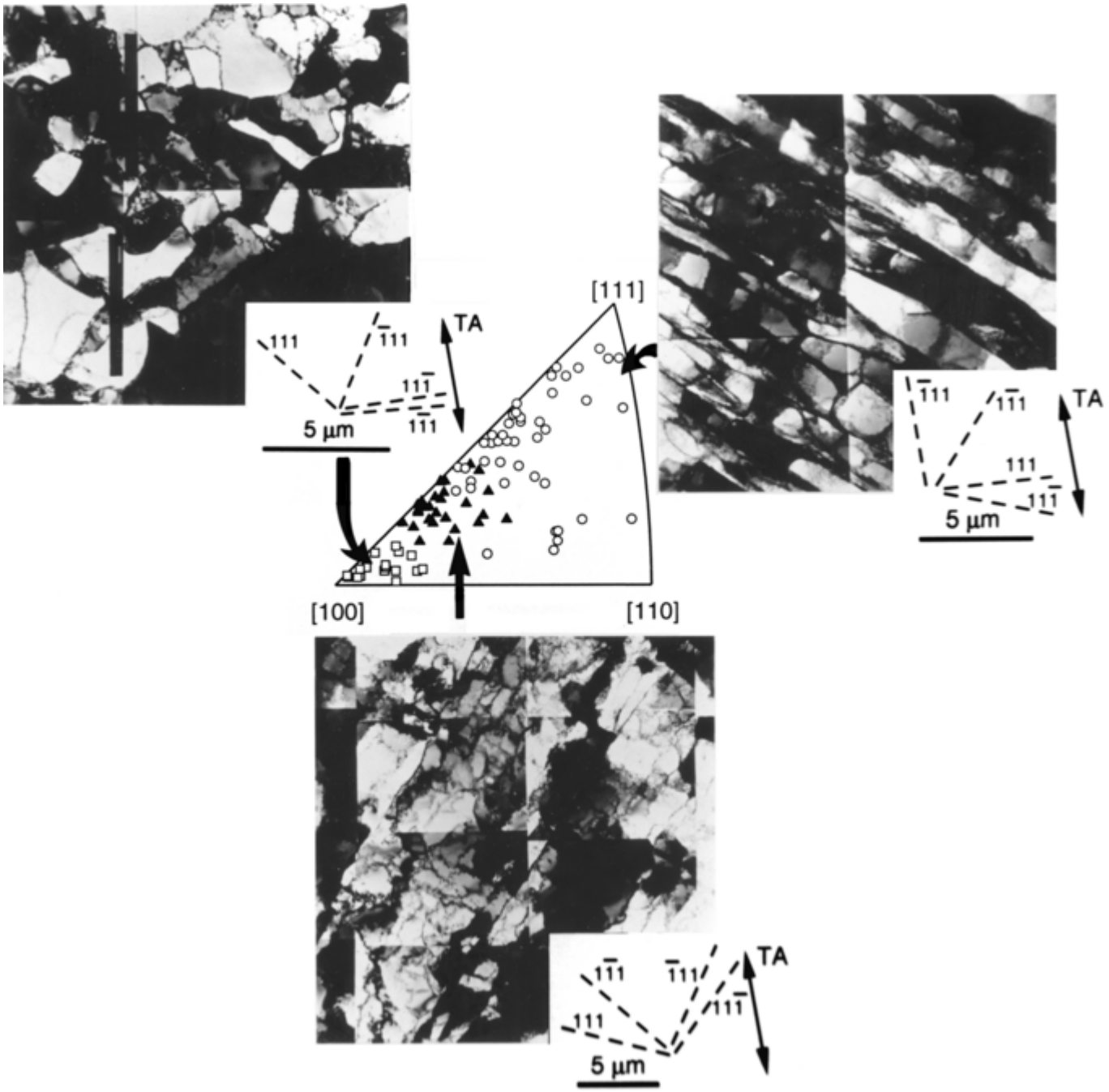

Fig. 22 Relationship between deformation microstructure and grain orientation in polycrystalline aluminum (99.99%) following tension. Three types of cell block structures have been identified. Source: Ref 51

The general observation of a correlation between the crystallographic orientation of a grain and the deformation microstructure has been used in an analysis of the relationship between the microstructure and the slip pattern to predict the microstructure evolution under given load conditions (Ref 61). An example is the prediction that GNBs in cold-rolled aluminum should be approximately parallel to a slip plane when a large fraction of the slip in a grain occurs on one or two slip planes. For example, an empirically quantitative relation has been determined for rolled aluminum polycrystals, and it has been found that boundary traces deviate less than 5° from the slip-plane traces when the fraction of slip exceeds 45% (Ref 62). In tensile deformation, single crystals oriented for single or double slip, that is, where all slip is predicted to occur on one or two slip planes, have boundaries almost parallel to these planes. Grains of these orientations in a polycrystal also have boundaries lying within 10° of these planes. On the other hand, the macroscopic direction of slip causes the macroscopic directionality of boundaries. These results, and others, point to the grain orientation as a very important factor underlying the microstructural evolution. This is in contrast to interaction between grain neighbors, which appear to be less influential.

Similar relationships between crystal orientation and microstructure are also found in bcc metals, for example, the wide spacing of lamellar boundaries (LBs) in grains oriented along the alpha fiber compared with the more narrow spacing in the gamma fiber (Fig. 7d and Fig. 23).

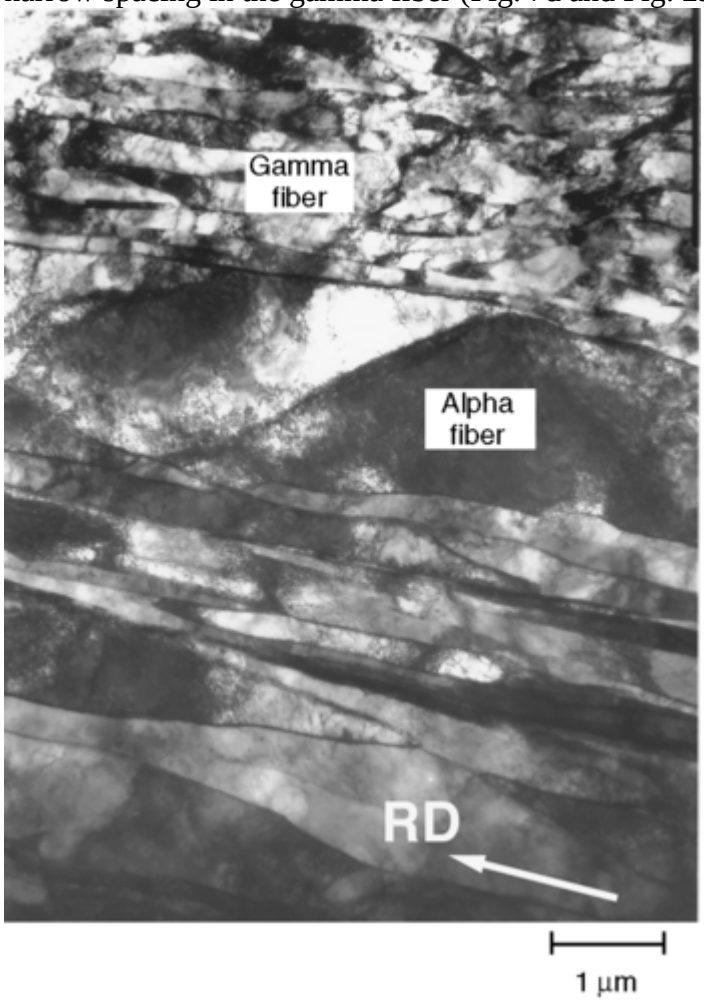

Fig. 23 Relationship between deformation microstructure and grain orientation in polycrystalline interstitial-free iron (99.99%) following rolling, 90% cold reduction. Courtesy of X. Huang, Risø National Laboratory

While GNBs are very typical structures, created by most monotonic deformation modes, the pervasiveness and importance of the GNBs came to light in the 1980s and 1990s. Parallel families of GNBs, together with the crystal orientation with respect to the deformation, facilitate the "flow" of metal in certain directions. Geometrically necessary boundaries thereby control the ability to make desired shape changes in metals. Since GNBs form near the beginning of deformation, they are an important ingredient not only in understanding the creation of the mosaic microstructural pattern, but also in understanding the slip pattern and predicting the flow stress.

References cited in this section

7. D.A. Hughes, D.C. Chrzan, Q. Liu, and N. Hansen, Scaling of Misorientation Angle Distributions, *Phys. Rev. Lett.*, Vol 81, 1998, p 4664–4667

8. D. Kuhlmann-Wilsdorf, Theory of Plastic Deformation: Properties of Low Energy Dislocation Structures, *Mater. Sci Eng.*, Vol A113, 1989, p 1–41

11. Q. Liu and N. Hansen, Geometrically Necessary Boundaries and Incidental Dislocation Boundaries Formed During Cold Deformation, *Scr. Metall. Mater.*, Vol 32, 1995, p 1289

15. D.A. Hughes and N. Hansen, Microstructure and Strength of Nickel at Large Strains, *Acta Mater.,* Vol 48, 2000, p 2985–3004

17. A. Godfrey and D.A. Hughes, Determination of Boundary Area and Spacing in Prismatic Structures with Applications to Dislocation Boundaries, *Mater. Charac.,* Vol 48, 2002, p 89

21. Q. Liu, X. Huang, N. Hansen, and D.J. Lloyd, Microstructure and Strength of Commercial Purity Aluminium (AA1200) Cold-Rolled to Large Strains, *Acta Mater.,* Vol 50, 2002, p 3798–3802

24. D.A. Hughes and N. Hansen, Graded Nanostructures Produced by Sliding and Exhibiting Universal Behavior, *Phys. Rev. Lett.,* Vol 87 (No. 13), 2001, p 135503

35. H. Hu, Annealing of Silicon-Iron Single Crystals, *Recovery and Recrystallization,* L. Himmel, Ed., AIME, Interscience, 1963, p 311–378

42. G. Christiansen, J.R. Bowen, and J. Lindbo, Electrolytic Preparation of Metallic Thin Foils with Large Electron-Transparent Regions, *Mater. Charac.,* Vol 49, 2003, p 331–335

43. A.S. Malin and M. Hatherly, Microstructure of Cold-Rolled Copper, *Met. Sci.,* Vol 13, 1979, p 463–472

44. E.E. Underwood, *Quantitative Stereology,* Addison-Wesley, 1970

45. A. Godfrey and D.A. Hughes, Scaling of the Spacing of Deformation Induced Boundaries, *Acta Mater.,* Vol 48, 2000, p 1897–1905

46. B.L. Adams, S.I. Wright, and K. Kunze, Orientation Imaging: The Emergence of a New Microscopy, *Metall. Trans.,* Vol 24A, 1993, p 819–831

47. N.C. Krieger-Lassen, D. Juul-Jensen, and K. Conradsen, Automatic Recognition of Deformed and Recrystallized Regions in Partly Recrystallized Samples Using Electron Back Scattering Patterns, *Mater. Sci. Forum,* Vol 157–162, 1994, p 149–158

48. Q. Liu, A Simple Method for Determining Orientation and Misorientation of the Cubic Crystal Specimen, *J. Appl. Crystallogr.,* Vol 27, 1994, p 755–761

49. H. Hu, *Textures in Research and Practice,* J. Grewen and G. Wassermann, Ed., Springer Verlag, 1969, p 200

50. J. Alberdi, “Grandes Deformaciones Plasticas en Frio en Policristales de Cobre y Aluminio (Torsion),” PhD. thesis, Universidad de Navarra Facultad de Ciencias: San Sebastian, 1984

51. X. Huang and N. Hansen, Grain Orientation Dependence of Microstructure in Aluminum Deformed by Tension, *Scr. Mater.,* Vol 37, 1997, p 1–7

52. W. Pantleon and N. Hansen, Disorientations in Dislocation Boundaries: Formation and Spatial Correlation, *Mater. Sci. Eng.,* Vol A309–310, 2001, p 246–250

53. W. Pantleon, On the Statistical Origin of Disorientations in Dislocation Structures, *Acta Mater.,* Vol 46, 1998, p 451–456

54. D.A. Hughes, Q. Liu, D.C. Chrzan, and N. Hansen, Scaling of Microstructural Parameters: Misorientations of Deformation-Induced Boundaries, *Acta Mater.,* Vol 45, 1997, p 105–112

55. W. Pantleon and N. Hansen, Dislocation Boundaries—The Distribution Function of Disorientation Angles, *Acta Mater.*, Vol 49, 2001, p 1479–1493

56. F.C. Frank, *Report of the Symposium on the Plastic Deformation of Crystalline Metals,* Carnegie Institute of Technology and Office of Naval Research, 1950, p 150–154

57. W.T. Read and W. Shockley, Dislocation Models of Crystal Grain Boundaries, *Phys. Rev.*, Vol 78, 1950, p 275–289

58. Q. Liu and N. Hansen, Deformation Microstructures and Orientation of FCC Crystals, *Phys. Stat. Solids (a)*, Vol 149, 1995, p 187–199

59. R.A. Vandermeer and J.W.B. Snyder, Recovery and Recrystallization in Rolled Tantalum Single Crystals, *Metall. Trans. A*, Vol 10A, 1979, p 1031–1044

60. Y. Kawasaki and T. Takeuchi, Cell Structure in Copper Single Crystals Deformed in the [100] and [111] Axes, *Scr. Metall.*, Vol 14, 1980, p 183–188

61. G. Winther, X. Huang, and N. Hansen, Crystallographic and Macroscopic Orientation of Planar Dislocation Boundaries—Correlation with Grain Orientation, *Acta Mater.*, Vol 48, 2000, p 2187–2198

62. G. Winther, D. Juul-Jensen, and N. Hansen, Dense Dislocation Walls and Microbands Aligned with Slip Planes—Theoretical Considerations, *Acta Mater.*, Vol 45, 1997, p 5069–5068

D.A. Hughes and N. Hansen, Plastic Deformation Structures, *Metallography and Microstructures*, Vol 9, *ASM Handbook*, ASM International, 2004, p. 192–206

Plastic Deformation Structures

Darcy A. Hughes, Sandia National Laboratories; Niels Hansen, Risø National Laboratory

---

Macroscopic Properties

The quantitative and theoretical analysis of microstructural parameters is applied in many areas in materials science, engineering, and technology. One application is process optimization to obtain prescribed microstructure and texture, thereby producing materials with excellent formability during both bulk and sheet forming. Another application is to develop thermomechanical processes that produce metals and alloys with uniform and fine grain microstructures having both good strength and ductility. An important part of this optimization is to establish general relationships between the microstructural parameters and properties, for example, flow stress and flow-stress anisotropy. This analysis is shown below in a calculation of the stress-strain curves for pure polycrystalline nickel.

Based on the observations of the cell block structure, the suggestion has been made that two strengthening contributions should be considered: (a) dislocation strengthening due to the presence of low-angle boundaries and (b) boundary strengthening due to medium- to high-angle boundaries (Ref 15, 63). In the following paragraphs, average parameters are used to predict an average flow stress, although on a finer scale, the grain orientation, slip pattern, and the local structures will affect the local flow stresses.

Dislocation density in the diffuse low-angle boundaries, that is, IDBs, is calculated from the IDB misorientation angles and spacing, $\rho = S_v \cdot 1.5\theta/b$, in which S_v is the boundary area per unit volume (S_v is inversely related to the spacing D_{av}^{IDB}) and $1.5\theta/b$ is the dislocation density per unit of a mixed twist-tilt boundary (Ref 57). The strength contribution is then:

$$\sigma_{IDB} = M\alpha G\mathbf{b}\sqrt{\left(1.5S_v\theta_{av}^{IDB}/\mathbf{b}\right)} \quad \text{(Eq 1)}$$

where M is the Taylor factor, α is a constant taken to be 0.24 (Ref 64), **b** is the Burgers vector (0.249 nm for nickel), G is the shear modulus (79 GPa for nickel). An average M factor of 3.06 is used in the calculations.

The GNBs separate differently, deforming regions like grain boundaries. Thus, their strength contribution should not generally be associated with a dislocation content spread throughout the volume. Instead for the GNBs, boundary strengthening via a Hall-Petch equation is introduced:

$$\sigma_{GNB} = K_{HP}\Big/\sqrt{D_{av}^{GNB(i)}} \quad \text{(Eq 2)}$$

where K_{HP} is the slope of the straight line relating the flow stress of a polycrystalline metal to the inverse square root of grain size. For nickel, K_{HP} is 158 MPa · $\mu m^{1/2}$ (Ref 65). Note that $D_{av}^{GNB(i)}$ is a slip distance that is related to the perpendicular spacing, D_{av}^{GNB}. Since a detailed slip-pattern analysis is yet in progress for $D_{av}^{GNB(i)}$, the random spacing, ${}^{r}D = 2/S_v$, will be substituted for $D_{av}^{GNB(i)}$.

The total flow stress can be determined by the sum of these two different strengthening mechanisms:

$$\sigma = \sigma_0 + \sigma_{IDB} + \sigma_{GNB} \quad \text{(Eq 3)}$$

The friction stress, σ_0 is 20 MPa (Ref 65).

A more inclusive treatment is to include the density of the unassociated dislocations within the cells whose density is ρ_0. While this is a trivial addition for pure metals, it becomes more important for alloys as ρ_0 increases. Combining equations 1, 2, and 3 with ρ_0, one obtains:

$$\sigma = \sigma_0 + M\alpha G\mathbf{b}\sqrt{\left(\left(1.5S_v\theta/\mathbf{b}\right)_{IDB} + \rho_0\right)} + K_{HP}\Big/\sqrt{D_{av}^{GNB(i)}} \quad \text{(Eq 4)}$$

Equation 4 has been used for cold-rolled nickel based on a detailed characterization of microstructural parameters up to very large strain (ε_{vM} = 4.5 or 98% cr), and the results are shown in Fig. 24 together with hardness data and flow-stress values from the literature (Ref 66, 67). The calculated individual strength contributions evolve differently with the strain, and their addition leads to flow-stress values and hardening rates in good agreement with those observed experimentally (Fig. 24). A smooth transition from stage III to stage IV was observed and no saturation of the calculated and experimental flow stress was found (Fig. 24). This lack of saturation in the flow stress agrees with the structural observation, showing a continuous structural evolution with increasing strain. Similar absence of saturation in flow stress and microstructure has been observed in cold-rolled and cold-drawn aluminum (99.5 and 99.99% purity) and in torsion-deformed aluminum and nickel. The suggested strength structural relationship may also have predictive capabilities when combined with an analysis of the evolution of microstructural parameters as a function of the applied strain.

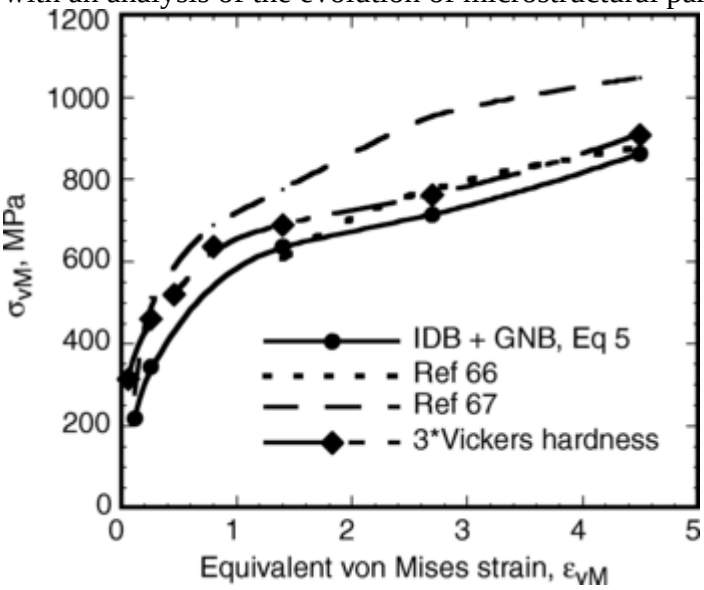

Fig. 24 Flow-stress calculations for cold-rolled nickel (99.99%) based on microstructural measurements compared with Vickers hardness and literature data. Source: Ref 15

References cited in this section

15. D.A. Hughes and N. Hansen, Microstructure and Strength of Nickel at Large Strains, *Acta Mater.,* Vol 48, 2000, p 2985–3004

57. W.T. Read and W. Shockley, Dislocation Models of Crystal Grain Boundaries, *Phys. Rev.,* Vol 78, 1950, p 275–289

63. N. Hansen, Flow Stress and Microstructural Parameters, *Proc. 15th Risø International Symposium on Materials Science: Numerical Predictions of Deformation Processes and the Behavior of Real Materials,* S.I. Andersen, J.B. Bilde-Sørensen, et al., Ed., Risø National Laboratory, 1994, p 325–334

64. N. Hansen and X. Huang, Microstructure and Flow Stress of Polycrystals and Single Crystals, *Acta Mater.,* Vol 46, 1998, p 1827–1836

65. A.W. Thompson, Yielding in Nickel as a Function of Grain or Cell Size, *Acta Metall.,* Vol 23, 1975, p 1337–1342

66. J. Nuttall and J. Nutting, Structure and Properties of Heavily Cold-Worked fcc Metals and Alloys, *Met. Sci.,* Vol 12, 1978, p 430–437

67. W.H. Zimmer, S.S. Hecker, D.L. Rohr, and L.E. Murr, Large-Strain Plastic Deformation of Commercially Pure Nickel, *Met. Sci.,* Vol 17, 1983, p 198–206

D.A. Hughes and N. Hansen, Plastic Deformation Structures, *Metallography and Microstructures,* Vol 9, *ASM Handbook,* ASM International, 2004, p. 192–206

Plastic Deformation Structures

Darcy A. Hughes, Sandia National Laboratories; Niels Hansen, Risø National Laboratory

---

Conclusion

The microstructural evolution during plastic deformation follows a pattern of grain subdivision on a finer and finer scale down to the nanometer range. Structural parameters such as boundary spacing and misorientation angle across boundaries show scaling, which has led to physically based models for the formation and evolution of dislocation boundaries. In parallel, correlations between the crystallographic orientation of a grain and the deformation microstructure have led to a slip-pattern analysis based on the crystallographic orientation of the dislocation boundaries. Thereby, a tool has been provided for relating load conditions with resulting microstructures. This type of physical and mechanical analysis leads toward general relationships among processing conditions, structure, and properties vital for future development of processes and materials.

D.A. Hughes and N. Hansen, Plastic Deformation Structures, *Metallography and Microstructures,* Vol 9, *ASM Handbook,* ASM International, 2004, p. 192–206

Darcy A. Hughes, Sandia National Laboratories; Niels Hansen, Risø National Laboratory

Acknowledgment

This work was supported by the Office of Basic Energy Sciences, the U.S. Department of Energy under contract No. DE-AC04-94AL85000 and by the Danish National Research Foundation through the Center for Fundamental Research: Metal Structures in Four Dimensions.

D.A. Hughes and N. Hansen, Plastic Deformation Structures, *Metallography and Microstructures,* Vol 9, *ASM Handbook,* ASM International, 2004, p. 192–206

Plastic Deformation Structures

Darcy A. Hughes, Sandia National Laboratories; Niels Hansen, Risø National Laboratory

References

1. J.W. Ewing and W. Rosenhain, *Philos. Trans. R. Soc., London A,* Vol A193, 1899, p 353–375

2. J.W. Steeds, Dislocation Arrangement in Copper Single Crystals as a Function of Strain, *Proc. R. Soc. A,* Vol 292, 1966, p 343–373

3. J. Gil-Sevillano, P. van-Houtte, and E. Aernoudt, Large Strain Work Hardening and Textures, *Prog. Mater. Sci.,* Vol 25, 1980, p 69–412

4. S.S. Hecker and M.G. Stout, Strain Hardening of Heavily Cold Worked Metals, *Deformation Processing and Structure,* G. Krauss, Ed., ASM, 1982, p 1–46

5. M.F. Ashby, C.M. Sellars, et al., Deformation Processing of Metals, *Philos. Trans. R. Soc., London A,* Vol 357, 1999, p 1441–1729

6. N. Hansen, New Discoveries in Deformed Metals, *Metall. Mater. Trans. A,* Vol 32A, 2001, p 2917–2935

7. D.A. Hughes, D.C. Chrzan, Q. Liu, and N. Hansen, Scaling of Misorientation Angle Distributions, *Phys. Rev. Lett.,* Vol 81, 1998, p 4664–4667

8. D. Kuhlmann-Wilsdorf, Theory of Plastic Deformation: Properties of Low Energy Dislocation Structures, *Mater. Sci Eng.,* Vol A113, 1989, p 1–41

9. B. Bay, N. Hansen, D.A. Hughes, and D. Kuhlmann-Wilsdorf, Evolution of fcc Deformation Structures in Polyslip, *Acta Metall. Mater.,* Vol 40, 1992, p 205–219

10. D. Kuhlmann-Wilsdorf and N. Hansen, Geometrically Necessary, Incidental and Subgrain Boundaries, *Scr. Metall. Mater.,* Vol 25, 1991, p 1557–1562

11. Q. Liu and N. Hansen, Geometrically Necessary Boundaries and Incidental Dislocation Boundaries Formed During Cold Deformation, *Scr. Metall. Mater.,* Vol 32, 1995, p 1289

12. D.A. Hughes, Microstructure Evolution, Slip Patterns and Flow Stress, *Mater. Sci. Eng.,* Vol 319–321, 2001, p 46–54

13. D.A. Hughes, R. Lebensohn, H.R. Wenk, and A. Kumar, Stacking Fault Energy and Microstructure Effects on Torsion Texture Evolution, *Proc. R. Soc. (London) A,* Vol 456, 2000, p 921–953

14. D.A. Hughes and N. Hansen, Deformation Structures Developing at Fine Scales, *Philos. Mag.,* Vol 83, 2003, p 3871–3893

15. D.A. Hughes and N. Hansen, Microstructure and Strength of Nickel at Large Strains, *Acta Mater.,* Vol 48, 2000, p 2985–3004

16. D.A. Hughes and N. Hansen, Microstructural Evolution in Nickel During Rolling to Large Strains, *Metall. Trans. A,* Vol 24A, 1993, p 2021–2037

17. A. Godfrey and D.A. Hughes, Determination of Boundary Area and Spacing in Prismatic Structures with Applications to Dislocation Boundaries, *Mater. Charac.,* Vol 48, 2002, p 89

18. G. Langford and M. Cohen, Strain Hardening of Iron by Severe Plastic Deformation, *Trans. Am. Soc. Met.,* Vol 62, 1969, p 623–638

19. G. Langford and M. Cohen, Microstructural Analysis by High-Voltage Electron Diffraction of Severely Drawn Iron Wires, *Metall. Trans.,* Vol 6A, 1975, p 901–910

20. J.D. Embury and R.M. Fisher, Structure and Properties of Drawn Pearlite, *Acta Metall.,* Vol 14, 1966, p. 147

21. Q. Liu, X. Huang, N. Hansen, and D.J. Lloyd, Microstructure and Strength of Commercial Purity Aluminium (AA1200) Cold-Rolled to Large Strains, *Acta Mater.,* Vol 50, 2002, p 3798–3802

22. Y. Saito, H. Utsunomiya, N. Tsuji, and T. Sakai, Novel Ultrahigh Straining Process for Bulk Metals—Development of the Accumulative Roll Bonding (ARB) Process, *Acta Mater.,* Vol 47, 1999, p 579–583

23. R.Z. Valiev, R.K. Islamgaliev, and I.V. Aleksandrov, Bulk Nanostructured Materials from Severe Plastic Deformation, *Prog. Mater. Sci.,* Vol 45, 2000, p 103–189

24. D.A. Hughes and N. Hansen, Graded Nanostructures Produced by Sliding and Exhibiting Universal Behavior, *Phys. Rev. Lett.,* Vol 87 (No. 13), 2001, p 135503

25. D.A. Hughes, Microstructural Evolution in a Non-Cell Forming Metal: Al-Mg, *Acta Metall. Mater.,* Vol 41, 1993, p 1421–1430

26. R. Neuhaus and C. Schwink, On the Flow Stress of [100]- and [111]-Oriented Cu-Mn Single Crystals: A Transmission Electron Microscopy Study, *Philos. Mag.,* Vol 65, 1992, p 1463–1484

27. B.J. Duggan, M. Hatherly, W.B. Hutchinson, and P.T. Wakefield, Deformation Structures and Textures in Cold-Rolled 70:30 Brass, *Met. Sci.,* Vol 12, 1978, p 343–351

28. J.K. Solberg, H.J. McQueen, N. Ryum, and E. Nes, Influence of Ultra-High Strains at Elevated Temperature on the Microstructure of Aluminum, Part I, *Philos. Mag.,* Vol 60A, 1989, p 447–471

29. V.M. Segal, Materials Processing by Simple Shear, *Mater. Sci. Eng.,* Vol A197, 1995, p 157–164

30. P.E. Armstrong, J.E. Hockett, and O.D. Sherby, Large Strain Multidirectional Deformation of 1100 Aluminum at 300 K, *J. Mech. Phys. Solids,* Vol 30, 1982, p 37–58

31. C.Y. Barlow, Y.L. Liu, and N. Hansen, Fine Scale Structures from Deformation of Aluminium Containing Alumina Particles, *Acta Mater.,* Vol 50, 2002, p 171–182

32. V. Randle, N. Hansen, and D. Juul-Jensen, The Deformation Behaviour of Grain Boundary Regions in Polycrystalline Aluminium, *Philos. Mag.,* Vol 73, 1996, p 265–282

33. C.S. Barrett and L.H. Levenson, The Structure of Aluminum after Compression, *Trans. AIME,* Vol 137, 1940, p 112–127

34. J.L. Walter and E.F. Koch, Electron Microscope Study of the Structure of Cold-Rolled and Annealed (100)[001] Crystals of High-Purity Silicon-Iron, *Acta Metall.,* Vol 10, 1962, p 1059–1075

35. H. Hu, Annealing of Silicon-Iron Single Crystals, *Recovery and Recrystallization,* L. Himmel, Ed., AIME, Interscience, 1963, p 311–378

36. B.C. Wonsiewicz and G.Y. Chin, Inhomogeneity of Plastic Flow in Constrained Deformation, *Metall. Trans.,* Vol 1, 1970, p 57–61

37. I.L. Dillamore and H. Katoh, The Mechanisms of Recrystallization in Cubic Metals with Particular Reference to their Orientation Dependence, *Met. Sci.,* Vol 8, 1974, p 73–83

38. D. Kuhlmann-Wilsdorf, Overview No. 131 "Regular" Deformation Bands (DBs) and the LEDS Hypothesis, *Acta Mater.,* Vol 47, 1999, p 1697–1712

39. J.A. Wert, X. Huang, et al., *Proc. 20th Risø Int. Symposium on Materials Science,* J. Bilde-Sørensen, J.V. Carstensen, et al., Ed., Risø National Laboratory, 1999, p 529–534

40. C.S. Lee, B.J. Duggan, and R.E. Smallman, A Theory of Deformation Banding in Cold Rolling, *Acta Metall. Mater.,* Vol 41, 1993, p 2265–2270

41. Q. Liu and N. Hansen, Macroscopic and Microscopic Subdivision of a Cold-Rolled Aluminum Single Crystal of Cubic Orientation, *Proc. R. Soc. (London),* Vol 454, 1998, p 2555–2591

42. G. Christiansen, J.R. Bowen, and J. Lindbo, Electrolytic Preparation of Metallic Thin Foils with Large Electron-Transparent Regions, *Mater. Charac.,* Vol 49, 2003, p 331–335

43. A.S. Malin and M. Hatherly, Microstructure of Cold-Rolled Copper, *Met. Sci.,* Vol 13, 1979, p 463–472

44. E.E. Underwood, *Quantitative Stereology,* Addison-Wesley, 1970

45. A. Godfrey and D.A. Hughes, Scaling of the Spacing of Deformation Induced Boundaries, *Acta Mater.,* Vol 48, 2000, p 1897–1905

46. B.L. Adams, S.I. Wright, and K. Kunze, Orientation Imaging: The Emergence of a New Microscopy, *Metall. Trans.,* Vol 24A, 1993, p 819–831

47. N.C. Krieger-Lassen, D. Juul-Jensen, and K. Conradsen, Automatic Recognition of Deformed and Recrystallized Regions in Partly Recrystallized Samples Using Electron Back Scattering Patterns, *Mater. Sci. Forum,* Vol 157–162, 1994, p 149–158

48. Q. Liu, A Simple Method for Determining Orientation and Misorientation of the Cubic Crystal Specimen, *J. Appl. Crystallogr.,* Vol 27, 1994, p 755–761

49. H. Hu, *Textures in Research and Practice,* J. Grewen and G. Wassermann, Ed., Springer Verlag, 1969, p 200

50. J. Alberdi, "Grandes Deformaciones Plasticas en Frio en Policristales de Cobre y Aluminio (Torsion)," PhD. thesis, Universidad de Navarra Facultad de Ciencias: San Sebastian, 1984

51. X. Huang and N. Hansen, Grain Orientation Dependence of Microstructure in Aluminum Deformed by Tension, *Scr. Mater.,* Vol 37, 1997, p 1–7

52. W. Pantleon and N. Hansen, Disorientations in Dislocation Boundaries: Formation and Spatial Correlation, *Mater. Sci. Eng.,* Vol A309–310, 2001, p 246–250

53. W. Pantleon, On the Statistical Origin of Disorientations in Dislocation Structures, *Acta Mater.,* Vol 46, 1998, p 451–456

54. D.A. Hughes, Q. Liu, D.C. Chrzan, and N. Hansen, Scaling of Microstructural Parameters: Misorientations of Deformation-Induced Boundaries, *Acta Mater.,* Vol 45, 1997, p 105–112

55. W. Pantleon and N. Hansen, Dislocation Boundaries—The Distribution Function of Disorientation Angles, *Acta Mater.,* Vol 49, 2001, p 1479–1493

56. F.C. Frank, *Report of the Symposium on the Plastic Deformation of Crystalline Metals,* Carnegie Institute of Technology and Office of Naval Research, 1950, p 150–154

57. W.T. Read and W. Shockley, Dislocation Models of Crystal Grain Boundaries, *Phys. Rev.,* Vol 78, 1950, p 275–289

58. Q. Liu and N. Hansen, Deformation Microstructures and Orientation of FCC Crystals, *Phys. Stat. Solids (a),* Vol 149, 1995, p 187–199

59. R.A. Vandermeer and J.W.B. Snyder, Recovery and Recrystallization in Rolled Tantalum Single Crystals, *Metall. Trans. A,* Vol 10A, 1979, p 1031–1044

60. Y. Kawasaki and T. Takeuchi, Cell Structure in Copper Single Crystals Deformed in the [100] and [111] Axes, *Scr. Metall.,* Vol 14, 1980, p 183–188

61. G. Winther, X. Huang, and N. Hansen, Crystallographic and Macroscopic Orientation of Planar Dislocation Boundaries—Correlation with Grain Orientation, *Acta Mater.,* Vol 48, 2000, p 2187–2198

62. G. Winther, D. Juul-Jensen, and N. Hansen, Dense Dislocation Walls and Microbands Aligned with Slip Planes—Theoretical Considerations, *Acta Mater.,* Vol 45, 1997, p 5069–5068

63. N. Hansen, Flow Stress and Microstructural Parameters, *Proc. 15th Risø International Symposium on Materials Science: Numerical Predictions of Deformation Processes and the Behavior of Real Materials,* S.I. Andersen, J.B. Bilde-Sørensen, et al., Ed., Risø National Laboratory, 1994, p 325–334

64. N. Hansen and X. Huang, Microstructure and Flow Stress of Polycrystals and Single Crystals, *Acta Mater.*, Vol 46, 1998, p 1827–1836

65. A.W. Thompson, Yielding in Nickel as a Function of Grain or Cell Size, *Acta Metall.*, Vol 23, 1975, p 1337–1342

66. J. Nuttall and J. Nutting, Structure and Properties of Heavily Cold-Worked fcc Metals and Alloys, *Met. Sci.*, Vol 12, 1978, p 430–437

67. W.H. Zimmer, S.S. Hecker, D.L. Rohr, and L.E. Murr, Large-Strain Plastic Deformation of Commercially Pure Nickel, *Met. Sci.*, Vol 17, 1983, p 198–206

Revised by W.L. Mankins, Recovery, Recrystallization, and Grain-Growth Structures, *Metallography and Microstructures*, Vol 9, *ASM Handbook*, ASM International, 2004, p. 207–214

Recovery, Recrystallization, and Grain-Growth Structures

Revised by William L. Mankins, Metallurgical Services Incorporated

---

Introduction

RECOVERY, RECRYSTALLIZATION, AND GRAIN GROWTH are the stages that a cold-worked metal undergoes when it is annealed. Cold working produces a large number of imperfections within the material, and thermal treatments are necessary to restore certain properties, especially ductility. Some overlap of the previously mentioned processes occurs due to microstructural heterogeneities within the material. Slight variations in composition within samples of the same alloy, variations in the amount and type of cold work, and the entire processing history of the specimen influence its response to thermal treatments.

Plastically deforming a metal by cold working results in a small portion of the expended mechanical energy being stored within the specimen. Grains are deformed and move relative to one another. The effects of the stored energy (visually observed only, using thin-foil transmission electron microscopy) are present as point defects, dislocations, and stacking faults.

Dislocations, flaws in the linear array of atoms, are generated and become rearranged due to the applied forces. The number of dislocations increases with increasing strain, and, due to their interactions, they become entangled, until at very large strains the original microstructure becomes unrecognizable. Cold-worked materials are in a higher energy state and are thermodynamically unstable. The effect of annealing is to provide thermal activation energy that transforms the material to lower energy states accompanied by a series of microstructural changes. Other properties of the material will also change as a result of the annealing process. Typically, the strength of materials decreases as a result of annealing, and the ductility increases.

Revised by W.L. Mankins, Recovery, Recrystallization, and Grain-Growth Structures, *Metallography and Microstructures,* Vol 9, *ASM Handbook*, ASM International, 2004, p. 207–214

Recovery, Recrystallization, and Grain-Growth Structures

Revised by William L. Mankins, Metallurgical Services Incorporated

The Deformed State

It is essential to understand the changes that metal undergoes when cold worked, in order to absorb the concepts of recovery and recrystallization. As described in the article “Plastic Deformation Structures” in this Volume, the nature of highly deformed structures and the mechanisms responsible for their development aid in understanding the microstructural changes occurring as a material changes from a deformed state to a fully annealed state as a result of thermal treatment.

Plastic deformation is achieved principally by the passage and redistribution of dislocations as they move through the lattice. Figure 1, 2, 3, and 4 show the effect of increasing amounts of cold work on type 304 stainless steel. The strain energy required to reduce the thickness of the material is stored within the strip, as evidenced by the increasing number of lattice defects (dislocations). Figure 1 shows the relatively long, straight dislocations that have the freedom to move within the matrix. The dislocations from the slip systems that require the least energy move first, followed by those produced from other slip systems. Figure 2 shows the initiation of cells as the dislocations from various slip systems begin to tangle and pile up. These small areas, or cells, exhibit very few or no individual dislocations and therefore are outlined by broad boundaries. Note that these thin-foil specimens for transmission electron microscopy (TEM) were prepared parallel to the rolling plane of the strip.

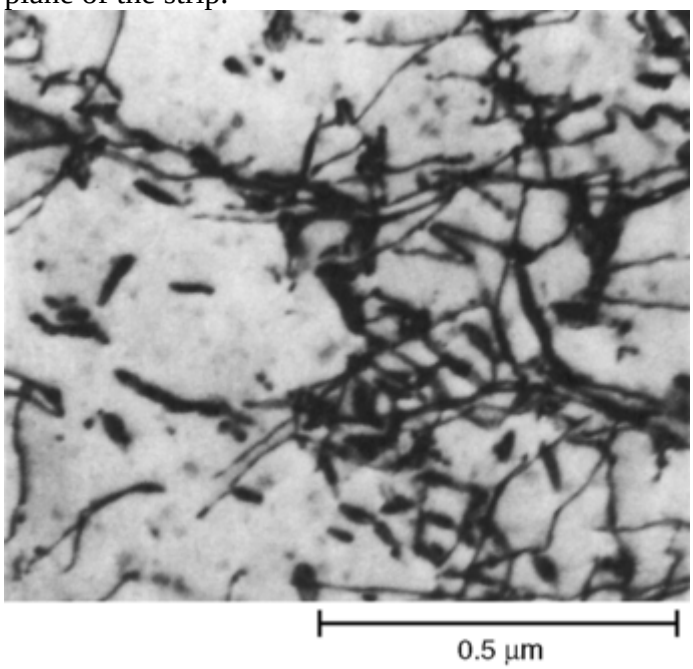

Fig. 1 Fe-3Si single crystal, cold rolled 5% in the (111)[11$\bar{2}$] orientation. Trails of small dislocation loops, edge dislocation dipoles, and cusps on dislocation lines. Thin-foil TEM specimen prepared parallel to the rolling plane. 62,000×

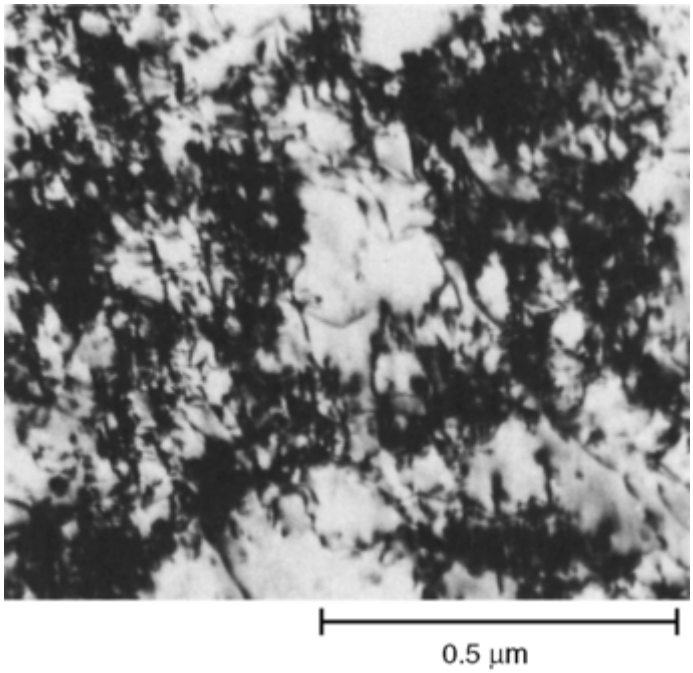

Fig. 2 Fe-3Si single crystal, cold rolled 20% in the (111)[11$\bar{2}$] orientation showing increased density of dislocations and clusters of short dislocation loops. Thin-foil TEM specimen prepared parallel to the rolling plane. 62,000×

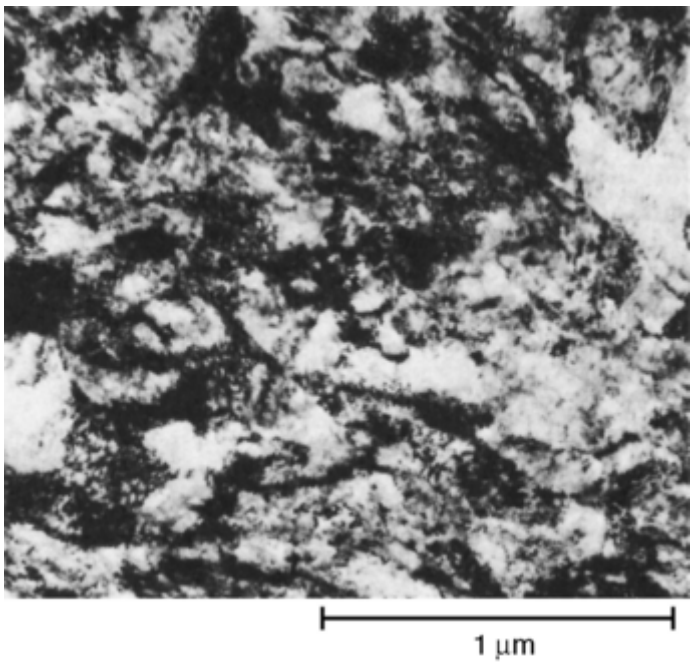

Fig. 3 Type 304 stainless steel, cross rolled 90% at 200 °C (390 °F). Highly irregular cell structure and numerous microtwins and stacking faults. Thin-foil TEM specimen prepared parallel to the rolling plane. 30,000×. Source: Ref 1

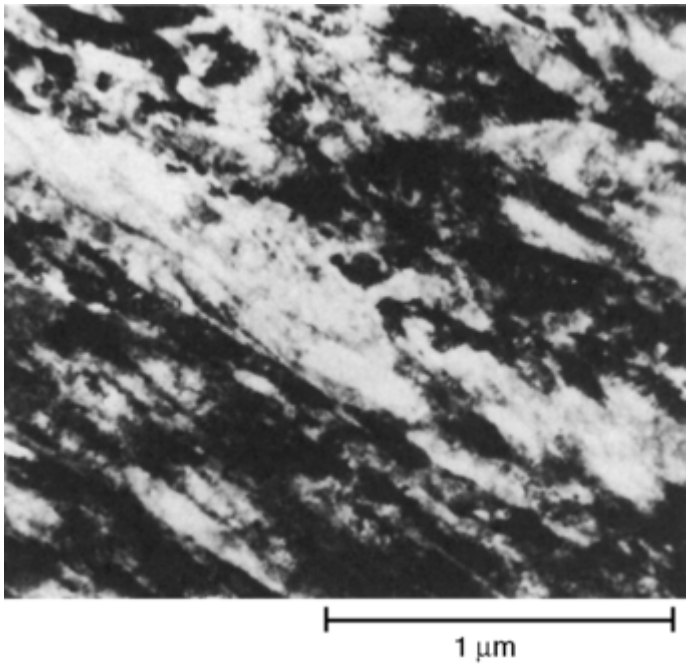

Fig. 4 Same as Fig. 3. Deformation cells (resembling ribbons) of very small thicknesses lying parallel to the rolling plane of the sheet. Thin-foil TEM specimen prepared parallel to the longitudinal cross section. 30,000×. Source: Ref 1

The heavily cold-worked (90%) strip examined parallel to the rolling direction and shown in Fig. 3 has such a high dislocation density that it is not possible to resolve the microstructure. Figure 4 is a TEM specimen prepared parallel to the cross section of the strip, and a better-defined cell structure with thin ribbons can be seen. Optical micrographs of severely cold-worked materials do not provide much useful information. With increasing deformation, a strong preferred orientation or crystallographic texture is developed in the specimen, even when the grains in the initial microstructure are randomly oriented.

Reference cited in this section

1. R.S. Cline and H. Hu, “Abstract Bulletin,” TMS-AIME Fall Meeting, 1970, p 54

Revised by W.L. Mankins, Recovery, Recrystallization, and Grain-Growth Structures, *Metallography and Microstructures,* Vol 9, *ASM Handbook,* ASM International, 2004, p. 207–214

Recovery, Recrystallization, and Grain-Growth Structures

Revised by William L. Mankins, Metallurgical Services Incorporated

---

Recovery

The earliest change in structure and properties that occurs on annealing a cold-worked metal is considered the beginning of recovery. As recovery proceeds, a sequence of structural changes emerge:

1. The annealing out of point defects and their clusters
2. The annihilation and rearrangement of dislocations into lower-energy configurations
3. Polygonization (subgrain formation and subgrain growth, with dislocations “knitting” or interlocking into subboundaries, as shown in Fig. 5)

4. The formation of recrystallization nuclei energetically capable of further growth

These structural changes do not involve high-angle boundary migration. Therefore, during this stage of annealing, the texture of the deformed metal essentially does not change.



Fig. 5 Dislocations, which have "knitted" themselves into small-angle subboundaries, in a specimen of unalloyed nickel that was cold rolled to a reduction of 8% and then annealed for 2 h at 600 °C (1110 °F). Thin-foil TEM specimen. 10,000×

Changes in Properties. During the early stages of recovery, in which the annealing out of point defects and the annihilation and rearrangement of dislocations have occurred only to a limited extent, the change in microstructure may not be apparent in conventional optical or transmission electron micrographs. However, some physical or mechanical properties of the metal, such as electrical resistivity, x-ray line broadening, or strain-hardening parameters, may show the changes due to recovery with high sensitivities. Figure 6 and 7 show the changes in resistivity and residual strain hardening, respectively, during isothermal recovery annealing. These figures indicate that isothermal recovery of the various properties share the following features:

- There is no incubation period.
- The rate of change is highest at the beginning, decreasing with increasing time.
- At long times, the property approaches the equilibrium value very gradually.

Hardness is less sensitive to early stages of recovery in comparison with other properties, such as electrical resistivity, x-ray line broadening, strain hardening, and density.

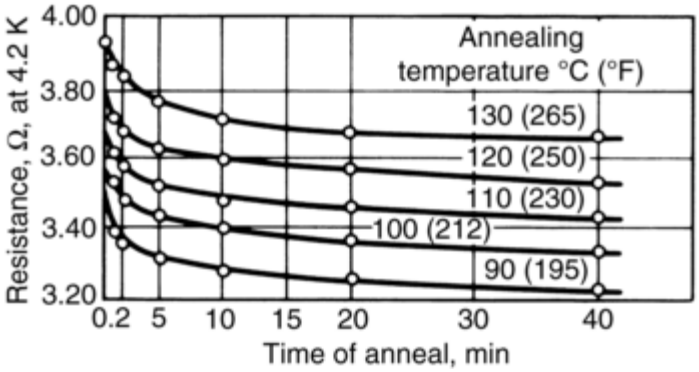

Fig. 6 Change in electrical resistivity during isothermal recovery for copper deformed by torsion at 4.2 K. Source: Ref 2

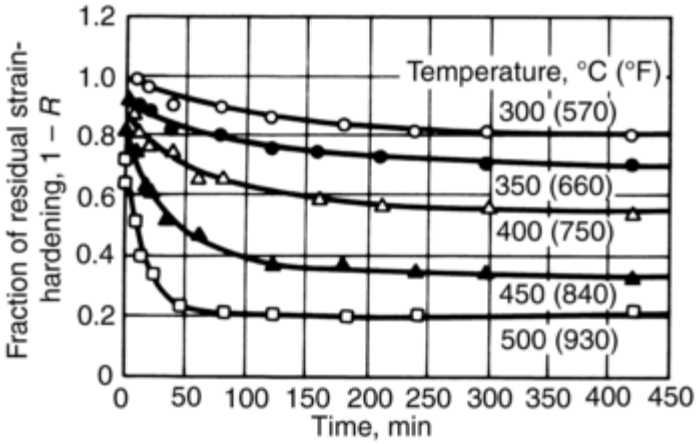

Fig. 7 Change in residual strain hardening during isothermal recovery for zone-melted iron deformed 5% in tension at 0 °C (32 °F). The fraction of residual strain hardening, $1 - R = (\sigma - \sigma_0) \div (\sigma_m - \sigma_0)$, where R is the fraction of recovery, σ_0 the flow stress of the fully annealed material, σ_m the flow stress of the strain-hardened material at a predetermined constant strain, and σ the initial flow stress after a recovery anneal. Source: Ref 3

Changes in microstructure during recovery cannot be seen optically but become readily observable by TEM when the density of dislocations is considerably reduced and the appreciable rearrangement of the remaining dislocations has occurred. Figure 8(a) to (d) show the sequence of dislocation substructure changes for a single crystal of Fe-3Si (wt%) that was cold rolled 80% in the (001)[110] orientation and subsequently annealed at various temperatures. From a structure of random arrays of dislocation tangles (Fig. 8b) to that of well-defined subgrains (Fig. 8c) is a process commonly referred to as polygonization. Further annealing may gradually increase the average size of the subgrains (Fig. 8c, d).

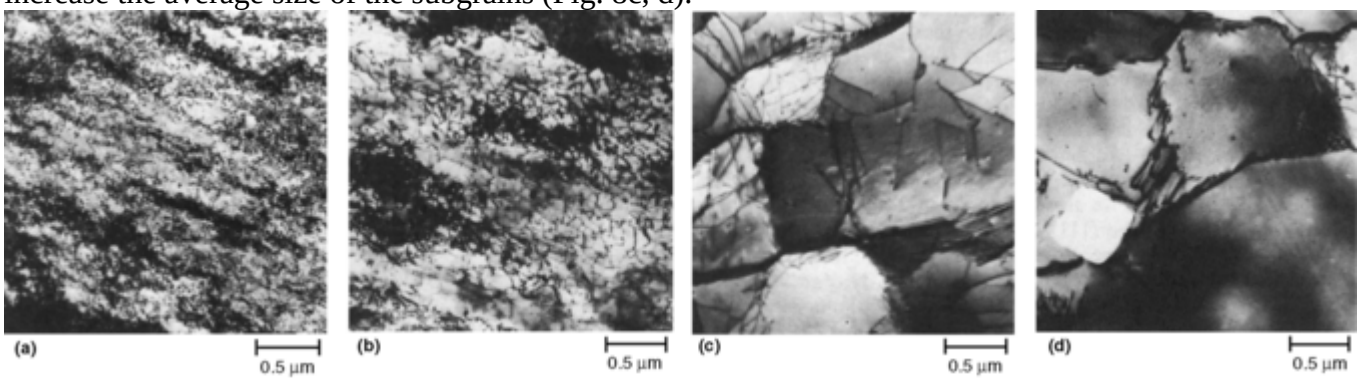

Fig. 8 Effect of annealing time and temperature on the microstructure of an Fe-3Si single crystal, cold rolled 80% in the (001)[110] orientation. (a) High density of dislocations and no well-defined cell structure is revealed in the as-rolled condition. (b) Annealed at 400 °C (750 °F) for 1280 min. Reduced

dislocation density and random arrays of dislocations are evident. (c) Annealed at 600 °C (1110 °F) for 1280 min. Well-defined subgrains resulting from polygonization are shown. (d) Annealed at 800 °C (1470 °F) for 5 min. Increased average diameter of the subgrains is due to subgrain growth. All thin-foil TEM specimens prepared parallel to the rolling plane. All at 17,200×

Prolonged heating of the samples of Fig. 8(a) through (c) at the temperatures shown would not alter the microstructures, but it can be seen in Fig. 8(d) that an increase in temperature enhances the subgrain growth in only 5 min. Typically, at lower temperatures, an extended time is required to produce the same microstructural changes resulting from a short time exposure at a higher temperature. Higher temperatures cause deformed metals to approach their undeformed state; the fully annealed state cannot be reached by recovery temperatures, even after long time exposures.

When the microstructure of a heavily rolled crystal is revealed using thin-foil specimens parallel to the cross sections of the strip, the thin, ribbonlike deformation cells are readily observed. Figure 9(a) shows the dislocation substructure of an as-deformed iron crystal cold rolled in the (111)[$\bar{1}$10] orientation to 70% reduction (also see Fig. 4 for a much finer microstructure in a heavily rolled polycrystalline stainless steel). During recovery, the thickness of the ribbonlike subgrains increases, as shown in Fig. 9(b). Subgrain growth at these early stages cannot be clearly observed when thin-foil specimens parallel to the rolling plane are used for TEM examination. As mentioned earlier, this is because a clearly defined subgrain structure can be observed in a thin-foil specimen parallel to the rolling plane only when the thickness of the subgrains exceeds that of the foil.

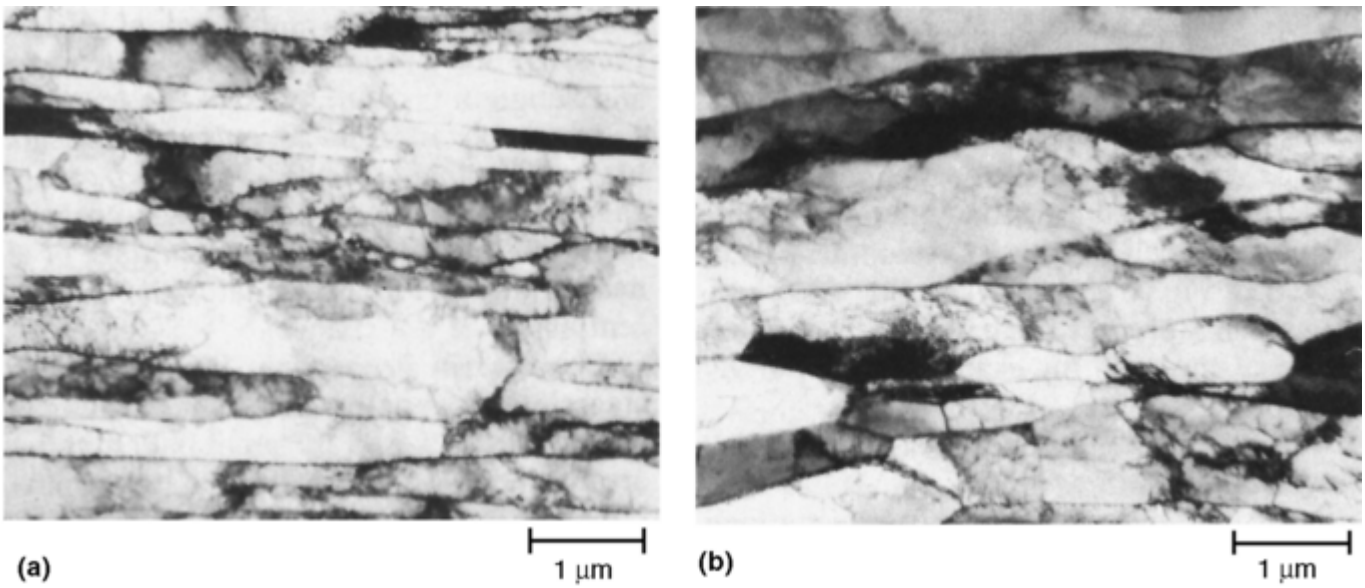

Fig. 9 Electrolytic iron single crystal, cold rolled 70% in the (111) [$\bar{1}$10] orientation. (a) Thin, ribbonlike cells stacked up in the thickness dimension of the as-rolled crystal. (b) Annealed at 550 °C (1020 °F) for 20 min. Increased cell thickness resulting from subgrain growth. Thin-foil TEM specimens prepared parallel to the transverse cross section. Both at 11,000×. Source: Ref 4

References cited in this section

2. R.R. Eggleston, *J. Appl. Phys.,* Vol 23, 1952, p 1400

3. J.T. Michalak and H.W. Paxton, *Trans. AIME,* Vol 221, 1961, p 850

4. B.B. Rath and H. Hu, *Proceedings of the 31st Annual Meeting of the Electron Microscopy Society of America,* San Francisco Press, 1973, p 160

Revised by W.L. Mankins, Recovery, Recrystallization, and Grain-Growth Structures, *Metallography and Microstructures,* Vol 9, *ASM Handbook*, ASM International, 2004, p. 207–214

Recovery, Recrystallization, and Grain-Growth Structures

Revised by William L. Mankins, Metallurgical Services Incorporated

Recrystallization

Extensive experimental primary recrystallization studies have been conducted for nearly one hundred years. Studies by Burke and Turnbull (Ref 5) are summarized with six laws of recrystallization:

- A certain minimum amount of cold work or deformation and a certain minimum temperature are necessary to initiate recrystallization.
- The smaller the amount of deformation, the higher the temperature required to initiate recrystallization.
- Recrystallization is time-temperature dependent, and increased time decreases the temperature required for recrystallization.
- Final grain size is more dependent on the amount of deformation or cold work than either the temperature or the time of anneal.
- The larger the original grain size of the material, the greater the amount of cold work required to achieve an equivalent recrystallization for a given temperature and time.
- For a given amount of work hardening, a higher working temperature is accompanied by a coarser grain size and requires a higher temperature to cause recrystallization.

Two additional laws (Ref 6) can be added:

- New grains first originate at grain-boundary triple points and do not grow into deformed grains having identical or slightly deviated crystallographic orientations.
- (Aside from primary recrystallization) heating after the recrystallization process is complete causes grain growth to occur.

Applications of the laws of recrystallization are provided in subsequent examples.

Following recovery, recrystallization (or primary recrystallization) occurs by the nucleation and growth of new grains, which are essentially strain-free, at the expense of the polygonized matrix. During incubation, stable nuclei are formed by the coalescence of subgrains, leading to the formation of high-angle boundaries. From that time on, subsequent growth of new grains can proceed rapidly because of the high mobility of the high-angle boundaries. The rate of recrystallization later decreases toward completion as concurrent recovery of the matrix occurs and more of the new grains impinge on each other. Accordingly, isothermal recrystallization curves are typically sigmoidal. Because recrystallization is accomplished by high-angle boundary migration, a large change in the texture occurs.

With a low degree of deformation and a low annealing temperature, the specimen may recover only without the occurrence of recrystallization. In situ recrystallization, or complete softening without the nucleation and growth of new grains at the expense of the polygonized matrix, is a process of recovery, not recrystallization, because it does not involve high-angle boundary migration. Consequently, there is no essential change in texture following in situ recrystallization.

Nucleation Sites. Because of the highly nonhomogeneous microstructure of a plastically cold-worked metal, recrystallization nuclei are formed at preferred sites. Examples of preferred nucleation sites include the grain-boundary triple points; the original grain boundaries (Fig. 10); the boundaries between deformation bands within a crystal or grain; the intersections of mechanical twins, such as Neumann bands in body-centered cubic crystals; the distorted twin-band boundaries; and the regions of shear bands. Limited recrystallization may also occur by the growth of grains nucleated at large and hard inclusion particles (Fig. 11).

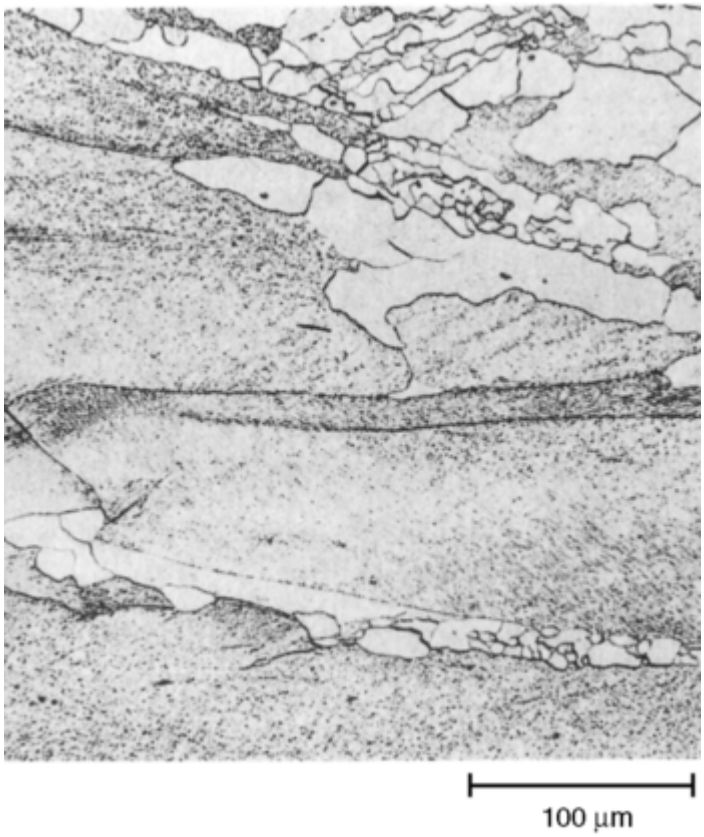

Fig. 10 Iron that was rolled and partially recrystallized, showing new grains (light) that were nucleated at the grain boundaries of the as-rolled grains. 2% nital etch. 200×

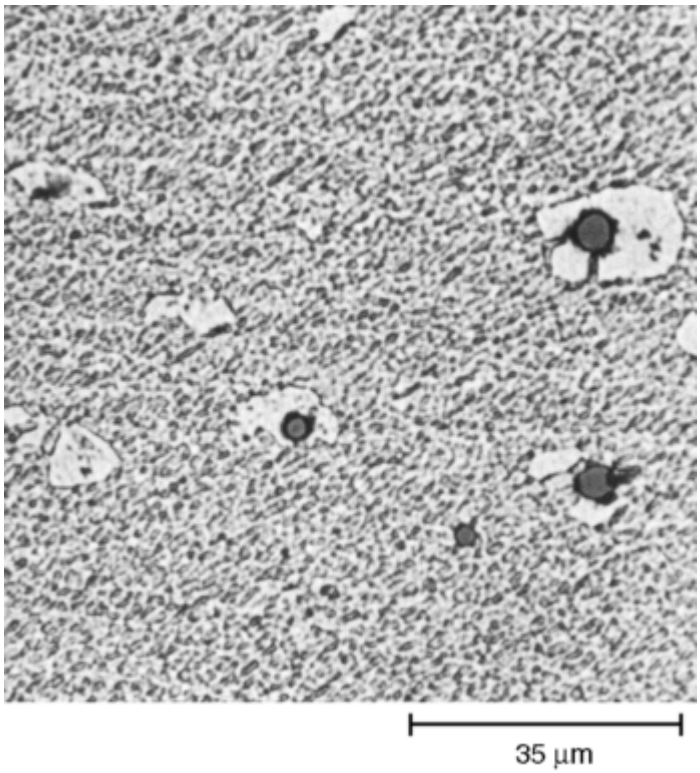

Fig. 11 Fe-0.07% oxygen alloy that was deformed and partially recrystallized, showing new grains (light) that were nucleated at iron oxide particles (dark). 2% nital etch. 750×

In general, preferred nucleation sites are regions of relatively small volume where the lattice is highly distorted (having high lattice curvature). In such regions, the dimension of the substructure is fine, and the orientation gradient is high. Therefore, the critical size for a stable nucleus to form in these regions is relatively small and

thus can be attained more readily. Furthermore, the nucleus needs only to grow through a relatively short distance to form a high-angle boundary with the matrix.

Figure 12, 13, and 14 show a low-carbon steel sheet that had been severely cold worked (90%). It was subsequently annealed at 550 °C (1025 °F) for increasing times. Very fine grain can be seen forming between the highly elongated grains in Fig. 12. The percent recrystallization is approximately 10%, and the hardness is 79 Rockwell on the 30-T scale. The effects of longer time at temperature are shown in Fig. 13 and 14, where the percent recrystallization becomes larger, accompanied by a decrease in hardness. The first recrystallized grains grow as a function of time at temperature, and later recrystallized grain are very fine in size and also grow after an incubation period.

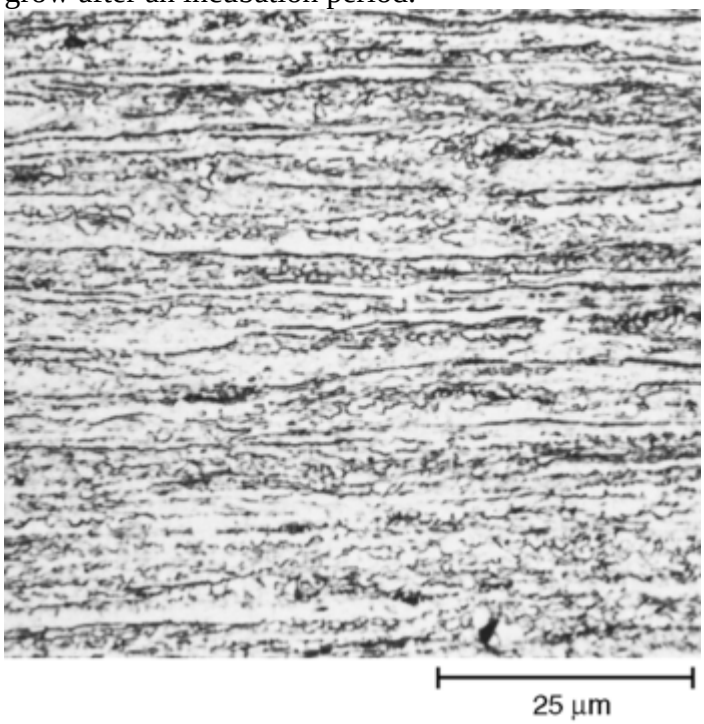

Fig. 12 0.10% carbon steel cold rolled 90% to a thickness of 0.25 mm (0.010 in.) with a Rockwell hardness of 81 (on 30-T scale), then annealed at 550 °C (1025 °F) for 106 s. Recrystallized 10% with Rockwell hardness of 79 (on 30-T scale). Nital etch. 1000×

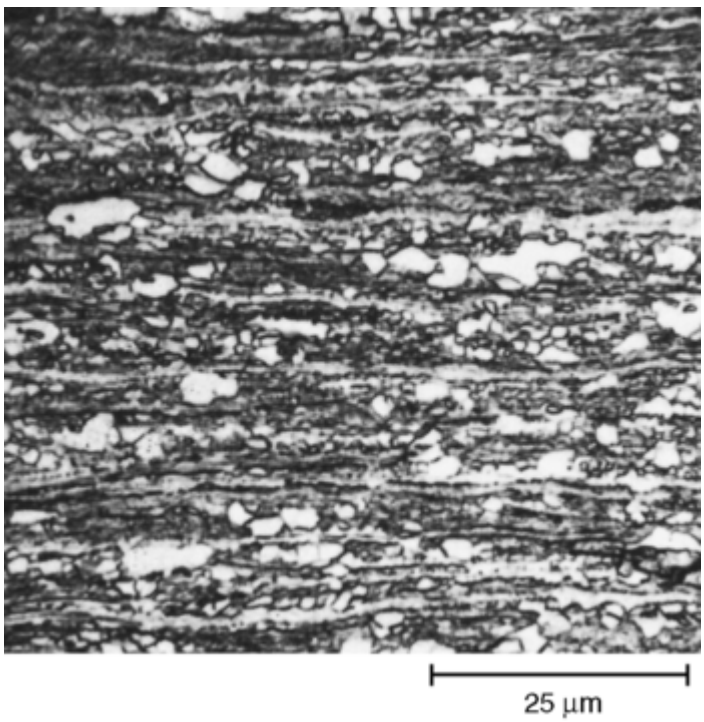

Fig. 13 0.10% carbon steel cold rolled the same as in Figure 12 but annealed at 550 °C (1025 °F) for 430 s. Recrystallization increased to 40%, with a reduction in hardness to 76 on Rockwell 30-T scale. Nital etch. 1000×

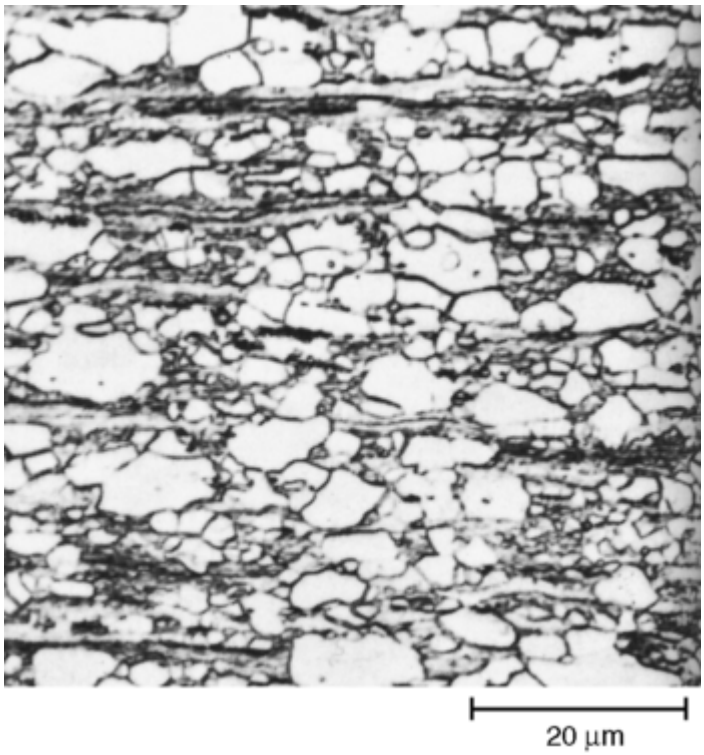

Fig. 14 0.10% carbon steel cold rolled the same as in Figure 12 but annealed at 550 °C (1025 °F) for 865 s. Recrystallization increased to 80%, with a reduction in hardness to 70 on Rockwell 30-T scale. Nital etch. 1000×

In moderately deformed samples with relatively coarse initial grains, the microstructure near the grain boundaries and the evolution of the microstructure during nucleation can be studied in considerable detail, even when thin-foil specimens parallel to the rolling plane are used for TEM examinations. Figure 15 shows the grain-boundary bands observed adjacent to an initial grain boundary in commercial-purity aluminum that was cold rolled 50%. The cumulative misorientations across the bands (16.5°), as shown in the inset, indicate similarity in feature between these grain-boundary bands and the transition bands. These grain-boundary bands obviously would not form at every grain boundary but would depend on the relative orientations of the two adjacent grains.

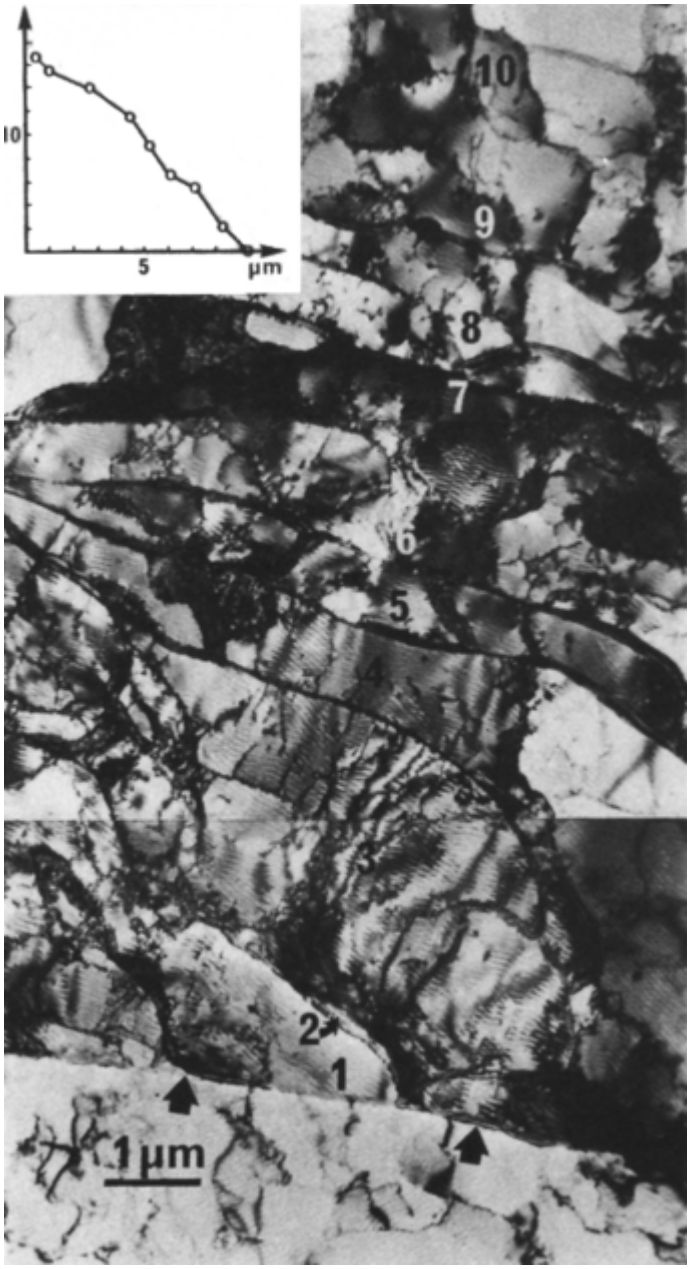

Fig. 15 Fine-grained commercial-purity aluminum, cold rolled 50%. A 9 μm wide grain-boundary band consisting of elongated subgrains that was developed along an initial grain boundary marked by arrows. The inset shows the misorientations regarding the grain interior as a function of the distance from the grain boundary. Thin-foil TEM specimen prepared parallel to the rolling plane. 7300×. Source: Ref 7

Grain-boundary nucleation by the bulging out of a section of an initial boundary from the region of a low dislocation content into a region of high dislocation content is frequently observed in large-grained materials deformed at low and medium strains. This bulging mechanism of nucleation for recrystallization is a consequence of the strain-induced boundary migration. Figure 16 shows a recrystallization nucleus that has formed by straddling a grain boundary in a coarse-grained aluminum that was cold rolled 30% and annealed at 320 °C (610 °F) for 30 min. Such grain-boundary nucleation was observed to have three types of structural detail. As shown in Fig. 17, the nucleus may be formed by subgrain growth to the right of the original grain boundary (Fig. 17a); by grain-boundary migration to the right and subgrain growth to the left, forming a new high-angle boundary (Fig. 17b); and by grain-boundary migration to the right and subgrain growth to the left but without forming a new high-angle boundary (Fig. 17c).

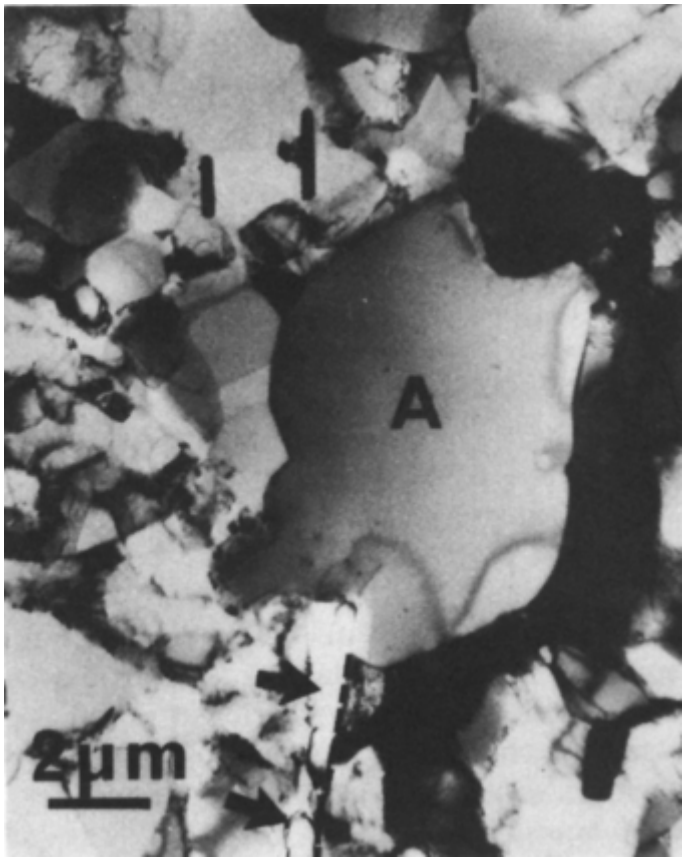

Fig. 16 Coarse-grained commercial-purity aluminum, cold rolled 30% and annealed at 320 °C (610 °F) for 30 min. A recrystallization nucleus (denoted A) developed near arrow-marked $FeAl_3$ particles and is shown straddling an initial grain boundary (marked by dotted line). Thin-foil TEM specimen prepared parallel to the rolling plane. 3650×. Source: Ref 7

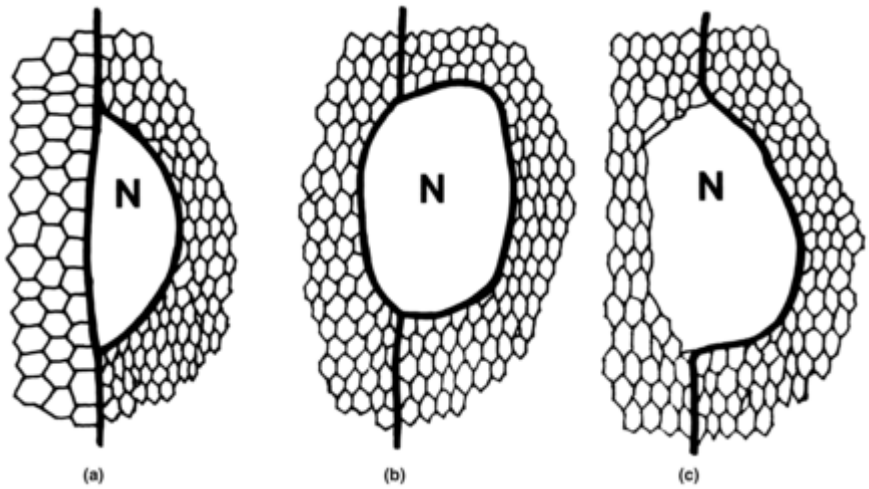

Fig. 17 Schematic showing three types of grain-boundary nucleation and the growth of the nucleus (N) at the expense of the polygonized subgrains. See text for detailed explanation. Source: Ref 7

When a polycrystalline specimen is deformed with a very small strain—less than 2 or 3%, for example—then annealed at a sufficiently high temperature, recrystallization occurs by strain-induced boundary migration of only a few grains. These few grains grow very large at the expense of the small matrix grains. The maximum level of strain below which such coarsening occurs is commonly termed critical strain. This behavior has been used to grow single crystals in the solid state by the so-called strain-anneal technique.

Figure 18 shows recrystallized grains nucleated and grown at a large and hard $FeAl_3$ inclusion particle in 90% cold-rolled aluminum after annealing in a high-voltage electron microscope at 264 °C (507 °F) for 6 min. Compare with Fig. 11. Unless the volume fraction of the inclusion particles is substantially large, the

contribution of particle-nucleated grains constitutes only a small fraction of the total recrystallization volume. From the previous discussions on nucleation sites, it is easy to understand that the size of the recrystallized grains, as recrystallization is complete, decreases with increasing deformation, because the number of nuclei increases with increasing deformation.

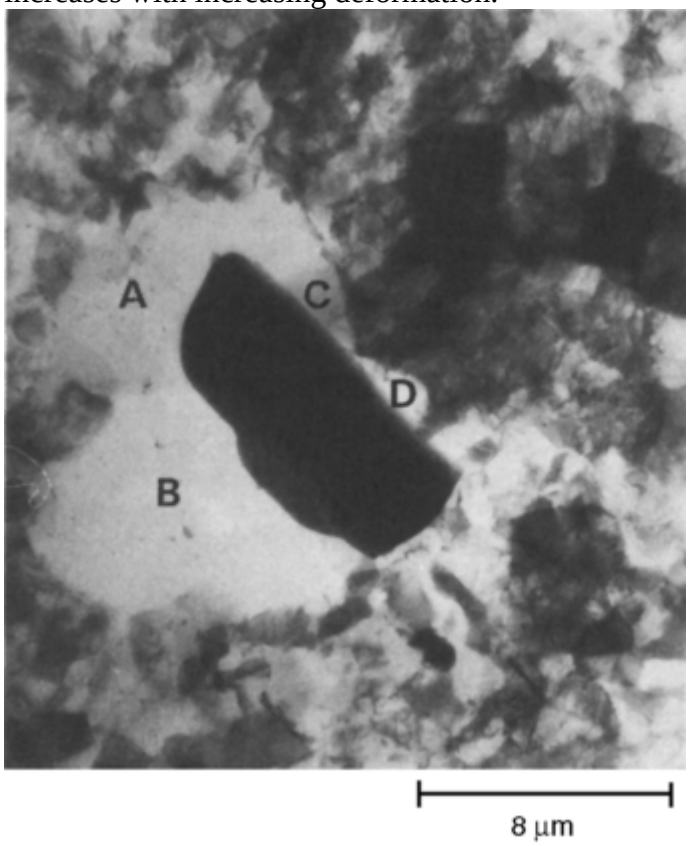

Fig. 18 Fine-grained commercial-purity aluminum, cold rolled 90% and heated in a high-voltage electron microscope at 264 °C (507 °F) for 480 s. Recrystallized grains (denoted by letters) nucleated at a large $FeAl_3$ particle and grew into the polygonized matrix. Thin-foil TEM specimen prepared parallel to the rolling plane. 2810×. Source: Ref 7

Growth of Nucleated Grains. The growth of the newly formed strain-free grains at the expense of the polygonized matrix is accomplished by the migration of high-angle boundaries. Migration proceeds away from the center of boundary curvature. The driving force for recrystallization is the remaining strain energy in the matrix following recovery. This strain energy exists as dislocations mainly in the subgrain boundaries. Therefore, the various factors that influence the mobility of the high-angle boundary or the driving force for its migration will influence the kinetics of recrystallization. For example, impurities, solutes, or fine second-phase particles will inhibit boundary migration; therefore, their presence will retard recrystallization. Figure 19 shows the pinning of a mobile low-angle boundary by a fine alumina (Al_2O_3) particle in an aluminum-alumina specimen during recovery. In connection with the driving force for recrystallization, a fine-subgrained matrix has a higher strain-energy content than does a coarse-subgrained matrix. Accordingly, recrystallization occurs faster in a fine-subgrained matrix than in a coarse-subgrained matrix. During recrystallization, continuous recovery may occur in the matrix by subgrain growth, resulting in a reduction of the driving energy for recrystallization and therefore a decrease in the recrystallization rate. From driving-energy considerations, it is understandable that the tendency for recrystallization is stronger in heavily deformed than in moderately or lightly deformed specimens. For a given deformation, the finer the original grain size, the stronger the tendency for recrystallization. Figure 20 shows such effects in low-carbon steel.

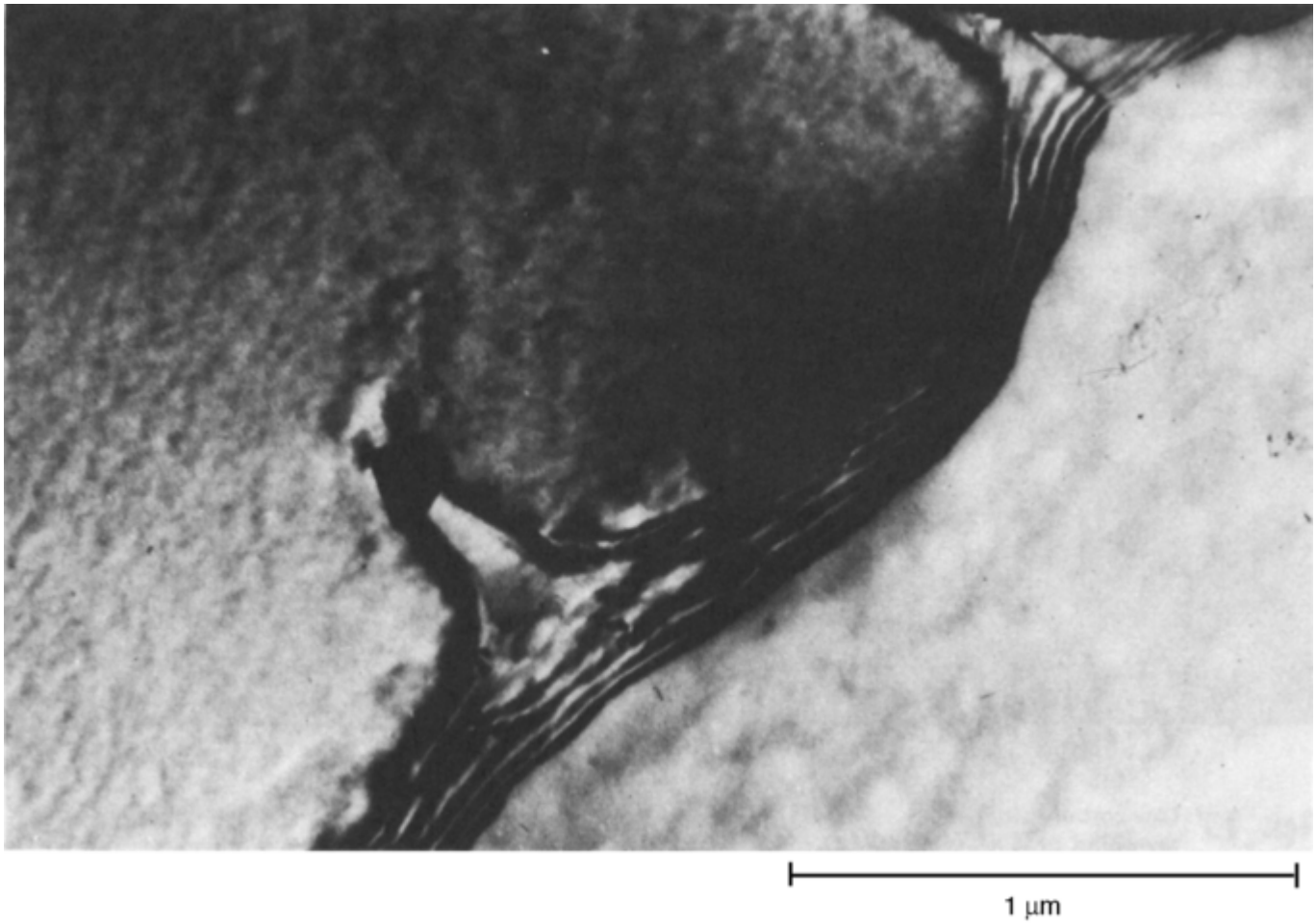

Fig. 19 Aluminum-aluminum oxide specimen, cold rolled and annealed. Shown is the pinning of a mobile low-angle boundary by a small Al_2O_3 particle during a recovery anneal. Thin-foil TEM specimen. 47,000×. Source: Ref 8

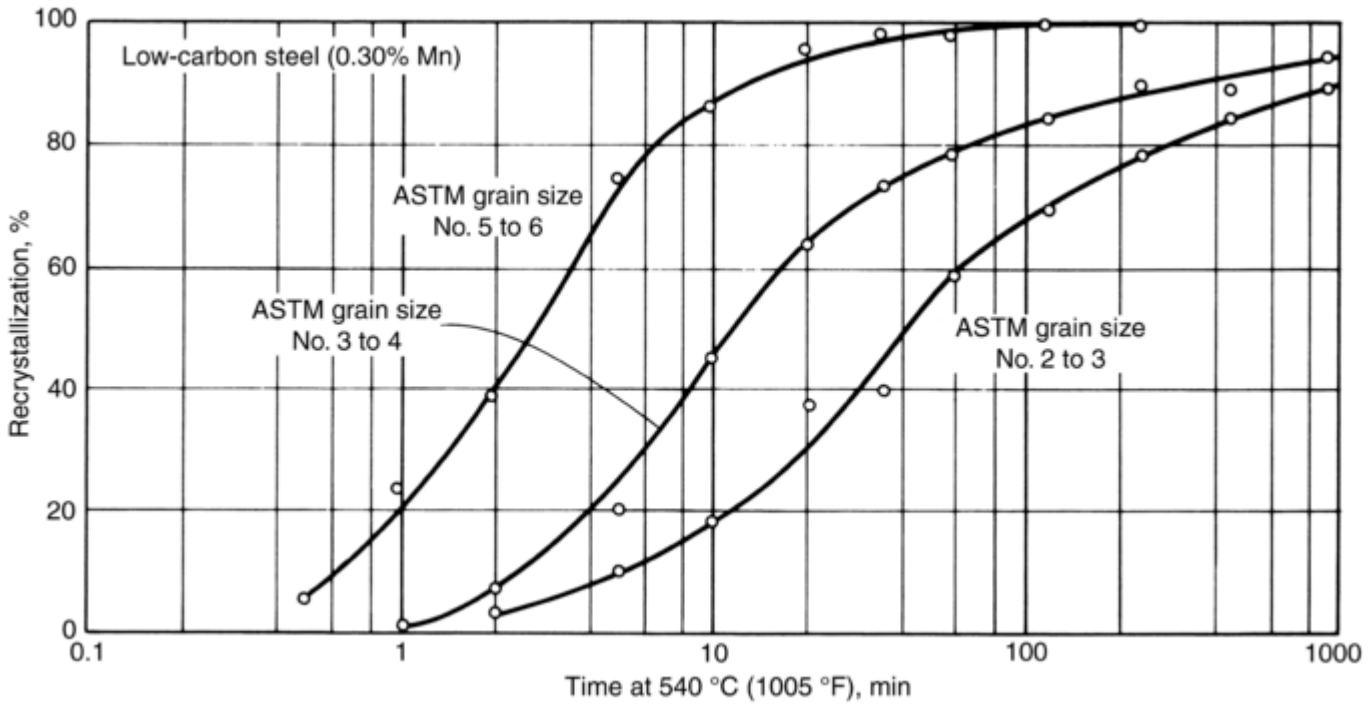

Fig. 20 Effect of penultimate grain size on the recrystallization kinetics of a low-carbon steel, cold rolled 60% and annealed at 540 °C (1005 °F). Note the incubation time is shortened as the penultimate grain size before cold rolling is decreased. Source: Ref 9

References cited in this section

5. J.E. Burke and D. Turnbull, *Prog. Met. Phys.*, Vol 3, 1952, p 220

6. R.W. Cahn, *Physical Metallurgy*, 2nd rev. ed., American Elsevier Publishing Company, 1970, p 1149, 1181, 1186–1187

7. B. Bay and N. Hansen, *Metall. Trans. A*, Vol 10, 1979, p 279; Vol 15, 1984, p 287

8. A.R. Jones and N. Hansen, *Recrystallization and Grain Growth of Multiphase and Particle Containing Materials*, N. Hansen, A.R. Jones, and T. Leffers, Ed., Riso National Laboratory, Denmark, 1980, p 19

9. D.A. Witmer and G. Krauss, *Trans. ASM*, Vol 62, 1969, p 447

Revised by W.L. Mankins, Recovery, Recrystallization, and Grain-Growth Structures, *Metallography and Microstructures*, Vol 9, *ASM Handbook*, ASM International, 2004, p. 207–214

Recovery, Recrystallization, and Grain-Growth Structures

Revised by William L. Mankins, Metallurgical Services Incorporated

---

Grain Growth

After recrystallization is complete, that is, when the polygonized matrix is replaced by the new strain-free grain (although the grain structure is not stable), further annealing increases the average size of the grains. The process, known as grain growth, is accomplished by the migration of grain boundaries. Recrystallization consumes the retained energy of deformation, but the grain boundaries still have a finite interfacial energy. The material is metastable, with thermodynamic stability only being achieved if the structure becomes a single grain or crystal (Ref 6). In contrast to recrystallization, the boundary moves toward its center of curvature. Some of the grains grow, but others become smaller and vanish. Typically, the smaller the number of sides on the recrystallized grain, the sharper the curvature of the sides and the quicker the grain becomes absorbed by adjacent grains. Because the volume of the specimen is a constant, the number of the grains decreases as a consequence of grain growth. The driving force for grain growth is the grain-boundary free energy, which is substantially smaller in magnitude than the driving energy for recrystallization.

According to the growth behavior of the grains, grain growth can be further classified into two types: normal or continuous grain growth and abnormal or discontinuous grain growth. The latter has also been termed exaggerated grain growth, coarsening, or secondary recrystallization.

Normal or continuous grain growth occurs in pure metals and single-phase alloys. During isothermal growth, the increase in the average grain diameter obeys the empirical growth law, which can be expressed as $D_{ave} = Kt^n$, where D_{ave} is the average grain diameter, t is the annealing time, and K and n are constants depending on the material and temperature. When D_{ave} and t are plotted on a logarithmic scale, a straight line is drawn, with K as the intercept and n as the slope of the curve. The value of n, the time exponent in isothermal grain growth, is usually 0.5 or less. A typical example for isothermal grain growth in zone-refined iron is shown in Fig. 21. The deviations from a straight-line relationship for very short annealing times at low temperatures are due to recrystallization, and long annealing times at high temperatures show the limiting effect of the thickness of the sheet specimen.

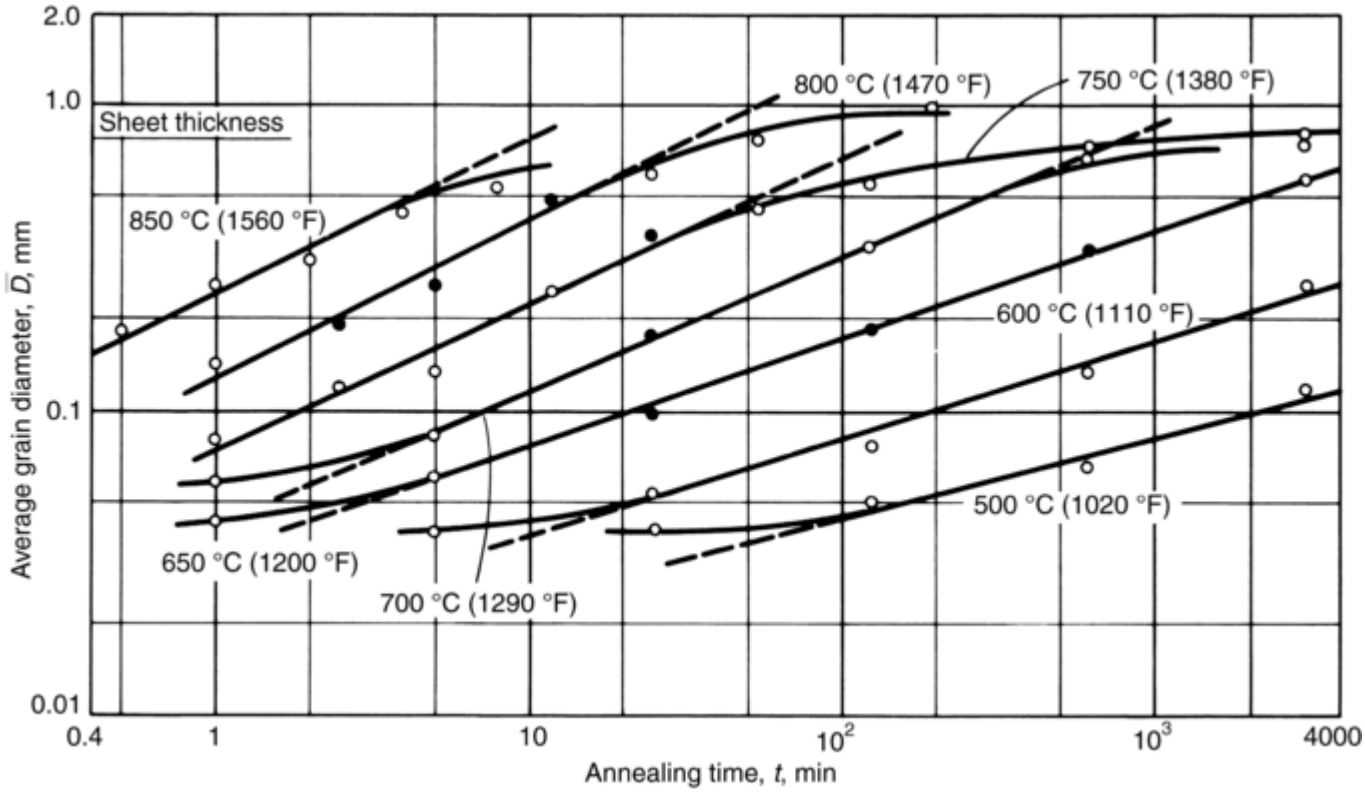

Fig. 21 Normal grain growth in zone-refined iron during isothermal anneals. Closed circles represent specimens for which statistical analysis of grain-size and grain-shape distributions was conducted.

One of the structural characteristics during normal grain growth is that the grain-size and grain-shape distributions are essentially invariant; that is, during normal grain growth, the average grain size increases, but the size and shape distributions of the grains remain essentially the same before and after the growth, differing only by a scale factor. Figure 22 and Figure 23 show, respectively, the size and shape distributions of the grains in zone-refined iron after normal grain growth at 650 °C (923 K) for various lengths of time. The data points fit the same distribution curves. Therefore, to a first approximation, normal grain growth is equivalent to photographic enlargement.

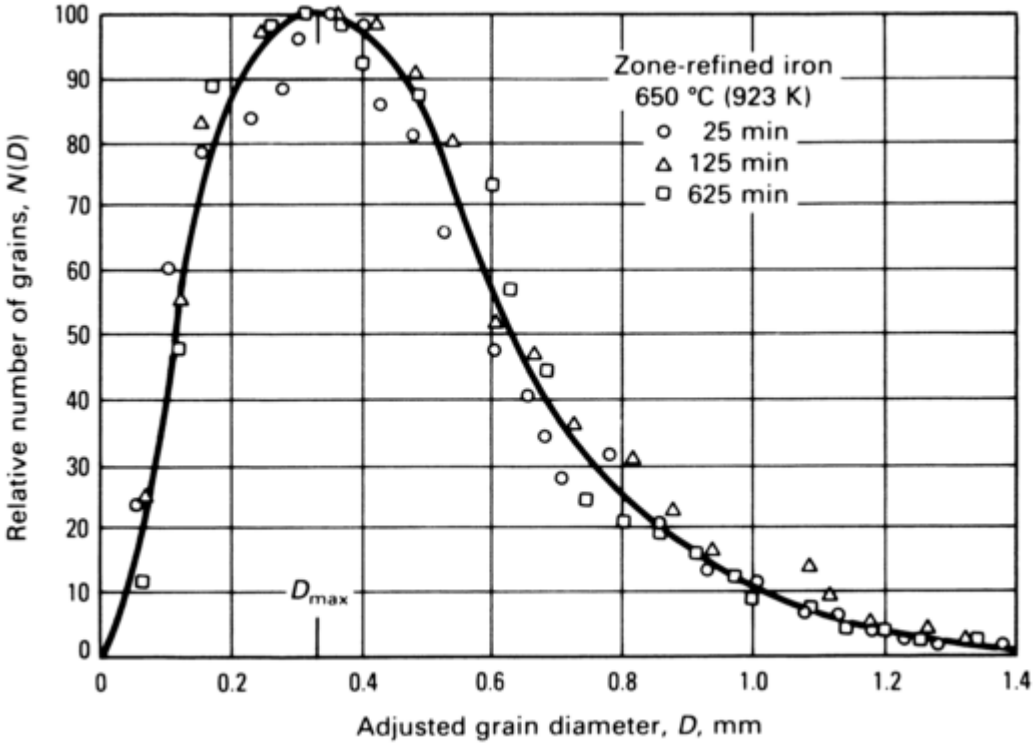

Fig. 22 Grain-size distribution in zone-refined iron during isothermal grain growth at 650 °C (923 K), using a scalar-adjusted grain diameter for each specimen. The plot indicates that the grain-size distribution remains essentially unchanged during normal grain growth.

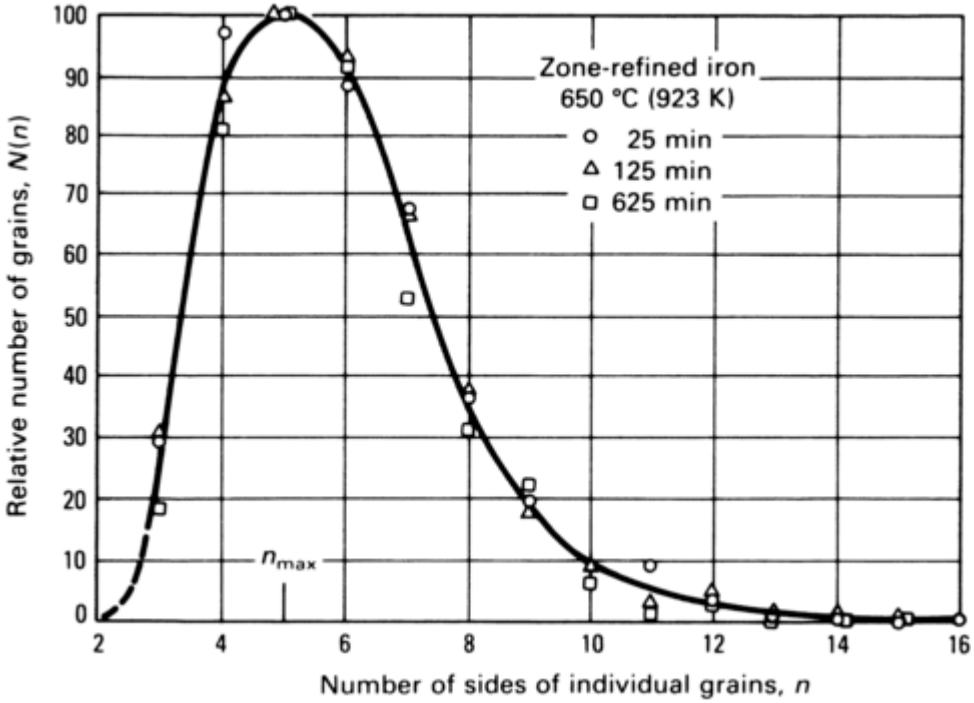

Fig. 23 Grain-shape distribution in zone-refined iron during isothermal grain growth at 650 °C (923 K), using the number of sides of individual grains. The plot indicates that the grain-shape distribution remains essentially unchanged during normal grain growth.

During the normal grain growth, the change in texture is small and gradual. Assuming the initial grains are nearly randomly oriented, after extensive normal grain growth, some weak preferred orientations may be developed among the final grains, depending on such a factor as the energies of the free surfaces of the grains. If the initial grains are strongly textured, normal grain growth may be inhibited as a consequence of low mobility of the matrix-grain boundaries (see the following section on secondary recrystallization). Figure 24 shows the grain aggregate of a zone-refined iron specimen after normal grain growth at 800 °C (1470 °F) for 12 min. The size and shape distributions of these grains are essentially the same as those of the much finer grains before growth.

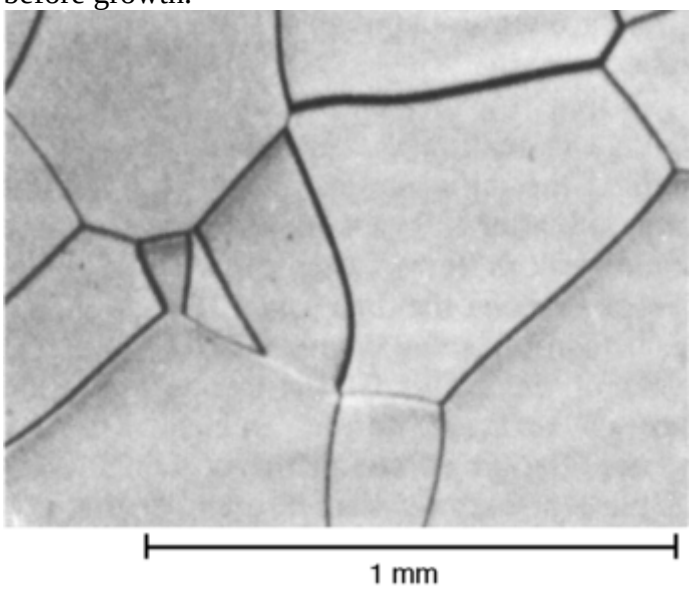

Fig. 24 Zone-refined iron, cold rolled to a moderate reduction and annealed for recrystallization for several cycles to refine the penultimate grain size without introducing preferred orientation. Micrograph shows grain structure after normal grain growth at 800 °C (1470 °F) for 12 min. 2% nital. 45×

Abnormal grain growth, also known as secondary recrystallization or coarsening, occurs when normal growth of the matrix grains is inhibited and when the temperature is high enough to allow a few special grains to overcome the inhibiting force and to grow disproportionately. The start of secondary recrystallization has some common characteristics (Ref 6):

- The grains that grow large are not newly nucleated but of the primary structure.
- The very large grains initially grow slowly, followed by rapid growth to sizes of the order of centimeters in some cases.
- The grains that coarsen possess many sides.
- The explanation for the growth of the favored grains is the least understood part of the process, but it has been observed that these grains have orientations different from the primary texture of the material.
- Normal grain growth must be impeded. The commonly known conditions for inhibiting grain growth are a fine dispersion of second-phase particles, a discrete grain-boundary precipitate, a strong single-orientation texture, and a stabilized two-dimensional grain structure imposed by sheet thickness. These conditions for inhibiting grain growth are readily understandable, because the fine particles exert a pinning force on the boundary motion, the matrix grain boundaries are predominantly low-angle boundaries, and therefore, both low mobilities and the boundary grooving at the sheet surfaces retard boundary motion.
- The large grains of the secondary structure frequently exhibit a unique texture always different from the texture of the former primary structure.
- Localized or shallow working of the material creates a critical amount of strain required for secondary recrystallization.
- After working the material, a well-defined minimum temperature must be exceeded for secondary recrystallization to take place. It has been observed that the largest grains are formed at temperatures just above the minimum, and increases in temperature produce smaller secondary grains.
- Critical strain producing grain-boundary energy provides the driving force for secondary recrystallization.

Figure 25 shows abnormal grain growth or secondary recrystallization in the cube-textured matrix of a type 304 stainless steel. The cube-textured matrix is characterized by the small grains; the twin traces within the cube grains are oriented at 45° to the rolling direction. This particular example of abnormal grain growth or secondary recrystallization in cube-textured type 304 stainless steel probably represents the combined effect of particle inhibition and texture inhibition on secondary recrystallization.

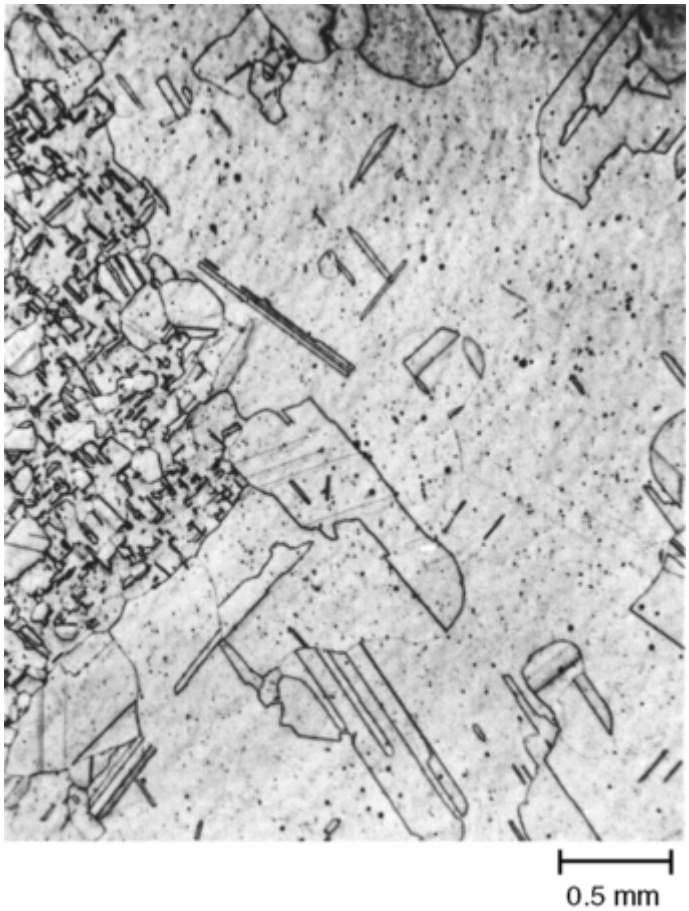

Fig. 25 Type 304 stainless steel, rolled 90% at 800 °C (1470 °F) to produce a copper-type rolling texture, recrystallized to cube texture by annealing at 1000 °C (1830 °F) for 30 min, then annealed at 1000 °C (1830 °F) for 96 h to cause secondary recrystallization. Large secondary grains are shown in a cube-textured primary matrix. Rolling direction: left to right. Electrolytic etch. 20×. Source: Ref 10

References cited in this section

6. R.W. Cahn, *Physical Metallurgy,* 2nd rev. ed., American Elsevier Publishing Company, 1970, p 1149, 1181, 1186–1187

10. S.R. Goodman and H. Hu, *Trans. Met. Soc. AIME,* Vol 233, 1965, p 103; Vol 236, 1966, p 710

Revised by W.L. Mankins, Recovery, Recrystallization, and Grain-Growth Structures, *Metallography and Microstructures,* Vol 9, *ASM Handbook,* ASM International, 2004, p. 207–214

Recovery, Recrystallization, and Grain-Growth Structures

Revised by William L. Mankins, Metallurgical Services Incorporated

---

Acknowledgment

This article is adapted from H. Hu, Recovery, Recrystallization, and Grain-Growth Structures, *Metallography and Microstructures,* Vol 9, *ASM Handbook,* 1985, p 692–699.

Revised by W.L. Mankins, Recovery, Recrystallization, and Grain-Growth Structures, *Metallography and Microstructures,* Vol 9, *ASM Handbook,* ASM International, 2004, p. 207–214

Recovery, Recrystallization, and Grain-Growth Structures

Revised by William L. Mankins, Metallurgical Services Incorporated

References

1. R.S. Cline and H. Hu, "Abstract Bulletin," TMS-AIME Fall Meeting, 1970, p 54
2. R.R. Eggleston, *J. Appl. Phys.,* Vol 23, 1952, p 1400
3. J.T. Michalak and H.W. Paxton, *Trans. AIME,* Vol 221, 1961, p 850
4. B.B. Rath and H. Hu, *Proceedings of the 31st Annual Meeting of the Electron Microscopy Society of America,* San Francisco Press, 1973, p 160
5. J.E. Burke and D. Turnbull, *Prog. Met. Phys.,* Vol 3, 1952, p 220
6. R.W. Cahn, *Physical Metallurgy,* 2nd rev. ed., American Elsevier Publishing Company, 1970, p 1149, 1181, 1186–1187
7. B. Bay and N. Hansen, *Metall. Trans. A,* Vol 10, 1979, p 279; Vol 15, 1984, p 287
8. A.R. Jones and N. Hansen, *Recrystallization and Grain Growth of Multiphase and Particle Containing Materials,* N. Hansen, A.R. Jones, and T. Leffers, Ed., Riso National Laboratory, Denmark, 1980, p 19
9. D.A. Witmer and G. Krauss, *Trans. ASM,* Vol 62, 1969, p 447
10. S.R. Goodman and H. Hu, *Trans. Met. Soc. AIME,* Vol 233, 1965, p 103; Vol 236, 1966, p 710

D.P. Field, Textured Structures, *Metallography and Microstructures,* Vol 9, *ASM Handbook*, ASM International, 2004, p. 215–226

Textured Structures

David P. Field, Washington State University

Introduction

THE WORD TEXTURE connotes, among other definitions, the arrangement or manner of union of the particles of a body or substance. In describing polycrystalline microstructures, the word texture is used to describe any feature of the microstructure that lends to the anisotropic behavior of the polycrystalline body. Anisotropy refers to the directional dependence of properties. The value of a given property of an anisotropic material will differ for any randomly chosen direction. Anisotropy of strength is well appreciated in wood, for example, where the strength is greater along the grain of the wood than it is in a direction normal to the grain. The properties of a single crystal are often strongly anisotropic. Mechanical, magnetic, and electronic properties can all vary widely as a function of crystallographic direction in a single crystal. In polycrystalline materials, this directionality of properties can be a consequence of crystallite or cell-shape anisotropy, particle morphology, or preferred orientation. In the present discussion, texture refers only to preferred orientation of the crystallite lattice, or crystallographic texture.

Although the properties of single crystals can be strongly anisotropic, if all possible crystallite lattice orientations occur with equal frequency and without spatial correlation, the properties of a polycrystalline material can be quite isotropic, on the average. Figure 1(a) shows a two-dimensional depiction of a polycrystalline material with cubes representing unit cells of the crystallite lattice. In this microstructure, the cells are oriented randomly with equal probability of occurrence for any given orientation. The properties of such a material will be globally isotropic even though local anisotropy prevails on the scale of the crystallite. When there exists a preferred orientation such that a significant fraction of the crystallite lattices are oriented in a similar manner, the polycrystal begins to take on the anisotropic nature of the single crystal. Figure 1(b) depicts such a structure in a manner similar to that of Fig. 1(a). When preferred orientation exists, the structure is said to be textured or that it has a strong texture. When the lattices are randomly oriented, the structure has no texture or is termed randomly textured.

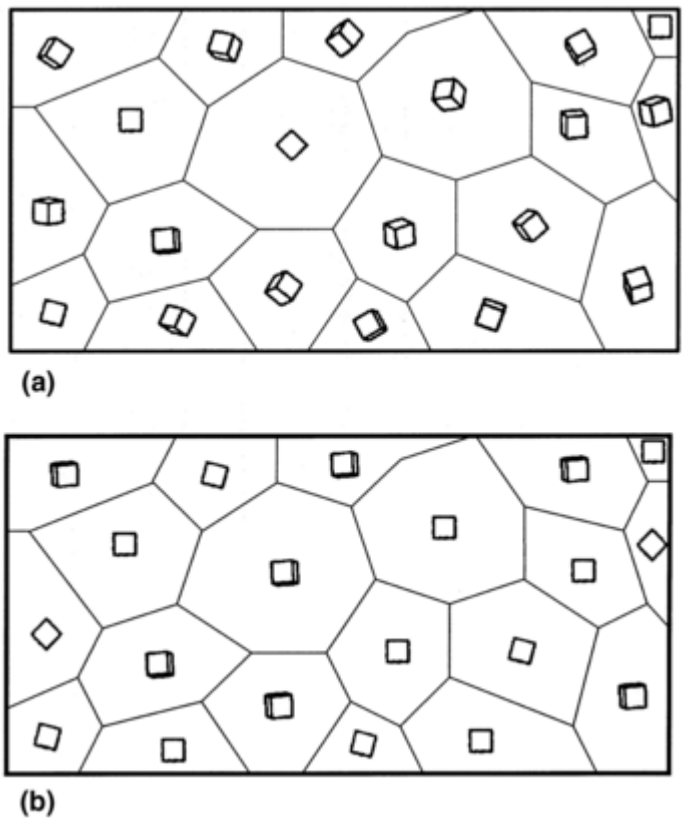

Fig. 1 A two-dimensional depiction of a polycrystalline material with cubes representing unit cells of the crystallite lattice for (a) a randomly textured material and (b) a material with preferred orientation

Anisotropy is undesirable when uniform material properties are desired. One of the most commonly cited examples of this behavior is that of deep-drawing sheet metal. When a metal blank with a nonrandom distribution of crystallite lattice orientations, or a nonrandom texture, is deformed by the deep-drawing process, nonuniform deformation occurs and certain directions in the sheet deform more readily than others. This nonuniform deformation results in undulations along the top of the can where the peaks correspond to easy deformation directions in the sheet and the valleys to directions in the sheet that are more resistant to deformation. This phenomenon is commonly known as earing and is generally undesirable in deep-drawing processes. Figure 2 shows the resulting “ears” formed along the flange of a test specimen during the drawing of a textured aluminum sheet. The rolling direction in the sheet is the horizontal direction in the image, and the major ears are oriented at 45° from the rolling direction. To avoid earing, the material should have a random texture before drawing (or at least random in the sense that uniform in-plane deformation occurs). This is only achieved through strategic processing of the rolled sheet (Ref 1, 2, 3, 4, 5).

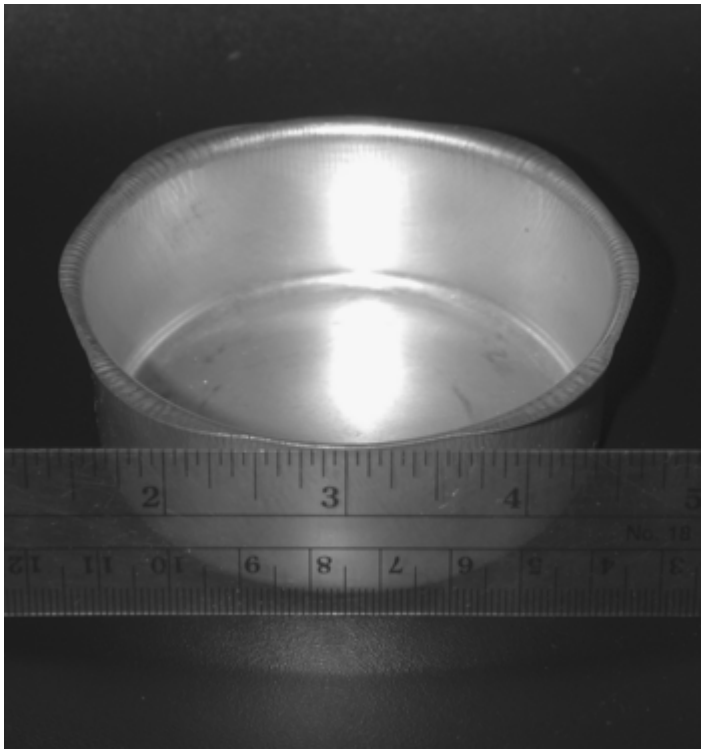

Fig. 2 A cup showing ears formed during the deep-drawing process of aluminum. The rolling direction in the sheet is horizontal in the image.

On the other hand, a very strong texture is useful for optimizing the properties of an engineering component in a given direction. The fact that many structural and electronic properties are anisotropic allows for the design of components with properties significantly better in a direction of interest than those that could be obtained from a randomly textured material. For example, the critical current density, J_c, of most superconducting compounds (such as bismuth-, tellurium-, or YBCO- [that is, $YBa_2Cu_3O_x$]-base materials) is highly anisotropic. Typically, J_c in the direction of the *c*-axis is significantly higher than that in a direction 90° from the *c*-axis at a given temperature. To optimize the superconducting properties of these materials, researchers have developed fabrication procedures that result in strong biaxial textures with grains separated only by low-angle grain boundaries (Ref 6, 7). Grain-oriented silicon steels are another example of where a strong biaxial texture is desirable. In the case of these transformer steel applications, the magnetic properties of the materials are optimized by taking advantage of the magnetocrystalline anisotropy that exists in iron. The sheet is fabricated such that one axis of the cubic unit cell is preferentially aligned with the rolling direction of the sheet (Ref 8, 9, 10, 11, 12, 13). This results in maximum magnetic permeability in the transformer along the desired direction to achieve optimal efficiency. The following properties are anisotropic in cubic crystals: Young's modulus, Poisson's ratio, yield strength, tensile strength, elongation, coefficient of friction, magnetic permeability, and magnetostriction. Also, in cubic metals, the following are isotropic (but may be anisotropic in noncubic metals): coefficient of thermal expansion, thermal conductivity, electrical resistivity, dielectric constant, Thomson coefficient, Peltier coefficient, and index of refraction. Table 1 contains an example set of values of various properties for given materials indicating their anisotropic nature.

Table 1 Directional dependence of certain mechanical and physical properties

Property	Metal	Crystal direction	Value
Young's modulus	Copper	⟨111⟩	193 GPa (28×10^6 psi)
		⟨100⟩	69 GPa (10×10^6 psi)
Yield strength	Magnesium	*c*-axis 5° from tensile axis	10 MPa (1450 psi)
		c-axis 45° from tensile axis	1.7 MPa (247 psi)
Thermal expansion	Uranium	*a*-axis	33×10^{-6}/K (59.4×10^{-6}/°F)
		b-axis	-6.5×10^{-6}/K (-11.7×10^{-6}/°F)

Electrical resistivity	Tellurium	*c*-axis	6×10^{-4} Ω · m (60,000 μΩ · cm)
		90° from *c*-axis	15×10^{-4} Ω · m (150,000 μΩ · cm)
Magnetic flux density	Cobalt	*c*-axis	1.8 T (18,000 G)[(a)]
		90° from *c*-axis	0.6 T (6,000 G)[(a)]

(a) At a magnetic field strength of 1.6×10^5 A/m (2016 Oe)

References cited in this section

1. F. Barlat, S. Panchanadeeswaran, and O. Richmond, Earing in Cup Drawing Face-Centered Cubic Single-Crystals and Polycrystals, *Metall. Trans.,* Vol A22, July 1991, p 1525–1534

2. W.B. Hutchinson and H.E. Ekstrom, Control of Annealing Texture and Earing in Non-Hardenable Aluminum Alloys, *Mater. Sci. Technol. Ser.,* Vol 6, Nov 1990, p 1103–1111

3. S.X. Ding and J.G. Morris, Processing of AA3004 Alloy Can Stock for Optimum Strength and Formability, *Metall. Mater. Trans.,* Vol A28, Dec 1997, p 2715–2721

4. J. Savoie, Y. Zhou, J.J. Jonas, and S.R. MacEwen, Textures Induced by Tension and Deep Drawing in Aluminum Sheets, *Acta Mater.,* Vol 44, Feb 1996, p 587–605

5. X.M. Cheng and J.G. Morris, Texture, Microstructure and Formability of SC and DC Cast Al-Mg Alloys, *Mater. Sci. Eng. A,* Vol A323, Jan 2002, p 32–41

6. R.P. Reade, P. Berdahl, R.E. Russo, and S.M. Garrison, Laser Deposition of Biaxially Textured Yttria-Stabilized Zirconia Buffer Layers on Polycrystalline Metallic Alloys for High Critical Current Y-Ba-Cu-O Thin-Films, *Appl. Phys. Lett.,* Vol 61, Nov 1992, p 2231–2233

7. A. Goyal, D.P. Norton, D.K. Christen, E.D. Specht, M. Paranthaman, D.M. Kroeger, J.D. Budai, Q. He, F.A. List, R. Feenstra, H.R. Kerchner, D.F. Lee, E. Hatfield, P.M. Martin, J. Mathis, and C. Park, Epitaxial Superconductors on Rolling-Assisted Biaxially-Textured Substrates (RABiTS): A Route towards High Critical Current Density Wire, *Appl. Superconduct.,* Vol 4, Oct–Nov 1996, p 403–427

8. A. Bottcher and K. Lucke, Influence of Subsurface Layers on Texture and Microstructure Development in RGO Electrical Steel, *Acta Metall. Mater.,* Vol 41, Aug 1993, p 2503–2514

9. I. Samajdar, S. Cicale, B. Verlinden, P. Van Houtte, and G. Abbruzzesse, Primary Recrystallization in a Grain Oriented Silicon Steel: On the Origin of Goss{110}[001] Grains, *Scr. Mater.,* Vol 39, Sept 1998, p 1083–1088

10. P. Gangli and J.A. Szpunar, The Role of Sigma-5 Coincidence Boundaries in the Growth Selection of Fe-3-Percent Si, *J. Mater. Process. Technol.,* Vol 47, Dec 1994, p 167–184

11. S. Nakashima, K. Takashima, and J. Harase, Effect of Tin Addition on Process of Secondary Recrystallization of Fe-3-Percent-Si, *Tetsu-to-Hagané,* Vol 80, Feb 1994, p 137–142

12. S. Suzuki, Y. Ushigami, H. Homma, S. Takebayashi, and T. Kubota, Influence of Metallurgical Factors on Secondary Recrystallization of Silicon Steel, *Mater. Trans.,* Vol 42, June 2001, p 994–1006

13. J. Harase, R. Shimizu, K. Takashima, and T. Watanabe, Effect of AlN on the Secondary Recrystallization of 3%Si-Fe Alloy, *Trans. Iron Steel Inst. Jpn.,* Vol 27, 1987, p 965–973

D.P. Field, Textured Structures, *Metallography and Microstructures,* Vol 9, *ASM Handbook,* ASM International, 2004, p. 215–226

Textured Structures

David P. Field, Washington State University

Texture Evolution and Control

In general, preferred orientations will be generated in a material during fabrication, resulting in anisotropy of properties. This occurs in virtually all of the conventional metal-fabrication procedures including thermomechanical processing or any deformation or annealing procedure, casting, and deposition. Specific procedures must be followed to generate given types of textures for property optimization in a given direction or to avoid the creation of texture components during metal fabrication altogether. Processes that do not generally result in significant preferred orientations include conventional powder metallurgy processing (in the absence of external fields), spray forming, and various processes used to create nanocrystalline metals (such as severe plastic-deformation processes).

The mechanisms involved in creating texture are briefly described for each of the metal-fabrication processes given below. Also, Table 2 shows the texture components formed by various processes in given metals or metal classes.

Table 2 Textures developed by various processes

Material	Stable texture component
Casting (solidification direction)	
fcc	⟨100⟩
bcc	⟨100⟩
hcp	
Cd, Zn	$\langle 10\bar{1}0\rangle \parallel$, {0001} $\perp$
Mg	$\langle 21\bar{1}0\rangle \parallel$, {2025} $\perp$
hex, $(Co, Cu)_5Sm$, $(Co, Cu)_5Ce$	[0001]
tet, β-Sn	⟨110⟩
rhom, Bi	⟨111⟩
Film deposition	
fcc	⟨111⟩
bcc	⟨110⟩
hcp	[0001]
Electrodeposition (thick deposits) (Ref 14)	
fcc	
Ag, Cu—low overvoltage	⟨111⟩
Ag, Cu—intermediate overvoltage	⟨100⟩
Ag, Cu—high overvoltage	⟨110⟩ or ⟨210⟩
bcc	
Fe—low overvoltage	⟨110⟩
Fe—intermediate overvoltage	⟨112⟩ or ⟨310⟩
Fe—high overvoltage	⟨111⟩
hcp	
Co—low overvoltage	[0001]

Co—intermediate overvoltage	⟨11$\bar{2}$0⟩
Co—high overvoltage	⟨11$\bar{2}$0⟩ or ⟨11$\bar{2}$2⟩
tet	
Sn—low overvoltage	⟨100⟩
Sn—intermediate overvoltage	⟨110⟩
Sn—high overvoltage	⟨101⟩
Wiredrawing, swaging, extrusion	
fcc	⟨111⟩ + ⟨100⟩
bcc	⟨110⟩
hcp	
Zn, small strain	[0001]
Zn, large strain	[0001] 70° from wire axis
Mg, <450 °C (842 °F); Be, Hf, Ti, Zr	⟨10$\bar{1}$0⟩
Mg, >450 °C (842 °F)	⟨2$\bar{1}\bar{1}$0⟩
ortho, U	⟨010⟩ + ⟨410⟩
Recrystallization after wiredrawing	
fcc	⟨111⟩ + ⟨100⟩ ; also ⟨112⟩
bcc	⟨110⟩
hcp	
Be	⟨10$\bar{1}$0⟩
Ti, Zr	⟨11$\bar{2}$0⟩
Ortho, U	⟨431⟩ + ⟨100⟩
Uniaxial compression	
fcc	⟨100⟩
bcc	⟨111⟩ + ⟨110⟩
hcp	
Mg, Co (?)	[0001]
Hf, Ti	[0001] 10–30° from compression axis
Recrystallization after uniaxial compression or forging	
fcc, Al, Cu, α-brass	⟨110⟩
bcc, Fe	⟨111⟩
hcp, Mg	[0001]
Cold rolling	
fcc	{110} ⟨$\bar{1}$12⟩ + {112} ⟨11$\bar{1}$⟩
Al, Cu, Cu-Ni, Au, Ni, Ni-Fe, Pd, Th, Rh, Pb-0.26Ca	
Ag, Yb, Ni-15Mo, Ni-50Co, Co-10Fe, 18-8 stainless steel, Cu alloys	{110} ⟨$\bar{1}$12⟩ + spread around {110} to {110} ⟨001⟩
bcc	{001} ⟨110⟩ + spread around ⟨110⟩ to {$\bar{1}$12} ⟨110⟩ ; also {11$\bar{1}$} ⟨112⟩
hcp	
Zn, Cd	[0001] at 20–25° from ND toward RD
Mg, Co	[0001] ‖ ND
Ti-Al (>2% Al)	(0001) ⟨10$\bar{1}$0⟩
Be, Hf, Zr, Ti, Ti-Nb, Ti-Ta, Ti-Zr	[0001] at 20–40° from ND toward TD, ⟨10$\bar{1}$0⟩ ‖ RD
ortho	
U, <300–400°C (572–752°F)	{103} ⟨010⟩
U, >500°C (932°F)	{1$\bar{4}$6} ⟨410⟩ + {103} ⟨010⟩

Fiber textures and ideal components in rolled fcc metals	
Cube	{100}〈001〉 (primarily a recrystallization texture component)
Goss	{110}〈001〉
Brass	{110}〈112〉
S1	{124}〈21$\bar{1}$〉
S2	{123}〈41$\bar{2}$〉
S3	{123}〈63$\bar{4}$〉
Copper	{112}〈11$\bar{1}$〉
Taylor	{4 4 11}〈11 11 $\bar{8}$〉
α-fiber	{110}〈110〉 to {110}〈$\bar{1}$12〉, 〈110〉 parallel to the RD
β-fiber	{110}〈$\bar{1}$12〉 to {112}〈11$\bar{1}$〉, 〈111〉 parallel to the ND
Fiber textures in rolled bcc metals	
α 〈110〉	{001}〈110〉 to {111}〈1$\bar{1}$0〉, 〈110〉 parallel to the RD
γ{111}	{111}〈1$\bar{1}$0〉 to {111}〈112〉, 〈111〉 parallel to the ND
η	{001}〈100〉 to {011}〈100〉, 〈100〉 parallel to the RD
ε	{001}〈110〉 to {111}〈112〉, 110 parallel to the TD
Recrystallization after cold rolling	
fcc	
Al, Au, Cu, Cu-Ni, Fe-Cu-Ni, Ni, Ni-Fe, Th	{100}〈001〉
Ag, Ag-30Au, Ag-1Zn, Cu-(5-39)Zn, Cu-(1-5Sn),	
Cu-0.5Be, Cu-0.5Cd, Cu-0.05P, Co-10Fe	{113}〈21$\bar{1}$〉
bcc	
Mo	Same as deformation texture
Fe, Fe-Si, V	{111}〈21$\bar{1}$〉, and {001} + {112} with 〈$\bar{1}$10〉 15° from RD
Fe-Si	{110}〈001〉 after two-step rolling and annealing (Goss method); also {110}〈001〉, {100}〈001〉 after high-temperature anneal (>1100 °C or 2012 °F)
Ta	{111}〈$\bar{2}$11〉
W, <1800 °C (<3272 °F)	Same as deformation texture
W, >1800 °C (>3272 °F)	{001}〈110〉 12° from RD
hcp	Same as deformation texture
ortho, U	{103}〈010〉

fcc, face-centered cubic; bcc, body-centered cubic; hcp, hexagonal close-packed; hex, hexagonal; ortho, orthogonal; tet, tetragonal; rhom, rhombohedral; ND, normal direction; RD, rolling direction; TD, transverse direction. Source: Ref 14

Solidification. In a simple analysis of casting, the liquid metal begins solidification by nucleation of crystallites along the surface of the mold. The nuclei then grow in the direction of greatest temperature gradient—usually normal to the mold walls. Nucleation is generally considered to be a random event that produces a uniform distribution of lattice orientations. As the metal solidifies, certain growth directions become dominant and columnar grains are formed with the growth direction becoming the preferred texture component. Figure 3 shows an orientation image of columnar grain growth during casting of a nickel-base alloy. (The orientation image is formed by automated mapping of crystal orientations; see the section “Approach Using Individual Orientation Measurements” in this article.) Grains that are oriented to within 10° of {100} aligned with vertical in the image are shaded gray. Apparent in the image is a random distribution of nuclei (image bottom) followed by preferential growth of orientations with {100} planes aligned normal to the direction of solidification. Since the growth orientation follows the direction of maximum temperature gradient, the texture of a casting gives an

indication of the temperature gradients present during solidification. Conversely, specific textures can be created by imposition of controlled temperature gradients during casting.

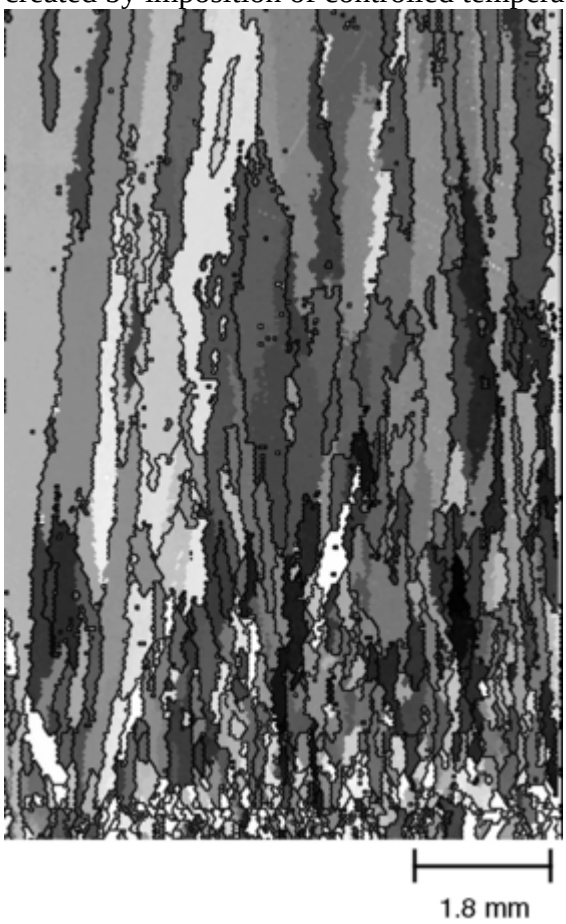

Fig. 3 Orientation image (obtained by mapping of automated electron backscatter diffraction data) of a columnar grain formation during solidification of a nickel-base alloy. The small grains at image bottom are solidification nuclei with the extended columnar grains growing into the melt. The shaded grains are those oriented in the preferred growth direction.

Many casting processes and alloys include grain-refinement techniques that result in uniform nucleation throughout the structure. This results in a refined grain size and generally a more random texture.

Deformation. Plastic deformation of polycrystalline materials is strongly dependent on crystallographic texture, and texture evolution is dependent on the imposed deformation on a material. At low and intermediate temperatures, deformation occurs in crystalline materials by two main processes: dislocation motion and twinning. For most metals, twins are constrained to occur on certain planes and dislocations are confined to motion along given slip systems. These slip systems are defined by a slip plane and a direction of dislocation glide, with the slip plane and direction typically being the most atomically close-packed planes and directions in the lattice. At high temperatures, additional slip systems become active and dislocations are free to move on a larger selection of planes. When dislocation glide is confined to a few slip systems, deformation can only occur by shearing on these planes and directions. As the shearing occurs, the crystallite lattice reorients itself to allow for easier dislocation glide during continued deformation until stable orientations are achieved for the given deformation state. These stable orientations become the preferred orientations in the final product. A similar analysis can be made when deformation occurs by twinning.

While slip occurs simultaneously on many slip systems in polycrystalline materials and dislocation interactions make the process rather complicated, it is instructive to consider a simple case of single-crystal deformation with dislocation glide on a single slip system. In this simplification, the single crystal can be construed as a deck of cards with individual cards acting as slip planes on which deformation will occur. Figure 4(a) depicts a single-crystal tensile bar with the slip system that will become active shown as thin lines across the bar (Ref 15). The stress required to initiate slip is a function of the orientation of the slip system (and, hence, the lattice) to the imposed deformation. The Schmid factor defines this relationship for single crystals. Since slip is confined to the slip planes indicated, deformation would cause a displacement of the top of the specimen

relative to the bottom of the specimen as shown in Fig. 4(b). Since the grips are constrained, however, the condition is satisfied by rotation of the slip planes as deformation occurs, resulting in an evolution of the lattice orientation during deformation as indicated by Fig. 4(c). The shaded slip planes in Fig. 4(c) are the regions where strain accommodation bending occurs, whereas the unshaded region indicates pure lattice rotation. The lattice would continue to rotate until a stable orientation is achieved.

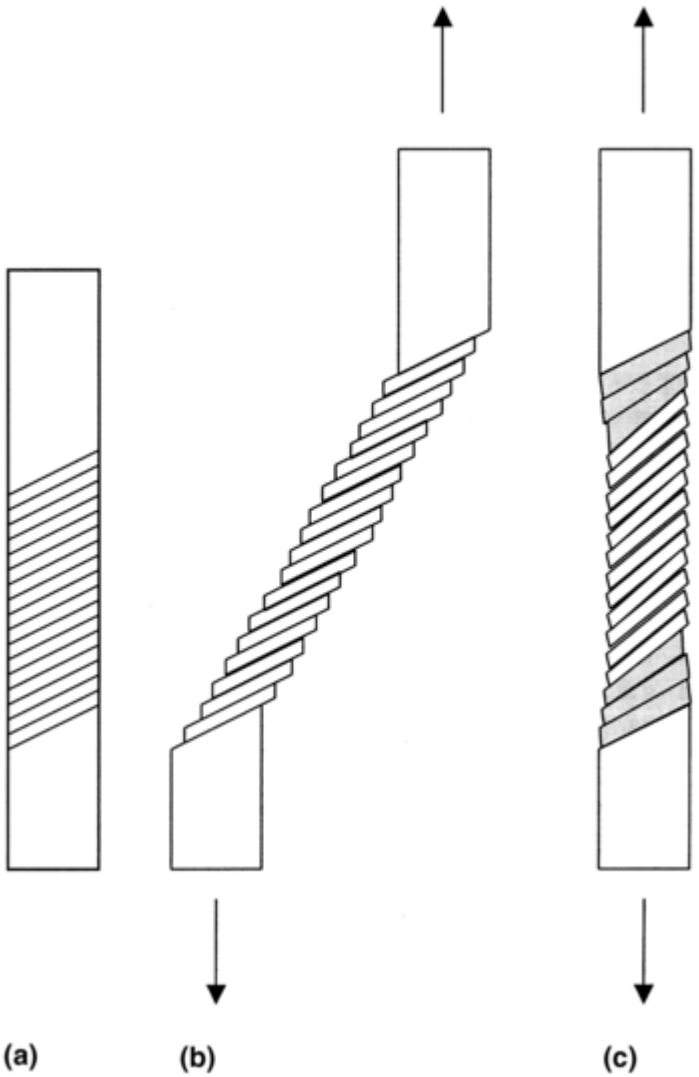

Fig. 4 Slip in a single-crystal tensile bar showing the slip systems (a) before deformation, (b) after pure slip with unconstrained grips, and (c) with constrained grips and rotated slip planes. After Hertzberg (Ref 15)

Deformation of polycrystalline metals is more complicated than this simple example in that it occurs by simultaneous slip on several slip systems in each crystallite. In a similar manner, however, the lattice in each grain will rotate according to the imposed deformation state until a stable orientation is achieved (Ref 16, 17, 18, 19). The paths along which the grains rotate to the stable orientations are the observed deformation fiber textures listed in Table 2. Deformation texture evolution has been a subject of substantial research interest over the past several decades, both experimentally and theoretically. For a more complete discussion of deformation texture development, the reader is referred to Ref 16, 17, 18, 19, 20, 21, 22, 23.

Recrystallization and Grain Growth. When a deformed metal is annealed at high temperatures, the structure responds by recovery, recrystallization, and grain growth. Recovery is a process by which stresses at dislocation tangles and pileups are relieved by dislocation climb. The dislocations move to grain boundaries or cell walls, leaving a dislocation cell that is relatively free from dislocations. Recovery results in negligible lattice rotation and only removes any orientation spread caused by lattice curvature to accommodate the dislocation pileups and tangles.

Recrystallization occurs by nucleation of new crystallites that rapidly grow through the deformed matrix, creating a set of texture components unique to those that were created during deformation. The nuclei are

generated from complex dislocation structures and are usually observed to take on the orientation of the local lattice. After nuclei form, growth is dependent on the nuclei lattice misorientation with the surrounding deformed matrix and the strain energy in the deformed structure, among other factors. Considerable discussion has occurred over the past several years about whether oriented nucleation or oriented growth dominates texture development during recrystallization. It is generally accepted that both processes occur and that both nucleation and growth contribute to the development of preferred orientation. For example, particle-stimulated nucleation (PSN) has been shown to randomize the recrystallization texture, providing support to the argument that nucleation is orientation dependent and the nuclei orientations determine the final texture (Ref 24, 25). Conversely, secondary recrystallization and grain growth in silicon steel has been shown to be a function of the grain-boundary character, resulting in the important Goss texture for these structures (Ref 10, 11, 12, 13). This provides evidence that preferred growth of certain types of orientations aid in determination of the final structure. A more complete discussion of recrystallization textures can be found in Ref 23, 24, 25, 26. Selected recrystallization textures are listed in Table 2.

Thin-Film Deposition. Thin films can be deposited by any of several techniques including physical vapor deposition (PVD), chemical vapor deposition (CVD), and electrochemical deposition (ECD), among others. Regardless of deposition technique, epitaxial relationships with the substrate may develop. In some instances, epitaxy supersedes any other factors contributing to texture evolution. Apart from epitaxy, texture development in films is driven either by surface energy minimization, by strain energy minimization, or by a combination of these with interface and grain-boundary energy considerations that dominate recrystallization and grain growth of the films. For thinner films, the major driving force for texture evolution is surface energy minimization, so metals with a face-centered cubic (fcc) structure will develop a {111} out-of-plane texture. As the film thickness increases, strain energy becomes more dominant and {002} textures develop (for fcc materials).

In addition, texture can also be controlled in films using specialized deposition processes. Ion-beam-assisted deposition (IBAD), for example, can add a directional component to the film resulting in textures with both in-plane and out-of-plane components. Texture evolution in thin films has been described by many researchers (Ref 27, 28, 29, 30, 31, 32).

Magnetic Fields. For many materials, an external magnetic field can be imposed on the material during casting or powder processing, resulting in strong textures. These develop because of the anisotropic nature of magnetic properties in the films. Powder particles can align themselves in the direction of highest magnetic susceptibility and remain in that position during compaction. During casting, metal will solidify in the configuration that is most energetically favorable. An imposed magnetic field can dictate the lattice orientation of the solidifying crystallites, resulting in preferred orientation.

References cited in this section

10. P. Gangli and J.A. Szpunar, The Role of Sigma-5 Coincidence Boundaries in the Growth Selection of Fe-3-Percent Si, *J. Mater. Process. Technol.,* Vol 47, Dec 1994, p 167–184

11. S. Nakashima, K. Takashima, and J. Harase, Effect of Tin Addition on Process of Secondary Recrystallization of Fe-3-Percent-Si, *Tetsu-to-Hagané,* Vol 80, Feb 1994, p 137–142

12. S. Suzuki, Y. Ushigami, H. Homma, S. Takebayashi, and T. Kubota, Influence of Metallurgical Factors on Secondary Recrystallization of Silicon Steel, *Mater. Trans.,* Vol 42, June 2001, p 994–1006

13. J. Harase, R. Shimizu, K. Takashima, and T. Watanabe, Effect of AlN on the Secondary Recrystallization of 3%Si-Fe Alloy, *Trans. Iron Steel Inst. Jpn.,* Vol 27, 1987, p 965–973

14. N.A. Pangarov, *J. Electroanal. Chem.,* Vol 9, 1965, p 70–85

15. R.W. Hertzberg, *Deformation and Fracture Mechanics of Engineering Materials,* 4th ed., John Wiley & Sons, 1995

16. G.I. Taylor, Plastic Strain in Metals, *J. Inst. Met.,* Vol 62, 1938, p 307–324

17. J.F.W. Bishop and R. Hill, A Theory of the Plastic Distortion of a Polycrystalline Aggregate under Combined Stresses, *Philos. Mag.,* Vol 42, 1951, p 414–427

18. J. Gil-Sevillano, P. Van Houtte, and E. Aernoudt, Large Strain Work Hardening and Textures, *Prog. Mater. Sci.,* Vol 25, 1980, p 69–412

19. J.H. Driver, D. Juul-Jensen, and N. Hansen, Large Strain Deformation Structures in Aluminum Crystals with Rolling Texture Orientations, *Acta Metall. Mater.,* Vol 42, Sept 1994, p 3105–3114

20. W. Gambin, *Plasticity and Textures,* Kluwer Academic Publishers, 2001

21. D. Raabe, M. Sachtleber, Z. Zhao, F. Roters, and S. Zaefferer, Micromechanical and Macromechanical Effects in Grain Scale Polycrystal Plasticity Experimentation and Simulation, *Acta Mater.,* Vol 49, Oct 2001, p 3433–3441

22. C.S. Lee and B.J. Duggan, Simple Theory for the Development of Inhomogeneous Rolling Textures, *Metall. Trans. A,* Vol A22, Nov 1991, p 2637–2643

23. U.F. Kocks, C.N. Tome, and H.-R. Wenk, *Texture and Anisotropy: Preferred Orientations in Polycrystals and Their Effect on Materials Properties,* Cambridge University Press, 1998

24. M. Ferry and F.J. Humphreys, Deformation and Recrystallization of Particle-Containing {011}[100] Aluminum Crystals, *Acta Mater.,* Vol 44, Aug 1996, p 3089–3103

25. H.E. Vatne, O. Engler, and E. Nes, Effect of Precipitates on Texture Development, *Mater. Sci. Forum,* Vol 157, 1994, p 1501–1506

26. F.J. Humphries and M. Hatherly, *Recrystallization and Related Annealing Phenomena,* Pergamon Press, 1995

27. C.V. Thompson and R. Carel, Texture Development in Polycrystalline Thin Films, *Mater. Sci. Eng. B,* Vol B32, 1995, p 211–219

28. J.M.E. Harper and K.P. Rodbell, Microstructure Control in Semiconductor Metallization, *J. Vac. Sci. Technol.,* Vol B15, July 1997, p 763–779

29. C. Lingk, M.E. Gross, and W.L. Brown, X-Ray Diffraction Pole Figure Evidence for (111) Sidewall Texture of Electroplated Cu in Submicron Damascene Trenches, *Appl. Phys. Lett.,* Vol 74, Feb 1999, p 682–684

30. J.E. Sanchez Jr., Effects of Crystallographic Orientation on Film Morphological Evolution, *Materials Research Society Symposium Proceedings,* Vol 343, 1994, p 641–652

31. D.P. Tracy and D.B. Knorr, Texture and Microstructure of Thin Copper Films, *J. Electron Mater.,* Vol 22, 1993, p 611–616

32. E.M. Zielinski, R.P. Vinci, and J.C. Bravman, Effects of Barrier Layer and Annealing on Abnormal Grain Growth in Copper Thin Films, *J. Appl. Phys.,* Vol 76, Oct 1994, p 4516–4523

D.P. Field, Textured Structures, *Metallography and Microstructures,* Vol 9, *ASM Handbook,* ASM International, 2004, p. 215–226

Textured Structures

David P. Field, Washington State University

Texture Characterization and Experimental Determination

Description of a crystallite lattice orientation is a problem of coordinate transformation. One coordinate frame is fixed to the crystal lattice and another to an external reference frame that is generally defined by the processing symmetry of the specimen (such as rolling direction, normal direction, and transverse direction of a rolled sheet). The orientation, *g*, is given by the rotation required to bring the two coordinate frames into coincidence. A direction cosine matrix relating the two coordinate frames to one another is one mathematical description of the "orientation." Texture researchers have generally adopted the passive approach where the "orientation" is defined as the coordinate transformation that rotates the specimen reference coordinate frame into coincidence with that of the crystallite lattice. In other words, for a vector $\mathbf{x}^c$ defined in the crystal frame, and the corresponding vector $\mathbf{x}^s$ defined in the specimen coordinate frame, the transformation for the vectors follows the rule:

$$\mathbf{x}^c = g\mathbf{x}^s$$

It must be emphasized that for the passive description, these $\mathbf{x}^c$ and $\mathbf{x}^s$ vectors are column vectors so that:

$$\text{When } \mathbf{x}^s = \begin{pmatrix} 0 \\ 0 \\ 1 \end{pmatrix}, \quad \mathbf{x}^c = \begin{pmatrix} g_{13} \\ g_{23} \\ g_{33} \end{pmatrix}$$

Additional descriptions of orientations exist in the literature, such as the active formalism, where "orientation" is defined as the coordinate transformation that rotates the coordinate frame attached to the crystallite lattice into the reference coordinate frame defined by specimen directions. The relationship between the orientations obtained from the active and passive descriptions are simply the inverse of each other, but confusing these two conventions can result in significant error.

Many equivalent orientations exist that are mathematically distinct, but physically indistinguishable. The number of equivalent orientations and their exact definitions are dependent on the symmetry of the crystal lattice. Processing symmetry is also considered in texture analysis where the occurrence of a given orientation is considered to be statistically identical in various directions. For example, a rolled sheet is said to have orthotropic processing symmetry, where 180° rotations about the rolling, transverse, and normal directions are said to be statistically equivalent. A thorough presentation of these considerations is made in Bunge (Ref 33).

Three parameters are required for a unique description of an orientation. These parameters are typically given by either an axis and a rotation angle ($\mathbf{n}$,θ), a triplet of Euler angles (φ_1,Φ, φ_2), or by a set of Miller indices $\{hkl\}\langle uvw\rangle$. The axis-angle description defines an axis of rotation ($\mathbf{n}$) about which a rotation of (θ) will result in the required transformation. The Euler angle parameterization in Bunge's notation calls for a rotation of φ_1 about the specimen *z*-axis, followed by a rotation of Φ about the newly formed *x*-axis, and finally a rotation of φ_2 about the final *z*-axis. The Miller index description defines a plane $\{hkl\}$ normal to the *z*-axis in the specimen coordinate frame and a direction $\langle uvw\rangle$ aligned with the *x*-direction of the specimen coordinate frame. These three parameterizations are described in Fig. 5 with the transformation from the ($\mathbf{X}^s$,$\mathbf{Y}^s$,$\mathbf{Z}^s$) specimen coordinate frame to the ($\mathbf{X}^c$,$\mathbf{Y}^c$,$\mathbf{Z}^c$) crystal coordinate frame. Table 3 lists the mathematical relationships between the various orientation descriptions and the direction cosine matrix. Additional parameterizations exist, such as quaternions and Rodrigues vectors, but these are generally based on the axis-angle description or variants of the Euler angle definitions (Ref 33, 34).

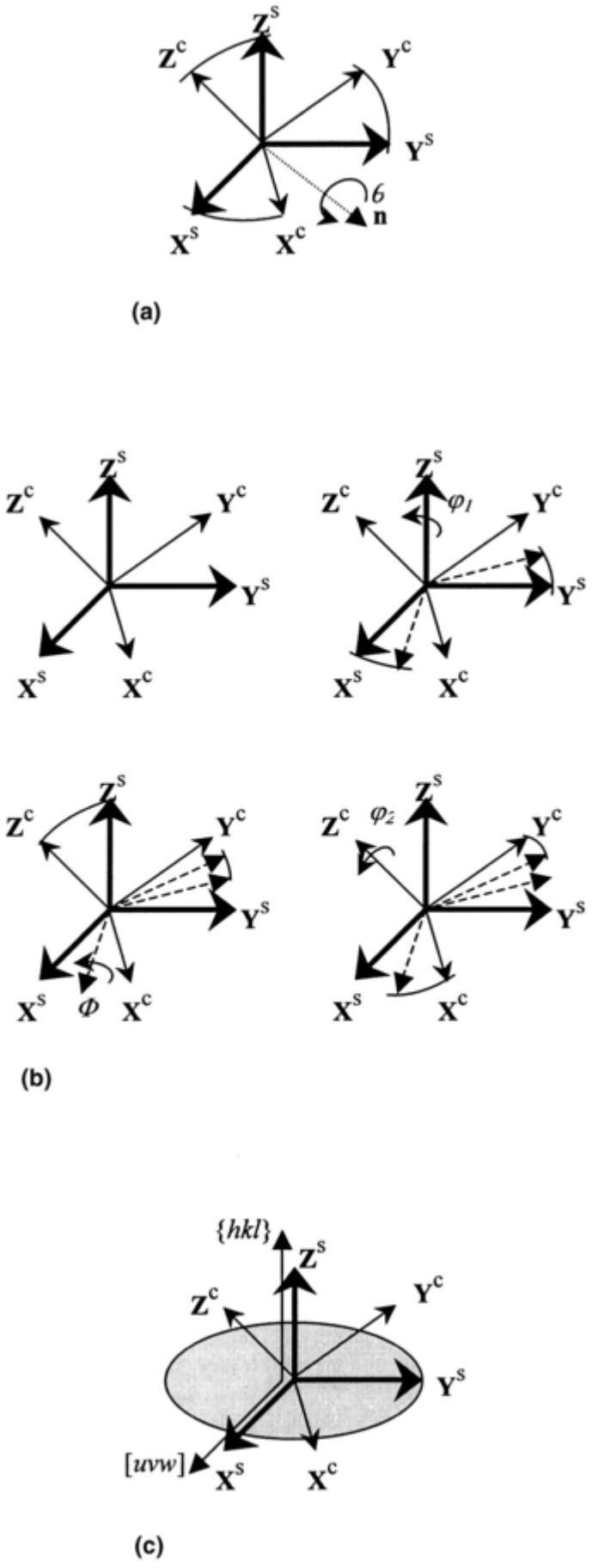

Fig. 5 Orientation parameterizations. (a) Axis-angle description. (b) Euler angles (Bunge notation). (c) Miller indices

Table 3 Relations between orientation parameterizations

Euler Angles
Bunge notation: (φ_1,Φ,φ_2)
Roe notation: (Ψ,Θ,Φ) - (φ_1 - 90°,Φ, φ_2 + 90°)
Kocks notation: (Φ,Θ,φ) - (φ_1 - 90°,Φ, φ_2 + 90°)
Orientation matrix (direction cosine matrix)—passive convention
$$g=\begin{bmatrix} \cos\varphi_1\cos\varphi_2-\sin\varphi_1\sin\varphi_2\cos\Phi & \sin\varphi_1\cos\varphi_2-\cos\varphi_1\sin\varphi_2\cos\Phi & \sin\varphi_2\sin\Phi \\ -\cos\varphi_1\sin\varphi_2-\sin\varphi_1\cos\varphi_2\cos\Phi & -\sin\varphi_1\sin\varphi_2-\cos\varphi_1\cos\varphi_2\cos\Phi & \cos\varphi_2\sin\Phi \\ \sin\varphi_1\sin\Phi & -\cos\varphi_1\sin\Phi & \cos\Phi \end{bmatrix}$$
Axis angle
$$g=\begin{bmatrix} \left(1-n_1^2\right)\cos\theta+n_1^2 & n_1n_2\left(1-\cos\theta\right)-n_3\sin\theta & n_1n_3\left(1-\cos\theta\right)-n_2\sin\theta \\ n_1n_2\left(1-\cos\theta\right)-n_3\sin\theta & \left(1-n_2^2\right)\cos\theta+n_2^2 & n_2n_3\left(1-\cos\theta\right)-n_1\sin\theta \\ n_1n_3\left(1-\cos\theta\right)-n_2\sin\theta & n_2n_3\left(1-\cos\theta\right)-n_1\sin\theta & \left(1-n_3^2\right)\cos\theta+n_3^2 \end{bmatrix}$$
$$2\cos\theta=Trace(g)-1=g_{11}+g_{22}+g_{33}-1$$
$$n_1=\frac{g_{23}-g_{32}}{2\sin\theta},\quad n_2=\frac{g_{31}-g_{13}}{2\sin\theta},\quad n_3=\frac{g_{12}-g_{21}}{2\sin\theta}$$
Miller Indices—{*hkl*} 〈*uvw*〉
***h* = *n* sin φ_2 sinΦ**
***k* = *n* cos φ_2 sinΦ**
***l* = *n* cosΦ**
***u* = *n′* cos φ_1 cos φ_2 - sin φ_1 sin φ_2 cosΦ**
***v* = *n′*(-cos φ_1 sin φ_2 - sin φ_1 cos φ_2 cosΦ)**
***w* = *n′* sin φ_1 sinΦ**
$$\cos\Phi=\frac{l}{\sqrt{h^2+k^2+l^2}}$$
$$\cos\varphi_2=\frac{k}{\sqrt{h^2+k^2}}\sin\varphi_2\frac{h}{\sqrt{h^2+k^2}}$$
$$\sin\varphi_1=\frac{w}{\sqrt{u^2+v^2+w^2}}\sqrt{\frac{h^2+k^2+l^2}{h^2+k^2}}$$

Experimental determination of texture requires the measurement of the orientations of crystallite lattices. Texture measurement almost always is accomplished by means of diffraction experiments, typically using x-rays, but also with electron or neutron diffraction. The ability to measure texture derives from Bragg's law:

$$n\lambda = 2d_{hkl}\sin\theta$$

where n is an integer, λ is the wavelength of the diffracting media, d_{hkl} is the interplanar spacing on the {*hkl*} plane, and θ is the incident and diffracting angle. X-ray diffraction yields orientation information over relatively large areas of the specimen surface, while neutron diffraction can be used to obtain volume information and electron diffraction to obtain information from individual points on the specimen surface. X-ray and neutron diffraction techniques yield measurements of orientation distributions over large areas or volumes. Electron diffraction techniques obtain orientations of individual crystallites. When many individual measurements are made over large areas of the specimen surface, electron diffraction is considered to be an area probe, yielding texture information similar to that obtained by x-ray diffraction. Some microdiffraction x-ray systems can yield

diffraction information from fairly small spot sizes (on the order of a few microns, or even submicron volumes in some instances) making micro-x-ray diffraction an additional technique for obtaining orientations of individual crystallites.

Approach Using Classical Diffraction and Pole Figure Measurement Techniques. The experimental and analytical approach to texture measurement and the graphical and numerical presentation of the texture depends on the information required. Texture measurement and presentation may involve only one or two parameters instead of the full three-parameter description of the crystallite lattice orientation distribution. The crudest texture measurement is made by performing a simple theta 2-theta (θ-2θ) x-ray diffraction scan such as that shown in Fig. 6 for polycrystalline aluminum. Theta 2-theta scans by themselves do not yield complete texture information, but give the maximum intensities of planes aligned exactly with the specimen surface for those planes matching the diffraction criterion. The relative orientation intensities for various {*hkl*} planes are not obtained by simply comparing the relative peak heights seen in the scans since these are dependent on the structure factor of the crystallite. To obtain useful information, the intensities must be determined by integration of each peak and by comparing these values against a random standard. Such measurements can be used to obtain relative textures for use in comparing one material to the other, but care must be taken since similar textures could produce quite different θ-2θ scan intensities. The relative intensities of the diffraction peaks at the angle corresponding to a given plane, for example, {200}, will indicate whether one specimen has more or less area covered by crystallites oriented exactly so that the {200} plane is aligned with the specimen surface. Rocking curves (phi scans) should always be employed in conjunction with θ-2θ scans for texture comparisons (Ref 35) since these curves yield the spread in texture about an ideal component. Other approaches to using θ-2θ scans for texture measurements have also been proposed. One such analysis employs multiple scans on section planes of differing orientation and an analytical approach based on the Rietveld technique for analysis of powder diffraction patterns (Ref 36).

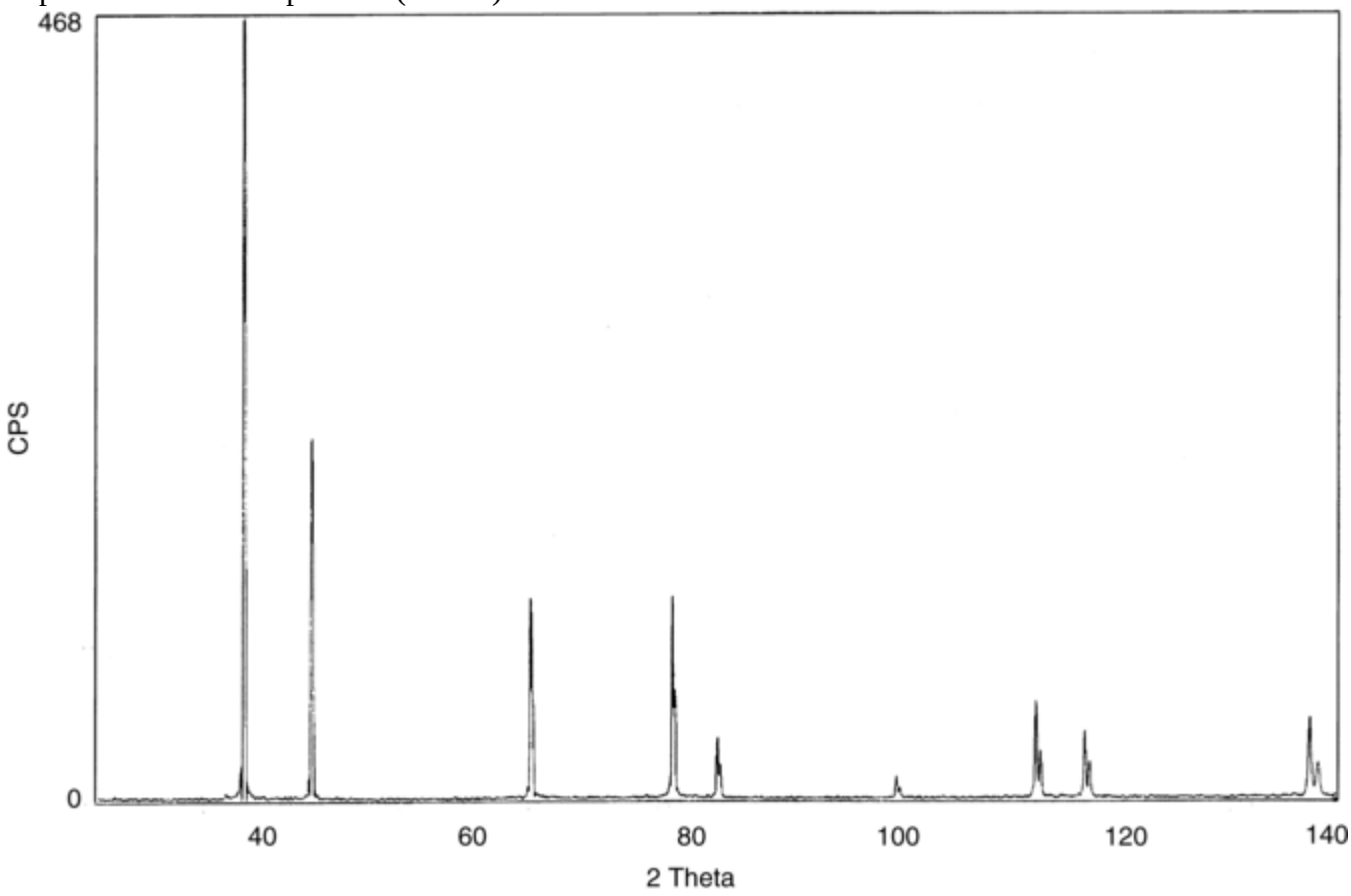

Fig. 6 Theta 2-theta x-ray diffraction scan for polycrystalline aluminum. CPS, counts per second. Courtesy of M.G. Norton

One of the most common presentations of texture information is that of a pole figure. Pole figures are two-parameter projections of the orientation of a given pole or distribution of poles. The pole is defined as the normal vector to a specific lattice plane and is given by {*hkl*} in the Miller index description. (For crystals with

cubic symmetry, the pole is coincident with the direction $\langle uvw \rangle$ of the same indices; that is, for a given vector in cubic crystal space, $h = u$, $k = v$, $l = w$.)

The pole figure plot is a projection showing the orientation of a given family of poles in the reference or specimen coordinate frame. Pole figures are typically presented as stereographic projections, but alternate projections, such as equal angle or equal area projections, are sometimes employed. It is instructive to consider the discrete presentation of a single crystallite in describing the construction of a pole figure. The pole figure uniquely contains the orientations of a given family of poles described by Miller indices. Figure 7(a) shows the projections of the {100} poles from a cubic crystal onto the surface of a reference sphere. Figure 7(b) shows the creation of a {111} pole figure (stereographic projection) from a single crystallite of cubic symmetry that is oriented in the "cube" orientation where the specimen and crystal coordinate frames are coincident with one another (as shown in Fig. 7a). The small black diamonds indicate the intersection points of the {111} poles with the reference sphere. The round dots show the positions of the intersections of the projection lines to the black diamonds, where the {111} poles intersect the reference sphere. The equatorial plane is shaded and is the projected {111} pole figure for the indicated orientation. The discrete {111}, {110}, and {100} pole figures of the "cube" orientation are shown in Figure 7(c). Pole figures are generally used to present distributions of orientations, and the orientation intensities are represented as contour lines or shading levels instead of discrete points in the projection. Figure 8 contains a {111} pole figure of a cold-rolled copper plate. The orientation distribution is similar for any fcc metal deformed by cold rolling.

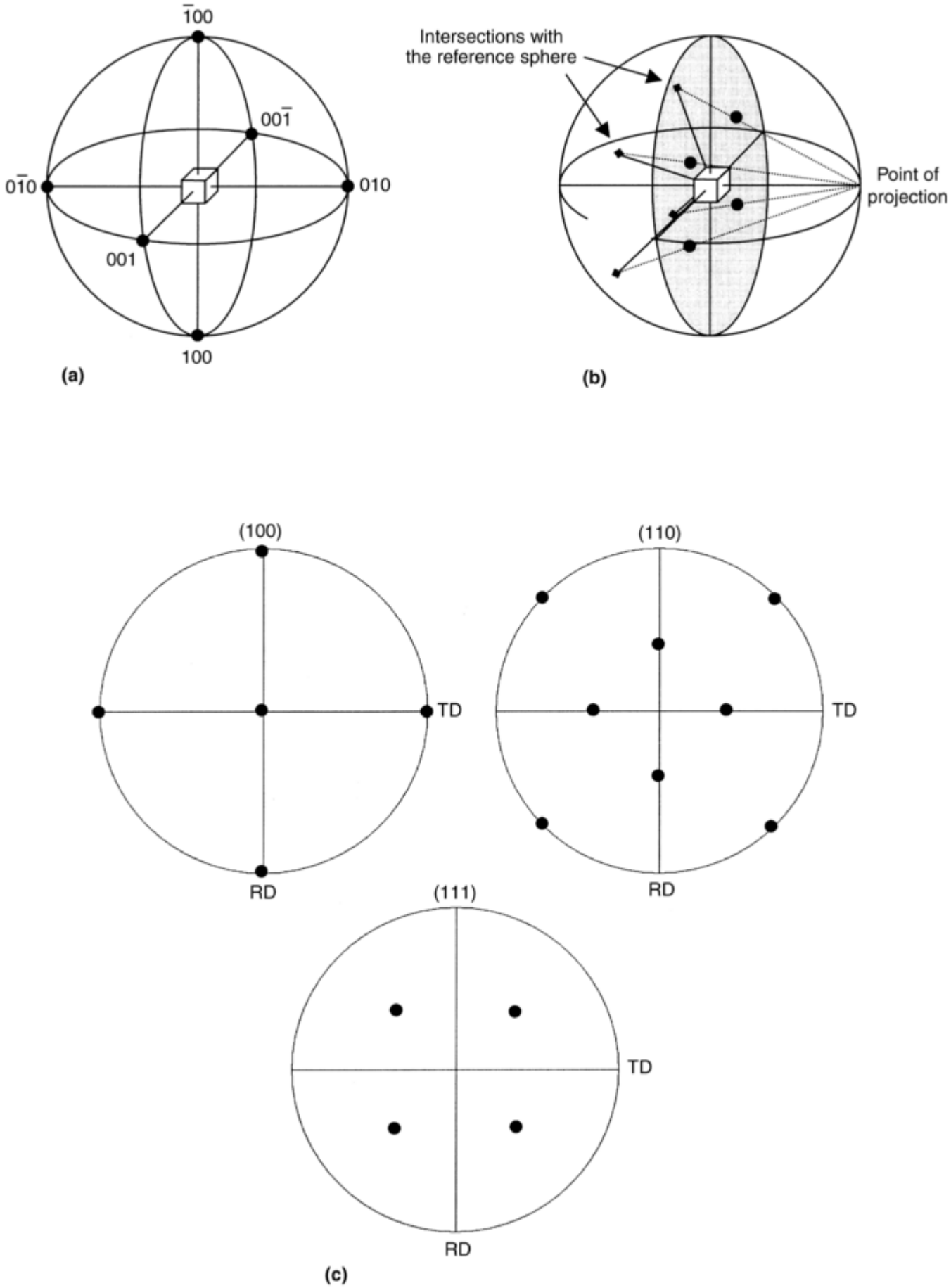

Fig. 7 (a) The projection of the {100} poles onto the surface of a reference sphere. (b) The creation of a {111} pole figure for a crystallite in the "cube" orientation. (c) Discrete {100}, {110}, and {100} pole figures. ND, normal direction; RD, rolling direction; TD, transverse direction

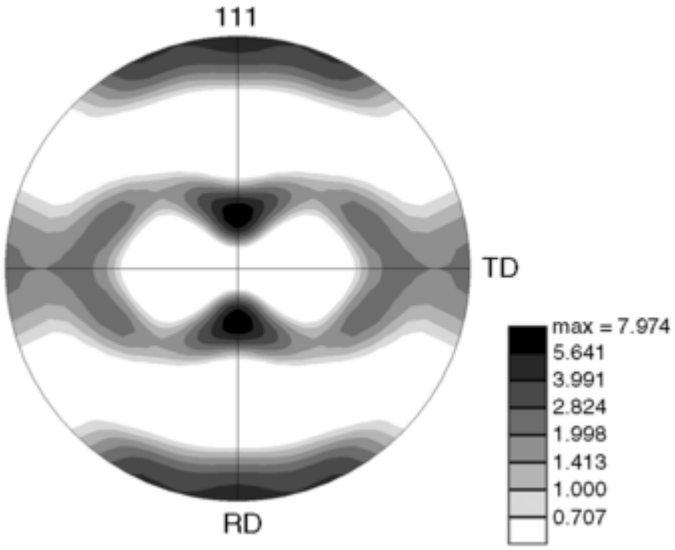

Fig. 8 {111} pole figure of a cold-rolled copper plate (scale is in units of times random)

The measurement of pole figures is typically done using x-ray diffraction, though electron or neutron diffraction will yield similar information (Ref 37, 38). The x-ray pole figure is measured by first selecting the angle of diffraction corresponding to the desired family of poles. This angle is given theoretically by Bragg's equation, but is generally obtained experimentally using a θ-2θ scan prior to pole figure measurement. The incident beam and detector are positioned at the given angles, and the specimen is rotated through increments of the azimuthal and polar angles noting the relative x-ray intensities at each position. The resulting measured intensity distribution for a given family of poles is plotted as discussed previously. It should be noted that geometry of the pole figure measurement renders it impossible to cover the entire space of the pole figure. The pole figures are generally measured to polar angles of about 75 to 80°, and the crystallite orientation distribution function (ODF, a three-dimensional description, discussed below) is calculated from the available data. The complete pole figures are often recalculated from the full distribution and presented in their complete form.

Inverse pole figures are similar to pole figures in that they are a two-parameter description of the orientation distribution, plotted using a stereographic projection. The difference is that inverse pole figures contain a single direction defined by the specimen coordinate frame plotted in the space of the crystal frame, while pole figures show poles from the crystallite lattice, plotted in the specimen coordinate frame. Usually, a prominent direction such as a rolling direction or the axis of a tensile specimen is used to plot the inverse pole figure. Also, the projection is typically restricted to the asymmetric domain; therefore, for cubic crystallites, the plot consists of only the unit triangle with vertices defined by the {001}, {111}, and {101} poles. The inverse pole figure cannot be easily measured directly. Theta 2-theta scans give data for specific points in the inverse pole figure corresponding to the low-index diffracting planes that satisfy the diffraction criterion, but yield no information on orientation spread or on nondiffracting or low-index planes. Similar to the pole figures, inverse pole figures are most often presented as recalculated from the complete ODF.

Some materials exhibit a texture dominated by the alignment of a particular crystal direction with a given sample direction. This type of texture, known as a fiber texture, is often observed in thin films where surface energy minimization dominates texture evolution. (Fiber textures are also common in cast and various additional structures.) Metal films with an fcc Bravais lattice often exhibit alignment of {111} poles with the film normal direction. Such a texture is commonly termed a (111) fiber texture. X-ray rocking curves are often used to characterize such textures when the assumption is reasonably made that no additional texture components exist with significant intensity and no in-plane preferred orientation is likely. Again, this measurement is a gross simplification and should not be used to characterize the full texture of a material, but only to give an indication of orientation spread about a given peak.

Other fiber textures exist in many materials that derive from specimen processing. Descriptions of any fiber texture can be made using a one-parameter description. Some common fiber textures are listed in Table 2. Additionally, one-dimensional skeleton lines through the space of the full orientation distribution are often used to describe certain special textures with the reduced parameterization. Some of these are described below,

following the discussion of the crystallite ODF, which is the full three-parameter description of the orientation distribution.

The ODF is a probability density function containing the probability of occurrence of an orientation lying within some incremental volume of orientation space. The statistical description of the volume fraction of each component of the orientation distribution is contained in this function. The distribution is most often presented in the space of Euler angles since these are the arguments for the basis functions used in the mathematical description of the ODF (spherical harmonic functions). Various other parameterizations, such as Rodrigues vectors, are sometimes used in the mathematical description of the function along with piecewise polynomial functions. The distributions are determined from x-ray or neutron diffraction pole figure measurements by obtaining pole figures from several families of poles and combining the information to obtain the complete function. The mathematics for doing this is well developed in the literature and is beyond the scope of the present discussion (Ref 33).

It should also be mentioned that textures are generally presented in the space that requires the least amount of redundant information. As discussed previously, with the exception of the triclinic crystal system, all crystallites have more than one mathematically distinct definition. This is because of symmetry in both the crystal system and in the processing of the material (statistical symmetry). The set of possible orientations can be reduced significantly by requiring all orientations to lie within an asymmetric domain of orientation space where all orientations are physically distinct. To present a pole figure of a rolled sheet, for example, requires only one quadrant of the projection since the information presented in the other quadrants is redundant. The mathematics of asymmetric domains in texture analysis has been clearly established (Ref 33, Ref 39).

Figure 9 contains a typical plot of a ODF from rolled steel plotted in Euler space using the Bunge notation convention. The plot is made by drawing contours or shading levels indicating constant orientation density in two-dimensional slices through orientation space. In Fig. 9, each two-dimensional plot represents a slice through orientation space at increments of constant φ_2. Intensities of the ODF are generally given in units of "times random" with the random texture determined experimentally.

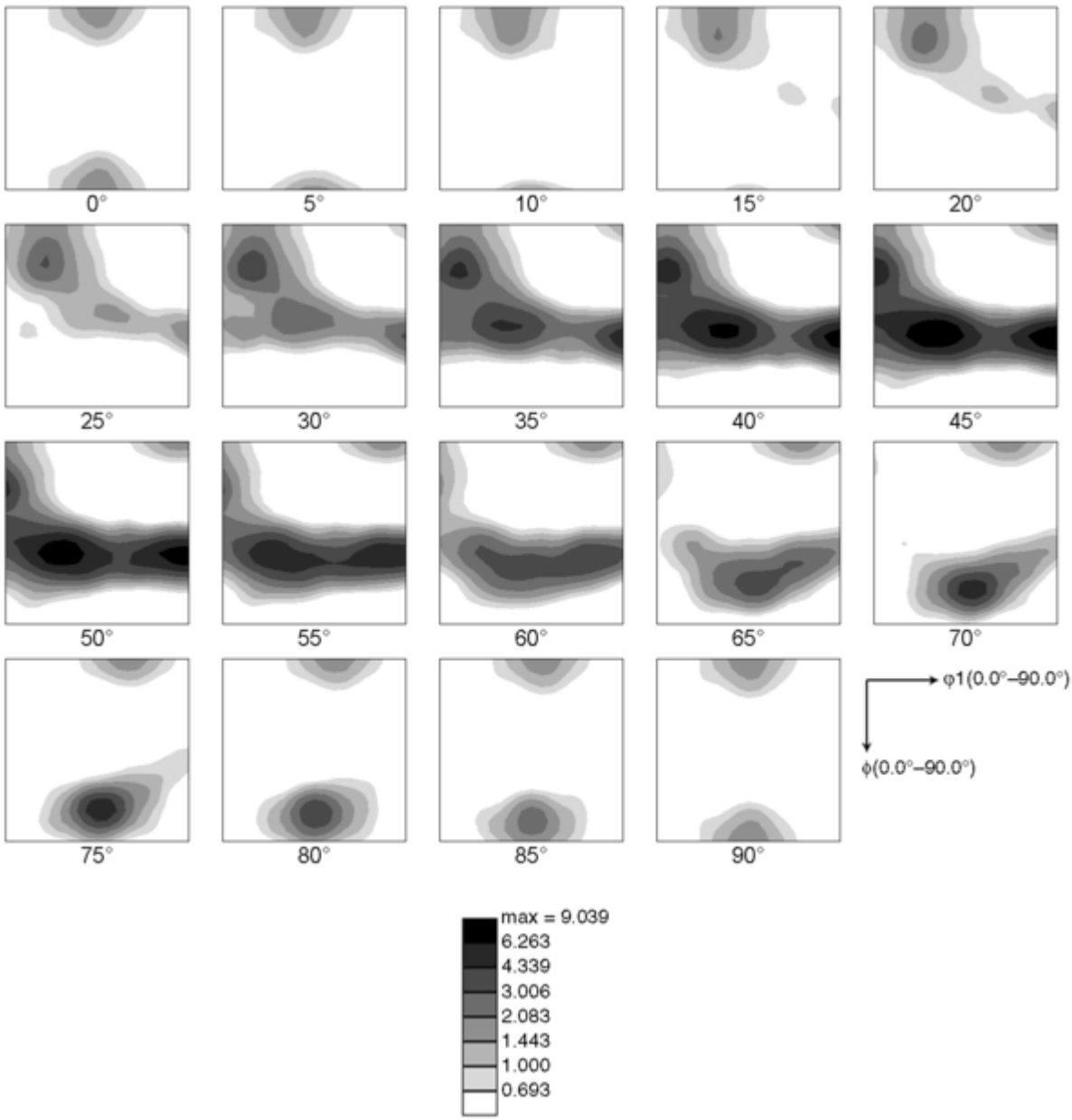

Fig. 9 Orientation distribution function (ODF) of rolled steel plotted in the space of Euler angles using Bunge's notation

The two-dimensional sections plotted incrementally give a graphical presentation of the three-dimensional distribution. As discussed previously, pole figures are two-parameter descriptions of the orientation distribution that can be determined from the full function, and fiber texture plots (such as rocking curves) are one-dimensional characterizations. Figure 10 shows sections through Euler space, a pole figure, and a fiber plot showing the texture of a thin aluminum film. A rocking curve is essentially an intensity profile of the pole figure along an arbitrary line passing through the center of the pole figure.

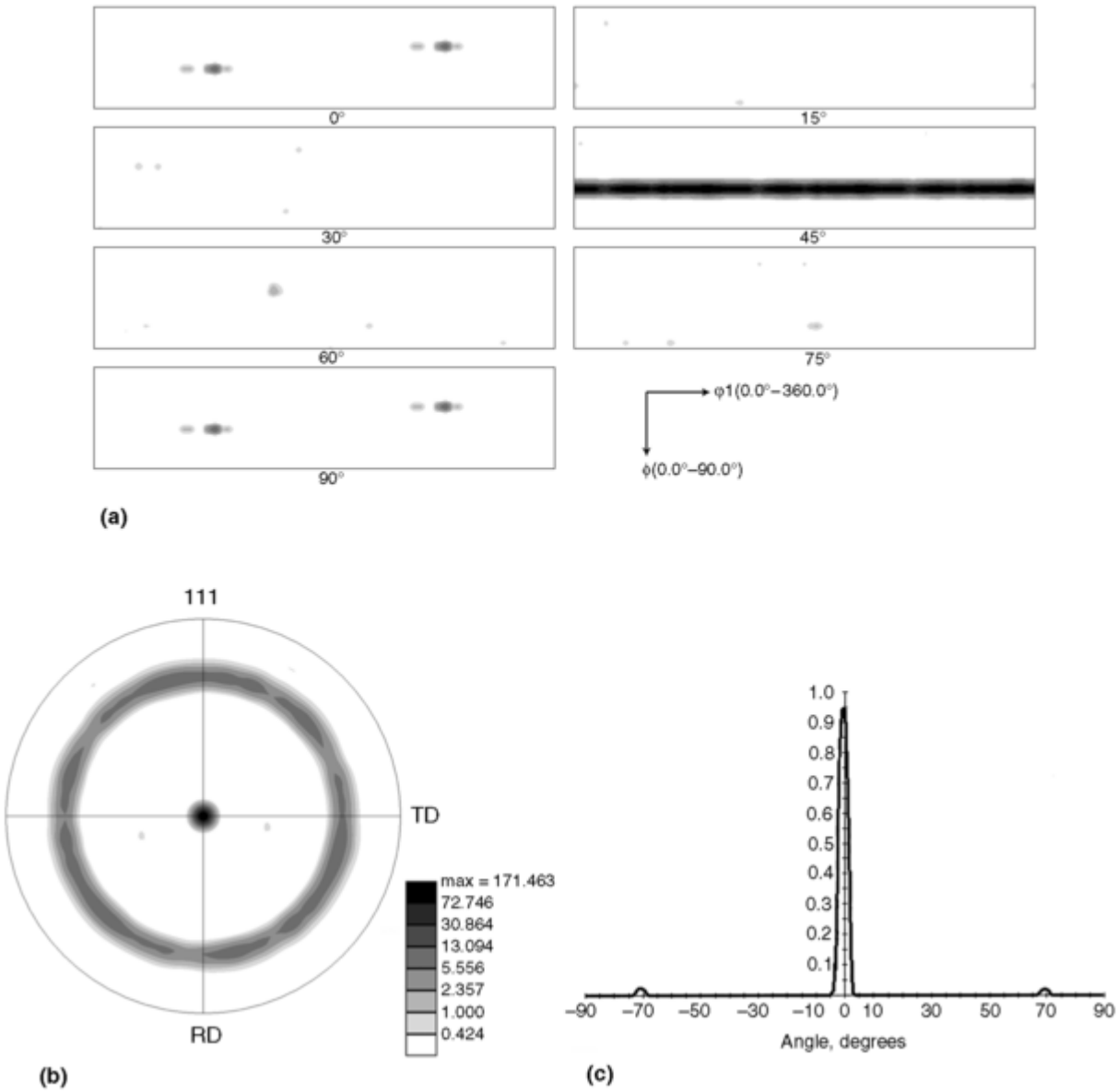

Fig. 10 (a) Orientation distribution function (ODF). (b) {111} pole figure. (c) {111} fiber plot showing the texture of an aluminum thin film

Rocking curves can be analyzed to further simplify the parameterization of the texture. The key parameters are the width of the peak (ω, full-width, half-max), the fraction of randomly oriented material, and the fraction of material in the peak (Fig. 10c). In Fig. 10(c), the large peak at φ = 0° is due to a strong alignment of {111} poles with the sample normal. The smaller peak at φ = 70.5° is due to symmetrical variants of {111} poles. If a {111} pole is exactly aligned with the sample normal, then the other three ⟨111⟩ variants are located at 70.5° from the sample normal as shown in the schematic. A {100} fiber texture would exhibit a similar secondary peak at 90°, and a {110} fiber texture would exhibit a secondary peak at 60° and a tertiary peak at 90°. The fact that these secondary peaks appear as rings of uniform intensity in the pole figure and as constant lines through Euler space indicates that the material has no in-plane preferred orientation.

Other fiber textures exist, such as those described in Table 2, but these generally cannot be directly measured. Instead, the orientation intensity along these fibers is obtained by analysis of the complete orientation distribution and the one-dimensional graphical presentation of the results is shown in simplified form. Fiber textures that occur in rolled metals, for example, are well defined and are often given in the literature as fiber plots. Figure 11 contains a typical gamma fiber from a cold-rolled steel sheet. The gamma fiber is defined in Table 2, and the major rolling texture components along the fiber are indicated in the figure.

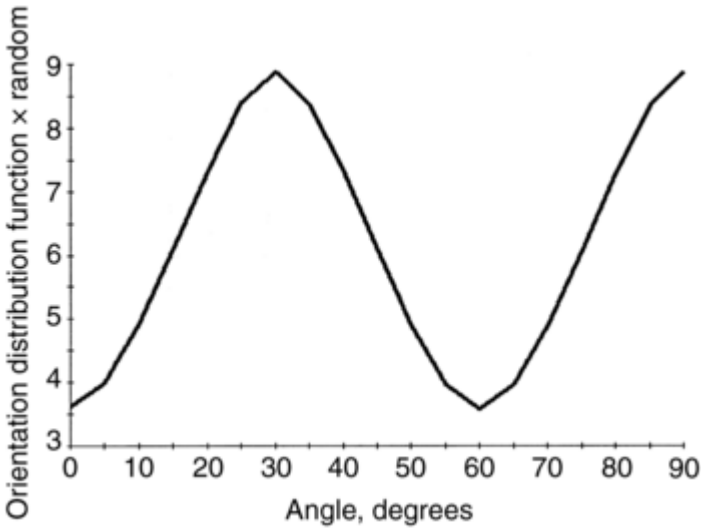

Fig. 11 Gamma fiber plot of rolled steel (γ-fiber is for {111} || ND)

Finally, skeleton line plots are often shown to indicate relative intensities of specific texture components. These are similar to fiber plots in that only one dimension of the orientation distribution is indicated. The skeleton lines, however, do not follow any typical fiber texture, but merely trace a line through orientation space that intersects several important texture components.

Approach Using Individual Orientation Measurements. There are a number of techniques that can be used to determine the orientations of individual crystallites. Using x-rays, Laue diffraction measurements can be made on single crystals to determine the orientation. This technique is usually restricted to large single crystals and is not practical for texture measurement. On the other hand, electron diffraction measurements generally give the orientations of single crystallites and distributions are obtained by making many measurements over a given area or through a given volume of material. (Diffraction measurements in the transmission electron microscope, or TEM, can give information for either single crystallites, spot patterns, or for distributions of crystallites, ring patterns.) X-ray diffraction generally gives information over the surface of the specimen, neutron diffraction through the volume, and electron diffraction at specific points. X-ray and neutron diffraction techniques typically yield the relative orientation density of a given family of planes, but do not uniquely determine the in-plane component of the orientation. The full information is only obtained after several pole figures are measured, and the ODF is calculated. Electron diffraction measurements of orientations commonly include Kikuchi patterns or spot patterns in the TEM and electron channeling diffraction (ECD) patterns or electron backscatter diffraction (EBSD) patterns in the scanning electron microscope (SEM) among other techniques (Ref 37, 40, 41). Each of these electron-diffraction-based techniques yields the full orientation directly for each crystallite.

Unlike the other techniques mentioned, automated EBSD analysis can measure large numbers of discrete, spatially specific orientations in a short time. As of the end of 2002, as many as 60 measurements per second were possible on well-prepared specimens. These point measurements are generally made over a regular array on the specimen surface, making the technique essentially an area measurement, similar to x-ray diffraction, but obtaining complete orientation information. Using a field emission source electron beam, the spatial resolution of EBSD in the transverse direction is of the order of 10 to 20 nm, depending on the backscattering coefficient of the material (Ref 41, Ref 42, 43). Because of its ease of use and wealth of experimental information, EBSD has become a popular texture measurement technique over the past decade or so for both local and bulk textures. Figure 12 shows a schematic of the specimen and electron beam geometry for EBSD measurements.

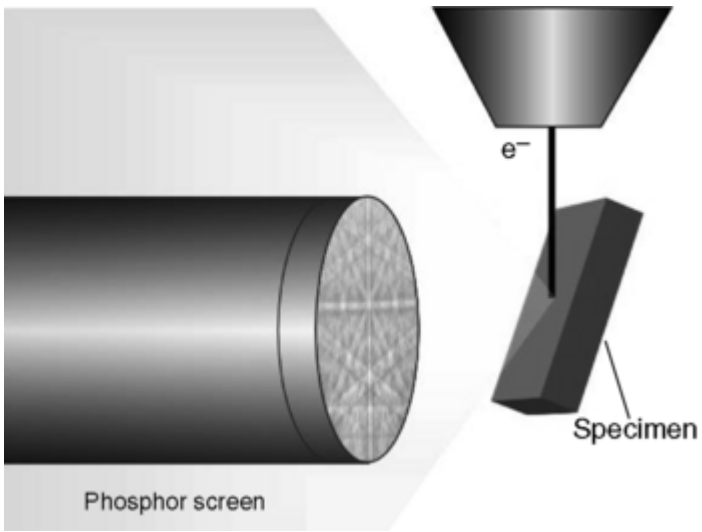

Fig. 12 Electron backscatter diffraction (EBSD) geometry showing the position of the phosphor screen relative to the specimen-beam interaction position

To obtain the orientation distributions from individual measurements requires the measurement of a large number of orientations obtained over a representatively large region. For random to weak textures the number of discrete measurements from individual grains required for reasonable statistical reliability is of the order of 10^3 to 10^4 (Ref 41). Stronger textures require correspondingly fewer measurements from individual crystallites. This information can be assimilated in a binning fashion to produce the desired result. Alternatively, the ODF can be determined by what amounts to an algebraic averaging of the coefficients for each crystallite in a Fourier series expansion representation of the function.

When ODFs are determined from discrete measurements, there is typically a Gaussian spread associated with each orientation instead of treating each measurement as a Dirac delta function (Ref 41, 44). Doing this requires appropriately distributing the fraction of each Gaussian peak into adjacent bins, effectively smoothing the function. The calculated texture strength for individual components is a function of the half-width of the Gaussian spread associated with each measurement. The correct half-width to use in texture determination is proportional to the strength of the texture and inversely proportional to the number of individual measurements collected. From the measured ODF, any of the previously described presentations of the texture are possible. The real strength of the individual orientation measurement techniques is in the spatially resolved nature of the measurements. This aspect of texture analysis is described in the following section.

References cited in this section

33. H.-J. Bunge, *Texture Analysis in Materials Science,* Butterworths, 1982

34. S.L. Altmann, *Rotations, Quaternions and Double Groups*, Clarendon Press, 1996

35. M.D. Vaudin, M.W. Rupich, M. Jowett, G.N. Riley Jr., and J.F. Bingert, Method for Crystallographic Texture Investigations Using Standard X-Ray Equipment, *J. Mater. Res.*, Vol 13, Oct 1998, p 2910–2919

36. H.-R. Wenk, Texture Analysis with TOF Neutrons, *Trans. Am. Crystallogr. Assoc.,* Vol 29, 1994, p 95–108

37. H. Weiland and R. Schwarzer, Determination of Preferred Orientations with the TEM, *Proceedings of the Seventh International Conference on Textures of Materials (ICOTOM 7),* Netherlands Society for Materials Science, 1984, p 857–862

38. H.-G. Brokmeier, Texture Analysis by Neutron Diffraction, *Mater. Sci. Forum,* Vol 156–157, 1994, p 59–70

39. A. Morawiec and D.P. Field, Rodrigues Parameterization for Orientation and Misorientation Distributions, *Philos. Mag. A*, Vol 73A, 1996, p 1113–1130

40. D.J. Dingley, A Comparison of Diffraction Techniques for the SEM, *Scanning Electron Microsc.*, Vol 258, 1981, p 273–286

41. A.J. Schwartz, M. Kumar, and B.L. Adams, *Electron Backscatter Diffraction in Materials Science*, Kluwer Academic/Plenum Publishers, 2000

42. K. Troost and J.-D. Kamminga, BKD in the SEM: Toward a Smaller Information Volume, *Proceedings—Annual Meeting, Microscopy Society of America*, 1994, p 606–607

43. F.J. Humphreys, Grain and Subgrain Characterisation by Electron Backscatter Diffraction, *J. Mater. Sci.*, Vol 36, Aug 2001, p 3833–3854

44. F. Wagner, H.-R. Wenk, C. Esling, and H.-J. Bunge, Importance of Odd Coefficients in Texture Calculations for Trigonal-Triclinic Symmetries, *Phys. Status Solidi A*, Vol A67, Sept 1981, p 269–285

D.P. Field, Textured Structures, *Metallography and Microstructures*, Vol 9, *ASM Handbook*, ASM International, 2004, p. 215–226

Textured Structures

David P. Field, Washington State University

Microtexture, Grain-Boundary Character, and Texture Gradients

Adjacent crystallites are related to one another by the misorientation, or the rotation required to bring the two lattices into coincidence with one another. The misorientation is easily determined by discrete measurement of the orientations making up the grain boundary. The probability density function describing the probability of occurrence for a specific type of misorientation is termed the misorientation distribution function (MDF). This function can be estimated from the ODF using the assumption that the orientation components are randomly distributed throughout the microstructure (Ref 45, 46). This assumption is rarely true, so the MDF is best obtained using discrete measurement techniques. In addition to the misorientation between neighboring grains, the grain-boundary plane normal orientation is often important in describing the structure of the interface. This five-parameter description of grain-boundary geometry is used in defining the grain-boundary character distribution (GBCD). The terms microtexture, or mesotexture, denote the statistics of spatially resolved orientations (Ref 47). The term microtexture is often used to describe grain-boundary geometry whether the full five-parameter description of the boundaries is used or the reduced description using only the three parameters required for the MDF. Similar to the ODF, the MDF can be described in certain instances with a reduced set of parameters. For example, the misorientation angle, sometimes called the disorientation, is commonly employed as a one-parameter description of the microtexture. Grain-boundary specific phenomena, such as second-phase growth or void coalescence, often occur heterogeneously with the structure of the crystallite interface controlling interface properties. The microtexture of the material controls the extent to which these phenomena manifest themselves in the structure.

Inherent in microtextural statistics is a description of orientation gradients through the material. Texture gradients often form during processing of the metal, resulting in heterogeneity of certain anisotropic material properties. Gradients can be defined over a large distance, such as across the width of a rolled sheet or over a distance consisting of only a few grains. An example of texture gradients affecting the properties of a product can be taken from the microelectronics industry where uniform film thickness is of highest importance.

Sputtering yield from a fabricated metal target is a function of texture. Tantalum is employed as a barrier layer for copper interconnects in integrated circuit (IC) fabrication and is useful as a case study since sputtering yield is high for {111} textures and low for {100} textures. Fabrication of tantalum plate by rolling typically results in inhomogeneous crystallographic texture with a strong through-thickness texture gradient (Ref 48). Depending on the through-thickness position in the plate at which texture is measured, one might find a predominantly (100) or (111) texture component (among other variants), resulting in significantly differing sputtering performance as a function of through-thickness position. A sputtering target made from such a structure would have widely varying sputtering rates both spatially and temporally. Such unpredictable performance would cause nonuniform and unpredictable thickness variation of the tantalum layer, potentially resulting in lost batches, poor IC performance, and frustrated process development engineers. Texture gradients are typically represented by plotting the variation in the strength of a texture as a function of distance. Figure 13 shows an orientation image of the through-thickness microstructure of a tantalum target containing bands of {111} and {100} texture components along with the corresponding angular deviation from the {100} fiber as a function of distance through the plate thickness (Ref 49).

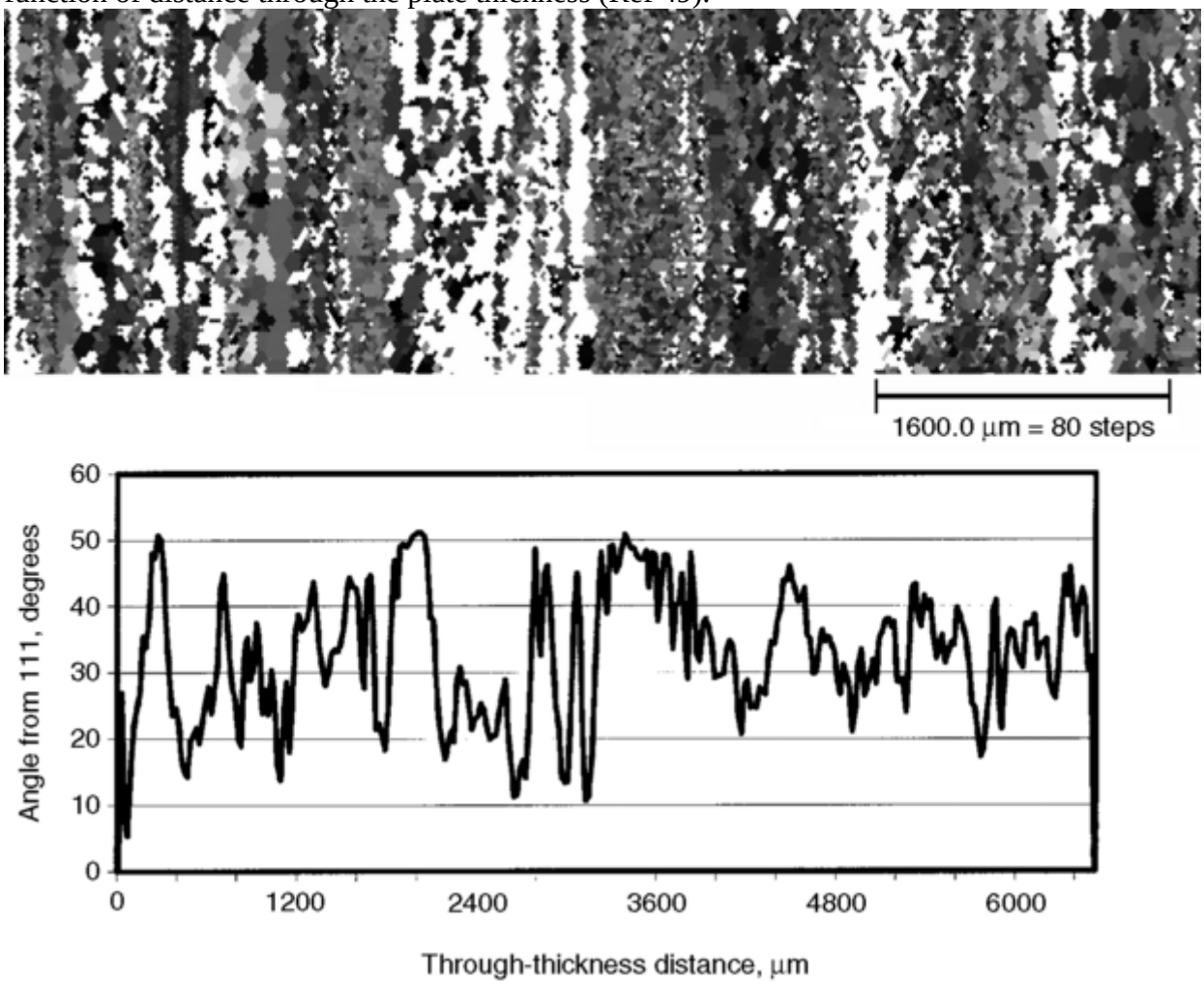

Fig. 13 Orientation image of tantalum plate showing the cross-section view. Shaded grains are near-{111} oriented. Also shown is a chart plotting the angular deviation from {100} as a function of position through the plate thickness.

References cited in this section

45. J. Zhao, B.L. Adams, and P.R. Morris, A Comparison of Measured and Texture-Estimated Misorientation Distributions in Type 304 Stainless Steel Tubing, *Textures Microstruct.*, Vol 8–9, 1988, p 493–508

46. F. Haessner, J. Pospiech, and K. Sztwiertnia, Determination of the Misorientation Distribution Function, *Mater. Sci. Eng.*, Vol 57, 1983, p 1–15

47. V. Randle, B. Ralph, and D.J. Dingley, Relationship between Microtexture and Grain Boundary Parameters, *Acta Metall.*, Vol 36, Feb 1988, p 267–273

48. S.I. Wright, A.J. Beaudoin, and G.T. Gray III, Texture Gradient Effects in Tantalum, *Mater. Sci. Forum*, Vol 157–162, 1994, p 1695–1700

49. S.I. Wright, D.P. Field, R.A. Witt, and C.A. Michaluk, On the Development of New Scalar Measures of Heterogeneity, *Mater. Sci. Forum*, Vol 408–412, 2002, p 107–112

D.P. Field, Textured Structures, *Metallography and Microstructures*, Vol 9, *ASM Handbook*, ASM International, 2004, p. 215–226

Textured Structures

David P. Field, Washington State University

Modeling of Texture Evolution

Since anisotropy of properties is important in understanding material behavior and in optimizing microstructure through processing, it is necessary to gain an understanding of texture evolution through modeling. Since the work of Taylor in 1938 (Ref 16), researchers have modeled individual lattice rotations as a function of imposed deformation. Modifications to Taylor's theory have resulted in improved predictive capability for modeling global texture evolution during metal deformation. Even though many of the assumptions of the Taylor model give cause to doubt its predictive capability, it is surprisingly successful in predicting deformation textures in many cases. Both slip and twinning mechanisms are taken into account in the models, and recovery mechanisms through dislocation climb have been explicitly incorporated in models of elevated-temperature processes. Self-consistent models describing global texture evolution using either a deterministic or stochastic approach contain both the kinematics and kinetics of deformation. The success of these models depends largely on the specific constitutive and hardening laws employed. Texture evolution is also built into finite-element based models by way of polycrystalline plasticity procedures (Ref 23, 48, 50, 51, 52, 53, 54). Finite-element calculations that include the proper constitutive relationships and crystal plasticity equations show that the agreement between observed and predicted rotations during plastic deformation is substantially improved by taking into account the interactions of neighboring grains. Much of the successful deformation modeling work has been done on single-phase fcc or body-centered cubic (bcc) metals using many of the simplifying assumptions of Taylor. Modeling of hexagonal close-packed (hcp) metals has also been attempted with similar approaches with a modicum of success.

Phase transformations that occur during cooling after high-temperature deformation of many metals and alloys introduces an additional complication into the modeling effort. The well-known Kurdjumov-Sachs orientation relationship between the austenite and ferrite structures, for example, gives a means of predicting the texture of grains deformed at high temperature in one phase, but transformed to a different phase during cooling. Similar orientation relationships exist in other metals. High-temperature deformation of titanium alloys often occurs in the β-phase (bcc) range with the final structure being primarily α-phase (hcp). Recent experimental observations and models predicting the texture evolution during processing of these materials have been presented in the literature (Ref 55).

Fundamental approaches to modeling of recrystallization textures require knowledge of the physics of both the nucleation and growth events. In general, nucleation is considered to be a random event, or the nuclei are artificially constrained to match the components observed in the recrystallization texture. Growth models employ either a Potts model approach or the recently more popular cellular automata technique. In some cubic metals, it has been observed that the primary recrystallization texture components are related to the deformed

structure by a 40° rotation about a 〈111〉 axis. Some recrystallization models are based on this observation (Ref 56, 57, 58, 59, 60, 61).

Models also exist that predict texture evolution during deposition and further processing of thin films and narrow metal lines fabricated for integrated circuits (Ref 27, 28, 29, 30). These have been developed because of the observed relationship in aluminum interconnect lines between electromigration resistance and a strong {111} fiber texture. The models are based on considerations of balancing surface and interface energy minimization, which result in a {111} texture for fcc films, with strain energy minimization, which results in a {100} texture for fcc metals. Texture evolution during further processing into narrow lines is additionally a function of grain-boundary energy minimization.

References cited in this section

16. G.I. Taylor, Plastic Strain in Metals, *J. Inst. Met.,* Vol 62, 1938, p 307–324

23. U.F. Kocks, C.N. Tome, and H.-R. Wenk, *Texture and Anisotropy: Preferred Orientations in Polycrystals and Their Effect on Materials Properties,* Cambridge University Press, 1998

27. C.V. Thompson and R. Carel, Texture Development in Polycrystalline Thin Films, *Mater. Sci. Eng. B,* Vol B32, 1995, p 211–219

28. J.M.E. Harper and K.P. Rodbell, Microstructure Control in Semiconductor Metallization, *J. Vac. Sci. Technol.,* Vol B15, July 1997, p 763–779

29. C. Lingk, M.E. Gross, and W.L. Brown, X-Ray Diffraction Pole Figure Evidence for (111) Sidewall Texture of Electroplated Cu in Submicron Damascene Trenches, *Appl. Phys. Lett.,* Vol 74, Feb 1999, p 682–684

30. J.E. Sanchez Jr., Effects of Crystallographic Orientation on Film Morphological Evolution, *Materials Research Society Symposium Proceedings,* Vol 343, 1994, p 641–652

48. S.I. Wright, A.J. Beaudoin, and G.T. Gray III, Texture Gradient Effects in Tantalum, *Mater. Sci. Forum,* Vol 157–162, 1994, p 1695–1700

50. R.J. Asaro and A. Needleman, Texture Development and Strain Hardening in Rate Dependent Polycrystals, *Acta Metall.,* Vol 33, June 1985, p 923–953

51. W. Gambin, *Plasticity and Textures,* Kluwer Academic Publishers, 2001

52. A.J. Beaudoin, P.R. Dawson, K.K. Mathur, and U.F. Kocks, Hybrid Finite Element Formulation for Polycrystal Plasticity with Consideration of Macrostructural and Microstructural Linking, *Int. J. Plast.,* Vol 11, May 1995, p 501–521

53. M.F. Horstemeyer and D.L. McDowell, Modeling Effects of Dislocation Substructure in Polycrystal Elastoviscoplasticity, *Mech. Mater.,* Vol 27, 1998, p 145–163

54. L. Delannay, S.R. Kalidindi, and P. Van Houtte, Comparison of Two Grain Interaction Models for Polycrystal Plasticity and Deformation Texture Prediction, *Int. J. Plast.,* Vol 18, March 2002, p 359–377

55. N.R. Barton and P.R. Dawson, On the Spatial Arrangement of Lattice Orientations in Hot-Rolled Multiphase Titanium, *Model. Simul. Mater. Sci. Eng.,* Vol 9, Sept 2001, p 433–463

56. O. Engler and H.E. Vatne, Modeling the Recrystallization Textures of Aluminum Alloys After Hot Deformation, *J. Mater. (JOM),* Vol 50, June 1998, p 23–27

57. B.J. Duggan, M. Sindel, G.D. Kohlhoff, and K. Lucke, Oriented Nucleation, Oriented Growth and Twinning in Cube Texture Formation, *Acta Metall.,* Vol 38, Jan 1990, p 103–111

58. A.D. Rollett and D. Raabe, A Hybrid Model for Mesoscopic Simulation of Recrystallization, *Comput. Mater. Sci.,* Vol 21, Jan 2001, p 69–78

59. L. Kestens and J.J. Jonas, Modeling Texture Change During the Static Recrystallization of Interstitial Free Steels, *Metall. Mater. Trans.,* Vol A27, Jan 1996, p 155–164

60. G. Gottstein and R. Sebald, Modelling of Recrystallization Textures, *J. Mater. Proc. Technol.,* Vol 117, Nov 2001, p 282–287

61. D.N. Lee, Strain Energy Release Maximization Model for Evolution of Recrystallization Textures, *Int. J. Mech. Sci.,* Vol 42, Aug 2000, p 1645–1678

D.P. Field, Textured Structures, *Metallography and Microstructures,* Vol 9, *ASM Handbook*, ASM International, 2004, p. 215–226

David P. Field, Washington State University

Acknowledgment

Some data used in preparation of this manuscript and helpful discussions with S.I. Wright and R.A. Witt of TexSEM Laboratories are gratefully acknowledged.

D.P. Field, Textured Structures, *Metallography and Microstructures,* Vol 9, *ASM Handbook*, ASM International, 2004, p. 215–226

Textured Structures

David P. Field, Washington State University

References

1. F. Barlat, S. Panchanadeeswaran, and O. Richmond, Earing in Cup Drawing Face-Centered Cubic Single-Crystals and Polycrystals, *Metall. Trans.,* Vol A22, July 1991, p 1525–1534

2. W.B. Hutchinson and H.E. Ekstrom, Control of Annealing Texture and Earing in Non-Hardenable Aluminum Alloys, *Mater. Sci. Technol. Ser.,* Vol 6, Nov 1990, p 1103–1111

3. S.X. Ding and J.G. Morris, Processing of AA3004 Alloy Can Stock for Optimum Strength and Formability, *Metall. Mater. Trans.,* Vol A28, Dec 1997, p 2715–2721

4. J. Savoie, Y. Zhou, J.J. Jonas, and S.R. MacEwen, Textures Induced by Tension and Deep Drawing in Aluminum Sheets, *Acta Mater.,* Vol 44, Feb 1996, p 587–605

5. X.M. Cheng and J.G. Morris, Texture, Microstructure and Formability of SC and DC Cast Al-Mg Alloys, *Mater. Sci. Eng. A,* Vol A323, Jan 2002, p 32–41

6. R.P. Reade, P. Berdahl, R.E. Russo, and S.M. Garrison, Laser Deposition of Biaxially Textured Yttria-Stabilized Zirconia Buffer Layers on Polycrystalline Metallic Alloys for High Critical Current Y-Ba-Cu-O Thin-Films, *Appl. Phys. Lett.,* Vol 61, Nov 1992, p 2231–2233

7. A. Goyal, D.P. Norton, D.K. Christen, E.D. Specht, M. Paranthaman, D.M. Kroeger, J.D. Budai, Q. He, F.A. List, R. Feenstra, H.R. Kerchner, D.F. Lee, E. Hatfield, P.M. Martin, J. Mathis, and C. Park, Epitaxial Superconductors on Rolling-Assisted Biaxially-Textured Substrates (RABiTS): A Route towards High Critical Current Density Wire, *Appl. Superconduct.,* Vol 4, Oct–Nov 1996, p 403–427

8. A. Bottcher and K. Lucke, Influence of Subsurface Layers on Texture and Microstructure Development in RGO Electrical Steel, *Acta Metall. Mater.,* Vol 41, Aug 1993, p 2503–2514

9. I. Samajdar, S. Cicale, B. Verlinden, P. Van Houtte, and G. Abbruzzesse, Primary Recrystallization in a Grain Oriented Silicon Steel: On the Origin of Goss{110}[001] Grains, *Scr. Mater.,* Vol 39, Sept 1998, p 1083–1088

10. P. Gangli and J.A. Szpunar, The Role of Sigma-5 Coincidence Boundaries in the Growth Selection of Fe-3-Percent Si, *J. Mater. Process. Technol.,* Vol 47, Dec 1994, p 167–184

11. S. Nakashima, K. Takashima, and J. Harase, Effect of Tin Addition on Process of Secondary Recrystallization of Fe-3-Percent-Si, *Tetsu-to-Hagané,* Vol 80, Feb 1994, p 137–142

12. S. Suzuki, Y. Ushigami, H. Homma, S. Takebayashi, and T. Kubota, Influence of Metallurgical Factors on Secondary Recrystallization of Silicon Steel, *Mater. Trans.,* Vol 42, June 2001, p 994–1006

13. J. Harase, R. Shimizu, K. Takashima, and T. Watanabe, Effect of AlN on the Secondary Recrystallization of 3%Si-Fe Alloy, *Trans. Iron Steel Inst. Jpn.,* Vol 27, 1987, p 965–973

14. N.A. Pangarov, *J. Electroanal. Chem.,* Vol 9, 1965, p 70–85

15. R.W. Hertzberg, *Deformation and Fracture Mechanics of Engineering Materials,* 4th ed., John Wiley & Sons, 1995

16. G.I. Taylor, Plastic Strain in Metals, *J. Inst. Met.,* Vol 62, 1938, p 307–324

17. J.F.W. Bishop and R. Hill, A Theory of the Plastic Distortion of a Polycrystalline Aggregate under Combined Stresses, *Philos. Mag.,* Vol 42, 1951, p 414–427

18. J. Gil-Sevillano, P. Van Houtte, and E. Aernoudt, Large Strain Work Hardening and Textures, *Prog. Mater. Sci.,* Vol 25, 1980, p 69–412

19. J.H. Driver, D. Juul-Jensen, and N. Hansen, Large Strain Deformation Structures in Aluminum Crystals with Rolling Texture Orientations, *Acta Metall. Mater.,* Vol 42, Sept 1994, p 3105–3114

20. W. Gambin, *Plasticity and Textures,* Kluwer Academic Publishers, 2001

21. D. Raabe, M. Sachtleber, Z. Zhao, F. Roters, and S. Zaefferer, Micromechanical and Macromechanical Effects in Grain Scale Polycrystal Plasticity Experimentation and Simulation, *Acta Mater.,* Vol 49, Oct 2001, p 3433–3441

22. C.S. Lee and B.J. Duggan, Simple Theory for the Development of Inhomogeneous Rolling Textures, *Metall. Trans. A*, Vol A22, Nov 1991, p 2637–2643

23. U.F. Kocks, C.N. Tome, and H.-R. Wenk, *Texture and Anisotropy: Preferred Orientations in Polycrystals and Their Effect on Materials Properties,* Cambridge University Press, 1998

24. M. Ferry and F.J. Humphreys, Deformation and Recrystallization of Particle-Containing {011}[100] Aluminum Crystals, *Acta Mater.,* Vol 44, Aug 1996, p 3089–3103

25. H.E. Vatne, O. Engler, and E. Nes, Effect of Precipitates on Texture Development, *Mater. Sci. Forum,* Vol 157, 1994, p 1501–1506

26. F.J. Humphries and M. Hatherly, *Recrystallization and Related Annealing Phenomena,* Pergamon Press, 1995

27. C.V. Thompson and R. Carel, Texture Development in Polycrystalline Thin Films, *Mater. Sci. Eng. B,* Vol B32, 1995, p 211–219

28. J.M.E. Harper and K.P. Rodbell, Microstructure Control in Semiconductor Metallization, *J. Vac. Sci. Technol.,* Vol B15, July 1997, p 763–779

29. C. Lingk, M.E. Gross, and W.L. Brown, X-Ray Diffraction Pole Figure Evidence for (111) Sidewall Texture of Electroplated Cu in Submicron Damascene Trenches, *Appl. Phys. Lett.,* Vol 74, Feb 1999, p 682–684

30. J.E. Sanchez Jr., Effects of Crystallographic Orientation on Film Morphological Evolution, *Materials Research Society Symposium Proceedings,* Vol 343, 1994, p 641–652

31. D.P. Tracy and D.B. Knorr, Texture and Microstructure of Thin Copper Films, *J. Electron Mater.,* Vol 22, 1993, p 611–616

32. E.M. Zielinski, R.P. Vinci, and J.C. Bravman, Effects of Barrier Layer and Annealing on Abnormal Grain Growth in Copper Thin Films, *J. Appl. Phys.,* Vol 76, Oct 1994, p 4516–4523

33. H.-J. Bunge, *Texture Analysis in Materials Science,* Butterworths, 1982

34. S.L. Altmann, *Rotations, Quaternions and Double Groups,* Clarendon Press, 1996

35. M.D. Vaudin, M.W. Rupich, M. Jowett, G.N. Riley Jr., and J.F. Bingert, Method for Crystallographic Texture Investigations Using Standard X-Ray Equipment, *J. Mater. Res.,* Vol 13, Oct 1998, p 2910–2919

36. H.-R. Wenk, Texture Analysis with TOF Neutrons, *Trans. Am. Crystallogr. Assoc.,* Vol 29, 1994, p 95–108

37. H. Weiland and R. Schwarzer, Determination of Preferred Orientations with the TEM, *Proceedings of the Seventh International Conference on Textures of Materials (ICOTOM 7),* Netherlands Society for Materials Science, 1984, p 857–862

38. H.-G. Brokmeier, Texture Analysis by Neutron Diffraction, *Mater. Sci. Forum,* Vol 156–157, 1994, p 59–70

39. A. Morawiec and D.P. Field, Rodrigues Parameterization for Orientation and Misorientation Distributions, *Philos. Mag. A,* Vol 73A, 1996, p 1113–1130

40. D.J. Dingley, A Comparison of Diffraction Techniques for the SEM, *Scanning Electron Microsc.,* Vol 258, 1981, p 273–286

41. A.J. Schwartz, M. Kumar, and B.L. Adams, *Electron Backscatter Diffraction in Materials Science,* Kluwer Academic/Plenum Publishers, 2000

42. K. Troost and J.-D. Kamminga, BKD in the SEM: Toward a Smaller Information Volume, *Proceedings—Annual Meeting, Microscopy Society of America,* 1994, p 606–607

43. F.J. Humphreys, Grain and Subgrain Characterisation by Electron Backscatter Diffraction, *J. Mater. Sci.,* Vol 36, Aug 2001, p 3833–3854

44. F. Wagner, H.-R. Wenk, C. Esling, and H.-J. Bunge, Importance of Odd Coefficients in Texture Calculations for Trigonal-Triclinic Symmetries, *Phys. Status Solidi A,* Vol A67, Sept 1981, p 269–285

45. J. Zhao, B.L. Adams, and P.R. Morris, A Comparison of Measured and Texture-Estimated Misorientation Distributions in Type 304 Stainless Steel Tubing, *Textures Microstruct.,* Vol 8–9, 1988, p 493–508

46. F. Haessner, J. Pospiech, and K. Sztwiertnia, Determination of the Misorientation Distribution Function, *Mater. Sci. Eng.,* Vol 57, 1983, p 1–15

47. V. Randle, B. Ralph, and D.J. Dingley, Relationship between Microtexture and Grain Boundary Parameters, *Acta Metall.,* Vol 36, Feb 1988, p 267–273

48. S.I. Wright, A.J. Beaudoin, and G.T. Gray III, Texture Gradient Effects in Tantalum, *Mater. Sci. Forum,* Vol 157–162, 1994, p 1695–1700

49. S.I. Wright, D.P. Field, R.A. Witt, and C.A. Michaluk, On the Development of New Scalar Measures of Heterogeneity, *Mater. Sci. Forum,* Vol 408–412, 2002, p 107–112

50. R.J. Asaro and A. Needleman, Texture Development and Strain Hardening in Rate Dependent Polycrystals, *Acta Metall.,* Vol 33, June 1985, p 923–953

51. W. Gambin, *Plasticity and Textures,* Kluwer Academic Publishers, 2001

52. A.J. Beaudoin, P.R. Dawson, K.K. Mathur, and U.F. Kocks, Hybrid Finite Element Formulation for Polycrystal Plasticity with Consideration of Macrostructural and Microstructural Linking, *Int. J. Plast.,* Vol 11, May 1995, p 501–521

53. M.F. Horstemeyer and D.L. McDowell, Modeling Effects of Dislocation Substructure in Polycrystal Elastoviscoplasticity, *Mech. Mater.,* Vol 27, 1998, p 145–163

54. L. Delannay, S.R. Kalidindi, and P. Van Houtte, Comparison of Two Grain Interaction Models for Polycrystal Plasticity and Deformation Texture Prediction, *Int. J. Plast.,* Vol 18, March 2002, p 359–377

55. N.R. Barton and P.R. Dawson, On the Spatial Arrangement of Lattice Orientations in Hot-Rolled Multiphase Titanium, *Model. Simul. Mater. Sci. Eng.,* Vol 9, Sept 2001, p 433–463

56. O. Engler and H.E. Vatne, Modeling the Recrystallization Textures of Aluminum Alloys After Hot Deformation, *J. Mater. (JOM),* Vol 50, June 1998, p 23–27

57. B.J. Duggan, M. Sindel, G.D. Kohlhoff, and K. Lucke, Oriented Nucleation, Oriented Growth and Twinning in Cube Texture Formation, *Acta Metall.,* Vol 38, Jan 1990, p 103–111

58. A.D. Rollett and D. Raabe, A Hybrid Model for Mesoscopic Simulation of Recrystallization, *Comput. Mater. Sci.,* Vol 21, Jan 2001, p 69–78

59. L. Kestens and J.J. Jonas, Modeling Texture Change During the Static Recrystallization of Interstitial Free Steels, *Metall. Mater. Trans.,* Vol A27, Jan 1996, p 155–164

60. G. Gottstein and R. Sebald, Modelling of Recrystallization Textures, *J. Mater. Proc. Technol.,* Vol 117, Nov 2001, p 282–287

61. D.N. Lee, Strain Energy Release Maximization Model for Evolution of Recrystallization Textures, *Int. J. Mech. Sci.,* Vol 42, Aug 2000, p 1645–1678

D.P. Field, Textured Structures, *Metallography and Microstructures,* Vol 9, *ASM Handbook,* ASM International, 2004, p. 215–226

Textured Structures

David P. Field, Washington State University

Selected References

- B.L. Adams, S.I. Wright, and K. Kunze, Orientation Imaging: The Emergence of a New Microscopy, *Metall. Trans.,* Vol 24A, 1993, p 819–831
- S.L. Altmann, *Rotations, Quaternions and Double Groups,* Clarendon Press, 1996
- H.-J. Bunge, *Texture Analysis in Materials Science,* Butterworths, 1982
- H.-J. Bunge, R. Grossterlinden, A. Haase, R. Ortega, J.A. Szpunar, and P. Van Houtte, Advanced Experimental Techniques in X-Ray Texture Analysis, *Mater. Sci. Forum,* Vol 156–157, 1994, p 71–96
- B.D. Cullity and S.R. Stock, *Elements of X-Ray Diffraction,* 3rd ed., Prentice Hall, 2001
- W. Gambin, *Plasticity and Textures,* Kluwer Academic Publishers, 2001
- G. Gottstein and O. Engler, Local Texture Measurement with the Scanning Electron Microscope, *J. Phys.,* Vol 3, Nov 1993, p 2137–2142
- H. Hu, Texture of Metals, *Texture,* Vol 1, 1974, p 233–243
- F.J. Humphries and M. Hatherly, *Recrystallization and Related Annealing Phenomena,* Pergamon Press, 1995
- U.F. Kocks, C.N. Tome, and H.-R. Wenk, *Texture and Anisotropy: Preferred Orientations in Polycrystals and Their Effect on Materials Properties,* Cambridge University Press, 1998
- N.C. Krieger-Lassen, K. Conradsen, and D. Juul-Jensen, Image Processing Procedures for Analysis of Electron Back Scattering Patterns, *Scanning Microsc.,* Vol 6, 1992, p115–121
- Proceedings of the International Conference on Textures of Materials (ICOTOM); Meetings held every third year
- V. Randle and O. Engler, *Introduction to Texture Analysis: Macrotexture, Microtexture, and Orientation Mapping,* Taylor and Francis, 2000
- A.J. Schwartz, M. Kumar, and B.L. Adams, *Electron Backscatter Diffraction in Materials Science,* Kluwer Academic/Plenum Publishers, 2000
- Website of the International Committee of Texture of Materials: http://www.texture-anisotropy.org/Default2.htm

D. Aliya, Metallographic Sectioning and Specimen Extraction, *Metallography and Microstructures,* Vol 9, *ASM Handbook,* ASM International, 2004, p. 229–241

Metallographic Sectioning and Specimen Extraction

Debbie Aliya, Aliya Analytical, Inc.

Introduction

SECTIONING, the removal of a conveniently sized and representative specimen from a larger piece, is the first major operation in the preparation of metallographic specimens. The other operations, discussed in subsequent articles, include mounting (not always performed), grinding/polishing, etching (not always performed), and examination of the specimen. Metallurgical sectioning may also be used to prepare specimens for tests other than macrostructure or microstructure evaluation. In this case, the term specimen extraction may be more appropriate. Many of the techniques described in this article apply to extracting metallurgical test coupons for hardness or other mechanical tests, or for scanning electron microscopy or energy-dispersive spectroscopy or other microchemical analysis procedures that may precede metallography in complete materials characterization programs or failure analysis protocols.

Metallurgical sectioning is important and critical when preparing specimens for physical or microscopic analysis. First and foremost, metallography is, by its nature, a destructive test, whereby some material is lost in the preparation process. In classical metallography, where a cross section is used, the kerf, or width of the cut, is material lost (Fig. 1). Grinding and polishing create additional losses. Even in field metallography work, where the component evaluated is left intact, some surface layers must be removed. Therefore, extreme care must be taken in selecting test locations, even when the sectioning operation only involves sanding and grinding to a particular depth. In particular, the careful metallographer should take precautions before sectioning any component that appears as though it may have been returned from the field in a damaged condition. Company policy may or may not protect individual workers from potential legal repercussions when evidence is knowingly or unknowingly destroyed in a failure analysis investigation.

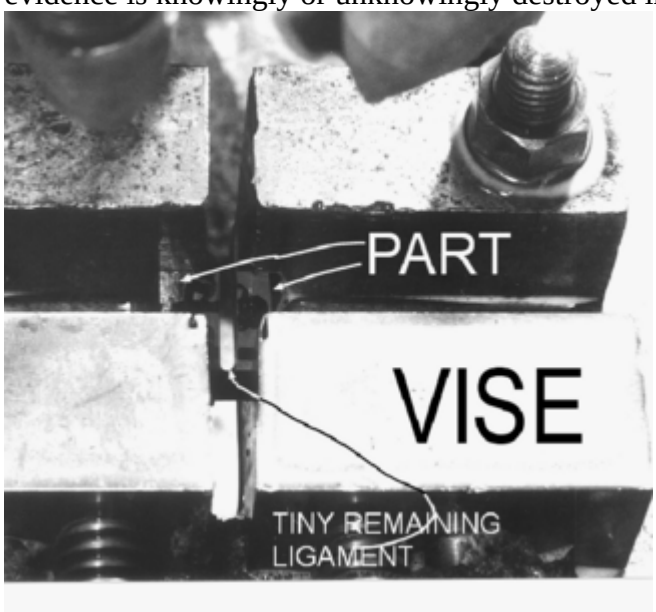

Fig. 1 Final portion of section being cut. Very slow cutting at the final portion of the section can minimize the risk of burning the specimen.

In addition to the obvious issue of material loss, sectioning also alters the material condition at the test location. For example, residual stress patterns and many dimensional characteristics, especially of formed parts, will be

altered in unpredictable ways. These consequences should be understood prior to making any cuts, especially if metallography is part of a component or process failure analysis. In this case, it is necessary to describe dimensional characteristics and make decisions about the need for determination of residual stress before any sectioning. Incorrect preparation techniques can also cause microstructural changes that lead to erroneous conclusions.

Ideally, changes in microstructure from the sectioning process should be avoided. However, because some hot and cold working inevitably occurs from most sectioning methods, compromises must be made in order to get the job done. The damage to the specimen during sectioning depends on the material being sectioned, the nature of the cutting device used, the cutting speed and feed rate, and the amount and type of coolant used. On some specimens, surface damage near the cut is inconsequential and can be removed during subsequent grinding and polishing. The depth of damage varies with material and sectioning method (Fig. 2) (Ref 1). In any case, the competent metallographer develops a habit of checking every single specimen for burn or deformation damage at the area of interest before embedding it in a mounting compound, where it is usually much more difficult to evaluate. Burn damage is visible and in the less severe cases is confined to the area near the final separation. See Fig. 3.

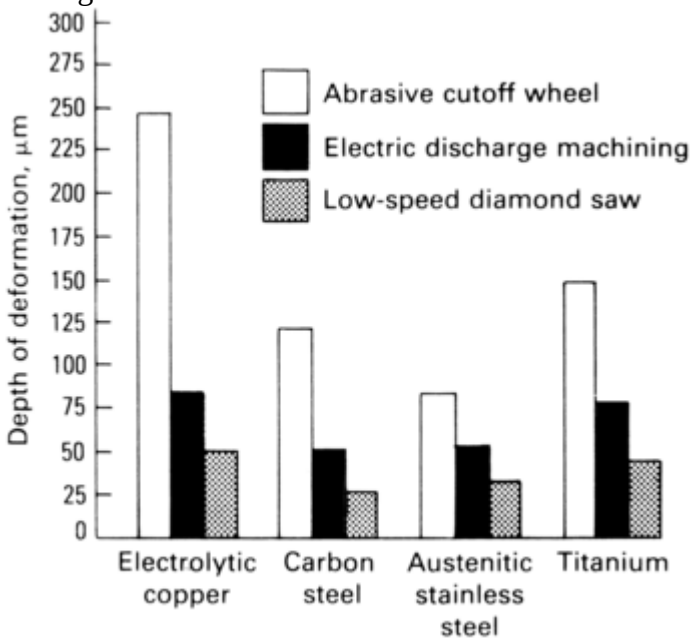

Fig. 2 Depth of deformation in different metals due to cutting method. Source: Ref 1

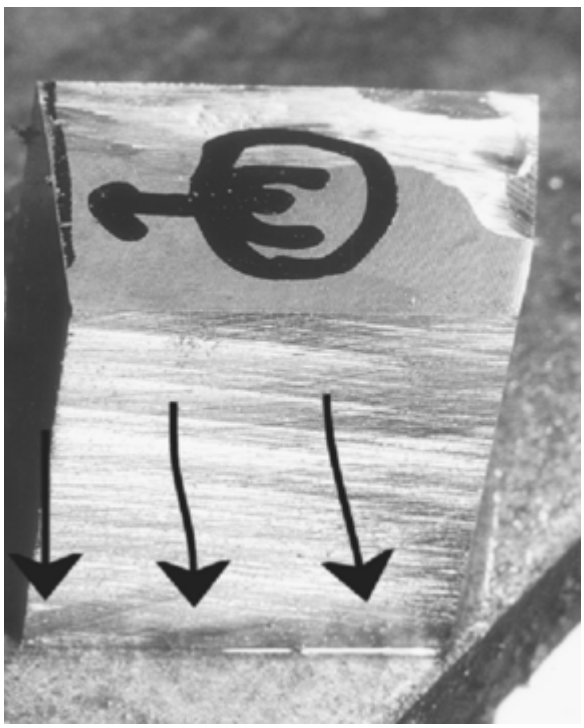

Fig. 3 Burn marks (arrows) confined to the area near final separation. Sometimes, in order to speed the cutting operation, one may allow burn marks, as long as they are not near the area of interest. However, this practice is only considered advisable for experienced and skilled practitioners.

This article describes the sectioning process, some general practices, common tools, and guidelines on how to select a cutting tool for a given metallographic sectioning operation. This article also covers issues related to specimen test location for certification work as well as for process troubleshooting and component failure analysis. For much metallography work, company procedures define test locations for "in process" certification work. The technician who is performing the work does not need to ask where the best location is, because the location is standardized for each component. While there are many benefits of standardizing the test location, especially those related to process control issues, most process control metallographic work is done with ease of specimen preparation in mind. This is natural, and there is nothing wrong with making the choice of test locations for pragmatic reasons. However, when a component problem arises, if the metallographic work is to actually provide information about the problem, the test location selection process should include more inputs than ease and speed of making the cut. Thus, this article gives significant coverage to issues related to specimen test location for certification work as well as for process troubleshooting and component failure analysis.

Reference cited in this section

1. G.F. Vander Voort, *Metallography: Principles and Practice*, McGraw-Hill, 1984, reprinted by ASM International, 1999

D. Aliya, Metallographic Sectioning and Specimen Extraction, *Metallography and Microstructures*, Vol 9, *ASM Handbook*, ASM International, 2004, p. 229–241

Metallographic Sectioning and Specimen Extraction

Debbie Aliya, Aliya Analytical, Inc.

Process and Practices

Metallographic sectioning is a technology that is best performed by skilled workers. It requires skill, knowledge, and craftsmanship in the proper use of tools, which is a key part of any technology. A skilled metallographer with good communication abilities is an essential part in helping beginners and those with a lower skill level. Much of the information in this first part is that which has traditionally been passed on more by word of mouth from experienced to less experienced metallography technicians or among metallurgists within particular companies.

This section describes some things to think about before making the first cut. On the surface, metallographic sectioning appears to be a type of machining process, although this is not the best way to consider metallographic sectioning. The dominant principle in machining is to produce a certain shape with stable fixturing of the workpiece and efficient feeds and speeds. In contrast, the dominant principle in sectioning is to prevent damage and reduce changes in the specimen condition from the heat or deformation of the sectioning process. Thus, the habit of selecting and using a suitable cutting medium, rather than simply using whatever is most convenient, is the first step in becoming a professional metallographer. Likewise, the ingrained habit of stopping to think about test location and orientation issues before cutting the specimen is an important part of metallography.

In selecting a test location, it is important to note that metallography attempts to represent a three-dimensional object using only two-dimensional images. Many metallography texts describe early work done by geologists and mathematicians that shows that this is a legitimate assumption, because the characteristics of the material are the same in all directions, or isotropic. However, most real metallic components that are manufactured by

humans are not isotropic. This means that, depending on the orientation of the cut, the characteristics revealed may differ. In order to ensure that one has an overall understanding of the characteristics of the component, multiple sections may be required. To select the appropriate sections, a detailed understanding of how the component was manufactured, step by step, is necessary.

Variation of macrostructural and microstructural characteristics revealed by sectioning in different orientations or directions has many sources, including rate of heat extraction as a function of position in the component during solidification, deformation of grains during hot- or cold-working operations, thermal conductivity and diffusion rate variations during heat treating operations, as well as surface effects. The only really completely isotropic metals may be some types of spheroidal powder metal particles, prior to being compressed into an actual component blank. Performing metallography over time will allow the attentive worker many insights into materials science and engineering concepts.

Other things that affect the characteristics revealed by the properly performed metallographic process include the thickness or size of the component at the section location. An example of a strong dependence of section thickness on microstructure would be components made of heat treated unalloyed or low-alloy steel, as well as most castings. In addition, many nonferrous materials are very susceptible to significant structural changes with very small process variations. Layers near the surface of a component may have totally different characteristics from those in the interior of the component. Forgings (including hot- or cold-headed components), extrusions, stampings, and castings may all have very different characteristics depending on the test position and orientation.

Cutting of Cross Sections for Macroscale, Mesoscale, and Microscale Examination. When metallographic preparations are being planned and performed, it is always necessary to keep the specific goal of the work in mind. Despite the fact that much metallographic sectioning resembles a cutting or machining process, it is best to keep in mind the ultimate objective of obtaining a suitable specimen for metallographic analysis. One must also realize that the best test orientation to allow easy measurement of one characteristic may be different from another. One may decide to compromise and “make do” with a nonideal test location for one of the measurements, or one may decide to make an additional section, if possible. In any case, it is necessary to keep in mind the limitations of the essentially two-dimensional metallographic test method.

Metallographic sectioning may be performed for many different specific reasons. The specific purpose of the test will determine how much of the component or material cross section will be evaluated. The types of sections can be grouped into the categories macroscale, mesoscale, and microscale.

Macroscale Structure Evaluation. Macrostructure is that level of structure that may be best evaluated by the unaided eye, with proper lighting. Macrostructure analysis is used to evaluate for such features as consistency of composition in large sections and presence of large-scale imperfections in castings or forgings. Grain flow in forgings and extrusions are generally considered to be macroscale evaluations and are performed either on complete cross sections of the component, or specific critical sections, if the part is too large for a complete section (see Fig. 4). If a partial section is to be used for macroanalysis, it is important that the test location be determined by someone who understands both the use of the component (subsequent manufacturing or in-service stress distribution) and the details of the manufacturing process that is being evaluated. High-stress locations and heavily worked locations, for example, might be considered as having high priorities for evaluation. Depending on the cutting method used, grinding and rough polishing may be required, and etching is often required following sectioning.

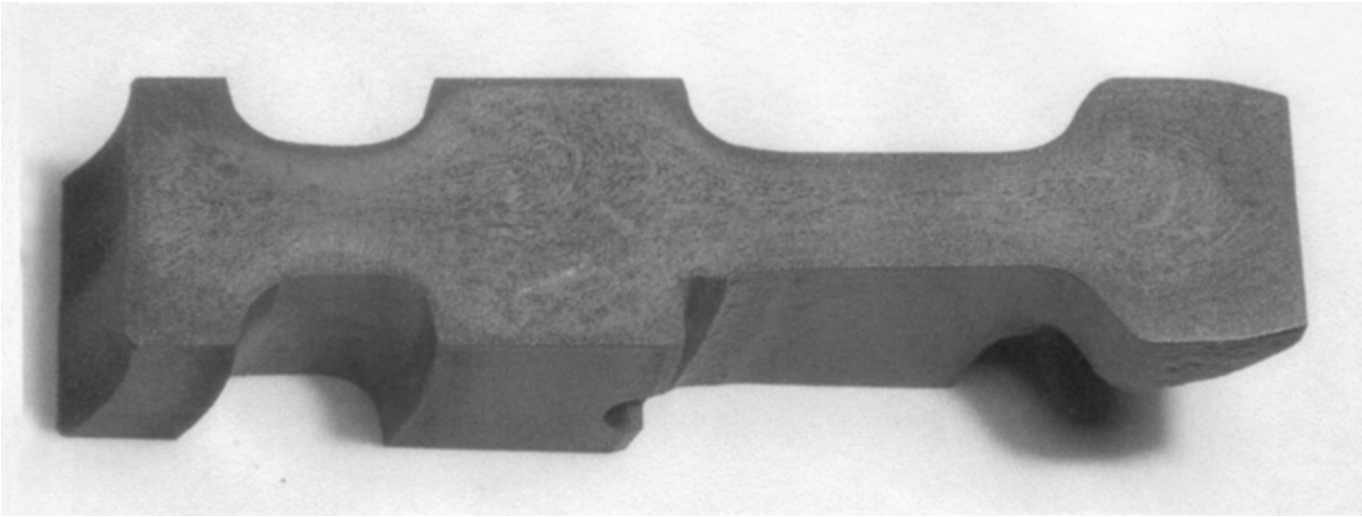

Fig. 4 Macroetch coupon prepared by heating smooth ground specimen in hot acid. This shows macroscale features related to the grain flow during forging. Macroetch sections do not need to be as smooth as microetch sections.

Mesoscale structure analysis is a term without significant historical precedence in metallography, but is useful to help one avoid overlooking a characteristic that might be of interest. This level of focus, between macrolevel and microlevel metallography, includes the types of features revealed on polished metallographic coupons, but visible to the naked eye or at low magnification (up to 10×). Uniformity of case depth and microsegregation are examples of using the mesolevel of metallography (see Fig. 5). A metallographic specimen of a small fastener as-cold-headed for grain flow may also be considered a mesoscale structure analysis.

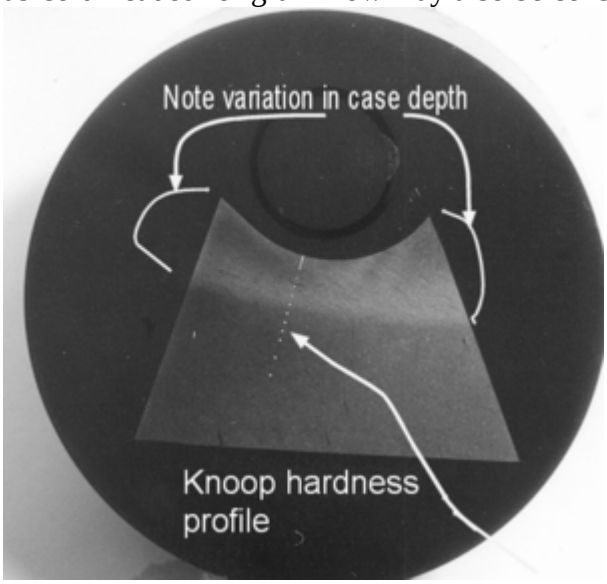

Fig. 5 Microetch coupon of a case-hardened steel with Knoop microindentation hardness profile. This section allows mesoscale evaluation of structure, in this case, variation of case depth.

When the decision is made to include only a small testpiece instead of a larger one, some mesoscale information is lost. Because the scale of mesofeatures is (generally) finer than that of macrofeatures, at least grinding, and often rough or fine polishing, may be required to eliminate interference from surface finish features created by the sectioning operation.

Microscale analysis, possibly the most familiar to people who work outside of primary metal production facilities or forging companies, is performed with the goal of observing features that cannot be seen with low-level magnification and requires use of a higher-powered microscope. Microstructure evaluation work includes identification and distribution of phases present, measurement of depth of thin surface layers, and determination of the presence of objectionable imperfections that cannot be seen with the naked eye (see Fig. 6). Microlevel analysis requires careful preparation of a true metallographically polished specimen, usually a deformation-free

mirror finish. Before selecting a specific location for microstructural examination, it is wise to perform at least a cursory mesoscale evaluation, so that one knows whether the area one has selected is typical or not. Again, although only a tiny specimen may be required to perform the measurement or evaluation, extracting very small sections prevents meaningful mesoscale analysis, and thus important information regarding whether the viewed features are typical of the whole component is left in doubt. When imperfections of any type are being looked for in a microlevel metallographic cross section, the less material in the sample, the lower the chance of finding the imperfection, even if it is present.

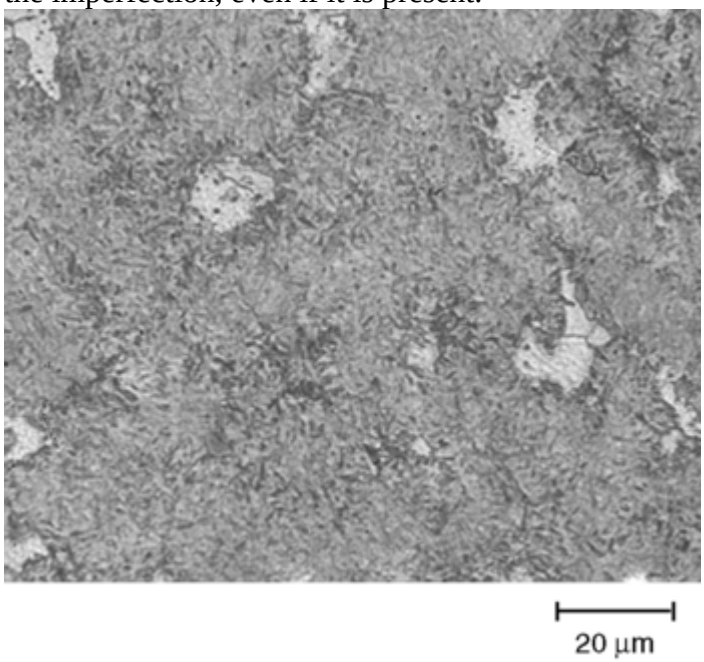

Fig. 6 Micrograph used to evaluate localized differences in the structure Original magnification. 500×

Preparation and planning of the sectioning process depends on several factors. Skill, knowledge, and craftsmanship are especially required when planning to cross section a damaged component. In fracture analysis, for example, the fracture area must be carefully protected. The failure analyst must also consider where the high-stress locations or imperfections in a given component might be. Since most heat treat shop floor employees, and most metallurgists for that matter, are not skilled in the art of guessing, it is to be expected that the convenient location and orientation will be chosen. When a corrosion failure is suspected, cutting operations must proceed only after careful examination by a qualified or authorized individual has shown that contamination by the cutoff saw coolant will not interfere with the corrosion analysis. If contamination by the coolant is not allowed, some other cutting tool must be selected. (For more information on metallurgical sectioning in failure analysis see “Sectioning” on page 398 and pages 501–503 of *Failure Analysis and Prevention,* Volume 11 of the *ASM Handbook*, 2002.)

In more routine instances, product specifications may indicate a particular test location or is left to the judgment of the metallographer. In externally threaded fasteners, for example, certification calls out for a decarburization test at half the thread flank height (see Fig. 7). In many other cases, the section may be cut at a convenient location and orientation. The most convenient position will probably depend on the type of fixture and saw available, so this may be difficult for an outside design engineer to guess. Cylindrical or rectangular sections are generally easier to clamp than tapered or spherical sections. If an axial (or longitudinal) section is required, rectangular sections are easier to clamp than cylindrical sections. Thus, unless someone specifies a longitudinal section on a cylindrical section, for example, which is required if the evaluation is being performed to classify nonmetallic inclusions in wrought steel, it is likely that the metallographer, on his own, will make a transverse cut on a cylindrical section.



Fig. 7 Midheight of the thread flank (arrows). This is the standard test location for evaluating decarburization or carburization by Knoop or Vickers microindentation hardness methods.

Metallographers and machining technicians should be aware, when making axial (radial or longitudinal) cuts on heat treated or heavily deep-drawn hollow components, of the possibility of the presence of residual stresses that often tend to close the newly created surfaces toward each other, thus pinching the blade. This can be a particular problem (saw blade damage) as the last bit of the cut is made. Some hints for dealing with this situation are provided later in this article. It is also possible that cylindrical parts will tend to pop open when sectioned along an axial direction. As-welded, roll-formed tubing and some extruded shapes may be susceptible to this type of postmachining shape change. A little bit of thought about the test setup can minimize the chances of this “springback”-related wheel damage.

Another common practical consideration that the metallographer is likely to evaluate is the amount of material to be cut. Obviously, it will take less time to section the thinner portion of a component with a nonconstant cross section. This should raise an alarm for the designer of the component, because the thinner area will tend to have different characteristics than the thicker one. In the case of many carbon and low-alloy steels, the thinner area may have a more uniform microstructure than the thicker area. If the purpose of the evaluation is to find residual lack of uniformity, checking the thinnest part of the component may not be the most desirable action. Mechanical properties associated with the structure differences obviously vary as well. While many design engineers are not aware of these issues, metallography lab personnel at heat treating companies can help raise their customers' awareness of these structure and associated property variation issues. Ideally, the metallographic cross-section location should be indicated on the engineering drawing, after consideration of the manufacturing and use issues previously noted.

The key point here is that the tool(s) available for cutting play a significant role in determining the test location. In many routine metallography laboratory operations, a metallurgical abrasive cutoff saw will be the standard choice. This is also the preferred choice for routine certification work for many alloys, including evaluation of grain size and most other microstructural characteristics of ferrous alloys, and many other alloys as well. Metallurgical cutoff saws are specifically designed to minimize changes in the structure of the material due to excessive heat buildup and deformation next to the cut. A combination of properly directed water jets and appropriate choice of abrasive medium keeps the part cool. Proper subsequent metallographic grinding and polishing should remove the thin layers of remaining deformed material (see the article “Mechanical Grinding and Polishing” in this Volume).

Small parts with reasonably stiff cross sections can be easily clamped in a standard vise with only minimal deformation of the adjacent layers. Thin curved parts may be more difficult to clamp without deforming adjacent areas. Some imagination must be exercised to allow the material to be clamped securely without deforming the specimen at the relevant test location. For example, sectioning of thin annealed cylindrical stainless steel or brass components may be particularly challenging, because of their low resistance to plastic deformation. If the purpose of the metallographic section is to evaluate the effectiveness of the annealing process, for example, even small amounts of deformation can introduce artifacts by producing deformation (mechanical) twins (subgrains).

It is best to take every practical measure to avoid confusion by creative fixture design, such as clamping directly on a small segment of the rim of the component with a vise grip, and clamping the vise grip in the saw

vise. It is possible to make both transverse and axial cuts with this fixturing device. Small fasteners and other small cylindrical components may also be held this way to make otherwise difficult longitudinal cuts. Tiny parts that do not have a critical test location may be laid directly in a mounting press without sectioning. The grinding-and-polishing process then acts as the sectioning operation.

Also note that new automatic grinder polishers may sometimes be set to remove a specified amount of material. This may be the only way for the less experienced technician to get reliably close to the diameter, for example, on a longitudinal specimen on small-diameter wire. Small screw heads may be ground flush with the thread major diameter, using a water-cooled metallurgical grinding wheel or belt prior to mounting, in order to avoid fixturing difficulties.

Small components in general pose some unique challenges. Obviously, if a component is being held by one end instead of being securely clamped on both ends, the amount of force that can be applied at any location away from the clamp is lower than the amount that could otherwise be applied before objectionable deflection occurs. Deflection of the component is undesirable for several reasons. First of all, if a transverse section is desired, especially if numerical data are to be obtained, only a cut that is perpendicular to the part axis will have a direct relationship between distances measured on the cross section and actual distances from position to position within the component. In other words, a transverse specimen cut from a hollow cylindrical part that has an elliptical or oval cross section will have an apparently varying wall thickness, even if the wall thickness itself is uniform. Likewise, a uniformly case-hardened cylindrical part will appear to have a varying case depth if the cut is not perpendicular to the axis of the cylinder surface. If the parts are mounted before being polished and etched, and if the mounting compound is not transparent, it can be impossible to tell whether the variations in wall thickness or case depth are real or apparent.

Secondly, a part that is not securely clamped may shift due to the forces of the abrasive wheel during the cutting operation. If the part shifts after the wheel has made a partial cut, a high lateral force may be exerted on the wheel. Since most abrasive wheels have little ductility, this lateral force will often result in shattering the wheel. Since most metallurgical cutoff saw abrasive wheels are reasonably highly engineered components sold by specialty companies, they are expensive. Prematurely broken wheels are generally undesired. Here one can begin to understand that, except for the most routine metallographic sectioning, much judgment is required in making trade-offs between getting what might be the ideally desired cross section and getting a deformation-free cross section that is not heat affected both in a timely manner and without breaking the abrasive wheels at an unacceptable rate.

In addition to the clamping geometry, the wheel material itself has a significant effect on controlling undesired heat buildup in the component. In many cases, it is helpful to consult the technical sales departments at the specialty metallography companies that sell the wheels to get advice on which wheel to choose for routine and special sectioning jobs. The technology and science of preparing metallographic cross sections has been under development for many decades. When preparing cross sections of unfamiliar materials, it is a good idea to consult with the experts in the technical support departments at the metallography supply houses. Some of these companies have gone to great effort to document successful sectioning procedures for almost every alloy that humans have developed. Some sectioning methods may not be self-evident. For example, it is recommended that the sectioning of a part coated with thermal spray be accomplished using an abrasive silicon carbide blade, rather than a diamond wheel to avoid debonding of the coating from the substrate. It is also important to keep the coating in compression—not tension—during cutting.

Any part with a nonuniform cross section may present challenges in fixturing. Fragments to be sectioned as part of a failure analysis, for example, must be sectioned with additional considerations kept in mind. It is generally unacceptable to clamp on the fracture surface. If the visual examination and photo documentation have been completed, and any areas to be subject to scanning electron microscopy have been determined, it may be acceptable to clamp adjacent areas of the fracture surface with a rubber pad between the clamp and the fracture surface. This will generally do a reasonable job of protecting macroscale features, although it is not advised to touch the area of most interest with anything at all. This includes the water-based coolant in the saw. So before sectioning any part containing a fracture surface, precautions must be made to prevent loss of evidence related to contamination or corrosion processes that might have been a factor in the failure. In addition to these issues, when only one end of the sample must be gripped, assess whether the part can be held in a manner such that the region of interest remains in the clamp after the sectioning is performed. This will reduce the risk of damage to a fracture surface once the piece has been sectioned and is free from the sample.

Protection from contamination by the coolant fluid itself may be performed by use of acetate or silicone replicas, which can trap some of the loose contaminant on the fracture surface and hold it in position for future evaluation. However, if the contaminant or corrosion product contains carbon or oxygen, acetate replicas will make any subsequent chemical analysis of the contaminant more difficult, and if the specimen contains silicon or oxygen, silicone replicas will have the same disadvantage for silicon- and oxygen-containing contaminant or corrosion product. In addition, bits of the acetate or silicone can get stuck in the crevices of the specimen. This is a bigger problem for fracture surfaces than for part surfaces, although heavily corroded part surfaces can have many crevices as well. The silicone material is more rubbery and can thus be pulled out of somewhat more difficult geometries than the acetate material. If the part is small enough, it is wise to perform energy dispersive spectrometry/wavelength dispersive spectrometry (EDS/WDS) prior to metallographic sectioning.

The metallographer or lab technician may consider making one or several replicas to trap the contaminants, leaving another replica in place during the sawing (see Fig. 8). It is a good idea to experiment with a similarly shaped component with comparable fracture features before depending on the replica material to act as a barrier during the sectioning operation. The replica material may become loose or fall off, which would then allow the coolant to contaminate the specimen.

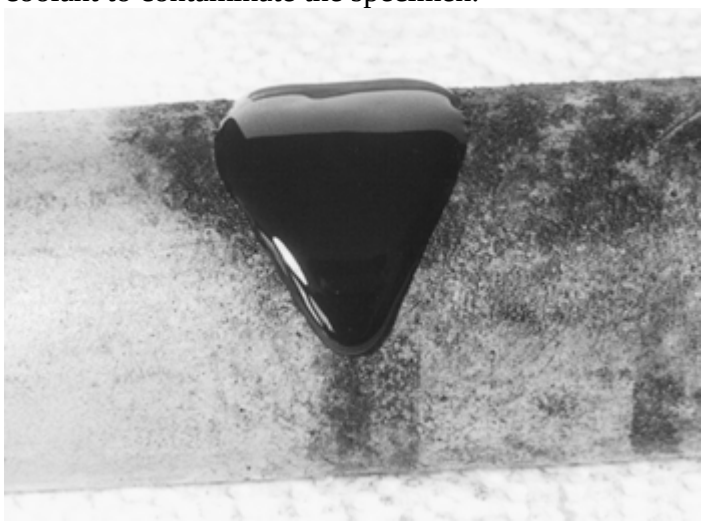

Fig. 8 Silicone replicating material to preserve evidence of corrosion processes, corrosion product position, as well as fracture features. In some fixturing setups, replicating material left in place may protect the underlying surface from contamination by the coolant.

Skill, knowledge, and craftsmanship are required to select and cross section components that have failed by a corrosion process. Such cutting operations must proceed only after careful examination by a qualified or authorized individual has shown that contamination by the cutoff saw coolant will not interfere with the corrosion analysis. If contamination by the coolant is not to be allowed, some other cutting tool must be selected.

D. Aliya, Metallographic Sectioning and Specimen Extraction, *Metallography and Microstructures,* Vol 9, *ASM Handbook*, ASM International, 2004, p. 229–241

Metallographic Sectioning and Specimen Extraction

Debbie Aliya, Aliya Analytical, Inc.

Abrasive Cutting

Abrasive cutting is the sectioning of material using a relatively thin rotating disk composed of abrasive particles supported by a suitable medium. The thousands of particles contacting the material in rapid succession and at

very high speeds section the material. Methods of abrasive cutting offer various cutting characteristics useful for most material-sectioning situations. The quality of the cut surface obtained is often superior to that obtained by other means, and fewer subsequent steps may be required. Metal-matrix diamond blades handle such specialized applications as ceramics, rocks, very hard metallics, and printed circuit boards.

Abrasive cutting is the most widely used method of sectioning materials for microscopic examination and other material investigations. Conventional abrasive cutting using consumable wheels is the most popular method for routine metallographic sectioning, because it is fast, accurate, and economical. Other methods include the use of hacksaws, shears, burning torches, wire saws, and electrical discharge machining discussed in the section "Other Cutting Methods" in this article.

Equipment

The metallurgical cutoff saw is designed and engineered to provide a means of metallographic sectioning, typically with a consumable cutting wheel and the application of a coolant to ensure an almost plane surface without serious mechanical or thermal damage.

When equipped with a properly selected abrasive wheel, a water-cooled metallurgical cutoff saw is typically the safest and most efficient cutting method for most metallographic work, such as certification work involving determination of grain size, inclusion ratings, case depth, plating thickness, and the volume fraction of microstructural phases. Despite the benefits of this method, it is still possible, even easy, to burn or overheat specimens while cutting them. Certain specimen configurations and material types also are prone to deformation. Therefore, care must be exercised in order to avoid these problems, and a brief review is given here on how the cut is made.

An abrasive cutoff saw includes a high-speed motorized drive for a consumable, replaceable wheel. The most common type of wheel contains abrasive particles held in place by some type of polymeric material (rubber is also used, or a mixture of rubber and resin). In summarizing this information, since harder materials require more force of wheel against specimen, more heat is generated at the cut. Each abrasive particle acts somewhat like a knife edge, scraping away a bit of the material. The deformation associated with the scraping generates heat. If the water jets are properly aimed at the cut location, and an excessive amount of force is not applied, then the water cools the part as fast as the heat is generated, and the part is protected (see Fig. 9).

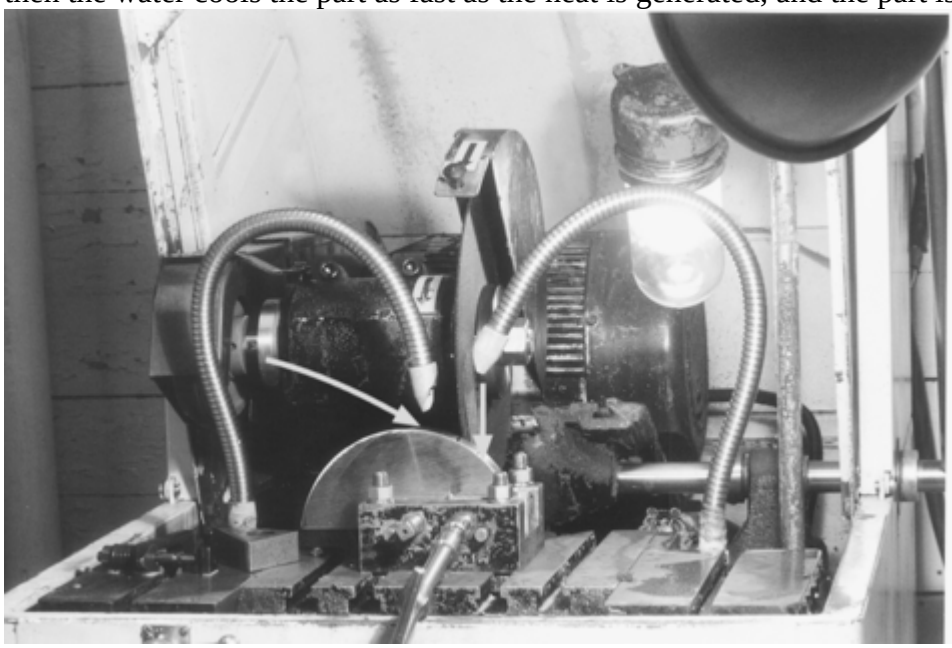

Fig. 9 Flexible nozzle hoses can be used to direct coolant to the area to be cut (arrows).

The most critical part of the cut is the last bit to separate, since it is difficult to get the coolant to the bottom of the cut, unless an immersion-type saw is used. Even so, as the last bit of material is being removed, the connecting ligament available to conduct heat away from the cut site becomes very small (see Fig. 1, where the cutting was stopped just before the final separation). On most metallurgical abrasive saws, the experienced operator can learn to detect a change in the way the saw sounds as the last part of the cut is being approached.

For some common fixture setups, a constant force will allow a noticeable increase in speed of cut just before the end. Slowing down as the last bit of material is cut away helps to avoid local overheating. Alternatively, the metallographer can maximize efficiency by clamping any critical areas in such a manner as to cut them first, so that he is not delayed by protecting against a small burn in a location that is not of interest (see Fig. 10).

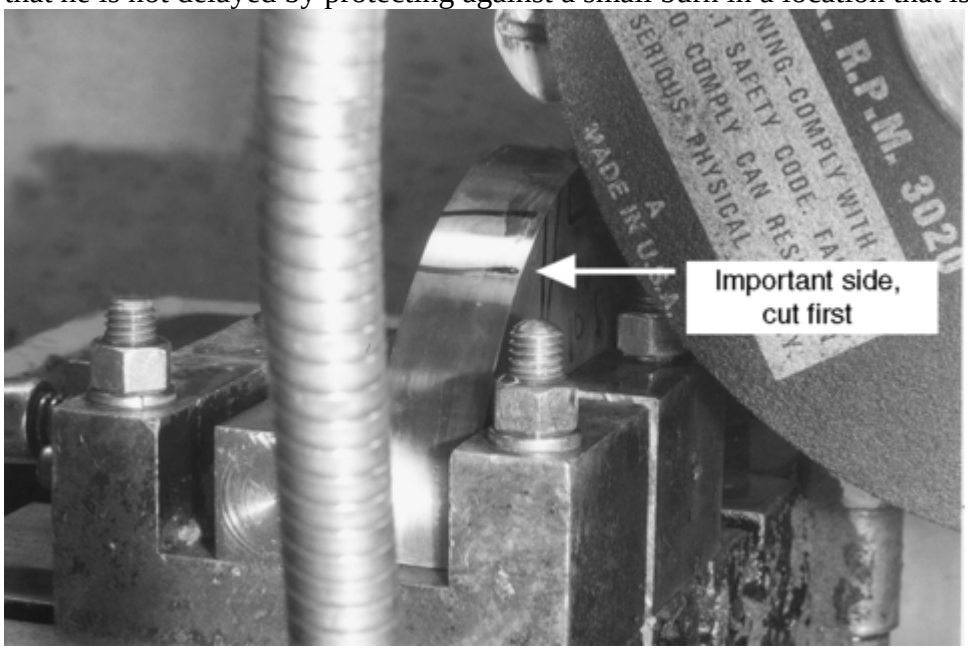

Fig. 10 Setup to cut the critical surface first (arrow). Cutting the critical surface first is one way to optimize cutting speed and also to prevent burning of the specimen at the critical location

In general, it is desired to clamp in a way that the force of the blade will not be able to move the fragments of the part. Note that pushing the blade into the surface of the component generates a force, which will attempt to move the component. Only the fixture keeps the two sides of the cut in position. Many fixturing setups appear to be acceptable when checked by pushing on the parts by hand prior to initiating the cut. However, as the cut progresses, and the remaining material thins, the three-point bending condition tends to close the part onto the blade, creating a pinching condition that in turn tends to cause undesired catastrophic damage to the blade. Sometimes it may be desirable to clamp only one side of a part held in a vise, if the unclamped side can fall away from the blade at the end of the cut. Alternatively, the cut may be stopped just short of complete separation, and the fragments can be broken apart by hand or pried apart with a screwdriver, for example. The fragment of interest can be easily deburred on a sanding disk or belt.

One other challenging fixture setup situation involves tapered or rounded parts. If the component edge where the blade first contacts is not perpendicular to the blade, the edge of the blade will tend to wander. If the blade does “bite into” the component while the blade is deflected from its flat, rest position, it may turn the rotating blade into a flattened cone shape! Again, this is not a stable situation. Aside from the greatly increased likelihood of breaking a blade, the component may get damaged in the area of interest. Very slow cutting (with minimal force) at the beginning of such cuts on tapered components may help to avoid annoying wheel fractures.

Use of a cutoff saw with a T-slot table gives flexibility to metallographers to cut parts of many configurations. However, some parts are just too big to be efficiently cut or to be clamped in the saw at all. In these cases, other cutting tools can be used, often to get the part down to a size that will fit into the metallurgical saw for the final cut. Small cutoff saws generally do not have T-slot tables, but are equipped only with a small vise.

Handheld Electric or Pneumatic Rotary Abrasive Cutters. For small, light parts that must be kept free from liquid contamination, a high-speed rotary abrasive cutter offers a lot of flexibility. These tools do generate dust from the specimen itself as well as the wheel as it breaks down. If information on corrosion products or suspected contaminants that are adhering to the specimen is required, it may be worth making an acetate or silicone replica or replicas prior to cutting the part. The dust can be blown off the component with a stream of dry compressed air after sectioning. In addition, there is a lot of local heat generated at the cut. Stainless steel, of the common industrial materials, is particularly easy to burn or overheat with this method. Aluminum and magnesium also burn easily.

In general, the part will have to be clamped or held in place by some device, such as a bench vise, during the cutting. Attention to clamping-related deformation must be considered with this method. High-speed rotary devices can create a fair amount of damage. In addition, high-speed rotary devices have also been known to be associated with human injuries. Attention to recommended safety procedures is important. Care should be taken to wear a protective eyewear and an air-filtering mask or to perform this sectioning under a fume hood.

Consumable-Abrasive Cutting

Wheel Selection. In selecting a wheel for a particular application, the abrasive, bonding material, bond hardness, and density must be considered. Coolant, wheel speed, applied pressure, and wheel edge wear affect the quality of the cut (Table 1) (Ref 2). Abrasive wheels afford more control over the conditions used than do other types of specimen sectioning. Many factors determine the suitability of a particular wheel when cutting a given material:

- The nature of the abrasive
- The size of the abrasive grains
- The nature of the bond
- The hardness of the bond
- The porosity of the wheel

Table 1 Solutions for problems encountered in abrasive cutoff sectioning

Problem	Possible cause	Solution
Burning (bluish discoloration)	Overheated specimen	Increase coolant rate; lessen cutting pressure; choose softer wheel.
Rapid wheel wear	Wheel bond breaking down too rapidly	Choose harder wheel; lessen cutting pressure.
Frequent wheel breakage	Uneven coolant distribution, loose specimen fixturing	Distribute coolant uniformly; fix specimen rigidly.
Resistance to cutting	Slow wheel breakdown	Choose softer wheel; use oscillating stroke.
Cutter stalls	Cutter too light for the work	Use heavier cutter; limit sample size.

Source: Ref 2

Silicon carbide is preferred for cutting nonferrous metals and nonmetals. Alumina (Al_2O_3) is recommended for ferrous metals. Coarse-grain wheels generally cut heavier sections faster and cooler, but fine-grain wheels produce smoother cuts with less burring. Fine-grain wheels are therefore recommended for cutting delicate materials, such as thin-wall tubing. Cutoff wheels with grit sizes from 60 to 120 are recommended for sectioning metallographic specimens. The surface finish does not require coarse grinding, and the grinding sequence usually can begin with a 180-grit silicon carbide.

Resin-bonded wheels, which have very high cutting rates, are generally used for dry cutting and find application in plant production cutting. Wet cutting wheels require a rubber or rubber-resin bond and are used in metallographic laboratories.

The rate of wheel deterioration depends on the type of bond used. Resin- and resinoid-bonded wheels generally break down more rapidly than rubber-bonded wheels. The rubber bond retains abrasive particles more tenaciously, resulting in slower wheel wear and more cuts per wheel. In addition, the rubber forms a solid bond; that is, there are no pores. However, resin used as a bond sets up in a polymerization process and there are extremely small pores throughout the wheel that may or may not be near abrasive grains. Therefore, resin-bonded wheels wear away faster, but always present a fresh cutting surface, because each abrasive grain is ejected before it becomes dull. The abrasive used is more important than the bond. Selection of bond is usually based on objections to the odor of burning rubber as the wheel degrades.

Two terms used in selecting abrasive cutoff wheels are “hard” and “soft.” These terms do not refer to the hardness of the abrasive grains, but to how the wheel breaks down. Silicon carbide (approximately 9.4 on the Mohs scale) and Al_2O_3 (approximately 9.0) differ only slightly in hardness. A hard wheel (one made with hard bonding material) is usually best for cutting soft stock, because it will last longer and because the lower forces to cut the soft material will not create the danger of burning. A soft wheel is preferred for cutting hard

materials, specifically to prevent burning. A good general-purpose cutoff wheel is a medium-hard silicon carbide abrasive wheel.

In rubber-resin wheels, the amount of bonding material and the percentage of free space determine the hardness or wheel grade. A more porous, less dense (softer) wheel breaks down faster because the abrasive particles are held more loosely. Softer wheels are used because fresh, sharp abrasive grains are more frequently exposed. Less porous, more dense wheels are harder, break down slower, and are better for softer materials.

Coolants. Water alone should not be used as a coolant for wet sectioning. A coolant should contain a water-soluble oil with a rust-inhibitor additive, which protects the moving parts of the cutoff machine, minimizes the possibility of burning, and produces better cuts. Some foaming of the coolant is desirable.

The preferred cooling condition is submerged sectioning, in which the entire piece is under water. Submerged sectioning is recommended for heat-sensitive materials that undergo microstructural changes at low temperatures. For example, as-quenched alloy steels with an untempered martensitic microstructure can readily transform to tempered martensite with the frictional heat developed. The quality of a submerged cut is excellent, and the specimens produced will not require extensive grinding. Section size, material, and hardness dictate whether submerged cutting can be employed. Submerged cutting will tend to make a wheel bond act harder.

Wheel Speed and Edge Wear. Wheel speed must be carefully considered in the design of a cutter and the selection of wheels for a given cutter. In the interest of safety, maximum operating speeds printed on the specific blade or wheel should never be exceeded. Also, increased wheel speed may introduce frictional heat, which damages the microstructure.

Wheel edge wear may be used to determine whether the correct wheel has been selected. Abrasive wheels that show little or no wear are not performing satisfactorily. Controlled wheel loss indicates that the wheel bond is breaking down, exposing fresh abrasive grains for faster, more effective, and cooler cutting. Wheels that do not deteriorate fast enough may become glazed with specimen material, resulting in poor cutting and excessive specimen heating. Exerting additional pressure will most likely cause overheating.

The acceptable rate of wheel loss is:

$$LR = \frac{M}{W}$$

where LR is wheel life ratio, M is area of material cut, and W is area of abrasive wheel consumed. In plant production cutting, resin-bonded wheels are commonly used without a coolant. Rate of cutting is the main concern, because this step probably precedes any heat treating. In this application, an M/W ratio of 1.5 to 1 is acceptable. In other words, 1.5 times more material should be cut as wheel area consumed.

Surface Damage. Abrasive-wheel sectioning can produce damage to a depth of 1 mm (0.04 in.). However, control of cutting speed, wheel pressure, and coolant application minimizes damage.

Nonconsumable-Abrasive Cutting

The exceptional hardness and resistance to fracturing of diamond make it an ideal choice as an abrasive for cutting. Because of its high cost, however, diamond must be used in nonconsumable wheels. Diamond bort (imperfectly crystallized diamond material unsuitable for gems) that has been crushed, graded, chemically cleaned, and properly sized is attached to a metal wheel using resin, vitreous, or metal bonding in a rimlock or a continuous-rim configuration.

Metal-bonded rimlock wheels consist of metal disks with hundreds of small notches uniformly cut into the periphery. Each notch contains many diamond particles, which are held in place with a metal bond. The sides of the wheel rim are serrated and are considerably thicker than the core itself, a construction that does not lend itself to delicate cutting. When cutting more ductile materials, the blades will require more frequent dressing.

Rimlock blades are recommended for the bulk cutting of rocks and ceramics where considerable material loss may be tolerated. Kerosene or mineral spirits are used as the coolant/lubricant, and a constant cutting pressure or feed must be maintained to avoid damaging the rim.

Continuous-rim resin-bonded wheels consist of diamond particles attached by resin bonding to the rim of a metal core. These blades are suitable for cutting very hard metallics, such as tungsten carbide, and nonmetals, such as high-alumina ceramics, dense-fired refractories, and metal-ceramic composites. Water-based coolants are used.

Wafering Blades. For precision cutting of metallographic specimens or thin-foil specimens for transmission electron microscopy, very thin, small-diameter wafering blades are used. These blades are usually constructed of diamond, metal powders, and fillers that are pressed, sintered, and bonded to a metal core. Wafering blades are available in high and low diamond concentrations. Lower concentrations are better for harder materials, particularly the nonmetals; higher concentrations are preferred for softer materials.

Wafering blades may be used with diamond saws. Unlike some other methods of sectioning, the diamond saw uses relatively low speeds (300 rpm maximum) and a thin, continuous-rim diamond-impregnated blade to accomplish true cutting of nearly all solid materials. Applications include cutting of hard and soft materials, brittle and ductile metals, composites, cermets, laminates, miniature devices, and honeycombs. The as-cut surface is generally free of damage and distortion and is ready for microscopic examination with minimum polishing or other preparation. Figure 11illustrates a typical low-speed diamond saw.

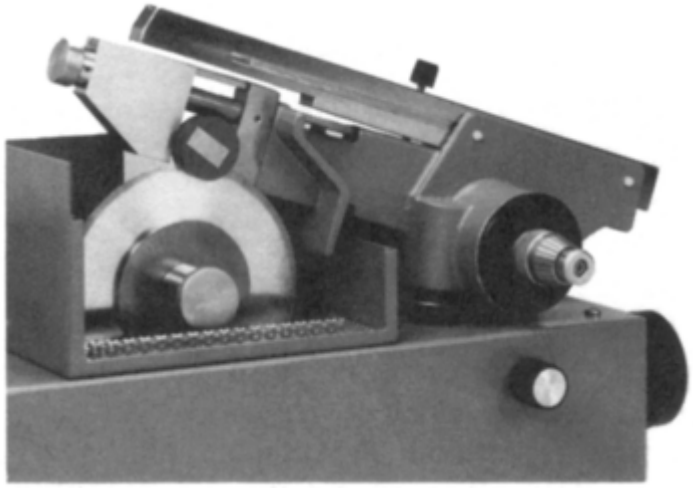

Fig. 11 Typical low-speed diamond saw

Wire Saws (Ref 3)

The need to produce damage-free, single-crystal semiconductor surfaces for the electronics industry has generated interest in using the wire saw in the metallographic laboratory. Applications include:

- Removing samples from the bulk material
- Cutting electronic assemblies for failure analysis
- Cutting thin-wall tubing
- Cutting fiber-reinforced and laminated composite materials
- Cutting honeycomb structural materials (Fig. 12, 13)
- Cutting polymers (Fig. 14)
- Cutting metallic glasses (Fig. 15)
- Preparing thin specimens for transmission electron microscopy, electron probe microanalysis, ion probe analysis, and x-ray diffraction analysis

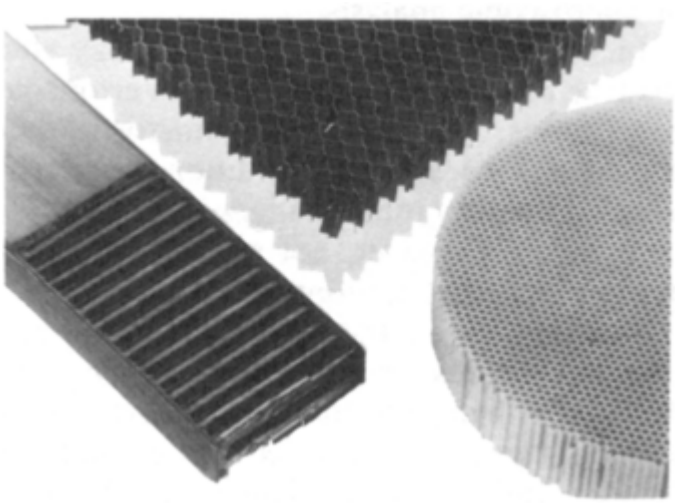

Fig. 12 Three pieces of honeycomb cut with a diamond wire saw. Note the absence of burrs and breakout. From left: titanium; section from helicopter rotor blade consisting of plastic, paper honeycomb, epoxy, stainless steel screws, and Kevlar; extruded ceramic honeycomb used in automotive catalytic converters

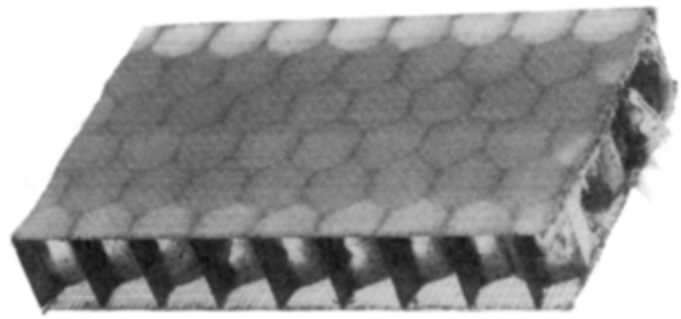

Fig. 13 Kevlar honeycomb cut with a wire saw

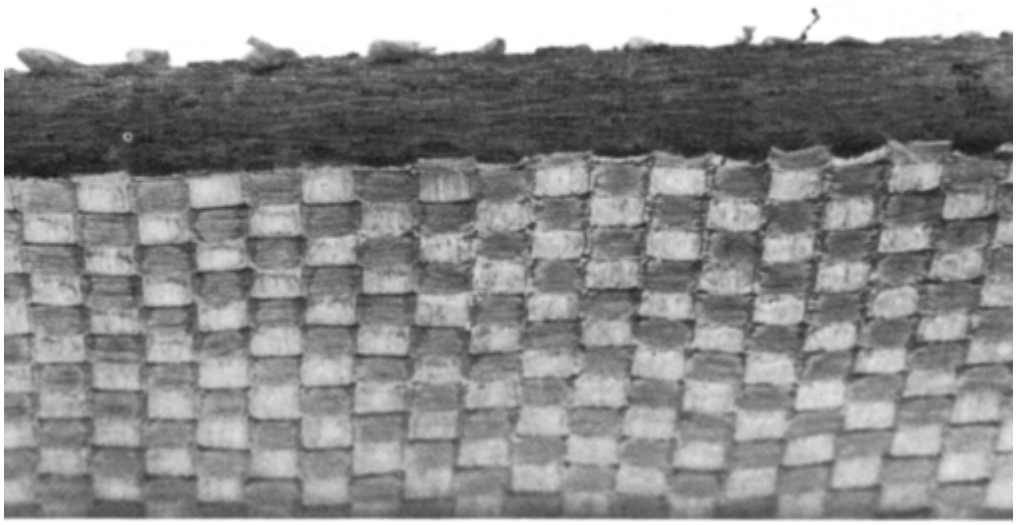

Fig. 14 Woven Kevlar cut with a wire saw. This material is used in bulletproof vests. When woven into thick pieces, it is used in tanks and is comparable to armor steel plate of equal thickness.

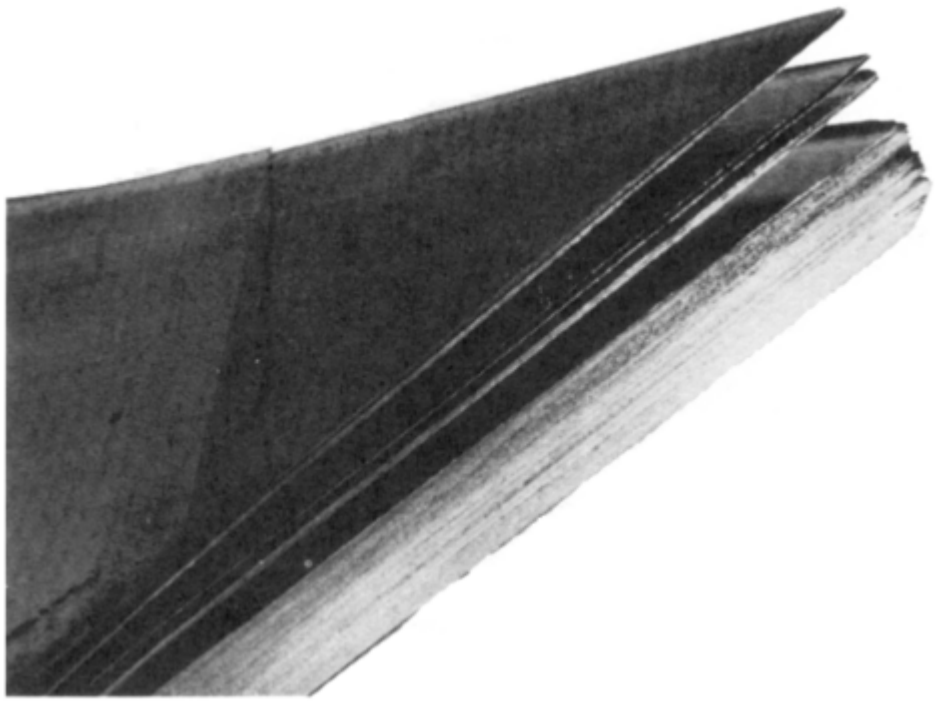

Fig. 15 Amorphous iron (Metglas) cut with a wire saw. Each laminate is 0.1 mm (0.004 in.) thick.

In principle, a fine wire is continuously drawn over the sample at a controlled force. Cutting is accomplished using an abrasive slurry applied to the wire, a chemical solution (generally acidic) dripped onto the wire, or electrolytic action. Although cutting rates are much lower than those of abrasive cutoff wheels, hacksaws, or band saws, the deformation produced is negligible, and subsequent grinding and polishing is often unnecessary.

Wire saws are available in a variety of designs. Some move the specimen into the wire, some move the wire into the specimen, some run horizontal, and some run vertical. A saw in which the wire runs vertical is advantageous if a specimen is to be removed from bulk material. In this case, the material is attached to an *x-y* table and is moved into the saw.

Various methods have been devised for drawing the wire across the specimen. The endless-wire saw consists of a loop of wire fastened together at its ends and driven in one direction (Fig. 16). The oscillating wire saw passes a wire back and forth across the sample, usually with a short stroke. A variation of this technique employs a 30 m (100 ft) length of wire that is fed from a capstan across the workpiece and back onto the capstan. The direction of the capstan is reversed at the end of each stroke. The capstan is further shuttled back and forth to maintain the alignment of the wire regarding the pulleys.

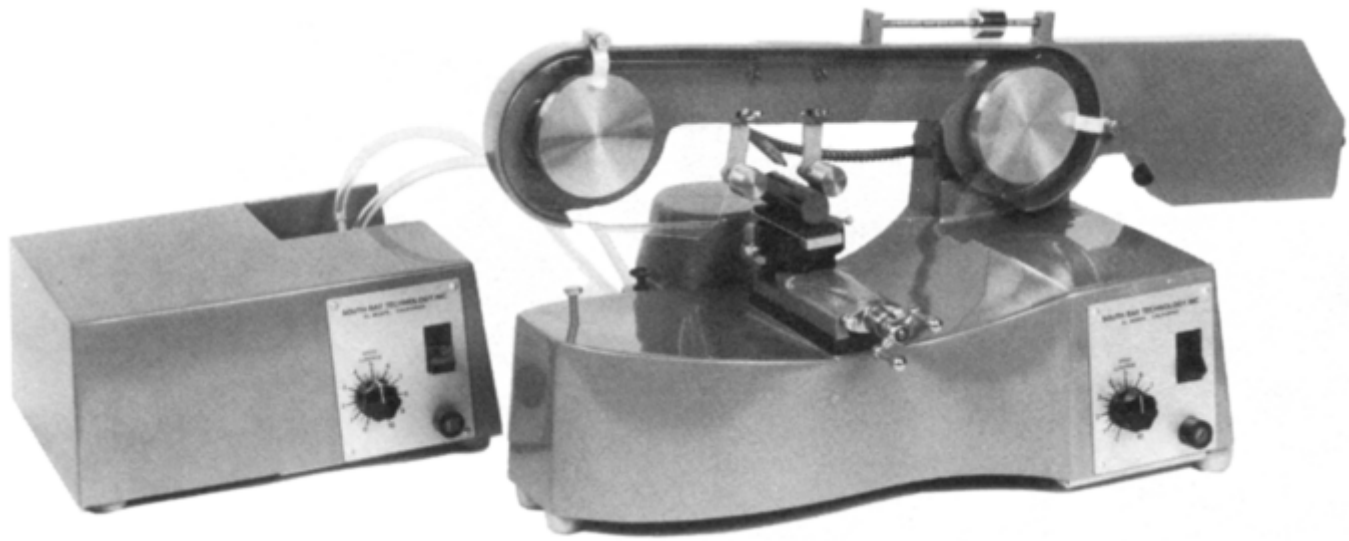

Fig. 16 Wire saw with an endless loop

Abrasives. Any crystalline material can be used as an abrasive in wire sawing if the abrasive is harder than the specimen to be cut. Although natural abrasives, such as emery and garnet, have been used extensively, the best overall abrasive currently available is synthetic diamond. There are two methods for applying abrasives to the wire. Loose abrasive can be mixed with a liquid vehicle as a slurry to be applied at the kerf behind the wire, or the abrasive can be bonded to a stainless steel wire core.

In the first method, part of the abrasive remains with the specimen and erodes the wire. Furthermore, much of the abrasive is wasted, which precludes using diamond in a slurry. In the second method, all the abrasive moves with the wire to cut the specimen. Therefore, only a fixed quantity of abrasive is employed; diamond then becomes economically feasible. Figure 17 illustrates typical diamond-impregnated wires.

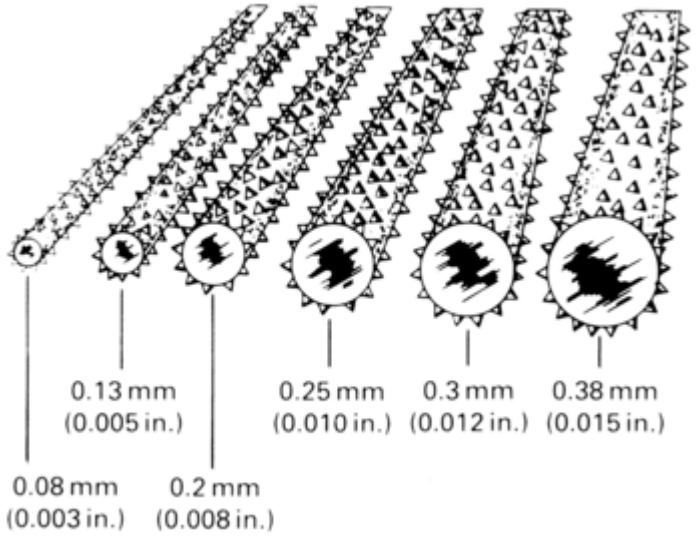

Wire size		Diamond size, μm	Kerf size	
mm	**in.**		**mm**	**in.**
0.08	0.003	8	0.08	0.00325
0.13	0.005	20	0.14	0.0055
0.2	0.008	45	0.23	0.009
0.25	0.010	60	0.29	0.0115
0.3	0.012	60	0.34	0.0135
0.38	0.015	60	0.42	0.0165

Fig. 17 Diamond-impregnated wires

Lubricants. Water is used in wire sawing with diamond-impregnated wire. This is not used to lubricate the cut, nor is it used to prevent heat buildup. The amount of heat generated is negligible, and lubrication of the wire is unnecessary. Water is used to wash out the debris that would accumulate above the wire and prevent the easy exit of the wire when the cut is complete.

Force. As force is increased between the wire and the specimen, the bow in the wire increases, even though the wire is under maximum tension. Little is gained in cutting time by increasing the force. When the force is increased excessively, the bow becomes so great that the wire has a tendency to wander, which increases the kerf. When wandering occurs, more material is being cut away, and cutting time increases. This also shortens wire life. Therefore, high force with the resulting wider kerf is a poor alternative to lighter force with a straighter wire and a more accurate cut. Lighter force also yields a better finish. If the cut is to be flat at the bottom, the saw should be allowed to dwell for a short time with no force.

The force between the wire and the specimen ranges from 10 to 500 gf. As an example, for a specimen that is in limited supply, fragile, high priced, and/or delicate, a 0.08 mm (0.003 in.) diam wire impregnated with 8 μm diamonds would be selected. The force between the wire and the crystal would range from 10 to 35 gf. The tension on the wire would be 500 to 750 gf, and the wire would travel 20 to 30 m/min (60 to 100 ft/min).

When a firm, hard, tough specimen is to be cut and when surface damage poses little or no problem, the fastest and most economical method of cutting usually is best. For example, a 0.4 mm (0.015 in.) diam wire impregnated with 60 μm diamonds would be chosen. The tension on the wire would be approximately 6000 to

8000 gf. The machine would operate at 60 m/min (200 ft/min). The force between the wire and the specimen would range from 200 to 500 gf.

References cited in this section

2. J.A. Nelson and R.M. Westrich, Abrasive Cutting in Metallography, *Metallographic Specimen Preparation—Optical and Electron Microscopy,* J.L. McCall and W.M. Mueller, Ed., Plenum Press, 1974, p 41–54

3. H.B. McLaughlin, The Use of Wire Saws for Metallographic Sectioning, *Metallographic Specimen Preparation—Optical and Electron Microscopy,* J.L. McCall and W.M. Mueller, Ed., Plenum Press, 1974, p 55–68

D. Aliya, Metallographic Sectioning and Specimen Extraction, *Metallography and Microstructures,* Vol 9, *ASM Handbook,* ASM International, 2004, p. 229–241

Metallographic Sectioning and Specimen Extraction

Debbie Aliya, Aliya Analytical, Inc.

Other Cutting Methods

Band saws are another good selection for metallographic sectioning. Sometimes they are available in a water-cooled model, but many of the most common structural steels (low carbon, not hardened) may be cut on a dry band saw. Very soft alloys with low melting points, such as some grades and tempers of aluminum, as well as lead and tin alloys must be cut with a hand hacksaw to avoid heat damage. Band saws generate much more damage than abrasive cut-off saws.

Band saws are often used in steel mills, foundries, and forge shops to rough cut ingots, slabs, billets, castings, and forgings for macroetch coupons. Band saws are a good alternative to metallurgical cutoff saws for odd-shaped sheet metal components (stampings) or large pieces of raw sheet metal that are difficult to fixture in the limited closed-in area of the water-cooled saw. Dry band saws are a good choice for cutting parts that must be kept free of contamination by the coolant, such as in failure analysis where contamination or corrosion is or may be an issue. It is a good idea in such cases to make sure that the band saw and adjacent area are clean and free of dirt, oils, grease, or other shop materials. As with metallurgical cutoff saws, proper selection of a saw blade is important. Most machinists should be able to advise metallographers on appropriate selection of tooth geometry, feed and speed rates, and desirable clamping methods.

Band saws are limited to cutting relatively soft materials, unless they have special diamond-tipped blades. If fixturing is set up so that one or both of the fragments can fall off of the saw when it is cut, care must be taken to prevent that from happening, especially if the fall may produce denting or damage in an area of interest. Band saw accidents have injured people in the past, and operators must pay closer attention to their actions for the sake of their own safety, than with a completely enclosed, properly maintained water-cooled metallurgical cutoff saw. Proper safety techniques should be researched and followed. Classes in industrial shop techniques may be available at local high schools or community colleges for the untrained or more academically trained readers who intend to perform this type of work themselves.

A handheld hacksaw is an indispensable aid to the metallographer who has multiple odd-shaped parts. Aside from the same types of previously mentioned clamping-related deformation problems, and similar problems created by the sawing itself, the hacksaw is a fine tool. In addition to being useful for thin and light parts, or soft parts that must be kept clean, the hacksaw is a very useful tool for making the final portion of an abrasive saw cut that would otherwise tend to pinch and break the wheel or overheat the specimen. A hacksaw is the least expensive tool listed here. The operator has the added advantage of close-up evaluation of the part during

cutting, and the slow pace of the cut may allow thought processes and new insights that might otherwise have been lost.

Handheld Shears or “Tin Snips.” A regular or compound handheld shear is a good way to cut small, thin specimens that must be kept free of contamination. By wearing gloves and precleaning the shear, contamination worries may be nearly eliminated. However, large amounts of undesired deformation usually accompany this process. Depending on what the particular test is, this may or may not be acceptable.

Floor Model Flat Shears. Large flat shears are particularly helpful for cutting sheet metal. Depending on how closely the shear is set up to the ideal for the particular strength and thickness of the material being cut, a reasonably small amount or an unacceptably large amount of deformation may be associated with the cut. When using a shear, a large enough piece should be cut so that the final cross section will not be affected by the deformation.

Burning Torch. Especially for large components, such as structural steel shapes or plate, or large castings or forgings, the most convenient and often only practical way to extract a specimen is with a burning torch. Such specimen extraction from very large components is probably most common in failure analysis work, although some steel mills burn their continuous cast billets to length with a torch. Extreme care must be used to minimize heat damage to the portion of the component to be analyzed. The cut should be made far enough away from the area of interest so that a human with normal sensory perception in their fingers can keep their hand on the portion of interest without being burned. It may be more practical to use a surface-temperature measuring device, such as a contact thermometer or an infrared (IR) gun, to monitor the temperature during cutting. If one of the devices (other than the hand) is being used, for structural steel and cast iron, temperatures of up to 200 °C (390 °F) may be acceptable. A metallurgist with adequate background as to the history and manufacture of the component should be consulted when considering burning as a sectioning method for a failure analysis. If litigation is or may be involved, all sides should agree to any destructive testing protocol before it is carried out.

Electric Discharge Machining (EDM). Very hard and bulky specimens, such as dies or other tool steel components, may be most efficiently sectioned by electric discharge machining (EDM). Electric discharge machining, or spark machining, is a process that uses sparks in a controlled manner to remove material from a conducting workpiece in a dielectric fluid (usually kerosene or transformer oil). With EDM, less cutting is required for some geometries than would be needed when using a round wheeled abrasive cutoff saw. Thus, even though the cost per square inch of cut is high for the EDM process, in some situations EDM may be the method of choice.

Because of the immersion in dielectric fluid, EDM is not a contamination-free sectioning method. A spark gap is generated between the tool and the sample, and the material is removed from the sample in the form of microscopic craters. The material produced by the disintegration of the tool and workpiece as well as by the decomposition of the dielectric is called swarf. Sparking is done while the sample and tool are immersed in the dielectric.

The dielectric must be kept clean to achieve the full accuracy capability of the instrument, and this is routinely accomplished by using a pump and filter attachment. Depending on the polarity of discharge, type of generator, and particularly the relative hardness of the sample and tool, material can be removed effectively and accurately. No contact is required between the tool and workpiece.

Resulting samples have a surface finish of 0.13 μm (5 μin.), exhibit excellent edge definition, and can be less than 0.13 mm (0.005 in.) thick. A melted and recast layer is generated at the cut area. As is the case with a burning torch, the cut position must be selected with regard for the test position. The damaged layer of an EDM cut is generally much thinner than that of a burning torch.

Depth of Damage (Ref 4). Electric discharge machining will damage the specimen to several millimeters or more in depth if precautions are not taken. Two criteria for assessing depth of damage are, first, depth of detectable damage, which is the depth at which the structure is altered as measured by the most sensitive process available, and, second, the depth of significant damage, which is the depth to which damage can be tolerated for the application intended.

Four zones can be defined in the spark-affected surface layer. The most strongly affected layer is the melted zone, which can extend from fractions of a micron to hundreds of microns, depending on the instrumentation used. In EDM, sparks melt a shallow crater of metal in the melted zone. Most of this is ejected at the end of the spark. Some residual liquid material remains and freezes epitaxially onto the solid below, leaving the melted layer in tension and the layer beneath in compression. Deep melted layers can cause cracking.

The second layer is the chemically affected zone, in which the chemical composition has changed perhaps because of reaction with the dielectric and the tool and diffusion of impurities. This zone is generally very small due to the time involved. The third layer is the microstrained zone, which is subjected to large compressive forces during the heating cycle and later during the shrinkage of the rapidly frozen molten layer. This zone can be detected by optical microscopy and is characterized by the presence of twins, slip, phase changes, and, sometimes, microcracks. The fourth layer is the submicrostrained zone. Damage in this layer can be detected only by counting dislocations. Slip, twinning, or cracking do not occur.

Reference cited in this section

4. J. Barrett, Electric Discharge Machining, *Metallographic Specimen Preparation—Optical and Electron Microscopy*, J.L. McCall and W.M. Mueller, Ed., Plenum Press, 1974, p 69–76

D. Aliya, Metallographic Sectioning and Specimen Extraction, *Metallography and Microstructures,* Vol 9, *ASM Handbook,* ASM International, 2004, p. 229–241

Metallographic Sectioning and Specimen Extraction

Debbie Aliya, Aliya Analytical, Inc.

Certification Work

Certification work is performed in order to determine whether a specimen meets the requirements of a specification. Common features tested by microscopic metallographic examination include:

- Nonmetallic inclusion content
- Grain size
- Graphite flake type
- Nodularity
- Shapes of grains and shapes and sizes of second-phase particles
- Carburized layer or decarburization layer thickness
- Amount of pearlite, ferrite, martensite, alpha phase, beta phase, eutectic, and so forth
- Presence and severity of microsegregation (banding) or other measures of uniformity of microphases

There are many other microstructural features that might be evaluated by qualitative or quantitative means.
Product specifications written by standards organizations (such as ISO) also often include metallographic evaluation requirements. In such cases, the product specification may refer to a test method specification written by the same organization or other organizations. For example, the Society of Automotive Engineers (SAE) created a test method for nonmetallic inclusion rating of steels (SAE J422). This specification cross references ASTM E 45, which gives a much more complete description of nonmetallic inclusion content determination in steels, detailing specific concerns relating to data interpretation. Both specifications tell how much square area should be evaluated. Nonmetallic inclusion ratings must be performed on longitudinal cross sections or cross sections whose plane lies in the rolling or working direction. Sometimes, as in the SAE specification just mentioned, the test methods or product specifications will call out a particular test position as well as size of specimen. Such a position, for example, might be halfway from the edge to the center of the rolled or forged cross section. Both product and test method specifications should be consulted carefully to determine if the test location is specified.
Considerations for Parts with Curved Surfaces. For cylindrical- or almost cylindrical-shaped parts, such as fasteners, that are being evaluated on a longitudinal section for plating thickness or depth of decarburization or carburization on thread flanks, the metallographer must realize that any deviation from the exact diameter

position will cause the layer in question to appear thicker than it really is. In addition, for threaded fasteners, the threads themselves will appear to be shorter than they really are if the cut is not made as specified on a true diameter. This could affect the accuracy of the position along the thread height where the measurement is made. This is of concern for microscopic visual measurements, as well as for microindentation hardness tests.

This important aspect in obtaining quality test results may be overlooked in commercial grade testing for high-volume or other “medium technology level” components. Test results may not be reviewed in terms of deviations from ideal test location, perhaps because audit procedures may have a tendency to get caught up in documentation details, while ignoring more important evaluations of conceptual understanding of the employees. Perhaps they have not thought about the error introduced into quantitative measurements by deviations from an ideal test procedure.

The competent metallographer should have a good idea of where the actual cross section is with respect to the true diameter. For small fasteners, wires, and other small-diameter cylindrical parts, if the diameter showing is within 10% of the actual diameter, any error is likely to be within the expected precision of the test method and certainly within the same level of expertise with which most such specifications are written. If the test is particularly critical, additional care should be considered when obtaining such layer-depth-related measurements. A good way to gage accuracy for routine certification work is to measure the amount of material lost on a mount with a similar amount of metal with similar plastic mounting compound that goes through the intended grinding and polishing procedure. The cut should be made in accordance with the expected material loss. In this case, make an off-center longitudinal section, mount the larger portion, and grind down to the desired diameter.

Before issuing a report stating that the case depth is over the maximum limit, it would be a good idea to make sure that the cross-section position tested was at the correct location. This type of error will never give a false low value. Of course, this does not address the issue of parts that are barely at the minimum case depth. If they are not at a true diameter, it is likely that the true case depth is below the specified range. Again, it is very difficult for a technician who does not have a specific fixture for each fastener size to be tested to be at an ideal test location.

One other issue related to cylindrical shapes is that if the longitudinal cut is made so that a semicircular cross section results, and the subsequent grinding of the mount results in a less than half circle, it is easier for the metal to become somewhat loose in the mount. For this reason, it may be preferable to actually leave about 55 to 65% of the original part embedded in the mount. The exact amount left will depend on the original diameter of the part and how much will be removed during grinding and polishing. The mounting compound can seal better, and there is less chance of the specimen falling out of the mount. The suggestions for preventing specimens from falling out of the mount given for cylindrical specimens here may be applied similarly to spherical shapes.

Ball bearings are particularly challenging to section, especially if they are large. There is no easy way to hold onto them without a special fixture, and it is difficult to cut just far enough away from the diameter so that the diameter is exposed after grinding and polishing. The geometric shape effect of making a surface layer appear thicker and making the cross section appear smaller is even greater with a sphere than a cylinder. Any quantitative data must be obtained with great care on such shapes. One option for some ball sizes might be to embed them in cold mount so that a cylindrical surface is available for clamping. The large disadvantage to this method is the extremely slow cutting rate needed to prevent burning, since the coolant cannot contact very much of the ball. Figure 18shows two ball bearings mounted whole and then “sectioned” by grinding. Special calculations were made to compensate for the fact that section was on a nondiametral chord.

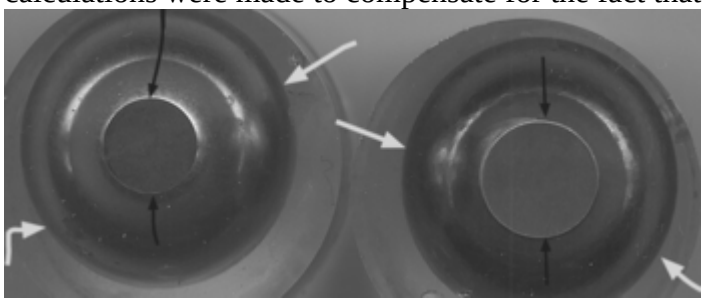

Fig. 18 Sections from ball bearings. These sections were not made by cutting at all, but by grinding to the depth required. The use of a transparent mounting compound could allow the component to be marked prior to mounting. This technique is useful for small, thin soft parts as well. Here, the bright

arrows show the ball diameters, and the dark arrows show the circle-shaped chord of the sphere that has been revealed by the grinding operation.

If no test position is specified for a particular product to be certified, using a standardized position is a good idea. Case depths on gear teeth, for example, are usually to be tested at a position halfway between the flat surface and the center of the width of the tooth (see Fig. 19). Since the required test position is so specific, for small gears it is a good idea to have several teeth available in the mount. Beveled gears or worm gears can be challenging to fixture so that the correct test position is obtained, perpendicular to the tooth crest surface. Keeping all of the material that is not turned into kerf segregated by specimen identification code, until after the metallographic evaluation, will allow easier confirmation of test location should any questions develop.

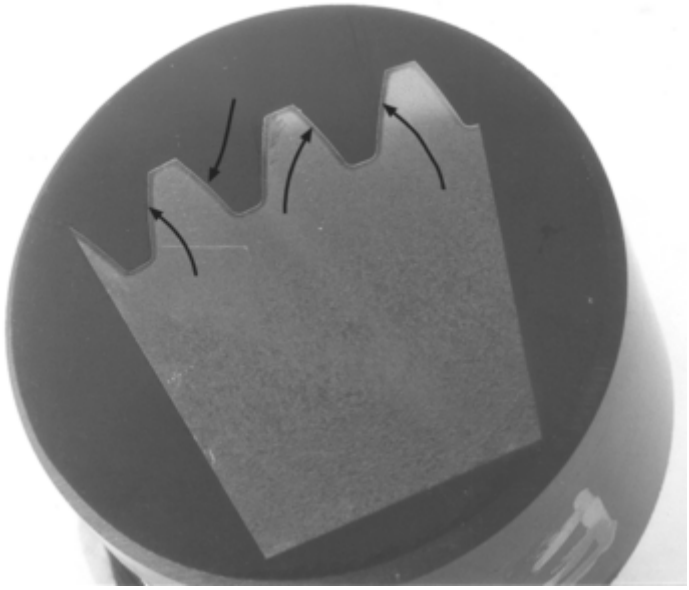

Fig. 19 Midheight of the gear tooth at the middle of the gear thickness. This is a frequently specified standard test position for case depth of gears. It is not possible to tell from this view whether the middle position of the gear thickness is the actual test surface.

Considerations for Plating and Coating Thickness Measurements. When performing certification tests on plated parts, the plating specification will commonly refer to the “significant surfaces.” It is necessary to understand the particular definition of a significant surface for the specification in question. However, the term often refers to the most obvious surface on the part after it is in the final assembly. To a metallographer working at a commercial plating company or an independent test lab, it may not be obvious which surfaces are going to be the most visible in the final product.

While the experienced industry practitioner may find it relatively simple to identify the visible surface on a casting that has a recognizable function, such as a bathtub spout, some components do not have any visible clues. Likewise, engineering prints may have no clues that are decipherable to someone outside of the design team. In an effort to overcome these difficulties, significant surfaces are often designated as those to which it is possible to touch the surface of a ball of given diameter, often 10 mm. This definition would then require any “large” surface to meet the plating thickness specification, whether or not it would be visible. This is an important distinction. Some parts have decorative plating on components with planned obsolescence and are required only to be tested in the visible areas. On other components, where the plating is intended to provide freedom from corrosion that could affect structural integrity, the entire plating layer may in some way be “significant.”

In either of the common definitions of significant surface, the insides of small-diameter holes, groove bottoms, and thread flanks are generally overlooked. Since these locations may be sites of enhanced susceptibility to crevice corrosion, for example, it is important that component designers be aware of the limitations of standard certification testing of plated parts. For some (few) coating processes, the coating is very uniform, even within holes, if the holes are not too deep. For many coating and plating processes, the coating thickness may vary greatly from location to location on the same part. An understanding of the intricacies of the particular coating process to be evaluated is a useful prerequisite to selecting a test location.

It is also important to note that metallographic coupons for coating or plating thickness measurements are commonly made in one of two orientations. If the plating thickness to be measured is more than 0.5 μm (20 μin.), it is usually suitable for sectioning with a cut perpendicular to the surface to be evaluated. If the plating or coating thickness is thinner than 0.5 μm (20 μin.), then the coupon may be set in a micromount so that it is at a low angle to the surface to be exposed by the grinding and polishing operation. Commercially available specimen alignment clips help to keep the coating layer at a known angle to simplify the trigonometric calculations necessary to convert the measurements to actual layer thicknesses. Again, when selecting test position and orientation, one must know in advance which procedure will be used.

Multiple Specimens. It is generally good laboratory practice to keep all of the fragments left over from the sectioning identified by specimen code until the test results are of no further interest. It is unusual that laboratories in manufacturing companies take this extra trouble, although it is considered standard practice in most quality commercial test labs. While it does sometimes take a few minutes to find the bits of a small sectioned component in an abrasive saw, it is helpful to keep the scraps to be able to show others where the cut was actually made. Finding the scraps after cutting is obviously easier and less time consuming in a clean saw. If all else fails, the micromount can be broken open to confirm correct or incorrect test location (see Fig. 20). Drawing a schematic of the sectioning performed on the piece also aids in future understanding of where the cuts were made, especially when multiple sections are involved.



Fig. 20 View that shows the order of the three cuts made to extract the section of interest (three marker arrows in a row at lower left of image.) Keeping all of the scraps until after the test is complete can help to confirm that the test was taken at the correct position.

D. Aliya, Metallographic Sectioning and Specimen Extraction, *Metallography and Microstructures,* Vol 9, *ASM Handbook*, ASM International, 2004, p. 229–241

Metallographic Sectioning and Specimen Extraction

Debbie Aliya, Aliya Analytical, Inc.

Process Control and Troubleshooting

When metallography is to be performed for the purpose of ensuring that a manufacturing process is running smoothly (i.e., no significant changes have taken place that make the material fall outside of the specification to which it is being produced), the metallographer who sets up the process control evaluation procedure has somewhat more freedom than the metallographer who is performing a certification test. With process control work, there is nothing wrong with giving a higher value to convenience of testpiece extraction than can be given in certification work, where the test location is often defined quite precisely.

However, convenience alone should not rule. Rather than selecting a test position based on standard industry procedure, it is wise to consider the metallurgy of the process. For example, when performing metallographic analysis on large section through-hardened steel parts, it would be a good idea to evaluate the smallest cross section for evidence of overheating, decarburization, or excessive case depth. The largest cross section might be selected for evaluation of complete homogenization and evidence of adequate quenching rate (see Fig. 21). Obviously, it would be a waste of effort to cut, mount, polish, and examine the specimens for only the particular characteristics of greatest concern. Metallography gives the operations personnel an excellent tool for evaluation of incoming material and process consistency. A properly trained metallographer is a great asset to the operating system, if the operations personnel understand and value the potential contribution to maintenance of product quality level that may be gained through his or her knowledge.



Fig. 21 Possible section locations when selecting test specimens to evaluate heat treating processes. When no particular test position is specified, it is worthwhile spending a few minutes to think about what sections might reveal from different test positions. In this example, an area near the center of the large pieces was selected to evaluate for uniformity of microstructure, and an area near the edge of the small piece was selected to evaluate for surface damage.

A properly trained metallographer, as opposed to a machinist performing metallographic tests, is one who understands phase diagrams and cooling transformation curves, along with the basic principles of solidification and diffusion in metals, and how these concepts relate processing variables to material structure and property variations. The professional metallographer can do much more than tell the operations people whether their process is in control. The professional metallographer may often be able to determine what went wrong when the process was not in control. Knowing where to take the cross section is at least as important in these cases as knowing how to mount, polish, and photograph the specimen.

Sometimes it is very difficult to determine a specific single cause for a process control failure. However, using an example from heat treating of steel, it should be relatively straightforward for the thoughtful and observant metallographer to determine whether a low hardness condition is due mainly to a slack quench or alternatively to overtempering. Of course there may be other reasons, such as incomplete homogenization, variations in incoming microstructure, and so forth. Knowing when (with respect to the process sequence) to collect a specimen as well as where to cut it, is important in process control and troubleshooting related metallographic operations.

Special Issues for Large Components. Foundries and forging operations personnel have particular challenges in using metallography for process control, especially for large components. For such large components, whose cost would preclude making extra full-sized specimens to be destroyed for evaluation, a small coupon is often specified to be processed along with the component or components in a batch or lot. Since a small coupon will heat up and cool down/solidify faster than a large one, the properties of the small coupon may bear little relationship to the large component. In this case, the coupon will only show some of the many potential deviations from intended processing that could possibly occur. If the test coupon has a problem, it is likely that the component does also. Evaluation of the test coupon may shed light on whether salvage operations are possible. However, it may be necessary to actually sacrifice a component in some cases to determine the extent of the lack of conformity within the entire component. Again, even if the test coupon is normal, it does not imply that the components are normal. Some of the drawbacks of using a small separate coupon in heat treating

operations may be minimized by attaching the coupon to the large component to more closely match the heating and cooling rate of the surface of the component. Because the surface layers are the most critical in many engineering applications, this may be a helpful procedure.

A common practice among heat treaters that should be questioned is that of making up a large group of small test coupons for the purpose of metallographic evaluation of many subsequent same-grade material lots. Whether the test coupon is to be used for evaluation of uniformity of microstructure, case depth, effective case depth, grain size, decarburization, or any other feature, no conclusions may be drawn about the conformity of the actual components to post-heat-treatment requirements based on evaluation of a coupon from another heat. The cumulative effect of composition variation, homogeneity variation, and size differences makes this practice virtually meaningless as a process control check.

Issues in Cleaning, Coating, Plating, and Other Surface Treatments. Metallography is often a useful tool in troubleshooting cleaning, coating, and other surface treatment processes. Especially when stains, discoloration, blisters, or residues are left on the surface of cast or molded components, subsurface porosity may be suspected. Even parts that are produced from wrought materials may have subsurface discontinuities that are contributing to the surface treatment process problems. Often it is useful to evaluate any stain or discoloration using the EDS microchemical analyzer in conjunction with a scanning electron microscope, or if the stain is thought to be related to an organic contaminant, with a microscope-equipped Fourier transform infrared (FTIR) analyzer. If such methods are to be used prior to cutting a cross section for metallographic analysis, the specimen should be kept clean and dry during any necessary initial cutting.

Determining exactly where to make a cut to evaluate subsurface conditions relating to surface blemishes is as much due to luck as to skill in many cases. The subsurface imperfection may or may not be directly under the center of the blemish. Some blemishes or blisters are very tiny. Sectioning with standard care setups may cause the entire blister or underlying feature to be consumed by the kerf. A useful procedure when using grinding equipment with no direct measurement of material removal is to cut about 1 mm (0.04 in.) from the plane to be revealed and gradually hand grind to a location just short of the desired location. Gradually may mean 3 to 5 s on a 600-grit sandpaper (see Fig. 22). Multiple, repeated polishing steps may be necessary to reach the desired position. Multiple repeated polishing steps may still reveal no evidence of the suspected subsurface imperfection. Patience is required in this part of metallographic section selection more than in other areas. Mounting in a transparent medium and marking the surface with a fine-point permanent marker can help the metallographer keep track of the position.

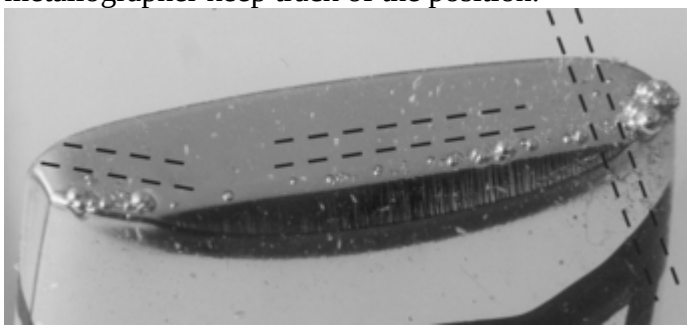

Fig. 22 Possible cut locations (pairs of dashed lines) for a part with multiple plating imperfections. When choosing a cross-section location for evaluation of small paint or plating blemishes, it is helpful to make sure the kerf will leave the entire blemish intact. The final position can then be reached by careful hand grinding.

D. Aliya, Metallographic Sectioning and Specimen Extraction, *Metallography and Microstructures,* Vol 9, *ASM Handbook,* ASM International, 2004, p. 229–241

Metallographic Sectioning and Specimen Extraction

Debbie Aliya, Aliya Analytical, Inc.

Component Failure Analysis

Many steps are necessary prior to sectioning a component that is part of a failure analysis. Evidence preservation is extremely important. This information may be found in *Failure Analysis and Prevention,* Volume 11 of the *ASM Handbook* (2002) and in many other references on performing failure analysis work. Only an overview of specific issues related to sectioning of components is covered in this article. Many of the issues, those relating to selection of a cutting tool that will not cause contamination of corrosion products, for example, are described in earlier sections of this article. This section specifically addresses the area of where the section should be obtained in various situations.

Failure analysis protocols or associated testing often require evaluation of parts similar to the one that is the subject of the investigation in order to determine if they meet specification. Where the cut is to be made depends on what characteristic is being evaluated. The guidelines previously described in this article may be consulted for a general discussion of the issues involved. However, if the failure being analyzed originated or happened in a specific position or location, regardless of any standard test location for certification, it may be helpful to analyze the location associated with the failure. However, more so than with other types of metallographic work, preservation of evidence must be the key guiding principle when both choosing preferred test locations and selecting a cutting method and fixturing setup.

Failure analysis of fractures often benefits from cross sections that contain crack profiles. If the crack is relatively clean and free from corrosion product, normal failure analysis protocol would usually delay the metallography until scanning electron microscopy had been completed, and the preferred test position for the cross section, once evidence preservation guidelines have been satisfied, would be the crack initiation or origin area. If the crack is totally covered with corrosion product or other contaminant, or for some other reason scanning electron microscopy is not part of the protocol, it may be wise to set the main crack or the suspected initiation area aside and make the metallographic section from a secondary crack, if available. If a more complete picture of the crack process is desired on a large component, it may be necessary to select several areas of the crack surface for examination of the microstructure and any microphase preferences the crack seems to exhibit.

A dilemma often faced by the failure analyst is whether to section through a fracture surface. A benefit of this sectioning is the ability to observe metallographically the region in and around the known fracture origin. Obviously, a determination of the fracture origin location must be made with a high degree of accuracy prior to sectioning. Precise sectioning must follow to be able to examine the desired region. It should be noted that fracture surface sectioning should generally be performed only if one has mating sides of the fracture.

Sectioning is also helpful to the failure analyst if secondary cracks are to be opened. Often this useful laboratory procedure allows examination of fracture surfaces that do not possess the marring and smearing accompanying primary fractures. The failure analyst must make an assessment as to the depth and length of the crack that is unseen. The sample is aligned so that the crack opening is opposite the saw blade. The sample is then sectioned a certain distance and then removed.

Wear failures may also benefit from metallographic analysis. The edges of a worn area may be useful areas to obtain insight into the wear mechanisms. Again, cross sectioning should follow any planned or required scanning electron microscopy, which generally follows other less destructive documentation.

Corrosion failures to be analyzed by metallography may benefit from sections being obtained from less and more severely affected areas. Metallographic analysis of components that have failed by stress or temperature associated deformation may prove useful when sections are made from both affected and unaffected or less affected areas.

D. Aliya, Metallographic Sectioning and Specimen Extraction, *Metallography and Microstructures,* Vol 9, *ASM Handbook,* ASM International, 2004, p. 229–241

Acknowledgments

The author gratefully acknowledges Marc Pepi, Naval Air Warfare Center, China Lake, CA; Dr. William T. Becker, Emeritus, University of Tennessee, Knoxville, TN; Brett Miller, IMR Testing, Louisville, KY; and Daniel Aliya, Aliya Analytical, Inc. for reading and offering helpful comments on the manuscript.
Appreciation also goes to previous Handbook authors for the details of how abrasive cutting disks are to be selected, and the information on wire saws, EDM, and some of the other less commonly used cutting methods.

D. Aliya, Metallographic Sectioning and Specimen Extraction, *Metallography and Microstructures,* Vol 9, *ASM Handbook,* ASM International, 2004, p. 229–241

Metallographic Sectioning and Specimen Extraction

Debbie Aliya, Aliya Analytical, Inc.

References

1. G.F. Vander Voort, *Metallography: Principles and Practice,* McGraw-Hill, 1984, reprinted by ASM International, 1999

2. J.A. Nelson and R.M. Westrich, Abrasive Cutting in Metallography, *Metallographic Specimen Preparation—Optical and Electron Microscopy,* J.L. McCall and W.M. Mueller, Ed., Plenum Press, 1974, p 41–54

3. H.B. McLaughlin, The Use of Wire Saws for Metallographic Sectioning, *Metallographic Specimen Preparation—Optical and Electron Microscopy,* J.L. McCall and W.M. Mueller, Ed., Plenum Press, 1974, p 55–68

4. J. Barrett, Electric Discharge Machining, *Metallographic Specimen Preparation—Optical and Electron Microscopy,* J.L. McCall and W.M. Mueller, Ed., Plenum Press, 1974, p 69–76

D. Aliya, Metallographic Sectioning and Specimen Extraction, *Metallography and Microstructures,* Vol 9, *ASM Handbook,* ASM International, 2004, p. 229–241

Metallographic Sectioning and Specimen Extraction

Debbie Aliya, Aliya Analytical, Inc.

Selected References

- B.L. Bramfitt and A.O. Benscoter, Chapter 7: Metallographic Specimen Preparation, in *Metallographer's Guide: Practices and Procedures for Irons and Steels,* ASM International, 2002
- L.E. Samuels, Chapter 2: Sectioning and Mounting, *Metallographic Polishing by Mechanical Methods,* 4th Edition, ASM International, 2003

Mounting of Specimens, *Metallography and Microstructures,* Vol 9, *ASM Handbook,* ASM International, 2004, p. 242–256

Mounting of Specimens

Introduction

AFTER a metallographic specimen is cut to an appropriate size, mounting of the specimen is often desirable or necessary for subsequent handling and metallographic polishing. Mounting may done by encapsulating the specimen in a polymeric material or by clamping with a mechanical device. In some cases, specimens are not mounted. For example, large-sized specimens may not be mounted. Also, automatic grinding and polishing machines have holders that may not require mounted samples. For best results, however, mounting has several benefits, especially in hand polishing when specimen flatness and edge retention are important. Advantages of encapsulating specimens in a mount include:

- Edge retention of mounted specimens is markedly superior to that of unmounted specimens
- Easier handling of specimens that are too small, fragile, or awkwardly shaped
- Containment of sharp edges or corners that may damage the papers and cloths used in polishing equipment or pose a hazard during handling
- Convenient and uniform configuration for either manual or automatic grinding and polishing machines
- Specimen identification of unmounted specimens is difficult and nonpermanent. More details can be listed on the back of a mount, and this information is not easily degraded with time
- Filling of holes and cracks in the specimen with mounting material to prevent “bleeding” of water, alcohol, and etching solutions
- Standard size for ease of storage in desiccator cabinets

Before mounting a specimen, the metallographer must think about the procedures that will be used to polish and etch the specimen. There are many different mounting methods and materials, and special mounting methods may be required for some specimens, such as thin-sheet specimens, small-diameter wire and tube specimens, powders, and techniques for edge retention (see the section “Special Mounting Techniques” in this article). The size and configuration of the specimen mount depends on several factors, as discussed in the section “Mount Size and Configuration” in this article.

Cleaning

Prior to mounting, the overall plan of the metallographic examination should be understood. The first step is to clean the specimen, either before mounting or before plating. Specimens are plated either before sectioning or mounting in order to protect surface layers in the specimens and/or to ensure good edge retention (see the section "Coatings for Specimen Protection and Edge Retention" in this article).

With certain samples, such as those in which surface oxide layers are to be examined, cleaning must be limited to very simple treatments, or the detail to be examined may be lost. A distinction can be made between physically and chemically clean surfaces. Physical cleanliness implies freedom from solid dirt, grease, or other debris; chemical cleanliness implies freedom from any contaminant. In metallographic work, physical cleanliness is usually adequate and nearly always necessary.

Vapor degreasing is frequently used to remove oil and grease left on metal surfaces from machining operations, but ultrasonic cleaning is usually the most effective method for routine use. Specimens that require cleaning may be placed directly in the tank of the ultrasonic cleaner, but the cleaning solution must be changed frequently. This can be avoided by placing approximately 25 mm (1 in.) of water in the tank, then placing inside the tank a beaker containing the cleaning solution and the specimen. Cleaning times are usually 2 to 5 min, but very soft specimens can be damaged by the cavitation; therefore, ultrasonic cleaning should be limited to 30 s or less for these materials (Ref 1).

Reference cited in this section

1. G.F. Vander Voort, *Metallography: Principles and Practice*, McGraw-Hill, 1984, reprinted by ASM International, 1999, p 71–93

Mounting of Specimens, *Metallography and Microstructures,* Vol 9, *ASM Handbook*, ASM International, 2004, p. 242–256

Mounting of Specimens

Mechanical Clamps

Although mounting often involves encapsulation of the specimen in a cylindrical mold of plastic, mechanical mounting is still an effective method. It is quick, provides excellent edge retention, and does not require any special equipment other than a clamp, vise, and screwdriver. Clamps provide very good edge retention because the specimens are directly against the clamp and against each other.

Typical examples of mechanical clamps are illustrated in Fig. 1. Mechanical clamping devices can be very effective in preparing transverse or longitudinal sheet surfaces. Clamps for this type of work are usually fabricated from approximately 6 mm (0.25 in.) thick plate stock, which can be cut into blocks of various sizes. The material of the clamp should preferably be similar in nature to the specimen material with respect to both composition and hardness. If this is not possible, it should at least have similar abrasion and polishing characteristics when retention of the specimen edges is important. If the specimen is to be etched after polishing, the clamp material must also have similar etching characteristics, or be inert to the etching solutions, or be insulated electrically from the specimen.

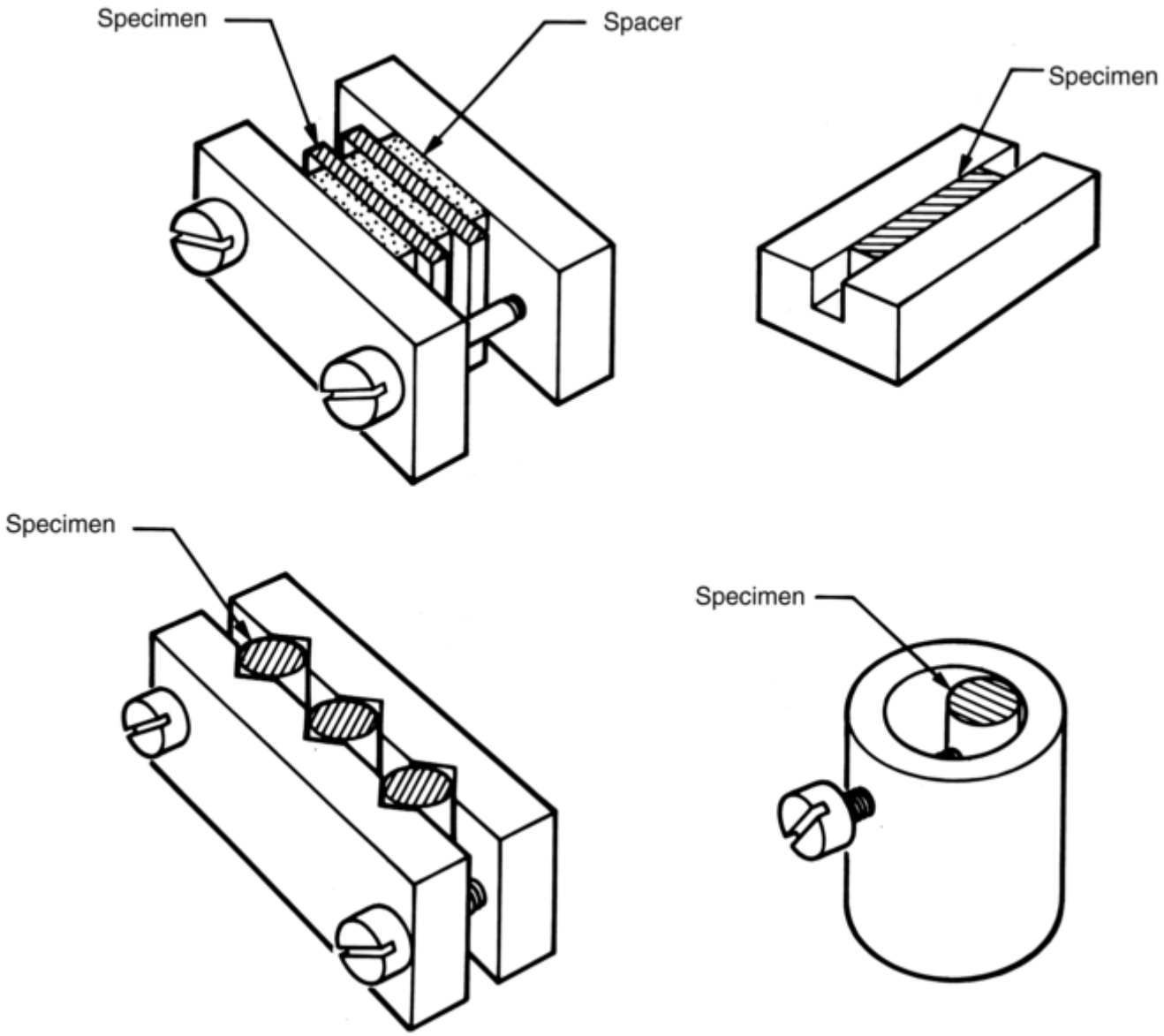

Fig. 1 Mechanical methods of mounting small specimens

Another problem after etching may be the difficulty of obtaining close contact between the specimen and clamp. The etchants tend to seep out of the resultant gap, causing staining along the specimen edges. This difficulty can sometimes be overcome by inserting thin spacers of a soft metal between the clamp and the specimen, but the spacer material also must not interfere with the etching process itself. Films of a plastic material can also be used. A rather similar result is achieved if the surfaces of the specimen are precoated with a thick layer of phenolic or epoxy resin lacquer, particularly if the assembly is clamped up before the resin sets.

The clamp is placed in a vise, and the clamp bolts are tightened. Clamping pressure is important. Specimens may be damaged if it is too high. Insufficient pressure can result in formation of gaps between assembled components and encourage seepage and abrasive entrapment. Thus, the very nature of the clamping procedure, and the precautions that have to be associated with it, limit its application, and the method is cumbersome at best. All of this tends to further restrict application of mechanical clamping to cases where mounting in plastics is not possible for some special reason.

Spacers are also used when clamping flat specimens, especially if specimen surfaces are rough or are thin sheets of such materials as copper, lead, or plastic. Specimens can also be coated with a layer of epoxy or lacquer before being placed in the clamp. For maximum edge retention, a spacer should have abrasion and polishing rates similar to those of the specimen. Material for the spacer and the clamp should be selected to avoid galvanic effects that would inhibit etching of the specimen. If the etchant more readily attacks the clamp or spacer, the specimen will not etch properly.

Another common mechanical mount is a cylinder or other convenient shape in which the specimen is held by a set screw. Again, abrasion and polishing rates should approximate those of the specimen, and the mount should be inert to any solvents and etchants used or have the same reactivity as the specimen.
When mounting with mechanical clamps, cleaning of the assembly between preparation stages needs to be particularly thorough (Ref 2). One disadvantage of mounting specimens in a mechanical mount is that grinding and polishing debris tend to collect in open areas of the mount. When using mechanical mounts, the mount must be placed in a beaker of alcohol in an ultrasonic cleaner after the last grinding step and after each polishing step. Alcohol is used because it dries quickly and does not leave a residue on the specimen. Also, after etching the mounted specimen, all traces of etching solution must be washed from the specimen by rinsing in warm water, followed by a rinse in alcohol and blow drying. Any etchant remaining on the specimen may seep from between the clamp and specimen and create a stain. Any acid fumes remaining from the etchant may attack the optical system of the microscope and cause damage.

Reference cited in this section

2. B.L. Bramfitt and A.O. Benscoter, Chapter 7: Metallographic Specimen Preparation, *Metallographer's Guide for Irons and Steels,* ASM International, 2002, p 169–214

Mounting of Specimens, *Metallography and Microstructures,* Vol 9, *ASM Handbook*, ASM International, 2004, p. 242–256

Mounting of Specimens

Plastic Mounts

The two general types of polymer compounds for mounting of metallographic specimens are:

- Compression molding resins that require the application of heat and pressure for the curing of the polymer
- Castable (“cold”-mounting) resins, where a liquid mixture of two or more polymers solidifies at room temperature after being poured into a mold containing the specimen

Castable mounting materials are more expensive than compression molding resins, but the major advantage is that a mounting press is not required. Castable mounting compounds are relatively easy to mix and use, and many mounts can be made at one time. Resins for castable mounts include epoxies, acrylics, and polyester, as described in more detail in the section “Cast Mounts” in this article.
Compression molding is done with either thermosetting resins or thermoplastics resins. Since the first introduction of phenolic as a compression molding mount in the 1930s, many other polymeric resins have been evaluated for mounting of metallographic specimens. Thermosetting resins for compression molding include phenolic, diallyl phthalate, and epoxies. Thermoplastic resins for compression molding have included acrylics and polyvinyl compounds; currently only methyl methacrylate is used. Typical resins and methods are described in more detail in the section “Compression Molded Mounts” in this article.
Selection of the most appropriate mounting method and resin depends on several factors. Table 1 and Table 2 are brief summaries of compression molding and castable resins, respectively. Selection depends on the relative importance of several factors, as discussed in this section. Some general comparisons are as follows (Ref 3):

- Phenolics are low cost, readily available, and quite adequate when the mount is used merely as a holding device.
- Acrylics give poor edge retention and exhibit poor chemical resistance, particularly to solvents, which virtually restricts their use to applications where extreme clarity is required in the mount.

- Epoxies find application as either liquid casting resins or powders for compression molding. True adhesion to the specimen is obtained with cast epoxies. Epoxies with appropriate fillers also have polishing rates similar to metals and thus can result in specimens with good edge retention after polishing.
- Small amounts of polyester are used, but they have no advantage.

The following are no longer or very seldom used:

- Allyls were once used for improved apparent adhesion and specimen-edge preservation compared to phenolics. They are less satisfactory in both of these respects compared to Formvar and polyvinyl chloride types. They are expensive and not readily available. Other disadvantages are low polishing rate and poor resistance to strong acids.
- Formvar (polyvinyl formal) is sometimes used for good adhesion and edge-retention characteristics. Main deficiencies are unsatisfactory resistance to some strong acids, restricted availability, and a marked tendency to stick in the mold.
- Polyvinyl chloride is comparable to Formvar with respect to both apparent adhesion and edge-retention characteristics yet is less expensive and more readily available. It is comparable to phenolics with respect to cost, availability, and ease of handling and consequently should be considered for general-purpose mounting as well according to Ref 3.

Table 1 General comparison of compression mounting resins

Factor	Phenolics	Acrylics	Epoxy	Diallyl phthalates
Cost	Low	Moderate	Moderate	Moderate
Ease of use	Excellent	Moderate	Excellent	Excellent
Availability of colors	Yes	Clear	Black only	Blue only
Cycle times	Excellent	Poor	Excellent	Excellent
Edge retention[(a)]	Fair	Poor	Excellent	Moderate
Clarity	Opaque	Excellent	Opaque	Opaque
Hardness[(a)]	Low	Good	High	High
Form	Granular	Powder	Granular or powder	Granular
Specific gravity, g/cm^2	1.4	0.95	1.75–2.05[(b)]	1.7–1.9
Colors	Black, red, green	Clear	Black	Blue
Shrinkage (compression), in./in.	0.006	…	0.001–0.003[(b)]	0.001–0.003
Coefficient of linear thermal expansion, (in./in.)°C×10^{-6}	50	…	28[(b)]	19
Heat (boiling) etchant	Seriously degraded	Soften	Holds up in heated etchant	Degrades but not as badly as phenolics
Molding temperature, °C (°F)	150–165 (300–330)	…	143–177 (290–350)	160–177 (320–350)
Molding pressure, MPa (psi)	21–28 (3050–4000)	…	17–28 (2500–4000)	24–41 (3500–6000)
Curing time (at temperature and pressure) for 12 mm (0.5 in.) mount	90–120 s	2–4 min	90–120 s	90–120 s

(a) No polymer is hard compared to metal, except for lead. Abrasion/polishing rate relative to metals is the important comparison. Epoxies are very good, because fillers make their grinding/polishing rates similar to metals.
(b) Glass-filled epoxy

Table 2 General comparison of castable (cold-mounting) resins

Factor	Epoxy	Acrylic	Polyester resin
Type	Epoxy resin and hardener	Acrylic resin and powder	Polyester resin and hardener
Peak temperature, °C (°F)	28 (82)	27 (80)	38 (100)
Shore D hardness	82	80	76
Cure time	6–8 h. Some cure in 45 min.	5–8 min	6–8 h
Comments	Moderate hardness, low shrinkage, transparent	Very fast cure, translucent, some shrinkage, inexpensive, and widely used on printed circuit boards; high exotherm during polymerization	Transparent, clear, rarely used

Selection of a mounting plastic for a specific application requires detailed consideration of key performance factors that sometimes can be quite demanding. Some key factors are (Ref 3):

- The mounting process must not physically damage the specimen by causing either distortion or structural changes that would be detectable in the subsequent microscopic examination. Similarly, it must not heat the specimen to an extent that would cause detectable structural changes. These are mandatory requirements.
- Adequate resistance to physical distortion at elevated temperatures is desirable if the specimen must be heated during etching or washing.
- Adequate resistance is required for chemical reagents and solvents into which the mounted specimen must be immersed. Attack of this nature becomes significant when it causes marked deterioration of the plastic or when the specimen surface is stained by reaction or solution products.
- It is desirable that a fissure should not form at the specimen-plastic interface. This becomes a necessary requirement when seepage of solutions from the fissure would cause staining of the prepared surface. This is also advantageous when good edge retention of the specimen edges is desired—particularly when thin, irregular surface films (such as oxides) are present on the specimen.
- It may be desirable for the plastic to penetrate and fill small pores and crevices in the specimen (e.g., when the pores and crevices allow seepage of solutions during preparation and etching).
- The abrasion and polishing rates of the plastic must be similar to those of the specimen when good retention of the edges of the specimen is desired.
- Significant electrical conductance is desirable if, for example, the specimen is to be electrolytically polished or etched or examined with a scanning electron microscope or an electron probe microanalyzer.
- Sufficient transparency to permit recognition of features on the side surfaces of the specimen is an advantage in certain cases.
- The reflectivity of the plastic may need to be such as to provide good contrast against the edges of the specimen.
- Other factors being equal, the plastic should be simple to mold and readily available.

None of the many plastics available at present meets all of these demands, so proper selection requires that the needs of the particular application be carefully compared with the known properties of the available plastics. Availability of several mounting compounds is desirable in choosing the most suitable for a particular application.

Damage to Specimen. With compression molding resins, the molding pressure can cause specimen damage, such as fracture of friable materials, distortion of fragile specimens, and introduction of deformation artifacts in certain alloys (e.g., brass and zirconium). Temperatures should not exceed 170 °C (340 °F) during compression molding to avoid structural changes in the specimen, such as tempering or aging of a precipitation-hardened alloy. Some temperature rise is also possible in cold mounting with epoxy casting plastics, although it can be kept small. Pressure damage is completely avoided by the use of casting plastics.

Distortion of Plastics by Creep Deformation. Rigidity of plastics can be a concern because of temperature effects on the viscoelasticity of plastics. Plastics can be susceptible to distortion when elevated temperatures

cause a reduction in rigidity and the onset of creep deformation. One measure of this effect is the so-called heat-deflection temperature (or deflection temperature under load, DTUL), which is a general indication of the temperature at which the material deforms under load. It is also sometimes referred to as the heat-distortion temperature, but DTUL is the preferred term. The measurement of DTUL values is based on deflection of a simple cantilever beam under load at high temperature (ASTM D 648).

Rigidity of plastics is influenced by a number of factors, such as the use of fillers and the crystallinity of a plastic. Thus, the values of DTUL measurements are strictly comparative only, although they can roughly indicate temperatures that a plastic can withstand without severe distortion. Thermoplastics generally have lower DTUL values than those of thermosetting plastics, because the cross linking of thermosets during curing is equivalent to an increase in crystallinity. Table 3 lists some general DTUL values of major types of resins.

Table 3 Typical properties of plastics suitable for metallographic mounts

Plastic	Type	Molding conditions			Deflection temperature under load[a], °C (°F)	Coefficient of thermal expansion[b], mm/mm/°C	Transparency	Chemical resistance
		Temperature, °C (°F)	**Pressure, MPa (lbf/in.^{2})**	**Curing time**				
Phenolic molding powder	Thermosetting[c]	170 (340)	27 (4000)	5 min	140 (285)	3.0–4.5 × 10^{-5}	Opaque	Not resistant to strong acids or alkalis
Acrylic (polymethyl methacrylate) molding powder	Thermoplastic	150 (300)	27 (4000)	8–12 min	65 (150)	5–9 × 10^{-5}	Water white	Not resistant to strong acids
Epoxy casting resin	Thermosetting[d]	20–40 (70–105)	…	45 min to 20 h	60 (140)[e]	4–7 × 10^{-5}	Clear but light brown in color	Fair resistance to most alkalis and acids. Poor resistance to conc. nitric and glacial acetic acids
Allyl molding compound[f]	Thermosetting[g]	160 (320)	17 (2500)	6 min	150 (300)	3–5 × 10^{-5}	Opaque	Not resistant to strong acids and alkalis
Formvar (polyvinyl formal) molding compound[f]	Thermoplastic	220 (430)	27 (4000)	nil	75 (170)	6–8 × 10^{-5}	Clear but light brown in color	Not resistant to strong acids
Polyvinyl chloride (PVC) molding compound[f]	Thermoplastic[h]	160 (320)[i]	20 (3000)	nil	60 (140)	5–18 × 10^{-5}	Opaque	Highly resistant to most acids and alkalis

(a) As determined by the method described in ASTM D 648–56, at a fiber stress of 1.8 MPa (264 lb/in.^{2}).
(b) The coefficient of thermal expansion in most metals is in the range 1–3 × 10^{-5} mm/mm/°C.
(c) Wood-filled grade, preferably with low filler content.
(d) A liquid epoxy resin with an aliphatic amine hardener.
(e) Depends on the curing schedule; can be as high as 110 °C (230 °F) with heat curing.
(f) Allyl, Formvar, and PVC are seldom if ever used today. Listed only for information.
(g) A diallyl phthalate polymer with a mineral filler.
(h) A stabilized rigid polyvinyl chloride. For example, a mixture of 100 parts of a paste-making grade of polyvinyl chloride, 2 parts dibasic lead phosphate, and 2 parts tribasic lead sulfate.
(i) Must not exceed 200 °C (390 °F). Source: Ref 3

Resistance to Chemical Attack. All the plastics listed in Table 3 have adequate resistance to the comparatively mild reagents used for many metallographic etchants. However, they may have unsatisfactory resistance to stronger reagents sometimes used, for example, for etching refractory metals. Epoxy plastics are more resistant in this regard.

Plastics also exhibit various levels of resistance to the solvents likely to be used for cleaning and drying operations, but a satisfactory solvent may be chosen to match the plastic. For example, all the plastics listed have good resistance to alcohol, while epoxy may be liable to staining when acetone is used for drying. Acrylic plastics are severely attacked by acetone and by chlorinated hydrocarbons.

Fissure Formation at Specimen-Plastic Interface. Of the different types of resins, only epoxies physically adhere to metals. This characteristic of epoxies helps eliminate fissuring between specimen and mount. Fissuring can be kept to an almost indiscernible level for some of the remaining plastics, provided that suitable precautions are taken. Fissuring complicates the metallography, because the gap will allow seepage (or bleeding) of etching and rinse solutions and entrapment of grinding and polishing debris, and promotes poor edge retention.

The first factor of importance with nonepoxy plastics is the relative coefficients of thermal expansion (CTEs) of the plastic and the specimen. The CTEs of plastics (Table 3) are greater than that of metals, and the difference may vary depending on the metal and the choice of filler content in the plastic mount. A large difference generally is desirable in compression molding with nonepoxy resins, because it increases the tendency for the plastic to shrink onto the specimen during cooling from the molding temperature. Similarly, it is desirable to maintain the molding pressure during cooling to as low a temperature as possible. However, there is no point in lowering molding temperatures below the DTUL value, and so this precaution is less effective with compression molding plastics that have higher DTUL characteristics.

Acrylics have high shrinkage and the biggest gaps from fissuring. Satisfactory absence of fissuring cannot be obtained with these materials if the shape of the specimen precludes free contraction onto any portion of the surface. For example, satisfactory absence of fissuring may be obtained on the outer surface but not on the inner surface of a transverse section of a tube. With sheet specimens, shrinkage tends to cause the plastic to be drawn tightly against the ends but to pull away from the faces of the sheet. If the affected surface is the one of interest, it may then be more effective to use a plastic with a comparatively low CTE.

Although epoxy resins adhere to metals and hence have the potential to produce mounts with no interface fissures at all, it does not follow that epoxy mounts are completely immune from fissure formation. Stresses can be induced at the interface during curing, and the differences in the thermal expansion of the specimen and resin may be sufficiently large to rupture the interface bond. The differential thermal contraction during cooling of the resin from the curing (cross-linking) temperature can cause strains. Thus, the problem is more likely to arise when the metal specimen and the epoxy resin undergo large differences in thermal expansion/contraction during heating/cooling. Thus, the first precaution against fissuring of epoxies is to reduce the effective curing temperature. Another step is to reduce the difference in CTE values. The CTE values of epoxies can vary depending on fillers (Fig. 2).

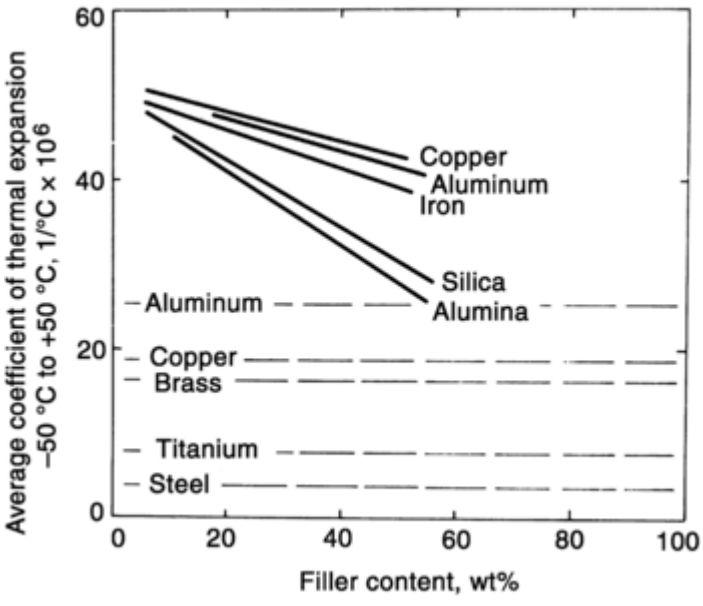

Fig. 2 Variation in the coefficient of thermal expansion of epoxy resin with the addition of various filler materials. The coefficients of five common metals are indicated for comparison. Source: Ref 3

Modified molding techniques can also be adopted to reduce the possibility of fissuring—techniques that are based on, first, reducing to the minimum the volume of epoxy that is polymerized with the specimen and, secondly, transferring the shrinkage fissure to a less-adherent dummy specimen (Ref 4). For example, a sheet specimen can be cast into a slot machined in an epoxy preform, together with a number of stainless steel strips, as indicated in Fig. 3. Adhesion between the epoxy and the specimen is then maintained along the full length of the specimen. Any fissures that develop form along the stainless steel strips.

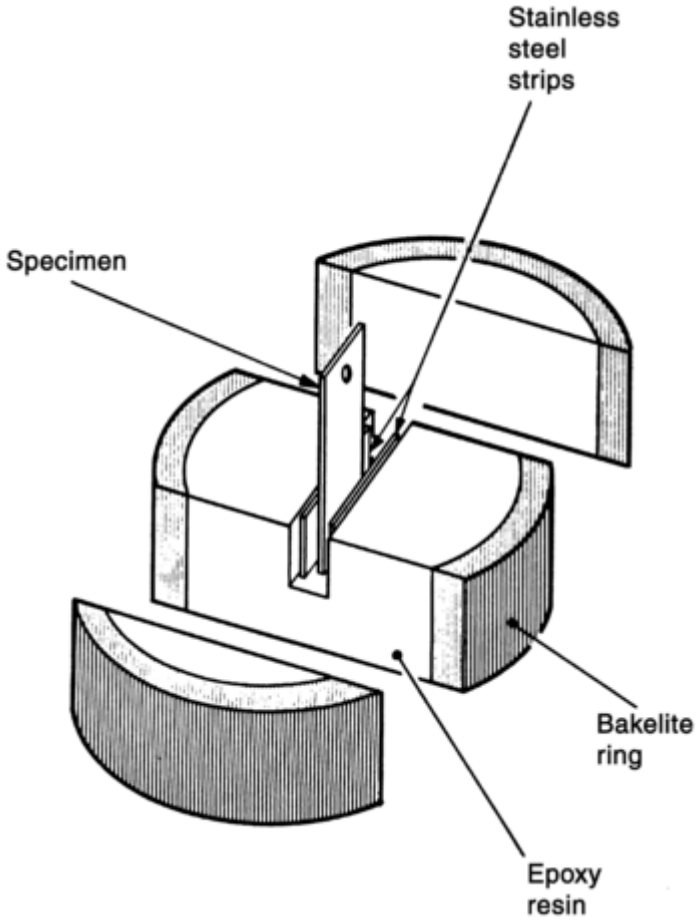

Fig. 3 Technique for reducing the tendency for fissures to form along the side faces of sheet specimens cast in epoxy. The specimen is cast in a slot machined in an epoxy preform, together with several dummy specimens. Source: Ref 4

Finally, if all else fails, it is usually possible to repair an interface fissure after it has been exposed by using a preliminary abrasion operation. A small volume of epoxy casting liquid is placed over the section surface, and the mount is subjected to the vacuum impregnation process discussed later. Cyanocrylate ester glues often can be used as an alternative and do not require vacuum impregnation.

Ability to Fill Pores and Crevices. Only liquid casting plastics show any significant tendency to fill pores and crevices in the specimen. Even then, the tendency is only slight, and vacuum treatment of cast mounts is usually necessary when this factor is of importance.

Abrasion Rates. Representative abrasion rates are listed in Table 4 for common types of mounting plastics, such as phenolics filled with cellulose, phenolics filled with a small volume fraction of a mineral such as glass or silica, acrylics, casting epoxides, and polyvinyl chlorides. The abrasion rates can be compared directly with those for metals listed in Table 5. The abrasion rates vary by as much as an order of magnitude, where the rate for epoxy casting resin is notably high, while those for polyvinyl chloride are low. The rates for papers coated with silicon carbide and alumina do not differ significantly. Of course, abrasion rates of the plastic mount are markedly affected by filler materials that can be added to match wear rates of the specimen and mount for good edge retention.

Table 4 Abrasion rates of common specimen-mounting plastics that cause only minor deterioration of papers coated with conventional abrasives

Plastic		Abrasion rate[(a)], μm/m	
Type	**Filler**	**Silicon carbide abrasive**	**Alumina abrasive**
Phenolic	Cellulose[(b)]	11.0	11.6
	Mineral, 7 wt%[(c)]	8.0	8.5
Acrylic	nil	10.5	11.5
Epoxy, casting	nil	20	20.5
Formvar	nil	5.0	5.0
Polyvinyl	nil	…	3.0

(a) Determined under the same conditions and by the same methods as for Table 5.
(b) Wood flour.
(c) Probably mica and asbestos. Source: Ref 3

Table 5 Abrasion rates obtained with various metals that cause little deterioration of abrasive papers

Metal or alloy		Abrasion rate[(a)], μm/m		
Description	**Hardness, HV**	**Silicon carbide, P240**	**Aluminum oxide, P240**	**Diamond 220**
Aluminum:	24	2.61	1.93	1.76
High purity, annealed				
Alloy, heat treated	105	1.29	0.85	0.65
Cadmium: commercial purity, annealed	21	2.4	2.0	…
Chromium: high purity, annealed	200	0.25	0.20	0.16
Copper:				
High purity, annealed	50	0.61	0.28	0.19
Brass 30% Zn, annealed	45	0.81	0.72	0.40
Brass 40% Zn, leaded	155	2.06	1.48	0.77
Aluminum bronze	200	0.78	0.66	0.18
Gold: high purity, annealed	22	0.26	0.16	0.08
Lead: commercial purity	4.2	1.3	1.3	…
Nickel:				
Commercial purity, annealed	130	0.08	0.17	0.14
Alloy (Nimonic 100), heat treated	260	0.10	0.21	0.06
Steel: austenitic, type 304	155	0.09	0.36	…
Silver: high purity, annealed	35	1.17	0.41	0.21
Tin: high purity	9	3.5	3.45	…
Titanium:				
Commercial purity, annealed	200	0.25	0.15	0.11
Alloy (6Al/4V), heat treated	295	0.15	0.07	0.07
Zinc: commercial purity, annealed	35	1.24	1.22	…

(a) Abrasion rates obtained after approximately 500 traverses on a track of paper. Pressure applied to specimen, 38.7 kPa (395 g/cm^2). Abrasion rates in μm/min for a specimen abraded on a track 16 cm (6 in.) in diameter on a wheel rotating at 200 rpm can be obtained by multiplying these figures by 100. Source: Ref 3

Polishing Rates. In polishing operations, the general characteristics of material removal from the plastics commonly used in metallography are similar to those for metals. The material removal rate increases over the first few hundred specimen traverses and then decreases slowly over some tens of thousands of further

traverses. A plastic can therefore be characterized by the maximum polishing rate achieved in the same manner that is used for metals. As with metals, the highest polishing rate is obtained with a 2 to 4 μm abrasive grade, although the difference between 2 to 4 and 4 to 8 μm grades usually is only small (Ref 3). Considerably higher polishing rates are obtained for most plastics with polycrystalline rather than monocrystalline diamonds; mineral-filled molding epoxy is an exception (Table 6).

Table 6 Polishing rates of common specimen-mounting plastics

Plastic		Polishing rate[(a)], μm/100 m	
Type	**Filler**	**Monocrystalline diamond**	**Polycrystalline diamond**
Phenolic	Cellulose	14	19
	Mineral, 7 wt%[(b)]	8.8	14
Acrylic	nil	11	19
Epoxy, casting	nil	4.1	11
Formvar	nil	2.0	3.0
Polyvinyl	nil	5.0	6.0
Epoxy, casting	Alumina, 20 wt%[(c)]	2.6	4.2
Epoxy, molding	Mineral, 7 wt%[(d)]	0.8	0.5
Allyl	Mineral, 55 wt%[(e)]	4.5	5.2

(a) Polished on a 4 to 6 μm grade of diamond abrasive.
(b) Wood flour.
(c) Added as 600-mesh abrasive powder to the polymer-hardener mixture before polymerization commenced.
(d) Probably silica.
(e) Probably mica and glass. Source: Ref 3

An important feature to note is that the polishing rates of plastics are 2 orders of magnitude smaller than their abrasion rates (compare Table 6 with Table 4 and Table 7). A consequence is that their polishing rates are of the same order as those of metals (compare Table 6 with Table 8). In absolute terms, the polishing rates of the commonly used mounting plastics (e.g., cellulose-filled phenolic, acrylic, and casting epoxy resins) are somewhat higher than those of most metals. Material removal from the metal then would not be impeded when mounted in the plastic. However, the rates for some plastics (notably, Formvar and polyethylene) are considerably lower than for most common metals. In this event, the rate of material removal from a metal in the plastic would be reduced to a value approaching that of the plastic in proportion to their relative areas. Any plastic with large volume fraction of an abrasive filler is also likely to be in this category (such as the epoxy plastic listed in Table 6).

Table 7 Abrasion rates of common specimen-mounting plastics that cause severe deterioration of papers coated with conventional abrasives

Plastic		Abrasion rate, μm/m		Maximum thickness removable, μm
Type	**Filler**	**100[(a)]**	**1000[(b)]**	
Epoxy, casting	Alumina, 20 wt%[(c)]	15	1.5	2500
Epoxy, molding	Mineral, 70 wt%[(d)]	3.5	0.2	450
Allyl	Mineral, 55 wt%[(e)]	11	2.5	2500

Note: Determined under the conditions and by the same methods as for Table 5. Figures listed are for P240-grade silicon carbide paper. The values for P240-grade alumina paper are not greatly different.
(a) Average abrasion rate for the first 100 specimen traverses on a track of the paper.
(b) Abrasion rate after 1000 specimen traverses on a track of the paper.
(c) Added to the polymer-hardener mixture before polymerization commenced.
(d) Probably silica.
(e) Probably a mixture of silica and glass. Source: Ref 3

Table 8 Maximum polishing rate obtained in polishing various metals and alloys with two grades of polycrystalline diamond (6 and 3 μm) on a synthetic suede cloth

Metal or alloy	Hardness, HV	Maximum polishing rate[(a)], μm/100 m	
		4–8 μm grade	**2–4 μm grade**
Aluminum:	24	9.9	17.2
High purity			
Alloy (4.5% Cu)	105	9.0	15.0
Chromium: high purity	200	0.42	0.1
Copper:			
Commercial purity	50	5.6	8.8
Brass (30% Zn)	45	8.5	12.5
Brass (40% Zn), leaded	155	10	14.5
Aluminum bronze (11% Al)	200	4.0	6.5
Gold: high purity	22	0.10	0.18
Lead:			
Commercial purity	4	4.0	4.9
Alloy (40% Sn)	13	5.6	6.5
Nickel:			
Commercial purity	130	2.8	3.8
Alloy	260	1.8	2.0
Platinum: high purity	40	1.9	1.9
Steel:			
0.15% C, annealed	130	2.2	3.1
0.75% C, heat treated	340	1.8	3.0
0.75% C, heat treated	800	1.4	2.0
1.4% C, heat treated	840	2.1	1.6
Austenitic, type 304	105	2.2	2.8
Silver: high purity	35	3.0	7.8
Tin: high purity	9	2.5	4.4
Titanium:			
Commercial purity	200	1.8	1.8
Alloy (6% Al, 4% V)	295	1.6	2.1
Tungsten carbide (12% Co)	1550	1.3	1.4
Zinc:			
Commercial purity	35	8.3	10.4
Alloy (4% Al, 1% Cu)	90	7.3	11.8

Note: The abrasive was applied in the reference carrier paste, and kerosene was used as the polishing fluid. Conditions otherwise optimized.

(a) Under the particular conditions used, this corresponds to depth removed per minute of polishing time. Source: Ref 3, p 185

Electrical Conductivity. Conductive mounts are needed for electrolytic polishing of specimens or for scanning electron microscopy. Plastic mounting materials are electrical insulators, but several methods are available that allow electricity to flow to the specimen. For example, mechanical arrangements on the back surface of mounts can be done for electrolytic polishing. For examination by scanning electron microscopy, adequate electrical contact can be made to one point on the prepared surface by means of a dab of a special electrically conducting paint or with a special conducting adhesive tape.

Conductive fillers can also be incorporated into the resin of a plastic mount. Electrical resistance on the order of 100 ohms between the prepared surface and the back surface of the mount is needed. Filler materials of iron, aluminum, carbon, and copper have been used for this purpose. Copper diallyl phthalate is a widely known conductive mounting material. Good conductivity can be achieved with approximately 10 vol% metal mixed with mounting plastic. However, the resistance of mounts prepared by this technique can be unpredictable, because a low-resistance mold is only obtained under circumstances when the metallic particles form connecting chains by chance.

More reliable results are obtained when the individual plastic particles are coated with a conductive material. For example, polyvinyl chloride powder can be milled with carbon black to produce a conductive mounting material. Details of a method of preparing a polyvinyl chloride powder coated with carbon black and suitable for this purpose are given in Table 9. Standard mounts made with this powder consistently have a resistance in the range from 100 to 200 ohms. A disk of an appropriate metal may be molded in the back surface of such a mount, and electrical contact can be made to this disk.

Table 9 Method of preparing a conducting plastic

Ingredients	
Plastersol grade of polyvinyl chloride	100 parts by weight
Tribasic lead sulfate	2.5 parts by weight
Dibasic lead phosphite	2.0 parts by weight
Carbon black	15 parts by weight
Molding conditions	
Pressure	17 to 21 MPa (2500 to 3000 psi)
Temperature	160 °C (320 °F) (must not exceed 200 °C, or 390 °F)
Cooling	Cool to below 40 °C (105 °F) before ejecting mount from mold.

Note: Ball mill ingredients together for 24 h. Some separation of the ingredients may occur during storage after several years. In this event, the resin can be reconstituted by further ball milling. Source: Ref 3

If, for any reason, the conducting plastic has a detrimental effect on the characteristics of the working face of the mount, a mount with a more appropriate distribution of plastics can be achieved by the method illustrated in Fig. 4. The specimen is placed in a normal molding set, and a tube is inserted temporarily (Fig. 4a). Powder of the plastic required for the section surface of the mount is poured into the annulus between the tube and the mold until the base of the mold is covered and the annulus filled, the back surface of the specimen remaining uncovered (Fig. 4a). The tube is then filled with the conducting plastic (Fig. 4b) and withdrawn gently (Fig. 4c). The mold, when finally processed, has the distribution of plastic illustrated in Fig. 4(d).

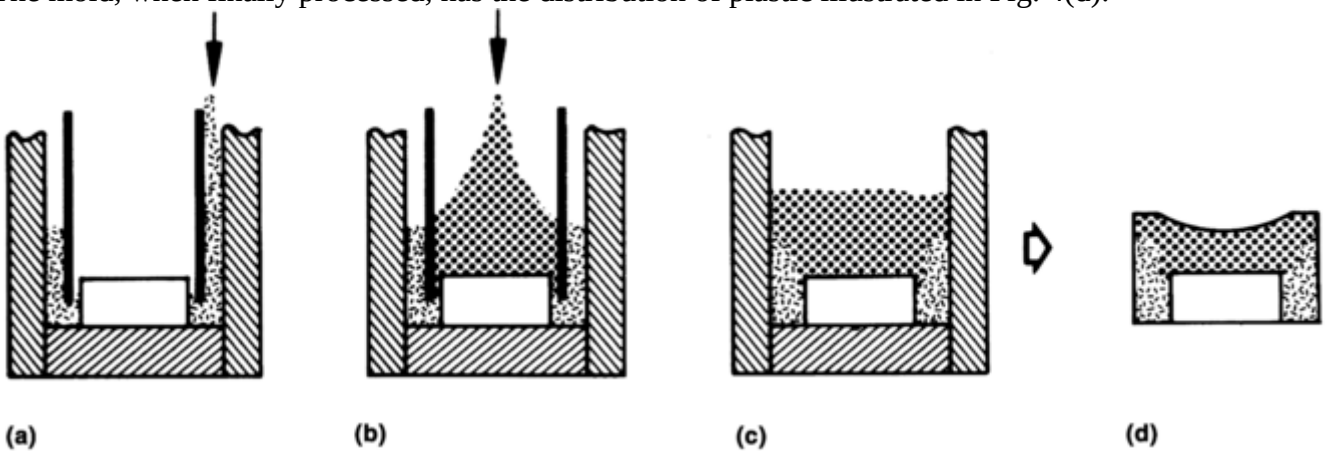

Fig. 4 Technique for making a mount with a conducting plastic (large dots) at the back of the specimen and a different plastic (small dots) at the section surface. Source: Ref 5

Transparency. Acrylics are the only plastics listed that are highly transparent. The epoxy and Formvar types, although translucent, are sufficiently transparent for many purposes.

Reflectivity. Plastics all have poor reflectivity in vertical bright-field illumination. They thus appear in strong contrast against the edge of a clean metal specimen but not when a nonmetallic layer (such as an oxide scale or a corrosion product) is present on the surface. It may, in the latter case, become difficult, particularly in a photographic print, to clearly distinguish the interface between the surface layer and the plastic mount. Deposition of a metallic layer on the nonmetallic layer before sectioning obviates this problem. Otherwise, all that can be done is to adjust the photographic technique to reduce the contrast in the final image. In these respects, plastic-mounted specimens are not very different from unmounted specimens, although the mismatch in reflectivity with respect to nonmetallic surface layers does tend to be smaller.

The reverse problem arises with translucent plastics, such as epoxy resins, during examination under polarized light. The mount may reflect strongly and the specimen poorly, in which event the flare from the plastic significantly reduces the contrast observed in the specimen. A good solution is to use epoxy with a colored pigment. The use of a black epoxy with an additive of black pelletized aluminum oxide also has been suggested for this problem (Ref 3, 6). However, pelletized alumina can cause serious grinding/polishing problems.

References cited in this section

3. L.E. Samuels, Chapter 2: Sectioning and Mounting, *Metallographic Polishing by Mechanical Means,* 4th ed., ASM International, 2003, p 9–32

4. R.J. Hussey, P.E. Beaubein, and D. Caplan, *Metallography,* Vol 6, 1973, p 27

5. W.L. Ladroga, *Met. Prog.,* Vol 83(No. 2), 1963, p 108

6. D.V. Miley and A.E. Calabra, A Review of Specimen Mounting Methods for Metallography, *Metallographic Specimen Preparation,* J.L. McCall and W.M. Mueller, Ed., Plenum Press, 1974, p 1–40

Mounting of Specimens, *Metallography and Microstructures,* Vol 9, *ASM Handbook,* ASM International, 2004, p. 242–256

Mounting of Specimens

Mount Size and Configuration

In addition to the selection of an appropriate mounting plastic, the size and configuration of the mount must be considered. This depends on specimen size, handling, and the type of metallographic examination to be performed. For example, square or rectangular mounts are often used in x-ray diffraction examination, which requires a relatively large surface.

Molds are commonly available for producing mounts with diameters of 25 mm (1 in.), 32 mm ($1\frac{1}{4}$ in.), and 38 mm ($1\frac{1}{2}$ in.). Smaller-diameter mounts tend to rock excessively during hand abrasion and polishing operations; larger-diameter molds give reduced abrasion and polishing rates for a given applied load. A diameter of approximately 25 mm (1 in.) is optimal, unless specimen dimensions dictate otherwise. The thickness of the mount ideally should be approximately half its diameter; thinner mounts are more difficult to handle, and thicker ones tend to rock during manipulation.

Another consideration is the position and number of specimens in a mount. This depends, in part, on the type of specimen holder to be used with a semiautomatic polishing machine (or alternatively, whether polishing is done manually). There are two types of specimen holders for semiautomatic polishing machines: a nonfixed holder (Fig. 5a) or a more rigid fixed holder (Fig. 5b). In both cases, the specimen holders attach to a power head that moves a mount holder over a polishing platen. The difference is how pressure is applied to the specimens in the holder.

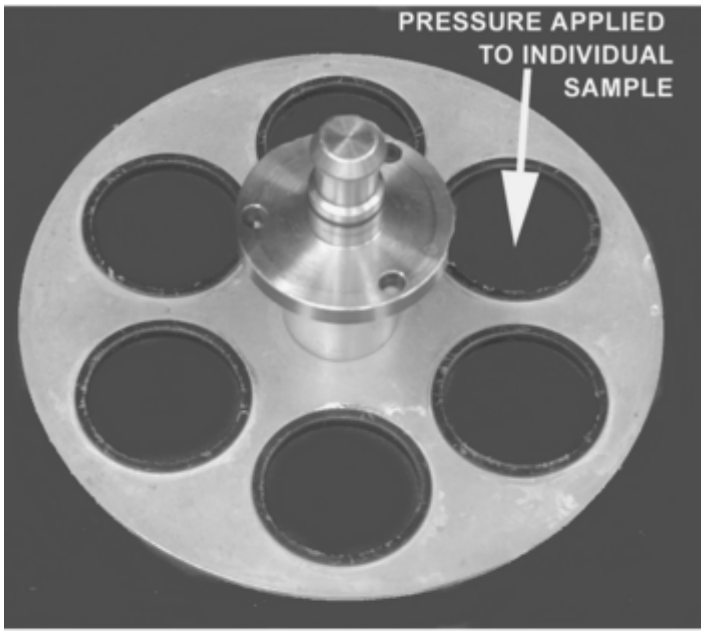

(a)

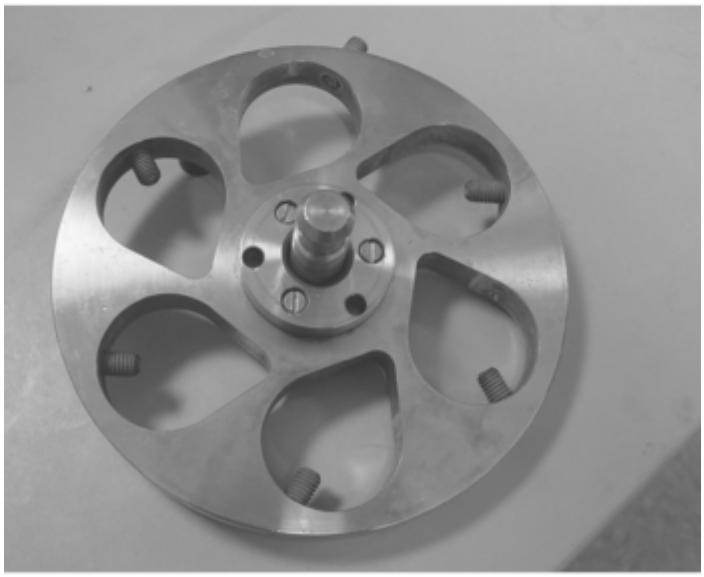

(b)

Fig. 5 Sample holders for semiautomatic polishing machines. (a) Nonfixed holder. (b) Fixed (rigid) holder

In semiautomated polishing with a fixed specimen holder, pressure is applied via the central column of the specimen holder. In this case, it is mandatory that three to six sample mounts be symmetrically placed in the specimen holder (Fig. 6). Each mount remains fixed in the sample holder during polishing. The mount surface will remain flat, because the samples are held in-plane by the sample holder. This method provides optimal edge retention and flatness and is the recommended sample-preparation method for operators requiring larger volumes of throughput.

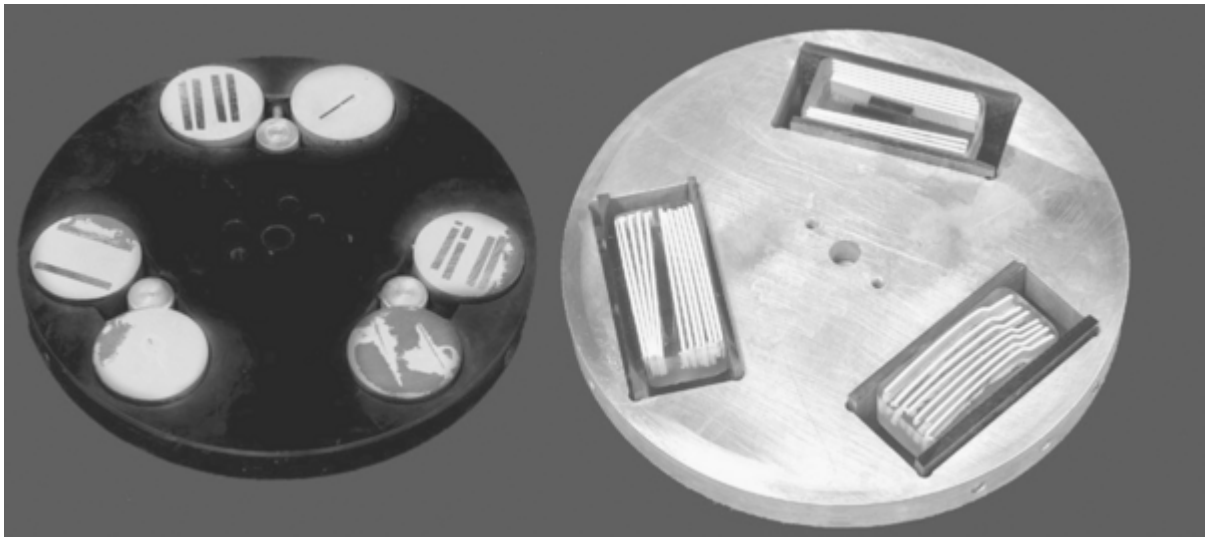

Fig. 6 Arrangement of specimen mounts in a rigid (fixed) sample holder

Polishing on a semiautomatic machine can also be done with a so-called nonfixed specimen holder. This method involves the same machine as mentioned previously, but the holder is not as rigid as a fixed holder, and the pressure is applied to each sample mount individually (Fig. 5a). In this case, two or more specimens should always be placed in each mount. By centering them in each side of the mount (Fig. 7), the specimens support the mount and eliminate the tendency for the mount to rock back and forth. The result is a flatter sample with better edge retention.

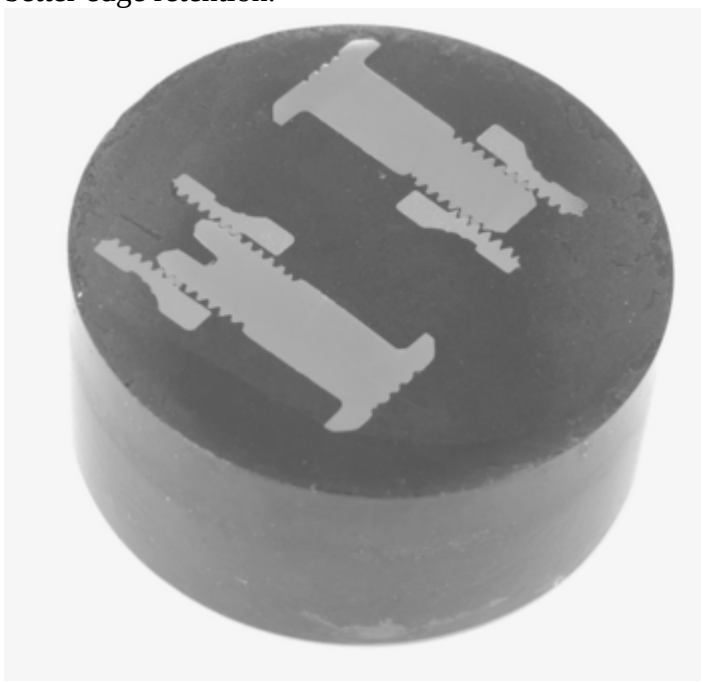

Fig. 7 Dual-specimen mount for a nonfixed sample holder

The nonfixed method is still not as good as the more rigid, centrally loaded fixed-specimen holder, but a dual-specimen mount can improve flatness after polishing. A single specimen should never be mounted in the center of a mount when polishing with a nonfixed specimen holder. The result is usually a convex and/or faceted mount surface with poor edge retention. The mount will have the tendency to rock back and forth about the small, hard specimen, rounding the mount surface and degrading the quality of the edge. This convex surface will have an adverse effect on the appearance of the microstructure. A similar-sized mount with two small samples in the holders will reduce the rocking effect, making it possible to prepare a more flat sample.

Manual or hand polishing is similar to polishing with a nonfixed specimen holder on a semiautomatic machine. Two or more specimens should be mounted in each sample. The only difference with respect to the

semiautomatic nonfixed method is that the specimen size in the mount for hand preparation should be kept to a minimum to facilitate grinding and to maintain a uniform applied pressure across the mount.

Mounting of Specimens, *Metallography and Microstructures*, Vol 9, *ASM Handbook*, ASM International, 2004, p. 242–256

Compression Molded Mounts

Thermal-compression mounting with either thermosetting or thermoplastic compounds requires a temperature and pressure cycle in a mounting press in order to produce the desired mount. Mounting generally takes place by rapid heating of the specimen and mounting material in a pressurized cylinder. The specimen is placed upside down on the bottom piston of the cylinder. The mounting material is poured over the specimen, and the top piston is placed inside the cylinder. Both heat and pressure are applied to the cylinder.

Many satisfactory presses and molding die sets are manufactured specifically for metallographic purposes. A mounting press should have an automatic temperature controller and an ejection device to remove the specimen. They vary from simple hand presses to automatically controlled hydraulic or pneumatic presses. The following should be considered when selecting from this range of equipment options (Ref 3):

- It is important to measure the amount of material so that the specimen is completely covered in the final mount.
- A hydraulic or pneumatic press should be of robust design, because maintenance of the desired pressure for a lengthy period is a severe requirement.
- A heater of high capacity (approximately 500 W) is desirable to ensure the minimum cycle time, particularly when starting from cold. Preheating of preformed blanks reduces the cycle time.
- An automatic temperature cutoff control is a desirable feature. Mount, specimen, and mold all can be severely damaged by accidental overheating.
- It is desirable that the mold-ejection arrangement load the press symmetrically.

Molding techniques are also straightforward if the equipment manufacturer's recommendations are followed, although the following points should be noted:

- The specimen should be clean and should be at least 1 cm (0.4 in.) smaller than the diameter of the mounting cylinder in any lateral dimension.
- Sharp corners should be eliminated from the specimen, if possible.
- Sufficient plastic must be placed in the mold to ensure that the upper ram of the molding die set does not contact the specimen.
- The die set must be cold enough when loaded with plastic powder to ensure that partial setting of the powder does not occur before loading of the mold has been completed.
- The pressure applied is not critical, provided that it exceeds a certain minimum. Excessive pressures are undesirable, however, because of the increased risk of damaging the specimen.
- Pressure must be applied immediately on commencement of mold heating in the case of thermosetting plastics, but it may be delayed with thermoplastic materials; this is even desirable when the specimen is fragile.
- Control of temperature is more critical than control of pressure. A certain minimum temperature must be exceeded in all cases, although this is, to some extent, dependent on the curing time allowed in the case of thermosetting plastics. Excessively high temperatures result in charring of the plastic or, in the case of thermoplastics, in the plastic becoming so fluid that it penetrates into clearances in the molding die set. In general, temperature should not exceed 180 °C (355 °F) or preferably 170 °C (340 °F).

- Thermosetting plastics may be ejected while hot after they have become fully cured, but slow cooling under pressure to well below the DTUL value of the plastic is desirable to reduce the width development of the fissure between specimen and plastic.
- Slow cooling under pressure is required with thermoplastics; this, for example, reduces the tendency for crack networks to develop in acrylic mounts.
- Difficulties in ejection usually are experienced only when the working surfaces of the die set are damaged. It is good practice, however, to treat these surfaces with a silicone mold-release agent, for which purpose pressure-pack sprays are available; this is virtually obligatory with Formvar plastics.

Mount Defects

Various types of defects (Table 10) may occur with compression molding of either thermosetting resins or thermoplastic resins. Some common mount defects and their causes are described in the following paragraphs. These defects are rarely seen today with modern mounting presses. Cottonball can still be observed, usually when specimen volume is small and powder volume is large.

Table 10 Typical problems of compression mounting materials

Problem	Cause	Solution
Thermosetting resins		
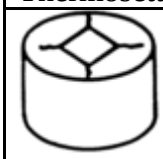 **Radial split**	Too large a section in the given mold area; sharp-cornered specimens	Increase mold size; reduce specimen size.
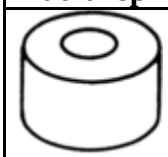 **Edge shrinkage**	Excessive shrinkage of plastic away from sample	Decrease molding temperature; cool mold slightly prior to ejection.
 **Circumferential splits**	Absorbed moisture; entrapped gasses during molding	Preheat powder or premold; momentarily release pressure during fluid state.
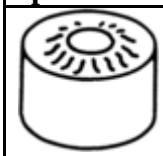 **Burst**	Too short a cure period; insufficient pressure	Lengthen cure period; apply sufficient pressure during transition from fluid state to solid state.
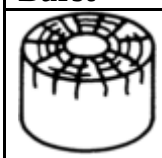 **Unfused (woody)**	Insufficient molding pressure; insufficient time at cure temperature; increased surface area of powdered materials	Use proper molding pressure; increase cure time. With powders, quickly seal mold closure and apply pressure to eliminate localized curing.
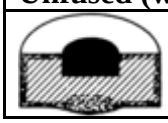	Excessive mold temperature	Decrease mold temperature. Momentarily release pressure during flow stage.

Case hardening and blister		
Thermoplastic resins		
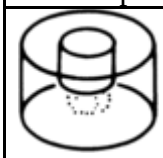 **Cottonball**	Powdered media did not reach maximum temperature; insufficient time at maximum temperature	Increase holding time at maximum temperature.
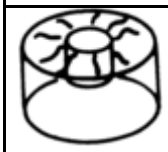 **Crazing**	Inherent stresses relieved on or after ejection	Allow cooling to a lower temperature prior to ejection; temper mounts in boiling water.

Radial cracks in thermosetting plastics usually result from attempts to mold a specimen whose dimensions are too large for the particular size of mount, especially when the specimen contains sharp corners. Such cracking can be alleviated by reducing the molding temperature and by allowing the mold to cool to a lower temperature before removing the applied pressure. In thermoplastics, radial cracks may develop even around small, smoothly shaped specimens as well as after a time delay. These cracks form because high internal stresses have developed in the mount due to ejection at too high a temperature.

Reducing the ejection temperature usually eliminates the form of cracking that develops immediately after ejection but perhaps not that which develops after a time delay. In this event, the mount should be annealed at 100 °C (210 °F) for a period by immersing it in boiling water.

Transverse cracking usually results from evolution of gases from either the plastic or the specimen; baking out the plastic or the specimen prior to mounting may help alleviate this problem. Transverse cracking may also result from use of a mold that initially was too hot.

Porous friable areas may result from low molding pressure, short curing time, or charging into an excessively hot mold, either singly or in combination. The cause is almost certainly insufficient time at temperature when the porous area is in the center of the mount; this is most obvious with transparent plastics.

Bulging of front or back surface is usually caused by insufficient curing time or insufficient pressure while the material is above the DTUL value.

Internal cloudy regions in thermoplastics result when the polymer powder has not reached a sufficiently high temperature in the center of the mount. The use of a longer dwell time at the molding temperature is indicated.

Thermosetting Molding Resins

Thermosetting resins, such as phenolic compounds, undergo the liquid and hardening stages before reaching the final curing temperature of approximately 150 °C (300 °F). The final mount can be removed from the mounting press once the curing temperature is achieved. However, to produce a better mount, it is advisable to allow these materials to remain under pressure until they have cooled, preferably to room temperature, or perhaps at least 65 °C (150 °F) in the case of some thermosets. This produces a better mount with reduced shrinkage and elimination of gaps and other defects. Once cured, a thermosetting material will not remelt but will char if exposed to high temperature.

Thermosetting mounting materials are widely used in the metallographic laboratory. They are resistant to most solvents and acids (although some etchants may break down the material and cause swelling). Thermosetting mounts are resistant to softening during grinding and polishing operations. The filled diallyl phthalates and thermosetting epoxies can match the rate of abrasion of most steels and cast irons.

Phenolics. Phenolic resins are the oldest type of mounting resin, first used in the early 20th century as a mounting material. The first commercial use was marketed under the trade name of Bakelite, after Leo Baekeland the inventor. Bakelite (Georgia-Pacific Corp.), or phenolic resins in general, are popular because of their low cost and good availability. Phenolic powders and granules can be purchased in various colors, including red, green, black, and mottled (filled with a wood flour). They also can be obtained as premolds,

which are cylinders of partially compacted granules ready to form a standard-sized mount. The premold is manufactured to fit into the cylinder of the mounting press. In mounting fragile specimens, a premold should not be used, because of potential damage to the specimen when pressure is applied to the cylinder.

Depending on mold diameter, curing times for phenolics vary from 5 to 9 min at 29 MPa (4200 psi) and 150 °C (300 °F). They are at heat only a few minutes before cooling is started. A lower pressure (down to 8 MPa, or 1200 psi) can be used for the same curing time, but few people bother to change the pressure setting. Curing times for premolds range from 3 to 7 min at the same pressure and temperature.

As a thermosetting material, a phenolic resin has the advantage of a shorter cycle in the mounting press operation. Its curing time is shorter than other mounting thermosets. It can be ejected from the mold after a short hold at 65 °C (150 °F). This can be important in a production metallographic laboratory, although it is still desirable to allow cooling to room temperature before removal. Better results are obtained when cooled under pressure. Never remove a hot phenolic mount from the mounting press and cool the hot mount in water. This practice will save time but will definitely cause fissuring or separation between the specimen and the mount.

Phenolics exhibit relatively low hardness, limited abrasion resistance, and limited edge protection. A phenolic mount can be attacked by certain etching solutions. For example, boiling alkaline sodium picrate, an etchant used to darken cementite, will attack a phenolic mount. Bakelite normally contains wood flour fillers but is also available as 100% resin (Bakelite amber).

Diallyl phthalate is another thermosetting material. This material is more expensive than a phenolic resin and is marketed with various fillers, including mineral and glass particles for added hardness and strength. A filled diallyl phthalate mount will have greater wear resistance than a phenolic mount. Usage as a mounting material is low compared to that of phenolics or compression molding epoxies.

Diallyl phthalate mounts require a pressure of approximately 22 MPa (3200 psi) at 150 °C (300 °F) and a curing time of 7 to 12 min, depending on mold diameter. It is advisable to cool the mount under pressure to room temperature before removing it from the mounting press. Like phenolics, do not cool hot mounts in water. Diallyl phthalates may adhere to metals better than phenolics, but rapid cooling can still cause loss of adhesion to the specimen surface. The adhesion is not as good as that of the epoxy materials.

Diallyl phthalate is available as a powder with mineral or glass filler. In glass-filled form, it will provide harder mounts and better edge retention than phenolics (but not as good as filled epoxies). Mineral-filled and glass-filled diallyl phthalate exhibit good resistance to chemical attack, which is useful when using powerful etchants or etching at elevated temperatures.

Electrically Conductive Diallyl Phthalate Mounts. Conductive particles may be added to diallyl phthalate for mounts in electrolytic polishing or scanning electron microscopy. Additives include particles of aluminum, copper, iron, or graphite. However, the filled diallyl phthalates contaminate grinding and polishing wheels. Many laboratories restrict the use of copper-filled diallyl phthalates. In an aqueous environment, the copper can be inadvertently plated onto the specimen surface. In the light microscope, one can actually observe the copper plating by its reddish color. If metallographic specimens are contaminated with copper-filled diallyl phthalate, the elemental analysis also may lead the investigator to false conclusions.

Compression Mounting Epoxies. Compression molding mounts are also produced from premixed powders of epoxy compounds (usually with a filler added for higher abrasion resistance). As with the other thermosetting materials, thermosetting epoxy requires a mounting press and heating. The advantage is that epoxies provide low shrinkage and produce excellent edge retention with appropriate filler. Thermosetting epoxy is also resistant to solvents and acids. Thermosetting epoxy compounds are more expensive than phenolics.

Thermosetting epoxy has better flow characteristics than phenolics and diallyl phthalates. This is an important feature in filling cracks and voids in the specimen. Thermosetting epoxy compounds require lower pressures than the phenolic materials, for example, a pressure as low as 8 MPa (1200 psi) versus the 29 MPa (4200 psi) required for the phenolic materials. Molding time, pressure, and temperature are similar to those used for diallyl phthalate, but molding defects are less common. It adheres well to metal, and thus the occurrence of fissuring is reduced. Conversely, a mold-release agent also is generally required to prevent the mount from adhering to the ram.

Thermosetting epoxy mounts provide good wear/polishing characteristics, because the polishing rate of filled epoxy is low (Table 6). It thus can provide excellent edge retention when reinforced with an appropriate abrasive filler. This is shown in Fig. 8, where a steel screw is mounted in a thermosetting epoxy (Fig. 8a) and Bakelite (Fig. 8b). There is excellent edge retention in the epoxy, because the specimen and mount are both in focus. Also, there is a thin oxide-scale layer on the surface of the screw. In the Bakelite mount, there is poor

edge retention, with the mount out of focus and the oxide-scale layer not evident. There is also a gap between the mount and the specimen.

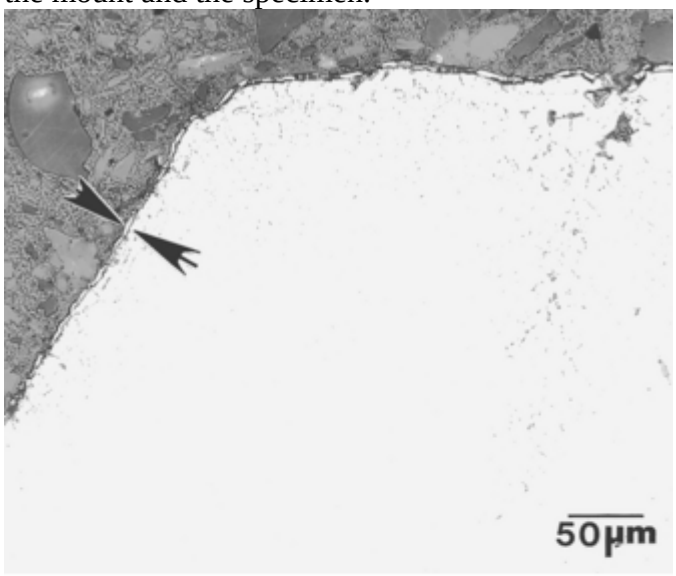

(a)

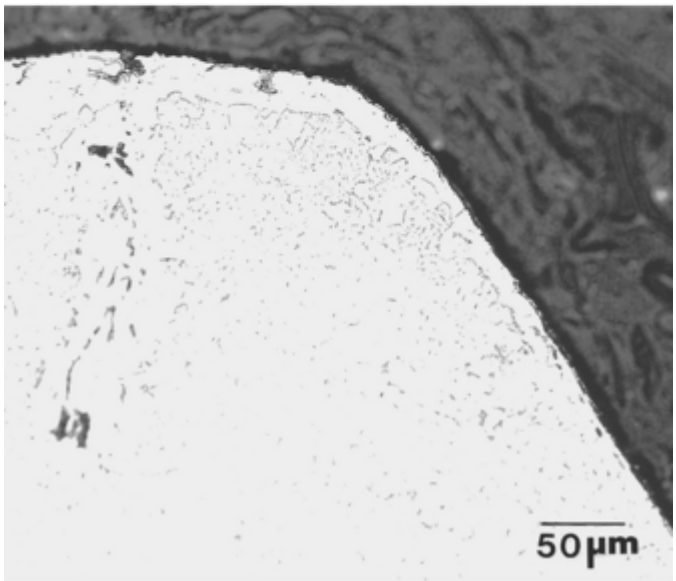

(b)

Fig. 8 Micrographs showing the polished edge of a steel screw mounted in (a) thermosetting epoxy and (b) a thermosetting phenolic resin (Bakelite). Excellent edge retention is obtained with the epoxy mount, where a thin oxide layer can be seen on the screw surface. The edge of the screw in the Bakelite mount is rounded, and the oxide layer cannot be seen. 200×. Source: Ref 2

Thermoplastic Molding Resins

Compression molding of mounts with thermoplastic resins also requires heat and pressure during molding, but the mounts must be cooled to ambient temperature under pressure. These materials can be used with delicate specimens, because the required molding pressure can be applied after the resin is molten. However, because they must be completely cooled under pressure, thermoplastic resins are more difficult to use than thermosetting materials. They are also more susceptible to heat distortion, as indicated by comparison of general deflection temperature under load (DTUL) values (Table 3).

In using thermoplastic powders, the mounting practice differs somewhat from that used for thermosetting materials. During the initial heating of the cylinder, a low pressure of approximately 0.7 MPa (100 psi) is applied. Once the temperature reaches 150 °C (300 °F), the pressure is increased to 29 MPa (4200 psi). The

mount is then cooled within the cylinder at this pressure until the temperature drops to below 40 °C (105 °F) or, preferably, to room temperature. In the early type of presses (~1960s), this process took approximately 40 min (although it could be shortened by applying chill blocks or other cooling devices to the outside of the cylinder during the cooling cycle). This is not a problem with modern presses that have integral water cooling. If removed from the cylinder too early, the mount will not hold its shape.
Thermoplastic molding resins include:

- Acrylic (methyl methacrylate) also known by trade names such as Lucite, E.I. DuPont de Nemours and Co., or Transoptic, Buehler, Ltd.
- Polystyrene
- Polyvinyl chloride (PVC)
- Polyvinyl formal (Formvar)

Acrylic (methyl methacrylate) and polyvinyl formal have become prevalent because of their transparency, which can be a useful property when grinding and polishing must be controlled to locate a particular defect or area of interest.
Linear shrinkage of thermoplastics on cooling is high. Abrasion and polishing rates are generally lower than those of thermosetting materials, and fairly low DTUL values can result in softening of the mount if frictional heat generated during grinding and polishing is not controlled. Of the thermoplastics, PVC and polyvinyl formal display the best polishing characteristics (Ref 6) (see also Table 6). The chemical resistance of thermoplastics is fair at best; most are attacked by strong acids. Some are at least partially soluble in organic solvents, but all show good resistance to dilute acids and to alcohol, except methyl methacrylate, which is partially soluble in alcohol.
Acrylic (Methyl Methacrylate). The acrylics are transparent in the solid form and thus can be an advantage when the sides of the embedded specimen need to be observed. Identification labels also can be placed inside the mount (facing outward) or, in some cases, the identification code can be placed on the specimen itself. However, the acrylics suffer from many disadvantages.
First, acrylics are not resistant to nitric and acetic acids and many solvents (alcohol, acetone, and ethyl methyl ketone). An improperly prepared (insufficient melting) acrylic will easily dissolve in alcohol, and even a properly prepared mount may craze in etchants containing alcohol, for example, nital and picral. Second, an acrylic mount has a tendency to pull away from specimens such as steel that have a CTE much lower than acrylic. Third, the acrylics require longer curing times than the thermosetting materials, because the mount must remain in the mounting press cylinder, under pressure, until it is cooled to room temperature.
Finally, the metallographer must prevent the mount from heating during grinding operations. A coolant (usually water) must be used, because the acrylic material will soften with heat. A thermosetting material will not soften under the same circumstances.
Polyvinyl Compounds. Other thermoplastic materials are polyvinyl formal and PVC. Polyvinyl formal is marketed under the trade name Formvar. It has similar characteristics to the acrylics but is not widely used as a mounting material. It does have the advantage of being one of the hardest of the organic compounds used as mounting materials. One of its disadvantages is its short shelf life. Apparently, the mount continues to cure with time and will eventually deteriorate and crack during storage.

References cited in this section

2. B.L. Bramfitt and A.O. Benscoter, Chapter 7: Metallographic Specimen Preparation, *Metallographer's Guide for Irons and Steels,* ASM International, 2002, p 169–214

3. L.E. Samuels, Chapter 2: Sectioning and Mounting, *Metallographic Polishing by Mechanical Means,* 4th ed., ASM International, 2003, p 9–32

6. D.V. Miley and A.E. Calabra, A Review of Specimen Mounting Methods for Metallography, *Metallographic Specimen Preparation,* J.L. McCall and W.M. Mueller, Ed., Plenum Press, 1974, p 1–40

Mounting of Specimens, *Metallography and Microstructures,* Vol 9, *ASM Handbook,* ASM International, 2004, p. 242–256

Cast Mounts

Mounting is done with a mixture of liquid resins that are castable at room temperature. The specimen is placed inside the mold, where both mold and specimen are on a flat surface. The castable compound is poured around the specimen in a mold, and then the compound solidifies (cures) at room temperature. The method is called "cold" mounting, because it does not require external heating.

However, the term "cold" mount is a misnomer because even cast resins get hot during curing. For example, acrylics are popular because they are cheap and cure quickly (in 5–8 min), but temperatures can reach well over boiling (100 °C, or 212 °F) during curing (polymerizing). In addition, mixing a large quantity of epoxy resins (100–200 mL is not uncommon), can cause the blend to smoke and even boil after curing for a few minutes in a cup. Thus, many people use insulative-type molds (silicone rubber or plastic). Conductive molds with aluminum foil are also desirable; if the volume of epoxy to sample volume is not high, then the exotherm may be as little as 10 °C (~20 °F) above ambient with an Al-foil mold. Conversely, the opposite problem can occur when epoxy volume is low and cannot generate enough heat to start or hasten the polymerization process.

Castable resins include acrylics, polyesters, and epoxies, as discussed in this section. Castable mounting materials are more expensive than the thermosetting and thermoplastic mounting materials. They also require longer curing times than compression molding resins. However, castable compounds have several advantages over the thermal-compression materials. One major advantage is that a mounting press is not required. They also are relatively easy to mix and use, and many mounts can be made at one time.

Castable compounds usually consist of a resin and a hardener. Because hardening is based on the chemical reaction of the components, the resin and hardener must be carefully measured and thoroughly mixed, or the mount may not harden. Because all castable resins produce vapors, mounting under a ventilation hood is preferred. Skin damage can also result from frequent contact with some materials, but these hazards are minimal if reasonable care is taken. As part of preparations, the Material Safety Data Sheets should be carefully read for the materials being used.

Preparation may also influence the extent of heating. Many consider the process heat from curing a cast resin to be much less than the heat required for compression mounting. However, this is not necessarily true. For example, an experiment (Ref 8) was done with a tube of commerical pure titanium that contained an extensive amount of titanium hydrides (TiH). It has been suggested that such specimens should never be compression molded, as the amount of TiH would be reduced or eliminated from heat exposure. In the experiment, specimens were mounted with a compression molding epoxy (press, 150 °C), in an acrylic resin (8 min cure), in a fast curing epoxy (45 min), and in a slow curing epoxy. Molds for the castable resins included both insulative polyethylene cups and the Al-foil conductive method. The latter did maintain the most TiH. However, there was little, if any, difference in the amount of TiH in the compression-mounted specimen versus any of the other "cold" mounted specimens. They all exhibited less TiH than the specimen mounted with slow curing (low viscosity) epoxy using the Al foil-bakelite ring method.

Molds for Castable Mounts

For a castable mount, the specimen is placed in the center of a mold. The mold can be a simple receptacle, such as an aluminum or phenolic tube cut to a height of approximately 20 to 25 mm ($\frac{3}{4}$ to 1 in.). Various mold shapes can be used, but cylindrical mounts are the most common in various standard-sized diameters between 25 to 50 mm (1 to 2 in.), depending on specimen size. There are three basic types of molds:

- A cylinder open at both ends
- A cylinder with a removable end

- A flexible cylinder with a closed end

The open-ended mold is the least expensive but must be glued to a flat surface.
A simple mold procedure begins by covering a flat plate with aluminum foil. Rubber cement is applied to one end of a disposable phenolic (Bakelite) ring form of the desired mount diameter, and this end is pressed against the foil. The specimen is placed inside the ring form with the side to be polished against the foil, and the mixed mounting material is poured around the specimen after the rubber cement hardens. After curing, the mount, permanently enclosed by the ring, can be easily removed from the foil.
Possible mold materials include glass, disposable phenolic (Bakelite) or aluminum rings, aluminum foil, and polyethylene cups or silicone rubber cups. When using epoxy resins, one important consideration is that epoxy resins adhere strongly to many materials. Thus, if the mold is to be reclaimed, a mold-release agent, such as silicone oil or vacuum grease, may be needed, depending on the mold material. Release agents are not necessary if flexible silicone rubber molds are employed; however, rubber molds tend to deteriorate when exposed to the epoxy hardener.
Simple molds machined from a metal such as aluminum can be used, provided that the mold surfaces are maintained in a highly polished condition and are treated regularly with an appropriate release agent. However, epoxy plastics contract very little during curing, and the mounts consequently are difficult to eject from a rigid mold of this type, unless further mechanical complications are introduced into the mold system. Similar molds can be machined from acrylic plastics, to which epoxy plastics do not adhere, but acrylics also are relatively rigid and thus also cause ejection difficulties.
More flexible plastics ease mount ejection, and, among these, PVC has acceptable, and polyethylene has excellent, parting characteristics. Coating the molds with a silicone release agent is desirable with these materials but not essential. Satisfactory mold designs employing available solid forms of these materials are sketched in Fig. 9(a) and (c). An even simpler form of mold (Fig. 9d) can be formed from a dipping-grade PVC, as described subsequently. This type of mold has a comparatively limited life but is inexpensive and is easy to make in any size.

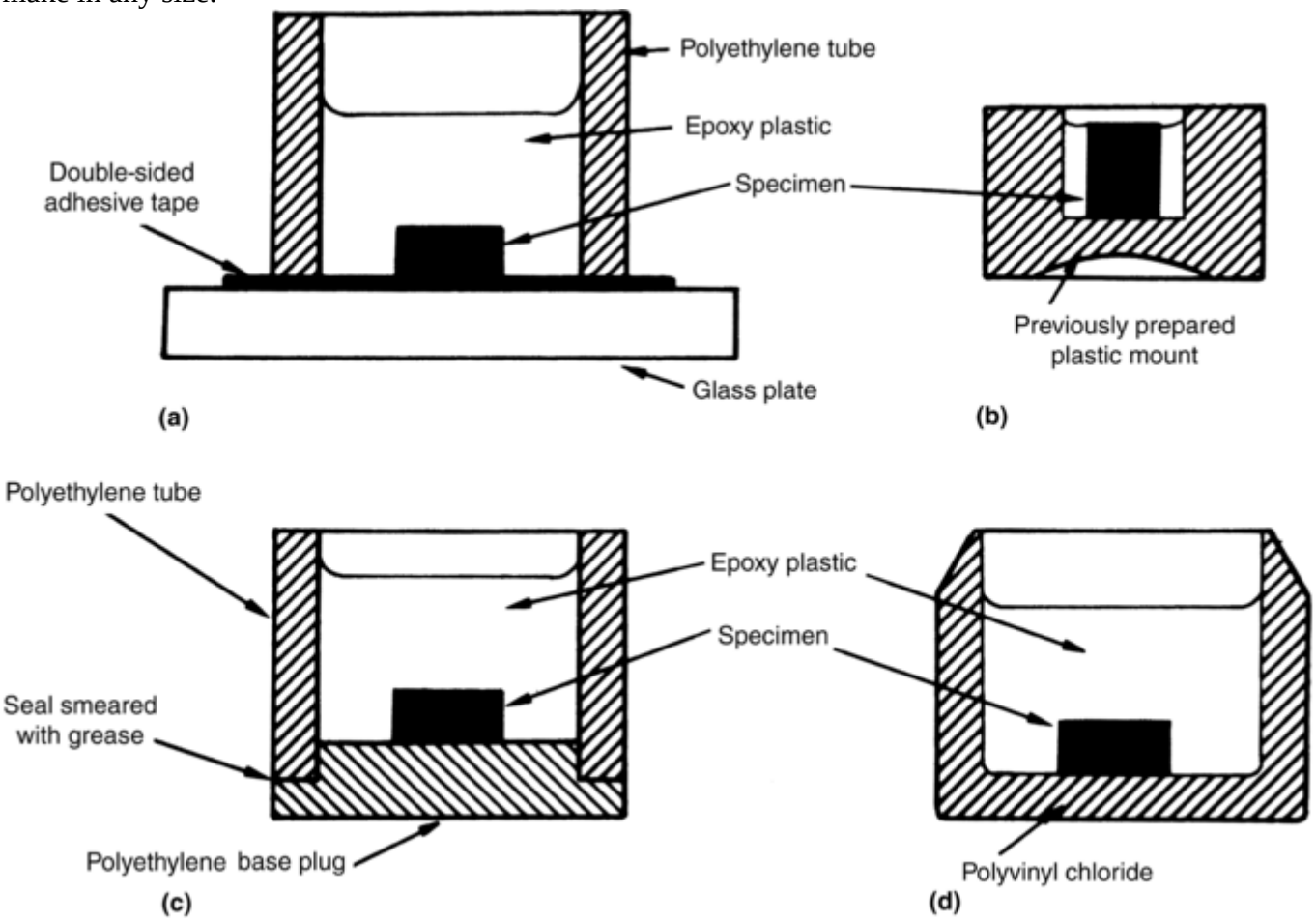

Fig. 9 Molds suitable for casting plastics of the epoxy type. The base of the mold tube in (a) must be dressed regularly against an abrasive paper to ensure a leak-free joint. A mold of similar form can be manufactured from silicone rubber. Source: Ref 3

Silicone Rubber Molds. Silicone rubber is the most satisfactory mold material presently available in terms of parting characteristics. Even thick-wall molds are flexible enough to permit easy mount ejection, and silicone rubber molds are simple to make, as described in Ref 3. A reasonably fluid grade of elastomer should be chosen and the catalyst addition adjusted to give a pot life of at least 20 min. Mixing can be carried out in a paper cup or a metal, glass, or plastic container and by either simple hand or mechanical mixing. Care must be taken to minimize air entrapment. The catalyzed rubber mix is poured around a properly prepared pattern and allowed to stand for at least 24 h at room temperature to allow the rubber to cure. This may be followed (if possible) by heating in an air oven at 70 °C (160 °F) for 16 h. It also may be necessary to remove entrapped air by vacuum treatment.

Castable Resins for Mounts

Castable resins for mounts include acrylics, polyesters, and epoxies. Table 11 lists common mold defects of these castable materials. Epoxies have the lowest shrinkage of the castable resins. They adhere well to most other materials and are chemically resistant, except in concentrated acids. The epoxies are sensitive to variations in the resin-hardener mixture; however, premeasured packets are available. Curing times vary according to the specific formula used. Epoxies generate significant stresses during curing, which may damage delicate specimens.

Table 11 Typical problems of castable mounting materials

Problem	Cause	Solution
Acrylics		
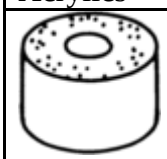 **Bubbles**	Too violent agitation while blending resin and hardener	Blend mixture gently to avoid air entrapment.
Polyesters		
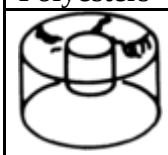 **Cracking**	Insufficient air cure prior to oven cure; oven cure temperature too high; resin-to-hardener ratio incorrect	Increase air cure time; decrease oven cure temperature; correct resin-to-hardener ratio.
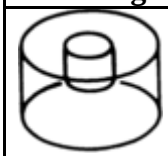 **Discoloration**	Resin-to-hardener ratio incorrect; resin has oxidized	Correct resin-to-hardener ratio; keep containers tightly sealed.
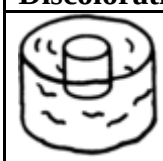 **Soft mounts**	Resin-to-hardener ratio incorrect; incomplete blending of resin-hardener mixture	Correct resin-to-hardener ratio; blend mixture completely.

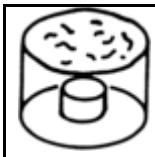 **Tacky tops**	Resin-to-hardener ratio incorrect; incomplete blending of resin-hardener mixture	Correct resin-to-hardener ratio; blend mixture completely.
Epoxies		
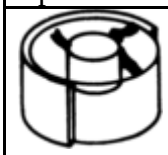 **Cracking**	Insufficient air cure prior to oven cure; oven cure temperature too high; resin-to-hardener ratio incorrect	Increase air cure time; decrease oven cure temperature; correct resin-to-hardener ratio.
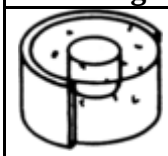 **Bubbles**	Too violent agitation while blending resin and hardener mixture	Blend mixture gently to avoid air entrapment.
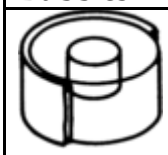 **Discoloration**	Resin-to-hardener ratio incorrect; oxidized hardener	Correct resin-to-hardener ratio; keep containers tightly sealed.
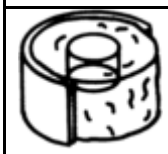 **Soft mounts**	Resin-to-hardener ratio incorrect; incorrect blending of resin-hardener mixture	Correct resin-to-hardener ratio; blend mixture completely.

Epoxy Casting Resins. Castable epoxies consist of two or more liquid resins that are mixed in certain proportions. One liquid is the resin, and the other liquid is the hardener (also called activator or catalyst). The proper proportion of resin to hardener is very important for optimal curing of the mount. Also, the two liquids must be thoroughly mixed. To ensure a better mix, a flat paddle should be used instead of a rod to mix the two liquids. After the two liquids are thoroughly mixed, there will be a slight amount of heat generated by the reaction of the hardener and the resin. Because of this heat of reaction, polystyrene (e.g., Styrofoam, The Dow Chemical Co.) and wax-coated mixing cups should be avoided as a mixing container.

Care must be taken in mixing the two constituents of epoxy plastics. Shelf life is critical with epoxy. It is advisable not to buy more than a six-month supply. Date the container when purchased. Always follow the instructions for mixing (as generally any suggestion to alter mixing ratios of epoxy is prone to mistake by the average person). Then impregnate the epoxy and oven cure about 60 °C (140 °F). It is difficult to remove a specimen from a partially cured epoxy mount and start over. In general, the lower the viscosity of the epoxy, the longer the curing time. Low-viscosity epoxies are desired for vacuum impregnation. One type is heated to about 50–60 °C (120–140 °F), which significantly lowers the viscosity.

One disadvantage of epoxy mounts is their gumminess when grinding and polishing, which increases machine vibrations. Hand polishing is more difficult. An inadequate amount of hardener results in soft mounts; an excessive amount causes large temperature rises during hardening and perhaps even cracking of the mount. Once established, the proportions must be measured accurately and the ingredients must be very thoroughly mixed; otherwise, locally uncured regions may develop in the mount.

Vigorous mixing inevitably entraps small air bubbles. These bubbles can create pockets on the polished surface that will be undesirable. The air pockets will fill with grinding and polishing contamination, which will produce scratches and an unacceptable polish. Elimination of air bubbles may require that the mixture be allowed to stand for sufficient time before casting to permit most of these bubbles to escape. Vacuum treatment is also done to remove air bubbles.

To prevent the epoxy from bonding with the flat surface in an open-end mold, place a sheet of aluminum foil over the surface. After the mount has cured, the foil can be peeled away from the mount or will easily disappear in the first grinding operation. To prevent the epoxy from seeping under the mold while pouring the liquid, the mold must be bonded to the foil. Usually, this is done with a fast-drying glue.

Curing of Epoxy. Generally, metallographic mounts are prepared for an overnight cure at room temperature. Epoxies cure in 45 min to 20 h after mixing, depending on mount size and the resin. Some epoxy materials on the market have a catalyst that shortens the curing time, but this material generates much more heat during the curing reaction, and this can lead to shrinkage. If, after a long cure time at room temperature, the mount is not completely cured, place the mount in an oven at 60 to 70 °C (140 to 160 °F) or under a heat lamp for a few hours for a more wear-resistant mount. An epoxy mount should not shrink away from the specimen, and usually, there is an excellent bond between the mount and specimen.

The curing time required for epoxy resins can be reduced considerably by heating to a slightly elevated temperature (50 to 75 °C, or 120 to 170 °F). Heat curing also has the advantage of increasing the DTUL value of the plastic. Different procedures are possible. For example, one recommendation is that the plastic cure at room temperature for approximately 1 h after mixing; curing is then completed after a further 15 to 30 min at 70 °C (160 °F) (Ref 3). Another recommendation to accelerate the solidification process is that the mount be placed in an oven at 65 °C (150 °F) for 1 h, followed by curing at room temperature for 2 h (Ref 2). Vendor recommendations should be followed carefully, because the ratio of hardener to resin must also be reduced when curing at high temperatures. Control of temperature is important, because the curing process is exothermic. Development of excessive temperatures in the curing plastic can cause frothing, cracking, and development of fissures between specimen and plastic.

To cast a mount larger than 38 mm ($1\frac{1}{2}$ in.) in diameter, the ratio of hardener to resin must be lowered or the mount will crack during the curing period from the excess heat generated during the reaction. Other options include adding the epoxy in layers or placing the mount in a refrigerator for approximately 16 h (overnight). Remove from the refrigerator and let the mount stabilize at room temperature for 8 to 12 h. This technique will prevent the epoxy from producing a high exothermic reaction that would result in a gap between the specimen and a mount.

Acrylics. Castable acrylics usually have a faster curing time (5 to 8 min) than castable mounting epoxies. Acrylics are simple to use and transparent. However, acrylics do not provide good edge retention. As with the acrylic thermoplastic mounting material, attack by solvents and strong acids could be a problem. Also, acrylics have the greatest shrinkage of any of the castable mounting materials.

In addition, although referred to as cold-mounting materials, acrylics generate considerable heat during curing (Ref 7). Depending on the amount of heat generated and the temperature excursion in the specimen itself, this could alter the microstructure. To minimize heating of the specimen, a conductive mold material such as copper and aluminum can be used to extract the excess heat.

Polyesters. Castable polyesters generally require slightly longer curing times than acrylics and are not very sensitive to slight variations in the mixture. They cure within 1 to 3 h and have less shrinkage than castable acrylic mounting materials. However, they are more expensive than acrylic resins. Polyester mounts generally have lower hardness than other castable mounts. A finished polyester mount is transparent. They have good chemical resistance to typical metallographic reagents.

Vacuum Treatment

To remove bubbles and avoid the formation of air pockets, the epoxy mixture (while still in the liquid state) can be placed in a vacuum chamber. The chamber must be of ample size and should be fitted with a transparent, vacuum-sealed lid to act as both an entrance port and an observation window. A common transparent glass or plastic vacuum desiccator can be used for this purpose. The chamber has to be connected to a vacuum pump that produces a vacuum approaching, but not exceeding, 25 MPa (600 mm Hg). Epoxies boil at room temperature at lower pressures, causing severe frothing. A laboratory-type water-injection vacuum pump is suitable, or the vacuum pump can be an inexpensive mechanical “roughing” pump. The three different methods of vacuum treatment are described in Ref 2. The simplest method is to pour the mixture around the specimen in the mold and then place it in the vacuum chamber. However, it may be more effective to outgas while the liquid is put into the mold. This requires the addition of a mechanism inside the chamber.

Placing a Freshly Mixed Epoxy Mount in the Vacuum Chamber. In this method, the epoxy mixture is prepared in air and poured around the specimen in the mold. The mold is then placed in the vacuum chamber, and the chamber is evacuated. The mount should remain under vacuum until foam forms on top of the exposed side of the mount. After evacuation is completed, air is slowly bled into the chamber. For best results, this evacuation-bleeding process should be repeated several times. This technique assists the epoxy in flowing into cracks and voids in the specimen. In this method, bubble-free mounts usually are obtained if the polymer-hardener mixture is first outgassed in the chamber and then poured into the mold outside the chamber (Ref 3). In each outgassing cycle, the chamber is pumped out and the vacuum maintained for a few minutes or until all visible signs of gas evolution have ceased.

Drawing the Epoxy Mixture into the Vacuum Chamber. The epoxy is mixed in the air. However, in this method, the mold and specimen are placed inside the vacuum chamber without adding the epoxy mixture. The chamber is then evacuated, and the epoxy mixture is drawn into the chamber through a plastic tube to fill the mold. This type of vacuum desiccator requires an excess amount of epoxy mixture in order to prevent air from being drawn into the chamber. The plastic tube must be discarded after use because of the hardened epoxy inside the tube.

Pouring Inside the Vacuum Chamber. In this method, the epoxy is mixed and then poured into a cup that is mounted inside the vacuum chamber. After evacuation of the chamber, the cup is tipped and the mixture is poured directly into the mold. As in the previous method, because the pouring takes place under vacuum, the epoxy can fill all the voids and cracks in the specimen. After pouring, air can be bled into the chamber, or the chamber can be placed under positive pressure.

References cited in this section

2. B.L. Bramfitt and A.O. Benscoter, Chapter 7: Metallographic Specimen Preparation, *Metallographer's Guide for Irons and Steels,* ASM International, 2002, p 169–214

3. L.E. Samuels, Chapter 2: Sectioning and Mounting, *Metallographic Polishing by Mechanical Means,* 4th ed., ASM International, 2003, p 9–32

7. J.A. Nelson, Heating of Metallographic Specimens Mounted in `Cold Setting' Resins, *Prakt. Metallogr.,* Vol 7, 1970, p 510–521

8. G. Vander Voort, private communication

Mounting of Specimens, *Metallography and Microstructures,* Vol 9, *ASM Handbook,* ASM International, 2004, p. 242–256

Special Mounting Techniques

Edge Retention. In many metallographic specimens, the features at the edge of the specimen are of vital importance. These features could include a metallic or organic coating, an oxide scale, or a decarburized layer. Unfortunately, during polishing, the specimen edge tends to abrade faster than the remaining specimen. This rounding of the specimen edge is unacceptable, because features at the edge become imperceptible or blurred due to the limited depth of field of a light microscope at high magnifications.

One of the easiest techniques for edge retention is to mount the specimen in a clamp of similar material. This way, the interface between the clamp and specimen is preserved. In a thermal-compression or castable mount, it is advisable to place a steel sheet next to the edge of interest. A small gap is allowed between the steel sheet and the specimen in order to fill the gap with the mounting material. If the sheet abuts the specimen directly, a space

may develop that will allow seepage of etching and rinsing solutions at the final preparation stage. During mounting, there is not enough pressure between the sheet and the specimen to ensure a tight interface.
As noted in the section “Mount Size and Configuration,” a flatter sample with better edge retention can be obtained when two or more specimens are centered in a mount (Fig. 7). Placing two specimens in a mount provides support, so the mount does not tend to rock back and forth when polishing on a machine with a nonfixed specimen holder. Another approach is to place rods (of material comparable to that of the specimen) at the outer quadrants of the specimen (Fig. 10b). This mounting method is geared mainly toward using cast epoxy, which may be the only resin that will do the job (filling voids and cracks, holding loose oxides, etc., to the surface, etc.). Cast epoxy does not give great edge retention and there are many problems with using it (including health hazards). An alternate approach is to use mineral-filled thermosetting epoxy (with proper grinding/polishing practices) for good edge retention.

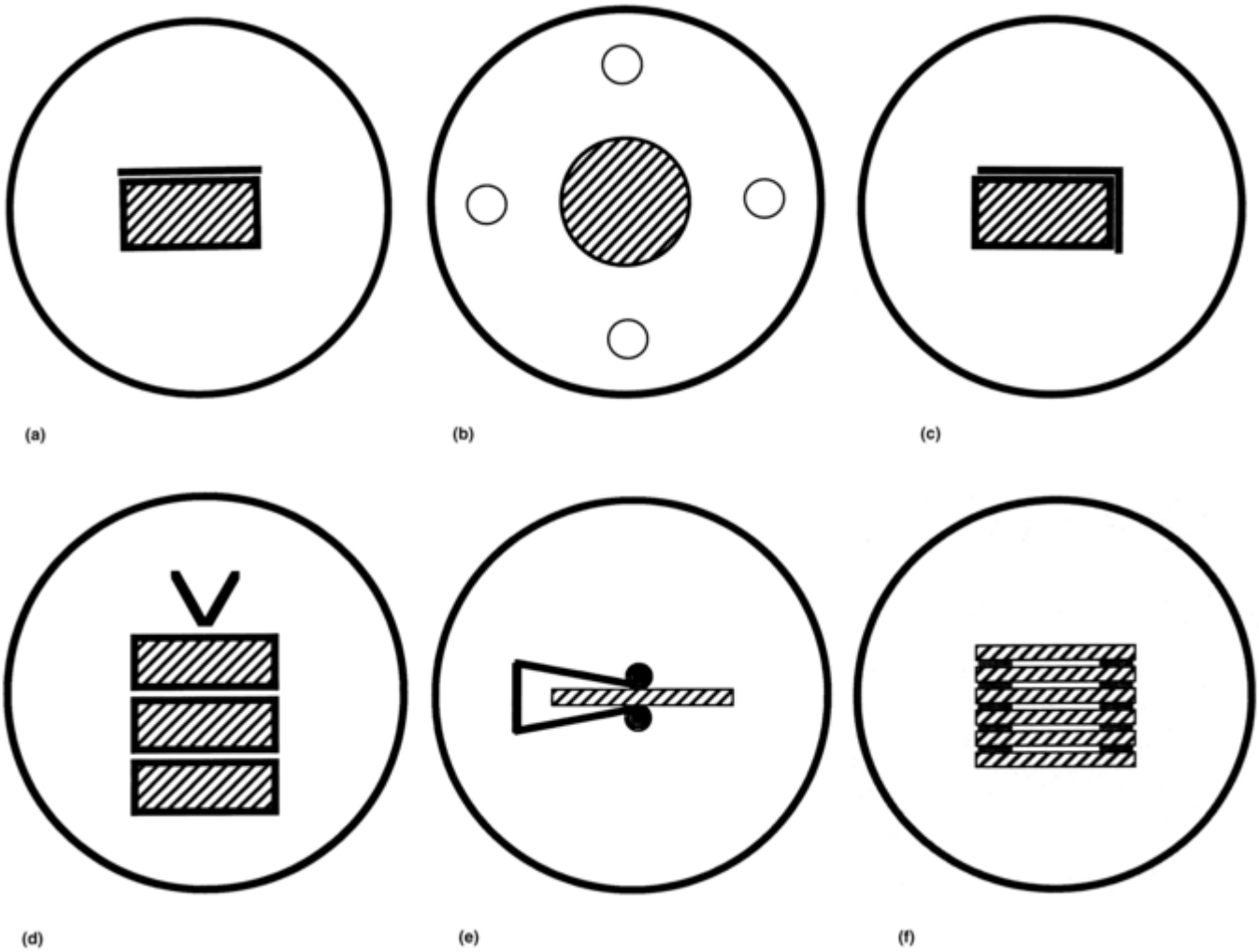

Fig. 10 Examples of special mount arrangements. (a) Sheet placed next to the specimen in an epoxy mount for edge retention. (b) Epoxy mount with rod at each quadrant for specimen flatness and edge retention. (c) Mount with an L-shaped strip to indicate specimen orientation. (d) V-shaped metal strip in a mount to indicate orientation. (e) Epoxy mounts with binder clips to hold the specimen perpendicular to the polished surface. (f) Mount with sheet specimens separated by double-sided tape at the ends. Source: Ref 2

Plastic Mount Fillers for Edge Retention. Edge retention can also be improved by selecting a mounting material that closely matches the abrasion resistance of the specimen. Most plastic mounting materials abrade somewhat faster than most metals, and so particulate fillers are added to the mount plastic for better matching of polishing rates of the mount and specimen. Plastic mount fillers for enhanced edge retention include silica particles, ground glass, cast iron grit, metal flakes, and pelletized alumina (Al_2O_3). For example, a mixture of zirconia and silica with a -250 mesh size is a soft ceramic that helps support the edge but is not incompatible in

grinding/polishing. It has a hardness of about 775 HV and has been used with soft steels at about 120–150 HV without problems (Ref 8).

Coatings for Specimen Protection and Edge Retention. For good edge retention and protection of surfaces, a protective coating can be applied either before or after sectioning. These coatings ensure that the surface layers after polishing are sufficiently coplanar for high-magnification examination with a light microscope. The coatings can be deposited by either electrolytic methods (which require application of an external electric current for deposition) or chemical (electroless) methods that do not require application of an external current. Electroless nickel plating is by far the most common technique. Electroless nickel plating procedures are preferred over electrolytic methods, because it is a simple procedure and the coating has lower internal stresses.

The protective coating does not necessarily have to be of the same material as the specimen. The essential need is that its abrasion and polishing characteristics be similar to those of the base material. The coating may also need to have sufficiently similar chemical/electrochemical properties, so that it does not interfere with any etching operations. It may also be desirable that its light reflectivity be somewhat different, so that it can be easily distinguished from the base material during the final microscopic examination.

Various plating methods are listed in Table 12. Before plating can begin, it is important that the specimen surface be clean. Premixed solutions can be obtained from vendors, or a solution can be prepared in the laboratory. The time in the solution depends on the thickness of the coating required. In the case of electroless nickel, the solution plates a layer thickness of 10 to 15 μm/h. With a layer of nickel on the surface, subtle features can be retained, because the nickel layer will become rounded during polishing instead of the edge of the steel or cast iron specimen.

Table 12 Chemical (electroless) and electrolytic plating methods

Copper: electrolytic; acid bath	
Solution	$CuSo_4 \cdot 5H_2O$, 170 g/L H_2SO_4 (conc.), 60 g/L
Temperature	15–50 °C (60–120 °F)
Voltage	1–4 V
Current density	10–20 mA/cm^2
Agitation	Mild stirring preferable
Anode	Copper
Anode bags	Desirable but not essential
Uses	General use for copper alloys
Copper: electrolytic; cyanide bath	
Solution	CuCN, 20 g/L NaCN, 30 g/L NaOH, 1.5–3 g/L
Temperature	45–60 °C (115–140 °F)
Voltage	4–6 V
Current density	0.5–1 mA/cm^2
Agitation	Mild stirring
Anode	Copper
Anode bags	Desirable but not essential
Uses	As a preliminary to an acid deposit to improve adhesion and contrast at the section line, particularly in the case of taper sections
Copper: chemical	
Solution A	$KNaC_4H_4O_6 \cdot 4H_2O$ (Rochelle salt), 170 g

	NaOH, 50 g $CuSO_4 \cdot 5H_2O$, 35 g Water (distilled), 1 L
Solution B	Formaldehyde, 37 wt%
Procedure	Mix 5 parts of solution A and 1 part of solution B at 20–30 °C (70–85 °F) just before use.
Uses	Most metals. Plastics can also be coated if their surface is first sensitized by being immersed in a 0.1 wt% solution of methyl ethyl ketone at room temperature.
Iron: electrolytic	
Solution	$FeCl_2 \cdot 4H_2O$, 288 g NaCl, 57 g Water (distilled), 1 L Filtered for use
Temperature	70–100 °C (160–210 °F) (This necessitates a constant-level device to make up for evaporation losses with distilled water.)
Current density	0.5–4 A/dm^2
Agitation	Specimen (cathode) suspended from a spindle and rotated at 50 rpm
Anode	Ingot iron plate
Uses	Excellent for all ferrous specimens but usefulness restricted by the difficulties in operating and maintaining the bath
Nickel: electrolytic	
Solution	$NiSO_4 \cdot 7H_2O$, 300 g/L $NiCl_2 \cdot 6H_2O$, 60 g/L Boric acid, 40 g/L pH 4 (Note: Add 1 part of 30% H_2O_2 per 200 parts of solution once a day.)
Temperature	40–70 °C (105–160 °F)
Voltage	1–3 V
Current density	30 mA/cm^2
Agitation	Vigorous stirring
Anode	Anode nickel
Anode bags	Essential
Uses	Ferrous alloys; nickel alloys; convenient for most metals of moderately high melting point
Nickel: chemical	
Solution	$NiCl_2 \cdot 6H_2O$, 45 g $Na_2HPO_2 \cdot H_2O$, 11 g $Na_3C_6H_2O_7 \cdot H_2O$, 100 g NH_4Cl, 50 g

	Water (distilled), 1.0 L Dissolve in order in warm (90–100 °C, or 195–210 °F) distilled water. Adjust pH to 8.5–9.0 by adding NH_4OH.
Procedure	Bring solution to a rolling boil (95–100 °C, or 200–210 °F) Immerse specimen for 1–2 h.
Uses	The following metals can be plated directly: Fe, Co, Ni, Ru, Pd, Os, Ir, and Pt. A wide variety of nonmetals, such as plastics, wood, glass, carbides, and porcelain, can also be plated. The following metals can be plated if deposition is initiated galvanically: Cu, Ag, Au, Be, Al, V, Mo, W, Cr, Ti, U, and C. The following metals cannot be plated directly but can be plated if first coated electrolytically with copper; Bi, Cd, Sn, Pb, and Zn.
Silver: chemical	
Solution A	$AgNO_3$, 9.6 g NH_4OH, 4.4 g Water (distilled), 1.0 L
Solution B	Hydrazine sulfate, 19.2 g NaOH, 4.8 g Water (distilled), 1.0 L
Procedure	Mix equal parts of solutions A and B. To decrease the speed of deposition, eliminate the NaOH and increase the NH_4OH.
Use	Coating nonconductors prior to electrodeposition
Zinc	
Solution	$Zn(CN)_2$, 60 g/L NaCN, 23 g/L NaOH, 53 g/L
Temperature	Room temperature
Voltage	1–4 V
Current density	10–15 mA/dm^2
Anode	Zinc
Anode bags	Not necessary
Uses	Zinc alloys

Source: Ref 3

A difficulty of electrolytic coating is that it has limited ability to penetrate into deep, narrow regions in the specimen surface. Another difficulty is that nonconducting materials cannot be plated, and so metals covered with oxide or scale layers cannot be plated directly. However, this problem can be overcome if a thin layer of silver is first deposited on the surface by a nonelectrolytic method.

Electroless methods are generally preferred, because they suffer less from the major disadvantages of electrolytic processes. Rough, porous, or irregular surfaces are penetrated more effectively; internal stresses in the deposit are comparatively low. Many types of metals can be deposited and coated as well, although

pretreatments may be needed in some cases. Nonconducting materials can be coated. Processes are available for depositing nickel, copper, and silver (Table 12) at rates comparable to those obtained by electrolytic methods.

Maintaining Specimen Orientation. For a single specimen in a mount, an L-shaped sheet can be mounted along with the specimen, as shown in Fig. 10(c). The long dimension of the "L" can be aligned along the rolling direction. Often, more than one specimen is placed in the same mount. It is necessary that the orientation of the specimens be arranged so that they are easily identified after mounting. If a number of sheet or thin-plate specimens are in the same mount, a small V-shaped metal sheet placed at one side of the arrangement will suffice as an orientation marker, as shown in Fig. 10(d).

Mounting of wire and tube is a challenge, and several methods have been used. Holes or slots just large enough to hold the specimen can be machined into a preformed blank of cured or uncured resin, into which the specimen is then inserted. For thermoplastic resins, simply repeating the molding cycle will hold the specimen in place. Thermosetting resins require more resin before the molding cycle is repeated. Another technique involves mounting the specimen horizontally in any plastic mounting material. This mount is then cut to reveal the cross section of the specimen, and the sectioned mount is remounted, with the specimen in the desired position.

Mounting of Tubes and Cylinders. In tubular specimens, the epoxy pulls away from the internal diameter of the tube. One method to prevent this shrinkage is to mix 0.5 g of 0.05 μm aluminum oxide (used for specimen polishing) with 20 g of epoxy. When the mount is cured, the powder will minimize shrinkage.

Mounting of Wires. One simple technique for mounting wire includes coiling the specimen into a spring, which is placed longitudinally in the mold. Polishing reveals transverse and longitudinal sections of the specimen. Wire specimens can also be fused inside Pyrex (Corning, Inc.) glass capillary tubing. The tubing is heated until it collapses around the wire. If the specimen cannot be heated, it can be placed inside a capillary tube and vacuum impregnated with epoxy to produce a tight bond.

If the cross-sectional area of wire is to be observed, the wires must be mounted on end, that is, perpendicular to the polished surface. To ensure that the wires are aligned properly, an L-shaped sheet is placed in an empty but fully cured thermosetting mount. In the central region of the mount, rows of equally spaced holes are drilled, with hole diameters slightly larger than the wire diameter. The wires are placed into the drilled holes, and a castable epoxy is poured, after damming the sides with masking tape. After curing, the epoxy side of the mount is prepared to reveal the wire cross sections.

Mounting of Sheet Specimens. In most cases, only the cross section of the sheet is of microstructural interest. This means that the sheet must be mounted perpendicular to the prepared surface. To ensure that the sheet specimen remains in the correct alignment during mounting, the sheet can be bent in the shape of an "L," or a metal or plastic binder clip can be secured to one end of the sheet. Figure 10(e) illustrates the use of binder clips. In some cases, the triangular-shaped spring portion of a paper binder clip can be used. Plastic clips are better because etching problems can occur with metal clips. The placement of the clip or short leg of the "L" can indicate specimen orientation. This technique can be used with both thermal-compression or castable mounts.

Many thin-sheet specimens can be mounted by stacking the sheets. The specimens can be separated by placing a small strip of double-sided tape (adhesive on both sides) on the outer edges of each sheet specimen, as shown in Fig. 10(f). In stacking the taped specimens into a sandwich, the specimens themselves will not touch each other, and there will be a small space between layers for epoxy to fill. Use vacuum impregnation with epoxy. Keeping the specimens closely spaced will prevent edge rounding.

Shearing during sectioning results in massive damage that must be removed. It's best to avoid shearing as much as possible by cutting with an abrasive wheel. However, for those specimens that have a shear burr, the thickness of the mount should be measured beforehand, so that an ample amount of mount is removed during grinding. This ensures that all cold work from shearing is removed in the grinding process.

References cited in this section

2. B.L. Bramfitt and A.O. Benscoter, Chapter 7: Metallographic Specimen Preparation, *Metallographer's Guide for Irons and Steels,* ASM International, 2002, p 169–214

3. L.E. Samuels, Chapter 2: Sectioning and Mounting, *Metallographic Polishing by Mechanical Means,* 4th ed., ASM International, 2003, p 9–32

8. G. Vander Voort, private communication

Mount Marking and Storage

After mounting, specimens are usually identified using hand scribers or vibrating-point engravers. Markings made with these tools can then be inked over to increase their visibility.

If a transparent mounting material is used, a small metal tag or piece of paper bearing the identification can be included in the mount. An indelible ink must be used, but identification is then permanently visible and protected with the specimen.

Specimens are usually stored in a desiccator to minimize surface oxidation during preparation and examination. Surfaces also can be coated with clear lacquer for preservation. The microstructure can be viewed through the lacquer, or the coating can be removed with acetone.

Mounting of Specimens, *Metallography and Microstructures,* Vol 9, *ASM Handbook*, ASM International, 2004, p. 242–256

Mounting of Specimens

Acknowledgments

Portions of this article include text adapted from Ref 1, 2 and 3.

References cited in this section

1. G.F. Vander Voort, *Metallography: Principles and Practice,* McGraw-Hill, 1984, reprinted by ASM International, 1999, p 71–93

2. B.L. Bramfitt and A.O. Benscoter, Chapter 7: Metallographic Specimen Preparation, *Metallographer's Guide for Irons and Steels,* ASM International, 2002, p 169–214

3. L.E. Samuels, Chapter 2: Sectioning and Mounting, *Metallographic Polishing by Mechanical Means,* 4th ed., ASM International, 2003, p 9–32

Mounting of Specimens, *Metallography and Microstructures,* Vol 9, *ASM Handbook,* ASM International, 2004, p. 242–256

References

1. G.F. Vander Voort, *Metallography: Principles and Practice,* McGraw-Hill, 1984, reprinted by ASM International, 1999, p 71–93

2. B.L. Bramfitt and A.O. Benscoter, Chapter 7: Metallographic Specimen Preparation, *Metallographer's Guide for Irons and Steels,* ASM International, 2002, p 169–214

3. L.E. Samuels, Chapter 2: Sectioning and Mounting, *Metallographic Polishing by Mechanical Means,* 4th ed., ASM International, 2003, p 9–32

4. R.J. Hussey, P.E. Beaubein, and D. Caplan, *Metallography,* Vol 6, 1973, p 27

5. W.L. Ladroga, *Met. Prog.,* Vol 83(No. 2), 1963, p 108

6. D.V. Miley and A.E. Calabra, A Review of Specimen Mounting Methods for Metallography, *Metallographic Specimen Preparation,* J.L. McCall and W.M. Mueller, Ed., Plenum Press, 1974, p 1–40

7. J.A. Nelson, Heating of Metallographic Specimens Mounted in `Cold Setting' Resins, *Prakt. Metallogr.,* Vol 7, 1970, p 510–521

8. G. Vander Voort, private communication

Mechanical Grinding and Polishing, *Metallography and Microstructures,* Vol 9, *ASM Handbook,* ASM International, 2004, p. 257–280

Mechanical Grinding and Polishing

Introduction

INVESTIGATIONS OF THE STRUCTURES of metals are generally carried out on sections that have been cut from a bulk specimen. Frequently, only a single section surface is prepared, and the structural features exposed on this surface may be investigated using various techniques. All these techniques involve the reflection of some form of radiation from the section surface; an image of the surface is formed from the reflected radiation that allows variations in crystal structure or composition over the surface to be discerned.

Visible light is commonly used for this purpose. The surface is examined by the human eye with or without magnification. Optical macrography and microscopy are examples. It is usually necessary first to treat the section surface by some chemical or physical process that alters the way light is reflected by the various structural constituents that have been exposed.

Alternatively, a section surface may be investigated by probing with a beam of electrons in a high vacuum. Structures are revealed that in effect depend on how electrons are reflected off the surface; this may be

determined by variations in topography or composition. Scanning electron microscopes and electron probe microanalyzers are examples of investigative techniques operating on these principles. It is possible also to use x-rays to determine variations in composition, as in x-ray fluorescent analysis, or to determine structural features that depend on crystal lattice spacing and orientation, as in x-ray microscopy and x-ray methods of determining internal stresses.

Another group of techniques requires preparation of section surfaces on two parallel planes in close proximity. The radiation used is transmitted through the thin slice so formed. Transmission electron microscopy and diffraction are important examples of techniques that require this type of specimen.

Three operations are generally involved in determining the structures of metals: (1) the preparation of a section surface, (2) the development of features on the surface that are related to the structure and can be detected by the examination technique used, and (3) the examination itself. The overall effectiveness of the examination often is determined by the operation carried out least effectively, which too frequently is the preparation of the section surface.

A preparation procedure must produce a surface that accurately represents the structure as it existed in the metal before sectioning. All structural features that should be detected by the particular examination technique being used must be detectable, and false structures must not be introduced. This is a more demanding requirement.

Successful specimen preparation requires information based on systematic and objective experiments. Therefore, this article will illustrate how objective experiments and comparisons can be used to develop procedures that not only give better results, but also are simpler and less laborious. Principles useful as guidelines in the development of practical preparation procedures are emphasized, rather than the details of those procedures.

The other investigative techniques mentioned earlier are doubtless crucial in many research investigations and have pushed the frontiers of metallography far beyond what would have been possible by optical metallography alone. Nevertheless, most metallography in industry and in general investigations is still carried out by optical microscopy, so this article also considers the preparation of surfaces for examination by optical microscopy.

Because it is possible to deal here with only a limited number of concepts involved in preparing fully representative surfaces, the concepts selected illustrate the types of problems that arise and how their solutions may be approached systematically.

Mechanical Grinding and Polishing, *Metallography and Microstructures,* Vol 9, *ASM Handbook*, ASM International, 2004, p. 257–280

Surface Preparation

Any classification of the numerous processes used to cut a section, then to prepare the cut surface suitably for metallographic examination, inevitably is arbitrary and arguable. One convenient system, however, is to classify the processes as machining, grinding and abrasion, or polishing.

Machining involves the use of tools having cutting edges of controlled shape, as in conventional machine shop practice. Examples are sawing, lathe turning, milling, and filing. These processes normally are used only for the preliminary stages of preparation and do not require particular attention here.

Grinding and abrasion employ an array of fixed abrasive particles whose projecting points act as the cutting tools. In some of these processes, the particles are in effect cemented together into a block whose exposed surface is the working surface. This surface is “dressed” by fracturing the exposed abrasive particles to form an array of sharp points. Examples are abrasive cutoff wheels, grinding wheels, abrasive laps, and abrasive stones. In other processes, a layer of abrasive particles is cemented onto a cloth or paper backing, creating coated abrasive products such as papers, cloths, or belts. In still other processes, the abrasive particles are forced into a flat surface of a comparatively soft material where they are held as an array similar to that in a coated abrasive product.

A range of surface speeds may be employed in any of these processes; it is convenient, therefore, to distinguish between grinding and abrasion. The term “grinding” denotes processes that employ high surface speeds with the possibility that significant heating of the surface layers of the specimen may occur. The term “abrasion” refers to processes that use low surface speeds and copious liquid coolant; significant heating of the specimen surface cannot occur.

Polishing uses abrasive particles that are not firmly fixed, but suspended in a liquid among the fibers of a cloth. The objective is to produce a bright mirrorlike, or specularly reflecting, surface, commonly referred to as a polished surface.

Typical metallographic preparation procedures employ a sequence of machining or grinding stages of increasing fineness, then a sequence of abrasion processes of increasing fineness, followed by a sequence of polishing processes of increasing fineness until the desired surface finish has been achieved. Increasing fineness refers to the use of finer grades of abrasive to produce finer grooves or scratches in the surface.

Therefore, metallographic preparation processes employ abrasive particles to remove material and to improve surface finish, two objectives that are not always compatible. It is not possible to discuss in detail how the processes operate (see Ref 1 for a more detailed treatment). Briefly, in grinding and abrasion, the abrasive points that contact the surface may be regarded as V-point cutting tools. The rake angles of these tools vary widely. Only a small proportion of the points have a configuration suitable for removing metal by cutting a chip, as in normal machining. The others plow a groove in the surface, displacing material laterally. Both processes produce scratches and impose severe plastic deformations on the outer layers of the surface.

Most mechanical polishing procedures are similar to those for abrasion, except that only small forces are applied to individual abrasive particles by the fibers of the cloth that supports them. They therefore produce comparatively shallow, narrow scratches. Some very fine polishing procedures, however, remove material by less drastic mechanical processes that remove very small flakes of material. Some others occur largely by chemical dissolution processes. Barring these exceptions, the processes involved in grinding, abrasion, and polishing differ in degree rather than in kind. This is why any classification of preparation processes necessarily is arbitrary.

Sections to be prepared are usually no larger than about 5 cm^2 (0.78 $in.^2$), although larger areas can be prepared if necessary. The specimen is mounted to facilitate handling; it is often molded into a plastic cylinder. Various plastics are available for this purpose, each with advantages and disadvantages in particular applications. A simple phenolic resin is often used when the sole requirement is to facilitate handling.

At the simplest level the section surface, after preliminary machining, is rubbed by hand against the working surface of an abrasive paper supported on a flat backing surface. The working surface of the paper is flooded with a liquid. Waterproof abrasive papers, usually those coated with silicon carbide abrasive, are convenient because their working surfaces can be flushed continuously with water to remove the abrasion debris as it forms. The section surface is treated in this way, using successively finer grades of abrasive paper, usually to the finest available. The surface is then polished by rotating it by hand against a cloth that has been charged with a fine abrasive and an appropriate liquid, and then has been stretched across a flat backing surface. Several stages of polishing employing increasingly finer abrasives usually are necessary. Diamond, alumina (Al_2O_3), and magnesium oxide (MgO) are the abrasives most commonly used for polishing; colloidal silica is sometimes used.

Mechanized processes are less time consuming and laborious than manual operations. The first step in mechanization is to drive the abrasive paper or polishing cloth. The paper or cloth is attached to the surface of a wheel that is rotated at a comparatively low speed in a horizontal plane. The specimen is held against the working surface of a wheel and rotated slowly in a direction opposite that of the wheel.

The next step involves handling the specimen. This is more difficult because the specimen must be held and rotated so that the section surface is maintained precisely in a horizontal plane against the working surface of the abrasive or polishing wheel. The full surface must maintain contact with the working surface. The specimen should be rotated counter to the direction of wheel rotation. Several commercially available devices can perform this procedure. Most of them handle a batch of specimens that must be processed through the full preparation cycle on the machine. Some of these machines are highly automated, providing control of rotation speeds, pressure applied to the specimen, and polishing time.

Mechanization is particularly useful when a large number of specimens must be handled. In addition, once optimal preparation parameters are established, they can be reproduced exactly without having to rely on the operator. Moreover, flatter surfaces are produced. Nevertheless, only the mechanics of the preparation

procedure are affected, not the mechanisms or principles involved. The various steps proposed for an automated preparation sequence should be judged on this basis. See the section “Semiautomatic Preparation Systems” in this article for more information.

Reference cited in this section

1. L.E. Samuels, *Metallographic Polishing by Mechanical Methods*, 4th ed., ASM International, 2003

Mechanical Grinding and Polishing, *Metallography and Microstructures,* Vol 9, *ASM Handbook*, ASM International, 2004, p. 257–280

Abrasion Damage and Abrasion Artifacts

The obvious result of abrasion is a system of comparatively fine, uniform scratches on the surface of the specimen. Abrasion also produces a plastically deformed surface layer (disturbed metal) of considerable depth. The microstructure of this layer may be recognizably different from the true structure of the specimen.

The general pattern of a surface layer that has been plastically deformed is shown in Fig. 1(a),* which depicts abraded 70-30 brass, an alloy in which the effects of prior plastic deformation can be easily revealed by a range of etchants. Also illustrated in Fig. 1(a) is a shallow, dark-etching, unresolved band contouring the surface scratches that is known as the outer fragmented layer; here the strains have been very large and the crystal structure has been altered as a result. Beneath this extends a layer in which the strains have been comparatively small and in which they tend to concentrate in rays extending beneath individual surface scratches. This is shown by the bands of etch markings, which develop at the sites of slip bands, and by the more diffuse rays, which indicate the presence of kink bands. These effects extend for many times the depth of the surface scratches.

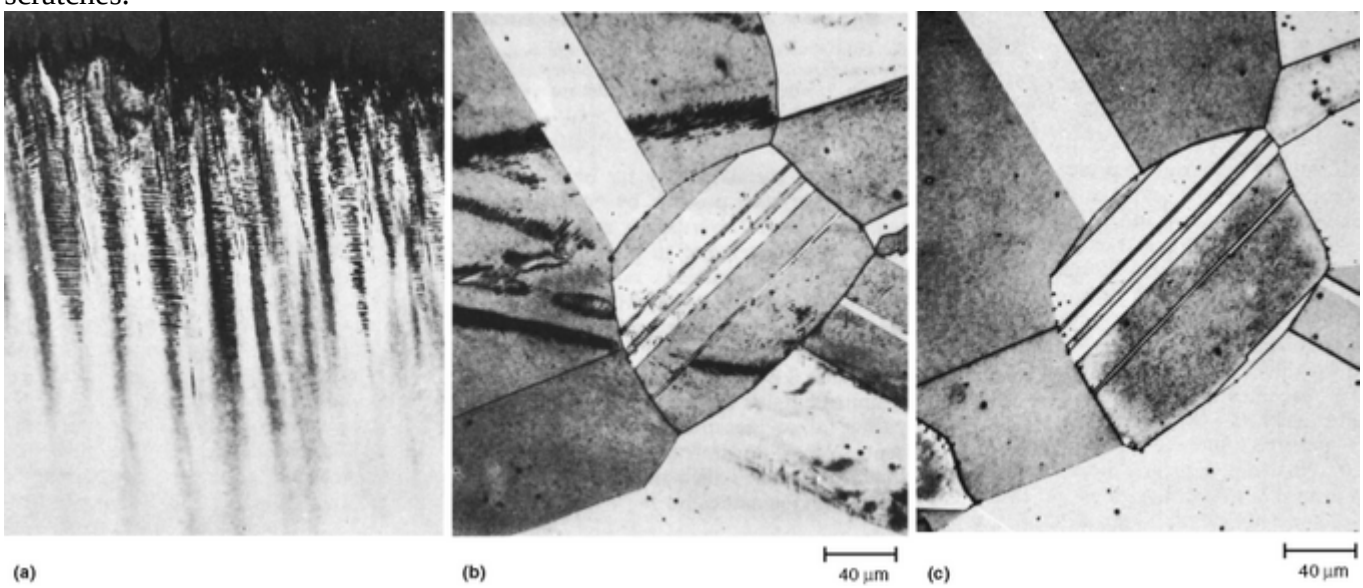

Fig. 1 Annealed 70-30 brass. (a) Taper section (horizontal magnification 600×, vertical magnification 4920×) of surface layers that were abraded on 220-grit silicon carbide paper. (b) and (c) Results of abrading on 220-grit silicon carbide paper and then polishing until about 5 μm (b) and 15 μm (c) of metal are removed. The banded markings in (b) are false structures (abrasion artifacts). The true structure is shown in (c). Aqueous ferric chloride. 250×

The importance of the surface damage in Fig. 1(a) is shown in Fig. 1(b) and (c). A sample of annealed 70-30 brass was abraded on 220-grit silicon carbide paper, then polished to remove a surface layer about 5 μm thick. Although all traces of the abrasion scratches were removed and what appeared to be a satisfactory surface was produced, the bands of deformation etch markings shown in Fig. 1(b) appeared when the surface was etched. When layers of greater thickness were removed during polishing, these bands were gradually reduced in number and intensity; they eventually were eliminated, as can be seen in Fig. 1(c), which shows the true structure.

The bands of deformation etch markings in Fig. 1(b) are false structures introduced by the preparation process, or artifact structures. They clearly are related to the rays of deformation produced during abrasion, as shown in Fig. 1(a). Because the artifacts are the result of deformation introduced into the surface during abrasion, they may be called abrasion artifacts.

Detectable microstructural changes in the abrasion-damaged layer are potential sources of abrasion artifacts in the final surface. Metals vary markedly in their susceptibility to the formation of abrasion artifacts. Highly alloyed copper alloys such as 70-30 brass, for example, are among the most sensitive. Etchants also vary in their ability to delineate abrasion damage. Because a major objective of metallographic preparation is to ensure that unrepresentative structures are not present in the surface to be examined, the metallographer must recognize abrasion artifacts, understand how these artifacts originate, and eliminate them when they are found.

Each successive abrasion stage should remove the artifact-containing layer produced by the preceding abrasion stage. This takes longer than the time required simply to remove existing scratches and places a premium on obtaining maximum possible material-removal rates. The effectiveness of an abrasion stage must be judged on how quickly it removes the preexisting deformed layer. Also considered are the depths of the damaged layer and the scratches that abrasion produces. Similarly, the first objective of rough polishing must be effective removal of abrasion damage. This necessitates obtaining maximum material-removal rates. The polishing processes with fast cutting rates usually produce comparatively coarse finishes. They must be followed by polishing processes that produce finer finishes. Only after the abrasion damage has been removed effectively by a rough-polishing process should attention be given to producing a final polish.

The depth of the artifact-containing layer generally decreases as specimen hardness increases. It also decreases with increasing fineness of the abrasion stage until the working surface of the abrasion device clogs with metallic abrasion debris. Deep artifact-containing layers are then produced. The material-removal rate achieved by an abrasion stage depends on many factors, and of those factors, specimen hardness is only marginally important. The most important parameter is often how the specimen material causes the abrasion device to deteriorate; this can be established only by experimentation.

The material-removal rates achieved by conventional polishing stages can vary more than those of abrasion. Diamond abrasives produce the highest removal rates, but the removal rate even with this abrasive varies by several orders of magnitude, depending on the nature of the specimen material and how the abrasive is used. Many of the commonly recommended methods of using this abrasive yield far from optimal removal rates. Quantitative, or at least semiquantitative, data on the material-removal rates of the abrasion and polishing stages proposed for a preparation system should be obtained to ensure optimal conditions and that abrasion and polishing artifacts are removed effectively.

Abrasion Artifacts in Austenitic Steels. Austenitic steels generally are susceptible to abrasion artifacts, and the common etchants reveal effects due to prior deformation with considerable sensitivity. The structure of a typical abrasion-damaged layer (see Fig. 2a) is comparable to that for brass. A shallow, unresolved layer contours the surface scratches, and deep rays of deformation etch markings extend beneath the surface scratches. Bands of these deformation etch markings may appear in a final-polished surface as abrasion artifacts (see Fig. 2b). Good abrasion practice and efficient polishing will remove the abrasion artifacts in an acceptable polishing time (see Fig. 2c).

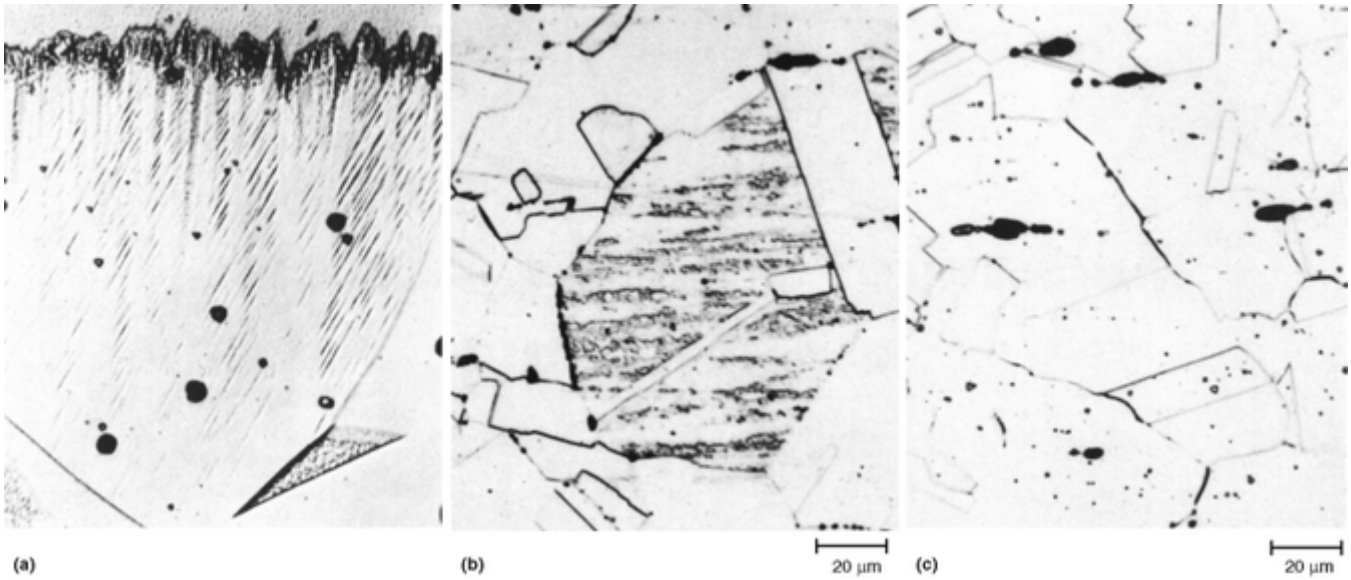

Fig. 2 Austenitic stainless steel (18Ni-8Cr). (a) Taper section (horizontal magnification 600×, vertical magnification 6060×) of surface layers that were abraded on 220-grit silicon carbide paper. (b) and (c) Results of abrading on 600-grit silicon carbide paper and then polishing until about 1 µm (b) and 3 µm (c) of metal are removed. Abrasion artifacts are shown in (b). The true structure is shown in (c). Electrolytic: oxalic acid. 500×

When a surface contains artifacts of the type shown in Fig. 2(b), it can be assumed that a deep surface layer will have to be removed to obtain an artifact-free surface. Therefore, the specimen must be returned to rough polishing to attain a sufficiently high cutting rate. Alternate polishing and etching at the final-polishing stage, as is sometimes recommended, is not likely to be effective.

Abrasion Artifacts in Zinc. Metals of noncubic crystal structure, such as zinc, characteristically form large mechanical twins during plastic deformation. This is reflected in the abrasion-damaged layer in Fig. 3(a), where deformation twins are present to considerable depth. In metals with low melting points, such as tin and zinc, recrystallization of the outer layers of the deformed structure may also occur at ambient temperature; this accounts for the recrystallization of the outermost portion of the abrasion-damaged layer in Fig. 3(a). The grain size of a recrystallized layer usually is fine and becomes finer as the surface is approached; only by coincidence will the grain size be similar to that of the parent metal.

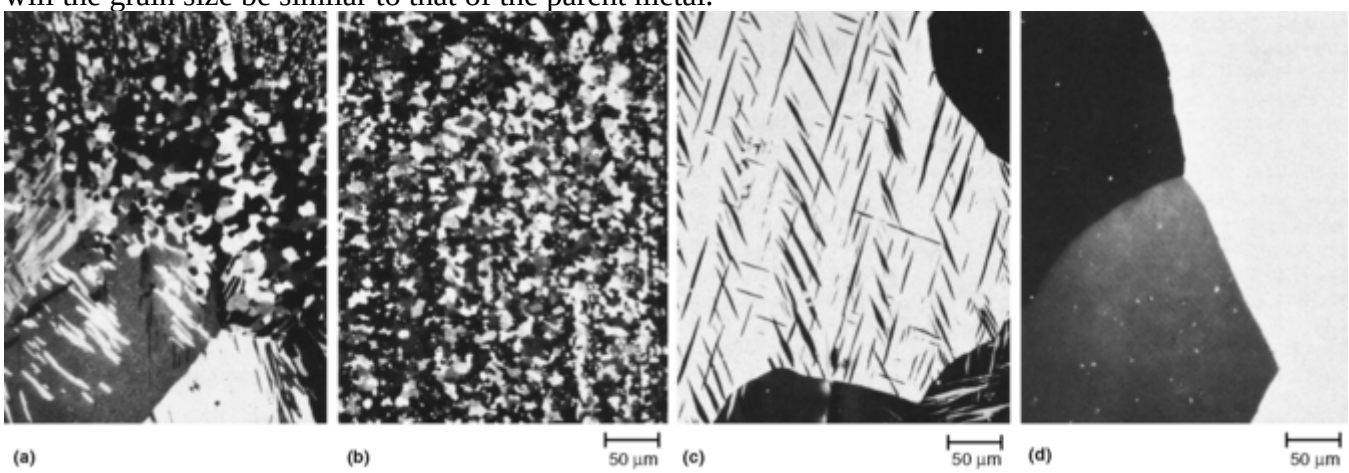

Fig. 3 Annealed zinc. (a) Taper section (horizontal magnification 150×, vertical magnification 2040×) of surface layers that were abraded on 220-grit silicon carbide paper. Note recrystallization at the top. Polarized light was used. (b) to (d) Results of abrading on 220-grit silicon carbide paper and polishing until about 2.5 µm (b), 15 µm (c), and 45 µm (d) of metal are removed. The small grains in (b) and the twins in (c) are artifact structures. The true structure is shown in (d). As-polished. 150×

The following range of artifact structures may be observed if an abraded surface of zinc is polished for progressively longer times:

- A fully recrystallized structure of different grain size than the parent metal (Fig. 3b)
- A mixed structure of recrystallized grains and parent-metal grains containing deformation twins
- Parent-metal grains containing deformation twins that are likely to be aligned in bands in the direction of the initiating abrasion scratches (Fig. 3c)

When polishing has been continued long enough for removal of the abrasion-damaged layer, the true structure may be observed (Fig. 3d). Efficient preparation procedures depend on avoiding the production of deep abrasion-damaged layers prior to polishing, eliminating the need for removing them by excessive polishing.
Abrasion Artifacts in Ferritic Steels. The deep abrasion-damage effects discussed so far cause difficulties in a limited range of alloys, but effects due to an outer fragmented layer are likely to be found in all metals. For example, a section of the outer fragmented layer in a ferritic steel is shown in Fig. 4(a). The structure of the fragmented layer cannot be properly resolved by optical microscopy, but it is clearly different from that of the parent-metal ferrite grains. The types of artifacts that may be found in final-polished surfaces of ferritic steel are shown in Fig. 4(b) and (c). These artifacts obscure the true structure, shown in Fig. 4(d); they can be developed in virtually all metals. However, as shown in Fig. 4(a), the damaged layer is quite thin, and a polishing treatment continued for twice the time it takes to remove the abrasion scratches will eliminate the abrasion artifacts. Therefore, abrasion artifacts are usually the result of inadequate preparation procedures.

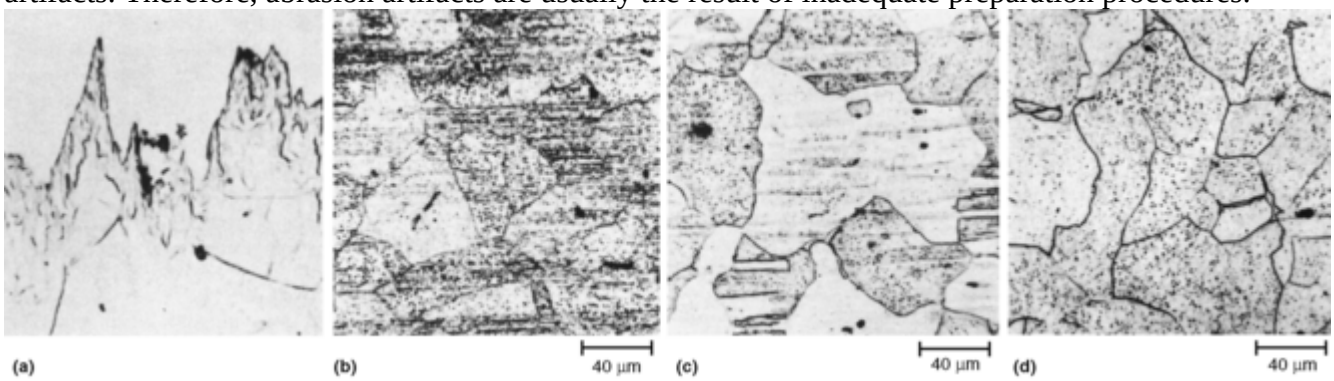

Fig. 4 Ferritic steel. (a) Taper section (horizontal magnification 1000×, vertical magnification 10,000×) of surface layers that were abraded on 220-grit silicon carbide paper. Note the outer fragmented layer. (b) Results of abrading on 000 emery paper and then polishing only long enough to remove abrasion scratches. (c) Results of abrading on 600-grit silicon carbide paper and polishing only long enough to remove abrasion scratches. (b) and (c) Banded markings and generally artifact-dominated structure. (d) Results of abrading on 600-grit silicon carbide paper and polishing for a longer time than for (c); it shows the true structure of the steel. Nital. 250×

Abrasion Artifacts in Pearlitic Steels. Distinctive artifacts caused by disturbance in the outer fragmented layer are observed in pearlitic steels. Taper sections of abraded surfaces of these steels show that the cementite plates of pearlite may simply be bent adjacent to some scratches (Fig. 5a) and may be completely fragmented adjacent to others (Fig. 5b). As a result, artifact structures of the types shown in Fig. 6(a) and (b) may be observed in surfaces after final polishing. The cementite plates in Fig. 6(a) have been so fragmented that the pearlite structure is unrecognizable; the appearance, in fact, is more like that found after hardening and tempering. The structure in Fig. 6(b) is recognizable as lamellar pearlite, but the kinking of the cementite plates represents an artifact structure. The true pearlite structure, free of artifacts, is shown in Fig. 6(c). The affected layer in Fig. 6(a) and (b) is quite shallow, and the artifacts shown are likely to be found only after inefficient preparation procedures.

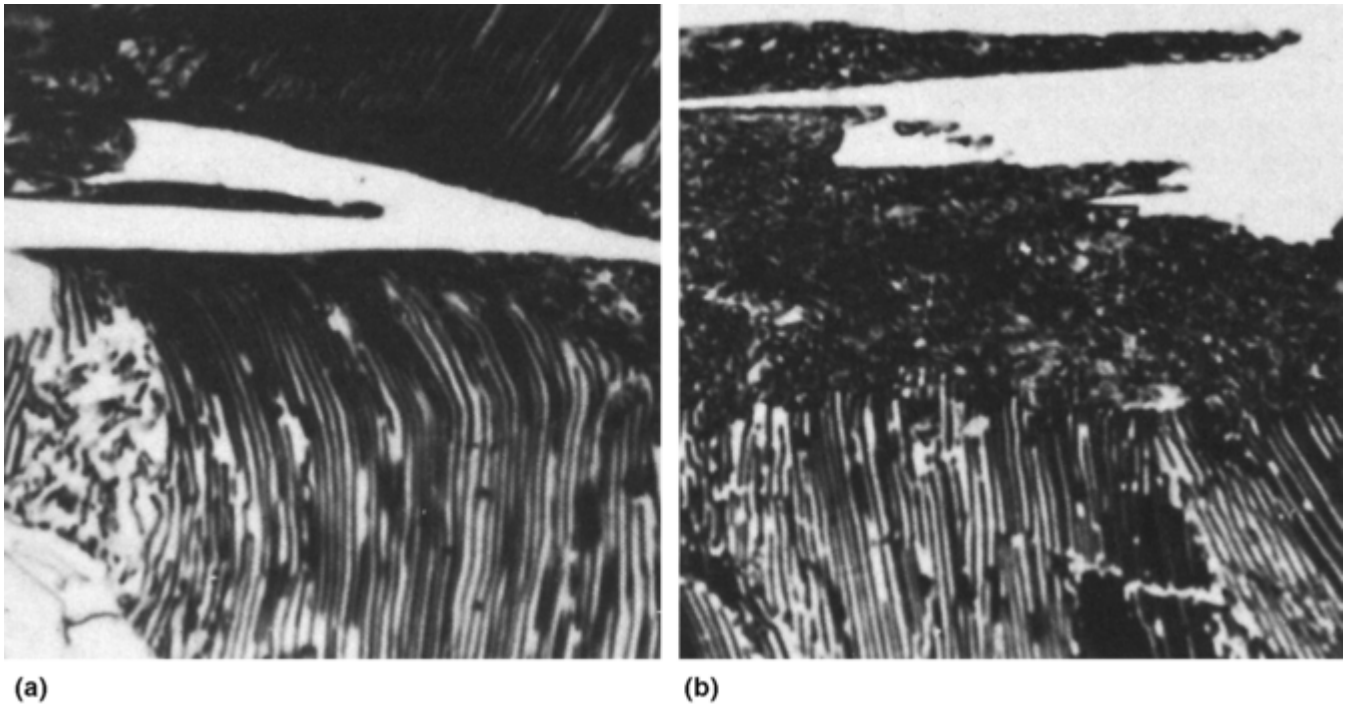

Fig. 5 Pearlitic steel. Longitudinal taper sections of surface layers that were belt abraded on 100-mesh Al_2O_3, showing that cementite plates of pearlite are merely bent adjacent to some scratches (a) and are completely fragmented adjacent to others (b). Picral. Horizontal: 2000×; vertical: 20,000×

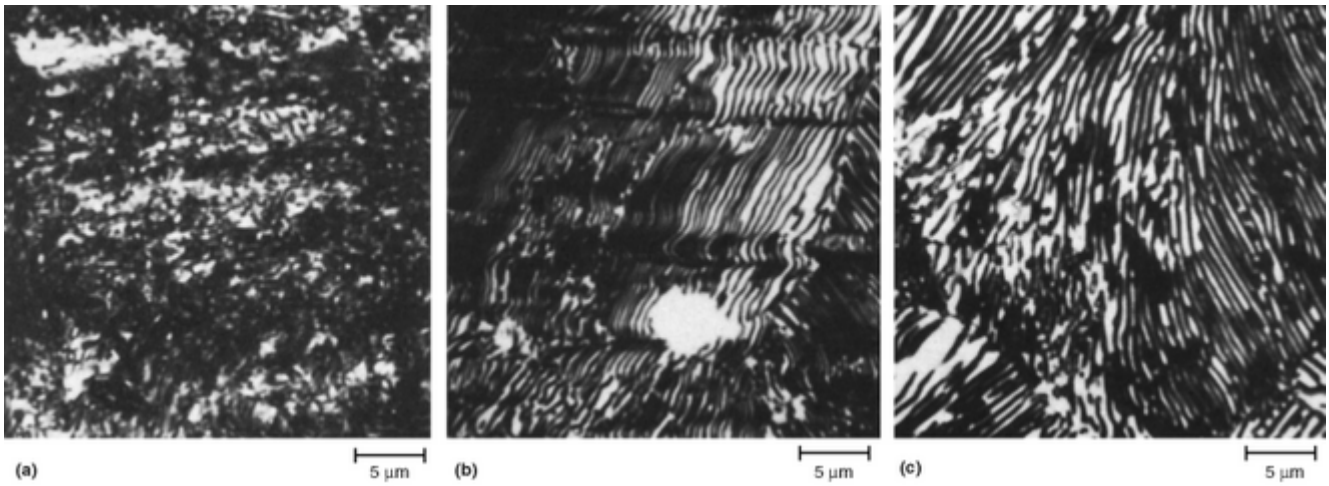

Fig. 6 Pearlitic steel. (a) Results of abrading on an abrasive belt and then polishing for only long enough to remove abrasion scratches; structure contains abrasion-deformation artifacts. (b) Results of abrading on 600-grit silicon carbide paper and then polishing only long enough to remove abrasion scratches; kinking of cementite plates is an abrasion-deformation artifact. (c) Results of abrading on 600-grit silicon carbide paper and polishing for a longer time than for (b). The true structure is shown in (c). Picral. 2000×

Tempering Artifacts in Steel. When steels with medium to high carbon content are ground abusively, especially with inadequate coolant, the surface may be heated sufficiently to develop a rehardened martensitic surface layer, such as the outer white-etching layer shown in Fig. 7(a). A martensitic layer is likely to be quite thin. If the steels initially are in the hardened-and-untempered condition, the rehardened layer will be accompanied by a tempered layer that is much deeper and highly variable in depth; the tempered layer is dark etching. The bands of tempered structure (see Fig. 7b) are much more likely to produce artifact structures than the martensitic layer. The artifact structure is banded, because the grinding that caused the damage produced unidirectional scratches. When compared to the true structure in Fig. 7(c), it is apparent that artifact banding

could be mistaken for segregation banding in steel. Similar effects may occur in any alloy system in which structural changes can result from reheating.

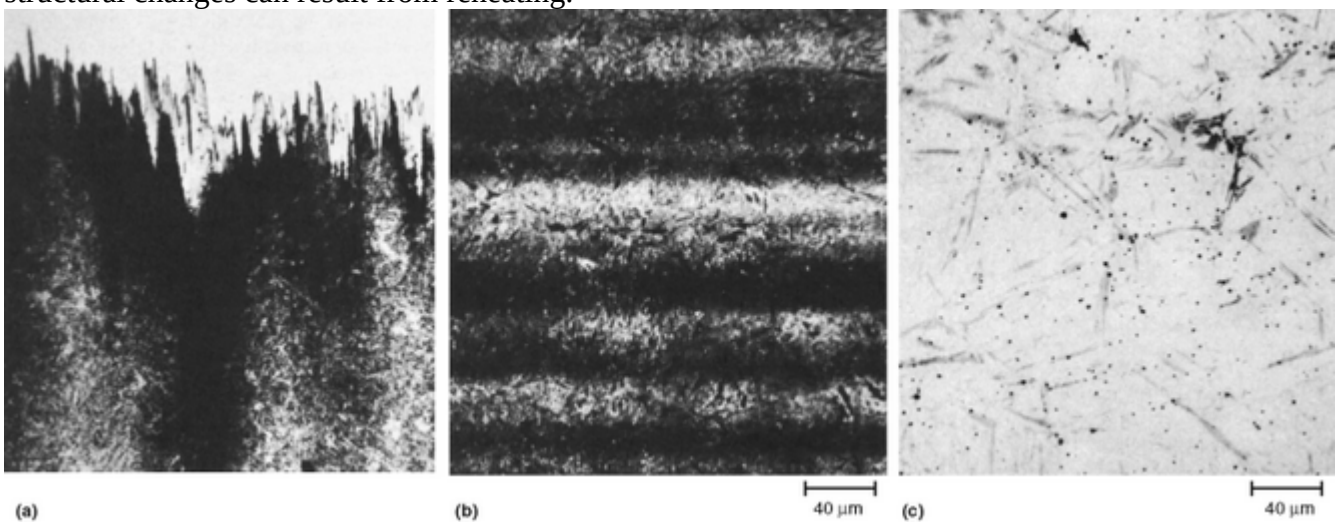

Fig. 7 Plain carbon steel, hardened but not tempered. (a) Taper section (horizontal magnification 1200×, vertical magnification 13,080×) of surface layers that were abusively ground, producing martensite (white-etching constituent) and tempering (dark-etching bands). (b) Dark-etching bands of tempered structure that originated from dry belt grinding. (c) The true structure. Picral. 250×

Tempering artifacts can be avoided by ensuring that the specimen is continuously flooded with liquid coolant during abrasive machining, particularly those involving high speeds. Dry, mechanized abrasion processes should be avoided.

Abrasion Damage in Gray Iron. Cast irons are an important group of alloys for which a purpose of metallographic examination often is the determination of the true size and shape of the particles of free graphite that are present (Fig. 8, 9). The apparent size and shape of the graphite can be severely altered at several stages of the preparation sequence, causing false structures.

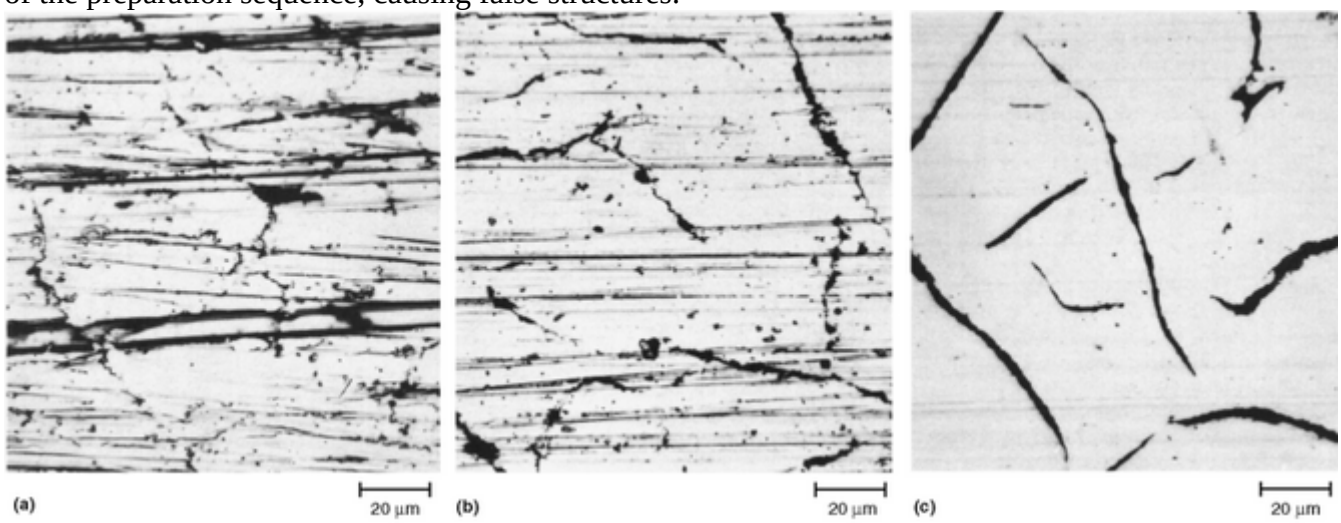

Fig. 8 Effects of abrasion on flake graphite in gray iron. (a) Results of abrading on 220-grit silicon carbide paper. (b) Results of abrading on 600-grit silicon carbide paper. (c) Results of abrading on a fine fixed-abrasive lap. See also the taper section in Fig. 9. As-polished. 500×

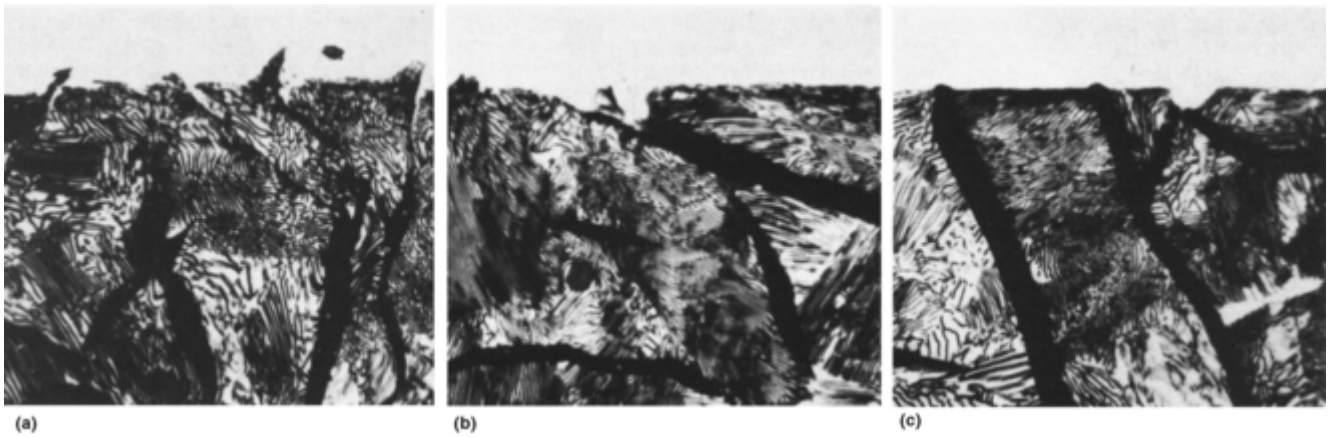

Fig. 9 Longitudinal taper sections of abraded surfaces in gray iron (horizontal magnification 1000×, vertical magnification 10,000×). (a) Results of abrading on 220-grit silicon carbide paper. (b) Results of abrading on 600-grit silicon carbide paper. (c) Results of abrading on a fine fixed-abrasive lap. Picral

The true graphite form for a particular gray iron is most closely represented in Fig. 8(c). This can be confirmed by examining a taper section of the surface (Fig. 9c), which shows that most of the graphite flakes are accurately sectioned. Those few that were acutely aligned to the section surface are slightly enlarged. On the other hand, the majority of flakes on a coarsely abraded surface appear much narrower than their true width (Fig. 8a), because the graphite has been removed from its cavity for a considerable depth and the empty portion of the cavity has collapsed (Fig. 9a). An intermediate abrasion treatment gives an intermediate result (Fig. 8b); the flakes in some areas are of true width and in others are greatly contracted. On the other hand, the flakes appear to be much wider than their true width at occasional areas in Fig. 8(a) and (b), because the graphite has been removed from its cavity, then the cavity has been enlarged (Fig. 9b), presumably by erosion.

Because problems in correctly preserving graphite also arise during polishing, it is unwise to rely on subsequent polishing to correct damage introduced by abrasion. The graphite should be retained as fully as possible during abrasion; elimination of water lubrication during fine grinding steps (400- and 600-grit abrasives) is beneficial.

Other Effects of Abrasion Damage. The effects of abrasion damage discussed so far represent those that can be recognized by optical microscopy. Other indirect effects are also noticeable. For example, a hardness measurement made on the prepared surface may be unusually high if the depth of the damage layer is comparable to that of the hardness indentation and if the strains in the layer are large enough to increase detectably the hardness of the material. True hardness values are obtained only after sufficient material has been removed during polishing to ensure that the strains in the residual layer are not high enough to affect hardness. This usually is achieved because small deformations often do not greatly affect hardness. At the other extreme, surfaces prepared for examination by transmission electron microscopy must be free of residual abrasion strains. Small strains introduce crystal defects detectable by transmission electron microscopy.

Flatness of Abraded Surfaces. Finishing abrasion on a fixed-abrasive lap often yields more satisfactory results than those obtained by finishing on abrasive papers. In general, a flatter surface is obtained from a dressed lap or stone, resulting, for example, in improved preservation of edges (compare Fig. 10a and b), improved retention of nonmetallic inclusions (compare Fig. 11a and b), and reduction in the difference in level between different phases (compare Fig. 12a and b). A slightly finer finish is also obtained. However, because fixed-abrasive laps clog easily, producing deep, damaged layers, and are more difficult to use than abrasive paper, it is necessary to decide if the improvement in finish justifies the additional effort.

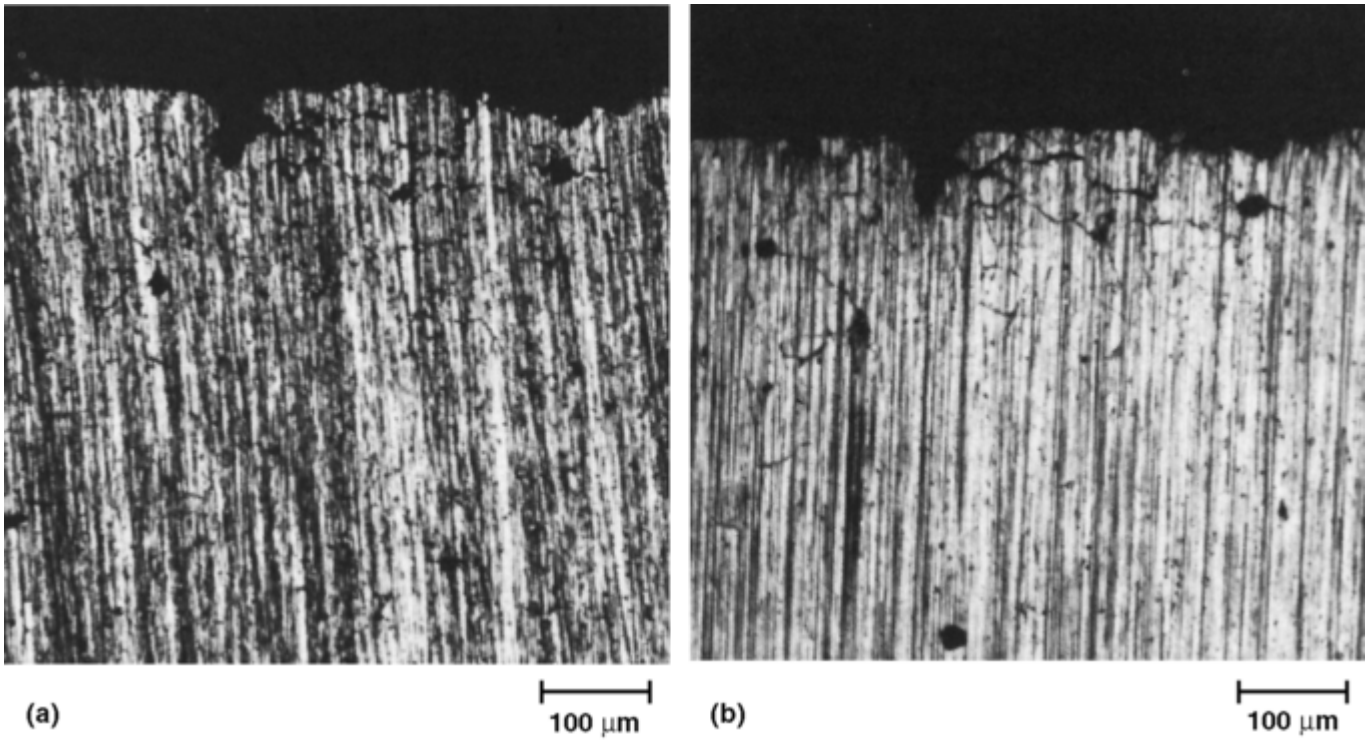

Fig. 10 Comparison of abrasives for preservation of corroded surface of aluminum alloy. (a) Results of abrading on 600-grit silicon carbide paper. (b) Improvement in finish and edge preservation obtained by abrading on a fine fixed-abrasive lap. As-polished. 100×

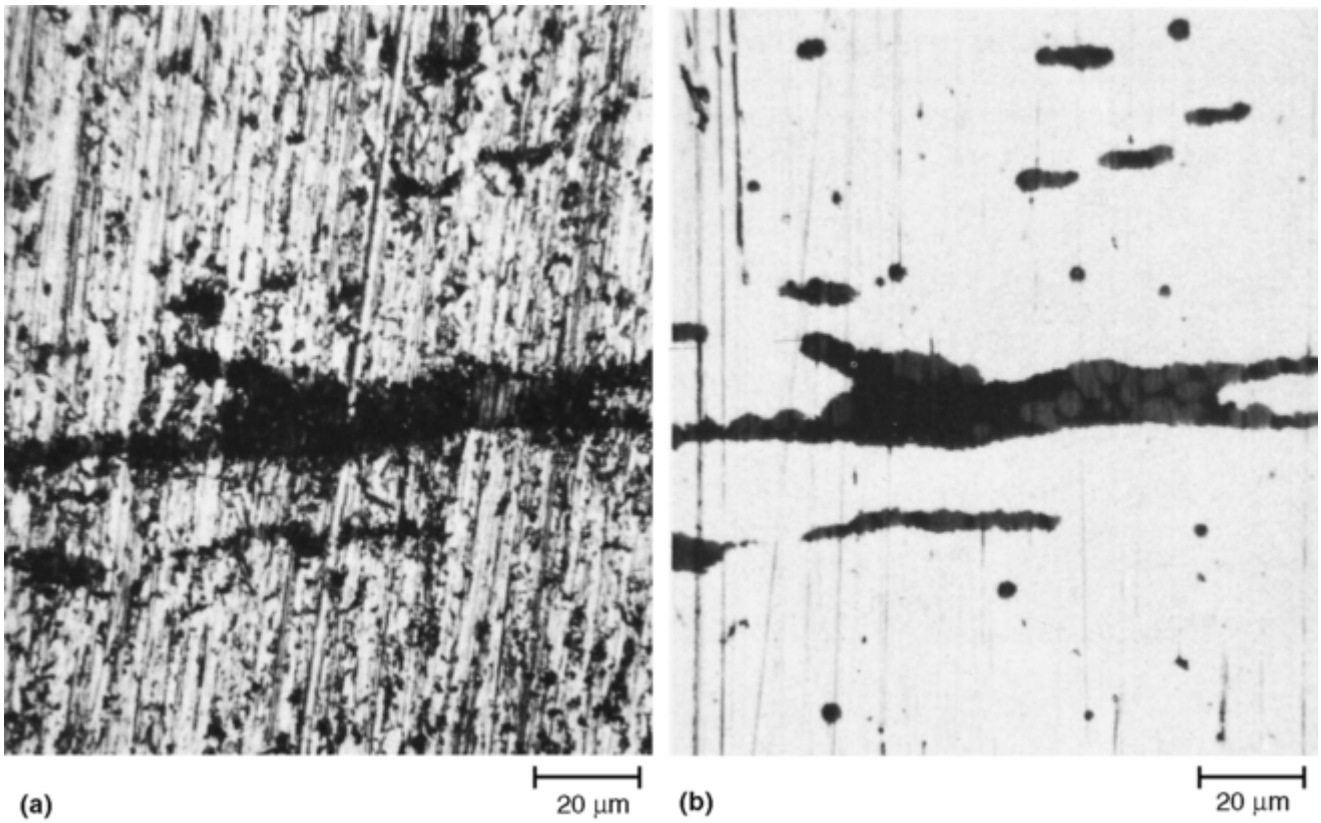

Fig. 11 Comparison of abrasives for preservation of a nonmetallic inclusion in wrought iron. (a) Results of abrading on 600-grit silicon carbide paper. (b) Improved results obtained by abrading on a fine fixed-abrasive lap. As-polished. 500×

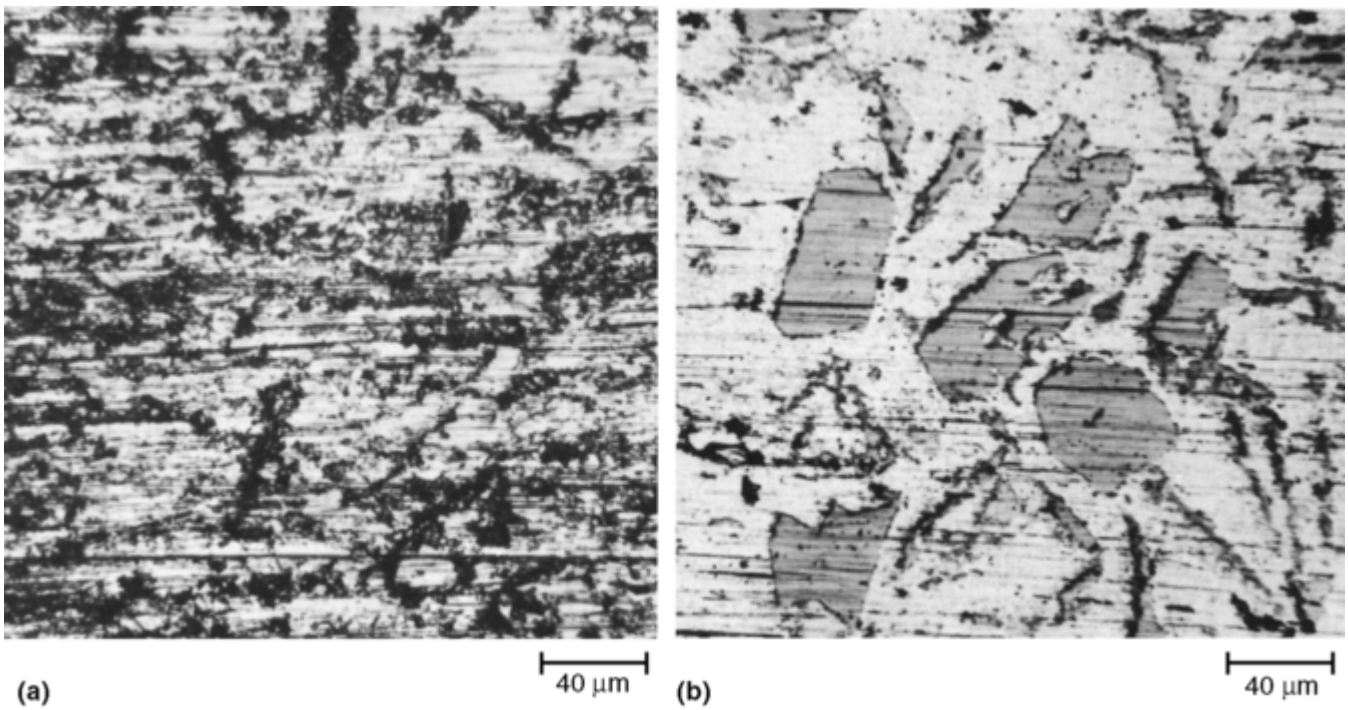

Fig. 12 Comparison of abrasives for reduction of the differences in level of different phases in Al-13Si alloy. (a) Results of abrading on 600-grit silicon carbide paper. (b) Improved results obtained by abrading on a fine fixed-abrasive lap. As-polished. 250×

Embedding of Abrasive. The points of the contacting abrasive particles of an abrasive paper fracture readily during abrasion. These fragments may become embedded in the surface of a very soft metal, such as lead or annealed high-purity aluminum, where they are difficult to discern by optical microscopy. However, a surface with a high concentration of embedded abrasive characteristically has a rough, torn appearance (Fig. 13a), quite different from the regular grooves of a normal abraded surface. It is difficult to prepare such a surface through subsequent stages.

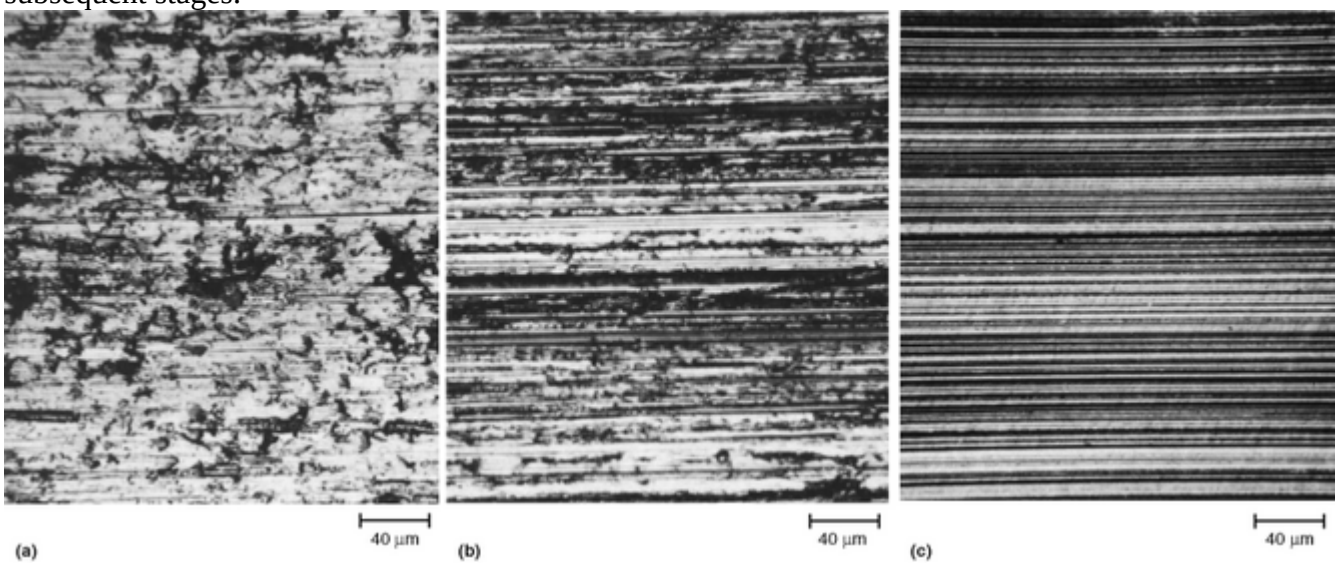

Fig. 13 (a) Results obtained by finishing high-purity lead on 600-grit silicon carbide paper using water as the fluid. (b) Results obtained on 600-grit silicon carbide paper using wax on the abrasion surface. (c) Results obtained using a sledge microtome. As-polished. 250×

Embedding of abrasive fragments can be avoided by filling the surface of the abrasive paper with a soft wax; the fragments will then embed in the wax rather than in the specimen. The result of finishing high-purity lead on a silicon carbide paper lubricated with wax is shown in Fig. 13(b). The surface of soft metals may also be prepared by cutting with a heavy microtome. This produces the highest quality surface, as shown in Fig. 13(c).

Footnote

* Figure 1(a) shows a taper section in which the apparent magnification in depth (vertically in the micrograph) is 8.2 times the nominal magnification. Here the section line is perpendicular to a set of unidirectional abrasion scratches. Similar taper sections are shown in Fig. 2(a), 3(a), 4(a), 7(a), 14(a), and 19. When the section line is parallel to the abrasion scratches (as in Fig. 5 and 9), the section is referred to as a longitudinal taper section.

Mechanical Grinding and Polishing, *Metallography and Microstructures,* Vol 9, *ASM Handbook*, ASM International, 2004, p. 257–280

Polishing Damage

The mechanical polishing procedures most commonly used in metallography remove metal by mechanical cutting processes analogous to those of abrasion. This type of mechanical polishing produces a series of scratch grooves on the surface of the specimen that are difficult to detect by optical microscopy, particularly with bright-field illumination, but are readily detected by scanning electron microscopy. Moreover, a plastically deformed, damaged layer is also introduced. The layer is much shallower than that produced by abrasion, but its structure is similar.

The damaged layer produced on the surface of annealed 70-30 brass by polishing (Fig. 14a) can be compared with that produced by abrading (Fig. 1a). A layer, analogous to the outer fragmented layer in abraded surfaces, can be recognized contouring the surface scratches, and occasional rays of deformed metal extend to depths many times that of the polishing scratches. The gradient of plastic strains on the layer is the same as for the fragmented layer in abraded surfaces, but the layer is shallower by one or two orders of magnitude. The presence of this damaged layer affects the response of the surface to etching.

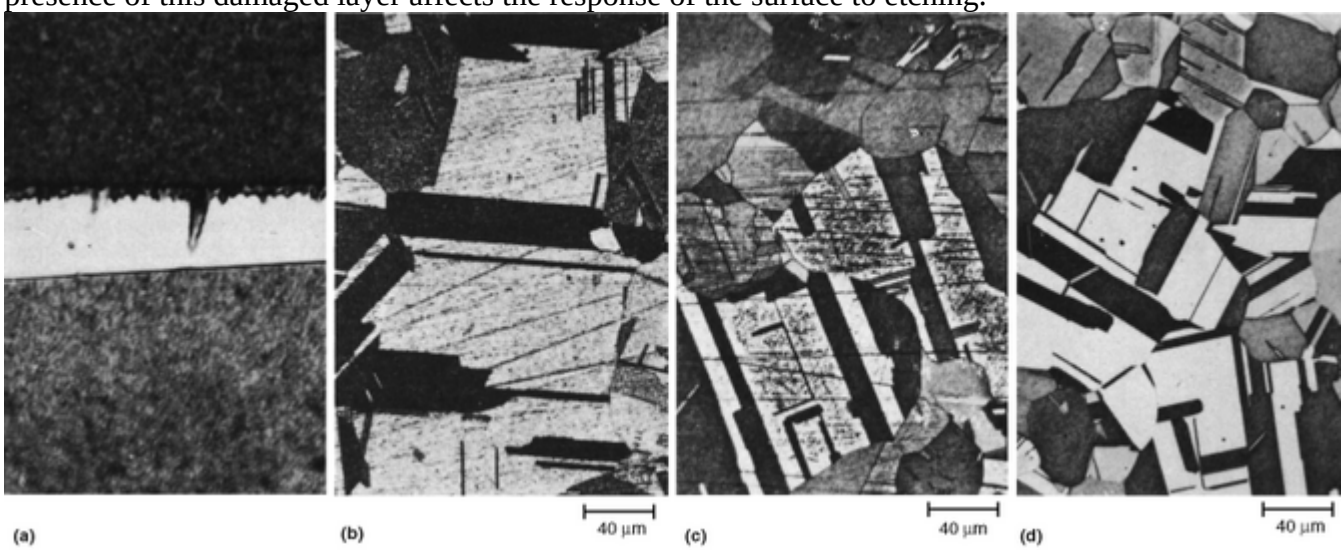

Fig. 14 Effect of polishing damage on response to etching for annealed 70-30 brass. (a) Taper section (horizontal magnification 2000×, vertical magnification 21,800×) of surface layers that were polished on 1 μm diamond abrasive. (b) Results of etching immediately after polishing on a 1 μm diamond abrasive. (c) Fine polishing for a short time before etching. (d) Fine polishing for a longer time before etching. The fine polishing process is skid polishing on magnesium oxide abrasive, a chemical-mechanical polishing process that does not produce a damaged layer. Aqueous $FeCl_3$. 250×

This damaged layer cannot be avoided in a polishing that removes material primarily by chip cutting. Several fine polishing processes, however, do not operate in this way. In the first group of these processes, polishing occurs by detaching small flakes of material from the surface. The surface strains introduced by this polishing are so small and the strained layer so shallow that often it would be removed by etching.

The second group consists of polishing processes in which, intentionally or otherwise, the liquid in which the polishing abrasive is suspended is chemically active with respect to the specimen material. The function of the abrasive then appears to be that of continuously removing protective films, ensuring more rapid and more uniform dissolution of the surface by chemical attack. This combination of actions may be referred to as a chemical-mechanical polishing mechanism. The surface produced is damage-free when the chemical component is large enough.

However, an excessive chemical component in a mechanical-chemical process may cause such detrimental effects as severe etch pitting. Proper balance between the mechanical and chemical components can preserve most of the benefits provided by mechanical polishing and yet produce a damage-free surface—a most desirable combination in a final polishing.

Degradation of Etching Contrast. The orientation of the grain sectioned in Fig. 14(a) is such that it should have appeared white on the original polished surface under the etching conditions indicated, as it does in the middle portions of this micrograph. However, it is covered by a fragmented layer that etches darkly. Therefore, this grain would have appeared much darker than it should have if the original surface had been etched and examined. Consequently, the contrast between this grain and the others would have been less than it should have been. This is why the grain contrast in Fig. 14(b) is poor compared to that in Fig. 14(d). This phenomenon can be expected whenever an etchant develops contrast by differential coloring; it may be described as a polishing artifact.

Scratch Traces. If a surface is subjected to coarse polishing, followed by finer polishing until the first series of scratches but not all the rays of deformation in the layer damaged by polishing have been removed, the residuals of the rays of deformation left in the surface may be preferentially attacked during etching, as shown in Fig. 14(c), giving the impression that some of the first series of scratches have reappeared. These effects can be avoided by continuing finer polishing long enough to remove all the preexisting polishing damage, as shown in Fig. 14(d).

This phenomenon, common in metallography, is frequently ascribed to the reappearance of the scratches themselves. However, the features developed should be thought of as “ghosts” of the original scratches; they are not the grooves of the original scratches. They may more properly be termed scratch traces, another type of polishing artifact.

Enlargement of Polishing Scratches by Etching. A surface that appeared to be free of scratches when examined as-polished under bright-field illumination often appears severely scratched after etching (see Fig. 15). The numerous fine scratches were not detected on the unetched specimen; they were enlarged, or shown in greater contrast, by etching.

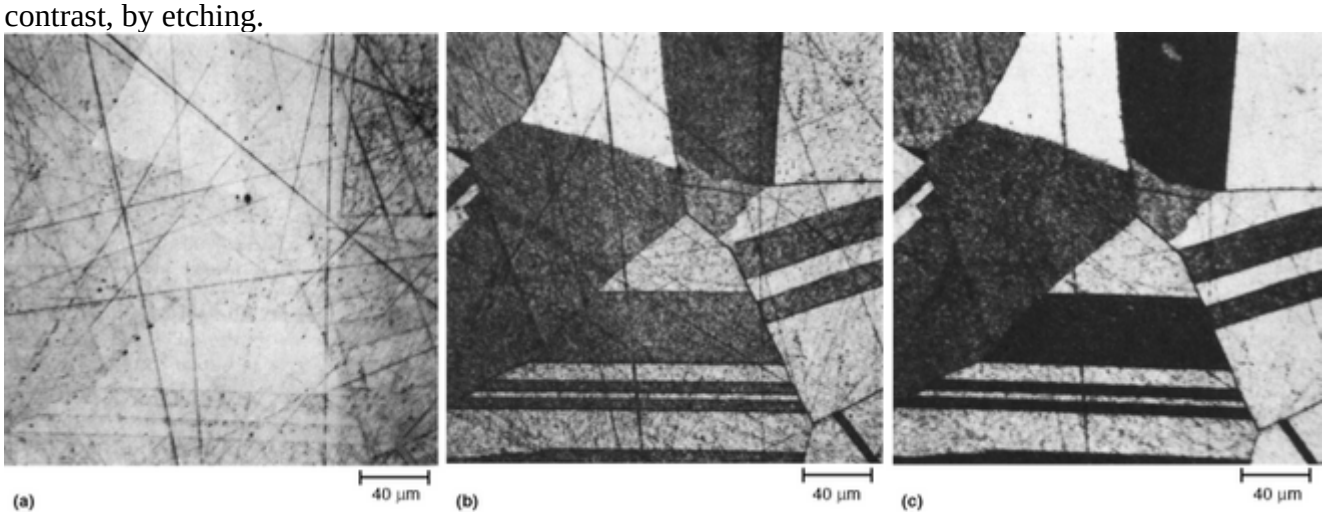

Fig. 15 Effect of incremental increases in etching time on appearance (a) and (b) and disappearance (c) of scratches on a specimen of annealed 70-30 brass that was polished on fine Al_2O_3. (c) Longer etching time removes scratches and the damaged layer. Aqueous $FeCl_3$. 250×

Scratches are attacked preferentially during etching because of the disturbed metal, or damaged layer, associated with them. Severity of attack varies directly with the ability of the etchant to reveal deformation. The appearance of scratches also depends on the etching time. A certain minimum etching time is necessary to develop the scratches to maximum visibility, after which the scratches recede with increasing etching time, because etching progressively removes the damaged layer.

Metals vary in their susceptibility to this effect; the greater the sensitivity of the metal-etchant combination to plastic deformation, the more likely that enlargement of scratches during etching will be troublesome. On the other hand, the phenomenon becomes less troublesome when the depth of the damaged layer is less than that of the layer removed during etching. Polishing processes that do not introduce a damaged layer cause no such problems.

It may be difficult to distinguish scratches enlarged by the final-polishing stages from scratch traces introduced during the previous polishing stage. This can be resolved by making the earlier set of scratches unidirectional and parallel to a known direction in the specimen surface. The originating system of scratches can then be recognized. This technique was used in preparing the specimen for Fig. 14(c).

Flatness. Surfaces should be adequately free of confusing polishing scratches and should be sufficiently flat for examination of all constituents and local regions. Two examples of how markedly the choice of polishing abrasive and polishing cloth can affect surface flatness in specimens of duplex structure are given in Fig. 16 and 17. These micrographs show that Al_2O_3 abrasive on billiard cloth produced a result inferior to diamond abrasive on synthetic suede cloth in polishing wrought iron and an aluminum alloy. The Al_2O_3 on billiard cloth produced marked relief between the silicon constituent and the aluminum matrix of the aluminum alloy (Fig. 17a) and removed a portion of the silicate inclusion in the wrought iron (Fig. 16a). These are not the only types of polishing cloths available, but the examples demonstrate the wide variation in quality of results that is possible and the type of systematic experiment that can be carried out to compare polishing processes.

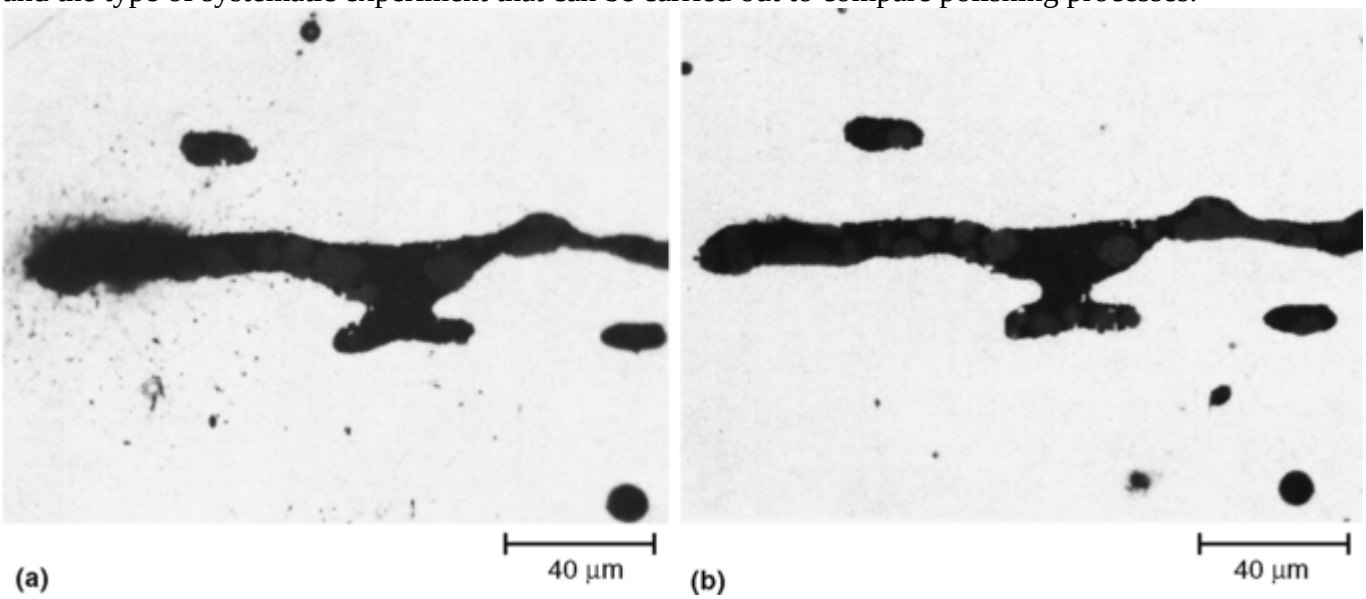

Fig. 16 Comparison of polishing methods for showing inclusions in wrought iron. (a) Specimen was polished on 10 to 20 μm Al_2O_3 on billiard cloth. (b) Specimen was polished on 4 to 8 μm diamond on synthetic suede cloth. Both specimens were abraded on a fixed-abrasive lap before polishing. As-polished. 350×

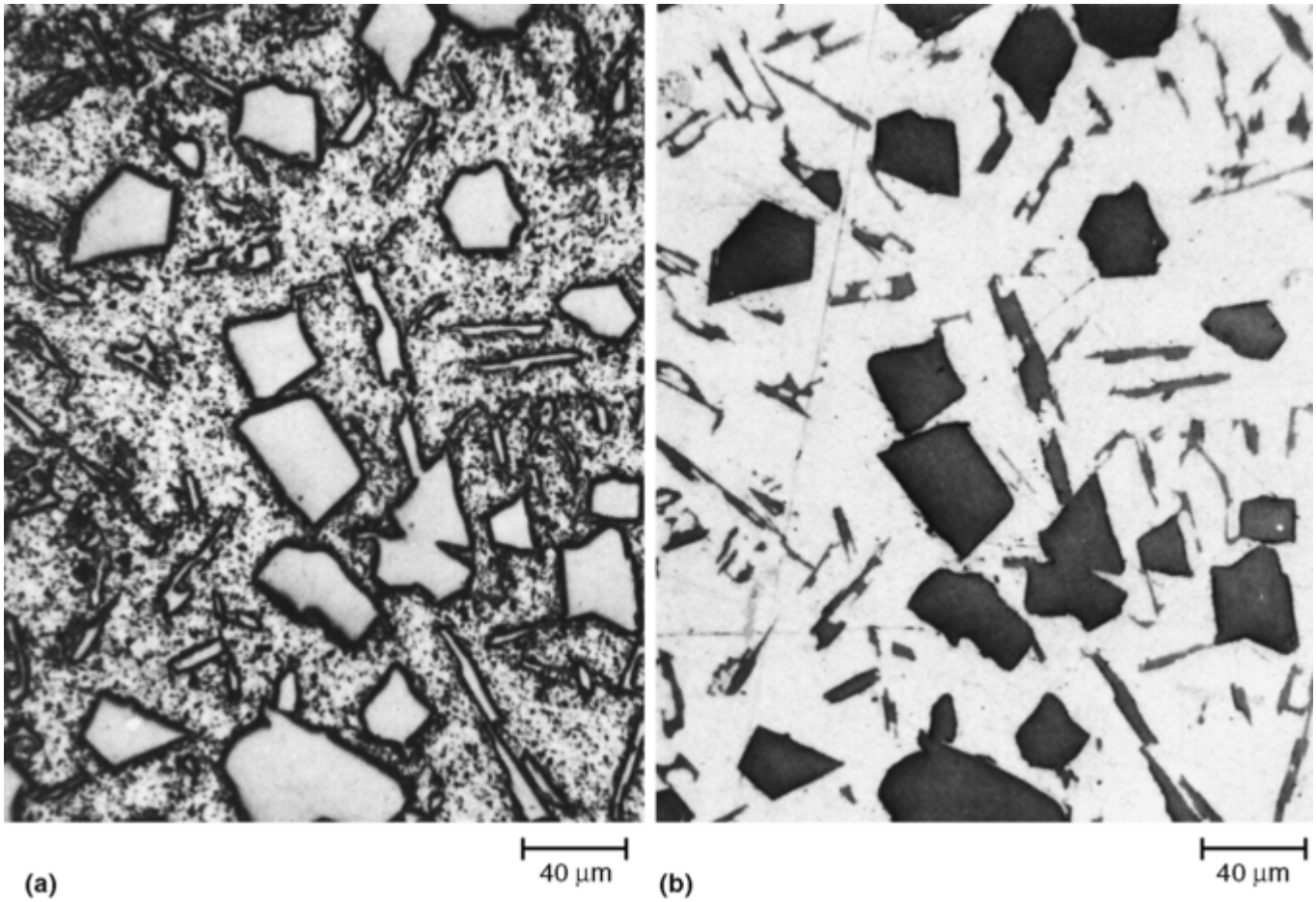

Fig. 17 Comparison of polishing methods for showing phases in Al-13Si alloy. (a) Specimen was polished on 10 to 20 μm Al_2O_3 on billiard cloth. (b) Specimen was polished on 4 to 8 μm diamond on a synthetic suede cloth. Both specimens were abraded on a fixed-abrasive lap before polishing. As-polished. 250×

Retention of Graphite in Gray Iron. Earlier in this article it was demonstrated that although the graphite in cast iron can be damaged severely by abrasion, it is possible by suitable choice of abrasion process to obtain a reasonably true representation of the structure. However, there is the problem of retaining the graphite during polishing. The solution to the problem depends heavily on the length of the nap of the polishing cloth.

Graphite flakes in a gray iron invariably look much larger when a long-nap cloth is used for polishing, as demonstrated in Fig. 18(a). This apparent enlargement is caused by erosion, which occurs at the interface between graphite and matrix, producing an enlarged cavity from which the flake itself eventually is removed (see Fig. 19a). With a cloth of reasonably short nap, many of the flakes are well retained, although some appear slightly larger (see Fig. 18b and 19b). Examination of sections of such a surface indicates that flakes aligned perpendicular to the surface are not eroded (flakes at right in Fig. 19b), but that slight erosion occurs around flakes that happen to be acutely aligned at the section surface (flake at left in Fig. 19b). Correct representation of the graphite flakes is obtained after polishing with a napless cloth, as shown in Fig. 18(c).

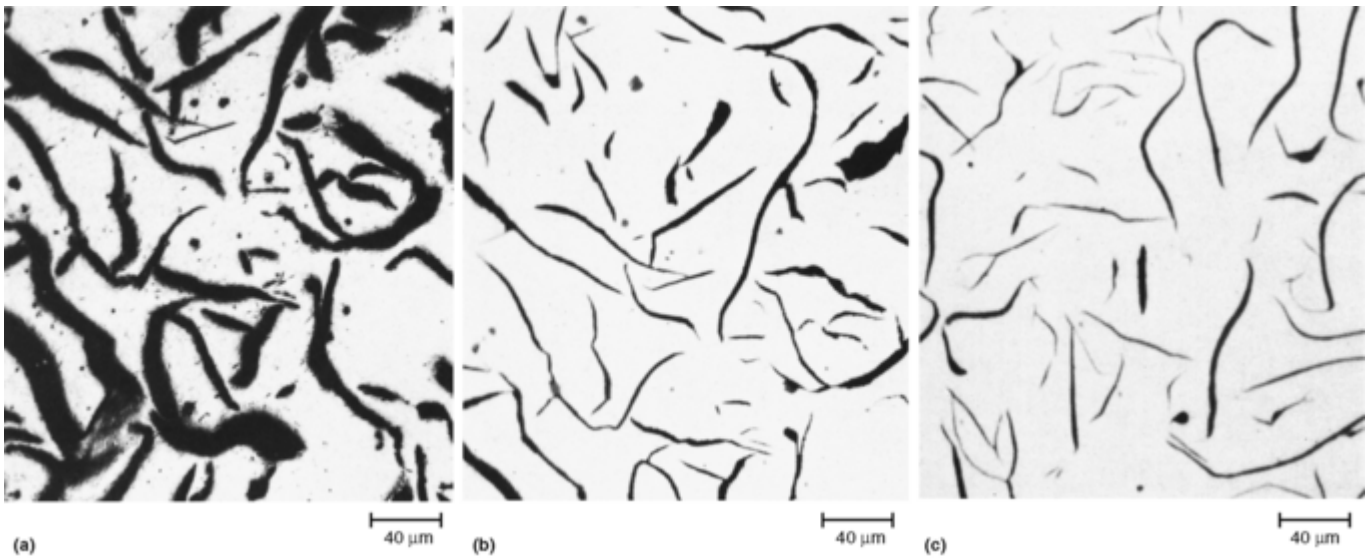

Fig. 18 Comparison of polishing methods for retention of graphite in gray iron. (a) Results of polishing on 10 to 20 µm Al_2O_3 on long-nap billiard cloth. (b) Results of polishing on 1 µm diamond on a synthetic suede short-nap cloth. (c) Results of polishing on 1 µm diamond on cotton drill. All specimens were abraded on a fixed-abrasive lap before polishing. As-polished. 250×

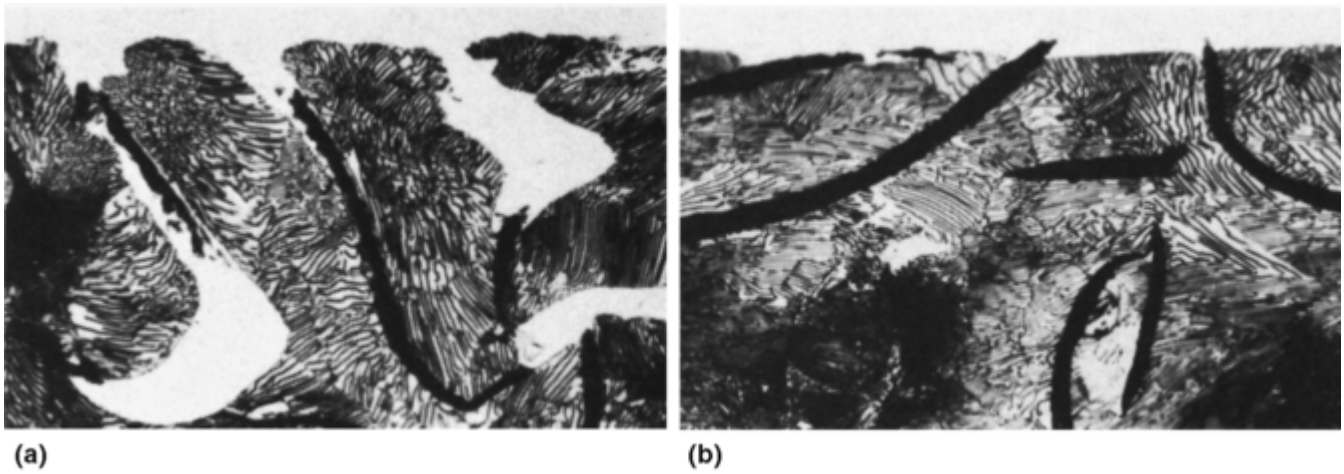

Fig. 19 Taper sections (horizontal magnification 1000×, vertical magnification 10,000×) comparing polishing methods for retention of graphite in gray iron. (a) Results of polishing on 10 to 20 µm Al_2O_3 on long-nap billiard cloth. (b) Results of polishing on 1 µm diamond on short-nap synthetic suede. Picral

Only certain abrasives, notably diamond abrasives, produce satisfactory results on napless cloths. Even then, a moderately heavily scratched polish is obtained. If this finish is unacceptable, a finishing treatment with a fine abrasive on a napped cloth is necessary. The treatment must be brief to avoid enlargement of the cavities.

Mechanical Grinding and Polishing, *Metallography and Microstructures,* Vol 9, *ASM Handbook,* ASM International, 2004, p. 257–280

Final-Polishing Processes

Only rarely must final-polished surfaces be totally free of scratches. Rather, no scratches should be detectable under the particular conditions of examination. Attaining this will depend, therefore, on the specimen material (more difficult with soft materials), the etching conditions (more difficult with etchants that are sensitive to deformed structures), and the optical conditions of examination. In general, high-standard polishing processes are more laborious and require greater operator skill. A variety of final-polishing processes should be available that can produce increasingly higher qualities of finish from which to select the most suitable and simplest for a particular need.

Skid Polishing. The nap of the polishing cloth is filled with a thick paste of a fine polishing abrasive and an appropriate polishing fluid, and the specimen is rotated lightly against the surface of the paste so that it skids over the paste without touching the fibers of the polishing cloth. Alternatively the nap is filled with an abrasive-free paste of an appropriate material, and the polishing abrasive is sprinkled onto the surface of the paste. These procedures should eliminate the scratches that would ordinarily result from contact with the fibers of the polishing cloth. In addition, because the abrasive particles are more lightly supported than usual, they produce finer scratches. Processes carried out in this way can also involve a chemical-mechanical mechanism of material removal, particularly if active chemicals are added to the abrasive paste. They sometimes operate entirely by such a mechanism. The skidding technique with MgO abrasive used for Fig. 14(d) is an example. Skid-polishing methods, however, are tedious and difficult.

Vibratory polishing methods, in which the specimen is made to track automatically around the polishing cloth by imparting a suitable vibratory motion to the polishing head, are useful for final polishing because they operate automatically and permit accurate control of polishing conditions. Results are highly reproducible once the controlling variables have been identified and optimized. A further advantage of vibratory polishing is that it can be adapted to chemical-mechanical polishing. The important variables in vibratory polishing are the abrasive, the nature of the liquid in which the abrasive is suspended, and the load applied to the specimen.

The results of varying the suspending liquid are shown in Fig. 20. The polishing rate with straight glycol as the suspending liquid was so low that scratch traces from the previous polishing stage were retained even after a protracted polishing time (Fig. 20a). Water as the suspending liquid provided fast polishing, but caused severe etch pitting (Fig. 20c). A suitable mixture of the two provided an adequate polishing rate and a satisfactory polish (Fig. 20b).

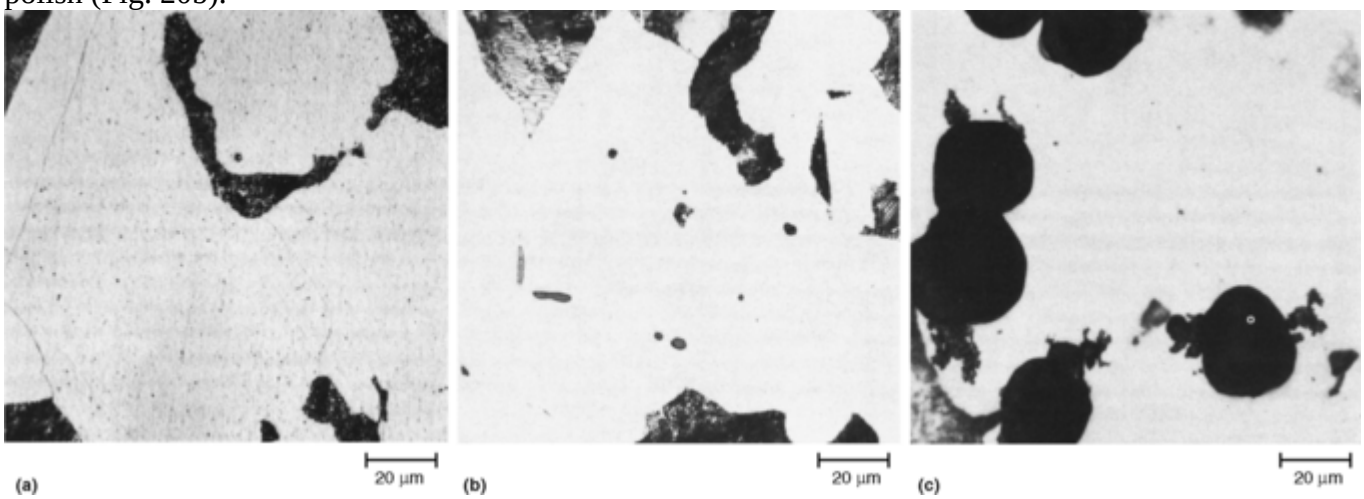

Fig. 20 Effect of type of suspending liquid used in vibratory polishing of low-carbon steel. Specimens were rough polished on 1 μm diamond and finish polished for 4 h on 0.1 μm Al_2O_3. (a) Using propylene

glycol; scratches have not been removed. (b) Using a 2-to-1 mixture of propylene glycol and water; results are satisfactory. (c) As-polished; using water; large corrosion pits have developed. Nital. 500×

Some etch attack occurs with the glycolwater suspending liquid, even with optimal adjustment of the liquid; the etching varies directly with the load applied to the specimen, increasing with increasing load, as shown in Fig. 21. This behavior offers evidence that the polishing process is occurring by a chemical-mechanical mechanism, with the water acting as the active ingredient and the glycol (a chelating agent) acting as a modifier.

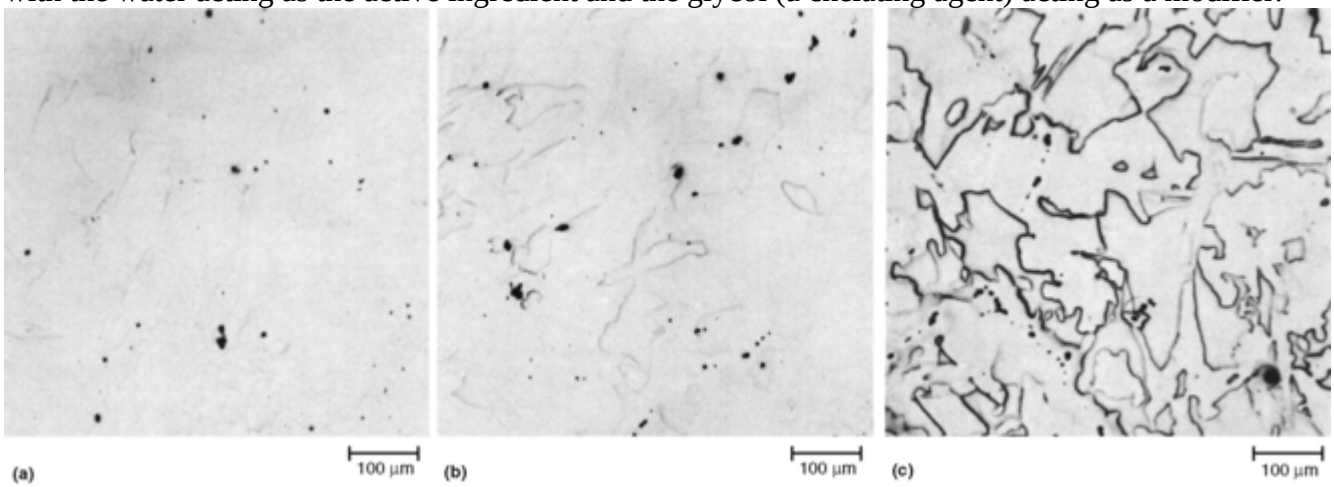

Fig. 21 Effect of load applied to the specimen in vibratory polishing of low-carbon steel. Specimens were rough polished on 1 μm diamond and finish polished for 4 h on 0.1 μm Al_2O_3 suspended in a 2-to-1 mixture of propylene glycol and water. (a) Using a 40 g load. (b) Using a 70 g load. (c) Using a 380 g load. Etch relief develops during polishing, being greater the larger the applied load. As-polished. 100×

The most appropriate suspending fluid varies with the specimen material. Sometimes it is also necessary to add a more aggressive etching reagent to the suspending liquid to ensure an adequate chemical component in the polishing mechanism. For example, the mechanism for an α-β brass that was polished with the use of a straight glycol-water mixture had an excessive mechanical component, and final-polishing scratches became apparent as a result (Fig. 22a). The addition of a large amount of ammonium hydroxide (NH_4OH) caused the chemical mechanism to predominate, and an unacceptable degree of relief developed between the two phases of the microstructure (Fig. 22c). Adjustment of the NH_4OH addition balanced the two mechanisms to give an acceptable result (Fig. 22b).

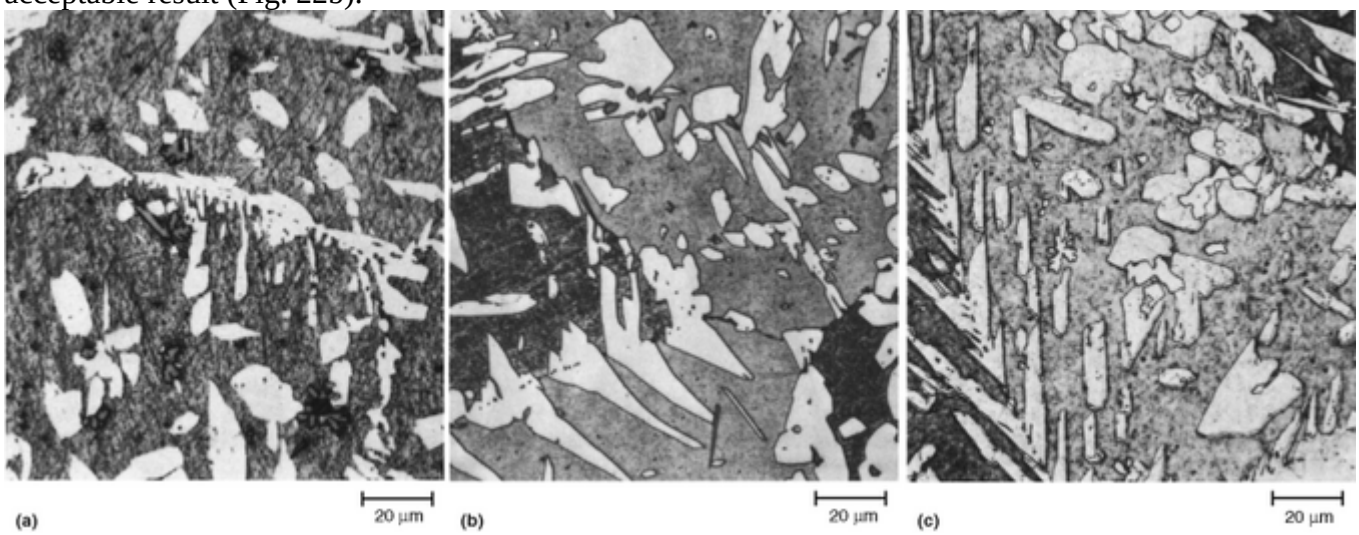

Fig. 22 Effect of addition of different amounts of NH_4OH to the suspending liquid in vibratory polishing of a cast α-β brass. Specimens were polished with magnesia suspended in a 3-to-1 mixture of propylene glycol and water. (a) Using no addition of NH_4OH; note numerous polishing scratches. (b) Using an optimal addition of NH_4OH. (c) Using excessive NH_4OH; note excessive relief between the two phases. As-polished (etched during polishing). 500×

The optimal polishing conditions are arrived at largely by experimentation, guided by a few broad principles. However, highly reproducible results are achieved once the optimal conditions have been determined.

Etch-Attack and Electromechanical Polishing. The material-removal rate obtained with some metals, particularly the refractory metals, is very small with conventional polishing methods. This inhibits the removal of preexisting abrasion and polishing damage as well as the production of adequately scratch-free final surfaces. It is possible in many cases to increase the polishing rate acceptably by adding an active chemical etchant to the abrasive slurry. Unfortunately, because the reagents necessary are frequently very aggressive to other metals and human tissue, they require the use of special corrosion-resistant equipment and specimen-handling arrangements. Less than ideal results, however, often are obtained, as shown in Fig. 23(a).

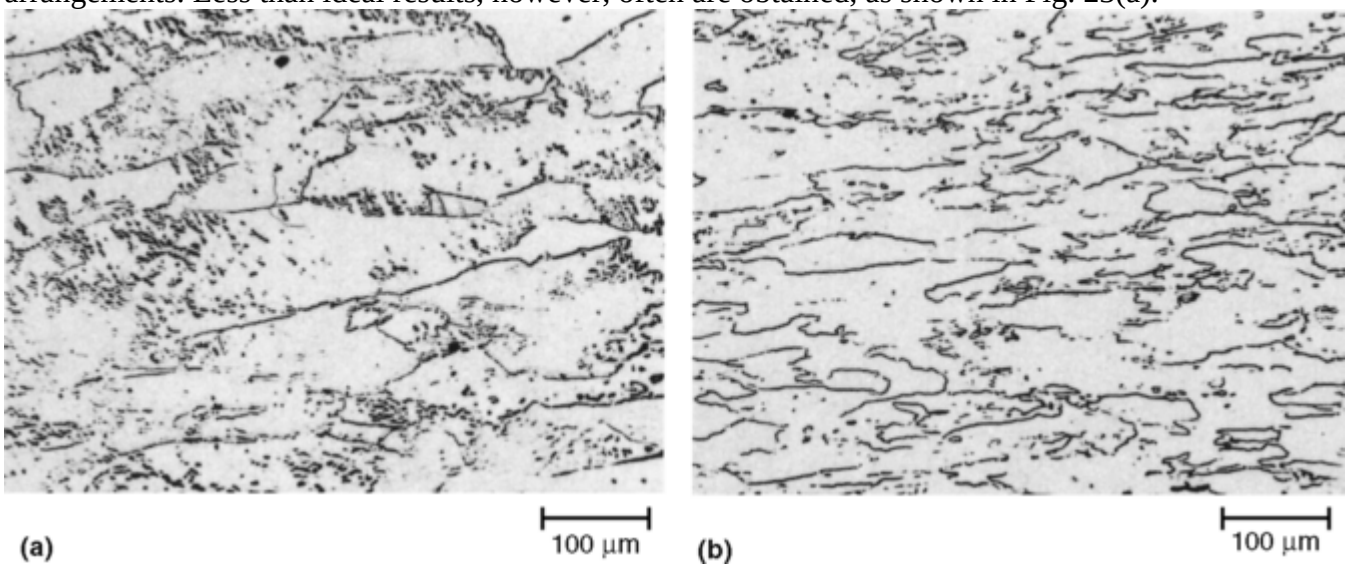

Fig. 23 Comparison of etch-attack and electrochemical methods of polishing tungsten, a representative refractory metal. (a) Polishing by an etch-attack technique using Al_2O_3 abrasive suspended in an aqueous solution of potassium ferricyanide (KCN) and sodium hydroxide (NaOH). (b) Polishing by an electromechanical technique using Al_2O_3 abrasive suspended in a saturated aqueous solution of NaOH. The etch-attack technique produced some grain relief and many wiping marks. The electromechanical technique produced a surface in which no structure could be seen before etching. A satisfactory artifact-free result was obtained on etching. 100×

Less aggressive reagents can be employed if an electrical potential is applied between the specimen and the polishing wheel; the two act as electrodes of an electrolytic cell. Suitable electromechanical processes of this type have been developed for various difficult metals and alloys. Only minor modifications to standard polishing equipment are required to use these techniques, and a more uniform polish is achieved than by straight etch-attack techniques (compare Fig. 23a and b).

Polishing with Special Abrasives. Two fine abrasives are available that produce unusually scratch-free surfaces, particularly in soft materials, when used conventionally. Apparently, the improved results are obtained because these abrasives act by different mechanisms than conventional fine polishing processes. For example, 0 to $\frac{1}{4}$μm grade of polycrystalline diamond used conventionally as a carrier paste added to a short-nap cloth produces a surface with a shallow low-strain-damaged layer.

Another example is a proprietary material that is a colloidal suspension of silica (SiO_2). This material is widely used for polishing silicon in the semiconductor industry. A number of precautions are essential for its use; the solution must not be allowed to freeze or to dry out on the polishing cloth, and it may be necessary to adjust its pH for particular types of specimens. This polishing process appears to act largely by a chemical-mechanical mechanism. Although some relief is produced between the grains and constituents, it is usually well within acceptable limits.

Mechanical Grinding and Polishing, *Metallography and Microstructures,* Vol 9, *ASM Handbook,* ASM International, 2004, p. 257–280

Edge Retention

For metallographic examination, the surface produced should be flat up to an edge of the specimen. The criterion is that the regions adjacent to the edge should all be focused sharply by the particular microscope system that is used for the examination of the section. This may require adopting special procedures during specimen preparation, because unsupported edges of a section normally round off slightly when the specimen rocks during preparation, particularly during manual operations. Special procedures may also be required because of the elasticity of the working surfaces on the abrasion and polishing devices. An acceptable degree of rounding and therefore the extent of the precautions necessary during specimen preparation depend on the depth of field of the microscope system to be used. Comparatively large degrees of rounding are acceptable in scanning electron microscopy, but much lesser degrees are acceptable in optical microscopy. The higher the magnification in use in optical microscopy, the lesser the degree of rounding that is acceptable.

Many techniques, which usually require a degree of operator skill, have been devised to improve edge retention, yet few have general application. The basic problems involved and methods by which they may be overcome by the simplest possible modifications of standard procedures are discussed below. Although the difficulties involved in edge retention are alleviated by the use of mechanized preparation machines, the same principles apply to manual operations. Additional information on edge retention (or preservation) can be found in the article “Mounting of Specimens” in this Volume.

With few exceptions, the abrasion rates of the plastics in which metallographic specimens are mounted greatly exceed those of metals. The plastic abrades to a lower general level than the metal, and rounding of the specimen edge occurs to blend in the differences in level. The degree of edge rounding may be increased or decreased during polishing; long-nap polishing cloths increase edge rounding.

However, the abrasion rates of different types of plastic differ significantly, and edge retention can be improved by choosing a mounting plastic that has an abrasion rate matching as closely as possible that of the specimen. For example, progressively improved edge retention is obtained, as shown in Fig. 24, with the change from a phenolic (Fig. 24a) to an allyl (Fig. 24b) to a polyvinyl formal (Fig. 24c) mounting plastic. Metals such as chromium and tungsten, which have very low abrasion rates, show poorer edge retention than that illustrated in Fig. 24(c), even when mounted in a polyvinyl formal plastic. Metals such as copper and aluminum, which have high abrasion rates, show good edge retention, even when mounted in phenolic or epoxy plastics.

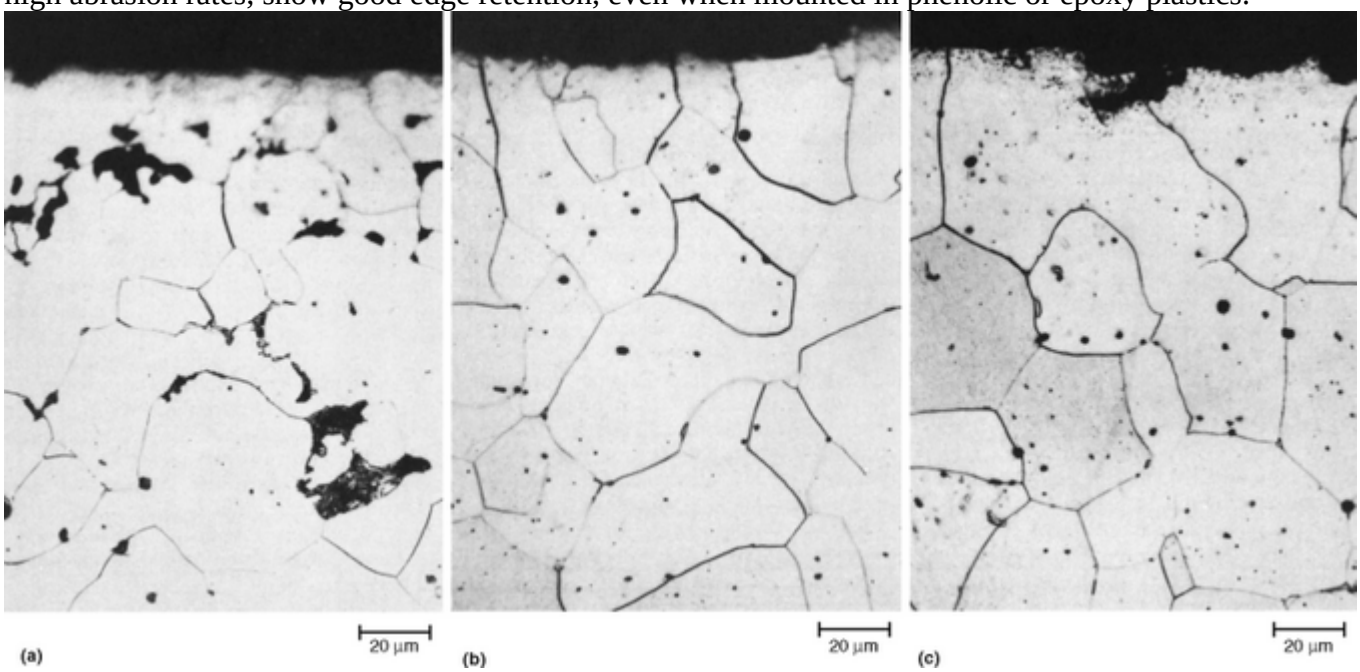

(a) (b) (c)

Fig. 24 Effect of type of mounting plastic on edge retention of steel specimens polished by standard technique. (a) Specimen mounted in a phenolic plastic; also representative of edge retention using an epoxy. (b) Specimen mounted in an allyl plastic. (c) Specimen mounted in a polyvinyl formal plastic; also representative of edge retention using polyvinyl chloride plastic. Nital. 500×

Reducing the difference in abrasion rate between the specimen and mount improves edge retention. This may be accomplished by incorporating chips or pellets of a metal similar to the specimen in the mount face (see Fig. 25a). Any included material that reduces the abrasion rate of the plastic will also be effective. Plastics are available to which a substantial volume fraction of mineral or ceramic (for example, mica, SiO_2, or Al_2O_3) has been added as a filler. They are effective for edge retention, but cause rapid deterioration of abrasive papers. The potential for removing preexisting damaged layers is therefore considerably reduced, an important factor when considering mineral- or ceramic-filled plastics.

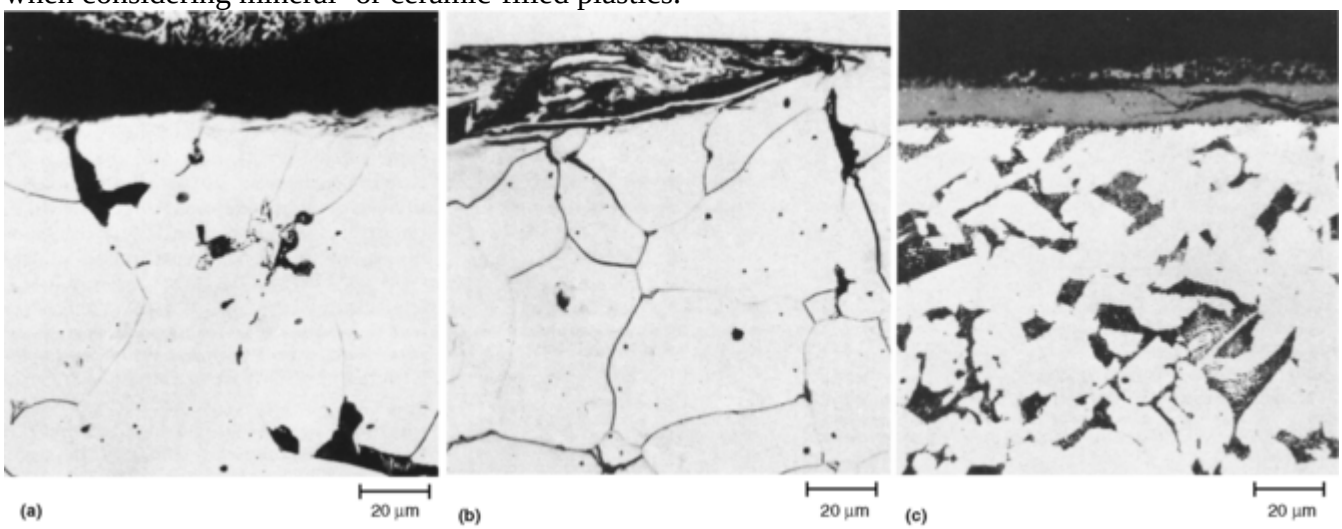

Fig. 25 Effect of special techniques for improving edge retention of steel specimens mounted in an epoxy resin. (a) Steel shot incorporated in the mount; specimen finish polished by a standard technique. (b) Edge protected by an electrodeposited coating of nickel; specimen finish polished by a standard technique. (c) Specimen finish polished using a fairly rigid napless pad and diamond abrasive. Nital. 500×

The polishing rates of plastics are small compared to their abrasion rates. They can now be either less than or greater than that of the metal specimen itself. If the former, any edge rounding that developed during abrasion will increase during polishing; if the latter, it will decrease to a degree that also depends on the elasticity of the polishing cloth. Consequently, it is easier to achieve good edge retention with some metals than with others using standard procedures. If the polishing ratio of metal and plastic is adverse, anything that reduces the polishing rate of the plastic will improve edge retention, such as adding a mineral or ceramic filler. However, the overall polishing rate of the metal-plastic combination is then reduced correspondingly, with an attendant increase in the difficulty of removing the abrasion-damaged layer.

The napped cloths used in standard polishing procedures are likely to worsen the edge rounding developed during abrasion, because these soft cloths tend to conform locally to the contour of the abraded surface. If polishing is done on a fairly rigid pad so that contact is made during polishing only with high spots on the abraded surface, the specimen surface can be polished down to the level of the plastic. Edge retention, therefore, will be improved. Results obtained by this procedure are shown in Fig. 25(c). When polishing on a rigid pad, careful selection of the polishing abrasive and cloth will prevent the development of excessive polishing scratches.

A high standard of edge retention is achieved ideally by depositing on the surface concerned, before sectioning, a layer of material with abrasion and polishing removal rate characteristics similar to those of the specimen material. This is illustrated in Fig. 25(b). In addition, the deposited layer sometimes must have electrochemical characteristics similar to those of the specimen material so that it does not interfere with etching of the specimen material. Good adhesion between deposit and base metal is also essential. Electrodeposition is the most common method of forming the protective layer, but the number of metals that can be deposited in this

way is limited. A similar result is achieved by clamping a pack of like specimens together, but this applies only to specimens in the form of thin sheet.

Mechanical Grinding and Polishing, *Metallography and Microstructures*, Vol 9, *ASM Handbook*, ASM International, 2004, p. 257–280

Special Techniques for Unusual Materials

Very Hard Materials. An abrasive particle generally will not embed in a specimen material and remove material by machining a chip unless it is at least two times and preferably three times harder than the specimen material. This applies also to individual constituents in an alloy when their size is comparable to that of the scratches being produced. The hardnesses of the commonly used abrasives are 2500 HV (silicon carbide), 2000 HV (Al_2O_3), and 8000 HV (diamond). In practice for example, very little material can be removed by silicon carbide and Al_2O_3 abrasives from materials with a hardness of about 1000 HV. Such materials usually are cermets or ceramics, such as tungsten carbide or Al_2O_3. Diamond abrasives clearly are desirable for all stages of the preparation of materials of these types and are mandatory for the hardest of them.

Diamond abrasive laps suitable for the abrasion stages of preparation are available commercially in a range of grades. In the most common form, the abrasive is held onto a metal disk by a covering layer of metallic material, often an electrodeposit of nickel. Very hard materials are invariably brittle. Abrasion then occurs by irregular blocky chips fracturing out of the surface. This leaves deep pits on the surface (see Fig. 26a), with systems of cracks extending beneath the pits. These pits and chips become the artifacts that must be removed during polishing (compare the micrographs in Fig. 26). This is important, because the pits may be mistaken for the porosity often present in hard materials when they have been fabricated by sintering, as is commonly the case.

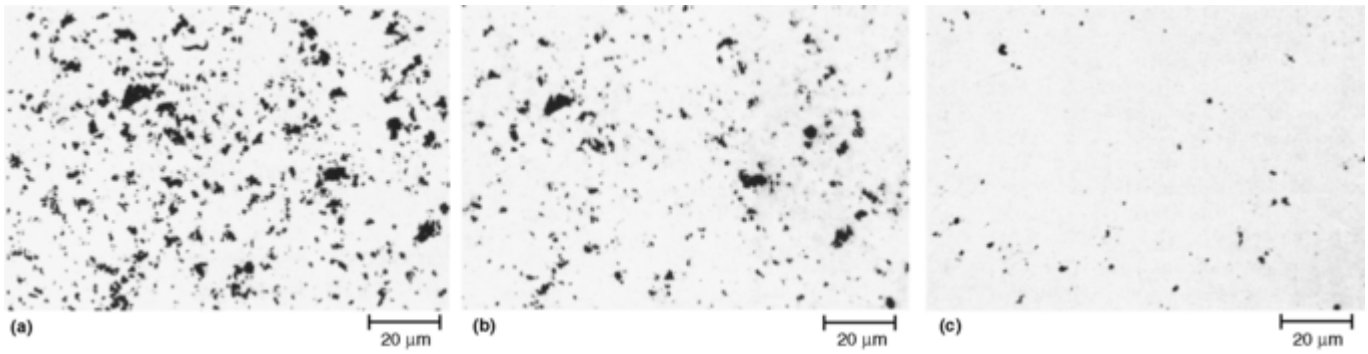

Fig. 26 Sintered WC-15Ti. (a) Dark, angular areas are artifacts due to chipping during abrasion of 6 μm diamond-plastic lap. (b) Result of polishing the abraded surface for comparatively short period on a cotton drill cloth charged with 6 μm diamond abrasive. Many of the deeper pits produced during abrasion remain and might be mistaken for sintering pores. They are abrasion artifacts. (c) Result obtained after polishing further. The chipping artifacts have been removed, and the true distribution of the sintering pores can now be seen. As-polished. 500×

Polishing of these materials occurs by the normal mechanisms, but the rates of material removal obtained even with diamond abrasives are low. The polishing times required to remove abrasion artifacts consequently may be long—much longer than for soft materials. It is important, therefore, to establish the polishing parameters that achieve maximum removal rates. Automated polishing also becomes useful. Even then, long polishing times will still be necessary, and it becomes desirable to check using the experiment shown in Fig. 26 that the true result will be obtained. Final polishing must be carried out on the finest diamond abrasive available.

Surface Oxide Layers. Determination of the structure of a surface layer of oxide, or scale, on a specimen is sometimes the principal reason for metallographic examination. A specimen with such a surface layer presents

a problem in edge retention. The oxide is usually brittle and friable, being therefore susceptible to chipping and cracking during preparation. Because the detection of porosity or cracking in the layer is usually an important feature of the examination, it is essential to avoid the development of preparation artifacts that might be mistaken for such features. The development of such artifacts during abrasion is likely, because treatment on standard abrasive papers often results in extensive chipping of the oxide layer (see Fig. 27a). Even a fixed-abrasive lap produces some artifact chipping (see Fig. 27b), but a special diamond-abrasive leadfoil lap produces a satisfactorily artifact-free result (see Fig. 27c). Then polishing with diamond abrasive on a hard napless cloth ensures that a high degree of surface flatness will be maintained and that no polishing damage will be introduced (see Fig. 27d).

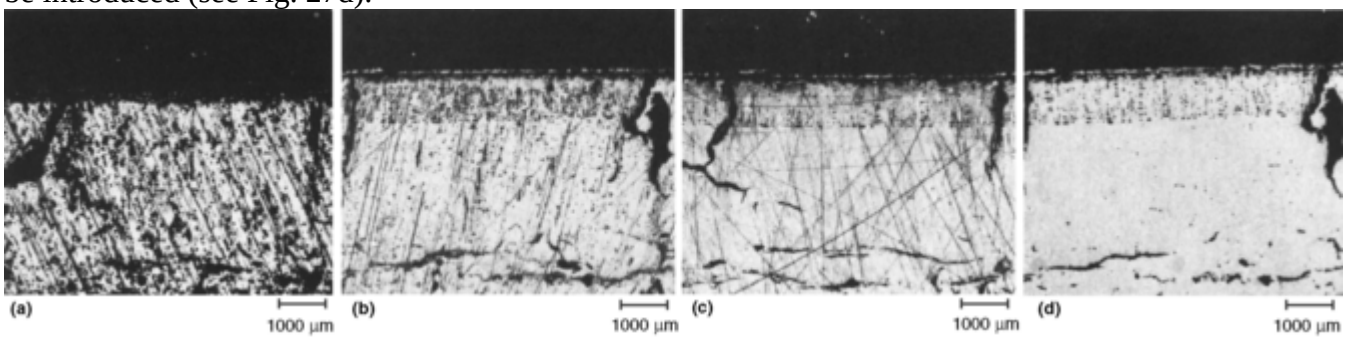

Fig. 27 Effect of different abrading and polishing techniques on the appearance of oxide scale on high-purity iron. (a) Specimen abraded on 400-grit silicon carbide paper; numerous chipping artifacts are present in the oxide. (b) Specimen abraded on a fine fixed-abrasive lap; minor chipping artifacts are present in the oxide. (c) Specimen abraded on a leadfoil lap coated with 1 μm diamond paste; oxide and metal are free from chipping artifacts, but are badly scratched. (d) Specimen polished on 1 μm diamond abrasive on a cotton drill cloth after being abraded as described for (c); oxide is free from chipping artifacts, and the surface of the specimen has an adequately scratch-free finish. As-polished. 70×

Very Soft Materials. Metals and alloys with a hardness of less than about 20 HV require special treatments, because many abrasive particles can embed in the section during abrasion and because it is difficult to obtain an adequately scratch-free final polish (see Fig. 28a). These materials are also sensitive to abrasion artifact of the types illustrated in Fig. 3.

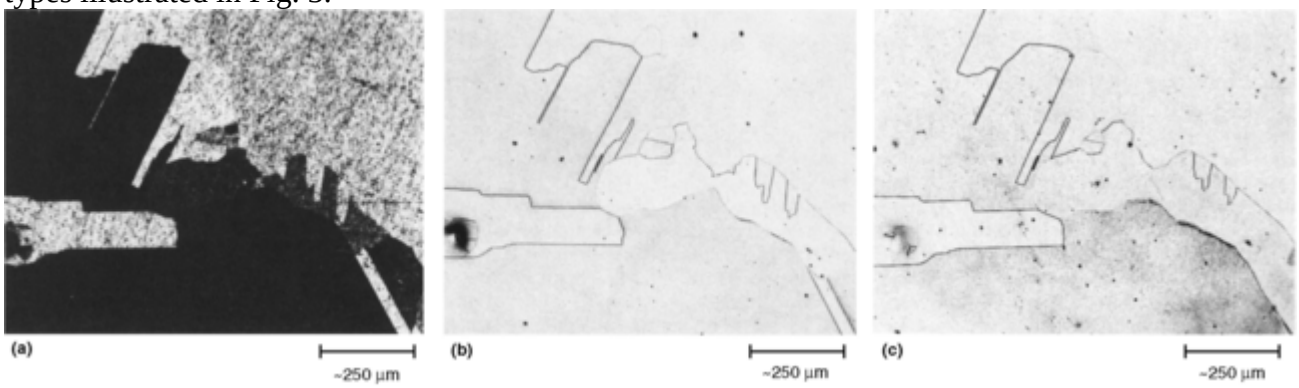

Fig. 28 Comparison of three methods of final polishing commercially pure lead. (a) Final polishing by a conventional method using fine Al_2O_3. Many polishing artifacts, principally in the form of polishing scratches enlarged by etching, are present. Dark grain contrast has been developed by etching after polishing. (b) Final polishing by a vibratory method using a proprietary colloidal silica solution. No polishing artifacts are present, and a lighter, clearer grain contrast has been developed by etching. (c) Final polishing by chemical polishing. No artifacts and clear etching grain contrast, but some etch pitting and grain relief were developed during chemical polishing. 10% ammonium molybdate, 10% citric acid. 55×

Methods of preventing the embedment of abrasive during conventional abrasion were discussed previously. As an alternative, the preliminary surface preparation of these soft metals can be carried out by machining in a heavy microtome. Rough polishing can be carried out conventionally, but final polishing is most effectively

performed by special methods. Polishing with a colloidal silica solution using very low pressures is effective (Fig. 28b). A number of chemical polishing methods are also available that can be used as brief treatments after polishing by conventional methods (Fig. 28c).

Electrochemical Differences. Some specimens contain phases or areas whose electrochemical characteristics are quite different from those of the main areas of the section surface. The electrochemically negative phase or area may then dissolve preferentially during conventional polishing processes and thus will not be obtained in a properly polished condition. This is most likely to occur during a final polish using an electrolytic polishing fluid. For example, marked electrochemical differences arise between the zinc-rich coating and the steel base of galvanized steels. Severe etching of the coating occurs when a section is polished using water, even normal distilled water, as the suspending liquid for the polishing abrasive, as shown in Fig. 29(a). The effect in this instance can be eliminated by using a suspending liquid that has a pH close to 7.0. This pH can be conveniently achieved by using a standard pH 7 buffer solution to prepare the slurry of polishing abrasive; results are shown in Fig. 29(b). Liquids with other pH values may be necessary with other types of specimens.

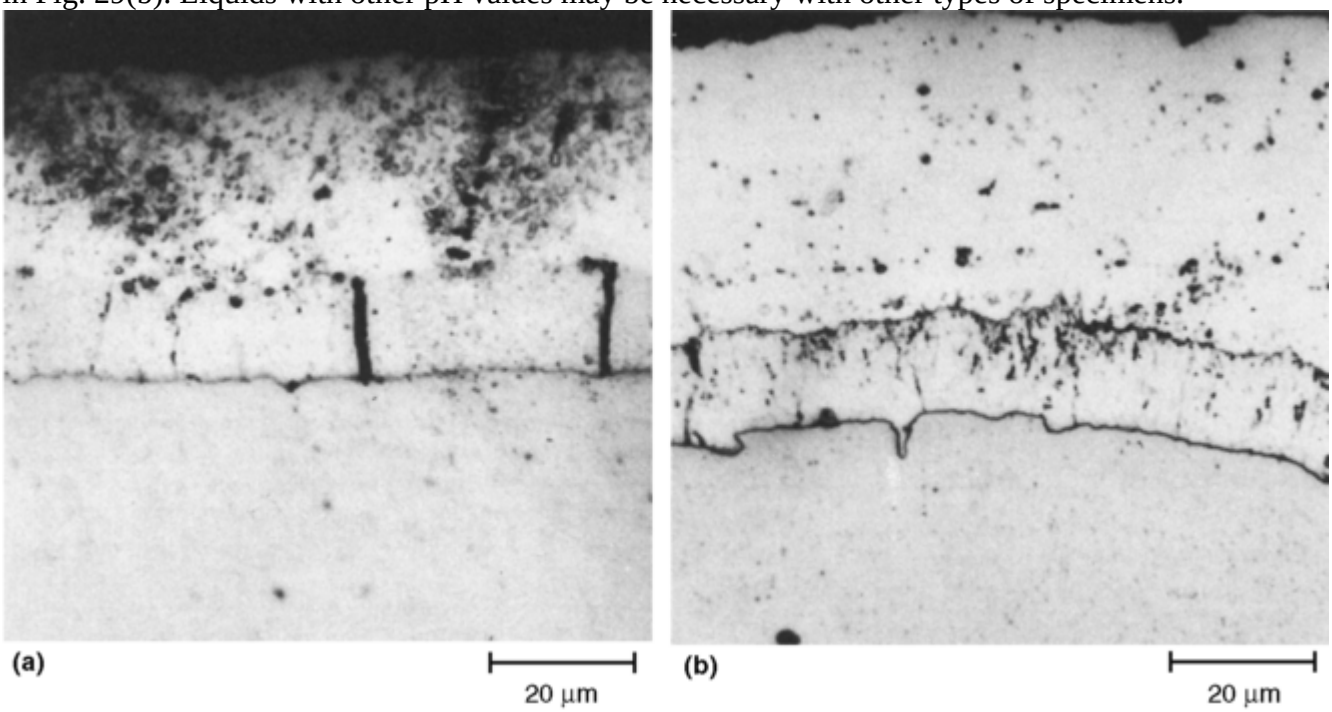

Fig. 29 Effect of pH of suspending liquid in the final polishing of specimens of galvanized iron. (a) Using a good-quality tap water. (b) Using a buffer solution with a pH of 7. The severe etching of the coating in (a) occurred as the result of electrochemical differences between the zinc coating and the steel base. As-polished. 700×

Mechanical Grinding and Polishing, *Metallography and Microstructures,* Vol 9, *ASM Handbook,* ASM International, 2004, p. 257–280

Semiautomatic Preparation Systems*

Similar to manual methods, semiautomatic preparation procedures must be developed by integrating a series of processing steps. The basic requirement again is to reduce in stages the depth of the surface scratches and associated damage to an acceptable level in the surface that is finally examined. It follows that the primary requirement of each processing step is to remove the damage produced by the preceding step in an acceptable

processing time, while forming a damaged layer that either can be removed in an acceptable time by the process that follows or, in the case of the final stage, that does not interfere with the examination to be carried out.

The development of semiautomatic procedures is driven by several additional factors. First, a major requirement may be that productivity be maximized, in which event it is desirable that the smallest possible number of processing stages be used. This increases the desirability of processes that have comparatively high material-removal rates and produce comparatively shallow deformed layers. A mitigating factor in this respect is that longer processing times than those that reasonably can be expected to be used in manual procedures are acceptable. Secondly, it is desirable that the parameters of each processing step be definable precisely enough to ensure that they can be reproduced successfully by even comparatively unskilled operators. Finally, process selection may be weighted toward the better achievement of some desirable feature of the final finish; in particular, to the attainment of a high degree of surface flatness.

A restricting factor is that much less information is available on candidate processes than for the manual procedures. Thus, the discussion is necessarily less extensive and less definitive than the corresponding discussions regarding manual procedures. This difficulty is increased by the fact that many parameters must be considered adequately to define a semiautomatic process. They include the material used for the working surface of the abrasion/polishing wheel, the type and grade of abrasive applied to the working surface, the rate at which the abrasive is applied, and the type of polishing fluid applied to the working surface. Other relevant parameters are the rate at which the polishing fluid is applied to the working surface, the speed of rotation of the working surface, the method of holding the specimen, the speed of rotation of the specimen holder, and the force applied to the specimen. Other necessary considerations include the relative directions of rotation of the specimen holder and the abrasion/polishing wheel and the polishing time. Another factor that should be considered, but rarely is, is the elastic stiffness of the preparation system.

Commercial specimen preparation machines permit control of most of these parameters within appropriate limits. The selection of a set of operating parameters consequently is usually not quite the overwhelming task that it might appear to be from the length of the above list. Core procedures have been developed that provide guidelines to procedures suitable for a range of similar specimen types. The discussion that follows mainly is concerned with these core procedures.

Procedures Based on the Use of Diamond Abrasives Charged in a Carrier Paste

A basic procedure of this type suitable, sometimes with modifications, for alloys ranging in hardness from soft to medium high, is outlined in Table 1 (Ref 2, 3, 4, 5).

Table 1 Semiautomatic procedure employing diamond abrasives in a carrier paste

	Abrasive parameters			Mechanical parameters			
Stage	**Type**	**Grade**	**Fluid**	**Speed[(a)], rpm**	**Direction**	**Force[(b)], N**	**Time, min**
1	SiC	240	Water	250	Comp[(c)]	20–25	[(d)]
2	Diamond[(e)]	9 μm	[(f)]	150	Comp[(c)]	20–40	5
3	Diamond[(g)]	3 μm	[(f)]	150	Comp[(c)]	20–35	3
4	Diamond[(g)]	1 μm	[(f)]	150	Contra[(h)]	20–25	2
5	Silica[(i)]	…	…	150	Contra[(h)]	20–30	2

(a) Speed of rotation of the work wheel.
(b) Applied to a 25 mm diam specimen mount.
(c) Comp, work wheel and specimen holder rotated in similar directions.
(d) Until the preexisting damaged layer is judged to have been removed.
(e) Diamond abrasive charged in a carrier paste on a hard woven silk cloth.
(f) A proprietary fluid that emulsifies the carrier paste.
(g) Diamond abrasive charged in a carrier paste on a napless woven acetate cloth.
(h) Contra, work wheel and specimen holder rotated in opposite direction.
(i) Proprietary colloidal silica charged on a napped cloth.
Source: Ref 2

Abrasion Stages. The purpose of the first abrasion stage (stage 1 in Table 1) is merely to produce a flat surface in which the specimen material and the plastic mount are reasonably coplanar. Internally charged diamond laps

and coated diamond laps tend to damage excessively softer metals of this group when used for this purpose. As a consequence, coated silicon carbide abrasive papers are preferred even though they deteriorate rapidly when used to prepare steels and hard alloys, and perhaps also soft alloys when the preparation system is elastically stiff, for example, Fig. 30.

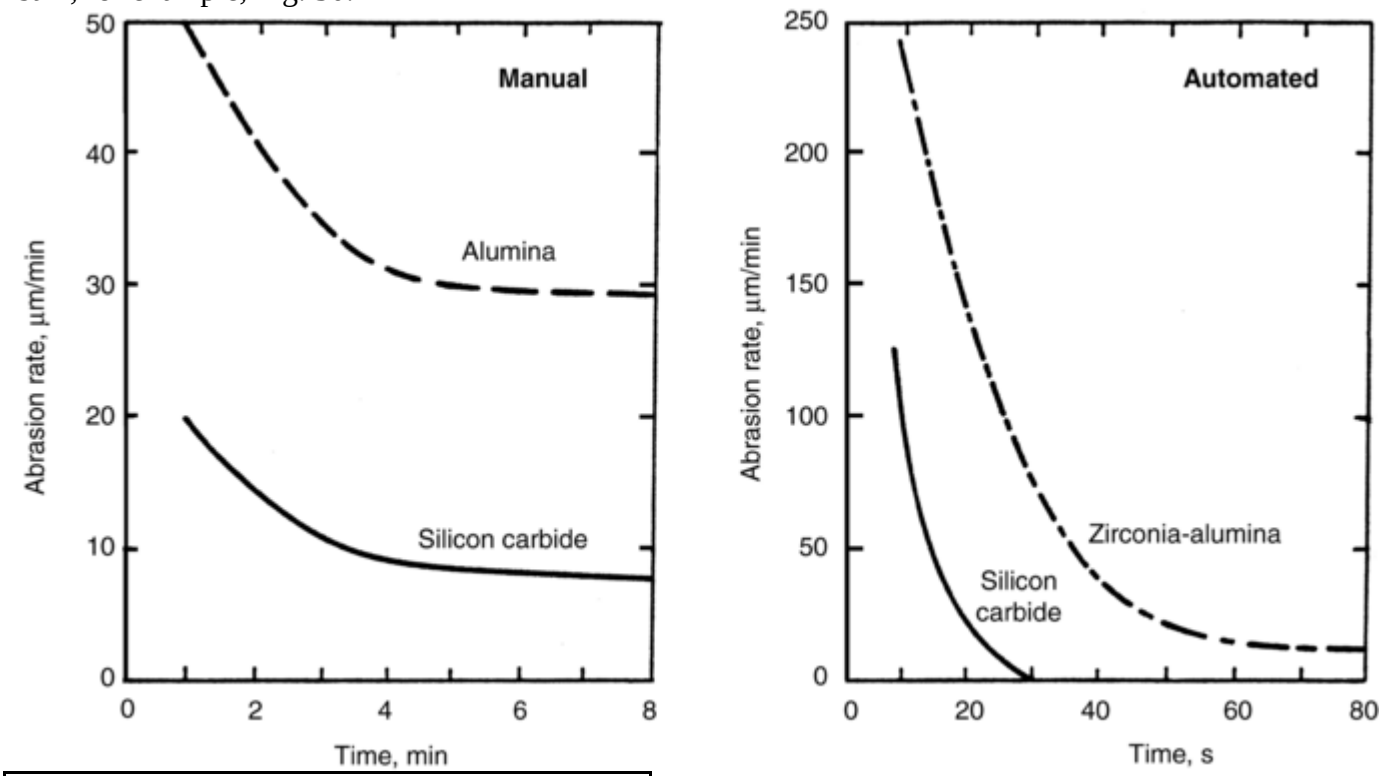

	Manual	Automatic
Abrasive mesh grade	220	120
Specimen pressure, kPa	39	25
Translation speed, m/s	1.7	1.5[(a)]
Abrasion fluid	Water	Water

(a) Varied from zero to this maximum value, depending on the position on the epicyclic path followed by the specimens.

Source: Ref 6

Fig. 30 Comparison of the abrasion rates obtained by manual and semiautomatic elastically hard abrasive machining systems with an 18%Cr-8%Ni austenitic steel. The coating abrasives are as indicated in the figure. Other abrasive parameters are in the accompanying table. Source: Ref 1, p 94

Experience in other types of applications (see, for example, Fig. 31) suggests that grades in the P150 to P240 range would then achieve abrasion rates close to the maximum attainable. Moreover, experience indicates that the abrasion rate is then high enough to achieve the objective of the stage in a reasonable processing time only if the sectioning process produced a reasonably flat surface (Ref 4). If not, consideration must be given to the use of either a different or an additional preliminary abrasion stage, such as a metal-bonded or polymer-bonded diamond lap. The use of an alternative abrasion process of this nature is likely always to be required when harder alloys, particularly harder steels, are being processed.

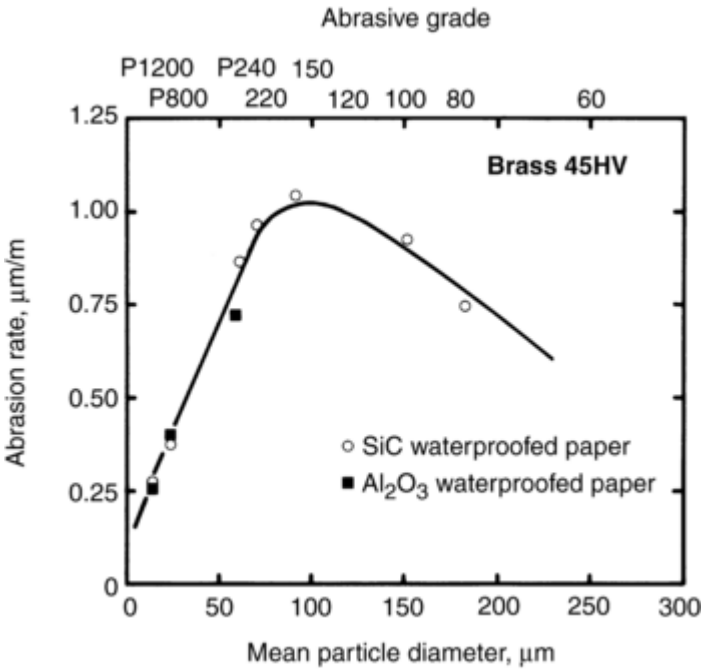

Fig. 31 Variation of abrasion rate with grade of abrasive paper for annealed 30% Zn brass. Source: Ref 1, p 73

Moreover, it is often desirable with softer metals to employ an additional final abrasion stage, such as one using P1200 or P2400 grade silicon carbide papers. It is also desirable to use an additional stage of this type with alloys that contain large particles of a brittle constituent.

Preliminary Polishing Stages. In the first three preliminary polishing stages (stages 2 to 4, Table 1), the abrasive is charged in a standard carrier paste on an elastically hard napless woven silk cloth for stage 2 and a somewhat less rigid napless woven acetate cloth for stages 3 and 4. The objective is to achieve a high degree of surface flatness and retention of edges.

The use of elastically hard polishing cloths is conducive to the attainment of this objective, but comparatively deep surface scratches and damaged layers are produced (Ref 1, chapter 11). The cloth used in stage 2 is chosen principally with the establishment of a high level of surface flatness in mind, but a compromise is made in stages 3 and 4. A less rigid cloth that achieves an acceptable level of surface damage while retaining an adequate standard of surface flatness is used. A relatively high standard of edge retention is still achieved at both the edges of external surfaces and the walls of internal cavities. An example of the standard achieved in the retention of the walls of an internal cavity is illustrated in Fig. 32(b).

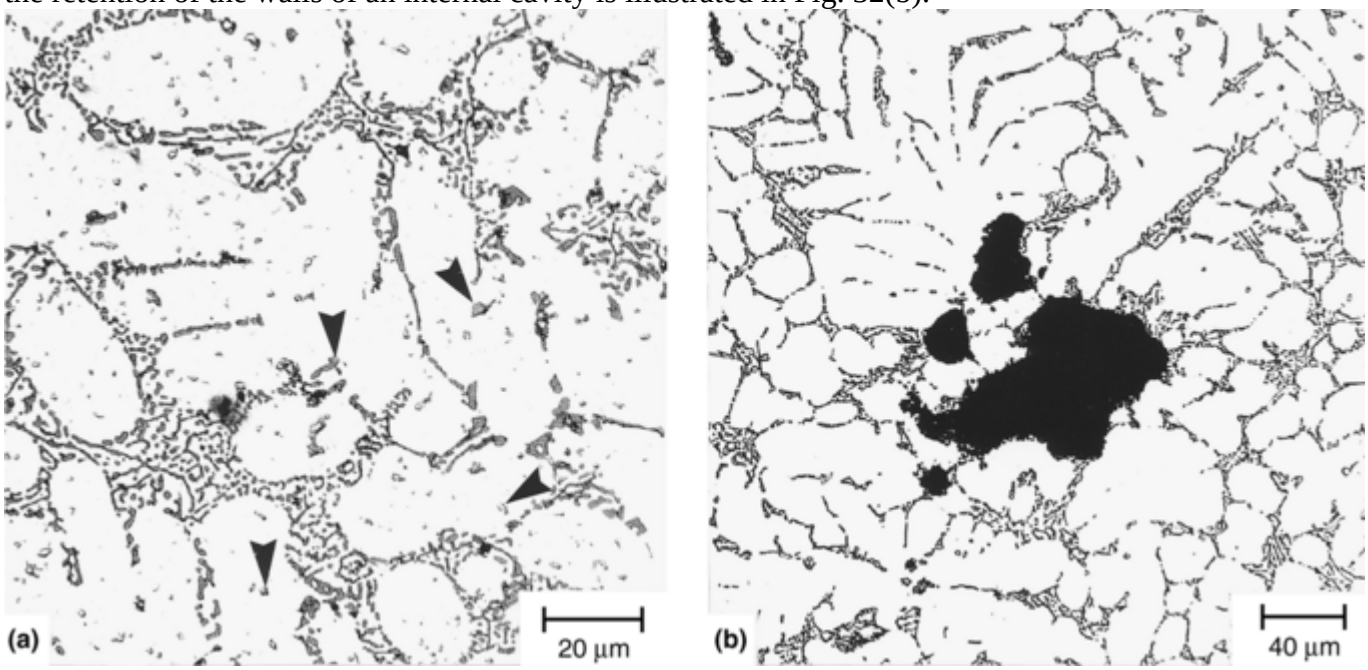

Fig. 32 Sections of a cast Al-2.8% Si alloy finish polished using a semiautomatic machine and a napped cloth charged in (a) a suspension in alcohol and (b) a carrier paste. Etched in 0.5% hydrofluoric acid solution. (a) 500×. (b) 200×. A large number of embedded diamond particles, some indicated by arrows, are visible in (a), but none are visible in (b). Courtesy of G.F. Vander Voort, Buehler Ltd. Source: Ref 1, p 216

Nevertheless, there are applications where the attainment of quite this high a standard of surface flatness is not required. The use of elastically less rigid polishing cloths can then be considered, first in stage 4 and then in stage 3. Higher polishing rates and improved surface finishes are obtained, and the likelihood of abrasive particles embedding in soft specimen materials is greatly reduced (Ref 1, p 214).

Experience has also shown that it is not necessary to use all the stages listed in Table 1 with some materials. Titanium and titanium alloys, for example, can be prepared satisfactorily using a procedure comprising only stages 1, 2, and 5, although modifications, which are discussed later, then have to be made to stage 5 (Ref 5). Note also that the material-removal rate obtained with 3 μm grade diamond abrasive is greater than that obtained using a 9 μm grade for all the methods of using this abrasive that have so far been investigated quantitatively (see, for example, Fig. 33). If this relationship also applies to the process being considered, it is possible that stage 2 could be eliminated. Quantitative measurements of polishing rates would be required to settle this question.

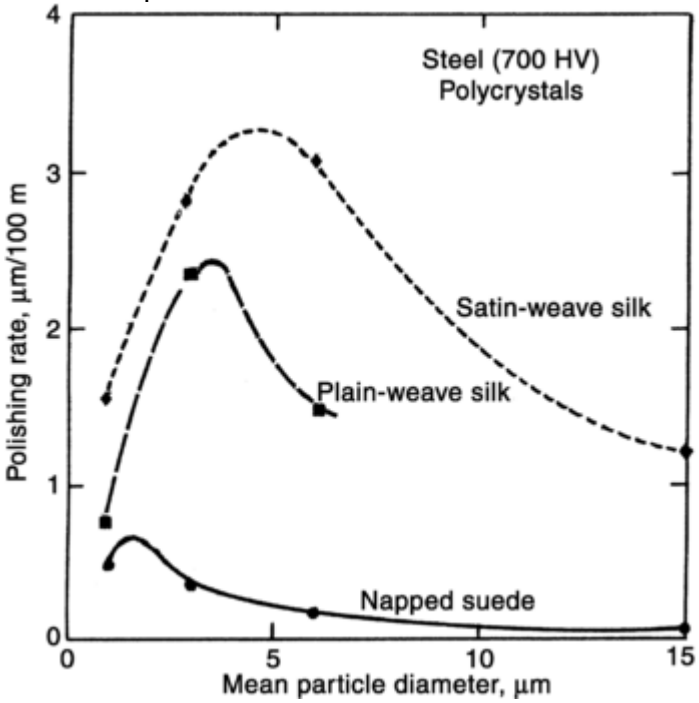

Fig. 33 Variation in polishing rate in a semiautomatic machine with type of polishing cloth and particle diameter of polycrystalline diamond abrasives. The specimen polished was a ferritic steel (hardness, 700 HV), and the specimen pressure was 43 kPa. Courtesy of K. Geels, Struers A/S. Source: Ref 1, p 201

It is recommended in Table 1 that the specimen holder be rotated in the same (complementary) direction as the work wheel. This is to take advantage of the higher material-removal rate then obtained. The rotation direction should be changed to a contra direction, however, if scouring effects then develop.

Final-Polishing Stage. The structure of the surface-damaged layer produced during semiautomatic polishing with 1 μm diamond can be expected to be about the same as that produced when the grade is used in a manual process. The damaged layer can be expected to be somewhat deeper, however, because elastically harder polishing cloths are used. It can be expected, therefore, that it would be more difficult to remove the damaged layer by a final-polishing process (stage 5 in Table 1). Recourse consequently may have to be made, when colloidal silica is used as the polishing agent, to the technique of adding a mild etching reagent to the sol to increase the polishing rate.

For example, the addition of a mixture of 10 mL hydrogen peroxide (30%) and 5 mL Kroll's reagent has also been found effective in this respect when polishing titanium and titanium alloys (Ref 5). It is advisable to use a

chemical-resistant polishing cloth when additions of this nature are made. It has also been found (Ref 4) that precharging the polishing cloth with 1 μm grade diamond in a carrier paste, then moistening the paste with the appropriate emulsifying fluid before adding the colloidal silica, increases the polishing rate (Ref 4). The reasons for this are not clear. Note that, as a general rule, the specimen holder needs to be rotated in a direction contra to the work wheel with all of these final-polishing processes. Otherwise, scouring effects might develop.

The final-polishing treatment can also be carried out in a vibratory machine external to a semiautomatic machine. Treatment times of several hours can then be used (Ref 2). This has a further advantage. As was pointed out earlier, apparatus in which colloidal silica has been used must be cleaned meticulously to remove all traces of sol that may have dried out before it is reused. This is less difficult to do with a vibratory polishing machine than with semiautomatic apparatus.

An example of results that can be achieved by these procedures when colloidal silica is used for final polishing is shown in Fig. 34. These micrographs are representative of commonly encountered structures, but the example presented in Fig. 35 illustrates one of the principal advantages of the procedure—namely, only very small differences in level have developed between constituents that have widely different abrasion and polishing characteristics. The material is a cast hypereutectic aluminum-silicon alloy in which large idiomorphic crystals of silicon are distributed in a matrix of silicon-aluminum eutectic. This alloy has been used throughout this text as a testing indicator of the degree to which the preparation procedure has suppressed the development of relief between phases. Relief can, as shown Fig. 36(b), be suppressed to a reasonable level when the preparation is carried out by the basic manual method, but not quite to the standard attainable by the semiautomatic procedure.

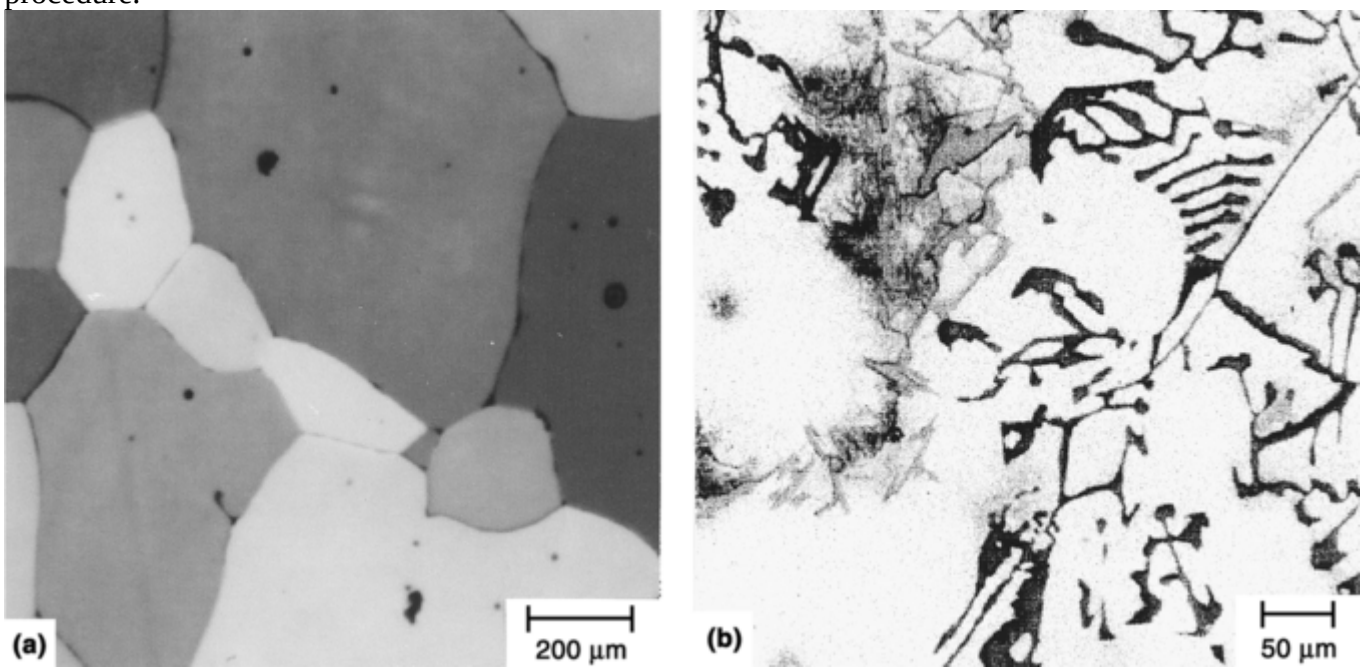

Fig. 34 Examples of a soft wrought aluminum alloy and a cast aluminum alloy finish polished using colloidal silica. (a) Annealed superpure aluminum, anodized in Barker's solution after polishing. Viewed using cross polarizers and sensitive tint plate. Reproduction of a color micrograph. 50×. (b) Cast aluminum-6.0%Si-3.5%Cu alloy finish polished using colloidal silica. Etched with Keller's reagent. 150×. Courtesy of G.F. Vander Voort, Buehler Ltd. Source: Ref 1, p 262

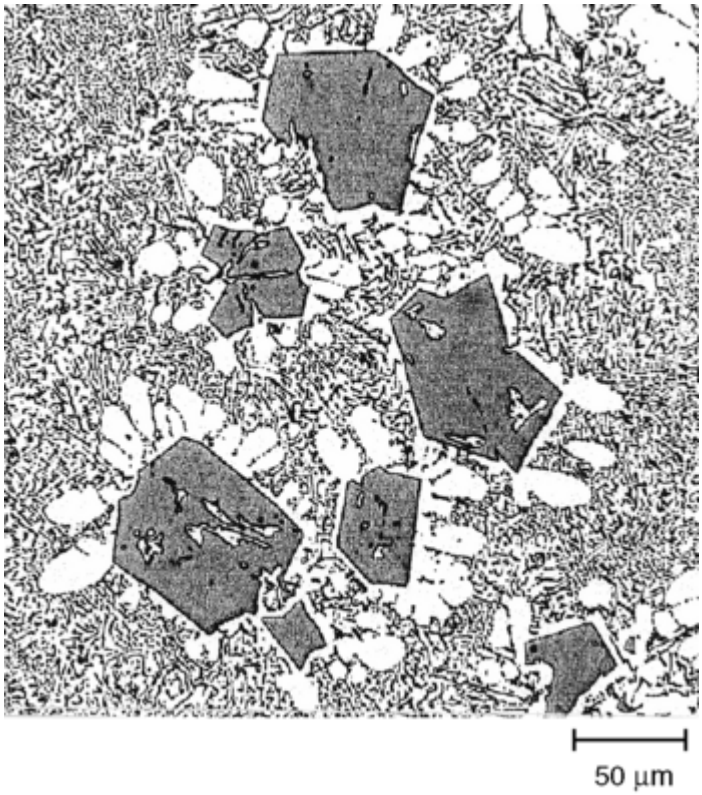

Fig. 35 Section of a cast hypereutectic Al-19.9%Si alloy prepared by a semiautomatic procedure using diamond abrasives charged in a carrier paste. The treatment was as outlined in Table 1. Final polishing was carried out on a napped cloth charged with a 1 µm diamond carrier paste as a preliminary stage and then with colloidal silica. Compare with Fig. 36(b), which shows a section of a similar alloy prepared by a manual method. Etched in a 0.5% HF solution. 200×. Source: Ref 4

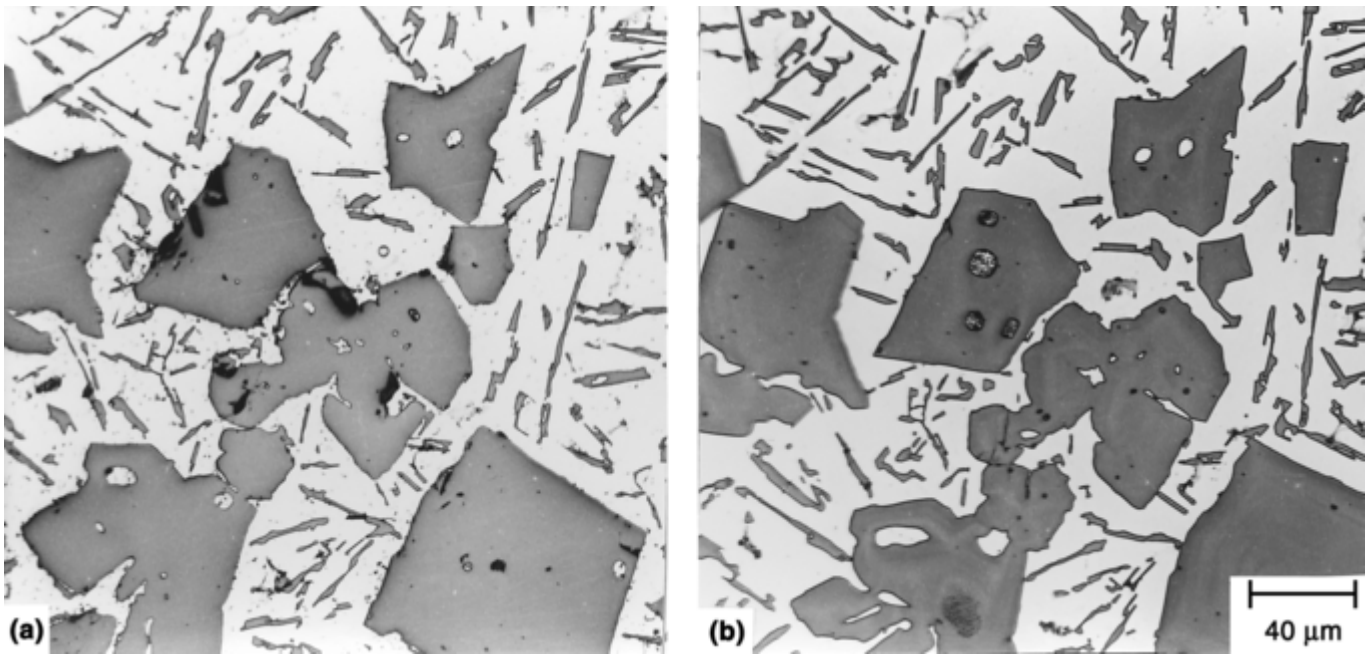

Fig. 36 Crack artifacts in the primary silicon constituent of a cast Al-13%Si alloy. 250×. (a) Abraded on P800-grade silicon carbide paper and then polished on 1 µm diamond until all surface irregularities had been removed. (b) Same area as in (a), but polished for a longer time. Note the cracks and pits in the primary silicon present in (a) but not in (b). Source: Ref 1, p 241

Final polishing could also be carried out by procedures using diamond abrasives, the suitability of these procedures being dependent on the specimen material and the standard of polish required. The alternatives

available can be considered in steps of increasing improvement in quality of polish. For a start, a finish that is acceptable for harder materials in more routine application may be produced at stage 4, Table 1. Preparation can then be terminated at this stage. A further improvement, if needed, can be achieved by using finer grades of diamond (e.g., 0.5 and 0.25 μm grades) instead of a 1 μm grade in stage 4. The use of 0.1 μm polycrystalline diamond could also be considered as a substitute for colloidal silica in stage 5 (Ref 1, p 246). This abrasive is probably best used in an external operation, particularly as only short polishing times would be required. Acceptable, if somewhat inferior, finishes may also be obtained with many materials by using aqueous slurries of gamma alumina (0.05 μm grade) as external operations.

Procedures with Diamond Abrasives Charged in a Suspension

A large number of permutations and combinations are again possible when the processes that have been developed to use suspensions of diamond abrasives are integrated into a specimen preparation procedure. Fortunately, however, experience has also shown that a limited number of basic procedures can, with modifications, deal with the great bulk of the specimens encountered in practice.

Medium- to High-Hardness Materials. This group includes materials ranging in hardness from about 100 to 900 HV. Ferritic steels, austenitic steels, and cast irons are included. A procedure that incorporates the range of procedures that are likely to be needed is summarized in Table 2.

Table 2 Semiautomatic procedure employing suspensions of diamond abrasives suitable for alloys of medium to high hardness

	Abrasive parameters			Mechanical parameters			
Stage	**Type**	**Grade**	**Fluid**	**Speed[a], rpm**	**Direction[b]**	**Force[c], N**	**Time, min**
1	SiC[d]	120	Water	150	Contra	10–20	[e]
2	Diamond[f]	9 μm	[g]	150	Comp	30	5
3	Diamond[h]	3 μm	[g]	150	Comp	30	3
4	Diamond[h]	1 μm	[g]	150	Contra	20	2
5	Silica[i]	…	…	150	Contra	10	2

(a) Speed of rotation of the work wheel.
(b) Specimen holder rotated in same direction as the work wheel (comp) or in the opposite direction (contra).
(c) Force applied to a 25 mm diam specimen.
(d) Coated waterproofed paper.
(e) Until a plane surface has been produced.
(f) Proprietary suspension of polycrystalline diamond sprayed onto a polymer lap.
(g) Proprietary fluid sprayed onto the work surface.
(h) Proprietary suspension of polycrystalline diamond sprayed onto an elastically hard satin-weave silk cloth.
(i) Proprietary colloidal silica sprayed onto an elastically soft napped cloth.
Source: Ref 7

Abrasion Stages with Materials of Medium to High Hardness. The objective of the first abrasion stage (stage 1 in Table 2) is to provide a reasonably flat surface in which the specimen and mounting plastic are approximately coplanar. As discussed earlier, internally charged diamond laps generally are not favored for this purpose because they tend to damage excessively the surface being generated, particularly with hardnesses at the lower end of the range being considered. Consequently, conventional silicon carbide coated papers in the P240 to P120 grade range are most commonly the first choice for use in this first abrasion stage.

This is true in spite of the fact that the papers deteriorate comparatively rapidly when used to abrade many of the alloys being considered. Moreover, they can generate an acceptably flat surface in an acceptable treatment time only if the surfaces of the mount and specimen are reasonably flat and coplanar to start with. If not, an additional abrasion stage that achieves a higher material-removal rate may have to be used first. An internally charged diamond lap is acceptable for this purpose, as are a number of the similar lap types. The use of an additional stage is most likely to be needed with materials such as ferritic steels that cause particularly rapid deterioration of coated papers (see Fig. 37) and with the harder materials of the group.

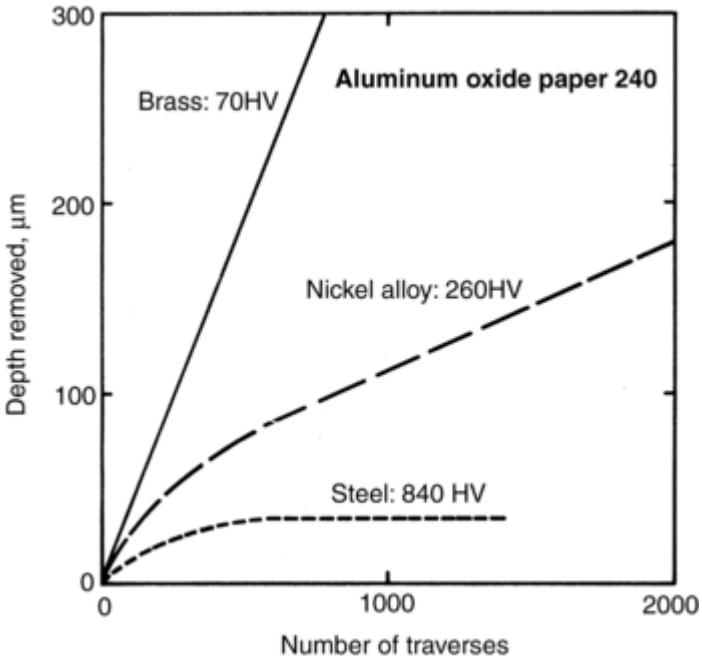

Fig. 37 Variation of the depth removed with number of traverses for alloys representing three groups of materials. For brass, the abrasion rate does not change significantly with increasing use of the paper. For nickel alloys, the abrasion rate decreases initially, but then stabilizes to a steady value. For steel, the abrasion rate decreases rapidly to zero. Source: Ref 1, p 72

The flatness of the surfaces abraded with coated papers can be of a lower standard than is desirable (Ref 1, chapter 11). Specifically regions adjacent to the edges of the specimens may not be adequately flat, and differences in level may develop between phases that have widely different abrasion characteristics. The principle objective of the process listed as stage 2 in Table 2 is to correct this deficiency. It can be described as an elastically hard, fine abrasion process.

A suspension of 9 µm diamond abrasive is applied to a lap coated with segments of an epoxy-type polymer; polycrystalline diamond is generally preferred (Ref 1, chapter 4). The reason a 1 µm grade of abrasive is chosen is that the abrasion rate increases with particle size under these conditions, but the working surface wears excessively when grades of abrasive exceeding 15 µm mean diameter are used. The abrasion rate when a 9 µm grade abrasive is used is comparable to that obtained with 220 grade metal-bonded diamond laps. The abrasion rate remains at this level for as long as the abrasive supply is maintained.

Consequently, it is usually possible, using this lap, to remove in an acceptable time the damaged layer present after abrasion with 220 grade silicon carbide papers. At the same time, a high standard of surface flatness is achieved both at specimen edges and between dissimilar phases. An example demonstrating these features is shown in Fig. 38. Note that material removal from the brittle silicon phase in the alloy shown in Fig. 38 has occurred by micromachining and not by chip fracturing

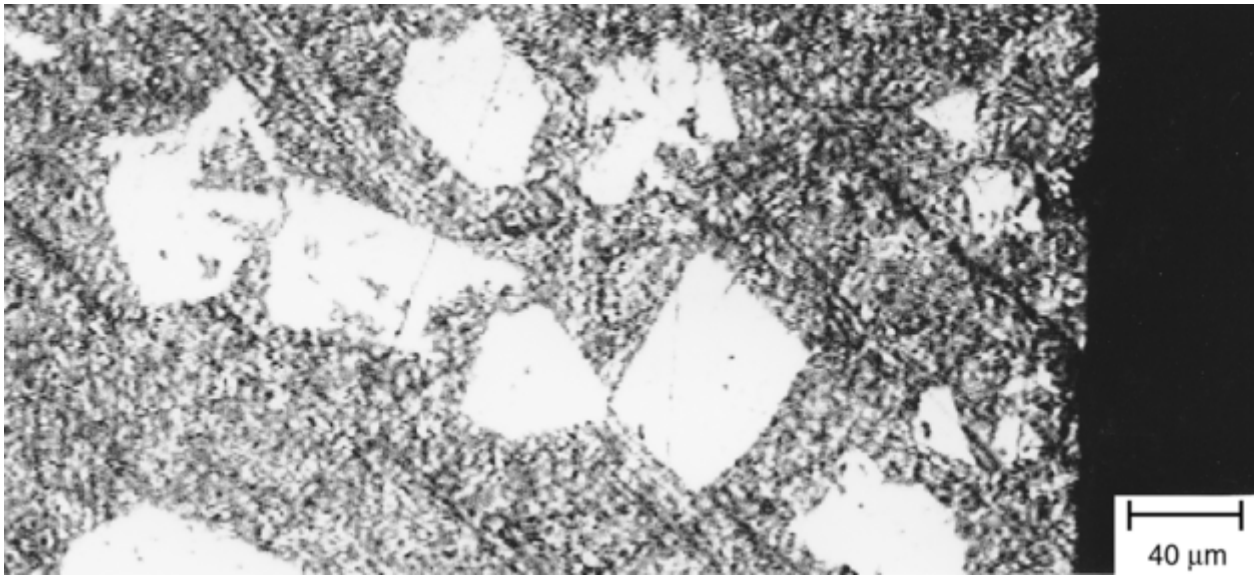

Fig. 38 Result obtained by abrading a cast aluminum 19.9% Si alloy with a polymer lap extrinsically charged with 9 µm grade diamond abrasive. 250×. Source: Ref 1

Preliminary Polishing Stages with Materials of Medium to High Hardness. Stage 3 listed in Table 2 can be regarded as a rough polishing stage. Its objective is to remove the abrasion damage, for which purpose a high material-removal rate is desirable. In addition, however, it is required to maintain the high standard of surface flatness achieved during stage 2. This requires that an elastically hard polishing cloth be used. A fine satin-weave silk cloth recommended in Table 2 is representative of the type of cloth that can meet these two requirements.

Quantitative investigations have indicated that a maximum polishing rate is achieved when an approximately 3 µm grade of diamond abrasive is used with this cloth when used to polish a hard steel (Fig. 38). It is reasonable to suppose, from experience with other methods of applying diamond abrasives, that this is also likely to be the optimal grade to use for a wide range of specimen materials, although the matter needs to be confirmed experimentally. To obtain an acceptable quality of polish, however, this stage must be followed by one using a finer grade of abrasive.

A 1 µm grade is usually used and is charged on the same type of elastically hard polishing cloth (stage 4, Table 2). An optimal combination of surface flatness and polish quality is then obtained. The specimen shown in Fig. 39 is representative, indicating the high standard of edge retention that is achieved in steel specimens without special precautions being taken. A similar standard of edge retention can be achieved by manual methods of specimen preparation, but only if special precautions are taken (see Ref 1, p 269–270).

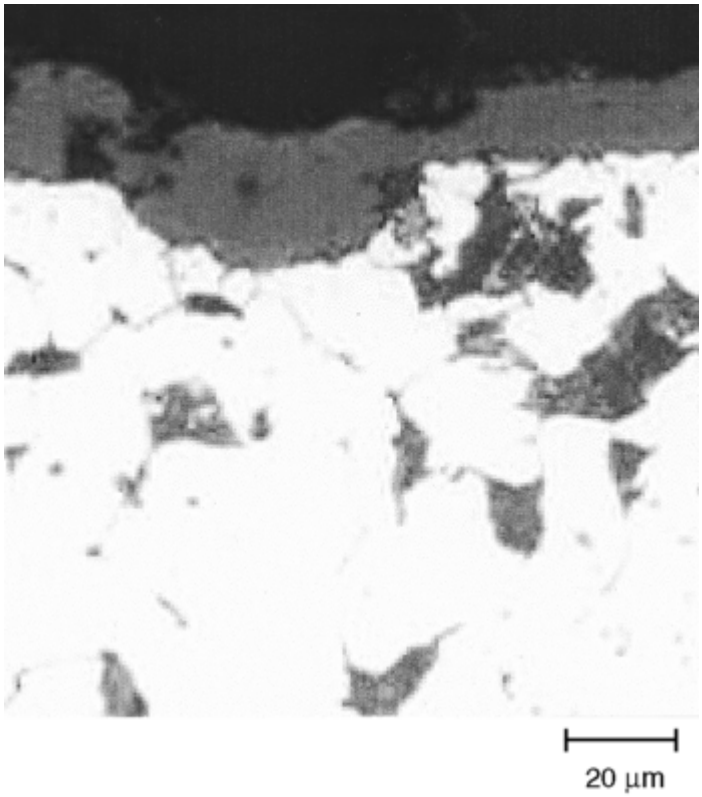

Fig. 39 Section of an oxidized surface of a low-carbon steel prepared by a semiautomated procedure using suspensions of diamond abrasives. The section was prepared using the procedure outlined in Table 3. Final polishing was carried out using 1 μm grade diamond abrasive sprayed onto a satin-weave silk cloth (stage 4 in Table 3). Etched in 5% nital. 500×. Source: Ref 1

Note also that the oxide layer present on the surface of the specimen shown in Fig. 39 has been well polished and, so far as can be discerned, has been polished to the same level as the steel substrate. Thick oxide layers are equally well retained, and cavities and similar structures in the layer are correctly represented (Fig. 40). The reason is that stage 2, Table 2, of the procedure has removed material by micromachining. Consequently, chip artifacts formed during the preceding abrasion stages have been removed easily without introducing a new generation of chip-fracture artifacts.

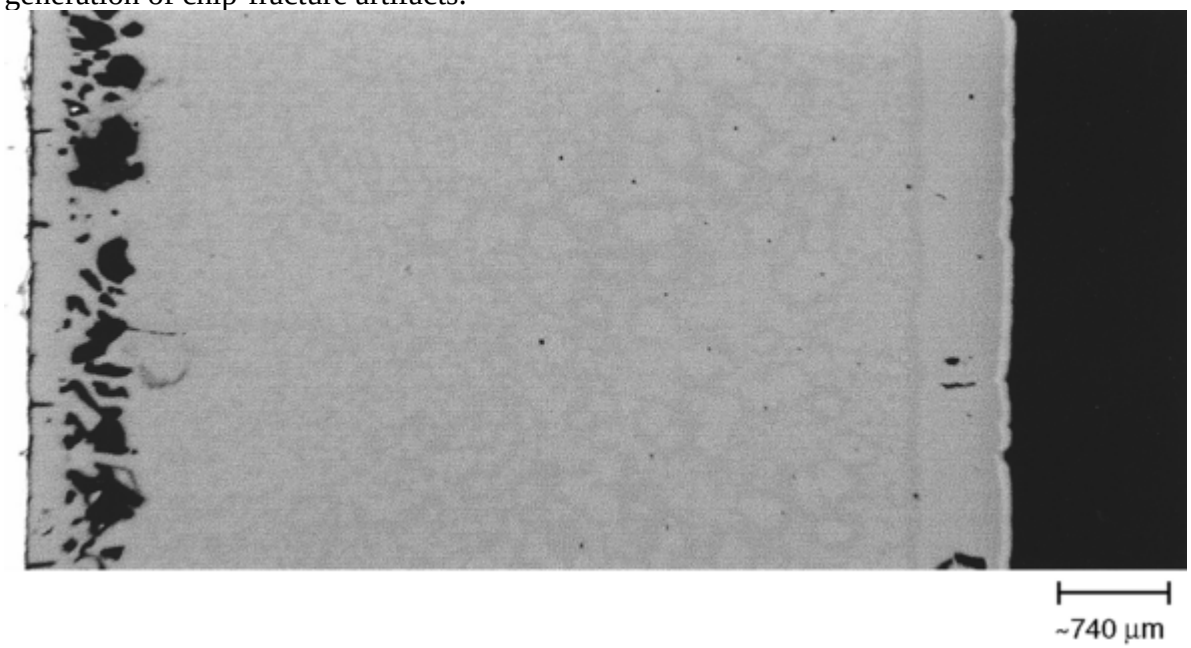

Fig. 40 Section of a thick oxide layer on a low-carbon steel prepared by a semiautomatic preparation procedure using suspensions of diamond abrasives. The section was prepared by the procedure

summarized in Table 2, stage 4 of this procedure being the final-polishing stage. The phases present in the layer, starting from the outer surface, are hematite, magnetite, and decomposed wustite. The dark features in the hematite and wustite layers are genuine cavities. Not etched. 135×. Source: Ref 8

Stages 3 and 4 also remove material by micromachining and so do not introduce any chip-fracture artifacts either.* These desirable characteristics can be expected with bases and constituents encountered in the types of specimens being considered. For example, stage 2, Table 2, also removes material from the primary particles of silicon in aluminum alloys by micromachining (Fig. 38). So also do stages 3 and 4. Consequently, the prepared surfaces of particles of this phase are also artifact free. Moreover, the elastic stiffness of the cloths with which the abrasive is backed ensures that discernible differences in level do not develop between the silicon particles and the eutectic matrix (Fig. 41).

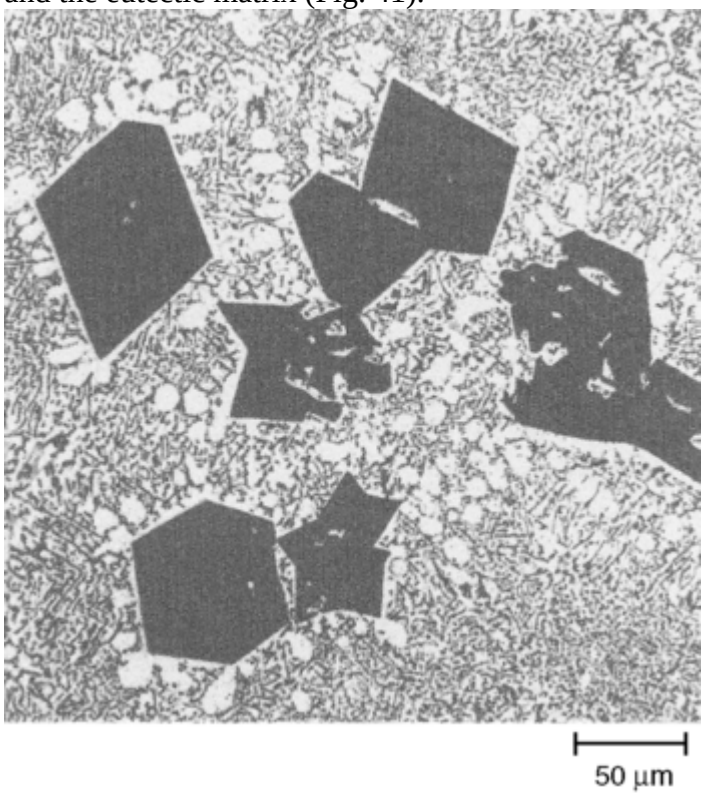

Fig. 41 Section of a cast Al-13.9%Si alloy prepared by a semiautomatic procedure using suspensions of diamond abrasives. The section was prepared using the procedure outlined in Table 2. Final polishing was carried out using a 1 μm grade of diamond abrasive sprayed onto a satin-weave silk cloth (stage 4 in Table 2). Not etched. 200×. Source: Ref 1

Final-Polishing Stage with Materials of Medium to High Hardness. The finish obtained using the stage 3 polishing process is adequate for some applications but not for others. For example, the finish obtained on the section shown in Fig. 39 would have been acceptable if the purpose of an examination had been only to investigate the oxide layer and its interface with the steel substrate. However, although it is not apparent from Fig. 39, it would not be acceptable if the purpose was to investigate the fine structure of the steel. The finish obtained on the specimen shown in Fig. 41 would not be acceptable either if the purpose of the examination included establishing the structure of the eutectic matrix. There is often a need, therefore, for a final-polishing stage that produces a less damaged surface by using alternative finishing processes, including processes used externally to the semiautomatic machine. These alternative final-polishing processes are discussed in an earlier section.

Graphite-Containing Alloys. Difficulties can arise in retaining and polishing inclusions of graphite in many important iron-carbon alloys with substantial volume fractions of free graphite. Manual polishing using suspensions of conventional abrasives on napped polishing cloth can remove the graphite inclusions from their containing cavity. This does not occur, however, when suspensions of diamond abrasive are used on woven polishing cloths (Ref 1, p 289–291). Graphite particles of all sizes and morphologies encountered in industrial

alloys are fully retained in sections prepared to stage 4 listed in Table 2, although in some instances extended treatment times may be required at stage 4 to achieve full retention.

However, the finish obtained by polishing with a 1 μm grade abrasive may not appear adequately free from polishing scratches after metallographic etching. A final-polishing treatment, such as that listed as stage 5 in Table 2, must then be used to achieve an adequately scratch-free finish on the matrix structure and an improved finish on the graphite. A polishing treatment of this type requires the use of an elastically soft (napped) polishing cloth, which inevitably causes some deterioration in the standard of retention of the graphite. The treatment time consequently must be restricted to the minimum consistent with production of an acceptable finish on the matrix. Examples representative of the results then obtained are presented in Fig. 42.

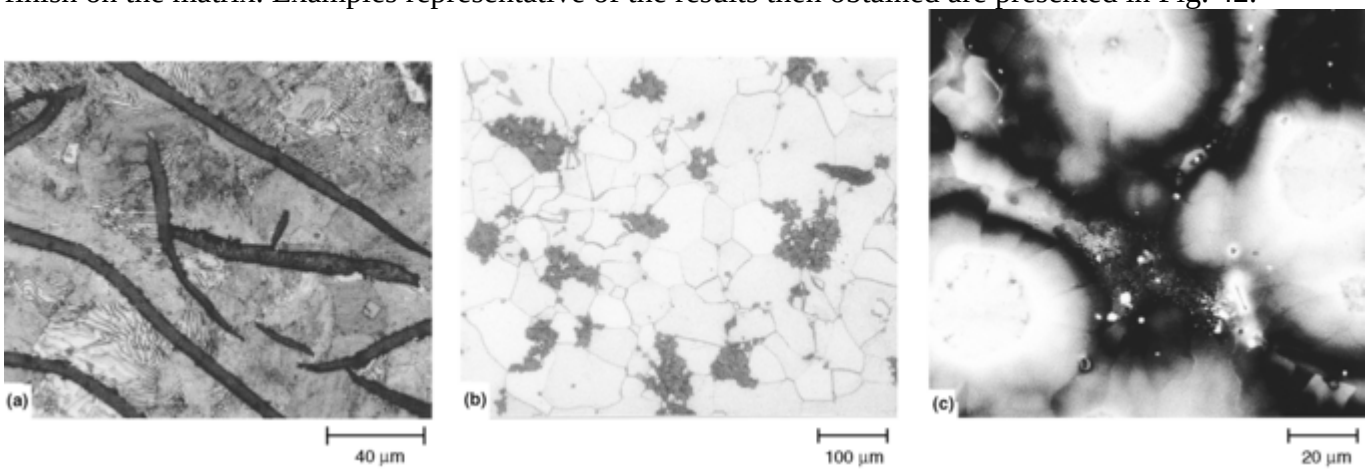

Fig. 42 Sections of graphite-containing cast irons prepared by a semiautomatic procedure using suspensions of diamond abrasives. (a) A gray cast iron containing comparatively large graphite flakes. Finish polished using 1 μm diamond abrasive. Etched in nital. 350×. (b) A blackheart malleable cast iron containing nodules of temper graphite. Finish polished using 1 μm diamond abrasive. Etched in nital. 100×. (c) An iron containing spheroidal graphite. Finish polished using colloidal silica. Etched in Klemm's reagent. 500×. Source: Ref 7

Soft Metals and Alloys. The metals of this group, which include unalloyed metals with a hardness below 50 HV, are in general more difficult to prepare than the harder metals and alloys considered in the preceding section. A preparation procedure is outlined in Table 3, but it will emerge that it is desirable to make significant modifications to this procedure in specific applications.

Table 3 Semiautomatic procedure employing suspensions of diamond abrasives suitable for soft alloys

	Abrasive parameters			Mechanical parameters			
Stage	**Type**	**Grade**	**Fluid**	**Speed[(a)], rpm**	**Direction[(b)]**	**Force[(c)], N**	**Time, min**
1	SiC[(d)]	220	Water	150	Contra	10	[(e)]
2	Diamond[(f)]	15 μm	[(g)]	150	Comp	30–50	5
3	Diamond[(h)]	3 μm	[(g)]	150	Comp	20	5
4	Diamond[(i)]	1 μm	[(g)]	150	Comp	20	5
5	Silica[(j)]	Sol	nil	150	Contra	10	2–5

(a) Speed of rotation of the work wheel.
(b) Specimen holder rotated in same direction as the work wheel (comp) or in the opposite direction (contra).
(c) Force applied to a 25 mm diam specimen.
(d) Coated waterproofed paper.
(e) Until a plane surface has been produced.
(f) Proprietary suspension of polycrystalline diamond sprayed onto a polymer-impregnated synthetic paper.
(g) Proprietary fluid sprayed onto the work surface.
(h) Proprietary suspension of polycrystalline diamond sprayed onto an elastically hard satin-weave silk cloth.
(i) Proprietary suspension of polycrystalline diamond sprayed onto an elastically soft napped cloth.
(j) Proprietary colloidal silica sprayed onto an elastically soft napped cloth.

Source: Ref 7

Abrasion Stages for Soft Metals and Alloys. Metal-bonded or polymer-bonded diamond laps cannot satisfactorily be used to abrade most metals of this group, particularly the softer ones. This is because the surfaces formed are severely damaged. Coarser grades of silicon carbide papers, on the other hand, can usually be used successfully, and their use is suggested in Table 3 for stage 1 for all metals of the group.

In elastically soft machine systems, the abrasion rates obtained decrease slowly with use, and the papers can be used for extended periods. The maximum abrasion rate can be expected to be obtained with approximately 220 or P240 grade (Fig. 31), and one or other of these grades is probably the best choice for the first abrasion stage.

Externally charged polymer laps of the type used for the last abrasion stage with harder alloys (stage 2 in Table 2) are not suitable for abrading most alloys of the group either. This is again because the surfaces formed are severely damaged. However, polymer-impregnated papers with a suspension of a diamond abrasive are suitable for use with the harder alloys of the group. The abrasion rate obtained with this type of process increases with increase in abrasive particle diameter. So also does the depth of the scratches formed on the specimen surface. A 15 μm grade is usually selected as providing the best compromise between abrasion rate and surface finish. Polycrystalline diamonds are preferred to monocrystalline diamonds because a higher abrasion rate is obtained without the depth of damage being affected.

However, surface damage may still be too severe to be acceptable with the softest metals and alloys of the group. When this is so, finer grades of silicon carbide abrasive papers can be used for the abrasion stages provided that comparatively low specimen pressures (~10 N on a 25 mm diam specimen) and short treatment times (<1 min) are used (Ref 9). A sequence of grades, such as P600, P1200, and P2400, can be used. A finish from which the damaged layer can be removed successfully by the polishing stage that is to follow is produced.

However, the possibility of the occurrence of several detrimental phenomena must be kept in mind. The first is that the finer abrasive papers may load with abrasion debris, in which event severe damage is likely to be caused to the surface being formed. If loading does occur, abrasion must be terminated before it becomes too severe, hence the proviso mentioned earlier that abrasion be carried out for a short period only. A loaded abrasive paper must either be cleaned before being reused or be abandoned. The second possible detrimental phenomenon is that of the embedding of abrasive in the specimen surface.

Preliminary Polishing Stages for Soft Metals and Alloys. The scratches developed when metals are polished using a 1 μm grade diamond on an elastically hard woven cloth are typically more severe than is desirable in a precursor to a final-polishing stage. Recourse consequently must be made to the use at this stage of a more resilient napped cloth of the type described earlier as a “synthetic suede” (stage 4 in Table 3). If the polishing rates obtained with steel specimens are a true guide, the polishing rates obtained are then considerably smaller than when elastically hard polishing cloths are used (Fig. 33).

The reason for this has not been established, but a possible reason is that a much smaller density of abrasive particles comes into contact with the specimen surface with a napped than with a woven cloth. In any event, it follows that the desirable practice is to continue stage 3 of the procedure until the significant abrasion damage has been removed with certainty. Stage 4 is expected only to remove the damage introduced at stage 3.

Soft metals are prone to embedding of polishing abrasives under the conditions used in stages 3 and 4, less so in stage 4 than stage 3. It is difficult to avoid embedding when polishing very soft metals, and it may even be difficult to discern embedded particles by light microscopy.

Final-Polishing Stages for Soft Metals and Alloys. In general, an acceptably scratch-free surface will not be produced by the process used in stage 4. A further, finer polishing stage is normally required, and it is more difficult to produce an acceptable final polish on these metals than on any other metal that has been considered. The difficulties are likely to be essentially the same as for the manual procedure. Previous discussions in the section “Final-Polishing Stage with Materials of Medium to High Hardness” in this article are also relevant, although the problems are likely to be less severe because an elastically softer polishing cloth is used during the last rough polishing stage.

A general approach would be first to assess the efficacy of the process using colloidal silica, as suggested in Table 3 and then to investigate alternatives if an acceptable result has not been obtained.

It is necessary to remember, in this context, that properties other than hardness can influence polishing characteristics. Chemical reactivity to the polishing solutions is, for example, one possibility. Figure 43 illustrates this point. The material sectioned is a Mg-3%Al-1%Zn alloy that is soft (~50 HV), has a hexagonal crystal structure, and is more reactive to oxygenated water than most of the metals commonly encountered. The section was abraded on a succession of silicon carbide papers and then polished using a suspension of 3 μm

diamond on napped cloth (stage 3 in Table 3). A force of 10 N was applied to a 25 mm diam specimen, and the polishing time was 1 min. The results (Fig. 43) were obtained by etching this surface in a reagent commonly used for this alloy, although the section had first to be immersed in nital for a short period before the etching reaction would proceed. An obscuring reaction product formed on the surface of this section if an attempt was made to polish it using a 1 μm grade of abrasive under the same conditions (Ref 9).

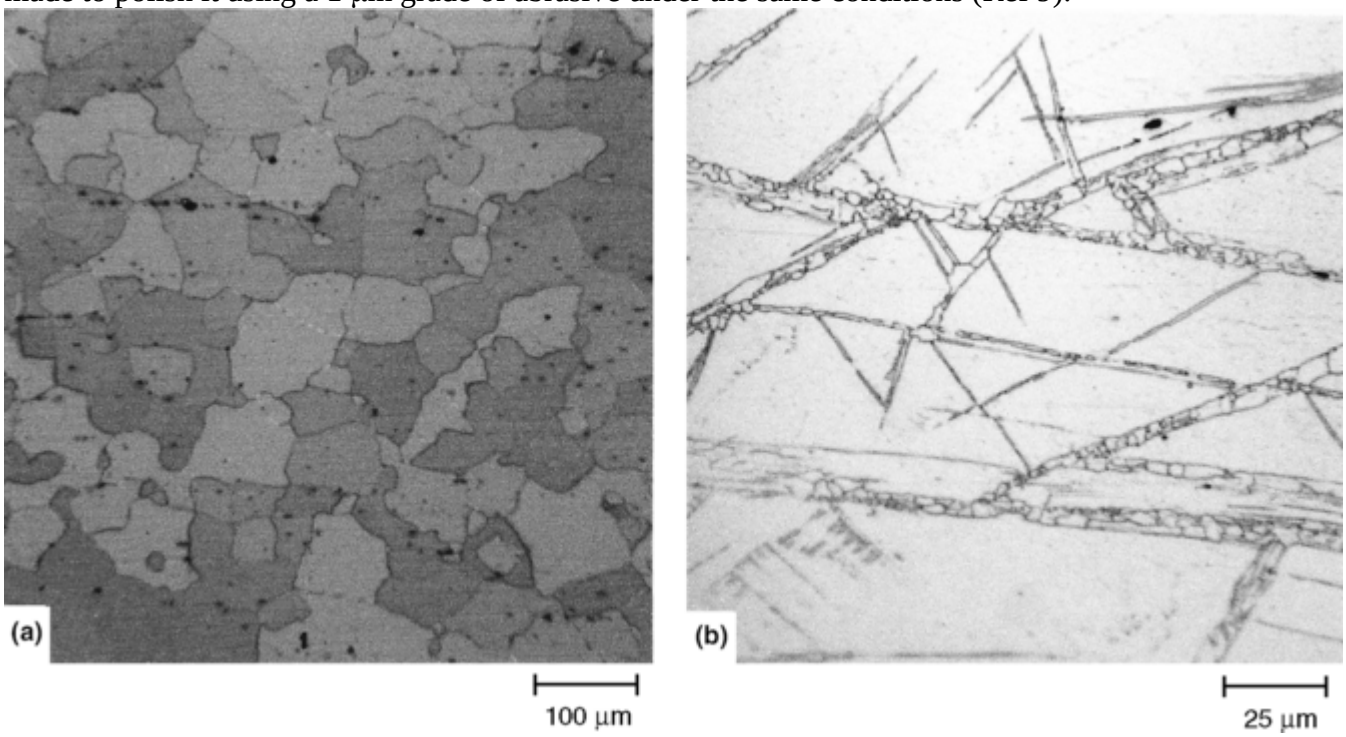

Fig. 43 Sections of a wrought magnesium alloy prepared by a modified procedure using a suspension of a diamond abrasive for polishing. (a) Hot extruded tube. Etched in a picric acid-acetic acid-ethanol reagent. Viewed in polarized light. 100×. (b) Compressed uniaxially at 200 °C. Etched in a picric acid-acetic acid-ethanol reagent. Viewed in bright-field illumination. 400×. Source: Ref 9

It is apparent that it is not yet possible to generalize too widely on suitable polishing treatments for metals and alloys of this group. Moreover, further experience will be required before it will become possible to discern principles on which the development of procedural modifications can be based.

Very Hard Materials. This group includes materials with hardnesses exceeding ~1000 HV for which the use of diamond abrasives is obligatory in all preparation processes. The materials typically concerned are compounds (oxides, carbides, or nitrides) of high-melting-point metals.

A generally applicable procedure is outlined in Table 4. The first or preliminary abrasion stage (stage 1 in Table 4) is carried out using a polymer lap intrinsically charged with a comparatively coarse grade of diamond abrasive. A second, finer abrasion stage (stage 2 in Table 4) uses a plain, extrinsically charged polymer lap by spraying a suspension of a 9 μm grade polycrystalline diamond over the working surface. A flat surface is formed by these processes, but both remove material from these hard, brittle materials by fracture chipping. Numerous small, angular cavities consequently are present in the surface that is produced (Fig. 44a). These cavities are *abrasion artifacts* that could be mistaken for cavities formed during the processing of the material. They must be removed, as a first priority, by the polishing stages that follow.

Table 4 Semiautomatic procedure employing suspensions of diamond abrasives suitable for very hard materials

	Abrasive parameters			Mechanical parameters			
Stage	**Type**	**Grade**	**Fluid**	**Speed[(a)], rpm**	**Direction**	**Force[(b)], N**	**Time, min**
1	Diamond[(c)]	220	Water	150	Comp[(d)]	20–30	[(e)]
2	Diamond[(f)]	9 μm	[(g)]	150	Comp[(d)]	30	5
3	Diamond[(h)]	3 μm	[(g)]	150	Comp[(d)]	30	5
4	Diamond[(i)]	1 μm	[(g)]	150	Comp[(d)]	20	5

(a) Speed of rotation of the work wheel.
(b) Force applied to a 25 mm diam specimen.
(c) Internally charged polymer lap.
(d) Specimen holder rotated in the same direction as the work wheel.
(e) Until a plane surface has been produced.
(f) Proprietary suspension of polycrystalline diamond sprayed onto a polymer lap.
(g) Proprietary fluid sprayed onto the working surface.
(h) Proprietary suspension of polycrystalline diamond sprayed onto an elastically hard satin-weave silk cloth.
(i) Proprietary suspension of polycrystalline diamond sprayed onto a plain-weave silk cloth.
Source: Ref 7

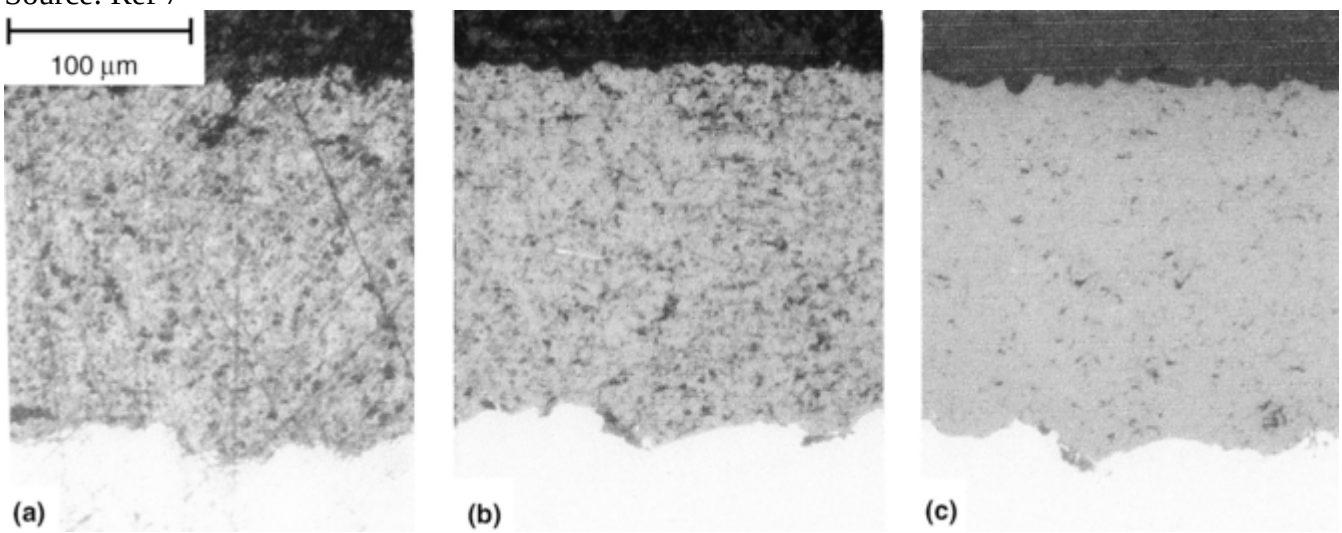

Fig. 44 Section of a sprayed coating of chromic oxide on steel prepared by a semiautomatic procedure using suspensions of diamond abrasives. The section was prepared by the procedure outlined in Table 4. (a) Abraded on a polymer lap charged with 9 μm grade diamond. Most of the dark angular features are abrasion artifacts. (b) Same area as in (a), but then polished on a woven silk cloth charged with a 6 μm grade diamond abrasive for 3 min. Some of the abrasion artifacts remain. (c) Same area as for (b) but further polished on a napped cloth charged with a 1 μm grade diamond abrasive. This is the true structure. All 150×. Source: Ref 10

The two polishing stages listed (stages 2 and 3 in Table 4) consequently must be continued until, between them, all of the abrasion artifacts have been removed, as illustrated in Fig. 44. A test that can be used to determine whether all the artifacts have been removed or not is described in Ref 1, p 287–288. The finish obtained by polishing with 1 μm grade (preferably polycrystalline) diamond is adequate for most purposes. If not, finer grades of diamond abrasive could be used for final polishing. Colloidal silica can also be used on a napped cloth for this purpose (Ref 3).

Footnotes

* Adapted from Chapter 12 of Ref 1, pages 297–307

** See Ref 1, p 284–285 for a method to distinguish true cavities from chip artifacts.

References cited in this section

1. L.E. Samuels, *Metallographic Polishing by Mechanical Methods*, 4th ed., ASM International, 2003
2. G.F. Vander Voort, Copper Color Metallography, *Adv. Mater. Process.*, Vol 158 (No. 1), 2000, p 37
3. G.F. Vander Voort, Contemporary Concepts in Specimen Preparation, *Buehler Tech-Notes*, Vol 3 (No. 2)
4. G.F. Vander Voort, Preparation of Cast Aluminum Alloys, *Buehler Tech-Notes*, Vol 3 (No. 2)
5. G.F. Vander Voort, Metallographic Preparation of Titanium and Its Alloys, *Buehler Tech-Notes*, Vol 3 (No. 2)
6. G.A. Blann, in *Microstructural Science*, American Society for Metals, 1974, p 327
7. T. Palmer, Radiometer Pacific Pty. Ltd., personal communication, 2002
8. D.S. O'Neill, "An Investigation of Surface Hot Shortness in Low-Carbon Steels," Ph.D. dissertation, University of New South Wales, 2002
9. Y. Lizama and A. Grosvenor, Cast Metals Manufacturing Co-operative Research Centre, Monash University, personal communication, 2002
10. L. Bjerregaard, K. Geels, B. Ottesen, and M. Ruckert, *Metalog Guide*, Struers A/S, 2000, available http://www.struers.com/

Mechanical Grinding and Polishing, *Metallography and Microstructures*, Vol 9, *ASM Handbook*, ASM International, 2004, p. 257–280

Mechanical Grinding and Polishing

Acknowledgment

Adapted from L.E. Samuels, Mechanical Grinding, Abrasion, and Polishing, *Metallography and Microstructures*, Volume 9, *ASM Handbook*, 1985, p 33–47. Some of the information and micrographs presented in this article originally appeared in Ref 1. Reference should be made to that publication for full details of the mechanical abrasion processes, the mechanisms by which they operate, their effects on the surfaces being produced, and the most efficient methods of carrying them out.

Reference cited in this section

1. L.E. Samuels, *Metallographic Polishing by Mechanical Methods*, 4th ed., ASM International, 2003

References

1. L.E. Samuels, *Metallographic Polishing by Mechanical Methods,* 4th ed., ASM International, 2003
2. G.F. Vander Voort, Copper Color Metallography, *Adv. Mater. Process.,* Vol 158 (No. 1), 2000, p 37
3. G.F. Vander Voort, Contemporary Concepts in Specimen Preparation, *Buehler Tech-Notes,* Vol 3 (No. 2)
4. G.F. Vander Voort, Preparation of Cast Aluminum Alloys, *Buehler Tech-Notes,* Vol 3 (No. 2)
5. G.F. Vander Voort, Metallographic Preparation of Titanium and Its Alloys, *Buehler Tech-Notes,* Vol 3 (No. 2)
6. G.A. Blann, in *Microstructural Science,* American Society for Metals, 1974, p 327
7. T. Palmer, Radiometer Pacific Pty. Ltd., personal communication, 2002
8. D.S. O'Neill, "An Investigation of Surface Hot Shortness in Low-Carbon Steels," Ph.D. dissertation, University of New South Wales, 2002
9. Y. Lizama and A. Grosvenor, Cast Metals Manufacturing Co-operative Research Centre, Monash University, personal communication, 2002
10. L. Bjerregaard, K. Geels, B. Ottesen, and M. Ruckert, *Metalog Guide,* Struers A/S, 2000, available http://www.struers.com/

Chemical and Electrolytic Polishing, *Metallography and Microstructures*, Vol 9, *ASM Handbook*, ASM International, 2004, p. 281–293

Chemical and Electrolytic Polishing

Introduction

METALLOGRAPHIC PREPARATION of many materials can be difficult by mechanical means. For example, metals and alloys with a hardness of less than approximately 20 HV require special treatments, because many abrasive particles can embed in the section during abrasion, and because it is difficult to obtain an adequately scratch-free final polish (e.g., see the section "Very Soft Materials" in the article "Mechanical Grinding and Polishing" in this Volume). Certain pure refractory metals (e.g., titanium, zirconium, niobium, and uranium) are soft and readily twin at low strain rates, and artifact-free mechanical polishing of these metals is difficult. In these cases, the elimination of artifacts or scratches from fine polishing may be achieved by methods such as attack polishing, vibratory polishing, chemical polishing, electrolytic polishing, and electromechanical polishing. Attack polishing, vibratory polishing, and electromechanical polishing employ some mechanical means and are described in the preceding article, "Mechanical Grinding and Polishing," in this Volume.

This article, adapted from Ref 1 and 2, describes methods of chemical polishing and electrolytic polishing for metallographic preparation. Electrolytic polishing (also known as electropolishing) can be a fast and efficient method in sample preparation of difficult metals, but there are important limitations. Difficulties include polishing heterogeneous alloys and edge protection in examining surface layers. In two-phase alloys, one phase is polished at a different rate than another, leading to excessive relief or perhaps preferential attack of one phase. Thus, electropolishing and chemical polishing are best suited for pure metals and single-phase alloys. Electropolished surfaces also tend to be wavy rather than flat, and so, stage movement and focus control over a reasonable area are difficult. This restricts the use of electropolishing for image analysis work (Ref 3). Chemical polishing has similar limitations and restrictions.

References cited in this section

1. G.F. Vander Voort, *Metallography: Principles and Practice*, McGraw-Hill, 1984, Reprinted ASM International, 1999

2. E. Weidmann, Electrolytic Polishing, *Metallography and Microstructures*, Vol 9, *ASM Handbook*, American Society for Metals, 1985, p 48–56

3. *Practical Guide to Image Analysis*, ASM International, 2000, p 53

Chemical and Electrolytic Polishing, *Metallography and Microstructures*, Vol 9, *ASM Handbook*, ASM International, 2004, p. 281–293

Chemical Polishing (Ref 1)

Chemical polishing is a controlled corrosion process, where a polished surface is obtained by immersion in or swabbing with a suitable solution. It is similar to electropolishing, except that chemical polishing does not

require an external current. Solutions contain an oxidizing agent, such as nitric acid or hydrogen peroxide, that takes the place of the electric current used in electropolishing. An anion is used to dissolve the film formed at a controlled rate. For many metal-polishing solution combinations, a surface film forms during chemical polishing. These films are either oxides or hydroxides, because the solutions are strongly oxidizing. In cases where the sample is immersed in an unstirred solution, a clearly visible viscous layer is present. In some polishing solutions, gas evolution is observed, which is indicative of polishing. Uniform dissolution of the surface of a particular metal in a specific solution is due to the presence of either a passivating oxide film or a viscous diffusion layer.

Chemical polishing is generally simple to employ and fast, requiring little physical exertion. Elaborate equipment is not required. Metal removal rates are high enough to remove scratches and deformation from fine grinding. The method is applicable to round or curved surfaces or for simultaneous polishing of all of the sides of a square, rectangular, or flat specimen. Thus, the technique has wide applicability and versatility.

However, routine use of chemical polishing by metallographers is limited. The disadvantages are that a given volume of solution can only polish a limited number of samples. Some solutions must be mixed fresh and must be discarded immediately after use; they cannot be stored as stock solutions. Many of the solutions are somewhat dangerous to use. Most should be used under a chemical hood, with the operator avoiding contact with the solution or its vapors. No universally applicable solution exists; most must be tailored to the specific alloy. Therefore, some experimentation may be required with a new alloy to obtain good results.

As with electropolishing, inclusions and pores are preferentially attacked, which is a serious drawback. Both techniques produce edge rounding. Results are best with pure metals or single-phase alloys, but some chemical polishes work well with two-phase alloys.

Chemical polishing is usually performed in a beaker placed on a magnetic stirring device. The sample is hung in the bath or held with tongs. If stirring is not desired, the sample can be placed on the bottom of the beaker. Some chemical polishes work better by swabbing. With these chemical polishes, the solution is placed in a shallow, wide dish. The sample is held with tongs, and the solution is rubbed against the surface using cotton held with tongs. With some samples, the solution volume relative to the sample size is important. Therefore, for best results, attention must be given to technique.

Most samples are ground to 600-grit SiC, although in a few instances, a coarser final grind works best. In general, the finer the mechanical finish, the less time is required for chemical polishing, and difficulties with pitting and other preferential attack are reduced. A film sometimes forms on the specimen surface, which must be removed by treatment with an appropriate solution. Comments regarding these problems, when available, are noted in Table 1, which lists various solutions for chemical polishing.

Table 1 Chemical-polishing solutions

Material	Chemical-polishing solution	Comments
Alumina	H_3PO_4	Use at 425 °C (795 °F); remove sample from mount before polishing, 2–3 min required
Alumina	Borax glass	Use at 800–900 °C (1470–1650 °F); rotate sample periodically for approx. 5 min. Dissolve adherent glass with dilute acid
Alumina-0.04%Cr	H_3PO_4	Heat sample slowly in gas flame to 425 °C (795 °F), then immerse in acid at 425 °C (795 °F) for 1–2 min
Aluminum	60 mL H_2SO_4 30 mL H_3PO_4 10 mL HNO_3	Use at 100 °C (212 °F) for 2–5 min
Aluminum	25 mL H_2SO_4 70 mL H_3PO_4 5 mL HNO_3	Use at 85 °C (185 °F) for 30 s to 2 min. Good for alloys with intermetallic phases

Material	Chemical-polishing solution	Comments
Al-Mg alloys, Al-Mg-Si alloys, Al-Zn-Mg alloys, Al-Cu-Mg alloys	Solution A: 30–60 mL H_3PO_4 60–30 mL H_2SO_4 5–10 mL HNO_3 Solution B: 70–90 mL H_3PO_4 25–5 mL H_2SO_4 3–8 mL HNO_3 Solution C: 90 mL H_3PO_4 10 mL HNO_3	Use solution A at 95–120 °C (205–250 °F); good for preliminary polish. Use solution B at 85–110 °C (185–230 °F); good for final polish. Use solution C at 85 °C (185 °F); etches grain boundaries
Aluminum	70 mL H_3PO_4 15 mL acetic acid 15 mL water	Use at 100–120 °C (212–250 °F) for 2–6 min
Aluminum	83 mL H_3PO_4 15 mL acetic acid 5 mL HNO_3	Use at 100–105 °C (212–220 °F) for a few minutes
Aluminum	70 mL H_3PO_4 3 mL HNO_3 12 mL acetic acid 15 mL water	Use at 100–120 °C (212–250 °F), 2–6 min. Good for many Al alloys
Aluminum	90 mL H_3PO_4 5 mL HNO_3 5 g sodium nitrate 0.2 g copper nitrate	Grind through 600-grit SiC, immerse in solution at 90 °C (195 °F) for 4 min
Aluminum	80 mL H_3PO_4 15 mL H_2SO_4 5.5 mL HNO_3	Grind through 600-grit SiC, immerse in solution at 95 °C (205 °F) for 4 min
Aluminum	77.5 mL H_3PO_4 16.5 mL H_2SO_4	Use for 1½–2 min. Temperature not given, probably approx. 100 °C (212 °F)

Material	Chemical-polishing solution	Comments
	6 mL HNO_3 3.9 g $CuSO_4 \cdot 5H_2O$ 1000 mL water	
Aluminum	47.7 mL H_3PO_4 6.4 mL HNO_3 6.0 mL acetic acid 25.0 mL H_2SO_4 12.5 mL water 0.3 g $Ni(NO_3)_2$	Use at 90–110 °C (195–230 °F) for 30–120 s. Good for Al alloys
Pure Al, Al-1%Si-1%Fe-0.1%Cu alloy	15 mL HNO_3 4 mL HCl 46 mL H_3PO_4	Use at 100 °C (212 °F) for 8–10 min
Beryllium	44 mL H_3PO_4 3 mL H_2SO_4 13 mL water 7 g CrO_3	Use at 49 °C (120 °F). Removes 1 mil (25 μm) in 20 min
Cadmium	2 parts H_2O_2 (30%) 2 parts ethanol 1 part HNO_3	Immerse sample in solution for 2 min—always add HNO_3 to ethanol when preparing solution
Cd-1.5%Zn alloy	320 g CrO_3 20 g Na_2SO_4 1000 mL water	If staining occurs, use above solution
Cadmium, Cd-Ag alloys (up to 3% Ag)	Solution A: 1 part H_2O_2 (3%) 1 part NH_4OH Solution B: 2 mL HF 28 mL HCl 50 mL water Solution C: 25 mL	Immerse or gently swab with solution A for 1 min to remove grinding scratches. Follow with very fine diamond on satin, 500 rpm, for 15 min. Wipe with a solution of HCl and ethanol, swab with solution B for 50–60 s. Remove surface deposit by immersing in solution C for 30 s

Material	Chemical-polishing solution	Comments
	water 25 mL H_2O_2 25 mL NH_4OH	
Cadmium	3–6 g $K_2Cr_2O_7$ 100 mL HNO_3	Prepolish through alumina. Use solution at 40–60 °C (105–140 °F), immerse sample for 8–10 s, wash with water. Repeat cycle 6–7 times until polished
Cobalt	40 mL lactic acid 30 mL HCl 5 mL HNO_3	Good for Co alloys also
Cobalt	1 part acetic acid 1 part HNO_3	…
Copper, Alpha brass	55 mL H_3PO_4 20 mL HNO_3 25 mL acetic acid	0.5 mL HCl can be added. Use at 55–80 °C (130–175 °F) for 2–4 min. Agitate solution
Copper	6 mL HNO_3 65 mL acetic acid 27 mL H_3PO_4	Grind samples through 600-grit SiC. Immerse in solution at 60 °C (140 °F) for 1 min
Copper	80 mL H_2SO_4 20 mL HNO_3 1 mL HCl 55–60 g CrO_3 200 mL water	Use at 20–40 °C (70–105 °F) for 1–3 min. Good for Cu alloys also
Cu-8%Al alloy, Cu-0.5%Be alloy, Cu-5%Al-2%Si alloy	1 part HNO_3 1 part H_3PO_4 1 part acetic acid	Use at 60–70 °C (140–160 °F) for 1–2 min
Cu-4.85%Si alloy	30 mL HNO_3 10 mL HCl 10 mL H_3PO_4 50 mL acetic acid	Use at 70–80 °C (160–175 °F) for 1–2 min. Agitate sample
Alpha brass	17 mL HNO_3 17 mL H_3PO_4 66 mL acetic acid	Use at 50 °C (120 °F) for 30–120 s

Material	Chemical-polishing solution	Comments
OFHC copper(a), Cu-Zn alloys (10–15% Zn), Cu-7.5%Al alloy	57 mL H_3PO_4 20 mL HNO_3 16 mL acetic acid	Use at 50–60 °C (120–140 °F) for 20 s
Gallium arsenide	5 mL HCl 5 mL HNO_3 40 mL glycerin	Suspend sample in solution, agitate lightly to dislodge bubbles. Polishing rate is 0.37 mg/(cm^2 · min)
Gallium phosphide	100 mL methanol Saturate with chlorine	Use under hood, 5–20 min
Germanium	15 mL HF 25 mL HNO_3 15 mL acetic acid 3–4 drops bromine	Use at 20 °C (70 °F) for 5–10 s
Iron, Low-carbon steels	30 mL HNO_3 70 mL HF 300 mL water	Use at 60 °C (140 °F)
Iron, Low-carbon steels	25 g oxalic acid 10 mL H_2O_2 (13 g) 1 drop H_2SO_4 (0.1 g) 1000 mL water	Grind through 600-grit SiC. Immerse sample for 5 min at 20 °C (70 °F)
Iron, Low-carbon steels, Fe-20%Ni-5% Mn alloy	80 mL H_2O_2 (30%) 15 mL water 5 mL HF	Prepolish sample through 6 μm diamond. Swab with fresh solution at 20–25 °C (70–75 °F) for 4–10 s. Flush immediately with cold water
Iron, Low-carbon steels, Low-alloy steels	3 mL HF 97 mL H_2O_2 (30%)	Adjust HF concentration to obtain gas evolution. Good for thinning transmission electron microscopy samples
Steels (0.1–0.8% C, up to 3% alloys)	14 mL HF 100 mL H_2O_2 (30%) 100 mL water	The finer the mechanical polish, the smaller the pits produced. Use a fresh, cold solution. Immerse sample for 3–30 s and shake vigorously. Rinse in 30% H_2O_2
Cast iron, Low-alloy steels	70 mL H_2O_2 (30%)	Use at 15–25 °C (60–75 °F)

Material	Chemical-polishing solution	Comments
	5 mL HF 40 mL H_2O	
Carbon steel	7 parts oxalic acid (100 g/L) 1 part H_2O_2 (100%) 20 parts water	Grind to 0-grade emery or equivalent. Immerse sample 15 min at 35 °C (95 °F)
Low-carbon steels, Magnesium	90 mL H_2O_2 (30%) 10 mL water 15 mL H_2SO_4	Use at 25 °C (75 °F) for 2–5 min
Carbon steels	Solution A: 25 g oxalic acid 1000 mL water Solution B: 100 vol H_2O_2	Use fresh for 30 min. Ratio of solution A to B varies with carbon content
Pure iron	5 mL HF 70 mL H_2O_2 (30%)	Grind through 600-grit SiC. Immerse in solution at 20 °C (70 °F) for 25–45 s
Fe-3%Si alloy	100 mL H_3PO_4 115 mL H_2O_2 (30%)	Grind through 600-grit SiC. Immerse in solution at 25 °C (75 °F) for 8–10 min. Cool during use
Stainless steel	% by weight: 30% HCl 40% H_2SO_4 5.5% titanium tetrachloride 24.5% water	Use by immersion of sample at 70–80 °C (160–175 °F) for 2–5 min. Can add 0.5% HNO_3 to solution
Low-carbon steels	3 parts H_3PO_4 1 part H_2SO_4 1 part HNO_3	Use at 85 °C (185 °F)
Low-carbon steels	1 part H_2O_2 (30%) 2 parts 20% oxalic acid in water	Used at 30–70 °C (85–160 °F)
Medium-carbon steels	10 parts H_2O_2 (30%)	Use at room temperature

Material	Chemical-polishing solution	Comments
	10 parts water 1 part HF	
Steels	Solution A: 3 parts H_2O_2 (30%) 10 parts water 1 part HF Solution B: 1 part H_3PO_4 15 parts water	Steels > 0.3% C: Grind to 150 grit, immerse in solution A for 15–25 s, wash with water, clean with solution B with cotton, wash in water, dry Steels 0.15–0.30% C: Grind to 320 grit, immerse in solution A for 12–18 s, then same procedure as for steels > 0.3% C Steels < 0.15% C: Grind to 600 grit, immerse in solution A for 3–5 s, then same procedure as for steels > 0.3% C Extrasoft sheet steels: Grind to 200 grit, immerse in solution A for 3–5 s, mechanical polish with chromium oxide, then with alumina
Iron, Fe-Si alloys	6 mL HF 94 mL H_2O_2 (30%)	Use at room temperature. Wash in successive baths of H_2O_2, water, and ethanol, dry
Austenitic stainless steel	4 parts HNO_3 1 part HCl 1 part H_3PO_4 5 parts acetic acid	Use at 70 °C (160 °F) for 3 min
Austenitic stainless steel	4 parts HNO_3 3 parts HCl 5 parts acetic acid	First, passivate surface by dipping in boiling 4% aq. H_2SO_4. Then, chemical polish at 70 °C (160 °F) for 1 min
Pure lead	20 mL acetic acid 30 mL H_2O_2 50 mL methanol	…
Pure lead, Lead alloys	75 mL acetic acid 25 mL H_2O_2	Pour solution rapidly over sample (50 mL in 3–4 s) in a random pattern. Quickly wash in running water, rinse with alcohol, dry. Repeat until good polish is obtained
Lithium fluoride	H_3PO_4	Use at 60–120 °C (140–250 °F) for 6–12 h; cool to ambient temperature, rinse in water, ethanol, and anhydrous ether

Material	Chemical-polishing solution	Comments
Magnesium	10 mL HNO_3 90 mL methanol	Use at 20 °C (70 °F)
Magnesium	0.4 g potassium dichromate 6 g boric acid 140 mL water 15 drops HNO_3	Use for 1–2 min. Good for polarized-light work
Magnesium, Mg-MgO alloys (0–5% MgO)	8 mL HNO_3 12 mL HCl 100 mL ethanol	Grind to 600-grit SiC. Use at 20 °C (70 °F) for 30 s
Pure nickel	3 parts HNO_3 1 part H_2SO_4 1 part H_3PO_4 5 parts acetic acid	Grind through 600-grit SiC. Use at 85–95 °C (185–205 °F) for less than 1 min. Wash immediately in water
Pure nickel, Ni-Co alloys	65 mL acetic acid (ice cooled) 35 mL HNO_3 0.5 mL HCl	Fine grinding not required for pure Ni. Use at 20 °C (70 °F) for 2–4 min. For Ni-Co alloys, grind through 600-grit SiC, use at 20 °C (70 °F) for 1–2 min
Niobium, Vanadium,Tantalum	6 g $FeCl_3$ 30 mL HCl 120 mL water 16 mL HF	Use at room temperature, 1 min for V, 2 min for Nb, 3 min for Ta
Niobium, Vanadium, Tantalum	30 mL water 30 mL HNO_3 30 mL HCl 15 mL HF	Use at room temperature
Platinum	20 mL HF 5 mL HNO_3	Use hot (temperature not specified) under hood
Rare earth metals:Erbium, Dysprosium, Gadolinium, Holmium, Lanthanum	Solution A: 20 mL lactic acid 5 mL H_3PO_4 10 mL acetic acid	Solution A: Polish through 3 μm diamond. Do not add water to solution. Swab sample gently for 10–15 s (good for samples with low amount of inclusions)

Material	Chemical-polishing solution	Comments
	15 mL HNO_3 1 mL H_2SO_4 Solution B: 10 mL H_3PO_4 10 mL lactic acid 30 mL HNO_3 20 mL acetic acid	Solution B: Etches with a slight chemical-polishing action. Use for samples with larger amounts of inclusions. Polish through $\frac{1}{2}$–1 μm diamond, then use solution A for 2–3 s
Cerium	20 parts of solution A above 10 parts dimethyl-formamide (inhibits oxidation)	Do not add water to solution. Use for 10–15 s
Silicon	93 mL HNO_3 70 mL HF 17 mL water 30 mL acetic anhydride 30 mL acetic acid	Use at 20 °C (70 °F) for 10–15 min. Discard after use
Silicon	20 mL HNO_3 5 mL HF	Use at 20 °C (70 °F) for 5–10 s (CP-4 Reagent)
SiO_2	1 part HF 2 parts acetic acid 3 parts HNO_3	Stir solution
Silver	100 g CrO_3 65 mL water 5 drops HCl	Polish to 6 μm diamond, swab with solution (rinse frequently with water) for approx. 5 min. If a film forms, swab with H_3PO_4
Silver	21 g NaCN 78 g H_2O_2 (30%) 1000 mL water	Use at 32 °C (90 °F) for a few seconds. When gas evolution begins, remove and wash with 37.5 g NaCN per liter of water. Immerse in chemical polish and repeat cycle until polished
Ag-30%Zn alloy	4 g Cr_2O_3 7.5 g NH_4Cl	Use at 60 °C (140 °F)

Material	Chemical-polishing solution	Comments
	150 mL HNO_3 52 mL H_2SO_4 Water to 1 L	
Sodium	5–50% methanol in acetone	Use at room temperature for less than 10 s. Dip in pure acetone, wash immediately in petroleum ether. Place in mineral oil for viewing
Tantalum	2 parts acetic acid 5 parts H_2SO_4 1 part HF	…
SnTe	0.35 g I_2 40 mL ethanol (or methanol) 10 mL water 4 mL HF	To prepare solution, dissolve iodine in ethanol (or methanol). Add water, then add HF. Prepolish sample to Linde A abrasive. Saturate cloth with solution. Lightly rub sample over wet cloth in figure-eight motion for 15–20 min. Add solution periodically. Rinse in methanol, then water, dry
Iodide titanium	60 mL H_2O_2 (30%) 30 mL water 8–10 mL HF	Swab for 30–60 s
Titanium	1 part HF 1 part HNO_3	Immerse sample and agitate vigorously. When polishing action becomes violent, continue for approx. 10 s. Discard solution when it turns green
Titanium	30 mL HF 70 mL HNO_3	Polish through gamma alumina. Chemical polish for 10 s
TiO_2	KOH	Heat to 650 °C (1200 °F), immerse sample (remove from mount) for 8 min
Zinc	20 g CrO_3 95 mL water 5 mL HNO_3 4 g zinc sulfate	Use at 20 °C (70 °F) for 2–5 min. Use fresh solution. Discard when done. Hold sample vertical to minimize pitting. Remove chromic acid film by dip in 5–7% aq. HCl
Zinc	1 part HNO_3 1 part H_2O_2 (30%) 1 part ethanol	Immerse sample for approx. 2 min. When preparing solution, always add HNO_3 to ethanol
Zinc	43 mL H_2O_2 27 mL H_2SO_4 900 mL water	Immerse for 30 s

Material	Chemical-polishing solution	Comments
Zinc, Cadmium	200 g $Na_2Cr_2O_7$ 6–9 mL H_2SO_4 1000 mL water	Use at 20 °C (70 °F) for 5–10 min
Zinc	200 g CrO_3 15 g Na_2SO_4 52.5 mL HNO_3 950 mL water	Use at 20–30 °C (70–85 °F) for 10–30 s
Zinc	25 wt% CrO_3 10 wt% HCl 65 wt% water	Use at 20–30 °C (70–85 °F) for 10–30 s
Zirconium, Zircaloys, Hafnium	45 mL HNO_3 45 mL glycerol 8–10 mL HF	Use under hood. Swab (preferred) or dip sample. A few seconds after contact, NO_2 is given off (do not inhale)—polishing has started. Continue 5–10 s
Zirconium, Zr-2½%Nb alloy, Zircaloy-2, Zircaloy-4, Hafnium	45 mL NHO_3 45 mL water 8–10 mL HF	Use as above
Zirconium, Hafnium	45 mL H_2O_2 (30%) 45 mL HNO_3 8–10 mL HF	Use as above
Zircaloy-2, Hafnium	70 mL water 30 mL HNO_3 2–5 mL HF	Use as above
Zr-Cr-O alloys, Zr alloys other than Zircaloys	45 mL lactic acid 45 mL HNO_3 8 mL HF	Polish to 6 μm diamond
Zircaloy-4	50 mL HNO_3 50 mL water 10 mL HF	…
Zirconium	15 mL HF 80 mL HNO_3	Use for 2 min

Material	Chemical-polishing solution	Comments
	80 mL water	

Note: When water is specified, always use distilled water. (a) OFHC, oxygen-free high conductivity. Source: Ref 1

Reference cited in this section

1. G.F. Vander Voort, *Metallography: Principles and Practice,* McGraw-Hill, 1984, Reprinted ASM International, 1999

Chemical and Electrolytic Polishing, *Metallography and Microstructures,* Vol 9, *ASM Handbook*, ASM International, 2004, p. 281–293

Electrolytic Polishing (Ref 2)

Electrolytic polishing, or electropolishing, is used widely in the metallography of stainless steels, copper alloys, aluminum alloys, magnesium, zirconium, and other metals that are difficult to polish by conventional mechanical methods. When electropolishing is correctly performed, the prepared surfaces are scratch-free and the deformation from cutting and grinding is removed. Hence, the method is ideal for preparation of metals that are difficult to polish mechanically, especially where disturbed metal or mechanical twinning artifacts are problems. These characteristics are valuable for very low-load microhardness testing or for transmission electron microscopy thin-foil work. When electropolishing is used in metallography, it is preceded by mechanical grinding (and sometimes polishing) and followed by etching.

Mechanism of Electropolishing

Although the mechanism of electropolishing is not completely understood, the process is generally considered to include both a leveling (or smoothing) action and a brightening action. Current-voltage relations also affect the polishing results and vary with electrolytes and metals. A preground sample is made the anode in an electrolytic cell, and the surface is smoothed and brightened by the anodic solution when the correct combination of bath temperature, voltage, current density, and time is applied. Variables that influence electropolishing include (Ref 1):

- Surface area to be polished
- Orientation of sample in bath
- Orientation of cathode in bath
- Choice of cathode material
- Ratio of cathode-to-anode surface area
- Anode-to-cathode spacing
- Depth of sample below solution surface
- Composition of sample, including impurities
- Electrolyte bath age and composition changes
- Bath temperature
- Degree of bath agitation
- Current density and voltage
- Time
- Degree of preliminary mechanical treatment

- Manner of specimen removal from bath
- Washing procedure
- Safety precautions in mixing of electrolytes (which may be dangerous or even explosive)

The need to control all these variables can be an obstacle and has reduced the utilization of the method. However, for laboratories that routinely examine the same materials, once the operating conditions are fully established, an inexperienced metallographer can be quickly trained and can obtain excellent results. In some instances, electropolishing can reduce the overall time required for preparation. Etching can often be accomplished in the same electrolyte merely by reducing the applied voltage to approximately 10% of that required for polishing.

Smoothing is accomplished by preferential solution of the hills or ridges on a rough surface, which commonly result from mechanical grinding (Ref 4). When such a rough surface is made the anode of a suitable electrolytic cell, a viscous liquid layer immediately adjacent to this surface is produced by the reaction between the metal and the electrolyte. This layer of solution, known as the polishing film (Fig. 1), has a greater electrical resistance than the remainder of the solution. As such, it controls the smoothing action.

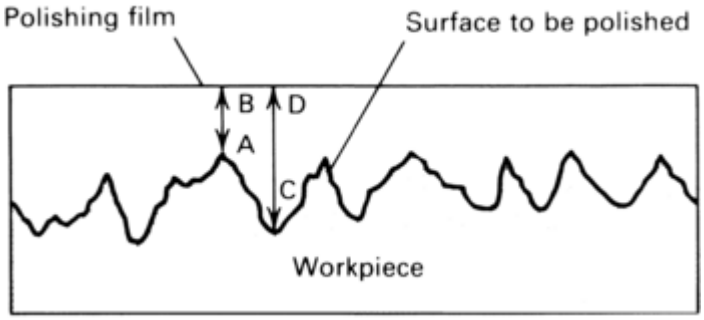

Fig. 1 Mechanism of electrolytic polishing

The resistance at peak A, represented by the distance A-B, will be lower than at depression C, represented by the distance C-D, because the film is thinner at A-B. The current at A will be much higher than at C, causing metal to dissolve faster at A than at C and producing a nearly level, gently undulating surface by removing asperities 1 μm or more in size. More rapid ionic and molecular diffusion through the thinner polishing film at A, as well as differences in anodic polarization phenomena at A and C, may also contribute to the leveling or smoothing action.

The brightening action is related to the elimination of irregularities as small as approximately 0.01 μm and to the suppression of etching on the metal surface. This behavior is generally attributed to the formation of a thin, partly passivating film directly on the surface of the metal and following its contours.

Optimal brightening conditions are related to local differences in anodic passivation at heterogeneities and between secondary peaks and crevices, as well as to the effects of passivation inhibitors that influence oxide-film formation and gas evolution. Similar factors may also contribute to the primary leveling or smoothing action in electropolishing (Ref 5).

Current-voltage relations in electropolishing vary in different electrolytes and for different metals. The simple relation, wherein polishing occurs over an extensive continuous range of currents and voltages, is shown in Fig. 2. At low voltages, a film forms on the surface, and little or no current passes. Thus, etching occurs but not polishing. At higher voltages, polishing occurs. The perchloric acid ($HClO_4$) electrolytes used for aluminum conform to this relation.

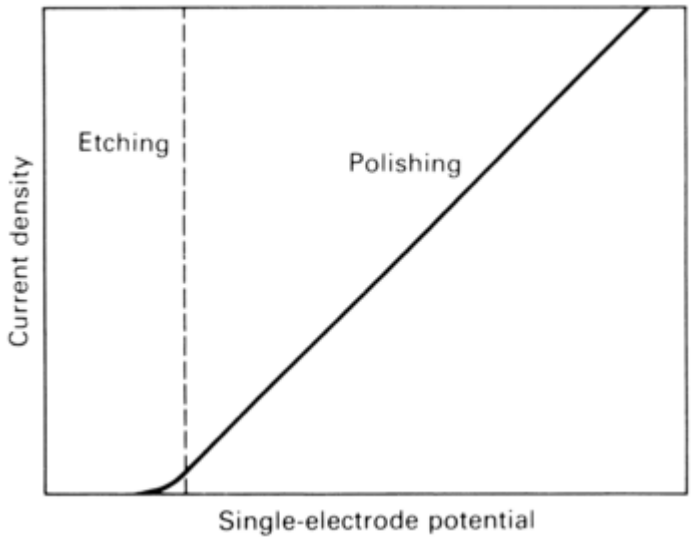

Fig. 2 Relationship between current density and single-electrode potential for electrolytes possessing polishing action over a wide range of voltages and currents

A more complex relation that is frequently encountered is illustrated in Fig. 3. Cell voltage is depicted as a function of anode current density for electropolishing copper in an aqueous solution of orthophosphoric acid (ortho-H_3PO_4), using a potentiometric circuit.

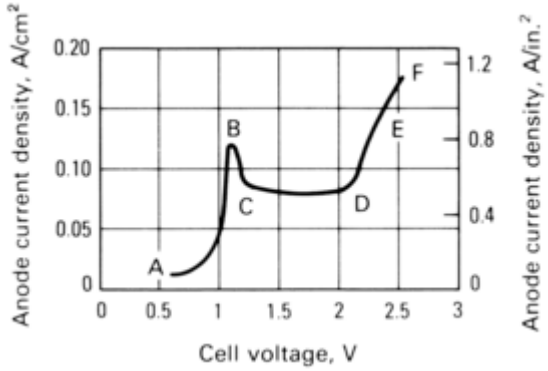

Fig. 3 Cell voltage as a function of anode current density for electropolishing copper in ortho-H_3PO_4 (900 g per 1000 mL H_2O), using a potentiometric circuit

Five distinct regions can be distinguished on the cell-voltage curve. In the region A-B, current density increases with potential, some metal dissolves, and the surface has a dull, etched appearance. The region B-C reflects an unstable condition, while region C-D indicates a stable plateau. At this stage, the previously formed polishing film reaches equilibrium, and polishing occurs. During the polishing stage, current density remains constant.
Optimal polishing conditions occur along C-D near D. In the region D-E, gas bubbles evolve slowly, breaking the polishing film and causing severe pitting. Polishing with rapid evolution of gas is represented by the region E-F. In general, the higher the plateau current density, the shorter the time required. Some electrolytes require only a few seconds and can be difficult to control.
Electrolytes of the sulfuric-phosphoric acid (H_2SO_4 + H_3PO_4) and chromic-acetic acid (CrO_3 + CH_3COOH) types used for stainless steels also typify the complex, multistage relationship shown in Fig. 3.
In establishing voltage-current curves, electrolysis must be allowed to proceed under fixed conditions until enough metal has dissolved to produce a steady-state condition at the anode.

Mounting Specimens

To properly conduct metallography studies involving electropolishing techniques, only the portion of the specimen to be polished should be in contact with the electrolyte. Small specimens may be hot mounted using

conductive or nonconductive resins. On nonconductive mounts, electrical contact can be made via a small hole drilled through the back of the mount into the metal specimen, or by an indirect connection, as shown in Fig. 4.

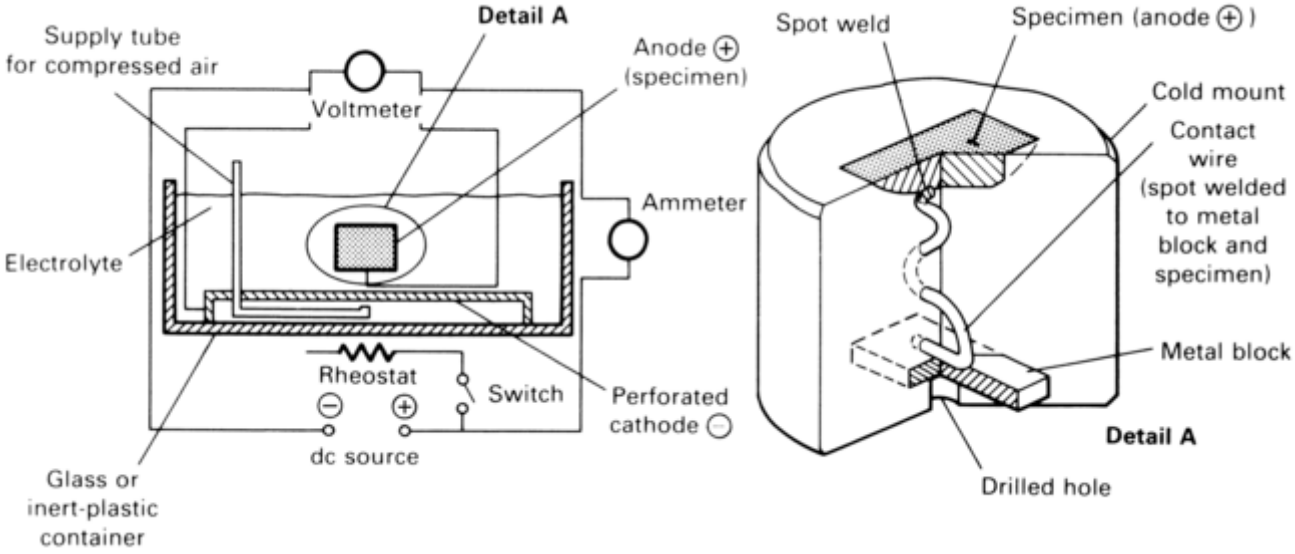

Fig. 4 Equipment setup for electropolishing. Air agitation of electrolyte is provided through a perforated cathode. Detail at right shows an indirect electrical connection to a mounted specimen.

When specimens are mounted in plastic, violent reactions may occur between the plastic and some electrolytes. For example, phenol-formaldehyde and acrylic-resin mounting materials and cellulose-based insulating lacquers and materials should not be used in solutions containing $HClO_4$ because of the danger of explosion. However, polyethylene, polystyrene, epoxy resins, and polyvinyl chloride can be used as mounting materials in $HClO_4$ solutions without danger.

Mounting of specimens in dissimilar metals is undesirable, because the metal in contact with the electrolyte is likely to interfere with polishing and also because fusible mounting alloys containing bismuth may be dangerously reactive in certain electrolytes that contain oxidizing agents. Bismuth-containing alloys may form explosive compounds in $HClO_4$ solutions.

In preparing an unmounted specimen for electropolishing, a suitable chemically inert, electrically insulating coating can be applied to all surfaces of the specimen and specimen holder, except the surface to be polished. Plastic electrical tape is also an effective stopoff, because it is impervious to most electrolytes and is readily removable from the specimen after electropolishing.

Most commercially available equipment features plastic tops with different sized apertures that are placed over the polishing cell. The surface to be polished is clamped face down over the aperture.

Apparatus and Procedure

Electrical equipment used for electropolishing can vary from the simplest arrangement of dry cells to complex arrays of rectifiers and electronic control devices. Various types of apparatus are available commercially. Selection of equipment depends on the number and type of specimens to be treated and the versatility and control desired.

Current Source. Direct current usually is used in electropolishing. The current source may consist of a battery, a direct-current generator, or a rectifier. Generally, a battery supply is used for low voltages only, because a bank of batteries is required to produce higher voltages.

Electrical Circuits. Figure 5 illustrates two typical circuits—one for low and one for high current densities. For solutions in which a small drop in potential occurs across the cell, a potentiometric circuit for low current densities is more suitable (Fig. 5a). Conversely, when the drop in potential across the cell is large, a series circuit for high current densities should be used (Fig. 5b). Provision must be made for controlling voltage and current.

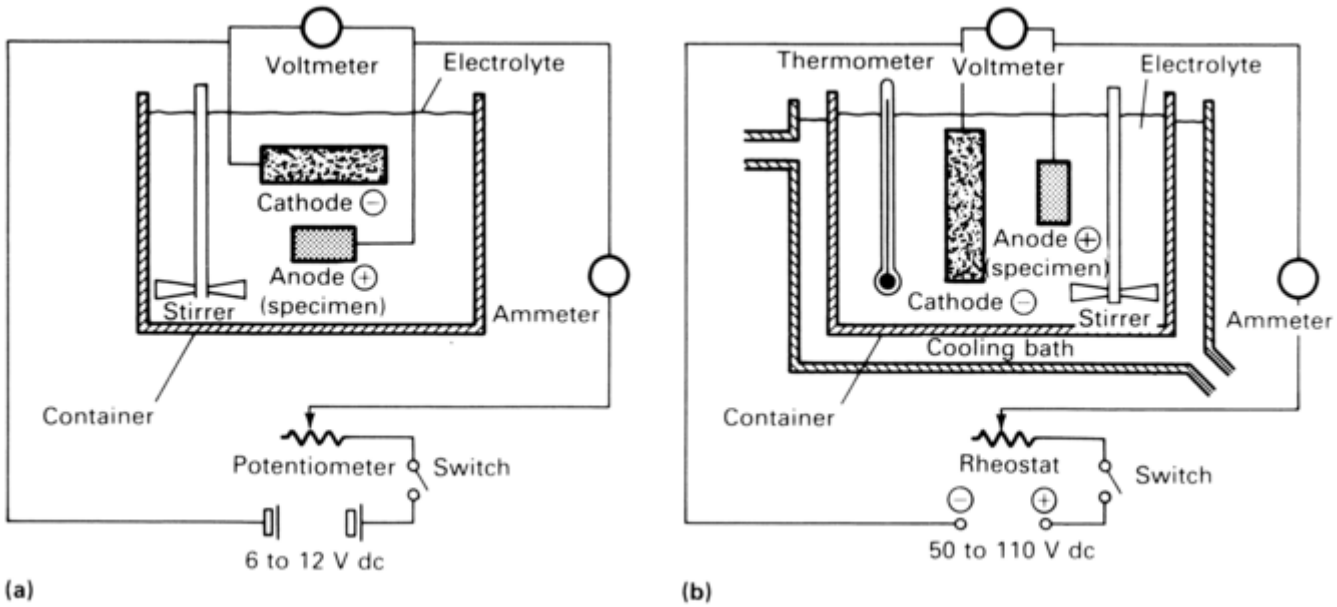

Fig. 5 Typical electrical circuits and equipment setups used for electropolishing. (a) Potentiometric circuit (for low current densities). (b) Series circuit (for high current densities)

Alternating current is used for electropolishing and electroetching metals of the platinum group (platinum, iridium, palladium, rhodium, osmium, and ruthenium), in conjunction with a series circuit and test setup similar to that shown in Fig. 5(b) with an alternating-current source.

The electrolytic cell is simply a container for the electrolyte, in which the cathode and anode are suspended. The cell usually is made of glass, but polyethylene or polypropylene may be used for solutions containing fluoride ions. Sometimes, a stainless steel cell is used, which may also serve as the cathode. Frequently, the cell is surrounded by water or an ice bath or is cooled in another manner.

The specimen to be polished (anode) should be arranged to facilitate rapid removal from the electrolyte. The electrical connection to the specimen should be simple and easily broken, so that the specimen can be rinsed immediately after polishing.

The cathode should be made of a metal that is inert in the electrolyte being used. Generally, stainless steel is satisfactory for most applications.

For many applications, stirring or air agitation of the electrolyte is necessary. During electropolishing under steady-state conditions, the anodic reaction products accumulate on the surface of the polished metal. Frequently, natural diffusion and convection processes cannot remove these products from the anode surface into the bulk of the electrolyte rapidly enough, and excessive accumulation of reaction products interferes with the electropolishing process. Stirring or air agitation hastens the removal of these products, prevents localized heating of the surface, maintains a uniform bath temperature, and removes gas bubbles that may adhere to the surface and cause pitting. However, the use of agitation usually requires an increase in the current density to maintain a sufficiently thick polishing film.

In some applications, vibratory motion of the specimen can be substituted for stirring. In other applications, agitation of the electrolyte in the cell and simultaneous control of the electropolishing temperature can be accomplished by circulating the electrolyte with a pump and an external cooling bath or device. To prevent furrowing of the surface being electropolished, the movement of the electrolyte (and gas) across the metal surface should be gentle and nondirectional.

Anode and Cathode. Figure 5 illustrates two methods of positioning the specimen (anode) and cathode. In each arrangement, only the portion of the specimen to be polished is exposed to the electrolyte.

In Fig. 5(a), the surface to be polished is horizontal and facing upward, toward the cathode. This arrangement helps to maintain a stable layer near the surface being polished and is used when polishing occurs under a viscous layer.

In Fig. 5(b), the surface to be polished is vertical and facing toward the cathode. This arrangement is sometimes used when polishing occurs with gas evolution, because it allows the gas bubbles to escape easily. However, unless special attention is given to positioning and agitation, directional streaming can cause furrowing of the surface being polished. Reciprocating movement of the specimen helps prevent furrowing.

Pitting and furrowing are prevented in the cell arrangement shown in Fig. 4, in which gentle, nondirectional movement of the electrolyte at the surface being polished is provided by introduction of air through perforations in a horizontal cathode at the bottom of the cell. Although the electrical circuit shown in Fig. 4 (a series circuit, same as in Fig. 5b) is ordinarily used, the potentiometric circuit shown in Fig. 5(a) can also be used.

The electrical connection to the specimen is made indirectly through a metal block and a contact wire that is spot welded to the back of the specimen and the metal block before the assembly is mounted in epoxy resin or other suitable material (see detail A in Fig. 4). After mounting, a hole is drilled through the back of the mount to the metal block to permit attachment of the electrical connector wire. The indirect connection lessens the danger of loosening the bond of specimen to mount that would exist with a direct connection through a hole drilled into the specimen.

The arrangement shown in Fig. 4 is particularly well suited for electropolishing at medium to high current densities. The mount is conveniently held in an alligator clip with stainless steel extensions welded to the jaws. The clip is attached to a hook that can be supported on a horizontal anode bar for ease of manipulation.

By placing the hook on the bar, electrical contact to the specimen is made almost simultaneously with immersion in the electrolyte. Contact is broken almost simultaneously with removal from the electrolyte when the hook is lifted from the anode bar, thus allowing immediate rinsing to prevent staining of the polished surface. A similar setup, in which the cathode is an L-shaped strip and agitation is provided by means of a magnetic stirrer below the cathode, is illustrated in Fig. 6.

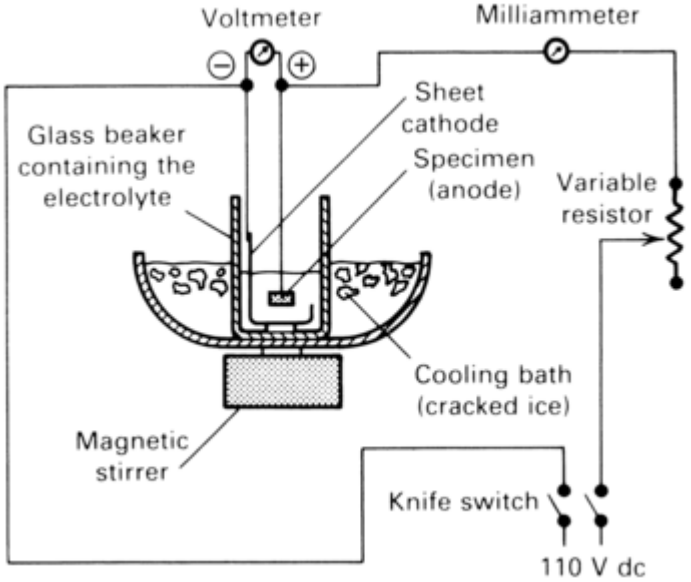

Fig. 6 Basic laboratory setup for electropolishing and electrolytic etching

For electropolishing at low current densities, agitation is not ordinarily used. Any of the cell arrangements described previously can be used in these applications. However, when low current densities are used, it is advantageous to place the specimen horizontally at the center of a circular, vertical-walled cell of glass or inert plastic, in which the cathode is a vertical stainless steel sheet that has been formed into a circular shape slightly smaller than the cell.

Developing an Electropolishing Procedure

In developing a suitable procedure for electropolishing a metal or alloy, it is generally helpful to compare the position of the major component of the alloy with elements of the same general group in a periodic table and to study the phase diagram, if available, to predict the number of phases and their characteristics. Single-phase alloys generally are easy to electropolish, whereas multiphase alloys are likely to be difficult or impossible to polish with electrolytic techniques. Even minor alloying additions to a metal may significantly affect the response of the metal to polishing in a given electrolyte.

The possibility of polishing a metal and the conditions for polishing metal in a given electrolyte can sometimes be ascertained by plotting current density versus electrode potential. The curve illustrated in Fig. 2 is typical of electrolytes that polish over a very wide range or that will not polish at all. The curve depicted in Fig. 3 is

characteristic of electrolytes that form an ionic film; polishing will occur between points C and D on this curve and is usually best near point D.

In a cell designed so that the anode is clearly visible during electrolysis, the polishing plateau can be determined by observing the anode while gradually increasing the current. For stable and reproducible results, current is passed for 30 min before recording data, and the current is increased slowly.

In working with radioactive metals, the specimen is held close to a thin, transparent window in a special cell, and the polishing action is observed using an external optical system that has a focal length of 5 mm (0.2 in.) or more, while circulating electrolyte between the specimen and the window.

After the polishing range is determined, other constants such as preparation, agitation, and time can be determined experimentally. The amount of preparation required depends on the nature of the specimen and on the results desired.

Specimen Preparation. Prior to electropolishing, the specimen must be ground with 600-grit abrasive paper. With some materials, such as beryllium and lithium, it may be necessary to polish to a finer finish with a 4000 fine-grain abrasive paper or 6 μm/3 μm diamond paste. The surface to be polished should be clean to allow uniform attack by the electrolyte. To avoid contamination with hand oil, the specimen should be handled with forceps or tongs after final preparation for electropolishing.

In general, the time required to electropolish a sample decreases as the degree of preliminary mechanical polishing increases. However, more time may be required to establish polishing conditions when starting with a fine mechanically polished surface. Indeed, the curves for voltage versus current density will be somewhat different when comparing coarsely ground versus finely polished samples in the same electrolyte. Thus, there appears to be an optimal initial surface roughness.

If the initial surface roughness is too coarse, electropolishing times will be long, with excessive metal removal and waviness, and other problems, such as preferential attack of inclusions, may be emphasized. For most work, the optimal surface finish is obtained by grinding to approximately a 600-grit finish.

Test Cells. A simple method to determine optimal electropolishing conditions after a suitable polishing solution has been selected involves the use of test cells, as shown in Fig. 7. In Fig. 7(a), the rod anode, the 360° glass insulating cylinder surrounding it, and the 360° circular cathode rest on the bottom of the cell, while the liquid level is maintained some distance above the upper end of the cathode and the glass cylinder.

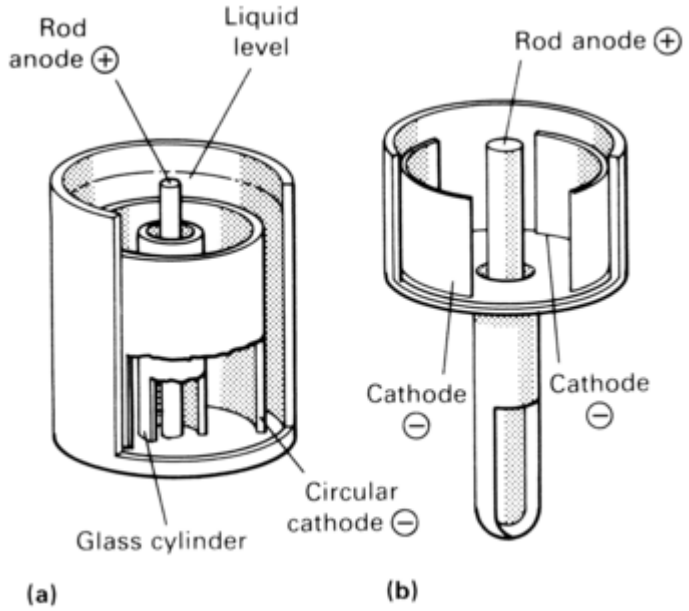

Fig. 7 Test cells for use in evaluating operating conditions in electropolishing over a range of anode current densities

In the cell shown in Fig. 7(b), the cathode consists of two opposing circular segments. The rod anode does not extend to the bottom of the cell, and the liquid level is maintained slightly below the upper end of the anode and the two-segment cathode.

In each cell, the anode current density is greater near the liquid level and is progressively lower at greater depths. In operation, when a constant current is passed through the cell, the finish at any depth on the anode is related to the current density at that depth.

If the electrolyte is of a composition that makes it suitable for electropolishing, the optimal ranges of current density can be estimated roughly from the positions and lengths of the polished zones. Additional information can be obtained from such cells by measurements of anode potential.

The cell shown in Fig. 7(b) allows accurate temperature control and observation of the anode during the passage of current. Similar results can be obtained in a Hull cell, which is widely used for evaluating operating conditions in electroplating. When the bath temperature rises, the resistance of the bath decreases, and the potential required to produce the plateau current density decreases. In addition, the bath viscosity decreases, making it more difficult to maintain a viscious anode layer. The optimal bath temperature, which must be determined, is the temperature at which the power requirement is minimum and surface quality is maximum. Control of bath temperature is of extreme importance with electrolytes that are explosive. With many samples, lower bath temperatures produce better surface quality, but the temperature cannot be lowered beyond the point where precipitation of solid particles occurs on the anode surface.

Electrolytes

Table 2 lists the formulas of several groups of electrolytes and conditions for their use in electropolishing various metals and alloys. Table 3 summarizes the applicability of these electrolytes to electropolishing specific metals.

Table 2 Electrolytes for electropolishing of various metals and alloys

Class	Formula	Use	Cell voltage	Time	Notes
Group I: Electrolytes composed of $HClO_4$ and alcohol with or without organic additions(a)					
I-1	800 mL ethanol (absolute), 140 mL distilled H_2O (optional), 60 mL $HClO_4$ (60%)	Aluminum and aluminum alloys with less than 2% Si	30–80	15–60 s	…
		Carbon, alloy, and stainless steels	35–65	15–60 s	…
		Lead, lead-tin, lead-tin-cadmium, lead-tin-antimony	12–35	15–60 s	…
		Zinc, zinc-tin-iron, zinc-aluminum-copper	20–60	…	…
		Magnesium and high-magnesium alloys	…	…	(b)
I-2	800 mL ethanol (absolute), 200 mL $HClO_4$ (60%)	Stainless steel; aluminum	35–80	15–60 s	…
I-3	940 mL ethanol (absolute), 6 mL distilled H_2O, 54 mL $HClO_4$ (70%)	Stainless steel	30–45	15–60 s	…
		Thorium	30–40	15–45 s	…
I-4	700 mL ethanol (absolute), 120 mL distilled H_2O, 100 mL 2-butoxyethanol, 80 mL $HClO_4$ (60%)	Steel, cast iron, aluminum, aluminum alloys, nickel, tin, silver, beryllium, titanium, zirconium, uranium, heat-resistant alloys	30–65	15–60 s	(c)
I-5	700 mL ethanol (absolute), 120 mL distilled H_2O, 100 mL glycerol, 80 mL $HClO_4$ (60%)	Stainless, alloy, and high-speed steels; aluminum, iron, iron-silicon alloys, lead, zirconium	15–50	15–60 s	(d)
I-6	760 mL ethanol (absolute), 30 mL distilled H_2O, 190 mL ether, 20 mL $HClO_4$ (60%)	Aluminum, aluminum-silicon alloys, iron-silicon alloys	35–60	15–60 s	(e)
I-7	600 mL methanol (absolute), 370 mL 2-butoxyethanol, 30 mL $HClO_4$ (60%)	Molybdenum, titanium, zinc, zirconium, uranium-zirconium	60–150	5–30 s	…

		alloy			
I-8	840 mL methanol (absolute), 4 mL distilled H_2O, 125 mL glycerol, 31 mL $HClO_4$ (70%)	Aluminum, aluminum-silicon alloys, iron-silicon alloys	50–100	5–60 s	…
I-9	590 mL methanol (absolute), 6 mL distilled H_2O, 350 mL 2-butoxyethanol, 54 mL $HClO_4$ (70%)	Germanium	25–35	30–60 s	…
		Titanium	58–66	45 s	(f)
		Vanadium	30	3 s	(g)
		Zirconium	70–75	15 s	(h)
I-10	950 mL methanol (absolute), 15 mL HNO_3, 50 mL $HClO_4$ (60%)	Aluminum	30–60	15–60 s	…
Group II: Electrolytes composed of $HClO_4$ (60%) and glacial acetic acid					
II-1	940 mL acetic acid, 60 mL $HClO_4$	Chromium, titanium, uranium, zirconium, iron, cast iron, carbon, alloy, and stainless steels	20–60	1–5 min	(j)
II-2	900 mL acetic acid, 100 mL $HClO_4$	Zirconium, titanium, uranium, steels, superalloys	12–70	½–2 min	…
II-3	800 mL acetic acid, 200 mL $HClO_4$	Uranium, zirconium, titanium, aluminum, steels, superalloys	40–100	1–15 min	…
II-4	700 mL acetic acid, 300 mL $HClO_4$	Nickel, lead, lead-antimony alloys	40–100	1–5 min	…
II-5	650 mL acetic acid, 350 mL $HClO_4$	3% silicon iron	…	5 min	(k)
Group III: Electrolytes composed of H_3PO_4 (85%) in water or organic solvent					
III-1	1000 mL H_3PO_4	Cobalt	1.2	3–5 min	…
III-2	175 mL distilled H_2O, 825 mL H_3PO_4	Pure copper	1.0–1.6	10–40 min	(m)
III-3	300 mL H_2O, 700 mL H_3PO_4	Stainless steel, brass, copper, and copper alloys except tin-bronze	1.5–1.8	5–15 min	(m)
III-4	600 mL H_2O, 400 mL H_3PO_4	α or α + β brass, copper-iron, copper-cobalt, cobalt, cadmium	1–2	1–15 min	(n)
III-5	1000 mL H_2O, 580 g $H_4P_2O_7$ (pyrophosphoric acid)	Copper, copper-zinc	1–2	10 min	(m)
III-6	500 mL diethylene glycol monoethyl ether, 500 mL H_3PO_4	Steel	5–20	5–15 min	(p)
III-7	200 mL H_2O, 380 mL ethanol (95%), 400 mL H_3PO_4	Aluminum, magnesium, silver	25–30	4–6 min	(q)
III-8	300 mL ethanol (absolute), 300 mL glycerol (cp), 300 mL H_3PO_4	Uranium	…	…	…
III-9	500 mL ethanol (95%), 250 mL glycerol, 250 mL H_3PO_4	Manganese, manganese-copper alloys	18	…	…
III-10	500 mL distilled H_2O, 250 mL ethanol (95%), 250 mL H_3PO_4	Copper and copper-base alloys	…	1–5 min	…
III-11	Ethanol (absolute) to make 1000 mL of solution; 400 g $H_4P_2O_7$	Stainless steel, all austenitic heat-resistant alloys	…	10 min	(r)
III-12	625 mL ethanol (95%), 375 mL H_3PO_4	Magnesium-zinc	1.5–2.5	3–30 min	…
III-13	445 mL ethanol (95%), 275 mL ethylene glycol, 275 mL H_3PO_4	Uranium	18–20	5–15 min	(s)
Group IV: Electrolytes composed of H_2SO_4 in water or organic solvent					
IV-1	250 mL H_2O, 750 mL H_2SO_4	Stainless steel	1.5–6	1–2 min	…

IV-2	400 mL H_2O, 600 mL H_2SO_4	Stainless steel, iron, nickel	1.5–6	2–6 min	…
IV-3	750 mL H_2O, 250 mL H_2SO_4	Stainless steel, iron, nickel	1.5–6	2–10 min	…
		Molybdenum	1.5–6	$\frac{1}{3}$–1 min	(t)
IV-4	900 mL H_2O, 100 mL H_2SO_4	Molybdenum	1.5–6	$\frac{1}{3}$–2 min	(t)
IV-5	70 mL H_2O, 200 mL glycerol, 720 mL H_2SO_4	Stainless steel	1.5–6	$\frac{1}{2}$–5 min	…
IV-6	220 mL H_2O, 200 mL glycerol, 580 mL H_2SO_4	Stainless steel, aluminum	1.5–12	1–20 min	…
IV-7	875 mL methanol (absolute), 125 mL H_2SO_4	Molybdenum	6–18	$\frac{1}{2}$–1$\frac{1}{2}$ min	(u)
Group V: Electrolytes composed of CrO_3 in water					
V-1	830 mL H_2O, 620 g CrO_3	Stainless steel	1.5–9	2–10 min	…
V-2	830 mL H_2O, 170 g CrO_3	Zinc, brass	1.5–12	10–60 s	…
Group VI: Electrolytes composed of mixed acids or salts in water or organic solution					
VI-1	600 mL H_3PO_4 (85%), 400 mL H_2SO_4	Stainless steel	…	…	…
VI-2	150 mL H_2O, 300 mL H_3PO_4 (85%), 550 mL H_2SO_4	Stainless steel	…	2 min	(v)
VI-3	240 mL H_2O, 420 mL H_3PO_4 (85%), 340 mL H_2SO_4	Stainless and alloy steels	…	2–10 min	(w)
VI-4	330 mL H_2O, 550 mL H_3PO_4 (85%), 120 mL H_2SO_4	Stainless steel	…	1 min	(x)
VI-5	450 mL H_2O, 390 mL H_3PO_4 (85%), 160 mL H_2SO_4	Bronze (to 9% Sn)	…	1–5 min	(y)
VI-6	330 mL H_2O, 580 mL H_3PO_4 (85%), 90 mL H_2SO_4	Bronze (to 6% Sn)	…	1–5 min	(y)
VI-7	140 mL H_2O, 100 mL glycerol, 430 mL H_3PO_4 (85%), 330 mL H_2SO_4	Steel	…	1–5 min	(z)
VI-8	200 mL H_2O, 590 mL glycerol, 100 mL H_3PO_4 (85%), 110 mL H_2SO_4	Stainless steel	…	5 min	(aa)
VI-9	260 mL H_2O, 175 g CrO_3, 175 mL H_3PO_4 (85%), 580 mL H_2SO_4	Stainless steel	…	30 min	(bb)
VI-10	175 mL H_2O, 105 g CrO_3, 460 mL H_3PO_4 (85%), 390 mL H_2SO_4	Stainless steel	…	60 min	(cc)
VI-11	245 mL H_2O, 80 g CrO_3, 650 mL H_3PO_4 (85%), 130 mL H_2SO_4	Stainless and alloy steels	…	5–60 min	(dd)
VI-12	100 mL HF, 900 mL H_2SO_4	Tantalum	…	9 min	(ee)
VI-13	210 mL H_2O, 180 mL HF, 610 mL H_2SO_4	Stainless steel	…	5 min	(ff)
VI-14	800 mL H_2O, 100 g CrO_3, 46 mL H_2SO_4 310 g sodium dichromate, 96 mL acetic acid (glacial)	Zinc	…	…	(gg)
VI-15	260 mL H_2O_2 (30%), 240 mL HF, 500 mL H_2SO_4	Stainless steel	…	5 min	(hh)

VI-16	520 mL H_2O, 80 mL HF, 400 mL H_2SO_4	Stainless steel	…	½–4 min	(jj)
VI-17	600 mL H_2O, 180 g CrO_3, 60 mL HNO_3, 3 mL HCl, 240 mL H_2SO_4	Stainless steel	…	…	…
VI-18	750 mL glycerol, 125 mL acetic acid (glacial), 125 mL HNO_3	Bismuth	12	1–5 min	(kk)
VI-19	900 mL ethylene glycol monoethyl ether, 100 mL HCl	Magnesium	50–60	10–30 s	(mm)
VI-20	685 mL methanol (absolute), 225 mL HCl, 90 mL H_2SO_4	Molybdenum, sintered and cast	19–35	20–35 s	(nn)
VI-21	885 mL ethanol (absolute), 100 mL *n*-butyl alcohol, 109 g $AlCl_3 \cdot 6\ H_2O$ (hydrated aluminum chloride), 250 g $ZnCl_2$ (zinc chloride) (anhydrous)	Titanium	30–60	1–6 min	…
VI-22	750 mL acetic acid (glacial), 210 mL distilled H_2O, 180 g CrO_3	Uranium	80	5–30 min	(pp)
VI-23	720 mL ethanol (95%), 90 g $AlCl_3 \cdot 6H_2O$, 225 g ZnCl (anhydrous), 120 mL distilled H_2O, 80 mL *n*-butyl alcohol	Pure zinc	25–40	½–3 min	(qq)
VI-24	870 mL glycerol, 43 mL HF, 87 mL HNO_3	Zirconium(h)	9–12	1–10 min	(rr)
VI-25	980 mL saturated solution of KI (potassium iodide) in distilled H_2O, 20 mL HCl	Bismuth	7	30 s	(ss)
Group VII: Alkaline electrolytes					
VII-1	Water to make 1000 mL, 80 g KCN (potassium cyanide), 40 g K_2CO_3 (potassium carbonate), 50 g $AuCl_3$ (gold chloride)	Gold, silver	7.5	2–4 min	(tt)
VII-2	Water to make 1000 mL, 100 g NaCN (sodium cyanide), 100 g potassium ferricyanide	Silver	2.5	To 1 min	(tt)
VII-3	Water to make 1000 mL, 400 g KCN, 280 g silver cyanide, 280 g K_2CrO_7 (potassium dichromate)	Silver	…	To 9 min	(uu)
VII-4	Water to make 1000 mL, 160 g $Na_3PO_4 \cdot 12\ H_2O$ (trisodium phosphate)	Tungsten	…	10 min	(vv)
VII-5	Water to make 1000 mL, 100 g NaOH	Tungsten, lead	…	8–10 min	(ww)
VII-6	Water to make 1000 mL, 200 g KOH	Zinc, tin	2–6	15 min	(xx)
Group VIII: Electrolyte composed of methanol and HNO_3					
VIII-1	600 mL methanol (absolute), 300 mL HNO_3	Nickel, copper, zinc, Monel, brass, Nichrome, stainless steel	40–70	10–60 s	(yy)

Note: Chemical components of electrolytes are listed in the order of mixing. Except where otherwise noted, the electrolytes are intended for use at ambient temperatures, in the approximate range of 18 to 38 °C (65 to 100 °F), and with stainless steel cathodes.

(a) In electrolytes I-1 through I-6, absolute SD-3A or SD-30 ethanol can be substituted for absolute ethanol. (b) Nickel cathode. (c) One of the best electrolytes for universal use. (d) Universal electrolyte comparable to I-4. (e) Particularly good with Al-Si alloys. (f) Polish only. (g) 3 s cycles repeated at least seven times to prevent heating. (h) Polish and etch simultaneously. (j) Good general-purpose electrolyte. (k) 0.06 A/cm^2 (0.4 A/in.^{2}). (m) Copper cathode. (n) Copper or stainless steel cathode. (p) 49 °C (120 °F). (q) Aluminum cathode; 38 to 43 °C (100 to 110 °F). (r) 38 °C (100 °F) plus. (s) 0.03 A/cm^2 (0.2 A/in.^{2}). (t) Particularly good for sintered

molybdenum; 0 to 27 °C (32 to 80 °F). (u) 0 to 27 °C (32 to 80 °F). (v) 0.3 A/cm^2 (1.9 A/in.^{2}). (w) 0.1 to 0.2 A/cm^2 (0.65 to 1.3 A/in.^{2}). (x) 0.05 A/cm^2 (0.3 A/in.^{2}). (y) 0.1 A/cm^2 (0.65 A/in.^{2}). (z) 1 to 5 A/cm^2 (6.5 to 32 A/in.^{2}); 38 °C (100 °F) plus. (aa) 1 A/cm^2 (6.5 A/in.^{2}); 27 to 49 °C (80 to 120 °F). (bb) 0.6 A/cm^2 (3.9 A/in.^{2}); 27 to 49 °C (80 to 120 °F). (cc) 0.5 A/cm^2 (3.2 A/in.^{2}); 27 to 49 °C (80 to 120 °F). (dd) 0.5 A/cm^2 (3.2 A/in.^{2}); 38 to 54 °C (100 to 130 °F). (ee) Graphite cathode; 0.1 A/cm^2 (0.65 A/in.^{2}); 32 to 38 °C (90 to 100 °F). (ff) 0.5 A/cm^2 (3.2 A/in.^{2}); 21 to 49 °C (70 to 120 °F). (gg) 0.002 A/cm^2 (0.013 A/in.^{2}); 21 to 38 °C (70 to 100 °F). (hh) 0.5 A/cm^2 (3.2 A/in.^{2}). *Caution:* Dangerous. (jj) 0.08 to 0.3 A/cm^2 (0.52 to 1.9 A/in.^{2}). (kk) 0.5 A/cm^2 (3.2 A/in.^{2}). *Caution:* This mixture will decompose vigorously after a short time; do not try to keep. (mm) Bath should be stirred. Cool below 2 °C (35 °F) with cracked ice. (nn) Mix slowly. Heat is developed. Avoid contamination with water. Use below 2 °C (35 °F). (pp) Chromic acid is dissolved in the water, and this solution is then added to the acetic acid. Electrolyte is used below 2 °C (35 °F). (qq) Electrolyte is used below 16 °C (60 °F). (rr) *Caution:* Electrolyte will decompose on standing and is dangerous if kept too long. (ss) Polish 30 s, but allow to remain in electrolyte until brown film is dissolved. (tt) Graphite cathode. (uu) Graphite cathode; 0.003 to 0.009 A/cm^2 (0.02 to 0.06 A/in.^{2}). (vv) Graphite cathode; 0.09 A/cm^2 (0.58 A/in.^{2}). 38 to 49 °C (100 to 120 °F). (ww) Graphite cathode; 0.03 to 0.06 A/cm^2 (0.02 to 0.4 A/in.^{2}). (xx) Copper cathode; 0.1 to 0.2 A/cm^2 (0.65 to 1.3 A/in.^{2}). (yy) An extremely useful electrolyte for certain applications, but dangerous; see text.

Table 3 Applicability of electrolytes in Table 2 to electropolishing of various metals and alloys

Metal	Electrolyte
Aluminum	I-1, I-2, I-4, I-5, I-6, I-8, I-10, II-3, III-7, IV-6
Aluminum-silicon alloys	I-6, I-8
Antimony	II-4
Beryllium	I-4
Bismuth	VI-18, VI-25
Cadmium	III-4
Cast iron	I-4, II-1
Chromium	II-1, VIII-1
Cobalt	I-5, III-1, III-4
Copper	III-2, III-3, III-4, III-5, III-10, VIII-1
Copper-nickel alloys	III-3, III-10, VIII-1
Copper-tin alloys	III-10, VI-5, VI-6, VIII-1
Copper-zinc alloys	III-3, III-4, III-5, III-10, V-2, VIII-1
Germanium	I-9
Gold	VII-1
Iron, pure	I-5, II-1, IV-2, IV-3
Iron-copper alloys	III-3, III-4
Iron-nickel alloys	I-5, II-1, II-2, II-4, IV-3, VIII-1
Iron-silicon alloys	I-5, I-6, I-8, II-5
Lead	I-1, I-5, II-4, VII-5
Magnesium	I-1, III-7, III-12, VI-19
Manganese	III-9
Molybdenum	I-7, IV-3, IV-4, IV-7, VI-20
Nickel	I-4, II-4, IV-2, VII-1
Nickel-chromium alloys	II-4, VIII-1
Silver	I-4, III-7, VII-1, VII-2, VII-3
Steel: austenitic stainless and superalloys	I-1, I-2, I-3, I-4, I-5, II-1, II-2, II-3, III-3, III-6, III-11, IV-1, IV-2, IV-3, IV-5, IV-6, V-1, VI-1, VI-2, VI-3, VI-4, VI-7, VI-8, VI-9, VI-10, VI-11, VI-13, VI-15, VI-16, VI-17, VIII-1
Steel: carbon and alloy	I-1, I-4, I-5, II-1, II-2, II-3, III-6, VI-3, VI-7, VI-11
Tantalum	VI-12
Thorium	I-3

Tin	I-4, VI-5, VI-6, VII-6
Titanium	I-4, I-7, I-9, II-1, II-2, II-3, VI-21
Tungsten	VII-4, VII-5
Uranium	I-4, I-7, II-1, II-2, II-3, III-8, III-13, VI-22
Vanadium	I-9
Zinc	I-1, I-5, III-12, VI-2, VI-14, VI-23, VII-6, VII-1
Zirconium	I-4, I-5, I-7, I-9, II-1, II-2, II-3, VI-24

Desirable electrolyte characteristics include the following (Ref 6):

- Should be a somewhat viscous solution
- Should be a good solvent during electrolysis
- Should not attack the sample with the current off
- Should contain one or more large ions, for example, PO_4^{3-}, ClO_4^{1-}, or SO_4^{2-}, or large organic molecules
- Should be simple to mix, stable, and safe
- Should be operable at room temperature and be insensitive to temperature changes

ASTM standard E 3 (Ref 6) lists commonly encountered problems in electropolishing and recommendations for their elimination, as shown in Table 4.

Table 4 Electropolishing procedural problems and corrections

Trouble	Possible cause	Suggested correction
Center of specimen deeply etched	No polishing film at center of specimen	Increase voltage
		Decrease agitation
		Use more viscous electrolyte
Pitting or etching at edges of specimen	Too viscous or thick film	Decrease voltage
		Increase agitation
		Use less viscous electrolyte
Sludge settling on surface	Insoluble anode product	Try new electrolyte
		Increase temperature
		Increase voltage
Roughness or matte surface	Insufficient or no polishing film	Increase voltage
		Use more viscous electrolyte
Waviness or streaks on polished surface	Insufficient time	Increase or decrease agitation
	Incorrect agitation	Use better preparation
	Inadequate preparation	Increase voltage and decrease time
	Too much time	
Stains on polished surface	Attack after polishing current is off	Remove specimen while current is still on
		Try less corrosive electrolyte
Unpolished spots (bullseyes)	Gas bubbles	Increase agitation
		Decrease voltage
Phases in relief	Insufficient polishing film	Increase voltage
		Use better preparation
		Decrease time
Pitting	Polishing too long	Use better preparation
	Voltage too high	Decrease voltage
		Decrease time
		Try different electrolyte

Source: Ref 6

Advantages and Limitations

When properly applied, electropolishing can be a useful tool for the metallographer and offers several advantages. For some metals, electropolishing can produce a high-quality surface finish that is better than or equivalent to the best surface finish obtained by mechanical methods. Once a procedure has been established, good results can be obtained with less operator skill than required for mechanical polishing.

A significant saving of time can be achieved if many specimens of the same material are to be polished sequentially. Electropolishing is particularly well suited to softer metals, which may be difficult to polish by mechanical methods. Scratching does not occur in electrolytic polishing. The absence of scratches is advantageous in viewing high-quality electropolished surfaces of optically active materials under polarized light.

Artifacts resulting from mechanical deformation, such as disturbed metal or mechanical twins, which are produced on the surface even by careful grinding and mechanical polishing, do not occur in electropolishing. Surfaces are completely unworked by the polishing procedure, which is particularly beneficial in low-load hardness testing, x-ray studies, and electron microscopy.

In some applications, etching can be accomplished by reducing the voltage to approximately one-tenth the potential required for polishing and then continuing electrolysis for a few seconds. In general, electropolishing is frequently useful in electron microscopy, in which high resolution is important, because it can produce clean, undistorted metal surfaces.

Metallographic preparation by electropolishing is subject to several limitations, which should be recognized to prevent misapplication of the method and inappropriate results (Ref 7).

Generally, the chemicals and combinations of chemicals used in electropolishing are poisonous; many are highly flammable or potentially explosive. Only well-trained personnel who are thoroughly familiar with chemical laboratory procedures should be permitted to handle or mix the chemicals or to operate the polishing baths (see the article “Contrast Enhancement and Etching” in this Volume).

The conditions and electrolytes required to obtain a satisfactorily polished surface differ for different alloys. Consequently, considerable time may be required to develop a procedure for a new alloy, if it can be developed at all. This limitation does not apply if appropriate procedures exist.

In multiphase alloys, the rates of polishing of different phases often are not the same. Polishing results depend significantly on whether the second or third phases are strongly cathodic or anodic with respect to the matrix. The matrix is dissolved preferentially if the other phases are relatively cathodic, thus causing the latter to stand in relief.

Preferential attack may also occur at the interface between two phases. These effects are most pronounced when phases other than the matrix are virtually unattacked by the polishing bath. The effects are reversed when the matrix phase is relatively cathodic.

A large number of electrolytes may be needed to polish the variety of metals encountered by a given laboratory. Plastic or metal mounting materials may react with the electrolyte.

Electropolished surfaces exhibit an undulating rather than a plane surface and, in some cases, may not be suited for examination at all magnifications. Under some conditions, furrowing and pitting may be produced. Also, edge effects limit applications involving small specimens, surface phenomena, coatings, interfaces, and cracks.

Attack around nonmetallic particles and adjacent metal, voids, and various inhomogeneities may not be the same as that of the matrix, thus exaggerating the size of the voids and inclusions. Additionally, electropolished surfaces of certain materials may be passive and difficult to etch.

Safety Precautions

Many electrolytes used for electropolishing can be dangerous if improperly handled. Although general safety precautions are discussed as follows, the bulk of the subsequent discussion relates directly to the electrolyte groups listed in Table 2 (groups I to VIII). *It is essential that the following instructions be read before any electrolyte is mixed or used.*

Mixtures of $HClO_4$ and acetic anhydride are extremely dangerous to prepare and are even more unpredictable to use. Many industrial firms and research laboratories forbid their use. Some municipalities also have ordinances prohibiting the use of such potentially explosive mixtures, which have caused fatalities and property damage in some accidents. These mixtures are highly corrosive to the skin, and the vapors of acetic anhydride can cause

severe damage by inhalation. These hazards are considered sufficient reason for recommending that mixtures of $HClO_4$ and acetic anhydride not be used, despite their effectiveness as electropolishing electrolytes.

Mixtures of oxidizable organic compounds and powerful oxidizing agents are always potentially dangerous. After some use, any electrolyte will become heavily laden with ions of the metals polished. These ions may catalyze the decomposition of the electrolyte, and the metallic salts that can crystallize from some reagents may be explosive. Electrolytes must be discarded immediately after use by flushing down a chemical waste drain with a large amount of water.

Mixing, storing, and handling of electrolytes should be done using containers and equipment made of materials suitable for the chemicals used. Glass is resistant to nearly all chemicals.

Polyethylene, polypropylene, and similarly inert plastics are resistant to hydrofluoric (HF), fluosilicic (H_2SiF_6), and fluoboric (HBF_4) acids, as well as to solutions containing salts of these acids. These materials are also recommended for prolonged storage of strongly alkaline solutions and strong solutions of phosphoric acid (H_3PO_4), both of which attack glass (particularly, ordinary grades of glass).

Electrolytes must not be allowed to become heavily laden with dissolved metals in use. They must never be allowed to become more concentrated by evaporation during storage or use.

The electrolytes listed in Table 2 are classified by chemical type (Ref 8). Their chemical components are listed in the order of mixing. Although contrary to common practice, listing in this order is done to prevent possibly dangerous mistakes. Unless other instructions are given, the electrolytes are intended to be used in the temperature range of 20 to 40 °C (65 to 100 °F). The use of a stainless steel cathode with these electrolytes is also presumed unless otherwise stipulated.

Use of Perchloric Acid. Electrolytes of groups I and II contain $HClO_4$ because of its unique effectiveness in electropolishing many metals. No attempt should be made to store, handle, or prepare mixtures of $HClO_4$ without a thorough understanding of all the precautions that must be observed to avoid accidents.

Some highly concentrated mixtures of $HClO_4$ can be exploded by detonation; others that are not detonatable can be ignited by sparks or by general heating, and the ensuing fire may result in an explosion. Perchloric acid solutions should not be used in contact with organic materials; polyethylene, polystyrene, epoxy resins, and polyvinyl chloride are among the mounting materials considered safe for use with $HClO_4$. For a detailed discussion of the hazards of $HClO_4$ solutions and the precautions that must be observed in their use, see Ref 1 and 8.

Group I electrolytes (composed of $HClO_4$ and alcohol with or without organic additions) are believed to be safe to mix and use, provided the following precautions are observed:

- The baths should be made up only in small quantities and should be stored in glass-stoppered bottles that are filled completely with the electrolyte.
- Any evaporated solvents should be promptly replaced by refilling the bottle.
- Spent or exhausted baths should be promptly discarded.
- No departure should be allowed from the prescribed formula, the method of mixing, or the strength of the acid used.
- The electrolytes should always be protected from heat or fire.

Group II electrolytes are composed of $HClO_4$ and glacial acetic acid in varying proportions. Very little heat is developed when $HClO_4$ is mixed with glacial acetic acid. In mixing, $HClO_4$ should be added to the acetic acid while stirring. Although these mixtures are considered safe to mix and use, great care should be exercised in their use. Temperatures should not exceed 30 °C (85 °F).

These electrolytes are flammable and must be guarded against fire or the evaporation of the acetic acid. Plastic parts are likely to be damaged quickly by exposure to such mixtures.

Group III electrolytes (composed of H_3PO_4 in water or organic solvent) are generally quite easy to prepare. In mixing, the acid must be slowly poured into the water or solvent with constant stirring to prevent the formation of a heavy layer of acid at the bottom of the vessel. Pyrophosphoric acid reacts vigorously when dissolved in water. It hydrolyzes slowly in water at room temperature and rapidly in hot water to form ortho-H_3PO_4.

Group IV electrolytes are composed of H_2SO_4 in water or organic solvent. Dilution of H_2SO_4 with water is somewhat difficult, because it is accompanied by an extremely exothermic reaction. The acid must always be poured into the water slowly and with constant stirring to prevent violent boiling. Great care should be taken to prevent spattering.

Mixing should be done in an exhaust hood, and a face shield and protective laboratory apron should be worn. Even dilute solutions of H_2SO_4 strongly attack the skin or clothing. Such solutions are also very hygroscopic.
These solutions vigorously attack most plastics; only certain mounting materials, such as polyvinyl chloride, provide satisfactory resistance. Mixtures of H_2SO_4 with other inorganic acids are generally more useful as electrolytes.
Group V electrolytes are composed of chromic acid in water. Dissolving of crystalline chromic acid or chromium trioxide (CrO_3) in water is not hazardous, because very little heat is developed. Chromic acid, however, is a powerful oxidant and, under certain conditions, reacts violently with organic matter or other reducing substances.
Chromic acid generally is dangerous and may be incendiary in the presence of oxidizable materials. It cannot be safely mixed with most organic liquids. It generally can be mixed with saturated organic acids. Chromic acid solutions cannot be used in contact with plastic parts without eventually destroying them. Care should be taken to prevent contact of these solutions with the skin, because repeated exposure to even dilute solutions of CrO_3 or chromates in acidic solutions causes persistent and painful ulcers that are difficult to heal.
Group VI electrolytes (mixed acids or salts in water or organic solutions) are safe to mix and use, provided the mixing is done carefully and in the specified sequence. In all cases, the acid must be added to the solvent slowly and with constant stirring. If H_2SO_4 is contained in the formula, it should be added last and with extreme care, after cooling the initially prepared mixture to room temperature if necessary.
If HF or fluorides are contained in the electrolyte formula, the vessels used should be made of polyethylene or other material that is resistant to HF. Particular care should be taken to avoid skin contact with acid fluorides; exposure, which may pass unnoticed at the time of occurrence, may result in serious burns.
In mixing electrolytes containing anhydrous aluminum chloride ($AlCl_3$), extreme care must be exercised. The reaction between this compound and water is almost explosive. Chromic acid cannot be safely mixed with most organic liquids but can be mixed with saturated organic acids. Care should be taken to prevent contact with the skin.
Group VII (alkaline) electrolytes are classified into two general groups: those that contain cyanide and those that do not. Use of cyanide by untrained personnel is extremely dangerous. Cyanides are among the most rapid acting and most potent poisons encountered in the laboratory, and lethal concentrations of hydrogen cyanide gas may not be detected readily by odor or irritant action. Cyanide is so quick-acting and deadly that the administration of an antidote is usually ineffective.
Extreme care must be taken that neither a droplet of the solution nor a crystal of the salt is left where it can be accidentally picked up and carried to the mouth. If any spillage occurs, as much as possible should be mopped up with a sponge and water. The remainder can then be destroyed by washing the area with very dilute nitric acid (HNO_3).
Solutions of the alkali hydroxides are very useful for the polishing of certain amphoteric metals, such as lead, tin, tungsten, and zinc. The attack of these solutions on the skin is drastic, so great care should be exercised in their use.
These solutions evolve considerable amounts of heat in contact with water and should be dissolved with constant stirring, using cooling and adding the hydroxide in small portions when preparing concentrated solutions. Incomplete mixing can cause layering, with danger of a delayed violent reaction.
Group VIII electrolyte is a mixture of methanol and HNO_3. With careful handling, HNO_3 can be safely mixed with methanol. The acid should be added gradually to the alcohol, with constant stirring. Nitric acid cannot be safely mixed with ethanol or higher alcohols, except in solutions not stronger than approximately 5 vol% HNO_3.
If pure chemicals are used, the mixture of HNO_3 and methanol is quite stable, provided it is never heated or confined in any way. Consequently, it must not be stored in a closed container.
Under certain conditions, extremely unstable or explosive nitro compounds, azides, or fulminates can be formed. The spontaneous decomposition of the mixture can also be catalyzed by impurities or heat. The electrolyte should be discarded immediately after use.
For some applications, group VIII electrolyte is extremely useful, but because of its dangerous nature, it should be used only when necessary.

Local Electropolishing

Special techniques for local polishing extend the application of electropolishing from use on conventional small metallographic specimens to the examination of selected regions on large objects, and to almost any metal. Several types of portable cathode probes for in situ local electropolishing (complete with current sources and controls) are available commercially. These devices vary in design and complexity.

In one type of unit, electrolyte is circulated from an external container through a replaceable pencil-type plastic polishing chamber that can be clamped against the area (approximately 7 mm, or $\frac{1}{4}$ in., in diameter) to be polished. Both conventional and proprietary electrolytes are used, and polishing is conveniently followed by electrolytic etching at greatly reduced current, or by chemical etching where needed.

A typical simple unit for local electropolishing is the portable, handheld tampon-type probe (Fig. 8). In this application, it is used to polish a recessed portion of a large roll. The probe consists of an austenitic stainless steel head (cathode) attached to the end of an electrically insulating plastic body.

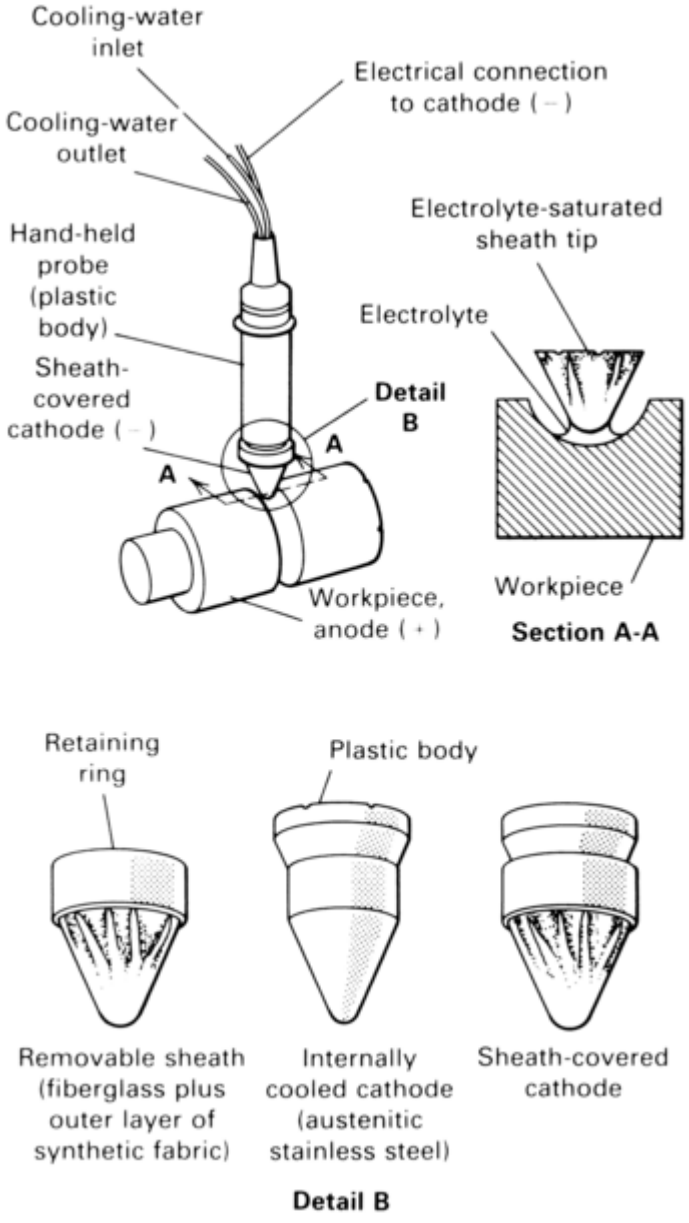

Fig. 8 Arrangement for nondestructive local electropolishing on a recessed portion of a large object, using a small-radius tampon-type portable probe. Cathode shown has a radius of approximately 1.6 mm ($\frac{1}{16}$ in.); for polishing flat surfaces or larger areas, a cathode with a more rounded tip (radius of approximately 9.5 mm, or $\frac{3}{8}$ in.) is used.

The stainless steel head is cooled by internal circulation of water to maintain the tip and the electrolyte at a predetermined optimal temperature for electropolishing, usually between 0 and 10 °C (32 and 50 °F). The head is covered by a removable sheath made of an inner layer of fiberglass and an outer layer of chemically resistant

woven synthetic fabric. The sheath is flexible, electrically insulating, and spongy enough to retain the electrolyte.

In use, a small amount of electrolyte is retained by capillarity between the specimen and the cathode by keeping the sheath saturated with electrolyte. The sheath tip is held at approximately 1.6 mm ($\frac{1}{16}$ in.) from the specimen (see section A-A in Fig. 8).

Conical stainless steel cathodes with tips having radii of approximately 9.5 and 1.6 mm ($\frac{3}{8}$ and $\frac{1}{16}$in.) are available; the sharper tip is used where access is difficult and where high current densities are needed. The diameter of the spot on the specimen covered by the drop of electrolyte is approximately 9.5 mm ($\frac{3}{8}$ in.) when the sharper tip is used and approximately 19 mm ($\frac{3}{4}$ in.) with the more rounded tip.

The electrolyte held by the sheath is renewed approximately once a minute by dipping the sheath in a beaker of electrolyte. To polish larger areas, the probe is moved in a circular pattern and back and forth, as desired. Polishing usually takes approximately 3 min. The sheath is removed and washed after each use and can be used 20 to 50 times.

Specimen Preparation. Before electropolishing, specimen surfaces usually are mechanically ground with 220-, 320-, 400-, and 600-grit papers in sequence and then polished with 6 and 1 μm diamond paste. A portable mechanical grinding/polishing machine is well suited for this purpose.

Electrolytes and Recommended Voltages. Not all conventional electrolytes are suitable for local electropolishing by the tampon method, and special electrolytes are available for this purpose. Recommended electrolytes and voltages for polishing various metals are listed in Table 5.

Table 5 Electrolytes and voltages for tampon-type local electropolishing of various metals

Electrolyte composition	Metal	Voltage
9 mL $HClO_4$ (60%), 91 mL butyl cellosolve	Steel, iron, and iron-base alloys	35–40
	Aluminum and aluminum alloys	30–45
	Beryllium and beryllium alloys	43–46
10 mL $HClO_4$ (60%), 45 mL acetic acid (glacial), 45 mL butyl cellosolve	Steel	30–35
	Chromium-base alloys	32–37
	Nickel and nickel-base alloys	30–40
	Cobalt-base alloys	30–60
54 mL H_3PO_4 (85%), 22 mL ethanol (absolute), 3 mL H_2O, 21 mL butyl cellosolve	Copper and copper alloys	4–6
11 mL $HClO_4$ (60%), 65 mL methanol (absolute), 24 mL butyl cellosolve	Titanium alloys	26–28

Examination. After polishing, the surface can be observed under a metallographic microscope. However, the range of the technique can be extended considerably by the use of plastic replicas. After removal, the replica can be examined by transmission in an ordinary microscope, by reflection in a metallographic microscope, or in an electron microscope after coating with carbon and metal (two-stage replica).

Advantages and Applications. The polishing current used is usually lower than that used in a conventional cell. Convex and concave surfaces with small radii can be examined, and voltage and current density can be controlled accurately.

With the aid of replication techniques, the fine structure on large objects or parts for which removal of a conventional specimen would be costly or impractical can be examined with an optical or electron microscope. The surface changes during fatigue of parts in service can be followed, and structures of highly radioactive specimens can be examined (with special precautions).

The surface macrostructure, microstructure, and submicrostructure of parts as large as a ship propeller and a crankshaft and a connecting rod of a diesel engine have been inspected during manufacture, in service, and after

damage. The tampon method can also be used for laboratory metallographic work and is particularly useful for examining thin sheets and tubes.

Another use has been the study of crack growth in fatigue and fracture toughness specimens—polishing areas approximately 50 by 125 mm (2 by 5 in.) to measure crack length and optically examining deformation markings related to the plastic zone at the tip of a crack. In addition, longitudinal sections of fatigue and fracture toughness specimens have been locally electropolished for measurement of plastic zone sizes by microhardness indentations, using special edge-retention techniques. The equipment, procedures, and applications of local electropolishing by the tampon technique are discussed in Ref 9 and 10.

Electrolytic Etching. Immediately after an electropolishing operation is completed, electrolytic etching can be accomplished in some applications by reducing the voltage to approximately one-tenth the potential required for electropolishing and then continuing electrolysis for a few seconds. For more information on the procedures, apparatus, and applications of electrolytic etching, see the article “Contrast Enhancement and Etching” in this Volume and Ref 1 and 11. Specific applications of electrolytic etching are also described in articles for specific metals and alloys in this Volume. Information on anodizing, an electrolytic etch process for depositing an oxide film on a metal surface, and electrolytic-potentiostatic etching can be found in the article “Color Metallography” in this Volume.

References cited in this section

1. G.F. Vander Voort, *Metallography: Principles and Practice*, McGraw-Hill, 1984, Reprinted ASM International, 1999

2. E. Weidmann, Electrolytic Polishing, *Metallography and Microstructures,* Vol 9, *ASM Handbook,* American Society for Metals, 1985, p 48–56

4. P.A. Jacquet, Electrolytic Polishing of Metallic Surfaces, *Met. Finish.,* May 1949, p 48–54; June 1949, p 83–92; July 1949, p 58–64; Sept 1949, p 60–67; Oct 1949, p 68–73; Jan 1950, p 56–62; Feb 1950, p 55–62

5. P.V. Schigolev, *Electrolytic and Chemical Polishing of Metals,* Freund, Holon, Israel, 1970

6. “Standard Practice for Preparation of Metallographic Specimens,” E 3, *Annual Book of ASTM Standards,* ASTM International

7. L.E. Samuels, A Critical Comparison Between Mechanical and Electrolytic Methods of Metallographic Polishing, *Metallurgia,* Vol 66 (No. 396), 1962, p 187–199

8. R.L. Anderson, “Electrolytic Polishing of Metallographic Specimens,” Research Report 60-94402-11-R2, Westinghouse Research Laboratories, 20 April 1955

9. T.C. Bathias and R.M.N. Pelloux, Electropolishing System Ideal for Small Areas of Large Structures, *Met. Prog.,* Aug 1972, p 69

10. W.J.McG. Tegart, *The Electrolytic and Chemical Polishing of Metals in Research and Industry,* 2nd ed., Pergamon Press, 1959

11. G. Petzow, *Metallographic Etching,* 2nd ed., ASM International, 1999

References

1. G.F. Vander Voort, *Metallography: Principles and Practice,* McGraw-Hill, 1984, Reprinted ASM International, 1999

2. E. Weidmann, Electrolytic Polishing, *Metallography and Microstructures,* Vol 9, *ASM Handbook,* American Society for Metals, 1985, p 48–56

3. *Practical Guide to Image Analysis,* ASM International, 2000, p 53

4. P.A. Jacquet, Electrolytic Polishing of Metallic Surfaces, *Met. Finish.,* May 1949, p 48–54; June 1949, p 83–92; July 1949, p 58–64; Sept 1949, p 60–67; Oct 1949, p 68–73; Jan 1950, p 56–62; Feb 1950, p 55–62

5. P.V. Schigolev, *Electrolytic and Chemical Polishing of Metals,* Freund, Holon, Israel, 1970

6. "Standard Practice for Preparation of Metallographic Specimens," E 3, *Annual Book of ASTM Standards,* ASTM International

7. L.E. Samuels, A Critical Comparison Between Mechanical and Electrolytic Methods of Metallographic Polishing, *Metallurgia,* Vol 66 (No. 396), 1962, p 187–199

8. R.L. Anderson, "Electrolytic Polishing of Metallographic Specimens," Research Report 60-94402-11-R2, Westinghouse Research Laboratories, 20 April 1955

9. T.C. Bathias and R.M.N. Pelloux, Electropolishing System Ideal for Small Areas of Large Structures, *Met. Prog.,* Aug 1972, p 69

10. W.J.McG. Tegart, *The Electrolytic and Chemical Polishing of Metals in Research and Industry,* 2nd ed., Pergamon Press, 1959

11. G. Petzow, *Metallographic Etching,* 2nd ed., ASM International, 1999

Contrast Enhancement and Etching, *Metallography and Microstructures,* Vol 9, *ASM Handbook,* ASM International, 2004, p. 294–312

Contrast Enhancement and Etching

Introduction

ETCHING is used in metallography primarily to reveal the microstructure of a specimen under the optical (light) microscope. A specimen suitable for etching must include a carefully polished plane area of the material free of changes caused by surface deformation, flowed materials (smears), pullout, and scratches. The edges of the specimens often must be preserved.

Although some information may be obtained from as-polished specimens, the microstructure is usually visible only after etching. Only features that exhibit a 10% or greater difference in reflectivity can be viewed without etching. This is true of microstructural features with strong color differences or with large differences in hardness that cause relief formation. Crack, pores, pits, and nonmetallic inclusions may be observed in the as-polished condition.

A polished specimen frequently will not exhibit its microstructure, because light is uniformly reflected. The eye cannot discern small differences in reflectivity; therefore, image contrast must be produced. Although this has become known as etching, it does not always refer to the selective chemical dissolution of various structural features. Metallographic contrasting methods include various electrochemical, optical, and physical etching techniques. These can be subdivided into methods based on processes that alter the surface or leave it intact. The latter include nondestructive techniques such as optical enhancement of contrast or the development of structural contrast by the deposition of interference layers on the surfaces of polished specimens. Conversely, etching techniques enhance contrast by preferential attack of constituents on the surface of the specimen to be examined. Etching methods include electrochemical and physical techniques. Of these methods, the classical electrochemical/chemical etching procedures are used more frequently. Physical etching methods, such as ion etching or thermal etching, are used primarily when other techniques fail.

This article primarily discusses etching in conjunction with light microscopy, although polished and etched sections are increasingly examined using the scanning electron microscope with magnifications between those of the optical and transmission electron microscopes. For scanning electron microscopy (SEM), polished specimens are electrochemically etched as for optical examination. However, the depth of etching will generally be quite different, depending on the microstructural features to be examined and the large depth of field characterizing the scanning electron microscope. Fine microstructures from polished surfaces can often be contrasted in secondary electron images when they are selectively coated with chemical layers or when the surface is uniformly coated with a thin physically deposited film. For additional information, see the article “Scanning Electron Microscopy” in this Volume.

Contrast Enhancement and Etching, *Metallography and Microstructures,* Vol 9, *ASM Handbook,* ASM International, 2004, p. 294–312

Etching Nomenclature

The most commonly used metallographic etching terms can be classified on the basis of distinctive features. Optical, electrochemical, and physical etching may be differentiated by kinetic phenomena occurring at the specimen surface. Further distinctions are changes in microsection surface, such as dissolution and precipitation etching; the state of aggregation of etchant, for example, wet and dry etching; etching conditions, such as time

and temperature; magnifications used; etching methods and techniques; and etching phenomena dependent on microstructure. Terms are often used that refer to the major component of the etchant, for example, dilute nitric acid, aqua regia, and sodium thiosulfate; to the originator of the etchant, such as Vilella, Murakami, and Beraha; or to alloys of chief constituents for which the etchant is intended, for example, carbide, phosphide, and steel etchant. Combinations of etching procedures may be used, usually in increasing severity.

Commonly used etching terms are defined in the "Glossary of Terms" of this Volume. The "Reference Information" section in this Volume also contains a "Table of Common Etchant Designations" that lists names and treatment conditions of commonly used etch methods. In addition, Table 1 lists short descriptions of commonly used terms for various etching techniques.

Table 1 Definitions of etching methods

Method	Definition
Anodic etching	Reveals the microstructure by selective anodic dissolution of the polished surface using a DC current. Variation with layer formation: anodizing
Attack polishing	Simultaneous etching while mechanical polishing
Cathodic etching	See *ion etching.*
Cold etching	Reveals the microstructure at room temperature and below
Controlled etching	Electrolytic etching with selection of suitable etchant and voltage, resulting in a balance between current and dissolved metal ions
Crystal figure etching	Discontinuity in etching depending on crystal orientation. Distinctive sectional figures form at polished surface. Closely related to *dislocation etching*
Deep etching	Macroetching, especially for steels, to determine the overall character of the material (presence of imperfections such as seam defects, rolling defects, forging bursts, remnant shrinkage voids, cracks, and coring)
Dislocation etching	Reveals exit points of dislocations on the sample surface. Etching of dislocations is caused by their strain field ranging over a distance of several atoms. Crystal figures (etch pits) are formed at the exiting points. For example, etch pits for cubic materials are cube faced.
Dissolution etching	Reveals the microstructure by surface removal
Double etching	Two etchants are used sequentially, the second one will accentuate a particular microstructural feature.
Drop etching	Placing a drop of an etchant on a selected area of the sample surface to develop the alloying microconstituents (drip reaction)
Dry etching	Develops the microstructure by gaseous exposure
Electrochemical (chemical etching)	General term for revealing the microstructure by redox reactions
Electrolytic etching	See *anodic etching.*
Etch rinsing	Pouring the etchant over a tilted sample surface until the structure is revealed. Used for etching with severe gas evolution
Eutectic cell etching	Reveals eutectic grains (cells)
Grain-boundary etching	Reveals the intersections of individual grains. Grain boundaries have a higher dissolution potential than the individual grains because of their high density of structural defects. Accumulation of impurities in grain boundaries increases this effect.
Grain-contrast etching	Etching the surface of the grains according to their crystal orientation. They become distinct by the different reflectivity caused by reaction layers or surface roughness.
Heat tinting	Formation of interference colors in air or other gases, usually at elevated temperature
Hot etching	Development and stabilization of the microstructure at elevated temperature in etching solutions or gases
Identification (selective) etching	Etching for the identification of particular microconstituents without attacking any others
Immersion etching	The sample is immersed in the etchant with the polished surface up and is agitated. This is the most common etching method.

Immersion etching (cyclic)	Alternate immersion into two etchants: 1, the actual etchant; 2, solution to dissolve the layer formed during the etching process of 1
Ion etching	Surface removal by bombardment with accelerated ions in a vacuum (1 to 10 kV)
Long-term etching	Etching times of a few minutes to several hours
Macroetching	Reveals the macrostructure for the examination with the unaided eye or at a magnification of 50× or less
Microetching	Reveals the microstructure for microscopic observation at a magnification of 50× or higher
Multiple etching	A sample is etched sequentially with specific etchants to reveal certain constituents.
Network etching	Formation of networks (subgrain boundaries), especially in mild steels after etching in nitric acid
Optical etching	Develops the microstructure by using special illumination techniques (dark-field, phase contrast, interference contrast, polarized light)
Physical etching	Develops the microstructure through removal of surface atoms or lowering the grain surface potential
Plasma etching	High-frequency electromagnetic vibrations produce radicals in a gas mixture that react with the sample surface and cause its removal.
Potentiostatic etching	Anodic development of the microstructure at a constant potential enables a defined etching of singular phases.
Precipitation etching	Develops the microstructure by the formation of reaction products at the sample surface
Primary etching	Develops the cast microstructures including coring
Print etching (printing)	A carrier material is soaked with an etching solution and is pressed onto the sample surface. The etchant reacts with one of the microstructural constituents forming substances that affect the carrier material. The result is a direct imprint as a life-size image. It is used for the identification of specific elements, for example, sulfur.
Secondary etching	Develops the microstructures that differ from primary structures through transformation and heat treatment in the solid state
Segregation (coring) etching	Develops segregation (coring) mainly in macrostructures and microstructures of castings
Short-term etching	Etching time of seconds to a few minutes
Shrink etching	Produces a precipitate coating on the grain surfaces and shrinks upon drying, generating cracks. Crack orientation depends on the underlying crystal structure.
Staining	Precipitation etching that causes contrast by distinctive staining of microconstituents; different interference colors originate from surface layers of varying thickness. Identifies inhomogeneities
Strain etching	Reveals regions of high deformation within undeformed areas. Strained areas show increased segregations of precipitates.
Swabbing	Wiping the sample surface with cotton saturated with the etchant; this will simultaneously remove undesired reaction products.
Thermal etching	Annealing the specimen in a vacuum or inert atmosphere. This is a preferred technique for high-temperature microscopy and for ceramics.
Wet etching	The sample surface has been wetted before immersion into the etching solution. This is important when using color etchants.
Wipe etching	See *swabbing.*

Source: Ref 1

Reference cited in this section

1. G. Petzow, *Metallographic Etching*, 2nd ed., ASM International, 1999

Contrast Enhancement and Etching, *Metallography and Microstructures,* Vol 9, *ASM Handbook,* ASM International, 2004, p. 294–312

Optical Enhancement of Contrast

As noted, the observed contrast of metallographic specimens can be enhanced by nondestructive techniques or by altering the surface with etchants. Optical methods allow nondestructive enhancement of contrast by various illumination modes common to metallurgical reflected light microscopes. These optical techniques include dark-field illumination, polarized light microscopy, phase contrast microscopy, and differential interference contrast, all of which use the Köhler illumination principle known from the most common bright-field illumination mode. These illumination modes are available in many commercially produced metallurgical microscopes and are discussed in the article “Light Microscopy” in this Volume. Optical methods may involve a few simple manipulations in the operation of a metallurgical microscope or in other cases the addition of accessories. These methods can be applied to reveal details of the microstructure even in the as-polished condition and thus should be considered prior to etching of specimens.

Contrast Enhancement and Etching, *Metallography and Microstructures,* Vol 9, *ASM Handbook,* ASM International, 2004, p. 294–312

Contrast Enhancement and Etching

Contrast Enhancement by Film Deposition

Microstructural contrast can be enhanced by the formation of a thin transparent film on the specimen surface. Incident light is partially absorbed by the film and is repeatedly reflected at the layer/specimen interface before exiting. This optical effect can enhance the reflectivity difference (ΔR) between different phases, as shown in Fig. 1 (Ref 1). The reflected rays may also interfere with one another and produce color contrast. Contrast differences between phases is achieved by optimizing the optical absorption coefficient (k) and refractive index (n) of the film with respect to the optical properties of the phases. Thickness of the film is also controlled to produce interference effects and color contrast. A very thin layer absorbs all the wavelengths and gives a gray contrast. Thickening of the layer causes interference effects, which result in cancellation of particular wavelengths and the intensification of color contrast.

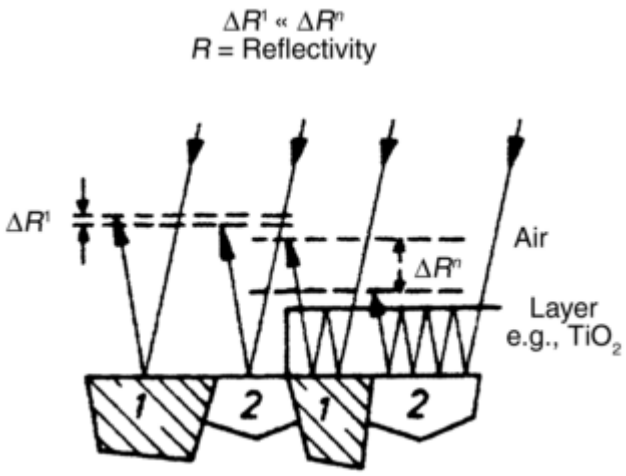

Fig. 1 Concept of improved contrast between two phases from film deposition. The difference in reflectivity (ΔR) between phases 1 and 2 is much greater with a film (ΔR^n) than without (ΔR^1).

Several methods exist for film formation on specimen surfaces in metallography:

- Heat tinting (thermal oxidation)
- Color (tint) etching
- Anodizing
- Potentiostatic etching (with controlled conditions that can etch or allow film formation)
- Vapor deposition
- Film deposition by sputtering (which can be reversed to result in etching, as described in the section "Etching by Ion Bombardment" in this article)

Unlike the removal of material from the specimen surface by etching techniques, the various methods of film deposition can improve optical contrast mechanism without altering the chemical or morphological character of the specimen surface. Reproducibility of results can also be improved by the more highly controlled methods such as potentiostatic etching and physical sputtering/etching. Depending on their setup conditions, these two methods can remove (etch) material from the specimen surface or deposit film on the surface. Potentiostatic etching and physical sputtering/etching provide good reproducibility of results and are thus particularly useful in quantitative metallography. The reproducibility of the results can be guaranteed only if the surface quality of the specimen is maintained, as scratches may become more evident from interference effects.

Interference Films

An interference film is a thin transparent layer whose thickness is small compared to the resolving power of the optical microscope. When light rays impinge on a thin transparent adherent film, reflection occurs at the film/air and film/metal interfaces (see Fig. 2). Phase shifts also occur at either or both of these interfaces. Consequently, selected wavelengths are cancelled between the incident and reflected light, resulting in the reflected light having colors characteristic of uncancelled wavelengths. The revealed color of a phase is determined by film thickness, the optical properties of the phase, and the structure of a film (particularly whether it is single crystalline, polycrystalline, amorphous, and sensitive to polarized light).

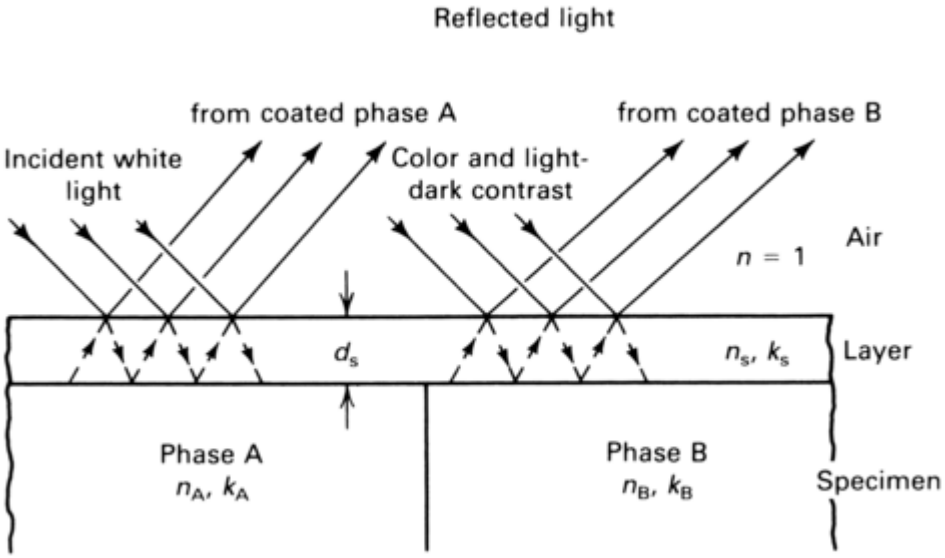

Fig. 2 The function of a physically deposited interference layer. Contrast between phase A and B is achieved by optimizing the refractive index (n_s) and absorption coefficient (k_s) of the layer with respect to the optical constants of the phases (n_A, k_A, n_B, k_B) and adjusting the layer thickness, d_s.

Interference may be expected whenever the effective paths traveled by light reflected at the film and metal surfaces differ by an odd number of λ/2 (half wavelength). That is, the difference in the effective paths (with

refraction effects) of the reflective light is proportional to twice the film thickness. If the phase changes due to the slower speed of light in the film are disregarded, interference would occur at film thicknesses that differ by an odd number of λ/4 (quarter wavelength). When the effect of the slower speed of light in the film is included, interference will occur at odd values of $\lambda/(4n)$, where n is the refractive index of the film. The effect also is a function of the wavelengths in the incident light and will be sensitive to the light source and any filtering in the source or reflected light paths. Within a good approximation, cancellation of a specific wavelength, λ, occurs for the thickness, $t \simeq N(\lambda/4n)$, where n is the refractive index of the film and N the integer order of the interference.

The color of the interference film is related to its thickness. As film thickness is increased, and with incident unfiltered light of all wavelengths, interference occurs first for the shorter wavelengths of the blue limit of the visible wavelength range. The longer wavelengths are reflected, giving the first color of red-yellow. With progressive thickening of the film, the color passes through the spectral range to blue, then repeats for successive values of the order, *N*. For *N* greater than 3 or 4, excessive film thickness leads to absorption and poor color development.

When the film is very thin and exposed to white light, interference will occur in the ultraviolet region (≃350 nm, or 3500 Å), and no color will be observed with white light. Considering that light passes into and from the film at an angle, interference for violet light having a wavelength of 400 nm (4000 Å) begins for films approximately 40 nm (400 Å) thick; these films produce yellow. The first blue will occur for films somewhat thinner than 70 nm (700 Å). Thus, when the film is thickened progressively so that the interference reaches the blue-violet region (≃450 nm, or 4500 Å), the blue light reflected from the surface will be out of phase, and the complementary yellow will be visible.

Upon further thickening of the film, the green waves (≃500 nm, or 5000 Å) will suffer interference, and the light will be magenta, which is the complement to green. The magenta will appear several times: at thicknesses of $\lambda_G/(4n)$, $3\lambda_G/(4n)$, $5\lambda_G/(4n)$, …, where λ_G is the wavelength of green light in air. Interference in the yellow region (≃600 nm, or 6000 Å) will provide the complementary blue.

Finally, when the end of the first band of colors (band I) is reached, the interference passes out of the visible spectrum into the infrared region. This occurs before the film thicknesses comprising band II, and after it band III, of interference are reached. The colors in band I are called first-order colors. The repetition of the color sequence as second-order yellow, magenta, blue, and so on, in band II will be the same, but the interval between them will differ (see Table 2). Not all colors will appear in every band. Successive sequences occur for progressively thicker films, but clarity of color based on interference decreases for films thicker than 500 nm (5000 Å).

Table 2 Colors obtained at various thicknesses of interference films of silver iodide on silver

Film color	Interference band No.					
	I		**II**		**III**	
	nm	**Å**	**nm**	**Å**	**nm**	**Å**
Yellow	20	200	115	1150	245	2450
Reddish	43	430	165	1650	290	2900
Blue	55	550	195	1950	…	…
Green	…	…	225	2250	340	3400

Source: Ref 2

Use of Polarized Light and Phase Contrast. The color of interference films is frequently enhanced using polarized light, sensitive-tint plates, and phase-contrast devices (see descriptions in the article “Light Microscopy” in this Volume). These rely on the ability of some films to alter the plane of polarization, or they provide a phase shift that is sensitive to wavelength.

Irregularities in the surface, such as grain boundaries, etch pits, and faceting, and, to a lesser extent, films with rough surfaces allow the repeated reflection of incident polarized light within an irregularity. If the emerging ray enters the microscope objective with a fractional shift in path length relative to light reflected from an adjacent region of different elevation, the resulting light is elliptically polarized and, upon passing through a sensitive tint plate or phase contrast device, results in differences in color. Because upon etching different grains or phases can develop surface topology sensitive to the crystal lattice orientation, such as facets, microstructural detail becomes distinguishable by color without the formation of surface films. The optical

principles dictating development of color to enhance microstructural detail are discussed in Ref 2, 3, 4, 5, 6, 7, 8, and 9.

Heat Tinting

Oxide films can be formed by heat tinting. The polished specimen is heated in an oxidizing atmosphere. Coloration of the surface takes place at different rates according to the reaction characteristics of different microstructural elements under the given conditions of atmosphere and temperature. The thickness of the film is influenced by differences in chemical composition and crystallographic orientation, and the observed interference colors allow the distinction of different phases and grains.

Different metals require different oxidation durations and temperatures. High temperatures may induce phase transformations on the surface, an effect that sometimes limits application of this technique. Some specimens may oxidize after exposure to ambient atmospheres. This was demonstrated during research on uranium-zirconium alloys (Ref 10). A U-14Zr (at.%) alloy was oxidized 40 min at 900 °C (1650 °F). Several conventional etching techniques were used without success to reveal the characteristics of the oxide/metallic interface. However, after exposing the specimen to ambient atmosphere for 48 h, a thin zirconium-rich layer with slender fingerlike penetrations into the bulk oxide was visible at 2000×.

Heat tinting can also be performed using a more sophisticated procedure in which temperature and oxidation are closely monitored in an enclosed system. This procedure has been used in studies of surface reactions of single crystals (Ref 11). Heat tinting is also be preceded by chemical etching to reveal grain and phase boundaries. This has proved successful with uranium alloys, uranium carbides (Ref 12, 13), zirconium and its alloys, high-speed tool steels, and austenitic stainless steel weldments.

Color Etching

Color etching, also commonly referred to as tint etching, has been used to color many metals and alloys, such as cast irons, steels, stainless steels, nickel-base alloys, copper-base alloys, molybdenum, tungsten, lead, tin, and zinc. Satisfactory color, or tint, etchants are balanced chemically to produce a stable film on the specimen surface. This is contrary to ordinary chemical etching (discussed in the section “Etching” of this article), when the corrosion products produced during etching are redissolved into the etchant.

Immersion color etchants that produce color contrast are associated with Klemm and Beraha, whose work is described in Ref 14 and 15. Color etchants work by immersion, never by swabbing, which would prevent film formation. Externally applied potentials are not used. Color etchants have been classified as anodic, cathodic, or complex systems, depending on the nature of the film precipitation (Ref 2). Tint etchants generally color one anodic phase. Some success has been attained in developing color etchants for steels that are selective to the phases that are normally cathodic. However, most tint etchants color the anodic phases. Color etchants are usually acidic solutions, using water or alcohol as the solvent. They have been developed to deposit a 0.04 to 0.5 μm (1.6 to 19.7 μin.) thick film of an oxide, sulfide, complex molybdate, elemental selenium, or chromate on the specimen surface.

The colors produced by color (tint) etchants are visible under bright-field illumination, and in many cases further enhancement is attained using polarized light. Colors are developed by interference in the same manner as with heat tinting or vacuum deposition. As noted, color is determined by the thickness of the film, usually in the sequence of yellow, red, violet, blue, and green when viewed using white light. With anodic systems, the film forms only over the anodic phase, but its thickness can vary with the crystallographic orientation of the phase. For cathodic systems, because the film thickness over the cathodic phase is generally consistent, only one color is produced, which will vary as the film grows during etching. Therefore, to obtain the same color each time, the etching duration must be constant. This can be accomplished by timing the etch and observing the macroscopic color of the specimen during staining.

Specimens for color etching must be carefully prepared during polishing. Control of scratches is the most challenging difficulty, particularly for alloys such as brass. Scratches are often observed after color etching, even if the specimen appeared to be free of scratches before polishing. This is a common problem with techniques that use interference effects to produce an image. However, preparation is carried out in virtually the same way as for specimens that would be chemically etched, but greater attention must be given to fine scratch removal.

Color etchants have been developed that deposit a thin sulfide film over a wide range of metals, such as cast irons, steels, stainless steels, nickel-base alloys, copper, and copper alloys (Ref 15, 16). These films are produced in two ways. For reagents containing potassium metabisulfite ($K_2S_2O_5$) or sodium metabisulfite ($Na_2S_2O_5$), the iron, nickel, or cobalt cation in the sulfide film originates from the specimen, and the sulfide anion derives from the reagent after decomposition.

The second type of film is produced by a metal-thiosulfate complex in the reagent that consists of an aqueous solution of sodium thiosulfate ($Na_2S_2O_3 \cdot 5H_2O$), citric acid (organic acid), and lead acetate ($Pb(C_2H_3O_2)_2$) or cadmium chloride ($CdCl_2$) (metal salt). In such etchants, the specimen acts as the catalyst, and the film formed is lead sulfide (PbS) or cadium sulfide (CdS). These reagents color only the anodic constituents; the film is not formed over the cathodic features. Color etchants that use reduction of the molybdate ion have also been developed (Ref 17). Sodium molybdate ($Na_2MoO_4 \cdot 2H_2O$) is used. Molybdenum in the molybdate ion, MoO_4^{2-} has a valence of +6. In the presence of suitable reducing compounds, it can be partially reduced to +4. A dilute (1%) aqueous solution of $Na_2MoO_4 \cdot 2H_2O$ is made acidic by the addition of a small amount of nitric acid (HNO_3). This produces molybdic acid (H_2MoO_4). Addition of a strong reducing agent, such as iron sulfate ($FeSO_4$), colors the solution brown.

When the 1% aqueous Na_2MoO_4 solution (made acidic with HNO_3) is used to color etch steels, the molybdate is reduced at the cathodic cementite phase. This produces a yellow-orange to brown color, depending on etching duration. If a small amount of ammonium bifluoride (NH_4HF_2) is added, the carbides are colored red-violet, and ferrite is colored yellow. Perhaps the most widely applicable color etchant is that developed by Klemm (Ref 14), which colors ferrite in steels, reveals overheating or burning in steels, and develops the grain structure of copper and many copper alloys, as well as those of lead, tin, and zinc.

Common constituents in color etchants include $Na_2S_2O_5$, $K_2S_2O_5$, and $Na_2S_2O_3 \cdot 5H_2O$. These are used with water as the solvent and generally color anodic phases. To tint more acid-resistant metals, hydrochloric acid (HCl) is added. Color etchants containing these compounds produce sulfide films; during use, the odor from sulfur dioxide and hydrogen sulfide can be detected. Although this is a minor nuisance, etching should be conducted under a hood.

Color etchants based on selenic acid (H_2SeO_4) or $Na_2MoO_4 \cdot 2H_2O$ generally color cathodic constituents, such as cementite in cast irons and steels. Because H_2SeO_4 is dangerous to handle, its use should be restricted to those well aware of the necessary safety precautions. Fortunately, the reagents based on $Na_2MoO_4 \cdot 2H_2O$ are relatively safe to use. Reagents containing additions of NH_4HF_2 should also be handled carefully.

Mixing of Reagents. With most chemical etchants, precise adherence to the stated formula is not necessary. However, formulas for color etchants must be followed closely. For some color etchants, the order of mixing of the various components is also critical. Generally, the recommendations of the developer of the reagent should be followed closely.

Many color etchants can be prepared as 500 to 1000 mL stock solutions. In some cases, one ingredient is omitted until the quantity needed for etching is poured into a beaker. The activating agent is then added. Klemm's I reagent can be used in this manner. However, after mixing, this reagent can be stored for many days by covering the beaker tightly with aluminum foil to prevent evaporation. If evaporation does occur, crystals will form that are very difficult to dissolve. When a color etchant contains NH_4HF_2, a polyethylene beaker should be used.

Applications of several color etchants are listed in Table 3 and described in more detail in the article “Color Metallography” in this Volume. Additional examples are also provided in Fig. 3, 4, 5, 6, 7, 8, 9, 10 and 11. Color etching is particularly well suited to copper and copper alloys. Klemm's I reagent (Table 3) is effective with most of these compositions. It will also color ferrite grains in iron or steel varying shades of blue-brown, depending on crystallographic orientation. Phosphorus segregations are colored yellow or white, depending on concentration. Cementite can be detected using this reagent because it does not become colored; instead, it remains white to contrast with the colored matrix (Ref 14).

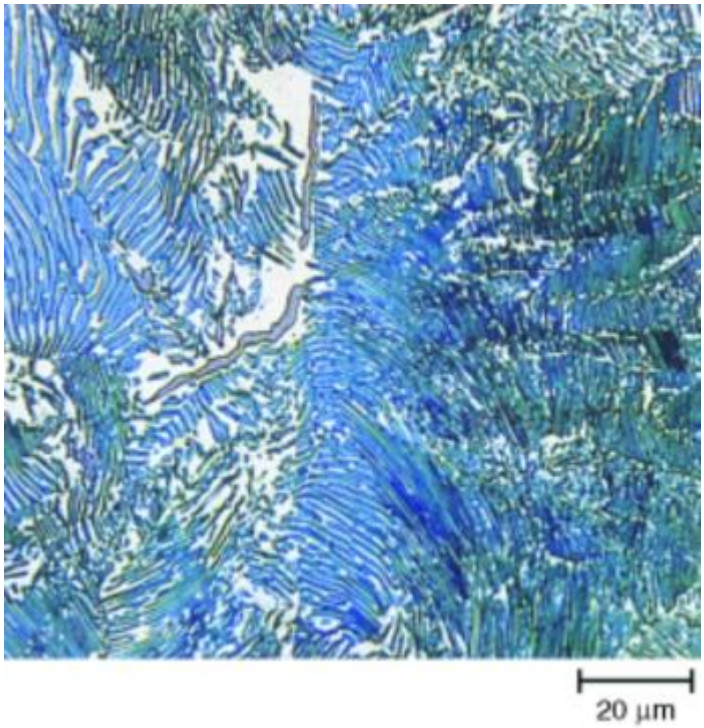

Fig. 3 Fe-1C alloy etched with acidified 1 g Na_2MoO_4 in 100 mL H_2O to color the cathodic cementite. The cementite in the pearlite is blue; grain-boundary cementite is violet. 500×. (G.F. Vander Voort)

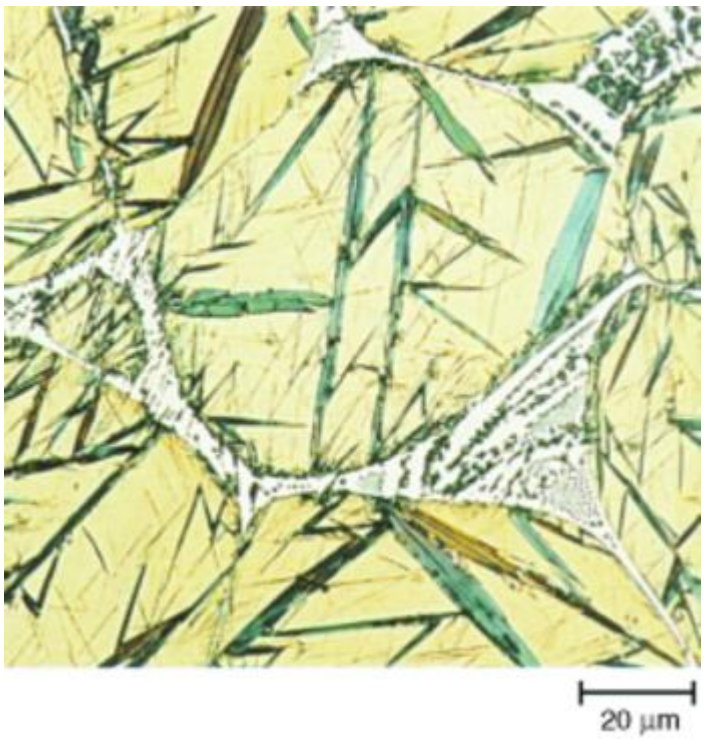

Fig. 4 Fe-1.86C alloy color etched with 2% nital to reveal plate martensite within austenite grains and ledeburite in the grain boundaries. 500×. (A.O. Benscoter)

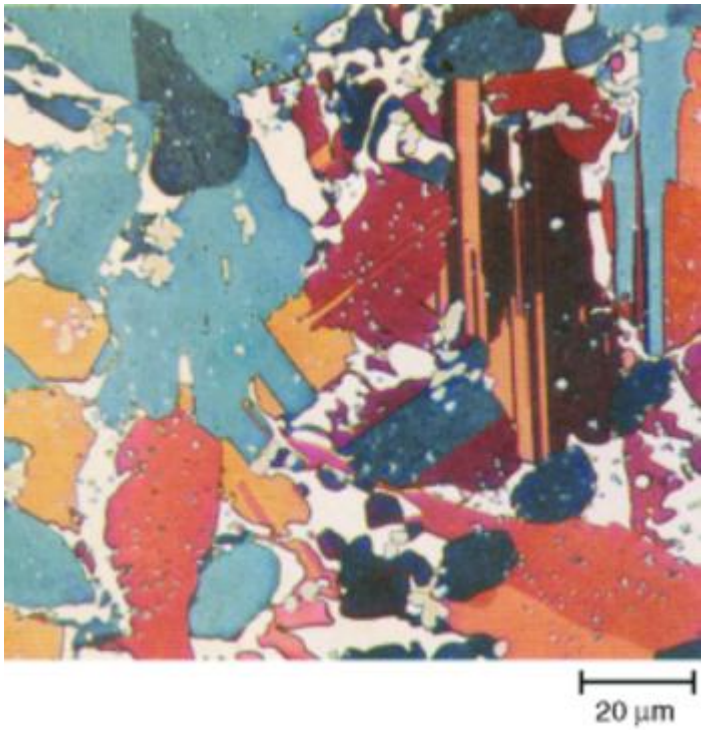

Fig. 5 Aluminum bronze (ASTM B 148, grade 9C) heat treated to form Al_4Cu_9. Pre-etched with aqueous 10% $(NH_4)_2S_2O_8$ and color etched with Beraha's lead sulfide reagent. 500×. (G.F. Vander Voort)

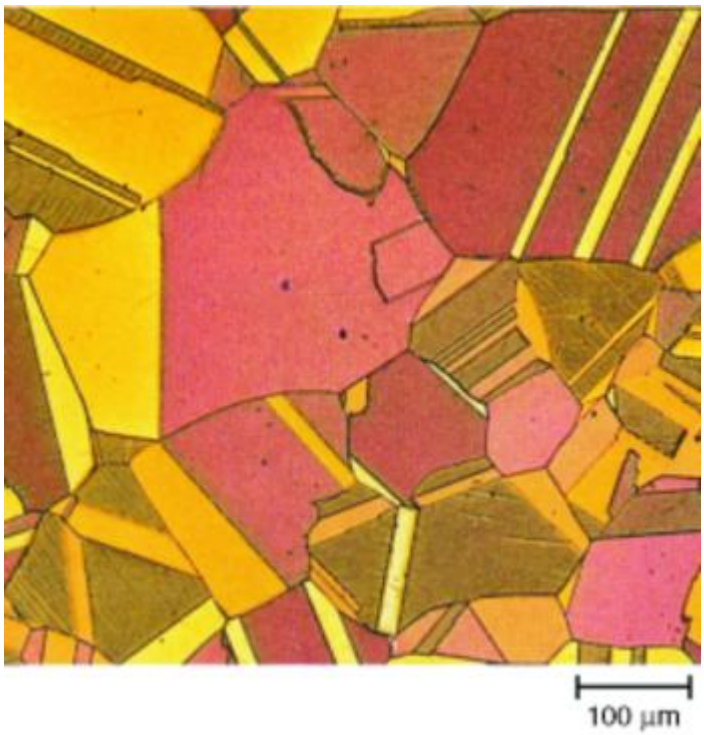

Fig. 6 Alpha brass (Cu-30Zn) cold worked and annealed. Color etching with Klemm's I reagent, which required approximately 1 h, revealed all the grains and annealing twins. 100×. (G.F. Vander Voort)

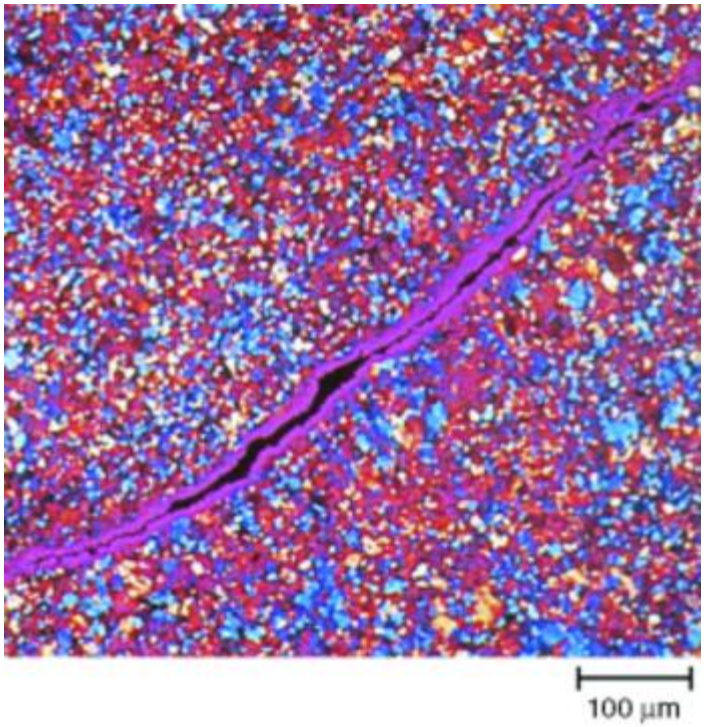

Fig. 7 Recrystallized Ti-6Al-4V alloy with a crack resulting from creep-rupture testing. Attack polished and color etched in 100 mL distilled H_2O, 4 mL HCl, and 3 g NH_4HF_2. Polarized light illumination. 100×. (G. Müller)

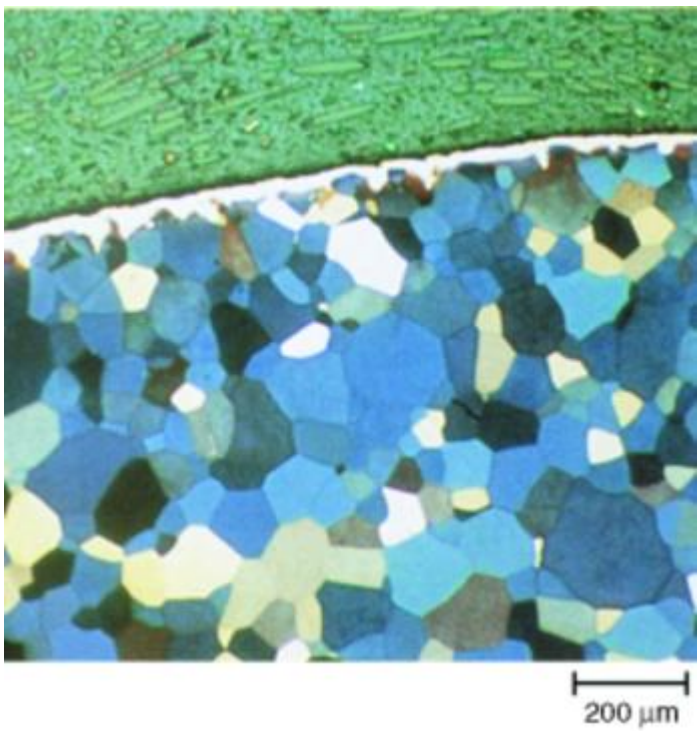

Fig. 8 Equiaxed *α* structure of pure titanium. The white surface layer is oxygen-stabilized *α*. The green at the top is mounting resin. Color etched with 100 mL distilled H_2O and 5 g NH_4HF_2. 50×. (G. Müller)

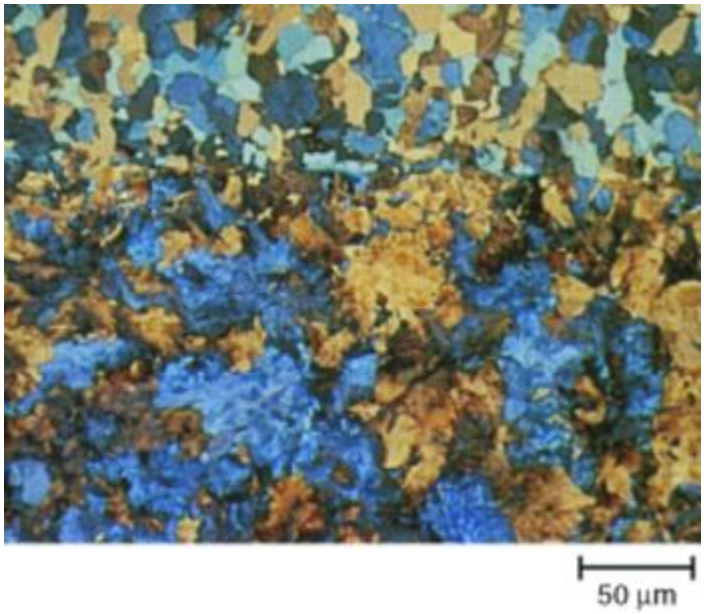

Fig. 9 Armco iron friction welded to carbon steel. Structure is ferrite (smaller grains) and pearlite plus ferrite (large grains). Color etched with Klemm's I reagent. 200×. (G. Müller)

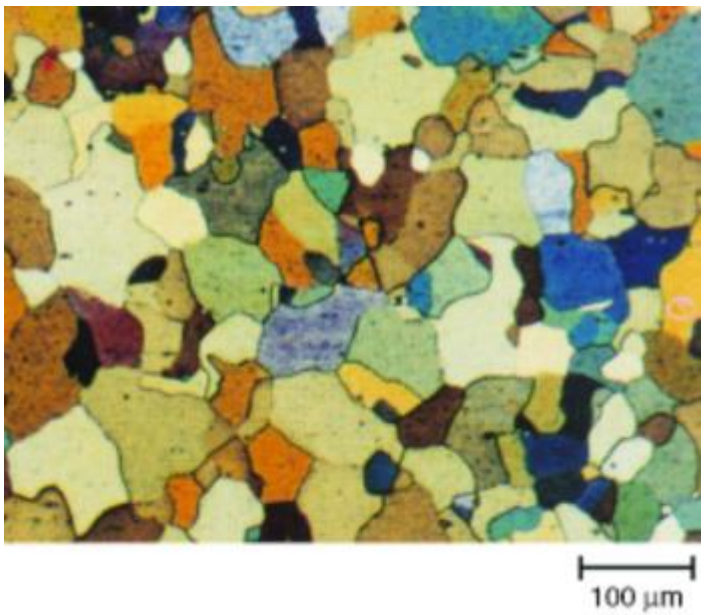

Fig. 10 Chromized sheet steel (Fe-0.06C-0.35Mn-0.04Si-0.40Ti) color etched to delineate ferrite structure. 3 g $K_2S_2O_5$, 10 g $Na_2S_2O_3$, and 100 mL H_2O. 100×. (A.O. Benscoter)

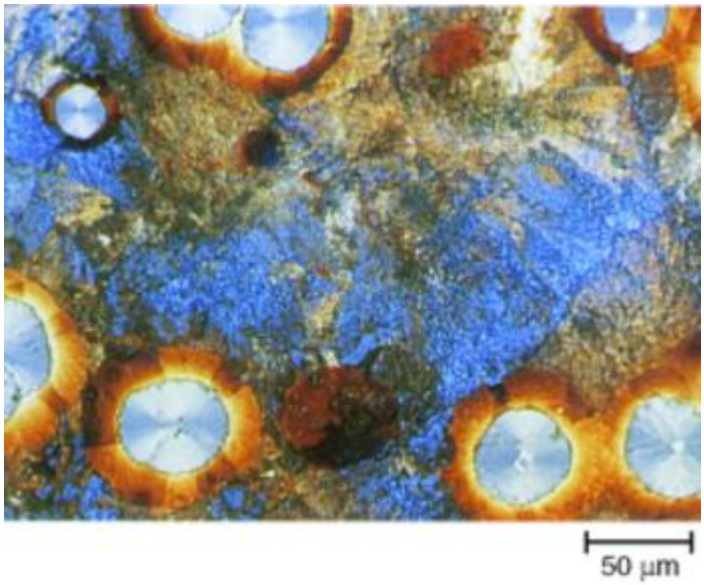

Fig. 11 Ductile iron (3.63 to 3.69% C, 2.74% Si, 0.26% Mn, 0.084% S, 0.13% Cu, 0.060% Mg) as-cast alloy. Structure consists of graphite nodules in envelopes of free ferrite in a pearlite matrix. Color etched with Klemm's I reagent. 200×. (G. Müller)

Table 3 Selected color etchants

Additional tint etchants are listed in Ref 2 and 3.

Composition[(a)]	Comments
200 g CrO_3, 20 g Na_2SO_4 (sodium sulfate), 7 mL HCl, 1000 mL H_2O	Beraha's tint etch for aluminum alloys; pre-etch with 10% aqueous NaOH followed by 50% aqueous HNO_3; rinse in water, dip immediately into tint etch for 1–5 s; rinse and dry; colors matrix grains, outlines second phase particles.
1 g $(NH_4)_6Mo_7O_{24}$ (ammonium molybdate), 6 g NH_4Cl (ammonium chloride), 200 mL H_2O	Tint etch of Lienard and Pacque for aluminum alloys; colors $CuAl_2$ violet; immerse approximately 2 min.
(1) Stock solution: 1:2, 1:1, or 1:0.5 HCl-H_2O **(2) 100 mL stock solution plus 0.6–1.0 g $K_2S_2O_5$** **(3) Optional additions: 1–3 g $FeCl_3$, 1 g $CuCl_2$ (cupric chloride), or 2–10 g NH_4HF_2**	Beraha's tint etch for iron-, nickel-, or cobalt-base heat-resistant alloys; colors the matrix—carbides and nitrides are unaffected; immerse specimen in solution at room temperature for 60–150 s; move specimen during etching; start with lowest HCl concentration; if coloration does not result, increase HCl or etch longer.
50 mL saturated $Na_2S_2O_3$[(b)], 1 g $K_2S_2O_5$	Klemm's I tint etch; good for many alloys; immerse 3 min or more for β-brass, α-β brass, and bronzes; use 10–60 min for α-brass; use 40–100 s for coloring ferrite in steels; reveals phosphorus segregation and overheating; longer time produces line etching of ferrite; etch 30 s for zinc alloys.
50 mL $Na_2S_2O_3$, 5 g $K_2S_2O_5$	Klemm's II tint etch; immerse 6 min or more for α-brass; immerse 30–90 s for steels; reveals phosphorus segregation; good for austenitic manganese alloys; immerse 60–90 s for tin and its alloys.
5 mL $Na_2S_2O_3$, 45 mL H_2O, 20 g $K_2S_2O_5$	Klemm's III tint etch; immerse 3–5 min for bronze; immerse 6–8 min for Monels.
240 g $Na_2S_2O_3$, 30 g citric acid, 24 g $Pb(C_2H_3O_2)_2$, 1000 mL H_2O	Beraha's lead sulfide tint etch; dissolve in order given; allow each to dissolve before adding next (cannot get complete dissolution); age in dark bottle at least 24 h before using; do not remove precipitate; when stock solution turns gray after prolonged storage, discard; immerse in solution until surface is

	violet or blue; excellent for copper and its alloys; to color MnS in steels, add 200 mg $NaNO_3$ sodium nitrate (optional) to 100 mL solution—good for 30 min; colors MnS white; pre-etch with nital or picral.
21–28% aqueous $NaHSO_3$	Beaujard and Tordeux's tint etch for steels; immerse 10–25 s; reveals grain boundaries and ferrite orientations; darkens as-quenched martensite.
1 g $Na_2S_2O_5$, 100 mL H_2O	Tint etch for lath or plate martensite; immerse 2 min.
8–15 g $Na_2S_2O_5$, 100 mL H_2O	Darkens as-quenched martensite; immerse approximately 20 s.
3–10 g $K_2S_2O_5$, 100 mL H_2O	Darkens as-quenched martensite; immerse 1–15 s.
1 g Na_2MoO_4, 100 mL H_2O	Beraha's tint etch for cast iron and steels; add HNO_3 to pH 2.5–4.0 (approximately 0.4 mL); immerse 20–30 s for cast iron, Fe_3P and Fe_3C, yellow-orange and ferrite, white; for low-carbon steel add 0.1 g NH_4HF_2, immerse 45–60 s; for medium-carbon steel add 0.2 g NH_4HF_2; for high-carbon steel add 0.3–0.4 g NH_4HF_2; carbides, yellow-orange to violet and ferrite, white or yellow.
3 g $K_2S_2O_5$, 10 g $Na_2S_2O_3$, 100 mL H_2O	Beraha's tint etch for iron and steel; immerse 1–15 min; colors ferrite, martensite, pearlite, and bainite; sulfides are brightened.
0.5–1.0 mL HCl, 100 mL H_2O, 1 g $K_2S_2O_5$	Beraha's tint etch for irons, steels, tool steels; agitate strongly during etching, then hold motionless until surface is colored; 10–60 s total time; colors ferrite, martensite, pearlite, bainite; reveals grain boundaries.
20 mL HCl, 100 mL H_2O, 0.5–1 g $K_2S_2O_5$	Beraha's tint etch for stainless steels; immerse 30–120 s with agitation; colors austenite.
Stock solution: 20 mL HCl, 100 mL H_2O, 2.4 g NH_4HF_2	Beraha's tint etch for stainless steels; before use, add 0.6–0.8 g $K_2S_2O_5$ (0.1–0.2 g for martensitic grades); after mixing, reagent is good for 2 h; use plastic tongs and beaker; immerse 20–90 s, shake gently during etching; colors matrix phases.
40–60 mL $FeCl_3$ solution (1300 g/L H_2O), 25 mL HCl, 75 mL ethanol	Hasson's tint etch for molybdenum; immerse without agitation for 40–50 s (do not exceed 70 s); $FeCl_3$ can be dissolved in ethanol but etch is slower, 2–3 min; colors vary with grain orientation.
70 mL H_2O, 20 mL 30% H_2O_2, 10 mL H_2SO_4	Tint etch for molybdenum alloys (Oak Ridge National Laboratory); immerse 2 min, wash, and dry; swab removes colors, produces grain-boundary attack.
5 g NH_4HF_2, 100 mL H_2O	Weck's tint etch for α-titanium; for pure titanium, immerse a few seconds, longer times for titanium alloys; colors vary with grain orientation.
3 g NH_4HF_2, 4 mL HCl, 100 mL H_2O	Weck's tint etch for α-titanium alloys; immerse for a few seconds; colors vary with grain orientation.
94% mL 10% aqueous HCl, 20 g CrO_3	Tint etch for tungsten; immerse at 55 °C (130 °F); use 2 or 3 stages (view between etches) of 15, 10, and 10 min; pre-etch with grain-boundary etch.

(a) Whenever water is specified, use distilled water.

(b) Maximum solubility of anhydrous $Na_2S_2O_3$ is 50 g/100 mL H_2O at 20 °C (70 °F); that of the crystal form ($Na_2S_2O_3 \cdot 5H_2O$) is 79.4 g/100 mL H_2O at 0 °C (32 °F) or 291.1 g/100 mL H_2O at 45 °C (115 °F).

Beraha's reagent is also useful for etching carbon and low-alloy steels (Ref 15). After approximately 5 s, martensite is colored an intense bluish brown, and austenite remains white. Used to etch alloy steels, Beraha's reagent will color martensite blue to brown; ferrite and sulfide inclusions remain unetched and retain their inherent colors.

Another advantage of color etching is revealing microstructural and chemical changes after exposure to elevated temperatures. For example, many ferritic and austenitic stainless steels can form σ phase after prolonged exposure to temperatures from 480 to 900 °C (900 to 1650 °F). Sigma phase is a hard, brittle, nonmagnetic, intermediate phase with a tetragonal crystal structure (space group $P4_2/mnm$). It occurs in many binary and ternary alloys of transition elements. The presence of δ-ferrite in the microstructure of austenitic stainless steel also accelerates the formation of σ phase (Ref 18).

Anodizing

Anodizing is an electrolytic process for depositing a thin oxide film on the surface of the specimen in a standard electropolishing unit. The resulting interference colors are a function of the anodic film thickness, which depends on the anodizing voltage, the anodizing solution, and the composition and/or structures of the phases present in the specimens. Anodizing is used for phase identification, improvement of optical contrast in bright-field and polarized light examination, and for preservation of the etched surface of the specimen.

The specimen to be anodized is mounted in a standard thermoset or epoxy resin mount that hardens at room temperature. After grinding, polishing, and etching, the specimen is placed in a standard electropolishing unit. The specimen, acting as the anode, is placed face up in the anodizing solution inside a stainless steel container, which acts as the cathode. Approximately 6 mm ($\frac{1}{4}$ in.) of solution should cover the top of the mounted specimens. The electrolyte composition depends on the composition of the alloy. For example, an electrolyte used for zirconium-base alloys is 60 mL ethyl alcohol, 35 mL H_2O, 5 mL 85% phosphoric acid (H_3PO_4), 10 mL 85% lactic acid, 20 mL glycerine, and 2 g citric acid. This solution is also applicable to titanium, niobium, and tantalum specimens.

Voltages are 15 to 180 V dc, depending on the purpose (constituents or phases observed) and the color desired. The anodizing voltage, which is applied for 5 to 10 s, is usually selected by trial and error, using successively higher voltages on the basis of the greatest color contrast between the phases. Once selected, the voltage is used for other specimens of the same alloy.

Potentiostatic Etching (Adapted from Ref 19)

Potentiostatic etching is the selective corrosion of one or more morphological features of a microstructure that results from holding the metal to be etched in a suitable etching electrolyte at a controlled potential relative to a reference electrode (Fig. 12). The basis of the method is that the products of electrochemical dissolution reactions and the rates of formation of these products for a given electrolyte are a function of the potential at which a metal or alloy is held relative to a suitable reference electrode. Because specific surface topology, with or without films, is necessary for color contrast metallography, potentiostatic etching can enhance control in producing the requisite surface characteristics. This can produce more reliable and reproducible results from etching.

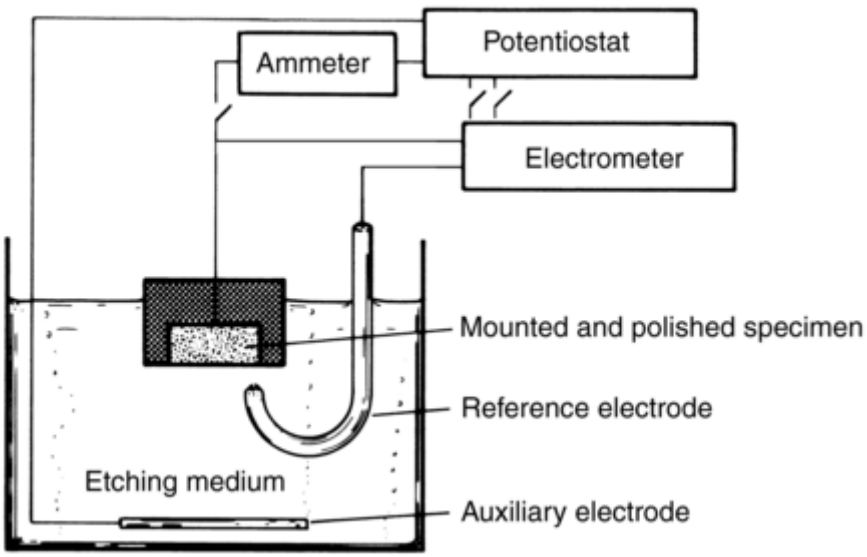

Fig. 12 Setup for potentiostatic etching

In this process, the specimen is placed in an electrolytic cell and used as an anode. Its potential is measured against the electrolyte by a reference electrode. During etching, a defined solution pressure (potential of solution) is maintained. This method is based on the different rate of material removal from different phases and on interference film deposition. A comparison of the current density versus potential curves for the different phases identifies the range of potential corresponding to a specific phase. A conventionally mounted and polished metal specimen is modified to provide electrical contact with the specimen without access of the

electrolyte to the connecting wire. An auxiliary electrode, usually fabricated of platinum or specially prepared graphite, permits current to pass from or to the specimen through the electrolyte.

The potential of the specimen is measured with respect to the potential of a reference electrode placed a few millimeters from the surface. The common reference electrodes are the calomel half-cell [mercury in contact with mercurous dichloride (Hg_2Cl_2)] and the silver-silver chloride half-cell. The potential depends on the chloride ion concentration contacting the metal and insoluble metal chloride. The potentials of these half-cells are established with respect to the hydrogen gas (1 atm)/hydrogen ion (unit activity) half-cell assigned the value of zero potential. In Fig. 13 and 14, the potentials are given relative to the standard hydrogen electrode (SHE), although essentially all measurements are made regarding one of the secondary reference half-cells.

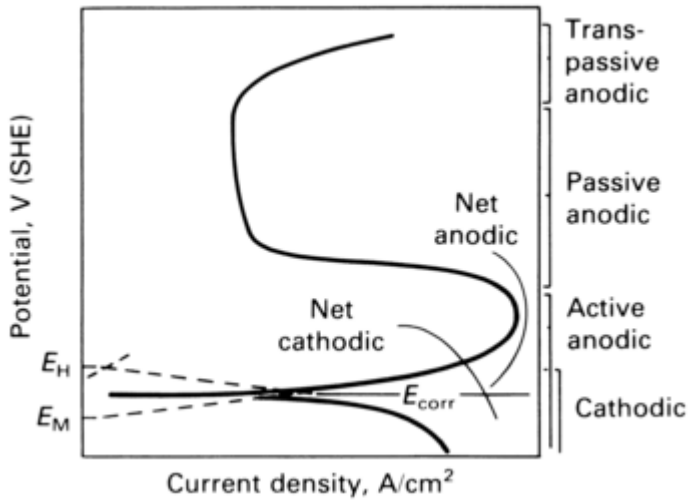

Fig. 13 Polarization curves representative of an alloy in a deaerated-acid environment showing active/passive behavior. E_H is the equilibrium potential for the hydrogen reaction. E_M is the indefinite potential near which metal dissolution is very small. E_{corr} is the corrosion potential. SHE, standard hydrogen electrode

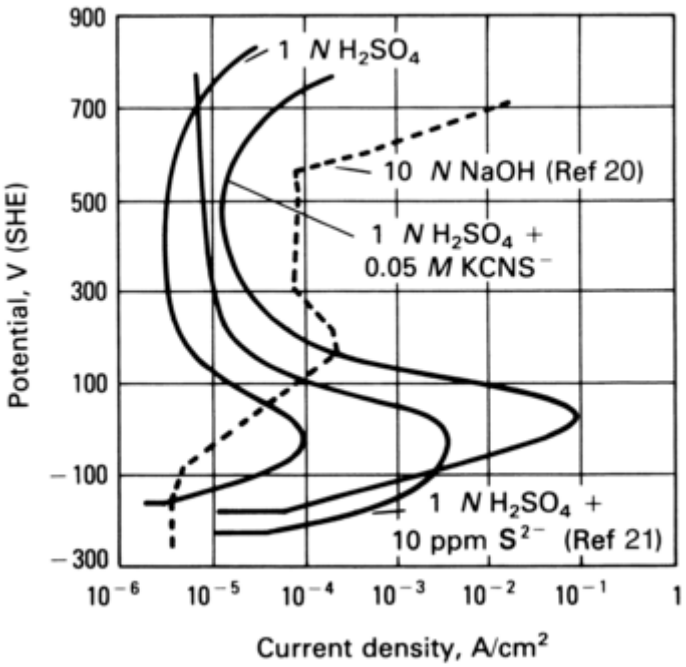

Fig. 14 Polarization curves for 18–8 austenitic stainless steel showing effects of the indicated environments. SHE, standard hydrogen electrode

Electrochemical Principles. Surfaces containing irregularities or interference films may be produced by several methods, ranging from direct aqueous chemical attack to thermal oxidation (heat tinting) and color, or tint, etching. Aqueous chemical attack involves electrochemical processes in which anodic dissolution—for

example, electrons lost, oxidation, or corrosion—occurs spontaneously, supported by cathodic reactions (electrons gained or reduced) of etchant species. The electrochemical potential at which oxidation occurs is established largely by the oxidizing characteristics of the etchant; this potential and etchant species determine the rate of oxidation and the mode of attack. Metal atoms are released from the surface as ions that pass into solution, leaving unfilmed surfaces, or react to form films.

Anodic dissolution is also controlled by removing electrons through an external circuit, which is completed by an auxiliary electrode placed in the etchant solution. If the external circuit is designed to control the current, the process is termed galvanostatic etching. The current causes a shift in electrochemical potential of the metal specimens. For small currents, the effect is superimposed on the potential and currents resulting from the etchant described previously; with higher external currents, removal of electrons to the external current dominates the change in potential and current density and therefore etching response. However, the modes of attack remain sensitive to etchant composition. More importantly, though, the type of interface reaction depends largely on electrochemical potential, and often the establishment and control of the potential can be accomplished only by a potentiostat using the arrangement shown in Fig. 12.

The dependence of the dissolution rate of a metal or alloy on the electrochemical potential is represented by the polarization or potential/current-density curve. A representative, experimentally determined curve for a metal forming a corrosion-product film in a deaerated acid environment is shown in Fig. 13. Sections of the curve are identified as potential ranges of net cathodic, net active anodic, passive anodic, and transpassive anodic behavior. Dashed extensions of the curves indicate the potential and current-density ranges over which cathodic and anodic reactions occur when the net current density is anodic and cathodic, respectively. In the net cathodic potential range, the rate of metal dissolution may be slow with little etching.

Upon increasing the potential, the current reverses at E_{corr}, the natural corrosion potential of the specimen in the absence of a potentiostat. Further increase in potential causes a net removal of electrons. The entire anodic curve is the potential range of anodic dissolution (oxidation) of the metal to soluble or insoluble corrosion products. In the cathodic potential range, there is a net flow of electrons to the specimen; the predominant effect is a reduction of hydrogen ions to hydrogen gas. In the active anodic region, the dissolution rate increases as potential increases; etching may occur, but corrosion product films do not form. A maximum in current density results from the initiation and growth of films that reduce current density until an adherent oxide film characteristic of the passive state forms. Increasing the potential in the passive range results in progressive thickening of the film such that the current density remains relatively constant. In the transpassive range, the passive film becomes unstable regarding soluble species in solution, such as CrO_4^{2-}. The film disappears, and current density increases.

The polarization curve is sensitive to the composition of the environment or, for present purposes, etchant composition. Representative examples for type 304 stainless steel are shown in Fig. 14. The reference curve is for 1 *N* sulfuric acid (H_2SO_4), the environment most commonly used to compare corrosion behaviors of various materials. The pH is a major variable, and because much of the reported work on potentiostatic etching relates to 1 to 10 *N* sodium hydroxide (NaOH), the curve shown in the figure is for a strongly alkaline environment. The curves for 1 *N* H_2SO_4 with additions of 10 ppm S^{2-} and potassium thiocyanate ($KCNS^-$) ions are examples of additives to the 1 *N* H_2SO_4 to increase the dissolution rate in the active range, an important consideration in increasing current density to accomplish etching within a reasonable time. Chloride ions significantly influence the polarization of most active/passive alloys; these and other halide ions increase current density and may break down the passive film at potentials below the transpassive range. This occurs as localized attack on the passive film in the form of pitting. For some alloys, high halide ion concentrations can prevent formation of the passive film, complicating enhancement of potentiostatic etching by chloride ions.

The polarization curve is usually determined by a continuous scan of potentials from the cathodic range or from E_{corr} at 6 V/h. The experimental curve is sensitive to scan rate and surface topology, and films at any potential may be very sensitive to the potential/time history, that is, whether a specimen is scanned to or is initially set at the given potential. Because of this sensitivity, reference to polarization curves in the literature as guides for conditions for potentiostatic etching may be limited to qualitative value, because etching will usually be carried out by directly setting the potential and holding for a specified time to produce the desired etching response. However, polarization curves indicate potential ranges of dissolution with and without film formation and readily reflect changes in etchant composition.

In potentiostatic etching, the desired information is the current density as a function of time at various potentials along the polarization curve. Grain-boundary attack, faceting, etch pitting, and preferential dissolution of grains

and phases occur predominantly in the active and high-transpassive potential ranges where films do not form. Under these circumstances, the current density is a relatively constant function of time. The major variables, in addition to selection of potential, are time and the environment. The environment influences the mode of attack—for example, faceting. Time determines the extent to which the mode of attack must progress to develop a surface that adequately reveals the microstructure, including development of color under available optical conditions. The major etchant variables to consider are pH and additives, such as $KCNS^-$, which increase current density and therefore decrease etching time if acceptable surface topology develops.

Selective etching of multiphase alloys depends on differential rates of dissolution and on formation of film-free or filmed surfaces on the phases providing color contrast. The principle is illustrated in Fig. 15 (Ref 22), which depicts differences in dissolution rates for austenite, ferrite, and σ phases in an austenitic stainless steel. Such curves are constructed by adding curves for the individual phases displaced along the current density axis proportional to the relative areas exposed at the surface. The latter are directly related to the volume fractions of the phases in the alloy. Where current density maxima are indicated for a specific phase, preferential etching of the phase is expected. However, the mode of attack and the optical methods applied will determine if differentiation of phases by color contrast results.

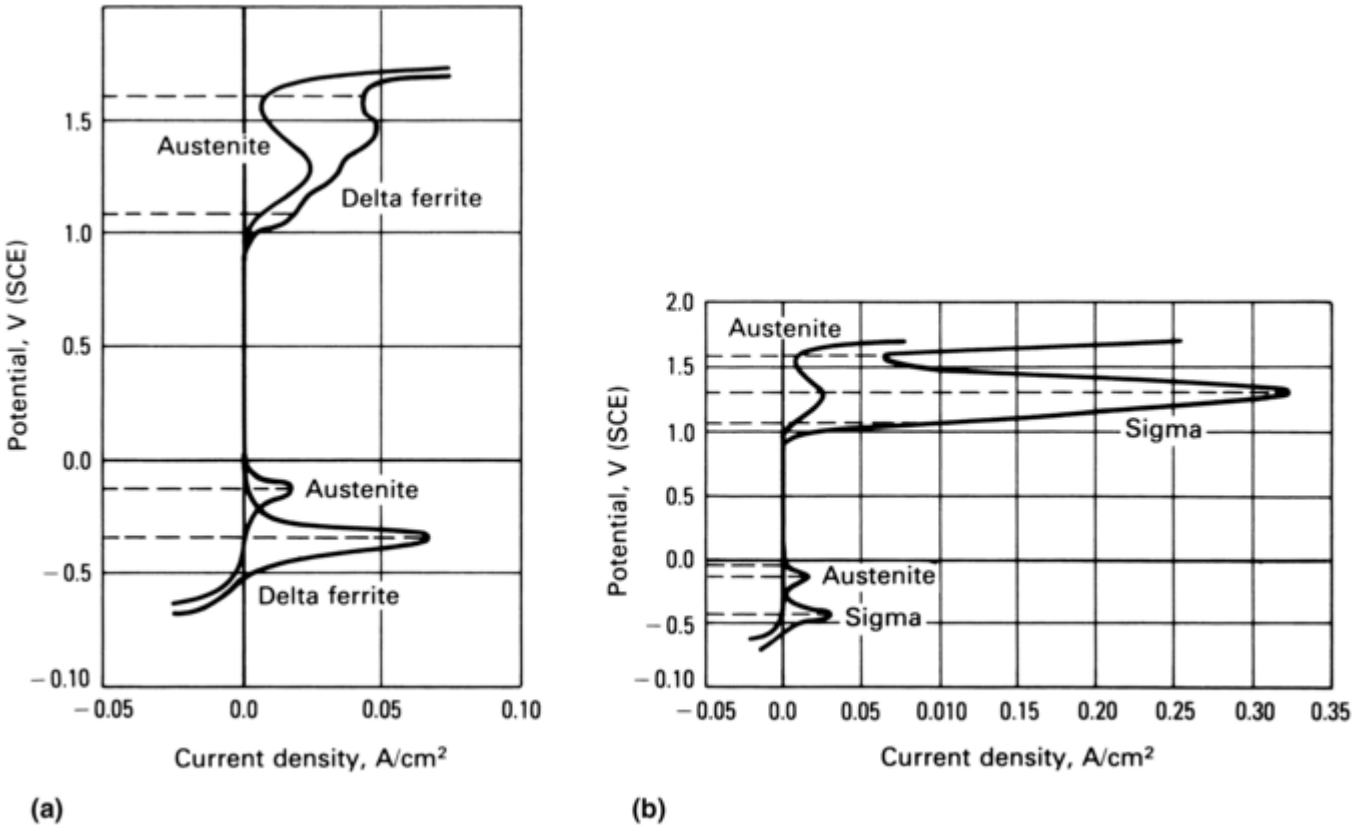

Fig. 15 Polarization curves for 18–8 stainless steel showing potential ranges for selective etching of (a) austenite and δ-ferrite and (b) austenite and σ phase. SCE, saturated calomel electrode. Source: Ref 22

Conditions for Color Response. Color contrast from film formation depends on interference effects, rotation of the plane of polarization, and optical effects associated with surface topology. For color to develop due to interference, films 40 to 500 nm (400 to 5000 Å) thick must be produced. Film thickness is directly proportional to charge density, which is the integration of the time/current-density product to a given time expressed in coulombs per square centimeter (C/cm^2), if all metal ions oxidized by the anodic current density remain in the film and do not go into solution. Otherwise, a correction must be made for this loss. The relationship (Ref 23) for film thickness (D) is:

$$D = \frac{M'}{m'z'd'F} Q\alpha \qquad \text{(Eq 1)}$$

where the primes refer to average values, and M' is molecular weight of the oxide, m' is metal atoms per molecule of oxygen, d' is density of the oxide, and z' is metal ion valence. F is the Faraday constant, Q is the

charge density, and α is the fraction of the metal retained in the film, which allows preferential loss of selected metal atoms to the environment, such as iron and nickel, relative to chromium in an austenitic stainless steel, resulting in an oxide approaching chromic oxide (Cr_2O_3). For an austenitic stainless steel, Eq 1 reduces to:

$$D \text{ (in nm)} = 0.5Q\alpha \qquad \text{(Eq 2)}$$

where Q is expressed in mA · s/cm^2, or mC/cm^2.

Theoretical and empirical investigations indicate that the time dependence of current density during film formation is frequently:

$$\log i = A + \log (1/t^n) \qquad \text{(Eq 3)}$$

where A is a constant and values of n have been evaluated from 0.6 to 1 (Ref 20, 23). Further analysis leads to thickening of the films as cubic, parabolic, or logarithmic functions of time. The parameters of the functions depend on the alloy, environment, and potential range in which dissolution occurs. Therefore, the rate of thickening decreases with time and may lead to excessive etching durations to form films capable of yielding interference effects. A limiting thickness may also be reached if the growth rate slows sufficiently that additional growth is balanced by dissolution of the film into the etchant. Growth-rate characteristics complicate estimates from a conventional polarization curve of the time required to form a 40 to 500 nm (400 to 5000 Å) thick film, which is necessary for interference contrast.

In the passive potential range of most stainless steels and nickel-base alloys, the passive film in acid environments usually attains a steady thickness under 10 nm (100 Å), which is too thin to produce interference colors. In general, as will be shown, good color contrast has been developed by etching in strong NaOH (5 to 40%) in potential ranges just above the current density peak or in the early stages of the transpassive potential range. Because the rate of dissolution of the film quickens with increases in potential in the transpassive range, careful control of potential and time is required to obtain desired film properties. A significant factor that correlates with the formation of thicker films on stainless steel in strongly alkaline solutions is the preferential loss of chromium and formation of iron- and nickel-rich films, which contrasts with the chromium-rich films observed in acid solution.

For example, potentiostatic etching of a Fe-27.7Cr alloy (Ref 20, 24) at 540 mV (SHE) resulted in:

- A yellow color with an estimated thickness of 35 nm (350 Å) after 20 s
- Brown at 38 nm (380 Å) after 60 s; orange at 40 nm (400 Å) after 2 min
- Purple at 44 nm (440 Å) after 6 min
- Blue at 48 nm (480 Å) after 20 to 60 min

Reference 20 and 24 discuss the interrelationship among compositions of several stainless steels, potential, charge density, current density as a function of time, and the development of color for 10 *N* NaOH etching solution. Observations are correlated with potentiostatic polarization curves obtained by holding the alloys at successive potential intervals for 5 min. For example, a 27.7% Cr ferritic stainless steel developed a golden yellow at 440 mV (SHE) in 5 min, corresponding to a charge density of 106 mA · s/cm^2. As an example of the decay of the current density with time, during the time required to produce this charge density, the current density decreased from 10 mA/cm^2 at 10 s to 0.1 mA/cm^2 at 5 min.

The difference in charge density of the ferrite and austenite phases in a two-phase alloy required to give color contrast between the phases has been discussed (Ref 20). After 5 min at +240 mV (SHE), the charge density of a 44.77% Cr σ phase alloy is 208 mA · s/cm^2 greater than that of the 27.7% Cr ferritic alloy. In a two-phase alloy of 60% ferrite and 40% s, the ferrite was blue and the σ phase was brown. A carbide phase was light yellow. These observations are consistent with the polarization curve shown in Fig. 16, in which current density for the σ phase exceeds that for the α phase and therefore would produce a thicker film. The curve for the two-phase α/σ phase alloy generally lies between the curves for the individual phases. The effect of the higher chromium content of the σ phase in lowering the potential for onset of transpassivity is evident when curves for the high- and low-content alloys are compared in the potential range of 450 to 650 mV. Therefore, at 500 mV the difference in current density is large and corresponds to excessive attack of the σ phase in the 5 min holding time used in generating these data. The curves suggest that useful etching might result for shorter times, but that the selection and control of the potential becomes critical.

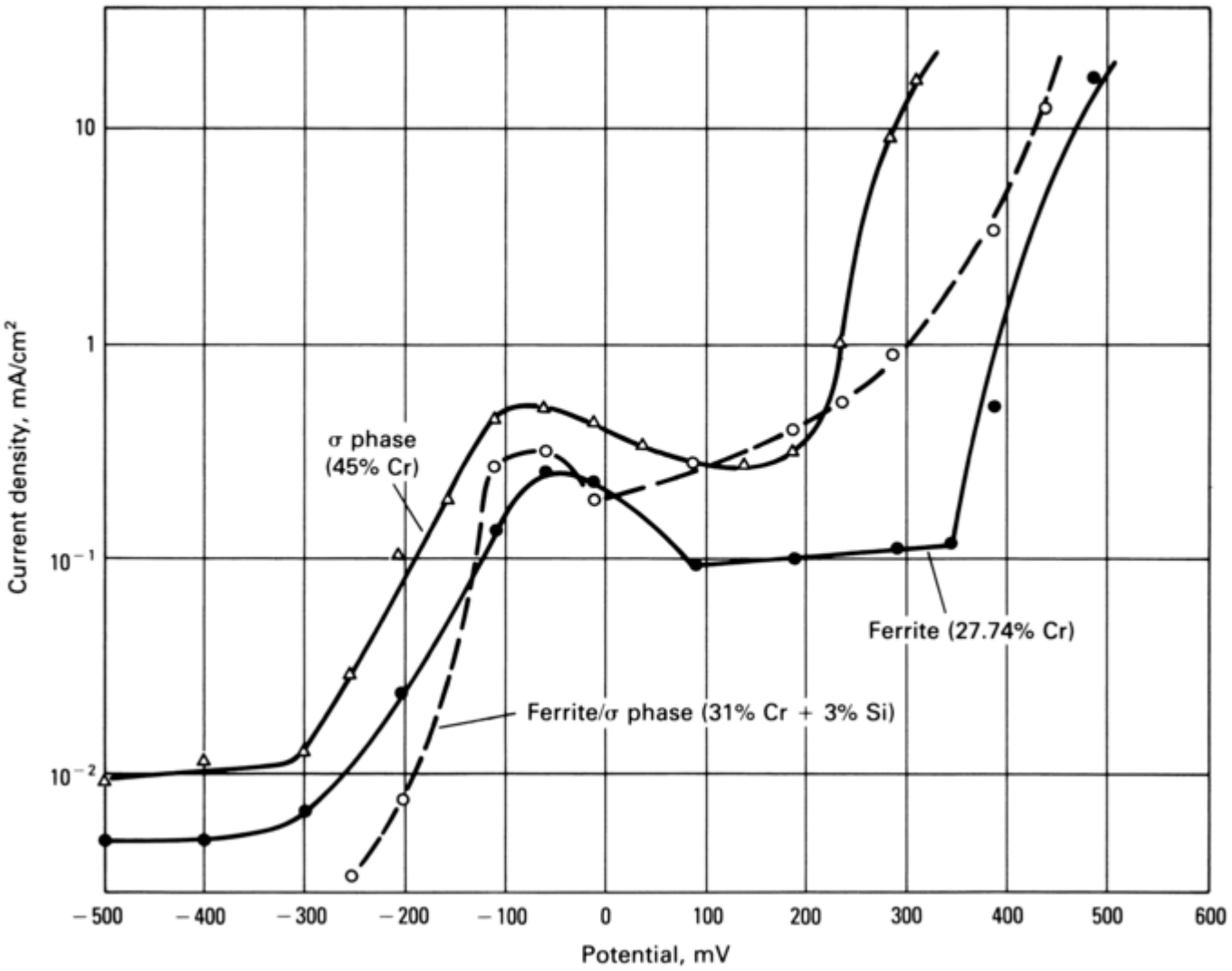

Fig. 16 Polarization curves for iron-chromium alloys. Source: Ref 20

Interference contrast films providing color differentiation of microconstituents are also produced by the controlled potential oxidation or reduction of species in solution in contrast to dependence on films produced by corrosion products. The method depends on depositing films having thicknesses and/or properties that are sensitive to the substrate phase and its crystal lattice orientation. Again, for interference color development, these films must attain thicknesses of 40 to 500 nm (400 to 5000 Å), although optically active films may be thinner. Examples are the anodic (oxidation) deposition of lead dioxide (PbO_2) and manganese dioxide (MnO_2), according to the reactions:

$$Pb_2 + 2H_2O \rightarrow PbO_2 + 4H^+ + 2e \quad \text{(Eq 4)}$$

and

$$Mn^{2+} + 2H_2O \rightarrow MnO_2 + 4H^+ + 2e \quad \text{(Eq 5)}$$

For example, a yellow film was obtained in 1 min at 660 mV (SHE) in a $Pb(C_2H_3O_2)_2$ solution; blue was developed in 3 min, and the next order of yellow at 4 min (Ref 24). Potentiostatic deposition of MnO_2 from a 10% manganese sulfate ($MnSO_4$) solution has been reported (Ref 25). Higher valent soluble species can be reduced (cathodic deposition) to insoluble film-forming species, such as molybdenum dioxide (MoO_2), according to the reaction:

$$MoO_4^{2-} + 4H^+ + 4e \rightarrow MoO_2 + 2H_2O \quad \text{(Eq 6)}$$

Although formation of deposit films by immersion using similar reagents, including formation of sulfide films, has been described (Ref 26), investigation of deposition by control of potential appears limited. Because the film-forming species are in solution, an advantage of the technique is that growth occurs at the film/solution interface without necessity of diffusion of cations or anions through the film. As a consequence, current density

and therefore film growth rate are constant and do not decrease with time, as occurs during thickening of corrosion-product films. Problems may be encountered if the potential required for the formation of deposit films is in the range of rapid dissolution of the substrate. The problem is alleviated by the possibility of solutions used for depositing films being relatively neutral and thus not as aggressive in the required potential range, as would result if film formation required extreme values of pH.

Color differentiation of microconstituents by etching in the active and high-transpassive potential ranges depends on development of surface topology containing irregularities, such as facets, etch pits, and differences in elevation. If the dissolution is uniform, within a factor of approximately 2, a current density of 1 mA/cm^2 will remove 50 nm (500 Å) per min. Because films are not forming, this dissolution rate is relatively constant with time. Optical features of the microscope, such as sensitive tint and quarter-wave plates as well as phase contrast devices, can develop color for surface irregularities with widths and depths of approximately one-quarter of a wavelength or less. For wavelengths at the lower end of the visible range—for example, violet at 40 nm (400 Å)—the dimension of the irregularities can approximate 10 nm (100 Å). Considering that the exposed surface area per unit area of specimen increases rapidly as the surface topology becomes progressively irregular, these approximations lead to current densities of approximately 1 mA/cm^2 for 1 min to produce surfaces with irregularities capable of yielding color. Whether or not the desired surface topology develops depends on the etchant; unfortunately, systematic investigations of the interrelationship of these factors in producing useful microstructural contrast, particularly in color, have not been reported.

Potentiostatic Etchants for Color. Table 4 surveys potentiostatic etchants that have been reported to develop color useful for microconstituent identification for the indicated materials. The wide range of potentials, times, and temperatures precludes reasonable inclusion of these variables in tabular form. The previous discussion provides a guide to the variables that should be investigated to establish useful techniques.

Table 4 Potentiostatic etching

Solution	Material	Morphology developed	Ref
10 *N* NaOH	Fe: 0–62% Cr, 0.78–8% C	Pure Fe_3C, $M_{23}C_6$, M-C_3, and as-distributed phases	27
	Fe: 18–41% Cr, 2.5–39% Ni	Martensite, austenite, α-ferrite, δ phase	28
	Fe: 25–45% Cr, 2% Mo, 6.4% Ni	$Cr_{23}C_6$, α-ferrite, δ phase	29
	Fe: 13% Cr, 1.5% Ti, 4% V	TiC, M_7C_3	30
	Fe: 17–45% Cr, 0–10% Ni, 0–2% Mo	Austenite, α-ferrite, δ phase	20
10% NaOH	Co: 20% Cr, 20% Ni, 4% (Nb, W, Mo)	Differentiation of M_6C, NbC	31
	Co: 31% Cr, 13% W, 2.2% C (cast)	M_2C	31
	Fe: Cr, Ni, Mo, Nb	NbC[(a)]	31
20% NaOH	Cast iron: C, Si, P	Segregation; nodular and flake graphite (effect of etchant temperature)	32
40% NaOH	Low-alloy steels	Differentiation of bainite and martensite	31
	Fe: 27% Cr	Ferrite, δ phase	31
	Co: 26% Cr, 10% Ni(Mo, W, Nb, Fe)	M_6C[(a)]	31
$NH_4C_2H_3O_2$ (ammonium acetate)	Tool steels	Mo, W, and V segregation in metal carbides	31
10% Na_2CO_3 (sodium carbonate)	Fe: Cr, Ni, Mo	$M_{23}C_6$	31
	Co: 26% Cr, 20% Ni, 4% (Nb, W, Mo)	$M_{23}C_6$[(a)]	31
	Co: 31% Cr, 13% W,	M_7C_3[(a)]	31

	2.2% C (cast)		
85% H_3PO_4	Cu: Be, Zr, Ni	Grain boundaries, dendritic segregation, dispersed phases	33, 34
$Pb(C_2H_3O_2)$	Fe: 13% Cr, 1.5% Ti, 4% V	VC, M_7C_3	30
10% NH_4Ac (ammonium acetate)	Fe: 10% W, 4% Mo, 4% Cr, 1.3% C	(V, W)C	31
10% $MnSO_4$ (manganese sulfate)	Fe: 25% Cr, 20% Ni	M_7C_3, $M_{23}C_6$, MnO_2	25

(a) Multiple potential and/or etchant

Vapor Deposition (Adapted from Ref 1, 3, and 35)

Vapor deposition, also referred to as vacuum deposition, involves film formation from a coating material that is vaporized or sublimated inside a vacuum chamber at approximately 10^{-3} Pa (10^{-5} torr). The coating material is heated by an electric current and then accumulates on the surface of specimens in the chamber. A typical experimental arrangement is shown in Fig. 24, where a tungsten wire basket is filled with material for evaporation. The temperature of the filament basket is raised slowly, and when the material melts and coats the wire, the wire is then raised to white heat for a few seconds, which evaporates the coating material.

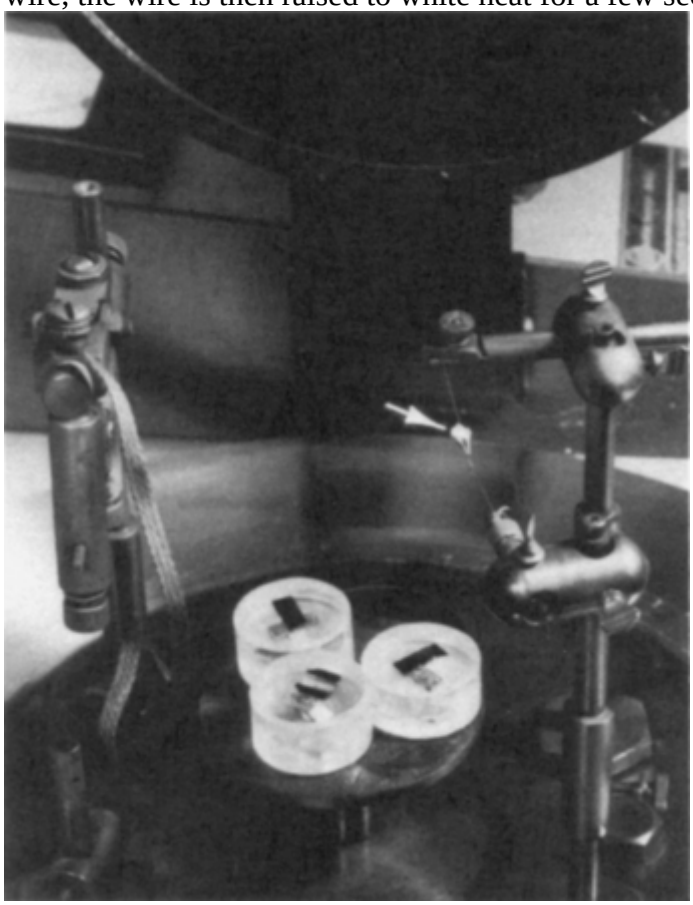

Fig. 17 Typical arrangement for vacuum deposition of interference films. The arrow indicates the tungsten wire basket filled with material for evaporation.

Interference films may be applied by vacuum deposition to metallic systems unsuited to oxidation or anodization. This was demonstrated by Pepperhoff in 1960 (Ref 36) and adapted and extended in 1966 (Ref 37). The Pepperhoff interference film method has been applied to the study of a very wide range of materials, as summarized in Ref 38. It is a simple technique to employ, but does require use of a vacuum evaporator. Striking results can be obtained, and the method is useful for phase identification and image analysis. Microstructural contrast is developed by deposition of a suitable material onto the sample surface to produce a thin, low-absorption, dielectric film with a high refractive index. The film enhances small differences in

intensity and optical phase angles between the microstructural constituents of polished specimens so that invisible or barely visible phases under bright-field illumination become more visible. The introduction of a thin interference film amplifies these minor differences by successive light reflection at the specimen surface.

In general, as the reflectivity of the polished surface increases, the refractive index of the deposited film must increase for proper contrast development. Thus, for high-reflectivity metals, materials with refractive index equal to or greater than that of zinc selenide (ZnSe) must be used. Zinc telluride (ZnTe), titanium dioxide (TiO_2), ZnSe, and zinc sulfide (ZnS) are some of the more popular vapor-deposited materials. Zinc telluride and TiO_2 are slightly absorbent, while ZnS and ZnSe are transparent. The high refractive index of the deposited film increases the brightness contrast between the phases and also increases the phase displacements between the waves reflected from the constituents producing color differences. Phase-contrast discrimination with interference films is more sensitive than phase-contrast illumination. Optical properties of the slightly absorbent ZnTe are $n_s = 3.25$ and $k_s = 0.4$ (at $\lambda = 550$ nm, or 5500 Å). The nonabsorbing materials zinc selenide ($n_s = 2.65$ at $\lambda = 550$ nm, or 5500 Å) and zinc sulfide ($n_s = 2.36$ at $\lambda = 550$ nm, or 5500 Å) have negligible absorption coefficients. For poorly reflective materials such as ceramics, cryolite (Na_3AlF_6) is used.

Other materials that have been found to produce phase contrast and color when vacuum deposited include silicon dioxide (SiO_2), zirconium dioxide (ZrO_2), tin oxide (SnO_2), and carbon. These alternate coating materials may be considered when the need for subsequent x-ray microanalysis necessitates using a film that does not contain elements to be analyzed. Frequent usage of this technique necessitates experimenting with controlled amounts of material, different compounds, and variable angles of deposition. Because the final mechanical polishing easily removes the film from the specimen, recoating can be carried out quickly. It cannot be predicted when the maximum contrast or desired color will be obtained; trial and error must be used. Additional material may be deposited by simply repeating the procedure.

For maximum contrast, the optical constants, that is, the refractive index and absorption coefficient for the different phases, should be known. Bühler and his associates have developed the needed information for several systems. Bühler and Kossel determined optical constants (absorption coefficients and refractive indexes) for carbides in ferritic and austenitic steels (Ref 39) with plotted graphs that show the relationship between the absorption coefficient as a function of the refracting indexes of commonly used vapor-deposited films. Reference 39 also provides optical constants for aluminum and some common intermetallic phases. Zogg et al. have shown the usefulness of vapor-deposited ZnTe for identification of constituents in aluminum alloys (Ref 40).

Good sample preparation procedures with particular attention to cleanliness is imperative for best results. Introduction of a slight amount of relief during final polishing, or a light pre-etch, are useful for obtaining better resolution of details. Residues left on the surface from polishing, cleaning, or handling must be removed. Vapor deposition is generally conducted under a vacuum of about 0.1 to 10^{-3} Pa (10^{-3} to 10^{-5} torr), with the sample about 10 to 15 cm (4 to 6 in.) from the deposition material. The compound should be evaporated slowly while being observed. As the film thickness increases, the macroscopic surface color changes in the following sequence: yellow, green, red, purple, violet, blue, silvery blue. Evaporation should be halted when the surface color is purple to violet, although with a few samples a green or red color has produced excellent results. To obtain a uniform film thickness, the sample is placed perpendicular to the flow of evaporated material and the sample can be slowly rotated. It sometimes helps to angle the sample surface so that a range of film thicknesses and colors is obtained. In this way, the conditions for best color contrast can be established in a single experiment.

Applications. Interference films produced by vacuum deposition apply to practically any polished metallographic specimen. The materials required are relatively inexpensive and readily available, and the technique is simple and easy. Figures 18, 19 and 20 in this article illustrate three examples of how vapor-deposited films have been used to help define microstructure. Figure 24 is an example of a TiO_2 coating on a specimen of oxidized type 316 stainless steel to provide better contrast between two different oxides (and also to distinguish the oxides from epoxy that infiltrated from the mounting medium). Figure 23 is another example of a TiO_2 coating deposited on siliconized silicon carbide to greatly improve contrast between the phases of silicon carbide, silicon, and an Fe-Ni-Si intermetallic. Figure 25 is an example of color contrast developed from a ZnSe coating deposited on a cermet, where tungsten carbide grinding debris resulting from ball milling the alumina-titanium carbide raw materials is highly visible using vapor deposition. These examples represent typical situations where such interference films have produced contrast and characteristic colors that aid microstructural analysis.

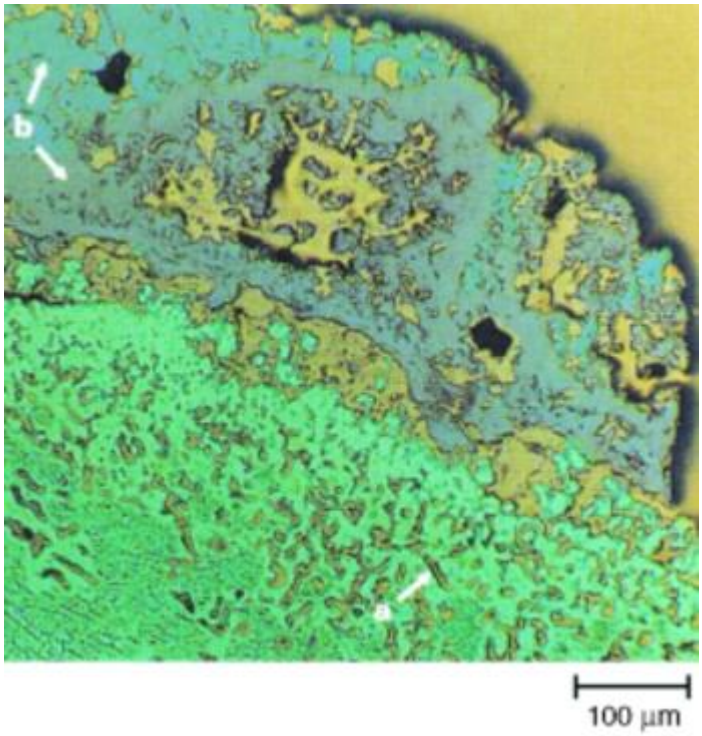

Fig. 18 Type 316 stainless steel exposed to air for 3000 h at 870 °C (1600 °F). Vapor deposition of a TiO_2 coating onto the as-polished surface provides color differences between two oxide compositions (arrow b) and subsurface void formation. Epoxy-filled voids are shown by arrow a. This was determined by noting that the material in the voids was the same color as the mounting material. 100×. (R. Crouse)

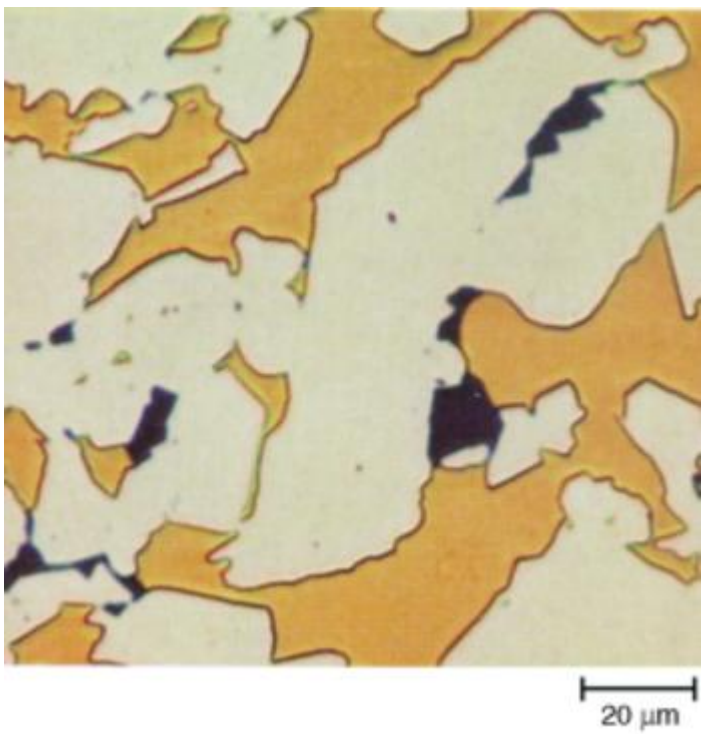

Fig. 19 Siliconized silicon carbide heat-exchanger tube vapor deposited with TiO_2. Silicon carbide is gray-tan, silicon is yellow, and an iron-nickel-silicon intermetallic is violet. 500×. (R. Crouse)

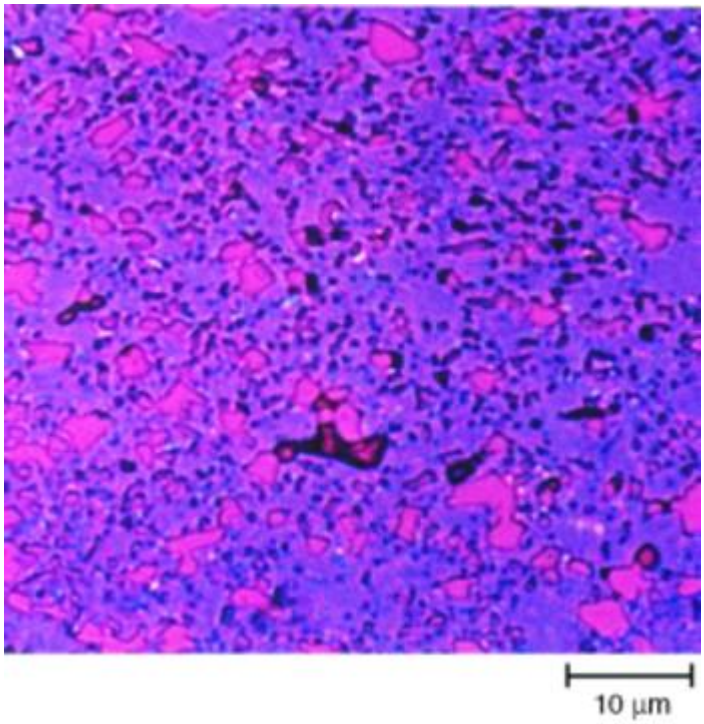

Fig. 20 Use of vapor deposition to reveal entrapped tungsten carbide inclusions in an Al_2O_3-TiC cermet cutting tool. The as-polished surface was vapor deposited with ZnSe. The tungsten carbide is dark red, the titanium carbide is pink, and the Al_2O_3 is blue. 1125×. (G.F. Vander Voort)

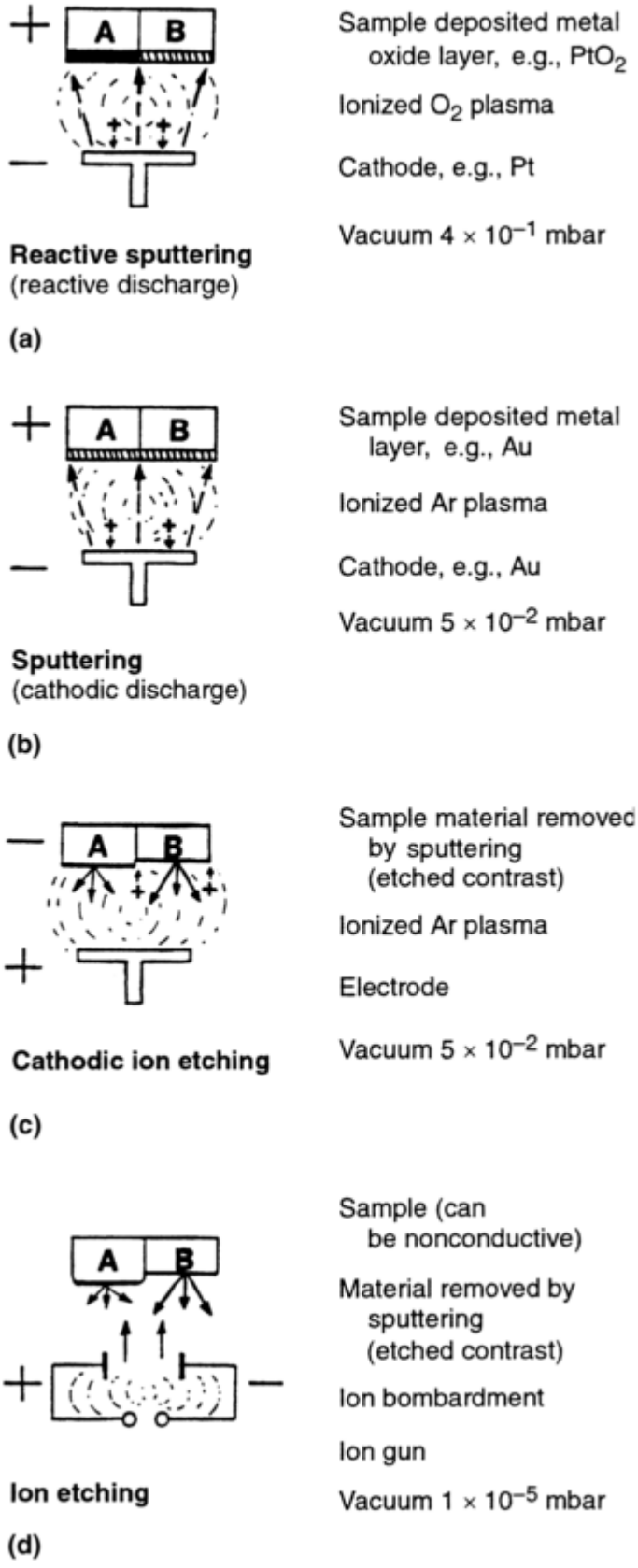

Fig. 21 Gas-discharge methods for deposition of interference films (a) and (b) and physical etching (c) and (d) by ion bombardment. (a) Reactive sputtering. (b) Cathodic discharge or sputtering. (c) Cathodic ion etching. (d) Ion etching. Source: adapted from Ref 1

Some microstructures have such variable composition as to be virtually impossible to chemically etch properly. For example, brazed joints frequently pose this problem, where a brazed joint may contain several phases that are chemically etched at different rates, resulting in a microstructure that does not fully reveal all phases. Deposition coating may provide enhancement that will completely reveal all details of the microstructure.

Figure 22 is an example of a titanium alloy brazed with an alloy of aluminum and silicon. Titanium is difficult to polish and etch, especially in combination with a brazing alloy. The specimen was coated with ZrO_2, rather than TiO_2, because titanium was one of the elements to be analyzed. All phases are well contrasted and quite colorful. The phases were identified using electron probe x-ray microanalysis.

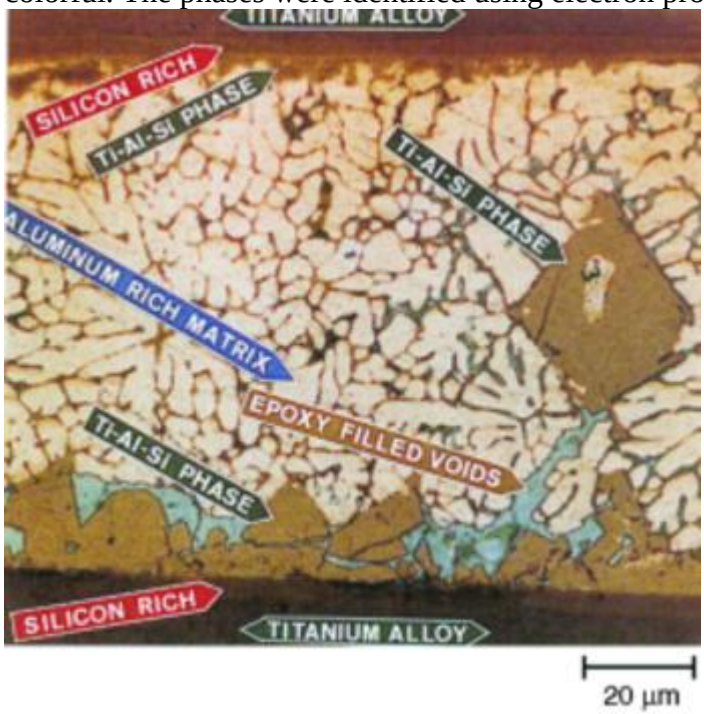

Fig. 22 Titanium alloy brazed with an aluminum-silicon brazing alloy. As-polished and vapor deposited with zirconium dioxide. 500×. (R. Crouse)

Sputtered Films (Adapted from Ref 1 and 3)

Physical deposition of thin films on specimens involves processes known as reactive sputtering (or gas contrasting) and cathodic vaporizing (or, simply, sputtering). Reactive sputtering (Fig. 21a) involves gas discharge in an ionized (plasma) atmosphere of a reactive gas (typically oxygen) at a pressure of about 4×10^{-5} mbar. Cathodic vaporization (Fig. 21b) also involves glow-discharge technology, but is done in an inert atmosphere instead of oxygen. The latter is done on specimens of low reflectivity, such as ceramics.

Reactive sputtering, also referred to as gas contrasting, is done in glow-discharge tubes, where positive ions bombard a cathode material (Fig. 21a). During the gas-discharge process, positively charged ions accelerate near the cathode. They impact on the cathode with energies of approximately 100 eV to more than 1 keV and atomize its surface. The atoms or ions, respectively, liberated in this process move in the direction of the specimen surface. They react, at least in part, with the atoms of the reactive carrier gas during passage through the gas chamber before their deposition as interference films on the specimen surface.

Reactive sputtering (Ref 41) can be applied to various metal alloys, composite materials, coatings, and joined materials. Good contrast is obtained for aluminum alloys, high-temperature nickel and cobalt alloys, cemented carbides, plasma sprayed layers, brazed joints, and sintered metals. The glow chamber can be attached directly to the microscope (Fig. 23) and is partially filled with oxygen or a mixture of various gases. The anode is the specimen; the cathode is of different metals—iron, for example. The as-polished specimen (anode) is brought into position in front of the cathode, or gas-discharge electron gun. During the gas discharge, a film forms on the specimen.

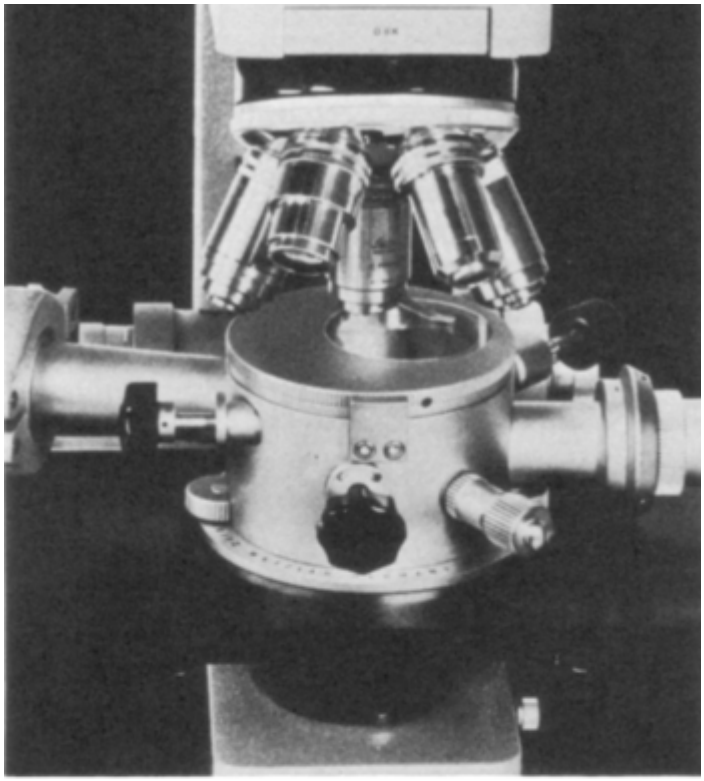

(a)

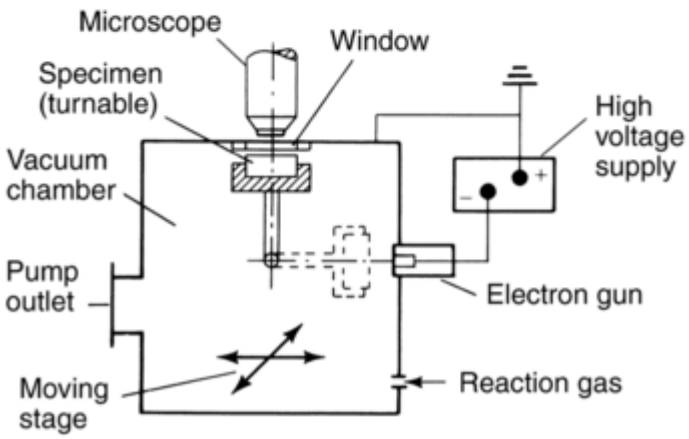

(b)

Fig. 23 Gas-discharge chamber for reactive sputtering and optical examination of interference layers on polished specimens. The results of the reactive sputtering process can be monitored through the viewing window. (a) Chamber mounted on a microscope stage. (b) Schematic of the various components.

The protective atmosphere is not filled statically into the chamber, but flows through it, even during deposition. After the voltage is adjusted to the respective distance of the specimen from the cathode (up to a 2500 V maximum is applied), a glow discharge is ignited in the gas chamber.

Determination of the optimal contrasting conditions is greatly simplified, because results of reactive sputtering can be directly observed by placing the coated specimen under a microscope without removing the specimen from the chamber. The composition of the reactively sputtered interference layers is determined only by the cathode material and the reactive gas. If oxygen is selected as the reactive carrier gas, an oxidic interference film is formed, but it does not necessarily consist of a stoichiometric oxide of the cathode materials (Ref 42). Depending on process parameters, different fractions of the reaction gas and the nonoxidized atoms of the cathode material may be incorporated into the interference film.

The most frequently used cathode materials are iron, lead, and platinum (although gold, copper, indium, nickel, and palladium have also been used). The oxide layers formed by reactive sputtering of these metals have refractive indices, n_s, of 1.8 to 2.8 and absorption coefficients, k_s, of 0.01 to 0.5 (which are a function of the light wavelength, λ). Cathode material selection depends on the specimen material and the optical contrast conditions to be controlled. For example, optical properties of various cathode materials are given in Table 5. Cathode distance may be varied over a wide range. Values from 5 to 15 mm (0.2 to 0.6 in.) are favorable for metals. Smaller cathode distances cause higher specimen temperatures. Specimen temperature influences the optical constants of the deposited film.

Table 5 Optical constants of some cathode materials used in interference film metallography

Cathode material		Wavelength, nm (Å)				
		500 (5000)	**525 (5250)**	**550 (5500)**	**575 (5750)**	**600 (6000)**
Platinum	n_z	2.78	2.55	2.66	2.61	2.57
	k_z	0.4	0.3	0.3	0.25	0.25
Palladium	n_z	2.45	2.58	2.65	2.65	…
	k_z	0.2	0.25	0.3	0.35	…
Lead	n_z	2.6	2.5	2.45	2.48	2.5
	k_z	0.1	0.05	0.04	0.04	0.1
Gold	n_z	2.28	2.35	2.3	2.3	2.3
	k_z	0.3	0.215	0.25	0.25	0.25
Iron	n_z	2.61	2.65	2.65	2.65	2.6
	k_z	0.35	0.3	0.25	0.175	0.1

Data measured with glass substrates. n_z is the refractive index; k_z is the absorption coefficient.

Cathode size may be selected at random and is principally a function of the technical limitations of the gas ion chamber. Larger cathodes necessitate a flatter thickness profile of the deposited interference film. Discharge current may vary from 0.5 to 2.5 kV in the installation at hand. This value substantially influences specimen temperature and therefore the optical constants of the interference film being formed. This value must be kept low for temperature-sensitive specimen materials.

Achieving specific color contrast effects requires control of film thickness, which is a function of time, voltage, the spacing between the sample and the electron gun, the type of gas, and the gas pressure. The time required decreases with increasing potential and decreasing spacing. The coating time t can be calculated using (Ref 41):

$$t = \frac{A}{\mathrm{kV} - B}$$

where A is 4.4 min and B is 0.3 kV. Contrast effects can be changed by varying the time or the cathode material. In general, optimal contrast is obtained when the macroscopic surface color is red to blue, as in heat tinting or in the Pepperhoff vapor-deposition method. Typically, times of 3 to 20 min are required using potentials of 1.5 to 2.5 kV and sample-to-gun spacings of 5 to 10 mm.

The gas pressure influences coating time and coating area (generally 1 cm^2). High gas pressure (50 Pa) reduces contrasting time, but the area coated is reduced. If the coated area is inadequate, lower pressures can be used. Although most early work employed an iron cathode, Exner and Roth experimented with silver, gold, copper, indium, lead and platinum cathodes (Ref 41). In general, only a few cathode materials produced significant differences if the coating time is adjusted. They also reported that changes in the gas used produced no significant differences. Typically, argon, air, or oxygen is used. The time required for contrasting can be significantly influenced by the gas used. The use of noble-metal cathode and inert gases reduced the coating time by at least a factor of 3 (Ref 41).

Phase contrast of most metals can be successfully improved by this method. Typical results of contrasting by interference layers are shown in Fig. 24; four phases can be differentiated on the polished microsection of a cast Sn-Ag-Cu alloy coated with a platinum oxide layer. If the contrast requirements are given, the optimal optical constants of the coating materials can be calculated from the optical constants of the phases present. However, contrasting calculations are often empirically or semiempirically formulated, because of the lack of knowledge of the optical constants of the phases. Measurement of the missing values is hampered because the composition

of the phases changes with heat treatment and specimen composition, with the optical constants varying accordingly.

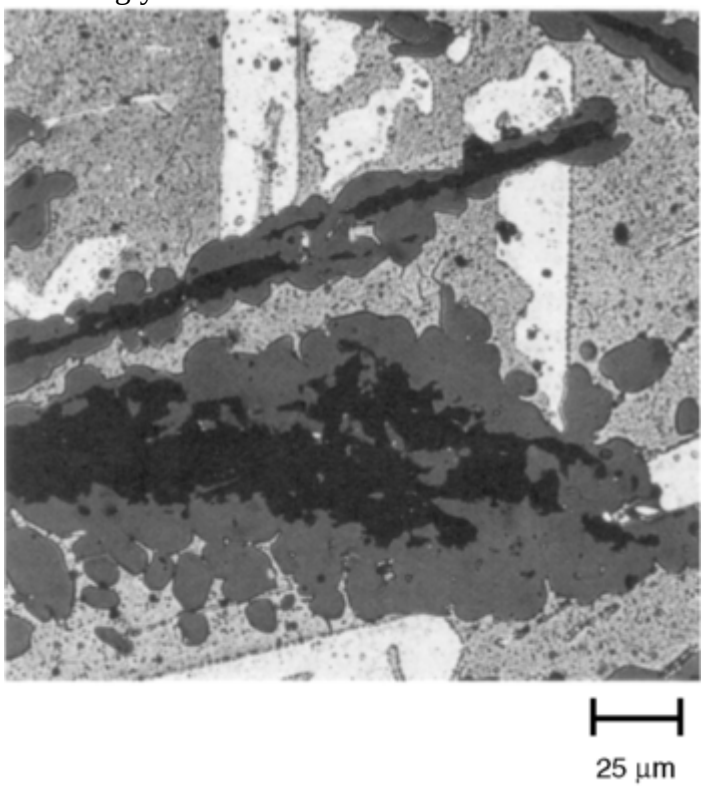

Fig. 24 Interference-layer micrograph of a cast Sn-18Ag-15Cu alloy. Polished specimen coated with a platinum oxide layer by reactive sputtering. Structure consists of Ag_3Sn (white), Sn (light gray), Cu_6Sn_5 (medium gray), and Cu_3Sn (dark gray). 300×

Cathodic vaporization (sputtering) involves physical deposition of a film inside vacuum chamber filled with an inert gas (instead of a reactive atmosphere, such as oxygen in reactive sputtering). The target material is deposited without reaction as a pure metal layer onto the sample surface. This metal layer reflects light and has no interference qualities. This technique is useful in the reflective light microscopy of materials with low reflectivity such as ceramic materials. Gold and aluminum are suitable coating materials.

References cited in this section

1. G. Petzow, *Metallographic Etching*, 2nd ed., ASM International, 1999

2. E. Beraha and B. Shpigler, *Color Metallography*, American Society for Metals, 1977

3. G.F. Vander Voort, *Metallography—Principles and Practice*, McGraw-Hill, 1984, p 180–181, 316–317, Reprinted by ASM International, 1999

4. S. Bradbury, *An Introduction to the Optical Microscope*, Vol 1, *Microscopy Handbooks*, Springer Verlag; rev. ed., Nov 1993

5. P. Torok and F.-J. Kao, Ed., and T.S. Han, *Optical Imaging and Microscopy: Techniques and Advanced Systems*, Vol 87, Springer Series in Optical Sciences, Springer Verlag, Aug 2003

6. H. Gahm and F. Jeglitsch, *Microstruc. Sci.*, Vol 9, 1981, p 65–80

7. J.H. Richardson, *Optical Microscopy for the Materials Sciences*, Marcel Dekker, 1971

8. H. Modin and S. Modin, *Metallurgical Microscopy*, Butterworths, 1973

9. V.A. Phillips, *Modern Metallographic Techniques and Their Applications,* Wiley-Interscience, 1971

10. R.J. Gray, R.S. Crouse, and B.C. Leslie, Decorative Etching, *Metallographic Specimen Preparation: Optical and Electron Microscopy,* J.L. McCall and W.M. Muller, Ed., Plenum Press, 1974

11. J.V. Cathcart, G.F. Peterson, and C.J. Sparks, Oxidation Rate and Oxide Structural Defects, *Surfaces and Interior Chemical and Physical Characteristics,* Burke, Reed, and Weiss, Ed., Syracuse University Press, 1967

12. R.J. Gray, W.C. Thurber, and C.K.H. Dubose, Preparation of Arc-Melted Uranium Carbides, *Met. Prog.,* Vol 74 (No. 1), July 1958, p 65–70

13. R.J. Gray, E.S. Bomar, and R.W. McClung, Evaluating Coated Particles of Nuclear Fuel, *Met. Prog.,* Vol 86 (No. 1), July 1964, p 90–93

14. E. Weck and E. Leistner, *Metallographic Instructions for Colour Etching by Immersion—Part I: Klemm Colour Etching,* Deutscher Verlag für Schweisstechnik, 1982

15. E. Weck and E. Leistner, *Metallographic Instructions for Colour Etching by Immersion—Part II: Beraha Colour Etchants and Their Different Variants,* Deutscher Verlag für Schweisstechnik, 1983

16. E. Beraha, Metallographic Reagents Based on Sulfide Films, *Prakt. Metallogr.,* Vol 7, 1970, p 242–248

17. E. Beraha, Metallographic Reagents Based on Molybdate Solutions, *Prakt. Metallogr.,* Vol 11, 1974, p 271–275

18. R.J. Gray, V.K. Sikka, and R.T. King, Detecting Transformation of Delta Ferrite to Sigma-Phase in Stainless Steels by Advanced Metallographic Techniques, *J. Met.,* Nov 1978, p 18–26

19. E.E. Stansbury, Potentiostatic Etching, *Metallography and Microstructures,* Vol 9, *ASM Handbook,* 1985, p 143

20. G. Grutzner and J.H. Schuller, *Werkst. Korros.,* Vol 20, 1969, p 3203–3251

22. V. Cihal and M. Prazak, *J. Iron Steel Inst.,* Vol 193, 1959, p 360–367

23. W.A. Mueller, *Corrosion,* Vol 18, 1962, p 73t–79t

24. G. Grutzner and H.J. Schuller, *Pract. Metallogr.,* Vol 6, 1969, p 246–258

25. P. Helbach and E. Bullock, "Potentio-static Etching of Carburized Steels," Petten, Establ., Netherlands: Committee of European Communities, EUR 8138, 1982

26. G.F. Vander Voort, Tint Etching, *Met. Prog.,* Vol 127, 1985, p 31

27. F.K. Naumann and G. Langenscheid, *Arch. Eisenhüttenwes.,* Vol 38, 1967, p 463–468

28. W. Schaarwachter, H. Ludering, and F.K. Naumann, *Arch. Eisenhüttenwes.,* Vol 31, 1960, p 385–391

29. F.K. Naumann, *Arch. Eisenhüttenwes.,* Vol 34, 1963, p 187–194

30. P. Lichtenegger, A. Kulmburg, and R. Bloch, *Pract. Metallogr.,* Vol 6, 1969, p 535–539

31. R. Bloch and P. Lichtenegger, *Pract. Metallogr.,* Vol 12, 1975, p 186–193

32. H. Ludering, *Arch. Eisenhüttenwes.,* Vol 2, 1964, p 153–159

33. A. Mance, *Metallography,* Vol 4, 1971, p 287–296

34. A. Mance, V. Perovic, and A. Mihajlovic, *Metallography,* Vol 6, 1973, p 123–130

35. R.S. Crouse, Interference Films by Vacuum Deposition, *Metallography and Microstructures,* Vol 9, *ASM Handbook,* 1985, p 147

36. W. Pepperhoff, Sechtbarmachung von Gefügestrukturen durch Interferenz—Aufdampfoschichten, *Naturwissenschaften,* Vol 16, 1960, p 375

37. J.O. Stiegler and R.J. Gray, Microstructural Discrimination by Deposition of Surface Films, *Advances in Metallography,* Technical Papers of the 20th Metallographic Conference, R.J. Jackson and A.E. Calabra, Ed., RFP-658, The Dow Chemical Co., Oct 1966, p 11–17

38. H.E. Bühler and H.P. Hougardy, *Atlas of Interference Layer Metallography,* Deutsche Gesellschaft für Metallkunde, Oberursel, Germany, 1980

39. H.E. Bühler and D. Kossel, Guidelines for the Development and Application of Interference Film Metallography, *Prakt. Metallogr.,* Vol 18, 1981, p 385–391

40. H. Zogg, S. Weber, and H. Warlimont, Optical Enhancement for Al-Alloys by Vacuum Deposited ZnTe Interference Layers, *Pract. Metallogr.,* Vol 14, 1977, p 553

41. H.E. Exner and J. Roth, Metallographic Contrasting by Reactively Sputtered Interference Layers, *Pract. Metallogr.,* Vol 18, 1980, p 365

42. S. Hofmann and H.E. Exner, Auger-elektronenspektroskopische Untersuchungen von Kontrastierschichten auf Metallen, *Z. Metallkde.,* Vol 65 (No. 778), 1974

Contrast Enhancement and Etching, *Metallography and Microstructures,* Vol 9, *ASM Handbook,* ASM International, 2004, p. 294–312

Etching

The term etching refers to the preferential chemical, electrochemical, or physical attack of different constituents on the surface of a specimen to reveal structural details for macroscopic or microscopic examination. In some cases, contrast can also originate from layers formed simultaneously with material dissolution. For example, precipitation etching and potentiostatic etching are two methods that involve controlled etching and the possible formation of interference films. The process of film deposition by sputtering (Fig. 21a and b) can also be reversed to result in physical etching (Fig. 21c and d). Another type of etching is magnetic etching, which is a special technique to examine domain structures of magnetic materials.

For the most part, metallographic etching continues to be an empirical method. This condition results from the abundance of etching methods, nonuniform nomenclature, and, frequently, the lack of knowledge of etchant mechanisms. Conventional etching in particular is difficult to reproduce, regardless of its simplicity. During the electrochemical processes, numerous side effects must be considered. For example, changes in the electrolyte and inhibiting reactions at the specimen surface that cause polarization phenomena, overpotential, and so on,

must be appraised. In some respects, metallographic etching is as much art as science with various techniques (e.g., Table 1) available to the metallographer.

To achieve more reproducibility and dependable structural contrast, various methods have been developed in recent years. Electrolytic potentiostatic etching, ion etching, and contrasting by physically deposited interference layer are gaining more acceptance. These methods can provide more reproducible results, which is of particular importance for quantitative image analysis. These instruments are used to determine automatically the area fraction of various phases and are not sensitive to subtle differences. Therefore, sharply reproducible etching contrast is necessary to obtain accurate information.

Electrochemical (Chemical) Etching

The chemical methods of etching processes involve a process of controlled corrosion from cathodic (reducing) reactions and anodic (oxidizing) reactions. Reduction (cathodic reaction) involves the absorption of electrons, while oxidation (anodic reactions) involves the emission of electrons. For example:

$$\text{Oxidizing agent} + \text{electron} \leftrightarrow \text{reducing agent}$$

$$Fe^{3+} + e \leftrightarrow Fe^{2+}$$

Etchants provide an electrolytic action that results in different reduction-oxidation (redox) rates for the different phases on the specimen surface. All metals contacting the etching solutions tend to become ionized by releasing electrons. The extent of this reaction can be compared from the electromotive series for the potential of metal versus the standard potential of a reference electrode. The tabulation of various metals listed in order of decreasing electroaffinity is:

$$Li^{+}, Na^{+}, K^{+}, Ca^{2+}, Ba^{2+}, Be^{2+}, Mg^{2+}, Al^{3+},$$
$$Mn^{2+}, Zn^{2+}, Cr^{3+}, Cd^{2+}, Ti^{+}, Co^{2+}, Ni^{2+},$$
$$Pb^{2+}, Fe^{3+}, H^{+}, Sn^{4+}, Sb^{3+}, Bi^{3+}, As^{3+},$$
$$Cu^{2+}, Ag^{+}, Mg^{2+}, Au^{3+}, Pt^{3+}$$

Acids attack all elements preceding hydrogen (H_2) as it evolves. All elements following hydrogen cannot be attacked without the addition of an oxidizing agent. Therefore, microstructural elements of different electrochemical potential are attacked at varying rates, producing differential etching, which results in microstructural contrast.

The difference in potential of the microstructural elements causes a subdivision into a network of miniature cells consisting of small, adjoining anodic and cathodic regions. These local elements originate not only from differences in phase composition, but also from irregularities in the crystal (e.g., grain boundaries), as well as from other inhomogeneities such as:

- Inhomogeneities resulting from deformation (deformed zones), which are less resistant to attack than undeformed material
- Unevenness in the formation of oxidation layers (regions free of oxides are preferentially etched)
- Concentration fluctuation in the electrolyte (low concentration is less resistant)
- Differences in electrolyte velocity (higher circulation rates reduce resistance to attack)
- Differences in the oxygen content of the electrolyte (aerated solutions are more resistant)
- Differences in the illumination intensity, which can initiate differences in potential

For pure metals and single-phase alloys, a potential difference exists between grain boundaries and grain interiors, grains with different orientations, between impurity phases and the matrix, or at concentration gradients in single-phase alloys. For multiphase alloys, a potential also exists between phases. These potential differences alter the rate of attack, revealing the microstructure when chemical etchants are used. For a two-phase alloy, the potential of one phase is greater than that of the other. During etching, the more electropositive (anodic) phase is attacked; the more electronegative (cathodic) phase is not attacked appreciably. The magnitude of the potential difference between two phases is greater than the potential differences existing in single-phase alloys. Therefore, alloys with two or more phases etch more rapidly than single-phase metals or alloys.

A wide variety of etchants are available, including acids, alkaline solutions, neutral solutions, mixtures, molten salts and gases. Most chemical etchants are empirically derived recipes that can be easily modified or applied to various materials. The etch also may be done strictly as a chemical technique (without the use of an external current supply), or it may involve dissolution with the aid of electrochemical techniques. Electrochemical etching may be regarded as “forced corrosion,” while conventional chemical etching proceeds by selective dissolution according to the electrochemical characteristics of the microstructural constituents. With most chemical etchants, the same phase will usually be anodic or cathodic. It is difficult with standard etchants to reverse the attack, that is, to make the anodic phase cathodic. Only by using the potentiostatic method can phases be etched selectively in the same electrolyte by changing the applied voltage.

Electrolytic etching involves the process of electrolysis, which is also the basis for electropolishing. In some cases electrolytic etching can be accomplished immediately after an electropolishing operation by reducing the voltage to approximately one-tenth the potential required for electropolishing (see the article “Chemical and Electrolytic Polishing” in this Volume for more details on voltage-current conditions of electrolysis). In electrolytic (anodic) etching, electrical potential is applied to the specimen using an external circuit. Figure 25 shows a typical setup consisting of the specimen (anode) and its counterelectrode (cathode) immersed in an electrolyte (etchant). During electrolytic etching, positive metal ions leave the specimen surface and diffuse into the electrolyte; an equivalent number of electrons remain in the material. This results in direct etching, shown as segment A—B of the current density versus voltage curve in Fig. 26. Specimen dissolution without formation of a precipitated layer occurs in this instance. However, if the metal ions leaving the material react with nonmetal ions from the electrolyte and form an insoluble compound, precipitated layers will form on the specimen surface whose thicknesses are a function of the composition and orientation of the microstructural features exposed to the solution.

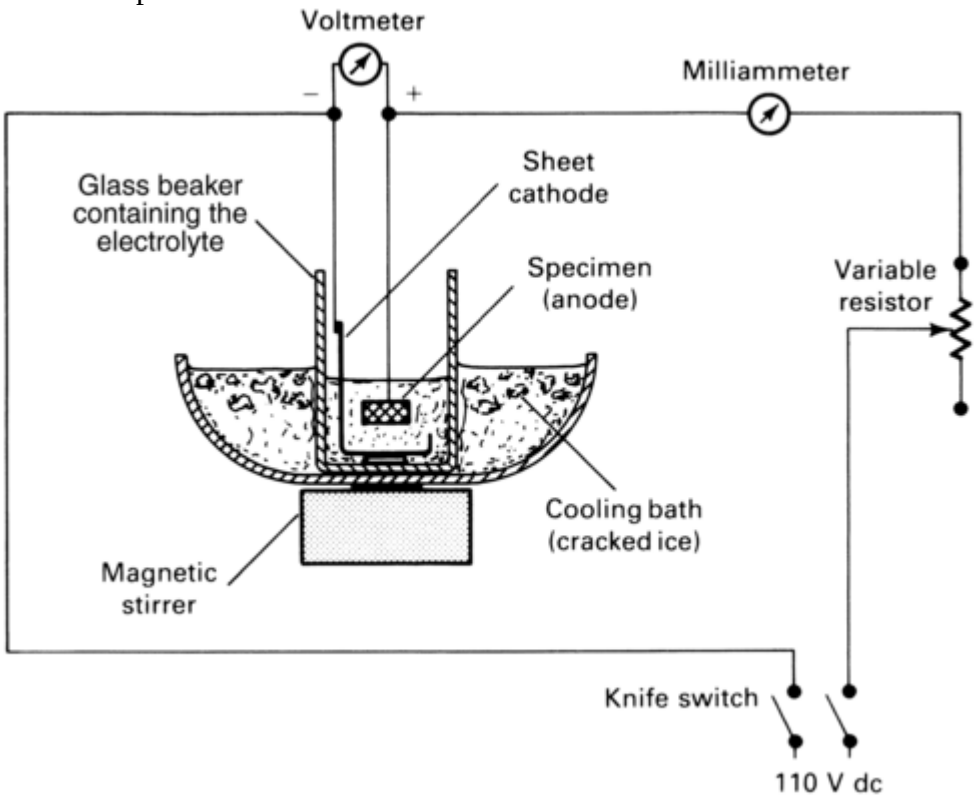

Fig. 25 Basic laboratory setup for electrolytic etching and polishing

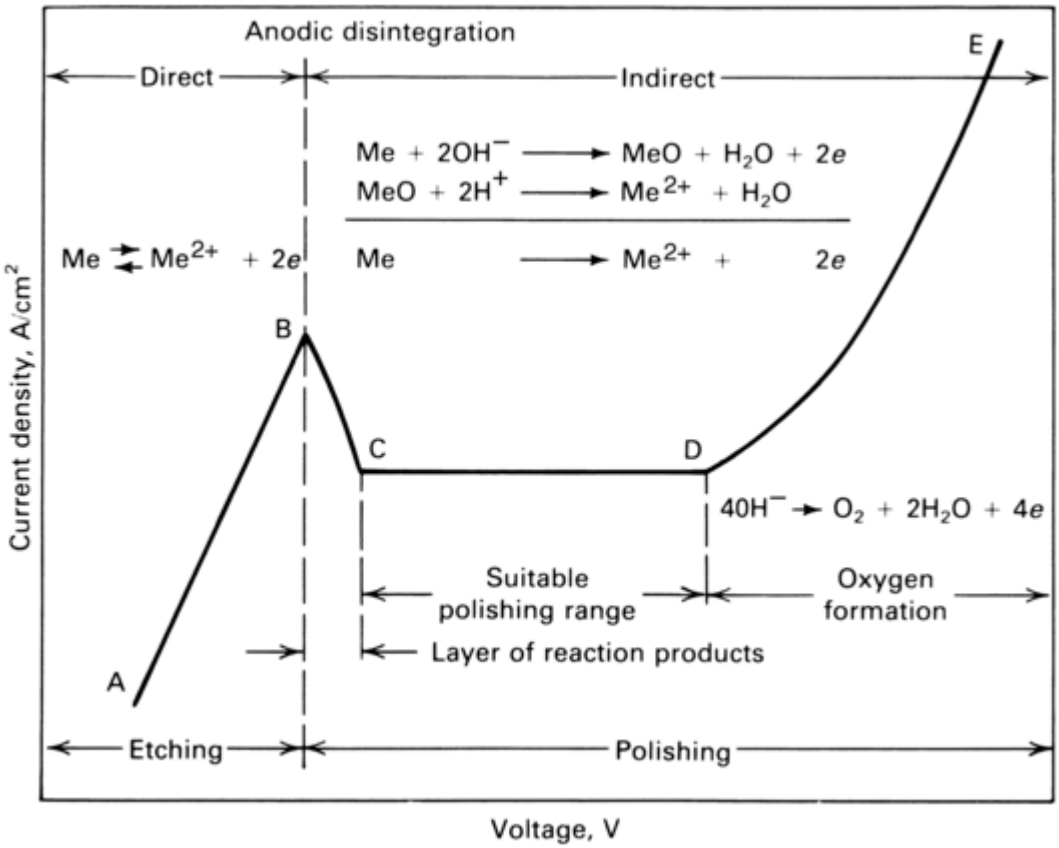

Fig. 26 Idealized current density versus applied voltage for many common electrolytes. Regions for electrolytic etching and polishing are indicated.

Potentiostatic etching (Fig. 12 and Fig. 27) is an advanced form of electrolytic etching that produces the ultimate etching contrast through highly controlled conditions. It can also result in film formation and interference effects as noted in the section “Potentiostatic Etching” in this article. Clearly pronounced contrast can be produced with this method, where it would not be possible otherwise, because the potential of the specimen is maintained at a fixed level through the use of a potentiostat and suitable reference electrodes (Fig. 27). The potential of the specimen usually changes with variations in electrolytic concentration.

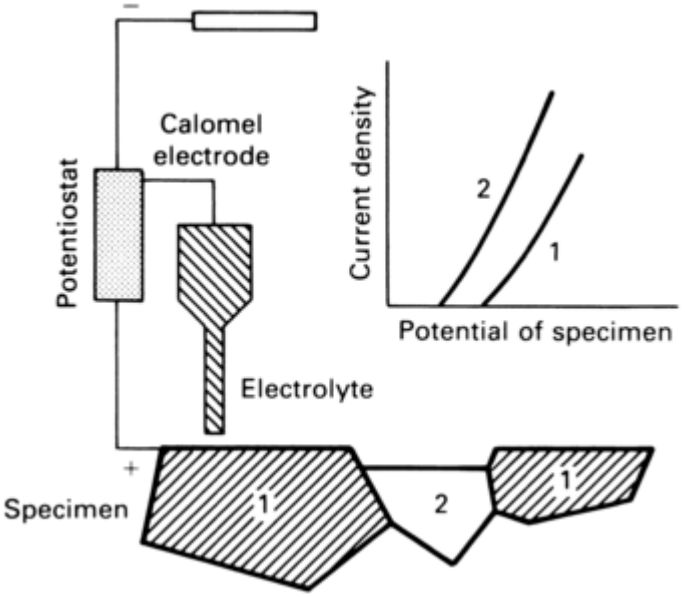

Fig. 27 Principles of electrolytic potentiostatic etching

Potentiostatic etching provides very reproducible results. In some cases, the cell current can be maintained with a coulombmeter to determine the extent of etching (controlled etching). For more details on these methods, see

the section “Potentiostatic Etching” in this article. Additional information on potentiostatic etching also can be found in Ref 43, Ref 44, Ref 45, Ref 46, Ref 47, Ref 48, Ref 49, Ref 50, Ref 51.

Precipitation (deposit) etching is an immersion technique that allows formation of interference layers as a by-product of the etching from material dissolution. In precipitation etching, the material is dissolved at the surface; it then reacts with certain components of the etchant to form insoluble compounds. These compounds precipitate selectively on the surface, causing interference colors or heavy layers of an inherent color. Thus, precipitation (deposit) etching can be considered as a color immersion technique. This technique has produced excellent results in the examination of grain orientation and inhomogeneities such as coring. Additional information on precipitation etching can be found in Ref 52.

Other Etching Methods

Etching by Ion Bombardment. Ion bombardment is a form of physical etching that leaves the surface free of chemical residues. It offers an advantage when electrochemical etching is difficult—for example, when there is an extremely large difference in electrochemical potential between microstructural elements, or when chemical etchants cause stains or residues that could produce false microstructures. The two methods of ion bombardment are based on glow-discharge devices, where specimen is the cathode of the glow tube (Fig. 21c), or where a glow tube produces ions that bombard the specimen (Fig. 21d). Additional information on ion etching can be found in Ref 53, 54, and 55.

Cathodic ion etching (Fig. 21c) is an inert-gas-discharge method like cathodic discharge sputtering (Fig. 21c), except that the specimen is the cathode, so that the specimen is etched instead of coated. The discharge gas is typically argon. This method produces structural contrast by selective removal of atoms from the specimen surface. Etching is accomplished by using high-energy argon ions, accelerated by voltages of 1 to 10 kV. Individual atoms are removed at various rates, depending on their atomic number, their bonding state, and the crystal orientation of the individual grains.

Ion etching also involves ion bombardment, but the specimen is not the cathode of a glow-discharge chamber. The specimen is etched by an ion gun, which consists of a glow-discharge tube (Fig. 21d) of inert gas such as argon. High-energy ions from the discharge tube traverse a vacuum chamber and bombard the specimen. The different phases are etched at different rates by the ions. This method is especially useful for nonconductive specimens.

Thermal etching is used in high-temperature microscopy and to etch polished surfaces of ceramic materials well below their sintering or hot-pressing temperature. Thermal etching is also partially based on atoms leaving the material surface as a result of additional energy. However, the predominant force in thermal etching is the formation of slightly curved equilibrium surfaces having individual grains with minimum surface tension. Thermal etching of ceramic materials in air, vacuum, or inert gases is often better than conventional chemical etching. Figure 28 shows as an example the grain structure of a diffusion-welded ceramic joint revealed by thermal etching. Additional information on thermal etching can be found in Ref 56, 57, 58, 59, 60, and 61 for metals and Ref 62, 63, 64, 65, 66, and 67 for ceramics. Thermal etching is compared with other techniques in Ref 68, 69, and 70.

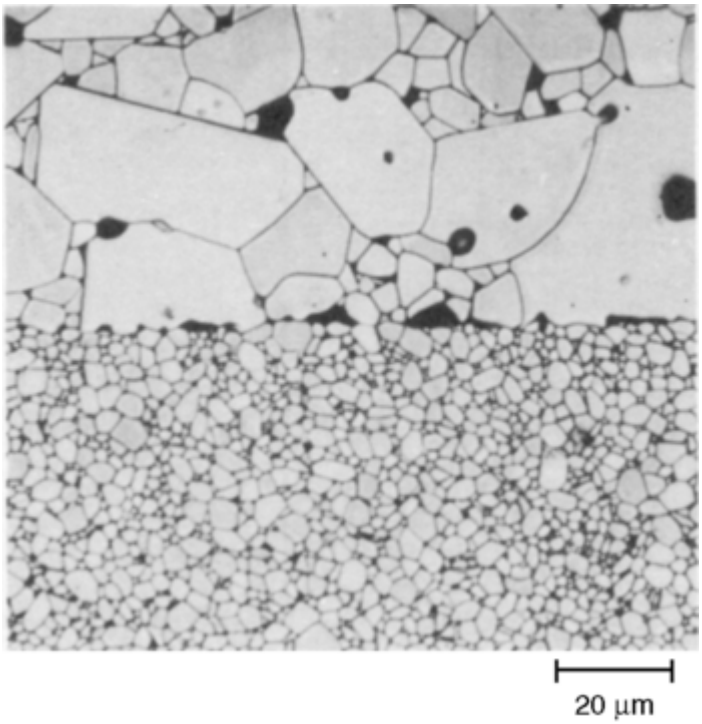

Fig. 28 Polished section of a diffusion-bonded joint between a coarse-grained and a fine-grained alumina ceramic (99.7% Al_2O_3) thermally etched in air at 1400 °C (2550 °F) for 1 h. 500×

Magnetic etching (adapted from Ref 3) can be used to examine domain structures of magnetic materials to relate metallographic and domain structures to properties. Magnetic etching uses magnetism to reveal specific features in the microstructure of fully magnetic (ferromagnetic) materials or strongly magnetic (ferrimagnetic) materials. The technique originates from the work of Bitter and others (Ref 71, 72) in the 1930s. The basic technique involves sprinkling magnetic powder on the surface of a material in a magnetic field and observing the distribution of the particles. The distribution of powder, sometimes referred to as "Bitter patterns," help in the visual observation of magnetic domains, which are regions with distinct transition in magnetic orientation. Although the domain patterns are visible on some materials, the use of this technique to reveal ferromagnetic conditions can serve a more practical role. Other methods used to observe magnetic domains include magnetooptic Kerr and Faraday effect, Lorentz microscopy, and x-ray tomography. More information on the metallography of magnetic materials is in the article "Microstructure and Domain Imaging of Magnetic Materials" in this Volume.

The Bitter method is commonly used because of its simplicity. The technique initially employed finely ground particles of gamma ferric oxide suspended in ethyl acetate. Colloidal (i.e., permanent) suspensions of gamma ferric oxide are used today, either by preparing colloidal suspensions or by using a commercially prepared colloidal magnetic suspension known as Ferrofluid (Ferrotec, Nashua, NH). To use the Bitter technique, samples must be carefully prepared to eliminate artifact structures and residual stresses. Electropolishing is generally preferred. A drop of the colloidal suspension of magnetic iron oxide is applied to the sample surface. The particles are attracted by stray magnetic fields, thus outlining domain structures. The sample is observed with either bright-field or dark-field illumination. A magnetic coil or yoke is used to alter the magnetic structure. Examination can be made using magnifications of up to several hundred fold; if replicas are prepared, electron microscopy (Ref 73) can be used or optical microscopy at high magnification can be performed if the suspension is dried after application ("dry Bitter technique") (Ref 74).

References cited in this section

3. G.F. Vander Voort, *Metallography—Principles and Practice,* McGraw-Hill, 1984, p 180–181, 316–317, Reprinted by ASM International, 1999

43. G. Hertsleb and P. Schwaab, Fundamentals of the Potentiostatic Development of Structures Using High-Alloy Steels as an Example, *Pract. Metallogr.,* Vol 15, 1978, p 213

44. M.G. Pujar, R.K. Dayal, T.P.S. Gill, and S.N. Malhotra, Microstructural Evaluation of Molybdenum-Containing Stainless Steel Weld Metals by a Potentiostatic Etching Technique, *J. Mater. Sci.,* Vol 33 (No. 10), 15 May 1998, p 2691–2700

45. X. Ma and S.J. Luo, Potentiostatic Etching and Etching Quantitative Analysis of Carbides in Die Steel, *J. Iron Steel Res. Int.,* Vol 2 (No. 1), Sept 1995, p 47–52

46. H. Worch, K. Nocke, C. Blank, W. Oelssner, and F. Bertholt, Potentiostatic Etching—Presentation of a New Etching Technique, *Prakt. Metallogr.,* Vol 31, May 1994, p 245–251

47. E.M. Jackson, P.E. de Visser, and L.A. Cornish, Distinguishing between Chi and Sigma Phases in Duplex Stainless Steels Using Potentiostatic Etching, *Mater. Charact.,* Vol 31 (No. 4), Dec 1993, p 185–190

48. A. Sato, K. Kon, S. Tsujikawa, and Y. Hisamatsu, Dependence of Dissolution Rate of Inconel Alloy 600 with Coarse Columnar Crystals on Crystallographic Orientation in Potentiostatic Etching, *J. Jpn. Inst. Met.,* Vol 57 (No. 7), July 1993, p 790–796

49. Y. Wang, F. Yu, and Y. Wang, Check the Sensitivity of Non-Sensitive Intergranular Corrosion Using Potentiostatic Etching in Transpassive Region, *Huagong Jixie (Chem. Eng. Mach.),* Vol 19 (No. 3), 1992, p 129–133, 134

50. J.H. Potgieter, L.M. Matthews, and P. De Visser, Experimental Study of Quantitative Phase Characterization in Duplex Stainless Steels by Potentiostatic Etching, *J. Mater. Sci.,* Vol 27 (No. 13), 1 July 1992, p 3667–3679

51. K. Takiazawa and Y. Nakayama, Effects of MnS Inclusion and the Potentiostatic Etching Treatment on Pitting Corrosion Resistance of 18-8 Stainless Steels, *Hyomen Gijutsu (J. Surf. Fin. Soc. Jpn.,* Vol 42 (No. 6), June 1991, p 649–654

52. H. Gahm, F. Jeglitsch, and E.M. Hörl, Investigations of the Structure of Chemically Deposited Films Produced by Precipitation Etching, *Pract. Metallogr.,* Vol 19, 1982, p 369

53. I. Graf, Ion Etching—State of the Art and Perspectives for Contrasting the Microstructure of Ceramic and Metallic Materials: I. Development and Physics in Ionetching, *Prakt. Metallogr.,* Vol 35 (No. 5), May 1998, p 235–254

54. M. Pohl and W.-G. Burchard, Ion Etching in Metallography, *Pract. Metallogr.,* Special Edition 11, 1980, p 42 (in German)

55. R.C. Sanwald and D.J. Gould, Ion Etching Metallographic Samples, *Metallography,* Vol 7, 1974, p 73

56. Y. Iino, Creep Plastic Zone and Crack Initiation at 923 K of 304 Stainless Steel Compact Tension Specimen, Proc. Conf. *ECF 10—Structural Integrity: Experiments—Models—Applications,* Vol I (Berlin, Germany), 20–23 Sept 1994, Engineering Materials Advisory Services Ltd., 1994, p 291–296

57. B. Hoffmann-Millack, C.J. Roberts, and W.S. Steer, Observation of Rhombic Facets on Platinum Wire after Heating in Air Using Scanning Tunnelling Microscopy, *J. Microsc.,* Vol 166 (No. 2), May 1992, p 247–252

58. G.D. Bruce, P. Fortier, G. Palumbo, J.E. Guillet, and G.J. Vancso, Scanning Tunneling Microscopy Imaging of Grain Boundaries and Triple Junctions in Copper, *Mater. Charact.,* Vol 28 (No. 2), March 1992, p 133–137

59. C.I.H. Ashby, Laser-Driven Etching, *Thin Film Processes II,* Academic Press, 1991, p 783–856

60. J. Wolfenstine, R.P. Kershaw, W.J. Kim, and O.D. Sherby, Thermal—Chemical Etching Technique for Hypereutectic Irons, *Mater. Charact.,* Vol 24 (No. 4), June 1990, p 375–378

61. J. Frohm, U. Linke, and K. Besocke, Thermal Etching of Platinum Crystals in Air, Hydrogen and Oxygen—Some STM Observations, *Prakt. Metallogr.,* Vol 21 (No. 10), Oct 1989, p 518–528

62. G. Willmann and G. Heimke, Thermal Etching of α-Alumina and Na-β-Alumina, *Pract. Metallogr.,* Vol 15, 1978, p 11

63. M. Asano, T. Kobayashi, and Y. Takasu, Bending Strength, Fracture Toughness and Crack Propagation Characteristics of Si_3N_4 Ceramic at High Temperature, *J. Soc. Mater. Sci., Jpn.,* Vol 45 (No. 2), Feb 1996, p 189–194

64. G. Nicoletto, A. Tucci, and L. Esposito, The Effect of Microstructure on Fracture Toughness of Polycrystalline Alumina, *Fat. Fract. Eng. Mater. Struct.,* Vol 19 (No. 1), 1996, p 119–128

65. M. Asano, T. Kobayashi, and Y. Takasu, Analysis of Crack Growth Behavior for Silicon Nitride Ceramics at High Temperature, *Strength of Materials,* ICSMA 10 (Sendai, Japan), 22–26 Aug 1994, Japan Institute of Metals, 1994, p 615–618

66. V.A. Knapp, D.E. Wittmer, and J.J. Conover, Microwave Plasma Etching of Si_3N_4, 18th Annual Conference on Composites and Advanced Ceramic Materials, 9–14 Jan 1993, *Ceram. Eng. Sci. Proc.,* Vol 15 (No. 5), Sept–Oct 1994, p 1118–1127

67. R.H. Plovnick and J.O. Kiggans, Microwave Thermal Etching of Stabilized Zirconia, *J. Am. Ceram. Soc.,* Vol 75 (No. 12), Dec 1992, p 3462–3464

68. I.O. Owate and R. Freer, Thermomechanical Etching Methods for Ceramics, *J. Am. Ceram. Soc.,* Vol 75 (No. 5), May 1992, p 1266–1268

69. V.L. Smith-Wackerle and D.V. Miley, Nontraditional Mounting Media for the Preparation of Advanced Materials, *Metallographic Characterization of Metals after Welding, Processing and Service,* 4–5 Aug 1992, ASM International, 1993, p 539–545

70. J.D. Katz and G. Hurley, Etching Alumina with Molten Vanadium Pentoxide, *J. Am. Ceram. Soc.,* Vol 73 (No. 7), July 1990, p 2151–2152

71. F. Bitter, On Inhomogeneities in the Magnetization of Ferromagnetic Materials, *Phys. Rev.,* Vol 38, 1931, p 1903

72. L. von Hamos and P.A. Thiessen, Uber die Sicharmachung von Bezirken verschiedemen ferromagnetersehen Zustanden festen Korpen, *Z. Phys.,* Vol 71, 1931, p 442

73. D.J. Craig and P.M. Griffiths, New Techniques for the Study of Bitter Figures, *Br. J. Appl. Phys.,* Vol 9, 1958, p 276, 277, 279–282

74. A. Tanasouiu, D. Feldmann, and I. Schulz, A Dry Bitter Technique for High Resolution Studies of Magnetic Domains by Optical Microscopy, *Prakt. Metallogr.,* Vol 10, 1978, p 210–219

Contrast Enhancement and Etching, *Metallography and Microstructures,* Vol 9, *ASM Handbook,* ASM International, 2004, p. 294–312

Etching for Effect

Etching techniques are developed in practical metallography by optimizing the effects they produce regarding the intended examination of the specimens. Considering the size of structural details revealed by etching as a distinguishing feature, metallographic etching can be subdivided into microetching and macroetching. Among the various microetching procedures, etch pitting and line etching are two typical examples of etching for special effects.

Macroetching is based on conventional chemical etching methods. Macroetching reveals the structure of a section or displays surface imperfections of a workpiece to magnifications of 25× (50× in Europe). These low magnifications enable examination of surface regions having large differences in height produced by very aggressive macroetchants (deep etching). However, many macroetching procedures, which are based on the application of modified or regular microetchants, may be used for macrostructural and microstructural observations if a coarse structure prevails and the surface irregularities due to etching are within the depth of field at higher magnifications.

Typical macrostructural details revealed are variations in grain size, solidification structure, segregation, inclusions, voids, porosity, flow lines, and cracks. Macroetching is used extensively for quality control and failure analysis of weld structures, heat treated parts, extrusions, forgings, and castings. Because macroetching yields an overall view of the inhomogeneity of the structure under examination, it also provides the necessary information about the location of sections to be used for subsequent microstructural investigations. Specimen preparation need not be elaborate. Wet grinding on silicon carbide papers is normally sufficient. When examining surface imperfections, etching is performed directly.

Microetching is based on electrochemical, physical, or optical etching methods and is used mainly to reveal microstructural features under the optical microscope at magnifications exceeding 25× and up to 1500×. This approximate practical limit of magnification is dictated by the resolving power of the optical microscope. It can be shifted to higher values if microetched sections are examined with the scanning electron microscope. Most commonly used magnifications of secondary electron and backscattered electron images taken from microsections are from 300 to 10,000×.

Microetching techniques reveal the shape, size, and arrangement of such structural components as phases, inclusions, and pores. Although grain and phase boundaries will clearly be revealed if proper chemical, electrolytic, potentiostatic, or physical microetching procedures are used, contrasting by physically deposited interfaces uncovers phase boundaries only because of the light-dark or color contrast of the adjacent phases. Microetching is particularly useful for disclosing structural changes caused by chemical, mechanical, and/or thermal treatments rendered during manufacture or service.

Dislocation Etch Pitting. Suitable etchants produce etch pits on polished surfaces of single crystalline or polycrystalline metals. The geometric shape of these pits depends on the crystallographic orientation of the examined grain or crystal. The etchant first attacks local defects, such as dislocations, vacancies, inclusions, or impurities. The ratio of the dissolution rates at the specimen plane and at the facets of etch pits governs the observed variety of the shapes of the etch pits.

Quantitative evaluation of etch pits having geometrically well-defined facets yields information on the crystallographic position of the sectioning plane of the examined grain, the crystallographic directions in the sectioning plane, and the orientation of the examined grain relative to a fixed reference direction. Etch pitting can also be applied to investigate the crystallographic correlation of a precipitated phase and the matrix as well as to study the orientation effect of domain structures. The dislocation density of single crystals can be estimated from the number of etch pits when surfaces of the crystals are oriented parallel to low-index planes and when proper etchants are used. Additional information on etch pitting can be found in Ref 3, 75, 76, 77, 78, 79, 80, 81, 82, and 83.

Line Etching. The technique for line etching presupposes a reaction layer formed on the surface of the specimen by precipitation (deposit) etching. With extended etching and upon subsequent drying, shrinking stresses crack the layer. Under certain experimental conditions, the crack formation leads to a pattern of lines visible on the individual grain surfaces that relates to their crystallographic orientation (Fig. 29).



Fig. 29 Line-etched grains of α-brass (Cu-33Zn). 200×

Line etching is used to determine preferred directions and to study recrystallization effects. Suitable etching procedures exist for copper and copper alloys (α-brass and α-bronze), aluminum alloys containing copper, low-carbon steels, and austenitic stainless steels. Etchants based on sodium thiosulfate ($Na_2S_2O_3$) are preferentially used (Ref 84). They form sulfur-containing layers whose nature depends on the chemical composition of the reagent and the specimen.

A modified line-etching technique is used to carry out metallographic texture control on silicon steel transformer sheets. In this double-etch procedure, precipitation etching using sodium picrate is followed by a brief etch in dilute nitric acid (HNO_3). This solution penetrates the crack, attacks the metal surface, and lifts off the layer. The exposed surface exhibits parallel lines on grains oriented at or near {110}. The relationship between the deviation of the direction of the parallel lines from the rolling direction of transformer sheets and the magnitude of the coercive force has been demonstrated (Ref 85).

References cited in this section

3. G.F. Vander Voort, *Metallography—Principles and Practice,* McGraw-Hill, 1984, p 180–181, 316–317, Reprinted by ASM International, 1999

75. J.D. Livingstone, Etch Pits at Dislocations in Copper, *J. Appl. Phys.,* Vol 31, 1960, p 1071

76. L. Yang, W. Zhen-chin, and L. Wen-chen, Forming Conditions and Geometric Variety of Etch Pits, *Pract. Metallogr.,* Vol 20, 1980, p 194, 232

77. K.T. Lee, G. de Wit, A. Morawiec, and J.A. Szpunar, The Application of the Etch-Pit Method to Quantitative Texture Analysis, *J. Mater. Sci.,* Vol 30 (No. 5), 1 March 1995, p 1327–1332

78. Th. Baudin, F. Cruz, P. Paillard, and R. Penelle, Characterization of Local Texture by Etch Pit Method, *Arch. Metall.*, Vol 38 (No. 3), 1993, p 317–325

79. F. Cruz, T. Baudin, E. Estevez, R. Penelle, and F. Caleyo, Semiautomatic Measurement of Individual Orientation of Crystals by Using Etch Pits and Digitized Images, *Mater. Charact.*, Vol 34 (No. 3), April 1995, p 189–194

80. T. Baudin, P. Paillard, F. Cruz, and R. Pennelle, Microtexture Determination in Fe-Si Alloy Sheets by Etch Pitting. Comparison with the Electron Back-Scattering Pattern Technique, *J. Appl. Crystallogr.*, Vol 27 (No. 6), 1 Dec 1994, p 924–933

81. S. Fortunati, G. Abbruzzese, and P.E. Di Nunzio, An Etch-Pitting Technique for Statistical Analysis of Grain Size Distributions as a Function of Orientation in Fe-Si Alloys, Proc. Conf.: Grain Growth in Polycrystalline Materials. I, 18–21 June 1991, *Mater. Sci. Forum*, Vol 94–96 (No. 1), 1992, p 431–436

82. E. Henault, M. Coster, and J.L. Chermant, Grain Boundary Reconstruction by Automatic Image Analysis on Etch Pits, *Mater. Res. Bull.*, Vol 26 (No. 7), July 1991, p 569–575

83. I. Fejfarova, J. Brezina, and A. Orlova, Etch-Pitting of Substructures in Silicon Iron, *Prakt. Metallogr.*, Vol 33 (No. 8), Aug 1996, p 409–420

84. H. Klemm, Uses of Thiosulphate (Klemm's Reagent) as an Etchant, *Pract. Metallogr.*, Vol 5, 1968, p 163

85. W. Schatt, Control of Textured Sheet by Means of Line Etching, *Pract. Metallogr.*, Vol 4, 1967, p 620

Contrast Enhancement and Etching, *Metallography and Microstructures*, Vol 9, *ASM Handbook*, ASM International, 2004, p. 294–312

Etchants and Etching Practice

The wide variety of chemicals for metallographic etching include acids, bases, neutral solutions, mixtures of solutions, molten salts, and gases. Many examples are provided in this Volume in the individual articles on metallography of alloys. Etchants for one type of alloy may also apply to other alloys.

Most etchant formulas are derived empirically. Their composition and mode of application may be varied and modified, and combinations of etching procedures also may be used, usually in increasing severity. The rate of attack is determined chiefly by the degree of dissociation of the etchant and its electrical conductivity. Both are often influenced by small additions of other chemicals. This may explain why many formulas contain small amounts of substances whose significance is not immediately apparent. The stability of many etching solutions is limited; oxidation-reduction (redox) potentials vary with time. Changes that necessitate discarding after a limited time may also occur while the etchant is in use.

Etching times range from several seconds to several hours. When no instructions are given, progress is judged by the appearance of the surface during etching. The surface will usually become less reflective (duller) as etching proceeds.

Etching temperature and etching time are closely related; increasing the temperature usually allows the duration to be decreased. However, this may not be advisable, because the contrast could become uneven when the rate of attack is too rapid. Most etching is performed at room temperature.

Errors. Sources of error are numerous, especially in electrochemical etching. Etching errors may lead to microstructural misinterpretation. For example, precipitates from etching or washing solutions could be interpreted as additional phases.

Cleaning. Upon completion of any chemical or electrochemical etching, the specimen should be rinsed in clean water to remove the chemicals and halt any reactions. For example, etching to reveal segregations in irons and steels using copper-containing compounds sometimes requires rinsing in alcohol first, or copper could precipitate on the specimen surface because of the change in the degree of dissociation. After specimens are water rinsed, they should be rinsed in alcohol and dried in a stream of warm air.

Alcohol hastens drying and prevents the formation of water spots. If etching produces water-soluble layers, water must be avoided in rinsing. Mounted specimens must be cleaned thoroughly to avoid the destructive effects of etchants and solvents seeping from pores, cracks, or mounting clamp interfaces. An ultrasonic cleaner will help avoid these problems. If specimens are highly porous or if highly concentrated acids are used for etching—for example, as in deep etching—the chemicals should be neutralized before rinsing and drying the specimen.

Specimen Storage. When polished and etched specimens are to be stored for long periods of time, they must be protected from atmospheric corrosion. Desiccators and desiccator cabinets are the most common means of specimen storage, although plastic coating and cellophane tape are sometimes used.

Contrast Enhancement and Etching, *Metallography and Microstructures*, Vol 9, *ASM Handbook*, ASM International, 2004, p. 294–312

Preparation and Handling of Etchants

This section summarizes general procedures and precautions for etchants and reagents used in metallographic microetching, macroetching, electropolishing, chemical polishing, and similar operations. Additional information is also contained in the article “Laboratory Safety in Metallography” in this Volume.

Applications and compositions of the reagents are described in individual articles that discuss metallographic techniques for specific metals and alloys. The formulations of etchants given in articles in this Volume are adequate for most applications, but may require modification. Adjustments in etchant composition, time, and technique, based on the experience and skill of the metallographer and depending on the specific application and the magnification to be used, are frequently indicated for satisfactory results. Details of etching to reveal specific aspects of structure are discussed in the articles on metallographic techniques for specific metals and alloys.

Expression of Composition

Etchants are generally aqueous or alcoholic solutions containing one or more active chemicals (acids, bases, or salts). Liquids other than water or alcohol are used as solvents in some formulations. Compositions of most etchants described in this Volume are expressed in terms of the amounts of the substances to be used in preparing small quantities of these reagents.

For etchants that are solutions of solid substances in liquids, the amounts of the solid substances are usually expressed in grams, and the amounts of liquids (or the total volumes of solution) are expressed in milliliters. The liquids may be individual commercially available substances or stock solutions containing two or more substances.

To prepare large quantities, as for some macroetching, kilograms and liters may be taken instead of grams and milliliters, or the amounts specified may be converted to pounds (1 kg = 2.2 lb) and gallons (1 L = 0.264 gal).

Other generally accepted methods for expressing composition are also used where appropriate. Compositions of some etchants prepared by mixing together two or more liquids are given in parts by volume or percentage by

volume. Compositions of some etchants consisting of solutions of solid substances in liquids are described in terms of percentage by weight.
In long-established, although nonstandard, usage in metallography, such terms as 1%, 2%, and 4% have been used to describe the approximate strength of picral and are understood to mean 1, 2, and 4 g, respectively, of picric acid per 100 mL alcohol. These approximate expressions are used in this sense in many articles in this Volume.

Purity of Chemicals

In the preparation of solutions for microetching and electropolishing, recommended practice is to use chemicals meeting the requirements of NF (National Formulary), USP (U.S. Pharmacopoeia), "laboratory," or "purified" grades or grades of still higher purity, such as reagent, ACS (American Chemical Society), or "certified" grades. The commercial or technical grades of certain special-purpose industrial chemicals, such as chromium trioxide (CrO_3) and synthetic methanol are extremely pure and are equivalent to reagent, ACS, or "certified" grades for use in microetching and electropolishing.
Where water is specified, distilled water is preferred because of wide variations in the purity of tap water. For macroetching, technical grades of chemicals are satisfactory, unless specifications indicate otherwise, and potable water of good quality is generally acceptable.

Identification of Chemicals

The practices generally followed in the technical literature on metallography are used in this Volume to identify the chemicals used in the preparation of etchants.
Aqueous Acids. In identification of aqueous acids, the name or formula alone, sometimes followed by "conc" or "concentrated," refers to the common commercially available concentrated laboratory grade (see Table 6). Where more than one concentration is commonly available, the percentage by weight of the active constituent follows the name or formula.

Table 6 Characteristics of aqueous liquid chemicals used in metallographic etchants.

Except for H_2SO_4, all data apply to laboratory and technical or commercial grades of chemicals.

Name	Active constituent	Nominal composition[(a)], wt%	Specific gravity
Aqueous acids			
Acetic acid, glacial	$HC_2H_3O_2$	99.5	1.05
Fluoboric acid	HBF_4	48	1.32
Hydrochloric acid[(b)]	HCl	37	1.18
Hydrofluoric acid	HF	48	1.15
Lactic acid	$HC_3H_5O_3$	85	1.20
Nitric acid	HNO_3	70	1.42
Perchloric acid	$HClO_4$	70	1.67
		60	1.53
Phosphoric acid (ortho)	H_3PO_4	85	1.70
Sulfuric acid	H_2SO_4	96[(c)]	1.84
Miscellaneous aqueous chemicals			
Ammonium hydroxide	NH_4OH	28[(d)]	0.90
Hydrogen peroxide	H_2O_2	3[(e)]	1.01
		30[(f)]	1.11
		50[(g)]	1.20

(a) Nominal percentage of the active constituent; remainder is water. Reagents made by different manufacturers may differ slightly in nominal concentration and allowable range of concentration.
(b) Technical grade is also called muriatic acid.
(c) Laboratory grade. Technical grade has concentration of 93%.
(d) Percent NH_3.

(e) Sometimes called 10 volume.
(f) Sometimes called 100 volume.
(g) Sometimes called 170 volume

An acid designated "tech" indicates the technical grade having the same concentration as the common laboratory grade. The concentration of technical grades is sometimes expressed by suppliers in terms of specific gravity, as shown in Table 6. Most technical-grade chemicals are available in several concentrations.

Miscellaneous aqueous chemicals, such as ammonium hydroxide (NH_4OH) and hydrogen peroxide (H_2O_2) (Table 6), which are used in various etchants, are identified similarly to aqueous acids (see above). Concentration must always be specified for H_2O_2, which is available in several widely differing concentrations.

The alcohols most frequently used in etchants are methanol and ethanol, which are described in Table 7. It is important to use alcohol that has the desired water content—anhydrous or "95%" alcohol, whichever is specified—in etchants that contain a small percentage of water. However, either grade can be used when the etchant is a dilute aqueous solution. Practice regarding the substitution of methanol for ethanol (or conversely) and the use of some grades of denatured ethanol in etchants varies greatly.

Table 7 Characteristics of pure methanol and ethanol

Name	Active constituent	Nominal composition[(a)], wt%
Methanol	CH_3OH	99.5[(b)]
Methanol, 95%	CH_3OH	95[(c)]
Ethanol, anhydrous	C_2H_5OH	99.5[(d)(e)]
Ethanol, 95%	C_2H_5OH	95[(e)]

(a) Nominal percentage of the active constituent; remainder is H_2O, unless otherwise specified.
(b) Synthetic methanol; the commercial grade is of high purity and is satisfactory for use in all ordinary metallographic etchants where methanol is specified; wood alcohol has not been manufactured commercially in the United States since 1969. Methanol is available only as an anhydrous, or absolute, grade containing less than 0.1 or 0.2% H_2O as packaged, and usually not more than approximately 0.5% H_2O at time of use, depending on storage and handling.
(c) Where methanol, 95%, is called for, the ordinary anhydrous grade must be diluted with 5% H_2O by volume.
(d) The anhydrous, or absolute, grade of ethanol is ordinarily used only where no significant amount of H_2O can be tolerated. It contains less than 0.1 or 0.2% H_2O as packaged and usually not more than approximately 0.5% H_2O at time of use, depending on storage and handling.
(e) Available only with special governmental permit

Although many etchant formulations show the use of methanol or ethanol as alternate materials, caution should be exercised in substituting one for the other in formulations where their equivalence is not indicated. Safety precludes changing accepted formulations for electropolishing without a thorough chemical study (see the article "Chemical and Electrolytic Polishing" in this Volume). In addition, ethanol or higher alcohols should not be substituted for methanol in nital containing more than 5% by volume concentrated nitric acid (HNO_3) or in other methanol-base etchants that contain strong oxidants and only a small percentage of water.

In a variety of applications for which the etchant is specified to contain ethanol, excluding electropolishing electrolytes, a proprietary solvent or denatured "reagent" alcohol having suitable water content (see Table 8) may substitute for pure "anhydrous" or "absolute" (99.5%) ethanol and for pure 95% ethanol (see Table 7). These substitutes are available without permit from suppliers of laboratory chemicals. These grades have been formulated in accordance with U.S. government regulations to be suitable for general laboratory purposes and have been denatured with small percentages of volatile solvents; they may substitute for pure ethanol having the same water content, except where pure ethanol is required.

Table 8 Nominal compositions of various grades of denatured alcohol (ethanol) used in some metallographic etchants

Component	Parts by volume in specially dentured alcohol[a]					
	Formula SD-1[b]		**Formula SD-3A**		**Formula SD-30**	
	Anhydrous	**95%[c]**	**Anhydrous**	**95%[c]**	**Anhydrous**	**95%[c]**
Ethanol, anhydrous	100	95	100	95	100	95
Water	…	5	…	5	…	5
Methanol	4	4	5	5	10	10
Methyl isobutyl ketone	1	1	…	…	…	…

Component	Parts by volume in proprietary solvent[d]		Parts by volume in "reagent" alcohol[d]	
	Anhydrous	**95%[c]**	**Anhydrous**	**95%[c]**
SD-1, anhydrous[b]	100	…	…	…
SD-1, 95%[b][c]	…	100	…	…
SD-3A, anhydrous	…	…	95	…
SD-3A, 95%[c]	…	…	…	95
Methyl isobutyl ketone	1	1	…	…
Hydrocarbon solvent or gasoline	1	1	…	…
Ethyl acetate	1	1	…	…
Isopropyl alcohol	…	…	5	5

(a) See text for discussion of suitability of the various grades for use in etchants.

(b) Specially denatured alcohol is available only with special governmental permit.

(c) The formula shown here has replaced the obsolete SD-1 formula in which wood alcohol was specified; wood alcohol has not been manufactured commercially in the United States since 1969.

(d) The designation of type of denatured alcohol as "95%" means that the denatured product contains 5 parts H_2O for every 95 parts anhydrous (absolute) ethanol, plus denaturants as specified.

(e) Available without governmental permit from suppliers of laboratory chemicals for scientific and general laboratory purposes

The specially denatured (SD) alcohols described in Table 8 are generally suitable for use in etchants. However, SD alcohol is obtainable only with special governmental permits and usually can be purchased only in larger quantities than the proprietary solvent and "reagent" alcohol in Table 8 and only from major suppliers. The metallographic laboratories of at least one large governmental scientific and engineering facility denature all the pure ethanol they use by adding less than 1% by volume isopropyl alcohol.

Water of Hydration. With some exceptions, it has been common practice to identify solid salts and acids used in etchants only by name and abbreviated formula, without indicating the presence or absence of water of hydration (see Table 9). Historically, in developing and preparing etchants, the most stable hydrate, which was the common commercial form, was ordinarily used, except for salts that do not form hydrates. Current practice varies.

Table 9 Description of miscellaneous chemicals used in metallographic etchants

aluminum chloride, anhydrous. **Solid; $AlCl_3$; reacts violently with water, evolving HCl gas; use of hydrated form, $AlCl_3 \cdot 6H_2O$, is preferred**
ammonium molybdate. **Crystals; also called ammonium paramolybdate or heptamolybdate; $(NH_4)_6Mo_7O_{24} \cdot 4H_2O$; can be used interchangeably with "molybdic acid, 85%"**
benzalkonium chloride. **Crystals; essentially alkyl-dimethyl-benzyl-ammonium chloride. May not be readily available in this form. See *zephiran chloride.***
1-butanol. **See *n-butyl alcohol.***
2-butoxyethanol. **See *butyl cellosolve.***
n-butyl alcohol. **Liquid; normal butyl alcohol; also called butyl alcohol and 1-butanol**
butyl carbitol. **Liquid; diethylene glycol monobutyl ether**
butyl cellosolve. **Liquid; ethylene glycol monobutyl ether; also called 2-butoxyethanol**
carbitol. **Liquid; diethylene glycol monoethyl ether**
cellosolve. **Liquid; ethylene glycol monoethyl ether**
chromic acid. **Dark-red crystals or flakes; CrO_3; also called chromic anhydride, chromic acid anhydride, and chromium trioxide. See *chromic oxide.***
chromic anhydride. **See *chromic acid.***
chromic oxide. **Fine green powder; Cr_2O_3; a polishing abrasive; do not confuse with CrO_3, which is a strong acid and a component of many etchants**
cupric ammonium chloride. **Crystals; a double salt, $CuCl_2 \cdot 2NH_4Cl \cdot 2H_2O$; if not available, substitute 0.6 g $CuCl_2 \cdot 2H_2O$ plus 0.4 g NH_4Cl for each gram of the double salt**
diethylene glycol. **Syrupy liquid; also called 2,2′-oxydiethanol and dihydroxydiethyl ether; $(HOCH_2CH_2)_2O$; more viscous than ethylene glycol—otherwise similar in behavior**
diethylene glycol monobutyl ether. **See *butyl carbitol.***
diethylene glycol monoethyl ether. **See *carbitol.***
diethyl ether. **See *ether.***
ether. **Liquid; also called ethyl ether and diethyl ether; very low flash point, highly explosive; boiling point is 34.4 °C (94 °F)**
ethylene glycol. **Syrupy liquid; also called 1,2-ethanediol and dihydroxyethane; $(CH_2)_2/(OH)_2$. Less viscous than diethylene glycol; otherwise similar in behavior**
ethylene glycol monobutyl ether. **Liquid; also called 2-butoxyethanol or butyl cellosolve**
ethylene glycol monoethyl ether. **See *cellosolve.***
ethyl ether. **See *ether.***
ferric nitrate. **Crystals; $Fe(NO_3)_3 \cdot 9H_2O$; there is no anhydrous form of this salt**
fluoboric acid, 48%. **Liquid; HBF_4; if not readily available in small quantities, substitute 10.3 mL HF (48%) plus 4.4 g H_3BO_3 for each 10 mL 48% HBF_4 specified**
glycerol. **Syrupy liquid; also called glycerin or glycerine; $C_3H_5(OH)_3$; contains to 5% (by weight) H_2O**
molybdic acid, 85%. **Crystals or powder containing the equivalent of 85% MoO_3. This misnamed chemical consists mostly of ammonium molybdate, or paramolybdate, which is $(NH_4)_6Mo_7O_{24} \cdot 4H_2O$; the two chemicals can be used interchangeably. See *ammonium molybdate.***
muriatic acid. **Liquid; technical grade HCl; see Table 6.**
picric acid. **Crystals; 2,4,6-trinitrophenol; crystals of laboratory chemical contain 10 to 15% H_2O; explosive; its crystalline metallic salts are even more explosive; do not use grades that do not have the 10 to 15% H_2O content**
pyrophosphoric acid. **Crystals or viscous liquid; $H_4P_2O_7$, anhydrous; hydrolyzes to H_3PO_4 slowly in cold H_2O and rapidly in hot H_2O**
zephiran chloride. **Aqueous solution; a proprietary material produced in grades containing approximately 12% and 17% (by weight) benzalkonium chloride (alkyl-di-methyl-benzyl-ammonium chloride) as the active constituent, plus some ammonium acetate; also called sephiran chloride; available from pharmacies or pharmaceutical distributors. See *benzalkonium chloride.***

Using the specified amount of the anhydrous or a hydrated form of a solid salt or acid in preparing an etchant will in most cases produce essentially the same etching behavior; any difference in results will usually be small

compared to the effects of normal differences in technique and other variables in specimen preparation. Exceptions are the preparation of etchants that must be anhydrous or must contain only a small and fairly critical percentage of water for proper etching activity; for such etchants, the need to use specific anhydrous or hydrated forms of each component should be clearly stated.

Some salts, such as ferric nitrate ($Fe(NO_3)_3 \cdot 9H_2O$), do not exist in an anhydrous form. Conversely, some nominally water-free compounds contain a substantial percentage of water. One of these is picric acid, for which the 10 to 15% H_2O content found in laboratory grades is necessary for satisfactory performance of etchants based on it (see Table 9).

Miscellaneous chemicals may be difficult to identify because of similarity in names of different chemicals or because of misleading or nonstandard nomenclature and trade names. The chemicals are described in Table 9. Also included are certain chemicals for which some aspects of composition or behavior are important.

Safety Precautions

All chemicals are potentially dangerous; formulating and using etchants requires thorough knowledge of the chemicals involved and the proper procedures for handling and mixing. The discussion that follows indicates many of the potential hazards of using chemicals and describes precautions and safe practice. Additional guidelines are described in the article "Laboratory Safety in Metallography."

Ventilation. Etchants should be mixed, handled, and used in a well-ventilated area, preferably under an exhaust hood, to prevent exposure to or inhalation of toxic and corrosive fumes. Use of an exhaust hood is mandatory whenever large quantities of chemicals are handled or large areas of metal are etched (as in macroetching), when executing lengthy electropolishing operations, or when electropolishing large areas.

Protection of Personnel. Pouring, mixing, handling, and use of chemicals and etchants necessitate the wearing of suitable protective equipment and clothing, such as glasses, face shield, gloves, apron, and so on, to prevent contact of chemicals with the eyes, skin, or clothing.

Chemicals that contact the skin should be washed off promptly using water and soap. Medical attention should be sought immediately for chemical burns, especially if at cuts or abrasions in the skin. If chemicals contact the eyes, the eyes should be flushed at once with large quantities of water, and medical attention should be obtained without delay. A face-and-eye fountain should be available for use where chemicals or etchants are stored or handled. A safety shower is also required where quantities large enough to be hazardous are stored or handled. This washing equipment should be readily available and should be tested at scheduled intervals to ensure dependable performance in an emergency.

Hydrofluoric acid (HF) and fluosilicic acid (H_2SiF_6) can cause painful and serious ulcers upon contacting the skin, unless washed off immediately. Also especially harmful to the skin are concentrated HNO_3, sulfuric acid (H_2SO_4), CrO_3, 30 or 50% H_2O_2, sodium hydroxide (NaOH), potassium hydroxide (KOH), bromine (Br_2), and anhydrous aluminum chloride ($AlCl_3$). Inhalation of vapors or mist from these chemicals or etchants containing them can also cause irritation or serious damage to the respiratory system.

Container Material and Design. Preparation, storage, and handling of etchants dictates using containers and equipment made of materials suitable for the chemicals used. Glass resists nearly all chemicals. Polyethylene, polypropylene, and similarly inert plastics resist HF, H_2SiF_6, and fluoboric acid (HBF_4), as well as solutions containing salts of these acids. These inert plastics are also recommended for prolonged storage of strongly alkaline solutions and strong solutions of phosphoric acid (H_3PO_4), both of which attack glass, especially ordinary grades of glass.

Certain mixtures of chemicals can generate gaseous reaction products over a period of time or if inadvertently exposed to heat and can build up dangerous pressures if stored in tightly sealed containers. One example is the methanol-HNO_3 solution used for electropolishing. The use of vented or pressure-relief stoppers instead of tightly sealed screw caps or conventional stoppers on bottles of etchants that are prepared in quantity and stored is recommended.

Heat Evolution in Preparing Etchants. Caution should be exercised and accepted laboratory procedures followed when mixing chemicals. In general, heat is evolved, sometimes in large amounts, when strong acids (particularly H_2SO_4), alkalis (NaOH and KOH), anhydrous $AlCl_3$, or their concentrated solutions are added to water, alcohols, or solutions of other chemicals and when combining acidic with alkaline substances or solutions.

The acid, alkali, or anhydrous $AlCl_3$ should always be added to the water, alcohol, or solution. These chemicals should be introduced slowly while stirring continuously to avoid local overheating. Incomplete mixing can permit layering, with danger of a delayed violent reaction. Special attention and special cooling procedures may be necessary when large quantities of etchants are prepared and large areas of metal are etched, as in some macroetching, and when high currents are used in electropolishing.

Mixing of Oxidizing Agents with Reducing Agents. Mixing oxidizing agents, such as HNO_3, H_2SO_4, perchloric acid ($HClO_4$), CrO_3, salts of these acids, persulfates, Br_2, and H_2O_2, with reducing agents—for example, alcohols and other organic solvents, acetic acid, acetic anhydride [$(CH_3CO)_2O$] and most organic compounds—requires special care. Failure to follow accepted safe procedures can result in violent or explosive reactions. The use of $(CH_3CO)_2O$ is not safe in electropolishing solutions, except in limited ranges of composition and water content, and is therefore not recommended. The article "Chemical and Electrolytic Polishing" in this Volume contains special precautions for procedures and the reagents used in electropolishing.

Care with Cyanides. Etchants containing cyanides present special toxicity hazards, because poisoning can result from inhaling hard-to-detect small amounts of HCN gas evolved from acidic solutions, from ingesting small amounts of cyanides, and from absorbing cyanides through the skin or exposed body tissues. Careful handling and the use of an effective exhaust hood are especially important. Used cyanide-containing solutions should be rendered slightly alkaline with ammonia and poured into a chemically resistant waste-disposal drain, and the drain flushed thoroughly with copious water.

Disposal of Etchants. Spent etchant solutions should be individually poured slowly into a chemically resistant waste-disposal drain in an exhaust hood promptly after use while running a substantial flow of tap water down the drain. The drain should then be flushed thoroughly with abundant water. Strongly acidic, strongly alkaline, corrosive, or toxic solutions should be handled with extra care during disposal, because of the hazards described in the section "Protection of Personnel" in this article. The safe disposal of used solutions containing substantial amounts of volatile solvents requires special attention to avoid the creation of toxicity, fire, or explosion hazards from vapors of the solvents.

Contrast Enhancement and Etching, *Metallography and Microstructures,* Vol 9, *ASM Handbook,* ASM International, 2004, p. 294–312

Contrast Enhancement and Etching

Acknowledgment

Portions of this article were adapted from the following publications:

- Color Metallography, *Metallography and Microstructures,* Vol 9, *ASM Handbook,* 1985
- G. Petzow and G. Elssner, Etching, *Metallography and Microstructures,* Vol 9, *ASM Handbook,* 1985, p 57–70
- G. Petzow, *Metallographic Etching,* 2nd ed., ASM International, 1999
- G.F. Vander Voort, *Metallography—Principles and Practice,* McGraw-Hill, 1984, p 180–181, 316–317, reprinted by ASM International, 1999

References

1. G. Petzow, *Metallographic Etching,* 2nd ed., ASM International, 1999

2. E. Beraha and B. Shpigler, *Color Metallography,* American Society for Metals, 1977

3. G.F. Vander Voort, *Metallography—Principles and Practice,* McGraw-Hill, 1984, p 180–181, 316–317, Reprinted by ASM International, 1999

4. S. Bradbury, *An Introduction to the Optical Microscope,* Vol 1, *Microscopy Handbooks,* Springer Verlag; rev. ed., Nov 1993

5. P. Torok and F.-J. Kao, Ed., and T.S. Han, *Optical Imaging and Microscopy: Techniques and Advanced Systems,* Vol 87, Springer Series in Optical Sciences, Springer Verlag, Aug 2003

6. H. Gahm and F. Jeglitsch, *Microstruc. Sci.,* Vol 9, 1981, p 65–80

7. J.H. Richardson, *Optical Microscopy for the Materials Sciences,* Marcel Dekker, 1971

8. H. Modin and S. Modin, *Metallurgical Microscopy,* Butterworths, 1973

9. V.A. Phillips, *Modern Metallographic Techniques and Their Applications,* Wiley-Interscience, 1971

10. R.J. Gray, R.S. Crouse, and B.C. Leslie, Decorative Etching, *Metallographic Specimen Preparation: Optical and Electron Microscopy,* J.L. McCall and W.M. Muller, Ed., Plenum Press, 1974

11. J.V. Cathcart, G.F. Peterson, and C.J. Sparks, Oxidation Rate and Oxide Structural Defects, *Surfaces and Interior Chemical and Physical Characteristics,* Burke, Reed, and Weiss, Ed., Syracuse University Press, 1967

12. R.J. Gray, W.C. Thurber, and C.K.H. Dubose, Preparation of Arc-Melted Uranium Carbides, *Met. Prog.,* Vol 74 (No. 1), July 1958, p 65–70

13. R.J. Gray, E.S. Bomar, and R.W. McClung, Evaluating Coated Particles of Nuclear Fuel, *Met. Prog.,* Vol 86 (No. 1), July 1964, p 90–93

14. E. Weck and E. Leistner, *Metallographic Instructions for Colour Etching by Immersion—Part I: Klemm Colour Etching,* Deutscher Verlag für Schweisstechnik, 1982

15. E. Weck and E. Leistner, *Metallographic Instructions for Colour Etching by Immersion—Part II: Beraha Colour Etchants and Their Different Variants,* Deutscher Verlag für Schweisstechnik, 1983

16. E. Beraha, Metallographic Reagents Based on Sulfide Films, *Prakt. Metallogr.,* Vol 7, 1970, p 242–248

17. E. Beraha, Metallographic Reagents Based on Molybdate Solutions, *Prakt. Metallogr.,* Vol 11, 1974, p 271–275

18. R.J. Gray, V.K. Sikka, and R.T. King, Detecting Transformation of Delta Ferrite to Sigma-Phase in Stainless Steels by Advanced Metallographic Techniques, *J. Met.*, Nov 1978, p 18–26

19. E.E. Stansbury, Potentiostatic Etching, *Metallography and Microstructures*, Vol 9, *ASM Handbook*, 1985, p 143

20. G. Grutzner and J.H. Schuller, *Werkst. Korros.*, Vol 20, 1969, p 3203–3251

21. N.D. Greene and B.E. Wilde, *Corrosion*, Vol 26, 1970, p 533–538

22. V. Cihal and M. Prazak, *J. Iron Steel Inst.*, Vol 193, 1959, p 360–367

23. W.A. Mueller, *Corrosion*, Vol 18, 1962, p 73t–79t

24. G. Grutzner and H.J. Schuller, *Pract. Metallogr.*, Vol 6, 1969, p 246–258

25. P. Helbach and E. Bullock, "Potentio-static Etching of Carburized Steels," Petten, Establ., Netherlands: Committee of European Communities, EUR 8138, 1982

26. G.F. Vander Voort, Tint Etching, *Met. Prog.*, Vol 127, 1985, p 31

27. F.K. Naumann and G. Langenscheid, *Arch. Eisenhüttenwes.*, Vol 38, 1967, p 463–468

28. W. Schaarwachter, H. Ludering, and F.K. Naumann, *Arch. Eisenhüttenwes.*, Vol 31, 1960, p 385–391

29. F.K. Naumann, *Arch. Eisenhüttenwes.*, Vol 34, 1963, p 187–194

30. P. Lichtenegger, A. Kulmburg, and R. Bloch, *Pract. Metallogr.*, Vol 6, 1969, p 535–539

31. R. Bloch and P. Lichtenegger, *Pract. Metallogr.*, Vol 12, 1975, p 186–193

32. H. Ludering, *Arch. Eisenhüttenwes.*, Vol 2, 1964, p 153–159

33. A. Mance, *Metallography*, Vol 4, 1971, p 287–296

34. A. Mance, V. Perovic, and A. Mihajlovic, *Metallography*, Vol 6, 1973, p 123–130

35. R.S. Crouse, Interference Films by Vacuum Deposition, *Metallography and Microstructures*, Vol 9, *ASM Handbook*, 1985, p 147

36. W. Pepperhoff, Sechtbarmachung von Gefügestrukturen durch Interferenz—Aufdampfoschichten, *Naturwissenschaften*, Vol 16, 1960, p 375

37. J.O. Stiegler and R.J. Gray, Microstructural Discrimination by Deposition of Surface Films, *Advances in Metallography*, Technical Papers of the 20th Metallographic Conference, R.J. Jackson and A.E. Calabra, Ed., RFP-658, The Dow Chemical Co., Oct 1966, p 11–17

38. H.E. Bühler and H.P. Hougardy, *Atlas of Interference Layer Metallography*, Deutsche Gesellschaft für Metallkunde, Oberursel, Germany, 1980

39. H.E. Bühler and D. Kossel, Guidelines for the Development and Application of Interference Film Metallography, *Prakt. Metallogr.*, Vol 18, 1981, p 385–391

40. H. Zogg, S. Weber, and H. Warlimont, Optical Enhancement for Al-Alloys by Vacuum Deposited ZnTe Interference Layers, *Pract. Metallogr.,* Vol 14, 1977, p 553

41. H.E. Exner and J. Roth, Metallographic Contrasting by Reactively Sputtered Interference Layers, *Pract. Metallogr.,* Vol 18, 1980, p 365

42. S. Hofmann and H.E. Exner, Auger-elektronenspektroskopische Untersuchungen von Kontrastierschichten auf Metallen, *Z. Metallkde.,* Vol 65 (No. 778), 1974

43. G. Hertsleb and P. Schwaab, Fundamentals of the Potentiostatic Development of Structures Using High-Alloy Steels as an Example, *Pract. Metallogr.,* Vol 15, 1978, p 213

44. M.G. Pujar, R.K. Dayal, T.P.S. Gill, and S.N. Malhotra, Microstructural Evaluation of Molybdenum-Containing Stainless Steel Weld Metals by a Potentiostatic Etching Technique, *J. Mater. Sci.,* Vol 33 (No. 10), 15 May 1998, p 2691–2700

45. X. Ma and S.J. Luo, Potentiostatic Etching and Etching Quantitative Analysis of Carbides in Die Steel, *J. Iron Steel Res. Int.,* Vol 2 (No. 1), Sept 1995, p 47–52

46. H. Worch, K. Nocke, C. Blank, W. Oelssner, and F. Bertholt, Potentiostatic Etching—Presentation of a New Etching Technique, *Prakt. Metallogr.,* Vol 31, May 1994, p 245–251

47. E.M. Jackson, P.E. de Visser, and L.A. Cornish, Distinguishing between Chi and Sigma Phases in Duplex Stainless Steels Using Potentiostatic Etching, *Mater. Charact.,* Vol 31 (No. 4), Dec 1993, p 185–190

48. A. Sato, K. Kon, S. Tsujikawa, and Y. Hisamatsu, Dependence of Dissolution Rate of Inconel Alloy 600 with Coarse Columnar Crystals on Crystallographic Orientation in Potentiostatic Etching, *J. Jpn. Inst. Met.,* Vol 57 (No. 7), July 1993, p 790–796

49. Y. Wang, F. Yu, and Y. Wang, Check the Sensitivity of Non-Sensitive Intergranular Corrosion Using Potentiostatic Etching in Transpassive Region, *Huagong Jixie (Chem. Eng. Mach.),* Vol 19 (No. 3), 1992, p 129–133, 134

50. J.H. Potgieter, L.M. Matthews, and P. De Visser, Experimental Study of Quantitative Phase Characterization in Duplex Stainless Steels by Potentiostatic Etching, *J. Mater. Sci.,* Vol 27 (No. 13), 1 July 1992, p 3667–3679

51. K. Takiazawa and Y. Nakayama, Effects of MnS Inclusion and the Potentiostatic Etching Treatment on Pitting Corrosion Resistance of 18-8 Stainless Steels, *Hyomen Gijutsu (J. Surf. Fin. Soc. Jpn.,* Vol 42 (No. 6), June 1991, p 649–654

52. H. Gahm, F. Jeglitsch, and E.M. Hörl, Investigations of the Structure of Chemically Deposited Films Produced by Precipitation Etching, *Pract. Metallogr.,* Vol 19, 1982, p 369

53. I. Graf, Ion Etching—State of the Art and Perspectives for Contrasting the Microstructure of Ceramic and Metallic Materials: I. Development and Physics in Ionetching, *Prakt. Metallogr.,* Vol 35 (No. 5), May 1998, p 235–254

54. M. Pohl and W.-G. Burchard, Ion Etching in Metallography, *Pract. Metallogr.,* Special Edition 11, 1980, p 42 (in German)

55. R.C. Sanwald and D.J. Gould, Ion Etching Metallographic Samples, *Metallography,* Vol 7, 1974, p 73

56. Y. Iino, Creep Plastic Zone and Crack Initiation at 923 K of 304 Stainless Steel Compact Tension Specimen, Proc. Conf. *ECF 10—Structural Integrity: Experiments—Models—Applications,* Vol I (Berlin, Germany), 20–23 Sept 1994, Engineering Materials Advisory Services Ltd., 1994, p 291–296

57. B. Hoffmann-Millack, C.J. Roberts, and W.S. Steer, Observation of Rhombic Facets on Platinum Wire after Heating in Air Using Scanning Tunnelling Microscopy, *J. Microsc.,* Vol 166 (No. 2), May 1992, p 247–252

58. G.D. Bruce, P. Fortier, G. Palumbo, J.E. Guillet, and G.J. Vancso, Scanning Tunneling Microscopy Imaging of Grain Boundaries and Triple Junctions in Copper, *Mater. Charact.,* Vol 28 (No. 2), March 1992, p 133–137

59. C.I.H. Ashby, Laser-Driven Etching, *Thin Film Processes II,* Academic Press, 1991, p 783–856

60. J. Wolfenstine, R.P. Kershaw, W.J. Kim, and O.D. Sherby, Thermal—Chemical Etching Technique for Hypereutectic Irons, *Mater. Charact.,* Vol 24 (No. 4), June 1990, p 375–378

61. J. Frohm, U. Linke, and K. Besocke, Thermal Etching of Platinum Crystals in Air, Hydrogen and Oxygen—Some STM Observations, *Prakt. Metallogr.,* Vol 21 (No. 10), Oct 1989, p 518–528

62. G. Willmann and G. Heimke, Thermal Etching of α-Alumina and Na-β-Alumina, *Pract. Metallogr.,* Vol 15, 1978, p 11

63. M. Asano, T. Kobayashi, and Y. Takasu, Bending Strength, Fracture Toughness and Crack Propagation Characteristics of Si_3N_4 Ceramic at High Temperature, *J. Soc. Mater. Sci., Jpn.,* Vol 45 (No. 2), Feb 1996, p 189–194

64. G. Nicoletto, A. Tucci, and L. Esposito, The Effect of Microstructure on Fracture Toughness of Polycrystalline Alumina, *Fat. Fract. Eng. Mater. Struct.,* Vol 19 (No. 1), 1996, p 119–128

65. M. Asano, T. Kobayashi, and Y. Takasu, Analysis of Crack Growth Behavior for Silicon Nitride Ceramics at High Temperature, *Strength of Materials,* ICSMA 10 (Sendai, Japan), 22–26 Aug 1994, Japan Institute of Metals, 1994, p 615–618

66. V.A. Knapp, D.E. Wittmer, and J.J. Conover, Microwave Plasma Etching of Si_3N_4, 18th Annual Conference on Composites and Advanced Ceramic Materials, 9–14 Jan 1993, *Ceram. Eng. Sci. Proc.,* Vol 15 (No. 5), Sept–Oct 1994, p 1118–1127

67. R.H. Plovnick and J.O. Kiggans, Microwave Thermal Etching of Stabilized Zirconia, *J. Am. Ceram. Soc.,* Vol 75 (No. 12), Dec 1992, p 3462–3464

68. I.O. Owate and R. Freer, Thermomechanical Etching Methods for Ceramics, *J. Am. Ceram. Soc.,* Vol 75 (No. 5), May 1992, p 1266–1268

69. V.L. Smith-Wackerle and D.V. Miley, Nontraditional Mounting Media for the Preparation of Advanced Materials, *Metallographic Characterization of Metals after Welding, Processing and Service,* 4–5 Aug 1992, ASM International, 1993, p 539–545

70. J.D. Katz and G. Hurley, Etching Alumina with Molten Vanadium Pentoxide, *J. Am. Ceram. Soc.,* Vol 73 (No. 7), July 1990, p 2151–2152

71. F. Bitter, On Inhomogeneities in the Magnetization of Ferromagnetic Materials, *Phys. Rev.,* Vol 38, 1931, p 1903

72. L. von Hamos and P.A. Thiessen, Uber die Sicharmachung von Bezirken verschiedemen ferromagnetersehen Zustanden festen Korpen, *Z. Phys.,* Vol 71, 1931, p 442

73. D.J. Craig and P.M. Griffiths, New Techniques for the Study of Bitter Figures, *Br. J. Appl. Phys.,* Vol 9, 1958, p 276, 277, 279–282

74. A. Tanasouiu, D. Feldmann, and I. Schulz, A Dry Bitter Technique for High Resolution Studies of Magnetic Domains by Optical Microscopy, *Prakt. Metallogr.,* Vol 10, 1978, p 210–219

75. J.D. Livingstone, Etch Pits at Dislocations in Copper, *J. Appl. Phys.,* Vol 31, 1960, p 1071

76. L. Yang, W. Zhen-chin, and L. Wen-chen, Forming Conditions and Geometric Variety of Etch Pits, *Pract. Metallogr.,* Vol 20, 1980, p 194, 232

77. K.T. Lee, G. de Wit, A. Morawiec, and J.A. Szpunar, The Application of the Etch-Pit Method to Quantitative Texture Analysis, *J. Mater. Sci.,* Vol 30 (No. 5), 1 March 1995, p 1327–1332

78. Th. Baudin, F. Cruz, P. Paillard, and R. Penelle, Characterization of Local Texture by Etch Pit Method, *Arch. Metall.,* Vol 38 (No. 3), 1993, p 317–325

79. F. Cruz, T. Baudin, E. Estevez, R. Penelle, and F. Caleyo, Semiautomatic Measurement of Individual Orientation of Crystals by Using Etch Pits and Digitized Images, *Mater. Charact.,* Vol 34 (No. 3), April 1995, p 189–194

80. T. Baudin, P. Paillard, F. Cruz, and R. Pennelle, Microtexture Determination in Fe-Si Alloy Sheets by Etch Pitting. Comparison with the Electron Back-Scattering Pattern Technique, *J. Appl. Crystallogr.,* Vol 27 (No. 6), 1 Dec 1994, p 924–933

81. S. Fortunati, G. Abbruzzese, and P.E. Di Nunzio, An Etch-Pitting Technique for Statistical Analysis of Grain Size Distributions as a Function of Orientation in Fe-Si Alloys, Proc. Conf.: Grain Growth in Polycrystalline Materials. I, 18–21 June 1991, *Mater. Sci. Forum,* Vol 94–96 (No. 1), 1992, p 431–436

82. E. Henault, M. Coster, and J.L. Chermant, Grain Boundary Reconstruction by Automatic Image Analysis on Etch Pits, *Mater. Res. Bull.,* Vol 26 (No. 7), July 1991, p 569–575

83. I. Fejfarova, J. Brezina, and A. Orlova, Etch-Pitting of Substructures in Silicon Iron, *Prakt. Metallogr.,* Vol 33 (No. 8), Aug 1996, p 409–420

84. H. Klemm, Uses of Thiosulphate (Klemm's Reagent) as an Etchant, *Pract. Metallogr.,* Vol 5, 1968, p 163

85. W. Schatt, Control of Textured Sheet by Means of Line Etching, *Pract. Metallogr.,* Vol 4, 1967, p 620

Contrast Enhancement and Etching, *Metallography and Microstructures,* Vol 9, *ASM Handbook,* ASM International, 2004, p. 294–312

Selected References

- M. Beckert and H. Klemm, *Handbook of Metallographic Etching Techniques,* VEB Deutscher Verlag für Grundstoffindustrie, 1976 (in German)
- B. Bousfield, *Surface Preparation and Microscopy of Materials,* John Wiley & Sons, Ltd., 1992
- B.L Bramfitt and A.O Benscoter, *Metallographer's Guide: Practice and Procedures for Irons and Steels,* ASM International 2002
- H.-E. Bühler and H.P. Hougardy, *Atlas of Interference Layer Metallography,* Deutsche Gesellschaft für Metallkunde, 1980
- R.E. Chinn, *Ceramography: Preparation and Analysis of Ceramic Microstructures,* ASM International, 2002
- G. Elssner and G. Petzow, Modern Ceramographic Preparation and Etching Methods for Incident Light and Scanning Electron Microscopy, in *Microstructural Science,* Vol 9, American Elsevier, 1981, p 83
- P.M. French and J.L. McCall, Ed., *Interpretive Techniques for Microstructural Analysis,* Plenum Press, 1977
- J.L. McCall and W.M. Mueller, Ed., *Metallographic Specimen Preparation,* Plenum Press, 1971
- J.L. McCall and W.M. Mueller, Ed., *Microstructural Analysis, Tools and Techniques,* Plenum Press, 1973
- G. Petzow, *Metallographic Etching,* 2nd ed., ASM International, 1999
- L. Samuels, *Light Microscopy of Carbon Steels,* ASM International, 1999
- A. Tomer, *Structure of Metals through Optical Microscopy,* ASM International, 1991
- G.F. Vander Voort, *Metallography: Principles and Practice,* McGraw-Hill, 1984; reprinted by ASM International, 1999

S.M. Purdy, Macroetching, *Metallography and Microstructures,* Vol 9, *ASM Handbook*, ASM International, 2004, p. 313–324

Macroetching

Samuel M. Purdy, National Steel Corp. (Retired)

Introduction

MACROETCHING is a procedure for revealing the large-scale structure of a metallic specimen, that is, structure visible with the unaided eye, by etching an appropriately prepared surface. The procedure is used in process metallurgy as both a quality-control tool and an investigatory tool. For example, segregation and inclusion stringers in billets and slabs, flow lines in forgings, and depth of weld penetration are made evident.

Microscopic examination of a specimen will reveal detailed information about a small area but cannot provide information about variation in the sample unless numerous fields or multiple specimens are examined. Macroetching, on the other hand, will provide information about a large area, that is, structures such as columnar structure, flow lines, dendrites, and other features that may not be recognizable at normal microscopical magnifications. Chemical segregation, coring, inclusion streaks, and depth of decarburization, which would be missed in a microscopic specimen, can be seen. Macroetching will not provide quantitative information about chemical variation but will display the location of extremes of segregation or coring where sampling for chemical analysis should be conducted.

Macroetching will also reveal discontinuities such as laps, seams, porosity, flakes, cracks, and extrusion rupture. Often, these defects can be seen without etching but are rendered more clearly by etching. The ends of cracks, for example, are better revealed by etching. Variation in grain size is often easily detected in macroetched specimens.

In metal fabrications, macroetching can reveal the quality characteristics of welds, the depth of penetration, the dilution of filler metal by base metal, the entrapment of flux, porosity and cracks, and the extent of the heat-affected zone (HAZ). In the heat treating shop, macroetching will reveal soft spots, tong marks, quenching cracks, case depth in shallow hardening steels, case depth in carburizing steels, and the effectiveness of stopoff coatings during carburization. In the machine shop, grinding burns and cracks can be found easily. In forge shops, macroetching is used to determine flow lines and internal defects. In the aluminum industry, macroetching is used to evaluate extrusions for porthole defects as well as defects in forgings, castings, bars, and sheet products.

S.M. Purdy, Macroetching, *Metallography and Microstructures,* Vol 9, *ASM Handbook*, ASM International, 2004, p. 313–324

Macroetching

Samuel M. Purdy, National Steel Corp. (Retired)

Procedures

Sampling. The choice of the sample and its orientation to the workpiece are crucial to obtaining good results. In most cases, the problem in hand will point to the location and orientation of the specimen plane as well as the stage of manufacture at which the sample is taken. For example, in quality control of wrought primary products, a transverse cross-sectional sample should be taken as soon as possible to avoid processing unsuitable product. In ingot products, this would be just after initial breakdown, that is, after blooming or slabbing. In continuously

cast product, sample just after casting. Examination for coring or segregation usually requires a longitudinal sample.

Sampling of forgings, extrusions, and castings is more complicated. To look for flow lines in a forging, the piece should be sectioned longitudinally. Transverse sections will reveal flakes and bursts. In extrusions, an etched longitudinal section at the back end of the extrusion will reveal coring and coarse grains. To find shrinkage cavities in a casting, the section should be taken through the largest section or beneath the choke points in headers and feeders.

Weldments should be sampled transverse to the weld to look for weld penetration, undercutting, porosity, and depth of HAZ. The transverse plane should be in the steady-state section of the weld and not close to the end points. Weldments of dissimilar metals will cause problems in etching. The usual approach is to etch the least corrosion-resistant metal and then to etch the more resistant metal.

When examining machined and ground parts to reveal cracks and grinding burns, the part may be etched directly without further preparation.

Whenever possible, samples should be cut from the piece using cold methods, for example, sawing or abrasive machining. Even so, copious cooling should be used. When hot methods must be used, such as gas torching or hot sawing, the sample should be large enough so that a second cold cut can be made to expose a surface outside of the HAZ.

Specimen preparation is simple. Sometimes, when using a cold abrasive cutoff machine, the specimen can be etched without preparation other than cleaning. Other times, planing or facing a slice on a lathe using a sharp V-tip tool with a light feed will be sufficient. When more detail is required, grind the specimen on a surface grinder, finishing with a fine, smaller-than-150-grit wheel using light feeds with a clean wheel. The greatest detail can be obtained using metallographic techniques (Ref 1), but the size of the specimen will be limited by the capacity of the apparatus. Some metallographers have success with lapping machines.

Because etching is essentially a surface reaction, the surface must be cleaned after surface preparation to remove all traces of grease or oil. Any method of cleaning that removes oil and grease and does not contaminate or oxidize the surface will be satisfactory. Solvents or hot water with a detergent are satisfactory. If brushing is required, a brush with nonmetallic fibers should be used. After cleaning, the last rinse is made with clean liquid that drains off and evaporates, leaving no residue behind. Alcohol or acetone are popular final rinses. Vapor degreasing, when available, is effective. Once the surface has been cleaned, great care must be taken to make sure that the surface is not recontaminated. Touching the surface with a finger often will contaminate the surface sufficiently to interfere with etching.

Reference cited in this section

1. “Standard Guide for Preparation of Metallographic Specimens,” E 3, *Annual Book of ASTM Standards*, Vol 3.01, ASTM International, 2002, p 1

S.M. Purdy, Macroetching, *Metallography and Microstructures,* Vol 9, *ASM Handbook*, ASM International, 2004, p. 313–324

Macroetching

Samuel M. Purdy, National Steel Corp. (Retired)

Apparatus

In large-scale operations, where large numbers of specimens are examined, steel tanks lined with rubber, lead, or corrosion-resistant alloys may be used to hold the etchant. The choice of material is important. Slow leaching of ions from the lining can seriously impact the etching process, producing misleading artifacts. Wooden tanks

have been used, but leaching of resins can lead to artifacts. Similarly, rinse tanks must be fabricated from corrosion-resistant material to prevent artifacts.

In the laboratory, ordinary laboratory vessels, dishes, and trays manufactured from glass, porcelain, or porcelain-coated steel may be used. These should be large enough to contain the specimen as well as sufficient etchant for efficient etching. The specimen must be covered to a sufficient depth so that the etchant composition will remain homogeneous.

An electrolytic apparatus (Ref 2) has been introduced in which the specimen is mounted in a tray immersed in an etchant and moved slowly beneath an electrode to etch the surface. After etching, the specimen moves on to a rinsing station and, if necessary, is sprayed with a neutralizing or stabilizing solution. When this process is used to replace the conventional 1 to 1 hot hydrochloric acid etch for iron and steel, the amount of hydrochloric acid fumes produced by the consumption of acid solutions is reduced.

In all etching operations, industrial and laboratory, careful thought must be given to safety and the environment, because these processes can produce copious amounts of fume and hydrogen gas. Material safety data sheets and suppliers' safety precautions must be consulted. For more information, see the article “Laboratory Safety in Metallography” in this Volume.

Reference cited in this section

2. Steltech Ltd., 2800 Speakman Drive, Sheriden Science and Technology Park, Mississauga, Ontario, Canada

---

S.M. Purdy, Macroetching, *Metallography and Microstructures,* Vol 9, *ASM Handbook,* ASM International, 2004, p. 313–324

Macroetching

Samuel M. Purdy, National Steel Corp. (Retired)

Etching Solutions

Lists of etching solutions and their application can be found in Ref 3, 4, 5, and 6. These lists are comprehensive and, initially, overwhelming. However, most of the etchants are for special purposes. Those at the head of any given list are ones that can be used for general purpose.

Most etchants can be prepared from technical-quality reagents, but superior results often can be obtained by using analytical-quality reagents. In preparing etching solutions, the laboratory safety procedures must be followed. These include using a fume hood, pouring acids into solvents slowly while mixing, and wearing protective clothing and safety glasses.

When mixing a solution, measure out the solvent first, then add each component in the order listed in the formulation, waiting for each component to dissolve or mix completely before making the next addition. If the solution heats up during mixing, cool it before adding the next ingredient.

Hydrochloric Acid (HCl). Hot 1 to 1 HCl in water is a common etching solution for iron, steel, and iron-base alloys. It is an azeotropic mixture, meaning that it does not change in composition as it evaporates. Hot, fresh solution can be added as replenishment without fear that the composition of the batch will change. Of course, eventually the batch will accumulate iron salts that will slow down etching, and the bath will have to be replaced. Other etching solutions are not azeotropes and will change in composition as they are used, even at room temperature. Reaction products will accumulate with use, retarding or altering etching behavior.

Hydrofluoric Acid (HF). A few etchants contain HF or fluorine salts. These require particular care in use. Hydrofluoric acid and its salts can generate painful ulcers on contact with the skin unless flushed off immediately. Solutions containing fluorine will react with glass, etching the vessel and causing artifacts on the specimen. Polyethylene vessels are recommended.

References cited in this section

3. "Standard Test Methods for Macroetching Metals and Alloys," E 340-00, *Annual Book of ASTM Standards,* Vol 3.01, ASTM International, 2002, p 397

4. "Standard Test Method for Macroetch Testing Steel Bars, Billets, Blooms, and Forgings," E 381-01, and adjuncts (ordered separately), *Annual Book of ASTM Standards,* Vol 3.01, ASTM International, 2002, p 413, Section 5.2

5. G. F. Vander Voort, *Metallography: Principles and Practice,* McGraw-Hill, 1984; reprinted by ASM International, 1999

6. G. Petzow, *Metallographic Etching,* 2nd ed. ASM International, 1999

S.M. Purdy, Macroetching, *Metallography and Microstructures,* Vol 9, *ASM Handbook,* ASM International, 2004, p. 313–324

Macroetching

Samuel M. Purdy, National Steel Corp. (Retired)

Etching Operations

The basic procedure for macroetching is simply to immerse the cleaned specimen into the etching solution, remove it after it has developed a clear structure, rinse it to remove the etchant, and dry.

The etchant solution is raised to the specified temperature before immersing the specimen. Small specimens can be picked up with tongs and immersed in the solution. Larger ones can be handled with gloved hands when using less aggressive etchants. Slings made from polyethylene, synthetic fluorine-containing resin tape, or braided fiberglass can be used to lower large specimens into hot baths. A mesh tray or corrosion-resistant material can also be used to lower the specimen into the bath. Often, glass rods are placed in the bath to lift the specimen off the bottom, in order to allow circulation of the solution. This is especially important when the solution is heated.

At the completion of etching, when a clear macrostructure has developed, the specimen is removed from the etching solution and rinsed in hot, running water. Smut, or reaction products, can be removed from the surface of the specimen by scrubbing with a stiff brush containing vegetable or synthetic fibers. Do not use a metal brush. Some smuts can be removed with a chemical treatment. Smut can also be removed as it forms by swabbing the surface with a wad of cotton. Surgical or cosmetic cotton is recommended, because ordinary cotton often contains coarse fibers that can scratch the etched surface.

Certain copper-bearing etchants, as noted in the tables of Ref 3, 4, 5, and 6, will deposit copper if rinsed in water. Alcohol should be used for rinsing.

After rinsing with hot water, specimens can be dried using a compressed gas blast. Cans of clean gas are available from metallographic or microscope supply houses. Of course, laboratory compressed air can be used if it is clean and free of oil or water. The best rinsing and drying technique, especially for large specimens, is to remove the specimen from the batch, flood it with hot water, continue to rinse the specimen in running hot water until the specimen is warm, remove it from the rinse, and set it on edge so that the water drains off. A clean air gun or heat gun can be used to "wipe" the water down the specimen.

References cited in this section

3. “Standard Test Methods for Macroetching Metals and Alloys,” E 340-00, *Annual Book of ASTM Standards,* Vol 3.01, ASTM International, 2002, p 397

4. “Standard Test Method for Macroetch Testing Steel Bars, Billets, Blooms, and Forgings,” E 381-01, and adjuncts (ordered separately), *Annual Book of ASTM Standards,* Vol 3.01, ASTM International, 2002, p 413, Section 5.2

5. G. F. Vander Voort, *Metallography: Principles and Practice,* McGraw-Hill, 1984; reprinted by ASM International, 1999

6. G. Petzow, *Metallographic Etching,* 2nd ed. ASM International, 1999

S.M. Purdy, Macroetching, *Metallography and Microstructures,* Vol 9, *ASM Handbook,* ASM International, 2004, p. 313–324

Macroetching

Samuel M. Purdy, National Steel Corp. (Retired)

Macroetching of Iron and Steel

Probably the most common use of macroetching is in the routine quality control of iron and steel wrought products. Prepared specimens are immersed in the solution until the desired degree of etching is developed, then rinsed, desmutted, and dried. Ingots and continuously cast products can be compared with plates I, II, and III that are published as adjuncts to ASTM E 381 (Ref 4) or other such standards.

Structure Revealed

Etching often reveals a dendritic structure that results from the solidification of the ingot and is observable even in steel that has been subjected to repeated mechanical reduction. This is not detrimental if the steel has been worked enough and the segregation accompanying the dendritic structure is not in the form of excessively large nonmetallic inclusions.

Dendritic structure present in cast steel and persisting in wrought steels can be revealed by etchants 3 and 4 in Table 1 and by etchants composed of ferric chloride (30 g $FeCl_3$), cupric chloride (1 g $CuCl_2$), stannous chloride (0.5 $SnCl_2$), 50 mL HCl , 500 mL ethanol, and 500 mL water. A polished specimen is etched by immersion for 30 s to 2 min. Etching for too long a period deposits excessive copper, which may obliterate the details of the dendritic structure. Dendritic structure can also be revealed by the use of an etchant that contains 40 g $FeCl_3$, 3 g $CuCl_2$, 40 mL HCl, and 500 mL water. The specimen surface, which may be smoothly ground through 00 emery paper or metallographically polished, is etched 10 to 20 s using 10% nital, washed and dried, then immersed 15 to 30 s in the previously mentioned etchant. The dendritic pattern developed is revealed by visual examination in incident light.

Table 1 Selected etchants for iron and steel

No.	Composition	Temperature		Time, min	Comments
		°C	°F		
1	50% HCl (conc.), 50% H_2O	70–80	160–180	15–60	General etch. Desmut by brushing or washing with 10% HNO_3 after rinsing.
2	38% HCl (conc.), 12% H_2SO_4 (conc.), 50% H_2O	70–80	160–180	15–60	General etch
3	6% HCl and 1% HBO_3 in water	Room temperature	Room temperature	Varies	Electrolytic etch
4	Saturated solution of picric acid in H_2O (~20 g/L) with 1–10% sodium tridecyl benzene sulfonate. Add 1% HCl to etch alloy steels.	50 (approx.)	120 (approx.)	5–30	Primary structure in cast and welded steels. Swab during etching to remove smut.
5	10 g $(NH_4)_2S_2O_8$ in 100 mL H_2O	Room temperature	Room temperature	1–10	Segregation, flow lines, ghost lines. Swab with cotton balls to remove smut.
6	10–30 mL HNO_3 (conc.) in 100 mL water	Room temperature	Room temperature	0.5–2	Grinding burns, general structure
7	2.5 g $CuCl_2$, 10 g $MgCl_2$, 5 mL HCl (conc.), 250 mL ethanol. Dissolve salts in HCl with minimum of hot water; dilute to 250–500 mL with ethanol.	Room temperature	Room temperature	5–30	Stead's reagent; reveals phosphorus segregation
8	90 g $CuCl_2$, 120 mL HCl (conc.), 100 mL H_2O	Room temperature	Room temperature	5–30	Fry's reagent. Rinse with alcohol or acetone. Rinsing with water will deposit copper. Use alcohol. Used to reveal discontinuous yielding in temper-rolled steel sheet and formed parts

Segregations are revealed by differences in the severity of the acid attack on the affected areas. Segregations at the center may be attacked so deeply that they appear as a pipe or may be grouped in some fairly regular form about the center, depending on the shape of the ingot and the mechanical work done on it. ASTM International plate I has a graded series of photographs for center segregation. Figure 1(a) and 317(b) are not from the plate but show the extent of center segregation represented in that series. The intended use of the product usually determines the acceptability of center segregation.

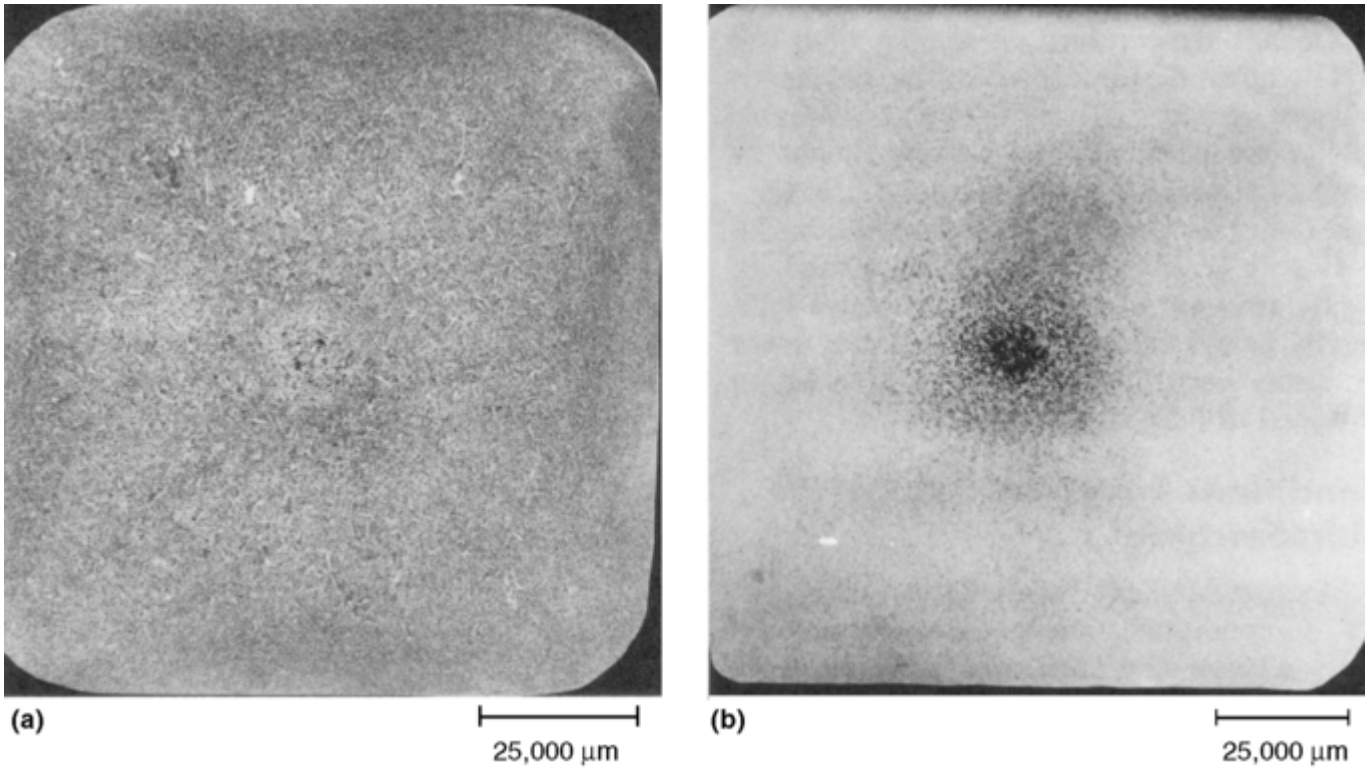

Fig. 1 Center segregation in an alloy steel billet (a) Graded C-1 in the graded series (Ref 4). 0.625×. (b) Graded C-5 in the graded series (Ref 4). 0.5×. Both samples etched in 50% aqueous HCl. Source: Ref 7, courtesy of Republic Steel

Ingot Pattern. The conditions leading to the formation of ingot pattern develop during solidification of the ingot and can remain even after forging. The pattern appears as a zone of demarcation between the columnar and heterogeneous regions of ingot solidification, which may persist during reduction of the ingot to billets and bars. Because inclusions, particularly sulfides, may segregate to a minor degree in this region, macroetching may reveal the presence of ingot pattern through preferential etching effects. In the absence of large amounts of sulfide and silicate inclusions, ingot pattern is of no serious consequence. One such pattern is presented in Fig. 2.

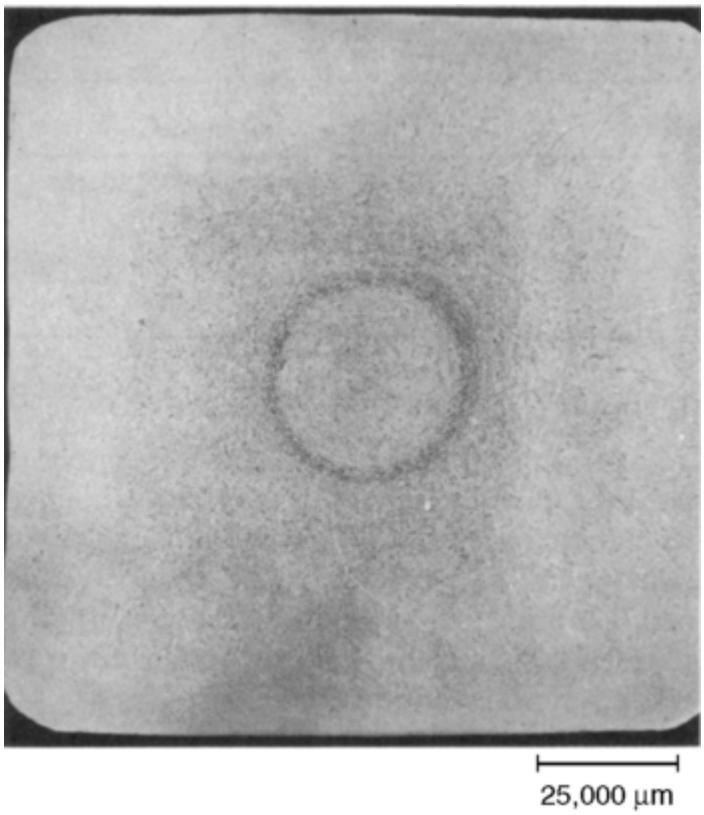

Fig. 2 Ingot pattern in a low-carbon alloy steel billet. Acceptable in any degree (Ref 4). Etch: 50% HCl. 0.5×. Source: Ref 7, courtesy of Republic Steel

Carbon spots are a type of segregation that is most likely to occur in carbon or alloy steels that contain more than 0.40% C. A degree of segregation no greater than that illustrated in Fig. 3(a) is usually considered acceptable.

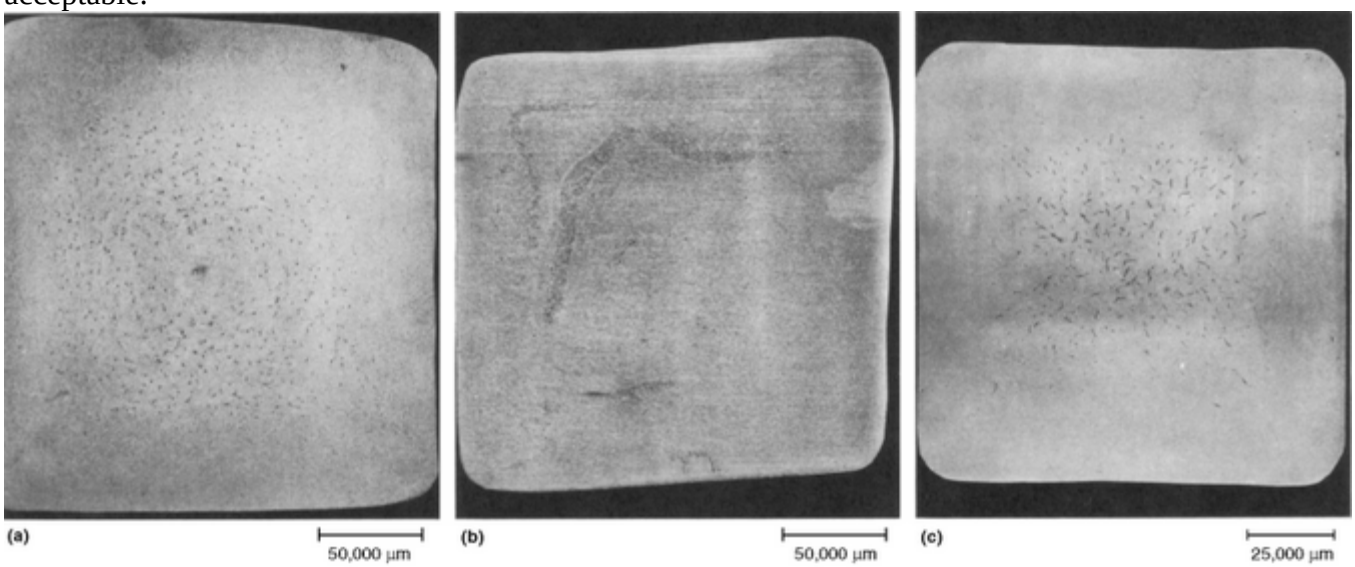

Fig. 3 Conditions revealed by macroetching with 50% HCl solution. (a) Carbon spot segregation in top billet of medium-carbon alloy steel. This degree of separation is acceptable (Ref 4). 0.33×. (b) Splash in bottom billet of an alloy steel ingot. Unacceptable in any degree (Ref 4). 0.33×. (c) Flakes in a billet of alloy steel. Unacceptable in any degree (Ref 4). 0.5×. Source: Ref 7, courtesy of Republic Steel

Splash is a condition sometimes found in steel billets taken from the bottom of an ingot. Such a condition may take place when the mold is too cold or if it has not been coated. When the molten steel first strikes the bottom of the ingot mold, some may splash and freeze immediately, which causes the type of segregation depicted in Fig. 3(b). Splash is not acceptable and is easily detected by macroetching.

Cracks such as flakes, butt tears, and flute marks are unacceptable (Ref 4). Flakes are internal cracks, which are sometimes called cooling cracks or thermal cracks (Fig. 3c). They can be detected by macroetching, and their identity can be verified by a fracture test of a hardened specimen in which the cracks are revealed as bright crystalline spots. Butt tears (Fig. 4b) are internal cracks that resemble bursts, and flute marks (Fig. 4c) are cracks that appear at the surface.

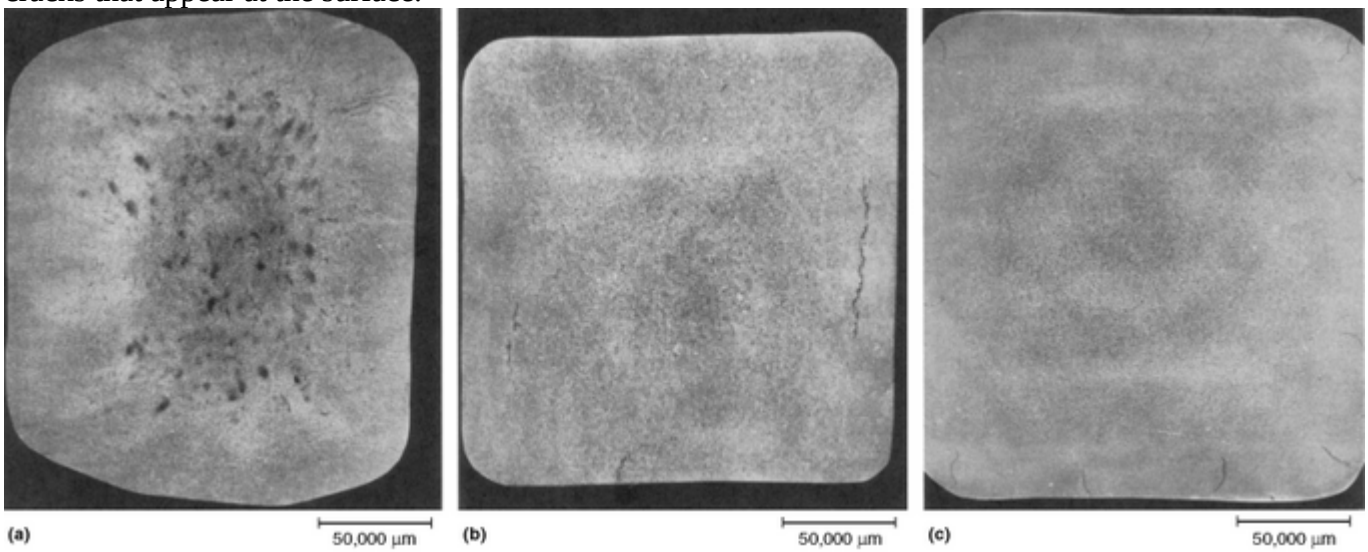

Fig. 4 Conditions revealed by macroetching with 50% HCl solution. (a) Bleeding (gassy) in top billet of alloy steel. Unacceptable in any degree (Ref 4). 0.33×. (b) Butt tears in bottom billet of alloy steel. Unacceptable in any degree (Ref 4). 0.33×. (c) Flute marks in bottom billet of alloy steel. Unacceptable in any degree (Ref 4). 0.33×. Source: Ref 7, courtesy of Republic Steel

Bleeding results from a gassy condition that is most likely to occur in billets from near the top of an ingot (Fig. 4a). This condition is unacceptable in any degree.

Bursts usually display a distinct pattern of cracks and do not show spongy areas, thus distinguishing them from pipes. Bursts are readily detected by macroetching; a typical burst is illustrated in Fig. 5.

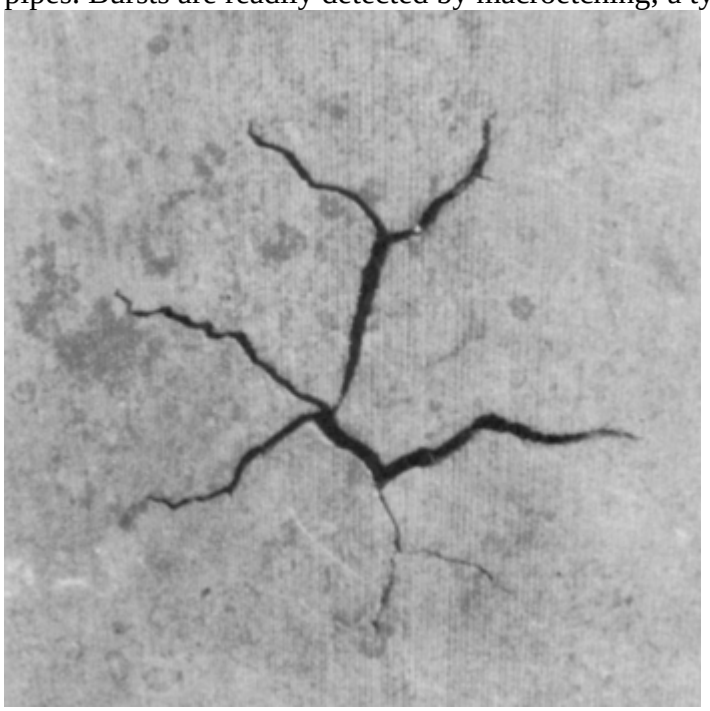

Fig. 5 Center burst in an alloy steel forging caused by improper processing. Etch: 50% aqueous HCl. Approximately actual size

Pipe is an internal shrinkage cavity formed during solidification of ingots of fully deoxidized steel that may be carried through the various manufacturing processes to the finished product. Pipe invariably is associated with

segregated impurities, which are deeply attacked by the etchant. Cavities in the center that are not associated with deeply etched impurities often are mistaken for pipe, but such cavities usually can be traced to bursts caused by incorrect processing of the steel during forging or rolling. Pipe should be visible after deep etching; it usually can be distinguished from bursts by the degree of sponginess surrounding the defect.

Other conditions revealed by etching in transverse sections of as-cast continuously cast steel and in ingot steel after primary reduction are available from plate III, an adjunct to ASTM E 381 (Ref 4).

One feature not included in the plate is refilled crack, which is defined as a defect formed during the solidification of continuously cast steel in which either external (bulging) or internal (shrinkage) forces produce a separation of crystallites, permitting solute-rich liquid to fill the gap as it forms. Figure 6 displays a particularly strong illustration of this defect.

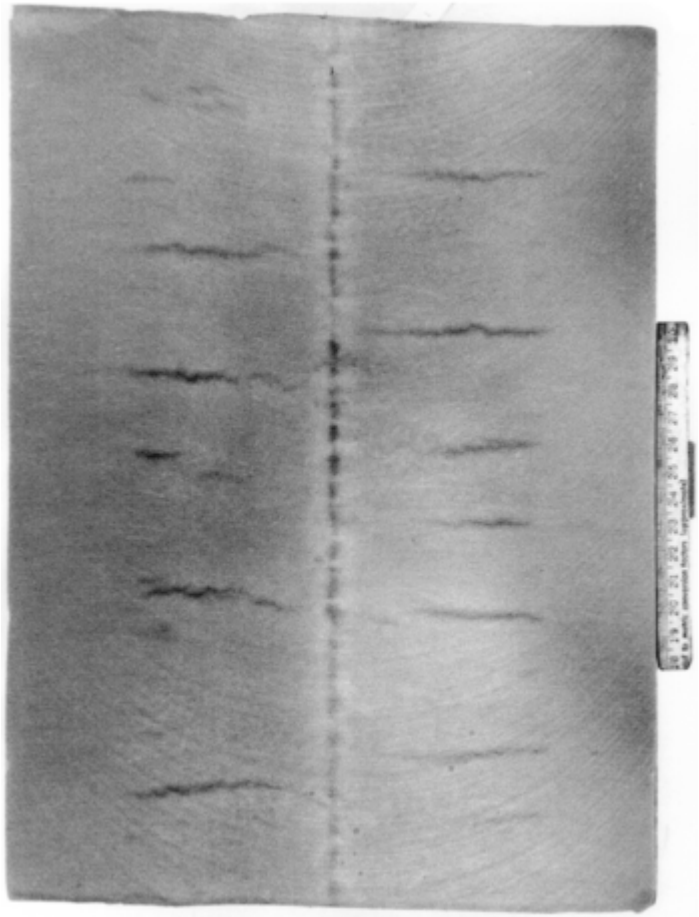

Fig. 6 Refilled cracks in a low-carbon steel slab, longitudinal section. Electrolytic macroetch. Courtesy of J. Kelly, Steltech Ltd.

Flow lines, which indicate the direction in which the steel was mechanically worked, have become part of the engineering specifications for certain designs of forgings and other parts, especially aircraft engine components. The contrast in deep-etched specimens can be increased by wiping the etched surface with ink and then wiping off the excess ink, as illustrated in Fig. 7.

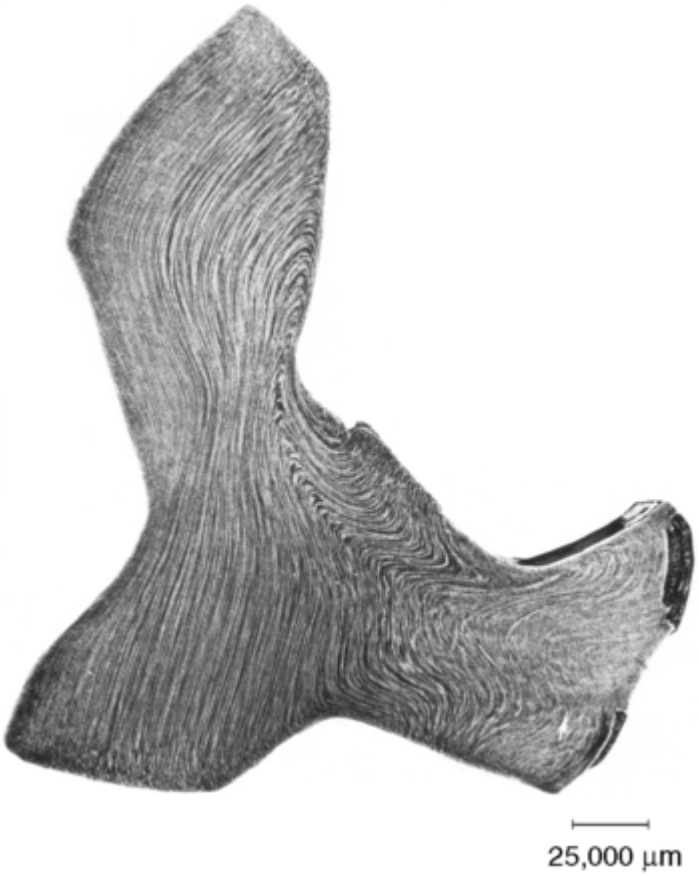

Fig. 7 Flow lines in closed-die-forged UNS G41400 steering knuckle revealed by cold deep-acid etching with 10% aqueous HNO_3 (0.5×) and enhanced with inking

Grain Size. Macroetching can be used to reveal areas of excessive grain size in some highly alloyed steels. It is not used for routine determination of grain size in the standard carbon and alloy steels. Figure 8 illustrates how localized coarse grain can be revealed in high-alloy steels by macroetching.

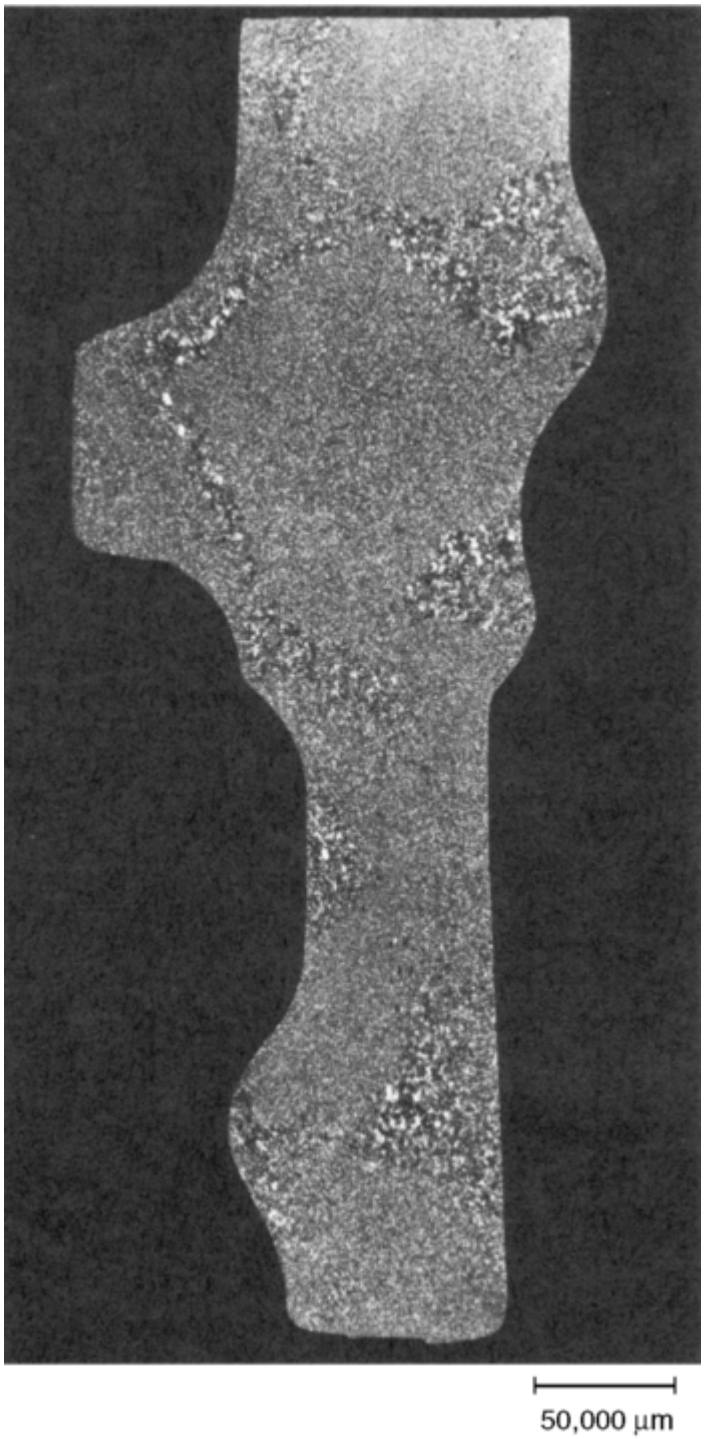

Fig. 8 Localized coarse grain, also called germinative grain growth, in a cross section of a high-alloy steel disk forging. 50% HCl. 0.25×. Source: Wyman-Gordon Co.

Macroetchants

Commonly used macroetchants are listed in Table 1.

Etchant No. 1, 1 to 1 HCl in water, is popular because it is easy to mix, easy to use, relatively inexpensive, and does not change in acidity as it is used. Being azeotropic, both water and HCl evaporate at the same rate. Specimen preparation is neither complicated nor expensive. A simple ground surface suffices. Sometimes, even the surface produced by an abrasive cutoff machine will do.

Etchant No. 2, a modification of the 1 to 1 composition, has been reported (Ref 4) to produce a clearer structure but never has achieved popularity, probably because of the difficulty in maintaining a constant composition over time.

Etchant No. 3, a variant of No. 1, is an electrolytic solution of 6% HCl and 1% HBO_3 in water at room temperature and is used in an electrolytic apparatus (Ref 2) in which the specimen, with a current density of 4.6 to 6.2 A/cm^2 (30 to 40 $A/in.^2$), passes beneath a cathode bar. A transverse section from a continuously cast stainless steel slab, etched in this apparatus, revealed a clear structure of the triple point (Fig. 9). Dendrites with long arms are well delineated.



Fig. 9 Macrostructure at a triple point of a stainless steel slab, transverse section. Electrolytic etch. Courtesy of J. Kelly, Steltech Ltd.

Etchant No. 4, hot aqueous picric acid, can be used to reveal primary structure in as-cast steels. A longitudinal cross section on an as-cast slab through a deep oscillation mark etched in hot aqueous picric acid (Fig. 10), reveals that the chill zone folded but did not rupture or shear. A dark band marks the bottom of the chill zone beneath the mark. Fine dendrites are seen to radiate from the bottom of the dark band. The bright spot at the corner is a photographic artifact. The use of etchant No. 4 requires care in specimen preparation and in etching. Because the etch is shallow, the specimen requires a fine finish, such as several light passes on a surface grinder using a 150-grit or finer alumina wheel. The detergent, sodium tridecyl benzene sulfonate, may be difficult to obtain; the dodecyl version works well also. As a last resort, dishwashing detergents can be tried. After cleaning, the specimen is immersed in the hot solution with at least 1 cm (0.5 in.) of solution over the specimen surface. Swabbing with a surgical cotton ball will remove the smut that generates pits. After etching, the specimen is rinsed in hot flowing water followed by acetone, to remove any remnants of smut. Any exposed sides and the bottom of the specimen should also be rinsed with acetone to remove smut, which is soft and will stain skin and clothes.

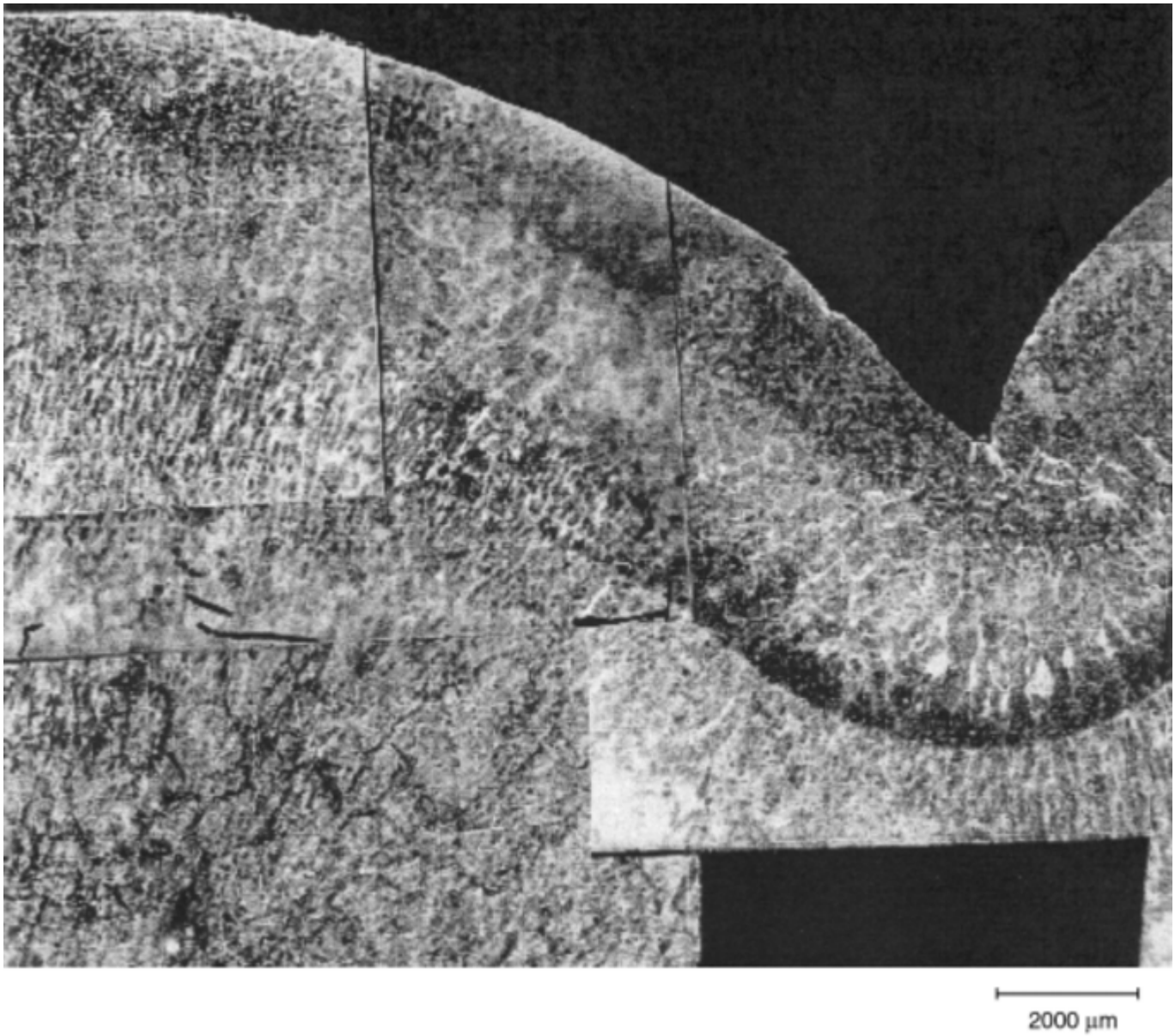

Fig. 10 A longitudinal cross section through a deep oscillation mark in a low-carbon steel slab. Etched in hot aqueous picric acid solution. 10×

Cold macroetchants do not produce the deep etch that hot 1 to 1 HCl in water does, hence better surface preparation is required. Fine grinding, 150 grit or smaller, will usually produce a satisfactory finish. Again, careful cleaning preparation is required.

Etchant No. 5, 10% ammonium persulfate in water, reveals segregation and flow lines in wrought products and general structure in weldments. Note the fine structure and flow lines in the HAZ at the bottom of the weld in Fig. 11. Swabbing with a surgical cotton ball to remove smut is essential. Contrast is improved by submersing the specimen in a water bath.

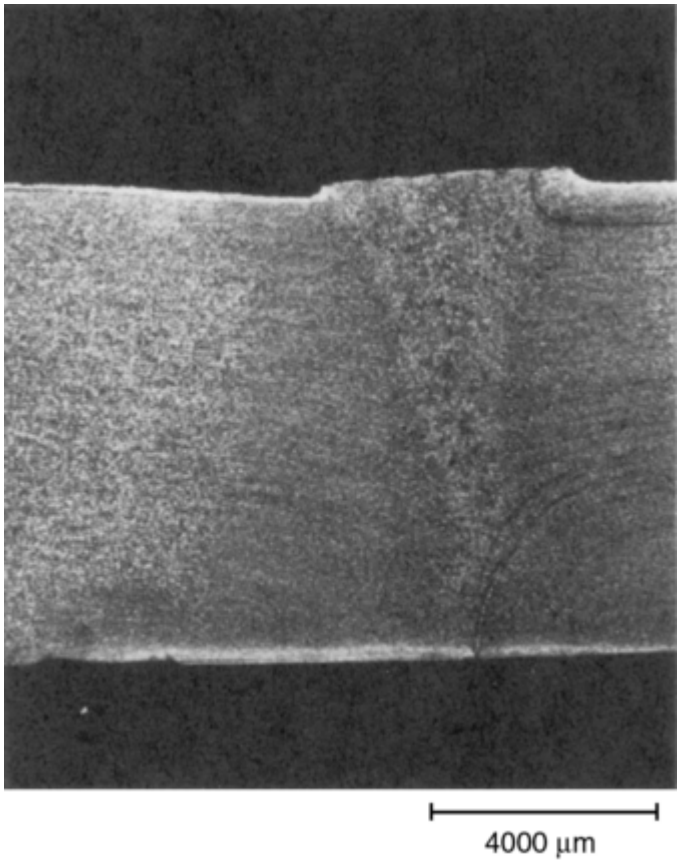

Fig. 11 View of a cross section taken through a resistance weld in American Petroleum Institute 5L-X46 steel pipe, 46 cm (18 in.) in outside diameter and with 9.5 mm ($\frac{3}{8}$ in) wall thickness. Weld is sound. Etch: ammonium persulfate. 5×

Etchant No. 6, 10 to 30% HNO_3 in water, is usually used on finished or heat treated parts to show the depth of hardening (Fig. 12a), decarburization (Fig. 12b), grinding burns (Fig. 12c), and soft spots from improper quenching.

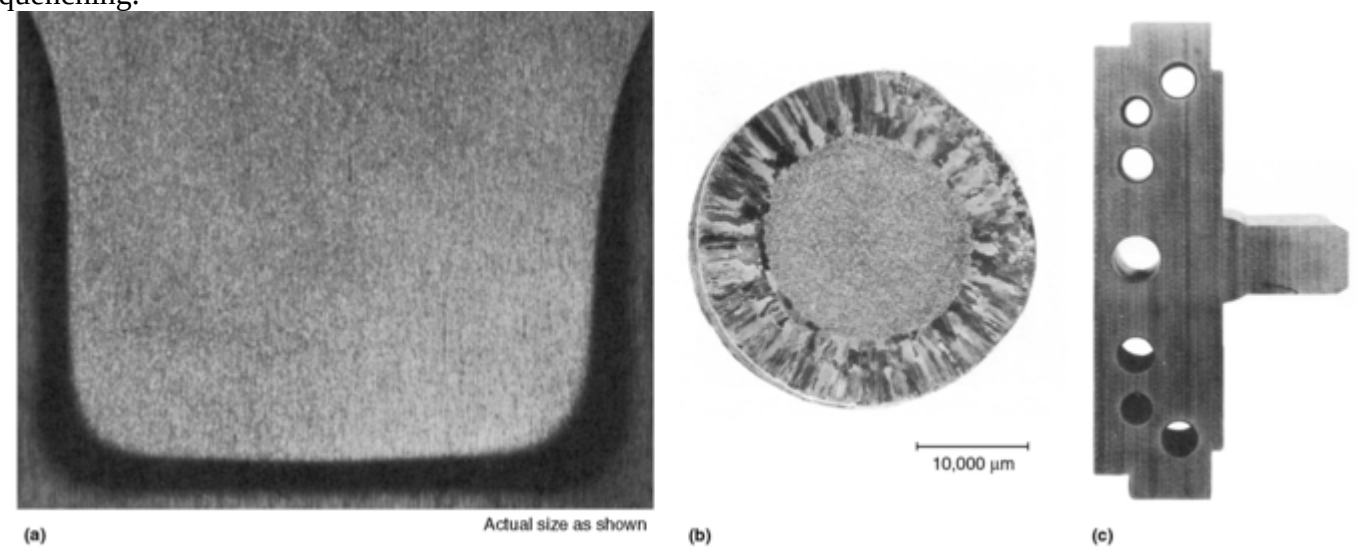

Fig. 12 Characteristics of heat treated or finished parts. (a) One end of a cross section through a flame-hardened UNS G10600 steel guide bar showing the hardened case. Dark-gray area at outside edges is a fully hardened martensitic structure; black area is the transition zone between the martensitic exterior and the core. Etch: 10% nital. Figure width is 9 cm (3.5 in.). Courtesy of Cincinnati Milacron. (b) Macroetching of a section cut from a UNS G10200 (semikilled) basket handle used in a continuous annealing furnace revealed coarse dendritic grain growth associated with decarburization (Ref 5). 2×. (c)

Macroetching (10% aqueous HNO_3) was used to reveal grinding scorch on the surface of this AISI D2 die. Grinding damage resulted because the die had not been tempered (Ref 5).

Etchant No. 7, Stead's reagent, is used to reveal phosphorus segregation. Specimen preparation is critical. It is reported (Ref 8) that Stead's reagent is widely used, but papers recommending its use offer contradictory procedures. The author's experience has been that careful specimen preparation to eliminate cold work, followed by careful cleaning, will be sufficient without pre-etching or complicated etching procedures.
Etchant No. 8, Fry's reagent, is used to detect discontinuous yielding. Again, numerous papers have been published concerning its application (Ref 8) and suggesting complicated procedures, but with careful specimen preparation and cleaning, the author has been able to avoid them. The specimen is prepared carefully to as fine a polish as is practicable, cleaned carefully, and immersed in solution. Polishing and etching several times to remove cold work is advised.

References cited in this section

2. Steltech Ltd., 2800 Speakman Drive, Sheriden Science and Technology Park, Mississauga, Ontario, Canada

4. "Standard Test Method for Macroetch Testing Steel Bars, Billets, Blooms, and Forgings," E 381-01, and adjuncts (ordered separately), *Annual Book of ASTM Standards,* Vol 3.01, ASTM International, 2002, p 413, Section 5.2

5. G. F. Vander Voort, *Metallography: Principles and Practice,* McGraw-Hill, 1984; reprinted by ASM International, 1999

7. Macroetching of Carbon and Alloy Steels, *Metallography, Structures, and Phase Diagrams,* Vol 8, *Metals Handbook,* 8th ed., American Society for Metals, 1973, p 70

8. G. F. Vander Voort, *Metallography: Principles and Practice,* McGraw-Hill, 1984; reprinted by ASM International, 1999, p 5, 8

S.M. Purdy, Macroetching, *Metallography and Microstructures,* Vol 9, *ASM Handbook*, ASM International, 2004, p. 313–324

Macroetching

Samuel M. Purdy, National Steel Corp. (Retired)

Macroetching of High-Alloy Steels, Stainless Steels, and High-Temperature Alloys

This group of alloys requires more aggressive etchants than ordinary irons and steels. The basic 1 to 1 HCl in water (No. 1a) is sometimes usable but often requires augmenting, as suggested in Table 2.

Table 2 Selected etchants for high-alloy steels, stainless steels, and high-temperature alloys

No.	Composition	Temperature	Time	Comments
1a	50% HCl (conc.), 50% H_2O	70–80 °C (160–180 °F)	15–60 min	General etch. Desmut by brushing or washing with 10% HNO_3 after rinsing.
1b	Etch No. 1a with an addition of H_2O_2 (30% conc.) or 5–10% HNO_3	Room temperature; may be heated to 70–80 °C (160–180 °F)	15–60 min	General etch used when No. 1a does not work. HNO_3 may be added and stirred before immersion of the specimen. Immerse specimen and add the H_2O_2 in steps. Add more H_2O_2 after foaming from the previous addition has stopped. Do not stir. Etch must be used fresh
2	50 mL (conc.), 10 g $CuSO_4$, 50 mL H_2O	Room temperature; may be heated	Indefinite, a few seconds to a few minutes	Marble's reagent. General purpose. Etch until the desired contrast is obtained.
3	10–40 mL HNO_3 (conc.), 3–19 mL HF (48% conc.), 25–50 mL H_2O	70–80 °C (160–180 °F)	Until desired degree of etching is achieved	Use great caution when using HF.
4	1 part HNO_3 (conc.), 3 parts HCl (conc.); make dilute solutions by mixing acids in water	Room temperature	Until desired degree of etching is achieved	Aqua regia, an extremely powerful etchant, gives off noxious fumes; must be used in a fume hood

Etchants. Straight chrome stainless steels may be etched in etchant No. 1a. Etches No. 1a and 1b present bright surfaces, compared to the matte surface of etchant No. 1 on low-alloy steel, but reveal the same features as etchant No. 1, Table 1. Nickel-containing stainless steel may require the addition of oxidizing agents. Similarly, etchant No. 1 for tool and alloy steels may require the use of oxidizing agents.

A 20 cm (8 in.) as-forged billet of UNS N07718 (Inconel 718, 50Ni-19Cr-3Mo-5Nb-1.0Ti-0.5Al, bal Fe) was sectioned using a cold abrasive cutoff machine and etched directly, without further preparation, in etchant No. 1b (Table 2), using a 20% addition of H_2O_2 (Fig. 13). A rim of coarse grains, produced by finish rounding the billet using light hammer blows, is evident. The faint, dark etching horizontal bands are artifacts produced by sectioning. They could be eliminated by further grinding.

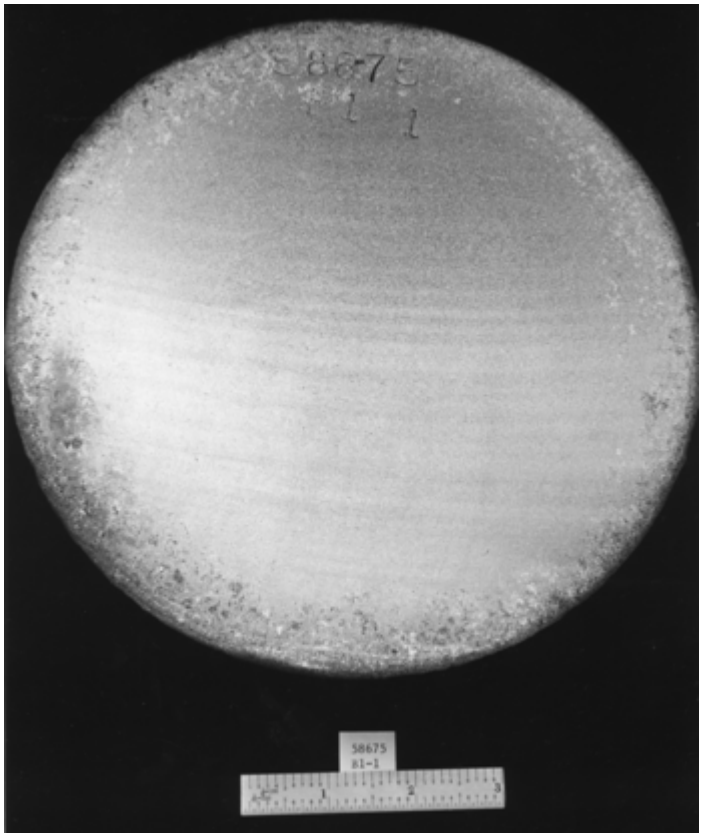

Fig. 13 Transverse section of an as-forged billet of UNS N07718 (Inconel 718) alloy. The rim of coarse grains was produced by hammer blows during finish rounding. Etchant: 1 to 1 HCl in water. Courtesy of F. Warmuth, Warmuth-Gordon

Some features are better revealed by not removing etch smut (Fig. 14). This specimen, an Inconel 718 forging, was immersed in etchant No. 1b of Table 2 (H_2O_2), rinsed gently so that the smut was not removed, and dried. The white spots, evidence of low hardener concentrations from vacuum arc remelting, are quite evident.

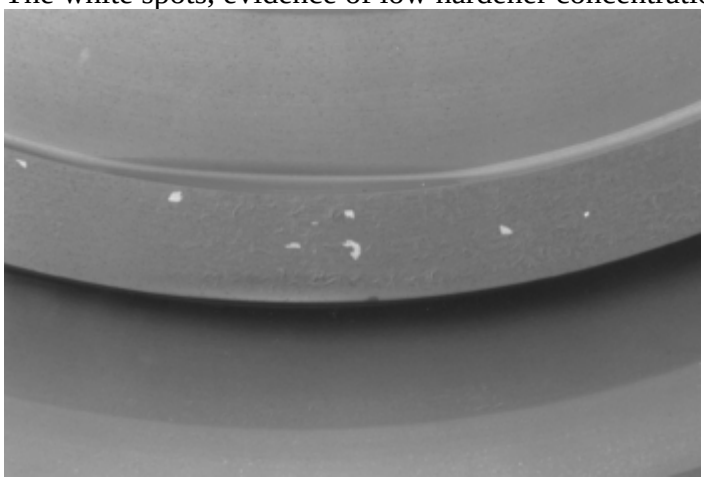

Fig. 14 Transverse section of a turbine wheel manufactured from UNS N07718 (Inconel 718) alloy. Etched in 1:1 HCl in water with H_2O_2 (Table 2, etchant 1b) but without removing the smut. White spots are indicative of low hardener concentration from unstable vacuum arc remelting. Courtesy of F. Warmuth, Warmuth-Gordon

With careful specimen preparation, fine and subtle details of structure can be developed. A cross section of the rim of a gas turbine disc was finely ground with 9 μm diamond abrasive and etched in etchant No. 1b of Table 2 (H_2O_2), cleaned carefully, and dried to reveal the structure seen in Fig. 15. Faintly darker marks, called stress chevrons, can be seen in the center of the rim, and remanent dendritic structures can be picked out in the upper

left corner of the rim. Stress chevrons are related to adiabatic heating by local rapid metal movement during forging. They appear in macros only and are almost impossible to relate to microstructure.

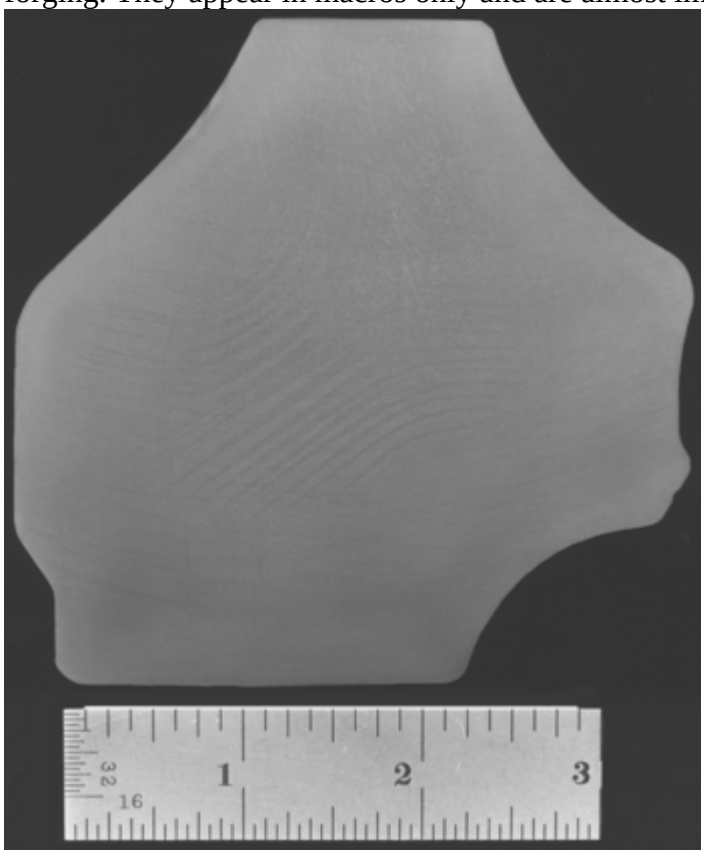

Fig. 15 Transverse section of a turbine disk, stage 3, manufactured from Inconel 718 alloy. Note faint stress chevrons. Etched in 1:1 HCl in water with H_2O_2 (Table 2, etchant 1b). Courtesy of F. Warmuth, Warmuth-Gordon. ~1×

S.M. Purdy, Macroetching, *Metallography and Microstructures,* Vol 9, *ASM Handbook,* ASM International, 2004, p. 313–324

Macroetching

Samuel M. Purdy, National Steel Corp. (Retired)

Macroetching of Titanium

The reactive metals are difficult to machine or grind, having a strong tendency to gall or seize up. Sharp tools and fresh grinding papers are required to prevent cold work from blurring the structure. The best results in specimen preparation are obtained by grinding with fresh, sharp SiC abrasives or diamond abrasives, both with copious lubrication.

Solutions for macroetching titanium and its alloys are not standardized. The most common ones contain HNO_3 and HF in varying ratios but always with HNO_3 well in excess of HF. Two of the more popular ones are listed in Table 3. Etchant No.1 requires more HF but is used at room temperature. Etchant No. 2 uses less HF but must be heated. Both will require fume hoods vented outdoors. Etchant No. 3 is used to etch certain titanium alloys.

Table 3 Selected etching solutions for titanium and titanium alloys

No.	Composition	Temperature		Time, min	Comments
		°C	°F		
1	15 mL HNO_3 (conc.), 10 mL HF (48%), 75 mL H_2O	Room temperature	Room temperature	10–20	General etch
2	42 mL HNO_3 (conc.), 4 mL HF (48%), 50 mL H_2O	50–65	120–150	20–30	General etch
3	20 mL HCl (conc.), 40 mL HF (48%), 50 mL H_2O	50–65	120–150	20–30	Desmut in aqueous 30% H_2SO_4 for 3 min, if required. Use for Ti-13V-11Cr and Ti-11Cr-3A1 alloys

A longitudinal cross section of a compressor disc forged from a Ti-17 alloy billet was etched in solution No. 2 to reveal flow lines (Fig. 16). A band of coarser grains is observed along the right side of the disc section, curving around the bottom and spreading out toward the right.

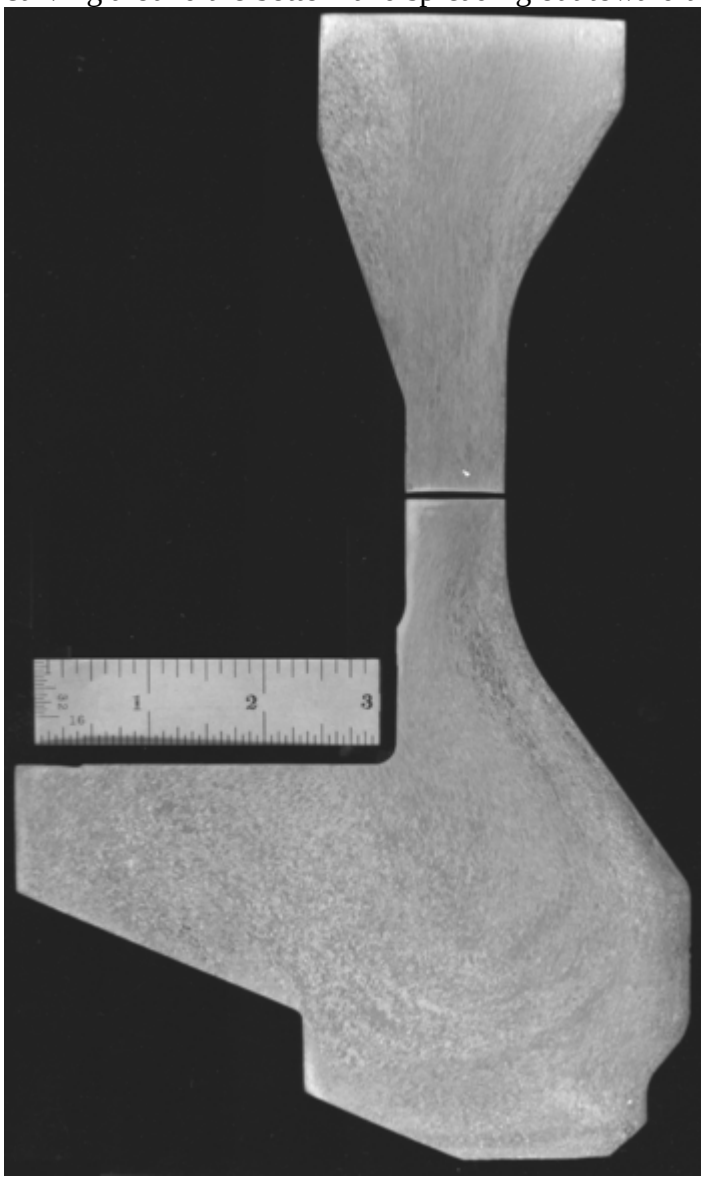

Fig. 16 Transverse section of a forged compressor disc, Ti-17 alloy. Flow lines and variations in grain size are revealed. Section is approximately 25 cm (10 in.) high; scale is in inches. Etched in 15 mL HNO_3 (conc.), 10 mL HF (48%), and 75 mL H_2O at room temperature. Courtesy of F. Warmuth, Warmuth-Gordon

S.M. Purdy, Macroetching, *Metallography and Microstructures,* Vol 9, *ASM Handbook,* ASM International, 2004, p. 313–324

Macroetching

Samuel M. Purdy, National Steel Corp. (Retired)

Macroetching of Aluminum and Aluminum Alloys*

Because of its tendency to cold work, sharp tools and abrasives must be used in preparing aluminum specimens. Machining and grinding aluminum also generates heat, so that copious lubrication is required to prevent overheating the specimen and changing the structure. Usually, a fine-machined surface without cold work is sufficient for macroetching. Softer alloy and temper combinations can be difficult to prepare due to the tendency to gall. Never use composition cutoff blades, diamond saw blades, or grinding stones to prepare aluminum for macroetching. Generally, a sharp skip-tooth steel band saw blade or a coarse carbide-tipped blade will give less smearing than the tools commonly used for steel. For a smoother surface, a lathe or fly cutter with a sharp V-point tool is used after the saw cut. Use a lubricant or coolant to avoid redistributing the swarf back onto the sample.

Macroetchants

Aluminum macroetchants can be divided into two basic categories: etches that show aluminum phase grains and etches that show macrosegregation of other phases. To show aluminum grains, a mixed acid etch is commonly used; to show segregation, a caustic etch is often used. The mixed acids are nearly reagent-strength mixtures of concentrated (70%) nitric, concentrated (40%) HCl, and concentrated (48%) HF acids. The most common caustic etch is 10% sodium hydroxide in hot water. Caustic etches may cause a smut of non-aluminum residues to accumulate on the surface. This can be removed by desmutting in dilute nitric acid. However, the sample may be more photogenic with the smut intact, if care is taken not to disturb the surface. Dye penetrants can also be classed as macroetchants.

Caution: Hydrofluoric acid is highly toxic and its use is so prevalent in aluminum metallography that its safety demands special attention. Hydrofluoric acid is a rather weak acid. This is not the mechanism of its toxicity. Hydrofluoric acid is a contact poison; it travels through tissue and attacks nerve endings directly, causing excruciating pain. Untreated, concentrated HF exposure often results in the loss of all tissue between the exposure site and the bone, where it is sequestered by the calcium in the bone. It also depletes calcium and potassium in the blood, sometimes fatally. Exposures may not be immediately painful, so any suspected exposure to concentrated HF requires immediate first aid and hospitalization. Dilution of HF by other concentrated acids in the mixed acid etches substantially reduces the toxicity, but these mixtures still require the respect one would give strong acids and dilute HF. Solutions of HF will attack glass, so synthetic fluorine-containing resin or polyethylene containers and personal protective equipment are required. This safety note is not a substitute for safety training and is included to emphasize the need for that training.

Acid etches are used to evaluate the amount of recrystallization in annealed wrought alloys where it is desirable (O-temper) or where it is undesirable (H2*x* tempers). They are used to visualize clusters of similar orientation that cause “Looper lines” in deep drawing. Acid etchants can distinguish an H2*x* product from an H1*x* product. They can be used on sample cast buttons to evaluate grain refiner effectiveness prior to casting or on annealed products to check for grain growth. They can be used in evaluating the amount of cold work on formed products by re-annealing and evaluating the grain size gradations.

Caustic etchants are used to evaluate the thickness of the chill zone in direct chill cast slab and billet, to evaluate the expected cosmetic appearance of a product to be etched and anodized, to remove smeared metal from machining, to evaluate porosity and cracks in cross-sectioned castings, and to evaluate other cosmetic defects such as structural streaking. One of the reasons caustic etches are useful for evaluating cosmetic defects is that many products are finished using a caustic etch to generate a consistent matte surface prior to anodizing. So, a uniform appearance after caustic etching generally means the end users will be satisfied after their

processing. The high grain contrast from an acid etch often confounds other features, such as pores, cracks, and segregation. These features are usually, but not exclusively, evaluated by caustic etch.

Conditions Revealed by Macroetching of Aluminum

Example 1: Deformation in Formed Sheet. Macroetching can be used as an aid to visualize the amount of deformation in a formed sheet. Figure 17(a) shows a part formed from O-temper aluminum alloy that was subsequently reannealed. The gradations from large grain (low deformation) to small grain (high deformation) clearly show the gradation in cold work during forming. It is quite easy to partially pull tensile specimens to varying elongations and to anneal along with the formed part according to cold work calibration standards. Figure 17(b) is a closeup showing the gradations in grain size more clearly. Figure 17(c) is a similar part, but here, the abrupt change from coarse to fine grain at the top of the image is from an entirely different cause. The fine grain is not recrystallized, because it received subcritical cold work in forming. Whenever the grain size changes discontinuously from very large to very small without passing through intermediate sizes, this is probably the reason. The sharp transition at the top indicates a transition from a fine-grained unrecrystallized area of subcritical cold work to a large-grained recrystallized area of barely sufficient cold work. Figure 17(b) shows detail of the transition from subcritical cold work (unrecrystallized) above to barely critical cold work (recrystallized to a large grain) below. Continuing down the piece, the gradual transition to finer grain indicates increasing deformation, as in Fig. 17(a).

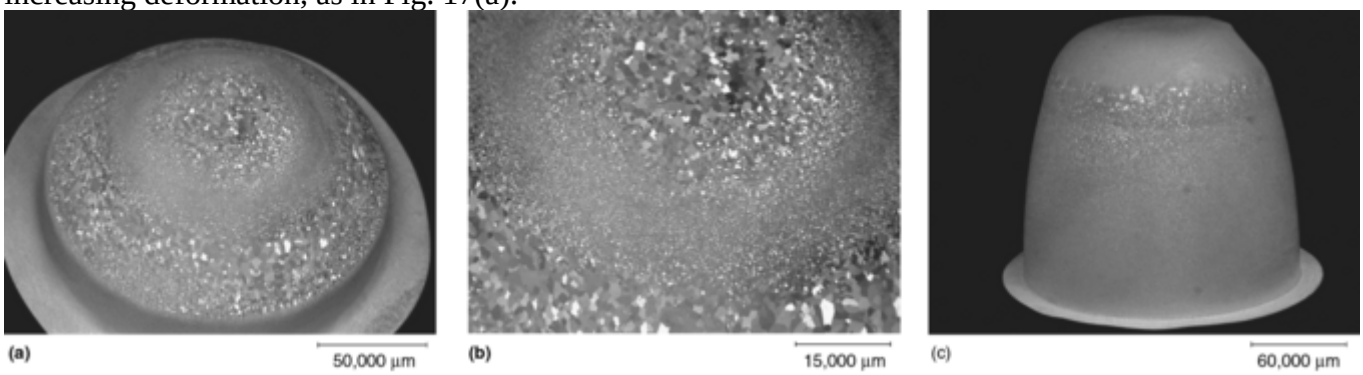

Fig. 17 Deformation in formed sheet. (a) Reannealed formed part illustrating distribution of cold work. Etchant: mixed acids. 0.67×. (b) Detail showing transition. Etchant: mixed acid. 2×. (c) Re-annealed formed reflector showing abrupt transition between recrystallized and unrecrystallized areas. Etchant: mixed acid. 0.5×

Example 2: Cast 5052 Ingot (UNS A95052). Figure 18 shows a corner of a transverse cross section of a direct chill cast rolling ingot alloy 5052 (A1-2.5 Mg-0.25 Cr). It was etched in Poulton's reagent (etchant 2 in Table 4). In this case, very little grain refiner was added, resulting in a structure containing columnar surface grains in the chill zone and massive twin columnar or feather grains in the interior, particularly in the center toward the top. Because in liquid aluminum it is easier to grow a grain at the side of an existing grain than from a seed, large patches of similarly oriented dendrites can grow from a few seeds. This sort of coarse structure can result in inhomogeneous properties under some conditions.

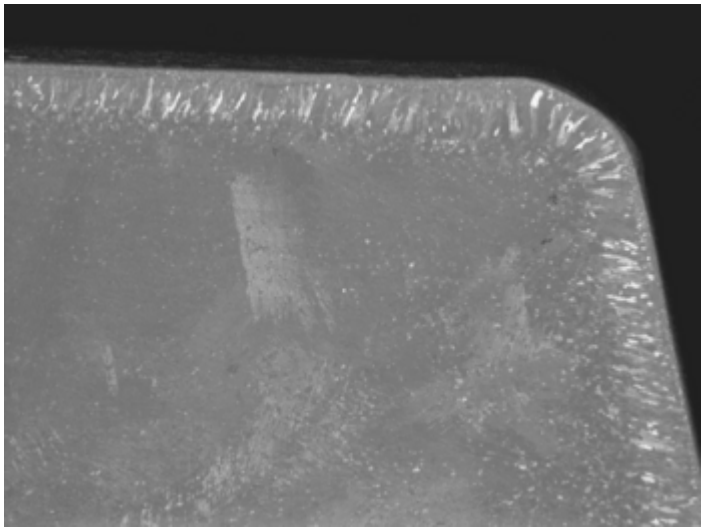

Fig. 18 Transverse cross section of 5052 as-cast direct chill rolling ingot—corner of 64 × 152 cm (25 × 60 in.) slice. Width shown is 13.5 cm (5.3 in.). Etchant: mixed acid

Table 4 Selected etchants for aluminum and aluminum alloys

No.	Composition	Temperature		Time	Comments
		°C	**°F**		
1	10 g KOH or NaOH, 100 mL H_2O	60–70	140–160	1–10 min	Good general etch; does not require fine grinding. Rinse in hot water, then dip specimen in 50% HNO_3 in H_2O to remove smut.
2	120 mL HCl, 60 mL HNO_3, 10 mL HF, 10 mL H_2O	Room temperature	Room temperature	5 s–1 min	Poulton's reagent. May be stored at room temperature. Use a water bath to keep solution cool. Etch specimen with brief, repeated immersions until desired contrast is obtained. Rinse specimen in cool water.
3	45 mL HCl, 15 mL HNO_3, 15 mL HF, 250 mL H_2O	Room temperature	Room temperature	10–15 s	Tucker's reagent. Mix fresh before using. Rinse specimen in warm water.

Example 3: Rolled Sheet. Figure 19 shows a comparison of unrecrystallized, partially recrystallized, and fully recrystallized rolled sheet. In some conditions, a recrystallized product would result in unacceptably large grains that would “pop” or “orange peel” in areas of high deformation. The best combination of formability and appearance could then arise from a back-annealed product that never underwent recrystallization. The structure in Fig. 19(a) is H25 temper, but H18 would look the same. The structure in Fig. 19(b) is an unintentional H23, and the structure in Fig. 19(c) is a true O-temper.

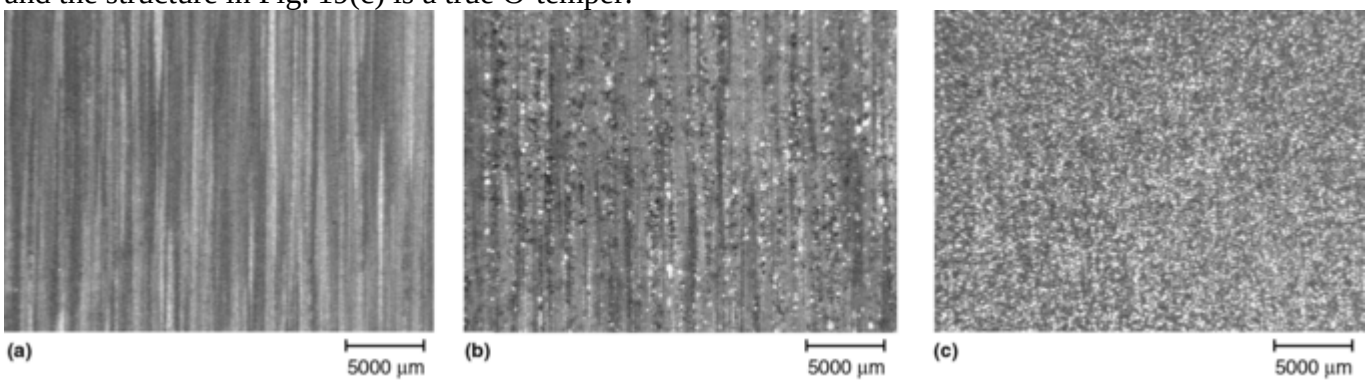

Fig. 19 Rolled sheet. (a) Unrecrystallized, H25 temper (H18 would look the same). (b) Partially recrystallized, H23 temper. (c) Fully recrystallized, O-temper. Etchant: mixed acid. 2×

Example 4: Billet Extrusion, 6*xxx* Alloy. Just as a sheet mill will "sell" surface quality and mechanical properties, a billet-casting facility will sell ingot integrity and homogeneity. Some customers require photos as part of the certification. Figure 20(a) shows a fine, uniform grain size with insignificant cortical zone. A somewhat larger grain in the center is expected, due to the lower temperature gradient in solidification.

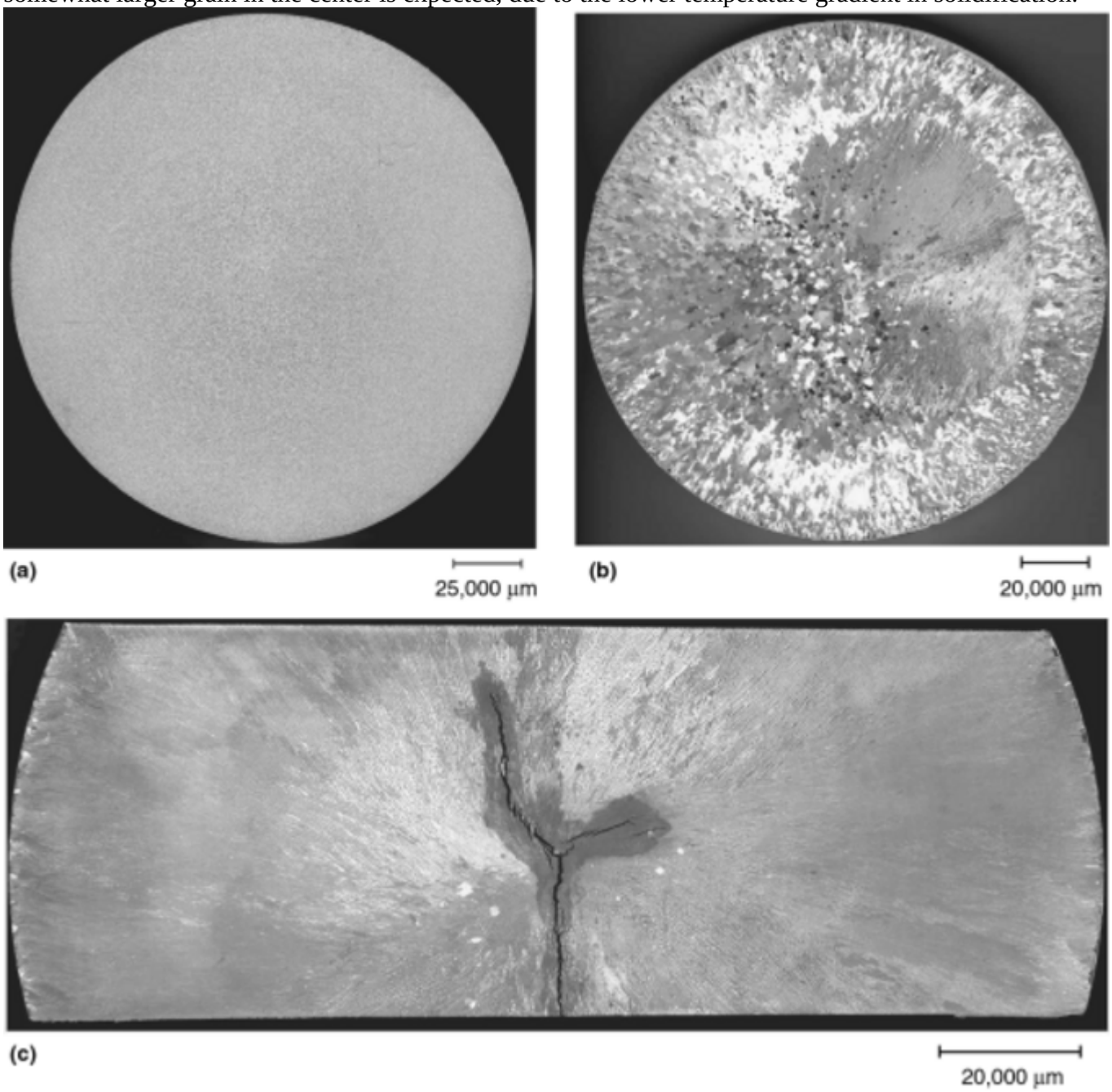

Fig. 20 6*xxx* alloy extrusion billet. (a) Transverse cross section showing fine equiaxed grain structure. Original, 0.75×. (b) Billet showing coarse grain structure and massive twin columnar grains on upper right side. Original, 1×. (c) Extrusion billet with massive twin columnar grains and central cracks. Original, 1×. Etchant: mixed acid. Courtesy of Marlene Reisinger, Eastalco

Figure 20(b) shows the opposite extreme: a coarse structure with massive twin columnar (feather) grains. This sort of structure can cause production problems, such as cracking (Fig. 20c), and may cause problems for the customer. The twin columnar structure is a massive array of parallel dendrites originating from the same nucleus. Smaller grains, nucleated in the melt, can be seen included in the twin columnars. The predominant recrystallization nucleation mechanism in some alloys occurs at grain boundaries, so orientation effects may carry through to recrystallized products. Thus, a large-grained initial structure may create forming problems due to similar-sized clusters of local anisotropy variations in the final product.

Example 5: Architectural Panels, 5005 Alloy. Figure 21(a) and (b) show the use of caustic etch to evaluate casting parameters for structural streaking, a phenomenon that shows up as streaks of matteness differences in 5005 architectural panel that is to be etched and anodized to a uniform matte finish. The cause has been linked to an abrupt change in the iron constituent phase from the metastable Al_6Fe near the surface to the stable Al_3Fe in the interior of the direct chill cast rolling slab. The surface aluminum phase appears to etch more aggressively, possibly due to a difference in electrical potentials. Either structure is generally acceptable, but stripes are not, nor is it good to change appearance from lot to lot. Because the outer 1.3 cm (0.5 in.) or so of a rolling slab is scalped off to remove the chill zone, the iron phase transition zone should be in that 1.3 cm (0.5 in.) or else uniformly deeper than the etch depth of the final gage product. The top piece in Fig. 21(a) has a fairly even transition zone near enough to the surface to be removed with the chill zone, while the bottom piece may also be an acceptable product where the transition zone is deep enough to remain below the surface even after scalping and etching. The center practice makes zebra stripes.

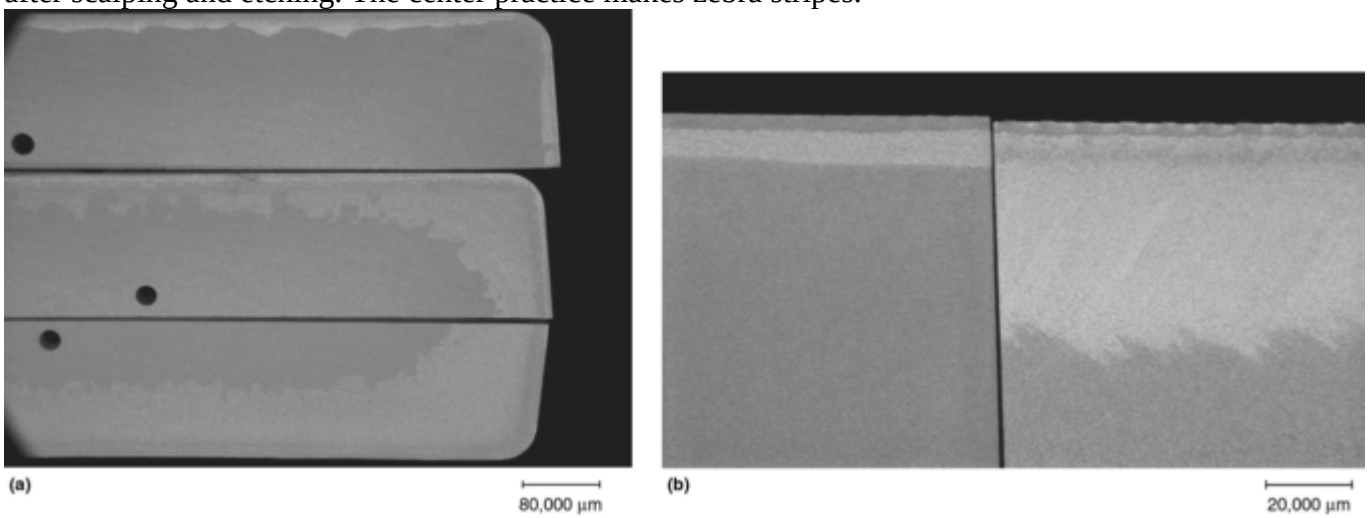

Fig. 21 5005 alloy slabs for architectural panels. (a) Corners of transverse cross sections of three 64 × 152 cm (25 × 60 in.) direct chill cast 5005 rolling slabs cast under different conditions. Etchant: 10% NaOH in hot water. 0.25×. (b) Longitudinal cross sections from a slab with a shallow iron phase transition point (left) and a deep iron phase transition point (right). Etchant: 10% NaOH in hot water. 1×

A longitudinal cross section shows a sawtooth-or “fir-tree”-shaped transition from meta-stable to stable structure instead of the cloud-shaped transition zone in the transverse section. Figure 21(b) shows a closer view of the chill zones and transitions in longitudinal section of the two acceptable structures shown in transverse section in Fig. 21(a).

Example 6: Clad Aluminum, 4047 on 3005 Core. Visualizing deformation through differential etching of natural and artificial segregation is a task for which caustic etching is well suited. Figure 22(a) shows a transverse section of the outer 20 cm (8 in.) at the edge of a brazing sheet clad composite hot rolled from approximately 64 cm (25 in.) total thickness to approximately 10 cm (4 in.). This particular trial involved a 4047 liner on a (scalped) direct chill cast 3005 core. Among the features visible in this image are:

- A liquation or chill zone is visible on the edge of the core (right side) but not at the liner interface, because the rolling face was scalped approximately 1 cm (0.5 in.).
- The edge foldover at the right side of the image is due to a light pass schedule used in sealing the liner to the core. (Some lateral flow is common at the edges of a rolling ingot, so the molds are beveled to compensate for the most common breakdown mill pass schedule.)
- The edge effects that affect the liner thickness can be seen from left to right:
    1. The majority of the width (not shown) is of uniform thickness due to elongation in the rolling direction.
    2. Approaching the edges, the liner thins due to bilateral deformation. It must elongate with the rest of the ingot, but it is not supported against lateral flow, as is the central portion of the slab.

3. Where the foldover relieves the compressive forces of the mill, the major deformation force is tensile elongation, and the bilateral thinning stops.

- Some inhomogeneity in the silicon distribution is visible in the liner.

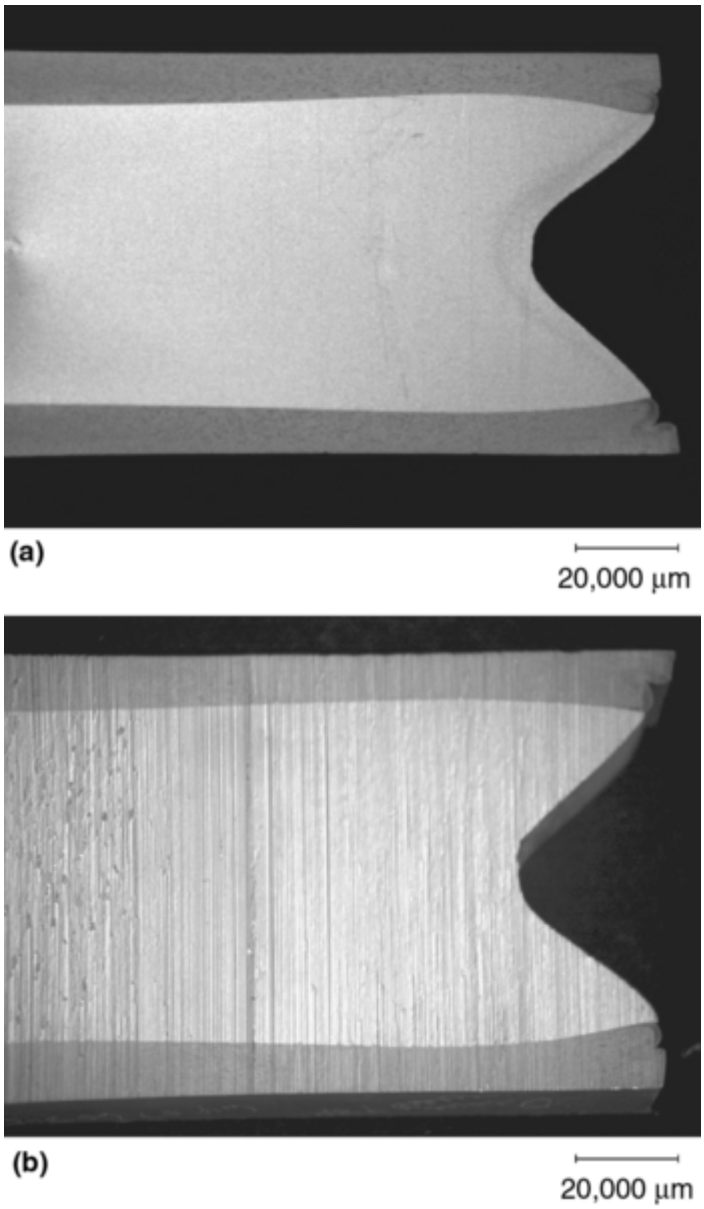

Fig. 22 Experimental 4047 on 3005 clad aluminum product. (a) Transverse cross section of near the edge at 10 cm (4 in.) reversing mill pass. Etchant: 10% NaOH in hot water. 1×. (b) Backside of same slice shows saw marks, but information on material flow behavior still is evident. Etchant: 10% NaOH in hot water. 1×

This sample was fly cut, because actual profile measurements were taken and graphed. Most of the features are readily discernible on the as-sawed surface, as can be seen in Fig. 22(b).

Example 7: Liquid Dye Penetrant. Liquid dye penetrant (Zyglo, Magnaflux) can be classed as a non-destructive macrostructural test method, that can be valuable in evaluating porosity, cracks, cold shuts, or any discontinuity in the metal. Its primary use is for quality-control inspection (Fig. 23).

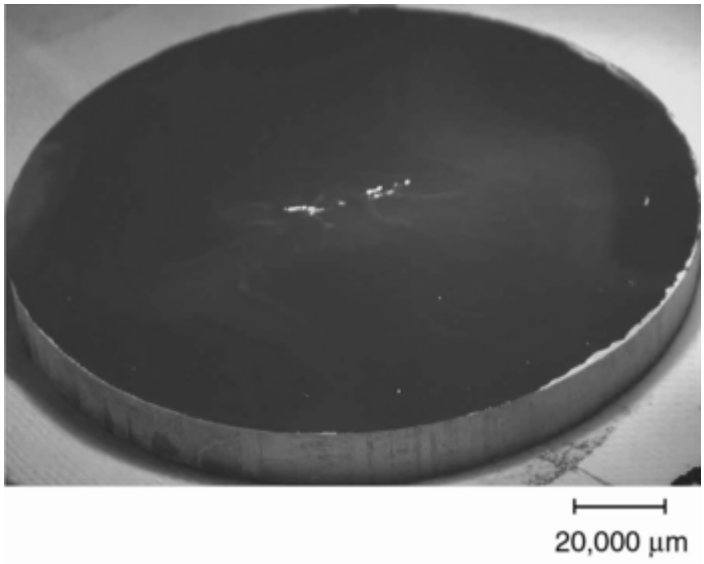

Fig. 23 Center crack observed in billet due to poor grain refinement. Dye penetrant (Zyglo) was used. 1×. Courtesy of Marlene Reisinger, Eastalco

Footnote

* This section is based on the contributions of Timothy Eck of Alcoa.

S.M. Purdy, Macroetching, *Metallography and Microstructures,* Vol 9, *ASM Handbook,* ASM International, 2004, p. 313–324

Macroetching

Samuel M. Purdy, National Steel Corp. (Retired)

Macroetching of Copper and Copper Alloys

Specimen preparation of copper and its alloys is fairly straightforward. Use sharp tools in a two-stage process. First, use a heavy cut to prepare a flat surface, and then use a fine cut with a V-shaped tool to remove cold work from the previous operation. Further preparation, using finer abrasives such as diamond on a hard disc, will improve resolution and detail. Common etchants are listed in Table 5.

Table 5 Selected macroetchants for copper and copper alloys

No.	Composition	Temperature	Time, min	Comments
1	10 mL HNO_3, 100 mL H_2O	Room temperature	1–5	Emphasizes grains and cracks
2	50 mL HNO_3, 50 mL H_2O	Room temperature	1–5	Brings up grain contrast
3	15 g $FeCl_3$, 30 mL HCl, 120 mL H_2O or ethanol	Room temperature	1–5	Develops good grain contrast
4	100 mL NH_4OH, 100 mL H_2O, 100 mL	Room temperature	1–5	Develops good grain contrast and brilliant tone. Mix NH_4OH and H_2O first, then add H_2O_2 and mix

H_2O_2	thoroughly before immersing the specimen. Etching action ceases when foaming ends.

Example 8: Cooling Plates. Three candidate materials for use as blast furnace bosh cooling plates with internal cooling passages were sectioned perpendicular to the cooling passages, ground down through 150-grit alumina, and etched in etchant No. 3.

Candidate 1, a hot rolled plate 24 cm (9.5 in.) thick with two passages gun drilled longitudinally (Fig. 24a), exhibited an equiaxed and uniform grain size. At the hot surface (top), some grain size coarsening is observed. Candidate 2, a plate continuously cast with two oblong passages produced by inserting graphite plugs into the mold, displayed a coarser grain size, with columnar grains at the hot surface (Fig. 24b). Grinding scratches not removed in preparation are evident. Candidate 3, a sand casting with water passages formed by cores, contained a wildly varying grain size, some regions of equiaxed grains, and two patches of coarse columnar grains (Fig. 24c). The choice between candidates 1 and 2 was made on a basis other than macrostructure. Candidate 3 was eliminated.



Fig. 24 Copper cooling plates. (a) Transverse section of candidate material 1, hot rolled copper slab. Etched in $FeCl_3$/HCl in water (Table 5, No. 3). Uniform, equiaxed grain size. (b) Transverse section of candidate material 2, continuously cast copper slab with integral cooling passages. Etched in $FeCl_3$/HCl in water (Table 5, No. 3). Coarse, equiaxed grains with columnar grains at the hot face (top). (c) Transverse section of candidate material 3, sand cast copper with water passages. Mixed grain sizes. Source: National Steel

---

S.M. Purdy, Macroetching, *Metallography and Microstructures,* Vol 9, *ASM Handbook,* ASM International, 2004, p. 313–324

Macroetching

Samuel M. Purdy, National Steel Corp. (Retired)

Other Metals and Alloys

Using the principles discussed in the section “Procedures” in this article, methods of macroetching other metals and alloys can be developed, using the solutions listed in ASTM E 340 (Ref 3).

Reference cited in this section

3. “Standard Test Methods for Macroetching Metals and Alloys,” E 340-00, *Annual Book of ASTM Standards,* Vol 3.01, ASTM International, 2002, p 397

S.M. Purdy, Macroetching, *Metallography and Microstructures,* Vol 9, *ASM Handbook*, ASM International, 2004, p. 313–324

Acknowledgment

Thank are extended to Timothy C. Eck of Alcoa for his contribution to the aluminum section of this article.

S.M. Purdy, Macroetching, *Metallography and Microstructures,* Vol 9, *ASM Handbook*, ASM International, 2004, p. 313–324

Macroetching

Samuel M. Purdy, National Steel Corp. (Retired)

References

1. "Standard Guide for Preparation of Metallographic Specimens," E 3, *Annual Book of ASTM Standards,* Vol 3.01, ASTM International, 2002, p 1

2. Steltech Ltd., 2800 Speakman Drive, Sheriden Science and Technology Park, Mississauga, Ontario, Canada

3. "Standard Test Methods for Macroetching Metals and Alloys," E 340-00, *Annual Book of ASTM Standards,* Vol 3.01, ASTM International, 2002, p 397

4. "Standard Test Method for Macroetch Testing Steel Bars, Billets, Blooms, and Forgings," E 381-01, and adjuncts (ordered separately), *Annual Book of ASTM Standards,* Vol 3.01, ASTM International, 2002, p 413, Section 5.2

5. G. F. Vander Voort, *Metallography: Principles and Practice,* McGraw-Hill, 1984; reprinted by ASM International, 1999

6. G. Petzow, *Metallographic Etching*, 2nd ed. ASM International, 1999

7. Macroetching of Carbon and Alloy Steels, *Metallography, Structures, and Phase Diagrams,* Vol 8, *Metals Handbook,* 8th ed., American Society for Metals, 1973, p 70

8. G. F. Vander Voort, *Metallography: Principles and Practice,* McGraw-Hill, 1984; reprinted by ASM International, 1999, p 5, 8

P.J. Goodhew, J. Humphreys, and R. Beanland, Light and Electron Microscopy, *Metallography and Microstructures,* Vol 9, *ASM Handbook*, ASM International, 2004, p. 325–331

Light and Electron Microscopy*

Peter J. Goodhew, University of Liverpool; John Humphreys, Manchester Materials Centre; Richard Beanland, Marconi Materials Technology

Introduction

IMAGES of microstructural features are obtained from microscopes that magnify images obtained by the transmission or reflection of either light or electrons. The choice of method depends on several factors, such as the type of specimen and the imaging requirements. For example, reflected light microscopy is common in the imaging of metallic microstructures, while transmitted light microscopy can be more effectively used in the microstructural imaging of polymers (where specimens may allow more light transmission). The choice of method also depends on imaging requirements such as resolution, magnification, depth of field, and lens aberration. These factors may influence the choice of light or electron microscopy (as detailed in the subsequent articles “Light Microscopy” and “Scanning Electron Microscopy” in this Handbook). However, these general factors are common to any imaging system, and an understanding of electron and light microscopy can be introduced with some general features of imaging systems and the ideas of magnification, resolution, and lens aberrations as they apply to simple and familiar light-optical systems.

Footnote

* Adapted with permission from P.J. Goodhew, J. Humphreys, and R. Beanland, Chapter 1, *Electron Microscopy and Analysis,* 3rd ed., Taylor & Francis Publishing, Inc., 2000, p 1–19

P.J. Goodhew, J. Humphreys, and R. Beanland, Light and Electron Microscopy, *Metallography and Microstructures,* Vol 9, *ASM Handbook*, ASM International, 2004, p. 325–331

Light and Electron Microscopy

Peter J. Goodhew, University of Liverpool; John Humphreys, Manchester Materials Centre; Richard Beanland, Marconi Materials Technology

Methods of Image Formation

There are three basic ways in which an image can be formed. Perhaps the simplest to imagine is the *projection* image, of which the most common example is the formation of shadows when an object is placed in front of a point source of illumination, as shown in Fig. 1. The second type of image is formed by conventional lens systems, as, for example, in Fig. 2, and this is called an *optical* image. This is not a strictly accurate term, because optical often refers to imaging systems involving light. However, the term *optical* also is sometimes used in the general sense of images formed using light electrons or ions. For clarification, the terms *electron-optical* and *ion-optical* may be used when appropriate.

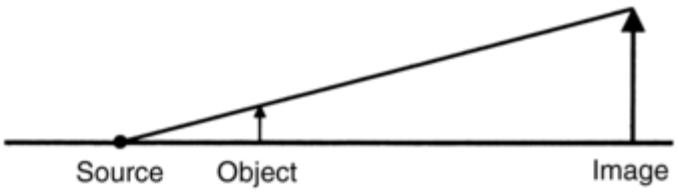

Fig. 1 The formation of a projection (or shadow) image. Each point in the object is projected directly at the equivalent point in the image.

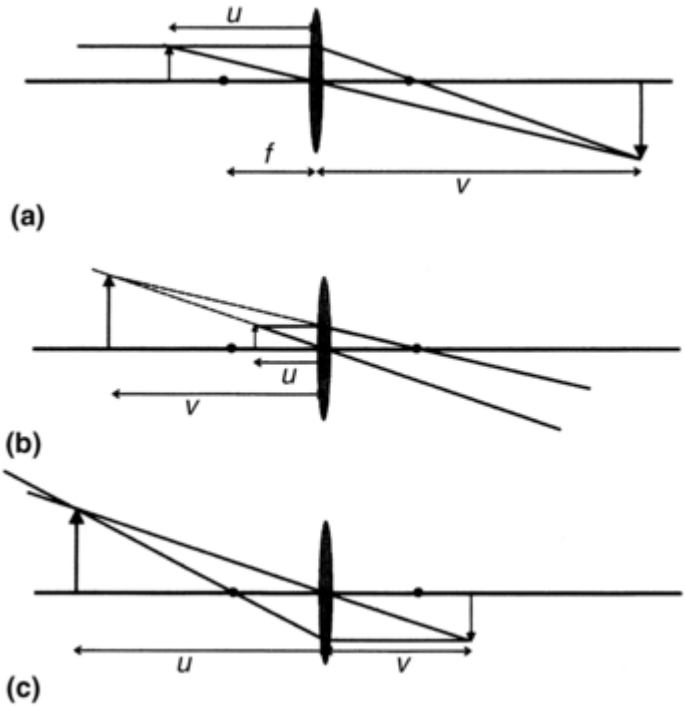

Fig. 2 Ray diagrams illustrating the formation of an image by a single lens of focal length f.

Both projection and optical images are formed in parallel; that is, all parts of the image are formed essentially simultaneously. However, a third type of image is the *scanning* image, in which each point of the picture is presented serially. With this type of image, several thousand picture points are displayed consecutively, but the process is repeated with such a high frequency that the image appears to the eye in its entirely.

P.J. Goodhew, J. Humphreys, and R. Beanland, Light and Electron Microscopy, *Metallography and Microstructures,* Vol 9, *ASM Handbook,* ASM International, 2004, p. 325–331

Light and Electron Microscopy

Peter J. Goodhew, University of Liverpool; John Humphreys, Manchester Materials Centre; Richard Beanland, Marconi Materials Technology

---

Pixels

One of the most important ideas concerned with images arises from the scanning image and digital imaging. The smallest piece of information in a scanned or digital image is contained in one *picture point* or pixel, which is short for picture element. The smallest detail that can possibly be shown in the image is a single pixel in size, each of which can be a different intensity or color. The idea of the pixel arose from consideration of scanned images, but it turns out to be universally applicable to images however they are formed. This is particularly

relevant when an image is to be stored by a computer, and again it must be broken down into the smallest necessary units of information. For example, the images produced by electron microscopes are often stored in computer memory and need to be in a digital form; that is, each pixel is coded so that its brightness is represented by a single number (usually between 0 and 255). Such images are often composed of a number of pixels that is a power of two, and common image sizes are 256 × 256 ($=2^8 \times 2^8$) pixels or 1024 × 1024 ($=2^{10} \times 2^{10}$) pixels. Large amounts of computer memory are then needed to store such images. If 256 ($=2^8$) brightness levels (known as gray levels) are permitted, each pixel takes up 8 bits of memory, and a complete 1024 × 1024 pixel image needs 1024 × 1024 × 8 bits, which, for many computers, is 1 megabyte (often abbreviated to 1 MB). Such an image will just fit on the conventional floppy disc of a microcomputer. However, image compression techniques are making it possible to reduce the storage requirement, often by an order of magnitude.

P.J. Goodhew, J. Humphreys, and R. Beanland, Light and Electron Microscopy, *Metallography and Microstructures,* Vol 9, *ASM Handbook*, ASM International, 2004, p. 325–331

Light and Electron Microscopy

Peter J. Goodhew, University of Liverpool; John Humphreys, Manchester Materials Centre; Richard Beanland, Marconi Materials Technology

The Light-Optical Microscope

Both optical and scanning types of microscope usually use lenses in some form. The simplest optical microscope, which has been in use since the early 17th century, is a single convex lens or magnifying glass. The ray diagram for this is shown in Fig. 2 and serves to illustrate the concepts of focal length, *f*, and magnification, *M*. The image is magnified, real, and inverted if the object distance *u* (between lens and object) is between *f* and 2*f*, as shown in Fig. 2(a). The image is erect but virtual if the object is within the focal distance (i.e., the object distance is between zero and *f*, as in Fig. 2b). If an image is to be recorded on a photographic plate or viewed on a screen, then it must be real; therefore, optical arrangements that give rise to virtual final images are not of concern here.

If the object is farther from the lens than 2*f* (Fig. 2c), the image is demagnified; that is, the magnification is less than unity. Notice that Fig. 2(a) and (c) are essentially the same (although drawn backwards) if the words "object" and "image" are interchanged. This illustrates one of the important features of an optical system: Its effect on the light rays does not depend on the direction in which they are supposed to be travelling. This *principle of reciprocity* was propounded by Helmholtz in 1886.

The aforementioned conclusions drawn about the behavior of a convex lens of focal distance *f* are summarized in the thin-lens equation:

$$\frac{1}{f} = \frac{1}{u} + \frac{1}{v} \qquad \text{(Eq 1)}$$

where *u* is the object distance (the distance from the lens to the object), and *v* is the image distance. Figure 2(b) shows that, by similar triangles, the magnification *M* produced by the single lens is given by *v*/*u*. Substitution in the lens equation gives:

$$M = \frac{f}{u - f} = \frac{v - f}{f} \qquad \text{(Eq 2)}$$

from which it can be deduced that for large magnification, *u* - *f* must be small and positive. This is achieved by placing the object just outside the focal point of the lens.

Magnification of an object without severe distortion is very limited using a single lens. Strictly the image in Fig. 2(a) should be curved so that all points on it are equidistant from the lens center. If the magnification is high, this effect is considerable, and the image seen in any one plane will appear distorted. For high

magnifications, therefore, combinations of lenses are used so that the total magnification is achieved in two or more stages. A simple two-stage photomicroscope will have the ray diagram shown in Fig. 3.

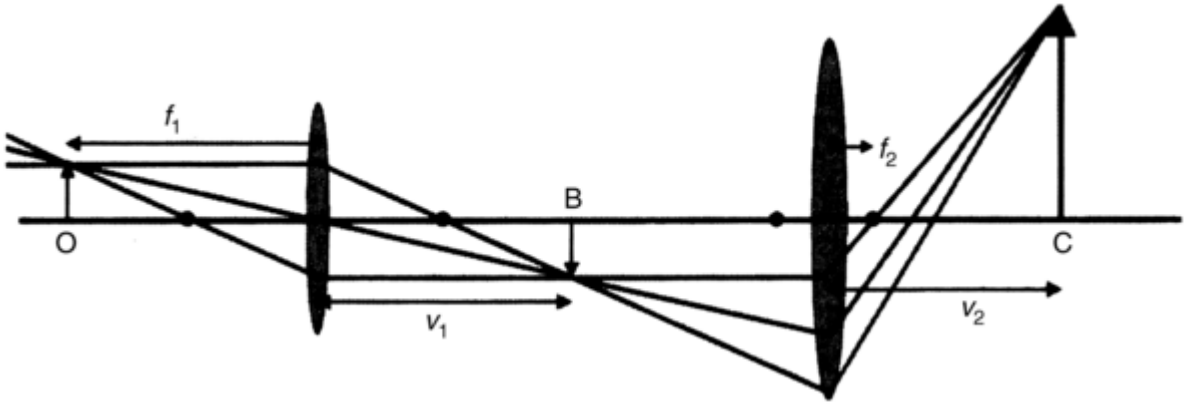

Fig. 3 The ray diagram of a simple two-stage projection microscope. The object is at O and the final image at C, with an intermediate image at B.

The first lens, the ***objective,*** provides an inverted image at B, with a magnification $(v_1 - f_1)/f_1$, and the second lens, the ***projector,*** gives a final upright image at a further magnification of $(v_2 - f_2)/f_2$. The image is viewed on a screen or recorded on a photographic plate at C, with a total magnification of:

$$M = \frac{(v_1 - f_1)(v_2 - f_2)}{f_1 f_2} \qquad \text{(Eq 3)}$$

If higher magnifications are required, it is quite straightforward to add a second projector lens to provide a third stage of magnification.

So far, it has been assumed that the object itself is self-luminous; that is, the rays start at the object and end at the viewing screen. In practice, this idealized situation is rare, as the specimen must be illuminated with light from a convenient source. If the object is mainly transparent, it is illuminated from behind, and the light (or electrons) are transmitted through the specimen. If the specimen is opaque, it is illuminated from the front, with the image formed from the reflection of light. Thus, there are two classes of optical microscope: a transmission arrangement such as shown in Fig. 4(a) to look at very thin sections, or a reflection arrangement as shown in Fig. 4(b) to examine the structure of a solid specimen. The same two types of electron-optical arrangement arise in electron microscopy, leading to transmission electron microscopy and scanning electron microscopy instruments. In this case, both types of instrument are used in almost all fields of science.

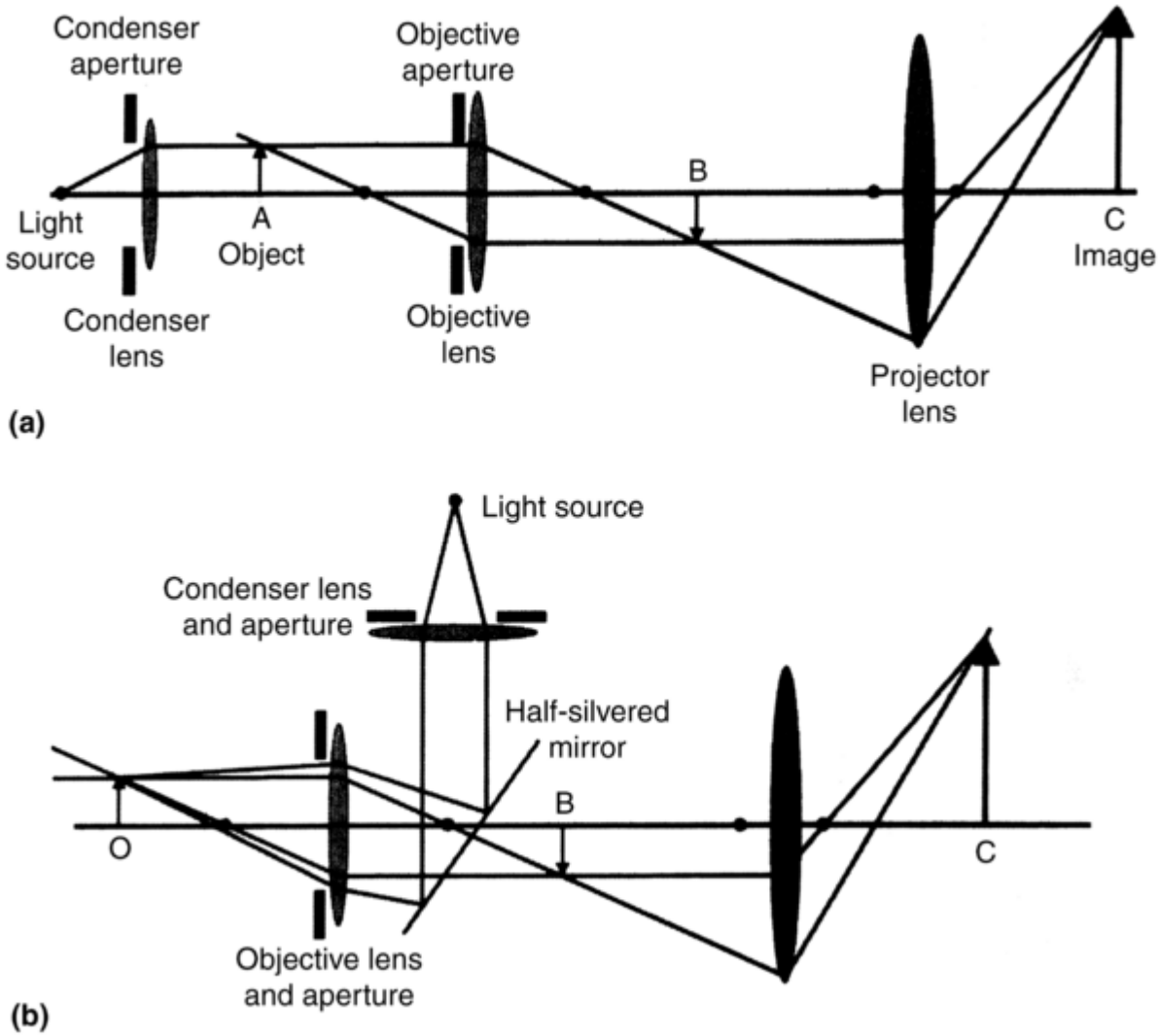

Fig. 4 The optical systems for the two common types of projection microscope. (a) Transmission illumination. (b) Reflected illumination

The essential parts of any illumination system are a light source and a condenser system. The condenser is necessary to collect the light that is diverging from the source and to direct it at the small area of the specimen that is to be examined. This serves two purposes: It makes the object appear brighter so that it can be seen more easily (also improving its *contrast*), and it also enables the microscopist to control the angle at which the illumination arrives at the specimen. The beam can be made to converge on the specimen or can illuminate it with parallel rays. In electron microscopy, the concepts of contrast and convergence angle are rather important.
In early light microscopes, the sun or ordinary diffuse daylight was used as a source, and a concave mirror was used to direct the light toward the specimen. For many purposes, this is adequate, but for more demanding work it is more usual to find a built-in light source and a condenser lens, as shown in Fig. 4. With the addition of two variable apertures near the condenser lens and the objective lens, it is possible to control the area of specimen that is illuminated and the angular spread of the light collected from the specimen. With a well-made microscope and proper specimen preparation, micrographs such as those shown in Fig. 5(a) and (b) can be taken.

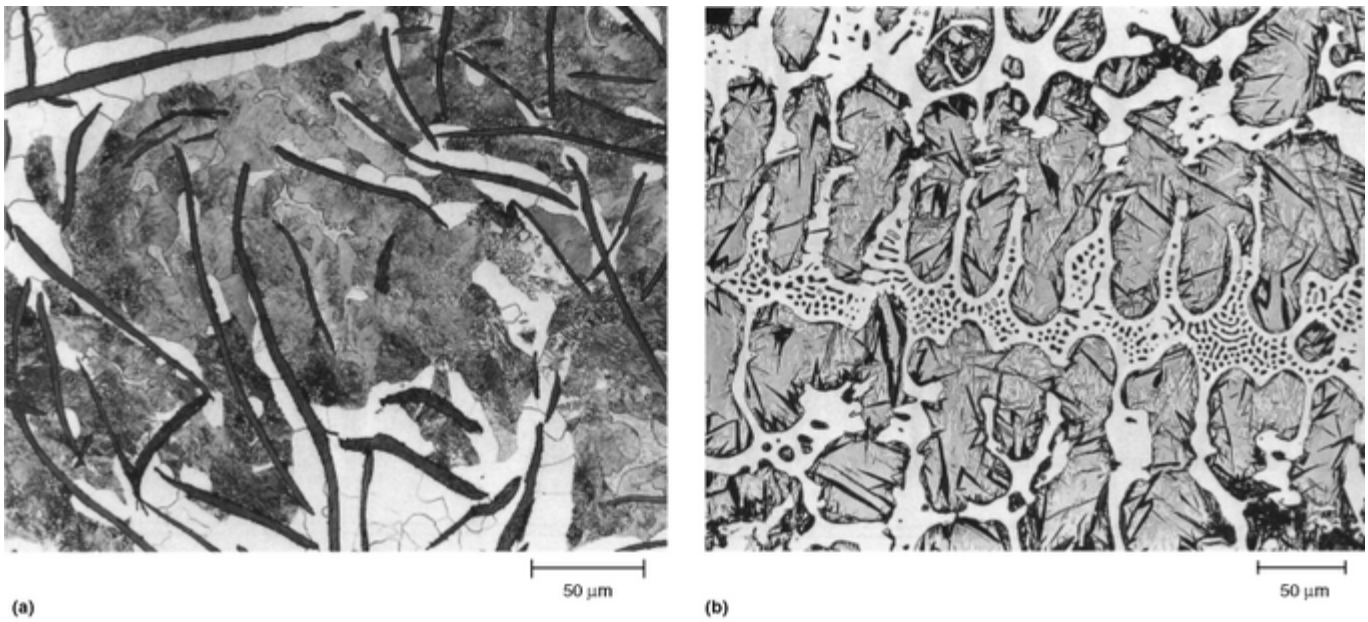

Fig. 5 Microstructures of (a) a gray cast iron with a ferrite-pearlite matrix, 4% picral etch, 320×, and (b) an alloy white cast iron. White constituent is cementite, and the darker constituent is martensite with some retained austenite. 4% picral etch. 250×. Courtesy of A.O. Benscoter, Lehigh University

P.J. Goodhew, J. Humphreys, and R. Beanland, Light and Electron Microscopy, *Metallography and Microstructures,* Vol 9, *ASM Handbook*, ASM International, 2004, p. 325–331

Light and Electron Microscopy

Peter J. Goodhew, University of Liverpool; John Humphreys, Manchester Materials Centre; Richard Beanland, Marconi Materials Technology

Magnification

In principle, it is possible to make a light microscope that will produce any selected magnification. However, because for convenience the instrument should be compact, without too many adjustments, it is usual to alter f_1 or f_2 in Eq 3 rather than v_1 or v_2. This means that in order to change the magnification, one lens is usually exchanged for another with a different focal length, giving a limited set of fixed magnifications. The alternative is to alter the distances between all the components of the microscope, and this is generally less convenient. This problem does not arise in electron microscopes, where all the parameters are more easily adjusted.

Although it was stated that the total magnification of the microscope can easily be increased by adding additional lenses, it turns out that for the vast majority of purposes the two-lens system shown in Fig. 3 is quite sufficient. The reason for this is simple: The smallest details that can usefully be distinguished in a light microscope are approximately 200 nm in size (2×10^{-7} m: 1000 nm = 1 μm; 1000 μm = 1 mm). The reason for this limit is discussed in the next section, but for the moment, consider its implication. The unaided human eye can easily detect detail only 0.2 mm (200 μm) in size. Therefore, there is very little point in magnifying the smallest details that can be resolved (200 nm) up to a larger size than 0.2 mm (200 μm). Thus, any magnification greater than 1000× only makes the details bigger. Finer details cannot be made visible by magnifying the image an extra ten times. An example of this "empty magnification," as it is called, is shown in Fig. 6. The first micrograph has a magnification of 70×, and a lot of detail can be seen. Magnifying this several times more, to 300×, reveals more detail. However, a further stage of magnification to 1400× or higher shows no more; the features are further apart but no clearer. If a large display is needed, for example, in order to view the micrograph at a distance, it is more sensible to enlarge a 1000× micrograph photographically than to build a

microscope capable of higher magnifications. Now it is relatively easy to provide magnifications of 1000× with only the two-lens system of Fig. 3, for example, using an 80× objective lens and a 15× projector lens. Consequently, it is not necessary to build a light microscope with three or more stages of magnification, because this will not improve the resolution but will rather degrade it by introducing extra aberrations (see the section “Aberrations in Optical Systems” in this article). However, the scanning electron microscope has inherently better resolution, and it makes sense to use it at higher magnifications, as Fig. 6 shows.

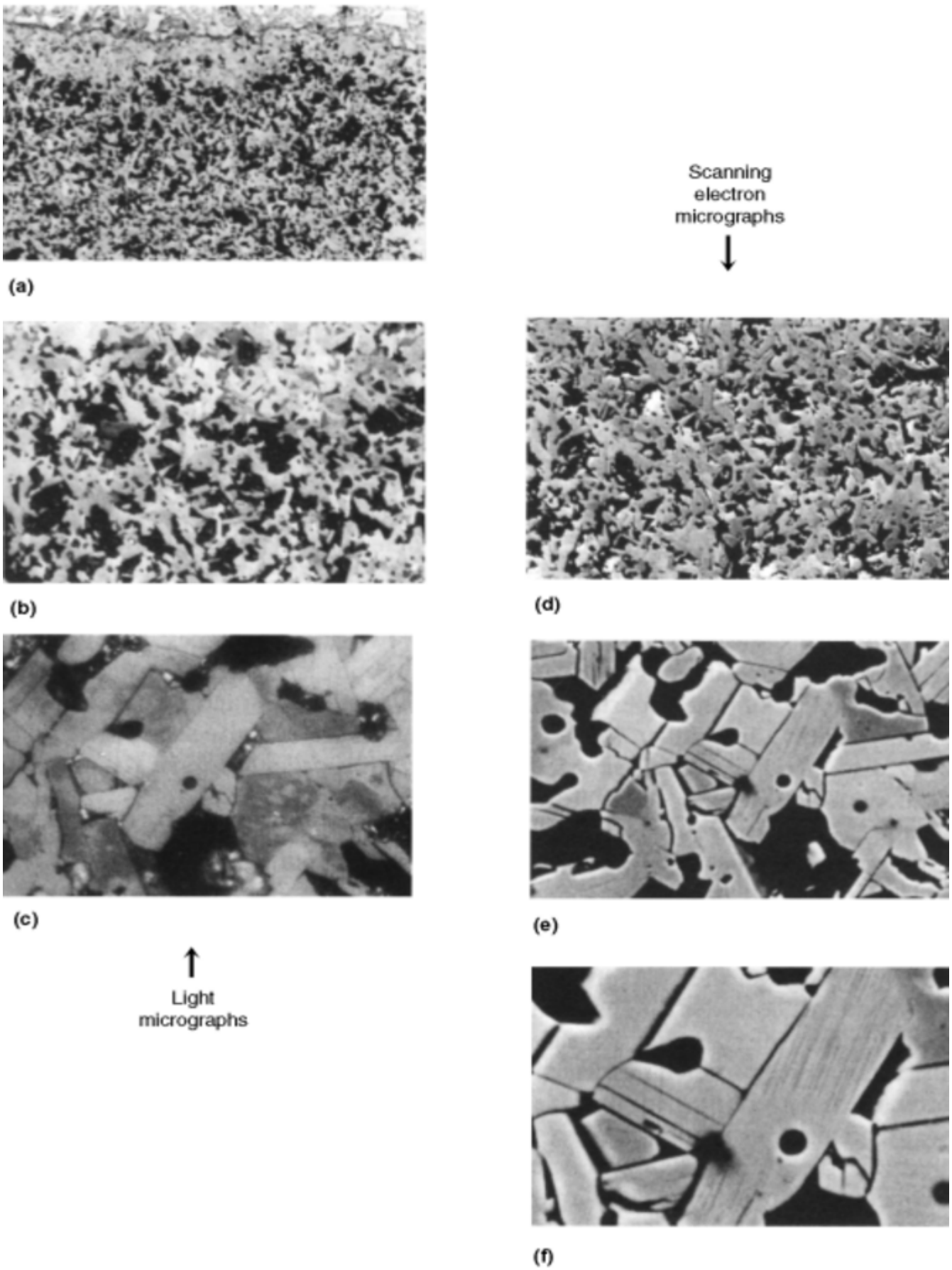

Fig. 6 A series of light and scanning electron micrographs of the high-temperature superconductor barium-yttrium copper oxide at increasing magnification. Original magnifications: (a) 70×, (b) and (d) 300×, (c) and (e) 1400×, and (f) 2800×

P.J. Goodhew, J. Humphreys, and R. Beanland, Light and Electron Microscopy, *Metallography and Microstructures,* Vol 9, *ASM Handbook*, ASM International, 2004, p. 325–331

Light and Electron Microscopy

Peter J. Goodhew, University of Liverpool; John Humphreys, Manchester Materials Centre; Richard Beanland, Marconi Materials Technology

Resolution

In order to compare the electron microscope with the light microscope, it is necessary to understand the factors that control the resolution (often called resolving power). Resolution may be defined as the closest spacing of two points that can clearly be seen through the microscope to be separate entities. Notice that this is not necessarily the same as the smallest point that can be seen with the microscope, which will often be smaller than the resolution limit.

Even if all the lenses of the microscope were perfect and introduced no distortions into the image, the resolution would nevertheless be limited by a diffraction effect. Inevitably, in any microscope the light must pass through a series of restricted openings—the lenses themselves or the apertures shown in Fig. 4. Wherever light passes through an aperture, diffraction occurs so that a parallel beam of light (which would be seen as a spot) is transformed into a series of cones, which are seen as circles and are known as Airy rings. Figure 7 shows this effect with a laser beam and two small pinholes. For light of a given wavelength, the diameter of the central spot is inversely proportional to the diameter of the aperture from which the diffraction is occurring. Consequently, the smaller the aperture, the larger is the central spot of the Airy disc. Very small apertures have been used in order to make the Airy disc clearly visible, but the same effects occur from the relatively larger apertures found in light microscopes. The diffraction effect limits the resolution of a microscope, because the light from every small point in the object suffers diffraction, particularly by the objective aperture, and even an infinitely small point becomes a small Airy disc in the image. In order to make this disc as small as possible, that is, to make the image of each point as small as possible, the aperture must be as large as is feasible.

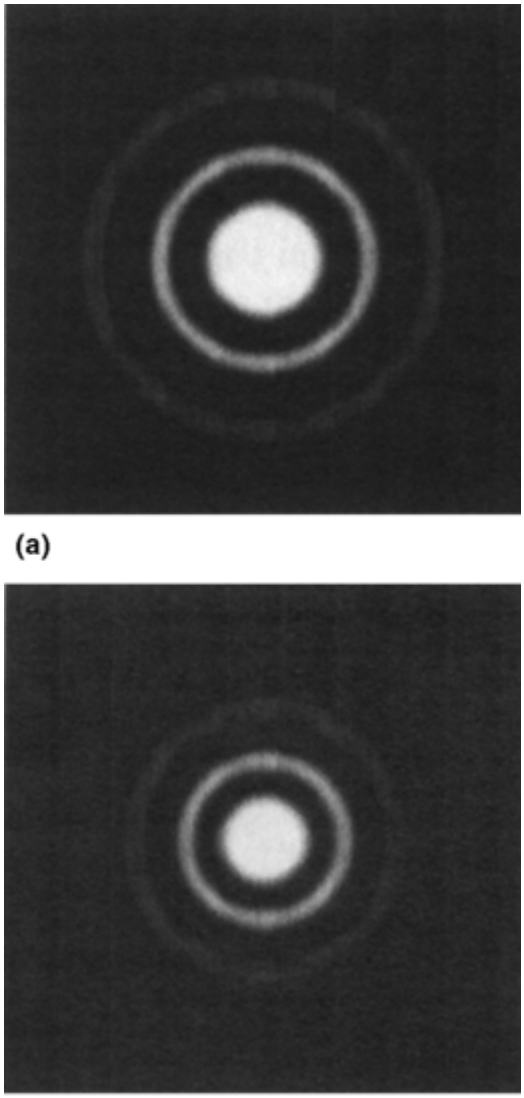

Fig. 7 Airy rings resulting from the diffraction of a laser beam by small pinholes. (a) 75 µm diameter. (b) 100 µm diameter

Now consider the resolution of the microscope in more detail, starting with the Airy disc. Figure 8 shows the variation of the light intensity across the series of rings that make up the disc. The central spot is very much more intense than any other ring and, in fact, contains 84% of all the light intensity. Consequently, for many purposes, the rings can be ignored, and it can be assumed that all the light falls in a spot of diameter d_1, where d_1 α 1/(aperture diameter). Consider how far apart two of these spots must be in the image before they are distinguishable as two—this distance is the resolution that was defined earlier. Lord Rayleigh proposed a criterion that works well in most cases and has been used extensively ever since: When the maximum of intensity of an Airy disc coincides with the first minimum of the second, then the two points can just be distinguished. This is illustrated in Fig. 9, from which it can be seen that the resolution limit is $d_1/2$. Microscope apertures are normally referred to in terms of the semiangle, α, which they subtend at the specimen (Fig. 10). It is then possible to derive from diffraction theory (see any text on optics) the relationship:

$$r_1 = \frac{d_1}{2} = \frac{0.61\lambda}{\mu \sin \alpha} \qquad \text{(Eq 4)}$$

where λ is the wavelength of the light, and µ is the refractive index of the medium between the object and the objective lens. The product, µ sin α, is usually called the *numerical aperture.*

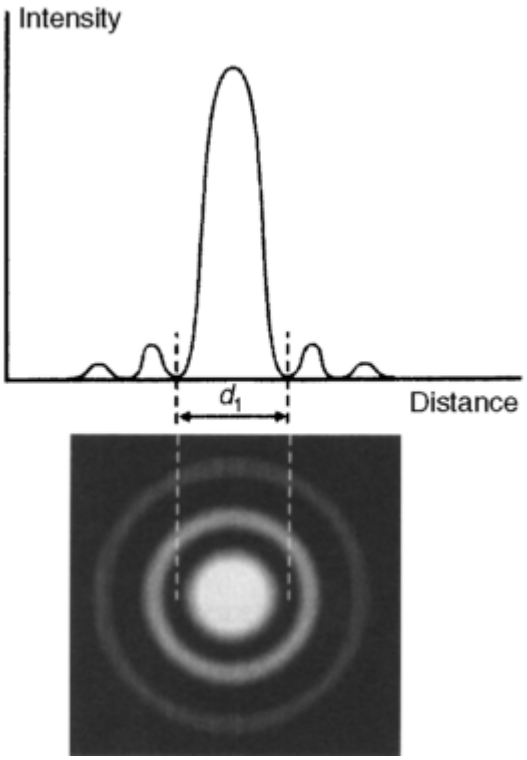

Fig. 8 The variation of light intensity across a set of Airy rings. Most of the intensity (84%) lies within the first ring, that is, within a spot of diameter d_1.

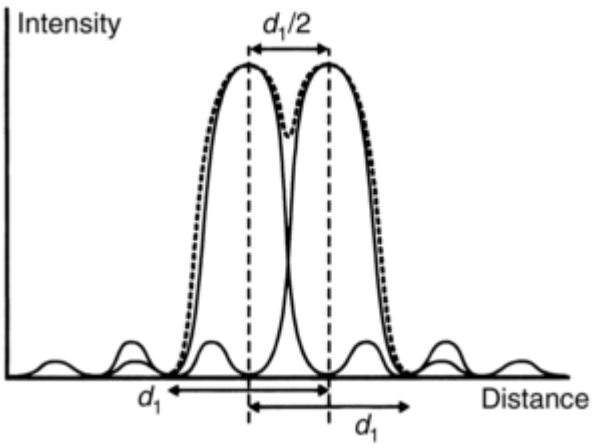

Fig. 9 The intensity of the Airy rings from two neighboring pinholes. The intensity distributions from each of the pinholes separately are shown as solid lines; the combined profile from the two pinholes acting together is shown dotted. At the Rayleigh resolution limit, as shown here, the maximum intensity from one pinhole coincides with the first minimum from the other. This gives a resolution limit of $d_1/2$.

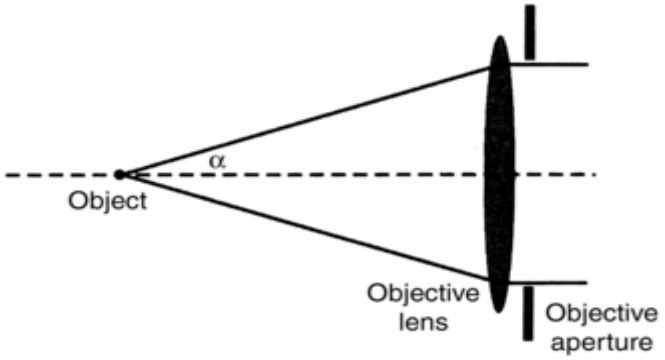

Fig. 10 The definition of the half-angle, α, subtended by an aperture (in this case, the objective aperture)

In order to obtain the best resolution (i.e., the smallest r_1), it is obviously possible to decrease λ or increase μ or α. With a light microscope, λ can be decreased to 400 nm by using green light (or to approximately 200 nm if it is possible to use ultraviolet light); sin α can be increased toward 1 by using as large an aperture as possible, and μ can be increased by using an oil immersion objective lens. However, it is impractical to make μ sin α much greater than approximately 1.6, because sin α must be less than unity, and even very exotic materials are limited to a refractive index of approximately 1.7. The absolute resolution limit using green light is therefore approximately 150 nm (0.15 μm). Even sophisticated image processing cannot improve on this fundamental limit.

P.J. Goodhew, J. Humphreys, and R. Beanland, Light and Electron Microscopy, *Metallography and Microstructures,* Vol 9, *ASM Handbook,* ASM International, 2004, p. 325–331

Light and Electron Microscopy

Peter J. Goodhew, University of Liverpool; John Humphreys, Manchester Materials Centre; Richard Beanland, Marconi Materials Technology

---

Depth of Field and Depth of Focus

In any microscope, the image is only accurately in focus when the object lies in the appropriate plane (strictly the surface of a sphere). If part of the object being viewed lies above or below this plane, then the equivalent part of the image will be out of focus. The range of positions for the object for which our eye can detect no change in the sharpness of the image is known as the *depth of field.* In most microscopes, this distance is rather small, and therefore, in order to produce sharp images, the object must be very flat. If a nonflat object (or a transparent object of appreciable thickness) is viewed at high magnification using a light microscope, then some out-of-focus regions will be seen. This is a useful feature for accentuating certain parts of the image at the expense of others but is a grave disadvantage for seeing all parts of a three-dimensional object clearly.

In the 1990s, clever optical design and the use of scanning led to the development of confocal light microscopes that exploit the intrinsic narrow depth of field to build up a three-dimensional image that, when viewed, is in focus over a range of depths. The term *confocal* simply means single focus. In a confocal microscope, confocality is achieved through the use of pinhole optics that prevent out-of-focus light from reaching the image plane. The sample is illuminated through an objective lens with a pinpoint of light, and a pinhole aperture is placed in the reflected light path. Light reflected from the sample at the focal plane of the objective lens passes back through the lens, through the pinhole, and forms an image of the illuminated spot. Reflected light from other regions of the sample is blocked by the aperture. An image of the sample is created by moving either the sample or the light source in an appropriate scan pattern, and either recording or viewing the resulting signals.

The depth of field can be estimated from Fig. 11, which shows rays converging at the specimen. Because the diffraction effect described in the section “Resolution” in this article will limit the resolution at the specimen to r_1 (given by Eq 4), it will not make any difference to the sharpness of the image if the object is anywhere within the range h shown in Fig. 11. Simple geometry then gives:

$$h = \frac{0.61\lambda}{\mu \sin\alpha \tan\alpha} \qquad \text{(Eq 5)}$$

from which it is evident that the only effective way to increase the depth of field is to decrease the convergence angle, which is controlled in most cases by the objective aperture, as Fig. 10 shows. Notice that conditions that maximize the depth of field simultaneously make the resolution worse (Eq 4).

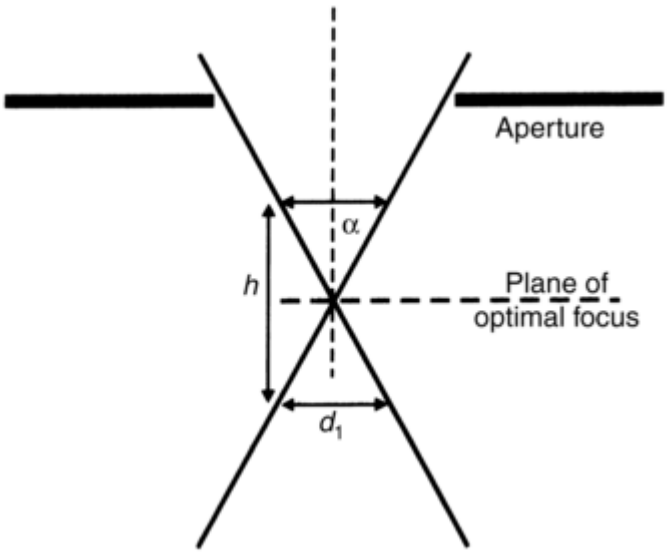

Fig. 11 The depth of focus of an optical system, *h*, is the distance from the plane of optimal focus within which the beam diverges by no more than the spot diameter d_1, d_1 will be limited by diffraction and aberrations.

For a light microscope, where α might be in the region of 45°, the depth of field is not very different from the resolution. Even if the objective convergence is limited to 5°, the depth of field will only be approximately 40 μm, while the resolution will then be limited to approximately 3 μm. For an electron microscope, the use of electrons for microscopy brings a number of advantages, among which are an improvement in both resolution and depth of field. The reason for this is that high-energy electrons have a much smaller wavelength than light, and the microscopes are usually operated with very small values of α.

A term that is often confused with depth of field is the *depth of focus*. This refers to the range of positions at which the image can be viewed without appearing out of focus, for a fixed position of the object. Depth of focus is often not as important as the depth of field to a microscopist but, in any case, tends to be larger, as the following calculation shows.

Equation 1 can be differentiated (for constant focal length) to give:

$$\frac{dv}{du} = \frac{-v^2}{u^2} = -M^2 \qquad \text{(Eq 6)}$$

This shows that *dv*, the effective shift in image position, is related to *du*, the change in position of the object, via the square of the magnification. The negative sign arises because the shifts are in opposite directions, which is of no concern here. Thus, if *du* is set to be the depth of field, calculated perhaps from Eq 5, the equivalent depth of focus is a factor M^2 bigger. At any reasonable magnification, the depth of focus will therefore be large, and at the high magnifications that are sometimes encountered in electron microscopy, it will be huge (often more than 10 m, or 33 ft). Microscopists should therefore experience little difficulty in positioning their viewing screen or photographic film.

P.J. Goodhew, J. Humphreys, and R. Beanland, Light and Electron Microscopy, *Metallography and Microstructures,* Vol 9, *ASM Handbook*, ASM International, 2004, p. 325–331

Light and Electron Microscopy

Peter J. Goodhew, University of Liverpool; John Humphreys, Manchester Materials Centre; Richard Beanland, Marconi Materials Technology

Aberrations in Optical Systems

In discussing resolution and depth of field, it has been assumed that all the components of the microscope are perfect and will focus the light from any point on the object to a similar unique point in the image. This, in fact, is rather difficult to achieve because of lens aberrations. The easiest lenses to make (for light) are those with spherical surfaces, but any single spherical lens suffers from two types of aberration: *chromatic* aberrations that depend on the spectrum of wavelengths in the light, and *monochromatic* or *achromatic* aberrations that affect even light of a single wavelength. The effect of each aberration is to distort the image of every point in the object in a particular way, leading to an overall loss of quality and resolution in the image. In order to correct these aberrations, it is necessary to replace the single lens in the figures with compound lenses containing several carefully shaped pieces of glass with different refractive indexes. Although this is not a correction technique that can be used in the electron microscope, the same types of aberration arise and are very important in determining the resolution of the instrument. Therefore, the most significant aberrations must be considered in more detail.

Chromatic aberrations occur when a range of wavelengths is present in the light (e.g., in white light) and arise because a single lens causes light to be deviated by an amount depending on its wavelength. Thus, a lens will have different focal lengths for light of different wavelengths. To take an extreme example, a red focus and a blue focus will be formed from white light. Figure 12 makes this clear in terms of ray paths and illustrates that wherever the image is viewed, a colored halo will surround each detail. For example, if the viewing screen is placed at A, the image of a point will appear as a bluish dot with a red halo, whereas if the screen were at B, the dot would be reddish with a blue halo. In neither case is a truly focused image of a small white dot formed. With the screen at the compromise position C, the smallest image is formed; however, it is not a point but a *disc of least confusion.*

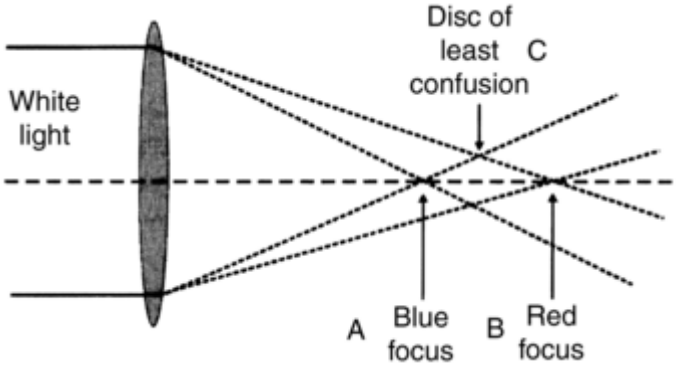

Fig. 12 Ray diagram illustrating the introduction of chromatic aberration by a single lens. Light of shorter wavelength (blue) is brought to a focus nearer the lens than the longer wavelength (red) light. The smallest focused spot is the disc of least confusion at C.

All aberration corrections are designed to reduce in size this disc of confusion. In the light microscope, there are two ways in which chromatic aberrations can be improved: either by combining lenses of different shapes and refractive indexes, or by eliminating the variation in wavelength from the light source by the use of filters or special lamps. Both methods are often used if the very best resolution is required.

Monochromatic aberrations arise because of the different path lengths of different rays from an object point to the image point. The simplest of these effects is *spherical aberration,* which is illustrated in Fig. 13. The portion of the lens furthest from the optical axis brings rays to a focus nearer the lens than does the central

portion of the lens. Another way of expressing this concept is to say that the optical ray path length from object point to focused image point should always be the same. This naturally implies that the focus for marginal rays is nearer to the lens than the focus for paraxial rays (those that are almost parallel to the axis). Again, a disc of least confusion exists at the best compromise position of focus.

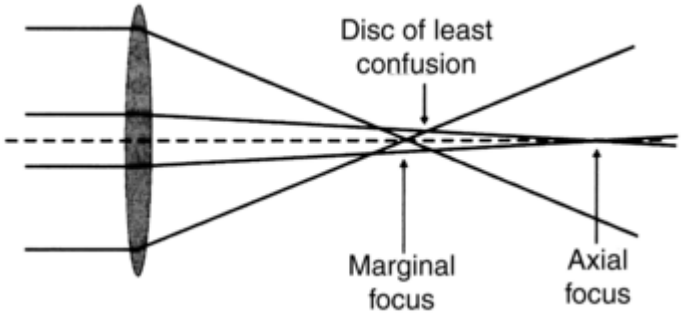

Fig. 13 Ray diagram illustrating spherical aberration. Marginal rays are brought to focus nearer the lens than near-axial rays.

A related effect is that of ***astigmatism.*** For object points off the optical axis, the path length criterion shows that there will be a focus for rays travelling in the horizontal plane at a different position from the focus for rays travelling in the vertical plane drawn in Fig. 2(a). A similar, but more serious, effect occurs if a lens does not have identical properties across the whole of its area. As an example, Fig. 14 shows the effect for a lens with slightly different properties in the horizontal and vertical planes. All the monochromatic aberrations are reduced if only the central portion of the lens is used, that is, if the lens aperture is "stopped down." Unfortunately, this limits the resolution of the microscope, as previously discussed.

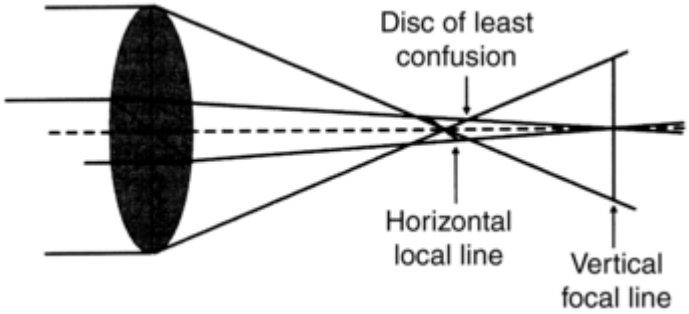

Fig. 14 Ray diagram illustrating the formation of astigmatism for a lens with slightly different optical properties in the horizontal and vertical directions. In this illustration, the lens is more powerful in the vertical plane.

Other aberrations are often discussed in textbooks on optics, but the three mentioned here are those of prime concern in electron microscopy. One further effect that is sometimes troublesome, particularly at low magnification, is distortion. This occurs if for some reason the magnification of the lens changes for rays off the optical axis. The two possible cases are when magnification increases with distance from the optical axis, leading to pincushion distortion, and when magnification decreases with distance from the optical axis, leading to *barrel* distortion (Fig. 15). These effects are obviously of great importance if measurements are to be made from micrographs, and manufacturers of both light microscopes and electron microscopes try to ensure that they are minimized.

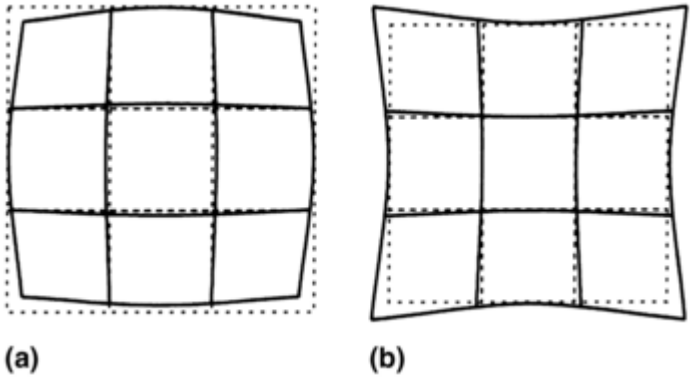

Fig. 15 The appearance of a square grid in the presence of (a) barrel and (b) pincushion distortion

P.J. Goodhew, J. Humphreys, and R. Beanland, Light and Electron Microscopy, *Metallography and Microstructures,* Vol 9, *ASM Handbook*, ASM International, 2004, p. 325–331

Light and Electron Microscopy

Peter J. Goodhew, University of Liverpool; John Humphreys, Manchester Materials Centre; Richard Beanland, Marconi Materials Technology

Electrons versus Light

In very many ways, electron optics is just the same as light optics—all the terminology used in this article applies, and ray diagrams can be used to illustrate the working of electron microscopes.

For many purposes, it is adequate to think of light as electromagnetic radiation with a wavelength λ and of electrons as subatomic particles. Both types of description (*wave* and *particle*) of course apply to both light and electrons; thus, light may be described in terms of photons or as radiation of wavelength 400 to 700 nm, while electrons can also be considered as radiation with wavelengths (useful in microscopy) between approximately 0.001 and 0.01 nm. The first obvious difference between electrons and light is that their wavelengths differ by a factor of many thousands. The implications of this for microscopy are immense but fortunately, in most cases, lead to a simplification.

Another major difference is that electrons are very much more strongly scattered by gases than is light. This is so severe an effect that in order to use electrons in a microscope, all the optical paths must be evacuated to a pressure of better than 10^{-10} Pa (approximately 10^{-7} of atmospheric pressure); the electrons would scarcely penetrate a few millimeters of air at atmospheric pressure.

Since the lenses in an electron microscope are merely magnetic fields, there is a negligible change of refractive index as the electrons pass through each lens. Hence, in electron-optical calculations, μ can be assumed to be unity. Furthermore, the angles through which the rays need to be deflected are generally very small (a few degrees), and the approximation sin α = tan α = α (Fig. 10, in radians) holds to a very high degree of accuracy. These simplifications mean that the theoretical resolution of the electron microscope (Eq 4) can be written as:

$$r_1 = \frac{0.61\lambda}{\alpha} \qquad \text{(Eq 7)}$$

which implies a resolution of approximately 0.02 nm, using reasonable values of λ = 0.0037 nm (the wavelength of 100 kV electrons) and α = 0.1 radians (approximately 5°). This is much smaller than the size of a single atom. Unfortunately, however, in the *transmission electron microscope* (TEM), this sort of resolution cannot be obtained because of the lens aberrations. Whereas in a light microscope it is possible to correct both chromatic and achromatic aberrations by using subtle combinations of lenses, this is very difficult using electron lenses and was only seriously attempted in the 1990s. Consequently, although chromatic aberrations

can be virtually eliminated by using electrons of a very small range of wavelengths, it is not possible to eliminate the monochromatic aberrations, principally spherical aberration. The only way of minimizing this is to restrict the electrons to paths very near the optical axis, that is, near the center of the lens, by using a small objective aperture. The importance of doing this can be seen from the equation for the degradation of resolution caused by spherical aberration in a lens of aberration coefficient, C_s:

$$r_2 = C_s\alpha^3 \qquad \text{(Eq 8)}$$

The use of a small aperture thus reduces spherical aberration but makes the diffraction-limited resolution worse. There is an optimal size of aperture (i.e., value of α) for which the net resolution is smallest. This can be calculated quite easily by assuming that the net resolution is given by $r = r_1 + r_2$ and minimizing r with respect to α. The result is:

$$\alpha_{opt} = 0.67\lambda^{1/4}C_s^{-1/4}$$
$$r_{opt} = 1.21\lambda^{3/4}C_s^{1/4} \qquad \text{(Eq 9)}$$

Under slightly different conditions, it turns out that the resolution can be improved, and the factor 1.21 can be reduced to as low as 0.7 in favorable circumstances. (Notice that a similar calculation is used, with an alternative derivation, to arrive at the resolution limit of the scanning electron microscope). Using the optimal aperture, it is now possible with a good TEM to resolve two points approximately 0.2 nm apart. This is approximately the separation of atoms in a solid.

Because it is necessary to keep α small in order to reduce the effect of spherical aberrations, electron microscopes always gain the advantage of a large depth of field. Equation 5 can be rewritten using the approximations appropriate to electrons as:

$$h = \frac{0.61\lambda}{\alpha^2} \qquad \text{(Eq 10)}$$

which shows that as α is reduced, the depth of field increases very rapidly. This is one of the major advantages of electron microscopy.

A further major difference between electrons and light is that electrons carry a charge. Not only does this mean that electromagnetic fields can be used as lenses for electrons, but it opens up the possibility of easily scanning a beam of electrons back and forth, as happens in a cathode ray tube or a television tube. The application of this approach has led to the development of the scanning electron microscope, which, over the past 35 years, has revolutionized attitudes to the study of surfaces.

With both types of electron microscope, transmission and scanning, the use of electromagnetic lenses and deflection coils means that it is possible to obtain an image of a specimen at any magnification within a wide range (say, up to 1,000,000×), without physically changing or moving lenses. Electron microscopy therefore offers higher resolution, higher magnification, greater depth of field, and greater versatility than the light microscope, albeit at a rather higher price.

G.F. Vander Voort, Light Microscopy, *Metallography and Microstructures,* Vol 9, *ASM Handbook,* ASM International, 2004, p. 332–354

Light Microscopy

George F. Vander Voort, Buehler Ltd.

Introduction

THE LIGHT OPTICAL MICROSCOPE remains the most important tool for the study of microstructure, despite the evolution of sophisticated electron metallographic instruments. Scanning electron microscopy (SEM) and transmission electron microscopy (TEM) are invaluable tools as well; however, they should be used in conjunction with light microscopy, rather than as a substitute. For more information on these methods, see the article "Scanning Electron Microscopy" in this Volume.

All examinations of microstructure should begin with use of the light microscope, starting at low magnification, such as 100×, followed by progressively higher magnifications for efficient assessment of the basic characteristics of the microstructure. Most microstructures can be observed with the light microscope and identified based on their characteristics. Identification of questionable or unknown constituents may be aided by observation of their hardness relative to the matrix, by their natural color, by their response to polarized light, and by their response to selective etchants. These observations are compared to known details about the physical metallurgy of the material being examined. If doubt still remains or if the structure is too fine to observe, more sophisticated techniques must be implemented.

General reviews on the use of the light microscope in metallography are given in Ref 1, 2, 3, 4, 5, 6, 7, 8, and 9.

With the equipment currently available, high-quality micrographs are easily produced. However, doing so requires careful attention to specimen preparation, etching, and use of the microscope. The specimen must be adequately prepared to ensure correct observation and interpretation of the microstructure without complications from artifacts due to sample preparation or etching. Specimen preparation is discussed in the Section, "Metallographic Techniques" in this Volume. Reproduction of false microstructures is all too common and a cause of inaccurate interpretations, rejection of good materials, and faulty conclusions in failure analyses.

The light microscope can be used to examine as-polished or etched metallographic specimens. Examination should be done before etching the specimen. Certain constituents are more readily observed as-polished because they are not obscured by etching detail. Inclusions, nitrides, certain carbides, and intermetallic phases can be readily observed without etching. Except for inclusions, the other phases may be more easily examined if some relief is introduced during final polishing. Specimens that respond to polarized light, such as materials with noncubic crystal structures, are generally examined without etching.

However, in most cases etching must be performed to observe the microstructure. A general-purpose etchant is normally used first to reveal the grain structure and the phases present, followed by selective etchants that attack or color specific phases of interest. Selective etchants are widely used for quantitative metallography, particularly if performed using an automated image-analysis device. In either case, etching must be carefully performed to reveal the microstructure with clarity.

References cited in this section

1. R.C. Gifkins, *Optical Microscopy of Metals,* American Elsevier, 1970
2. R.P. Loveland, *Photomicrography: A Comprehensive Treatise,* Vol 1 and 2, John Wiley & Sons, 1970
3. V.A. Phillips, *Modern Metallographic Techniques and Their Applications,* Interscience, 1971
4. J.H. Richardson, *Optical Microscopy for the Materials Sciences,* Marcel Dekker, 1971

5. H.W. Zieler, *The Optical Performance of the Light Microscope,* Microscope Publications Ltd., Part 1, 1972, Part 2, 1974

6. R.B. McLaughlin, *Accessories for the Light Microscope,* Microscope Publications, Ltd., 1975

7. R.B. McLaughlin, *Special Methods in Light Microscopy,* Microscope Publications, Ltd., 1977

8. H. Modin and S. Modin, *Metallurgical Microscopy,* Halsted Press, John Wiley & Sons, 1973

9. G.F. Vander Voort, *Metallography: Principles and Practice,* McGraw-Hill, 1984

G.F. Vander Voort, Light Microscopy, *Metallography and Microstructures,* Vol 9, *ASM Handbook*, ASM International, 2004, p. 332–354

Light Microscopy

George F. Vander Voort, Buehler Ltd.

Microscope Components

Light microscopes vary considerably in cost and capability. Reflected light is used for the study of metals. Transmitted-light microscopes are used to study minerals and polymers, which can also be examined using reflected light. Light microscopes are also classified as “upright” or “inverted”; these terms refer to the orientation of the light path to plane-of-polish of the specimen during observation (Fig. 1). Because each configuration has certain advantages and disadvantages, selection generally is based on personal preference.

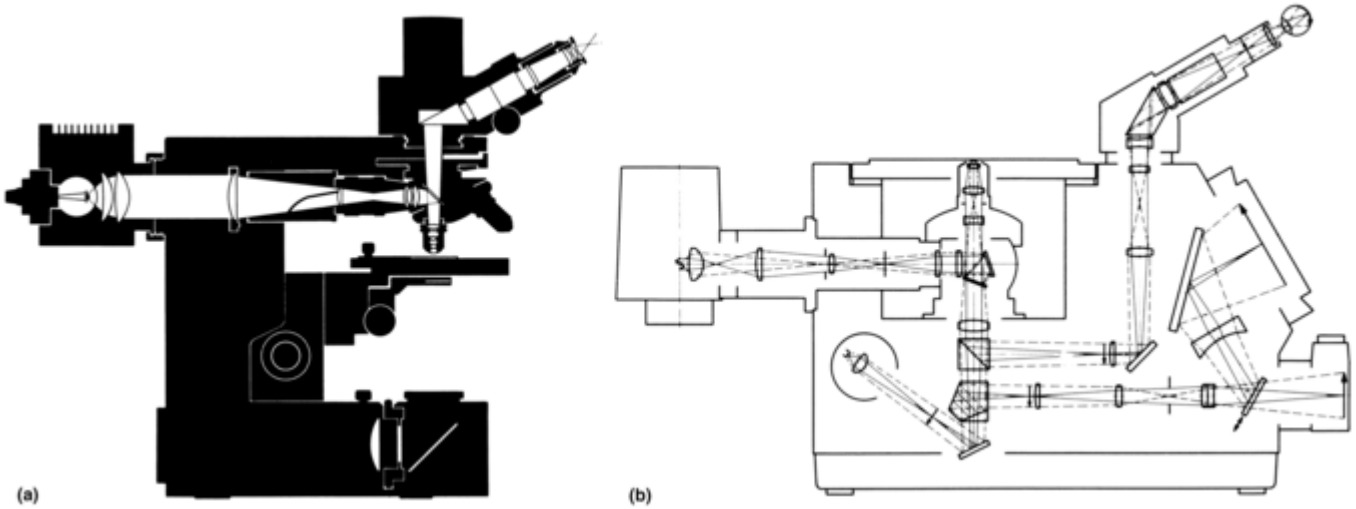

Fig. 1 Light paths in (a) an upright incident-light microscope and (b) an inverted incident-light microscope

Basic components of the light microscope are described below. The simplest light microscope is the bench type (usually upright). Examples of an upright and an inverted bench microscope are shown in Fig. 2. Photographic capabilities may include digital recording attachments or a bellows for the connection of a camera, depending on the rigidity of the stand and the size and weight of the camera. Figure 3 shows research-quality bench microscopes suitable for photographic work.

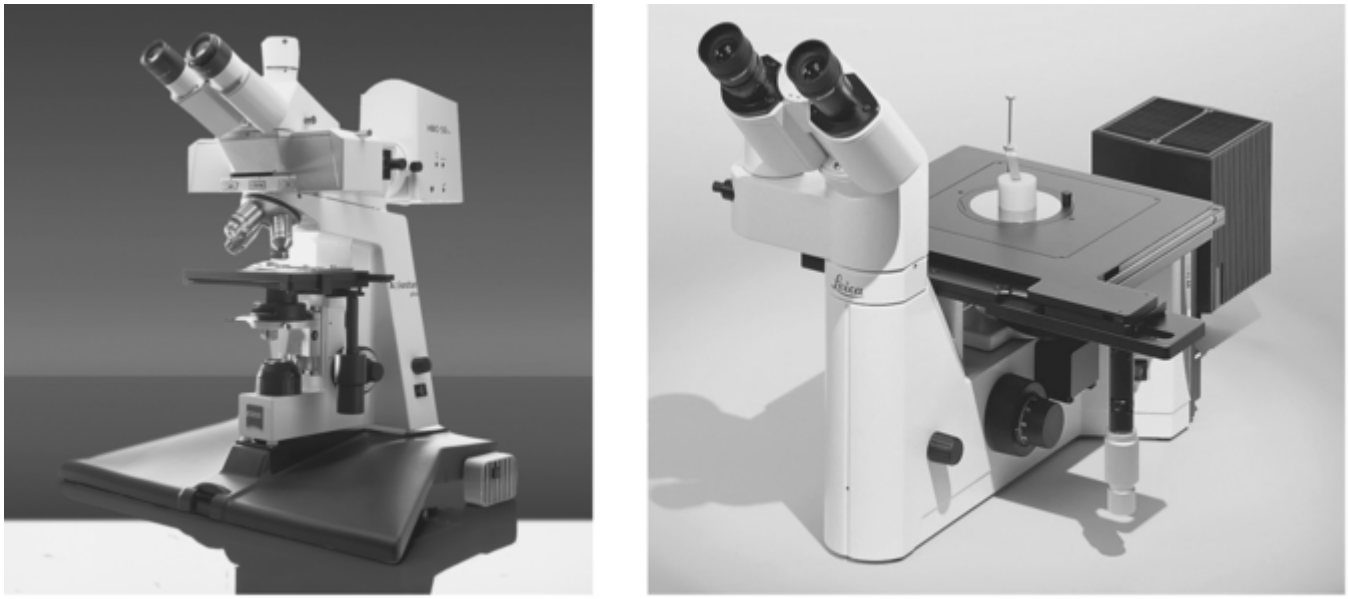

(a) (b)

Fig. 2 Upright (a) and inverted (b) bench-type microscopes. Courtesy of Carl Zeiss, Inc. and Leica, Inc.



(a) (b)

Fig. 3 Upright (a) and inverted (b) research-quality bench microscopes. Courtesy of Carl Zeiss, Inc. and Leica, Inc.

Various metallographs are available for visual observation, photomicrography, and image analysis of metallographic specimens. They include a high-intensity illuminating source, a microscope, and often capability for examination of specimen surfaces using polarized light, phase contrast, oblique illumination, dark-field illumination, and bright-field illumination. Metallographs can be rather simple units or full-scale research metallographs with assorted illumination modes, light sources, microhardness attachments, hot stages, and so on. An example of an inverted metallograph is shown in Fig. 4.

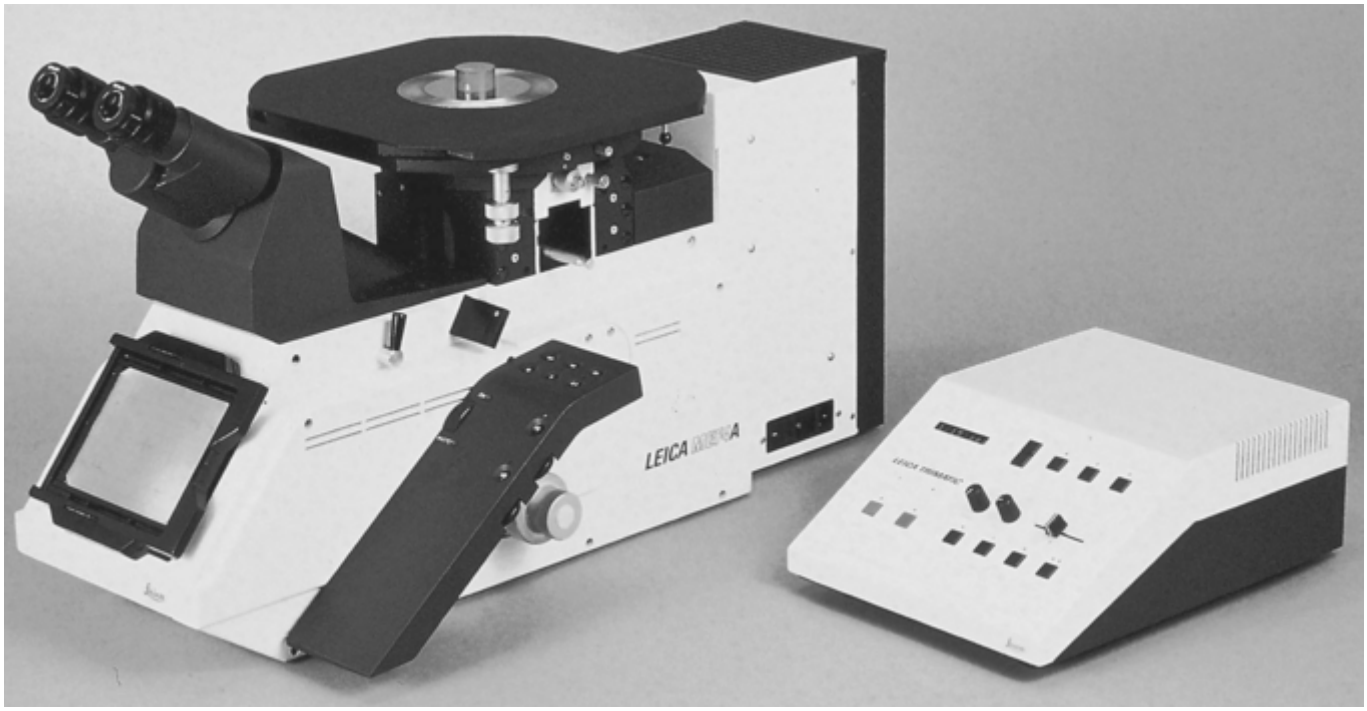

Fig. 4 Inverted metallograph. Features include selection of incident light, various contrasting methods, camera, and microhardness tester. Courtesy of Leica, Inc.

Illumination System

The illumination system for incident light microscopy consists of the lamp, lenses, filters, and diaphragms that are along the light path between the light source and the specimen. The control and interaction of these components is a consideration in achieving the optimal illumination of the specimen. Generally, a uniformly illuminated object field exactly the size of the field of view is desired. The light should be adjustable in intensity, color, and polarization.

In reflected light microscopes, special illumination techniques can be applied to reveal details of the microstructure even in the as-polished condition. These optical techniques (see the section “Examination Modes” in this article) include dark-field illumination, polarized light microscopy, phase contrast microscopy, and differential interference contrast, all of which use the Köhler illumination principle (Ref 1, 2, 3, 4, 5, 6, 7, 8, and 9) to provide uniform illumination of the microsection. A uniform light field at the object is desired, but the light source itself, such as a coiled filament is nonuniform.

The concept of the Köhler principle is illustrated in Fig. 5. The collector lens forms an image of the light source at the first condenser lens or at the illumination condenser aperture. The second condenser lens reproduces the image of the light source in the back focal plane of the objective lens after reflection of the light at the reflector (plane glass, half-silvered mirror, or prism). Therefore, the surface of the specimen is uniformly illuminated. The condenser lenses and the objective form an image of the radiant field stop in the plane of the specimen surface.

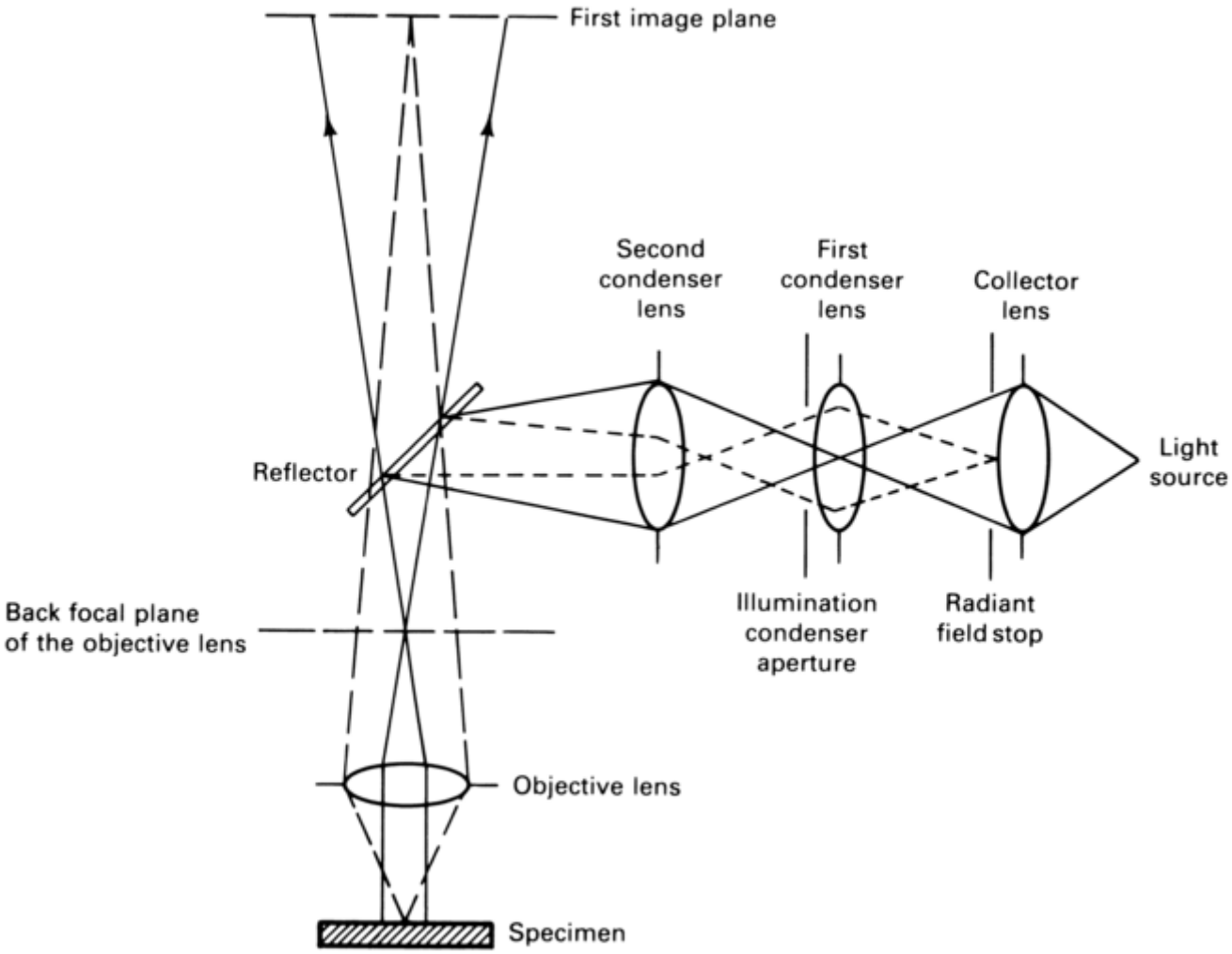

Fig. 5 The Köhler illumination principle in incident light microscopy

Light Sources. A variety of light sources are available for light microscopy. The low-voltage tungsten-filament lamp is used primarily with bench microscopes. The light intensity can be varied by controlling the power to the lamp according to need for observation. For photography, light sources in the 30 W range are inadequate. Carbon-arc illumination systems, once common on metallographs, have been replaced by arc or filament light sources. The xenon-arc light source is prevalent in older instruments (prior to 1980s) because of its high intensity and the daylight color of its emission spectra characteristics. Light intensity, however, can be adjusted only by the use of neutral-density filters.

Tungsten-halogen filament lamps (usually 100 W) are now widely used for their high intensity and high color temperature. Light intensity can be controlled by varying the current or by use of neutral-density filters. The color temperature of the light will shift as the applied voltage is varied, however. Lower voltages will lead to a shift toward red. Other light sources, such as the zirconium-arc, sodium-arc, quartz-iodine, or mercury-vapor lamps, are less common. Lasers are also used as light sources for scanning specimens, but the optical elements presented next apply to the classic light sources.

Collector Lens (Condenser). An adjustable lens free of spherical aberration and coma is placed in front of the light source to focus the light at the desired point in the optical path. A field diaphragm is placed in front of this lens to minimize internal glare and reflections within the microscope. The field diaphragm is stopped down to the edge of the field of view, so the size of the illuminated area is limited to the observed field to minimize stray light.

A second adjustable-iris diaphragm, the aperture diaphragm, is placed in the light path before the vertical illuminator. Opening or closing this diaphragm alters the amount of light and the angle of the cone of light entering the objective lens. The optimal setting for this aperture varies with each objective lens and is a compromise among image contrast, resolution, and depth of field. As magnification increases, the aperture diaphragm is stopped down. Opening this aperture increases image resolution, but reduces contrast; closing the aperture increases contrast, but diminishes image resolution. The aperture diaphragm should not be used for

reducing light intensity, but for adjusting contrast and resolution. Typically, the aperture diaphragm is 75% of the objective aperture. A simple procedure to check the aperture is to remove one eyepiece and observe the illuminated back aperture of the objective. By closing the aperture diaphragm, the illuminated field becomes smaller. It is rather easy to close down the aperture diaphragm to 75% of the possible field.

Light filters are used to modify the light for ease of observation, for improved photomicroscopy, or to alter contrast. Neutral-density filters are used to reduce the light intensity uniformly across the visible spectrum. Various neutral-density filters from approximately 85 to 0.01% transmittance are available. Most light microscopes offer at least two such filters.

Selective filters are used to balance the color temperature of the light source to that of the film. This is often necessary for faithful reproduction of color images, depending on the light source used and the film type. A green or yellow-green filter is widely used in black-and-white photography to reduce the effect of lens defects on image quality. Most objectives, particularly the lower-cost achromats, require such filtering for best results, as these objectives are not fully corrected for chromatic aberrations. Daylight filters are quite common to increases color temperature. In some applications, monochromatic filters are applied to increase sensitivity of detection (e.g., in phase difference measurements or with height measurements with interferometers).

Polarizing filters are used to produce plane-polarized light (one filter) or crossed-polarized light (two filters rotated to produce extinction) for examination of noncubic (crystallographic) materials. Materials that are optically anisotropic, such as beryllium, zirconium, α-titanium, and uranium, can be examined in the crossed-polarized condition without etching. A sensitive-tint plate (also called compensator plate, lambda plate, or gypsum plate) may also be used with crossed-polarized light to enhance coloration.

Optical Components

The choice of optics is always a compromise between cost and the need to minimize the effects of aberrations or errors in producing an image with an exact point-to-point representation of the object under view. Aberrations may be due to defects or to the inherent limitations of an optical system. The different types of aberrations include:

- Astigmatism
- Coma
- Distortion
- Chromatic aberration
- Lateral color
- Curvature of field
- Spherical aberration

These sources of aberration are discussed in the section “Optical Performance” in this article. It is impossible to completely remove all the source aberrations with an optical system, and removing or reducing the extent of aberrations can increase the complexity and costs of a lens systems. Thus, the choice of optics is a compromise of cost and viewing requirements.

The objective lens forms the primary image of the microstructure and is the most important component of the light microscope. It is the lens closest to the object of interest. It collects as much light as possible from the specimen and combines this light to produce the image. In reflected light microscopes, the condenser (or collector lens) and objective lens are the same.

The numerical aperture (*NA*) of the objective, a measure of the light-collecting ability of the lens, is defined as:

$$NA = n \sin \alpha \quad \text{(Eq 1)}$$

where n is the minimum refraction index of the material (air or oil) between the specimen and the lens, and α is the half-angle of the most oblique light rays that enter the front lens of the objective. Light-collecting ability increases with α. The setting of the aperture diaphragm will alter the *NA* of the condenser and therefore the *NA* of the system.

Objective lenses are usually mounted on a nosepiece turret that can accept four to six objectives. Older metallographs did not use nosepiece turrets, and only one objective at a time could be placed on the vertical illuminator using a bayonet mount. The vertical illuminator contains a reflector or prism that deflects the light down the objective onto the specimen surface. It usually holds the aperture and field diaphragms and filters as

well. The vertical illuminator usually provides only one or two types of illumination, such as bright-field and dark-field illumination or bright-field and polarized light illumination. However, universal vertical illuminators are now available that provide all types of illumination with one vertical illuminator and one set of objectives. Modern light microscopes are based on the principle of *infinity corrected optics*. In simple words, this means that the reflected light forms a parallel beam between the objective and the tube lens. This principle allows placement of reflectors, prisms, and other components in the vertical illuminator without altering the magnification or the formation of the secondary image in the eyepieces.

The tube length is the length of the body tube from the eye line of the eyepiece to the objective thread. This length is not standardized and can vary. Most objectives are designed for use with a certain tube length, generally 160 to 250 mm (6 to 10 in.) and generally cannot be interchanged without changing the total magnification of the optical system.

The most commonly used objective is the achromat, which is corrected for spherical aberration for one color (usually yellow-green) and for longitudinal chromatic aberration for two colors (usually red and green). Therefore, achromats are not suitable for color photomicroscopy, except at low magnifications. Use of a yellow-green filter and orthochromatic film yields optimal results for black-and-white photography. However, achromats do provide a relatively long working distance, that is, the distance from the front lens of the objective to the specimen surface. Modern optics design and manufacturing technology allows an increase of working distance for higher-quality objectives, as well. In addition, the parfocal distance of the objective is an even more important limiting factor for working distance. Working distance decreases as magnification of the objective increases. Most manufacturers make long-working-distance objectives for special applications, for example, in hot-stage microscopy. Achromats are strain free (or, due to fewer lenses, lower strain than “normal” plan objectives), which is important for polarized light examinations. Because they contain fewer lenses than other more highly corrected lenses, internal reflection losses are minimized.

Semiapochromatic or fluorite objectives provide a higher degree of correction of spherical and chromatic aberration. Therefore, they produce higher-quality images than achromats. The apochromatic objectives have the highest degree of correction, produce the best results, and are more expensive. Apochromatic lenses provide correction of color aberration for three primary colors and spherical correction for two colors. Apochromatic lenses are useful in color microscopy. These lenses are used now with infinity-corrected objectives, but not in the past, as some microscopes used a compensating eyepiece. With apochromatic lenses, all the aberrations are corrected in the objective and eyepiece correction is not needed. These lenses are useful when using digital cameras that do not require an eyepiece.

Flat-field, or plano-type, objectives correct for curvature of field, where the outer edges appear out of focus when the field of view appears focused in the center (Fig. 6). Field curvature occurs when a lens focuses on a rounded object. This problem may not be very noticeable in a good objective, and the human eye can adjust to some extent for this type of aberration. However, correction for flatness of field with plano objectives reduces eyestrain and are commonly found on modern microscopes. Flat-field objectives can be chromatic, semiapochromatic, or apochromatic with the complexity and cost increasing with more lens added for correction (Fig. 7). The barrel of the objective is coded as to the type of objective, its magnification, and numerical aperture. For example, Fig. 8 illustrates three plano-type objectives.

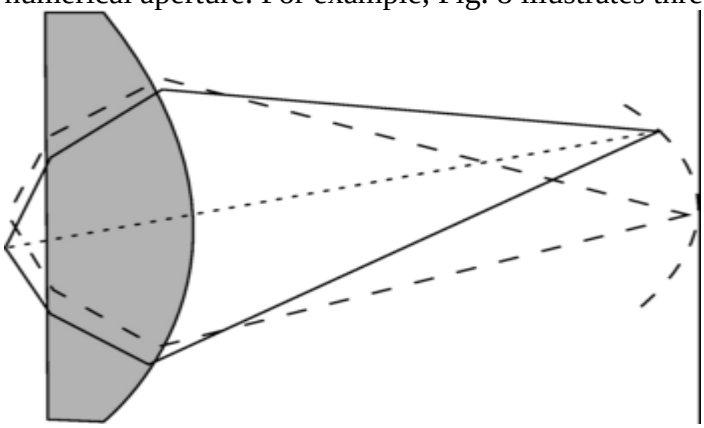

Fig. 6 Field curvature aberration. Even with correction of astigmatism, a plane object is imaged on a curved image surface whose radius of curvature roughly corresponds to the focal length of the objective. Source: Ref 10

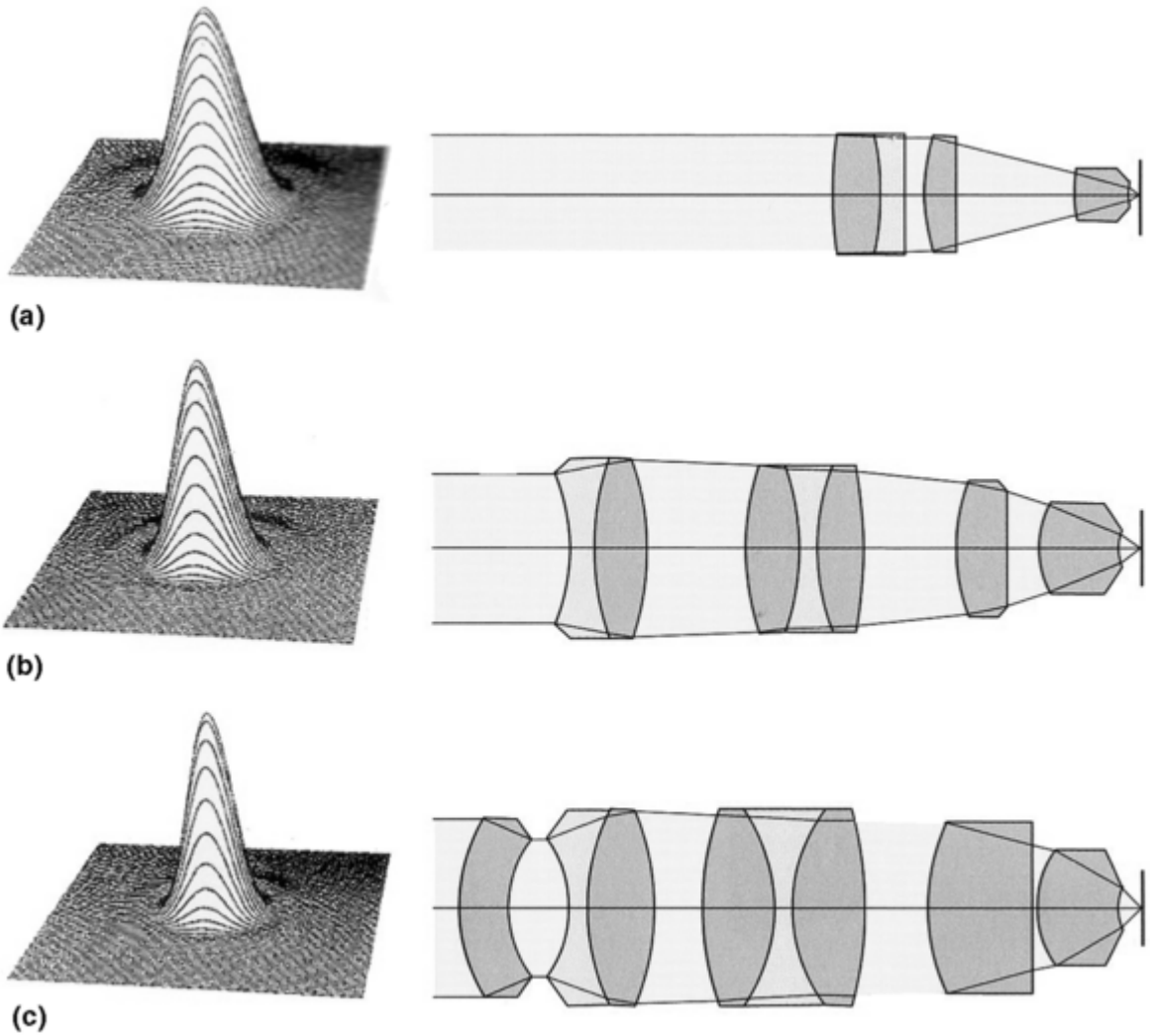

Fig. 7 Comparison of internal lens for objectives with increasing degrees of chromatic correction (a) achromatic, (b) semiapochromatic, and (c) apochromatic flat-field objectives. The point-spread plots (left) illustrate the gain in sharpness with increased correction. Adapted with permission from Leica Microsystems. Source: Ref 10

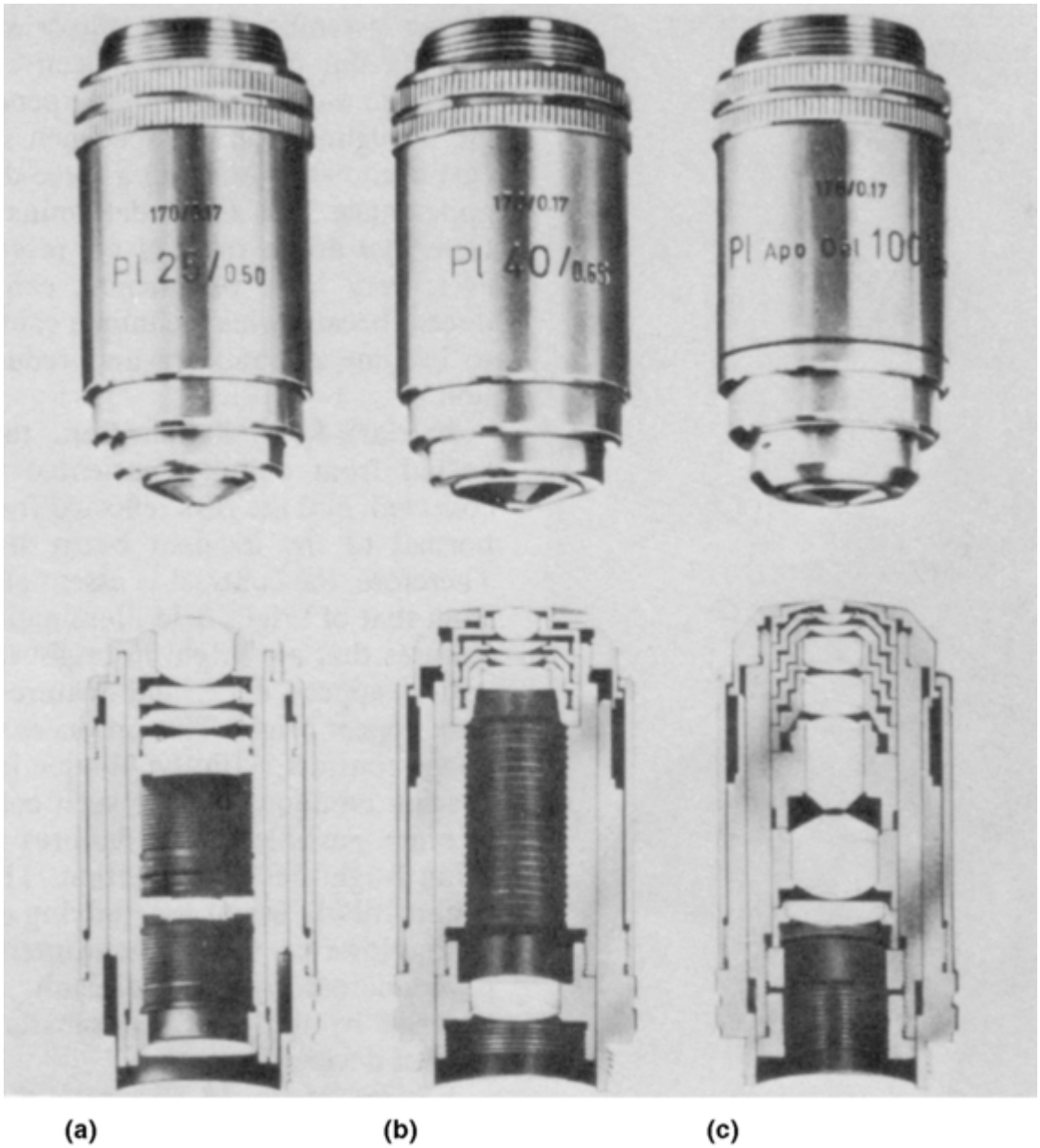

Fig. 8 Plano-type objective lenses and cross sections through each. The lens shown in (c) is a 14-element oil-immersion objective, with a numerical aperture (*NA*) of 1.32. Because the lens and specimen must be cleaned between each use, oil immersion is rarely used; it does provide higher resolution and a crisper image, which is valuable for examining low-reflectivity specimens. Courtesy of E. Leitz, Inc.

With parfocal lens systems, each objective on the nosepiece turret will be nearly in focus when the turret is rotated, preventing the objective front lens from striking the specimen when lenses are switched. Many objectives also are spring loaded, which helps prevent damage to the lens. This is more of a problem with high-magnification objectives, because the working distance can be very small.

Certain objectives are designed for use with oil between the specimen and the front lens of the objective. However, oil-immersion lenses are rarely used, because the specimen and lens must be cleaned after use. However, they do provide higher resolutions than can be achieved when air is between the lens and specimen. In the latter case, the maximum possible *NA* is 0.95; oil-immersion lenses produce a 1.3 to 1.45 *NA*, depending on the lens and the oil used. Magnifications from 25 to 160× are available. Use of oil also increases contrast and reducing glare of the image, which is valuable when examining low-reflectivity specimens, such as coal, polymers, or ceramics. Due to the higher *NA*, more light is collected, and therefore smaller differences in reflectivity of the specimen can be visualized. The dynamic range in the image is increased.

The eyepiece, or ocular, magnifies the primary image produced by the objective; the eye can then use the full resolution capability of the objective. The microscope produces a virtual image of the specimen at the point of

most distinct vision, generally 250 mm (10 in.) from the eye. The eyepiece magnifies this image, permitting achievement of useful magnifications. The standard eyepiece has a 24 mm diam field of view; wide-field eyepieces for plano objectives have a 30 mm diam field of view (Fig. 9), which increases the usable area of the primary image.

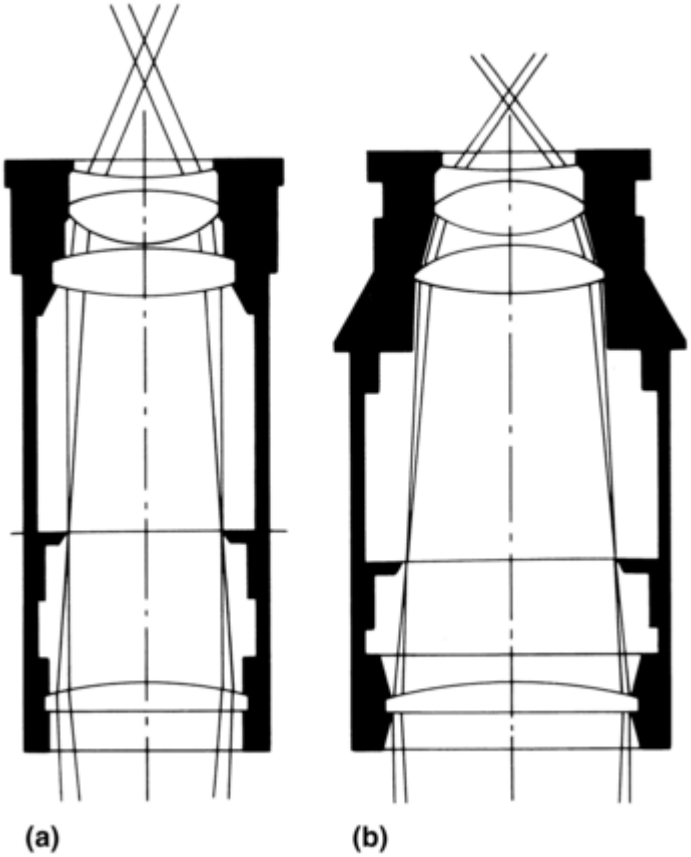

Fig. 9 Cross sections of typical eyepieces. (a) Standard (24 mm) field of view. (b) Wide (30 mm) field of view. The wide-field eyepiece increases the usable area of the primary image. Courtesy of E. Leitz, Inc.

The simplest eyepiece is the Huygenian, which is satisfactory for use with low- and medium-power achromat objectives. Compensating eyepieces are used with high *NA* achromats and the more highly corrected objectives. Because some lens corrections are performed using these eyepieces, the eyepiece must be matched with the type of objective used.

Eye clearance is the distance between the eye lens of the ocular and the eye. For most eyepieces, the eye clearance is 10 mm or less—inadequate if the microscopist wears glasses. Simple vision problems, such as nearsightedness, can be accommodated using the fine focus adjustment or the diopter adjustment provided with most eyepieces. Vision problems such as astigmatism cannot be corrected by the microscope, and glasses or contact lenses must be worn. High-eyepoint eyepieces are available to provide an eye clearance of approximately 20 mm necessary for wearing glasses (Fig. 10).

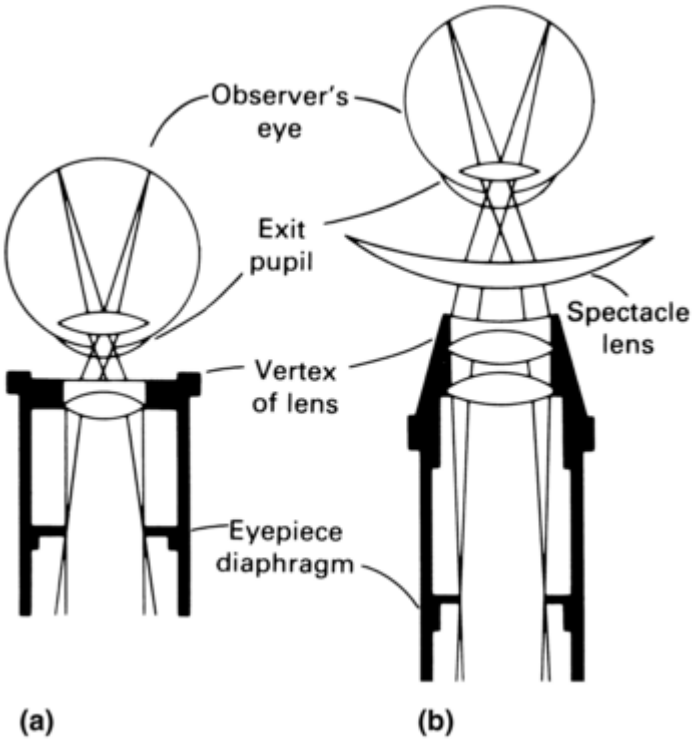

Fig. 10 Comparison between the position of the eye with (a) a standard eyepiece and (b) a high-point eyepiece. Eye clearance with a standard eyepiece is approximately 10 mm (0.4 in.); a high-point eyepiece allows clearances of approximately 20 mm (0.8 in.). Courtesy of E. Leitz, Inc.

Eyepieces are commonly equipped with various reticles or graticules for locating, measuring, counting, or comparing microstructures. The eyepiece enlarges the reticle or graticule image and the primary image. Both images must be in focus simultaneously. Special eyepieces are also produced to permit more accurate measurements than can be made with a graticule scale. Examples are the filar-micrometer ocular or screw-micrometer ocular.

A 10× magnification eyepiece is usually used; to obtain standard magnifications, some systems require other magnifications, such as 6.3×. Higher-power eyepieces, such as 12×, 15×, 20×, or 25×, are also useful in certain situations. The overall magnification is found by multiplying the objective magnification, M_o, by the eyepiece magnification, M_e. If a zoom system or bellows is also used, the magnification should be altered accordingly.

Mechanical Components

Stage. A mechanical stage is provided for focusing (upright microscopes) and moving the specimen, which is placed on the stage and secured using clips. On most inverted scopes, focusing is accomplished with the nosepiece and the objective while the stage is stationary. The stage of an inverted microscope has replaceable center-stage plates with different size holes. The polished surface is placed against the hole for viewing. However, the entire surface cannot be viewed, and at high magnifications it may not be possible to focus the objective near the edge of the hole due to the restricted working distance.

Using the upright microscope, the specimen is placed on a slide on the stage. Because the polished surface must be perpendicular to the light beam, clay is placed between the specimen bottom and the slide. A piece of lens tissue is placed over the polished surface, and the specimen is pressed into the clay using a leveling press. However, pieces of tissue may adhere to the specimen surface. An alternative, particularly useful with mounted specimens, is to use a ring instead of tissue to flatten the specimen. Aluminum or stainless steel ring forms of the same size as the mounts (flattened slightly in a vise) will seat on the mount rather than the specimen.

The upright microscope allows viewing of the entire surface with any objective, and the operator can see which section of the specimen is being viewed—a useful feature when examining specific areas on coated specimens, welds, and other specimens where specific areas are to be examined. Autoleveling stage holder for mounted specimens can eliminate leveling specimens on clay.

The stage must be rigid to eliminate vibrations. Stage movement, controlled by *x*- and *y*-micrometers (or coaxial knobs), must be smooth and precise; rack and pinion gearing is normally used. Many stages have scales for measuring the distances in the *x*- and *y*-directions, and some offer digital readout of these data. The focusing controls may contain rulings for estimating vertical movement. Some units have motorized stages and focus controls that allow automated movement of the sample often controlled by a PC and image-analysis programs.

A circular rotatable stage plate may facilitate polarized light examination. Such stages, common for mineralogical or petrographic studies, are graduated to permit measuring the angle of rotation. A rectilinear stage is generally placed on top of the circular stage.

Stand. Bench microscopes require a rigid stand, particularly if photomicroscopy is performed with the instrument. The various pieces of the microscope are attached to the stand when assembled. In some older instruments, the bench microscope is placed on a separate stand that also holds the photographic system.

References cited in this section

1. R.C. Gifkins, *Optical Microscopy of Metals,* American Elsevier, 1970
2. R.P. Loveland, *Photomicrography: A Comprehensive Treatise,* Vol 1 and 2, John Wiley & Sons, 1970
3. V.A. Phillips, *Modern Metallographic Techniques and Their Applications,* Interscience, 1971
4. J.H. Richardson, *Optical Microscopy for the Materials Sciences,* Marcel Dekker, 1971
5. H.W. Zieler, *The Optical Performance of the Light Microscope,* Microscope Publications Ltd., Part 1, 1972, Part 2, 1974
6. R.B. McLaughlin, *Accessories for the Light Microscope,* Microscope Publications, Ltd., 1975
7. R.B. McLaughlin, *Special Methods in Light Microscopy,* Microscope Publications, Ltd., 1977
8. H. Modin and S. Modin, *Metallurgical Microscopy,* Halsted Press, John Wiley & Sons, 1973
9. G.F. Vander Voort, *Metallography: Principles and Practice,* McGraw-Hill, 1984
10. K.-H. Schade, *Light Microscopy—Technology and Application,* 3rd ed., Verlag Moderne Industrie, 2001

G.F. Vander Voort, Light Microscopy, *Metallography and Microstructures,* Vol 9, *ASM Handbook,* ASM International, 2004, p. 332–354

Light Microscopy

George F. Vander Voort, Buehler Ltd.

Optical Performance

Image aberrations are a consequence of the laws of reflection and refraction. There is a strong relationship between the amount of aberration a lens will display, relative to its *NA.* Typically, optical aberration increases relative to the cubed power of the *NA.* If the diameter of a lens is increased, the theoretical resolution increases, while aberrations erode the image quality. This effect depends on the quality of the lens. High-quality objectives allow use of the full *NA.* For example, achromat lenses may be limited to about 70% of the *NA,* while apochromats allow use of 95% to 100% of *NA.*

Color aberration occurs because the focal length of the lens varies with lens refractive index, which depends on the wavelength of light. Therefore, focal length will change for different colors of light. A separate image for each wavelength present is focused at different distances from the lens (Fig. 11). This is longitudinal chromatic aberration. Moreover, magnification varies with focal length, altering the size of the image. This is lateral chromatic aberration (Fig. 12). The effects are apparent when color fringes are seen at the edge of the image detail. These differences must be eliminated to produce good color photographs. Because achromats have limited corrections for these problems, they must be used with yellow-green light filtering to obtain sharp images.

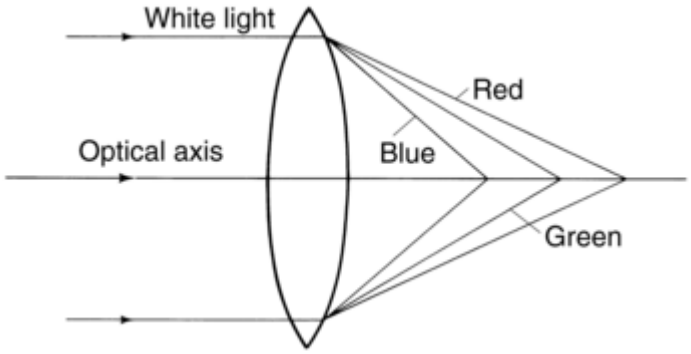

Fig. 11 Longitudinal chromatic aberration in an uncorrected lens. Different wavelengths cause each of the three primary colors to be focused at a different point along the optical axis.

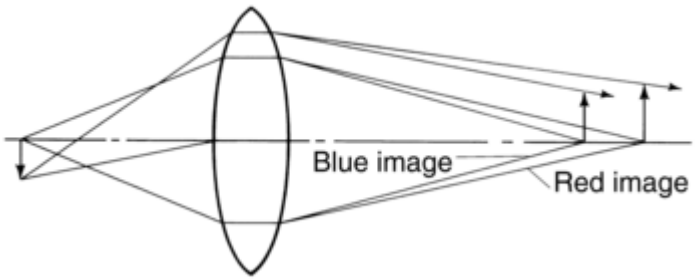

Fig. 12 Lateral chromatic aberration. As focal length is varied, magnification changes, altering image size.

Spherical aberration (Fig. 13) occurs when light from a point object on the optical axis is more strongly refracted at the center or at the periphery of the lens, producing a series of focal positions in which the point image appears as a circle of finite area. The result is no real point of a sharp focus. This can be minimized by using an aperture that restricts use of the objective to the central portion. Lens design also can correct part of this problem. A compensating lens may correct for this, but the correcting lens is only effective for a specific wavelength of color.

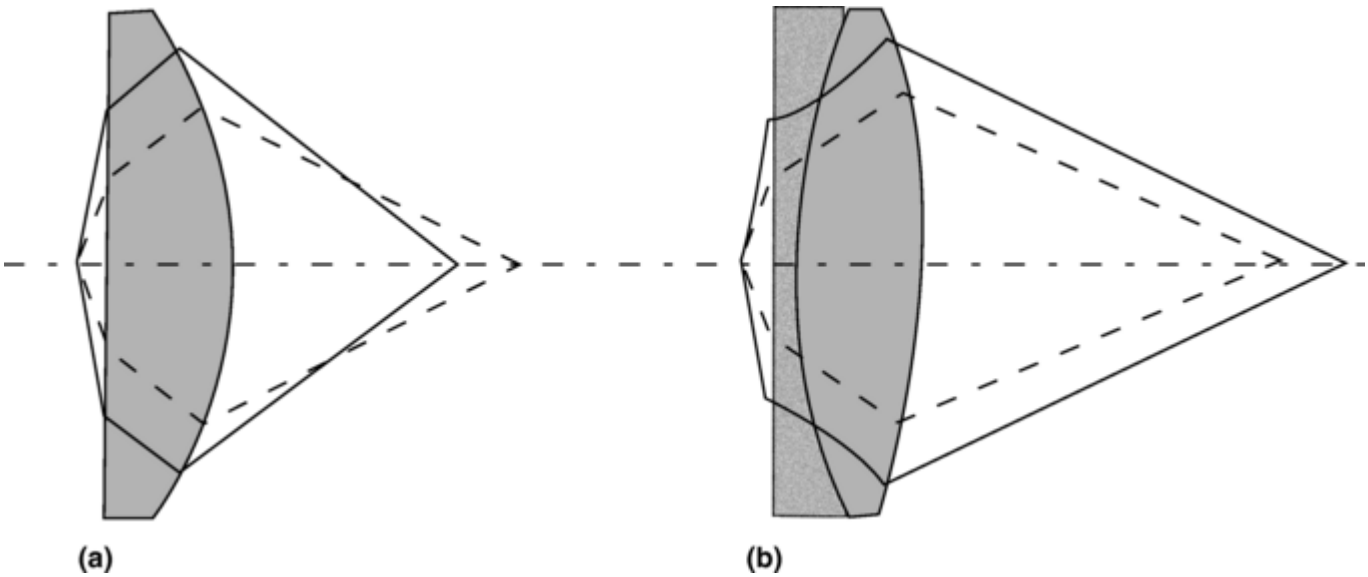

Fig. 13 Spherical aberration. Light rays passing through the outer portion of the lens are more strongly refracted than those passing through the central portion and are focused at a different point along the optical axis (a). This problem can be minimized by using an aperture to restrict the light path to the central part of the objective or with combinations of converging and diverging lens (b).

Because the image surface of optimal focus is curved, compensating eyepieces with equal but opposite curvature are used to produce a flat image (Fig. 14). In some instruments, this compensation is corrected in the objective and does not require further compensation. Other problems, such as coma and astigmatism (Fig. 15), can impair image quality unless corrected. Coma and astigmatism are defects because they can be eliminated by good design of the lens. If they occur, it is likely that the lens has been damaged.

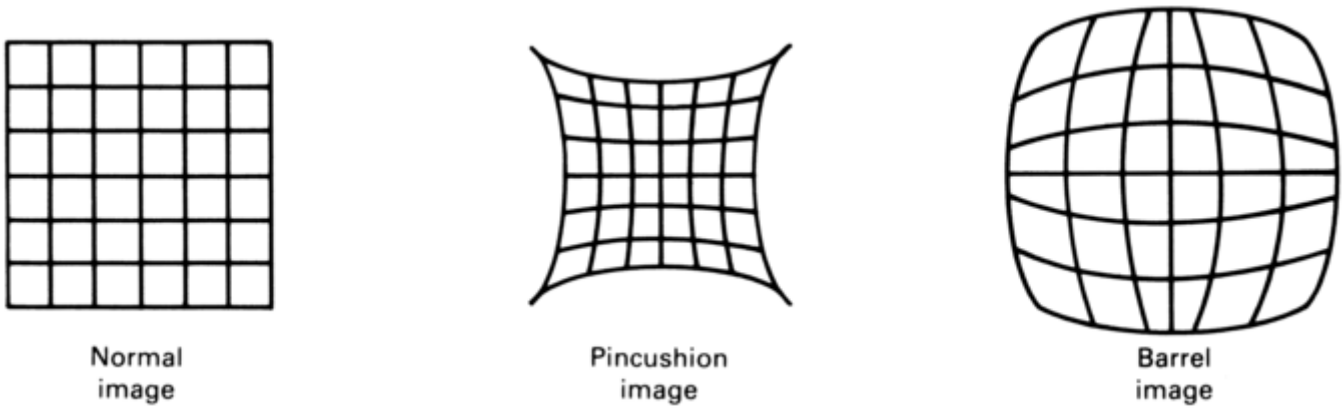

Fig. 14 Image distortions caused by curvature in the image surface of best focus. A compensating eyepiece, with a curvature equal to but opposite of that of the image surface, must be used to produce a normal image.

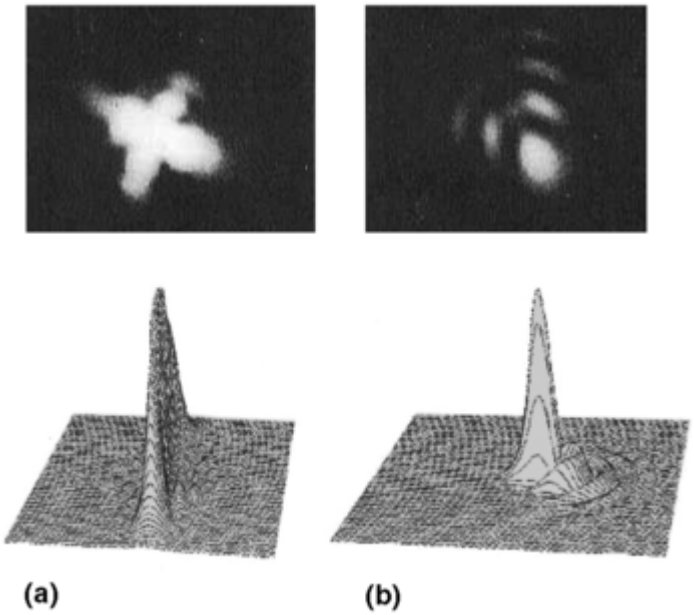

Fig. 15 Point density plots and black-white images of astigmatism (left) and coma (right). (a) The image of an off-axis point appears on two differently curved surfaces with astigmatism defect. (b) Coma is an asymmetrical spherical aberration of an off-axis point with an image that has cometlike tails.

Resolution. To see microstructural detail, the optical system must produce adequate resolution, or resolving power, and adequate image contrast. If resolution is acceptable but contrast is lacking, detail cannot be observed. In general, the ability to resolve two points or lines separated by a distance d is a function of the wavelength, λ, of the incident light and the numerical aperture, *NA*, of the objective:

$$d = k\lambda;t2/NA \qquad \text{(Eq 2)}$$

where k is 0.5 or 0.61. Figure 16 illustrates this relationship for k = 0.61 and four light wavelengths. Other formulas have also been reported (Ref 11). Equation 2 does not include other factors that influence resolution, such as the degree of correction of the objectives and the visual acuity of the microscopist. It was based on the work of Abbe under conditions not present in metallography, such as self-luminous points, perfect black-white contrast, transmitted-light examination, an ideal point-light source, and absence of lens defects (Ref 12).

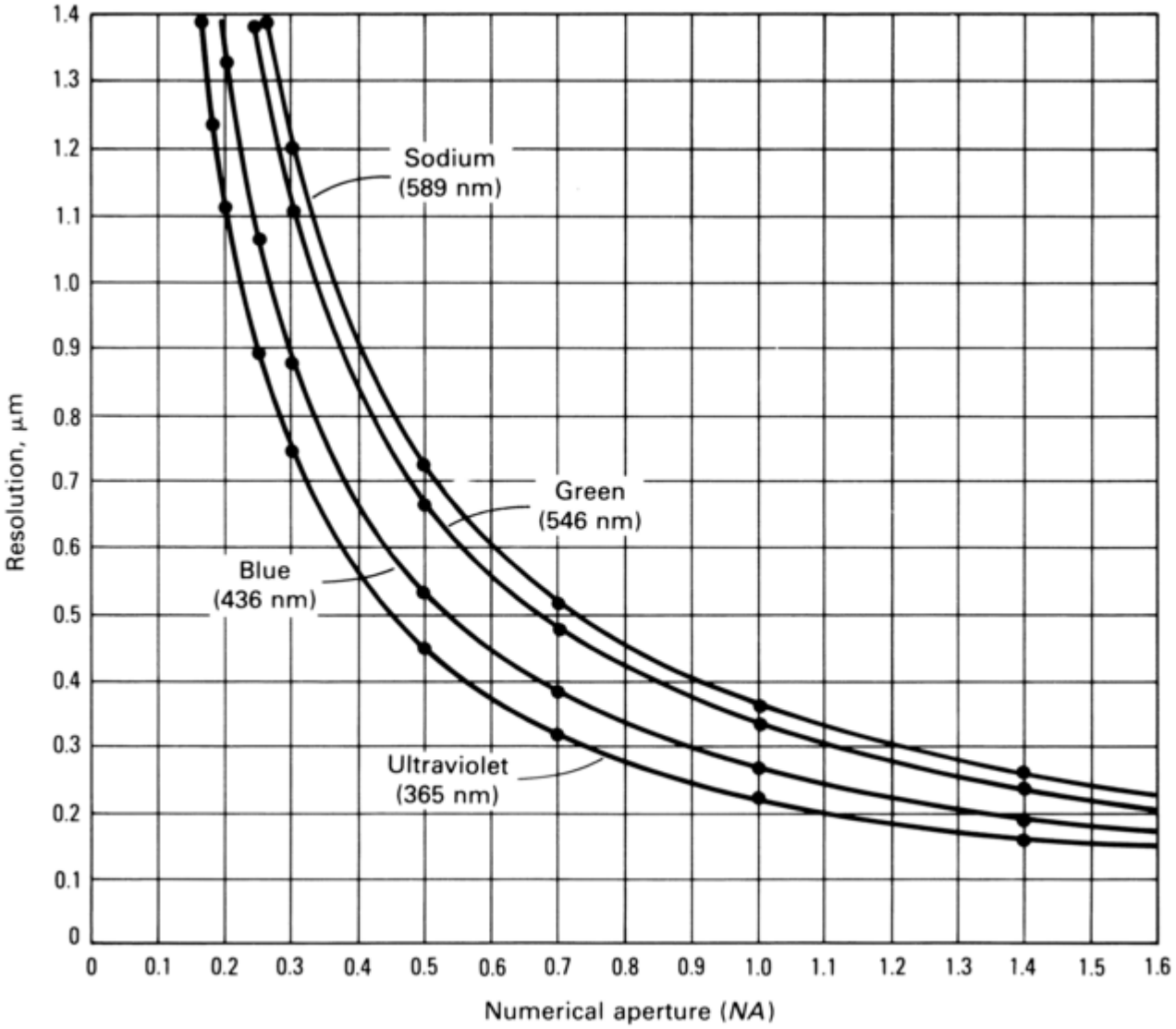

Fig. 16 Relationship between the resolution possible with an incident-light microscope and the numerical aperture of the objective lens used for four wavelengths of light

Using Eq 2, the limit of resolution for an objective with an *NA* of 1.4 is approximately 0.2 μm. To see lines or points spaced 0.2 μm apart, the required magnification must be determined by dividing the resolving power of the objective by the resolving power of the human eye, which is difficult to determine under observation conditions. Abbe used a value of 0.3 mm at a distance of 250 mm—the distance from the eye for optimal vision. For light with a mean wavelength of 0.55 μm, the required magnification is 1100 times the *NA* of the objective. This is the origin of the 1000 *NA* rule for the maximum useful magnification. Any magnification above 1000 *NA* is termed "empty," or useless.

Strict adherence to the 1000 *NA* rule should be questioned, considering the conditions under which it was developed, which are certainly far different from those encountered in metallography. According to the Abbe analysis, for a microscopist with optimal 20/20 vision and for optimal contrast conditions and a mean light wavelength of 550 nm, the lowest magnification that takes full advantage of the *NA* of the objective is 550 times the *NA.* This establishes a useful minimum magnification to use with a given objective. It has been suggested that the upper limit of useful magnification for the average microscopist is 2200 *NA*, not 1000 *NA* (Ref 12).

Depth of field, or depth of focus, is the distance along the optical axis over which image details are observed with acceptable clarity. Those factors that influence resolution also affect depth of field, but in the opposite direction. Therefore, a compromise must be reached between these two parameters, which becomes more difficult as magnification increases. This is one reason light etching is preferred for high-magnification examination. The depth of field, T_f, can be estimated from:

$$T_f = \frac{\lambda\sqrt{n^2 - NA^2}}{NA^2} \qquad \text{(Eq 3)}$$

where n is the refractive index of the medium between the specimen and the objective ($n \approx 1.0$ for air), λ is the wavelength of light, and *NA* is the numerical aperture. Equation 3 shows that depth of field increases as the *NA* decreases and when longer wavelength light is used, as shown in Fig. 17. Factors that improve the depth of field, however, reduce the resolution of the microscope.

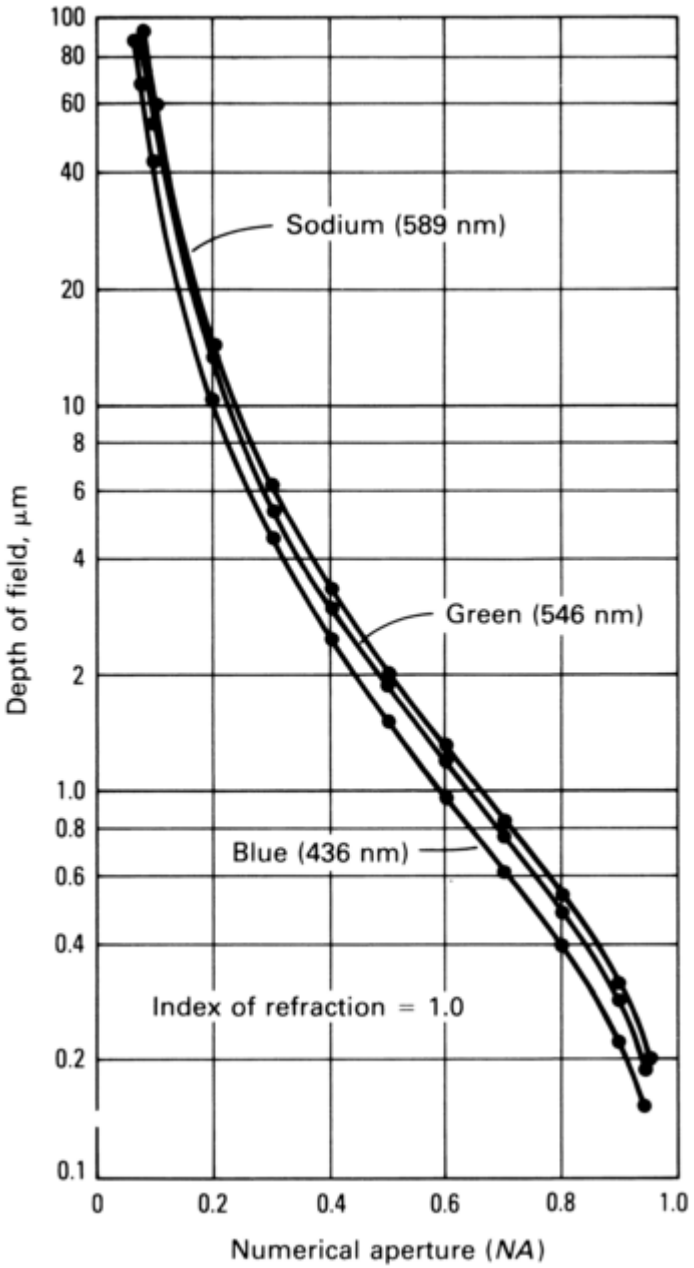

Fig. 17 Relationship among depth of field of the image produced, numerical aperture of the objective used, and wavelength of light employed

References cited in this section

11. H.W. Zieler, What Resolving Power Formula Do You Use? *Microscope,* Vol 17, 1969, p 249–270

12. C. Van Duijn, Visibility and Resolution of Microscopic Detail, *Microscope,* Vol 11, 1957, p 196–208

G.F. Vander Voort, Light Microscopy, *Metallography and Microstructures,* Vol 9, *ASM Handbook,* ASM International, 2004, p. 332–354

Light Microscopy

George F. Vander Voort, Buehler Ltd.

Examination Modes

To achieve the resolution capability of the selected objective, image contrast must be adequate. Image contrast depends on specimen preparation and optics. Differences in light reflectivity from the specimen surface produce amplitude features visible to the eye after magnification. Phase differences created by light reflection must be rendered visible by the use of interference-contrast attachments to the microscope.

Bright-Field Illumination. Bright-field vertical illumination, the most widely used method of observation, accounts for the vast majority of micrographs taken. In operation, light passes through the objective and strikes the specimen surface perpendicularly. Surface features normal to the incident light reflect light back through the objective to the eyepieces, where the surface features appear bright. Surfaces oblique to the light beam reflect less light to the objective and appear darker, depending on their angle.

Oblique Illumination. With some microscopes, it is possible to decenter the condenser assembly (aperture diaphragm) or the mirror so that the light passing through the objective strikes the specimen surface at a nonperpendicular angle. Roughness on the specimen surface will cast shadows, producing a three-dimensional (3-D) appearance. This allows determination of features that are in relief or are recessed. However, very little obliqueness can be introduced, because this technique causes lighting to become nonuniform and reduces resolution.

Dark-Field Illumination. The method of dark-field illumination is based on the effect of diffraction contrast, whereby light hitting the edge of an object bends and is diffracted out of the optical path. If the difference between the angle of incidence and half the aperture of the cone of light is larger than half the aperture angle of the objective, no regularly reflected light passes through the objective. This is realized in dark-field illumination (Fig. 18). Only those light rays deflected by diffuse scattering from their original direction toward the optical axis of the microscope are used for image formation. The light reflected from obliquely oriented features is collected, and the rays reflected from features normal to the incident beam are blocked. Therefore, surface regions perpendicular to the optical axis will appear dark, and angled surfaces will appear light.

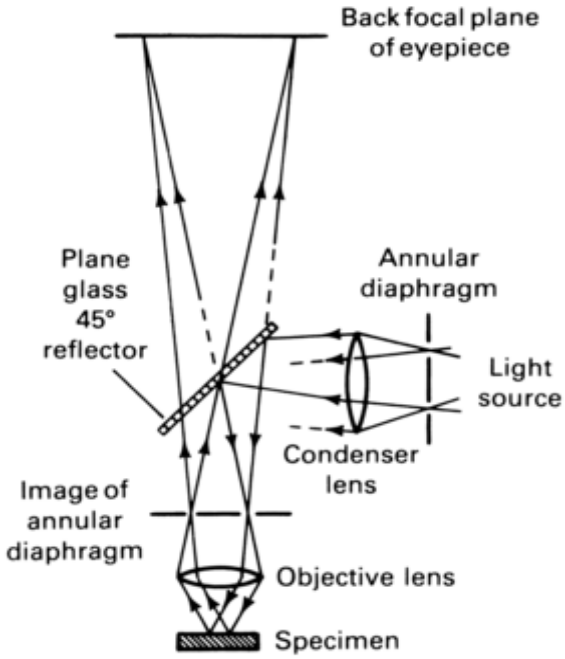

Fig. 18 Principles of dark-field illumination. Basic components of an opaque-stop microscope

Dark-field illumination produces contrast completely reversed from that obtained using bright-field illumination; that is, features that are bright in bright-field illumination appear dark, and features normally dark appear bright. This produces very strong image contrast, with the oblique features appearing luminous. Under such conditions, it is often possible to see features not visible using bright-field illumination. This method is particularly useful for studying grain-boundary structures. However, the low light intensity makes photomicroscopy more difficult, a problem lessened by the use of automatic exposure-control devices. With modern digital cameras, this is no longer a big issue. However, a camera capable of long exposure times (>10 s) should be used.

Dark-field illumination is applied to reveal cracks, pores, voids, and inclusions. Nonmetallic inclusions often undergo an intensive brightening by dark-field illumination. The surface quality of polished microsections can also be controlled using this method, because even very fine scratches and indications of relief formation are revealed. Figure 19 illustrates the value of dark-field illumination for examining grain structures. Figure 20 shows the eutectic in the copper-phosphorus system in bright-field, dark-field, and interference-contrast illumination. Note the strong contrast at the lamellae in dark-field. Figure 21 shows martensite formed in a copper-aluminum alloy using bright-field, dark-field, polarized light, and interference-contrast illumination. Note how the latter three illumination modes produce greater detail of the structure than bright-field illumination (even if the specimen is etched).

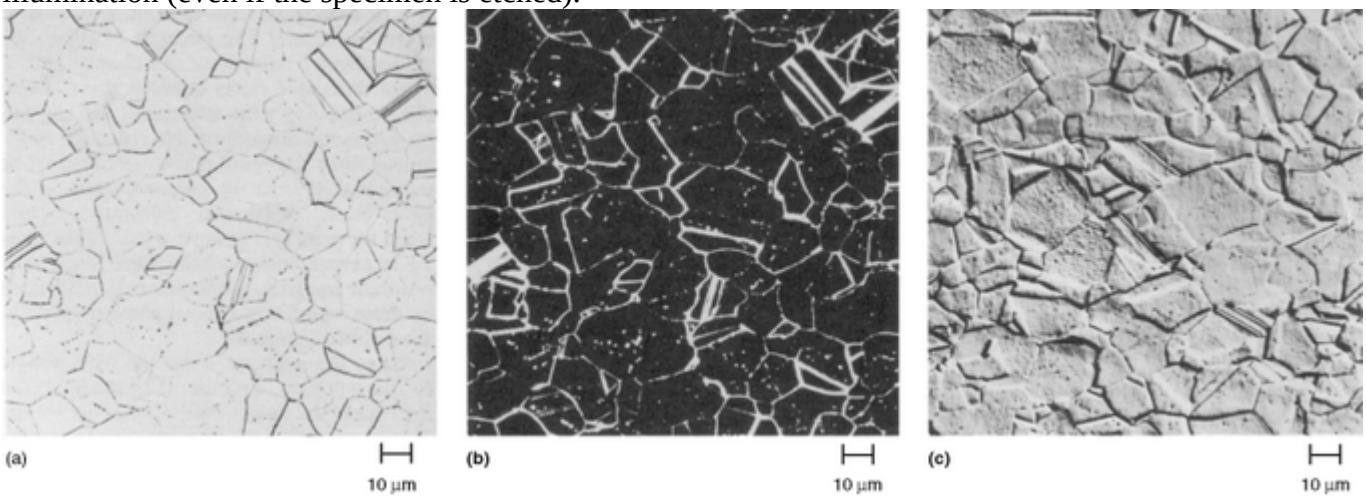

Fig. 19 Austenitic stainless steel (Fe-20Cr-33Ni-2.5Mo-3.5Cu and Nb + Ta), solution annealed. (a) Bright-field illumination. (b) Dark-field illumination. (c) Differential interference-contrast illumination. 15 mL HCl, 10 mL acetic acid, 10 mL HNO_3, and 2 drops glycerol. 400×

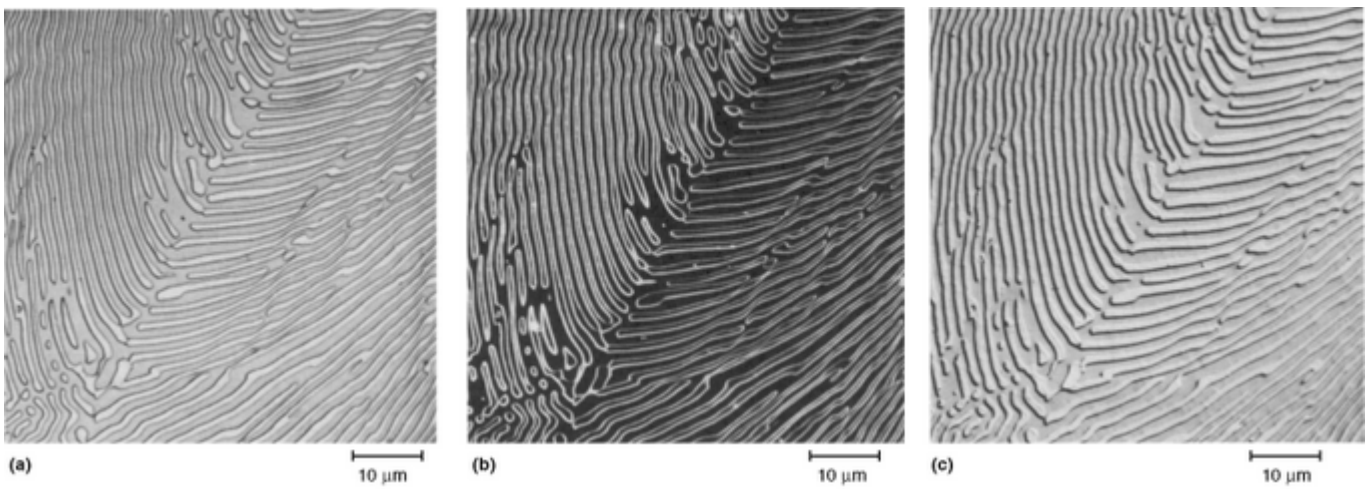

Fig. 20 Cu-8.9P sand cast alloy showing the α + Cu_3P eutectic. (a) Bright-field illumination. (b) Dark-field illumination. (c) Differential interference-contrast illumination. Swab etched using an aqueous solution of 3% $(NH_4)_2S_2O_8$ and 1% NH_4OH. 1000×

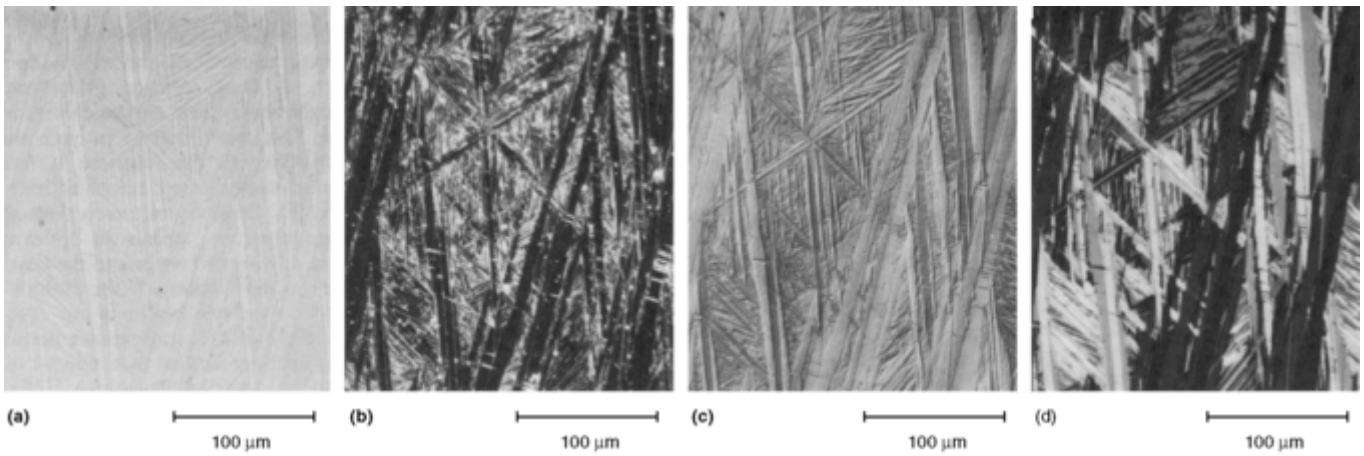

Fig. 21 Cu-11.8Al (aluminum bronze), heat treated, with martensite in the microstructure. (a) Bright-field illumination. (b) Dark-field illumination. (c) Differential interference-contrast illumination. (d) Crossed polarized light illumination. As-polished. 200×

Polarized light (Ref 13, 14, and 15), as used in metallography, has generally been limited to observation of certain optically anisotropic metals, such as beryllium, α-titanium, zirconium, and uranium, that are difficult to etch but respond well to polarized light when properly polished. Before development of the electron microprobe analyzer (EMPA) and energy-dispersive spectroscopy (EDS), polarized light examination was an integral part of the procedure for identifying inclusions. Since the development of these instruments, polarized light has been used less frequently for this purpose, because identification with the EMPA or EDS techniques is more definitive.

The basic arrangement for image enhancement by polarized light is shown in Fig. 22. Most metallurgical microscopes now use synthetic polarizing filters made of polymer films that are stretched in one direction to align the long chains of polymer molecules. The “polarizer” is placed in the light path before the objective. The “analyzer” is placed in the light path after the objective, generally just below the eyepiece or below the tube lens, to avoid strain from the eyepiece influencing the quality of polarization. The analyzer is normally in a crossed relationship regarding the polarizer, with the plane of polarization of the analyzer perpendicular to that of the polarizer.

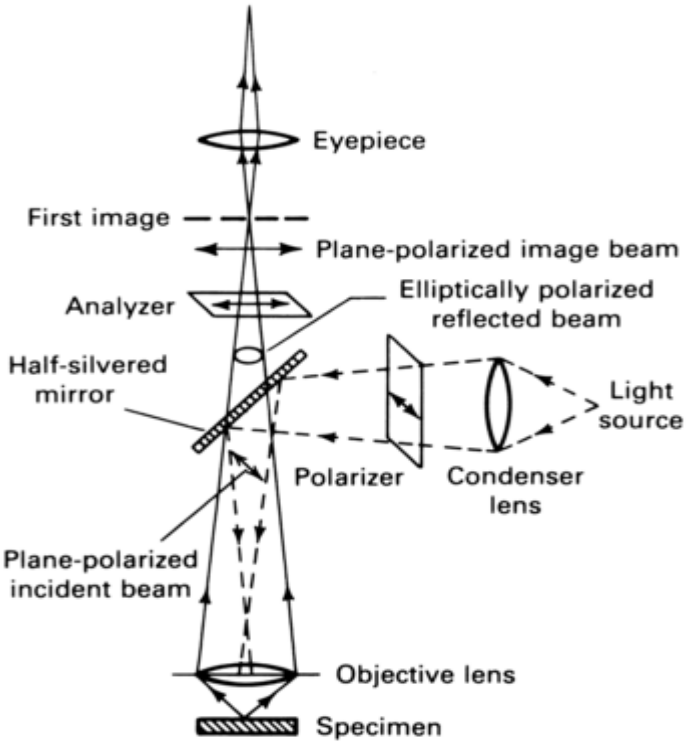

Fig. 22 Principles of polarized light microscopy

Application of this technique is based on the fact that optically anisotropic metals and phases reflect plane-polarized light as elliptically polarized light with a rotation of the plane of polarization. When light passes through a polarizing filter, the vibrations occur in only one plane in the direction of propagation, and the light is termed plane-polarized. This plane will change as the filter is rotated. When the analyzer filter is placed in the light path, plane-polarized light will pass through it if the plane of vibration of the light is parallel to the plane of vibration of the analyzer. If the plane of vibration of the analyzer is perpendicular to that of the light, the light will not pass through, and extinction results.

When plane-polarized light is reflected from the surface of an isotropic metal (any metal with a cubic crystallographic structure, such as iron) and then passes through the analyzer in the crossed position (plane of vibration perpendicular to that of the plane-polarized light), the image is extinguished, or dark. However, in practice, because the metallurgical microscopes with polarizing filters do not produce perfectly plane-polarized light, complete extinction will not occur. This is not a serious problem, because polarized light is used only in a qualitative manner in metallography.

Strain-free objectives, usually achromats, must be used. Fluorite or apochromatic objectives can be considered now, too, as modern production technology allows the assembly of fluorites and apochromatic objectives in a strain-reduced or even strain-free condition. Strain-free objectives are usually marked “SF,” “P,” or “POL.” Objectives for differential interference contrast (DIC) or Normarski (N or NIC) are so marked and normally offer a low level of strain and can be used for qualitative polarization microscopy. A strong white-light source is required to produce accurate color effects (for examples of color photomicrographs with polarized light, see Fig. 23, 24, 25, 26, 27, 28, and 29.

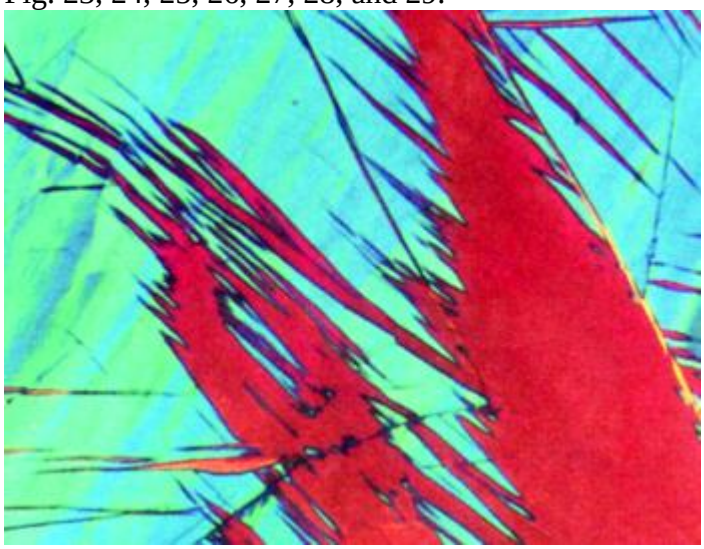

Fig. 23 Mechanically twinned hafnium weld. Specimen was attack polished and heat tinted (~400 °C, or 750 °F). Polarized light illumination. 60×. (P.E. Danielson)

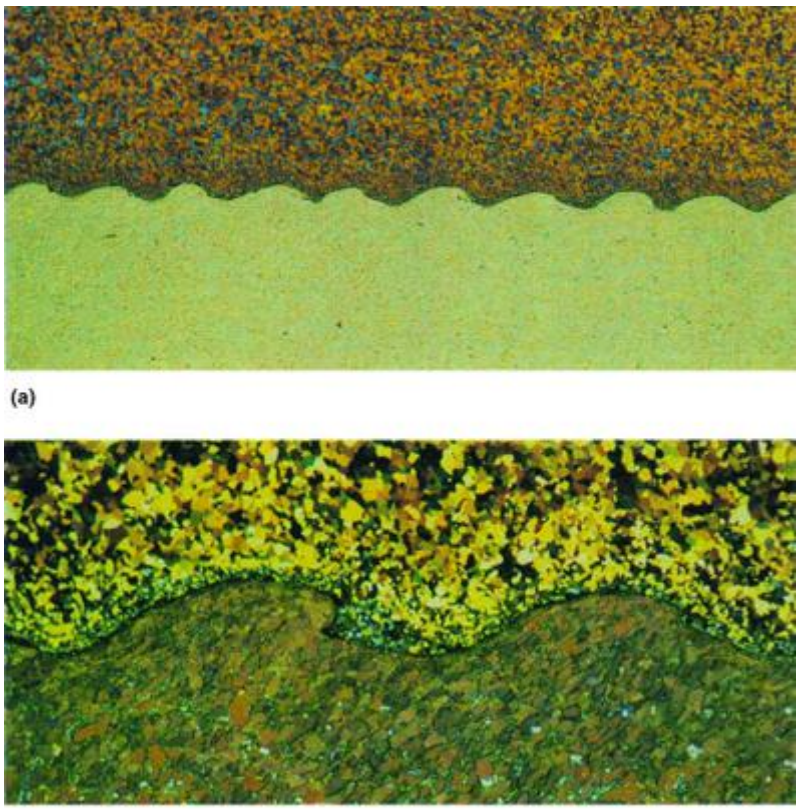

Fig. 24 Explosive-bonded 3.2 mm ($\frac{1}{8}$ in.) thick zirconium clad to 32 mm ($1\frac{1}{4}$ in.) thick carbon steel plate. Attack polished, swab etched with 97% methanol and 3% HNO_3, and heat tinted at 370 °C (700 °F). (a) Under bright-field illumination, the zirconium is brown-blue and shows some grain orientation. The steel is yellow-green. 15×. (b) Note the difference between the anisotropic zirconium (top) and the isotropic steel (bottom) under polarized light illumination. 85×. (P.E. Danielson)

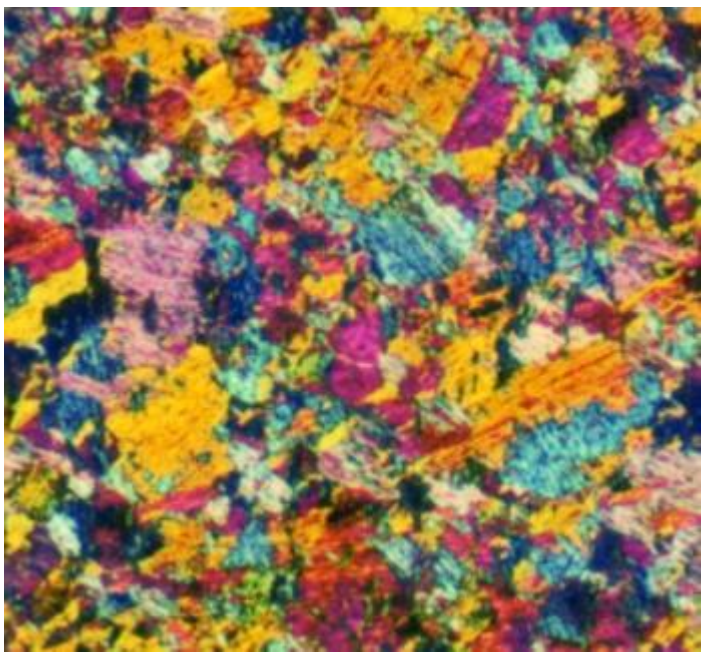

Fig. 25 Color etching (10% aqueous $Na_2S_2O_5$) revealed the lath martensite packet size of AF 1410 ultrahigh-strength steel that was heat treated (austenitized at 900 °C, or 1650 °F, water quenched, and tempered at 675 °C, or 1250 °F). Polarized light illumination. 100×. (G.F. Vander Voort)

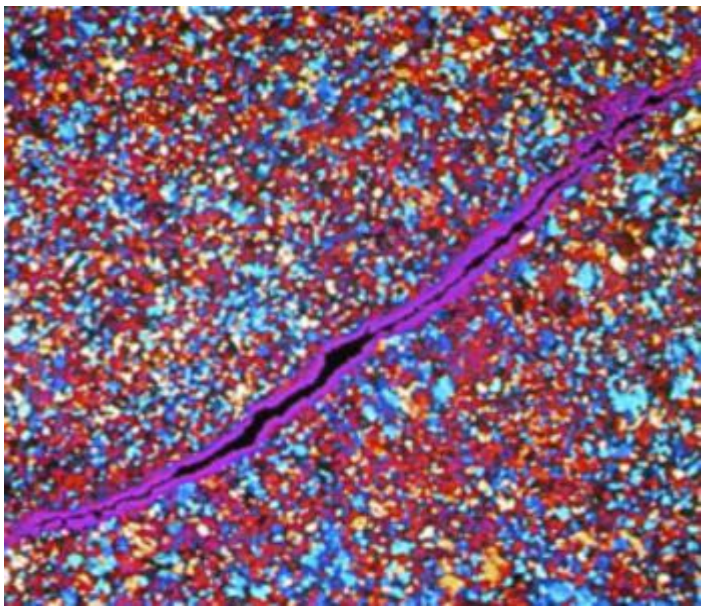

Fig. 26 Recrystallized Ti-6Al-4V alloy with a crack resulting from creep-rupture testing. Attack polished and color etched in 100 mL distilled H_2O, 4 mL HCl, and 3 g NH_4HF_2. Polarized light illumination. 100×. (G. Müller)

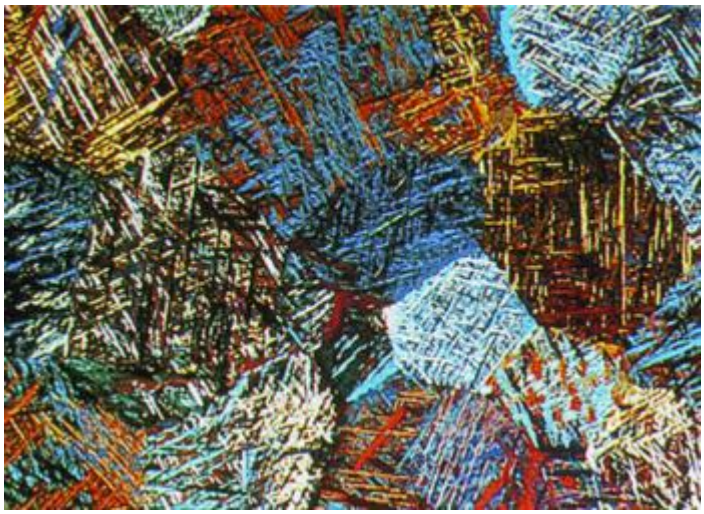

Fig. 27 Ti-6Al-4V alloy containing martensite needles formed at elevated temperature (>840 °C, or 1540 °F). Color etched in 100 mL H_2O, 4 mL HCl, 3 g NH_4HF_2. Polarized light illumination. 100×. (G. Müller)

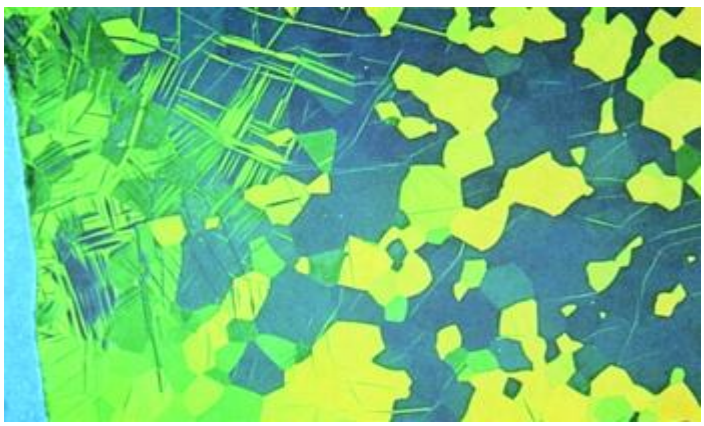

Fig. 28 Titanium alloy with a zone of mechanical deformation caused during shearing the specimen from an 8 mm (0.3 in.) diameter bar. The light-blue area on the side is mounting resin. Attack polished. Polarized light illumination. 200×. (G. Müller)

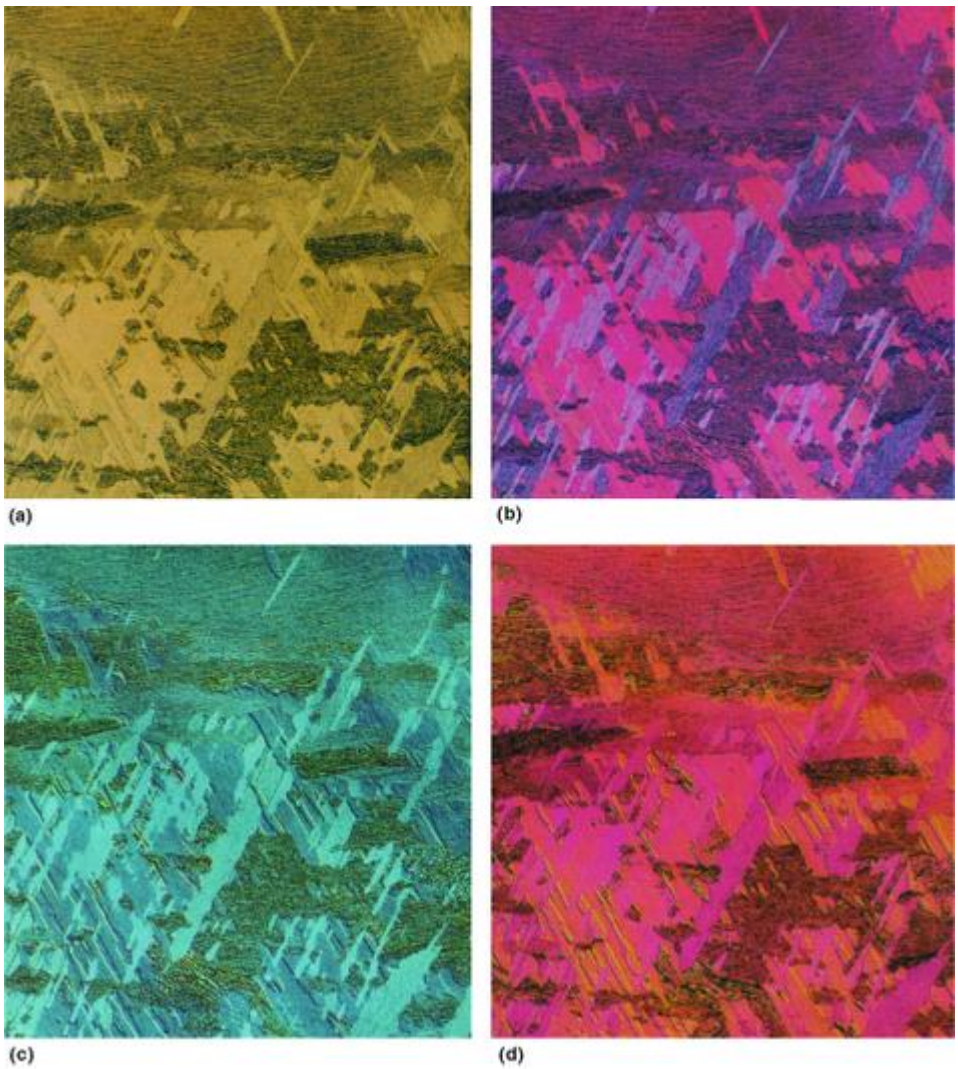

Fig. 29 Comparison of bright-field illumination (a), cross-polarized light (b), and differential interference contrast illumination (c and d) used to examine the basketweave pattern of an α-β Ti-6Al-4V alloy. Figures (c) and (d) illustrate the observation of reversed topography by adjusting the Wollaston prism. The same effect can be seen in Fig. 42 Kroll's reagent. 200×. (G.F. Vander Voort)

The quality of specimen preparation also is very important, and the surface must be perpendicular to the light path. Examination under polarized light requires well-polished microsections, because surface irregularities, smudges, and surface layers influence the state of polarization and may suppress anisotropic effects.

Anisotropic surface layers produced by chemical etching or by anodic oxidation of isotropic metals and metal alloys provide a stronger grain contrast when polarized light is used. For anisotropic material, an increase in grain contrast is observed when the surface of the polished microsection is coated with interference layers before examination under polarized light. A special application is the examination of polished cross sections of transparent resin, glass, or ceramic layers. Under polarized light, the inherent colors of these layers can be determined, and cracks or other flaws are revealed.

Image enhancement by polarized light is applied to anisotropic metals and to metal alloys containing anisotropic phases. Anisotropic metals include:

- Beryllium
- Bismuth
- Cadmium
- Magnesium
- Antimony
- Tin
- α-titanium

- α-uranium
- Zinc
- α-zirconium

Polarized light is used primarily for revealing grain structure (Fig. 30) and for distinguishing and identifying phases in multiphase alloys. Other uses include detecting preferred orientation in polycrystalline materials and identifying nonmetallic anisotropic inclusions in optically isotropic metal-matrix materials.

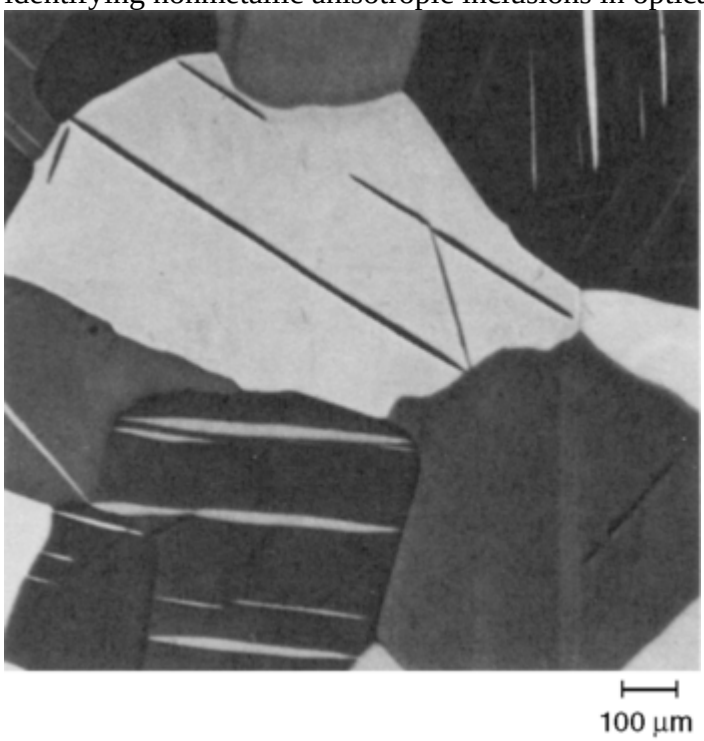

Fig. 30 Grains and deformation twins revealed by polarized light on an as-polished section of cast bismuth. 50×

When an optically anisotropic, polished metal is placed under the light beam with the polarizer and analyzer crossed, the microstructure will be revealed (Fig. 31). The anisotropic metal and phases react to polarized light and exhibit contrast effects under crossed polars as a variation in brightness and color. Rotation of the specimen under the beam changes light intensity and color. Because it may be difficult to set the polarizer and analyzer in the crossed position accurately when an anisotropic specimen is in place unless the crossed positions are marked on the polarizer and the analyzer, it is best to find this position first using an isotropic specimen or a mirror. An easy procedure to align the polarizers is to place a mirror on the stage, select a low power objective, adjust illumination (open aperture a bit wider than in normal work), and then cross polarizer and analyzer while observing the polarization cross in the eyepieces. To avoid misalignment, polarizer-analyzer components are equipped with fixing screws.

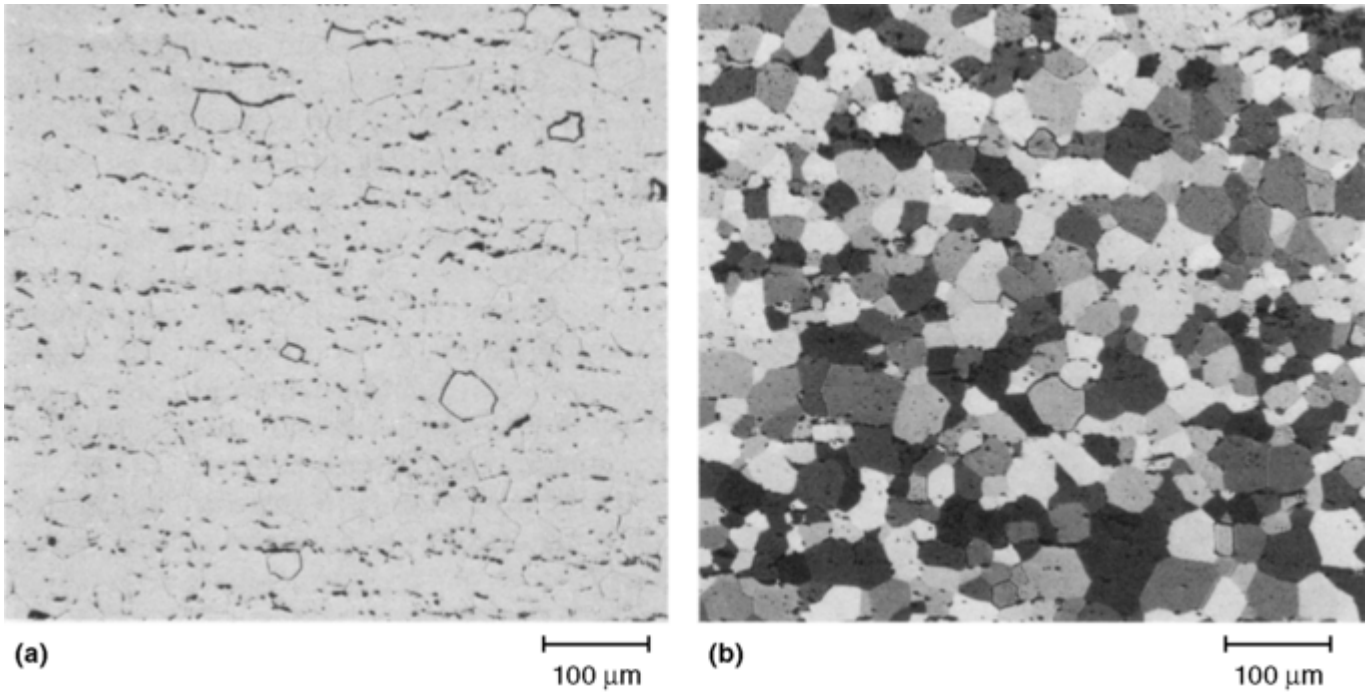

Fig. 31 Polycrystalline zirconium. (a) Bright-field illumination. (b) Crossed polarized light illumination. Chemically polished in 45 mL HNO_3, 45 mL H_2O_2, and 10 mL HF. 100×

When plane-polarized light strikes an anisotropic metal surface, reflection occurs as two plane-polarized components at right angles to each other. The directions vary with crystal structure. The strength of these two perpendicular reflections can change, and a phase difference exists between them. These differences vary with each metal and depend on the crystal orientation. No reflection is obtained when the basal plane of hexagonal or tetragonal crystals is perpendicular to the light beam. Maximum reflectance occurs when the principal symmetry axis of the crystal is perpendicular to the light beam. The resultant image is predominantly influenced by these orientation effects; phase differences are of little significance.

When the analyzer is crossed with respect to the polarizer, rotation of plane-polarized light from the anisotropic surface allows some light to pass through the analyzer, producing an image in which each grain has a different light intensity and color, depending on its crystal orientation relative to the light beam. As the stage is rotated, each grain changes four times in intensity from light to dark during a 360° rotation. If the phase difference is appreciable, the light will be elliptically polarized, the difference in intensity in each grain with rotation will be less, and extinction will not be observed. Color images are obtained when the reflected plane-polarized light varies with wavelength. When little color is present, a sensitive tint plate inserted between the polarizer and the objective may enhance coloration.

Isotropic metals can be examined using crossed-polarized light if the surface can be rendered optically active by etching, staining, or anodizing. Procedures have been developed for several metals (Ref 9); however, all etched surfaces do not respond to polarized light. Generally, the etch must produce etch pits or facets in each grain to cause double reflection at these features. Grains with different crystal orientations produce differently oriented pits or facets, yielding different degrees of elliptical polarization and therefore varying light intensity.

Anodizing may produce a thick oxide film on the specimen surface; irregularities in the film lead to double reflection. Although the polarization response of anodized specimens has been attributed to optical anisotropy of the film, experimentation has shown that the effect is due to surface irregularities (Ref 16). Tint etchants produce surface films that result in interference colors that can be enhanced using polarized light. In general, best results are obtained when the analyzer is shifted slightly from the crossed position.

In addition to its use in examining inclusions, anisotropic metals (antimony, beryllium, bismuth, cadmium, cobalt, magnesium, scandium, tellurium, tin, titanium, uranium, zinc, and zirconium, for example), and etched/anodized/tint-etched cubic metals, polarized light is useful for examination of coated or deformed metals. Phase identification may also be aided in some cases. The internal structure of graphite nodules in cast iron is vividly revealed using polarized light (Fig. 32). Martensitic structures are frequently better revealed

using polarized light, as shown in Fig. 33, which illustrates lath martensite in a high-strength iron-base alloy, AF 1410.

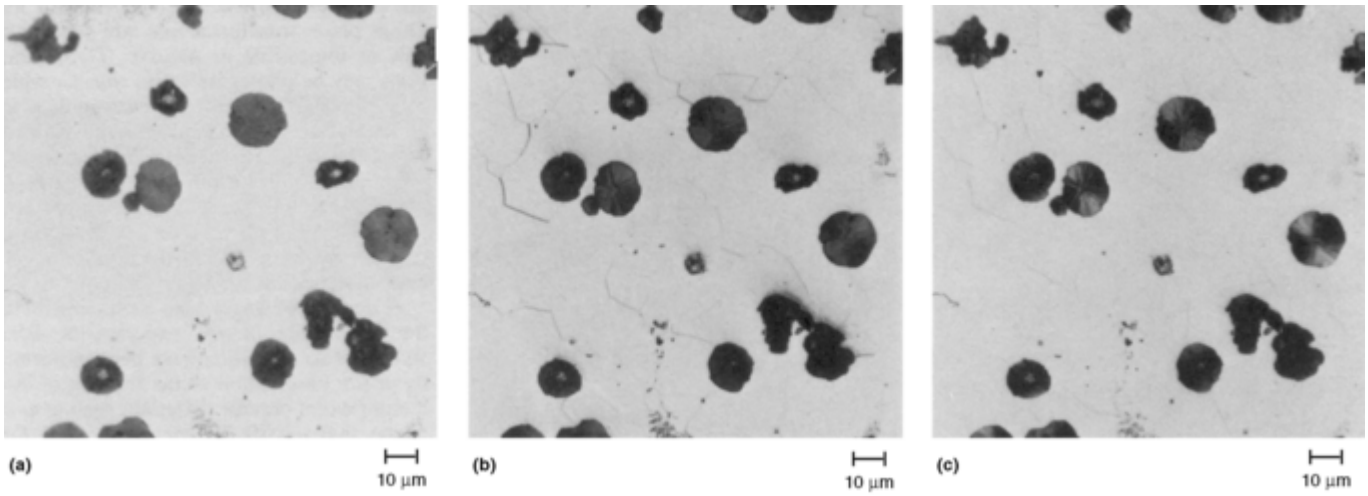

Fig. 32 Graphite nodules in cast iron. (a) Bright-field illumination. (b) Differential interference-contrast illumination. (c) Crossed polarized light illumination. 2% nital. 400×

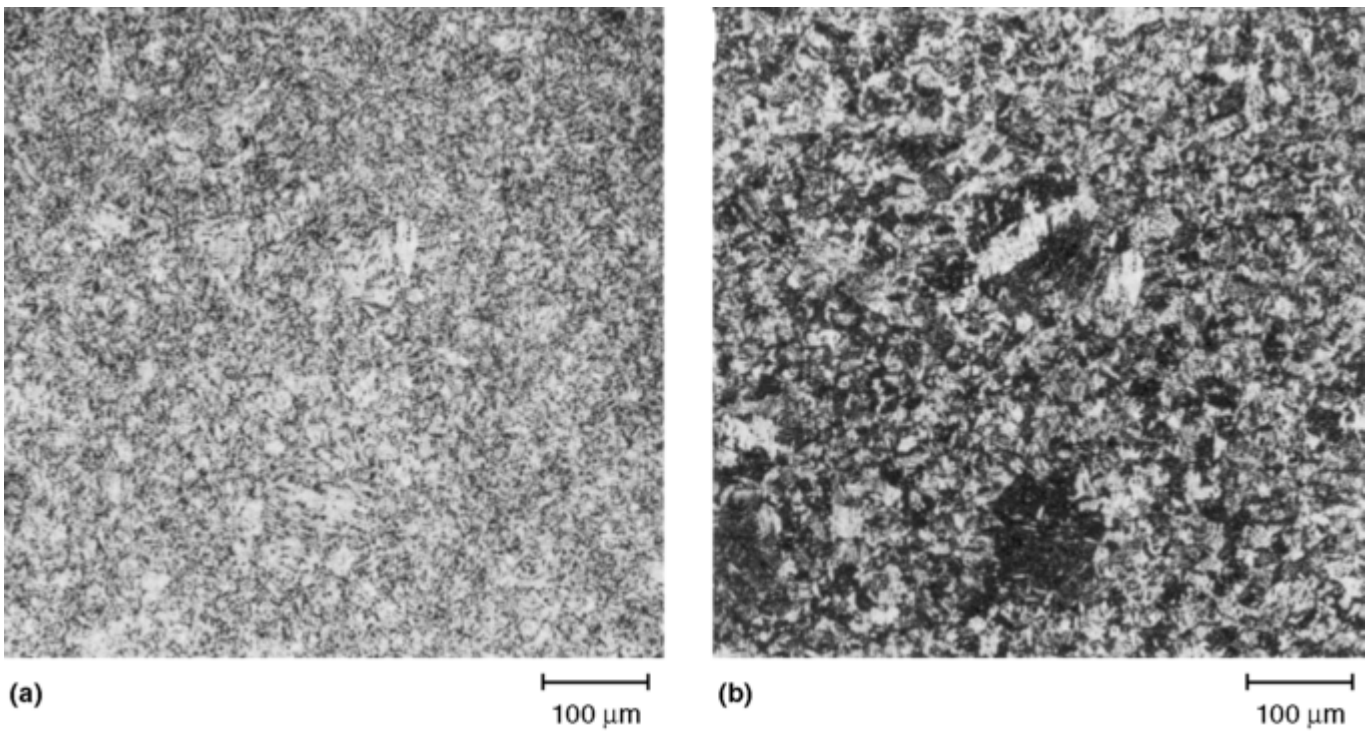

Fig. 33 AF 1410 alloy steel. (a) Highly tempered lath martensite is difficult to study under bright-field illumination. (b) Crossed polarized light reveals the packet size by contrast differences. Tint etched in 10% $Na_2S_2O_5$. 100×

Circularly polarized light is used in conjunction with differential interference contrast (C-DIC) techniques to enhance contrast. The structure is enhanced without the need to rotate the specimen. With circularly polarized light and total interference contrast (TIC) technique, instruments can measure specimen profiles in the nanometer range. Figure 3(a) shows an example of a research-quality microscope with C-DIC capability.

Sensitive tint, another important application of polarized light, is used to study materials that are weakly birefringent, that is, slightly responsive to polarized light. This is achieved by placing a special retardation plate (crystal quartz) into the optical path with the polarizer and analyzer (Fig. 34). Studies of this kind are accomplished by observing any change in the magenta tint as the specimen is rotated. Sensitive tint has been used to study anodized aluminum specimens, to detect pores in commercial graphite, and to determine grain orientation. Small structural differences not apparent in polarized light may be enhanced using sensitive tint.

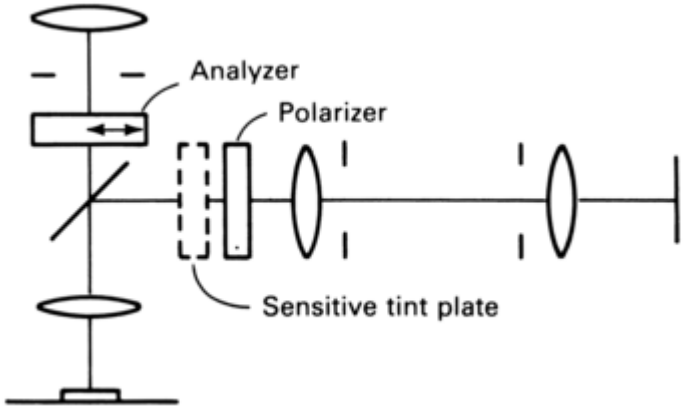

Fig. 34 Placement of the crystal quartz sensitive tint plate

Phase contrast illumination (Ref 17) permits examination of subtle phase variations in microstructures with little or no amplitude contrast from differences in the optical path at the surface (reflected light) or from differences in the optical path through the specimen (transmitted light). Slight differences in height on polished microsections are invisible in bright-field illumination, because they produce only phase differences between the reflected light waves. The phase-contrast technique transforms these phase differences into detectable variations in brightness. To achieve phase contrast, an angular disk is inserted at the front focal plane of the condenser lens, and a transparent phase plate of suitable size is placed in the back focal plane of the objective, as shown in Fig. 35. Depending on the type of transparent phase plate used, positive or negative phase contrast results. In positive phase contrast, higher areas of the specimen appear bright, and depressions dark. In negative phase contrast, lower areas on the specimen are brighter, and higher areas are darker than the background.

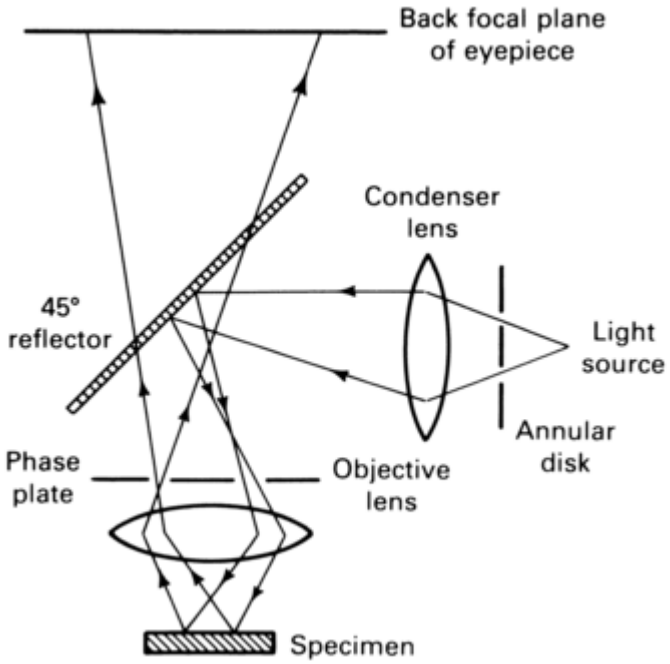

Fig. 35 Principles of phase contrast microscopy

Minimal differences in height of 1 to 5 nm (10 to 50 Å) are disclosed using this method. The optimal range of differences in surface level is approximately 20 to 50 nm (200 to 500 Å). The phase-contrast technique can be applied to reveal the microstructure of metals and alloys after polishing or light etching of the microsections. Examples are the identification of carbide and σ phase in ferritic chromium steel and the identification of σ phase in austenite. Other applications of phase-contrast microscopy include the study of cleavage surfaces and the observation of twins and slip lines. Phase contrast is also useful as an optical etching method in high-temperature (hot-stage) microscopy.

Application of phase-contrast illumination in metallography has been limited. The technique requires a separate set of objectives and a special vertical illuminator.

Interference-Contrast Illumination (adapted from Ref 18). Among the various techniques of interference-contrast microscopy, DIC illumination has found broad application in metallography. Differential interference contrast illumination (Ref 19, 20, and 21) produces images with emphasized topographic detail similar to those observed using oblique illumination. Detail that is invisible or faintly visible using bright-field illumination may be revealed vividly with interference-contrast illumination. For example, small variations in height on an apparently flat surface may be revealed by changes in brightness or color of the image. There is a sense of three-dimensionality as compared to the bright-field microscope (Fig. 36). Various color backgrounds may be selected, the colors being those of Newton's rings (Table 1).

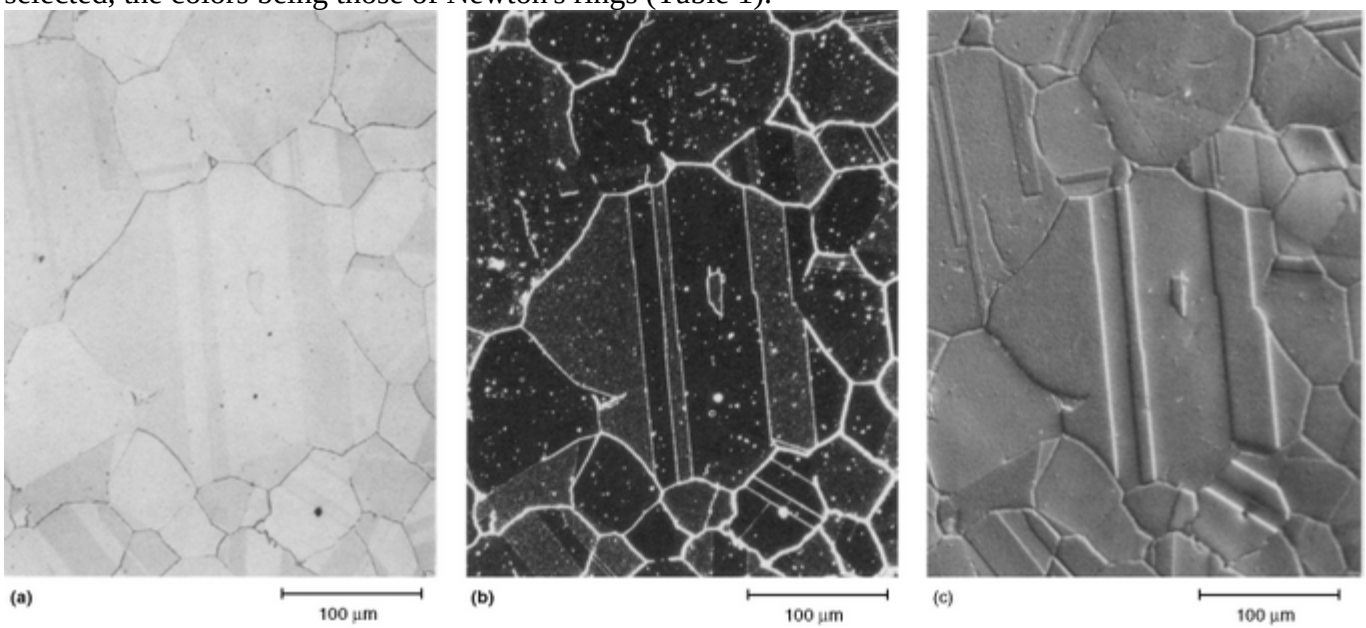

Fig. 36 Solution-annealed and aged Waspaloy (UNS N07001). (a) Bright-field illumination. (b) Dark-field illumination. (c) Differential interference-contrast illumination. Glyceregia. 200×

Table 1 Newton's rings: an abbreviated scale

Path difference		
nm	**Å**	**Color**
0	0	Black
40	400	Iron gray
158	1580	Bluish gray
234	2340	Greenish white
259	2590	White
332	3320	Bright yellow
430	4300	Brownish yellow
505	5050	Reddish orange
536	5360	Red
565	5650	Purple
575	5750	Violet
589	5890	Indigo
664	6640	Sky blue
747	7470	Green

The instruments for DIC illumination are usually based on systems proposed by Francon and Yamamoto (Ref 22) or Nomarski (Ref 23, 24). The systems are described in detail in Ref 20, 21, 25, and 26. The key feature is the device for splitting and recombining the beam. A Savart polaroscope and a modified Wollaston prism are used in the Francon-Yamamoto and Nomarski microscopes, respectively. The device is simply inserted behind

the objective lens of the microscope. It is matched to the objective lens and is available with most metallurgical microscopes. The same technique works for transmission electron microscopes, except separate units are needed for splitting and superimposing the beam.

If a complementary device, the polarization interferometer, is inserted instead, height differences can be qualitatively measured routinely down to λ/20, where λ is the wavelength of the light. Sodium illumination, for example, has a wavelength of 589 nm (5890 Å). Smaller height differences down to λ/200 are detectable and are reportedly measurable using special photographic procedures (Ref 21). In the DIC microscope, it is sometimes possible to detect height differences as small as 1 nm, or 10 Å (Ref 27). The more common Nomarski unit is described here. A description of the principles and use of the Francon-Yamamoto microscope can be found in Ref 20. The two microscopes yield equivalent results.

The Nomarski unit incorporates a Wollaston prism to split the incident polarized light beam into two coherent components of equal intensity that are linearly polarized perpendicular to each other. The basic arrangement for this examination mode is shown in Fig. 37. A ray of light emitted from the light source is linearly polarized after it passes through the polarizer. It then enters a Nomarski biprism (Wollaston prism), which consists of a double-quartz prism that provides uniaxial double refraction and splits the light into two rays of linearly polarized light. The planes of vibration of these rays are perpendicular to each other. Upon passing through the objective, the rays become parallel and impinge on the specimen. After reflection from the specimen surface, they are recombined by the biprism. Interference is produced when these recombined rays pass through the analyzer. Circularly polarized light and a rotatable prism are used in the C-DIC technique. This avoids stage rotation and the possible loss of information due to the unilateral directionality of standard DIC.

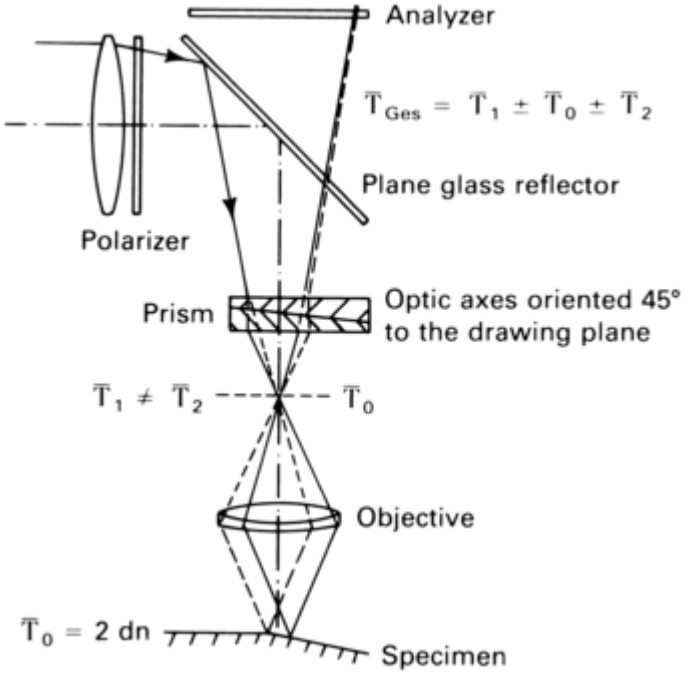

Fig. 37 Light path in an incident-light DIC microscope. Courtesy of C. Zeiss, Inc.

When the light passes through the Nomarski-modified Wollaston prism, it is split into two wave fronts with a path difference of T_1; that is, one wave front is slightly ahead of the other. When this light is reflected from the specimen surface, the path difference T_1 changes due to the height differences on the surface. The split wave fronts also cause phase jumps resulting from different refractive indices of the specimen phases. The change in path difference after reflection is T_0. When the reflected light re-enters the prism, the path difference is T_2. These wave fronts are recombined without interference, because they are still linearly polarized perpendicular to each other. The path difference before the analyzer is T_{total} (T_{Ges}):

$$T_{total} = T_1 \pm T_0 \pm T_2 \qquad \text{(Eq 4)}$$

Only those split wavefronts of $T_{total} = (2k + 1)\,\lambda/2$ where $k = 0, 1, 2$, and so on, pass through the analyzer. If the prism is symmetrical to the microscope axis, $T_1 = T_2$ and the image intensity in the field of view is a function of T_0 because of geometric height differences and phase jumps. Therefore, the intensity differences produce relief effects resembling unilateral, oblique illumination.

As with normal polarized light microscopy, the analyzer is in a crossed relationship with respect to the polarizer. Phase differences resulting from the two spatially separated beams reflecting from the specimen are due to differences in height of the surface relief, which are modified by the optical properties of the specimen. These phase differences cause the light-dark or color interference contrast. Lateral displacement of the biprism allows an additional phase difference to be superimposed that varies color contrast. The achievable contrast depends on the local gradient of the phase difference. Therefore, this type of contrast is termed differential interference contrast. Images produced using this examination mode are characterized by their 3-D appearance, as illustrated in Fig. 38. Another DIC technique, called circular DIC (C-DIC) uses circularly polarized light and a rotatable prism, which avoids stage rotation due to unilateral directionality of DIC and the possible loss of information.

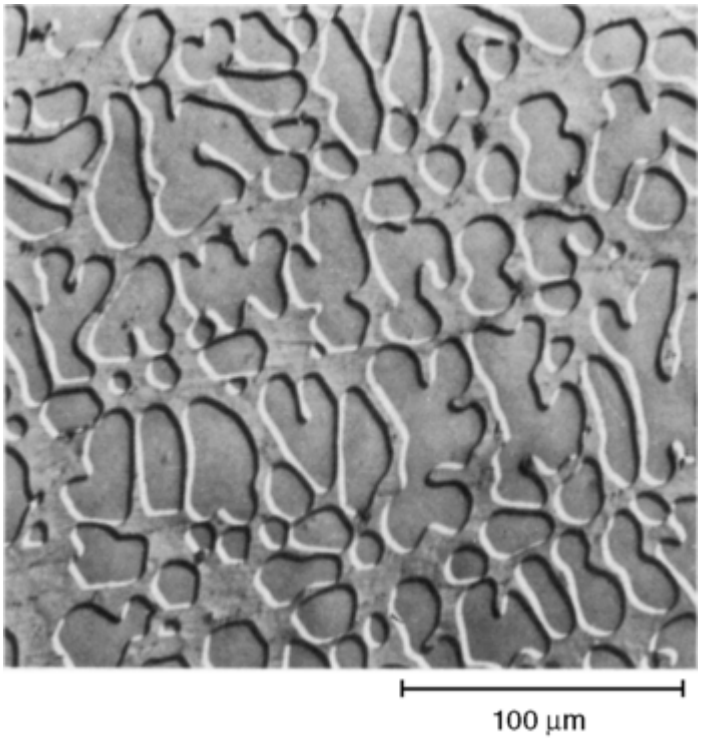

Fig. 38 Differential interference contrast after Nomarski showing the two-phase structure of a U-33Al-25Co (at.%) alloy. Electrolytically etched. 250×

Differential interference contrast can be used to reveal phases of different hardness in polished microsections of metal alloys, layered materials, and materials joints. Good results have been obtained in visualizing carbide particles in roller bearing and high-speed tool steels. A special field of application is the study of coherent phase transformations, which produce surface reliefs. Surface and subsurface defects of thin films evaporated or sputtered on metallic or nonmetallic substrates are also detectable using DIC.

Examples of the topographic detail that can be revealed using DIC illumination are illustrated in Fig. 19(c), 20(c), 21(c), and 32(b). This detail shows the relative hardness of the constituents or the nature of the etching process; that is, which areas or constituents were attacked by the etchant. In some instances, other aspects of the structure may be revealed that are invisible or faintly visible in bright-field illumination. Figure 36 shows the microstructure of solution-annealed and aged Waspaloy (UNS N07001), a nickel-base superalloy, etched in glyceregia. Interference contrast better reveals the austenitic twin structure and shows the roughness in the austenite matrix due to the presence of very fine γ' phase. Figure 39 depicts the structure of Inconel 718 (UNS N07718) after extended high-temperature exposure that has produced orthorhombic platelets of δ-Ni_3Nb. Differential interference contrast illumination clearly shows this phase and the massive MC-type carbides in relief.

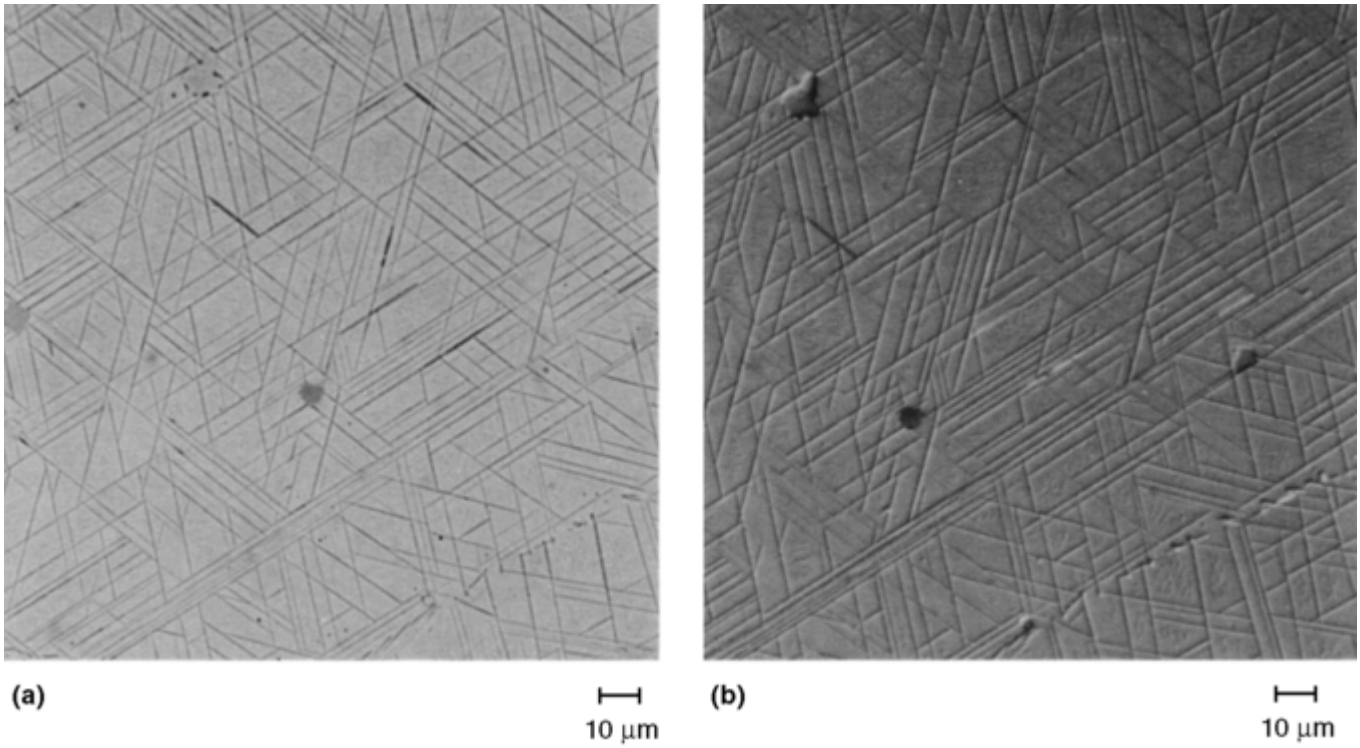

Fig. 39 Inconel 718 (UNS N07718) heat treated 100 h at 870 °C (1600 °F) to produce needlelike orthorhombic Ni_3Nb. (a) Bright-field illumination. (b) Differential interference-contrast illumination. Particles in relief in (b) are niobium carbides; particles flush with the surface are niobium nitride. As-polished. 400×

The Wollaston prism consists of two similar wedges of a birefringent crystal cemented together to produce a plane-parallel plate (Fig. 40). The divergence, ε, of the two beams is related to the wedge angle, α, by the equation:

$$\varepsilon = 2(n_e - n_o) \tan \alpha \qquad \text{(Eq 5)}$$

where n_o and n_e are the refractive indices of the two rays, termed the ordinary ray and extraordinary ray, respectively. In the Nomarski unit, the wedges are quartz, and (n_e - n_o) equals +0.009. The divergence of the two beams is such that they appear to originate inside the Wollaston prism and give rise to a series of interference fringes. In the polarization interferometer, these fringes are observed together with a double image, one from each beam. Any step on the specimen surface causes a displacement of the fringes at the interface between the two images, from which the height difference can be calculated.

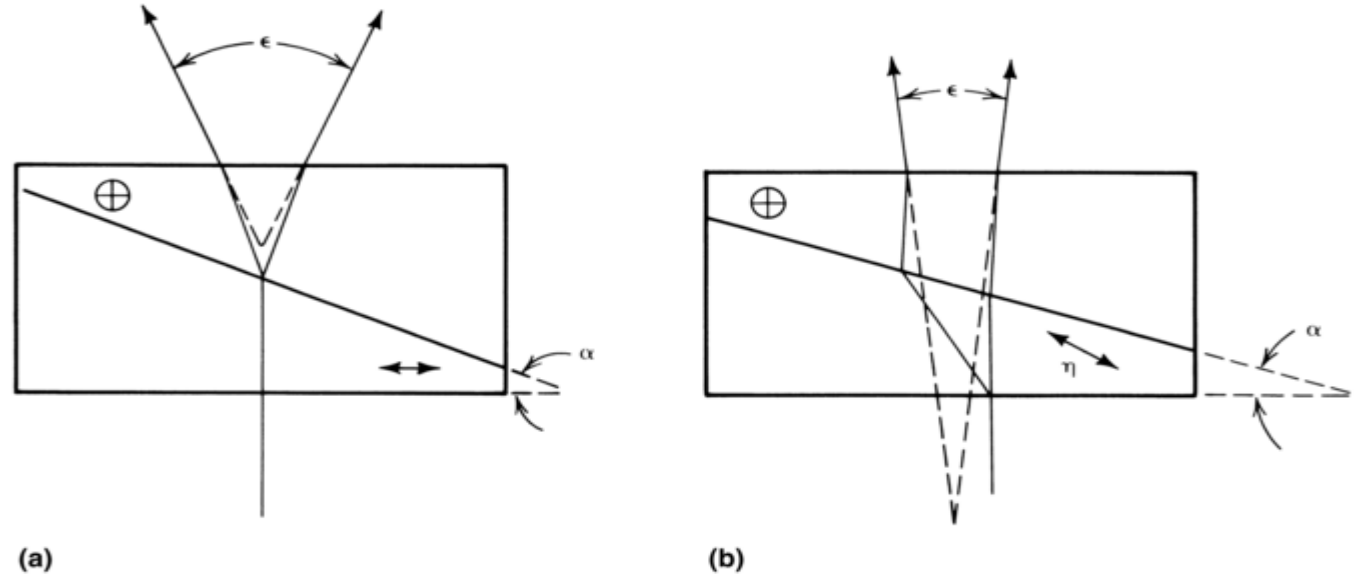

Fig. 40 (a) Wollaston prism. The divergent rays appear to originate inside the unit. (b) By inclining the optical axis of one of the component wedges, the apparent point of origin can be brought outside the unit. By opposite inclinations, the image plane can be made real or virtual.

The width of the interference fringes and their spacing can be varied somewhat by moving the Wollaston prism along the optical axis of the microscope. If the point of convergence of the two beams coincides with the rear focal plane of the objective, one interference fringe encompasses the field of view, and the appearance is uniform. To achieve this condition, the point of convergence must be brought outside the Wollaston prism, which could be achieved by modifying the Wollaston prism so that the optical axis of one prism is inclined at an angle η to the surface (Fig. 40b). This is the condition in the DIC microscope. Furthermore, the angle α of the wedge is reduced such that the separation of the two beams does not exceed the resolving power of the objective lens. Therefore, only one image is seen.

The ordinary and extraordinary rays travel at different velocities: $v_o = c/n_o$ and $v_e = c/n_e$, where c is the velocity (speed) of light in a vacuum. Because the optical axes of the two component prisms are at right angles, the ordinary ray in the first prism becomes the extraordinary ray for the second prism. Therefore, when the Wollaston prism is located along the optical axis of the microscope and the specimen is flat, the two split beams travel equal paths, and the crossed analyzer does not pass the resultant beam. A local difference in height of the specimen surface leads to a path difference, and this region appears bright. If the prism is moved sideways with respect to the optical axis, the two split beams do not travel equivalent paths (Fig. 41). Therefore, the analyzer will pass the spectrum, except for the wavelength corresponding to the path difference.

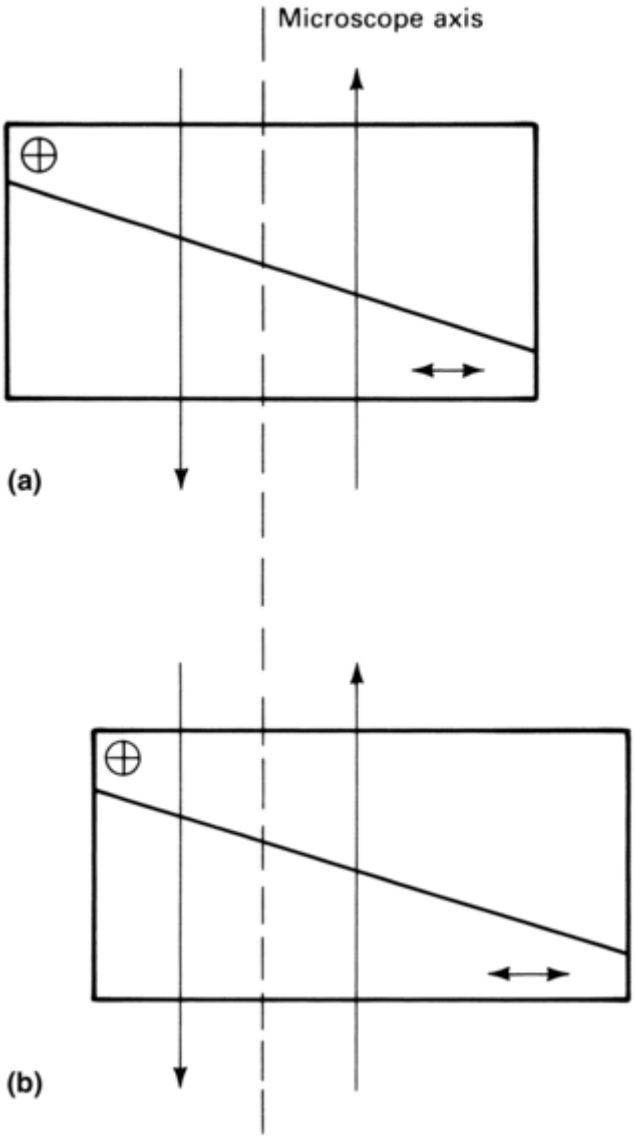

Fig. 41 Travel of ordinary (o) and extraordinary (e) rays. The o ray in the first prism becomes the e ray in the second prism. The rays travel at different velocities. (a) If the Wollaston prism is located

symmetrically relative to the microscope axis there is no resultant phase difference. (b) If the Wollaston prism is displaced sideways, there will be a resultant phase difference of approximately ε*x*, where *x* is the displacement. The relatively small divergence, ε, of the o and e rays is not shown here.

For example, if the path difference corresponds to a wavelength in the yellow region, the specimen appears blue or purple (white light minus the yellow). Any height difference on the specimen surface alters the path difference and therefore appears as a variation in color or brightness. The microscope is most sensitive in the gray region (see Fig. 44). The height differences are relative. A feature that appears as a depression upon moving the prism to the left will appear elevated upon moving the prism to the right (Fig. 42). A polishing scratch or a microhardness indentation can be used for reference to identify depressions correctly. When height changes, one slope is made brighter, and the reverse slope less bright (Fig. 43). This may also be visible in the micrographs.

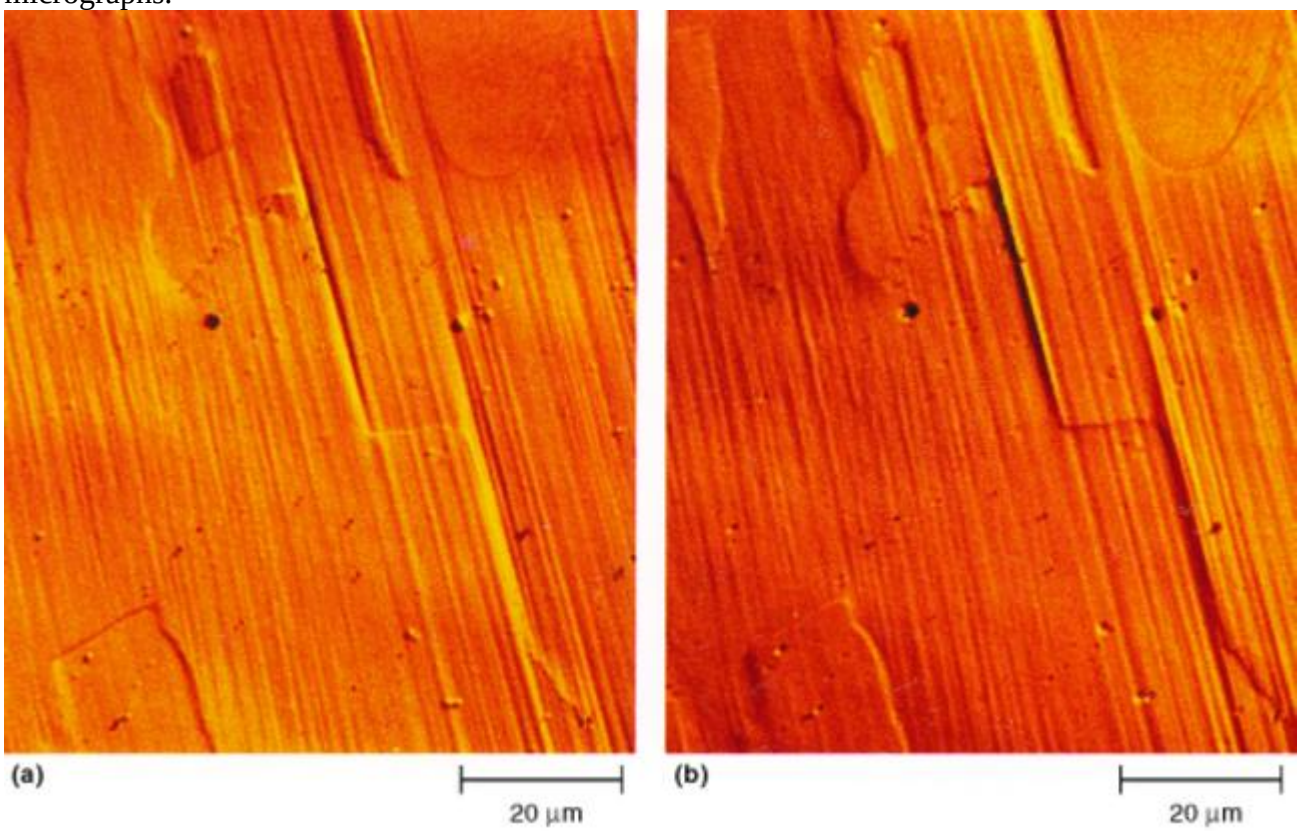

Fig. 42 Plastically deformed Nickel 200 specimen viewed under orange differential interference contrast illumination to either side of the Wollaston prism symmetry position so that the height differences appear reversed. Chemically polished. 800×. (C.E. Price).

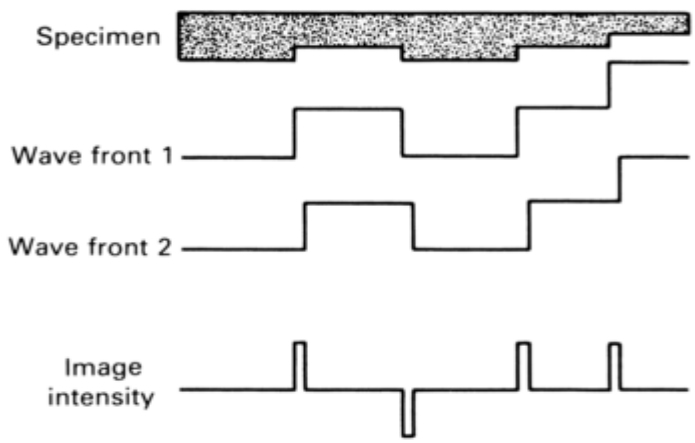

Fig. 43 When changes in height occur, one slope appears brighter, the other less bright. See text for details.

Color Metallography with DIC Illumination. An advantage of the DIC microscope is that without changing the specimen preparation technique, the image can be made to appear blue, orange, gray, and so on, by moving a lever. Bright-field view can be obtained for comparison without removing the device by rotating the analyzer 45°, which extinguishes one beam. There are specific advantages in any situation in which small height differences may arise on a prepared specimen surface. For example, the microstructure of chemically polished or electropolished specimens can usually be revealed without etching. This is also true for mechanically polished specimens having different phases of sufficiently different hardness levels that relief develops during preparation. Upon etching, such features as subgrain networks and dislocation etch pits may be revealed more clearly.

A different category of usage involves the development of height differences on a specimen in service or during experiments, for example, because of wear, corrosion, phase transformations, or mechanical deformation. The device is particularly useful for studying the progression of surface changes during a test. Therefore, the development of persistent slip bands and slip-band cracks during fatigue, the initiation of slip and/or stress-corrosion cracking during slow strain rate tensile tests, or the development of plastic zones around a stationary or propagating crack are clearly revealed under DIC, although during the early stages the surface may display little or nothing. Mechanical twins are similarly revealed. Interference contrast is useful for studying surface films or coatings and cleaved surfaces or for detecting incipient melting. Figures 44, 45 46, 47, 48, 49, 50, and 51 illustrate various applications of differential interference microscopy.

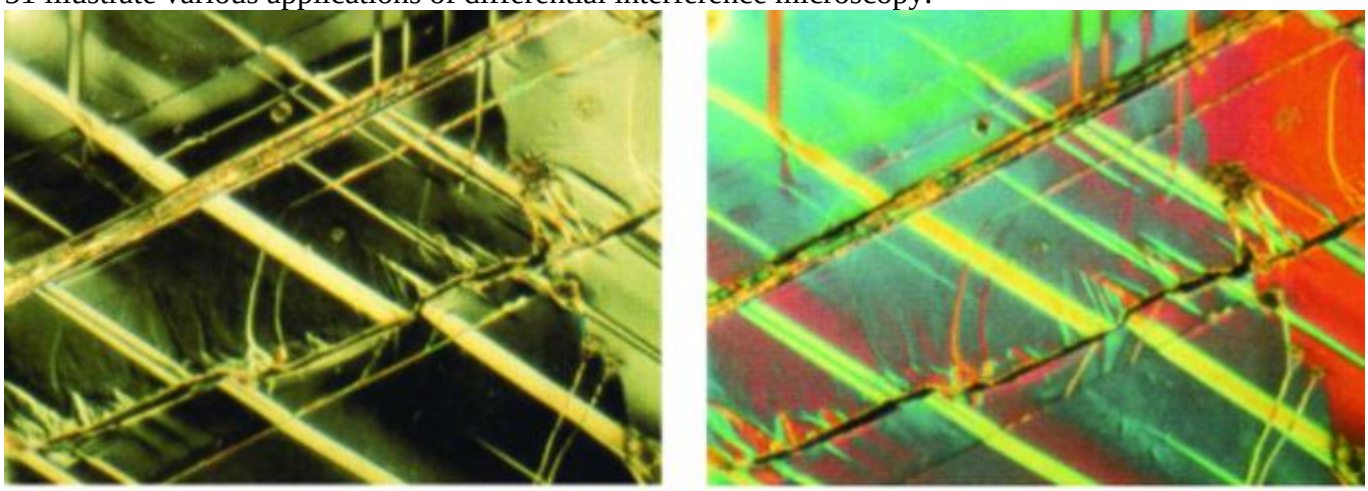

Fig. 44 As-cleaved antimony specimen viewed under differential interference contrast illumination. Views under different contrast conditions show the greater sensitivity in the gray regime (a) than in the nongray regime (b). Twins, river patterns, and cracks are present. As-polished. 200×. (C.E. Price)

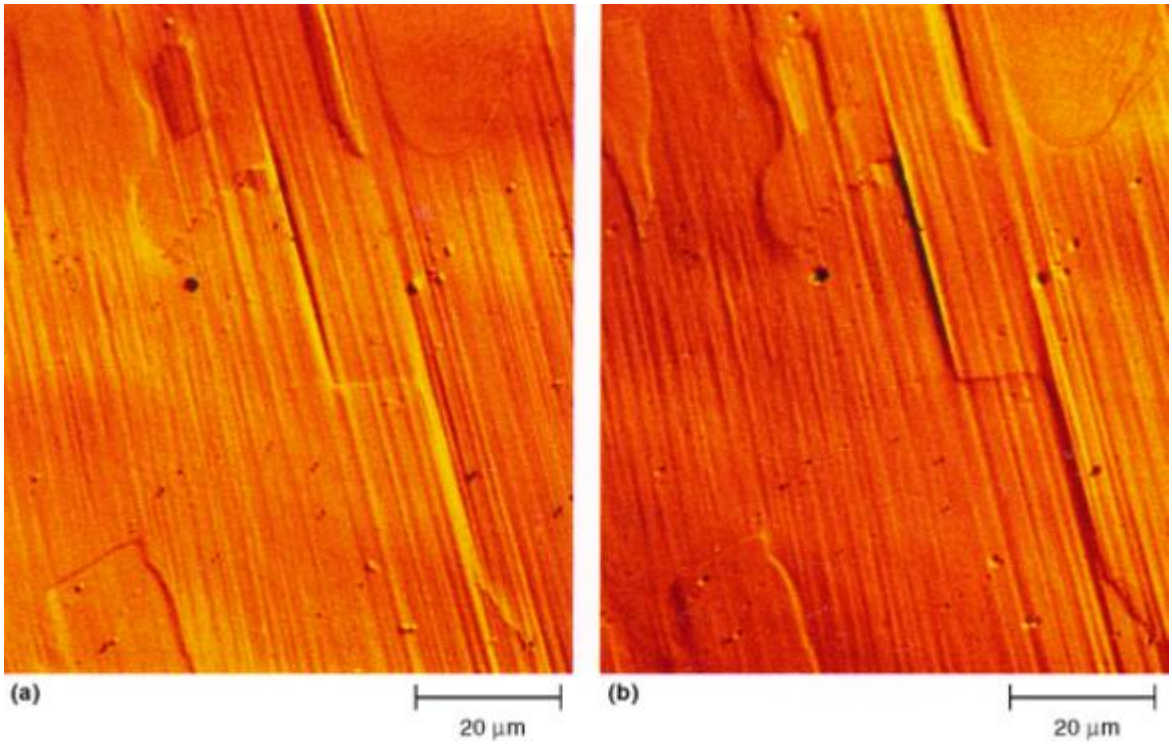

Fig. 45 Plastically deformed Nickel 200 specimen viewed under orange differential interference contrast illumination to either side of the Wollaston prism symmetry position so that the height differences appear reversed. Chemically polished. 800×. (C.E. Price).

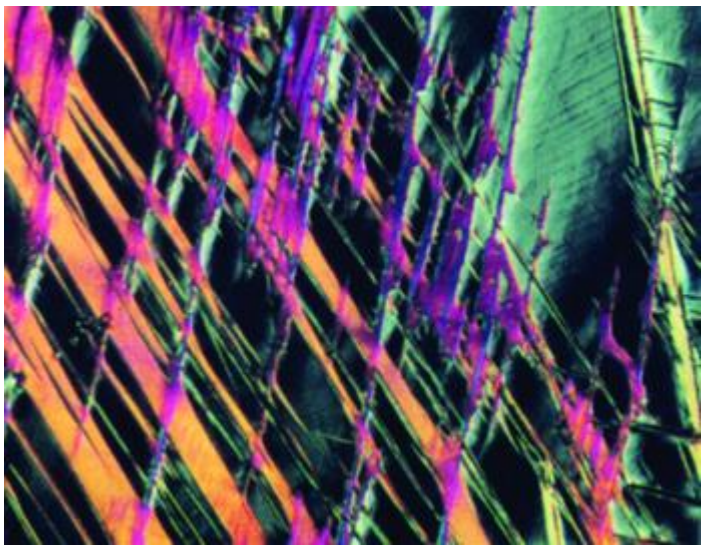

Fig. 46 Hafnium crystal bar showing twins caused by cold working. Attack polished, heat tinted at 480 °C (900 °F), and viewed under differential interference contrast illumination. 65×. (P.E. Danielson)

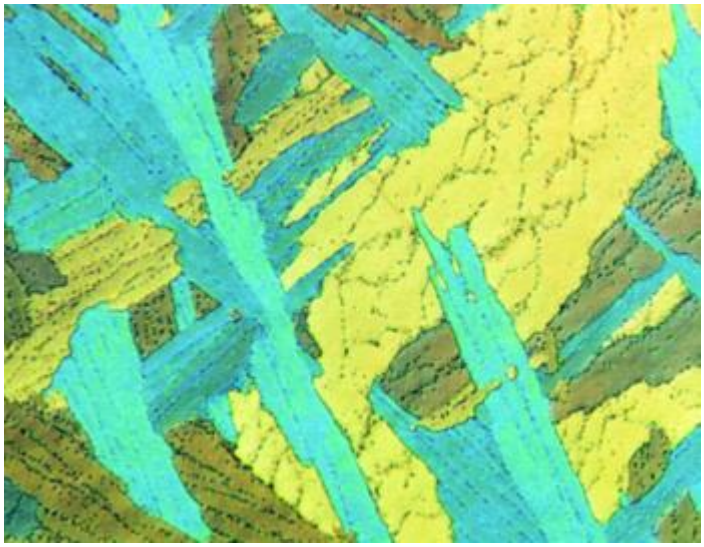

Fig. 47 Zircaloy 4 as-cast ingot. Use of attack polishing, heat tinting (425 °C, or 800 °F), and differential interference contrast illumination reveals the basic crystal structure and the iron-chromium second phase. 200×. (P.E. Danielson)

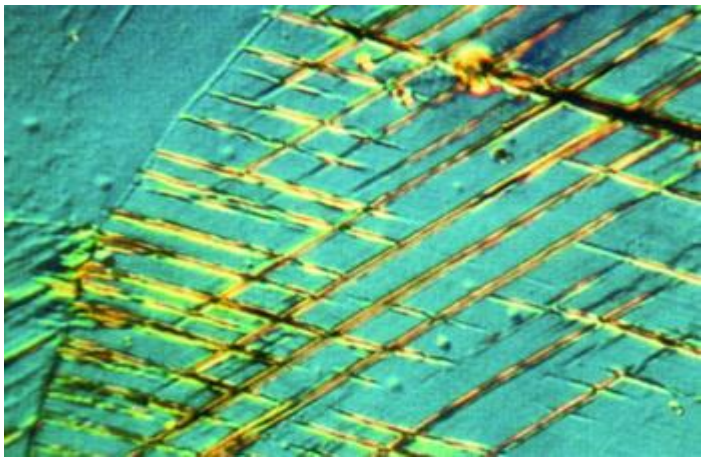

Fig. 48 Nickel 200 specimen fatigued in reverse bending for 10^4 cycles. Use of differential interference contrast illumination shows persistent slip bands with associated cracks outlined against a blue background. Chemically polished. 800×. (C.E. Price)

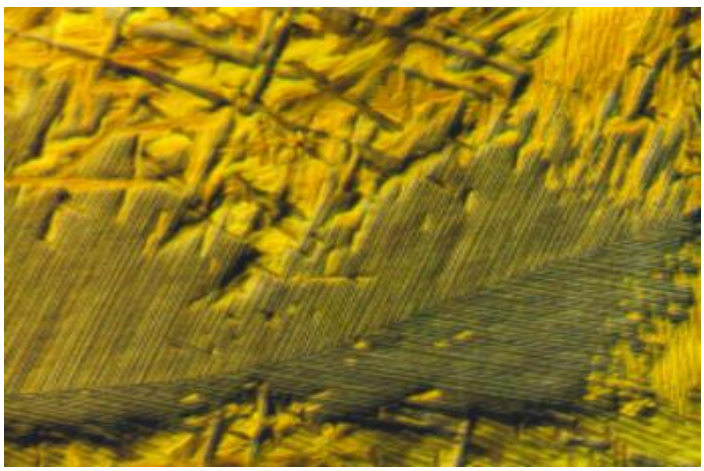

Fig. 49 Zircaloy forging as viewed under differential interference contrast illumination. The parallel platelet structure is an area lower in carbon content. Etched in 45 mL H_2O, 45 mL HNO_3, and 10 mL HF and heat tinted at 425 °C (800 °F). 100×. (P.E. Danielson)

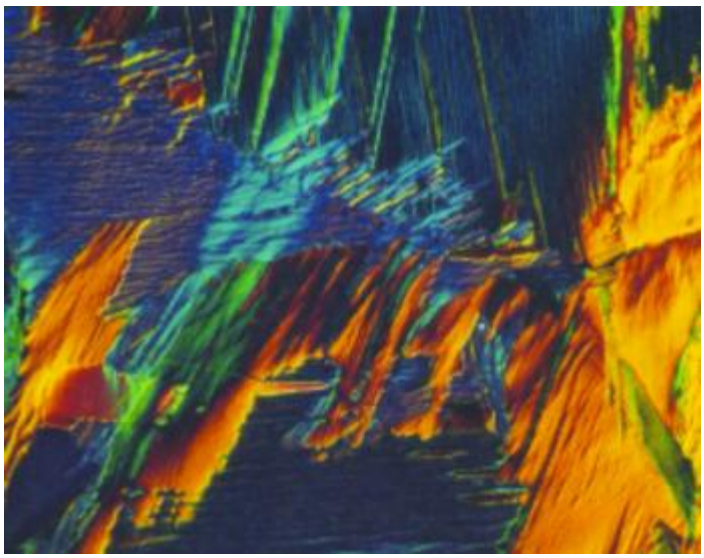

Fig. 50 As-cast Zircaloy structure as viewed under differential interference contrast illumination. The high mechanical deformation evident was induced deliberately during specimen preparation. Attack polished and heat tinted at 425 °C (800 °F). 100×. (P.E. Danielson)

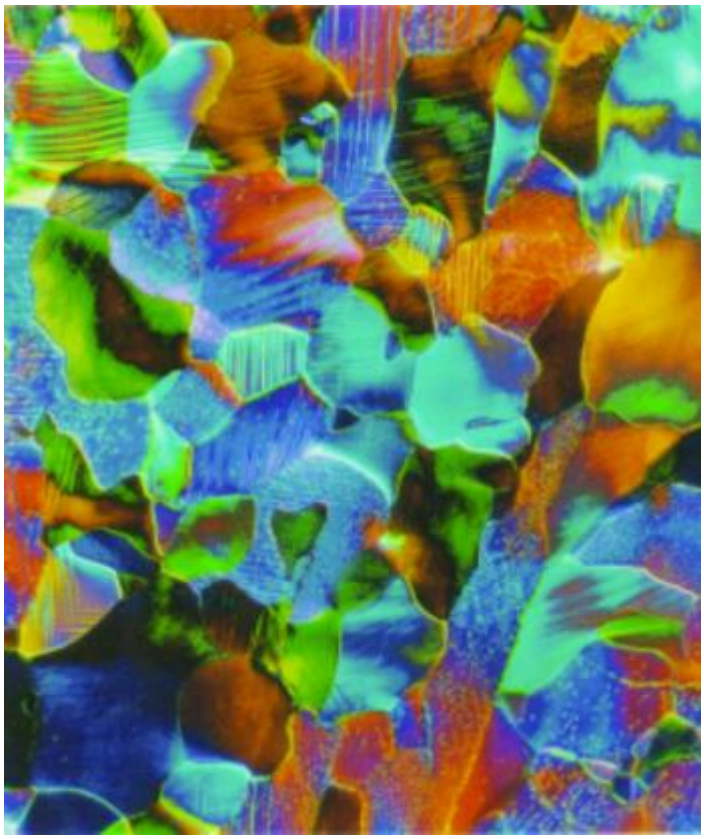

Fig. 51 Heat-tinted niobium alloy (C103) plate as viewed under differential interference contrast illumination. Some of the grains exhibit a second phase (note small, particle-like features) due to alloying additions. 65×. (P.E. Danielson)

Interference Techniques. Several interference techniques (Ref 28, 29) are used to measure height differences on specimens. Interference fringes on a perfectly flat surface appear as straight, parallel lines of equal width and spacing. Height variations cause these fringes to appear curved or jagged, depending on the unit used. The interference microscope divides the light from a single point source into two or more waves that are superimposed after traveling different paths. This produces interference. Two-beam and multiple-beam instruments are the two basic types of interferometers used. The measurements are based on the wavelength of

the light used. Two-beam interferometers can measure height differences as small as λ/20; multiple-beam interferometers, as small as λ/200.

The Linnik-type interferometer is a two-beam reflecting microscope that uses nonpolarized light. A beam-splitting prism produces two light beams from a monochromatic light source. One beam travels through the testpiece objective to the testpiece surface and is reflected back through the objective to the eyepiece. The other beam travels through the reference objective, strikes an optically flat reference mirror, and returns to the beam splitter, then to the eyepiece. If the path difference between the two beams is not equal or not a multiple of λ/2, interference occurs and contour lines are formed that indicate locations of equal elevation. The height difference between adjacent fringes is λ/2.

The Tolansky multiple-beam interferometer produces interference between many light beams by placing a reference mirror that is partially transmitting and partially reflecting very near the specimen surface but slightly out of parallel. The reference mirror has a known reflectivity selected to approximate that of the surface. Light passes through the reference mirror and strikes the specimen surface, is reflected by the specimen surface, and interferes with the rays reflected between the reference mirror and the specimen. The fringes produced by the multiple-beam interferometer are sharper than those from the two-beam interferometer, which accounts for the greater accuracy. The distance between the fringes is also λ/2. Elevations produce displacements of the fringes from parallel alignment. The displacement is compared to the distance between the fringes to obtain height measurements.

Light-section microscopy is used to measure surface topography and complements interferometry techniques. Roughness differences from 1 to 400 μm can be measured, which is useful in examining machined surfaces and for measurement of surface layers or films.

In operation, a slit is placed near the field iris in the illumination system and is imaged by an objective as a light line on the surface to be measured. Oblique illumination is used with a dark background. The light band is observed using a second objective that is identical to the first. The objectives are 45° to the specimen surface and 90° to each other. A reticle in the eyepiece is used for measurements, or they are made on photographs. Vertical resolution is not as good as with interferometers, but lateral resolution is better.

Laser scanning microscopy is a type of light microscopy that is especially suited to the study of surface structures, thin films, and providing quantitative information for the 3-D analysis of material structures and two-dimensional (2-D) surface profiling. Using confocal optical principles, scanning laser-based microscopes produce an image by scanning the beam across the sample in a TV-like raster pattern, and the data are stored, point by point, until a complete image area has been scanned on a selected focal plan. (Ref 30). Laser scanning modules can be adapted to certain light microscope, or the instruments can be dedicated to laser scanning microscopy. Software is available to analyze the topography. With a motorized stage, software can stitch images together so samples larger than the field of view can be analyzed.

References cited in this section

9. G.F. Vander Voort, *Metallography: Principles and Practice,* McGraw-Hill, 1984

13. G.K. Conn and F.J. Bradshaw, Ed., *Polarized Light in Metallography,* Butterworths, 1952

14. W.C. McCrone et al., *Polarized Light Microscopy,* Ann Arbor Science Publishers, 1978

15. A.F. Hallimond, *The Polarizing Microscope,* 3rd ed., Vickers Instruments, 1970

16. E.C.W. Perryman and J.M. Lack, Examination of Metals by Polarized Light, *Nature,* Vol 167 (No. 4247), 1951, p 479

17. A.H. Bennett et al., *Phase Microscopy,* John Wiley & Sons, 1951

18. C.E. Price, Differential Interference Contrast, *Metallography and Microstructures,* Vol 9, *ASM Handbook,* American Society for Metals, 1985, p 150–152

19. J. Padawer, The Nomarski Interference-Contrast Microscope: An Experimental Basis for Image Interpretation, *J. R. Microsc. Soc.,* Vol 88 (Part 3), 1968, p 305–349

20. R. Hoffman and L. Gross, Reflected-Light Differential-Interference Microscopy: Principles, Use and Image Interpretation, *J. Microsc.,* Vol 91 (Part 3), 1970, p 149–172

21. A.S. Holik, Surface Characterization by Interference Microscopy, *Microstruct. Sci.,* Vol 3B, 1975, p 991–1010

22. M. Francon and T. Yamamoto, A New and Very Simple Interference System Applicable to the Microscope, *Optica Acta,* Vol 9, 1962, p 395–408

23. M.G. Nomarski, Microinterféromètrie Differentiel à Ondes Polarisées, *J. Phys. Radium,* Vol 16, 1955, p 9

24. M.G. Nomarski and A.R. Weill, Application à la Métallographie des Méthodes Interférentielles á Deux Ondes Polarisées, *Revue de Metall.,* Vol 52, 1955, p 121–134

25. F. Herzog, Polarization Interferometric Methods in Incident-light Microscopy, with Special Reference to Material Testing, *Ind. Anz.,* Vol 60, July 1962, p 27–31

26. M. Francon and S. Mallick, *Polarization Interferometers,* Wiley-Interscience, 1975

27. W. Lang, "Nomarski Differential Interference Contrast Microscopy, Part IV: Applications," Zeiss Information, No. 77/78, 1971, p 22–26

28. S. Tolansky, *Multiple-Beam Interferometry of Surface and Films,* Clarendon Press, 1948

29. S. Tolansky, *Surface Microtopography,* Interscience, 1960

30. A.M.A. Schmidt and R. D. Compton, Confocal Microscopy, *Friction, Lubrication, and Wear Technology,* Vol 18, *ASM Handbook,* ASM International, 1992, p 357–361

G.F. Vander Voort, Light Microscopy, *Metallography and Microstructures,* Vol 9, *ASM Handbook,* ASM International, 2004, p. 332–354

Light Microscopy

George F. Vander Voort, Buehler Ltd.

Auxiliary Techniques

Several special devices may be used with the optical microscope to obtain additional information. These procedures or techniques are described below.

Microhardness Testing. Microindentation hardness data may be obtained by adding indenter attachments to the microscope. Single-purpose units for semiautomatic testing also are made by most manufacturers of hardness test equipment. Loads are generally made from 1 to 1000 g, although some manufacturers have units for low loads (0.05 to 200 g). Knoop or Vickers indenters can be used. Single-purpose units for semiautomatic hardness testing include personal computers (PCs) for monitor viewing of the indentation and image-analysis software for giving hardness values from indentation readings.

Hot-Stage Microscopy. Hot-stage microscope cells are available from several manufacturers. Single-purpose units can also be used. Cold-cell attachments have also been produced, but have rather limited use in metallography. The hot-stage microscope has been used to study phase transformations on heating or cooling or at constant temperature (Ref 31, 32).

Examination of reactions in the hot-stage microscope cell requires use of long-working-distance objectives, because the specimen is held within the cell. Moreover, because the cell window is quartz, the objectives must be quartz-corrected for the specific thickness of the quartz window, especially those with magnifications of 20× or more.

Techniques other than chemical etching must be used to view phase changes. Grain boundaries will be thermally etched if the specimen is held at a constant temperature in the vacuum. Grain-boundary grooving is easily observed using bright-field illumination, as shown in Fig. 52. Phase transformations are visible by the relief produced at the surface. Therefore, shear reactions, such as those produced by martensite or bainite formation, are most easily observed (Fig. 53). Other phase transformations are more difficult or impossible to observe. Transformations may be photographed in situ, for which motion picture cameras are commonly used.

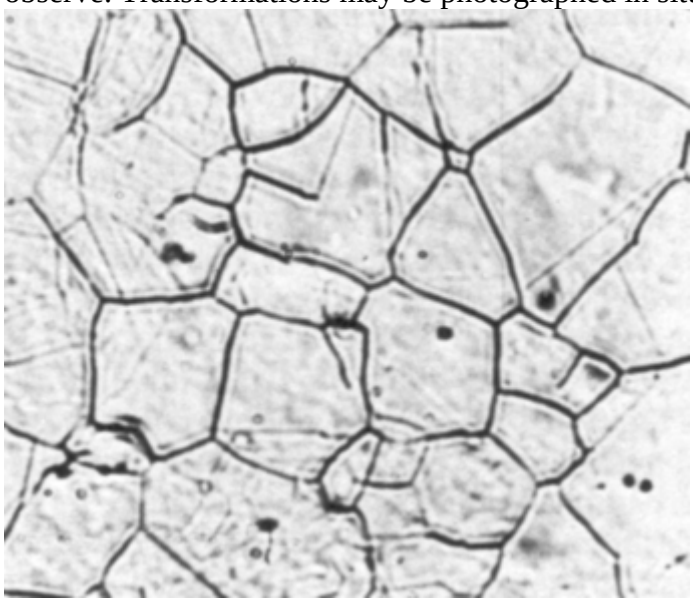

Fig. 52 Low-carbon Cr-Mo-V steel. Thermally etched austenite grain boundaries are shown in situ at 1000 °C (1830 °F) on a hot-stage microscope. 440×. Courtesy of A.O. Benscoter

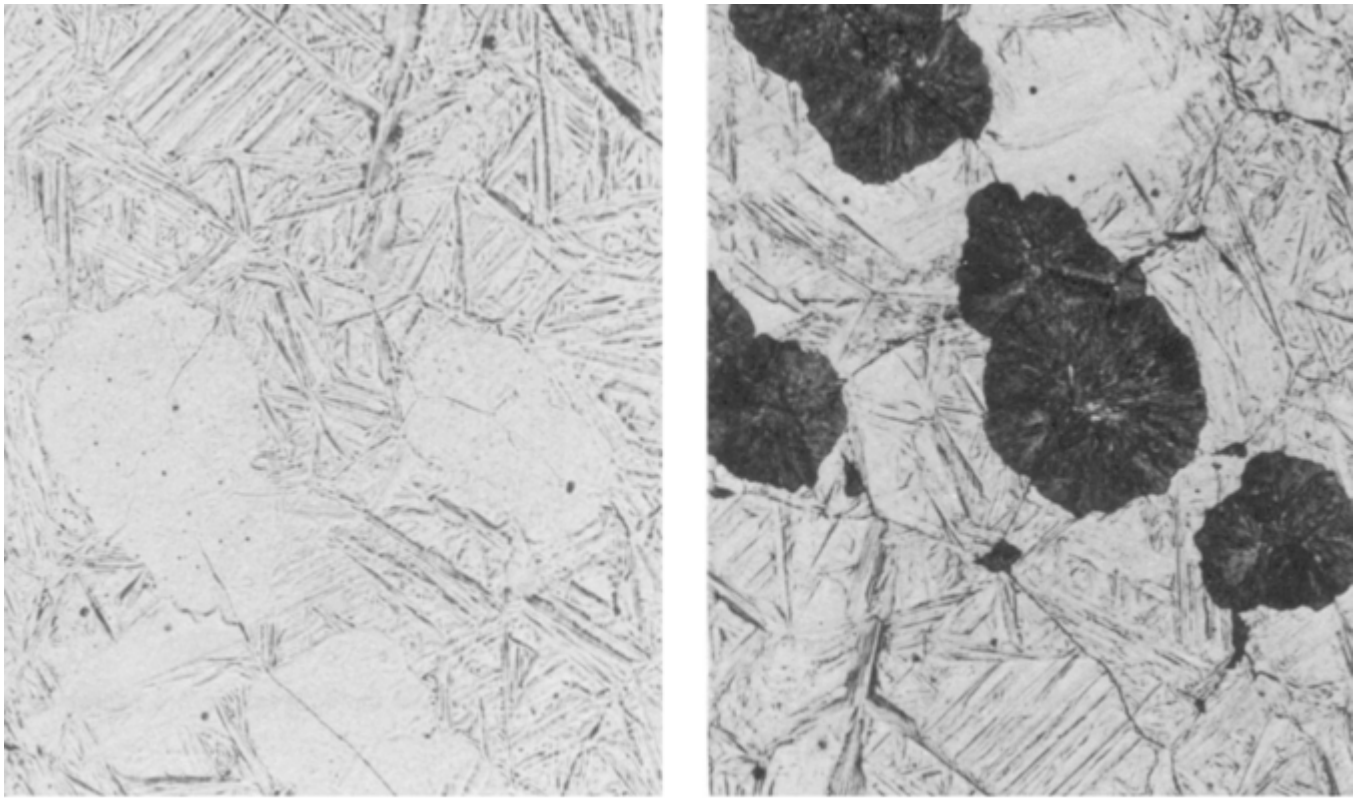

Fig. 53 High-carbon steel, quenched in the hot stage at a rate that allowed some pearlite (smooth areas) to form before the martensite (rough areas). In hot-stage microscopy, phase transformations are observed by the relief produced at the surface of the specimen, (b) shows the same area as (a) after light polishing and etching. 320×. Courtesy of J.R. Kilpatrick

Special stages are available in a variety of configurations. Autoleveling stages for mounted specimens are a typical example. Universal tilting stages have also been constructed for rapid manipulation of rough, irregular specimens. Special stages have also been designed for handling small objects.

A number of stages have been constructed for performing in situ experiments. Basic studies of solidification have been performed by in situ observation of the freezing of low-melting-point organic materials, such as camphene, that solidify like metals (Ref 33). Observation of the recrystallization of low-melting-point metals and alloys has been similarly observed (Ref 34).

Special stages have been used to observe the progress of electrolytic polishing and etching (Ref 35). Cells have also been used for in situ examination of corrosion processes (Ref 36). Stages have been designed to observe a variety of processes involving static or dynamic stress (Ref 37, 38, 39, 40, and 41), and devices have also been designed to permit physical extraction of inclusions (Ref 42).

Hot-Cell Microscopy. Metallographic preparation of radioactive materials requires remote-control preparation using specially designed hot cells (Ref 43, 44). Special metallographs have been designed for use with the hot cell, as part of a workstation containing a metallograph and associated remote controls that are connected to a shielded chamber containing the radioactive specimen.

Field Microscopy. When the microstructure of a component or large object that cannot be cut and moved to the laboratory must be examined, portable laboratory equipment, made by several manufacturers, can be used to polish a section in situ. A portable microscope (Fig. 54) may sometimes be used to examine and photograph the microstructure. If this cannot be done, replicas can be made and examined using an optical microscope (Ref 45, 46) or an electron microscope.

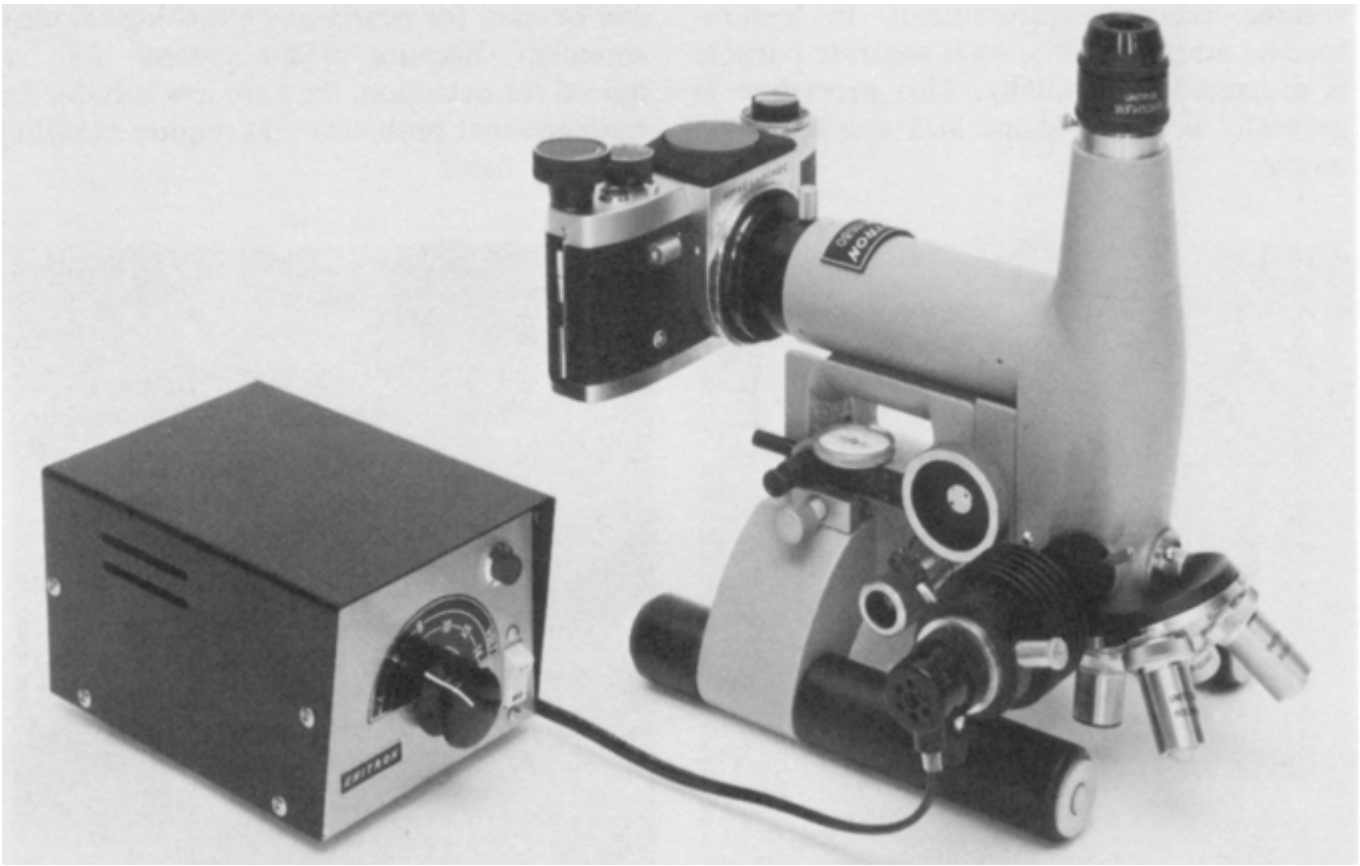

Fig. 54 Microscope designed for use away from the laboratory. Batteries for the light source are contained in the cylindrical stand of the instrument. Courtesy of Unitron Instruments, Inc.

Comparison Microscopes. The need occasionally arises to compare two microstructures. Generally, this is carried out by placing micrographs from each specimen side-by-side, but it can also be performed using special microscopes. A bridge comparator (Fig. 55) is used to combine images from two bench microscopes for simultaneous viewing.



Fig. 55 Comparison microscope, which allows simultaneous viewing of two specimens. Courtesy of Leica, Inc.

Image Monitors. With digital imaging, the use of monitors is common. Projection televisions also can be used for group viewing. A number of high-resolution closed-circuit systems are available.

Clean-Room Microscopy. The study of small particles is influenced by dust contamination during viewing. Therefore, such work must be performed in a clean box, clean bench, or clean room that is specially constructed to provide a dust-free environment.

Image Analyzers. The increased use of quantitative metallography, particularly for characterization of inclusions, is enhanced by the continuing improvement of automated image-analysis systems. Phases or constituents of interest are detected primarily by differences in light reflectivity that produce gray-level differences on the monitor. Most stereological measurements can be made using these systems, and considerable automation has been achieved using PC software to drive automated stages.

Features are detected on as-polished or etched specimens, depending on the nature of the feature of interest. If etching is required, selective techniques are generally used (Ref 9). Field and feature-specific measurements are utilized. Field measurements measure all the detected features simultaneously, as in volume fraction measurements. In feature-specific measurements, each separate particle is measured sequentially. This procedure is generally used for shape and size measurements. Typical presentations from image-analysis systems may display imaging enhancements and tabular data (such as grain size distributions) for a series of images.

Some structures do not lend themselves to accurate measurements using such systems. For example, quantification of fracture surface detail cannot be performed using an automatic image analyzer, because the device cannot separate fracture features by gray level. Many transmission electron micrograph structures also cannot be analyzed using these devices.

References cited in this section

9. G.F. Vander Voort, *Metallography: Principles and Practice,* McGraw-Hill, 1984

31. M.G. Lozinskii, *High Temperature Metallography,* Pergamon Press, 1961

32. B.L. Bramfitt et al., The Use of Hot-Stage Microscopy in the Study of Phase Transformations, in *Metallography—A Practical Tool for Correlating the Structure and Properties of Materials,* STP 557, ASTM, 1974, p 43–70

33. K.A. Jackson and J.D. Hunt, Transparent Compounds That Freeze Like Metals, *Acta Metall.,* Vol 3, 1965, p 1212–1215

34. P. Tardy, New Methods for Direct Observation of the Recrystallization of Low Melting Metals, *Pract. Metallog.,* Vol 9, 1968, p 485–493

35. M. Markworth, Preparation of Metallographic Specimens of Ferrous Materials by Electrolytic Polish Attack under Direct Microscope Observation, *Neue Hütte,* Vol 13 (No. 11), 1968, p 684–689

36. R. Wall and D.I. Roberts, A Cell Technique for Microscopic Observation of Selective Corrosion, *Metallurgia,* Vol 68 (No. 410), 1963, p 291–294

37. R.A. Flinn and P.K. Trojan, Examination of Microstructures under Varying Stress, *Met. Prog.,* Vol 68, July 1955, p 88–89

38. E. Brobery and R. Attermo, A Miniature Tensile-Testing Machine for Deformation During Microscopic Observation, *Jernkontorets Ann.,* Vol 152 (No. 10), 1968, p 525–526

39. D. Godfrey, "Investigation of Fretting by Microscopic Observation," Report 1009, National Advisory Committee for Aeronautics, 1951

40. J.L. Walter and H.E. Cline, Grain Boundary Sliding, Migration, and Deformation in High-Purity Aluminum, *Trans. AIME,* Vol 242, 1968, p 1823–1830

41. S. Takeuchi and T. Homma, Direct Observation for High Temperature Fatigue in Pure Metals by Means of Microscopic Cine-Camera, *Proc. First International Conference on Fracture* (Sendai, Japan), Vol 2, 1966, p 1071–1086

42. G.L. Kehl et al., The Removal of Inclusions for Analysis by an Ultrasonic "Jack Hammer" *Metallurgia,* Vol 55, March 1957, p 151–154

43. J.H. Evans, Remote Metallography, in *Interpretive Techniques for Microstructural Analysis,* Plenum Press, 1977, p 145–168

44. R.J. Gray et al., Metallography of Radioactive Materials at Oak Ridge National Laboratory, *Applications of Modern Metallographic Techniques,* STP 480, ASTM, 1970, p 67–96

45. L. Kosec and F. Vodopivec, Examples of the Replica Technique in Optical Metallography, *Pract. Metallog.,* Vol 6, 1969, p 118–121

46. J. Neri, Optical Replicas—A Nondestructive Metallographic Evaluation Technique, in *Failure Analysis,* American Society for Metals, 1969, p 241–268

G.F. Vander Voort, Light Microscopy, *Metallography and Microstructures,* Vol 9, *ASM Handbook,* ASM International, 2004, p. 332–354

Light Microscopy

George F. Vander Voort, Buehler Ltd.

Photomicroscopy

Photomicroscopy is important in metallography, because the photomicrograph can faithfully reproduce the detail observed for others to view. Prior to the development of photographic attachments, microstructures had to be sketched. Although the need for such documentation has long since past, sketching remains useful as a teaching method.

High-quality micrographs can be easily produced, but it requires careful attention to specimen preparation, etching, and use of the microscope. Regardless of whether the image is captured on film or a digital medium (such as charge-coupled device, CCD), obtaining good micrographs requires adequate image contrast and resolution, uniform focus over the entire field, uniform lighting, and adequate depth of field. The light source must be properly aligned, and the system should be free of vibration. The yellow-green filter should be employed to correct lens defects. The optics must be clean, and the field and aperture diaphragms must be adjusted correctly.

The magnification at the plane of the recording device (film or CCD) must be known. This is a simple procedure if the only variables are the objective and eyepiece magnification, but is more difficult when using a zoom system or bellows. A stage micrometer can be utilized to determine the true magnification.

Film Photography. Several film formats may be used, such as instant, sheet film of different size, or 35-mm roll film. Historically, darkroom photographic procedures were needed, but many photomicrographs have been made taking advantage of the speed and efficiency of instant photographic processes. However, image reproduction is sacrificed, and the process must be repeated for each extra copy. Use of an automatic exposure device is necessary with instant process film to minimize waste. Traditional darkroom photographic procedures require more effort, but yield better micrographs. Considerable automation in wet darkroom processes is possible, but frequent use of photomicroscopy is required to justify the cost of such equipment.

A range of black-and-white and color films is available for darkroom or instant techniques. The manufacturers of these films document film characteristics. Black-and-white films are most commonly used due to their lower cost. They exhibit better contrast control, are easier to process, and are generally quicker to use than color films. Color film has some important uses for which its cost is justified.

In traditional black-and-white photography, a negative image is produced first and is used to produce a positive image of the microstructure on suitable paper. The micrograph will last for many years without any apparent change. Selection of the negative film is based on the format available, color sensitivity, contrast, resolving power, speed, graininess, and exposure and development latitudes. Some black-and-white films are not sensitive to the entire visible spectrum.

Orthochromatic films are sensitive to all colors except orange and red; panchromatic films are sensitive to all colors, although they emphasize blue and deemphasize yellow. A yellow filter can be used to reduce this color bias. Orthochromatic films can be developed under a dark red safe light, but panchromatic films require total darkness. Orthochromatic films are excellent for photomicroscopy, particularly when a yellow-green filter is inserted to correct lens defects.

Film speed is a critical variable only when illumination is low, as in polarized light, interference-contrast, or dark-field illumination. Orthochromatic film has a medium contrast that is adequate for most structures. Contrast may be enhanced with a high-contrast film. The resolving power of a film defines its ability to record fine details in the image. Therefore, a high-resolving-power film is desirable. Graininess depends on the size of the silver grains in the emulsion, the developer used, and the development time and temperature. High-speed films are more grainy than low-speed films, making them less suitable for enlarging. Contact printing is preferred. It requires a large film size, but saves enlargement time. It produces better images and eliminates redetermining the magnification of the print. A fine-grain film provides the best resolution.

When a negative is exposed, there is an allowable range of exposures that will produce a useful, printable negative. A wide exposure latitude is quite valuable. Each film includes information on its characteristic relationship between exposure time and density. The exposure selected should be on the linear portion of the density-time curve. A good, dense negative allows suppression of some of the fine image defects during printing. An underexposed negative greatly restricts printing and generally results in a poor print. Development of negatives is rather simple and involves use of a developing solution, a stop bath, a fixing solution, as well as washing and drying.

The correct exposure is most easily determined using a built-in exposure meter. If this is not available, a test exposure series can be made. This is accomplished by pulling out the film slide completely and exposing the entire film for a time judged to be considerably shorter than that required. The slide is then inserted so that it covers about 10 to 20 mm (0.4 to 0.8 in.) of the film, and the exposure is repeated at double the initial exposure time. This is repeated incrementally, doubling the exposure time with each increment, until the slide is fully inserted, covering the film. After development, the correct time can be assessed based on the density of the negative in each band. Alternatively, the step exposure can be performed using an instant film of the same speed, saving the darkroom time.

Most black-and-white films are contact printed. The negative is placed emulsion side up on the contact printer, and a suitable paper is placed emulsion side down over the negative. The printer is closed, and light is passed through the film onto the paper. The print is developed, stopped, fixed, washed, and dried. Print contrast is controlled by the type of paper and development time. Print contrast types vary from extra-soft (flat) to extra-contrast (grades 1 to 5). Number 3 paper is used most often. Number 4 paper is used to increase contrast, and No. 2 paper to reduce contrast.

To illustrate the influence of film contrast and paper contrast on image quality, Fig. 56 and 57 compare images of a high-contrast microstructure with medium-contrast film and high-contrast film, respectively. Likewise, Fig. 58 and 59 compare medium-contrast and high-contrast films for a flat (low-contrast) microstructure. The negative images were printed on four grades of paper from F1 grade (low-contrast paper) through F4 (high-contrast paper). Figure 56 shows a ferrite-pearlite microstructure etched with picral at 500×. This high-contrast image produces excellent results with the medium-contrast film (Tri-X Orthochromatic) using paper grades F2 to F4. The same image taken with a high-contrast film (Fig. 57) (Contrast-Process Orthochromatic) is a bit harsh; the best images are on papers F1 and F2. Figure 58 and 59 show tempered martensite and sulfide inclusions in a medium-carbon alloy steel etched with 2% nital at 500×. This is a rather flat, low-contrast image that is greatly improved with high-contrast film and paper grades F2 to F4.

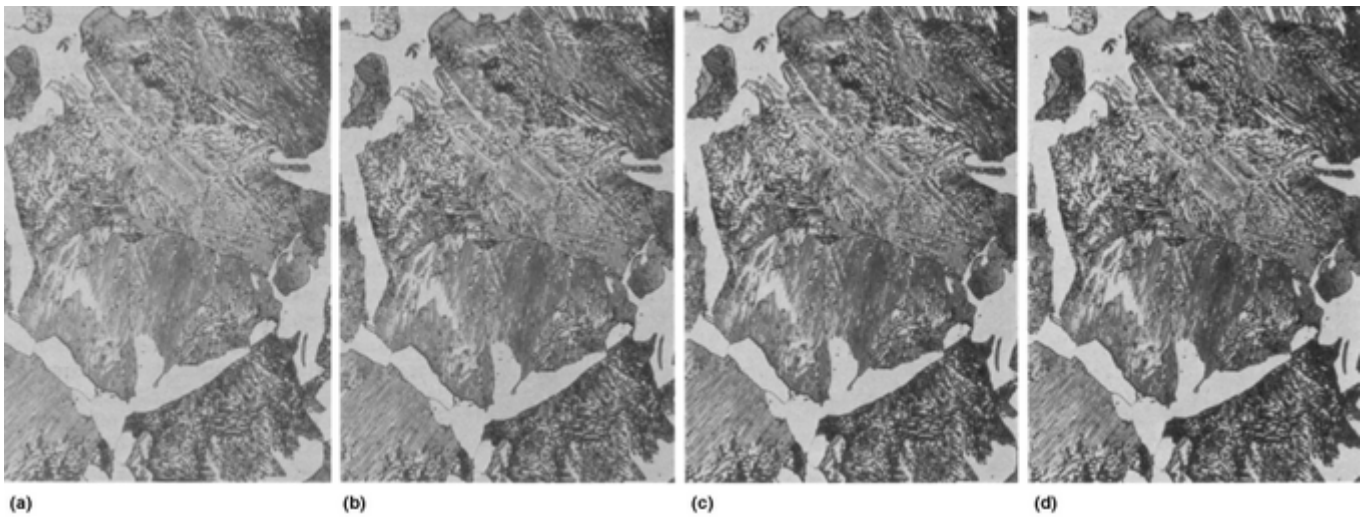

Fig. 56 High-contrast microstructure (ferrite and pearlite) photographed using a medium-contrast film (Tri-X Ortho) and printed with paper grades: (a) F1 (low contrast), (b) F2, (c) F3, and (d) F4 (high contrast). 500×

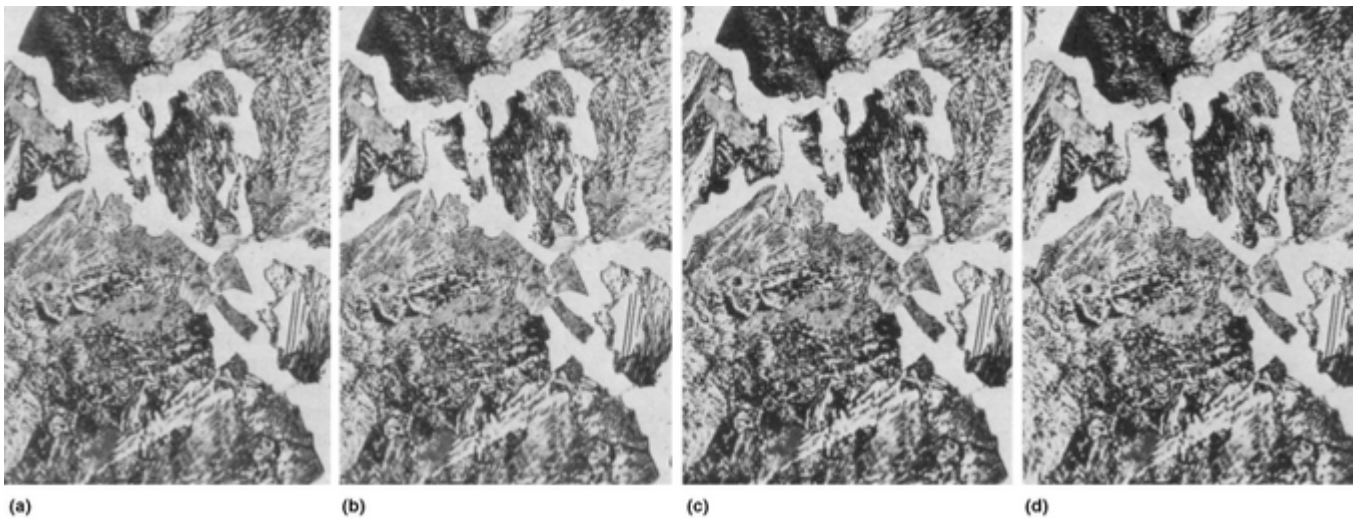

Fig. 57 Same microstructures as Figure 56 photographed with a high-contrast film (Contrast Process Ortho). Again, the negative was printed with paper grades: (a) F1 (low contrast), (b) F2, (c) F3, and (d) F4 (high contrast). 500×

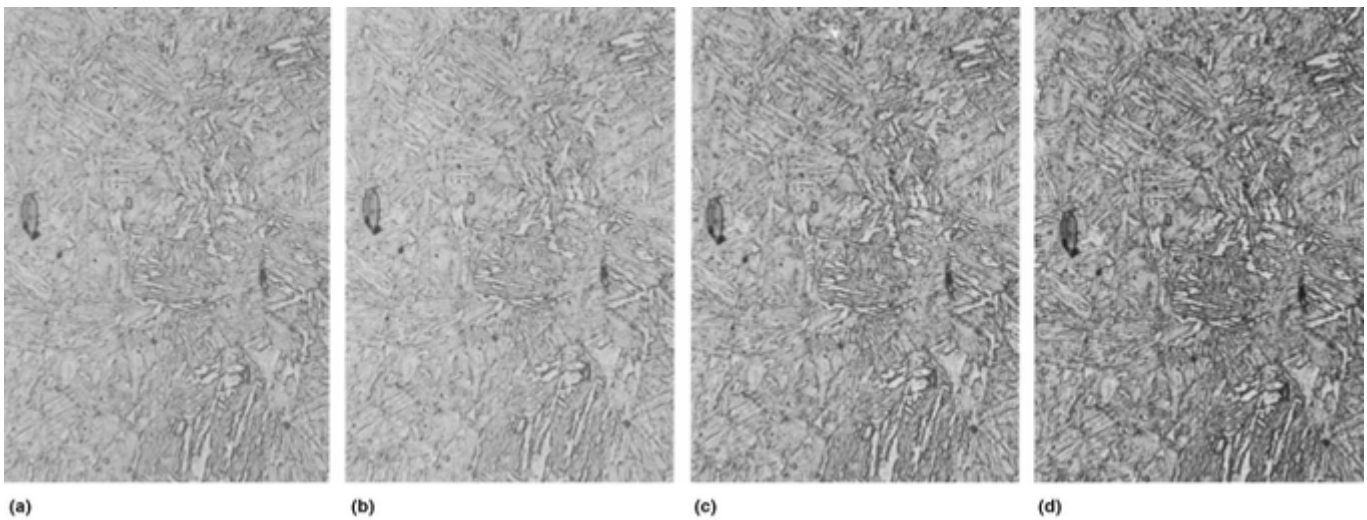

Fig. 58 Low-contrast microstructure (tempered martensite in a medium-carbon alloy steel) photographed with a medium-contrast film (Tri-X Ortho) and printed with paper grades: (a) F1 (low contrast), (b) F2, (c) F3, and (d) F4 (high contrast). 500×

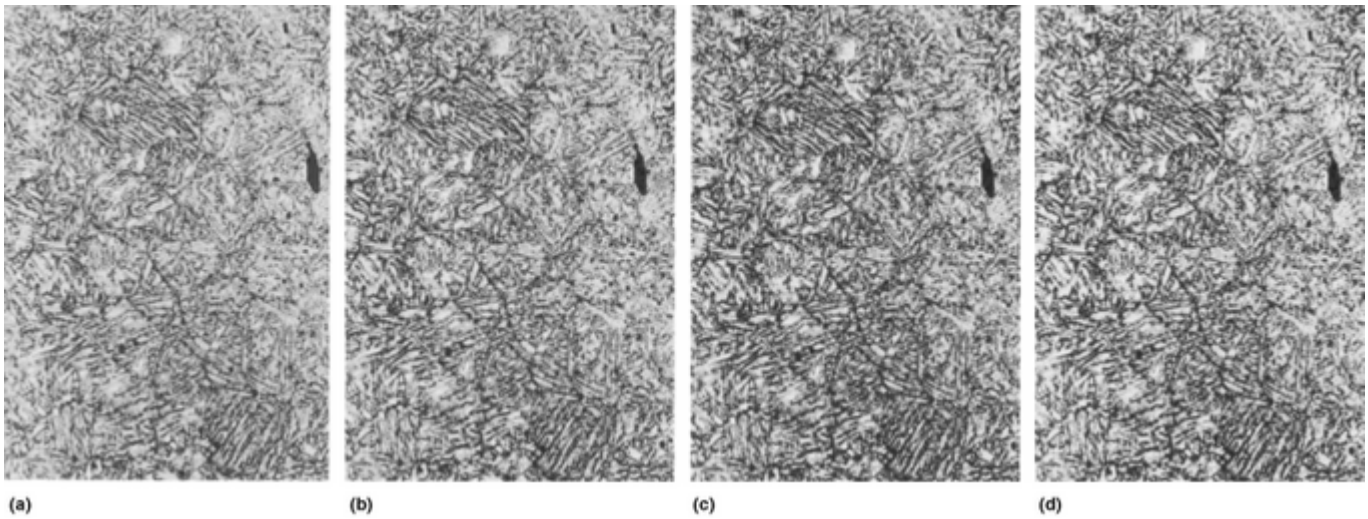

Fig. 59 Same microstructure as Figure 58 photographed with a high-contrast film (Contrast Process Ortho) and printed with paper grades: (a) F1 (low contrast), (b) F2, (c) F3, and (d) F4 (high contrast). 500×

Instant process films eliminate the darkroom work, thus hastening the process. Some instant films have very high speeds, an advantage in dim lighting. Some prints must be coated with a neutralizing stabilizer/protective varnish to prevent staining and fading. Also available are instant films (55P/N, for example) that produce a negative and a positive print; this negative must be cleared, but a darkroom is not required. Polaroid films used in microscopy are all panchromatic. They are available as roll film, film packs, or sheets. Exposure times must be more accurately controlled to obtain good prints than with traditional wet-process films. Additional information on color photomicroscopy is available in Ref 2, 47, 48, 49 50, 51, and 52.

Color Photography. Negative color film (print film) and positive transparency (reversal) color film are the two types available. Color negative films produce a negative with complementary colors. Printing is required to obtain the true colors, which are sometimes not achieved, because the film laboratory technician may not be familiar with the subject matter. Processing and printing one's own work yields optimal results. With slide films, or reversal color films, the colors are substantially the same as the image, lessening the chances of defective printing.

Selecting color film requires attention to the type of light source used, because films are balanced for artificial light or daylight. The xenon light source, particularly valuable in color photomicroscopy, provides a useful daylight spectrum. Other light sources necessitate using color-balancing filters to match the color temperature of the light to that of the film. Figure 60 is a copy of a National Bureau of Standards (now the National Institute of Standards and Technology) filter nomograph that aids in the selection of the best filter for a given light source and color photographic emulsion. The filters suggested may not be exact for accurate color reproduction, but will always be close enough to enable intelligent changes for achieving accuracy. A comparison of several color films has shown that differences in contrast and color rendition occur (Ref 51).

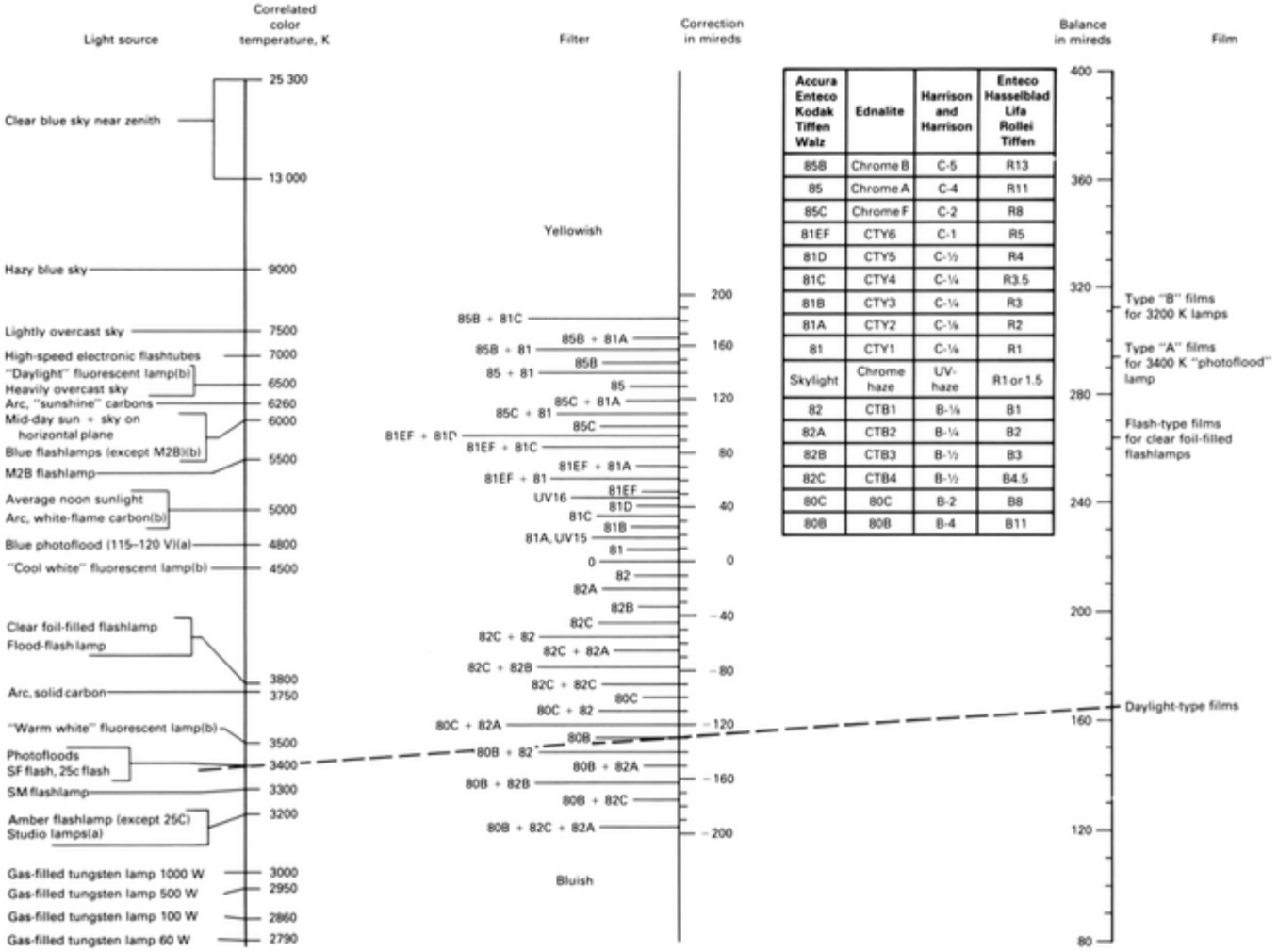

Accura Enteco Kodak Tiffen Walz	Ednalite	Harrison and Harrison	Enteco Hasselblad Lifa Rollei Tiffen
85B	Chrome B	C-5	R13
85	Chrome A	C-4	R11
85C	Chrome F	C-2	R8
81EF	CTY6	C-1	R5
81D	CTY5	C-½	R4
81C	CTY4	C-¼	R3.5
81B	CTY3	C-⅛	R3
81A	CTY2	C-⅛	R2
81	CTY1	C-⅛	R1
Skylight	Chrome haze	UV-haze	R1 or 1.5
82	CTB1	B-⅛	B1
82A	CTB2	B-¼	B2
82B	CTB3	B-½	B3
82C	CTB4	B-½	B4.5
80C	80C	B-2	B8
80B	80B	B-4	B11

Fig. 60 Color filter nomograph to aid photographers in determining which color-correcting filters are required to match the film with the light source. The dashed line presents an example. If daylight film is used in the camera with photoflood lamps (3400 K), the line between the film and light source shows that an 80B color-correction filter is required. (a) The correlated color temperature of these lamps increases approximately 11 K for each voltage increase in applied potential of approximately 115 V. As lamps are used, the correlated color temperature (at a given voltage) decreases, often from 50 K above to 50 K below the rated value during the life of the lamp. (b) Color temperature is only an approximate specification of these light sources. Source: National Bureau of Standards

Digital techniques involve digital processing of an analog signal or the more direct digitization of an image with solid-state camera. Cameras are mounted with C-mounts or a bayonet attachment. The C-mount will allow the image to be focused at the plane of the sensors in the camera. The image is focused through the eyepiece and then the object in the preview screen is made sharp and crisp by adjusting the C-mount. Good lighting and the correct microscope optics are still required to acquire a good image, just as in image acquisition on film.

Solid-state cameras employ charge-coupled or charge-injected devices, which are a matrix of small, accurately spaced photosensitive elements. When light passing through the camera lens strikes the array, each detector converts the light falling on it into a corresponding analog electrical signal. The entire image is thus broken down into an array of individual picture elements, or pixels. The magnitude of the analog voltage for each pixel is directly proportional to the intensity of light in that portion of the image. Charge-coupled and charge-injected device arrays differ primarily in how the voltages are extracted from the sensors.

The voltage from each pixel represents an average of the light-intensity variation on the area of the individual pixel. Incident light photons are converted into an analog voltage, which is then digitized into gray scale based on the intensity of light. Cameras may have an analog to digital converter (A/D) of 8 bits yielding 2^8 (256) levels, 14 bits giving 2^{14} (16,384) levels, or 16 bits 2^{16} (65,536) levels, and so on. Most commercial digital cameras offer at least 256 (2^8) gray levels, although there are 12-bit and 16-bit cameras. Naturally, the more levels available, the greater the sensitivity to subtle changes in the incident light. Color is captured in some

cameras by having sets of pixels where each pixel samples a specific primary color. For microscopy, most cameras use filters and all the pixels give information on each of the three primary colors. For the 8-bit A/D, 256 × 256 × 256 = 16,777,216 color variations can be assigned.

The necessary resolution and memory depend on contrast resolution (sensitivity) and spatial resolution requirements. In terms of contrast sensitivity (or dynamic range), the human eye can differentiate only 40 gray levels. However, because the human eye can discern several thousand shades of color, assigning individual shades of color to more than 250 gray levels can significantly increase the amount of information recognizable in an image. In addition, computerized image-analysis (IA) systems allow for gray-image processing and transformations. However, it is considered prudent to use gray-image processing as a last resort for metallographic specimens. Different etches and filters (other than the standard green filter) should be evaluated prior to gray-scale transformations (Ref 53).

Sufficient spatial resolution of the detector must also be compatible with the microscope. In microscopy with visible light, for example, the theoretical limit at which it is no longer possible to distinguish two adjacent lines is about 0.2 μm (or about 0.3 μm for dry objectives). The theoretical expression for optical resolution (*d*) of a light microscope is:

$$d = \frac{1.22 \times \lambda}{2 \cdot NA}$$

where λ is the wavelength of light (approximately 0.55 μm). In order to properly match resolution of the detector with that of the microscope, it is necessary to know the number of detectors and their size relative to the image projected onto the array surface by the microscope. Thus, required pixel size depends on the optical resolution (*d*), the objective magnification, and any additional zoom (commonly 2.5× zoom on many metallurgical microscopes). For a given optical resolution (*d*), required pixel size is larger as the objective magnification is increased (e.g., see Table 2 and Fig. 61). Conversely, required pixel size becomes smaller when optical resolution is increased at a given objective magnification (e.g.,Table 2 and Fig. 61). In addition, smaller pixels and a larger array size are required when a larger area is recorded by the CCD after zooming into a field of view at a given *NA* setting and objective magnification (compare Fig. 61a with c and compare Fig. 61b with d).

Table 2 Objective resolution and theoretical size of the CCD cell

Objective magnification	Numerical aperture	Objective resolution, μm	Theoretical cell size, μm	Number of cells per 22 mm
4×	0.10	3.36	13.4	1642
10×	0.25	1.34	13.4	1642
20×	0.40	0.84	16.8	1310
40×	0.65	0.52	20.6	1068
60×	0.95	0.35	21.2	1038
60×, oil	1.40	0.24	14.4	1528
100×, oil	1.40	0.24	24.0	917

(a) CCD, charge-coupled device. Source: Ref 54

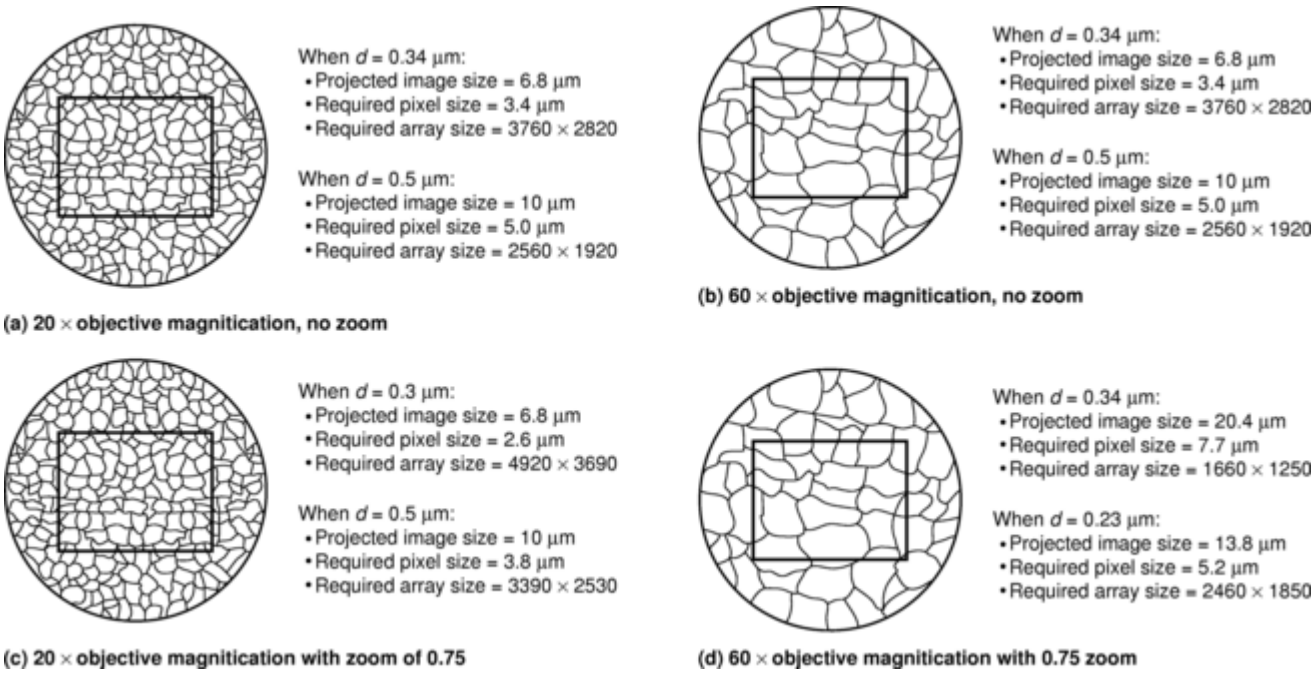

Fig. 61 Pixel requirements for a 12.8 × 9.6 mm CCD array (size not shown to scale) to match the optical resolution (*d*) and objective magnification of a microscope. (a) 20× objective magnification without zoom. (b) 60× objective magnification without zoom. (c) 20× objective magnification with 0.75 zoom. (d) 60× objective magnification with 0.75 zoom. Adapted from Ref 55

Currently available CCD arrays vary in size from several hundred to many thousands of pixels. Modern array sizes used in devices intended for scientific investigations range from 1000 × 1000 up to 5000 × 5000 sensor elements. The trend in consumer- and scientific-grade CCD manufacture is for the sensor size to continuously decrease, and digital cameras with photodiodes as small as 4 × 4 μm are currently available. Typical solid-state cameras have arrays ranging from 1×10^6 pixels (1024 × 1024 pixel array) to 4×10^6 pixels. In an average 35-mm silver halide film, there are about 20×10^6 pixels. The trend is to reduce the size of the photodetector for each pixel, but reducing pixel size can reduce dynamic range, or contrast sensitivity, of the pixel.

The determination of adequate pixel arrays for a given application also influences the sampling necessary to achieve adequate statistical relevance and the necessary revolving power to obtain accurate measurements. For example, if it is possible to resolve the features of interest using the same microscope setup and two cameras having differing resolutions, the camera having the lowest resolution should be used because it will cover a much greater area of the sample (Ref 56). The following is an example (Ref 56).

Consider a system using a 16× objective and a 1024 × 1024 resolution camera, each pixel is 0.3 μm^2. Measuring 10 fields to provide sufficient sampling statistics provides a total area of 0.94 mm^2 (0.001 $in.^2$). Using the same objective, but switching to a 760 × 574 pixel camera, the pixel size is 0.66 μm^2. To measure the same total area of 0.94 mm^2, it would only require the measurement of five fields. This could save substantial time if the analysis is complicated and slow, or if there are hundreds or thousands of samples to measure (assuming that it is possible to sufficiently resolve features of interest using either camera and the same optical setup, which often is not the case).

The key point is whether or not the features of interest can be sufficiently resolved. Additional information on processing, compression, and analysis of digital images are discussed in the articles, “Digital Imaging” and “Quantitative Image Analysis” in this Volume.

References cited in this section

2. R.P. Loveland, *Photomicrography: A Comprehensive Treatise,* Vol 1 and 2, John Wiley & Sons, 1970

47. *Photomicrography of Metals,* Kodak Scientific Publication P-39, 1971

48. *Photography through the Microscope,* Kodak Scientific Publication P-2, 1980

49. L.E. Samuels, Photographic Methods, in *Interpretative Techniques for Microstructural Analysis,* Plenum Press, 1977, p 17–42

50. B.H. Carroll et al., *Introduction to Photographic Theory,* John Wiley & Sons, 1980

51. R.S. Crouse, R.J. Gray, and B.C. Leslie, Applications of Color in Metallography and Photography, *Interpretative Techniques for Microstructural Analysis,* J.L. McCall and P.M. French, Ed., Plenum Press, 1977 p 43–64

52. H.E. Exner et al., Some Experiences in the Documentation of Colour Micrographs, *Pract. Metallog.,* Vol 17, 1980, p 344–351

53. D. Hetzner, Chapter 8 Applications, *Practical Guide to Image Analysis,* ASM International, 2000, p 204

54. L. Wojnar and K. Kurzydlowski, Chapter 7, Analysis and Interpretation, *Practical Guide to Image Analysis,* ASM International, 2000, p 172

55. http://www.microscopyu.com/tutorials/java/pixelcalculator/, Nikon MicroscopyU, Jan 2004

56. J.C. Grande, Chapter 4, Principles of Image Analysis, *Practical Guide to Image Analysis,* ASM International, 2000, p 78

G.F. Vander Voort, Light Microscopy, *Metallography and Microstructures,* Vol 9, *ASM Handbook,* ASM International, 2004, p. 332–354

Light Microscopy

George F. Vander Voort, Buehler Ltd.

Macrophotography

Examination and photography are often required for such objects as macroetched disks and broken parts. Examination can be performed visually or with the aid of a simple hand lens or stereomicroscope. Macrophotography can be performed using most cameras, perhaps aided by the use of close-up lens attachments, a bellows, or a macrolens. Stereomicroscopes are useful for macroexamination and can be used in preliminary examinations to point out specific features for more detailed study. Digital stereomicroscopes (Fig. 62) are capable of high-resolution photography or high-speed video for time-sensitive applications. Some will take stereopairs. A few manufacturers offer camera stands for macrophotography. Some metallographs also have low-magnification objectives that can perform certain types of macrophotography.



Fig. 62 Digital stereomicroscope with trinocular head allowing attachment of any C-mount compatible still or video camera. Courtesy of Olympus Corporation of America

Macrophotography utilizes magnifications from less than 1× to 50×. Most laboratories, especially those engaged in failure analyses, have various cameras, light sources, and stereoviewers to cover the wide range of objects photographed. Correct lighting is necessary to emphasize details and provide even illumination without glare or reflection. Adjustment of lighting requires some experimentation and experience. Available lighting includes flood lamps, rings, coaxial, or fiber optics. A light box is useful for eliminating shadows, but considerable creativity is required to obtain good results.

Depth of field and resolution are important variables. Many of the objects to be photographed are three-dimensional, which requires a certain depth of field and proper lighting to reveal shape and texture. Depth of field varies with the aperture diaphragm lens setting, the magnification, and the focal length of the lens. Stopping down the aperture improves depth of field, but decreases image brightness and clarity. Depth of field also increases as magnification decreases and focal length increases. Depth of field can be estimated by:

$$\text{Depth of field} = 2(f\text{-number})(C)[1 + 1/M] \quad \text{(Eq 6)}$$

where depth of field is in mm, C is the circle of confusion of the subject ($0.33/M$), and M is the magnification. Long-focal-length lenses are preferred for macrophotography to avoid distortion and astigmatism. For magnifications below 5×, focal lengths of 100 mm or more are preferred. Shorter-focal-length lenses are used for higher magnifications. Additional details concerning macrophotography can be found in Ref 57, 58, 59, and 60.

References cited in this section

57. *Simplified Photomacrography,* Kodak Scientific Publication P-53, 1970

58. *Photomacrography,* Kodak Technical Publication N-12B, 1972

59. J.R. Dvorak, Photomacrography in Metallography, *Microstruc. Sci.,* Vol 3B, 1975, p 1011–1025

60. *Photomacrography and Photomicrography,* Wild Heerbrugg, Ltd., Switzerland, 1979

G.F. Vander Voort, Light Microscopy, *Metallography and Microstructures,* Vol 9, *ASM Handbook,* ASM International, 2004, p. 332–354

Light Microscopy

George F. Vander Voort, Buehler Ltd.

References

1. R.C. Gifkins, *Optical Microscopy of Metals,* American Elsevier, 1970
2. R.P. Loveland, *Photomicrography: A Comprehensive Treatise,* Vol 1 and 2, John Wiley & Sons, 1970
3. V.A. Phillips, *Modern Metallographic Techniques and Their Applications,* Interscience, 1971
4. J.H. Richardson, *Optical Microscopy for the Materials Sciences,* Marcel Dekker, 1971
5. H.W. Zieler, *The Optical Performance of the Light Microscope,* Microscope Publications Ltd., Part 1, 1972, Part 2, 1974
6. R.B. McLaughlin, *Accessories for the Light Microscope,* Microscope Publications, Ltd., 1975
7. R.B. McLaughlin, *Special Methods in Light Microscopy,* Microscope Publications, Ltd., 1977
8. H. Modin and S. Modin, *Metallurgical Microscopy,* Halsted Press, John Wiley & Sons, 1973
9. G.F. Vander Voort, *Metallography: Principles and Practice,* McGraw-Hill, 1984
10. K.-H. Schade, *Light Microscopy—Technology and Application,* 3rd ed., Verlag Moderne Industrie, 2001
11. H.W. Zieler, What Resolving Power Formula Do You Use? *Microscope,* Vol 17, 1969, p 249–270
12. C. Van Duijn, Visibility and Resolution of Microscopic Detail, *Microscope,* Vol 11, 1957, p 196–208
13. G.K. Conn and F.J. Bradshaw, Ed., *Polarized Light in Metallography,* Butterworths, 1952
14. W.C. McCrone et al., *Polarized Light Microscopy,* Ann Arbor Science Publishers, 1978
15. A.F. Hallimond, *The Polarizing Microscope,* 3rd ed., Vickers Instruments, 1970
16. E.C.W. Perryman and J.M. Lack, Examination of Metals by Polarized Light, *Nature,* Vol 167 (No. 4247), 1951, p 479
17. A.H. Bennett et al., *Phase Microscopy,* John Wiley & Sons, 1951
18. C.E. Price, Differential Interference Contrast, *Metallography and Microstructures,* Vol 9, *ASM Handbook,* American Society for Metals, 1985, p 150–152

19. J. Padawer, The Nomarski Interference-Contrast Microscope: An Experimental Basis for Image Interpretation, *J. R. Microsc. Soc.,* Vol 88 (Part 3), 1968, p 305–349

20. R. Hoffman and L. Gross, Reflected-Light Differential-Interference Microscopy: Principles, Use and Image Interpretation, *J. Microsc.,* Vol 91 (Part 3), 1970, p 149–172

21. A.S. Holik, Surface Characterization by Interference Microscopy, *Microstruct. Sci.,* Vol 3B, 1975, p 991–1010

22. M. Francon and T. Yamamoto, A New and Very Simple Interference System Applicable to the Microscope, *Optica Acta,* Vol 9, 1962, p 395–408

23. M.G. Nomarski, Microinterféromètrie Differentiel à Ondes Polarisées, *J. Phys. Radium,* Vol 16, 1955, p 9

24. M.G. Nomarski and A.R. Weill, Application à la Métallographie des Méthodes Interférentielles á Deux Ondes Polarisées, *Revue de Metall.,* Vol 52, 1955, p 121–134

25. F. Herzog, Polarization Interferometric Methods in Incident-light Microscopy, with Special Reference to Material Testing, *Ind. Anz.,* Vol 60, July 1962, p 27–31

26. M. Francon and S. Mallick, *Polarization Interferometers,* Wiley-Interscience, 1975

27. W. Lang, "Nomarski Differential Interference Contrast Microscopy, Part IV: Applications," Zeiss Information, No. 77/78, 1971, p 22–26

28. S. Tolansky, *Multiple-Beam Interferometry of Surface and Films,* Clarendon Press, 1948

29. S. Tolansky, *Surface Microtopography,* Interscience, 1960

30. A.M.A. Schmidt and R. D. Compton, Confocal Microscopy, *Friction, Lubrication, and Wear Technology,* Vol 18, *ASM Handbook,* ASM International, 1992, p 357–361

31. M.G. Lozinskii, *High Temperature Metallography,* Pergamon Press, 1961

32. B.L. Bramfitt et al., The Use of Hot-Stage Microscopy in the Study of Phase Transformations, in *Metallography—A Practical Tool for Correlating the Structure and Properties of Materials,* STP 557, ASTM, 1974, p 43–70

33. K.A. Jackson and J.D. Hunt, Transparent Compounds That Freeze Like Metals, *Acta Metall.,* Vol 3, 1965, p 1212–1215

34. P. Tardy, New Methods for Direct Observation of the Recrystallization of Low Melting Metals, *Pract. Metallog.,* Vol 9, 1968, p 485–493

35. M. Markworth, Preparation of Metallographic Specimens of Ferrous Materials by Electrolytic Polish Attack under Direct Microscope Observation, *Neue Hütte,* Vol 13 (No. 11), 1968, p 684–689

36. R. Wall and D.I. Roberts, A Cell Technique for Microscopic Observation of Selective Corrosion, *Metallurgia,* Vol 68 (No. 410), 1963, p 291–294

37. R.A. Flinn and P.K. Trojan, Examination of Microstructures under Varying Stress, *Met. Prog.,* Vol 68, July 1955, p 88–89

38. E. Brobery and R. Attermo, A Miniature Tensile-Testing Machine for Deformation During Microscopic Observation, *Jernkontorets Ann.,* Vol 152 (No. 10), 1968, p 525–526

39. D. Godfrey, "Investigation of Fretting by Microscopic Observation," Report 1009, National Advisory Committee for Aeronautics, 1951

40. J.L. Walter and H.E. Cline, Grain Boundary Sliding, Migration, and Deformation in High-Purity Aluminum, *Trans. AIME,* Vol 242, 1968, p 1823–1830

41. S. Takeuchi and T. Homma, Direct Observation for High Temperature Fatigue in Pure Metals by Means of Microscopic Cine-Camera, *Proc. First International Conference on Fracture* (Sendai, Japan), Vol 2, 1966, p 1071–1086

42. G.L. Kehl et al., The Removal of Inclusions for Analysis by an Ultrasonic "Jack Hammer" *Metallurgia,* Vol 55, March 1957, p 151–154

43. J.H. Evans, Remote Metallography, in *Interpretive Techniques for Microstructural Analysis,* Plenum Press, 1977, p 145–168

44. R.J. Gray et al., Metallography of Radioactive Materials at Oak Ridge National Laboratory, *Applications of Modern Metallographic Techniques,* STP 480, ASTM, 1970, p 67–96

45. L. Kosec and F. Vodopivec, Examples of the Replica Technique in Optical Metallography, *Pract. Metallog.,* Vol 6, 1969, p 118–121

46. J. Neri, Optical Replicas—A Nondestructive Metallographic Evaluation Technique, in *Failure Analysis,* American Society for Metals, 1969, p 241–268

47. *Photomicrography of Metals,* Kodak Scientific Publication P-39, 1971

48. *Photography through the Microscope,* Kodak Scientific Publication P-2, 1980

49. L.E. Samuels, Photographic Methods, in *Interpretative Techniques for Microstructural Analysis,* Plenum Press, 1977, p 17–42

50. B.H. Carroll et al., *Introduction to Photographic Theory,* John Wiley & Sons, 1980

51. R.S. Crouse, R.J. Gray, and B.C. Leslie, Applications of Color in Metallography and Photography, *Interpretative Techniques for Microstructural Analysis,* J.L. McCall and P.M. French, Ed., Plenum Press, 1977 p 43–64

52. H.E. Exner et al., Some Experiences in the Documentation of Colour Micrographs, *Pract. Metallog.,* Vol 17, 1980, p 344–351

53. D. Hetzner, Chapter 8 Applications, *Practical Guide to Image Analysis,* ASM International, 2000, p 204

54. L. Wojnar and K. Kurzydlowski, Chapter 7, Analysis and Interpretation, *Practical Guide to Image Analysis,* ASM International, 2000, p 172

55. http://www.microscopyu.com/tutorials/java/pixelcalculator/, Nikon MicroscopyU, Jan 2004

56. J.C. Grande, Chapter 4, Principles of Image Analysis, *Practical Guide to Image Analysis,* ASM International, 2000, p 78

57. *Simplified Photomacrography,* Kodak Scientific Publication P-53, 1970

58. *Photomacrography,* Kodak Technical Publication N-12B, 1972

59. J.R. Dvorak, Photomacrography in Metallography, *Microstruc. Sci.,* Vol 3B, 1975, p 1011–1025

60. *Photomacrography and Photomicrography,* Wild Heerbrugg, Ltd., Switzerland, 1979

H.E. Exner and S. Weinbruch, Scanning Electron Microscopy, *Metallography and Microstructures,* Vol 9, *ASM Handbook,* ASM International, 2004, p. 355–367

Scanning Electron Microscopy

H.E. Exner and S. Weinbruch, Darmstadt University of Technology

Introduction

THE SCANNING ELECTRON MICROSCOPE is one of the most versatile instruments for investigating the microstructure of materials. Under electron bombardment, a variety of different signals is generated (including secondary electrons, backscattered electrons, characteristic x-rays, and long-wave radiation in the ultraviolet and visible region of the spectrum) that can be used for materials characterization. Using secondary electrons, scanning electron microscopy (SEM) expands the resolution range to a few nanometers (under favorable conditions), thus bridging the gap between optical (light) microscopy and transmission electron microscopy. In addition to the higher lateral resolution, SEM also has a much greater depth of field compared to optical microscopy, due to the small size of the final lens aperture and the small working distance. Scanning electron microscopy offers possibilities for image formation that are usually easy to interpret and will reveal clear pictures of as-polished and etched cross sections as well as rough surfaces and particles. Energy-dispersive x-ray microanalysis using equipment routinely attached to the scanning electron microscope features qualitative and quantitative analysis of the chemical composition with a typical lateral resolution of a micrometer and a typical depth resolution of a few tenths of a micrometer. Due to the relatively easy handling, SEM has found a wide range of applications in materials research, materials development, failure analysis, and quality control. There are several excellent monographs available on physical fundamentals, instrumental details, and applications of the scanning electron microscope (Ref 1, 2, 3, 4, 5). A short outline of beam/sample interactions, the basic instrumental design, the different types of contrast, SEM at elevated pressures, x-ray microanalysis, sample preparation, and a brief review of materials applications are presented in this article.

References cited in this section

1. J.I. Goldstein, D.E. Newbury, P. Echlin, D.C. Joy, A.D. Romig, C.E. Lyman, C. Fiori, and E. Lifshin, *Scanning Electron Microscopy and X-Ray Microanalysis,* 2nd ed., Plenum Press, 1992

2. L. Reimer, *Scanning Electron Microscopy,* 2nd ed., Springer, 1998

3. S.J.B. Reed, *Electron Microprobe Analysis,* 2nd ed., Cambridge University Press, 1993

4. S.J.B. Reed, *Electron Microprobe Analysis and Scanning Electron Microscopy in Geology,* Cambridge University Press, 1996

5. D.E. Newbury, D.C. Joy, P. Echlin, C.E. Fiori, and J.I. Goldstein, *Advanced Scanning Electron Microscopy and X-Ray Microanalysis,* Plenum Press, 1986

H.E. Exner and S. Weinbruch, Scanning Electron Microscopy, *Metallography and Microstructures,* Vol 9, *ASM Handbook,* ASM International, 2004, p. 355–367

Scanning Electron Microscopy

H.E. Exner and S. Weinbruch, Darmstadt University of Technology

Beam/Sample Interactions

Interactions between the primary electrons and the sample result in a variety of signals that can be used for sample characterization (Table 1).

Table 1 Overview of contrast mechanisms, detectors, and typical lateral and depth resolution of signals used for imaging and analyzing materials in the scanning electron microscope

The lateral resolution and the depth of information are strongly dependent on primary electron energy and sample composition; typical values are shown.

Detected signal	Type of detector	Information	Lateral resolution	Depth of information
Secondary electrons	Scintillator/photomultiplier	Surface topography, compositional contrast	5–100 nm	5–50 nm
Backscattered electrons	Solid-state detector or scintillator/photomultiplier	Compositional contrast, surface topography, crystal orientation, magnetic domains	50–1000 nm	30–1000 nm
Specimen current	No external detector necessary	Complementary contrast to backscattered plus secondary electron signal	Same as backscattered electrons	Same as backscattered electrons
Characteristic x-rays (primary fluorescence)	Semiconductor detector (energy-dispersive) or crystal/proportional counter (wavelength-dispersive)	Element composition, element distribution	0.5–2 μm	0.1–1 μm
Cathodoluminescence	Photomultiplier	Detection of nonmetallic and semiconductive phases	…	…

Backscattered Electrons. Elastic scattering (by single large-angle or multiple small-angle events) leads to a significant fraction of incident electrons that escape the sample. These electrons are termed backscattered electrons (BEs). The BEs have energies up to the incident electron energy, with the energy distribution depending on the average atomic number of components in the sample. The fraction of incident electrons that leave the target is quantified by the backscattering coefficient (η), which again strongly depends on the atomic number (Fig. 1) and the angle between incident beam and sample surface (Fig. 2). Due to the strong dependence of η on the atomic number, BEs can be employed for imaging the differences in the mean atomic number of different constituents of a sample (compositional contrast). Backscattered electrons may also be used to image the sample topography and the crystal orientation.

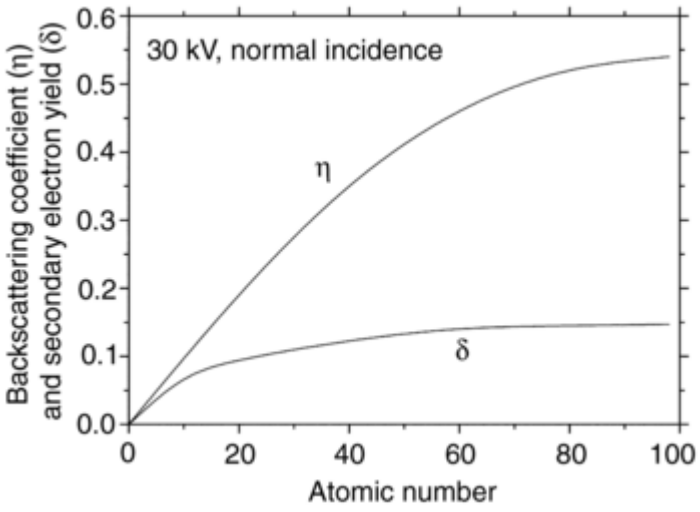

Fig. 1 Backscattering coefficient and secondary electron yield as functions of the atomic number at normal incidence

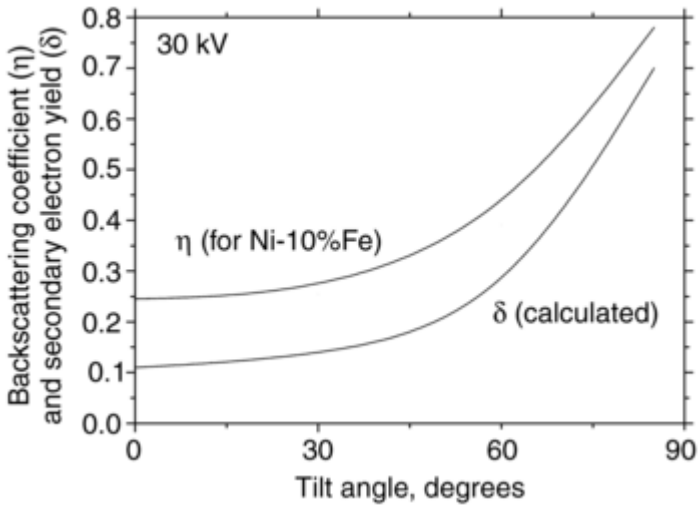

Fig. 2 Backscattering coefficient and secondary electron yield as functions of tilt angle (defined as the complement of the angle between primary beam and sample surface)

Secondary Electrons. Electrons that are produced as a result of interactions between the beam electrons and weakly bound conduction electrons of sample atoms are termed secondary electrons (SEs). The ratio of SEs to incident electrons is called secondary electron yield (δ). Because δ is almost independent of the atomic number (Fig. 1) but strongly depends on the angle between the incident beam and the sample surface (Fig. 2), SEs are mostly used to image the surface morphology (topographic contrast). Secondary electrons have much lower energies than BEs. The energy spectrum of SEs shows a pronounced maximum at approximately 3 eV; at approximately 50 eV, the frequency of SEs approaches 0. Therefore, all electrons leaving the sample with energies exceeding 50 eV are considered BEs. Secondary electrons are produced all along the way of the beam electrons through a sample. However, due to their low energy, only those SEs generated close to the surface can escape. The SEs generated by incident electrons entering the sample are called SE I; those generated by BEs when leaving the sample are called SE II. Because the number of SE II generated in a sample strongly depends on the backscattering coefficient, the contrast achieved with SEs may also contain a significant component of compositional contrast.

Absorbed Current. Electrons that flow from the sample to ground contribute to the absorbed current, which is equal to the incident beam current minus the current lost by BEs and SEs. In contrast to BE and SE images, regions that emit a large number of electrons appear dark in the absorbed current image.

X-Rays. Bombardment with electrons of sufficient energy leads to inner-shell ionization, and the target atoms are left in an excited state. Relaxation to the ground state occurs after approximately 10^{-12} seconds and results in

the emission of either characteristic x-rays or Auger electrons. Because the energy of the characteristic x-rays depends on the atomic number (Moseley's law), the chemical composition of a sample can be determined from the characteristic x-ray lines. The probability that inner-shell ionization is followed by x-ray emission (rather than the Auger electron emission) is called fluorescence yield. This probability increases rapidly with increasing atomic number. In addition to the characteristic x-ray lines, a continuous spectrum from zero energy up to the energy of the incident beam is excited. The continuum x-rays (also termed bremsstrahlung) originate from the deceleration of the beam electrons in the Coulombic field of an atom. Because the characteristic x-ray lines must be measured against the continuous background, the bremsstrahlung often limits the detection of minor or trace components in a sample. Characteristic x-rays may be excited by the beam electrons (primary fluorescence) or by characteristic x-rays or bremsstrahlung generated in the sample (secondary fluorescence).

Cathodoluminescence. Electron bombardment may lead, in some samples, to the emission of long-wave radiation (in the ultraviolet and visible region of the spectrum) by a process known as cathodoluminescence (CL), which results from the recombination of electron-hole pairs created by the primary electron beam. Compared to imaging with BEs, SEs, or characteristic x-rays, CL finds only limited use in materials investigations.

Phonons. The major fraction of energy deposited in a sample is transferred to heat, that is, to lattice oscillations (phonons). The temperature rise in a sample is directly proportional to the incident electron energy and the beam current, and inversely proportional to the thermal conductivity of a sample and the beam diameter. For metals, the temperature rise is negligible under normal operation conditions. In materials of low thermal conductivity (e.g., ceramics, minerals), however, the temperature rise may be so high that volatile components (e.g., sodium, sulfur) are lost during investigation.

Interaction Volume. For the processes discussed previously, the sample volume in which the incident beam interacts with the material is illustrated in Fig. 3 for a sample consisting of Ni-10Fe (E_0 = 20 keV, normal incidence). The distance traveled by an electron in a sample is called the electron range. According to Ref 6, the maximum electron range, R_{K-O} (micrometers), can be estimated from the following equation:

$$R_{K-O} = \frac{0.0276 \cdot A \cdot E_0^{1.67}}{\varphi \cdot Z^{0.889}}$$

where A is the atomic weight (grams/mole), E_0 is the incident electron energy (kiloelectron volts), φ is the density (grams/cubic centimeters), and Z is the atomic number. Therefore, the interaction volume for primary electrons can be approximated as a hemisphere with radius R_{K-O}, while the sampling volume of BEs may be approximated as a disk with a diameter equal to $2R_{K-O}$ and a height of $0.3R_{K-O}$ (Fig. 3). Secondary electrons have a much smaller depth of information. According to Ref 7, the maximum depth of emission of SEs is on the order of 5 nm for metals (and up to 50 nm for insulators). Thus, the sampling volume of SEs is shown in Fig. 3 as a disk with a diameter equal to $2R_{K-O}$ and a height of 5 nm. The lateral resolution achievable with BEs is inferior compared to SEs, because the majority of the latter leaves the sample closer to the point of impact of the primary electrons.

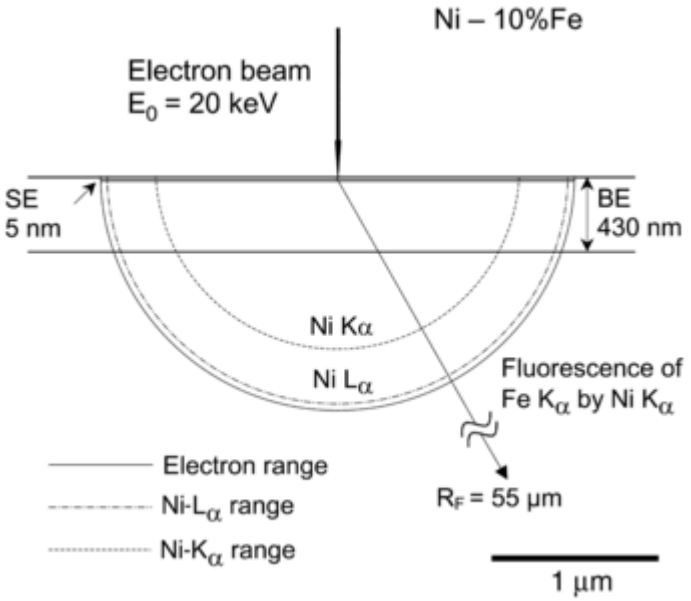

Fig. 3 Schematic illustration of the interactions between the electron beam and a sample (Ni-10%Fe alloy). Displayed are the electron range, the sampling depths of backscattered electrons (BE) and secondary electrons (SE), the x-ray generation ranges for Ni-K*α* and Ni-L*α*, and the range of fluorescence radiation, R_F, for Fe K*α* excited by Ni-K*α*.

The maximum x-ray generation range, R_X (micrometers), can be obtained from the maximum electron range, because characteristic x-rays can only be excited within the envelope containing electron energies above the critical ionization energy, E_c. The maximum x-ray generation range is, therefore, given by the following equation (Ref 1):

$$R_X = \frac{0.0276 \cdot A}{\varphi \cdot Z^{0.889}} \cdot \left(E_0^{1.67} - E_c^{1.67}\right)$$

The maximum x-ray generation range of Ni-K_α and Ni-L_α is shown in Fig. 3. Because the critical ionization energy is lower for the L-shell (0.854 keV) than for the K-shell (8.332 keV), R_X is smaller for Ni-K_α than for Ni-L_α. However, because absorption of the Ni-L_α line in nickel is much stronger than for the Ni-K_α line, the sampling volume for Ni-L_α radiation is smaller than for Ni-K_α radiation.

The x-ray generation range given previously considers only x-ray generation by beam electrons (primary fluorescence). Radiation excited by secondary fluorescence may originate in a much larger volume than the interaction volume of the electrons. Therefore, the spatial resolution of x-ray microanalysis may be strongly degraded in unfavorable cases. In the case of a Ni-10%Fe alloy, secondary fluorescence of Fe Kα by Ni Kα may take place in a distance up to approximately 55 μm away from the location of the original generation of the Ni Kα radiation (Fig. 3).

References cited in this section

1. J.I. Goldstein, D.E. Newbury, P. Echlin, D.C. Joy, A.D. Romig, C.E. Lyman, C. Fiori, and E. Lifshin, *Scanning Electron Microscopy and X-Ray Microanalysis,* 2nd ed., Plenum Press, 1992

6. K. Kanaya and S. Okayama, Penetration and Energy-Loss Theory of Electrons in Solid Targets, *J. Phys. D, Appl. Phys.,* Vol 5, 1972, p 43–58

7. H. Seiler, Einige aktuelle Probleme der Sekundärelektronenemission, *Z. Angew. Phys.,* Vol 22, 1967, p 249

H.E. Exner and S. Weinbruch, Scanning Electron Microscopy, *Metallography and Microstructures,* Vol 9, *ASM Handbook,* ASM International, 2004, p. 355–367

H.E. Exner and S. Weinbruch, Darmstadt University of Technology

Basic Design of the Scanning Electron Microscope

The main components of the scanning electron microscope include the electron gun, probe-forming column (consisting of magnetic electron lenses, apertures, and scanning coils), electron detectors, and vacuum system (Fig. 4).

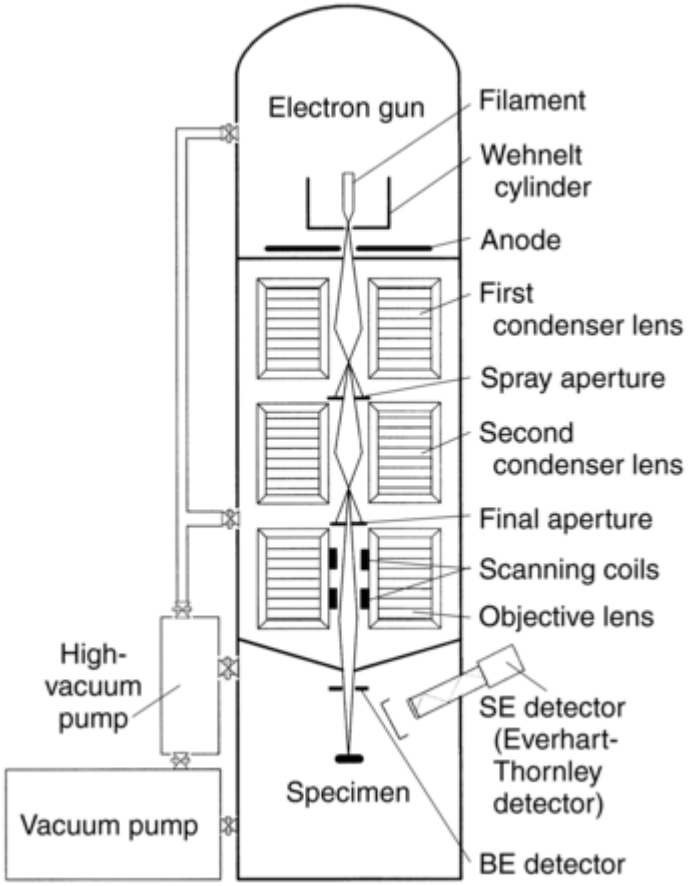

Fig. 4 Typical design (schematic) of a scanning electron microscope for secondary and backscattered electron imaging. SE, secondary electron; BE, backscattered electron

Electron Gun. Electrons are generated by thermionic emission or by an electric field. These electrons are then accelerated toward the sample. The most common type of electron gun consists of a tungsten filament that acts as a cathode. The anode consists of a grounded plate with a hole to let the electrons pass. The accelerating voltage is usually varied between 1 and 50 kV. A third electrode (Wehnelt cylinder) with a negative bias of a few hundred volts (relative to the cathode) is introduced to limit the emitting area to the tip of the tungsten filament. Lanthanum hexaboride (LaB_6) cathodes are used in order to obtain a higher brightness, which has additional benefits, such as improving the lateral resolution. Field emission sources, with still higher brightness than the LaB_6 cathode, recently became available for routine operation in commercial instruments.

Lenses and Scanning Systems. Magnetic electron lenses are used to demagnify the image of the electron source (cross over) to the final spot size on the sample surface. In most cases, three lenses are used to obtain the required demagnification. Apertures are placed between the lenses to limit the beam diameter. In order to scan the electron beam across the sample, two sets of scanning coils are placed in the bore of the objective lens. The magnification is varied by changing the size of the area scanned on a sample. The electron beam scans the sample in much the same way as in a cathode ray tube (CRT) used for image formation on a television screen, and the output of the electron detectors is displayed on the screen of a synchronously scanned CRT. In modern instruments, the analog scanning systems are replaced by digital systems in which the movements of the beam on a sample are controlled with a computer. The analog signal from the electron detectors is digitized and stored as a number for each pixel.

Vacuum System. The electron gun and the column must be evacuated in order to avoid damage to the electron source and high-voltage breakdown in the gun. High vacuum is also necessary to minimize scattering of the electrons during their travel from the gun to the sample surface. In general, the vacuum system consists of a high-vacuum pump (oil-diffusion pump, turbomolecular pump, or ion pump) and a mechanical rotary pump. Operation of a tungsten filament requires a vacuum in the gun better than $\approx 10^{-3}$ Pa, a LaB_6 cathode better than $\approx 10^{-5}$ Pa, and a thermal field emitter better than $\approx 10^{-7}$ Pa. The high vacuum in the instrument leads to evaporation of volatile compounds, especially under electron bombardment, and sample characterization may be limited by the stability of the material. Recently, environmental SEM (Ref 8) has become a routine

technique. In these instruments, pressures up to 2600 Pa are possible in the sample chamber during imaging with SEs and BEs. Due to multiple pressure-limiting apertures, a high vacuum can be retained at the same time in the electron gun and the column. The relatively high pressures in the sample chamber enable the study of fragile materials such as biological tissue, plastics, and grease. It is even possible to stabilize liquid water during electron microscopical investigation.

Detectors. The electron detector most commonly used in SEM is the Everhart-Thornley detector (Ref 9), which consists of a scintillator that, under electron bombardment, produces photons. The photons are converted to an electrical signal by means of a photomultiplier. The Everhart-Thornley detector can be used for SEs and BEs. However, there are more dedicated BE detectors, including large-area scintillator detectors, BE-to-SE conversion detectors, or solid-state diode detectors. The latter may be divided into sectors in order to obtain different contrast by combining the output of the individual sectors in different ways (see the following). In environmental SEM, special SE and BE detectors (gaseous SE detector and gaseous BE detector), which use gas ionization to detect and amplify the signal, are necessary.

In addition to the main components of a scanning electron microscope described previously, most instruments are equipped with an energy-dispersive x-ray detector (silicon or germanium solid-state detector). Energy-dispersive x-ray spectroscopy enables the qualitative and quantitative chemical analysis of elements with an atomic number ≥ 5 (boron). x-ray detection may also be carried out by wavelength-dispersive spectrometers, which consist of a crystal to reflect only radiation of a certain wavelength (Bragg's law) and a proportional counter for x-ray detection.

Additional detectors that may be fitted to a scanning electron microscope include a cathodoluminescence detector (photomultiplier) and acoustic or infrared detectors. No special detector is needed for registration of the absorbed current, because the sample itself acts as detector.

References cited in this section

8. G.D. Danilatos, Environmental Scanning Electron Microscopy and Microanalysis, *Mikrochim. Acta,* Vol 114, 1994, p 143–155

9. T.E. Everhart and R.F.M. Thornley, Wide-Band Detector for Micro-Microampere Low-Energy Electron Currents, *J. Sci. Instr.,* Vol 37, 1960, p 246–248

H.E. Exner and S. Weinbruch, Scanning Electron Microscopy, *Metallography and Microstructures,* Vol 9, *ASM Handbook,* ASM International, 2004, p. 355–367

Scanning Electron Microscopy

H.E. Exner and S. Weinbruch, Darmstadt University of Technology

---

Types of Contrast

The contrast, C, is defined as follows:

$$C = \frac{(S_2 - S_1)}{S_2} \quad S_2 > S_1$$

with S_1 and S_2 being the signals detected at two different locations in an image. By this definition, the contrast is restricted to values between 0 and 1 (or to 0 and 100%, if multiplied by a factor of 100).

Topographic Contrast. Secondary and backscattered electrons may be used to image the sample topography. Advantages in comparison to light optical microscopy include the greater depth of field and the higher lateral resolution. Topographic contrast is, in most cases, achieved with SEs. The topographic contrast in SE images results from the strong dependence of the SE yield on the tilt angle (Fig. 2), which is defined as the complement

of the angle between the primary beam and the sample surface. The resulting contrast is analogous to an optical image in which the light comes from the detector and the observation direction is that of the incident electron beam. The three-dimensional impression in SE images is not only a result of the large depth of field but is also caused by the fact that the Everhart-Thornley detector attracts SEs from regions hidden from the detector (e.g., the far side of a sample or from inside cavities). At an edge, more SEs can exit the specimen, leading to a bright appearance of this feature (edge effect). The lateral resolution achievable with SEs mainly depends on the beam diameter and can be as low as a few nanometers in favorable cases. Typical SE images with pronounced topographic contrast are shown in Fig. 5 (a–c) and 6(a) (see also Fig. 14a, 15b, 18a, 19a, and 20).

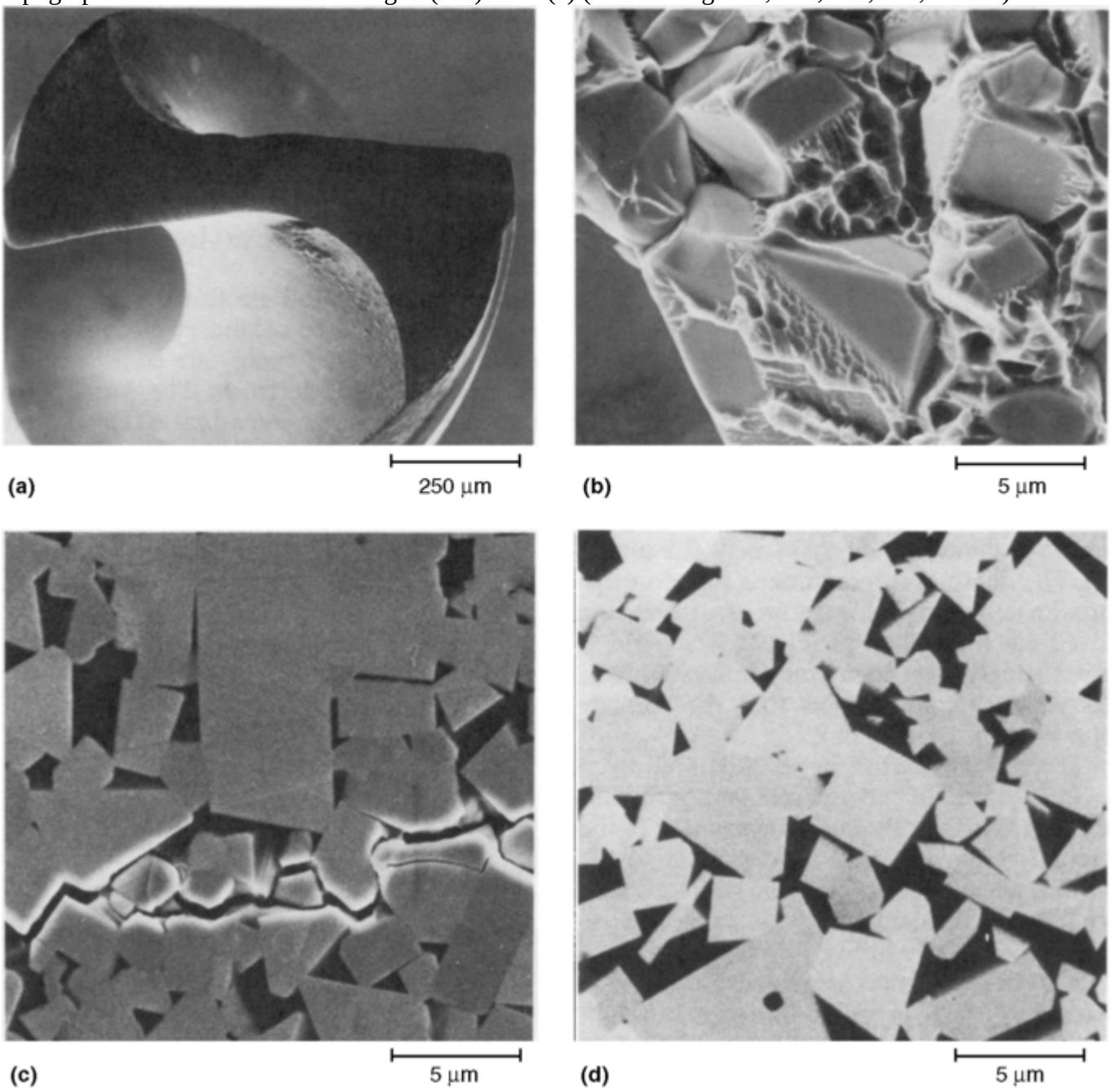

Fig. 5 Typical scanning electron micrographs of a sintered WC-12Co cemented carbide (hard metal used in metal cutting operations). (a) Secondary electron image of the surface of a worn drill (strong topographic contrast). 60×. (b) Secondary electron image of the fracture surface in a fracture toughness test specimen (strong topographic contrast). 3000×. (c) Secondary electron image of a plane section through a cracked region showing weak orientation contrast between the hexagonal carbide crystals and strong material contrast between the carbide and the binder (darker due to the lower atomic number). The crack edges appear bright due to the pronounced edge effect. 3000×. (d) Backscattered electron image (primary electron energy, 15 keV) of a plane section showing strong compositional contrast

between tungsten carbide (light) and the cobalt binder phase (black). In addition, some orientation contrast exists for the different tungsten carbide crystals. 3000×

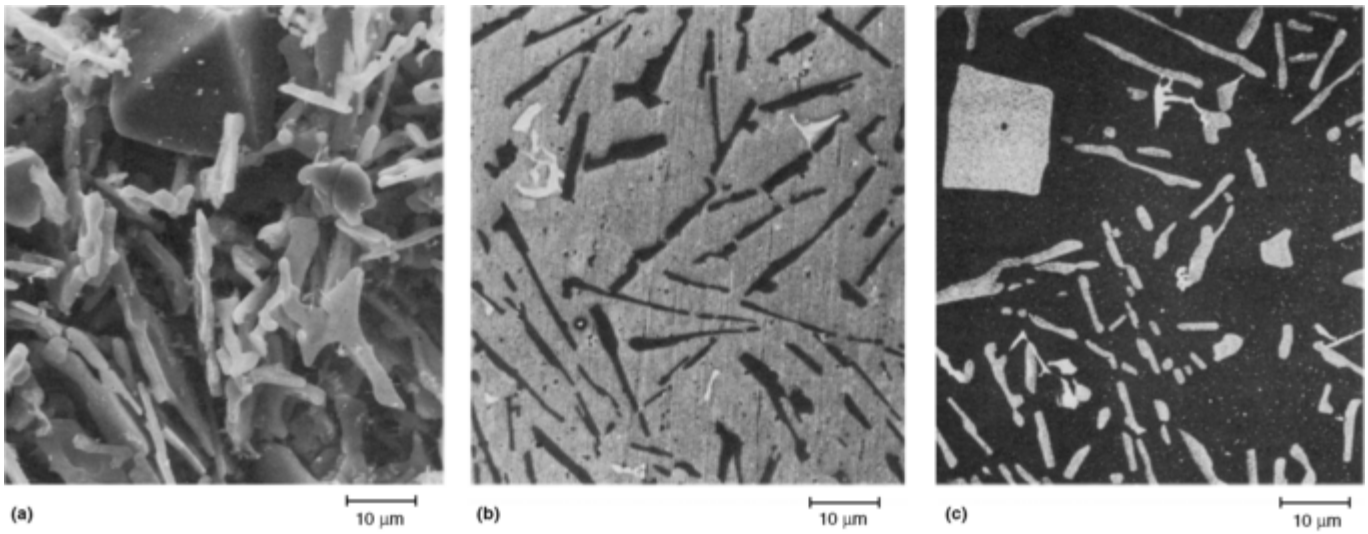

Fig. 6 Contrast formation in a cast Al-11.7Si-0.3Fe alloy by secondary electron (SE) and backscattered electron (BE) imaging. (a) Topographic contrast in a SE image. The aluminum matrix was deep etched using hot sodium hydroxide. The octahedral shape of a primary silicon crystal and the complex shapes of the eutectic silicon lamellae are clearly revealed. 1000×. (b) Topographic contrast BE image of a freshly polished cross section. The aluminum matrix appears brighter despite the lower atomic number due to the enhanced yield at the polishing scratches. The smooth silicon lamellae are dark; the intermetallic phases containing heavy elements (Fe, Ni) are bright. 1000×. (c) Backscattered electron image with the same imaging conditions as in (b) but contrasted by a molybdenum oxide layer formed selectively on the silicon particle by dipping the specimem into Mallete's reagent (400 mL CH_5OH, 10 mL H_2O_2, 10 mL HNO_3, and 4 g $(NH_4)2MoO_3$) for 15 s. The silicon appears much brighter due to the mean atomic number of the deposits. Artifacts from below the surface and blurred edges are avoided. 1000×

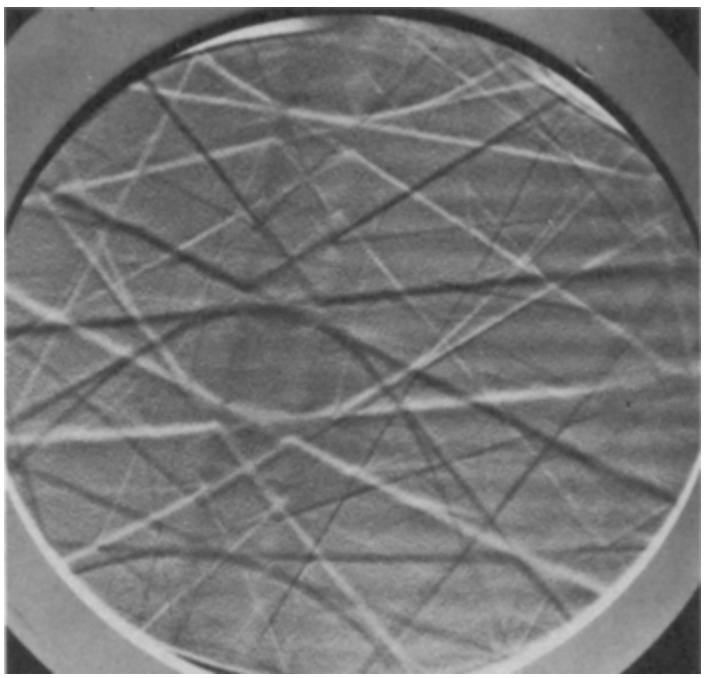

Fig. 7 Selected area electron channeling pattern from a W-10Ni heavy metal alloy. The grain orientation can be determined from the pattern arising from the penetration and absorption of electrons at those locations where lattice planes in Bragg orientation cut the specimen surface. Magnification not specified

The topographic contrast in BE images is caused by the strong dependence of the backscattering coefficient on the tilt angle (Fig. 2). In addition, pronounced shadowing effects may contribute to the topographic contrast when the detector is located to one side of the specimen (as it is in the case for the Everhart-Thornley detector). The shadowing effects result from the fact that BEs are not attracted to the detector (in contrast to SEs), due to their high energies. However, if a solid-state diode detector is used, which is divided into sectors, or if several diodes are placed in an instrument (as is the case in some commercial electron microprobes), the topographic contrast can be enhanced by using the difference in the signal of opposite sectors of one detector or two detectors placed on opposite sides of the sample, respectively. Lateral resolution with BEs is inferior compared to SEs, because BEs generally travel larger distances within a sample.

Compositional (Material) Contrast. The increase of the backscattering coefficient with increasing atomic number (Fig. 1) forms the basis for the compositional contrast. Areas with higher atomic number (or mean atomic number for compounds) appear brighter in the BE image than areas with lower atomic number. The atomic number (*Z*) dependence of the backscattering coefficient (η) can be fitted with the following equation (Ref 10):

$$\eta = -0.025 + 0.016Z - 1.86 \times 10^{-4} Z^2 + 8.3 \times 10^{-7} Z^3$$

This equation is quite useful for estimating the backscattering coefficient of compounds. However, it should be kept in mind that there are local deviations from the general increase that are not represented by the preceding equation. For example, the backscattering coefficient of cobalt ($Z = 27$) is higher than that of nickel ($Z = 28$). Because the slope of the η-versus-*Z* curve decreases with increasing *Z* (Fig. 1), compositional contrast is more pronounced in the lower range of atomic numbers. For illustration, the compositional contrast of pairs of elements separated by one atomic number is 14% for boron-carbon, 6.7% for aluminum-silicon, and 0.41% for gold-platinum (Ref 1). In order to minimize influences of topographic contrast, the specimen should be flat and well polished for compositional imaging. Compositional contrast is useful for qualitative identification of phases and is especially suitable for qualitative evaluation of microstructural geometry by image analysis. Figure 5(d) and 6(b) and (c) show examples of compositional contrast obtained with BEs, with Fig. 6(b) demonstrating the superposition of topographic contrast.

Electron Channeling Pattern and Orientation Contrast. Based on an observation of a pattern of lines superimposed on the topographic BE image dating back to 1967, a number of techniques developed, yielding information on the crystal orientation, crystal structure, and defect density and allowing new types of imaging with the scanning electron microscope (SEM) (Ref 11, 12, 13, 14, 15, 16). These techniques use the fact that the proportion of primary electrons backscattered and reaching the BE detector depends on the angle between the primary beam and the lattice planes. If the beam is parallel to certain crystallographic directions, the electrons follow the “channels” between densely packed planes and travel to a depth from which the probability of their reescape is small. Dark lines, forming patterns similar to Kikuchi lines in the transmission electron microscope, are thus formed (Fig. 14). When the direction of the primary beam deviates from these channeling directions, the proportion of electrons backscattered initially increases rapidly and then gradually with increasing angle of deviation.

There are several modes of SEM operation that use this effect (Ref 11, 12, 13, 14, 15, 16):

- *Electron channeling patterns (ECPs):* At small magnifications (approximately 20×), the electron beam scans a large specimen area (approximately 5 mm, or 0.2 in., square), over which the angle of the incident beam varies by approximately 12°. In coarse-grained materials, each grain shows a line pattern from which the orientation of the grain can be determined with reference to the angle of the primary beam or to neighboring grains. This technique is also called electron backscatter diffraction or backscatter Kikuchi diffraction.
- *Selected-area channeling pattern (SACP):* When the point mode is used and the crystal size is larger than the beam (20 to 50 μm), the crystal orientation can be precisely assessed (to approximately 1°) as follows. The cross-over point of the electron beam (under normal operating conditions, located at the last lens) is lowered to the specimen surface by adjusting the lens current, and the beam is tilted about this point by 5 to 15°, depending on the working distance. A typical pattern, called SACP, is obtained that is compared to standard patterns available for a number of materials (copper, steels, superalloys, silicon, and carbon, among others) or is indexed by commercially available computer software.
- *The step mode:* The SACP can be produced at small distances across the specimen surface by using the step mode. Every significant change of the pattern indicates a grain boundary. In contrast to most other

methods (e.g., light microscopy of etched surfaces), even twin boundaries or small-angle boundaries are safely detected. By automated registration and analysis, a map of the grain-boundary structure or a gray-level image of the grains (similar to an image obtained for some materials in polarized light) can be generated. Software for this technique (Ref 11) is available commercially under the term *orientation imaging microscopy.*

- *Electron channeling contrast imaging (ECCI):* The SEM is operated at higher magnifications (200 to 5000×) in the ECP mode. Tilting of the beam across the field of view is negligible at these magnifications, and the dependence of BE intensity on crystal orientation causes a contrast between individual crystals. Furthermore, similar contrast effects as in transmission electron microscopy are observed by concentrations of lattice defects, dislocation clusters, and subgrain boundaries. Persistent slide bands in a single crystal of copper and dislocation networks in porous materials undergoing cyclic deformation have been successfully imaged by ECCI, as well as the dislocation structure of deformation zones at the tip of cracks in massive samples and thin foils (Ref 13, 15).

Because the depth of information is restricted to 10 to 100 nm below the surface, care must be taken in surface preparation (see the section “Sample Preparation” in this article). Special recipes for a large number of materials have been published recently (Ref 12, 14). For metals, electropolishing is usually employed. For materials with stable oxide films and chemically resistant materials, ion beam polishing or plasma cleaning can provide good results. For ceramics, sample preparation is more intricate, due to their lack of electrical conductivity and their generally poor scattering behavior. Conductive coatings with a low absorption of electrons (e.g., carbon films of a maximum thickness of 1 nm), high beam currents, sensitive detectors, and low-light cameras are required.

The opportunities for applications of scanning electron microscope/electron channeling contrast imaging (SEM-ECCI) are manifold (see the following and Ref 11, 12, 13, 14, 15, 16). Because the advantages (little effort for sample preparation; destruction-free investigation of large areas, yielding statistically significant data; local combination of signals; and new types of information) are convincing, SEM-ECCI is becoming an additional routine technique in SEM.

Magnetic Contrast. Magnetic fields of ferromagnetic crystals can affect the emission of SEs and BEs, which makes it possible to image magnetic domains. The main contrast (C) mechanism is deflection of SEs immediately above the sample surface (type I magnetic contrast). For materials having strong fields (e.g., cobalt), type I magnetic contrast may amount to C = 20%. Type II magnetic contrast results from the deflection of BEs. However, this contrast mechanism is weak, leading to a magnetic contrast of approximately C = 0.1 to 0.3%. A third mechanism of magnetic contrast (type III) is the polarization of SEs. The different mechanisms of magnetic contrast are described in detail in Ref 5. An example is shown in Fig. 8 (Ref 17).

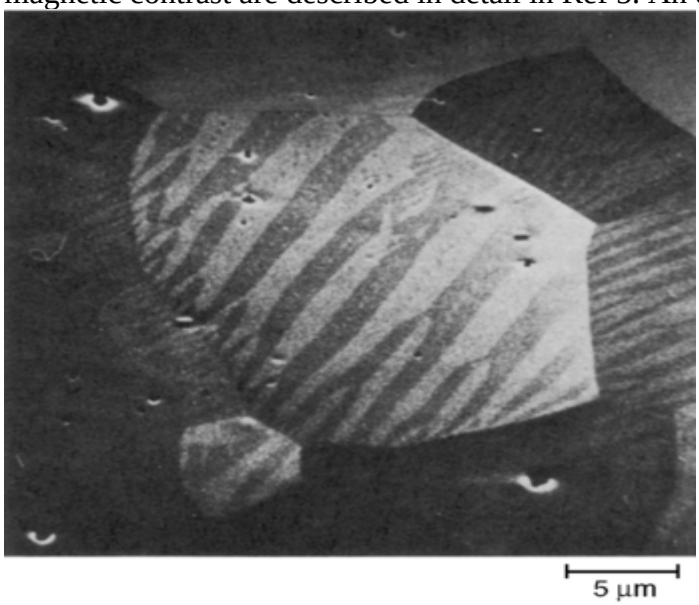

Fig. 8 Magnetic contrast in an Fe-3.5%Si sheet (mechanically lapped and electrolytically polished in 10% perchloric acid and 90% acetic acid). The magnetic domains are clearly revealed by the varying intensity of backscattered electrons due to the deflection of the primary beam by the Lorentz force.

Superimposed are the compositional contrast (bright inclusions), the topographic contrast (grain boundaries), and the orientation contrast (grain faces). 2000×

Voltage Contrast and Electron Beam Induced Current. Secondary electrons are sensitive to surface potentials. A negative bias of a few volts activates emission; a positive field impedes emission. Electron beam induced current depends on the creation of excess electron-hole pairs by the electron beam and provides useful information on diffusion length and the lifetime of minority carriers in semiconductor devices.

Image Processing and Contrast Enhancement. The signals from the detector system (output from a scintillator/photomultiplier, a semiconductor, or a specimen current preamplifier) can be modified before final amplification to control the brightness of the CRT. Techniques to improve the visibility of features of interest include black-level suppression (differential amplification that distributes contrast over the full range of the CRT), nonlinear amplification (contrast enhancement by preferential contrast expansion at either end of the gray-level scale), and differentiation of the electron signal (to emphasize boundaries between areas of uniform contrast).

The possibilities of image processing have dramatically increased with the development of digital systems, which allow software-controlled filtering, edge sharpness improvement, and contrast enhancement. In addition, powerful software packages are available for quantitative image analysis, including the measurement of size distributions, shape factors, and modal analysis of the phases present (Ref 18).

References cited in this section

1. J.I. Goldstein, D.E. Newbury, P. Echlin, D.C. Joy, A.D. Romig, C.E. Lyman, C. Fiori, and E. Lifshin, *Scanning Electron Microscopy and X-Ray Microanalysis,* 2nd ed., Plenum Press, 1992

5. D.E. Newbury, D.C. Joy, P. Echlin, C.E. Fiori, and J.I. Goldstein, *Advanced Scanning Electron Microscopy and X-Ray Microanalysis,* Plenum Press, 1986

10. W. Reuter, The Ionization Function and Its Application to the Electron Probe Analysis of Thin Films, *Proc. Sixth Int. Conf. on X-Ray Optics and Microanalysis,* G. Shinoda, Ed., Tokyo University Press, 1972, p 121

11. S.I. Wright, A Review of Automated Orientation Imaging Microscopy (OIM), *J. Comput.-Assist. Microsc.,* Vol 5, 1993, p 207

12. D. Katrakova, C. Maas, D. Hohnerlein, and F. Muecklich, Experiences on Contrasting Microstructure Using Orientation Imaging Microscopy, *Prakt. Metallogr.,* Vol 35, 1998, p 4–20

13. C. Stickler, D. Melisova, B. Mingler, B. Weiss, and R. Stickler, Advanced Microstructural Investigation Using the REM-ECC Imaging Technique, *Prakt. Metallogr.,* Vol 38, 2001, p 19–30

14. D. Katrakova and F. Muecklich, Specimen Preparation for Electron Backscatter Diffraction, Part I: Metals, *Prakt. Metallogr.,* Vol 38, 2001, p 547–565

15. C. Stickler, SEM-ECC Imaging and SAC Patterns—Procedures for the Non-Destructive Characterization of Microstructures and for Revealing the Global Dislocation Arrangement, *Prakt. Metallogr.,* Vol 38, 2001, p 566–590

16. J. Pospiech, K. Wiencek, A. Marawiec, and A. Piatzowski, Grain Boundary Contrasting on the Map of the Crystallographic Orientation Topography, *Prakt. Metallogr.,* Vol 39, 2002, p 126–139

17. G. Zwilling, Observation of Magnetic Domains in the Scanning Electron Microscope, *Prakt. Metallogr.,* Vol 11, 1974, p 716–728

18. J. Goldstein *et al, Scanning Electron Microscopy and X-Ray Microanalysis,* 3rd ed., Kluwer Academic/Plenum Publishers, 2003

H.E. Exner and S. Weinbruch, Scanning Electron Microscopy, *Metallography and Microstructures,* Vol 9, *ASM Handbook,* ASM International, 2004, p. 355–367

Scanning Electron Microscopy

H.E. Exner and S. Weinbruch, Darmstadt University of Technology

Special Instrumentation and Accessory Equipment

Scanning Electron Microscopy at Elevated Pressures. Conventional SEM is usually performed at pressures below 10^{-3} Pa (1.4×10^{-7} psi). Recently, a number of commercial instruments operating at elevated sample chamber pressures in the range of 10 to 2600 Pa became available (Ref 8). It is now common practice to classify the elevated-pressure instruments into two categories: low-vacuum scanning electron microscopy (LV-SEM) and environmental scanning electron microscopy (ESEM). The boundary between these two different types of elevated-pressure instruments is set at a pressure of 611 Pa (0.089 psi), which is the minimum equilibrium vapor pressure of liquid water. Working at pressures ≥611 Pa (0.089 psi) is considered ESEM; working at pressures below the equilibrium vapor pressure of liquid water is considered LV-SEM. Although this definition may appear somewhat arbitrary, it is quite useful from a practical point of view, because working with liquid water opens a complete new field of experiments never thought possible (Ref 8).

The high pressures in the sample chamber lead, of course, to pronounced scattering of the incident electrons. Each electron undergoes a finite number of collisions with gas atoms before it reaches the surface of the specimen. Based on the average number of collisions per electron (n_c) three different scattering regimes can be distinguished. Conventional SEMs operate in the minimal scattering regime, where n_c varies between 0 and 0.05. In the partial scattering regime, where LV-SEMs and ESEMs are operating, n_c varies between 0.05 and 3. The complete scattering regime, with $n_c > 3$, is not useful for imaging. In Fig. 9, the beam intensity profile is shown schematically for the different scattering regimes. With increasing extent of scattering, the beam loses intensity to a very broad skirt (with a diameter on the order of micrometers). However, the unscattered component does not broaden substantially. Therefore, the lateral resolution is not affected, as long as sufficient intensity to form an image remains in the unscattered component.

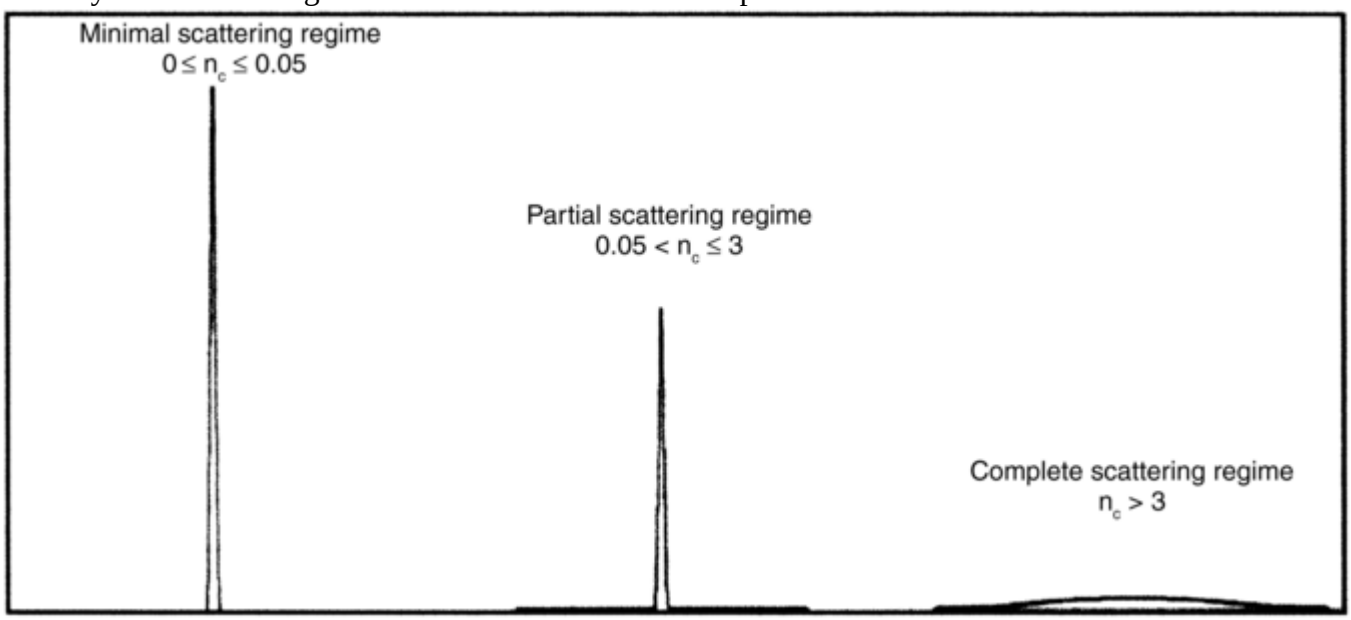

Fig. 9 Schematic of the beam intensity in the different scattering regimes (see text for details)

Both LV-SEMs and ESEMs have virtually eliminated sample preparation, because charging of insulating samples is avoided due to the high abundance of free electrons and positive ions in the gas phase. Consequently, insulating samples can be studied without any conductive coating (Fig. 10).

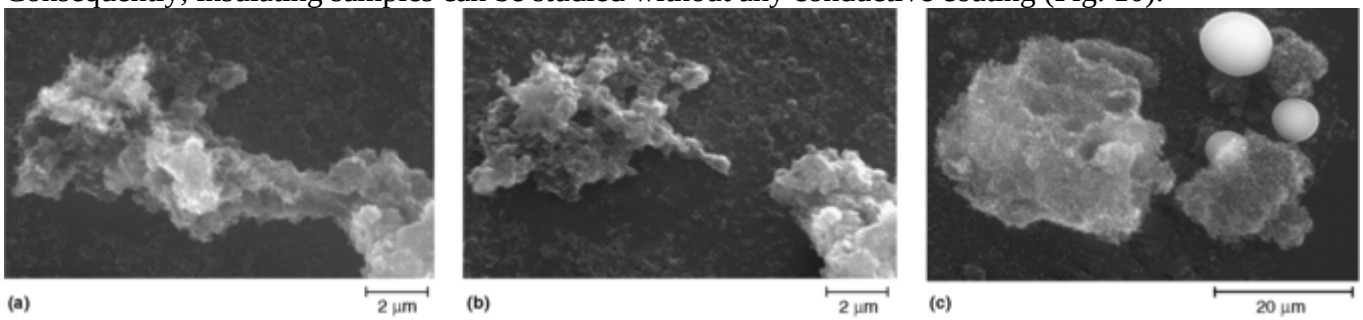

Fig. 10 Secondary electron images of a diesel soot agglomerate from a heavy-duty engine. (a) Environmental scanning electron microscopy at elevated pressures (600 Pa). Volatile components are preserved. 4000×. (b) Conventional scanning electron microscopy at high vacuum (10^{-3} Pa). Volatile components (hydrocarbons) are lost. 4000×. (c) Environmental scanning electron microscopy at a relative humidity of 91% (temperature = 5 °C, or 40 °F). Due to the presence of soluble components within the complex agglomerates, the formation of water droplets (bright spheres) is observed. 1000×

A variety of gases can be used in the sample chamber of an ESEM, including nitrogen, argon, carbon dioxide, and water vapor. By using appropriate gas mixtures, the oxygen fugacity in the sample chamber can be controlled. The temperature accessible for in situ experiments ranges from -196 (liquid nitrogen) to +1500 °C (-321 to +2730 °F). The ESEM has several benefits that open new fields of materials investigation:

- Many materials unstable under high-vacuum conditions (e.g., grease, plastics, delicate biological specimens) can be examined at elevated pressures (compare Fig. 10a and b).
- Liquid water/solid reactions (e.g., hydration/dehydration, crystallization from aqueous solutions) and hygroscopic properties (e.g., wetting of surfaces, adsorption of water) can be investigated in situ (Fig. 10c).
- High-temperature processes (e.g., oxidation, melting, sintering) can be studied in situ (Fig. 11).

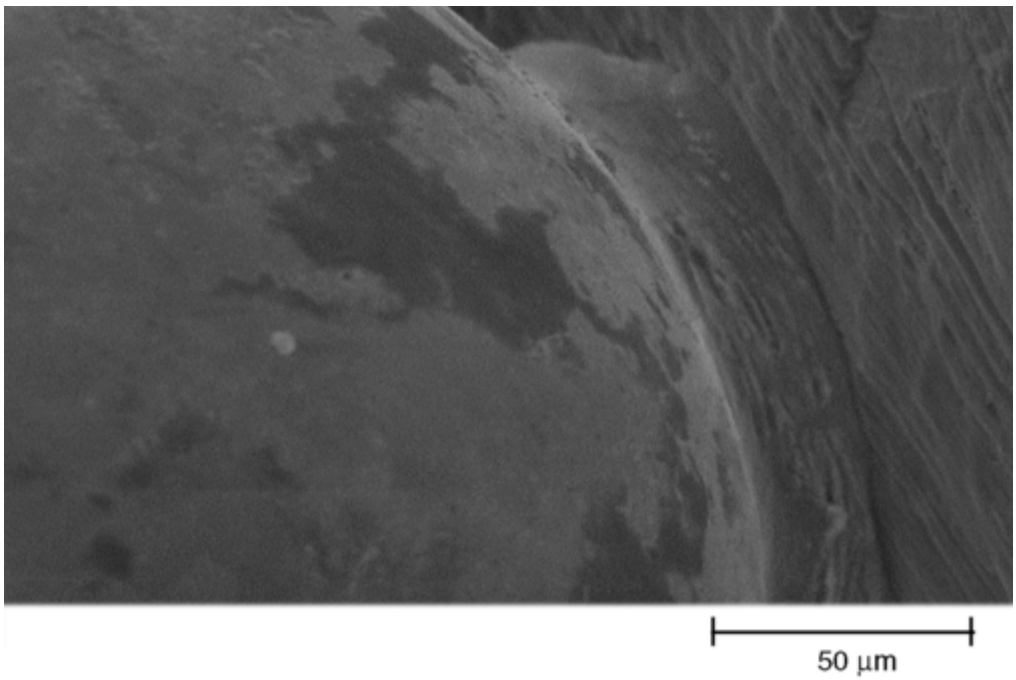

Fig. 11 Melting of a Sn36Pb2Ag alloy at a temperature of 217 °C (423 °F) studied in situ with an environmental scanning electron microscope. At this temperature, melting of the alloy (sphere) and wetting of the substrate can be observed. 460×

X-Ray Microanalysis. Although it is not a SEM technique in sensu strictu, x-ray microanalysis is discussed here briefly, because almost all instruments are equipped with an energy-dispersive x-ray detector and/or (less frequently) wavelength-dispersive spectrometers. A SEM equipped with several wavelength-dispersive spectrometers and optimized for chemical analysis is usually called an electron microprobe. Energy-dispersive x-ray (EDX) microanalysis has the advantages of higher count rates and the simultaneous recording of the complete spectrum. Due to the higher count rates, EDX microanalysis can be performed at lower beam currents (in the pA range), which is advantageous for the lateral resolution during imaging. Wavelength-dispersive x-ray (WDX) microanalysis has a higher peak/background ratio, which enables the analysis of minor and trace constituents. Detection limits achievable in WDX microanalysis are typically 1 order of magnitude lower (0.001 to 0.05 wt%) than in EDX (0.01 to 0.5 wt%). In addition, wavelength-dispersive spectrometers have a better spectral resolution, which reduces problems with line overlaps in complex samples.

Quantification of x-ray microanalysis (i.e., conversion of x-ray count rates into element concentrations) requires the measurement of standards (samples with known chemical composition) and complex calculations in order to correct matrix effects (Ref 1, 3, 19). Matrix effects arise due to the differences in chemical composition between the unknown sample and the standards investigated. The most widely used algorithm for matrix correction is the so-called ZAF correction (Ref 1, 3), where “Z” stands for atomic number, “A” for absorption, and “F” for fluorescence. The atomic number correction deals with the dependence of electron penetration and electron backscattering on the mean atomic number. The absorption correction takes account of the fact that x-rays travel a certain distance within a sample and then are absorbed. The fluorescence correction corrects the different extent of fluorescence by characteristic x-ray lines and by the continuum within the sample and standard. Quantitative chemical analysis usually requires flat and polished samples with dimensions larger than the interaction volume. However, special algorithms have been developed for small particles, rough surfaces, stratified samples, and depth profiles (Ref 1, 19). Most software packages for EDX microanalysis include procedures referred to as standardless analysis. However, because these procedures may lead to large errors that cannot be recognized without measuring standards, their use is strongly discouraged (Ref 1).

The two-dimensional distribution of chemical elements can be visualized by recording the intensity of characteristic x-ray lines as a function of the beam position, which is called an element distribution image. Because the x-ray signal is several orders of magnitude less intense than the SE and BE signal, much longer recording times are needed. Due to the higher peak/background ratio, wavelength-dispersive spectrometers are advantageous for aquisition of element distribution images. The classic approach to visualizing the element distribution in a sample is the x-ray dot map, in which each recorded photon produces a bright dot on a CRT. Because the electron beam is scanned synchronously with the CRT, a two-dimensional distribution image is obtained. However, due to the low count rates, x-ray dot maps are rather noisy, and digital recording is more appropriate. In a digital system, the number of x-ray counts is stored for each pixel. This information can then be used to modulate the brightness of a CRT. In addition, the digital information can be easily transferred to image processing and analysis software. The lateral resolution of element distribution maps is typically on the order of a few micrometers. In favorable circumstances (e.g., high concentration gradients), a resolution of a few hundred nanometers is possible. An example of an element distribution map (yttrium in the oxide scale of an iron-base oxide-dispersion-strengthened superalloy) is shown in Fig. 12 (Ref 20).

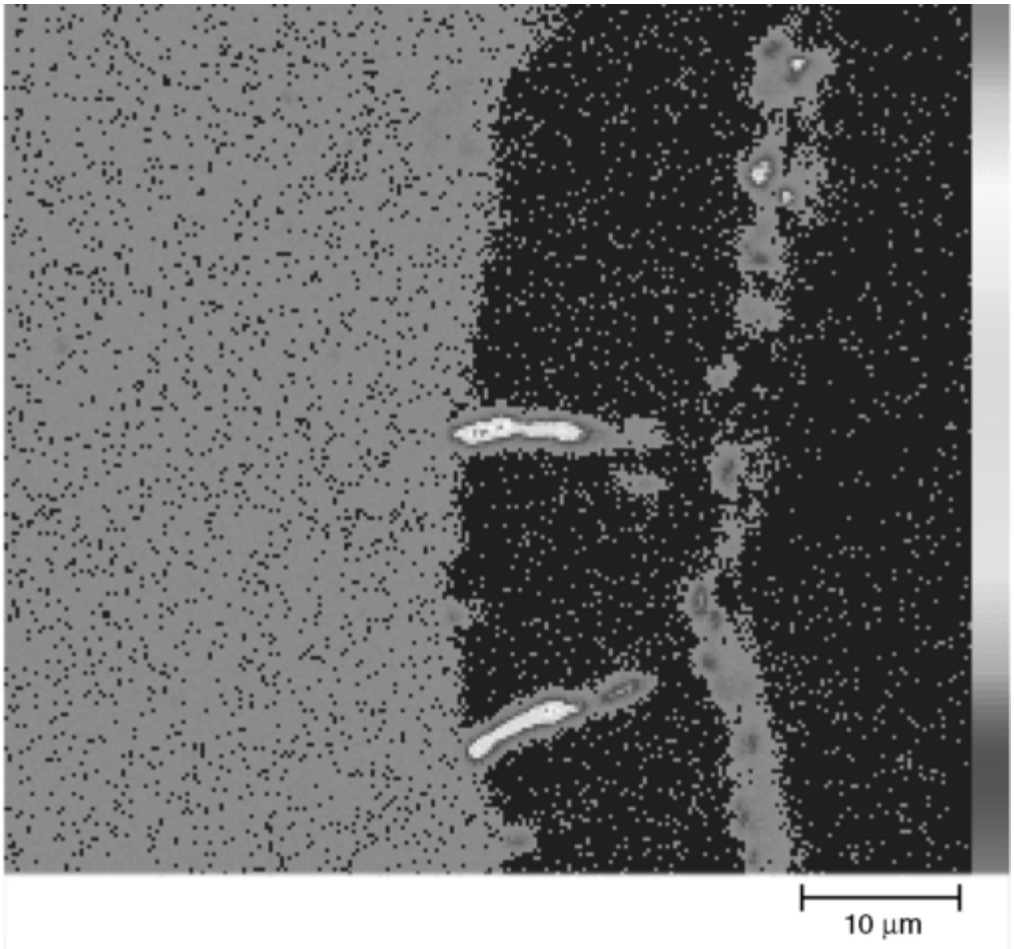

Fig. 12 Distribution map of yttrium in the oxide scale of an iron-base oxide-dispersion-strengthened superalloy. During annealing at high temperatures (1100 °C, or 2010 °F) in air, yttrium diffuses along cracks to the surface of the oxide scale. In the alloy, yttrium is distributed homogeneously. 1400×

Dynamic and Nonambient-Temperature SEM. Large depth of focus and the possibility of rapidly changing the magnification, in combination with mechanical or low- and high-temperature stages, are prerequisites for continuous observation of specimens subject to applied stress, magnetic or electric fields, chemical reaction, and the various effects of cooling or heating. Special stages to be inserted in the usually large specimen chambers of commercial microscopes have been constructed for heating, varying magnetic fields, and mechanical loading (Ref 21, 22, 23). Videorecording is ideal for registering events of interest, especially for such dynamic processes as cracking during cyclic loading or martensitic transformation. These events can be registered with markedly higher resolution than with optical micrographs using higher acceleration voltage, fast electron detectors, and wide band amplifiers; however, the maximum useful magnification may be significantly reduced in such studies. A number of results have been documented (Ref 21, 22, 23); a typical application is shown in Fig. 13 (Ref 21).

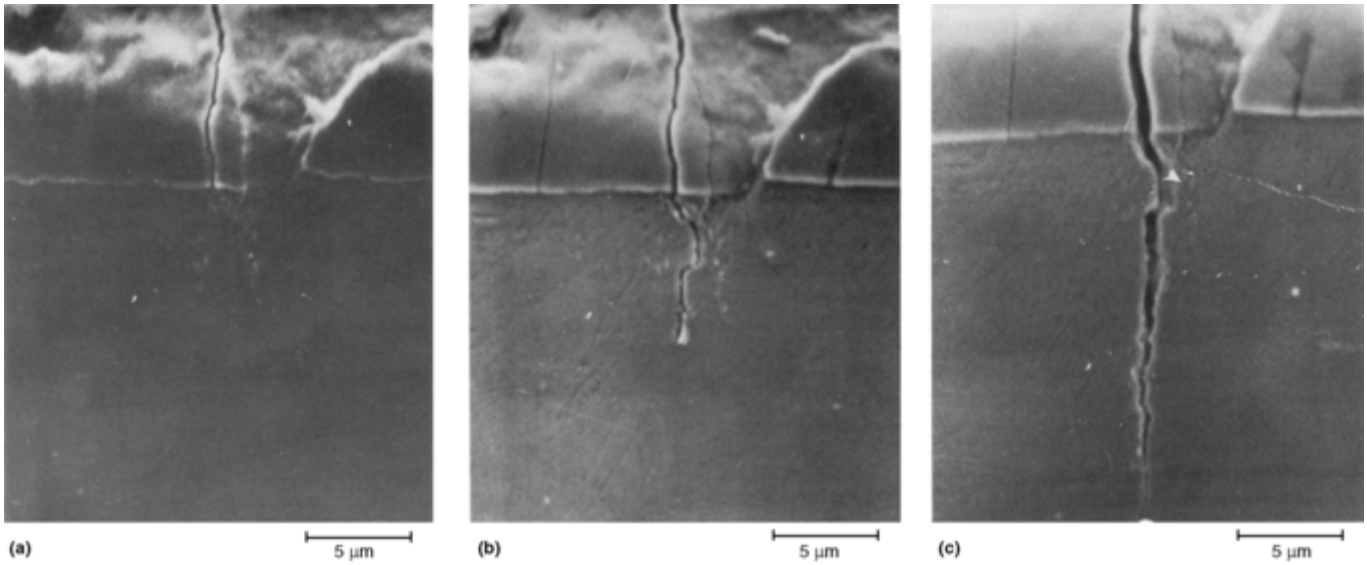

Fig. 13 Propagation of a fatigue crack from a hard surface coating into a steel specimen. The TiC coating (top) was produced by chemical vapor deposition at 970 °C (1780 °F) on C100W1 steel. The micrographs were taken in a bending stage built into the specimen stage without interrupting the fatigue test after the following number of cycles: (a) 80,000 cycles, (b) 190,000 cycles, and (c) 320,000 cycles. All 3000×

Stereoviewing and Quantitative Analysis. An excellent three-dimensional impression of fracture surfaces as well as other rough surfaces, powder particles, and other three-dimensional objects is provided by viewing stereopair micrographs (taken by using accessory tilting or goniometer stages) in a stereoscope. Some instruments are equipped to employ the anaglyphe method, in which one of the two stereopair pictures is colored red and the other one green or blue by using false colors. Using colored glasses gives a three-dimensional impression directly from the SEM screen.

The lateral shift of any picture point in the two pictures, the parallax, depends on the tilt angle and the viewing distance, which are known, and the height difference (distance in *z*-direction) between the tilt axes and the corresponding point on the sample surface. Measuring the parallax manually or by automatic image analysis yields accurate data on the *x-y-z* coordinates. These data can then be combined to construct height profiles or height maps. Also, characteristic parameters such as roughness indexes can be calculated and then used to classify fracture surfaces and other rough surfaces obtained in machining, after corrosion, or after wear. More detailed descriptions of techniques and applications can be found in the literature (Ref 24, 25, 26, 27, 28).

Quantitative analysis of SEM images follows the lines for quantitative assessment of microstructural geometry. Other recent reviews are available in the literature (Ref 28, 29, 30, 31, 32). Using the good resolution and the various capabilities of phase discrimination, quantitative SEM will frequently be the best solution when, using the optical microscope, the resolution limit is reached or contrast formation is not possible. On-line processing by interfacing a commercial automatic image analyzer to a SEM has become a powerful routine technique with the development of digital gray-level image storages. Highly sensitive discrimination of two or more phases is usually not a problem, because several signals can be used simultaneously, and noise reduction, filtering processes, contrast enhancement, and other image-processing techniques can be carried out. Processing time per field is only limited by the scanning time for producing the image. A special feature is geometric and chemical analysis of small powder particles and inclusions (for example, nonmetallic or carbide particles in steels) by means of computer-controlled positioning of the electron beam. The particles are localized and geometrically characterized in the image analyzer, then the electron beam locates their center, and the chemical composition is determined using x-ray microanalysis (Ref 33).

References cited in this section

1. J.I. Goldstein, D.E. Newbury, P. Echlin, D.C. Joy, A.D. Romig, C.E. Lyman, C. Fiori, and E. Lifshin, *Scanning Electron Microscopy and X-Ray Microanalysis*, 2nd ed., Plenum Press, 1992

3. S.J.B. Reed, *Electron Microprobe Analysis,* 2nd ed., Cambridge University Press, 1993

8. G.D. Danilatos, Environmental Scanning Electron Microscopy and Microanalysis, *Mikrochim. Acta,* Vol 114, 1994, p 143–155

19. K.F.J. Heinrich and D.E. Newbury, *Electron Probe Quantitation,* Plenum Press, 1991

20. S. Weinbruch, A. Anastassiadis, H.M. Ortner, H.P. Martinz, and P. Wilhartitz, On the Mechanism of High-Temperature Oxidation of ODS Superalloys: Significance of Yttrium Depletion within the Oxide Scales, *Oxid. Met.,* Vol 51, 1999, p 111–128

21. K. Wetzig, A. Maslov, and J. Edelmann, Development and Application of a Cyclic Bending Device for in-situ Fatigue Investigations in the Scanning Electron Microscope, *Prakt. Metallogr.,* Vol 21, 1984, p 161–172

22. D.L. Davidson and A. Nagy, A Low Frequency Cyclic-Loading Stage for the SEM, *J. Phys. E, Sci. Instrum.,* Vol 11, 1978, p 207–210

23. W. Krompp, P. Bajons, and B. Weiss, A Scanning Electron Microscope Accessory for the Observation of Deformation Processes, *Prakt. Metallogr.,* Vol 13, 1976, p 53–62

24. J. Stampfl, S. Scherer, M. Gruber, and O. Kolednik, Reconstruction of Surface Topographies by Scanning Electron Microscopy for Application in Fracture Research, *Appl. Phys. A,* 1996, p 341–346

25. C.O.A. Semprimoschnig, J. Stampfl, R. Pippan, and O. Kolednik, A New Powerful Tool for Surveying Cleavage Fracture Surfaces, *Fatigue Fract. Eng. Mater. Struct.,* 1997, p 1541–1550

26. H.E. Exner, Quantitative Metallography in Three Dimensions, *Prakt. Metallogr.,* Vol 38, 2001, p 370–384

27. H.E. Exner and M. Fripan, Quantitative Assessment of Three-Dimensional Roughness, Anisotropy and Angular Distribution of Fracture Surfaces by Stereometry, *J. Microsc.,* Vol 138, 1985, p 161–178

28. H.E. Exner, Quantitative Description of Microstructures by Image Analysis, *Materials and Technology,* Vol 2B, VCH, 1994, p 281–350

29. H.E. Exner, Qualitative and Quantitative Surface Microscopy, *Physical Metallurgy,* Vol 2, Elsevier, 1996, p 993–1032

30. J.C. Russ, *Computer-Assisted Microscopy—The Measurement and Analysis of Images,* Plenum Press, 1990

31. H.E. Exner and H.P Hougardy, *Quantitative Image Analysis of Microstructures,* DGM-Informationsgesellschaft-Verlag, 1988

32. M. Coster and J.L. Chermant, *Précis d'Analyse d'Images,* Editions du Centre National de la Recherche Scientifique, 1989

33. R.J. Lee, W.A. Spitzig, J.F. Kelly, and R.M. Fisher, Quantitative Metallography by Computer-Controlled Scanning Electron Microscopy, *Prakt. Metallogr.,* Vol 21, 1984, p 27–41

H.E. Exner and S. Weinbruch, Scanning Electron Microscopy, *Metallography and Microstructures,* Vol 9, *ASM Handbook,* ASM International, 2004, p. 355–367

Scanning Electron Microscopy

H.E. Exner and S. Weinbruch, Darmstadt University of Technology

Sample Preparation

Scanning electron microscopy often requires little effort in specimen preparation. Good imaging necessitates contamination-free surfaces, resistance of the specimen to the high vacuum and the electron beam, absence of electrical charging, and sufficiently high electron yield. Samples of electrically conductive material free of outgassing substances, which is often the case with solid materials, need only be sectioned to a suitable size and secured to the specimen holder of the microscope. In ESEM, insulators can be studied without any coating (Fig. 10a–c). Thus, surface morpholgy of these materials can be studied without any artifacts from sample preparation. Details of sample preparation techniques for a variety of different materials (including inorganic, biological, organic, polymeric, and hydrated materials) can be found in Ref 1.

Mounting. The upper limit of specimen size is defined by the size of the loading door of the specimen chamber. Specimens under 20 mm (0.8 in.) in height, width, or length are usually cut from larger pieces. To prevent charging, conductive adhesives, such as silver, aluminum-containing glues, or carbon adhesives (to avoid unwanted radiation), are used to secure the specimen. Difficulties are encountered in the investigation of small powder particles. Separation of a representative specimen from a large quantity of a powder material, deagglomeration, and uniform distribution are important when quantitative information on particle size and shape distribution is required. Affixing the specimen to the specimen holder using adhesive tapes or direct adhesion yields favorable results. For embedding of powders or small specimens, special resins with a low tendency toward outgassing should be used. Mechanical securing is often used for larger specimens to avoid contaminating the microscope.

Surface Treatment. Cross sections are prepared in the same manner as for optical microscopy, but care must be taken in cleaning, because residual polishing liquids or etchants trapped in pores or cracks contaminate the surface when placing the specimen into the vacuum chamber. Weak contrast mechanisms, such as magnetic or electron channeling contrast, are impossible to detect in the presence of a deformed layer or topographic variations. Therefore, deformation-free and plane cross sections must be prepared by careful polishing when studying microstructures using these contrast mechanisms. Scratches, height differences of hard and soft phases, and deformed layers, which are unavoidable in mechanical polishing, can usually be removed by electrolytic polishing. Fracture surfaces, if not freshly produced, usually must be washed clean. Reaction products formed during extended exposure to the atmosphere or by high-temperature reaction can be removed electrolytically, by hydrogen reduction, or chemically.

Conductive Coating. In conventional instruments, insulating materials, even nonconducting particles dispersed in a metallic matrix, build up a space-charge region by accumulation of absorbed electrons. This charging deflects the incident beam, leading to image distortion, and significantly changes the emission of SEs. Charging also affects x-ray microanalysis, because the energy of the incident electrons is reduced. Charging effects can be avoided by operating at a low acceleration voltage of the primary beam or by applying conductive coatings, which is the widely used technique. The coating layer must be thick enough to provide a conductive path but should be as thin as possible to avoid obscuring fine details. The minimum thickness depends on surface roughness and may range from 0.5 nm for microscopically flat to 10 nm for slightly profiled and up to 100 nm for extremely rough surfaces. Because the thickness of the layer can be irregular in the latter cases, only the average thickness can be monitored by adjusting the weight of the material chip used for evaporation or, more conventionally, by using a piezoelectric crystal monitor. Carbon, gold, platinum, palladium, silver, copper, or aluminum are applied by high-vacuum evaporation or cathode sputtering. The latter method is preferred, because sputtered layers exhibit better adhesion. Based on physical considerations, a gold coating approximately 10 nm thick is predicted to produce a maximum SE emission, and gold is used most often. Carbon, which is applied preferentially as a ground material for coating porous and rough surfaces, is often

used with a low vacuum (>0.1 Pa) to provoke scattering of the carbon and with a shield to avoid shadowing and heating of the object by direct radiation from the carbon source. When performing x-ray analysis, primary electrons, BEs, and x-rays emitted from the specimen can excite x-ray photons in the coating that can interfere with the x-ray lines of interest, for example, gold with zirconium, niobium, phosphorus, or platinum. Compared to carbon, aluminum, and gold-palladium, gold is to be preferred, due to its high electric conductivity (exceeding that of aluminum by a factor of approximately 3).

Contrast Enhancement by Coating. Coating is sometimes applied to enhance the plastic impression by using the shadowing effect. By using a coating substance with high SE emission, such as gold, a positive image with bright, outstanding details and dark shadows in the direction of oblique evaporation is obtained. Coatings can also enhance the contrast of materials, forming a layer on only one of the phases. As an example, Fig. 6(c) shows the dramatic improvement in contrast between aluminum and silicon compared to the normal BE image as the result of a MoO_2 layer formed on the silicon by reaction with a suitable solution (Ref 34). Chemical vapor deposition of hard coatings on and carbide particles in high-speed steel can be contrasted by evaporated, sputtered, and chemically deposited layers. Coated and uncoated arsenic selenide (AsSe) layers are illustrated in Fig. 14, demonstrating the improvement in image quality for this semiconducting material (Ref 35). Other developments of this type are numerous and are specific to certain alloys and based on varying chemical or physical principles not yet fully understood in some cases.

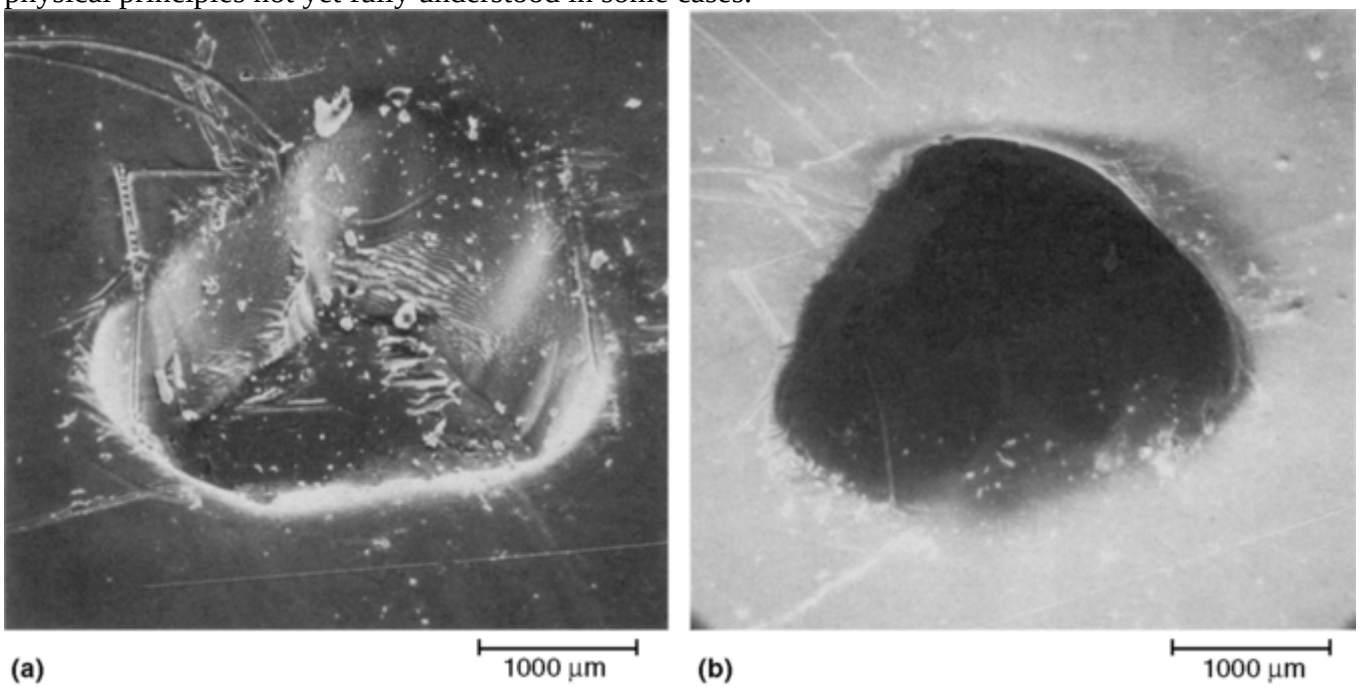

Fig. 14 Improvement of image quality by coating. (a) Secondary electron image of a depression in a gold-coated semiconductor layer (AsSe) showing the cavity wall and protuberances. (b) Same specimen and imaging conditions as (a) but uncoated. Both 15×

Etching. No special treatment is necessary when compositional contrast is used for image formation; differences in atomic number appear as variations in brightness, with the phase containing the lighter elements appearing darker. Etching, harmful in these cases, obscures the weaker effects of magnetic or orientation contrast. If topographic contrast is used for image formation, then chemical, electrolytic, or ion etching is applicable. Ion etching produces a uniform surface layer and leaves none of the residuals of liquid reagents. Etching is used to produce special effects, such as developing etch pits at dislocations (Fig. 21b). Deep etching is frequently used to study complexly shaped microstructural constituents. Figure 15(a) and (b) compare the appearance of intermetallic phases in a cross section imaged with BEs (compositional contrast) and in a deeply etched surface using SEs (topographic contrast). Further examples are shown in Fig. 5(b) and 6(a) and in Fig. 17(c) and (d) discussed subsequently.

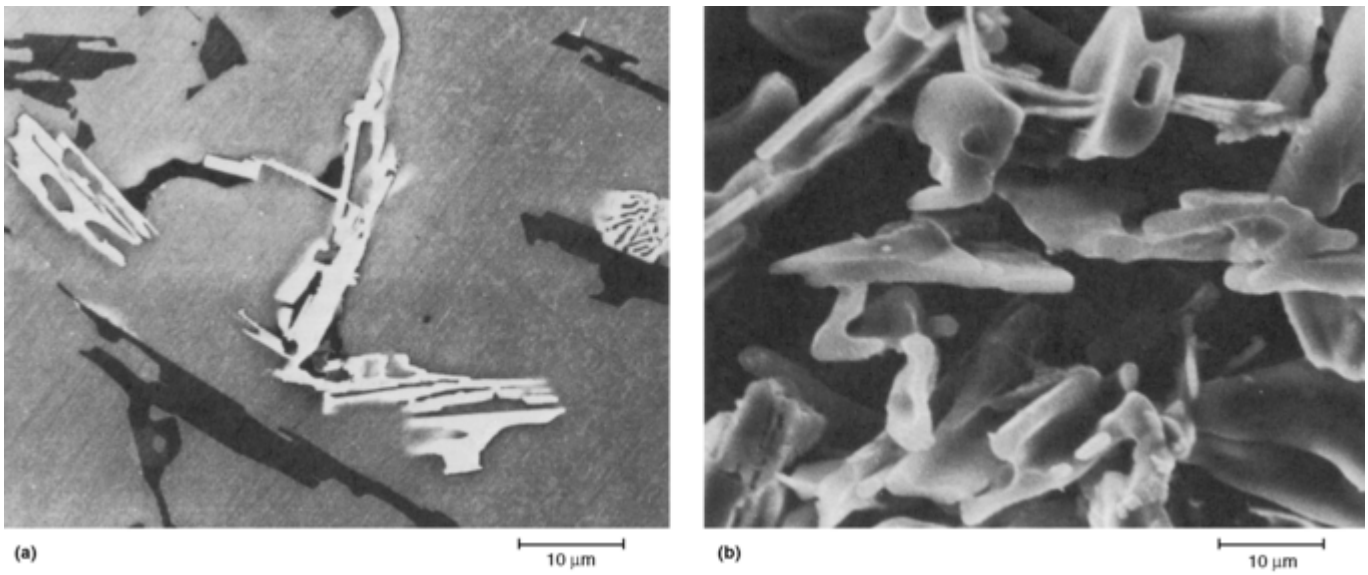

Fig. 15 Scanning electron micrographs of a cast Al-11.7Si-1Co-1Mg-1Ni-0.3Fe alloy. (a) Unetched cross section, backscattered electron image. The intermetallic phases are clearly revealed by the compositional contrast. AlFeSiNi appears bright due to the high content of heavy elements; Mg_2Si and Si appear dark. (b) Deep etched using sodium hydroxide, secondary electron image. The three-dimensional shape can be correlated to the two-dimensional cross sections shown in this micrograph. Both 1500×

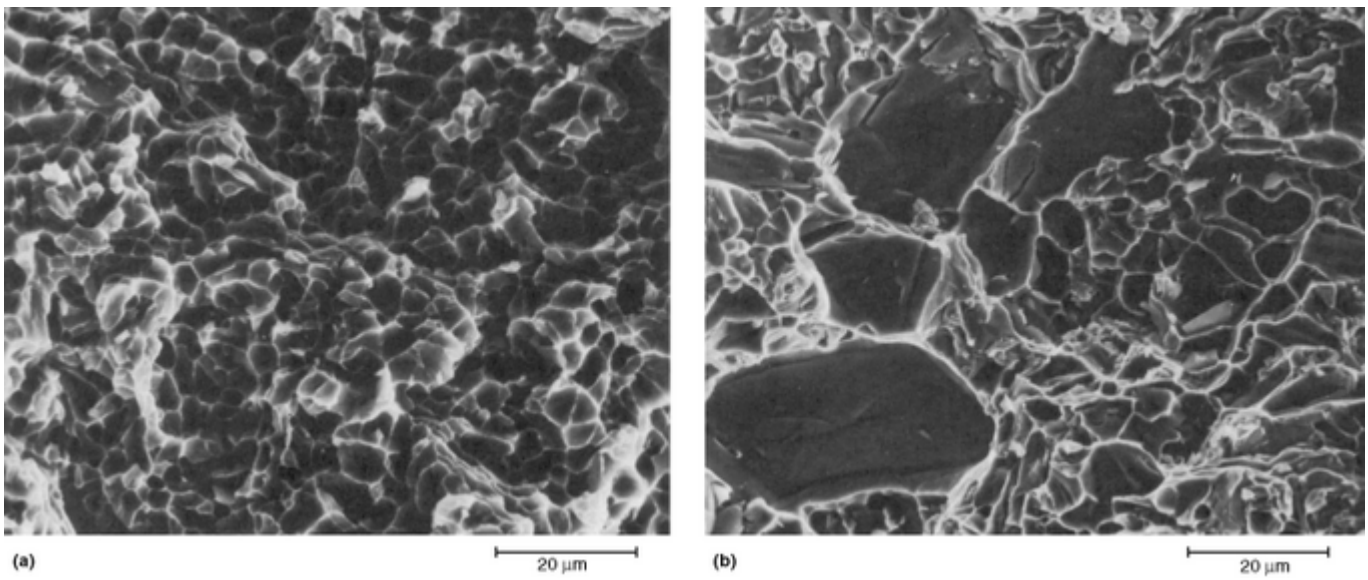

Fig. 16 Fracture surfaces of alloy Al-11.7Si-1Co-1Mg-1Ni-0.3Fe. (a) Ductile appearance of a fracture surface, backscattered electron image. The alloy was rapidly cooled during casting and has a fine microstructure, giving rise to high elongation to fracture. 1000×. (b) Brittle appearance of a fracture surface, backscattered electron image. The alloy was slowly cooled during casting and has a coarse microstructure. The large silicon plates (large, dark areas) and the intermetallic phases (small, light particles) cause a low elongation to fracture. 1000×

References cited in this section

1. J.I. Goldstein, D.E. Newbury, P. Echlin, D.C. Joy, A.D. Romig, C.E. Lyman, C. Fiori, and E. Lifshin, *Scanning Electron Microscopy and X-Ray Microanalysis,* 2nd ed., Plenum Press, 1992

34. J. Paul and B. Bauer, Contrast Techniques for Phase Separation in the Scanning Electron Microscope, *Prakt. Metallogr.,* Vol 20, 1983, p 213–221

35. T. Hillmer, Practical Experience in Materials Microanalysis with the Scanning Electron Microscope, Part 1: Methods of Preparation, *Prakt. Metallogr.*, Vol 16, 1979, p 465–479

H.E. Exner and S. Weinbruch, Scanning Electron Microscopy, *Metallography and Microstructures,* Vol 9, *ASM Handbook,* ASM International, 2004, p. 355–367

Scanning Electron Microscopy

H.E. Exner and S. Weinbruch, Darmstadt University of Technology

Applications in Materials Science and Technology

In all fields in which geometry and composition of microstructures are of interest, the SEM and most of its accessories have become routine instrumentation. The wide range of applications in earth and life sciences can best be appreciated by consulting the proceedings of special conferences on SEM. Excellent examples of applications in materials science and technology can be found in almost every volume, if not issue, of journals in these fields and thus cannot possibly be reviewed in detail. The examples discussed subsequently illustrate some typical areas in which the SEM provides useful information.

Fractography. The investigation of fracture processes and fracture surfaces is probably the most popular field of SEM. The large depth of focus, the possibility of changing magnification over a wide range, very simple nondestructive specimen preparation with direct inspection, and the three-dimensional appearance of SEM fractographs make the SEM an indispensable tool in failure studies and fracture research. Fracture types are classified by appearance in the SEM for steels and other materials. Figure 16(a) and (b) compare a ductile and a brittle fracture in the same alloy, cast at different cooling rates. Stereoviewing to identify the crack features unambiguously, quantitative assessment of the crack path in plane section or in three dimensions, in situ fracture studies for varying loading conditions, and the possibility of identifying the phases through which the crack has passed by locating the ductile/brittle appearance at the different locations of a fracture surface or by dot mapping in energy-dispersive x-ray analysis are special techniques generally practicable by using the various techniques of SEM. In a classical study (Ref 36), a combination of these techniques was used to quantify the fracture areas in the ductile and brittle phases and the depth of the dimples (Fig. 5b), the size of the process zone in front of the crack, and the mode of crack propagation by the SEM techniques discussed previously. These data were used to show the excellent agreement between experiments and a quantitative model for the fracture toughness of WC-Co cemented carbides (Ref 37). By computerized stereometry, the distribution of tilt angles and the size of surface facets were determined after critical and subcritical crack propagation in these materials, indicating no difference between these fracture modes (Ref 38). Scanning electron microscope stereometry was used also to measure the locations of fiber fracture (Fig. 17a) as an important ingredient of predicting the fracture probabilities of aluminum reinforced by ceramic fibers (Ref 39, 40).

Microstructural Morphology. Scanning electron microscopy studies have contributed extensively to understanding the development of materials microstructures and their influence on materials properties. Nucleation and growth instabilities during solidification produce a variety of shapes and arrangements of microstructural features in cast alloys. Examples are shown for cast aluminum alloys in Fig. 6, 15, and 17(b), which display the shapes of silicon and intermetallics and the morphology of dendrites. From the deep-etched section of the cast aluminum-copper alloy (Fig. 17b), the curvature distribution of the dendrites was assessed by computerized stereometry (Ref 41) and compared to theoretical predictions (Ref 42). Starting with interesting studies on primary graphite in gray cast iron in the 1960s, the shape of different types (i.e., lamellar, nodular, vermicular) of graphite was of great concern. Using stereoviewing of graphite particles etched out from the iron matrix, the complicated shapes were analyzed, and a systematic characterization of the multitude of graphite morphologies has become available.

Degradation of microstructures during use due to morphological changes (but also by grain growth, particle coarsening, recrystallization, and so forth) is also investigated using SEM. Image analysis is used to obtain quantitative data to assess the kinetics of microstructural transformations and their effect on materials properties. For example, because the size of ceramics determines their strength, it is of interest to understand the interaction between dispersed particles and grain boundaries in Al_2O_3-10%ZrO_2 composites. From SE micrographs taken after thermal etching (Fig. 17c), the grain and particle sizes can be quantitatively assessed, establishing a Zener-type relationship and a better understanding of the mechanical behavior of this technically important ceramic. Figure 17(d) shows the effect of heating on the microstructural geometry of a conduction material. It is obvious that the decay of the strong fibers during extended heating deleteriously affects the strength of this material. Another example of the large variety of SEM applications in materials science is the study of the degradation of an electronic component investigated using SEM imaging and x-ray dot mapping, shown in Fig. 18(a–c).

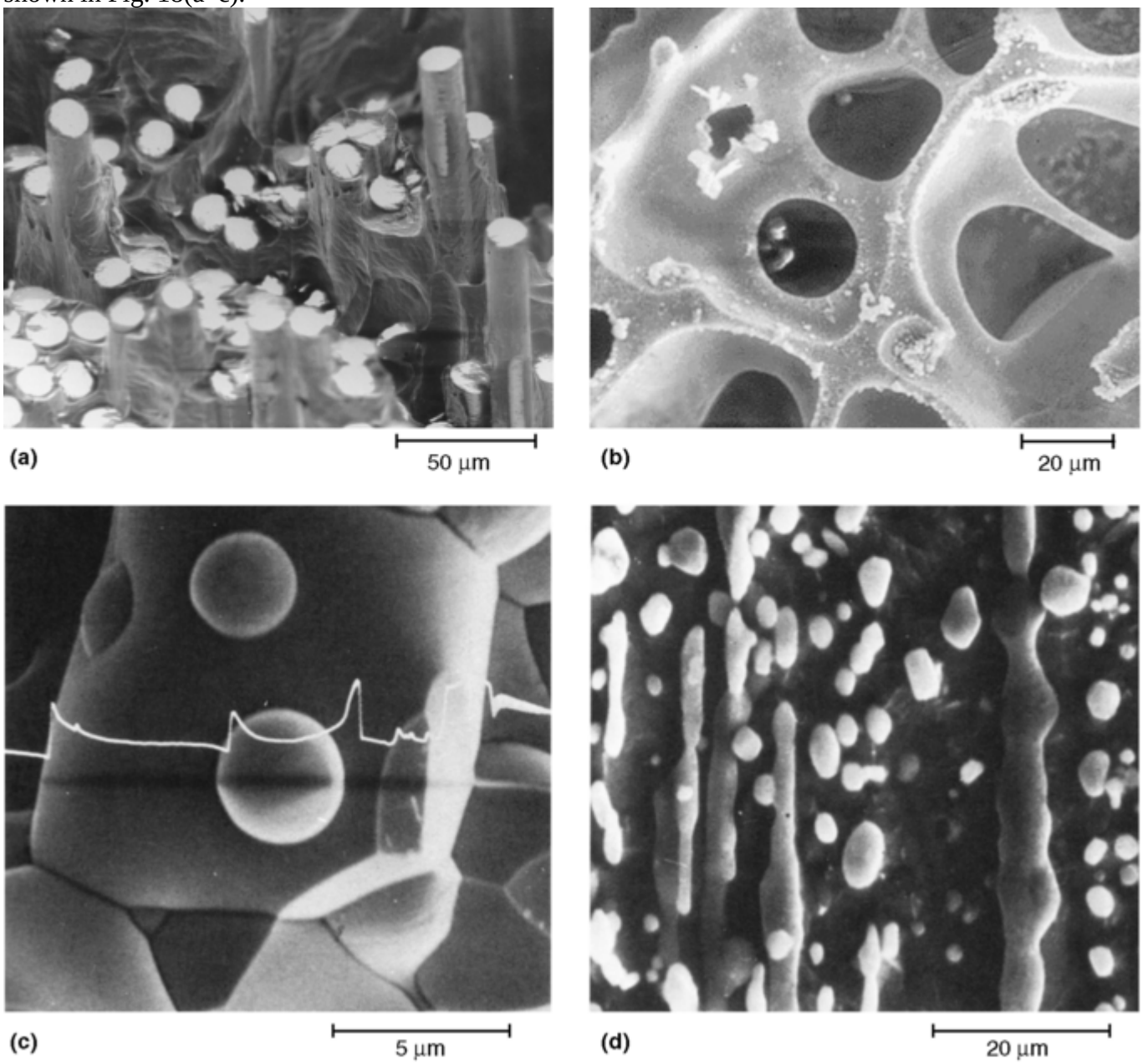

Fig. 17 Examples of SEM studies on materials microstructures. (a) Fracture surface of a ceramic-fiber-strengthened aluminum-matrix composite. From the measured distribution of relative heights of fiber fractures and known strength distribution along the fibers, the fracture probability of the composite can be calculated. 300×. (b) Cross section of a dendritic Al-20%Cu alloy, deep etched by soaking in 32% hydrochloric acid for 5 min at room temperature. 500×. (c) Thermally etched surface of an Al_2O_3-10%ZrO_2 ceramic. The height profile (white line) obtained by γ-modulation (in which the cathode ray tube beam is deflected proportionally to the detector signal) allows control of the depth of thermal

etching. 4000×. (d) Decay of nickel fibers in a silver matrix of an electrical conduction material produced by the drawing of bundled, coated rods. During annealing at 900 °C (1650 °F) for 5 h, the continuous nickel fibers break into short pieces or disintegrate into rows of spherical particles. 1000×

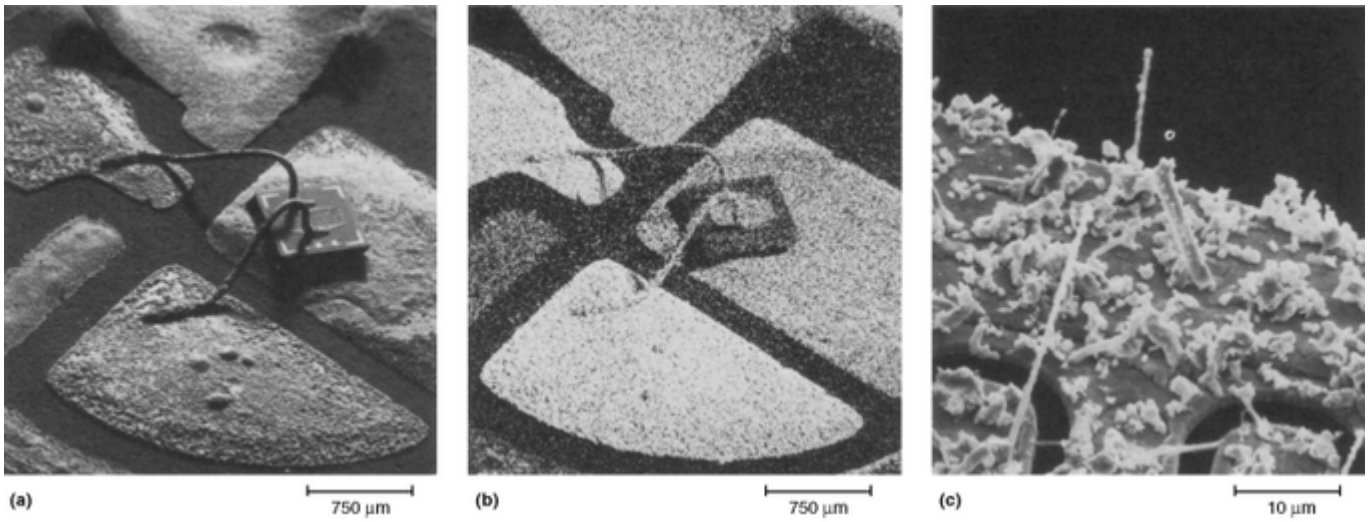

Fig. 18 Degradation of an electronic circuit due to silver diffusion and whisker formation during storage for 3000 h at 270 °C (520 °F). (a) Secondary electron image showing a general view of the transistor with gold-coated silver pads and gold wires. 20×. (b) X-ray dot map (silver distribution) showing that silver has diffused from the pads over the wires to the transistor. 20×. (c) Whiskers formed on the base and the emitter, secondary electron image. 1500×. Source: Ref 35

Powders and Porous Materials. Powder metallurgy and ceramic processing are also major application areas for SEM. Metal powders are produced by such methods as atomization, reduction of oxides, and electrolysis; each yields a specific type of powder (see the article “Metallography and Microstructures of Powder Metallurgy Alloys” in this Volume). Particle size distribution and the details of particle shape are controlled by adjusting the process parameters; the SEM is used to study these correlations and to ensure uniform powder quality (see the article “Particle Image Analysis” in *Powder Metal Technologies and Applications*, Volume 7 of *ASM Handbook*). This is important because the characteristics of the powder determine its behavior during pressing and sintering. The deformation of the powder particles and the change of the pore-space morphology during uniaxial, isostatic, and hot pressing have been confirmed by qualitative and quantitative evaluation of scanning electron micrographs. Fracture surfaces of porous materials or plastic replicas of the pore space are useful for evaluating the internal structures. The same techniques are used to study sintering (Ref 43).

As examples of fundamental studies, Fig. 19 shows the development of particle contacts and pore morphology during sintering of a spherical copper powder, and Fig. 20 shows a study of wetting phenomena during liquid phase sintering of spherical tungsten particles with copper (Ref 44). Important information on particle rearrangement during solid and liquid phase sintering has been obtained from in situ studies using a high-temperature stage.

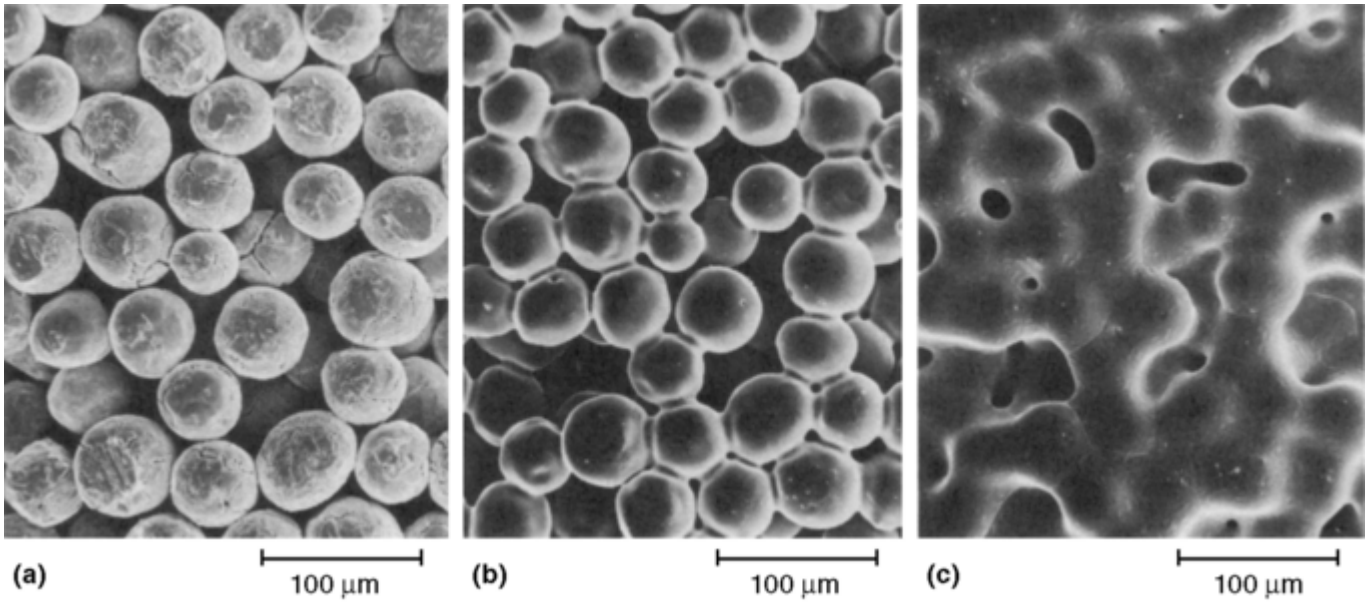

Fig. 19 Progress of sintering in a loose stack of copper powder spheres, secondary electron images. (a) Light bonding at 600 °C (1110 °F) during heating to sintering temperature. (b) After sintering for 1 h at 1050 °C (1920 °F). Clearly visible is the formation of necks between touching particles. (c) After sintering for 64 h at 1050 °C (1920 °F). The shape of the individual spheres is hardly recognizable; grain growth has occurred across prior particle boundaries, and a substantial increase in particle contact has taken place. All at 150×. Source: Ref 43

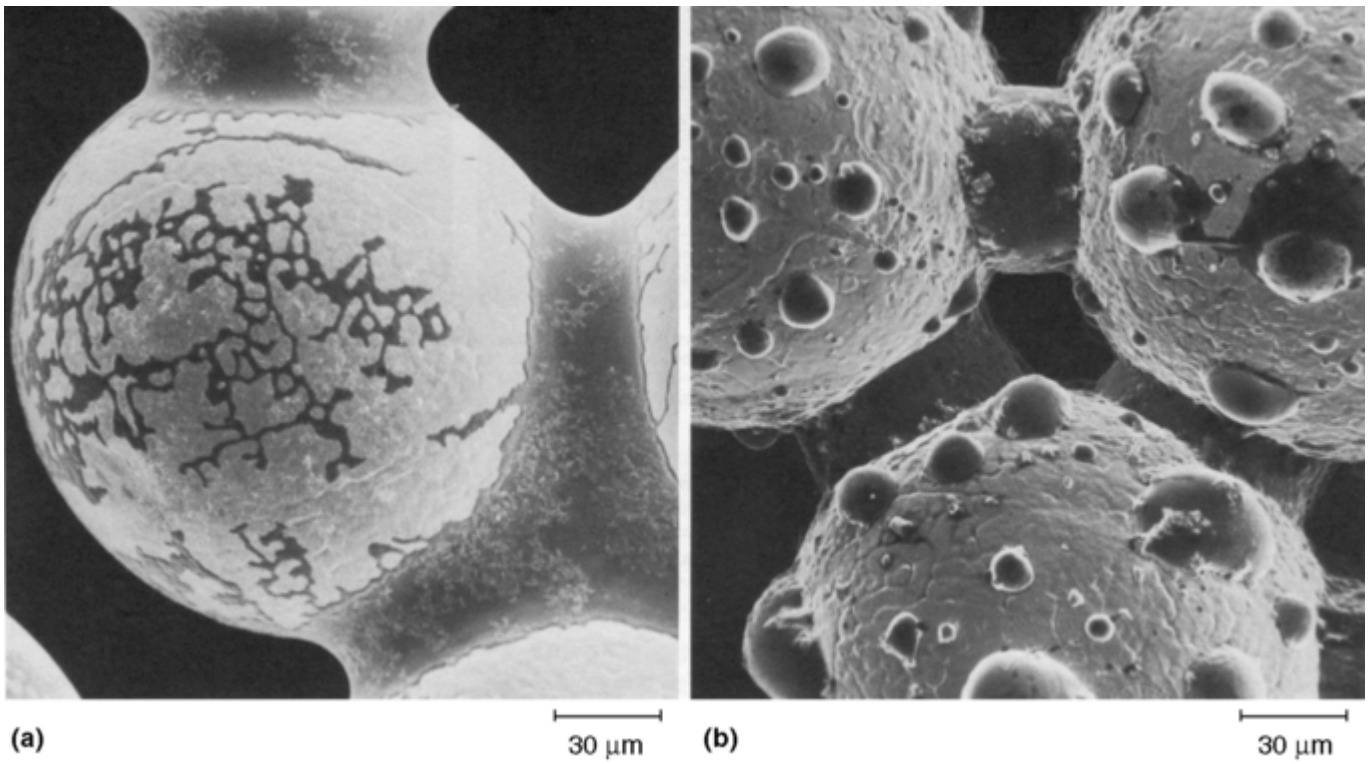

Fig. 20 Wetting of large, spherical tungsten particles by liquid copper during liquid phase sintering. (a) In vacuum, wetting is very good. Most of liquid copper fills the contact regions, and some of it spreads over the surface of the tungsten spheres. (b) In an oxygen-containing argon atmosphere, wetting is reduced. The contacts are connected by liquid bridges, and some of the copper is present in droplets, forming a wetting angle of approximately 90° to the surface of the tungsten particles. Both at 300×. Source: Ref 43

Fig. 21 Typical applications of SEM in physical metallurgy. (a) Deformation marks on the surface of a fatigued copper specimen with protuberances at glide bands. The hill-and-valley profile and the glide systems are quantitatively characterized by stereoscopic measurement of height and spacing using latex balls for exact scaling. Source: Ref 44. 1500×. (b) Etch pit at the surface of a sheet produced for electrical applications from an Fe-3Si alloy. After mechanical polishing and chemical removal of the deformed layer, preferential attack at a dislocation by three-step etching forms a pit with fixed crystallographic planes. The intersection of {100} and {110} planes forms edges. From the angles between these edges, the surface orientation is calculated to approximate {810}. 2500×. Source: Ref 45

Deformation Studies. Scanning electron microscopy studies have revealed various phenomena and processes occurring during working of metallic materials. Persistent slide bands in a single crystal of copper and dislocation networks in porous materials undergoing cyclic deformation have been successfully imaged by electron channeling contrast imaging as well as the dislocation structure of deformation zones at the tip of cracks in massive samples and thin foils (Ref 13, 15). Figure 21(a) shows the surface of a fatigued copper specimen with typical deformation marks. The appearance of the protuberances and hill-and-valley profiles has been qualitatively characterized and correlated to experimental conditions and to crack nucleation in fatigue testing (Ref 44). The study of local textures and the orientation relationships between grains during or after deformation and annealing are prominent examples of applications in physical metallurgy. A useful technique to determine the orientation of grains at the surface of rolled sheets involves the use of etch pits (Fig. 21b) formed at locations where dislocations penetrate the surface. Studies of local deformation during and after fracture (see Fig. 5b and c and 16a and b for examples) have contributed significantly to all relevant fields, such as fracture mechanics, modeling of fracture processes, and analysis of damage.

References cited in this section

13. C. Stickler, D. Melisova, B. Mingler, B. Weiss, and R. Stickler, Advanced Microstructural Investigation Using the REM-ECC Imaging Technique, *Prakt. Metallogr.,* Vol 38, 2001, p 19–30

15. C. Stickler, SEM-ECC Imaging and SAC Patterns—Procedures for the Non-Destructive Characterization of Microstructures and for Revealing the Global Dislocation Arrangement, *Prakt. Metallogr.,* Vol 38, 2001, p 566–590

35. T. Hillmer, Practical Experience in Materials Microanalysis with the Scanning Electron Microscope, Part 1: Methods of Preparation, *Prakt. Metallogr.,* Vol 16, 1979, p 465–479

36. L. Sigl and H.E. Exner, Experimental Study of the Mechanisms of Fracture in WC-Co Alloys, *Metall. Trans. A,* Vol 18, 1987, p 1299–1308

37. L. Sigl and H.F. Fischmeister, On the Fracture Toughness of Cemented Carbides, *Metall. Trans. A,* Vol 18, 1988, p 887–987

38. H.E. Exner, L. Sigl, M. Fripan, and O. Pompe, Fractography of Critical and Subcritical Cracks in Hard Materials, *Int. J. Refract. Met. Hard. Mater.,* Vol 19, 2001, p 329–334

39. M. Lienkamp, U. Kunaver, and H.E. Exner, Stereometric Quantitative Microscopy of Unidirectional Composite Materials, *J. Comput.—Assist. Microsc.,* Vol 6, 1994, p 103–107

40. M. Lienkamp and H.E. Exner, Prediction of the Strength Distribution for Unidirectional Fibre Strengthened Composites, *Acta Mater.,* Vol 44, 1996, p 4433–4446

41. D. Feijoo, B. Bauer, and H.E. Exner, Determination of Local Curvature and Its Frequency Distribution by Computer Assisted Stereometry, *J. Comput.—Assist. Microsc.,* Vol 2, 1990, p 3–23

42. D. Feijoo and H.E. Exner, Surface Curvature Distributions of Growing Dendrite Crystals, *J. Cryst. Growth*, Vol 113, 1991, p 449–455

43. H.E. Exner and E. Arzt, Sintering Processes, *Physical Metallurgy*, Vol 3, Elsevier, 1996, p 2627–2662

44. R. Wang, B. Bauer, and H. Mughrabi, The Study of Surface Roughness Profiles on Fatigued Metals by Scanning Electron Microscopy, *Z. Metallkd.*, Vol 73, 1982, p 30–34

45. E. Horn and U. Lotter, Assessment of Grain Orientations at the Surface of Electrical Sheets by Means of Etch Pits, *Prakt. Metallogr.*, Vol 22, 1985, p 397–406, 439, 453

Scanning Electron Microscopy

H.E. Exner and S. Weinbruch, Darmstadt University of Technology

---

H.E. Exner and S. Weinbruch, Scanning Electron Microscopy, *Metallography and Microstructures*, Vol 9, *ASM Handbook*, ASM International, 2004, p. 355–367

References

1. J.I. Goldstein, D.E. Newbury, P. Echlin, D.C. Joy, A.D. Romig, C.E. Lyman, C. Fiori, and E. Lifshin, *Scanning Electron Microscopy and X-Ray Microanalysis*, 2nd ed., Plenum Press, 1992

2. L. Reimer, *Scanning Electron Microscopy*, 2nd ed., Springer, 1998

3. S.J.B. Reed, *Electron Microprobe Analysis*, 2nd ed., Cambridge University Press, 1993

4. S.J.B. Reed, *Electron Microprobe Analysis and Scanning Electron Microscopy in Geology*, Cambridge University Press, 1996

5. D.E. Newbury, D.C. Joy, P. Echlin, C.E. Fiori, and J.I. Goldstein, *Advanced Scanning Electron Microscopy and X-Ray Microanalysis*, Plenum Press, 1986

6. K. Kanaya and S. Okayama, Penetration and Energy-Loss Theory of Electrons in Solid Targets, *J. Phys. D, Appl. Phys.*, Vol 5, 1972, p 43–58

7. H. Seiler, Einige aktuelle Probleme der Sekundärelektronenemission, *Z. Angew. Phys.*, Vol 22, 1967, p 249

8. G.D. Danilatos, Environmental Scanning Electron Microscopy and Microanalysis, *Mikrochim. Acta*, Vol 114, 1994, p 143–155

9. T.E. Everhart and R.F.M. Thornley, Wide-Band Detector for Micro-Microampere Low-Energy Electron Currents, *J. Sci. Instr.*, Vol 37, 1960, p 246–248

10. W. Reuter, The Ionization Function and Its Application to the Electron Probe Analysis of Thin Films, *Proc. Sixth Int. Conf. on X-Ray Optics and Microanalysis*, G. Shinoda, Ed., Tokyo University Press, 1972, p 121

11. S.I. Wright, A Review of Automated Orientation Imaging Microscopy (OIM), *J. Comput.-Assist. Microsc.,* Vol 5, 1993, p 207

12. D. Katrakova, C. Maas, D. Hohnerlein, and F. Muecklich, Experiences on Contrasting Microstructure Using Orientation Imaging Microscopy, *Prakt. Metallogr.,* Vol 35, 1998, p 4–20

13. C. Stickler, D. Melisova, B. Mingler, B. Weiss, and R. Stickler, Advanced Microstructural Investigation Using the REM-ECC Imaging Technique, *Prakt. Metallogr.,* Vol 38, 2001, p 19–30

14. D. Katrakova and F. Muecklich, Specimen Preparation for Electron Backscatter Diffraction, Part I: Metals, *Prakt. Metallogr.,* Vol 38, 2001, p 547–565

15. C. Stickler, SEM-ECC Imaging and SAC Patterns—Procedures for the Non-Destructive Characterization of Microstructures and for Revealing the Global Dislocation Arrangement, *Prakt. Metallogr.,* Vol 38, 2001, p 566–590

16. J. Pospiech, K. Wiencek, A. Marawiec, and A. Piatzowski, Grain Boundary Contrasting on the Map of the Crystallographic Orientation Topography, *Prakt. Metallogr.,* Vol 39, 2002, p 126–139

17. G. Zwilling, Observation of Magnetic Domains in the Scanning Electron Microscope, *Prakt. Metallogr.,* Vol 11, 1974, p 716–728

18. J. Goldstein *et al, Scanning Electron Microscopy and X-Ray Microanalysis,* 3rd ed., Kluwer Academic/Plenum Publishers, 2003

19. K.F.J. Heinrich and D.E. Newbury, *Electron Probe Quantitation,* Plenum Press, 1991

20. S. Weinbruch, A. Anastassiadis, H.M. Ortner, H.P. Martinz, and P. Wilhartitz, On the Mechanism of High-Temperature Oxidation of ODS Superalloys: Significance of Yttrium Depletion within the Oxide Scales, *Oxid. Met.,* Vol 51, 1999, p 111–128

21. K. Wetzig, A. Maslov, and J. Edelmann, Development and Application of a Cyclic Bending Device for in-situ Fatigue Investigations in the Scanning Electron Microscope, *Prakt. Metallogr.,* Vol 21, 1984, p 161–172

22. D.L. Davidson and A. Nagy, A Low Frequency Cyclic-Loading Stage for the SEM, *J. Phys. E, Sci. Instrum.,* Vol 11, 1978, p 207–210

23. W. Krompp, P. Bajons, and B. Weiss, A Scanning Electron Microscope Accessory for the Observation of Deformation Processes, *Prakt. Metallogr.,* Vol 13, 1976, p 53–62

24. J. Stampfl, S. Scherer, M. Gruber, and O. Kolednik, Reconstruction of Surface Topographies by Scanning Electron Microscopy for Application in Fracture Research, *Appl. Phys. A,* 1996, p 341–346

25. C.O.A. Semprimoschnig, J. Stampfl, R. Pippan, and O. Kolednik, A New Powerful Tool for Surveying Cleavage Fracture Surfaces, *Fatigue Fract. Eng. Mater. Struct.,* 1997, p 1541–1550

26. H.E. Exner, Quantitative Metallography in Three Dimensions, *Prakt. Metallogr.,* Vol 38, 2001, p 370–384

27. H.E. Exner and M. Fripan, Quantitative Assessment of Three-Dimensional Roughness, Anisotropy and Angular Distribution of Fracture Surfaces by Stereometry, *J. Microsc.,* Vol 138, 1985, p 161–178

28. H.E. Exner, Quantitative Description of Microstructures by Image Analysis, *Materials and Technology,* Vol 2B, VCH, 1994, p 281–350

29. H.E. Exner, Qualitative and Quantitative Surface Microscopy, *Physical Metallurgy,* Vol 2, Elsevier, 1996, p 993–1032

30. J.C. Russ, *Computer-Assisted Microscopy—The Measurement and Analysis of Images,* Plenum Press, 1990

31. H.E. Exner and H.P Hougardy, *Quantitative Image Analysis of Microstructures,* DGM-Informationsgesellschaft-Verlag, 1988

32. M. Coster and J.L. Chermant, *Précis d'Analyse d'Images,* Editions du Centre National de la Recherche Scientifique, 1989

33. R.J. Lee, W.A. Spitzig, J.F. Kelly, and R.M. Fisher, Quantitative Metallography by Computer-Controlled Scanning Electron Microscopy, *Prakt. Metallogr.,* Vol 21, 1984, p 27–41

34. J. Paul and B. Bauer, Contrast Techniques for Phase Separation in the Scanning Electron Microscope, *Prakt. Metallogr.,* Vol 20, 1983, p 213–221

35. T. Hillmer, Practical Experience in Materials Microanalysis with the Scanning Electron Microscope, Part 1: Methods of Preparation, *Prakt. Metallogr.,* Vol 16, 1979, p 465–479

36. L. Sigl and H.E. Exner, Experimental Study of the Mechanisms of Fracture in WC-Co Alloys, *Metall. Trans. A,* Vol 18, 1987, p 1299–1308

37. L. Sigl and H.F. Fischmeister, On the Fracture Toughness of Cemented Carbides, *Metall. Trans. A,* Vol 18, 1988, p 887–987

38. H.E. Exner, L. Sigl, M. Fripan, and O. Pompe, Fractography of Critical and Subcritical Cracks in Hard Materials, *Int. J. Refract. Met. Hard. Mater.,* Vol 19, 2001, p 329–334

39. M. Lienkamp, U. Kunaver, and H.E. Exner, Stereometric Quantitative Microscopy of Unidirectional Composite Materials, *J. Comput.—Assist. Microsc.,* Vol 6, 1994, p 103–107

40. M. Lienkamp and H.E. Exner, Prediction of the Strength Distribution for Unidirectional Fibre Strengthened Composites, *Acta Mater.,* Vol 44, 1996, p 4433–4446

41. D. Feijoo, B. Bauer, and H.E. Exner, Determination of Local Curvature and Its Frequency Distribution by Computer Assisted Stereometry, *J. Comput.—Assist. Microsc.,* Vol 2, 1990, p 3–23

42. D. Feijoo and H.E. Exner, Surface Curvature Distributions of Growing Dendrite Crystals, *J. Cryst. Growth,* Vol 113, 1991, p 449–455

43. H.E. Exner and E. Arzt, Sintering Processes, *Physical Metallurgy,* Vol 3, Elsevier, 1996, p 2627–2662

44. R. Wang, B. Bauer, and H. Mughrabi, The Study of Surface Roughness Profiles on Fatigued Metals by Scanning Electron Microscopy, *Z. Metallkd.,* Vol 73, 1982, p 30–34

45. E. Horn and U. Lotter, Assessment of Grain Orientations at the Surface of Electrical Sheets by Means of Etch Pits, *Prakt. Metallogr.,* Vol 22, 1985, p 397–406, 439, 453

S.Paciornik and M. H. de Pinho Mauricio, Digital Imaging, Vol 9, *ASM Handbook*, ASM International, 2004, p. 368–402

Digital Imaging

Sidnei Paciornik and Marcos Henrique de Pinho Mauricio, Catholic University of Rio de Janeiro

Introduction

DEVELOPMENTS IN COMPUTER HARDWARE AND SOFTWARE have contributed to major changes in materials characterization in the last decade. Electronic acquisition is replacing photographic film in laboratory use. Digitized images are efficiently stored in computer memory and can be processed and analyzed to extract quantitative information. Printers are approaching film quality and allow low-cost image output.

The move from traditional photographic film imaging to digital imaging is a complex one. It requires knowledge of different aspects such as image resolution and color depth, digital files sizes and formats, video cameras and frame grabbers, charge-coupled device (CCD) cameras, digital image processing and analysis, and printing methods.

The flowchart in Fig. 1 illustrates the sequence normally followed in digital image-acquisition, processing, analysis, and output.

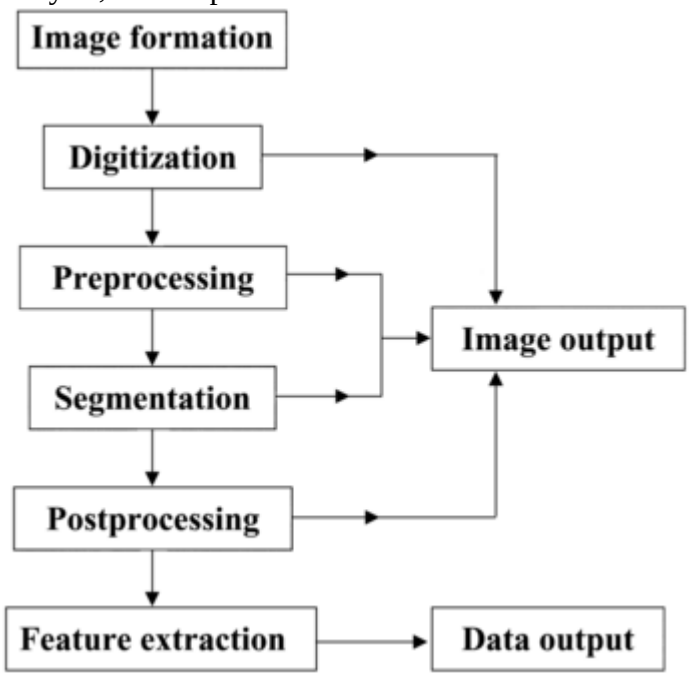

Fig. 1 The sequence of image acquisition, processing, analysis, and output

The sequence starts with an image from a given source—for example, a microstructure imaged through a light microscope and a video camera. The camera signal goes through the digitization step, and the resulting digital image is stored in the computer memory. At this point, if no further processing is required, the image can be output to a suitable printer.

In many situations, however, some degree of image processing may be required. Electronic noise and uneven illumination are typical examples of defects that can be successfully corrected in the preprocessing step.

If the goal is to further analyze the image to extract quantitative information, then the sequence follows with the segmentation step, in which the several objects in the image must be identified and discriminated from the background. This is a complex and critical step because the software must mimic a sophisticated human cognition capability. Due to this complexity, it is often necessary to correct the segmentation result in the postprocessing step where the so-called morphological operators are employed.

The resulting postprocessed image is then composed of the desired objects, which can be analyzed in the feature extraction step. A large number of quantitative parameters can be obtained including size, shape, position, texture, and so forth. The data can be output to various plotting and statistical analysis programs.
This article reviews the main theoretical and practical aspects of this sequence. In the following sections, each step in the sequence is thoroughly described.

S.Paciornik and M. H. de Pinho Mauricio, Digital Imaging, Vol 9, *ASM Handbook*, ASM International, 2004, p. 368–402

Digital Imaging

Sidnei Paciornik and Marcos Henrique de Pinho Mauricio, Catholic University of Rio de Janeiro

---

Image Acquisition

This first step in the sequence considers the terms used to describe how an image of a real object is converted to a set of digital information, instruments used accomplish this, and file and format convention.

Digitization Basics

Digitization is the first step of the sequence. An analog signal representing the image goes through analog-to-digital conversion (A/D), creating a digital file that is stored in the computer. Digitization is a fundamental step because it defines the quality of the digital image and therefore the quality of all further processing and analysis.
There are basically three different image-digitization methods:

- Images acquired in photographic film that must then be digitized through a scanner
- Images acquired with a video camera that are digitized with a frame-grabber board
- Images acquired through a digital camera that sends data directly to the computer

Each of these methods has its trade-offs. To understand them, the basic concepts of sampling, resolution, and quantization must be presented first.
Sampling, Spatial Frequency, Resolution, and Quantization. Figure 2(a) shows a cleaved silicon wafer in a scanning electron microscope (SEM), and Fig. 2(b) shows the intensity trace (gray graph) along the line drawn on the image. Digitizing this one-dimensional signal requires sampling both axes—distance and intensity—as represented by the grid of vertical and horizontal lines. The digital values are approximations of the intensity trace to the nearest grid intersection. This is shown with the small dots in the plot.

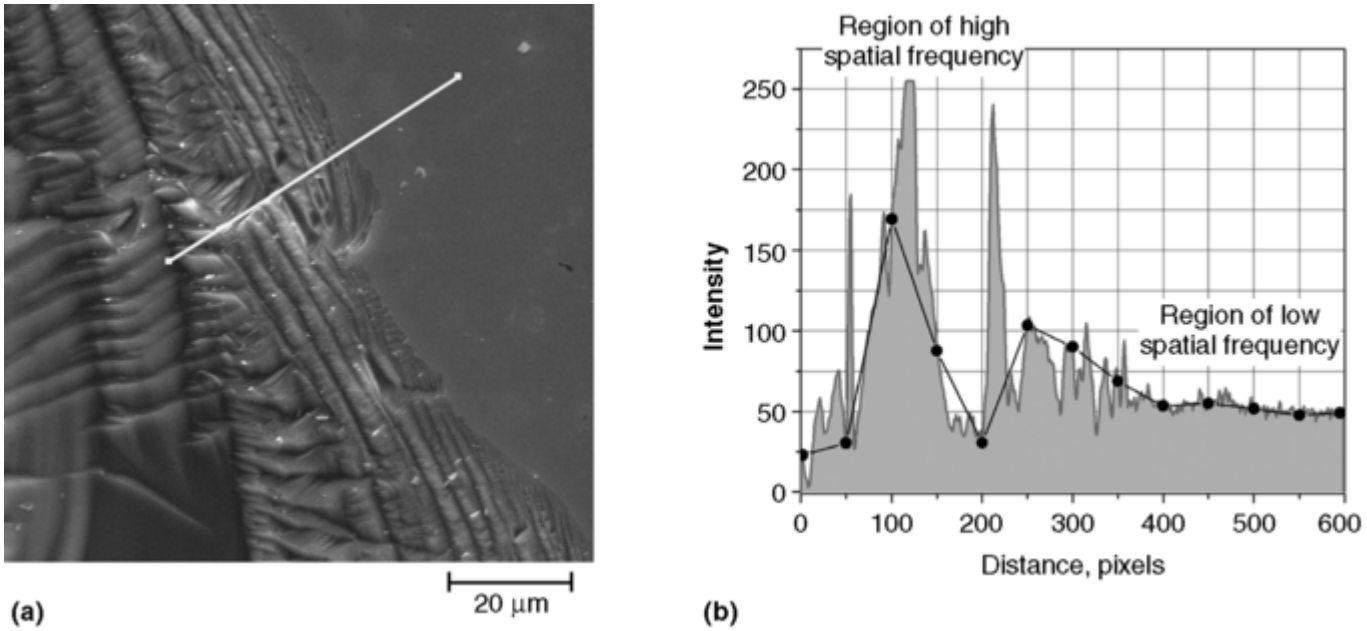

Fig. 2 Sampling, resolution, and quantization. (a) SEM image of a cleaved silicon wafer. (b) Intensity trace (gray graph) along the white line shown on the image. The black dots represent sampling points. The black line is the digital approximation given by the sampling shown.

The digital signal obtained from the sampling procedure is shown with the straight lines connecting the circles. Clearly, it is a poor representation of the original signal. It is particularly bad in the region labeled high spatial frequency, where the line trace shows abrupt changes in intensity, corresponding to edges in the original image. Many peaks and valleys in the line trace are completely ignored in the sampled signal. Conversely, the region labeled low spatial frequency, on the right end of the trace, corresponds to a part of the image with smooth variation of intensity and no sharp edges. The straight lines are a better approximation in this region.

This example brings up three fundamental concepts: spatial frequency, resolution, and quantization.

Similar to the concept of time frequency, which is the rate at which a signal oscillates in time, spatial frequency is the rate at which a signal changes in space. Thus, the regions of the image that show a lot of detail such as edges and small particles have high frequency content. The regions that show little detail, such as a smoothly varying background, have low frequency content.

The sampling at intervals of 50 pixels used in Fig. 2(b) leads to a poor approximation of the original signal. To improve the quality of the digital signal, one could sample at shorter intervals on both axes. The sampling frequency in the spatial axis is called resolution, while the sampling frequency in the intensity axis is called quantization. Each division on the spatial axis is called a picture element or pixel.

The concept of spatial frequency is present in many steps of the sequence depicted in Fig. 1. Besides its use in describing digitization quality, it appears in filters used in the preprocessing step.

Resolution is measured both intensively (for example, number of pixels per unit distance) and extensively (for example, total number of pixels on each axis of the image), depending on the digitization method. Typical values for a scanner range from 300 dpi (dots per inch) to several thousand dpi, while modern digital cameras can reach thousand pixels in each direction.

Quantization, sometimes called color depth or color resolution, is measured in number of color levels—gray levels for grayscale images and primary color levels for color images. Typical values range from 256 to 16,384 gray levels and 16.7 million colors levels.

The effect of these parameters can be evaluated both qualitatively and quantitatively. Figure 3 shows the effect of resolution and quantization on image quality. In Fig. 3(a), both resolution and quantization are low, 64 × 64 pixels and four gray levels. In Fig. 3(b), quantization is increased to 256 gray levels with no resolution improvement. In Fig. 3(c) the resolution is increased to 512 × 512 pixels, while keeping the quantization unchanged. Finally, Fig. 3(d) shows that increasing both resolution and quantization results in a clear improvement in image visual quality.

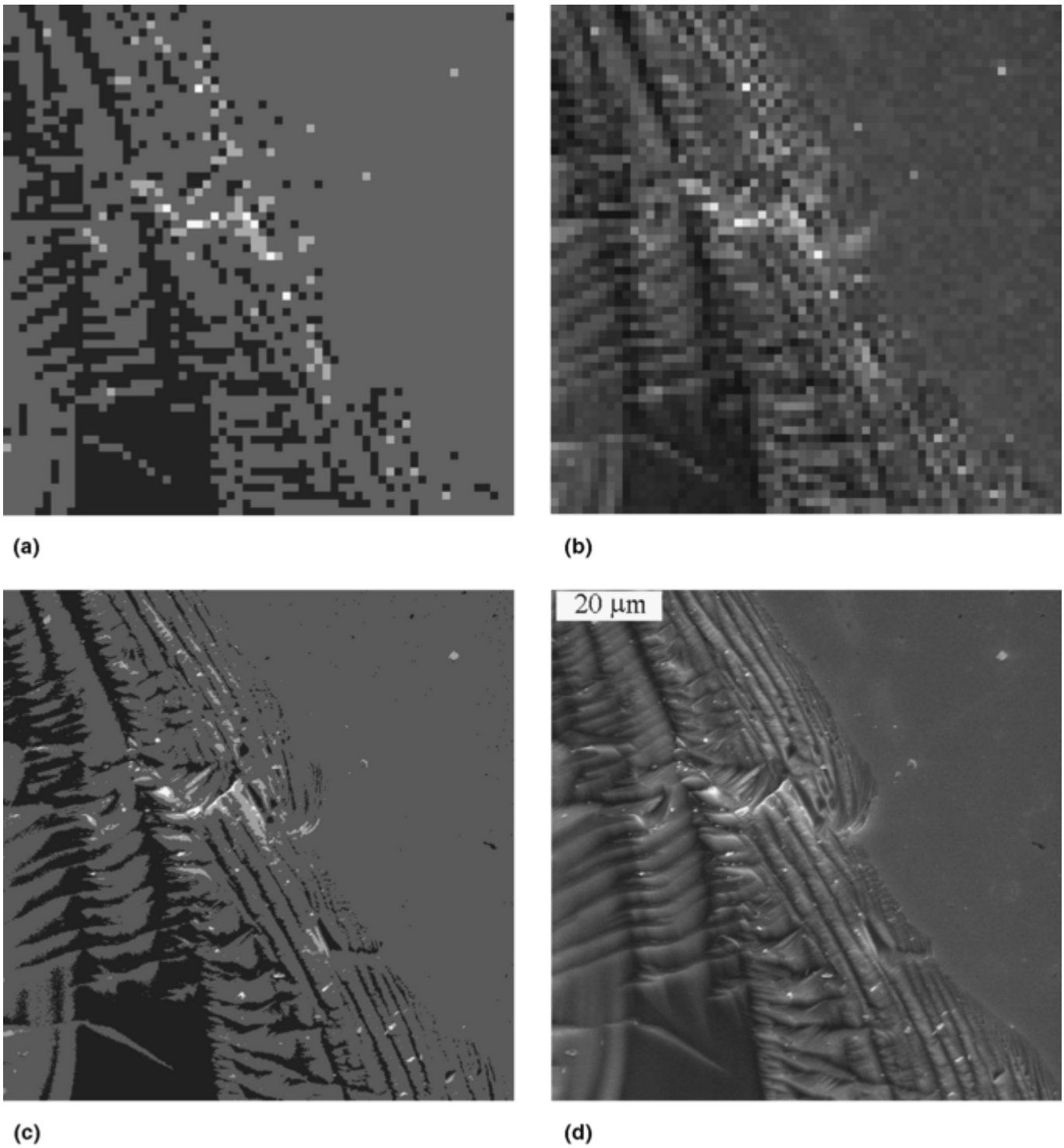

Fig. 3 The effect of resolution and quantization on a digital image. The same image as Fig. 2 in different levels of resolution and quantization. (a) 64 × 64 pixels and four gray levels. (b) 64 × 64 pixels and 256 gray levels. (c) 512 × 512 pixels and four gray levels. (d) 512 × 512 pixels and 256 gray levels

The quantitative effect can be evaluated if one considers the problem of measuring features in the image such as, for example, the width of the cleaved planes or the average intensity of a given region. It is quite clear that the low resolution/quantization images do not give accurate results, especially for features that have dimensions close to or smaller than the pixel size.

Thus, resolution and quantization should be chosen carefully for each case at hand. With the recent improvement of digitization equipment such as scanners and digital cameras, one could have the tendency to choose the highest available values for both parameters. However, this choice translates into large digital files and might lead to meaningless information as the digital file ends up with higher resolution than the original physical signal (Ref 1).

Image Representation

A digital image is a matrix of pixels with intensities. There are three basic ways of showing an image: raster format, spreadsheet, and three-dimensional (3-D) view (Fig. 4).

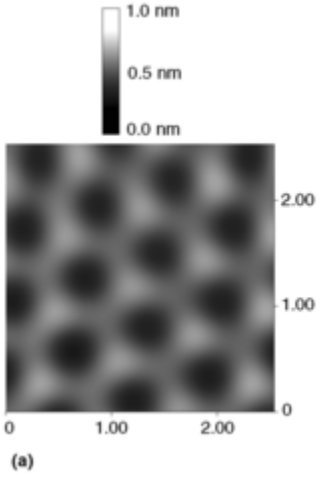

	Col 384	Col 385	Col 386	Col 387	Col 388	Col 389	Col 390	Col 391
Row 37	97	100	102	105	106	108	111	113
Row 38	99	100	102	105	106	108	111	113
Row 39	97	100	102	103	106	108	111	113
Row 40	99	100	102	103	106	108	111	111
Row 41	99	100	102	103	106	110	110	111
Row 42	97	100	103	105	106	106	108	110
Row 43	97	100	102	103	106	106	110	111
Row 44	97	100	102	103	105	106	110	111

(b)

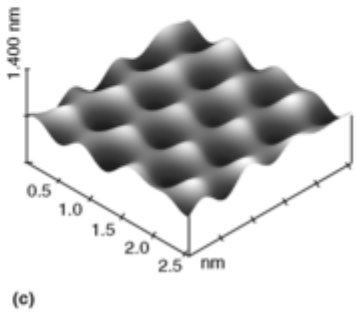

Fig. 4 Image representation. AFM image of boric acid crystal lattice. (a) Raster format. (b) Spreadsheet view of a small part of the image in (a). (c) Three-dimensional visualization. Courtesy of R. Prioli, PUC-Rio, Brazil

The raster format is the most common visualization mode. The intensity of each pixel is translated into the brightness of a screen pixel. The term raster comes from the scanning operation used in video signals. In the spreadsheet mode (Fig. 4b), the image is shown as a matrix where each cell represents a pixel and the intensity of the pixel is shown numerically. This can be useful in analyzing specific portions of the image and can help understand the effect of mathematical operation.

In 3-D view, the pixel intensities are converted into the height of a 3-D plot. There are many ways to show this plot. Figure 4(c) shows a shaded view where the shade intensity is proportional to the height. This kind of plot is particularly useful when the intensity in the original image represents a true height. This is the case, for example, of topographic images obtained with an atomic force microscope (AFM) or reconstructed with the parallax method in a SEM. Details of this last case are presented later in this article.

Digital Files

The digitized images are stored in computer memory as digital files that must be managed, copied, and transmitted over networks. A good understanding of how digital files are created and stored is extremely important.

File size is a pertinent issue, especially if one has to manage a large number of images. The amount of memory occupied by a digital image depends on resolution, quantization, and also on the use of compression, as discussed below.

The basic equation for estimating uncompressed file size is:

$$FileSize = N_h \cdot N_v \cdot b_{pp} \qquad \text{(Eq 1)}$$

where N_h and N_v are the number of pixels in the horizontal and vertical directions, respectively, and b_{pp} is the number of bytes occupied by each pixel.

The byte is the minimum memory allocation unit. By definition, a byte is composed of eight binary digits (bits). As each bit can assume only two values (0 and 1) a combination of n bits can represent 2^n values. Table 1 shows some relevant numbers.

Table 1 Number of stored values as function of number of bits and bytes

Number of bits, n	Number of occupied bytes	Number of values, 2^n
1	1[(a)]	2
4	1[(a)]	16
8	1	256
14	2	16,384
16	2	65,536 (64k)
24	3	16,777,216 (16.7M)

(a) Maximum values, depending on specific software. See text.

The number of bytes required by each pixel depends on quantization. A typical value for grayscale images is 256 gray levels; that is, each pixel may assume digital values from 0 (black) to 255 (white). In this case, each pixel would require 1 byte.

As an example, consider an image of 512 × 512 pixels. The total number of pixels is 512 · 512 = 262,144 pixels = 256 kpixels. (Note that the prefix "k" in computer science is not equivalent to the standard kilo [1000×] multiplier. Rather, it corresponds to 1024 [2^{10}].) Table 2 shows file sizes for different quantization levels.

Table 2 File sizes as a function of quantization for a 512 × 512 pixel image

Image type	Pixel type	Number of bits	Quantization	bpp[(a)]	File size
Typical grayscale	Integer	8	256 levels	1	256 Kbytes
High-quantization grayscale	Integer	14	16384 levels	2	512 Kbytes
Indexed color	Integer	8	256 levels	1	256 Kbytes
RGB color	Integer	24	16,777,216 colors	3	768 Kbytes
Processing result (simple precision)	Noninteger	32	NA	4	1 Mbyte
Processing result (double precision)	Noninteger	64	NA	8	2 Mbytes

(a) Byte per pixel

If a pixel requires less than a byte, for example, in a black-and-white image each pixel requires a single bit, the amount of memory it will occupy depends on how the program stores the data. Certain programs join several pixels in a byte, effectively compressing the used memory, while others use at least a byte per pixel, even if there are not enough bits to fill it. Normally the unused bits are wasted, assuming zero values.

Grayscale images, with 256 gray levels, are commonly obtained from scanners or video digitizer boards. High quantization grayscale, with up to 16,384 levels, is provided by specialized CCD cameras. This level of quantization is necessary to accurately represent signals with a wide range of intensities. For example, electron diffraction in the transmission electron microscope (TEM) creates images in which the brightest spot can be millions of times stronger than the weakest spot. Representing this range with just 256 gray levels would lead to a large loss of information. Note that 16,384 levels correspond to 14 bits that occupy 2 bytes, even though 2 bits always have a zero value.

Color images are normally represented by three channels corresponding to the three primary colors red, green, and blue, in the so-called RGB model. This model is based on the specific characteristics of the human eye, which has specific light sensors, the cones, tuned to three different regions of the visible spectrum, approximately corresponding to the red, green, and blue colors. The psychophysical sensation of color is created by the level of activation of these three types of cones. It is common to treat the three primaries as mutually orthogonal unit vectors of a 3-D color space. A given color is then constructed by linear combination of the R, G, and B components. That is why this model is also called an additive model.

If 1 byte is allocated to each primary, each pixel occupies 3 bytes (or 24 bits) and has a color quantization of $2^{24} \approx 16.7$ million colors (256 tones for each primary). Scanners often offer higher quantization, but these are normally converted to 24 bits before image storage or further processing. The higher quantization, even if invisible to the human eye, may provide better color rendition when images are printed.

There are many other color representation models (Ref 2) that are beyond the scope of the present text. Two of them are briefly discussed here.

The CMYK (cyan, magenta, yellow, and black) model, used for printing, is discussed in more detail in the section “Image Output—Printing” in this article. In this case, the superposition of inks creates a color that is the result of a subtractive process.

The HSB (hue, saturation, and brightness) model is very useful in image processing mainly because it concentrates the basic cognitive sensation of color in a single component, the hue. Thus, it becomes easier to discriminate regions of a given color in an image that would be otherwise be difficult to discriminate using the RGB model. Another relevant feature of the HSB model, which is sometimes confusing to the novice, is that its three components are *not* mutually orthogonal, and thus a change in one component affects the available range for the other two.

Certain programs allow the use of indexed color or palette (Ref 2). In this mode, each RGB color is converted to an approximation using just 1 byte per pixel, for a total of 256 colors. The result can be visually acceptable, and the file size is the same as for a typical grayscale image. However, no direct measurement of color values can be done on this kind of image.

When images are processed mathematically, the values of pixels in the resulting image may lie outside the range of the original images (see Fig. 5). In subtracting image B from image A, for example, the pixels of the result are negative where the pixels in image B have higher intensity than in image A (see Fig. 5a, b, and c). If both input images have 256 gray levels, the subtraction result may have pixels with intensities going from -256 to +256. This range of values cannot be represented by a single byte. Thus, in principle, the subtraction result may require 2 bytes per pixel and the file size doubles when compared with the original images.

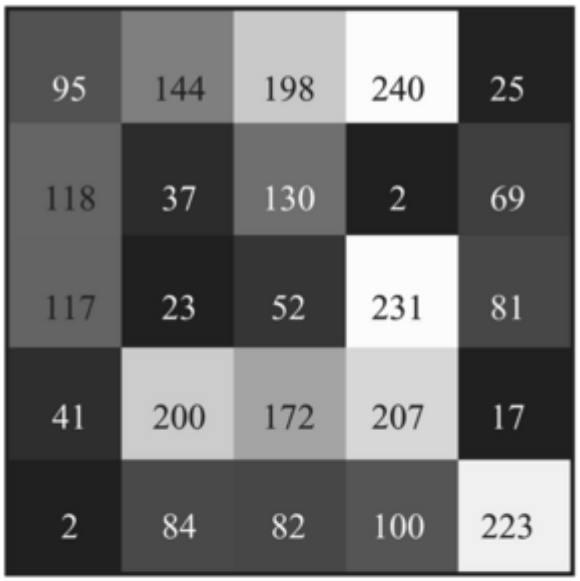

(a)

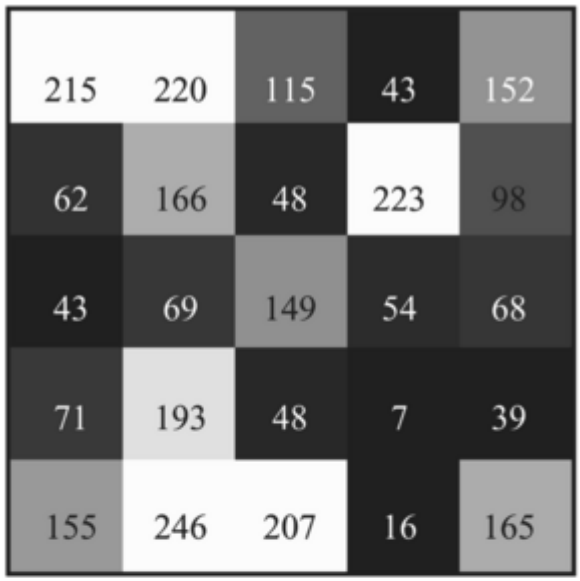

(b)

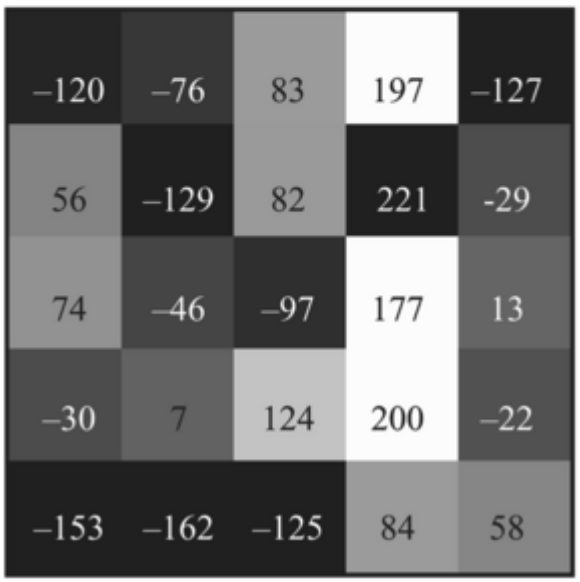

(c)

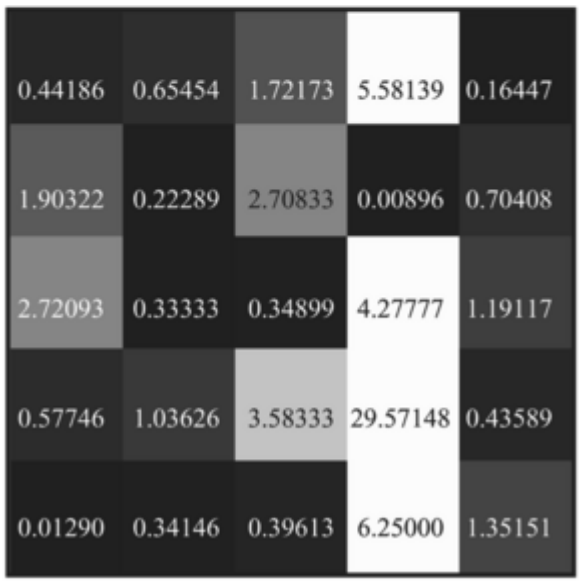

(d)

Fig. 5 Arithmetic operations and pixel types. (a) and (b) Integer pixel type images 256 gray levels (1 byte/pixel). (c) Image (a) - Image (b). (d) Image (a)/Image (b). The images in (c) and (d) were rescaled to 256 gray levels for visual representation only.

In the same fashion, dividing two images means dividing their corresponding pixel intensities, which generally creates noninteger values. Computers use the so-called floating-point format (Ref 3) to represent noninteger numbers. This format uses 4 bytes in single precision or 8 bytes in double precision. Again, the resulting image requires more bytes per pixel than the original ones, and the file size grows by a factor of four or eight, as shown in the last two entries of Table 2 (see also Fig. 5a, b, and d).

It is important to mention that different image-processing programs deal with these issues in different fashions. Most programs deal correctly only with typical grayscale and RGB images; if processing results fall outside the input range, they are scaled or clipped to 256 gray levels (or 256 levels per RGB primary). Many programs can read 16-bit (2-byte) images, but are limited in terms of processing, requiring first a conversion to 8 bits (1 byte) to use the full range of functions. Some programs keep the required extended precision data internally when doing calculations, but have to fall back to the original quantization when saving the resulting image. Others are able to preserve full precision when saving the image, but this normally requires proprietary file formats as described in the next section.

Finally, the reader must be aware that the file size calculations shown here are approximate. File sizes may actually be slightly larger because of control information that must be stored together with pixel values. Conversely, compressed formats reduce the file size. These issues are discussed in the next section.

File Formats. Images can be stored in different file formats that correspond to alternate ways of writing in computer memory the sequence of data that represents the image. Over the years, a wide variety of formats were developed by different companies or research communities. This can be a very confusing subject and can lead to problems when exchanging images between different computer platforms or over the Internet.

The main issues to be considered when selecting a file format are:

- Is there any limitation on image size? As image-acquisition devices develop, ever-larger images are created. It is not uncommon nowadays to work with files thousands of pixels on each axis.
- What pixel types does the format accept? As mentioned previously, pixel intensities may be integer numbers in different ranges, a triplet of integer intensities when dealing with color images, and noninteger values when mathematical operations are applied.
- Does the format allow data compression? Several compression methods exist to reduce the amount of memory occupied by the image. Compression methods may be lossy, meaning some image information is lost in the compression procedure, or lossless, meaning no information is lost.

Table 3 lists some of the most common formats with their main characteristics.

Table 3 Main file formats and characteristics

Format	Pixel types	Compression method
TIFF	Grayscale 8 and 16 bits (integer) RGB Color 24 bits (integer) Floating-point 32 and 64 bits (noninteger)	RLE, LZW, JPEG, JBIG, other
GIF	Color 8 bits (indexed)	LZW
BMP	Grayscale 8 bits (integer) RGB Color 24 bits (integer)	RLE
JPEG	Grayscale 8 bits (integer) RGB Color 24 bits (integer)	JPEG
PCX	Grayscale 8 bits (integer)	RLE

RGB Color 24 bits (integer)

Acronyms are explained in text.

Tagged Image File Format (TIFF) is the most flexible format. It was originally developed by Aldus Corporation in 1986 (Ref 4, 5) and has had many revisions since to increase its flexibility. Currently, Adobe Systems Inc. manages the TIFF format through its Developers Association. This format accepts most types of pixels, even though not all programs are prepared to read them.

TIFF files are easily exchanged between different computer platforms, for example, between PC-Windows and Macintosh machines. Actually, the only difference between TIFF files in both platforms is the so-called byte order, which refers to pixels that occupy more than 1 byte of memory; the order of storage is reversed between the Windows machines and the Macintosh, but this does not affect software that accurately follows the TIFF specification. (One must remember, however, that the Macintosh operating system does not require the three-letter name extension used in Windows. Thus, a file saved in a Macintosh without the name extension may not be recognized by PC software even though the data is readable.)

The TIFF format also accepts different kinds of compression methods. The most commonly used is the LZW (Lempel, Ziv, and Welsh, Ref 4), offered by several programs. LZW is a lossless compression scheme. However, not all programs are prepared to read LZW-compressed TIFF files and this may confuse the user. (The generic compression program WinZip uses the LZW algorithm to compress all kinds of documents.)

Given all these characteristics, TIFF has become the format of choice in a wide range of applications.

Graphics Interchange Format (GIF) was developed originally by CompuServe (Ref 4) to facilitate the transmission of graphics and images through a network. It is restricted to a total of 256 colors or gray shades and thus is not suitable for scientific applications. However, it is very common on the Internet because of two useful features: it allows the use of a transparent color that is ignored by the browser, and it can be recorded and displayed in an interlaced mode. This last characteristic allows the display of the image at increasing levels of detail, speeding up the interaction with the user. GIF is compressed, by default, with the LZW algorithm.

Bit Map (BMP) was developed by Microsoft (Ref 4) and is a native format under the Windows Operating System. It is restricted to 8-bit grayscale and 24-bit RGB color and is compressed with the lossless run length encoding (RLE) algorithm, which is a simple lossless method. Its use is mainly restricted to the Windows environment.

Joint Photograph Expert Group (JPEG, or JPG) (Ref 4) was the first attempt at creating a standard for image file formats with efficient compression while keeping good visual quality. To reach this goal, a complex *lossy* algorithm was developed. When recording an image in JPG format, the user has the choice of several compression levels. The higher the level, the smaller the file and the greater the loss of information.

JPG has become ubiquitous on the Internet because of its efficiency in creating small files that retain the main characteristics of the image. However, it must be used very carefully when quantitative data is to be extracted from the image. It must be remembered that once a file is saved in JPG format some information is lost and cannot be recovered. If measurements are made on an original image and it is then saved as JPG, further measurements will provide different results. The amount of difference will depend on the compression level and may be acceptable, but it must be tested for each different problem.

As an example, Fig. 6 shows a comparison between an original image of fibers in a composite material and compressed versions at three different levels. The visual difference is negligible; however, measurements are slightly different as shown in the statistics for fiber area. This example cannot be easily generalized because the influence of compression on measurements will depend strongly on the distribution of intensity levels in the original image and on the parameter to be measured. As JPEG affects directly the quantization of the image, intensity measurements are likely to be more affected. Geometrical measurements are less affected, but the effect changes from case to case. The rule of thumb is to experiment with typical images and decide which level of compression still allows an acceptable error.

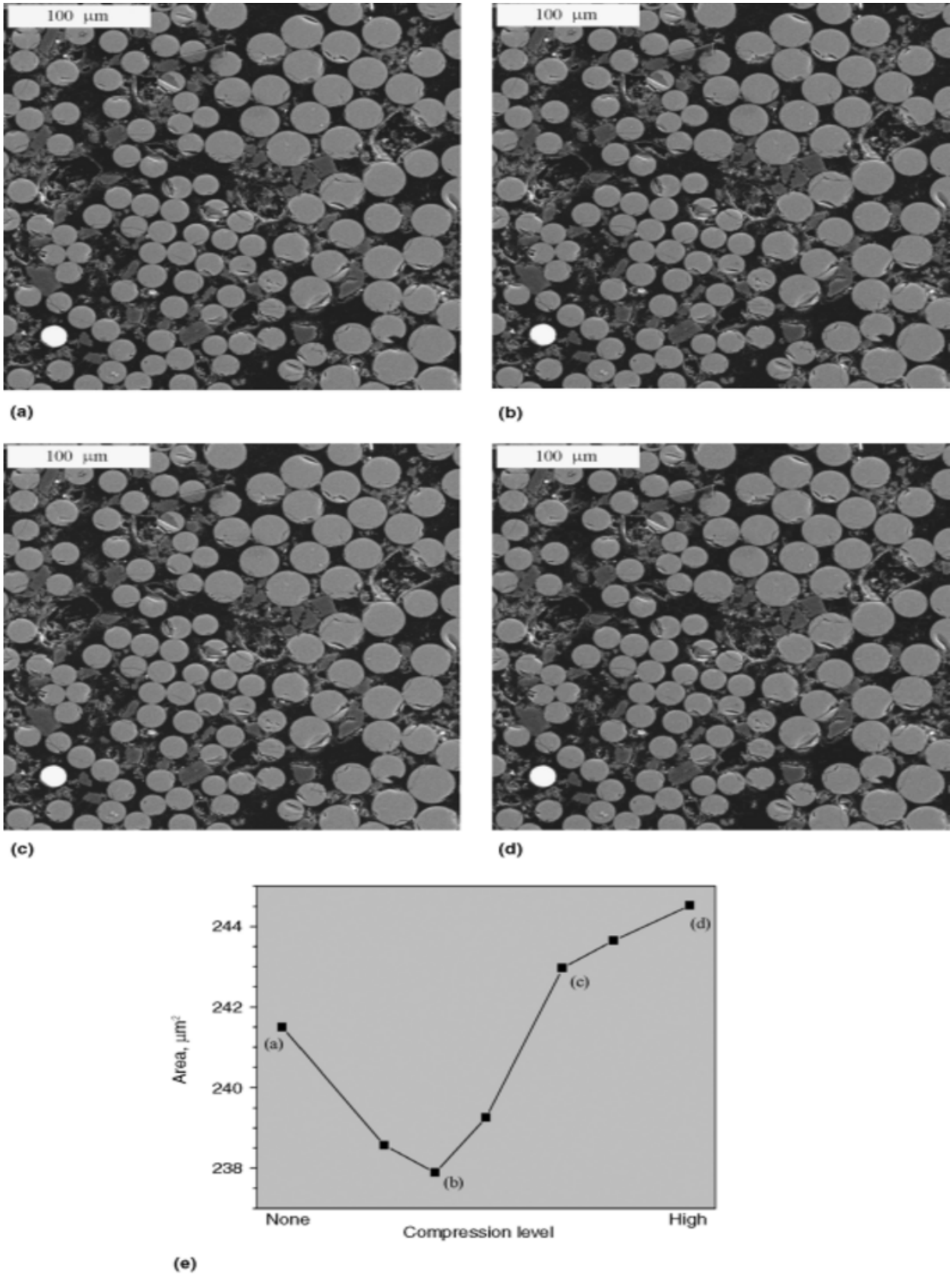

Fig. 6 The effect of lossy compression. (a) A SEM image of a fiber-reinforced composite. TIFF noncompressed. (b) JPEG low compressed. (c) JPEG medium compressed. (d) JPEG high compressed. (e) Measured area of the fiber highlighted in white against compression level

Many programs use proprietary formats that allow recording specific information that only that program is capable of recording. For example, many scientific image-processing programs have one or more annotation layers to store scale markers, drawings, and so forth, independently from the image pixels. When saving the image with these annotations, the program uses a specific file format because standard formats generally cannot store this kind of information. If it is necessary to use a standard format, the annotations must be "burned" in the image, that is, converted into image pixels, before recording the file.

Image Sensors

Image sensors are necessary to transform light intensity in a given scene into some permanent form of storage. There are two kinds of sensors with very different characteristics: film and image-acquisition electronic chips. Electronic sensors are evolving rapidly and are replacing film in laboratories worldwide. As image formation in the two kinds of sensors is based on distinct physical processes, an accurate comparison is very difficult. One of the main issues in digital imaging is the comparison of resolution between film and electronic sensors. The following sections aim at clarifying some of the aspects of this discussion.

Photographic film was the only practical image storage medium for nearly a century. Film sensitivity to light is based on its effect on an emulsion coating of silver salts or dyes. When exposed to light there is the formation of active centers—agglomerates that will appear as opaque points in the exposed negative.

The resolution of film depends directly on the size of these agglomerates, which are also referred to as film grain. Characteristics vary widely between color and black-and-white film, different film speeds (ISO settings), and different manufacturers. Film resolution is measured in lines per millimeter (lpm). This unit is more compatible with the analog (nondiscrete) characteristic of the medium and derives from the standard test normally used to characterize film and lens quality in photographic cameras. In this test, an array of periodic lines with different line spacings and contrasts is photographed under optimal conditions of focus and illumination. The resulting picture is analyzed to determine the film resolving power (Ref 6).

The detailed description of these tests is beyond the scope of the present text, except to say that film resolution is strongly dependent on the contrast between adjacent lines—the higher the contrast, the higher the resolution—and lies approximately between 50 and 150 lpm for typical film. Equating lpm to dpi translates into a resolution between 1270 and 3810 dpi. This explains why film scanners require high resolutions to accurately digitize film. A 35 mm film, which has an area of 24×36 mm^2, would require between 2,160,000 and 19,440,000 pixels.

Film can be considered a high-resolution medium. It is also relatively inexpensive and flexible. However, it has important limitations. Film responds nonlinearly to light intensity at low and high levels of illumination. The linear region may be relatively narrow, making accurate intensity measurements and comparison very difficult. Electronic sensors are generally superior in this regard. Light sensitivity varies among films of different ISO settings—higher settings mean higher sensitivity, but also larger grain, restricting resolution. Film is not suitable for capturing movement or for any kind of online acquisition and processing, as it requires separate chemical processing.

Electronic Sensors. The principle behind all electronic image sensors is the conversion of light intensity into a measurable electric signal. There are two types of devices: tube sensors and solid-state sensors.

Tubes. For many decades, cameras used the vidicon tube. This tube is coated with a light-sensitive material that changes its electrical conductivity when exposed to light. An electron beam that scans the internal surface of the tube probes the conductivity change. The principle is complementary to the operation of a TV picture tube. Although vidicons are still used in some specialized applications such as infrared detection, they have been supplanted by solid-state sensors in most situations.

Charge-coupled devices (CCDs) were developed in the 1960s and eventually became widespread from the mid-1980s. A CCD is an array of potential wells that store an amount of charge proportional to the integrated light intensity that hits each sensor over a period of time (Fig. 7). The name charge-coupled device comes from the fact that in original models the charge stored at each point needed to be displaced point by point in each line/column, therefore coupled to its neighbor, before the attached electronic circuit could read it.

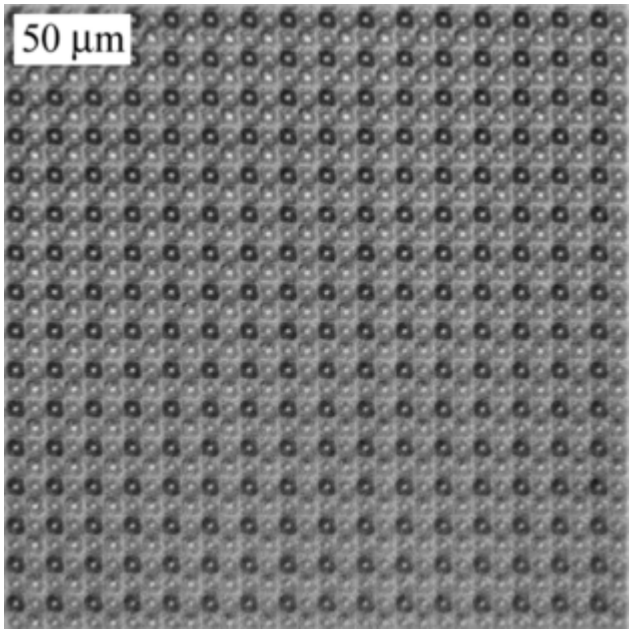

Fig. 7 Part of a CCD chip observed under a light microscope

Charge-coupled devices have several advantages over traditional vidicon tubes:

- They are manufactured as integrated circuits and thus have very accurate geometry, with essentially no distortion, excellent quality control, and relatively low price.
- The stored charge depends linearly on light intensity.
- They are sensitive to very low light levels and have large dynamic range. (Dynamic range is defined as the ratio of the maximum detectable signal to the noise.)
- They are flexible electronic devices, controllable by software.

Charge-coupled devices are currently used in all kinds of still and video cameras, both for consumer and scientific use. Some of the main parameters that specify a CCD are:

- The total number of pixels. Modern CCDs employed in scientific-grade cameras range from 1 to 16 megapixels (Ref 7), approaching film resolution.
- The pixel size. The larger the pixel, the more charge can be stored, improving the signal-to-noise ratio (SNR) but restricting resolution. Sizes range from $4 \times 4\ \mu^2$ to $15 \times 15\ \mu^2$. In consumer-grade cameras, the pixel has a 4-to-3 aspect ratio to conform to standard video formats. In scientific-grade cameras, the pixels are normally square to simplify image processing and analysis.
- The CCD chip area, essentially a function of the number of pixels and pixel size. It is limited by fabrication technology and cost. Sizes range from 7×7 mm^2 to 60×60 mm^2. The chip area defines the field of view. In general, CCDs still provide a smaller field than film for the same optical path. In light microscopy, it is sometimes necessary to use a demagnifier adapter (typically 0.63×) to reduce the image size on the CCD. Similar restrictions apply to transmission electron microscopy. A modern solution to these issues is the use of digital montage, discussed later.
- The dark current, the amount of charge stored due to thermal activation when there is no light hitting the camera. This noise image is added to all acquired images. In scientific-grade cameras the dark current is reduced by cooling the sensor with a Peltier diode. (Operating between -20 and -30 °C, or -4 and -22 °F, the dark current is reduced by a factor of 10 or more from that at room temperature.) This allows substantially longer exposure times to capture fainter signals, without degradation of the SNR. For the finest applications, the dark image for each used exposure time must be recorded and subtracted from the image. See the section “Algebraic and Logic Operations” in this article.
- Gain variations. Different pixels in the sensor may have different responses, and this may also vary with the distance of a given pixel to the output amplifier, as charge transfer between sensors may not be

perfect. Although these effects are minimized in modern scientific-grade cameras, it may be useful to acquire a gain reference image and use it to divide each image.

- The scan rate with which an image is formed. Consumer grade CCDs normally conform to video rates to allow easy output to VCRs and TV monitors. Scientific-grade CCDs are of the slow-scan kind, meaning the readout time is normally longer, with no compatibility with video scan rates. This improves charge-transfer efficiency, reducing gain variations, and also improves the SNR (Ref 8). The scan rate is normally adjustable to allow faster or slower image acquisition.
- Pixel binning, in which several pixels are treated as one, reducing the resolution but increasing the frame rate, allowing faster image acquisition. This is used to position or focus the sample, when faster visual feedback is necessary.
- Region of interest (ROI) acquisition. Software control allows easy selection of subregions of the sensor, allowing faster image acquisition and improved contrast in the desired region.

A typical interface for a scientific-grade camera is shown in Fig. 16. One can see controls for manual and automatic exposure time, subsampling, and so forth.

Part of the high cost associated with scientific-grade CCDs stems from the use of specialized microelectronics fabrication methods that are different from the methods for common computer chips. Thus, CCDs do not profit from the economy of scale of consumer-grade electronic circuits.

Complementary metal oxide semiconductor (CMOS) technology has been recently introduced for image sensors. These sensors use standard chip manufacturing techniques, thus allowing a substantial cost reduction. They also have better integration between the sensors and output electronics, improving and facilitating their connection to computers. Currently, CMOS cameras are still noisier than CCDs, but their performance is improving steadily (Ref 9). They are likely to supercede CCDs in the future.

Scanners

Scanners are used to digitize printed positives or negatives obtained from photographic film. Scanners are necessary whenever photographic film is employed, as they are the only method that reaches the very high film resolution.

There are basically three kinds of scanners:

- Flatbed scanners suitable for scanning positives and printed material in general and, with a suitable attachment, transparent material. Resolutions range from 300 to 2400 dpi.
- Dedicated film scanners suitable for scanning only photographic film. There are specific models for 35 mm film and mounted slides, and multiformat scanners. Resolutions range from 1200 to 4800 dpi.
- Drum scanners suitable for both positives and negatives, with very high resolution (10,000 dpi plus) and very low distortion.

Flatbed scanners are by far the most common kind due to their low price and ease of use. Figure 8 depicts the operation for opaque originals. A linear source of light, normally a fluorescent lamp, is focused to illuminate a line on the original. Light is reflected off the surface, filtered to detect the RGB components, and focused onto a linear CCD. The whole optical assembly is displaced by a stepper motor in the direction orthogonal to the CCD, thus scanning a rectangular area of the original.

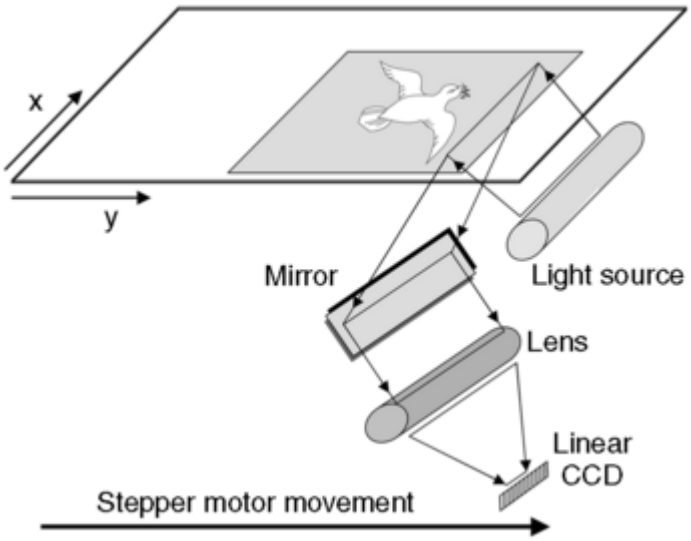

Fig. 8 Flatbed scanner internal scheme

When checking scanner specifications, it is common to see two different numbers for the resolution, for example, 400 × 800 dpi. The first number is the optical resolution of the CCD detector (*x*-direction resolution) and is the main factor in defining scanner quality. The second number is the stepper motor resolution and defines the mechanical resolution in the *y*-direction. Even if it is higher than the optical resolution, it does not improve overall scanning resolution. Higher mechanical resolution is only used to improve positioning accuracy when scanning a specific region of the original (Ref 10).

It is not uncommon to see much higher resolutions in the specifications for flatbed scanners, for example, 4800 × 9600 dpi. However, these numbers do not represent true physical resolution (optical/mechanical), but rather interpolated resolution that is obtained by calculating intermediate values between measured points. Interpolation can be useful in specific situations, but can always be obtained with image-processing software (discussed subsequently) and thus higher interpolated resolution does not represent higher scanner quality.

It is worth mentioning that flatbed scanners can reach near-micron resolution. A resolution of 1200 dpi means that in each inch, 25,400 μm, there are 1200 pixels. Thus each pixel is 25,400/1200 = 21.17 μm. In some situations, it is much more practical to use a scanner to image millimeter-sized objects than to use a low-magnification microscope or digital camera. The catalyst particles in Fig. 9 were imaged at 600 dpi (42.34 μm/pixel) with a flatbed scanner. The enlarged view illustrates the level of detail obtained. Use of the scanner simplifies sample preparation, focusing, and illumination. It is even possible to scan 3-D objects, as shown in the figure, even though shadows are likely to be present and must be dealt with properly (more details are provided in the section “Image Processing and Analysis” in this article).

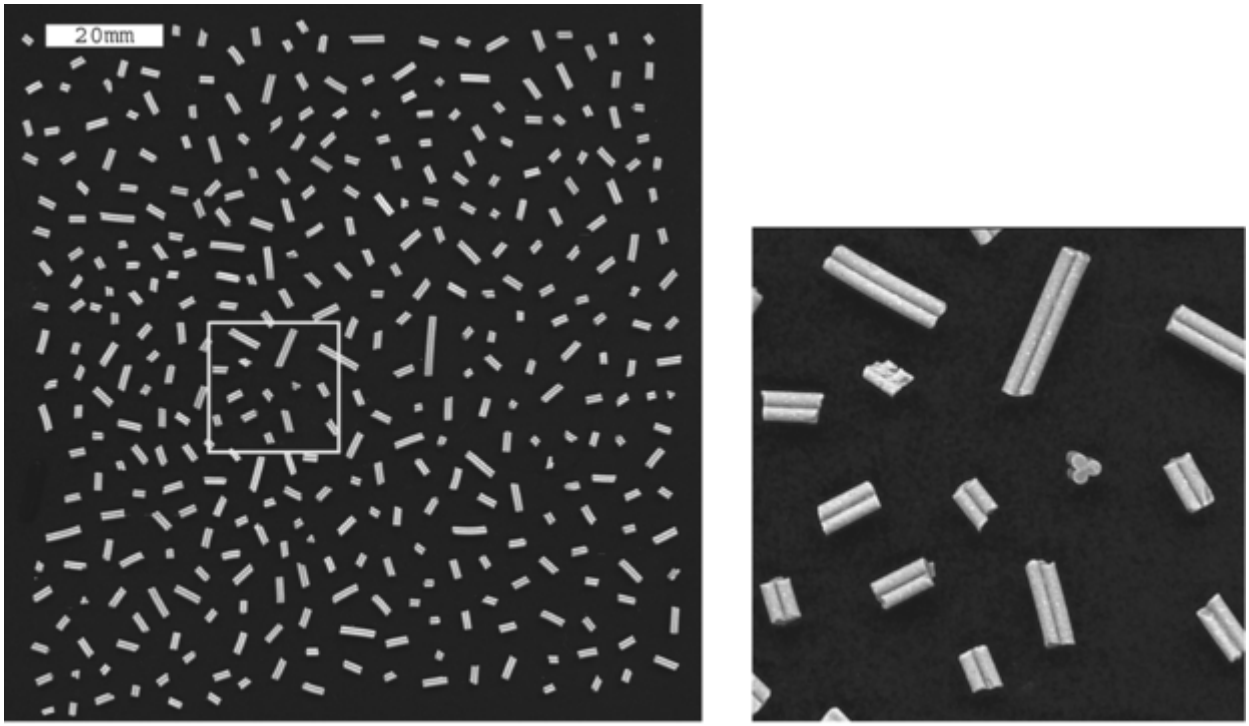

Fig. 9 The quality of scanned images. (a) An image of catalyst particles digitized with a flatbed scanner at 600 dpi. The square area is zoomed up in (b) to show the high level of detail obtained.

Film Scanners. Some flatbed scanners can be fitted with transparency adapters to allow digitizing transparent originals and even film, using special holders. However, these adapters are normally inferior to film scanners that have higher resolution and special optics. Higher resolution is required to reproduce the fine detail of film. The most common model is the 35 mm scanner that accepts either negatives or mounted slides. In these models, the light source and detector are fixed in relation to each other, and the film is displaced to scan the desired region. It is important to keep in mind that these scanners can create very large files. A 35 mm slide has an area of 24×36 mm^2 (0.95×1.42 in.^{2}). At 2700 dpi the total number of pixels is $2551 \times 3834 \approx 9.3$ Mpixels. For a color image with 3 bytes per pixel, the total file size is close to 30 Mbytes.

In electron microscopy, it is still relatively common to use large-format film. Multiformat film scanners have special adapters for different film formats and offer high resolution and superior optics. File sizes are even larger in this case.

Drum scanners are at the high end of the scanner family. Mainly used in advanced printing and graphics applications, they offer very high resolution (10,000 dpi and above) and very sophisticated optics. The material to be scanned, either positive or negative, is attached to a cylindrical drum that keeps optical distortions at a minimum over the whole scanned area. Drum scanners have a specific application in high-resolution transmission electron microscopy (HRTEM), where they are used to digitize the high-definition electron-sensitive film. However, they are quite expensive and relatively difficult to operate. Slow-scan CCD cameras are quickly replacing film in these applications.

Video Capture and Image Display

Video cameras have become ubiquitous in light microscopy labs in the last decade. They are relatively inexpensive, can capture movement, offer good color quality, and are compatible with TV monitors, VCRs, and DVDs, allowing easy display and recording. However they are restricted to very low resolutions due to limitations of the standards. A description of these standards is in order.

Video Standards. When TV broadcasting became commercial in the 1940s, two main standards were established, based on electronics capabilities of the time. These standards are still present in modern television and affect compatible cameras and VCRs.

The American standard, RS170A, for black-and-white TV later evolved into the NTSC (National Television Standards Committee) standard for color TV. It shares many characteristics with the CCIR (Comité Consultatif de la Radiodiffusion, or Radio Diffusion Consulting Committee) standard used in Europe, which later incorporated color through the PAL (Phase Alternate Lines) and SECAM (SÉquentiel Couleur Avec Mémoire, or Sequential Color with Memory) standards.

A TV image is formed through periodic scanning of an electron beam as shown in Fig. 10. The scanning follows horizontal lines from left to right, at the end of which there is a horizontal retrace line in which the beam is blanked. The beam hits an electron-sensitive material (normally a phosphor) that emits light. On each scan line the intensity of the electron beam, and thus the emitted brightness, is modulated by the intensity of the signal that is to be imaged. A sequence of lines forms a frame at the end of which there is a vertical retrace that brings the beam back to the starting position to start a new scan. Thus, even static images are formed of the periodic repetition of frames.

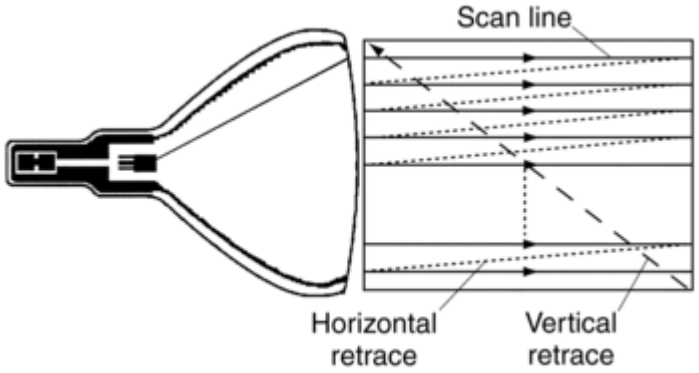

Fig. 10 A sketch of TV image formation through scanning

The repetition rate, measured in frames/s, must be high enough to prevent the image from blinking due to the natural brightness decline of the phosphor emission during a full frame scan, in a phenomenon called flicker. The effect of flicker depends on the time response of the human eye. The retina is not sensitive to brightness oscillations faster than ~1/60 s. Thus, in the original definition of TV standards the frame rate, also called refresh rate, was chosen to be 60 Hz in the American standard and 50 Hz for the European standard (the difference stems from the different frequencies employed in alternating-current line voltages).

The original standards defined a number of scan lines per frame, 525 for RS170A and 625 for CCIR, of which only 480 and 576, respectively, are visible lines. The two standards shared the same screen aspect ratio, 4 to 3. This means that when digitized, standard video signals must have 4/3 as many pixels in the horizontal direction as in the vertical direction, if square pixels are used. This leads to the well known 640 × 480 resolution employed when digitizing RS170 video signals and which is also used in the computer world with the name of VGA (video graphics array) resolution. All higher resolutions employed in computer screens follow the same aspect ratio.

At the time TV was developed, electronics were not fast enough to scan a full frame with more than 500 lines in 1/60 s. To bypass this limitation, the defined standards used the so-called interlaced scan in which each frame is divided into two fields containing the odd and even lines of the frame. The odd field is scanned first in 1/60 s, providing a fast low-resolution representation of the image. The even field is then scanned at the same rate, showing the other half of the image, for an effective frame rate of 1/30 s. The resulting image is not as good as a noninterlaced (NI) image. (This is analogous to the subsampling used to display gif and jpg images in web sites, where a low-resolution version is showed first and then the resolution is subsequently improved.)

Even though electronics has evolved tremendously since then, the original definitions of number of lines per frame, refresh rate, and interlaced scan have remained in all video-related equipment until today. This means the maximum video resolution that can be achieved with RS170 cameras, monitors, or VCRs is 640 × 480 and with CCIR is 768 × 576. Thus, when selecting a video camera to adapt to a light microscope; for instance, it is better to choose a CCIR camera that has over 135,000 more pixels. (Video signals are digitized with special computer boards called frame grabbers. These boards always provide compatibility with both RS170 and CCIR signals. Thus, choosing a European standard camera in an American environment or vice-versa is not a problem.)

With the advent of CCD sensors, the old-style vidicon was substituted in all kinds of video cameras. In some instances, the CCD array has even more pixels than the numbers mentioned above. However, regardless of the physical CCD resolution, when outputting a video signal the final resolution follows the standards.

It must remain clear that video cameras, even modern ones, suffer from all limitations entailed by the video standards, the main problem being low resolution. Modern digital cameras are much superior in this and other regards. On the other hand, video cameras provide fast image acquisition, allowing the capture of movement, which is not yet possible with the highest resolution digital cameras.

High-definition TV (HDTV) is a modern set of standards for TV broadcasting, which increase the number of lines/frame, the refresh rates, and aspect ratio. As for traditional TV, HDTV has different standards in different parts of the world, and it will take a few years before it becomes a de facto standard.

Display Adapters and Computer Monitors. Computer monitors evolved from TV and for a long time suffered from the same limitations described above. The first monitors were interlaced and had low refresh rate. Even at the low resolutions used at the time, flicker was a serious concern. As electronics evolved, computer monitors became somewhat independent of TV standards keeping only the same 4-to-3 aspect ratio.

The major evolution was in resolution. Nowadays few monitors are restricted to VGA resolution. Currently used resolutions are SVGA (super VGA, 800 × 600), XGA (extended VGA, 1024 × 768), UGA (ultra VGA, 1280 × 1024), and UXGA (1600 × 1200). Higher resolutions allow more comfortable display of several windows and increase productivity dramatically, specially when dealing with high-resolution images. However, as resolution increases, screen size becomes an issue. Even though smaller monitors can accept higher resolutions, the image normally becomes distorted, and most text and graphic objects become too small to be readable. Typical screen sizes range from 17 to 21 in.

As resolution and screen size increase, the refresh rate becomes a critical factor for image quality. Lower refresh rates may lead to some kind of flickering, ever more prominent as static, high-quality images are the focus of attention. Current refresh rates range from 60 to 120 Hz.

Video boards translate the computer binary signals into video signals compatible with the monitor. Each board has a certain amount of video memory that establishes the maximum resolution and quantization with which a picture can be displayed. The numerical relation among video memory, resolution, and quantization is the same as for digital file sizes, described earlier. Thus, for instance, a 1024 × 768 pixels image with 16.7 million colors (3 bytes/pixel) requires at least 1024 × 768 × 3 = 2,359,296 bytes = 2.25 Mbytes of video memory while a 1600 × 1200 image with 64 kcolors (2 bytes/pixel) requires 3,840,000 bytes = 3.66 Mbytes. Typical low-cost boards have 8 Mbytes or more. The best boards allow the choice of different combinations of resolution, quantization, and refresh rate to adapt to the monitor characteristics and specific user needs.

In recent years, standard tube monitors have showed a steady improvement in image quality; the main evolution has been flat screens that have no curvature and reduce image distortion to a minimum. Flat plasma panels are a more recent, and still expensive, development, eliminating the electron tube. Through the direct access to integrated electronic light emitters, flat panels provide superior image stability and save substantial desktop space. As they do not emit any magnetic field, they are also ideal in applications such as transmission electron microscopy, where stray magnetic fields pose limitations to the microscope performance. As their price decreases, flat panel displays will replace traditional tube monitors in most applications.

Digital Imaging and Microscopy

The ability to acquire digital images from microscopes has opened up new possibilities in their interface with computers, in what is now called digital microscopy. The next three sections review some of the consequences of these new methods in light microscopy (LM), scanning electron microscopy (SEM), and transmission electron microscopy (TEM).

Light Microscopy. A new generation of light microscopes integrates digital image acquisition with microscope automation to provide many new features. A motorized/automated microscope has the following software-controlled options:

- Motorized sample-holder displacement in three axes (*x*, *y*, and *z* focus)
- Motorized objective change with automatic focus and illumination adjustment
- Contrast mode (bright field, dark field, differential interference contrast, or DIC, and polarization), filters, and diaphragms

These options allow many integrated tasks to be run under the control of routines developed by the user. Some examples are:

- *Field scanning* in any sequence and objective choice, integrated with image-acquisition, processing, and analysis, allows complete evaluation of a sample without user intervention. The program controls *x-y* scanning, digital camera operation, image processing, and analysis with automatic accumulation of results for any number of fields.
- *Automatic focusing* of the image for each field, through image analysis. The software automatically acquires a through-focus series and determines the in-focus image. This procedure can be integrated with the field scanning described previously to deal with sample height variations.
- *Extended focus* to improve the normally limited depth of field of light microscopes. The system acquires a sequence of images at different focus values, analyzes each image to extract the in-focus portion, adds these portions, and builds a resulting image with extended focus.
- *Digital montage* to improve the field size of objectives with larger magnification and higher resolution. Using the motorized stage, the system automatically acquires a series of partially superimposed images. The superposition region is used to calculate optimal montage position through cross-correlation (Ref 11). Then field brightness and contrast are equalized, resulting in a much larger image with the higher resolution of the higher-magnification objective lens.

Scanning Electron Microscopy. The main changes in SEM come from the digital control of electron beam and detectors, allowing acquisition of images with high pixel resolution and, especially, sophisticated x-ray spectroscopy (EDX). Given a reference image in either secondary electron (SE) or backscattered electron (BSE) modes, a full x-ray spectrum can be obtained for *each scan point* allowing powerful analysis.
Figure 11 illustrates some of these possibilities (Ref 12). The top-left reference image of a microcircuit was acquired with the SE detector. The image also shows the line marker that was used to define the path for the electron beam. Profiles of the Si-Kα and Al-Kα peak intensities along that line are displayed at the bottom. These profiles were extracted a posteriori from the spectra that were stored to disk. The spectrum at the top-right corresponds to the position of the marker in the profile display at the bottom. Spectra for any position can be recalled by moving the position markers in the profile display. The profiles clearly show how the aluminum and silicon intensity fluctuates as the probe is positioned on an aluminum line or on the silicon substrate.

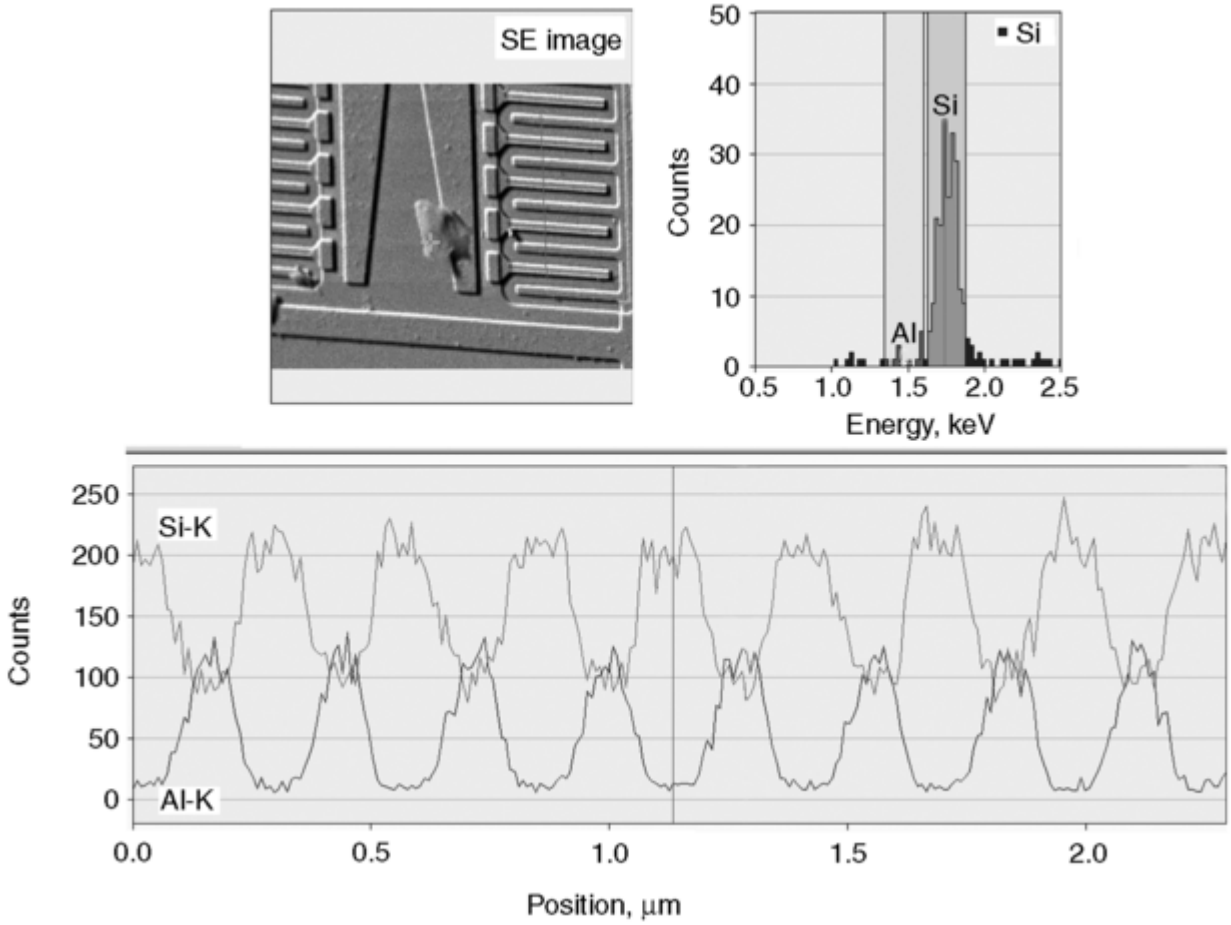

Fig. 11 Digital microscopy in the scanning electron microscope. See text for detailed explanation. Courtesy of Emispec Systems Inc.

Spectrum imaging is attracting renewed interest lately, mainly because it is now technologically feasible. There are obvious advantages to saving the spectra at each point in a scan, as opposed to discarding the original data after processing each point because it gives the user the opportunity to process the data as many times as are necessary to extract the useful content (Ref 13). The ability to perform sophisticated postprocessing not possible during real-time acquisition makes spectrum imaging very attractive, especially for systems with significant spectroscopic peak overlap, low signal-to-background ratios, low elemental concentrations, or spectral artifacts.

In a different approach, digital imaging allows extracting 3-D information from a stereo pair of tilted SEM images. Tilting the specimen by a known angle in relation to the electron beam provides the parallax needed to estimate heights (*z*-axis) based on *x*-axis translation between the two images in the pair (Ref 14, 15). Figure 12 shows an example of the procedure. This procedure is not practical in a light microscope because of limited depth of focus and restrictions in specimen tilting. In TEM, a similar principle has been applied to reconstruct 3-D structures with atomic resolution (Ref 16).

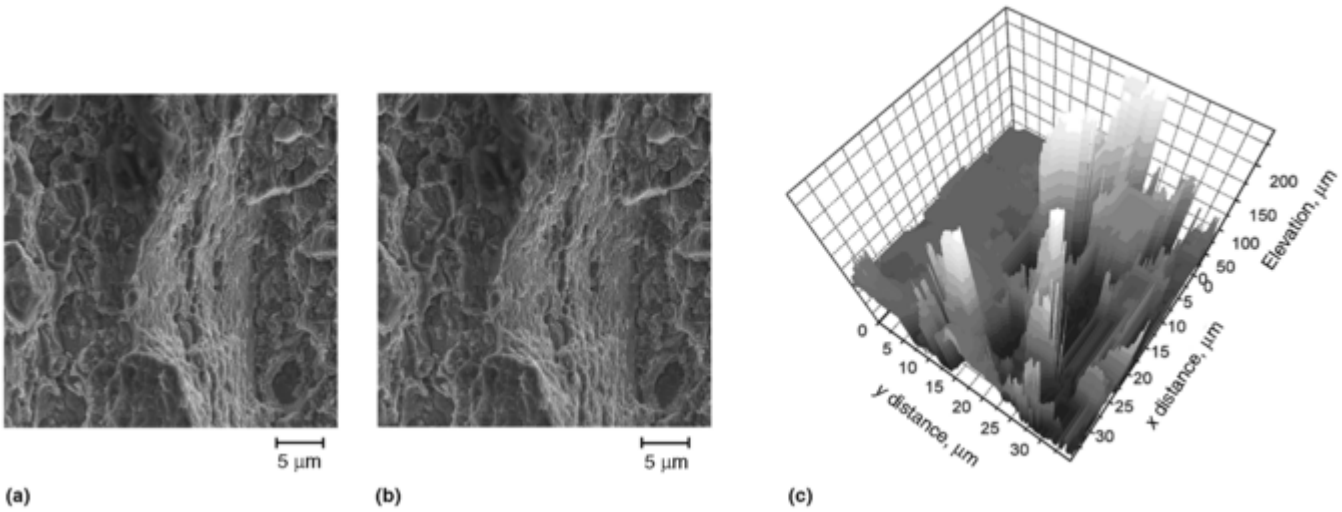

Fig. 12 Three-dimensional reconstruction from a stereo pair of SEM images. (a) Left parallax image. (b) Right parallax image. (c) Three-dimensional graph showing the surface reconstruction. Courtesy of L.R.O. Hein and C.R. de F. Azevedo, UNESP, Brazil

It must also be mentioned that when image processing is to be used, it may be better to acquire images in the BSE rather than in the SE mode. Secondary electrons provide strong topographic contrast that enhances the qualitative interpretation of an image. However, this information may be detrimental to image processing because it makes image contrast too complex. BSE images present atomic-number contrast and do not have the typical shading/illumination conditions of SE images, as the BSE detector is axially mounted. This kind of image is much easier to process, even though it may look less attractive visually. One should keep in mind, though, that there is no general rule in this regard, and that the choice of image mode or a combination of modes will depend on the specific sample/problem at hand.

Transmission electron microscopy has been strongly affected by digital microscopy methods, perhaps in a more sophisticated way. Both in conventional diffraction contrast mode and in HRTEM, the fine tuning of the microscope strongly affects the quality of images obtained. Astigmatism, for example, must be corrected, but, until recently, this correction required an experienced operator and would take several minutes for each sample. With the development of specialized CCD cameras for TEM, the ability to acquire digital images and analyze them online has opened the door to automatic tuning procedures.

Automatic tuning integrates image acquisition, image analysis, and microscope control (Ref 17). In the case of astigmatism correction (see Fig. 13), images of an amorphous region of the sample are continuously acquired with the CCD camera. The Fast Fourier Transform (FFT) of each image is obtained, and the rings representing the amorphous material are analyzed. The deviation from a circle is calculated, and the astigmatism intensity and direction are determined. These results are used in feedback to send signals to the TEM computer interface, allowing the modification of the current in the magnetic lenses, changing imaging conditions. In each cycle, the astigmatism is reduced until the procedure converges to an acceptable state.

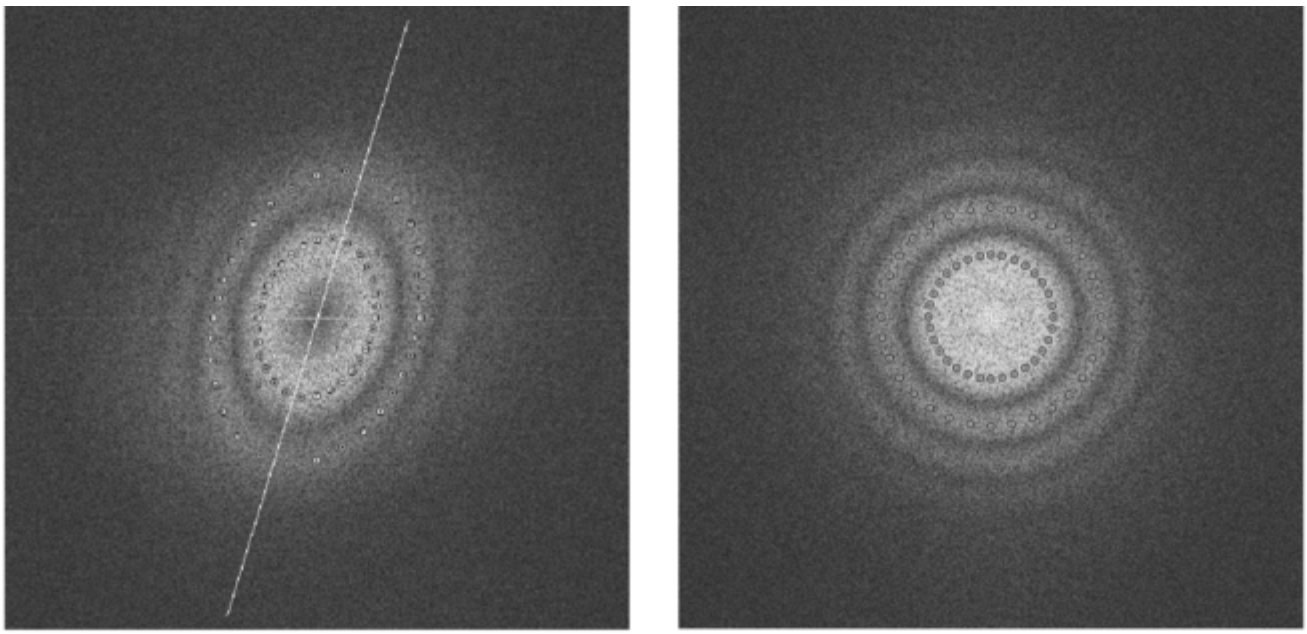

Fig. 13 Automatic tuning in TEM. (a) Digital diffractogram of an amorphous layer, showing astigmatism. (b) After automatic tuning of the microscope conditions, the astigmatism is reduced to negligible values. Courtesy of M. Pan, Gatan Inc.

One of the limitations of CCD cameras used in TEM is their limited field size when compared to standard film. In similar fashion to the digital montage described for light microscopy, several adjoining fields can be captured and stitched together to create a much larger digital image. In this case, each field is imaged through software-controlled tilting of the electron beam, effectively displacing the field of view.

References cited in this section

1. L. Wojnar and K.J. Kurzydlowski, Analysis and Interpretation, in *Practical Guide to Image Analysis*, ASM International, 2000, p 171–183

2. J.D. Foley, A. Van Dam, S.K. Feiner, and J.F. Hughes, *Computer Graphics: Principles and Practice*, 2nd ed., Addison-Wesley, 1991

3. "IEEE Standard for Binary Floating-Point Arithmetic," Std 754, IEEE Computer Society, 1985

4. J.D. Murray and W. van Ryper, *Encyclopedia of File Format*, 2nd ed., O'Reilly & Assoc., Inc., Bonn, Germany, 1996

5. partners.adobe.com/asn/develop/pdfs/tn/TIFF67.pdf, Adobe Systems, Inc.

6. http://www.normankoren.com/Tutorials/MTF.html, Norman Koren Photography

7. http://www.gatan.com/imaging/ultrascan.html, Gatan, Inc.

8. http://micro.magnet.fsu.edu/primer/digitalimaging/digitalimagingdetectors.html, Florida State University

9. C. Williams, CMOS vs. CCD: The Battle Continues, *Adv. Imag.*, Vol 16 (No. 9), Sept 2001, p 28–31

10. http://www.scantips.com/, Wayne Fulton, Scantips, self-published

11. J. Frank, The Role of Correlation Techniques in Computer Image Processing, *Computer Processing of Electron Microscope Images,* P.W. Hawkes, Ed., Springer, Berlin, 1998, p 187–222

12. http://www.emispec.com/EM/appnotes/edxprof.html?whichPage=3, Emispec, FEI, Co.

13. J. Bruley, M.W. Tseng, and D.B. Williams, Spectrum-Line Profile Analysis of a Magnesium Aluminate Spinel Sapphire Interface, *Microsc. Microan.,* Vol 6 (No. 1), Feb 1995, p 1–18

14. L.R.O. Hein, Quantitative Fractography by Digital Image Processing: NIH Image Macro Tools for Stereo Pair Analysis and 3-D Reconstruction, *J. Microsc.,* Vol 204 (Part 1), Oct 2001, p 17–28

15. L.R.O. Hein, F.A. Silva, A.M.M. Nazar, and J.J. Ammann, Three-Dimensional Reconstruction of Fracture Surfaces: Area Matching Algorithms for Automatic Parallax Measurements, *Scanning,* Vol 21 (No. 4), July–Aug 1999, p 253–263

16. M.A. O'Keefe, K.H. Downing, H.-R. Wenk and H. Meisheng, 3D Imaging of Crystals at Atomic Resolution, *Proc. MRS,* Vol 332, Materials Research Society, 1994, p 563

17. O.L. Krivanek and G.Y. Fan, Complete HREM Autotuning Using Automated Diffractogram Analysis, *Proc. Elect. Microsc. Soc. Am.,* Vol 50, Microscopy Society of America, 1992, p 96–97

S.Paciornik and M. H. de Pinho Mauricio, Digital Imaging, Vol 9, *ASM Handbook,* ASM International, 2004, p. 368–402

Digital Imaging

Sidnei Paciornik and Marcos Henrique de Pinho Mauricio, Catholic University of Rio de Janeiro

---

Image Output—Printing

One of the most common tasks in digital imaging is to prepare an image for printing. Different printing technologies impose different requirements on the characteristics of the digital image in order to produce the best quality prints. This section reviews some of the most important issues.

Just as for digital images, the two main parameters to describe a printer are its resolution (number of print points per unit distance) and quantization (number of different colors or gray shades that each point can assume).

Resolution is continuously increasing. Black-and-white laser printers regularly offer 1200 dpi. Inkjet printers can reach almost 3000 dpi. However, these numbers can be deceiving because the quantization of these printers is very limited, requiring a reduction in effective resolution to allow the creation of more colors.

The main question then is: What is the correct resolution for a digital image if it is to be printed? The answer is that it depends on the printer technology.

Quantization. In terms of quantization there are two basic kinds of printers: continuous tone, in which each printed point can assume essentially infinite values of color, and dithering printers, in which each point can assume a restricted number of tones, requiring the use of many points to simulate finer variations in color.

Continuous tone printers are generally very expensive, but can produce photo-quality prints. The best-established technology is dye sublimation (Ref 18). These printers use a transfer ribbon made of a plastic film. Page-sized panels on the ribbon consist of cyan, magenta, and yellow dye. A thermal print head, with thousands of heating elements, capable of precise temperature variations, moves across the transfer ribbon. Heat from the heating elements causes the color on the ribbon to vaporize and diffuse onto the surface of specially coated paper. Precise temperature variations are responsible for the varying densities of color.

Because each printed point can assume any color, the effective resolution of the printer is used to print a digital image. Typical resolution values for modern dye-sublimation printers are in the range of 300 dpi. Thus, when an image is to be printed in such a printer, it should have no less and no more than 300 dpi. Less resolution implies a loss of print quality. More resolution implies wasted information. Dye-sublimation prints are still much more expensive than laser or inkjet prints.

Dithering. Inkjet and laser printers, on the other hand, cannot produce tone variation in each printed point. It is easier to understand the principle with a black-and-white laser printer, but it applies in similar fashion to inkjet printers. A black-and-white laser printer can print black points or no points (white). It has no intermediate gray shades. To emulate these shades, the principle of dithering, used for many years in newspapers and magazines, is employed. In its simplest form, dithering is the use of a matrix of several print points, normally 6 × 6 points, in which intermediate shades are created printing a subset of the matrix points. Thus, to create a gray shade of 128, half of the full scale, 18 of the 36 points are printed in black while the other 18 points are kept white. This method can be improved by different algorithms that control how points are printed in each part of the image to optimize the emulation of gray shades. A well-known algorithm, that produces realistic shades, uses the error diffusion method (Ref 2). However, in any case, the effective resolution is reduced by a factor corresponding to the side of the dithering matrix. Thus, a 1200 dpi laser printer effectively prints grayscale images with a resolution of about 200 dpi. This means that the maximum required resolution for a digital image that is printed in such a laser printer is 200 dpi and not 1200 dpi.

These numbers vary depending on different dithering algorithms, and, especially in the case of inkjet printers, the final effect is strongly dependent on paper type and quality. A good practice is to divide the nominal resolution of the printer by 6 and add 50%. Thus, for a 1440 dpi inkjet printer, a reasonable image resolution would be 1440/6 + 50% = 240 + 120 = 360 dpi.

Programs. It is also important to understand how common word-processing and presentation programs deal with images. There are two basic ways of inserting images in such documents: inserting a file from disk or using copy and paste from an image-visualization program. When inserting from disk, the original picture resolution is preserved. When using copy and paste, the image gets the screen resolution, normally 96 dpi. Scaling the images inside the programs *does not* change image resolution, just the print size. Thus, copy and paste should be avoided when preparing an image to print because 96 dpi is too low for most printers. On the other hand, it does not make sense to insert a 1200 dpi grayscale image into a document to be printed in a laser or inkjet. This is three to four times the resolution required in each direction, resulting in a file size nine to 16 times larger than necessary. (When printing pure black-and-white line art, the full resolution should be used.)

Color Printing. The primary colors for printing—cyan, magenta, and yellow (CMY)—are different from the primary colors for image acquisition and display—red, green, and blue (RGB). The RGB model is called additive because the sensation of color is based on the addition of the excitations of three kinds of retina light sensors, the cones, which have sensitivity peaks close to these three primaries. The CMY model is subtractive because each ink deposited on a paper subtracts from white light a certain range of colors, allowing just the complement to reflect back. When two inks are superimposed, only the color that is in the intersection of both primaries is reflected. The intersection between pairs of primaries in one model gives a primary of the other model. Thus, for instance, red and green give yellow, while yellow and cyan give green. Many times, the pigments used in color printing do not provide enough color saturation when mixed together. It is then common to add black, giving rise to the four-color cartridges used in inkjet printers (CMYK). For more details refer to Ref 2 and 19.

References cited in this section

2. J.D. Foley, A. Van Dam, S.K. Feiner, and J.F. Hughes, *Computer Graphics: Principles and Practice,* 2nd ed., Addison-Wesley, 1991

18. http://www.kodak.com/US/en/digital/dlc/book2/chapter2/l1.shtml, Eastman Kodak Co.

19. J. Gomes and L. Velho, *Image Processing for Computer Graphics,* Springer Verlag, 1997

S.Paciornik and M. H. de Pinho Mauricio, Digital Imaging, Vol 9, *ASM Handbook*, ASM International, 2004, p. 368–402

Sidnei Paciornik and Marcos Henrique de Pinho Mauricio, Catholic University of Rio de Janeiro

Image Processing and Analysis

The previous sections have discussed how to acquire a digital image that accurately represents the sample under observation and how to output this image to a printer. The present section describes the methods to enhance the digital image and extract quantitative information as was pictured in the flowchart in Fig. 1.

Preprocessing

Preprocessing, or enhancement, is the first step after image digitization used to correct basic image defects, normally created during the image-acquisition step. Preprocessing can be used for qualitative purposes if the output image is to be just evaluated by a user. In this case, the image-processing sequence stops there. However, preprocessing is more relevant as a preparation for the segmentation step that eventually leads to the extraction of quantitative information.

Histograms, lookup tables, and point operations are preprocessing mathematical manipulations of pixel intensities.

The image histogram is actually the distribution of the pixel intensities in the image. For a grayscale image it corresponds to the gray-level distribution, while for a color image, there is one histogram for each component.

Figure 14(a) shows an image obtained through a light microscope and a CCD camera, and its respective histogram, Fig. 14(b). The horizontal axis represents the pixel intensities, in this case between 0 (black) and 255 (white). The vertical axis measures the number of pixels in each intensity value.

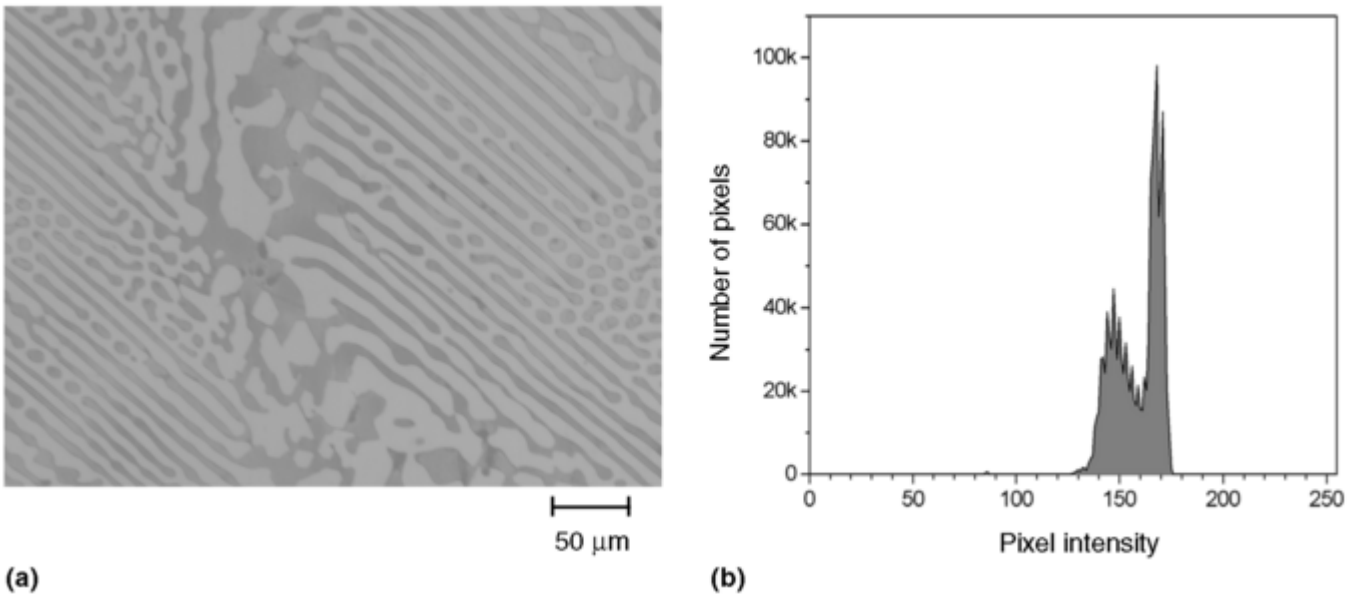

Fig. 14 An image and its histogram. (a) Light micrograph, hypereutectic cast iron, 200×, BF, CCD 1300 × 1030. (b) Intensity histogram. Note the limited spread of the plot, indicating low contrast in the image.

The histogram shows that this particular image does not have pixels at intensities close to the extremes of the range, 0 and 255. In other words, the contrast of the image is not maximized. This a relatively common situation when digitizing images directly from a microscope. The digitization equipment, a video camera plus frame grabber or a CCD camera, should be adjusted as a function of the microscope illumination and specimen

transmittance/reflectance to optimize contrast. Figure 15 shows the same sample imaged with careful contrast optimization. Notice the histogram is now widely spread over the full intensity range.

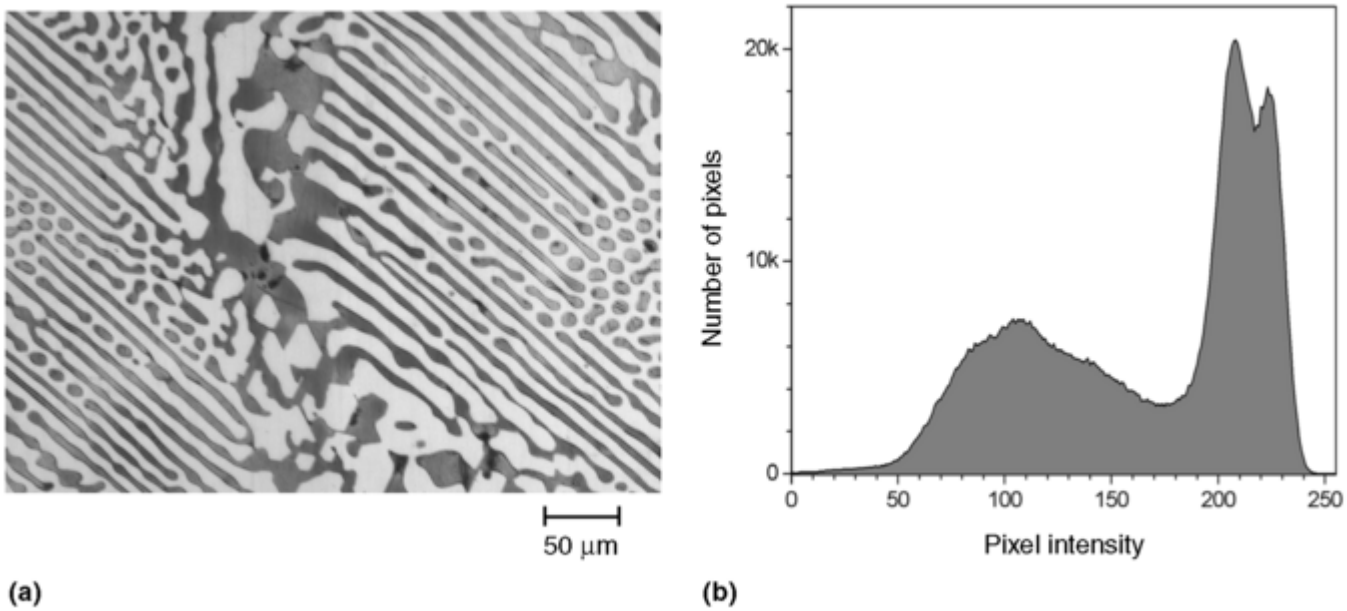

Fig. 15 Optimized acquisition. (a) The same sample shown in Fig. 14 captured to optimize contrast. (b) Note the wider spread of the histogram, occupying the full intensity range.

Modern image-acquisition software offers a *live* window that shows a preview of the image and its histogram. As illumination or exposure time is changed, the image and histogram change dynamically, allowing for optimal adjustment. Figure 16 shows such an interface (Ref 20). For given illumination conditions the software can automatically adjust camera exposure time to optimize the image histogram.

Actually, histogram optimization is a simple normalization operation that can be applied online or offline. The optimized image intensities can be calculated from:

$$I_o(x,y) = \left[I_i(x,y) - \min(I_i) \cdot \left(\frac{255}{\max(I_i) - \min(I_i)} \right) \right] \qquad \text{(Eq 2)}$$

where $I_o(x,y)$ and $I_i(x,y)$ are the output and input intensities at coordinate (x,y), and $\min(I_i)$ and $\max(I_i)$ are, respectively, the minimum and maximum input intensities. The 255 factor (2^8 - 1) is, in this case, the maximum allowable intensity for an 8-bit camera. In the case of 12- and 14-bit cameras, this factor is 2^{12} -1 = 4095 and 2^{14} -1 = 16,383, respectively.

This equation is implemented in most programs, and its application is almost instantaneous in most computers. It is referred to as contrast enhancement, contrast equalization, and histogram stretching, among other names. One must note, however, that it is preferable to adjust image-acquisition conditions than to use contrast enhancement offline. This is shown in Fig. 17, where an image captured with low contrast is enhanced using the equation above. The enhanced histogram is similar in overall shape to the one shown in Fig. 15, but there are many intensity values that have no pixels. This derives from the fact that in both the input and output images the *same number of pixels* is distributed in the *same number of intensity levels*, but in the enhanced image these levels are spread apart. As a consequence, the enhanced image shows the effect known as banding with regions of uniform intensity separated from adjoining regions by sharp boundaries.

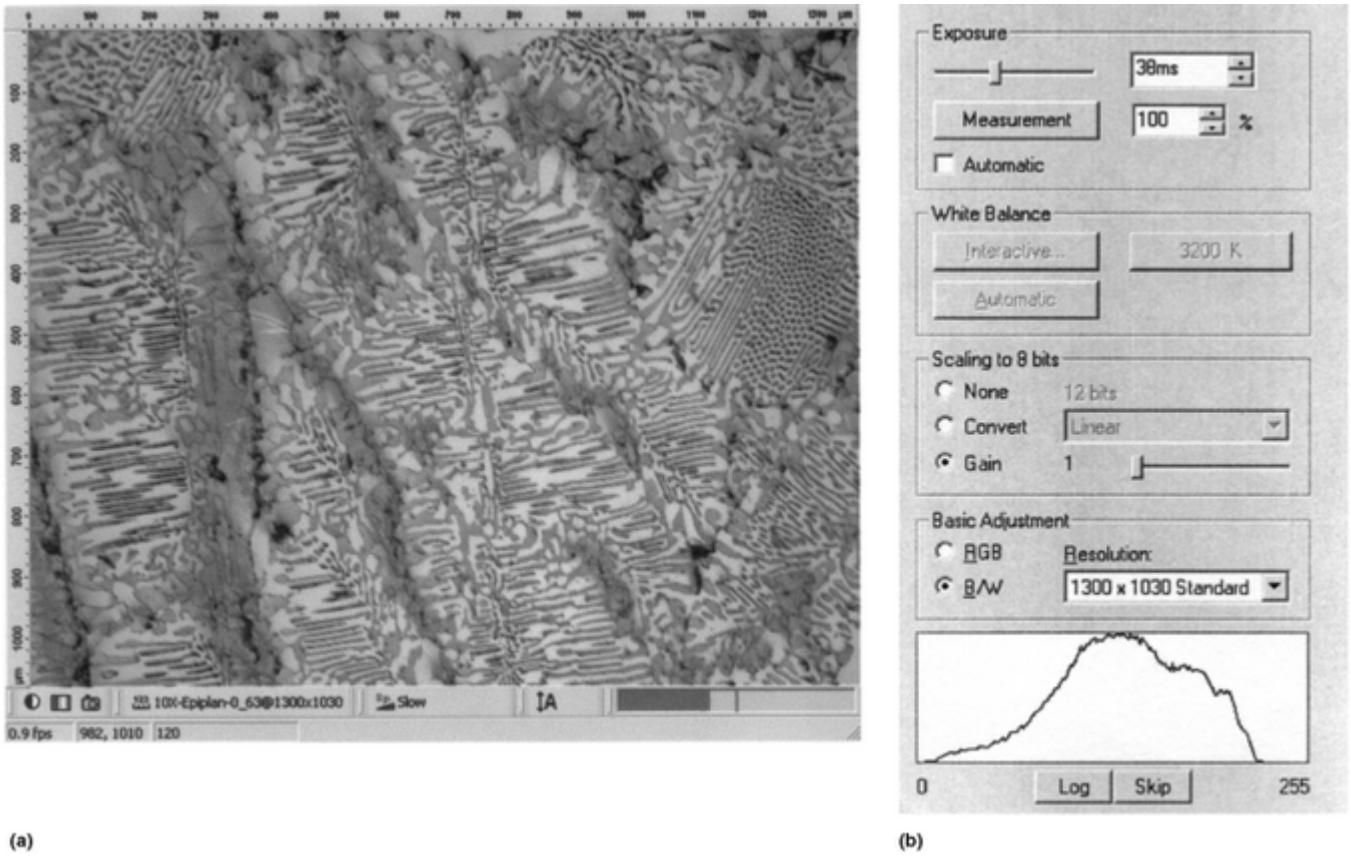

Fig. 16 Image-acquisition interface. (a) A dynamic image-acquisition window showing a live image. (b) The exposure controls and the image histogram

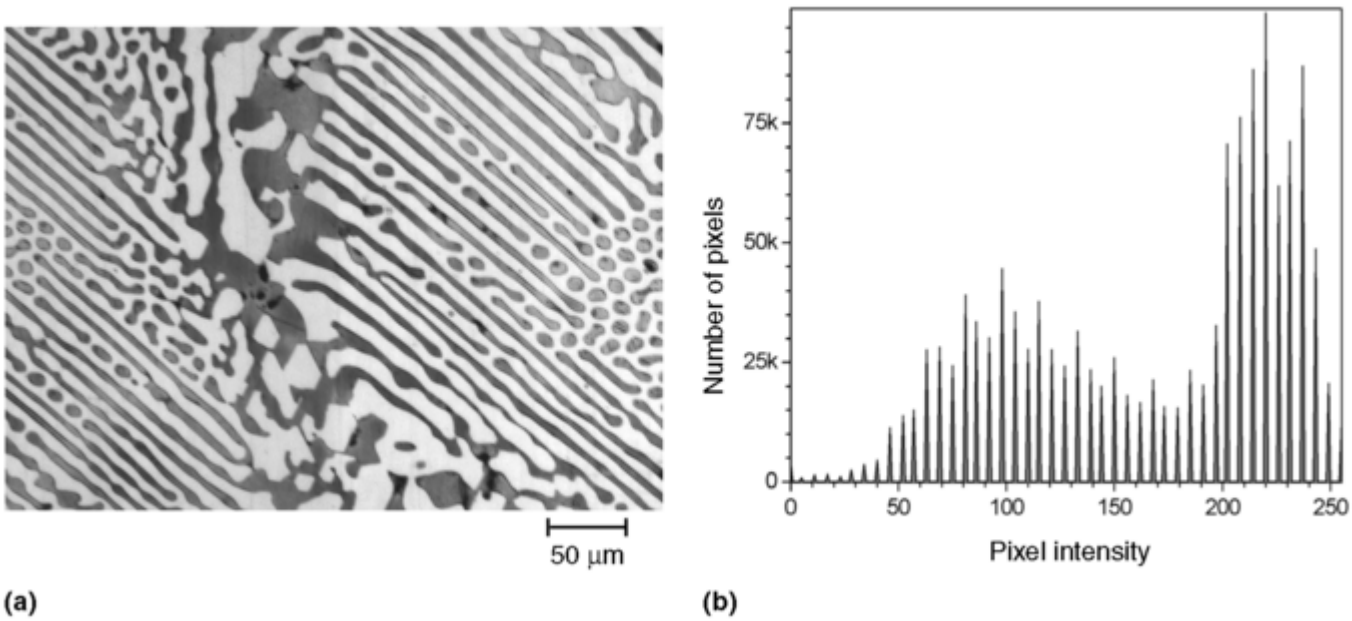

Fig. 17 (a) Offline contrast enhancement of the image in Fig. 14 (b) Note the empty bins in the resulting image histogram.

The histogram can also be used to identify intensity clipping, which happens when there is too little or too much brightness. This is shown in Fig. 18, where the same sample appears with high brightness, leading to many saturated pixels that appear as a peak in the histogram at intensity 255.

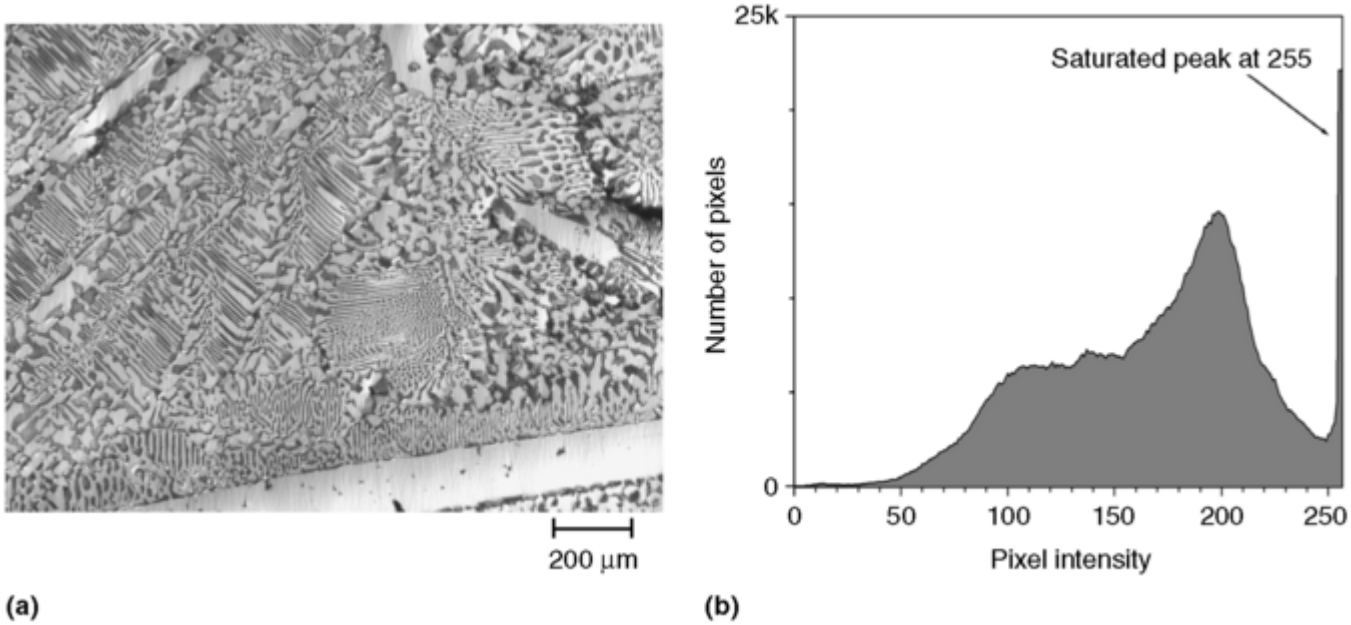

Fig. 18 Saturated image and its histogram. (a) Light micrograph, hypereutectic cast iron, 50×, BF, CCD 1300 × 1030. (b) Intensity histogram. Note the peak at intensity 255.

In summary, the histogram can be used to optimize image capture. One should look for a histogram as wide as possible, without peaks in the extremes of the intensity range.

The histogram is also extremely important in the segmentation step to be described later, where similar regions are identified and discriminated from the background through the intensity of their pixels. In this regard, regions in the image with relatively uniform intensity appear as bands in the histogram.

Lookup table (LUT) is another important tool in preprocessing. It can be represented by a numerical table or a mathematical function, and it describes the relationship between the pixel intensities in the input and output images or between pixel intensities and display intensities. As an example, the images in Fig. 5(c) and (d) are displayed with a LUT that converts the actual pixel intensities into gray levels in the display range, 0 to 255.

Applying a LUT to an image is a very fast operation. Image-processing programs use this fact to allow dynamic, interactive modification of parameters such as brightness, contrast, and other display characteristics. The modification affects only the display and not the actual pixel data. However, most programs also allow creating a new image with pixel intensities that are a copy of what is displayed. This operation might be called “Apply LUT” or “Create Image from Display.”

Simple changes of brightness and contrast are examples of linear LUTs. Equation 2 is another example of such a function. However, there are many situations where nonlinear LUTs can be useful. For instance, a logarithm expands the contrast of the low-intensity pixels of an image while compressing the contrast of the high-intensity range. This is useful when the intensity range is very wide and a linear LUT would obscure relevant information in the low-intensity range. As an example, Fig. 19 shows an image and its Fourier Transform (FT) both with a linear and a logarithmic LUT. The increase in the detail of darker regions with the nonlinear LUT is evident. An exponential LUT has an inverse effect and is useful when pixel intensities are predominantly bright.

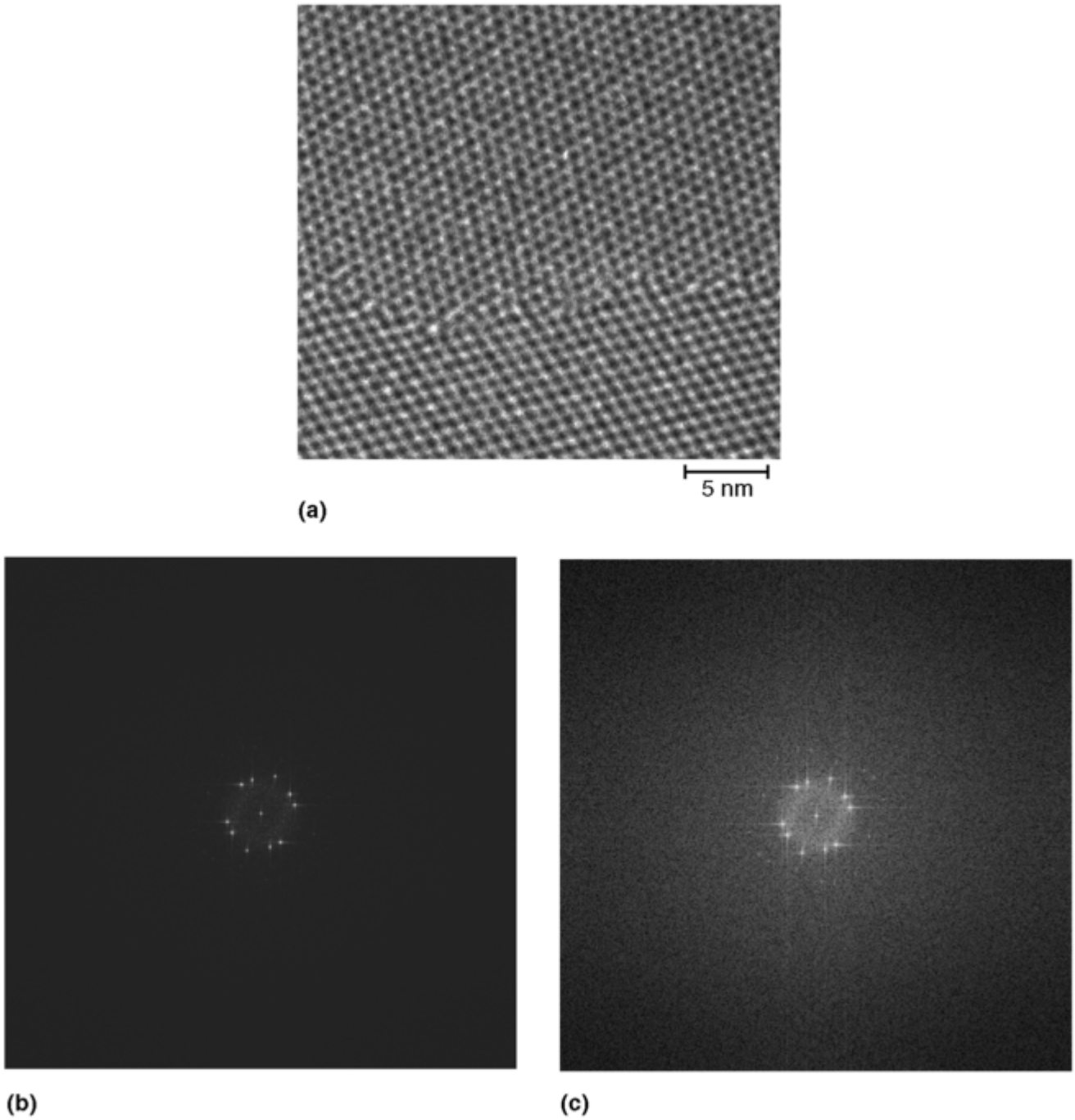

Fig. 19 Application of a nonlinear LUT. (a) HRTEM image of a grain boundary in aluminum and its Fourier transform (b) with a linear LUT and (c) with logarithmic LUT. Note the enhancement of details in the low-intensity range.

Many programs provide a simple interface to approximate a logarithmic or exponential LUT through the change of a single user-operated parameter, called gamma (γ), originally used to correct for the nonlinear response of photographic film. (The relationship between exposure, E, and intensity, I, in film is given by $E = I^{\gamma}$ over a wide range of exposure where γ is the gamma of the film.) When $\gamma < 1$, the power function approximates a logarithm; when $\gamma = 1$, the function is linear; and when $\gamma > 1$, the power function approximates an exponential. Thus, with a single control, the user can interactively change the LUT between linear and nonlinear behavior. Figure 20 shows this kind of interface. In this particular example, the gamma values are normalized between 0 and 1.

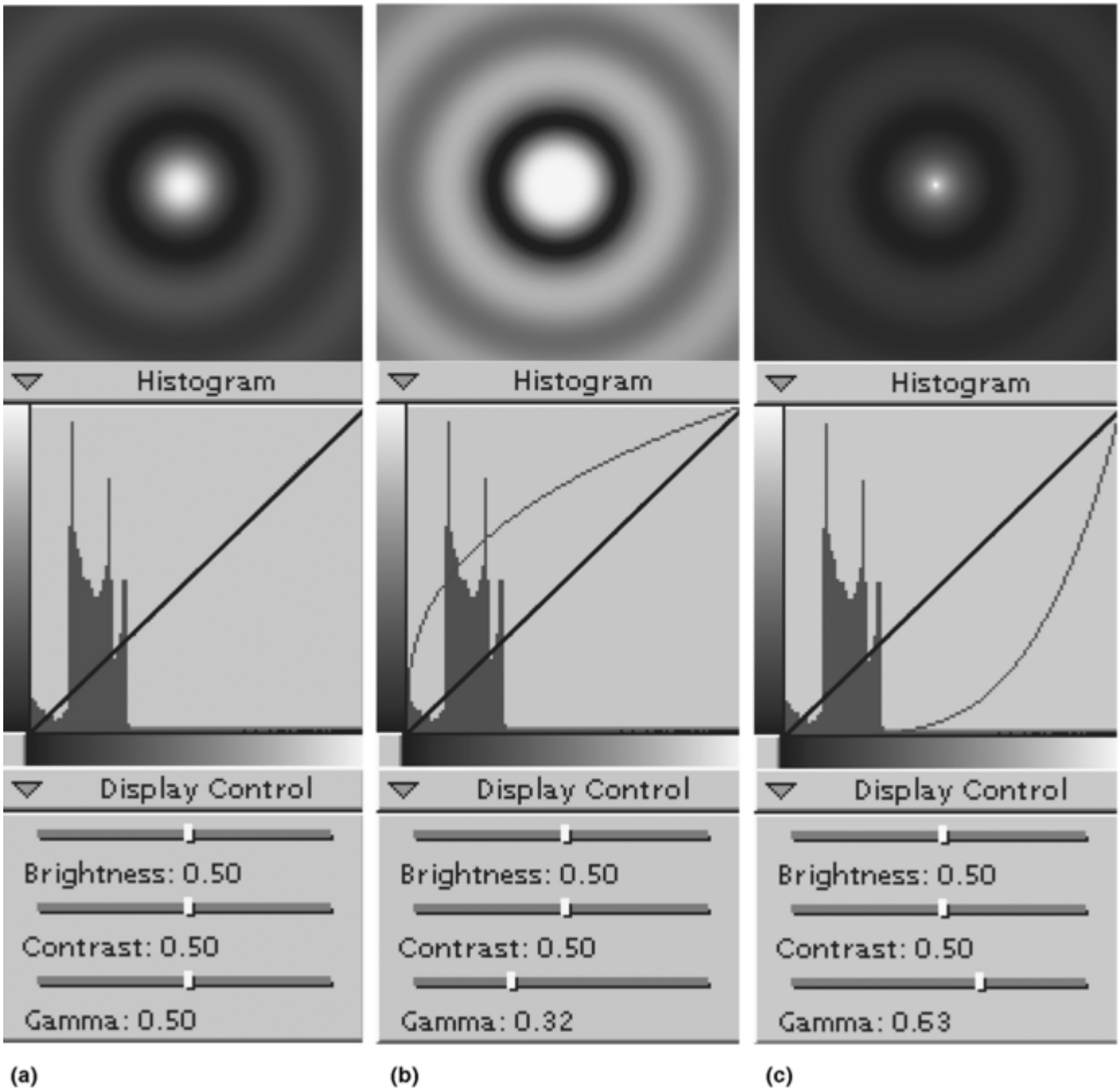

Fig. 20 A typical LUT control interface with sliders for brightness, contrast, and gamma. (a) Original image, $\gamma = 0.5$, linear LUT. (b) Modified image, $\gamma < 0.5$, approximately logarithmic LUT. Notice the contrast expansion in the dark regions. (c) Modified image, $\gamma > 0.5$, approximately exponential LUT. Note the contrast reduction in the dark regions. Gamma values are normalized between 0 and 1.

Another common use of LUTs is in the application of pseudocolor. In this case, the table converts gray levels to colors. This is useful because gray-level variations become more visible in color. This is shown in Fig. 21, where subtle uneven illumination is highlighted with two different color tables.

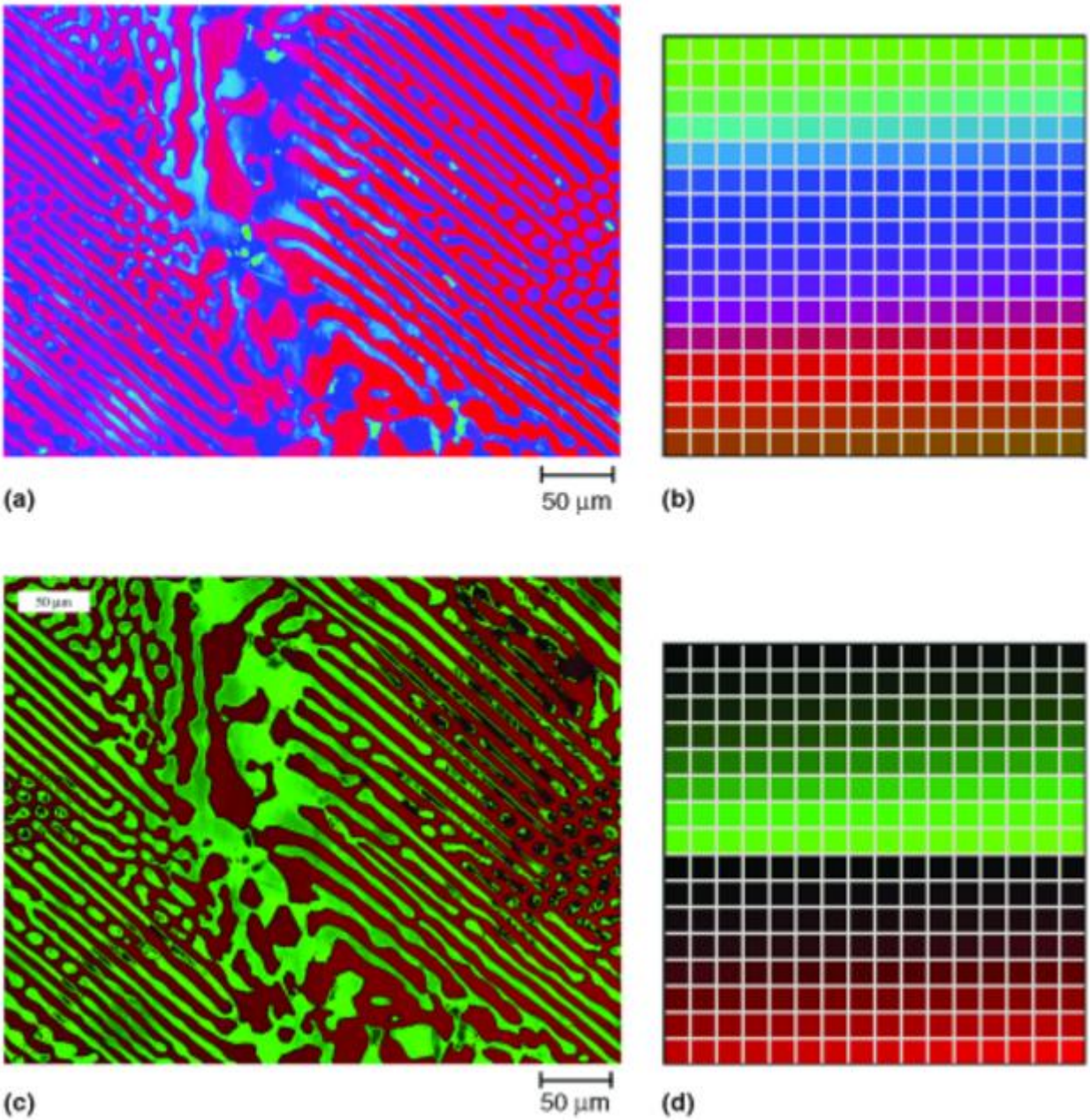

Fig. 21 The use of color tables. (a, c) An image with uneven illumination shown with two different color tables (b, d). Note the visual enhancement of the uneven background.

Point Operations. In general terms, all LUT operations are classified as point operations, where the intensity $I_o(x,y)$ of a pixel with coordinates (x,y) in the output image is a function only of the intensity $I_i(x,y)$ of a pixel with the same coordinates in the input image. That is:

$$I_o(x,y) = F[I_i(x,y)] \qquad \text{(Eq 3)}$$

where F is the function that relates input and output intensities.

Point operations are the basis of algebraic and logic operations, discussed in the next section. Operators that use the intensities in a certain neighborhood of a pixel at (x,y) to calculate the output intensity are also discussed.

Algebraic and Logic Operations. Two or more images of the same size can be combined with different kinds of operations in such a way that:

$$I_o(x,y) = F[I_{i1}(x,y), I_{i2}(x,y)] \qquad \text{(Eq 4)}$$

where $I_{i1}(x,y)$ and $I_{i2}(x,y)$ represent the intensities of pixels in the same positions of two input images, F is a function that relates the two images, and $I_o(x,y)$ is the output intensity.

The simplest functions are algebraic operations like addition, subtraction, multiplication, and division. Some of the applications of this kind of functions are described in this section.

Addition can be used to improve the signal-to-noise ratio (SNR) of a noisy static image. Acquiring several fields of the same image and adding them together improves the SNR by the square root of the number of fields if the noise has zero average and is uncorrelated between fields (Ref 21). Figure 22 shows the effect of adding 16 fields of a noisy image acquired in BSE mode in a SEM. (The same principle is behind the use of lower scan rates to improve image quality in SEM. Lower rates increase acquisition time, effectively adding up more information at each scan point.)

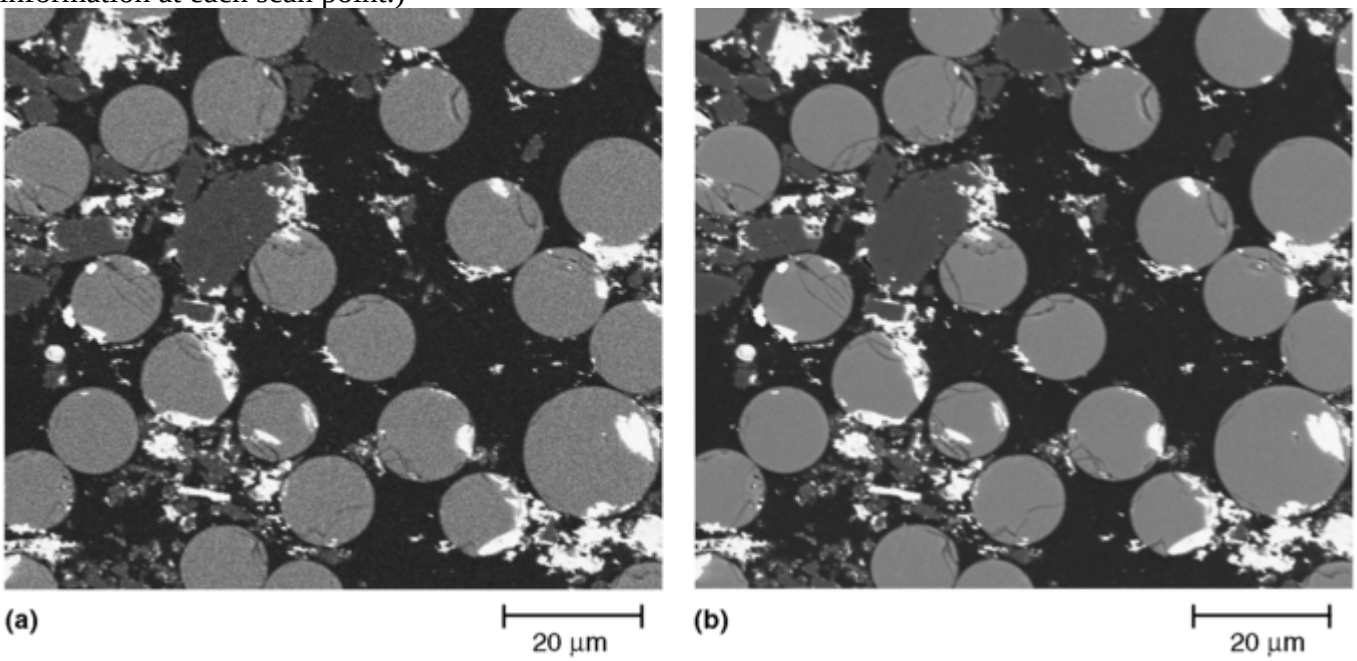

Fig. 22 The use of addition to improve the signal to noise ratio. (a) One noisy image of a composite material imaged in a SEM in BSE mode. (b) The effect of adding 16 independent fields at the same position

Subtraction is used to eliminate the contribution of noise or other intensity background in an image. A very useful application comes from image acquisition with a CCD camera. The CCD accumulates charge even when the camera is not exposed to light. A dark image must be subtracted from each image captured with a CCD to correct this problem.

In a similar fashion, subtraction can be used to compensate for an uneven illumination background, typical of light microscopy. Evidently, the best procedure is to correct image acquisition at the microscope, but there are situations in which this has not been done and the background is present. It is possible to estimate the separate contribution of the uneven illumination, as shown in Fig. 23, and subtract this estimate to obtain a corrected image.



Fig. 23 Background subtraction. (a) An image with uneven illumination (hypereutectic cast iron, 200×, BF, CCD 1300 × 1030). (b) Estimated background. (c) Background subtracted image

Subtraction can also be used to estimate changes and detect movement between images over time. The resulting image has zero intensity where the input images are the same and positive/negative values where there was a change due to movement.

Multiplication is used to change pixel intensities using another image as a mask. In the most common use, the mask image is binary; that is, it has only two intensities, 0 and 1 (or 255). This is important in the segmentation step. In Fourier filtering (Ref 22), masks are used to eliminate/preserve specific parts of the Fourier transform of an image, allowing the separation of periodic/nonperiodic contributions in the original image.
Division is sometimes used to normalize the response of a CCD camera.
Similar to algebraic operations, logic operations relate binary images. The fundamental operations, based on Boolean Logic, are negation (NOT), intersection (AND), union (OR), and difference (exclusive or, XOR). Figure 24 shows examples of these operations. Logic operations are particularly useful in the postprocessing step that follows image segmentation.

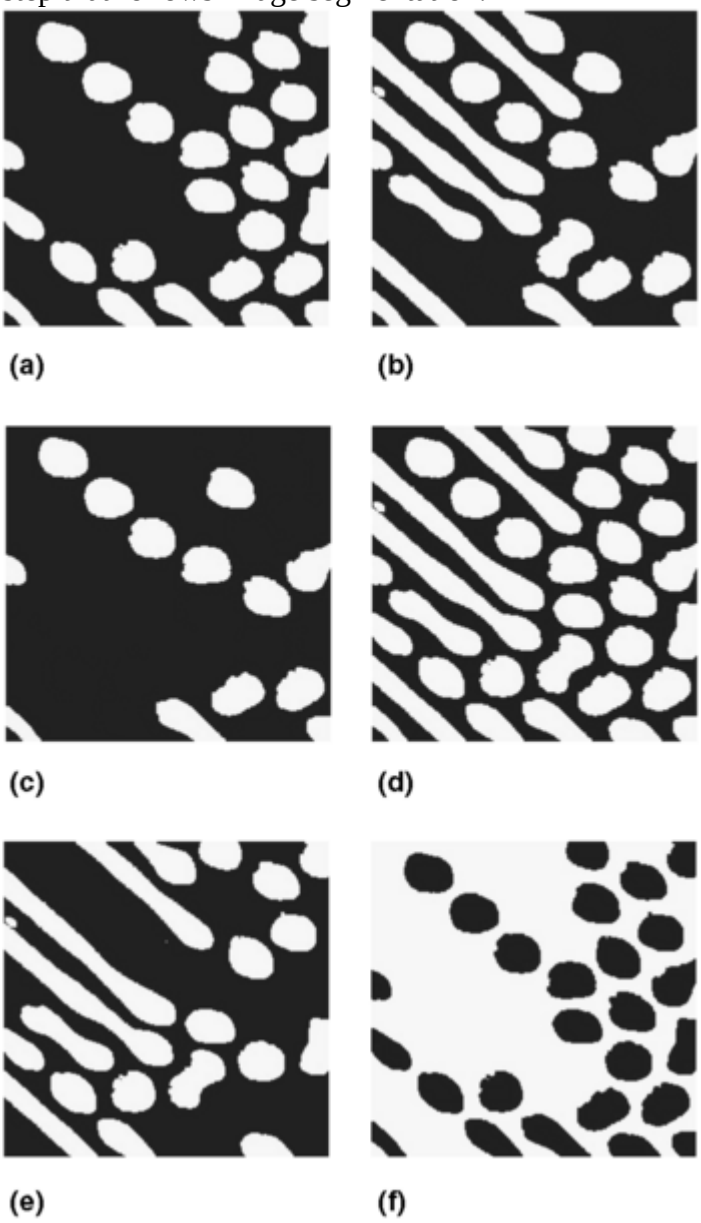

Fig. 24 Examples of logic operations between binary images. (a) Image A. (b) Image B. (c) A AND B. (d) A OR B. (e) A XOR B. (f) NOT A

Neighborhood operations differ fundamentally from the operations described so far, inasmuch as the output intensity of a given pixel at position (*x*,*y*) depends not only on the input intensity at the same position but also on the intensities of its neighbors. Also known as convolution, local, or kernel operations, they provide powerful and flexible processing of images. They are fundamental for noise filtering, background subtraction, edge detection, and other applications.
The basic principle of operation is shown in Fig. 25. A certain neighborhood size is chosen in the input image—in this example, 3 × 3 pixels. The intensity of each pixel in this neighborhood is multiplied by a certain weight; the results are summed together and divided by the total weight for all pixels. The resulting value is

written in the output image in a coordinate that corresponds to the neighborhood center. The process is repeated for a new neighborhood, one column to the right, and so on, until the right edge of the image is reached. Then the neighborhood moves to the next line, and the column scan is repeated. Eventually, the last line of the image is scanned.

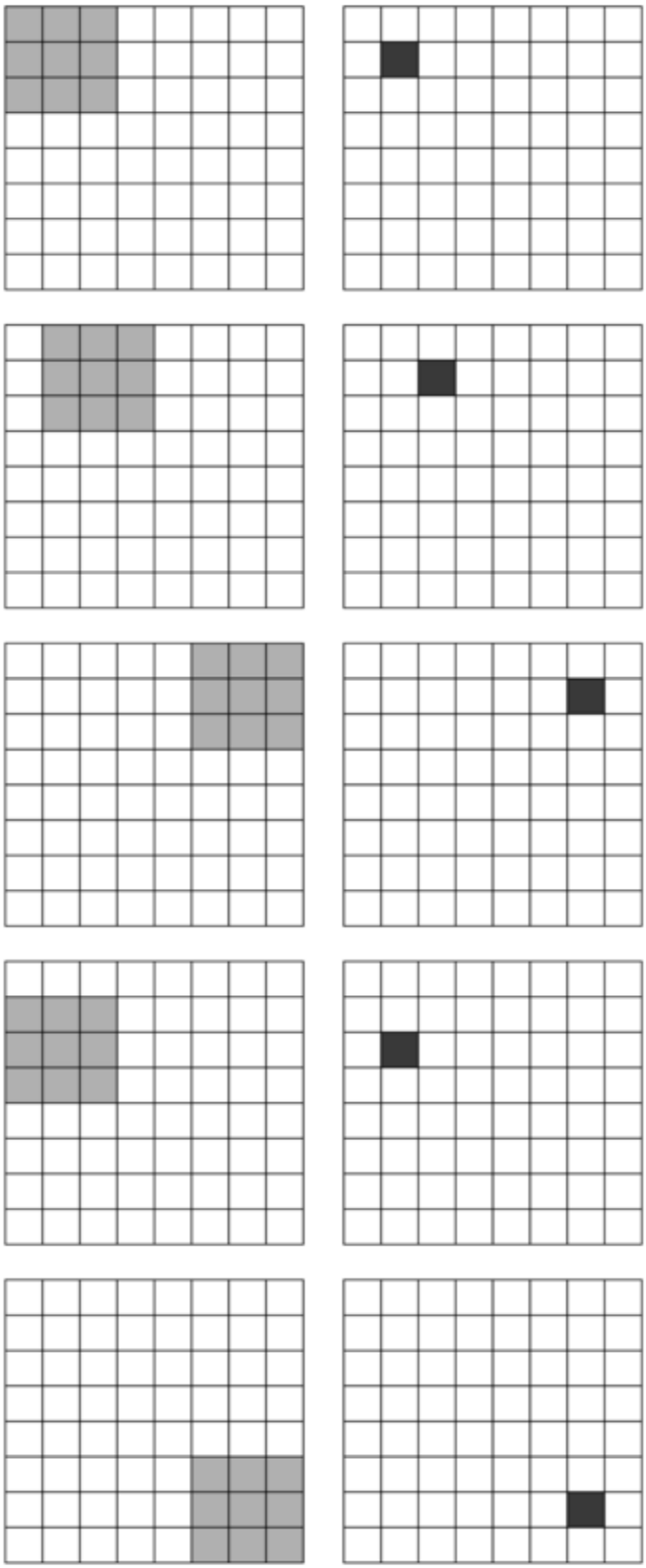

Fig. 25 The sequence of application of a neighborhood operation. Left column: neighborhood analyzed. Right column: output pixel calculated. The process begins at the top left, proceeds column by column, then line by line, until it reaches the last column of the last line. See text for details.

The effect of the operation depends on the neighborhood size and on the weights that multiply the intensities of the pixels. The neighborhood is always odd-sided, so that a central pixel can be chosen. The larger the neighborhood the stronger the effect of the operation. The weights are normally represented by a matrix with the size of the neighborhood, the kernel.

There are basically two different types of kernels—kernels with only positive values and kernels with both positive and negative values.

Low-Pass Filters. The positive-valued kernels are called low-pass filters because they reduce the high-frequency content of the image, preserving the low spatial frequencies. Both noise and fine details of the image are composed of high spatial frequencies. The effect of the low-pass filters is thus to reduce noise and blur the image. These filters are also called blurring or smoothing filters. Figure 26(a) shows the sequence of application of a simple low-pass filter, the 3 × 3 average or box filter, on an image with a sharp intensity edge. The effect of the filter is to smooth the edge by spreading its intensity change over several pixels. One can see that the mathematical effect of this filter is to calculate a local intensity average for each neighborhood.

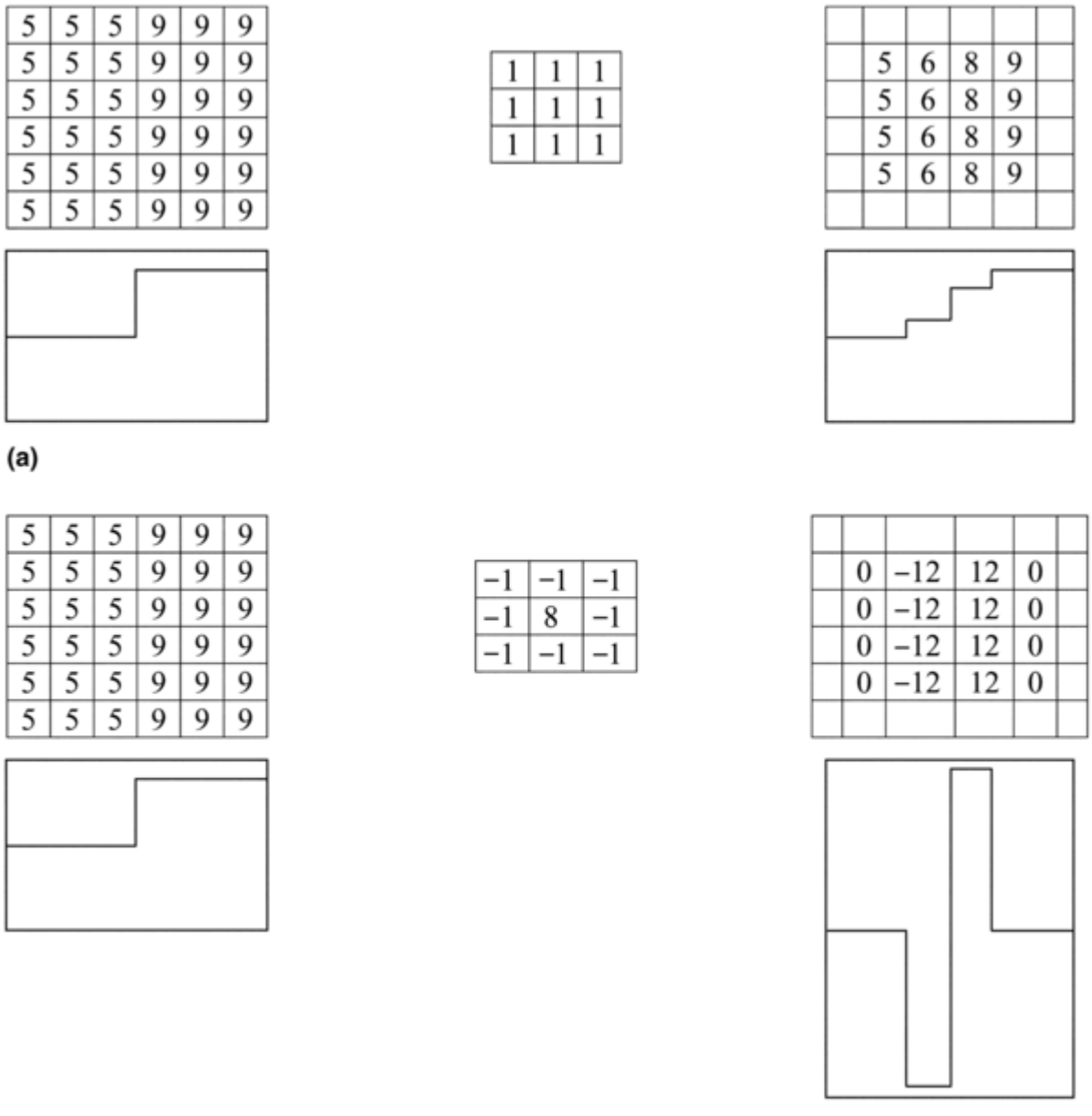

Fig. 26 Application of low-pass and high-pass filters to a simple image. (a) Left: Original image and line profile. Center: Low-pass kernel. Right: Output image and line profile. (b) Left: Original image and line profile. Center: High-pass kernel. Right: Output image and line profile

High-Pass Filters. Kernels with both positive and negative values work like high-pass filters. They increase high spatial frequencies and reduce low frequencies. Their effect is to increase noise and sharpen the image.

They are also called sharpening filters. Figure 26(b) shows the application of such a filter, called a Laplacian filter. The filter approximates the Laplacian of the image, that is:

$$\nabla^2 I = \frac{\partial^2 I}{\partial x^2} + \frac{\partial^2 I}{\partial y^2} \qquad \text{(Eq 5)}$$

The kernel proposed here is just one of several implementations of the Laplacian proposed in the literature.
Now the discontinuity at the edge is strongly increased. Note also that for regions of uniform intensity in the original image (both sides of the discontinuity), the filter result is zero. This is because uniform regions have zero spatial frequency, which is rejected by the high-pass filter. Moreover, the edge position in the output image is preceded by a negative value and followed by a symmetrical positive value.
The effect of these filters on an image is shown in Fig. 27. The blurring effect of the low-pass filter and the edge-enhancement effect of the high-pass filter are clearly visible. It must be mentioned that the blurred image was obtained with a 9 × 9 box filter to make changes visible in print.

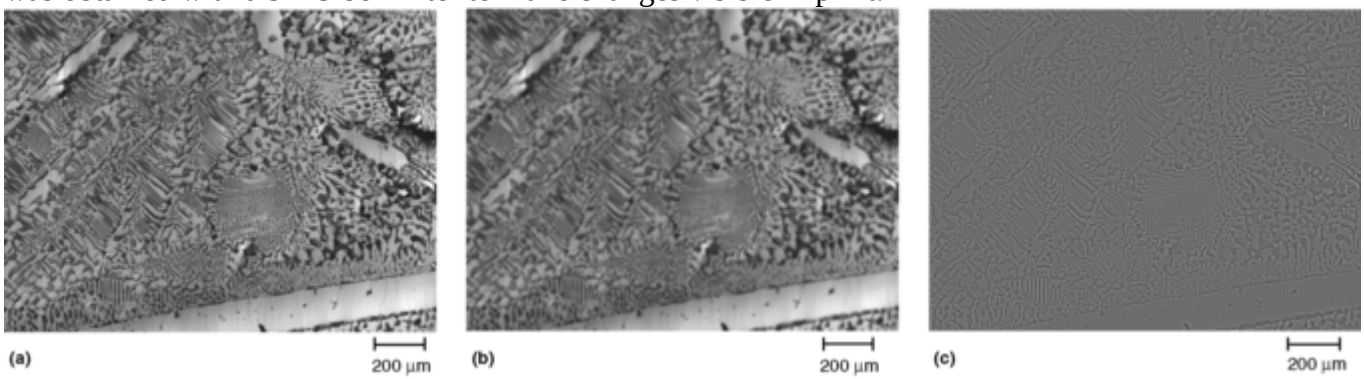

Fig. 27 Visual effect of low-pass and high-pass filters. (a) Original image. (b) Effect of 9 × 9 box low-pass filter. (c) Effect of 3 × 3 high-pass filter

Background Subtraction. The background estimation mentioned in Fig. 23 requires blurring the image to eliminate object edges, leaving behind only the low-frequency background due to uneven illumination. This can be achieved with a box filter with a kernel larger than the largest object in the image. Figure 28 shows this fact with an image low-pass filtered with kernels of three different sizes. The smaller size is smaller than many objects that are only partially blurred. The larger kernel is able to blur all objects, leaving behind an estimate of the background, which can then be subtracted from the original image to produce a background corrected image.

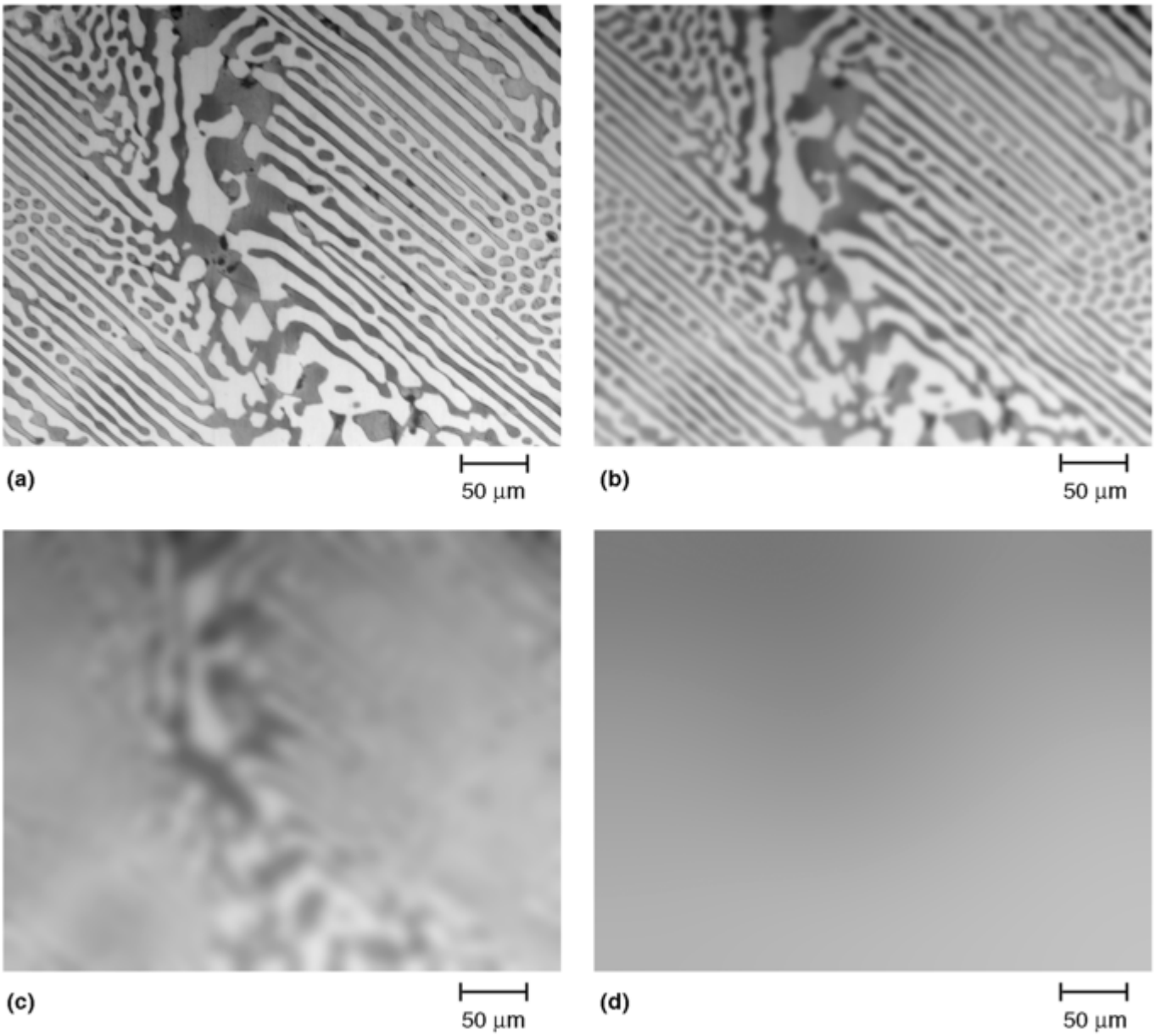

Fig. 28 Low-pass filter and background estimation. (a) The same image as Fig. 23 blurred with low-pass filters of different kernel sizes. (b) 9 × 9. (c) 29 × 29. (d) 249 × 249

The low-pass and high-pass filters presented here are complementary. It can be shown that:

$$\text{HighPass}[I(x,y)] = I(x,y) - \text{LowPass}[I(x,y)] \quad \text{(Eq 6)}$$

Thus, background subtraction can be achieved with a single operation—a high-pass filter with the same kernel size of the equivalent low-pass filter.

The edges of the image always pose a problem to the application of kernel filters. For an $n \times n$ kernel, a frame of $(n/2 - 1)$ pixels around the image does not have a well-defined result, because there are no pixels outside to allow the calculation of the kernel operation. This problem can be important if the kernel size is large compared to the image size. Consider, for example, an unevenly illuminated 512 × 512 pixel image with objects as large as 50 pixels. According to the procedure described previously, a high-pass filter with a kernel size of at least 51 pixels would be necessary. This would leave a 25 pixel wide frame around the image, which is nearly 10% of the image width.

Different programs offer different solutions to this problem. Some simply do not touch the edge pixels, leaving them with their original value. This is the worst option because a clear boundary between filtered and unfiltered pixels will appear. A better solution is to use “virtual” pixels outside the image. These pixels are many times obtained from a reflection of internal pixels around the image edges. The results are excellent, as shown by the images in Fig. 28.

Edge Detection. Besides their use for low-pass/high-pass filtering, neighborhood operations can be used to produce directional filters that may have different effects in different image directions. Consider for instance the filters defined in Fig. 29(b).

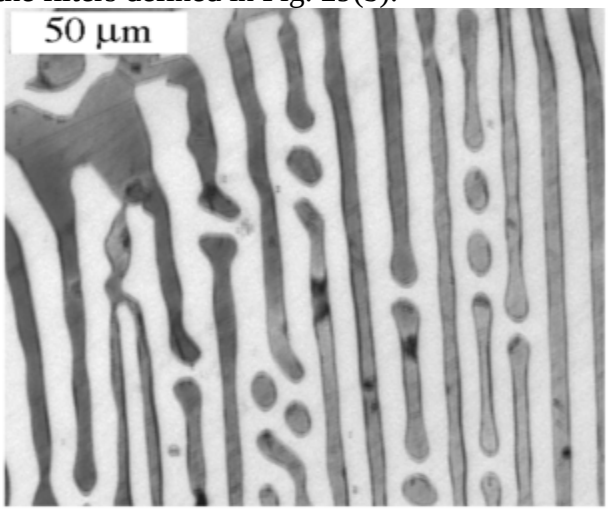

(a)

1	0	−1
2	0	−2
1	0	−1

$\frac{\partial}{\partial x}$

1	2	1
0	0	0
−1	−2	−1

$\frac{\partial}{\partial y}$

(b)

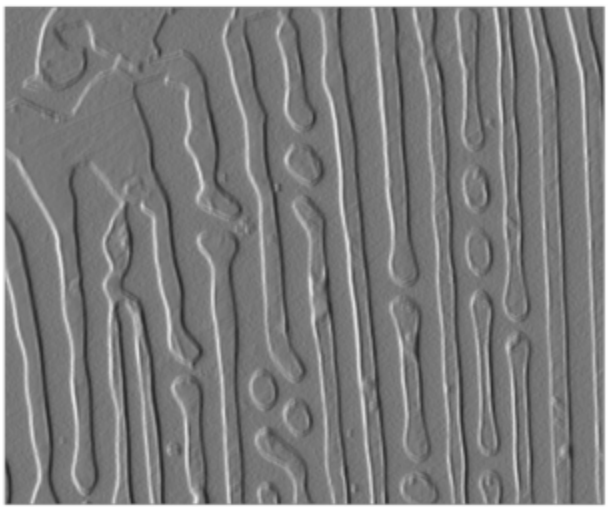

(c)

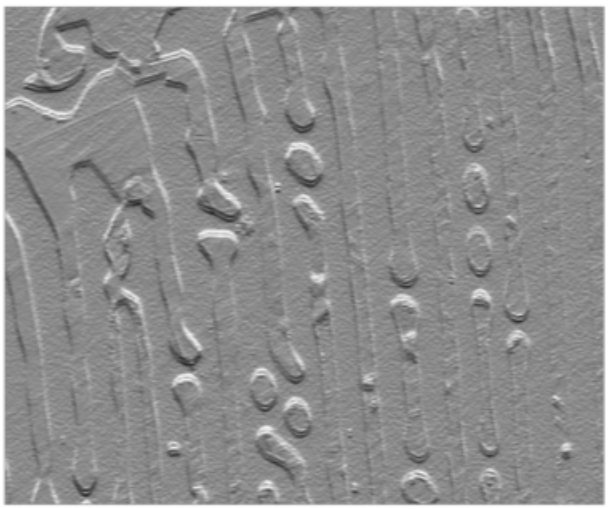

(d)

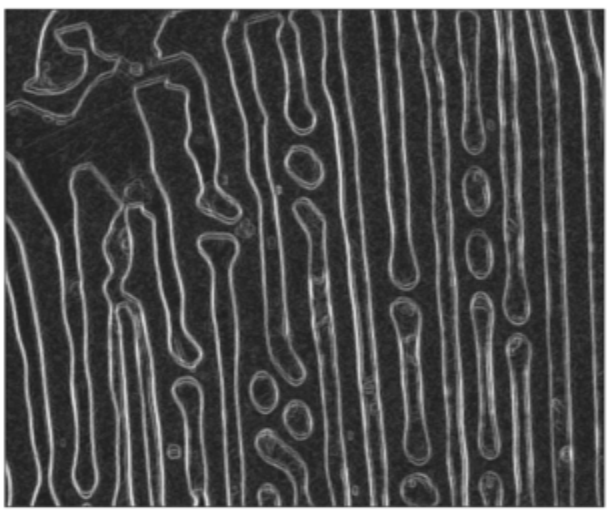

(e)

Fig. 29 The *x* and *y* partial derivatives and the Sobel operator. (a) A detail of the image Fig. 15(a). (b) The kernels for partial derivatives of *x* and *y*. (c) Image with x partial derivative applied. (d) Image with *y* partial derivative applied. (e) Sobel magnitude

Examination of these kernels shows that they are low-pass filters in one direction (in which all weights have the same sign) and high-pass in the perpendicular direction (where weights are both positive and negative). Thus, these filters enhance edges directionally, while blurring the image and reducing noise. They are approximations of derivatives in *x* and *y* directions, respectively, which is why they are referred to by the partial derivative symbols.

These two kernels are the basis of the Sobel edge detector. This detector creates an image that corresponds to the intensity gradient of the input image. The Sobel filter magnitude is described by:

$$\text{Sobel}\left[I(x,y)\right] = \left|\nabla\left[I(x,y)\right]\right| = \sqrt{\left(\frac{\partial I(x,y)}{\partial x}\right)^2 + \left(\frac{\partial I(x,y)}{\partial y}\right)^2} \qquad \text{(Eq 7)}$$

where ∇ represents the gradient operator and the partial derivatives correspond to the two kernels shown in Fig. 29(b).

The effect of these operations on an image is shown in Fig. 29. Note how the edges are enhanced while uniform regions become black. The Sobel is somewhat similar to the Laplacian filter described previously, but it has the advantage of reducing noise. The Sobel operator can be used in the segmentation step. Being a local operator, it is insensitive to low-frequency background variations and is thus capable of detecting objects without the need for a previous step of background subtraction.

Noise Reduction. The concept of neighborhood operations can be extended to define filters that do not use a numerical kernel as described so far. Instead, the neighborhood can be analyzed to create a result that is a statistical function of the input pixel intensities. The most common of these filters is the median filter. For each neighborhood, this filter sorts pixel intensities in ascending order and takes the median value of the sequence, which is then written in the central pixel of the neighborhood in the output image. In a 3 × 3 neighborhood, for example, the median value is the fifth in the sequence of ascending order. In a 5 × 5 neighborhood the median is the 13th in the sequence and so on.

The median is an excellent filter for the so-called “salt-and-pepper” noise, localized intensity peaks much brighter or darker than their neighborhood. These “outliers” will always end up at the extremes of the sequence after the intensity sorting in each neighborhood and will be substituted by a reasonable estimate of the local background.

Figure 30 shows the effect of a 3 × 3 median filter on a noisy image and compares it with the effect of a 3 × 3 low-pass box filter. The noise was artificially added to the original image to help illustrate the concept. The median filter eliminates the noise much more efficiently while preserving edge quality. The median should always be tried first when there is noise to be filtered out in an image. There are several variants to the simple median described previously. The interested reader can find further information in Ref 23 and 24.

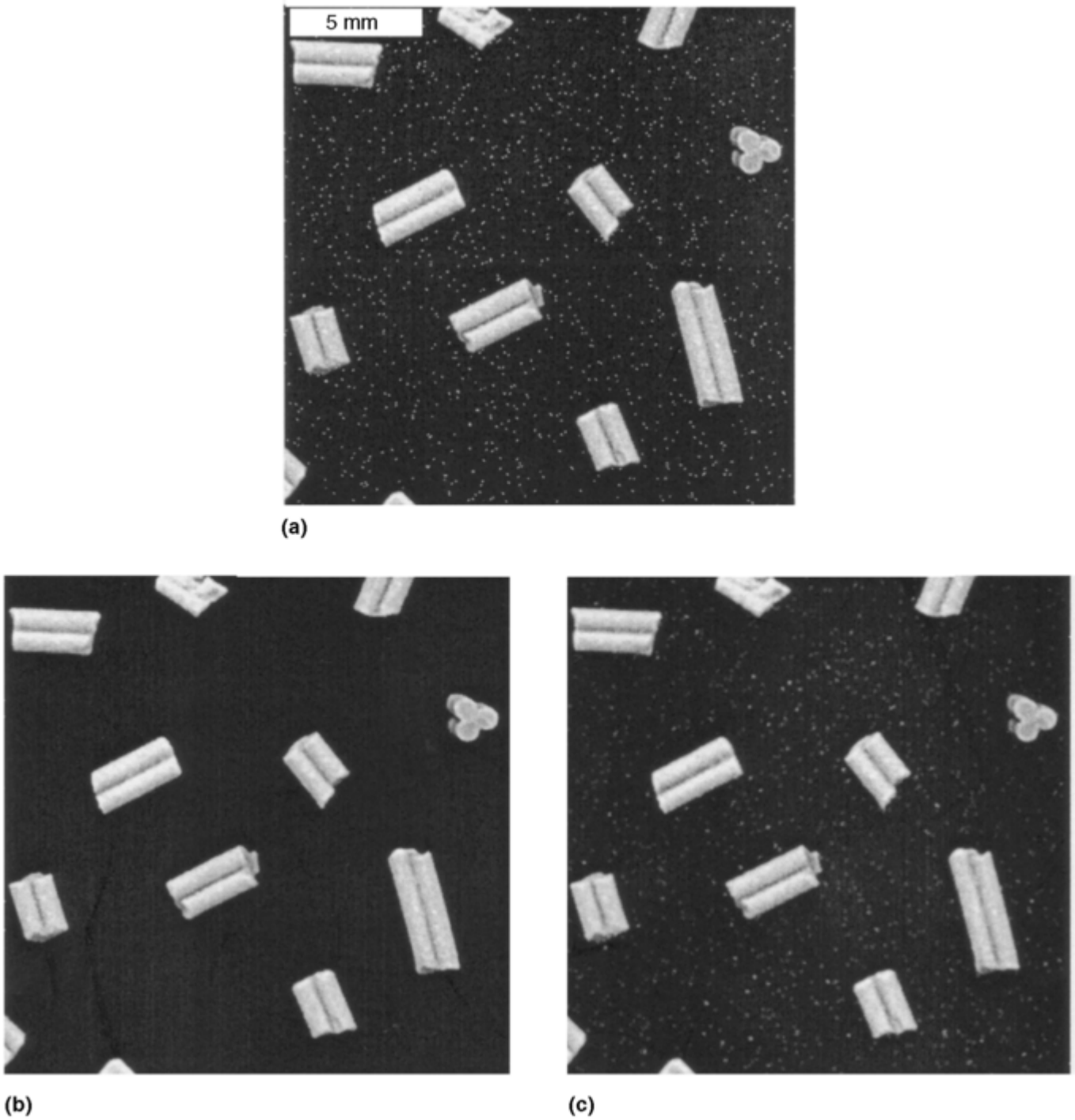

Fig. 30 Comparing the median filter with a low-pass filter. (a) Original noisy image. (b) Median filtered image. (c) Low-pass filtered image

Geometrical Operations. The operations described so far—point, algebraic, logic, and neighborhood—do not change the positional relationship between the pixels of an image. Two neighboring pixels in the input image will remain neighbors in the output image, albeit with different intensities.

However, there are many situations where this positional relationship must change. Consider, for example, the operation of zooming in an image, shown in Fig. 31. A 2 × 2 pixel image has the intensities show by the numbers. When a 2× zoom is applied, a 4 × 4 pixel is created (Fig. 31b), in which originally neighboring pixels are spread apart. Thus, new pixels must be created.

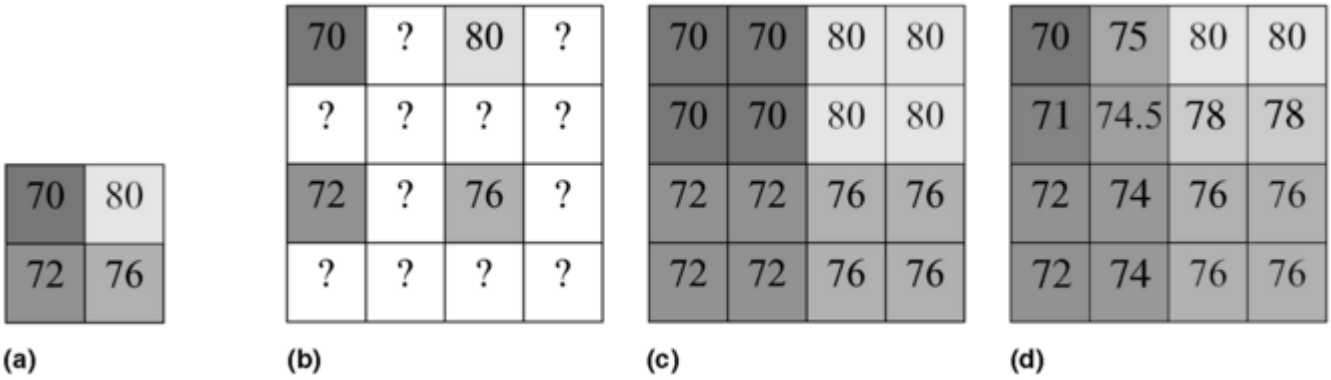

Fig. 31 Zoom, replication, and interpolation. (a) A 2 × 2 pixel image. (b) The same image after a 2× zoom (interrogation marks indicate new pixels). (c) Result of the replication method. (d) Result of the bilinear interpolation method

There are different methods for calculating the unknown pixel intensities. In the simplest method, called replication or nearest neighbor, each original pixel has its intensity repeated into its new neighbors (Fig. 31c). The effect is to form “super-pixels” with the same intensity, as if each original pixel has grown, simulating the proximity effect of a magnified view. This is very similar to the binning operation used in CCD cameras. Replication is extremely fast to compute, and all programs use this method to zoom in the image when the user selects the zoom or magnifying tool. The goal in this case is to get a fast, interactive response, without concern for image quality.

A better estimate for the intensities of the unknown pixels can be obtained through an interpolation procedure. Figure 31(d) shows the result of a bilinear interpolation where each unknown pixel has an intensity that is the average of the neighboring pixels. Higher-order interpolations can also be used, but generally do not bring a lot of improvement.

Thus, all geometrical operations involve two steps: a spatial transformation and an intensity transformation. Examples of spatial transformations are translation, magnification, rotation, perspective change, and other higher-order distortions. The intensity transformations include replication, bilinear, and higher-order interpolations.

When dealing with magnification, the use of interpolation creates new intensities for the new pixels and to some degree masks the original resolution of the image. This is the “trick” used by scanners, as mentioned in the section “Scanners” in this article. Interpolation becomes more important with other spatial transformations such as rotation, for example. Depending on the kinds of features present in the image and on the rotation angle, the “pixelization” effect of simple replication can be very annoying. Figure 32 shows a rotated image with and without interpolation. Notice the difference in edge quality.

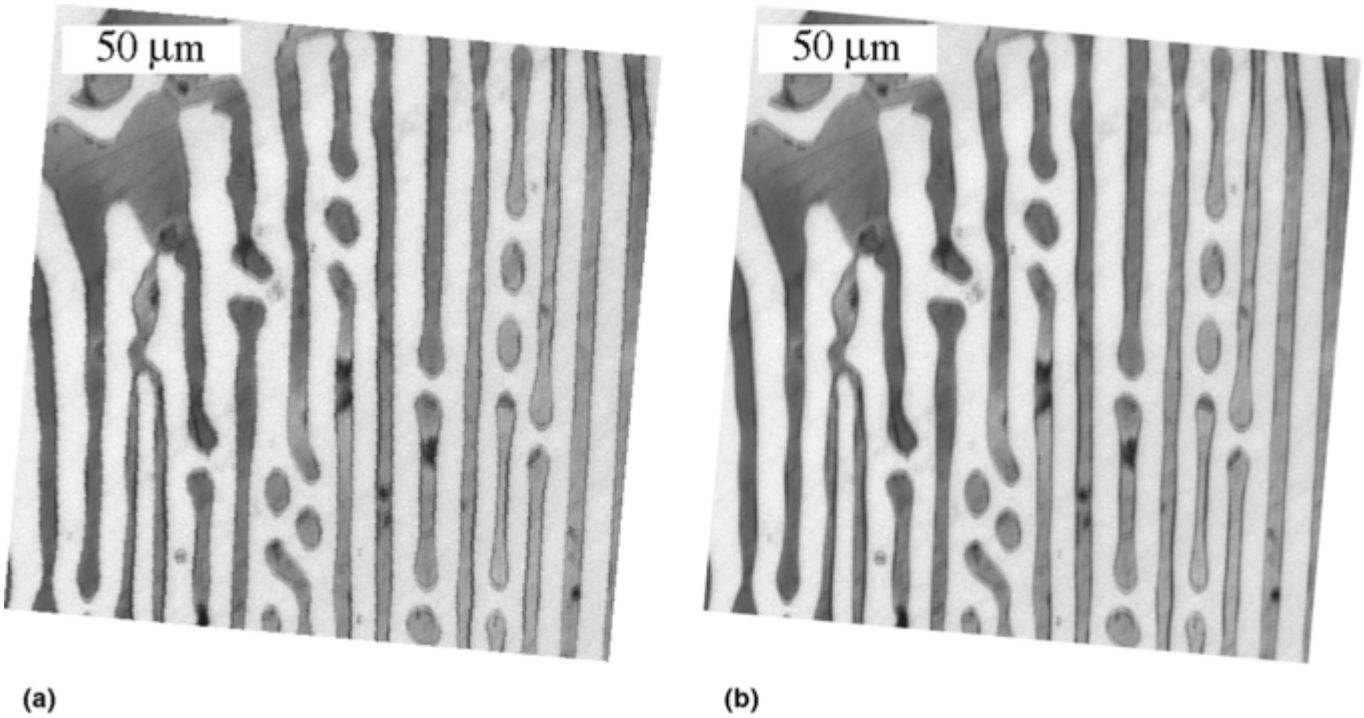

Fig. 32 The importance of interpolation in image rotation. The same image as Fig. 29(a) rotated with replication and (b) rotated with bilinear interpolation

Sometimes it is necessary to compare two images where one is distorted in relation to the other because it was obtained at a slightly different magnification, position, or rotation. Before any quantitative comparison can be done, the images must be put in register using a geometrical operation. The spatial transformation uses reference marks or fiduciary points that represent equivalent points in the two images. At least three points are sequentially marked in both images, either by the user or by some automatic detection procedure, and the program distorts one image to match the coordinates of the three points in both images.

Figure 33 shows an example. In this case it is desired to measure the area fraction of ferrite, pearlite, and graphite in cast iron. The contrast in the unetched sample (Fig. 33a) discriminates between the dark graphite particles and the gray ferrite/pearlite matrix. In the etched sample (Fig. 33b) ferrite can be discriminated from pearlite/graphite. Thus, to be able to measure each phase independently, both the etched and the unetched images must be used, but they are out of register because the sample had to be removed from the microscope for etching. Using the three Vickers indentations shown as reference points, the image after etching is displaced, rotated, and zoomed (Fig. 33b) to put it into register with the image before etching. Then a common field, marked with a white frame in the images, is analyzed and the desired area fractions can be measured.

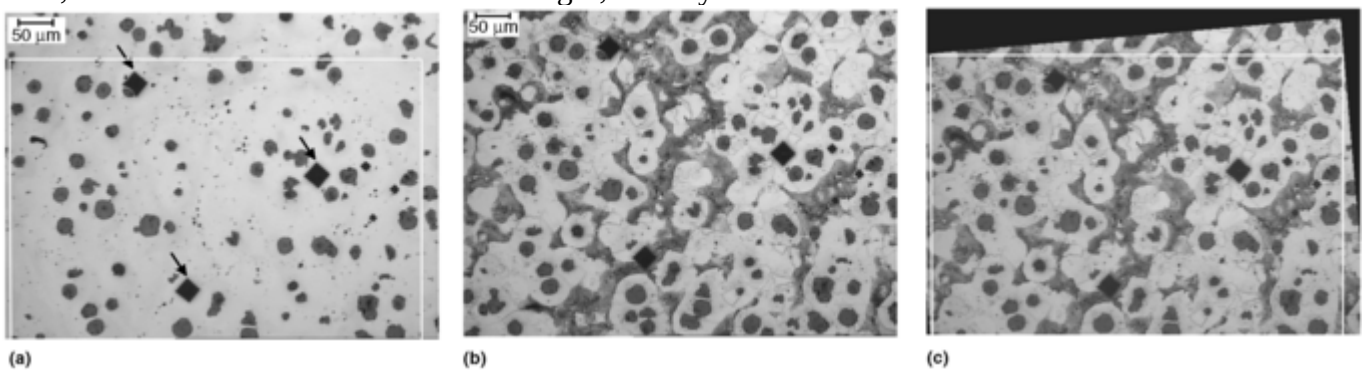

Fig. 33 The use of reference points and geometrical operations to put two images in register. (a) Unetched cast iron sample showing graphite particles. Arrows point to Vickers indentation marks used for reference. (b) A similar field of the sample after etching. Note the displacement and rotation of the reference marks. (c) Geometrical transformation of the image in (b) to put it in register with the image in (a). The white frame shows the resulting coincident field.

Image Segmentation

Segmentation is the technical term used for the discrimination of objects in an image. Segmentation is probably the most complex step in the flowchart in Fig. 1 because it tries to represent computationally a cognitive process that is inherent to the human eye/brain. When one looks at an image one uses many different inputs to distinguish the objects: brightness, boundaries, specific shapes, or textures. The brain processes this information in parallel at high speed, using previous experience. Computers, on the other hand, do not have the same associative power. The recognition of objects in an image is made through the classification of each pixel of the image as pertaining or not to an object.

As an example, Fig. 34 shows a simple image composed of bright objects on a dark background. The eyes and brain have no difficulty telling what is an object and what is the background; all objects can be easily identified and counted. For the computer, however, the concept of object does not exist a priori. All it knows are pixels with a coordinate in space and an intensity. The "vision" of the computer is mimicked in Fig. 34(b), where part of the image is shown as a spreadsheet. With this representation, it becomes harder to visually distinguish objects. Thus, the digital identification of objects is done through the measurement of some parameter that distinguishes between the several classes of pixels.

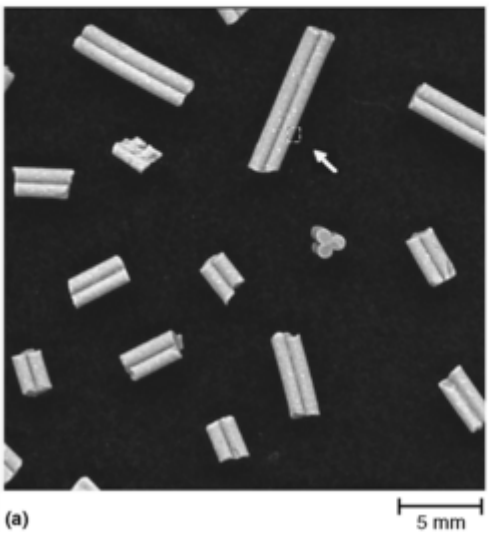

(a)

192	186	179	170	170	166	159	146	116	69	6	0	4	2
206	200	187	168	166	160	149	131	97	41	0	9	2	0
220	214	200	181	161	150	135	114	71	15	0	6	1	0
209	202	179	158	155	146	131	103	57	0	5	4	1	0
198	184	165	152	148	145	129	84	26	0	7	3	1	0
179	169	159	156	148	134	120	61	4	9	5	3	1	0
189	166	155	158	146	125	94	32	0	5	4	2	0	0
186	172	164	152	145	115	67	14	0	3	3	1	0	0
186	176	162	142	131	97	35	0	9	3	2	1	0	0
175	171	161	142	119	71	9	0	6	3	2	2	2	2
175	166	157	141	104	58	0	10	3	2	1	1	1	1
178	164	149	135	91	34	0	5	0	0	0	0	1	1
164	157	137	115	65	13	9	4	2	0	0	0	0	0
158	149	127	91	34	1	5	3	2	0	0	0	0	0
152	141	111	69	6	0	3	3	2	0	0	0	0	0
154	140	101	44	0	5	2	1	1	1	1	1	1	1

(b)

Fig. 34 Image and pixel intensities. (a) An image composed of bright objects on a dark background. (b) The pixel intensities in the square region (see arrow) of (a)

Intensity Thresholding. The simplest and most commonly used parameter is the intensity of the pixel. In Fig. 34, a pixel is considered part of an object if it is bright enough. The segmentation then proceeds through the choice of a certain threshold level *T* and the application of the simple decision rule:

If $I(x,y) \geq T$ then the pixel at (x,y) belongs to the object class.

If $I(x,y) < T$ then the pixel at (x,y) belongs to the background class.

The main point issue, evidently, is the choice of the value for *T*. Figure 35 shows a choice based on the analysis of the image histogram and the resulting pixels selected. In the binary image of Fig. 35(b), the selected object pixels are marked white, while the background pixels are marked black.

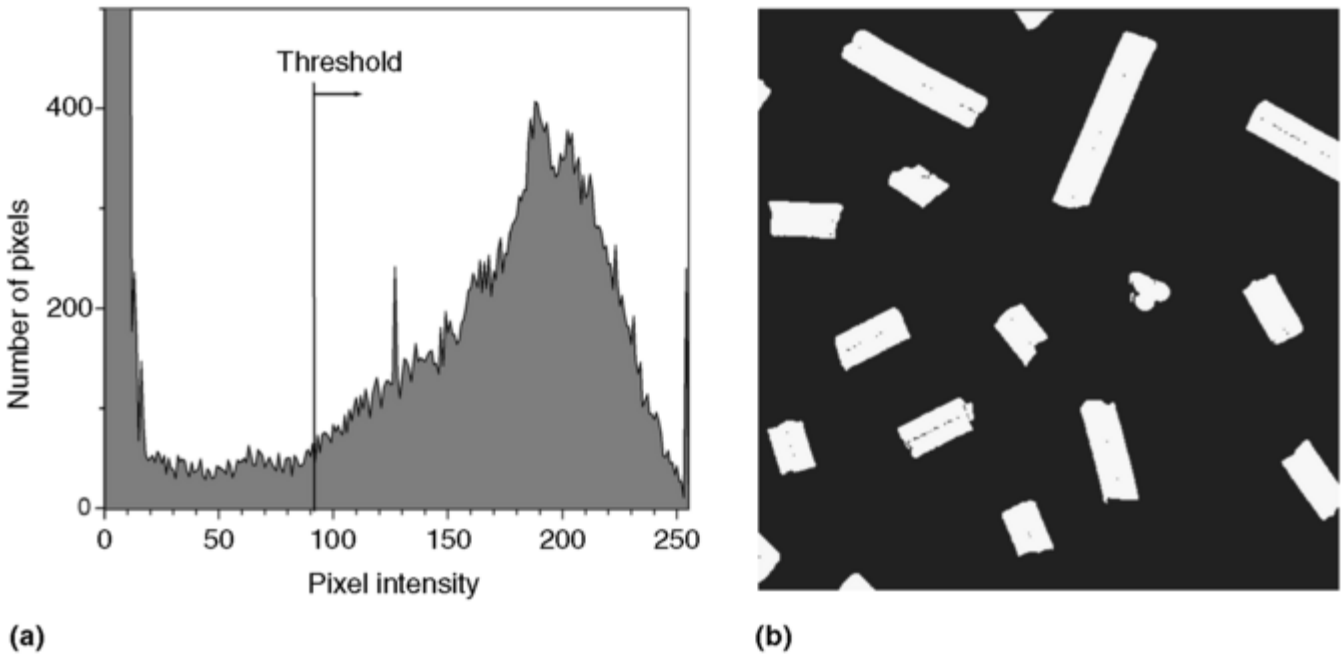

Fig. 35 Threshold selection and application. (a) The histogram of the image in Fig. 34 with a given threshold level highlighted. (b) The segmentation obtained with the threshold level

Threshold selection methods can require user intervention or be fully automatic.

In interactive thresholding the operator chooses the threshold T manually and adjusts it until a reasonable segmentation is obtained. The image histogram is always used as a reference, and most programs show selected pixels as a color overlay on top of the image.

Figure 36 depicts this interface for two different threshold values, T_1 and T_2. The histogram for this simple two-phase image is bimodal—the band in the brighter range of the plot corresponds to the brighter pixels that form the objects while the band in the darker range of the plot represents the background pixels. This relationship provides relevant aid to choosing the threshold. Intuitively, one would choose a threshold that lies between the two bands, in a region where the histogram goes through a minimum. Clearly the choice of T_2, which lies in this region, gives a better identification of the desired objects in Fig. 36.

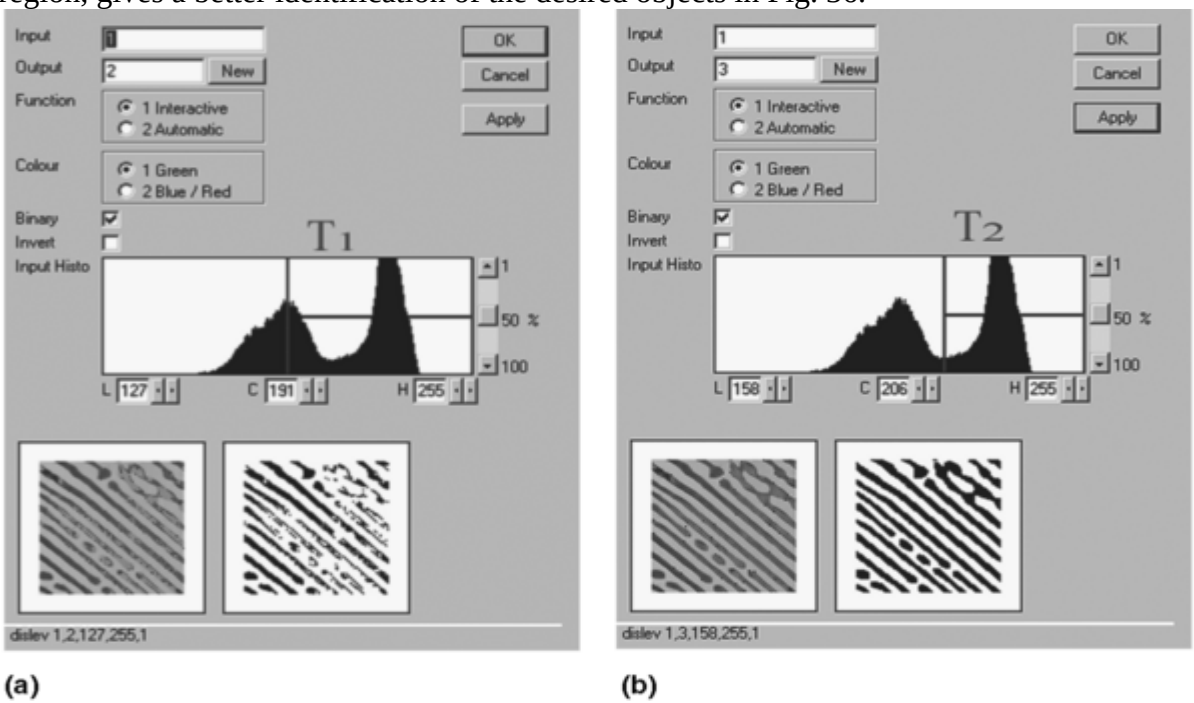

Fig. 36 The interface for interactive thresholding. (a) The segmentation obtained with threshold T_1. (b) The segmentation obtained with threshold T_2

The relationship can be extended to multiphase systems and multimodal histograms, and many programs provide interfaces for selecting several threshold levels simultaneously. Interactive thresholding can be very efficient and provide fast, accurate results—it is always the first method to try. However, being operator dependent, it is not always reproducible and robust. Different operators may choose different threshold levels for the same image. Besides, if a collection of images is to be analyzed, interactive thresholding can become a burden if a different threshold needs to be chosen for each image. This problem can be minimized if all images are acquired with similar brightness and contrast. In this case, an optimal interactive threshold can be chosen based on a few images and then applied automatically to the whole collection without further user intervention.

In general, though, it is of interest to have a threshold level selection that is fully independent of operator interference and that adapts to each analyzed image.

Automatic Thresholding. There are several methods for automatic selection of the threshold level. Two of them—the minimum method and the Otsu method—are described here.

The minimum method automates the location of the minimum between histogram bands described previously. A minimum can be found through mathematical analysis of the histogram without user intervention. However, this method suffers from two important limitations (Ref 25). First, if the two bands are widely separated by a relatively flat histogram region, the minimum is not well defined. Second, the minimum region is composed of intensity levels for which there are not many pixels in the image. Thus, it is more sensitive to noise and may be affected by local minima that do not represent an optimal choice. Sometimes it may be necessary to low-pass filter the histogram to improve the minimum detection. This is usually impractical, and few programs allow these options.

The Otsu method (Ref 26) is one of the most common methods in image-processing programs. It chooses a threshold level through an automatic optimization procedure in which the ideal threshold maximizes the interclass variance, that is, the separation between objects and background, while minimizing the intraclass variance, that is, the grouping of object pixels and background pixels in their respective classes. Figure 37 shows the application of the Otsu method and compares its results with the minimum method. It can be shown that, in this case, besides being more sensitive to small particles in the background, the Otsu segmentation discriminates larger objects more accurately.

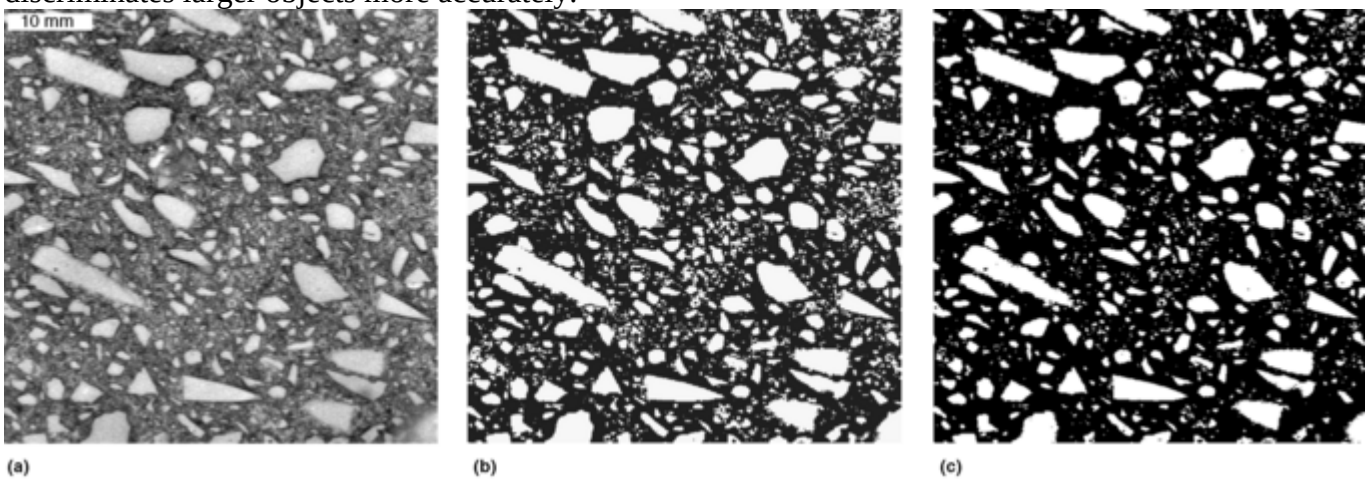

Fig. 37 The Otsu method. (a) Original image. (b) Otsu segmentation. (c) Minimum point segmentation. Original image, courtesy of Vito Smolej, Carl Zeiss Vision

The Otsu method is automatic and very fast. Its principle can be extended to multiphase systems and multimodal histograms. However, computing time grows with the number of intensity levels to the power of the number of histogram modes (Ref 27). Thus, for a 256-level grayscale image, the time to compute a trimodal segmentation is 256× longer than for a bimodal segmentation. In practice, this precludes the use of the Otsu method for five or more histogram modes. Most commercial programs have only the bimodal implementation.

Global versus Local Thresholding. The methods described so far, both interactive and automatic, are global methods inasmuch as they are based on the histogram, which is a statistical representation of the whole image. Their success depends basically on the association of histogram bands with phases in the image. Global thresholding fails for images with uneven illumination, as shown in Fig. 38, the same image as Fig. 23, captured with even worse conditions, to illustrate the point. The histogram is not bimodal, and it is clear that no single threshold level will be able to segment object pixels in the whole image. However, after background

subtraction (as discussed earlier in this article), the histogram becomes bimodal and global thresholding gives a good result, as shown.

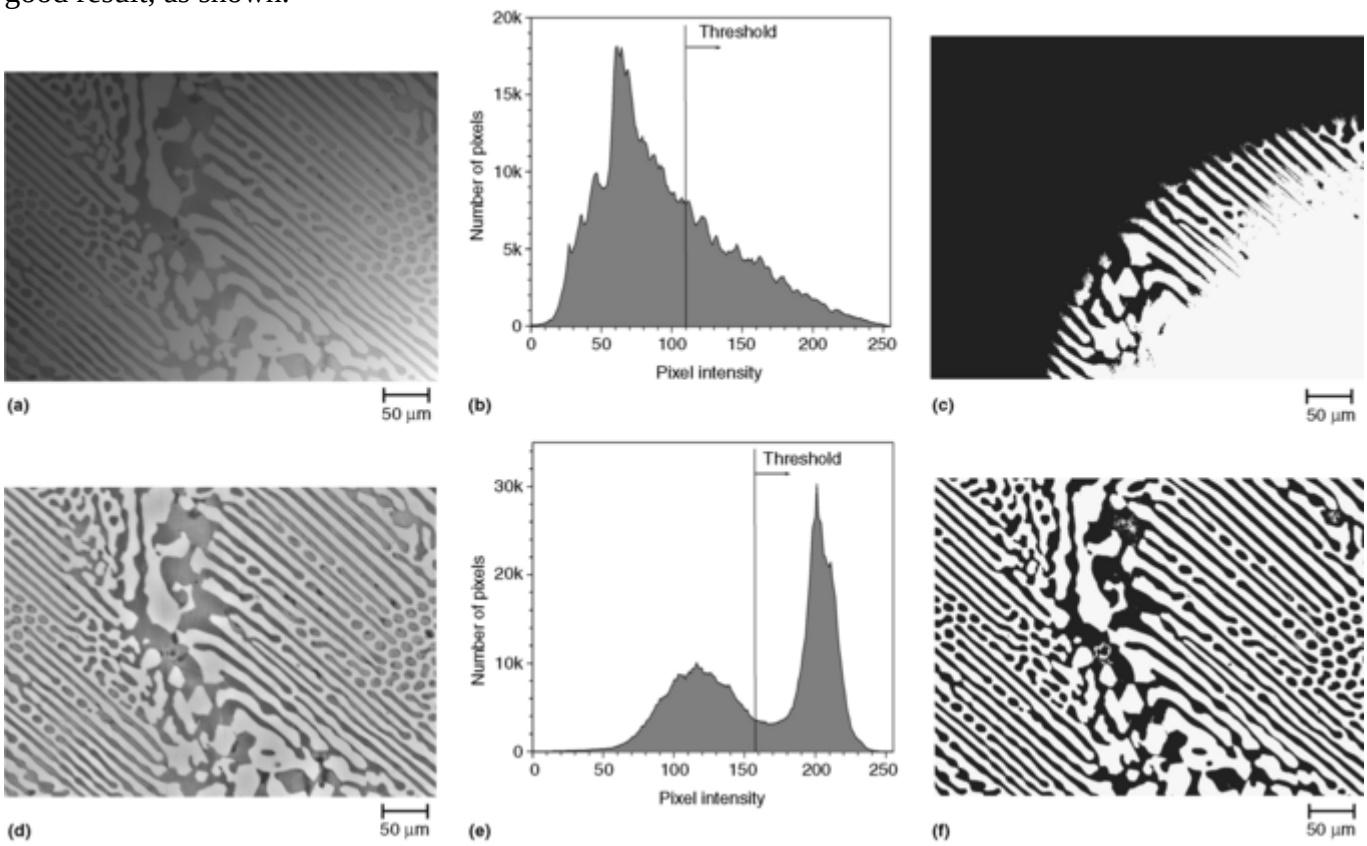

Fig. 38 Limitations of global thresholding. (a) Image with uneven illumination. (b) Histogram and tentative threshold. (c) Incorrect segmentation. (d) Background corrected image. (e) Bimodal histogram and optimal threshold. (f) Correct segmentation

As an alternative to background subtraction, adaptive, or local, thresholding can be useful. The basic principle is to treat the image at a local instead of a global level, supposing that at the local level the histograms are better behaved. There are several implementations of this approach. The simplest is to divide the image in a certain number of subimages and apply one of the previously described methods to each subimage.

The result of one such implementation, an adaptive Otsu algorithm for 5 × 5 subimages, is shown in Fig. 39. The use of adaptive segmentation poses a few problems. First of all, if the results for each subimage are just pasted together to rebuild the complete image, boundaries between subdivisions appear and corrupt the result. This is shown in Fig. 39(a). This is caused by sudden changes in the threshold value used for segmentation of adjoining subimages. To eliminate this problem, it is necessary to use the concept of bilinear interpolation, described earlier, to calculate intermediate threshold values for all pixels in the image. The result is shown in Fig. 39(b).

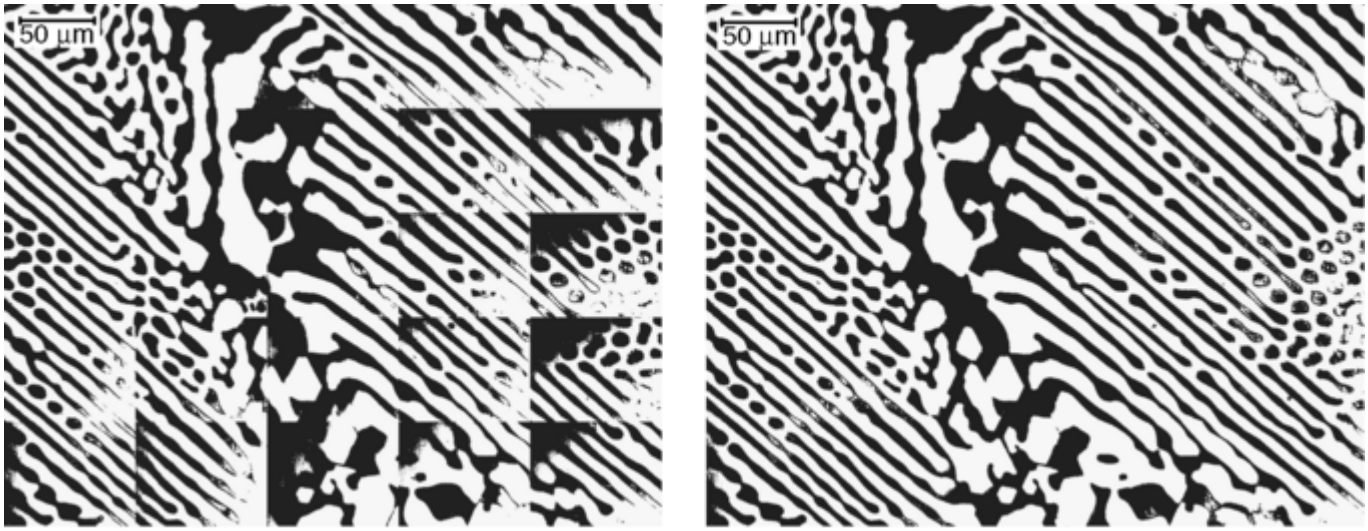

Fig. 39 Adaptive segmentation of the same image as Fig. 38 (a) Adaptive Otsu segmentation with 5 × 5 subimages, without interpolation. (b) Adaptive Otsu segmentation with 5 × 5 subimages, with interpolation

In principle, one could think that increasing the number of subdivisions would lead to an improvement in the result. However, when subimage dimensions decrease below the typical dimensions of the present phases, the sampling of pixel intensities ceases to be representative and the results are meaningless. Clearly, if the subimage contains just one phase, there is no threshold to be found.

As in interactive thresholding, adaptive segmentation always requires some operator influence, at the very least to choose the number of subdivisions.

Contour-Based Segmentation. Differently from thresholding, where objects are understood as adjoining pixels sharing a range of intensities, contour-based segmentation tries to identify objects by first identifying a closed boundary. These methods are somewhat similar to the adaptive methods described previously, inasmuch as they look at local characteristics of the images. However, contour methods do not subdivide the image, but rather use the principles of edge detection as a basis for object detection.

Contour-based segmentation is particularly useful when there is strong local variation of brightness and contrast in an image. As mentioned before, SEM images in the SE mode have these characteristics and are generally difficult to segment. One such example is shown in Fig. 40(a). Global thresholding or background subtraction would not work in this case. Even adaptive thresholding would not produce good results.

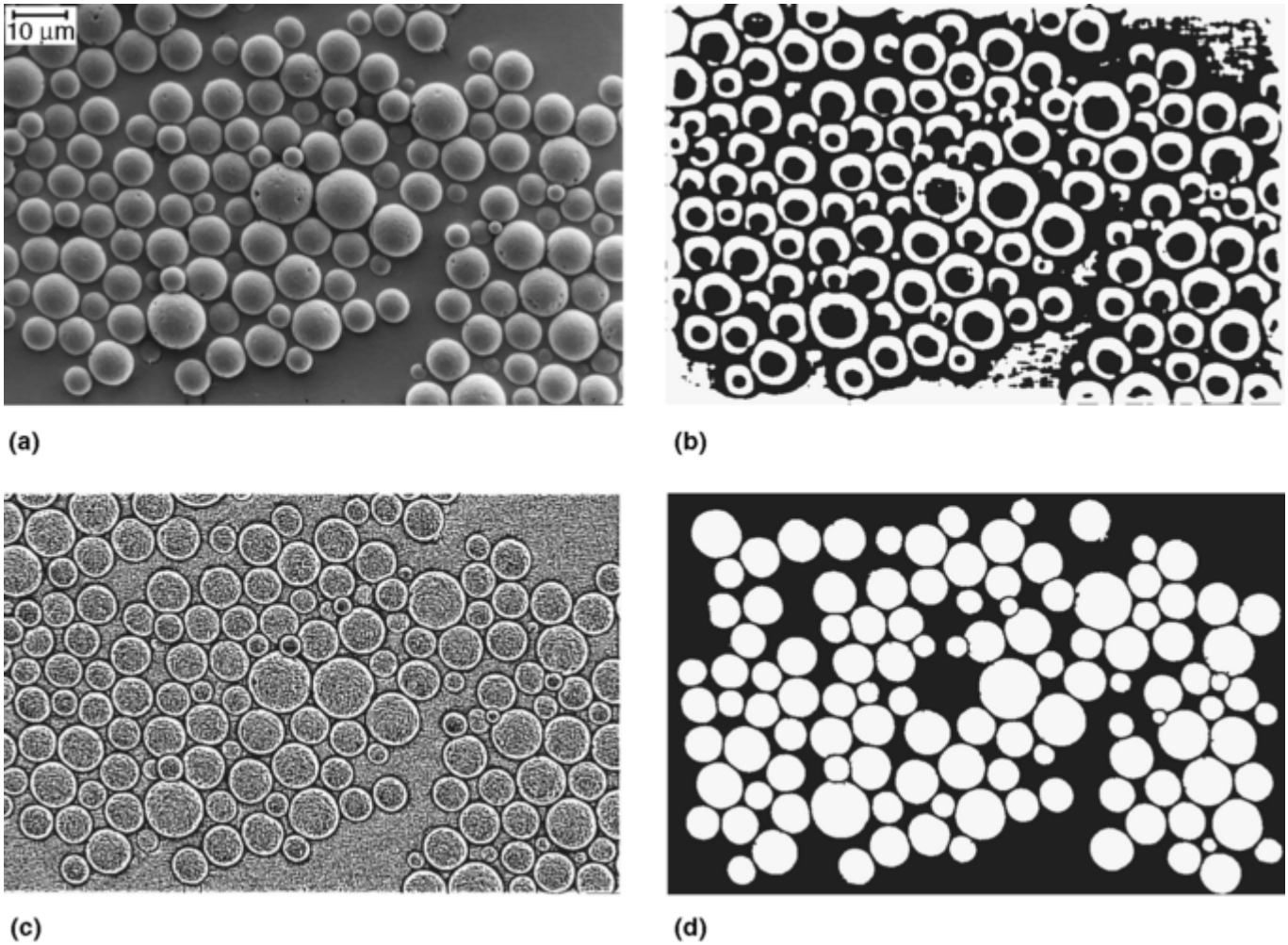

Fig. 40 The Marr-Hildreth segmentation method. (a) Original image. (b) Segmentation for σ = 5. (c) Segmentation for σ = 0.8. Notice the detection of subtle variations in the background and inside the particles. (d) The image in (c) after postprocessing. Original image, courtesy of Vito Smolej, Carl Zeiss Vision

The simplest contour-based method uses the Sobel edge detector. An interactive threshold is applied to the Sobel magnitude image to segment the preeminent edges in the original image. Some of these edges form closed boundaries that can be identified with objects. However, many incomplete contours prevent complete object detection. This limitation, together with the need for operator influence in the threshold selection, severely restricts the use of this method.

Several more sophisticated contour-based methods try to surpass the limitations of the Sobel method. Among those, the Marr-Hildreth and the Canny methods deserve description here.

The Marr-Hildreth method (Ref 28) derives from research in human vision in which the ability of the eye/brain to detect objects is described as based on the detection of closed boundaries at several simultaneous resolution levels. The mathematical emulation of this ability uses the so-called Laplacian of Gaussian (LoG) filter (this filter has no relation to the logarithmic point operation described previously). The sequence of application of the filter is:

- The original image is low-pass filtered with a Gaussian kernel. The operator must choose the standard deviation of the Gaussian. The larger the standard deviation the more the image is blurred.
- A Laplacian high-pass filter is applied to the Gaussian filtered image (hence the LoG name). The Laplacian functions as a kind of edge detector in which every edge in the blurred image is marked by a transition from negative to positive values (see Fig. 26). The Gaussian filter reduces the noise enhancement effect of the Laplacian.

- The points of zero-intensity crossings of the LoG image are detected. These points correspond to the exact positions of the edges in the original image. The fundamental consequence here is that these points *always* form closed contours.

Thus, the LoG filter creates closed contours from the detected edges. The standard deviation of the Gaussian controls if fine or coarse structures are detected. Figure 40(b) and (c) illustrate the sequence. The small standard deviation used to allow detection of small objects also leads to the detection of subtle variations in the background and inside the objects, as shown in Fig. 40(c). To eliminate these undesired features, it is necessary to postprocess the result using the methods described in subsequent sections of this article. In this case, only large, round objects that do not touch the edges of the image were preserved (Fig. 40d). This sequence was only possible because the segmentation created closed contours.

The Marr-Hildreth method requires a single user-selected parameter and can provide good results where other methods fail. However, it is not commonly found in commercial image-processing programs.

The Canny edge detector (Ref 29) is similar to the Marr-Hildreth method. It also begins by low-pass filtering the image with a Gaussian kernel. Then a derivative operator similar to the Sobel is applied to detect edges in the original image and transform them into ridges. The ridge tops are then tracked and points not on the ridge tops are erased, effectively thinning the ridges and locating the edges. In most implementations, the user must choose the standard deviation of the Gaussian and a sensitivity parameter that controls the detection of shallow/steep edges. Figure 41 illustrates the operation for the same image as Fig. 40. Postprocessing is also necessary and is complicated because the method does not guarantee closed contours. In this example, the Canny segmentation was inferior to the Marr-Hildreth segmentation, which detected many more objects. However, there are situations where the Canny method provides results where the Marr-Hildreth method fails. The user must experiment for each type of image.

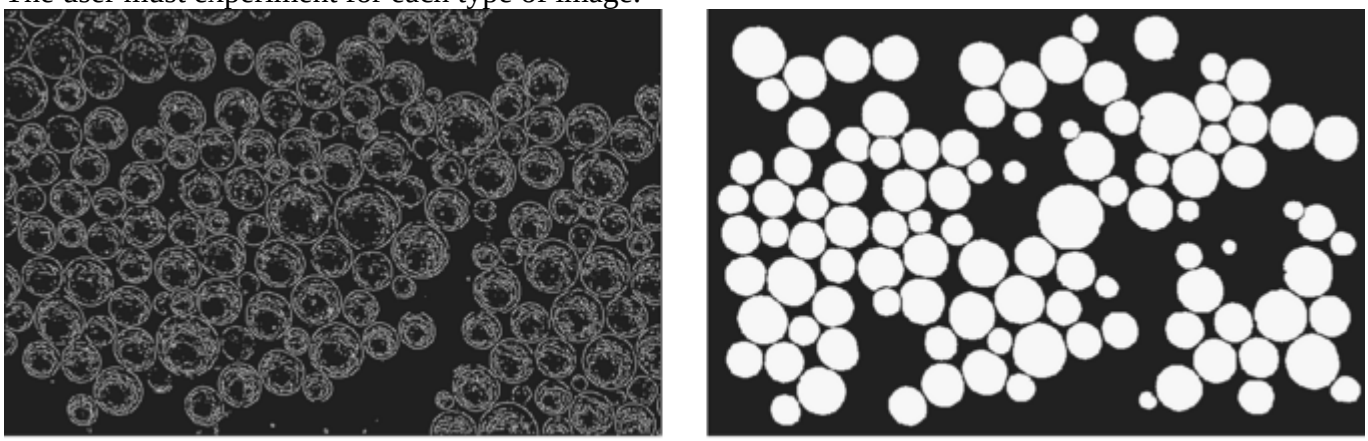

(a) (b)

Fig. 41 The Canny edge detector applied to the same image as Fig. 40 (a) Edges detected with σ = 0.5. (b) Objects detected after suitable postprocessing. Original image, courtesy of Vito Smolej, Carl Zeiss Vision

As mentioned previously, segmentation is the most difficult step in the image processing and analysis sequence. The results depend on image complexity, operator experience, and availability of segmentation options in the programs. This last characteristic should be taken into consideration when specifying software because it may well mean the difference between success and failure in the analysis of an image.

Postprocessing

Even with the best conditions, segmentation is seldom a single-step procedure. Even the most sophisticated methods can leave behind spurious objects and other defects that must be dealt with in the postprocessing step of the basic flowchart.

There are basically two ways to improve segmentation results: methods based on morphological operations and methods based on measurements of the segmented objects. The former are used to correct segmentation defects. The latter are used to further discriminate object classes that are lumped together by segmentation.

Basic Morphological Operators. Morphological operators are part of mathematical morphology (Ref 30), a powerful approach to process images, mainly developed at the Ecole des Mines, in France. Only the simplest and most commonly found operators are discussed here. Morphological operators are similar to the neighborhood operators described previously—they look at a given pixel and its neighbors. The main difference is that morphological operators are more commonly applied to the binary images created by segmentation; grayscale morphology is also defined and provides powerful tools for image analysis. The analysis of a pixel neighborhood defines if the pixel keeps its original black or white color, or if it is inverted.
Morphological operators depend on three parameters: a structuring element (se), a rule for keeping or inverting a pixel, and the number *n* of applications of the rule. The structuring element essentially defines the shape of the neighborhood analyzed around each pixel and, as the name says, will affect the final shape of objects submitted to the operations.
The rules define a set of operators. The two basic ones are erosion and dilation.
In erosion, each white pixel is inverted if it does not have enough white neighbors to cover the se used. Figure 42 shows the effect of $n = 1$ cycle of erosion with a square (eight-neighborhood) se on a magnified binary image. As indicated by the name of the operator, the white objects are eroded as a one pixel wide layer is removed from their periphery. This happens because white pixels at the edge of objects fail the test stated previously as they necessarily have black neighbors in the neighborhood defined by the se. White pixels in the interior of objects are not touched because they pass the test. The net effect is to reduce the area of objects and eliminate altogether objects that are smaller or narrower than *n* times the size of the se.

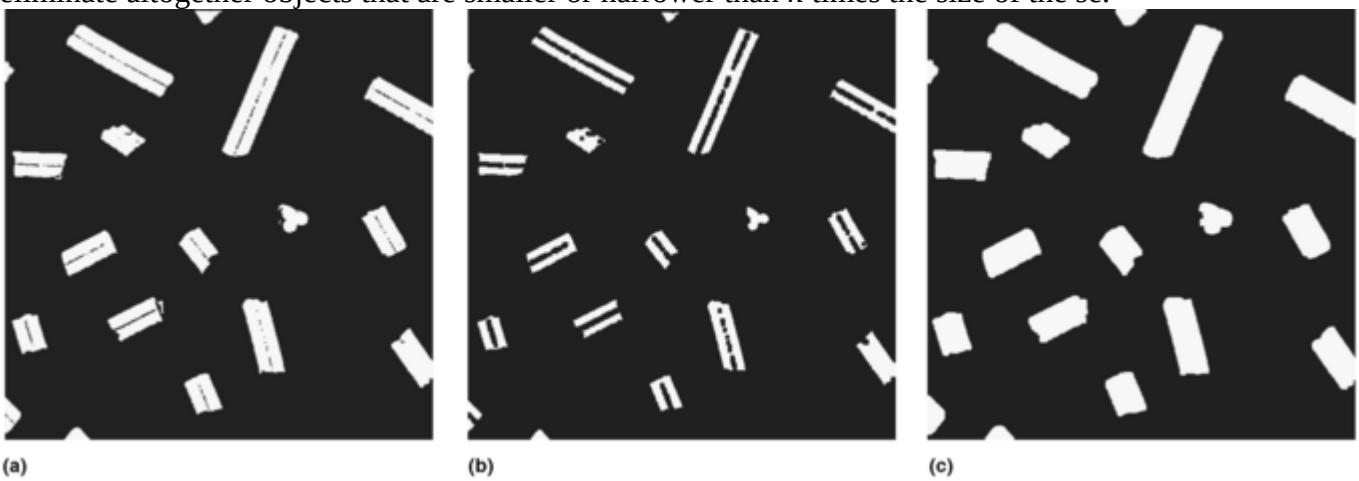

Fig. 42 Erosion and dilation in action. (a) A magnified binary image. (b) Erosion and (c) dilation, using a square (eight-neighborhood) structuring element, with one iteration

Dilation is complementary to erosion because it follows the same rule but for the black pixels. Its effect is also shown in Fig. 42. The net effect is to increase the area of the white objects, possibly merging neighboring objects.
These two operators are many times used “in tandem,” providing powerful options. A certain number *n* of erosions followed by (normally) the same number of dilations is called opening. It eliminates objects smaller than ($n \cdot$ se), breaks narrow connections between objects while keeping the area of the larger objects unchanged. Figure 43(a) illustrates the procedure. Opening is useful when segmentation leaves behind spurious bridges between objects, which must be eliminated without changing the larger objects.

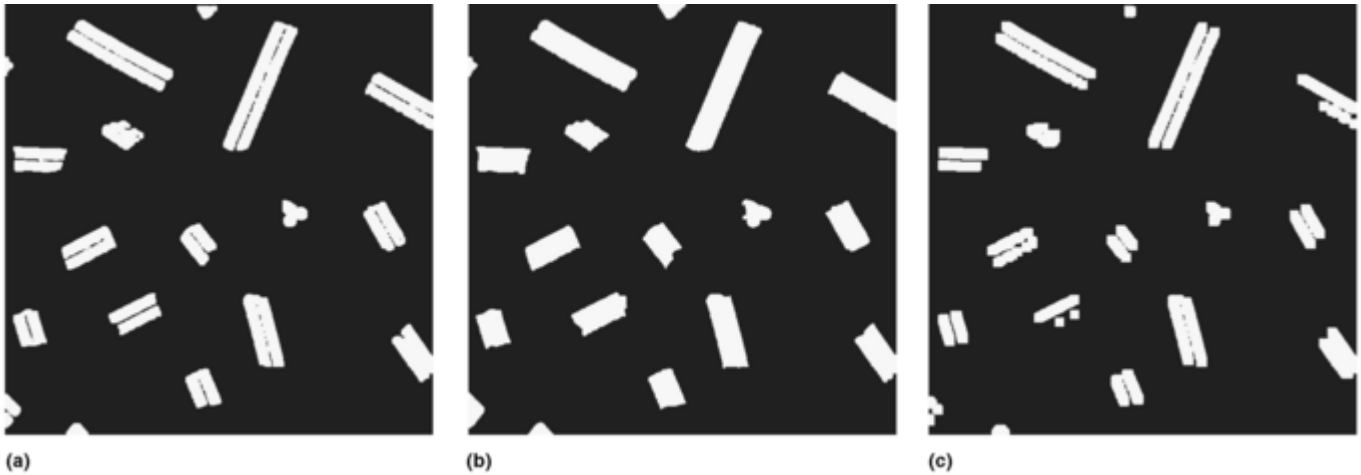

Fig. 43 Opening and closing. (a) Opening and (b) closing of the image in Fig. 42, using the same structuring element. (c) Shape distortion after five cycles of closing with the same square structuring element

Closing is *n* cycles of dilation followed by (normally) the same number of erosions. Its effect is to bridge gaps smaller than the se, as mentioned before for dilation, but it keeps the area of larger objects unchanged. Closing can be used to smooth a rough contour created during segmentation, eliminating the “entrance of bays” in the objects and allows filling of the resulting holes, as discussed below. See Fig. 43(b).

Even though opening and closing are meant to keep unchanged the area of objects larger than the employed se, they will nevertheless influence the shape of the objects. As *n* increases, the remaining objects get distorted and assume a shape similar to the se used. This is shown in Fig. 43(c), where the remaining objects assume square shapes identical to the se employed.

Fill is another useful operator, which can also be derived from erosion and dilation (Ref 23). It fills holes; the islands of black pixels completely surrounded by white pixels. Different from the well-known paint bucket of common image-editing programs, which is controlled manually by clicking on each region to be filled, the fill operator is automatically applied to all holes in an image (see Fig. 44).

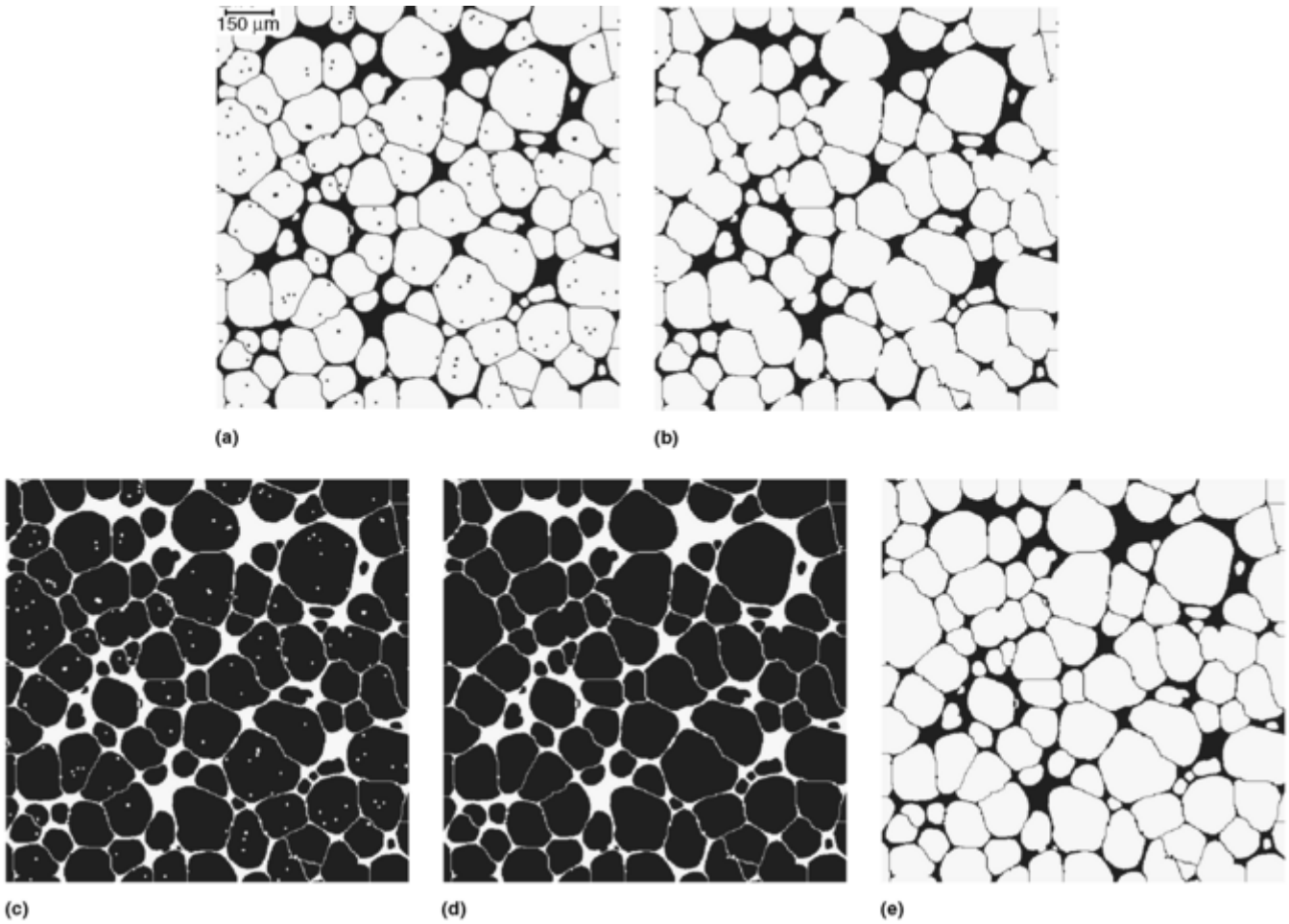

Fig. 44 The fill and scrap operators. (a) A binary image with holes in the objects. (b) After fill. Note the merging neighboring objects. (c) The original binary image after inversion with the NOT operator. Small black holes in objects have become small white objects. (d) Elimination of small objects with the scrap operator. (e) Another inversion to recover the original image without holes

One has to be careful, though, when using the fill operator in images where objects touch each other. Some background regions end up surrounded by white regions and end up filled as if they were holes. This is also shown in Fig. 44.

There are different solutions to this problem, based on the expectation that "true" holes are generally smaller than "false" holes.

Scrap. The simplest solution, also shown in Fig. 44, is to use a combination of the NOT logical operator with a scrap operator. This last operator eliminates objects based on their pixel count. It is not based on erosion and dilation and does not affect the remaining objects. The scrap operator is a basic type of measurement-based postprocessing. Thus, to eliminate holes in the objects without filling background regions, the image is first inverted with the NOT operator. The holes become small objects that can be eliminated with the scrap operator tuned to their typical size. The image is inverted again to produce the final result, with object holes eliminated.

One could think that the best solution to this problem would be to first disconnect the touching objects. However, as discussed in the next section, the method for separating objects is strongly affected by holes in the objects and cannot be used directly.

Separating Touching Objects. Images with touching or partially overlapping objects are relatively common. They can originate from a physical situation, for example, a sintered material, from acquisition limitations, for example, nearly touching objects that are merged together due to limited microscope/camera resolution, or from the preprocessing and segmentation steps that may lead to spurious connections.

Touching objects are treated as a single object by the computer because there are no boundaries between objects, even though a human operator would easily separate them, "imagining the boundaries." Therefore, to be able to count and measure objects accurately, one has to find a way to establish these boundaries on the image.

The best-known method for the separation of touching objects is the watershed method (Ref 31, 32). It uses the fill and scrape operators shown in Fig. 44. Beginning with a binary image, steps of fill, inversion with NOT operator, scrap operator, and another inversion follow.
Figure 45 shows the watershed method for a sintered tungsten carbide sample:

- Using any segmentation method, produce a binary image where objects are still touching.
- From the binary image, compute the Euclidian Distance Map (EDM), explained below.
- From the EDM, obtain the watersheds, which will function as boundaries between objects.

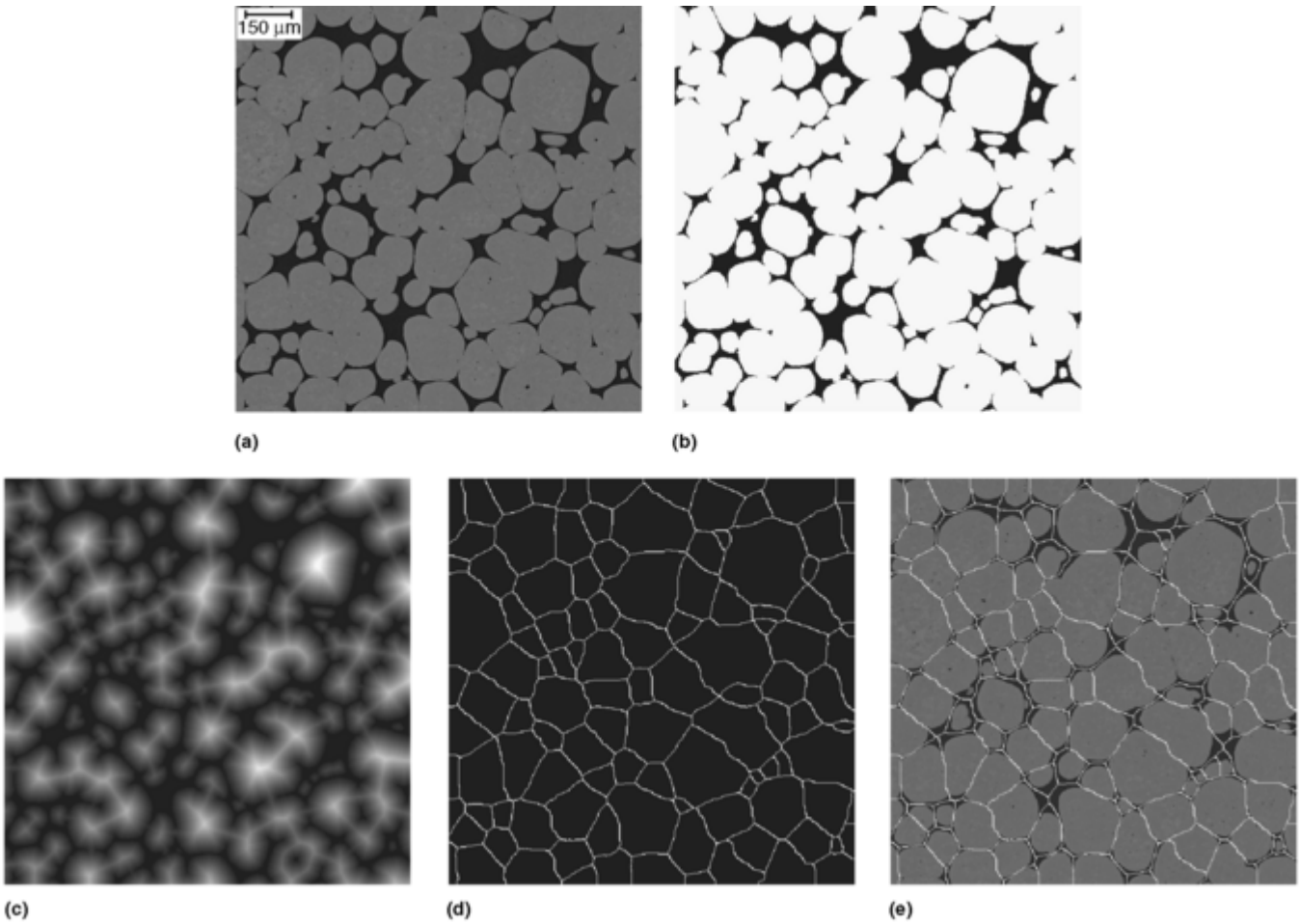

Fig. 45 The watershed method. (a) Original image. (b) Binary image with touching objects. (c) The EDM of the binary image (with contrast enhancement). (d) The watersheds derived from (c). (e) The boundaries superimposed on the original image. Original image, courtesy of Vito Smolej, Carl Zeiss Vision

The EDM (Ref 25) is a grayscale image where the pixel gray value is the distance between that pixel and the nearest object edge in the binary image. This operation transforms the white “plateaus” that correspond to objects in the binary image into mountains separated by valleys. One way to describe the ensuing operation is to invert the EDM so that objects become valleys separated by ridges. The location of the ridges is then determined by slowly filling the valleys with water up to a level at which the water would start flowing from one valley to a neighboring one. At this point the watersheds between valleys (that actually correspond to objects) are found. These watersheds are shown in Fig. 45(e) and can then be superimposed onto the original binary image as shown in Fig. 45(e).
The watersheds found are sensitive to holes in the binary objects. These defects normally give rise to spurious boundaries. Thus, it is important to fill holes, as described previously, before obtaining the EDM. The EDM itself is sensitive to irregularities in the contours of the binary objects. Therefore, it is common to smooth the EDM through a low-pass filter before obtaining the watersheds.

The watershed method is not perfect and cannot find boundaries between objects when there is no curvature change in the boundary (just imagine trying to separate two adjoining rectangular objects). The results also depend on the specific algorithm implemented by the software used as there are many possible variations. The interested reader should look for more detailed information in the literature on mathematical morphology. Furthermore, when objects are actually overlapping, the watershed is at most a reasonable boundary, but, evidently, the correct shape of the object is not recovered. There are specific methods for deagglomeration of partially overlapping circles (Ref 33), which use shape fitting to reconstruct the correct shapes.

Measurements

Once the image has gone through preprocessing, segmentation, and postprocessing, the regions in the binary image can be used as a mask to measure several different parameters of the original objects in the grayscale or color image.

There is a basic distinction between field features and region features. Field features refer to the image as a whole. Parameters such as total object count, total area, total perimeter, area fraction, and number of intercepts, commonly used in traditional metallographic analysis, are field features. Region features refer to each object in the image. Parameters such as object area, perimeter, major axes, shape, average intensity, and so forth are region features. Evidently, all field features can be derived from region features, but most programs provide this separation to facilitate basic measurements.

Region features are extremely diverse and flexible, and literally hundreds of parameters are defined. It is common to group the parameters into four classes (Ref 25)—size, shape, position/distance, and intensity/texture. The most commonly used of these are described in the following sections.

As in traditional metallography, the operator must choose a strategy for collecting a sequence of fields from a sample and decide how to deal with field edges. Most programs provide options to eliminate objects that touch all or some edges of the image, as their region-specific parameters cannot be measured accurately.

Size. The simplest measurement of size is the area (A), obtained digitally by simply counting the number of pixels in the object. Notice that there is no simple way of measuring area manually. All traditional metallographers know that. The procedure always requires some kind of sampling and has limited accuracy. In this regard, the digital measurement of area also involves sampling with a given pixel size, but it is much more accurate and faster.

Another useful size parameter is the convex area (A_C), which is the area enclosed by a taut string around the object (Fig. 46). For convex objects, it is the same as A, but it is larger for nonconvex shapes. The convex area is useful when one wants to measure the area without considering irregularities in the contour of the object that may have been caused by some spurious effect of sample preparation or image processing. As discussed previously, morphological closing can be used to reduce the irregularities. However, the direct measurement of A_C provides a reasonable estimate for the true area of the objects. The A_C is also used in the measurement of shape, as described in the following section.

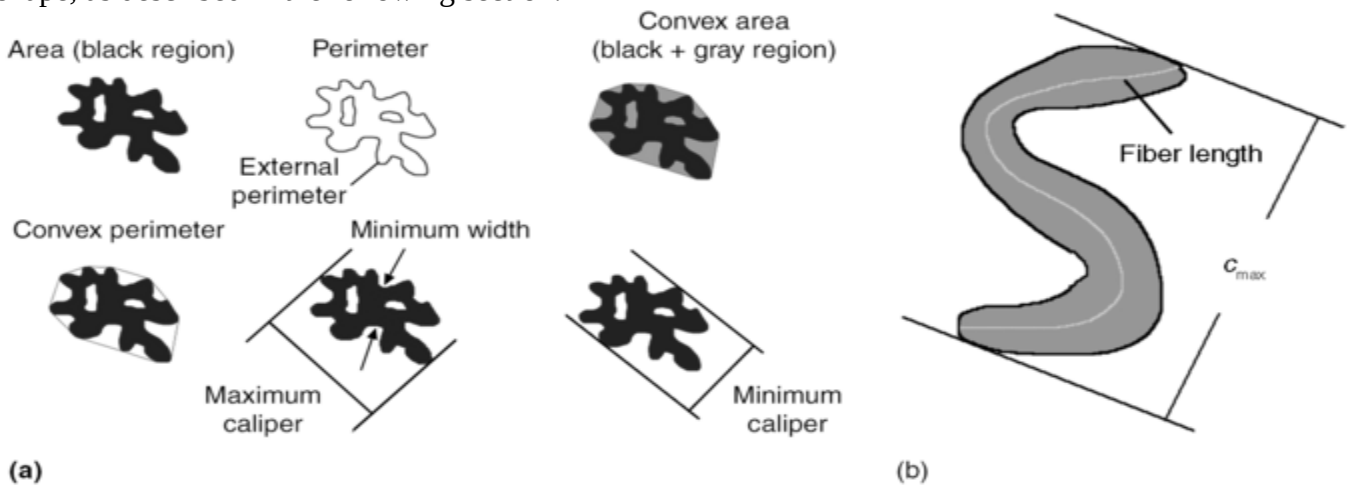

Fig. 46 Basic size parameters. (a) Definitions of area, perimeter, their convex equivalents, and basic calipers. (b) The fiber length compared to C_{max}

The filled area (A_F) is the area of the object including internal holes and can be used, in conjunction with A, to assess superficial porosity.

As for the area, one can define the perimeter (P), convex perimeter (P_C), and filled perimeter (P_F). The perimeter includes the external perimeter and the internal perimeter of holes. The convex perimeter is measured for the taut string around the object and is used with the perimeter to estimate convexity, as described in the following section. The filled perimeter measures only the external perimeter, ignoring holes.

The computational measurement of the perimeter is complex due to the digital character of the images. Depending on how neighboring pixels in the horizontal, vertical, and diagonal directions are considered, the results can be overestimated or underestimated. A very accurate way for obtaining the perimeter is the Crofton method (Ref 34). The best image-analysis programs provide this method.

Another set of commonly used size parameters are the calipers (also known as Ferets), linear measurements that correspond to the projections of the particle in different directions. It is common to define the x and y calipers (C_x, C_y), corresponding to projections onto the two axes, and the maximum (C_{max}) and minimum (C_{min}) calipers (Fig. 46).

Note that C_{min} does not correspond to the minimum width of the particle (breadth), also marked in the figure. Moreover, generally C_{min} is not perpendicular to C_{max}. Certain programs measure the caliper perpendicular to the maximum (C_{Pmax}) independently. The angle of C_{max} ($Angle_{Cmax}$) in relation to a reference axis can be used as a measurement of particle orientation.

The parameters described so far are primary parameters. Secondary parameters are obtained from primary ones through some calculation. The most common is the equivalent circular diameter (*Dcirc*) that computes a diameter for the particle, based on the assumption that it approximates a circle. There are two basic options for *Dcirc,* namely:

$$\text{Based on the area: } Dcirc_A = \sqrt{\frac{4 \cdot A}{\pi}} \qquad \text{(Eq 8)}$$

$$\text{Based on the perimeter: } Dcirc_P = \frac{P}{\pi} \qquad \text{(Eq 9)}$$

For elongated, nonlinear fiberlike structures, C_{max} may not be a good measurement of the true length, as shown in Fig. 46(b). It is possible to define a parameter fiber length (*FLength*), based on the filled area and perimeter. There are several equations (Ref 25) for the *FLength;* a commonly used option is:

$$FLength = \frac{P_F + \sqrt{(P_F)^2 - 16A_F}}{4} \qquad \text{(Eq 10)}$$

This and other equations are approximations for the true fiber length and should be checked for accuracy in each application.

Shape. The shape of an object is more complex to describe and is nearly impossible to measure manually.

The simplest measure of shape is the aspect ratio (*AR*) that can be conveniently obtained from the minimum and maximum calipers as:

$$AR = \frac{C_{min}}{C_{max}} \qquad \text{(Eq 11)}$$

AR is a measure of elongation. A long object has $C_{min} \ll C_{max}$ and *AR* approaches 0, while a more isotropic object has $C_{min} \approx C_{max}$ and *AR* approaches 1. The *AR* of a circle equals 1. Note that for a square, *AR* = 0.707 because $C_{min} = L$ (square side) while $C_{max} = L\sqrt{2}$ (square diagonal). This definition of *AR* is preferable to the inverse (with C_{max} in the numerator) found in some references, because the values are bound in the range [0–1] and can be more easily compared.

A shape factor is a measurement of similarity of an object with a specific shape. Thus, for example, a circular shape factor (*CSF*) can be written as:

$$CSF_P = \frac{4\pi \cdot A_F}{(P_F)^2} \qquad \text{(Eq 12)}$$

This parameter assumes the value 1 for a perfect circle. As any other shape has more perimeter in relation to area, it decreases for less circular objects. As it depends quadratically on the perimeter, it is very sensitive to contour irregularities that increase the perimeter. Thus, it is also a measurement of contour smoothness for similarly shaped objects.

Alternatively, a circular shape factor can use the maximum caliper instead of the perimeter, making it more sensitive to elongation than to contour changes. In this case:

$$CSF_{C\max} = \frac{4A_F}{\pi \cdot (C_{\max})^2} \qquad \text{(Eq 13)}$$

Other shape factors can be defined for other simple geometrical shapes. For example, suppose one wants to measure how close to a square is a Vickers hardness indentation. A square shape factor can be defined as:

$$SSF = \frac{16A_F}{(P_F)^2} \qquad \text{(Eq 14)}$$

that is, 1 only for perfect squares and <1 for other shapes. Shape factors are especially useful in measurement-based postprocessing.

Another set of shape parameters that is less related to the specific shape or elongation of an object, but rather estimates contour roughness and convexity, can be defined using the standard and convex measurements of area and perimeter. Two parameters are typically defined. The perimeter-based convexity uses the fact that the convex perimeter, P_C, is always less than or equal to the filled perimeter, P_F.

$$Conv_P = \frac{P_C}{P_F} \qquad \text{(Eq 15)}$$

that is, 1 for a convex object and approaching 0 for nonconvex objects. This parameter is very sensitive to the occurrence of thin, long "peninsulas," because P_C decreases sharply.

The area-based convexity uses the convex area, A_C, which is always greater than or equal to the filled area A_F. Thus:

$$Conv_A = \frac{A_F}{A_C} \qquad \text{(Eq 16)}$$

that is 1 for a convex object and approaching 0 for nonconvex objects.

Many other parameters can be devised to describe shape (Ref 35). The choice of the best set of parameters to deal with a specific problem is normally a matter of trial and error. A case study is presented regarding the classification of cast iron based on the shape description of graphite particles, using different shape parameters.

Position and Distance. The spatial distribution of objects in an image can also be measured. The simplest parameter is the center of gravity (*CG*), described by its *x* and *y* coordinates. This position can be obtained from the binary mask of the object or weighted by the pixel intensity in the original image.

Perhaps more important is the interparticle distance and its distribution. This distribution is important because it can reveal characteristics of the spatial arrangement of the particles, distinguishing between uniform, clustered, periodical, and random organizations. Figure 47(a), (d), and (g) show three synthetic structures composed of the same number of circles with constant diameter, but with different spatial organizations. Even though basic parameters such as area fraction and diameter distribution are the same for the three structures, mechanical properties of materials with these spatial distributions of a second phase would probably be different.

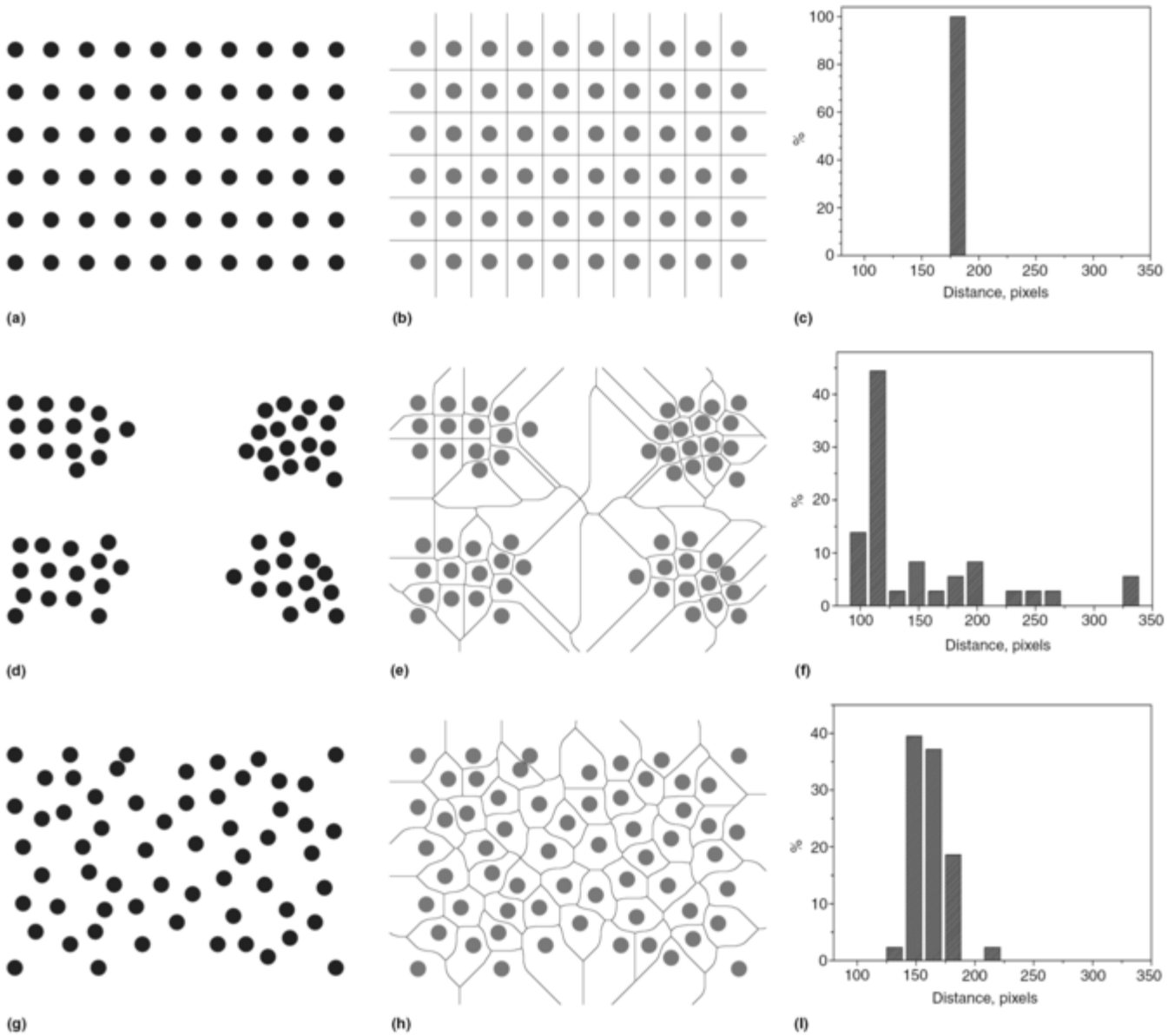

Fig. 47 Synthetic structures with different spatial distributions, influence zones map, and distance distribution. (a), (b), and (c) Square lattice. (d), (e), and (f) Clustered. (g), (h), and (i) Random

The easiest way to describe the difference between these structures is through their interparticle distances. At first thought, one would think of measuring the distance between each particle and all other particles in the field, using the *CG* as a reference for each particle. However, this procedure is too computer intensive and does not reveal the basic characteristics of the spatial distribution, which depend more closely on the distance between each particle and its nearest neighbors. These local characteristics are also more important in terms of the mechanical properties of the material.

The most efficient approach to measuring the spatial distribution uses a special morphological operator, ultimate dilation, an extension of the dilation operator described previously. This operator dilates each object a certain number of times, with a given structuring element, with the condition of avoiding merging any two or more objects. As dilation evolves and each object grows, it will stop if a new cycle would merge the object with a neighboring one, leaving a background line between them. This means that an object will grow more in a direction in which the nearest neighbor is farther away, and less in a direction were the neighbor is closer. The result of the procedure, repeated until no further change occurs in the image, is called an influence zone map (also known as a Voronoi diagram). These are shown in Fig. 47(b), (e), and (h), where the particles are shown in gray inside their influence zones shown in white. It is also referred to as the SKIZ (from skeletonization by influence zones). In this case the image is inverted and the skeleton (Ref 30) of the background is determined, leading to the same result.

Once the influence zone map is determined, the zone of each particle can be treated as an object that can be measured (Ref 36). Thus, for instance, the equivalent circle diameter (D_{circ}) of each zone can be used as an estimate of the average distance to nearest neighbors. The histograms of D_{circ} for the three structures are shown in Fig. 47(c), (f), and (i). The square lattice shows a strong peak for the lattice spacing. The clustered structure shows peaks corresponding to the intracluster and intercluster typical distances. The random structure shows a continuous distribution of distances. These results are normally biased by edge effects. Thus it may be desirable to eliminate the influence zones that touch the edges of the image. Figure 48 shows this kind of analysis applied to two different fiber-reinforced composite materials. The composite in Fig. 48(a) has both agglomerated and spread apart fibers. This leads to the wider distance histogram in Fig. 48(b), with two separate peaks. The composite in Fig. 48(c) has uniformly distributed fibers leading to the histogram of Fig. 48(d) that shows a single narrower peak at a smaller distance.

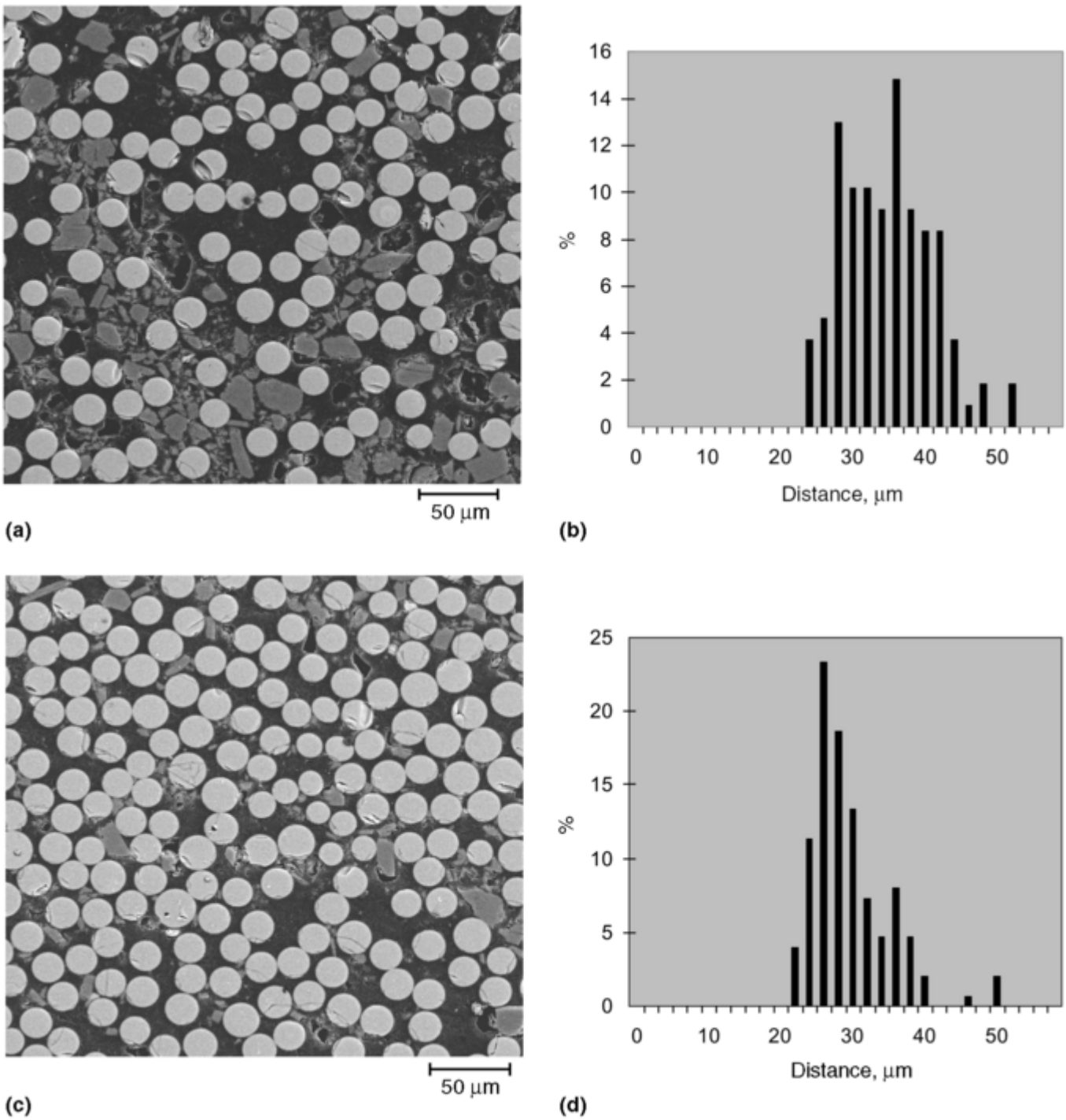

Fig. 48 Two fiber-reinforced composite materials with different fiber distance distributions. (a) and (c) Original SEM images. (b) and (d) Respective fiber distance histograms

Intensity and Texture. Measures based on the pixel intensities, also called densitometric, can be grouped in two classes: occurrence statistics and co-occurrence statistics.

Occurrence statistics include simple measurements such as the average and standard deviation of the gray levels of an object. The standard deviation is a basic assessment of local contrast in an object. Higher-order statistics, such as skewness and kurtosis, can reveal anisotropic intensity distributions. The same measurements can be applied to each channel in a color image.

Co-occurrence statistics, as the name says, refer to the simultaneous occurrence of specific intensities in pairs of neighboring pixels. These statistics are much more sophisticated and allow the measurement of texture parameters. (The term texture is not used here in its metallographical sense, meaning preferred orientation, but rather in its colloquial sense.) These parameters were originally proposed in Ref 37 in the context of remote sensing to distinguish between different surfaces such as ocean, lake, land, forest, city, and so forth.

Consider the images shown in Fig. 49, for two very similar textures observed with HRTEM—a pure amorphous resin (Fig. 49a) and the same resin with dispersed carbon nanoparticles (Fig. 49b). The presence of carbon is nearly invisible in the image, but it affects dielectric measurements (Ref 38) and electron energy loss (EELS) spectra. Regular grayscale analysis would not be able to distinguish the two textures. However, the use of the so-called Haralick parameters for uniformity and entropy reveals strong differences between the two, as shown by the graphs in Fig. 49(c) and (d) (Ref 39).

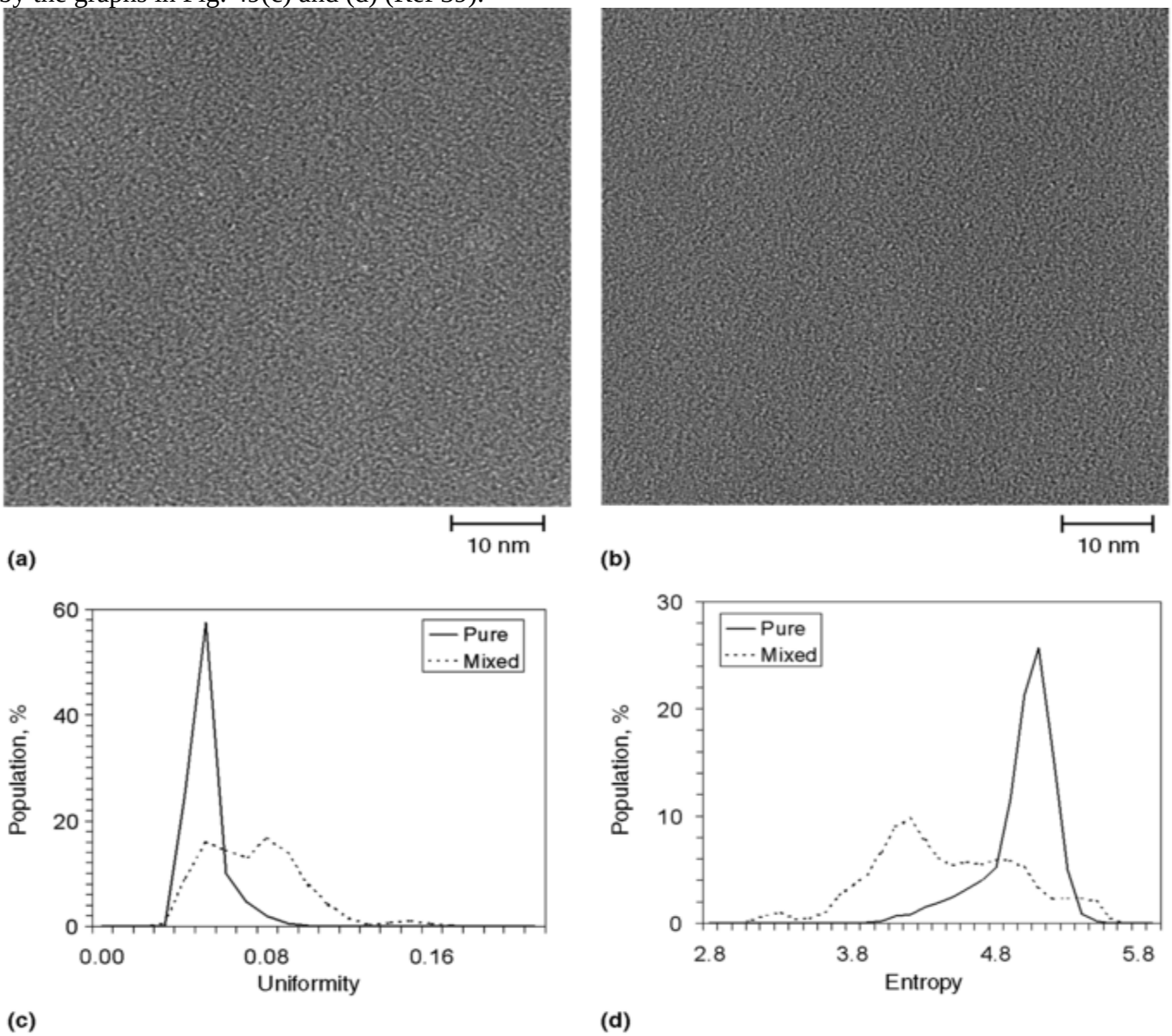

Fig. 49 The use of co-occurrence statistics in texture analysis. (a) HRTEM image of an amorphous resin. (b) HRTEM image of the same resin with diluted nanoparticles of carbon. (c) and (d) The histograms for uniformity and entropy for the two images. Courtesy Dr. Alain Thorel, ENSMP

Measurement-Based Postprocessing. All segmentation methods presented in the section “Image Segmentation” are based, in one way or another, on the pixel intensities. However, when morphological postprocessing and measurements are successful, there is a wealth of information about the objects in the image, which can be used to separate the segmented objects into classes based on other parameters besides intensity. This is called measurement-based postprocessing to distinguish from typical morphological postprocessing. It can be understood as a statistical analysis of the measured data and can be undertaken with specific software unrelated to image analysis. However, when integrated in image-analysis programs this approach can be very powerful, as shown in the following.

The image of the fiber-reinforced composite shown in Fig. 50 serves as an example. In the segmented image (Fig. 50b), many fibers appear distorted due to defects from specimen preparation. The goal of the analysis is to accurately measure several parameters such as fiber diameter distribution, fiber distance, and so forth. On one hand, one would like to measure as many fibers as possible. On the other hand, lumping together measurements of regular fibers and corrupted fibers biases the results. For instance, the D_{circ} of a fiber with irregular contour is different from the true fiber diameter. Thus, it is important to first separate regular and corrupted fibers.

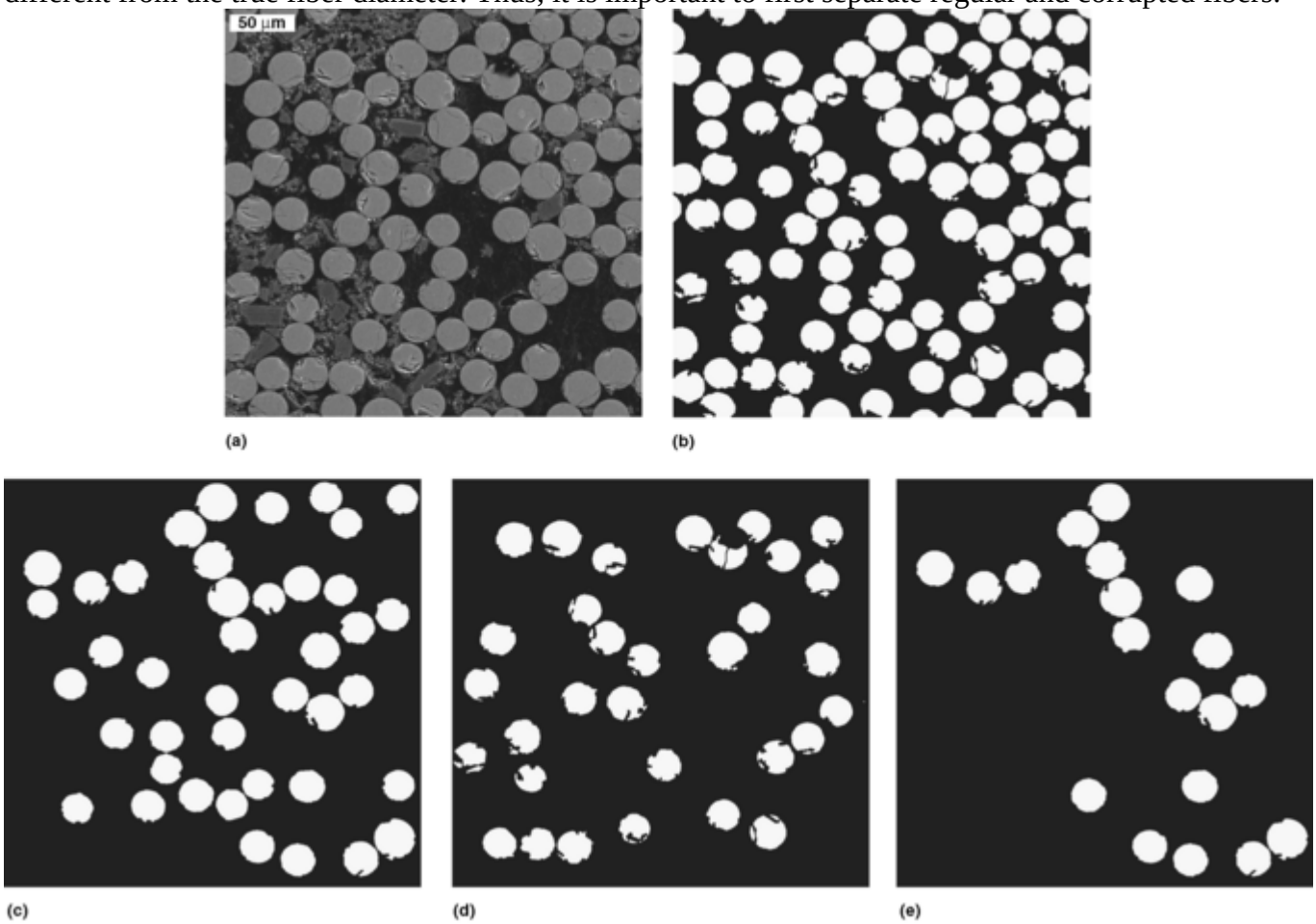

Fig. 50 Shape-based postprocessing. (a) Original composite image. (b) Segmented and postprocessed binary image. (c) Regular fibers with $CSF_P < 0.85$. (d) Irregular fibers with $CSF_{Cmax} \leq 0.85$. (e) Regular fibers with equivalent convex diameter ≥26 µm. Fibers touching the edges were discarded.

This separation can be achieved with shape-based postprocessing using the circular shape factor based on the maximum caliper (Eq 12). Figure 50(c) shows fibers for which $CSF_{Cmax} > 0.85$, closer to a circle, leaving behind the corrupted fibers, Fig. 50(d).

More sophisticated analysis can be achieved by combining criteria for different parameters. Figure 50(e) shows the result of selecting, among the more circular fibers, the ones with $D_{circ} > 26$ µm. The convex area was used to calculate D_{circ} to avoid influence of residual irregularities. Any logical combination of parameters can be used.

As another example, the images in Fig. 40(c) and 41(d), representing the final results of the Marr-Hildreth and Canny segmentation methods, respectively, were obtained using criteria for circularity.

These principles can be extended, in many cases, to achieve fully automatic classification of objects in an image.

References cited in this section

20. Axio Vision Control Release 3.0, *Manual: B40-640 e,* Carl Zeiss Vision GmbH, 2000

21. K.R. Castleman, *Digital Image Processing,* Prentice-Hall, 1979

22. J.C. Russ, *The Image Processing Handbook,* CRC, 1992

23. R.C. Gonzalez and R.E. Woods, *Digital Image Processing,* Addison-Wesley, 1993

24. M. Sonka, V. Hlavac, and R. Boyle, *Image Processing, Analysis and Machine Vision,* 2nd ed., PWS, 1998

25. J.C. Russ, *Computer Assisted Microscopy, The Measurement and Analysis of Images,* Plenum Press, 1990

26. N. Otsu, A Threshold Selection Method from Grayscale Histograms, *IEEE Trans. Sys. Man. Cyb.,* SMC-9, 1979, p 62–66

27. P.-Y. Yin and L.-H. Chen, A New Method for Multilevel Thresholding Using Symmetry and Duality of the Histogram, *International Symposium on Speech, Image Processing and Neural Networks,* IEEE, Hong Kong, 1994, p 43–48

28. D. Marr and E. Hildreth, On the Theory of Edge Detection, *Proc. R. Soc. (London) B,* Vol 207, Royal Society of London, 1980, p 127–217

29. J. Canny, A Computational Approach to Edge Detection, *IEEE Trans. Pattern An. Mach. Intell.,* Vol. 8 (No. 6), Nov 1986, p 679–698

30. J. Serra, *Image Analysis and Mathematical Morphology,* Academic Press, 1982

31. S. Beucher and C. Lantejoul, Use of Watersheds in Contour Detection, *Proc. Int. Workshop Image Processing, Real-Time Edge and Motion Detection/Estimation,* CCETT/INSA/IRISA, IRISA Report No. 132, Rennes, France, 1979, p 2.1–2.12

32. S. Beucher, The Watershed Transformation Applied to Image Segmentation, *Scanning Microscopy Supplement,* Vol 6, 1992, p 299–314

33. F. Meyer and S. Beucher, Morphological Segmentation, *J. Vis. Commun. Image Represen.,* Vol 1 (No. 1), 1990, p 21–46

34. M.P. do Carmo, *Geometry of Curves and Surfaces,* Prentice-Hall, 1976, p 41

35. J. Grum and R. Strum, Computer Supported Recognition of Graphite Particle Forms in Cast Iron, *Acta Stereol.,* Vol 14 (No. 1), 1995, p 91–96

36. M.T. Shehata, Characterization of Particle Dispersion, *Practical Guide to Image Analysis,* ASM International, 2000, p 141–143

37. R.M. Haralick, K. Shanmugam, and I. Dinstein, Textural Features for Image Classification, *IEEE Trans. Systems, Man and Cybernetics,* Vol SMC-3 (No. 6), 1973, p 610–621

38. S. Paciornik, O.F.M. Gomes, A. Delarue, S. Schamm, D. Jeulin, and A. Thorel, *Eur. Phys. J. Appl. Phys*, Vol 21, 2003, p 17–26

39. S. Paciornik et al., Texture Analysis in the Detection of Subtle Structural Changes in HRTEM, *15th International Congress on Electron Microscopy*, CIASEM, 2002

S.Paciornik and M. H. de Pinho Mauricio, Digital Imaging, Vol 9, *ASM Handbook*, ASM International, 2004, p. 368–402

Sidnei Paciornik and Marcos Henrique de Pinho Mauricio, Catholic University of Rio de Janeiro

Case Studies

The previous sections have provided the main theoretical aspects of the application of image processing and analysis to materials characterization. The two case studies in this section describe real-life applications where these concepts are used, and their sequence and interrelation can be better appreciated.

The first case study illustrates the use of preprocessing, different types of segmentation, and extensive preprocessing to discriminate precipitates located either at grain boundaries or inside grains of a metallic alloy. The second case study requires very simple preprocessing, segmentation, and postprocessing, but uses sophisticated shape measurements to achieve fully automatic classification of graphite inclusions in cast iron.

Example 1: Discrimination of Intragrain and Boundary Inclusions. The spatial distribution of precipitates in metallic alloys is relevant to the mechanical properties. The relative population of intragrain versus grain-boundary precipitates is of interest.

An image-processing procedure to automate the discrimination between these two kinds of inclusions is shown in Fig. 51. A Galfan aluminum-zinc alloy (Ref 40) was imaged in an SEM, and BSE mode images were acquired at 512 × 480 pixels. Even though both intrinsic and digital resolution of the images are limited, there is enough contrast to allow visualization of the precipitates (Fig. 51a).

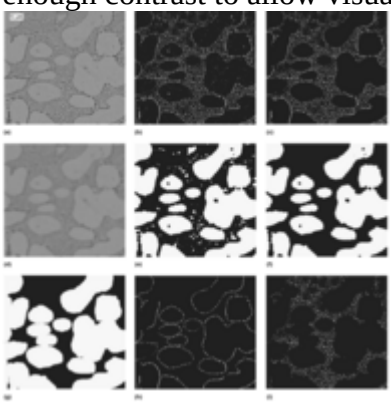

Fig. 51 Discrimination of intragrain and grain-boundary precipitates. (a) Original image (SEM, BSE, 512 × 480). (b) After median filter to reduce noise and adaptive segmentation to reveal the precipitates. (c) After dilation, scrap, and logical AND to eliminate "lonely" precipitates. (d) Strong low-pass filtering. (e) Otsu automatic segmentation of (d). (f) After opening and scrap to eliminate spurious objects. (g) After dilation to overlap boundary precipitates. (h) Boundary precipitates detected. (i) Intragrain precipitates detected

After median filtering to reduce noise, adaptive segmentation was used to create the binary image of Fig. 51(b), where all precipitates are visible. The isolated precipitates were first eliminated through a sequence of dilation

(to merge neighboring precipitates), scrap (to eliminate small objects), and a logical AND to recover the original shape of precipitates (Fig. 51c).

Strong low-pass filtering of the original image then created regions of lower-average intensity where the precipitates are concentrated (Fig. 51d), allowing automatic thresholding to discriminate these regions (Fig. 51e). Opening and scrap were then used to erase spurious objects (Fig. 51f). Controlled dilation allowed selective overlap of boundary precipitates (Fig. 51g), which were then revealed through a logical AND (Fig. 51h). Remaining intragrain precipitates were then obtained with a logical XOR (Fig. 51i).

All procedure parameters can adapt automatically to average image contrast, effectively eliminating operator influence to adjust to varying image conditions. The whole sequence takes just a few seconds per image and automatically calculates area fraction and size distribution for both precipitate classes.

This is an excellent example of how the various steps of the flowchart in Fig. 1 can be ingeniously combined to achieve a discrimination that would be nearly impossible with manual methods.

Example 2: Automatic Classification of Cast Iron. When carbon is diluted in iron with a concentration above 2.1%, it precipitates to form graphite particles. The shape of these particles can vary widely depending on the presence of other impurities and on the cooling rate from the melt. The thermomechanical properties of cast iron are strongly affected by these shapes. For example, nodular cast iron, in which the particles assume a roughly spherical shape, is normally less brittle than gray iron, where sharp graphite flakes contribute to stress concentration and crack initiation (Ref 41).

Thus, it is relevant to classify cast iron according to graphite shape. The ISO-945 (Ref 42) standard defines six classes for cast iron, based on the graphite shape. These classes are represented by the drawings in Fig. 52. In the traditional classification method by chart comparison, an operator chooses the correct class for a given experimental field through visual comparison with these reference drawings. Using image processing and analysis, the classification procedure can be completely automated, as described in the following paragraphs.

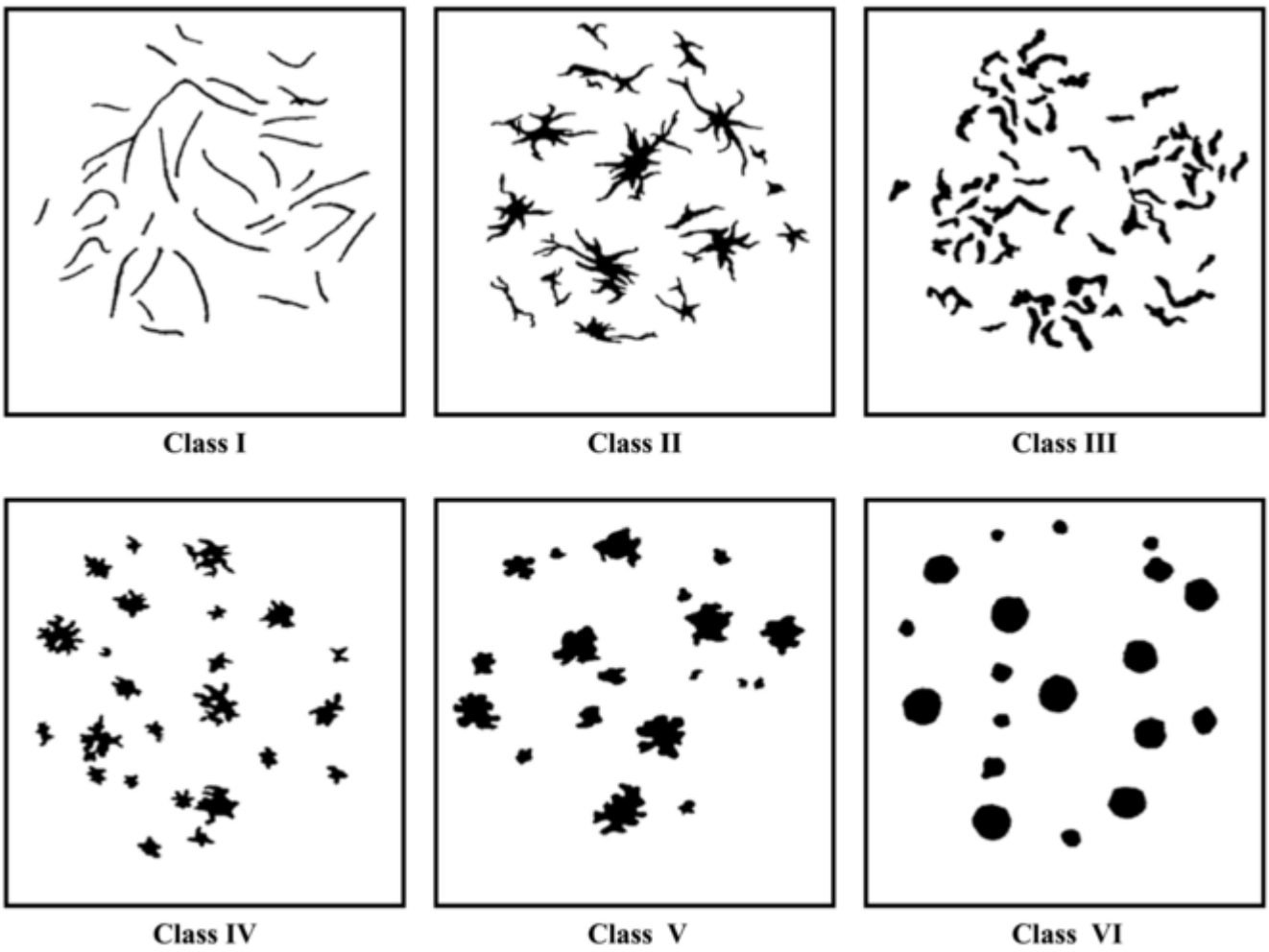

Fig. 52 Reference images for the six classes of cast iron, based on the ISO-945 standard. Ref 42

Using a subset of the particles in the reference images as a training set, several shape parameters can be used to build a classifier in a typical supervised classification routine (Ref 43). The classifier can be validated using the same reference images with the subset of the particles that was not used for training. The performance of a specific classifier is shown in Fig. 53, where the graphite particles in the reference images appear color-coded according to the classification results. A "perfect" classifier would return a single color to all particles in a given reference image. In the case shown, only the extreme classes, I and VI, get 100% classification rate. The others present some kind of mixture with neighboring classes. Nevertheless, the recognition rate is very high, as shown by Table 4. The statistics are not particularly strong because the total number of graphite particles in each reference image is not very large, but the results are intuitively reasonable.

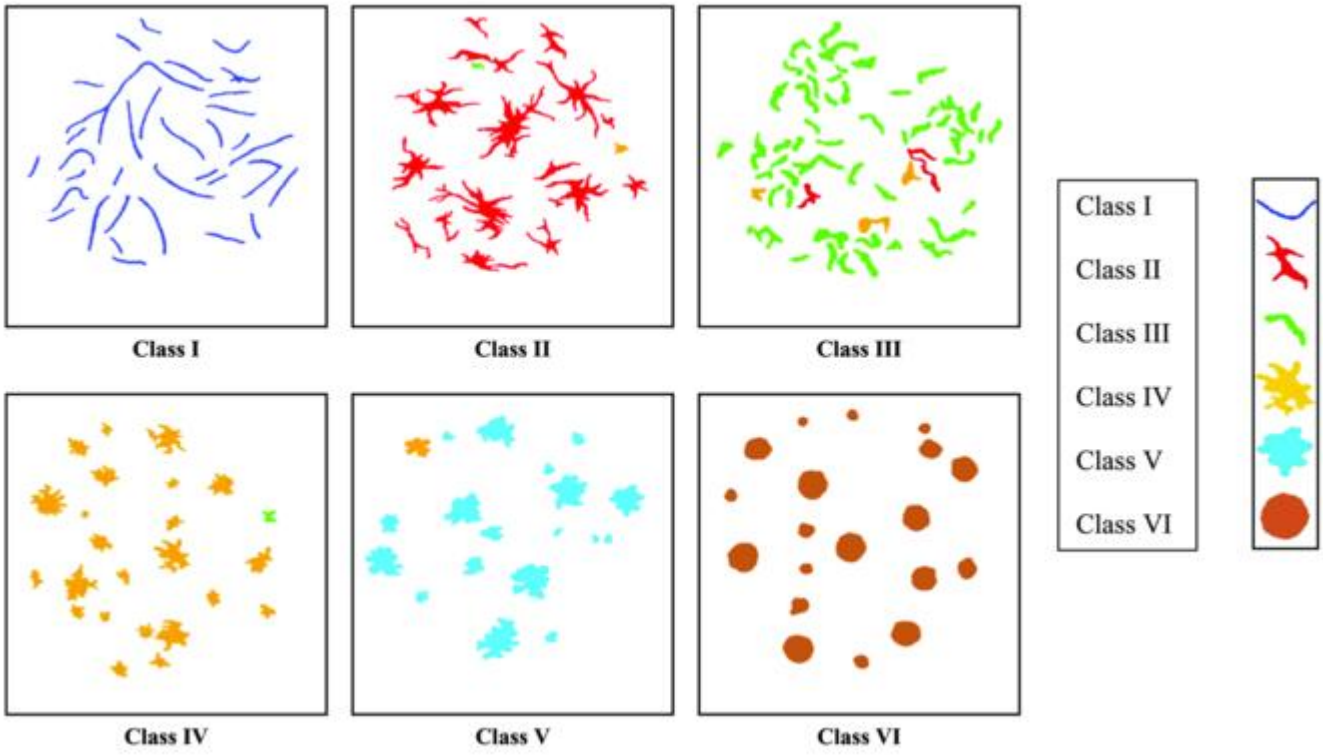

Fig. 53 Performance evaluation for a color-coding classifier. (a) Classified reference images are color coded according to attributed graphite class. (b) Graphite class color code based on ISO-945 standard. See also Table 4.

Table 4 Class recognition rates in the validation of the classifier used in Fig. 53

Class	Recognition rate, %
I	100.0
II	88.9
III	91.1
IV	95.8
V	94.7
VI	100.0
Global	94.7

Once the proposed classifier has been validated, it can be applied to real images. This is shown in Fig. 54, where two different cast irons are automatically classified. In this procedure, unetched cast iron samples are imaged through light microscopy and captured with a video camera. The contrast between graphite particles and the iron matrix is very good, allowing simple automatic thresholding. The binary image can be postprocessed to eliminate spurious objects and to separate touching particles using the methods described. The resulting binary image can then be submitted to the classifier that automatically selects the class for each particle and provides a class statistics table (Table 5).

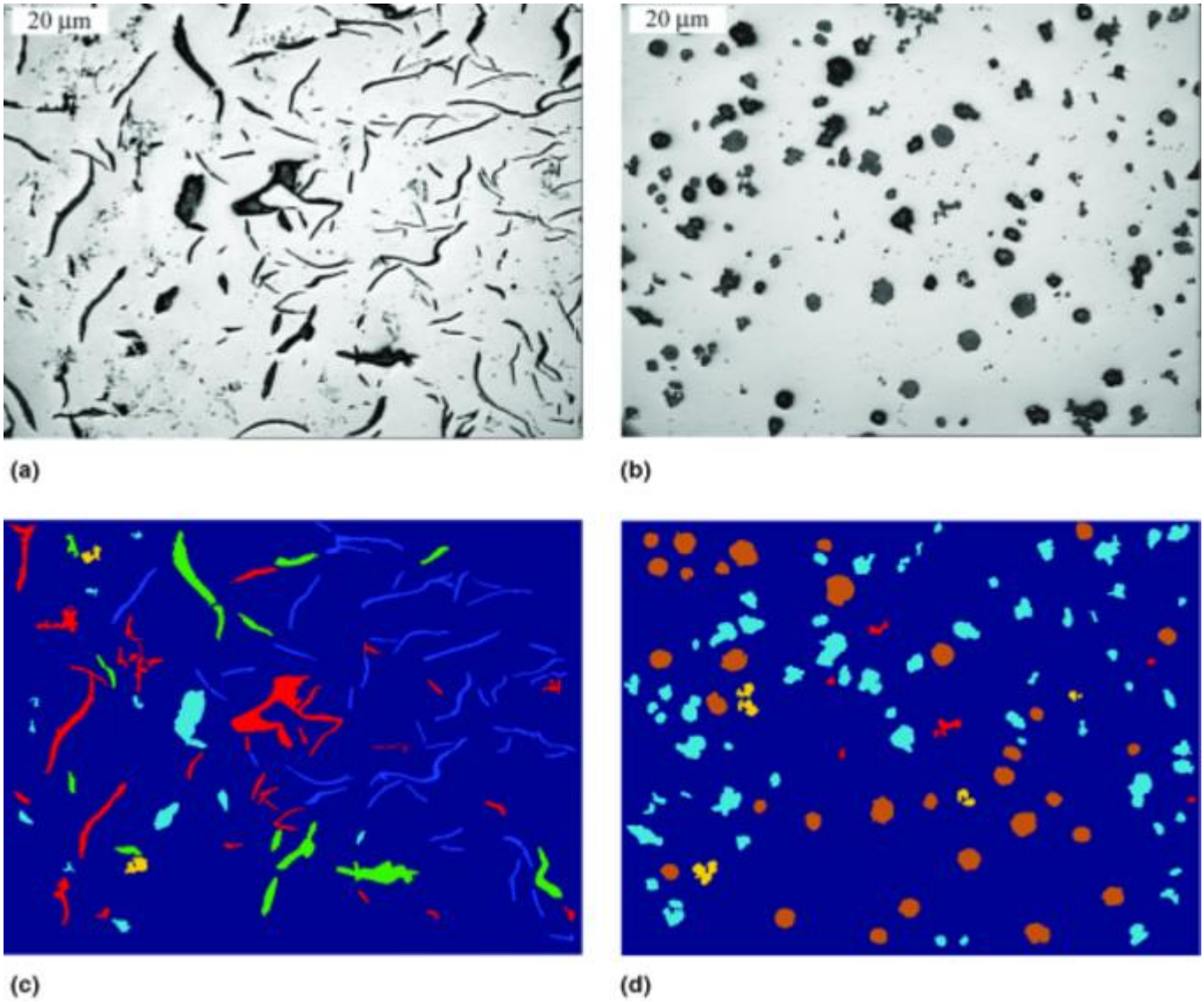

Fig. 54 Automated classification of real cast iron samples. (a, b) Light microscopy images of samples. (c, d) Color-coded classification results based on scheme given in Fig. 53. See also Table 5.

Table 5 Classification tables for the two samples shown in Fig. 54

Class	Sample(a)		Sample(b)	
	No. of particles	**Percent**	**No. of particles**	**Percent**
I	42	42.4	0	0.0
II	29	29.3	6	5.7
III	14	14.1	0	0.0
IV	2	2.0	5	4.8
V	12	12.1	62	59.1
VI	0	0.0	32	30.5
Total	99	100.0	105	100.0

It is important to notice that once the classifier has been trained, which is done only once, the classification itself takes just a few seconds per image. Moreover, this method provides a class for each graphite particle in the field differently from traditional chart comparison that returns a single overall class for the whole field.

References cited in this section

40. "Standard Specification for Zinc-5% Aluminum-Mischmetal Alloy in Ingot Form for Hot-Dip Coatings," B 750, *Annual Book of ASTM Standards*, ASTM, 1999

41. D.R.R. Lesuer, O.D. Sherby, and C.K. Syn, Ed., *Thermomechanical Processing and Mechanical Properties of Hypereutectoid Steels and Cast Irons*, The Minerals, Metals, & Materials Society, 1997

42. "Cast Iron—Designation of Microstructure of Graphite," ISO 945, 1975

43. R.O. Duda, P.E. Hart, and D.G. Stork, *Pattern Classification*, Wiley-Interscience, 2nd ed., 2000, p 1–62

Conclusions

This article has discussed the main methods of digital imaging, image processing, and analysis, as applied to microscopy of materials. The strong integration of microscope and computer hardware and software is giving rise to a new set of techniques and possibilities, in a field often called digital microscopy. The main advances to be seen in the near future are the improvement of electronic image acquisition to substitute for film and complete automation of routine tasks in the microscopes. These developments will open new possibilities in the microstructural characterization of materials, making it faster, deeper, and more accurate.

S.Paciornik and M. H. de Pinho Mauricio, Digital Imaging, Vol 9, *ASM Handbook*, ASM International, 2004, p. 368–402

Digital Imaging

Sidnei Paciornik and Marcos Henrique de Pinho Mauricio, Catholic University of Rio de Janeiro

Acknowledgment

The authors wish to thank George Vander Voort for the invitation to write this article. The support of Alain Thorel from Ecole Nationale Superieure des Mines de Paris, France, is greatly appreciated. Vito Smolej, from Carl Zeiss Vision, Germany, L.R.O. Hein and C.R. de F. Azevedo, from UNESP, Brazil, Rodrigo Prioli, from PUC-Rio, Brazil, Ulrich Dahmen, from NCEM LBNL, Mike Mizell, from EMISPEC Systems, USA and Ming Pan, from Gatan Inc., USA, provided example images for which the authors are grateful. The help of Marcelo S. Malheiros, from DCMM PUC-Rio in specimen preparation is also acknowledged.

S.Paciornik and M. H. de Pinho Mauricio, Digital Imaging, Vol 9, *ASM Handbook*, ASM International, 2004, p. 368–402

Digital Imaging

Sidnei Paciornik and Marcos Henrique de Pinho Mauricio, Catholic University of Rio de Janeiro

References

1. L. Wojnar and K.J. Kurzydlowski, Analysis and Interpretation, in *Practical Guide to Image Analysis,* ASM International, 2000, p 171–183

2. J.D. Foley, A. Van Dam, S.K. Feiner, and J.F. Hughes, *Computer Graphics: Principles and Practice,* 2nd ed., Addison-Wesley, 1991

3. "IEEE Standard for Binary Floating-Point Arithmetic," Std 754, IEEE Computer Society, 1985

4. J.D. Murray and W. van Ryper, *Encyclopedia of File Format,* 2nd ed., O'Reilly & Assoc., Inc., Bonn, Germany, 1996

5. partners.adobe.com/asn/develop/pdfs/tn/TIFF67.pdf, Adobe Systems, Inc.

6. http://www.normankoren.com/Tutorials/MTF.html, Norman Koren Photography

7. http://www.gatan.com/imaging/ultrascan.html, Gatan, Inc.

8. http://micro.magnet.fsu.edu/primer/digitalimaging/digitalimagingdetectors.html, Florida State University

9. C. Williams, CMOS vs. CCD: The Battle Continues, *Adv. Imag.,* Vol 16 (No. 9), Sept 2001, p 28–31

10. http://www.scantips.com/, Wayne Fulton, Scantips, self-published

11. J. Frank, The Role of Correlation Techniques in Computer Image Processing, *Computer Processing of Electron Microscope Images,* P.W. Hawkes, Ed., Springer, Berlin, 1998, p 187–222

12. http://www.emispec.com/EM/appnotes/edxprof.html?whichPage=3, Emispec, FEI, Co.

13. J. Bruley, M.W. Tseng, and D.B. Williams, Spectrum-Line Profile Analysis of a Magnesium Aluminate Spinel Sapphire Interface, *Microsc. Microan.,* Vol 6 (No. 1), Feb 1995, p 1–18

14. L.R.O. Hein, Quantitative Fractography by Digital Image Processing: NIH Image Macro Tools for Stereo Pair Analysis and 3-D Reconstruction, *J. Microsc.,* Vol 204 (Part 1), Oct 2001, p 17–28

15. L.R.O. Hein, F.A. Silva, A.M.M. Nazar, and J.J. Ammann, Three-Dimensional Reconstruction of Fracture Surfaces: Area Matching Algorithms for Automatic Parallax Measurements, *Scanning,* Vol 21 (No. 4), July–Aug 1999, p 253–263

16. M.A. O'Keefe, K.H. Downing, H.-R. Wenk and H. Meisheng, 3D Imaging of Crystals at Atomic Resolution, *Proc. MRS,* Vol 332, Materials Research Society, 1994, p 563

17. O.L. Krivanek and G.Y. Fan, Complete HREM Autotuning Using Automated Diffractogram Analysis, *Proc. Elect. Microsc. Soc. Am.,* Vol 50, Microscopy Society of America, 1992, p 96–97

18. http://www.kodak.com/US/en/digital/dlc/book2/chapter2/l1.shtml, Eastman Kodak Co.

19. J. Gomes and L. Velho, *Image Processing for Computer Graphics,* Springer Verlag, 1997

20. Axio Vision Control Release 3.0, *Manual: B40-640 e,* Carl Zeiss Vision GmbH, 2000

21. K.R. Castleman, *Digital Image Processing,* Prentice-Hall, 1979

22. J.C. Russ, *The Image Processing Handbook,* CRC, 1992

23. R.C. Gonzalez and R.E. Woods, *Digital Image Processing,* Addison-Wesley, 1993

24. M. Sonka, V. Hlavac, and R. Boyle, *Image Processing, Analysis and Machine Vision,* 2nd ed., PWS, 1998

25. J.C. Russ, *Computer Assisted Microscopy, The Measurement and Analysis of Images,* Plenum Press, 1990

26. N. Otsu, A Threshold Selection Method from Grayscale Histograms, *IEEE Trans. Sys. Man. Cyb.,* SMC-9, 1979, p 62–66

27. P.-Y. Yin and L.-H. Chen, A New Method for Multilevel Thresholding Using Symmetry and Duality of the Histogram, *International Symposium on Speech, Image Processing and Neural Networks,* IEEE, Hong Kong, 1994, p 43–48

28. D. Marr and E. Hildreth, On the Theory of Edge Detection, *Proc. R. Soc. (London) B,* Vol 207, Royal Society of London, 1980, p 127–217

29. J. Canny, A Computational Approach to Edge Detection, *IEEE Trans. Pattern An. Mach. Intell.,* Vol. 8 (No. 6), Nov 1986, p 679–698

30. J. Serra, *Image Analysis and Mathematical Morphology,* Academic Press, 1982

31. S. Beucher and C. Lantejoul, Use of Watersheds in Contour Detection, *Proc. Int. Workshop Image Processing, Real-Time Edge and Motion Detection/Estimation,* CCETT/INSA/IRISA, IRISA Report No. 132, Rennes, France, 1979, p 2.1–2.12

32. S. Beucher, The Watershed Transformation Applied to Image Segmentation, *Scanning Microscopy Supplement,* Vol 6, 1992, p 299–314

33. F. Meyer and S. Beucher, Morphological Segmentation, *J. Vis. Commun. Image Represen.,* Vol 1 (No. 1), 1990, p 21–46

34. M.P. do Carmo, *Geometry of Curves and Surfaces,* Prentice-Hall, 1976, p 41

35. J. Grum and R. Strum, Computer Supported Recognition of Graphite Particle Forms in Cast Iron, *Acta Stereol.,* Vol 14 (No. 1), 1995, p 91–96

36. M.T. Shehata, Characterization of Particle Dispersion, *Practical Guide to Image Analysis,* ASM International, 2000, p 141–143

37. R.M. Haralick, K. Shanmugam, and I. Dinstein, Textural Features for Image Classification, *IEEE Trans. Systems, Man and Cybernetics,* Vol SMC-3 (No. 6), 1973, p 610–621

38. S. Paciornik, O.F.M. Gomes, A. Delarue, S. Schamm, D. Jeulin, and A. Thorel, *Eur. Phys. J. Appl. Phys,* Vol 21, 2003, p 17–26

39. S. Paciornik et al., Texture Analysis in the Detection of Subtle Structural Changes in HRTEM, *15th International Congress on Electron Microscopy,* CIASEM, 2002

40. "Standard Specification for Zinc-5% Aluminum-Mischmetal Alloy in Ingot Form for Hot-Dip Coatings," B 750, *Annual Book of ASTM Standards,* ASTM, 1999

41. D.R.R. Lesuer, O.D. Sherby, and C.K. Syn, Ed., *Thermomechanical Processing and Mechanical Properties of Hypereutectoid Steels and Cast Irons*, The Minerals, Metals, & Materials Society, 1997

42. “Cast Iron—Designation of Microstructure of Graphite,” ISO 945, 1975

43. R.O. Duda, P.E. Hart, and D.G. Stork, *Pattern Classification*, Wiley-Interscience, 2nd ed., 2000, p 1–62

L. Wojnar, K.J. Kurzydłowski, and J. Szala, Quantitative Image Analysis, *Metallography and Microstructures,* Vol 9, *ASM Handbook,* ASM International, 2004, p. 403–427

Quantitative Image Analysis

Leszek Wojnar, Kraków University of Technology, Kraków, Poland; Krzysztof J. Kurzydłowski, Warsaw University of Technology, Warsaw, Poland; Janusz Szala, Silesian University of Technology, Katowice, Poland

Introduction

PROGRESS in production technology and materials science has forced extensive research on the structures of materials. The discovery of the existence of stable structure-property relationships has led to the development of various methods of microstructural quantification, known as quantitative metallography or, more generally, stereology (Ref 1, 2, 3, 4, 5). Stereological methods have proven their usefulness during decades of application but were extremely laborious and time-consuming. This led to extensive research toward the automation of microstructural quantification, which, fortunately, the era of digital imaging made relatively easy and inexpensive. The application of stereological methods in the analysis of digitally processed microstructural images is fairly straightforward and is done successfully in many laboratories all over the world. However, some problems arise due to the fact that digital images have, by definition, a discrete character. This forces some modifications in classical stereological formulas. On the other hand, measurement can be simpler in digital space than in real space (Ref 6, 7, 8, 9, 10, 11, 12, 13, 14).

Automatic microstructural quantification requires an understanding of quantitative metallography and digital imaging, which are discussed respectively in the next and preceding articles in this Volume. Nevertheless, some problems exist that are not apparent to a novice and require experience to solve. The aim of this article is to help those who want to apply automatic image analysis in their laboratories. In preparing this article, there was a challenge to select suitable information without repeating extensive parts of other articles on quantitative metallography and digital imaging. Essential parts of the complex process of quantitative image analysis are reviewed in this article, and care was taken to limit duplicate information on image processing procedures and algorithms as well as basic methods and the background of stereology.

References cited in this section

1. R.T. De Hoff and F.N. Rhines, *Quantitative Microscopy,* McGraw-Hill, 1968
2. J.C. Russ, *Practical Stereology,* Plenum Press, 1986
3. J. Ryś, *Stereology of Materials,* Fotobit-Design, Kraków, Poland, 1995, p 323 (in Polish)
4. E.E. Underwood, *Quantitative Stereology,* Addison Wesley, 1970
5. E.R. Weibel, *Stereological Methods,* Academic Press, 1980, 1989
6. G. Gauthier, M. Coster, L. Chermant, and J.L. Chermant, Morphological Segmentation of Cutting Tools, *Microsc. Microanal. Microstruct.,* Vol 7, 1996, p 339
7. G. Gauthier, J.L. Quenec'h, M. Coster, and J.L. Chermant, Segmentation of Grain Boundaries in WC-Co Cermets, *Acta Stereol.,* Vol 13, 1994, p 209
8. S. Gentier, D. Billaux, D. Hopkins, F. Davias, and J. Riss, Images and Modelling of the Hydromechanical Behaviour of a Fracture, *Microsc. Microanal. Microstruct.,* Vol 7, 1996, p 513

9. K.J. Huebner, Application of Colour Metallography of Microstructural Images in Research Studies, *Proc. Q-Mat'97, International Conference on the Quantitative Description of Materials Microstructure* (Warsaw, Poland), Polish Society for Stereology, 1997, p 299

10. F. Le Pennec and D. Malewicz, Automatic Grain Size Measurement in Low Carbon Steels by Image Analysis, *Microsc. Microanal. Microstruct.*, Vol 7, 1996, p 433

11. *Practical Guide to Image Analysis*, ASM International, 2000

12. C. Redon, "Morphology and Mechanical Behavior of Amorphous Cast Iron Fiber Reinforced Concrete," Ph.D. dissertation, University of Caen, France, 1997

13. H. Talbot, D. Jeulin, and D. Hanton, Image Analysis of Insulation Mineral Fibers, *Microsc. Microanal. Microstruct.*, Vol 7, 1996, p 361

14. H. Wendrock and R. Huebel, Characterization of Microstructural Anisotropy of Steels by Means of Mathematical Morphology, *Acta Stereol.*, Vol 13, 1994, p 143

L. Wojnar, K.J. Kurzydłowski, and J. Szala, Quantitative Image Analysis, *Metallography and Microstructures*, Vol 9, *ASM Handbook*, ASM International, 2004, p. 403–427

Quantitative Image Analysis

Leszek Wojnar, Kraków University of Technology, Kraków, Poland; Krzysztof J. Kurzydłowski, Warsaw University of Technology, Warsaw, Poland; Janusz Szala, Silesian University of Technology, Katowice, Poland

Digital versus Manual Methods

Digital image analysis is a relatively new tool. The first powerful, commercial image analyzers, such as the Quantimet 720 or Texture Analysis System (TAS) (Leitz) emerged in the 1970s. These machines were extremely expensive, with prices similar to scanning electron microscopes. In the 1990s, the progress in computer technology allowed for the construction of relatively inexpensive personal-computer-based digital image analyzers (Ref 11). In spite of this enormous progress and the introduction of user-friendly, usually icon-based software, the image analysis tools have been implemented on a limited scale. It is observed that numerous systems are not fully and properly exploited. Many people are afraid of using computerized tools in the metallographic laboratory and declare that machines will never do as good and thorough an analysis as an experienced metallographer. The main reasons for reservations are (Ref 11, 15, 16, 17):

- The significant cost of the apparatus, which includes a charge-coupled device (CCD) camera and frame grabber or equivalent hardware, personal computer, and specialized image analysis software
- The necessity to learn how to operate new, complex equipment and software
- The difficulty in preparation of adequate automatic procedures for nontypical research tasks, which requires some experience or usually costly help from experts in this field
- The necessity to use the highest-quality specimens for digital imaging, which often requires modernization of the specimen preparation laboratory and additional investments comparable with the image processing equipment

In spite of the previously listed concerns, automatic image analysis is more frequently a prerequisite for adequate quality control of materials. Among the factors forcing implementation of digital tools into laboratory practice are:

- The significant increase in the objectivity of the results obtained, which lowers the probability of introducing subjective errors into the analysis
- The almost full reproducibility of the methods (especially in the case when the same software is applied) and very good repeatability of the results obtained
- The high speed of the analysis, which can be decisive, for example, in the foundry industry when control analysis of the microstructure should be done prior to the final cast
- The low cost, relative to the whole process, when used every day for routine analysis. Note that the image analysis system can be used not only for microstructural quantification but it also adds value by documenting results.

Computerized image analysis has advantages as well as drawbacks in comparison with analysis carried out by a human observer. Table 1 indicates that digital imaging and analysis is the best choice in the following conditions:

- The laboratory can ensure specimens of very good quality.
- Frequent routine analysis dominates over the investigation of case histories.
- High repeatability of the results and high speed of analysis are important factors.

Table 1 Comparison of selected properties of human and computerized vision systems when applied in metallography

Analyzed feature or property	Traditional analysis using human visual system	Computer-aided image analysis
Human fatigue after prolonged work	Very sensitive	Insensitive
Sensitivity to illusions (we see what we want to see)	Very sensitive	Insensitive
Required image quality	Medium quality acceptable for quantitative analysis	Highest quality standards
Repeatability of results	Low	Full repeatability in totally automatic analysis. High repeatability in semiautomatic analysis
Reproducibility of the analysis	Low	Full reproducibility
Qualitative assessment of microstructure	Can be very good	Poor and difficult
Quantitative assessment of microstructure	Time-consuming; some parameters cannot be evaluated	Can be very good
Cost of analysis	Low for single specimen; rapid growth with increasing number of specimens	High for single specimen; significant drop per unit as number of routine investigations increases
Speed of analysis	Slow, especially in quantitative analysis	Fast, especially for on-line analysis
Operator experience	Significant effect on the results	Negligible effect for routine tasks; very important during implementation of the system

Source: Ref 17

These factors match contemporary industry requirements, and therefore, image analysis tools are implemented in a continuously growing number of laboratories. Consequently, the number of appropriate textbooks increases (Ref 11, 18, 19, 20), and some methods of analysis are standardized (Ref 21, 22, 23, 24, 25, 26). Studying such literature gives relatively thorough knowledge, but the reader often needs instant answers to some questions that arise in everyday practice. The rest of this article is organized to quickly provide solutions for the most common problems. Every effort was made to prepare this text in an easy-to-understand format; however, some

knowledge from the articles “Quantitative Characterization and Representation of Global Microstructural Geometry” and “Digital Imaging” in this Volume may aid the understanding of more complex items.

References cited in this section

11. *Practical Guide to Image Analysis,* ASM International, 2000

15. J. Chrapoński, “Analysis of Applicability of Stereological Methods of Evaluation of Grain Size in Polycrystalline Materials,” Ph.D. thesis, Silesian University of Technology, Katowice, Poland, 1997 (in Polish)

16. M. Coster, and J.L. Chermant, *Introduction to Image Analysis,* Presses du CRNS, Paris, 1989 (in French)

17. L. Wojnar, Semiautomatic Image Analysis System—Ease of Use and Accelerated Analysis, *Second Conference on Metallography in Industrial Laboratories* (Ustron, Poland), Institute of Ferrous Metals, April 1999, p 32–40 (in Polish)

18. K.J. Kurzydlowski and B. Ralph, *The Quantitative Description of the Microstructure of Materials,* CRC Press, 1995

19. J. Szala, Application of Computer-Aided Image Analysis Methods for a Quantitative Evaluation of Material Structure, *Zesz. Nauk. Politech. Slask., Hutn.,* Vol 61, 2001, p 1–167 (in Polish)

20. L. Wojnar, *Image Analysis, Applications in Materials Engineering,* CRC Press, 1999

21. “Test Methods for Estimating the Largest Grain Observed in a Metallographic Section (ALA Grain Size),” E 930-92, *Annual Book of ASTM Standards, Section 3: Metals Test Methods and Analytical Procedures,* ASTM International, 1999, p 683–687

22. “Practice for Obtaining JK Inclusion Ratings Using Automatic Image Analysis,” E 1122-96, *Annual Book of ASTM Standards, Section 3: Metals Test Methods and Analytical Procedures,* ASTM International, 1999, p 729–736

23. “Test Methods for Characterizing Duplex Grain Sizes,” E 1181-87, *Annual Book of ASTM Standards, Section 3: Metals Test Methods and Analytical Procedures,* ASTM International, 1999, p 741–755

24. “Practice for Determining the Inclusion or Second Phase Constituent Content of Metals by Automatic Image Analysis,” E 1245-95, *Annual Book of ASTM Standards, Section 3: Metals Test Methods and Analytical Procedures,* ASTM International, 1999, p 789–796

25. “Practice for Assessing the Degree of Banding or Orientation of Microstructures,” E 1268-94, *Annual Book of ASTM Standards, Section 3: Metals Test Methods and Analytical Procedures,* ASTM International, 1999, p 797–823

26. “Test Methods for Determining Average Grain Size Using Semiautomatic and Automatic Image Analysis,” E 1382-97, *Annual Book of ASTM Standards, Section 3: Metals Test Methods and Analytical Procedures,* ASTM International, 1999, p 867–890

L. Wojnar, K.J. Kurzydłowski, and J. Szala, Quantitative Image Analysis, *Metallography and Microstructures,* Vol 9, *ASM Handbook,* ASM International, 2004, p. 403–427

Quantitative Image Analysis

Leszek Wojnar, Kraków University of Technology, Kraków, Poland; Krzysztof J. Kurzydłowski, Warsaw University of Technology, Warsaw, Poland; Janusz Szala, Silesian University of Technology, Katowice, Poland

Basic Definitions

Most of the image analysis terms are intuitively understood, but precise definition of the basic terms helps avoid possible misinterpretations.

Image is defined as (a) "a likeness or copy of the shape of someone or something, especially in wood, stone, or other material"; and (b) "a reflection seen in a mirror or through the lens of a camera" (Ref 27, 28). ASTM E 7 defines image as a representation of an object produced by means of radiation, usually with a lens or mirror system (Ref 29). This article deals with images that are digital, electronic representations. The image is a data set, stored in a computer memory or in a digital file, that can then be displayed on-screen or printed for human observation.

Pixels. The elementary unit of a digital image is the pixel. When the image is displayed in a computer monitor, it is a mosaic of pixels. Enlarging this image leads to a situation in which one observes individual pixels as uniform squares. Spacing of the pixels in reality defines the resolution of digital image (for example, 1.5 μm/pixel). The location of each pixel is defined by the image format (Tagged Image File Format, or TIFF; BMP; Joint Photographic Expert Group, or JPEG; Graphics Interchange Format, or GIF; etc.). The body of the digital file contains information concerning pixel intensity or color. Usually, 1, 8, or 24 bits are used for storing information about individual pixels (consequently, there are 1-, 8-, or 24-bit images). Binary images require 1 bit/pixel, 8-bit files are used for storage of gray-tone images (8 bits allow for recording of 256 gray levels), and 24-bit images allow coding of 16,777,216 colors.

Stereology is a body of procedures, mainly geometrico-statistical, that has the aim of obtaining information about three-dimensional structure from two-dimensional, flat images (Ref 30).

Image analysis and image processing are similar terms; they have no commonly accepted definitions and are frequently misinterpreted. The following is most appropriate interpretation.

Image processing is a process of data transformation in which the initial data set is an image or a collection of images (for example, any digital movie is a collection of images), and the final, resulting data set is also an image or a collection of images. Image processing also can be called digital imaging, as is done within this Volume. The aim of image processing is to highlight the features under investigation (for example, grain boundaries) or to suppress the unwanted features (scratches, noise, etc.). The process of image acquisition is usually interpreted as the introductory part of image processing.

Image analysis is, similarly, a process of data transformation in which the initial data set is an image or a collection of images, but the final, resulting data set has another format; this can be a number or set of numbers, text, logical decisions, or movements. So, image processing is just a part of the image analysis process. Note that the contents of commercial software for image analysis encompass the previous definition. Some textbooks interpret image analysis as only the very moment of analyzing data obtained from images. This seems to be an erroneous interpretation.

The previously mentioned terms are described in ASTM E 7 as follows (Ref 29): "image processing, in image analysis—the computer modification of a digitized image on a pixel-by-pixel basis to emphasize or de-emphasize certain aspects of the image." This definition can be judged as correct; however, it does not define what image analysis is. Nevertheless, similar to previous remarks, image processing is considered here as a part of image analysis.

According to the definition proposed previously, the final step of image analysis can be of various characters. For example, in quality control, one usually wants to obtain a single number characterizing the grain size. This is, however, insufficient if one studies subtle changes in recrystallization. In such a case, one would prefer analysis of grain size distribution. Generally speaking, in quantitative metallography, some numerical characterization of the structure under investigation is desired.

Computer-Aided Image Analysis. The term *image analysis* is usually used instead of a longer term, computer-aided image analysis, which infers some automation, generally not obligatory in stereology. Moreover, in stereological investigation, it is usually stressed that one is looking for three-dimensional descriptors of a structure from two dimensional sections, whereas image analysis, in most cases, concentrates on extracting some data that are eventually used for further stereological interpretation. As a consequence, one can easily adapt numerous stereological methods to the needs of automatic image analysis, as is shown by the examples in this article.

In order to perform any measurements, the image has to be binarized, that is, transformed into binary form, which consists of two families of pixels having the values of 0 (black) and 1 (white), respectively. In these images, one can count objects and measure their geometrical characteristics, such as section area, perimeter, and projection length. So, binary images are the final step of image processing in metallography. Usually, the microstructural features under consideration are visualized in binary images as white objects (Fig. 1). Sometimes, a few different families of objects are to be analyzed in the same image. Pores, matrix grains, and precipitation particles in a sintered material are examples. In such a case, a series of binary images is prepared, and each one corresponds to a microstructural constituent. Various procedures can be applied to obtain this result (see the article “Digital Imaging” in this Volume), and the appropriate choice is the researcher's responsibility (Ref 16, 31, 32, 33).

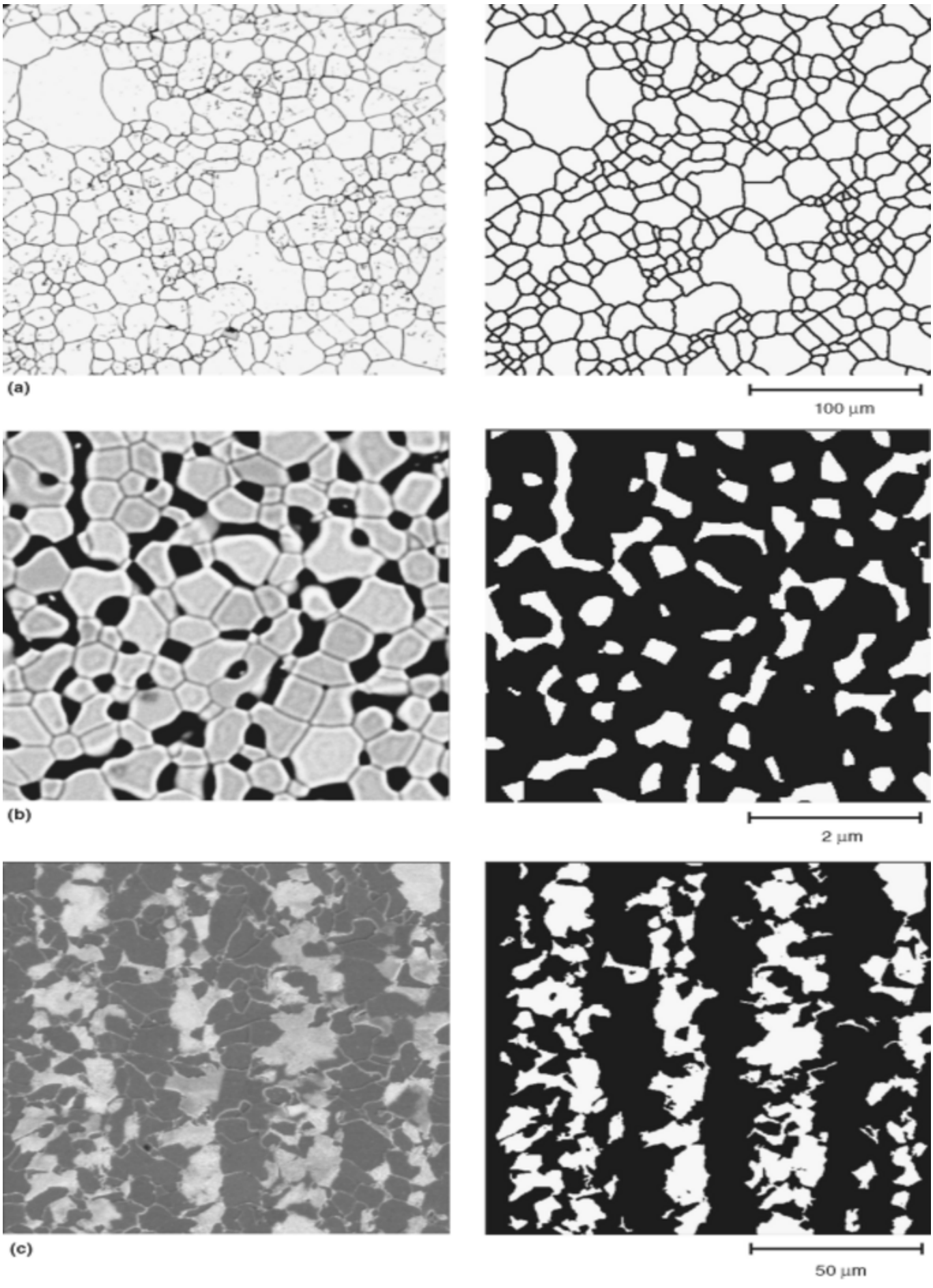

Fig. 1 Gray-scale images of microstructures (left) and binary representations of selected features (right). (a) Grains in austenitic stainless steel. (b) Pores in sintered CeO_2. (c) Pearlite areas in carbon steel bar

One should take into consideration that images can be transferred into binary form in various ways. The most common is the thresholding technique, based on pixel intensities. All the pixels with chosen intensities are assigned the value of 1, whereas the rest are 0. The choice of threshold intensities can be manual or automatic. Other characteristics can be used for segmentation as well. For example, grain boundaries are often established on the case of edge detection, and very fine structures are characterized by means of texture analysis. Nevertheless, the final result is stored as a binary image. In some cases, different phases can be detected in one pass, for example, by applying a multithreshold technique. This leads to the collection of a few sets of pixels with different intensities. A set belonging to any intensity can be treated as a binary image in such a case.
Using some software, the analyzed features also also can be presented in other forms, for example, object sets that can be drawn as overlays of the initial or intermediate images. However, even in these cases, the same rules of detection are used, and one can easily obtain only the binary image if necessary. So, the general rule that binary images are necessary for digital measurements remains valid.

References cited in this section

16. M. Coster, and J.L. Chermant, *Introduction to Image Analysis,* Presses du CRNS, Paris, 1989 (in French)

27. *Collins English Dictionary and Thesaurus,* Diamond Books, 1992

28. A.S. Hornby, *Oxford Advanced Learner's Dictionary of Current English,* Oxford University Press, London, 1974

29. "Terminology Relating to Metallography," E 7-99, *Annual Book of ASTM Standards, Section 3: Metals Test Methods and Analytical Procedures,* ASTM International, 1999, p 28–56

30. E.R. Weibel, Ideas and Tools: The Invention and Development of Stereology, *Acta Stereol.,* Vol 6/Suppl. II, 1987, p 23–33

31. J. Serra, *Image Analysis and Mathematical Morphology,* Academic Press, 1982

32. J. Serra, Ed., *Image Analysis and Mathematical Morphology, Volume 2: Theoretical Advances,* Academic Press, 1988

33. J. Serra, Morphological Image Segmentation, *Acta Stereol.,* Vol 14, 1995, p 99

L. Wojnar, K.J. Kurzydłowski, and J. Szala, Quantitative Image Analysis, *Metallography and Microstructures,* Vol 9, *ASM Handbook,* ASM International, 2004, p. 403–427

Quantitative Image Analysis

Leszek Wojnar, Kraków University of Technology, Kraków, Poland; Krzysztof J. Kurzydłowski, Warsaw University of Technology, Warsaw, Poland; Janusz Szala, Silesian University of Technology, Katowice, Poland

---

Specimen Preparation and Image Acquisition

If the initial image is of very poor quality, one cannot obtain excellent results, even if the best processing is applied. The problem of appropriate image quality is very complex, due to the multitude of factors affecting the process of specimen preparation and image acquisition (Ref 11, 34). This section is a brief primer concerning

specimen and apparatus preparation as well as image acquisition. More details can be found in the article “Digital Imaging” in this Volume.

Preparation. Special care is necessary when preparing polished sections for automatic detection. In general, the rules are similar to those applied for normal microscopic observations. The main difference lies in the fact that the polished section quality (flatness, lack of artifacts, etc.) should be higher. Unfortunately, the number of different factors that has to be taken into account during specimen preparation is so large that “each laboratory should develop its own specific procedure to prepare specimens conforming to the necessarily high standard” (Ref 35). It is often surprising for people not experienced in image analysis that, in general, the quality of specimens has to be significantly higher than in the case of classical analysis by a human observer. Some artifacts, which can be easily neglected by an experienced researcher, are extremely difficult to remove using automatic image analysis (Fig. 2).

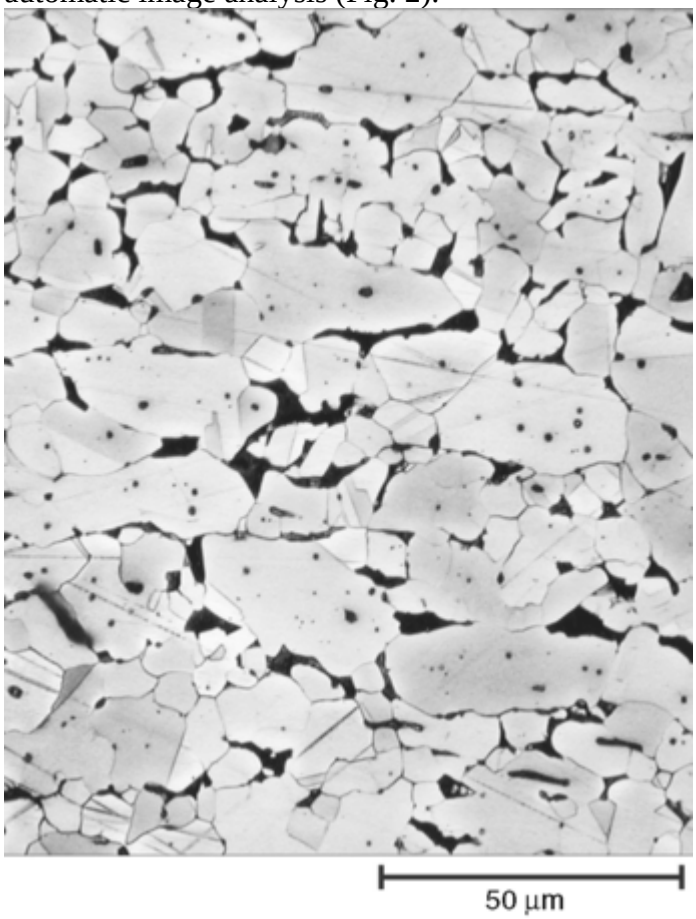

Fig. 2 Microstructure of a Cu-Zn-Pb alloy with various defects that are difficult to eliminate automatically

Practical experience shows that the vast majority of problems in using image analysis stem from inadequate specimen preparation and choosing the wrong etching technique to reveal the structure. Once a decent image is captured, the rest is relatively simple (Ref 36, 37, 38).

The most important factor during specimen preparation is recognizing the final goal of the analysis. As shown in Fig. 3, the image judged as very good for manual analysis is not necessarily the best one for automatic methods. A medium-quality image containing some scratches is sufficient (due to good contrast between various phases) for fully automatic detection of SiC fiber cores (Fig. 3a) as well as full sections of fibers (Fig. 3b). The best-quality image, with all the scratches removed, seems to be ideal for a human observer, who can still discriminate the fiber core from the whole fiber (Fig. 3c, left side). Unfortunately, using fully automatic methods, one can correctly detect only full sections of the SiC fibers (Fig. 3c, right side) (Ref 19). This example illustrates very well how subtle problems can be faced when applying image analysis methods. Please note that the aforementioned example does not change the general rule that only specimens of the highest quality are useful for automatic image analysis. A good metallographic practice requires the selection of a preparation method that correctly reveals all the structural constituents to be analyzed. This can be difficult, but contemporary materials and methods for specimen preparation help to solve most of the practical cases.

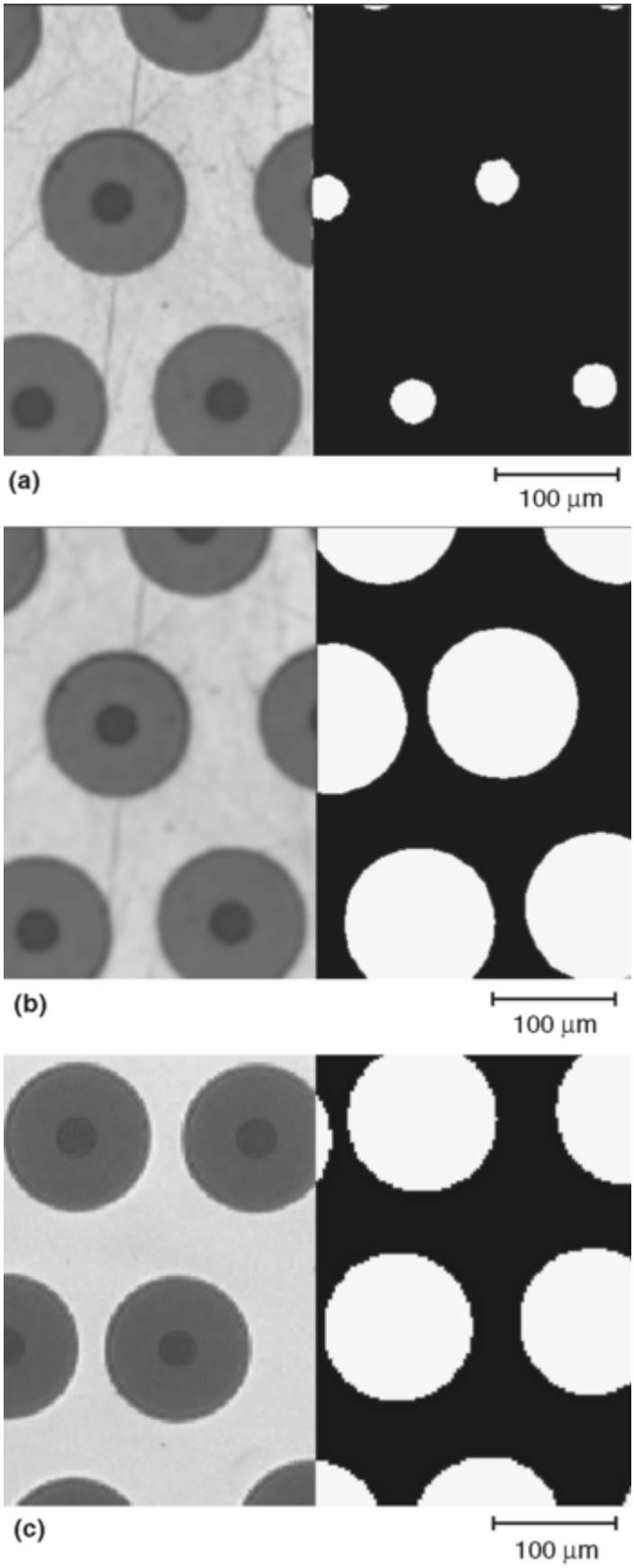

Fig. 3 Gray-scale images of microstructures (left) and binary representations of selected features (right) of a titanium-matrix SiC fiber-reinforced composite. (a) Medium-quality specimen, fiber core detectable. (b) Medium-quality specimen, full sections of fibers detectable. (c) High-quality specimen with fiber core not detectable in an automatic way

There is a similar problem with specimen preparation that involves etching following the final polishing (Ref 39). This obstacle is especially clear when one wants to image grain boundaries. Even if the initial image seems to be clear and simple for analysis (Fig. 4a), automatic detection will either lose a part of the grain boundaries or produce some nonexisting ones (Fig. 4b–d). Three different detection algorithms were used to produce the binary images presented in Fig. 4 (Ref 40). The first algorithm (Fig. 4b) was based on a combination of three well-known edge-detection filters, namely, Sobel, Prewitt, and Roberts (Ref 20, 41, 42). Following edge detection, some fine-tuning of the image led to smooth and continuous grain-boundary lines. More information on appropriate techniques can be found in the article “Digital Imaging” in this Volume. The second algorithm (Fig. 4c) was based on the detection of local minima, called the “black top hat.” Grain boundaries are visible as the locally darkest objects in the image, so the results are satisfactory as a detection method that is not sensitive to local changes in image brightness. The third algorithm (Fig. 4d) uses a Laplacian filter that detects grain boundaries as regions of the highest local contrast in the image.

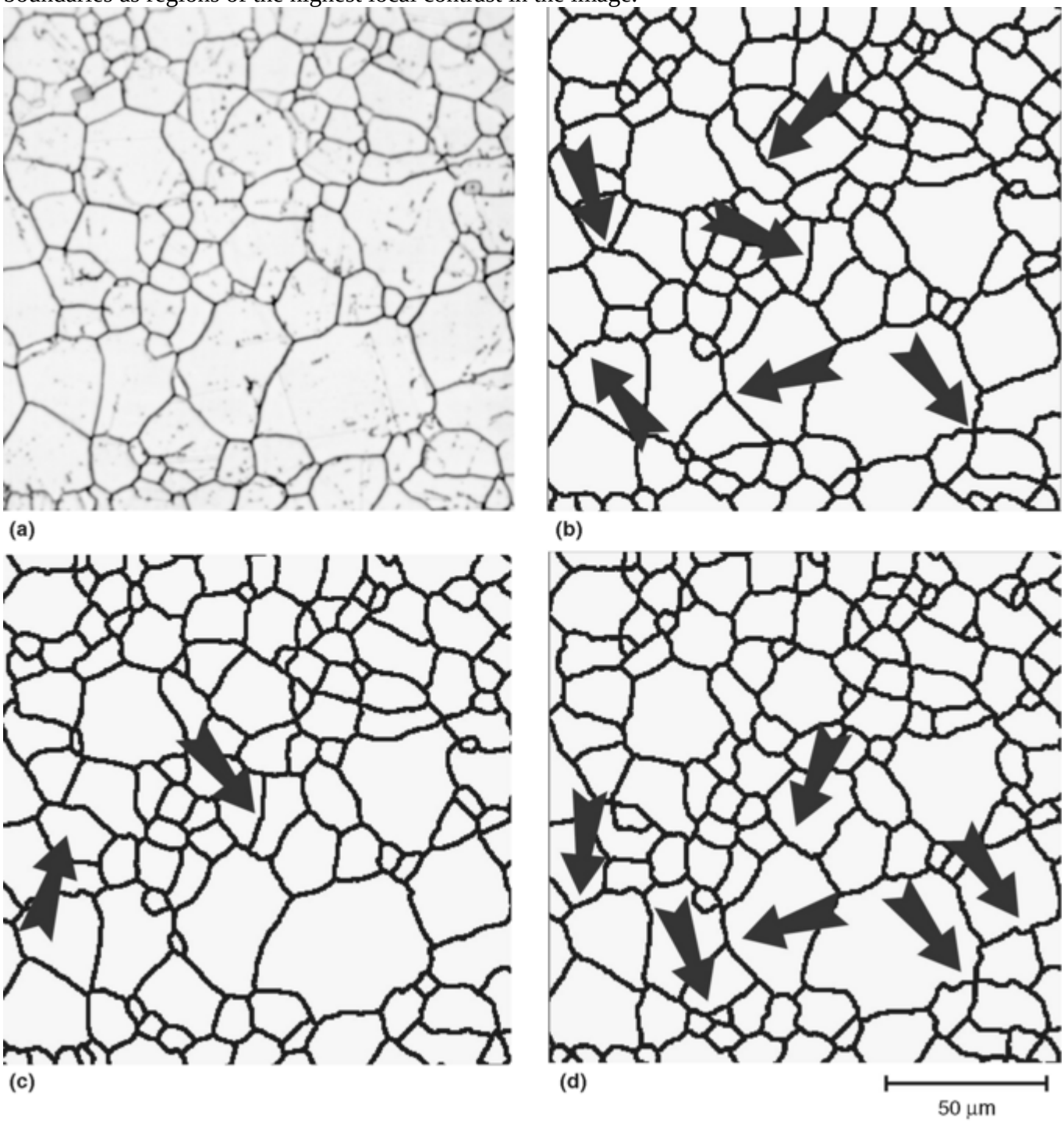

Fig. 4 Gray-scale image and binary images of austenitic stainless steel. (a) Original gray-scale grains. Binary images of grains detected using various algorithms. (b) Edge detection. (c) Local minima detection. (d) Laplacian detection. Black arrows indicate location of lost or extra grain-boundary lines

There is no need to carry out any deeper analysis of these procedures. What should be stressed is the multitude of small errors in detection that accompanies each method. Some lost or extra grain-boundary lines are marked by black arrows in each image in Fig. 4 (this marking is not exhaustive). As a consequence of these errors, some scatter is evident in the results of the measurements of ASTM grain numbers made by using various algorithms: 9.45 for the algorithm based on edge detection, 9.49 for top-hat transformation, and 9.56 for detection based on Laplacian filtering. It should be noted that the computer technique provides unique and repeatable results automatically, and it is almost 100 times quicker than manual computations. All the algorithms used led to identical materials classification. If the results of manual methods were applied to the same structures, similar values and scatter (within a range of approximately 10%) would occur. Unfortunately, the materials classification was not so stable as in the case of the automatic methods, and, generally, a considerable effect of subjective factors was evident (Ref 40).

Resolution. Most of the microstructural images used for quantitative image analysis in quality control are recorded from optical microscopes. The operator faces the problem of how to optimize the choice of the camera resolution for the recorded image. Older systems used mainly square masks of size 256 by 256, 512 by 512, or 1024 by 1024 pixels. Currently, simple CCD cameras offer resolutions of 640 by 480 or 768 by 576 pixels or something similar. This may seem insufficient, especially if one takes into account that digital cameras for microscopy offer extremely high resolutions (for example, 3840 by 3072 pixels in the case of the Nikon DXM 1200). Because this challenge is faced in everyday laboratory practice, it is discussed in more detail.

The resolving power of an objective is the parameter that defines the closest distance of two points that can still be recognized as separate. It seems to be natural that the image should be digitized with resolution (pixel size) of the same order of magnitude as the resolving power of the instrument. If the pixels represent a large area, part of the information recognized by the microscope will be lost. By contrast, very small pixels will produce an image with empty magnification, an effect similar to images scanned with unnecessarily high resolution. Such an image requires a needlessly large memory size and contains no more details than images taken at optimal resolution (Ref 11, 20).

The resolving power of the objective, *d*, can be expressed as:

$$d = \frac{0.61 \cdot \lambda}{\mathrm{NA}} \qquad \text{(Eq 1)}$$

where λ is the wavelength of light used for observation (usually, approximately 0.55 μm), and NA is the numerical aperture of the objective. On the basis of the known resolving power of the objective, one can evaluate the optimal resolution of the camera (dimension of a single cell in the CCD matrix) as:

$$L = d \cdot M \qquad \text{(Eq 2)}$$

where L is the optimal dimension of a single CCD element, and M is the objective magnification.

Taking into account that the field of view (FOV) in contemporary microscopes has a diameter of 22 mm (0.87 in., or 22,000 μm), one can easily evaluate the theoretical number of pixels per FOV diameter (Table 2) as:

$$N_{22} = \frac{22{,}000}{L} \qquad \text{(Eq 3)}$$

where N_{22} is the number of pixels per 22 mm (0.87 in.) diameter. For example, taking into account an objective with M = 50× and NA = 0.80, one obtains: $d = 0.61 \cdot 0.55/0.80 = 0.4194$, $L = 0.4194 \cdot 50 = 20.97$, and $N_{22} = 22{,}000/20.97 = 1049$, respectively (Table 2).

Table 2 Resolving power of objectives and theoretical size of a single pixel in charge-coupled device (CCD) elements

Objective magnification (M)	Numerical aperture (NA)	Resolving power of the objective (d), μm	Theoretical size of a single CCD cell (pixel) (L), μm	Number of pixels on a 22 mm (0.87 in.) diameter (N_{22})	Number of pixels on a 13 mm (0.5 in.) diagonal
5×	0.15	2.24	11.2	1967	1137
10×	0.30	1.12	11.2	1967	1137
20×	0.45	0.75	14.9	1475	852
50×	0.80	0.42	21.0	1049	606
100×	0.90	0.37	37.3	590	341
150×	1.25	0.27	40.3	546	315
100× oil	1.40	0.24	24.0	918	530

Data for Nikon CFI60 objectives. Objectives produced by other vendors can exhibit slightly different values.

Similarly, one can compute the necessary resolution of a typical camera with the CCD element of 13 mm (0.5 in.) diagonal size. If one considers an image of low size, 640 by 480 pixels, one arrives at approximately 16 μm/pixel. Comparing this value with the data from Table 2 (fourth column), it can be seen that this image size is sufficient for objective magnifications of 50× or higher.

The CCD elements consist of pixels lying within a square grid, as shown in Fig. 5. It is clearly visible that the number of pixels along the diagonal line (denoted by the gray color) is equal to the number of pixels on the longer side of the image. So, the number of pixels along the diagonal defines the necessary resolution of the CCD element. The appropriate number of pixels at low magnification is significantly higher, but one should take into mind two factors:

- Most objectives of low magnification have lower apertures than those listed in Table 2, and, consequently, the number of necessary pixels will be somewhat lower.
- Usually, in order to improve the depth of focus, microscopic observations are carried out with a partially closed aperture diaphragm that decreases the resolving power.

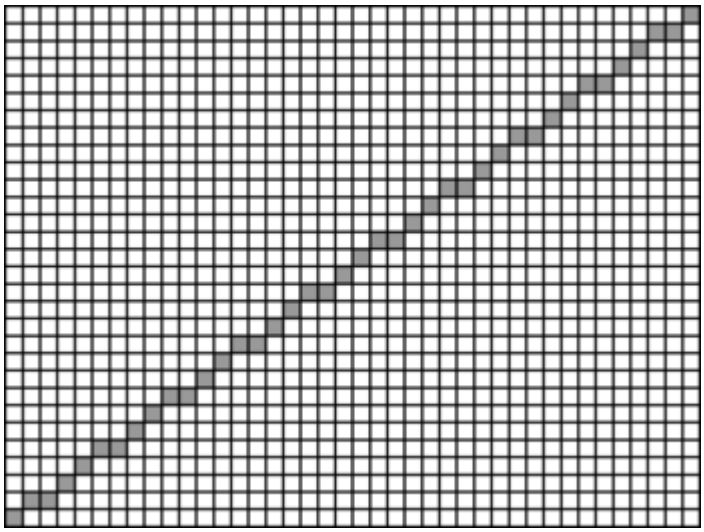

Fig. 5 Square grid with pixels along the diagonal filled in in gray. See text for details.

To summarize, if a simple CCD camera is used without any additional optical elements, a resolution of 640 by 480 or, better, 800 by 600 pixels seems to be acceptable. However, the CCD element of 13 mm (0.5 in.) is, in fact, a rectangle of the dimensions 10.16 by 7.62 mm (0.40 by 0.30 in.) that gives only 20% of the 22 mm (0.87 in.) diameter FOV (Fig. 6).

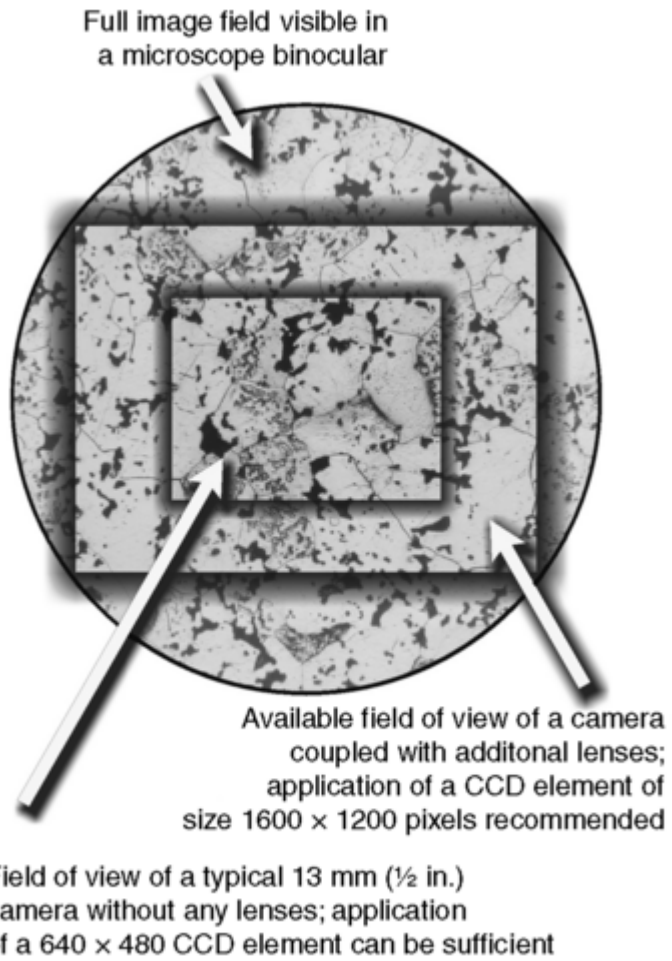

Fig. 6 Comparison of the sizes of circular field of view of a microscope binocular and rectangular images captured by digital charge-coupled devices (CCD)

One can mount additional optical elements between the camera and the microscope body (usually of magnification 0.4 to 0.7×) that enable the capture of a rectangular area as inscribed into the FOV (Fig. 6). If a device of 1600 by 1200 pixels is used, its resolution is sufficient for registration of the full information given by the objective. The use of lower resolutions will result in the loss of some data. For extremely detailed observations, or if the image will be reproduced in a large format (A4 or letter size), one can use a camera with a resolution 1.5 times larger. Further increase in the image resolutions will not improve the image quality in a noticeable way and leads to unnecessary increase of the size of memory needed to store the image.

Obviously, the previous discussion of the optimal image resolution refers only to the properties of the optical system. When preparing images for automatic quantitative analysis, it is a good practice to select such resolution and magnification that allow for the best possible reproduction of the microstructural features under consideration. Both too high and too low resolutions can deteriorate the result of the analysis (Fig. 7).

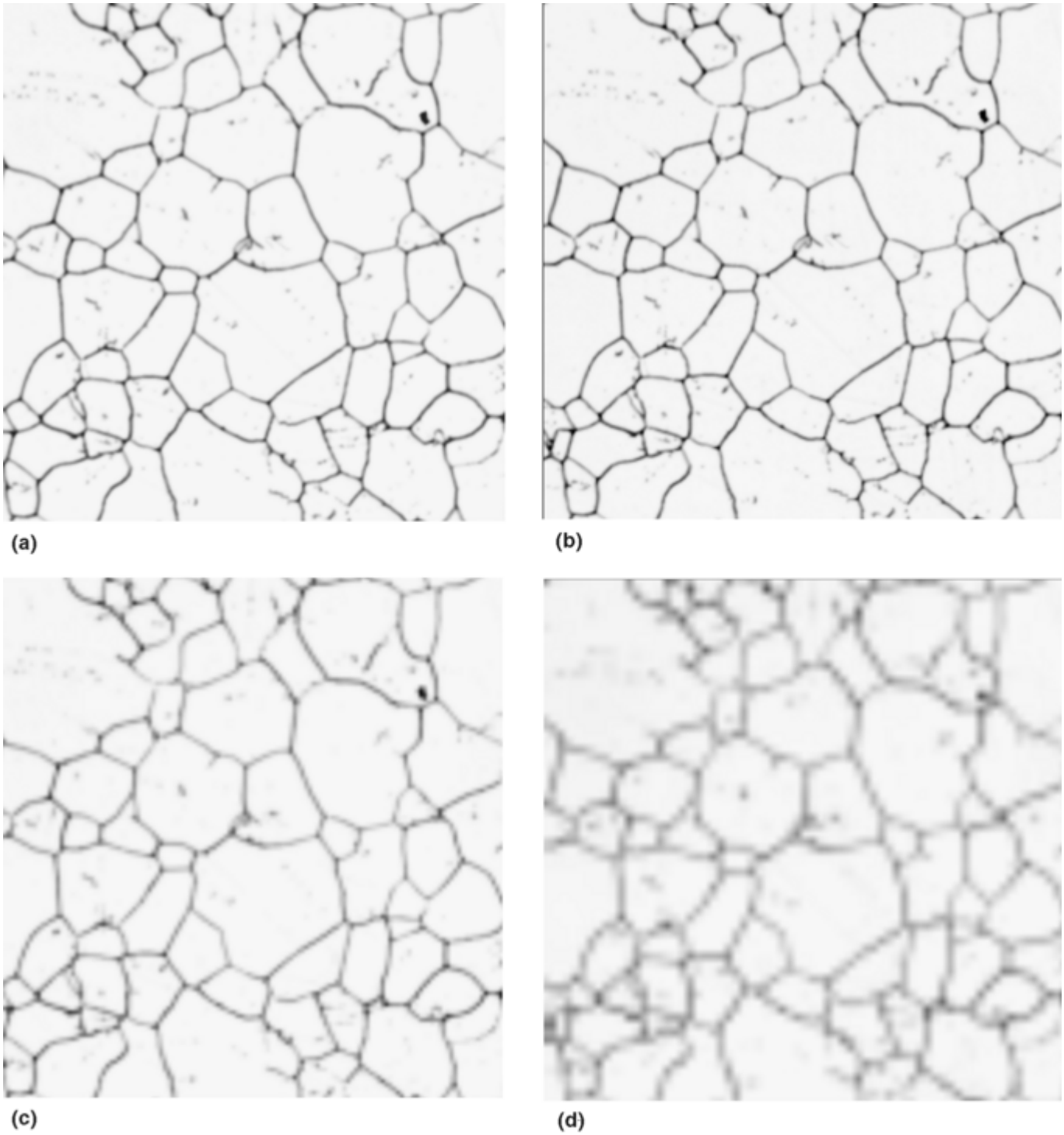

Fig. 7 The same image stored with decreasing spatial resolution. Image sizes, in pixels, are (a) 560 × 560, (b) 280 × 280, (c) 140 × 140, and (d) 70 × 70. 150×

Figure 7(a) is oversampled; that is, its resolution is too high. All the details noticeable in this image are also visible in Fig. 7(b), which represents optimal resolution. If the microstructure from Fig. 7(a) is being analyzed, one can easily obtain erroneous results, because most digital filters take into account predefined pixel neighborhoods. Some features in the oversampled image can be too large (or thick, in the case of grain boundaries) for correct detection. An undersampled image (Fig. 7c) looks a little out of focus. However, most features are still detectable. This example shows that, usually, one has some margin in image resolution that enables correct detection. Further resolution decrease (Fig. 7d) leads to images that are obviously inadequate for automatic analysis.

If a system of isolated particles (Fig. 8) is being analyzed, slightly different rules of proper image resolution choice should be used. The upper bound is similar to the previous case; that is, oversampling the image can lead to detection of some artifacts. The lowest resolution, however, depends on the size and shape of the particles to

be analyzed. First, the resolution should be high enough to detect all the desired objects. This condition allows for correct counting of the particles. Second, to analyze any geometrical properties of the particles (dimensions, section area, or shape), the particles should have an area greater than 10 pixels (16, which is an equivalent of 4 by 4 pixels square, is better). Selecting smaller particles leads to quite serious errors in quantification of their geometrical parameters. This problem is discussed in further detail in this article.

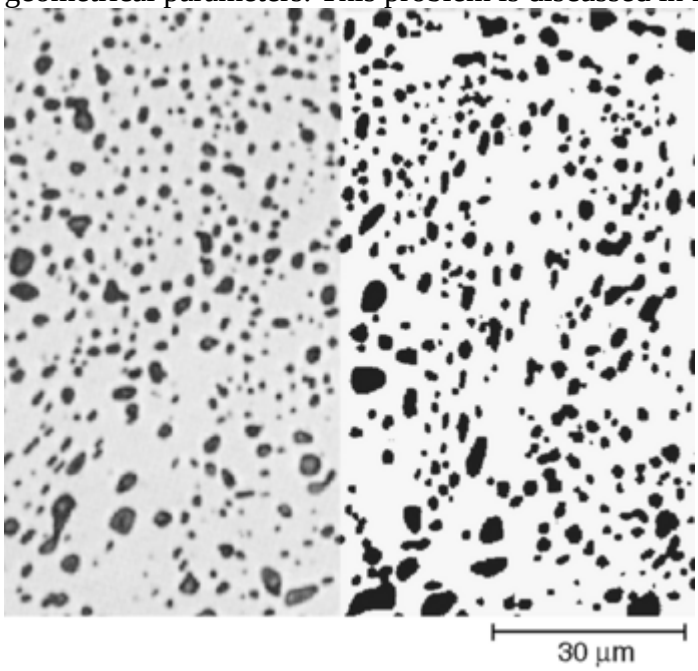

Fig. 8 Cementite particles in the microstructure of AISI W2 steel. Gray-scale (left) and binary (right) images of the particles are visible.

To summarize, the appropriate choice of objective magnification and camera resolution is not very simple and straightforward. In the case of digital images, there is, in fact, no rigid and precisely defined magnification. The same image can be printed the size of a postage stamp, displayed on a 13 in. laptop or 21 in. cathode ray tube (CRT) monitor, or on the wall using a multimedia projector. Each time the final magnification will be entirely different, but the amount of information remains unaltered. Therefore, instead of magnification, digital images can be characterized by their size in pixels (for example, 800 by 600) and their resolution (for example, 0.8 µm/pixel). Exact resolution values can be computed on the basis of scale bars, as shown in Fig. 9. The black segment, covering 0.1 mm (0.004 in.) of the scale, is 420 pixels long in this image. This resolution is 0.238 µm/pixel. Note that the same resolution is obtained if computing the whole image; its horizontal dimension is 800 pixels, and this distance corresponds to 0.19 mm (0.007 in.) of the scale.

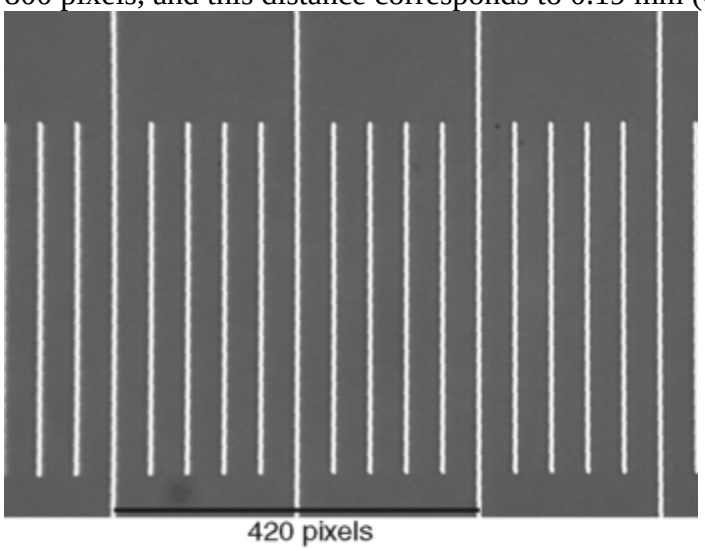

Fig. 9 Image calibration. Spacing between line segments of the micrometer reticle is 0.01 mm. Consequently, the segment length of 420 pixels corresponds with the distance of 0.1 mm.

In most cases, microscope magnification is the product of the objective and ocular magnifications (usually 10×). Therefore, if the recommended magnification is 100×, an objective magnification of 10× is needed if the ocular lens is in place. Appropriate image size (in pixels) can be determined taking into account these remarks and the data given in Table 2. Sometimes, it is necessary to choose the appropriate magnification without prior guidelines and personal experience. Suggestions based on practical experience are summarized in Table 3 (Ref 11).

Table 3 Guidelines for adequate magnification for digital measurements

Exemplary structure	Feature analyzed	Proposed criterion for magnification choice	Suggested secondary criterion
Austenitic steels, single-phase materials	Grains filling the space	Area of the image equal to approximately 200× (mean grain section area)	100–300 grains in a single field of view
Graphite in cast iron	Shape and/or size distribution of dispersed particles, approximately 10–15% area fraction	Mean diameter or length of precipitates equal to 5–10% of the diagonal of the field of view	Approximately 100 precipitates visible in a single field of view
Carbides in tool steels	Size distribution of small, dispersed particles	Mean area of precipitates equal to at least 25 pixels	At least 50 prior-austenite grains visible (in order to preserve spatial distribution)
Ferritic-pearlitic steels	Mixture of two constituents	A mean from magnifications optimal for both constituents	Magnification optimal for analysis of the constituent more important for subsequent analysis
Pores in sintered materials, nonmetallic inclusions	Pores and inclusions	…	Preservation of the spatial distribution of features analyzed

References cited in this section

11. *Practical Guide to Image Analysis,* ASM International, 2000

19. J. Szala, Application of Computer-Aided Image Analysis Methods for a Quantitative Evaluation of Material Structure, *Zesz. Nauk. Politech. Slask., Hutn.,* Vol 61, 2001, p 1–167 (in Polish)

20. L. Wojnar, *Image Analysis, Applications in Materials Engineering,* CRC Press, 1999

34. L. Bjerregaard, K. Geels, B. Ottesen, and M. Ruckert, *Metalog Guide. Your Guide to the Perfect Materialographic Structure,* Struers, Denmark, 1992

35. "Practice for Preparing and Evaluating Specimens for Automatic Inclusion Assessment of Steel," E 768-80 (1993), *Annual Book of ASTM Standards, Section 3: Metals Test Methods and Analytical Procedures,* ASTM International, 1999, p 635–636

36. G.F. Vander Voort, *Metallography: Principles and Practice,* ASM International, 1999

37. G.F. Vander Voort, Etching Techniques for Image Analysis, *Microstructural Science,* Vol 9, Elsevier, 1981, p 135–154

38. G.F. Vander Voort, Phase Identification by Selective Etching, *Applied Metallography,* G.F. Vander Voort, Ed., Van Nostrand Reinhold Co., 1986, p 1–19

39. "Practice for Microetching Metals and Alloys," E 407-93, *Annual Book of ASTM Standards, Section 3: Metals Test Methods and Analytical Procedures,* ASTM International, 1999, p 453–470

40. Z. Latala and L. Wojnar, Computer-Aided versus Manual Grain Size Assessment in a Single Phase Material, *Mater. Charact.,* Vol 46 (No. 2/3), 2001, p 227–233

41. W. Pratt, *Digital Image Processing,* John Wiley & Sons, 1978

42. J.C. Russ, *The Image Processing Handbook,* 2nd ed., CRC Press, 1995

L. Wojnar, K.J. Kurzydłowski, and J. Szala, Quantitative Image Analysis, *Metallography and Microstructures,* Vol 9, *ASM Handbook,* ASM International, 2004, p. 403–427

Quantitative Image Analysis

Leszek Wojnar, Kraków University of Technology, Kraków, Poland; Krzysztof J. Kurzydłowski, Warsaw University of Technology, Warsaw, Poland; Janusz Szala, Silesian University of Technology, Katowice, Poland

---

Image Processing Necessary for Quantitative Image Analysis

Image processing, in general, lies outside the scope of this article; therefore, only very basic remarks are made. The reader should refer to the article "Digital Imaging" in this Volume for more detailed information. However, some very general rules and guidelines can be defined that allow for optimization of the image processing algorithms from the point of view of further quantification (Ref 43, 44, 45, 46, 47, 48, 49, 50).
First, the algorithms used should be as short as possible; the fewer the steps of processing in the algorithm, the lower the probability of serious errors in analysis. An optimal solution is image acquisition followed by simple binarization, as in Fig. 8. Obviously, this ideal case can be achieved only relatively rarely in reality. There are numerous methods that allow for reduction of the necessary processing, including (Ref 16, 19, 20, 51, 52):

- Selective etching, that is, etching oriented toward emphasizing only the selected phases. An example is the use of alkaline sodium picrate for detection of cementite in steels.
- Color etching, which allows for discrimination of a larger number of different phases than in the case of gray-scale images. Unfortunately, color etching is not very easy to control, and strong color variation can derive from different acquisition methods, illumination, camera calibration, and etching itself (Ref 11).
- Application of special observation techniques in optical light microscopy, such as polarized light. In older microscopes, one can use phase contrast. In contemporary microscopes, differential interference contrast (DIC), also known as Nomarsky contrast, is used. Surprisingly, observations under DIC, offering very nice-looking and impressive images, suffer from overloading with a multitude of very small details and are not suitable for digital processing (Fig. 10). Moreover, all of the aforementioned methods are restricted only to phases sensitive to these observation techniques.
- Applications of different signals in scanning electron microscopy, for example, back-scattered and secondary electrons. If the apparatus also allows for the analysis of chemical composition, this option can be used for producing a series of images offering partial information about the interesting features. The appropriate use of this information can lead to the discrimination of different phases not accessible using other tools (Fig. 11) (Ref 53).

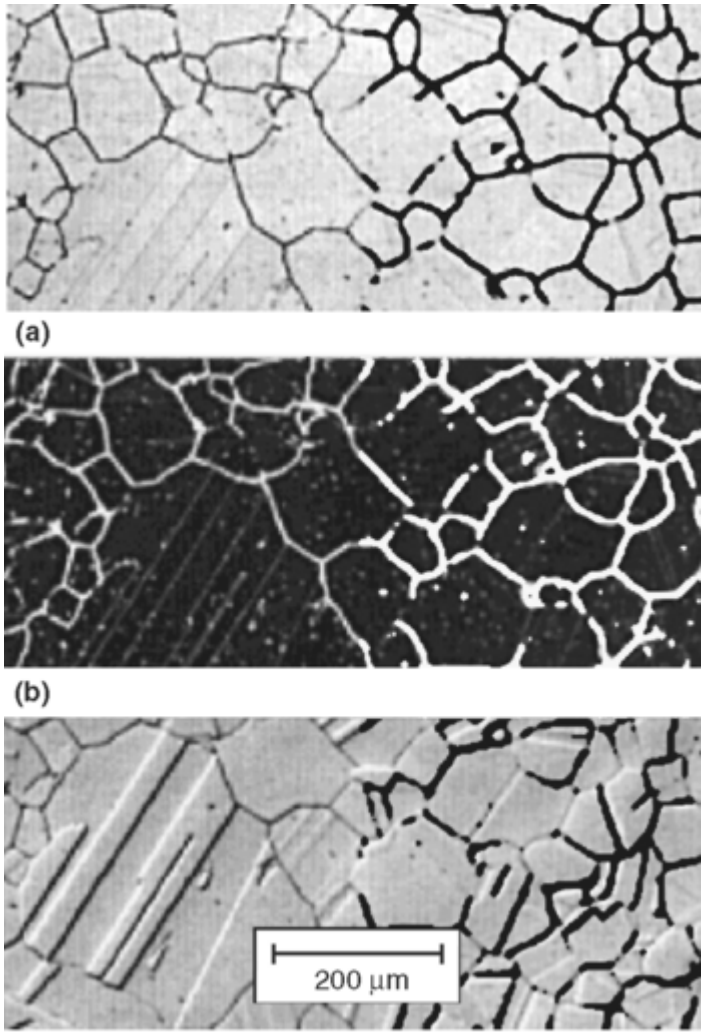

Fig. 10 Microstructure of a stainless steel observed using different techniques of optical microscopy: (a) bright field, (b) dark field, and (c) differential interference contrast (DIC). Grain boundaries detected using simple binarization are marked on the right side as black (a and c) or white (b) lines. Note that observation in DIC leads to the worst detection.

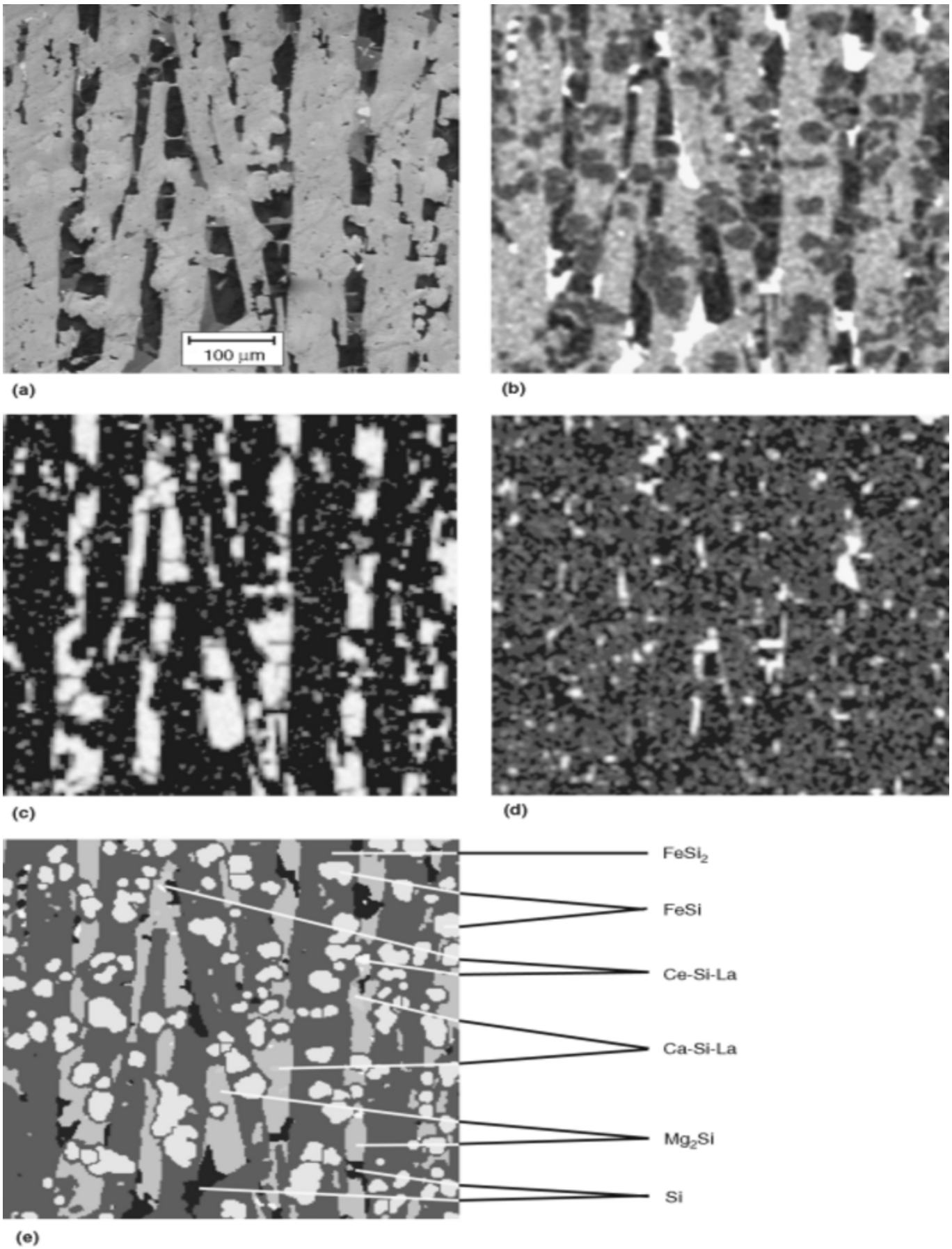

Fig. 11 Detection of different phases in ferro-silicon. (a) Secondary electron image. (b) Distribution of silicon. (c) Distribution of magnesium. (d) Distribution of calcium. (e) Phase distribution. Images (b) to (d) have gray-level distributions distorted in comparison with the originals for better visualization.

Second, one should concentrate only on the final goal of the processing, that is, the correct detection of the phases or structure constituents under consideration. Many intermediate steps in such an analysis can look as if the process was ill organized. For example, blurring the image produces the impression of losing all the appropriate data, which is not necessarily true (Fig. 12). By contrast, sharpening transformations produce images with locally increased contrast that look better for the human observer but, simultaneously, contain an increased amount of noise not present in the initial image. This additional noise can make correct detection extremely difficult. Some knowledge of image processing algorithm properties can prevent errors in specimen preparation and/or image acquisition.

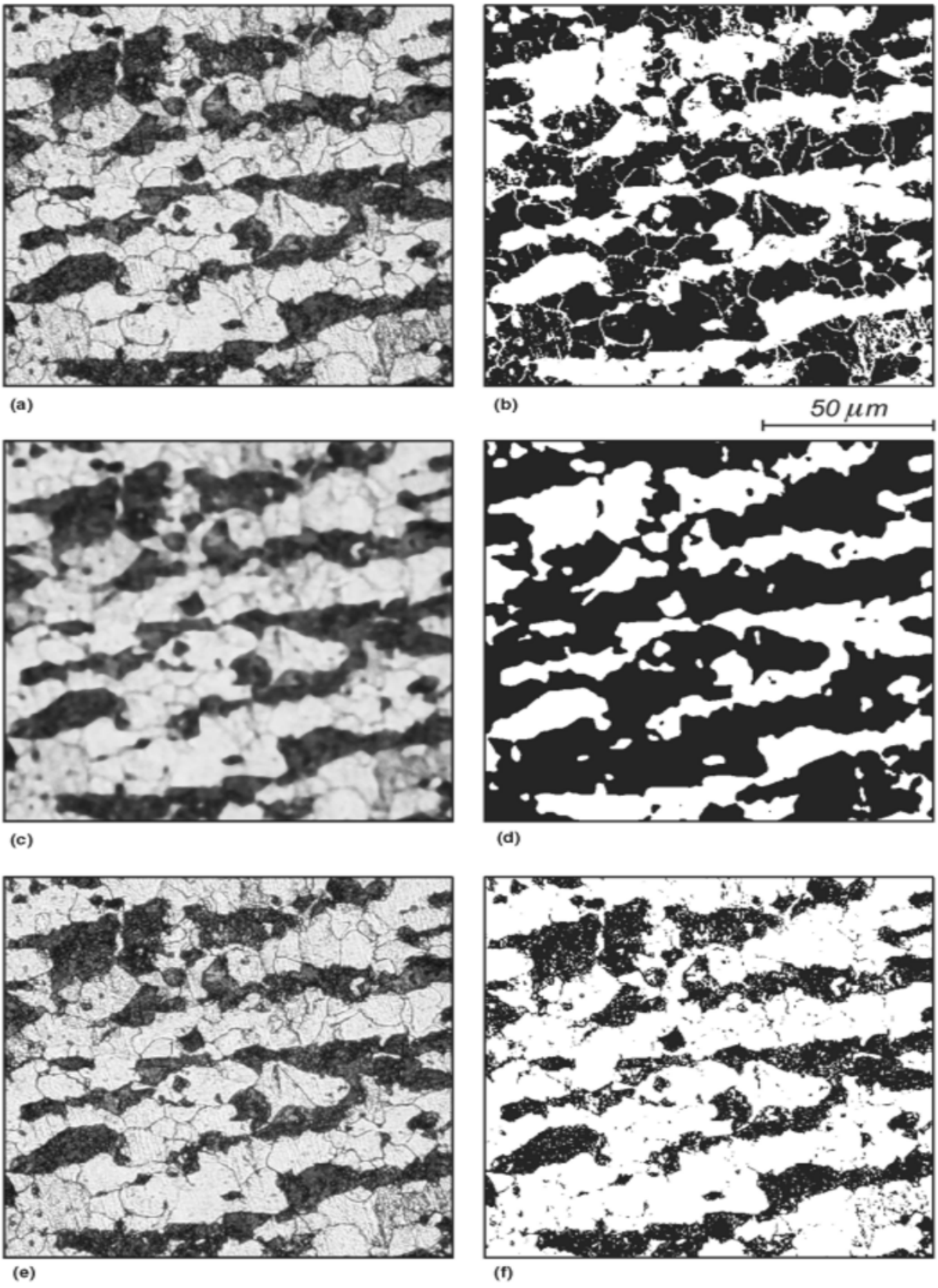

Fig. 12 Detection of pearlite colonies in a carbon steel. (a) Initial image of medium quality. (b) Binarization of the initial image, which produces numerous artifacts. (c) Initial image after blurring. (d)

Binarization of the blurred image, which produces perfect detection. (e) Sharpened image of (a). (f) Binarization of the sharpened image, which gives a very poor result.

Lastly, some images are really not suitable for automatic detection based on gray-level thresholding (Fig. 13). In some cases, other techniques, for example, based on correlation techniques, texture analysis, color segmentation, or Fourier transformation, offer satisfactory segmentation (Ref 42). More detailed discussion of these possibilities lies outside the scope of this article. Moreover, one can encounter structures that cannot be segmented in an automatic way, even with the help of these advanced tools. However, even in such apparently hopeless cases, one can perform manual detection and still benefit from the speed of digital measurements, which are much faster than manual ones.

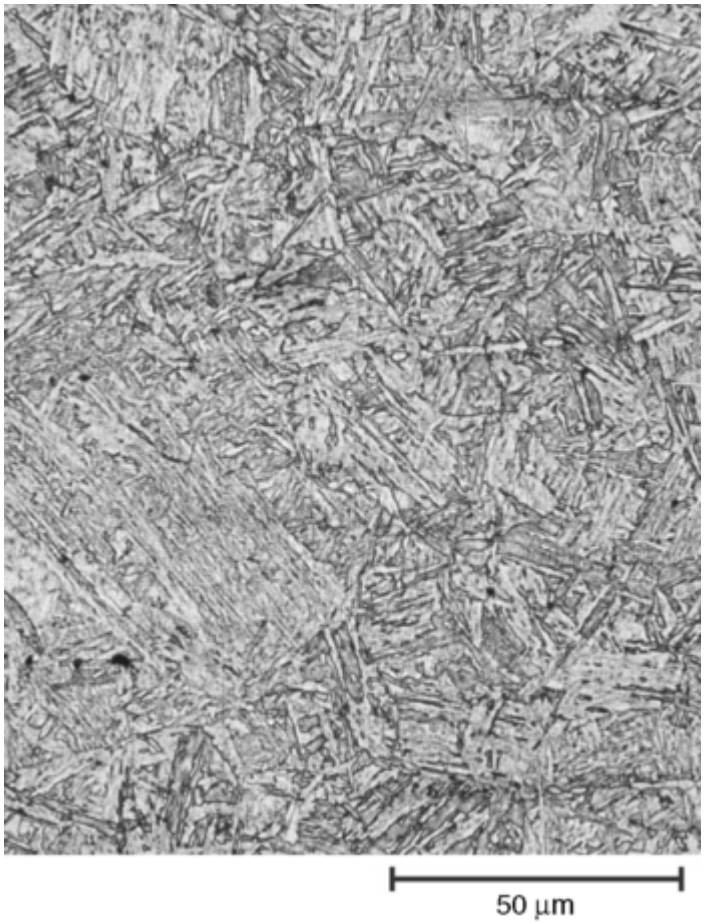

Fig. 13 Images of martensitic structures are not suitable for automatic detection. 500×

To summarize, every possible effort should be made to obtain initial images of the highest quality. This simplifies image processing, prevents the majority of processing errors, and speeds the whole process of analysis. Sophisticated image processing can be helpful in cases that appear hopeless at first glance, but it may lessen the accuracy of the final results.

References cited in this section

11. *Practical Guide to Image Analysis,* ASM International, 2000

16. M. Coster, and J.L. Chermant, *Introduction to Image Analysis,* Presses du CRNS, Paris, 1989 (in French)

19. J. Szala, Application of Computer-Aided Image Analysis Methods for a Quantitative Evaluation of Material Structure, *Zesz. Nauk. Politech. Slask., Hutn.,* Vol 61, 2001, p 1–167 (in Polish)

20. L. Wojnar, *Image Analysis, Applications in Materials Engineering,* CRC Press, 1999

42. J.C. Russ, *The Image Processing Handbook,* 2nd ed., CRC Press, 1995

43. J.R. Beveridge, J. Griffith, R.R. Kohler, A.R. Hanson, and E.M. Riseman, Segmenting Images Using Localized Histograms and Region Merging, *Int. J. Comput. Vision,* Vol 2, 1989, p 311

44. J.L. Chermant and M. Coster, Introduction à l'Analyse d'Images (Introduction to Image Analysis), *J. Microsc. et de Spectrosc. Électron.,* Vol 12, 1987, p 1

45. J.L. Chermant and M. Coster, Granulometry and Granulomorphy by Image Analysis, *Acta Stereol.,* Vol 10, 1991, p 7

46. B. Ralph and K.J. Kurzydlowski, Microscopical Quantification as an Input to Microscopical Modelling, *Proc. Q-Mat'97, International Conference on the Quantitative Description of Materials Microstructure* (Warsaw, Poland), Polish Society for Stereology, 1997, p 141

47. F. Robert and G. Lefebvre, Distance Mapping for Image Filtering, *Acta Stereol.,* Vol 14, 1995, p 209

48. J. Serra and L. Vincent, lecture notes on morphological filtering, Paris School of Mining, Center for Mathematical Morphology, Fontainebleau, 1989

49. R. Tadusiewicz, *Vision Systems for Industrial Robots,* WNT, Warsaw, Poland, 1992 (in Polish)

50. H. Talbot, The Pre-Processing in Mathematical Morphology, *Rev. Métall.,* Vol 91, 1994, p 211

51. E. Henault, and J.L. Chermant, Parametrical Investigation of Gray Tone Image, *Acta Stereol.,* Vol 11/Suppl., 1992, p 665

52. J.C. Russ and J.C. Russ, Automatic Discrimination of Features in Gray-Scale Images, *J. Microsc.,* Vol 148, 1987, p 263

53. G.F. Vander Voort, The SEM as a Metallographic Tool, *Applied Metallography,* Van Nostrand Reinhold Co., 1986, p 139–170

L. Wojnar, K.J. Kurzydłowski, and J. Szala, Quantitative Image Analysis, *Metallography and Microstructures,* Vol 9, *ASM Handbook,* ASM International, 2004, p. 403–427

Quantitative Image Analysis

Leszek Wojnar, Kraków University of Technology, Kraków, Poland; Krzysztof J. Kurzydłowski, Warsaw University of Technology, Warsaw, Poland; Janusz Szala, Silesian University of Technology, Katowice, Poland

---

Digital Measurements

Digital measurements are the core of quantitative image analysis. Most of them are performed in binary images. A detailed description of the algorithms used for digital measurements can be found in textbooks on image processing and analysis (Ref 16, 20, 31, 42, 54). Fortunately, in-depth knowledge of the construction of these algorithms is not necessary for solving practical problems. Therefore, this article concentrates only on understanding the basic properties of digital measurements.

Counting various objects is one of the most natural and simple tasks. However, in digital images stored in squared matrices, one should define the rules of connectivity prior to making any measurements. There are two basic cases:

- Four-connected pixels (any pixel has four neighbors, similar to the black pixel in Fig. 14a)
- Eight-connected pixels (any pixel has eight neighbors, similar to the black pixel in Fig. 14b)

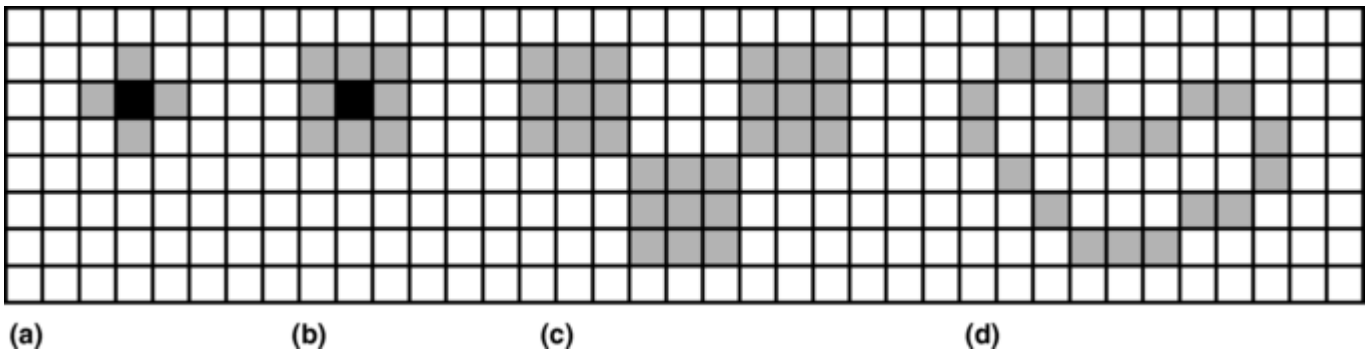

Fig. 14 Effect of connectivity rules on the results of detection. See text for details.

Individual objects in an image are recognized as coherent sets of pixels of given connectivity. In other words, any object consists of all the pixels arranged in such a way that one can move from any pixel of this object to any other one, moving only through the pixels of this object and using the rules of connectivity. If one wants to count relatively big particles, it is better to assume four-connected neighborhood, as in the case of the objects shown in Fig. 14(c), which will be considered as three separate squares. In the case of eight-connected neighborhood, all three squares will be treated as a single, complex object. Another solution is recommended for thin lines or curves, as shown in Fig. 14(d). This object will be recognized as a closed loop only in terms of assumed eight-connected neighborhood. If one chooses a four-connected one, the curve in Fig. 14(d) will be treated as ten separate objects.

Volume Fraction. Problems can be encountered when trying to apply some concepts of classical stereology to digital imaging. The first such case is the application of point-sampled methods, with the most commonly used method of estimation of volume fraction:

$$V_V = P_P \qquad \text{(Eq 4)}$$

where V_V is the estimated volume fraction, and P_P is the ratio between the number of points that hit the analyzed phase and all the points of a test grid.

Sometimes, novices in image analysis try to use a grid of points overlying the image in order to reproduce the classical, stereological solution. This is obviously not necessary, and one should simply count (in a binary image) all the pixels that represent the analyzed phase and use the number of all the pixels in the image as a reference value:

$$V_V = A_A = \frac{N_p}{N_0} \qquad \text{(Eq 5)}$$

where A_A denotes area fraction, N_p denotes the number of pixels that belong to the phase being analyzed, and N_0 is the total number of pixels in the image.

Intersections. The digital realization of counting intersection points, typical for linear methods widely used in classical stereology, appears to be more difficult. Sometimes, people draw a set of section lines manually or automatically and look for the number of intersection points, as indicated in by the arrows Fig. 15. This is an approach that unnecessarily complicates the analysis. Note that all the potential intersection points have the configuration shown in the small, two-pixel-sized object in Fig. 15: two pixels along a horizontal line, one having the value corresponding to the matrix (usually 0), and one having the value corresponding to the analyzed phase (usually 1). This is sufficient to count all the pairs of such pixels existing in the image and to obtain the number of intersection points, in accordance with the test line of a length equal to the horizontal image dimension multiplied by the vertical image dimension expressed in pixels.

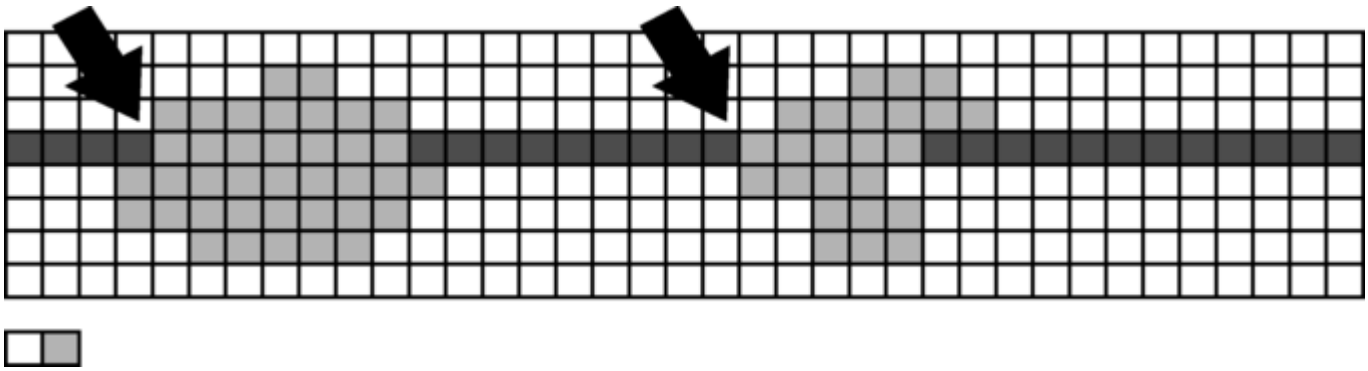

Fig. 15 Counting the intersection points in linear analysis. See text for details.

Compared to classical manual stereological methods, digital image analysis allows very fast and convenient evaluation of various geometrical characteristics related to individual objects. The commonly used parameters are summarized in Table 4, along with the basic properties of each. This list is not exhaustive. Some other parameters, such as moments of inertia or various shape factors (discussed later), can be introduced.

Table 4 Basic geometrical parameters available in quantitative image analysis

Quantity	Schematic illustration	Properties and comments
Surface area		In the case of noncalibrated images, surface area is equal to the number of pixels building the object. Surface area is one of the simplest and most accurate parameters that can be evaluated in image analysis.
Perimeter	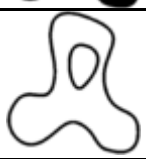	Should be used with special care, because it often gives biased results. It is a good practice to check the precision of perimeter evaluation using test figures prior to any measurements. Usually, the best results are obtained when the Crofton formula is applied for perimeter evaluation.
Feret diameter (horizontal and vertical)	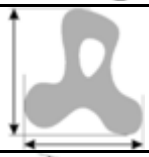	Very popular measure of the size of various objects. Especially useful for characterization of elongated, convex objects that are parallel to the horizontal or vertical direction in the image
Feret diameter (oriented at a given angle)	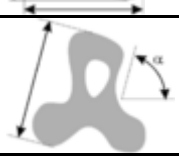	Not available in all systems. A pair of parameters, length and angle, is given as a result of this measure. Usually, it is less accurate than the Feret diameters evaluated horizontally or vertically.
Maximum intercept (maximum Feret diameter)	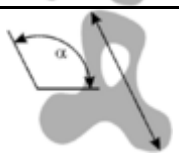	This is simply the maximum of the previously defined Feret diameters. This measure also can be interpreted as the longest projection length of the object. The value of the angle is useful in analysis of the orientation of elongated, approximately linear objects.
Maximum width	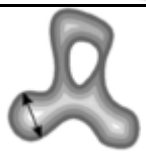	This measure also can be interpreted as the maximum diameter of a circle inscribed into the analyzed object. In most cases, its value is approximated by a doubled value of the maximum of the distance function (sum of erosions of the figure—see the article “Digital Imaging” in this Volume for details).
Center of gravity	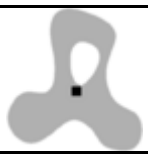	A pair of numbers, describing the location of the center of gravity, is returned. This measure is useful for analysis of the spatial distribution of the objects.
First point		There are coordinates of the very left pixel belonging to the upper row of pixels of the object. Location of the first point is used mainly for filtering of the objects. However, the use of the center of gravity is

		usually preferred.
Convex hull		In fact, this is not a measure but a new object generated on the basis of the initial one. It can be useful for shape quantification. In most cases, due to the digital nature of images, it is only a rough interpolation of the exact convex hull.
Minimum bounding rectangle		Minimum bounding rectangle defines the nature of this object, which has a character similar to the convex hull. Orientation of the minimum bounding rectangle can be useful when looking for preferred directions in the image. It can also be used as the starting point for some shape factors.
Number of holes		An important parameter for quantification of the topology of objects. In metallography, it is used only occasionally.

The parameters listed in Table 4 are commonly known, but one should remember that they have been initially defined for Euclidean space, whereas, during image analysis, their values are obtained from a simplified, two-dimensional grid. This can introduce some errors in the values obtained. One should check the accuracy of the image analysis system on simple test objects in order to obtain information on how the system measures the object parameters. Results of such an analysis are shown in Table 5 (Ref 11, 16, 20).

Table 5 Estimated versus theoretical measures for circles of different diameters obtained from the Aphelion v.3.2 image analysis package

							
Diameter, pixels	100	75	50	25	16	10	7
Relative error of Crofton perimeter, %	<1	-1	-6	-10	-10	-10	-14
Relative error of surface area, %	<1	<1	<1	<1	<1	+1	-4

Note: Measurements with errors of estimation smaller than 1% are treated as error-free. Underestimated and overestimated values are marked by "-" and "+," respectively.

In order to quantify the bias of digital measurements, one needs to define an appropriate test object. In most cases, this is a circle, because its geometrical characteristics are well known and it has a curvilinear edge, causing most of the errors in digital quantification. As shown in Table 5, section area is estimated almost perfectly for all the diameters, whereas the circle perimeter is estimated with a noticeable error for diameters of 50 pixels or less. The bias of perimeter shows a stable value of 10% for diameters in the range of 10 to 25 pixels, and rapid growth of the bias is observed for circles of a diameter smaller than 10 pixels. Although the values shown in Table 5 are obtained from the Aphelion v.3.2 package (Apogee Software, Inc.), similar values will be found for other digital image analysis systems.

Perimeter evaluation requires some additional comments, because various methods are used to estimate this parameter. In most cases, the best results are given when the Crofton formula is used. For a square grid of pixels, this formula has the following form:

$$L = \frac{\pi a}{4} \cdot \left[N_0 + N_{90} + \frac{N_{45} + N_{135}}{\sqrt{2}} \right] \qquad \text{(Eq 6)}$$

where L denotes perimeter, a is the pixel spacing in the grid, and N_x is the number of object boundary pixels hit by lines oriented at 0, 90, 45, and 135°, respectively. This formula is especially useful in the analysis of curvilinear objects and less accurate for rectangular shapes. For example, the Crofton perimeter of a square with sides of 100 equals 378.113 instead of 400. However, this 5.5% error still seems to be acceptable.

To conclude, one should avoid quantification of individual objects having a section area smaller than approximately ten pixels. In addition, perimeter evaluation for objects with a radius of curvature smaller than approximately five pixels may lead to serious errors, greater than 10% of the measured value.

References cited in this section

11. *Practical Guide to Image Analysis,* ASM International, 2000

16. M. Coster, and J.L. Chermant, *Introduction to Image Analysis,* Presses du CRNS, Paris, 1989 (in French)

20. L. Wojnar, *Image Analysis, Applications in Materials Engineering,* CRC Press, 1999

31. J. Serra, *Image Analysis and Mathematical Morphology,* Academic Press, 1982

42. J.C. Russ, *The Image Processing Handbook,* 2nd ed., CRC Press, 1995

54. R. Tadeusiewicz and P. Korohoda, *Computer-Aided Analysis and Processing of Images,* Foundation for Telecommunication Development, Kraków, Poland, 1997 (in Polish)

L. Wojnar, K.J. Kurzydłowski, and J. Szala, Quantitative Image Analysis, *Metallography and Microstructures,* Vol 9, *ASM Handbook,* ASM International, 2004, p. 403–427

Quantitative Image Analysis

Leszek Wojnar, Kraków University of Technology, Kraków, Poland; Krzysztof J. Kurzydłowski, Warsaw University of Technology, Warsaw, Poland; Janusz Szala, Silesian University of Technology, Katowice, Poland

---

Counting Objects and Size Distributions

Counting objects is one of the most natural tasks in quantification of any structure. Counting the objects visible in an image and dividing their number by a section area of the image gives the well-known N_A stereological parameter. This parameter allows for estimation of the mean object section area:

$$\bar{a} = \frac{A_A}{N_A} \qquad \text{(Eq 7)}$$

where $\bar{a}$ is the mean object area, A_A is the area fraction of the objects analyzed, and N_A denotes their density, that is, number of objects per unit section area.

Digital counting of objects (this can be done only in binary images) is a very fast and simple process that requires only definition of the connectivity rules (Fig. 14). However, new problems arise when some objects are cut by the image edge (Fig. 16a). The hitting of some particles or grains by image edges obviously has no effect on the estimation of volume fraction or the number of intersection points in linear methods. The problem arises when counting these particles.

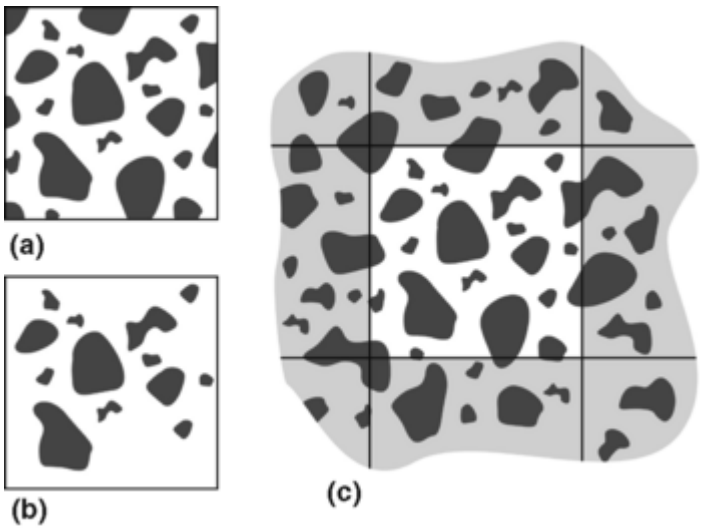

Fig. 16 Counting particles visible in an image. Objects intersected by the image edge have to be counted with the appropriate correction factor. (a) An image with some objects cut by the image edges. (b) The same image after border kill procedure, that is, removal of particles cut by the image edge. (c) The analyzed image treated as one element from a series of images. See text for details.

If one takes into account all the objects visible, the result will be overestimated, because the particles at image edges also belong to other images touching the analyzed one (Fig. 16c). One can easily remove all the objects cut by the image edges (this procedure is sometimes called border kill), but this leads to underestimated counting (Fig. 16b). The appropriate solution can be derived from the sketch in Fig. 16(c). In this figure, one can see a series of images touching each other. The backgrounds of these images are marked in gray, with one exception—the analyzed image, which has a white background. Note that any particle lying on the image edge belongs to two separate images, whereas any particle lying on the corner of the image belongs to four separate ones. This leads to a universal formula for counting the number of particles in the image, known as the Jeffries method (Ref 3):

$$N = N_i + \frac{1}{2}N_b + \frac{1}{4}N_c \qquad \text{(Eq 8)}$$

where N is the number of particles to be estimated, N_i is the number of internal (wholly included in the image) particles, N_b is the number of particles cut by the image edges, and N_c is the number of particles cut by the image corners.

The previously described procedure allows for the unbiased estimation of the number of objects per unit image area, N_A:

$$N_A = \frac{N}{A} \qquad \text{(Eq 9)}$$

where A is the area of the image analyzed.

Size distribution of particles represents another analysis challenge. In such a case, one can take into account only those particles that are wholly included in the image. Such an analysis is independent from the area in which the particles are placed. So, this seems to be the most natural solution to analyze particles after border kill, as shown in Fig. 16(b). Unfortunately, such an analysis leads to a distorted distribution. This problem is subsequently explained in detail (Ref 20).

Size distribution of circles that simulate particles is shown in Fig. 17. In order to demonstrate some properties of the border kill operation, only two sizes of circles are used. In Fig. 17(a), one can see equal numbers of bigger and smaller circles. In Fig. 17(b) to (d), respectively, smaller and smaller images are sampled, with borders drawn by dashed lines. After the removal of particles cut by the edges (filled in in gray), there remain particles wholly included in these images, which are filled in in black. It is clear that the proportion between the bigger and smaller ones is no longer equal to 1, as observed in Fig. 17(a). The probability of particle removal is proportional to its dimension in a direction perpendicular to the image edge. Thus, border kill, is more likely to remove bigger particles than smaller ones, and the fraction of small objects is overestimated.

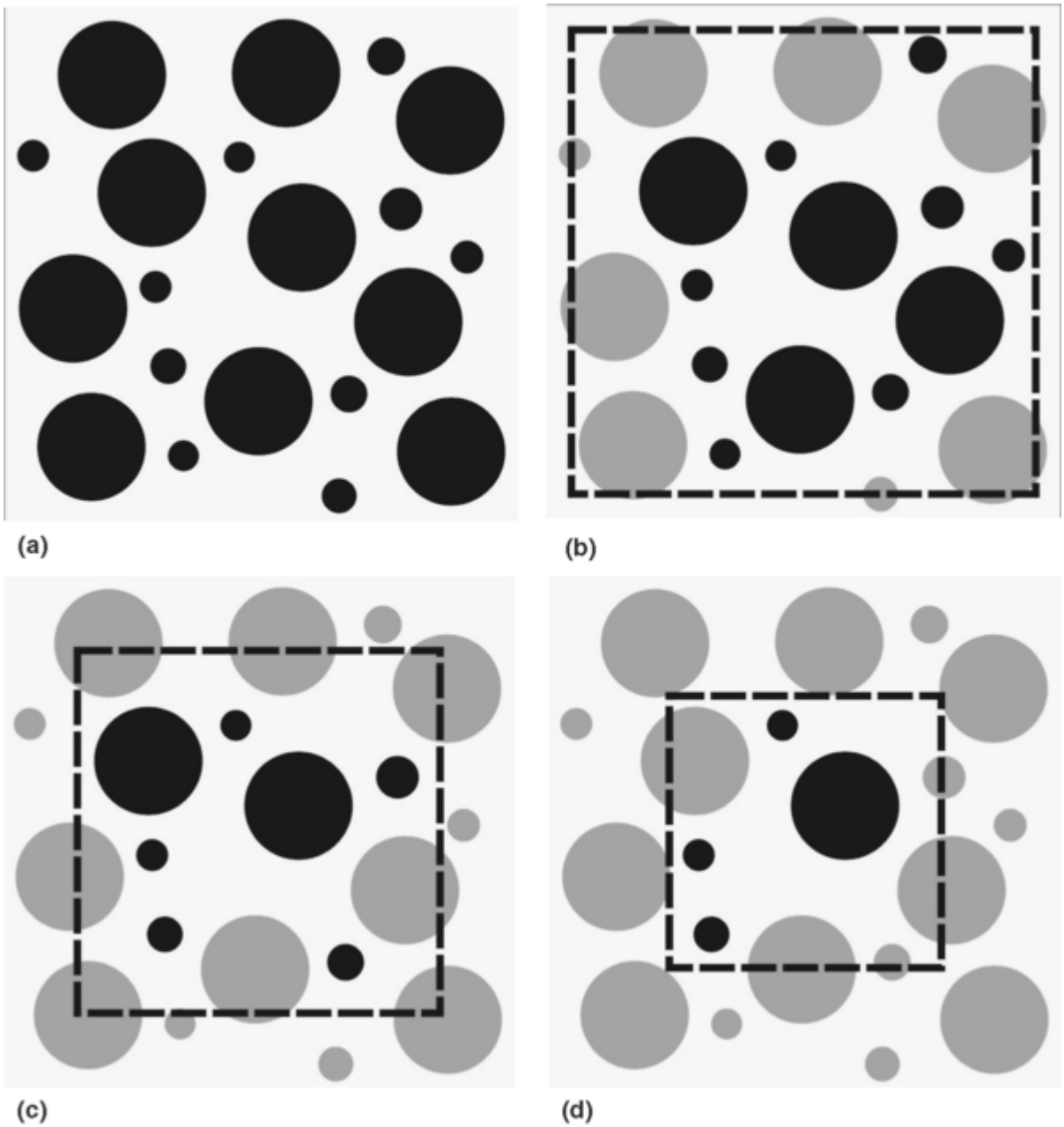

Fig. 17 Effect on the size distribution of removal of particles cut by the image edges or lying outside the area of interest. Counted particles are darkened.

A possible correction of the previously described effect can be obtained relatively easily by using the guard frame (Fig. 18). An image containing some objects to be analyzed is seen in Fig. 18(a). In this image, one should define the guard frame (cut by dashed lines and filled in in light gray in Fig. 18b). The general rule is that all the objects cut by the image edges should lie outside the guard frame. In practice, this rule is a little too restrictive, but this solution is both safe and easy for implementation in automatic systems for image analysis. The most common way of useing this tool is to analyze all the objects completely included inside the guard frame and those cut only by its right or bottom edge (marked using a solid line in Fig. 18b). In most cases, this solution gives satisfactory and unbiased results. However, one should take into account that in the case of guard frames touching each other (such a case can occasionally be found in practical applications), some objects can be hit by two guard frames, as indicated by an arrow in Fig. 18(c).

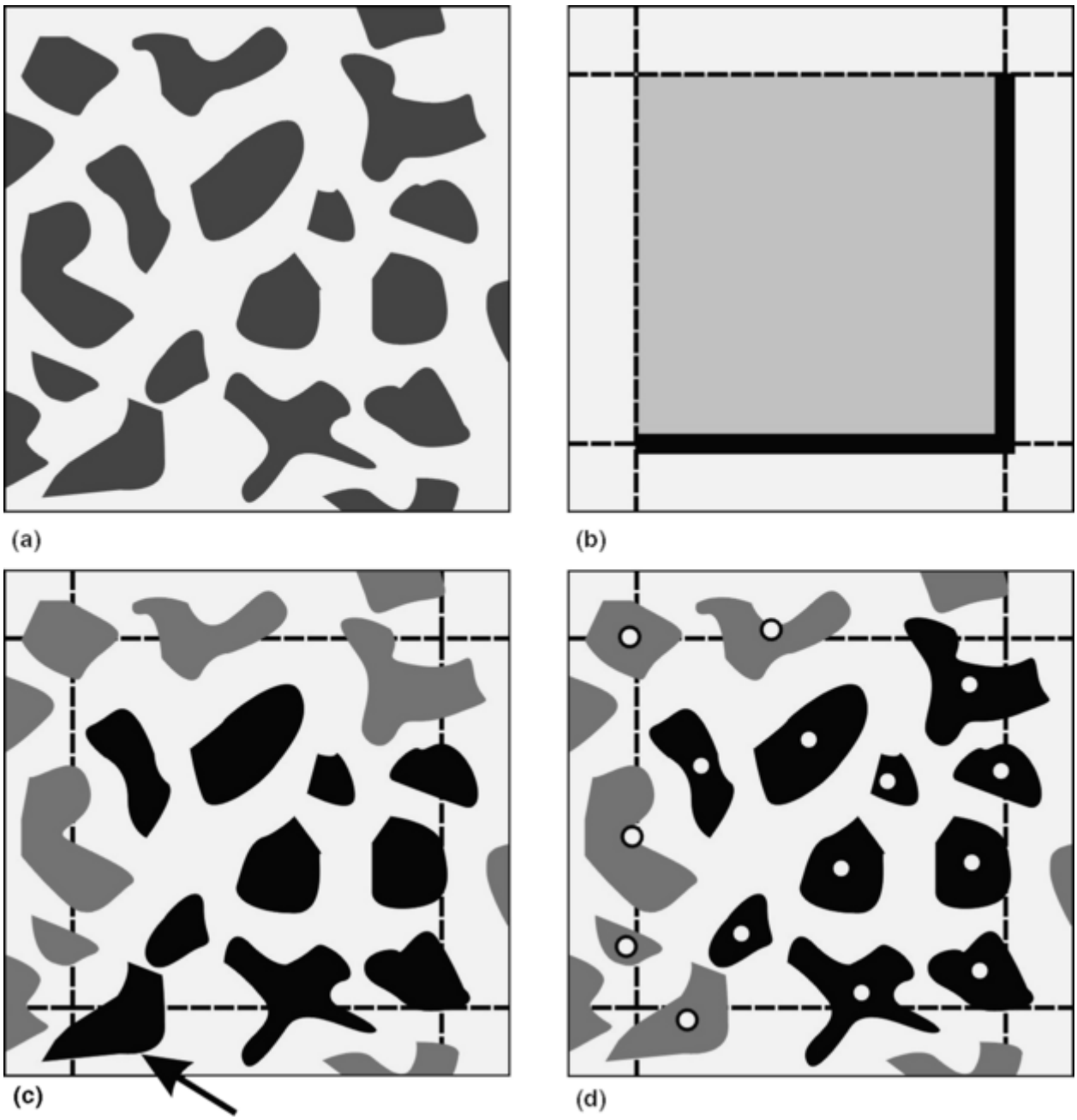

Fig. 18 Unbiased choice of particles for size distribution purposes using the guard frame. (a) Initial object. (b) Guard frame with right and bottom edges darkened. (c) Particles within frame or intersected by either the bottom or right edge, or both, are selected. (d) Objects selected based on a single characteristic point, the center of gravity

A somewhat better solution is illustrated in Fig. 18(d). Each object is bounded with a single characteristic point—the center of gravity, in this case. It can be virtually any site, if each object has only one such characteristic point. For further analyses, only objects whose characteristic points are placed inside the guard frame are selected. Presuming the consecutive guard frames touch each other, this solution assures that every object will be analyzed (nothing will be neglected), and no object will be counted twice. In that way, application of the guard frame concept assures unbiased estimation of the object size distribution (Ref 20, 55).

An example that illustrates the application of the previously described correction procedures is shown in Fig. 19. It is clearly visible that corrections based on a border kill procedure and a guard frame produce different sets of objects (Fig. 19b, c). These two concepts lead to different mean sizes and size distributions, as shown in Fig. 20. It is clear that the use of a border kill procedure leads to an overestimated fraction of the smallest grains. The previously described overestimation is a systematic error that can even be found in some standardized procedures. It should be stressed, however, that this effect is relatively small if the number of objects in the image is high.

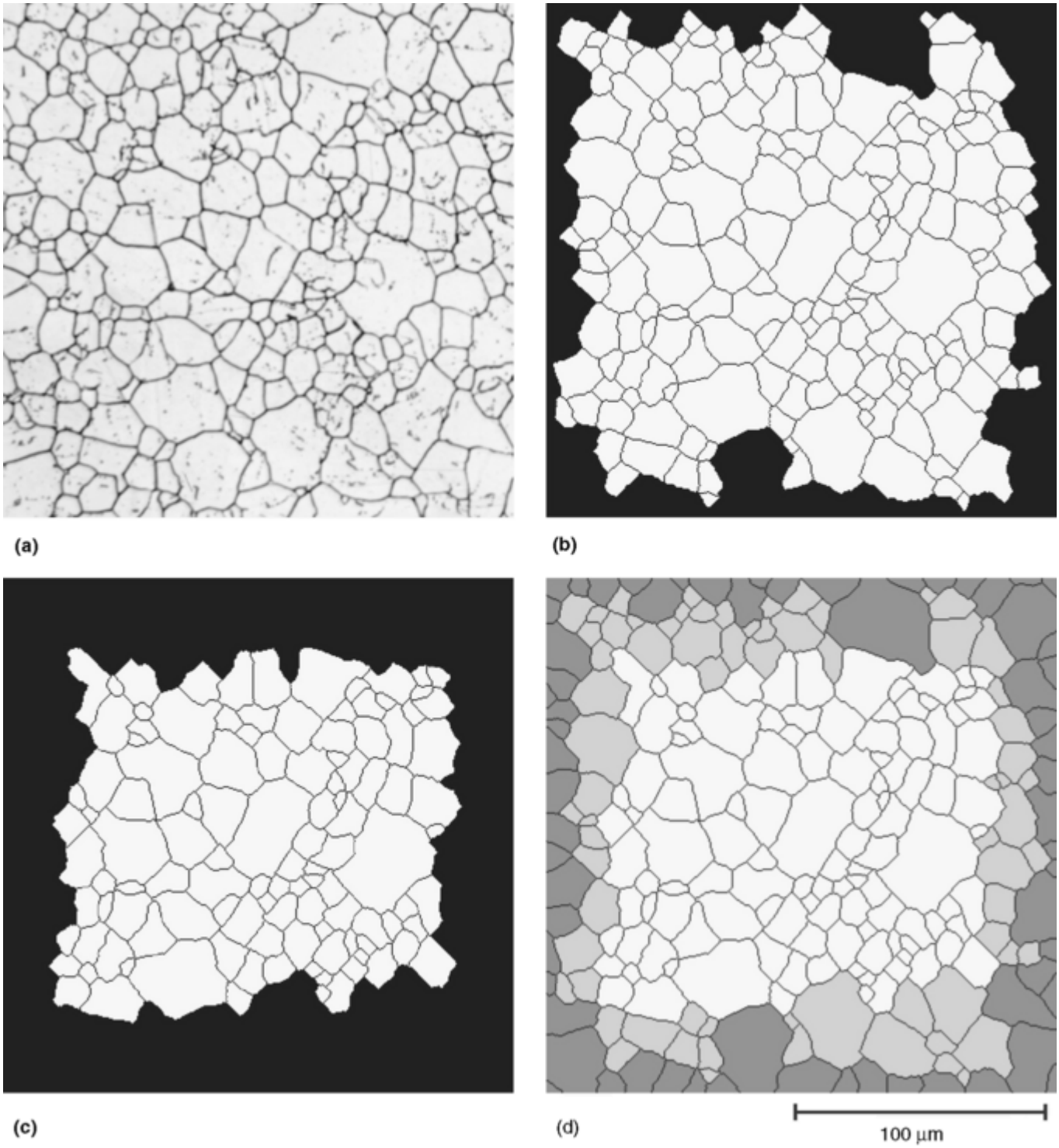

Fig. 19 Microstructure of austenitic steel and its analysis. (a) Initial image. (b) Binary image after border kill. (c) Binary image after correction based on guard frame. (d) Comparison of different sets of grains: dark gray, removed using border kill; light gray, additionally removed using guard frame; white, the same set as in (c)

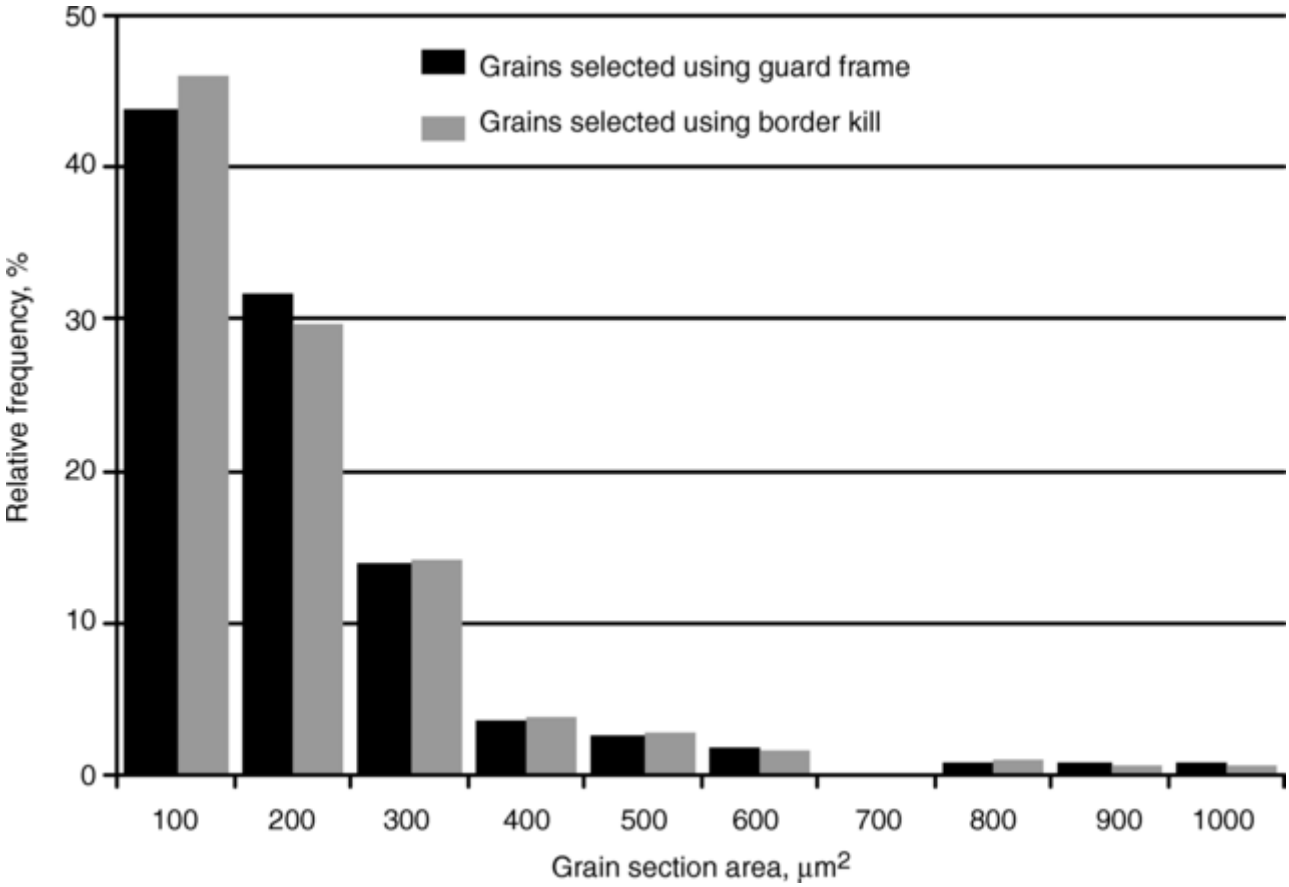

Fig. 20 Comparison of grain size distributions for the structure from Fig. 19 after different correction procedures. The border kill procedure overestimates the fraction of the smallest grains.

Another important factor that should be taken into account in the analysis of size distributions is the way in which the results are weighted. The most frequently used solutions are number-weighted and area-weighted distributions. In the first case, one computes the fraction of grains (objects) in a given class as follows (Ref 11, 18, 19, 20):

$$f_i = \frac{n_i}{N} \qquad \text{(Eq 10)}$$

where f_i is the fraction (relative frequency) of the ith class, n_i is the number of objects with a size that fits the ith class, and N is the overall number of objects.

In the case of area-weighted distribution, the fractions are computed in a slightly different way:

$$f_i = \frac{a_i}{A} \qquad \text{(Eq 11)}$$

where f_i is the fraction (relative frequency) of the ith class, a_i is the total section area of objects with a size that fits the ith class, and A is the overall section area of objects.

A comparison of the results given by these two methods is shown in Fig. 21. One can notice from this plot that area-weighted distribution produces results that are more suitable for any further statistical analysis, for example, checking if they fit any standardized distributions, such as normal, log normal, or Rayleigh distributions. In addition, parameters of such distributions usually give a better reflection of structure-property relationships (Ref 3, 4).

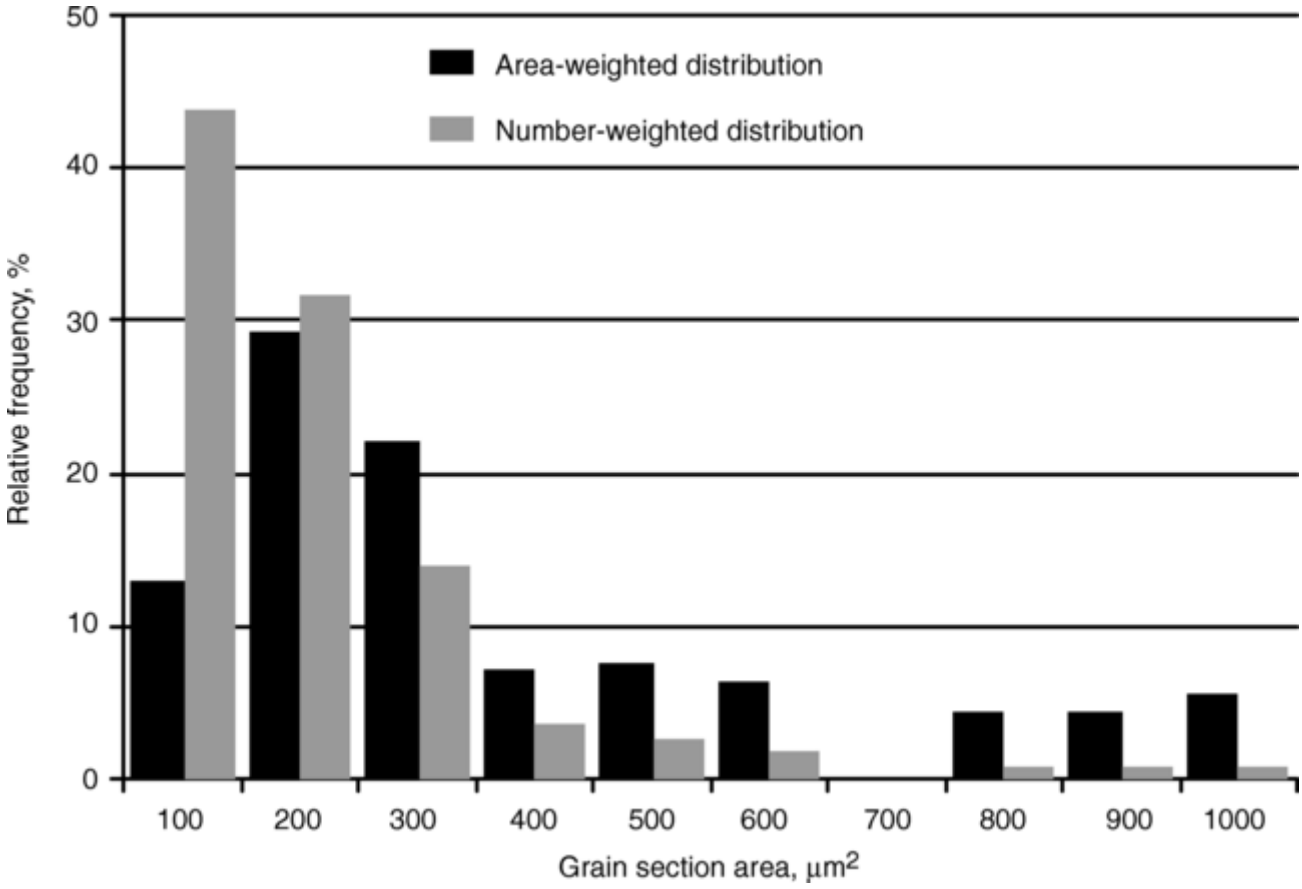

Fig. 21 Comparison of different methods of weighting the results of measurements: number- and area-weighted distributions of grain section areas

Area-weighted distributions are also very useful in the separation of single distributions that form bimodal or even more complex distributions. However, analysis of such cases is the aim of advanced statistical procedures and lies outside the scope of this article.

Mean Area. Often, one needs to evaluate the mean object size, usually the mean area, $\bar{a}$. This seems to be quite straightforward, but this evaluation can be performed in at least three ways that do not necessarily give identical results.

Method 1. Evaluate the overall section area of objects in the image (without any correction at the edges), and divide this area by the number of objects, N, evaluated using Eq 8.

Method 2. Do the same procedure in the corrected image that contains only particles that are not cut by the edges. If the correction procedure is done correctly (using a guard frame), one should obtain results statistically identical with those obtained using method 1. The results can be similar because in method 1, objects cut by the image edges are taken into account with the weight of 0.5 or 0.25, depending on their location. Method 1 is less complicated than method 2. However, method 2 is quite straightforward if one needs to simultaneously obtain the size distribution of the objects. Note also that simple removal of objects cut by the image edges (without guard frame and proper correction) will produce underestimated results.

Method 3. Measure areas a_i of individual objects, and count the mean value (assuming there are n objects) as an arithmetic mean:

$$\bar{a} = \frac{\sum_{i=1}^{n} a_i}{n} \qquad \text{(Eq 12)}$$

The results will be the same as in other methods except in one case: the analysis of grain size in a single-phase material (Fig. 19) where the image is filled with grains. Usually, one assumes in such a case that the grains occupy the whole image area. So, in the case of method 1, the total area of grains is equal to the area of the entire image. Similarly, in method 2, one can treat all the objects as being glued together for evaluation of their total section area. Unfortunately, when applying method 3, underestimated results are obtained because a part

of the image area is lost for drawing grain boundaries. Moreover, the difference between methods 1 or 2 on one side and method 3 on the other side increases with decreasing grain size. So, one should avoid method 3 in the case of grain size evaluation.

There is a simple yet successful method that allows for improving the results of method 3. One should simply correct the area of individual grains by adding half of the area of pixels surrounding a given grain. Nevertheless, using such a procedure is not recommended in the case of analyzing individual objects. In such a case, there are no pixels acting as boundary lines. There are (in the case of binary image) only two families of pixels: belonging to the particles (usually of value 1) and belonging to the matrix (usually of value 0). So, in this case, quantification of the size and phase contents is free of a systematic error.

References cited in this section

3. J. Ryś, *Stereology of Materials,* Fotobit-Design, Kraków, Poland, 1995, p 323 (in Polish)

4. E.E. Underwood, *Quantitative Stereology,* Addison Wesley, 1970

11. *Practical Guide to Image Analysis,* ASM International, 2000

18. K.J. Kurzydlowski and B. Ralph, *The Quantitative Description of the Microstructure of Materials,* CRC Press, 1995

19. J. Szala, Application of Computer-Aided Image Analysis Methods for a Quantitative Evaluation of Material Structure, *Zesz. Nauk. Politech. Slask., Hutn.,* Vol 61, 2001, p 1–167 (in Polish)

20. L. Wojnar, *Image Analysis, Applications in Materials Engineering,* CRC Press, 1999

55. H.E. Exner and H.P. Hougardy, *Einführung in die Quantitative Gefügeanalyse (Introduction to Quantitative Analysis of Microstructures),* DGM Informationsgesellschaft Verlag, Oberursel, 1986

L. Wojnar, K.J. Kurzydłowski, and J. Szala, Quantitative Image Analysis, *Metallography and Microstructures,* Vol 9, *ASM Handbook,* ASM International, 2004, p. 403–427

Quantitative Image Analysis

Leszek Wojnar, Kraków University of Technology, Kraków, Poland; Krzysztof J. Kurzydłowski, Warsaw University of Technology, Warsaw, Poland; Janusz Szala, Silesian University of Technology, Katowice, Poland

---

Evaluation of Basic Stereological Parameters

Many stereological parameters can be evaluated on the basis of the results of measurements made on individual objects (Table 4). Some problems arise when one has to evaluate the simplest stereological parameters, based on the linear method or point counting. It is not necessary to draw test lines or test points; the adaptation of tools typical for image analysis seems to be much more efficient. Such adaptation is quite simple if one takes into account the definition of the parameter to be evaluated. Some examples are shown in Table 6. Other stereological parameters can be evaluated using the rules of classical stereology and therefore are not discussed here. More information on quantitative metallography is in the article "Quantitative Characterization and Representation of Global Microstructural Geometry."

Table 6 Image analysis estimation methods for selected stereological parameters

Symbol	Description of the symbol	Evaluation procedure	Explanations
V_V	Volume fraction	$V_V = A_A = \frac{N_p}{N_0}$	N_p, number of pixels that belong to the phase being analyzed
A_A	Area fraction		N_0, total number of pixels in the image
L_A	Length per unit area	$L_A = \frac{L_t}{A_0}$	L_t, total length of edges of all the objects selected using guard frame A_0, total section area of the guard frame Both values should be calibrated.(a)
N_A	Number per unit area	$N_A = \frac{n}{A_0}$	n, number of objects selected using guard frame A_0, total section area of the guard frame; this value should be calibrated.(a)
P_L	Number of objects cut per unit length (in horizontal direction)	$P_L = \frac{n_{01}}{h \cdot L}$	n_{01}, number of pixels of value of 1 having the left neighbor of value equal to 0 h, number of rows of pixels in the image L, horizontal dimension of the image; this value should be calibrated.(a)
P_L	Number of objects per unit length (in any direction)		The image should be rotated prior to measurements by the angle, assuring evaluation in the horizontal direction.

(a) The image is calibrated if the physical length and area represented by a single pixel are known.

L. Wojnar, K.J. Kurzydłowski, and J. Szala, Quantitative Image Analysis, *Metallography and Microstructures,* Vol 9, *ASM Handbook,* ASM International, 2004, p. 403–427

Leszek Wojnar, Kraków University of Technology, Kraków, Poland; Krzysztof J. Kurzydłowski, Warsaw University of Technology, Warsaw, Poland; Janusz Szala, Silesian University of Technology, Katowice, Poland

Shape Analysis

Quantification of shape is one of the most frequent tasks of quantitative image analysis. The main problem in shape quantification is the lack of a precise and universal definition of this quantity. There is some feeling of the nature of shape, and it is known that any object can be quantified by its shape and size. However, it is often quite difficult to separate shape from size. For example, small buildings generally have different shapes than big ones. A similar relation can be observed in the case of cars, plants, or animals. The next difficulty is that a single number usually cannot describe shape. For example, when making a loop from a piece of rope, one obtains a loop of different shape at each attempt. So, the number of loops with different shapes is unlimited, and, consequently, it is impossible to differentiate all of them by a single number. By contrast, volume fraction (describing the amount of any phase) always falls in the range from 0 to 1 (0 to 100%), and the size of any structural constituent never exceeds the size of the tested piece of a material. Having no possibility to describe shape with ultimate precision leads to the introduction of new parameters sensitive to the changes in shape, the so-called shape factors. Similar to the loops discussed previously, one can define countless shape factors. However, in order to obtain useful microstructural quantification, all of them should have the following common properties (Ref 11, 20, 56):

- The shape factor should be dimensionless in order to keep its value unaltered in the case of particles of the same shape but different size.
- The shape factor should describe in a quantitative way how far a given shape deviates from the theoretically ideal or model one.
- The shape factor should be sensitive to particular shape changes occurring in a process under consideration. Consequently, it is impossible to define a universal shape factor. This is a clear consequence of the fact that one cannot define the shape of even a simple loop by a single number.

In general, shape factors quantify a deviation of the analyzed object from the ideal or model one. The most frequently used reference shape is a circle, because it is the most simple and natural figure in two-dimensional (2-D) images. The objects presented in metallographic images can exhibit shapes that are very far from the circle, but finding the reference circle can be intuitively easy, as illustrated in Fig. 22. The rows of objects in Fig. 22 illustrate three types of distortion: elongation, irregularity, and composition.

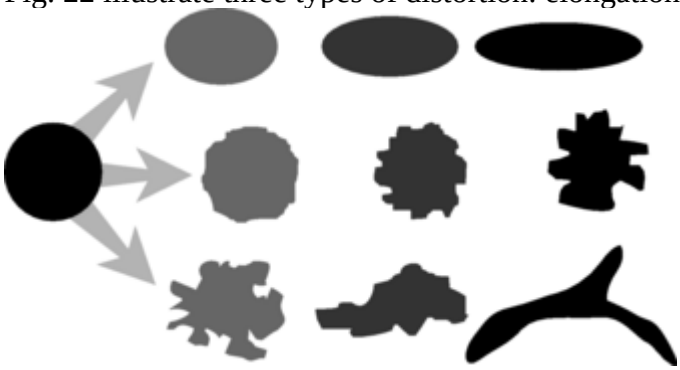

Fig. 22 Three models of distortion from the ideal circular shape (from top to bottom): elongation, irregularity, and composition. The more distorted the shape, the darker the object.

Elongation, or aspect ratio, is commonly used to describe the shape of particles after plastic deformation and can be effectively measured using the following shape factor (Fig. 23) (Ref 20):

$$f_1 = \frac{b}{a} \qquad \text{(Eq 13)}$$

where *a* is the maximum Feret diameter, while *b* is the Feret diameter measured perpendicularly to it.

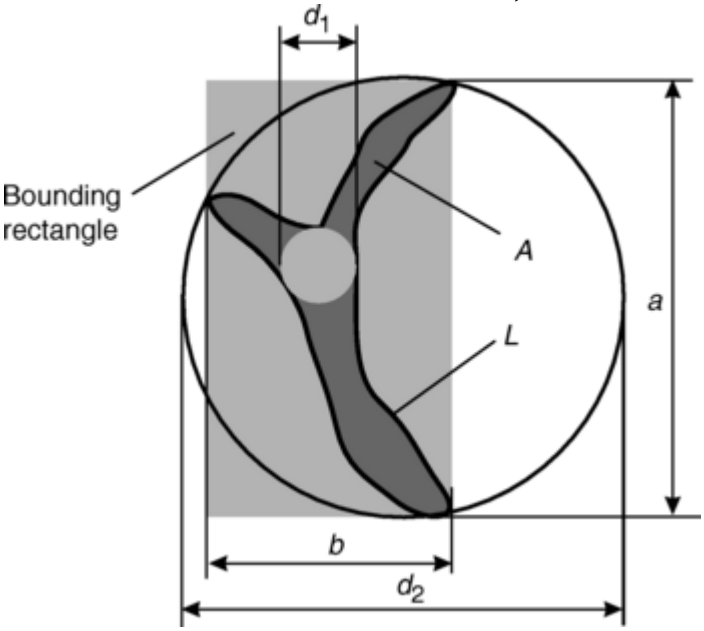

Fig. 23 Various geometrical characteristics used for shape factor evaluation. The symbols are further identified in text.

The aspect ratio is equal to 1 in the case of an ideal circle or a square and is less than 1 but greater than 0 in elongated shapes. Unfortunately, this parameter cannot be applied for quantification of irregularity, because objects with an irregular border can have f_1 values very close to 1 despite the fact that they profoundly differ in their shape. A good solution to quantify this case is one of the most popular shape factors, also called circularity:

$$f_2 = \frac{4\pi A}{L^2} \qquad \text{(Eq 14)}$$

where L is the perimeter, and A is the section area of the analyzed particle (Fig. 23).

The f_2 shape factor is very sensitive to any irregularity of circular objects. It reaches its maximum value of 1 for a circle and smaller values for all the other shapes. In contrast, it is almost completely insensitive to small elongation.

Composition. An even more complex problem is to quantitatively characterize composition, which can be understood as the summation of both cases (elongation and irregularity) discussed previously. An example of such variable shapes is graphite precipitates formed during transition from the nodular to flake cast iron. This transition cannot be effectively described by using alone any of the shape factors presented previously. One of the tempting solutions is to apply very complex shape factors, designed in an experimental way, as various functions of numerous geometrical parameters, which fulfill the basic properties of shape factors. Although one can successfully manipulate the weights and obtain good correlation between the shape factor and material properties, the result cannot be directly interpreted, because it has no physical interpretation. So, it is advised (but also more difficult) to try to construct a new shape factor capable of detecting the necessary changes in shape.

One can note that all objects illustrating the composition type of deformation (lower row of objects in Fig. 22) have approximately the same section area, but when moving across the sequence to the left, systematically greater circles can be inscribed within the particle. This observation leads to a definition of a new shape factor (Fig. 23) (Ref 11):

$$f_3 = \frac{d_1}{d_2} \qquad \text{(Eq 15)}$$

where d_1 and d_2 are the diameters of the maximum inscribed and circumscribed circles, respectively.

The aforemantioned defined shape factor returns very good results in the case of complex deviations from ideal circularity. In addition, this shape factor is more universal than the previous two, because it is sensitive to both elongation and irregularity. However, as already mentioned, shape cannot be quantified by a single number, and therefore, the f_3 factor cannot be a universal solution for shape classification. Usually, for classification purposes, more than one parameter must be applied.

One can find many other shape factors in image analysis packages. One is the proportion between areas of the analyzed object and the minimum bounding rectangle (Fig. 23):

$$f_4 = \frac{A}{S} \qquad \text{(Eq 16)}$$

where S is the area of the minimum bounding rectangle.

Note that although the edges of the minimum bounding rectangle shown in Fig. 23 are parallel to the Feret diameters, this is not always the case in real structures. However, the length-to-width ratio of the minimum bounding rectangle usually gives values very close to elongation, f_1.

Fuzzy Logic. Classification of any object can be successfully performed if one applies the rules of fuzzy logic. In contrast to binary logic, in which a particle can be regular or irregular, fuzzy logic allows the same particle to be regular, irregular, somewhat regular, nearly regular, and so on. The application of fuzzy logic has some advantages, which are briefly outlined as follows.

By using this technique, one can quantify particles that do not perfectly fit the assumed basic, ideal shapes. In addition, one can easily apply weighted averages or even more sophisticated functions of various quantities for classification needs. So, fuzzy logic is suitable for the development of turnkey applications and less useful for research applications. What is important when using fuzzy logic is that the results always lie in the 0 to 100% range. So, there is no difficulty in interpretation of the results. One can build classification rules that return results relatively close to the human way of classification.

Figure 24 illustrates both the idea and application of fuzzy logic to a collection of graphite particles, detected from cast irons of various grades. A number describes each particle: flake graphite is denoted as 0%, whereas a circular shape is marked as 100%. Intermediate shapes have various values in the 0 to 100% range. Calculations are based on the f_3 shape factor. It is clearly visible that four particles at the left side of Fig. 24 are recognized as fully circular, the particles in the middle are rated as partially circular, whereas the graphite flakes (right side of Fig. 24) are judged as absolutely not circular. This classification fits quite well to human feelings. Note that it also allows for quantifying intermediate shapes. For example, there are three shapes (indicated by arrows) that have similar outer shapes but are judged as entirely different—9, 40, and 71%, respectively. This is caused by the different arrangement of internal holes. So, quantitative image analysis allows for classification that is not possible for a human observer.

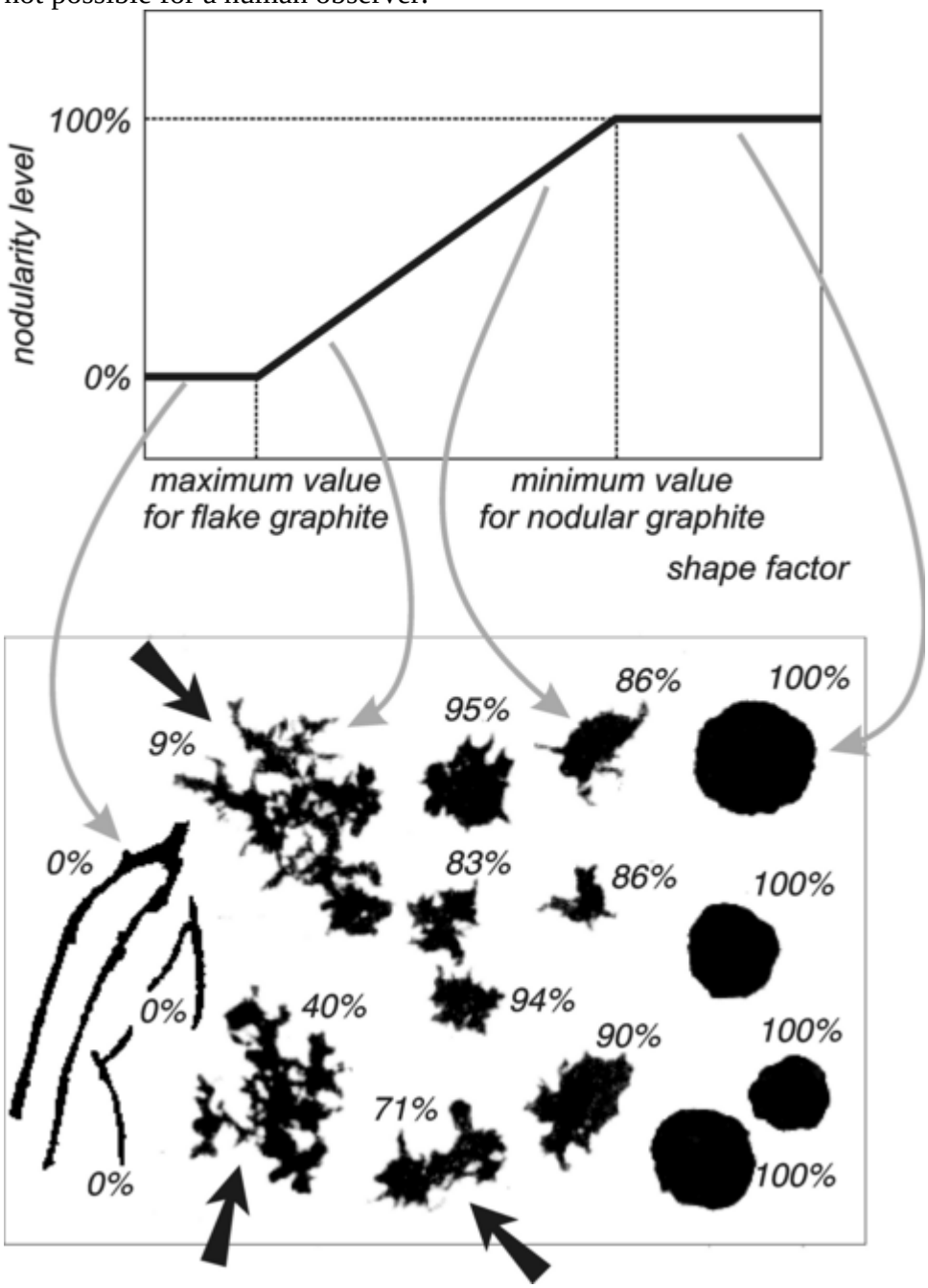

Fig. 24 Various shapes of graphite precipitations in cast iron with a rating of circularity (100% for nodular graphite and 0% for flake graphite). Arrows indicate three objects with similar outlines but different shape ratings caused by internal holes.

Even the most sophisticated shape factors are not sufficient for characterization of large sets of particles of different shapes. For example, even in cast iron with well-defined flake graphite, there are some precipitations that are almost ideally circular. Therefore, in order to obtain overall characterization of the shape of particles, it

is necessary to analyze the distribution of individual particle shapes, with special emphasis on the largest ones. The rules of such classification should be fixed individually, depending on the structure analyzed.

References cited in this section

11. *Practical Guide to Image Analysis*, ASM International, 2000

20. L. Wojnar, *Image Analysis, Applications in Materials Engineering*, CRC Press, 1999

56. J.L. Chermant, M. Coster, and G. Gougeon, Shape Analysis in R^2 Space Using Mathematical Morphology, *J. Microsc.*, Vol 145, 1987, p 143

L. Wojnar, K.J. Kurzydłowski, and J. Szala, Quantitative Image Analysis, *Metallography and Microstructures*, Vol 9, *ASM Handbook*, ASM International, 2004, p. 403–427

Quantitative Image Analysis

Leszek Wojnar, Kraków University of Technology, Kraków, Poland; Krzysztof J. Kurzydłowski, Warsaw University of Technology, Warsaw, Poland; Janusz Szala, Silesian University of Technology, Katowice, Poland

---

Spatial Distribution and Three-Dimensional Analysis

There are four characteristic structural parameters of any microstructure that are necessary to describe its properties: amount, size, shape, and spatial distribution of all the phases. Distribution is most difficult to quantify. Until now, stereology had no fully satisfactory means to characterize distribution. This is caused by the nature of the material itself. Any material built of two or more phases is, by definition, nonhomogeneous. This becomes clear during observations at very high magnifications, where only one or a few phase precipitates are observed and the geometrical characteristics change significantly from one field of view (FOV) to another. On the other hand, when observed by a human eye, the same material seems to be homogeneous. Therefore, the results of homogeneity quantification are highly dependent on the magnification applied. Image analysis techniques do not offer significantly better tools in comparison with classical stereology. This situation dramatically changes if one uses three-dimensional (3-D) images (described in detail in the article "Three-Dimensional Microscopy" in this Volume). Therefore, only remarks related directly to quantification of such images are given here (Ref 57, 58, 59, 60).

The oldest technique for obtaining 3-D data is to prepare a series of polished sections with a systematic shift in direction (usually called *z*-direction) perpendicular to the section plane (Fig. 25). Such a procedure is not very precise, because it is practically impossible to ensure the same step in *z*-direction. Moreover, resolution in this direction is significantly lower than in the section plane. Despite these drawbacks, systematic sectioning allowed for evaluation of real 3-D shapes of grains.

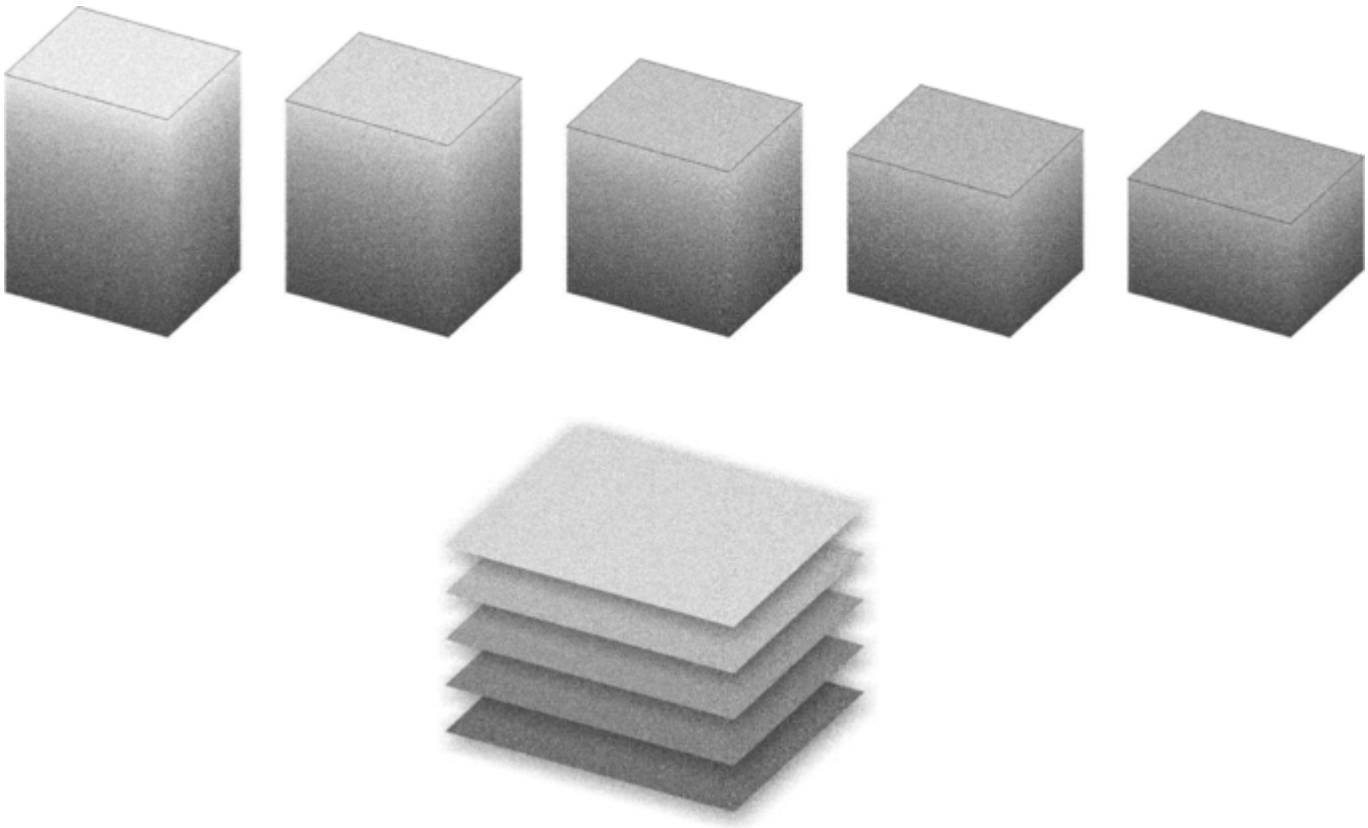

Fig. 25 Three-dimensional reconstruction can be obtained by systematic thinning of the specimen.

Much better results can be obtained using special x-ray scanners, which work in ways similar to computer tomography used in medicine. The result of scanning is a series of images that represent microstructural sections, as shown in Fig. 26. The white areas visible in this image are pores that, if observed in classical x-ray image, could be easily misinterpreted as local changes in the material density.

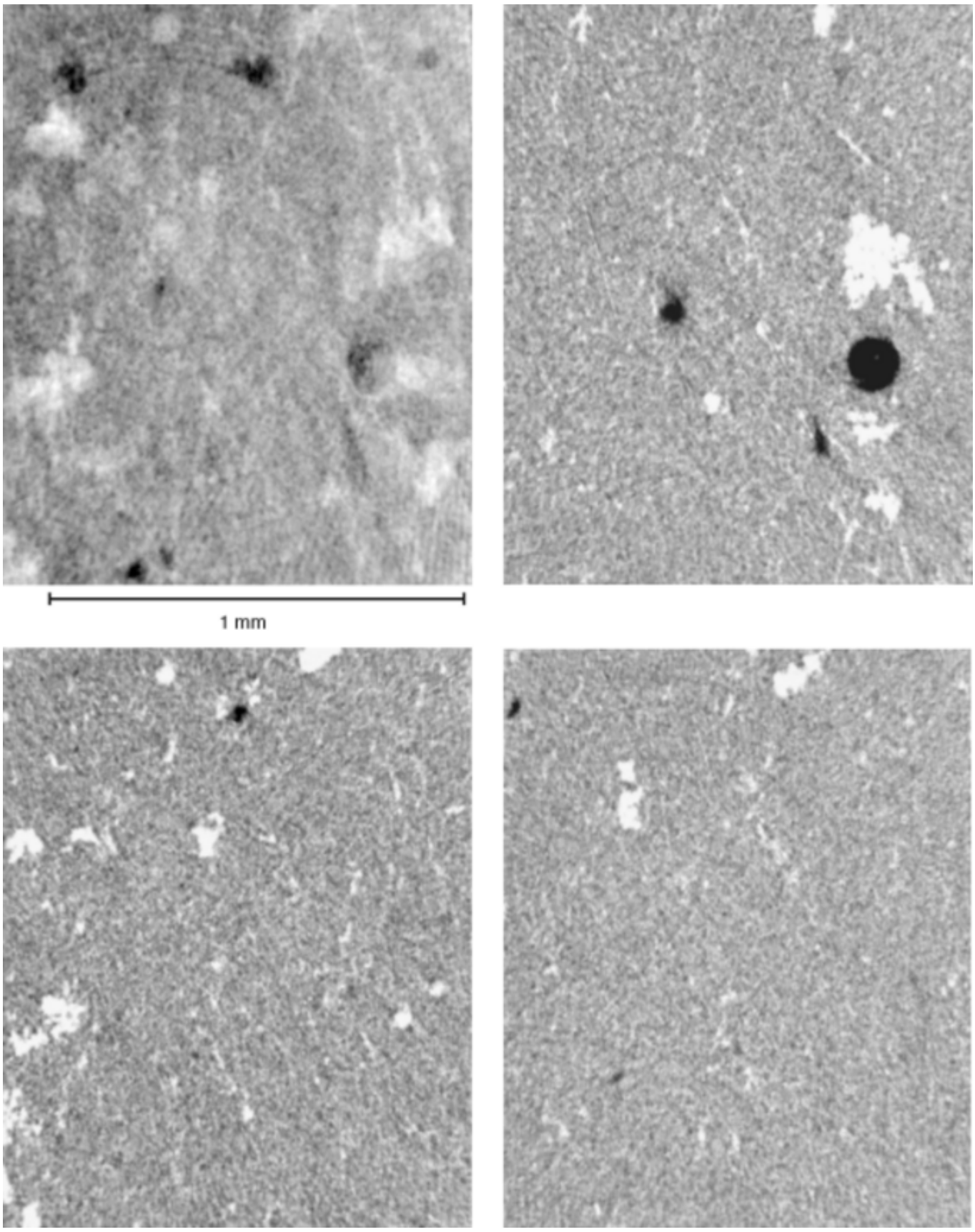

Fig. 26 Simulated x-ray image, computed on the basis of 126 sections (upper left image) and three sample sections of a silicon-aluminum-base composite material. White areas denote pores.

During this examination, similar resolution in all directions is possible. Thanks to this, the subsequent 3-D reconstruction can provide real shape and arrangement of features not available in other methods (Fig. 27). It is important to discriminate between software packages devoted to 3-D reconstruction or rendering and programs for image analysis. Software dedicated to reconstruction is more frequently available and allows for creation of

breathtaking illustrations. However, such packages do not allow for any analysis of 3-D images. By contrast, image analysis packages equipped with 3-D analysis tools allow for filtering, binarization, and measurements similar to those used for typical 2-D image analysis. Unfortunately, such programs are relatively expensive and require much computing power and computer memory for processing. For example, a relatively small, gray-scale 3-D image of resolution 256 by 256 by 256 pixels needs nearly 17 megabytes of memory without compression. However, only 3-D analysis offers the ability to obtain real, volumetric distribution of some features in the analyzed microstructure (Fig. 28). Thanks to the complexity of 3-D images, one can obtain precise information concerning size, shape, and spatial position of the objects analyzed. This is especially important if one discusses problems of continuity of neighboring objects and their spatial orientation. Obviously, similar to other tools, 3-D image analysis has its own limitations. For example, available resolutions are lower than in the case of microscopic techniques, and it is practically impossible to detect grain boundaries. To summarize, this modern tool seems to be especially suitable for assessment of porosity and homogeneity of materials built of phases, with composition enabling good contrast in x-ray images. More data can be found in the article “Three-Dimensional Microscopy” in this Volume.

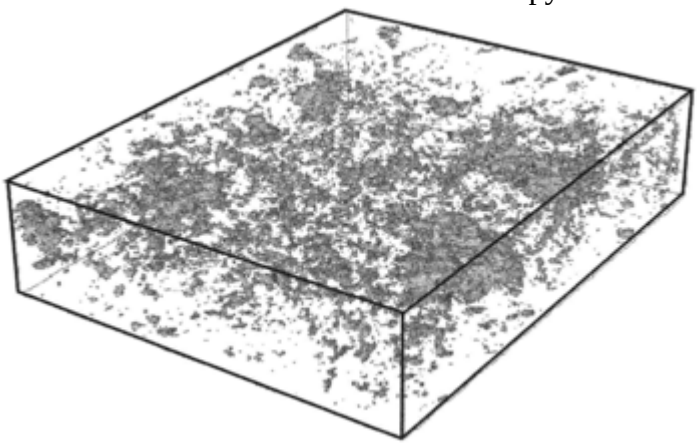

Fig. 27 Three-dimensional reconstruction of the pores

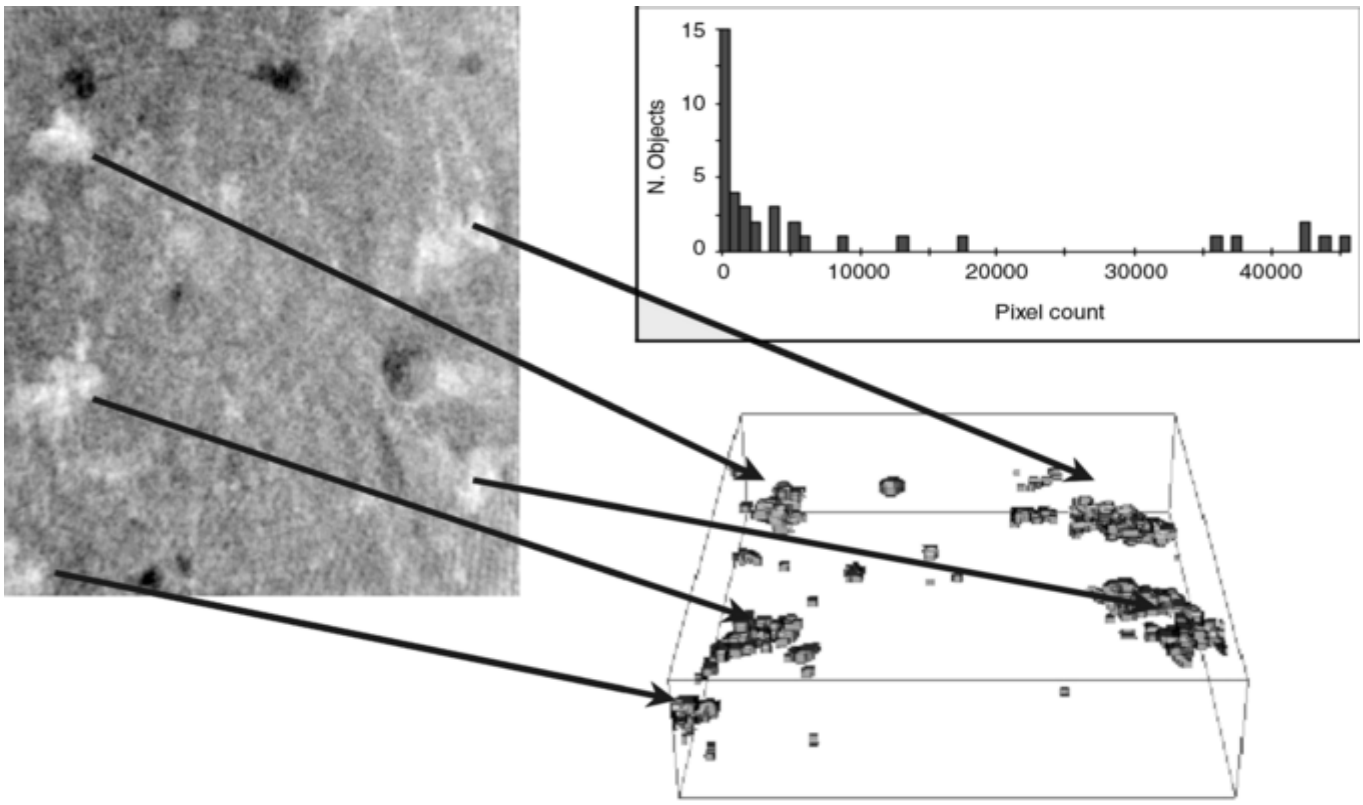

Fig. 28 Spatial arrangement of the pores compared with the x-ray image. The plot illustrates the volume distribution of the largest pores.

References cited in this section

57. J.D. Bryant, Stereo-Photogrammetry as Applied to Fractography, *Advances in Fracture Research Proc. ICF7,* (Houston, TX), International Congress on Fracture, 1989, p 3365

58. J. Chrapoński, M. Maliński, and J. Cwajna, The Algorithm of Three-Dimensional Reconstruction and Its Application in the Materials Science Investigations, *Inz. Materialowa,* Vol 17, 1996, p 206 (in Polish)

59. O. Faugeras, *Three-Dimensional Computer Vision,* MIT Press, 1993

60. M. Maliński and J. Chrapoński, 3-D Modelling of Polycrystalline Grain Structures, Part I and II, *Proc. Q-Mat'97, International Conference on the Quantitative Description of Materials Microstructure* (Warsaw, Poland), Polish Society for Stereology, 1997, p 383

L. Wojnar, K.J. Kurzydłowski, and J. Szala, Quantitative Image Analysis, *Metallography and Microstructures,* Vol 9, *ASM Handbook,* ASM International, 2004, p. 403–427

Quantitative Image Analysis

Leszek Wojnar, Kraków University of Technology, Kraków, Poland; Krzysztof J. Kurzydłowski, Warsaw University of Technology, Warsaw, Poland; Janusz Szala, Silesian University of Technology, Katowice, Poland

---

Quantification and Minimizing the Bias of Measurements

There is a basic difference between the bias of classical manual stereological analysis and quantitative image analysis. Most of the manual methods are based on one of the following methods (Ref 11, 18):

- Counting the number of points selected from the set chosen by random point selection or a grid of points (usually points of intersection of a square grid)
- Counting the number of points lying on the intersection between the system of test lines (chords) and edges of the analyzed features
- Measuring the lengths of intercepts created by test lines (chords) hitting the analyzed features

It is assumed that the choice of test points or lines fulfills the rules of randomness, and, consequently, the result obtained is a random variable. By knowing the parameters of the probability density function for this variable, one can evaluate the bias of the method itself. On the basis of such analysis, it is possible, for example, to estimate the number of test points or FOV necessary to estimate the volume fraction with a predefined relative error. Such analysis cannot be done in the case of image analysis methods, because all the pixels in the image are taken into account, not just selected ones. Computer-aided image measurements take into account the whole set of information available in the image. In that way, the measurements done in a single FOV are accurate in such a sense that any repeated analysis will give the same result. Obviously, results obtained using quantitative image analysis also can be heavily biased, but the sources of this bias are different in nature from that of manual analysis. The main sources of bias in image analysis are:

- Nonhomogeneity of the microstructure, which causes the results obtained from several FOV to be different (this source of bias also affects the results of manual analysis)
- Errors in specimen preparation and image acquisition that can lead to significantly distorted initial images (this source of bias can be minimized in manual analysis performed by an experienced operator and, consequently, amplified by a novice)

- Errors in introductory image processing, such as noise reduction, shade correction, and edge detection
- Erroneous binarization (most of the measurements are performed in binary images)
- Errors in digital measurements (such as errors of perimeter evaluation, as shown in Table 5)

Many sources of errors are unavoidable, even if the best care and procedures are used. However, some knowledge of the nature of these faults allows for minimizing or even eliminating their effect on the final microstructural quantification.

The effect of structural nonhomogeneity on the analysis results is a problem similar to quantification of the phase distribution, discussed earlier in this article. One can compute the mean value of the measurements as an arithmetic mean, denoted here by $\overline{x}$, which estimates the expected value of the measured parameter. Next, one should quantify the scatter, for example, using the standard deviation *s*, defined as a square root of the variance:

$$s = \sqrt{\frac{1}{n-1}\sum_{i=1}^{n}(x_i - \overline{x})^2} \qquad \text{(Eq 17)}$$

where x_i is the *i*th individual result, and *n* denotes the number of measurements.

Assuming the results obtained from different FOV have normal distribution (this condition should be checked using appropriate statistical tests), one can estimate the confidence interval for the mean value *CI* (Note: This is not the confidence interval for all the results under analysis), which can be computed as:

$$CI = t_{\alpha,n-1} \cdot \frac{s}{\sqrt{n}} \qquad \text{(Eq 18)}$$

where $t_{\alpha,n-1}$ is the value of the *t* (student) statistics for the significance level α and *n* - 1 degrees of freedom. Exact values of *t*-statistics can be found in statistical tables or are easily accessible in any software for statistical evaluation, including most popular spreadsheets. Note that the *t*-statistics are used for computations in the case of normal distribution and statistical probes (here, the number of FOV) smaller than 25. In the case of larger sets, both statistics, that is, student and normal (Gaussian), are practically identical.

The confidence interval has a straightforward interpretation. If its value is estimated for, say, α = 0.05, one can expect that after performing a whole series of measurements, in 95% (1 - α) of the cases, the mean value obtained from a single series of measurmements will be greater than $\overline{x} - CI$ and smaller than $\overline{x} + CI$. If the number of FOV is not very large (usually smaller than 30), the standard deviation tends to decrease as the number of FOV increases. This observation can be used for estimation of the necessary number of FOV. A criterion for such analysis can be, for example, the assumed relative error γ:

$$\gamma = \frac{CI}{\overline{x}} \qquad \text{(Eq 19)}$$

One should remember, however, that even if the number of measurements increases to very high values, the scatter of results never reaches a zero value.

The analysis of large sets of images has allowed for defining very simple, practical guidelines for the analysis of selected features in metallography. It has been demonstrated that measuring approximately 500 grains leads to stable grain size distribution. Increasing the number of quantified grains does not affect the results in a noticeable way. Similar observations in the case of isolated particles led to the conclusion that 1000 particles is the upper limit of our needs. Obviously, the aforementioned numbers will not ensure correct results if the rules of specimen preparation and choice of FOV are not satisfied (Ref 61, 62, 63).

Bias induced by errors in specimen preparation and image acquisition can be impossible for quantification and statistical analysis to deal with, because it can be qualitative in character. For example, using an as-polished specimen instead of an etched one will lead to obvious misinterpretation of the microstructure. To avoid such errors, one should carefully follow the guidelines for specimen preparation.

Errors introduced during quantitative image analysis can be catagorized as those introduced by image processing and binarization. It is difficult to quantify them, because one usually has no reference values to compare to the values obtained from the measurements. Reference values, if available, can also be biased. There are two solutions that allow for optimization of the research methods: interlaboratory round-robin programs and simulation.

Round-robin programs involve the same specimens or images being analyzed in several independent laboratories. The results obtained, together with detailed descriptions of the procedures applied, are collected

and analyzed. Such analysis helps to develop commonly accepted, standardized research procedures. Unfortunately, this method cannot prevent systematic errors that can be made in every laboratory involved in such a research program.

Simulation. The only way for objective quantification of the image-processing procedures is to test them on the simulated images with a priori known values of the parameters to be estimated.

Binarization would be very easy if the gray-scale images were very well contrasted, as shown in Fig. 29(a). Unfortunately, even if the best equipment and specimen preparation are used, some gradation in the gray levels is observed at the object boundary (Fig. 29b). It is clear from this image that the area and perimeter of detected features change with the threshold level. On the basis of numerous tests, it is advisable to apply a threshold level that is the arithmetic mean of two gray levels, representative for the feature analyzed (pore, particle, etc.) and the surrounding matrix, respectively. Regrettably, this criterion can be fulfilled only by images of perfect quality. In reality, most images exhibit some irregularities, called (not necessarily correctly) shade. A simulated image (Fig. 30) illustrates this problem.

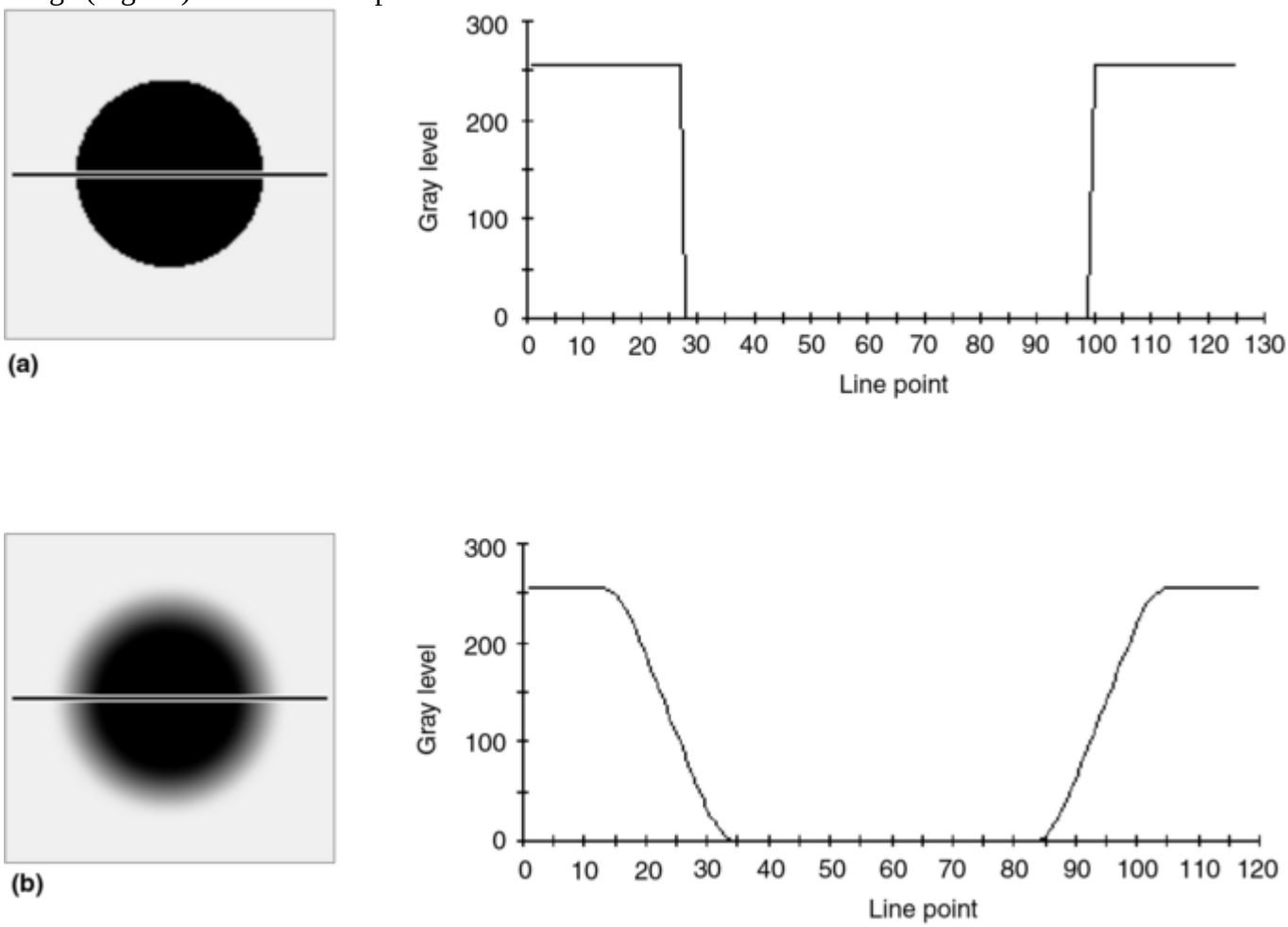

Fig. 29 Simulated images of a single pore or particle. (a) Idealized. (b) Simulated, more realistic image. Gray-level distribution functions are plotted along the line segments shown in each image.

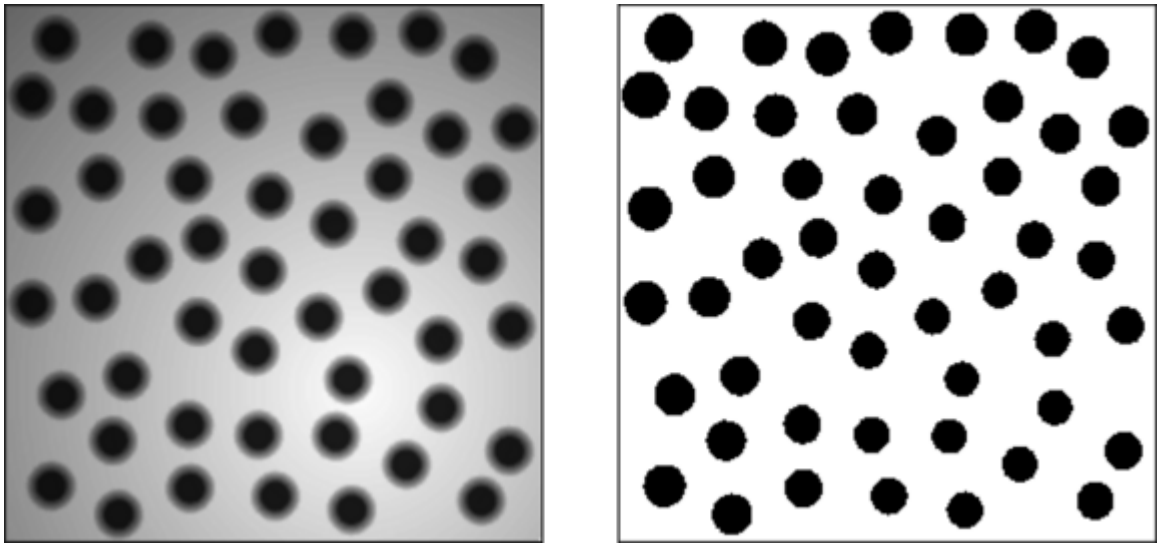

Fig. 30 Simulated image with uneven illumination (left) and the result of simple binarization (right)

Prior to the discussion of shade correction methods, some comments on automatic binarization should be added. There are numerous methods of automatic binarization. Most of them assume bimodal character of the gray-level histogram of the image. Among these methods, one can list, for example, the following criteria (Ref 19):

- Local minimum of the histogram
- Maximum histogram variance (the result is good when the two phases have similar fractions—in the range of approximately 40 to 60%) (Ref 64)
- Maximum entropy (the result is good when the two phases have different fractions—approximately 90 and 10%) (Ref 65)
- Maximum contrast (Ref 66)

For more detailed explanations, the reader should refer to specialized papers (Ref 64, 65, 66). Here, the authors would like to stress that none of these methods is universal. Each one has its own limitations and can be applied on a limited scale only.

Shade Correction. Uneven illumination visible in the left image in Fig. 30 simulates problems that frequently occur in practice. Figure 31(a) further illustrates the difficulties met by researchers. An image with a line overlying the microstructure is given on the left. The gray-level distribution along this selected line is shown in the middle column, and the right column of Fig. 31(a) contains a binarized image of the original. It is clear from the plots in Fig. 31(a) that binarization will lead to detection of overestimated features in dark regions and underestimated features in bright areas. The image on the right side of Fig. 31(a) supports this prediction. In order to suppress this phenomenon, various types of shade correction are used.

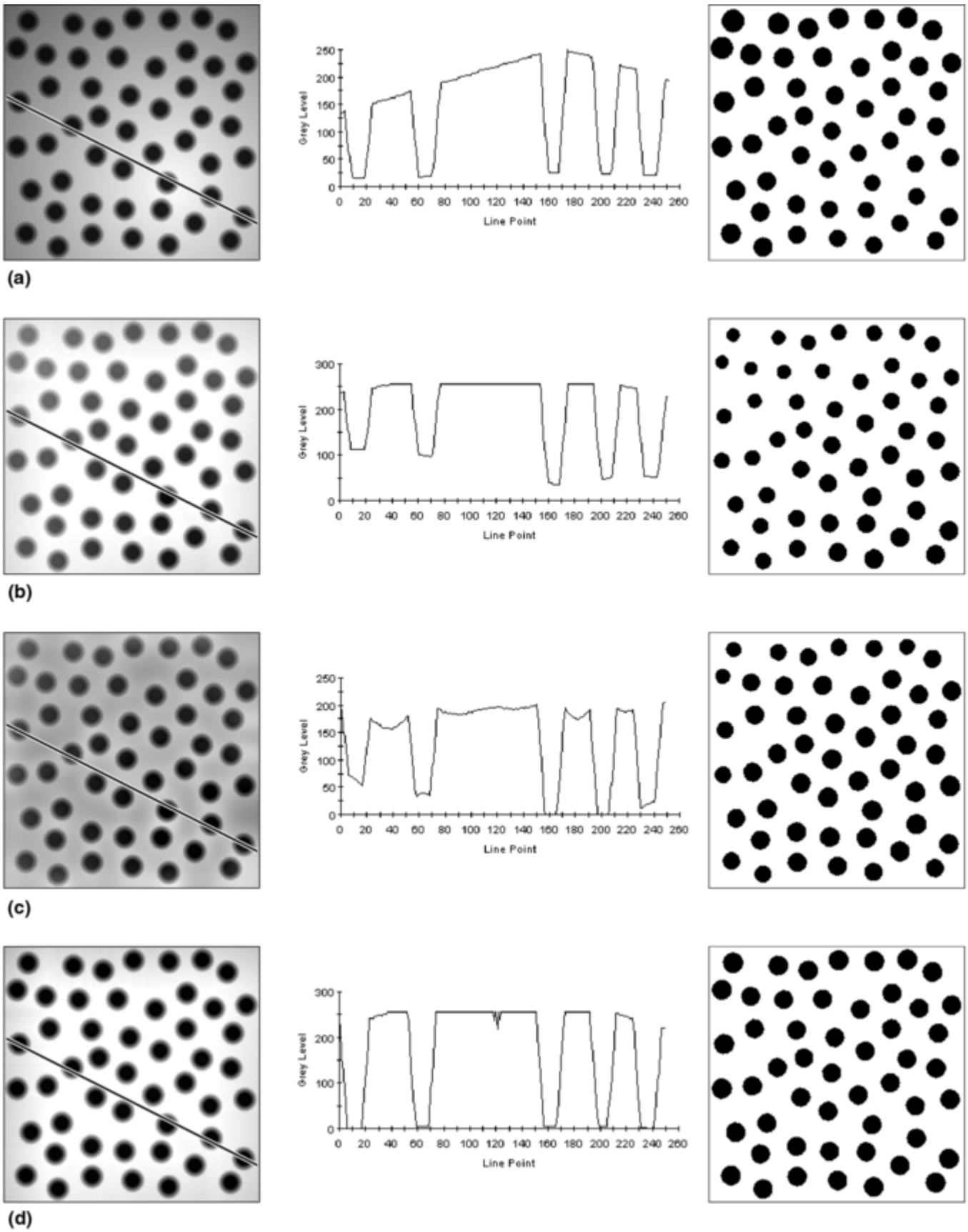

Fig. 31 Effect of shade correction procedures on initial and binary images. (a) Initial image with simulated uneven illumination. (b) Shade correction based on summation of the initial image and the negative of the matrix. (c) Shade correction based on removal of the lowest frequencies from the initial image. (d) Shade correction based on summation proportional to the gray values of the initial image. See text for detailed description.

Simple addition is the most common method and consists of two steps. The first step produces a generalized image of the background, usually using closing (dilation with erosion following it) or some interpolation methods. This image, after inversion (negative), is added to the initial image in the second step. The results of such shade correction are presented in Fig. 31(b). The background is almost perfectly uniform (small errors can be observed at the edges of the image; this effect is a consequence of the application of a fully automatic correction method and has no significant effect on the final results), but some of the dark objects are too bright (Fig. 31b, middle). As a consequence, objects situated in the bright regions of the initial image are correctly detected, whereas objects from the dark regions are (in contrast to the previous case) underestimated. This method of correction gives underestimated values of area (volume fraction, V_V), but the results are better than those obtained without any correction (Table 7) (Ref 19, 20, 42).

Table 7 Effect of correction method on the results of porosity estimation in a simulated image with uneven illumination

	Test image without shade fault	Test image with imposed shade fault	Simple addition	Removal of low frequencies	Proportional
Reference figure	…	Fig. 31(a)	Fig. 31(b)	Fig. 31(c)	Fig. 31(d)
Area (volume) estimate, V_V	0.205	0.32	0.17	0.24	0.215

The removal of low frequencies concept is based on the observation that the background illumination usually changes smoothly and slowly. If the image is interpreted as a collection of waves describing gray level (this is the basic principle of Fourier transformation), then shade can be recognized as waves of the lowest frequency. Consequently, removal of these lowest frequencies should lead to a corrected image (Fig. 31c). The result is slightly better than in the case of the previous correction method and leads to a binary image with more homogeneous-sized objects. Unfortunately, this correction still leads to a biased value of V_V (Table 7).

The proportional correction method presented in Fig. 31(d) is similar in principle to the first in that it uses simple addition of the negative of the background to the initial image. The difference is that the values of the inverted background are added proportionally to the initial values. Consequently, the darkest points remain dark irrespective of the value that is added. This new concept leads to the best results, as illustrated in Fig. 31(d), middle. The binary image obtained after this correction consists of objects of nearly identical size, as in the initial test image. The obtained values of the V_V fraction are in good agreement with the ones obtained from images without shade.

It is noteworthy that the distortion presented in the simulated image used for this analysis is much higher than in the majority of real images. Therefore, the application of correction techniques described here can lead to almost perfect correction of uneven illumination and results that are free of systematic bias. Another solution is the application of adaptive segmentation methods, but this solution requires good knowledge of both the analyzed structure and the method applied. Discussion on these items lies outside the scope of this article.

References cited in this section

11. *Practical Guide to Image Analysis,* ASM International, 2000

18. K.J. Kurzydlowski and B. Ralph, *The Quantitative Description of the Microstructure of Materials,* CRC Press, 1995

19. J. Szala, Application of Computer-Aided Image Analysis Methods for a Quantitative Evaluation of Material Structure, *Zesz. Nauk. Politech. Slask., Hutn.,* Vol 61, 2001, p 1–167 (in Polish)

20. L. Wojnar, *Image Analysis, Applications in Materials Engineering,* CRC Press, 1999

42. J.C. Russ, *The Image Processing Handbook,* 2nd ed., CRC Press, 1995

61. J. Chrapoński and M. Maliński, Estimation of Grain Size, Part I–III, *Proc. Q-Mat'97, International Conference on the Quantitative Description of Materials Microstructure* (Warsaw, Poland), Polish Society for Stereology, 1997, p 215

62. J. Cwajna, Quantitative Structural Criteria of Steel Quality Control, *Acta Stereol.,* Vol 13, 1994, p 409

63. J. Cwajna, J. Richter, and J. Szala, Quantitative Metallography and Fractography of Modern Tool Alloys, *Proc. Q-Mat'97, International Conference on the Quantitative Description of Materials Microstructure* (Warsaw, Poland), Polish Society for Stereology, 1997, p 125

64. N. Otsu, A Threshold Level Selection Method from Gray Level Histograms, *IEEE Trans. Syst. Man. Cybern.,* Vol 9, 1979, p 62–66

65. J.N. Kapur, P.K. Sahoo, and A.K.C. Wong, A New Method for Gray Level Picture Thresholding Using the Entropy Histogram, *Comput. Vis. Graph. Image Proc.,* Vol 29, 1985, p 273–285

66. R. Kohler, A Segmentation System Based on Thresholding, *Comput. Graphics Image Process.,* Vol 15, 1981, p 319–338

L. Wojnar, K.J. Kurzydłowski, and J. Szala, Quantitative Image Analysis, *Metallography and Microstructures,* Vol 9, *ASM Handbook,* ASM International, 2004, p. 403–427

Quantitative Image Analysis

Leszek Wojnar, Kraków University of Technology, Kraków, Poland; Krzysztof J. Kurzydłowski, Warsaw University of Technology, Warsaw, Poland; Janusz Szala, Silesian University of Technology, Katowice, Poland

---

Examples of Automatic Quantitative Image Analysis

The examples presented are selected to demonstrate the usefulness of automatic image analysis in comparison to manual methods. There are many well-documented examples of successful simple as well as complex applications of quantitative image analysis in materials science literature (Ref 6, 10, 13, 15, 19, 20, 42, 63, 67, 68, 69, 70, 71, 72, 73, 74, 75, 76, 77, 78, 79). Many more applications are described in other articles of this Volume.

Example 1: Estimating the Volume Fraction of Graphite in Cast Iron. This example demonstrates how the correct shade correction and binarization allows for fully automatic and unbiased estimation of the graphite volume fraction. Three different grades of cast iron were made from the same initial cast, thus ensuring practically identical chemical composition. Depending on final modification and cooling rates, three types of cast iron with graphite of various shapes were obtained (Ref 80):

- Malleable cast iron with vermicular and thin flake graphite (Fig. 32a)
- Gray iron with flake graphite (Fig. 32b)
- Nodular iron with spheroidal graphite (Fig. 32c)

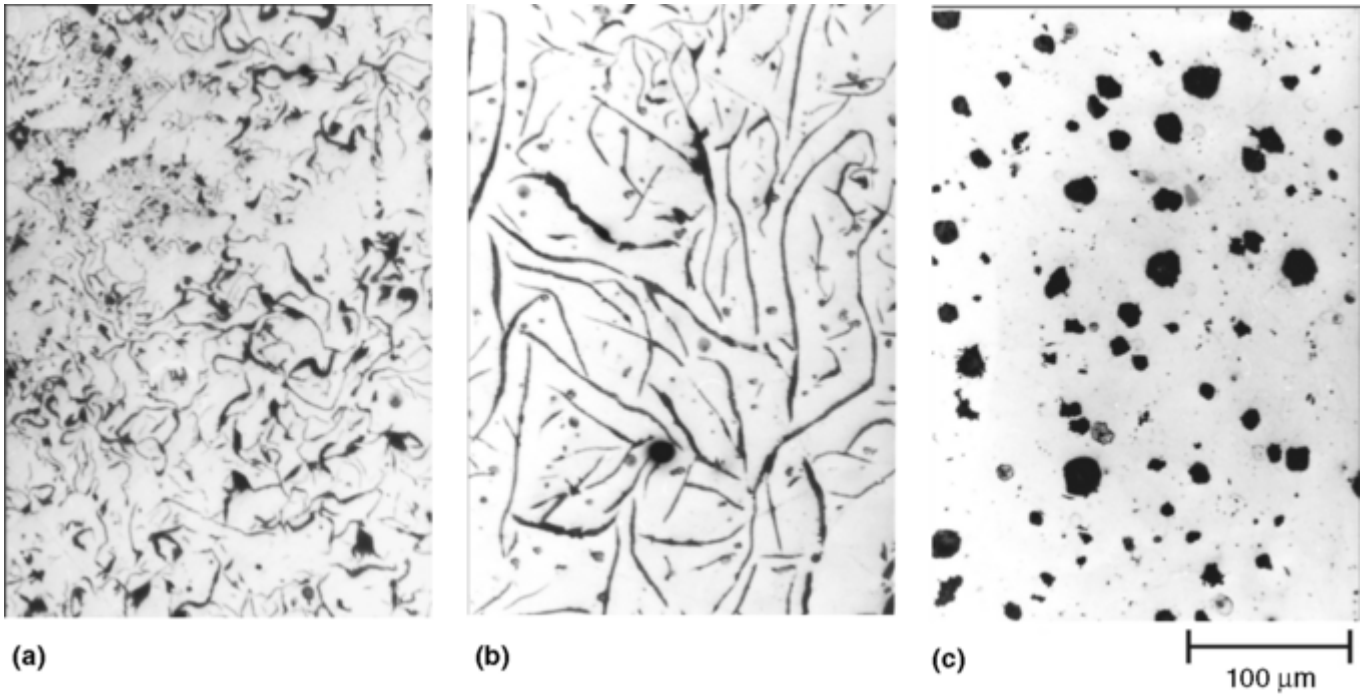

Fig. 32 Three types of cast iron, (a) malleable, (b) gray, and (c) nodular, made from the same basic cast. See text for details.

All the materials tested had a ferritic matrix in the as-cast condition; therefore, the whole content of carbon was observed as graphite precipitates. Knowing the chemical composition of the cast iron, one can approximate the content of graphite as (Ref 81):

$$V_V\left(\text{graphite}\right)=\frac{7.8\cdot\%\text{C}}{222+5.6\cdot\%\text{C}} \qquad \text{(Eq 20)}$$

where %C denotes the carbon content present in the form of graphite. The carbon content in the cast iron under study was relatively low, namely, 2.65%. Consequently, one can estimate the expected graphite content as being equal to 8.7%.

The digital images of the microstructures (Fig. 33) covered the whole range of gray levels (0 to 255), so the optimal threshold level was chosen at 128. The gray and nodular iron at this threshold level gave slightly higher values of V_V, equal to 9.1% graphite, whereas malleable iron gave a significant overestimate of 11%.

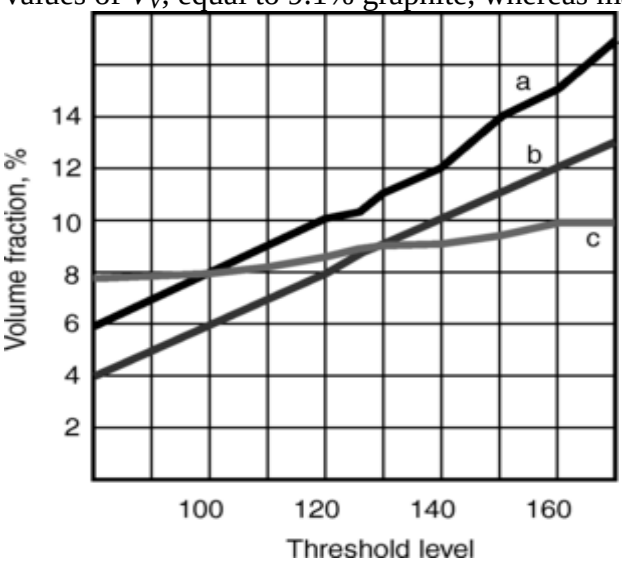

Fig. 33 Effect of threshold level on the estimated volume fraction of graphite for the (a) malleable, (b) gray, and (c) nodular cast irons shown in Fig. 32 Detection of graphite was performed without shade correction.

The analysis was repeated after shade correction performed according to the rules described in this article, and all the cast irons gave nearly the same value, namely, 8.5 to 8.7 at the threshold level 128 (Fig. 34). These results demonstrate that correct analysis, including all the steps of specimen preparation, image acquisition, image processing, and binarization, can lead to correct results. What is important is that these results can be obtained quickly in a fully automatic way that ensures maximum objectivity of the analysis.

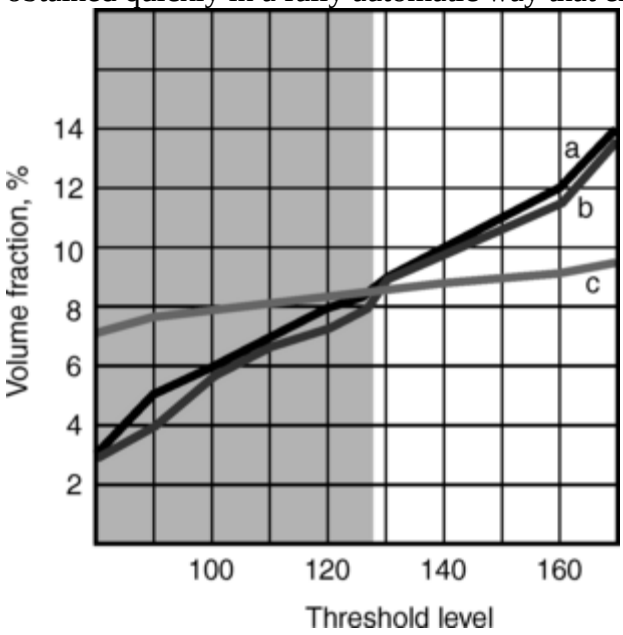

Fig. 34 Effect of threshold level on the estimated volume fraction of graphite for the (a) malleable, (b) gray, and (c) nodular cast irons shown in Fig. 32 Detection of graphite was performed after shade correction. The right edge of the grayed region in the plot represents the theoretically optimal threshold level. Note that the same volume fraction was estimated for every cast iron, if the threshold level was equal to 128.

Moreover, Fig. 33 and Fig. 34 demonstrate how the improper choice of threshold level can affect the results. The nodular iron (curve “c”) has a relatively low sensitivity to the changes in threshold level. The malleable and gray irons (curves “a” and “b”) have resulting values overestimated or underestimated up to approximately 60% if the threshold level was only approximately 30% too high or too low. It is noteworthy that variation of the threshold level in such a range can easily happen during manual detection.

Example 2: Automatic Classification of the Shape of Graphite in Cast Iron. Two microstructures, demonstrating different graphite morphology, are shown in Fig. 35(a) and (c). Note that the brightness and contrast of these images differ significantly. In spite of this, thanks to appropriate image processing, both types of images can be processed automatically to produce a quantitative description of the shape distribution of the graphite precipitates. This classification is based on the shape factor f_3 (Eq 15). The whole spectrum of shapes is divided into four classes: (regular) nodular graphite, irregular graphite, vermicular, and flake graphite. Graphite distribution is illustrated in the plots in Fig. 35(b) and (d), respectively. Gray levels in the image mark graphite particles of different shapes and correspond with the shade of the bars. The height of the microstructural image represents the value of 50%. So, the fractions of particles with irregular graphite in Fig. 35(b) and particles with flake graphite in Fig. 35(d) are both equal to approximately 47%.

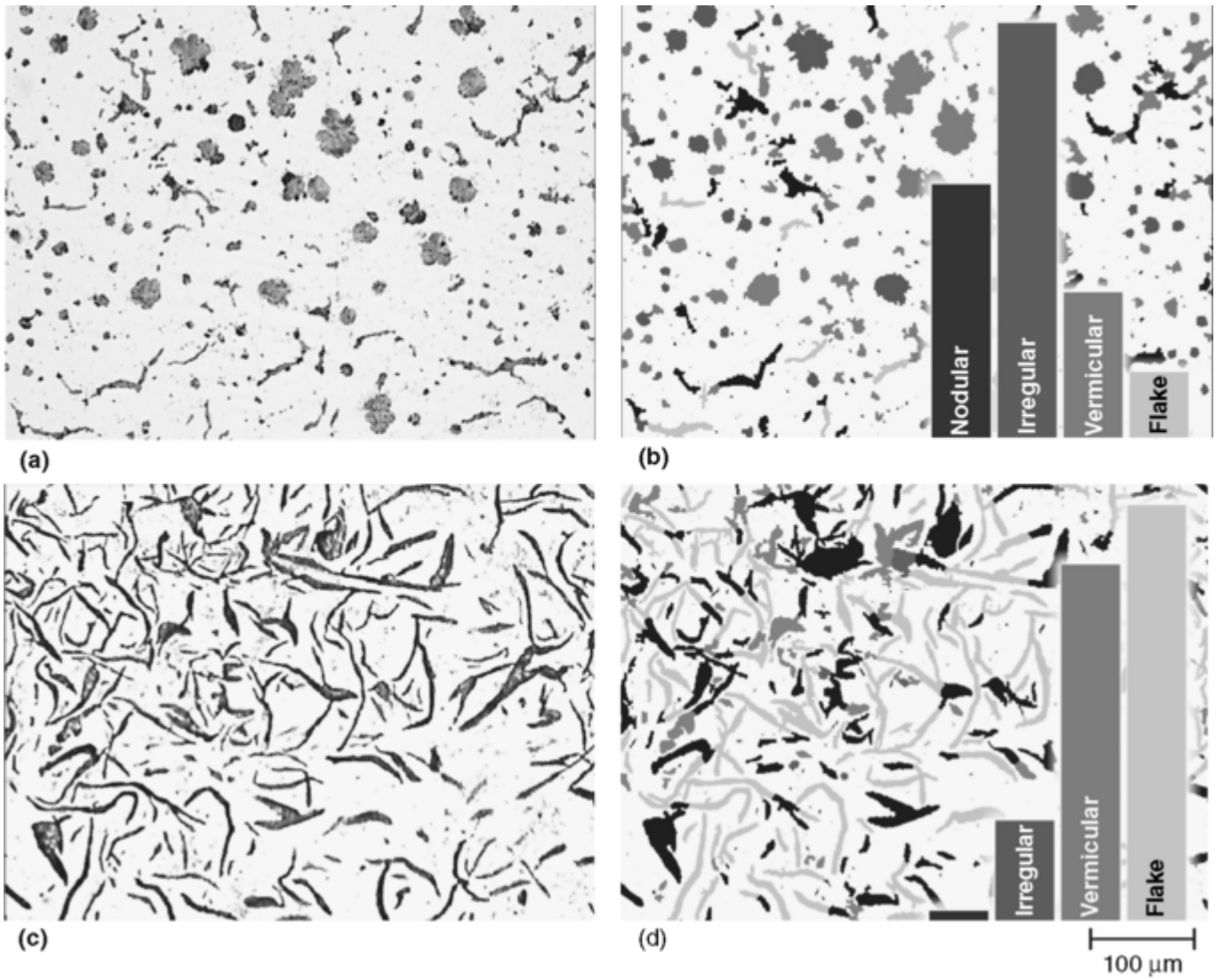

Fig. 35 Automatic classification of shape of graphite precipitates in cast iron. Two different morphologies are given in (a) and (c). Each is categorized and quantified in (b) and (d), respectively, where the particle shades correspond to the bar chart. The full height of the image corresponds to 50% on the bar chart, so both irregular graphite in (b) and flake graphite in (d) comprise approximately 47%.

Obviously, this classification is not absolutely perfect. For example, some graphite flakes are segmented into smaller particles, thus increasing the fraction of vermicular precipitations. Nevertheless, this is only a small, systematic shift that has no influence on the classification. The main advantages of the presented solution are speed and objectivity. As a consequence, one obtains almost immediate quantitative information. These results are sufficient for optimization of cast iron modification in the foundry industry (Ref 20, 82).

Example 3: Automatic Grain Size Assessment. Grain size evaluation is one of the most common applications of image analysis. However, there are still some doubts about how the results of automatic quantification are related to manual analysis. Therefore, this example is devoted to a comparison of these methods. A series of 12 microstructures of austenitic steel with well-defined grain boundaries (Fig. 4, which shows a fragment of one of the images investigated), each containing more than 250 grains, was used for comparison.

Digital images, used for image analysis, were printed on a laser printer, and these printouts were used for manual measurements. Thus, manual analysis was performed on the same images as automatic quantification. In order to test the scatter of the results, six independent observers examined all the images, and every person analyzed all 12 microstructures. Image analysis was performed in a fully automatic way, using four different algorithms for grain-boundary detection. As expected, such research produced a set of results with some scatter (Fig. 36) (Ref 40).

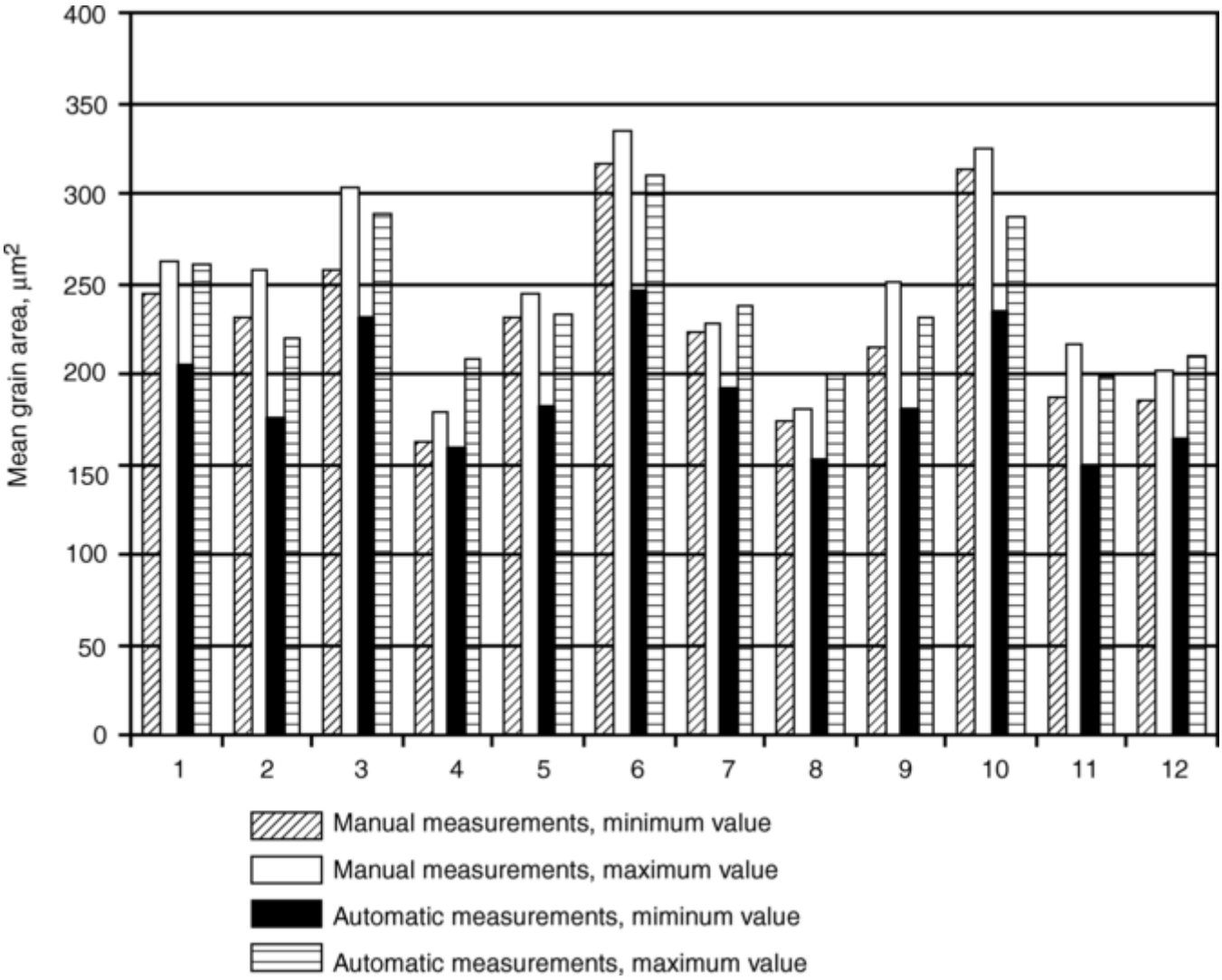

Fig. 36 Comparison of the results of grain size assessment using manual and image analysis methods

Detailed analysis of the results leads to the following observations and conclusions:

- Automatic analysis is dramatically faster than the manual technique (15 s versus 25 min). Therefore, in any extended research program, automatic analysis has practically no alternative.
- Very small grains are rejected in automatic analysis, because they can be mixed with artifacts. Consequently, in most cases, automatic analysis gives slightly lower values than the manual method (this difference can reach approximately 30% of the higher value). Therefore, one should check the results of detection prior to their subsequent use. It should be noted, however, that the automatic analysis was performed without any manual correction. In practical applications, the operator can visually check the correctness of detection and, in case of poor results, change the algorithm.
- In spite of the differences, all the methods applied give a similar classification of the microstructures under study. This is a very important observation, supporting the opinion that any detection errors in the automatic methods have a systematic character. Consequently, they do not affect the classification results.

Finally, the scatter of results can be neglected if one expresses the grain size by means of ASTM grain size number. All of the methods discussed return the same values. In such circumstances, automatic analysis remains the best available tool for quality control.

Example 4: Automatic Porosity Control. This example is described in the section “Shade Correction” (Fig. 30, Fig. 31). Pores, due to their contrast with the rest of the image, are relatively easy to detect automatically. The correction procedures described previously allowed for an almost perfect fit with semiautomatic analysis (differences lower than 3% of the measured value). Moreover, the scatter of results obtained from manual

methods, measured by means of standard deviation, was comparable with the automatically measured values. Consequently, the ease of use and the speed of fully automatic analysis makes it the preferred tool in porosity assessment.

The method discussed here was successfully implemented for industrial quality control of cast blades for jet engines.

Example 5: Structural Maps. Materials may exhibit significant variation in their microstructure, called nonhomogeneity. Quantifying this property is difficult. However, one can use a semiquantitative tool that is sufficient for practical applications. Structural maps show the variation of a chosen quantity over large areas. The preparation of structural maps on the basis of manual measurements is practically impossible, because the local inhomogeneity causes large scatter of the results of manual quantification (Fig. 37). Moreover, the necessity to analyze tens or hundreds of FOV is a natural argument toward automation of this process (Ref 19, 62, 70, 83, 84).

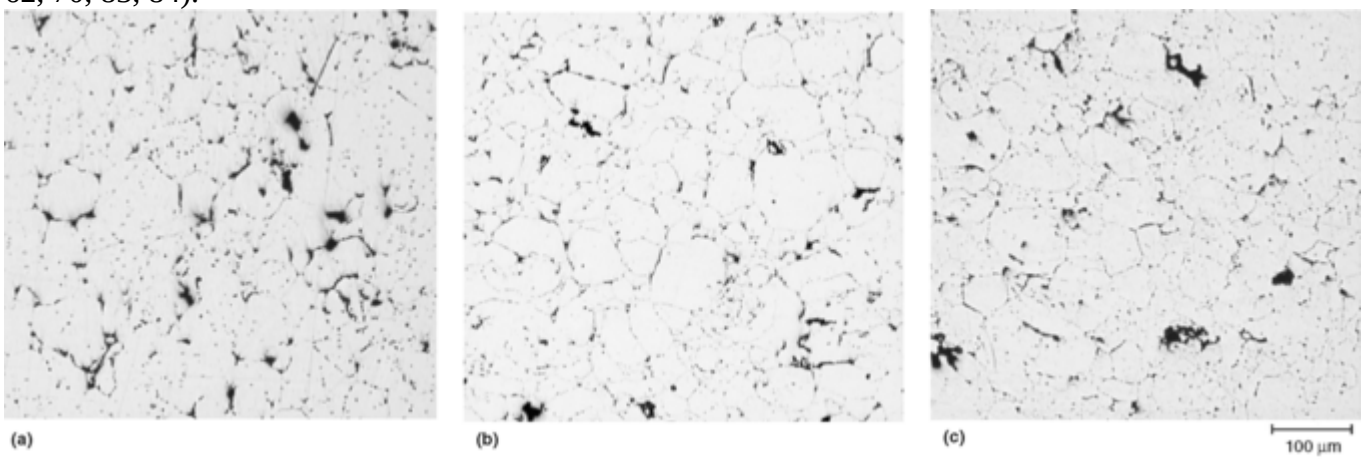

Fig. 37 Comparison of porosity visible in polished sections of three sintered materials, (a), (b), and (c), each having a different heat treatment, as explained in text

Figure 37 shows typical sections of disk-shaped specimens, obtained from sintering a vitallium-type Co-Cr-Mo alloy. Three specimens, designated (a), (b), and (c), respectively, were used for experiments:

- Material A was sintered for 1 h at 1150 °C (2100 °F) in a pure argon atmosphere.
- Material B was additionally subjected to cold rotary pressing at a nominal pressure of 600 MPa (87 ksi).
- Material C was processed similar to B and was additionally subjected to 1 h of annealing in a pure argon atmosphere, with subsequent cooling in the furnace cool zone.

The previously described processing should theoretically change the porosity level and distribution. Unfortunately, this effect is not visible on single-polished sections (Fig. 37). However, the effect of additional treatment is clearly visible in structural maps that show a continuous, systematic drop in porosity (Fig. 38). Moreover, the structural maps are not ideally symmetrical, which demonstrates some lack of symmetry during the initial pressing of the samples. Such a conclusion could not be drawn without the preparation of structural maps.

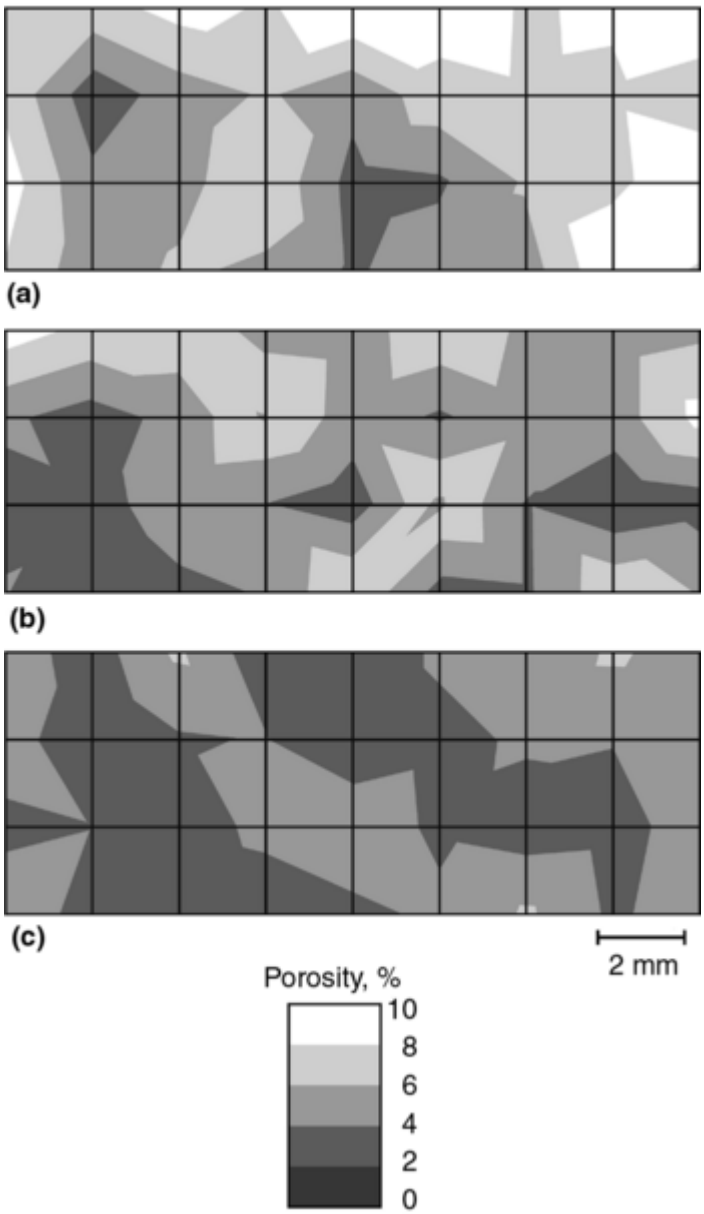

Fig. 38 Structural maps, illustrating porosity variation, taken from cross sections of cylindrical, sintered specimens

The construction of the maps shown in Fig. 38 is very simple. A set of systematically shifted FOV was used to evaluate local porosity. Locations of these FOV correspond with the nodes in the square grid of the maps. The areas of various porosity have been evaluated on the basis of the porosity values at the nodes and subsequent linear interpolation. In spite of its apparent simplicity, the maps provide very useful, graphic information concerning the nonhomogeneity of the porosity.

Another example is shown in Fig. 39, which illustrates the effect of liquid-state modification of SKC high-speed steel on the contents of carbide eutectics. Significant improvement is observed in the homogeneity after modification. Structural maps of such type can be very helpful in the optimization of the production process.

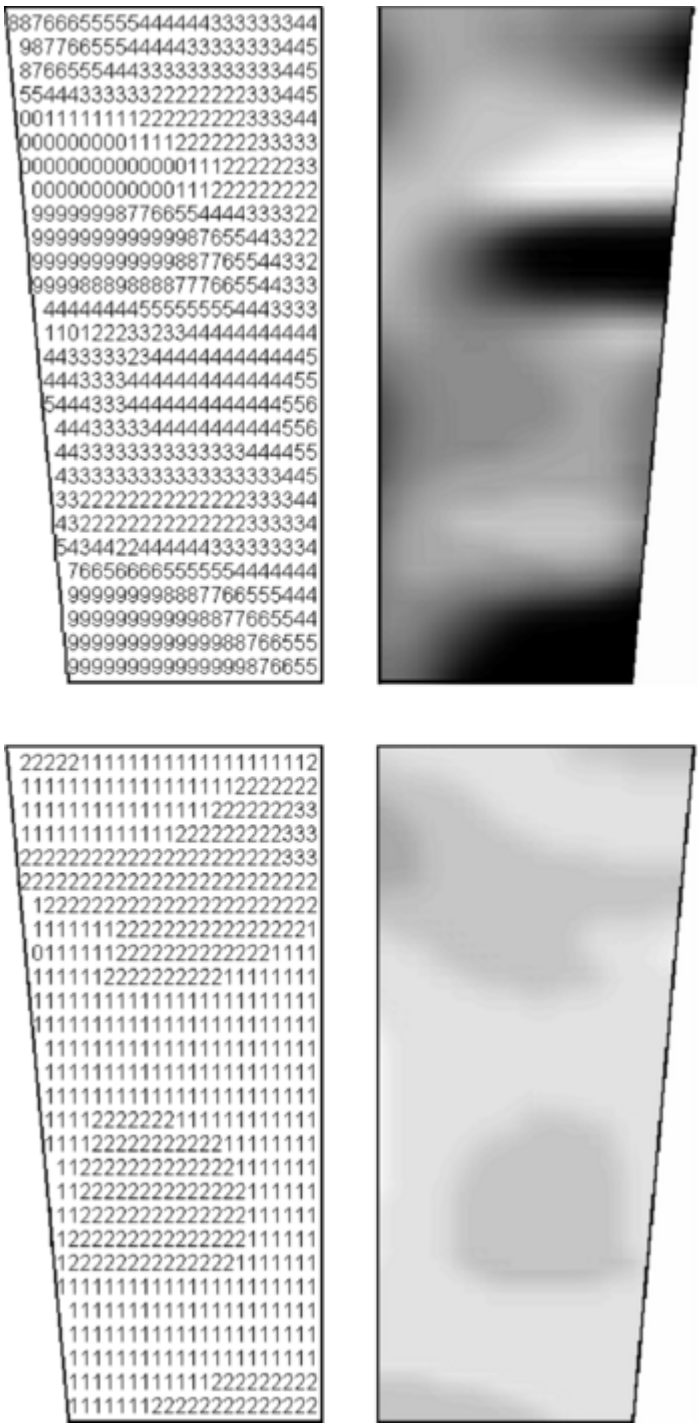

Fig. 39 Structural maps showing changes in carbide eutectics area fraction on the longitudinal cross section of an ingot of nonmodified (top) and modified (bottom) SKC high-speed steel

References cited in this section

6. G. Gauthier, M. Coster, L. Chermant, and J.L. Chermant, Morphological Segmentation of Cutting Tools, *Microsc. Microanal. Microstruct.,* Vol 7, 1996, p 339

10. F. Le Pennec and D. Malewicz, Automatic Grain Size Measurement in Low Carbon Steels by Image Analysis, *Microsc. Microanal. Microstruct.,* Vol 7, 1996, p 433

13. H. Talbot, D. Jeulin, and D. Hanton, Image Analysis of Insulation Mineral Fibers, *Microsc. Microanal. Microstruct.,* Vol 7, 1996, p 361

15. J. Chrapoński, “Analysis of Applicability of Stereological Methods of Evaluation of Grain Size in Polycrystalline Materials,” Ph.D. thesis, Silesian University of Technology, Katowice, Poland, 1997 (in Polish)

19. J. Szala, Application of Computer-Aided Image Analysis Methods for a Quantitative Evaluation of Material Structure, *Zesz. Nauk. Politech. Slask., Hutn.,* Vol 61, 2001, p 1–167 (in Polish)

20. L. Wojnar, *Image Analysis, Applications in Materials Engineering,* CRC Press, 1999

40. Z. Latala and L. Wojnar, Computer-Aided versus Manual Grain Size Assessment in a Single Phase Material, *Mater. Charact.,* Vol 46 (No. 2/3), 2001, p 227–233

42. J.C. Russ, *The Image Processing Handbook,* 2nd ed., CRC Press, 1995

62. J. Cwajna, Quantitative Structural Criteria of Steel Quality Control, *Acta Stereol.,* Vol 13, 1994, p 409

63. J. Cwajna, J. Richter, and J. Szala, Quantitative Metallography and Fractography of Modern Tool Alloys, *Proc. Q-Mat'97, International Conference on the Quantitative Description of Materials Microstructure* (Warsaw, Poland), Polish Society for Stereology, 1997, p 125

67. J.L. Chermant, *Les Ceramiques Thermomechaniques (Thermomechanical Ceramics),* Presses du CRNS, Paris, 1989

68. M. Coster, J.L. Chermant, and M. Prod'homme, Quantification of Ceramic Microstructures, *Proc. Q-Mat'97, International Conference on the Quantitative Description of Materials Microstructure* (Warsaw, Poland), Polish Society for Stereology, 1997, p 115

69. M. Coster, M. Prod'homme, L. Chermant, and J.L. Chermant, Morphological Study during a Ceramic Process, *Microsc. Microanal. Microstruct.,* Vol 7, 1996, p 407

70. J. Cwajna, Quantitative Description of the Microstructure of Tool Alloys and Its Applications, *Zesz. Nauk. Politech. Slask., Hutn.,* Vol 39, 1991 (in Polish)

71. A. Hazotte, and J. Lacaze, Quantitative Analysis of the Microstructure of Nickel Based Superalloys, *Rev. Métall.,* Vol 91, 1994, p 217

72. D. Jeulin, “Mathematical Morphology and Materials Image Analysis,” Rapport N-31/87/G, Center for Geostatics, Fontainebleau, 1987

73. M. Maliński, J. Cwajna, and J. Chrapoński, Grain Size Distribution, *Acta Stereol.,* Vol 10, 1991, p 73

74. M. Mlynarczuk and S. Beucher, Directional Fiber Analysis by Mathematical Morphology, *Proc. Q-Mat'97, International Conference on the Quantitative Description of Materials Microstructure* (Warsaw, Poland), Polish Society for Stereology, 1997, p 403

75. F. Montoya, S. Michelland, L. Chermant, M. Coster and J.L. Chermant, Size Distribution from Gray Tone Level Images: Case of Granular Materials, *Acta Stereol.,* Vol 14, 1989, p 401

76. E. Pirard, Morphometric Analysis of Powders: A Systematic and Robust Approach Using Mathematical Morphology, *Rev. Métall.,* Vol 91, 1994, p 295

77. J.L. Quenec'h, J.L. Chermant, M. Coster, and D. Jeulin, Example of Application of Probabilistic Models: Determination of the Kinetics Parameters during Liquid Phase Sintering, *Microsc. Microanal. Microstruct.,* Vol 7, 1996, p 573

78. J. Richter, J. Cwajna, and J. Szala, Verification of Empirical Structure-Properties Relations through Automatic Image Analysis of Sintered Carbides, *Proc. Q-Mat'97, International Conference on the Quantitative Description of Materials Microstructure* (Warsaw, Poland), Polish Society for Stereology, 1997, p 451

79. L. Vincent and D. Jeulin, Minimal Paths and Crack Propagation Simulations, *Acta Stereol.,* Vol 14, 1989, p 487

80. L. Wojnar and Z. Latala, On the Validity of Specimen Preparation in Automatic Analysis of the Microstructure of Cast Iron, *Proc. First Conference: Materials Science - Foundry - Quality,* (Kraków, Poland), Kraków University of Technology, 1997, p 165 (in Polish)

81. L. Wojnar, "Effect of Nodular Graphite on Fracture Toughness of Ductile Cast Iron," Ph.D. thesis, Kraków University of Technology, Kraków, Poland, 1985 (in Polish)

82. K. Huebner, Quantitative Characteristics of the Shape of Graphite Precipitates in Nodular Cast Iron, *Przegl. Odlew.,* Vol 3, 1977, p 60 (in Polish)

83. L. Wojnar, J.R. Dąbrowski, and Z. Oksiuta, Porosity of the Sintered Co-Cr-Mo Alloy Subjected to Additional Envelope Pressing and Heat Treatment, *Proc. Sixth International Conference Stereology and Image Analysis in Materials Science* (Kraków, Poland), Polish Society for Stereology, 2000, p 437–442

84. L. Wojnar, J.R. Dąbrowski, and Z. Oksiuta, Porosity Structure and Mechanical Properties of Vitallium-Type Alloy for Implants, *Mater. Charact.,* Vol 46 (No. 2/3), 2001, p 221–226

L. Wojnar, K.J. Kurzydłowski, and J. Szala, Quantitative Image Analysis, *Metallography and Microstructures,* Vol 9, *ASM Handbook,* ASM International, 2004, p. 403–427

Quantitative Image Analysis

Leszek Wojnar, Kraków University of Technology, Kraków, Poland; Krzysztof J. Kurzydłowski, Warsaw University of Technology, Warsaw, Poland; Janusz Szala, Silesian University of Technology, Katowice, Poland

---

References

1. R.T. De Hoff and F.N. Rhines, *Quantitative Microscopy,* McGraw-Hill, 1968

2. J.C. Russ, *Practical Stereology,* Plenum Press, 1986

3. J. Ryś, *Stereology of Materials,* Fotobit-Design, Kraków, Poland, 1995, p 323 (in Polish)

4. E.E. Underwood, *Quantitative Stereology,* Addison Wesley, 1970

5. E.R. Weibel, *Stereological Methods,* Academic Press, 1980, 1989

6. G. Gauthier, M. Coster, L. Chermant, and J.L. Chermant, Morphological Segmentation of Cutting Tools, *Microsc. Microanal. Microstruct.,* Vol 7, 1996, p 339

7. G. Gauthier, J.L. Quenec'h, M. Coster, and J.L. Chermant, Segmentation of Grain Boundaries in WC-Co Cermets, *Acta Stereol.,* Vol 13, 1994, p 209

8. S. Gentier, D. Billaux, D. Hopkins, F. Davias, and J. Riss, Images and Modelling of the Hydromechanical Behaviour of a Fracture, *Microsc. Microanal. Microstruct.*, Vol 7, 1996, p 513

9. K.J. Huebner, Application of Colour Metallography of Microstructural Images in Research Studies, *Proc. Q-Mat'97, International Conference on the Quantitative Description of Materials Microstructure* (Warsaw, Poland), Polish Society for Stereology, 1997, p 299

10. F. Le Pennec and D. Malewicz, Automatic Grain Size Measurement in Low Carbon Steels by Image Analysis, *Microsc. Microanal. Microstruct.*, Vol 7, 1996, p 433

11. *Practical Guide to Image Analysis*, ASM International, 2000

12. C. Redon, "Morphology and Mechanical Behavior of Amorphous Cast Iron Fiber Reinforced Concrete," Ph.D. dissertation, University of Caen, France, 1997

13. H. Talbot, D. Jeulin, and D. Hanton, Image Analysis of Insulation Mineral Fibers, *Microsc. Microanal. Microstruct.*, Vol 7, 1996, p 361

14. H. Wendrock and R. Huebel, Characterization of Microstructural Anisotropy of Steels by Means of Mathematical Morphology, *Acta Stereol.*, Vol 13, 1994, p 143

15. J. Chrapoński, "Analysis of Applicability of Stereological Methods of Evaluation of Grain Size in Polycrystalline Materials," Ph.D. thesis, Silesian University of Technology, Katowice, Poland, 1997 (in Polish)

16. M. Coster, and J.L. Chermant, *Introduction to Image Analysis*, Presses du CRNS, Paris, 1989 (in French)

17. L. Wojnar, Semiautomatic Image Analysis System—Ease of Use and Accelerated Analysis, *Second Conference on Metallography in Industrial Laboratories* (Ustron, Poland), Institute of Ferrous Metals, April 1999, p 32–40 (in Polish)

18. K.J. Kurzydlowski and B. Ralph, *The Quantitative Description of the Microstructure of Materials*, CRC Press, 1995

19. J. Szala, Application of Computer-Aided Image Analysis Methods for a Quantitative Evaluation of Material Structure, *Zesz. Nauk. Politech. Slask., Hutn.*, Vol 61, 2001, p 1–167 (in Polish)

20. L. Wojnar, *Image Analysis, Applications in Materials Engineering*, CRC Press, 1999

21. "Test Methods for Estimating the Largest Grain Observed in a Metallographic Section (ALA Grain Size)," E 930-92, *Annual Book of ASTM Standards, Section 3: Metals Test Methods and Analytical Procedures*, ASTM International, 1999, p 683–687

22. "Practice for Obtaining JK Inclusion Ratings Using Automatic Image Analysis," E 1122-96, *Annual Book of ASTM Standards, Section 3: Metals Test Methods and Analytical Procedures*, ASTM International, 1999, p 729–736

23. "Test Methods for Characterizing Duplex Grain Sizes," E 1181-87, *Annual Book of ASTM Standards, Section 3: Metals Test Methods and Analytical Procedures*, ASTM International, 1999, p 741–755

24. "Practice for Determining the Inclusion or Second Phase Constituent Content of Metals by Automatic Image Analysis," E 1245-95, *Annual Book of ASTM Standards, Section 3: Metals Test Methods and Analytical Procedures*, ASTM International, 1999, p 789–796

25. “Practice for Assessing the Degree of Banding or Orientation of Microstructures,” E 1268-94, *Annual Book of ASTM Standards, Section 3: Metals Test Methods and Analytical Procedures,* ASTM International, 1999, p 797–823

26. “Test Methods for Determining Average Grain Size Using Semiautomatic and Automatic Image Analysis,” E 1382-97, *Annual Book of ASTM Standards, Section 3: Metals Test Methods and Analytical Procedures,* ASTM International, 1999, p 867–890

27. *Collins English Dictionary and Thesaurus,* Diamond Books, 1992

28. A.S. Hornby, *Oxford Advanced Learner's Dictionary of Current English,* Oxford University Press, London, 1974

29. “Terminology Relating to Metallography,” E 7-99, *Annual Book of ASTM Standards, Section 3: Metals Test Methods and Analytical Procedures,* ASTM International, 1999, p 28–56

30. E.R. Weibel, Ideas and Tools: The Invention and Development of Stereology, *Acta Stereol.,* Vol 6/Suppl. II, 1987, p 23–33

31. J. Serra, *Image Analysis and Mathematical Morphology,* Academic Press, 1982

32. J. Serra, Ed., *Image Analysis and Mathematical Morphology, Volume 2: Theoretical Advances,* Academic Press, 1988

33. J. Serra, Morphological Image Segmentation, *Acta Stereol.,* Vol 14, 1995, p 99

34. L. Bjerregaard, K. Geels, B. Ottesen, and M. Ruckert, *Metalog Guide. Your Guide to the Perfect Materialographic Structure,* Struers, Denmark, 1992

35. “Practice for Preparing and Evaluating Specimens for Automatic Inclusion Assessment of Steel,” E 768-80 (1993), *Annual Book of ASTM Standards, Section 3: Metals Test Methods and Analytical Procedures,* ASTM International, 1999, p 635–636

36. G.F. Vander Voort, *Metallography: Principles and Practice,* ASM International, 1999

37. G.F. Vander Voort, Etching Techniques for Image Analysis, *Microstructural Science,* Vol 9, Elsevier, 1981, p 135–154

38. G.F. Vander Voort, Phase Identification by Selective Etching, *Applied Metallography,* G.F. Vander Voort, Ed., Van Nostrand Reinhold Co., 1986, p 1–19

39. “Practice for Microetching Metals and Alloys,” E 407-93, *Annual Book of ASTM Standards, Section 3: Metals Test Methods and Analytical Procedures,* ASTM International, 1999, p 453–470

40. Z. Latala and L. Wojnar, Computer-Aided versus Manual Grain Size Assessment in a Single Phase Material, *Mater. Charact.,* Vol 46 (No. 2/3), 2001, p 227–233

41. W. Pratt, *Digital Image Processing,* John Wiley & Sons, 1978

42. J.C. Russ, *The Image Processing Handbook,* 2nd ed., CRC Press, 1995

43. J.R. Beveridge, J. Griffith, R.R. Kohler, A.R. Hanson, and E.M. Riseman, Segmenting Images Using Localized Histograms and Region Merging, *Int. J. Comput. Vision,* Vol 2, 1989, p 311

44. J.L. Chermant and M. Coster, Introduction à l'Analyse d'Images (Introduction to Image Analysis), *J. Microsc. et de Spectrosc. Électron.,* Vol 12, 1987, p 1

45. J.L. Chermant and M. Coster, Granulometry and Granulomorphy by Image Analysis, *Acta Stereol.,* Vol 10, 1991, p 7

46. B. Ralph and K.J. Kurzydlowski, Microscopical Quantification as an Input to Microscopical Modelling, *Proc. Q-Mat'97, International Conference on the Quantitative Description of Materials Microstructure* (Warsaw, Poland), Polish Society for Stereology, 1997, p 141

47. F. Robert and G. Lefebvre, Distance Mapping for Image Filtering, *Acta Stereol.,* Vol 14, 1995, p 209

48. J. Serra and L. Vincent, lecture notes on morphological filtering, Paris School of Mining, Center for Mathematical Morphology, Fontainebleau, 1989

49. R. Tadusiewicz, *Vision Systems for Industrial Robots,* WNT, Warsaw, Poland, 1992 (in Polish)

50. H. Talbot, The Pre-Processing in Mathematical Morphology, *Rev. Métall.,* Vol 91, 1994, p 211

51. E. Henault, and J.L. Chermant, Parametrical Investigation of Gray Tone Image, *Acta Stereol.,* Vol 11/Suppl., 1992, p 665

52. J.C. Russ and J.C. Russ, Automatic Discrimination of Features in Gray-Scale Images, *J. Microsc.,* Vol 148, 1987, p 263

53. G.F. Vander Voort, The SEM as a Metallographic Tool, *Applied Metallography,* Van Nostrand Reinhold Co., 1986, p 139–170

54. R. Tadeusiewicz and P. Korohoda, *Computer-Aided Analysis and Processing of Images,* Foundation for Telecommunication Development, Kraków, Poland, 1997 (in Polish)

55. H.E. Exner and H.P. Hougardy, *Einführung in die Quantitative Gefügeanalyse (Introduction to Quantitative Analysis of Microstructures),* DGM Informationsgesellschaft Verlag, Oberursel, 1986

56. J.L. Chermant, M. Coster, and G. Gougeon, Shape Analysis in R^2 Space Using Mathematical Morphology, *J. Microsc.,* Vol 145, 1987, p 143

57. J.D. Bryant, Stereo-Photogrammetry as Applied to Fractography, *Advances in Fracture Research Proc. ICF7,* (Houston, TX), International Congress on Fracture, 1989, p 3365

58. J. Chrapoński, M. Maliński, and J. Cwajna, The Algorithm of Three-Dimensional Reconstruction and Its Application in the Materials Science Investigations, *Inz. Materialowa,* Vol 17, 1996, p 206 (in Polish)

59. O. Faugeras, *Three-Dimensional Computer Vision,* MIT Press, 1993

60. M. Maliński and J. Chrapoński, 3-D Modelling of Polycrystalline Grain Structures, Part I and II, *Proc. Q-Mat'97, International Conference on the Quantitative Description of Materials Microstructure* (Warsaw, Poland), Polish Society for Stereology, 1997, p 383

61. J. Chrapoński and M. Maliński, Estimation of Grain Size, Part I–III, *Proc. Q-Mat'97, International Conference on the Quantitative Description of Materials Microstructure* (Warsaw, Poland), Polish Society for Stereology, 1997, p 215

62. J. Cwajna, Quantitative Structural Criteria of Steel Quality Control, *Acta Stereol.,* Vol 13, 1994, p 409

63. J. Cwajna, J. Richter, and J. Szala, Quantitative Metallography and Fractography of Modern Tool Alloys, *Proc. Q-Mat'97, International Conference on the Quantitative Description of Materials Microstructure* (Warsaw, Poland), Polish Society for Stereology, 1997, p 125

64. N. Otsu, A Threshold Level Selection Method from Gray Level Histograms, *IEEE Trans. Syst. Man. Cybern.,* Vol 9, 1979, p 62–66

65. J.N. Kapur, P.K. Sahoo, and A.K.C. Wong, A New Method for Gray Level Picture Thresholding Using the Entropy Histogram, *Comput. Vis. Graph. Image Proc.,* Vol 29, 1985, p 273–285

66. R. Kohler, A Segmentation System Based on Thresholding, *Comput. Graphics Image Process.,* Vol 15, 1981, p 319–338

67. J.L. Chermant, *Les Ceramiques Thermomechaniques (Thermomechanical Ceramics),* Presses du CRNS, Paris, 1989

68. M. Coster, J.L. Chermant, and M. Prod'homme, Quantification of Ceramic Microstructures, *Proc. Q-Mat'97, International Conference on the Quantitative Description of Materials Microstructure* (Warsaw, Poland), Polish Society for Stereology, 1997, p 115

69. M. Coster, M. Prod'homme, L. Chermant, and J.L. Chermant, Morphological Study during a Ceramic Process, *Microsc. Microanal. Microstruct.,* Vol 7, 1996, p 407

70. J. Cwajna, Quantitative Description of the Microstructure of Tool Alloys and Its Applications, *Zesz. Nauk. Politech. Slask., Hutn.,* Vol 39, 1991 (in Polish)

71. A. Hazotte, and J. Lacaze, Quantitative Analysis of the Microstructure of Nickel Based Superalloys, *Rev. Métall.,* Vol 91, 1994, p 217

72. D. Jeulin, "Mathematical Morphology and Materials Image Analysis," Rapport N-31/87/G, Center for Geostatics, Fontainebleau, 1987

73. M. Maliński, J. Cwajna, and J. Chrapoński, Grain Size Distribution, *Acta Stereol.,* Vol 10, 1991, p 73

74. M. Mlynarczuk and S. Beucher, Directional Fiber Analysis by Mathematical Morphology, *Proc. Q-Mat'97, International Conference on the Quantitative Description of Materials Microstructure* (Warsaw, Poland), Polish Society for Stereology, 1997, p 403

75. F. Montoya, S. Michelland, L. Chermant, M. Coster and J.L. Chermant, Size Distribution from Gray Tone Level Images: Case of Granular Materials, *Acta Stereol.,* Vol 14, 1989, p 401

76. E. Pirard, Morphometric Analysis of Powders: A Systematic and Robust Approach Using Mathematical Morphology, *Rev. Métall.,* Vol 91, 1994, p 295

77. J.L. Quenec'h, J.L. Chermant, M. Coster, and D. Jeulin, Example of Application of Probabilistic Models: Determination of the Kinetics Parameters during Liquid Phase Sintering, *Microsc. Microanal. Microstruct.,* Vol 7, 1996, p 573

78. J. Richter, J. Cwajna, and J. Szala, Verification of Empirical Structure-Properties Relations through Automatic Image Analysis of Sintered Carbides, *Proc. Q-Mat'97, International Conference on the Quantitative Description of Materials Microstructure* (Warsaw, Poland), Polish Society for Stereology, 1997, p 451

79. L. Vincent and D. Jeulin, Minimal Paths and Crack Propagation Simulations, *Acta Stereol.,* Vol 14, 1989, p 487

80. L. Wojnar and Z. Latala, On the Validity of Specimen Preparation in Automatic Analysis of the Microstructure of Cast Iron, *Proc. First Conference: Materials Science - Foundry - Quality,* (Kraków, Poland), Kraków University of Technology, 1997, p 165 (in Polish)

81. L. Wojnar, "Effect of Nodular Graphite on Fracture Toughness of Ductile Cast Iron," Ph.D. thesis, Kraków University of Technology, Kraków, Poland, 1985 (in Polish)

82. K. Huebner, Quantitative Characteristics of the Shape of Graphite Precipitates in Nodular Cast Iron, *Przegl. Odlew.,* Vol 3, 1977, p 60 (in Polish)

83. L. Wojnar, J.R. Dąbrowski, and Z. Oksiuta, Porosity of the Sintered Co-Cr-Mo Alloy Subjected to Additional Envelope Pressing and Heat Treatment, *Proc. Sixth International Conference Stereology and Image Analysis in Materials Science* (Kraków, Poland), Polish Society for Stereology, 2000, p 437–442

84. L. Wojnar, J.R. Dąbrowski, and Z. Oksiuta, Porosity Structure and Mechanical Properties of Vitallium-Type Alloy for Implants, *Mater. Charact.,* Vol 46 (No. 2/3), 2001, p 221–226

L. Wojnar, K.J. Kurzydłowski, and J. Szala, Quantitative Image Analysis, *Metallography and Microstructures,* Vol 9, *ASM Handbook,* ASM International, 2004, p. 403–427

Quantitative Image Analysis

Leszek Wojnar, Kraków University of Technology, Kraków, Poland; Krzysztof J. Kurzydłowski, Warsaw University of Technology, Warsaw, Poland; Janusz Szala, Silesian University of Technology, Katowice, Poland

---

Selected References

- J.M. Chaix, P.H. Yang, M. Ardin, and M. Durrand-Charre, Image Analysis of Austenite and Carbides Coarsening in a Fe-Mo-C Steel, *Microsc. Microanal., Microstruct.,* Vol 7, 1996, p 387
- "Guide for Calibrating Reticles and Light Microscope Magnifications," E 1951-98, *Annual Book of ASTM Standards, Section 3: Metals Test Methods and Analytical Procedures,* ASTM International, 1999, p 1101–1107
- "Guide for Metallographic Preparation of Thermal Sprayed Coatings," E 1920-97, *Annual Book of ASTM Standards, Section 3: Metals Test Methods and Analytical Procedures,* ASTM International, 1999, p 1055–1059
- K.J. Kurzydlowski, Quantitative Studies of Recrystallization in Polycrystalline Materials, *Acta Stereol.,* Vol 13, 1994, p 277
- "Practice for Metallographic Laboratory Evaluation," E 807-96, *Annual Book of ASTM Standards, Section 3: Metals Test Methods and Analytical Procedures,* ASTM International, 1999, p 641–644
- "Practice for Preparation of Metallographic Specimens," E 3-95, *Annual Book of ASTM Standards, Section 3: Metals Test Methods and Analytical Procedures,* ASTM International, 1999, p 1–8
- "Test Methods for Determining Average Grain Size," E 112-96, *Annual Book of ASTM Standards, Section 3: Metals Test Methods and Analytical Procedures,* ASTM International, 1999, p 237–259
- "Test Methods for Determining the Inclusion Content of Steel," E 45-96, *Annual Book of ASTM Standards, Section 3: Metals Test Methods and Analytical Procedures,* ASTM International, 1999, p 163–176

- "Test Method for Determining Volume Fraction by Systematic Manual Point Count," E 562-95, *Annual Book of ASTM Standards, Section 3: Metals Test Methods and Analytical Procedures,* ASTM International, 1999, p 522–527

A.M. Gokhale, Quantitative Characterization and Representation of Global Microstructural Geometry, *Metallography and Microstructures,* Vol 9, *ASM Handbook,* ASM International, 2004, p. 428–447

Quantitative Characterization and Representation of Global Microstructural Geometry

Arun M. Gokhale, Georgia Institute of Technology

Introduction

IT IS THE CENTRAL PRECEPT of materials science that processing governs microstructure and the microstructure influences the properties and performance of materials. Consequently, quantitative characterization and mathematical representation of microstructure are of considerable importance in materials science. The discipline of quantitative characterization of microstructural geometry is called quantitative metallography or stereology. The objective of quantitative metallography/stereology is to describe the geometric characteristics of the features (for example, grains, voids, precipitates, dislocations) present in the microstructure in quantitative terms, such as amounts (how much?), numbers (how many?), and sizes (how large?).

Material microstructures are three-dimensional and, therefore, the attributes of three-dimensional microstructural geometry are of core interest. Nonetheless, as most of the materials are opaque, the microstructural observations are usually on the two-dimensional (2-D) metallographic sections through the three-dimensional (3-D) microstructural domains of interest. The microstructure observed in a metallographic section consists of intersections of the features in the 3-D microstructure with the sectioning plane. Therefore, in a metallographic plane, the volumes (e.g., grains, voids, particles) in a 3-D microstructure appear as areas, and the surfaces (e.g., grain boundaries, precipitate interfaces) appear as lines. Clearly, a 2-D metallographic section does not contain all the information concerning the true 3-D microstructural geometry. Even so, numerous important geometric attributes of 3-D microstructures can be estimated from the measurements that can be performed on 2-D metallographic sections.

It is well known that material microstructures are of stochastic nature. Consequently, no two microstructures are exactly alike; no two fields of view in a microstructure are exactly alike; and in most microstructures, no two particles/grains in a field of view are exactly alike. It follows that microstructure characterization must be couched in statistical terms. Further, microstructural features have complex morphologies, their locations and orientations are often nonuniform, and spatial clustering and correlations frequently exist. Accordingly, quantitative metallographic techniques must be free of any restrictive geometric assumptions so that they can be successfully applied to any arbitrary microstructure. Despite these complexities, quantitative metallographic procedures are straightforward to use in practice. Numerous geometric attributes of three-dimensional microstructures can be estimated in an unbiased manner from the counting measurements that can be performed on representative metallographic planes, without involving any assumptions whatsoever.

Modern quantitative metallographic/stereological methods typically involve statistical sampling of 3-D microstructure using lower dimensional geometric test probes such as planes, lines, and points. In many cases, the basic measurements simply consist of counting the number of times the test probe intersects (or hits) the microstructural features of interest; the average value (or more precisely, statistical expected value) of such "hits" is uniquely related to specific geometric attributes of the 3-D microstructure through simple stereological equations. The stereological techniques have rigorous theoretical foundations that are anchored in the

disciplines of stochastic geometry (Ref 1), integral geometry and global analysis (Ref 2), and differential geometry (Ref 3). The stereological methods are completely general, and therefore they are also applicable to microstructures encountered in many other disciplines, including biology (Ref 4) and mineralogy (Ref 5).

The basic principles of classical quantitative metallography are covered in numerous books (Ref 6, 7, 8). Nevertheless, during the past decade or so, there has been substantial progress in the development of new design-based stereological techniques for efficient characterization of anisotropic microstructures (Ref 9, 10, 11, 12, 13, 14, 15, 16, 17, 18) and new techniques for unbiased estimation of number density of microstructural features (Ref 19, 20, 21). Further, advances in digital image processing techniques (Ref 22, 23, 24, 25, 26, 27, 28), new microscopy techniques (Ref 29, 30, 31), and availability of powerful digital image analysis systems have opened up a whole new era of quantitative metallography dealing with new efficient techniques for reconstruction of 3-D microstructure from serial sections (Ref 32, 33, 34, 35) and new techniques for characterization parameters such as microstructural spatial correlations and clustering (12, 22, 23, 35, 36, 37), coordination number distributions (Ref 35), and bivariate and trivariate size-shape-orientation distributions of particles/inclusions in 3-D microstructures (Ref 38, 39). There has also been a steady rise in the practical applications of quantitative metallography during the recent years (Ref 40, Ref 41, 42, 43, 44, 45, 46, 47, 48, 49, 50, 51, 52, 53, 54, 55, 56, 57, 58, 59, 60).

The geometric attributes of microstructural features can be divided into the following categories:

- Numerical extents of microstructural features (how much?)
- Number density of microstructural features (how many?)
- Derived microstructural properties (grain size, mean free path, etc.)
- Feature specific size, shape, and orientation distributions
- Descriptors of microstructural spatial clustering and correlations

The classical methods as well as new design-based quantitative metallographic techniques for the estimation of the above categories of microstructural attributes are presented in this article; the emphasis is on the practical aspects of the measurement techniques and applications. The next section of this article describes the quantitative metallographic procedures for estimation of the numerical extents (amounts) of the features in microstructure, and that is followed by the techniques for estimation of number density, derived properties, and particle size distributions.

References cited in this section

1. D. Stoyan, S. Kendall, and J. Mecke, *Stochastic Geometry and Its Applications,* 2nd ed., John Wiley and Sons, 1995

2. L.A. Santalo, *Integral Geometry and Geometric Probability,* Addison-Wesley, 1976

3. A. Gray, *Modern Differential Geometry of Curves and Surfaces,* 2nd ed., CRC Press, London, 1997

4. P.R. Mouton, *Principles and Practices of Unbiased Stereology: An Introduction for Bioscientists,* The Johns Hopkins University Press, 2002

5. F. Chayes, *Petrographic Modal Analysis,* John Wiley, 1956

6. E.E. Underwood, *Quantitative Stereology,* Addison Wesley, 1970

7. R.T. DeHoff and F.N. Rhines, *Quantitative Microscopy,* McGraw Hill, 1968

8. S.A. Saltykov, *Stereometric Metallography,* 2nd ed., Metallurgizdat, Moscow, 1958

9. A.J. Baddeley, H.J.G. Gundersen, and L.M. Cruz Orive, Estimation of Surface Area Using Vertical Sections, *J. Microsc.,* Vol 142, 1986, p 259–276

10. A.M. Gokhale and W.J. Drury, Efficient Estimation of Microstructural Surface Area Using Trisector, *Metall. Trans. A,* Vol 25A, 1994, p 919–928

11. B.R. Morris, A.M. Gokhale, and G.F. Vander Voort, Estimation of Grain Size in Anisotropic Materials, *Metall. Mater. Trans. A,* Vol 29A, 1998, p 237–244

12. J. Ohser and F. Muecklich, *Statistical Analysis of Microstructures in Material Science,* John Wiley & Sons, 2000

13. A.M. Gokhale, Unbiased Estimation of Curve Length in 3D Using Vertical Slices, *J. Microsc.,* Vol 159, 1990, p 133–141

14. A.M. Gokhale, Estimation of Length Density L_v from Vertical Slices of Unknown Thickness, *J. Microsc.,* Vol 167, pt. I, 1992, p 1–8

15. A.M. Gokhale, Utility of Horizontal Slice for Stereological Characterization of Lineal Features, *J. Microsc.,* Vol 170, pt. 1, 1993, p 3–8

16. L.M. Cruz Orive and X. Gual-Arnau, Precision of Circular Systematic Sampling, *J. Microsc.,* Vol 207, 2002, p 225–242

17. A.M. Gokhale and N.U. Deshpande, Stereology of Anisotropic Microstructures, *Quantitative Microscopy and Image Analysis,* D.J. Diaz, Ed., ASM International, 1994, p 73–82

18. P.R. Mouton, A.M. Gokhale, N.L. Ward, and M.J. West, Unbiased Length Estimation Using Isotropic Spherical Probes, *J. Microsc.,* Vol 206, 2002, p 54–64

19. D.C. Sterio, The Unbiased Estimation of Number and Size of Arbitrary Particles Using Disector, *J. Microsc.,* Vol 134, 1984, p 127–136

20. A.M. Gokhale and A. Tewari, Efficient Estimation of Number Density in Opaque Material Microstructures Using Large Area Disector (LAD), *J. Microsc.,* Vol 200, pt. 3, 2000, p 277–283

21. J.P. Kroustrup and H.J.G. Gundersen, Estimating the Number of Complex Particles Using the ConnEulor Principle, *J. Microsc.,* Vol 203, 2001, p 314–320

22. L. Pascal and A.M. Gokhale, Application of Image Analysis for Characterization of Spatial Arrangement of Features in Microstructures, *Metall. Mater. Trans.,* Vol 26A, 1995, p 1449–1456

23. S. Yang, A. Tewari, and A.M. Gokhale, Modeling of Non-Uniform Spatial Arrangement of Fibers in a Ceramic Matrix Composite, *Acta Mater.,* Vol 45, 1997, p 3059–3069

24. C. Babu Rao, P. Kalyansundaram, K.K. Ray, and B. Raj, *Image Analysis in Materials and Life Sciences,* Oxford and IBH, New Delhi, India, 2000

25. J. Serra, *Image Analysis and Mathematical Morphology,* Academic Press, 1982

26. J.C. Russ, *The Image Processing Handbook,* CRC Press, London, 2001

27. P. Velecky and J. Pospisil, Digital Image Processing for Evaluation of the Internal Microstructure Characteristics of Cemented Carbides, *Optik,* Vol 111, 2000, p 493–496

28. A. Balasundaram and A.M. Gokhale, Quantitative Characterization of Spatial Arrangement of Shrinkage and Gas (Air) Pores in Cast Magnesium Alloys, *Mater. Charact.,* Vol 46, 2001, p 419–426

29. A.J. Schwartz, M. Kumar, and B.L. Adams, *Electron Backscatter Diffraction in Materials Science*, Plenum Press, 2000

30. F.J. Humphreys, Quantitative Metallography by Electron Backscattered Diffraction, *J. Microsc.,* Vol 195, 1999, p 170–185

31. J.K. Stevens, L.R. Mills, and J.E. Trogadis, *Three-Dimensional Confocal Microscopy,* Academic Press, London, UK, 1994

32. A. Tewari and A.M. Gokhale, Application of Serial Sectioning for Estimation of 3D Grain Size Distribution in a Liquid Phase Sintered Microstructure, *Mater. Charact.,* Vol 46, 2001, p 329–335

33. A. Tewari, M.D. Dighe, and A.M. Gokhale, Application of Digital Image Processing for Reconstruction of Three-Dimensional Microstructure From Serial Sections, *Mater. Charact.,* Vol 44, 2000, p 259–269

34. M.V. Kral, and G. Spanos, 3D Analysis of Cementite Precipitates, *Acta Mater.,* Vol 47, 1999, p 711–724

35. A. Tewari, A.M. Gokhale, and R.M. German, Effect of Gravity on Three-Dimensional Coordination Number Distribution in Liquid Phase Sintered Microstructures, *Acta Mater.,* Vol 47, 1999, p 3721–3734

36. S. Yang, A. Tewari, and A.M. Gokhale, An Experimental Method for Quantitative Characterization of Spatial Distribution of Fibers in Composites, *Developments in Materials Characterization Technologies,* G.F. Vander Voort and J.J. Frial, Ed., ASM International, 1996 p 33–43

37. A. Tewari, A.M. Gokhale, J.E. Spowart, and D.B. Miracle, Quantitative Characterization of Spatial Clustering in Three-Dimensional Microstructures Using Two-Point Correlation Functions, *Acta Mater.,* Vol 52, 2004, p 307–319

38. A.M. Gokhale, Estimation of Bivariate Size and Orientation Distribution of Microcracks, *Acta Metall.,* Vol 44, 1996, p 475–485

39. V. Benes, V. Jiruses, and M. Slamova, Estimation of Trivariate Size-Shape-Orientation Distributions from Vertical Sections, *Acta Mater.,* Vol 45, 1997, p 1105–1110

40. L. Hengcheng, Y. Sun, and S. Guoxiong, Correlation between Mechanical Properties and Amount of Dendritic Alpha-Al Phase in As-Cast Near-Eutectic Al-11.6% Si Alloys Modified with Strontium, *Mater. Sci. Eng. A,* Vol 335, 2002, p 62–66

41. M. Sozanska, A. Maciejny, C. Dagbert, J. Galland, and L. Hyspecka, Use Of Quantitative Metallography in the Evaluation of Hydrogen Action During Martensitic Transformations, *Mater. Sci. Eng. A,* Vol A273, 1999, p 485–490

42. Q. Meng, Y. Rong, S. Chen, and T.Y. Hsu, The Relationship of the Volume Fraction of Martensite vs. Plastic Strain in a Fe-Mn-Si-Cr-N Shape Memory Alloy, *Mater. Lett.,* Vol 50, 2001, p 328–332

43. H. Agarwal, A.M. Gokhale, S. Graham, and M.F. Horstemeyer, Quantitative Characterization of Three-Dimensional Damage Evolution in a Wrought Al-Alloy under Tension and Compression, *Metall. Mater. Trans.,* Vol 33A, 2002, p 2599–2606

44. M.P. Black, R.L. Higginson, and C.M. Sellars, Effect of Strain Path on Recrystallization Kinetics During Hot Rolling of Al-Mn, *Mater. Sci. Technol.,* Vol 17, 2001, p 1055–1060

45. K. Bodlak, A. Balasundaram, A.M. Gokhale, and V. Benes, Unfolding of Three-Dimensional Bivariate Size-Orientation Distribution of Microcracks, *Acta Mater.,* Vol 51, 2003, p 3131–3143

46. R.A. Vandermeer, N. Hansen, X. Huang, J. Jensen, E.M. Laurdisen, T. Leffers, W. Pantleon, T.J. Sabine, and J.A. Wert, Kinetic Aspects of Nucleation and Growth in Recrystallization, *Proc. 21st Riso International Symposium on Materials Science* (Roskilde, Denmark), 2000, p 179–200

47. J.A. Griggs, K.J. Anusavice, and J.J. Mecholsky, Jr., Devitrification and Microstructural Coarsening of a Fluoride-Containing Barium Aluminosilicate Glass, *J. Mater. Sci.,* Vol 37, 2002, p 2017–2022

48. K.-W. Moon, W.J. Boettinger, U.R. Kattner, C.A. Handwerker, and D.-J. Lee, The Effect of Pb Contamination on the Solidification Behavior of Sn-Bi Solders, *J. Electron. Mater.,* Vol 30, 2001, p 45–52

49. F.G. Caballero, C. Garcia de Andres, and C. Capdevila, Characterization and Morphologic Analysis of Pearlite in a Eutectoid Steel, *Mater. Charact.,* Vol 45, 2000, p 111–116

50. K.J. and H. Conrad, Microstructure Coarsening During Static Annealing of 60Sn40Pb Solder Joints. I. Stereology, *J. Electron. Mater.,* Vol 30, 2001, p 1294–1302

51. S. Spangel, E. Matthaei-Schulz, A. Schulz, H. Vetters, and P. Mayr, Influence of Carbon and Chromium Content and Preform Shape on the Microstructure of Spray Formed Steel Deposits, *Mater. Sci. Eng. A,* Vol A326, 2002, p 26–39

52. J. Wosik, H.J. Penkalla, K. Szot, B. Dubiel, and F.C. Schubert, The Influence of Various Microscopic Techniques on the Quantification of Stereological Structure Parameters in Waspaloy Alloy, *Prakt. Metallogr.,* Vol 39, 2002, p 140–154

53. W. Yunxin, R.M. German, D. Blaine, B. Marx, and C. Schlaefer, Effects of Residual Carbon Content on Sintering Shrinkage, Microstructure and Mechanical Properties of Injection Molded 17-4 PH Stainless Steel, *J. Mater. Sci.,* Vol 37, 2002, p 3573–3583

54. M. Grange, J. Besson, and E. Andrieu, An Anisotropic Gurson Type Model to Represent the Ductile Rupture of Hydrided Zircaloy-4 Sheets, *Int. J. Fract.,* Vol 105, 2000, p 273–293

55. N.U. Deshpande, A.M. Gokhale, D.K. Denzer, and J. Liu, Relationship between Fracture Toughness, Fracture Path, and Microstructure of 7050 Aluminum Alloy—I: Quantitative Characterization, *Metall. Mater. Trans. A,* Vol 29A, 1998, p 1191–1201

56. H. Agarwal, A.M. Gokhale, S. Graham, and M.F. Horstemeyer, Anisotropy of Intermetallic Particle Cracking Damage Evolution in an Al-Si-Mg Base Wrought Aluminum Alloy under Uniaxial Compression, *Metall. Mater. Trans. A,* Vol 33A, 2002, p 3443–3448

57. H. Agarwal, A.M. Gokhale, and S. Graham, Void Growth in 6061 Al-Alloy under Triaxial Stress State, *Mater. Sci. Eng.,* Vol 341 (No. 1–2), 2003, p 35–42

58. A.K. Balasundaram, A.M. Gokhale, S. Graham, and M.F. Horstemeyer, Three Dimensional Particle Cracking Damage Development in an Al-Mg Base Alloy, *Mater. Sci. Eng.,* Vol 355 (No. 1–2), 2003, p 368–383

59. Z. Zhang and F. Wang, Research on the Deformation Strengthening Mechanism of a Tungsten Heavy Alloy by Hydrostatic Extrusion, *Int. J. Refract. Met. Hard Mater.,* Vol 19, 2001, p 177–182

60. Y. Wu, R.M. German, D. Blaine, B. Marx, and C. Schlaefer, Effects of Residual Carbon Content on Sintering Shrinkage, Microstructure and Mechanical Properties of Injection Molded 17-4 PH Stainless Steel, *J. Mater. Sci.*, Vol 37, 2002, p 3573–3583

A.M. Gokhale, Quantitative Characterization and Representation of Global Microstructural Geometry, *Metallography and Microstructures*, Vol 9, *ASM Handbook*, ASM International, 2004, p. 428–447

Quantitative Characterization and Representation of Global Microstructural Geometry

Arun M. Gokhale, Georgia Institute of Technology

Numerical Extents of Microstructural Features (How Much?)

Numerical extent specifies total "amount" of microstructural features of interest per unit volume of microstructure. Volume fraction (or volume percentage) is the numerical extent of the amount of a phase (or constituent) in a unit volume of 3-D microstructure. On the other hand, total surface area per unit volume characterizes the numerical extent of two-dimensional internal surfaces/interfaces. Similarly, total length per unit microstructural volume (or so-called length density) represents the amount of one-dimensional lineal features of interest in a 3-D microstructure. These first-order microstructural parameters are of central importance in materials science as they influence numerous material properties. The classical quantitative metallographic techniques permit efficient estimation of volume fraction, total surface area per unit volume, and total length of lineal features of interest per unit volume in any isotropic uniform random 3-D microstructure from the counting measurements that can be performed in 2-D metallographic sections/projected images (Ref 6, 7, 8, 61). Such measurements have been used in numerous experimental studies on processing-microstructure-properties relationships (Ref 27, 40, 41, 42, 44, 46, 48, 51, 52, 53, Ref 54). Recent developments in design-based stereology enable efficient estimation of total surface area per unit volume and total length per unit volume in the anisotropic microstructures as well (Ref 9, 10, 11, 12, 13, 14, 15, 16, 17, 18). These design-based stereological measurements have also been used in several recent experimental studies (Ref 11, 43, 45, 55, 56, 57, 58, 62, 63, 64, 65, 66, 67, 68, 69). The quantitative metallographic methods for estimation of volume fraction, total surface area per unit volume, and the total length of per unit volume are described in the following sections.

Volume Fraction

Volume fraction is an important measure of the relative amount of a phase in a microstructure. It is equal to the sum of the volumes of the regions of a phase of interest in a material specimen divided by the volume of the specimen. Therefore, the volume fraction of a phase is the fraction of the 3-D microstructural space occupied by that phase. Volume fraction is denoted by the symbol, V_V where the subscript V signifies the normalization by the specimen volume. Obviously, the volume fraction of a phase must always be in the range $0 \leq V_V \leq 1$. Further, the sum of the volume fractions of all the phases in a microstructure must be equal to one. Volume fraction is often represented in terms of volume percentage, which is simply equal to volume fraction multiplied by 100.

The volume fraction of a phase in a microstructure is governed by the chemistry and processing history of the material. Numerous material properties depend on volume fractions of different phases in microstructure (Ref 40, 42, 46, 47, 48, 49, 52, 55). For example, the tendency of delayed cracking of quenched steel depends on the relative amount of retained austenite, the volume fraction of porosity in alumina controls its optical properties, and the strength of a fiber composite depends on the relative amounts of the fibers and the matrix. Accordingly, volume fraction is the most frequently measured microstructural attribute.

Volume fraction of a phase in any arbitrary 3-D microstructure can be estimated from the measurements performed in the 2-D metallographic sections without involving any assumptions concerning the shapes, sizes,

orientations, or spatial randomness of the features of interest. Interestingly, as volume fraction is a dimensionless microstructural parameter, it is not necessary to know the microscope (or micrograph) magnification for its estimation. Volume fraction can be estimated from the measurements performed in the metallographic planes either by using the areal analysis method, or by using the point counting method. These techniques are described in the following paragraphs.

Areal Analysis. In 1848, French geologist Delesse developed the areal analysis technique for estimation of volume fraction (Ref 6). The areal analysis involves the measurement of the fraction of the area of representative metallographic planes A_A occupied by the phase of interest. The population average value (or more precisely, "expected value") $\langle A_A \rangle$ of the area fraction A_A is equal to the volume fraction V_V of that phase in the 3-D microstructure (Ref 4, 5, 6, 7, 8):

$$V_V = \langle A_A \rangle \qquad \text{(Eq 1)}$$

The area fraction of the phase of interest A_A can be measured in the microstructural fields observed in a microscope, or from micrographs. Obviously, there are statistical variations in the local area fraction A_A measured in different microstructural fields. Therefore, it is essential to perform the measurements on numerous microstructural fields to obtain a representative average value of the area fraction. Areal analysis is a convenient method for estimation of volume fraction using digital image analysis. Once a gray-scale microstructural image (Fig. 1a) is converted into its binary image (Fig. 1b), the local area fraction of the phase of interest is simply equal to the number of pixels in the phase of interest divided by the total number of pixels in the measurement frame. Modern image analyzers can be interfaced with automatic specimen movement stage and autofocus modules of the microscope to automatically scan large number (~100 or more) of microstructural fields at certain fixed distance intervals and perform area fraction measurements in such microstructural fields automatically to yield a precise average value of the volume fraction. Nonetheless, in some microstructures, it is difficult to obtain a representative binary image from gray scale microstructural image (for example, microstructure in Fig. 2a). In such cases, digital image analysis is not useful, and one must resort to manual measurements. Areal analysis is not an efficient technique for estimation of volume fraction if manual measurements are required. In such cases, volume fraction can be efficiently estimated by using the point counting method discussed next.

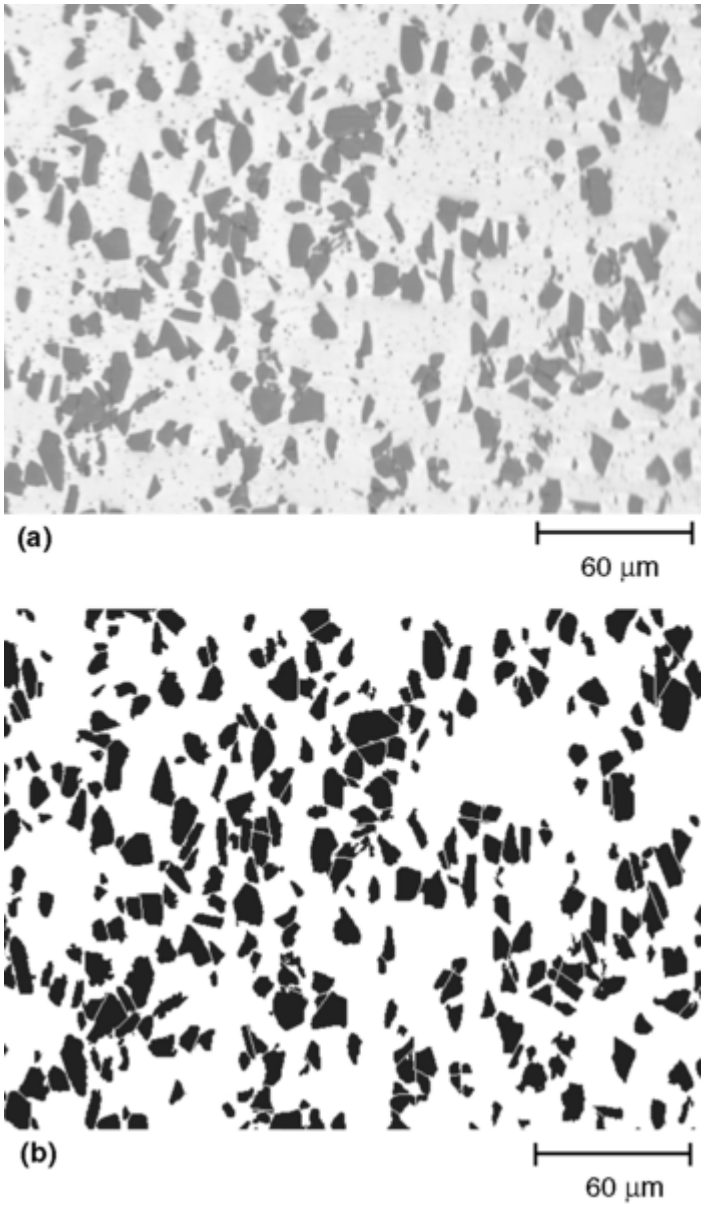

Fig. 1 Areal analysis. (a) Gray scale microstructural image of a metal-matrix composite depicting SiC particles in an aluminum alloy matrix. (b) Binary image of microstructure in (a) depicting excellent segmentation of the SiC particles as the dark phase. The area fraction of SiC particles in this image is equal to the number of black pixels divided by the total number of pixels in the image.

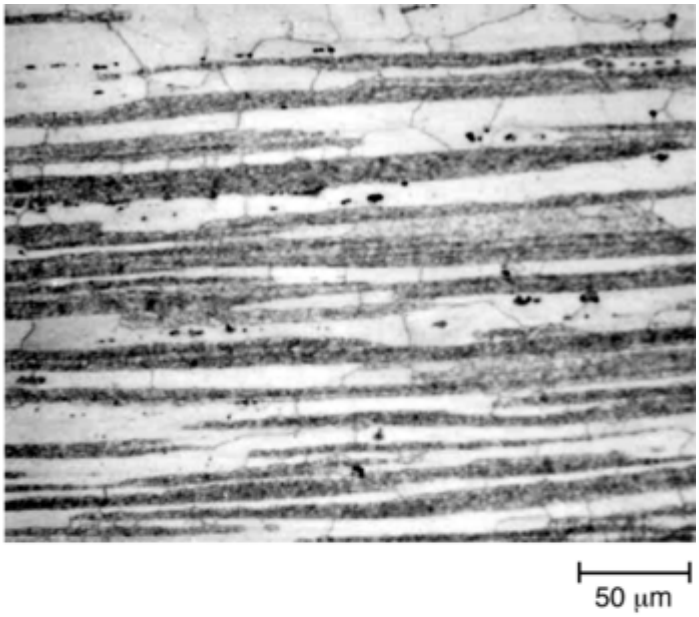

(a)

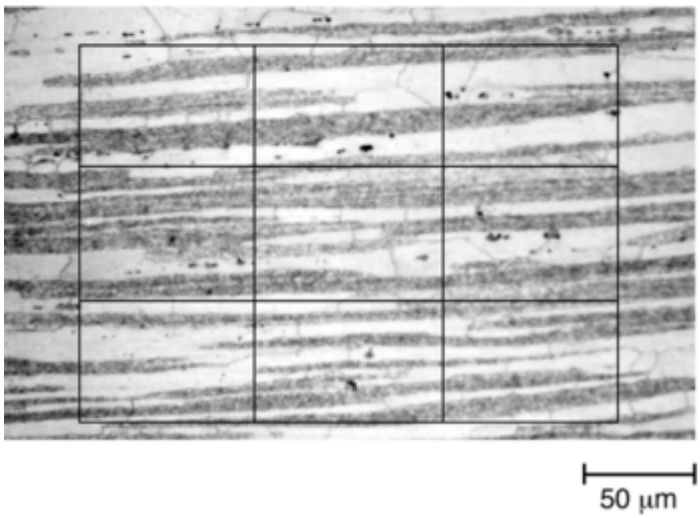

(b)

Fig. 2 Microstructure that is not suitable for areal analysis techniques. (a) Microstructure of a hot-rolled partially recrystallized 7050 aluminum alloy containing large anisotropic recrystallized grains and unrecrystallized regions containing subgrains. In such microstructures digital image analysis is not useful for estimation of volume fraction of recrystallized regions as such regions cannot be accurately segmented by the image analyzer. (b) A systematic grid of 16 test points overlaid on the microstructure in (a) to estimate volume fraction of recrystallized regions manually using point counting. Out of total of 16 test points, 7 are contained in the large bright anisotropic recrystallized regions. Therefore, the local point fraction P_P for the recrystallized regions is equal to $\frac{7}{16}$.

Point Counting. In this method, a set of test points is overlaid on a microstructural field, and the number of test points contained in the phase of interest is counted. The fraction of test points in the phase of interest P_P is calculated by dividing the number of test points in phase of interest by the total number of test points. The population average value of this point fraction $\langle P_P \rangle$ is precisely equal to the volume fraction of the phase of interest (Ref 4, 5, 6, 7, 8):

$$V_V = \langle P_P \rangle \qquad \text{(Eq 2)}$$

The point counting can be performed by using a grid of regular array of test points, or by using randomly distributed test points. The procedure is called “systematic” point counting, when a regular array of points is used, and it is called “random” point counting when random test points are used. The systematic point counting is easier to perform in practice, and it is more efficient than the random point counting. Figure 2(b) illustrates

the systematic point counting procedure using an array of test points. The efficiency of systematic point counting can be further increased by placing the test point grid at regular intervals in the metallographic plane rather than at independent random locations, and sampling multiple planes (if necessary) at different locations at fixed distance intervals in the specimen of interest. Figure 3 illustrates such a multilevel systematic sampling scheme, where all the regions of the specimen get equal "weightage." Such systematic sampling procedure is superior to the independent random sampling for all the quantitative microstructural measurements (Ref 6, 7, 16, 70, 71, 72, 73, 74). Volume fraction measurements are extremely useful for characterizing the effects of process parameters on microstructure as well as to correlate the effects of relative amounts of different phases on the properties and performance of materials. For example, Figure 4 illustrates the effect of hot-rolling temperature on the volume fraction of recrystallized regions in a set of specimens of 7050 wrought aluminum alloy, where the recrystallized volume fraction was measured manually using the systematic point counting method (Ref 55).

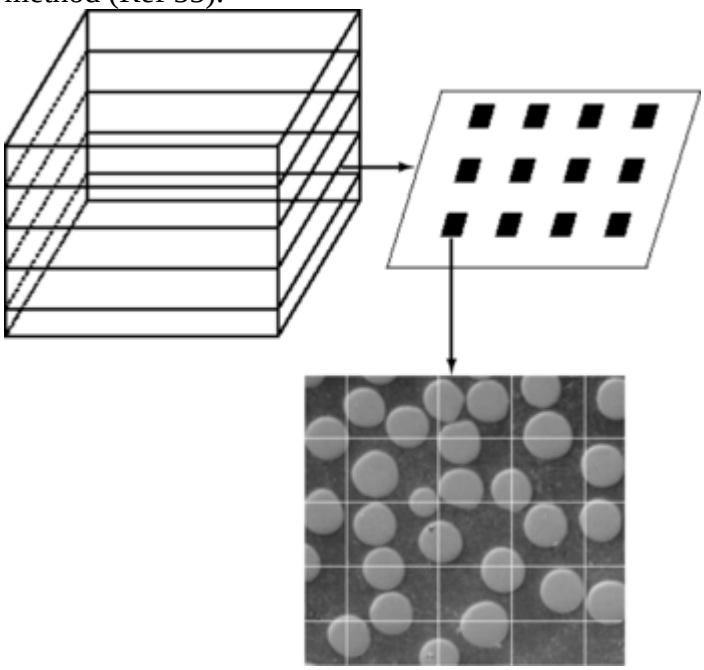

Fig. 3 Multilevel systematic sampling. The first metallographic plane is chosen at a random location in the specimen, and the subsequent planes are sampled such that the planes uniformly cover the specimen and the distance between the planes is approximately the same. Next, in each metallographic plane, the first field is chosen at a random location, and the subsequent fields are systematically chosen such that the distance between consecutive fields is approximately the same and the set of fields uniformly cover the plane. Finally, in each field of view a systematic test probe is placed. For point counting, the probe consists of grid of test points, and the test points contained in the phase of interest are counted.

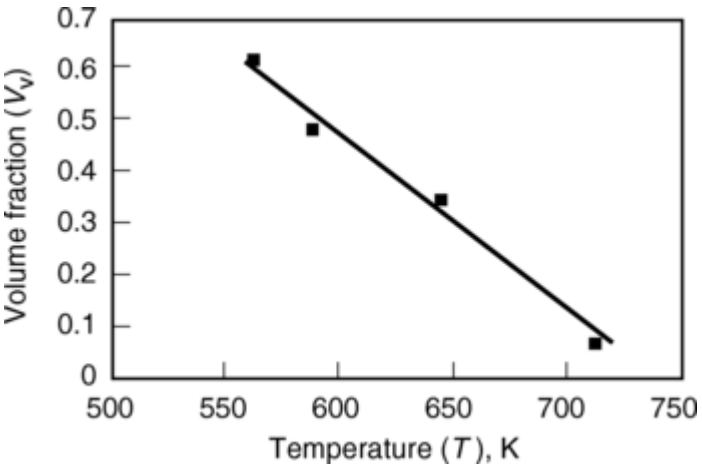

Fig. 4 Experimentally observed quantitative correlation between the volume fraction of recrystallized regions and hot-rolling temperature in a wrought 7050 aluminum alloy (Ref 55)

Several stereologists have carried out rigorous statistical analyses of the bias, efficiency, and precision of different measurement procedures for volume fraction estimation. Their conclusions are (Ref 6, 7, 70, 71, 72):

- Both the areal analysis and point counting are statistically unbiased and general methods. These techniques do not involve any assumptions concerning sizes and/or shapes of the features of the phase of interest.
- The angular orientations of the regions of the phase of interest need not be random; the techniques are equally applicable to anisotropic microstructures.
- It is not necessary to randomize the angular orientation of the sectioning plane, even for anisotropic microstructures. The measurements can be performed in a set of parallel planes of any one convenient angular orientation at systematic random locations in the 3-D microstructure.
- The regions of the phase of interest need not be randomly located in the sample; they may be at any arbitrary location, as long as the sampling is systematic random (or independent random) with respect to the phase of interest. Further, as this locational randomness of the sectioning plane is required only with respect to the phase of interest, if the regions of the phase of interest are randomly located in the microstructure, then measurements in a single sectioning plane (not necessarily randomly located or oriented) can yield a reliable estimate of V_V.
- If the microstructure contains a gradient, then it is more efficient to perform the measurements on the metallographic planes that contain the gradient.
- For optimal efficiency and precision, the measurements should be performed at the lowest magnification where all the features of interest are clearly resolved. Any further increase in the magnification decreases the efficiency.
- For manual measurements, systematic point counting (Fig. 2 and 3) is the most efficient sampling procedure.

Estimation of volume fraction involves statistical sampling of microstructure, and consequently there is always a statistical sampling error associated with the estimated value of the volume fraction. Nevertheless, the sampling error can be kept as small as desired simply by performing the measurements on more microstructural fields in more metallographic planes. The nature of the statistical sampling error and its estimation are described in the next paragraph.

Estimation of Sampling Error. Consider the estimation of volume fraction using a grid of test points containing P_T number of points. Suppose this grid is placed at n different locations in the microstructure, and each time, the number of test points in the phase of interest is counted. Let P_1, P_2, …, P_i, … P_n represent these data, which essentially constitute a statistical sample of size n. The estimated value of the population average point fraction $\langle P_P \rangle$ with the associated confidence interval is given as:

$$\langle P_P \rangle = [\Sigma P_i/(n \cdot P_T)] \pm E_n \qquad \text{(Eq 3)}$$

where E_n is the sampling error. If the sample size n is sufficiently large (for most microstructures, $n > 50$) then E_n can be computed by using (Ref 6, 7):

$$E_n = 2\{\Sigma(\langle P_P \rangle - P_i)^2/[n(n-1)(P_T)^2]\}^{1/2} \qquad \text{(Eq 4)}$$

where $\langle P_P \rangle$ is equal to $[\Sigma P_i/n]$, which is the average number of test points in the phase of interest in the sample consisting of n placements of the grid having P_T test points. Combining Eq 2, 3, 4 gives the following working equation for calculation of the confidence interval in volume fraction estimated from the experimental point counting data:

$$V_V = \langle P_P \rangle = \left[\Sigma P_i/(n \cdot P_T)\right] \pm 2\left\{\Sigma\left(\langle P_P \rangle - P_i\right)^2 \Big/ \left[n(n-1)(P_T)^2\right]\right\}^{1/2} \qquad \text{(Eq 5)}$$

Equation 5 states that there is 95% probability that the true volume fraction of the phase of interest is within the interval given by this equation. Note that the sampling error E_n strongly depends on the sample size n, and therefore it can be kept as small as desired by increasing the sample size n, that is, the number of grid placements. If the sample size is not sufficiently large (i.e., $n < 50$), then other statistical procedures must be used to compute the confidence interval, which are explained elsewhere (Ref 75).

Total Surface Area Per Unit Volume. Microstructures often contain internal surfaces or boundaries such as grain boundaries, precipitate-matrix interfaces, surfaces of internal voids/cavities, and so forth. The total area of the internal microstructural surfaces of interest per unit volume of microstructure is the ratio of the sum of the areas of all the internal surfaces of interest contained in a specimen divided by the volume of the specimen, and it is denoted by the symbol S_V, where the subscript V signifies the normalization by the specimen volume. Figure 5 illustrates this definition of total surface area per unit volume. In two microstructures having the same volume fraction of a phase, S_V is higher in the microstructure having a finer dispersion of that phase. Therefore, S_V can be used to characterize how fine (or coarse) a microstructure is. The mechanical and physical properties of materials strongly depend on the geometric characteristics of the microstructural internal surfaces such as the total area of the grain boundaries. For example, yield stress of a polycrystalline metal increases with the increase in the total surface area of the grain boundaries per unit volume, S_V. This is also a useful parameter for monitoring evolution of microstructure during the processes such as particle coarsening and grain growth, where the driving force is reduction in the total area of the microstructural interfaces. The dimensions of S_V are $\mu m^2/\mu m^3$ or $(\mu m)^{-1}$. Since S_V is not a dimensionless parameter, it is essential to know the magnification of microscope (or micrographs) for its estimation.

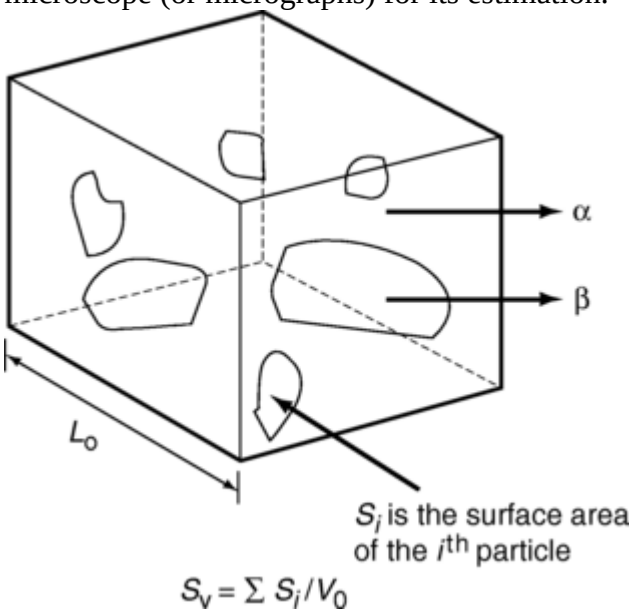

Fig. 5 Definition of S_V. See text for details.

Estimation of S_V involves statistical sampling of the 3-D microstructure by test lines. The number of intersections between the test lines and the surfaces of interest is counted. The population average value of the number of intersections between the test lines and the surfaces of interest per unit test line length $\langle I_L \rangle$ is related to the total surface area per unit volume S_V through the stereological equation given by Smith and Guttman (Ref 61) and Saltykov (Ref 8):

$$S_V = 2 \langle I_L \rangle \qquad \text{(Eq 6)}$$

Equation 6 is general: it is applicable to microstructural surfaces of any arbitrary geometry. I_L has units of $(\mu m)^{-1}$ because it is the number of intersections per unit test line length. In practice, the test lines are placed in a metallographic plane to perform the intersection counting.

An alternate general and unbiased stereological relationship is available for estimation of S_V, which is particularly attractive when the measurements are performed using automatic digital image analysis. This method requires measurements of the total length of all the boundary traces observed per unit area of metallographic plane, L_A. It can be shown that (Ref 61):

$$S_V = [4/\pi] \langle L_A \rangle \qquad \text{(Eq 7)}$$

where $\langle L_A \rangle$ is the population average value of the total boundary length per unit area.

It is easier to program an image analyzer to measure the lengths of all the boundaries of interest in the measurement frame as compared to counting the number of intersections of test lines with the boundaries of interest. Some commercial image analyzers are not even equipped with the computer codes for automatic line

intersection counting (i.e., I_L measurements). Therefore, if automatic image analysis is to be used, Eq 7 is useful for estimation of S_V. Although, in principle, Eq 6 and Eq 7 are applicable to isotropic as well as anisotropic microstructures, to maximize the efficiency and precision of the estimation procedure somewhat different sampling strategies are needed for practical applications of these stereological equations to isotropic and anisotropic microstructures.

Estimation of S_V in Isotropic Microstructures. In an isotropic microstructure (for example, Fig. 6), the microstructural surfaces have uniform random angular orientations. Consequently, the number of intersections between the test lines and the boundaries/surfaces of interest does not vary systematically with the angular orientation of the test lines. For example, in Fig. 6, on the average, horizontal, or vertical test lines (or lines having any other orientation) of the same length yield statistically similar number of intersections with the pore surfaces. Therefore, in an isotropic microstructure, it is not necessary to perform the intersection counts with test lines and/or metallographic planes of different angular orientations: the measurements on metallographic plane(s) of any one convenient angular orientation using test lines of any one convenient angular orientation can yield a reliable estimate of the population average value of the intersection count $\langle I_L \rangle$. An example of I_L measurements in the isotropic microstructure of sintered NiAl and aluminum mixture containing porosity is given in Fig. 6. In such homogeneous isotropic microstructures, the measurements on about 50 systematic random microstructural fields in just one metallographic plane can yield a reliable estimate of S_V. Even when the measurements are performed manually, this does not take more than about 40 min. Thus, unbiased and precise stereological estimation of S_V in the isotropic microstructures is straightforward and efficient.

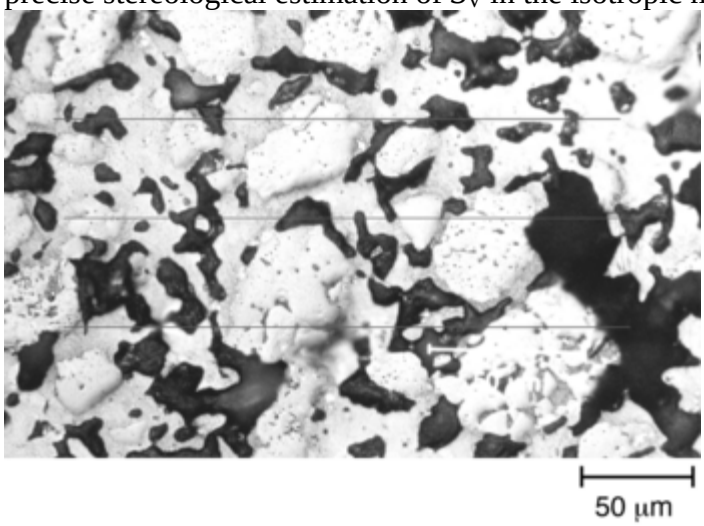

Fig. 6 Intersection counting is illustrated using a set of three horizontal test lines overlaid on the microstructure of a sintered material containing NiAl, aluminum, and porosity. In this microstructure, the pores (dark regions) have no preferred orientations, and the pore surfaces are randomly oriented. The total number of intersections between the pore surfaces and three horizontal test lines is equal to 10 + 13 +17 = 40. The effective length of each test line is 190 μm. Therefore, I_L = 40/(3 × 190) = 0.070 per μm.

Estimation of S_V in Anisotropic Microstructures. In an anisotropic microstructure, the microstructural surfaces have preferred orientations. As a result, the intersection count I_L systematically varies with the angular orientation of the test lines. Figure 7 shows an anisotropic microstructure depicting grain boundaries in a cold-rolled extra-low-carbon steel specimen. Clearly, in such a microstructure, on the average, a horizontal test line is expected to intersect significantly fewer grain boundaries as compared to a vertical test line of the same length. If I_L varies systematically with angular orientation of the test lines, it is essential to perform the intersection counts using test lines of several random angular orientations placed in numerous metallographic planes having random angular orientations to obtain an unbiased and precise estimate of the population average value $\langle I_L \rangle$, which makes the procedure very laborious. Further, in such an isotropic uniform random (IUR) sampling process, it is not known a priori on the test lines and test planes of how many different orientations the measurement need to be performed for a reliable estimate of S_V, because the answer depends on the morphological orientation distribution function of the surfaces of interest (which is usually unknown). During the recent years, a practical and efficient solution to this complex problem has been developed using design-based stereology and vertical section sampling technique (Ref 9) described below.

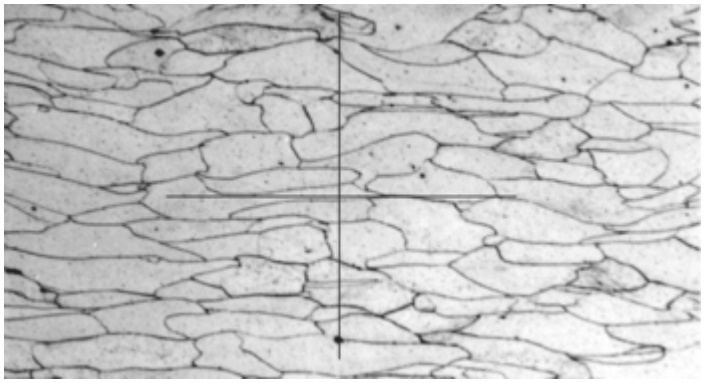

Fig. 7 Anisotropic microstructure of a specimen of cold rolled extra-low-carbon steel, where the number of intersections between a test line and grain boundaries strongly depends on the angular orientation of the test line. For example, in this microstructure, a vertical test line is expected to intersect a significantly higher number of grain boundaries than a horizontal test line of the same length.

To begin the sampling process, choose a reference direction in the 3-D space. In the present context, this reference direction is called vertical axis or vertical direction (it has no relation whatsoever to the gravitational vertical). Any plane that contains the vertical axis is called a vertical plane (see Fig. 8 and 9). Baddeley, Gundersen, and Cruz Orive (Ref 9) have shown that the set of vertical planes belonging to any chosen vertical axis contains test lines of all possible angular orientations in the 3-D space. Therefore, for estimation of S_V, it is sufficient to perform the intersection counts using the test lines in any one set of vertical metallographic planes (i.e., there is no need to perform the measurements in the metallographic planes that are inclined with respect to the chosen vertical axis). Nonetheless, the frequency of the angular orientations of the lines in the vertical planes is not equal to that in the 3-D space, and therefore it is essential to correct for this bias, when the intersection counts are performed only in the vertical planes. Baddeley et al. (Ref 9) showed that this bias can be eliminated if the intersection counts are performed using cycloid shape test lines (see Fig. 10) that are oriented such that the cycloid minor axis is parallel to the vertical axis. In such a case, the following equation (Ref 9) can be used for an unbiased estimation of S_V:

$$S_V = 2 \langle C_L \rangle \qquad \text{(Eq 8)}$$

where $\langle C_L \rangle$ is the population average value of the number of intersections between the cycloid shape test lines and the microstructural surfaces of interest per unit test line length, when the cycloids are placed in the vertical sections with their minor axis parallel to the vertical axis. Figure 11 illustrates such intersection counting using cycloid test lines.

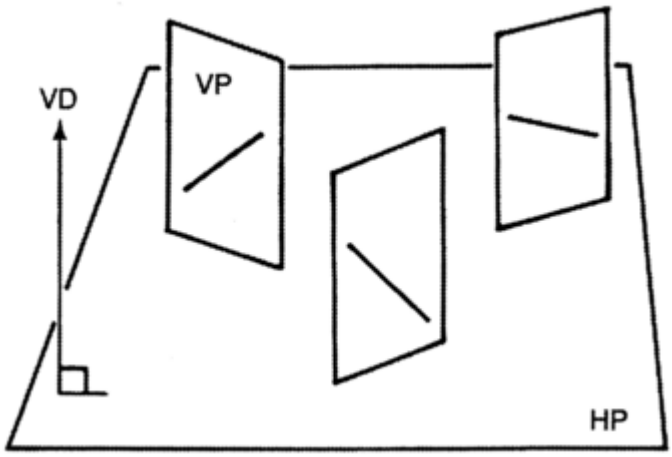

Fig. 8 Concept of vertical direction/axis (VD) and vertical planes (VP). HP is horizontal plane. Source: Ref 9

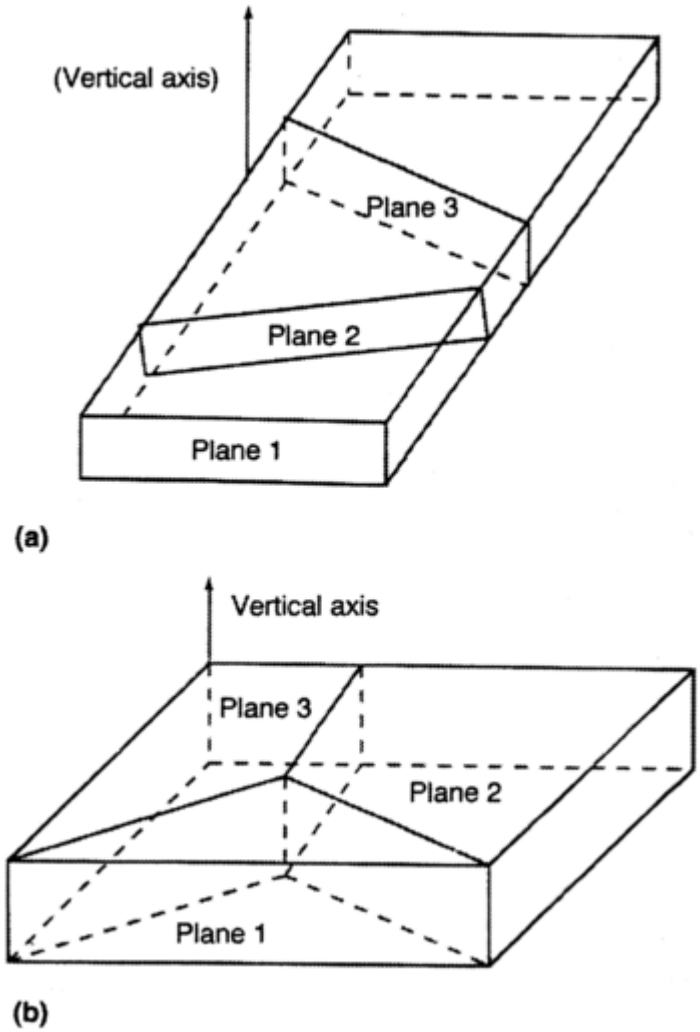

Fig. 9 Vertical planes. (a) At different locations in the specimen. (b) At the same location in the specimen

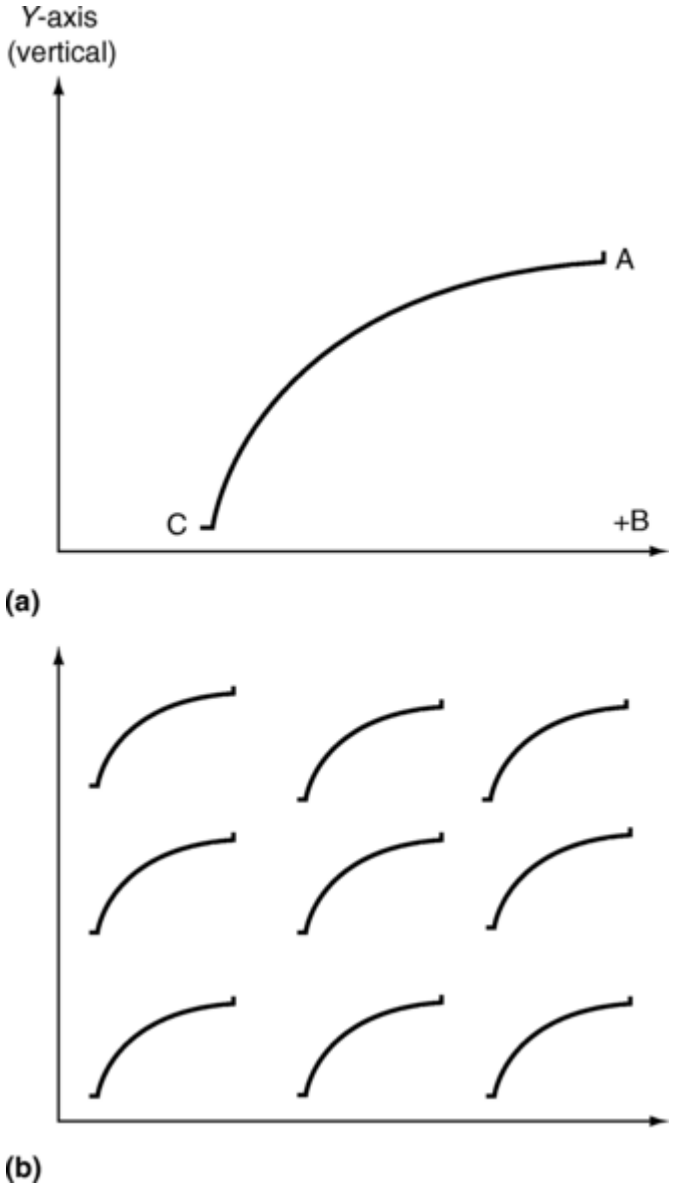

Fig. 10 Cycloid shape test lines. (a) Cycloid curve oriented with its minor axis (AB) parallel to the *Y*-axis (vertical axis). The length of the cycloid curve is equal to two times the length of its minor axis (AB). Parametric equation of cycloid is $Y = 1 - \cos\theta$ and $X = \theta - \sin\theta$. The parameter θ takes values from 0 to π. (b) A measurement grid containing nine cycloids. For the surface area measurements the grid must be oriented so that the arrow is parallel to the vertical axis.

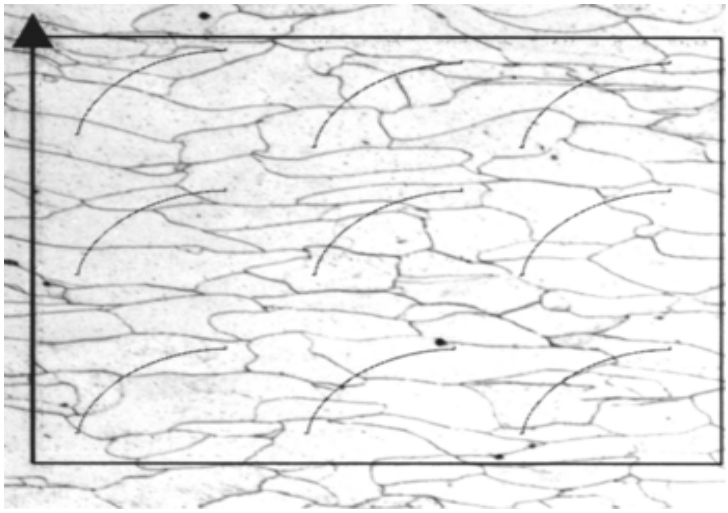

Fig. 11 A set of nine cycloid test lines superimposed on the microstructure observed in a vertical metallographic plane of a specimen of cold rolled extra-low-carbon steel (Ref 11). In this case, the chosen vertical axis (*Y*-axis) is the direction perpendicular to the faces of the rolled plate. The number of intersections between these nine test lines and the anisotropic grain boundaries is equal to 36. The effective length of cycloid minor axis was 138 μm. The length of a cycloid arc is two times the length of its minor axis. Therefore, the number of intersections per unit test line length is equal to [36]/{9 × (2 × 138)} = 0.0145 per μm.

Numerous materials processes lead to the microstructural anisotropy that has a natural rotational symmetry axis. For example, the morphological anisotropy of the grain boundaries in an extruded (or wire drawn) polycrystalline metal is rotationally symmetric with respect to the extrusion direction (wire axis). In such a material, all the metallographic planes containing the symmetry axis present statistically similar 2-D microstructures. Therefore, if the symmetry axis is chosen as the vertical axis, then all the corresponding vertical planes yield statistically similar intersection counts. Consequently, in such homogenous anisotropic microstructures, S_V can be estimated by performing the intersection counts using cycloid shape test lines placed in a single vertical plane containing the symmetry axis (vertical axis) using Eq 8. Thus, the methodology developed by Baddeley and coworkers (Ref 9) provides a very efficient practical solution for the estimation of S_V in the anisotropic microstructures that have a symmetry axis.

Several materials processes lead to the microstructural anisotropy that does not have a rotational symmetry axis. For example, the morphological anisotropy of the grain boundaries in a cold-rolled metal is not rotationally symmetric with respect to the rolling direction (or with respect to any other direction). In such cases, Eq 8 is still applicable, but the measurements must be performed on vertical planes of numerous different orientations. Further, it is not known a priori on vertical planes of how many different orientations the measurement need to be performed for a reliable estimation of S_V, because the answer depends on the morphological orientation distribution function of the surfaces of interest (which is usually unknown). This problem has been analyzed by Gokhale and Drury (Ref 10) using theoretical analysis and computer simulations. It has been shown that the measurements on vertical planes of at the most three orientations are always sufficient for an estimation of S_V with a bias of less than 5% in a microstructure of any arbitrary anisotropy, if the sampling and the intersection counts are performed using a trisector probe (which consists of three vertical planes) using the following procedure (Ref 10):

1. The vertical axis should be chosen such that it is *not* parallel to most of the surfaces of interest. For example, in a cold-rolled plate or sheet, the thickness direction can serve as such vertical axis.
2. The first vertical plane (obviously, it must contain the chosen vertical axis) is chosen in a completely arbitrary fashion.
3. The second and the third vertical planes of the trisector are chosen such that they are at an angle of 120° to the first vertical plane and to one another. This yields a set of three vertical planes that are mutually at angle of 120° and contain a common direction that is the chosen vertical axis (see Fig. 12). The three planes of the trisector need not be at the same location in microstructure, and to optimize the efficiency and to minimize the bias, they should not be at the same location.

4. On each vertical plane of the trisector, place a set of cycloid shape test lines and sample the plane in a systematic manner. The cycloid minor axis must be parallel to the vertical axis.
5. Count the number of intersections between the cycloid test lines and the microstructural surfaces of interest, and calculate the average number of intersections per unit test line length (see Fig. 11 for an illustration of the counting procedure).

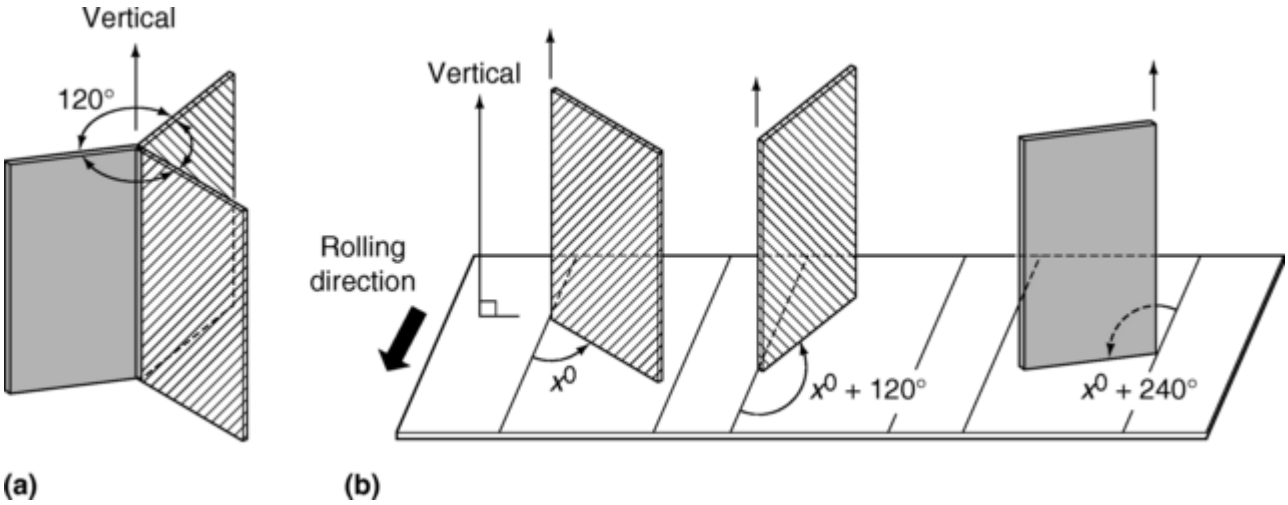

Fig. 12 Use of a trisector probe. (a) The trisector consists of three vertical planes that are mutually at an angle of 120° where the vertical axis is not parallel to most of the surfaces of interest. (b) In a rolled metal plate, most of the grain boundaries are parallel to the rolling directions, and therefore the vertical axis of the trisector can be the direction perpendicular to the faces of the plate. For the trisector sampling, the angular orientation x^0 of the first vertical planes is chosen at random. The orientations of the remaining two planes are obtained by adding 120° and 240°, respectively, to the first one. The three planes of the trisector need not be at the same location. Source: Ref 10, 64

The total surface area per unit volume S_V can be then estimated using a stereological equation (Ref 10):

$$S_V = 2\,\langle T_L \rangle \qquad \text{(Eq 9)}$$

where $\langle T_L \rangle$ is the population average value of the number of intersections of the microstructural surfaces with the cycloid shape test lines in the trisector planes per unit test line length. Note that Eq 6, Eq 8, and Eq 9 are formally identical: they differ only in the sampling procedures used for the intersection counting. The trisector technique has been used in several recent studies for estimation of S_V in anisotropic microstructures (Ref 10, 11, 17, 55, 56, 62, 63, 64).

Figure 13 shows a plot of the total surface area of the grain boundaries per unit volume estimated using the trisector technique versus the amount of cold work in a set of specimens of cold-rolled extra-low-carbon steel (Ref 11). In these specimens, the initial microstructure before the cold rolling was the same. The data show that the total grain boundary area increases with amount of cold work. Therefore, the plastic deformation creates new grain boundary surfaces.

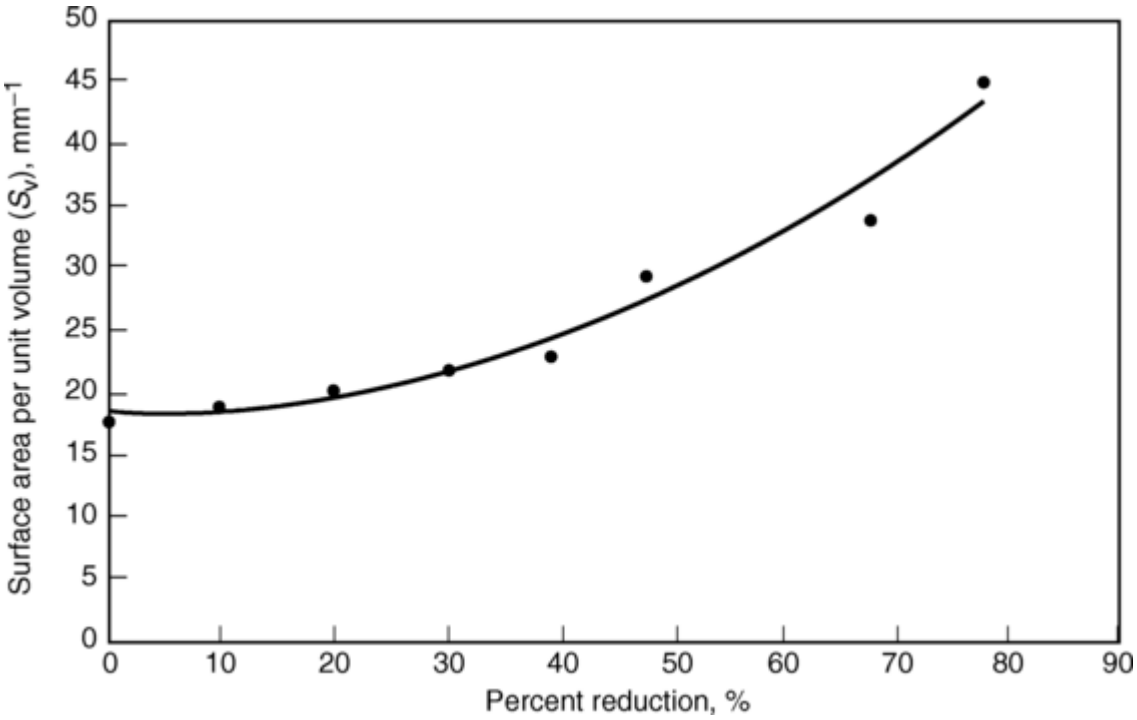

Fig. 13 Plot of total surface area of the grain boundaries per unit volume measured using the trisector technique versus the amount of cold work in a set of specimens of cold-rolled extra-low-carbon steel. Source: Ref 11

Estimation of Total Projected Surface Area per Unit Volume

In the microstructure-properties correlation studies involving anisotropic microstructures, another microstructural parameter of interest is the total projected surface area of the microstructural surfaces of interest on a plane of specific angular orientation (θ, φ) per unit volume, $A_V(\theta, \varphi)$. This parameter can also be estimated in a straightforward manner. Let $\langle I_L(\theta, \varphi) \rangle$ be the average number of intersections between straight test lines of orientation (θ, φ) and the microstructural surfaces per unit test line length. It can be shown that (Ref 6, 7, 8, 61):

$$A_V(\theta, \varphi) = \langle I_L(\theta, \varphi) \rangle \quad \text{(Eq 10)}$$

In other words, the intersection counts using straight test line of specific angular orientation essentially represent the total projected area of the surfaces on a plane perpendicular to the direction of the test lines. Figure 14 shows a plot of plane strain fracture toughness K_{Ic} versus the total projected area of the high angle grain boundaries between recrystallized and unrecrystallized regions on the plane perpendicular to the loading direction, in a set of specimens of partially recrystallized hot-rolled 7050 aluminum alloy having different degrees of recrystallization and orientations (Ref 55). The K_{Ic} decreases with the increase in the projected area of the boundaries indicating that these boundaries adversely affect the fracture toughness of the alloy.

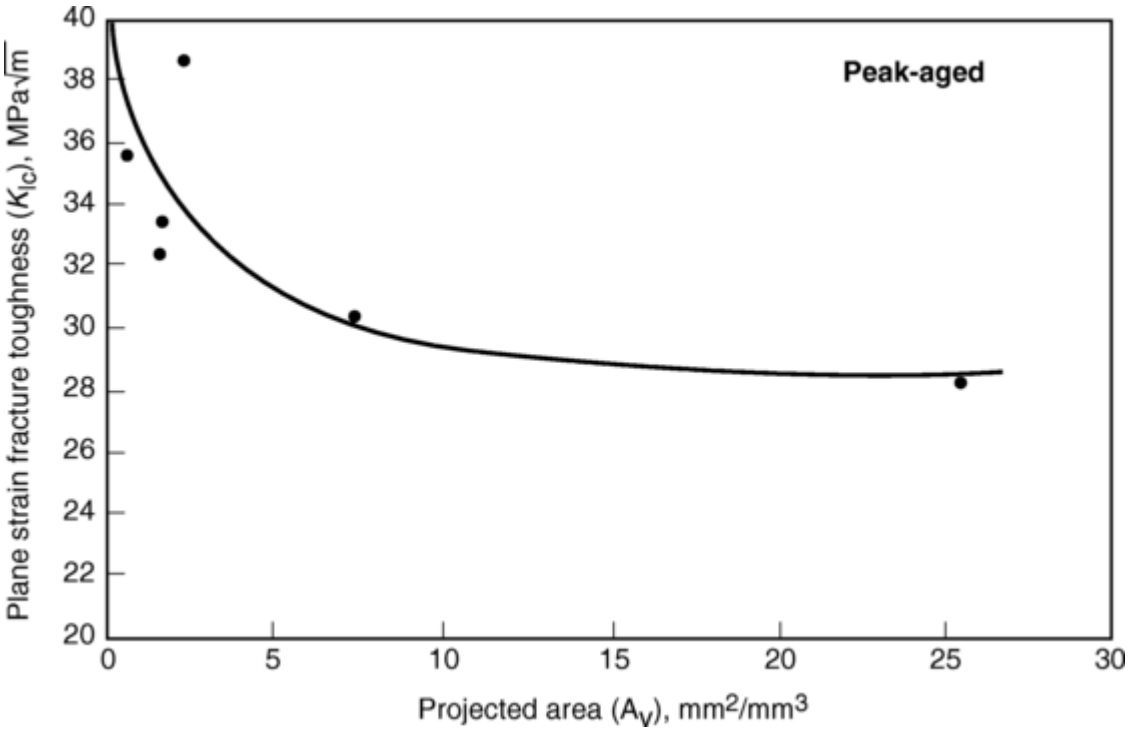

Fig. 14 Plot of plane strain fracture toughness K_{Ic} versus the total projected area of the high-angle grain boundaries between recrystallized and unrecrystallized regions per unit volume A_V on the plane perpendicular to the loading direction in a set of specimens of partially recrystallized hot-rolled 7050 aluminum alloy having different degrees of recrystallization and orientations. Source: Ref 55

Estimation of Sampling Error. To estimate the sampling error in the total surface area per unit volume S_V, let L_T be the total effective length of the set of test lines used for the intersection counting. Suppose that these test lines are placed in n number of fields of view, and the intersections between the test lines and the surfaces of interest are counted. Let $I_1, I_2, \ldots, I_i, \ldots I_n$ represent these intersection count data, which essentially constitute a statistical sample of size n. In this sample, the average number of intersections $\langle I \rangle$, that is, the sample average, is given as:

$$\langle I \rangle = \Sigma I_i/n \qquad \text{(Eq 11)}$$

If the sample size is sufficiently large (for most microstructures, $n > 50$), then the following working equation gives the confidence interval in the S_V estimated from the experimental intersection counts data:

$$E_n = 4\{\Sigma(\langle I \rangle - I_i)^2/[n(n-1)(L_T)^2]\}^{1/2} \qquad \text{(Eq 12a)}$$

$$S_V = [2\langle I \rangle/L_T] \pm E_n \qquad \text{(Eq 12b)}$$

Equation 12b implies that there is 95% probability that the true value of the total surface area per unit volume S_V is in the interval $\{2[\langle I \rangle/L_T] \pm E_n\}$. Note that the sampling error E_n strongly depends on the sample size n, and therefore it can be kept as small as desired by simply increasing the sample size n, that is, number of microstructural fields on which the measurements are performed. If the sample size is not sufficiently large (i.e., $n < 50$) then other statistical procedures must be used to compute the confidence interval (Ref 75). Note that Eq 12a and Eq 12b are applicable for calculation of confidence interval when the intersection counts are performed by using straight test lines, or by using cycloid shape test lines.

Total Length per Unit Volume

One-dimensional lineal features are usually present in material microstructures. Dislocation lines, grain edges, triple lines, and necks in the sintered microstructures are examples of the microstructural features that are truly one-dimensional. Further, the features such as needle-shaped precipitates, whiskers in composites, slag stringers, and so forth can be modeled as one-dimensional lineal features. An important attribute of the lineal microstructural features is their total length per unit volume, or so-called length density. Numerous material

properties depend on the length density of the lineal features present in microstructure. For example, almost all the plastic-deformation-related mechanical properties of crystalline materials depend on the dislocation density. The total line length per unit volume is denoted by the symbol L_V. It is equal to the sum of the lengths of the lineal features of interest in a specimen divided by the specimen volume. In the symbol L_V, the subscript V signifies the normalization with the specimen volume. The units of L_V are μm/μm^3 or (μm)$^{-2}$. Since L_V is not dimensionless, it is necessary to know the microscope magnification for its estimation. The length density can be estimated from the measurements performed in the metallographic planes, or in the projected images of a 3-D microstructure. These two techniques are described in the paragraphs that follow.

Estimation of L_V from Measurements Performed in Metallographic Planes. The 2-D metallographic planes serve as geometric probes for the estimation of L_V. The intersections of lineal features with a metallographic plane result in "points." These points can be observed in a metallographic plane. For example, the triple junctions in Fig. 15(a) are the intersections of the grain edges with the metallographic plane. One can count the number of such points per unit area of the metallographic plane, Q_A. The population average value of number of points per unit area $\langle Q_A \rangle$ is related to the length density of the lineal features as follows (Ref 8, 61):

$$L_V = 2 \langle Q_A \rangle \qquad \text{(Eq 13)}$$

Note that $\langle Q_A \rangle$ has units of (μm)$^{-2}$. The triple-point counting procedure is illustrated in Fig. 15. For isotropic microstructures, it is not necessary to randomize the angular orientation of the metallographic plane. In such a case, the measurements in the metallographic planes of any one convenient orientation can give a reliable estimate of L_V. If the microstructure is isotropic and homogeneous (i.e., no gradients), then the measurements performed in a single metallographic plane of any one angular orientation and at any convenient location in the specimen should yield a reliable estimate of L_V. For most homogeneous isotropic material microstructures, measurements on about 50 to 60 uniformly distributed microstructural fields can yield a reliable estimate of L_V.

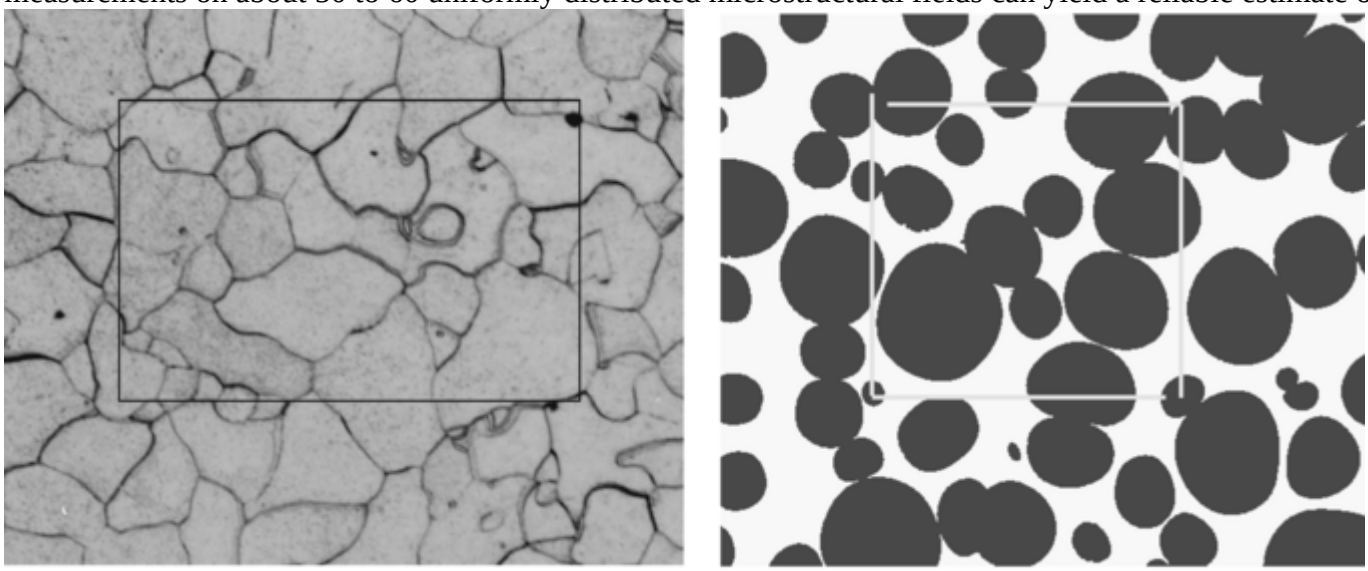

Fig. 15 Triple-point counting procedure. (a) Microstructure of well-annealed extra-low-carbon steel containing equiaxed grains. The triple junction points (i.e., junctions of three grain boundary traces) are points of intersections of grain edges in the 3-D microstructure with the metallographic plane. In the measurement frame there are 45 triple junction points in the measurement frame having the effective area of 36.5 × 10^4 μm^2. Therefore, Q_A is equal to 45/[36.5 × 10^4] = 1.23 × 10^{-4} per μm^2. (b) Microstructure of liquid phase sintered tungsten heavy alloy depicting tungsten grains. The "necks" are the loops that bound the grain boundary between each pair of abutting tungsten grains in the 3-D microstructure. The intersections of these necks with the metallographic plane yield solid-solid-liquid triple junction points (i.e., common junction points of two tungsten grains and matrix). In the measurement frame, there are 16 such triple junction points, and the frame has effective area of 10^4 μm^2. Therefore, Q_A is equal to 16/[10^4] = 1.6 × 10^{-3} per μm^2.

In an anisotropic microstructure, Q_A varies systematically with the angular orientation of the metallographic plane. Consequently, it is essential to perform the measurements on numerous metallographic planes of

different random angular orientations to obtain a reliable estimate of the population average $\langle Q_A \rangle$. At present, no stereological technique is available for efficient estimation of the length density in an anisotropic microstructure from the measurements performed on few metallographic planes. However, an efficient stereological technique for the estimation of the length density in any anisotropic microstructure is available if the measurements can be performed on the projected images of the microstructure. This alternate method is described below.

Estimation of L_V from Measurements Performed in Projected Images. For numerous microstructures, transmission microscopy (for example, transmission electron microscopy, radiography, and so forth) is the microscopy technique of choice. In such cases, efficient estimation of the length density of lineal features from the projected microstructural images is of particular interest. This design-based stereological method involves vertical slices sampling procedure developed by Gokhale (Ref 13, 14, 15):

1. Choose a convenient reference direction in the 3-D space. This reference direction is called vertical axis.
2. A slice is a microstructural volume contained between two parallel planes that are separated by distance, Δ, which is the thickness of the slice. A vertical slice is a slice whose parallel faces contain the chosen vertical axis (see Fig. 16). Uniformly sample the 3-D microstructure with vertical slices.
3. Observe the projected images of the lineal features contained in the vertical slices (Fig. 17).
4. Place cycloid shape test lines on the projected images of the vertical slices such that the cycloid minor axis is perpendicular to the vertical axis. Such test lines essentially represent the projections of hypothetical cycloidal test surfaces in the vertical slices as illustrated in Fig. 17.
5. Count the number of intersections between the cycloid shape test lines and the projected images of the lineal features of interest, and calculate the number of intersections per unit length (see Fig. 18).

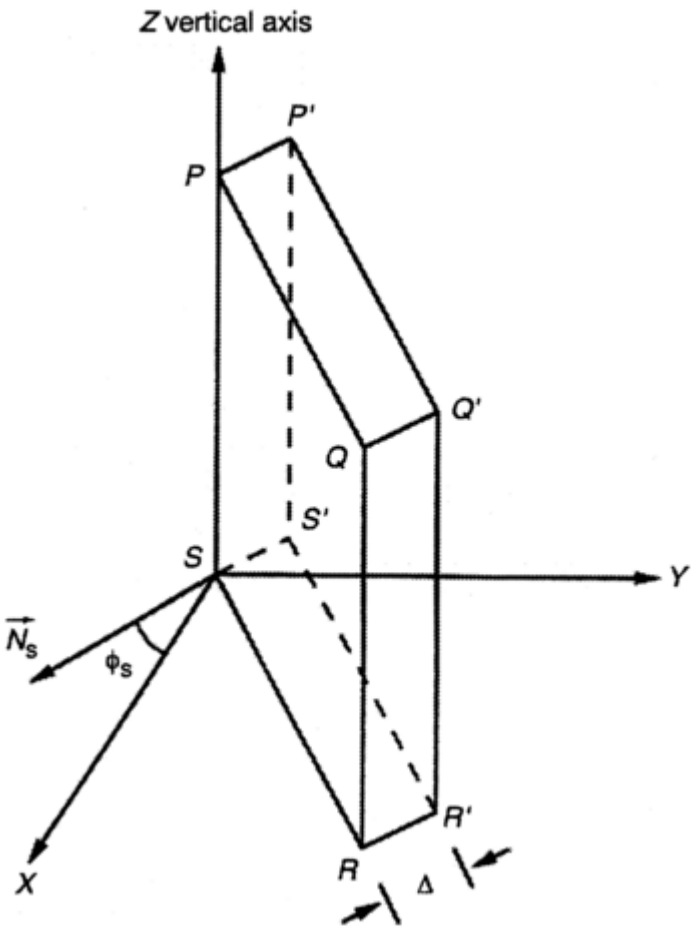

Fig. 16 Concept of vertical slice. A vertical slice is any microstructural volume contained between two vertical planes (faces of the slice) separated by distance, Δ, which is the slice thickness. Source: Ref 13, Ref 14

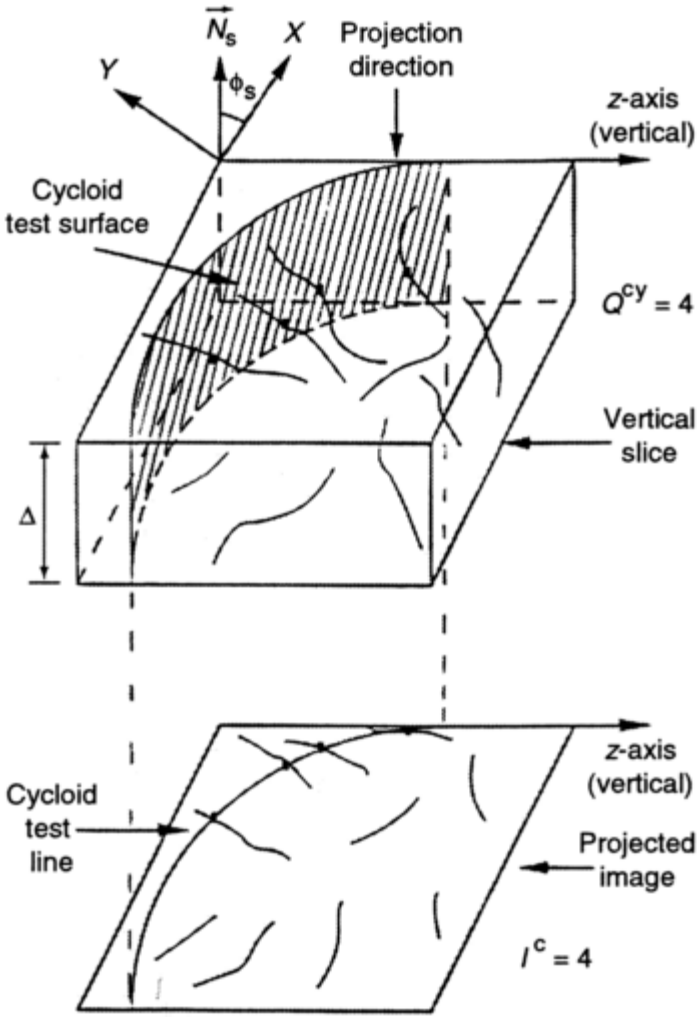

Fig. 17 A cycloid placed in the projected image of a vertical slice can be treated as projected image of hypothetical cycloidal surface contained in the slice. The number of intersections *Q* between the lineal features of interest in the slice and such cycloidal surface is exactly equal to the number of intersections *J* between the corresponding cycloid in the projected image and the projected images of the lineal features. Source: Ref 13

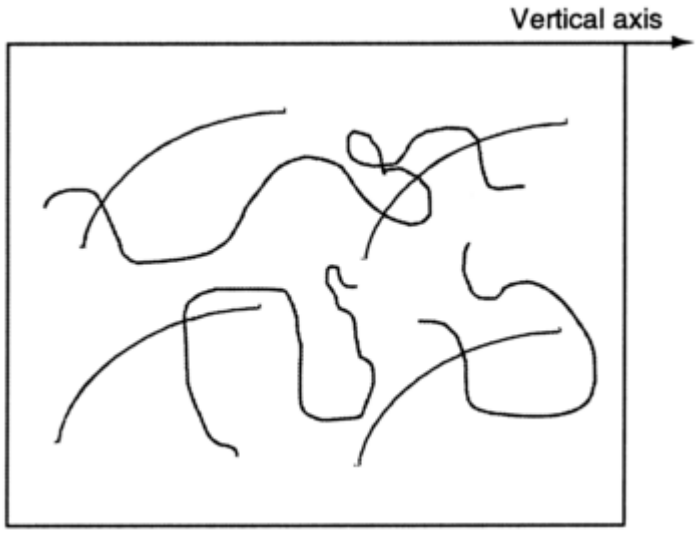

Fig. 18 Four cycloid shape test lines superimposed on the projected image of a vertical slice containing lineal features. Note that, for the length estimation, the cycloid minor axis must be perpendicular to the vertical axis. In this example, there are a total of six intersections between the four cycloid test lines and

the projected images of the lineal features. For the cycloids having minor axis equal to 20 μm, the length of each test line would be 40 μm, and J_L would be equal to 6/[4 × 40] = 0.0375 per μm.

The population average value of this quantity $\langle J_L \rangle$ is related to the length density L_V through the stereological equation (Ref 13, 14, 15):

$$L_V = 2 \langle J_L \rangle / \Delta \qquad \text{(Eq 14)}$$

This result has been utilized to estimate the length density of anisotropic lineal biological features in numerous biological tissues (Ref 65, 66, 67, 68); the technique is equally applicable for the estimation of dislocation density from transmission electron microscopy (TEM) images.

If the anisotropy of the lineal features of interest has a natural rotational symmetry axis, then the projected images of all the vertical slices containing the symmetry axis present statistically similar projected microstructures. Therefore, if the symmetry axis is chosen as the vertical axis, then all the corresponding vertical slices yield statistically similar intersection counts. Consequently, in such anisotropic microstructures, L_V can be estimated by performing intersection counts on the projected images of vertical slices of just one orientation containing the symmetry axis (vertical axis). If the anisotropy of the lineal features does not have a natural symmetry axis, then sampling similar to the trisector consisting of three vertical slices mutually at an angle of 120° yields a reliable estimate of L_V, if the vertical axis is not parallel to most of the lineal features (Ref 69).

Estimation of Sampling Error. For computation of the sampling error in the estimated total length per unit volume L_V from the measurements performed in the metallographic planes, let A_T be the total effective area of the measurement frame used for counting. Suppose this measurement frame is placed in n number of fields of view, and the intersections between the frame and the lineal features of interest are counted. Let Q_1, Q_2, …, Q_i, … Q_n represent these data, which essentially constitute a statistical sample of size n. In this sample, the average number of intersections $\langle Q \rangle$; that is, the sample average, is given as:

$$\langle Q \rangle = \Sigma Q_i / n \qquad \text{(Eq 15)}$$

If the sample size is sufficiently large (for most microstructures, $n > 50$) then the L_V estimated from this sample and the associated confidence interval are given as:

$$L_V = 2[\langle Q \rangle / A_T] \pm E_n \qquad \text{(Eq 16)}$$

$$E_n = 4\{\Sigma(\langle Q \rangle - Q_i)^2 / [n(n-1)(A_T)^2]\}^{1/2} \qquad \text{(Eq 17)}$$

Equation 16 states that there is 95% probability that the true value of the total length per unit volume is within the interval given by the right-hand side of the equation. As mentioned earlier, other statistical procedures need to be used for small samples (Ref 75).

References cited in this section

4. P.R. Mouton, *Principles and Practices of Unbiased Stereology: An Introduction for Bioscientists,* The Johns Hopkins University Press, 2002

5. F. Chayes, *Petrographic Modal Analysis,* John Wiley, 1956

6. E.E. Underwood, *Quantitative Stereology,* Addison Wesley, 1970

7. R.T. DeHoff and F.N. Rhines, *Quantitative Microscopy,* McGraw Hill, 1968

8. S.A. Saltykov, *Stereometric Metallography,* 2nd ed., Metallurgizdat, Moscow, 1958

9. A.J. Baddeley, H.J.G. Gundersen, and L.M. Cruz Orive, Estimation of Surface Area Using Vertical Sections, *J. Microsc.,* Vol 142, 1986, p 259–276

10. A.M. Gokhale and W.J. Drury, Efficient Estimation of Microstructural Surface Area Using Trisector, *Metall. Trans. A,* Vol 25A, 1994, p 919–928

11. B.R. Morris, A.M. Gokhale, and G.F. Vander Voort, Estimation of Grain Size in Anisotropic Materials, *Metall. Mater. Trans. A,* Vol 29A, 1998, p 237–244

12. J. Ohser and F. Muecklich, *Statistical Analysis of Microstructures in Material Science,* John Wiley & Sons, 2000

13. A.M. Gokhale, Unbiased Estimation of Curve Length in 3D Using Vertical Slices, *J. Microsc.,* Vol 159, 1990, p 133–141

14. A.M. Gokhale, Estimation of Length Density L_v from Vertical Slices of Unknown Thickness, *J. Microsc.,* Vol 167, pt. I, 1992, p 1–8

15. A.M. Gokhale, Utility of Horizontal Slice for Stereological Characterization of Lineal Features, *J. Microsc.,* Vol 170, pt. 1, 1993, p 3–8

16. L.M. Cruz Orive and X. Gual-Arnau, Precision of Circular Systematic Sampling, *J. Microsc.,* Vol 207, 2002, p 225–242

17. A.M. Gokhale and N.U. Deshpande, Stereology of Anisotropic Microstructures, *Quantitative Microscopy and Image Analysis,* D.J. Diaz, Ed., ASM International, 1994, p 73–82

18. P.R. Mouton, A.M. Gokhale, N.L. Ward, and M.J. West, Unbiased Length Estimation Using Isotropic Spherical Probes, *J. Microsc.,* Vol 206, 2002, p 54–64

27. P. Velecky and J. Pospisil, Digital Image Processing for Evaluation of the Internal Microstructure Characteristics of Cemented Carbides, *Optik,* Vol 111, 2000, p 493–496

40. L. Hengcheng, Y. Sun, and S. Guoxiong, Correlation between Mechanical Properties and Amount of Dendritic Alpha-Al Phase in As-Cast Near-Eutectic Al-11.6% Si Alloys Modified with Strontium, *Mater. Sci. Eng. A,* Vol 335, 2002, p 62–66

41. M. Sozanska, A. Maciejny, C. Dagbert, J. Galland, and L. Hyspecka, Use Of Quantitative Metallography in the Evaluation of Hydrogen Action During Martensitic Transformations, *Mater. Sci. Eng. A,* Vol A273, 1999, p 485–490

42. Q. Meng, Y. Rong, S. Chen, and T.Y. Hsu, The Relationship of the Volume Fraction of Martensite vs. Plastic Strain in a Fe-Mn-Si-Cr-N Shape Memory Alloy, *Mater. Lett.,* Vol 50, 2001, p 328–332

43. H. Agarwal, A.M. Gokhale, S. Graham, and M.F. Horstemeyer, Quantitative Characterization of Three-Dimensional Damage Evolution in a Wrought Al-Alloy under Tension and Compression, *Metall. Mater. Trans.,* Vol 33A, 2002, p 2599–2606

44. M.P. Black, R.L. Higginson, and C.M. Sellars, Effect of Strain Path on Recrystallization Kinetics During Hot Rolling of Al-Mn, *Mater. Sci. Technol.,* Vol 17, 2001, p 1055–1060

45. K. Bodlak, A. Balasundaram, A.M. Gokhale, and V. Benes, Unfolding of Three-Dimensional Bivariate Size-Orientation Distribution of Microcracks, *Acta Mater.,* Vol 51, 2003, p 3131–3143

46. R.A. Vandermeer, N. Hansen, X. Huang, J. Jensen, E.M. Laurdisen, T. Leffers, W. Pantleon, T.J. Sabine, and J.A. Wert, Kinetic Aspects of Nucleation and Growth in Recrystallization, *Proc. 21st Riso International Symposium on Materials Science* (Roskilde, Denmark), 2000, p 179–200

47. J.A. Griggs, K.J. Anusavice, and J.J. Mecholsky, Jr., Devitrification and Microstructural Coarsening of a Fluoride-Containing Barium Aluminosilicate Glass, *J. Mater. Sci.,* Vol 37, 2002, p 2017–2022

48. K.-W. Moon, W.J. Boettinger, U.R. Kattner, C.A. Handwerker, and D.-J. Lee, The Effect of Pb Contamination on the Solidification Behavior of Sn-Bi Solders, *J. Electron. Mater.,* Vol 30, 2001, p 45–52

49. F.G. Caballero, C. Garcia de Andres, and C. Capdevila, Characterization and Morphologic Analysis of Pearlite in a Eutectoid Steel, *Mater. Charact.,* Vol 45, 2000, p 111–116

51. S. Spangel, E. Matthaei-Schulz, A. Schulz, H. Vetters, and P. Mayr, Influence of Carbon and Chromium Content and Preform Shape on the Microstructure of Spray Formed Steel Deposits, *Mater. Sci. Eng. A,* Vol A326, 2002, p 26–39

52. J. Wosik, H.J. Penkalla, K. Szot, B. Dubiel, and F.C. Schubert, The Influence of Various Microscopic Techniques on the Quantification of Stereological Structure Parameters in Waspaloy Alloy, *Prakt. Metallogr.,* Vol 39, 2002, p 140–154

53. W. Yunxin, R.M. German, D. Blaine, B. Marx, and C. Schlaefer, Effects of Residual Carbon Content on Sintering Shrinkage, Microstructure and Mechanical Properties of Injection Molded 17-4 PH Stainless Steel, *J. Mater. Sci.,* Vol 37, 2002, p 3573–3583

54. M. Grange, J. Besson, and E. Andrieu, An Anisotropic Gurson Type Model to Represent the Ductile Rupture of Hydrided Zircaloy-4 Sheets, *Int. J. Fract.,* Vol 105, 2000, p 273–293

55. N.U. Deshpande, A.M. Gokhale, D.K. Denzer, and J. Liu, Relationship between Fracture Toughness, Fracture Path, and Microstructure of 7050 Aluminum Alloy—I: Quantitative Characterization, *Metall. Mater. Trans. A,* Vol 29A, 1998, p 1191–1201

56. H. Agarwal, A.M. Gokhale, S. Graham, and M.F. Horstemeyer, Anisotropy of Intermetallic Particle Cracking Damage Evolution in an Al-Si-Mg Base Wrought Aluminum Alloy under Uniaxial Compression, *Metall. Mater. Trans. A,* Vol 33A, 2002, p 3443–3448

57. H. Agarwal, A.M. Gokhale, and S. Graham, Void Growth in 6061 Al-Alloy under Triaxial Stress State, *Mater. Sci. Eng.,* Vol 341 (No. 1–2), 2003, p 35–42

58. A.K. Balasundaram, A.M. Gokhale, S. Graham, and M.F. Horstemeyer, Three Dimensional Particle Cracking Damage Development in an Al-Mg Base Alloy, *Mater. Sci. Eng.,* Vol 355 (No. 1–2), 2003, p 368–383

61. C.S. Smith and L. Guttman, Measurement of Internal Boundaries in Three-Dimensional Structures by Random Sectioning, *Trans. AIME,* Vol 97, 1953, p 81

62. A.M. Gokhale and W.T. Whited, Measurements of Growth Rates of Thermally Induced Micro-cracks in a Metal Matrix Composite, *Developments in Ceramics and Metal Matrix Composites,* K. Upadhya, Ed., TMS, 1992, p 273–286

63. A.M. Gokhale, W.J. Drury, and W.T. Whited, Quantitative Microstructural Analysis of Anisotropic Materials, *Mater. Charact.,* Vol 31, 1993, p 11–18

64. L. Karlsson and A.M. Gokhale, Stereological Estimation of Mean Linear Intercept Length in Metallography Using Vertical Sections and Trisector, *J. Microsc.,* Vol 186, 1997, p 143–152

65. E.A. Stocks, J.M. McArthur, J.W. Griffin, and P.R. Mouton, An Unbiased Method for Estimation of Total Epidermal Nerve Fiber Length, *J. Neurocyt.,* Vol 25, 1996, p 11–18

66. P.J. McMillan, J.O. Archambeau, and A.M. Gokhale, Morphometric and Stereological Analysis of Cerebral Cortical Microvessels Using Optical Sections and Thin Slices, *Acta Stereol.,* Vol 13, 1994, p 33–38

67. S. Batra, M.F. Konig, and L.M. Cruz Orive, Unbiased Estimation of Capillary Length from Vertical Slices, *J. Microsc.,* Vol 178, 1994, p 152–159

68. C.V. Howard, L.M. Cruz Orive, and H. Yaegashi, Estimating Neuron Dendritic Length in 3D From Total Vertical Projections and Vertical Slices, *Acta Neurol. Scand., Suppl.,* Vol 137, 1992, p 14–19

69. M. Hlawiczkova, A.M. Gokhale, and V. Benes, Efficiency and Bias of Length Density Estimator, *J. Microsc.,* Vol 204, 2001, p 2226–2231

70. J.E. Hilliard and J.W. Cahn, An Evaluation of Procedures in Quantitative Metallography for Volume Fraction Analysis, *Trans. AIME,* Vol 221, 1961, p 344–354

71. H.J.G. Gundersen and E.B. Jensen, The Efficiency of Systematic Sampling in Stereology and Its Prediction, *J. Microsc.,* Vol 121, 1987, p 65–73

72. L.M. Cruz Orive, Systematic Sampling in Stereology, *Bull. Int. Stat. Inst.,* Vol 55, 1993, p 451–468

73. L.M. Cruz Orive, On the Precision of Systematic Sampling: A Review of Matheron's Transitive Methods, *J. Microsc.,* Vol 153, 1985, p 518–530

74. H.J.G Gundersen, E.B. Kiru, and J. Neilsen, The Efficiency of Systematic Sampling in Stereology, *J. Microsc.,* Vol 193, 1999, p 199–211

75. E. Kreyszig, *Advanced Engineering Mathematics,* 6th ed., John Wiley & Sons, 1988

A.M. Gokhale, Quantitative Characterization and Representation of Global Microstructural Geometry, *Metallography and Microstructures,* Vol 9, *ASM Handbook,* ASM International, 2004, p. 428–447

Quantitative Characterization and Representation of Global Microstructural Geometry

Arun M. Gokhale, Georgia Institute of Technology

Number Density of Microstructural Features (How Many?)

Number density of a given type of microstructural features (for example, voids, particles, grains) is equal to the average value of the number of such features per unit microstructural volume. This is an important microstructural parameter of interest in processing-microstructure-properties studies. Unfortunately, in general, the number density of the features in a 3-D microstructure cannot be estimated from any measurements performed on independent 2-D metallographic sections, unless the particles/grains have a known simple convex shape (Ref 2, 6, 7, 8). Consequently, in the past, reliable estimation of number density was problematic. In 1984, Sterio (Ref 19) showed that the number density of the features in a 3-D microstructure can be estimated using a test probe (called disector) consisting of two parallel metallographic planes that are a small distance apart (i.e., two closely spaced serial sections). In 2000 (Ref 20), a combination of this sampling principle and modern image analysis techniques led to an efficient stereological method for an unbiased and efficient estimation of the number density from the measurements performed on the digital images of two closely spaced large-area high-resolution montage serial sections, called large-area disector (LAD). To understand these 3-D

techniques, first an unbiased method for counting particles/grains in a 2-D metallographic plane is presented, and then the estimation of the number density in the 3-D microstructures is described.

Estimation of Number of Particles/Grains per Unit Area in a Metallographic Plane. In any microscope, a limited area of the metallographic plane is observed in one field of view. Therefore, there are usually some features that cross the boundaries of the field of view (or measurement frame), which can lead to a counting bias due to an "edge effect." This is because such partly-in-partly-out features raise the question whether to include them in the number count, to exclude them, or to count them as one-half. Gundersen (Ref 76) has shown that none of these is a statistically unbiased and correct procedure. The correct statistical procedure to account for the edge effect requires the use of an unbiased counting frame (Ref 76). An unbiased counting frame consists of a square measurement frame of area A_f that has two forbidden edges (solid lines in Fig. 19), and two permissible edges (dashed lines in Fig. 19). The counting procedure is:

1. Count all the features that are completely contained in the measurement frame and therefore do not intersect any edges of the counting frame.
2. Do not count any feature that intersects a forbidden edge.
3. Count all the features that intersect the permissible edge(s), if they do not also intersect any forbidden edge.
4. The average value of the number of features counted in this manner divided by the area of the measurement frame A_f is an unbiased estimator of the two-dimensional number density of the features of interest in the metallographic plane.

This procedure for unbiased counting of the number of features in a metallographic section is shown in Fig. 19.

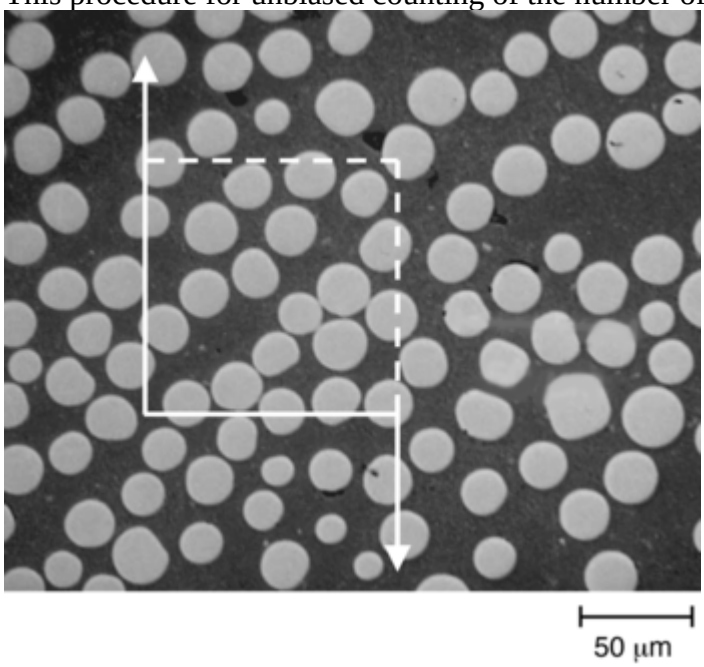

Fig. 19 Microstructure of a ceramic-matrix composite containing unidirectional continuous nicalon (SiC) fibers in MAS glass ceramic matrix observed in a transverse metallographic plane. An unbiased square counting frame consisting of two forbidden edges (solid line) and two permissible edges (dashed lines) is overlaid on the microstructure. There are 11 fibers completely inside the counting frame; there are nine fibers that intersect one or both forbidden edges (therefore, not to be included in the number count); and there are five fibers that intersect one or both permissible edges but do not intersect any forbidden edge (therefore, to be included in the number count). Thus, effectively there are 16 fibers in the measurement frame of area 3953 μm^2. Thus, the local value of the number of fiber per unit area is equal to 4.05 × 10^{-3} per μm^2.

Disector Principle for Unbiased Estimation of Number Density in 3-D Microstructure. Sterio (Ref 19) has developed a three-dimensional stereological sampling probe, disector, for an unbiased estimation of the number density of the features of interest in any three-dimensional microstructure. The disector consists of two parallel metallographic planes (i.e., two serial sections) that are separated by a known distance *t.* The distance *t* between

the disector planes must be less than one-fifth of the average size of the features of interest. Observations on both the planes of the disector are required for the estimation of the number density. An unbiased counting frame of area A_f is placed in the first disector plane to sample the features of interest using the counting procedure described in the previous subsection (and shown in Fig. 19), and these features are followed in the second plane. Out of the features sampled by the unbiased counting frame in the first disector plane, those that are not present in the second plane, Q^-, are counted. The average value of the quantity $[Q^-]/[A_f t]$ is an unbiased estimator of number of features per unit volume (i.e., number density) N_V in the three-dimensional microstructure. Alternately, an unbiased counting frame can be placed in the second metallographic plane of the disector, and the features sampled by the unbiased frame that are not present in the first plane, Q^+, may be counted in exactly the same way. In practice, it is efficient to count both Q^+ and Q^- and use the following equation for an unbiased estimation of the number density, N_V (Ref 19):

$$N_V = [Q^+ + Q^-]/[2A_f t] \quad \text{(Eq 18)}$$

The disector procedure is shown in Fig. 20. In the opaque material microstructures, a practical application of the disector probe requires storing of an image (or a micrograph) of a field of view in the first disector plane, physical removal of small known thickness of the specimen by polishing, followed by suitable etching to reveal microstructure, and the observations in the second sectioning plane to determine how many features sampled by the unbiased counting frame placed in the field of view in the first plane are not present in the second sectioning plane. In this process, the least amount of effort is required for the actual stereological counting; most of the effort (about 90%) goes into the specimen preparation steps such as physical sectioning, polishing, etching of disector planes, identification of the same microstructural region in the two sectioning planes, alignment of the images in the two planes, and measurement of thickness (i.e., distance between disector planes) of the material removed. After all the tedious metallographic work, very small numbers of particle counts are obtained. The number density estimated from such a small statistical sample (although unbiased) has a large sampling error. Therefore, to obtain a reasonably precise estimate of the number density and to decrease the sampling error, it is necessary to repeat the procedure on (typically) 25 to 50 different disectors, which requires physical sectioning of a large number of metallographic planes and involves tedious metallographic work. A practical solution to this problem has been recently developed (Ref 20) that utilizes a combination of the disector principle and modern digital image processing techniques; the resulting sampling technique, called large-area disector (LAD), is described below.

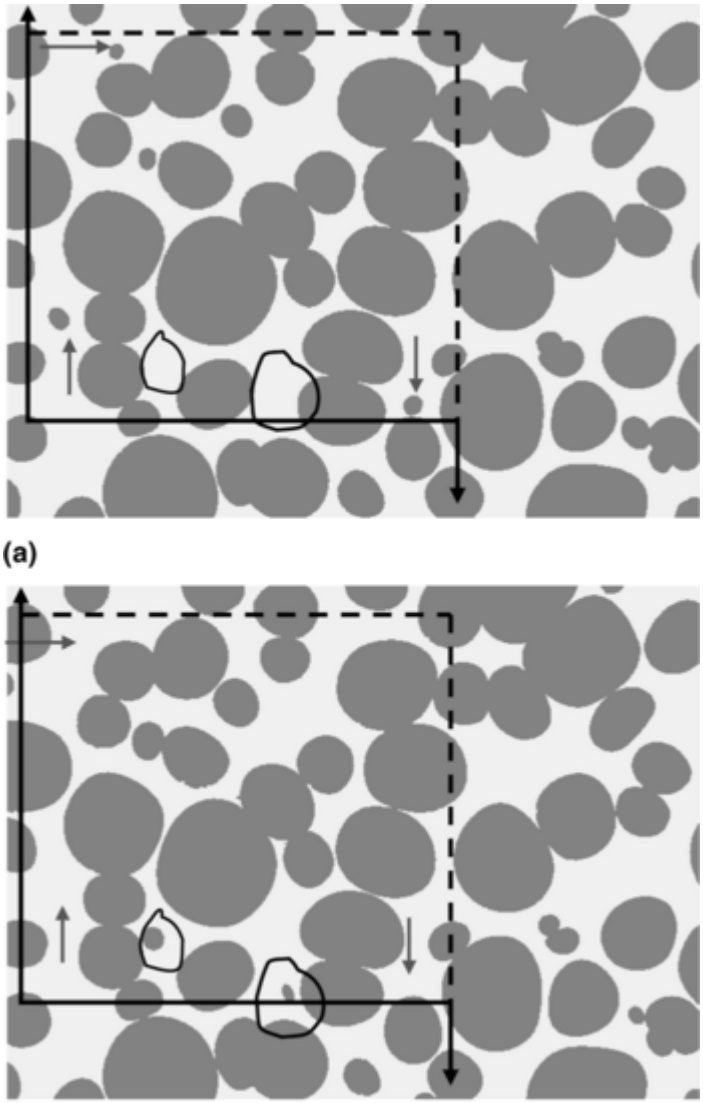

Fig. 20 Disector sampling method for estimation of number density of tungsten grains in the 3-D microstructure of liquid phase sintered W-Ni-Fe alloy. The three grains in (a) at the arrows are sampled by the unbiased counting frame, which are not present in the second disector plane segment shown in (b). Therefore, Q^- is equal to 3. On the other hand, the two grains that are circled in (b) are not present in (a). Therefore, Q^+ is equal to 2. The area of the sampling frame is 2×10^5 μm^2. In this case, the distance between the two disector planes was 1 μm. Thus, using Eq 18, the estimate of number density of tungsten grains N_V is $[2 + 3]/\{(2 \times 10^5) \times 1\} = 2.5 \times 10^{-5}$ per μm^3 of microstructural volume. Source: Ref 20

Large Area Disector (LAD) for Efficient and Unbiased Estimation of Number Density. The major limitation of the conventional disector technique is that it is inefficient for the estimation of the number density in opaque material microstructures due to low Q^+ and Q^- counts usually obtained from a disector whose area is equal to one field of view. The counts can be increased by increasing the absolute area of the field of view selected in the first sectioning plane simply by observing the structure at a much lower magnification. This is often not acceptable because the loss of resolution can lead to significant measurement errors. In almost all microscopy techniques, to obtain a higher resolution the structure must be observed at a higher magnification, and that decreases the area of the observed microstructural field of view. Therefore, it is not possible to observe a large area of a metallographic plane at a high resolution using the conventional microscopy techniques. However, it is possible to obtain a large microstructural area at a high resolution by creating a “seamless montage” of a very large number of contiguous microstructural fields grabbed at a high resolution and “stitched together” using the digital image analysis procedure given elsewhere (Ref 22, 23, 35). Using such a methodology, the number density can be efficiently estimated:

1. Identify a sufficiently large region in the first disector plane covering about 25 to 100 microstructural fields, and "tag" this region by placing sufficient number of deep microhardness indents around its four boundaries.
2. Create a seamless "montage" covering all the microstructural fields in this region of the first disector plane at sufficiently high resolution such that all the features of interest are clearly resolved, using the "montage" image analysis technique described in detail in Ref 22, 23, and 35. Figure 21 illustrates one such large-area-high-resolution montage.
3. Remove a small amount of material by polishing and identify the same region in the second disector plane by using the positions of the microhardness indents for reference.
4. Create the seamless montage of all the microstructural fields of the same region in the second disector plane, and align the two montages using the micro-hardness indents as the reference points (Ref 20). The two montages then constitute the LAD (see Fig. 22).
5. Measure the disector thickness *t* by measuring the decrease in the sizes of microhardness indents in the second disector plane (Fig. 23).
6. Place a large unbiased counting frame in the first LAD plane and note the features that can be effectively assigned to that frame using the unbiased counting procedure given by Sterio (Ref 19).
7. Out of the features sampled by the first plane of the LAD, identify the number of features that are absent in the second plane (i.e., Q^-), or vice versa (i.e., Q^+), as illustrated in Fig. 20, and estimate the number density using Eq 18.

In the uniform random microstructures (i.e., no gradients), a reliable and precise estimation of the three-dimensional number density of the particles (or any other features of interest) can be made by systematically sampling with three LADs at three different systematic random locations (Ref 20). The LAD sampling has been successfully used to estimate the 3-D number density of tungsten grains in a liquid phase sintered W-Ni-Fe alloy processed in normal gravity and microgravity (Ref 20) and the 3-D particle cracking damage in some wrought aluminum alloys as a function of strain under uniaxial tension and compression (Ref 43, 58).

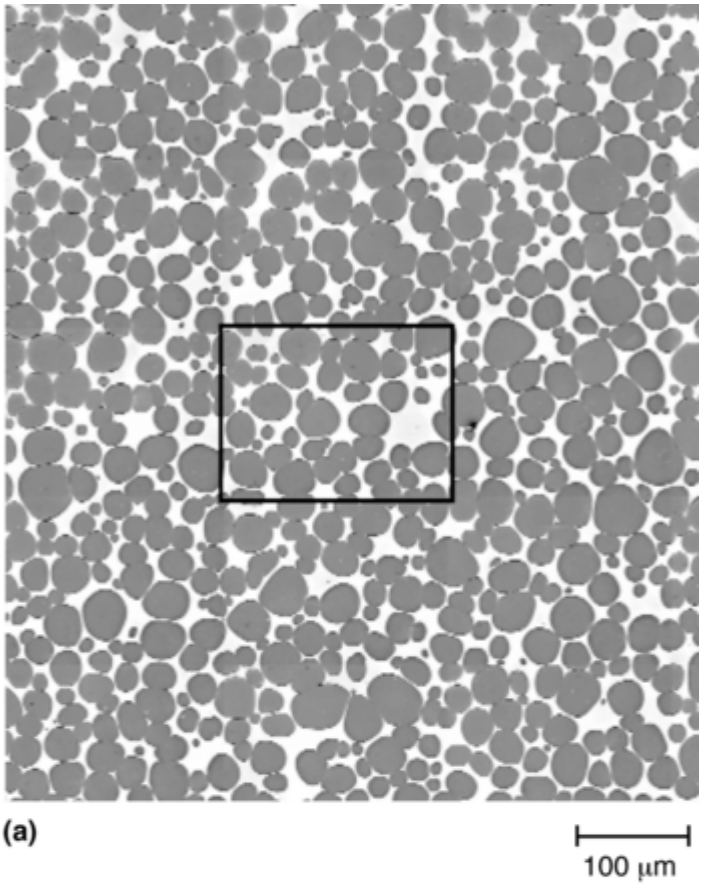

Fig. 21 Microstructure of liquid phase sintered W-Ni-Fe alloy containing tungsten grains (dark) in nickel-iron alloy matrix. (a) Seamless montage of a large number of contiguous microstructural fields grabbed at high resolution and then digitally compressed for presentation. Each field of the montage was grabbed at a magnification and resolution of the field of view shown in (b), which is the central bordered microstructural field in the compressed montage. Source: Ref 20

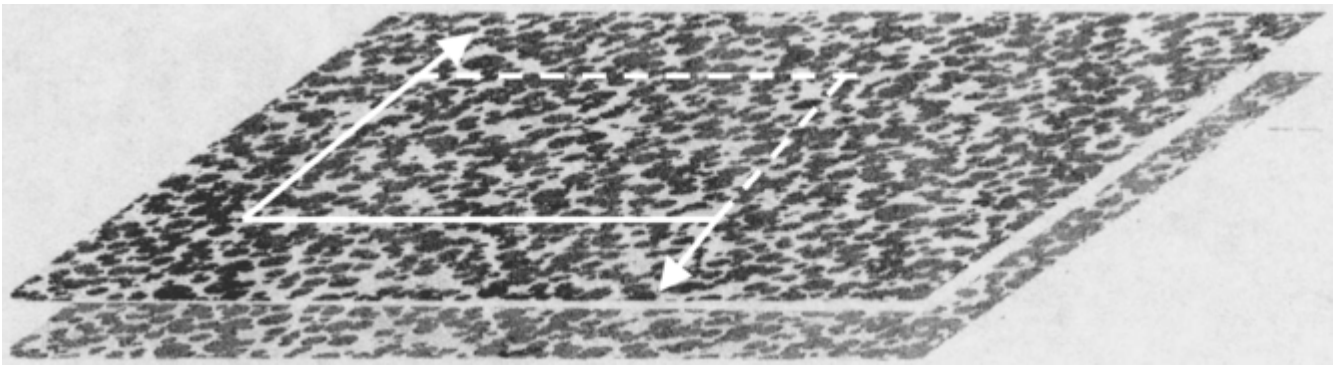

Fig. 22 Two planes of large-area disector (LAD), each of which is a seamless montage of large number of contiguous microstructural fields grabbed at a high resolution. A large area unbiased counting frame is overlaid on the first LAD plane. Source: Ref 20

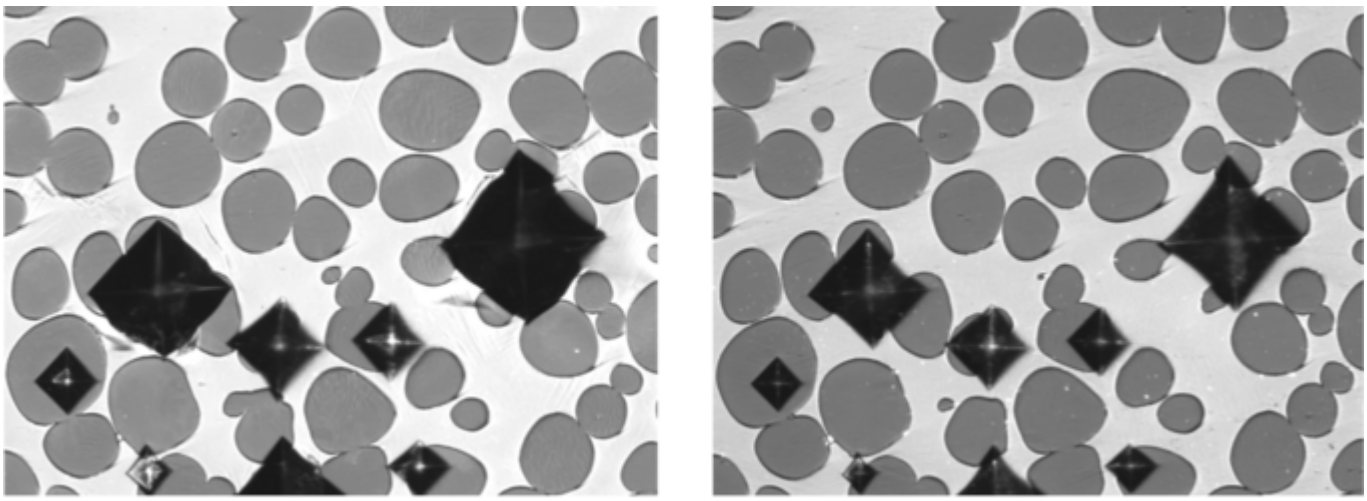

Fig. 23 Use of microhardness indents to measure disector thickness. (a) Microhardness indents placed in the first large-area disector (LAD) plane become smaller in the second LAD plane (b). The change in the size of the indents can be used to compute the amount of material removed (i.e., LAD thickness *t*), and the locations of the indents can be used to align the two LAD planes. Source: Ref 20

References cited in this section

2. L.A. Santalo, *Integral Geometry and Geometric Probability,* Addison-Wesley, 1976

6. E.E. Underwood, *Quantitative Stereology,* Addison Wesley, 1970

7. R.T. DeHoff and F.N. Rhines, *Quantitative Microscopy,* McGraw Hill, 1968

8. S.A. Saltykov, *Stereometric Metallography,* 2nd ed., Metallurgizdat, Moscow, 1958

19. D.C. Sterio, The Unbiased Estimation of Number and Size of Arbitrary Particles Using Disector, *J. Microsc.,* Vol 134, 1984, p 127–136

20. A.M. Gokhale and A. Tewari, Efficient Estimation of Number Density in Opaque Material Microstructures Using Large Area Disector (LAD), *J. Microsc.,* Vol 200, pt. 3, 2000, p 277–283

22. L. Pascal and A.M. Gokhale, Application of Image Analysis for Characterization of Spatial Arrangement of Features in Microstructures, *Metall. Mater. Trans.,* Vol 26A, 1995, p 1449–1456

23. S. Yang, A. Tewari, and A.M. Gokhale, Modeling of Non-Uniform Spatial Arrangement of Fibers in a Ceramic Matrix Composite, *Acta Mater.*, Vol 45, 1997, p 3059–3069

35. A. Tewari, A.M. Gokhale, and R.M. German, Effect of Gravity on Three-Dimensional Coordination Number Distribution in Liquid Phase Sintered Microstructures, *Acta Mater.*, Vol 47, 1999, p 3721–3734

43. H. Agarwal, A.M. Gokhale, S. Graham, and M.F. Horstemeyer, Quantitative Characterization of Three-Dimensional Damage Evolution in a Wrought Al-Alloy under Tension and Compression, *Metall. Mater. Trans.*, Vol 33A, 2002, p 2599–2606

58. A.K. Balasundaram, A.M. Gokhale, S. Graham, and M.F. Horstemeyer, Three Dimensional Particle Cracking Damage Development in an Al-Mg Base Alloy, *Mater. Sci. Eng.*, Vol 355 (No. 1–2), 2003, p 368–383

76. H.J.G. Gundersen, Note on Estimation of Number Density of Arbitrary Profiles: The Edge Effect, *J. Microsc.*, Vol 11, 1977, p 219–223

A.M. Gokhale, Quantitative Characterization and Representation of Global Microstructural Geometry, *Metallography and Microstructures,* Vol 9, *ASM Handbook*, ASM International, 2004, p. 428–447

Quantitative Characterization and Representation of Global Microstructural Geometry

Arun M. Gokhale, Georgia Institute of Technology

Derived Microstructural Properties

Derived microstructural properties such as grain size, mean free path, and mean particle volume often appear as parameters in the models and theories of materials behavior. These attributes can be computed from experimentally measured numerical extents and number densities of the microstructural features of interest, and therefore they are not independent microstructural characteristics. Nonetheless, they are extremely useful for understanding microstructure-properties interrelationships, and consequently these microstructural parameters are used in many studies (Ref 11, 43, 47, 49, 52, 58, 59, 60 77, 78, 79, 80). Important derived microstructural properties are described in the paragraphs that follow.

Mean Free Path. The average uninterrupted surface-to-surface distance between precipitates (or regions of any phase of interest) through the matrix in a three-dimensional microstructure is called mean free path (see Fig. 24). The mean free path is denoted by the symbol, $\langle\lambda\rangle$. Numerous mechanical properties (for example, yield stress) of microstructures containing a population of precipitates depend significantly on the mean free path of the precipitates. The mean free path $\langle\lambda\rangle$ is related to the volume fraction of precipitates, V_V, and their total surface area per unit volume, S_V through (Ref 81, 82):

$$\langle\lambda\rangle = 4[1 - V_V]/S_V \qquad \text{(Eq 19)}$$

Equation 19 is applicable to any arbitrary microstructure containing precipitates or particles or inclusions: it does not involve any assumptions. The microstructure need not be isotropic; and all the particles need not be of the same size or shape. The mean free path is also a measure of the length scale of a microstructure, and it has been used in numerous studies to correlate the microstructure to the material properties, as well as to monitor microstructural evolution processes. For example, this parameter has been utilized to monitor devitrification and microstructural coarsening in some aluminosilicate glasses (Ref 47).

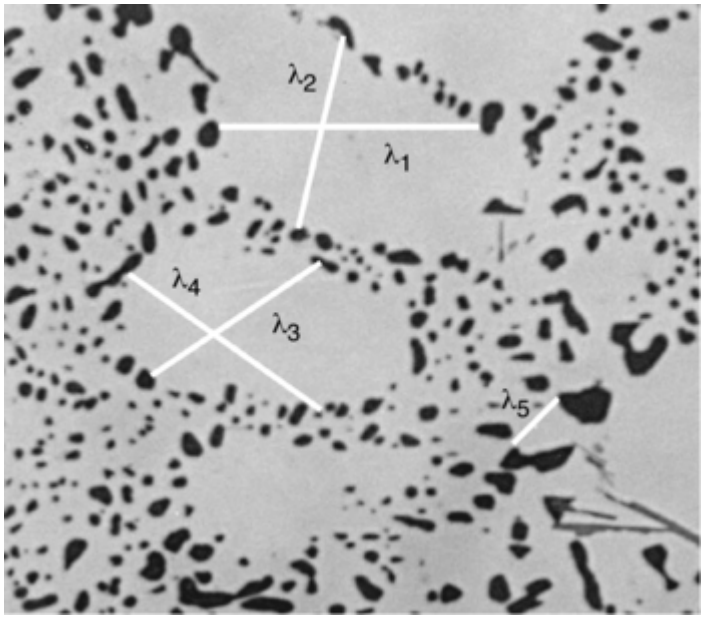

Fig. 24 Microstructure of a cast Al-Si-Mg base alloy containing silicon particles in the interdendritic eutectic regions. The "free path" is an uninterrupted surface-to-surface distance between the particles through the matrix. The distances λ_1 to λ_5 are few examples of such free paths between the silicon particles. The mean free path is the average of obtained by averaging the free path lengths over all locations and all angular orientations.

Mean Free Path along a Specific Direction. In an isotropic microstructure, the average free path is the same along all the directions in the three-dimensional microstructural space. However, in an anisotropic microstructure, the average free path varies with the direction, and therefore, average free path along a specific direction (for example, rolling direction in a cold-rolled steel) may be of interest. The average free path through the matrix $\lambda(\theta, \varphi)$ along the direction having the orientation (θ, φ) can be computed by using the general stereological equation:

$$\lambda(\theta, \varphi) = 2(1 - V_V)/I_L(\theta, \varphi) \quad \text{(Eq 20)}$$

where $I_L(\theta, \varphi)$ is the average number of intersections between the particle matrix interfaces and the straight test lines of orientation (θ, φ) per unit length.

Grain Size. The mean intercept grain size in a single-phase polycrystalline material, G, is equal to the average length of the chords formed by intersections of the grains with random straight test lines. The mean intercept grain size G can be computed using:

$$G = 1/\langle I_L \rangle \quad \text{(Eq 21)}$$

where $\langle I_L \rangle$ is the average number of intersections between the test lines and the grain boundaries per unit test line length. Combining Eq 6 and Eq 21 gives:

$$G = 2/S_V \quad \text{(Eq 22)}$$

where S_V is the total area of the grain boundaries per unit volume of the material. The ASTM grain size number n can be calculated from G by using the following equation given in ASTM E 112 (Ref 83):

$$n = [-6.644 \log G] - 3.288 \quad \text{(Eq 23)}$$

where the mean intercept grain size G is expressed in the units of millimeters.

Combining Eq 22 and Eq 23 gives:

$$n = 6.644 \log S_V - 5.288 \quad \text{(Eq 24)}$$

Therefore, the mean intercept grain size G is inversely proportional to the total surface area of the grain boundaries per unit volume, S_V. Alternately, it can be said that the mean intercept grain size G (and the ASTM grain size number calculated from it) reports the total surface area of the grain boundaries. Figure 25 illustrates the procedure for measurement of mean intercept grain size and ASTM grain size number. The grain size measurement procedures have also been discussed in detail elsewhere (Ref 11, 64, 77, 78, 83).

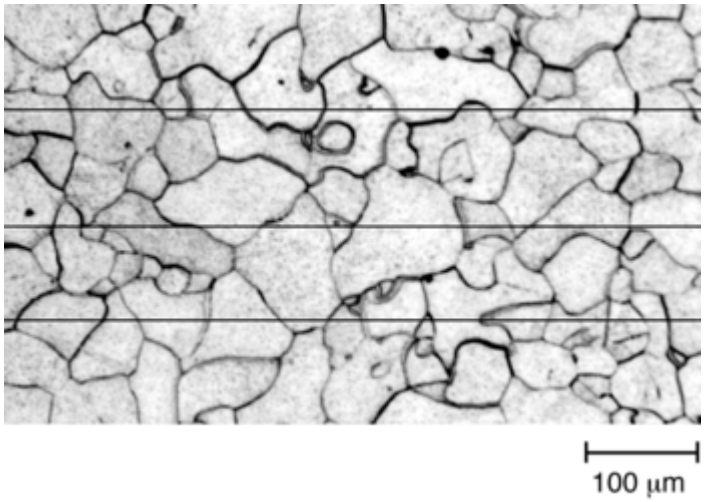

Fig. 25 Microstructure of well-annealed extra-low-carbon steel depicting ferrite grains and grain boundaries. Source: Ref 11. The total number of intersections between the three test lines and the grain boundaries is equal to {10 + 11 + 14} = 35. The total effective length of the test lines is equal to 3.625 mm. Therefore, number of intersections per unit test line length is equal to 9.65 per mm. Mean intercept grain size calculated from these data is equal to {1/9.65} = 0.103 mm (or 103 μm), and the ASTM grain size number calculated using Eq 23 is equal to 3.27.

The mean intercept grain size in an anisotropic microstructure can be also estimated by using Eq 21 and Eq 22. However, $\langle I_L \rangle$ must be obtained by averaging the intersection counts over all angular orientations of the test lines (and metallographic planes), which can be efficiently done by using the trisector methodology (Ref 10, 64) explained earlier. This methodology has been used to characterize the effects of cold rolling on the mean intercept grain size and ASTM grain size number in the microstructure of an extra-low-carbon steel (Ref 11).

ASTM E 112 gives an alternate method for the estimation of grain size number that requires measurement of average number density of grains observed in metallographic sections (i.e., counting the average number of grains per unit area). According to the standard, the ASTM grain size number n can be computed from such data using:

$$n = 1 + 3.3226 \log \langle N \rangle \quad \text{(Eq 25)}$$

where $\langle N \rangle$ is the average number of grains per square inch area of metallographic plane observed at 100× magnification. It is important to recognize that the grain size number calculated from Eq 25 using the 2-D number density of grains and the one calculated from Eq 24 using the intersection counts in the same specimen may not necessarily be equal! This is because the mean intercept grain size (and consequently, the grain size number calculated from such data) is directly related to the total grain boundary area per unit volume S_V, whereas the average number density of grains in metallographic planes (and consequently grain size number calculated from such data, as in Eq 25) is related to the total length of grain edges per unit volume L_V (Ref 84), which is an independent microstructural parameter.

Surface Area Averaged Particle Size. In numerous microstructures, it is of interest to quantify a measure of average particle size. Caliper diameter d of a particle is the distance between two parallel planes tangent to the particle surface at different points. For a sphere, the caliper diameter is equal to the diameter of the sphere, and its value does not depend on the angular orientation of the tangent planes. However, for most of the other shapes (for example, ellipsoid), the caliper diameter varies with the tangent plane orientation. In the case of particles of convex shape, the "average particle size" can be defined as a suitable average value of the caliper diameter. One such measure of average size is the surface area averaged particle size, d_s, where the size is averaged over the surface areas of the particles. The surface area averaged particle size (caliper diameter), d_s is given as (Ref 79):

$$d_s = 6V_V/S_V \quad \text{(Eq 26)}$$

where V_V is the volume fraction and S_V is the total surface area of the particles per unit volume. This equation is applicable to any collection of convex particles; not all the particles need be of the same shape or size, as long

as all of them are convex. Further, the microstructure need not be isotropic. It is important to emphasize that, in general, d_S is not equal to the arithmetic average particle size.

Arithmetic Mean Caliper Diameter. The arithmetic mean caliper diameter (average size) of convex particles (or voids, inclusions, etc.) $\langle d \rangle$ can be calculated from experimentally measured three-dimensional number density of particles N_V and the mean value of the number of particles per unit area of sectioning plane $\langle N_A \rangle$ using the following equation given by DeHoff (Ref 7):

$$\langle d \rangle = \langle N_A \rangle / N_V \quad \text{(Eq 27)}$$

Note that in Eq 27, $\langle N_A \rangle$ must be obtained by averaging over the angular orientations of the sectioning planes in 3-D space if the particle has anisotropic (nonrandom) morphological orientations.

Arithmetic Mean Particle Volume. Another measure of average size is the mean particle volume ν. If the number density of particles in the three-dimensional microstructure N_V and their volume fraction V_V are known, then the mean particle volume ν can be computed by using:

$$\nu = V_V/N_V \quad \text{(Eq 28)}$$

Similarly, the arithmetic mean particle surface area can be computed from the total surface area per unit volume and number density of the particles.

Contiguity Parameter. In a microstructure containing particles or grains of one phase (e.g., α) in a matrix of another phase (e.g., β), there can be three types of interfaces, namely, αα, ββ, and αβ. The contiguity parameter of the particles, *U*, is given as (Ref 6, 80).

$$U = 2(S_V)_{\alpha\alpha}/[2(S_V)_{\alpha\alpha} + (S_V)_{\alpha\beta}] \quad \text{(Eq 29)}$$

where $(S_V)_{\alpha\alpha}$ is the total surface area of the αα interfaces per unit volume, and $(S_V)_{\alpha\beta}$ is the total surface area of the αβ interfaces per unit volume. Although, the contiguity parameter is useful for characterization of the extent of particle contiguity, it is not a measure of the topological connectivity of the particles in the 3-D microstructure. The contiguity parameter is frequently used to characterize microstructures of sintered materials (Ref 59, 60).

Dendrite Arm Spacing/Mean Intercepts. Dendrite arm spacing (DAS) is commonly used to characterize cast microstructural fineness. The DAS influences numerous mechanical properties such as strength, fracture toughness, and fatigue life of the cast components. The DAS can be measured in a metallographic section as the mean distance between the dendrite arms, if the dendrite arms are well defined in the observed microstructure (for example as in Fig. 26). Nonetheless, the mean dendrite arm spacing observed in a 2-D section is not necessarily equal to the true mean 3-D arm spacing. It is also important to recognize that a significant operator bias may be introduced in the selection of dendrite arms for the measurement of DAS, and not all cast microstructures containing eutectic constituents have well-defined dendrite arms (for example, see Fig. 27). There are two 3-D stereological parameters of cast microstructures that can be measured in 2-D sections, have a rigorous geometric interpretation, and can equally well characterize cast microstructural fineness: these parameters are mean linear intercept through dendrites, Ω, and mean intercept through the interdendritic eutectic, ρ. These derived microstructural parameters can be computed:

$$\Omega = 4[1 - (V_V)_e]/(S_V)_e \quad \text{(Eq 30)}$$

$$\rho = 4(V_V)_e/(S_V)_e \quad \text{(Eq 31)}$$

where $(V_V)_e$ is the volume fraction of the interdendritic eutectic and $(S_V)_e$ is the total surface area of between the eutectic and dendrites per unit volume. Note that Ω and/or ρ are not equal to (or directly related to) the DAS, but these attributes provide an alternate measure of the cast microstructural fineness.

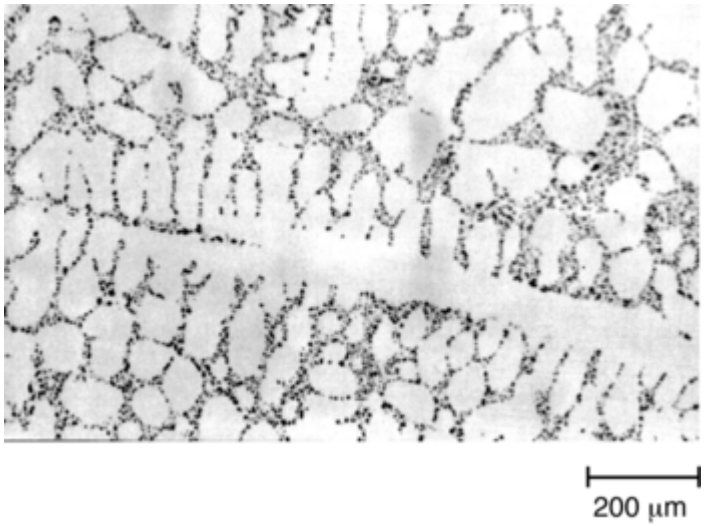

Fig. 26 Microstructure of a cast aluminum-silicon alloy depicting well-developed dendritic structure. The dendrite arm spacing (DAS) is the mean center-to-center distance between the dendrite arms.

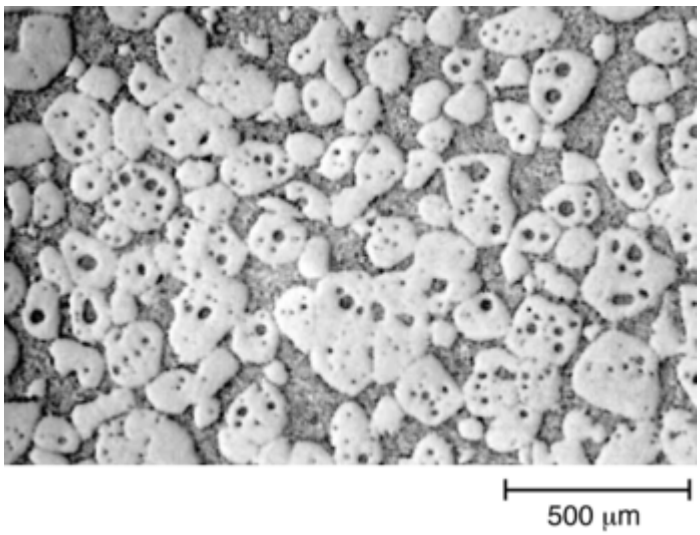

Fig. 27 Microstructure of A356 (Al-Si-Mg base alloy) alloy casting produced by semisolid process. Note that the dendrite cells do not have any well-defined dendrite arms. Therefore, for such cast microstructures, dendrite arm spacing (DAS) does not have any physical meaning. Nonetheless, the microstructural fineness can be still characterized in terms of the stereological parameters such as mean linear intercept of dendrites Ω and mean linear intercept in the interdendritic eutectic ρ.

References cited in this section

6. E.E. Underwood, *Quantitative Stereology,* Addison Wesley, 1970

7. R.T. DeHoff and F.N. Rhines, *Quantitative Microscopy,* McGraw Hill, 1968

10. A.M. Gokhale and W.J. Drury, Efficient Estimation of Microstructural Surface Area Using Trisector, *Metall. Trans. A,* Vol 25A, 1994, p 919–928

11. B.R. Morris, A.M. Gokhale, and G.F. Vander Voort, Estimation of Grain Size in Anisotropic Materials, *Metall. Mater. Trans. A,* Vol 29A, 1998, p 237–244

43. H. Agarwal, A.M. Gokhale, S. Graham, and M.F. Horstemeyer, Quantitative Characterization of Three-Dimensional Damage Evolution in a Wrought Al-Alloy under Tension and Compression, *Metall. Mater. Trans.,* Vol 33A, 2002, p 2599–2606

47. J.A. Griggs, K.J. Anusavice, and J.J. Mecholsky, Jr., Devitrification and Microstructural Coarsening of a Fluoride-Containing Barium Aluminosilicate Glass, *J. Mater. Sci.,* Vol 37, 2002, p 2017–2022

49. F.G. Caballero, C. Garcia de Andres, and C. Capdevila, Characterization and Morphologic Analysis of Pearlite in a Eutectoid Steel, *Mater. Charact.,* Vol 45, 2000, p 111–116

52. J. Wosik, H.J. Penkalla, K. Szot, B. Dubiel, and F.C. Schubert, The Influence of Various Microscopic Techniques on the Quantification of Stereological Structure Parameters in Waspaloy Alloy, *Prakt. Metallogr.,* Vol 39, 2002, p 140–154

58. A.K. Balasundaram, A.M. Gokhale, S. Graham, and M.F. Horstemeyer, Three Dimensional Particle Cracking Damage Development in an Al-Mg Base Alloy, *Mater. Sci. Eng.,* Vol 355 (No. 1–2), 2003, p 368–383

59. Z. Zhang and F. Wang, Research on the Deformation Strengthening Mechanism of a Tungsten Heavy Alloy by Hydrostatic Extrusion, *Int. J. Refract. Met. Hard Mater.,* Vol 19, 2001, p 177–182

60. Y. Wu, R.M. German, D. Blaine, B. Marx, and C. Schlaefer, Effects of Residual Carbon Content on Sintering Shrinkage, Microstructure and Mechanical Properties of Injection Molded 17-4 PH Stainless Steel, *J. Mater. Sci.,* Vol 37, 2002, p 3573–3583

64. L. Karlsson and A.M. Gokhale, Stereological Estimation of Mean Linear Intercept Length in Metallography Using Vertical Sections and Trisector, *J. Microsc.,* Vol 186, 1997, p 143–152

77. G.F. Vander Voort, Examination of Some Grain Size Measurement Problems, *Metallography: Past, Present, and Future,* G.F. Vander Voort, F.J. Warmuth, S.M. Purdy, and A. Szirmae, Ed., STP 1165, ASTM, 1993, p 266–294

78. G.F. Vander Voort, *Metallography: Principles and Practice,* ASM International, 1999

79. A.M. Gokhale, Estimation of Average Size of Convex Particle, *Metall. Trans. A,* Vol 17A, 1986, p 742–745

80. J. Gurland, Measurement of Grain Contiguity in Two-Phase Alloys, *Trans. AIME,* Vol 212, 1958, p 452–456

81. R.L. Fullman, Measurement of Particle Sizes in Opaque Bodies, *Trans. AIME,* Vol 197, 1953, p 47

82. H.W. Chalkley, J. Cornfield, and H. Park, A Method for Estimating Volume-Surface Ratio, *Science,* Vol 110, 1949, p 295

83. "Standard Test Methods for Determining Average Grain Size," E 112, *Annual Book of ASTM Standards,* ASTM

84. A.M. Gokhale, Interpretation of Grain Size Descriptors, *Trans. Ind. Inst. Metals,* Vol 35, 1982, p 595–600

A.M. Gokhale, Quantitative Characterization and Representation of Global Microstructural Geometry, *Metallography and Microstructures,* Vol 9, *ASM Handbook,* ASM International, 2004, p. 428–447

Quantitative Characterization and Representation of Global Microstructural Geometry

Arun M. Gokhale, Georgia Institute of Technology

Feature-Specific Size, Shape, and Orientation Distributions

Microstructures often contain ensembles of precipitates/inclusions/voids/grains having different sizes, shapes, and morphological orientations. These distributions often evolve during material processing (and/or during service), and they affect material properties and performance. Until recently, most of the stereological techniques for estimation of microstructural distributions were limited to the estimation of the size distributions of randomly oriented geometrically similar particles/voids of simple shapes (for example, spheres, ellipsoids) that differ only in size (Ref 6, 7, 8, 12, 85, 86, 87, 88, 89, 90, 91). Progress in stereology now enables efficient estimation of true bivariate size-shape (Ref 92) and size-orientation (Ref 38, 45) distributions, as well as trivariate size-shape-orientation distributions of particles/voids (Ref 39) in a three-dimensional microstructure from the measurements performed on few metallographic planes. Nonetheless, all of these techniques do require that the particles/voids of interest be of known convex shape.

Size Distribution of Spherical Particles. Numerous stereological procedures have been developed for the estimation of the three-dimensional size distribution of an ensemble of spherical particles in a microstructure from the measurements of the size distribution of the corresponding circular particle sections observed in a representative metallographic plane (Ref 6, 7, 8, 12, 85, 86, 87, 93, 94). The unfolding technique developed by Saltykov (Ref 8) is the most simple and most frequently used. In this method, the three-dimensional distribution of the sphere diameters is approximated by dividing it into K discrete sizes, where K can be any integer from 7 to 15. The size class interval Δ is defined as:

$$\Delta = D_m/K = d_m/K_m \quad \text{(Eq 32)}$$

where D_m is the diameter of the largest sphere in the three-dimensional microstructure, which is equal to the diameter d_m of the largest circular particle section observed in the metallographic plane. Let $(N_v)_1$, $(N_v)_2$, $(N_v)_3$, …, $(N_v)_j$, … $(N_v)_K$ be the number of spheres per unit volume having diameters, Δ, 2Δ, 3Δ, …, $j\Delta$, … $K\Delta$, respectively. The continuous apparent size distribution of the circular particle sections in the metallographic plane is divided into K number of size classes. Let $(n_A)_1$, $(n_A)_2$, $(n_A)_3$, …, $(n_A)_i$, … $(n_A)_k$ be the number of circles in a two-dimensional metallographic plane per unit area, having the diameters in the size range, (0 to Δ), (Δ to 2Δ), (2Δ to 3Δ), …, [$(i - 1)\Delta$ to $i\Delta$], … [$(K - 1)\Delta$ to $K\Delta$], respectively. Saltykov has shown that $(N_v)_j$ are related to $(n_A)_i$:

$$(N_V)_j = \sum_{i=j}^{i=K} b(j, i).(n_A)_i/\Delta \quad \text{(Eq 33)}$$

where $b(j, i)$ are Saltykov's coefficients given in Table 1. Note that the Saltykov's coefficients $b(j, i)$ are negative for $i > j$, they are positive for $i = j$, and there are no coefficients for $i < j$. Therefore, in the summation in Eq 33, all the terms except the first are negative.

Table 1 Saltykov's coefficients *b* (*j*, *i*)

i = 1	*i* = 2	*i* = 3	*i* = 4	*i* = 5	*i* = 6	*i* = 7	*i* = 8	*i* = 9	*i* = 10	*i* = 11	*i* = 12	*i* = 13	*i* = 14	*i* = 15	
***j* = 1**	+1.000	-0.1547	-0.0360	-0.130	-0.0061	-0.0033	-0.0020	-0.0013	-0.0009	-0.0006	-0.0005	-0.0004	-0.0003	-0.0002	-0.0001
***j* = 2**		+0.5774	-0.1529	-0.0420	-0.0171	-0.0087	-0.0051	-0.0031	-0.0021	-0.0015	-0.0010	-0.0009	-0.0006	-0.0006	-0.0004
***j* = 3**			+0.4472	-0.1382	-0.0408	-0.0178	-0.0093	-0.0057	-0.0037	-0.0026	-0.0018	-0.0013	-0.0010	-0.0007	-0.0007
***j* = 4**				+0.3779	-0.1260	-0.0386	-0.0174	-0.0095	-0.0058	-0.0038	-0.0027	-0.0020	-0.0016	-0.0012	-0.0009
***j* = 5**					+0.3333	-0.1161	-0.0366	-0.0168	-0.0094	-0.0059	-0.0040	-0.0028	-0.0021	-0.0016	-0.0013
***j* = 6**						+0.3015	-0.1081	-0.0346	-0.0163	-0.0091	-0.0058	-0.0041	-0.0028	-0.0022	-0.0016
***j* = 7**							+0.2773	-0.1016	-0.0329	-0.0155	-0.0090	-0.0057	-0.0040	-0.0029	-0.0022
***j* = 8**								+0.2582	-0.0961	-0.0319	-0.0151	-0.0088	-0.0056	-0.0039	-0.0028
***j* = 9**									+0.2425	-0.0913	-0.0301	-0.0146	-0.0085	-0.0055	-0.0039
***j* = 10**										+0.2294	-0.0872	-0.0290	-0.0140	-0.0083	-0.0054
***j* = 11**											+0.2182	-0.0836	-0.0280	-0.0136	-0.0080

| | | |

For a reliable estimation of the three-dimensional sphere size distribution, it is necessary to measure the diameters of more than 1000 circular particle sections in a metallographic plane, which can be facilitated via automated digital image analysis. The calculation of the sphere size distribution from the section size distribution data using Eq 33 can be done in a straightforward manner using a spreadsheet. As an example, consider Fig. 28(a) depicting gas (air) and shrinkage pores in the microstructure of a high-pressure die-cast AM60 magnesium alloy. The gas pores are round and can be approximated as spheres in the 3-D microstructure, whereas the shrinkage pores are elongated (cracklike) and they form a network that partially connects the gas pores. In this microstructure, to measure the sizes of the round gas pores in the metallographic plane using digital image analysis it is first necessary to separate them from the shrinkage pores, which can be done using an image analysis technique described elsewhere (Ref 28). Figure 28(b) shows the binary image of the field of view shown in Fig. 28(a) that contains only the gas pores because the shrinkage pores have been removed using image processing (Ref 28). The apparent two-dimensional diameter distribution of the gas pores measured from 100 microstructural fields such as Fig. 28(b) is shown in Table 2, and the three-dimensional size distribution of the diameters of the gas pores computed from these data using Saltykov's method is shown in Table 3. Saltykov's method has been modified by numerous investigators to introduce nonuniform size class intervals, to increase the number of size class intervals beyond 15, and to increase the precision of the estimated three-dimensional size distributions using sophisticated computational algorithms (Ref 85, 93, 94), which are discussed in detail elsewhere (Ref 12).

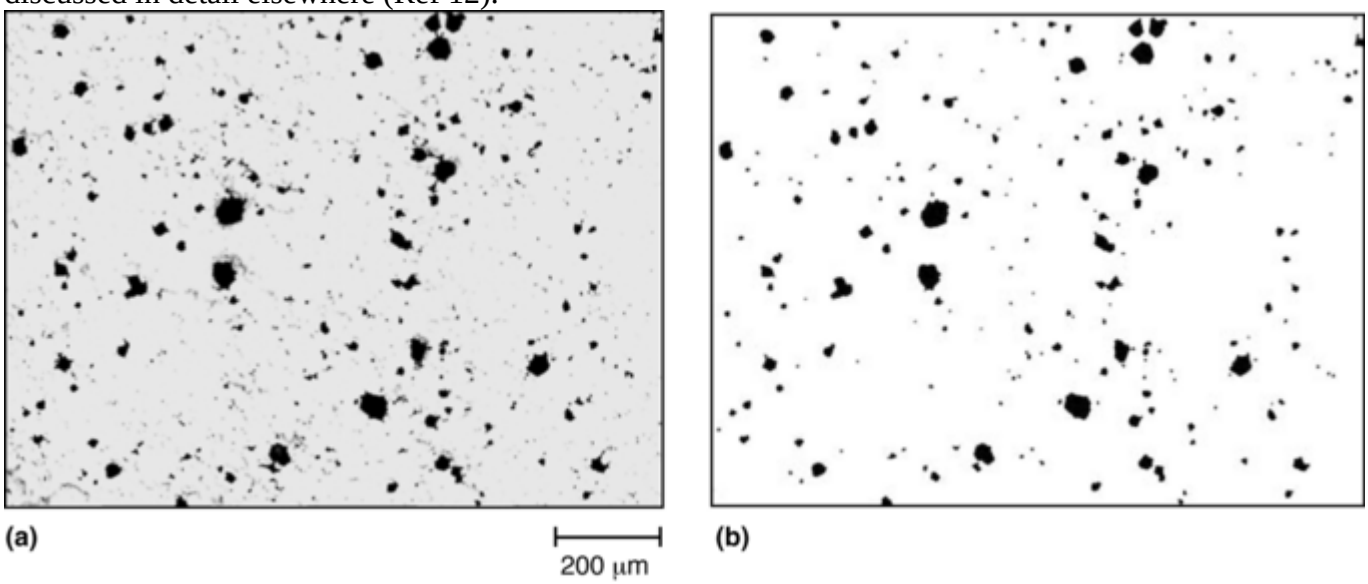

Fig. 28 Use of image processing in estimating size distributions of spherical particles. (a) Unetched microstructure of high-pressure die-cast AM60 Mg-alloy depicting round gas (air) pores and cracklike shrinkage pores. (b) The microstructure in (a) with shrinkage pores removed by using image analysis techniques

Table 2 Two-dimensional section size distribution of gas pores in AM 60 magnesium alloy

See Fig. 28 for microstructure.

Size class (i)	Range of gas pore section diameters [$(i - 1)\Delta$ to $i\Delta$], μm	Number of gas pore sections per mm^2 $(N_A)_i$
1	0–9	39
2	9–18	31
3	18–27	18
4	27–36	7
5	36–45	3
6	45–54	3
7	54–63	1
8	63–72	1

Table 3 Three-dimensional size distribution of the gas pores computed from the section size distribution (Table 2) and Saltykov's coefficients (Table 1) using Saltykov's technique

Size class (j)	Gas pore diameters ($j\Delta$), μm	Number of gas pores in three-dimensions $(N_V)_j$ per mm^3
1	9	3715
2	18	1641
3	27	766
4	36	236
5	45	66
6	54	85
7	63	20
8	72	29

Source: Ref 6, 8

Size Distribution of Geometrically Similar Nonspherical Particles. DeHoff (Ref 88) has developed a stereological technique for the estimation of the size distribution of ellipsoidal particles from the measurements performed on metallographic plane sections. In this technique, it is assumed that:

- All the particles are either prolate ellipsoids of revolution (for example, cigar-shaped particles), or all of them are oblate ellipsoids of revolution (for example, pancake- shaped particles).
- All the particles have the same axial ratio, and therefore, they are geometrically similar.
- The particles are randomly oriented.

The intersections of the ellipsoidal particles with a metallographic plane yield elliptical particle sections of different sizes and shapes. In the case of oblate ellipsoids of revolution, the major axis of the elliptical particle sections observed in a metallographic plane are measured and the size parameter for the ellipsoids is their major axis. On the other hand, for prolate ellipsoids of revolution, the minor axis of the elliptical sections observed in the metallographic plane are measured, and the ellipsoid size is specified by its minor axis. With this interpretation of the section size and true size parameters, and an introduction of shape factor C, an equation analogous to the one given by Saltykov holds for the ellipsoidal particles (Ref 88):

$$(N_V)_j = C.\sum_{i=j}^{i=K} b(j, i).(n_A)_i/\Delta \qquad \text{(Eq 34)}$$

The shape factor C depends on the axial ratio of the ellipsoidal particles, and it can be calculated by using the formula given by DeHoff (Ref 88). As before, $b(j, i)$ are Saltykov's coefficients given in Table 1. Analogous procedures are also available for the estimation of the size distribution of cubic (Ref 89) and polyhedral (Ref 90) particles, and lens-shaped grain boundary precipitates (Ref 91).

Multivariate Distributions. Numerous material microstructures contain particle/void/microcrack distributions, where all the features are not geometrically similar and/or are not randomly oriented. In such microstructures, there may also be correlations among the feature sizes, shapes, and their morphological orientations. Bivariate or trivariate distributions are required to characterize such particle/void/microcrack populations. Cruz-Orive (Ref 92) has given a stereological procedure for the estimation of the three-dimensional bivariate size-shape distribution of randomly oriented ellipsoids from the measurements of apparent bivariate size-shape distribution performed in the plane sections, if all the particles can be modeled as either oblate ellipsoids, or prolate ellipsoids (a mixture of prolate and oblate ellipsoids is not permitted). In many material microstructures where the particles/voids can be modeled as ellipsoids (for example, inclusions, creep cavities, etc.), the particles/voids are not randomly oriented (for example, inclusions in a hot-rolled metal, microcracks in particles, creep cavities, etc.), and in such cases, Cruz-Orive's stereological procedure is not useful. The correlations between size and orientation are particularly strong for the features such as microcracks and creep cavities on grain boundaries. For such microstructural features, Gokhale (Ref 38) has given the following stereological equation that relates the three-dimensional bivariate size-orientation distribution of population of features such as microcracks, plate shaped inclusions, and so forth, to the corresponding apparent size-orientation distribution in the vertical metallographic sections:

$$f(r,\alpha)=\frac{4rN_v}{\pi N_A \sin^2\alpha}\cdot\int_r^{r_m}\int_{\pi/2-\alpha}^{\pi/2}\frac{\cos^2\theta\sin\theta g(R,\theta)\,d\theta dR}{(R^2-r^2)^{1/2}(\sin^2\alpha-\cos^2\theta)^{1/2}} \quad \text{(Eq 35)}$$

where $f(r, \alpha)$ is the joint bivariate frequency distribution function in a representative vertical sectioning plane such that $f(r, \alpha)drd\alpha$ is equal to the fraction of the microcrack/plate section traces having the size in the range r to $(r + dr)$ and the orientation in the range α to $(\alpha + d\alpha)$. The function $f(r, \alpha)$ can be estimated from the experimental measurements of r and α on the microcrack traces observed in the vertical planes. The distribution $g(R, \theta)$ is the three-dimensional bivariate microcrack/plate size-orientation distribution function of interest, N_v is the number of microcracks/plates per unit volume in the three-dimensional microstructure, N_A is the average number of microcrack/plate section traces observed per unit area of vertical plane, and r_m is the size of the largest microcrack/plate section trace, which is equal to the true size R_m of the largest microcrack. In practice, $f(r, \alpha)$ is the measured quantity and $g(R, \theta)$ is to be estimated from these data. The numerical procedure for such estimation is described in detail elsewhere (Ref 45). This stereological technique has been recently applied for the estimation of the bivariate size-orientation distribution function of the microcracks observed in the intermetallic inclusions in two wrought aluminum alloys loaded in tension and compression (Ref 45); some of these results are shown in Fig. 29. Benes and coworkers (Ref 39) have given a stereological procedure for the estimation of the three-dimensional trivariate size-shape-orientation distribution of ellipsoidal particles/voids from the measurements of the corresponding apparent trivariate particle section size-shape-orientation distribution performed in the vertical sections under the condition that all the particles are either oblate ellipsoids, or they are all prolate ellipsoids.

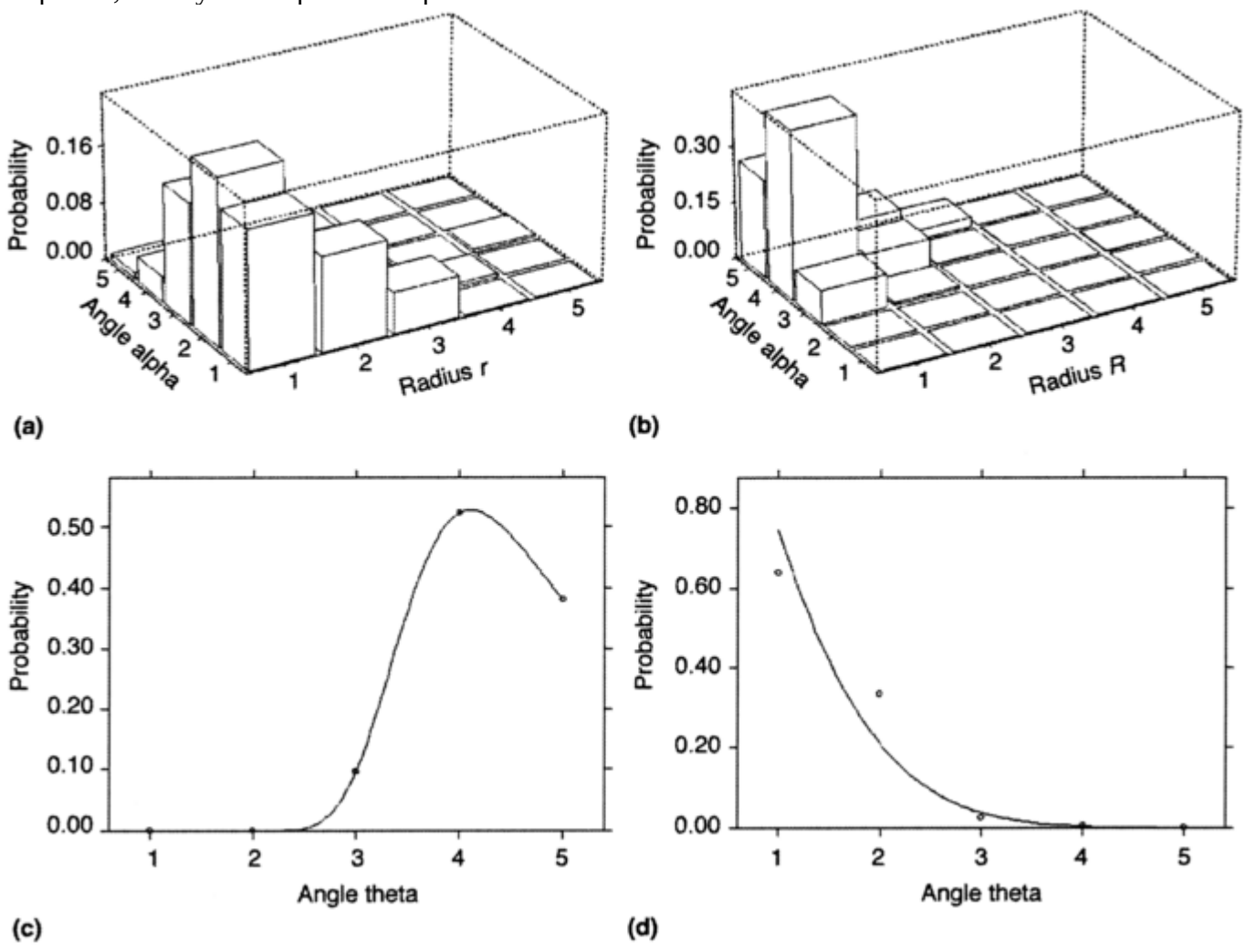

Fig. 29 Estimation of the bivariate size-orientation distribution function of microcracks. (a) Bivariate size-orientation distribution of the microcrack traces in a vertical metallographic plane where the

vertical axis is the loading direction, in the 6061 aluminum alloy under a uniaxial compressive stress deformed to 0.7 strain. (b) The estimated 3-D bivariate size and orientation distribution of the microcracks. All angles are measured with respect to the loading direction (vertical axis). In compression, the majority of the microcracks are parallel to the direction of applied compressive load. (c) Marginal 3-D orientation distribution of the microcracks under uniaxial compression at 0.7 strain. (d) Marginal 3-D orientation distribution of the microcracks under uniaxial tension. Observe that majority of the microcracks are now perpendicular to the loading direction. For all the distributions, the size class interval for radius is 0.69 μm, and for the orientation angle, it is 18°. Source: Ref 45

References cited in this section

6. E.E. Underwood, *Quantitative Stereology,* Addison Wesley, 1970

7. R.T. DeHoff and F.N. Rhines, *Quantitative Microscopy,* McGraw Hill, 1968

8. S.A. Saltykov, *Stereometric Metallography,* 2nd ed., Metallurgizdat, Moscow, 1958

12. J. Ohser and F. Muecklich, *Statistical Analysis of Microstructures in Material Science,* John Wiley & Sons, 2000

28. A. Balasundaram and A.M. Gokhale, Quantitative Characterization of Spatial Arrangement of Shrinkage and Gas (Air) Pores in Cast Magnesium Alloys, *Mater. Charact.,* Vol 46, 2001, p 419–426

38. A.M. Gokhale, Estimation of Bivariate Size and Orientation Distribution of Microcracks, *Acta Metall.,* Vol 44, 1996, p 475–485

39. V. Benes, V. Jiruses, and M. Slamova, Estimation of Trivariate Size-Shape-Orientation Distributions from Vertical Sections, *Acta Mater.,* Vol 45, 1997, p 1105–1110

45. K. Bodlak, A. Balasundaram, A.M. Gokhale, and V. Benes, Unfolding of Three-Dimensional Bivariate Size-Orientation Distribution of Microcracks, *Acta Mater.,* Vol 51, 2003, p 3131–3143

85. W.M. Visscher and A.S. Goldman, Estimating the Distribution of Spherical Particles from Plane Sections: An Optimal Algorithm for Solution of the Abel Integral Equation, *Siam. J. Sci. Stat. Comput.,* Vol 4, 1983, p 280–290

86. G.M. Tallis, Estimating the Distribution of Spherical and Elliptical Bodies from Plane Sections, *Biometrics,* Vol 26, 1970, p 87–90

87. P. Luchini, A. Pozzi, and C. Ronchi, Evaluation of Statistical Distribution of Spherical Objects from Measurements of Metallographic Cross-Sections, *Meccanica,* Vol 19, 1984, p 127–133

88. R.T. DeHoff, The Determination of Size Distribution of Ellipsoidal Particles from Measurements Made on Random Plane Sections, *Trans. Metall. Soc. AIME,* Vol 224, 1962, p 474–477

89. J. Osher and M. Nippe, Stereology of Cubic Particles: Various Estimators for the Size Distribution, *J. Microsc.,* Vol 187, 1997, p 22–30

90. J. Osher and F. Mucklich, Stereology of Some Classes of Polyhedrons, *Adv. Appl. Probabil.,* Vol 27, 1995, p 384–396

91. A.M. Gokhale and A.K. Jena, Size Distribution of Grain Boundary Precipitates, *Metallography,* Vol 13, 1980, p 307–317

92. L.M. Cruz-Orive, Particle Size-Shape Distributions; the General Spheroid Problem, *J. Microsc.,* Vol 107, 1976, p 235–253

93. B.W. Silverman, M.C. Jones, D.W. Nychka, and J.D. Wilson, A Smoothed EM Approach to Indirect Estimation Problems, With Particular Reference to Stereology, *J. Royal Stat. Soc.*, Vol B52, 1990, p 271–324

94. S. Mase, Stereological Estimation of Particle Size Distributions, *Adv. Applied Probabil.,* Vol 27, 1995, p 350–366

A.M. Gokhale, Quantitative Characterization and Representation of Global Microstructural Geometry, *Metallography and Microstructures,* Vol 9, *ASM Handbook*, ASM International, 2004, p. 428–447

Quantitative Characterization and Representation of Global Microstructural Geometry

Arun M. Gokhale, Georgia Institute of Technology

Spatial Clustering and Correlations

A location is associated with each feature in a microstructure. The statistical distribution of the relative locations of the microstructural features of interest represents their spatial arrangement in a microstructure. Spatial patterns, correlations, clustering, spatial affinity, short- and long-range interactions, pair correlations and higher-order correlations, microstructural gradients, segregations, and so forth, are important facets of the spatial arrangement of microstructural features. It is well known that these attributes of microstructural geometry affect numerous mechanical and physical properties of materials. Although theoretical statistics literature contains numerous quantitative descriptors that reflect various aspects of the spatial arrangement of ensembles of features in two- and three-dimensional space (Ref 1), flexible and general experimental techniques for estimation of such descriptors in the opaque material microstructures are still under development. Nevertheless, during the past decade or so, considerable progress has been made in the development of practical stereological techniques for the estimation of some important descriptors of spatial arrangement such as two-point correlation function (Ref 37), radial distribution function (Ref 22, 23, 36), nearest-neighbor distributions (Ref 22, 23, 36, 95), and coordination number distribution (Ref 35, 95). These recent developments are briefly described in the paragraphs that follow.

Two-Point Correlation Function. In a 3-D microstructure containing two phases, for example, particles (phase 1) and matrix (phase 2), the two-point correlation function $P_{11}(r, \theta, \varphi)$ is the probability that both the end-points of a randomly located straight line of length r and angular orientation (θ, φ) are contained in phase 1 (i.e., particles). One can similarly define $P_{22}(r, \theta, \varphi)$, where both the end points are in phase 2 (matrix), and $P_{12}(r, \theta, \varphi)$, where one end of the line is in phase 1 and the other is in phase 2. Although for a two-phase microstructure there are four possible two-point correlation functions, only one of the four is independent. Therefore, in this contribution, only the two-point function $P_{11}(r, \theta, \varphi)$ is considered. If the microstructure has a symmetry axis, then it is most efficient to choose the symmetry axis as the Z-axis of the reference frame (vertical axis). In such a case, $P_{11}(r, \theta, \varphi)$ does not depend on φ, and consequently, $P_{11}(r, \theta)$ measured in any one vertical plane (having symmetry axis as vertical axis) completely specifies the direction dependence of the two-point correlation function.

To capture the short-range as well as long-range spatial patterns, in a majority of material microstructures the two-point correlation data are required over the distances ranging from 1 to 500 μm at a resolution of about 0.5 μm. Therefore, the two-point correlation function cannot be measured from the usual “single field of view” microstructural images because such images either lack resolution (when magnification is low) or they lack the long-range spatial information (when magnification is high). Consequently, for the experimental measurement of the two-point correlation function, it is essential to create a seamless “montage” of very large number of

contiguous microstructural fields of view (~100 fields), as explained in section “Large-Area Disector (LAD) for Efficient and Unbiased Estimation of Number Density” (see Fig. 21). As a montage can be at a high resolution (typically 0.5 μm resolution) and of very large area (typically few mm^2 or so), it can capture both short- and long-range spatial patterns and correlations.

A computer code has been recently developed for the calculation of the two-point correlation function from the input image of a binary microstructural montage (Ref 37). The program reads the binary image and asks the user for the input to the maximum length (l_m) to which the two-point function is to be measured. A virtual rectangle inside the binary image, known as measurement frame, is then created such that each point inside this frame is at least l_m distance from the nearest edge. The computation begins with the reading of the gray value of the first pixel (base point) in the measurement frame to identify whether the point belongs to phase 1 (black) or phase 2 (white). The next step consists of reading of gray value of all the pixels inside a circle of radius l_m drawn around the base point, and computation of their Cartesian distance r from the base point and angle θ with the vertical axis. The program separately stores all the length segments whose both end pixels are black. This process is repeated for all the base points inside the measurement frame. Once the occurrences of all the required distances and angles are recorded, the probability is computed by dividing the number segments of given length and orientation whose both end pixels are black by the total number of the segments having the same length and orientation. The process is then repeated for different distances and orientation angles to generate detailed data on the direction-dependent two-point correlation function $P_{11}(r, \theta)$. Since a montage is a large image, calculation of the two-point function over the distances from 1 to 500 μm typically involves measurements on about 7 million base pixels, and 4 million top pixels for each base pixel. This amounts to about 28×10^{12} measurements, with the distance and angle computed for each such measurement.

This technique has been recently applied to quantify spatial clustering in the microstructures of an extruded metal matrix composite containing SiC particles in an aluminum alloy matrix (Ref 37). Figure 30(a) and (b) show two of the microstructures that have exactly the same volume fraction and size distribution of SiC particle: the only difference in these two microstructures is the spatial clustering of the SiC particles. Figure 30(c) depicts the normalized two-point correlation function in these microstructures along the extrusion direction (chosen vertical axis), and Fig. 30(d) depicts the normalized two-point correlation for the transverse direction. Observe that these correlation functions nicely capture the differences in the clustering tendencies and long-range spatial patterns in the two microstructures in Fig. 30(a) and (b), which demonstrates the utility of two-point correlation functions for mathematical representation of the clustering and spatial heterogeneity in microstructures (Ref 37).

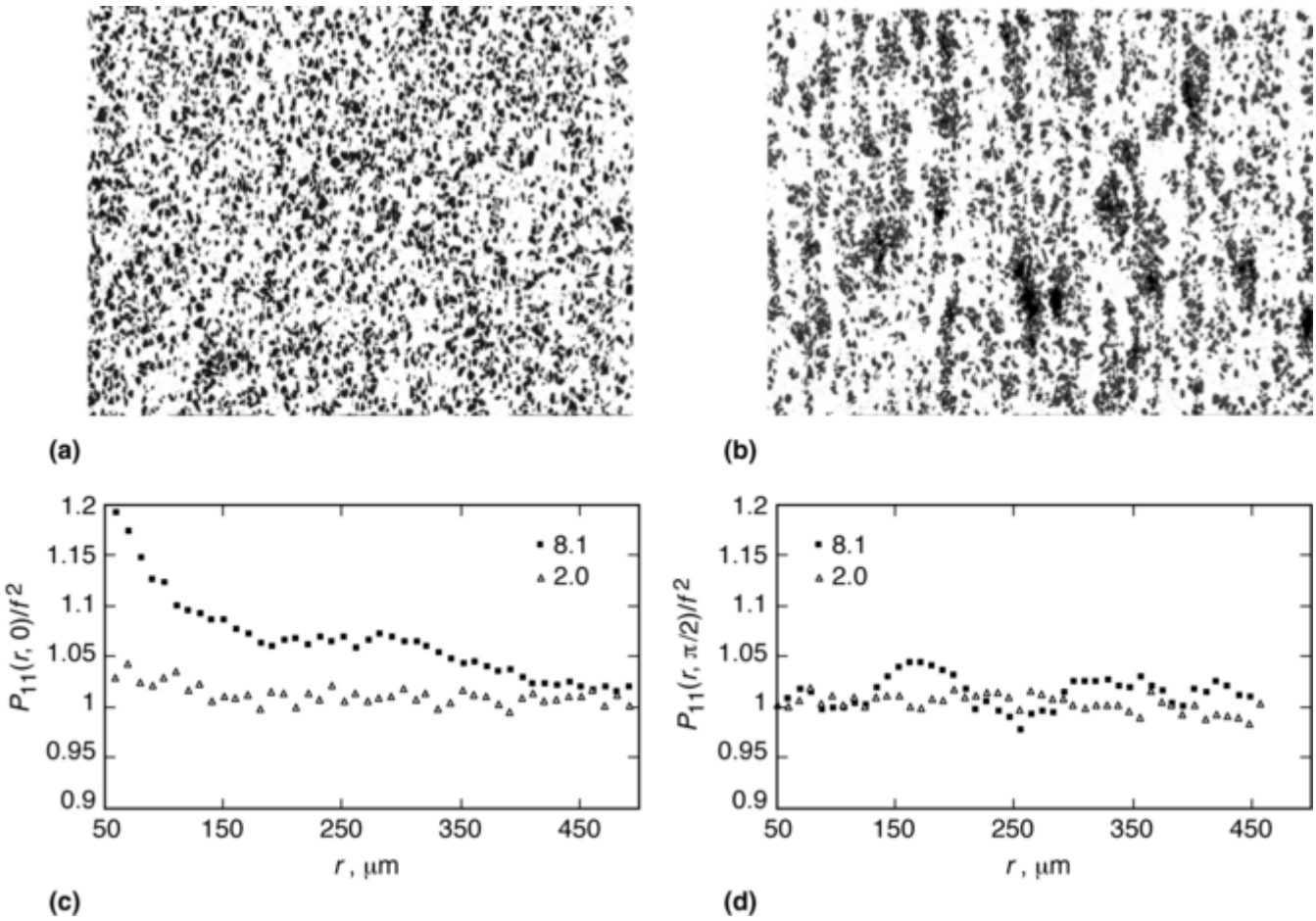

Fig. 30 Two-point correlation function. (a) Microstructure of a metal-matrix composite having uniform random distribution of SiC particles in an aluminum alloy matrix. The data points in (c) and (d) for this specimen are the open triangles. (b) Metal-matrix composite having highly clustered distribution of SiC particles in the particle-rich bands parallel to the extrusion direction (*Y*-axis of the micrograph). This specimen has exactly the same volume fraction and size distribution of the SiC particles as that in (a). The data points in (c) and (d) for this specimen are the dark rectangles. (c) Normalized two-point correlation function $P_{11}(r, 0)$ along the direction parallel to the extrusion direction (*Y*-axis). The dark rectangle data points for the composite having clustered SiC particles—i.e., (b)—do not reach the saturation value even at distances of 450 μm. (d) The normalized two-point correlation function $P_{11}(r, \pi/2)$ along the transverse direction. The data corresponding to the specimen with clustered SiC particles—i.e., (b)—show long-range oscillations that correspond to particle-rich and particle-poor regions. Source: Ref 37

Coordination Number Distribution. In the microstructures containing contiguous grains/particles, coordination number is an important geometric parameter. The coordination number of a grain/particle is the number of other grains/particles in direct contact with it. In general, a distribution of coordination numbers exists, which is an important descriptor of the short-range spatial arrangement of grains/particles. The mean coordination number (often referred to as just coordination number or connectivity in the sintering literature) is the average value of the coordination number distribution in the three-dimensional microstructure. The mean coordination number affects the mechanical response of liquid phase sintered materials (Ref 96), and it appears as a parameter in the theories of densification (Ref 97). There is often a correlation between the size of a grain and its coordination number. Therefore, a bivariate distribution of the 3-D coordination numbers that expresses the fraction of the grains having a given coordination number and having size in a certain narrow range is of importance. The mean coordination number and its distribution cannot be estimated from any measurements performed on independent 2-D metallographic sections. Direct observations on the 3-D microstructure are required for the estimation of the coordination number distribution. Further, to minimize the edge effects, the measurements must be performed on a large volume of the 3-D microstructure observed at a high resolution. Recently, a montage serial sectioning technique has been developed for creation of such a large volume of 3-D

microstructure of an opaque material at a high resolution (~1 μm). The method combines the montage technique for creation of a large contiguous area of a metallographic plane at a high resolution with the serial sectioning method and 3-D digital image processing (see Fig. 31). The montage serial sections are stacked together and aligned (Fig. 31b and c), and the 3-D microstructure is reconstructed using 3-D image analysis software (Ref 32, 33, 34, 35, 95). Figure 32 depicts small segments of two surface-rendered 3-D microstructures reconstructed in this manner, where the matrix was removed using image processing. To determine the coordination number of a grain/particle, it is then necessary to examine its local microstructural environment and count the number of other grains/particles in contact with it. These observations are repeated over a large number of grains/particles sampled in an unbiased manner, and the coordination number distribution is computed from such data. Figure 33 shows one such three-dimensional bivariate coordination number distribution of tungsten grains in a W-Ni-Fe alloy that was liquid phase sintered in the microgravity environment of the NASA's space shuttle Columbia. Table 4 shows the data on the mean coordination number of the tungsten grains in this alloy processed in the microgravity and normal gravity environments. Observe that the microgravity environment leads to the microstructure that is more open and therefore has a lower mean coordination number.

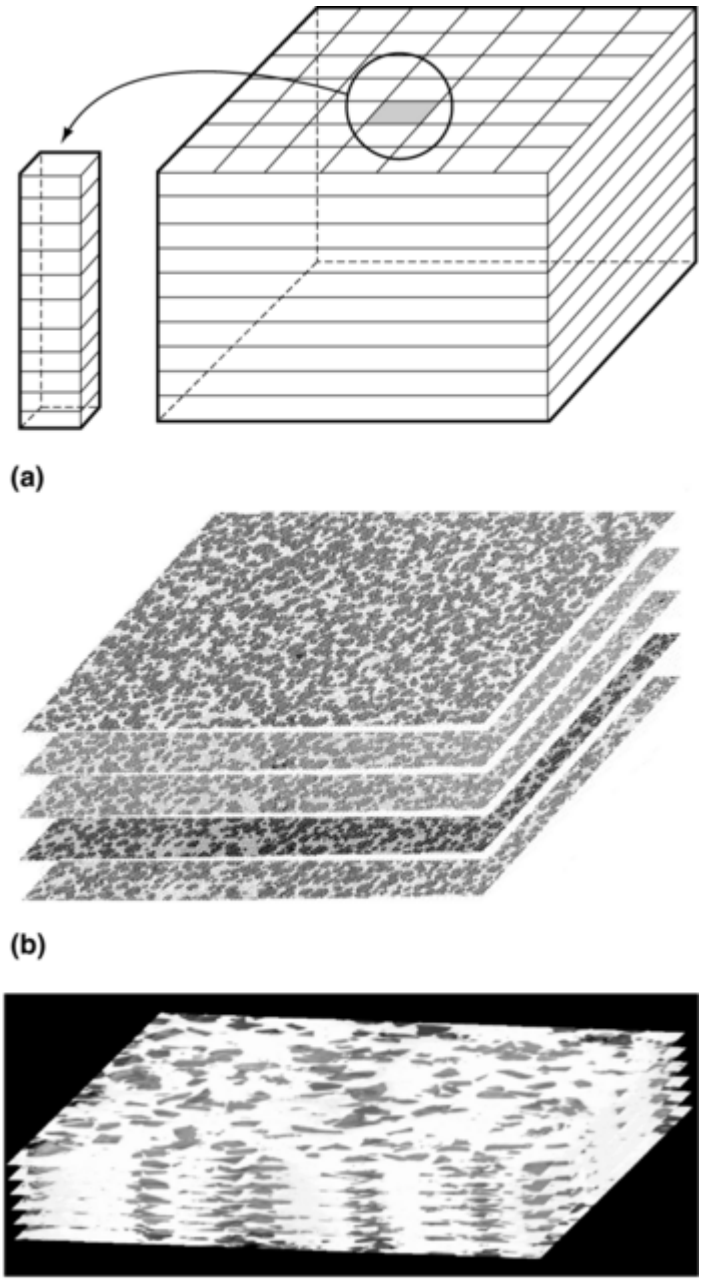

Fig. 31 Montage serial sectioning. The process involves creation of montages of large number of serial sections grabbed at a high resolution and then (a) aligned and stacked together to reconstruct a 3-D

microstructure. (b) A stack of five montage serial sections of microstructure of a liquid phase sintered W-Ni-Fe alloy showing tungsten grains. The montages have been digitally compressed for presentation. Source: Ref 95. (c) A stack of aligned five serial sections of microstructure of metal-matrix composite showing SiC particles in aluminum alloy matrix. Each serial section shown here is a very small segment of the actual montages created. Source: Ref 98

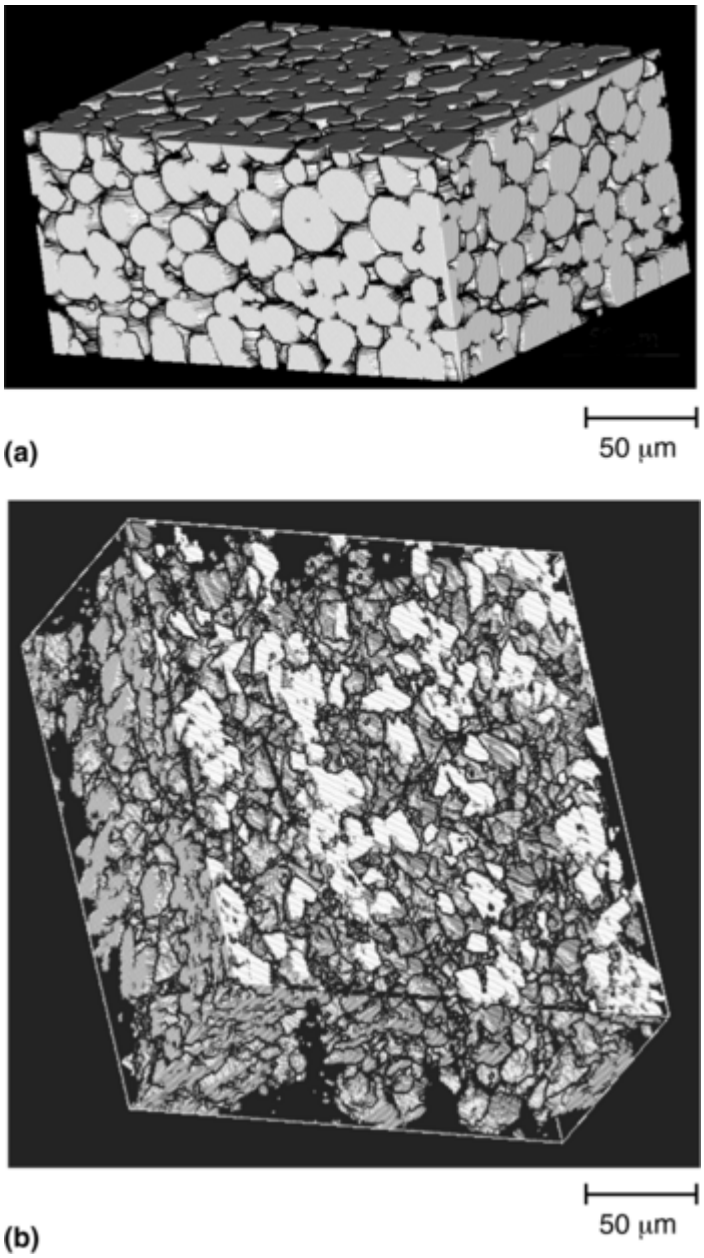

Fig. 32 Surface-rendered images of small volume segments from large-volume high-resolution 3-D microstructures reconstructed from large number (~100) of montage serial sections. (a) 3-D image depicting tungsten grains in a liquid phase sintered W-Ni-Fe-alloy. Source: Ref 35, Ref 95. (b) SiC particles clustered in the bands in the microstructure of a metal-matrix composite. Source: Ref 98

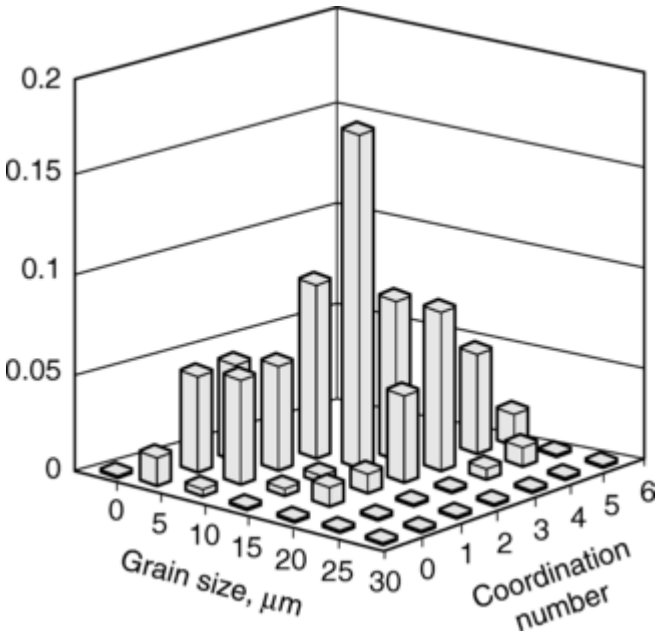

Fig. 33 Bivariate distribution of three-dimensional coordination numbers of tungsten grains in a 83 wt% W-Ni-Fe alloy specimen liquid phase sintered in microgravity environment for 1 min at 1507 °C (2745 °F). The *Z*-axis is the fraction of grains having a given coordination number, and grain size in a given range. Source: Ref 35, 95

Table 4 Mean three-dimensional coordination number of tungsten grains in 83 wt% W-Ni-Fe alloy liquid phase sintered at 1507 °C (2745 °F)

Normal gravity		Microgravity	
1 min	**120 min**	**1 min**	**120 min**
3.7	4.3	2.9	2.9

Nearest-Neighbor Distribution Functions. The spatial arrangement of particle/grain centers in the 3-D microstructure can also be characterized in terms of a series of nearest-neighbor distribution functions. The first nearest-neighbor distribution function is given by the probability density function $\psi_1(r)$, such that $\psi_1(r)dr$ is the probability that there is no other particle/grain center in a sphere of radius r around a typical particle/grain, and there is at least one particle/grain center in the spherical shell of radii r and $(r + dr)$. The second nearest-neighbor distribution function is characterized by the probability density function $\psi_2(r)$ such that $\psi_2(r)dr$ is the probability that there is exactly one other particle/grain center in a sphere of radius r around a typical particle/grain, and there is at least one particle/grain center in the spherical shell of radii r and $(r + dr)$. In general, nth nearest-neighbor distribution function $\psi_n(r)$ is the probability density function such that $\psi_n(r)dr$ is the probability that there are exactly $(n - 1)$ other particle centers in a sphere of radius r around a typical particle, and there is at least one particle center in the spherical shell of radii r and $(r + dr)$. The first nearest-neighbor distribution describes the short-range spatial arrangement of the particle/grain centers; progressively higher-order nearest-neighbor distributions characterize the spatial arrangement of the particles at the larger distances.

The nearest-neighbor distributions and the corresponding mean nearest-neighbor distances in the 3-D microstructure cannot be estimated from any measurements performed on independent 2-D metallographic sections, or by using a disector. Direct measurements on the 3-D microstructure are required for the estimation of these statistical distributions. Further, to minimize the edge effects, the measurements must be performed on a large volume of 3-D microstructures observed at a high resolution, which is possible via the montage serial sectioning technique (Fig. 33) explained in the previously. The coordinates of the centroids of the particles/grains can be measured in the reconstructed 3-D images; the nearest-neighbor distributions can be then computed from such data in a straightforward manner. Figure 34 shows normalized first and second nearest-neighbor distribution of the centers of the tungsten grains in the liquid phase sintered microstructures of a W-Ni-Fe alloy processed in the normal gravity and microgravity (Ref 95). In these plots, the nearest-neighbor distances are normalized by the average grain diameters. Observe that the normalized nearest-neighbor

distributions are almost time invariant, indicating that the grain-coarsening process only leads to a scale change in the short-range spatial arrangement of the tungsten grains in these microstructures.

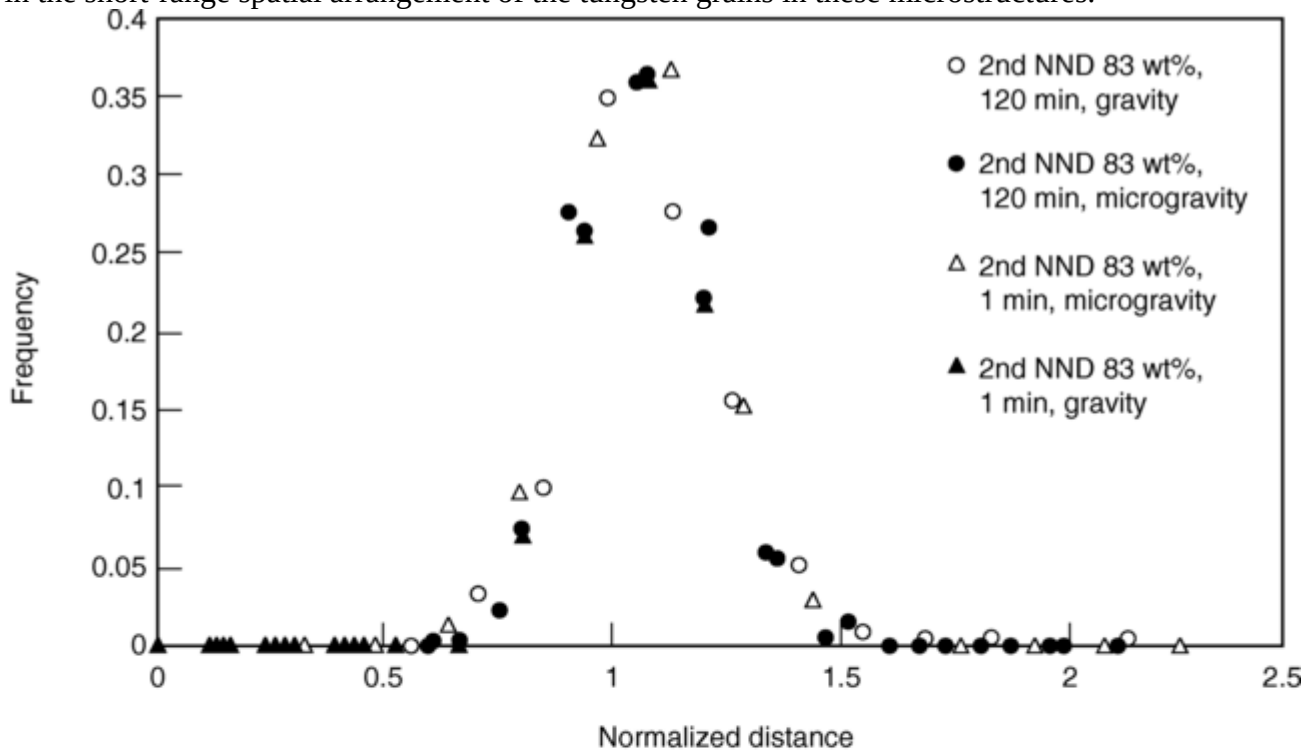

(a)

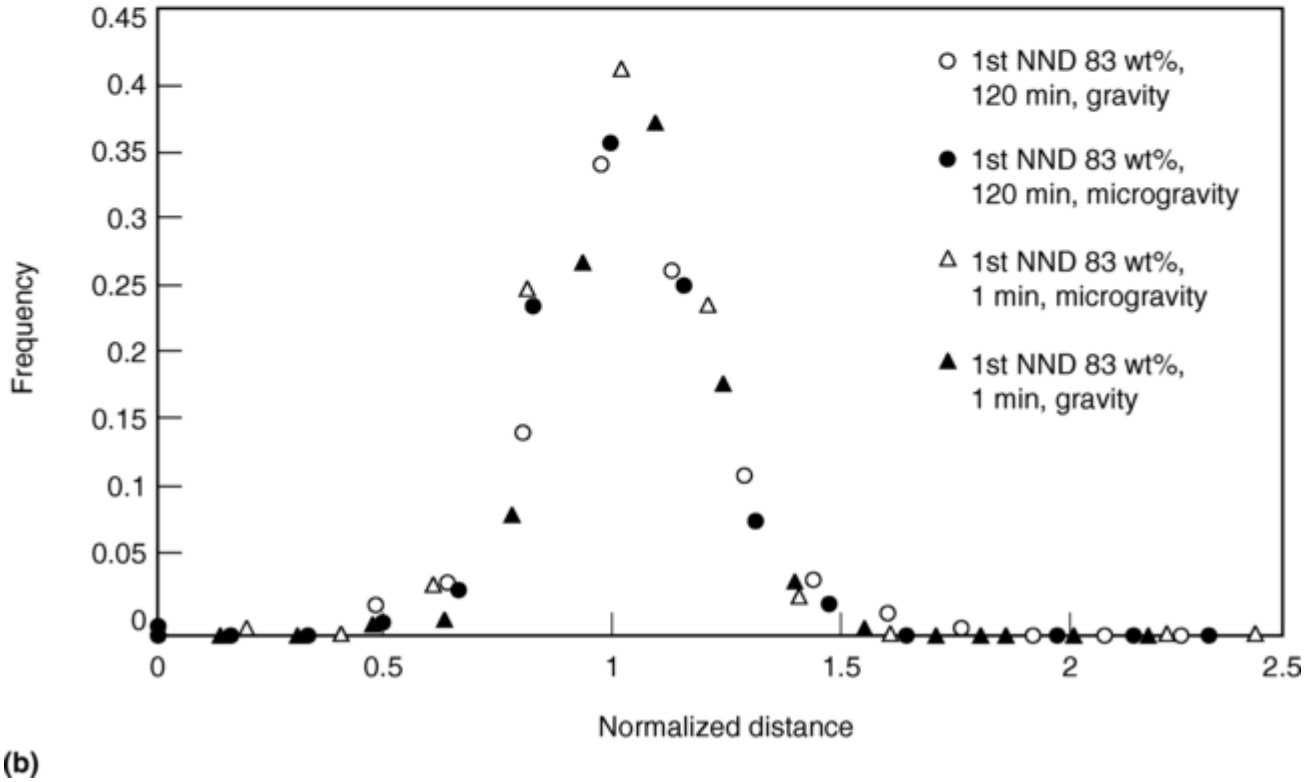

(b)

Fig. 34 Normalized 3-D nearest-neighbor distributions of tungsten grain centers in the specimens of W-Ni-Fe alloys under different processing conditions. (a) First nearest-neighbor distribution. (b) Second nearest-neighbor distribution. Source: Ref 95

Radial distribution function is another important descriptor of the short-range, intermediate-range, long-range spatial arrangement of particle/grains centroids in a microstructure. The radial distribution function $g(R)$ is equal to the ratio of the number of particle centers in a spherical shell of radii R and $(R + dR)$ around a typical

particle and ($4\pi R^2 N_V dR$), where N_V is the number density of the particles. For any microstructure, as $R \rightarrow \alpha$, $g(R) \rightarrow 1$. The radial distribution function of the particle/grain section centers in a 2-D metallographic plane or in a 2-D microstructure can be defined in an analogous manner. The 3-D radial distribution function cannot be estimated from any measurements performed on independent 2-D metallographic sections, or by using a disector. Practical stereological techniques for the estimation of 3-D radial distribution function have not been yet developed. However, the 2-D radial distribution function of the particle/fiber sections can be estimated efficiently in an unbiased manner (free of edge effects) using large area high-resolution montages as described elsewhere (Ref 22). In the materials such as composites containing continuous aligned fibers, the radial distribution function of the fiber centers in the transverse section essentially contains all the 3-D information on the spatial arrangement of fibers. In such microstructures, the 2-D radial distribution function in the transverse section is useful for characterization of the spatial arrangement of fibers. Figure 35(a) shows microstructure of such a composite containing aligned continuous SiC (nicalon) fibers in a glass ceramic (MAS) matrix observed in the transverse section. Observe that the spatial distribution of the fibers is not uniformly random, because there are fiber-rich and fiber-poor bands in the microstructure. Figure 35(b) shows the experimentally measured radial distribution function of the centers of the fibers in this microstructure (Ref 23). The radial distribution function of a uniform random microstructure having the same fiber volume fraction and size distribution obtained via computer simulations is superimposed on the experimental data. Observe that the first peak in the simulated data is much lower than that in the experimental data indicating short clustering of the fibers in the composite. Further, at the distances larger than 40 μm, the experimental data consistently remain slightly below 1.0 indicating presence of fiber-poor regions in the microstructure. These experimental data have been used to develop a computer-simulated nonuniform microstructure that has the nonuniform spatial arrangement that is statistically similar to that in the composite. Such microstructure models can be used to predict the effects of microstructural variations on the mechanical response of the composite using the finite elements (FE) based or other computational mechanics techniques (Ref 99).

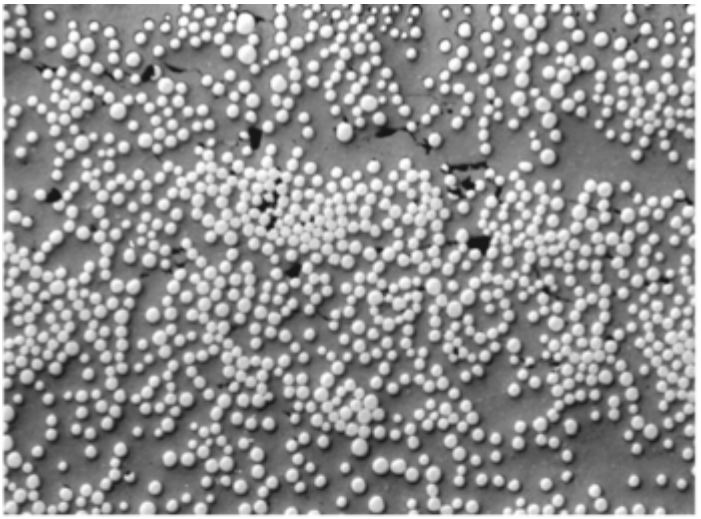

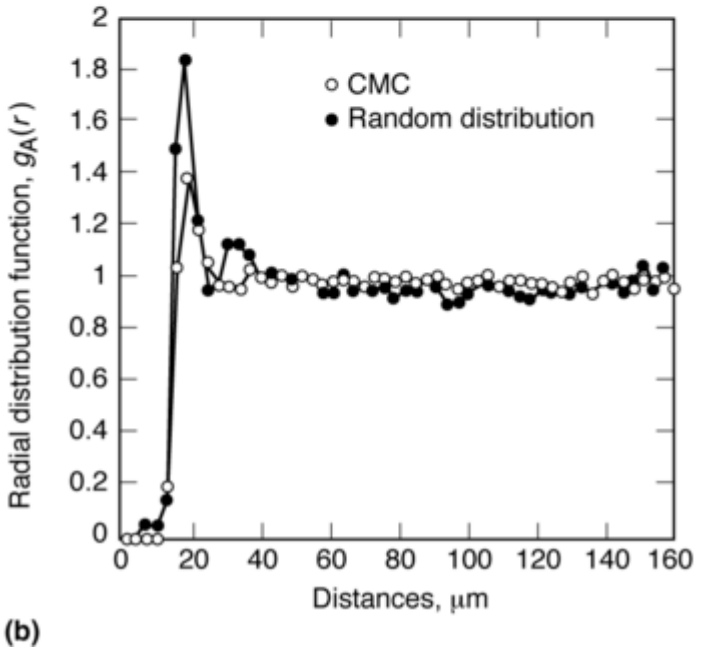

Fig. 35 Radial distribution function. (a) Microstructure of a ceramic-matrix composite containing aligned continuous fibers of SiC (nicalon) having a nonuniform spatial distribution, consisting of fiber-rich and fiber-poor regions, observed in the transverse section. (b) Radial distribution function $g_A(r)$ of the fiber centers in the composite (dark circles) and the corresponding radial distribution function in a computer-simulated composite having the same volume fraction and size distribution of the fibers, but a uniform random spatial distribution (open circles). Source: Ref 36

References cited in this section

1. D. Stoyan, S. Kendall, and J. Mecke, *Stochastic Geometry and Its Applications,* 2nd ed., John Wiley and Sons, 1995

22. L. Pascal and A.M. Gokhale, Application of Image Analysis for Characterization of Spatial Arrangement of Features in Microstructures, *Metall. Mater. Trans.,* Vol 26A, 1995, p 1449–1456

23. S. Yang, A. Tewari, and A.M. Gokhale, Modeling of Non-Uniform Spatial Arrangement of Fibers in a Ceramic Matrix Composite, *Acta Mater.,* Vol 45, 1997, p 3059–3069

32. A. Tewari and A.M. Gokhale, Application of Serial Sectioning for Estimation of 3D Grain Size Distribution in a Liquid Phase Sintered Microstructure, *Mater. Charact.,* Vol 46, 2001, p 329–335

33. A. Tewari, M.D. Dighe, and A.M. Gokhale, Application of Digital Image Processing for Reconstruction of Three-Dimensional Microstructure From Serial Sections, *Mater. Charact.,* Vol 44, 2000, p 259–269

34. M.V. Kral, and G. Spanos, 3D Analysis of Cementite Precipitates, *Acta Mater.,* Vol 47, 1999, p 711–724

35. A. Tewari, A.M. Gokhale, and R.M. German, Effect of Gravity on Three-Dimensional Coordination Number Distribution in Liquid Phase Sintered Microstructures, *Acta Mater.,* Vol 47, 1999, p 3721–3734

36. S. Yang, A. Tewari, and A.M. Gokhale, An Experimental Method for Quantitative Characterization of Spatial Distribution of Fibers in Composites, *Developments in Materials Characterization Technologies,* G.F. Vander Voort and J.J. Frial, Ed., ASM International, 1996 p 33–43

37. A. Tewari, A.M. Gokhale, J.E. Spowart, and D.B. Miracle, Quantitative Characterization of Spatial Clustering in Three-Dimensional Microstructures Using Two-Point Correlation Functions, *Acta Mater.,* Vol 52, 2004, p 307–319

95. A. Tewari, Ph.D. dissertation, Georgia Institute of Technology, 1999

96. K.S. Churn and R.M. German, *Metall. Trans. A,* Vol 15A, 1984, p 331–340

97. R.M. German, *Liquid Phase Sintering,* Plenum Press, 1985

98. H. Singh and A.M. Gokhale, Unpublished research, Georgia Institute of Technology, 2004

99. Z. Shan and A.M. Gokhale, Representative Volume Element for Non-Uniform Microstructure, *Comput. Mater. Sci.,* Vol 24, 20002, p 361–379

A.M. Gokhale, Quantitative Characterization and Representation of Global Microstructural Geometry, *Metallography and Microstructures,* Vol 9, *ASM Handbook,* ASM International, 2004, p. 428–447

Quantitative Characterization and Representation of Global Microstructural Geometry

Arun M. Gokhale, Georgia Institute of Technology

Acknowledgment

The Division of Materials Research of the U.S. National Science Foundation (NSF) and the Metallic Materials Program of the Air Force Office of Scientific Research (AFOSR) supported this work through the research grants DMR-9816618 and F49620-01-1-0045, respectively. Joseph Akkara and Bruce MacDonald are the Program Managers for the NSF grant, and C.S. Hartley is the Program Manager for the AFOSR grant. Additional financial support was provided by American Foundry Society (AFS)/United States Consortium for Automotive Research (USCAR) Project through the Structural Cast Magnesium Development (SCMD) program for which Richard Osborne, Donald Penrod, and Joseph Santner are the Program Managers. The financial support from the funding agencies is gratefully acknowledged. Published/unpublished research results of numerous past and present students of the author have been used in this contribution. The author gratefully acknowledges the contributions of his students K. Bodlak, A. Cottet, N.U. Deshpande, M.D. Dighe, W.J. Drury,

M. Hlawiczkova, T. Joenes, Z. Shan, A. Tewari, S. Yang, H. Agarwal, A. Balasundaram, Felipe Correa, Soon Gi Lee, Scott Lieberman, Pascal Louis, Yuxiong Mao, T. H. Mirabelli, B.R. Morris, S. Mukherjee, G. R. Patel, H. Singh, and W.T. Whited.

A.M. Gokhale, Quantitative Characterization and Representation of Global Microstructural Geometry, *Metallography and Microstructures,* Vol 9, *ASM Handbook,* ASM International, 2004, p. 428–447

Quantitative Characterization and Representation of Global Microstructural Geometry

Arun M. Gokhale, Georgia Institute of Technology

References

1. D. Stoyan, S. Kendall, and J. Mecke, *Stochastic Geometry and Its Applications,* 2nd ed., John Wiley and Sons, 1995

2. L.A. Santalo, *Integral Geometry and Geometric Probability,* Addison-Wesley, 1976

3. A. Gray, *Modern Differential Geometry of Curves and Surfaces,* 2nd ed., CRC Press, London, 1997

4. P.R. Mouton, *Principles and Practices of Unbiased Stereology: An Introduction for Bioscientists,* The Johns Hopkins University Press, 2002

5. F. Chayes, *Petrographic Modal Analysis,* John Wiley, 1956

6. E.E. Underwood, *Quantitative Stereology,* Addison Wesley, 1970

7. R.T. DeHoff and F.N. Rhines, *Quantitative Microscopy,* McGraw Hill, 1968

8. S.A. Saltykov, *Stereometric Metallography,* 2nd ed., Metallurgizdat, Moscow, 1958

9. A.J. Baddeley, H.J.G. Gundersen, and L.M. Cruz Orive, Estimation of Surface Area Using Vertical Sections, *J. Microsc.,* Vol 142, 1986, p 259–276

10. A.M. Gokhale and W.J. Drury, Efficient Estimation of Microstructural Surface Area Using Trisector, *Metall. Trans. A,* Vol 25A, 1994, p 919–928

11. B.R. Morris, A.M. Gokhale, and G.F. Vander Voort, Estimation of Grain Size in Anisotropic Materials, *Metall. Mater. Trans. A,* Vol 29A, 1998, p 237–244

12. J. Ohser and F. Muecklich, *Statistical Analysis of Microstructures in Material Science,* John Wiley & Sons, 2000

13. A.M. Gokhale, Unbiased Estimation of Curve Length in 3D Using Vertical Slices, *J. Microsc.,* Vol 159, 1990, p 133–141

14. A.M. Gokhale, Estimation of Length Density L_v from Vertical Slices of Unknown Thickness, *J. Microsc.,* Vol 167, pt. I, 1992, p 1–8

15. A.M. Gokhale, Utility of Horizontal Slice for Stereological Characterization of Lineal Features, *J. Microsc.,* Vol 170, pt. 1, 1993, p 3–8

16. L.M. Cruz Orive and X. Gual-Arnau, Precision of Circular Systematic Sampling, *J. Microsc.,* Vol 207, 2002, p 225–242

17. A.M. Gokhale and N.U. Deshpande, Stereology of Anisotropic Microstructures, *Quantitative Microscopy and Image Analysis,* D.J. Diaz, Ed., ASM International, 1994, p 73–82

18. P.R. Mouton, A.M. Gokhale, N.L. Ward, and M.J. West, Unbiased Length Estimation Using Isotropic Spherical Probes, *J. Microsc.,* Vol 206, 2002, p 54–64

19. D.C. Sterio, The Unbiased Estimation of Number and Size of Arbitrary Particles Using Disector, *J. Microsc.,* Vol 134, 1984, p 127–136

20. A.M. Gokhale and A. Tewari, Efficient Estimation of Number Density in Opaque Material Microstructures Using Large Area Disector (LAD), *J. Microsc.,* Vol 200, pt. 3, 2000, p 277–283

21. J.P. Kroustrup and H.J.G. Gundersen, Estimating the Number of Complex Particles Using the ConnEulor Principle, *J. Microsc.,* Vol 203, 2001, p 314–320

22. L. Pascal and A.M. Gokhale, Application of Image Analysis for Characterization of Spatial Arrangement of Features in Microstructures, *Metall. Mater. Trans.,* Vol 26A, 1995, p 1449–1456

23. S. Yang, A. Tewari, and A.M. Gokhale, Modeling of Non-Uniform Spatial Arrangement of Fibers in a Ceramic Matrix Composite, *Acta Mater.,* Vol 45, 1997, p 3059–3069

24. C. Babu Rao, P. Kalyansundaram, K.K. Ray, and B. Raj, *Image Analysis in Materials and Life Sciences,* Oxford and IBH, New Delhi, India, 2000

25. J. Serra, *Image Analysis and Mathematical Morphology,* Academic Press, 1982

26. J.C. Russ, *The Image Processing Handbook,* CRC Press, London, 2001

27. P. Velecky and J. Pospisil, Digital Image Processing for Evaluation of the Internal Microstructure Characteristics of Cemented Carbides, *Optik,* Vol 111, 2000, p 493–496

28. A. Balasundaram and A.M. Gokhale, Quantitative Characterization of Spatial Arrangement of Shrinkage and Gas (Air) Pores in Cast Magnesium Alloys, *Mater. Charact.,* Vol 46, 2001, p 419–426

29. A.J. Schwartz, M. Kumar, and B.L. Adams, *Electron Backscatter Diffraction in Materials Science,* Plenum Press, 2000

30. F.J. Humphreys, Quantitative Metallography by Electron Backscattered Diffraction, *J. Microsc.,* Vol 195, 1999, p 170–185

31. J.K. Stevens, L.R. Mills, and J.E. Trogadis, *Three-Dimensional Confocal Microscopy,* Academic Press, London, UK, 1994

32. A. Tewari and A.M. Gokhale, Application of Serial Sectioning for Estimation of 3D Grain Size Distribution in a Liquid Phase Sintered Microstructure, *Mater. Charact.,* Vol 46, 2001, p 329–335

33. A. Tewari, M.D. Dighe, and A.M. Gokhale, Application of Digital Image Processing for Reconstruction of Three-Dimensional Microstructure From Serial Sections, *Mater. Charact.,* Vol 44, 2000, p 259–269

34. M.V. Kral, and G. Spanos, 3D Analysis of Cementite Precipitates, *Acta Mater.,* Vol 47, 1999, p 711–724

35. A. Tewari, A.M. Gokhale, and R.M. German, Effect of Gravity on Three-Dimensional Coordination Number Distribution in Liquid Phase Sintered Microstructures, *Acta Mater.,* Vol 47, 1999, p 3721–3734

36. S. Yang, A. Tewari, and A.M. Gokhale, An Experimental Method for Quantitative Characterization of Spatial Distribution of Fibers in Composites, *Developments in Materials Characterization Technologies,* G.F. Vander Voort and J.J. Frial, Ed., ASM International, 1996 p 33–43

37. A. Tewari, A.M. Gokhale, J.E. Spowart, and D.B. Miracle, Quantitative Characterization of Spatial Clustering in Three-Dimensional Microstructures Using Two-Point Correlation Functions, *Acta Mater.,* Vol 52, 2004, p 307–319

38. A.M. Gokhale, Estimation of Bivariate Size and Orientation Distribution of Microcracks, *Acta Metall.,* Vol 44, 1996, p 475–485

39. V. Benes, V. Jiruses, and M. Slamova, Estimation of Trivariate Size-Shape-Orientation Distributions from Vertical Sections, *Acta Mater.,* Vol 45, 1997, p 1105–1110

40. L. Hengcheng, Y. Sun, and S. Guoxiong, Correlation between Mechanical Properties and Amount of Dendritic Alpha-Al Phase in As-Cast Near-Eutectic Al-11.6% Si Alloys Modified with Strontium, *Mater. Sci. Eng. A,* Vol 335, 2002, p 62–66

41. M. Sozanska, A. Maciejny, C. Dagbert, J. Galland, and L. Hyspecka, Use Of Quantitative Metallography in the Evaluation of Hydrogen Action During Martensitic Transformations, *Mater. Sci. Eng. A,* Vol A273, 1999, p 485–490

42. Q. Meng, Y. Rong, S. Chen, and T.Y. Hsu, The Relationship of the Volume Fraction of Martensite vs. Plastic Strain in a Fe-Mn-Si-Cr-N Shape Memory Alloy, *Mater. Lett.,* Vol 50, 2001, p 328–332

43. H. Agarwal, A.M. Gokhale, S. Graham, and M.F. Horstemeyer, Quantitative Characterization of Three-Dimensional Damage Evolution in a Wrought Al-Alloy under Tension and Compression, *Metall. Mater. Trans.,* Vol 33A, 2002, p 2599–2606

44. M.P. Black, R.L. Higginson, and C.M. Sellars, Effect of Strain Path on Recrystallization Kinetics During Hot Rolling of Al-Mn, *Mater. Sci. Technol.,* Vol 17, 2001, p 1055–1060

45. K. Bodlak, A. Balasundaram, A.M. Gokhale, and V. Benes, Unfolding of Three-Dimensional Bivariate Size-Orientation Distribution of Microcracks, *Acta Mater.,* Vol 51, 2003, p 3131–3143

46. R.A. Vandermeer, N. Hansen, X. Huang, J. Jensen, E.M. Laurdisen, T. Leffers, W. Pantleon, T.J. Sabine, and J.A. Wert, Kinetic Aspects of Nucleation and Growth in Recrystallization, *Proc. 21st Riso International Symposium on Materials Science* (Roskilde, Denmark), 2000, p 179–200

47. J.A. Griggs, K.J. Anusavice, and J.J. Mecholsky, Jr., Devitrification and Microstructural Coarsening of a Fluoride-Containing Barium Aluminosilicate Glass, *J. Mater. Sci.,* Vol 37, 2002, p 2017–2022

48. K.-W. Moon, W.J. Boettinger, U.R. Kattner, C.A. Handwerker, and D.-J. Lee, The Effect of Pb Contamination on the Solidification Behavior of Sn-Bi Solders, *J. Electron. Mater.,* Vol 30, 2001, p 45–52

49. F.G. Caballero, C. Garcia de Andres, and C. Capdevila, Characterization and Morphologic Analysis of Pearlite in a Eutectoid Steel, *Mater. Charact.,* Vol 45, 2000, p 111–116

50. K.J. and H. Conrad, Microstructure Coarsening During Static Annealing of 60Sn40Pb Solder Joints. I. Stereology, *J. Electron. Mater.,* Vol 30, 2001, p 1294–1302

51. S. Spangel, E. Matthaei-Schulz, A. Schulz, H. Vetters, and P. Mayr, Influence of Carbon and Chromium Content and Preform Shape on the Microstructure of Spray Formed Steel Deposits, *Mater. Sci. Eng. A,* Vol A326, 2002, p 26–39

52. J. Wosik, H.J. Penkalla, K. Szot, B. Dubiel, and F.C. Schubert, The Influence of Various Microscopic Techniques on the Quantification of Stereological Structure Parameters in Waspaloy Alloy, *Prakt. Metallogr.,* Vol 39, 2002, p 140–154

53. W. Yunxin, R.M. German, D. Blaine, B. Marx, and C. Schlaefer, Effects of Residual Carbon Content on Sintering Shrinkage, Microstructure and Mechanical Properties of Injection Molded 17-4 PH Stainless Steel, *J. Mater. Sci.,* Vol 37, 2002, p 3573–3583

54. M. Grange, J. Besson, and E. Andrieu, An Anisotropic Gurson Type Model to Represent the Ductile Rupture of Hydrided Zircaloy-4 Sheets, *Int. J. Fract.,* Vol 105, 2000, p 273–293

55. N.U. Deshpande, A.M. Gokhale, D.K. Denzer, and J. Liu, Relationship between Fracture Toughness, Fracture Path, and Microstructure of 7050 Aluminum Alloy—I: Quantitative Characterization, *Metall. Mater. Trans. A,* Vol 29A, 1998, p 1191–1201

56. H. Agarwal, A.M. Gokhale, S. Graham, and M.F. Horstemeyer, Anisotropy of Intermetallic Particle Cracking Damage Evolution in an Al-Si-Mg Base Wrought Aluminum Alloy under Uniaxial Compression, *Metall. Mater. Trans. A,* Vol 33A, 2002, p 3443–3448

57. H. Agarwal, A.M. Gokhale, and S. Graham, Void Growth in 6061 Al-Alloy under Triaxial Stress State, *Mater. Sci. Eng.,* Vol 341 (No. 1–2), 2003, p 35–42

58. A.K. Balasundaram, A.M. Gokhale, S. Graham, and M.F. Horstemeyer, Three Dimensional Particle Cracking Damage Development in an Al-Mg Base Alloy, *Mater. Sci. Eng.,* Vol 355 (No. 1–2), 2003, p 368–383

59. Z. Zhang and F. Wang, Research on the Deformation Strengthening Mechanism of a Tungsten Heavy Alloy by Hydrostatic Extrusion, *Int. J. Refract. Met. Hard Mater.,* Vol 19, 2001, p 177–182

60. Y. Wu, R.M. German, D. Blaine, B. Marx, and C. Schlaefer, Effects of Residual Carbon Content on Sintering Shrinkage, Microstructure and Mechanical Properties of Injection Molded 17-4 PH Stainless Steel, *J. Mater. Sci.,* Vol 37, 2002, p 3573–3583

61. C.S. Smith and L. Guttman, Measurement of Internal Boundaries in Three-Dimensional Structures by Random Sectioning, *Trans. AIME,* Vol 97, 1953, p 81

62. A.M. Gokhale and W.T. Whited, Measurements of Growth Rates of Thermally Induced Micro-cracks in a Metal Matrix Composite, *Developments in Ceramics and Metal Matrix Composites,* K. Upadhya, Ed., TMS, 1992, p 273–286

63. A.M. Gokhale, W.J. Drury, and W.T. Whited, Quantitative Microstructural Analysis of Anisotropic Materials, *Mater. Charact.,* Vol 31, 1993, p 11–18

64. L. Karlsson and A.M. Gokhale, Stereological Estimation of Mean Linear Intercept Length in Metallography Using Vertical Sections and Trisector, *J. Microsc.,* Vol 186, 1997, p 143–152

65. E.A. Stocks, J.M. McArthur, J.W. Griffin, and P.R. Mouton, An Unbiased Method for Estimation of Total Epidermal Nerve Fiber Length, *J. Neurocyt.,* Vol 25, 1996, p 11–18

66. P.J. McMillan, J.O. Archambeau, and A.M. Gokhale, Morphometric and Stereological Analysis of Cerebral Cortical Microvessels Using Optical Sections and Thin Slices, *Acta Stereol.,* Vol 13, 1994, p 33–38

67. S. Batra, M.F. Konig, and L.M. Cruz Orive, Unbiased Estimation of Capillary Length from Vertical Slices, *J. Microsc.,* Vol 178, 1994, p 152–159

68. C.V. Howard, L.M. Cruz Orive, and H. Yaegashi, Estimating Neuron Dendritic Length in 3D From Total Vertical Projections and Vertical Slices, *Acta Neurol. Scand., Suppl.,* Vol 137, 1992, p 14–19

69. M. Hlawiczkova, A.M. Gokhale, and V. Benes, Efficiency and Bias of Length Density Estimator, *J. Microsc.,* Vol 204, 2001, p 2226–2231

70. J.E. Hilliard and J.W. Cahn, An Evaluation of Procedures in Quantitative Metallography for Volume Fraction Analysis, *Trans. AIME,* Vol 221, 1961, p 344–354

71. H.J.G. Gundersen and E.B. Jensen, The Efficiency of Systematic Sampling in Stereology and Its Prediction, *J. Microsc.,* Vol 121, 1987, p 65–73

72. L.M. Cruz Orive, Systematic Sampling in Stereology, *Bull. Int. Stat. Inst.,* Vol 55, 1993, p 451–468

73. L.M. Cruz Orive, On the Precision of Systematic Sampling: A Review of Matheron's Transitive Methods, *J. Microsc.,* Vol 153, 1985, p 518–530

74. H.J.G Gundersen, E.B. Kiru, and J. Neilsen, The Efficiency of Systematic Sampling in Stereology, *J. Microsc.,* Vol 193, 1999, p 199–211

75. E. Kreyszig, *Advanced Engineering Mathematics,* 6th ed., John Wiley & Sons, 1988

76. H.J.G. Gundersen, Note on Estimation of Number Density of Arbitrary Profiles: The Edge Effect, *J. Microsc.,* Vol 11, 1977, p 219–223

77. G.F. Vander Voort, Examination of Some Grain Size Measurement Problems, *Metallography: Past, Present, and Future,* G.F. Vander Voort, F.J. Warmuth, S.M. Purdy, and A. Szirmae, Ed., STP 1165, ASTM, 1993, p 266–294

78. G.F. Vander Voort, *Metallography: Principles and Practice,* ASM International, 1999

79. A.M. Gokhale, Estimation of Average Size of Convex Particle, *Metall. Trans. A,* Vol 17A, 1986, p 742–745

80. J. Gurland, Measurement of Grain Contiguity in Two-Phase Alloys, *Trans. AIME,* Vol 212, 1958, p 452–456

81. R.L. Fullman, Measurement of Particle Sizes in Opaque Bodies, *Trans. AIME,* Vol 197, 1953, p 47

82. H.W. Chalkley, J. Cornfield, and H. Park, A Method for Estimating Volume-Surface Ratio, *Science,* Vol 110, 1949, p 295

83. "Standard Test Methods for Determining Average Grain Size," E 112, *Annual Book of ASTM Standards,* ASTM

84. A.M. Gokhale, Interpretation of Grain Size Descriptors, *Trans. Ind. Inst. Metals,* Vol 35, 1982, p 595–600

85. W.M. Visscher and A.S. Goldman, Estimating the Distribution of Spherical Particles from Plane Sections: An Optimal Algorithm for Solution of the Abel Integral Equation, *Siam. J. Sci. Stat. Comput.,* Vol 4, 1983, p 280–290

86. G.M. Tallis, Estimating the Distribution of Spherical and Elliptical Bodies from Plane Sections, *Biometrics,* Vol 26, 1970, p 87–90

87. P. Luchini, A. Pozzi, and C. Ronchi, Evaluation of Statistical Distribution of Spherical Objects from Measurements of Metallographic Cross-Sections, *Meccanica,* Vol 19, 1984, p 127–133

88. R.T. DeHoff, The Determination of Size Distribution of Ellipsoidal Particles from Measurements Made on Random Plane Sections, *Trans. Metall. Soc. AIME,* Vol 224, 1962, p 474–477

89. J. Osher and M. Nippe, Stereology of Cubic Particles: Various Estimators for the Size Distribution, *J. Microsc.,* Vol 187, 1997, p 22–30

90. J. Osher and F. Mucklich, Stereology of Some Classes of Polyhedrons, *Adv. Appl. Probabil.,* Vol 27, 1995, p 384–396

91. A.M. Gokhale and A.K. Jena, Size Distribution of Grain Boundary Precipitates, *Metallography,* Vol 13, 1980, p 307–317

92. L.M. Cruz-Orive, Particle Size-Shape Distributions; the General Spheroid Problem, *J. Microsc.,* Vol 107, 1976, p 235–253

93. B.W. Silverman, M.C. Jones, D.W. Nychka, and J.D. Wilson, A Smoothed EM Approach to Indirect Estimation Problems, With Particular Reference to Stereology, *J. Royal Stat. Soc.,* Vol B52, 1990, p 271–324

94. S. Mase, Stereological Estimation of Particle Size Distributions, *Adv. Applied Probabil.,* Vol 27, 1995, p 350–366

95. A. Tewari, Ph.D. dissertation, Georgia Institute of Technology, 1999

96. K.S. Churn and R.M. German, *Metall. Trans. A,* Vol 15A, 1984, p 331–340

97. R.M. German, *Liquid Phase Sintering,* Plenum Press, 1985

98. H. Singh and A.M. Gokhale, Unpublished research, Georgia Institute of Technology, 2004

99. Z. Shan and A.M. Gokhale, Representative Volume Element for Non-Uniform Microstructure, *Comput. Mater. Sci.,* Vol 24, 20002, p 361–379

M.V. Kral, G. Ice, M.K. Miller, M.D. Uchic, and R.O. Rosenberg, Three-Dimensional Microscopy, *Metallography and Microstructures,* Vol 9, *ASM Handbook,* ASM International, 2004, p. 448–467

Three-Dimensional Microscopy

M.V. Kral, University of Canterbury, Christchurch, New Zealand; Gene Ice and M.K. Miller, Oak Ridge National Laboratory; M.D. Uchic, Wright-Patterson Air Force Research Laboratory; R.O. Rosenberg, Naval Research Laboratory

Introduction

THREE-DIMENSIONAL MICROSCOPY can be used to reveal the shape, distribution, and connectivity of three-dimensional (3D) features that lie buried within an opaque material. Serial-sectioning techniques used to accomplish this task involve removing material from a bulk sample layer by layer, imaging each layer, and then reconstructing the resultant series of images using computer programs. Some methods, such as electrolytic dissolution or focused ion beam ablation, involve imaging taking place periodically at a known increment in a continuous material-removal process. Other methods, such as x-ray tomography, can nondestructively reveal the nature of the hidden 3D structure. It should be noted that any characteristic that can be associated with a particular location within a sample, such as crystallographic orientation, chemical composition, or phase, can be used to produce a 3D image.

Traditional two-dimensional (2D) metallographic methods provide single polished-and-etched sections for observation. Quantitative metallography can then be applied to estimate some parameters that describe 3D features of polycrystalline or multiphase materials. While some microstructural parameters can be accurately deduced in this manner, more precise descriptions of sizes, spatial distributions, shapes, and interconnectivities of complex microstructural features can only be obtained via true 3D characterization methods (Ref 1). To cite an instance, Lund and Voorhees (Ref 2) were able to observe for the first time the true 3D morphologies, distributions and interactions between γ' particles in a γ-γ' alloy. The benefits of 3D analysis extend to the results of studies inspired by 3D observations. For example, subsequent to a 3D analysis of proeutectoid cementite (Ref 3), Mangan et al. (Ref 4) determined that the two different morphologies of Widmanstätten cementite precipitates, which were revealed by 3D analysis, correspond to the two known orientation relationships between cementite and austenite.

Continuous improvements to computer software and hardware are now making the representation and dissemination of 3D images, via the Internet or CD-ROMs for example, a compelling possibility. Ongoing improvements in material-removal methods offer the greatest opportunity for making 3D microscopy a justifiable effort to more materials scientists and engineers. Semiautomated serial-sectioning machines used in conjunction with optical or scanning electron microscopes, such as the micromilling apparatus at Northwestern University (Ref 5), have been developed to reduce the time required for sectioning. Material can also be removed semiautomatically or automatically using focused ion beam (Ref 6) techniques. Going to the extreme, the 3D atom probe has been used to strip individual atoms from a specimen, while recording the atomic position and species (Ref 7). Three-dimensional reconstructions of microstructures can thus be made over a range of volumes from cubic millimeters down to the atomic level. The reader should keep in mind that 3D analysis of microstructures is a rapidly developing field. This article presents several experimental techniques that can be used to generate 3D images (serial sectioning, focused ion beam tomography, atom probe tomography, and x-ray microtomography) as well as techniques used to visualize 3D microstructures.

References cited in this section

1. R.T. DeHoff, Quantitative Serial Sectioning Analysis: Preview, *J. Microsc.,* Vol 131 (No. 3), 1983, p 259–263

2. A.C. Lund and P.W. Voorhees, The Effects of Elastic Stress on Microstructural Development: The Three-Dimensional Microstructure of a Gamma-Gamma′ Alloy, *Acta Mater.,* Vol 50 (No. 10), p 2585–2598

3. M.V. Kral and G. Spanos, Three Dimensional Analysis of Proeutectoid Cementite Precipitates, *Acta Metall.,* Vol 47 (No. 2), 1999, p 711–724

4. M.V. Mangan, M.V. Kral, and G. Spanos, Correlation between the Crystallography and Morphology of Proeutectoid Widmanstatten Cementite Precipitates, *Acta Mater.,* Vol 47 (No. 17), 1999, p 4263–4274

5. T.L. Wolfsdorf, W.H. Bender, and P.W. Voorhees, The Morphology of High Volume Fraction Solid-Liquid Mixtures: An Application of Microstructural Tomography, *Acta Mater.,* Vol 45 (No. 6), 1997, p 2279–2295

6. B.J. Inkson, M. Mulvihill, and G. Möbus, 3D Determination of Grain Shape in a FeAl-Based Nanocomposite by 3D FIB Tomography, *Scr. Mater.,* Vol 47 (No. 7), 2001, p 753–758

7. A. Cerezo et al., Visualisation of Three-Dimensional Microstructures, *Surf. Sci.,* Vol 266 (No. 1–3), 1991, p 471–480

M.V. Kral, G. Ice, M.K. Miller, M.D. Uchic, and R.O. Rosenberg, Three-Dimensional Microscopy, *Metallography and Microstructures,* Vol 9, *ASM Handbook,* ASM International, 2004, p. 448–467

Three-Dimensional Microscopy

M.V. Kral, University of Canterbury, Christchurch, New Zealand; Gene Ice and M.K. Miller, Oak Ridge National Laboratory; M.D. Uchic, Wright-Patterson Air Force Research Laboratory; R.O. Rosenberg, Naval Research Laboratory

Serial Sectioning

The history of 3D analysis of microstructures via serial sectioning spans at least from 1918 (Ref 8) with Forsman's effort to understand the 3D structure of pearlite. By projecting the images of each section onto cardboard layers of appropriate thickness, solid models of cementite lamellas were constructed. In 1962, M. Hillert (Ref 9) and N. Lange produced a motion picture of serial sections to show the true 3D structure of an entire pearlite colony. Eichen et al. (1964) studied the growth of Widmanstätten ferrite by measuring the changing length of plates with increasing depth through serial sections (Ref 10). Hopkins and Kraft (1965) used a unique "cinephotomicrographic recording of the microstructure of a specimen undergoing controlled electrolytic dissolution" (Ref 11). Their results were subsequently represented by building a 3D physical Plexiglas model to show the eutectic fault structure in a copper-aluminum alloy. Hawbolt and Brown (1967) used serial sectioning to study the shapes of grain-boundary precipitates in a silver-aluminum alloy (Ref 12). Barrett and Yust (1967) showed the interconnectivity of voids in a sintered copper powder (Ref 13). Ziolkowski (1985) used a "mikrotom" to perform a serial-sectioning study of grain-boundary precipitates in an α/β brass alloy (Ref 14). In most of the aforementioned cases, 3D results were represented by hand-drawn sketches, graphical plots of length versus depth, or motion pictures. In 1983, R.T. DeHoff wrote (Ref 1): "In its current embryonic state of development, the use of serial-sectioning analysis for all but the most rudimentary of measurements is prohibitively expensive and tedious."

Recent improvements in image processing and 3D visualization capabilities in addition to the development of automatic sectioning devices have made 3D reconstruction and visualization of serial sections much more practical. In 1991, Hull et al. (Ref 15) were among the first to use computer software to contain 3D wire-frame drawings of microstructural features, in this case titanium prior-beta grain sizes and shapes. Brystrzycki and

Przetakiewicz (1992) used a similar technique to study the sizes and shapes of annealing twins in Ni-2%Mn alloy (Ref 16). A significant innovation was made by Wieland, Rouns, and Liu (1994) in serial sectioning a recrystallized aluminum-manganese alloy and simultaneously capturing the crystallographic orientation and location of recrystallized grains using electron backscatter electron diffraction (EBSD) with a scanning electron microscope (SEM) (Ref 17).

Visual representations of 3D data sets, such as microstructural data via optical or SEM images or crystallographic data via EBSD, obtained through serial sectioning have continued to improve with advancements in computer visualization software. Probably the first to take full advantage of advanced computer reconstructions of serial sectioning was Shiflet's group at the University of Virginia (Ref 18).

The effort required for serial sectioning and the subsequent 3D analysis may always be a concern. Over recent years, steady improvements in semiautomated material removal, digital image acquisition, and visualization of 3D reconstructions using advanced computer software and hardware have made 3D analysis techniques more accessible to materials researchers. Even with the relative slowness of manual serial sectioning, at 20 to 30 min/section on average and approximately 100 person-hours per 250 sections, the time to visualize and understand the volume data set will still far exceed the time required to acquire it. Three-dimensional analyses have already produced important new insights into microstructural evolution that not only had immediate rewards, but also led to new avenues of research. Unfortunately, an unknown number of 3D analysis experiments have been left unpublished due to the difficulty of reproducing 3D representations onto 2D media. An easily accessible archival medium and common software are needed to enhance the utility of and encourage the practice of 3D characterization of microstructures.

References cited in this section

1. R.T. DeHoff, Quantitative Serial Sectioning Analysis: Preview, *J. Microsc.,* Vol 131 (No. 3), 1983, p 259–263

8. O. Forsman, Undersökning av rymdstrukturen hos ett kolstål av hypereutektoid sammansättning, *Jern-Kontorets Ann.,* Vol 102, 1918, p 1–30

9. M. Hillert, The Formation of Pearlite, *The Decomposition of Austenite by Diffusional Processes,* V.F. Zackay and H.I. Aaronson, Ed., Interscience, 1962, p 197–237

10. E. Eichen et al., Thermionic Emission Microscope Study of the Formation of Ferrite Sideplates, *Acta Metall.,* Vol 12, 1964, p 1298–1301

11. R.H. Hopkins and R.W. Kraft, A Rapid Technique for Observation of Three-Dimensional Microstructures, *Trans. AIME,* Vol 233, 1965, p 1526–1532

12. E.B. Hawbolt and L.C. Brown, Grain Boundary Precipitation in Ag-5.64 wt pct Al Alloys, *Trans. AIME,* Vol 239, 1967, p 1916–1924

13. L.K. Barrett and C.S. Yust, Progressive Shape Changes of the Void During Sintering, *Trans. AIME,* Vol 239, 1967, p 1172–1180

14. P.M. Ziolkowski, *The Three Dimensional Shapes of Grain Boundary Precipitates in a/b Brass,* Michigan Tech., 1985

15. D.A. Hull et al., Titanium Prior-Beta Grain Volume Distribution by Quantitative Serial Sectioning Techniques, *Mater. Charact.,* Vol 26, 1991, p 63–71

16. J. Brystrzycki and W. Przetakiewicz, 3-Dimensional Reconstruction of Annealing Twins Shape in FCC Metals by Serial Sectioning, *Scr. Metall. Mater.,* Vol 27, 1992, p 893–896

17. H. Wieland, T.N. Rouns, and J. Liu, The Role of Particle Stimulated Nucleation During Recrystallization of an Aluminum-Manganese Alloy, *Z. Metallkd.*, Vol 85, 1994, p 592–597

18. M.A. Mangan, P.D. Lauren, and G.J. Shiflet, Three-Dimensional Reconstruction of Widmanstatten Plates in Fe-12.3Mn-0.8C, *J. Microsc.*, Vol 188, Oct 1997, p 36–41

M.V. Kral, G. Ice, M.K. Miller, M.D. Uchic, and R.O. Rosenberg, Three-Dimensional Microscopy, *Metallography and Microstructures,* Vol 9, *ASM Handbook,* ASM International, 2004, p. 448–467

Three-Dimensional Microscopy

M.V. Kral, University of Canterbury, Christchurch, New Zealand; Gene Ice and M.K. Miller, Oak Ridge National Laboratory; M.D. Uchic, Wright-Patterson Air Force Research Laboratory; R.O. Rosenberg, Naval Research Laboratory

Serial-Sectioning Experimental Techniques

Anyone undertaking a serial-sectioning project will have identified a microstructural feature for which some three-dimensional information is desired. Once the subject of the study has been selected, the most important experimental option, that is, the material-removal technique, will probably have been decided by default since each technique is only practical for a certain range of material-removal rates. The basic serial-sectioning material-removal methods involve manual or semiautomated polishing, which can remove between approximately 0.05 and 1.0 μm/section and micromilling (which removes between approximately 1.0 and 20 μm/section).

Other experimental parameters that may be applicable include the number of sections required, whether an etchant is required, the use of fiducial marks, imaging method, image acquisition, and visualization software. A general procedure for serial sectioning is shown in Fig. 1.

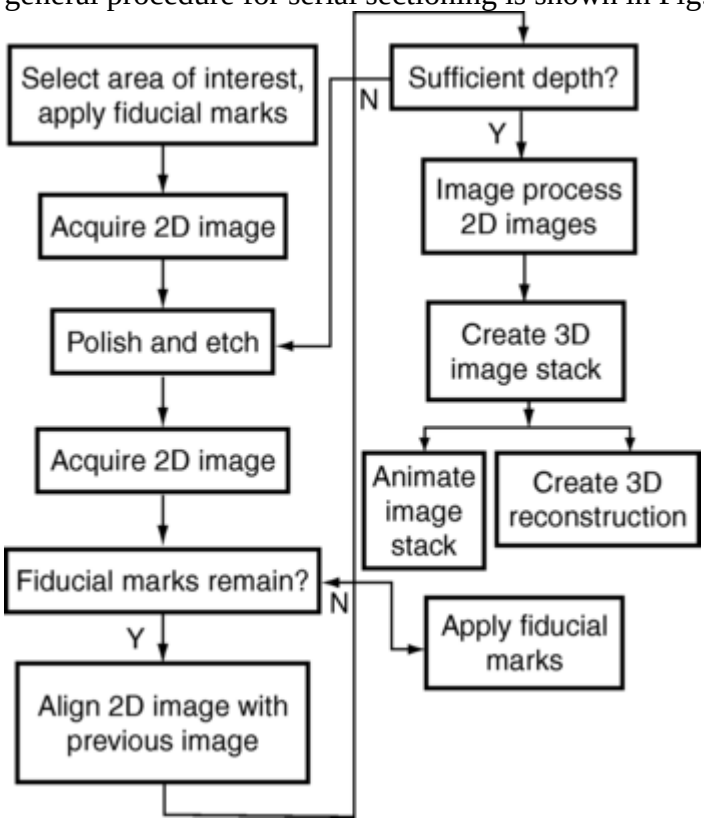

Fig. 1 The serial-sectioning process flow chart

Etching. Some materials require etching to obtain sufficient contrast between phases subsequent to the removal of each layer. Potential problems include inconsistent etching between layers, boundaries that do not respond to the etchant due to their orientation, and etching artifacts such as pits due to overetching. It is essential that subsequent polishing steps remove all pits to prevent the pitting from continuing or even accelerating.

Imaging. Digital optical micrographs can be acquired via video cameras with approximately 300,000 pixels as well as digital cameras with megapixel image size. Film is no longer a practical alternative. As digital cameras improve their resolution, a compromise must be obtained between the requirement for additional information and the size of the volume data set acquired (the number of pixels per image multiplied by the number of images). There are a number of digital cameras now available specifically for optical microscopy from manufacturers such as Olympus, Zeiss, and Diagnostics Instruments. Scanning electron microscopes may also be used, although with a considerable increase in the time required to remove and insert the sample into a vacuum chamber for each section. It should also be noted that the pixels in a SEM may not be square, and unless there is a calibration or correction for the pixel aspect ratio, the sample must be placed into the SEM chamber in the same orientation for each section to make subsequent registration more convenient. Obviously, the resulting 3D images will be distorted without a calibration or adjustment of pixel aspect ratio.

Fiducial Marks. With manual or semiautomated polishing or grinding, fiducial marks such as microhardness indents are often necessary to mark the area of interest, to align (or register) images in the *x*-*y* plane, and to track the actual material-removal rate. Prior to the commencement of actual image acquisition, the material-removal rate may be calibrated by measuring the change in the diagonal length of an indent when the indent diagonal-to-depth ratio is known. Figure 2 illustrates that fiducial hardness indents must be renewed at intervals.

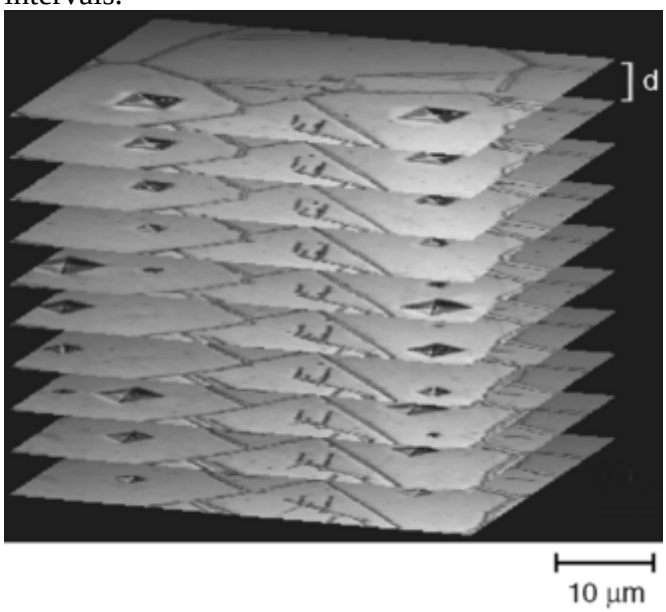

Fig. 2 A stack of serial sections showing the fiducial hardness indents

Sectioning Increment and Number of Sections Required. In studies of grain shape and size in a single-phase polycrystalline material, Rhines et al. (Ref 19) recommended using a magnification sufficient to show several grains simultaneously and sectioning to a depth of about twice the span of the largest grain in about 250 sections. In the general application of this rule of thumb, one must take into account the scale of the features being studied and the limitations of the material-removal technique being used. The resolution of the final 3D representations in every serial-sectioning project to date has been limited by the thickness of each serial section layer. This compromise is due, at least in part, to the total amount of manual labor involved and the problems of storing and properly registering the images once they had been obtained. Solutions for reducing the amount of labor required were to microtome (Ref 14) or micromill (Ref 5) or to avoid sectioning altogether (Ref 6, 11). Regarding the computational challenge, consider that 250 images captured at 640 by 480 pixels resolution (low resolution by current standards) result in a 3D image of 75 megabytes for gray-scale images (8 bits/pixel). Typical gray-scale image file sizes are currently approximately 1 to 2 megapixels. One method of quickly capturing larger areas at a useful magnification is to automatically montage (Ref 20), but again this quickly multiplies the overall size of the 3D data set.

Registration. The importance of proper alignment through the use of fiducial marks has been previously demonstrated (Ref 21). Alignment, or registry, of serial sections can be performed manually by overlaying fiducial marks in subsequent images using common image-processing software (e.g., Adobe Photoshop or NIH Image). Fiducial marks such as microhardness indents are also used to determine the distance between sections, *d*, as shown in Fig. 1. If the sectioning depth is known, it may be faster to align automatically using microstructural features of individual cross sections either before or after an image is acquired (Ref 22).

Three-Dimensional Reconstruction Software. There are a number of computer software packages currently available for 3D reconstruction and visualization of 3D data. Some programs are “shareware” (e.g., NIH Image or etdips), while others are commercially available (e.g., Interactive Data Language, Advanced Visual Systems' AVS Express or Vaytek's VoxBlast). Some researchers have chosen to develop their own software (Ref 18). There are many options available within any given computer program to enhance the appearance or utility of the 3D images. These options are discussed later in this article.

References cited in this section

5. T.L. Wolfsdorf, W.H. Bender, and P.W. Voorhees, The Morphology of High Volume Fraction Solid-Liquid Mixtures: An Application of Microstructural Tomography, *Acta Mater.*, Vol 45 (No. 6), 1997, p 2279–2295

6. B.J. Inkson, M. Mulvihill, and G. Möbus, 3D Determination of Grain Shape in a FeAl-Based Nanocomposite by 3D FIB Tomography, *Scr. Mater.*, Vol 47 (No. 7), 2001, p 753–758

11. R.H. Hopkins and R.W. Kraft, A Rapid Technique for Observation of Three-Dimensional Microstructures, *Trans. AIME*, Vol 233, 1965, p 1526–1532

14. P.M. Ziolkowski, *The Three Dimensional Shapes of Grain Boundary Precipitates in a/b Brass*, Michigan Tech., 1985

18. M.A. Mangan, P.D. Lauren, and G.J. Shiflet, Three-Dimensional Reconstruction of Widmanstatten Plates in Fe-12.3Mn-0.8C, *J. Microsc.*, Vol 188, Oct 1997, p 36–41

19. F.N. Rhines, K.R. Craig, and D.A. Rousse, Measurement of Average Grain Volume and Certain Topological Parameters by Serial Section Analysis, *Metall. Trans.*, Vol 7A, 1976, p 1729–1734

20. A. Tewari, A.M. Gokhale, and R.M. German, Effect of Gravity on Three-Dimensional Coordination Number Distribution in Liquid Phase Sintered Microstructures, *Acta Mater.*, Vol 47 (No. 13), 1999, p 3721–3734

21. J.C. Russ, *Image Processing Handbook*, CRC Press, 1994

22. J. Alkemper and P.W. Voorhees, Quantitative Serial Sectioning Analysis, *J. Microsc.*, Vol 201, 2000, p 1–8

M.V. Kral, G. Ice, M.K. Miller, M.D. Uchic, and R.O. Rosenberg, Three-Dimensional Microscopy, *Metallography and Microstructures,* Vol 9, *ASM Handbook,* ASM International, 2004, p. 448–467

M.V. Kral, University of Canterbury, Christchurch, New Zealand; Gene Ice and M.K. Miller, Oak Ridge National Laboratory; M.D. Uchic, Wright-Patterson Air Force Research Laboratory; R.O. Rosenberg, Naval Research Laboratory

Serial-Sectioning Case Study Examples

Every serial-sectioning study that has been performed to date has been different from every other, either in its basic purpose or in the details of the experimental procedure or the way the 3D data has been used to enlighten. The following nine case studies are intended not to be an exhaustive list, but to represent the work of the various research groups currently working on 3D microscopy using serial sectioning and to illustrate the variants of the basic experimental techniques. These case studies are based on papers available in the open literature and are fully referenced if further information is desired.

Example 1: Proeutectoid Cementite (Ref 3). The purpose of the study was to characterize the 3D morphology, distribution, and connectivity of proeutectoid cementite precipitates in a hypereutectoid steel (Fe-1.34%C-13.0%Mn alloy). The alloy was vacuum induction melted and hot rolled by LTV Steel Company of Independence, OH. A 20 by 20 by 80 mm (0.8 by 0.8 by 3 in.) bar was cut from the as-received plate, sealed in a quartz tube backfilled with $\frac{1}{3}$ atmosphere of argon at room temperature, and homogenized for three days at 1100 °C (2010 °F). Specimens approximately 5 by 5 by 5 mm (0.2 by 0.2 by 0.2 in.) were cut from the homogenized bar and rapidly solidified using an electromagnetic levitation/splat quenching apparatus (Ref 23) to refine the initial austenite grain size. The purpose of refining the austenite grain size to approximately 25 μm (1 mil) was to allow entire matrix austenite grains to be completely sectioned through using sectioning increments fine enough (~0.2 μm) to allow enhanced resolution, facilitating 3D reconstruction of entire austenite grains and groups of cementite precipitates within these grains. The splat-quenched specimens were austenitized for 30 s at 1100 °C (2010 °F) in a deoxidized barium chloride salt bath, isothermally reacted at 650 °C (1200 °F) in stirred, deoxidized lead baths for times ranging from 1 to 50 s to form the cementite precipitates, and finally quenched in room-temperature brine to halt the cementite transformation. Isothermal transformation at 650 °C (1200 °F) for 50 s produced an adequate number of cementite precipitates of appropriate size and was selected for the 3D analyses shown in the present work. A typical microstructure for this heat treatment is shown in Fig. 3. A 3 mm (0.12 in.) diam specimen was mechanically punched, ground, and mounted on a VCR Dimpler platen. Each layer was polished with a 0.06 μm (2.4 μin.) silica slurry using a 7 mm (0.3 in.) wide, 25 mm (1 in.) diam “flatting” tool covered with a Buehler Texmet cloth. Control of the sectioning depth was achieved through calibration of polishing load and time. The polished surface of each layer was lightly etched with 4% nital.

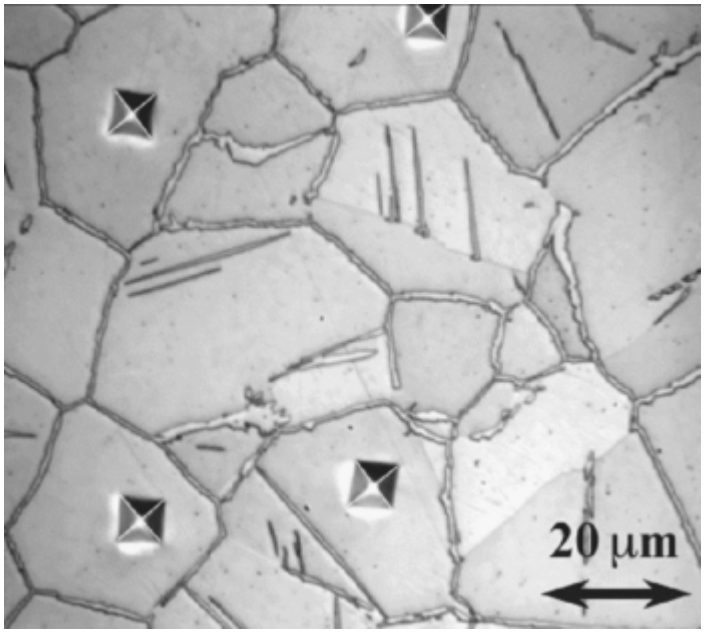

Fig. 3 Typical optical micrograph of an isothermally transformed Fe-13Mn-1.3C alloy showing proeutectoid cementite precipitates. Source: Ref 3

Fiducial hardness indents were applied using a Buehler Micromet II hardness tester with a Vickers hardness indenter at a 10 g (0.4 oz) load. Optical microscopy was performed at a magnification of 1000× using an oil immersion objective lens, with digital acquisition of video images using PGT Imagist image analysis software on a Sun SPARC station 5 computer. The images were "registered" with respect to each other in the plane of the image by aligning the hardness indents using Adobe Photoshop version 3.0 on a Power Macintosh 7200/120 personal computer. Thickness increments were calculated from the known indenter diagonal-to-depth ratio by measuring the change in diagonal length of the hardness indents after each polishing step. It was assumed that each successive polishing plane was parallel. Four overlapping areas encompassing a total of approximately 150 by 180 μm (6 by 7 mil) were documented for each of 250 layers with an average spacing of 0.17 ± 0.07 μm (6.7 ± 2.8 μin.) between layers. NIH Image software was used to store and view the resultant four "stacks" of TIFF images as video sequences that "step through" the microstructure slice by slice.

Each stack of TIFF images was saved to separate files using NIH Image's Stacks Macro, "Save Slices as files …" The separate TIFF images were then converted to ASCII Portable Pixel Map (PPM) images and concatenated to a single file, resulting in a uniform volumetric data set. AVS 5.5 on a Silicon Graphics Onyx workstation was used to read in these ASCII datasets, filter, and render them as isosurfaces and ray-traced images. Spot noise was removed using a "Median" image-processing filter with a 5 by 5 pixel cross-structuring element.

In this case, the austenite and the etched boundaries between austenite and cementite were easily distinguished by the different gray-scale value ranges of their pixels. The austenite matrix gray-scale values ranged from 0 to 100, and the etched boundaries were over 100 thus allowing a threshold to be set to automatically differentiate one phase from the other. After inverting the image, assigning translucency to the austenite phase, and assigning a large opacity value to the etched boundary between the cementite and austenite phases, ray-traced images were generated using a gray-scale, histogram-equalized color map along with Phong shading in order to best bring out the details of the surface. This gives the appearance of opaque cementite precipitates. The opacity is a linear ramp from low to high pixel intensity. A single, uninterpolated ray-traced image requires about 10 s of CPU time on an SGI Onyx 1 (R10K processor) to complete. A series of ray-traced images can be generated to produce an animation of the microstructure as it is rotated about any axis.

Alternatively, isosurfaces are generated using the standard Marching Cubes algorithm. The exact isosurface value used is selected to be the average voxel intensity of the data set. A simple Gouraud lighting model was used to shade the isosurfaces along with employing depth cuing. Surface- or volume-rendered models offer the capability of "real-time" manipulations on computer-display devices that can take advantage of "stereo" images, giving the visual impression of 3D objects in space.

The dimensions of individual precipitates were directly measured by digitally removing obstructing features (i.e., hardness indentations and overlapping precipitates) from a series of images and then projecting the resultant stack of images onto a projection plane using NIH Image version 1.61 software on a Power Macintosh 7200/120 personal computer. The length, width, and thickness of more than 200 individual precipitates were measured from appropriately rotated projected images with a calibrated scale. The length was taken as the maximum dimension of the precipitate when rotated into plan view. The width was the largest dimension perpendicular to the length. The thickness was the maximum dimension measured with the precipitate rotated to an edge-on orientation. An error of approximately ±0.4 μm (±15.7 μin.) was introduced by the apparent thickness of the etched boundaries of each precipitate and by the resolution of the image (approximately 5 pixels/μm).

Also, even with light etching, etch pits were often formed over the course of 250 sections, making subsequent image processing more difficult. Nevertheless, at least 20 entire grains and more than 200 precipitates were completely sectioned. A 3D reconstruction showing a portion of a representative grain is shown in Fig. 4, and a precipitate selected from this grain is shown in Fig. 5. The ability to digitally remove individual precipitates for study enabled the measurement of each precipitate in three dimensions. Among other results, it was observed that all precipitates were either connected to an austenite grain boundary or another cementite precipitate. Also, in addition to grain-boundary precipitates there appeared to be only two distinct types of Widmanstätten precipitates, those with relatively large length-to-width aspect ratios made up of several subunits (lathlike) and those with relatively small aspect ratios (platelike). Thus the Dubé morphological classification system (Ref 24, 25) was simplified from nine types to only three for proeutectoid cementite.

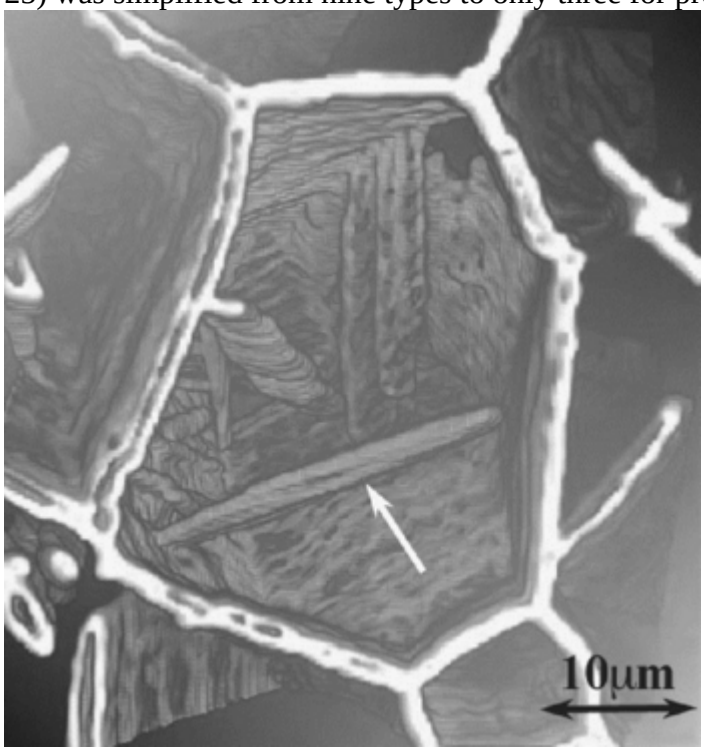

Fig. 4 Three-dimensional reconstruction of proeutectoid cementite precipitates in an isothermally transformed Fe-13Mn-1.3C alloy. Arrow indicates precipitate selected from grain for imaging in Fig. 5 Source: Ref 3

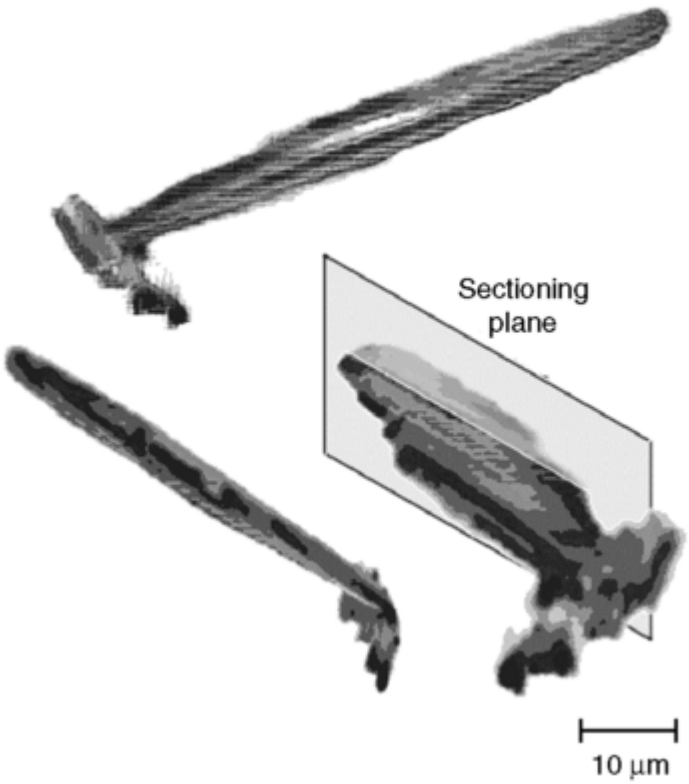

Fig. 5 Three perspective views of the Widmanstätten cementite precipitate indicated by an arrow in Fig. 4 Source: Ref 3

Example 2: Proeutectoid Ferrite (Ref 26). The purpose of the study was to characterize the 3D morphology, distribution, and connectivity of proeutectoid cementite precipitates in a Fe-0.12%C-3.28%Ni alloy. Homogenized specimens of the alloy were austenitized for 30 s at 1100 °C (2010 °F) in a deoxidized barium chloride salt bath, isothermally reacted for 2 to 3 s at 650 °C (1200 °F) in deoxidized lead baths, and then quenched into iced brine. This produced a structure of proeutectoid grain boundary and Widmanstätten ferrite in a martensitic matrix. The serial-sectioning and 3D reconstruction procedures were identical to the aforementioned except that a Buehler Minimet was used to polish the material, and picral and nital were used as etchants. A “motion-picture” sequence of serial sections was produced. Individual precipitates were reconstructed by cropping and editing images to contain only regions of interest. The total number of sections was only 125, although this number of sections was sufficient to clearly reveal the shape and interconnectivity of several ferrite grains.

This study of proeutectoid ferrite precipitates revealed a different set of experimental challenges than the study of proeutectoid cementite. Most importantly, there was little difference between the gray-scale levels of ferrite/martensite boundaries and martensite/martensite boundaries. Also, the alloy responded variably to the etchant (picral). The final digital images did not allow automatic thresholding, and therefore extensive manual editing on the computer was required. A typical light optical micrograph of this material is shown in Fig. 6. It was shown that proeutectoid ferrite precipitates (unlike proeutectoid cementite, which quickly wets austenite grain boundaries almost entirely) were not necessarily all interconnected. Although proeutectoid ferrite forms preferentially at prior-austenite grain corners and edges, it is also distributed as isolated primary Widmanstätten sideplates along grain boundaries. The 3D rendering of several ferrite precipitates along a former austenite grain boundary shown in Fig. 7 illustrates this observation.

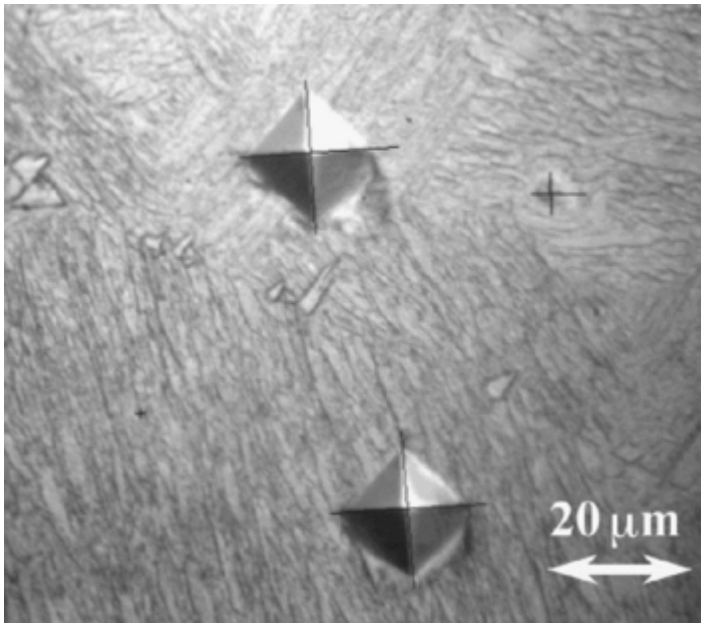

Fig. 6 Typical optical micrograph of an isothermally transformed Fe-3Ni-0.1C alloy showing proeutectoid ferrite precipitates. Source: Ref 26

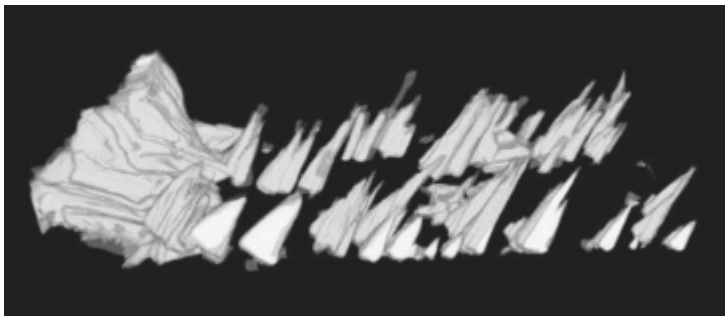

Fig. 7 A three-dimensional reconstruction of the ferrite precipitates shown in Fig. 6 taken from 113 sections spaced 0.3 mm apart in depth. Source: Ref 26

Example 3: Pearlite. Hillert (Ref 9) and Lange undertook serial sectioning of an entire pearlite colony to study its true 3D morphology. An electrolytic iron was carburized, grain-boundary cementite was formed just above the eutectoid temperature, and the transformation to austenite was completed just below this temperature. The microstructure was polished and etched repeatedly after approximately 1 μm (40 μin.) had been removed. The micrographs were originally transferred to a motion-picture film. Recently, the 241 original micrographs were digitized and processed for 3D reconstruction as shown in Fig. 8 (Ref 27). There were some challenges to the 3D reconstruction of this data set. First, there were no consistent fiducial marks with which to carry out translation/rotation registry between successive images. Occasionally, etch pits could be used to align subsequent images, but when etch pits were not available it was assumed that the colony boundaries and individual lamellas remained in the same relative orientation between slices. Second, there was no way to calibrate exactly the thickness of each section, reported to be approximately 1 μm (40 μin.). Finally, as with all materials, contrast between phases was variable. Extraneous data, such as etch pits, uneven gray-scale levels, and scratches were removed by manual editing using image-processing software such as Adobe Photoshop or NIH Image, while missing boundaries often had to be added. During image processing, some information was lost. For example, although not the focus of this study, the ferrite subboundaries arrowed at the top center of Fig. 1(a) are missing from Fig. 1(b). Viewing 3D reconstructions of all 241 sections at once has marginal utility because there is too much information to be seen at one time without confusion.

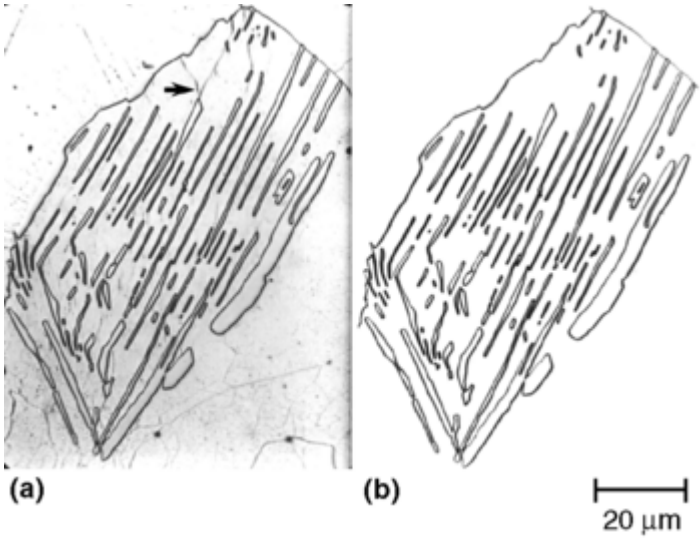

Fig. 8 Original optical micrograph of pearlitic iron by Hillert (Ref 9) and Lange showing an example of the difference between a preprocessed image (a) and a postprocessed image (b). Source: Ref 27

Reducing the number of slices shown, as well as cropping the dimensions of individual images, results in more meaningful 3D images such as Fig. 9. Even with a reduced data set (cropped from 713 pixels by 851 pixels by 241 sections to 236 by 280 by 160), it becomes difficult to understand the 3D morphology of this colony without viewing multiple perspectives. (Note: Scale markers are not given for the 3D reconstructions of pearlite because the images have been compressed in the thickness dimension. Each volume picture element, or voxel, is 0.29 μm, or 11.4 μin., in the *x*-*y* plane and 1 μm, or 40 μin., in the *z*-direction (the sectioning thickness). The reconstruction software used here requires cubic voxels; therefore the *z*-dimension was scaled down by a factor of 3.4. In the case of pearlite, the 3D shape of a colony is not as much of an issue as the connectivity and shapes of individual lamellas within a colony. Hillert and Lange's work showed that lamellas within a pearlite colony have extensive branching and are all interconnected. On reviewing any of their 241 optical micrographs individually, there appear to be many isolated cementite precipitates. However, by stepping through the image sequence back and forth, following precipitates as they branch out and intertwine, it can be shown that nearly every portion of the colony is somehow connected to the main branches that bound the lower portions of Fig. 1. NIH Image software is convenient for tracking and marking features directly on the image files so that the general interconnectivity of lamellas quickly becomes apparent. However, there are individual lamellas for which the connection is nearly lost due to the relatively coarse sectioning increment such as shown in Fig. 10. Smaller precipitates than the one shown in Fig. 1 even appear to be disconnected from any other cementite, indicating that the sectioning increment was small relative to the smallest cementite precipitates.

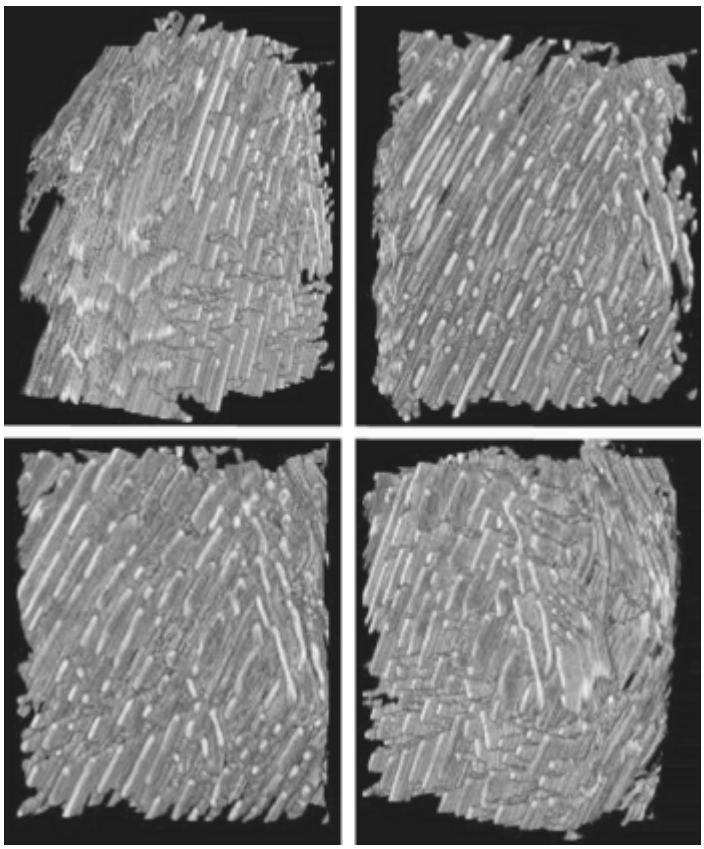

Fig. 9 Viewing several perspectives of a 3D reconstruction of a portion of a pearlite colony aids understanding the 3D morphology. Source: Ref 27

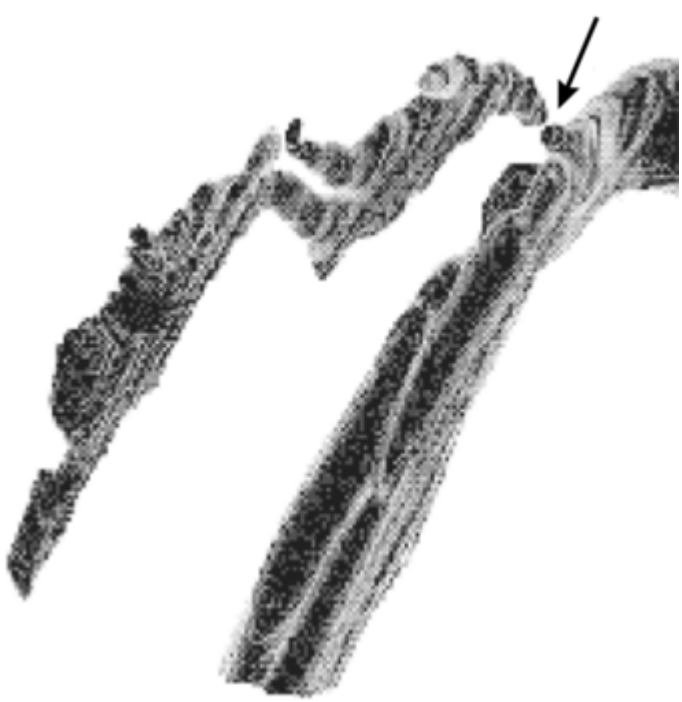

Fig. 10 Three-dimensional reconstruction of cementite lamellas in pearlite. Connections between lamellas are often too small to be resolved easily by optical microscopy. Source: Ref 27

In every serial-sectioning project, the sectioning thickness must be chosen based on a compromise between the scale of the microstructural features of interest and the number of sections that can be realistically obtained within a reasonable amount of time. Recent results (Ref 9) have confirmed Hillert's conclusions of interconnectivity (which likewise confirmed similar conclusions made by Forsman, Ref 8) by sectioning a smaller, less degenerate pearlite colony with proportionally smaller sectioning increments. Three-dimensional

reconstructions of individual lamellas were achieved by simply cropping or editing out all other features. In Fig. 11, two parallel lamellas change their apparent habit plane, twisting noticeably about their long-dimension axis. Among other possibilities, this apparent twisting could be a result of impingement or interaction with ferrite subboundaries. There are many other aspects of this 3D data set that will continue to be studied.



Fig. 11 Three-dimensional reconstruction of cementite lamellas in pearlite. The broad faces of these lamellas twist counterclockwise from the rear to the front of this perspective view. Source: Ref 27

Example 4: Aluminum Dendrites in an Aluminum-Copper Alloy. Alkemper and Voorhees (Ref 22) used a micromilling apparatus to obtain serial sections from a directionally solidified Al-15wt%Cu alloy. The experimental apparatus, shown in Fig. 12, allows one to take approximately 20 sections/h with interlayer spacings of 1 to 20 μm (0.04 to 0.8 mils). Because the sample remains attached to the micromiller at all times, the processing time is reduced dramatically over other serial-sectioning methods. The step height was measured using a profilometer and was shown to have a small systematic error from the set point of the Leitz Ultramiller. It has been shown that no translation between sections occurs in the *x*-direction, normal to the translation. The alignment of the cross sections in the *y*-direction was accomplished with a linear variable differential transformer (LVDT) and did not require the use of fiducial markers. The alignment procedure is illustrated in Fig. 13. Assume that the original image is 1000 by 1000 pixels, the *y*-direction positions do not vary by more than 50 μm (2 mils), there is a resolution of 1 μm/pixel and the LVDT measures within 0.5 μm (0.02 mil). A subset of images with which to form a stack can be created by deleting rows of pixels along the *x*-direction to produce a fully registered image without any intervention. In this case, the sections were 4.75 μm (0.19 mil) apart. A typical cross section is shown in Fig. 14. The resulting 3D microstructure is shown in Fig. 15. The mean and Gaussian curvatures of the interfaces were measured and used to better understand microstructural evolution of coarsening dendritic structures.

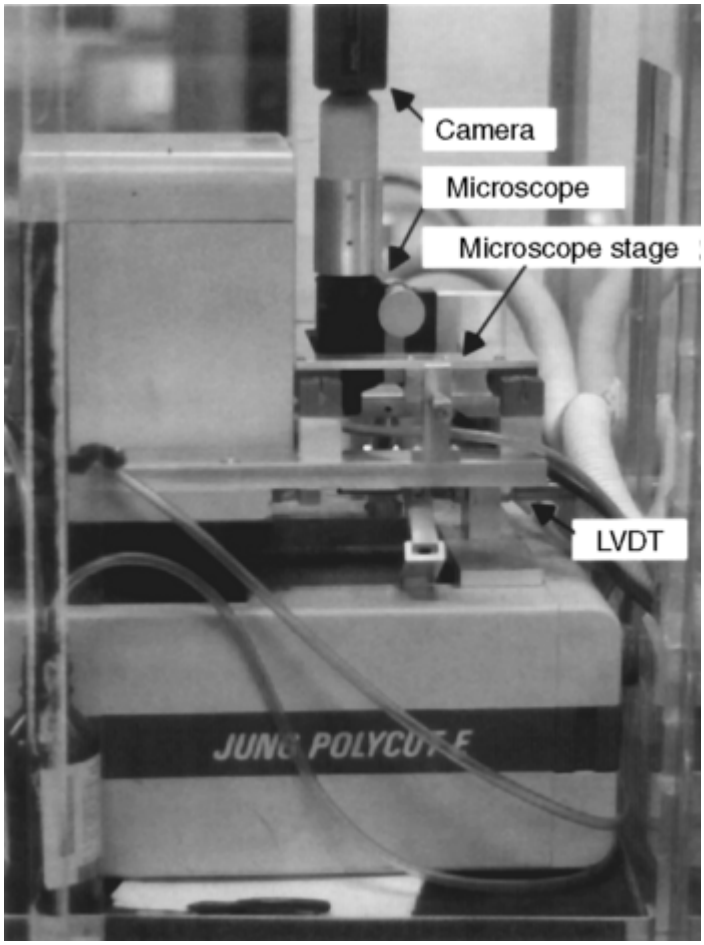

Fig. 12 Micromilling apparatus used for sectioning the aluminum-copper alloy. LVDT, linear variable differential transformer used to position the stage. Source: Ref 22

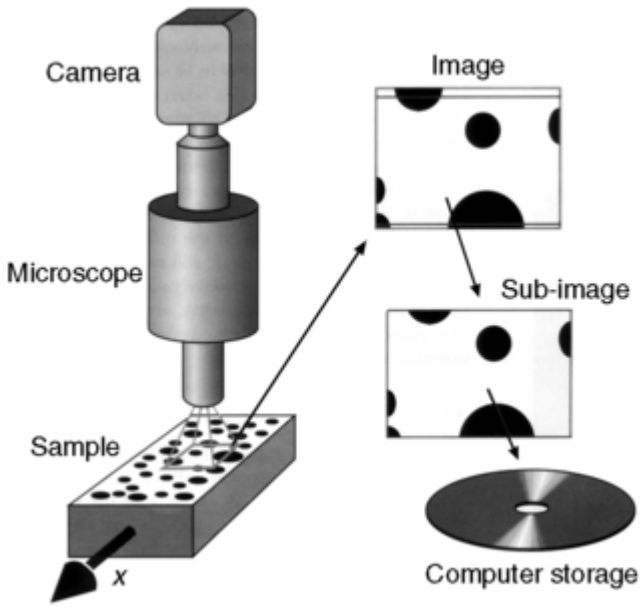

Fig. 13 Automated registration of images via a linear variable differential transformer (LVDT—not shown). The LVDT permits alignment of cross sections on the micromilling device without the need for fiducial markers. Source: Ref 22

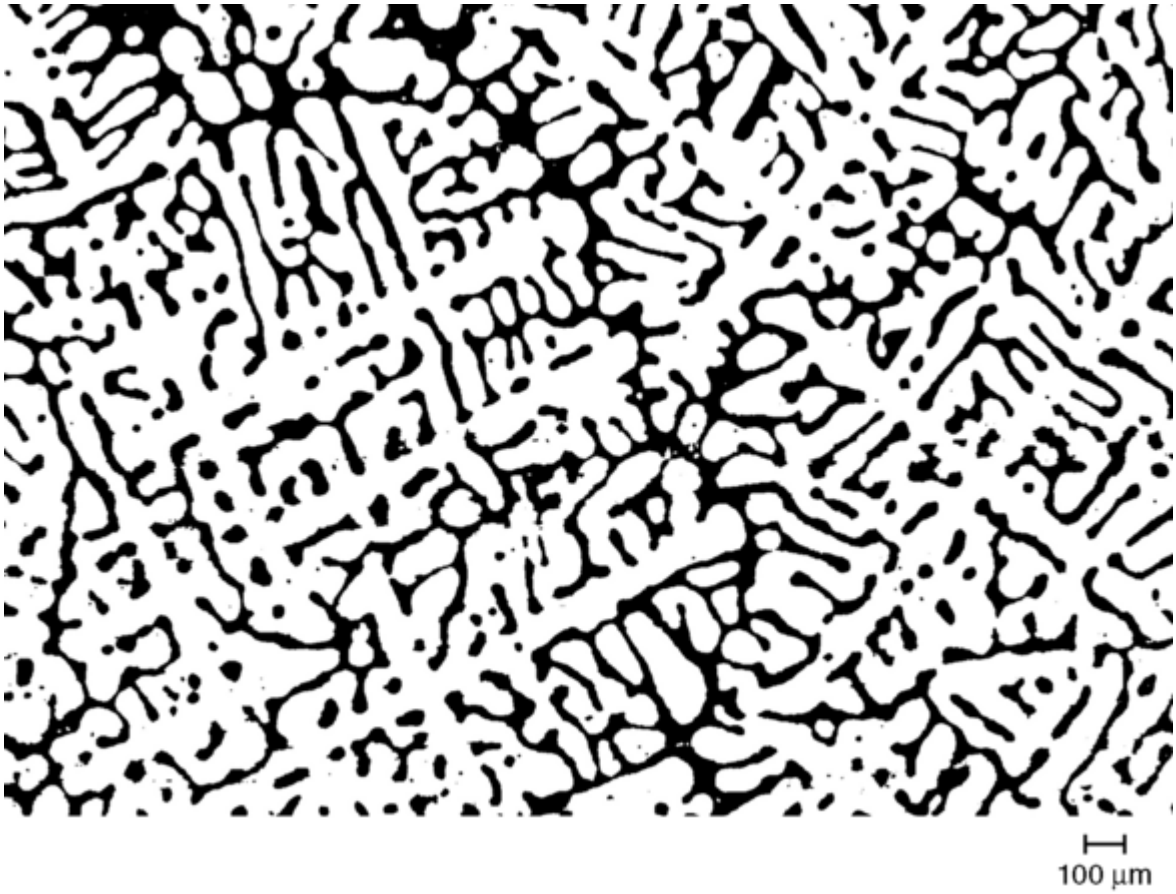

Fig. 14 A typical microstructure of an aluminum-copper alloy (coarsened for 10 min at 553 °C, or 995 °F) made binary to differentiate between the proeutectic aluminum-rich dendrite and the eutectic. Source: Ref 22



Fig. 15 A three-dimensional reconstruction of an aluminum dendrite in an aluminum-copper alloy with the eutectic phase omitted for clarity. Source: Ref 22

Example 5: Gamma-Prime Precipitates in a Nickel-Base Alloy (Ref 2). The composition of the alloy investigated was Ni-24.0Co-5.0Cr-2.5Mo-4.0Al-4.0Ti by weight percent. The molybdenum content of the alloy was adjusted to yield nonequiaxed rectangular-parallelepiped-shaped particles large enough to be studied by serial sectioning. The alloy button was solution treated at 1200 °C (2190 °F) for 135 h, and quenched into iced brine. Following the solution treatment, a portion of the alloy button was sectioned off and heat treated for 141.7 h at 1050 °C (1920 °F) to achieve the final microstructure investigated in this experiment. The heat treatment time and temperature were chosen so that distinctly nonspherical and noncuboidal particle morphologies were present in the microstructure. At longer heat treatment times on the same alloy the particles were observed to be incoherent with the particle/matrix interfaces no longer parallel to the ⟨100⟩ crystallographic directions. The γ′ volume fraction of the alloy following heat treatment was 0.272. The heat treated specimen was polished using to a 0.05 μm (2 μin.) alumina suspension and then marked with a series of Knoop hardness indents that were used both to realign one section with another and to measure the polishing depth. As serial sectioning proceeded, these hardness indents needed to be periodically replaced as the cumulative polishing depth approached the depth of the indent.

The serial sectioning consisted of repeatedly polishing, etching, and imaging the specimen surface. The polishing was performed in an automatic polisher to ensure repeatability of the polish. The hardness indents used to measure the depth of the polish were protected from the etchant to ensure that etching effects did not confound the measurements. The polish was deeper than the depth of matrix material removed during the etching procedure, so measuring unetched hardness indents provided a reasonable measure of the polishing depth of the etched region. The polishing depth was 0.078 ± 0.018 μm (3 ± 0.7 μin.) per polish over 46 polishes. Very little deviation was observed in the direction normal to the sectioning plane, a total of approximately 0.005° over the course of the experiment. After each polish, the area of the specimen to be imaged was electrolytically etched in a mixture of 17 parts deionized water, 1 part glacial acetic acid, and 2 parts nitric acid for 8 s at 2 V. This area was then imaged using a Hitachi S4500 SEM. Since the sample had to be remounted in the SEM after each polish and etch, alignment of the sections with one another was necessary. This alignment was achieved using additional hardness indents placed within the field of view of the recorded area. The image was then cropped to the desired viewing area and made binary. The 2D SEM images were combined into a volume measuring 11.33 by 11.33 by 3.6 μm (446 by 446 by 141 μin.), with a resolution of 0.025 μm (1 μin.) within the imaging plane and a resolution of 0.078 μm along the polishing direction. It was not possible to reconstruct reasonably smooth γ-γ′ interfaces with such a large difference in resolution between the lateral and polishing directions, and thus the resolution in the lateral directions was reduced by a factor of two before rendering the interfaces. Due to the small γ′-interparticle separation distances, artificial bridging occasionally occurred between precipitates in the reconstructed images after this reduction in resolution. As this bridging is not present in the higher-resolution lateral directions, and thus is a known artifact of the reconstruction process, such bridges are ignored in the analysis of the 3D microstructure.

A 2D cross section of the γ-γ′ microstructure is shown in Fig. 16(a). If the serial sections are taken on {100} planar sections, the particle cross sections on consecutive sections are relatively constant and the end of the particle is abrupt, making it difficult to determine the particle dimensions in the sectioning direction. On serial non-{100} planar sections the particle cross sections change gradually with each section, and the endpoint can be reasonably interpolated from this gradual evolution. Thus, the reconstruction plane was intentionally chosen not to be a {100} section of the microstructure.

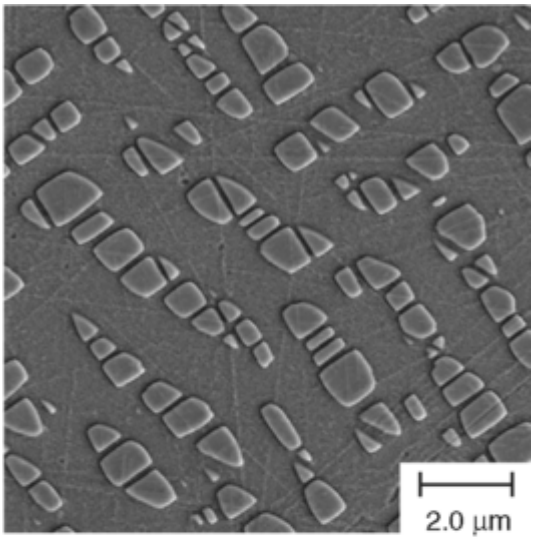

Fig. 16 An example of the 2D cross sections of the microstructure showing γ′ precipitates in a Ni-24.0Co-5.0Cr-2.5Mo-4.0Al-4.0Ti (wt%) alloy, solution treated at 1200 °C (2190 °F) for 135 h, quenched into iced brine, and heat treated for 141.7 h at 1050 °C (1920 °F). The scanning electron micrograph, (a), and the binary image after processing, (b). Source: Ref 2

For the digital reconstruction, each picture was converted into a binary image so that the matrix and particle phases could be easily differentiated. An example of this is shown in Fig. 16(b), which is the binary image obtained from Fig. 16(a). As mentioned earlier, despite the small interparticle separation distances there are no connections between the particle cross sections evident in Fig. 16. This is characteristic of all of the 2D planar sections of the microstructure.

In the 3D images in Fig. 17, the matrix has been made transparent, and the surfaces of the γ′ particles are represented in metallic gray. As this is a 2D projection of a 3D volume, a traditional scale bar is not appropriate. Instead, the volume has been framed in a box of known dimensions, and these dimensions are reported to give the approximate scale of the shown microstructure. Some of the characteristics of the 3D γ-γ′ structure can be seen in Fig. 17. The particles align with each other in three dimensions along the three 〈100〉 crystallographic directions. From the viewing angle in Fig. 17(b), it becomes obvious that the particles in region B are aligned in 2D sheets that are perpendicular to the 〈100〉 direction along which no alignment appears to be occurring in Fig. 17(a). The separation distances between the sheets are far larger than the interparticle separation distances within the sheets and appear to be relatively constant. In Fig. 17(c), the microstructure has again been rotated, this time so that the sheets in region B are approximately parallel to the viewing plane, and the regions A, B, and C have again been labeled. From this viewing angle it can be seen that the alignment of

the particles into 2D sheets observed in region B is also occurring in regions A and C, but that the sheets in regions A and C are perpendicular to a different 〈100〉 direction than those in region B. The nature of this microstructure would not have been obvious from single 2D sections.

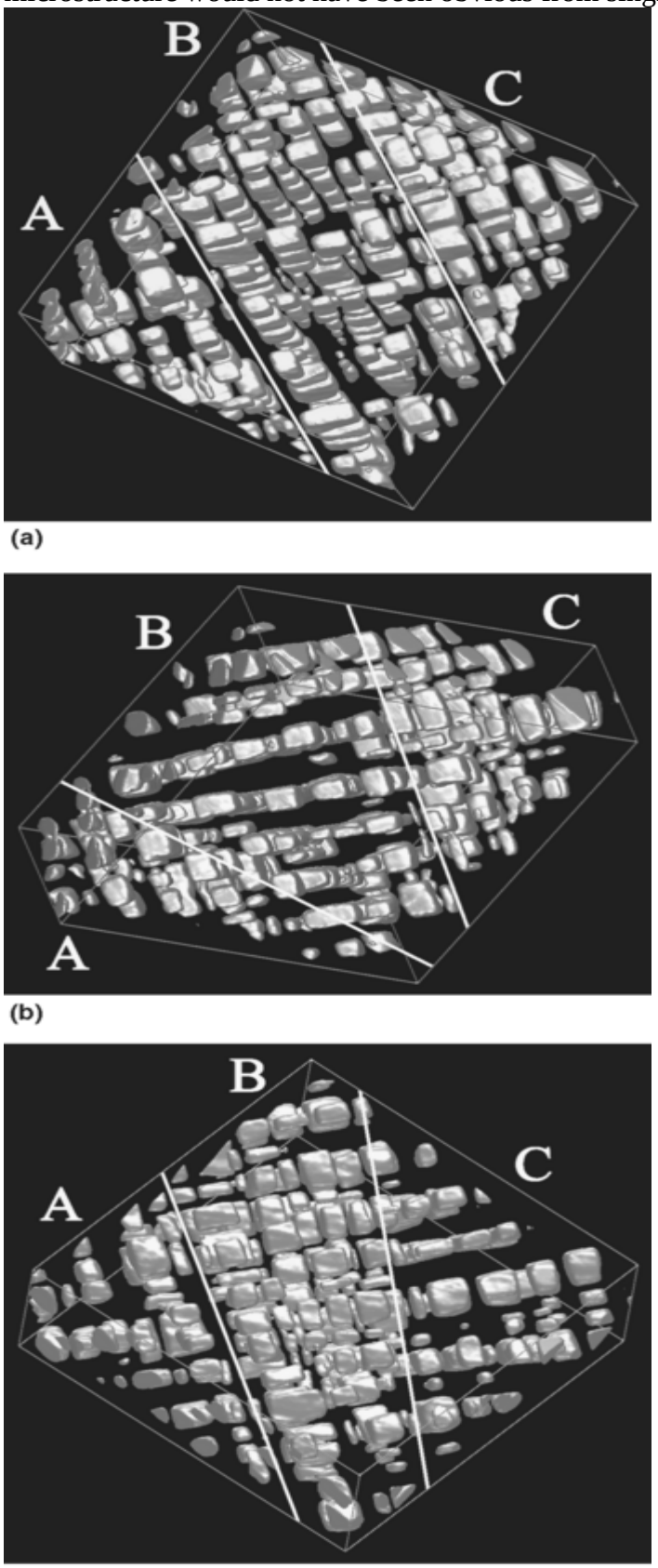

Fig. 17 A 10 × 10 × 3.6 μm (0.4 × 0.4 × 0.14 mil) portion of the reconstructed microstructure of γ′ precipitates in a Ni-24.0Co-5.0Cr-2.5Mo-4.0Al-4.0Ti (wt%) alloy at three different viewing angles. A, B, and C are regions described in the text. Source: Ref 2

Example 6: Intragranular Ferrite Precipitates (Ref 28). The Fe-0.1C-1.5Mn (mass%) alloy was melted in a vacuum induction furnace using electrolytic iron, high-purity carbon, and manganese. A considerable amount of sulfur, vanadium, and nitrogen were added to form VN and MnS and induce intragranular ferrite nucleation. Specimens of 0.01 by 0.01 by 0.0004 mm (0.4 by 0.4 by 0.016 μin.), machined from a hot-rolled plate and coated with antioxidation colloidal paint, were austenitized at 1250 °C (2280 °F) for 10 min under an argon atmosphere, isothermally reacted in a salt bath at 640 °C (1185 °F) for 40 s, and ice-brine quenched to form idiomorphic ferrite. The austenite grain size was about 200 to 300 μm (8 to 12 mils). The specimens were mechanically polished to remove 0.3 to 0.5 μm/section (12 to 20 μin./section). The amount of material removed was calibrated from the size of microhardness indents. The optical images of 200 to 250 sections were aligned and edited using image-processing software on a personal computer. A stack of these images were then transformed into a 3D image by means of visualization software (AVS) on a SUN work station (Ref 3). The size of 3D reconstructed volumes was typically 300 by 400 by 125 μm (12 by 16 by 5 mils). Ferrite idiomorphs were often composed of a few grains.

Figure 18 is an optical micrograph of a specimen reacted at 640 °C (1185 °F) for 40 s. MnS particles are observed as small dark dots (indicated by arrows). Figure 19 shows the distribution of MnS (red) and ferrite idiomorphs (white) in the sampling volume. It is noted that some ferrite idiomorphs are apparently not associated with inclusions. It is likely that a number of these ferrite particles may not have been completely reconstructed and may thus connect to inclusions that lie outside the reconstructed volume (the rectangular box in Fig. 1). These ferrite idiomorphs may also have been formed on undetectably small MnS particles and/or the MnS particles could have dropped out during polishing due to a larger thermal expansion coefficient of MnS as compared to that of ferrite.

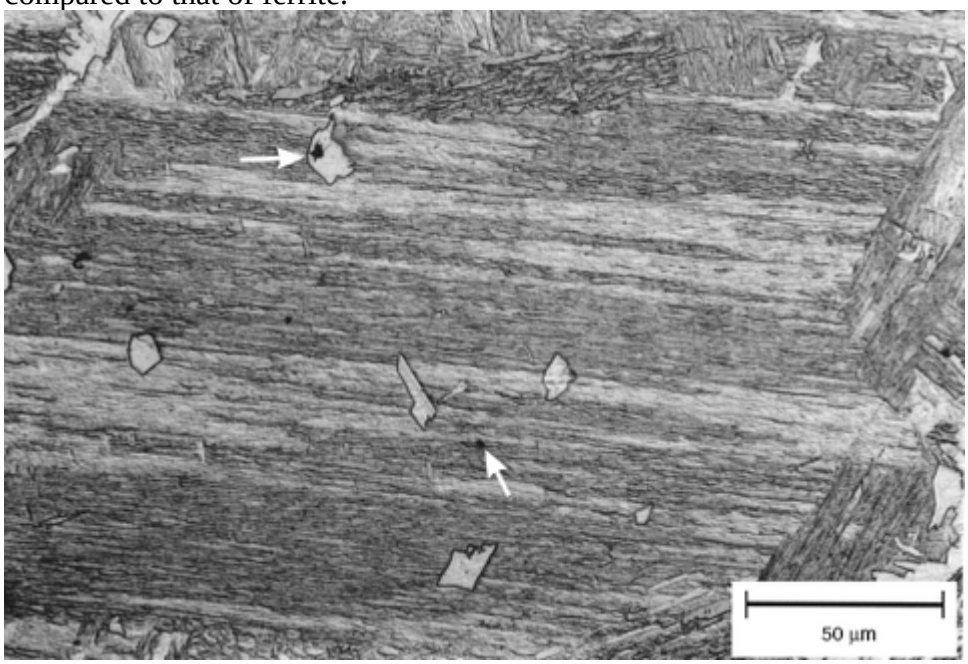

Fig. 18 Optical micrograph of intragranular idiomorphic ferrite formed in a Fe-0.1 C-1.5Mn (mass%) alloy specimen reacted at 640 °C (1185 °F) for 40 s. Source: Ref 28

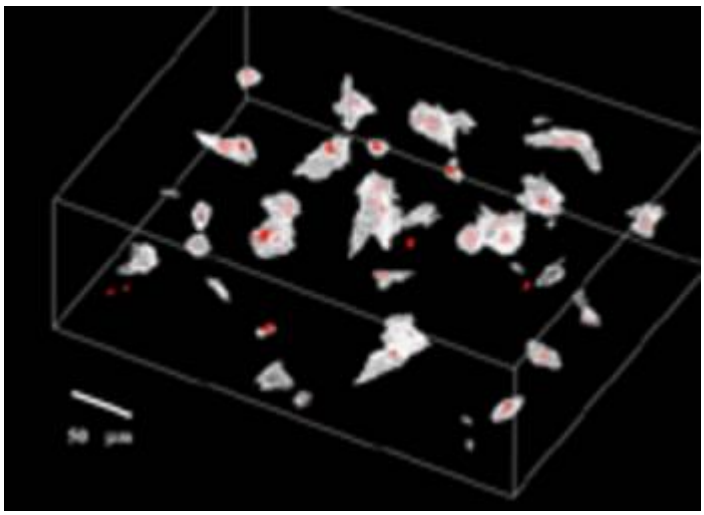

Fig. 19 Three-dimensional reconstruction showing the distribution and shapes of inclusions and ferrite particles formed at 640 °C (1185 °F) for 40 s in Fe-0.1C-1.5Mn (mass%) alloy. Source: Ref 28

Example 7: Distribution of MnS in Cold-Rolled and Annealed Ferrite (Ref 29). To investigate the effects of boundary pinning on grain growth in ferrite, a specimen of Fe-0.8Mn-0.03S (wt%) alloy was cold rolled 70% and annealed at 850 °C (1560 °F) for 48 h. A series of approximately 80 sections were taken with optical microscopy after the technique described earlier (Ref 28). Figure 20 and 21 (Ref 29) illustrate the distribution of MnS particles at the grain-boundary faces and interiors, respectively. A larger proportion of MnS particles are trapped by grain boundaries than calculated assuming random distribution. In addition, particles only a few hundred nanometers in size cannot be resolved.

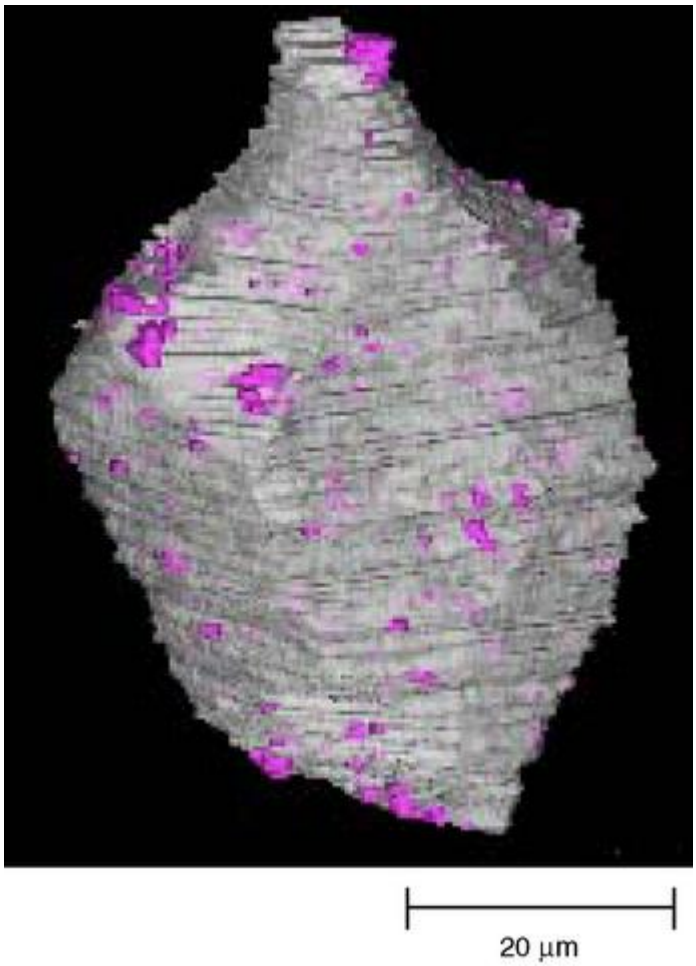

Fig. 20 Three-dimensional reconstruction showing the distribution of MnS particles located on grain boundaries in an Fe-0.8Mn-0.03S alloy. Source: Ref 29

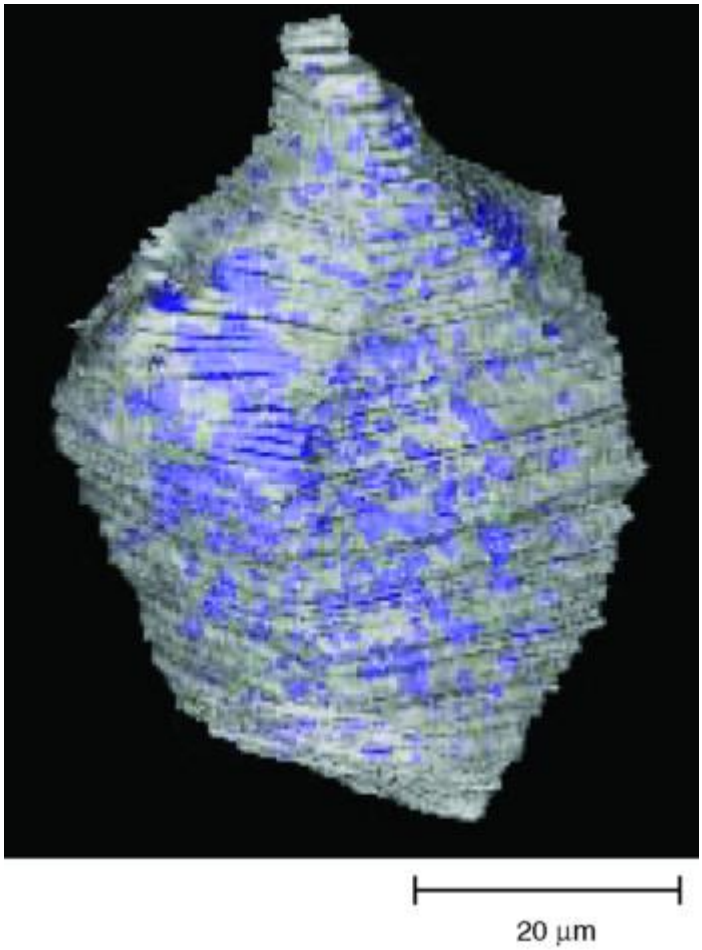

Fig. 21 Three-dimensional reconstruction showing the distribution of MnS particles located within grain interiors in an Fe-0.8Mn-0.03S alloy. The MnS particles are evident in this color version. Source: M. Uno and M. Enomoto, *Distribution of MnS Particles during Grain Growth of Ferrite,* Ibaraki University, 2002

Example 8: Grain-Size Distribution Measurements in a Liquid Phase Sintered Alloy (Ref 30). Grain-size distribution measurements were performed on a 83W-11.9Ni-5.1Fe (wt%) alloy specimen, liquid phase sintered at 1780 K for 1 min in a microgravity environment. The specimen was sectioned along central vertical plane containing gravity direction during presintering, and then it was mounted and polished with diamond polishing medium using standard techniques. For digital image analysis, good contrast between tungsten grains and the matrix was achieved by using interface-layering technique in which the sample was coated with a thin layer of platinum oxide by sputtering platinum on the sample kept in oxygen atmosphere. All metallographic measurements were performed in the region 1 to 2 mm from the "bottom" of the specimen. Figure 22(a) illustrates microstructure of the tungsten grains in this alloy. Observe that both tungsten grains and matrix have high topological connectivity, and they are almost cocontinuous. Therefore, the topological number density of tungsten grains is extremely low (zero for all practical purposes). The tungsten grains are connected to other grains by contacts known as "necks" (Fig. 22b). Each neck represents a boundary between two tungsten single crystals. In the present context, these single crystals are called "grains," and the size distribution of these grains (single crystals) is quantitatively characterized in the present investigation.

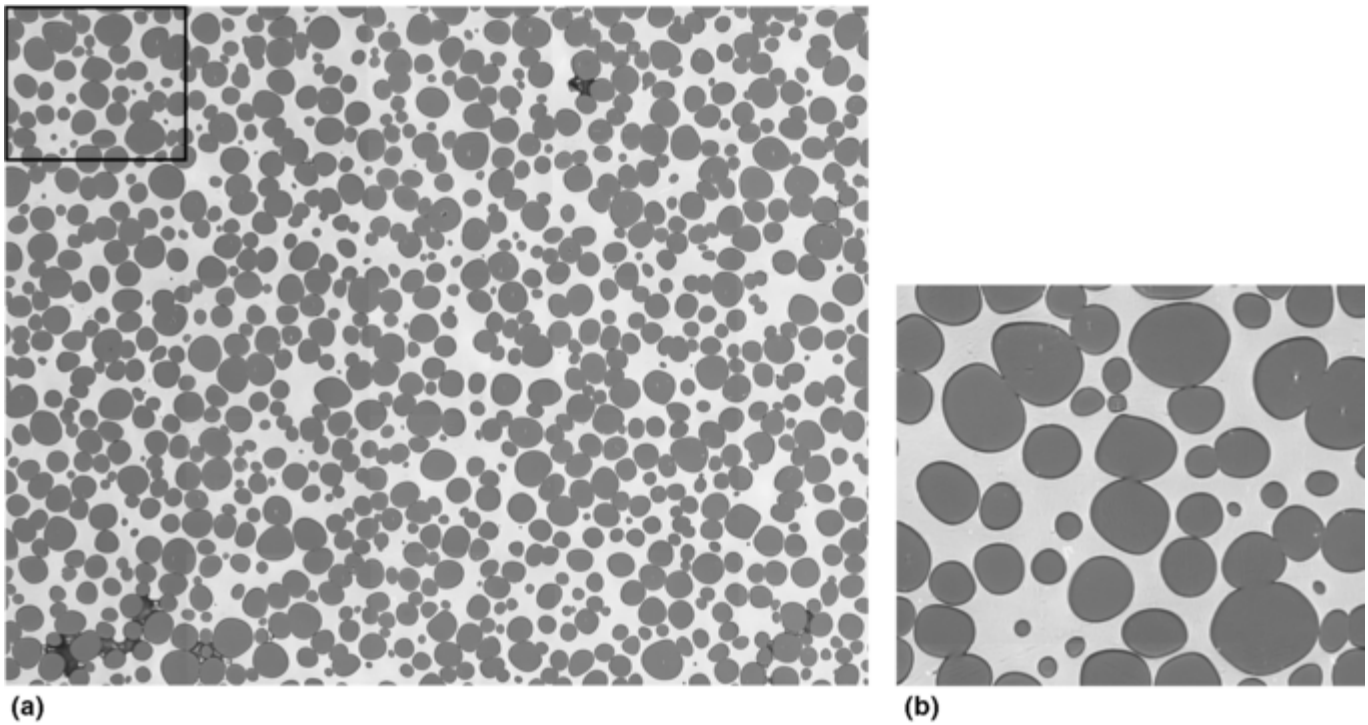

Fig. 22 Typical microstructure of an 83W-11.9Ni-5.1Fe (wt%) alloy specimen, liquid phase sintered at 1780 K for 1 min in a microgravity environment. (a) A montage of 25 microstructural fields, which is digitally compressed for display. (b) Each field of view (FOV) (e.g., PQRS) in montage (a) has the same resolution as that of the field shown here. Source: Ref 30

To generate a large volume of 3D microstructure at high resolution, one may first reconstruct a small microstructural volume such as the one in Fig. 23(a) and then reconstruct many contiguous small volumes surrounding it, perfectly match their boundaries, and paste them together to generate a large volume of 3D microstructure, as shown in Fig. 23(b). In the present work, first a "montage" of 25 (or more if necessary) contiguous microstructural fields observed at a high magnification (500× for the present microstructure) is created by using a large-area high-resolution montage procedure developed by Louis and Gokhale (Ref 31). To create the montage, a field of view (FOV) is arbitrarily chosen in the region of interest in the metallographic plane, and the image of this FOV is stored in the memory of the image analysis computer as an image file. The right border (of about 60 pixel width) of this image is recalled on the left edge of a blank image. This semiblank image is then displayed along with the live image. This results in a superimposed image on the left border of the screen (of the previous right border and live image) with the rest of the screen having the live image. The microscope stage is then moved so that the right border of the live image moves to the left border and gives a reasonable match with the superimposed image. The physical movement of the automatic stage has a large least count and thus cannot achieve a perfect match with the previous image. Therefore, small movements (to a least count of 1 pixel) of the live image are made manually using an image analyzer to achieve a perfect match. This results in a match of the first and the second images with an accuracy of 1 pixel (in the present case, the pixel resolution was 0.2 μm and microscope resolution was 1 μm). The second image is then stored in the computer memory as another image file. All successive contiguous images are grabbed by using the same procedure, and finally a seamless montage of a large number of contiguous microstructural fields is created. Figure 22(a) shows such a montage of 25 FOVs, which has been compressed for display. Each region of this montage has the high resolution of the image shown in Fig. 22(b). Therefore, montage is a microstructural image of a large area (25 FOVs at 500× magnification) having high resolution. The present montages contain about 1200 to 1500 tungsten grain sections. Once the montage of the first serial section is created and stored in the computer memory, small thickness of material is removed (about 1 μm) by polishing, and then a second montage is created at the region exactly below that in the first metallographic plane. In the present study, this polish-montage-polish procedure was repeated to obtain stack of 90 montage serial sections. Microhardness indents were used to locate the exact region of interest in successive serial sections and to measure the distance between consecutive serial sections. The 90 montage serial sections were then precisely aligned in the *z*-direction. Each montage serial section was stored in the computer memory as a separate image file. The effort involved in this

process of creating a stack of montage serial sections is comparable to that for creating the same number of conventional serial sections, but the montage microstructural volume is 25 times larger than that generated by the same number of conventional serial sections, and it contains a few thousand grains. Therefore, such a high-resolution large-volume segment can be used to quantitatively characterize the grain-size distribution in three dimensions with high precision.

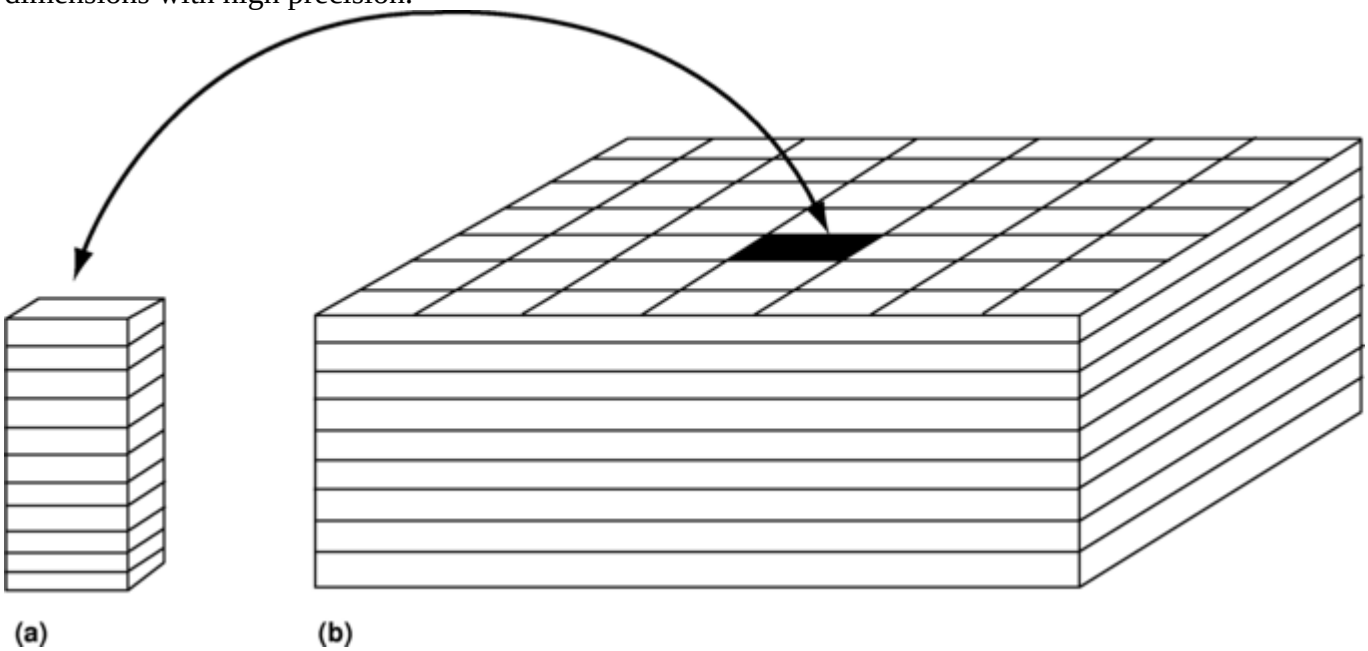

Fig. 23 (a) Volume generated by a stack of conventional serial sections. (b) Volume generated by a stack of montage serial sections. Source: Ref 30

Figure 24 shows a surface-rendered view of a segment of 3D volume generated from serial sections. This segment is about 5% of the total 3D microstructural volume generated from the montage-based serial sections. This specimen had about 61 vol% of liquid phase at the liquid phase sintering temperature. After inspecting a few thousand grains in the serially sectioned 3D microstructural volume, only one or two very small grains were observed to be completely isolated. To the best of the authors' knowledge, these are the first direct experimental measurements of a 3D grain/particle size distribution from serial sections of an opaque microstructure. Measurements of the 3D grain-size distribution (see Fig. 25) showed that the true grain-size distribution is quite broad. Grains sizes ranging from 1.5 to about 35 μm (0.06 to 1.4 mils) are present in the microstructure, and the average grain size is equal to 12.2 μm (0.5 mils).

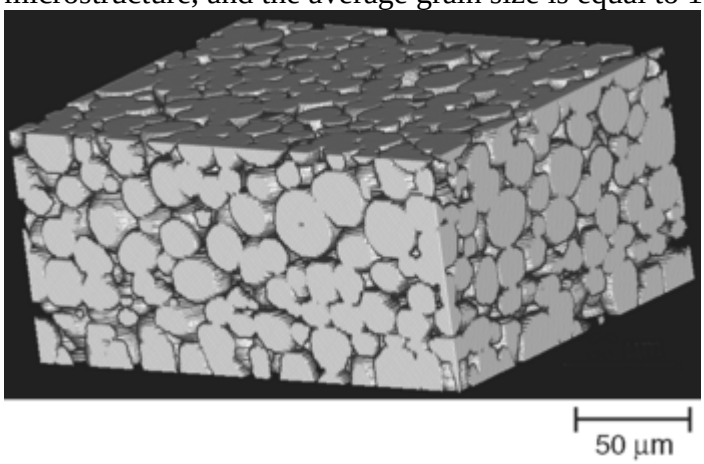

Fig. 24 Surface-rendered 3D microstructure of tungsten grains reconstructed from a stack of serial sections for specimens processed in microgravity for 1 min. This segment is about 5% of the total serially sectioned microstructural volume. Source: Ref 30

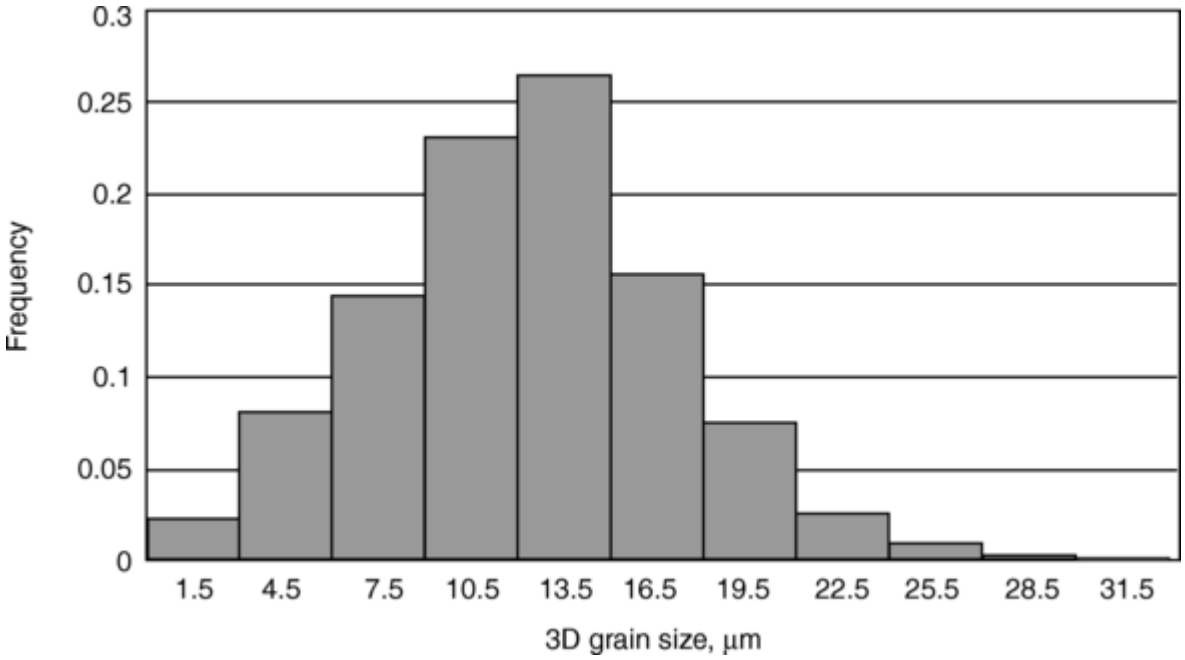

Fig. 25 The measured 3D size distribution of tungsten grains. Mean grain size is 12.2 μm (0.48 mil). Source: Ref 30

Example 9: Three-Dimensional Reconstruction of Ferrite Formed Below the Bay in an Fe-C-W Alloy (Ref 32). The limits of 2D metallography are encountered when less common, less regular structures are examined. These more complex microstructures can be revealed through the analysis and 3D reconstruction of serial sections. Degenerate ferrite found in a particular class of low-carbon steels is an example of a microstructure that requires such 3D methods. In all low-carbon steels, the decomposition of austenite at high temperatures begins with the nucleation and growth of allotriomorphic ferrite (with or without carbides) at austenite grain boundaries; it grows into the austenite with a more or less uniform growth front. At lower temperatures (but above the temperature at which martensite starts to form, M_s) the product morphology transitions to elongated forms identified as Widmanstätten structure. At these intermediate temperatures, most steels containing low to moderate amounts of alloy elements transform to grain-boundary nucleated Widmanstätten laths or plates that rapidly penetrate the interior of the austenite grains; the 3D shapes of these types of Widmanstätten ferrite are reasonably well understood.

This morphological transition is quite different in steels containing sufficient amounts of hardenability-enhancing alloying elements such as chromium, molybdenum, and tungsten. Firstly, it is coupled to the slow-to-fast kinetic transition found at a bay (local maximum) in the time-temperature-transformation (TTT) diagram start curve (other steels show only minor kinetic transitions). Secondly, the intermediate-temperature product is described as a degenerate form of the more ideal Widmanstätten ferrite laths and plates encountered in other steels. These forms of degenerate ferrite precipitate throughout the interior of the austenite grains; they are no longer confined to grain-boundary regions. The term “degenerate” encompasses not a single morphology, but instead a group of morphologies that can vary widely depending on alloy and heat treatment. Overall, degenerate ferrite connotes an image of a random and ill-defined microstructure with no obvious deference to crystallographic constraints. Although many explanations have been proposed to account for the occurrence of ferrite degeneracy in these steels (and the puzzling growth behavior of this product, Ref 33), the continuing lack of a 3D understanding of its morphology is one barrier holding back progress in this area. In response to this, serial sectioning and 3D reconstruction of degenerate ferrite formed in a well-characterized Fe-C-W alloy (Ref 34) was undertaken. Of specific interest are the connectivity and preferred growth directions of ferrite (if any).

A high-purity ternary Fe-0.30C-6.3W (wt%) steel was vacuum induction melted, hot rolled, and homogenized 3 days at 1200 °C (2190 °F) under argon. A specimen was encapsulated under argon, austenitized 30 min at 1200 °C (2190 °F) (in the single-phase austenite region), then isothermally transformed 10 min at 590 °C (1095 °F) (10 °C or 18 °F below the bay, Ref 34) and ended by a water quench. This heat treatment yielded a small amount of degenerate ferrite suitable for serial sectioning.

The specimen was mounted in Lucite (which resists repeated etchant attack) and then ground with abrasive paper in water, polished with 1.0 μm alumina, and etched in nital. Vickers microhardness (HV) indents were

placed in the martensitic regions (quenched from austenite) near the degenerate ferrite area of interest (Fig. 26). A micrograph of the ferrite and HV indents was then acquired with a digital camera attached to a metallograph; this is the first section. Serial sectioning provides adequate information for subsequent 3D reconstruction (which interpolates between sections) only when the vertical (depth) separation between successive sections is less than the length scale of the microstructural feature of interest. In this case, the degenerate ferrite subunits have a minimum dimension of roughly 1 μm (0.04 mil), necessitating submicron distances between sections. This was accomplished in a reproducible manner by polishing the specimen with 1.0 μm (0.04 mil) alumina in an automatic polisher for a fixed duration of 4 min; the polishing arm speed and pressure were held constant at moderate levels. This resulted in an average distance between sections of 0.127 μm (0.005 mil). After polishing, the specimen was etched and imaged like before; care was taken not to overetch, as the overetched state (having too much surface relief) will only get worse as it propagates down to later sections, given the small depth between sections. The sequence polish-etch-image was repeated until 81 sections were acquired, spanning a total depth of 10.3 μm (0.4 mil). The depth between sections was evaluated using the fixed pyramidal geometry of the HV indents; the result is that the change in the diagonal length of an indent measured on the plane of polish in two different sections is approximately 7.0 times the vertical distance separating these two sections. Periodically, fresh HV indents were placed to ensure continuity of depth measurement and image alignment beyond the disappearance of the original indents.

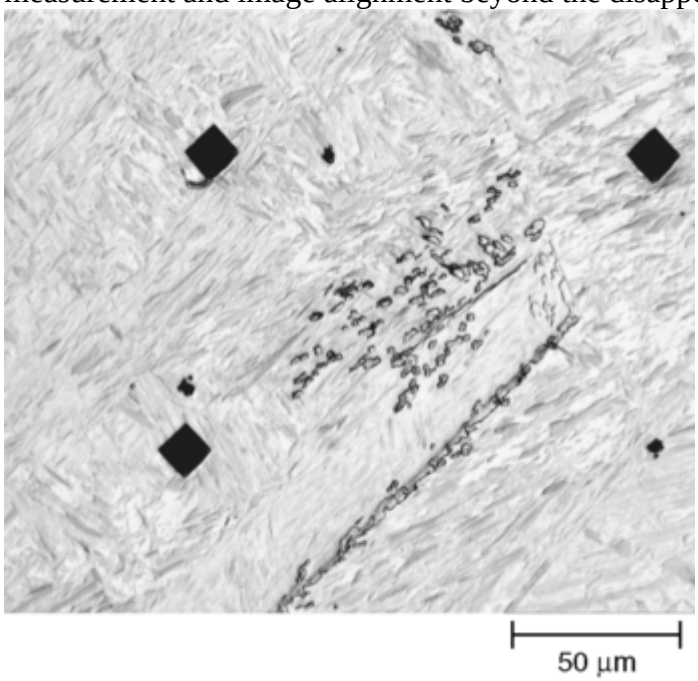

Fig. 26 Low-magnification optical micrograph of serial section 81. The degenerate ferrite sheaf of interest is between the diamond-shaped Vickers hardness indents. Source: Ref 32

The digital micrographs of the 81 sections were then processed using commercially available software. The sections were registered (aligned in a stack) by translating and rotating the images to move the HV indents on adjacent sections into coincidence, as the indents were the only fixed points of reference in the field of view. The registered sections were then cropped in an identical manner to reduce the area to be reconstructed to an acceptable size (Fig. 27), in light of the computationally intensive nature of the 3D reconstruction. The registered and cropped gray-scale images were then converted into a black-and-white format suitable for the 3D reconstruction. Specifically, the ferrite regions were outlined with a single pixel wide white line; all other pixels were set to black. Although various software tools assisted in locating these boundaries (they worked best when the contrast was high), all processed black and white outlines were compared with the gray-scale original to check for accuracy; any needed corrections were manually done. The full 3D reconstruction was then carried out on a computer workstation running a custom-made program (Ref 18, 35) similar to the description outlined previously (Ref 36). The 3D reconstruction computer program works by interpolating the 2D ferrite areas outlined in each section into 3D filled volumes; it is capable of handling randomly curved boundaries.

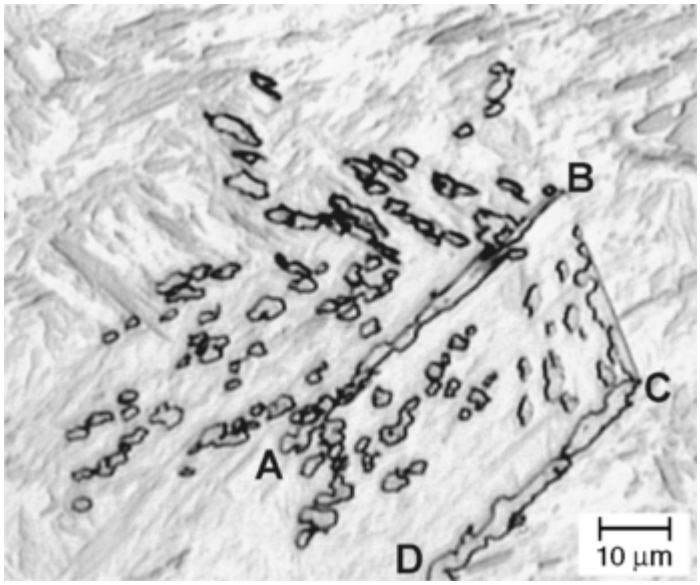

Fig. 27 Optical micrograph of section 33 after cropping. The outlines of individual ferrite subunits were subsequently converted into a white line against a black background prior to 3D reconstruction. Source: Ref 32

Figure 28 shows the reconstructed 3D volume of this bainite sheath. Most subunits have an elongated, rodlike shape. Tilting the 3D image reveals that the subunits in a given area are elongated in the same direction. This strongly suggests that crystallographic factors influenced the evolution of this ferrite morphology. Three bundles of subunits sharing a common elongation direction are identified by color in Fig. 28 (Ref 32). The angles between these bundles were determined by tilting the reconstructed volume to minimize the profile of each bundle and recording the *x* and *y* tilts, from which the angle was evaluated using a Wulff net. The measured angles were 34°, 85°, and 92°. If the ferrite alignment direction within each bundle corresponds to a crystallographically equivalent variant of a preferred growth direction, then these measured intervariant angles are most consistent with a 〈310〉-type direction in ferrite and/or austenite (since both phases have cubic symmetry).

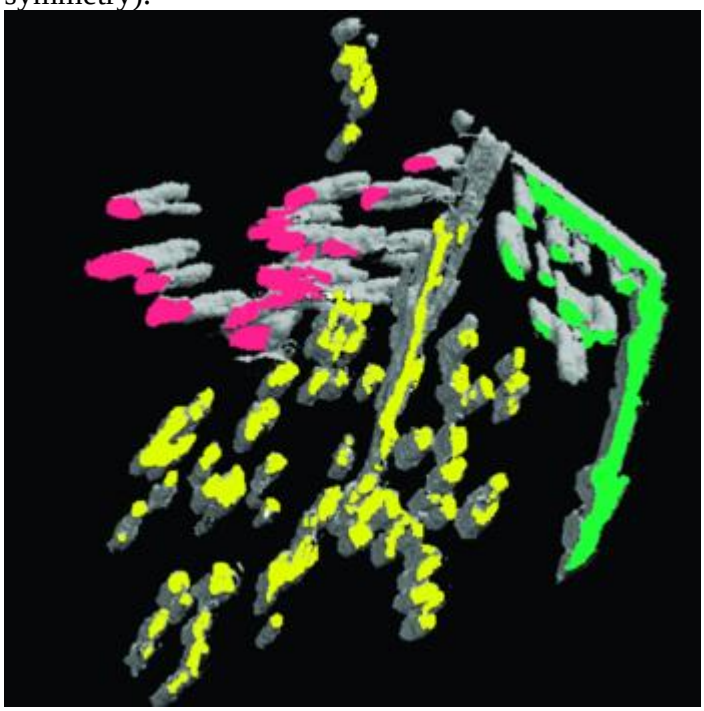

Fig. 28 Three-dimensional isosurface view of the reconstructed degenerate ferrite sheaf. This rendering of the three-dimensional body highlights the sidewalls as different shades of gray, depending on their orientation with respect to the light source (emanating from the top right). The colored surfaces demarcate the plane of polish of the first section, which truncates the intersecting subunits. Bundles of

subunits having a common elongation direction are marked with the same color. Source: R.E. Hackenberg, D.P. Nordstrom, and G.J. Shiflet, Morphology and the Three-Dimensional Structure of Ferrite Formed below the Bay in an Fe-C-W Alloy, *Scr. Mater.*, Vol 47 (No. 6), 2002, p 357–361

This 3D reconstruction revealed three key morphological characteristics of degenerate ferrite formed in this alloy: (1) the ferrite subunits were interconnected in many places (e.g., emanating from a common spine), (2) the subunits were elongated in one direction (like rods), and (3) the bundles of commonly oriented subunits showed a crystallographic growth pattern. This gives a much richer view of this microstructure than that obtained by 2D techniques and suggests reasons why this ferrite morphology appears so complex on 2D sections (Ref 32, 34). This apparent complexity is a consequence of the individual ferrite subunits being elongated in only one direction (like rods), and the many crystallographically equivalent growth directions (if the tentative 〈310〉 preferred growth direction is correct). Thus, within any given austenite grain, the intersection of many variants of rodlike subunit groupings with a random plane of polish results in much more varied 2D microstructures than in well-formed Widmanstätten plates, which appear quite regular on a 2D section due to their elongation in two directions and the smaller multiplicity of the preferred {111} austenite habit planes. The ferrite microstructures that appeared random and ill-defined with no obvious deference to crystallographic constraints on 2D sections are now revealed by 3D techniques to have a well-developed, crystallographically driven arrangement, albeit more complex than conventional, well-formed Widmanstätten plates found in other steels. The 3D examination of degenerate ferrite in this steel provided much-needed information, unavailable from 2D methods, that contributes to a better understanding of this morphologically (and kinetically) complex transformation product.

References cited in this section

2. A.C. Lund and P.W. Voorhees, The Effects of Elastic Stress on Microstructural Development: The Three-Dimensional Microstructure of a Gamma-Gamma′ Alloy, *Acta Mater.*, Vol 50 (No. 10), p 2585–2598

3. M.V. Kral and G. Spanos, Three Dimensional Analysis of Proeutectoid Cementite Precipitates, *Acta Metall.*, Vol 47 (No. 2), 1999, p 711–724

8. O. Forsman, Undersökning av rymdstrukturen hos ett kolstål av hypereutektoid sammansättning, *Jern-Kontorets Ann.*, Vol 102, 1918, p 1–30

9. M. Hillert, The Formation of Pearlite, *The Decomposition of Austenite by Diffusional Processes*, V.F. Zackay and H.I. Aaronson, Ed., Interscience, 1962, p 197–237

18. M.A. Mangan, P.D. Lauren, and G.J. Shiflet, Three-Dimensional Reconstruction of Widmanstatten Plates in Fe-12.3Mn-0.8C, *J. Microsc.*, Vol 188, Oct 1997, p 36–41

22. J. Alkemper and P.W. Voorhees, Quantitative Serial Sectioning Analysis, *J. Microsc.*, Vol 201, 2000, p 1–8

23. G.A. Bertero et al., *Metall. Trans.*, Vol 22A, 1991, p 2723

24. C.A. Dubé, H.I. Aaronson, and R.F. Mehl, La formation de la ferrite proeutectoide dans les aciers au carbon, *Rev. Metall.*, Vol 55 (No. 3), 1958, p 201–210

25. H.I. Aaronson, *The Decomposition of Austenite by Diffusional Processes*, V.F. Zackay and H.I. Aaronson, Ed., Interscience, 1962, p 387

26. G. Spanos and M.V. Kral. Three Dimensional Reconstruction and Classification of Ferrite Precipitates, *International Conference on Solid-Solid Phase Transformations '99*, Japan Institute of Metals, 1999

27. M.V. Kral et al., Three-Dimensional Analysis of Microstructures, *Mater. Charact.,* Vol 45 (No. 1), 2000, p 17–23

28. T. Yokomizo et al., Three-Dimensional Distribution, Morphology, and Nucleation Site of Intragranular Ferrite Formed in Association with Inclusions, *Mater. Sci. Eng. A,* Vol 344 (No. 1–2), 2003, p 261–267

29. M. Uno and M. Enomoto, *Distribution of MnS Particles During Grain Growth of Ferrite,* Ibaraki University, 2002

30. A. Tewari and A.M. Gokhale, Estimation of Three-Dimensional Grain Size Distribution from Microstructural Serial Sections, *Mater. Charact.,* Vol 46 (No. 4), 2001, p 329–335

31. P. Louis and A. Gokhale, Application of Image Analysis for Characterization of Spatial Arrangement of Features in Microstructures, *Metall. Mater. Trans.,* Vol 26A, 1995, p 1449–1456

32. R.E. Hackenberg, D.P. Nordstrom, and G.J. Shiflet, Morphology and the Three-Dimensional Structure of Ferrite Formed below the Bay in an Fe-C-W Alloy, *Scr. Mater.,* Vol 47 (No. 6), 2002, p 357–361

33. W.T. Reynolds et al., Incomplete Transformation Phenomenon in Fe-C-Mo Alloys, *Metall. Trans. A,* Vol 21 (No. 6), 1990, p 1433–1463

34. R.E. Hackenberg, D.G. Granada, and G.J. Shiflet, Austenite Decomposition to Carbide-Rich Products in Fe-0.30C-6.3W, *Metall. Mater. Trans. A,* Vol 33, 2002, p 3619–3633

35. D.N. Dunn, G.J. Shiflet, and R. Hull, Quantitative Three-Dimensional Reconstruction of Geometrically Complex Structures with Nanoscale Resolution, *J. Sci. Instrum.,* Vol 73, 2002, p 330–334

36. M.A. Mangan and G.J. Shiflet, Three-Dimensional Reconstruction of Pearlite Colonies, *Solid-Solid Phase Transformations Proc.,* TMS, 1994

M.V. Kral, G. Ice, M.K. Miller, M.D. Uchic, and R.O. Rosenberg, Three-Dimensional Microscopy, *Metallography and Microstructures,* Vol 9, *ASM Handbook,* ASM International, 2004, p. 448–467

Three-Dimensional Microscopy

M.V. Kral, University of Canterbury, Christchurch, New Zealand; Gene Ice and M.K. Miller, Oak Ridge National Laboratory; M.D. Uchic, Wright-Patterson Air Force Research Laboratory; R.O. Rosenberg, Naval Research Laboratory

---

Focused Ion Beam Tomography

M.D. Uchic, Wright-Patterson Air Force Research Laboratory

The application of focused ion beam (FIB) instruments to microstructural tomography fills a void between methods that examine very small volumes with high lateral and depth resolution (such as 3D atom probe tomography, field ion microscopy, and transmission electron tomography) and methods that examine very large volumes with much coarser resolution (such as mechanical serial sectioning coupled to light microscopy and x-ray tomography). Focused ion beam instruments operate by rastering a focused beam of ions (usually Ga^{+}) over the surface of a sample. The interaction of the ion beam with the sample allows for direct imaging of the sample surface and also results in material removal through sputtering. Ion beam spot sizes are routinely of the order of tens of nanometers for modern FIB systems, and so these instruments are capable of both high-precision

material removal and high-resolution imaging. In particular, the micromachining capability of the FIB can be used to replace traditional mechanical polishing or cutting processes in a serial-sectioning experiment, and FIB instruments can be used to examine volumes of material greater than 1000 μm^3 with high spatial resolution (<100 nm).

M.V. Kral, G. Ice, M.K. Miller, M.D. Uchic, and R.O. Rosenberg, Three-Dimensional Microscopy, *Metallography and Microstructures*, Vol 9, *ASM Handbook*, ASM International, 2004, p. 448–467

Three-Dimensional Microscopy

M.V. Kral, University of Canterbury, Christchurch, New Zealand; Gene Ice and M.K. Miller, Oak Ridge National Laboratory; M.D. Uchic, Wright-Patterson Air Force Research Laboratory; R.O. Rosenberg, Naval Research Laboratory

Sectioning

In using the FIB for sectioning, the FIB can be oriented in two different positions with respect to the sample surface. One position is to have the FIB orientation normal to the surface of interest—here, the FIB is used to mill the surface and collect structural or chemical data at the same time. This technique is termed image depth profiling (Ref 37) and is usually associated with surface science measurements using an ion beam (for example, 2D elemental mapping using secondary ion mass spectrometry, or SIMS). Using image depth profiling, modern FIB instrumentation offers the potential for nanometer-level resolution in both the image plane and in the sectioning depth. For image depth profiling, one of the most important considerations is the ability to accurately control the removal of a planar section of material, and this can only be accomplished if the erosion rate of the selected area is both uniform and constant. Uniform erosion rates occur when the initial surface is flat and smooth and the microstructural constituents have similar sputtering rates. Because the local erosion rate is very sensitive to surface topology, chemical composition, and crystallographic orientation, this technique works best for single crystals of uniform composition with a flat surface. As the ion beam is rastered over the surface, material is removed at a nominally fixed rate, and microstructural information can be collected via secondary electron imaging, ion imaging, and/or chemical analysis such as SIMS.

An alternate method for using the FIB for sectioning is to have the FIB orientation parallel to the surface of interest, that is, to use the FIB as a “nanoknife” to prepare a series of cross-section surfaces (Ref 6, 38, 39, 40). Unlike image depth profiling, this technique does not require that the microstructural constituents have the same milling rates in order to produce a series of planar surfaces. Note that the typical beam current can range from 100 to 1000 pA when preparing a cross section, as the user can determine whether to trade speed for cutting accuracy. For FIB instruments with a single ion beam, imaging the cross-sectioned surfaces requires tilting the sample so that the ion beam can be scanned across the newly prepared cross-section surface; after imaging, the sample is tilted back to prepare another cross section. Fiducial marks can be placed into the material surface to help with realignment and to ensure that the section slice thickness remains constant (Ref 6, 39).

Dual-beam FIB-SEM instruments—microscopes that have both an electron and ion column—eliminate the need to tilt between cutting and imaging operations by using the SEM column to image the cross-section surface. Dual-beam instruments are relatively new and offer significant advantages for microstructural tomography applications, as the incorporation of an electron column potentially allows for additional characterization methods to be included into the 3D characterization process (Ref 41). As noted by Phaneuf, modern FIB systems can be equipped with chemical and crystallographic analysis capabilities such as energy dispersive spectroscopy (EDS) and electron backscatter diffraction (EBSD) and thus allow for sectioning with submicron resolution while providing structural, chemical, and crystallographic analysis on each imaging plane (Ref 38). In addition, for one commercial instrument, the sectioning and imaging processes have been automated (FEI Company Strata DB 235 microscope using the “Auto(Slice and View)” software package); automation ensures that the sectioning slice thickness is consistent and allows for the examination of much larger volumes of material than could be reasonably examined manually. The increasing availability of these

systems to the materials science community will undoubtedly make FIB instruments a viable choice for microstructural tomography experiments.

References cited in this section

6. B.J. Inkson, M. Mulvihill, and G. Möbus, 3D Determination of Grain Shape in a FeAl-Based Nanocomposite by 3D FIB Tomography, *Scr. Mater.*, Vol 47 (No. 7), 2001, p 753–758

37. A.J. Patkin and G.H. Morrison, Secondary Ion Mass Spectrometric Image Depth Profiling for Three-Dimensional Elemental Analysis, *Anal. Chem.*, Vol 54 (No. 1), 1982, p 2–5

38. M.W. Phaneuf and J. Li, FIB Techniques for Analysis of Metallurgical Specimens, in *Microscopy & Microanalysis 2000*, Cambridge University Press, Cambridge, England, 2000

39. B.J. Inkson et al., Subsurface Nanoindentation Deformation of Cu-Al Multilayers Mapped in 3D by Focused Ion Beam Microscopy, *J. Microsc.*, Vol 201 (No. 2), 2001, p 256–269

40. D.N. Dunn and R. Hull, Reconstruction of Three-Dimensional Chemistry and Geometry Using Focused Ion Beam Microscopy, *Appl. Phys. Lett.*, Vol 75 (No. 21), 1999, p 3414–3416

41. T. Sakamoto et al., Development of an Ion and Electron Dual Beam Focused Beam Apparatus for Three-Dimensional Microanalysis, *Jpn. J. Appl. Phys.*, Vol 37 Part 1 (No. 4A), 1998, p 2051–2056

M.V. Kral, G. Ice, M.K. Miller, M.D. Uchic, and R.O. Rosenberg, Three-Dimensional Microscopy, *Metallography and Microstructures*, Vol 9, *ASM Handbook*, ASM International, 2004, p. 448–467

Three-Dimensional Microscopy

M.V. Kral, University of Canterbury, Christchurch, New Zealand; Gene Ice and M.K. Miller, Oak Ridge National Laboratory; M.D. Uchic, Wright-Patterson Air Force Research Laboratory; R.O. Rosenberg, Naval Research Laboratory

---

Case Study

The nickel superalloy selected for this study has a nominal composition of 70Ni-20Cr-10Al (wt%). Experimental quantities of the alloy (400 g, or 14 oz) were prepared by arc melting followed by thermomechanical processing. A thin slice approximately 1 mm (0.04 in.) thick was sectioned from the thermomechanically processed material, and from this slice a 3 mm (0.12 in.) diam disk was core drilled. The 3 mm disk was polished with SiC grinding paper and diamond lapping films and epoxied to a stub for insertion into a Strata DB 235 FIB-SEM manufactured by FEI Company. The DB 235 Dual Beam microscope was used to section and image the superalloy microstructure. The DB 235 allows for the use of various electron/ion detectors to be used with the ion beam, and for these experiments an Everhart-Thornley Thru-the-Lens Detector (TLD) was used to acquire the secondary electron signal. The secondary electron signal measured with the TLD provides reasonable contrast between the γ' precipitates and the γ matrix. As the ion beam is rastered over the surface, images of the microstructure are collected and saved, and these images are later reconstructed into the 3D volume representation. The single slice image shown in Fig. 29 has been slightly processed (using Adobe Photoshop and Image Processing Toolkit, background has been leveled, histogram adjusted, and a median filter has been applied).

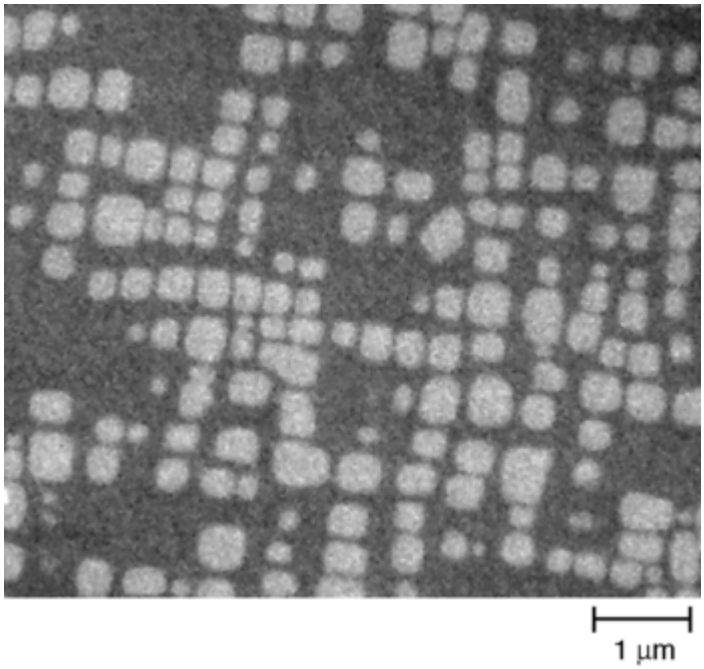

Fig. 29 A single 2D secondary electron image of γ′ precipitates in a γ matrix of a 70Ni-20Cr-10Al (wt%) alloy

Prior to sectioning and imaging, the FIB was used to prepare a smooth surface for imaging; a flat surface is necessary for producing uniform removal rates during milling. In order to produce an initially flat surface, a platinum cap was deposited at the cutting surface to minimize surface roughness (or curtaining) during preparation of the imaging surface. An initial surface trench is prepared using a 5000 pA beam, followed by 1000 and 300 pA beams to remove roughness produced during the previous cutting steps. After a smooth surface has been prepared, the sample is rotated so that the surface normal is parallel to the ion beam. The ion beam is simply rastered over the surface (using a 300 pA beam), and images are collected at a selected interval. Figure 30 shows a low-magnification view after completion of an image depth profiling experiment and the sectioned area is visible in the middle of the trenched area. The method allows for the simultaneous milling/sectioning of the surface and the acquisition of microstructural information without moving the sample. In addition, the Model 235 Dual Beam is supplied with scripting software, which was used to automate the image acquisition process, so that the sectioning and image collection took place without user intervention.

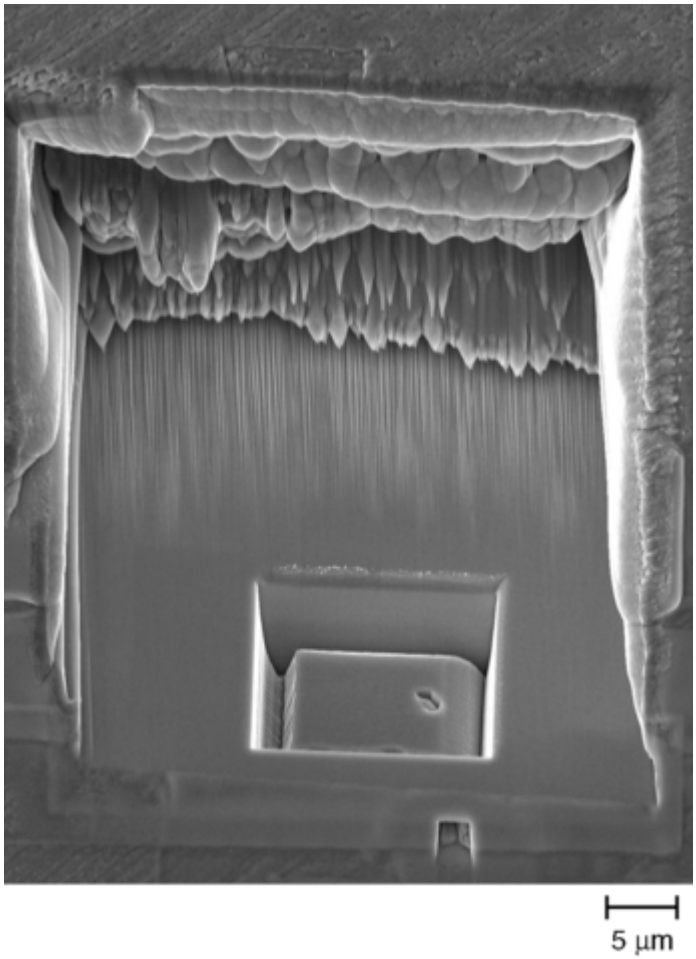

Fig. 30 A low-magnification secondary electron image of an area sectioned using a focused ion beam

In this case, the time interval was approximately 3 min between 160 consecutive images, and thus the experiment took about 8 h. The distance interval is 11 nm per section and lateral resolution is 14.9 nm. For this material, the milling rates of γ and γ′ in the 〈001〉 orientation are very similar, and the surface is uniformly milled away during the sectioning process. Note that because the secondary electron signal (TLD-S) is noisy, the signal-to-noise ratio is improved by averaging images, and each individual image used in the volume reconstruction is an integrated set of 32 images. After the sequence of images was captured, commercially available software (Interactive Data Language, from Research Systems, Inc.) was used to process and render the stack of collected images into the 3D volume reconstruction, as shown in Fig. 31.

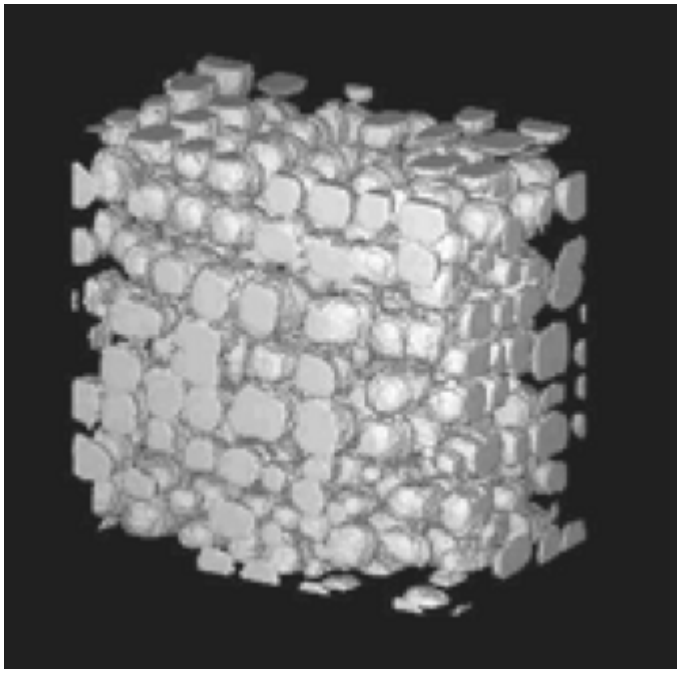

Fig. 31 Three-dimensional volume reconstruction of γ′ precipitates in a 70Ni-20Cr-10Al (wt%) alloy. The 3D image was generated from the stack of collected images (Fig. 29) from a dual beam FIB-SEM.

M.V. Kral, G. Ice, M.K. Miller, M.D. Uchic, and R.O. Rosenberg, Three-Dimensional Microscopy, *Metallography and Microstructures,* Vol 9, *ASM Handbook,* ASM International, 2004, p. 448–467

Three-Dimensional Microscopy

M.V. Kral, University of Canterbury, Christchurch, New Zealand; Gene Ice and M.K. Miller, Oak Ridge National Laboratory; M.D. Uchic, Wright-Patterson Air Force Research Laboratory; R.O. Rosenberg, Naval Research Laboratory

---

Atom Probe Tomography

M.K. Miller, Oak Ridge National Laboratory

Serial sectioning of microstructural features may also be performed at the atomic level with atom probe tomography (Ref 42). This technique is a remarkable evolution of atom probe field ion microcopy (Ref 43). The basic principles of atom probe field ion microscopy and the techniques for the preparation of metallic specimens are described in Ref 42, 43, 44, 45. Data obtained by atom probe tomography permit 3D visualization of the solute distribution in the sample and the quantification of the size, composition, and morphology of the microstructural features present.

References cited in this section

42. M.K. Miller, *Atom Probe Tomography: Analysis at the Atomic Level,* Kluwer Academic/Plenum Press, 2000

43. E.W. Müller, J.A. Panitz, and S.B. Mclane, *Rev. Sci. Instrum.,* Vol 36, 1968, p 83

44. M.K. Miller et al., *Atom Probe Field Ion Microscopy,* Oxford University Press, Oxford, UK, 1996

45. G.D.W. Smith, Field Ion Microscopy and Atom Probe Microanalysis, *Materials Characterization,* Vol 10, 9th ed., *Metals Handbook,* American Society for Metals, 1986, p 583–602

M.V. Kral, G. Ice, M.K. Miller, M.D. Uchic, and R.O. Rosenberg, Three-Dimensional Microscopy, *Metallography and Microstructures,* Vol 9, *ASM Handbook,* ASM International, 2004, p. 448–467

Three-Dimensional Microscopy

M.V. Kral, University of Canterbury, Christchurch, New Zealand; Gene Ice and M.K. Miller, Oak Ridge National Laboratory; M.D. Uchic, Wright-Patterson Air Force Research Laboratory; R.O. Rosenberg, Naval Research Laboratory

---

Principles of Atom Probe Tomography

In atom probe tomography, the sampled volume is reconstructed atom by atom from many hundreds of thousands of 2D layers, each of which contain a few atoms. Individual atoms are removed from the surface of a needle-shaped specimen at a precise time by a short-duration (10 ns) high-voltage pulse that is superimposed on a standing voltage. The three-dimensional atom probe (3DAP) features a position-sensitive detector at the end of a time-of-flight mass spectrometer. The volume analysis is defined by the number of layers of atoms field evaporated from the specimen and by the effective lateral extents of the position-sensitive detector rather than a small aperture in the microchannel plate and phosphor screen assembly used to view the field ion image that is used in the original atom probe. In the 3DAP, the *x* and *y* coordinates of each atom field evaporated from the specimen are derived from the highly magnified impact position on this position-sensitive detector, as shown in Fig. 32. The magnification, η, which is typically several million times, is given to a first approximation by:

$$\eta = d/\xi r_t$$

where d is the specimen-to-detector distance, ξ is a projection parameter known as the image compression factor, and r_t is the radius of curvature of the specimen ($r_t \approx 50$ nm), which is proportional to the applied voltage. The third *z* coordinate is derived from the position of the atom in the evaporation process (Ref 42). The mass-to-charge ratio, m/n, of each atom and hence its element identity are derived from its flight time, t, from the specimen to the detector, and the applied voltage, V:

$$m/n = (\text{constant}) \cdot V \cdot t^2/d^2$$

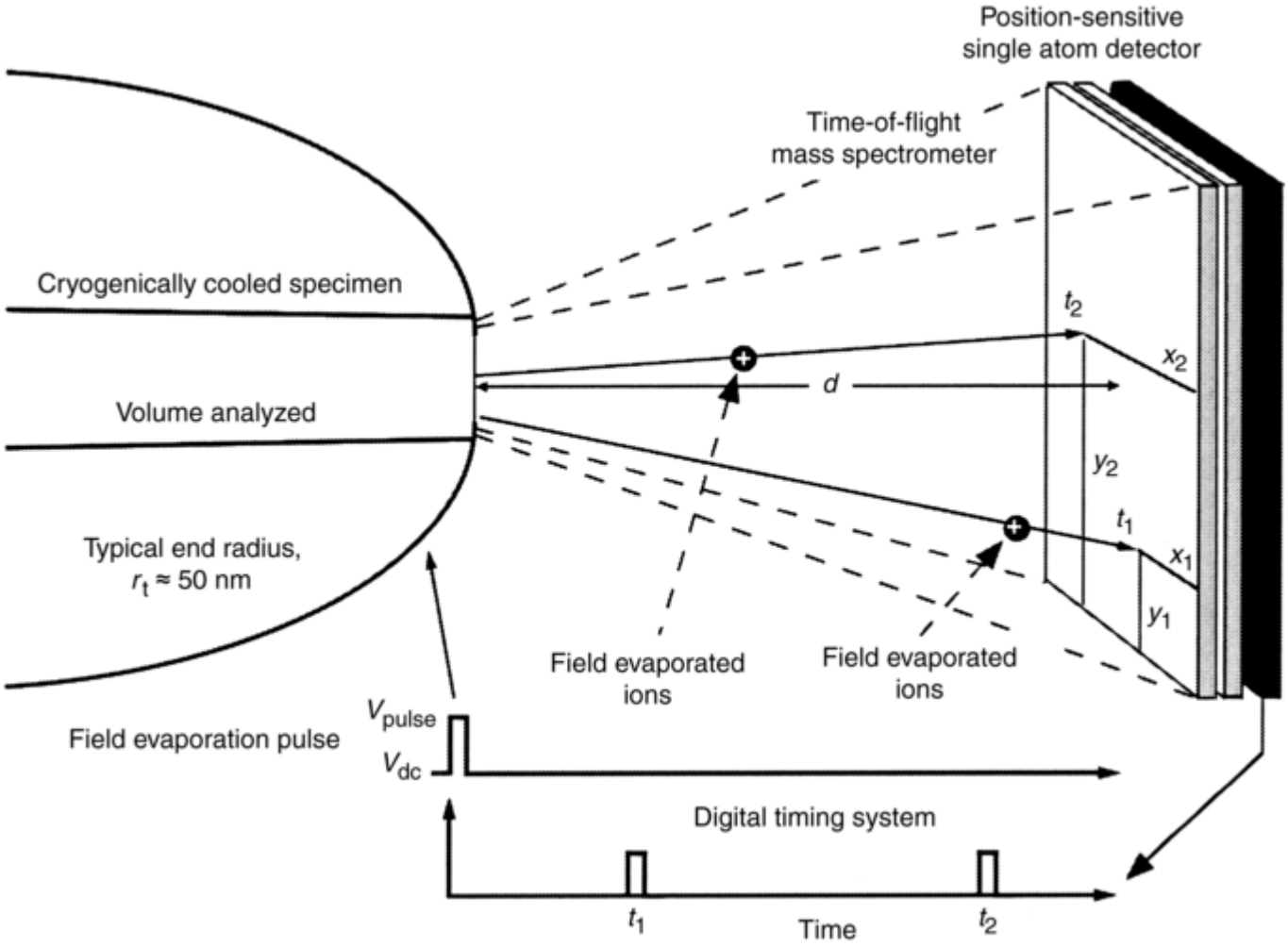

Fig. 32 The principle of operation of a 3D atom probe. The *x* and *y* coordinates of each atom are determined from the impact position on the position-sensitive detector. The *z* coordinate is determined from its position in the evaporation sequence. The mass-to-charge ratio and hence the elemental identity of each atom is determined from its flight time in the time-of-flight mass spectrometer and the applied voltages.

Most recent instruments feature energy compensation to minimize the effects of small energy deficits that arise during the field-evaporation process (Ref 42) and thereby improve the mass resolution so that the individual isotopes of all the elements are fully resolved. Compositions are estimated directly from the number of atoms of each solute species in the volume of interest.

Reference cited in this section

42. M.K. Miller, *Atom Probe Tomography: Analysis at the Atomic Level,* Kluwer Academic/Plenum Press, 2000

M.V. Kral, G. Ice, M.K. Miller, M.D. Uchic, and R.O. Rosenberg, Three-Dimensional Microscopy, *Metallography and Microstructures,* Vol 9, *ASM Handbook*, ASM International, 2004, p. 448–467

Three-Dimensional Microscopy

M.V. Kral, University of Canterbury, Christchurch, New Zealand; Gene Ice and M.K. Miller, Oak Ridge National Laboratory; M.D. Uchic, Wright-Patterson Air Force Research Laboratory; R.O. Rosenberg, Naval Research Laboratory

Methods of Representation

Several different methods are used to visualize features in the microstructure. In atom maps, color-coded spheres are used to represent the positions of the atoms, as shown in Fig. 33 for a neutron irradiated pressure vessel steel. Phases and solute segregation at interfaces and grain boundaries are distinguished from differences in the local density of atoms. The atoms associated with types of features may be distinguished from those in the matrix with the maximum separation method. This method is based on the principle that the solute atoms in a solute-enriched feature are closer together than those in the surrounding matrix. A critical distance between solute atoms may be defined such that solute atoms that are closer together than this critical distance are apportioned to the feature and the remainder to the surrounding matrix. The value of the critical distance depends on the solute level in the alloy. Once the atoms in each feature are identified, characteristic parameters such as the radius of gyration and the composition of small precipitates and the Gibbsian interfacial excess of solutes at interfaces can be estimated (Ref 42).

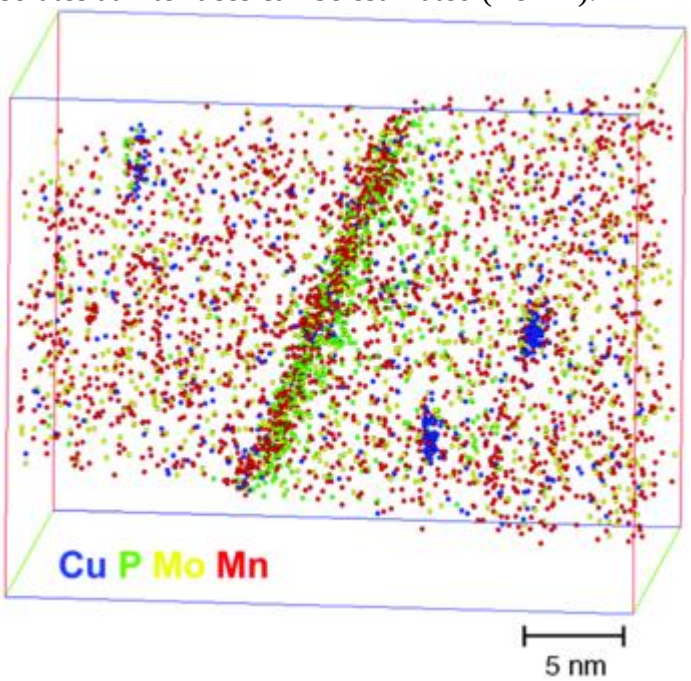

Fig. 33 Atom map of the solute distribution in a neutron-irradiated pressure vessel steel in which each sphere represents the position of an individual atom. The iron atoms are omitted for clarity. Three nanometer-sized copper-enriched precipitates are visible on either side of a lath boundary. Phosphorus, manganese, and molybdenum are enriched at the boundary.

The morphology of the products of phase separation may be investigated, as demonstrated for a spinodally decomposed Fe-32Cr alloy that was aged for ~10,000 h at 470 °C (880 °F) (Fig. 34). To produce this isoconcentration surface, all the atoms in the sampled volume are allocated to cells arranged in a 3D grid depending on their position. The composition of each cell is calculated from the number of atoms of each element. An isoconcentration surface is constructed through the cells with a solute concentration that is intermediate to that of the coexisting phases to represent the interface. The complex interconnected network structure of the chromium-enriched α′ phase that is responsible for the 475 °C embrittlement problem in iron-

chromium alloys is clearly seen. The compositions of the coexisting phases may also be estimated from statistical analysis of the frequency distribution of the concentrations of the cells. The scale of the microstructure may be estimated from these concentration fluctuations with the use of the autocorrelation function (Ref 46). In addition, topological parameters of this complex microstructure may also be estimated (Ref 46).

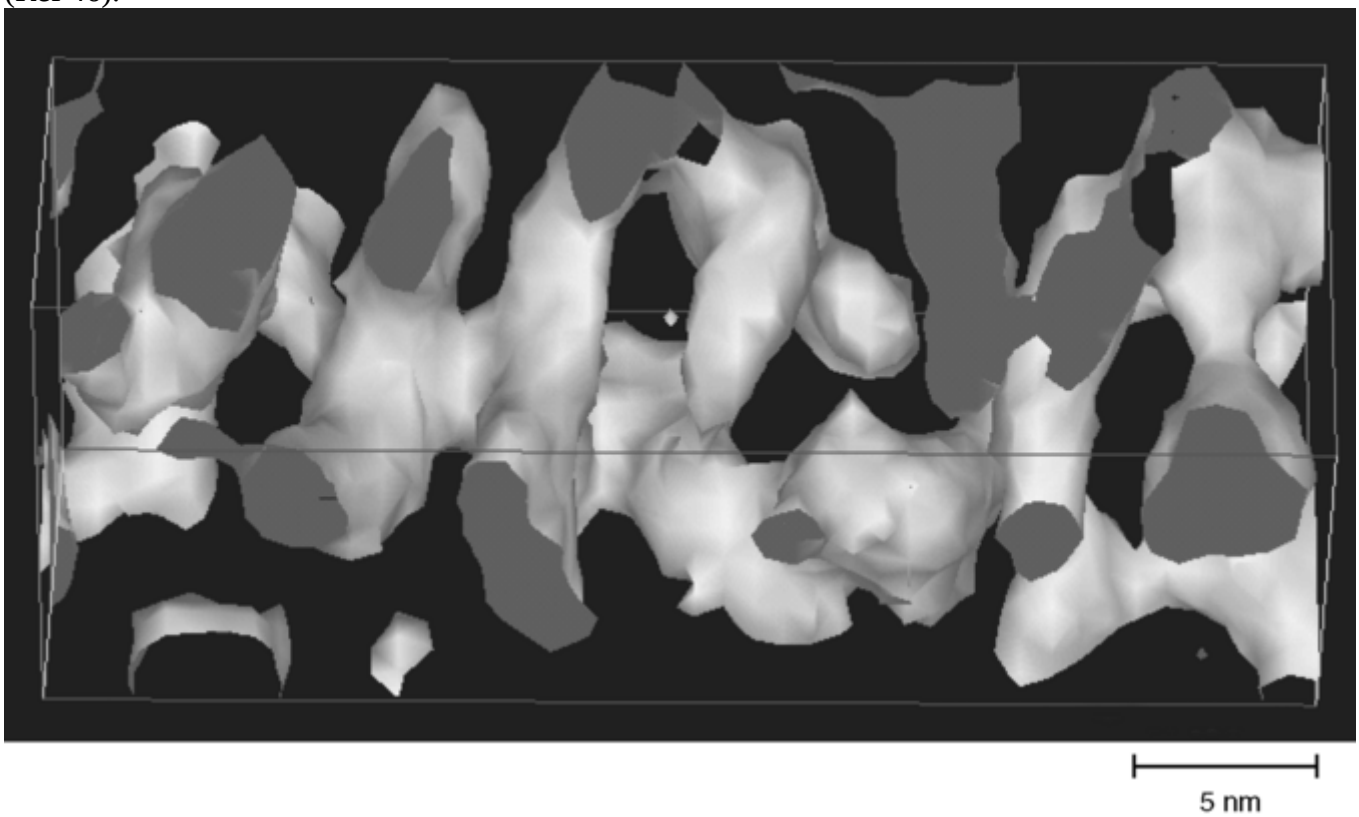

Fig. 34 Chromium isoconcentration surface in an Fe-32Cr alloy isothermally annealed for ~10,000 h at 470 °C (880 °F). The complex interconnected network structure of the chromium-enriched α′ phase is clearly evident.

References cited in this section

42. M.K. Miller, *Atom Probe Tomography: Analysis at the Atomic Level*, Kluwer Academic/Plenum Press, 2000

46. M.K. Miller et al., Spinodal Decomposition in Fe-Cr Alloys: Experimental Study at the Atomic Level and Comparison with Computer Models—I. Introduction and Methodology, *Acta Metall. Mater.*, Vol 43 (No. 9), 1995, p 3385–3401

M.V. Kral, G. Ice, M.K. Miller, M.D. Uchic, and R.O. Rosenberg, Three-Dimensional Microscopy, *Metallography and Microstructures,* Vol 9, *ASM Handbook,* ASM International, 2004, p. 448–467

M.V. Kral, University of Canterbury, Christchurch, New Zealand; Gene Ice and M.K. Miller, Oak Ridge National Laboratory; M.D. Uchic, Wright-Patterson Air Force Research Laboratory; R.O. Rosenberg, Naval Research Laboratory

X-Ray Microtomography

G.E. Ice, Oak Ridge National Laboratory

The remarkable ability of x-rays to penetrate through visually opaque materials, and to nondestructively reveal the nature of the hidden 3D structure within, revolutionized medicine and made Röentgen a household name. Following the discovery of x-rays, projection x-ray images in medicine and science almost immediately became a standard diagnostic tool of inner structure and defects. Tomographic reconstruction methods have evolved much later to provide detailed 3D structure images. X-ray microtomography in particular is still an emerging nondestructive tool for studying the 3D structure of materials. The field is now advancing rapidly due to the availability of intense synchrotron x-ray sources and the development of efficient x-ray optics and area detectors.

Although the fundamental principles of x-ray microtomography are similar to those of conventional medical tomography, the vastly different spatial resolution and sample dimensions create both new challenges and new opportunities. For example, a number of contrast mechanisms can be used with microtomography, some of which are impractical with medical imaging; microtomography may use familiar transmission (absorption) contrast, or more novel phase contrast, and fluorescence tomography contrast. Other related x-ray approaches to 3D imaging include direct imaging of 3D structure by triangulation (Ref 47, 48), or by defining a small gage volume in the sample with incident-beam and exit-beam localization. For example, some powder diffraction measurements of strain and the recently developed 3D x-ray crystal microscope (Ref 49) determine structure by limiting the gage volume from which a signal can be recovered. This section reviews evolving x-ray microtomography methods with an emphasis on novel contrast mechanisms.

References cited in this section

47. B.C. Larson et al., 3D Measurement of Deformation Microstructure in Al(0.2%) Mg Using Submicron Resolution X-Ray Microbeams, *Mater. Res. Soc. Symp. Proc.,* Vol 590, 2000, p 247–252

48. C.R. Patterson et al., Nondestructive Determination of the Depth of Different Texture Components in Polycrystalline Samples, *Mater. Res. Soc. Symp. Proc.,* Vol 590, 2000, p 253–258

49. G.E. Ice and B.C. Larson, 3D X-Ray Crystal Microscope, *Adv. Eng. Mater.,* Vol 2, 2000, p 643–646

M.V. Kral, G. Ice, M.K. Miller, M.D. Uchic, and R.O. Rosenberg, Three-Dimensional Microscopy, *Metallography and Microstructures,* Vol 9, *ASM Handbook,* ASM International, 2004, p. 448–467

Three-Dimensional Microscopy

M.V. Kral, University of Canterbury, Christchurch, New Zealand; Gene Ice and M.K. Miller, Oak Ridge National Laboratory; M.D. Uchic, Wright-Patterson Air Force Research Laboratory; R.O. Rosenberg, Naval Research Laboratory

General Concepts

X-ray tomography is based on the realization that as an x-ray beam passes through an object, it samples a prismatic volume consisting of many small volume elements (voxels) along its path (Fig. 35). If some property of the sample such as the attenuation of the beam density or the fluorescence yield is measured, it can be used to help reconstruct the structure along the beam path. Different combinations of the sample volume elements must be measured to accurately determine the internal structure of the object. With a small "pencil" beam, this is accomplished by translation and rotation of the sample (Fig. 1).

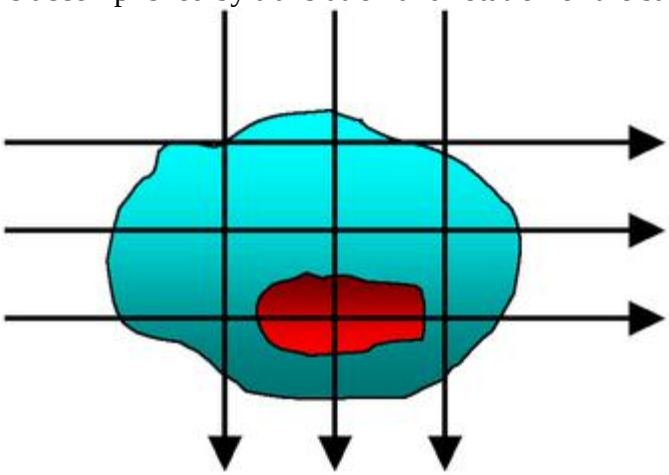

Fig. 35 The x-ray attenuation (excitation) through an object depends on the ray path. A "pencil" beam of x-rays must pass through more material near the center of the object but must pass through denser material near the bottom of the object. By translating and rotating the sample (or the beam), the 3D structure of the sample can be determined.

The key problem in microtomography is achieving adequate spatial resolution while simultaneously retaining good counting statistics. The time to collect data grows with the fourth power of linear resolution. This means that with similar source brilliance and optical efficiency, the counting time for 1 μm^3 resolution will be 12 orders of magnitude greater than for 1 mm^3 resolution. Because of this intrinsic need for a high-brilliance source to produce reasonable counting statistics with micron resolution, and because of the need for advanced x-ray optics and high-resolution detectors, microtomography has lagged medical tomography. High-brilliance synchrotron sources are highly desirable for microtomography. As described later, however, remarkable advances in microtomography with laboratory sources have now made it possible to achieve <0.1 μm^3 resolution with even conventional sources (Ref 50).

The most common strategy to obtain good spatial resolution with reasonable counting rates is to use a nearly parallel x-ray beam that floods the sample. The transmitted image is collected after magnification by an area detector. The projected resolution is given by the pixel resolution of the detector divided by the magnification. Defects even smaller than the measurement resolution can be detected if they provide sufficient contrast.

At least four schemes have been used to magnify the transmitted x-ray beam:

- Asymmetric Bragg crystals (Ref 51)
- Visible light magnification from an x-ray sensitive fluorescent single crystal (Ref 52)
- X-ray zone plate magnification (Ref 50)

- Projection imaging

These arrangements are illustrated in Fig. 36(a) to (d). In Fig. 36(a), the magnification is provided by asymmetrically cut single crystals set to magnify the x-ray beam before an x-ray sensitive detector. Although only one crystal is shown in the diagram, in real applications, two crystals are used to magnify the image in orthogonal directions. In Fig. 26(b), the transmitted image at a fluorescing crystal is reimaged by an optical lens that produces a magnified image at a visible-light-sensitive area detector (Ref 52). In Fig. 26(c), the transmitted beam is magnified by an x-ray zone plate, which magnifies the x-ray image onto an x-ray sensitive area detector. In Fig. 26(d), a divergent beam from a small source is used to project the image onto an x-ray sensitive area detector.

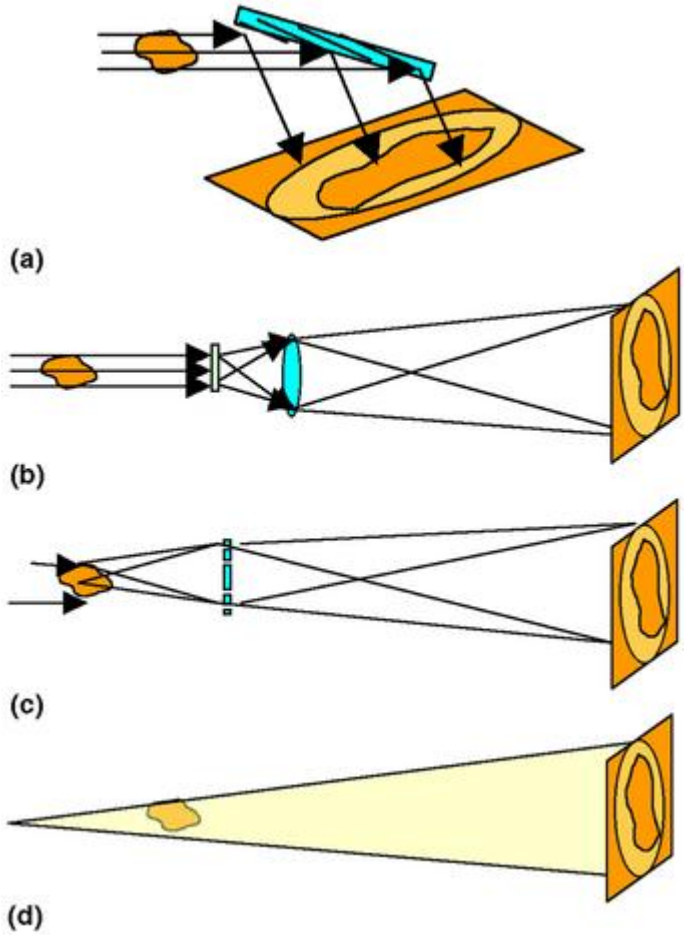

Fig. 36 The transmitted image through a beam can be magnified by a number of techniques: (a) asymmetric crystals, (b) optical magnification of projected scintillator, (c) zone plate magnifier, or (d) projection magnification.

References cited in this section

50. W.-B. Yun, personal communication, 2002

51. Q.C. Johnson et al., *Proc. Mater. Soc. Symp.,* Vol 69, 1986, p 203

52. J.H. Dunsmuir, personal communication, 1991

M.V. Kral, G. Ice, M.K. Miller, M.D. Uchic, and R.O. Rosenberg, Three-Dimensional Microscopy, *Metallography and Microstructures,* Vol 9, *ASM Handbook,* ASM International, 2004, p. 448–467

Three-Dimensional Microscopy

M.V. Kral, University of Canterbury, Christchurch, New Zealand; Gene Ice and M.K. Miller, Oak Ridge National Laboratory; M.D. Uchic, Wright-Patterson Air Force Research Laboratory; R.O. Rosenberg, Naval Research Laboratory

Transmission Tomography

The underlying principles of transmission microtomography are identical to those of computed tomography as used in medical diagnostic radiology. The transmission of x-rays through matter is dominated by photoabsorption, which has a ~Z^4 dependence on atomic number (Z). The attenuation of an x-ray beam through an object is therefore sensitive to the x-ray density of the object and depends on the incident x-ray energy spectrum, as well as the sample elemental composition and mass density. Kinney et al. (Ref 53) describe the transmitted intensity as a double integral that includes an integration over the energy spectrum and a line integral along the path of the x-rays through the sample:

$$I = \int I_0(E)\left\{e^{-\int \mu(x,y,z,E)dl}\right\}dE \qquad \text{(Eq 1)}$$

Here I is the transmitted beam intensity, $I_0(E)$ is the incident-beam intensity, $\mu(x, y, z, E)$ is the x-ray absorption coefficient in inverse units of length, and the line integral is taken over the path of the beam through the sample. The determination of the 3D contrast density of the sample from a series of line integrals of the kind in Eq 1 is known as image reconstruction. Image reconstruction is one of the great triumphs of modern science. The development of reconstruction techniques led to the award of the 1979 Nobel Prize in Physiology/Medicine to Allan M. Cormack and Sir Godfred N. Hounsfield. There are two general classes of reconstruction techniques: analytical methods and iterative methods. With analytical methods, the available data are inverted to estimate the x-ray contrast density distribution in the sample. Analytic inversions formally require an infinite number of projections, but can give good approximations with a finite number of projections. Analytical methods include such techniques as back-projection of filtered projection and 2D Fourier slice techniques (Ref 54). With iterative methods the attenuation coefficient map is estimated and then refined by successive iteration. An example of this technique is the maximum entropy algorithm (Ref 54, 55).

Although measurements with small x-ray beams allow for excellent spatial resolution (Ref 56) and are essential for fluorescence tomography and for 3D x-ray crystal microscopy (Ref 49), they are intrinsically slow; only one line integral is determined for each measurement. In most practical applications, transmission-tomography measurements are accelerated by ~10^6 through the use of area detectors (Fig. 1). Typically, the sample is bathed with a highly collimated x-ray beam and the transmitted intensities of the many “pencil beams” that are transmitted through the sample are measured with an x-ray area detector as shown in Fig. 1. The intensity distribution of the transmitted beam therefore simultaneously measures many line integrals of form shown in Eq 1. High spatial resolution is achieved by magnifying the transmitted x-ray beam.

The spatial resolution of transmission tomography is limited by a number of factors including the sample contrast, the number of projections, the beam collimation, and the spatial resolution of the detector. Ultimately, microtomography is brilliance limited, photons/($s \cdot eV \cdot \mu m^2 \cdot mrad^2$). Sensitivity to variations in the absorption depends on photon statistics and contrast that is typically best for monochromatic radiation.

Transmission tomography has been applied to a wide range of problems including studies of bone (Ref 57), porosity (Ref 56), and crack propagation (Ref 58). The power of x-ray microtomography to characterize 3D structure is clearly illustrated in a study of nuclear fuel particles by Dunsmuir and coworkers (Ref 52). As illustrated in Fig. 37, the internal structure of a small, less than 1 mm diam particle, is clearly resolved including the high Z core, and a SiC shell. A huge advantage of x-ray microtomography for these measurements is the ability to nondestructively determine the internal structure. This allows for measurements before and after irradiation and minimizes the generation of hazardous waste.



Fig. 37 An x-ray microtomographic image of a nuclear fuel particle with a high atomic number (Z) core and spherical layers of carbon and SiC

A very interesting study by Guvenilir et al. (Ref 58) followed the morphology of crack propagation in a series of in situ real-time measurements. These direct observations of the crack opening as a function of cyclic loading illustrate how nondestructive real-time measurements can be used to study not only 3D structures, but also dynamic processes. Whereas sectioning studies can (with a great deal of work) study the morphology of a crack in three dimensions, x-ray microtomography allowed the dynamics of a propagating crack to be studied at various stages of its evolution. This totally new information tests existing theoretical treatments of crack propagation and in this case allowed for a critical evaluation of the mechanisms leading to low crack-propagation rates in Al-Li 2090 alloys.

Recently, Yun and coworkers at Xradia Corporation have reported transmission tomographic images with better than 0.1 μm (3.9 μin.) resolution made with a laboratory source (Fig. 38) (Ref 50). Their highly optimized x-ray optics and software pioneers high-performance microtomographic imaging with laboratory x-ray sources.

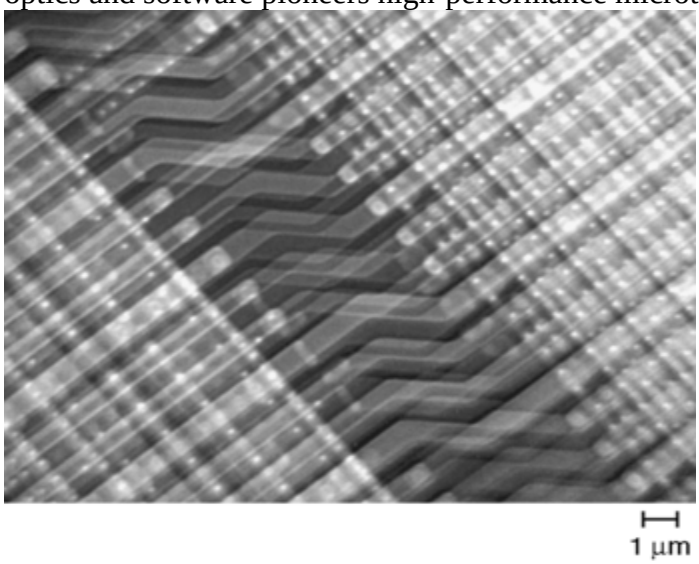

Fig. 38 Laboratory x-ray image of a six-layer copper interconnect structure in an integrated circuit. The smallest features on the chip are about 160 nm in size and are easily resolved by the system with ~80 nm resolution.

References cited in this section

49. G.E. Ice and B.C. Larson, 3D X-Ray Crystal Microscope, *Adv. Eng. Mater.*, Vol 2, 2000, p 643–646

50. W.-B. Yun, personal communication, 2002

52. J.H. Dunsmuir, personal communication, 1991

53. J.H. Kinney et al., The X-Ray Tomographic Microscope-3 Dimensional Perspectives of Evolving Microstructures, *Nucl. Inst. Meth. A*, Vol 347, 1994, p 480–486

54. R.H. Huesman et al., *Pub. 214—RECLBL Library Users Manual, Donner Algorithms for Reconstruction Tomography*, Lawrence Berkeley Laboratory, University of California, Berkeley, CA, 1977

55. G.T. Herman, *Image Reconstruction from Projections: Implementation and Applications*, Springer-Verlag, Berlin, 1979

56. P. Spanne et al., Synchrotron Computed Microtomography of Porous-Media-Topology and Transports, *Phys. Rev. Lett.*, Vol 73, 1994, p 2001–2004

57. J.H. Kinney, N.E. Lane, and D.L. Haupt, In-vivo, 3-Dimensional Microscopy of Trabecular Bone, *J. Bone Min. Res.*, Vol 10, 1995, p 264–270

58. A. Guvenilir et al., Direct Observation of Crack Opening as a Function of Applied Load in the Interior of a Notched Tensile Sample of Al-Li 2090, *Acta Mater.*, Vol 45, 1997, p 1977–1987

M.V. Kral, G. Ice, M.K. Miller, M.D. Uchic, and R.O. Rosenberg, Three-Dimensional Microscopy, *Metallography and Microstructures*, Vol 9, *ASM Handbook*, ASM International, 2004, p. 448–467

Three-Dimensional Microscopy

M.V. Kral, University of Canterbury, Christchurch, New Zealand; Gene Ice and M.K. Miller, Oak Ridge National Laboratory; M.D. Uchic, Wright-Patterson Air Force Research Laboratory; R.O. Rosenberg, Naval Research Laboratory

---

Phase Contrast Imaging

Away from a Bragg reflection, x-rays have an index of refraction slightly less than unity that can be described by:

$$n = 1 - \delta + i\beta \qquad \text{(Eq 2)}$$

Here the real component, δ, is on the order of 10^{-6}, while the imaginary component, β, is on the order of 10^{-9} for x-rays between 8 and 20 keV. The negative decrement from unity indicates that phase is advanced as an x-ray penetrates matter. Whereas straightforward absorption contrast imaging utilizes the imaginary component, β, phase contrast imaging is sensitive to the real component, δ, which is approximately three orders of magnitude larger. In order to utilize this increased sensitivity, however, specialized instrumentation is required and/or the source should have a significant coherent component.

Three techniques are used to produce phase contrast images: interferometry, angular deflectometry, and propagation-based Fresnel diffraction. With interferometry, the phase shift is measured directly against a reference. This technique is difficult and has particular trouble with rapid changes in phase contrast at edges. Angular deflectometry on the other hand is less difficult and ideally suited to the measurement of edges and

sharp features. This technique has recently evolved from a synchrotron-only method to a laboratory prototype (Ref 59). Propagation-based Fresnel diffraction requires a coherent source, but is by far the simplest of the three techniques. Like angular deflectometry this method is well suited to identifying edges, but has trouble with smoothly varying density distributions.

The principle behind propagation-based Fresnel diffraction is illustrated in Fig. 39. A plane wave has its phase shifted by a variation in sample density. At the edge, a Fresnel diffraction pattern is generated that interferes with the propagated wave. This interference develops with distance, and highest contrast depends on the size of the phase shift and the distance of the detector from the sample. Phase contrast tomography is particularly useful for measuring low-*Z* samples. For example, biological samples such as insects can be imaged in real time to reveal the action of working structures inside the living organism. These measurements provide important new insights into the structure of both organic and inorganic samples.

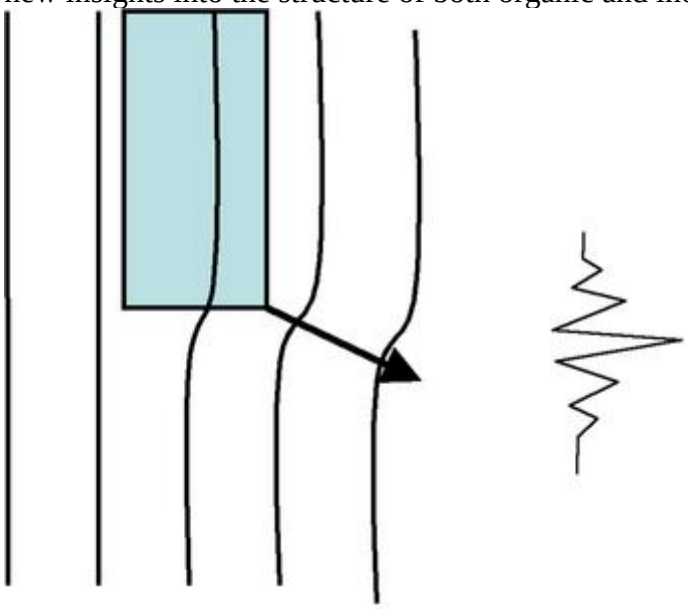

Fig. 39 A plane wave passing through a sample has its phase advanced with respect to vacuum. At the edge, an interference pattern is generated that develops with distance away from the sample. Although the experiment is very simple, a coherent source is required to detect the interference.

Reference cited in this section

59. M. Hasnah et al., Single-Exposure Simultaneous Diffraction-Enhanced Imaging, *Nucl. Instrum. Methods,* Vol 492, 2002, p 236–240

M.V. Kral, G. Ice, M.K. Miller, M.D. Uchic, and R.O. Rosenberg, Three-Dimensional Microscopy, *Metallography and Microstructures,* Vol 9, *ASM Handbook,* ASM International, 2004, p. 448–467

M.V. Kral, University of Canterbury, Christchurch, New Zealand; Gene Ice and M.K. Miller, Oak Ridge National Laboratory; M.D. Uchic, Wright-Patterson Air Force Research Laboratory; R.O. Rosenberg, Naval Research Laboratory

---

Edge Contrast Tomography

In addition to x-ray absorption density and phase contrast, x-ray tomography can be used to detect 3D elemental distributions. The most sensitive way to measure elemental distributions with transmission tomography is by comparing the transmitted beam intensity between x-ray energies above and below the absorption edge of a

trace element. In a real measurement, the detectable limit with this technique can be about 1 to 20 ppm/μm feature size.

M.V. Kral, G. Ice, M.K. Miller, M.D. Uchic, and R.O. Rosenberg, Three-Dimensional Microscopy, *Metallography and Microstructures,* Vol 9, *ASM Handbook*, ASM International, 2004, p. 448–467

Three-Dimensional Microscopy

M.V. Kral, University of Canterbury, Christchurch, New Zealand; Gene Ice and M.K. Miller, Oak Ridge National Laboratory; M.D. Uchic, Wright-Patterson Air Force Research Laboratory; R.O. Rosenberg, Naval Research Laboratory

---

X-Ray Fluorescence Tomography

Fluorescence microtomography is a pencil-beam technique that can extend elemental sensitivity at the expense of data collection time. For a uniform sample, the estimated minimum detectable limit (MDL) of a modern x-ray fluorescence microbeam is ~5 to 80 ppb/s · μm^2 (Ref 60). X-ray fluorescence microtomography is at least two orders of magnitude more sensitive to trace element distributions than transmission microtomography (Ref 61). The elemental sensitivity of fluorescence microtomography has been demonstrated in a study of elemental distributions in a thin SiC shell from a TRISO nuclear fuel particle. (TRISO is an acronym that evolved from bilayer isotropic coatings, or BISO. As the layers got more complex they became TRISO even though they have more than three layers). TRISO-coated fuel particles contain a small kernel of nuclear fuel encapsulated by alternating layers of carbon and SiC as shown in Fig. 40. The TRISO-coated fuel particle is used in an advanced nuclear fuel designed for passive containment of the radioactive isotopes. The SiC layer provides the primary barrier for radioactive elements in the kernel. The effectiveness of this barrier layer under adverse conditions is critical to containment.

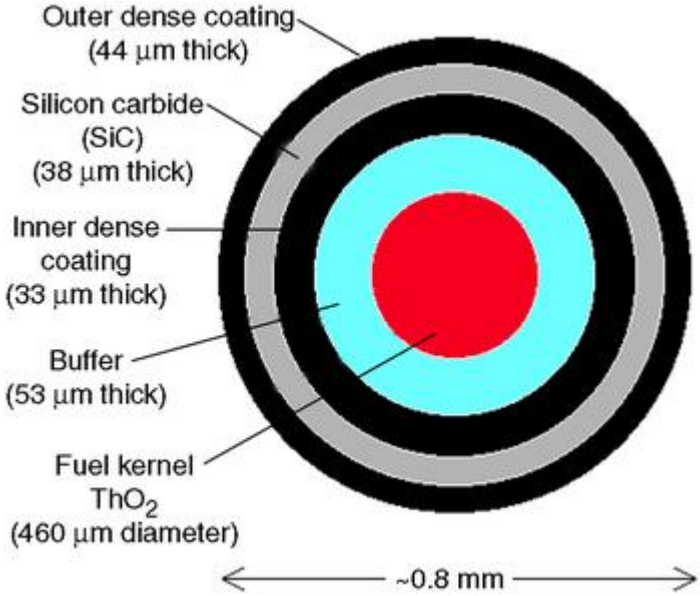

Fig. 40 Multilayer isotropic coatings (TRISO) fuel element. After Ref 61

The experimental setup for an x-ray fluorescence tomography measurement is conceptually very simple and is nearly identical to pencil-beam transmission experiments (Fig. 41). The sample is placed on a stage that rotates and translates the sample. A detector is placed in the plane of the storage ring and at 90° to the incident beam. This detector geometry allows efficient measurement of the characteristic fluorescence from the trace elements while minimizing the x-ray elastic and Compton scattering (Ref 60). The elemental distribution in a slice through the sample can be reconstructed after translating the sample through the x-ray beam and rotating the

sample at least 180° for every *x* position. Finer resolution is achieved by decreasing both the translation and rotational step size.

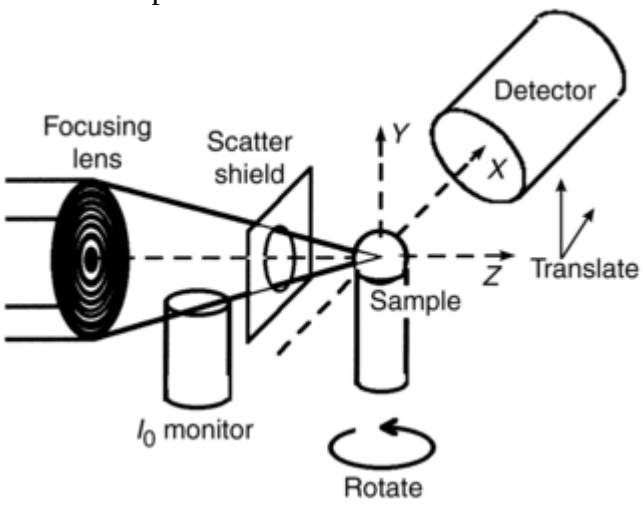

Fig. 41 Key elements of an x-ray fluorescence tomography arrangement. I_0 monitor measures the incident-beam intensity. The x-ray fluorescence is monitored while the sample is rotated and translated by a precision stage. Both the step size of the stage motions and the focal spot size of the probe beam determine the spatial resolution in the reconstructed image. Adapted from Ref 61

The elemental distribution through the SiC shell was measured with x-ray microfluorescence tomography to study the transport of trace elements in the SiC barrier after being subjected to various neutron fluences (Ref 61). Microfluorescence tomography by x-ray is an ideal tool for this work because it is nondestructive (no spread of contamination), it is sensitive to heavy elements in a low-*Z* matrix, and because it provides a 3D picture of the elemental distribution. For example, the zinc distribution in a plane of the SiC shell is illustrated in Fig. 42.

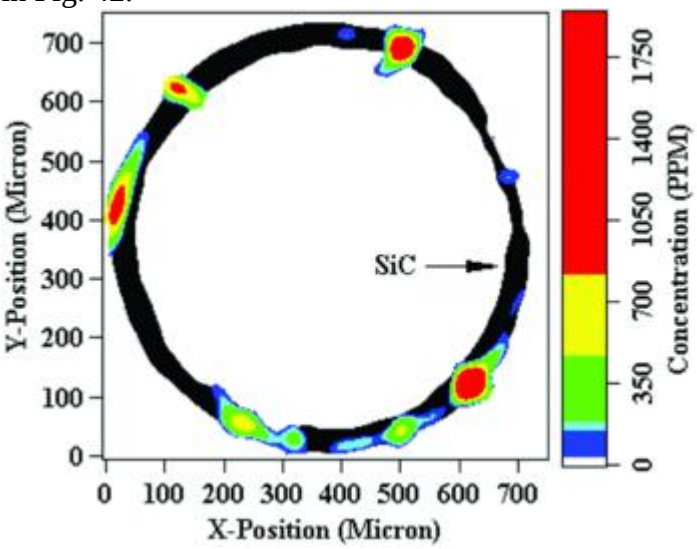

Fig. 42 Zinc distribution in a SiC shell after reconstruction from x-ray microfluorescence data. The spatial resolution was limited because available counting time restricted the number of steps. Source: Adapted from M. Naghedolfeizi et al., X-Ray Fluorescence Microtomography Study of Trace Elements in a SiC Nuclear Fuel Shell, *J. Nucl. Mater.*, 2002

References cited in this section

60. C.J. Sparks, X-Ray Fluorescence Microprobe for Chemical Analysis, *Synchrotron Radiation Research,* H. Winick and S. Doniach, Ed., Plenum Press, 1980, p 459–512

61. M. Naghedolfeizi et al., X-Ray Fluorescence Microtomography Study of Trace Elements in a SiC Nuclear Fuel Shell, *J. Nucl. Mater.*, Vol 312 (No. 2–3), 2003, p 146–155

M.V. Kral, G. Ice, M.K. Miller, M.D. Uchic, and R.O. Rosenberg, Three-Dimensional Microscopy, *Metallography and Microstructures,* Vol 9, *ASM Handbook,* ASM International, 2004, p. 448–467

Three-Dimensional Microscopy

M.V. Kral, University of Canterbury, Christchurch, New Zealand; Gene Ice and M.K. Miller, Oak Ridge National Laboratory; M.D. Uchic, Wright-Patterson Air Force Research Laboratory; R.O. Rosenberg, Naval Research Laboratory

---

Direct-Imaging Methods

Direct-imaging methods can sometimes be used to study 3D structure with micron to submicron resolution. The advantage of direct imaging is that only one or a few images are needed to determine the location of a particular voxel that is scattering into a particular location. This greatly reduces the noise that is typically introduced in a tomographic reconstruction.

Direct imaging is carried out typically with one of two possible methods: ray tracing or gage volume restriction. With ray-tracing methods, the detector-to-sample distance is changed and features in the pattern are correlated at the several distances to determine the origin along the incident pencil beam. This approach is illustrated in Fig. 43(a). This method works well for very distinct features such as Laue reflections from undeformed crystalline grains.

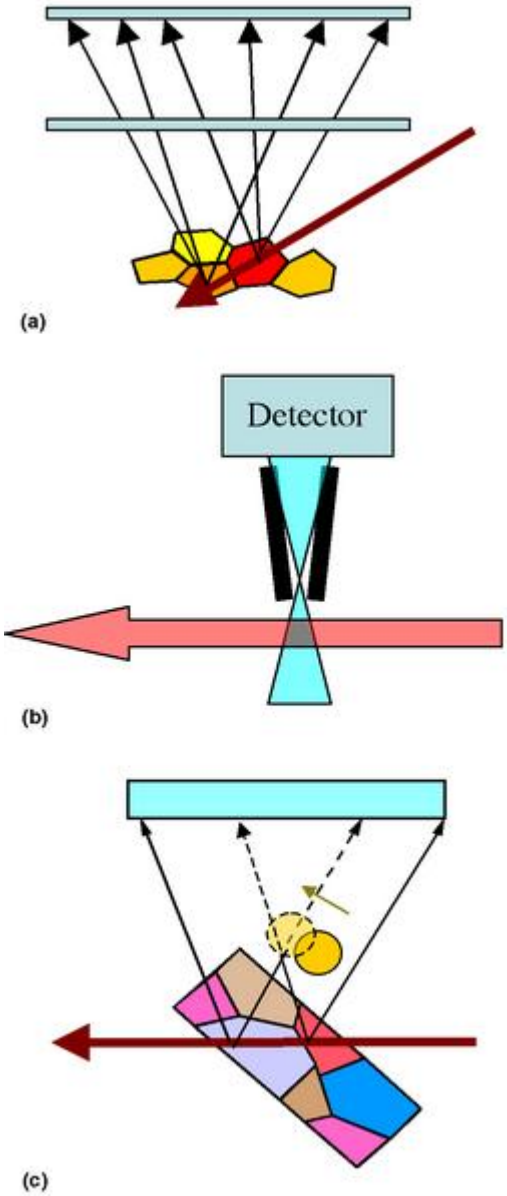

Fig. 43 Zinc distribution in a SiC shell after reconstruction from x-ray microfluorescence data. The spatial resolution was limited because available counting time restricted the number of steps. Source: Adapted from M. Naghedolfeizi et al., X-Ray Fluorescence Microtomography Study of Trace Elements in a SiC Nuclear Fuel Shell, *J. Nucl. Mater.*, 2002

An alternative method of determining 3D structure by direct imaging is by restricting the gage volume within which signal can be generated. For example, a focused beam defines the gage volume in two dimensions and beam-defining slits define the beam in a third dimension (Fig. 1b). This method is commonly used to define the scattering volume for powder diffraction and can be used with fluorescence imaging and other scattering processes.

An important variant of gage-volume defining techniques uses a differential aperture with an opening determined by the change in position of a wire (shown by the two overlapping circles) between successive images (Fig. 1c). This method has the advantage that it is automatic (such as standard gage volume methods) and also allows the gage volume studied to become submicron in size (Ref 62).

Reference cited in this section

62. B.C. Larson et al., Three-Dimensional X-Ray Structural Microscopy with Submicrometre Resolution, *Nature,* Vol 415, 2002, p 887

M.V. Kral, G. Ice, M.K. Miller, M.D. Uchic, and R.O. Rosenberg, Three-Dimensional Microscopy, *Metallography and Microstructures,* Vol 9, *ASM Handbook,* ASM International, 2004, p. 448–467

M.V. Kral, University of Canterbury, Christchurch, New Zealand; Gene Ice and M.K. Miller, Oak Ridge National Laboratory; M.D. Uchic, Wright-Patterson Air Force Research Laboratory; R.O. Rosenberg, Naval Research Laboratory

Computer Reconstruction and Visualization of Three-Dimensional Data

R.O. Rosenberg, Naval Research Laboratory, Scientific Visualization Laboratory

Characterization of materials by analysis of 3D microstructures is placing a strong demand for visualization tools and techniques. On-line sources of these tools are found in Table 1.

Table 1 On-line sources of further information

Web site name	URL	Note
San Diego Supercomputer Center	vis.sdsc.edu/download/downloads.html#VisTools	Image format conversion
Portable Pixel Map (PPM)	sourceforge.net/projects/netpbm	Image conversion
NIH Image	rsb.info.nih.gov/nih-image	Public domain preprocessing
Aphelion	hallogram.com/apheliondev	Commercial
Noesis Images	www.norpix.com/visilog.htm	Commercial
3D Doctor	www.ablesw.com/3d-doctor/3dhome.html	Image processing
Quadric Mesh Simplification	graphics.cs.uiuc.edu/~garland/software/qslim.html	Algorithm
STRIPE	www.cs.sunysb.edu/~stripe/	Public domain algorithm
Amira, Template Graphics, Inc. (TGS)	www.amiravis.com/	Commercial algorithm
AVS Express, Advanced Visual Systems	www.avs.com	Commercial algorithm
Imaris, Bitplane, Inc.	www.bitplane.com/products/imaris/imaris_product.shtml	Commercial algorithm
Silicon Graphics, Inc. (SGI)	www.sgi.com/software/volumizer	Commercial texture mapping algorithm
VolVis, SUNY, Stony Brook	www.cs.sunysb.edu/~vislab/volvis_home.htm	Public domain ray tracing
SCIRun, University of Utah	software.sci.utah.edu/scirun.html	Public domain ray tracing
Volpack, Stanford University	graphics.stanford.edu/software/volpack/	Public domain ray tracing
Mitsubishi Electronics Research Laboratory (MERL)	www.rtviz.com/products/volumepro_prod.html	Graphics card for ray tracing
Voxblast RT, VayTek, Inc.	www.vaytek.com/VoxBlast.html	Imaging package
WorkSpace	www.fakespacesystems.com/index.htm	Virtual reality
CAVE, NCSA	www.vrco.com/	Virtual reality

Three-dimensional data sets comprise a series of light optical or electron micrographs obtained via serial sectioning or computed tomography (CT). Spacing between serial-section images is usually on the order of 0.1 μm (3.9 μin.). A high enough resolution in the *x*, *y*, and *z* planes is recommended so that the desired features can be clearly elucidated, so that there is no confusion in characterizing complex structural features. Many visualization tools address "uniform" data that has the same spacing between each slice as between each pixel within each image. If micrographs are on the order of hundreds of pixels on a side, such uniform data sets will require hundreds of slices. The visualization tools must be able to compensate when the spacing between slices differs from the spacing between pixels, which is a common situation. The data set is still uniform, but with a larger spacing in the *z* direction.

Images can have many formats, the most common being GIF, JPEG, TIFF, and RGB. Many tools exist to convert between image formats. San Diego Supercomputer Center's "imconv" is a public domain package that converts between a large number of formats. The Portable Pixel Map (PPM) utilities are also useful for image conversion and simple image editing such as scaling, cropping, pasting, and copying.

M.V. Kral, G. Ice, M.K. Miller, M.D. Uchic, and R.O. Rosenberg, Three-Dimensional Microscopy, *Metallography and Microstructures,* Vol 9, *ASM Handbook,* ASM International, 2004, p. 448–467

Three-Dimensional Microscopy

M.V. Kral, University of Canterbury, Christchurch, New Zealand; Gene Ice and M.K. Miller, Oak Ridge National Laboratory; M.D. Uchic, Wright-Patterson Air Force Research Laboratory; R.O. Rosenberg, Naval Research Laboratory

Preprocessing

The images can be preprocessed to facilitate reconstruction and visualization of meaningful 3D images. Public domain tools such as NIH Image, along with commercial packages such as Aphelion and Noesis Images, can create image stacks. Images can then be realigned or masked by hand or filtered using standard image-processing operators such as dilation and erosion, edge detection, Fast Fourier Transforms, and despeckling. Commercial software, such as 3D Doctor automate realignment and have special functions to improve degraded images using point spread functions with maximum entropy deconvolution.

M.V. Kral, G. Ice, M.K. Miller, M.D. Uchic, and R.O. Rosenberg, Three-Dimensional Microscopy, *Metallography and Microstructures,* Vol 9, *ASM Handbook,* ASM International, 2004, p. 448–467

Three-Dimensional Microscopy

M.V. Kral, University of Canterbury, Christchurch, New Zealand; Gene Ice and M.K. Miller, Oak Ridge National Laboratory; M.D. Uchic, Wright-Patterson Air Force Research Laboratory; R.O. Rosenberg, Naval Research Laboratory

Segmentation

In medical applications, image segmentation is one of the most important operations. Segmentation requires a histogram of pixel values that shows which pixels values are the most frequent. For medical images, there is usually a peak around the skin/soft tissue area and another peak around the bone values. Based on the range of pixel values, either skin or bone can be visualized by making the appropriate range of pixel values either opaque, transparent, or some specific color. Pixel values can be assigned a color (a red, green, blue, opacity quartet) by use of a transfer function. A transfer function maps a pixel value to a color and can be as simple as using a red-orange-yellow-green-blue color ramp. (In hue-saturation-value space, hue is varied from red to

blue, i.e., form 0 to 255, pure red being the highest pixel value and blue the lowest). The opacity can be assigned to elucidate features. For example, in medical applications, either the bone values or the skin values can be assigned zero opacity in order to make them completely transparent.

M.V. Kral, G. Ice, M.K. Miller, M.D. Uchic, and R.O. Rosenberg, Three-Dimensional Microscopy, *Metallography and Microstructures,* Vol 9, *ASM Handbook,* ASM International, 2004, p. 448–467

Three-Dimensional Microscopy

M.V. Kral, University of Canterbury, Christchurch, New Zealand; Gene Ice and M.K. Miller, Oak Ridge National Laboratory; M.D. Uchic, Wright-Patterson Air Force Research Laboratory; R.O. Rosenberg, Naval Research Laboratory

---

Algorithms

Once the images have been aligned, masked, and segmented, they can be converted to a volumetric data set. One technique is to convert images to PPM format, strip off the top four lines, and append successive images. (The body of a PPM file is just the sequence of pixel values with the *x*-direction incremented first). With a volumetric data set, there is a voxel value for every image pixel in every slice.

There are two basic algorithms for viewing volumetric data sets, isosurface generation and ray tracing.

Isosurface generation renders an isosurface within each volumetric data set as a set of geometric primitives, such as triangles. These geometric descriptions of data have been very useful in modeling jets and submarines, as well as in finite-element calculations and, finally, with the advent of the Marching Cubes algorithm (Ref 63), in volumetric data.

The Marching Cubes algorithm is a simple technique to generate an isosurface. The volumetric data is decomposed into little cubes consisting of just eight voxels (volume elements) constituting the corners of the cube. Each corner vertex is checked to see if it is above or below the isosurface value. If all vertex values are above or below the isosurface value, then there is no isosurface intersection and one goes on to the next cube. If the isosurface does intersect the cube (some vertex values are above and some below the isosurface value), then the edges where the intersections occur are noted and intersection points are calculated using trilinear interpolation. A set of triangles is selected based on the edge intersection list and the resulting triangles, that is, the vertices and their normals, are saved to a triangle list. The algorithm continues until there are no more cubes to evaluate.

The Marching Cubes algorithm results in a list of independent triangles, that is, a list of vertices where each consecutive three vertices constitute a triangle. The lower the number of triangle vertices, the faster the rendering. Converting the independent triangle list to a shared vertex list—simply a list of vertices and their connectivities—usually results in about 60% fewer vertices. Still more efficient are triangle strips, which require only two vertices to specify the next triangle in the strip.

Model data sets, such as those used in engineering or computer gaming, are “smooth” and can consist of 50,000 to a million triangles. Natural data sets, such as those found in medicine and material science, are not smooth and can result in 10 million to hundreds of millions of triangles or more. In order to render these large and more complex data sets, the triangle mesh must be simplified. A number of algorithms exist to simplify (reduce the number of triangles) in a mesh in such a way as to preserve appearance of the mesh. The Visualization Tool Kit (VTK) (Ref 64) has such an algorithm available. One algorithm often employed is the Quadric Mesh Simplification by M. Garland (see Table 1). This algorithm is an “edge-collapsing” algorithm that constructs a list of edges from the triangle mesh and then prioritizes them according to the surface curvature about each edge. The user simply specifies the desired number of triangles to remain, and the triangle mesh is reduced in a speedy fashion with high-fidelity results comparable to algorithms that are an order of magnitude slower.

The simplified mesh can be converted to triangle strips for still faster rendering. On Silicon Graphics workstations, “ivfix” is typically used to convert triangles meshes to triangle strips of about length 6. “STRIPE,” a public domain package for triangles strip generator, attempts to construct triangle strips as long as possible.

In 1983, Jim Clark invented the Geometry Engine, a hardware device that accelerates the rendering of triangles a hundredfold by performing triangle vertex operations, such as rotation and lighting scan line rasterization and texture mapping, all in hardware (Ref 65). Jim Clark went on to found Silicon Graphics (SGI). Current graphics cards are geared toward gaming, but can render millions of triangles per second and are therefore well suited for visualization. There are a number of 3D reconstruction software kits that can take advantage of these new graphic cards, including Amira from Template Graphics, Inc. (TGS), Imaris from Bitplane, Inc., and AVS Express from Advanced Visual Systems.

Ray tracing, the other method of rendering a volume, is based on the physical illumination equation and does not depend on approximating data with geometric primitives. Typical ray-tracing algorithms are implemented in software and are much more time consuming to run than isosurface generation. However, they do result in very detailed, realistic images. With very large, multigigabyte data sets, it has been estimated that ray tracing, in software, will be competitive with geometry rendering in hardware (Ref 66).

There are many ray-tracing algorithms. Whitted developed the original ray-casting algorithm in 1980 (Ref 67). Splatting (Ref 68), shear-warp (Ref 69), and 3D texture mapping (see Table 1) are also popular algorithms.

Ray casting involves casting rays from the user's viewpoint through the volumetric data and compositing color along the ray based on the color and transparency values of each voxel. Each ray assigns a color for each pixel in the image plane. When another view is required, the image plane is rotated, not the volumetric data, thus saving much rendering time. Optimized algorithms store the data on a hierarchical grid in order to save time casting rays, or they rotate the volumetric data in an efficient way. The shear-warp algorithm converts the three Euler angle rotations to two shears and an image warp. The splatting algorithm loops over the data voxels, instead of the image plane pixels, thus achieving a greater degree of data parallelism for massively parallel computers. A number of public domain ray-tracing packages are available, including VolVis from SUNY Stony Brook, SCIRun from University of Utah, and Volpack from Stanford University.

Finally, hardware texture mapping stores the volumetric data in 3D texture memory. Geometry slices, parallel to the image plane, are texture mapped with the 3D texture, and compositing is done with in the graphics card for high-speed ray tracing. The only limitation is the amount of texture memory available on the graphics card. SGI's OpenGL Volumizer renders in hardware providing a tenfold to hundredfold speedup over the algorithm in software.

Mitsubishi Electronics Research Laboratory (MERL) recently developed the first commercially available graphics card specifically designed for ray tracing. The commercial product is known as the VolumePro Graphics card. TeraRecon, Inc. can provide a workstation with the latest card able to render a 512^3 data set at 30 frames/s. A number of 3D imaging packages support the VolumePro graphics card including Voxblast RT from VayTek, Inc. and Amira from TGS.

References cited in this section

63. W.E. Lorensen and H.E. Cline, Marching Cubes: A High Resolution 3D Surface Construction Algorithm, *Comput. Graph.*, Vol 21 (No. 4), p 163–169

64. W. Schroeder, K. Martin, and B. Lorensen, *The Visualization Toolkit,* Prentice Hall, 1996

65. J.D. Foley et al., *Computer Graphics Principles and Practice,* Addison-Wesley, 1990

66. S. Parker et al., Interacting with Gigabyte Volume Datasets on the Origin 2000, *The 41st Annual Cray User's Group Conference,* 1999

67. T. Whitted, An Improved Illumination Model for Shaded Display, *CACM,* Vol 23 (No. 6), 1980, p 343–349

68. L. Westover, Footprint Evaluation for Volume Rendering, *Computer Graphics (SIGGRAPH '90 Proceedings),* 1990

69. P. Lacroute and M. Levoy, Fast Volume Rendering using a Shear-Warp Factorization of the Viewing Transformation, *Computer Graphics (SIGGRAPH '94 Proceedings),* 1994

M.V. Kral, G. Ice, M.K. Miller, M.D. Uchic, and R.O. Rosenberg, Three-Dimensional Microscopy, *Metallography and Microstructures,* Vol 9, *ASM Handbook,* ASM International, 2004, p. 448–467

M.V. Kral, University of Canterbury, Christchurch, New Zealand; Gene Ice and M.K. Miller, Oak Ridge National Laboratory; M.D. Uchic, Wright-Patterson Air Force Research Laboratory; R.O. Rosenberg, Naval Research Laboratory

Virtual Reality

Virtual Reality (VR) provides the ultimate in visualization environments for high-end visualization. These are immersive environments that the user can interact with through a pair of head-tracked stereo liquid crystal display (LCD) shutter glasses and a 3D tracking wand. Virtual reality environments range from a head-mounted display—essentially a helmet with stereo LCD displays—to Fakespace Systems WorkWall, WorkDesk, and WorkSpace. The latter is an immersive room with 3 by 3 m (10 by 10 ft) screens that are rear projected (affording the user intimate interaction with the environment without obstructing the projector beam). Each screen typically has its own graphics engine controlling the view. The trick is to coordinate the views on all the screens so that the visual environment is seamless. National Center for Supercomputer Applications (NCSA) provides the CAVE software and Iowa State provides "Juggle." Both kits can be used to program and control these immersive VR environments. Older CAVEs ran only with SGI platforms, but current environments can be supported by Linux clusters. These virtual environments use high-speed rendering to achieve interactivity. With the human-scale interaction afforded by large-scale VR, visualization is performed in a very natural way, providing a realistic depiction that makes quite an impact. Often the user will notice details that just were not seen using the desktop visualization environment. A number of commercial packages support VR environments, including AVS Express multipipe edition and Amira by TGS.

M.V. Kral, G. Ice, M.K. Miller, M.D. Uchic, and R.O. Rosenberg, Three-Dimensional Microscopy, *Metallography and Microstructures,* Vol 9, *ASM Handbook,* ASM International, 2004, p. 448–467

Three-Dimensional Microscopy

M.V. Kral, University of Canterbury, Christchurch, New Zealand; Gene Ice and M.K. Miller, Oak Ridge National Laboratory; M.D. Uchic, Wright-Patterson Air Force Research Laboratory; R.O. Rosenberg, Naval Research Laboratory

Acknowledgments

For the section "Atom Probe Tomography," research at the Oak Ridge National Laboratory SHaRE Collaborative Research Center was sponsored by the Division of Materials Sciences and Engineering, U.S. Department of Energy, under contract DE-AC05-00OR22725 with UT-Battelle, LLC.

For the section "X-Ray Microtomography," work was sponsored by the Division of Materials Sciences. Oak Ridge National Laboratory (ORNL) is operated by UT-Battelle, LLC, for the U.S. Department of Energy under contract DE-AC05-00OR22725.

M.V. Kral, G. Ice, M.K. Miller, M.D. Uchic, and R.O. Rosenberg, Three-Dimensional Microscopy, *Metallography and Microstructures,* Vol 9, *ASM Handbook,* ASM International, 2004, p. 448–467

Three-Dimensional Microscopy

M.V. Kral, University of Canterbury, Christchurch, New Zealand; Gene Ice and M.K. Miller, Oak Ridge National Laboratory; M.D. Uchic, Wright-Patterson Air Force Research Laboratory; R.O. Rosenberg, Naval Research Laboratory

References

1. R.T. DeHoff, Quantitative Serial Sectioning Analysis: Preview, *J. Microsc.,* Vol 131 (No. 3), 1983, p 259–263

2. A.C. Lund and P.W. Voorhees, The Effects of Elastic Stress on Microstructural Development: The Three-Dimensional Microstructure of a Gamma-Gamma′ Alloy, *Acta Mater.,* Vol 50 (No. 10), p 2585–2598

3. M.V. Kral and G. Spanos, Three Dimensional Analysis of Proeutectoid Cementite Precipitates, *Acta Metall.,* Vol 47 (No. 2), 1999, p 711–724

4. M.V. Mangan, M.V. Kral, and G. Spanos, Correlation between the Crystallography and Morphology of Proeutectoid Widmanstatten Cementite Precipitates, *Acta Mater.,* Vol 47 (No. 17), 1999, p 4263–4274

5. T.L. Wolfsdorf, W.H. Bender, and P.W. Voorhees, The Morphology of High Volume Fraction Solid-Liquid Mixtures: An Application of Microstructural Tomography, *Acta Mater.,* Vol 45 (No. 6), 1997, p 2279–2295

6. B.J. Inkson, M. Mulvihill, and G. Möbus, 3D Determination of Grain Shape in a FeAl-Based Nanocomposite by 3D FIB Tomography, *Scr. Mater.,* Vol 47 (No. 7), 2001, p 753–758

7. A. Cerezo et al., Visualisation of Three-Dimensional Microstructures, *Surf. Sci.,* Vol 266 (No. 1–3), 1991, p 471–480

8. O. Forsman, Undersökning av rymdstrukturen hos ett kolstål av hypereutektoid sammansättning, *Jern-Kontorets Ann.,* Vol 102, 1918, p 1–30

9. M. Hillert, The Formation of Pearlite, *The Decomposition of Austenite by Diffusional Processes,* V.F. Zackay and H.I. Aaronson, Ed., Interscience, 1962, p 197–237

10. E. Eichen et al., Thermionic Emission Microscope Study of the Formation of Ferrite Sideplates, *Acta Metall.,* Vol 12, 1964, p 1298–1301

11. R.H. Hopkins and R.W. Kraft, A Rapid Technique for Observation of Three-Dimensional Microstructures, *Trans. AIME,* Vol 233, 1965, p 1526–1532

12. E.B. Hawbolt and L.C. Brown, Grain Boundary Precipitation in Ag-5.64 wt pct Al Alloys, *Trans. AIME,* Vol 239, 1967, p 1916–1924

13. L.K. Barrett and C.S. Yust, Progressive Shape Changes of the Void During Sintering, *Trans. AIME,* Vol 239, 1967, p 1172–1180

14. P.M. Ziolkowski, *The Three Dimensional Shapes of Grain Boundary Precipitates in a/b Brass,* Michigan Tech., 1985

15. D.A. Hull et al., Titanium Prior-Beta Grain Volume Distribution by Quantitative Serial Sectioning Techniques, *Mater. Charact.,* Vol 26, 1991, p 63–71

16. J. Brystrzycki and W. Przetakiewicz, 3-Dimensional Reconstruction of Annealing Twins Shape in FCC Metals by Serial Sectioning, *Scr. Metall. Mater.,* Vol 27, 1992, p 893–896

17. H. Wieland, T.N. Rouns, and J. Liu, The Role of Particle Stimulated Nucleation During Recrystallization of an Aluminum-Manganese Alloy, *Z. Metallkd.,* Vol 85, 1994, p 592–597

18. M.A. Mangan, P.D. Lauren, and G.J. Shiflet, Three-Dimensional Reconstruction of Widmanstatten Plates in Fe-12.3Mn-0.8C, *J. Microsc.,* Vol 188, Oct 1997, p 36–41

19. F.N. Rhines, K.R. Craig, and D.A. Rousse, Measurement of Average Grain Volume and Certain Topological Parameters by Serial Section Analysis, *Metall. Trans.,* Vol 7A, 1976, p 1729–1734

20. A. Tewari, A.M. Gokhale, and R.M. German, Effect of Gravity on Three-Dimensional Coordination Number Distribution in Liquid Phase Sintered Microstructures, *Acta Mater.,* Vol 47 (No. 13), 1999, p 3721–3734

21. J.C. Russ, *Image Processing Handbook,* CRC Press, 1994

22. J. Alkemper and P.W. Voorhees, Quantitative Serial Sectioning Analysis, *J. Microsc.,* Vol 201, 2000, p 1–8

23. G.A. Bertero et al., *Metall. Trans.,* Vol 22A, 1991, p 2723

24. C.A. Dubé, H.I. Aaronson, and R.F. Mehl, La formation de la ferrite proeutectoide dans les aciers au carbon, *Rev. Metall.,* Vol 55 (No. 3), 1958, p 201–210

25. H.I. Aaronson, *The Decomposition of Austenite by Diffusional Processes,* V.F. Zackay and H.I. Aaronson, Ed., Interscience, 1962, p 387

26. G. Spanos and M.V. Kral. Three Dimensional Reconstruction and Classification of Ferrite Precipitates, *International Conference on Solid-Solid Phase Transformations '99,* Japan Institute of Metals, 1999

27. M.V. Kral et al., Three-Dimensional Analysis of Microstructures, *Mater. Charact.,* Vol 45 (No. 1), 2000, p 17–23

28. T. Yokomizo et al., Three-Dimensional Distribution, Morphology, and Nucleation Site of Intragranular Ferrite Formed in Association with Inclusions, *Mater. Sci. Eng. A,* Vol 344 (No. 1–2), 2003, p 261–267

29. M. Uno and M. Enomoto, *Distribution of MnS Particles During Grain Growth of Ferrite,* Ibaraki University, 2002

30. A. Tewari and A.M. Gokhale, Estimation of Three-Dimensional Grain Size Distribution from Microstructural Serial Sections, *Mater. Charact.,* Vol 46 (No. 4), 2001, p 329–335

31. P. Louis and A. Gokhale, Application of Image Analysis for Characterization of Spatial Arrangement of Features in Microstructures, *Metall. Mater. Trans.,* Vol 26A, 1995, p 1449–1456

32. R.E. Hackenberg, D.P. Nordstrom, and G.J. Shiflet, Morphology and the Three-Dimensional Structure of Ferrite Formed below the Bay in an Fe-C-W Alloy, *Scr. Mater.,* Vol 47 (No. 6), 2002, p 357–361

33. W.T. Reynolds et al., Incomplete Transformation Phenomenon in Fe-C-Mo Alloys, *Metall. Trans. A,* Vol 21 (No. 6), 1990, p 1433–1463

34. R.E. Hackenberg, D.G. Granada, and G.J. Shiflet, Austenite Decomposition to Carbide-Rich Products in Fe-0.30C-6.3W, *Metall. Mater. Trans. A,* Vol 33, 2002, p 3619–3633

35. D.N. Dunn, G.J. Shiflet, and R. Hull, Quantitative Three-Dimensional Reconstruction of Geometrically Complex Structures with Nanoscale Resolution, *J. Sci. Instrum.,* Vol 73, 2002, p 330–334

36. M.A. Mangan and G.J. Shiflet, Three-Dimensional Reconstruction of Pearlite Colonies, *Solid-Solid Phase Transformations Proc.,* TMS, 1994

37. A.J. Patkin and G.H. Morrison, Secondary Ion Mass Spectrometric Image Depth Profiling for Three-Dimensional Elemental Analysis, *Anal. Chem.,* Vol 54 (No. 1), 1982, p 2–5

38. M.W. Phaneuf and J. Li, FIB Techniques for Analysis of Metallurgical Specimens, in *Microscopy & Microanalysis 2000,* Cambridge University Press, Cambridge, England, 2000

39. B.J. Inkson et al., Subsurface Nanoindentation Deformation of Cu-Al Multilayers Mapped in 3D by Focused Ion Beam Microscopy, *J. Microsc.,* Vol 201 (No. 2), 2001, p 256–269

40. D.N. Dunn and R. Hull, Reconstruction of Three-Dimensional Chemistry and Geometry Using Focused Ion Beam Microscopy, *Appl. Phys. Lett.,* Vol 75 (No. 21), 1999, p 3414–3416

41. T. Sakamoto et al., Development of an Ion and Electron Dual Beam Focused Beam Apparatus for Three-Dimensional Microanalysis, *Jpn. J. Appl. Phys.,* Vol 37 Part 1 (No. 4A), 1998, p 2051–2056

42. M.K. Miller, *Atom Probe Tomography: Analysis at the Atomic Level,* Kluwer Academic/Plenum Press, 2000

43. E.W. Müller, J.A. Panitz, and S.B. Mclane, *Rev. Sci. Instrum.,* Vol 36, 1968, p 83

44. M.K. Miller et al., *Atom Probe Field Ion Microscopy,* Oxford University Press, Oxford, UK, 1996

45. G.D.W. Smith, Field Ion Microscopy and Atom Probe Microanalysis, *Materials Characterization,* Vol 10, 9th ed., *Metals Handbook,* American Society for Metals, 1986, p 583–602

46. M.K. Miller et al., Spinodal Decomposition in Fe-Cr Alloys: Experimental Study at the Atomic Level and Comparison with Computer Models—I. Introduction and Methodology, *Acta Metall. Mater.,* Vol 43 (No. 9), 1995, p 3385–3401

47. B.C. Larson et al., 3D Measurement of Deformation Microstructure in Al(0.2%) Mg Using Submicron Resolution X-Ray Microbeams, *Mater. Res. Soc. Symp. Proc.,* Vol 590, 2000, p 247–252

48. C.R. Patterson et al., Nondestructive Determination of the Depth of Different Texture Components in Polycrystalline Samples, *Mater. Res. Soc. Symp. Proc.,* Vol 590, 2000, p 253–258

49. G.E. Ice and B.C. Larson, 3D X-Ray Crystal Microscope, *Adv. Eng. Mater.,* Vol 2, 2000, p 643–646

50. W.-B. Yun, personal communication, 2002

51. Q.C. Johnson et al., *Proc. Mater. Soc. Symp.,* Vol 69, 1986, p 203

52. J.H. Dunsmuir, personal communication, 1991

53. J.H. Kinney et al., The X-Ray Tomographic Microscope-3 Dimensional Perspectives of Evolving Microstructures, *Nucl. Inst. Meth. A,* Vol 347, 1994, p 480–486

54. R.H. Huesman et al., *Pub. 214—RECLBL Library Users Manual, Donner Algorithms for Reconstruction Tomography,* Lawrence Berkeley Laboratory, University of California, Berkeley, CA, 1977

55. G.T. Herman, *Image Reconstruction from Projections: Implementation and Applications,* Springer-Verlag, Berlin, 1979

56. P. Spanne et al., Synchrotron Computed Microtomography of Porous-Media-Topology and Transports, *Phys. Rev. Lett.,* Vol 73, 1994, p 2001–2004

57. J.H. Kinney, N.E. Lane, and D.L. Haupt, In-vivo, 3-Dimensional Microscopy of Trabecular Bone, *J. Bone Min. Res.,* Vol 10, 1995, p 264–270

58. A. Guvenilir et al., Direct Observation of Crack Opening as a Function of Applied Load in the Interior of a Notched Tensile Sample of Al-Li 2090, *Acta Mater.,* Vol 45, 1997, p 1977–1987

59. M. Hasnah et al., Single-Exposure Simultaneous Diffraction-Enhanced Imaging, *Nucl. Instrum. Methods,* Vol 492, 2002, p 236–240

60. C.J. Sparks, X-Ray Fluorescence Microprobe for Chemical Analysis, *Synchrotron Radiation Research,* H. Winick and S. Doniach, Ed., Plenum Press, 1980, p 459–512

61. M. Naghedolfeizi et al., X-Ray Fluorescence Microtomography Study of Trace Elements in a SiC Nuclear Fuel Shell, *J. Nucl. Mater.,* Vol 312 (No. 2–3), 2003, p 146–155

62. B.C. Larson et al., Three-Dimensional X-Ray Structural Microscopy with Submicrometre Resolution, *Nature,* Vol 415, 2002, p 887

63. W.E. Lorensen and H.E. Cline, Marching Cubes: A High Resolution 3D Surface Construction Algorithm, *Comput. Graph.,* Vol 21 (No. 4), p 163–169

64. W. Schroeder, K. Martin, and B. Lorensen, *The Visualization Toolkit,* Prentice Hall, 1996

65. J.D. Foley et al., *Computer Graphics Principles and Practice,* Addison-Wesley, 1990

66. S. Parker et al., Interacting with Gigabyte Volume Datasets on the Origin 2000, *The 41st Annual Cray User's Group Conference,* 1999

67. T. Whitted, An Improved Illumination Model for Shaded Display, *CACM,* Vol 23 (No. 6), 1980, p 343–349

68. L. Westover, Footprint Evaluation for Volume Rendering, *Computer Graphics (SIGGRAPH '90 Proceedings),* 1990

69. P. Lacroute and M. Levoy, Fast Volume Rendering using a Shear-Warp Factorization of the Viewing Transformation, *Computer Graphics (SIGGRAPH '94 Proceedings),* 1994

M.L. Wayman, Metallography of Archaeological Alloys, *Metallography and Microstructures*, Vol 9, *ASM Handbook*, ASM International, 2004, p. 468–477

Metallography of Archaeological Alloys

M.L. Wayman, University of Alberta

Introduction

ARCHAEOMETALLURGY is the field of research in which information about life in the past is obtained from the study of how past peoples produced and used metals and alloys. It is, in fact, a subdiscipline of archaeometry, a broader field in which all of the physical and natural sciences are applied to studies of the past. Archaeometallurgy involves the study of a wide range of metal-related objects that have survived over time and have come down to us in the present. These objects, the results of the original metal production and metalworking processes, reached their present states after having been subjected to one or more of many processes, including trade, use, modification, discard, and possibly some degradation in the ground and/or alteration in museum or private collections. These artifacts have been recovered from a variety of archaeological contexts, such as habitation sites, industrial sites, funerary (burial) contexts (i.e., grave goods), hoards, and ceremonial sites (including offerings, deposits into rivers or other sacred places, etc.). Some appear to have been simply discarded, either inadvertently or consciously, while others have been placed purposefully in specific locations, either with or without the intention of recovering them later. Unfortunately, all too often the material that is available for the archaeometallurgist to analyze has no well-defined provenance, either because of imprecise record keeping in the past (e.g., incompletely documented museum collections) or because the objects were removed from their archaeological contexts without proper recording, which can happen, for example, by the actions of an overenthusiastic artifact collector or an illicit tombrobber.

The actual artifacts include not only metallic objects but also related material, including debris from metal producing and metalworking sites, for example ore (as-mined, as-concentrated, as-roasted), slag, crucibles, molds, and the remains of furnaces, kilns, and hearths. Other material includes hammers, anvils, and other shaping tools, along with partially formed objects and casting debris such as molds, misruns, sprues and runners, defective castings waiting for remelt, and various other forms of scrap.

It is useful to think of each of the objects that comes down to us from the past as having a story to tell, a story that, if read, can contribute to our general understanding. This story is inscribed or recorded in the composition and microstructure of the object, and metallography serves as a language that is employed to read the story of the object in the same way that a written language can be employed to read an ancient text. This philosophy can be applied not only to truly ancient objects but also to historical objects from the more recent past, such as the Industrial Revolution. Because of poor record keeping, deliberately misleading patents, and other attempts to maintain control over industrial process secrets, an understanding of the prevailing technologies of the time has not yet been achieved.

The results of metallographic analysis are used in many ways to improve our understanding of life in the past (Ref 1 provides an anthropological perspective). In many cases, the analysis can provide us with a knowledge of the early technologies employed (i.e., how the objects were made) and the metallurgical traditions; innovations and possible origins can sometimes be identified. However, at a deeper level, studies of the objects can shed light on issues such as their original appearance, how they were used and recycled, and what processes occurred after they were deposited in the archaeological record. Information can be obtained about trade and exchange routes along which raw materials, finished products, and/or technical knowledge moved, and hence contributions can be made to assessing such questions as whether a particular technology is present in a particular geographic area as a result of diffusion as opposed to independent invention.

These interpretations can be extended to provide ideas about the place of metals and those who worked with them in ancient economies and societies, the extent to which their properties were understood, and the technical choices that guided the working strategies of the people involved. Information can be obtained about the living conditions of the people who were involved in some way with the object, including the miners; the smelters; the

metalworkers; the traders of raw materials and semifinished and finished objects; the owners, custodians, and users of the object; their families; their communities; and their cultures. Who were these people? In what types of society did they live? Were they full-time or part-time workers? Were they self-employed or employees of the state, of an aristocracy, or of a ruler? To what extent was there social stratification and differentiation? Were these family activities or caste activities? What were the gender roles in the technologies?

For example, in some cases objects were produced using holistic procedures (Ref 2), with each worker making judgment decisions while taking raw materials through to a finished object. In other cases the technologies were prescriptive, with each worker carrying out one or a few of many steps in the technological chain and then passing the object along to someone else for the ensuing steps to be carried out. In this situation, standards and specifications are indispensable, with associated control and direction making necessary the existence of bosses, managers, and all that this implies. Archaeometallurgical studies of objects can thus potentially yield a surprising range of information about many aspects of life in the past.

Dating of artifacts is an issue that arises frequently. Most archaeological metals cannot be dated directly, and hence dating is most often achieved by stylistic analyses and/or by dating of the contexts in which the objects were found. However, some metal-related objects do contain information that can be used to obtain dates indirectly; for example, if the detailed history of the use of a particular technology is known with confidence, then the determination that this technology was used for a particular object can be useful in assigning it a date. Often, it is sufficient to know what dates do *not* fit the object; for example, knowledge of the earliest possible date consistent with the characteristics of the object (its *terminus post quem*) or the latest possible date for the object (its *terminus ante quem*) can be invaluable aids to archaeological interpretation.

Archaeometallurgical analysis can be complemented by experiments in which postulated early technologies are replicated to assess their feasibility and to produce objects whose structures and properties can be compared with those of the originals; analytical techniques, including metallography, are indispensable tools in this regard as well.

Archaeometallurgical analyses of objects from earlier times can also be carried out for purposes other than furthering our understanding of the past. Museum curators and conservators benefit from the results of such analyses by a better understanding of their collections and improved treatments for maintaining stability of the objects under storage or display conditions. Furthermore, assessments of the authenticity of purportedly ancient objects make extensive use of archaeometallurgical studies. Finally, some archaeometallurgical research can be of benefit to modern materials developments; for example, the long-term behavior of archaeological materials in burial contexts is of interest to those working on long-term corrosion characteristics of modern materials, including the stability of radioactive wastes under various conditions of disposal.

References cited in this section

1. D. Killick, Optical and Electron Microscopy in Material Culture Studies, *Learning from Things. Method and Theory of Material Culture Studies,* W.D. Kingery, Ed., Smithsonian Press, 1996

2. U.M. Franklin, *The Real World of Technology,* House of Anansi, Toronto, 1990; revised 1999

M.L. Wayman, Metallography of Archaeological Alloys, *Metallography and Microstructures,* Vol 9, *ASM Handbook*, ASM International, 2004, p. 468–477

Metallography of Archaeological Alloys

M.L. Wayman, University of Alberta

Metallography and the Archaeometallurgist

Archaeometallurgists use metallography to reveal and interpret the microstructures of objects so that, in conjunction with the results of their chemical analyses and microanalyses, they can acquire as much information as possible about the history of the material, including its smelting, refining, alloying, and

processing history. In other words, they use materials characterization techniques to unravel as much as is possible about the chemical, thermal, and mechanical histories of the objects since production. Previous treatments of this topic are included in Ref 3, 4, 5.

In comparison with metallographic analysis carried out on modern materials, there are a number of special problems that confront people wishing to perform such analyses on archaeological materials. Some of these are now considered.

Sampling. The objects that the archaeometallurgist studies are normally valuable in their own rights, either as art objects or as rare representatives of past cultures. They are typically housed in storage collections of material excavated from specific sites or in museum collections, where they may be either on display or in storage. Because of their value and rarity, they are normally jealously guarded, and rightly so, by their custodians who wish to preserve them for posterity while still making use of the material to obtain information about the lives of the people with whom they have been associated in the past. Hence, it is often forbidden to carry out sampling for metallographic purposes, which is, after all, an invasive procedure. Where such sampling is permitted, it is usually only allowed under conditions that are far from optimal, from a metallographic perspective. Sampling may be permitted only on visually unobtrusive areas of objects, such as the rear or the base of a casting or other areas that may have microstructures that the archaeometallurgist realizes are unlikely to be representative of the object as a whole or of specific areas of interest. For example, if it is of interest to determine the method of production of a knife or other edged tool, a metallographic section through the appropriate edge is essential for a proper evaluation of the edge forming, hardening, and/or sharpening procedures. However, sampling may only be permitted on the hilt, possibly under a wrapping where the sampling site will not be visible when the object is on display (Ref 6). Alternatively, metallography may only be permissible on the external surface of an object without cutting a sample, for example, by polishing a flat on the rim of a coin (Ref 7). In such a case, it is necessary to assess whether there could be important differences between surface and interior microstructures, differences that could arise as a result of processing parameters (e.g., surface segregation of solute elements during casting), surface treatment, wear, corrosion, and so on. Another frequent occurrence is that sampling may be permitted but restricted to the removal of a sample that is too small to address questions of heterogeneity, so that it may not be possible to be confident that the results obtained are representative of the object as a whole. Alternatively, sampling may be permitted adjacent to some preexisting damage to the object, such as a hole where corrosion has penetrated. In summary, it frequently happens that the material must be sampled for metallography at a location that is far from ideal. Of course, the sampling location and extent must be decided in consultation with the custodian of the object and approved (in writing!) by that person.

Often, where permitted, a V-shaped wedge sample is cut from the surface inward, ideally to the midpoint of the cross section. This sample is then mounted in an orientation appropriate to assess the microstructure of the full cross section. Where it is only possible to perform metallography on the external surface of the object, without cutting a sample, the complexity of surface topography can dictate that unorthodox sample preparation techniques be employed. A small handheld grinder-polisher (such as a Dremel-type motor drive) can be used for this purpose, along with dental microgrinding and polishing tools. This can reveal the surface microstructure in an adequate manner. However, it is important to note that preparation of a planar surface is not possible using this technique, so the light microscope cannot be used for microstructural observation even at moderate magnifications. The scanning electron microscope (SEM), with its significantly greater depth of field, proves useful here, provided that the object is small enough to fit into the evacuated specimen chamber of the SEM in an orientation appropriate for examination of the polished area of the surface. Several examples of situations where this has been successful are described in the subsequent case studies.

If the custodian so desires, the damage caused by cutting a sample from the object can be disguised, so that the display value of the object is restored. For example, a conservator can make use of a polymer filler to replace the material removed. In such cases, it is important that all procedures carried out on the object be recorded and that the records are kept with the object, so that future analysts will not attribute to the original creators of the object the features caused by modern sampling. Record keeping is, in fact, important in other respects, notably, to avoid repeating sampling where results of previous analyses have been lost. When inspecting a museum object, it is not uncommon to recognize locations where the object had been sampled at some point in the past but with no extant record of when, by whom, and with what result the previous analyses were carried out. Lack of proper record keeping can therefore result in excessive sampling, with consequent unnecessary damage to the object. Other consequences of inadequate record keeping are discussed subsequently.

Condition. Many early objects are now in poor condition, increasing the difficulty of determining their original microstructures and compositions and limiting the amount of information that can be obtained. This is especially true of those objects that have been buried in the earth for long periods of time. Corrosion of various types can affect metallic materials, converting the surfaces into corrosion product. The penetration of corrosion into the interior of objects is not uncommon. In some cases, it has proven difficult to distinguish between natural corrosion products and surface treatments applied intentionally to the object. This is the case with the many glossy, black-surfaced cast bronze Chinese mirrors (see subsequent case study), where much controversy has developed over whether a surface treatment was applied intentionally to create a glossy black surface or whether the surface appearance is the result of corrosion. Furthermore, pseudomorphic replacement of phases can occur, notably, the selective mineralization of metallic second-phase particles, both in alloys and in slag phases.

Some objects have been completely consumed by corrosion, so that they survive only as corrosion product. Efforts to extract useful information about the original material from the corrosion product have had some success, but because the archaeometallurgist is working backward from the object in order to decipher the nature of the processing, major changes to the object increase the uncertainty of the interpretation of the analysis. This applies not only to the microstructure but also to the composition.

In other cases, it can prove difficult to decide whether an object was originally made of a naturally occurring mineral or of a metal that has subsequently been completely converted to a corrosion product with similar mineralogy. This can apply, for example, to early beads, some of which now consist of malachite, the hydrated copper carbonate, but may or may not have originally been metallic copper.

The corrosion itself can, in some cases, occur differently from modern corrosion that takes place under different conditions. For example, the slip band corrosion observed in copper-base alloys (see subsequent case study) is distinctive enough that it can potentially be used as a means of assessing the authenticity of a purportedly ancient object (provided that it is permissible to sample the internal microstructure of the object). On the other hand, there are cases where corrosion can attack some phases preferentially, creating a microstructure that is a mixture of unetched phases and fully corroded phases, so that the original microstructure is revealed without the need for metallographic etching. This is the case, for example, with some early cast irons, where the ferrite constituent of the pearlite is replaced by corrosion product, but the cementite is more resistant to corrosion. If composition is being assessed by surface analysis, it must be remembered that corrosion product composition can differ markedly from the overall composition of an alloy. This applies, for example, to corroded tin bronzes, where tin content can be enriched or depleted relative to its content in the uncorroded alloy. Microanalysis of corroded objects can yield even more complexity and uncertainty. For example, if meteoritic iron is being identified on the basis of nickel content (see subsequent case study), it must be remembered that the nickel content in a meteorite is inhomogeneous among the different phases, and the corroded remnants of the different phases may survive in the corrosion product in different proportions, as compared with the uncorroded material. Furthermore, if nickel content is determined by microanalysis, there is a possibility that only a large corroded grain of the low-nickel phase is analyzed, in which case the potential exists for meteoritic iron to be misidentified as smelted iron.

Corrosion is not the only way in which objects can be microstructurally changed after they enter the archaeological record. Such changes can occur as a result of intentional heating, which can cause recrystallization or other heat treating effects, even melting, for example, when the objects are grave goods that have been involved in a cremation burial. Alternatively, the heating may have been unintentional—a situation that could arise, for example, if a forest fire swept through the site after the object was in place. Furthermore, mechanical damage occurring during archaeological excavation (trowel trauma) is not uncommon nor is chemical or mechanical damage due to on-site cleaning of objects by enthusiastic excavators.

In trying to interpret the history of an object, its history since excavation is far from irrelevant. Many iron objects in museum collections are now in rapid states of degradation after having survived centuries in burial environments. Furthermore, many museum objects have been subjected to ill-advised conservation treatments in the past that have made significant changes to their chemical composition and microstructure. Even in relatively recent times, high-temperature treatments have been applied to many museum objects in order to combat museum degradation. Such high-temperature treatments frequently will have altered the microstructure, so that its present condition will be of little or no use in interpreting its prior thermal and mechanical history. In other cases, complex surface patination treatments have been applied to museum objects to bring them into conformity with the art historians' current speculation as to the original appearance of the object. In still other

cases, records such as “conservation treatment applied” may survive with an object but without indication of the nature of the actual treatment. All of this is bad enough when there is a full record of such treatments, but, sadly, such records are often lacking, so that the unsuspecting archaeometallurgist can be attempting to understand the results of a materials characterization study without realizing that these analytical results are no longer related to the state of the material in its original condition.

Sample Preparation. Metallographic mounting procedures must also be chosen with care. Heat damage to the microstructure can be a problem in many materials, such as native copper, so cold mounting is normally preferred. Furthermore, the custodian of the object may stipulate that the sample be removed from the mount after analysis and replaced in the object. In this case, the difficulties of demounting must be taken into consideration when selecting a mounting material.

Technical effects related to sample preparation can also be important. For example, particles of high-hardness corrosion product can become dislodged during grinding and polishing, making scratch-free surfaces difficult to achieve. Furthermore, cracks and pores can be present in the corrosion product, leaving open the question of whether these could be the original locations of second-phase particles that are no longer present. This applies, for example, to slag inclusions in corroded wrought iron, which can potentially fall out during grinding and polishing.

The small size of samples creates other important problems of a technical nature. Material can be removed from a mounted metallographic sample surprisingly quickly during coarse grinding, and hence care must be taken to avoid grinding away the entire specimen! Furthermore, the limited amount of sample material can restrict the amount of grinding and polishing to less than the optimal amount, so that compromise must be made with regard to the condition of the polished sample. It may be necessary to accept the presence of polishing scratches on the surface if the alternative is a repolish that would endanger the very existence of the sample.

Observation in Unetched Condition. Much of the useful information that is obtained from archaeometallurgical samples comes from observation and analysis of nonmetallic inclusions and other second-phase particles in the sample. Hence, it is always desirable to examine the specimen carefully in the unetched condition, where the characteristics of the inclusions are more clearly visible without interference from matrix structure. Furthermore, better quantitative microanalysis results can be obtained when the sample is unetched.

Uniqueness of Materials Used in Antiquity. The compositions of ancient materials can differ widely from those of ostensibly similar modern materials, so that it is not always possible to go to a modern reference book to obtain understanding of an observed microstructure. For example, white cast irons were extensively produced by early Chinese metallurgists and used for many purposes, including statuary, bells, and coinage. In modern times, white cast irons are not much used, and then normally only as a precursor for malleable iron. Furthermore, this early material can have sulfur and/or phosphorus contents that are far in excess of their normal levels in modern material, so that modern research on the effects of high impurity contents does not include material corresponding to the early irons (e.g., a modern definition of a high sulfur content is far below the values observed in some early irons). Similar situations apply in copper-base alloys containing, for example, arsenic and/or antimony.

Sources of Information. Although the previously mentioned factors can complicate metallographic analysis and the interpretation of results, nevertheless, many archaeometallurgical researchers have used metallography productively. Typical publications appear in journals such as *Historical Metallurgy* (the journal of the Historical Metallurgy Society), *Journal of Archaeological Science, Archaeometry,* and the *Bulletin of the Metals Museum* (Japan), as well as in many archaeological journals. The *Proceedings of the International Symposia on Archaeometry,* the Beginning of the Use of Metals and Alloys (BUMA) conferences, and the *Materials Research Society Symposia on Materials Issues in Art and Archaeology* also include archaeometallurgical applications of metallography, as do various publications of the British Museum and the University Museum of the University of Pennsylvania, for example. Useful treatments of the general history of metallurgy include the classic works of R.F. Tylecote (Ref 8, 9, 10) and P.T. Craddock (Ref 11).

References cited in this section

3. C.S. Smith, The Interpretation of Microstructures of Metallic Artifacts, *Application of Science in Examination of Works of Art,* W.J. Young, Ed., Boston Museum of Fine Arts, 1967, p 20–52; reprinted in *A Search for Structure: Selected Essays on Science, Art and History,* MIT Press, Cambridge, 1981

4. M.R. Notis, C.E. Lyman, H. Moyer, and C. Cowen, Tapping the Memory in Archaeological Materials, *Materials Issues in Art and Archaeology, Materials Research Society Symposium Proceedings,* Vol 123, E.V. Sayre, P.B. Vandiver, J. Druzik, and C. Stevenson, Ed., Materials Research Society, 1988

5. D.A. Scott, *Metallography and Microstructure of Ancient and Historic Metals,* Getty Conservation Institute, 1991

6. M.L. Wayman, J.S.H. King, and P.T. Craddock, *Aspects of Early North American Metallurgy,* British Museum Occasional Paper 79, British Museum, London, 1992

7. M.L. Wayman and H. Wang, Iron Coins of Song Dynasty China: A Metallurgical Study, *Hist. Metall.,* Vol 37, 2003, p 6–24

8. R.F. Tylecote, *The Prehistory of Metallurgy in the British Isles,* Institute of Metals, London, 1986

9. R.F. Tylecote, *The Early History of Metallurgy in Europe,* Longman, 1987

10. R.F. Tylecote, *A History of Metallurgy,* 2nd ed., Institute of Materials, London, 1992

11. P.T. Craddock, *Early Mining and Metal Production,* Edinburgh University Press, 1995

M.L. Wayman, Metallography of Archaeological Alloys, *Metallography and Microstructures,* Vol 9, *ASM Handbook,* ASM International, 2004, p. 468–477

Metallography of Archaeological Alloys

M.L. Wayman, University of Alberta

Case Studies

This selection of case studies illustrates situations where metallography has contributed to archaeometallurgical studies.

Example 1: The Earliest Use of Metallic Materials. The date when people first started using metals is not known, but it seems clear that the earliest metals used were native metals, i.e., those that occur in their metallic form in nature, so that they were available for use without the need for the smelting of ores. Only a few metals occur in native form, copper being the most important, and it is likely that native copper was the first metal used by people, perhaps as early as 8000 b.c. (Ref 12). The development of copper smelting techniques followed several thousand years later (Ref 13). It is of great interest to be able to trace these developments, but in order to do so by analysis of archaeological objects, it is necessary to be able to distinguish between native copper and early smelted copper. This is difficult to accomplish using compositional analysis (Ref 14), because, although native copper is highly pure in terms of most trace elements and hence can be distinguished from later smelted copper (Ref 15), the very early smelted copper has a high purity, comparable to that of native copper. The high purity is a consequence of its having been smelted from handpicked high-grade ore in small quantities and at low furnace (hearth) temperatures, so there were only limited opportunities for it to have become contaminated with impurities. In general, therefore, it is necessary to use a combination of metallography with trace element analysis by neutron activation or by inductively coupled plasma mass spectrometry techniques to distinguish between native and early smelted copper. The microstructure of native copper is usually distinctive in that the grain size is very large, and it contains a very low density of nonmetallic inclusions (a clean microstructure) (Fig. 1), in some cases with an abundance of long, thin twins. Furthermore, the inclusions that are present are typically silica and silicates, rather than the oxides and sulfides that are predominant in smelted

copper. In addition, inclusions of metallic silver can be present, even profuse, in native copper. The overall result is that metallography is of great use in distinguishing between native and smelted copper.

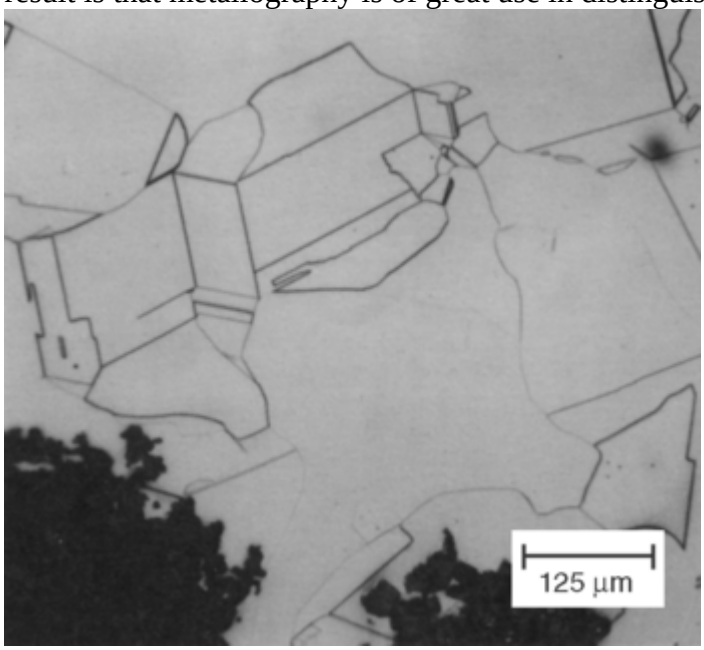

Fig. 1 Native copper showing a clean microstructure with a large grain size. Ammonium hydroxide/hydrogen peroxide etch. Source: Ref 16

Metallography has also been useful in studies of the early use of iron by people. Iron in native form is very rare (other than for a unique occurrence in Greenland), but meteoritic iron has been used by early people far back into the past (Ref 17, 18). Meteoritic iron is normally distinguished from smelted iron by its nickel content, which averages approximately 8%. However, in addition, it normally exhibits a distinctive two-phase matrix microstructure (Fig. 2), one phase being a high-nickel solid solution of nickel in face-centered cubic iron (above approximately 25% Ni and called taenite, corresponding to austenite), and the other being a lower-nickel solid solution of nickel in body-centered cubic iron (up to approximately 7% Ni and called kamacite, corresponding to ferrite). The kamacite normally occurs as Widmanstätten laths in the taenite, in a structure that can be so coarse as to be visible to the naked eye on an etched section. In addition, various types of nonmetallic inclusions can be present, including sulfides, phosphides, and chromite. Some meteorites have extremely large grain size, of the order of tens or even hundreds of centimeters, with proportionately large inclusions (Ref 17).

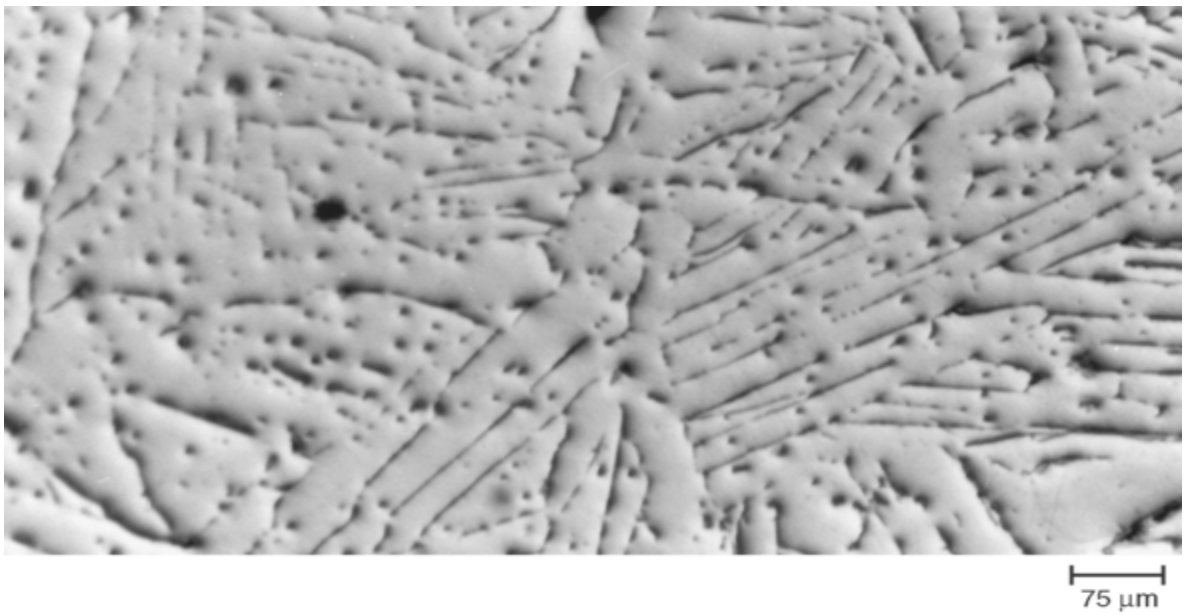

Fig. 2 Microstructure of the cross section of a meteoritic iron fragment from an archaeological site in the Canadian Arctic. The light areas are nickel-poor kamacite laths, which are separated by thin, dark bands of high-nickel taenite. Nital etch

Meteoritic iron has been used in many cultures over time, a particularly good example occurring in eastern Arctic North America. A meteorite fall in Northern Greenland was exploited by the local people, who beat flakes off the body of the meteorites and used them, for example, as inserts in a slotted bone to create a serrated cutting edge. On first direct contact with the outside world, in the early 19th century, these people were thus familiar with iron. However, smelted (wrought) iron was, by this time, becoming available to most of the maritime world in the form of nails and other ship fittings present in flotsam and jetsam adrift on the ocean currents. Objects are known that made use of both meteoritic and wrought iron (Ref 6).

Wrought iron is a material whose microstructure consists of silicate slag inclusions embedded in a matrix that can range from being completely ferritic to including major amounts of pearlite, frequently distributed in a highly heterogeneous manner (Fig. 3). The slag inclusions are normally elongated in the working directions by the hot forging processes that are used to process the as-smelted material and to shape the wrought iron objects. This is quite distinct from the meteoritic iron microstructure described previously, so that metallographic identification is unambiguous.

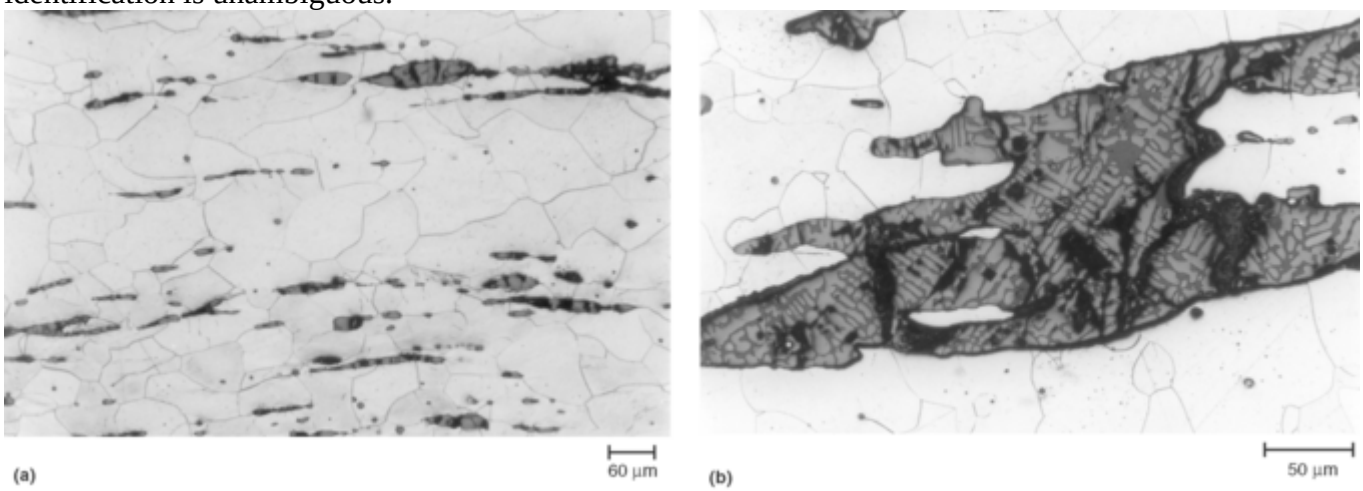

Fig. 3 Microstructure of a wrought iron axehead from St. Lawrence Island, Alaska. (a) Elongated slag inclusions in ferrite matrix. (b) Slag inclusion containing light-gray iron oxide dendrites in a darker-gray silicate matrix. Both etched in nital. Source: Ref 19

Wrought iron has been produced in many parts of the world over a time period ranging from the early Iron Age (second millennium b.c.) well into the 20th century a.d. It is produced by two distinctly different technologies.

One is the direct smelting of iron ore in a bloomery furnace, which yields a slag-metal composite bloom that is hot forged to expel as much slag as possible but inevitably leaves embedded slag inclusions in the microstructure. The alternative indirect method involves smelting iron ore in a blast furnace to produce liquid cast iron that is then decarburized by oxidation, using techniques referred to as fining or puddling. This again leaves slag inclusions in the wrought iron, because, although the blast furnace slag can be eliminated from the liquid cast iron, a slag produced during fining or puddling becomes incorporated into the wrought iron product. Most of the attempts to interpret slag analyses to identify the smelting process used for a particular piece of wrought iron have been unable to achieve a convincing success, and although some controversy remains, it is generally accepted that distinguishing the smelting process is not possible in most cases.

Example 2: Replicative or Experimental Archaeology. On occasion, the work at a particular archaeological site indirectly suggests that particular metallurgical processes may have been employed there in earlier times. Confirmation of the suggested or implied processes is desirable; however, such confirmation is not always possible. One such situation arose in a pre-Roman Iron Age site in South Italy, where excavation uncovered deposits of slag and appreciable quantities of what appeared to be scrap or miscast bronze objects. It was presumed that a bronze manufacturing operation and/or a bronze foundry had been operational, but the presence of modern steel fencing prevented the use of the remote sensing techniques that would otherwise have permitted the buried furnace remains to be located and then excavated. As an alternative, metallography was employed to characterize the slag, and attempts were made to reproduce the slag characteristics by reconstructing the plausible bronze-making technologies in the laboratory. These processes included the reduction of tin ore in the presence of metallic copper, the mixing of metallic tin and metallic copper, and the remelting of scrap bronze. A micrograph typical of both the archaeological and the replicated slag is shown in Fig. 4.

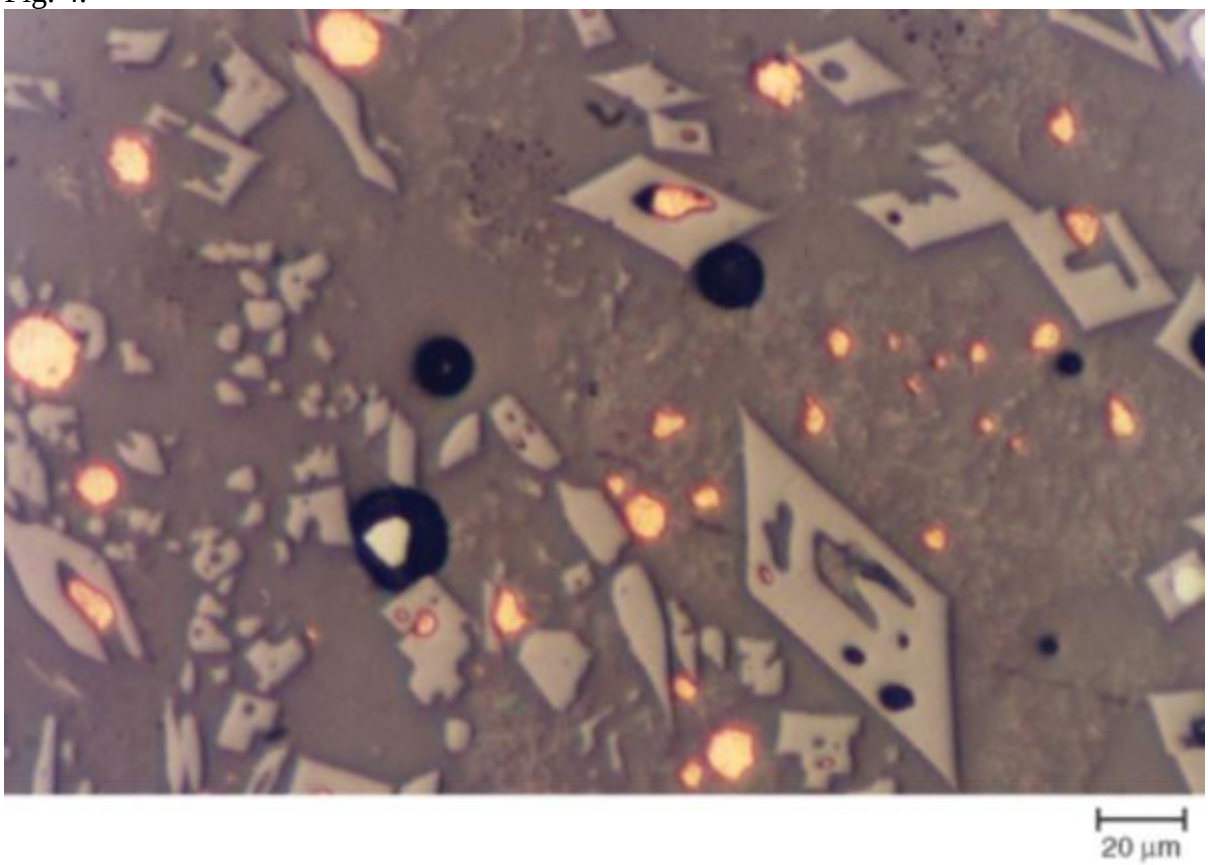

Fig. 4 Microstructure of replicated bronze-making slag. Visible are spheroids of metallic bronze, rhomboidal tin oxide crystals, and spherical voids in a glassy silicate matrix. Unetched

The scrap bronze found at the site was also analyzed and found to consist primarily of casting debris, including remnants of gating systems as well as spatter particles presumably ejected from the furnace, the crucible, or the mold during melting and casting. These were all leaded bronze whose dendritic microstructures exhibited abundant amounts of metallic lead inclusions (Fig. 5a). Such microstructures are in sharp contrast with those of worked bronze, which exhibits elongated grain structures that often contain deformation bands (Fig. 5b).

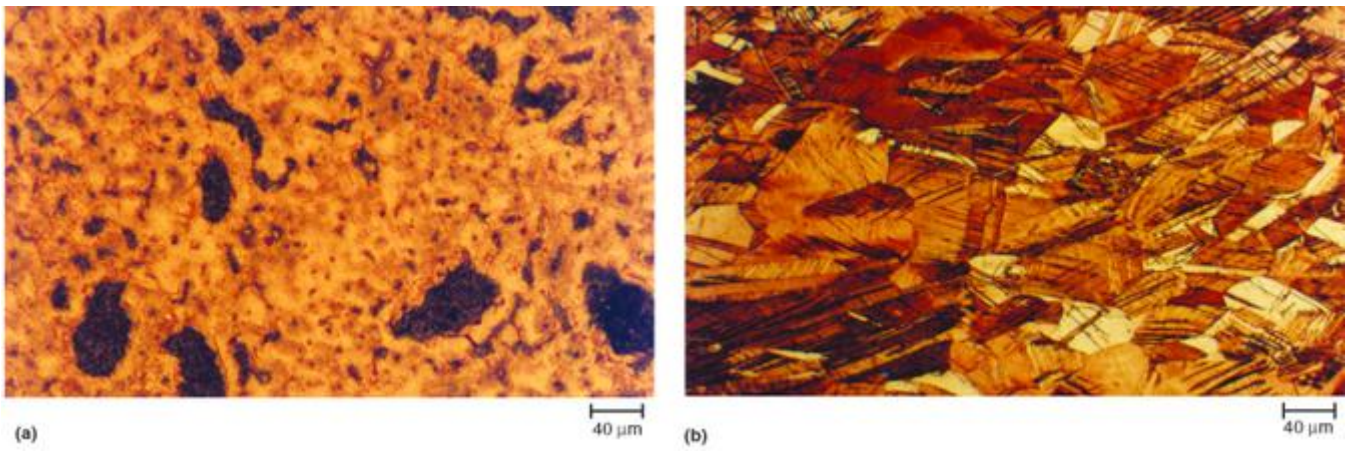

Fig. 5 The contrasting mircrostructure of (a) as-cast leaded bronze and (b) worked bronze. Both are ferric chloride etch.

One of the most successful applications of experimental archaeology has been the work of Dr. Gill Juleff in Sri Lanka. Dr. Juleff discovered large numbers of similar archaeological sites, all located on the west-facing sides of hills and all containing the remains of highly unusual furnace structures, with associated ceramics and slag deposits. She postulated that these were, in fact, iron-smelting sites where the strong monsoon winds were used to power wind-blown furnaces capable of smelting iron. In the face of considerable skepticism from the archaeometallurgical community, Dr. Juleff was able to construct furnaces corresponding to her postulate and to successfully smelt iron ore to produce good-quality iron and steel, including some cast iron (Fig. 6). Furthermore, the experimental smelts produced the same type of furnace remains, ceramics and slag, that were found in the archaeological record at these sites. Metallography played an important role in showing the correspondence between the archaeological material and the material produced by the experimental smelts.

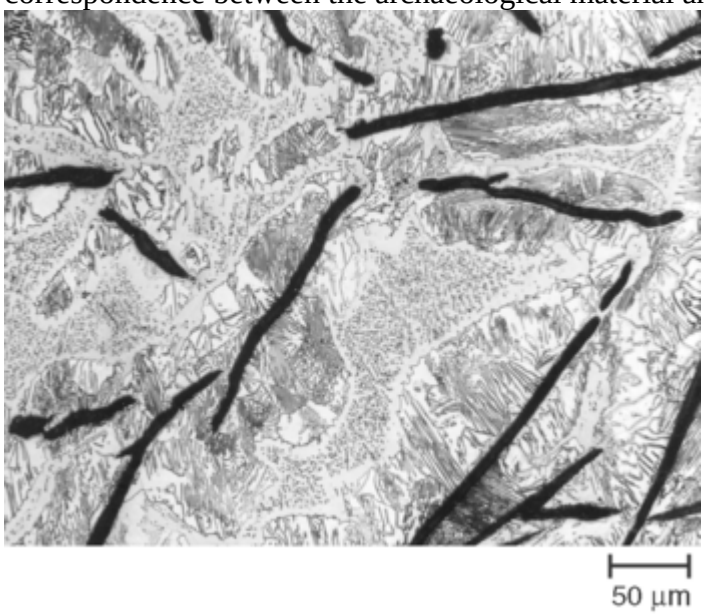

Fig. 6 Microstructure of gray cast iron showing graphite flakes and phosphorus-rich eutectic in a pearlite matrix. Nital etch

Another successful replicative archaeology experiment involved traditional iron-smelting technologies used in Cameroon. Here, ethnographer Dr. Nicholas David and his colleagues were able to arrange for a local ironmaster to construct, using a dimly remembered traditional technology, a bloomery furnace in the characteristic local style (Ref 20). Bloom iron was successfully smelted and transformed into wrought iron and steel, again using traditional technologies, for use in agricultural implements. Metallography was able to elucidate the nature of the smelting process in these unusual furnaces and to show that, contrary to expectations, some high-carbon iron was produced directly in the bloomery furnace, including some globules of cast iron (Fig. 7) that were also transformed into steel in the forge.

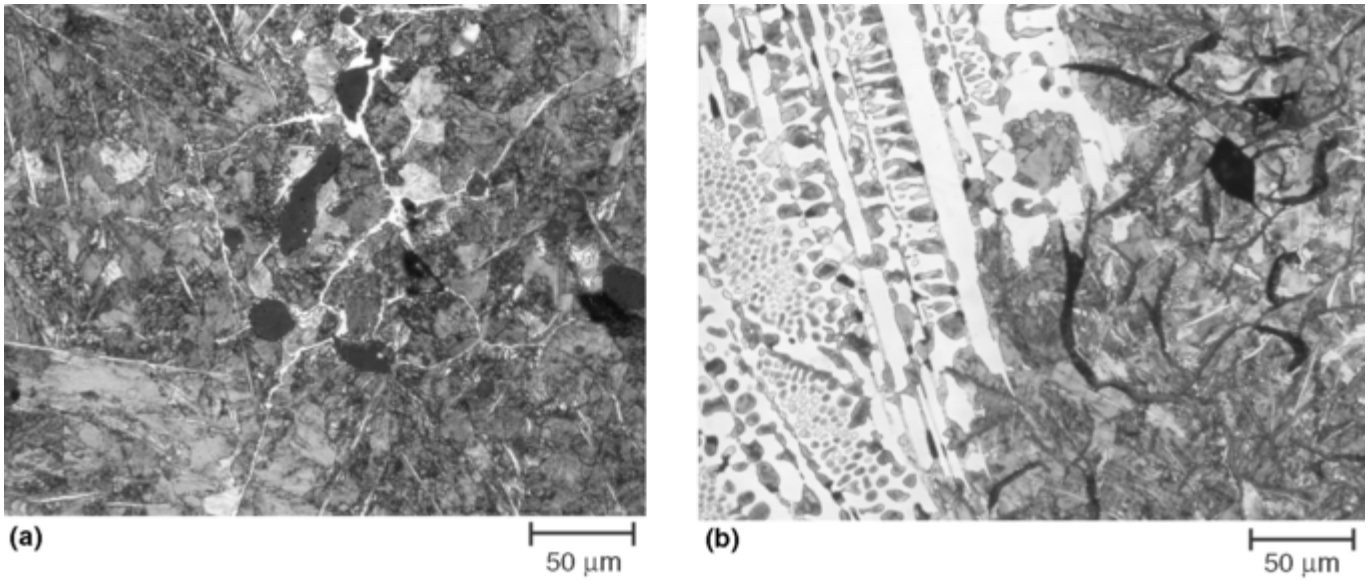

Fig. 7 Microstructures of high-carbon products from Cameroon bloomery furnace. (a) High-carbon hypereutectoid steel, with cementite and pearlite. (b) Mixture of gray and white cast iron, with pearlite, graphite, and free cementite. Both etched in nital. Source: Ref 20

Example 3: Postmedieval Steelmaking. Between 1500 and 1900 a.d., European steelmaking technology changed dramatically, with a number of new processes coming into use at different times. At the beginning of this period, steel was made by limited carburization of wrought iron, for example, on the cutting edges of tools and weapons. Alternatively, steel could be produced by smelting manganese-bearing ores either in a direct process (bloomery smelting) or an indirect process (blast furnace smelting followed by fining). These products were sometimes referred to as natural steel or German steel, but only certain ores were capable of being used for this purpose, and steel was not a common material. In the 16th and 17th centuries, the cementation process came into use, first on the European continent and shortly afterward in Britain. In the fully developed cementation process, bar iron, typically charcoal-smelted low-phosphorus iron from Sweden, was packed in a stone chest interspersed with layers of charcoal. The chest, which was constructed inside a furnace, was then sealed and heated for 5 to 10 days to allow carbon to diffuse into the iron bars, creating steel, either throughout the cross section or as a surface layer whose depth depended on the cementation time and temperature. The product, called blister steel, was repeatedly forged and folded (piled) to produce a somewhat heterogeneous but good-quality steel. The nonmetallic (slag) inclusions from the original wrought iron remained in the steel, although in modified form.

Beginning in the mid-18th century, the cementation process was supplemented and, to some extent, superseded by the crucible steel (Huntsman) process, wherein cementation steel was melted in a crucible, which homogenized the carbon content as well as allowed the inclusions to float to the surface of the steel bath, where they could be skimmed off. Later, in approximately the mid-19th century, the Bessemer and open-hearth steelmaking processes came into use, and steel became a high-volume, lower-cost commodity. It must be noted that this brief outline applies only to European steelmaking; the situation in China, for example, was quite different and is discussed subsequently.

It is possible to distinguish between cementation steel and crucible steel on the basis of several metallographic criteria. Cementation steel is, in general, more heterogeneous in its carbon content, which is typically banded. Banding is, however, not a sufficient criterion for differentiation, because forged natural steel with heterogeneous carbon content is likely to be banded. The low abundance of nonmetallic inclusions and their character (small, spheroidal silica inclusions) are also useful indicators and, when combined with carbon homogeneity, normally can allow the identification of crucible steel with some confidence.

Using this approach, the transition from cementation steel to crucible steel has been identified in the components (including springs) of clocks and watches dating from the 16th to the 19th centuries (Fig. 8). Knowledge of the technological history has also proven useful. For example, the knowledge that crucible steel was not introduced in Europe until the mid-18th century has also proven potentially applicable to the dating of North American fur trade sites where steel is present in the form of smithing tools, especially files (Fig. 9).

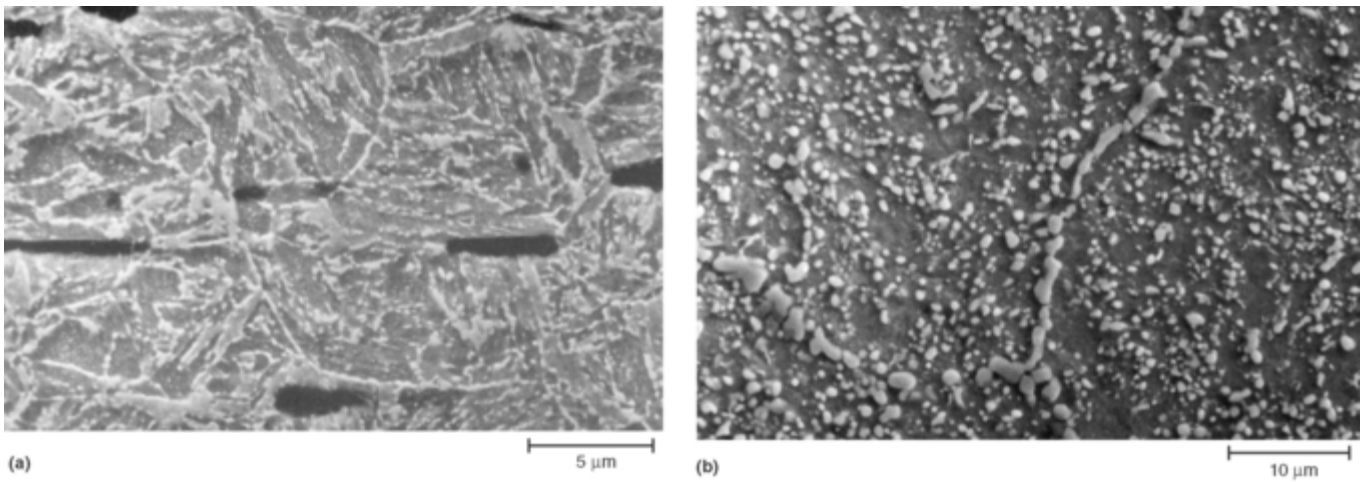

Fig. 8 Microstructures of cementation and crucible steel components of early clocks and watches. Due to sampling restrictions, it was necessary to employ surface metallography. Scanning electron microscope secondary electron images. (a) Cementation steel. Tempered martensite with slag inclusions. (b) Crucible steel. Cementite in ferritic or martensitic matrix. Both etched in nital. Source: Ref 21

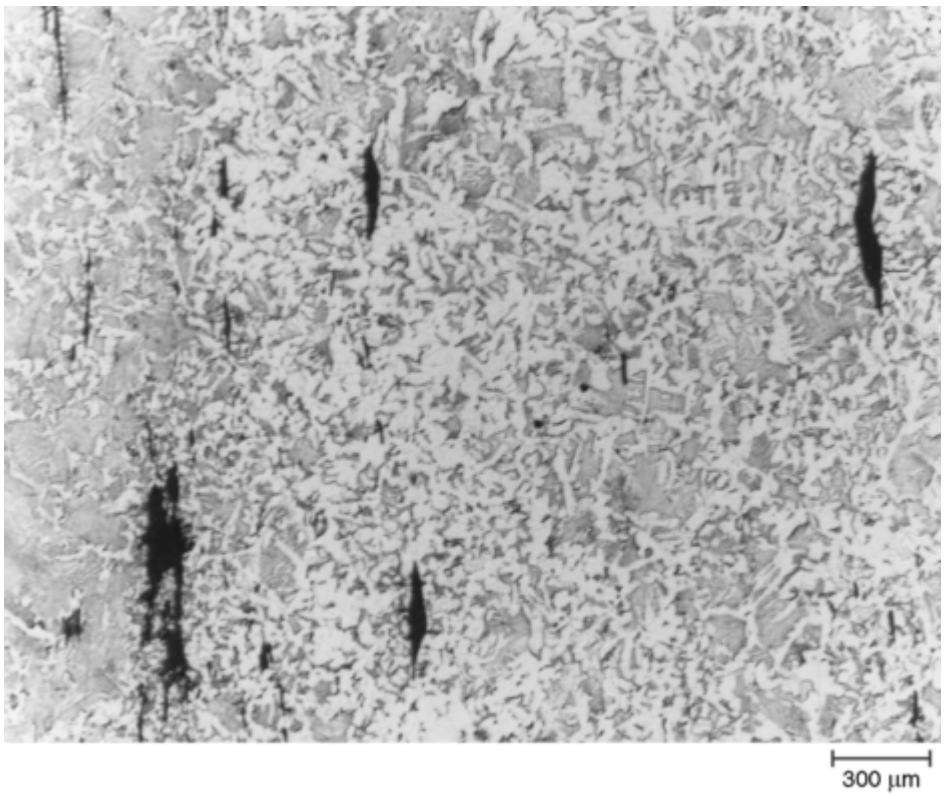

Fig. 9 Microstructure of steel file from Alberta fur trade site showing the heterogeneous carbon distribution and nonmetallic inclusions characteristic of a cementation steel. Nital etch. Source: Ref 22

Liquid steel has also been produced in crucibles in the Indian subcontinent and elsewhere in Asia, the Indian variant being the most famous because it was reputedly the raw material for the so-called Damascus swords. Metallography has been used in identifying such steels as well as in distinguishing between forged composite iron-steel laminar structures, as in the Japanese swords (Ref 23), and the cast and forged true Damascus steels. The work of John Verhoeven and colleagues (Ref 24, 25) has provided an excellent example of the importance of metallography to the understanding of ancient technologies. Here, the collaboration between a metallurgist and a bladesmith has led to an appreciation of the metallurgical factors involved in casting a steel ingot and forging it to yield a steel with the remarkable surface patterns characteristic of Damascus steel. Careful metallographic work comparing the microstructures of known Damascus swords with those of experimentally produced blades has played a vital role in these investigations (Fig. 10).

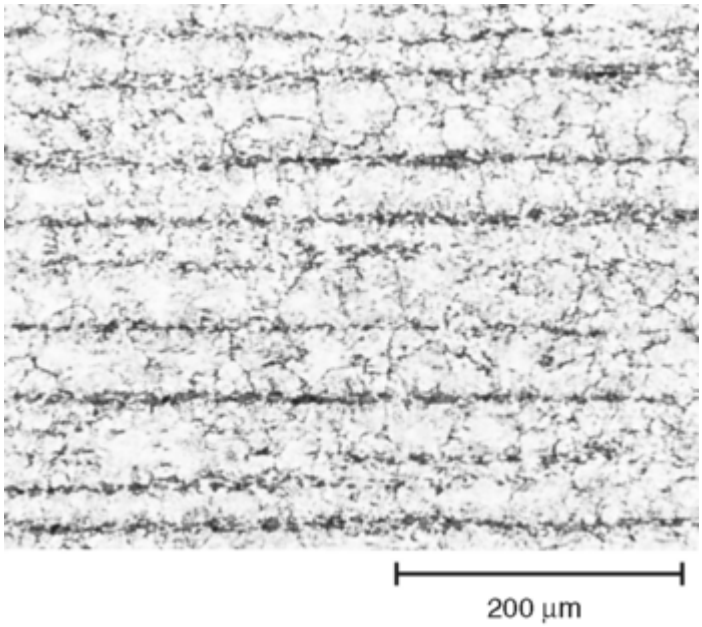

Fig. 10 Microstructure of longitudinal section of steel blade forged from an experimentally produced cast ingot. The observed carbide banding is very similar to that responsible for the surface appearance of Damascus steel blades. Picric plus boiling picric acid etch. Source: Ref 24

Example 4: Early Iron in China. In the West, early smelted iron was produced, beginning in approximately 1500 b.c., by the solid-state reduction of ore in bloomery furnaces, followed by forging to produce wrought iron. The indirect process, wherein blast furnaces produced liquid cast iron that was decarburized to wrought iron by fining, appears to have come into use early in the second millennium a.d., several millennia later. However, in China the situation was markedly different, with liquid cast iron being produced in blast furnaces early in the first millennium b.c. and used not only for fining to wrought iron but also as castings. Furthermore, the Chinese learned by the mid-first millennium b.c. to decarburize cast iron castings in the solid state, so as to produce steel, and also to malleablize the castings, producing malleable cast iron. Malleable cast iron in Europe dates from the late 17th century a.d.

Metallography is indispensable for differentiating among these various types of ferrous material, and it has been used in most studies of early Chinese iron (Ref 26). For example, Song Dynasty cast iron coins have been shown to be white cast iron with several types of microstructure (Fig. 11), reflecting variations in composition and cooling conditions after casting (Ref 7). Furthermore, the presence of high percentage levels of sulfur in the material, manifested as a high density of iron sulfide inclusions observed metallographically, can be interpreted as being evidence for the use of coal or coke, rather than charcoal, in the blast furnaces that produced the cast iron. A collection of Buddhist statuary dating from the past millennium has been shown to include not only white but also gray and mottled cast iron.

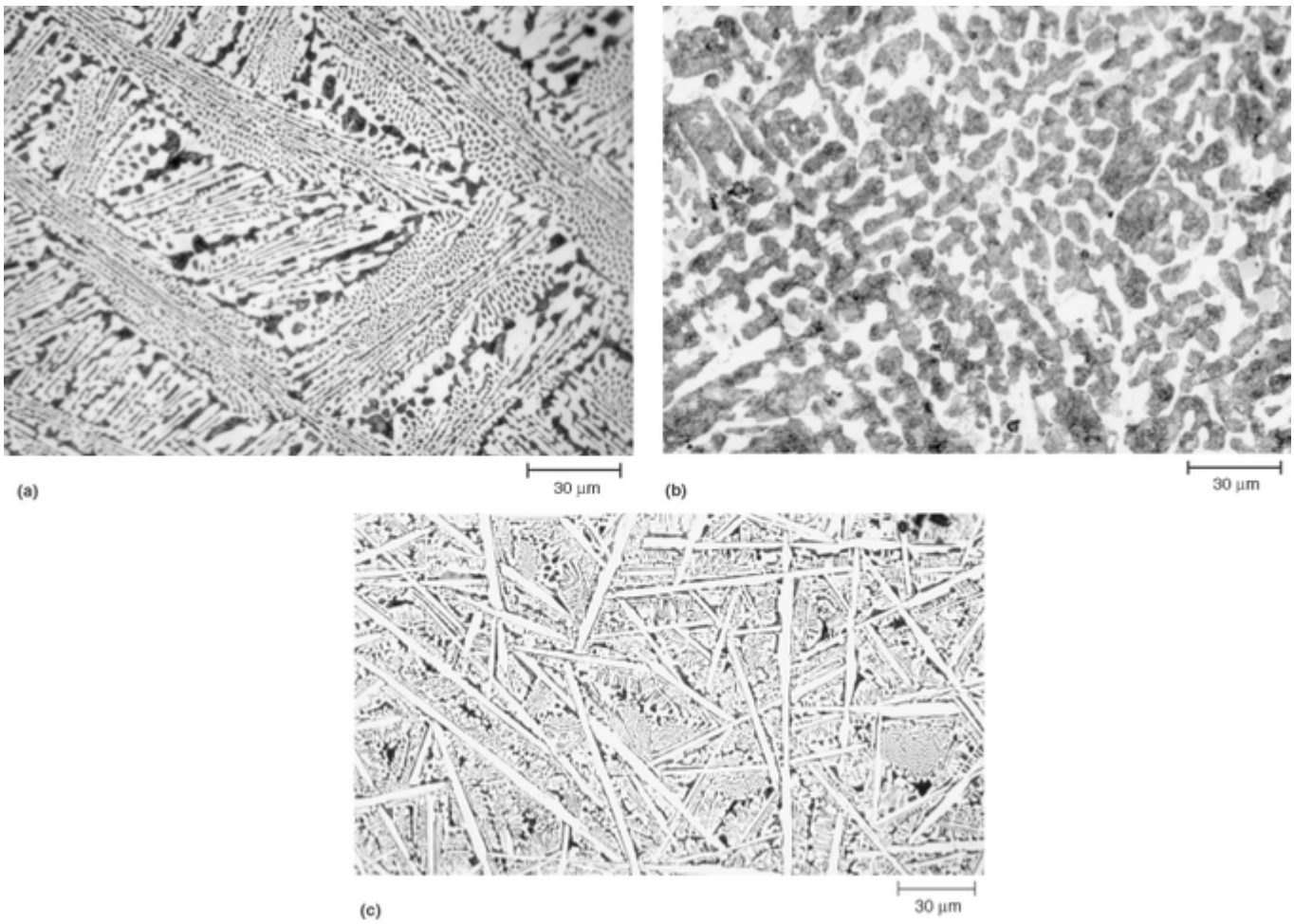

Fig. 11 Microstructures of Song Dynasty Chinese coins (circa 1200 a.d.). White cast iron. (a) Ledeburitic microstructure. (b) Hypoeutectic divorced eutectic microstructure. (c) Hypereutectic microstructure. All etched in nital

The use of the solid-state decarburization process to produce steel in early Chinese objects has been demonstrated metallographically by the occurrence of strong carbon gradients within the iron. Typically, the carbon contents rise from negligible values at the surface to high levels at the center of objects, in association with microstructural features (inclusions, casting defects) that show that the material is in the cast (unworked) condition. Also present in some of these materials are spheroidal nodules of graphite. There thus appears to be a continuous range of material, from steel to malleable cast iron, that was created by solid-state decarburization and is identifiable metallographically.

Example 5: Surface Treatments and Effects. There are many examples of the use of metallography to decipher the surface treatments applied to materials in the past. For example, it has been shown that in South America, several different surface treatments were developed and used in times prior to European contact (Ref 27). One of these was an electrochemical gilding treatment that used electrochemical replacement to deposit a thin surface layer, approximately 1 μm (40 μin.), of gold on a copper substrate. Subsequent heating created a diffusion bond between the surface gold layer and the substrate. Another technique employed was the surface enrichment of debased gold-bearing alloy objects, which was used to give a golden color to copper-gold and copper-silver-gold alloys with relatively small gold contents (often considerably less than 50% Au). This process, known as depletion gilding, involved cycles of heating to oxidize the more reactive copper in the surface layers, followed by pickling to remove the copper oxide, leaving a relatively thick surface layer of metallic gold. A similar technique was applied to copper-silver alloys to enrich the surface in silver. Metallography on archaeological objects and on the results of experimental simulations has been indispensable in identifying the gilding technologies employed.

Metallography has also been used in studies of the lustrous black coatings present on some early bronze objects, including Chinese mirrors (Ref 28, 29). The presence of a shiny black coating has been explained both as intentional patination and as the result of a corrosion reaction in a burial environment. After years of

controversy, metallographic characterization of the microstructure of the surface layers of high-tin bronze objects and comparison with bulk microstructure has led to the conclusion that this surface layer is a corrosion product.

The understanding of other surface decoration technologies has also benefited from metallographic studies. In one case, a silver-colored inlay into a blackened copper surface had been described ethnographically as being carried out by hammering a silver wire into an incised groove, where it was held by mechanical interlocking. However, metallographic studies (Ref 30) revealed that, in fact, the inlay was a Ag-Cu-Zn alloy with an as-cast microstructure, showing that it had been cast into position in the grooves (Fig. 12).

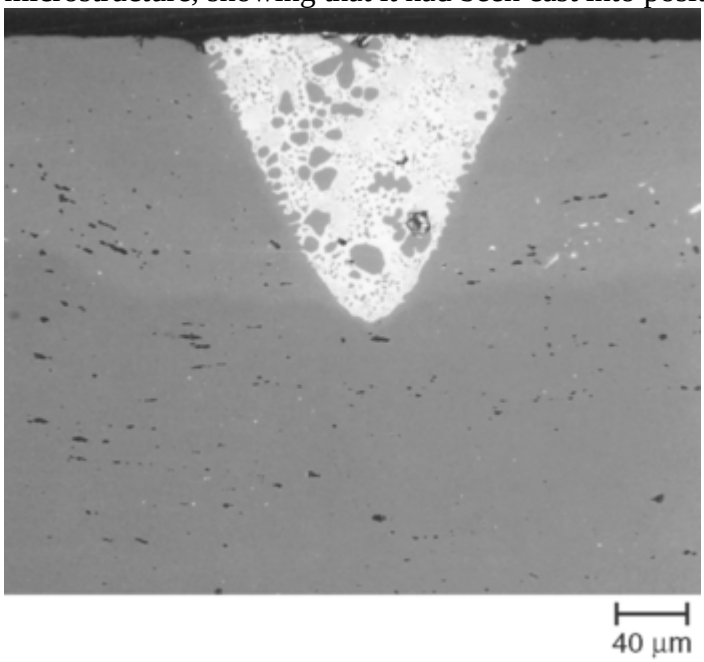

Fig. 12 Scanning electron micrograph showing cross section through inlaid silver-colored line on copper-alloy box. The dendritic nature of the inlay is clearly visible. Backscattered electron image

It must also be noted that long-term corrosion of archaeological objects can occur in ways that are not normal for modern shorter-term corrosion. In particular, the corrosion of bronzes frequently occurs along slip bands, presumably those on which plastic deformation has occurred (Fig. 13). The presence of this mode of corrosion can be interpreted as evidence for the authenticity of a purportedly old object, as opposed to a modern fake. Obviously, this authentication methodology is only possible when it is deemed permissible to carry out metallography on a section through the object.



Fig. 13 Corrosion penetrating a pre-Roman Carthaginian bronze mirror along slip bands and grain boundaries. Unetched

References cited in this section

6. M.L. Wayman, J.S.H. King, and P.T. Craddock, *Aspects of Early North American Metallurgy,* British Museum Occasional Paper 79, British Museum, London, 1992

7. M.L. Wayman and H. Wang, Iron Coins of Song Dynasty China: A Metallurgical Study, *Hist. Metall.,* Vol 37, 2003, p 6–24

12. R. Maddin, J.D. Muhly, and T. Stech, Early Metalworking at Cayonu, *The Beginnings of Metallurgy,* A. Hauptmann, E. Pernicka, T. Rehren, and U. Yalcin, Ed., Bergbau-Museum, 1999

13. V.C. Pigott, A Heartland of Metallurgy: Neolithic/Chalcolithic Metallurgical Origins on the Iranian Plateau, *The Beginnings of Metallurgy,* A. Hauptmann, E. Pernicka, T. Rehren, and U. Yalcin, Ed., Bergbau-Museum, 1999

14. R. Maddin, T. Stech Wheeler, and J.D. Muhly, Distinguishing Artifacts Made of Native Copper, *J. Archaeol. Sci.,* Vol 7, 1980, p 211–225

15. M.L. Wayman, R.R. Smith, C.G. Hickey, and M.J.M. Duke, The Analysis of Copper Artifacts of the Copper Inuit, *J. Archaeol. Sci.,* Vol 12, 1985, p 367–375

16. W.W. Vernon, New Perspectives on the Archaeometallurgy of the Old Copper Industry, *MASCA J.,* Vol 3 (No. 5), 1986

17. V.F. Buchwald, *Handbook of Iron Meteorites,* Vol 1, University of California Press, 1975

18. M.L. Wayman, On the Early Use of Iron in the Arctic, *CIM Bull.,* Vol 80 (No. 899), 1987, p 147–150

19. M.L. Wayman, Determining the Origin and Age of Metal Artifacts, *MRS Bull.,* Vol 14 (No. 3), 1989, p 31–35

20. N. David, R. Heimann, D. Killick, and M. Wayman, Between Bloomery and Blast Furnace: Mafa Iron-Smelting Technology in North Cameroon, *African Archaeol. Rev.,* Vol 7, 1989, p 183–208

21. M.L. Wayman, Ed., *The Ferrous Metallurgy of Early Clocks and Watches: Studies in Post-Medieval Steel,* British Museum Occasional Paper 136, British Museum, London, 2000

22. T.S. Wiltzen and M.L. Wayman, Steel Files as Archaeological Markers in North American Fur Trade Sites, *Archaeometry,* Vol 41, 1999, p 117–135

23. M.R. Notis, The History of the Metallographic Study of the Japanese Sword, *Mater. Charact.,* Vol 45, 2000, p 253–258

24. J.D. Verhoeven, A.H. Pendray, and E.D. Gibson, Wootz Damascus Steel Blades, *Mater. Charact.,* Vol 37, 1996, p 9–22

25. J.D. Verhoeven, F. Laabs, A.H. Pendray, and W.E. Dauksch, Microsegregation and Banding in Hypereutectoid Steel: Damascus Steel, *ISS Trans.,* Vol 18 (No. 11), 1998, p. 65–74

26. D.B. Wagner, *Iron and Steel in Ancient China,* Brill, 1993

27. W. Bray, Techniques of Gilding and Surface-Enrichment in Pre-Hispanic American Metallurgy, *Metal Plating and Patination,* S. La Niece and P.T. Craddock, Ed., Butterworth-Heinemann, 1993

28. N. Meeks, Patination Phenomena on Roman and Chinese High-Tin Bronze Mirrors and Other Artifacts, *Metal Plating and Patination,* S. La Niece and P.T. Craddock, Ed., Butterworth-Heinemann, 1993

29. Zhu Shoukang and He Tangkun, Studies of Ancient Chinese Mirrors and Other Bronze Artifacts, *Metal Plating and Patination,* S. La Niece and P.T. Craddock, Ed., Butterworth-Heinemann, 1993

30. M.L. Wayman and P.T. Craddock, Wu Tong, a Neglected Chinese Decorative Technology, *Metal Plating and Patination,* S. La Niece and P.T. Craddock, Ed., Butterworth-Heinemann, 1993

M.L. Wayman, Metallography of Archaeological Alloys, *Metallography and Microstructures,* Vol 9, *ASM Handbook*, ASM International, 2004, p. 468–477

Metallography of Archaeological Alloys

M.L. Wayman, University of Alberta

Acknowledgment

Some of the material included in this article appears in M.L. Wayman's article “Archaeometallurgical Contributions to a Better Understanding of the Past” from *Materials Characterization,* Volume 45, 2000, p 259–267.

M.L. Wayman, Metallography of Archaeological Alloys, *Metallography and Microstructures,* Vol 9, *ASM Handbook,* ASM International, 2004, p. 468–477

Metallography of Archaeological Alloys

M.L. Wayman, University of Alberta

References

1. D. Killick, Optical and Electron Microscopy in Material Culture Studies, *Learning from Things. Method and Theory of Material Culture Studies,* W.D. Kingery, Ed., Smithsonian Press, 1996

2. U.M. Franklin, *The Real World of Technology,* House of Anansi, Toronto, 1990; revised 1999

3. C.S. Smith, The Interpretation of Microstructures of Metallic Artifacts, *Application of Science in Examination of Works of Art,* W.J. Young, Ed., Boston Museum of Fine Arts, 1967, p 20–52; reprinted in *A Search for Structure: Selected Essays on Science, Art and History,* MIT Press, Cambridge, 1981

4. M.R. Notis, C.E. Lyman, H. Moyer, and C. Cowen, Tapping the Memory in Archaeological Materials, *Materials Issues in Art and Archaeology, Materials Research Society Symposium Proceedings,* Vol 123, E.V. Sayre, P.B. Vandiver, J. Druzik, and C. Stevenson, Ed., Materials Research Society, 1988

5. D.A. Scott, *Metallography and Microstructure of Ancient and Historic Metals,* Getty Conservation Institute, 1991

6. M.L. Wayman, J.S.H. King, and P.T. Craddock, *Aspects of Early North American Metallurgy,* British Museum Occasional Paper 79, British Museum, London, 1992

7. M.L. Wayman and H. Wang, Iron Coins of Song Dynasty China: A Metallurgical Study, *Hist. Metall.,* Vol 37, 2003, p 6–24

8. R.F. Tylecote, *The Prehistory of Metallurgy in the British Isles,* Institute of Metals, London, 1986

9. R.F. Tylecote, *The Early History of Metallurgy in Europe,* Longman, 1987

10. R.F. Tylecote, *A History of Metallurgy,* 2nd ed., Institute of Materials, London, 1992

11. P.T. Craddock, *Early Mining and Metal Production,* Edinburgh University Press, 1995

12. R. Maddin, J.D. Muhly, and T. Stech, Early Metalworking at Cayonu, *The Beginnings of Metallurgy,* A. Hauptmann, E. Pernicka, T. Rehren, and U. Yalcin, Ed., Bergbau-Museum, 1999

13. V.C. Pigott, A Heartland of Metallurgy: Neolithic/Chalcolithic Metallurgical Origins on the Iranian Plateau, *The Beginnings of Metallurgy,* A. Hauptmann, E. Pernicka, T. Rehren, and U. Yalcin, Ed., Bergbau-Museum, 1999

14. R. Maddin, T. Stech Wheeler, and J.D. Muhly, Distinguishing Artifacts Made of Native Copper, *J. Archaeol. Sci.,* Vol 7, 1980, p 211–225

15. M.L. Wayman, R.R. Smith, C.G. Hickey, and M.J.M. Duke, The Analysis of Copper Artifacts of the Copper Inuit, *J. Archaeol. Sci.,* Vol 12, 1985, p 367–375

16. W.W. Vernon, New Perspectives on the Archaeometallurgy of the Old Copper Industry, *MASCA J.*, Vol 3 (No. 5), 1986

17. V.F. Buchwald, *Handbook of Iron Meteorites*, Vol 1, University of California Press, 1975

18. M.L. Wayman, On the Early Use of Iron in the Arctic, *CIM Bull.*, Vol 80 (No. 899), 1987, p 147–150

19. M.L. Wayman, Determining the Origin and Age of Metal Artifacts, *MRS Bull.*, Vol 14 (No. 3), 1989, p 31–35

20. N. David, R. Heimann, D. Killick, and M. Wayman, Between Bloomery and Blast Furnace: Mafa Iron-Smelting Technology in North Cameroon, *African Archaeol. Rev.*, Vol 7, 1989, p 183–208

21. M.L. Wayman, Ed., *The Ferrous Metallurgy of Early Clocks and Watches: Studies in Post-Medieval Steel*, British Museum Occasional Paper 136, British Museum, London, 2000

22. T.S. Wiltzen and M.L. Wayman, Steel Files as Archaeological Markers in North American Fur Trade Sites, *Archaeometry*, Vol 41, 1999, p 117–135

23. M.R. Notis, The History of the Metallographic Study of the Japanese Sword, *Mater. Charact.*, Vol 45, 2000, p 253–258

24. J.D. Verhoeven, A.H. Pendray, and E.D. Gibson, Wootz Damascus Steel Blades, *Mater. Charact.*, Vol 37, 1996, p 9–22

25. J.D. Verhoeven, F. Laabs, A.H. Pendray, and W.E. Dauksch, Microsegregation and Banding in Hypereutectoid Steel: Damascus Steel, *ISS Trans.*, Vol 18 (No. 11), 1998, p. 65–74

26. D.B. Wagner, *Iron and Steel in Ancient China*, Brill, 1993

27. W. Bray, Techniques of Gilding and Surface-Enrichment in Pre-Hispanic American Metallurgy, *Metal Plating and Patination*, S. La Niece and P.T. Craddock, Ed., Butterworth-Heinemann, 1993

28. N. Meeks, Patination Phenomena on Roman and Chinese High-Tin Bronze Mirrors and Other Artifacts, *Metal Plating and Patination*, S. La Niece and P.T. Craddock, Ed., Butterworth-Heinemann, 1993

29. Zhu Shoukang and He Tangkun, Studies of Ancient Chinese Mirrors and Other Bronze Artifacts, *Metal Plating and Patination*, S. La Niece and P.T. Craddock, Ed., Butterworth-Heinemann, 1993

30. M.L. Wayman and P.T. Craddock, Wu Tong, a Neglected Chinese Decorative Technology, *Metal Plating and Patination*, S. La Niece and P.T. Craddock, Ed., Butterworth-Heinemann, 1993

B.L. Bramfitt and S.J. Lawrence, Field Metallography Techniques, *Metallography and Microstructures,* Vol 9, *ASM Handbook,* ASM International, 2004, p. 478–492

Field Metallography Techniques

Bruce L. Bramfitt and Samuel J. Lawrence, International Steel Group, Inc.

Introduction

FIELD METALLOGRAPHIC PROCEDURES are performed “on location” or in the “field” on components that are too large to bring to the metallographic laboratory. Generally, these components are still being used in service or must be returned to service and cannot be destructively sectioned or physically altered. Field metallography is also called in situ metallography, and it is sometimes called nondestructive metallography. This article focuses on several field metallographic techniques that have been successfully used by the authors. Although there are many other applications, the examples given in this article give the reader a solid idea how field metallographic techniques are employed. Basically, the metallographer should consider field metallography as simply an extension of the metallographic laboratory. Although the examples given in this article are mostly of steels and cast irons, they apply to all metals. For example, the grinding, polishing, and etching procedures (both mechanical and electrolytic) used for copper-base alloys would be the same as those used for copper-base alloys in the metallographic laboratory. Thus, the step-by-step techniques and the equipment used for iron and steels can be applied almost universally.

Performing life assessment investigations of nuclear and fossil-fuel power plant equipment established many of the techniques described in this article. Power plants routinely use field metallography to assess the useful life of turbine rotors and blades, steam piping, pressure vessels, and so forth. These components are very large, extremely expensive to replace, and are still being used to generate power and thus cannot be dismantled or sectioned to obtain a metallographic specimen. It is important to know how much “life” is left in these components before they need to be replaced. Years ago many turbine rotors failed catastrophically, creating costly damage, loss of life, and a complete shutdown of the power plant. To prevent this from happening, metallurgists and metallographers were called on to predict the useful life of these components so that decisions could be made to replace these components before failure. From these studies, field metallography became a routine technique.

Field metallographic work must be performed on-site without damaging the components. This means that portable metallographic instruments for grinding, polishing, and etching procedures are required. For example, Fig. 1(a) and (b) show a field metallographer working in different facilities. The equipment is portable, and the metallographer can be seen polishing an area on the steam piping in Fig. 1(b). Note the safety equipment including hardhat, safety glasses, respirator, and disposable work clothes in Fig. 1(b). Ample lighting is provided by a light source (on the left, outside the view of Fig. 1b). For power plants, an important goal in this kind of work is to examine the microstructure of a component in situ for creep damage and other microstructural changes at various time intervals while these components are in service. This type of study is called life assessment.



(a)



(b)

Fig. 1 Examples of field metallography. (a) Metallographer using field techniques to examine the microstructure of a hot strip work roll that spalled. Metallographer is in the mill roll shop where rolls are reconditioned. (b) Field metallography being conducted in a power plant. The metallographer is in tight quarters preparing a polished area on a steam pipe. Courtesy of A.O. Benscoter, Lehigh University

In the steel industry, the use of field metallography is also a very valuable tool. It is of particular importance in the examination of rolling-mill rolls and rolling-mill equipment. These components are far too large to examine in a metallographic laboratory, and in most cases a sample cannot be removed. In the case of rolls, where they are purchased to a hardness specification, field metallography is often used to evaluate the condition (proprietary microstructure) of rolls being purchased from different vendors. These rolls are very expensive, and the consistency of quality of different roll manufacturers can be evaluated. Many times field metallography is employed to determine the cause of a roll failure. Case examples are given later in this article.

One example involved a spalling and breakage problem in D2 tool steel rolls for a rotary straightener used to straighten railroad rails in production. In the case of D2 steel rolls, the steel is very hard and has exceptional wear resistance. However, D2 tool steel is also brittle and sensitive to abuse by an impact force. Certain rolls from the same vendor would perform adequately, whereas other rolls would break and spall immediately after being installed. Field metallography was employed in the roll shop to examine the microstructures of all the rolls being supplied from that particular vendor. It was revealed that the "bad" rolls had a microstructure consisting of coarse, continuous carbide networks on the dendritic boundaries while the "good" rolls did not have these networks. In the problem rolls, the brittle carbides were susceptible to cracking, and the cracks would follow a path along the continuous networks to the point that the roll spalled or fractured. The vendor was notified about the problem, and casting, forging, and heat treatment procedures were altered to minimize these networks. Based on the field metallography results, the roll shop developed stringent microstructural specifications to prevent problems in all future rolls purchased from that vendor and other vendors.

Another example involved work rolls that were prematurely spalling in the last stand of a seven-stand hot strip mill. Roll spalls are a serious problem because of lost productivity, damage to other rolls and equipment, and lost product and the roll itself. Figure 1(b) shows a field metallographer examining the microstructure of a spalled roll (note that part of the roll on the right has broken away or spalled from the roll barrel). In this case, all the equipment is portable and was assembled on-site in the roll shop. The rolls used in the later stands of this particular hot strip mill are called indefinite chill rolls. They are centrifugally cast and consist of a microstructure of 1 to 2.5% graphite in a white iron matrix of iron alloy carbide and bainite/tempered martensite. Field metallography revealed that the rolls that spalled had excessive graphite. The vendor was notified that his process was not in control, and the problem rolls were replaced. Thus, field metallography provided the "hard" evidence needed to solve the problem and saved hundreds of thousands of dollars in roll purchases and lost product/productivity. This is a prime example of a workpiece too large to bring to the metallography laboratory.

Techniques adapted from field metallographic procedures can also be performed in the metallographic laboratory to examine the microstructure of valuable archaeological artifacts, metallic artwork, Damascus swords, and meteor fragments. Since only a few microns of surface area are removed during grinding and polishing, the technique in most cases will not damage the component. With proper etching techniques the microstructure can be examined under the microscope. This article describes those nondestructive metallographic procedures used both in the field and in the laboratory.

B.L. Bramfitt and S.J. Lawrence, Field Metallography Techniques, *Metallography and Microstructures,* Vol 9, *ASM Handbook,* ASM International, 2004, p. 478–492

Field Metallography Techniques

Bruce L. Bramfitt and Samuel J. Lawrence, International Steel Group, Inc.

Background

Field metallography is an important tool and is practiced around the world. Some countries have developed standard practices for field metallography including the United States with ASTM E 1351 (Ref 1) and Germany with DIN 54-150 (Ref 2). There are also numerous published articles describing various techniques and applications of field metallography (see References at the end of this article). One of the most thorough publications on field metallography is a report prepared by Ontario Hydro for the Canadian Electrical Association (Ref 3). Although somewhat dated, this report describes surface preparation, replication practices, special techniques, and applications of field metallography. Henry and Ellis (Ref 4) and Viswanathan (Ref 5) describe field metallography replication techniques used for damage assessment of power-generating components. Damage assessment is the most significant application of field metallography. At some point in time, for example, the metallographic analysis will indicate that a rotor or steam pipe, exposed to superheated steam over 540 °C (1000 °F), needs to be replaced because creep voids are forming and these voids may link up

at grain boundaries to form the beginning of a crack. Figure 2 shows creep voids formed on the grain boundaries of steel exposed to elevated temperature. If damage is caught early by field metallography, a catastrophic failure can be prevented.

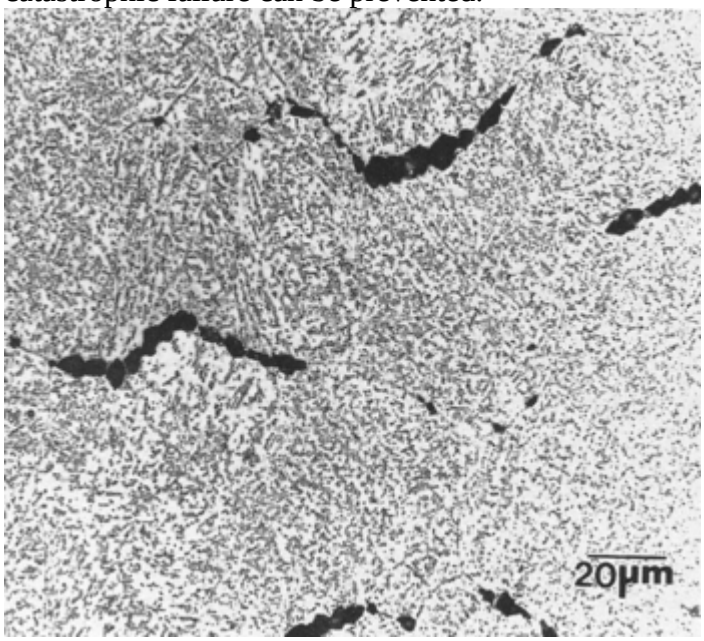

Fig. 2 Photomicrograph of voids at grain boundaries from intergranular creep cavitation.

Carbide coarsening in low-alloy steels and spheroidization of pearlite in carbon steels can also be monitored in those components subjected to continuous elevated temperatures. If the carbides can be extracted, their composition can be analyzed and lattice parameter measured. The extraction process is covered in detail elsewhere (Ref 3, 5, 6). At temperatures above 425 °C (800 °F), plain carbon steels can begin to graphitize with time (Ref 5). In this graphitization process, iron carbides (cementite particles) will begin to decompose into graphite and iron. The graphite weakens the component with time, and failure will occur.

For the tribologist, field metallography is a valuable technique to determine wear mechanisms. For example, wear surfaces can be examined to evaluate fretting, burnishing, and abrasion mechanisms as well as the effects of adiabatic heating. There are a selected number of papers listed in the references at the end of the article describing techniques and the use of field metallography for various applications (Ref 3, 4, 5, 6, 7, 8, 9, 10, 11, 12, 13, 14, 15, 16, 17, 18, 19, 20, 21, 22, 23, 24, 25, 26, 27, 28, 29, 30, 31, 32, 33, 34, 35, 36, 37, 38).

References cited in this section

1. "Standard Practice for Production and Evaluation of Field Metallographic Replicas," E 1351, *Annual Book of ASTM Standards,* 1990

2. "Nondestructive Testing Impression Methods for Surface Examination," DIN Standard 54–150, Deutsche Industrie-Normen, 1977

3. M. Clark and A. Cervoni, "In-Situ Metallographic Examination of Ferrous and Non-Ferrous Components," Report 314 G 429, Canadian Electrical Association, 1985

4. J.F. Henry and F.V. Ellis, "Plastic Replication for Damage Assessment," Report RP2253, Electric Power Research Institute, 1983

5. R. Viswanathan, *Damage Mechanisms and Life Assessment of High-Temperature Components,* ASM International, 1989

6. M.C. Askins et al., "Remaining Life of Boiler Pressure Parts—Base Material Model," Report RP 2253-1, Vol 3, Electric Power Research Institute, 1988

7. G. Kerzner, I. Sprung, and V. Zilberstein, “Field Metallography for Life Extension Studies of High-Temperature Components,” Proc. ASNT Conference on Characterization of Materials and Flaws, 1988

8. P.A. Jacquet, An Innovation in Inspection Tool and Control, *Met. Prog.*, Vol 85 (No. 2), Feb. 1964, p 114

9. D.E. Bradley, Replica and Shadowing Techniques, *Techniques for Electron Microscopy,* D.H. Kay, Ed., 2nd ed., Blackwell, Oxford, 1965, p 96–152

10. D. Vassallo, J. Fritzche, M. Savrato, and O. Wortman, Observation of Boiler Elements by Nondestructive Metallography, *Fifth Int. Conf. on Pressure Vessel Technology Part I, Design and Analysis,* American Society of Mechanical Engineers, 1969, p 451–461

11. M. Gell and T.T. Field, Detection of Deformation and Cracking on Oxide and Coated Surfaces by Light Microscopy, *Metall. Trans.,* Vol 1, 1970, p 317–318

12. M.W. Lui and I. LeMay, The Use of Plastic Replicas in Optical Metallography, *Metallogr. Rev.*, 1972, p 30–31

13. T.S. Akhmatova and L.G. Voronina, Use of Surface Prints for Nondestructive Investigation of Microstructure, *Ind. Lab.,* 1972, p 590

14. H. Crowder, Portable Laboratory for Field Metallography, *Met. Prog.,* Vol 105 (No. 4), 1974, p 76, 79

15. K. Dieser, The Nondestructive Metallographic Examination of Large Structural Components, *Prakt. Metallogr.,* Vol 11, 1974, p 441–455

16. E. Berner and R. Lohberg, Microstructural Investigations by Means of Replicas Taken from Components at Temperatures around 100 °C, *Prakt. Metallogr.,* Vol 17 (No. 1), 1980, p 14–22

17. B. Neubauer and U. Wedel, Restlife Estimation of Creeping Components by Means of Replicas, *Advances in Life Prediction Methods,* American Society of Mechanical Engineers, 1983, p 307–314

18. P. Auerkari, Remanent Creep Life Estimation of Old Power Plant Steam Piping Systems, *Advances in Life Prediction Methods,* American Society of Mechanical Engineers, 1983, p 353–356

19. B. Neubauer and U. Wedel, NDT: Replication Avoids Unnecessary Replacement of Power Plant Components, *Power Eng.,* Vol 88 (No. 5), 1984

20. M.E. Blum, On-Site Metallographic Investigations using the Replica Technique, *Microstructural Science,* Vol 12, American Society for Metals/International Metallographic Society, 1985, p 143–150

21. J.F. Henry, Field Metallography: The Applied Techniques of In-place Analysis, *Microstructural Science,* Vol 12, American Society for Metals/International Metallographic Society, 1985, p 537–549

22. Y. Lindblom, Refurbishing Superalloy Components for Gas Turbines, *Mater. Sci. Eng.,* Vol 1, 1985, p 636–643

23. E.V. Sullivan, Field Metallography Equipment and Techniques, *Microstructural Science,* Vol 15, International Metallographic Society, 1987, p 13–26

24. J.F. Henry and F.V. Ellis Field Metallography Techniques for Plant Life Extension, *Microstructural Science,* Vol 15, International Metallographic Society, 1987, p 3–11

25. J.J. Balaschak, Field Metallography in Assessment of Steam Piping in Older Fossil Power Plants, *Microstructural Science,* Vol 15, International Metallographic Society, 1987, p 12–35

26. A. Cervoni and M.A. Clark, Investigation of Turbine Disc Cracking by Field Metallography, *Microstructural Science,* Vol 15, International Metallographic Society, 1987, p 37–53

27. J.W. Simmons, On-Site Nondestructive Metallographic Examination of Materials, *Microstructural Science,* Vol 15, International Metallographic Society, 1987, p 55–67

28. N.G. Oh, "Replica Metallography," Publication NDE, Vol 5, American Society of Mechanical Engineers, 1989, p 231–236

29. W.L. Daugherty and P.R. Bormecker, "Assessment of Remaining Service Life of 1Cr-0.5Mo Steam Piping," Report W5RC-MS-94-0416, CONF-950288-1, DOE Westinghouse Savannah River Co., 1995, p 13

30. J.L. Han, Assessment of Fire Damage to Pressure Vessels in a Refinery Fire, *Corrosion,* Vol 49 (No. 5), 1993, p 420–437

31. B. Hahn and B. Melzer, Suitability of the Various Replica Materials for Use in Surface Replication on Warm Components, *Steel Res.,* Vol 67 (No. 9), 1996, p 390–393

32. M.E. Blum, P.M. French, R.M. Middleton, and G.F. Vander Voort, Ed., *Field Metallography, Failure Analysis, and Metallography,* ASM International, 1987

33. G. Kerzner, I. Sprung, and V. Zilberstein, Field Metallography for Life Extension Studies of High-Temperature Components, *Mater. Eval.,* Vol 47 (No. 9), 1989, p 1008, 1011–1014, 1017–1018

34. K.M. John, K.S. Kumar, and A. Natarajan, Application of Nondestructive Metallography in Materials Processing and Quality Control, *Prakt. Metallogr.,* Vol 28 (No. 6), 1991, p 285–294

35. I. LeMay, P. Cheung, and T.L. daSilveira, On Field Metallography Applications, *Microstructural Science,* Vol 22, International Metallographic Society/ASM International, 1987, p 87–92

36. G. Venkataraman, R. Veeraragavan, and S. Samidas, Recent Creep Damage Evaluation and Condition Assessment of Fossil Power Plant Components by in situ Metallography, *Trans. Indian Inst. Met.,* Vol 53 (No. 3), 2000, p 435–443

37. F. Ahrens, Characterising the Condition of Normalized Forged and Cast Steels by Combined Non-Destructive Metallography and Ultrasonic Attenuation Measurements, *Prakt. Metallogr.,* Vol 38 (No. 5), 2001, p 270–279

38. G.P. Kallenberg and T. Munsterman, Remaining Life Assessment of Catalytic Reforming Reactors, *Corrosion,* 2002, p 9

B.L. Bramfitt and S.J. Lawrence, Field Metallography Techniques, *Metallography and Microstructures,* Vol 9, *ASM Handbook,* ASM International, 2004, p. 478–492

Field Metallography Techniques

Bruce L. Bramfitt and Samuel J. Lawrence, International Steel Group, Inc.

Advantages and Disadvantages

Advantages. There are numerous advantages in using field metallography. Some are:

- The technique is portable and can be used on-site.
- Field metallography can be used to monitor quality of purchased components.
- A properly prepared surface and replica provides very good resolution of microstructural constituents.
- Replication techniques are nondestructive.
- Replicas are ideal for both flat and curved surfaces (see Fig. 3).
- Field metallography can be used to monitor the evolution of microstructural changes in a component during its lifetime. This is particularly useful in assessing creep damage in elevated-temperature components (turbine rotors/blades, steam piping, heat exchangers, chemical reactors, pressure vessels, etc.).
- The techniques can be applied to a wide variety of materials.
- Field metallography can complement nondestructive techniques such as ultrasonic testing.

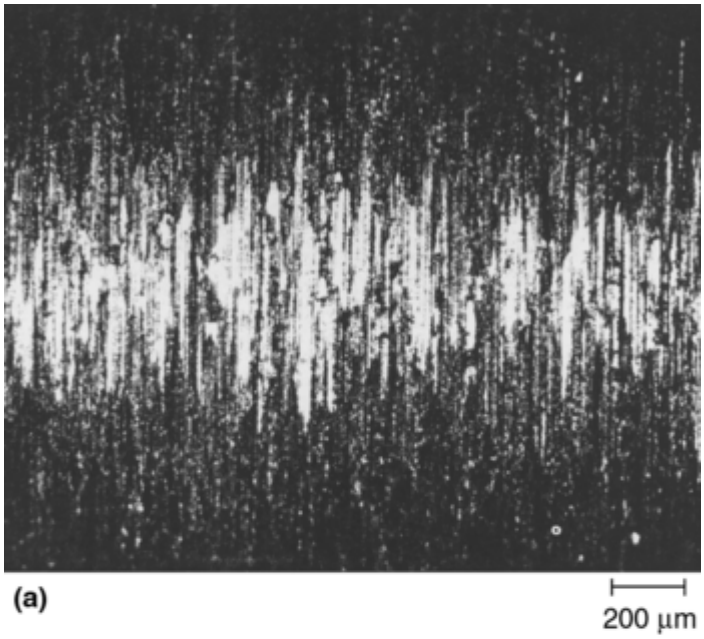

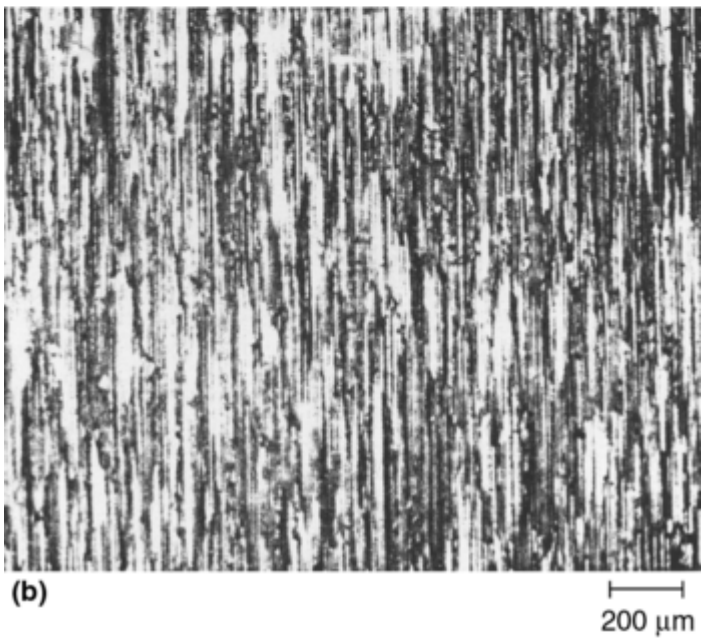

Fig. 3 Micrographs showing scratches on the surface of a roll. (a) Curved surface. (b) Replica of the curved surface. Note the limited field of view on the curved surface compared with the replica. Courtesy of LECO.

Disadvantages of field metallography include:

- The technique only analyzes the microstructure of the surface of a material/component. This must always be kept in mind when conducting an investigation because in many cases the surface microstructure can be different from the microstructure found in the interior of the component.
- The chemical composition of the constituents in the microstructure cannot be analyzed because the replica only reveals the topographic features at the surface. However, there are extraction replication techniques used for electron microscopy that can physically pull precipitates and particles from the component surface for analysis in the scanning electron microscope (SEM) or electron probe microanalyzer (EPMA), or scanning transmission electron microscope (STEM).
- Special portable equipment is required.
- Contamination may be a problem in harsh or dusty environments.

B.L. Bramfitt and S.J. Lawrence, Field Metallography Techniques, *Metallography and Microstructures,* Vol 9, *ASM Handbook,* ASM International, 2004, p. 478–492

Field Metallography Techniques

Bruce L. Bramfitt and Samuel J. Lawrence, International Steel Group, Inc.

Basic Equipment and Supplies

Since field metallography is a portable procedure, the equipment must be compact, easy to carry, and, if possible, battery operated. Basically a handheld motorized grinding and polishing device is required to prepare the polished surface. Metallographic equipment suppliers provide such equipment. An entire system can be purchased for grinding, polishing, etching, observation, and replication. The most expensive equipment purchase will be a good-quality observation microscope with a system to capture the image digitally. However, much of the basic equipment can be purchased in a hardware store. For simplicity, a battery-powered, handheld drill can be used as seen in Fig. 4. Conventional solvents are used to clean the surface, and routine etchants are used to reveal the microstructure. A small, portable, upright microscope is desirable in order to examine and possibly photograph the microstructure on-site. Surface replicas can be produced of the polished or etched surface to provide a permanent record of the microstructural details. The replicas can be enhanced and carefully studied back in the metallographic laboratory. The basic equipment and supplies are listed in Table 1.



Fig. 4 Use of a battery-operated handheld drill to grind and polish a region on a cast steel table roll for a hot strip mill

Table 1 Field metallography equipment

Process or requirement	Equipment
Grinding and polishing[(a)]	A portable, motorized handheld grinding and polishing device (Fig. 4 and 5)
	Several rubber stubs for grinding and polishing papers/cloths (Fig. 6)
	Disks of adhesive-backed grinding papers (120, 240, 320, 400, and 600 grit) in separate containers
	Disks of polishing cloths
	Diamond paste, slurry, suspension, or aerosol spray (6 and 1 μm)
	A plastic squeeze bottle of 0.03 μm alumina slurry (for nonferrous metals)
	A plastic squeeze-spray bottle containing alcohol
	A plastic squeeze-spray bottle containing water
	Cotton balls for swabbing and cleaning
Etching[(b)]	Plastic bottles of premixed etchants (screw caps)
	Plastic squeeze-spray bottles for water, solvent, and etchants
	Glass rods (6 mm diam × 20 m long, or $\frac{1}{4}$ in. diam × 8 in. long)
	Cotton balls for swabbing
	Cans of compressed air with spray nozzle
	Rubber gloves
In situ examination of microstructure	A portable upright microscope with reflected light source (Fig. 7 and 8); battery-operated is preferred
	5×, 10×, and 20× objectives
	Camera and attachment for microscope
	Battery-powered supply for light source
	Extra batteries and bulbs for light source
Replication	Sheets or rolls of cellulose acetate film (several different thicknesses)
	Bottle of acetone or methyl acetate solvent
	Squeeze bottle
	Roll of clear double-backed adhesive tape ($\frac{3}{4}$ in. wide)
	Tweezers
	Glass rod
	Boxes of standard glass slides
	Glass slide storage case
Miscellaneous	Absorbent cloths or paper towels
	Notebook and pencil
	Flashlight
	Safety equipment (safety goggles/glasses, hardhat, etc.)
	Extension cord
	Collapsible table to hold equipment
	Collapsible stool

(a) Electrolytic polishing equipment may be required for certain steels and nonferrous alloys; see the section "Polishing" in this article.

(b) Electrolytic etching procedures may be required for certain steels and nonferrous alloys; see the section "Etching" in this article.



Fig. 5 Portable handheld device made exclusively for grinding and polishing in the field

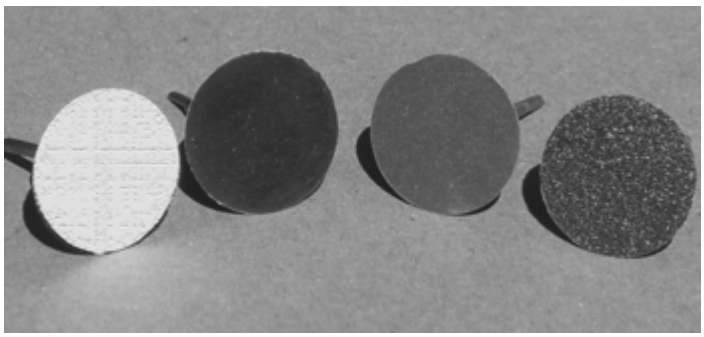

Fig. 6 Rubber stubs used to hold grinding papers and polishing cloths for field metallography. Three different mesh size grinding papers are on stubs on the right and a polishing cloth on the stub on the left



Fig. 7 Portable battery-operated microscope



Fig. 8 Portable battery-operated microscope with digital camera attached

B.L. Bramfitt and S.J. Lawrence, Field Metallography Techniques, *Metallography and Microstructures,* Vol 9, *ASM Handbook*, ASM International, 2004, p. 478–492

Field Metallography Techniques

Bruce L. Bramfitt and Samuel J. Lawrence, International Steel Group, Inc.

Planning for Field Metallography

Field metallography is actually an extension of the metallographic laboratory except that sample preparation is conducted with portable equipment in the field. Special equipment is required, but many of the items can be purchased in a hardware store or through a metallographic supply house. Also, sample preparation in a metallographic laboratory takes place in a rather clean environment. In the field, contamination can be a problem from airborne dust and other environmental emissions. Other factors such as the weather and the temperature of the component being examined can alter the way etchants respond. This section covers some of these issues.

Material Characteristics

Before any metallographic procedure is undertaken, the metallographer should know the characteristics of the material being prepared. The following three material characteristics are important:

- Hardness
- Type and composition of alloy
- Surface condition

Hardness. The hardness will determine what grinding papers, polishing cloths, and abrasives to use. For example, a very hard tool steel will require a different technique than a very soft copper alloy.
Alloy type and composition will determine what procedures to use. For example, an AISI 304 stainless steel will require electrolytic polishing and etching procedures, whereas an AISI/SAE 8620 steel will require conventional mechanical polishing and etching procedures. By knowing the materials to be examined, the metallographer can also bring the proper etchants to the field. For example, a plain carbon steel with a ferrite + pearlite microstructure will require a different etchant than a low-alloy steel with a martensitic microstructure. It must be kept in mind that these etchants will normally be premixed in the laboratory and placed in well-marked plastic bottles. However, in the field, the mode of shipment will be important since air travel prohibits pressurized aerosol cans as well as most chemicals and solvents in checked or carry-on baggage. Solvents will have to be purchased at location or shipped to the location from a chemical supply house. Picric acid, used in many etchants for steels and cast irons, may be prohibited from some localities and plant sites, and, if allowed, special permits may be required. Perchloric acid used for some electrolytic polishing and etching solutions requires special care and may require a permit. The metallographer must consider all these factors before going into the field.
Surface condition is also very important. If the component being examined has a fine-machined surface, as in the case of a rolling-mill roll, preparation will be simplified. In this case, the grinding process may start with 240 grit paper. If the surface is heavily oxidized or rusted, the procedure will require a more aggressive approach. If fairly shallow, a coarse grind starting with 60 grit paper may be adequate. However, the surface may be so corroded (oxidized) that the corrosion product must be mechanically chipped or scraped away to expose the metallic surface. This will require a grinding stone or a flapper wheel attached to a handheld drill. It may be important to save some of the corrosion product for analysis in the laboratory. In some cases, the metal surface below the corrosion will be affected (e.g., decarburized), and further grinding will be necessary to expose the true base microstructure deeper into the component. In some cases, the thickness of the corrosion or the depth of corrosion penetration may be important to the investigation. If the corrosion layer and associated microstructure below the surface is important to the investigation, it may be possible to prepare a tapered region at an edge of the workpiece. With this approach, the metallographer can get some idea about the extent of the oxidized layer and subsurface microstructure.

Other Considerations

Other aspects should also be considered before proceeding with a field investigation:

- Environment, e.g., outside in rain or snow
- Access to component
- Size and shape of component
- Location and number of areas to be examined
- Vibrations
- Dust, chemical fumes, and so forth

Environment. Knowing the environment is important for several reasons. Will the procedure be carried out on a component that is inside a building or outside in the elements of nature? If outside, very cold temperatures will extend etching response (longer times needed), and some etchants will freeze and become ineffective. It may be possible to heat the region with a hair dryer. If outside and exposed to precipitation (rain or snow), the area being prepared must be protected from the precipitation. If the components are hot, for example, steam piping, conventional solvents and etchants will evaporate very quickly and high boiling point solvents will be required. Thus, the metallographer must plan ahead for these conditions.
Access to the component must be known beforehand so that proper safety equipment can be worn and safety rules reviewed. For example, a weld on the inside of a 122 cm (48 in.) diam linepipe being installed for natural gas transmission may need to be examined. This will require the metallographer to be inside the pipe to prepare the surface. Ample ventilation (clean air flow) is mandatory, and all harmful gas must be removed. A safety mask or air supply and safety goggles must be worn during grinding, polishing, etching, and replication. Ventilation must be provided while using solvents. In some cases, access may be required for a component in an elevated location (as seen in Fig. 1). The metallographer may have to work from a scaffold or ladder using a

safety harness. A stepladder may be required to reach an elevated location. Access should always be carried out in a safe environment; that is, never work on or around moving machinery or at a site with poisonous gases or open flames. In some cases, the area of interest may be on a vertical surface or an overhead (inverted) surface. This can present a problem in utilizing a microscope in examining the area. However, some field microscopes have magnetic feet, which are ideal for such applications.

Component Size and Shape. It is important to know the size and shape of the component to be examined. For example, will the surface have curvature or will it be flat? Can the component be moved to a more convenient location? Will the component be in use during the investigation? With a description and understanding of the component, the metallographer can prepare accordingly.

Location and Number of Areas to be Examined. Advanced knowledge of the location and number of areas to be examined will be helpful for the metallographer to decide on the amount of consumable materials to be used. Another important aspect is the proper selection of the areas to be examined so as to obtain the critical information needed about the component. Several areas may need to be prepared to get a representative sampling of the microstructural details of the component. Finding creep damage will require many areas of observation. For example, welds and high-stress areas in piping would be an obvious location of damage. Also, locations that had a prior history of damage should be examined.

Vibrations, Dust, and Fumes. Vibrations can create a problem if the prepared microstructures need to be photographed with a microscope. Airborne dust can contaminate the area during grinding and polishing. The metallographer may have to improvise a way to protect himself or herself and the area being prepared. A temporary cloth or plastic hood can be set up over the area. The metallographer must wear a dust respirator in this situation. With chemical fumes, the metallographer must assess the environment and determine the danger involved. If harmful, the region must be avoided. The safety of the metallographer is paramount and much more important than conducting a metallographic investigation.

B.L. Bramfitt and S.J. Lawrence, Field Metallography Techniques, *Metallography and Microstructures,* Vol 9, *ASM Handbook*, ASM International, 2004, p. 478–492

Field Metallography Techniques

Bruce L. Bramfitt and Samuel J. Lawrence, International Steel Group, Inc.

Specimen Preparation

Once the location is determined, the surface condition will dictate the initial preparation steps required. Figure 9 shows the sequence of conducting an investigation using field metallography. The top portion of the sequence shown in Fig. 9 is for preparing and possibly preserving material on the surface of the workpiece. If the surface is coated with grease or paint, it is important to remove this organic material with a solvent.

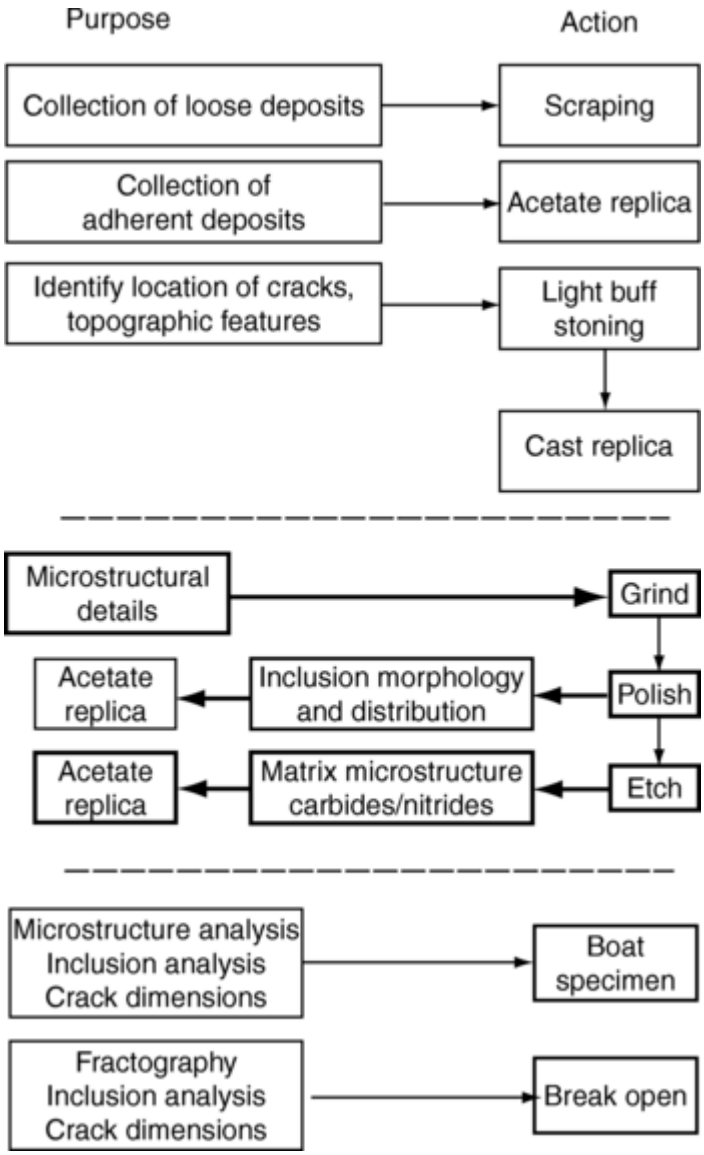

Fig. 9 An outline of the investigation steps for various stages of field metallography

Rust and corrosion can be removed by chipping away loose layers to expose the surface. A flap wheel or wire brush attached to a hand drill can be utilized for removal of corrosion products. A hand grinder can also be employed. In some cases it may be important to save this surface material for a more complete investigation. In fact, in some cases the surface material may be the focus of the investigation. A similar case is described later in this article. This can be accomplished by collecting the material in a clean container. In some cases, a replica can be applied to the surface to extract material and to preserve topological features. The types of replica materials required are discussed in a later section on replication.

For fine microstructural evaluation, the steps shown at the center of Fig. 9 are employed. In this case, the surface must be prepared by grinding and polishing to develop a smooth finish comparable to that produced in the metallographic laboratory. A photograph or replicas are made of the as-polished surface for determining inclusion size, shape, and distribution and of the etched surface for microstructural details. As shown in examples later in this article, the microstructure of an enhanced surface replica is practically identical to that produced on an actual specimen in the metallographic laboratory.

The bottom section of Fig. 9 shows that a small “boat” specimen may be needed of the actual material. Also, the component may be broken open to reveal a fractured surface for analysis.

The rotary straightener roll and the hot strip work roll described previously were utilized to illustrate the techniques of field metallography. The goal in these steps is to reveal the microstructure of the steel after the roll was initially machined or taken from service. The techniques shown here are proven techniques, although it is recognized that other procedures may work just as well. Remember, the techniques shown here are essentially the same as those used in the metallographic laboratory except that the equipment being used is

portable. Also, a replica is not necessary in the metallographic laboratory because the microstructure can be photographed with a metallograph or microscope with a digital camera attachment. A replica may not be necessary in the field if the portable observation microscope has photographic capability.

The series of photographs in Fig. 10 show the step-by-step technique for field metallography using mechanical methods (electrolytic methods are illustrated in a separate section). Basically the same equipment is used for grinding and polishing a small region on the workpiece. The grinding papers and polishing cloths/abrasives are the same as those used in the metallographic laboratory.

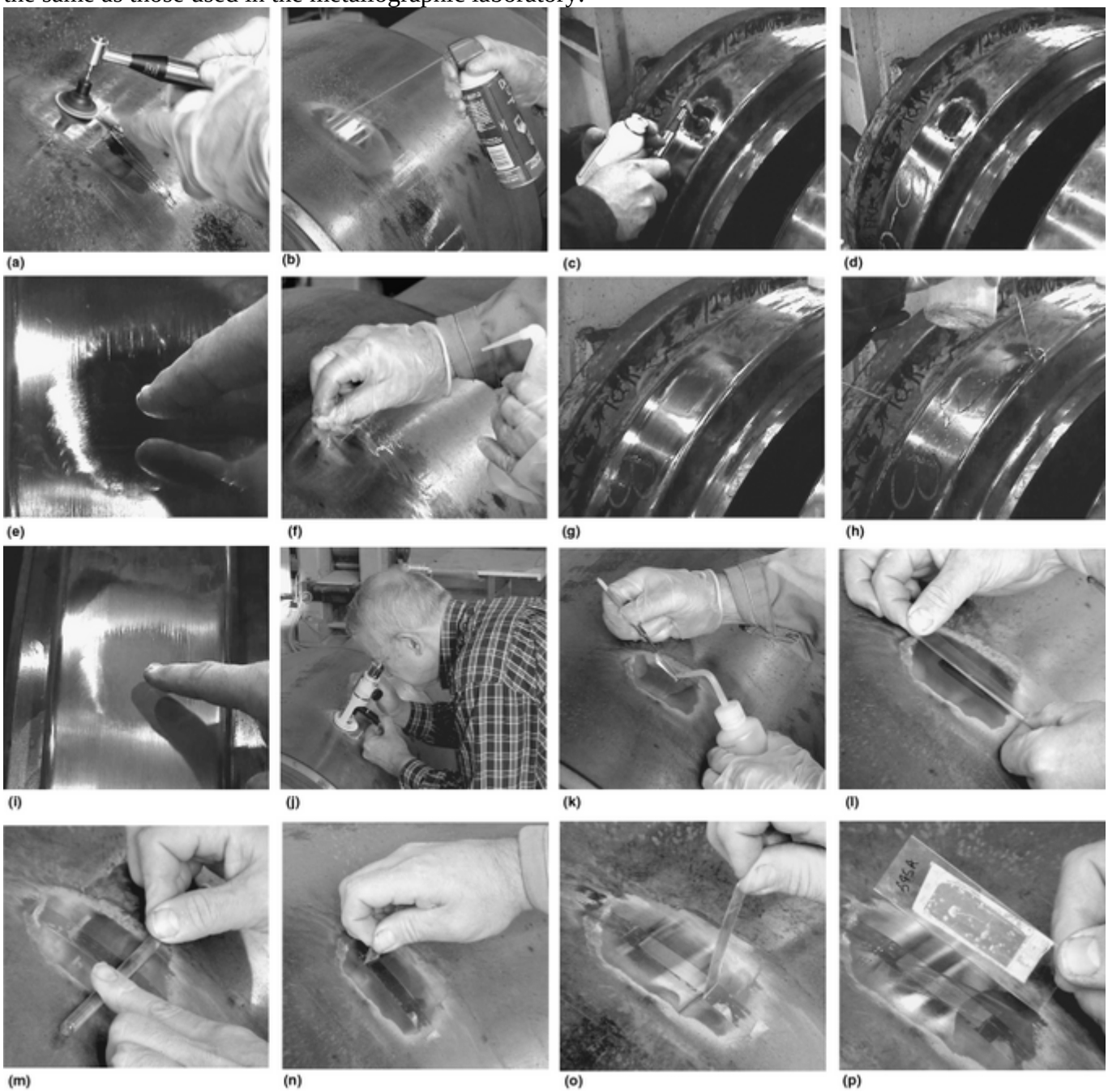

Fig. 10 The various steps in preparing a polished and etched surface on a roll surface. (a) Grinding an area on the roll. (b) Blow-drying the region with compressed air. (c) The polishing stage. Applying a diamond compound from an aerosol can. (d) The final polished area. (e) Reflection seen in the polished area. (f) Using a cotton swab to apply etchant to surface of polished area (note the use of rubber gloves to protect hands). (g) Etchant reacting with steel on the surface of polished area. (h) Flushing the etchant from the roll surface. (i) Note lack of reflection on matte finish of etch surface (compare with part e). (j) Using a portable microscope to examine the microstructure of the prepared surface. (k) An acetate film being applied to the polished surface with tweezers. The area is soaked in solvent from squeeze-bottle. (l) Placing double-backed transparent tape to dried replica. (m) Rolling a glass rod over the acetate film to minimize bubbles between two-sided adhesive-backed tape and the film. (n) Grabbing the end of the

double-backed tape to strip the dried acetate film from the surface. (o) Stripping the dried acetate film from the surface with double-backed tape. Note the region where the acetate film was on the roll surface. (p) The other side of the double-backed tape (opposite the acetate tape) is placed on a glass slide for protection and to keep the replica from curling. To ensure adherence to slide and keep the replica flat, roll a glass rod over the replica.

Grinding

As in conventional metallographic procedures, a series of progressively finer grinding papers are used to develop a smooth surface for the polishing steps. Details on grinding and grinding papers for ferrous and nonferrous alloys can be found elsewhere this Volume and in Ref 39. In the United States, grinding papers commonly used for metallography have grit sizes of 120, 240, 320, 400, and 600 grit designation. In Europe they differ. The relationship between U.S. and European designations is given below:

U.S. designation	European designation	Particle size, μm
60	60	260
80	80	200
100	…	160
120	120	125
150	…	93
180	180	76
220	220	68
…	…	58
240	…	52
…	320	46
280	…	39
320	…	35
…	500	30
360	…	25
400	800	22
600	1200	14

In field metallography, the same papers that are used in the metallography laboratory can be purchased from a supply house or can be hand-cut or punched from the larger papers. Usually, small adhesive-backed disks, 25 to 38 mm (1 to $1\frac{1}{2}$ in.) in diameter are required. The disks are attached to a flat rubber disk on a shaft (called a stub). Figure 6 shows a series of grinding papers attached to stubs. The stub shaft fits into a chuck of a handheld rotating tool as seen in Fig. 4 and 5. For convenience, the grinding papers can be purchased in the diameter desired. However, a less expensive option is to punch or cut disks from a conventional 200 or 300 mm (8 or 12 in.) adhesive-backed grinding paper. Dozens of disks of each grit size can be stored in separate containers, for example, a capped plastic cylinder or a zipper-type plastic bag. The container should be well marked with the grit size. It is of utmost importance not to mix or cross contaminate the grinding papers in these containers.

For a component with a fairly smooth surface, start with a disk of 240 grit paper and make a circular spot on the surface. For rougher surfaces, start with a 120 grit paper. Figure 10(a) shows the grinding stage of preparation. A lubricant such as water can be used except in cases where a galvanic cell is created (certain coated materials). In these special cases, alcohol-based extenders can be used. It is recommended to use a back-and-forth motion with moderate pressure to grind a spot about 40 to 50 mm ($1\frac{1}{2}$ to 2 in.) in diameter (smaller or larger diameter spots may be necessary for certain components). The speed of rotation should be about the same as grinding in the metallographic laboratory, 150 to 300 rpm.

Replace the grinding paper after grinding for about 10 to 20 s. Smaller grit size papers wear out faster than large grit size papers. Longer times may damage the surface. In fact, excessive grinding and rough polishing can actually burnish the surface and introduce plastic deformation. This deformation develops an artifact on the surface. Generally, two to four disks of each grit size are adequate to remove the scratches from the previous grind. Therefore, after the last grit paper, change to the next finer grit size and repeat. Before using the finer paper, rinse all grinding debris from the object being prepared. In this example, a plastic squeeze bottle of ethyl

alcohol was used. One thing to remember after each grinding step is that the back-and-forth motion should always be 90° to the previous grit size paper. Using this technique, the metallographer will be able to see if the previous set of scratches are removed. When finished grinding, rinse the surface with alcohol and dry with a blast of compressed air. Figure 10(b) shows compressed air being applied to dry the ground area. These pressurized cans are available in hardware stores and metallographic supply houses. They are called aerosol dusters. Do not use cans of compressed fluorocarbon-based gas since this gas has been shown to adversely affect the ozone layer in the atmosphere.

Polishing

Manual Polishing. A disk of adhesive-backed polishing cloth should be attached to a clean stub. The selection of the polishing cloth is the same as in conventional metallographic procedures. The procedures for polishing ferrous and nonferrous alloys are described elsewhere in this Volume. The cloth will depend on the type of material being polished. In general, for a very soft material a flocked twill rayon cloth is used, and for a hard material a medium-nap cloth is used. As with the grinding papers discussed previously, these cloths can be punched or cut from larger conventional polishing cloths to match the diameter of the rubber stub. The first polish should be performed with appropriate coarse polishing media; in this example, 6 μm diamond particles are applied to a canvas cloth from an aerosol can (Fig. 10c). In this figure, the aerosol can is held in the left hand and the right hand is used to polish the area. A moderate pressure is applied to the stub using the same type of back-and-forth motion described previously for grinding. For the first polishing step, use a motion that is 90° to the last grind. The polishing should take place for about 60 s. The time will depend on the rate of removal of the last set of grinding scratches. Examine the polished surface to ensure that these scratches are removed before proceeding to the next step. If the scratches are eliminated, rinse and swab the area with alcohol to remove all traces of grinding compound. Blow-dry the area with dry compressed air.

The next polishing step should be carried out with appropriately smaller size polishing media, in this example 1 μm diamond paste using a low-nap cloth. For convenience, a stub should be dedicated to each abrasive size, since the cloths can be used again for other areas of preparation. For this second polishing step, use a back-and-forth motion that is 90° to the previous polishing step. Polishing time should be between 60 s, or until the previous scratches are removed. After polishing with this cloth, swab the area with alcohol and blow dry.

The metallographer should have knowledge of the types of polishing cloths available. Some cloths are used for rough polishing, and a different cloth is used for final polishing. Some cloths are appropriate for inclusion retention, and some cloths “pull” inclusions from the surface. Examples of all these cloths for use with ferrous and nonferrous metals can be found elsewhere in this Volume; see for example, the article “Mechanical Grinding and Polishing.”

The final polishing step in this example will require a rayon cloth saturated with 0.3 μm aluminum oxide suspended in water. For very hard materials, this third polishing step may not be necessary as in the case of the D2 tool steel roll. Again, polish 90° to the previous step for 10 to 30 s. Once a scratch-free surface is produced, gently clean the surface with a cotton swab soaked in alcohol and blow dry. Figure 10(d) shows the final polished area on the roll surface. To show the mirror finish, note the reflection of the finger in the polished surface in Fig. 10(e).

Electrolytic Polishing. Some metallographers prefer electrolytic polishing to mechanical polishing especially in examining components in power-generating stations. Electrolytic polishing can take as little time as 15 s to polish an area as compared to 10 to 20 min for mechanical polishing. Some alloys require electrolytic polishing. In the case of ferrous alloys, electrolytic polishing is used for stainless steels. Suppliers of field metallographic equipment market portable electrolytic polishing and etching units that can be placed directly on the workpiece. Standard electropolishing solutions are listed elsewhere in this Volume; see, for example, the article “Chemical and Electrolytic Polishing.” Some of the components of these solutions are very dangerous, and the metallographer needs to be fully cognizant of these dangers. One such chemical is perchloric acid, which is highly explosive if used improperly (Ref 3). Perchloric acid is a strong oxidizer and can explode in contact with organic or carbonaceous materials (Ref 3).

An example of a portable electrolytic polishing/etching device can be seen in the bottom right corner of Fig. 11. The power supply is used to set the direct current and voltage of the cell. The cell is connected to a tube that supplies the electrolytic reagent to the workpiece. The workpiece is the anode. In the example shown in Fig. 11, the tube actually consists of an outer tube with an inner tube. The electrolyte solution passes through the inner

tube to the workpiece and returns to the cell in the outer tube. The voltage is applied to the workpiece by a wire wrapped around the outer tube. The tubes and wire are attached to a probe as seen in Fig. 12. By pushing downward on the probe, the electrolyte circulates across the area being polished and the circuit is completed. Once polishing is complete, the voltage is changed to etching. Most instruments have a switch that is turned on for polishing then turned on for etching. The result is a small round electrolytically polished and etched area on the workpiece. One of the advantages of this method is that many such areas can be produced as the probe is placed at different locations. The workpiece in this example is an AISI 304 stainless steel tank for liquid nitrogen storage. An example of a polished and etched surface can be seen in Fig. 13. It must be remembered that for an electrolytic unit to work effectively, the initial surface finish should be prepared to be at least 240 to 320 grit size.



Fig. 11 Portable electrolytic polishing/etching device being used to polish a region on a 304 stainless steel liquid nitrogen dewar. Note the polishing/etching cell and power source on the table at the bottom right and the metallographer holding the probe on the workpiece.

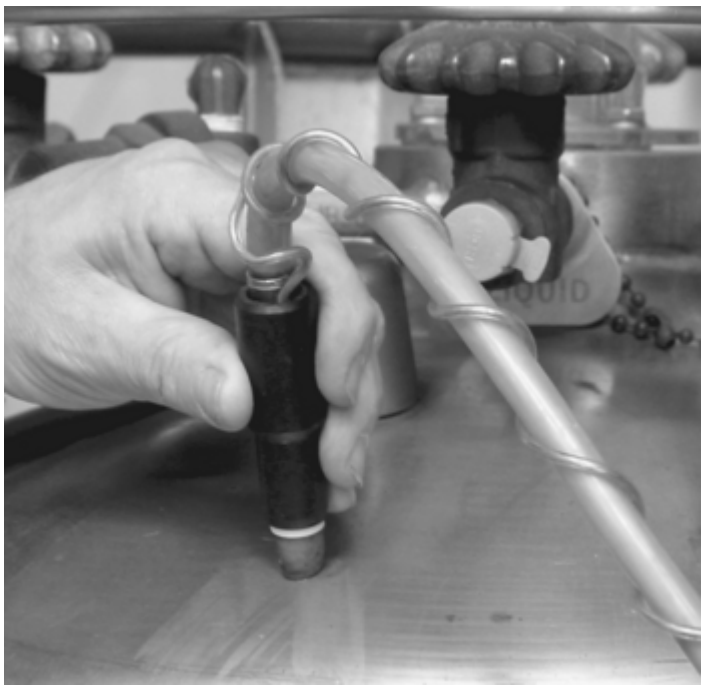

Fig. 12 Close-up view of the electrolytic probe being pressed onto the dewar surface

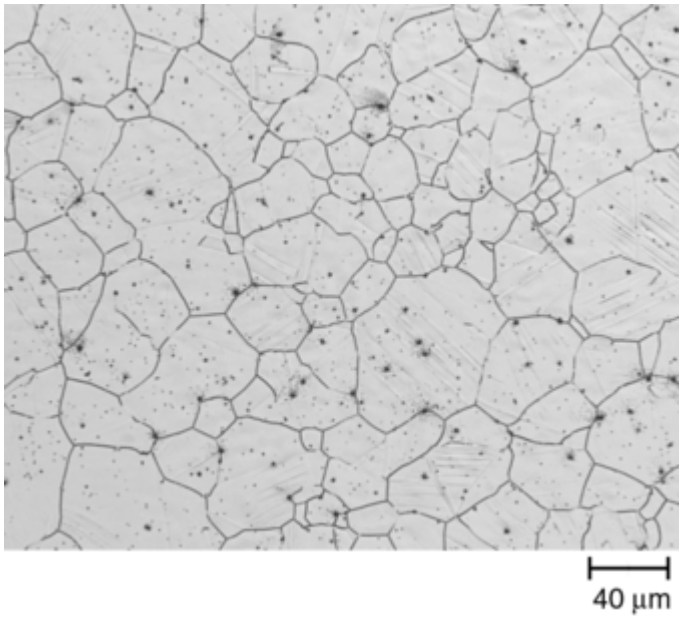

Fig. 13 Microstructure of the 304 stainless steel dewar after polishing and etching with the device shown in Fig. 11 and Fig. 12. Electrolytically etched in 10% oxalic acid solution. Original magnification 500×

Etching

Manual Etching. The metallographer must know the type of material being examined in order to select the proper etchant. The various etchants for steels, cast irons, and nonferrous metals can be found in this Volume.

A convenient way to apply an etchant to the polished surface is to use a cotton swab (Fig. 10f). In this case, the metallographer is using a cotton ball soaked in the etchant to gently swab the surface. Protective gloves are necessary. The cotton swab may be attached to a glass or wooden stick. The swab is dipped into the etchant and applied gently to the polished surface. Sometimes it may be necessary to construct a dam to hold the etchant. If this is the case, a dam of modeling clay pressed on the surface around the polished area will work. Etching time will depend on the type of etchant and the temperature of the component. Figure 10(g) shows the etchant reacting with the polished surface. For this example, Vilella's reagent was used. To avoid overetching, stop the etching process after a dull surface appears. This means that the etchant must be removed as in this example by flushing with ethyl alcohol (Fig. 10h). Here a squeeze bottle of ethyl alcohol is being used to flush the area. Dry the flushed surface with compressed air. Figure 10(i) shows a close-up of the etched surface. Note the “matte” finish and the absence of a reflection of the finger (a shadow is shown). Compare this figure with the mirrorlike polished surface in Fig. 10(e).

At this point, it is recommended that the metallographer or metallurgist examine the microstructure with a portable metallurgical microscope as seen in Fig. 10(j). If a microscope is not available, a surface replica of the prepared area can be brought back to the metallographic laboratory for examination (replication is described in the next step). If the microscopic examination reveals that a deeper etch is required, swab the area again with the etchant. Flush the surface with alcohol and blow dry. At this point reexamine the microstructure with the portable microscope. In general, a deeper etch is required for higher-quality microstructural replication.

Electrolytic Etching. The portable electrolytic polishing/etching cell described previously is also used to electrolytically etch the prepared surface. Standard electrolytic etchants can be found elsewhere in this Volume.

Replication

Preparing a replica of the as-polished or etched surface is quite simple and an essential feature of field metallography. Figure 14 shows the attributes of a replica. Figure 14(a) shows a carbide particle and a crack on the workpiece surface. Figure 14(b) shows a plastic film that was softened by a solvent as it adapts the surface. Figure 14(c) shows the film (replica) stripped from the surface of the workpiece. The replica is a “negative” impression of the features on the surface. This figure shows that deep cracks will not be completely filled with the replicating material, but the details of the carbide are duplicated.

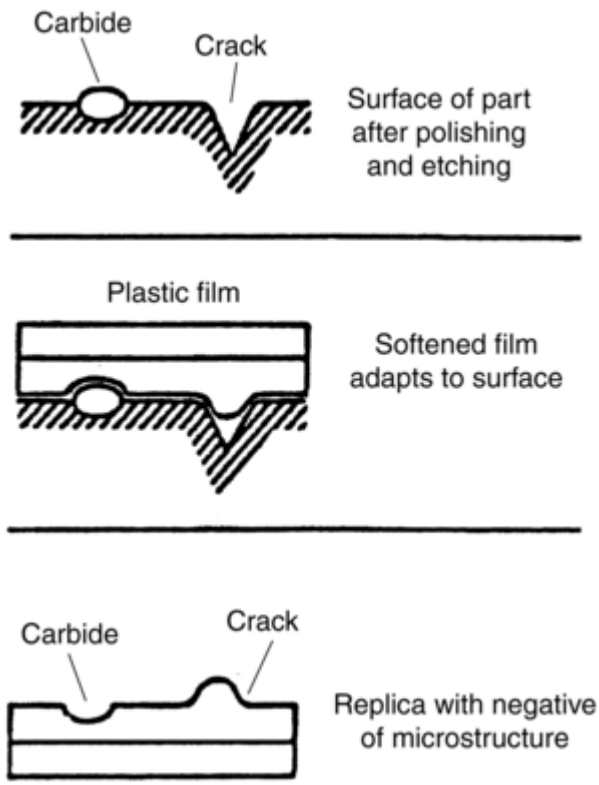

Fig. 14 Application of a replica to the surface of a workpiece. Courtesy of LECO.

Although the as-polished or etched surface can be examined directly with a portable microscope, a replica will provide a permanent record of the microstructure. This replica can be taken back to the metallographic laboratory and enhanced. It can then be studied under the light microscope or scanning electron microscope (SEM). However, as shown in the section "Case Studies" in this article, an acetate replica, enhanced by sputtering gold on its surface, provides a crisp image of the microstructure that is practically indistinguishable from the microstructure prepared on a standard metallographic specimen in the metallography laboratory. Also, in many cases, curved surfaces of the component are not conducive to photography because much of the field is out of focus (Fig. 3a). A replica, on the other hand, can be produced from a curved surface and then flattened on a glass slide and photographed in the metallographic laboratory.

Replication Materials. There are several different types of replication materials. Replication started about 50 years ago when surface replicas were common as specimens for observation in the transmission electron microscope (TEM). Initially collodion (ethyl or amyl acetate) was used as a replication material (Ref 8). Over the years other materials were used including nitrocellulose varnish, cellulose acetate (Ref 11, 12), polystyrene (Ref 13), cellulose nitrate, acetobutyrate (Ref 15), and silicone rubber. In 2004, a common replication material is a clear cellulose acetate film that is softened by a solvent, usually acetone or methyl acetate. There are also acrylic casting resins that can be poured directly onto the prepared area. An example of a casting resin is methyl methacrylate. A containment dam of modeling clay can be placed around the prepared area and the resin poured into the dammed region. Although these resins are used for metallographic replication, they are widely used for replicating a textured surface. The solid replica can then be taken to the laboratory and the surface roughness (R_a) can be measured using a profilometer. In addition to acetate film and acrylic resin, metal foils can be used to form a replica especially in applications requiring a replica of a hot component. The foil, for example, lead or aluminum is placed on the etched surface and pressed into the surface by an impact tool such as a rubber-head hammer. Since this is a specialized method it will not be covered in this article.

Replication with Acetate Film. To begin the replication process, soak the surface of the polished area with methyl acetate (acetone can also be used). A convenient way is to use a medicine dropper to add the proper amount of solvent or to squirt an ample amount of the solvent from a plastic squeeze bottle. The next step is to place a piece of cellulose acetate film on top of the surface that is wet with solvent. This is shown in Fig. 10(k), where a strip of acetate film is being placed by tweezers into a pool of methyl acetate that is continuously flooded on the prepared surface. Usually a rectangular piece (about 25 × 20 mm, or 1 × $\frac{3}{4}$ in.) is cut from a larger sheet or a roll of cellulose acetate strip. For convenience, the piece should be large enough to fit on a

glass slide. The long axis of the rectangle should be aligned to match a particular orientation of the component, for example, a rolling or forging direction. Keeping track of orientation may be an important aspect of the replication process. The thickness of the film is important. If the film is too thick, it will not fill all the valleys of the microstructure. If it is too thin, it may tear when the replica is removed from the component. For most replication, a film thickness between 20 and 45 μm is sufficient.

Once the film has wetted the surface, do not press the film to the surface with your finger. Just allow the film to naturally "soften" into the surface. This is the critical step since the softened acetate film must take the exact shape of the etched surface. Allow the film to soften in the solvent. The time will depend on the film thickness and temperature. During this time, the acetone will evaporate and the film will dry. Allow ample time for the film to dry, usually about 1 to 5 min. The next step is removal of the dried film from the surface. One convenient way is to lay one side of a two-sided adhesive-backed tape on top of the film (Fig. 10l) and then gently roll a glass rod over the tape to ensure good adherence (Fig. 10m). The tape should be longer than the replica itself. Next, carefully peel the tape, with the replica attached, from the surface (Fig. 10n and o). To keep the replica and tape from curling, the other side of double-backed tape is carefully placed on a glass slide so that the replica is face up as seen in Fig. 10(p). To ensure adhesion of the tape to the slide, simply roll the tape and replica with a glass rod. The identification code should be immediately placed on the slide and the slide placed in a covered slide storage box. This applies to an extraction replica where deep etching has exposed particles and inclusions in the microstructure. When the replica is applied, it encapsulates the particles and many will be removed from the surface as the replica is pulled from the surface. Usually a thicker acetate film is necessary for this type of replication. With some of the particles attached to the replica, they can be chemically analyzed in the laboratory using energy-dispersive spectroscopy (EDS) in the scanning electron microscope or scanning transmission electron microscope.

For convenience, metallographic supply houses market special adhesive-backed metallic sheets to attach to the back of the replica for easy removal from the surface.

The quality of the replica can be checked with a portable microscope. Many times, two or three replicas of the same spot are produced to ensure that the microstructural details are obtained from all areas of the prepared surface. Also, multiple replicas are necessary because air bubbles commonly form between the replica and the metal surface, and the structure in that area is not replicated. Another replica will ensure that the area is represented in the metallographic analysis. Also, the first replica can pick up debris from the surface. This debris may result from airborne dust particles.

Enhancement of the Replica. A plain cellulose acetate replica is not very useful. This is because it is transparent, and the light from the microscope simply penetrates the replica. Microstructural features are contained in the replica, but the replica needs some enhancement to reveal these features. To enhance the contrast of the microstructure in the replica, several methods can be employed. Some methods are seen in Fig. 15. In this example, a thick-walled AISI 440C stainless steel pipe was ground, polished, etched, and replicated as described previously. The actual microstructure from a metallographic sample destructively cut from the pipe is shown in Fig. 15(a). The microstructure consists of numerous rounded iron-chromium carbides in a ferritic matrix. A cellulose acetate replica of the same pipe is shown in Fig. 15(b). Note that the features of the carbides and the ferritic background are not as sharp as in the original bulk microstructure. Figure 15(c) shows the same replica with the back surface of the replica blackened. In this case, black ink from a marking pencil was coated on the back side of the glass slide containing the replica. Black paint or tape can also be used. Blackening can also be done to the back of the actual replica before attaching the replica to the double-back tape. The enhanced replica image in Fig. 15(c) is very similar to the image from the metallographic sample in Fig. 15(a).

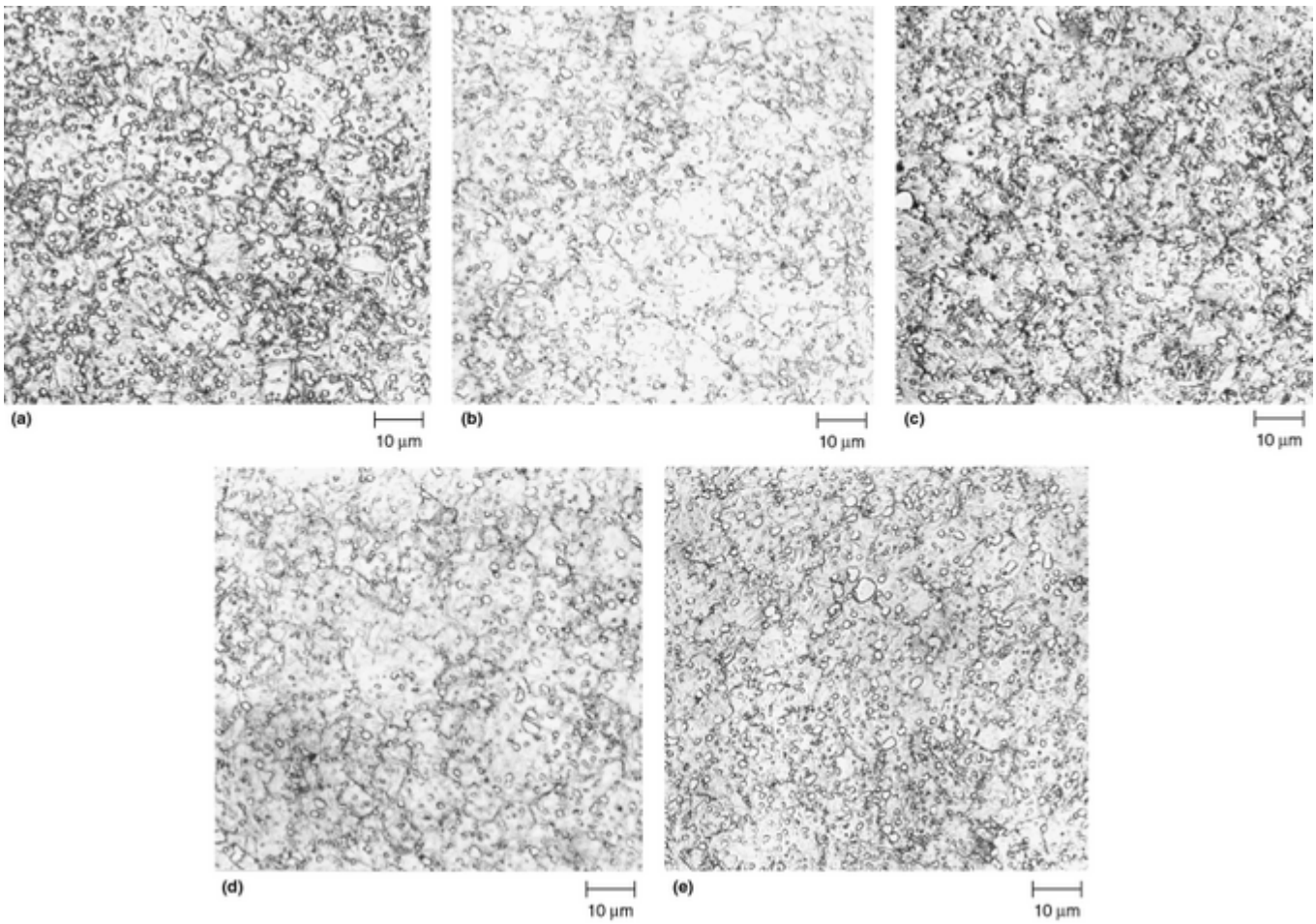

Fig. 15 Methods for replica enhancement. (a) Microstructure of actual AISI 440C stainless steel thick-wall pipe. (b) Microstructure represented by a plain acetate replica. (c) Microstructure enhanced by blackening the back of the replica. (d) Microstructure enhanced by coating the replica with a carbon layer. (e) Microstructure enhanced by coating the replica with a gold layer. Vilella's reagent. Original magnification 1000×

A better method is to enhance the contrast of the replica by a carbon or metallic coating process. The slide containing the replica is placed in a sputtering device or a carbon evaporator. These devices are described in Ref 39 and are commonly used to enhance the contrast of replicas produced for electron microscopy. The exposed surface is coated with carbon, gold, or gold-palladium alloy. Figure 15(d) shows the same replica described previously coated with carbon, and Fig. 15(e) shows the replica coated with gold. Note that the gold shadowing is particularly good at enhancing the features in the replica to the point that they match the actual bulk microstructure (Fig. 15a).

Another example of replica enhancement is shown in Fig. 16. In Fig. 16(a), the pearlite, iron carbide, and ferrite microstructure of a partially spheroidized AISI 1060 steel bar is shown. This micrograph was taken from a metallographic specimen. Fig. 16(b) shows a gold-enhanced replica of the microstructure from the same specimen. The two microstructures are practically indistinguishable. Another example, shown in Fig. 17, involves the welded area of a seam-welded API X70 steel linepipe. Figure 17(a) is the actual microstructure from a metallographic specimen at low magnification, and Fig. 17(b) is a gold-enhanced replica of the microstructure. Figure 18(a) represents the area at the edge of the weld bead interface in the weld shown in Fig. 17 (higher magnification). This micrograph was taken from a metallographic specimen. Figure 18(b) represents the same area, but the photo was taken from a gold-enhanced cellulose acetate replica. As seen, the actual microstructure and replicated microstructure are practically indistinguishable.

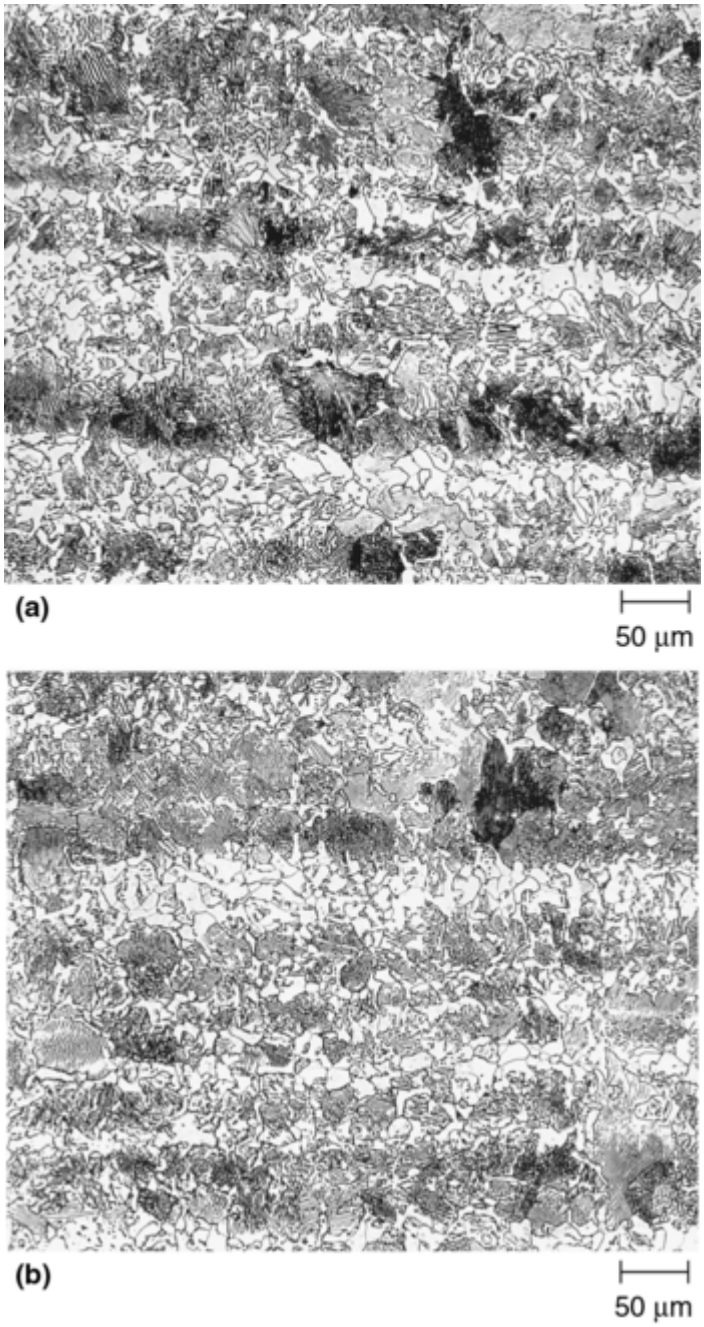

Fig. 16 Comparison of (a) the microstructure of an AISI 1060 steel bar and (b) the microstructure representing a gold-coated acetate replica of the same bar. (a) Etched in 4% picral. Original magnification 200×

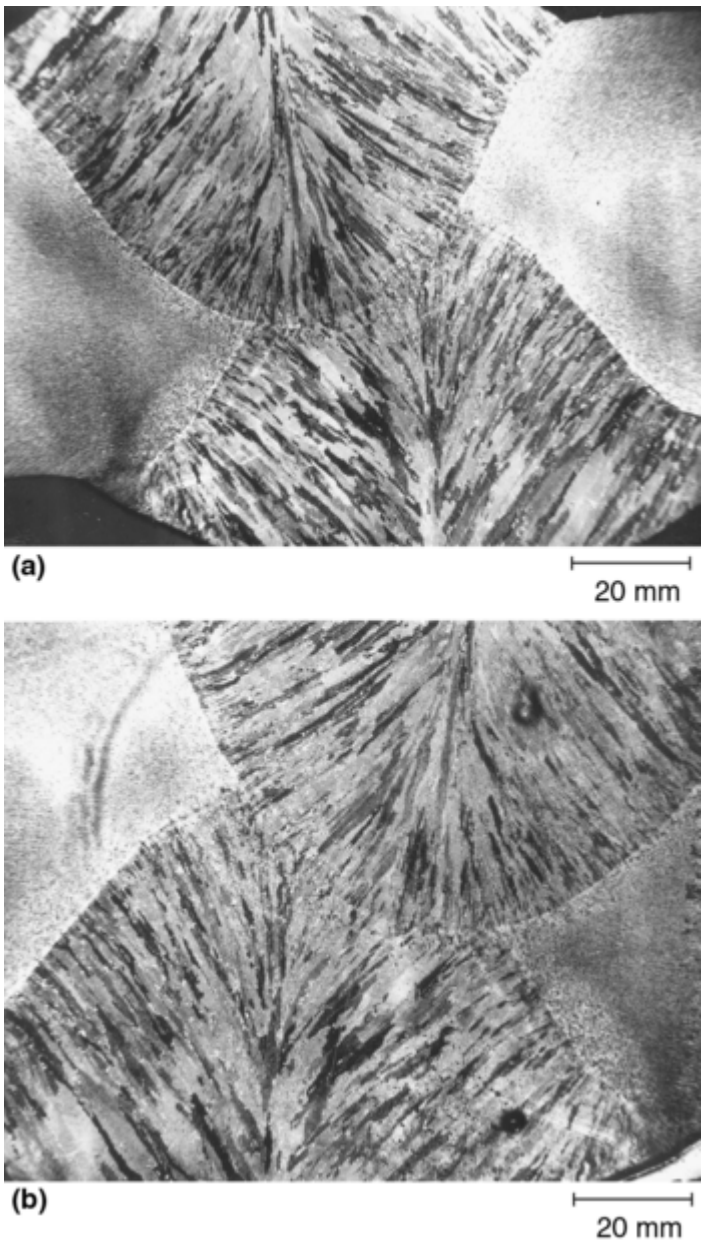

Fig. 17 Comparison between (a) the actual microstructure of a seam weld in an API X70 linepipe and (b) the microstructure of a gold-coated replica of the same area. (a) Etched in 2% nital. Original magnification 9×

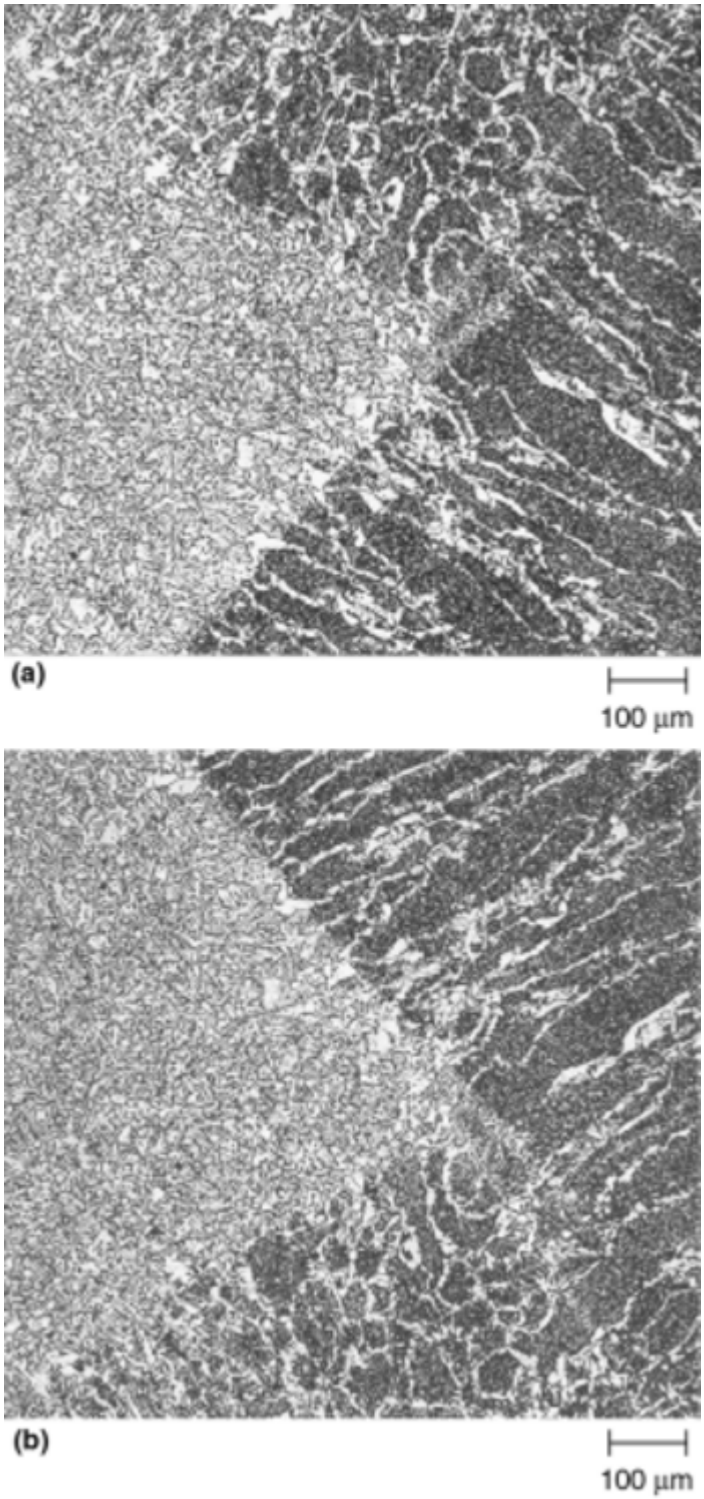

Fig. 18 Comparison between (a) the actual microstructure of a seam weld in an API X70 linepipe and (b) the microstructure representing a gold-coated replica of the same area. Different region of the weld shown in Fig. 17. Original magnification 100×

Replication with Silicone Rubber. Another method of replication is gaining popularity. This method utilizes a two-part silicone rubber compound that is applied to the prepared surface with a mixing gun (see Fig. 19). The snout of the gun as seen in Fig. 20 is designed to mix the two parts as it is applied to the surface of the workpiece. Once the mixture is cured, it can be easily peeled from the surface of the workpiece as seen in Fig. 21. In this case, a glass slide was pressed on the curing rubber replica before removing replica from surface. The silicone rubber compounds are formulated with different viscosities and for different temperature conditions and different curing times. Generally, curing takes 1 to 5 min. Although this is an advantage, the disadvantage is that the mixture in the snout or mixing tube also cures. This means that to economically take advantage of this method, several areas should be prepared ahead of time. This way, replication material can be

applied to all the areas before curing takes place in the snout. Otherwise, a new snout will be required for each application. The ideal procedure is to work as a team where one person prepares the polished surfaces electrolytically and another person applies the silicone rubber replica. Otherwise, if the prepared areas are allowed to stand for a long period of time they can collect dust and they can begin to corrode.



Fig. 19 A handheld device to apply a silicone rubber replica to the workpiece

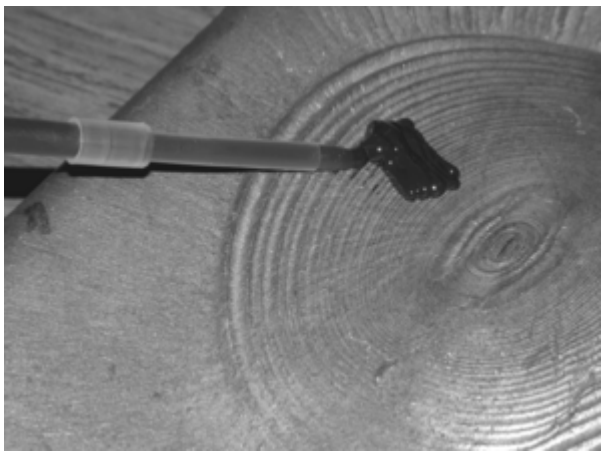

Fig. 20 Applying silicone rubber through mixing snout onto fatigue fracture surface

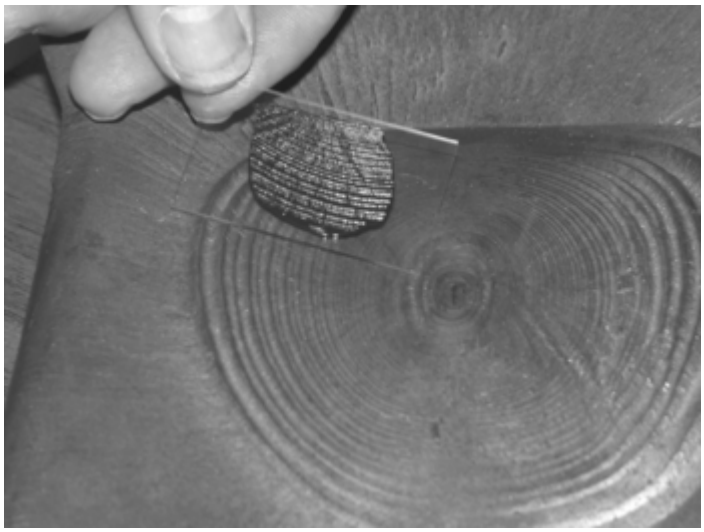

Fig. 21 Replica of surface on glass slide that was pressed onto silicone rubber patch in Fig. 20

These silicone rubber materials can be used overhead and on sloping surfaces. The advantage in using these materials is the simplicity and speed of replication. The disadvantages are that the consumable components (the two rubber components and the mixing tubes) are rather expensive and they lack the ability of enhancement as in the case of using an acetate replica. The resolution is satisfactory for most applications.
All these examples illustrate the effectiveness of the replication process as a powerful metallographic tool. Replication is what makes field metallography a valuable tool in the metallographer's arsenal.

Obtaining a Small Sample from the Workpiece

Since the replica cannot yield information about the chemical makeup of the workpiece, sometimes it may be necessary to cut a small sample from the component to conduct a bulk chemical analysis or to chemically analyze the constituents within the actual microstructure employing a SEM or electron probe microanalyzer (EPMA). Although this is a destructive test, there are times when a small “boat” sample or “plug” sample can be taken from a noncritical location on the workpiece. In this case, a handheld hack saw or a portable bandsaw can be used to remove the sample. Also, a handheld grinder can be fitted with an abrasive cut-off wheel. These tools, examples of which are shown in Fig. 22 and 23, can be obtained in a hardware store. For very hard materials, a boron nitride coated blade may be sufficient to cut a sample. In some cases, a diamond-impregnated hole-drilling saw blade can be used to extract a small cylinder of material. For hard materials, an electrodischarge machining (EDM) device can be used to provide a pin sample. Once the sample is removed, it can be prepared in the metallographic laboratory for further analysis.

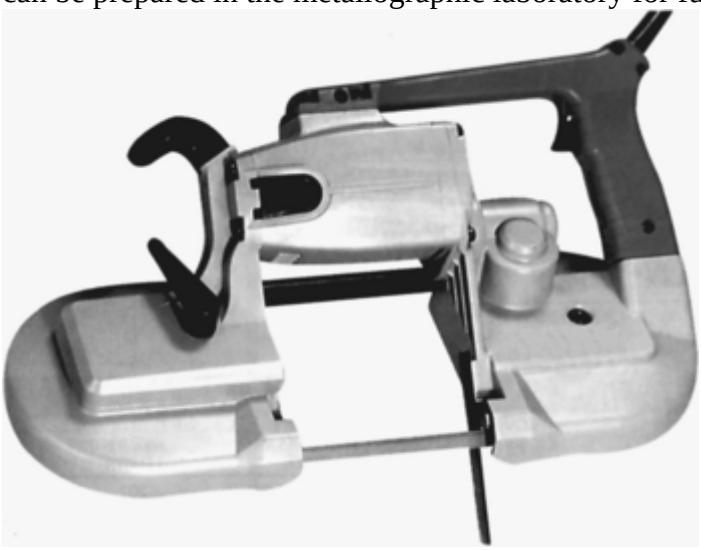

Fig. 22 A portable handheld band saw

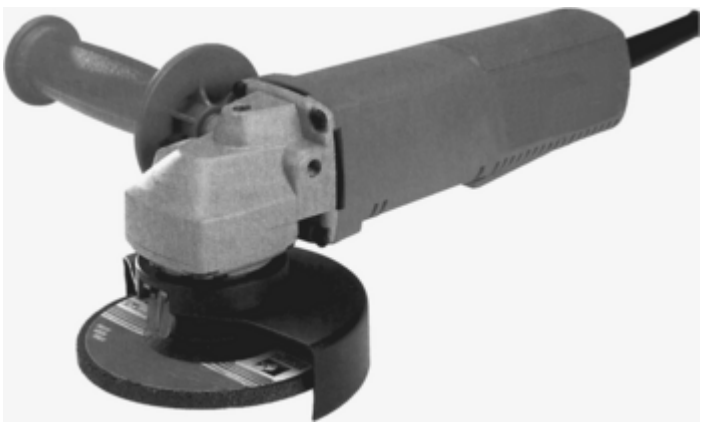

Fig. 23 A portable handheld disk sander/grinder. Thin abrasive cut-off wheels can be used to remove a “boat” sample.

References cited in this section

3. M. Clark and A. Cervoni, “In-Situ Metallographic Examination of Ferrous and Non-Ferrous Components,” Report 314 G 429, Canadian Electrical Association, 1985

8. P.A. Jacquet, An Innovation in Inspection Tool and Control, *Met. Prog.*, Vol 85 (No. 2), Feb. 1964, p 114

11. M. Gell and T.T. Field, Detection of Deformation and Cracking on Oxide and Coated Surfaces by Light Microscopy, *Metall. Trans.*, Vol 1, 1970, p 317–318

12. M.W. Lui and I. LeMay, The Use of Plastic Replicas in Optical Metallography, *Metallogr. Rev.*, 1972, p 30–31

13. T.S. Akhmatova and L.G. Voronina, Use of Surface Prints for Nondestructive Investigation of Microstructure, *Ind. Lab.*, 1972, p 590

15. K. Dieser, The Nondestructive Metallographic Examination of Large Structural Components, *Prakt. Metallogr.*, Vol 11, 1974, p 441–455

39. B.L. Bramfitt and A.O. Benscoter, *Metallographers Guide—Practices and Procedures for Irons and Steels*, ASM International 2002, p 158–159

B.L. Bramfitt and S.J. Lawrence, Field Metallography Techniques, *Metallography and Microstructures*, Vol 9, *ASM Handbook*, ASM International, 2004, p. 478–492

Field Metallography Techniques

Bruce L. Bramfitt and Samuel J. Lawrence, International Steel Group, Inc.

Using Field Metallography in the Laboratory

Sometimes, it is useful to apply the techniques of field metallography in the metallographic laboratory. An example would be polishing the edges of flat fatigue specimens to eliminate premature failure due to surface roughness. Figure 24 shows a set of fatigue specimens pressed together in a clamp and the edges of the gage area being polished to remove scratches and machining grooves. This requires portable handheld equipment. Other examples include preparation of welds for metallographic evaluation and the delicate examination of ancient artifacts.

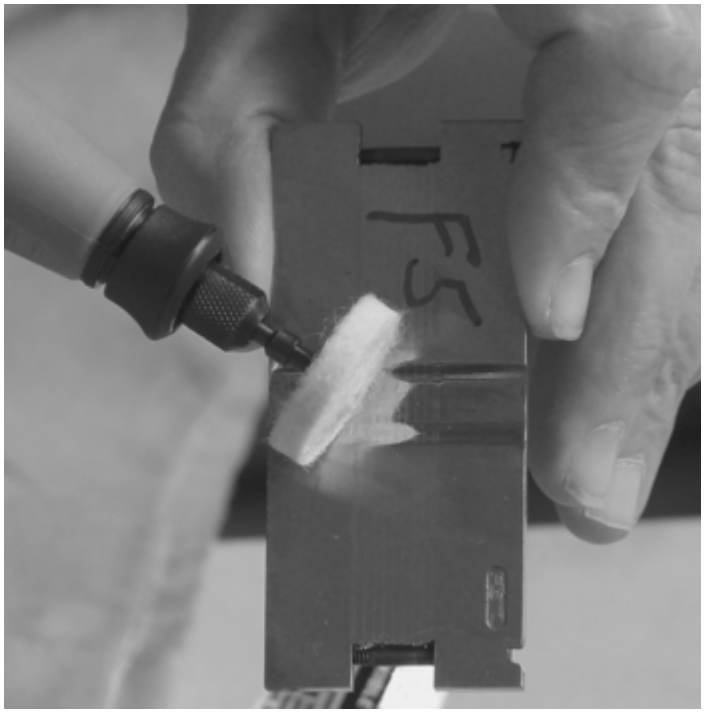

Fig. 24 Polishing the gage edges of a flat fatigue specimen using a handheld buffing tool

---

B.L. Bramfitt and S.J. Lawrence, Field Metallography Techniques, *Metallography and Microstructures,* Vol 9, *ASM Handbook,* ASM International, 2004, p. 478–492

Field Metallography Techniques

Bruce L. Bramfitt and Samuel J. Lawrence, International Steel Group, Inc.

Case Studies

In order to illustrate the application of field metallography, five actual case studies are presented. These cases were undertaken in an effort to solve a particular problem or to monitor the quality and consistency of components from the same or different vendors. Although these examples describe situations in a steel mill, the ideas can be applied to any situation.

Example 1: A Breakage Problem with D2 Tool Steel Rotary Straightener Rolls. Rotary straightening is employed as the final process step in the manufacture of long products such as structural shapes and railroad rails. In this particular case study, D2 tool steel rolls were used in a rotary straightening machine for railroad rails. The rolls were breaking and spalling immediately after being used for a short period of time. These rolls were from a recent shipment from the roll manufacturer and were expected to last for several months of continuous use. It was discovered that the roll manufacturer had changed his process from a forged roll to a spun-cast (centrifugally cast) roll without informing the roll shop of the rail mill. The recently spun-cast rolls were breaking.

Results. Field metallography of the problem rolls discovered that coarse carbide networks were providing an easy path for crack growth and propagation. Figure 25 shows the microstructure of a broken roll. Note that a continuous carbide network appears along the dendritic boundaries. This microstructure represents a spun-cast roll. Figure 26 shows the microstructure taken from a “good” roll that was used for 6 months and did not break. Note that the networks are not continuous, and the carbides are more dispersed in the unbroken roll. This microstructure represents a forged roll. If a coarse carbide network of the spun-cast rolls has been shown to be the cause of the breakage, what are the microstructural features of the other spun-cast rolls recently purchased

from this manufacturer and all the other rolls in stock in the roll shop? Also, how does one ensure the proper microstructure in rolls purchased in future orders to avoid coarse carbide networks? Since the rolls were too large to bring to the metallographic laboratory, field metallography was the only practical way to examine the microstructure of all the rotary straightener rolls in the roll shop (both new and used). Through field metallography it was discovered that all the broken and spalled rolls had these coarse carbide networks and all the unbroken used rolls had dispersed carbides. It was also found that not all of the newly purchased rolls had the coarse carbide networks. Some of these rolls did not break or spall and had a microstructure represented in Fig. 26. In these spun-cast rolls, the carbides did not connect as continuous networks. This meant that spun-cast rolls could work well, but only if they did not contain continuous carbide networks. The manufacturer was notified of the metallographic results, and specifications on all future rolls stated that continuous networks were not acceptable. Also, the manufacturer had to perform metallographic analysis on each roll before shipment to ensure a proper microstructure. A micrograph of the etched microstructure was requested in the shipment for each roll. Field metallography was crucial in sorting out this problem because the rolls could not be evaluated in the metallographic laboratory and microstructure was of utmost importance to solving the problem.

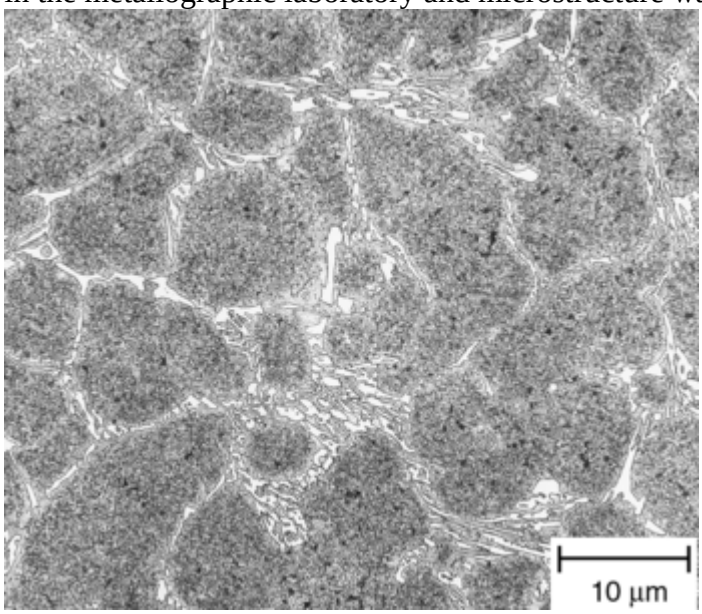

Fig. 25 An enhanced replica representing the microstructure of a D2 tool steel rotary straightener roll that broke prematurely in service. Note the carbide networks. Vilella's reagent on original surface. Original magnification 200×

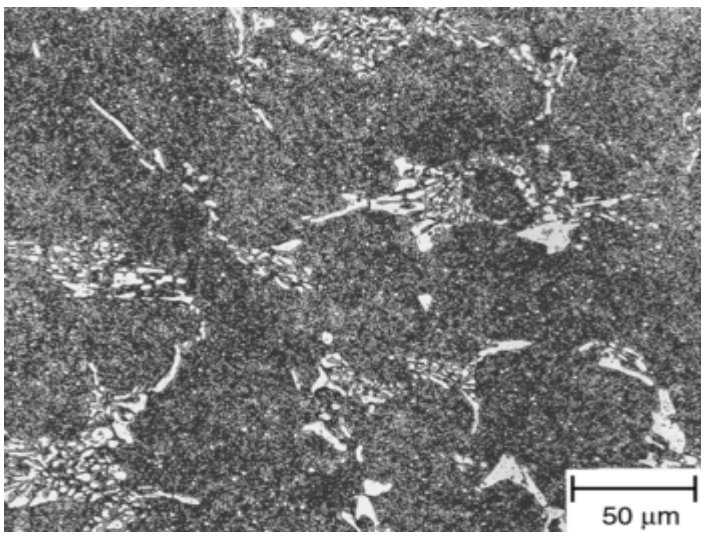

Fig. 26 An enhanced replica representing the microstructure of a D2 tool steel rotary straightener roll that worked well in service. Note that the carbides are not connected. Vilella's reagent on original surface. Original magnification 200×

Example 2: Premature Wear in Cast Iron Sleeves for Rotary Straightener Spindles. The same rotary straightener in example 1 employed cast iron sleeves around the shafts of the rolls. It was discovered that some of the sleeves were wearing much faster than others. These rapidly wearing sleeves were from a different manufacturer than the normal wearing sleeves. As in example 1, the sleeves were much too large to bring back to the metallographic laboratory and destructive sampling would render the sleeves useless. Field metallography was used to determine why certain sleeves were wearing at an accelerated rate.

Results. Upon in situ examination, it was discovered that the normal wearing sleeves had the specified austempered ductile iron microstructure shown in Fig. 27. This microstructure consisted of nodular graphite in a matrix of bainite. Field metallography of the faster wearing sleeves revealed a mixed microstructure of flake and nodular graphite as seen in Fig. 28(a). Also, the matrix microstructure was pearlite with some grain-boundary ferrite. This latter microstructure indicates that the inoculation process to produce the nodular graphite was done improperly at the foundry. It is also interesting that the surface of the faster wearing sleeve was decarburized as seen in Fig. 28(b). The soft decarburized ferrite layer enhanced wear. The matrix microstructure of the fast wearing sleeves was also improper for this application since the “good” sleeves had a microstructure of bainite. This is a case where field metallography can be used to uncover why the behavior of a particular component is substandard. It also illustrates that the metallographer must be aware that surface decarburization does not represent the real microstructure. If decarburization is suspected, caution must be used not to grind and polish through the decarburized layer. To check for carburization, prepare a surface at the edge (end) of the component and grind/polish a surface at an angle to the surface.

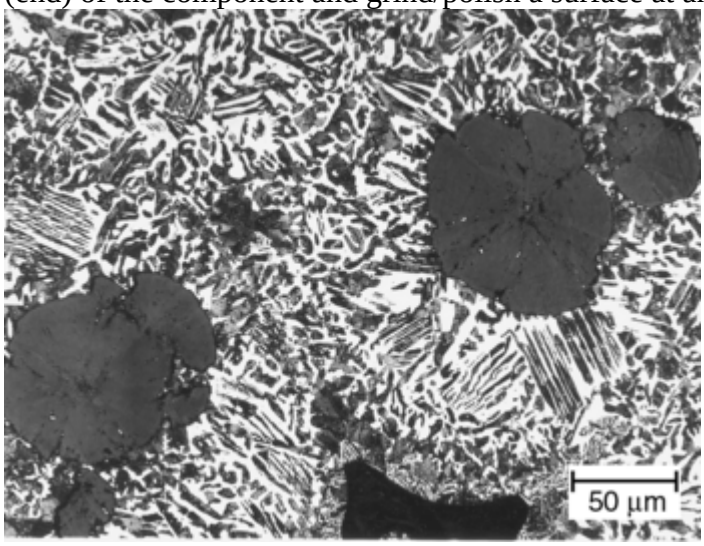

Fig. 27 An enhanced replica representing the microstructure of a cast iron rotary straightener roll sleeve that had normal wear in service. Note the nodular graphite particles in a bainitic matrix (austempered ductile cast iron). 4% picral on original surface. Original magnification 200×

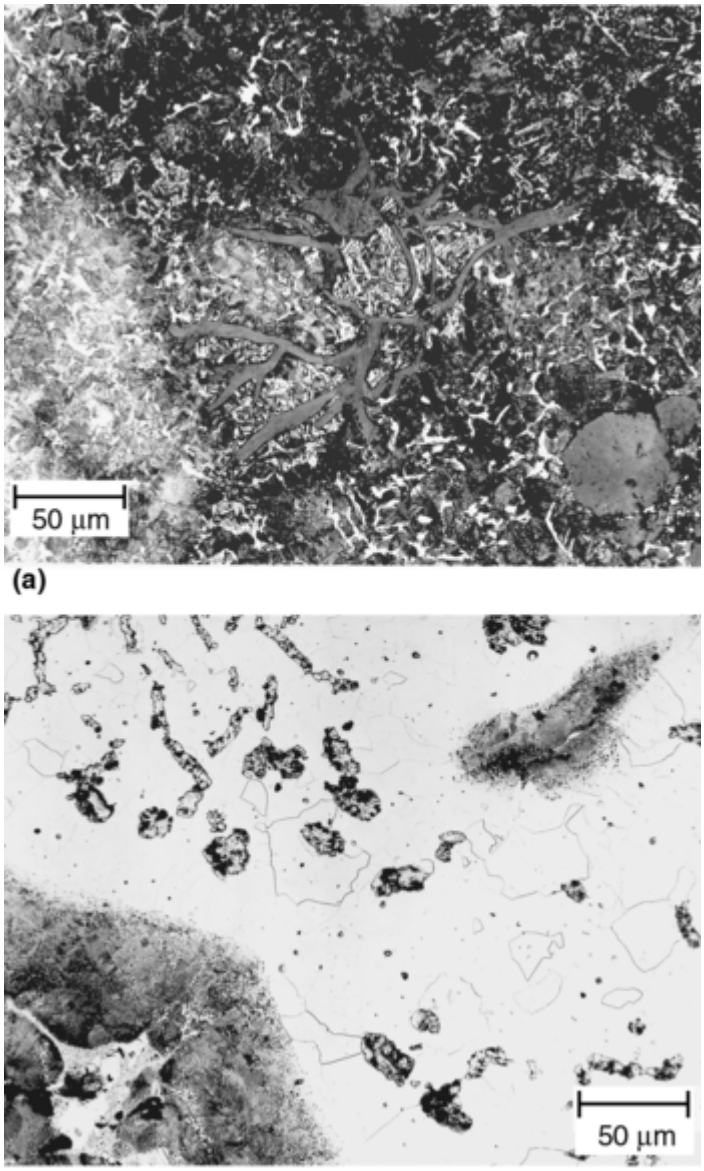

Fig. 28 An enhanced replica representing the microstructure of a cast iron rotary straightener roll sleeve that experienced wear in service. In (a) note the nodular graphite flakes and some graphite nodules on a ferrite + pearlite matrix and (b) a decarburized surface layer of ferrite. 4% picral on original surface. Original magnification 200×

Example 3: Spalling of Hot Strip Mill Work Rolls. One of the more serious problems with work rolls for a hot strip mill is spalling. A spall is a loose piece of roll that breaks away from the roll, and it creates damage to the sheet and surrounding equipment. Figure 2 shows a roll that spalled. With spalling, the mill must shut down to remove the damaged roll and sheet product. The roll must be reconditioned by grinding or by removing material in a lathe. Many roll shops now apply field metallographic procedures along with nondestructive tests to minimize the occurrence of a spall. In this example, rolls from a particular roll supplier were spalling at an unprecedented pace. To understand the cause of spalling, all the rolls from that supplier were examined using field metallography of areas prepared on the roll barrel. The rolls in this case were indefinite-chill double-poured rolls used in the last three stands of the hot strip mill. These rolls are produced by a process called centrifugal casting. The mold is in the vertical or horizontal position and spun at high speed, while molten metal is poured into the mold. The metal solidifies against a cylindrical steel chill. The outer portion of the roll is produced from alloyed cast iron to a thickness of about 50 mm (2 in.). Once the chill layer has solidified, the remaining portion of the mold cavity is filled with unalloyed cast iron. The resulting casting has a layer of alloy white iron at the surface of the roll barrel. In indefinite-chill, double-poured rolls, the outer white iron chill layer consists of a microstructure of eutectic carbide, martensite, and a small amount of graphite. Figure 29(a) and (b) show the typical microstructure of such a chill zone. These micrographs were taken from an acetate

replica enhanced by coating with gold. The white appearing component is Fe-Cr-Mo carbide and the dark gray appearing component is plate martensite. The graphite is seen as the black constituent in Fig. 29(b).

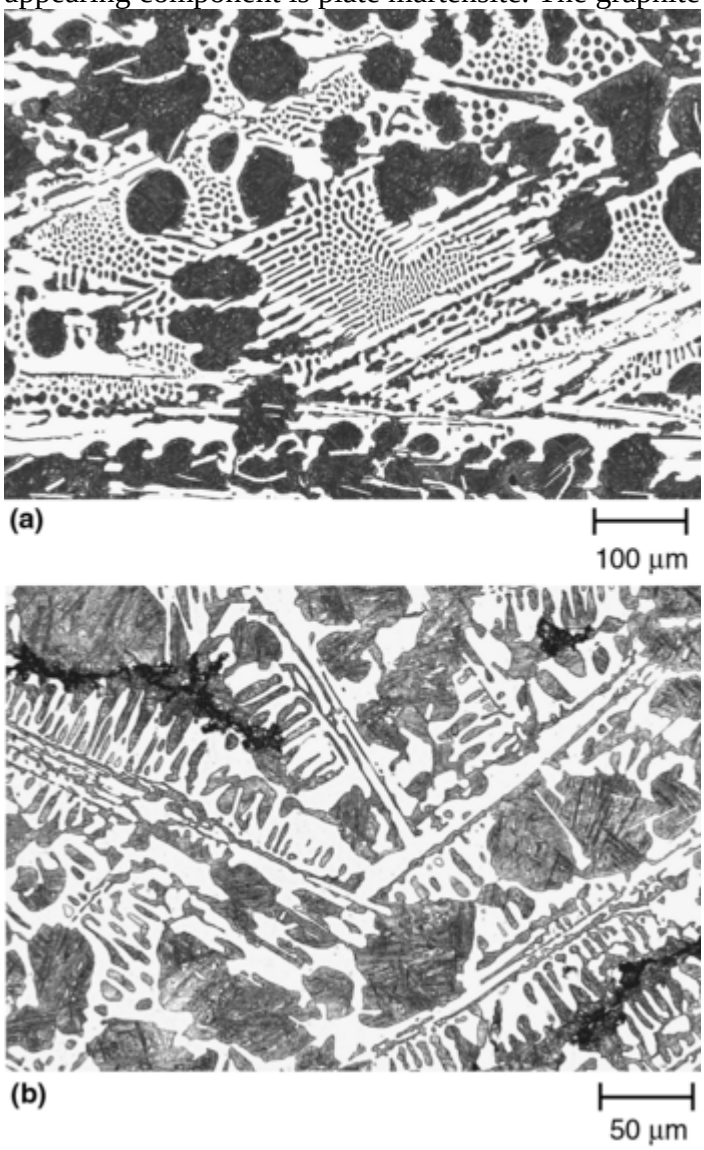

Fig. 29 Gold-enhanced replicas representing the microstructure of an indefinite-chill double-poured roll. Graphite seen as very dark (black) constituent in (b). Vilella's reagent on original surface. (a) Original magnification 100× and (b) Original magnification 200×

Results. Field metallography was used to grind and polish areas on the roll barrel to observe and measure the amount of graphite in the microstructure. Two methods were employed to measure the percent graphite. One method involved measurement in the portable observation microscope using a 100-point reticule in the eyepiece. The procedure outlined in ASTM E 562 was utilized on at least five fields of view. A more accurate method involved measurements taken from an enhanced acetate replica. The same point-counting method could be employed, and more fields could be measured. The results of the field metallographic investigation revealed that the amount of graphite in the rolls from this manufacturer was quite variable and the rolls that spalled had much higher levels of graphite than rolls that did not spall. Once this was determined, the various rolls were categorized and the spall-prone rolls were segregated from the normal rolls. The roll supplier was notified of the problem, and many of the problem rolls were replaced. Without field metallography, there was no way to sort out the good rolls from the problem rolls.

Example 4: Comparing Various High-Speed Steel Hot Strip Mill Work Rolls. High-speed steel (HSS or tool steel) work rolls are used in the early stands of a hot strip mill, and these rolls are much more expensive than the conventional high-chromium rolls they replace. However, they have the advantage of greater wear resistance, and they last far longer than the conventional rolls. In the very competitive roll market, each roll manufacturer has developed a proprietary chemistry and microstructure to provide the enhanced wear

resistance. These recipes include various combinations of chromium, molybdenum, vanadium, tungsten, and nickel. As a result, some HSS rolls outperform others. Performance is measured by calculating the number of tons rolled per mm of diameter consumed of the roll during its lifetime. Although field metallography is used mainly to solve a problem or to evaluate life assessment, it is also very useful in evaluating the microstructure of different vendor's products. In this case, it was applied to HSS work rolls to determine the microstructure and chemical composition of the various phases in the microstructure.

Results. Examples of two different high-speed roll microstructures are shown in Fig. 30. Note the different components in the microstructure. The white and gray appearing particles are metal carbides and the matrix is martensite. An important part of this investigation is to determine the composition of the various carbides. These carbides provide the exceptional wear resistance of these tool steel rolls. It is known that some carbides are harder than others. Since this type of information cannot easily be obtained by standard field metallography, a very small “boat” sample was physically taken from the end of the roll barrel. A portable hacksaw shown in Fig. 22 was used to carefully remove a sample. The sample was then mounted and prepared for the EPMA. This instrument has the capability to excite the particles in the microstructure with a beam of electrons. The excitation produces x-rays characteristic of the elements present in the particle. The x-ray energy and wavelength of each element is well known and is used for identification. Figure 31 shows the results of EPMA analysis where each element is represented by a map of intensity (the higher the intensity the lighter the image). In this set of x-ray maps, the image of the microstructure is shown in the upper left (called a backscattered electron image). Note the concentration of chromium, molybdenum, iron, and vanadium in each particle in the backscattered image. This case illustrates that a boat sample can be a valuable part of field metallography.

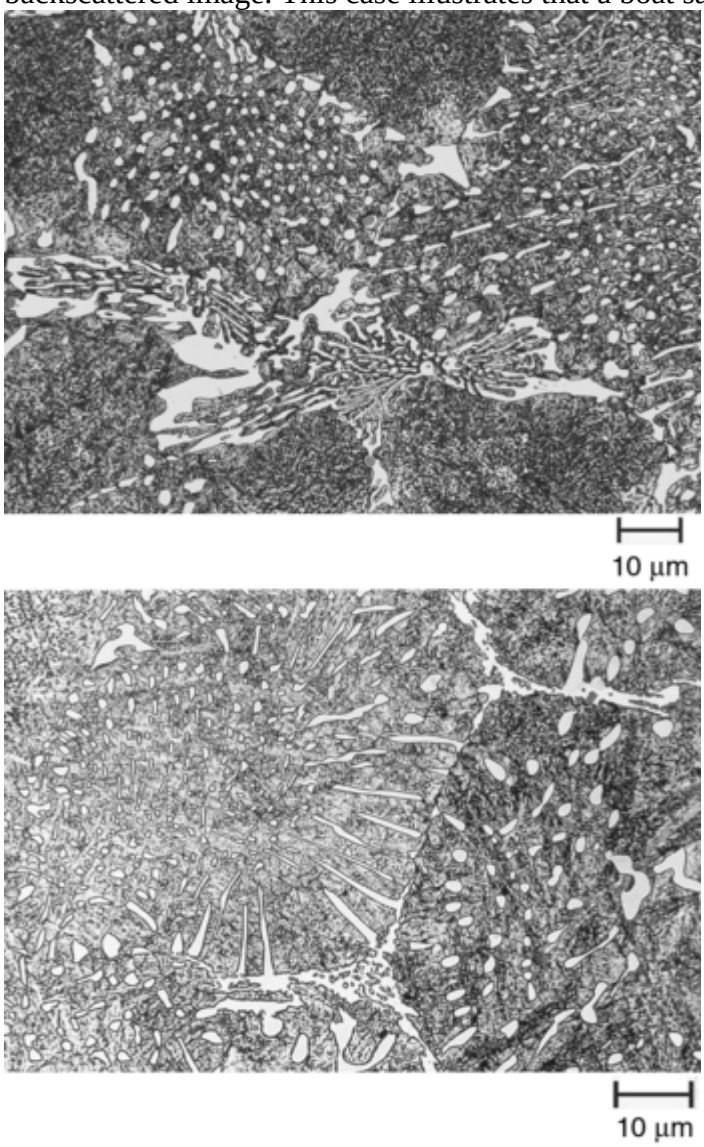

Fig. 30 Gold-enhanced replicas representing the microstructure of two different high-speed steel work rolls for the early stands of a hot strip mill. Vilella's reagent. Original magnification 500×

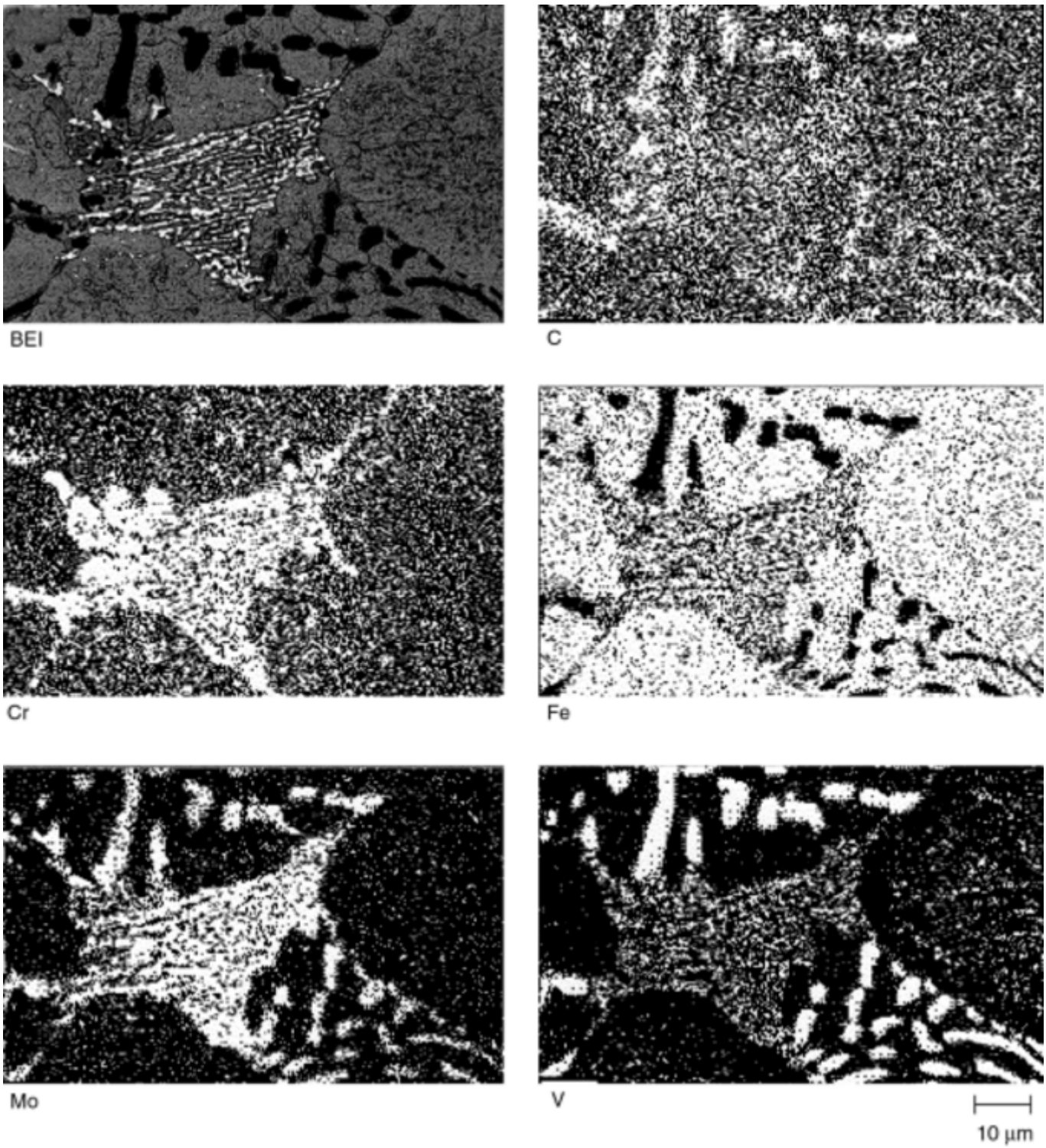

Fig. 31 X-ray dot maps showing the chemical elements in each constituent of a similar roll as in Fig. 30. BEI, backscattered electron image. Original magnification 1000×

Example 5: Austenitizing Furnace Rolls. To produce quenched-and-tempered steel plate, the plates are austenitized in a long roller-hearth furnace fired to 900 °C (1650 °F). The plates move from the entry end to the exit end on heat-resistant steel rolls. These 25% Cr + 20% Ni rolls (25 mm thick-walled cylinders) have a finite life and tend to sag and spall with time. This presents a serious problem in the operation of the furnace. An alternate material was needed. Nickel aluminide (Ni_3Al) alloys were being developed at the Oak Ridge National Laboratory for high-temperature applications (Ref 40). These intermetallic alloys have the unique high-temperature characteristic of getting stronger as they are heated. Nickel aluminides also have exceptional oxidation resistance. As part of commercial feasibility study to utilize these alloys, 101 rolls with length of 4.4 m (14 ft), 355 mm (14 in.) diameter, and 21 mm (~$\frac{3}{4}$ in.) wall thickness were centrifugally cast and installed in

the austenitizing furnace (Ref 41). In the early stages of utilization, there were several problems that had to be overcome in order to effectively employ these rolls. One problem was the adherence of material to the roll surface that was creating scratches on the bottom surface of the hot steel plates. Field metallographic techniques were employed to obtain actual specimens of the adherent surface particles for further analysis and to observe the actual microstructure at the surface of the rolls.

Results. The microstructure of a nickel aluminide roll can be seen in Fig. 32(a). This replicated image shows a dendritic structure with very fine domains of Ni_3Al as the primary dendritic arms and coarse domains of Ni_3Al as the secondary dendritic arms. The rectangular-shaped particle in the center of the bottom half of the micrograph was later determined to be zirconium oxide. In fact, numerous zirconium oxide particles were found on and near the surface of the roll. Figure 32(b) shows an area with many zirconium oxides (the white appearing square and rectangular particles). These particles were from a mold wash used by the foundry. These zirconium oxides were associated with the problem of adherent particles on the surface. From the analysis of the adherent particles removed from the roll surface, it was determined that the main component was iron oxide created from the steel plates. However, at the surface of the adherent particles and the roll, some zirconium oxide particles were found using EDS in the SEM. This can be seen in the SEM micrograph in Fig. 32(c). This case illustrates the use of field metallography in the analysis of surface material where careful procedures need to be followed to obtain uncontaminated samples and to prepare the surface microstructure.

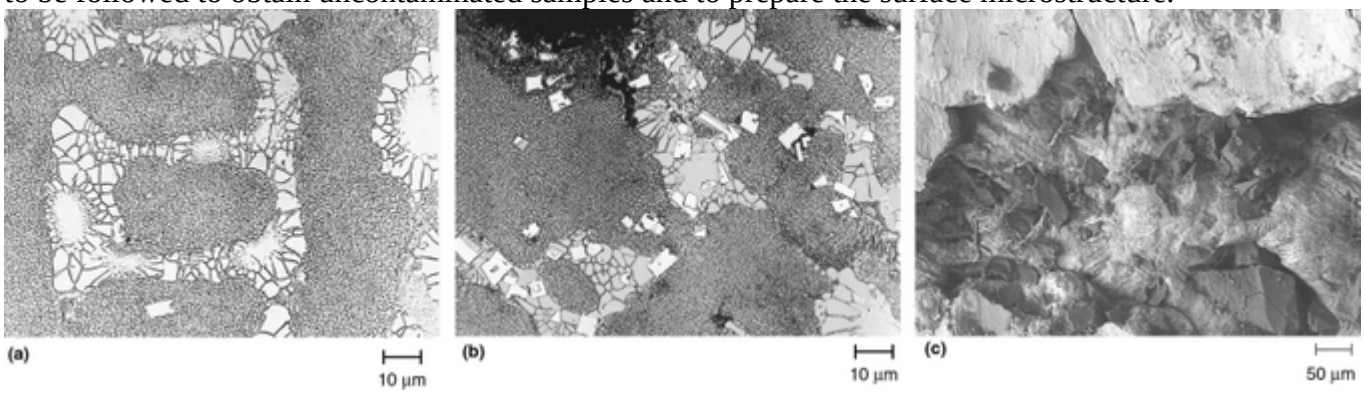

Fig. 32 Field metallography of a nickel aluminide austenitizing furnace roll. (a) and (b) Gold-enhanced replicas representing the microstructure of a nickel aluminide austenitizing furnace roll. The dendritic microstructure consists of primary dendrite arm of nickel aluminide with small domains and the interdendritic regions of nickel aluminide of large domains. Note the white appearing angular particles of zirconium oxide particularly in (b). (c) SEM micrograph of undersurface of surface particles showing oxide particles. (a) and (b) Original magnification of 100× and (c) taken at 200×

References cited in this section

40. C.T. Liu, Design of Ordered Intermetallic Alloys for High-temperature Use, *High Temperature Alloys; Theory and Design*, The Metallurgical Society, 1984, p 289–308

41. P. Angelini et al., “Large-Scale Evaluation of Nickel Aluminide Rolls in a Heat-Treat Furnace at Bethlehem Steel's (now ISG) Burns Harbor Plate Mill,” report DE-AC0500OR22725, Oak Ridge National Laboratory/Department of Energy, Sept 2003

B.L. Bramfitt and S.J. Lawrence, Field Metallography Techniques, *Metallography and Microstructures,* Vol 9, *ASM Handbook,* ASM International, 2004, p. 478–492

Conclusions

Field metallography is actually an extension of the metallography laboratory to the field or remote location. Essentially the same metallographic techniques are employed except that the metallographer must work with portable grinding/polishing tools and employ simple replication procedures to obtain a record of the microstructure. That replica, once enhanced in the laboratory, provides an almost exact image of the actual microstructure. Field metallography is employed when the component is too large to bring to the metallographic laboratory. Field metallographic techniques are widely used to determine the life assessment of components in nuclear and fossil-fuel power plants. Life assessment determines the useful life of a component still in service. In the high-temperature environment of turbine rotors and blades and steam piping and pressure vessels, field metallography can observe the onset of creep damage. If caught early, the component can be replaced in order to prevent catastrophic damage. Field metallography is also employed as a tool to examine the quality of large components in the steel industry. For example, the microstructure of rolling-mill rolls can be evaluated to check the consistency of a vendor's manufacturing process. A process out of control can lead to problems during the rolling process (spalling and roll breakage). The portable tools used by the field metallographer can also be used to observe the microstructure of valuable artifacts from archaeological sources. Field metallographic techniques are practically nondestructive in that they only affect a shallow surface layer of material.

In all, a valuable extension of the metallographic laboratory is the ability to perform a metallographic analysis in the field. The procedures are not difficult, and with practice proper technique can be mastered.

B.L. Bramfitt and S.J. Lawrence, Field Metallography Techniques, *Metallography and Microstructures,* Vol 9, *ASM Handbook,* ASM International, 2004, p. 478–492

Field Metallography Techniques

Bruce L. Bramfitt and Samuel J. Lawrence, International Steel Group, Inc.

References

1. “Standard Practice for Production and Evaluation of Field Metallographic Replicas,” E 1351, *Annual Book of ASTM Standards,* 1990

2. “Nondestructive Testing Impression Methods for Surface Examination,” DIN Standard 54–150, Deutsche Industrie-Normen, 1977

3. M. Clark and A. Cervoni, “In-Situ Metallographic Examination of Ferrous and Non-Ferrous Components,” Report 314 G 429, Canadian Electrical Association, 1985

4. J.F. Henry and F.V. Ellis, “Plastic Replication for Damage Assessment,” Report RP2253, Electric Power Research Institute, 1983

5. R. Viswanathan, *Damage Mechanisms and Life Assessment of High-Temperature Components,* ASM International, 1989

6. M.C. Askins et al., “Remaining Life of Boiler Pressure Parts—Base Material Model,” Report RP 2253-1, Vol 3, Electric Power Research Institute, 1988

7. G. Kerzner, I. Sprung, and V. Zilberstein, “Field Metallography for Life Extension Studies of High-Temperature Components,” Proc. ASNT Conference on Characterization of Materials and Flaws, 1988

8. P.A. Jacquet, An Innovation in Inspection Tool and Control, *Met. Prog.,* Vol 85 (No. 2), Feb. 1964, p 114

9. D.E. Bradley, Replica and Shadowing Techniques, *Techniques for Electron Microscopy,* D.H. Kay, Ed., 2nd ed., Blackwell, Oxford, 1965, p 96–152

10. D. Vassallo, J. Fritzche, M. Savrato, and O. Wortman, Observation of Boiler Elements by Nondestructive Metallography, *Fifth Int. Conf. on Pressure Vessel Technology Part I, Design and Analysis,* American Society of Mechanical Engineers, 1969, p 451–461

11. M. Gell and T.T. Field, Detection of Deformation and Cracking on Oxide and Coated Surfaces by Light Microscopy, *Metall. Trans.,* Vol 1, 1970, p 317–318

12. M.W. Lui and I. LeMay, The Use of Plastic Replicas in Optical Metallography, *Metallogr. Rev.,* 1972, p 30–31

13. T.S. Akhmatova and L.G. Voronina, Use of Surface Prints for Nondestructive Investigation of Microstructure, *Ind. Lab.,* 1972, p 590

14. H. Crowder, Portable Laboratory for Field Metallography, *Met. Prog.,* Vol 105 (No. 4), 1974, p 76, 79

15. K. Dieser, The Nondestructive Metallographic Examination of Large Structural Components, *Prakt. Metallogr.,* Vol 11, 1974, p 441–455

16. E. Berner and R. Lohberg, Microstructural Investigations by Means of Replicas Taken from Components at Temperatures around 100 °C, *Prakt. Metallogr.,* Vol 17 (No. 1), 1980, p 14–22

17. B. Neubauer and U. Wedel, Restlife Estimation of Creeping Components by Means of Replicas, *Advances in Life Prediction Methods,* American Society of Mechanical Engineers, 1983, p 307–314

18. P. Auerkari, Remanent Creep Life Estimation of Old Power Plant Steam Piping Systems, *Advances in Life Prediction Methods,* American Society of Mechanical Engineers, 1983, p 353–356

19. B. Neubauer and U. Wedel, NDT: Replication Avoids Unnecessary Replacement of Power Plant Components, *Power Eng.,* Vol 88 (No. 5), 1984

20. M.E. Blum, On-Site Metallographic Investigations using the Replica Technique, *Microstructural Science,* Vol 12, American Society for Metals/International Metallographic Society, 1985, p 143–150

21. J.F. Henry, Field Metallography: The Applied Techniques of In-place Analysis, *Microstructural Science,* Vol 12, American Society for Metals/International Metallographic Society, 1985, p 537–549

22. Y. Lindblom, Refurbishing Superalloy Components for Gas Turbines, *Mater. Sci. Eng.,* Vol 1, 1985, p 636–643

23. E.V. Sullivan, Field Metallography Equipment and Techniques, *Microstructural Science,* Vol 15, International Metallographic Society, 1987, p 13–26

24. J.F. Henry and F.V. Ellis Field Metallography Techniques for Plant Life Extension, *Microstructural Science,* Vol 15, International Metallographic Society, 1987, p 3–11

25. J.J. Balaschak, Field Metallography in Assessment of Steam Piping in Older Fossil Power Plants, *Microstructural Science,* Vol 15, International Metallographic Society, 1987, p 12–35

26. A. Cervoni and M.A. Clark, Investigation of Turbine Disc Cracking by Field Metallography, *Microstructural Science,* Vol 15, International Metallographic Society, 1987, p 37–53

27. J.W. Simmons, On-Site Nondestructive Metallographic Examination of Materials, *Microstructural Science,* Vol 15, International Metallographic Society, 1987, p 55–67

28. N.G. Oh, "Replica Metallography," Publication NDE, Vol 5, American Society of Mechanical Engineers, 1989, p 231–236

29. W.L. Daugherty and P.R. Bormecker, "Assessment of Remaining Service Life of 1Cr-0.5Mo Steam Piping," Report W5RC-MS-94-0416, CONF-950288-1, DOE Westinghouse Savannah River Co., 1995, p 13

30. J.L. Han, Assessment of Fire Damage to Pressure Vessels in a Refinery Fire, *Corrosion,* Vol 49 (No. 5), 1993, p 420–437

31. B. Hahn and B. Melzer, Suitability of the Various Replica Materials for Use in Surface Replication on Warm Components, *Steel Res.,* Vol 67 (No. 9), 1996, p 390–393

32. M.E. Blum, P.M. French, R.M. Middleton, and G.F. Vander Voort, Ed., *Field Metallography, Failure Analysis, and Metallography,* ASM International, 1987

33. G. Kerzner, I. Sprung, and V. Zilberstein, Field Metallography for Life Extension Studies of High-Temperature Components, *Mater. Eval.,* Vol 47 (No. 9), 1989, p 1008, 1011–1014, 1017–1018

34. K.M. John, K.S. Kumar, and A. Natarajan, Application of Nondestructive Metallography in Materials Processing and Quality Control, *Prakt. Metallogr.,* Vol 28 (No. 6), 1991, p 285–294

35. I. LeMay, P. Cheung, and T.L. daSilveira, On Field Metallography Applications, *Microstructural Science,* Vol 22, International Metallographic Society/ASM International, 1987, p 87–92

36. G. Venkataraman, R. Veeraragavan, and S. Samidas, Recent Creep Damage Evaluation and Condition Assessment of Fossil Power Plant Components by in situ Metallography, *Trans. Indian Inst. Met.,* Vol 53 (No. 3), 2000, p 435–443

37. F. Ahrens, Characterising the Condition of Normalized Forged and Cast Steels by Combined Non-Destructive Metallography and Ultrasonic Attenuation Measurements, *Prakt. Metallogr.,* Vol 38 (No. 5), 2001, p 270–279

38. G.P. Kallenberg and T. Munsterman, Remaining Life Assessment of Catalytic Reforming Reactors, *Corrosion,* 2002, p 9

39. B.L. Bramfitt and A.O. Benscoter, *Metallographers Guide—Practices and Procedures for Irons and Steels,* ASM International 2002, p 158–159

40. C.T. Liu, Design of Ordered Intermetallic Alloys for High-temperature Use, *High Temperature Alloys; Theory and Design,* The Metallurgical Society, 1984, p 289–308

41. P. Angelini et al., "Large-Scale Evaluation of Nickel Aluminide Rolls in a Heat-Treat Furnace at Bethlehem Steel's (now ISG) Burns Harbor Plate Mill," report DE-AC0500OR22725, Oak Ridge National Laboratory/Department of Energy, Sept 2003

G.F. Vander Voort, Color Metallography, *Metallography and Microstructures,* Vol 9, *ASM Handbook,* ASM International, 2004, p. 493–512

Color Metallography

George F. Vander Voort, Buehler Ltd.

Introduction

THE USE OF COLOR in metallography has a long history, with color micrographs published over the past eighty-some years. A number of general articles (Ref 1, 2, 3, 4, 5, 6, 7, 8, 9, 10, 11, 12, 13, 14, 15) have been published reviewing methods and applications.

Natural color is of use in only a few classic metallographic applications. Prior to the development of wavelength-dispersive spectrometers and energy-dispersive spectrometers used on electron microprobe analyzers and scanning electron microscopes, the color of inclusions using different illumination modes was part of the identification schemes used. However, natural color has limited applicability.

Color can be created by optical methods, such as with polarized light and differential interference contrast illumination. Polarized light examination is extremely useful for studying the structure of certain metals, without etching, that have noncubic crystal structures, such as beryllium, hafnium, α-titanium, uranium, and zirconium. In many cases, polarized light can be used with etched specimens, regardless of their crystal structure, to produce color. Differential interference contrast reveals height differences between constituents and the matrix, but in most cases, the color is of esthetic value only.

Color etching methods are widely used, although they are not universal. Color etchants have been developed for a limited number of metals and alloys, and they are not always easy to use, nor are they fully reliable. Color etchants are used by immersion or electrolytically. A complete listing of all color etchants is beyond the scope of this article, but good compilations are available (Ref 7, 10, 11, 12, 13, 14, 15). Aside from the immersion tint etchants, there are a number of older etchants that produced color either by immersion, sometimes in boiling solutions, or electrolytically. Historical information on these etchants can be found in Ref 16.

Tint etchants may color either the anodic (matrix) or cathodic constituents. There are also electrolytic reagents known as anodizing solutions. They have been used most commonly with aluminum and its alloys. These solutions may produce a thin film on the surface, with a degree of roughness. Examination in bright field reveals little, but polarized light reveals the structure clearly.

There are other procedures to create interference films using heat (heat tinting), vapor deposition, or by reactive sputtering. Color can be observed with bright-field illumination but often can be enhanced using polarized light.

References cited in this section

1. A. Portevin, Colored Films in Micrography, *Met. Prog.,* Vol 36, Dec 1939, p 761

2. R.P. Loveland, Metallography in Color, *ASTM Bull.,* May 1944, p 19

3. W.D. Forgeng, Color Metallography, *Iron Age,* Vol 162 (No. 16), 14 Oct 1948, p 130

4. *Symposium on Metallography in Color,* STP 86, ASTM, 1949

5. H. Yakowitz, Some Uses of Color in Metallography, *Applications of Modern Metallographic Techniques,* STP 480, ASTM, 1970, p 49

6. R.S. Crouse, R.J. Gray, and B.C. Leslie, Applications of Color in Metallography and Photography, *Interpretive Techniques for Microstructural Analysis,* Plenum Press, 1977, p 43

7. E. Beraha and B. Shpigler, *Color Metallography,* American Society for Metals, 1977

8. H. Gahm and F. Jeglitsch, Color Methods and Their Application in Metallography, *Met. Prog.,* Aug 1981, p 48

9. H. Gahm and F. Jeglitsch, *Microstructural Science,* Vol 9, Elsevier North Holland, Inc., 1981, p 65

10. G.F. Vander Voort, *Metallography: Principles and Practice,* McGraw-Hill Book Co., 1984; reprinted by ASM International, 1999

11. G.F. Vander Voort, Tint Etching, *Met. Prog.,* Vol 127, (No. 4), March 1985, p 31

12. E. Weck and E. Leistner, *Metallographic Instructions for Colour Etching by Immersion, Part I: Klemm Colour Etching,* Vol 77, D.V.S. Verlag GmbH, Düsseldorf, 1982

13. E. Weck and E. Leistner, *Metallographic Instructions for Colour Etchants by Immersion, Part II: Beraha Colour Etchants and Their Different Variants,* Vol 77/II, D.V.S. Verlag GmbH, Düsseldorf, 1983

14. E. Weck and E. Leistner, *Metallographic Instructions for Colour Etching by Immersion, Part III: Non-Ferrous Metals, Cemented Carbides and Ferrous Metals, Nickel-Base and Cobalt-Base Alloys,* Vol 77/III, D.V.S. Verlag GmbH, Düsseldorf, 1986

15. P. Skočovský, Colour Contrast in Metallographic Microscopy, *Slovmetal,* 1993

16. T. Berglund, *Metallographers' Handbook of Etching,* Sir Isaac Pitman & Sons, Ltd., London, 1931

G.F. Vander Voort, Color Metallography, *Metallography and Microstructures,* Vol 9, *ASM Handbook,* ASM International, 2004, p. 493–512

Color Metallography

George F. Vander Voort, Buehler Ltd.

Optical Methods for Producing Color

There are few instances where naturally occurring color differences are observed in metallic systems. Specimens plated with copper or gold are a common example. There are two main optical methods for

producing coloring: polarized light and differential interference contrast. In both cases, color per se is of minimal value beyond simple esthetics. The color of inclusion phases in bright field, dark field, and polarized light has been used for identification purposes for many years.

Natural color is not a common occurrence in metallic systems; many metals have a similar white color. When polished, only a few metals exhibit a color other than white; for example, gold and copper appear yellow when polished. Platings of these metals can be easily recognized by their color. A classic example of natural color differences is the detection of liquid metal embrittlement in steels due to copper. In this case, the natural color of copper is clearly seen against the steel matrix. It may be easier to see the copper color when the steel matrix is etched. Figure 1 shows an example of porous high-carbon steel that was partially infiltrated with liquid copper, where the natural color of the copper can be easily observed. There is a substantial difference in the reflectivity of iron and copper. Etching of the high-carbon martensitic/pearlitic matrix increases the image contrast difference, making it easier to see the copper color. The so-called “purple plague,” the intermetallic phase Al_2Au that can occur in brazing of integrated circuits, has a natural purple or red-violet color, as illustrated in Fig. 2. Nitrides and some inclusions exhibit specific colors when examined with bright-field illumination, but overall, natural color is uncommon with metals and alloys.

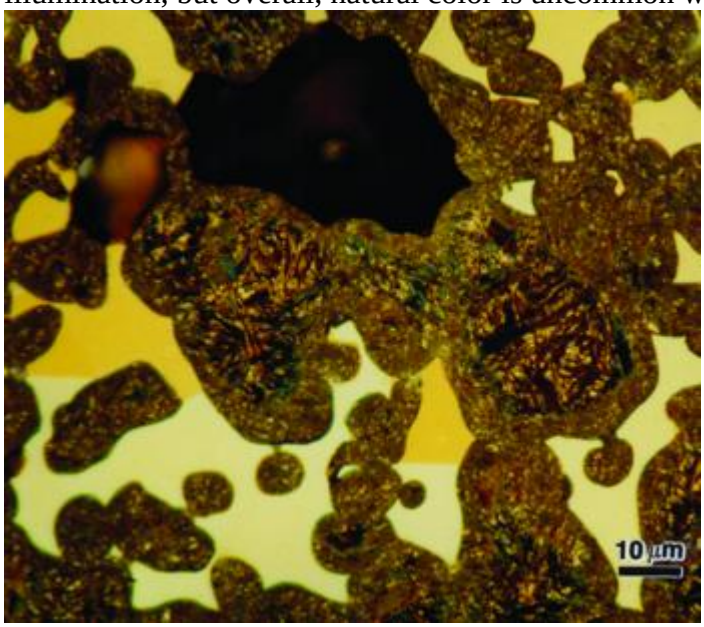

Fig. 1 Microstructure of a porous high-carbon steel powder metallurgy specimen infiltrated with copper showing the natural color of the copper, which is easier to see when the steel has been tint etched (revealing coarse plate martensite and retained austenite)

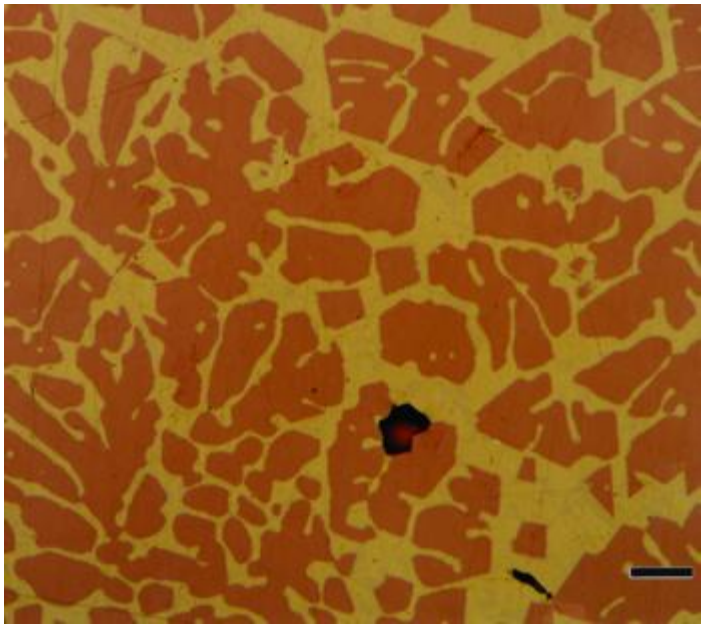

Fig. 2 Microstructure of as-cast Au-~22%Al showing the "purple plague," $AuAl_2$ intermetallic (reddish), surrounded by the Al-$AuAl_2$ eutectic after polishing to a 1 µm finish. Magnification bar is 50 µm long.

Dark-Field Illumination. Inclusions in metals have been identified using known colors when viewed with bright field, dark field, or polarized light (Ref 17). Cuprous oxide, Cu_2O, in tough pitch copper, for example, is easily recognized because it glows ruby red in dark-field illumination (Fig. 3) but appears bluish-gray in bright field. Cuprous sulfide, Cu_2S, has a similar color in bright field but remains dark and dull in dark field (Ref 18). Wood also exhibits natural color in dark field, as shown in Fig. 4.

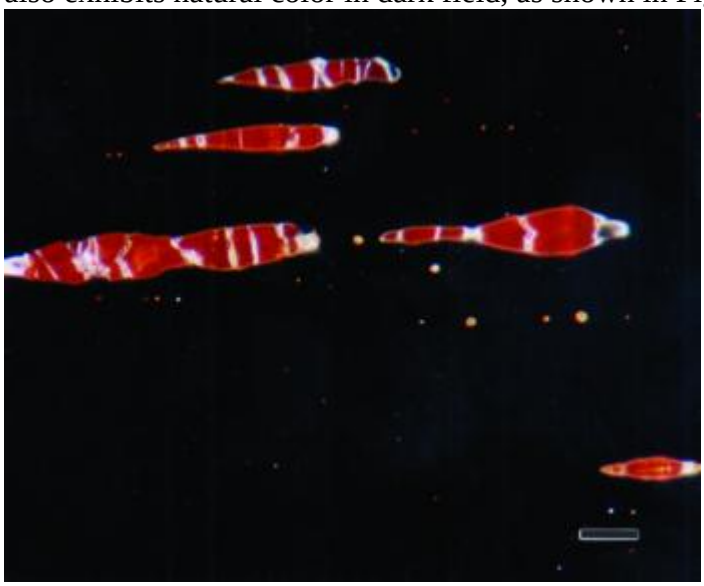

Fig. 3 Cuprous oxide in tough pitch arsenical copper (hot extruded and cold drawn) viewed in dark field, revealing the classic ruby-red color. Magnification bar is 10 µm long.

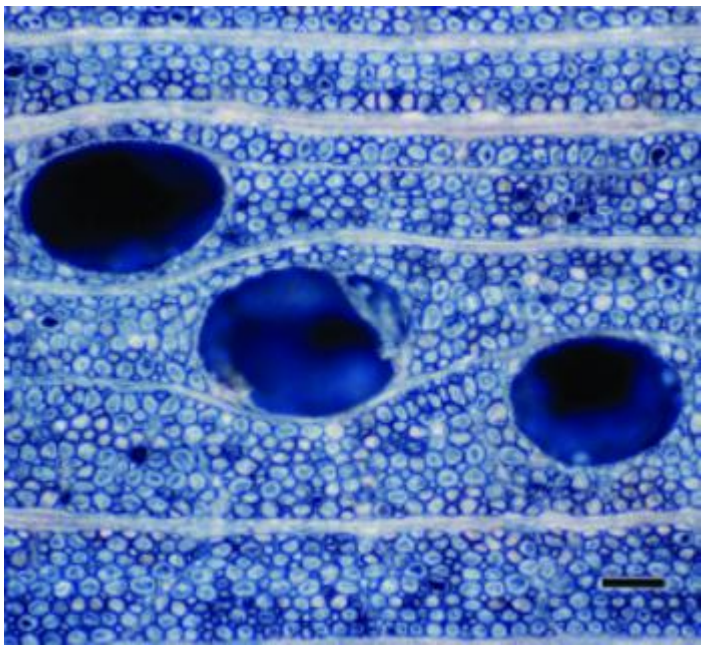

Fig. 4 Microstructure of walnut (plane perpendicular to the trunk axis) showing the cells and pores revealed using dark-field illumination. Magnification bar is 100 µm long.

Polarized Light. There are purely optical methods for generating color images employing polarized light and differential interference contrast illumination. Polarized light examination is useful with phases or anisotropic metals that have noncubic crystallographic structures (Ref 2), such as antimony, beryllium, cadmium, cobalt, magnesium, scandium, tellurium, tin, titanium, uranium, zinc, and zirconium. Figure 5 shows the grain structure near the surface of an electron-beam-melted crystal bar of high-purity zirconium (not etched) that was hot rolled, annealed, and cold drawn. The deformation process produces mechanical twins that are quite numerous at the surface but nearly absent in the interior. Other examples of color developed with polarized light on as-polished specimens of metals with noncubic crystal structures are shown in Fig. 6, hafnium; Fig. 7, ruthenium; and Fig. 8, Cd-20% Bi.

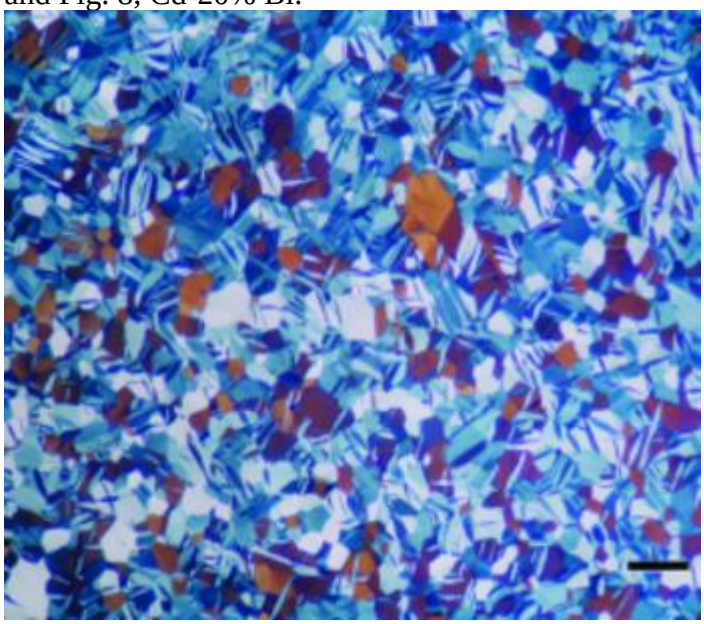

Fig. 5 Extensive mechanical twinning was observed in high-purity, electron-beam-melted zirconium after hot working and cold drawing. Viewed in polarized light. Magnification bar is 100 µm long.

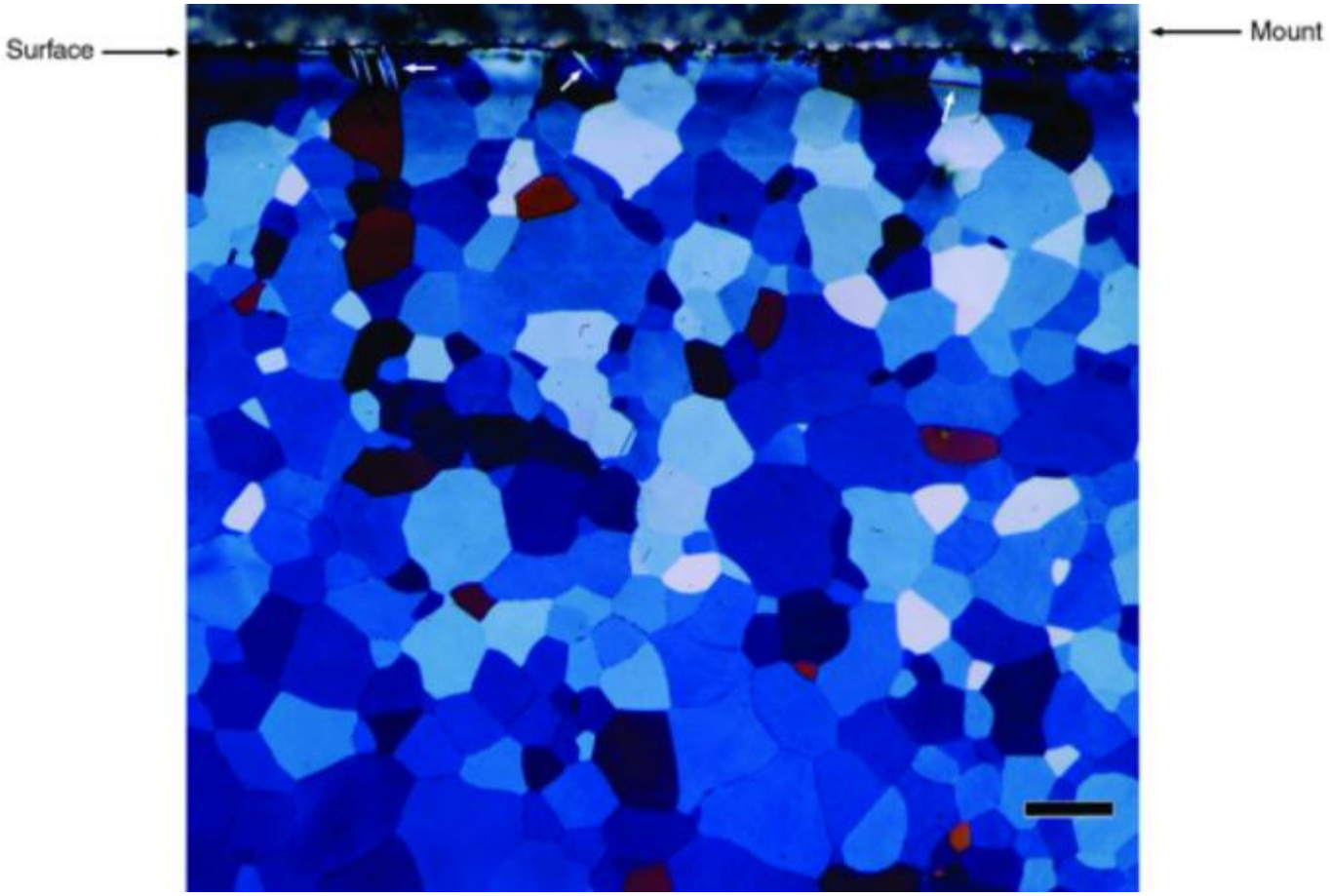

Fig. 6 Microstructure of wrought pure hafnium, with an as-polished specimen viewed in polarized light plus sensitive tint, revealing an equiaxed alpha hexagonal close-packed grain structure. A few mechanical twins can be seen at the surface (arrows). The magnification bar is 100 μm long.

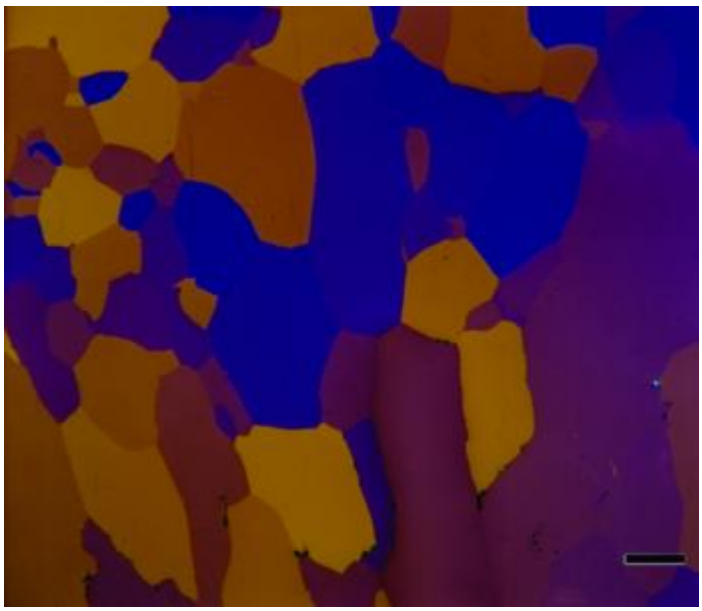

Fig. 7 Microstructure of as-cast pure ruthenium, as-polished and viewed in polarized light plus sensitive tint, revealing a mixture of equiaxed and columnar hexagonal close-packed grains and some small shrinkage cavities (black). The magnification bar is 200 μm long.

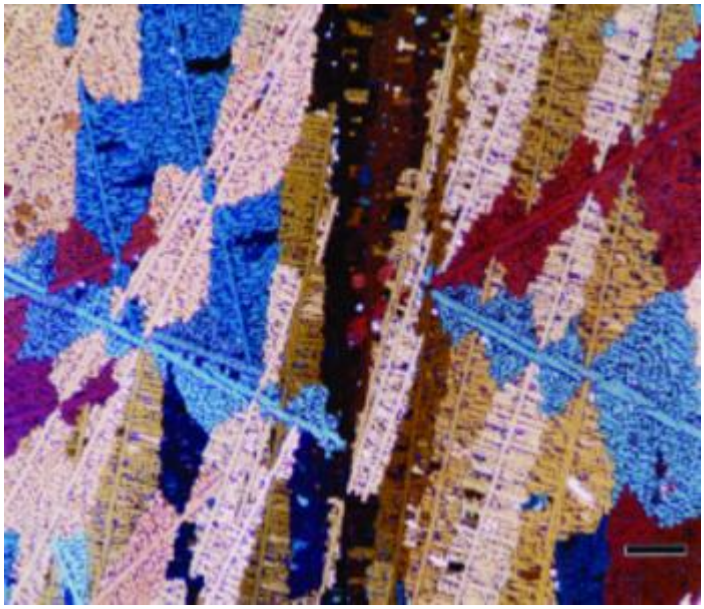

Fig. 8 Microstructure of Cd-20%Bi in the as-cast condition, unetched and viewed with polarized light (slightly off the crossed position) plus sensitive tint, revealing cadmium dendrites of various orientation. The interdendritic constituent is a eutectic of cadmium and bismuth but is too fine to resolve at this magnification. Magnification bar is 200 μm long.

Unfortunately, not all noncubic phases or metals respond well to polarized light. In some cases, a well-prepared specimen responds to polarized light, revealing the microstructure quite clearly but without appreciable color. The contrast produced, and the color intensity, may be a function of both the degree of anisotropy of the metal or alloy and the quality of specimen preparation. The quality of the surface appears to be the key factor, but the quality of the optical system is also very important. In some cases, the color response in polarized light can be markedly improved after etching specimens having noncubic crystal structures with some specific reagent. Figure 9 shows the grain structure of hot-rolled hexagonal close-packed (hcp) Zn-0.1%Ti-0.1%Cu in the as-polished condition and after etching, which improved polarized light response and color formation. Note that the fine precipitates between the elongated grains are much easier to see in polarized light after etching. Figure 10 shows pure hcp magnesium containing mechanical twins that were brought out vividly in color only after etching with the acetic-picral reagent (other standard etchants for magnesium did not provide this improvement).

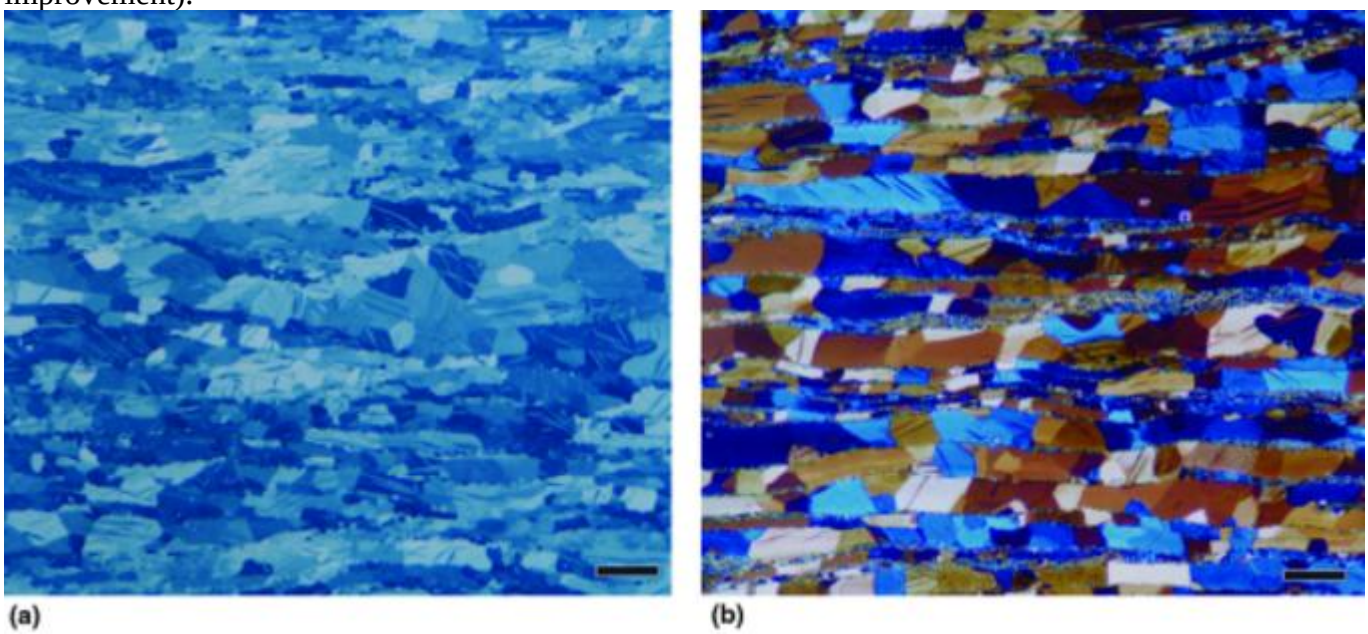

Fig. 9 Microstructure of Zn-0.1%Ti-0.1%Cu hot rolled to 6 mm (0.24 in.) thickness. (a) The as-polished condition, using polarized light, revealed elongated hexagonal close-packed grains containing mechanical

twins. Some fine precipitates are present in the grain boundaries but are not clearly revealed. (b) The structure after etching with Palmerton reagent and viewing with polarized light plus sensitive tint better reveals both the precipitates and grain structure. Magnification bars are 50 µm long.

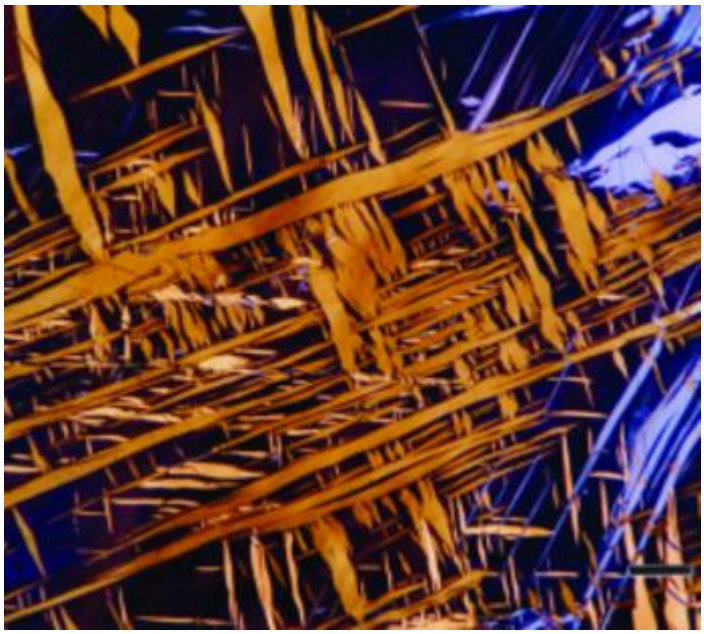

Fig. 10 Microstructure of wrought 99.98% Mg etched with acetic-picral reagent and viewed with crossed polarized light plus a sensitive tint filter. The magnification bar is 200 µm long.

In some cases, isotropic metals and alloys may respond to polarized light after being etched with a particular reagent that either produces an anisotropic film on the surface or roughens the surface. In some cases, anodizing solutions may produce an optically anisotropic film on the surface that produces color by interference. Color tint etchants form a film on the surface of certain metals that produces interference colors. If such a film is formed, color will be observed in bright field. In many cases, color contrast can be further enhanced when viewed with polarized light, due to the birefringence of these films. Anodizing and tint etching are discussed subsequently. The surfaces of many isotropic metals can be etched with a specific reagent that produces etch pits or furrows within the grains that respond to polarized light. Figure 11 shows an example of an aluminum brass (Cu-22%Zn-2%Al) that was cold worked and annealed at 750 °C (1380 °F). The specimen was etched with the classic potassium dichromate reagent, which produces a black-and-white grain contrast image in bright field that yields excellent color contrast in polarized light. The etch furrows are aligned crystallographically, and this produces grain-orientation coloring in crossed polarized light aided by a sensitive tint plate (also called a lambda plate, a full wave plate, or a first-order red plate). Fine lamellar structures will respond to polarized light regardless of the etchant used, producing strong coloration but often without any benefit except esthetics.

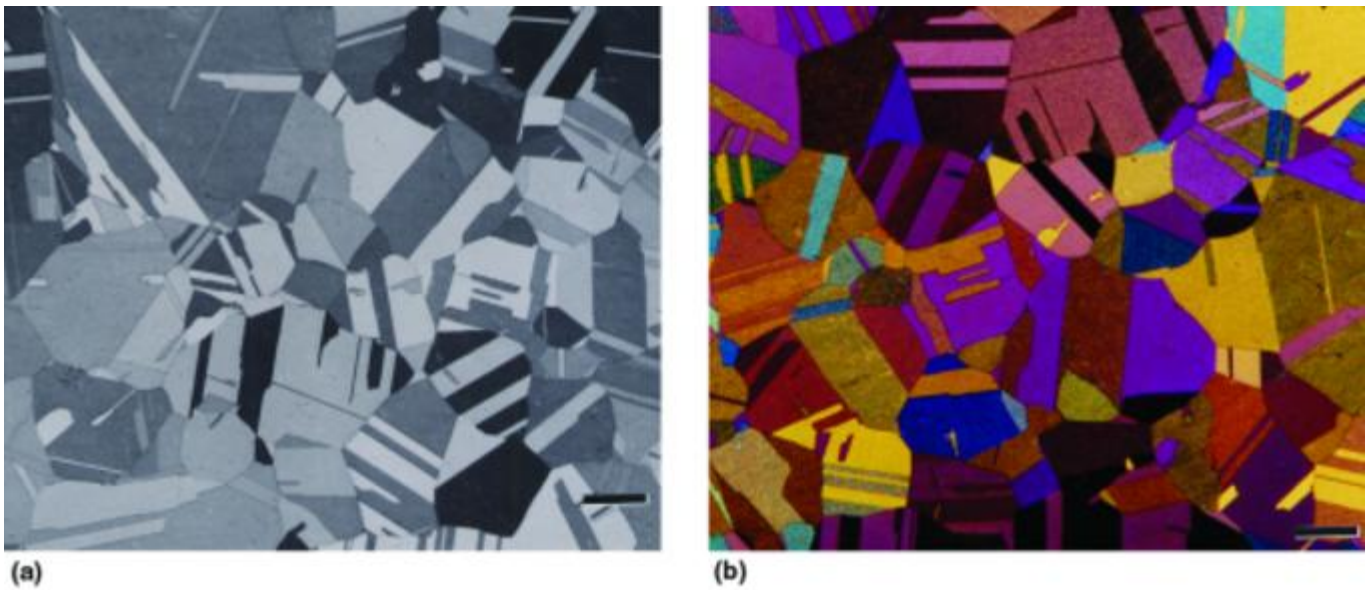

Fig. 11 Wrought aluminum brass (Cu-22%Zn-2%Al) annealed at 750 °C (1380 °F), producing equiaxed alpha grains containing annealing twins, and etched with potassium dichromate. Images in (a) bright field and (b) crossed polarized light plus sensitive tint. The magnification bars are 50 μm long.

Differential interference contrast illumination (DIC) (Ref 19) can be used to enhance height differences between constituent and matrix on a prepared surface. Introducing a small, controlled amount of relief in final polishing can enhance these height differences. Color is introduced using a sensitive tint plate. In most cases, the color is of no real value, but in some cases, it has more value. Figure 12 shows an example where Nomarski DIC was highly effective in revealing β_1 martensite in a Cu-26%Zn-5%Al shape memory alloy. A more complex example of a shape memory alloy is given in Fig. 13. This shows the structure of Spangold, a jewelry alloy (Au-19%Cu-5%Al), where some martensite was formed during hot mounting (it could be seen in polarized light). Then, the polished specimen was heated in boiling water and quenched, forming new martensite. The new martensite crosses the original martensite in some places (these are the areas with two crossing sets of parallel colored bands), referred to as antispangle by the alloy inventors.

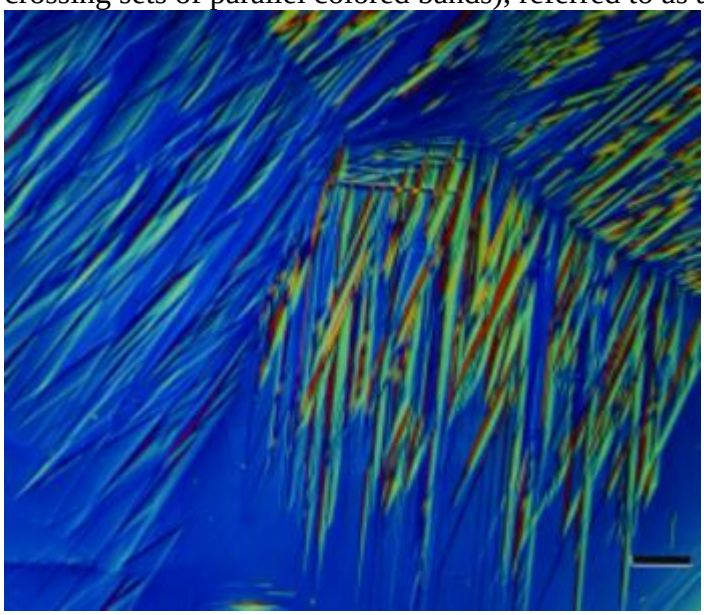

Fig. 12 Microstructure of a shape memory alloy (Cu-26%Zn-5%Al) showing β_1 martensite in a face-centered cubic alpha matrix, using Nomarski differential interference contrast without etching. The magnification bar is 25 μm long.

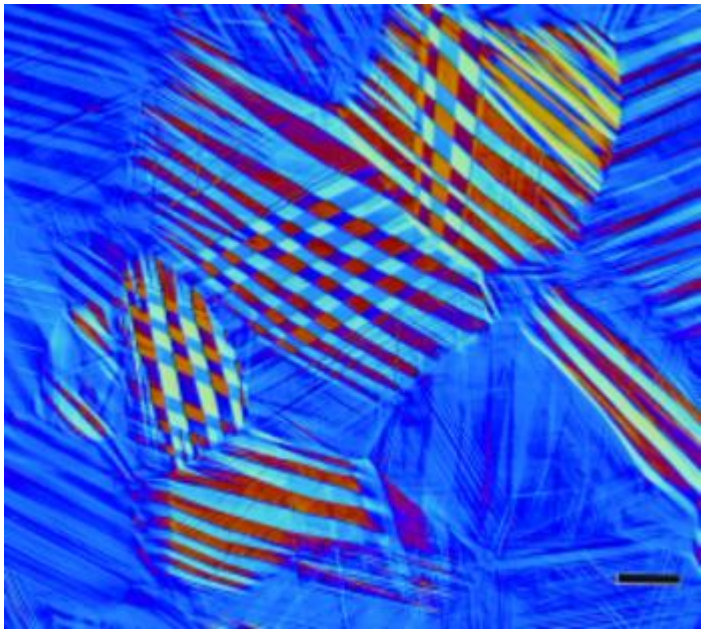

Fig. 13 Microstructure of Spangold (Au-19%Cu-5%Al), a new jewelry alloy, using martensite formation to create ripples ("spangles") on the surface. The specimen was polished, heated to 100 °C (212 °F) for 2 min, and quenched in water to form martensite, which produces shear at the free surface. This roughness can be seen using Nomarski differential interference contrast without etching. The crisscrossed pattern is produced by forming martensite, polishing, and then forming new martensite. The magnification bar is 50 μm long.

Figure 14 shows a rather interesting use of DIC. A metallographically prepared specimen of High-Expansion 22-3 alloy (Fe-22%Ni-3%Cr) was cooled to -73 °C (-100 °F), which caused martensite to form in areas where the austenite stability was low. When martensite forms, it does so by a shear transformation that produces surface movement at a free surface. The specimen was brought back to room temperature, cleaned off, dried, and viewed with Nomarski DIC, producing an excellent rendering of the martensite without etching. In some cases, DIC can be used effectively to study the structure of materials with significant variations in hardness and polishing rates. Figure 15 shows the microstructure of high-density polyethylene containing a filler material, viewed with DIC. In these examples, the color was produced by the use of the sensitive tint filter with the Wollaston prism. Without the sensitive tint filter, the images would exhibit gray tones.



Fig. 14 Martensite formed on the free polished surface of High-Expansion 22-3 alloy after refrigeration to -73 °C (-100 °F) to convert any unstable austenite to martensite. The specimen was brought back to room temperature, cleaned, and viewed with Nomarski differential interference contrast illumination without etching.

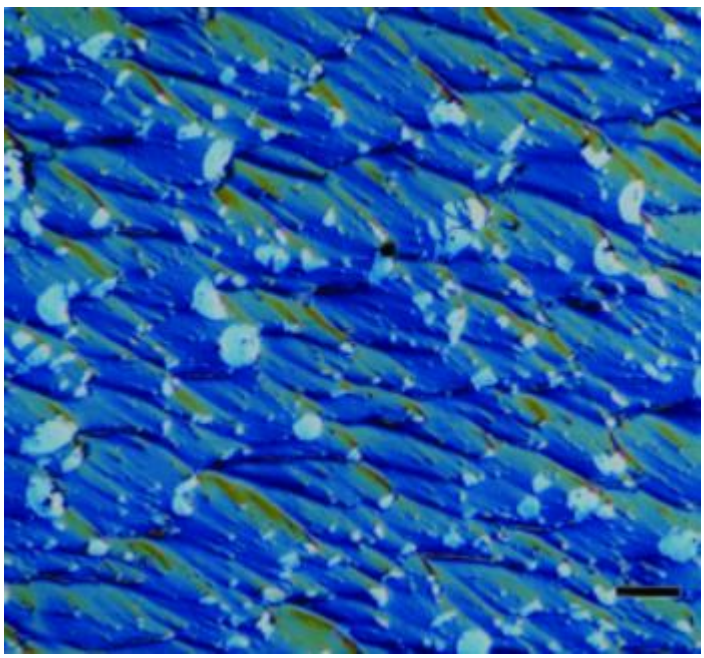

Fig. 15 Microstructure of high-density polyethylene containing a filler revealed using a polished specimen and Nomarski differential interference contrast. The magnification bar is 100 μm long.

References cited in this section

2. R.P. Loveland, Metallography in Color, *ASTM Bull.*, May 1944, p 19

17. T.R. Allmand, *Microscopic Identification of Inclusions in Steel*, British Iron and Steel Research Association, London, 1962

18. L.V. Foster and J.E. Wilson, The Examination of Metals in Polarized Light, *Proc. Am. Soc. Test. Mater.*, Vol 38 (Part II), 1938, p 315

19. H.E. Rosenberger, Differential Interference Contrast Microscopy, *Interpretive Techniques for Microstructural Analysis,* Plenum Press, 1977, p 79

G.F. Vander Voort, Color Metallography, *Metallography and Microstructures,* Vol 9, *ASM Handbook,* ASM International, 2004, p. 493–512

Color Metallography

George F. Vander Voort, Buehler Ltd.

Film Formation and Interference Techniques

Color can be produced by a number of techniques that rely on film formation and interference effects. These films can be formed thermally, as in heat tinting, or by chemical deposition, as in tint etching, or by vapor deposition, as in the Pepperhoff interference film method. These methods tend to be selective in nature, in that the films either color a specific phase, but not others, or color all constituents differently. In practice, the color produced is not a reliable means of phase identification compared to what is, or is not, colored.

Anodizing

Anodizing (Ref 20, 21, 22, 23, 24, 25, 26, 27, 28, 29) is an electrolytic procedure for depositing an anodic film on aluminum and certain other metals, for example, niobium, tantalum, titanium, uranium, and zirconium. Lacombe and Beaujard (Ref 20) first described the method in 1945. In was initially thought that this film varied in thickness from grain to grain, according to their crystallographic orientation, and that the birefringent properties of the oxide film varied the ellipticity produced by reflection of the beam. However, experiments have shown that a film is not formed on aluminum when anodized by reagents such as Barker's. Instead, the coloration effects in polarized light are due to double reflection from a furrowed surface produced by the anodizing solution, similar to certain chemical etchants discussed previously. Examination of aluminum specimens after anodizing with Barker's reagent should reveal color in bright-field illumination, if an anodic film is produced, but color is not observed. Instead, the surface looks etch-pitted when examined with the scanning electron microscope at high magnification. Figure 16 shows the surface of 1100 aluminum foil after anodizing with Barkers's reagent. The bright-field image (Fig. 16a) simply shows the intermetallic particles that have been slightly attacked by the solution. If Barker's had produced an anodic film, color should be observed. A classic experiment regarding this problem is discussed in the next section. Figure 16(b) shows the specimen viewed in polarized light; note that the grains are revealed in gray-level contrast. Figure 16(c) shows the same area viewed in polarized light with the addition of a sensitive tint filter; this yields the grains in color contrast. Figure 16(d) shows the microstructure of as-continuously cast 1100 aluminum after anodizing with Barker's reagent and viewing with polarized light plus sensitive tint. Dendrites with the same orientation have been colored uniformly. However, Barker's usually does not reveal the segregation within the dendrites. (Compare this result to that using Weck's color tint etch for aluminum, shown in Fig. 52.) Anodizing with Barker's, or other solutions, is the most universal procedure for revealing grain structures in cast and wrought aluminum alloys. Anodizing solutions have been developed for a number of metals and alloys, and some of these do deposit anodic films that produce color by interference effects, but Barker's does not.

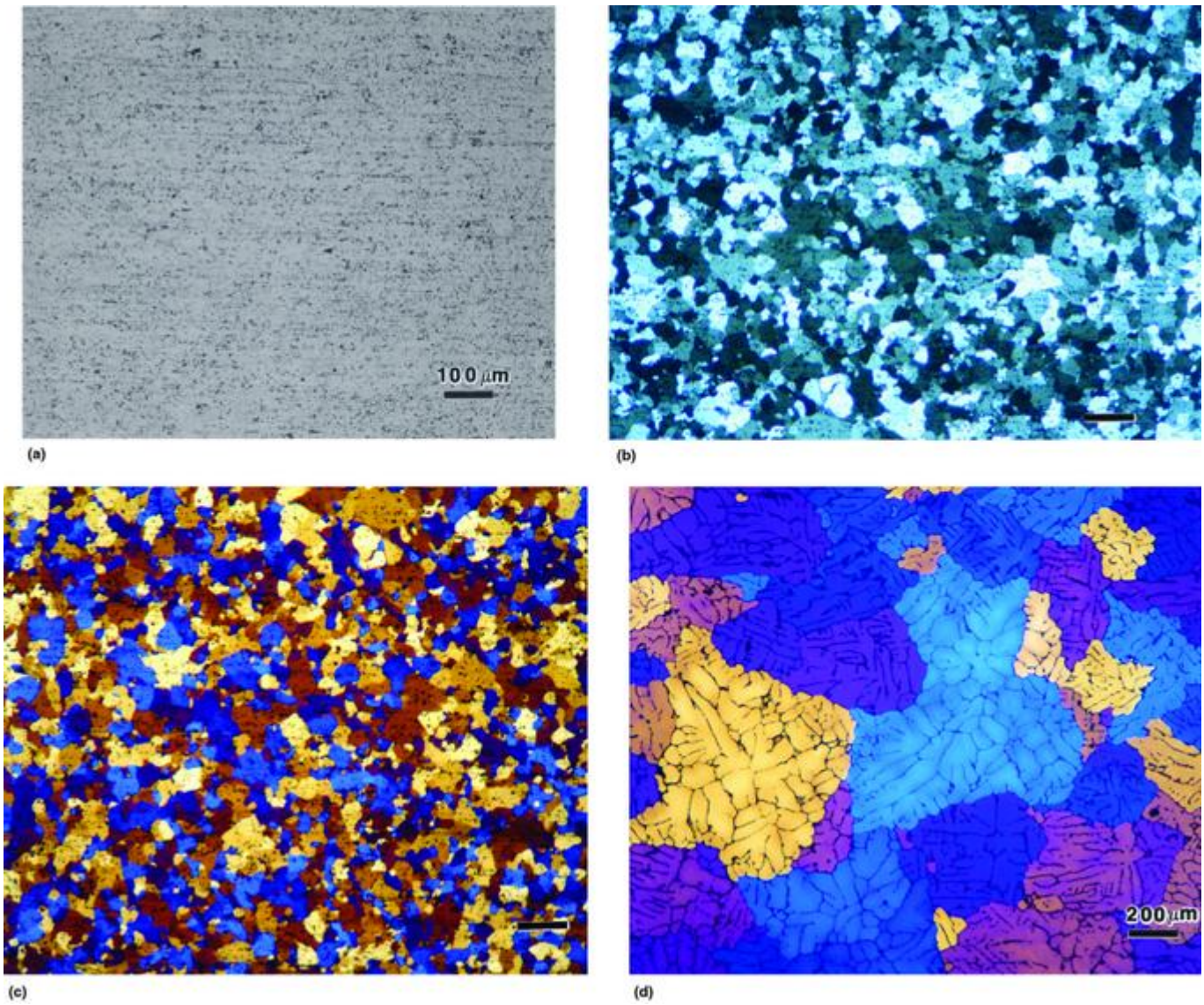

Fig. 16 Grain structure of wrought 1100-grade aluminum foil after electrolytic polishing and anodizing with Barker's reagent (20 V direct current, 2 min). (a) Viewed with bright-field illumination, revealing only the intermetallic precipitates. If anodizing had produced an interference film, colored grains should be visible. (b) Viewed with polarized light and (c) with polarized light plus a sensitive tint filter. The magnification bars in (b) and (c) are 100 µm long. (d) As-cast (concast) 1100 aluminum (>99% Al) anodized with Barker's reagent (30 V direct current, 2 min), revealing a dendritic solidification structure. Viewed with crossed polarized light plus sensitive tint

Chemical Etching

There are many cases where a chemical etchant, when used on an isotropic metal, results in grain-orientation coloration when viewed with polarized light and sensitive tint. Mott and Haines (Ref 30) and Gifkins (Ref 31) have described suitable preparation and etching procedures for a number of isotropic metals and alloys for producing color with polarized light. These procedures have been known and reported since at least the 1920s.

Woodard (Ref 32) studied the deformation of face-centered cubic (fcc) Monel using a grain contrast etchant (3 g chromic acid, 10 mL nitric acid, 5 g ammonium chloride, and 90 mL water) that produced an intensity contrast pattern with polarized light that he attributed to variations in crystal orientation. Woodard proposed that an anisotropic surface film, as in anodizing, produced the grain contrast effect. This is probably not the case, as suggested by the study of Perryman and Lack (Ref 33).

Perryman and Lack (Ref 33) performed a classic study to determine if polarization response was due to surface roughness or to the presence of an anisotropic surface film. The work used four specimens that respond to polarized light. The first two, electrolytically polished zinc and cadmium, are anisotropic metals with hcp

crystal structures that respond to polarized light when properly prepared (without need for etching). The second two specimens were isotropic metals with fcc crystal structures that were etched to respond to polarized light. They were electrolytically polished and anodized aluminum and Monel treated using Woodard's method (Ref 32). The surfaces were prepared and examined with polarized light, and all yielded good colored microstructures. Then, the surfaces were coated by vapor deposition of a thin (80 nm) film of silver. Silver has a fcc crystal structure and is isotropic. Hence, if the polarization effect is due to optical anisotropy, then the coated surface will no longer respond to polarized light. If, however, the polarization response is due to surface roughness, the silver film should not alter polarized light response. After deposition of the silver film, the anisotropic zinc and cadmium specimens did not respond to polarized light, but the anodized aluminum and the etched Monel did respond to polarized light. Thus, surface roughness is responsible for the polarized light response from anodizing or from etching with these specific reagents. This roughness was observed when these surfaces are examined by electron optical methods. Reed-Hill et al. (Ref 34) examined the surfaces of four fcc alloys (Ni 200, Ni 270, Monel 400, and Cu-10 Zn), etched to produce polarized light response, and confirmed the grooved surface roughness responsible for the response.

In general, any fine lamellar structure, etched with any general-purpose reagent, will exhibit color when viewed with polarized light plus sensitive tint. Also, any etchant that yields a grain contrast gray-scale image will exhibit color when viewed with polarized light plus sensitive tint, as shown in Fig. 11. In some cases, precipitation-hardened specimens can exhibit dramatic coloration after a standard etching reagent has been used, but mediocre coloration when a tint etchant is used. Figure 17 shows a classic example of this effect, where beryllium-copper that was solution annealed and aged to peak hardness was etched with equal parts ammonium hydroxide and hydrogen peroxide (3% concentration) (Fig. 17a) and with Klemm's I tint etch (Fig. 17b). Results with the standard etch are spectacular and come from the fine surface roughness created by etching a surface containing submicroscopic precipitates and their surrounding coherency strain fields. Klemm's I, like most tint etchants, does not do significant etching of the surface but deposits a film epitaxially with the underlying microstructure. Consequently, only a hint of the strain fields is seen.

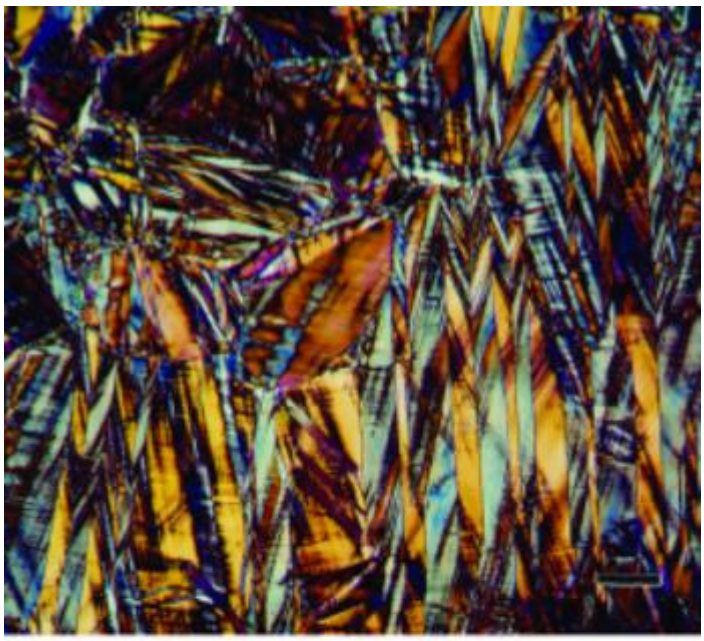

(a)

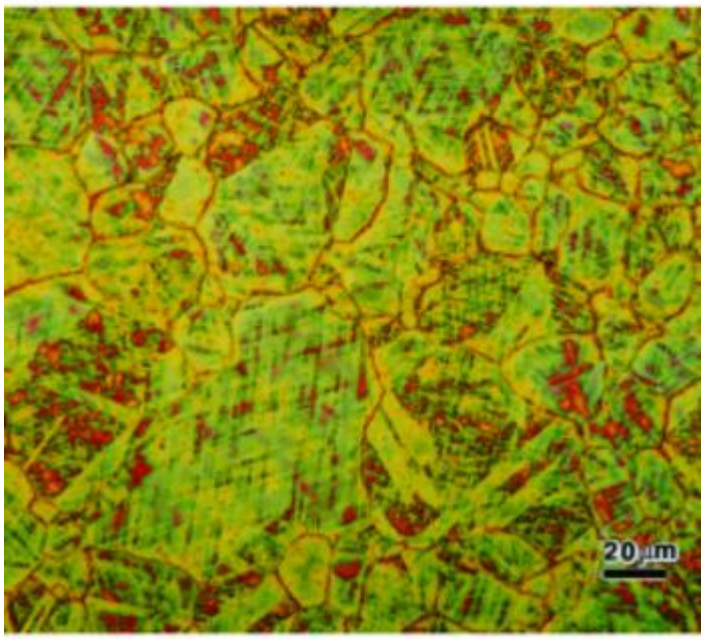

(b)

Fig. 17 Wrought, solution-annealed, and aged beryllium-copper (Cu-1.8%Be-0.3%Co) in the heat treated condition: 790 °C (1455 °F), held 1 h, oil quenched, and aged at 315 °C (600 °F) for 2 h (380 HV). (a) Swab etched with equal parts ammonium hydroxide and hydrogen peroxide (3% conc.). Polarized light and sensitive tint bring out the diffuse crisscross markings due to the submicroscopic γ′ precipitates and coherency strain fields. The magnification bar is 50 µm long. (b) Tint etching with Klemm's I did not reveal the structure as well, although the grain size is revealed. Tint etchants produce very little etch attack.

Tint Etching

Tint etching, also called stain etching or color etching, can be performed by using simple chemical immersion etchants, by electrolytic etching (such as, but not limited to, anodizing), and by potentiostatic etching. Immersion etching is the simplest; potentiostatic etching is the most complex. Deposition of color films on precipitates or matrix phases has been known for many years, because alkaline sodium picrate (Ref 35, 36), Murakami's reagent (Ref 37, 38), Groesbeck's reagent (Ref 39, 40), and Malette's reagent (Ref 41) have been used for many years. French metallographers (Ref 42, 43, 44, 45, 46, 47, 48) were very active in the 1950s developing color etchants based on aqueous solutions containing sodium bichromate, sodium nitrate, sodium

nitrite, and sodium bisulfite. Vilella and Kindle (Ref 49) at U.S. Steel tried the sodium bisulfite tint etch and found it useful for steels. However, these etchants are used infrequently today. Electrolytic etching with strong basic solutions also produces color films and is widely used with stainless steels to color delta ferrite or sigma phase (Fig. 18). Alkaline sodium picrate is widely used to color cementite in steels, as shown in Fig. 19. Murakami's reagent has been used to color certain alloy carbides (room-temperature immersion) or delta ferrite and sigma in stainless steels (immersion while boiling). Figure 20 illustrates the use of two modified versions of Murakami's to color delta ferrite and sigma in stainless steel welds. Groesbeck's reagent is used less frequently but is also useful for coloring alloy carbides, as shown in Fig. 21.

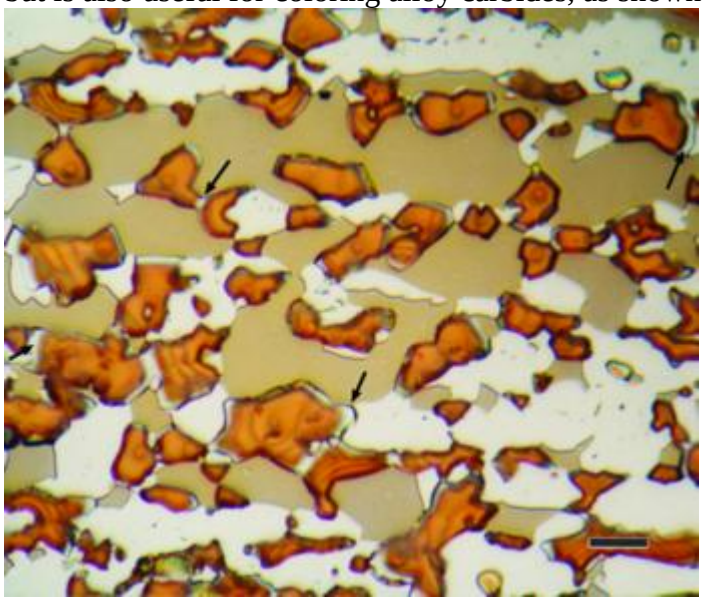

Fig. 18 Microstructure of wrought 7-Mo duplex stainless steel (Fe-<0.1%C-27.5%Cr-4.5%Ni-1.5%Mo) solution annealed and then aged 48 h at 816 °C (1500 °F) to form sigma. Electrolytic etching with aqueous 20% NaOH (3 V direct current, 10 s) revealed the ferrite as tan and the sigma as orange, while the austenite was not colored. The arrows point to austenite that formed during the conversion of ferrite to sigma. Magnification bar is 10 μm in length.

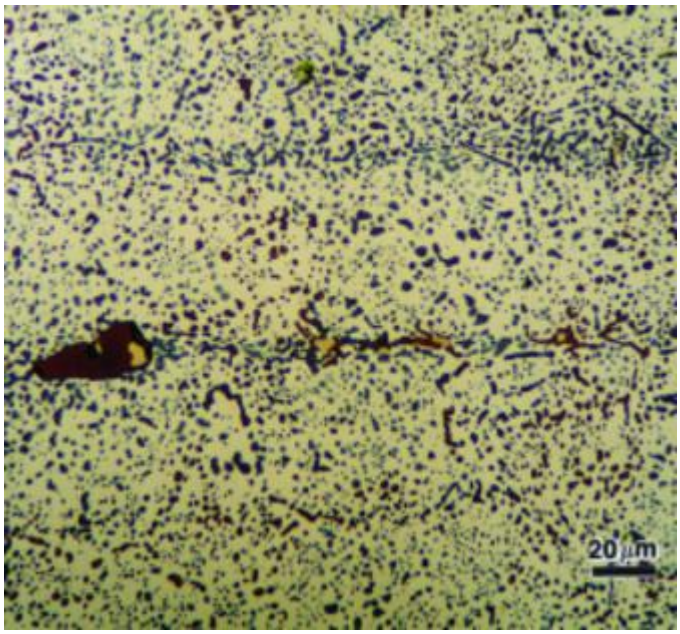

Fig. 19 High-carbon tool steel etched with boiling alkaline sodium picrate to color the cementite. Note the lighter-colored carbides in the segregation streak. These probably contain a small amount of molybdenum, present in this steel.

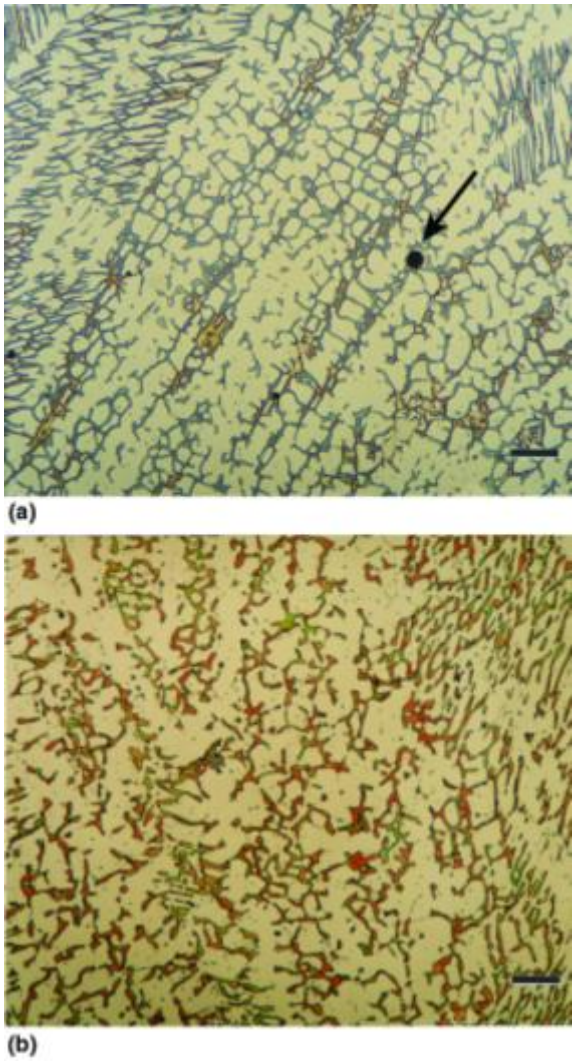

Fig. 20 Use of modified versions of Murakami's reagent to color delta ferrite and sigma phase in stainless steel welds. (a) Delta ferrite colored blue and brown in an austenitic matrix in type 312 stainless steel weld metal (as-welded) using modified Murakami's reagent (30 g sodium hydroxide, 30 g potassium ferricyanide, 100 mL water, at 100 °C, or 212 °F, for 10 s). The arrow points to a slag inclusion in the weld nugget. (b) Sigma phase formed in a type 312 stainless steel weld (from the delta ferrite phase) by aging at 816 °C (1500 °F) for 160 h. Sigma was colored green and orange by etching with Murakami's reagent (10 g sodium hydroxide, 10 g potassium ferricyanide, 100 mL water) for 60 s at 80 °C (175 °F). The magnification bars are 20 μm in length.

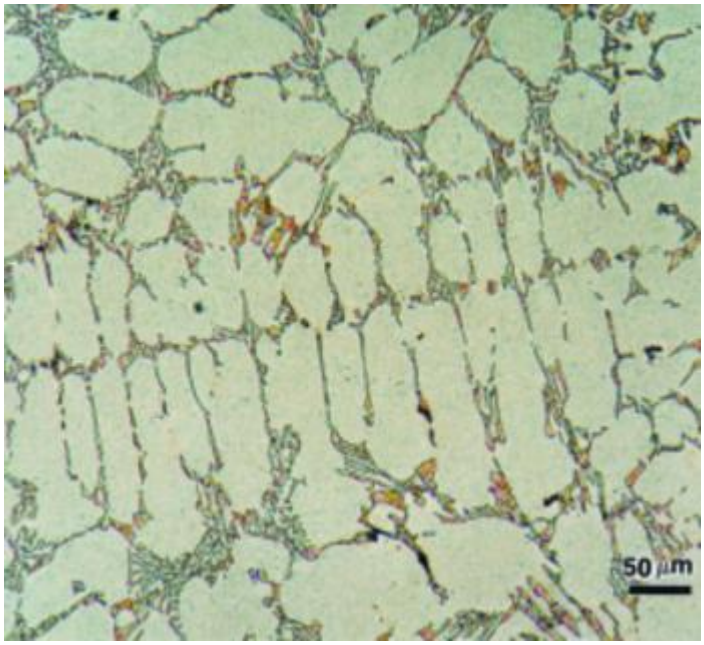

Fig. 21 Alloyed white cast iron (Fe-2.2%C-0.9%Mn-0.5%Si-12.7%Cr-0.4%Mo-0.1%V) with a martensitic matrix and a network of eutectic alloy carbides (colored). Etched with Groesbeck's reagent. (80 °C, or 175 °F, for 30 s) to color the alloy carbides

Color etching became a more useful and popular tool with the development of reagents by Klemm (Ref 50, 51) and Beraha (Ref 7, 52, 53, 54, 55, 56, 57, 58, 59, 60, 61, 62, 63, 64). These works were aided by developments by Benscoter, Kilpatrick, and Marder (Ref 65, 66, 67, 68), Lichtenegger and Blöch (Ref 69), Weck (Ref 14), and others. The books by Beraha and Shpigler (Ref 7) and by Weck and Leistner (Ref 12, 13, 14) have helped metallographers learn these useful techniques.

There are a number of processes, besides metallographic etching, that deposit thin films of various compositions on metals, but not all will reveal the microstructure. Film thickness is important; coloration due to interference effects is a function of film thickness. Passivation treatments, used on aluminum and stainless steels, produce thin, transparent films that do not reveal the microstructure. Oxides produced by high-temperature exposure are usually quite thick and also do not reveal the microstructure. Between these extremes, films of oxides, sulfides, and molybdates produce interference effects, revealing the structure in color as a function of thickness. The classic historical example of a process that yields oxide films of the correct thickness for interference-generated colors is heat tinting. Certain metals, when heated to temperatures that yield thin oxides, produce a visible color on the surface known as temper colors. At some low temperature, the film becomes thick enough to produce a straw-yellow color. As the temperature is increased, the film grows and the color changes to green, then red, violet, and blue. This same sequence is obtained when films are grown on a polished surface during tint etching. It may be difficult to grow a thick enough film to produce good color in bright field for some alloy compositions. In such a case, coloration can usually be improved, sometimes extensively, by viewing the specimen with polarized light plus sensitive tint. Figure 22 demonstrates this, where Monel 400 was color etched with Beraha's selenic acid reagent, producing a weak color image (Fig. 22a). However, polarized light plus sensitive tint yielded a very good color image of the grain structure (Fig. 22b). When a good film can be produced, as illustrated in Fig. 23(a) coloration is excellent in bright field. Using polarized light plus sensitive tint merely changes the color scheme (Fig. 23b) without any improvement in image quality.

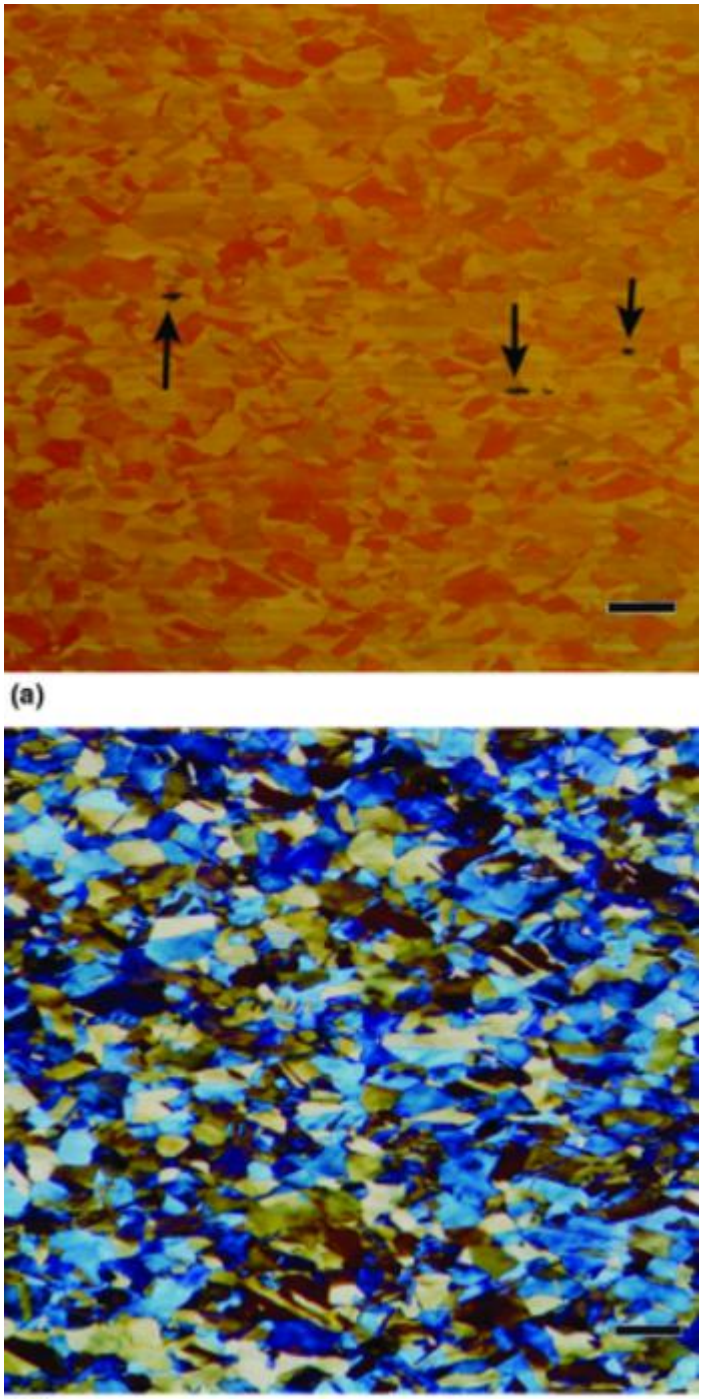

Fig. 22 The microstructure of hot-worked, annealed, and cold-drawn Monel 400 (Ni-32%Cu-<0.3%C-<2%Mn-<0.5%Si) revealed using Beraha's selenic acid etch for copper (longitudinal axis is horizontal). Monel alloys are very difficult to color etch, especially wrought alloys (as-cast alloys are easier). Bright field (a) revealed a weak image, because the interference film produced is thin (inclusions, arrows, can be seen). When this occurs, polarized light (b) will often enhance the image quality dramatically (the sensitive tint filter enhances coloration), as shown. Note the deformed, twinned face-centered cubic alpha grain structure. The magnification bars are 50 μm long.

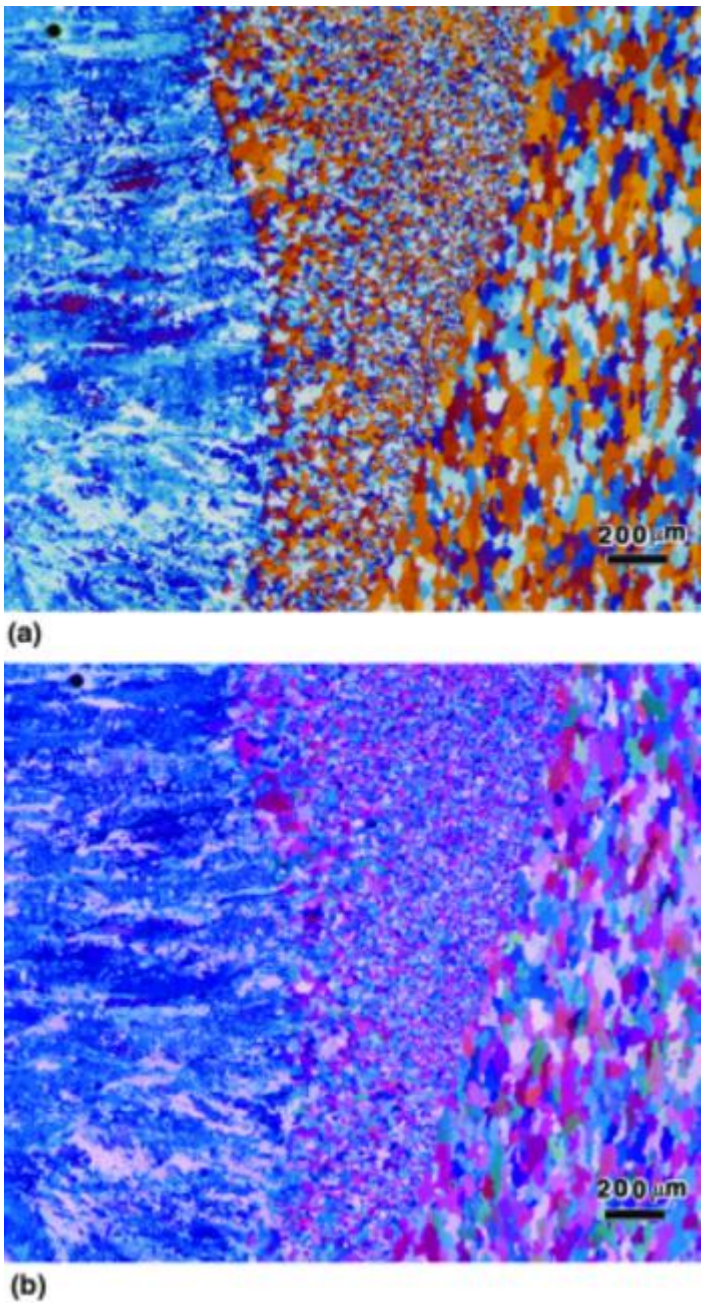

Fig. 23 This carbon steel weld developed an excellent interference film when tint etched with Klemm's I. Consequently, the bright-field image (a) reveals the grain structure very well, and the use of polarized light and sensitive tint (b) merely alters the color scheme without improving the image.

There are a great many tint etchants, and it is not possible to list, describe, and illustrate all of them in this article. Instead, some of the more useful and widely used color etchants are discussed. The films are the product of a controlled chemical reaction between the specimen surface and the reagent. The electrochemical potential on the surface of a polished specimen varies. For example, the potential at a grain boundary is different than the grain interior, while the potential of a second-phase particle may be greater than the matrix. In this case, which is quite common, the matrix is anodic while the particles are cathodic, that is, more noble. It is far easier to grow an interference film on the anodic matrix phase than on the cathodic second-phase particles. Anodic tint etchants are quite sensitive to crystallographic orientation, with the film thickness and the color being a function of crystal orientation. This is not the case for cathodic tint etches, which invariably color the noble phase uniformly, regardless of their crystallographic orientation. A few reagents will color both anodic and cathodic constituents and are referred to as complex reagents. In metallographic work, particularly for phase identification or for selective etching before performing quantitative measurements, anodic and cathodic etchants are generally more useful than complex reagents. Reagents that deposit sulfide films are usually anodic, while reagents that deposit selenium or molybdate films are usually cathodic.

Tint etching is always done by immersion, because swabbing would prevent formation of the interference film. Beraha often recommends lightly pre-etching the specimen with a general-purpose reagent before tint etching. This is not always necessary, and the author rarely does it. The author first etches specimens with a general-purpose reagent to see what the structure is. This is also useful because it may help determine what the best tint etchant may be, or at least which to try first. Immerse the specimen in the beaker, and watch the surface for coloration. This may be difficult, because the surface color can look quite different after drying than when immersed. If the solution contains ammonium bifluoride, NH_4FHF, it is best to use a plastic beaker and plastic tongs. Getting the specimen to form a film at the extreme edges can be difficult. This can be improved by wet etching, that is, squirting a small amount of distilled water on the surface before immersing it in the beaker. Then, agitate the specimen strongly for a few seconds. If the surface is not properly cleaned before etching, the results will be poor. Specimen preparation must be performed properly, with all preparation-induced damage removed.

Reagents that Deposit Sulfide Films. These are the best-known tint etches and usually the easiest to use. Klemm (Ref 50, 51) and Beraha (Ref 53, 54, 57, 58) have developed the most widely used sulfide-base tint etchants using sodium thiosulfate, $Na_2S_2O_3$, and potassium metabisulfite, $K_2S_2O_5$. Klemm's I, II, III and one of Beraha's reagents use both ingredients, while Beraha recommends a range of HCl concentrations used with potassium metabisulfite for etching a variety of iron-base alloys. To make Klemm's reagents, prepare a stock solution of cold water saturated with sodium thiosulfate. The compositions of Klemm's three reagents are given in Table 1.

Table 1 Klemm's reagents

Reagent	Composition[(a)]	Use
Klemm I	50 mL stock solution 1 g $K_2S_2O_5$	Immerse up to 3 min. Colors ferrite and martensite in cast iron, carbon and low-alloy steels; reveals segregation. Colors β-phase in brass (α-phase can be colored, but very slowly). Colors zinc and alloys
Klemm II	50 mL stock solution 5 g $K_2S_2O_5$	Immerse up to 8 min. Colors α-phase in copper brass, tin, and manganese steels
Klemm III	5 mL stock solution 45 mL water 20 g $K_2S_2O_5$	Immerse up to 8 min. Colors bronzes and Monel

(a) Stock solution: aqueous cold-saturated $Na_2S_2O_3$ solution

Klemm Color Etchants. To illustrate the use of the Klemm color etchants, Fig. 24(a) shows the microstructure of annealed cartridge brass etched with equal parts ammonium hydroxide and hydrogen peroxide (3%), which produced a weak grain contrast etch. Klemm's I is a bit weak to etch cartridge brass in a reasonable amount of time. After 3 min, weak coloration was obtained in bright field, but results were better in polarized light plus sensitive tint (Fig. 24b). Klemm's II is stronger, and after 2 min immersion, bright field produced a better image (Fig. 24c), while polarized light and sensitive tint yielded a much better image (Fig. 24d). Klemm's II often produces crystallographic line etching within many grains. This can be more easily seen in Fig. 24(c).

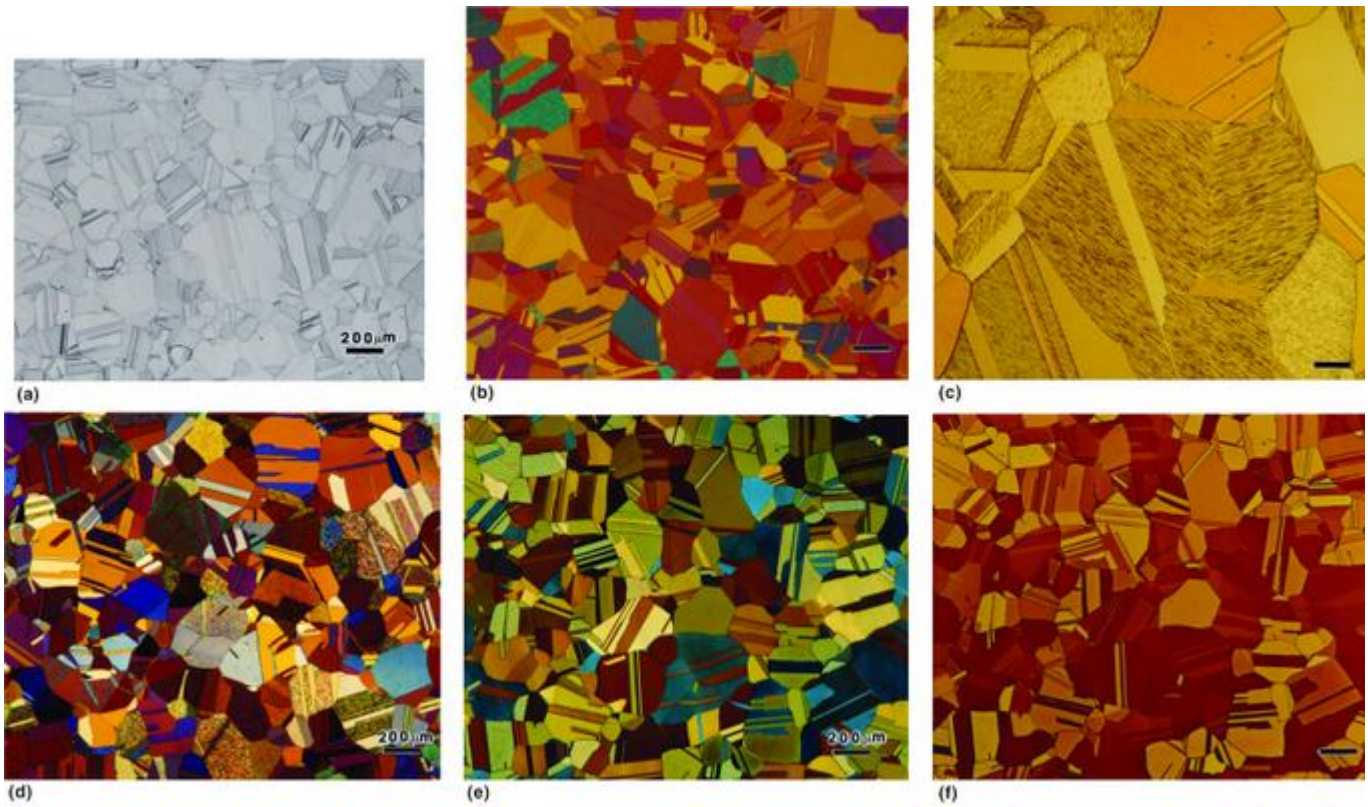

Fig. 24 Wrought cartridge brass (Cu-30%Zn) cold reduced 50% and annealed at 704 °C (1300 °F) for 30 min. Fully recrystallized and grown, equiaxed face-centered cubic grains with annealing twins. (a) Etched with equal parts ammonium hydroxide and hydrogen peroxide (3%). (b) The specimen was tint etched with Klemm's I reagent for 3 min, producing a lightly colored image in bright field. The structure was imaged with polarized light and sensitive tint, which dramatically improved the color contrast. The magnification bar is 200 µm long. (c) Etching with Klemm's II reagent for 2 min produced line etching within certain twins and grains. The lines are parallel to specific crystal planes. The specimen was viewed in bright field. The magnification bar is 50 µm long. (d) Tint etched with Klemm's II reagent and viewed with polarized light plus sensitive tint. This version line-etches many of the alpha grains. (e) Tint etched with Klemm's III reagent and viewed with polarized light and sensitive tint. (f) Viewed with bright-field illumination. Magnification bar is 200 µm long.

Klemm's III is an excellent tint etch for copper alloys and worked best for the cartridge brass (Fig. 24e). Results were very good in bright field (Fig. 24f), although the color range was limited, and even better in polarized light plus sensitive tint (Fig. 24e). Tint etchants produce noticeably different results on specimens that can be age hardened. Figure 25 shows a series of specimens of Kunial brass (Cu-20.34%Zn-5.87%Ni-1.39%Al) that were tint etched with Klemm's III. Figure 25(a) shows the grain structure of the alloy after solution annealing (73 HV hardness), revealing a multitude of colors in the grains and twins. Results were the same with aging at 300 °C (570 °F), which produced only a slight hardness increase (8 HV units). However, aging at 400 °C (750 °F), which increased the hardness to 143 HV, yielded a markedly different color response (Fig. 25b). Aging at the peak temperature, 500 °C (930 °F), increased the hardness to 192 HV, and the coloration within the grains was no longer uniform (Fig. 25c). The grain boundaries also appear to be wide. Overaging at 700 °C (1300 °F) reduced the hardness to 127 HV and produced a mottled-color appearance, precipitate in the grain boundaries, and denuding adjacent to the grain boundaries.

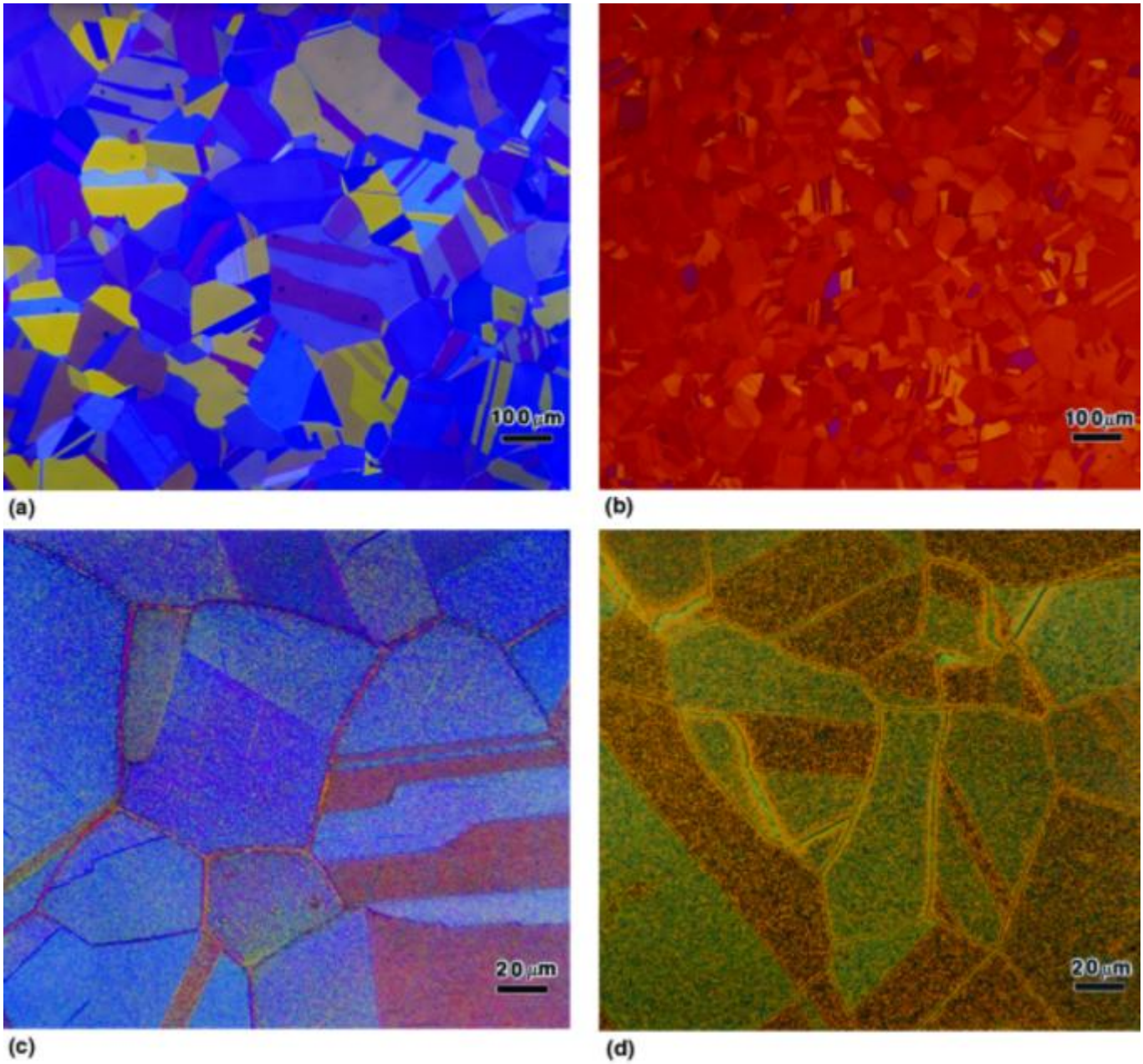

Fig. 25 Microstructure of Kunial brass (Cu-20.3%Zn-5.9%Ni-1.4%Al) that was (a) hot worked and solution annealed at 800 °C (1470 °F) (73 HV) and then tint etched with Klemm's III. (b) Solution annealing and aging at 400 °C (750 °F) (143 HV) and then tint etching with Klemm's III produced less color differences in a specimen with a finer grain size. The color difference may only be due to growth of a thinner interference film. Both specimens were viewed with polarized light plus sensitive tint. (c) The same alloy was hot worked, solution annealed at 800 °C (1470 °F), aged at 500 °C (930 °F) (192 HV, peak aged), and then tint etched with Klemm's III, which produced mottled grain coloring and some elongated features within grains. (d) Solution annealing and aging at 700 °C (1300 °F) (127 HV, overaged) and then tint etching with Klemm's III produced a narrower range of grain colors, and the strengthening precipitates are now visible with the light microscope.

Klemm's I has been used to color ferrite and martensite in carbon and low-alloy steels. Figure 26(a) shows the microstructure of an as-rolled 1.31% C water-hardened tool steel etched with 4% picral. The structure is fine pearlite, and there is a grain-boundary carbide film present, but this cannot be easily seen with nital, even at 500× magnification (2% nital was slightly poorer for revealing the cementite films). Figure 26(b) shows the specimen after color etching with Klemm's I and viewed with polarized light plus sensitive tint. Note that the grain-boundary cementite film is clearly visible, because Klemm's does not color cementite (neither does nital, but the contrast is too weak). Figure 27 shows an example of how Klemm's I colors ferrite in a wrought iron historic artifact. This is a section of a musket barrel that was hammer forged from wrought iron at the Henry

gun factory in Nazareth, Pennsylvania, in the 19th century. Across the top is a layer of iron oxide made magenta in color by the sensitive tint filter. At the surface, the grains are coarse and columnar in shape. The central region is fine grained and equiaxed, and uniform colors are seen within the grains. At the bottom of the image, the grains are larger and more irregular in shape, and the grain coloration is not uniform. This difference in the grain structure must be due to differences in the amount of deformation these two regions experienced. The mottled grain color suggests that the composition is more variable in these grains.

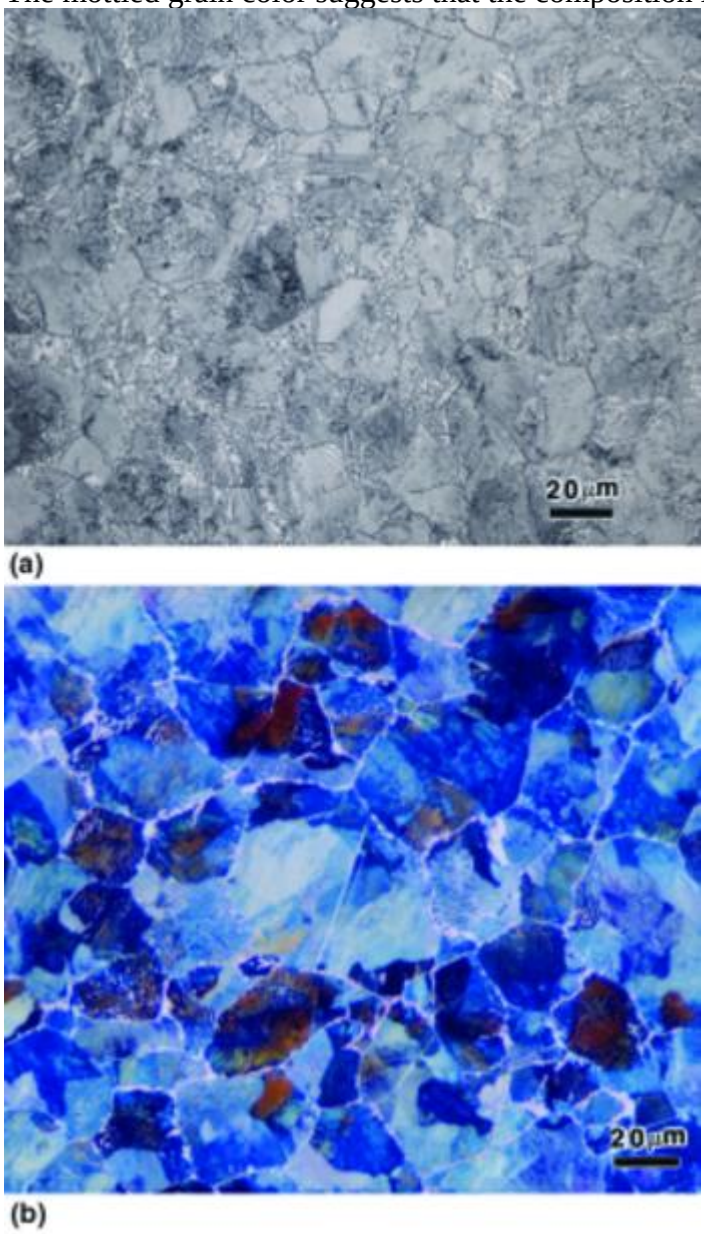

Fig. 26 Microstructure of as-rolled Fe-1.31%C-0.35%Mn-0.25%Si high-carbon water-hardenable tool steel. (a) Etching with picral revealed the Widmanstätten intragranular cementite that precipitated as proeutectoid cementite before the eutectoid reaction, but the intergranular cementite is not visible. Etching with nital was not as good as picral. (b) Color etching of the specimen with Klemm's I clearly revealed the intergranular and intragranular cementite films (viewed with polarized light and sensitive tint).

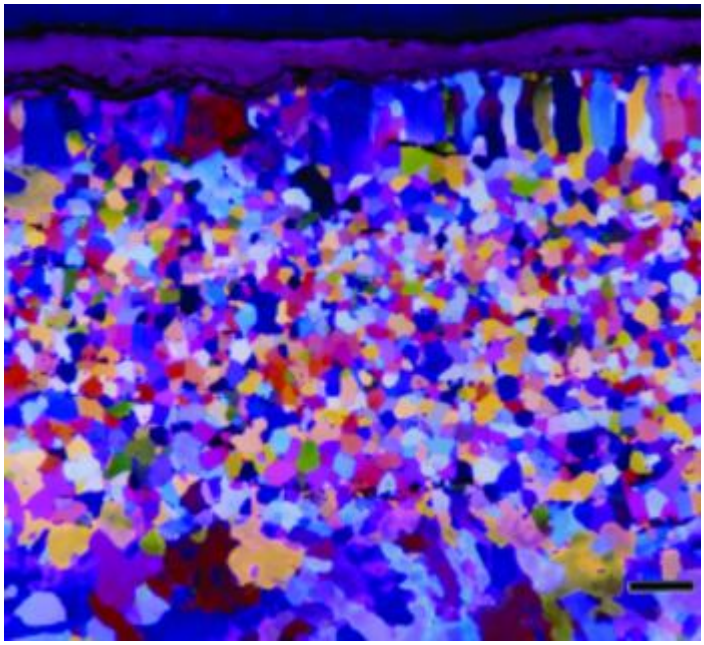

Fig. 27 Microstructure of a scrapped portion of a musket barrel made in the 19th century at the Henry gun factory near Nazareth, Pennsylvania, etched with Klemm's I and viewed with polarized light plus sensitive tint. The surface layer is scale (iron oxide) from forging the wrought iron. Beneath the scale is a layer of columnar ferrite grains. Below this zone, the grains are smaller and equiaxed. At the bottom of the field, the ferrite grains are larger and show evidence of segregation (the area probably saw less heat and forge work). The fine black spots are slag particles. The magnification bar is 200 μm long.

Figure 28 shows the microstructure of a powder-made gear that was not fully consolidated (note the dark voids). The structure is tempered martensite, and Klemm's I revealed the structure of the lath martensite. Prior-particle shapes are easily seen.

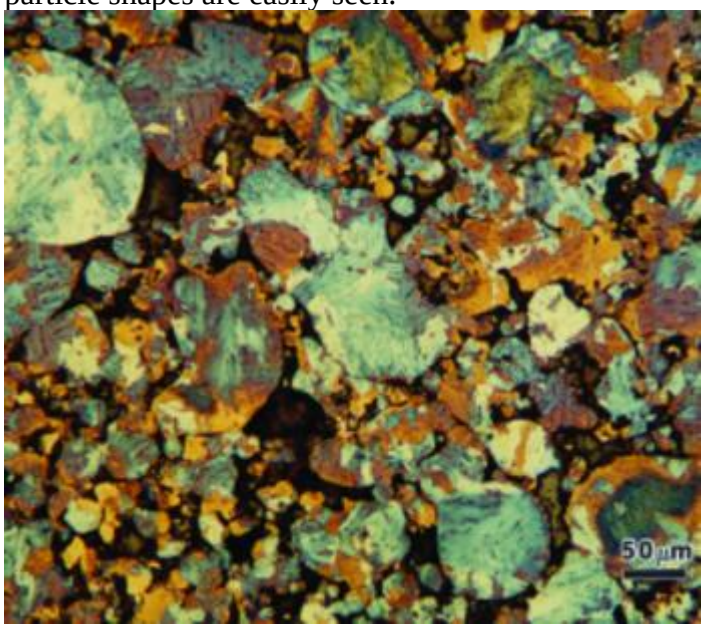

Fig. 28 Lath martensite microstructure of a low-density powder metallurgy alloy steel gear that was tint etched with Klemm's I and viewed with polarized light plus sensitive tint. Note that prior-particle shapes are quite visible due to the low density.

Figure 29 shows a dramatic example of the value of color etching. Figure 29(a) shows a montage of the microstructure of a weld in a low-carbon steel after etching with 2% nital. While the structure is visible, the grain boundaries are poorly revealed in the heat-affected zone and the base metal (center and right side). Figure

29(b) shows a montage of the specimen after etching with Klemm's I. It revealed the grain structure with exceptional clarity.

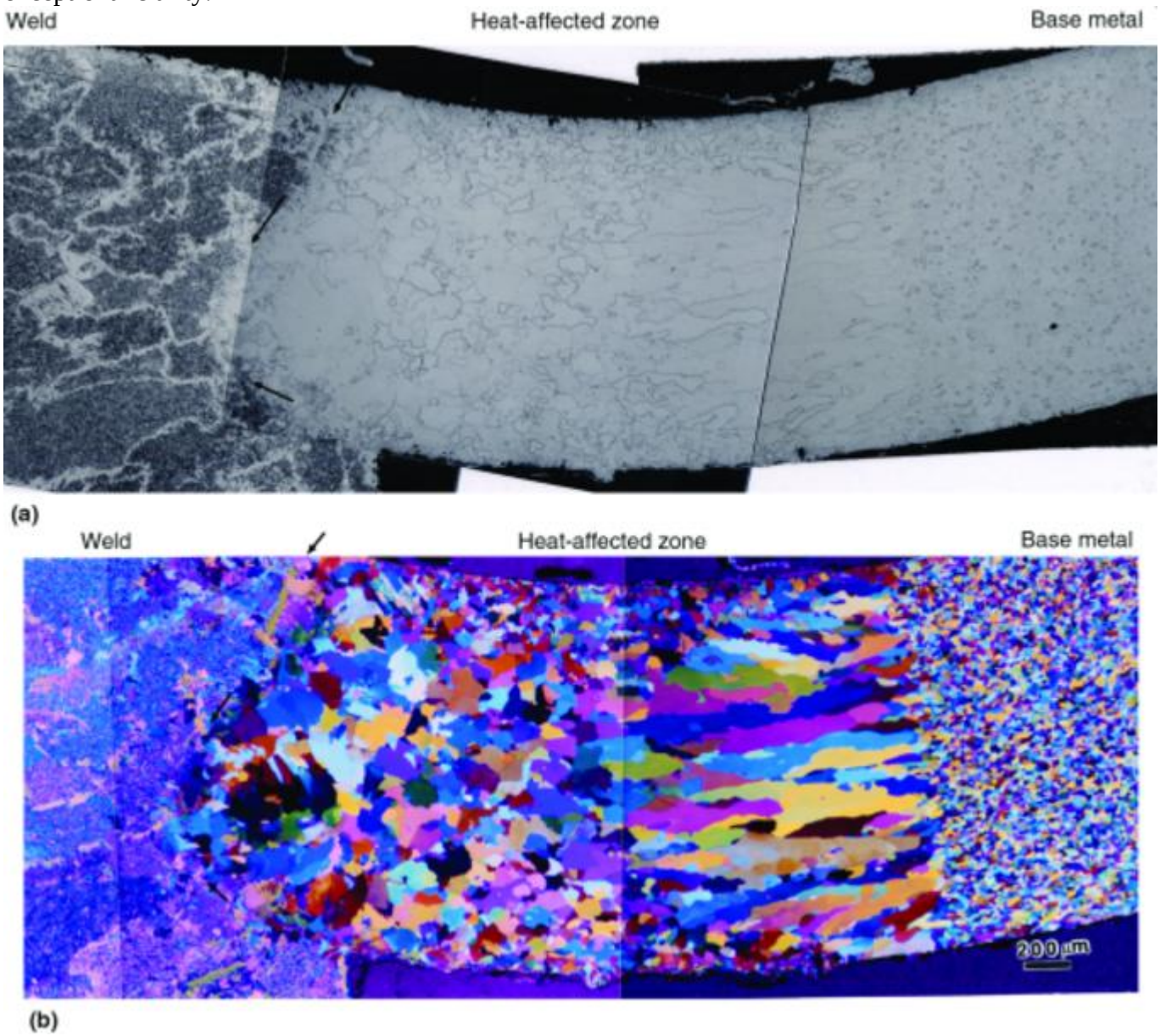

Fig. 29 Color etching to reveal weld microstructure. (a) Montage showing the structure of a large weld in a carbon steel as revealed using 2% nital. Note that the grain size and shape change dramatically from the fusion line (arrows) to the base metal at right. Nital did not fully reveal the grain structure, however. (b) Montage showing the structure of a weld in a carbon steel as revealed by Klemm's I reagent, viewed with polarized light plus sensitive tint. Note that the grain size and shape change dramatically from the fusion line (arrows) to the base metal. The magnification bar is 200 µm long.

Beraha Color Etching with Sulfide Films. Beraha has a somewhat similar composition (Ref 57) that works much like Klemm's I. It contains 10 g $Na_2S_2O_3$, 3 g $K_2S_2O_5$, and 100 mL water. In these reagents, the

metabisulfite ion ( ) decomposes in an aqueous solution in contact with a metallic surface, yielding SO_2, H_2S, and H_2. The SO_2 depassivates surfaces, particularly stainless steel surfaces, promoting film formation. The H_2S provides S^{2-} ions to form the sulfide film when ions of iron, nickel, or cobalt are present. Figure 46(c) discussed later in the text, shows the microstructure of as-continuously cast low-carbon, high-strength, low-alloy steel grade etched with Beraha's 10/3 version of Klemm's I. In general, this reagent performs much like Klemm's I but with slightly less aggressive coloring of ferrite.

Beraha also developed sulfide-film-forming reagents using a mineral acid (HCl) to permit tinting of stainless steels and nickel- and cobalt-base heat-resisting alloys (Ref 53, 56, 58). Beraha promoted these etches with a

wide range of acid content to accommodate variations in corrosion resistance and, with possible additions to the composition, to enhance coloration. These etchants include the BI, BII, and BIII reagents promoted by Weck and Leistner (Ref 13). The basic compositions recommended by Beraha are given in Table 2. The HCl-base reagents are mainly useful for the austenitic stainless steels and nickel- and cobalt-base alloys. The author has not had success with them for ferritic stainless steels, but they can be used to color high-alloy steels, such as tool steels, and martensitic and precipitation-hardenable stainless steels. While they can color duplex stainless steels, they are far more difficult to use than aqueous 20% NaOH electrolytically or Murakami's reagents (Fig. 18, Fig. 20, respectively).

Table 2 Beraha's reagents using HCl and potassium metabisulfite

Reagent (Ref)	Stock solution	Additions (per 100 mL stock solution)	Comments
B0 (58)	6 mL HCl 994 mL water	1 g $K_2S_2O_5$	For iron, carbon, alloy and tool steels. Immerse up to 60 s. Shake strongly to start etching, then leave motionless to color.
BI (13, 53, 58)	1000 mL water 200 mL HCl 24 g NH_4FHF	0.1–0.2 g $K_2S_2O_5$ (for martensitic stainless steels) 0.3–0.6 g $K_2S_2O_5$ (for ferritic and austenitic stainless steels)	Immerse up to 90 s. Best to use plastic tongs
BII (13, 53, 58)	800 mL water 400 mL HCl 48 g NH_4FHF	0.3–0.8 g $K_2S_2O_5$ 10–25 mg Na_2S[(a)]	For corrosion and heat-resistant alloys. Sodium sulfide can be added to improve color contrast.
BIII (13, 53, 58)	600 mL water 400 mL HCl 50 g NH_4FHF	0.3–0.8 g $K_2S_2O_5$ 1–1.5 g $FeCl_3 \cdot 6H_2O$[(a)] 1 g $CuCl_2$[(a)]	For corrosion and heat-resistant alloys. The optional additions (to improve coloration) can be made to the stock solution. Immerse up to 180 s.
BIV (58)	500 mL water 500 mL HCl 50 g NH_4FHF	0.3–0.8 g $K_2S_2O_5$ 1–1.5 g $FeCl_3 \cdot 6H_2O$[(a)] 1 g $CuCl_2$[(a)]	For difficult-to-etch corrosion- and heat-resisting alloys. The optional additions (to improve coloration) can be made to the stock solution.

(a) Optional additions used to improve color response. Note: When water is specified, use distilled water.

Figure 30 shows a portion of a weld made from Nitronic 50 and the heat-affected zone and base metal of 7-Mo PLUS duplex stainless steel color etched with Beraha's BI reagent. Note the coarseness of the heat-affected zone compared to the base metal and the acicular structure of the weld metal. Ferrite was colored, while the austenite was not. Figure 31 shows the austenitic grain structure of Custom Flo 302 HQ stainless steel in the

solution-annealed condition. Beraha's BI was used to color the grain structure. Figure 32 shows the austenitic grain structure of 316L stainless steel that was cold reduced 30% in thickness and then solution annealed from 1150 °C (2100 °F). It was color etched with Beraha's BII reagent. The streaks indicate alloy segregation, because they are parallel to the deformation axis. Color etchants are excellent for revealing segregation, and numerous studies have demonstrated that microprobe determinations of compositions can be made on an etched surface without impairment of the chemical analysis results. Figure 33 shows the microstructure of Waspaloy, a nickel-base superalloy, in the solution-annealed and double-aged condition. The specimen was tint etched with Beraha's BIV, with an addition of ferric chloride. Figure 34 shows the microstructure of Elgiloy, a cobalt-base alloy used for watch springs. The strip was hot rolled and then solution annealed at 1040 °C (1900 °F), not high enough for complete recrystallization. The specimen was tint etched with Beraha's BIV plus an addition of ferric chloride.

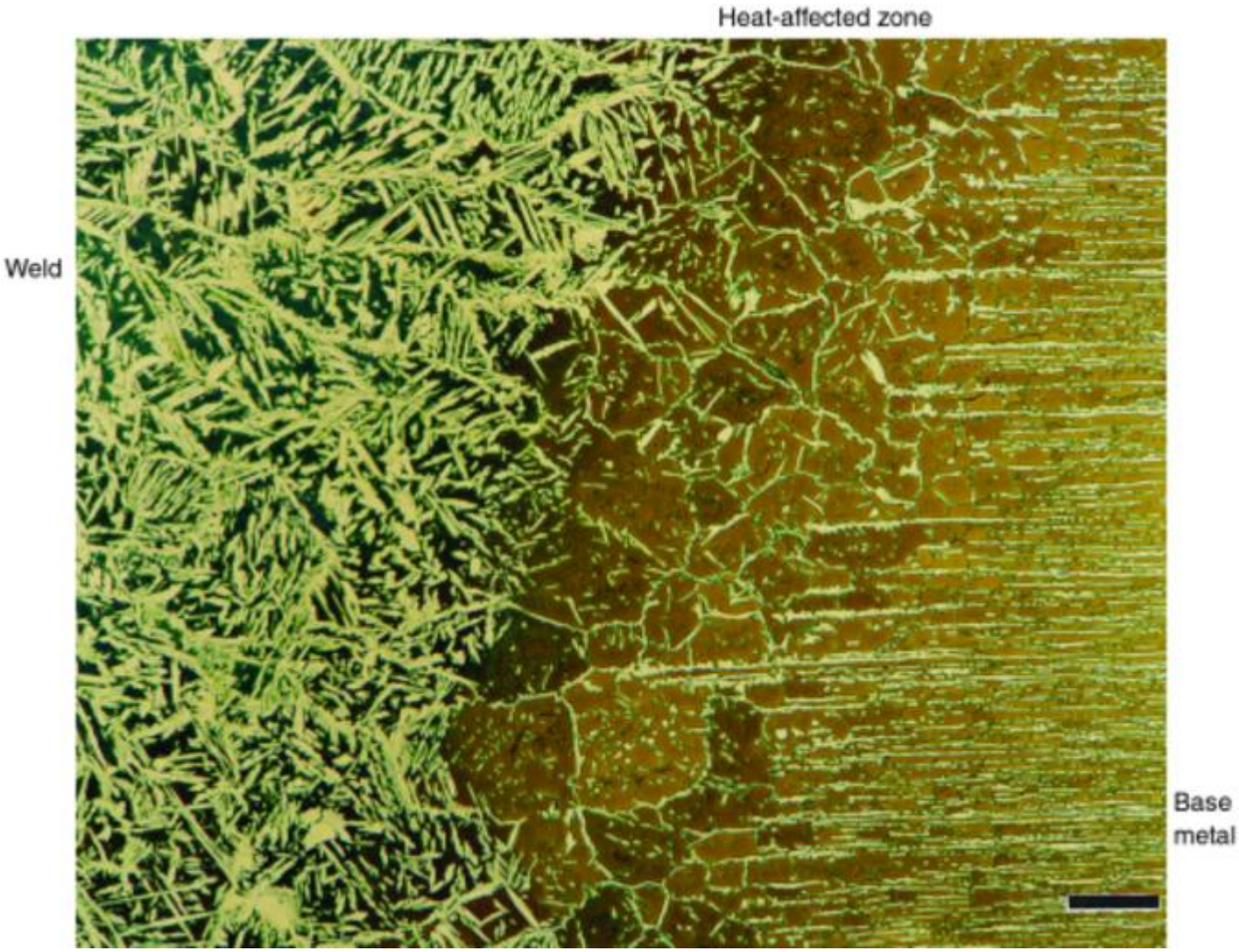

Fig. 30 Microstructure of 7-Mo PLUS duplex stainless steel (Fe-<0.03%C-<2%Mn-27.5%Cr-4.85%Ni-1.75%Mo-0.25%N) welded with Nitronic 50, etched with Beraha's BI reagent, and viewed with bright-field illumination. Ferrite is colored, and austenite is unaffected. The magnification bar is 200 µm long.

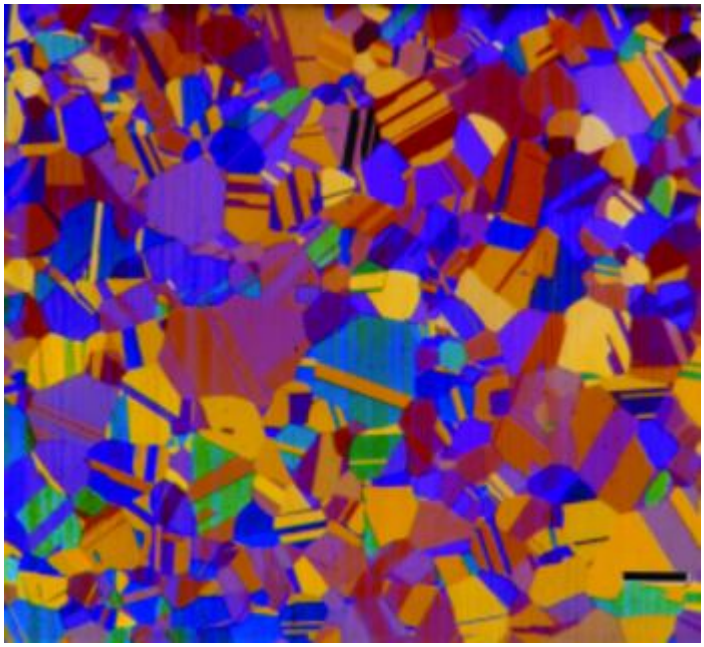

Fig. 31 Microstructure of Custom Flo 302 HQ austenitic stainless steel (Fe-<0.08%C-18%Cr-9%Ni-3.5%Cu) in the hot-rolled and solution-annealed condition after tint etching with Beraha's BI reagent. The structure is equiaxed, twinned, face-centered cubic austenite. The faint vertical lines are from alloy segregation (longitudinal direction is vertical). Viewed with polarized light plus sensitive tint. The magnification bar is 100 µm long.

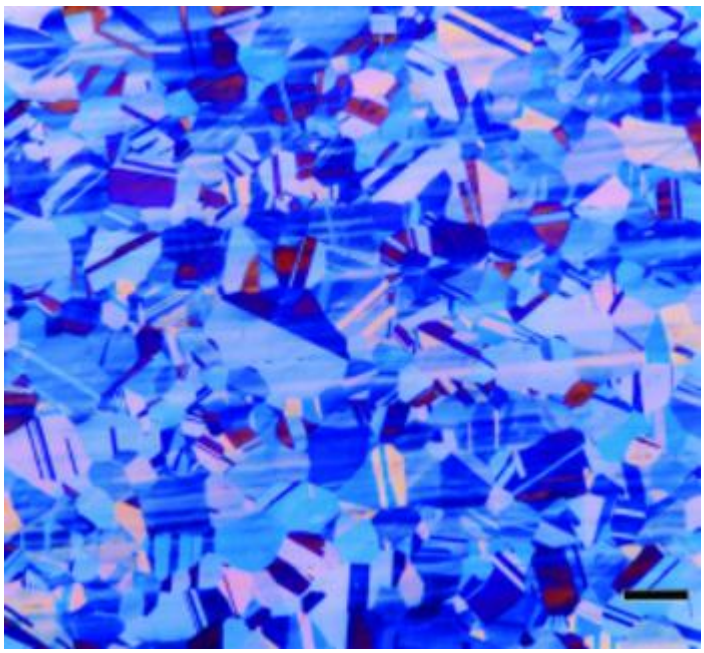

Fig. 32 Austenitic, twinned grain structure of 316L austenitic stainless steel (Fe-<0.03%C-17%Cr-12%Ni-2.5%Mo) that was hot rolled, solution annealed, cold reduced 30% in thickness, and solution annealed (1150 °C, or 2100 °F, for 1 h, water quenched). The specimen was tint etched with Beraha's BII reagent and viewed with polarized light plus sensitive tint. The faint lines, slightly off horizontal, are due to alloy segregation and are parallel to the longitudinal axis. The magnification bar is 200 µm long.

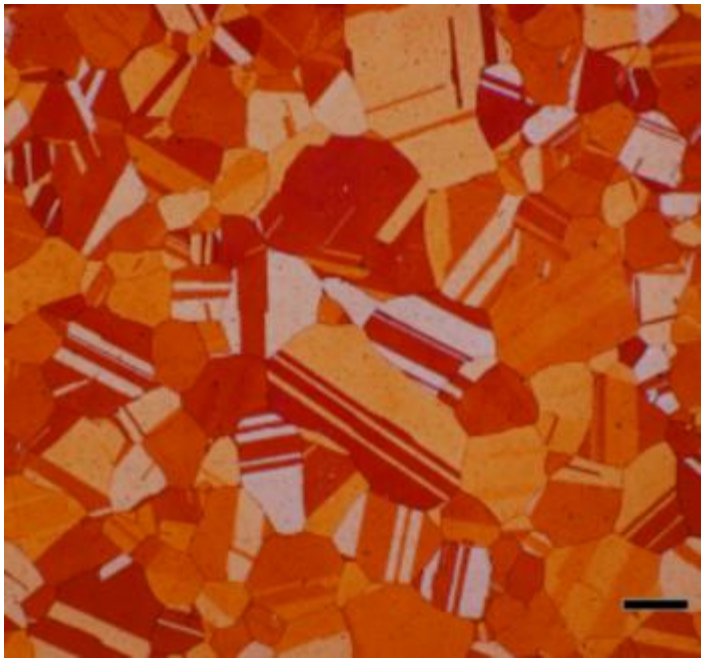

Fig. 33 Microstructure of wrought, solution-annealed, and double-aged (approximately 42 HRC) Waspaloy, a nickel-base superalloy (Ni-0.06%C-19.5%Cr-4.2%Mo-13.5%Co-3%Ti-1.35%Al-0.07%Zr-0.005%B-<2%Fe), tint etched with Beraha's BIV reagent, revealing twinned austenitic grains. Viewed in bright field. The magnification bar is 100 μm long.

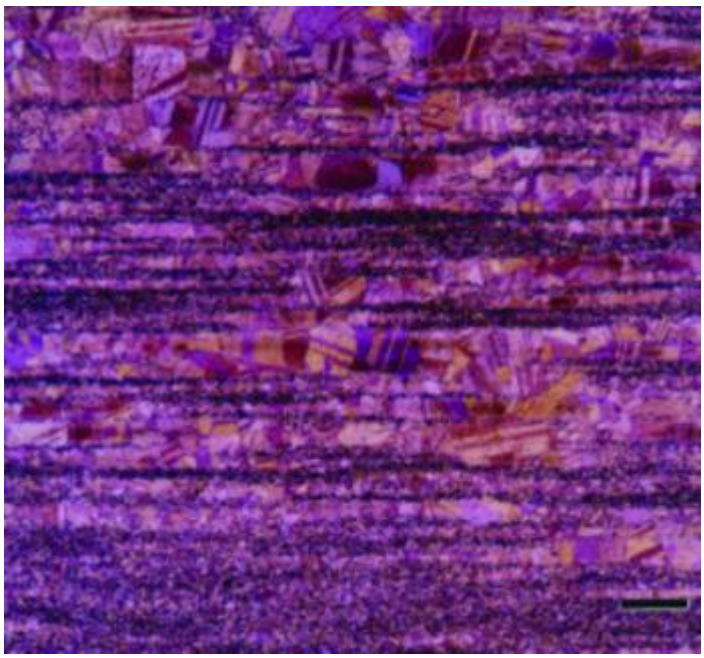

Fig. 34 Microstructure of Elgiloy, a cobalt-base alloy used for watch springs (Co-20%Cr-15%Fe-15%Ni-2%Mn-7%Mo-0.05%B-0.15%C), after hot rolling and solution annealing (1040 °C, or 1900 °F, for 2 h, water quenched). The specimen is partially recrystallized. The specimen was tint etched with Beraha's BIV plus 1 g $FeCl_3$ per 100 mL. The specimen was viewed with polarized light plus sensitive tint. The magnification bar is 100 μm long.

Beraha's etchants, based on sulfamic acid, a weak organic acid, have not been used much, although they are quite useful, reliable, and easy to employ (Ref 63). The sulfamic-acid-based reagents (Table 3) are applicable to iron, low-carbon and alloy steels, tool steels, and martensitic stainless steels. The author finds them to be highly reliable and simple to use.

Table 3 Beraha's sulfamic acid etchants

Reagent	Composition	Comments
1	100 mL water 3 g $K_2S_2O_5$ 1 g NH_2SO_3H	For cast iron, iron, carbon and alloy steels, manganese steels. Immerse up to 4 min. Good for 2–4 h. Discard when solution is yellow.
2	100 mL water 6 g $K_2S_2O_5$ 2 g NH_2SO_3H	Use as reagent 1, but faster acting
3	100 mL water 3 g $K_2S_2O_5$ 2 g NH_2SO_3H	Use as reagent 1, but faster acting. Immerse up to 90 s.
4	100 mL water 3 g $K_2S_2O_5$ 1 g NH_2SO_3H 0.5–1 g NH_4FHF	Use for martensitic stainless steels, tool steels, manganese steels. Immerse up to 3 min.

The sulfamic acid reagents are very useful for color metallography of iron-base alloys. Furthermore, they are easy to use and quite reliable. However, they do not seem to be used much. Figure 35 shows lath martensite in quenched and tempered 4118 alloy steel (the core of a carburized specimen) tint etched with Beraha's sulfamic reagent 1. Figure 36 shows the microstructure of a Hadfield manganese steel specimen that was solution annealed and tint etched with Beraha's sulfamic acid reagent 3. Figure 37 shows the fcc grain structure in an Fe-39%Ni magnetic alloy color etched with Beraha's sulfamic reagent 3. Figure 38 shows the decarburized surface of quenched and tempered 420 martensitic stainless steel tint etched with sulfamic reagent 4. Note that ferrite grains are present at the surface.

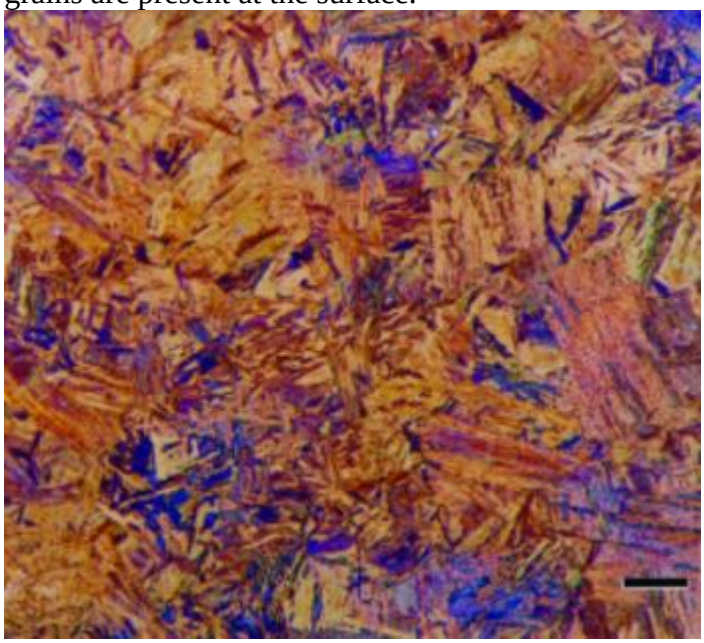

Fig. 35 Microstructure of the core of a carburized, heat treated 4118 alloy steel (Fe-0.2%C-0.8%Mn-0.5%Cr-0.12%Mo) tint etched with Beraha's sulfamic acid reagent (No. 1) and viewed with polarized light plus sensitive tint, revealing a lath martensite structure. The magnification bar is 20 μm long.

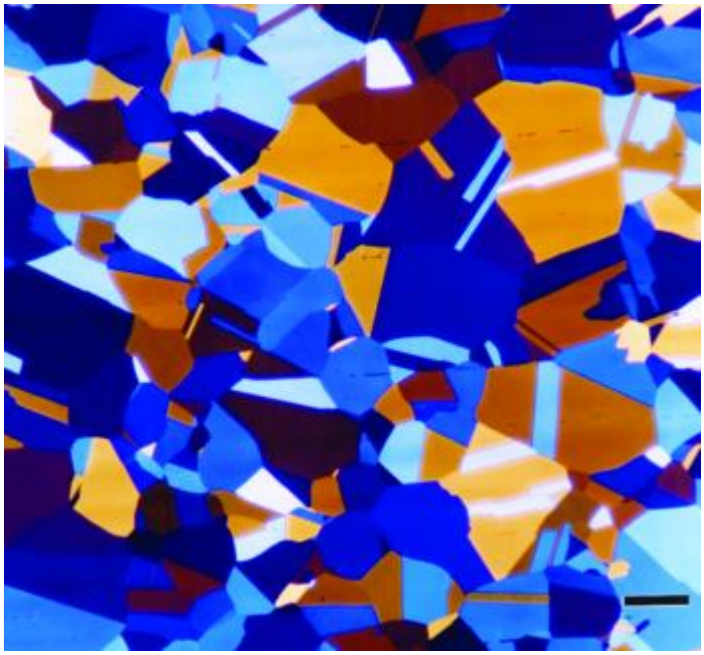

Fig. 36 Twinned austenitic grain structure of solution-annealed, wrought Hadfield manganese steel (Fe-1.12%C-12.7%Mn-0.31%Si) tint etched with Beraha's sulfamic acid reagent (No. 3) (100 mL water, 3 g potassium metabisulfite, and 2 g sulfamic acid) and viewed with polarized light plus sensitive tint. The magnification bar is 100 µm long.

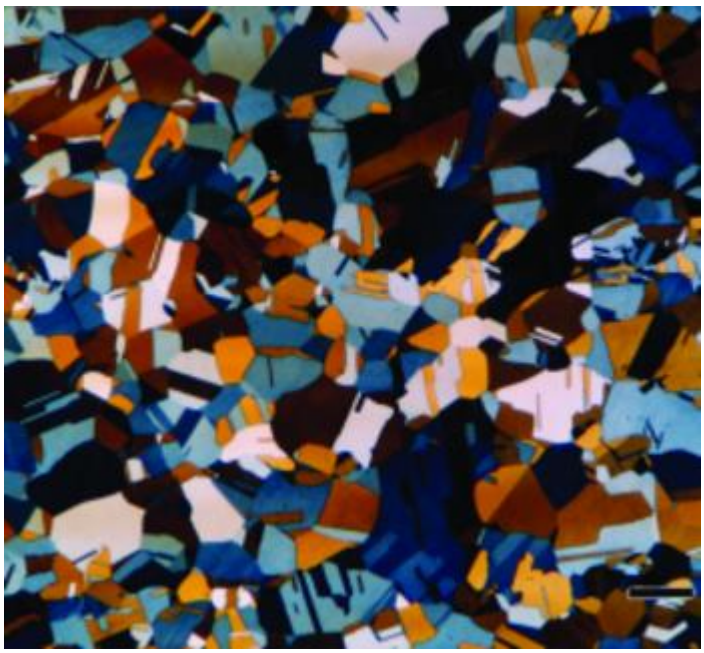

Fig. 37 Twinned austenitic grain structure of wrought, annealed Fe-39%Ni tint etched with Beraha's sulfamic acid solution (No. 3) and viewed with polarized light plus sensitive tint. The magnification bar is 100 µm long.

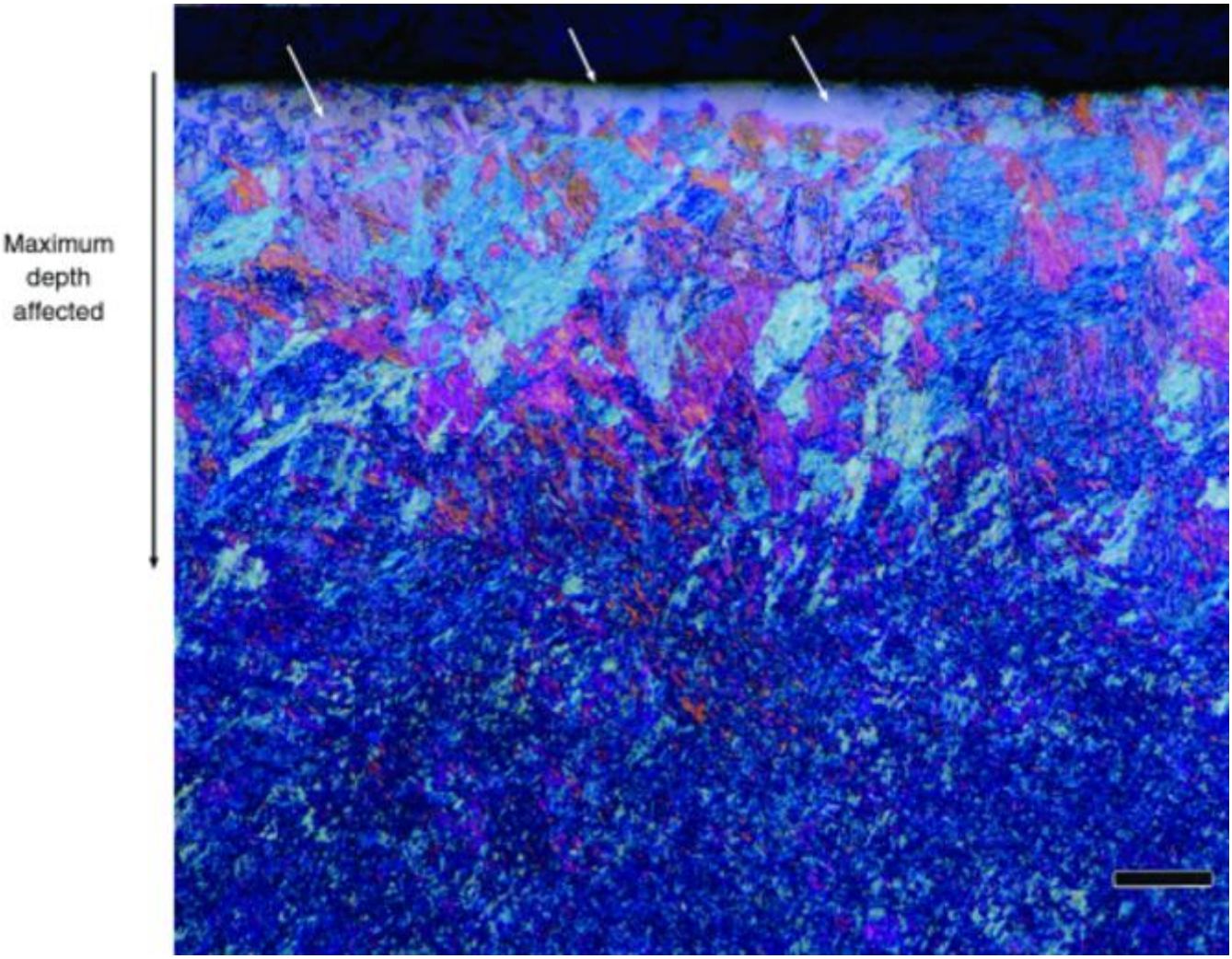

Fig. 38 Microstructure at the surface of a decarburized, hardened specimen of type 420 martensitic stainless steel (Fe-0.35%C-13%Cr) tint etched with Beraha's sulfamic acid reagent (No. 4) and viewed with polarized light plus sensitive tint. Note the free ferrite (arrows) at the surface (complete loss of carbon) and the change in the appearance of the martensite in the partial decarburized zone. The magnification bar is 100 μm long.

Beraha has also developed two rather specialized tint etches that deposit cadmium sulfide (CdS) or lead sulfide (PbS) films on the surfaces of steels and copper-base alloys (Ref 61, 62). These two etchants are quite useful. The CdS reagent is useful for carbon and alloy steels, tool steels, and ferritic, martensitic, and precipitation-hardenable stainless steels, while the PbS reagent does an excellent job on copper-base alloys and can be used to color sulfides in steels white (the specimen is pre-etched with nital, and the etch colors the darkened matrix, so that the white sulfides are visible). Table 4 lists these two reagents.

Table 4 Beraha's CdS and PbS reagents

Reagent	Composition	Comments
CdS	1000 mL water 240 g $Na_2S_2O_3 \cdot 5H_2O$ 30 g citric acid 20–25 g cadmium chloride Note: Cadmium sulfate or	For iron, steel, ferritic and martensitic stainless steel: Dissolve chemicals in the order shown. Age 24 h in a dark bottle in darkness at 20 °C (70 °F). Before use, filter 100 mL of the solution. Immerse 20–90 s. For steels, after 20–40 s, ferrite is colored red or violet; with longer times, ferrite is yellow or light blue, phosphide is brown, and carbides are violet or blue.

	cadmium acetate can be substituted for cadmium chloride.	For stainless steel: Immerse 60–90 s to color carbides red or violet-blue, matrix yellow; ferrite colors vary. Immersion >90 s colors the sulfides red-brown.
PbS	1000 mL water 240 g $Na_2S_2O_3 \cdot 5H_2O$ 30 g citric acid 24 g lead acetate	For copper and copper alloys: Dissolve in order given, and age as above. Do not filter stock solution. Immersion colors face-centered cubic matrix. For cast iron and steel: Pre-etch with nital. Add 0.2 g $NaNO_2$ to 100 mL of solution with vigorous stirring. Immerse until surface is colored as follows: ferrite, violet to blue; cementite, pale violet or blue; phosphide, yellow; and sulfides, white.

Figure 39 shows the microstructure of quenched and tempered 416 stainless steel, a grade designed for improved machinability. The CdS reagent has colored the martensitic matrix blue and brown but has not colored the delta ferrite. The sulfide inclusions (gray) were not attacked by this reagent. Figure 40 shows the microstructure of austempered ductile iron after isothermal heat treatment. The CdS reagent colored the ausferrite yellow, brown, and blue, while the retained austenite was not colored (it is tinted slightly by the sensitive tint filter). The nodule structure is visible in color due to the use of polarized light and sensitive tint. Figure 41 shows an as-cast specimen of Ni-Hard alloyed cast iron that was tint etched with Beraha's CdS reagent. Because retained austenite is the dominant matrix phase, the CdS reagent (it often acts as a complex reagent) colored the retained austenite light brown. The massive cementite particles are uncolored by the reagent but are tinted slightly by the sensitive tint filter. The plate martensite is colored light blue, dark blue, and shades of violet.

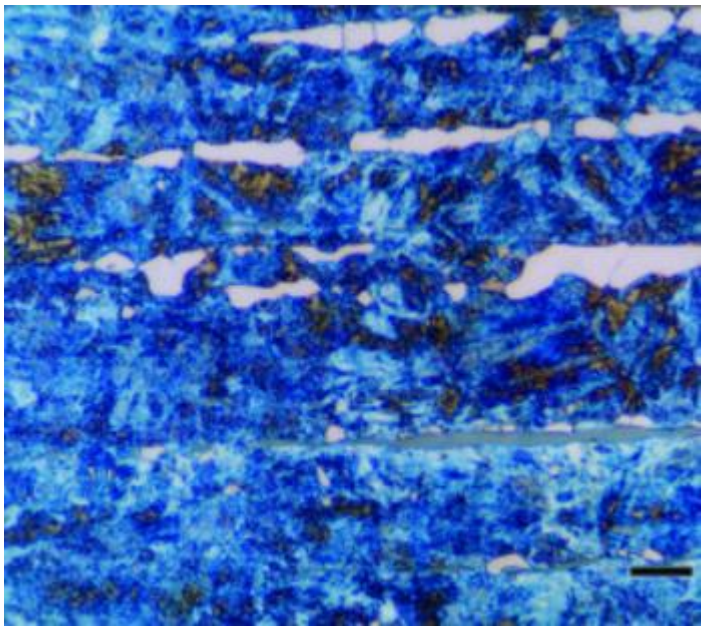

Fig. 39 Martensitic microstructure of Project 70 416 stainless steel (Fe->0.15%C->0.15%S-13%Cr) in the wrought heat treated condition (approximately 98 HRB) tint etched with Beraha's CdS reagent. The white grains are delta ferrite, and the elongated gray particles are manganese sulfides. The longitudinal direction is horizontal. The magnification bar is 200 μm long.

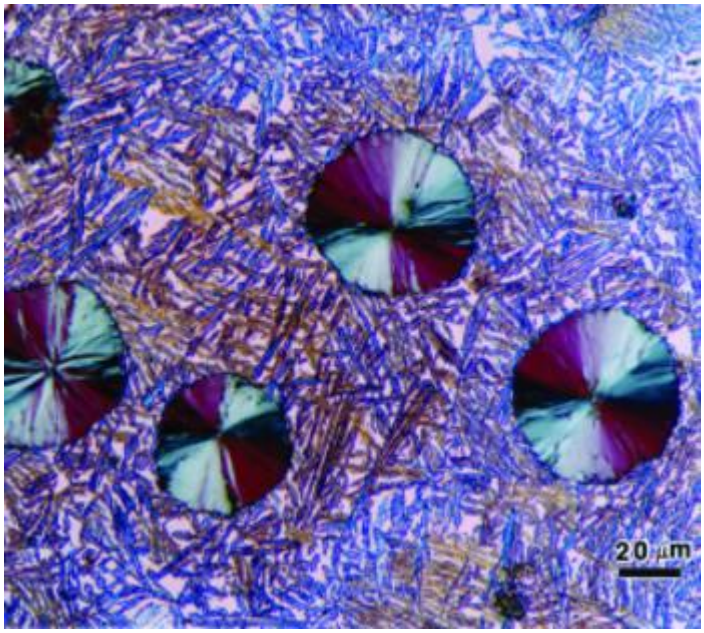

Fig. 40 Microstructure of austempered ductile iron tint etched with Beraha's CdS reagent. The microstructure shows large graphite nodules, ausferrite (blue and brown), and retained austenite (white) when viewed with polarized light plus sensitive tint.

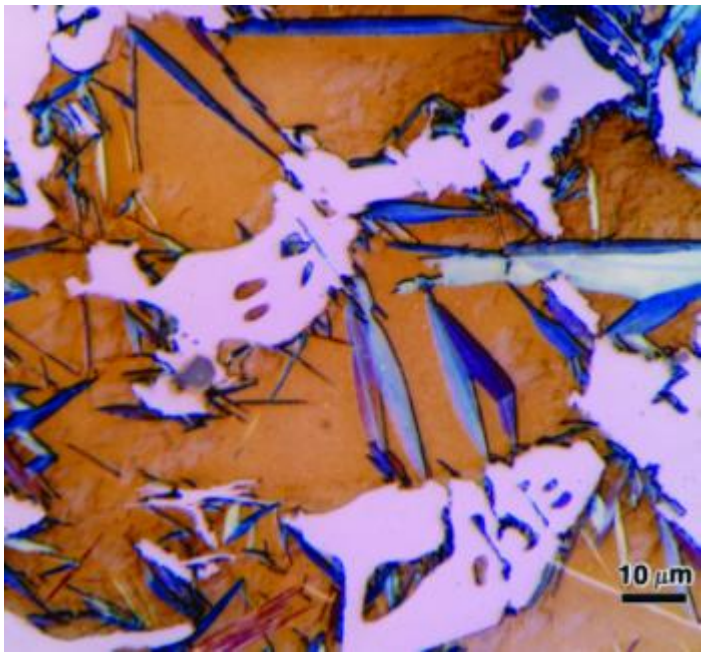

Fig. 41 As-cast Ni-Hard cast iron (Fe-2.98%C-0.64%Mn-0.85%Si-4.4%Ni-2.34%Cr) containing cementite (white), retained austenite (light brown), manganese sulfides (gray particles), and plate martensite needles (light blue and medium blue) after tint etching with Beraha's CdS reagent and viewing with polarized light plus sensitive tint.

Figure 42 shows Beraha's PbS reagent used to color the grain structure of the cartridge brass specimen previously shown in Fig. 24. The coloring is even more dramatic with the PbS reagent than with Klemm's III. Figure 43 shows the microstructure of aluminum brass (Cu-22%Zn-2%Al) that was cold drawn and then annealed at 750 °C (1380 °F). Tint etching with Beraha's PbS reagent gave a good rendering of the grain structure of the alloy.

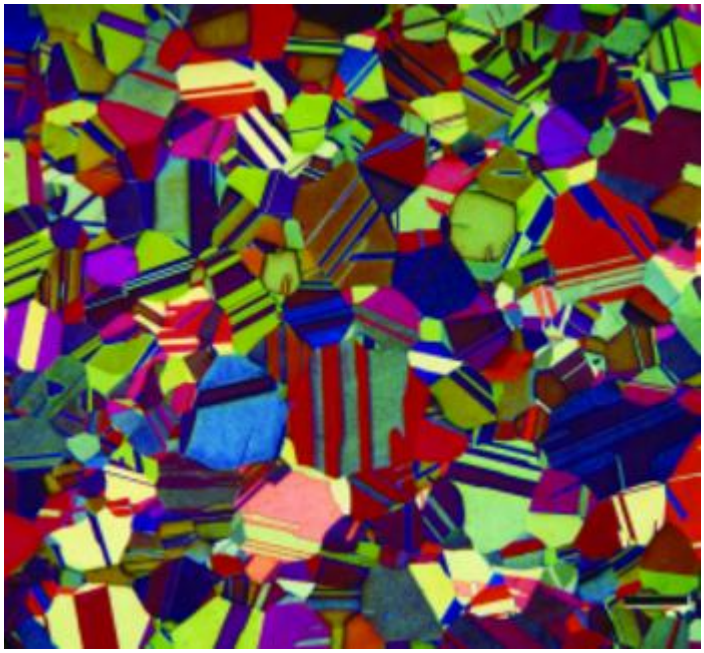

Fig. 42 Wrought cartridge brass (Cu-30%Zn) cold reduced 50% and annealed at 704 °C (1300 °F) for 30 min to produce a fully recrystallized, coarse-grained, equiaxed, face-centered cubic grain structure with annealing twins. Tint etched with Beraha's PbS. Viewed with polarized light and sensitive tint. The magnification bar is 200 µm long.

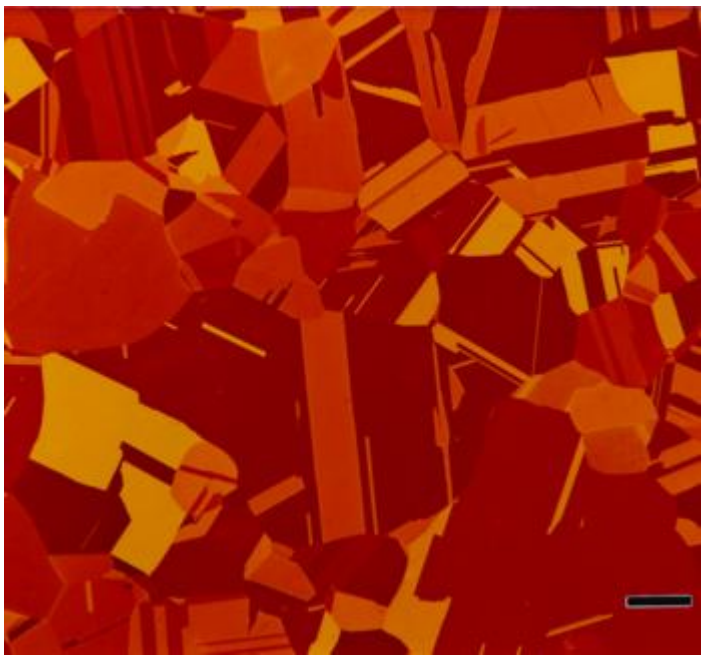

Fig. 43 Microstructure of aluminum brass (Cu-22%Zn-2% Al) that was cold drawn and annealed at 750 °C (1380 °F) after etching with Beraha's PbS reagent, revealing a coarse alpha face-centered cubic grain structure with annealing twins. The grain size is ASTM 0.8, and the hardness is 61 HV. The magnification bar is 200 µm long.

Sodium metabisulfite (Ref 66, 67, 70) has been used in a number of concentrations, from approximately 1 to 20 g per 100 mL water, as a safe, reliable, and useful color etch for irons and steels. It is not as strong a coloring etch as the others listed previously, and better results are usually obtained by viewing with polarized light and sensitive tint; but, this is not always a problem and sometimes can be an advantage. Figure 44 shows the microstructure of 5160 alloy steel that was austenitized at 830 °C (1525 °F) and then isothermally held at 538 °C (1000 °F) for 60 s (Fig. 44a) and 45 min (Fig. 44b) and then water quenched. The specimens were etched with aqueous 10% sodium metabisulfite and viewed with bright field (Fig. 44a) for the 60 s hold and with

polarized light plus sensitive tint (Fig. 44b) for the 45 min hold. After 60 s, only a small amount of upper bainite (colored white and blue—the blue areas are where the carbide has precipitated) has formed before the remaining austenite was quenched, forming martensite (colored light brown). However, after 45 min, more upper bainite has formed, and the remaining austenite transformed to very fine pearlite (colored violet, green, orange, and dark blue). It is hard to see the bainitic carbide regions, which were colored blue, against the slightly darker blues in the pearlite. Concentrations of 10 to 20% $Na_2S_2O_5$ have been used to color etch Hadfield manganese steels. Figure 45 shows martensite formed in the decarburized (<0.5% C) surface region of a wrought Hadfield manganese steel specimen etched with 10% sodium metabisulfite and viewed with polarized light plus sensitive tint.

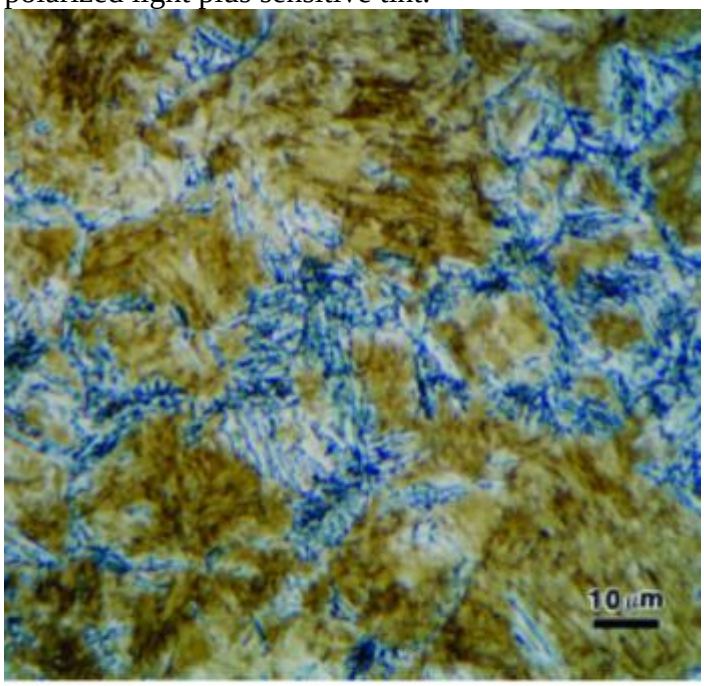

(a)

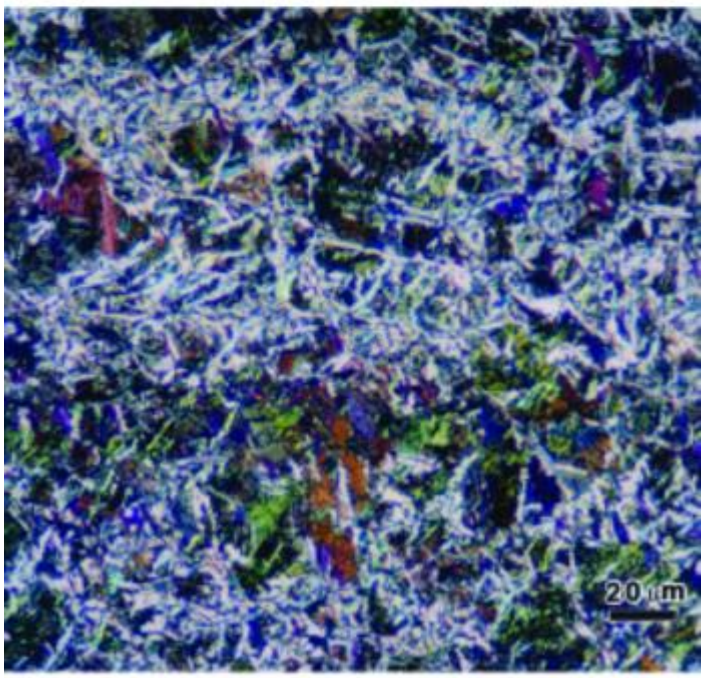

(b)

Fig. 44 Use of sodium metabisulfite to reveal structure in 5160 alloy steel (Fe-0.6%C-0.85%Mn-0.25%Si-0.8%Cr). (a) Upper bainite and as-quenched martensite in a specimen that was austenitized at 830 °C (1525 °F) for 30 min, isothermally held at 538 °C (1000 °F) for 60 s to partially transform the austenite, and then water quenched (untransformed austenite forms martensite). (b) Upper bainite and pearlite in a specimen held 45 min at 538 °C (1000 °F) to produce complete transformation. Both specimens etched

with aqueous 10% $Na_2S_2O_5$, which colored the martensite light brown, the upper bainite blue, and the pearlite various shades of orange, green, blue, and red.

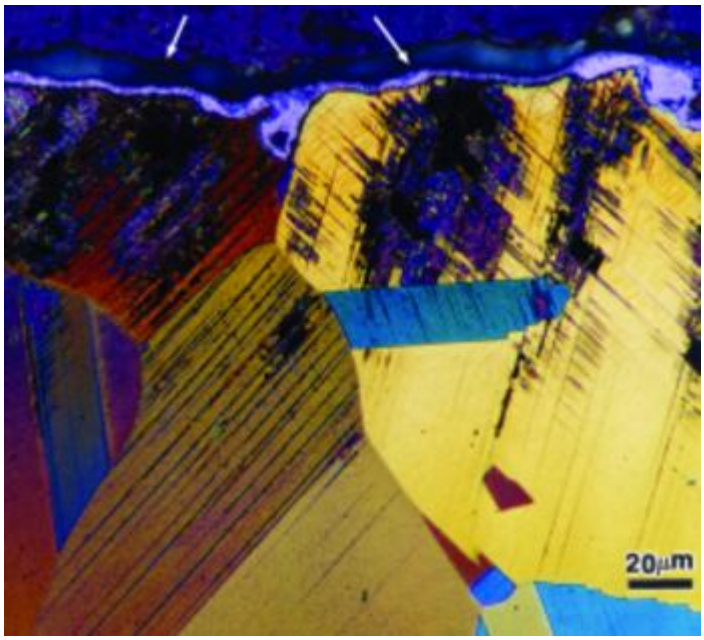

Fig. 45 Etching with 10% sodium metabisulfite revealed epsilon martensite at the surface of this hot-worked and solution-annealed specimen of Hadfield manganese steel. The arrows point to a substantial shrinkage gap between the phenolic mount and the specimen. The light-blue layer at the surface is iron oxide.

Comparison of Sulfide-Film-Forming Tint Etchants for Steels. As a comparison of these various sulfide-film-forming tint etchants for steels, Fig. 46(a) shows the microstructure of a low-carbon, high-strength, low-alloy steel in the as-rolled condition etched with nital. Segregation streaks were observed in this slab, and some segregated regions contained cracks. Bainite was observed in these streaks (some contained cracks), while the matrix was ferrite and pearlite. Figure 46(b) shows the specimen etched with Klemm's I, where the darkening of the ferrite grains is excessive, and there is poor contrast between the ferrite and the pearlite in the matrix and between the matrix and the segregate streak. Figure 46(c) shows the specimen etched with Beraha's version of Klemm's I. The coloring of the ferrite was less intense, and the structural elements in the matrix and in the streak are easily observed. Figure 46(d) shows the specimen etched with Beraha's sulfamic acid etch number 1. The coloring is less intense than with Klemm's I, and the streak is easily seen against the matrix, but the pearlite is hard to distinguish from the ferrite in the matrix. Figure 46(e) shows the specimen etched with 10% sodium metabisulfite, which yielded excellent contrast. The ferrite is not colored, except by the sensitive tint filter. The pearlite in the matrix is easily observed in the matrix, and the segregate streak stands out very well.

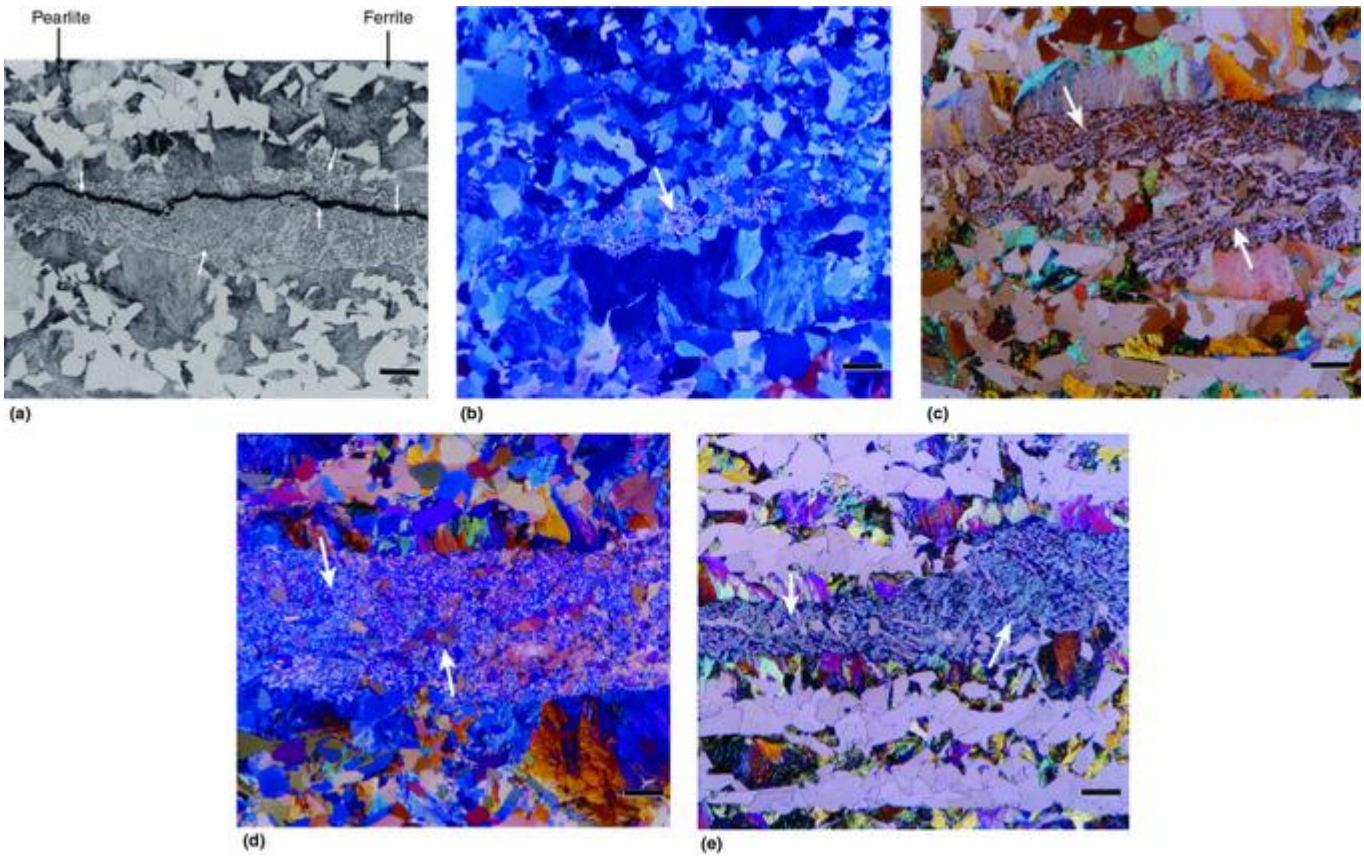

Fig. 46 Microstructures of as-rolled, continuously cast high-strength, low-alloy steel (Fe-0.19%C-1.24%Mn-0.37%Si-0.08%V). (a) Specimen containing segregation and some cracks (arrows) etched with 2% nital. The normal structure is ferrite and pearlite, but bainite was observed in the segregated regions (greater hardenability). Average hardness values were 180, 260, and 325 HV for the ferrite, pearlite, and bainitic segregation streaks, respectively. The magnification bar is 50 μm. (b) Specimen containing segregation etched with Klemm's I and viewed in polarized light plus sensitive tint. The normal structure is ferrite and pearlite, but bainite (arrow) is observed in the segregated regions. The segregated regions are hard to detect using Klemm's I, because it darkens the ferrite in the bainite as heavily as the matrix ferrite. The magnification bar is 50 μm long. (c) Specimen containing segregation etched with Beraha's 10/3 etch (10% $Na_2S_2O_3$ + 3% $K_2S_2O_5$) and viewed in polarized light plus sensitive tint. The normal structure is ferrite and pearlite, but bainite (arrows) is observed in the segregated regions. The magnification bar is 50 μm long. (d) Specimen containing segregation etched with Beraha's sulfamic acid etch (No. 1) (aqueous 3% $K_2S_2O_5$ + 1% H_2NSO_3H) and viewed with polarized light plus sensitive tint. The normal structure is ferrite and pearlite, but bainite (arrows) is observed in the segregated regions. The segregated regions are easier to detect with this etch than using Klemm's I, but 10% sodium metabisulfite and Beraha's 10/3 reagents were better, in this case. The magnification bar is 50 μm long. (e) Specimen containing segregation and some cracks (arrows) etched with aqueous 10% $Na_2S_2O_5$ (in polarized light plus sensitive tint). The magnification bar is 50 μm.

Reagents that Deposit Molybdate Films. Beraha developed two tint etchants that use molybdate ions in nitric acid (Ref 55, 62, 64). The MoO_4^{2-} contains molybdenum at a +6 valence state that can be reduced to a +4 valence state. Reduction can be partial with both the +6 and +4 ion valence levels present. This produces a blue color in the etchant, molybdenum blue. Partial reduction occurs at the local microcathodes on the specimen surface, leading to selective coloration. The sodium molybdate tint etchant for steels works well. It will color cementite in steels. Beraha also developed a molybdate-base tint etchant for aluminum alloys, although the author has not found that etchant easy to use. Table 5 lists the composition of the sodium molybdate reagent for steels.

Table 5 Beraha's sodium molybdate reagent

Composition	Comments
Stock solution: **1000 mL water** **10 g $Na_2MoO_4 \cdot 2H_2O$**	To color phosphide and cementite yellow-orange (ferrite unaffected): For cast iron: Add HNO_3 to the stock solution to bring the pH to 2.5–3.0. Immerse 45–60s. For low-carbon steel: Adjust pH and add 0.1 g NH_4FHF per 100 mL of stock solution. Immerse 45–60 s to color as above. For medium- and high-carbon steel: As above but add 0.3 g NH_4FHF per 100 mL of stock solution and immerse 30–45 s. To color carbides red-violet and ferrite yellow: For all steels: Add 0.5 g NH_4FHF and adjust the pH to 3–3.5. For low-carbon steels, immerse 20–30 s. For medium- and high-carbon steels, immerse 45–90 s. Beraha recommends pre-etching specimens with nital, but this is not absolutely necessary.

Figure 47 shows the microstructure of a hot-rolled Fe-1%C binary alloy (not a steel) that was tint etched with Beraha's sodium molybdate reagent. This reagent colors the cementite in carbon and low-alloy steels, as shown in this example. The arrow points to a grain-boundary cementite film. Figure 48 shows the microstructure of a spheroidize-annealed W1 carbon tool steel after etching with Beraha's sodium molybdate reagent. In this case, the ferrite is colored as well as the cementite.

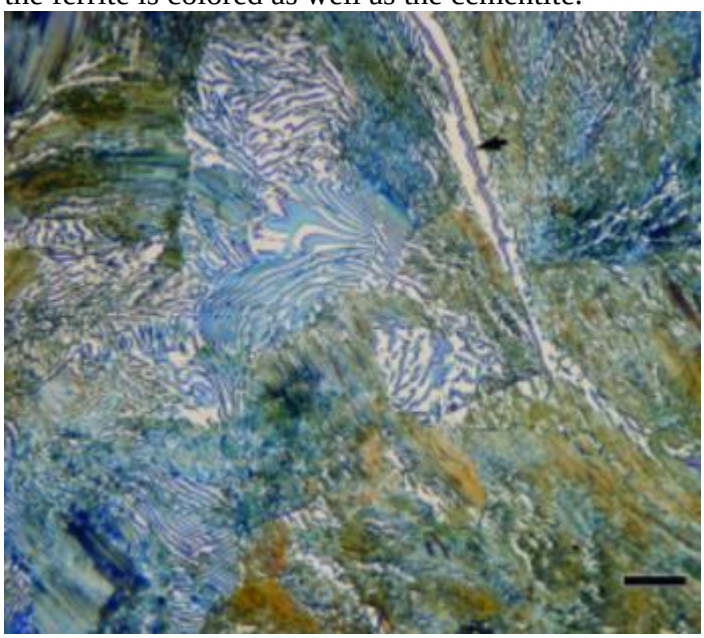

Fig. 47 Cementite in an as-hot-rolled Fe-1%C binary alloy revealed by tint etching with Beraha's sodium molybdate tint etch. The arrow points to proeutectoid cementite that precipitated in a prior-austenite grain boundary. The etch also colored the cementite in the pearlite. The specimen was viewed in bright-field illumination. The magnification bar is 20 µm long.

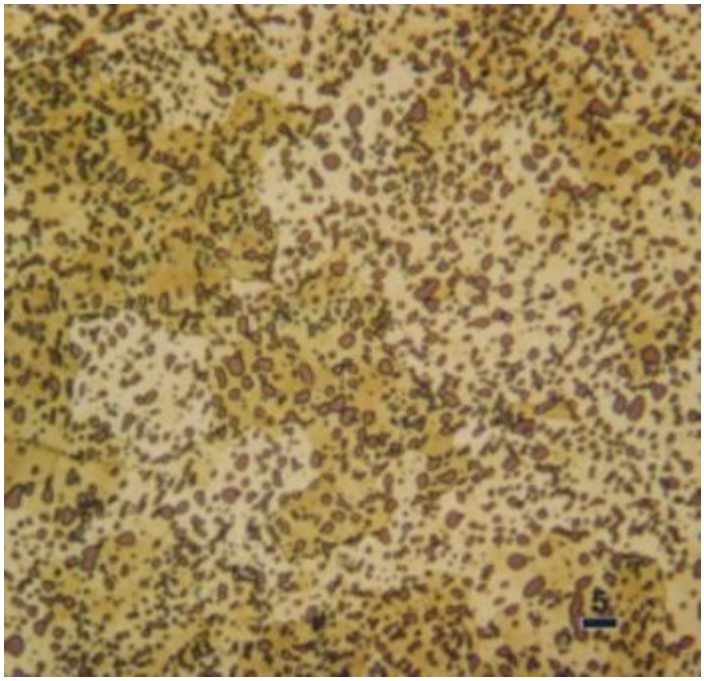

Fig. 48 Spheroidize-annealed microstructure of type W1 carbon tool steel (Fe-1.05%C-0.25%Mn-0.2%Si) etched with Beraha's sodium molybdate reagent, which colored both the cementite particles (brownish-red) and the ferrite matrix. The magnification bar is 5 μm long.

Reagents that Deposit Elemental Selenium. Beraha also developed tint etchants that deposit elemental selenium on the surface of steels and nickel- and copper-base alloys (Ref 59, 60). The selenium ion is reduced at the microcathodes on the surface of the specimens, producing coloration. It is recommended to use plastic tongs with these etchants. Selenic acid is a dangerous acid, and it should be handled with care. These etchants are quite useful. Compositions of seven selenic acid etchants and their characteristics are given in Table 6.

Table 6 Beraha's selenic acid reagents

Reagent	Composition	Comments
1	100 mL ethanol 2 mL HCl 1 mL selenic acid	For cast iron: Immerse 15–30 s. Colors phosphides red-brown or violet. Pre-etching is useful.
2	100 mL ethanol 1–2 mL HCl 0.5 mL selenic acid	For cast iron: (Use 2 mL HCl) Immerse 5–10 min to color phosphides blue or green and cementite red or violet (blue or green in white cast iron). For tool steels, martensitic or precipitation-hardenable stainless steels: Immerse 3–10 min if pre-etched and 5–15 min if as-polished to color carbides and nitrides orange, red-violet, or blue; ferrite, yellow or brown. Pre-etching is useful.
3	100 mL ethanol 10 mL HCl 3 mL selenic acid	For cast iron: Immerse up to 2 min to color phosphide red-brown or violet, while cementite and ferrite are unaffected. Pre-etching is useful.
4	100 mL	For austenitic stainless steel: Use 20–30 mL HCl for higher alloyed grades; do not

	ethanol 5–20 mL HCl 1 mL selenic acid	pre-etch. Immerse 1–10 min (depending on HCl content), until the surface is colored yellow or light brown to detect carbides and nitrides or longer (until the surface is colored orange-red). Delta ferrite is brighter than the matrix. Also good for maraging steels. Do not pre-etch.
5	100 mL ethanol 10–30 mL HCl 3 mL selenic acid	For nitrogen-base superalloys: Use 20 mL HCl to detect gamma prime, which is revealed after 1–3 min immersion (carbides colored red or violet). Immerse 3–15 min, until the surface is colored yellow to light brown to color carbides and nitrides red, violet, or blue.
6	100 mL ethanol 30–50 mL HCl 3 mL selenic acid	For higher alloy high-temperature alloys. Addition of 10–40 mL water may help increase etch rate. Use in same manner as number 5.
7	300 mL ethanol 2 mL HCl 0.5–1 mL selenic acid	For brass and copper-beryllium alloys: Store in a dark bottle. Pre-etch specimen for best results. Immerse until the surface is violet-blue to blue. Pre-etching is useful.

Figure 49 shows the microstructure of a chill-cast gray cast iron etched with Beraha's selenic acid reagent number 1. As it was chill cast, cementite formed in the chill region, along with regions containing small graphite flakes. The selenic acid etch colored the cementite reddish-orange, while the ferrite was not colored. Note the ferrite dendrites in the specimen. Beraha's selenic acid reagent will also color cohenite, $(Fe, Ni, Co)_3C$, a carbide found in certain meteorites (Ref 71). Figure 50 illustrates the use of Beraha's selenic acid reagent number 7 for copper-base alloys. The specimen is alpha-beta brass, Cu-40%Zn, that was hot extruded and cold drawn. The selenic acid reagent colors the twinned alpha phase nicely and produces a mottled-colored appearance in the beta phase. Thus, it acts as a complex tint etchant.

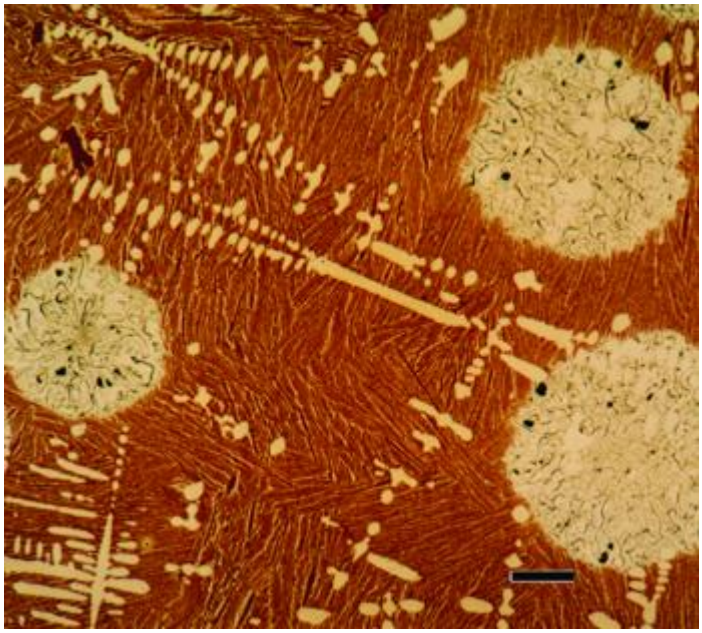

Fig. 49 Cementite colored in chill-cast hypoeutectic gray iron using Beraha's selenic acid reagent (No. 1) (bright field). The magnification bar is 100 µm long.

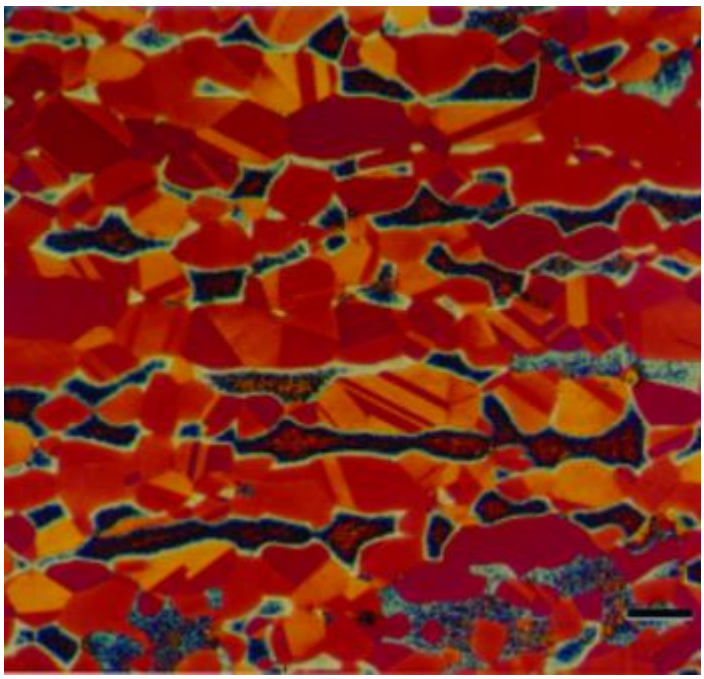

Fig. 50 Microstructure of hot-extruded and cold-drawn Muntz metal (Cu-40%Zn) tint etched with Beraha's selenic acid reagent (No. 7) for copper, which colored the twinned face-centered cubic alpha grain structure shades of yellow and red and nonuniformly colored the beta phase (note the light-blue border around the beta phase). Viewed in bright field. The magnification bar is 20 µm long.

Other Tint Etchants. There are many more tint etchants, but only a few that the author has tried and found to be useful are discussed. Lichtenegger and Blöch (Ref 69) developed an unusual reagent that will color austenite in duplex stainless steels, rather than ferrite (as nearly all others do). It consists of 20 g of ammonium bifluoride (NH_4FHF) and 0.5 g potassium metabisulfite ($K_2S_2O_5$) dissolved in 100 mL water. Although most chemicals, when dissolved in water, generate heat, that is, produce an exothermic reaction, ammonium bifluoride absorbs heat; that is, the reaction is endothermic. So, if the distilled water is at room temperature, the solution gets colder, and the ammonium bifluoride will not dissolve. Consequently, one must heat the water before dissolving the ammonium bifluoride. The etchant is generally used at approximately 25 to 30 °C (77 to 86 °F), rather than at room temperature. Weck (Ref 14) made several modifications of this etchant. Figure 51 shows the

microstructure of an as-cast duplex stainless steel, ASTM A 890, grade 5A, etched with the LB1 reagent, as it is generally called. It colored the austenite phase (no twins are observed, because this is an as-cast structure).

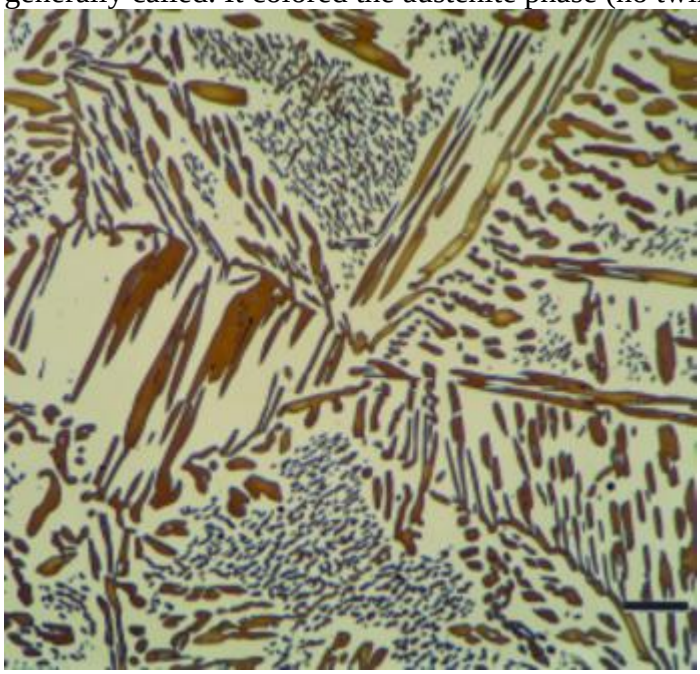

Fig. 51 Microstructure of as-cast ASTM A 890-5A duplex stainless steel (Fe-<0.03%C-<1.5%Mn-<1%Si-25%Cr-7%Ni-4.5%Mo-0.2%N) in the solution-annealed condition. Etched with LB1 (100 mL water, 20 g NH4FHF, and 0.5 g $K_2S_2O_5$). Austenite is colored, and ferrite is unaffected. Because it is as-cast, there are no annealing twins in the austenite. The magnification bar is 100 µm long.

Weck (Ref 12, 13, 14) developed a number of tint etchants, while using many of those shown in her research. While several have been developed for coloring aluminum, the most useful consists of 100 mL water, 4 g $KMnO_4$, and 1 g NaOH (similar to Groesbeck's carbide reagent, but 1 g instead of 4 g of NaOH). This tint etch is easier to use with cast aluminum alloys than with wrought alloys, but when successful, it will reveal the grain structure of many wrought aluminum alloys. Figure 52 shows the microstructure of the as-cast 1100 aluminum specimen shown in Fig. 16(d) after anodizing. Note that Weck's reagent reveals the segregation (coring) in the dendrites, while anodizing did not. Another example is shown in Fig. 53, where a cast 206 aluminum alloy was tint etched with Weck's reagent for aluminum. The intermetallic precipitates in the interdendritic regions can be easily seen, and the segregation within the dendrites is vividly revealed. Figure 54 shows the microstructure of wrought aluminum alloy 6061-T651 after etching with Weck's. It was successful in bringing up the grain structure, while other standard reagents failed. As a final example of the use of Weck's, Fig. 55 shows the interface between the base metal and the weld in a friction stir weld in alloy 2519.

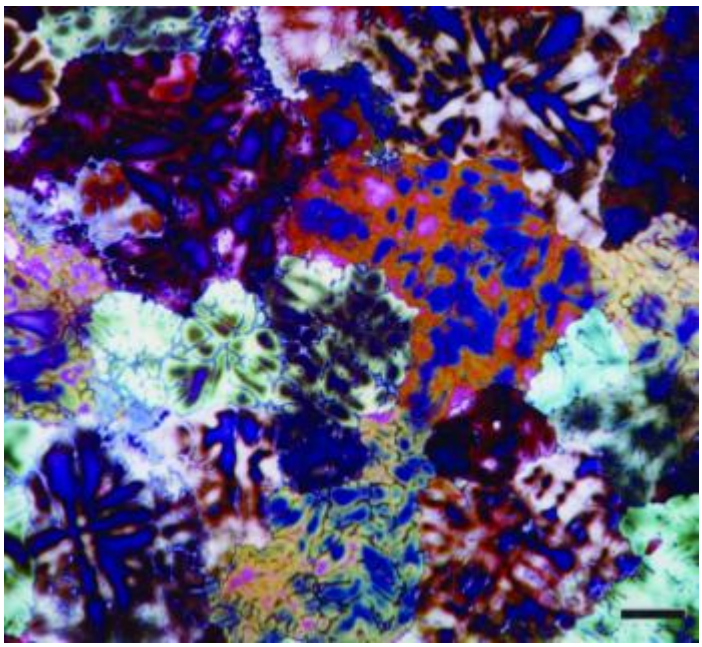

Fig. 52 As-cast (concast) 1100 aluminum (>99% Al) tint etched with Weck's reagent, revealing a dendritic solidification structure. Viewed with crossed polarized light plus sensitive tint. Magnification bar is 200 μm long.

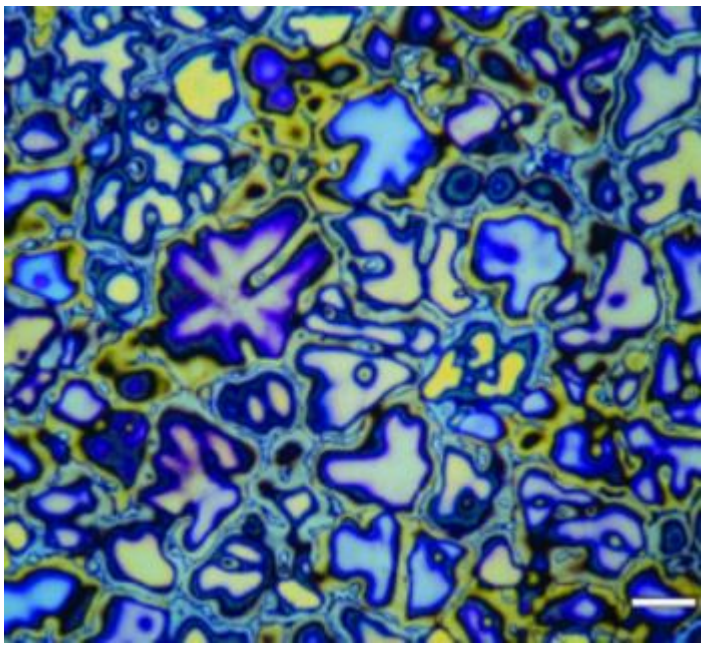

Fig. 53 As-cast 206 aluminum (Al-4.4%Cu-0.3%Mg-0.3%Mn) tint etched with Weck's reagent and viewed with crossed polarized light plus sensitive tint. See text. Magnification bar is 50 μm long.

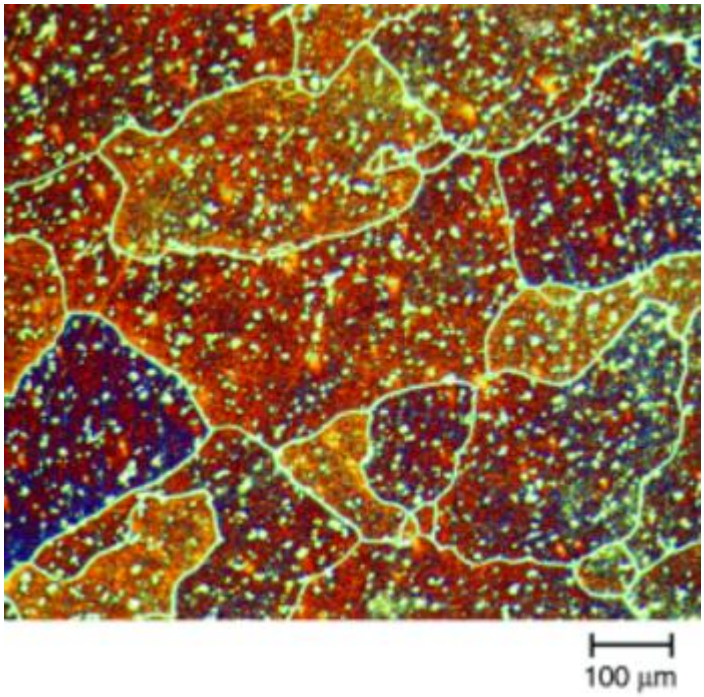

Fig. 54 Grain structure of 6061-T651 revealed by tint etching with Weck's reagent and viewing with polarized light plus sensitive tint. 200×

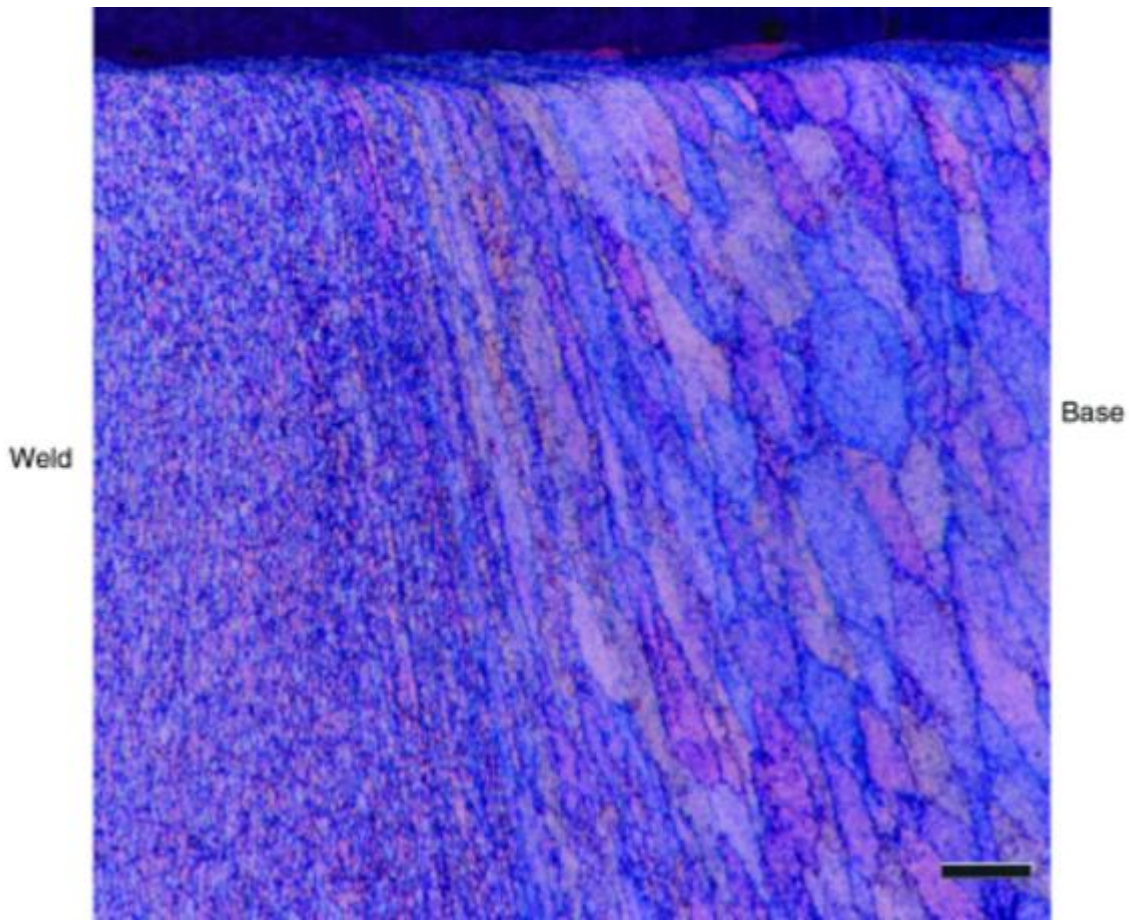

Fig. 55 Microstructure of a friction stir weld in 2519 aluminum (Al-5.8%Cu-0.3%Mn-0.3%Mg-0.06%Ti-0.1%V-0.15%Zr) etched with Weck's reagent and viewed with polarized light plus sensitive tint. Original at 100×. The magnification bar is 100 µm long.

Weck also developed several color etchants for titanium. Of them, one works better than the others, but it must be modified slightly. This reagent consists of 100 mL water, 50 mL ethanol, and 2 g ammonium bifluoride.

When the author has used this composition, small, white butterfly-shaped artifacts could be observed in the structure. Reducing the ethanol content to 25 mL (Ref 72) eliminates this problem, and good etch results are obtained. The solution colors the alpha phase in titanium and its alloys. Figure 56 shows commercial-purity titanium, ASTM F 67, grade 2, color etched with modified Weck's for titanium. Figure 57 shows the structure of as-cast Ti-6Al-4V color etched with Weck's reagent.

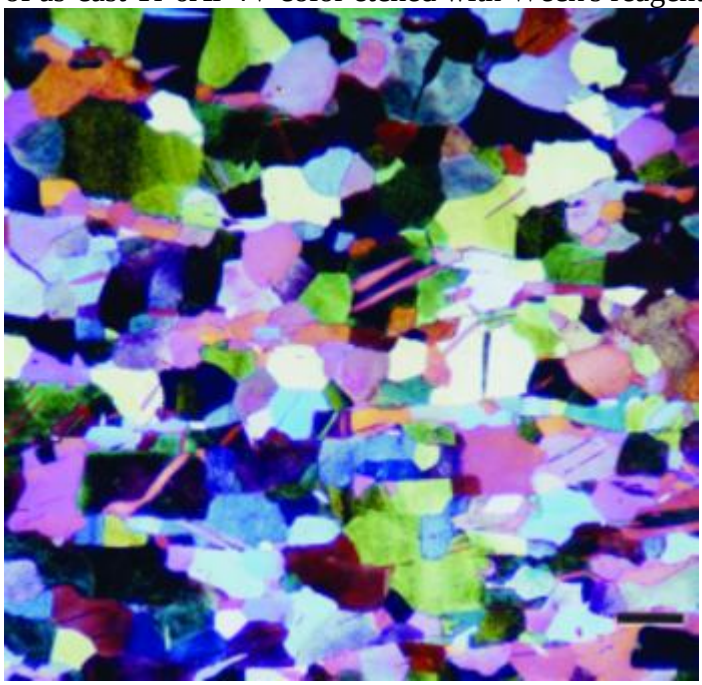

Fig. 56 Microstructure of commercially pure titanium (ASTM F 67, grade 2) (longitudinal plane) etched with modified Weck's reagent and viewed with crossed polarized light plus sensitive tint to reveal the grain structure. Magnification bar is 100 µm long.

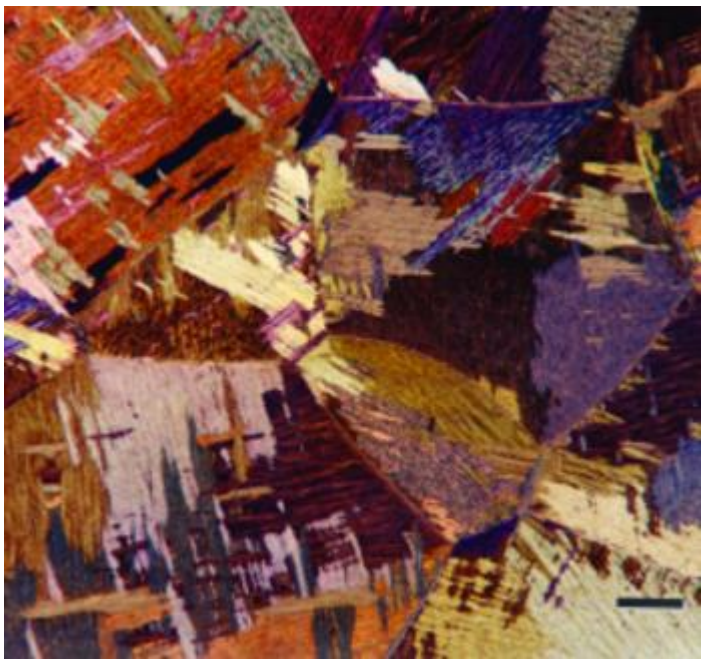

Fig. 57 Microstructure of as-cast Ti-6Al-4V etched with modified Weck's reagent, and viewed with polarized light to reveal a coarse basketweave alpha/beta matrix structure. The boundaries of several former beta grains can be seen. Magnification bar is 200 µm long.

Two etchants have been found useful for coloring theta phase, $AlCu_2$, in aluminum-copper alloys. The first was developed by Liénard (Ref 73, 74) and consists of 200 mL water, 1 g ammonium molybdate, and 6 g ammonium chloride. The specimen is immersed for up to 2 min, which colors the theta phase violet, as shown

in Fig. 58. The second etchant, of unknown origin, consists of a solution containing 20 mL water, 20 mL nitric acid, and 3 g ammonium molybdate. To use, add from 20 to 80 mL ethanol to this solution, and immerse until the surface is colored. This colors the theta blue, as shown in Fig. 59. Other solutions also exist for coloring theta or other constituents in aluminum alloys.

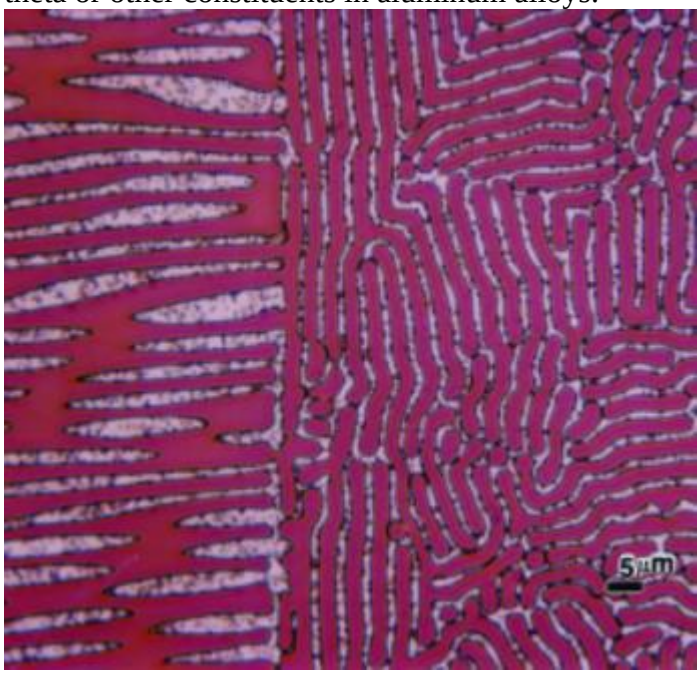

Fig. 58 Theta phase, $AlCu_2$, colored violet by Liénard's reagent in an as-cast Al-33%Cu eutectic alloy

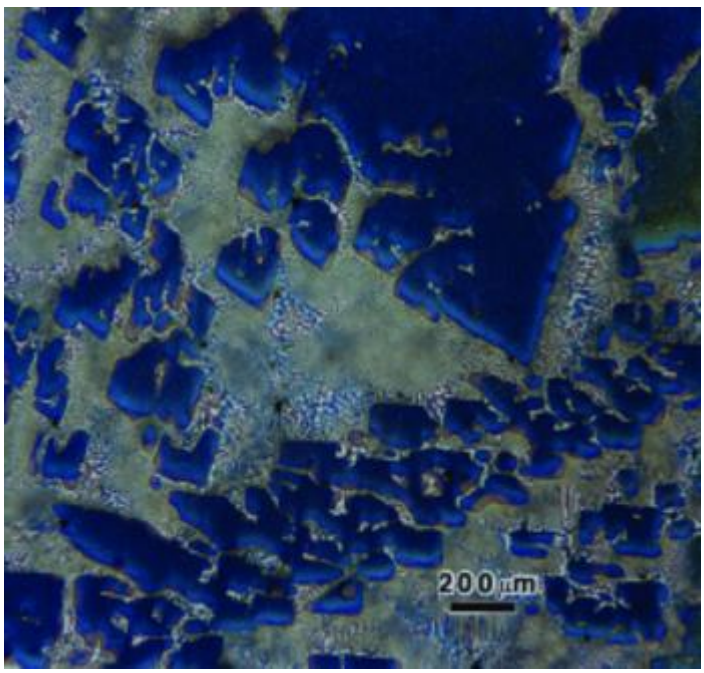

Fig. 59 Theta phase, $AlCu_2$, colored blue by an etchant consisting of water, nitric acid, and ammonium molybdate, diluted with ethanol (bright-field illumination) in a hypereutectic Al-45%Cu cast alloy

Several color etchants have been developed for molybdenum (Ref 10, 75, 76) and for tungsten (77). The author, however, has used an etchant for molybdenum that was developed at Oak Ridge National Laboratory (Ref 78) and consists of 70 mL water, 10 mL sulfuric acid, and 20 mL hydrogen peroxide (30% concentration). The specimen is immersed for 2 min. If the specimen is swabbed with the reagent, a color film will not form, but a grain-boundary flat etch will result. Figure 60 illustrates results with this reagent for pure molybdenum.

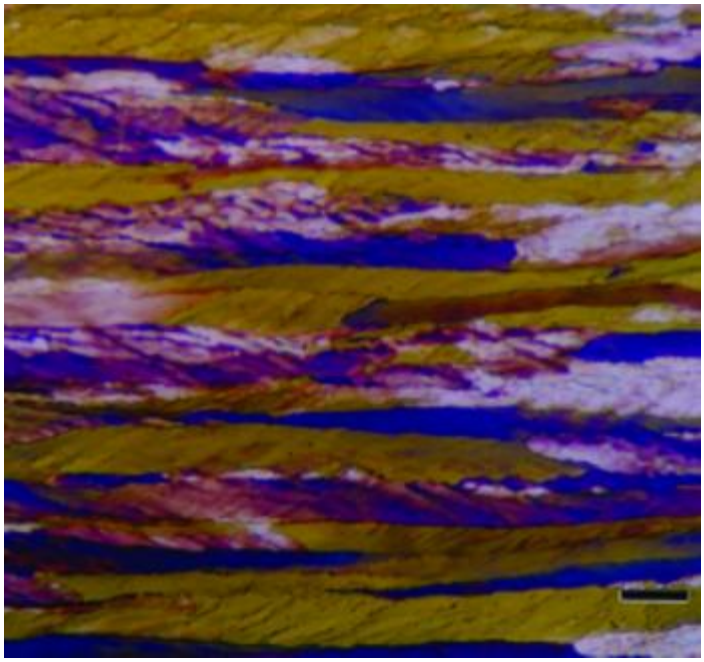

Fig. 60 Microstructure of wrought, nonrecrystallized pure molybdenum (longitudinal direction horizontal) tint etched with the Oak Ridge National Laboratory solution (90 mL water, 20 mL hydrogen peroxide [30% conc.], and 10 mL H_2SO_4) and viewed with polarized light plus sensitive tint, revealing highly elongated body-centered cubic alpha grains containing substantial deformation. The magnification bar is 20 μm long.

Thermal Methods to Produce Color

Although many textbooks state that heat tinting is not reproducible, the author's experience has been otherwise. Heat tinting is an almost universal method that can be applied to many metals and alloys. There are some restrictions. First, one must work with an unmounted specimen; otherwise, the polymeric mounting material will burn. Low-melting-point metals and alloys are unsuitable. If the heat tinting temperature will alter the microstructure, then the method should not be used. However, many metals and alloys can be successfully colored by heating them in air until a light oxide film forms on the surface. As the film grows, it will become thick enough to produce interference colors. When the surface reaches a visible color—generally, a red-violet color works well, but thinner films are often useful—remove the specimen from the furnace, and cool it back to room temperature. As with tint etching, polarized light and sensitive tint can improve the results. Heat tinting can also be quite selective, but the temperature must be kept low so as to not color everything. However, with practice, the best temperature can be determined for a particular alloy. Table 7 shows a listing of temperatures published in the literature for different metals and alloys. Figure 61 shows the structure of commercially pure titanium, ASTM F 67, grade 4, in the annealed condition after heat tinting, while Fig. 62 shows the structure of as-cast Ti-6Al-4V after heat tinting.

Table 7 Temperatures for heat tinting

Metal	Temperature and time in air	Comments
Beryllium	900 °C (1650 °F) for 30 min	Grain boundaries are revealed at a slightly higher temperature.
Cast iron	400 °C (750 °F) for 20 min	Fe_3C, blue; Fe_3P, cream
Stainless steel	500–700 °C (930–1290 °F) for ≤20 min	Gamma colored before sigma and sigma before carbides. 650 °C (1200 °F) for 20 min gave: γ, blue-green; α, light cream; σ, orange; and carbides, not colored
Nickel	600 °C (1110 °F) for 5–	…

	10 min	
Rare earth metals	200 °C (390 °F) for minutes to hours	…
Titanium	400–700 °C (750–1290 °F) for up to 30 min	…
Zirconium	400 °C (750 °F) for 5 min	…
Sintered carbides	300–600 °C (570–1110 °F) for 5 min	Cobalt binder colored brown at low temperatures, up to approximately 400 °C (750 °F); WC starts to color at approximately 540 °C (1000 °F). Time affects colors.

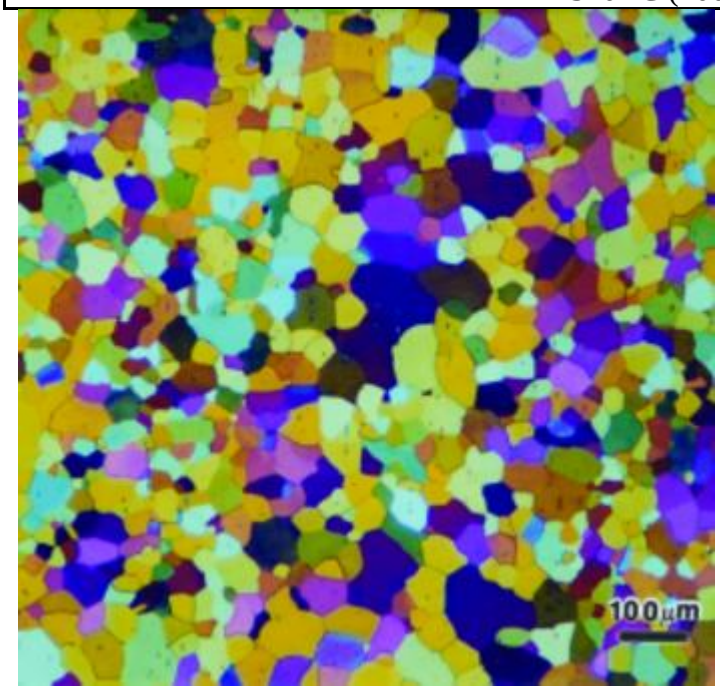

Fig. 61 Microstructure of commercially pure titanium (ASTM F 67, grade 4) (transverse plane, specimen was annealed) heat tinted on a laboratory hot plate, and viewed with polarized light plus sensitive tint to reveal the grain structure.

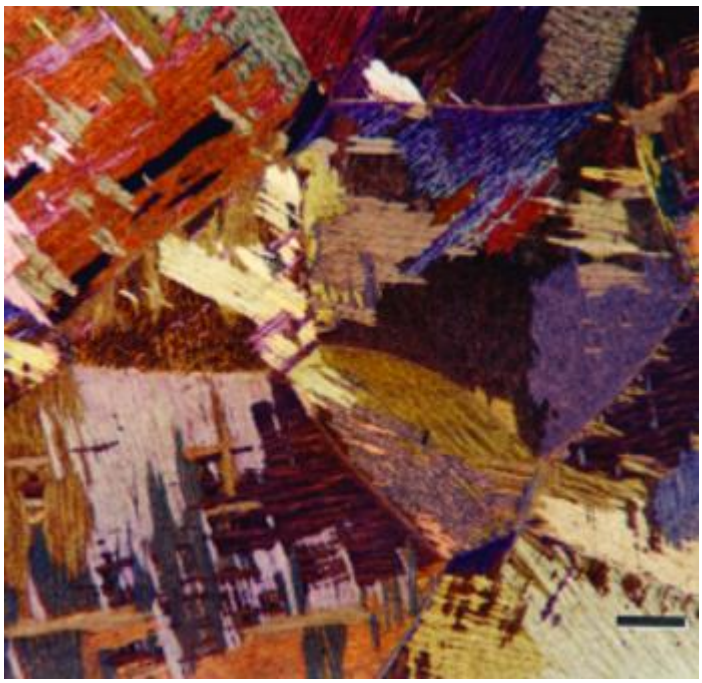

Fig. 62 Microstructure of as-cast Ti-6Al-4V heat tinted on a laboratory hot plate, and viewed with polarized light plus sensitive tint to reveal the coarse alpha-beta basketweave matrix structure. Magnification bar is 100 µm long.

Vapor Deposition Methods to Produce Color

In 1960, Pepperhoff showed that microstructures could be revealed without etching but by vacuum deposition of a suitable material onto the prepared surface. The deposition produced a thin, low-absorption, dielectric film with a high refractive index. Small differences in reflectivity usually exist between microstructural constituents, and therefore, they are invisible or barely visible in the as-polished condition. In such cases, Nomarski DIC may reveal the structure well but not always. The Pepperhoff method produces a thin interference layer in a different manner than by chemical etching or heat tinting, but the end results are similar. Contrast between two constituents is maximized when a film is produced using a material with a high refractive index. Suitable materials include ZnTe, ZnSe, TiO_2, and ZnS. The method is described in depth by Bühler and Hougardy (Ref 79). Reactive sputtering is a similar technique and equally useful.

References cited in this section

7. E. Beraha and B. Shpigler, *Color Metallography*, American Society for Metals, 1977

10. G.F. Vander Voort, *Metallography: Principles and Practice*, McGraw-Hill Book Co., 1984; reprinted by ASM International, 1999

12. E. Weck and E. Leistner, *Metallographic Instructions for Colour Etching by Immersion, Part I: Klemm Colour Etching,* Vol 77, D.V.S. Verlag GmbH, Düsseldorf, 1982

13. E. Weck and E. Leistner, *Metallographic Instructions for Colour Etchants by Immersion, Part II: Beraha Colour Etchants and Their Different Variants,* Vol 77/II, D.V.S. Verlag GmbH, Düsseldorf, 1983

14. E. Weck and E. Leistner, *Metallographic Instructions for Colour Etching by Immersion, Part III: Non-Ferrous Metals, Cemented Carbides and Ferrous Metals, Nickel-Base and Cobalt-Base Alloys,* Vol 77/III, D.V.S. Verlag GmbH, Düsseldorf, 1986

20. P. Lacombe and L. Beaujard, Anodic Oxidation Regarded as a Means for the Study of Surface Conditions of Aluminum and its Alloys, *Journees des Etats de Surface [Comptes Rendus],* 23–26 Oct 1945 (Paris), 1946, p 44

21. A. Hone and E.C. Pearson, Grain Orientation in Aluminum Revealed by Anodic Film, *Met. Prog.,* Vol 53, March 1948, p 363

22. L.J. Barker, Revealing the Grain Structure of Common Aluminum Alloy Metallographic Specimens, *Trans. ASM,* Vol 42, 1950, p 347

23. A. Hone and E.C. Pearson, A New Anodic-Film Method for Studying Orientation in Aluminum, *Met. Prog.,* Vol 58, Nov 1950, p 713

24. H.G. Cole and W.J.D. Brooks, A Simple Anodizing Process for Revealing the Grain Structure of Aluminum Alloys, *Metallurgia,* Vol 50, Aug 1954, p 97

25. H.S. Yang, An Electrolytic Etching/Anodizing Method for Revealing the Microstructures of Common Aluminum Alloys, *Pr. Metallogr.,* Vol 27, 1990, p 539

26. E. Ence and H. Margolin, Phases in Titanium Identified by Cumulative Etching, *J. Met.,* March 1954, p 346

27. R.H. Hiltz, Jr., "Metallographic Methods: Color Staining of Titanium and Its Alloys," Watertown Arsenal Laboratory Report WAL 132/24, 20 April 1956

28. R.S. Crouse, "Identification of Carbides, Nitrides and Oxides of Niobium and Niobium Alloys by Anodic Staining," Oak Ridge National Laboratory Report ORNL-3821, July 1965

29. M.L. Picklesimer, Anodizing for Controlled Microstructural Contrast by Color, *Microscope,* Vol 15, Oct 1967, p 472

30. B.W. Mott and H.R. Haines, Examination of Metals Under Polarized Light, Part II: Applications, *Research,* Vol 4, 1951, p 63

31. R.C. Gikfins, *Optical Microscopy of Metals,* American Elsevier Publishing Co., Inc., 1970, p 122

32. D.H. Woodard, Stages in the Deformation of Monel Metal as Shown by Polarized Light, *Trans. AIME,* Vol 185, 1949, p 722

33. E.C.W. Perryman and J.M. Lack, Examination of Metals by Polarized Light, *Nature,* Vol 167 (No. 4247), 1951, p 479

34. R.E. Reed-Hill, C.R. Smeal, and L. Lee, The Examination of fcc Metals with Polarized Light, *Trans. AIME,* Vol 230, Aug 1964, p 1019

35. W. Ischewsky, New Micrographic Structures on the Surface of Heat Treated Steels, *Stahl Eisen,* Vol 23, 1903, p 120

36. L. Loskiewicz, A Study of the Time Factor in the Etching of Iron-Carbon Alloys, *Rev. Métall.,* Vol 19, 1922, p 681

37. T. Murakami, The Structure of Iron-Carbon-Chromium Alloys, *Sci. Rep. Tohoku Imperial Univ.,* Vol 7 (Part I), 1918, p 217

38. T. Murakami, Note on the Structure of Iron-Carbon-Chromium Alloys, *J. Iron Steel Inst. Jpn.,* Vol 100 (No. 2), 1919, p 445

39. E.C. Groesbeck, Solutions for Carbides, etc., in Alloy Steels, appendix to report of Committee E-4 on Metallography, *Proc. ASTM,* Vol 26 (Part I), 1926, p 569

40. E.C. Groesbeck, Metallographic Etching Reagents, Part III: For Alloy Steels, *U.S. Bureau of Standards Scientific Papers*, S518, 1925, p 527

41. J. Malette, Color-Producing Reactions for Microscopic Examination of Carbon Steels, *Comptes Rendus,* Vol 201, 1935, p 1385

42. L. Beaujard, New Reagents for Revealing the Micrographic Structure of Steels by the Formation of Colored Films, *Comptes Rendus,* Vol 233, 1951, p 653

43. L. Beaujard and J. Tordeux, The Use of Sodium Bisulfite as an Etching Solution for Ferritic Steels, *Comptes Rendus,* Vol 235, 1952, p 1304

44. L. Beaujard, Micrographic Coloring Reagents for Iron and Steels, *Rev. Métall.,* Vol 49, July 1952, p 531

45. L. Beaujard, Color Etching of Iron and Steel, *Met. Treat. Drop Forg.,* Nov 1952, p 499

46. P Lacombe and M. Mouflard, The Application of Color Metallography by Formation of Very Thin Epitaxial Layers with Interference Colors for the Study of Aluminium, Iron and Copper, *Métaux-Corros.-Ind.,* No. 340, Dec 1953, p 471

47. L. Beaujard and J. Tordeux, A New Sodium Bisulfite Reagent for the Micrographic Investigation of Steels, *Rev. Métall.,* Vol 52, Sept 1955, p 750

48. B.V. Guellard, A New Etching Reagent for Steel and Cast Iron, *Metallurgia,* Vol 54, Aug 1956, p 93

49. J.R. Vilella and W.F. Kindle, Sodium Bisulfite as an Etchant for Steel, *Met. Prog.,* Vol 76, Dec 1959, p 99

50. H. Klemm, Color Etching of the Fine Structure of Metals with Sodium Thiosulfate, *Metallkundliche,* Vol 45, Verlag Technik Berlin, 1952

51. H. Klemm, Uses of Sodium Thiosulfate (Klemm's Reagent) as an Etchant, *Pr. Metallogr.,* Vol 5, April 1968, p 163

52. E. Beraha, Metallographic Reagent for the Identification of Cementite in Iron and Steel, *J. Iron Steel Inst. Jpn.,* Vol 203, May 1965, p 454

53. E. Beraha, New Metallographic Reagents for Stainless Steel and Heat-Resisting Alloys, *J. Iron Steel Inst. Jpn.,* Vol 204, March 1966, p 248

54. E. Beraha, Two New Metallographic Reagents, *Met. Prog.,* Vol 90, Sept 1966, p 135

55. E. Beraha, Etching Cast Iron, *Met. Prog.,* Vol 90, Oct 1966, p 13

56. E. Beraha, New Metallographic Reagent for Iron, Carbon-Alloy, and Tool Steels, *J. Iron Steel Inst. Jpn.,* Vol 205, Aug 1967, p 866

57. E. Beraha, Metallographic Reagents for the Determination of Chemical and Physical Heterogeneity in the Microstructure of Iron and Steels, *Pr. Metallogr.,* Vol 4, Aug 1967, p 416

58. E. Beraha, Staining Metallographic Reagent for Stainless Steels, Corrosion and Heat-Resisting Alloys, *Pr. Metallogr.,* Vol 5, Aug 1968, p 443

59. E. Beraha, Staining Metallographic Reagent for Detection of Phosphides, Carbides and Nitrides in Iron, Steel, Tool Steels, Stainless Steel and Heat-Resisting Alloys, *Pr. Metallogr.,* Vol 5, Sept 1968, p 501

60. E. Beraha, Staining Metallographic Reagent for Copper-Base Alloys, *Pr. Metallogr.,* Vol 7, March 1970, p 131

61. E. Beraha, Metallographic Reagents Based on Sulfide Films, *Pr. Metallogr.,* Vol 7, May 1970, p 242

62. E. Beraha, Staining Metallographic Reagents for Cast Iron, *Microstructures,* Vol 2, June/July 1970, p 23

63. E. Beraha, Staining Metallographic Reagents for Cast Iron, Steels, Tool Steels, Manganese Steels, and Ferritic and Martensitic Stainless Steel, *Pr. Metallogr.,* Vol 8, Sept 1971, p 547

64. E. Beraha, Metallographic Reagents Based on Molybdate Solutions, *Pr. Metallogr.,* Vol 11, May 1974, p 271

65. A.O. Benscoter, J.R. Kilpatrick, and A.R. Marder, An Etching Technique for Fe-Ni Massive Martensite, *Pr. Metallogr.,* Vol 15, Dec 1968, p 694

66. A.O. Benscoter, J.R. Kilpatrick, and A.R. Marder, Sulfate and Sulfite Compounds as Etchants for Low-Carbon Iron Martensite, *IMS Proceedings,* 1969, p 37

67. J.R. Kilpatrick, A.O. Benscoter, and A.R. Marder, Tint Etching Improves Resolution and Contrast of Microstructures, *Met. Prog.,* Dec 1971, p 79

68. J.R. Kilpatrick, A New Etching Technique for Galvanneal and Hot Dipped Galvanized Coatings, *Pr. Metallogr.,* Vol 28, Dec 1991, p 649

69. P. Lichtenegger and R. Blöch, Colour Etching of High Alloy Steels, *Pr. Metallogr.,* Vol 12, 1975, p 567

70. G.F. Vander Voort, Etching Isothermally Treated Steels, *Heat Treat. Prog.,* Vol 1, April/May 2001, p 25–32

71. G.F. Vander Voort, Metallography of Iron Meteorites, *Adv. Mater. Process.,* Vol 159, Feb 2001, p 37, 40, 41

72. J.M. Radzikowska, The Foundry Research Institute, Kraków, Poland, personal communication, 2000

73. P. Liénard and C. Pacqué, Analysis of the Selective Coloring Mechanism for Identification of Different Phases in Al-Si-Cu Foundry Alloys, *Hommes Fonderie,* No. 126, June/July 1982, p 27–35

74. P. Liénard, Etching of Aluminium Alloys, *Structure,* Vol 8, June 1984, p 17–20

75. R. Hasson, Metallography of Molybdenum in Color, *Microscope,* Vol 16, 1968, p 329–334

76. R. Hasson, An Improved Orientation-Dependent Chemical Anodizing Color Reagent for Molybdenum, *Microscope,* Vol 22, 1974, p 317–322

77. S. Lehwald et al., An Orientation-Sensitive Colour-Etching Method for Polycrystalline Tungsten, *Pr. Metallogr.*, Vol 9, Sept 1972, p 510–515

78. R.S. Crouse, Oak Ridge National Laboratory, personal communication, 1982

79. H.E. Bühler and H.O. Hougardy, *Atlas of Interference Layer Metallography*, Deutsche Gesellschaft für Metallkunde, Oberursel, Germany, 1980

G.F. Vander Voort, Color Metallography, *Metallography and Microstructures*, Vol 9, *ASM Handbook*, ASM International, 2004, p. 493–512

Conclusions

Color can be an extremely useful tool for examining the microstructure of many metals and alloys as well as other materials. Natural color is very limited but useful when it is present. Optical methods can introduce color with good results. Dark-field illumination has some limited applications. Polarized light, perhaps aided with a sensitive tint filter (always examine the structure with and without the sensitive tint filter, and a variable sensitive tint filter is very useful), is useful with metals and alloys that have noncubic crystal structures. However, some of these metals respond weakly to polarized light, and certain etchants may aid the response. Also, some cubic metals and alloys may respond to polarized light and sensitive tint after being etched.

This article has listed compositions of tint etchants that produce good results, and illustrations of these results were given. It is important to remember that the specimen must be properly prepared before using a tint etchant. Any residual preparation damage that is present and may be virtually invisible with a normal etch will be highly visible after color etching, and this will impair results. However, color etchants do reveal information that cannot be obtained with standard black-and-white etchants. First, they usually reveal grain structures much more fully than traditional etchants. Second, in single-phase structures, the degree of preferred crystallographic orientation can be gaged by looking at the range of colors produced. If a wide range of colors is observed, then there is a random orientation of the grains. If a narrow range of colors is obtained, then there may be a preferred texture present. Color etching cannot tell one the nature of the preferred orientation. That can be determined by x-ray diffraction methods. Color etchants reveal segregation and residual deformation quite well. Further, microprobe analyses can be conducted on a tint-etched surface, because the film will not interfere with the chemical analysis.

G.F. Vander Voort, Color Metallography, *Metallography and Microstructures*, Vol 9, *ASM Handbook*, ASM International, 2004, p. 493–512

Color Metallography

George F. Vander Voort, Buehler Ltd.

References

1. A. Portevin, Colored Films in Micrography, *Met. Prog.*, Vol 36, Dec 1939, p 761

2. R.P. Loveland, Metallography in Color, *ASTM Bull.,* May 1944, p 19

3. W.D. Forgeng, Color Metallography, *Iron Age,* Vol 162 (No. 16), 14 Oct 1948, p 130

4. *Symposium on Metallography in Color,* STP 86, ASTM, 1949

5. H. Yakowitz, Some Uses of Color in Metallography, *Applications of Modern Metallographic Techniques,* STP 480, ASTM, 1970, p 49

6. R.S. Crouse, R.J. Gray, and B.C. Leslie, Applications of Color in Metallography and Photography, *Interpretive Techniques for Microstructural Analysis,* Plenum Press, 1977, p 43

7. E. Beraha and B. Shpigler, *Color Metallography,* American Society for Metals, 1977

8. H. Gahm and F. Jeglitsch, Color Methods and Their Application in Metallography, *Met. Prog.,* Aug 1981, p 48

9. H. Gahm and F. Jeglitsch, *Microstructural Science,* Vol 9, Elsevier North Holland, Inc., 1981, p 65

10. G.F. Vander Voort, *Metallography: Principles and Practice,* McGraw-Hill Book Co., 1984; reprinted by ASM International, 1999

11. G.F. Vander Voort, Tint Etching, *Met. Prog.,* Vol 127, (No. 4), March 1985, p 31

12. E. Weck and E. Leistner, *Metallographic Instructions for Colour Etching by Immersion, Part I: Klemm Colour Etching,* Vol 77, D.V.S. Verlag GmbH, Düsseldorf, 1982

13. E. Weck and E. Leistner, *Metallographic Instructions for Colour Etchants by Immersion, Part II: Beraha Colour Etchants and Their Different Variants,* Vol 77/II, D.V.S. Verlag GmbH, Düsseldorf, 1983

14. E. Weck and E. Leistner, *Metallographic Instructions for Colour Etching by Immersion, Part III: Non-Ferrous Metals, Cemented Carbides and Ferrous Metals, Nickel-Base and Cobalt-Base Alloys,* Vol 77/III, D.V.S. Verlag GmbH, Düsseldorf, 1986

15. P. Skočovský, Colour Contrast in Metallographic Microscopy, *Slovmetal,* 1993

16. T. Berglund, *Metallographers' Handbook of Etching,* Sir Isaac Pitman & Sons, Ltd., London, 1931

17. T.R. Allmand, *Microscopic Identification of Inclusions in Steel,* British Iron and Steel Research Association, London, 1962

18. L.V. Foster and J.E. Wilson, The Examination of Metals in Polarized Light, *Proc. Am. Soc. Test. Mater.,* Vol 38 (Part II), 1938, p 315

19. H.E. Rosenberger, Differential Interference Contrast Microscopy, *Interpretive Techniques for Microstructural Analysis,* Plenum Press, 1977, p 79

20. P. Lacombe and L. Beaujard, Anodic Oxidation Regarded as a Means for the Study of Surface Conditions of Aluminum and its Alloys, *Journees des Etats de Surface [Comptes Rendus],* 23–26 Oct 1945 (Paris), 1946, p 44

21. A. Hone and E.C. Pearson, Grain Orientation in Aluminum Revealed by Anodic Film, *Met. Prog.,* Vol 53, March 1948, p 363

22. L.J. Barker, Revealing the Grain Structure of Common Aluminum Alloy Metallographic Specimens, *Trans. ASM,* Vol 42, 1950, p 347

23. A. Hone and E.C. Pearson, A New Anodic-Film Method for Studying Orientation in Aluminum, *Met. Prog.,* Vol 58, Nov 1950, p 713

24. H.G. Cole and W.J.D. Brooks, A Simple Anodizing Process for Revealing the Grain Structure of Aluminum Alloys, *Metallurgia,* Vol 50, Aug 1954, p 97

25. H.S. Yang, An Electrolytic Etching/Anodizing Method for Revealing the Microstructures of Common Aluminum Alloys, *Pr. Metallogr.,* Vol 27, 1990, p 539

26. E. Ence and H. Margolin, Phases in Titanium Identified by Cumulative Etching, *J. Met.,* March 1954, p 346

27. R.H. Hiltz, Jr., "Metallographic Methods: Color Staining of Titanium and Its Alloys," Watertown Arsenal Laboratory Report WAL 132/24, 20 April 1956

28. R.S. Crouse, "Identification of Carbides, Nitrides and Oxides of Niobium and Niobium Alloys by Anodic Staining," Oak Ridge National Laboratory Report ORNL-3821, July 1965

29. M.L. Picklesimer, Anodizing for Controlled Microstructural Contrast by Color, *Microscope,* Vol 15, Oct 1967, p 472

30. B.W. Mott and H.R. Haines, Examination of Metals Under Polarized Light, Part II: Applications, *Research,* Vol 4, 1951, p 63

31. R.C. Gikfins, *Optical Microscopy of Metals,* American Elsevier Publishing Co., Inc., 1970, p 122

32. D.H. Woodard, Stages in the Deformation of Monel Metal as Shown by Polarized Light, *Trans. AIME,* Vol 185, 1949, p 722

33. E.C.W. Perryman and J.M. Lack, Examination of Metals by Polarized Light, *Nature,* Vol 167 (No. 4247), 1951, p 479

34. R.E. Reed-Hill, C.R. Smeal, and L. Lee, The Examination of fcc Metals with Polarized Light, *Trans. AIME,* Vol 230, Aug 1964, p 1019

35. W. Ischewsky, New Micrographic Structures on the Surface of Heat Treated Steels, *Stahl Eisen,* Vol 23, 1903, p 120

36. L. Loskiewicz, A Study of the Time Factor in the Etching of Iron-Carbon Alloys, *Rev. Métall.,* Vol 19, 1922, p 681

37. T. Murakami, The Structure of Iron-Carbon-Chromium Alloys, *Sci. Rep. Tohoku Imperial Univ.,* Vol 7 (Part I), 1918, p 217

38. T. Murakami, Note on the Structure of Iron-Carbon-Chromium Alloys, *J. Iron Steel Inst. Jpn.,* Vol 100 (No. 2), 1919, p 445

39. E.C. Groesbeck, Solutions for Carbides, etc., in Alloy Steels, appendix to report of Committee E-4 on Metallography, *Proc. ASTM,* Vol 26 (Part I), 1926, p 569

40. E.C. Groesbeck, Metallographic Etching Reagents, Part III: For Alloy Steels, *U.S. Bureau of Standards Scientific Papers*, S518, 1925, p 527

41. J. Malette, Color-Producing Reactions for Microscopic Examination of Carbon Steels, *Comptes Rendus*, Vol 201, 1935, p 1385

42. L. Beaujard, New Reagents for Revealing the Micrographic Structure of Steels by the Formation of Colored Films, *Comptes Rendus*, Vol 233, 1951, p 653

43. L. Beaujard and J. Tordeux, The Use of Sodium Bisulfite as an Etching Solution for Ferritic Steels, *Comptes Rendus*, Vol 235, 1952, p 1304

44. L. Beaujard, Micrographic Coloring Reagents for Iron and Steels, *Rev. Métall.*, Vol 49, July 1952, p 531

45. L. Beaujard, Color Etching of Iron and Steel, *Met. Treat. Drop Forg.*, Nov 1952, p 499

46. P Lacombe and M. Mouflard, The Application of Color Metallography by Formation of Very Thin Epitaxial Layers with Interference Colors for the Study of Aluminium, Iron and Copper, *Métaux-Corros.-Ind.*, No. 340, Dec 1953, p 471

47. L. Beaujard and J. Tordeux, A New Sodium Bisulfite Reagent for the Micrographic Investigation of Steels, *Rev. Métall.*, Vol 52, Sept 1955, p 750

48. B.V. Guellard, A New Etching Reagent for Steel and Cast Iron, *Metallurgia*, Vol 54, Aug 1956, p 93

49. J.R. Vilella and W.F. Kindle, Sodium Bisulfite as an Etchant for Steel, *Met. Prog.*, Vol 76, Dec 1959, p 99

50. H. Klemm, Color Etching of the Fine Structure of Metals with Sodium Thiosulfate, *Metallkundliche*, Vol 45, Verlag Technik Berlin, 1952

51. H. Klemm, Uses of Sodium Thiosulfate (Klemm's Reagent) as an Etchant, *Pr. Metallogr.*, Vol 5, April 1968, p 163

52. E. Beraha, Metallographic Reagent for the Identification of Cementite in Iron and Steel, *J. Iron Steel Inst. Jpn.*, Vol 203, May 1965, p 454

53. E. Beraha, New Metallographic Reagents for Stainless Steel and Heat-Resisting Alloys, *J. Iron Steel Inst. Jpn.*, Vol 204, March 1966, p 248

54. E. Beraha, Two New Metallographic Reagents, *Met. Prog.*, Vol 90, Sept 1966, p 135

55. E. Beraha, Etching Cast Iron, *Met. Prog.*, Vol 90, Oct 1966, p 13

56. E. Beraha, New Metallographic Reagent for Iron, Carbon-Alloy, and Tool Steels, *J. Iron Steel Inst. Jpn.*, Vol 205, Aug 1967, p 866

57. E. Beraha, Metallographic Reagents for the Determination of Chemical and Physical Heterogeneity in the Microstructure of Iron and Steels, *Pr. Metallogr.*, Vol 4, Aug 1967, p 416

58. E. Beraha, Staining Metallographic Reagent for Stainless Steels, Corrosion and Heat-Resisting Alloys, *Pr. Metallogr.*, Vol 5, Aug 1968, p 443

59. E. Beraha, Staining Metallographic Reagent for Detection of Phosphides, Carbides and Nitrides in Iron, Steel, Tool Steels, Stainless Steel and Heat-Resisting Alloys, *Pr. Metallogr.,* Vol 5, Sept 1968, p 501

60. E. Beraha, Staining Metallographic Reagent for Copper-Base Alloys, *Pr. Metallogr.,* Vol 7, March 1970, p 131

61. E. Beraha, Metallographic Reagents Based on Sulfide Films, *Pr. Metallogr.,* Vol 7, May 1970, p 242

62. E. Beraha, Staining Metallographic Reagents for Cast Iron, *Microstructures,* Vol 2, June/July 1970, p 23

63. E. Beraha, Staining Metallographic Reagents for Cast Iron, Steels, Tool Steels, Manganese Steels, and Ferritic and Martensitic Stainless Steel, *Pr. Metallogr.,* Vol 8, Sept 1971, p 547

64. E. Beraha, Metallographic Reagents Based on Molybdate Solutions, *Pr. Metallogr.,* Vol 11, May 1974, p 271

65. A.O. Benscoter, J.R. Kilpatrick, and A.R. Marder, An Etching Technique for Fe-Ni Massive Martensite, *Pr. Metallogr.,* Vol 15, Dec 1968, p 694

66. A.O. Benscoter, J.R. Kilpatrick, and A.R. Marder, Sulfate and Sulfite Compounds as Etchants for Low-Carbon Iron Martensite, *IMS Proceedings,* 1969, p 37

67. J.R. Kilpatrick, A.O. Benscoter, and A.R. Marder, Tint Etching Improves Resolution and Contrast of Microstructures, *Met. Prog.,* Dec 1971, p 79

68. J.R. Kilpatrick, A New Etching Technique for Galvanneal and Hot Dipped Galvanized Coatings, *Pr. Metallogr.,* Vol 28, Dec 1991, p 649

69. P. Lichtenegger and R. Blöch, Colour Etching of High Alloy Steels, *Pr. Metallogr.,* Vol 12, 1975, p 567

70. G.F. Vander Voort, Etching Isothermally Treated Steels, *Heat Treat. Prog.,* Vol 1, April/May 2001, p 25–32

71. G.F. Vander Voort, Metallography of Iron Meteorites, *Adv. Mater. Process.,* Vol 159, Feb 2001, p 37, 40, 41

72. J.M. Radzikowska, The Foundry Research Institute, Kraków, Poland, personal communication, 2000

73. P. Liénard and C. Pacqué, Analysis of the Selective Coloring Mechanism for Identification of Different Phases in Al-Si-Cu Foundry Alloys, *Hommes Fonderie,* No. 126, June/July 1982, p 27–35

74. P. Liénard, Etching of Aluminium Alloys, *Structure,* Vol 8, June 1984, p 17–20

75. R. Hasson, Metallography of Molybdenum in Color, *Microscope,* Vol 16, 1968, p 329–334

76. R. Hasson, An Improved Orientation-Dependent Chemical Anodizing Color Reagent for Molybdenum, *Microscope,* Vol 22, 1974, p 317–322

77. S. Lehwald et al., An Orientation-Sensitive Colour-Etching Method for Polycrystalline Tungsten, *Pr. Metallogr.,* Vol 9, Sept 1972, p 510–515

78. R.S. Crouse, Oak Ridge National Laboratory, personal communication, 1982

J.M. Radzikowska, Metallography and Microstructures of Cast Iron, *Metallography and Microstructures,* Vol 9, *ASM Handbook*, ASM International, 2004, p. 565–587

Metallography and Microstructures of Cast Iron

Janina M. Radzikowska, The Foundry Research Institute, Kraków, Poland

Introduction

CAST IRON is an iron-carbon cast alloy with other elements that is made by remelting pig iron, scrap, and other additions. For differentiation from steel and cast steel, cast iron is defined as a cast alloy with a carbon content (min 2.03%) that ensures the solidification of the final phase with a eutectic transformation. Depending on chemical specifications, cast irons can be nonalloyed or alloyed. Table 1 lists the range of compositions for nonalloyed cast irons (Ref 1). The range of alloyed irons is much wider, and they contain either higher amounts of common components, such as silicon and manganese, or special additions, such as nickel, chromium, aluminum, molybdenum, tungsten, copper, vanadium, titanium, plus others.

Table 1 Range of chemical compositions for typical nonalloyed and low-alloyed cast irons

Type of iron	Composition, %				
	C	**Si**	**Mn**	**P**	**S**
Gray (FG)	2.5–4.0	1.0–3.0	0.2–1.0	0.002–1.0	0.02–0.025
Compacted graphite (CG)	2.5–4.0	1.0–3.0	0.2–1.0	0.01–0.1	0.01–0.03
Ductile (SG)	3.0–4.0	1.8–2.8	0.1–1.0	0.01–0.1	0.01–0.03
White	1.8–3.6	0.5–1.9	0.25–0.8	0.06–0.2	0.06–0.2
Malleable (TG)	2.2–2.9	0.9–1.9	0.15–1.2	0.02–0.2	0.02–0.2

FG, flake graphite; SG, spheroidal graphite; TG, tempered graphite. Source: Ref 1

Free graphite is a characteristic constituent of nonalloyed and low-alloyed cast irons. Precipitation of graphite directly from the liquid occurs when solidification takes place in the range between the temperatures of stable transformation (T_{st}) and metastable transformation (T_{mst}), which are, respectively, 1153 °C (2107 °F) and 1147 °C (2097 °F), according to the iron-carbon diagram. In this case, the permissible undercooling degree is $\Delta T_{max} = T_{st} - T_{mst}$. In the case of a higher undercooling degree, that is, in the temperatures below T_{mst}, primary solidification and eutectic solidification can both take place completely or partially in the metastable system, with precipitation of primary cementite or ledeburite. Graphitization can also take place in the range of critical temperatures during solid-state transformations. The equilibrium of phases $Fe_\gamma = Fe_\alpha + Fe_3C$ occurs only at the temperature 723 ± 2 °C (1333 ± 4 °F), while equilibrium of phases $Fe_\gamma = Fe_\alpha + C_{gr}$ occurs at the temperature 738 ± 3 °C (1360 ± 5 °F). So, in the range of temperatures 738 to 723 °C (1360 to 1333 °F), the austenite can decompose only into a mixture of ferrite with graphite instead of with cementite (Ref 2).

The previous considerations regard only pure iron-carbon alloys. In cast iron, which is a multicomponent alloy, these temperatures can be changed by different factors: chemical composition, ability of cast iron for nucleation, and cooling rate. Silicon and phosphorus both strongly affect the carbon content of the eutectic. That dependence was defined as a carbon equivalent (C_e) value that is the total carbon content plus one-third the sum of the silicon and phosphorus content (Ref 2). Cast iron, with a composition equivalent of approximately 4.3, solidifies as a eutectic. If the C_e is >4.3, it is hypereutectic; if it is <4.3, cast iron is hypoeutectic (Ref 3).

Eutectic cells are the elementary units for graphite nucleation. The cells solidify from the separate nuclei, which are basically graphite but also nonmetallic inclusions such as oxides and sulfides as well as defects and material discontinuities. Cell size depends on the nucleation rate in the cast iron. When the cooling rate and the degree of undercooling increase, the number of eutectic cells also increases, and their microstructure changes, promoting radial-spherical shape (Ref 2).

References cited in this section

1. Guide to Engineered Materials, Property Comparison Tables, *Adv. Mater. Process.*, Vol 159 (No. 12), Dec 2001, p 46

2. Cz. Podrzucki and Cz. Kalata, *Metalurgia i odlewnictwo żeliwa (Metallurgy and Foundrying of Cast Iron)*, Śląsk-Katowice, Poland, 1971, p 32, 54–59, 70

3. W. Sakwa, *Żeliwo (Cast Iron)*, Śląsk-Katowice, Poland, 1974, p 53

J.M. Radzikowska, Metallography and Microstructures of Cast Iron, *Metallography and Microstructures*, Vol 9, *ASM Handbook*, ASM International, 2004, p. 565–587

Metallography and Microstructures of Cast Iron

Janina M. Radzikowska, The Foundry Research Institute, Kraków, Poland

---

Preparation for Microexamination

Preparation of cast iron specimens for microstructural examination is difficult due to the need to properly retain the very soft graphite phase, when present, that is embedded in a harder matrix. Also, in the case of gray irons with a soft ferritic matrix, grinding scratches can be difficult to remove in the polishing process. When shrinkage cavities are present, which is common, the cavities must not be enlarged or smeared over.

Retention of graphite in cast iron is a common polishing problem that has received considerable attention. Coarse grinding is a critical stage, so, if the soft graphite is lost during coarse grinding, it cannot be recovered in subsequent steps and will be seen as an open or collapsed cavity. Silicon carbide (SiC) grinding papers are preferred to emery, because SiC cuts efficiently, while emery paper does not, and SiC produces less damage. Fresh paper should always be used; never grind with worn paper. White iron, by contrast, contains extremely hard iron carbides that resist abrasion and tend to remain in relief above the softer matrix after polishing (Ref 4).

Quality-control studies, based on image analysis measurements of the amount of phases and the graphite shape and size, also need perfectly prepared specimens with fully retained graphite phase and with microstructural constituents correctly revealed by etching.

Specimen Preparation. The metallographic specimen preparation process for microstructural investigations of cast iron specimens usually consists of five stages: sampling, cold or hot mounting, grinding, polishing, and etching with a suitable etchant to reveal the microstructure. Each stage presents particular problems in the case of cast iron. Of course, the graphite phase is studied after polishing and before etching.

Sampling is the first step—selecting the test location or locations to be evaluated metallographically. Usually, cast iron castings have a considerable variation in microstructure between surface and core. Selection of the test location is very important to obtain representative results from the microstructural examination. Samples can be obtained by cutting them out from either a large or small casting or from standard test bars, such as microslugs, ears, or keel bars; however, the microstructure of these pieces may not be representative for the actual casting due to substantial differences in the solidification rates. Production saws, such as large, abrasive cutoff saws, band saws, or power hacksaws, can be used for dividing medium-sized casting into smaller samples. In the case of very large castings, flame cutting may be used. Next, the pieces can be reduced to the desired size for metallographic specimens by using a laboratory abrasive cutoff saw or a band saw. If the casting was sectioned by flame cutting, the specimen must be removed well away from the heat-affected zone. The pieces cut out for metallographic examination may be ground prior to mounting (this may be done to round off sharp cut edges or to reduce the roughness of band-saw-cut surfaces) and subsequent preparation. Overheating is avoided by proper selection of the speed of cutoff saws, the use of the correct wheel, and adequate water cooling.

Overheating during grinding is avoided by using fresh abrasive paper and proper cooling. When metallographic specimens are cut out from the standard cast bars, they are sometimes prepared using standard machine shop equipment, such as turning in a lathe or milling. These devices can deform the testpiece surfaces to a considerable depth, so care must be exercised to remove any damage from these operations before starting specimen preparation.

Mounting. Specimens can be mounted in a polymeric material using either cold or hot mounting procedures. The mounting resin is chosen depending on the cast iron hardness (soft or hard) and the need to enhance edge retention. Use of an incorrect resin, or ignoring the mounting process, can make it very difficult to obtain properly polished graphite in the area close to the specimen edge. Figure 1 and 2 show the microstructure of spheroidal graphite in ductile iron close to the edge of the specimens, which were cut off from a 30 mm (1.2 in.) diameter bar and polished with and without embedding in a polymer resin, respectively. In the specimen prepared without embedding in a resin, the graphite was pulled out, while in the specimen that was embedded in a resin and prepared, the graphite nodules were perfectly retained. Figure 3 and 4 show that the uniform grinding of nonmounted specimens is more difficult, and the flake graphite in gray iron close to the edge of such a specimen is not polished perfectly, in comparison to well-polished graphite in the mounted specimen.

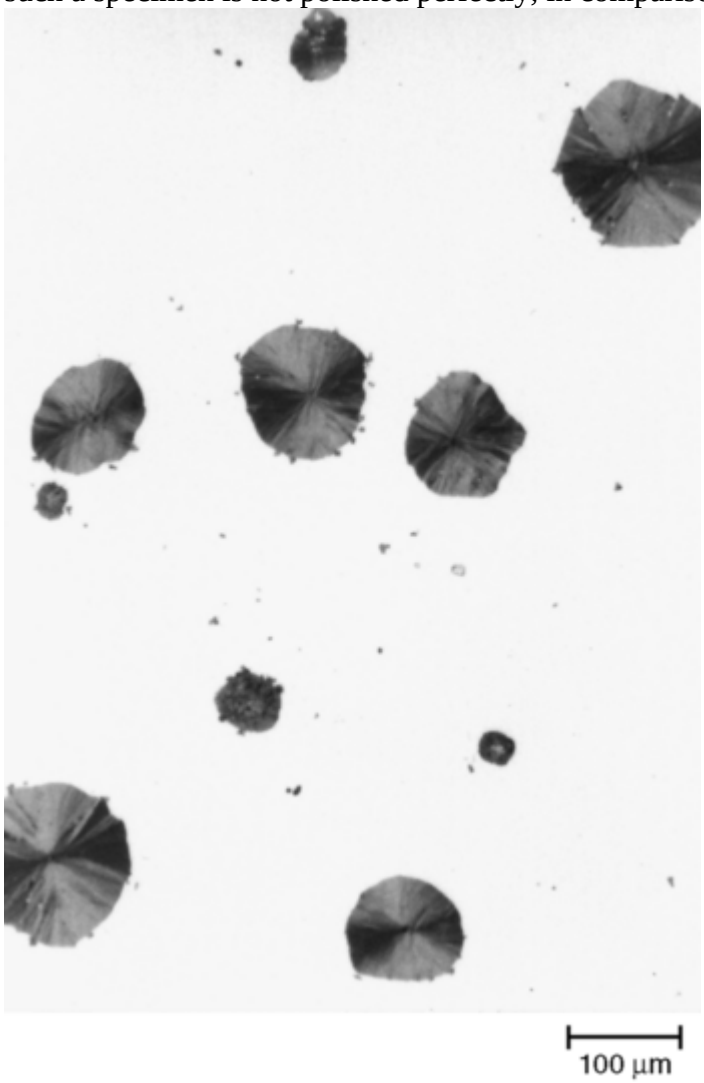

Fig. 1 Spheroidal graphite in as-cast ductile iron (Fe-3.7%C-2.4%Si-0.59%Mn-0.025%P-0.01%S-0.095%Mo-1.4%Cu) close to the edge of the specimen, which was 30 mm (1.2 in.) in diameter. The specimen was embedded. As-polished. 100×

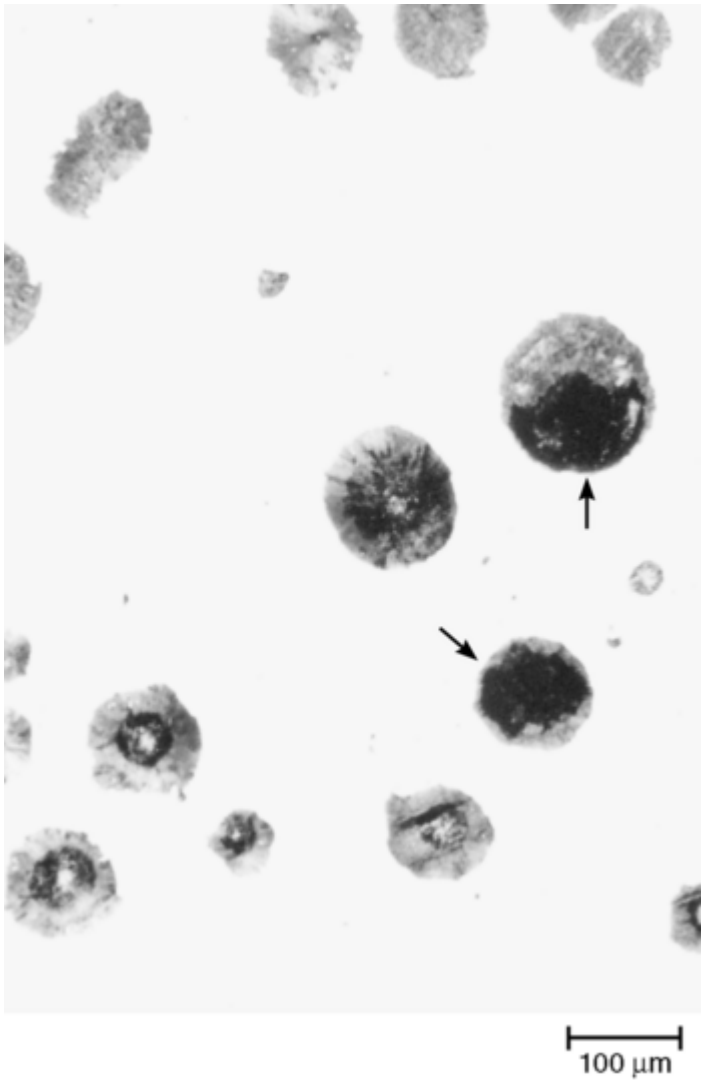

Fig. 2 Same as-cast ductile iron as in Fig. 1, but the specimen was not embedded. The arrows show the pulled-out graphite. As-polished. 100×

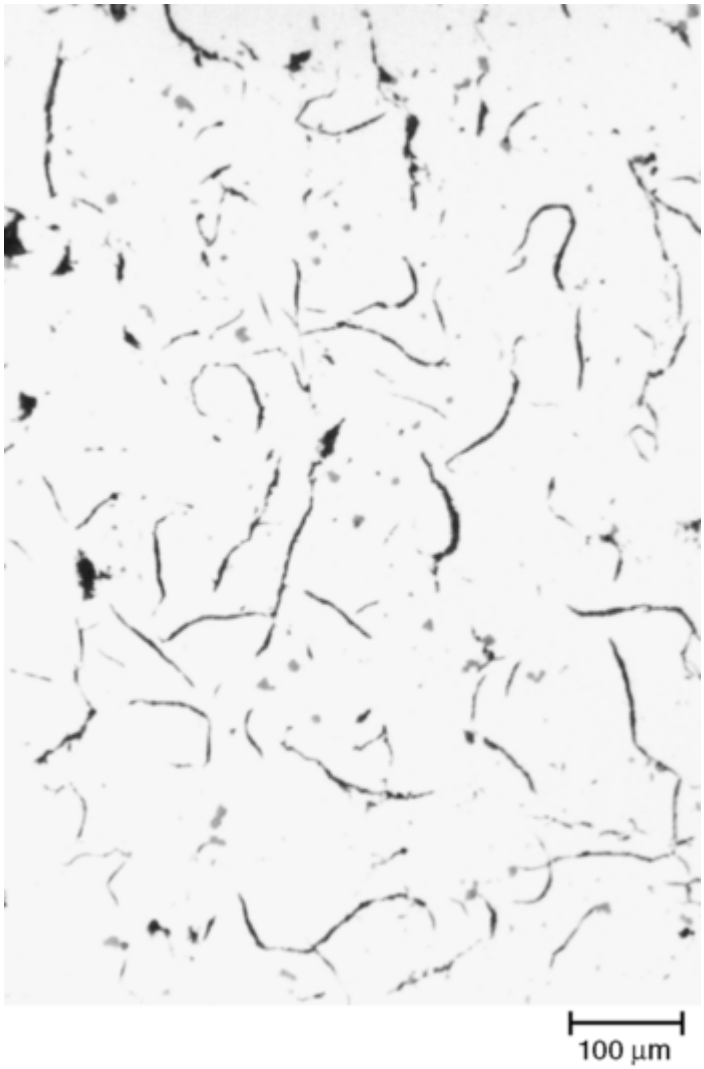

Fig. 3 Flake graphite in as-cast gray iron (Fe-3.5%C-2.95%Si-0.40%Mn-0.08%P-0.01%S-0.13%Ni-0.15%Cu) close to the edge of the unembedded specimen, which was 30 mm (1.2 in.) in diameter. As-polished. 100×



Fig. 4 Same as in Fig. 3 but close to the center of the specimen. As-polished. 100×

Grinding and Polishing. To ensure proper graphite retention, the use of an automated grinding-polishing machine is recommended over manual preparation. The automated equipment makes it possible, in comparison to manual specimen preparation, to properly control the orientation of the specimen surface relative to the grinding or polishing surface, to maintain constantly the desired load on the specimens, to uniformly rotate the specimens relative to the work surface, and to control the time for each preparation step. Proper control of these factors influences graphite retention, although other factors are also important.

A good, general principle is to minimize the number of grinding and polishing stages. Also, the load on each specimen, or on all specimens in the holder, must be chosen to obtain a correctly polished surface in the shortest possible time. This precludes the risk of pulling out the graphite phase and ensures that the graphite precipitates will be perfectly flat with sharp boundaries.

The recommended procedure for automated preparation of the specimens of nonalloyed and low-alloyed cast iron with graphite specimens is to grind with a high-quality, waterproof 220- or 240-grit (or equivalent) SiC paper until plane, with a load of 100 N for six specimens mounted in the sample holder, with central loading. Polishing is carried out in four steps with a different grain size diamond paste:

Step	Diamond paste grain size, µm	Load, N	Duration	Recommended polishing cloth
1	9	120[(a)]	5 min[(d)]	Napless woven
2	3	120[(a)]	3 min[(d)]	Napless woven
3	1	120[(a)]	2 min[(d)]	Napless woven
4	[(b)]	25[(c)]	45–60 s[(e)]	Napless synthetic polyurethane

(a) Load per six specimens.

(b) Aqueous 0.05 µm alumina suspension.

(c) Load per single specimen (switching to individual force to make specimen cleaning easier).

(d) Comp direction.
(e) Contra

Figure 5 shows temper graphite in malleable iron after the last step of grinding, which was carried out in three steps using, consecutively, SiC grit papers P220, P500, and P1000. Figure 6 shows the same specimen after grinding on P220 SiC paper and then polishing with 9 μm diamond paste according to the procedure given previously. In both cases, there is some pulled-out graphite after these steps. Each specimen was prepared further. The specimen ground with three SiC steps was polished with 3 μm diamond suspension on a napless cloth and then with 1 μm diamond suspension on a napped cloth. The pulled-out graphite was still visible. However, the specimen ground with P220 SiC and polished with 9 μm diamond paste, when finished with the recommended practice given previously, was free of any visible pullouts, as shown in Fig. 7. By using a napped cloth and an aqueous 1 μm diamond suspension for the final diamond polishing step, it was impossible to obtain perfectly retained graphite, as shown in Fig. 8. Napped cloths should not be used with diamond abrasive, either in paste, suspension, or aerosol form. Graphite retention appears to be slightly better using diamond paste and the preferred lubricant than with an aqueous suspension, although more work needs to be conducted to determine if this difference is important. Final polishing with an alumina suspension, such as Masterprep alumina (Buehler, Ltd.), makes the graphite boundaries sharper by removing the matrix, which was smeared over the edge of the graphite during grinding and was not removed by the diamond polishing steps.

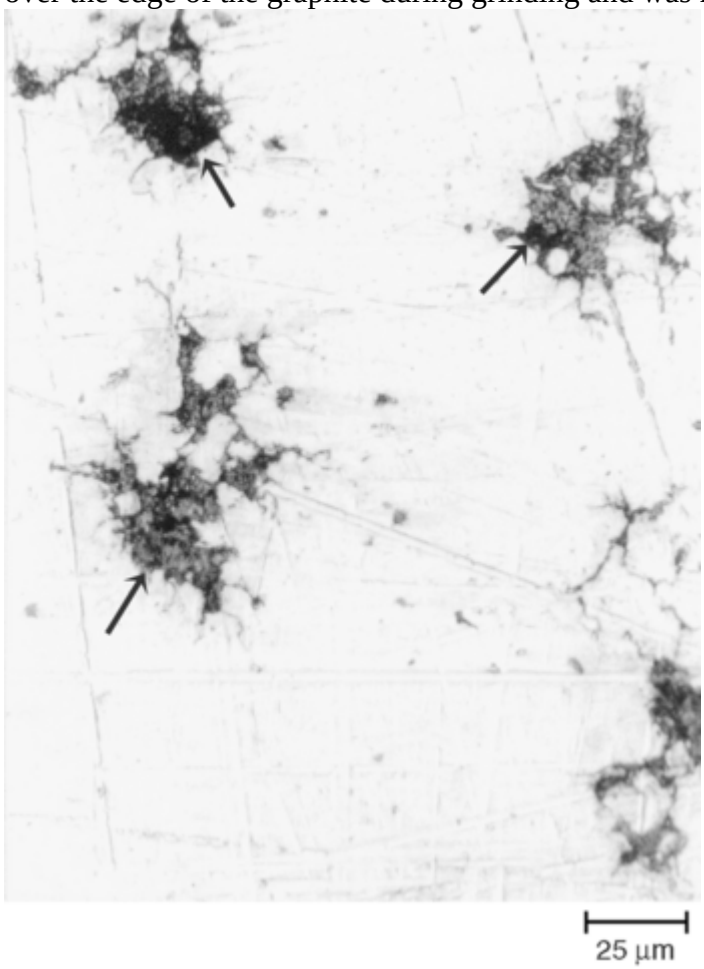

Fig. 5 Temper graphite in malleable iron (Fe-2.9%C-1.5%Si-0.53%Mn-0.06%P-0.22%S-0.08%Ni-0.1%Cu-0.09%Cr-0.003%Bi) after grinding on P1000 SiC waterproof paper. The casting was annealed at 950 °C (1740 °F), held 10 h, furnace cooled to 720 °C (1330 °F), held 16 h, and air cooled. The arrows show the pulled-out graphite. As-polished. 400×

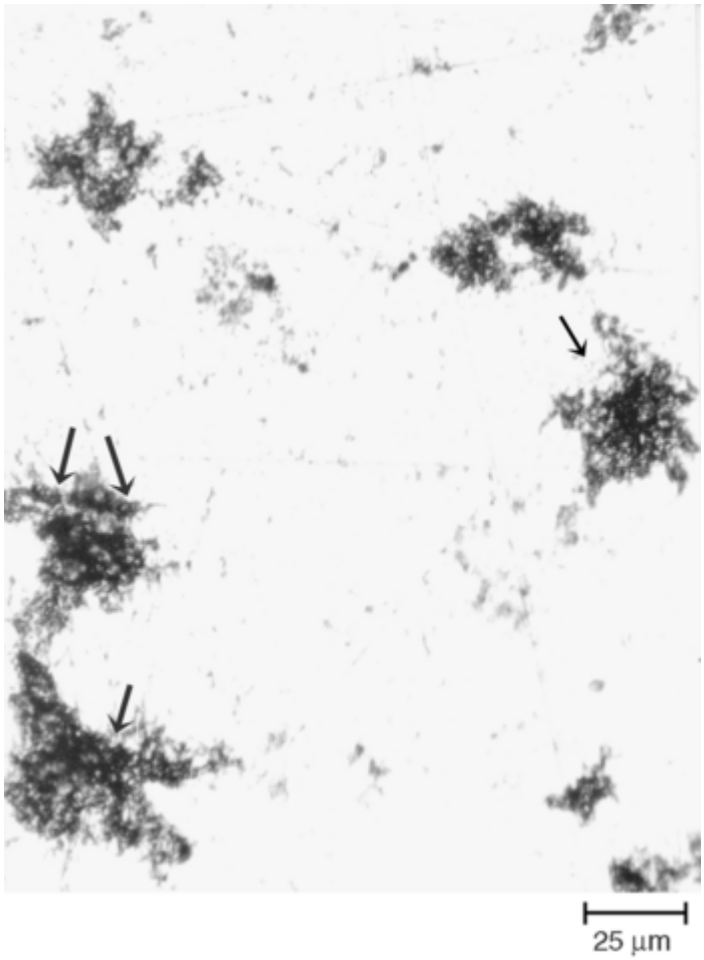

Fig. 6 Same as in Fig. 5 but after polishing with 9 µm diamond suspension. The arrows show the pulled-out graphite. As-polished. 400×

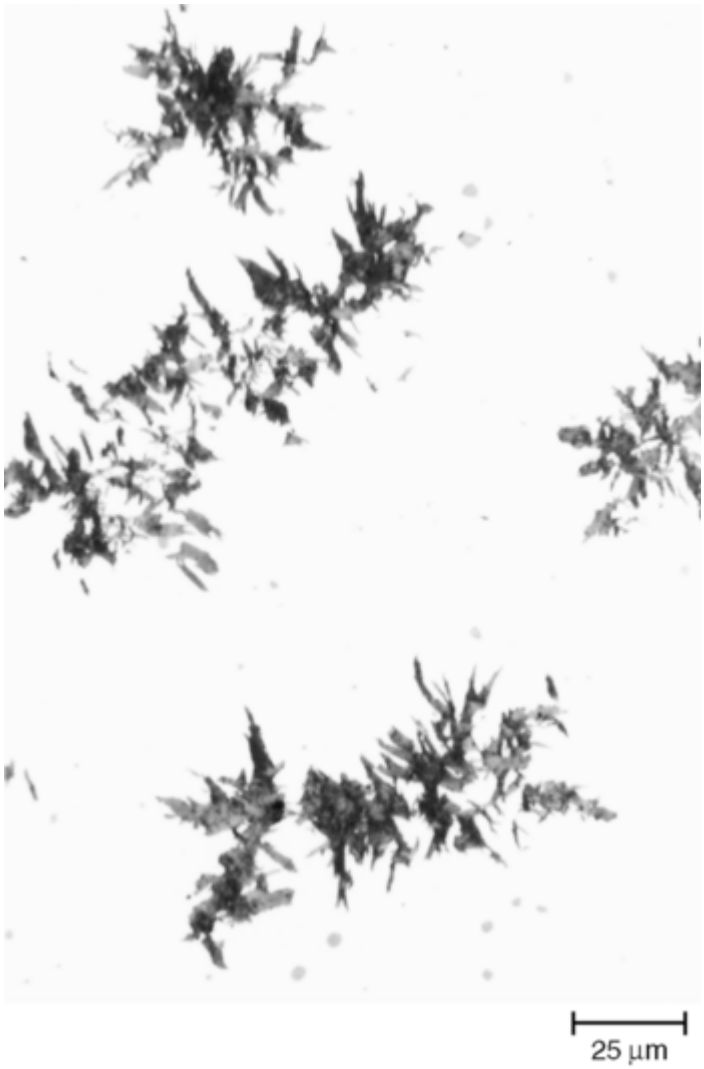

Fig. 7 Same as in Fig. 6 but after final polishing with the 1 µm diamond paste applied on a napless cloth. Graphite is free of any visible pullouts. As-polished. 400×

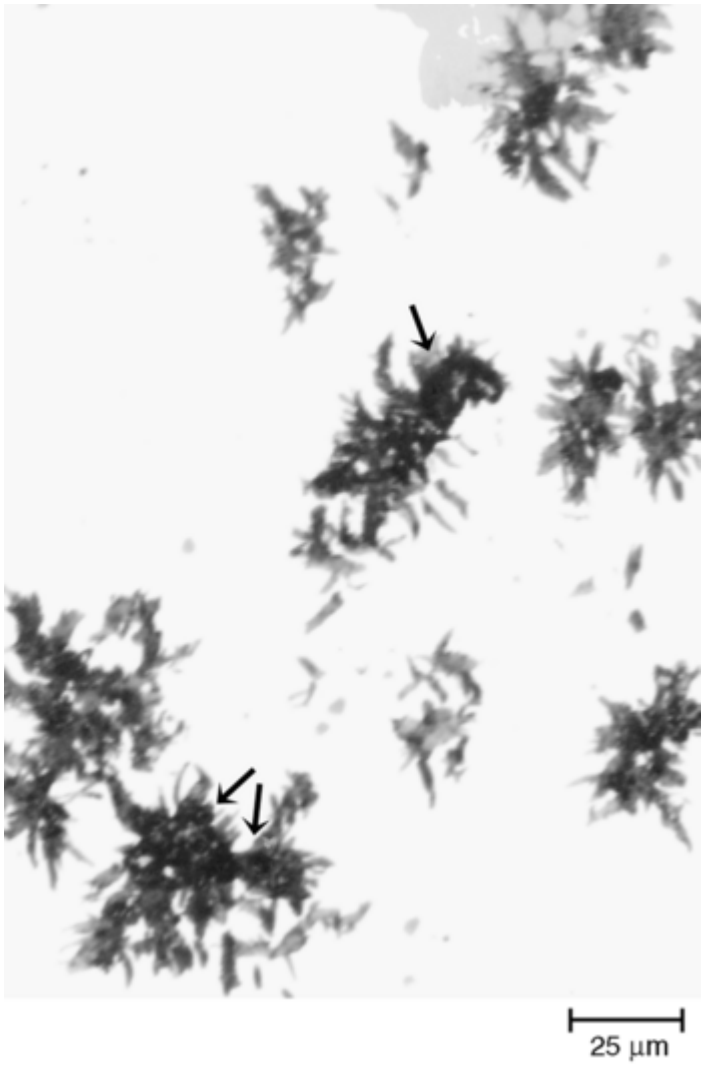

Fig. 8 Same as in Fig. 7 but after final polishing with the 1 μm diamond suspension applied on a napped cloth. The arrows show the pulled-out graphite. As-polished. 400×

Alloyed chromium iron is much harder, and a different preparation procedure must be used. The grinding process is carried out in three steps, and polishing is carried out in three steps, although only two polishing steps are needed for most routine work. Grinding of the specimens, mounted in the sample holder, used central loading (150 N/six specimens), with high-quality SiC waterproof paper (water cooled) with the following grit sizes:

- *First step:* P220 grit until plane.
- *Second step:* P500 grit for 3 min.
- *Third step:* P1000 grit for 3 min

Polishing is done in three steps, with different grain size diamond in paste for the first two steps:

- *First step:* 3 μm diamond, 120 N load/six specimens for 3 min with a napless cloth.
- *Second step:* 1μm diamond, 100 N load/six specimens for 3 min with a napless cloth

The last polishing step is carried out with a colloidal silica suspension on a napless synthetic polyurethane pad but in a single specimen holder with an individual load of 30 N for 1.5 min.
Figure 9 shows the microstructure of a heat treated chromium iron after this preparation. The carbides are perfectly flat, with very sharp edges and boundaries etched uniformly. Figure 10 shows the primary eutectic carbides in the microstructure of a high-chromium iron. They appear to be sticking out from the matrix, and their boundaries are not outlined uniformly. This result occurs if the load is too low or the final polishing time

on the silica suspension is too long. Both problems will result in too much removal of the softer matrix that was surrounding the primary carbides.

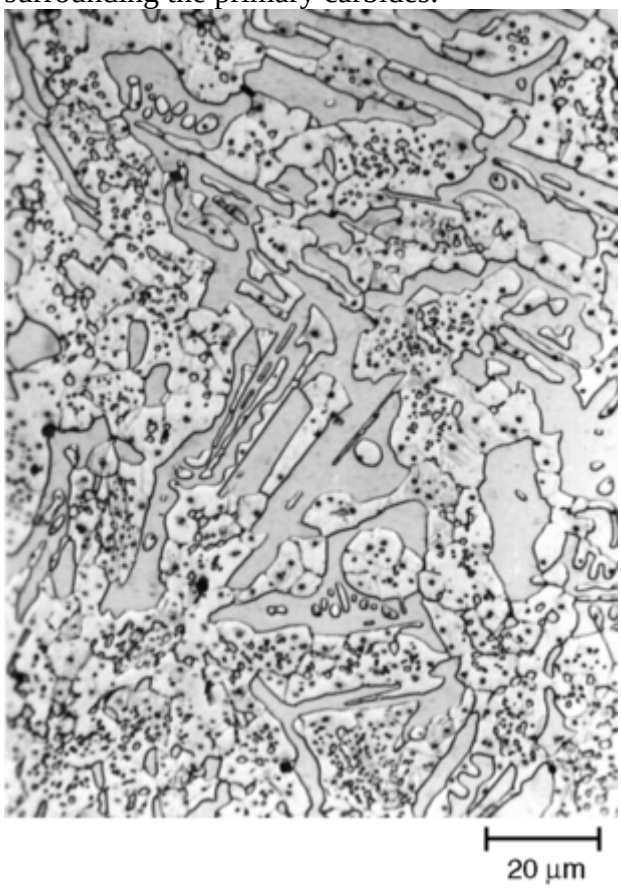

Fig. 9 White high-chromium iron (Fe-3.2%C-4.65%Cr-2.9%Mn-0.51%Si-0.050%P-0.024%S). Eutectic and secondary carbides in the matrix. Specimen was prepared correctly. The casting was austenitized at 1000 °C (1830 °F), held 1 h, furnace cooled to 400 °C (750 °F) for 2 h, taken to salt bath at 400 °C (750 °F), held for 4 h, and air cooled. Etched with glyceregia. 500×



Fig. 10 White high-chromium iron (Fe-3.16%C-8.86%Cr-0.50%Si-3.04%Mn-0.051%P-0.018%S). Eutectic and secondary carbides in the matrix. Specimen was prepared incorrectly. The casting was austenitized at 1000 °C (1830 °F), held 1 h, furnace cooled to 700 °C (1290 °F) for 2 h, taken to salt bath at 700 °C (1290 °F), held 4 h, and air cooled. Etched with glyceregia. 500×

During grinding, the paper must be moistened with flowing tap water, and the specimens should be washed with water after each step. Also, during the first planning step, the sheet of paper should be changed every 1 min. Used grit paper is not effective and will introduce heat and damage, impairing specimen flatness. During polishing with diamond paste from a tube, the cloth is moistened with the recommended lubricant for the paste. If a water-based diamond suspension is applied on the cloth, the use of an additional lubricant is not required.
The speed of the grinding-polishing head was 150 rpm, and it was constant. The speed of the platen during grinding was always 300 rpm, and during polishing was always 150 rpm. After each grinding step, the specimens were washed with running tap water and dried with compressed air, while after each polishing step, they were washed with alcohol and dried with hot air from a hair dryer.

Reference cited in this section

4. G.F. Vander Voort, *Metallography: Principles and Practice*, McGraw-Hill Book Co., 1984; Reprinted by ASM International, 1999, p 129, 294–303, 632, 634, 642–644, 646, 648

J.M. Radzikowska, Metallography and Microstructures of Cast Iron, *Metallography and Microstructures,* Vol 9, *ASM Handbook,* ASM International, 2004, p. 565–587

Metallography and Microstructures of Cast Iron

Janina M. Radzikowska, The Foundry Research Institute, Kraków, Poland

Microexamination Methods

Chemical Etching. The examination of the iron microstructure with a light optical microscope is always the first step for phase identification and morphology. One should always begin microstructural investigations by examining the as-polished specimen before etching. This is a necessity, of course, for cast iron specimens, if one is to properly examine the graphite phase.

Standard Etchants. To see the microstructural details, specimens must be etched. Etching methods based on chemical corrosive processes have been used by metallographers for many years to reveal structures for black-and-white imaging.

Specimens of nonalloyed and low-alloyed irons containing ferrite, pearlite, the phosphorus eutectic (steadite), cementite, martensite, and bainite can be etched successfully with nital at room temperature to reveal all of these microstructural constituents. Usually, this is a 2 to 4% alcohol solution of nitric acid (HNO_3) (Table 2, etch No. 1). Figure 11 shows a nearly ferritic annealed ductile iron with uniformly etched grain boundaries of ferrite and a small amount of pearlite. Nital is very sensitive to the crystallographic orientation of pearlite grains, so, in the case of a fully pearlitic structure, it is recommended to use picral, which is an alcohol solution of 4% picric acid (Table 1, etch No. 2). Figure 12 and 13 show the differences in revealing the microstructure of pearlite with nital or picral. Picral does not etch the ferrite grain boundaries, or as-quenched martensite, but it etches the pearlitic structure more uniformly, while nital leaves white, unetched areas, especially in the case where pearlite is very fine.

Table 2 Etchants

No. of etchant	Name of etchant	Composition	Comments	Ref
1	Nital	96–98 mL ethanol 2–4 mL nitric acid (HNO_3)	Most common etchant for iron, carbon, alloyed steels, and cast iron. Reveals alpha grain boundaries and constituents. The 2 or 4% solution is commonly used. Use by immersion of sample for up to 60 s.	Ref 4 p 648
2	Picral	4 g picric acid ($(NO_2)_3C_6H_2OH$) 100 mL ethanol	Recommended for structures consisting of ferrite and carbides. Does not reveal ferrite grain boundaries and martensite as-quenched. Addition of approximately 0.5–1% zephiran chloride improves etch rate and uniformity.	Ref 4 p 648
3	Glyceregia (modified)	3 parts glycerine 2 parts hydrochloric acid (HCl) 1 part nitric acid (HNO_3)	For austenitic stainless steels and cast irons. Reveals grain structure; outlines sigma and carbides. Mix fresh; do not store. Use by swabbing. Heat up to 50 °C (120 °F) when etching time at 20 °C (70 °F) does not bring results.	Ref 4 p 634
4	Alkaline sodium picrate (ASP)	2 g picric acid ($(NO_2)_3C_6H_2OH$)) 25 g sodium hydroxide	Immerse sample in solution at 60–70 °C (140–160 °F) for 1–3 min. Colors cementite (Fe_3C) dark brown to black, depending on etching time.	Ref 4 p 646

		(NaOH) 100 mL distilled water		
5	Klemm I	50 mL sat. aq. sodium thiosulfate ($Na_2S_2O_3·5H_2O$) 1 g potassium metabisulfite ($K_2S_2O_5$)	Immerse sample for 40–100 s. Reveals phosphorus segregation (white); colors ferrite blue or red; martensite brown; cementite and austenite are unaffected	Ref 4 p 642
6	Beraha CdS	240 g aq. sodium thiosulfate ($Na_2S_2O_3·5H_2O$) 30 g citric acid ($C_6H_8O_7·H_2O$) 20–25 g cadmium chloride ($CdCl_2·2.5H_2O$) 100 mL distilled water	Tint etch for iron, steel, cast irons, and ferritic and martensitic stainless steel. Dissolve in order shown. Allow each to dissolve before adding next. Allow to age 24 h at 20 °C (70 °F) in a dark bottle. Before use, filter 100 mL of solution to remove precipitates. Preetch with a general-purpose reagent. Etch 20–90 s; good for 4 h. For steels and cast irons, after 20–40 s only ferrite is colored, red or violet. Longer times color all constituents: ferrite is colored yellow or light blue; phosphide, brown; carbide, violet or blue. For stainless steels, immerse sample 60–90 s; carbides are colored red or violet-blue; matrix, yellow; colors of ferrite vary. Sulfides red-brown after 90 s	Ref 4 p 644
7	…	28 g sodium hydroxide (NaOH) 4 g picric acid ($(NO_2)_3C_6H_2OH$)) 1 g potassium metabisulfite ($K_2S_2O_5$)[(a)] 100 mL distilled water	Immerse sample in hot solution (close to boiling temperature) for 30–60 min. This reagent reveals silicon segregation in ductile iron. The colors of microstructure change themselves from green through red, yellow, blue, and dark brown to light brown as the silicon content is reduced from the graphite nodule to cell boundaries. The regions with lowest silicon content at the cell boundaries remain colorless. Before etching, ferritization of the specimen is recommended to enhance the visibility of the colors.	Ref 6
8	Murakami reagent	10 g potassium ferricyanide ($K_3Fe(CN)_6$) 10 g potassium hydroxide (KOH) or sodium hydroxide (NaOH) 100 mL distilled water	Use fresh, cold or hot. Cold, at 20 °C (70 °F) for up to 1.5 min, tints chromium carbides; Fe_3C unattacked or barely attacked. Hot, at 50 °C (120 °F) for 3 min, tints iron phosphide. The higher temperature or etching time also tints cementite into yellow color.	Ref 4 p 646
9	Beraha reagent with selenic acid	2 mL hydrochloric acid (HCl) 0.5 mL selenic acid (H_2SeO_4) 100 mL ethanol	For differentiation of the constituents in steadite in cast iron, immerse sample for 7–10 min; iron phosphide colored blue or green, cementite colored red, and ferrite is bright (unaffected). Preetching with nital is recommended.	Ref 4 p 643
10	Beraha-Martensite (B-M)	2 g ammonium bifluoride ($NH_4F·HF$)	Immerse sample for 1–3 s. Coarse martensite is blue or yellow; fine martensite and bainite are brown. Use fresh reagent, and wet sample with tap	Ref 6 p

		2 g potassium metabisulfite ($K_2S_2O_5$) 100 mL stock solution: 1:5, HCl to distilled water	water before etching.	26
11	10% sodium metabisulfite (SMB)[(b)]	10 g sodium pyrosulfite ($Na_2S_2O_5$) 100 mL distilled water	Tints as-quenched martensite into brown; bainite into blue; carbides, phosphides, and residual austenite, unaffected. Immerse sample in etchant solution approximately 20 s. Preetching sample with nital is recommended.	Ref 4 p 642
12	Lichtenegger and Bloech I (LB I)	20 g ammonium bifluoride ($NH_4F{\cdot}HF$) 0.5 g potassium metabisulfite ($K_2S_2O_5$) 100 mL hot distilled water	Dissolve in given order. In austenitic Cr-Ni alloys, it tints austenite and reveals dendritic segregation. Ferrite and carbides remain unaffected. Wet-etch for 1–5 min immediately after polishing.	Ref 7 p 51
13	…	50% aq. hydrochloric acid (HCl)	Immerse sample for 30–90 min. Every 15–20 min, wash sample with distilled water, quickly etch in hydrofluoric acid (conc.), and wash in tap water. When the etching process is finished, immerse sample in 5% aq. KOH or NaOH for 10–20 min, wash with distilled water in an ultrasonic washer, then in ethanol, and dry with blowing hot air.	Ref 8 p 97

(a) Potassium metabisulfite and potassium pyrosulfite are both synonomous with $K_2\ S_2\ O_5$.
(b) Sodium metabisulfite and sodium pyrosulfite are synonomous with $Na_2S_2O_5$.

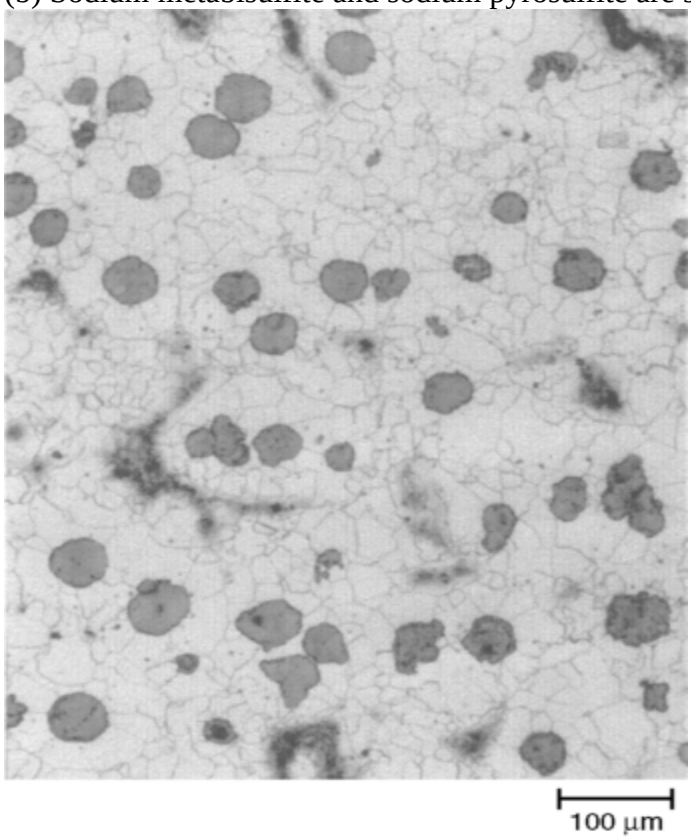

Fig. 11 Ductile iron (Fe-3.8%C-2.4%Si-0.28%Mn-1.0%Ni-0.05%Mg) after annealing. Ferrite and approximately 5% pearlite. Etched with 2% nital. 100×. Courtesy of G.F. Vander Voort, Buehler Ltd.



Fig. 12 As-cast gray iron (Fe-2.8%C-0.8%Si-0.4%Mn-0.1%S-0.35%P-0.3%Cr). Pearlite. Etched with 4% nital. Arrows show the white areas with weakly etched or nonetched pearlite. 500×

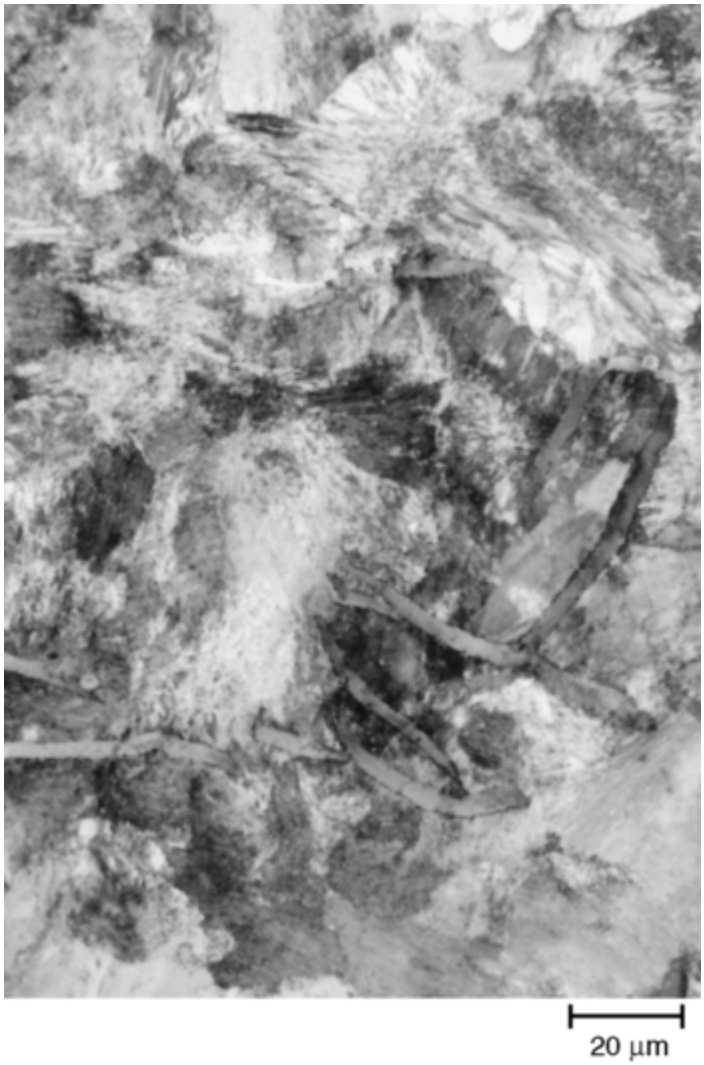

Fig. 13 Same as in Fig. 12 but after etching with 4% picral. Pearlite was etched uniformly. 500×

When the austempering heat treatment is very short, the microstructure of austempered ductile iron (ADI) consists of martensite and a small amount of acicular ferrite. After etching in 4% nital, martensite as well as acicular ferrite are both etched intensively, which makes it very difficult to distinctly see the needles of acicular ferrite. Picral reveals this phase very well; martensite is barely etched due to the very short austempering heat treatment of the specimen, which was 2 min, because the martensite was as-quenched. The needles of acicular ferrite are dark and very sharp (Fig. 32, 33). In this case, picral is very convenient for estimating the amount and morphology of the acicular ferrite in the ADI microstructure. Picral is safer to be stored in the lab than nital, which can be an explosive mixture under certain conditions when it is stored in a tightly closed bottle.

Glyceregia (Table 2, etch No. 3), which is a mixture of glycerine, hydrochloric acid (HCl), and nitric acid (HNO_3), is recommended for revealing the microstructure of high-chromium and chromium-nickel-molybdenum irons. Figure 14 shows the microstructure of a high-chromium cast iron after etching with glyceregia (see also Fig. 14, 40 and 96 Nital can be also used for revealing the carbide morphology in the microstructure of chromium or chromium-nickel irons when the carbon and chromium content promotes solidification of eutectic carbides. When the microstructure of a high-chromium white iron contains columnar primary carbides, glyceregia is recommended.

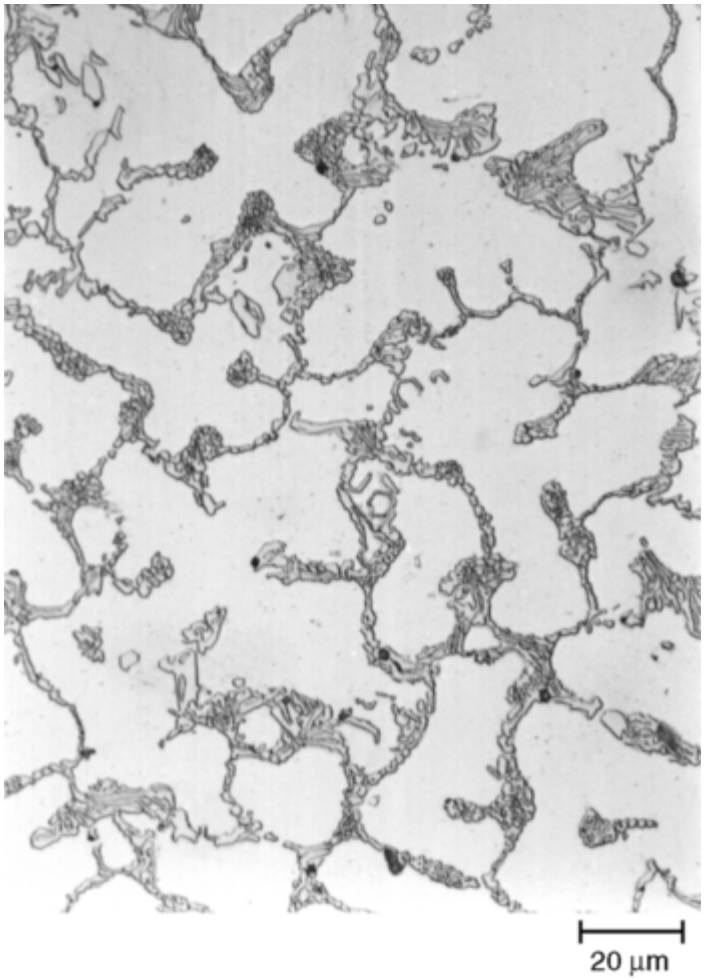

Fig. 14 As-cast high-chromium white iron (Fe-1.57%C-18.64%Cr-2.86%Mn-0.53%Si-0.036%P-0.013%S). Eutectic chromium carbides type M_7C_3 in austenitic matrix. Etched with glyceregia. 500×

Figure 15 shows the microstructure of the same cast iron as Fig. 14 but after etching with 4% nital (see also Figure 40 and 41). Both etchants reveal carbide boundaries sharply and uniformly.

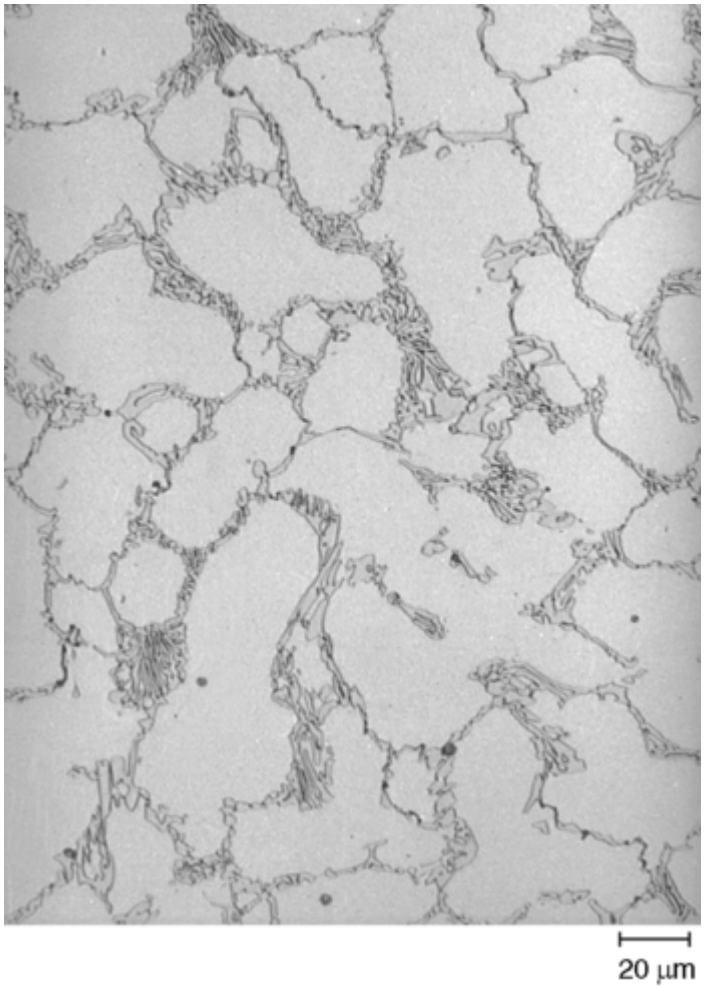

Fig. 15 Same as in Fig. 14 but after etching with 4% nital. 500×

Selective Color Etching. If the black-and-white etchants are inadequate for positive identification of the iron microstructures, other procedures must be used, such as selective color etching. The reagents referred to as tint etchants are usually acidic solutions with either water or alcohol as a solvent. They are chemically balanced to deposit a thin (40 to 500 nm), transparent film of oxide, sulfide, complex molybdate, elemental selenium, or chromate on the specimen surface. Coloration is developed by interference between light rays reflected at the inner and outer film surfaces. Crystallographic orientation, local chemical composition, and etching time affect film thickness and control color production. The use of selective etchants is invaluable for quantitative metallography, a field of growing importance (Ref 5).

When ferritic-pearlitic microstructures of cast iron contain large amounts of cementite and ledeburite, the differentiation of the white structural constituents is difficult after etching a specimen with nital. In such cases, hot alkaline sodium picrate (ASP) is recommended (Table 2, etch No. 4), which reveals cementite, tinted a brown color, while ferrite remains unaffected. This etch is a mixture of sodium hydroxide (NaOH), picric acid, and distilled water. Figure 16 shows the microstructure of a thin-walled, chilled ductile iron casting after etching with nital, while Fig. 17 shows the microstructure of the same specimen after etching with ASP; the brown-colored cementite and ledeburite are clearly visible in the pearlitic-ferritic matrix (the cementite in pearlite was also slightly tinted). It allows one to estimate the amount of cementite that should be removed from the casting microstructure in the annealing process.

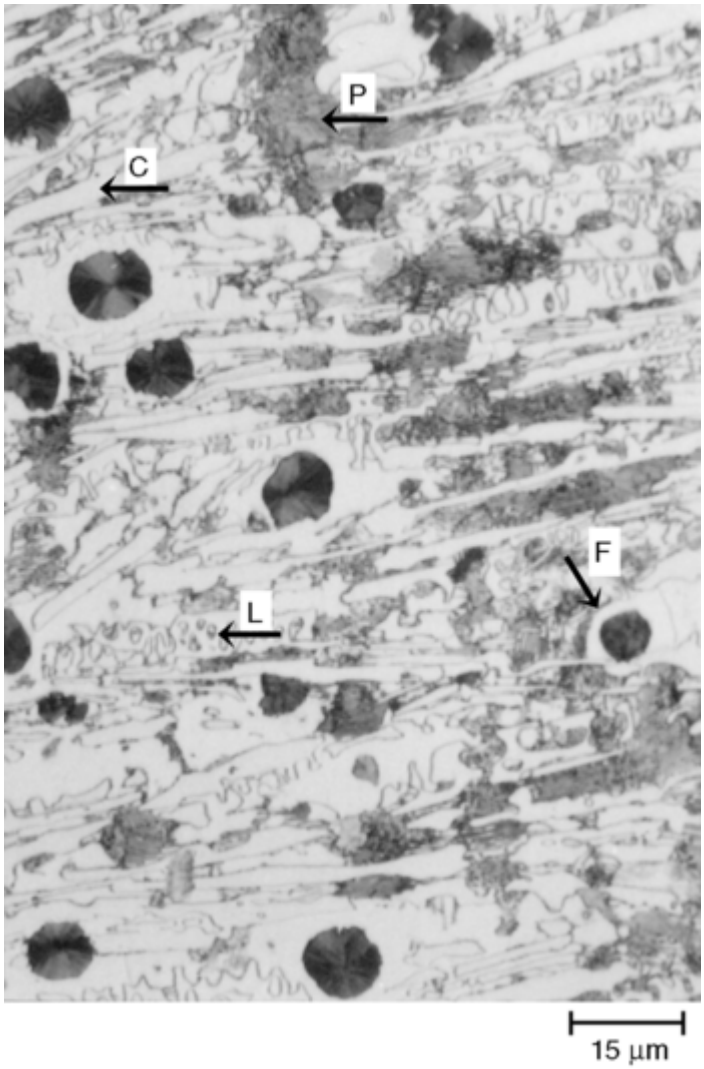

Fig. 16 As-cast ductile iron (Fe-3.07%C-0.06%Mn-2.89%Si-0.006%P-0.015%S-0.029%Mg). C, cementite; L, ledeburite; F, ferrite; and P, pearlite. Etched with 4% nital. 650× (microscopic magnification 500×)

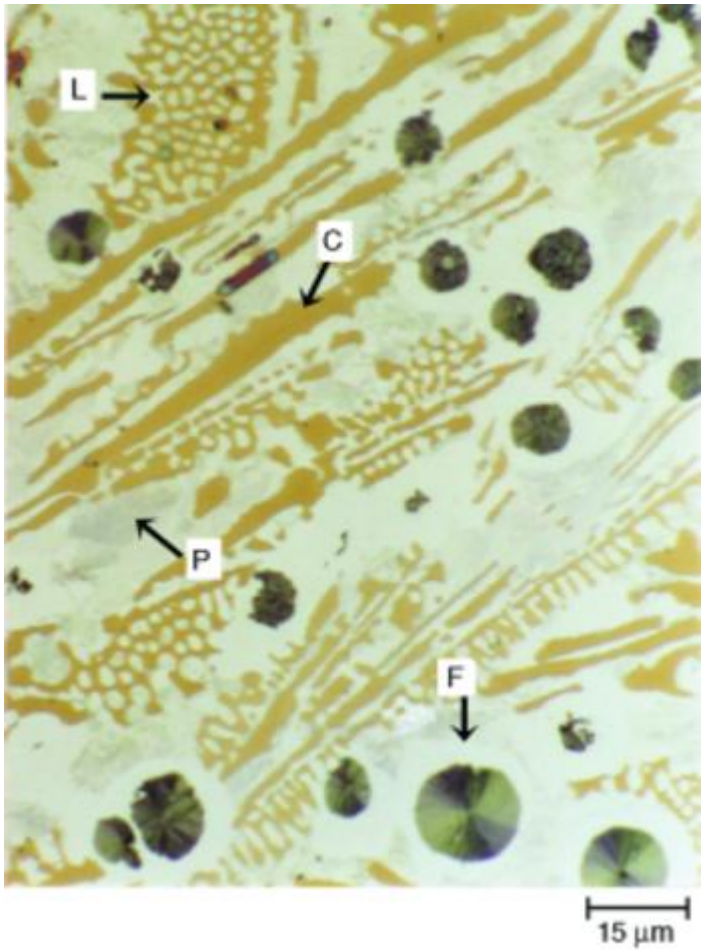

Fig. 17 Same as in Fig. 16 but after etching with hot alkaline sodium picrate. C, eutectic cementite; L, ledeburite; F, ferrite; and P, pearlite with slightly etched cementite. 650× (microscopic magnification 500×)

Segregation of silicon and phosphorus in iron is very strong and can be revealed with selective color etching methods. Klemm's I reagent (Table 2, etch No. 5), which tints ferrite while austenite and carbides remain colorless, consists of potassium metabisulfite ($K_2S_2O_5$) and a cold-saturated water solution of sodium thiosulfate ($Na_2S_2O_3 \cdot 5H_2O$) and is one of the etchants that can be used to reveal phosphorus and silicon segregation.

Usually, the distribution of the phosphorus eutectic, which solidifies in gray iron on the cell boundaries, is revealed by etching up to 4 min in 4% nital. Figure 18 shows the microstructure of as-cast gray iron with the ternary phosphorous eutectic. The cell boundaries, filled with steadite, are white, while their interiors are almost black due to overetching the pearlitic-ferritic matrix. Figure 19 shows the same microstructure after etching with Klemm's I reagent. The microregions inside the eutectic cells with a lower phosphorus content are tinted a blue color, while the areas with the ternary eutectic, situated at the boundaries of the eutectic cells, are almost colorless. In both cases, the cementite and iron phosphide in steadite are not etched, and the network is clearly visible.

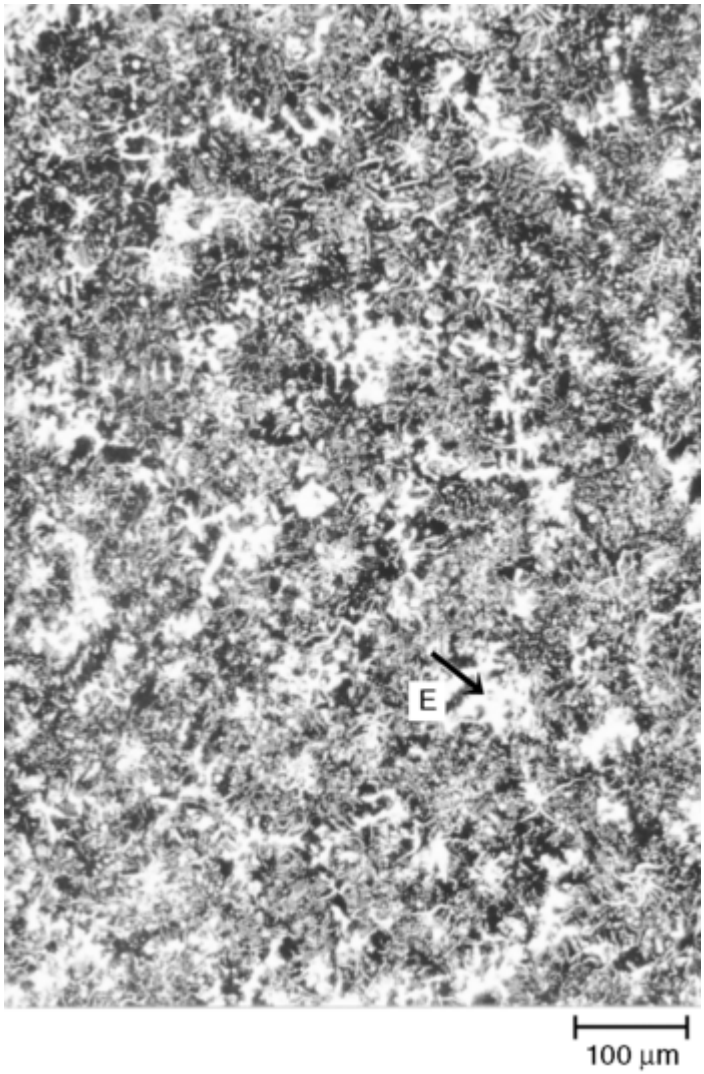

Fig. 18 As-cast gray iron (Fe-3.24%C-2.32%Si-0.54%Mn-0.71%P-0.1%S). E, phosphorous ternary eutectic. Etched with 4% nital. 100×

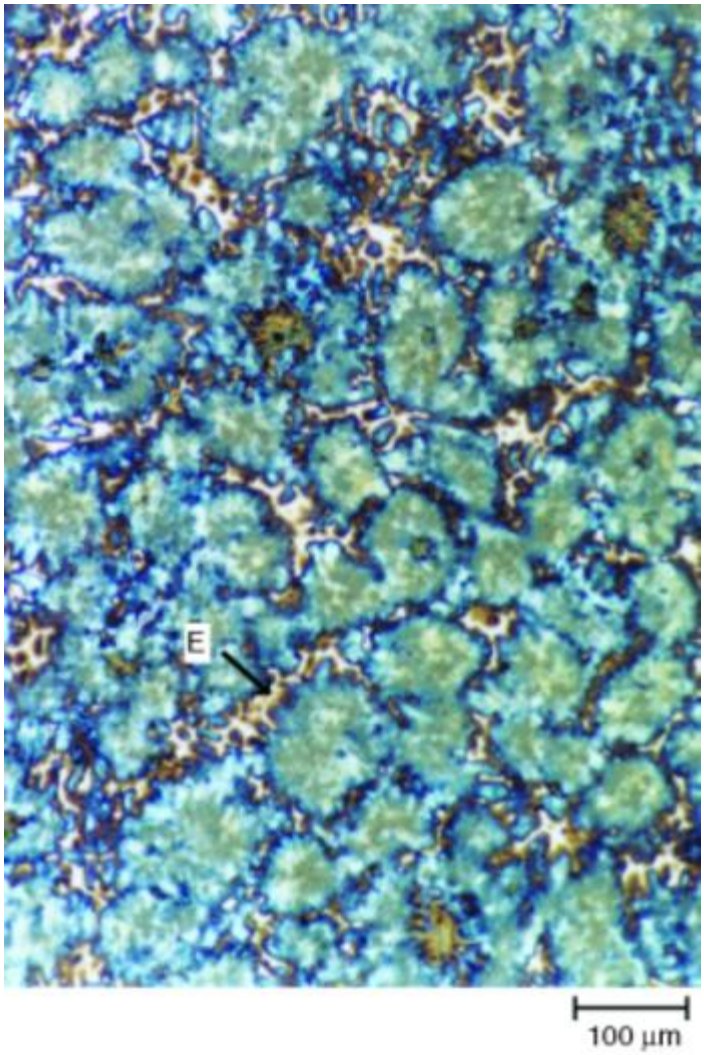

Fig. 19 Same as in Fig. 18 but after etching with Klemm I reagent. E, phosphorous ternary eutectic. 100×

Figure 20 shows silicon segregation in an ADI microstructure after etching with Klemm's I reagent. The regions outlining the cell boundaries, low in silicon, are tinted a blue color, while the very thin halos around the graphite nodules, where the silicon content is highest, remain colorless. Acicular ferrite is orange, and austenite is not tinted. Figure 21 shows the same microstructure after etching with Beraha's CdS reagent (Table 2, etch No. 6), an aqueous solution of sodium thiosulfate ($Na_2S_2O_3 \cdot 5H_2O$), citric acid ($C_6H_8O_7 \cdot H_2O$), and cadmium chloride ($CdCl_2 \cdot 2.5H_2O$). The silicon segregation is revealed the same way as after using Klemm's I reagent.

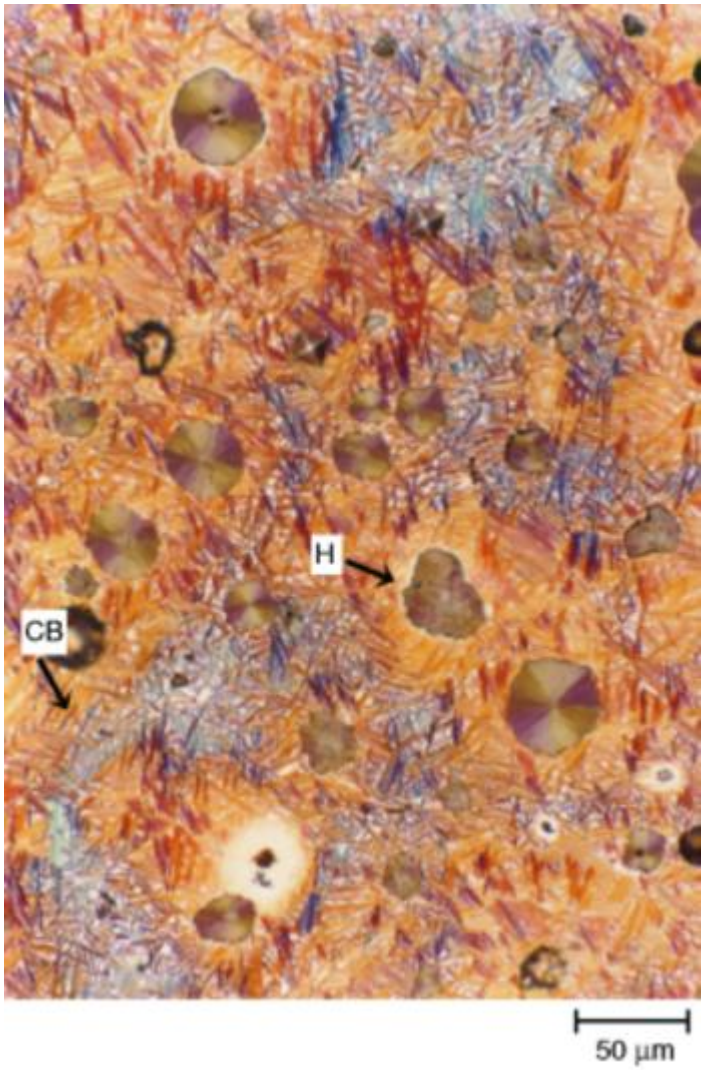

Fig. 20 Austempered ductile iron (Fe-3.6%C-2.5%Si-0.06%P-1.5%Ni-0.7%Cu). CB, cell boundaries; H, ferritic halo around the graphite nodules. Etched with Klemm I reagent. 200×

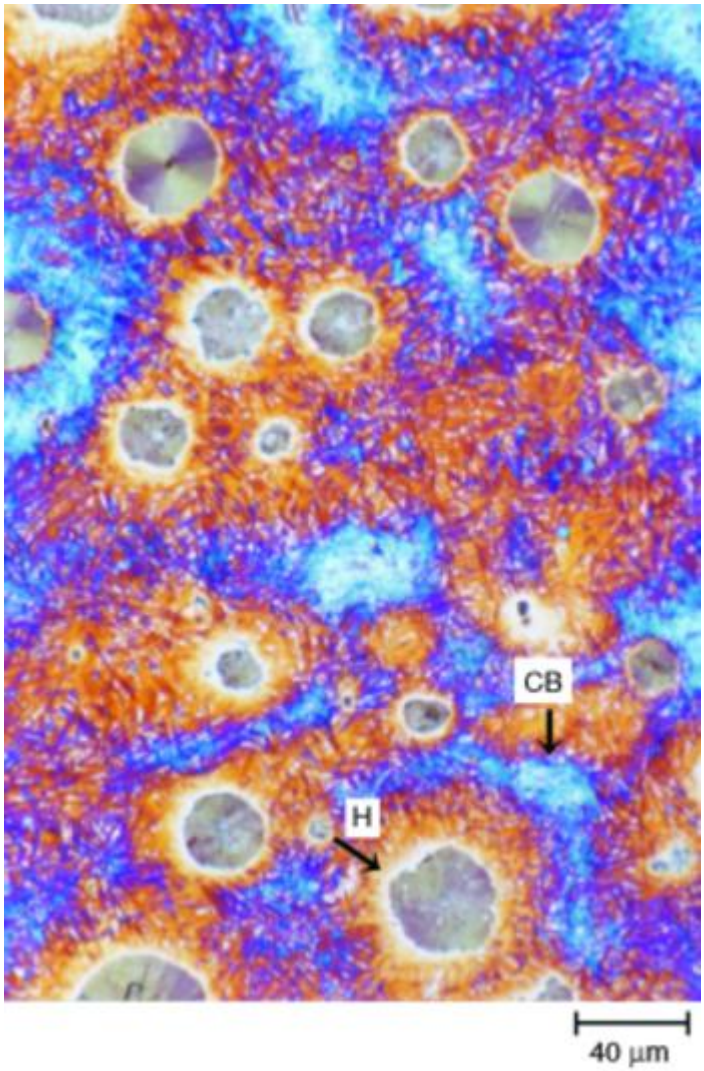

Fig. 21 Same as in Fig. 20 but after etching with Beraha's CdS reagent. H, ferritic halo; CB, cell boundaries. 250×

To reveal silicon segregation in nonalloyed ductile cast iron inside eutectic cells, the hot aqueous solution of sodium hydroxide, picric acid, and potassium pyrosulfite ($K_2S_2O_5$) can be used (Table 2, etch No. 7). Figure 22 shows the different colors of the microstructure, which change from green through red, yellow, blue, and dark brown to light brown as the silicon content is changing from the graphite nodule to the cell boundaries. The regions with the lowest silicon content at the cell boundaries remain colorless. Before etching, ferritization of the specimen was carried out to enhance the visibility of the microstructural colors.

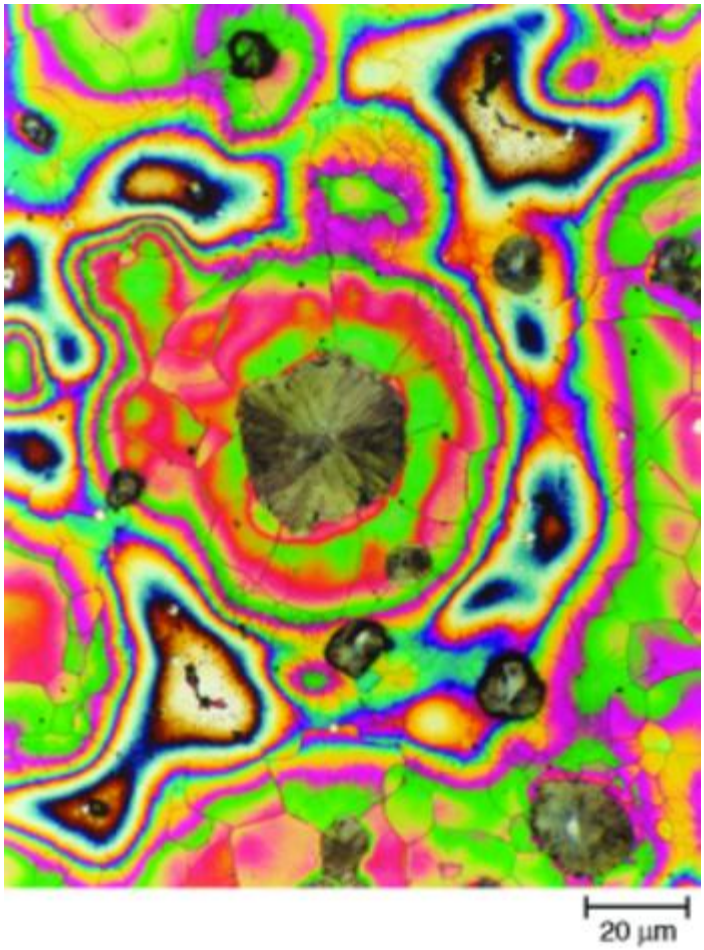

Fig. 22 Nodular iron (Fe-3.9%C-2.9%Si-0.32%Mn-0.06%P-0.037%Mg-1.5%Ni-0.57%Cu). Silicon microsegregation was revealed. The casting was annealed. Etched with hot aqueous solution of sodium hydroxide, picric acid, and potassium pyrosulfite (Table 2, etchant No. 7). 500×

The revealing and differentiation of all constituents in steadite is invaluable for the determination of the type of eutectic as well as the amount of each constituent. In the case of the ternary phosphorous eutectic, which consists of ferrite, cementite, and iron phosphide (Fe_3P), nital does not help in the identification of the constituents, nor does it provide enough information about distribution of the eutectic constituents. Figure 23 shows the microstructure of the ternary phosphorous eutectic in gray iron after etching in 4% nital. The white areas that surround the ternary eutectic and are also visible inside the eutectic can be either ferrite or cementite. Figure 24 shows the microstructure of the same specimen after selective color etching with hot ASP (Table 2, etchant No. 4). Cementite in the eutectic is tinted brown and blue colors (also in pearlite), while ferrite and iron phosphide are not tinted. To reveal the ferrite, the same specimen was etched with Klemm's I reagent. Figure 25 shows the eutectic regions with precipitates of brown ferrite (also in pearlite), while cementite and iron phosphide are not tinted.

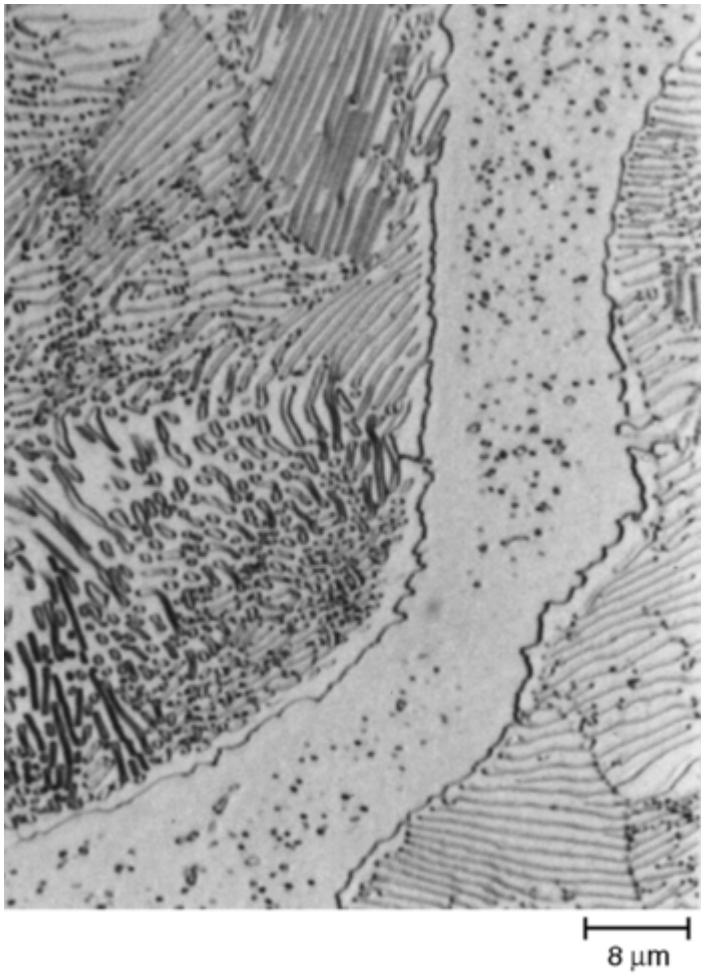

Fig. 23 As-cast gray iron (Fe-3.33%C-1.64%Si-0.31%Mn-1.37%P-0.107%S). Ternary phosphorus eutectic. Etched with 4% nital. 1300× (microscopic magnification 1000×)

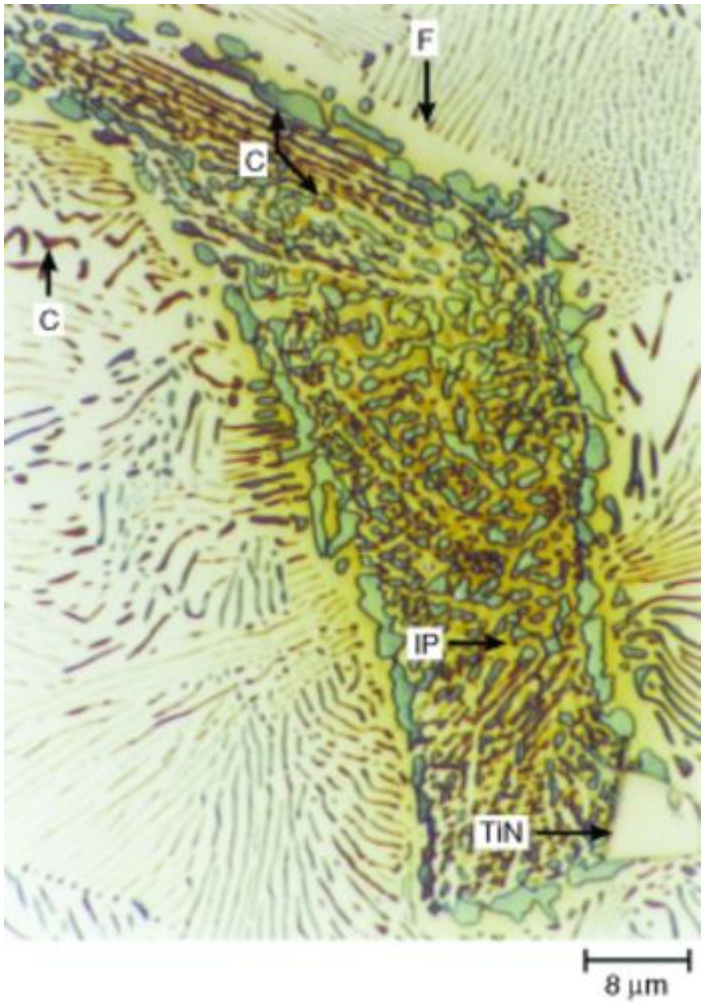

Fig. 24 Same as in Fig. 23 but after etching with hot alkaline sodium picrate. C, cementite; F, ferrite (unaffected); IP, iron phosphide + ferrite; and TiN, titanium nitride. 1300× (microscopic magnification 1000×)

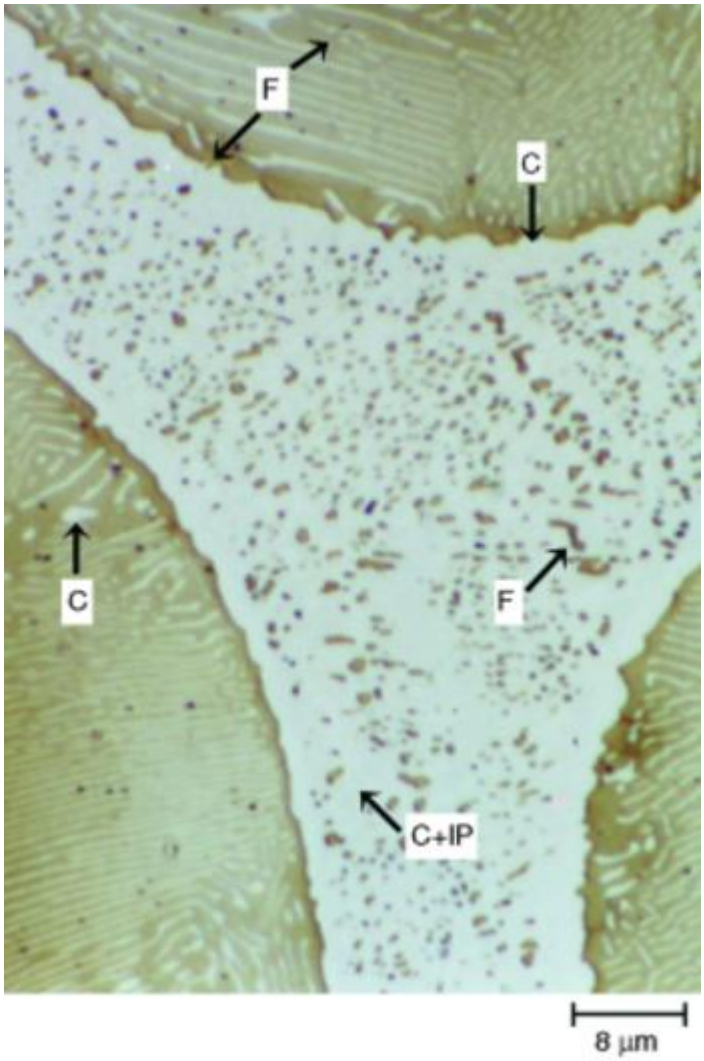

Fig. 25 Same as in Fig. 23 but after etching with Klemm I reagent. F, ferrite; C, cementite; and C + IP, cementite + iron phosphide inside the precipitate of phosphorous eutectic. 1300× (microscopic magnification 1000×)

Murakami's reagent (Table 2, etch No. 8), used at 50 °C (120 °F) for 3 min and containing potassium hydroxide (KOH), potassium ferricyanide ($K_3Fe(CN)_6$), and distilled water, can be used for revealing and estimating the amount of iron phosphide in steadite. Figure 26 shows this constituent of the ternary phosphorous eutectic microstructure, which was tinted a light-brown color, while cementite and ferrite remained colorless. The microstructure of the same specimen after overetching (5 min) with the same reagent is shown in Fig. 27. This time, cementite was also revealed and was tinted a yellow color, while ferrite remained white. The color of the iron phosphide changed to a dark-brown and gray-blue color. Nevertheless, extending the etching time beyond 3 min is not recommended, because this can falsify the true results of the microstructural examination.

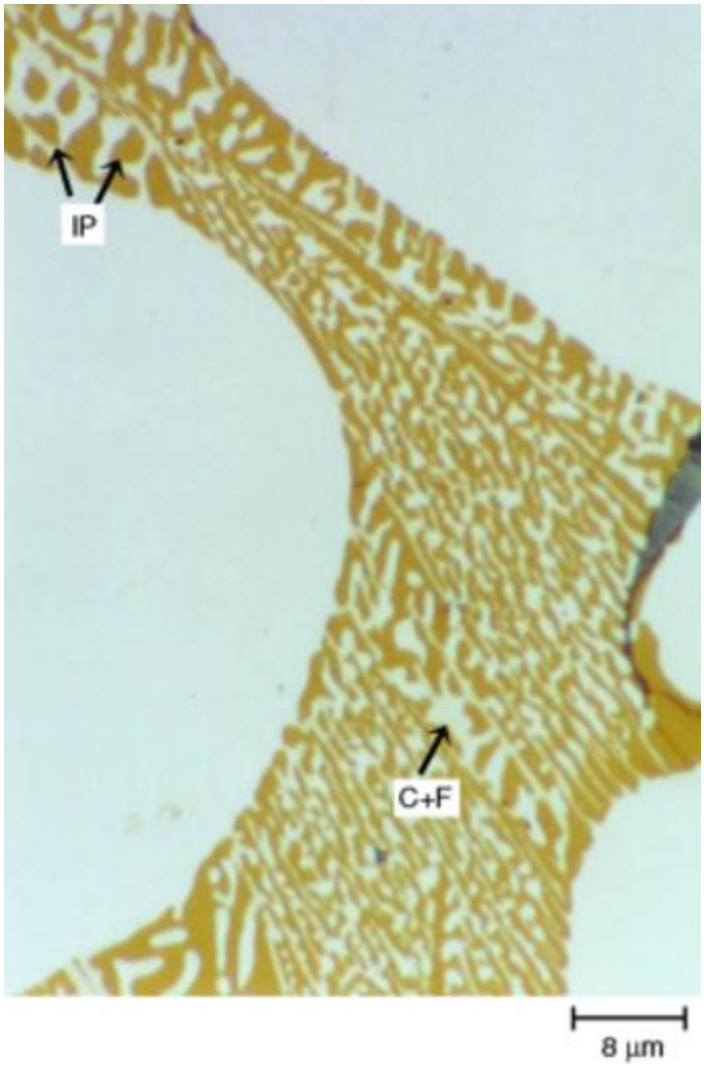

Fig. 26 Same as in Fig. 23 but after etching with hot Murakami's reagent. IP, iron phosphide; C + F, cementite + ferrite inside the precipitate of phosphorous eutectic. 1300× (microscopic magnification 1000×)

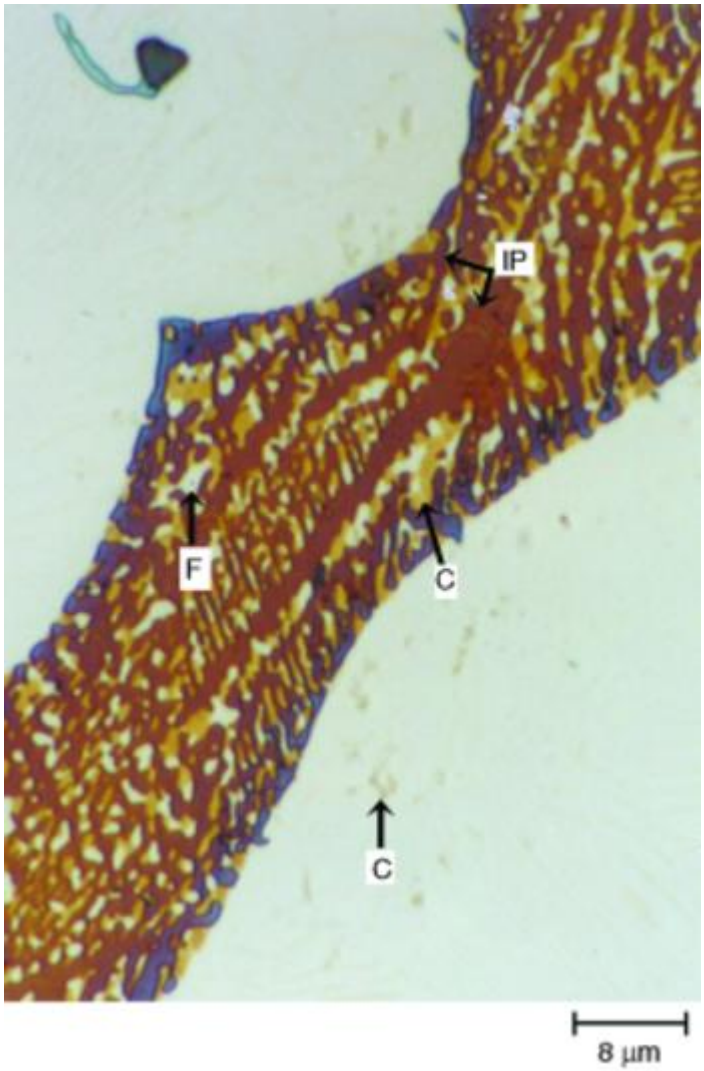

Fig. 27 Same as in Fig. 26 but after overetching with hot Murakami's reagent. IP, iron phosphide; C, cementite; and F, ferrite. 1300× (microscopic magnification 1000×)

Good differentiation of all constituents in the ternary phosphorus eutectic can be obtained with Beraha's reagent (Table 2, etch No. 9), a mixture of hydrochloric acid (HCl), selenic acid (H_2SeO_4), and ethanol. According to Beraha, this etchant tints iron phosphide a dark-blue color, cementite a violet or dark red, and ferrite remains white. Figure 28 shows the microstructure of the ternary eutectic, with cementite tinted a light-pink color, while the rest of the constituents were colored properly.

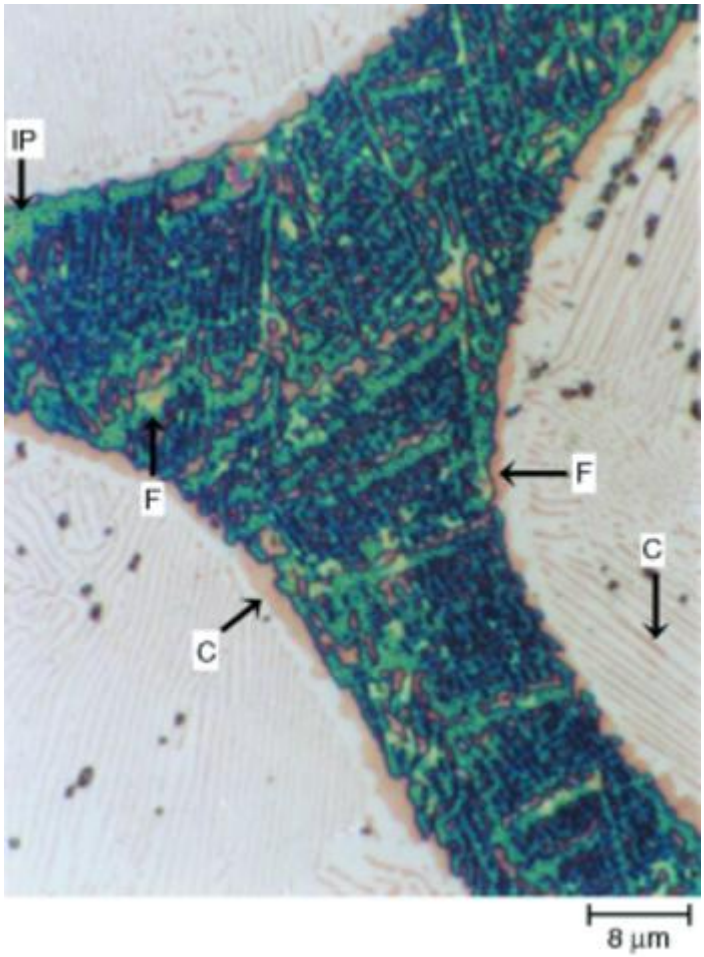

Fig. 28 Same as in Fig. 25 but after etching with Beraha's reagent with selenic acid. IP, iron phosphide; C, cementite; and F, ferrite. The dark points in pearlite, which look like artifacts, can be iron phosphide precipitates or fine, nonmetallic inclusions. 1300× (microscopic magnification 1000×)

Figure 29 shows the microstructure of the pseudobinary phosphorous eutectic, which consists of iron phosphide and ferrite, after etching with 4% nital. The same specimen was etched with hot ASP (Table 2, etchant No. 4). This did not tint the iron phosphide or the ferrite. Because cementite is not present in the eutectic, the only etching was of cementite in the pearlite, which showed up very lightly. To reveal the microstructure of the eutectic, the specimen was next etched with 4% nital. Figure 30 shows the results after using hot ASP and then nital. Hot Murakami's reagent perfectly tinted the iron phosphide in the binary phosphorous eutectic a brown color, while pearlite was colorless, as shown in Fig. 31.



Fig. 29 As-cast gray iron (Fe-3.62%C-2.03%Si-1.13%P-0.61%Mn-0.137%S-0.113%Cr-0.478%Ni-0.004%Al). E, binary phosphorous eutectic; F, ferrite at the graphite precipitate; and P, pearlite. Etched with 4% nital. 500×



Fig. 30 Same as in Fig. 29 but after etching with hot alkaline sodium picrate and 4% nital. Pearlitic matrix is revealed; phosphorous eutectic is unaffected. 500×

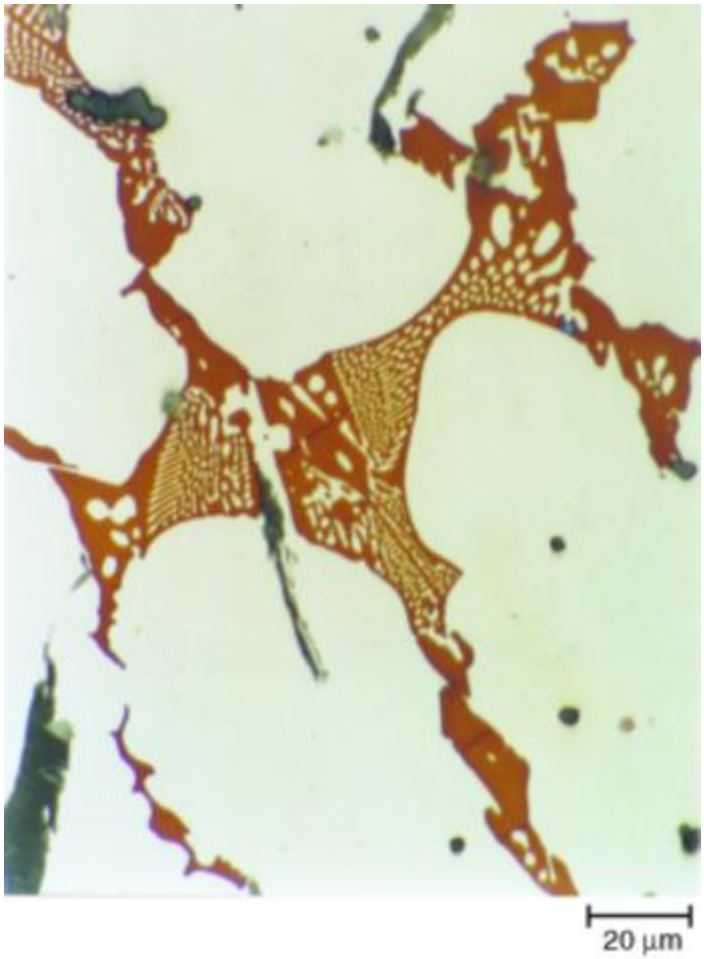

Fig. 31 Same as in Fig. 29 but after etching with hot Murakami reagent. Only brown-tinted iron phosphide was revealed. 500×

Beraha-Martensite (B-M) (Table 2, etch No. 10) and aqueous 10% sodium metabisulfite (SMB) (Table 2, etch No. 11) reagents for selective color etching are very useful in cases where microstructural details are very fine and barely visible after etching with nital. They reveal all of the constituents, tinting them to expected colors that are useful for verifying that the heat treatment process was carried out correctly.

The B-M etchant is a mixture of stock solution (1:5, HCl to water), potassium metabisulfite ($K_2S_2O_5$), and ammonium acid fluoride ($NH_4F{\cdot}HF$). According to Ref 6, B-M tints martensite a blue color and bainite a brown color, while the residual austenite and carbides remain unaffected.

The B-M etchant can be used for identification of the constituents after heat treatment of cast iron by tinting phases to different colors. It also improves microstructural contrast, enhancing visibility and permitting estimation of even small amounts of the residual austenite (although x-ray diffraction results are always more than 10% greater than by light microscopy) and fine carbides. Figure 32 shows the black-white microstructure of ADI after etching with 4% nital, while Fig. 33 shows the same microstructure after etching with 4% picral. Figure 34 and 35 show the microstructure of the same specimen after color etching, respectively, with B-M and with aqueous 10% SMB etchants. The SMB tints martensite a brown color and bainite a blue color, while austenite and carbides are colorless. Both etching time in B-M and the different crystallographic orientations affected the color of the coarse, high-carbon martensitic plates, which vary from blue to yellow. The brown areas in the microstructure (Fig. 34) are the patches of fine martensite. This color differentiation of microstructure occurs due to the change in size of the plate martensite as transformation progresses. However, this is not the only factor, because some of the larger plates are also brown. There is only a very small amount of austenite, which surrounds the acicular ferrite at the graphite nodules and in the matrix. The SMB etchant is even more useful than the B-M etchant in the case where the dominating phase in the ADI microstructure is martensite, and acicular ferrite is weakly visible. In ADI, the martensite of both types is tinted a brown color, the acicular ferrite is colored the same as bainite, that is, blue color, while austenite is colorless, which was shown in Fig. 35 (see the section “Ductile Iron” in this article).

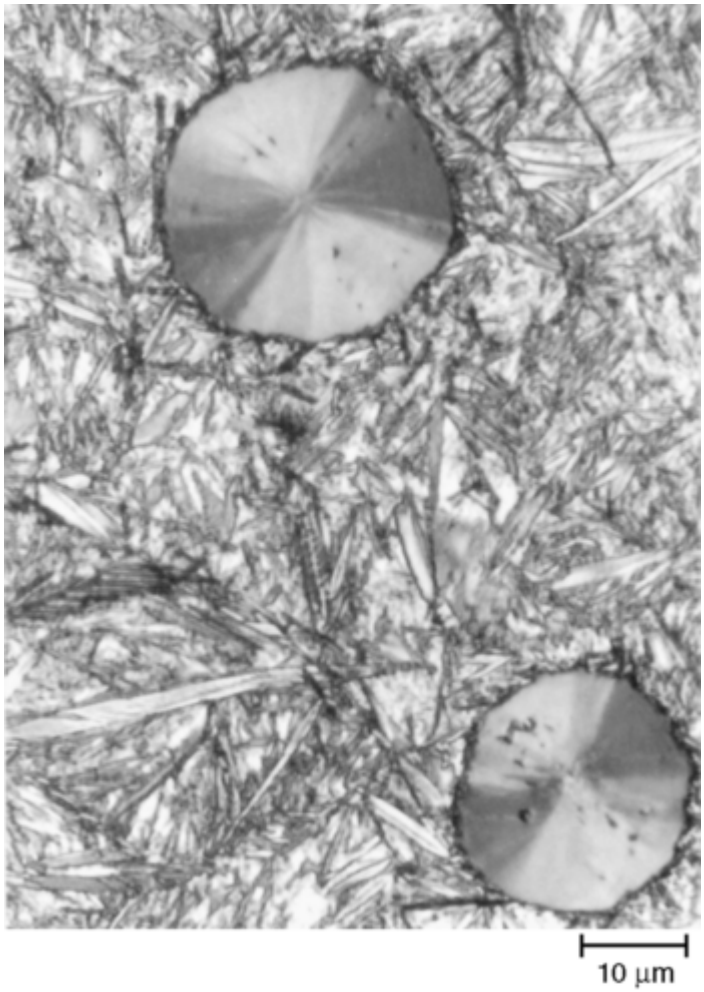

Fig. 32 Austempered ductile iron (Fe-3.6%C-2.5%Si-0.056%P-0.052%Mg-0.7%Cu). Martensite and acicular ferrite. The casting was austempered at 900 °C (1650 °F), held 2 h, taken to salt bath at 360 °C (680 °F), held 2 min, and air cooled. Etched with 4% nital. 1000×

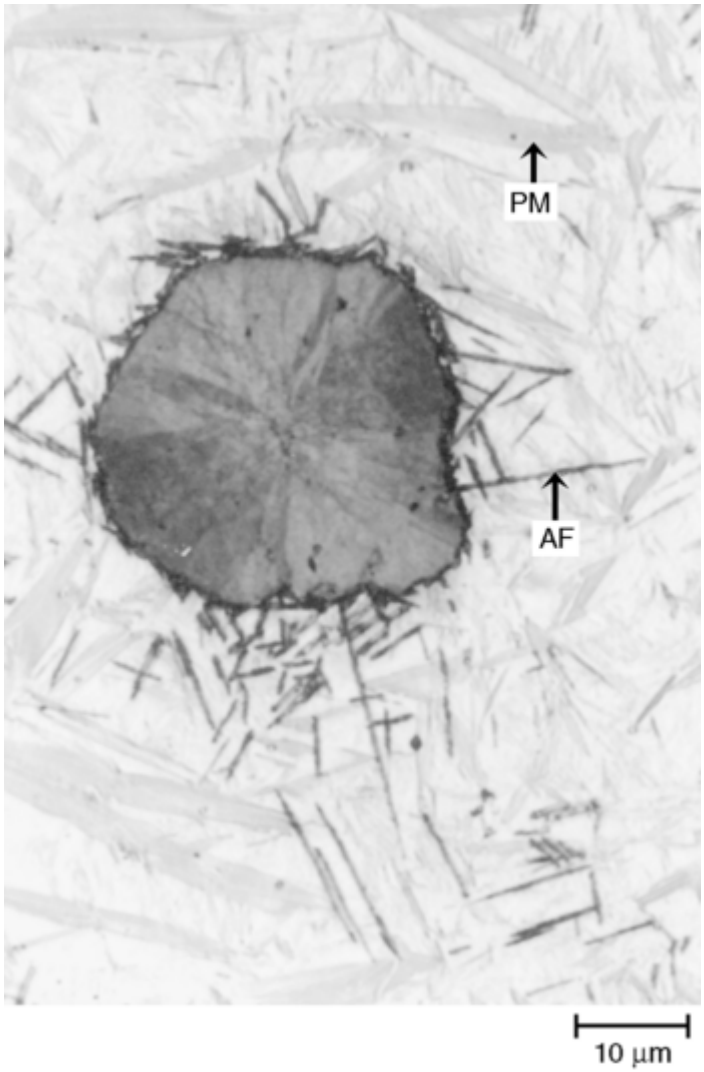

Fig. 33 Same as in Fig. 32 but after etching with 4% picral. AF, acicular ferrite; PM, plate martensite. 1000×

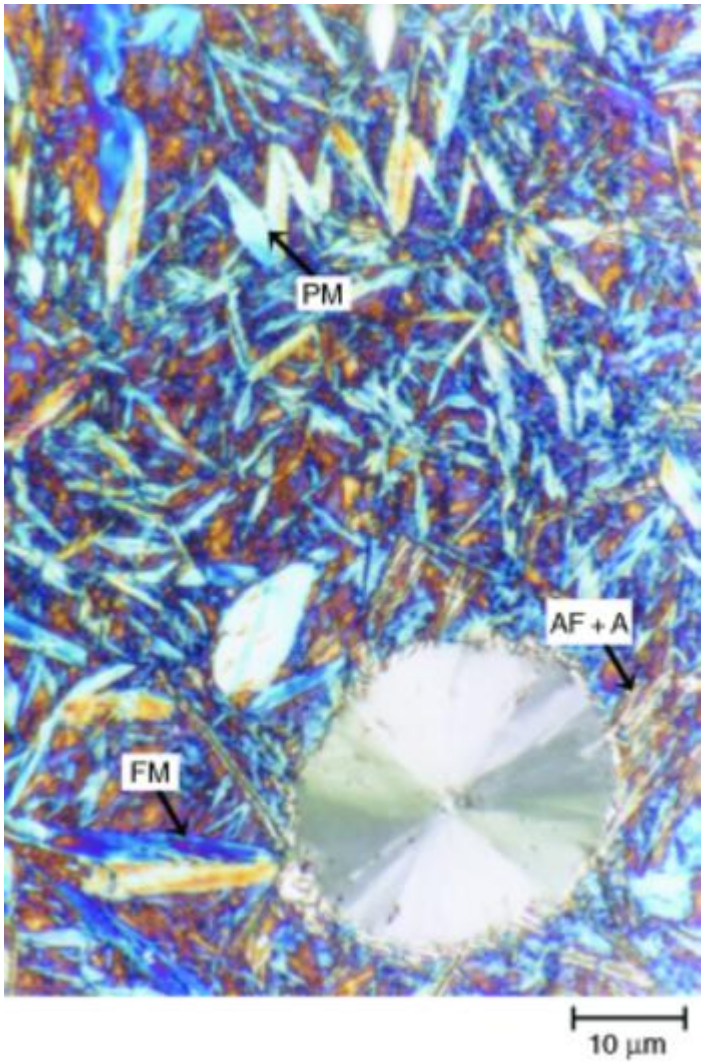

Fig. 34 Same as in Fig. 32 but after etching with Beraha-Martensite reagent. PM, blue-yellow plate martensite; FM, brown fine martensite; and AF + A, dark needles of acicular ferrite surrounded with colorless austenite. 1000×

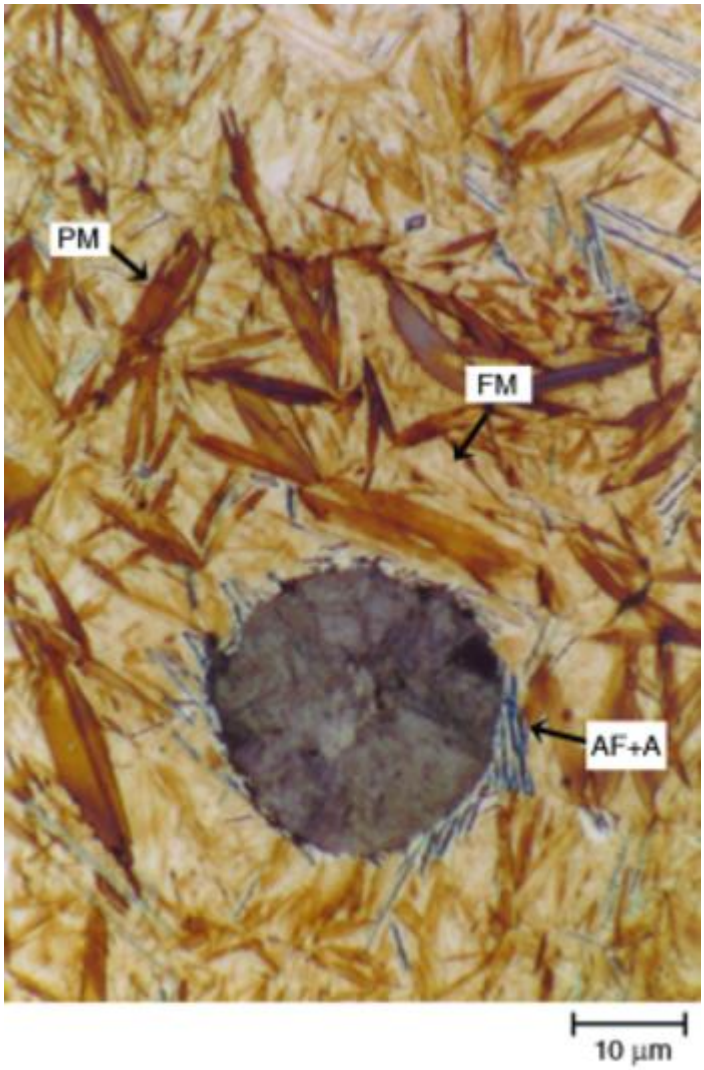

Fig. 35 Same as in Fig. 32 but after etching with 10% sodium metabisulfite. PM, plate martensite; FM, fine martensite; and AF + A, acicular ferrite and austenite. 1000×

Figure 36 shows the microstructure of ADI after etching with 4% nital, while Fig. 37 and 38 show the same microstructure after etching with B-M and 10% SMB, respectively. Nital etched the acicular ferrite, while the austenite is white. Some areas that were darkened may be martensite, but there is no clear distinction between martensite and acicular ferrite with nital. Selective color etching with the two previously mentioned reagents clearly revealed small patches of martensite, which were blue after etching with B-M and brown after etching with 10% SMB; acicular ferrite was colored blue (darker with B-M than with SMB), and austenite remained colorless.

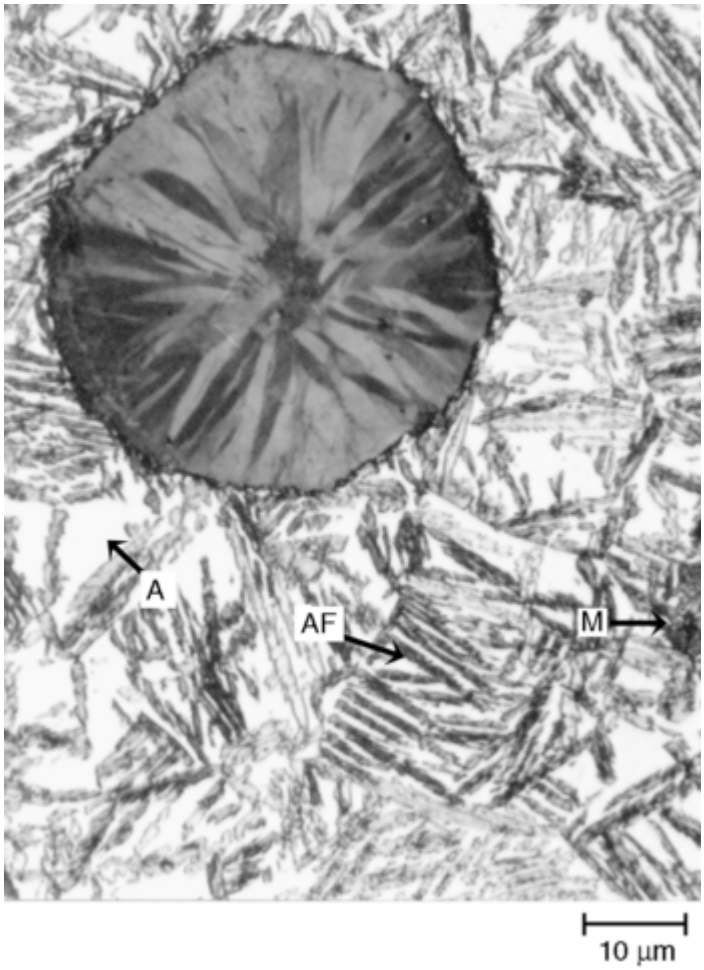

Fig. 36 Austempered ductile iron (Fe-3.6%C-2.5%Si-0.052%Mg-0.7%Cu). AF, acicular ferrite; A, austenite; and M, martensite. The casting was austempered at 900 °C (1650 °F), held 2 h, taken to salt bath at 360 °C (680 °F), held 30 min, and air cooled. Etched with 4% nital. 1000×

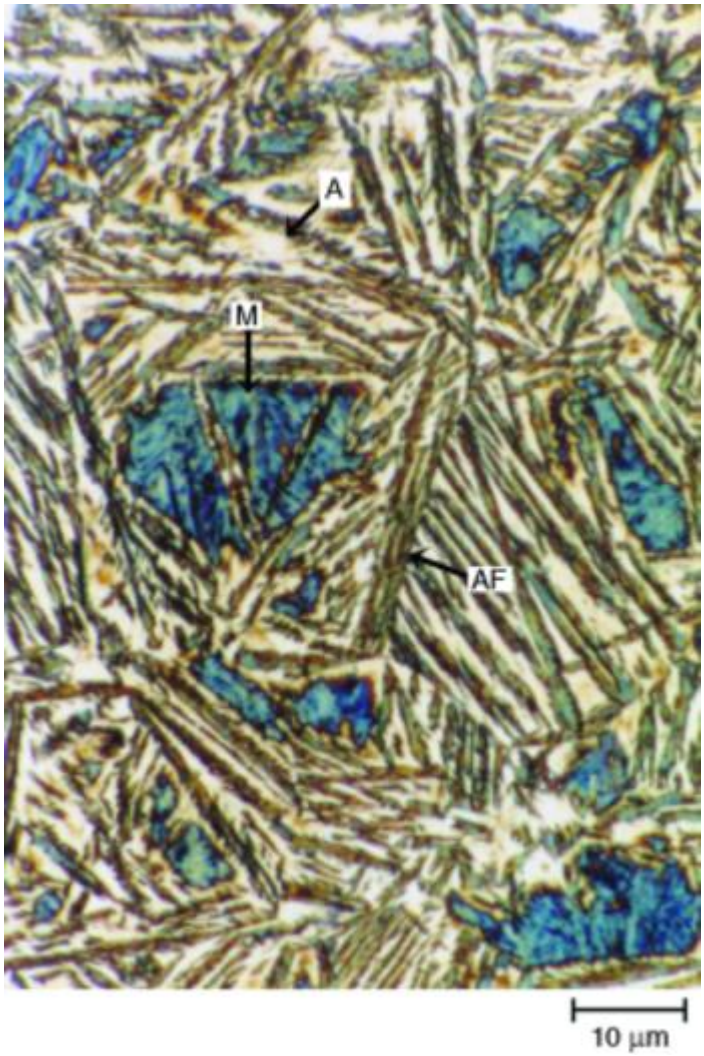

Fig. 37 Same as in Fig. 36 but after etching with Beraha-Martensite reagent. AF, acicular ferrite; A, austenite; and M, martensite. 1000×

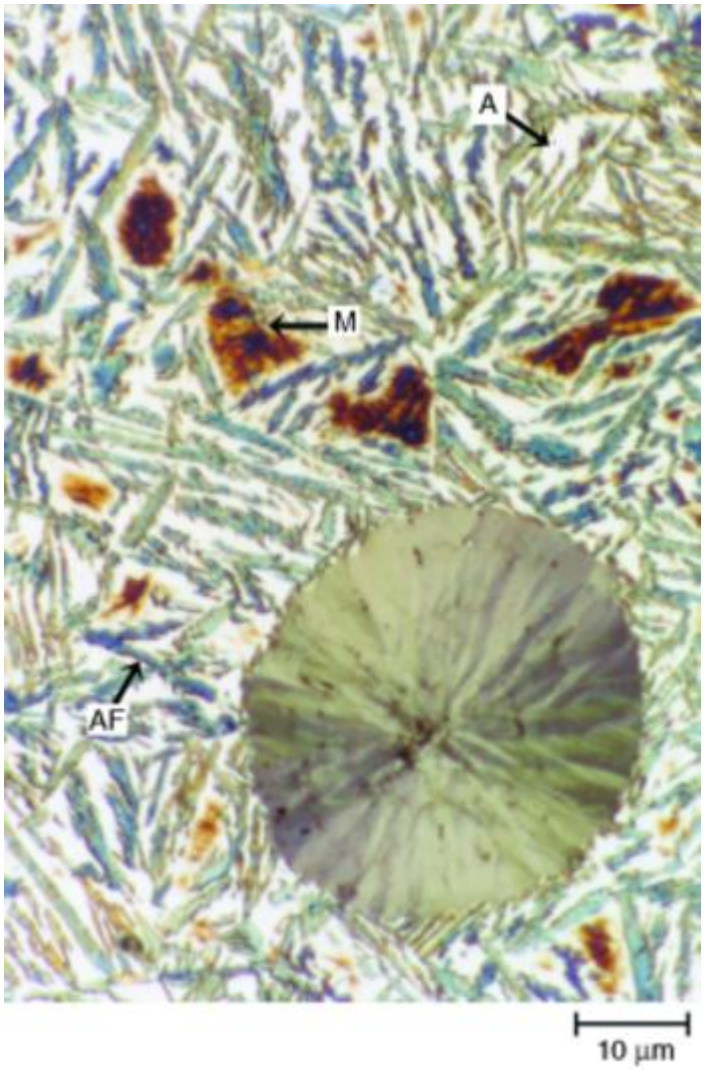

Fig. 38 Same as in Fig. 36 but after etching with 10% sodium metabisulfite. AF, acicular ferrite; A, austenite; and M, martensite. 1000×

The same results were achieved with the use of B-M reagent to reveal the microstructure of alloyed cast iron after heat treatment. The microstructure, which is shown in Fig. 39, consists of brown patches of fine martensite (which may have transformed from austenite during or after tempering), while the blue needles are high-carbon plate martensite. Figure 40 shows the microstructure of the same specimen after etching with 4% nital; in this case, the recognition of martensite is not straightforward.

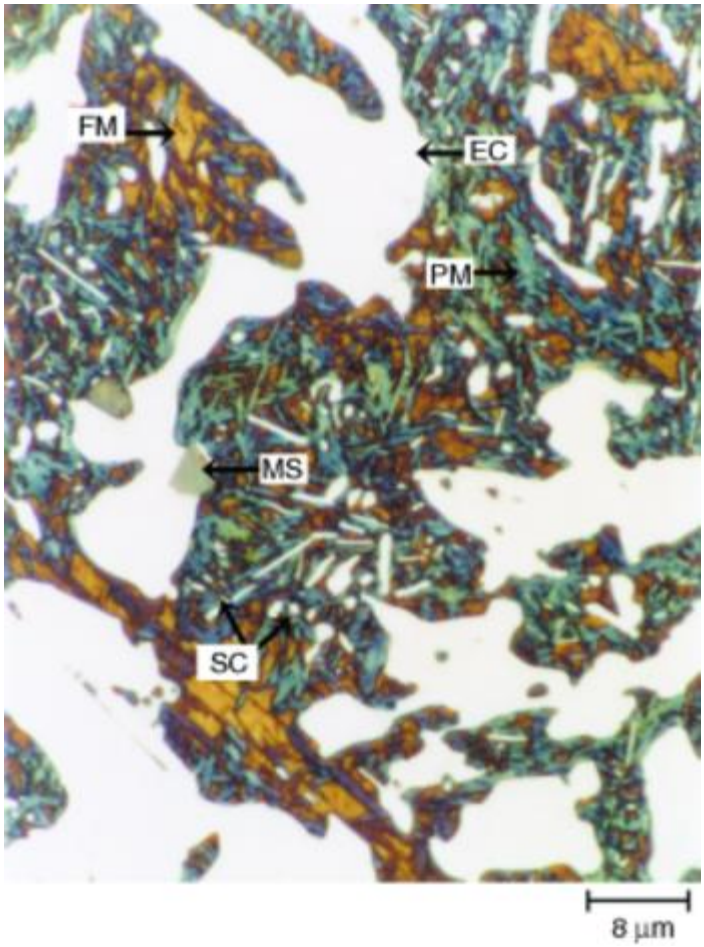

Fig. 39 White alloyed cast iron (Fe-3.4%C-0.92%Mn-1.89%Si-9.52%Cr-6.27%Ni). Etched with Beraha-Martensite. PM, plate martensite; FM, fine martensite; EC, eutectic carbides type M_7C_3; SC, secondary carbides; and MS, manganese sulfite. The casting was heat treated: austenitized at 750 °C (1380 °F), held 2 h, and air cooled; tempered at 250 °C (480 °F), held 4 h, and air cooled. 1300× (microscopic magnification 1000×)

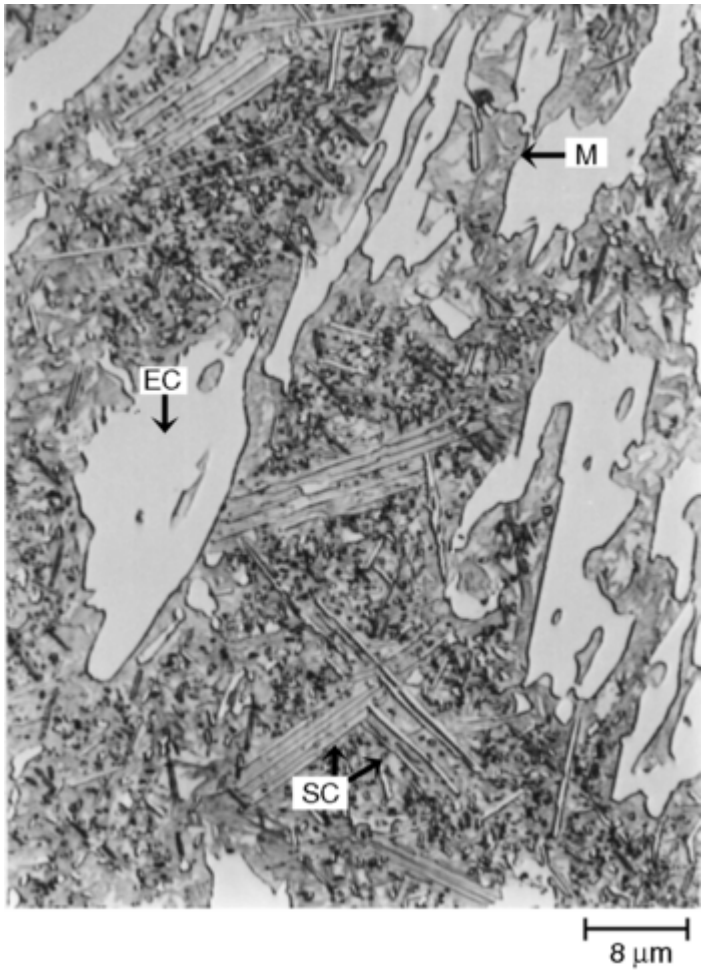

Fig. 40 Same white iron as in Fig. 39 but after etching with 4% nital. M, martensite; EC, eutectic carbides; and SC, secondary carbides. 1300× (microscopic magnification 1000×)

Figure 41 and 42 show the microstructure of the same iron but in the as-cast condition after etching with glyceregia and with Lichtenegger and Bloech I (LBI), respectively (Table 2, etchant No. 3 and 12). The LBI is an aqueous solution of ammonium bifluoride ($NH_4F{\cdot}HF$) and potassium metabisulfite ($K_2S_2O_5$) (Table 2, etch No. 12). In chromium-nickel alloys, LB I tints austenite, while carbides and ferrite (if present) remain unaffected (white). Glyceregia outlines only the eutectic carbides, while the LB I etchant also reveals microsegregation. The microstructure shown in Fig. 42 consists of austenite, tinted brown and blue color, and white (noncolored) carbides. The blue austenitic areas surrounding the eutectic carbides indicate regions with a lower concentration of carbide-forming elements, such as carbon and chromium, and perhaps a higher concentration of elements that are not present in the carbides, such as silicon and nickel.

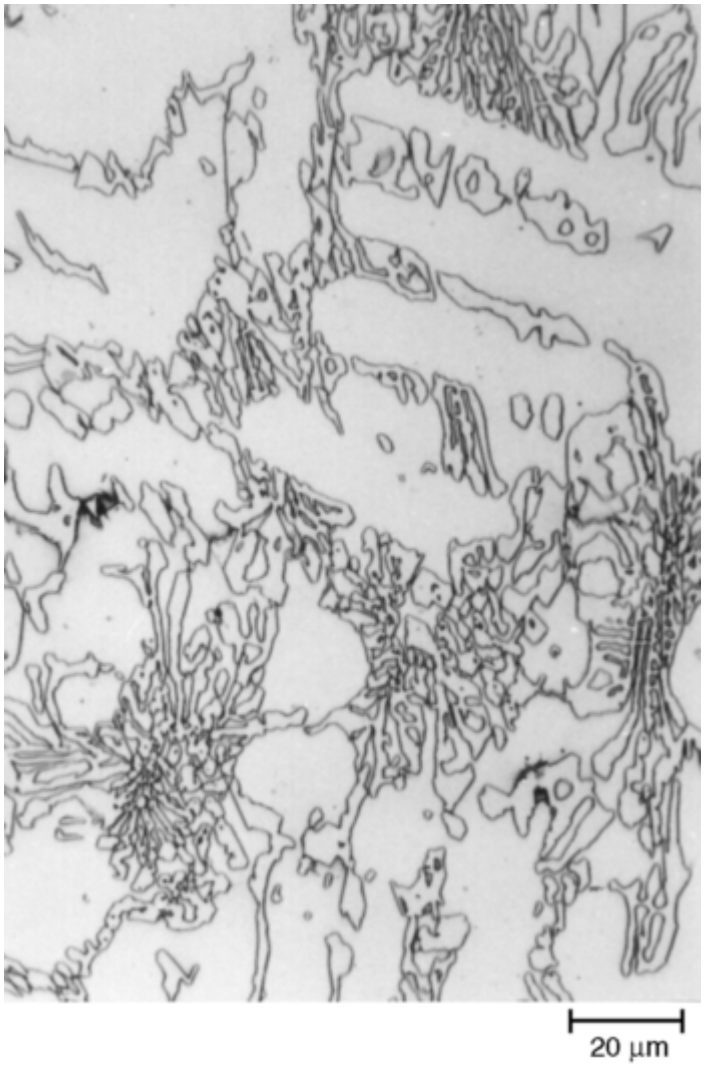

Fig. 41 Same white iron as in Fig. 39 and Fig. 40 but as-cast. Eutectic carbides in austenitic matrix. Etched with glyceregia. 500×

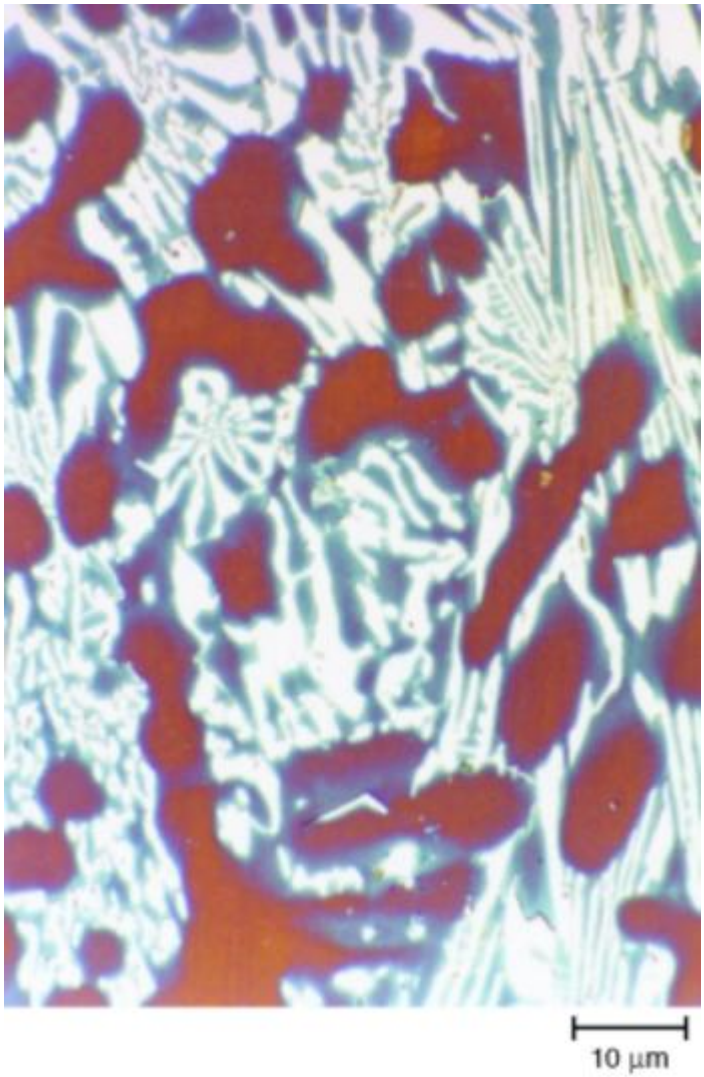

Fig. 42 Same as in Fig. 41 but after etching with Lichtenegger and Bloech I. Austenite is dark brown, and dendritic segregation is visible around unaffected carbides. 1000×

Figure 43 shows the microstructure of a high-chromium cast iron after etching with glyceregia, revealing columnar primary carbides and eutectic carbides, both $(FeCr)_7C_3$ type, uniformly distributed in the matrix. Figure 44 shows the microstructure of the same specimen after etching with the standard Murakami's etchant at room temperature. The carbides are tinted an orange color, while the matrix is not colored. X-ray diffraction determined that the matrix was austenitic-ferritic; the matrix was not colored using the LB I tint etchant due to missing nickel in that iron.

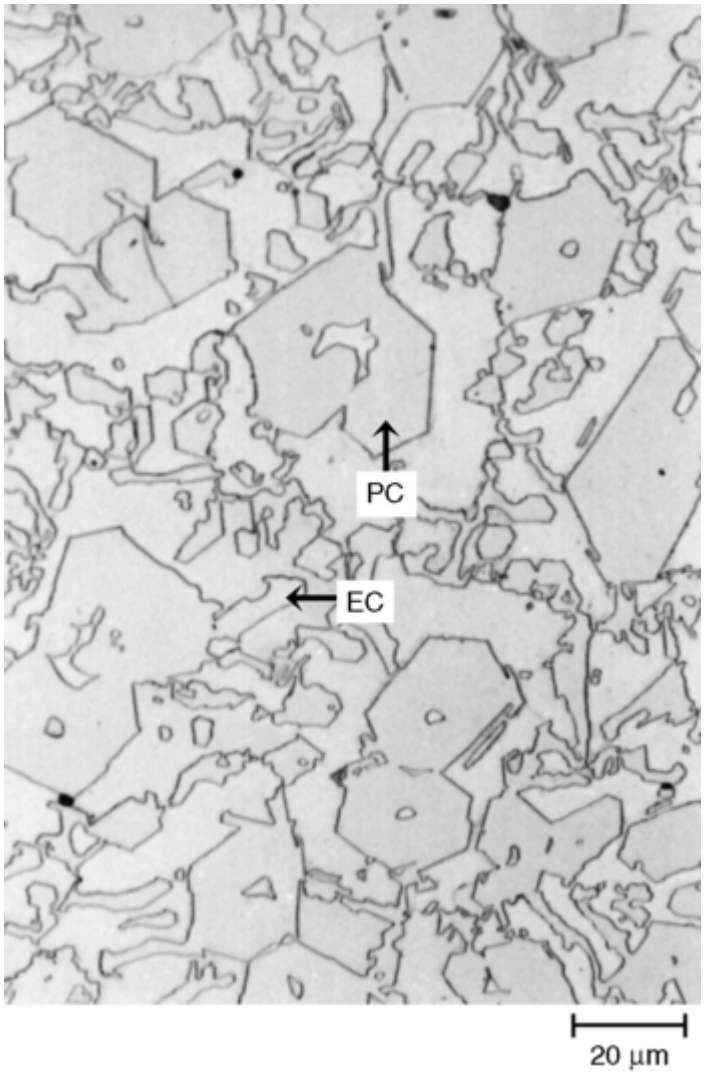

Fig. 43 As-cast high-chromium white iron (Fe-4.52%C-0.4%Si-2.86%Mn-35.0%Cr-0.06%P-0.012%S). PC, primary carbides; EC, eutectic carbides, both M_7C_3 type. Etched with glyceregia. 500×

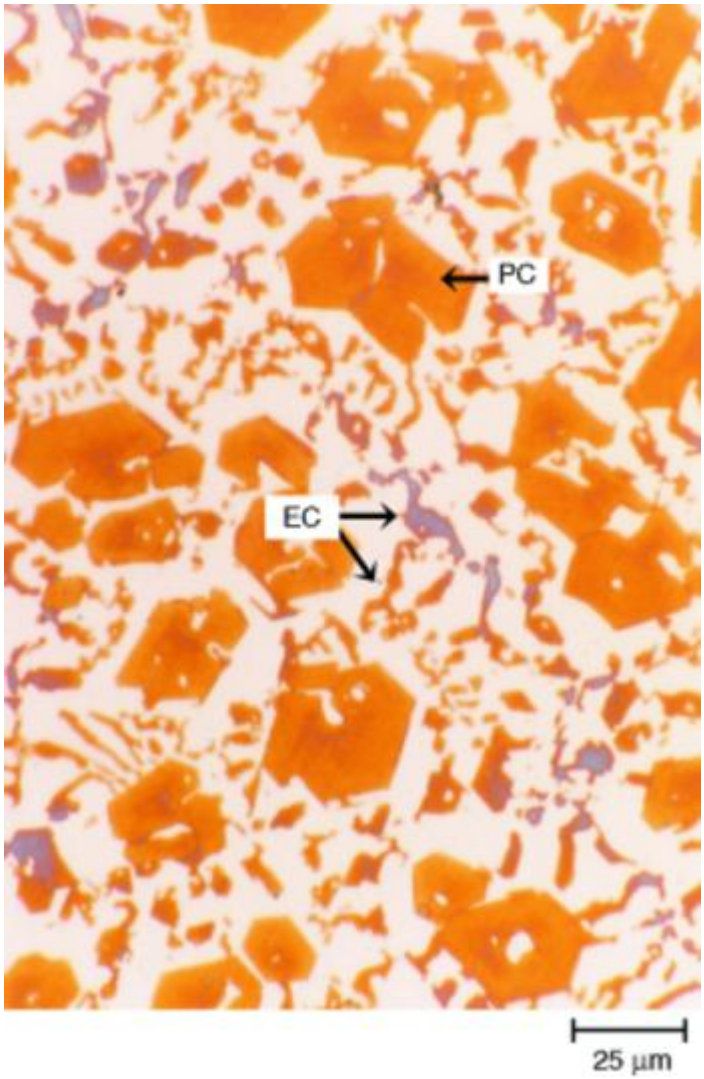

Fig. 44 Same as in Fig. 43 but after etching with Murakami's reagent (at room temperature). PC, orange primary carbides; EC, orange and gray eutectic carbides. 400×

The basic etchants mentioned previously, which are suitable for revealing microstructures as well as for phase identification in irons, are listed in Table 2.

Dark-Field Illumination and Differential Interference Contrast. Dark-field illumination (DFI) technique for microstructural examination produces a very strong image contrast that makes it possible to see features in the microstructure that are invisible or weakly visible in bright-field illumination (BFI) when the surface of the specimen is normal to the optical axis of the microscope and white light is used. This image contrast is a result of reversing the image, which is bright in BFI, into a dark one when DFI is used. Features that are perpendicular to the optic axis in BFI appear white, while in DFI they are black. Likewise, features that are at an angle to the surface, such as grain boundaries and phase boundaries, appear black in BFI but are white (self-luminous in appearance) in DFI.

When crossed polarized light is used along with a double-quartz prism (Wollaston prism) placed between the objective and the vertical illuminator, two light beams are produced that exhibit coherent interference in the image plane. This leads to two slightly displaced (laterally) images differing in phase ($\lambda/2$), which produces higher contrast for nonplanar detail. This is called differential interference contrast (DIC), and the most common system is the one developed by Nomarski. The image reveals topographic detail somewhat similar to that produced by oblique illumination but without the loss of resolution. Images can be viewed with natural colors similar to those observed in bright field, or artificial coloring can be introduced by adding a sensitive tint plate (Ref 4).

The microstructure of Fe-Cr-Mn cast irons can be examined in DIC after polishing. Figure 45 shows the microstructure of the high-chromium cast iron (shown previously in Fig. 43 and 44) but as-polished (unetched)

and examined in DIC. The chromium carbides, which are much harder than the matrix, stand above it in relief and can be seen very well.

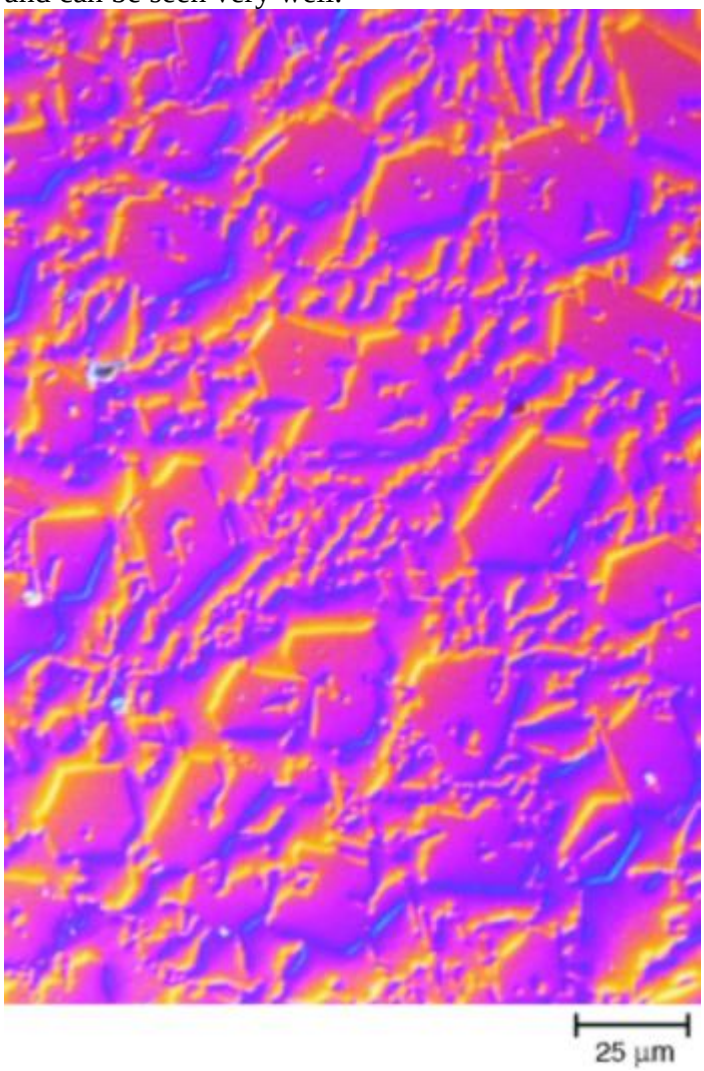

Fig. 45 Same as in Fig. 43 but as-polished and examined in differential interference contrast. Primary and eutectic carbides are sticking up from the softer austenitic matrix. 400×

The DFI and DIC methods also can be used for revealing the details of microstructures in alloyed irons, for example, a chromium-nickel iron after heat treatment, which were barely visible after etching with nital. Figure 46, 47, 48 show the microstructure of the Fe-Cr-Ni alloyed iron after heat treatment and after etching with 4% nital, but for a shorter time than usual. The three micrographs show the results for the same field after examination with BFI, DFI, and DIC, respectively. The BFI image reveals the martensite poorly, and the secondary carbides are barely visible. However, both the DFI and DIC images reveal the martensite, although not strongly, while the secondary carbides are very distinct (see also Fig. 39, 40).

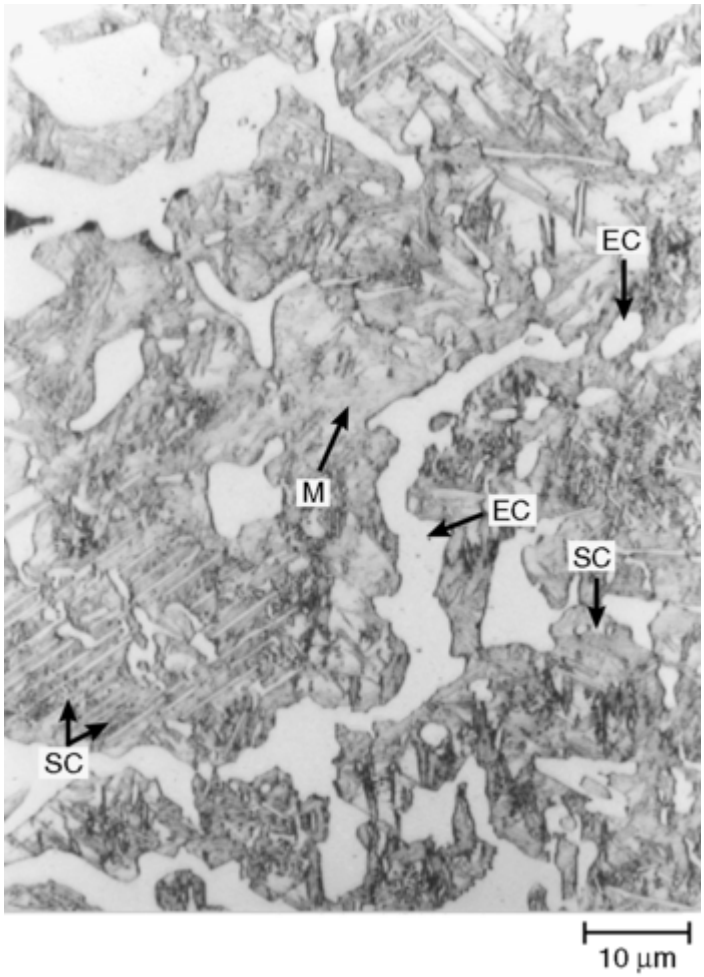

Fig. 46 Same white iron as in Fig. 39 but after slight etching with 4% nital and examined in bright-field illumination. EC, eutectic carbides type M_7C_3; SC, secondary carbides; and M, martensite. 1000×

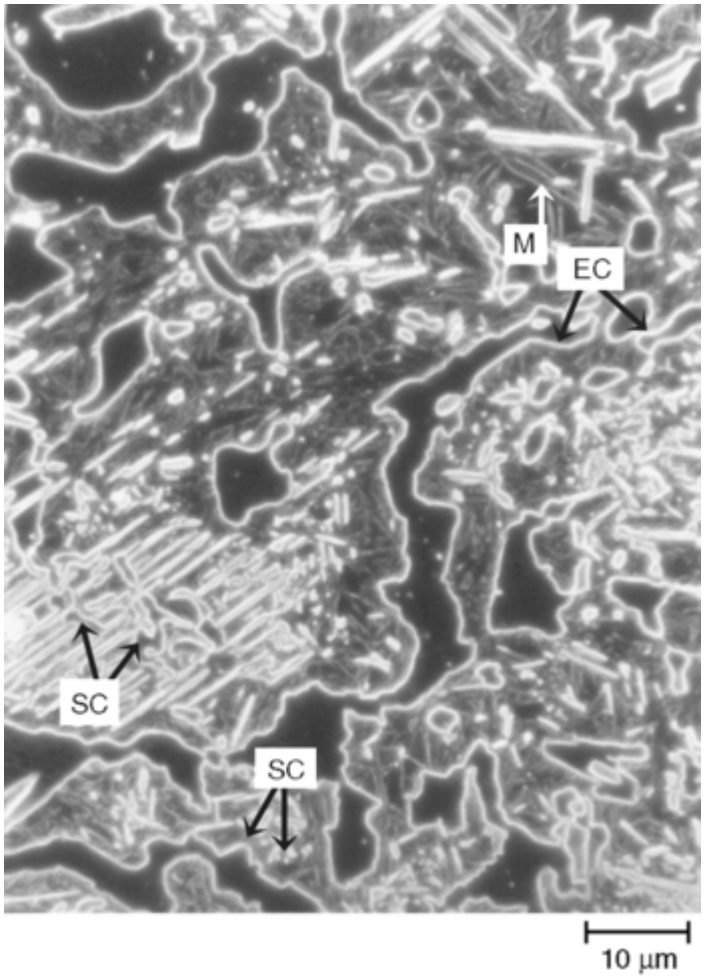

Fig. 47 Same as in Fig. 46 but examined in dark-field illumination. EC, eutectic carbides; SC, secondary carbides; and M, martensite. 1000×

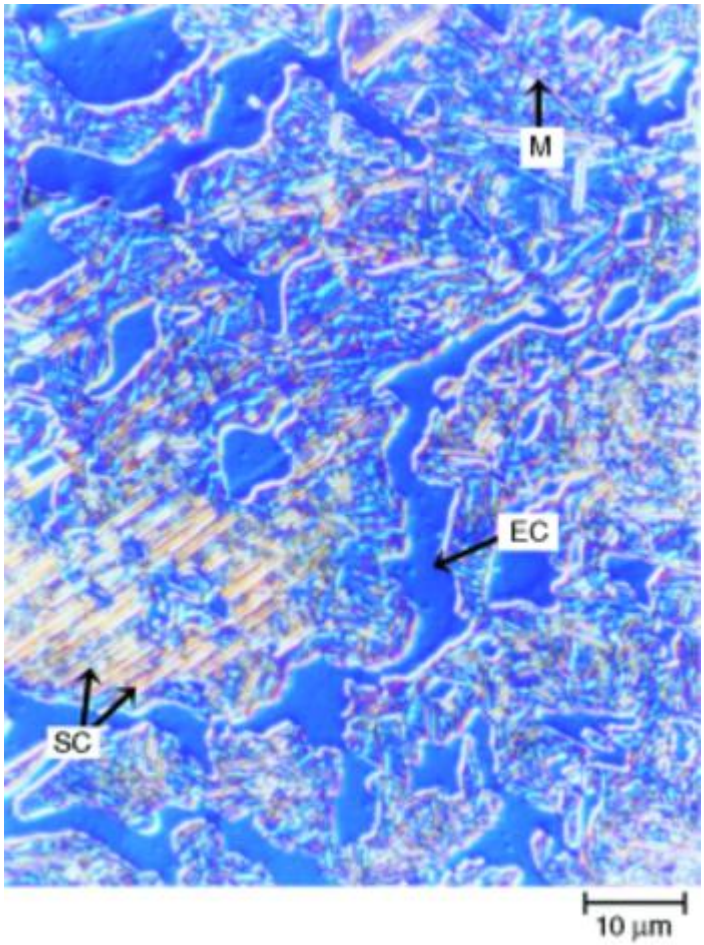

Fig. 48 Same as Fig. 46 but examined in differential interference contrast. EC, eutectic carbides; SC, secondary carbides; and M, martensite. 1000×

The microstructure of an Fe-C-Cr cast iron after heat treatment, revealed with glyceregia and examined with BFI and DFI, is shown in Fig. 49 and 50, respectively. The details of the microstructure were revealed much more strongly with DFI than with BFI.

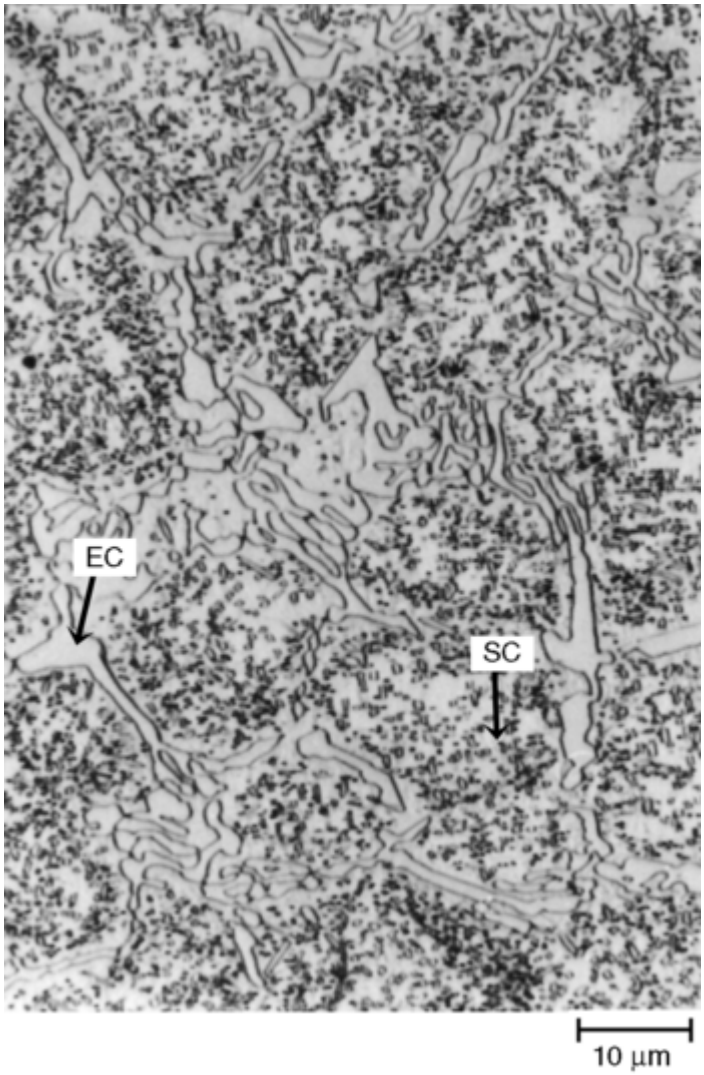

Fig. 49 Same white iron as in Fig. 14 and Fig. 15 but casting was heat treated at 1000 °C (1830 °F), held 1 h, furnace cooled to 400 °C (750 °F) for 2 h, taken to salt bath at 400 °C (750 °F), held 4 h, and air cooled. Examined in bright-field illumination. EC, eutectic carbides type M_7C_3; SC, secondary carbides. Etched with glyceregia. 1000×

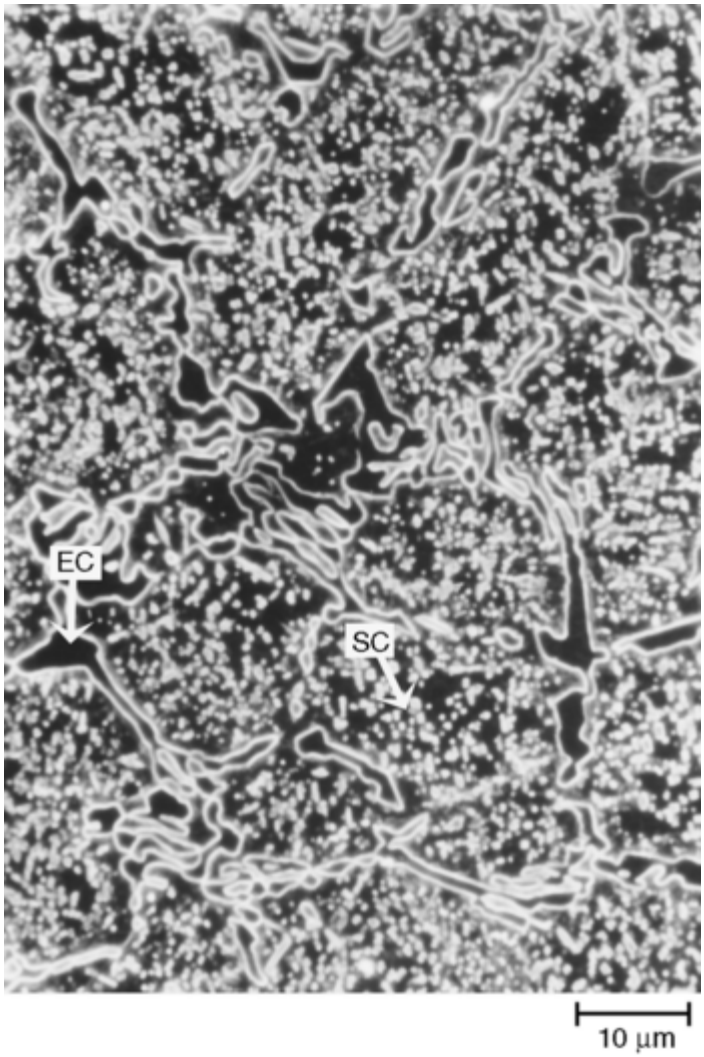

Fig. 50 Same as in Fig. 49 but examined in dark-field illumination. EC, eutectic carbides; SC, secondary carbides. 1000×

Polarized Light Response. Polarized light is obtained by placing a polarizer (usually a Polaroid filter, Polaroid Corp.) in front of the condenser lens of the microscope and placing an analyzer (another Polaroid filter) before the eyepiece. The polarizer produces plane-polarized light that strikes the surface and is reflected through the analyzer to the eyepieces. If an anisotropic metal is examined with the analyzer set 90° to the polarizer, the grain structure will be visible. However, viewing of an isotropic metal (cubic metals) under such conditions will produce dark, extinguished conditions (complete darkness is not possible using Polaroid filters). Polarized light is particularly useful in metallography for revealing grain structures and twinning in anisotropic metals and alloys as well as for identifying anisotropic phases and inclusions. This method also improves the contrast of microstructures, providing more structural details (Ref 4).

Figure 51 shows the microstructure of a graphite nodule in BFI, while Fig. 52 shows the same nodule in crossed polarized light. Polarized light reveals much better than BFI the radial structure of the graphite nodule that grows from the central nucleus. Also, the cross, which is characteristic of the perfectly formed graphite nodule, can be made visible only with the use of this technique. Figure 53 shows the anisotropic layered structure of graphite flakes, which also respond to polarized light. In both cases, the colors of graphite vary due to the anisotropy of graphite. Figure 54 shows the microstructure of ADI, consisting of martensite and a small amount of acicular ferrite. The specimen was etched with 4% picral to reveal the acicular ferrite in the background of the almost invisible martensite (see Fig. 33). When examination was carried out with crossed polarized light plus a sensitive tint filter, shown in Fig. 54, the ferritic needles can be seen by shining with a white color. Also, many of the coarsest martensitic plates (body-centered tetragonal crystal structure) with the proper lattice orientation were visible in polarized light but barely visible in BFI.

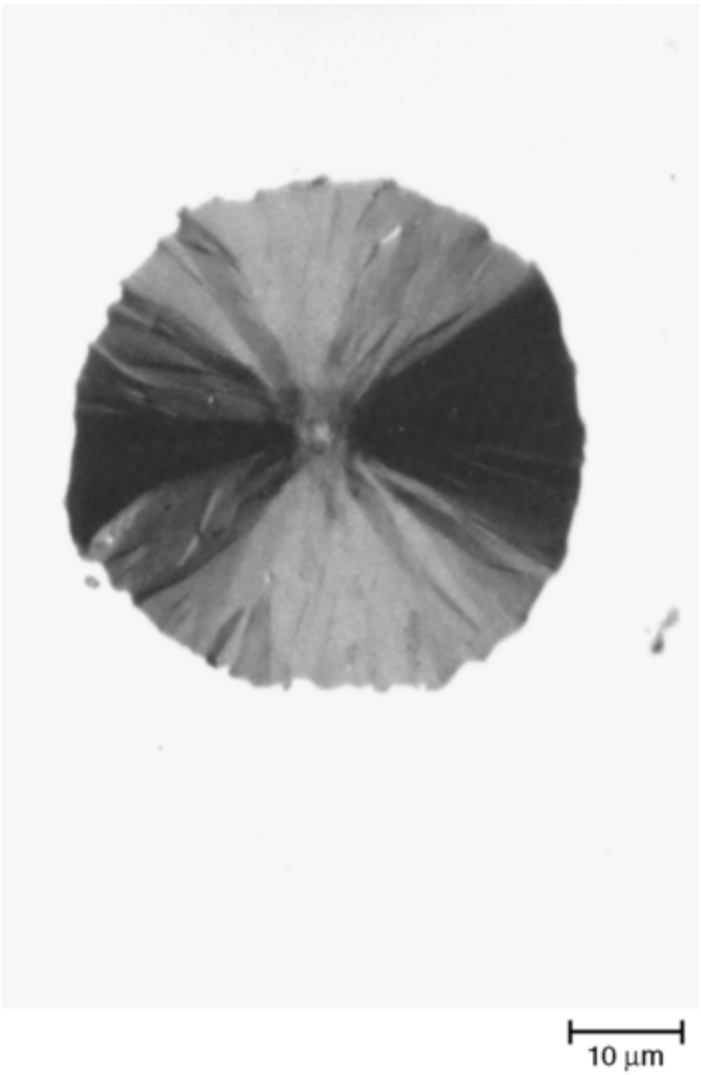

Fig. 51 Graphite nodule examined in bright-field illumination. As-polished. 1000×

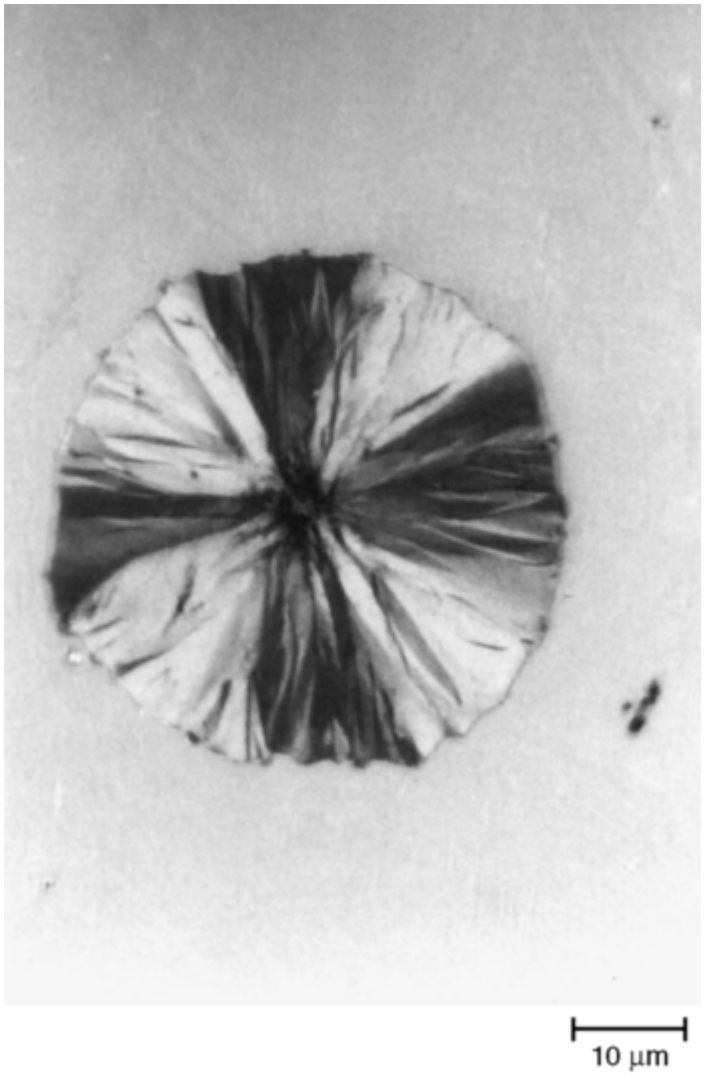

Fig. 52 Same as in Fig. 51, but graphite nodule was examined in crossed polarized light. 1000×

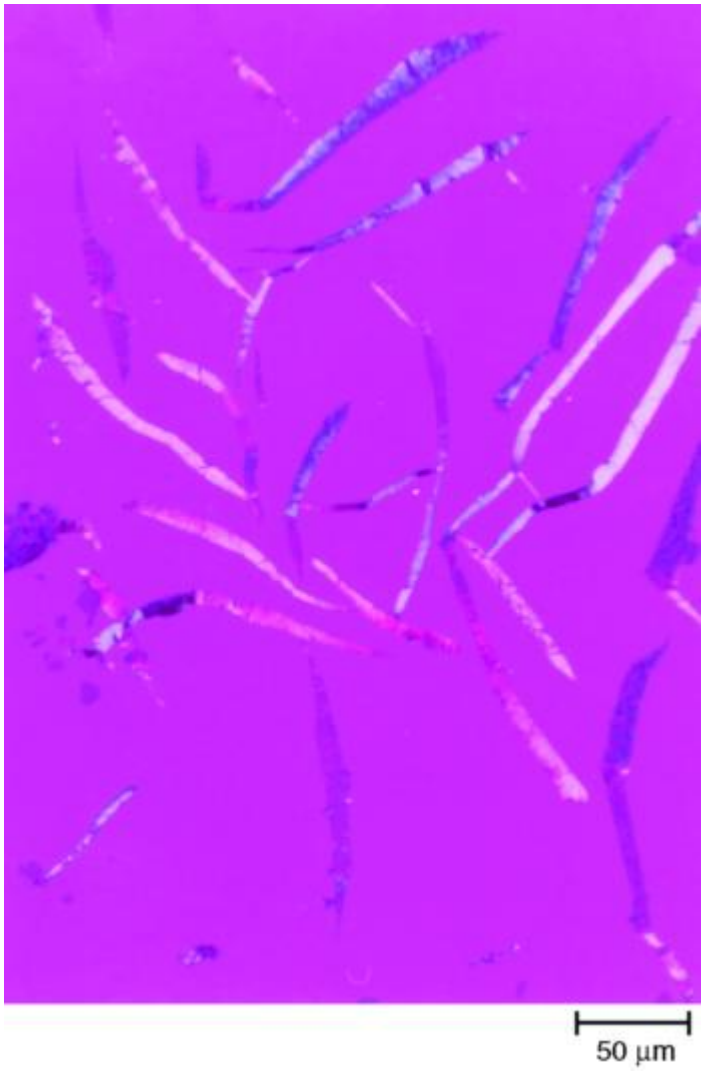

Fig. 53 Flake graphite in as-cast gray iron examined in crossed polarized light. As-polished. 200×

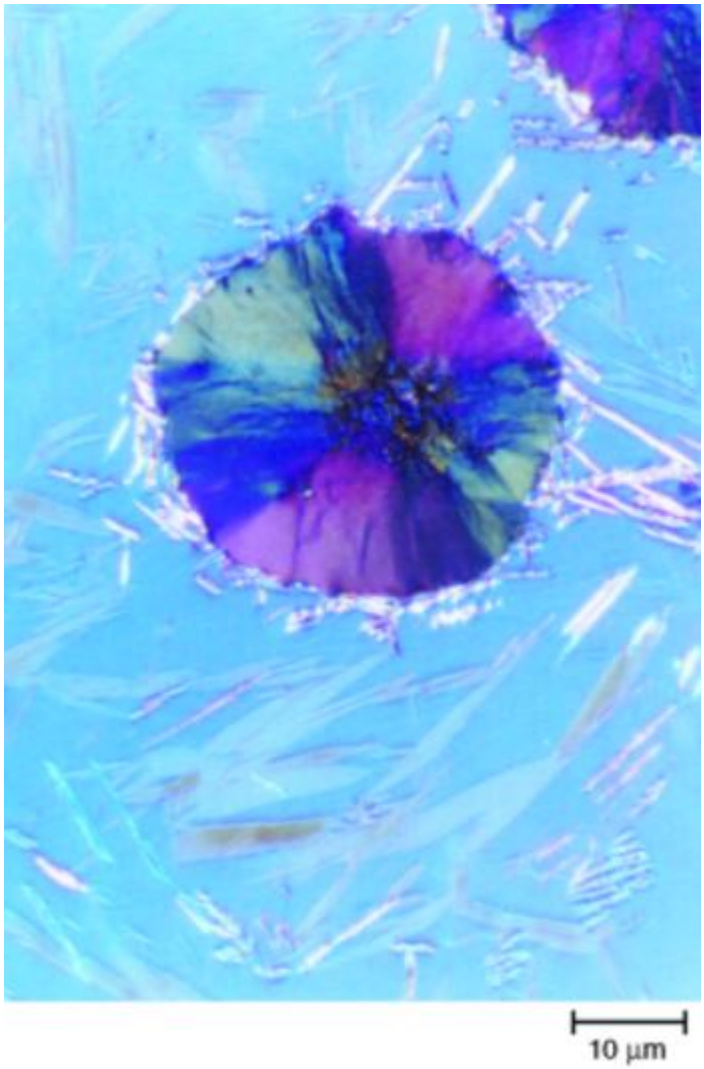

Fig. 54 Same as in Fig. 33 but microstructure was examined in crossed polarized light. Acicular ferrite is shining brightly; plate martensite is slightly gray-blue. 1000×

References cited in this section

4. G.F. Vander Voort, *Metallography: Principles and Practice*, McGraw-Hill Book Co., 1984; Reprinted by ASM International, 1999, p 129, 294–303, 632, 634, 642–644, 646, 648

5. G.F. Vander Voort, Phase Identification by Selective Etching, *Applied Metallography*, G.F. Vander Voort, Ed., Van Nostrand Reinhold Co., 1986, p 1–19

6. J. Zhou, Dalian, W. Schmitz, and S. Engler, Unterschung der Gefügebildung von Gußeisen mit Kugelgraphit bei langsamer Erstarrung, *Giessereiforschung*, Vol 39 (No. 2), 1987, p 55–70

7. P. Skočovský, *Colour Contrast in Metallographic Microscopy*, Žilina (Slovak Republic), 1993, p 26

8. E. Weck and E. Leistner, *Metallographic Instructions for Color Etching by Immersion, Part II: Beraha Color Etchants and Their Different Variations*, Deutscher Verlag für Schweißtechnik, GmbH, Düsseldorf, 1983, p 51

J.M. Radzikowska, Metallography and Microstructures of Cast Iron, *Metallography and Microstructures,* Vol 9, *ASM Handbook,* ASM International, 2004, p. 565–587

Metallography and Microstructures of Cast Iron

Janina M. Radzikowska, The Foundry Research Institute, Kraków, Poland

Microstructures

Table 3 lists the characteristics of typical constituents of cast iron microstructures and their effect on mechanical properties (Ref 3, 10).

Table 3 Constituents commonly found in cast iron microstructures, and their general effect on physical properties

Constituent	Characteristics and effects
Graphite (hexagonal crystal structure)	Free carbon; soft; improves machinability and damping properties; reduces shrinkage and may reduce strength severely, depending on shape
Austenite (γ-iron)	Face-centered cubic crystal structure. The character of the primary phase, which solidifies from the oversaturated liquid alloy in dendrite form, is maintained until room temperature. Austenite is metastable or stable equilibrium phase (depending upon alloy composition). Usually transforms into other phases. Seen only in certain alloys. Soft and ductile, approximately 200 HB
Ferrite (α-iron)	Body-centered cubic crystal structure. Iron with elements in solid solution, which is a stable equilibrium, low-temperature phase. Soft, 80–90 HB; contributes ductility but little strength
Cementite (Fe_3C)	Complex orthorhombic crystal structure. Hard, intermetallic phase, 800–1400 HV depending upon substitution of elements for Fe; imparts wear resistance; reduces machinability
Pearlite	A metastable lamellar aggregate of ferrite and cementite due to eutectoidal transformation of austenite above the bainite region. Contributes strength without brittleness; has good machinability, approximately 230 HB
Martensite	Generic term for microstructures that form by diffusionless transformation, where the parent and product phases have a specific crystallographic relationship. Hard metastable phase
Steadite (phosphorous eutectic)	A pseudobinary or ternary eutectic of ferrite and iron phosphide or ferrite, iron phosphide, and cementite, respectively. It can form in gray iron or in mottled iron with a phosphorous content >0.06%. Hard and brittle; solidifies from the liquid on cooling at the cell boundaries as a last constituent of the microstructure
Ledeburite	Massive eutectic phase composed of cementite and austenite; austenite transforms to cementite and pearlite on cooling. Produces high hardness and wear resistance; virtually unmachinable

Source: Ref 3, 10

Microstructure of Graphite

The eutectic graphite cell has a continuous graphite skeleton, but on the metallographic cross section, the three-dimensional nature is not obvious. Figure 55, 56, and 57 show scanning electron microscopy (SEM) micrographs of flake, nodular, and compacted graphite, respectively. Contrary to flake graphite, where the flakes solidify as an aggregate and each such agglomeration is one eutectic cell, both spheroidal and compacted

graphite solidify as separate precipitates. For SEM examination, the specimens were deeply etched (Table 2, etch No. 13).

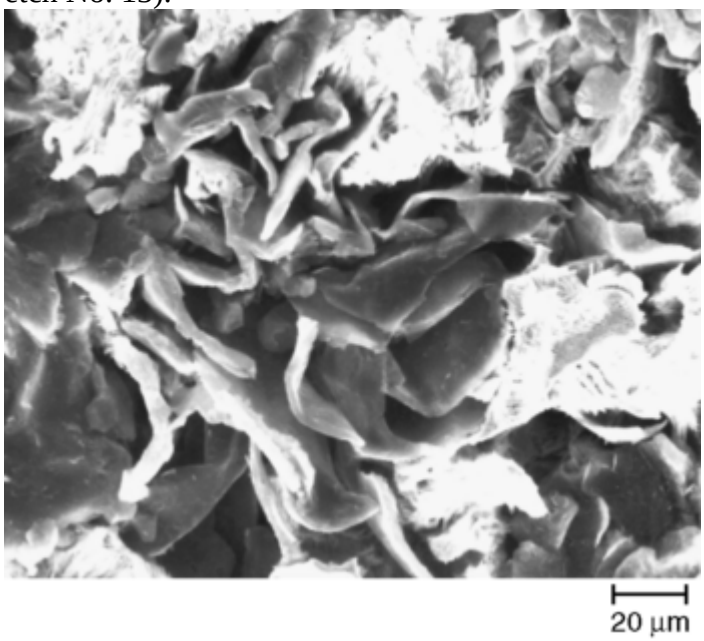

Fig. 55 Flake graphite in as-cast gray iron examined with SEM. Sample was deeply etched with 50% HCl. 500×

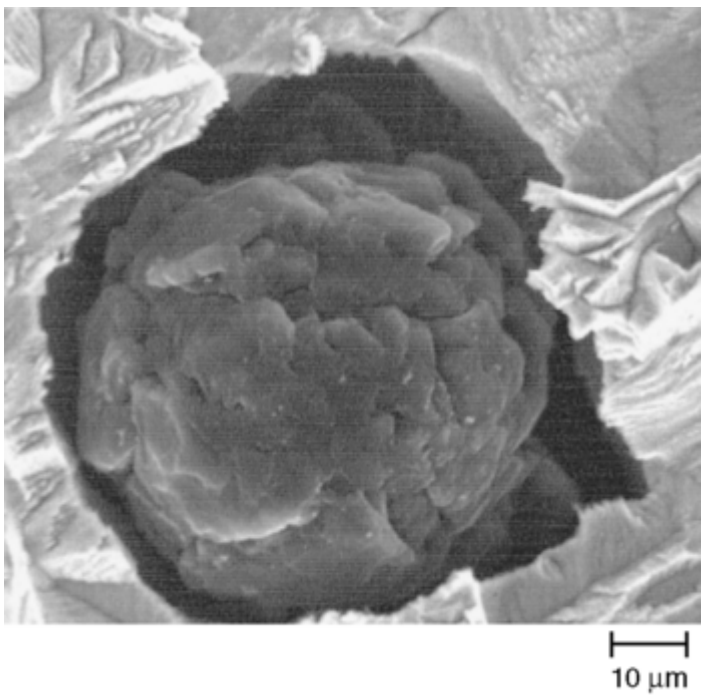

Fig. 56 Nodular graphite in as-cast ductile iron examined with SEM. Sample was deeply etched with 50% HCl. 1000×

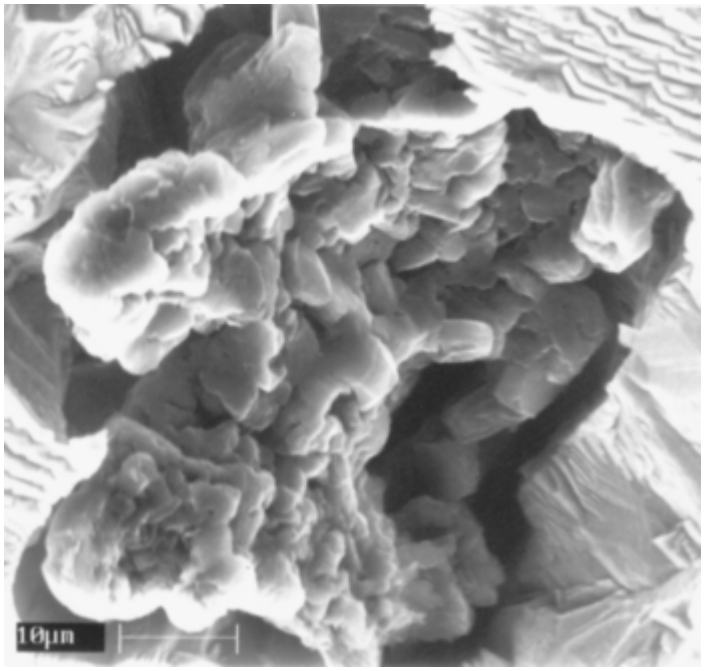

Fig. 57 Compacted graphite examined with SEM. Sample was deeply etched with 50% HCl. 1500×

Characteristic properties of graphite precipitations are shape, size, and distribution. There is a correlation between different graphite morphologies, the chemical composition, and the cooling rate.

Flake Graphite in Gray Iron. Flake (lamellar) graphite is characteristic of gray iron, and components such as aluminum, carbon, and silicon promote its formation. When the cooling rate increases, the flakes get finer, and their distribution tends to be interdendritic. Figure 58 shows a hypoeutectic gray iron with a uniform distribution of randomly oriented graphite flakes with a maximum length of 320 µm (type A flake graphite in the ASTM A 247 classifications). Figure 59 shows a fine, type D flake graphite with a maximum length of 40 µm, also in a hypoeutectic alloy, but it solidified at a higher cooling rate, which promoted the interdendritic distribution. Type A graphite in a hypereutectic gray iron is shown in Fig. 60. It has the most desired shape and distribution, and it is very characteristic of gray iron casts with high machinability. The maximum length of graphite flakes is 160 µm. Figure 61 and 62 show type E and type B graphite, respectively, which occur in hypereutectic gray iron at high cooling rates. Note in Fig. 62 that each rosette group of graphite represents one eutectic cell. That type of graphite is characteristic of thin-walled castings.



Fig. 58 Hypoeutectic as-cast gray iron (Fe-2.8%C-1.85%Si-0.5%Mn-0.04%P-0.025%S). Flake graphite type A. As-polished. 100×

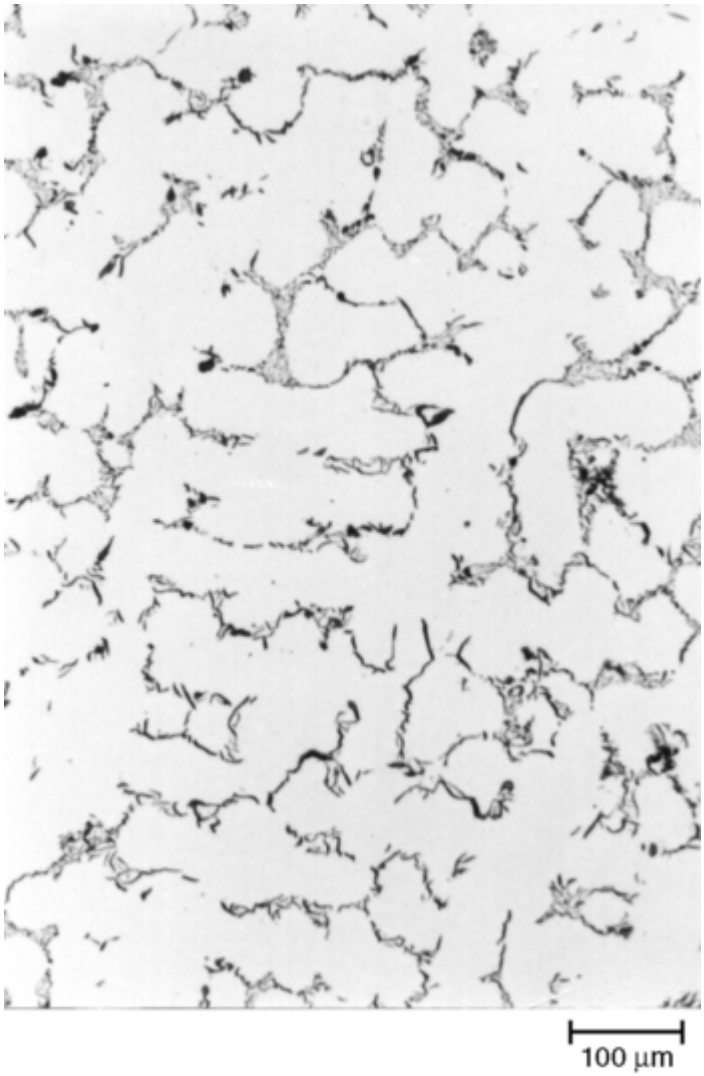

Fig. 59 Hypoeutectic as-cast gray iron (Fe-2.1%C-2.8%Si-0.38%Mn-0.06%P-0.03%S). Flake graphite type D. As-polished. 100×



Fig. 60 Hypereutectic as-cast gray iron (Fe-3.5%C-2.95%Si-0.4%Mn-0.08%P-0.02%S-0.13%Ni-0.15%Cu). Flake graphite type A. As-polished. 100×

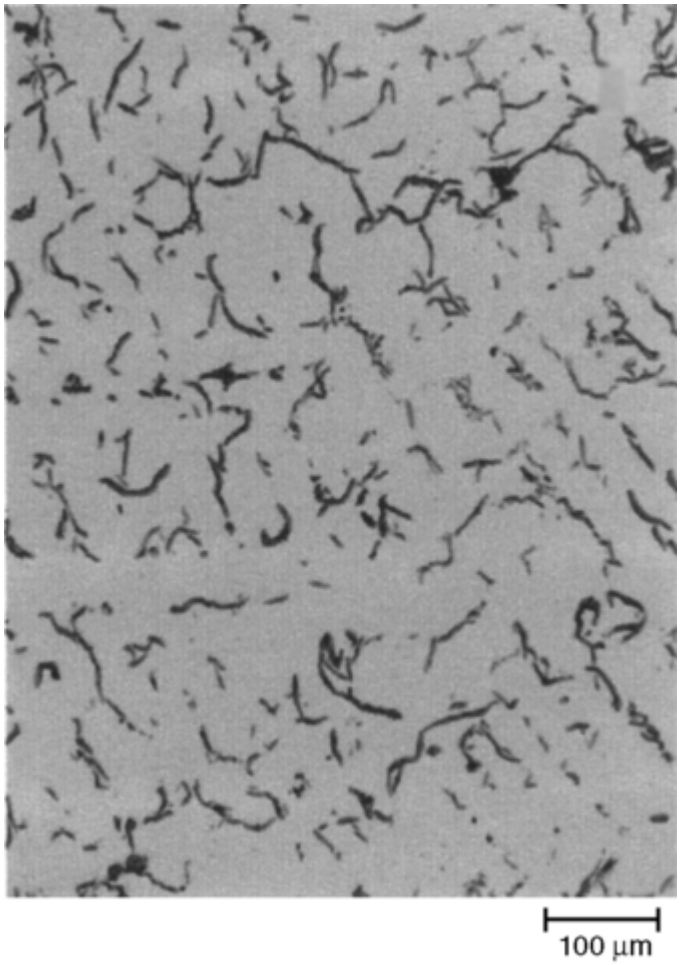

Fig. 61 Hypereutectic as-cast gray iron (Fe-2.18%C-2.49%Si-0.7%Mn-0.06%P-0.05%S). Flake graphite type E. As-polished. 100×. Courtesy of G.F. Vander Voort, Buehler Ltd.



Fig. 62 Hypereutectic as-cast gray iron (Fe-3.3%C-2.75%Si-0.88%Mn-0.42%P-0.086%S). Flake graphite type B. As-polished. 90× (microscopic examination 100×)

A high degree of undercooling of hypereutectic gray iron can promote the solidification of very fine, pointlike type D graphite with an interdendritic distribution, as shown in Fig. 63. In the other direction, undertreatment of the graphitizing inoculants, such as ferrosilicon, produces other flake graphite types in gray iron. For example, Fig. 64 shows a hypereutectic gray iron with graphite type C, where very coarse, needlelike flakes (kish graphite) form before the eutectic, which is very fine. Kish graphite, which is shown in Fig. 64, can be changed into a starlike graphite, shown in Fig. 65, under higher cooling rates, which is referred to as type V (plate I of ASTM A 247). The carbide-forming alloy elements, for example, chromium, manganese, and vanadium, and the low-melting-point metals, for example, bismuth, lead, and sulfur, also affect graphite morphology.

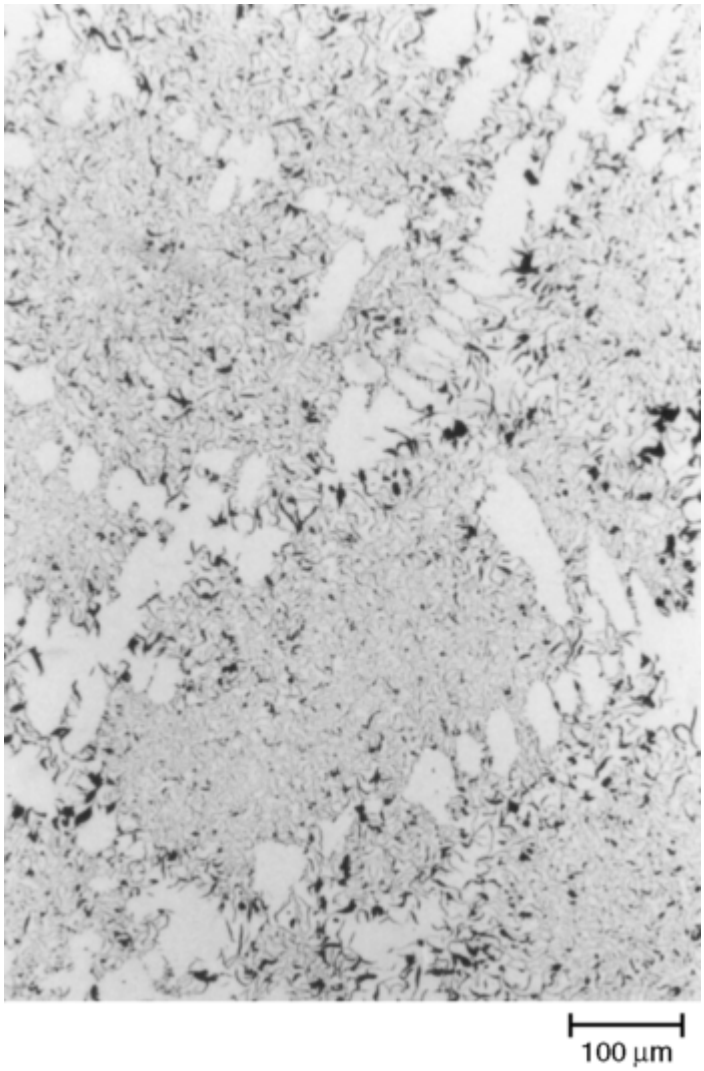

Fig. 63 Hypereutectic as-cast gray iron (Fe-3.4%C-3.4%Si-0.07%Mn-0.04%P-0.03%Cr-0.47%Cu). Pointlike flake graphite type D. As-polished. 100×

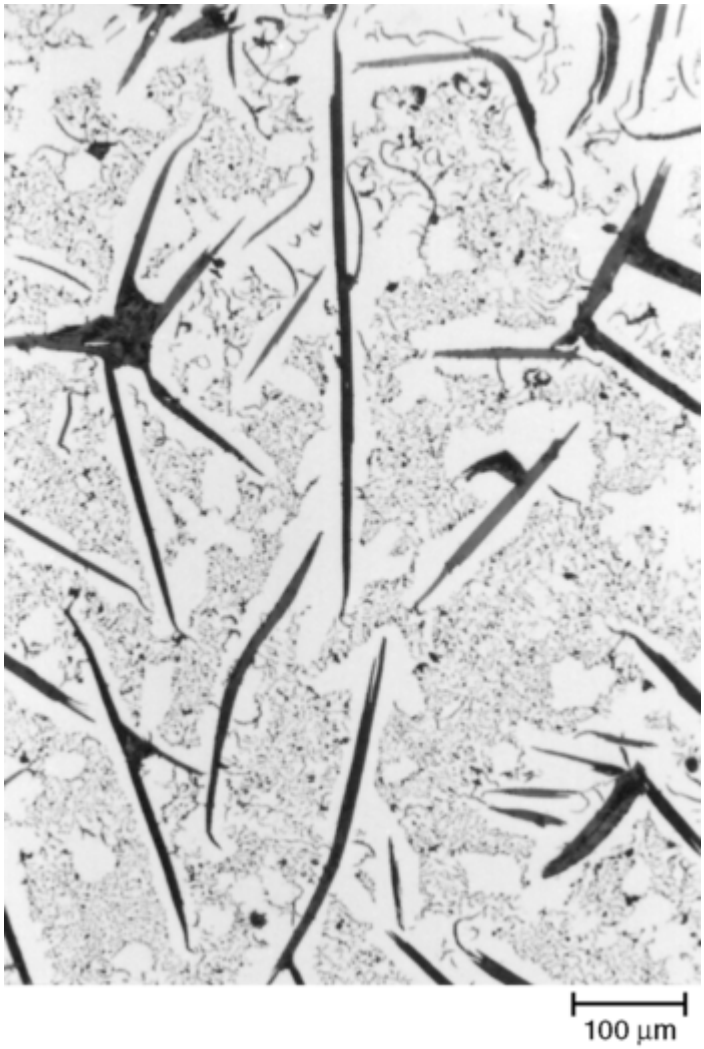

Fig. 64 Hypereutectic as-cast gray iron (Fe-4.3%C-1.5%Si-0.5%Mn-0.12%P-0.08%S). Flake graphite type C (kish graphite). As-polished. 100×

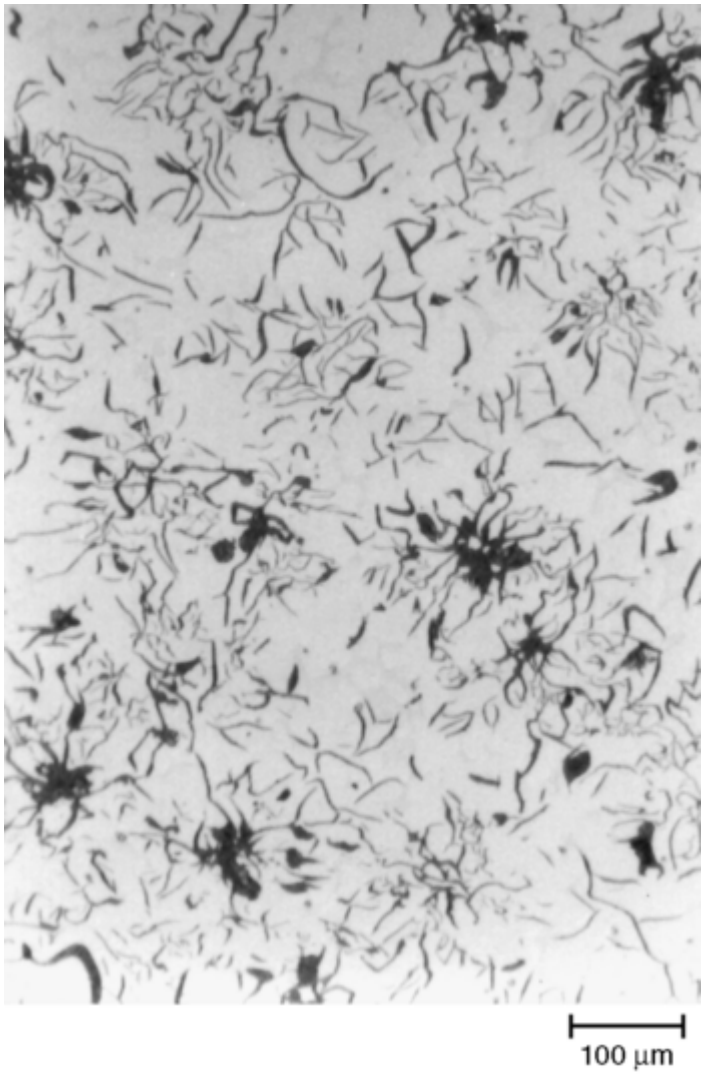

Fig. 65 As-cast gray iron. Flake graphite type V (star-like graphite). As-polished. 100×

Nodular Graphite in Ductile Iron. The addition of magnesium in the inoculation process desulfurizes the iron and makes graphite precipitate as nodules rather than flakes. Moreover, mechanical properties are greatly improved over gray iron; hence, nodular iron is widely known as ductile iron. Nodule size and shape perfection can vary, depending on composition and cooling rate. Figure 66 shows fine nodules with a maximum diameter of 20 μm in a chill-cast thin section, while Fig. 67 and 68 show coarser nodules, with maximum diameters of 40 and 100 μm, respectively. Note that the number of nodules per unit area is different and changes from approximately 350 to 125 to 22/mm^2, respectively, for Fig. 66, 67, and 68.

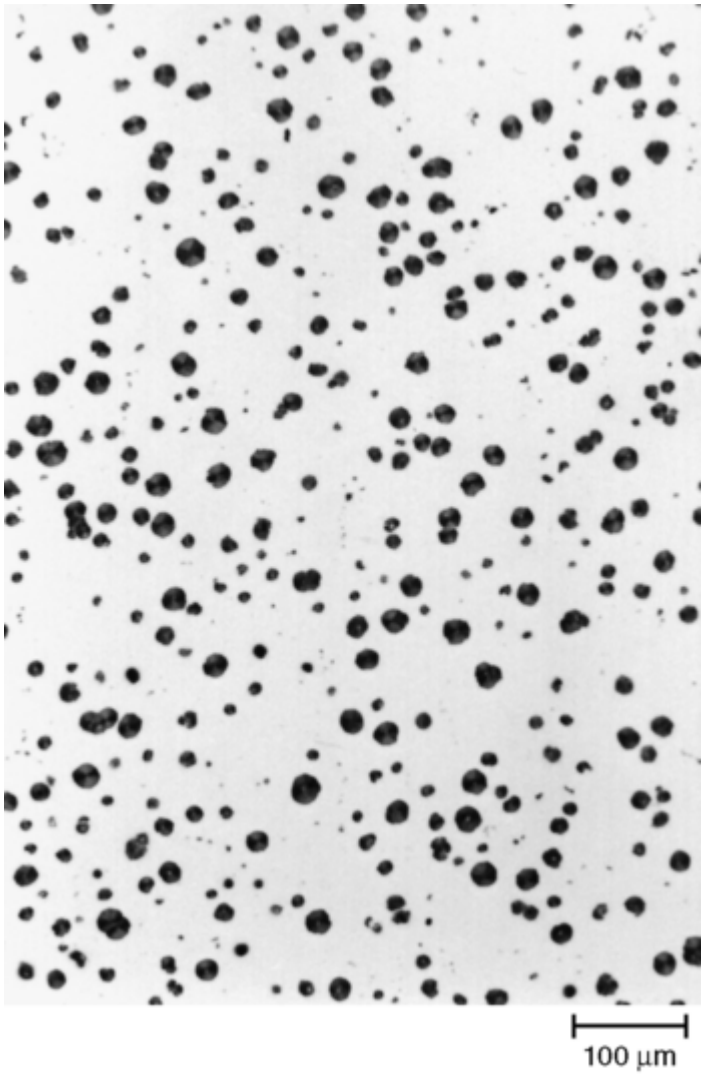

Fig. 66 As-cast ductile iron (Fe-3.45%C-2.25%Si-0.30%Mn-0.04%P-0.01%S-0.8%Ni-0.07%Mg-0.55%Cu). Nodular graphite size is 20 µm. As-polished. 100×

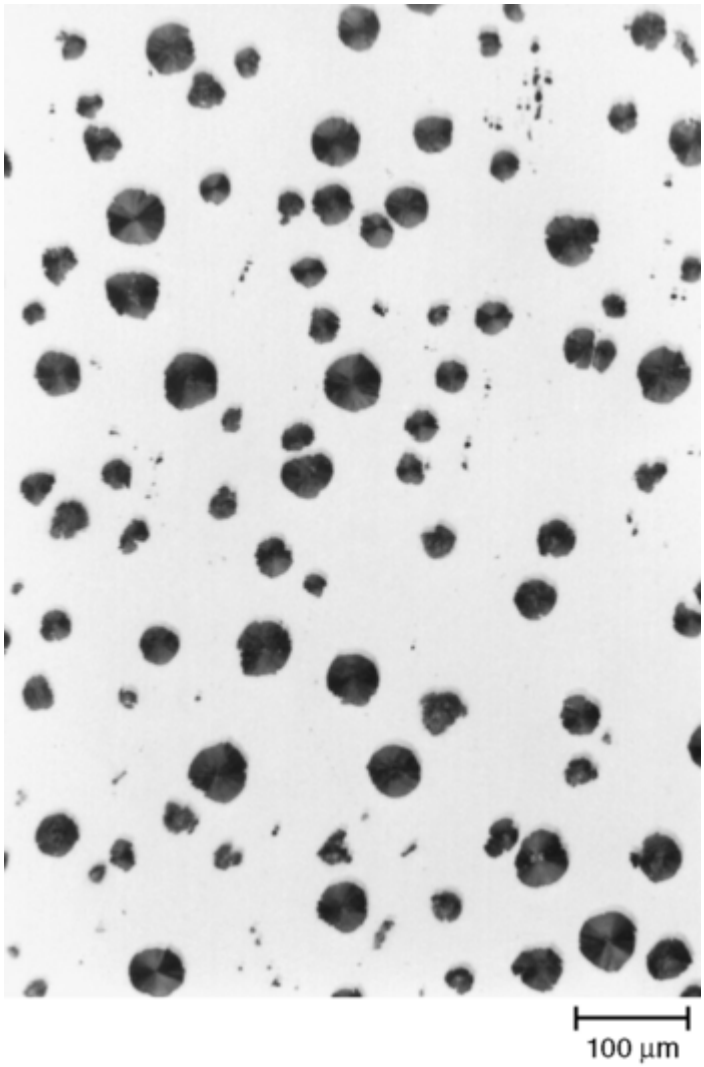

Fig. 67 As-cast ductile iron (Fe-3.6%C-2.9%Si-0.14%Mn-0.04%P-0.02%S-0.16%Ni-0.06%Mg). Nodular graphite size is 40 µm. As-polished. 100×

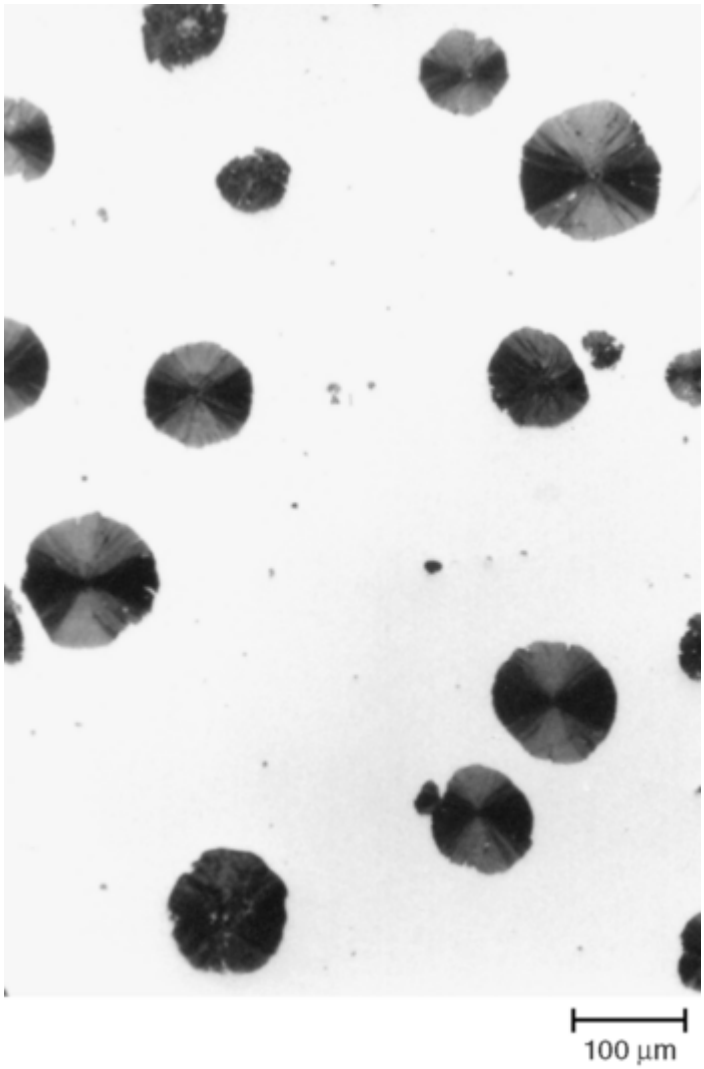

Fig. 68 As-cast ductile iron. Nodular graphite size is 100 µm. As-polished. 100×

Certain factors can cause weak nodularity. Figure 69 shows an irregular graphite shape due to poor inoculation or excessive fading of inoculant. Exploded graphite, shown in Fig. 70, may occur due to excessive rare earth additions. Normally, it is found in thick-section castings or at higher-carbon equivalents (Ref 11). Figure 71 shows chunky and spiky types of graphite. The first one is caused by high-purity charge materials and excess rare earth additions in high-carbon-equivalent compositions, while the second one is caused by small amounts of tramp elements, for example, lead, bismuth, tin, and titanium, in the absence of cerium (Ref 12).

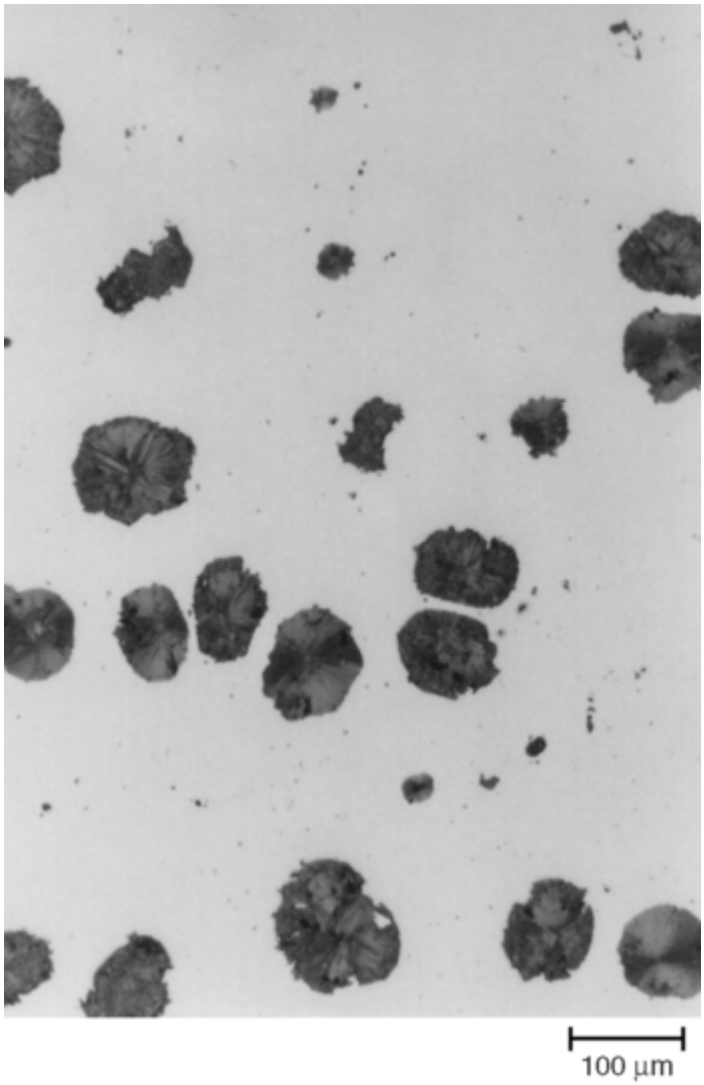

Fig. 69 As-cast ductile iron. Imperfectly formed graphite nodules. As-polished. 100×

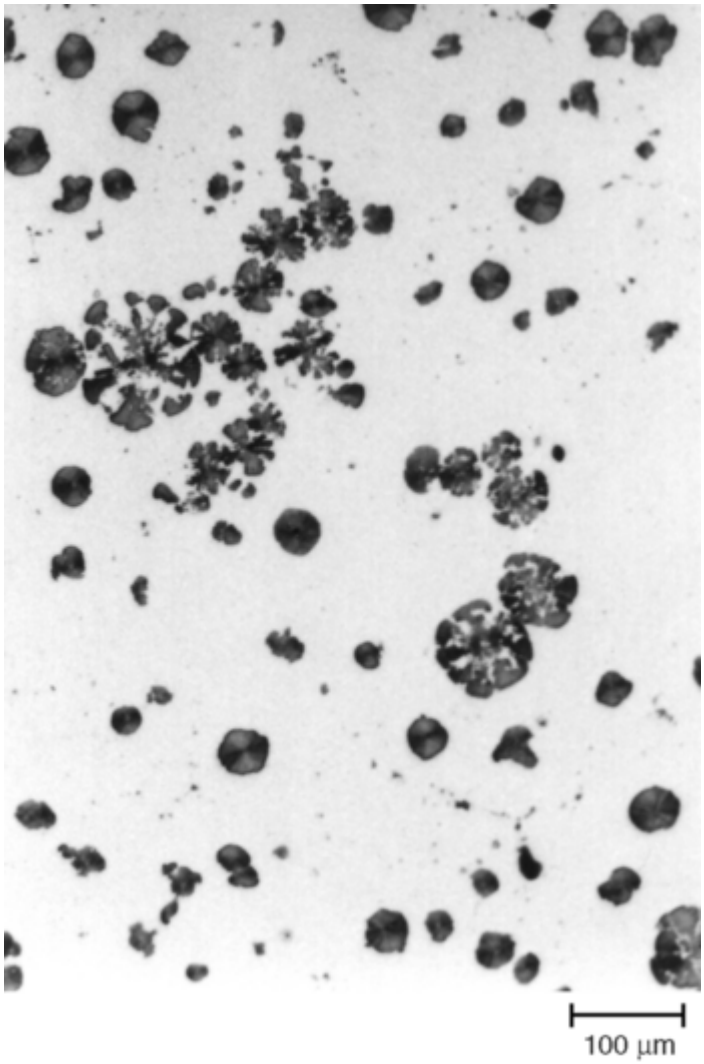

Fig. 70 As-cast ductile iron. Exploded graphite. As-polished. 100×

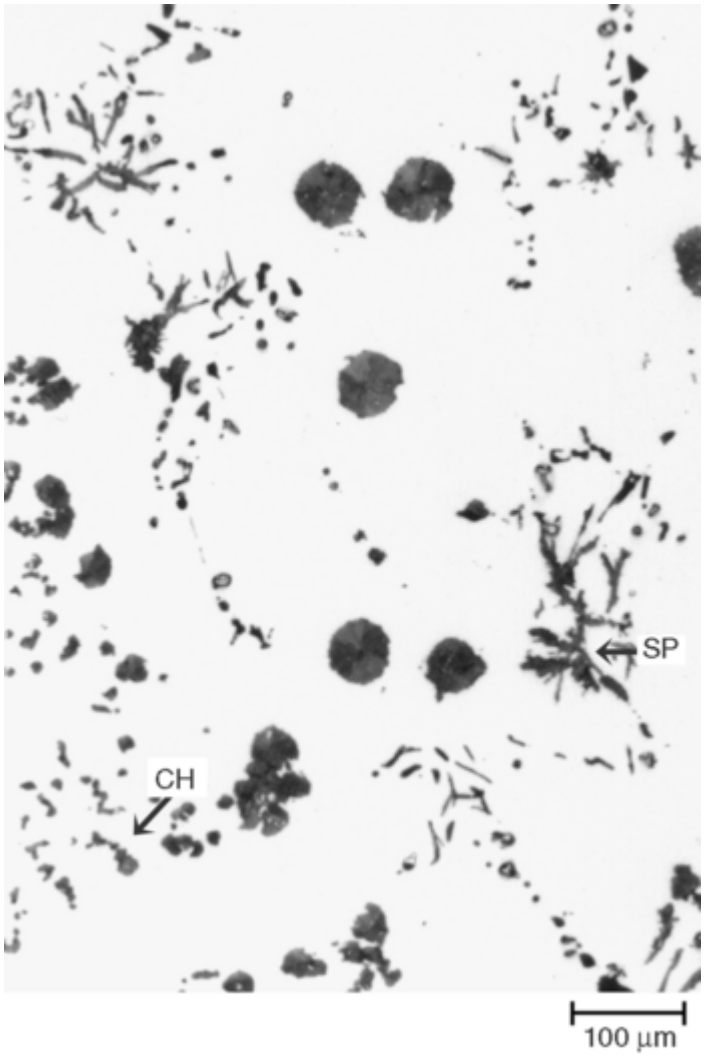

Fig. 71 Austempered ductile iron (Fe-3.6%C-2.5%Si-0.052%Mg-0.7%Cu). Chunky (CH) and spiky (SP) types of graphite. As-polished. 100×

Compacted Graphite. Methods that produce compacted graphite cast iron include the treatment of molten iron with rare earth inoculants, adding a lower amount of magnesium than is required to obtain nodular graphite, or adding elements such as titanium and aluminum that make it difficult to spheroidize graphite. This type of iron is a more recent development, made in an effort to improve the mechanical properties of flake gray iron. Figure 72 shows an example where the longest compacted graphite precipitations are in the 80 to 160 μm range.



Fig. 72 As-cast iron with compacted graphite (Fe-3.7%C-2.3%Si-0.21%Mn-0.03%P-0.01%S-0.82%Ni-0.02%Mg). Graphite size is 80 to 160 µm. As polished. 100×

Temper Graphite in Malleable Iron. Temper graphite is formed by annealing white cast iron castings to convert carbon in the form of cementite to graphite, called temper-carbon nodules. Figure 73 shows the type III graphite precipitation with 80 µm maximum size.

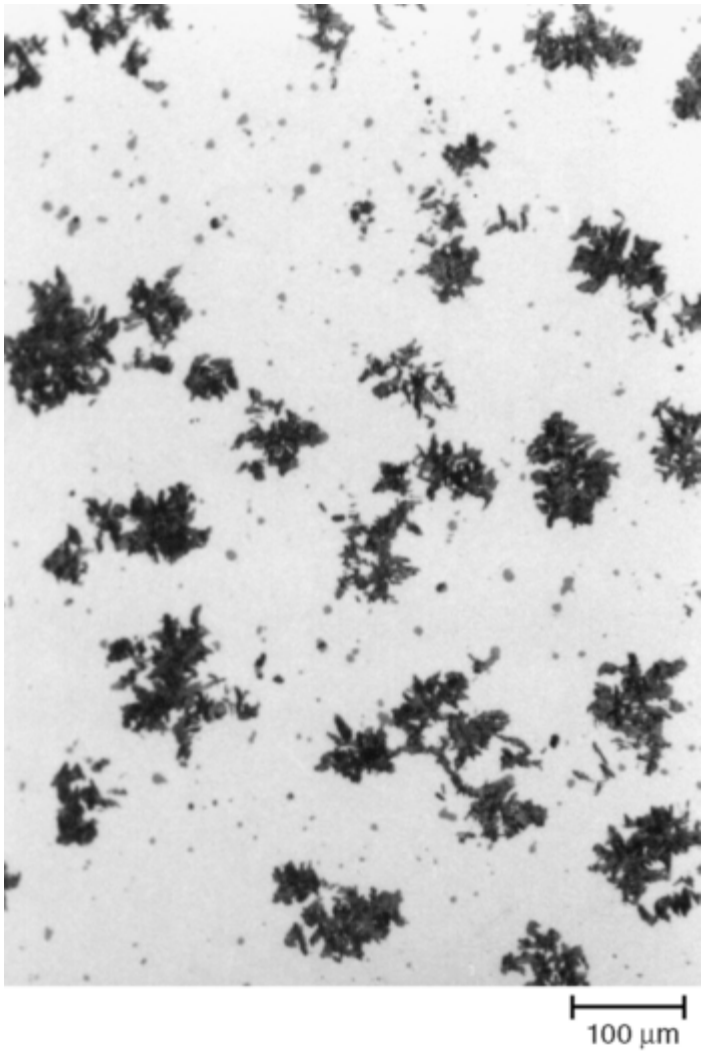

Fig. 73 Malleable iron (Fe-2.65%C-1.2%Si-0.53%Mn-0.06%P-0.21%S-0.08%Cr-0.10%Cu-0.07%Ni-<0.01%Al). Temper graphite type III with maximum size of 80 µm. As-polished. 100×

Microstructure of Matrix

The matrix of gray, nodular, compacted, and malleable cast irons can be pearlitic, pearlitic-ferritic, ferritic-pearlitic, or ferritic. The same matrix constituents can be present in white cast iron, but cementite precipitates from the melt, rather than graphite, due to crystallization in a metastable system.

The matrix microstructure depends on chemical composition as well as on the temperature of the eutectoidal transformation. Figure 74 shows the diagram of the correlation between the type of matrix in nonalloyed cast irons and the silicon and phosphorus content as well as the thickness, *R*, of the casting wall, which relates to the cooling rate. K_g = C (Si + log*R*) gives the coefficient of graphitization, and $C_E = C + \frac{1}{3}Si + \frac{1}{3}P$ is the coefficient of saturation (carbon equivalent). A low value of K_g promotes solidification of white cast iron, with cementite and pearlite as the microstructure, regardless of the total carbon content, C. When the K_g coefficient and the silicon content increase, the microstructure of the cast iron matrix tends to be pearlitic through pearlitic-ferritic to ferritic, and it depends on the C_E value (Ref 13).

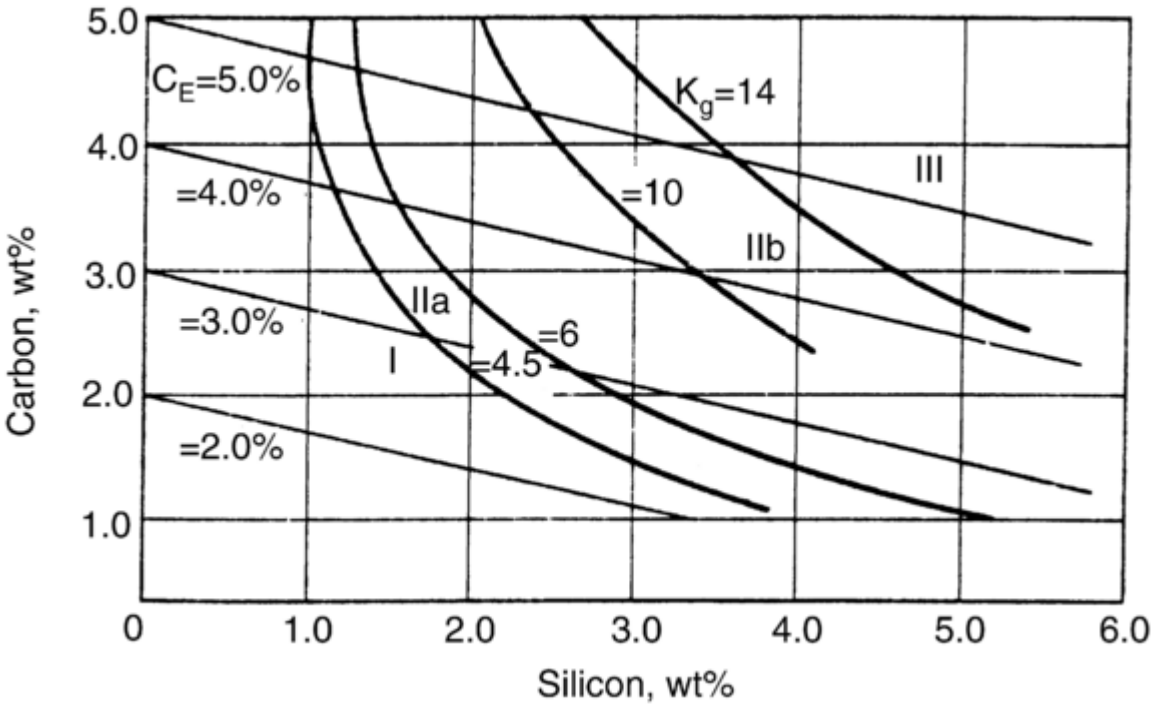

Fig. 74 The diagram of correlation between a type of matrix in nonalloyed cast irons and silicon and phosphorus content as well as the thickness, *R*, of the casting wall, which relates to the cooling rate. K_g = C (Si + log*R*) is a coefficient of graphitization, and C_E = C + $\frac{1}{3}$Si + $\frac{1}{3}$P is the coefficient of saturation (carbon equivalent). Region I is white cast iron (pearlite, cementite, no graphite); Region IIa is mottled cast iron (pearlite, graphite, cementite); Region IIb is ferritic-pearlitic cast iron; Region III is ferritic cast iron. Source: Ref 13

In pearlitic-ferritic cast irons, the regions with ferrite always occur within the eutectic cells and in the neighborhood of graphite precipitates due to microsegregation. The microregions of solidification, like the axis of dendrites and the interiors of eutectic cells, contain more silicon, which promotes ferrite formation. Slow cooling, as well as higher silicon contents, usually produces ferrite, while a very fast cooling rate can produce free cementite. Ferritic microstructures also can be obtained by annealing of pearlitic cast irons or in thick-walled castings (Ref 13).

Gray iron is classified according to minimum tensile strength of the test bars. The matrix is predominantly pearlitic (Fig. 75, 76) but also can be pearlitic-ferritic (Fig. 77, 78), ferritic-pearlitic (Fig. 79), or ferritic (Fig. 80).

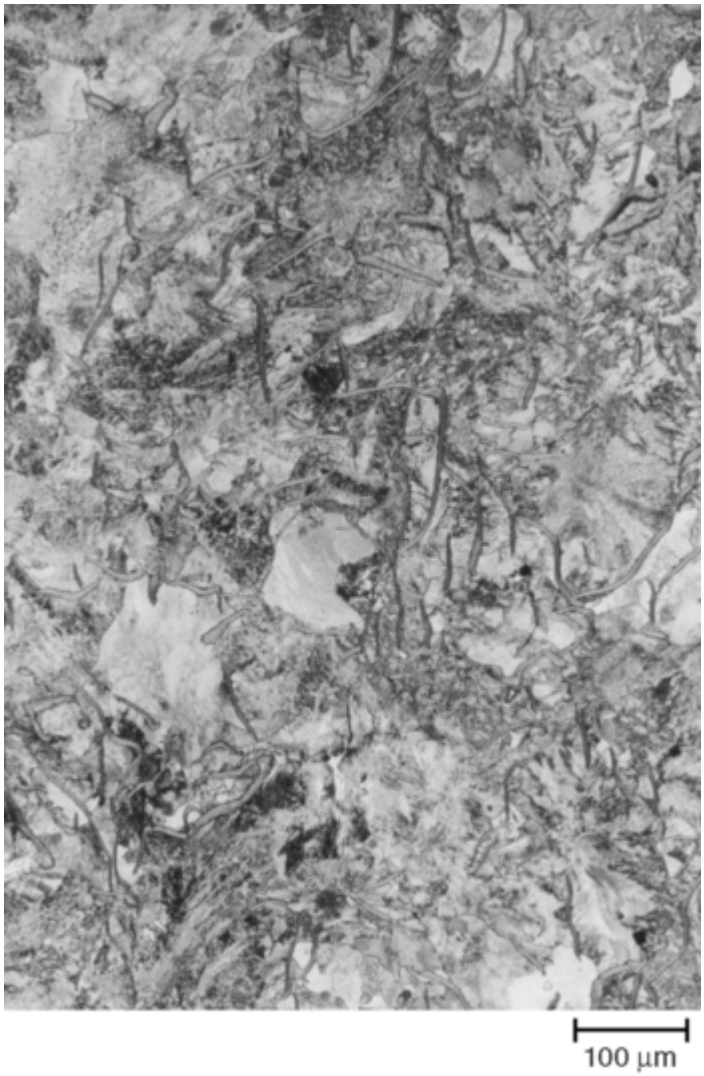

Fig. 75 As-cast gray iron (Fe-2.8%C-1.85%Si-1.05%Mn-0.04%P-0.025%S). Pearlitic matrix. Etched with 4% nital. 100×

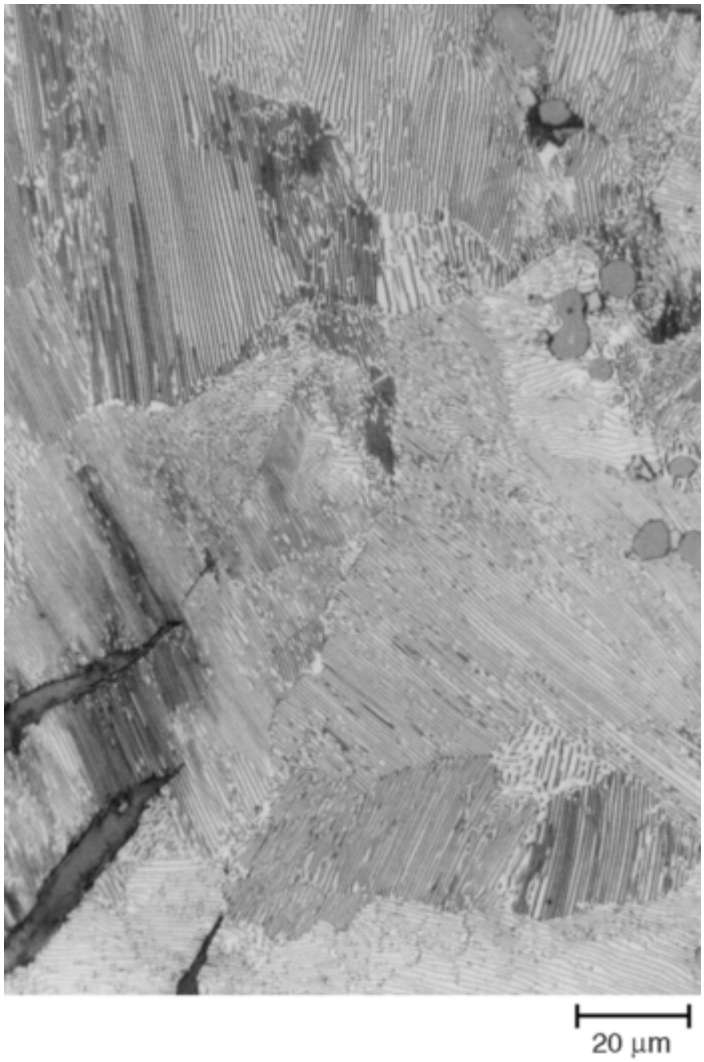

Fig. 76 Same as in Fig. 75. Fine pearlite. 500×



Fig. 77 As-cast gray iron. Pearlitic-ferritic matrix with phosphorous eutectic (E). Etched with 4% nital. 100×

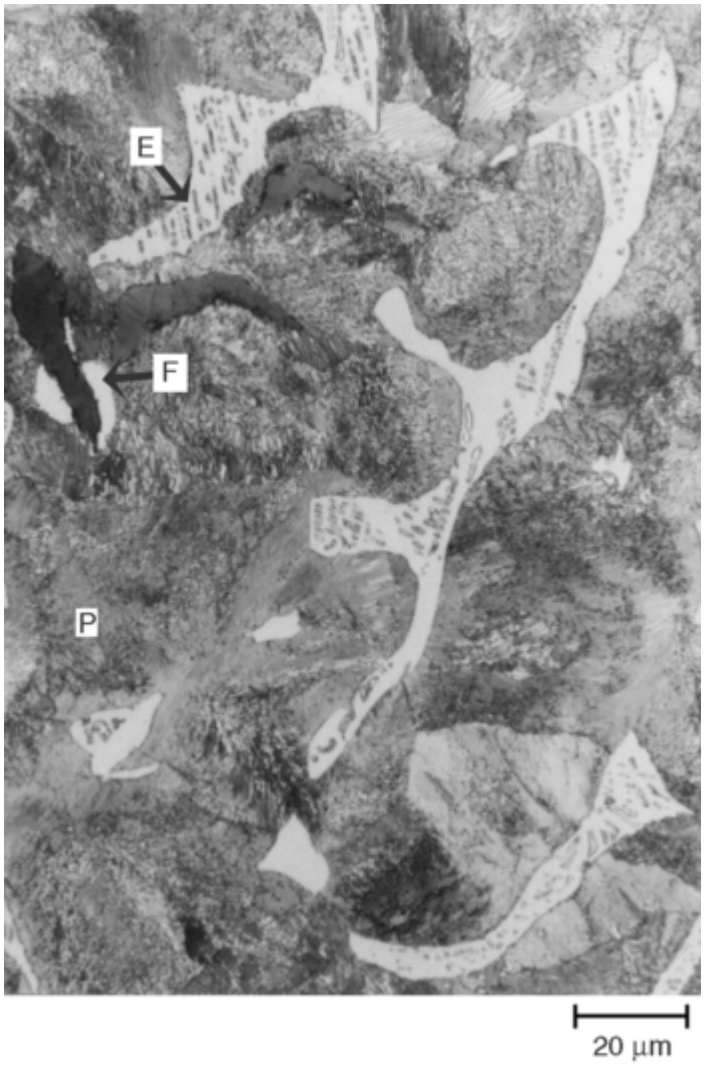

Fig. 78 Same as in Fig. 77. E, ternary phosphorous eutectic; P, pearlite; and F, ferrite. 500×

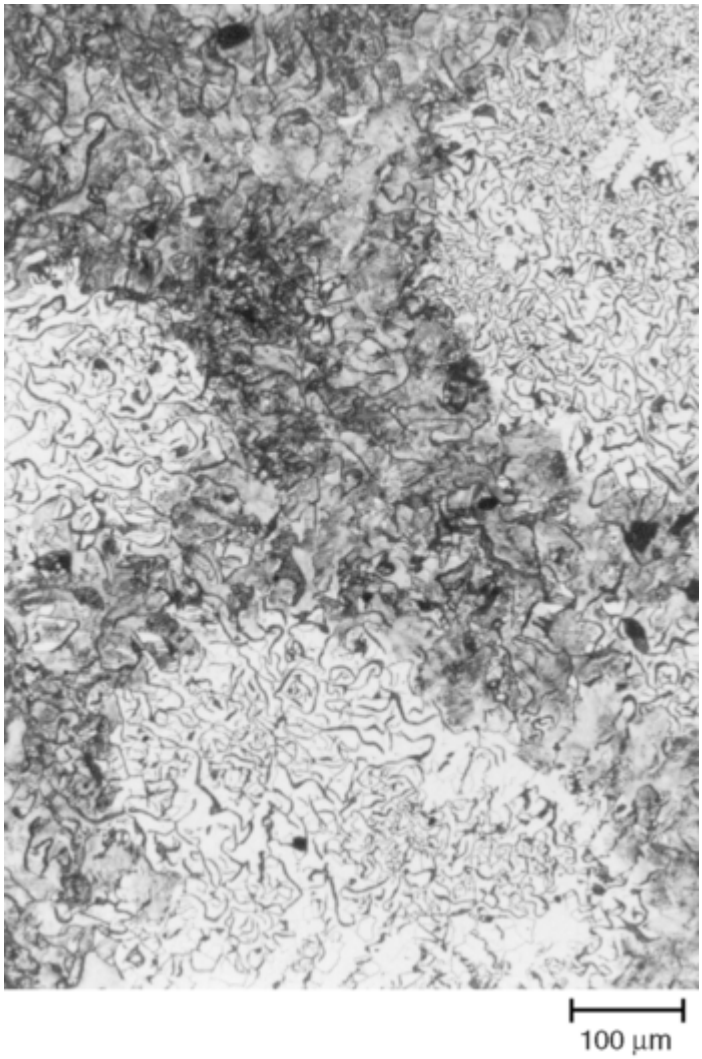

Fig. 79 As-cast gray iron (Fe-3.4%C-3.4%Si-0.07%Mn-0.04%P-0.03%Cr-0.47%Cu). Ferritic-pearlitic matrix. Etched with 4% nital. 100×

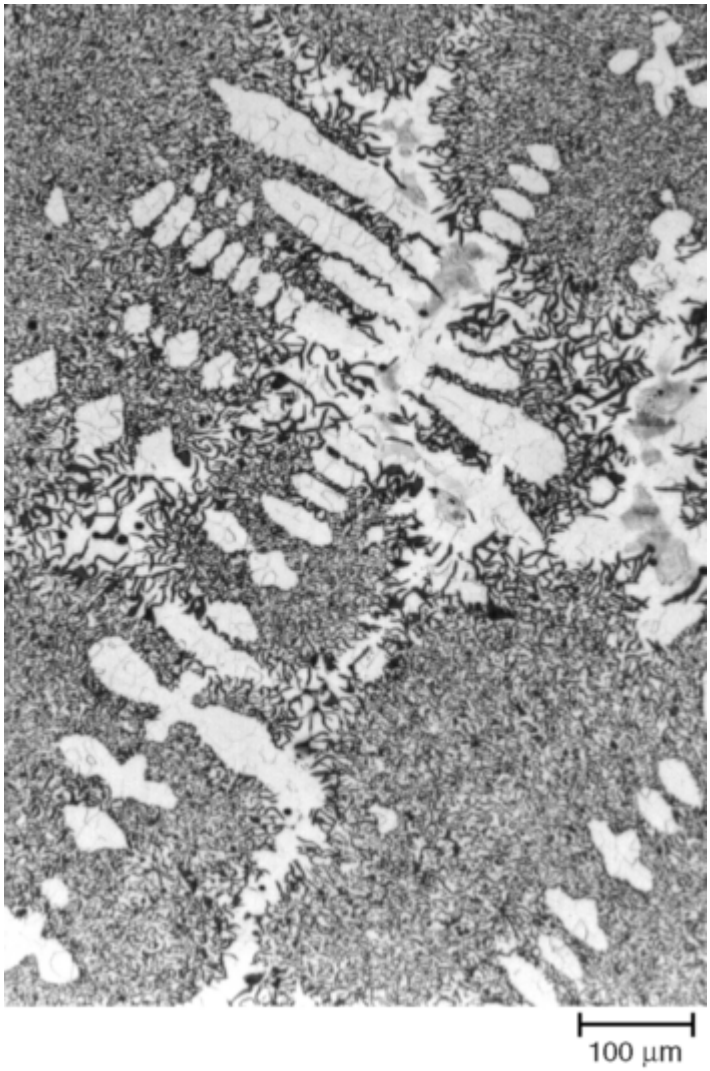

Fig. 80 As-cast gray iron (Fe-3.4%C-3.2%Si-0.09%Mn-0.04%P-0.01%S-0.86%Cu-<0.01%Mg). Ferritic matrix. Etched in 4% nital. 100×

A common characteristic constituent of gray iron microstructures is the phosphorus eutectic known as steadite. Figure 81 shows the Fe-C-P equilibrium diagram, while Table 4 shows the transformations that occur in this system during solidification as well as in the solid state. The characteristic property of this system is a large area of the ternary phosphorous eutectic due to the strong tendency for phosphorus to segregate. This type of eutectic appears in the microstructure of cast irons already at 0.07% P (Ref 13).

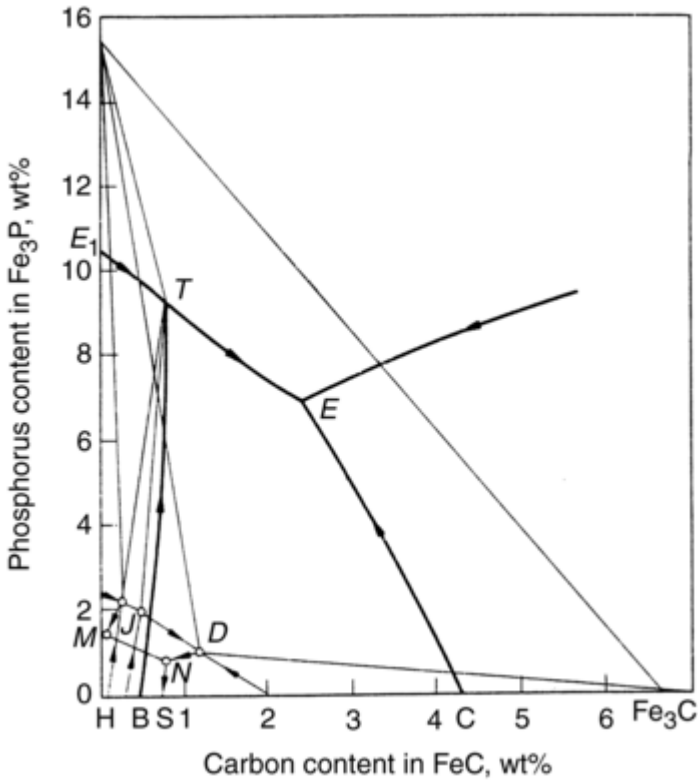

Fig. 81 The Fe-C-P equilibrium diagram. The *x*-axis is the carbon content, and the *y*-axis is the phosphorus content. Source: Ref 13

Table 4 Transformations in the range of solidification and in the solid state according to the Fe-C-P diagram (Fig. 81)

Symbol on the Fe-C-P diagram	Transformation[a]	Type of transformation	Temperature	Composition of phases[b]
TJ	$L + \alpha \leftrightarrow \gamma + Fe_3P$	Peritectic	1005 °C (1840 °F)	L = 0.8 C, 9.2% P α = 0.3% C, 2.2% P γ = 0.5% C, 2.0% P
E	$L \leftrightarrow \gamma + Fe_3P + Fe_3C$	Eutectic	950 °C (1740 °F)	L = 2.4% C, 6.89% P γ = 1.2% C, 1.1% P
MN	$\gamma + Fe_3P \leftrightarrow \alpha + Fe_3C$	Peritectoidal	745 °C (1375 °F)	γ = 0.8% C, 1.0% P α = 0.1% C, 1.5% P

(a) L, melt (liquid metal); α, ferrite (α-iron); γ, austenite (γ-iron); Fe_3P, iron phosphide; Fe_3C, cementite.
(b) Maximum solubility of chemical components in the particular phases. Source: Ref 13

The form of the phosphorus eutectic depends on the chemical composition of the gray iron. In irons with an average tendency to graphitization and a phosphorus content of approximately 0.4%, the fine-grain ternary eutectic solidifies from the liquid and consists of ferrite + Fe_3P + Fe_3C. In gray iron with a strong tendency for cementite solidification and with carbide-forming elements, the ternary eutectic may also contain large columnar precipitates of cementite.

Increasing the amount of strong graphitizing elements, such as silicon, promotes solidification of the binary phosphorous eutectic, ferrite + Fe_3P + C_{gr}, instead of the ternary one. The binary euetectic is called a pseudobinary eutectic, because carbon is removed from the eutectic during diffusion in the solid state (Ref 13).

Ductile iron microstructures normally consist of pearlite or pearlite and ferrite with graphite nodules surrounded with ferrite, which look like a white halo, although the more common name of this structure is the bull's-eye

structure. Figure 82 and 83 show this type of microstructure, while Fig. 84 shows a fully ferritic-matrix microstructure that was achieved after annealing a chilled casting with a microstructure containing cementite, ferrite, and pearlite (see also Fig. 11). In some cases, usually at a high cooling rate, cementite occurs as a separate constituent in the matrix.

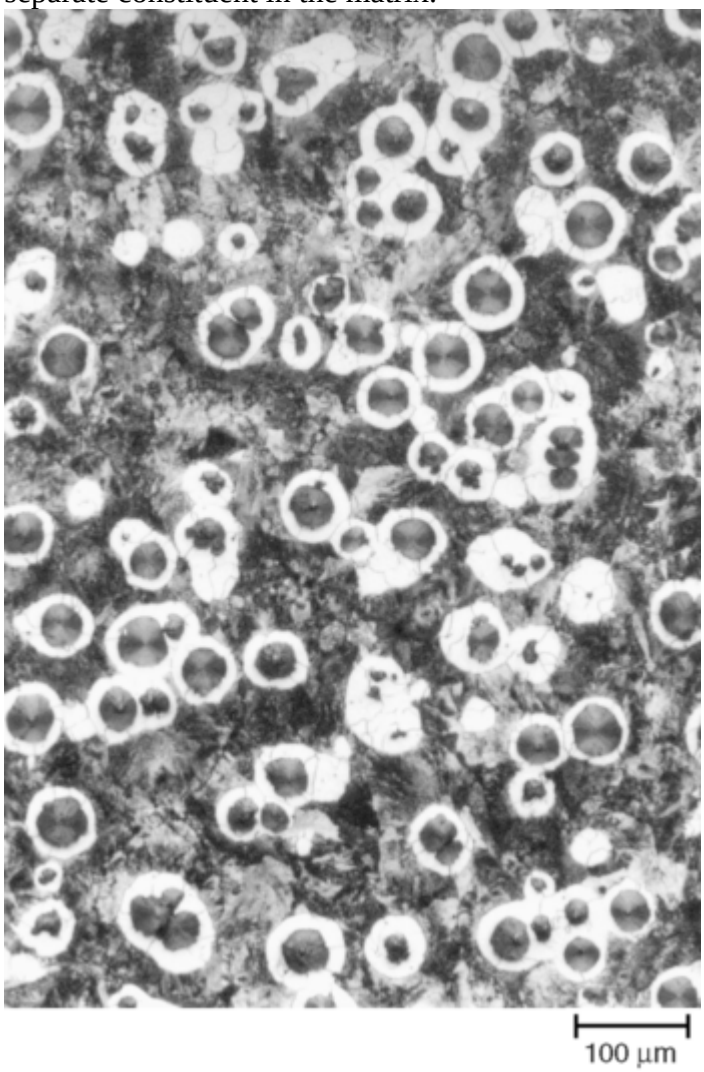

Fig. 82 As-cast ductile iron (Fe-3.7%C-1.25%Si-0.03%Mn-0.02%P-0.02%S-0.24%Ni-0.06%Mg). Pearlite matrix with ferritic halos around graphite nodules. Etched with 4% nital. 100×

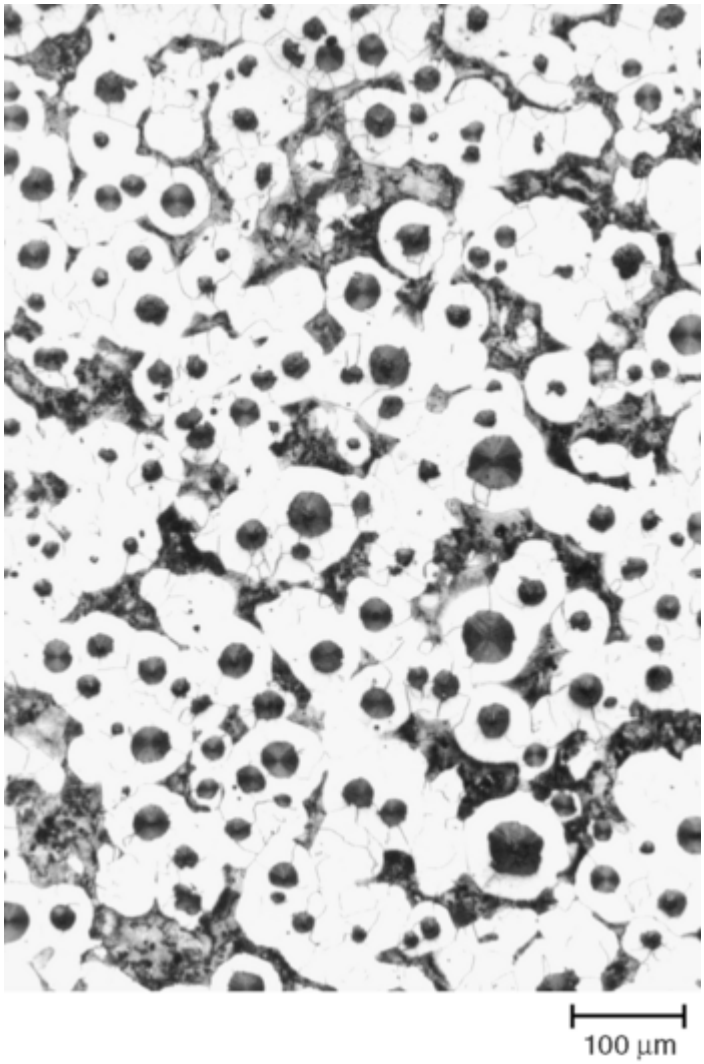

Fig. 83 As-cast ductile iron. Ferritic-pearlitic matrix. Etched with 4% nital. 100×

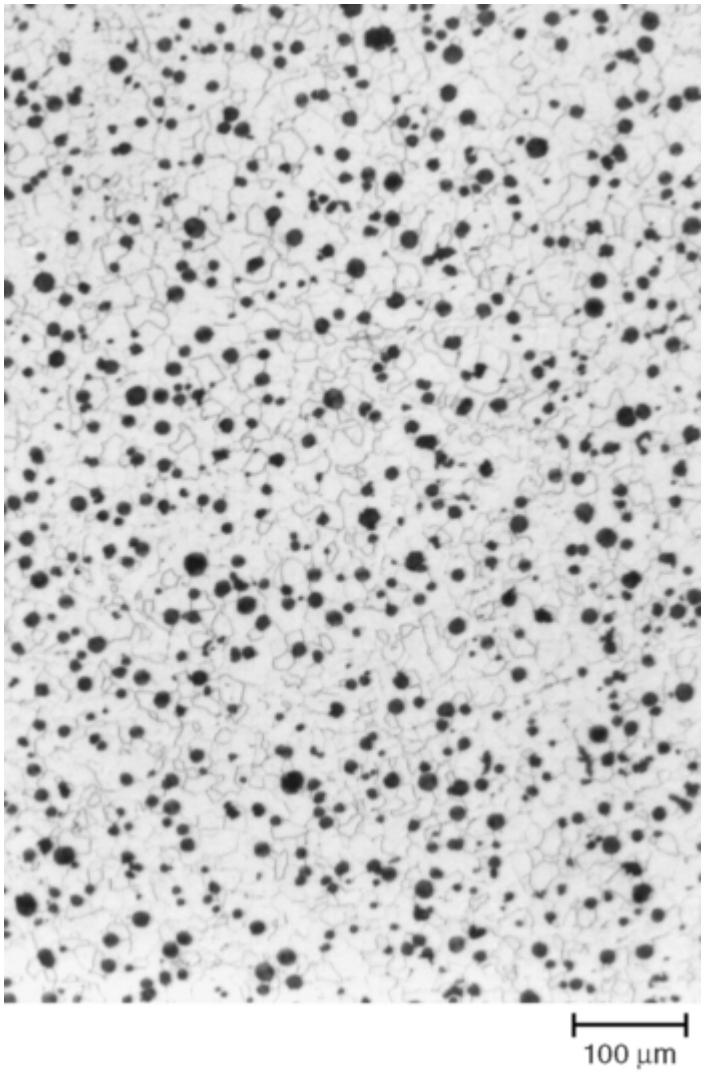

Fig. 84 Ductile iron. Ferritic matrix. The casting was annealed at 900 °C (1650 °F), held 2 h, quick furnace cooled to 730 °C (1345 °F), slow furnace cooled to 600 °C (1110 °F), and air cooled. Etched with 4% nital. 100×

The precipitates of cementite are situated in the exterior regions of the eutectic cells or in the interdendritic spaces of the transformed austenite due to the microsegregation of carbide-forming elements, such as manganese, chromium, or vanadium. Cementite appears very frequently in chill castings or in thin-walled sand castings (Ref 13). Figure 85 and 86 show the microstructure of pearlitic ductile iron with cementite and ledeburite. In this case, cementite was a desired constituent of the microstructure to improve the wear resistance of cast iron. It was achieved by feeding the melted metal with an iron-magnesium foundry alloy, without inoculation. The graphite nodules do not have a perfect shape. Figure 87 shows the microstructure of a heat- and wear-resistant ductile iron containing chromium and nickel, which consists of chromium carbides in an austenitic matrix.

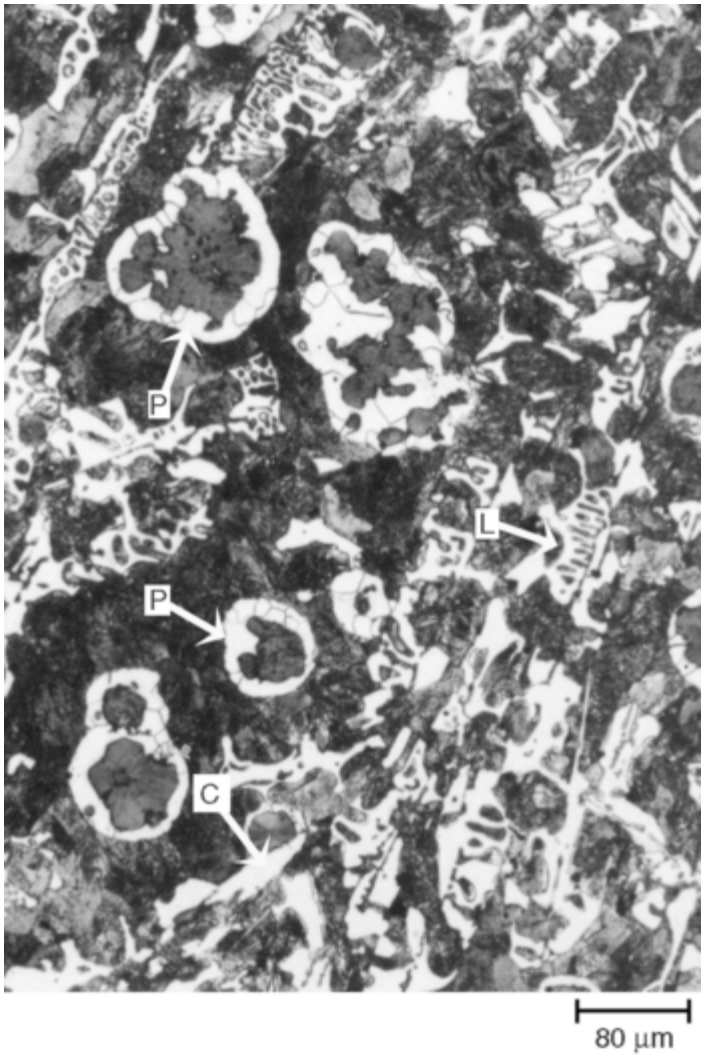

Fig. 85 As-cast ductile iron (Fe-3.35%C-2.05%Si-0.08%Mn-0.04%P-0.02%Cr-0.02%Ni-0.045%Mg). C, cementite; L, ledeburite; and P, pearlite and ferrite around graphite nodules. Etched with 4% nital. 125× (microscopic magnification is 100×)

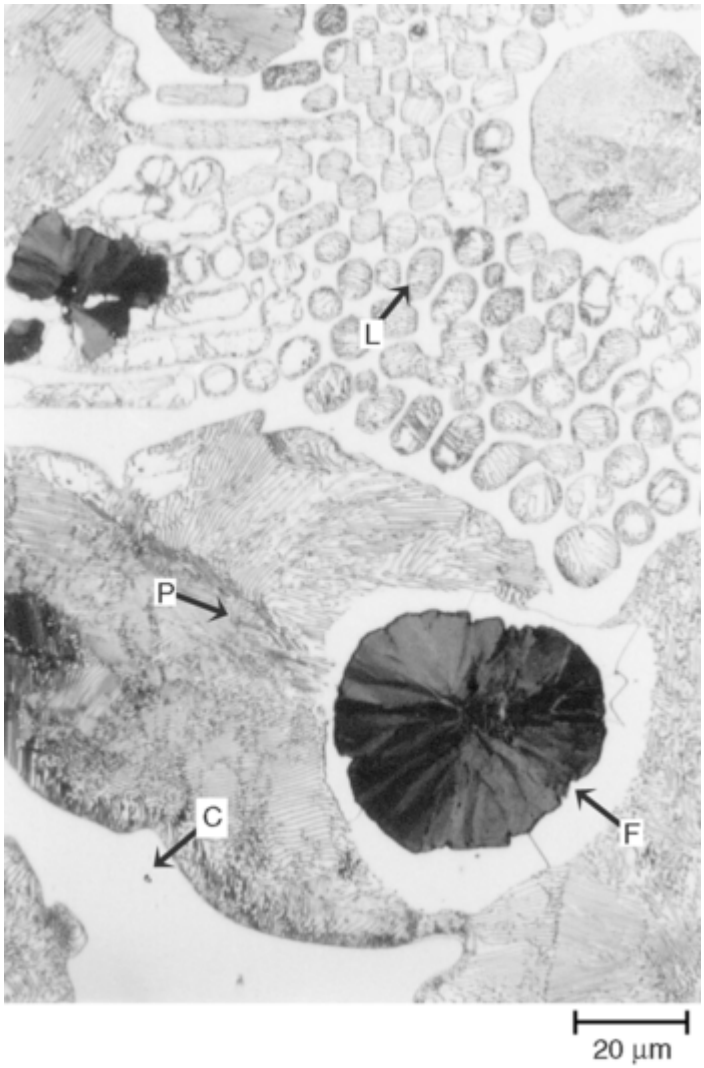

Fig. 86 Same as in Fig. 85. C, cementite; L, ledeburite; F, ferrite; and P, pearlite. 500×

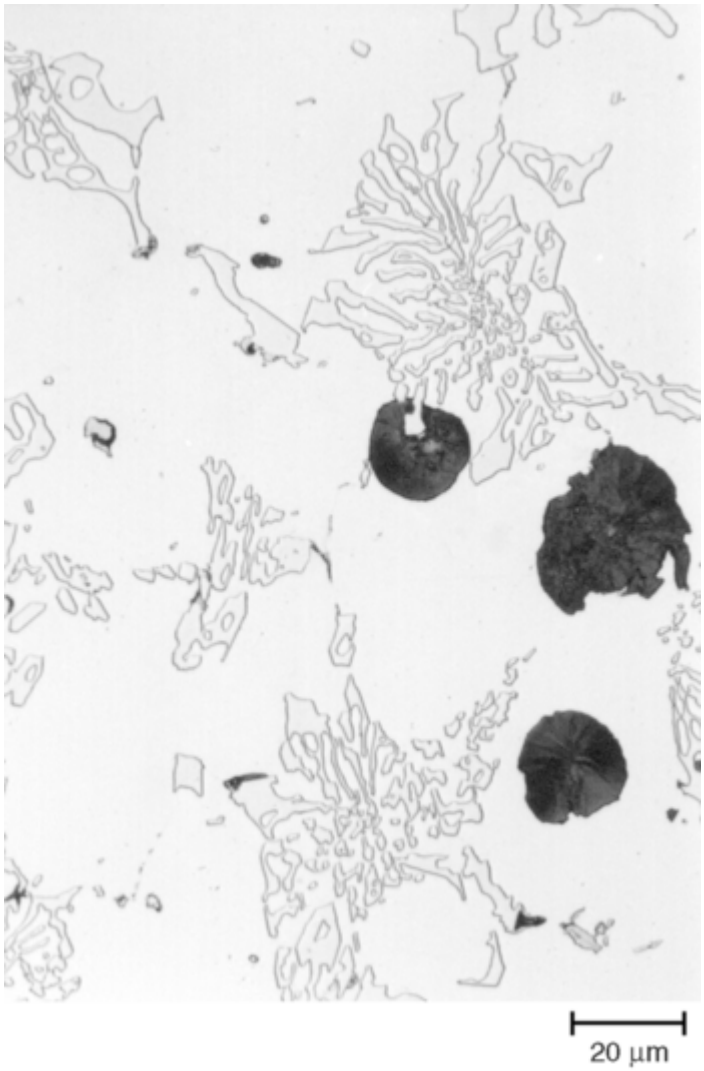

Fig. 87 As-cast austenitic ductile iron (Fe-2.7%C-2.85%Si-1.15%Mn-0.03%P-0.01%S-2.8%Cr-20.0%Ni-0.1%Mg). Austenite and eutectic carbides type M_7C_3. Etched with glyceregia. 500×

The austempering heat treatment is used to achieve better mechanical properties in ductile iron. The casting is heated to a temperature range of 840 to 950 °C (1545 to 1740 °F) and held at this temperature until the entire matrix is transformed to austenite saturated with carbon. The casting is then quenched rapidly to austempering temperature, between 230 and 400 °C (445 and 750 °F), and held at this temperature for the required time (Ref 14). When this cycle is properly performed, the final structure of the matrix, which is called ausferrite, consists of acicular ferrite and austenite, and the iron is called austempered ductile iron (ADI). The morphology and amount of ferrite depends on the time and temperature of the austempering process. Figure 88 and 89 show an ADI microstructure after austempering heat treatment, when the casting in both cases was held in the furnace for 180 min, and the annealing temperatures were different. The use of a higher temperature changed the morphology of the ferrite and increased the amount of austenite. Figure 90 shows the ADI microstructure after 2 min austempering heat treatment, when the transformation of austenite to acicular ferrite was just started, so martensite is the dominant phase, and there is only a small amount of acicular ferrite, mostly surrounding the graphite nodules (see also Fig. 31, 32, 33, 34, 35, . 36, 37).



Fig. 88 Austempered ductile iron (the same ductile iron as in Fig. 32). Acicular ferrite and austenite. The casting was austempered: 900 °C (1650 °F), held 2 h, taken to salt bath at 360 °C (680 °F), held 180 min, and air cooled. Etched with 4% nital. 500×

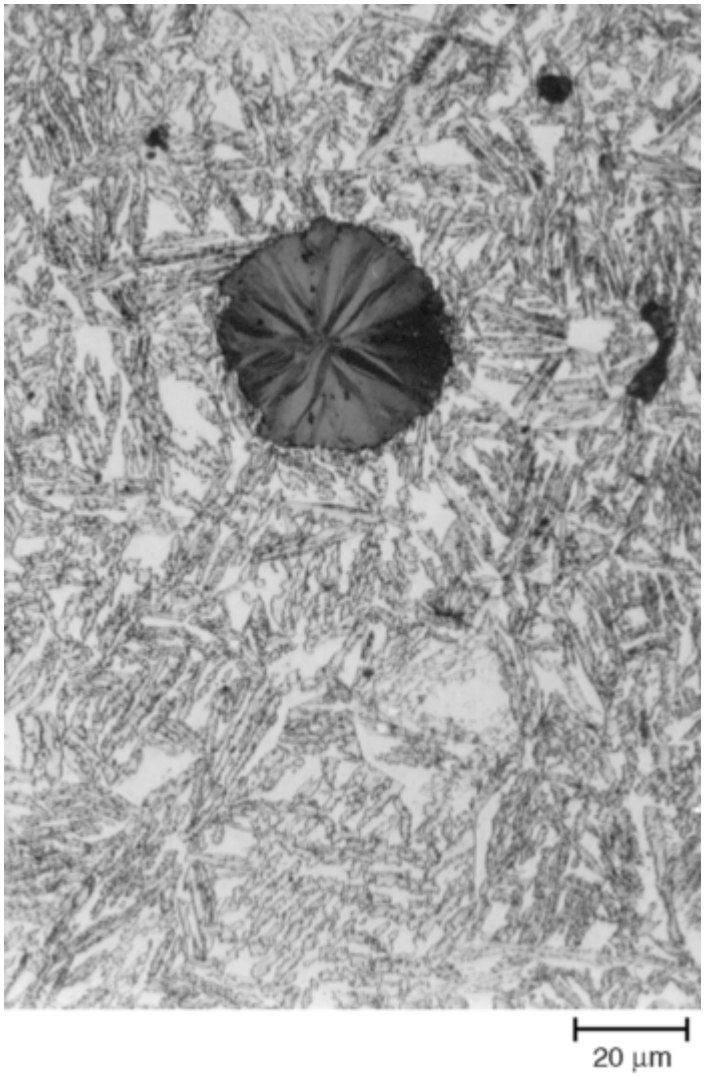

Fig. 89 Austempered ductile iron (the same composition as in Fig. 32). Acicular ferrite and austenite. The casting was austempered: 900 °C (1650 °F), held 2 h, taken to salt bath at 380 °C (715 °F), held 180 min, and air cooled. Etched with 4% nital. 500×

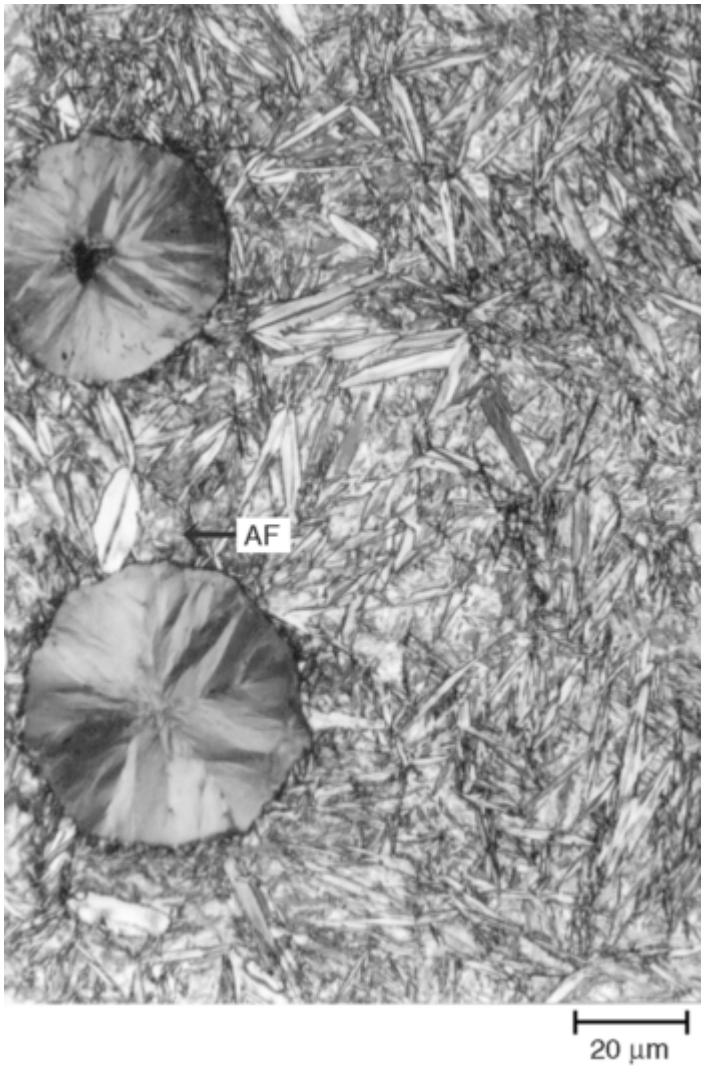

Fig. 90 Austempered ductile iron (the same composition as in Fig. 32). Martensite and small amount of acicular ferrite (AF). The casting was austempered: 900 °C (1650 °F), held 2 h, taken to salt bath at 300 °C (570 °F), held 2 min, and air cooled. Etched with 4% nital. 1000×

Compacted graphite-iron matrix microstructures consist of ferrite and pearlite; the amount of each constituent depends on the cooling rate and the chemical composition (elements that promote either ferrite or pearlite solidification). Figure 91 shows a ferritic-pearlitic microstructure with a small amount of nodular graphite.

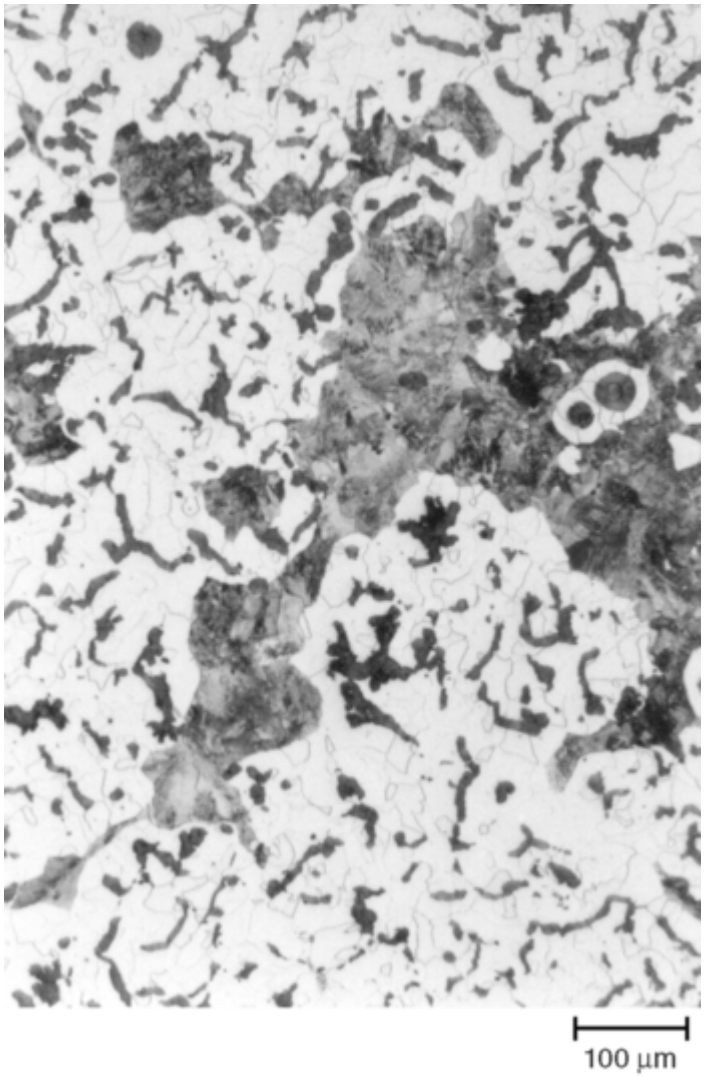

Fig. 91 As-cast iron with compacted graphite (Fe-2.8%C-1.9%Si-0.55%Mn-0.04%P-0.2%S-0.018%Mg). Ferritic-pearlitic matrix. Etched with 4% nital. 100×

Malleable iron matrix microstructures are mostly ferritic, ferritic-pearlitic, or pearlitic, depending on the cast-making process used. The type of matrix is a result of transformation in the solid state during the annealing of white cast iron. Figure 92 and 93 show the microstructure of the pearlitic-ferritic and ferritic malleable iron, respectively. The annealing process was the same one in both cases, but the final microstructures were achieved by the use of different foundry processes. In the case of the pearlitic-ferritic microstructure, the inoculation and deoxidation processes were not carried out. When these two processes were used, that is, deoxidation with aluminum and inoculation with iron-silicon and pure bismuth, the result was a ferritic microstructure after annealing.

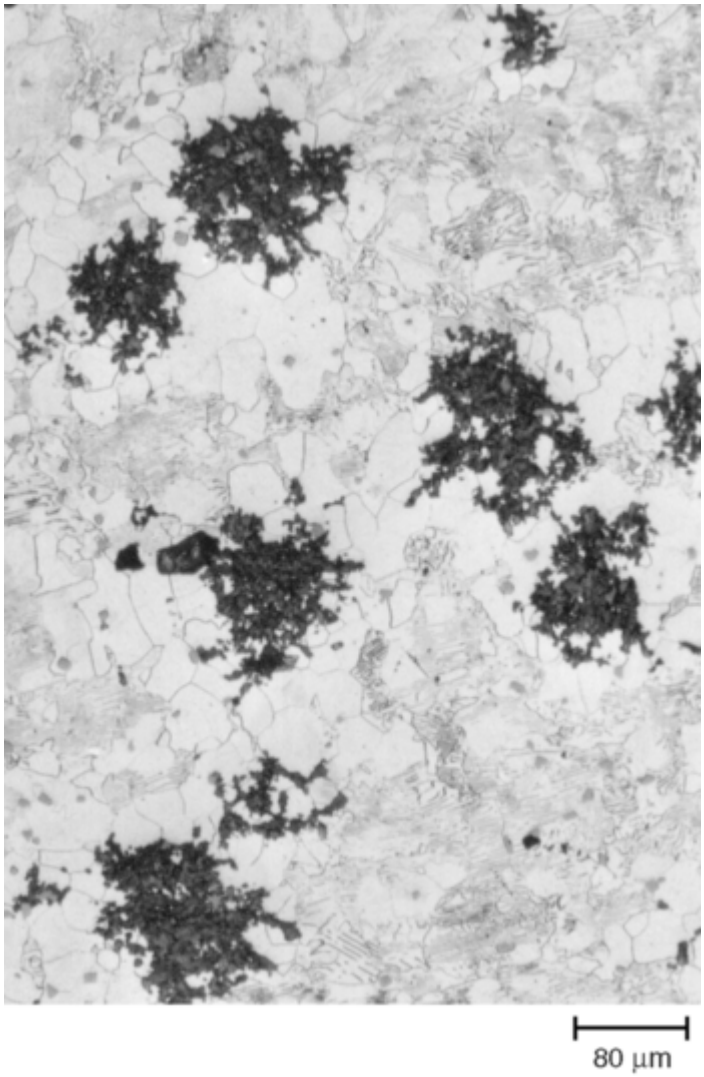

Fig. 92 Malleable iron (Fe-2.95%C-1.2%Si-0.53%Mn-0.06%P-0.21%S-0.08%Cr-0.10%Cu-0.07%Ni-<0.01%Al). The casting was annealed: at 950 °C (1740 °F), held 10 h, furnace cooled to 720 °C (1330 °F), held 16 h, and air cooled. Pearlitic-ferritic matrix. Etched with 4% nital. 125× (microscopic magnification 100×)

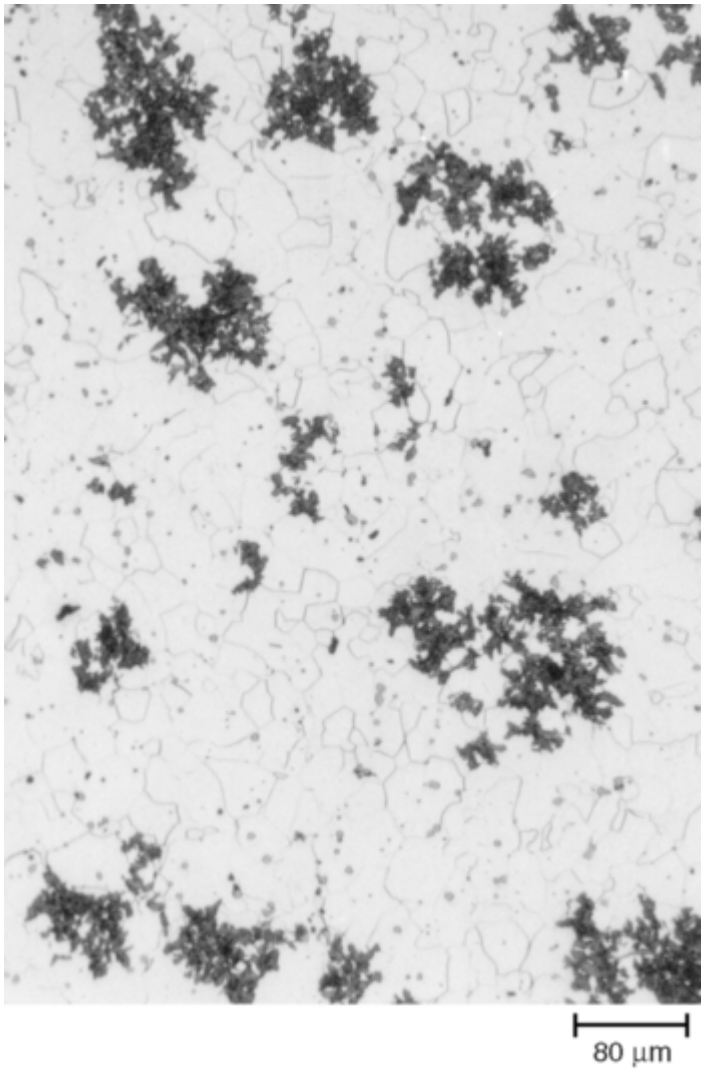

Fig. 93 Malleable iron (Fe-2.9%C-1.5%Si-0.53%Mn-0.06%P-0.22%S-0.09%Cr-0.10%Cu-0.08%Ni-0.02%Al). The casting was annealed as in Fig. 92. Ferrite. Etched with 4% nital. 125× (microscopic magnification 100×)

Unalloyed white iron microstructures are created when the castings solidify in the metastable system and the structure is free of graphite. The matrix may consist of cementite and pearlite, as shown in Fig. 94, or, after heat treatment, of cementite and martensite, as shown in Fig. 95. This type of white iron belongs to the class of abrasion-resistant cast irons and usually is produced as chill castings.

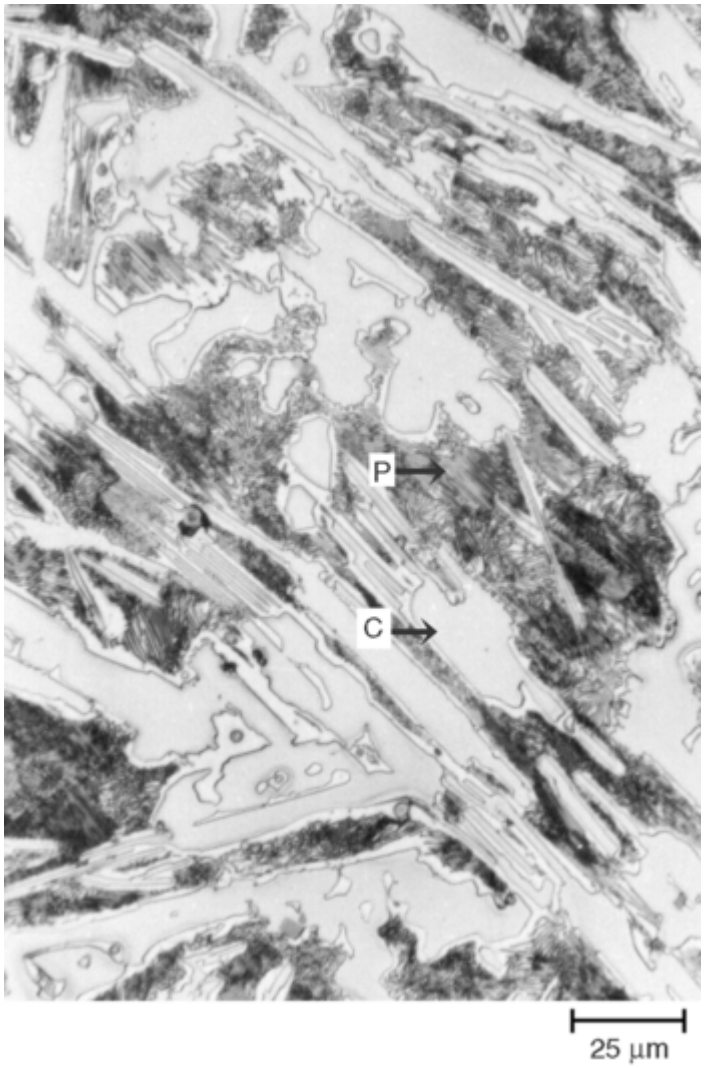

Fig. 94 As-cast white iron (Fe-3.0%C-2.7%Si-0.45%Mn-0.07%P-0.025%S). C, cementite; P, pearlite. Etched with 4% nital. 400×

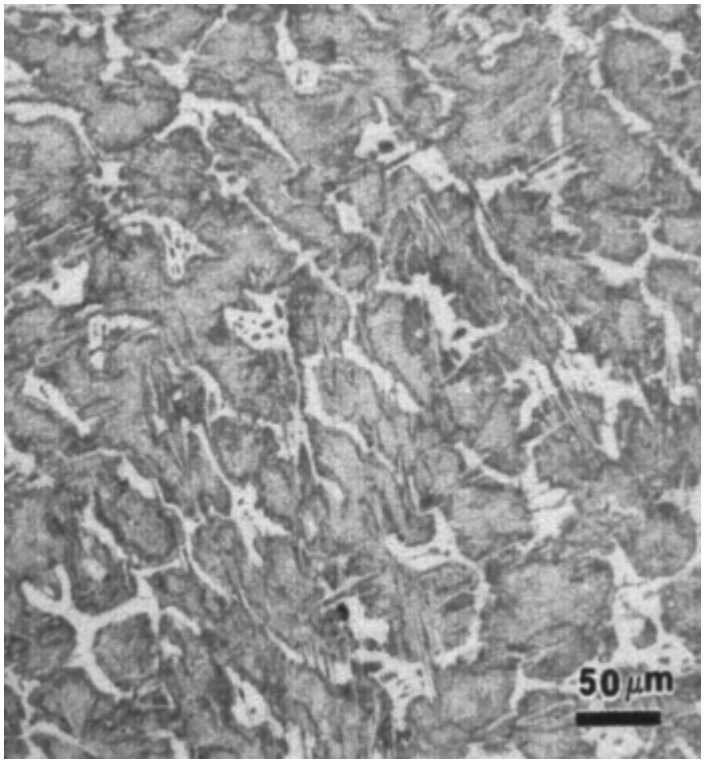

Fig. 95 White cast iron after heat treatment. A network of massive cementite and tempered martensite. Etched with 4% picral. 140×. Courtesy of G.F. Vander Voort, Buehler Ltd.

High-chromium white iron is a type of highly wear-resistant iron with a microstructure that consists of primary and eutectic carbides, for example, $(FeCr)_3C$, $(FeCr)_7C_3$, and $(FeCr)_{23}C_6$, depending on the chemical composition and cooling rate during solidification. The primary carbides have a typical shape, which in cross section is similar to the letter "L," and have the chemical formula M_3C at higher cooling rate and low chromium content. When the cooling rate slows down and the chromium content increases to, for example, 30% and higher, the primary chromium carbides have a hexagonal shape with a characteristic hole in the center. The eutectic carbides are always type M_7C_3, independent of chromium content and cooling rate (Ref 15).

The type $M_{23}C_6$ carbides solidify when the chromium content is approximately 50 to 60% (Ref 16). The same factors that affect the type of carbides also influence the type of matrix, which can be austenitic but also ferritic or pearlitic. When the cooling rate is respectively slow, secondary precipitations can occur around the austenitic dendrites (Ref 17).

It has been proven that the annealing heat treatment destabilizes the matrix, which will transform into either bainite or martensite with small secondary carbide precipitates. The resulting transformation product is a function of the cooling rate from annealing as well as the chemical composition; for example, when $Cr/C < 5$, the matrix microstructure was bainitic, while exceeding this value produced martensitic transformation (Ref 18). Figure 96 shows the microstructure of high-chromium white cast iron after isothermal heat treatment; the secondary, fine carbides precipitated from the austenitic matrix, which transformed into martensite (see also Fig. 43, 44, and 45).

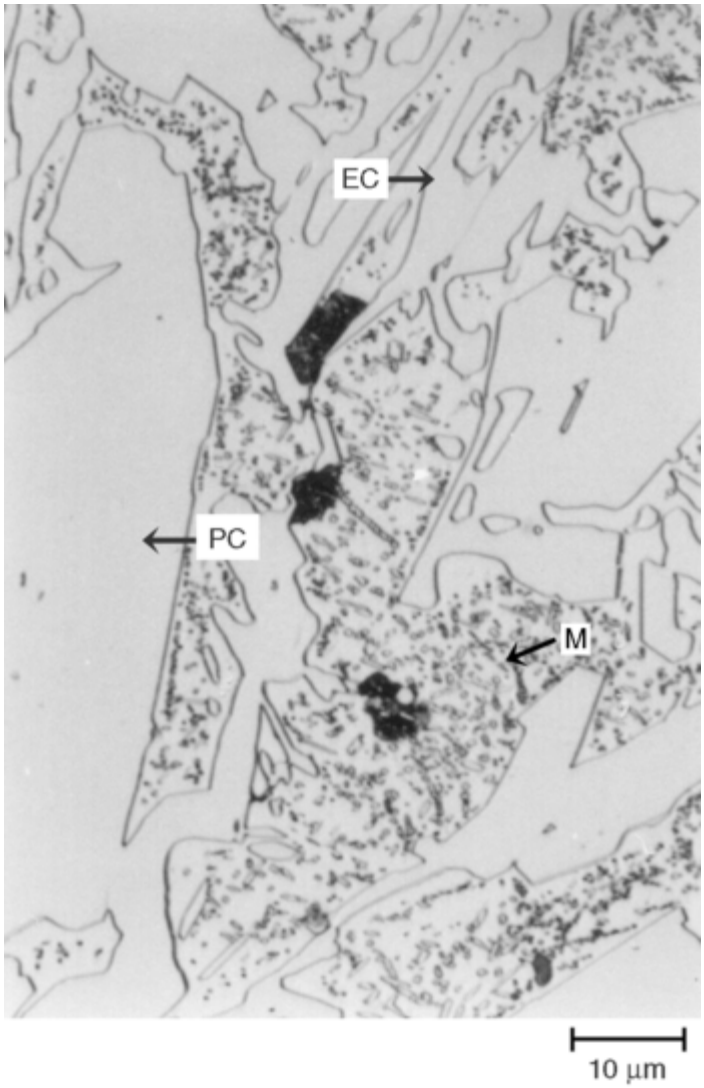

Fig. 96 White high-chromium cast iron (see Fig. 43). PC, primary carbides; EC, eutectic carbides in martensitic matrix with fine, globular secondary carbides. The casting was heat treated at 1000 °C (1830 °F), held 1 h, furnace cooled to 550 °C (1020 °F), held 4 h in a 400 °C (750 °F) salt bath, and air cooled. Etched with glyceregia. 1000×

References cited in this section

3. W. Sakwa, *Żeliwo (Cast Iron),* Śląsk-Katowice, Poland, 1974, p 53

10. J.A. Nelson, Cast Irons, *Metallography and Microstructures,* Vol 9, *ASM Handbook,* American Society for Metals, 1985, p 242

11. "Poor Nodularity in Ductile Iron," Technical Information 25, Revision No. 1, Elkem ASA, Silicon Division, 2001

12. "Graphite Structures in Cast Irons," poster, Elkem ASA

13. K. Sękowski, J. Piaskowski, and Z. Wojtowicz, Atlas struktur znormalizowanych stopów odlewniczych *(Atlas of the Standard Microstructures of Foundry Alloys),* WNT Warszawa, Poland, 1972, p 54–55, 74–77

14. B.V. Kovacs, On the Terminology and Structure of ADI, *Trans. AFS,* Vol 102, 1994, p 417–420

15. T. Ohide and G. Ogira, Solidification of High Chromium Alloyed Cast Irons, *Br. Foundryman,* Vol 76 (No. 1), 1983, p 7

16. M. Šittner, Primárni kristalizace chromovych litin, Časť II (Primary Solidification of the Chromium Cast Irons, Part II), *Slévárenství,* Vol 33 (No. 9), 1985, p 363

17. P. Dupin and J.M. Schissler, Etude structural de l'état brut de fontes blanches à 17% Cr, *Hommes et Fonderie,* No. 151, 1985, p 19

18. C.P. Tong, T. Suzuki, and T. Umeda, The Influence of Chemical Composition and Destabilization on Transformation Characteristics of High Chromium Cast Irons, *Imono (J. Jpn. Foundrymen's Soc.),* Vol 62 (No. 5), 1990, p 344

J.M. Radzikowska, Metallography and Microstructures of Cast Iron, *Metallography and Microstructures,* Vol 9, *ASM Handbook,* ASM International, 2004, p. 565–587

Metallography and Microstructures of Cast Iron

Janina M. Radzikowska, The Foundry Research Institute, Kraków, Poland

Acknowledgments

For samples and examination results, many thanks to:

- Colleagues at the Foundry Research Institute, Kraków, Poland: Adam Kowalski, W. Wierzchowski, J. Turzyński, W. Madej, K. Głownia, A. Pytel, and J. Bryniarska
- M. Sorochtej of The Kraków Technical University

Also, many thanks to M. Warmuzek at the Foundry Research Institute for making the SEM micrographs of different types of graphite.
Special thanks to G.F. Vander Voort from Buehler Ltd. for his advice and help in preparing this article.

J.M. Radzikowska, Metallography and Microstructures of Cast Iron, *Metallography and Microstructures,* Vol 9, *ASM Handbook,* ASM International, 2004, p. 565–587

Metallography and Microstructures of Cast Iron

Janina M. Radzikowska, The Foundry Research Institute, Kraków, Poland

References

1. Guide to Engineered Materials, Property Comparison Tables, *Adv. Mater. Process.,* Vol 159 (No. 12), Dec 2001, p 46

2. Cz. Podrzucki and Cz. Kalata, *Metalurgia i odlewnictwo żeliwa (Metallurgy and Foundrying of Cast Iron),* Śląsk-Katowice, Poland, 1971, p 32, 54–59, 70

3. W. Sakwa, *Żeliwo (Cast Iron),* Śląsk-Katowice, Poland, 1974, p 53

4. G.F. Vander Voort, *Metallography: Principles and Practice,* McGraw-Hill Book Co., 1984; Reprinted by ASM International, 1999, p 129, 294–303, 632, 634, 642–644, 646, 648

5. G.F. Vander Voort, Phase Identification by Selective Etching, *Applied Metallography,* G.F. Vander Voort, Ed., Van Nostrand Reinhold Co., 1986, p 1–19

6. J. Zhou, Dalian, W. Schmitz, and S. Engler, Unterschung der Gefügebildung von Gußeisen mit Kugelgraphit bei langsamer Erstarrung, *Giessereiforschung,* Vol 39 (No. 2), 1987, p 55–70

7. P. Skočovský, *Colour Contrast in Metallographic Microscopy,* Žilina (Slovak Republic), 1993, p 26

8. E. Weck and E. Leistner, *Metallographic Instructions for Color Etching by Immersion, Part II: Beraha Color Etchants and Their Different Variations,* Deutscher Verlag für Schweißtechnik, GmbH, Düsseldorf, 1983, p 51

9. P.C. Liu and C.R. Loper, Observation on the Graphite Morphology in Cast Iron, *Trans. AFS,* Vol 88, 1980, p 97

10. J.A. Nelson, Cast Irons, *Metallography and Microstructures,* Vol 9, *ASM Handbook,* American Society for Metals, 1985, p 242

11. "Poor Nodularity in Ductile Iron," Technical Information 25, Revision No. 1, Elkem ASA, Silicon Division, 2001

12. "Graphite Structures in Cast Irons," poster, Elkem ASA

13. K. Sękowski, J. Piaskowski, and Z. Wojtowicz, Atlas struktur znormalizowanych stopów odlewniczych *(Atlas of the Standard Microstructures of Foundry Alloys),* WNT Warszawa, Poland, 1972, p 54–55, 74–77

14. B.V. Kovacs, On the Terminology and Structure of ADI, *Trans. AFS,* Vol 102, 1994, p 417–420

15. T. Ohide and G. Ogira, Solidification of High Chromium Alloyed Cast Irons, *Br. Foundryman,* Vol 76 (No. 1), 1983, p 7

16. M. Šittner, Primárni kristalizace chromovych litin, Čast II (Primary Solidification of the Chromium Cast Irons, Part II), *Slévárenství,* Vol 33 (No. 9), 1985, p 363

17. P. Dupin and J.M. Schissler, Etude structural de l'état brut de fontes blanches à 17% Cr, *Hommes et Fonderie,* No. 151, 1985, p 19

18. C.P. Tong, T. Suzuki, and T. Umeda, The Influence of Chemical Composition and Destabilization on Transformation Characteristics of High Chromium Cast Irons, *Imono (J. Jpn. Foundrymen's Soc.),* Vol 62 (No. 5), 1990, p 344

A.O. Benscoter and B.L. Bramfitt, Metallography and Microstructures of Low-Carbon and Coated Steels, Metallography and Microstructures, Vol 9, ASM Handbook, ASM International, 2004, p. 588–607

Metallography and Microstructures of Low-Carbon and Coated Steels

Arlan O. Benscoter, Lehigh University; Bruce L. Bramfitt, International Steel Group, Inc.

Introduction

THIS ARTICLE distinguishes low-carbon steels from plain carbon and low-alloy steels described in the article "Metallography and Microstructures of Carbon and Low-Alloy Steels" in this Volume. Low-carbon steels generally contain less than approximately 0.10% C and are used in vast quantities in the automotive, appliance, and container industries. One of the major attributes of low-carbon steels is good formability, that is, the ease to form a part by stamping, pressing, bending, stretching, and so on. In the past few decades, there has been a swirl of activity in the metallurgy of low-carbon steels that has become quite sophisticated, and several new types of steels have evolved. These advanced steels include ultralow-carbon steels, bake-hardenable steels, interstitial-free steels, dent-resistant steels, electrical steels, dual-phase and transformation-induced plasticity (TRIP) steels, enameling steels, and microalloyed high-strength steels. These steels are produced in sheet form by hot rolling continuous-cast slabs on a hot strip mill. When produced from a hot strip mill, the steel is called hot-rolled sheet or hot band. Many low-carbon steels are further processed on a tandem mill or cold mill by cold rolling, where the thickness is reduced approximately 70 to 80% (e.g., from 0.110 in. to approximately 0.030 in.). Because of the cold work, the steel must be annealed by either batch annealing or continuous annealing to soften the steel and make it formable. These latter steels are the cold-rolled sheet steels that comprise a huge segment of the steel market around the world.

In the commodity cold-rolled sheet steel market, much of this steel is classified as commercial quality, drawing quality, or deep-drawing quality. For most of these low-carbon steels, the Unified Numbering System (UNS) does not apply. For example, the UNS classified steel G10080 can be marketed as several other classifications of sheet. These classifications depend on how the steel was produced and what chemical elements are contained in the steel. The steel may be aluminum-killed, or the steel may contain microalloying elements such as vanadium or niobium. The classification of these materials is discussed further in the article "Classification and Designation of Carbon and Low-Alloy Steels" in Properties and Selection: Irons, Steels, and High-Performance Alloys, Volume 1 of ASM Handbook.

For many critical applications, these steels are coated with metallic, organic, or oxide layers to impart corrosion resistance, cosmetic appeal, magnetic/electrical insulation, abrasion resistance, and color. Millions of tons of low-carbon sheet steel for automobiles are coated with zinc-base alloys for corrosion protection from road salts and moisture. These zinc-base coatings include conventional galvanized low-carbon steel sheet where the coated layer is applied in either a hot dipping (liquid bath) process or by electroplating, as in producing an electrogalvanized layer. There are also commercial hot dipped aluminum-zinc alloys, including Galvalume (a Zn-55% Al + 1.6% Si alloy) and Galfan (a Zn-5% Al alloy). There is also a zinc coating called galvanneal, which is a heat treated layer of a galvanized coating on a low-carbon steel. In some cases, an aluminum coating called aluminized is applied to protect low-carbon steel sheet for applications where moderate heat resistance is required. Such applications include automotive exhaust systems (tailpipes, mufflers, etc.).

The appliance industry coats ultralow-carbon sheet steel with a porcelain enamel layer to protect the steel from corrosion and to enhance surface appeal. These enameled steels are used in kitchen appliances (stovetops, ovens, sinks, etc.) and in lavatory fixtures (bathtubs and sinks). The food industry uses organic coatings or a metallic tin coating on low-carbon sheet steel containers for beverages and food. The tin can is a classic example of a food container. The metallographic techniques used for all these coatings are discussed later in this article.

Millions of tons of very-low-carbon sheet steels are used in the electrical appliance and power transmission industry. Electric motors contain hundreds of steel sheets called motor laminations that are stacked and wound with copper wire in the rotor and stator of the motor. Very-low-carbon 3.25% Si sheet steels are used as laminations in electrical power transformers. A thin iron oxide surface layer or organic coating electrically insulates these steel laminations from each other in order to minimize power losses.

This article discusses the techniques used to prepare metallographic specimens of low-carbon steels and coated steels. Simple and proven manual sample preparation techniques are described. Metallographic sample preparation for low-carbon steels may be only slightly more difficult than higher-carbon steels, because of the large volume percent of ferrite present in the microstructure. Ferrite is soft and can be mechanically cold worked during sample preparation. Mechanical cold work can be serious enough to range from a sloppy appearance of the microstructure to an artifact that leads to a complete misinterpretation of the metallographic features. Figure 1(b) shows an extreme example of a poorly prepared metallographic sample of UNS G10100 sheet. When the sheet was sheared into a metallographic specimen, the grains were heavily distorted, and the carbides were fractured into small particles. Figure 1(a) represents the same sample properly prepared. The actual microstructure consists of equiaxed (polygonal) grains of ferrite with some carbide (cementite) on the grain boundaries. An experienced metallographer will prepare a specimen properly to avoid artifacts in the microstructure.

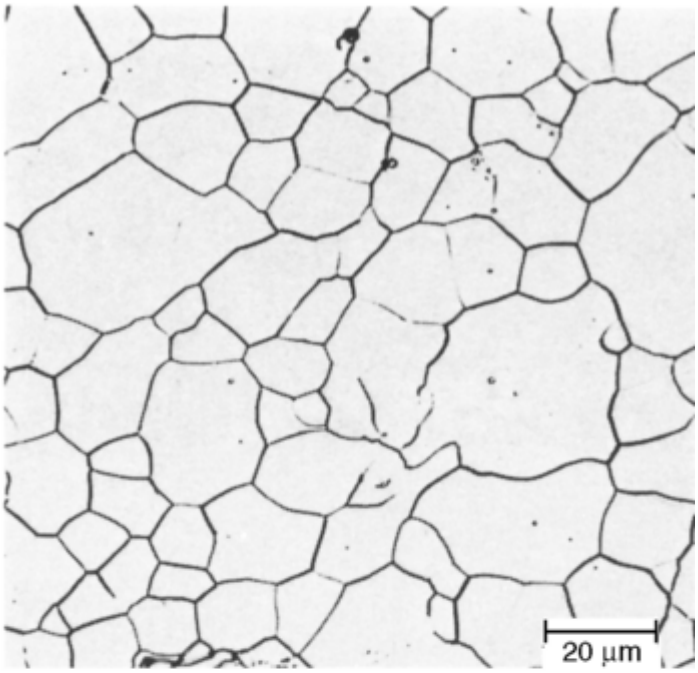

(a)

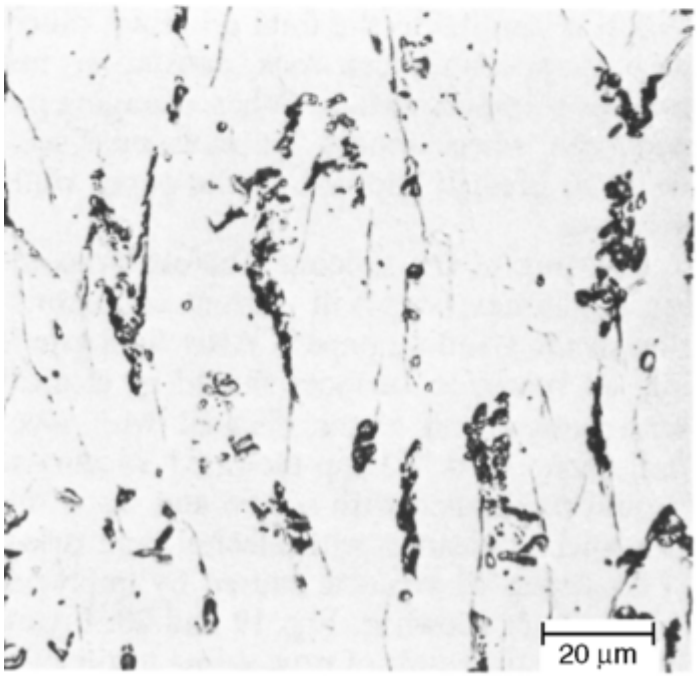

(b)

Fig. 1 Microstructure of a UNS G10100 steel sheet showing the effect of deformation during shearing of the specimen. (a) The proper microstructure of equiaxed ferrite grains. (b) An artifact microstructure showing elongated grains and broken carbides at sheared edge. Marshall's reagent. 500×

The metallographic preparation of coated steels requires different techniques; for example, it requires the absolute necessity to maintain edge integrity (flatness of the specimen and coated edge). Coatings are usually very thin, and they can be softer (zinc) or harder (enamel) than the steel base. Methods to preserve a flat edge are discussed in this article. Also, metallic coatings on steel, for example, zinc-base coatings, form an electrolytic cell in the presence of water and thus develop an electrochemical reaction. Thus, alcohol-based liquids are used in preparation. Many metallographic preparation steps require water, and thus special precautions are needed to deal with metallic-coated steels. These kinds of precautions are described in this article.

Before describing metallographic techniques, a quick review of the various phases and constituents found in the microstructures of low-carbon and coated steels is given as follows.

A.O. Benscoter and B.L. Bramfitt, Metallography and Microstructures of Low-Carbon and Coated Steels, Metallography and Microstructures, Vol 9, ASM Handbook, ASM International, 2004, p. 588–607

Metallography and Microstructures of Low-Carbon and Coated Steels

Arlan O. Benscoter, Lehigh University; Bruce L. Bramfitt, International Steel Group, Inc.

Microstructural Constituents

Most low-carbon steels are essentially pure iron (99.5% Fe) with small amounts of alloying elements, such as manganese, silicon, and aluminum, to enhance properties. In fact, many low-carbon steels, especially the very-low- and ultralow-carbon steels, are actually pure iron (99.99%), because carbon is at such a low level that it is considered a residual element and is no longer required to develop the properties of the material. In many cases, carbon is undesirable and detrimental to the properties of highly formable steels. This is true in steels used for enameling. In this case, the sheet steel for enameling is not called a steel but an enameling iron. In these steels, the microstructure is 100% ferrite.

Ferrite. With very few exceptions, ferrite is the major constituent in low-carbon steels. Ferrite is essentially pure iron and contains less than 0.005% C at room temperature. However, it can contain alloying elements such as manganese and silicon. An example of ferrite is seen in Fig. 2. In most low-carbon steels, ferrite appears as an equiaxed morphology (equal dimensions in all directions), as seen in Fig. 2. This form is also called polygonal ferrite. Ferrite can also appear in an elongated morphology in steels that have been cold worked. Figure 3 shows a low-carbon steel that has been cold rolled 30, 50, 70, and 90% from the original hot-rolled (hot band) thickness; for example, a 30% reduction would be from 2.55 to 1.78 mm (0.100 to 0.070 in.). Note how the ferrite grains are elongated and contain deformation bands (dark lines across the grains) from the cold working process. When this steel is annealed, these cold-worked ferrite grains recrystallize into new equiaxed grains, represented in Fig. 2. Another form of ferrite is epitaxial ferrite, formed when a steel is heated into the two-phase ferrite + austenite region. An example of epitaxial ferrite can be seen (arrows) in Fig. 4. During cooling, new ferrite has grown epitaxially on the existing ferrite grains. Some dual-phase steels show eptiaxial ferrite, because they were annealed in the two-phase region. In very-low-carbon steel (pure iron), a substructure called veining can be seen within the ferrite grains. Figure 5 shows an example of veining in pure iron.

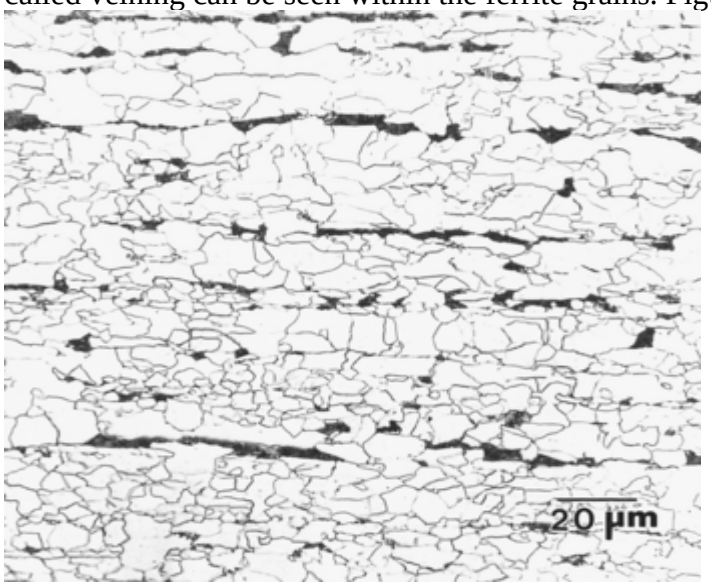

Fig. 2 Microstructure of equiaxed (polygonal) ferrite and pearlite (dark) in a low-carbon steel. 500×

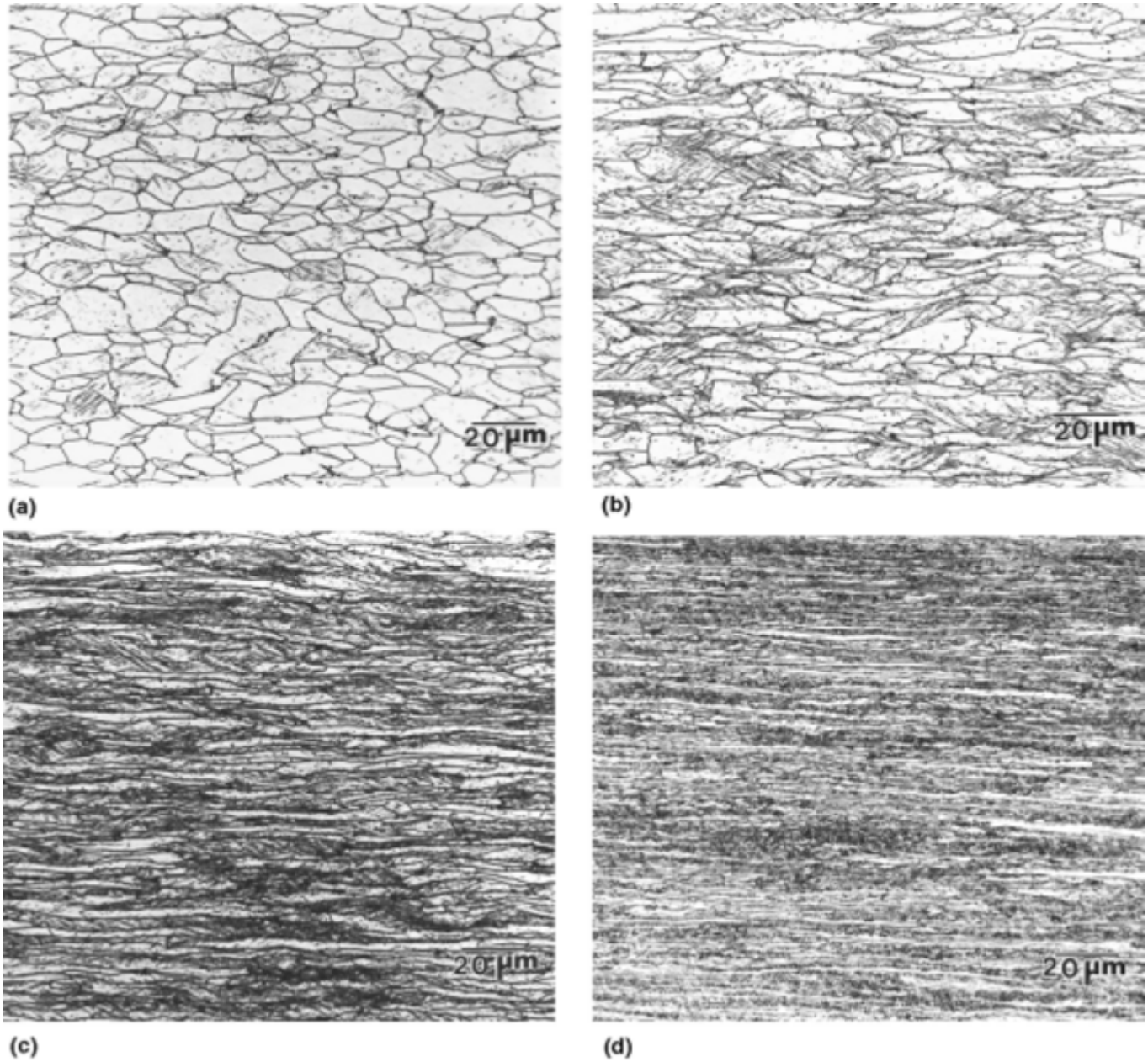

Fig. 3 Microstructure of a cold-rolled, low-carbon steel sheet showing ferrite grains at (a) 30%, (b) 50%, (c) 70%, and (d) 90% cold reduction. Marshall's reagent. 500×

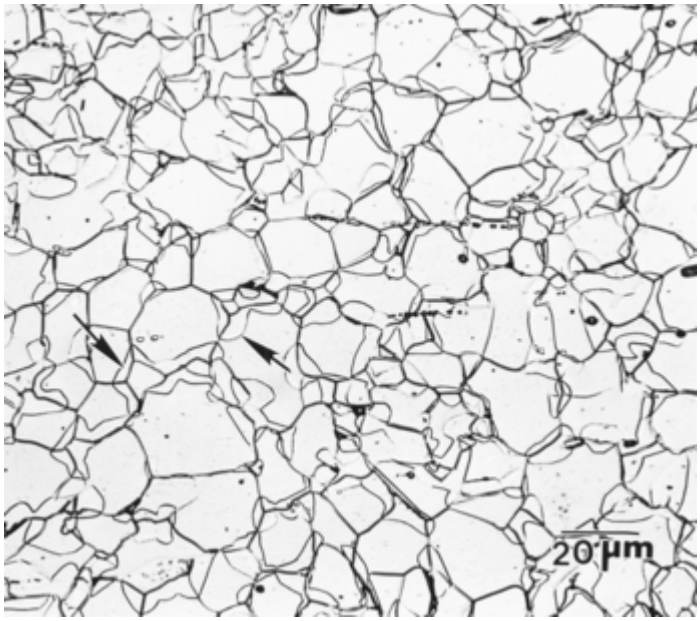

Fig. 4 Microstructure of epitaxial ferrite (arrows) formed by heating a low-carbon steel in the two-phase ferrite + austenite region. Marshall's reagent. 500×

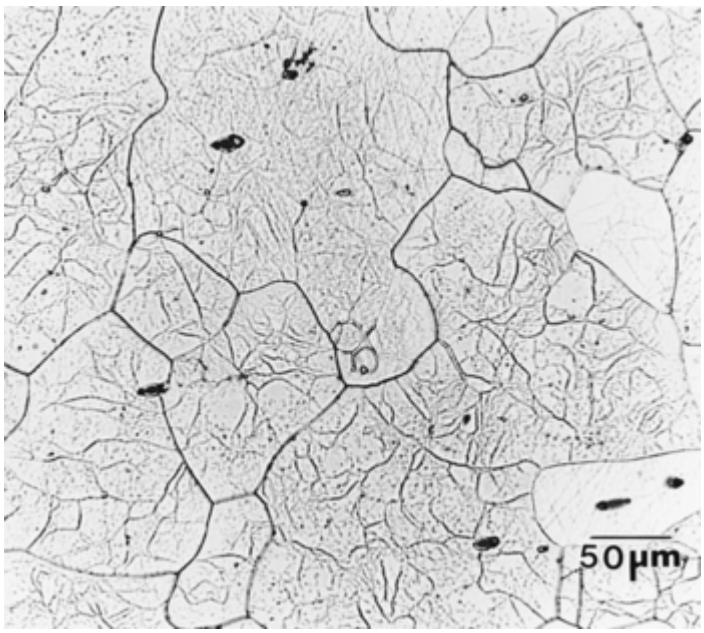

Fig. 5 Very-low-carbon steel (iron) showing large ferrite grains with veining. Marshall's reagent. 200×

Because of its low carbon content, ferrite is soft and easily deformed. This means that special care must be taken to avoid cold work and surface scratches in the sample during preparation. An experienced metallographer will prepare a metallographic specimen without cold work or surface scratches.

Cementite. When the carbon content of the steel exceeds the carbon solubility limit in ferrite (approximately 0.005 wt% C at room temperature), the excess carbon appears in the form of iron carbide (Fe_3C), a phase called cementite. Cementite is a hard phase and is usually not desired in most low-carbon steels because it is hard and brittle and is detrimental to formability. Examples of cementite in sheet steel containing 0.06% C are shown in Fig. 6. The carbides range from massive carbides (Fig. 6a) to smaller and rounded particles (Fig. 6c). These specimens were unetched in order to show the carbide morphology (the ferrite grains are not revealed). However, in these microstructures, the matrix is ferrite, and the cementite has nucleated and grown on the ferrite grain boundaries. This is seen more clearly in a specimen that has been attack-etched to reveal the ferrite grain boundaries. An example is seen in Fig. 7, where the cementite particles (arrows) are on the ferrite grain boundaries. Cementite can also be revealed in a different morphology, as described in a constituent called pearlite (discussed subsequently).

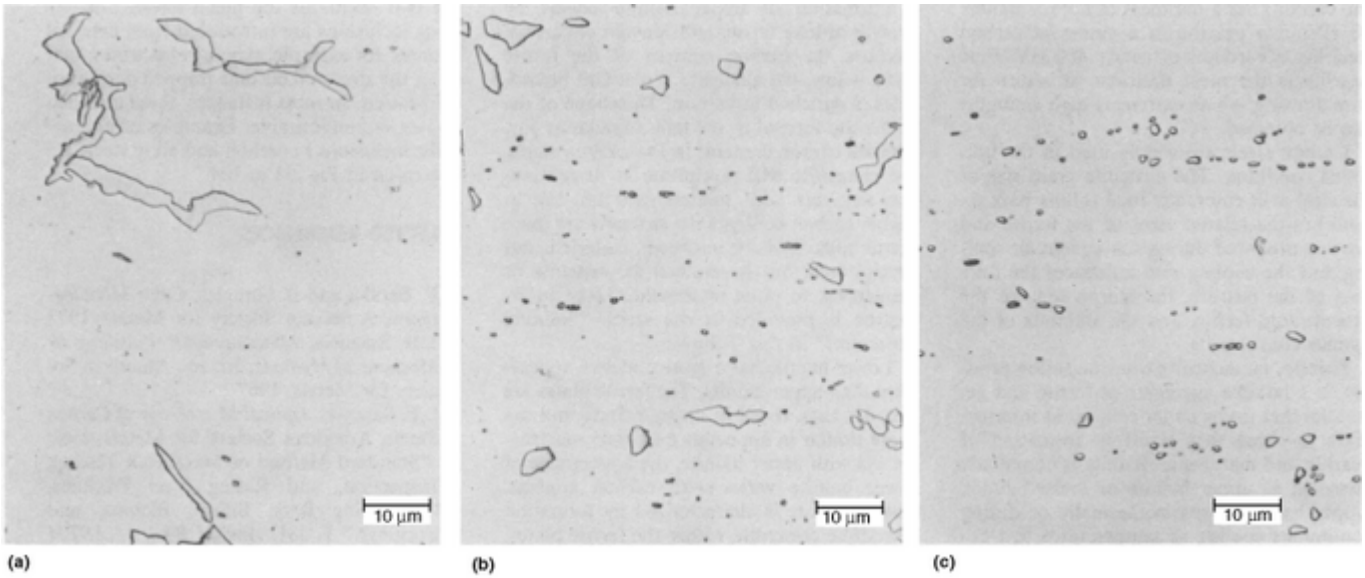

Fig. 6 Microstructure of a 0.06% C steel with various morphologies of cementite. (a) Massive carbides. (b) Medium-sized carbides. (c) Small, dispersed carbides. 4% picral etch. 1000×

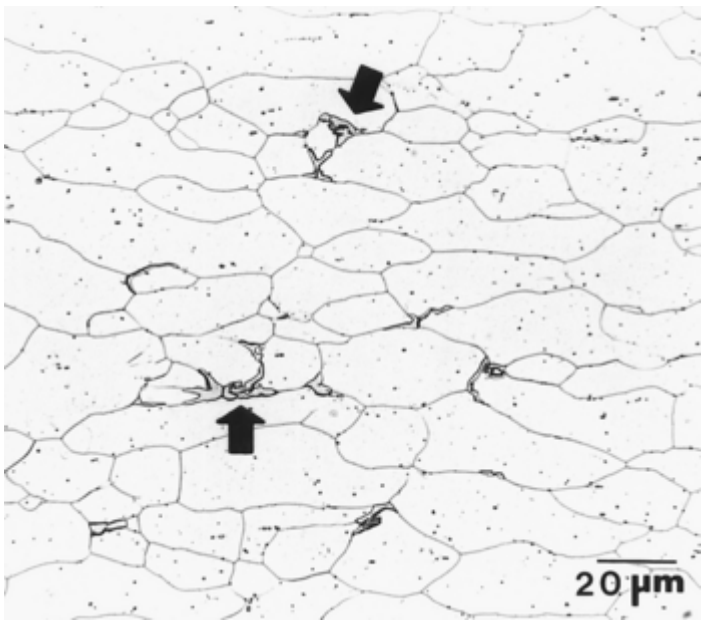

Fig. 7 Cementite (arrows) at ferrite grain boundaries in a batch-annealed 0.04% C steel. Marshall's reagent. 500×

Pearlite. In some low-carbon steels, the excess carbon appears in the distinctive lamellar morphology of pearlite, which is a two-phase constituent with alternating plates of cementite and ferrite. This morphology is classic for eutectoid transformations under slow (near-equilibrium) cooling (see the article “Invariant Transformation Structures” in this Volume). For example, pearlite in low-carbon UNS G10080 steel is seen in Fig. 8. Note the lamellar morphology of the cementite in the patches of pearlite. This steel was slow cooled during transformation from austenite to pearlite, and the pearlite interlamellar spacing is coarse. Another example can be seen in Fig. 9 for a faster cooled low-carbon steel, where dark patches of pearlite appear at the ferrite grain boundaries. The lamellar morphology of the cementite is not apparent in this micrograph, because the interlamellar spacing of the ferrite and cementite plates is not resolved, even at this magnification of 1000×. As seen in the next article (“Metallography and Microstructures of Carbon and Low-Alloy Steels”), pearlite is a major constituent in many higher-carbon plain carbon steels. The morphology of pearlite is also discussed extensively in the article “Physical Metallurgy Concepts in Interpretation of Microstructures” in this Volume.

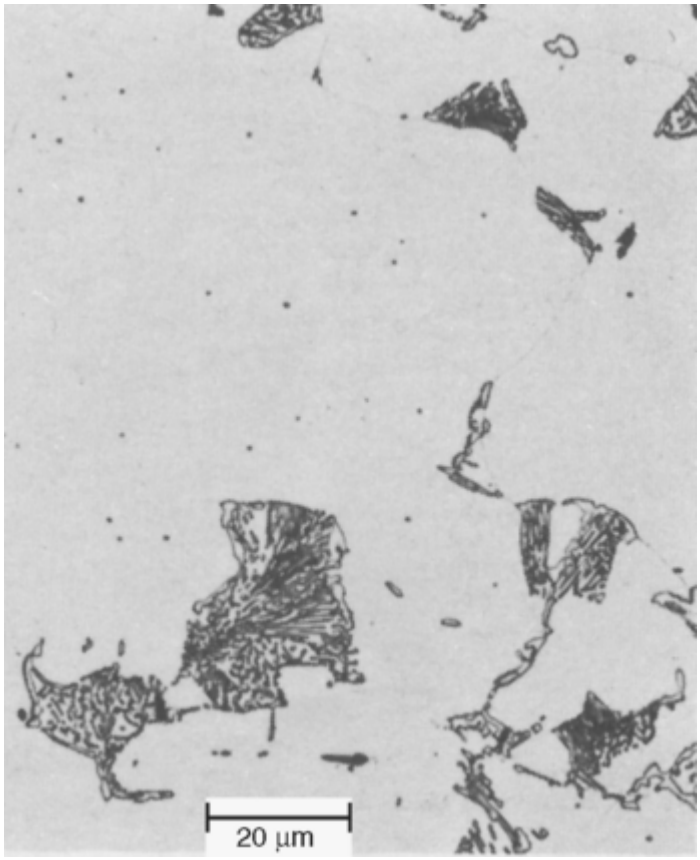

Fig. 8 Microstructure of a slow-cooled UNS G10080 steel showing pearlite islands in a ferritic matrix. The lamellar morphology of the pearlite is resolved. 4% picral etch. 500×

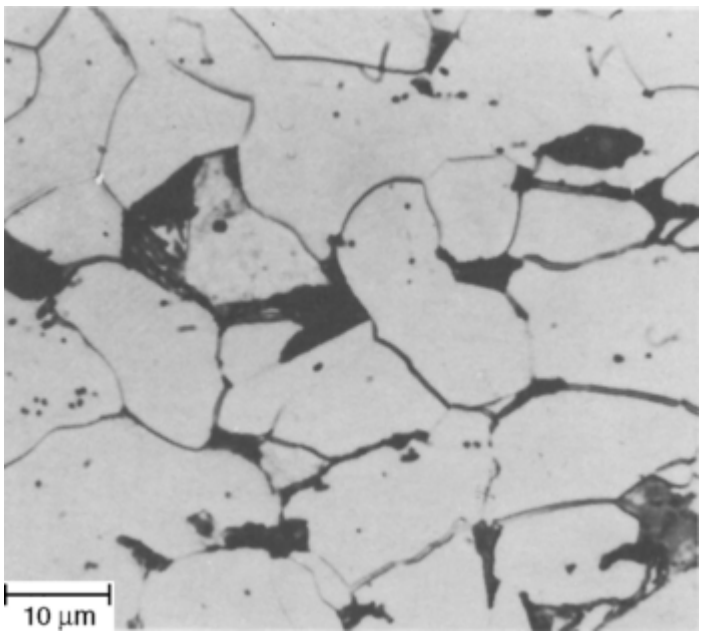

Fig. 9 Microstructure of a normalized UNS G10080 steel showing unresolved pearlite islands in a ferritic matrix. 4% picral etch. 1000×

Martensite. When low-carbon steels are moderately alloyed and rapidly cooled from the austenite phase field or the two-phase ferrite + austenite field, a constituent called martensite is formed. Martensite is not commonly found in low-carbon steels; in fact, in most cases it is highly undesirable. However, it is a desirable and necessary constituent in some special low-carbon advanced high-strength steels. These are the dual-phase and steels. Islands of martensite can be seen in the dual-phase steel microstructure in Fig. 10. Special etchants are required to distinguish these martensite islands from cementite particles, pearlite patches, and retained

austenite. In this particular microstructure, the martensite constituent is shown as dark islands, whereas the uncolored islands are retained austenite. The metallographic techniques are described later. There are special low-carbon fully martensitic high-strength steels that are employed in side impact beams in doors of some automobiles.

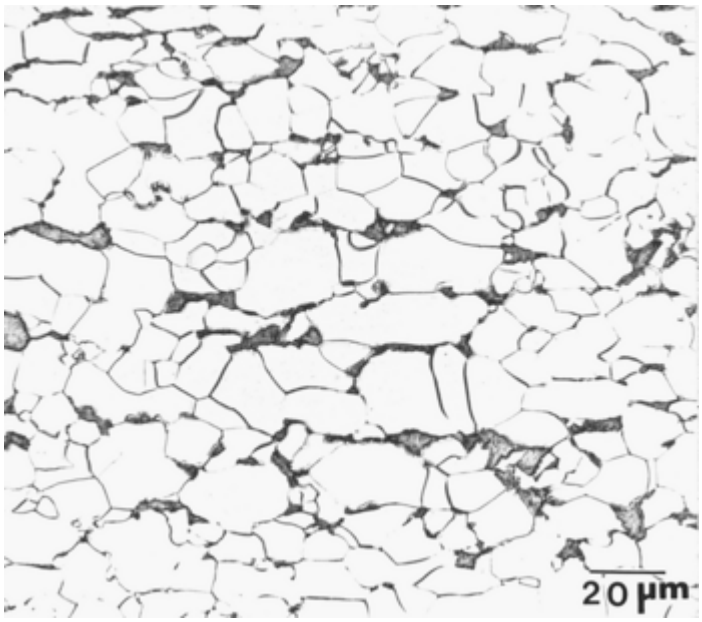

Fig. 10 Microstructure of a dual-phase sheet steel with islands of martensite in a matrix of ferrite. 4% picral etch. 500×

Austenite. The austenite phase is a high-temperature crystal structure that usually exists at temperatures above approximately 720 °C (1330 °F). However, if sufficient carbon or alloy is present, a small amount of austenite can be retained at room temperature. This is the case of the dual-phase steel shown in Fig. 11. This steel was accelerated-cooled from the two-phase ferrite + austenite region. During initial cooling, the regions of austenite were enriched with carbon as the ferrite grew and contained enough carbon (and alloy) to stabilize the austenite at room temperature (i.e., the martensite start temperature was lowered to below room temperature). Other than these special advanced high-strength steels, the metallographer should not see retained austenite in low-carbon steel.

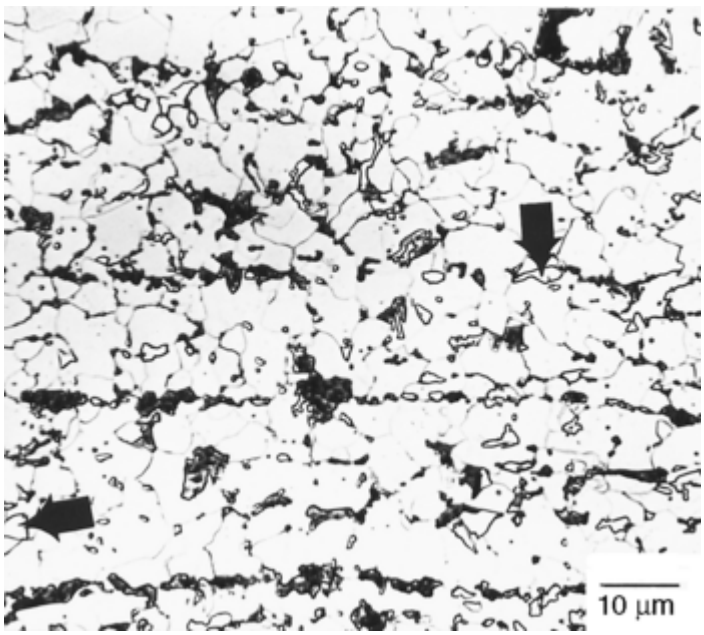

Fig. 11 Microstructure of a dual-phase sheet steel with islands of martensite (dark) and retained austenite (arrows) in a matrix of ferrite. 12% sodium metabisulfite tint etch. 1000×

A.O. Benscoter and B.L. Bramfitt, Metallography and Microstructures of Low-Carbon and Coated Steels, Metallography and Microstructures, Vol 9, ASM Handbook, ASM International, 2004, p. 588–607

Metallography and Microstructures of Low-Carbon and Coated Steels

Arlan O. Benscoter, Lehigh University; Bruce L. Bramfitt, International Steel Group, Inc.

Metallographic Procedures

Orientation of View. Before the sample preparation of any metallographic material can begin, the metallographer must consider which view (longitudinal, transverse, or planar) will yield the desired information. Figure 12 shows a sketch representing these three views. The longitudinal view will definitely reveal the most information about a material that has been rolled. This view, which is perpendicular to the surface and parallel to the rolling direction, more clearly illustrates the degree of grain elongation. For example, elongated ferrite grains in hot-rolled UNS G10200 steel plate are shown in Fig. 13(a), which represents the longitudinal view of the polished and etched specimen. The ferrite grains are equiaxed in morphology but extend in long bands, as does the pearlite (dark constituent). This morphology of ferrite and pearlite is called banding. Figure 13(b) affords a much different view of the same plate. This is a planar view, where the polishing is parallel to the bands of pearlite and ferrite.

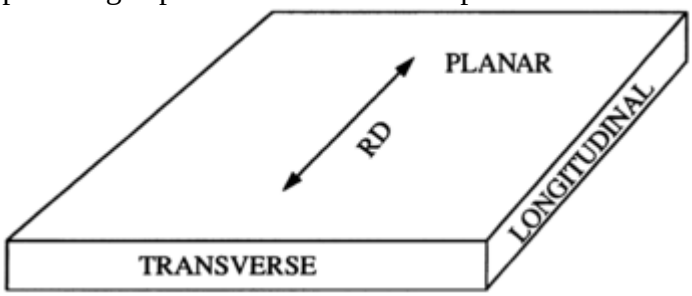

Fig. 12 Sketch showing the three planes of rolling. RD, rolling direction

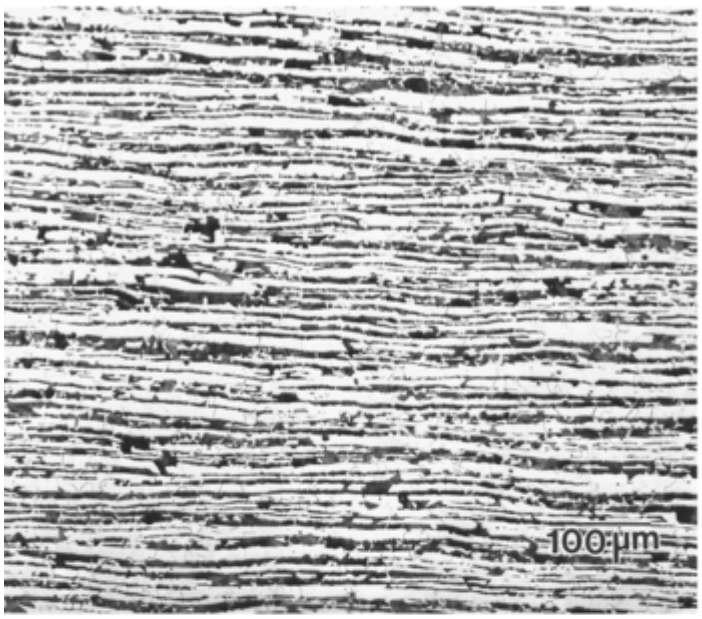

(a)

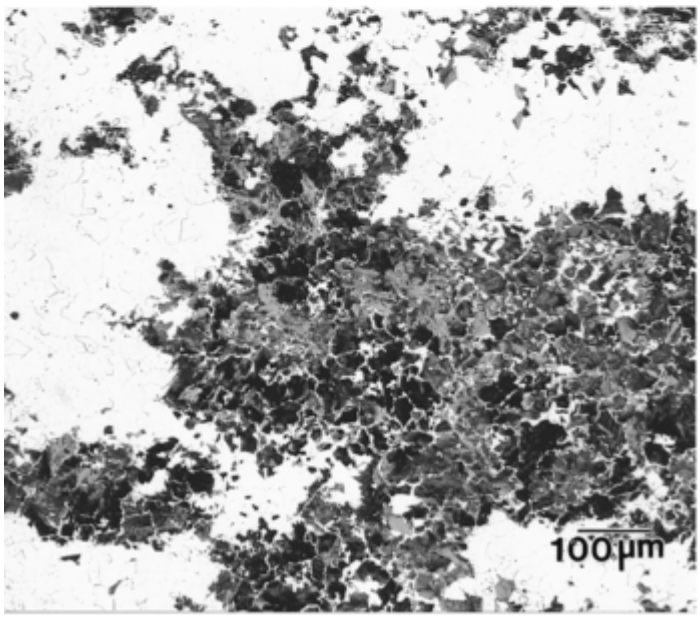

(b)

Fig. 13 Microstructure of an as-rolled UNS G10200 steel showing elongated bands of pearlite (dark) and ferrite grains. (a) Longitudinal plane. (b) Planar view. 4% picral etch. 100×

Sometimes, there are striking differences between the longitudinal and transverse views of a specimen. Figure 14(a) is a longitudinal view of an unetched wrought iron sample that was hand forged into a bar, showing the slag inclusions (gray constituent) as elongated particles or stringers in a matrix of ferrite running parallel to the forging axis. When viewed in the transverse plane (perpendicular to the longitudinal view in Fig. 14a), as seen in Fig. 14(b), the microstructure is much different. Here, the slag constituent appears as rounded particles, when, in fact, we know they are actually stringers. The examples shown in Fig. 13 and 14 make the point that the metallographer must think before preparing a metallographic specimen for observation. The rolling or forging directions must be known so that the proper information is presented in the polished specimen. If these directions are not known, then the metallographer must prepare specimens perpendicular to each other in order to determine the rolling (forging) direction.

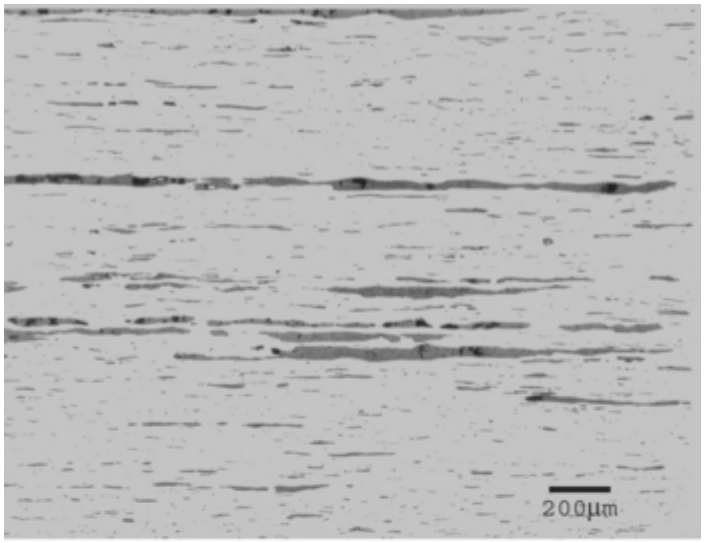

(a)

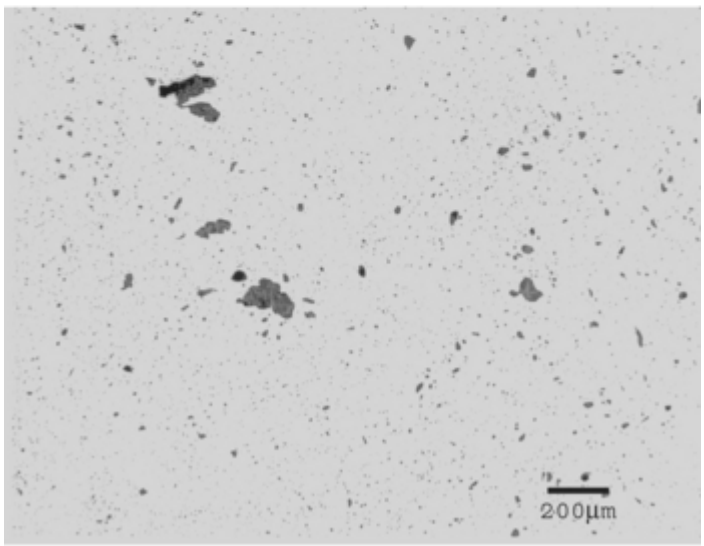

(b)

Fig. 14 Microstructure of forged wrought iron showing slag stringers in a ferrite matrix. (a) Longitudinal plane. (b) Transverse plane. As polished. 100×

Creation of Artifacts. The metallographer must be careful in the selection of the proper sectioning procedure. The procedure must cause minimal damage to the microstructure from excessive heat or mechanical deformation. An altered microstructure is called an artifact. Any artifact introduced into the microstructure points to poor metallographic practice. An artifact can lead to misinterpretation of the real microstructure hidden below the artifact. An example was shown previously in Fig. 1(b). Another example is seen in Fig. 15(a), where deformation (cold work) can be seen in a specimen that has been improperly prepared during grinding. Figure 15(b) shows the correct microstructure.

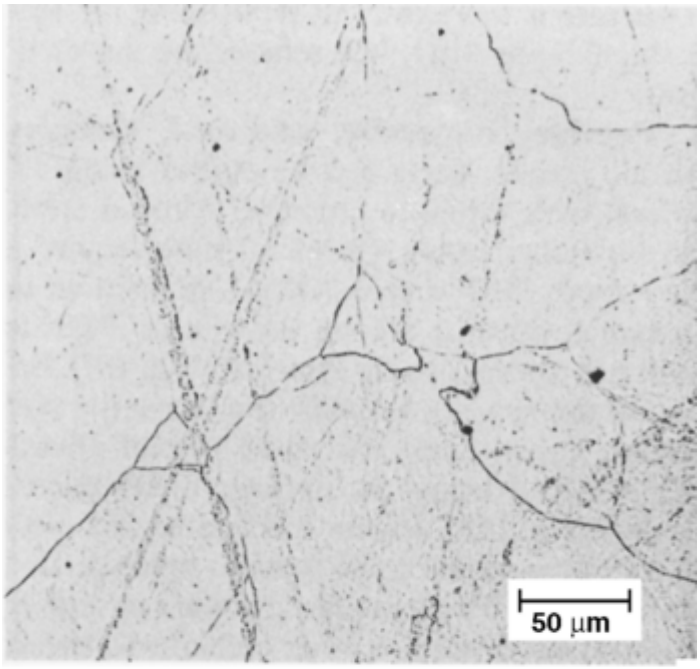

Fig. 15 Microstructure of a low-carbon steel showing the effect of improper grinding. (a) Scratches and deformation left on surface from previous grind. (b) The true microstructure. 2% nital etch. 200×

Figure 16(a) shows a low-carbon dual-phase microstructure that has been altered due to mechanical deformation during shearing, creating a microstructural artifact. As described previously, the microstructure of a dual-phase steel should consist of islands of retained austenite and martensite in a ferrite matrix. In the microstructure shown in Fig. 16(a), the severe cold working during shearing transformed the retained austenite to martensite, as seen in Fig. 16(b). The retained austenite of this particular grade of steel is fairly stable at room temperature and can even exist at temperatures as low as -200 °C (-330 °F) without transforming to a martensite, yet it can be readily transformed by mechanical deformation. This is a subtle example, but the metallographer must be cognizant that sample preparation itself can alter the microstructural constituents in ways that can mislead a person in the interpretation of the true microstructure.

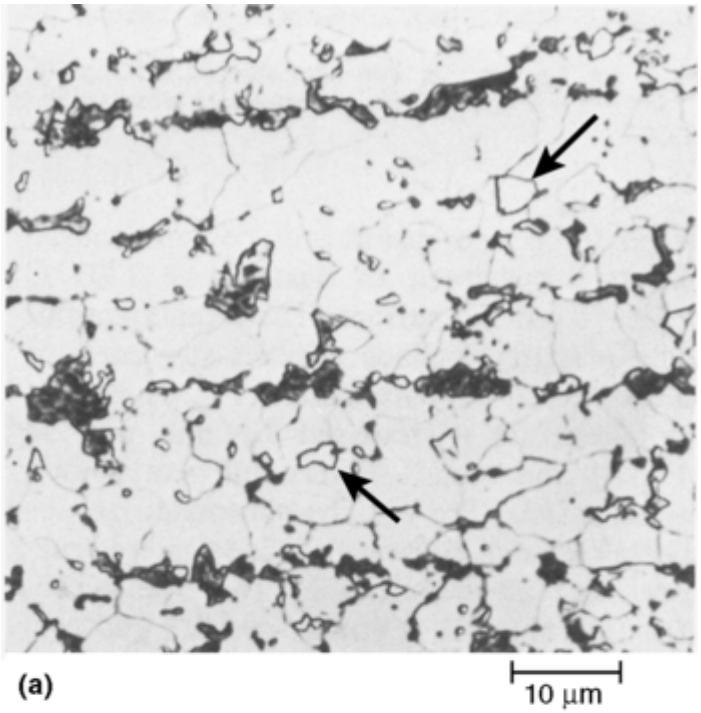

Fig. 16 Microstructure of a dual-phase steel sheet (0.11% C, 1.4% Mn, 0.58% Si, 0.12% Cr, and 0.08% Mo) showing islands of martensite (dark gray), pearlite (black), and retained austenite (white; see arrows) in a matrix of ferrite. (a) In as-cooled condition. (b) Same specimen but in deformation zone from shearing. In (b), the retained austenite transformed to martensite. 12% sodium metabisulfite tint etch. 1000×

A.O. Benscoter and B.L. Bramfitt, Metallography and Microstructures of Low-Carbon and Coated Steels, Metallography and Microstructures, Vol 9, ASM Handbook, ASM International, 2004, p. 588–607

Metallography and Microstructures of Low-Carbon and Coated Steels

Arlan O. Benscoter, Lehigh University; Bruce L. Bramfitt, International Steel Group, Inc.

Specimen Preparation

Sectioning. Generally, a sample to be metallographically examined must be sectioned to a convenient size before performing the preparation steps to reveal its microstructure. Methods to be considered, in the order of descending level of degradation of the microstructure, are as follows: acetylene cutting torch, plasma torch, electrical discharge machining (EDM), shear, band saw, abrasive cutoff machine, high-speed cutoff, gravity diamond saw, and wire saw. The microstructure is more vulnerable to alteration during sectioning than in any other metallographic preparation step. However, as mentioned previously, damage to the specimen during sectioning can alter the microstructure. Those surface artifacts, created by excessive heat or mechanical deformation, can normally be removed by rough grinding.

Oxyacetylene torch, plasma torch, and EDM cutting all leave a melted and heat-affected zone that must be removed by further sectioning by a less aggressive method before the sample is mounted. If a sample is cut using an oxyacetylene torch, approximately 50 mm (2 in.) of material needs to be removed before getting to an unaffected area. Plasma cutting leaves a much smaller heat-affected zone. Many metallographers do not realize that an EDM cut has a heat-affected zone that must be removed. The depth of the zone depends on the EDM parameters. Generally, the metallographer must use caution and common sense when preparing metallographic specimens from these sectioning methods.

Sectioning using a low-speed band saw or power hacksaw can be slow and tedious. The specimen should be softer than 35 HRC for the saw to be effective, unless a special bi-metal blade is used. The resulting surface is rough and generally uneven if manually fed. Using oil or water-soluble oil as the cutting fluid can minimize the frictional heat generated. The cutting fluid also prolongs the life of the saw blade by preventing tempering of the teeth.

Shearing thin specimens on a tabletop hand shear is a quick method of sectioning. However, shearing results in extreme mechanical deformation at the shear burr. Care must be taken to remove the deformation zone by rough grinding. If the sheared specimen is mounted in epoxy or a thermosetting material, the thickness of the mount should be measured to ensure that the deformed material is removed during grinding. An artifact microstructure caused by mechanical deformation as the result of shearing a dual-phase steel was previously shown in Fig. 16. The deformation produced during shearing can also be seen in Fig. 17(c)

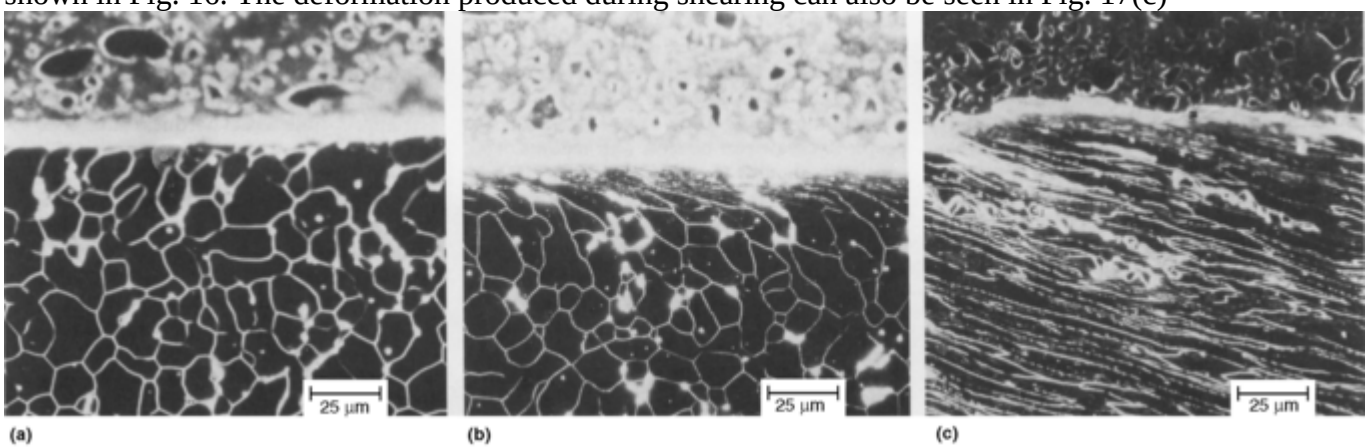

Fig. 17 Microstructures of a hot-rolled UNS G10100 sheet steel showing sectioning damage from (a) an abrasive cutoff wheel, (b) a band saw, and (c) from a shear. Marshall's reagent. Dark field illumination. 400×

Abrasive wheel cutting is another common method of sectioning steel samples. Most metallographic laboratories have an abrasive wheel device. Abrasive wheel cutting, if properly executed, is, by far, the best technique for obtaining a steel specimen surface that is smooth, has minimal deformation, and has minimal microstructural changes caused by overheating. Examples of surface deformation in a UNS G10100 hot-rolled steel specimen after abrasive wheel cutting, band saw cutting, and shearing are shown using dark-field illumination in Fig. 17. Figure 17(a) is a cross section illustrating the minimal depth of deformation caused by sectioning with an abrasive cutoff wheel. The specimen shown in Fig. 17(b) was sectioned using a band saw and shows that the ferrite grains have deformed at the cut surface. Figure 17(c) was obtained by shearing, and the deformation of the ferrite grains is extensive.

There are many abrasive wheel cutting machines available that range from small, gravity-fed models using 100 mm (4 in.) diameter wheels to large floor models with 355 mm (14 in.) diameter wheels 1.5 mm ($\frac{1}{16}$ in.) thick. Steel samples should be sectioned using alumina (Al_2O_3) wheels of the proper rubber-bonded hardness. The specimen is kept cool during cutting by an ample flow of water; cutting also can be performed with the specimen submerged in the coolant. The appropriate wheel hardness should be selected and the proper force applied during cutting. Manufacturers have developed different kinds of wheels, ranging from a soft bond that readily deteriorates and exposes fresh Al_2O_3 particles needed for cutting hard specimens, to hard-bonded wheels that break down slowly. The latter are preferred for softer materials (low-carbon steels).

Care must be taken when cutting with an abrasive wheel. If the specimen is not properly secured with a clamp, the wheel is likely to break. A steady, firm pressure must be maintained against the specimen. Careless use of an abrasive cutoff machine, even with coolant capability, can result in artifacts, as depicted in Fig. 18. In this example, too much force and insufficient coolant caused the steel specimen to heat above 720 °C (1330 °F) at the surface. The metallographically prepared surface exhibits structures of martensite in a ferrite matrix (Fig. 18a), islands of martensite surrounded by fine pearlite (Fig. 18b), and islands of very fine pearlite in a ferrite matrix (Fig. 18c). The micrographs display scratch-free, well-defined microstructures, but all are artifacts. The true microstructure shown in Fig. 18(d) is a coarse pearlite and carbide structure in a ferrite matrix and was revealed after regrinding and repolishing the specimen. The artifact microstructures in Fig. 18(a) to (c) were caused by frictional heating from insufficient cooling during the abrasive wheel cutting process. The patches of coarse pearlite (original microstructure) were heated into the austenitizing temperature range during cutting, and rapid cooling created the martensite and fine pearlite after the cutting stopped.

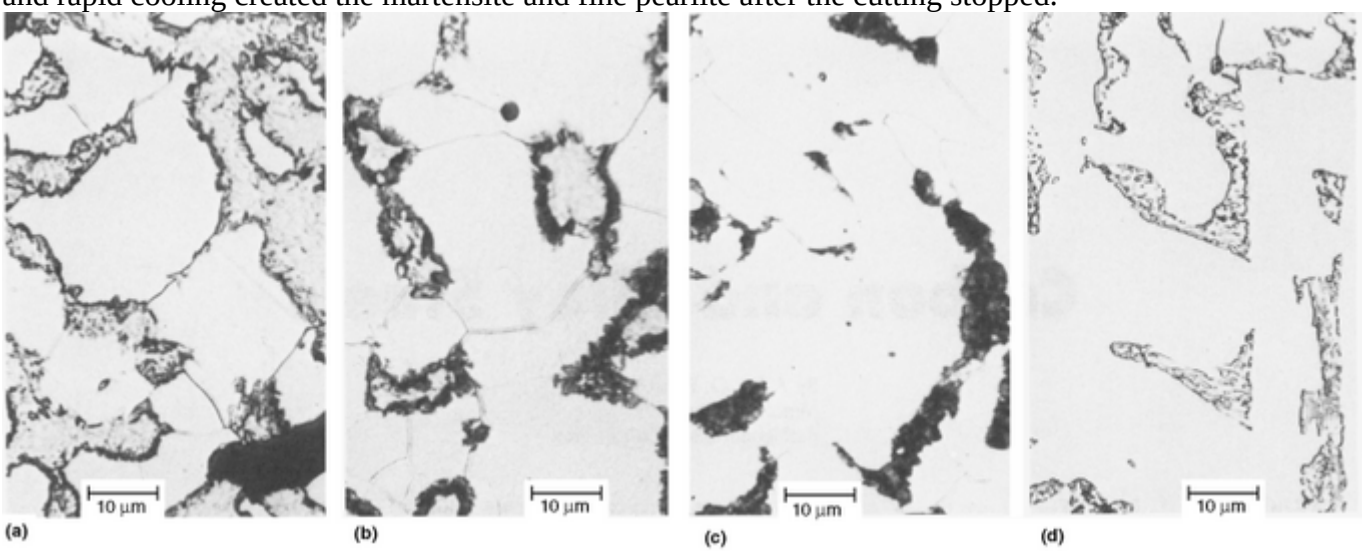

Fig. 18 Artifact microstructures in (a), (b), and (c) that developed by heating the specimen during sectioning on an abrasive cutoff wheel. (a) Tempered martensite (gray) in a ferrite matrix (white). (b) Tempered martensite (gray) and pearlite (dark) in a ferrite matrix (white). (c) Pearlite (dark) in a ferrite matrix. (d) The true microstructure consisting of islands of very coarse pearlite (gray) in a ferrite matrix. 4% picral etch. 1000×

Mounting. Not all metallographic specimens must be mounted before examination. A bulk specimen that is convenient to handle can be successfully prepared and examined at magnifications up to 1000×. This requires beveling the edges to prevent tearing or catching of the polishing cloths, which can cause an uneven surface.

However, most metallographic specimens, particularly sheet specimens, are mounted in castable epoxy, thermosetting resin, or a steel clamp for ease of preparation.
Various considerations must precede the mounting of a specimen, such as the use of an etchant to reveal the microstructure that may also attack the mounting medium. For example, alkaline sodium picrate (used to darken cementite) attacks phenolic thermosetting resin mounts. Thermosetting epoxy mounts are recommended when etching with alkaline sodium picrate.
In addition, examination of a specimen edge for decarburization, carburization, internal oxidation, depth of oxide scale, coating thickness, and so on will require a mounting material with minimal shrinkage properties, such as castable (liquid) epoxy resin or thermosetting epoxy powder. Further, if an oxide scale is to be examined, a compression-mounting resin may get in between and separate the scale from the base material during pressure molding of the mount.
If edge retention is important, it is advisable to closely match the polishing rate of the mount material with that of the specimen. However, in most cases this is not possible, and therefore, a number of different ways must be considered to maintain a flat edge. One possible way is to plate the surface with nickel (see the article "Mounting of Specimens" in this Volume). Some metallographic supply houses sell a two-part solution that, when mixed together and heated to 70 to 80 °C (160 to 180 °F), forms a electroless nickel coating. The nickel layer will plate out at a rate of 10 μm/h on the specimen surface. A solution for electroless nickel coating can also be prepared in the laboratory by adding the following chemicals to 1 L of water:

- 37.3 g $NiSO_4$ (nickel sulfate)
- 26.4 g NaH_2PO_2 (sodium hypophosphite)
- 15.9 g sodium acetate
- 5 to 6 drops H_2SO_4 (sulfuric acid)

Some specimens with coatings such as zinc-coated steel sheet (Galvalume, galvanneal, or galvanized) must first have a copper flash coating before the nickel layer, because the aqueous electroless nickel plating solution will attack the coating. The formula for a copper flash coating and other plating solutions can be found in Ref 1. The chemical formula and technique for copper flash plating is to first add the following to 1 L of water:

- 170 g $CuSO_4 \cdot 5H_2O$
- 60 g H_2SO_4 (concentrated)

with a solution temperature at 15 to 50 °C (60 to 120 °F), plating is done at 1 to 4 V, with a current density of 10 to 20 mA/cm^2. Agitation by mild stirring is preferred, and use a copper anode.
A second technique is to place a dummy steel specimen as close as possible to the edge of interest; this will minimize the degree of rounding during polishing. A third technique involves placing stabilizers (small steel pieces) every 90° around the specimen. A fourth method to maintain a flat edge can be accomplished by adding alumina particles to an epoxy mixture prior to casting; this filler material can be purchased through most metallographic supply houses. The alumina filler material is approximately 50 μm in size and very porous, to allow the epoxy to penetrate and hold it in place. However, this system will produce a metallographic mount that cannot be ground with silicon carbide papers, thus requiring a diamond disc for grinding, and that can only be polished with diamond compounds, except for the final polish with silicon dioxide.
Mounting methods can cause damage to the specimen, due to heat and pressure needed to cure a thermosetting resin or thermoplastic mount. Figure 19(a) illustrates the damage caused by the high pressure needed to process a thermosetting resin mount. The electroless nickel layer that was plated on a low-carbon steel sheet has separated from the teel. The mounting compound becomes fluid during the heating stage, then, at the high pressure of 30 MPa (4200 psi) needed to compact the compound, the coating was forced away from the base. In Fig. 19(b), the same sample was mounted using a castable epoxy, and the nickel coating is intact. Artifacts caused by improper mounting techniques are always permanent, and the sample is no longer representative of the original specimen.

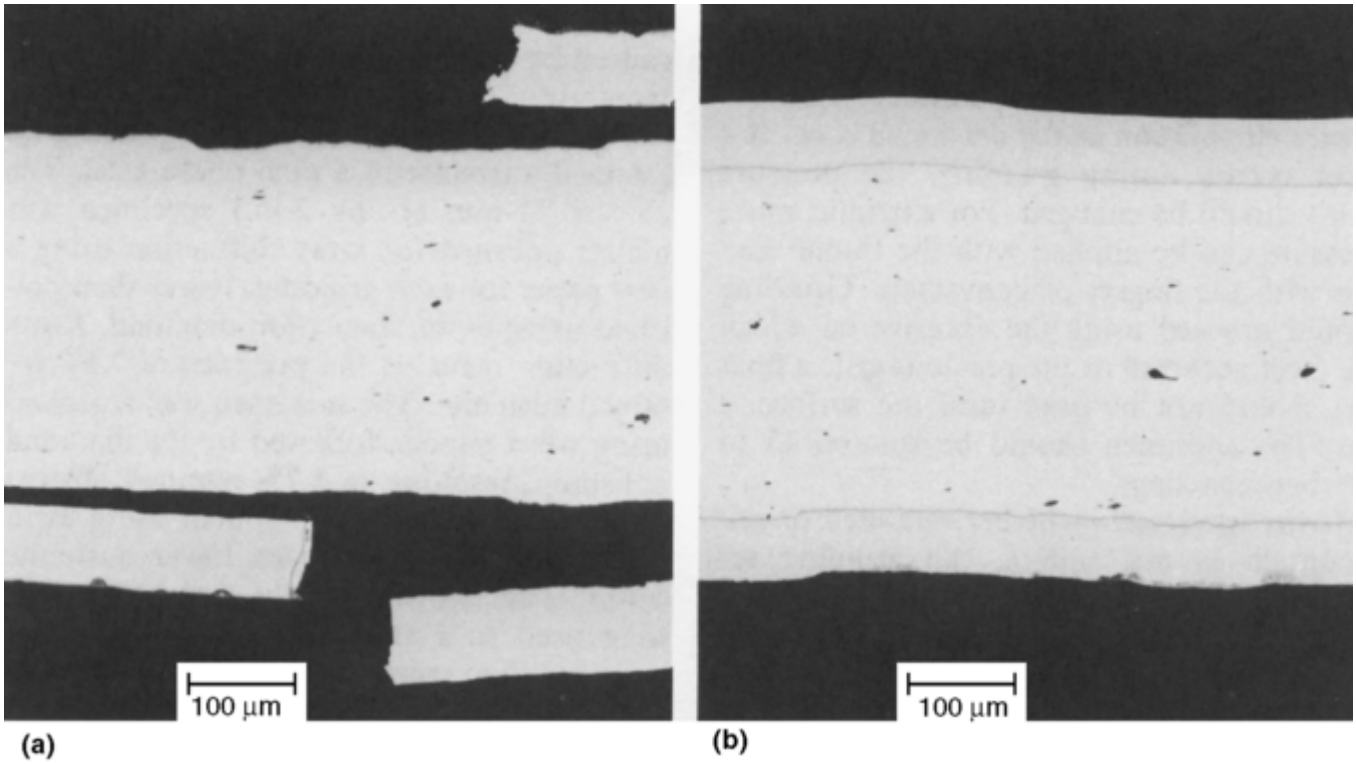

Fig. 19 A low-carbon steel sheet plated with electroless nickel showing (a) damage to the coating from mounting in a thermosetting phenolic resin and (b) the lack of damage when mounted in a castable epoxy. As-polished. 100×

Figure 20(a) shows that the pressure required for mounting can physically damage the thin sheet steel specimens in a thermosetting resin mount. The sheet specimens were separated by steel spacers, and the high pressure that developed during the mounting process caused the specimens to deform. Similar specimens in the castable epoxy mount (Fig. 20b) show no damage.

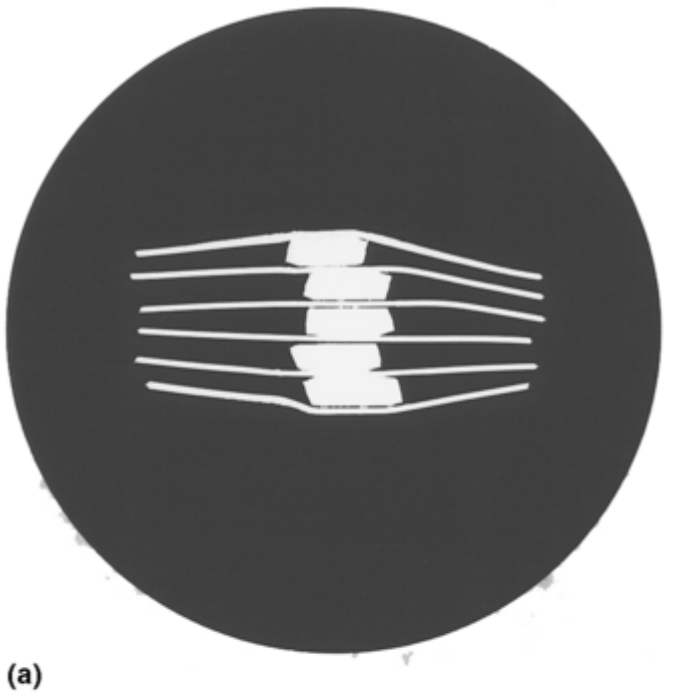

(a)

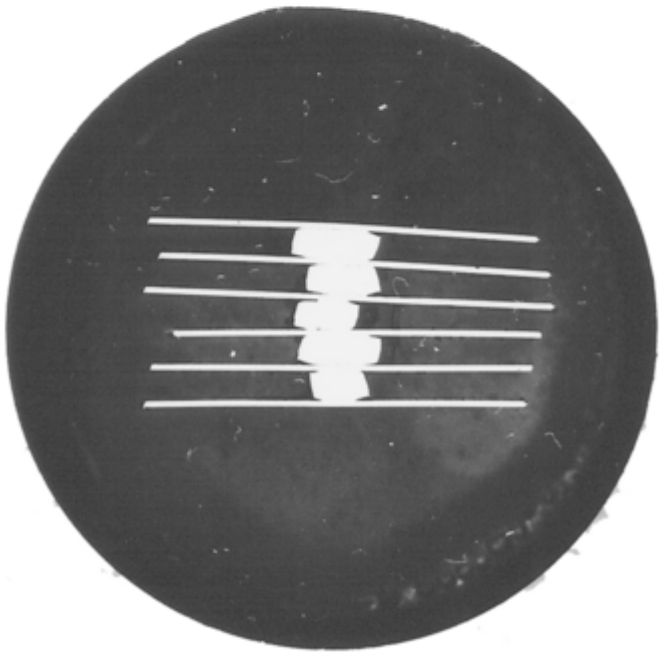

(b)

Fig. 20 Six low-carbon steel sheet specimens, separated by steel spacers, showing (a) damage from mounting in a thermosetting phenolic resin and (b) lack of damage when mounted in a castable epoxy

Castable Mounting Materials (Epoxy). For ease of preparation, many metallographers mount their specimens in castable epoxy. Epoxy mounts should be used when heat may affect the microstructure or when pressure may disturb a fragile surface condition, as mentioned previously. A common technique used for castable mounts is to glue a phenolic or aluminum ring form to a sheet of aluminum foil (the epoxy will not adhere to the aluminum foil) supported by a glass plate or thin sheet steel. Plastic or rubber molds can also be used. The specimen is placed face down in the ring. For sheet specimens, a steel or plastic clip can be used to hold the specimens upright. After the epoxy is poured into the mold, a vacuum is used to remove air bubbles trapped in small cracks and crevices in the specimen; it will also remove bubbles introduced during mixing.

If an epoxy mount does not completely cure due to improper mixing or due to an incorrect ratio of resin to hardener, this condition can be corrected if the mount, after setting up, is placed in an oven at 65 °C (150 °F)

for 4 h. Mounts larger than 38 mm (1.5 in.) in diameter should be placed in a refrigerator until they have set up, to prevent an exothermic reaction; otherwise, stresses resulting from such a reaction may cause the large mass of epoxy to crack.

Another possible application of epoxy is examination of a surface condition obscured by the mounting medium. An example is shown in Fig. 21. The coating material is a zinc powder mixed with a polymer. The coating is covered with a layer of black paint. If the specimen is mounted in an opaque mounting material (e.g., thermosetting resin), it is very difficult to distinguish the black paint layer from the mounting material. This is illustrated in Fig. 21(b). Even in an epoxy mount, the transparent mount absorbs the reflected light from the microscope. However, if the specimen is lighted from the back or side of the mount, the edge of the black paint can be clearly seen, as in Fig. 21(a).

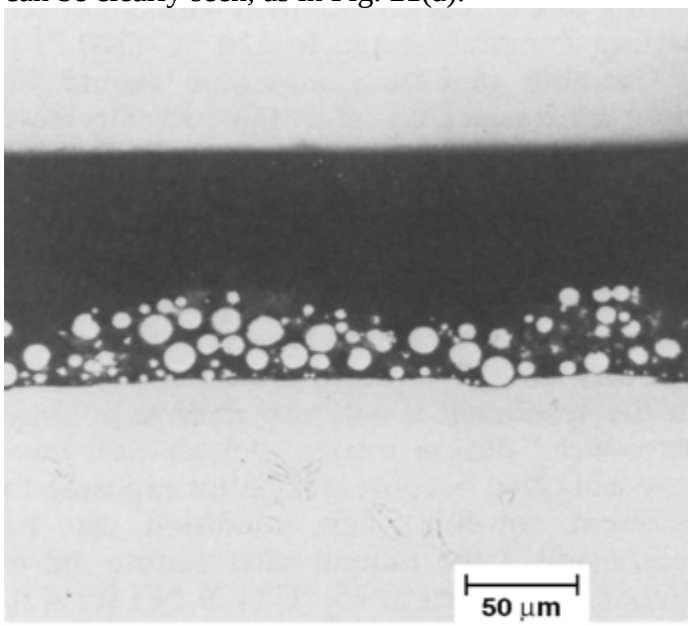

(a)

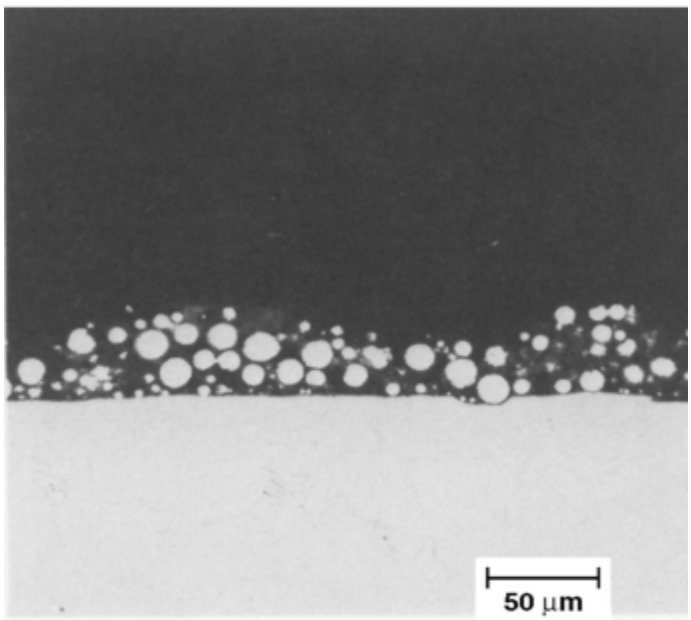

(b)

Fig. 21 A zinc-particle polymer coating (Zincrometal) with a top paint layer on a low-carbon steel sheet showing (a) the extent of the top paint layer, using transmitted light through a castable epoxy mount, and

(b) the difficulty of seeing the paint layer in a normal brightfield illumination (reflected light). As-polished. 200×

If edge retention (edge flatness) is important, a steel dummy sheet can be placed next to the sample edge to be examined. This will prevent rounding of the edge facing the dummy. An example where edge retention is important is shown in Fig. 22, where a thin layer of the steel has been penetrated by oxidation. This condition is called internal oxidation, and it occurred in this silicon-bearing electrical steel because silicon is less noble than iron and is preferentially oxidized. For very hard specimens (usually not the case for low-carbon steels), it is advisable to mix aluminum oxide spheres into the epoxy liquid. These particles add hardness to the final cured mount.

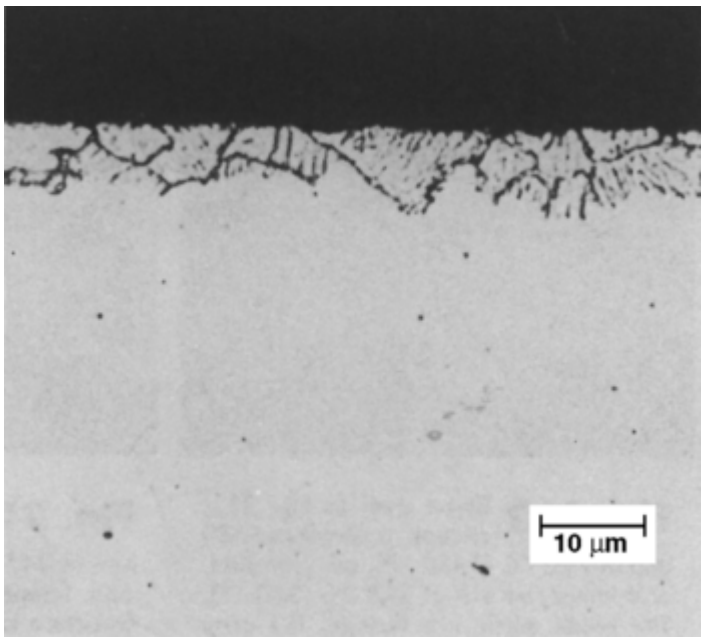

Fig. 22 Internal oxidation penetrating the surface of a motor lamination steel. Not only have oxides formed in the grain boundaries, but fine oxides have formed in the matrix. 4% picral etch. 1000×

Castable epoxy can also be used to salvage compression mounts having voids between the specimen and mount, which causes the etchant to bleed onto the specimen. Masking tape is wrapped around the mount, leaving the mount recessed approximately 6 mm (0.25 in.). Epoxy is then poured into the recess to a depth of approximately 1.5 mm (0.0625 in.), and a vacuum is used to remove air from the voids, allowing the epoxy to flow between the compression medium and the specimen.

In using castable epoxy mounts in the scanning electron microscope or electron probe microanalyzer, electron charging can be minimized by adding an electrically conductive material to the epoxy. For example, graphite powder (4.5 g per 15 g of epoxy) can be added for conductivity. However, caution must be used so that the additive does not contaminate the specimen.

Thermosetting Mounting Material. Ferrous specimens for routine examination are often mounted in a thermosetting material (phenolic resins such as Bakelite). A mounting press is required to soften and force the mounting material around the specimen. The specimen is placed on the steel insert of the pressure cylinder. Remember that the specimen(s) can move during this mounting process. There are metal and plastic clips that can be used to keep sheet specimens upright. The dry powder is measured and placed on top of the specimen. A steel piston is then placed into the cylinder, and the cylinder is heated and pressurized. The powder should be free of moisture, and sharp corners on bulk specimens should be rounded when possible. Follow the instructions of the mounting press manufacturer and read the safety warnings. The mount should be cooled before ejection from the mold. If ejected too hot, the mount may crack.

Bakelite or similar thermosetting materials can be used to mount any gage wire by first preparing a blank mount, then drilling holes slightly larger than the wire. The wire is placed into the holes, and masking tape is wrapped around the mount, extending approximately 6 mm (0.25 in.) above it. Epoxy is poured into the recess created by the tape; the mount is placed in a vacuum for several minutes, purged several times, then allowed to cure.

Steel Clamp. Using steel clamps to mount specimens is very rapid and versatile. Multiple sheet, small bulk, and wire specimens can be secured with clamps. The main disadvantage of this technique is that a clamp mount must be ultrasonically cleaned to remove debris after the final grinding and after each polishing step. Clamp mounts are shown in Fig. 23. The clamps are usually fabricated of 3 to 6 mm (0.125 to 0.25 in.) thick UNS G10200 steel plate. For best results, try to match the hardness of the clamp material with the hardness of the specimen. Each clamp is approximately 13 mm (0.5 in.) wide and 25 to 50 mm (1 to 2 in.) long, with holes at each end. One half is threaded to receive a bolt, and the other half has a mating hole through which the bolt can pass.

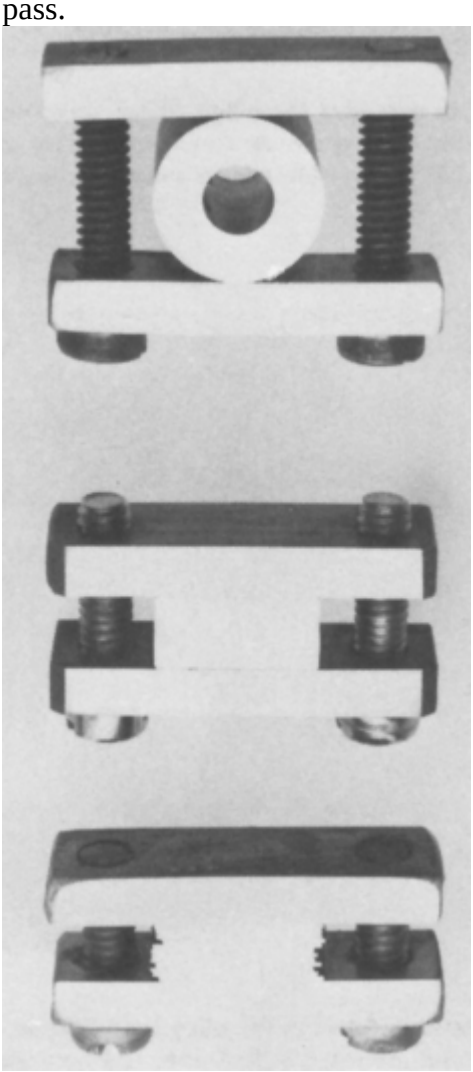

Fig. 23 Steel clamps used to mount tubular and sheet specimens

Mounting with clamps involves placing the specimen or specimens so that enough material protrudes from the clamp to ensure adequate removal during grinding of any deformation zone caused by sectioning. Once secured, the two bolts are then tightened, and the clamp with specimen(s) is secured in a vise, after which the bolts are tightened further. This will minimize seepage.

An example of a microstructure of a low-carbon steel specimen mounted in a clamp is shown in Fig. 24. In this micrograph, the clamp material is shown at the top. Note that a flat surface is maintained at the very edge of the specimen. This is called edge retention and is very important if the microstructural features at the edge are to be observed or if the steel has a coating. Edge retention is also maintained when several sheet specimens are stacked within a clamp, as shown in Fig. 25. The butting edges of the two specimens in this micrograph show excellent edge retention.

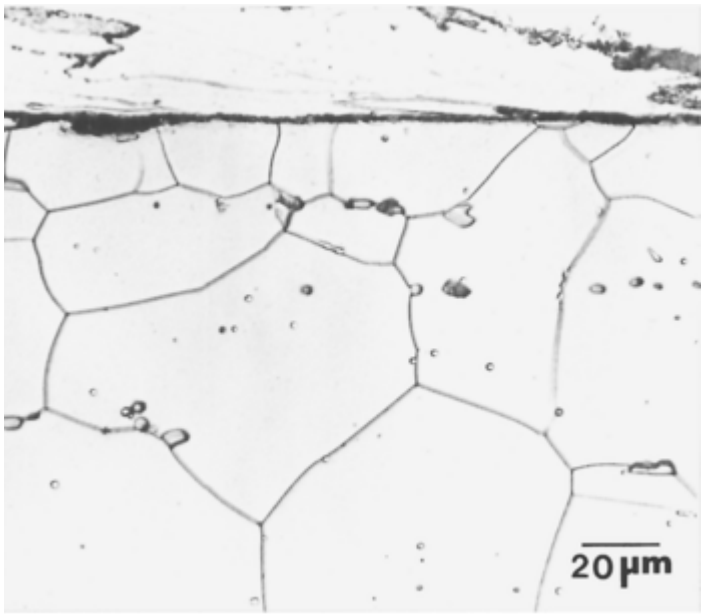

Fig. 24 Microstructure of a low-carbon steel sheet mounted in a steel clamp. The clamp is at the top. Note the excellent edge retention of the steel sample. Marshall's reagent. 500×

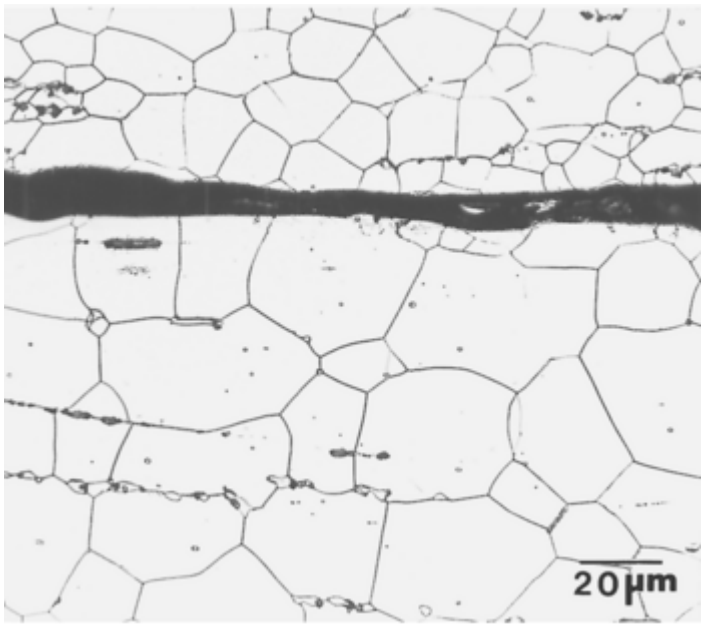

Fig. 25 Two low-carbon sheet specimens butted together in a steel clamp. Note the excellent edge retention of both specimens. Marshall's reagent. 500×

Grinding. As previously mentioned, regardless of the type of equipment used to section a sample, surface damage will be present to some degree. Always keep in mind that grinding, like sectioning, creates a zone of deformation on the specimen surface. The sketch in Fig. 26 illustrates the deformation zone that is created during grinding. A series of grinding steps, using successively finer-grit silicon carbide papers, must be used to remove most of the damaged layer and to produce a flat surface having minimal deformation (see Table 1 for a listing of standard grit sizes). Silicon carbide papers should be used to prepare ferrous materials. The first grit size that is selected depends on the sectioning method used in preparation of the specimen. The larger the grit-size numbers, the finer the particle size on the grinding paper. For example, a band-saw-cut or sheared surface may require an 80-grit paper, followed by 120-, 240-, 320-, 400-, and 600-grit papers, and a specimen sectioned using an abrasive wheel may require starting with a 320-grit paper (skipping the 80- and 240-grit papers). During grinding, water must be used to flush the abrasive disk and keep the specimen cool. The exception is when water-soluble particles (for example, aluminum nitrides) are present in the specimen. If water-soluble

particles are present and require examination, mineral spirits, kerosene, or commercial lapping oil that does not contain water must be used during grinding.

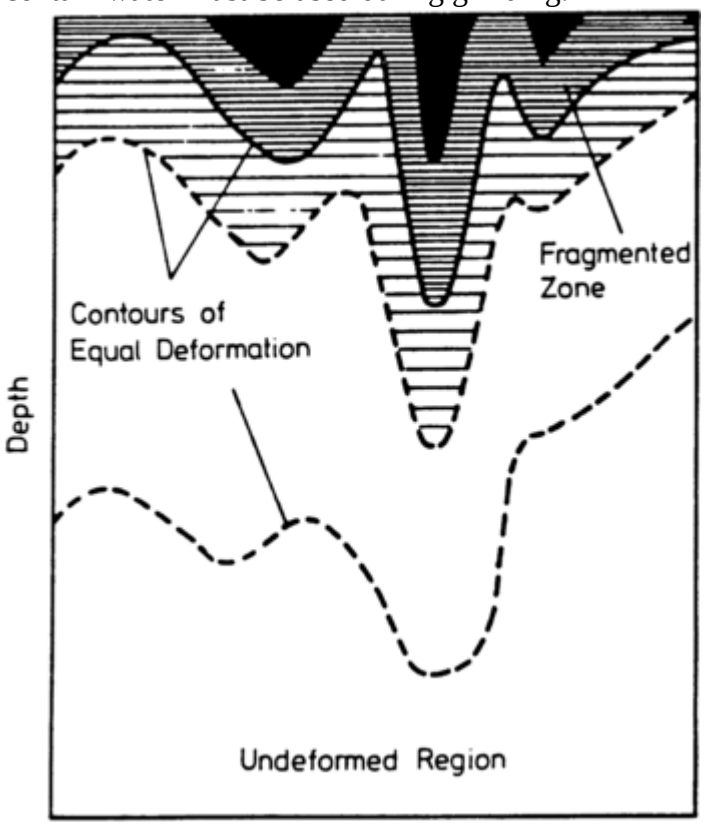

Fig. 26 Sketch showing depth of grinding scratches below the surface of a specimen

Table 1 Grit sizes for metallographic grinding papers

European grit No. (FEPA)	U.S. grit No. (ANSI/CAMI)	Approximate particle size, μm
Standard sizes		
P-60	60	250
P-80		180
P-120	120	125
P-180	180	75
P-220		63
	240	59
P-320		46
	320	41
P-500		30
	400	26
P-800		22
P-1000		18
P-1200	600	15
Finer sizes		
P-2400	800	8
P-4000	1200	3

FEPA, European Federation of Abrasive Particles; ANSI, American National Standards Institute; CAMI, Coated Abrasives Manufacturers Institute

To obtain a flat surface with minimal deformation, the specimen should be held with the fingertips as close as possible to the grinding paper. By using a moderately heavy pressure, slowly move the specimen back and forth from the center to the edge of the grinding disk. The specimen surface should be examined periodically to determine when scratches from the previous grinding have been removed. Grinding should continue two to

three times longer than the time required to remove the scratches from previous operations. This will ensure elimination of the deformed zone. If a bevel or facet occurs during grinding, the pressure point should be changed. For example, more pressure can be applied with the thumb and less with the fingers, or conversely. Grinding should proceed using the abrasive on which the facet occurred or the previous grit paper; a finer grit should not be used until the surface is flat. The specimen should be rotated 90° between steps. This will allow the metallographer to see if the scratches from the previous grinding paper were removed during the current step.

If the specimen—whether mounted or unmounted—is not square, the grinding sequence should be planned so that the longest length is parallel to the direction of wheel rotation in the final grinding step; otherwise, the specimen can rock, causing an uneven or rounded surface. When changing papers, the wheel should be moistened with water to prevent slippage of the paper while grinding.

Flushing of the specimen before proceeding to the next step will prevent contamination of the succeeding grinding papers. After final grinding, all specimen surfaces should be cleaned with cotton and water, flushed with alcohol, and then dried. Never allow water to sit on the surface of a ground (or polished) specimen between preparation steps, because corrosion will begin immediately. Clamp-mounted specimens should be cleaned with cotton and water, ultrasonically cleaned with alcohol, and dried.

An example of artifacts caused by improper grinding was shown previously in Fig. 15. Figure 15(a) depicts the result of proceeding to the next grinding step too soon. The scratches from the previous step have not disappeared, and random lines, mottled surface, and obscured grain boundaries are visible. When this occurs, the specimen must be reground to remove the artifacts. Figure 15(b) illustrates the same specimen after correct grinding. Deformation caused by grinding can also alter the microstructure.

Figure 27 shows the effect of grinding on retained austenite in a dual-phase steel. The 25 by 50 mm (1 by 2 in.) specimen was planar polished for x-ray diffraction, using a new paper for each grinding step; it was then polished using 6 μm diamond. X-ray diffraction revealed the presence of 7.8% retained austenite. Repetition of the experiment using worn papers resulted in a much lower austenite count. The two chemically polished planes were used as a standard. Both planes that were polished using worn papers resulted in the austenite transforming to martensite due to mechanical deformation.

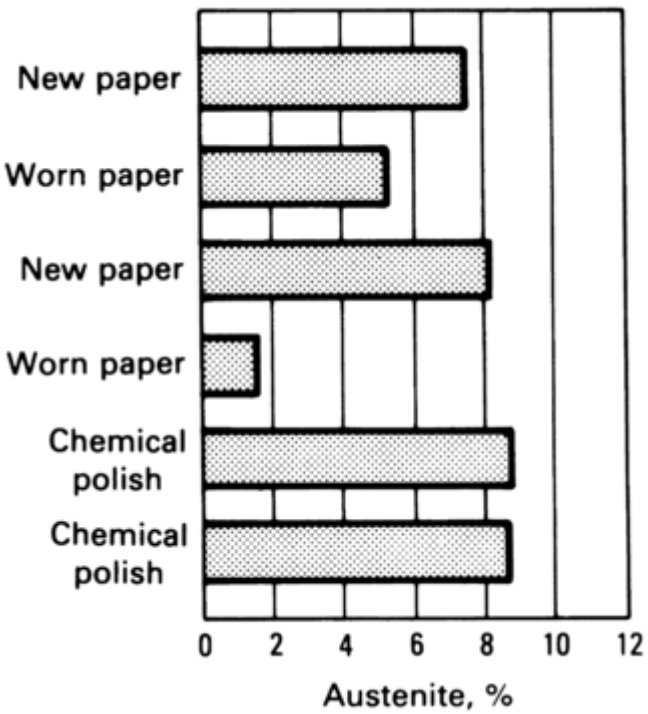

Fig. 27 A histogram showing the amount of retained austenite present in a dual-phase steel after grinding with new and worn grinding papers. The two bars for chemical polish represent the true percentage of retained austenite in the specimen. The lower percentages, from grinding with worn papers, indicate that much of the retained austenite transformed to martensite due to mechanical deformation.

Polishing is the last mechanical step, and its purpose is to remove the scratches and the surface deformation zone created by grinding. Usually, the metallographer will know when the specimen is prepared properly. For example, careful observation of the ferrite grains in Fig. 28 shows that the scratches from the last grinding step were not removed. The ferrite phase in this ferrite + pearlite microstructure is very soft, and the scratches and associated deformation zone are still present. When this is seen, the specimen needs to be repolished, or the specimen should be reground on a 600-grit paper. Polishing techniques for steel specimens depend on their microstructure. For a specimen with a pearlite or carbide microstructure, polishing times should be short and steps few to minimize relief. A specimen in which the ferrite grain boundaries are to be etched would require longer polishing times and an etch after each polishing step. Low-carbon steel specimens can be polished using 6 μm diamond on a canvas or low-nap cloth for 1 min with heavy pressure. This is followed by 3 μm alumina for 2 min with firm pressure on a medium-nap cloth. Use a low-speed polishing wheel while rotating the specimen clockwise (the opposite direction to wheel rotation).

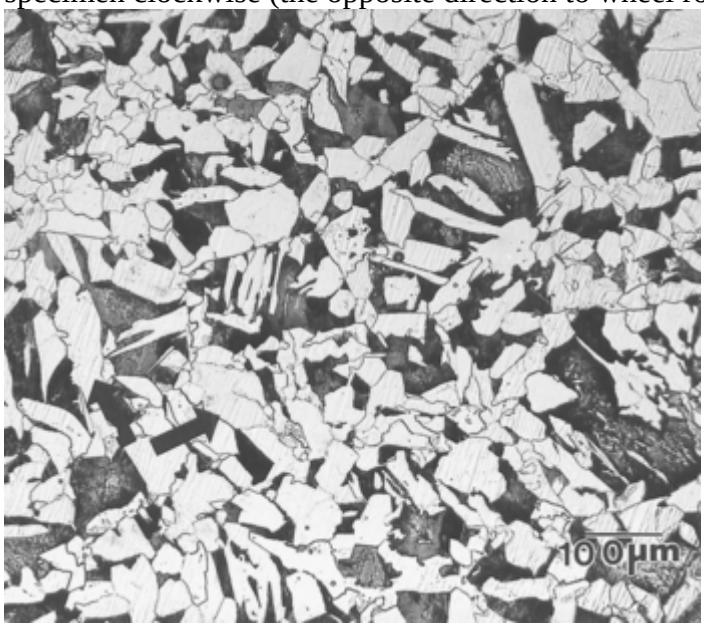

Fig. 28 Microstructure of an ASTM A36 structural steel showing ferrite + pearlite. Note the remnants of scratches in the softer ferrite phase. These subsurface deformation zones from grinding (as shown in Fig. 26) were not removed in the polish. 2% nital etch. 100×

If a water-soluble diamond compound is used, the specimen should be cleaned after polishing with a good grade of natural cotton and water, flushed with alcohol, then dried. The specimen should then be polished on a stationary wheel using a medium-nap cloth and a colloidal suspension of 0.04 μm silicon dioxide (SiO_2). If an adhesive-backed cloth is used, a thick glass or plastic plate can be substituted for the wheel. If the specimen contains 1.0% Si or more (electrical steels, dual-phase and TRIP steels), the SiO_2 polishing compound should be cleaned off with denatured alcohol and cotton to prevent staining; otherwise, the specimen should be cleaned with water, flushed with alcohol, and dried. Figure 29 shows a silicon-containing electrical steel specimen that was polished using this procedure.

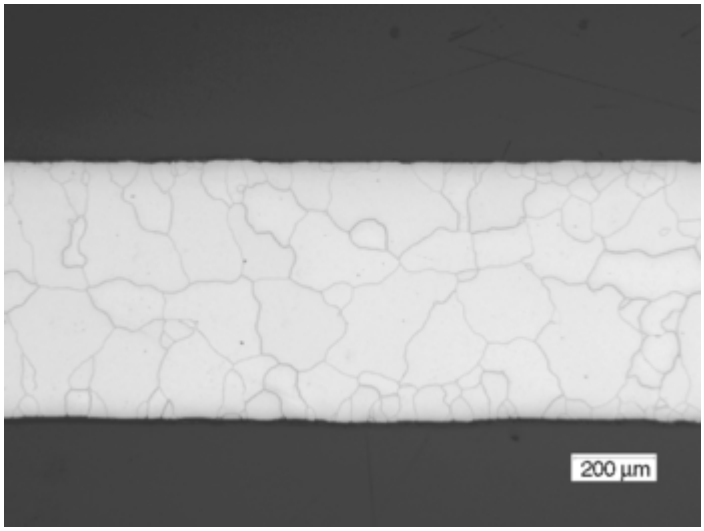

Fig. 29 Microstructure of a fully decarburized motor lamination steel showing large ferrite grains. Marshall's reagent. 200×

A specimen in which the ferrite grains are to be revealed can be polished 1 min using a low-speed wheel and 6 µm diamond on a low-nap cloth. The specimen is then etched 15 s in 2% nital, repolished 2 min using 0.3 µm Al_2O_3 on a medium-nap cloth and a low-speed polishing wheel, re-etched 15 s in 2% nital, and repolished 1 min using 0.3 µm Al_2O_3. The final polishing should be carried out with SiO_2 for 30 s on a stationary medium-nap cloth. After each step, the abrasive should be removed with cotton and water and the specimen flushed with denatured alcohol, then dried immediately. This etch-polish-etch technique will remove the deformed layer.
Nonmetallic inclusions can be retained by polishing with 6 µm diamond on a stationary napless cloth, then 1 µm diamond on a low-nap cloth for 1 min. After each polishing, the specimen should be cleaned with denatured alcohol and cotton, flushed with alcohol, and dried.
The following procedures will keep specimens flat and free of polishing artifacts during polishing. The edges of a clamp, mount, or bulk specimen should always be beveled to prevent catching on the polishing cloth, which can result in a rounded surface. Beveling also prevents tearing of the cloth. The specimen should always be rotated counter to wheel direction to avoid a comet tail effect, as shown in Fig. 30(a). Figure 30(b) illustrates the same specimen polished correctly. Comet tails are developed when inclusions are literally pulled from the specimen surface. In the pulling process, the inclusions leave a tail in the direction they were pulled.

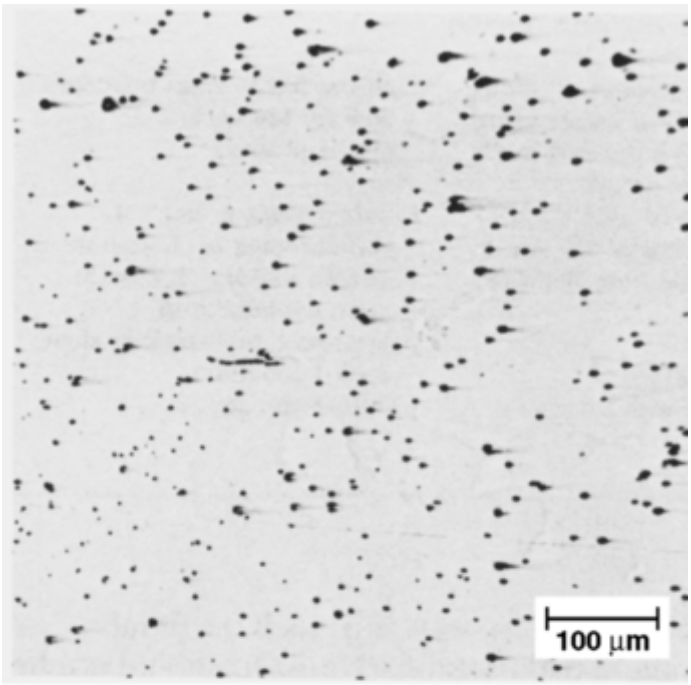

Fig. 30 A decarburized UNS G10100 steel sheet showing (a) comet tails from improper polishing and (b) the true microstructure. A comet tail is produced when inclusions (manganese sulfides) are pulled from the surface of the specimen. As-polished. 100×

Polishing abrasives should be removed from the specimen as quickly as possible to prevent them from drying and causing an artifact. For example, SiO_2 drying on the specimen can sometimes appear as coarse pearlite. A commercially available free-standing blow dryer (the type found in most restrooms) works well on metallographic specimens because of the large volume of warm air it produces.

During both grinding and polishing, it may be important to preserve the edge of the specimen, that is, maintain a flat surface right up to the edge. If precautions are not taken, the edges on a metallographic specimen are rounded, and the edge is not in focus on the same plane as the bulk of the specimen surface. An example where

edge retention is important is shown in Fig. 31, which represents the outer surface of a low-carbon steel sheet with carbides (cementite) on the surface. A planar view (looking at the sheet surface) of similar carbides can be seen in Fig. 32. The carbides formed from surface contamination of carbon during the batch annealing process. If the sheet from this batch anneal was to be galvanized, the zinc coating would not adhere to this portion of the sheet, and a coating defect would form. If good edge retention procedures were not followed, the metallographer may have missed these carbides on the surface. In this example, a higher-hardness thermosetting mounting material was used to minimize rounding of the edge of the specimen.

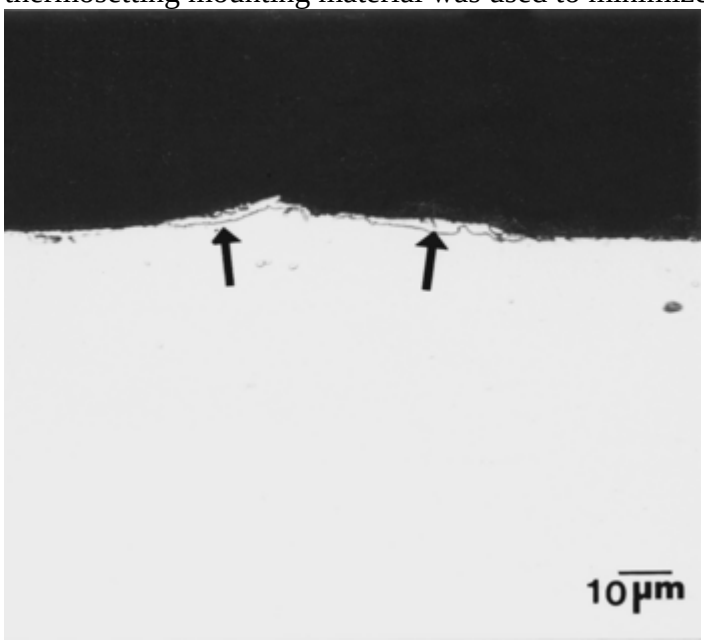

Fig. 31 Surface cementite (arrows) on a low-carbon batch-annealed sheet. This specimen was prepared with excellent edge retention. 4% picral + zephiran chloride wetting agent. 1000×

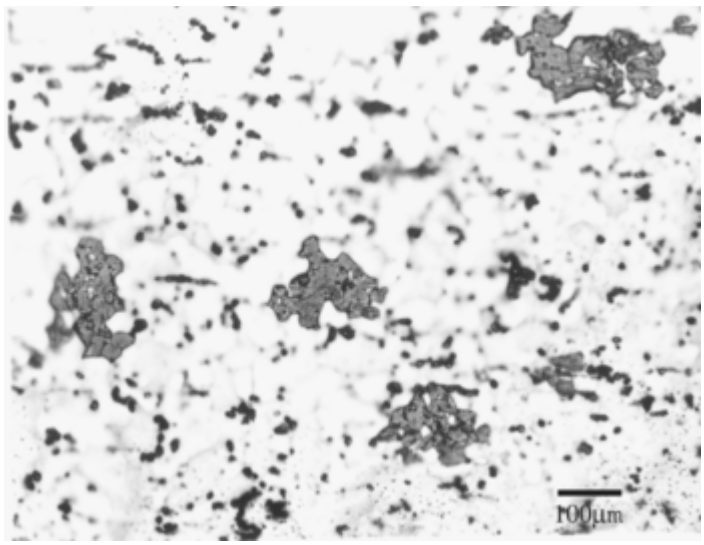

Fig. 32 Large surface carbides shown in a planar view. Marshall's reagent. 100×. Courtesy of Samuel Lawrence, International Steel Group

Etching. The specimen should be etched immediately after the final polishing. Etching solutions used to reveal the microstructures of low-carbon and coated steels are listed in Table 2 and 3, along with their primary characteristics. Nital and picral are the most widely used etchants for low-carbon steels.

Table 2 Common etchants for low-carbon steels

Etchant	Ingredients	Applications/remarks
2% nital	1–5 mL nitric acid (conc) 99 to 95 mL ethyl alcohol	Used to reveal ferrite grain boundaries and lath martensite (low carbon) The authors recommend a 2% solution with an etching time of 10 to 20 s. Use gentle agitation, with the polished surface upward. To reveal all ferrite boundaries, the last polishing step should be with silicon dioxide for at least 1 min and etched immediately to prevent a passive layer from forming on the polished surface.
Marshall's reagent	Part A: 5 mL sulfuric acid (conc) 8 g oxalic acid 100 mL water Part B: 30% solution hydrogen peroxide Part A can be mixed and stored, but do not store the mixture of parts A and B. Part B must be used fresh. Mix equal parts (A and B) just before using.	For ferrite grain boundaries (more uniform than nital). Colors cementite tan. Reveals prior-austenite grain boundaries in martensitic low-carbon steels Can pre-etch in 2% nital for better results. Hold polished surface vertical in solution to avoid pitting. Add 1 mL hydrofluoric acid per 100 mL of solution for deeper etching response, especially in interstitial-free steels. If a haze covers the surface, immerse specimen in a 3% aqueous EDTA[(a)] solution in an ultrasonic cleaner for several minutes, flush with water, then alcohol, and blow dry.
4% picral	4 g picric acid 96 mL ethyl alcohol 5 mL zephiran chloride (wetting agent) per 75 mL of solution	For structures consisting of ferrite and carbides (and pearlite). For bainitic steels and tempered martensite Does not reveal ferrite grain boundaries For pearlite and carbides, usually etch for 20 s The addition of zephiran chloride improves etch rate and uniformity. Etchant improves with age For chromium-bearing steels (above 0.5% Cr), add 5 drops of hydrochloric acid per 100 mL of solution.
4% picral + 2% nital	4 g picric acid 96 mL ethyl alcohol 5 mL zephiran chloride 2 mL nitric acid (conc)	For ferrite plus carbide (pearlite) structures and ferrite plus bainite or martensite Etch first in picral followed by nital, or mix the two solutions. Either technique produces good results.

	98 mL ethyl alcohol	
Sodium metabisulfite	10 to 12 g sodium metabisulfite 100 mL distilled water	Tint etch. Darkens martensite in quenched steels and dual-phase steels Pre-etch for 3 s in 2% nital Immerse in solution for 20 s. Etch, with polished surface facing upward, for 45 s and do not agitate. If over- or underetched, the specimen must be repolished, which can be done in approximately 15 s with 0.3 μm alumina.
Beraha's reagent	10 g sodium thiosulfate (anhydrous) 3 g potassium metabisulfite 100 mL water	Tint etch. For ferrite grain boundaries Pre-etch for 3 s in 2% nital for better results. Etch, with polished surface facing upward, for 45 s and do not agitate. If over- or underetched, the specimen must be repolished.
Klemm's reagent	50 mL water saturated with sodium thiosulfate Add 1 g potassium metabisulfite	Tint etch. Colors ferrite grains and ferrite in pearlite Etching time, 40–120 s
Alkaline sodium picrate	2 g picric acid 25 g sodium hydroxide 100 mL distilled water	Solution will darken pearlite and iron carbides. Add sodium hydroxide to water; when completely dissolved, add the picric acid. Bring the solution to a low boil; do not boil dry. Solution will attack phenolic mounts; thermosetting epoxy mounts are recommended.

(a) EDTA, ethylenediamine tetraacetic acid

Table 3 Common etchants for coated steels

Etchant	Ingredients	Applications/Remarks
1% Amyl Nital	1 mL nitric acid (concentrated) 99 mL amyl alcohol	Used to reveal the microstructure of zinc-based coatings (hot dipped galvanized, electrogalvanized, Galvalume and Galfan) This is basically a nital etchant but amyl alcohol replaces ethyl alcohol. Etch between 10 and 20 seconds to start.
2% Nital	2 mL nitric acid (concentrated) 98 mL ethyl alcohol	For aluminum-based (aluminized), tin, copper, nickel, brass and chromium coated steels. Does not etch the coating but contrasts the steel substrate. Works well with both Type 1 and Type 2 aluminized steel. 10–20 seconds.
Rowland's Reagent	0.075 g picric acid 13 mL ethyl alcohol 35–60 mL water	For etching galvanneal coatings Etching time varies between 5 and 30 seconds.
Modified Rowland's Reagent	50 mL water 45 mL ethyl alcohol	For etching zinc-based electrogalvanized coatings. Etching time varies between 5 and 30 seconds.

	5 mL of 4% picral solution	
Timofeef's Reagent	100 mL 4% picral solution; add 6 drops of a solution of 6 g CrO_3 in 100 mL of nitric acid	For etching galvanneal coatings Etching time varies between 5 and 30 seconds.
Amyl Nital + Amyl Picral	Part A, mix equal parts of: 1 mL nitric acid (conc.) 99 mL amyl alcohol 1 g picric acid 99 mL amyl alcohol Part B, mix equal parts of: 1 mL nitric acid (conc.) 99 mL amyl alcohol 1 g picric acid 99 mL amyl alcohol 3–4 drops hydrofluoric acid per 30 mL solution	For etching galvanneal coatings Etch for 20 seconds in Part A, flush with alcohol and etch for 10 seconds in Part B

Nital is generally used in concentrations of 1 to 3% nitric acid (HNO_3) in ethanol or methanol. In solutions containing more than 5% HNO_3, only methanol should be used, because the ethanol becomes unstable as the concentration of HNO_3 increases. However, for the lower concentrations, ethanol is preferred, because methanol is toxic and can be absorbed through the skin. An example of a low-carbon steel etched with 2% nital can be seen in Fig. 33. The nitric acid in this etchant chemically attacks the ferrite grains and is thus an “attack” etchant. The grain boundaries are delineated, because each ferrite grain has a different orientation with respect to the plane of polish. The boundaries between the grains can be seen, because the reflected light from the light microscope is scattered and not returned back through the objective of the microscope.

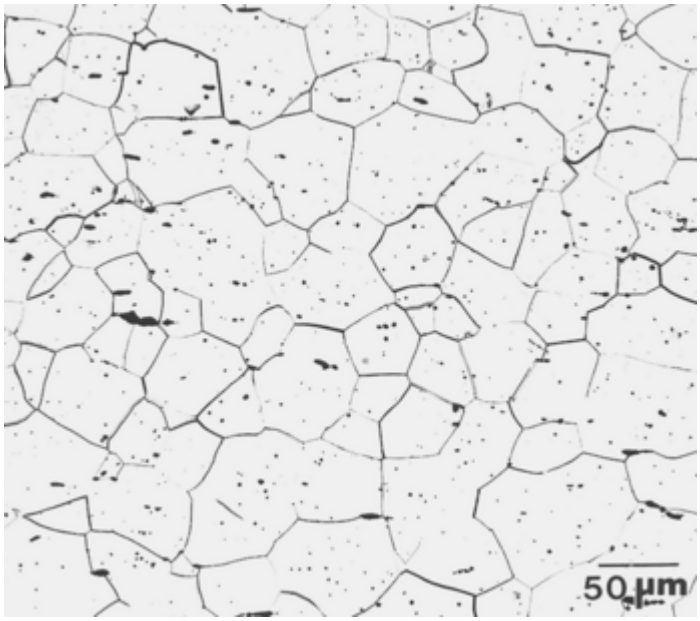

Fig. 33 Microstructure of ferrite grains and carbide particles in a nondecarburized motor lamination steel. 2% nital etch. 200×

Picral generally consists of a 4% solution of picric acid in ethanol. This etchant highlights the boundaries around carbides and is thus used when there are carbides present in the microstructure, for example, pearlite or cementite particles. An example of a specimen etched in 4% picral is seen in Fig. 34. In this case, cementite particles are clearly delineated from the ferrite matrix. Note in this example that the picral etch did not delineate the ferrite grain boundaries.

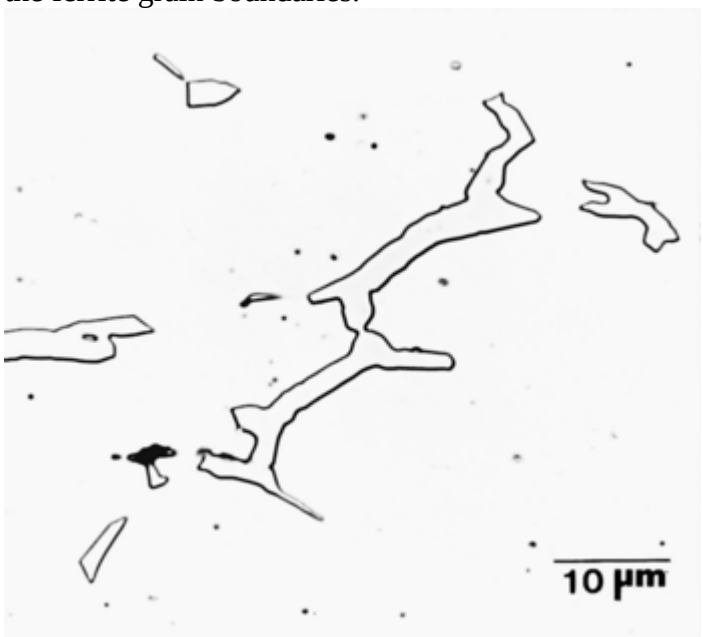

Fig. 34 Carbides in a low-carbon steel. 4% picral etch. 1500×

Four or five drops of 17% zephiran chloride per 100 mL of 4% picral solution will hasten the etching reaction and prevent preferential attack. Picral works best when it turns dark with use. Etching times generally range from 15 to 30 s, with the polished face held upward. The specimen should be held with tongs and agitated gently. After etching, the specimen should be held under water to remove excess etchant, flushed with denatured alcohol, and dried. If the water causes stains—for example, in steels containing more that 1% Si—the etching solution should be removed by placing the specimen in a sequence of alcohol baths, flushing with alcohol, and drying. Keep in mind that picric acid crystals in their dry form are highly explosive. Always keep the crystals moist and stored in a special storage cabinet. Maintain safe procedures when handling this

compound. As a standard practice, the metallographer should always check the Material Safety Data Sheet information that accompanies each chemical reagent.

Picral + Nital. A serial etch of 4% picral and 2% nital is sometimes used to delineate both the ferrite grain boundaries and the carbide particles. The specimen is etched using picral, then nital. This technique is useful for etching ferrite grain boundaries in a pearlite-ferrite microstructure without overetching the pearlite. Etching times are 10 to 15 s in 4% picral and 5 to 10 s in 2% nital.

Marshall's Reagent. Ferrite grain boundaries can be etched using nital in most steels, although Marshall's reagent appears to be the better etchant for low-carbon and decarburized steels. A 0.02% C steel etched in Marshall's reagent can be seen in Fig. 35. Note the sharpness and completeness of the ferrite grain boundaries. This is one advantage of Marshall's reagent over nital, in that it delineates all the ferrite grain boundaries in a low-carbon steel. This would be particularly important when measuring ferrite grain size using image analysis. An example showing the difference in etching response between Marshall's reagent (with a few drops of hydrofluoric acid) and 2% nital can be seen in Fig. 36. In this very-low-carbon interstitial-free steel, the Marshall's reagent (Fig. 36b) delineated all the ferrite grain boundaries, whereas the 2% nital (Fig. 36a) only delineated a few boundaries. The micrographs in Fig. 37 show a low-carbon steel etched in Marshall's reagent, where the ferrite grain size is duplex. This is an example where two micrographs were required to qualitatively represent the microstructure because of the large variability in ferrite grain size and distribution. Looking at only one field in the microscope would have been very misleading and would not have told the whole story about the microstructure.

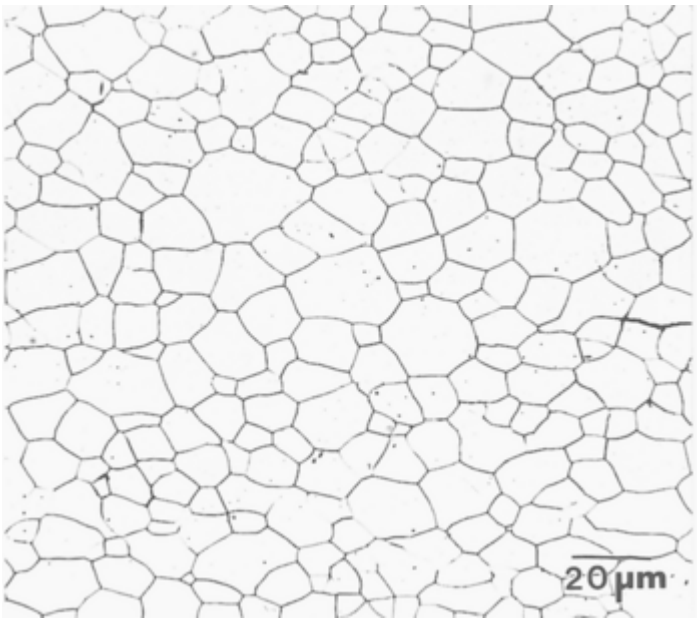

Fig. 35 Ferrite grains in a low-carbon (0.02% C) steel. Marshall's reagent. 500×

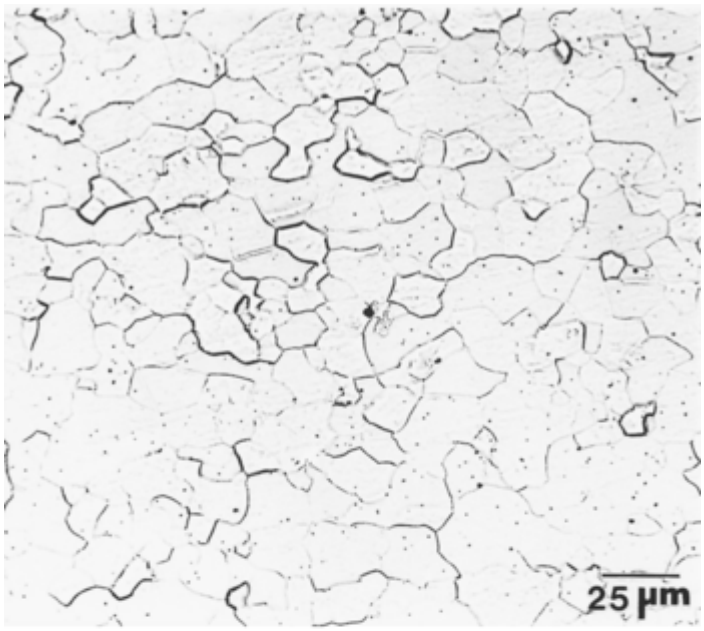

(a)

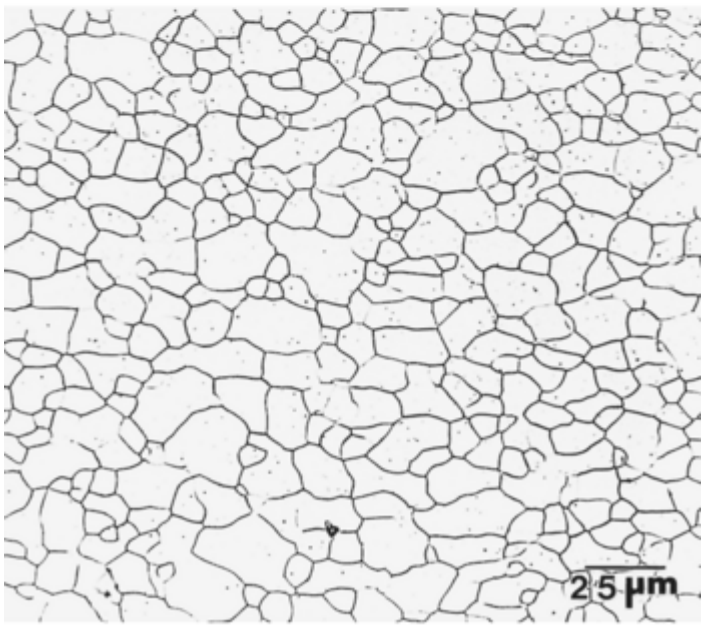

(b)

Fig. 36 Microstructure of a very-low-carbon interstitial-free steel etched in (a) 2% nital and (b) Marshall's reagent. Note that many of the ferrite grain boundaries are not delineated in the specimen etched in 2% nital. 400×

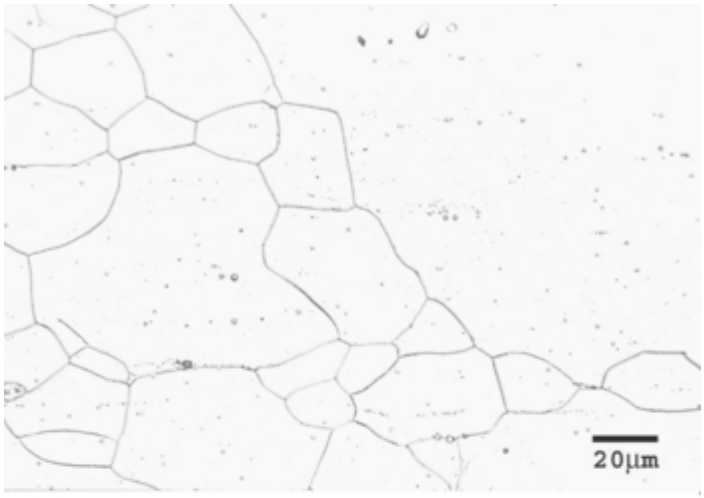

(a)

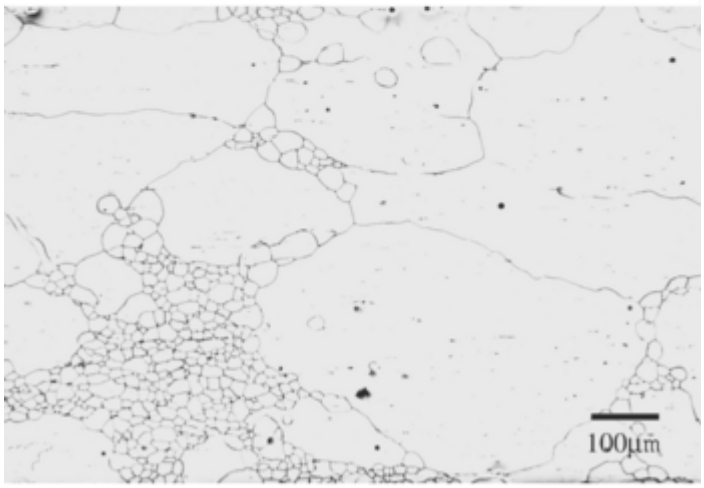

(b)

Fig. 37 Microstructures of a low-carbon sheet steel showing duplex ferrite grain size. (a) High magnification, masking the duplex severity. 100×. (b) Low magnification, showing true mixture of grain sizes. 100×. Both etched in Marshall's reagent

Another advantage of Marshall's reagent is that it not only sharpens ferrite grain boundaries, but it highlights carbide boundaries. An example can be seen in Fig. 38, where several cementite particles (arrows) are easily visible on the ferrite grain boundaries.

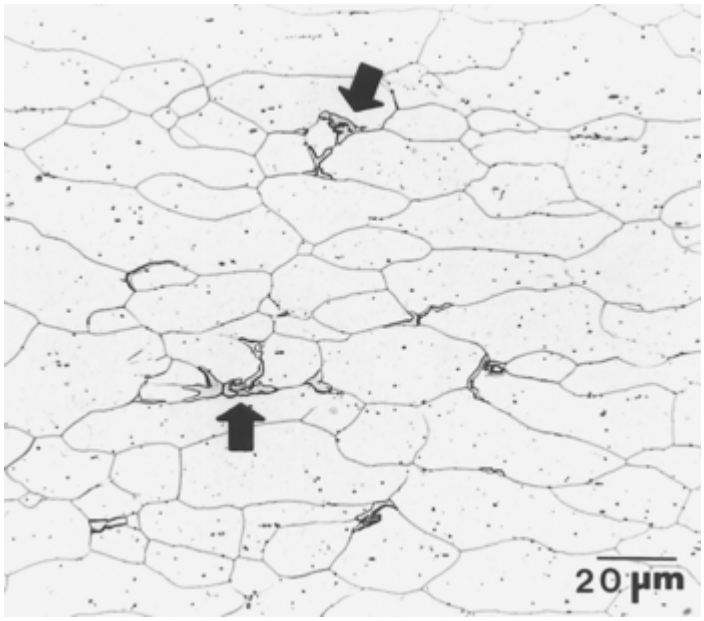

Fig. 38 Microstructure of a batch-annealed 0.04% C steel sheet showing ferrite grains with grain-boundary cementite (arrows). Marshall's reagent. 500×

Tint Etchants. Ferrite grain boundaries in low-carbon, 1% Si, and titanium-bearing steels are difficult to delineate. In this case, Beraha's tint etchant will differentiate the grains by color. Figure 39 shows ferrite grains tinted with Beraha's reagent. This specimen represents a very-low-carbon motor lamination steel containing silicon. Tint etchants such as Beraha's or sodium metabisulfate ($Na_2S_2O_5$) should not be agitated; the specimen should be pre-etched 2 to 3 s in picral or nital. A specimen etched in a tint etchant cannot be reimmersed if the structure is too light, but repolishing for 15 s using 0.3 µm Al_2O_3 will remove the tint etchant.

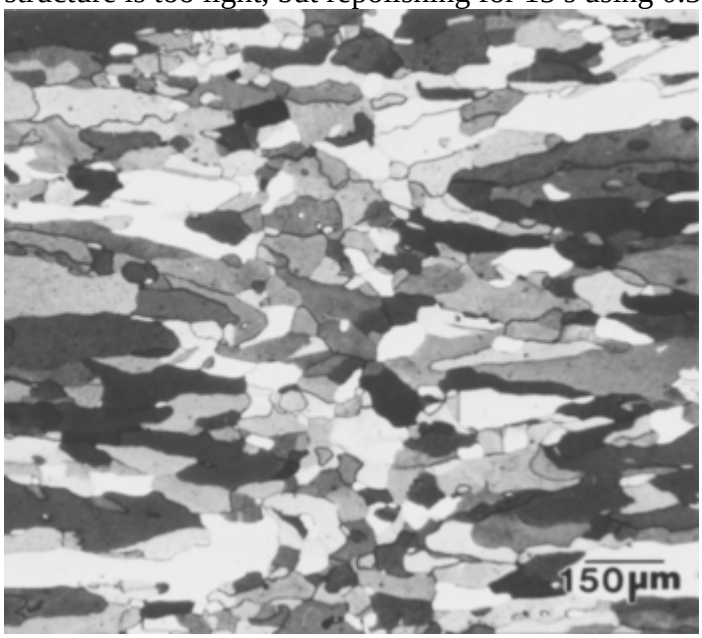

Fig. 39 Microstructure of a very-low-carbon (decarburized) motor lamination steel showing columnar ferrite grains that grew toward the two sheet surfaces. Beraha's tint etchant. 75×

Picral + Wetting Agent. Pearlite, cementite, and Fe_3C carbides in all carbon steels can be etched using 4% picral with zephiran chloride. The wetting agent improves the etching response of picral. Pearlite will not always appear lamellar, because the spacing between the cementite and ferrite cannot always be resolved using a light microscope. In Fig. 40, many islands of pearlite can be seen. However, the pearlite lamella cannot be resolved in most of the islands. Figure 40(b) is a replica electron micrograph of the pearlite patch circled in Fig. 40(a). The lamellar structure is visible when examined at this higher magnification.

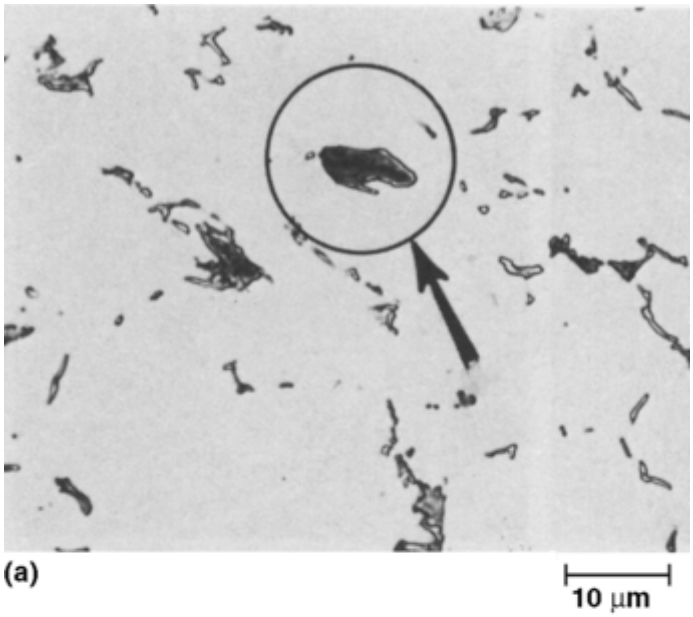

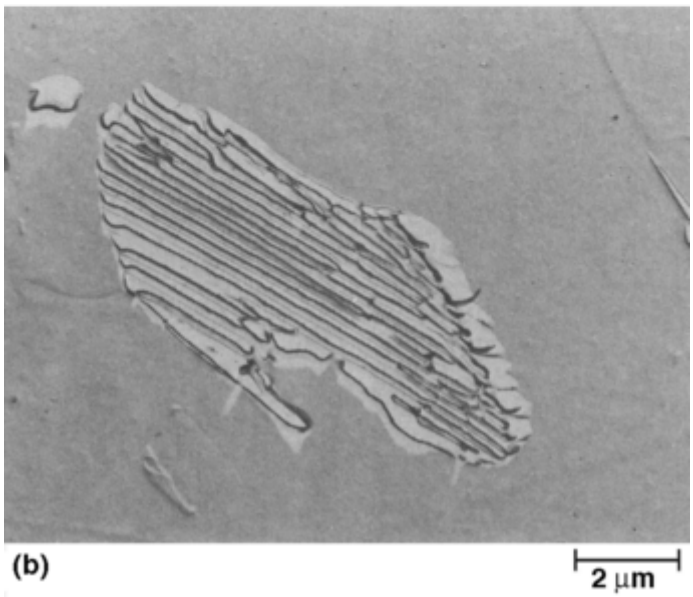

Fig. 40 Microstructure of a dual-phase steel showing islands of martensite and pearlite in a ferrite matrix. An island of pearlite is circled in (a) and shown at high magnification in (b). 4% picral etch. (a) 1000×. (b) A surface replica at 4970×

Selective etching is used to differentiate between various constituents in a complex microstructure. Some etchants darken cementite, and some do not. Some tint etchants darken martensite, and some etchants darken ferrite. This may be useful in trying to distinguish cementite from martensite and retained austenite in dual-phase and TRIP steels. Special cases require other etchants to reveal pearlite, cementite, and other carbides.
For example, Fig. 41 shows a number of pearlite colonies etched using Beraha's tint etchant to darken the ferrite and highlight the cementite white. Figure 42 illustrates a carburized UNS G10200 steel, where carbides at the prior-austenite grain boundaries were darkened using alkaline sodium picrate. If 4% picral had been used, the prior-austenite grain boundaries would not have been revealed; if nital had been used, the small carbides would not have appeared in the boundaries.

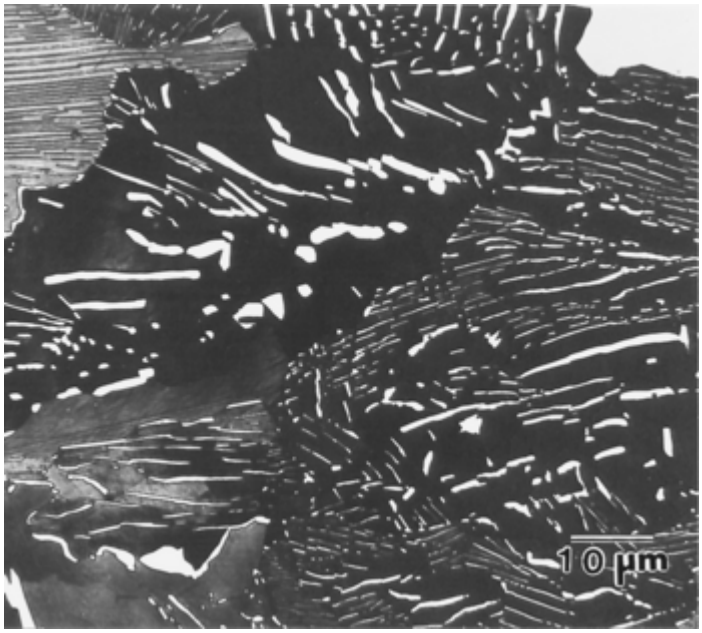

Fig. 41 A pearlitic microstructure showing ferrite darkened by the tint etch and cementite unaffected (white). Beraha's tint etch. 1000×

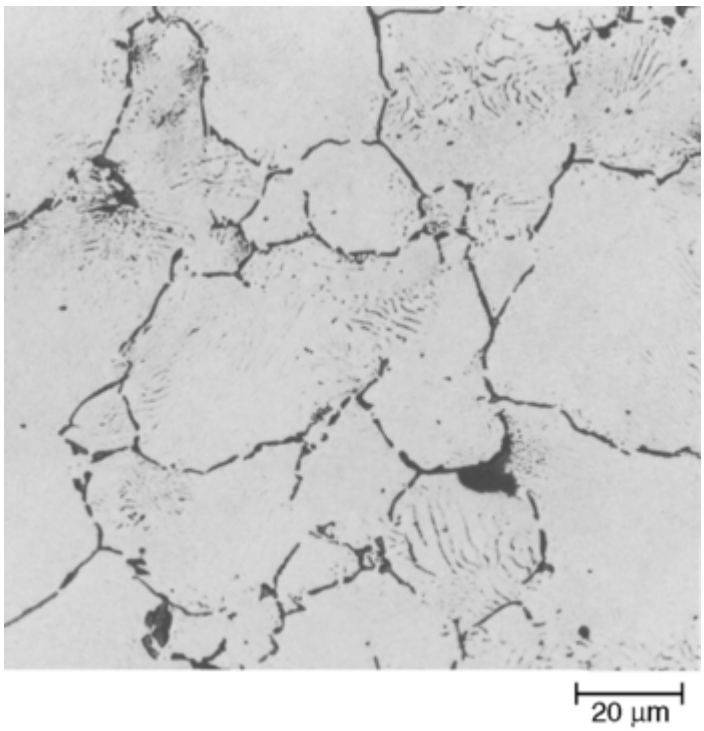

Fig. 42 Microstructure of a carburized UNS G10200 steel showing cementite at the prior-austenite grain boundaries. The cementite was darkened by the boiling alkaline sodium picrate etch. 500×

Reference cited in this section

1. L.E. Samuels, Metallographic Polishing by Mechanical Methods, ASM International, 2003

A.O. Benscoter and B.L. Bramfitt, Metallography and Microstructures of Low-Carbon and Coated Steels, Metallography and Microstructures, Vol 9, ASM Handbook, ASM International, 2004, p. 588–607

Metallography and Microstructures of Low-Carbon and Coated Steels

Arlan O. Benscoter, Lehigh University; Bruce L. Bramfitt, International Steel Group, Inc.

Manual Preparation of Coated Steel Specimens

In addition to the previously described preparation steps, there are a number of recommended sample preparation procedures for different groups of coated steel specimens. Some procedures were already briefly mentioned, but this section elaborates on a number of proven techniques used for coatings. Precautions unique to the preparation of coated steels are also described. This section describes preparation of metallic (zinc- and aluminum-base coatings as well as tin, copper, chromium, and nickel coatings) and nonmetallic coatings (porcelain enamel and organic coatings). This is preceded by a discussion on edge retention, which is of prime importance when dealing with coatings. Many of the coatings are thin, and a rounded edge makes it impossible to observe the coating. Also, most of the coatings on low-carbon steel are softer than the steel, and the coating tends to form a rounded edge. For most coated steel specimens, the authors have successfully used the specimen preparation procedure described as follows.

Manual Preparation for Coated Specimen Edge Retention

For most coated low-carbon steels, the following hand grinding/polishing procedure has been proven to provide a flat edge on the prepared specimen. This procedure augments the previously described procedure for low-carbon steel. More details can be found in Ref 2:

1. Sectioning: Use a tabletop hand shear with sharpened blades to cut specimens to proper size (this method is quick, convenient, and provides minimal damage). Remove the deformation from shearing during the grinding stage.
2. Mounting: Use a castable epoxy, and mount multiple specimens close together. A small piece of double-sided sticky tape is attached at the two ends of each specimen as spacers. A sketch of this procedure is shown in Fig. 43. The spacer allows the epoxy to penetrate the space between the specimens. Dummy sheet specimens can be placed at both sides of the stack of specimens. The coated edge should always face the same direction in the mount, and an indicator (small piece of bent sheet) can be in the mount to indicate the side the coating is facing. This indicator would be important, so that the metallographer would know the orientation of the specimen when grinding and polishing. The epoxy liquid should be poured to a height to just cover the specimens. At this point, the mount should be placed in a vacuum to remove air bubbles and to allow the epoxy to penetrate the space between specimens. Then, remove from the vacuum and fill the remaining space in the mount with epoxy (no vacuum required).
3. Grinding: During rough grinding, the deformation zone created by the shear must be fully removed. Also, during grinding, always rotate the specimen 90° after grinding on each paper. In one position, the coated edge of the specimen must be parallel to the direction of rotation, and the coated edge should be toward the center of the grinding wheel. When grinding perpendicular to the wheel rotation, the coated edge must be the leading edge (first edge to encounter the motion of the paper) to the direction of rotation. For the last step, it is recommended that the coated edge of the specimen be parallel to the direction of rotation to maintain complete flatness and that the specimen and the mount be on the same plane.
4. Polishing: During polishing, use the lowest nap (or napless) cloth possible. Polishing on a stationary wheel will maintain flatness (or a very low revolutions per minute rotation).

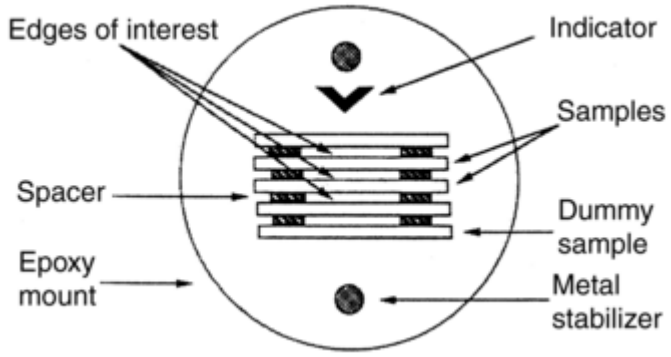

Fig. 43 A schematic of multiple zinc-base coated specimens showing the double-backed sticky tape spacers, indicator, dummy strips, and metal stabilizers

Specific procedures for both metallic and nonmetallic coatings on low-carbon steel are described in the remaining sections.

Metallic Coatings

All coatings on a steel surface must receive special attention. When preparing coated steels, the metallographer must keep in mind that, in most cases, the coating is there mainly to protect the steel from corrosion. This means that exposure to aqueous solutions will create an electrolytic cell that attacks the less-noble metal according to the electromotive series of chemical elements. Zinc coatings are less noble than iron, whereas tin coatings are more noble than iron. Also, the coating has different properties than the low-carbon steel substrate (hardness, thermal expansion, etc.). A soft coating will tend to form a rounded edge on the specimen. Thus, the general procedure described previously for edge retention should be followed.

Metallographic Preparation of Zinc-Base Coatings. In the case of zinc-base coatings, the zinc layer affords cathodic protection. This means that the zinc is the cathode and the steel (iron) is the anode of an electrolytic cell when exposed to an aqueous environment. In providing protection, the zinc coating is sacrificed (corroded away), while the steel remains intact. Thus, when a zinc-coated steel is etched in an aqueous solution, a cell is created, and the coating is attacked in preference to the steel (the zinc is less noble than the iron in the steel). This attack is usually uncontrolled, and thus, water-based etchants should be avoided for these types of coatings. Also, if water is used during the final stages of specimen preparation of the sample, a cell is created, and the microstructure of the coating is compromised. This means that zinc-coated specimens should be rinsed clean with cotton and alcohol, flushed with alcohol, and dried with a blast of warm air.

As mentioned in the introduction, there are a variety of commercial zinc-base coatings on steel. Passing the steel sheet through a bath of molten metal produces some of these coatings; other coatings are plated on the surface of the steel sheet by an electrolytic plating process. The former coatings are called hot dipped coatings and are galvanized (pure zinc), Galvalume (a Zn-55% Al alloy coating with 1.6% Si), and Galfan (a Zn-5% Al coating). The latter coating is called electrogalvanized steel. These coatings are mostly zinc with a small amount of alloying element (nickel, iron, etc.). Another important zinc-base coating is the galvannealed coating. This coating is formed when a hot dipped galvanized steel is annealed at 760 to 815 °C (1400 to 1500 °F) for 2 to 3 min. The metallographic procedures used to prepare these various zinc-base coatings are described as follows (see also Ref 3).

Sectioning. A convenient way to section a zinc-base coated steel is by a tabletop hand shear.

Mounting. Follow the procedure described in the previous section on edge retention of coated specimens.

Grinding. It is important to remove all evidence of deformation from the sheared surface during rough grinding. After rough grinding, continue with 120-, 240-, 320-, 400-, 600-, and 800-grit silicon carbide papers, finishing with the coating parallel to the 1200-grit paper. The specimen should be cleaned with cotton and alcohol, flushed with alcohol, and dried after each step to prevent an attack on the coating.

Polishing. Zinc-base coatings on low-carbon steel are particularly vulnerable during the polishing stage. When using a diamond-polishing medium (e.g., paste), use an extender. The extender pH should be adjusted to 9.6 ± 0.2; the authors found that this pH works well for all zinc-base coatings on low-carbon steel. If the pH is too

high or too low, a reaction may develop between the coating and the specimen. Thus, the metallographer must control the pH of the polishing medium to avoid a corrosion prob lem. Polishing with 3-μm diamond on a stationary napless cloth with heavy pressure for 1 min should remove all the scratches from the last grinding grit. Next, polish on a stationary low-nap cloth charged with 1 μm diamond with heavy pressure for 60 s; continue polishing for another 30 s but back off on the pressure. The last step should be on a low-nap stationary cloth with 0.25 μm diamond with firm pressure for 20 to 30 s. After each step, clean the specimen with alcohol and cotton, flush with alcohol, and dry.

Etching. A low-carbon sheet steel hot dip coated with Galvalume is shown in Fig. 44. In this example, the etchant was 1% nitric acid in amyl alcohol. Amyl-alcohol-based etchants react more slowly and the reaction is more easily controlled than with ethanol-based etchants (Ref 2). Also, ethyl alcohol is hygroscopic (absorbs water) and can easily contain residual water. A two-part mixture of equal parts (50 mL each) of 1% picric acid in amyl alcohol and 1% nitric acid in amyl alcohol can also be used. This is a modified version of Rowland's reagent, which is water based. Then, 50 mL of the mixture are placed in individual containers. In one container, add 3 to 4 drops of hydrofluoric acid. A separate container of ethyl alcohol is placed nearby. The first stage of etching is conducted with the specimen, face up, in the container of the mixture without the hydrofluoric acid. The specimen is slightly agitated for approximately 20 s. The specimen is then rinsed in the container of ethyl alcohol, then placed in the other container of the mixture with hydrofluoric acid. Slightly agitate the specimen for approximately 10 s. The specimen is flushed (rinsed) in ethyl alcohol and blown dry. Examine the specimen. If underetched, repeat the sequence but double the time in the first solution. The microstructure shown in Fig. 44 illustrates the various components of the hot dipped solidified coating. The solid gray particles are silicon, and the diffused gray patches are a zinc-rich eutectic; the white matrix is dendritic aluminum. Also, there is a silicon-rich intermetallic layer (light gray) at the interface between the steel and the coating. This etch, because of the nitric acid, also attacked the steel substrate, with some of the ferrite grain boundaries revealed.

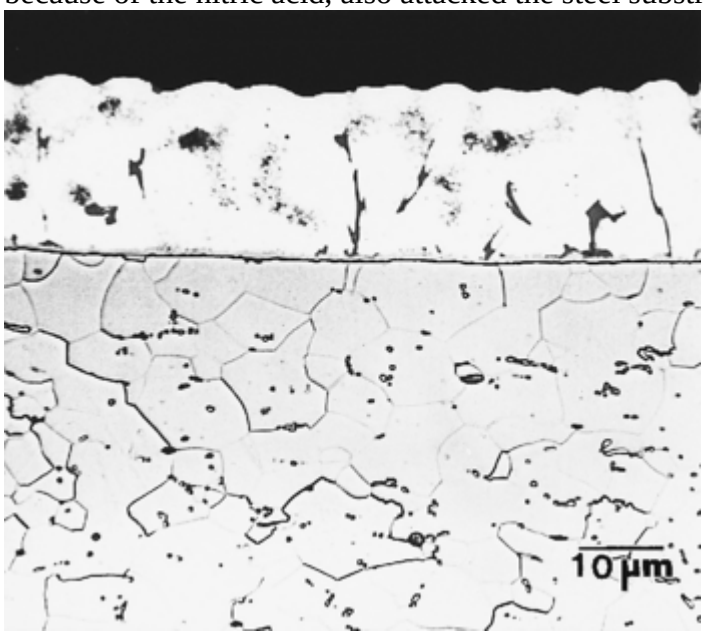

Fig. 44 Microstructure of a Galvalume (zinc-aluminum) coating on a low-carbon steel sheet. Etched in 1% nitric acid in amyl alcohol. 1000×

A 1% nitric acid in amyl alcohol can be used for etching a simple hot dipped galvanized sample. This coating is essentially pure zinc, an example of which can be seen in Fig. 45. Figure 46 shows a galvanized coating that was electroplated to the low-carbon steel surface. This is called an electrogalvanized coating. In general, electrogalvanized coatings are thinner than hot dipped galvanized coatings.

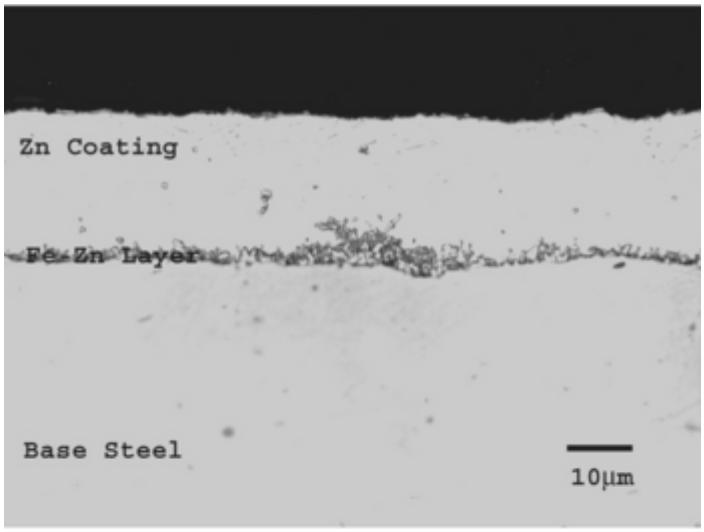

(a)

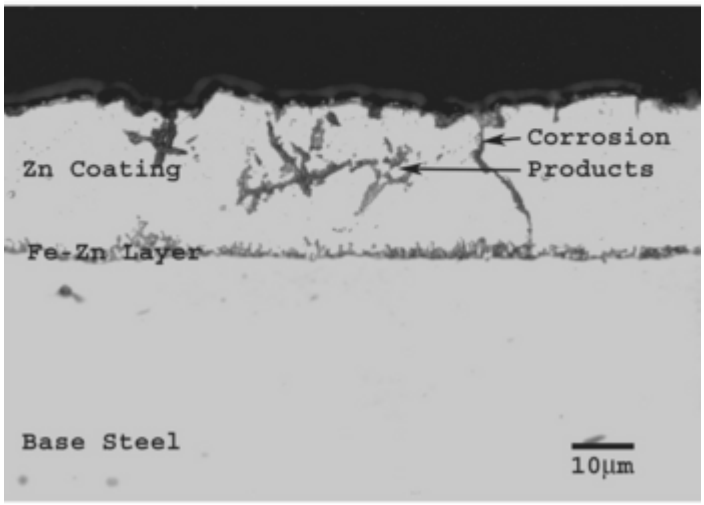

(b)

Fig. 45 Microstructure of a hot dipped galvanized coating on a low-carbon steel sheet. Etched in 1% nitric acid/amyl alcohol. 1000×

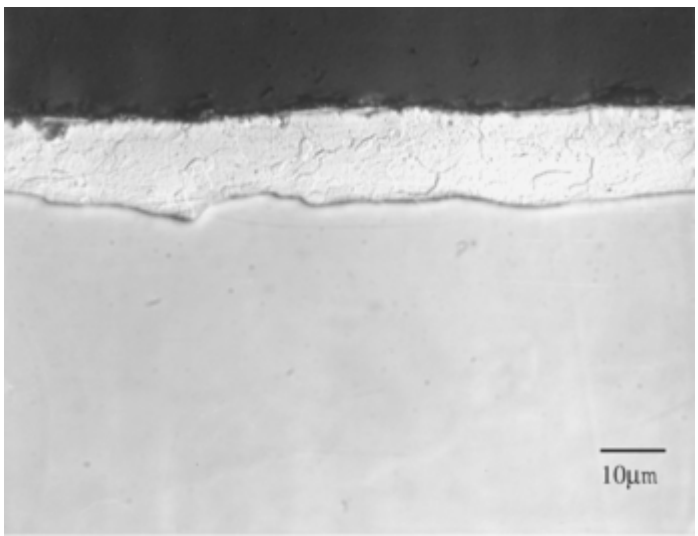

Fig. 46 Microstructure of an electrogalvanized coating on a low-carbon steel sheet. Etched in 1% nitric acid/amyl alcohol. 100×

Another form of zinc coating is a hot dipped galvanized coating that is heat treated. It is called a galvannealed coating. In a galvannealed coating, a number of iron-zinc intermetallic phases are formed during the heat treating process. Figure 47 shows an example of a galvannealed coating. The phases in the coating are zeta (the crystals at the top surface of the coating), delta (the matrix phase), and gamma (the phase at the steel/coating interface).

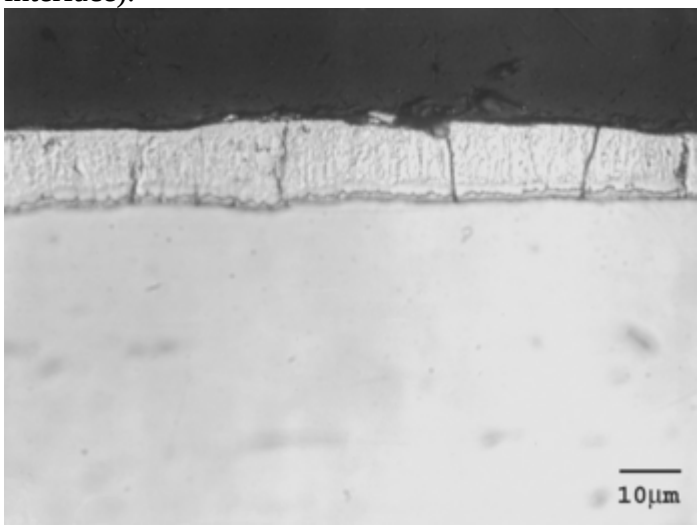

Fig. 47 Microstructure of a galvannealed coating on a low-carbon steel sheet. Note the various intermetallic compounds that developed. Etched in 100 mL amyl alcohol containing 1 mL nitric acid and 1 g picric acid for 20 s, followed by the same concentration solution plus 4 drops of hydrofluoric acid for 15 s. 100×

One more example of a zinc-base coating is Galfan. As described previously, it is a hot dipped Zn-5% Al coating. Figure 48 shows the microstructure of a Galfan coating on a low-carbon steel.

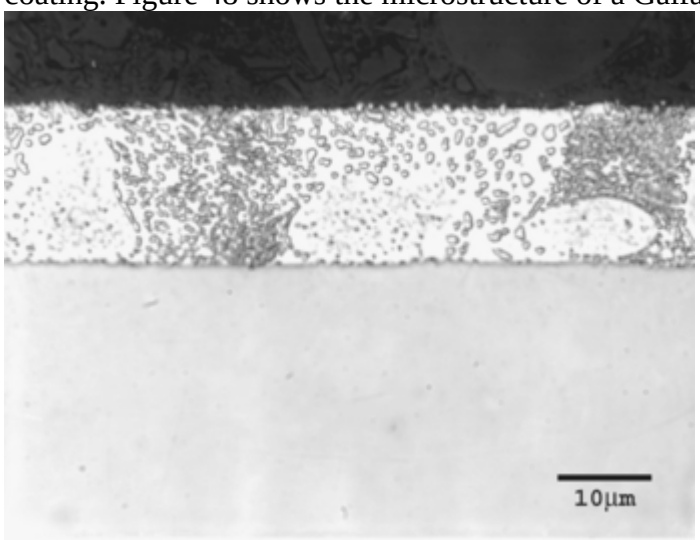

Fig. 48 Microstructure of a hot dipped Galfan coating on a low-carbon steel sheet. Etched in 2% nitric acid in amyl alcohol. Differential (Nomarski) interference contrast illumination. 1500×

Sometimes, the metallographer is asked to reveal the microstructure of the dendritic pattern (spangle pattern) of a zinc-base coating. An example of the dendrites in a spangle of Galvalume is shown in Fig. 49. In this case, the sheet specimen was suspended over a beaker of fuming nitric acid. The acid fumes attacked the surface of the coating, revealing the dendrites. A similar spangle, as viewed in the scanning electron microscope, is seen in Fig. 50. This technique is useful in that the secondary dendritic arm spacing can be measured. The spacing of the dendritic arms is directly related to the cooling rate during solidification of the coating.

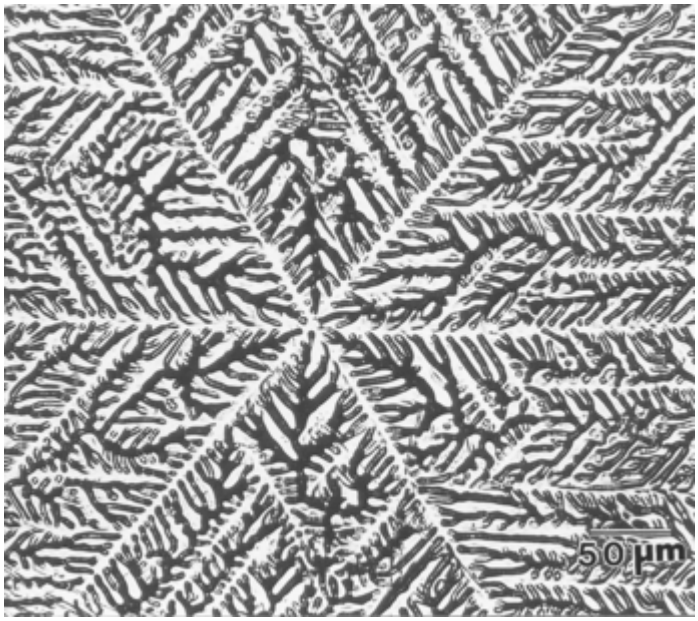

Fig. 49 Microstructure of the dendritic pattern in a spangle on the surface of a Galvalume coating. Etched by suspending the coated surface over fuming nitric acid. 200×

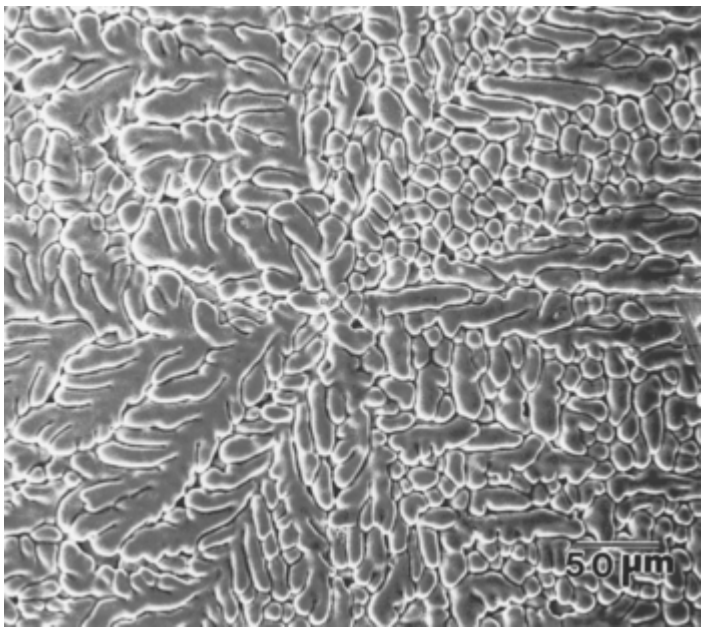

Fig. 50 A spangle dendrite similar to that shown in Fig. 49 viewed in the scanning electron microscope. Etched by suspending the coated surface over fuming nitric acid. 200×

Metallographic Preparation of Tin, Copper, Chromium, and Nickel Coatings. Some coatings, such as tin, copper, and nickel, have the opposite effect of corrosion protection from zinc-base coatings. These elements are more noble than iron, and thus the iron becomes the cathode and they become the anode. Tin coatings are used as a protective coating by preventing the corrosive environment from reaching the steel substrate. Tin coatings are applied to the steel sheet by either passing the steel sheet through a bath of molten tin or by an electrolytic plating process.

Sectioning. Generally, this type of material is sectioned with a tabletop hand shear to prevent distortion.

Mounting. Thin-coated specimens can be mounted in a thermosetting epoxy compound. One suggestion is to bend the specimens in the shape of an “L” in order to stand up in the mount. Also, place them as close together as possible to maintain edge flatness. For thin specimens, the observable coating thickness can be increased by placing them in a commercial holder designed to hold circuit boards that has been modified by cutting it on a 45° or less angle. The modified holder is then placed in a mold with the samples and cast with epoxy. Figure 51

shows a comparison of a normal cross-sectional view and a 45° view of two thin coatings on low-carbon steel. This technique can be used for other thin coatings.

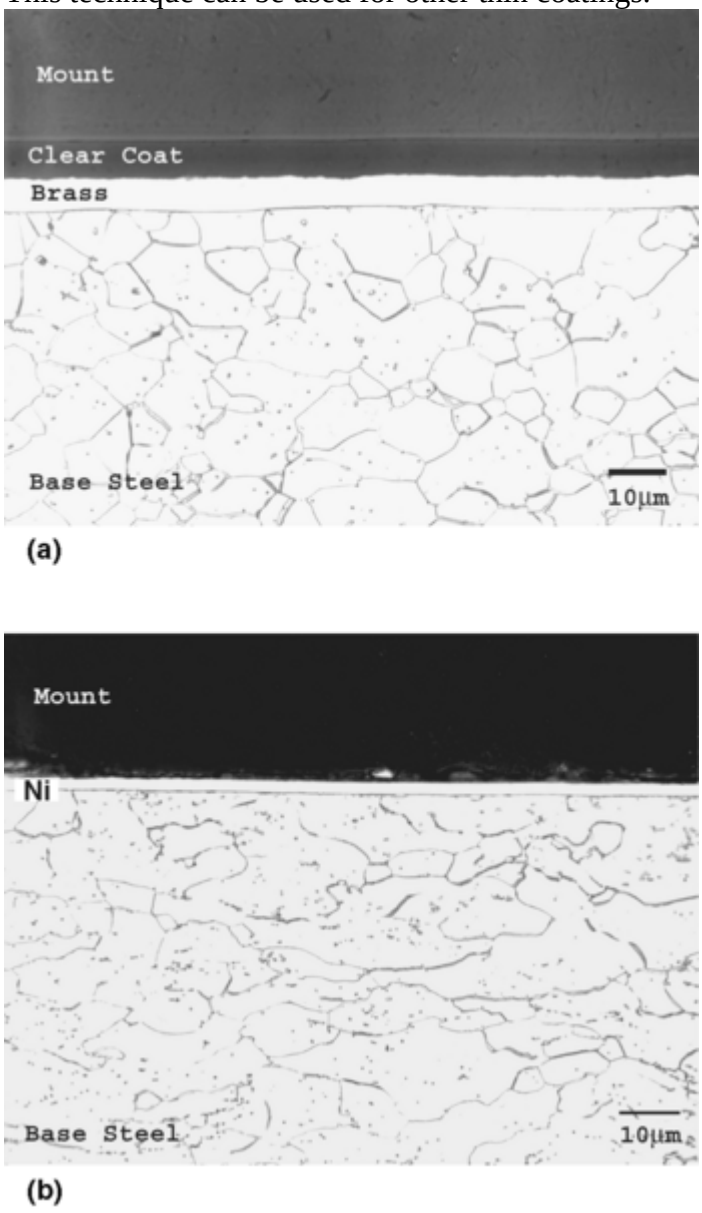

Fig. 51 (a) Microstructure of a brass coating with a clear lacquer film on a low-carbon sheet with a 45° mount. (b) Microstructure of a nickel coating on low-carbon sheet without the 45° angle. 2% nital etch. 1000×

Grinding should begin with coarse grit in order to remove the deformation caused by sectioning. Note: The deformation zone will increase as the sample thickness increases. If a certain side of interest is to be examined, it should always be facing the center of the wheel when grinding parallel to the rotation; when grinding perpendicular to rotation, the side of interest should be the leading edge. Also, on the last grinding step (600 or 800 grit), the coating should be parallel to the wheel rotation. This grinding procedure will minimize rounding of any coating.

Polishing is done on a very-low- or no-nap cloth charged with 6 μm diamond, using heavy pressure until the scratches from the last grinding step have disappeared. This usually takes 1 min. Next, polish the sample on low-nap rayon cloth with 0.3 μm aluminum oxide slurry for 2 min, using firm pressure, followed by 1 min on a low-nap rayon cloth with firm pressure with the wheel stationary. After all polishing steps, the sample is cleaned with cotton under running water, flushed with alcohol, and dried.

Etching for 10 to 20 s in 2% nital will develop sufficient contrast between the base steel and the coating.

Metallographic Preparation of Aluminum-Base Coatings. When aluminum is coated on steel, it comes under the classification of aluminized steel. The steel sheet is passed through a molten bath of the aluminum alloy. There

are generally two types of aluminized coatings: type 1, which is aluminum that contains 9% Si, and type 2, which is pure aluminum. The microstructure of types 1 and 2 aluminized sheet can be seen in Fig. 52. Both coatings have an alloy layer at the coating/steel interface that is essentially an iron aluminide intermetallic compound. In addition, type 1 aluminized steel (Fig. 52a) has particles of silicon (darker gray) in the coating.

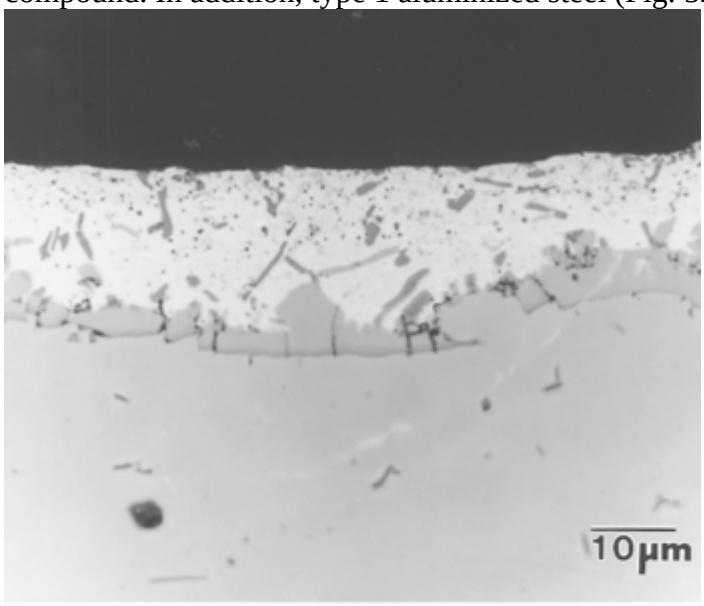

(a)

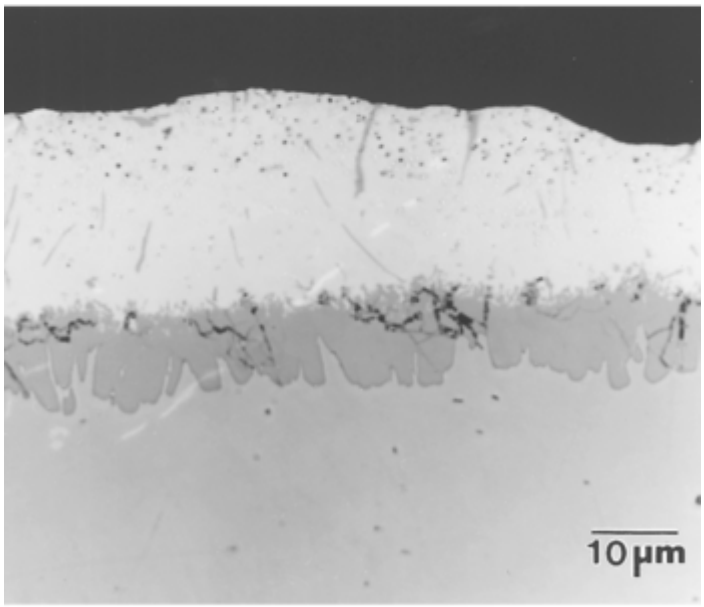

(b)

Fig. 52 Microstructure of aluminized low-carbon steel. (a) Type 1 aluminized (aluminum with 9% Si). (b) Type 2 aluminized steel. Both coatings have the alloy layer (iron aluminide intermetallic layer), and silicon particles can be seen in type 1 aluminized. 2% nital etch. 1000×

Sectioning. This type of material can be sectioned with a shear, band saw, or abrasive saw, as long as the effect of sectioning is removed during rough grinding. The sample prepared for this article was sectioned by shearing.
Mounting. When mounting in thermosetting epoxy, multiple samples are bent in an “L” shape in order for them to stand up in the mount. Place as close together as possible. Fine epoxy powder is poured on top, followed by normal-sized powder. The pressure needed to polymerize the thermosetting epoxy will push the samples closer together, thereby minimizing rounding during the polishing steps.

Grinding. Start grinding with 120-grit silicon carbide paper to remove the deformed microstructure caused by sectioning. Grind with the coated side of interest parallel to the direction of wheel rotation (coated edge facing the center of the wheel). During the next step (240 grit), the sample should be turned 90° to the previous grind, with the edge of interest as the leading edge to the rotation of the wheel. Continue for at least twice as long to remove the deformation layer caused by the silicon carbide grit of the 120-grit paper. Next, proceed to 320 grit, rotating the mount 90°, with the edge of interest again parallel to the rotation and facing the center of the wheel, and continue grinding twice as long as it took to remove the previous scratches. Then, proceed to 400 grit, rotating the mount 90°, with the edge of interest as the leading edge to the rotation of the wheel. Continue grinding for at least twice as long it took the 320-grit scratches to remove the deformation layer. For the last grinding step (with 600 grit), the sample is turned 90°, with the edge of interest again parallel and facing the center of the wheel; continue for at least twice as long as it took to remove the 400-grit scratches. Keeping the edge of interest parallel to the rotation and facing the center of the wheel, plus making the edge of interest the leading edge when grinding perpendicular to the wheel, will greatly reduce rounding. Also, on the last grinding step, the coating should be parallel to wheel rotation. Clean the sample with cotton under running water, flush with alcohol, and dry. The coating and mount should be on the same plane after the grinding step; if not, it must be corrected before polishing.

Polishing. Polish on a nylon cloth with 6 μm diamond abrasive with heavy pressure. Rotate the sample in the opposite direction to the wheel rotation (150 rpm) until the parallel scratches from the 600 grit have been removed. Clean with cotton under running water, flush with alcohol, and dry. The diamond paste remaining on the specimen can be mistaken for parallel grinding scratches; therefore, the sample must be cleaned to observe if the scratches have been removed. Next, polish with 0.3 μm alumina, using a firm pressure on a medium-nap rayon cloth for 2 min, with the wheel stationary. Clean with cotton under running water, flush with alcohol, and dry. The last step is with 0.05 μm silicon dioxide on a medium-nap rayon-cloth stationary wheel for 60 to 90 s, with firm pressure. Clean with cotton under running water, flush with alcohol, and dry. Polishing on a stationary wheel will minimize edge rounding.

Etching. In both types of aluminized steel shown in the examples, a simple 2% nital etch is generally sufficient to reveal the microstructure of the coating.

Nonmetallic Coatings

Metallographic Preparation of Enamel Coatings. Enamel coatings on steel are much different than metallic coatings. Enamel is a glass (porcelain) layer that is physically melted on the steel surface. Generally, a frit (crushed glass particles) suspended in an aqueous solution is applied to the steel surface, and the component is heated to the firing temperature, where the frit melts into a layer of glass. Some enamel coatings are applied and fired in multiple layers. Enamel coatings do not have an electrochemical problem, as found in zinc-base coatings. The coating is essentially an inert glass. The enamel coating is also harder than most metallic coatings, and usually, edge retention is not a problem. However, the enamel coating is brittle and can easily chip if the specimen is not handled properly (i.e., during sectioning).

Sectioning. Because of the brittleness of the enamel, the specimen should be sectioned with a low-speed gravity diamond saw, using mineral spirits as a cutting fluid. Align the sample in the holder so that the edge of interest is facing the blade. This will minimize damage to the coating. If a shear is used, the coating will crack and spall from the surface of the steel.

Grinding. Start grinding with 320-grit silicon carbide paper, with the coating side of interest parallel to the direction of wheel rotation and facing the center of the wheel. During the next step (400 grit), the sample should be turned 90° to the previous grind, with the edge of interest as the leading edge to the rotation of the wheel. When all the scratches from the 320-grit paper are removed, continue for at least twice as long to remove the deformation layer caused by the silicon carbide grit of the 320-grit paper. For the last grinding step (600 grit), the sample is turned 90°, with the edge of interest again parallel and facing the center of the wheel; continue for at least twice as long as it took to remove the 400-grit scratches. Clean the sample with cotton under running water, flush with alcohol, and dry. The coating and epoxy mount should be on the same plane after the grinding step.

Polishing. Polish on a nylon cloth with 6 μm diamond abrasive with heavy pressure, rotating the sample in the opposite wheel rotation (150 rpm) until the parallel scratches from the 600 grit have been removed. Clean the sample with cotton under running water, flush with alcohol, and dry. The diamond lubricant can be mistaken

for parallel grinding scratches; therefore, the sample must be cleaned to observe if the scratches have been removed.

Next, polish on a nylon cloth with 1 μm diamond abrasive for 1 min, using heavy pressure. Rotate the sample in the opposite direction of wheel rotation, which should be rotating at 150 rpm. Clean the sample with cotton under running water, flush with alcohol, and dry. Next, polish with 0.3 μm alumina abrasive with a medium-nap rayon cloth for 2 min. Use a firm pressure in a direction opposite the wheel rotation, which should be set to low speed. Clean with cotton under running water, flush with alcohol, and dry. The last step is with 0.05 μm silicon dioxide on a medium-nap rayon-cloth stationary wheel for 60 to 90 s, with firm pressure. Clean with cotton under running water, flush with alcohol, and dry.

Etching. First, etch with 4% picral to examine for carbides or pearlite. The sample can be re-etched with 2% nital to reveal the ferrite grains. If the sample is first etched in nital, grain-boundary carbides can be obscured. No etch is necessary to see the enameled coating. However, fiber optic lighting can assist in delineating the coating. Figure 53 shows a black-colored enameled steel sample prepared following this procedure. Figure 53(a) is without fiber optic lighting. The micrograph in Fig. 53(b) was taken using light from a fiber optic lamp transmitted through the transparent mount. This procedure assisted in delineating the enamel coating from the mounting material.

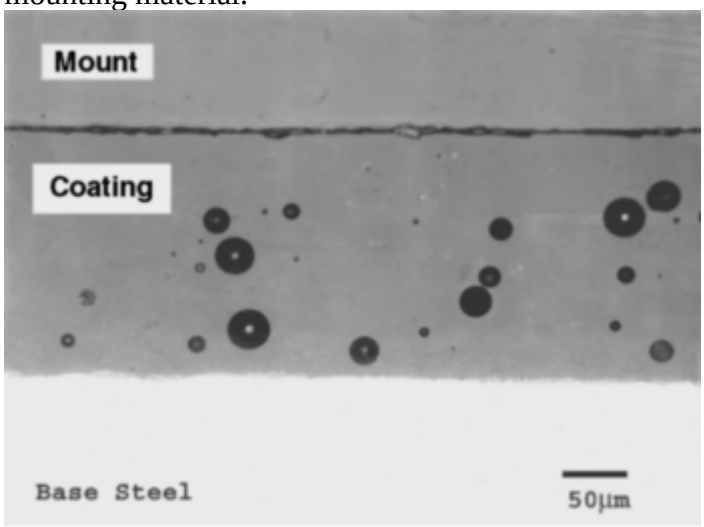

(a)

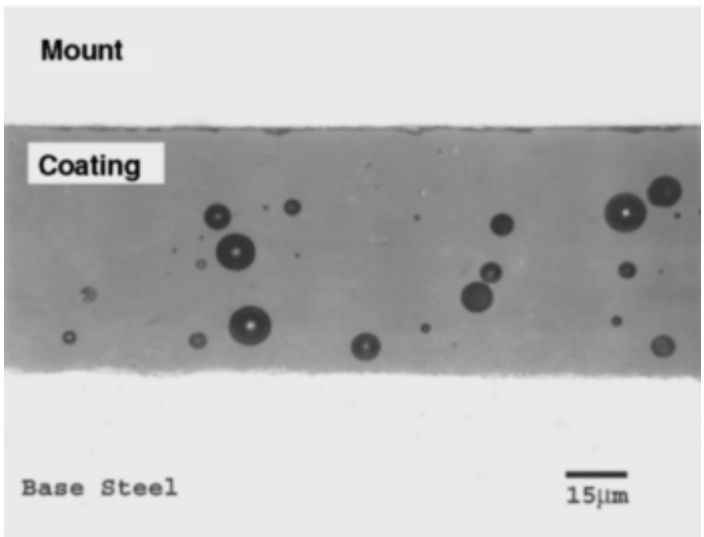

(b)

Fig. 53 Microstructure of a low-carbon sheet with a two-part enamel coating. (a) Without backlighting. (b) With backlighting through the epoxy mount to differentiate the coating from the mount. The bubbles are desired for trapping hydrogen gas.

By using dark-field illumination, coating defects and different enamel layers applied during pocessing will become apparent. Figure 54 was taken with dark-field illumination to show the ground coat. Note that dark-field illumination delineates a ground coat (first enamel layer) on the sheet. This initial coat could not be seen in the bright-field micrograph. Also, note that dark-field illumination highlights the bubbles in the enamel coating.

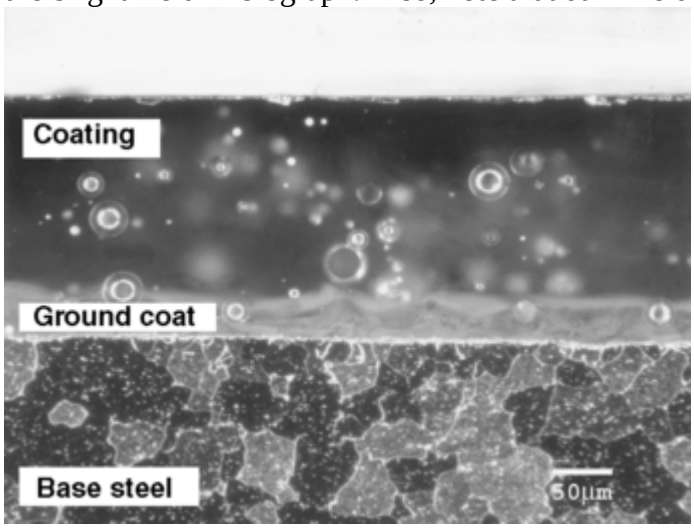

Fig. 54 Microstructure of an enamel coating, same as Fig. 53 shown with dark-field illumination to illustrate the ground coat

The steel used for enameling must have a low carbon content in order to eliminate the presence of cementite. Cementite particles on the sheet surface can decompose and react with the enamel layer to create a defect. Figure 55(b) shows a two-coat enamel coating on a low-carbon steel. The ground coat and the topcoat can both be seen in bright-field illumination, as opposed to the case shown previously. The bubbles in the enamel coating are desirable as traps for hydrogen gas. Hydrogen gas, if trapped between the steel and the coating, can expand and create a spall in the coating. This defect is called a fishscale because of its appearance. The enamel layer is usually not etched, but dark-field illumination and/or polarized light can sometimes be used to observe the structure of the enamel coating. For example, Fig. 56 shows a defect in an enamel coating on a low-carbon steel. Figure 56(a) shows the microstructure in bright-field illumination (standard illumination practice), and Fig. 56(b) shows the same field in dark-field illumination. Note the detail in the dark-field micrograph.

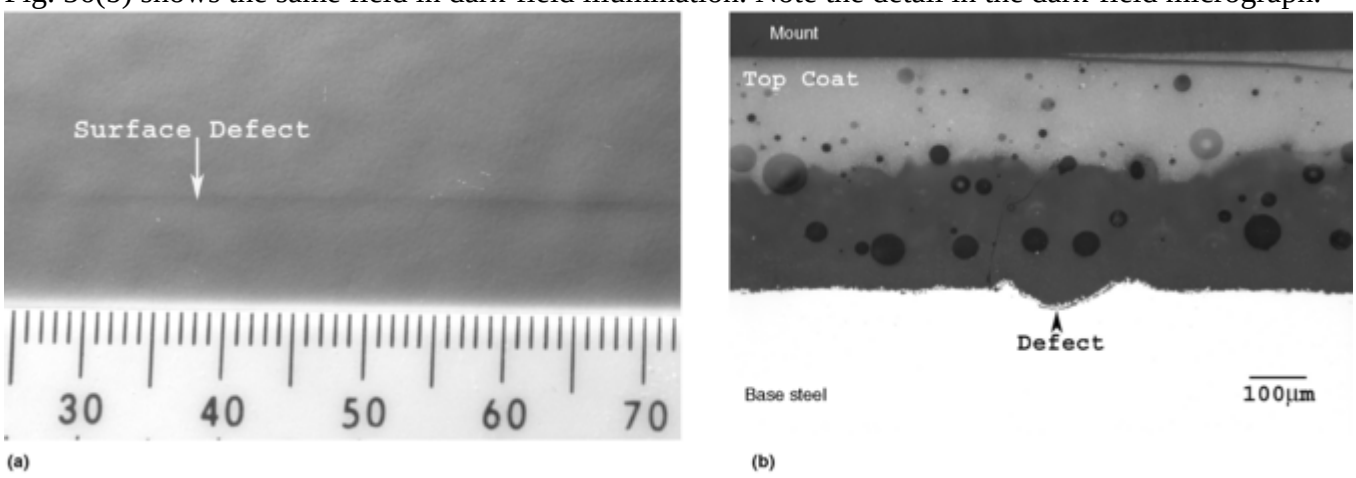

Fig. 55 Defect in an enamel coating on a low-carbon steel. (a) Defect shown through coating as a line in this macrograph (scale in mm). (b) Cause of line defect shown in (a). As-polished. 200×. Courtesy of Samuel Lawrence, International Steel Group

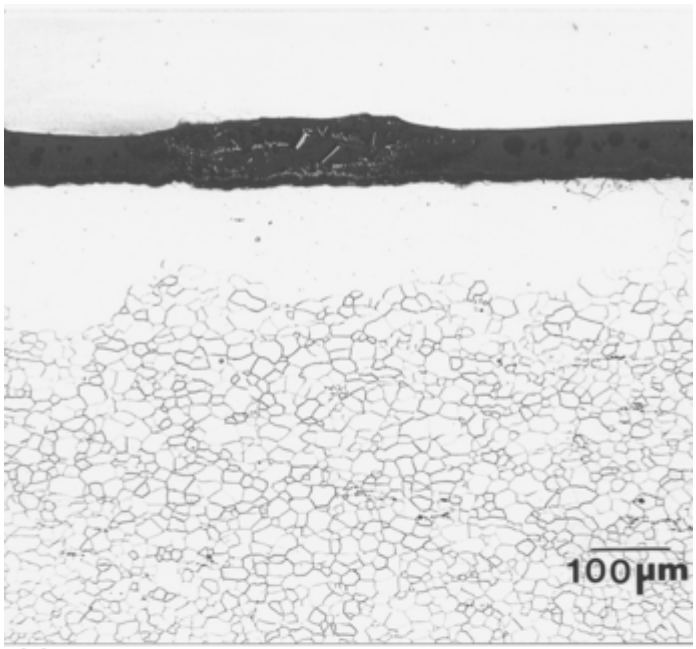

Fig. 56 Microstructure of a defect in an enamel coating on a low-carbon sheet. (a) Bright-field illumination. (b) Dark-field illumination. 2% nital etch. 100×

Metallographic Preparation of Organic (Paint) Coatings. The metallographer may encounter low-carbon steel specimens that have an organic coating such as paint. In fact, there may be multiple layers of paint. These painted specimens are prepared a little differently from specimens with metallic coatings.

Sectioning. Cutting into the painted surface is recommended; this will minimize the possibility of pulling the paint off the steel substrate. A thin-sheet specimen can also be sectioned with a tabletop hand shear.

Mounting. It is recommended to mount painted specimens in epoxy, keeping the specimens as close together as possible to prevent rounding. Making a sandwich out of the material, as described in the zinc-base coating section, will ensure good edge retention. Mounting in epoxy will not damage the paint and will allow lighting from the back-side of the mount if the paint contrast in reflected light is the same as the epoxy mount.

Grinding should begin with coarse grit in order to remove the deformation caused by sectioning. Note: The deformation zone will increase as the sample thickness increases. If a certain side of interest is to be examined,

it should always be facing the center of the wheel when grinding parallel to the rotation. When grinding perpendicular to rotation, the side of interest should be the leading edge. Also, on the last grinding step (600 or 800 grit), the coating should be parallel to the wheel rotation. This grinding procedure will minimize rounding of any coating.

Polishing is done on a very-low- or no-nap cloth charged with 6 μm diamond abrasive, using heavy pressure until the scratches from the last grinding step have disappeared. This usually takes 1 min. Next, the sample is polished on low-nap rayon cloth with 0.3 μm aluminum oxide slurry for 2 min, using firm pressure, followed by 1 min on a low-nap rayon cloth with firm pressure, with the wheel stationary. After all polishing steps, the sample is cleaned with cotton under running water, flushed with alcohol, and dried.

Etching for 10 to 20 s in 2% nital will develop sufficient contrast between the base steel and the paint. Polarized light or dark-field illumination will help separate multiple paint layers. See Fig. 57 for an example of a 0.06% C steel painted with a single layer of paint and backlighted through the back of the epoxy mount.

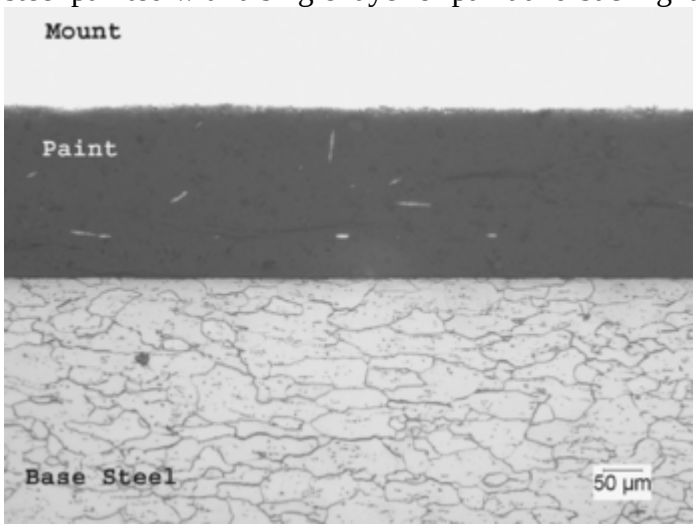

Fig. 57 Microstructure of a paint layer on a 0.06% C steel sheet, backlighted through the mount to differentiate the paint from the mount. Etched in 2% nital. 200×

References cited in this section

2. C.E. Gordan, K.M. Goggins, A.O. Benscoter, and A.R. Marder, Metallographic Preparation Technique for Hot-Dip Galvanized and Galvannealed Coatings on Steel, Mater. Charact., Vol. 31 (No. 2) 1993, p 107–114

3. E. Weidman, "Metallographic Preparation of Zinc Coatings," Application Notes, Struers, Copenhagen, 2002

A.O. Benscoter and B.L. Bramfitt, Metallography and Microstructures of Low-Carbon and Coated Steels, Metallography and Microstructures, Vol 9, ASM Handbook, ASM International, 2004, p. 588–607

Metallography and Microstructures of Low-Carbon and Coated Steels

Arlan O. Benscoter, Lehigh University; Bruce L. Bramfitt, International Steel Group, Inc.

References

1. L.E. Samuels, Metallographic Polishing by Mechanical Methods, ASM International, 2003

2. C.E. Gordan, K.M. Goggins, A.O. Benscoter, and A.R. Marder, Metallographic Preparation Technique for Hot-Dip Galvanized and Galvannealed Coatings on Steel, Mater. Charact., Vol. 31 (No. 2) 1993, p 107–114

3. E. Weidman, "Metallographic Preparation of Zinc Coatings," Application Notes, Struers, Copenhagen, 2002

A.O. Benscoter and B.L. Bramfitt, Metallography and Microstructures of Low-Carbon and Coated Steels, Metallography and Microstructures, Vol 9, ASM Handbook, ASM International, 2004, p. 588–607

Metallography and Microstructures of Low-Carbon and Coated Steels

Arlan O. Benscoter, Lehigh University; Bruce L. Bramfitt, International Steel Group, Inc.

Selected References

- E. Beraha and B. Shpigler, Color Metallography, American Society for Metals, 1977
- B.L. Bramfitt and A.O. Benscoter, The Metallographers Guide: Practices and Procedures for Irons and Steels, ASM International, 2002
- L.E. Samuels, Light Microscopy of Carbon Steels, ASM International, 1999
- G.F. Vander Voort, Metallography Principles and Practice, McGraw-Hill, 1984. Reprinted by ASM International, 1999

B.L. Bramfitt and S.J. Lawrence, Metallography and Microstructures of Carbon and Low-Alloy Steels, Metallography and Microstructures, Vol 9, ASM Handbook, ASM International, 2004, p. 608–626

Metallography and Microstructures of Carbon and Low-Alloy Steels

Bruce L. Bramfitt and Samuel J. Lawrence, International Steel Group, Inc.

Introduction

STEEL, by definition, must be at least 50% Fe and must contain one or more alloying element. These alloying elements include carbon, manganese, silicon, nickel, chromium, molybdenum, phosphorus, copper, vanadium, titanium, niobium, boron, and aluminum. In a previous article, "Metallography and Microstructures of Low-Carbon and Coated Steels," in this Volume, the metallographic practices used for low- and very-low-carbon steels (those with carbon contents generally lower than approximately 0.10% C) are discussed. This article describes the microstructure and metallographic practices used for medium- to high-carbon steels as well as low-alloy steels. Carbon steels, generally called plain carbon steels, range in carbon content from approximately 0.10% C to over 1% C. In the United States, examples of plain carbon steels are AISI/SAE 1020, 1040, and 1080. The American Iron and Steel Institute (AISI) and the Society of Automotive Engineers (SAE) developed this classification or numbering system for plain carbon, low-alloy, and stainless steels decades ago. The four-digit number describes the type of steel (three digits for stainless steel). In the three examples, the first

two digits, “10,” classify the steel as a plain carbon (nonresulfurized) steel, and the last two digits, “20,” “40,” and “80,” represent the nominal carbon content expressed in 0.01% increments of carbon. Thus, AISI/SAE 1040 steel is plain carbon steel with a nominal carbon content of 0.40% C. The Unified Numbering System (UNS) that unifies the grade codes is the joint effort of ASTM International and SAE. The UNS codes for the previously mentioned three examples are G10200, G10400, and G10800, respectively. Note that the UNS encompasses the AISI/SAE code. The AISI no longer maintains the designations. Listings of the complete composition ranges of these AISI/SAE and UNS steels can be found in the article “Classification and Designation of Carbon and Low-Alloy Steels” in Properties and Selection: Irons, Steels, and High-Performance Alloys, Volume 1 of ASM Handbook (Ref 1).

The microstructure of an as-rolled bloom of UNS G10400 steel is shown in Fig. 1. As is described later, this microstructure consists of ferrite grains (the light-appearing constituent) and pearlite (the dark-appearing constituent). The interesting feature of this microstructure is the ferrite formed on the original or prior-austenite grain boundaries during cooling from austenite. Ferrite in this form is called proeutectoid ferrite and is described later in this article. Figure 2 shows the microstructure of an as-rolled UNS G10150 steel plate. The microstructure also consists of ferrite and pearlite but is mostly ferrite with a small volume fraction of pearlite (dark-appearing constituent). The ferrite in this form is called equiaxed ferrite. The lower volume fraction of pearlite indicates that this steel has a much lower carbon content than the UNS G10400 steel shown in Fig. 1.

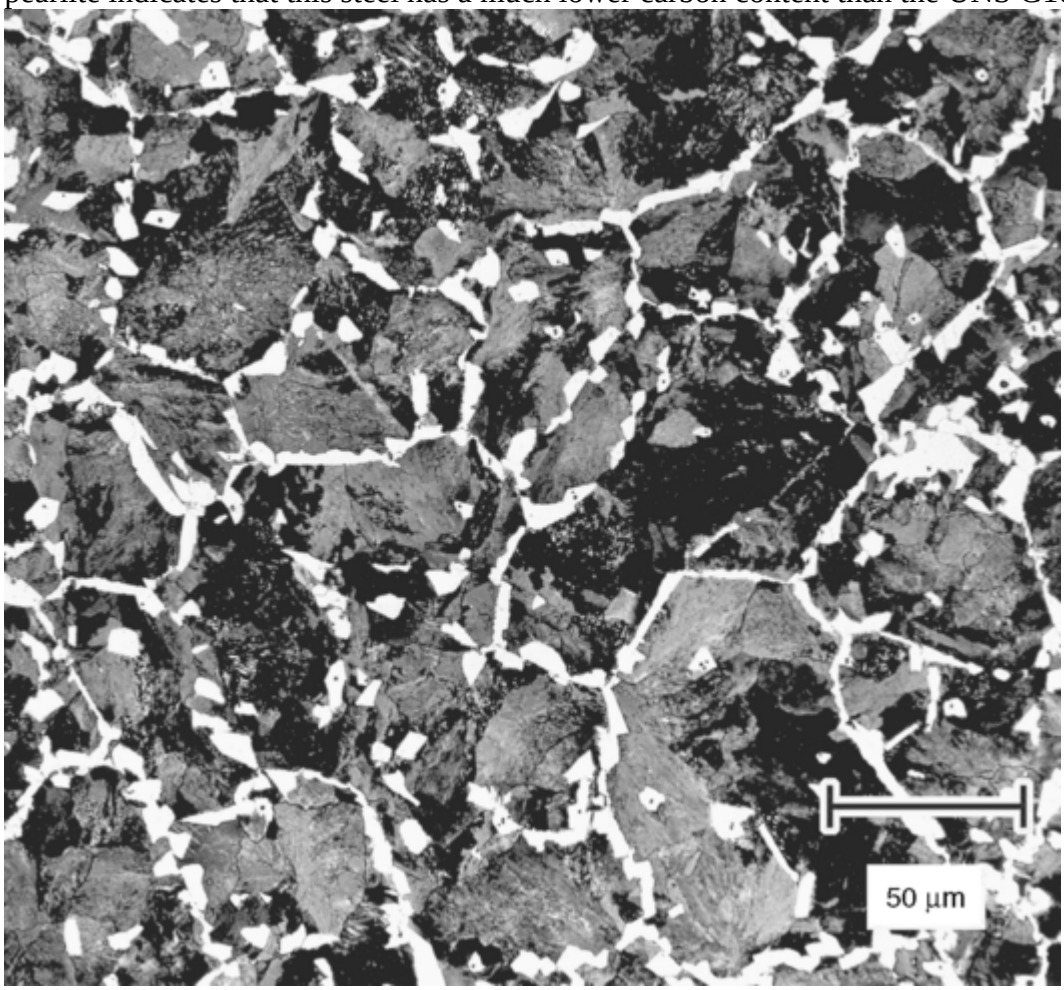

Fig. 1 Microstructure of plain carbon UNS G10400 steel showing equiaxed proeutectoid ferrite grains outlining the prior-austenite grain boundaries. The matrix is pearlite (dark etching constituent). 4% picral etch. Original magnification 200×

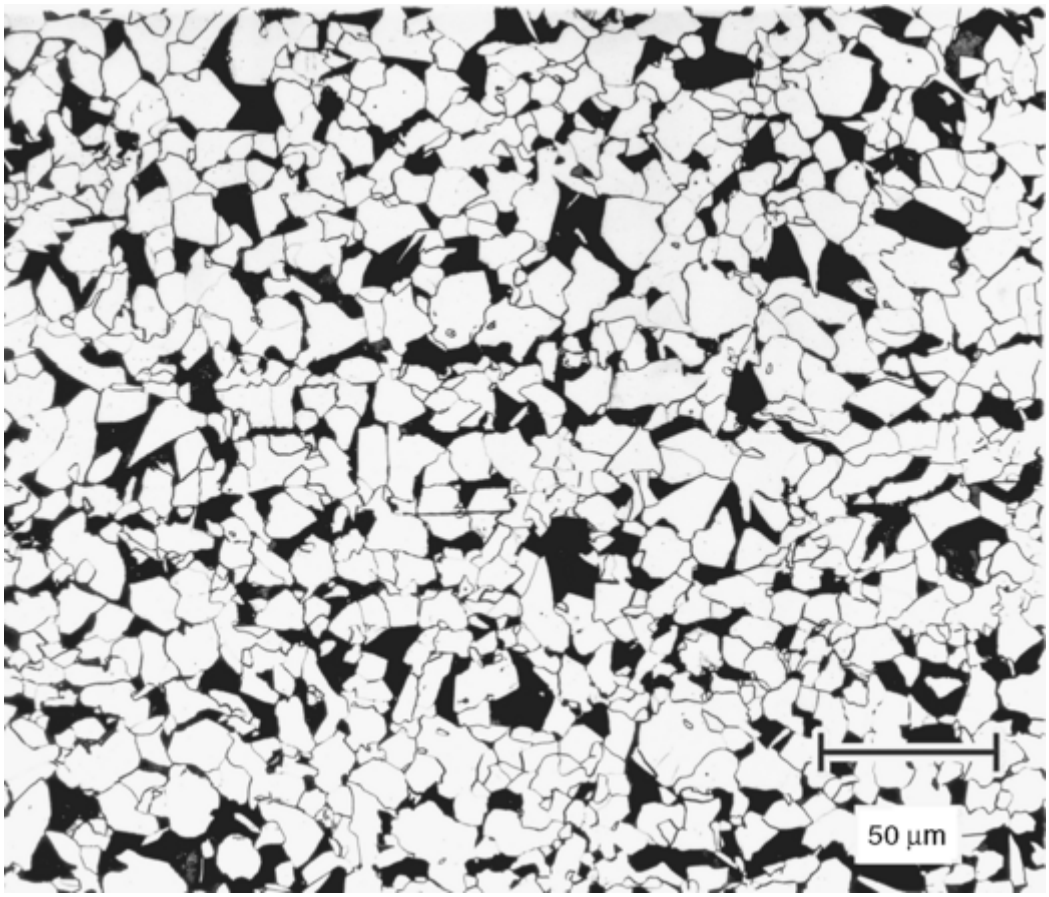

Fig. 2 Microstructure of plain carbon UNS G10150 steel showing equiaxed ferrite grains with pearlite islands. 4% picral + 2% nital etch. Original magnification 200×

Low-alloy steels are differentiated from alloy steels by having a total alloy content less than approximately 8%. Common examples of low-alloy steels are UNS G41300, G52986, G43400, and G86200. The letter “G” designates standard carbon and alloy steels. Following the AISI/SAE practice, the first two digits describe the class of steel, and the next two digits describe the nominal carbon content. The UNS 41xxx-series of low-alloy steels are chromium-molybdenum steels, the UNS 86xxx- and 43xxx-series are nickel-chromium-molybdenum steels, and the UNS 52xxx-series are chromium steels. G41300 contains 0.30% C, G52986 is 0.98 to 1.1% C, G43400 contains 0.40% C, and G86200 contains 0.20% C. (It was necessary at times to deviate from this system.) The microstructure of heat treated UNS G43400 steel is shown in Fig. 3. This microstructure is a mixture of martensite and bainite (dark constituent). These constituents are discussed later.

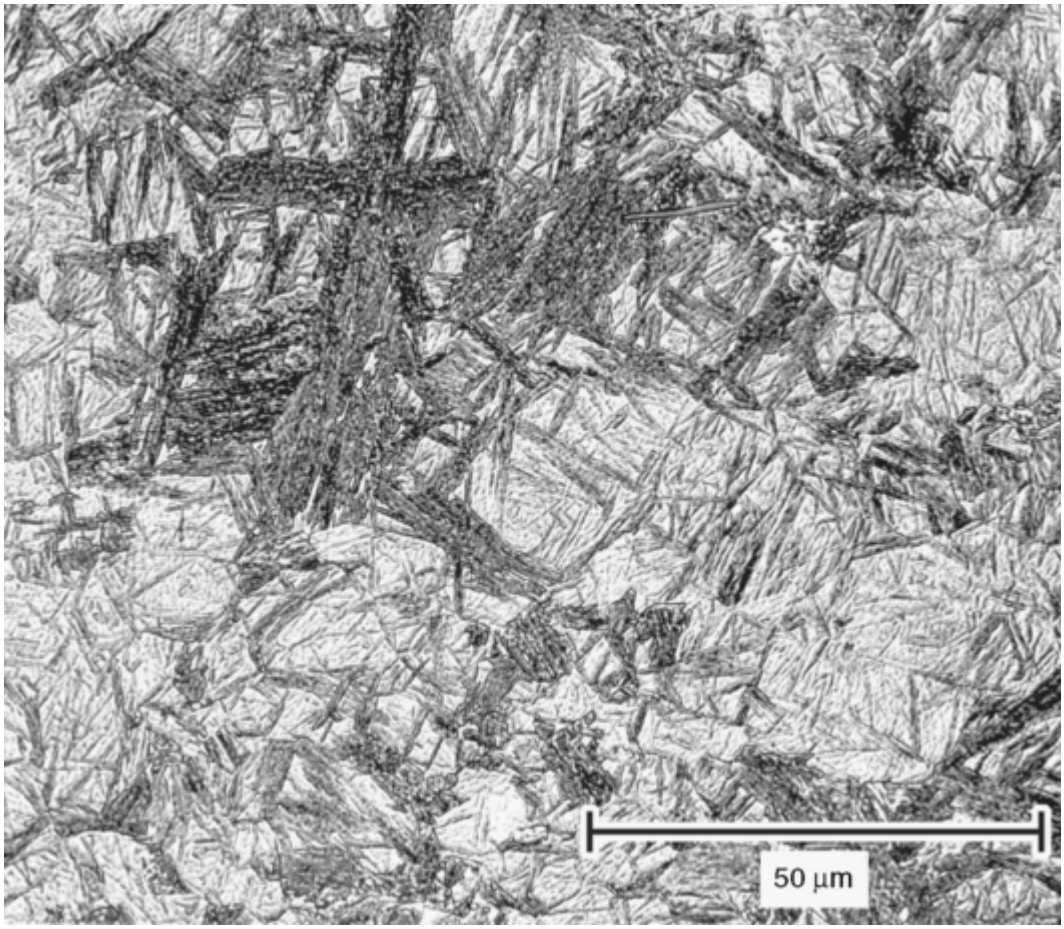

Fig. 3 Microstructure of quenched and tempered low-alloy UNS G43400 steel showing a mixture of bainite (dark etching constituent) and martensite (lighter gray). 4% picral + 2% nital etch. Original magnification 500×

Other classes of low-alloy steels include the high-strength, low-alloy (HSLA) steels. These HSLA steels contain vanadium, niobium, and/or titanium. These elements are referred to as microalloying elements because only small amounts of them are required, and the steels are called microalloyed steels. These are very popular high-strength steels that are used in a vast number of applications, including automobile frames, gas transmission pipelines, ship plate, bridge beams, and electrical power transmission poles. The microstructure of microalloyed HSLA steel is shown in Fig. 4. Although this microstructure is ferrite and pearlite, note how it differs from the plain carbon steels shown in Fig. 1 and 2. First of all, the carbon content is lower in the microalloyed steel, and thus, the pearlite content is lower. Second, the ferrite grain size is much smaller, and third, there is an elongated nature of the pearlite. This elongated morphology is called banding. The fine grain size and pearlite bands are the result of the thermomechanical processing of this microalloyed steel. Normal hot rolling involves rolling the steel at high temperatures, which produces a fairly coarse ferrite grain size (e.g.,Fig. 2). On the other hand, a microalloyed steel (Fig. 4) is rolled at much lower temperatures, generally at temperatures below what is called the recrystallization stop temperature, resulting in fine ferrite grains and an elongated microstructure. More about these steels can be found in Ref 1, 2, and 3.

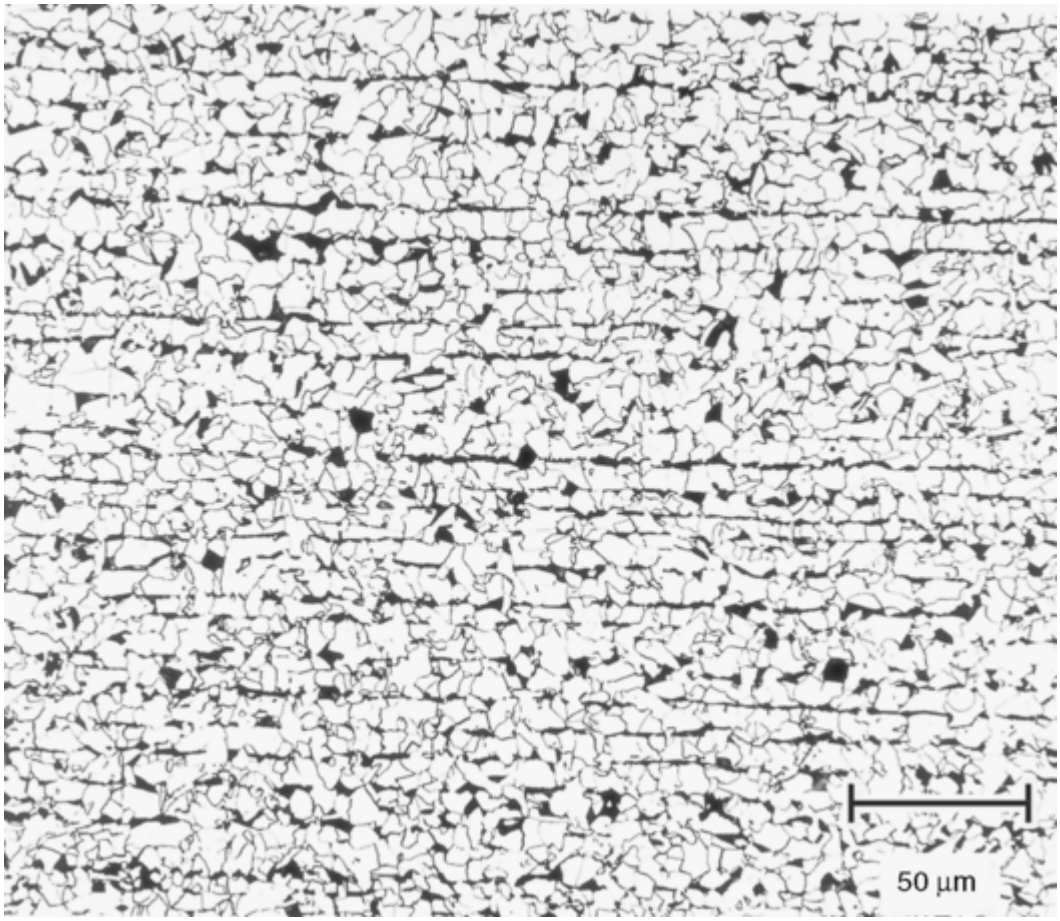

Fig. 4 Microstructure of an as-rolled microalloyed steel plate showing equiaxed ferrite grains with bands. Note the fine ferrite grain size when compared with Fig. 2. 4% picral + 2% nital etch. Original magnification 200×

It must be remembered that not only the composition but also the microstructure of these plain carbon and low-alloy steels is of importance in determining the properties of a particular steel product. The microstructure of these steels can be quite complex and can exhibit variations of the main constituents: ferrite, cementite, pearlite, bainite, and martensite. Some of the low-alloy steels may contain retained austenite. These microstructural constituents are subsequently described in brief. There are a number of references available that provide detailed information on these microstructural constituents and how they are developed by thermomechanical processing and heat treatment (Ref 2, 3, 4, 5).

References cited in this section

1. Properties and Selection: Irons, Steels, and High-Performance Alloys, Vol 1, ASM Handbook, ASM International, 1990

2. G. Krauss, Steels: Heat Treatment and Processing Principles, ASM International, 1990

3. C.R. Brooks, Principles of the Heat Treatment of Plain Carbon and Low-Alloy Steels, ASM International, 1996

4. B.L. Bramfitt, Annealing of Steel, Heat Treating, Vol 4, ASM Handbook, ASM International, 1991, p 43

5. B.L. Bramfitt and A.O. Benscoter, Metallographer's Guide: Practices and Procedures for Irons and Steels, ASM International, 2002

B.L. Bramfitt and S.J. Lawrence, Metallography and Microstructures of Carbon and Low-Alloy Steels, Metallography and Microstructures, Vol 9, ASM Handbook, ASM International, 2004, p. 608–626

Metallography and Microstructures of Carbon and Low-Alloy Steels

Bruce L. Bramfitt and Samuel J. Lawrence, International Steel Group, Inc.

Microstructural Constituents

Before describing the various constituents found in the microstructure of plain carbon and low-alloy steels, it is appropriate to provide some background on the physical metallurgy of these steels. The best way to understand the metallurgy is to examine the iron-carbon binary phase diagram (this is actually the iron-cementite diagram). A portion of this diagram that relates to steels is shown in Fig. 5 (more details of this diagram can be found in Ref 2, 3, 4, 5). It represents the phases that exist in the steel with respect to carbon content (up to 2.2%) and temperature (up to 1150 °C, or 2100 °F). Although the diagram is for equilibrium conditions, it can be roughly applied to steels that are annealed or have microstructures that have been cooled very slowly from an elevated temperature. However, this diagram cannot be used for steels that have been cooled quickly by quenching in water or oil, because the constituents (bainite and martensite) that develop are not represented on this diagram. From the diagram, the elevated temperature phase of steel is austenite. It is also called gamma (γ) iron and has a face-centered cubic crystal structure. Iron-carbon alloys exist as 100% austenite above the "V"-shaped lines labeled A_3 and A_{cm} and exist as mixtures of austenite and ferrite or austenite and cementite at temperatures between these lines and above the vertical line labeled A_1. Ferrite, also called alpha (α) iron, has a body-centered cubic crystal structure and transforms from austenite on cooling between the A_3 and A_1 temperatures. However, above 0.77% C, austenite transforms to cementite on cooling between the A_{cm} and A_1 temperatures. Cementite is iron carbide (Fe_3C) with an orthorhombic crystal structure. An important feature of the diagram is the reaction that takes place at 0.77% C. At this point, austenite transforms (reacts) to create pearlite (see the dotted vertical line in Fig. 5). The reaction is called a eutectoid reaction, and pearlite is a defined mixture of both ferrite and cementite. Thus, a steel with a specific carbon content, for example, 0.40% C, cooled from austenite will begin to transform to ferrite at the A_3 temperature of 780 °C (1435 °F), and then the remaining austenite transforms to pearlite once the A_1 temperature at 727 °C (1341 °F) is crossed. The ferrite that forms is called proeutectoid ferrite because it forms before the eutectoid reaction ("pro" meaning before). On the other side of the diagram, cementite will form as proeutectoid cementite. All steels below 0.77% C are called hypoeutectoid steels, and all steels above 0.77% C are called hypereutectoid steels ("hypo" meaning less than and "hyper" meaning more than). Thus, slow-cooled hypoeutectoid steels are mixtures of proeutectoid ferrite and pearlite, and slow-cooled hypereutectoid steels are mixtures of proeutectoid cementite and pearlite. Examples of these microstructures are shown as follows.

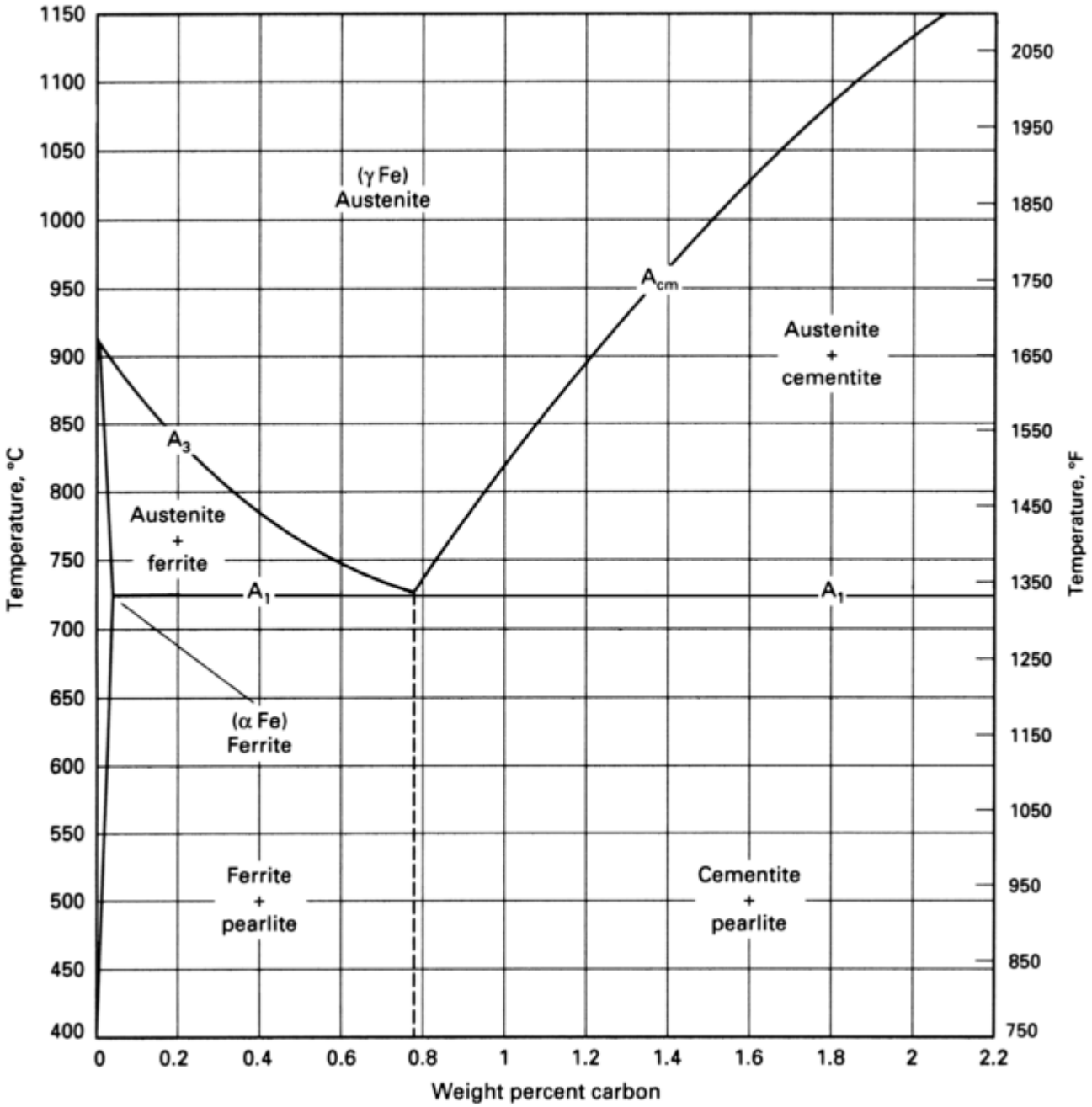

Fig. 5 The iron-carbon binary phase diagram. Source: Ref 4

Also discussed subsequently are constituents that do not appear on the iron-carbon equilibrium diagram. These are bainite and martensite, which form at faster cooling rates and thus are not represented by the equilibrium conditions of the iron-carbon diagram. However, microstructures with these constituents also can have proeutectoid ferrite or proeutectoid cementite present, and these steels are still considered hypoeutectoid or hypereutectoid, depending on the carbon content.

Ferrite is a constituent found in most as-rolled and annealed plain carbon steels with carbon contents less than approximately 0.77%. Examples of ferrite have already been seen in Fig. 1, 2, and 4. Ferrite is considered a phase because it consists of a single constituent. In the iron-carbon equilibrium diagram shown in Fig. 5, there is a field where 100% alpha iron (ferrite) exists on the far left side of the diagram below 910 °C (1670 °F). Ferrite is practically pure iron, having a carbon content less than 0.005% at room temperature (note that the alpha iron field is restricted at the bottom left corner of the iron-carbon diagram). Because the plain carbon steels shown previously have carbon contents well above 0.005%, the excess carbon appears as a constituent called pearlite (the dark etching constituent), which is described next. The excess carbon can also appear as cementite (iron carbide) particles, which are generally found in low-carbon steels (see the article “Metallography and Microstructures of Low-Carbon and Coated Steels” in this Volume). Ferrite can appear in

different forms or morphologies. In most as-rolled and annealed steels, it is equiaxed ferrite, which means that the dimensions of the grains of ferrite are approximately equal in all three axes. Equiaxed ferrite is shown in Fig. 1 and 4. Ferrite also can be seen at prior-austenite grain boundaries and is called grain-boundary ferrite or proeutectoid ferrite. Proeutectoid ferrite decorating prior-austenite grain boundaries can be seen in Fig. 6 (also seen in Fig. 1). The UNS G10400 steel in Fig. 6 has a very coarse prior-austenite microstructure that resulted from heating the steel to an excessively high temperature. Ferrite can also appear as needles. This form, called acicular ferrite, can be seen in Fig. 7. Acicular ferrite nucleates on prior-austenite grain boundaries, and these proeutectoid ferrite needles are called allotriomorphs. When needlelike ferrite forms a pattern similar to that shown in Fig. 8, it is called Widmanstätten ferrite, because it resembles the macrostructural features of meteorites first studied by 19th century Austrian museum curator Alois von Widmanstätten. These structures are usually the result of having a starting microstructure of very coarse austenite grain size.

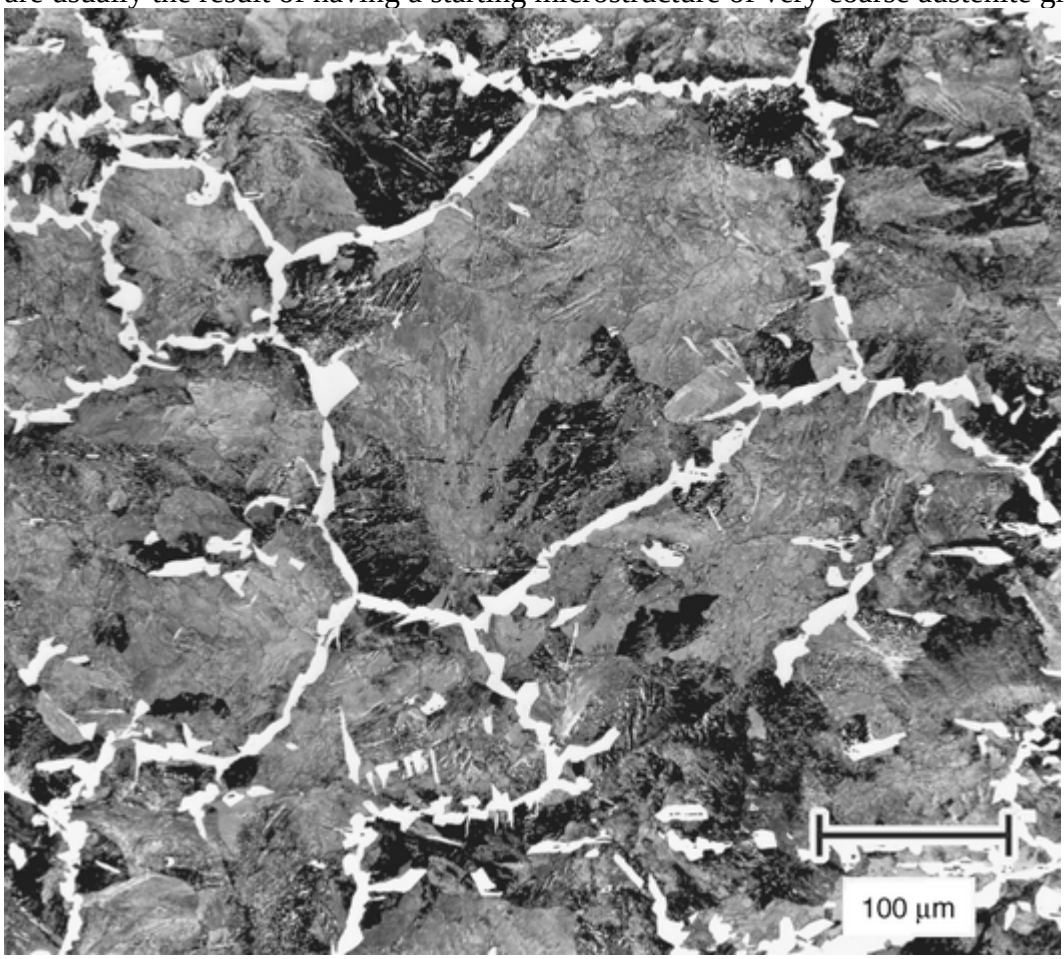

Fig. 6 Microstructure of coarse-grain plain carbon UNS G10400 steel showing a proeutectoid network of ferrite outlining the prior-austenite grain boundaries. The matrix is pearlite (dark etching constituent). 4% picral etch. Original magnification 100×

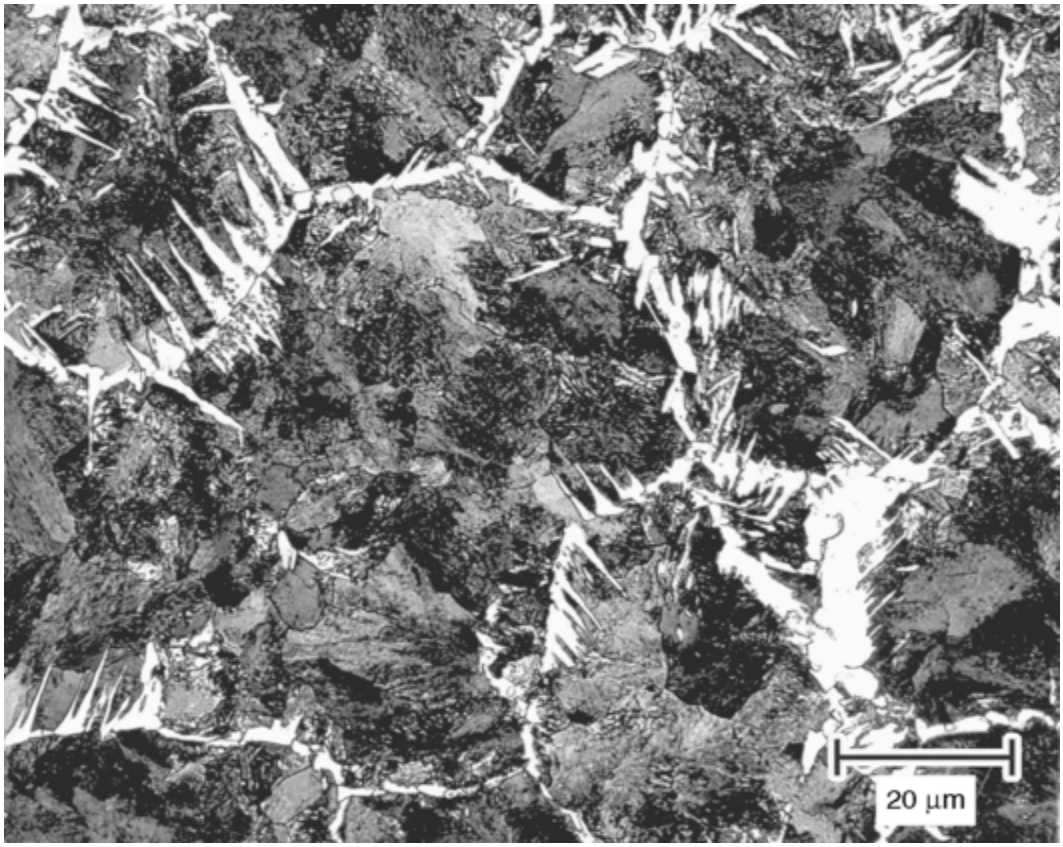

Fig. 7 Microstructure of plain carbon UNS G10400 steel showing acicular ferrite grains at the prior-austenite grain boundaries. This form of ferrite is different than that seen in Fig. 6. The matrix is pearlite (dark etching constituent). 4% picral etch. Original magnification 500×

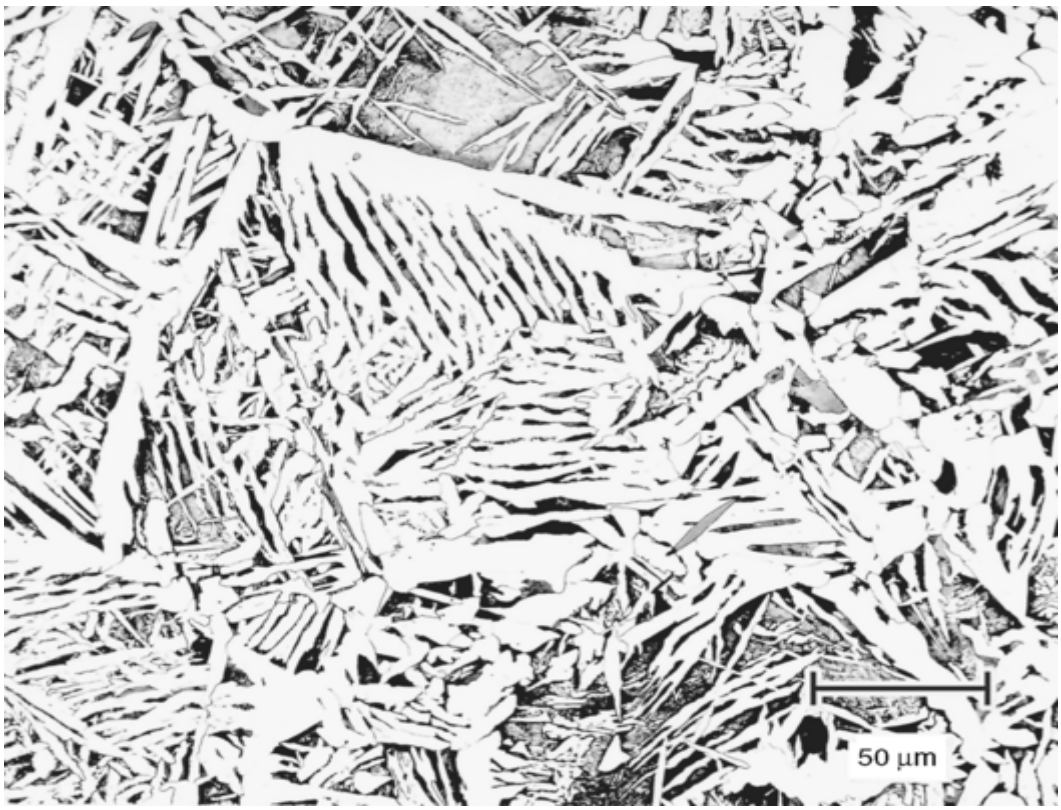

Fig. 8 Microstructure of plain carbon UNS G10200 steel showing acicular ferrite with some pearlite (dark etching constituent). This type of acicular appearance is called Widmanstätten structure. 4% picral etch. Original magnification 500×

With all these forms, ferrite is the most common constituent in plain carbon and low-alloy steels. Because ferrite contains very little carbon, it is very soft when compared with the other constituents described as follows.

Cementite is a hard iron carbide phase (Fe_3C) that is found in many low-carbon steels, as described in the article “Metallography and Microstructures of Low-Carbon and Coated Steels” in this Volume. However, it is a constituent found in plain carbon and low-alloy steels that have been spheroidized. An example of cementite in spheroidized steel is seen in Fig. 9. Here, cementite appears as rounded (spheroidal) particles of iron carbide in a matrix of ferrite. The spheroidized cementite in Fig. 9 resulted from heat treating UNS G10400 steel (like that shown in Fig. 1) at a temperature just below the A_1 in Fig. 5 for several hours. In this process, the platelike cementite in the pearlite constituent breaks down to form new rounded particles. Note that the ferrite grain boundaries in this microstructure (Fig. 1) are not delineated. This is because the metallographer chose to expose only the cementite by using a 4% picral etchant that highlighted the carbide particles but did not attack the ferrite. Etching procedures are covered in detail later in this article.

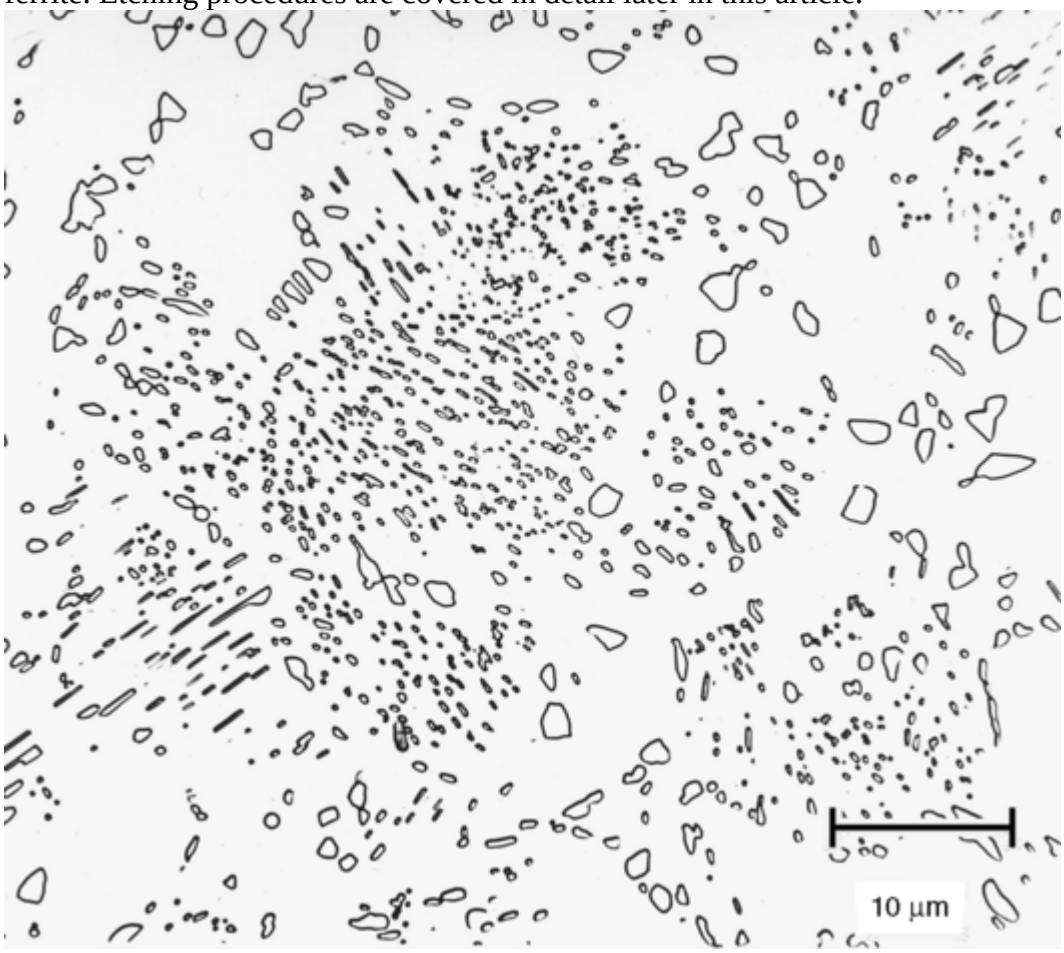

Fig. 9 Microstructure of UNS G10400 steel in the spheroidized condition where the cementite (carbides) appears as rounded particles. Alloy was heat treated for several hours just below the A_1 temperature (Fig. 5). 4% picral etch. Original magnification 1000×

Cementite can also appear as proeutectoid cementite in steels with carbon contents above approximately 0.77%. An example of proeutectoid cementite in a 1.2% C alloy is seen in Fig. 10. As in the case of proeutectoid ferrite (Fig. 1, 6, and 7), the proeutectoid cementite has also formed on the prior-austenite grain boundaries. There are also cementite needles extending across the pearlite colonies in Fig. 10. These are an allotriomorphic form of cementite. This microstructure is very undesirable, because the continuous network of cementite at the austenite grain boundaries and the cementite needles render the steel very brittle and unsuitable for most applications.

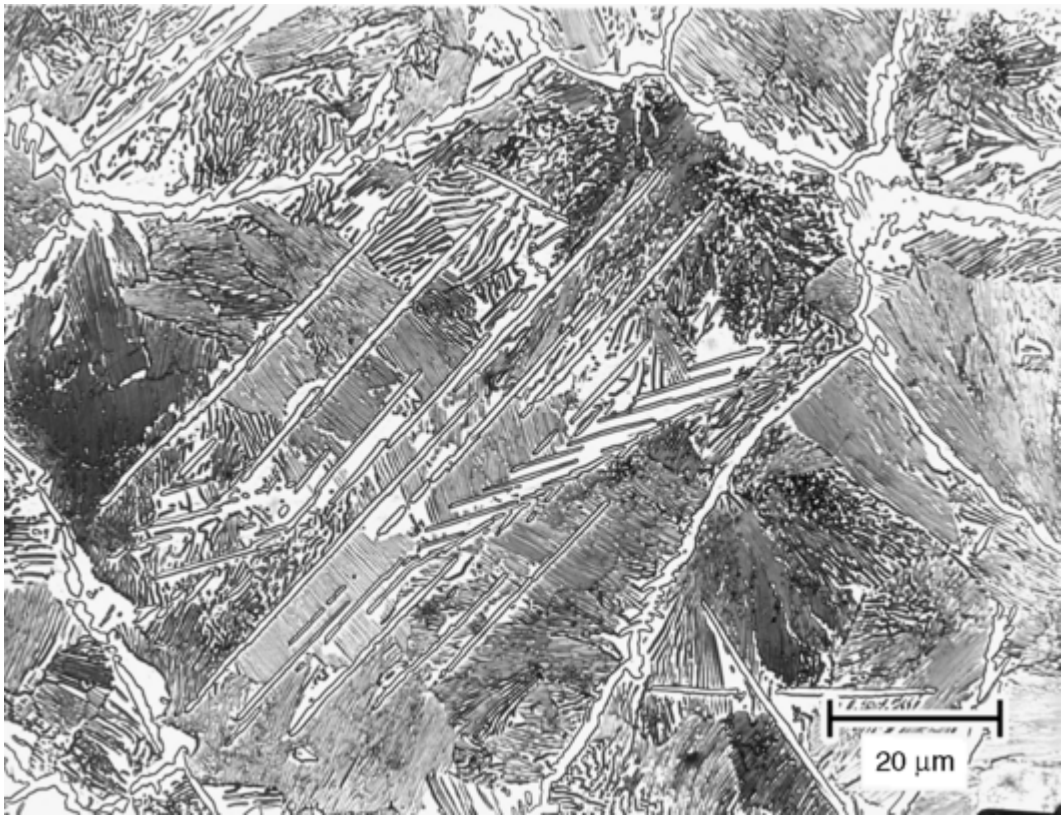

Fig. 10 Microstructure of 1.2% C-Fe alloy showing cementite outlining the prior-austenite grain boundaries and cementite needles in the grains of pearlite. The grain-boundary cementite is called proeutectoid cementite. This microstructure represents a hypereutectoid steel. 4% picral etch. Original magnification 200×

Pearlite is another common constituent in plain carbon and low-alloy steels and consists of two phases: ferrite and cementite. The ferrite and cementite phases form a platelike lamellar morphology. Examples of pearlite in hypoeutectoid steels have already been seen in Fig. 1, 2, . 4, 6, 7, 8, and 10. The pearlite appears dark in these microstructures, because the etchant attacked the ferrite phase in the pearlite, leaving the cementite phase untouched. In a metallurgical microscope, the incident beam of light was scattered (reflected) away from the microscope objective, and the area is perceived as dark. When resolved at higher magnification in the light microscope, pearlite consists of alternating plates of ferrite and cementite, as shown in Fig. 11. Many colonies of pearlite are shown in this micrograph. A colony represents a single orientation of the pearlite lamella. Often, it is very difficult to resolve the true structure of pearlite in the light microscope. However, when viewed at a higher magnification in the scanning electron microscope (SEM), the platelike morphology is more clearly seen (Fig. 12, 13). In these heavily etched specimens, the cementite plates are evident, because the ferrite between the plates has been dissolved by the etching solution. More details on these steels can be found in Ref 2, 3, 4, and 5.

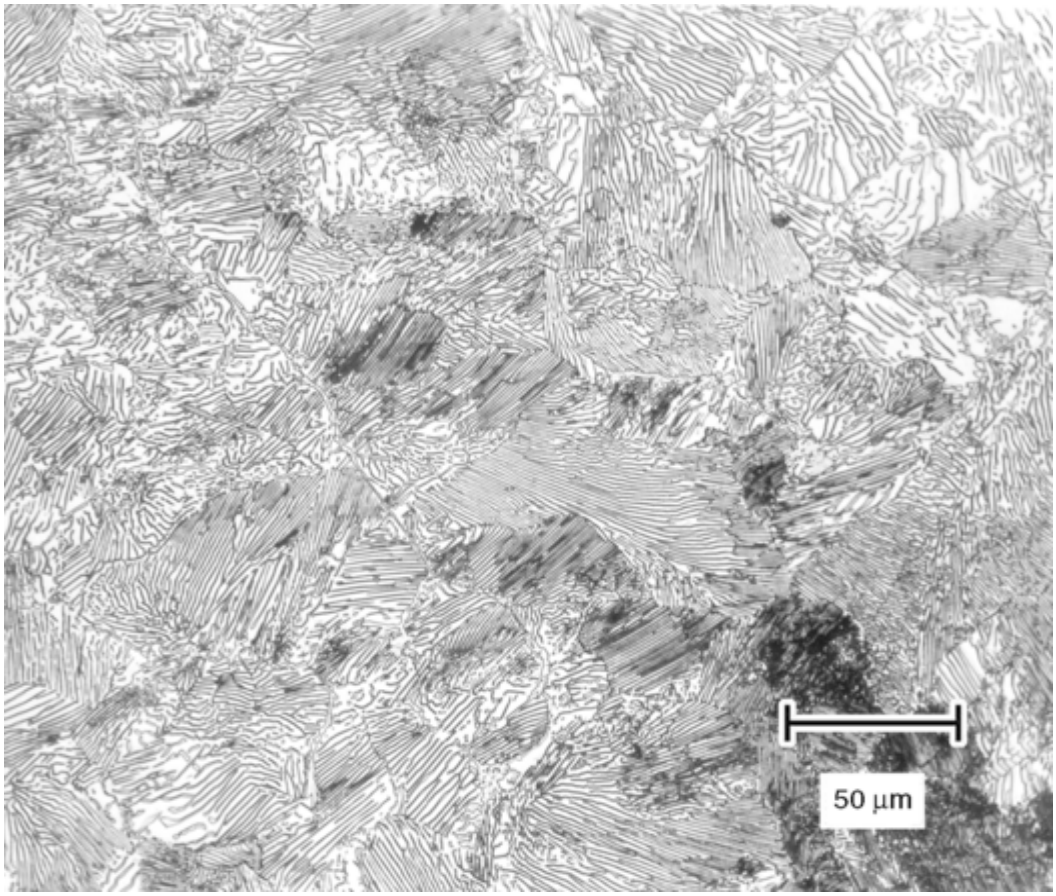

Fig. 11 Microstructure of plain carbon UNS G10800 steel showing colonies of pearlite. 4% picral etch. Original magnification 200×



Fig. 12 Microstructure of pearlite colonies in plain carbon UNS G10800 steel taken in the scanning electron microscope. 4% picral etch. Original magnification 2000×

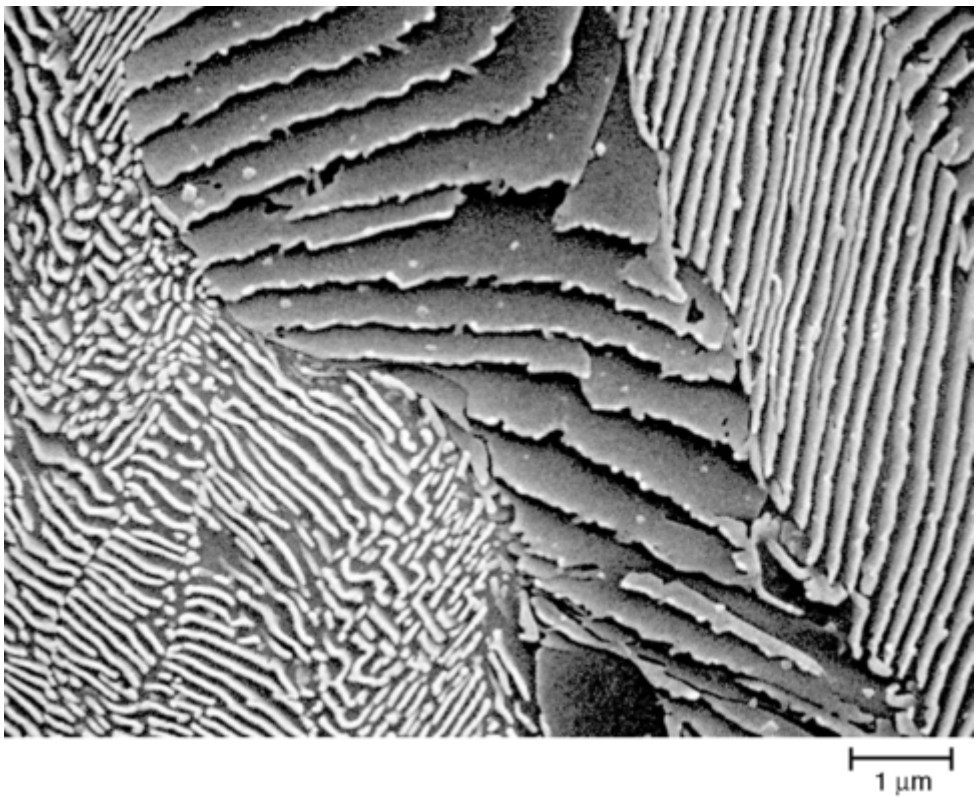

Fig. 13 Microstructure of pearlite colonies in plain carbon UNS G10800 steel taken in the scanning electron microscope. The plates of cementite are clearly revealed. 4% picral etch. Original magnification 10,000×

Bainite is also a constituent that consists of two phases: ferrite and cementite. The appearance of bainite (Fig. 14), which forms at much faster cooling rates than pearlite, is totally different than pearlite. Unfortunately, bainite can have vastly different morphologies. Classic bainites are called either upper bainite or lower bainite, because they form at higher (upper bainite) or lower (lower bainite) temperatures during transformation from austenite. Bainite, if viewed at high magnification, will appear as needles or laths of ferrite, with carbides at the lath boundaries (upper bainite) or within the laths themselves (lower bainite). Figure 15 shows upper bainite as observed in a transmission electron microscope (TEM). The specimen was a thin foil of a low-alloy steel. In the TEM, the electrons can penetrate the thin foil, and thus, the specimen becomes transparent. In this micrograph, cementite (dark particles) forms on the ferrite lath boundaries. Lower bainite, as observed in a thin foil in the TEM, is shown in Fig. 16. In this case, the carbide phase has formed within the ferrite laths at a discrete angular orientation. A similar view of lower bainite can be seen in the TEM from a surface replica (Fig. 17). This technique is detailed in the article “Transmission Electron Microscopy” in this Volume. Surface replicas are produced by coating the etched specimen surface with a carbon film (or other deposited material) and stripping the carbon film from the specimen surface. The film is usually shadowed with a heavy element such as gold to enhance the image and then placed on a copper grid and examined in the TEM. The actual specimen surface is not examined but a replica of the surface features. Unfortunately, for the metallographer using a light microscope, these subtle differences on the bainite cannot be seen; however, upper bainite has a coarser morphology than lower bainite.

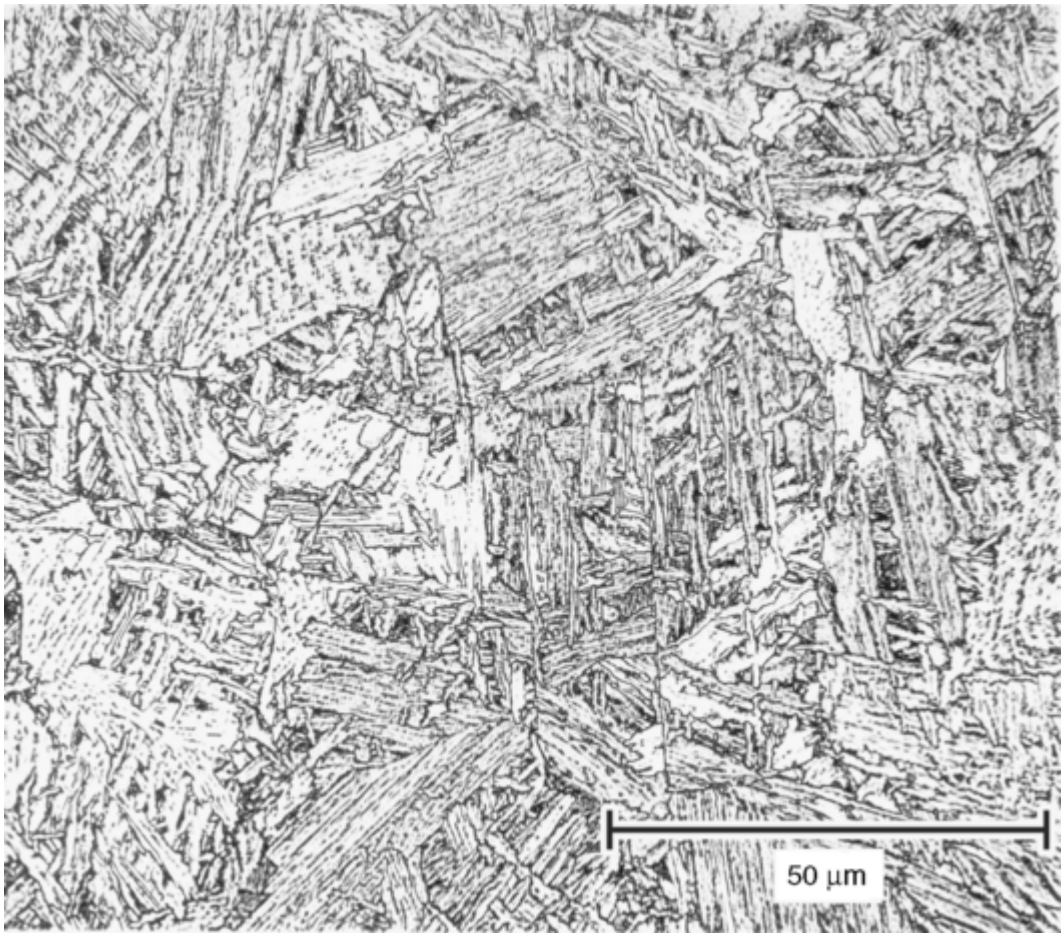

Fig. 14 Microstructure of heat treated low-alloy steel showing bainite. 4% picral + 2% nital etch. Original magnification 500×

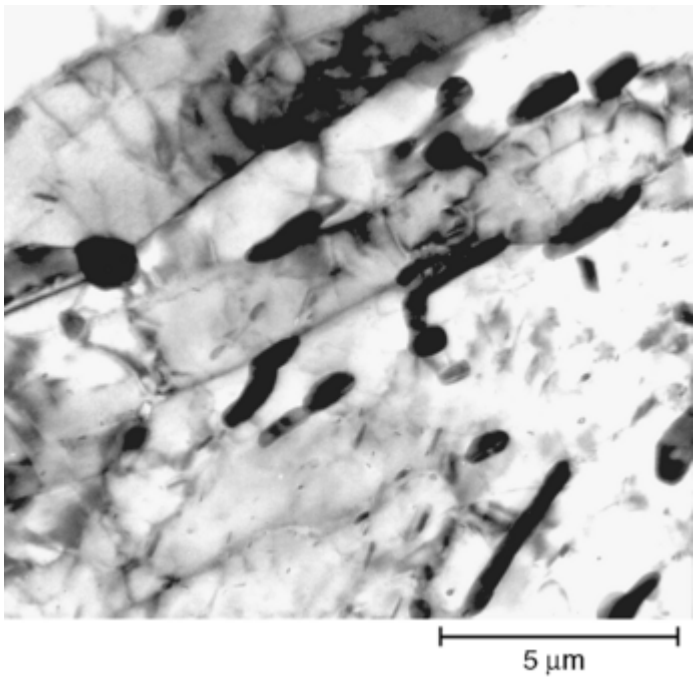

Fig. 15 Microstructure of upper bainite as seen in the transmission electron microscope. Note the carbides in the ferrite lath boundaries. Thin foil. Original magnification 5500×

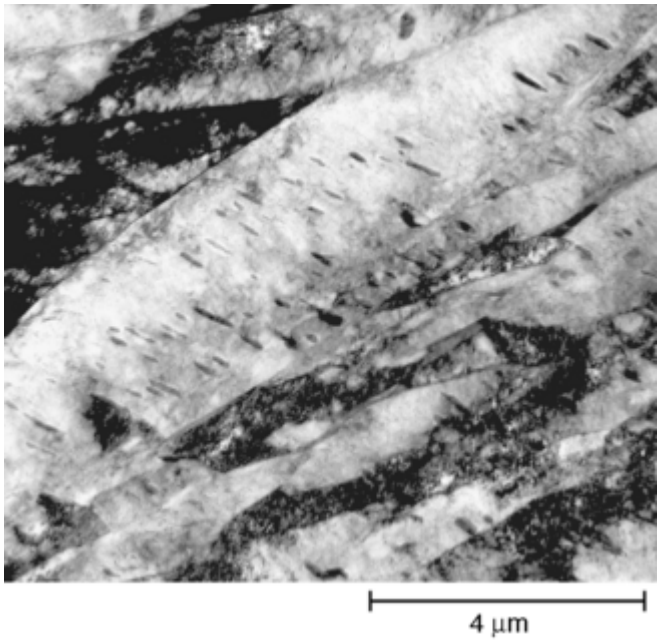

Fig. 16 Microstructure of lower bainite as seen in the transmission electron microscope. Note the carbides at a discrete angular orientation within the ferrite laths. Thin foil. Original magnification 8000×

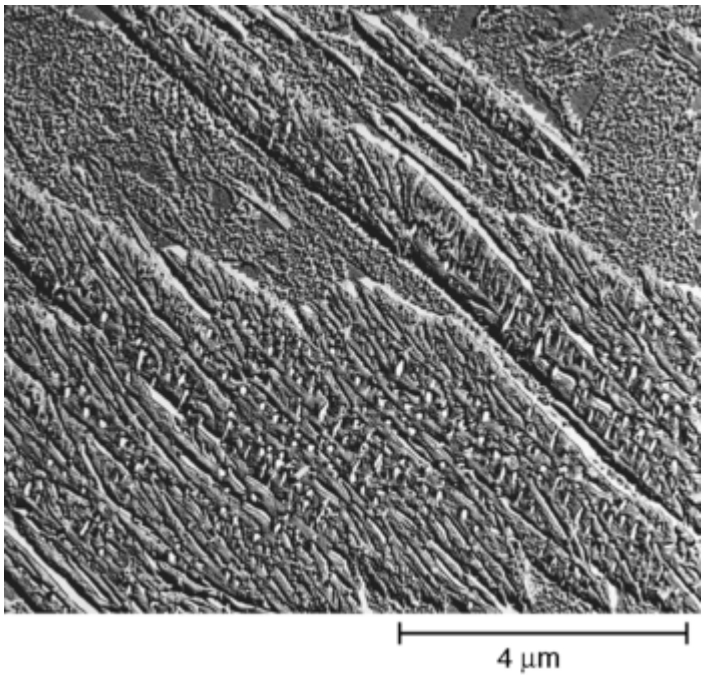

Fig. 17 Microstructure of lower bainite as seen in a carbon replica examined in the transmission electron microscope. As in Fig. 16, the carbides are at a discrete angular orientation within the ferrite laths. Original magnification 8000×

An unusual form of bainite is granular bainite (Fig. 18). Granular bainite consists of ferrite with islands of martensite and retained austenite, called M-A constituent. Granular bainite does not usually contain cementite, as in upper and lower bainite (it may contain regions of pearlite). It is called granular bainite because it has a somewhat granular appearance. However, granular bainite should not be called a bainite, because the ferrite phase lacks the lathlike morphology.

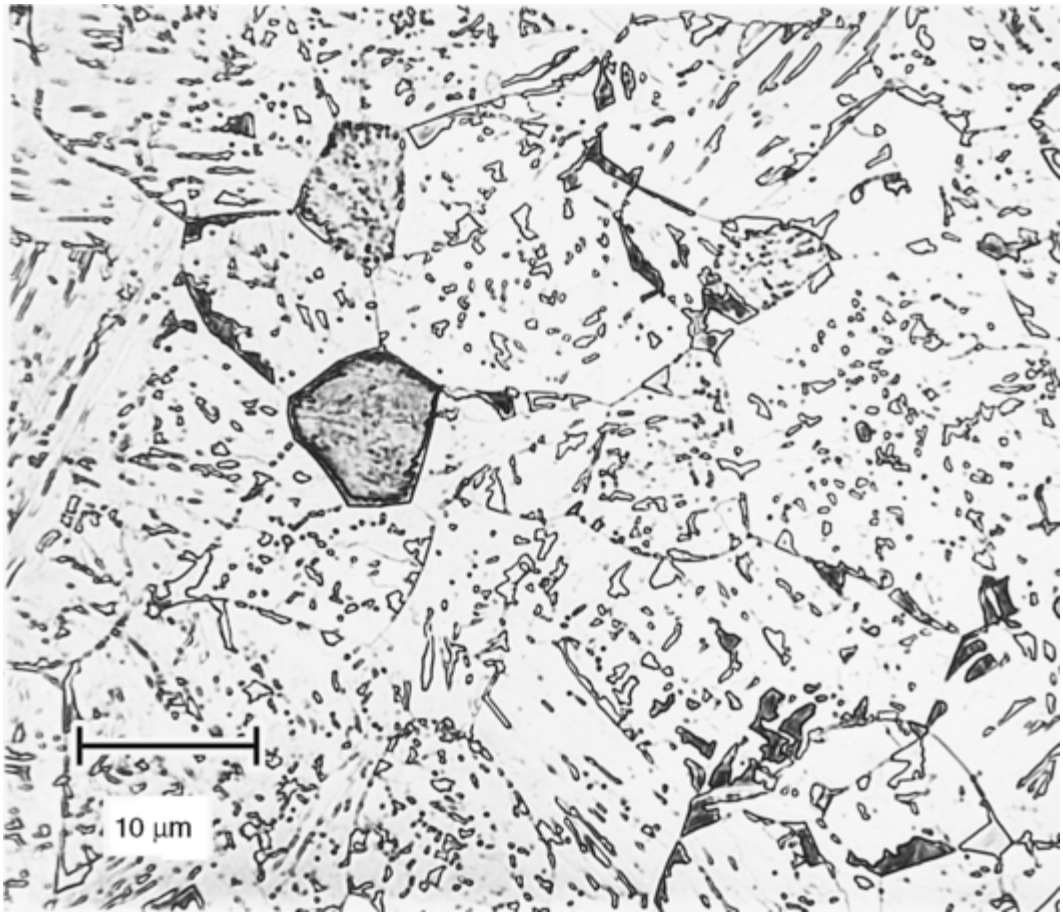

Fig. 18 Microstructure of granular bainite showing islands of martensite (dark) and retained austenite (white) in a matrix of ferrite. 10% sodium metabisulfite tint etch. Original magnification 1000×

Martensite is a constituent that is formed by rapid cooling (quenching) plain carbon or low-alloy steels from the high-temperature austenite phase. In essence, as-quenched martensite is ferrite that is supersaturated with carbon. This means that carbon is dissolved in the ferrite well past its room-temperature solubility limit of 0.005% C, and thus, the constituent is no longer considered ferrite. Because of the supersaturated carbon, martensite is a very hard constituent. To be useful, martensite is usually tempered (heated to a temperature between approximately 420 and 650 °C, or 800 and 1200 °F) to allow some of the carbon to precipitate out as a carbide phase, usually cementite. Examples of martensite are seen in Fig. 19 and 20. Figure 19 shows martensite in the form of lath martensite that is commonly found in lower-carbon steels (below approximately 0.6% C), and Fig. 20 shows the martensite in the form of plate martensite, which occurs in higher-carbon steels. Plate martensite differs from lath martensite in that the lenticular plates contain a midrib, as shown in Fig. 21. Tempered martensite can be seen in Fig. 22. In this micrograph, the carbides (cementite) appear as small, black-etching particles. Many times, it is difficult for the metallographer to distinguish between tempered martensite and bainite.

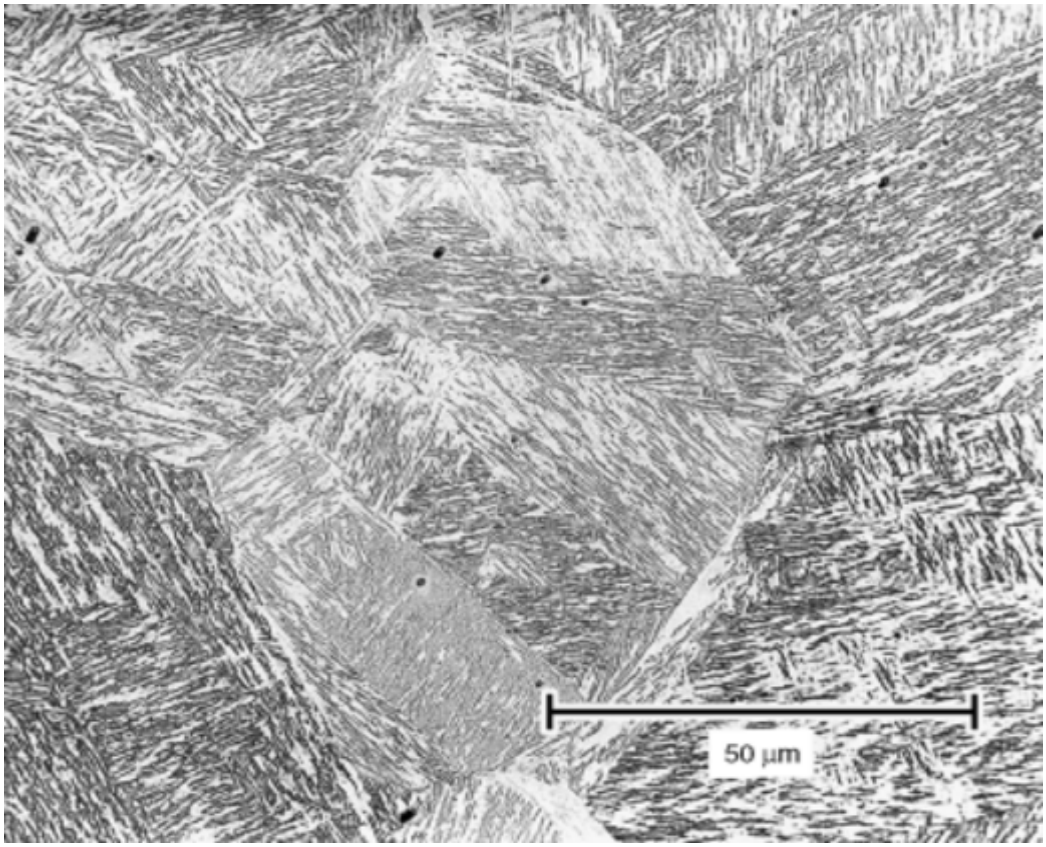

Fig. 19 Microstructure of water-quenched low-alloy steel showing lath martensite. 2% nital etch. Original magnification 500×

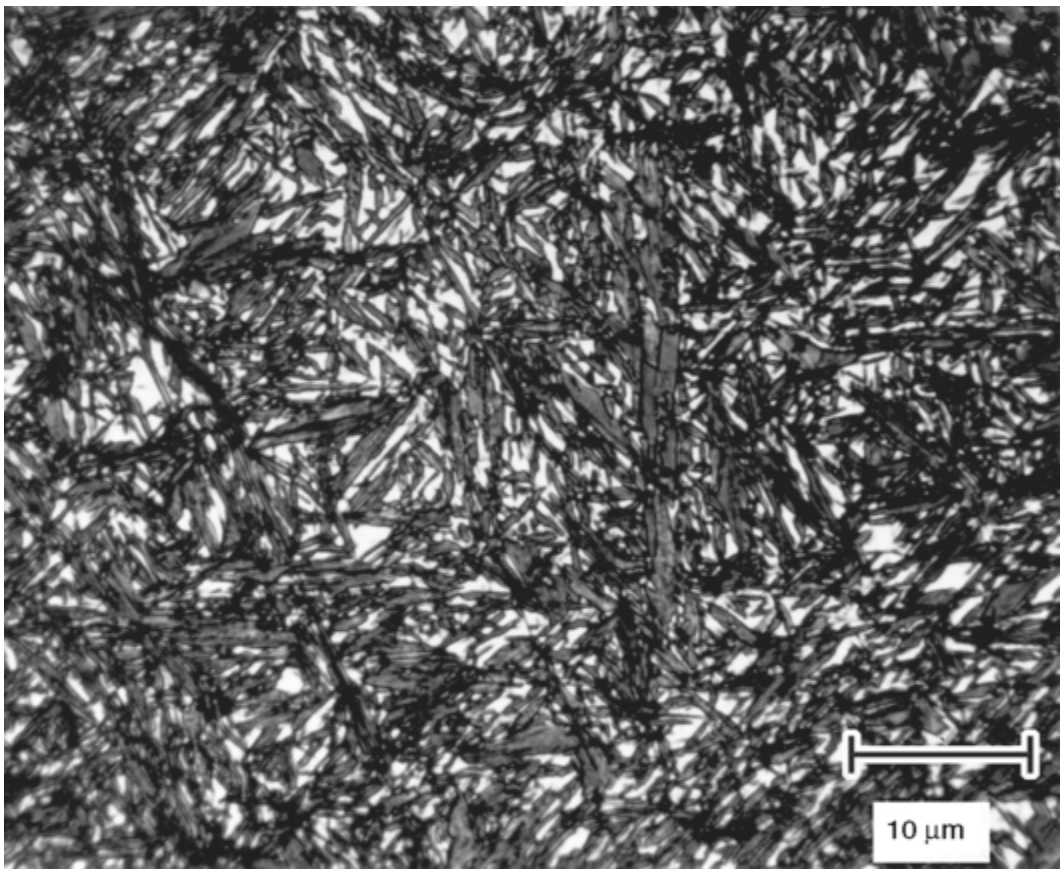

Fig. 20 Microstructure of water-quenched UNS G10800 steel showing plate martensite. The light regions between the martensite plates are retained austenite. 10% sodium metabisulfite etch. Original magnification 1000×

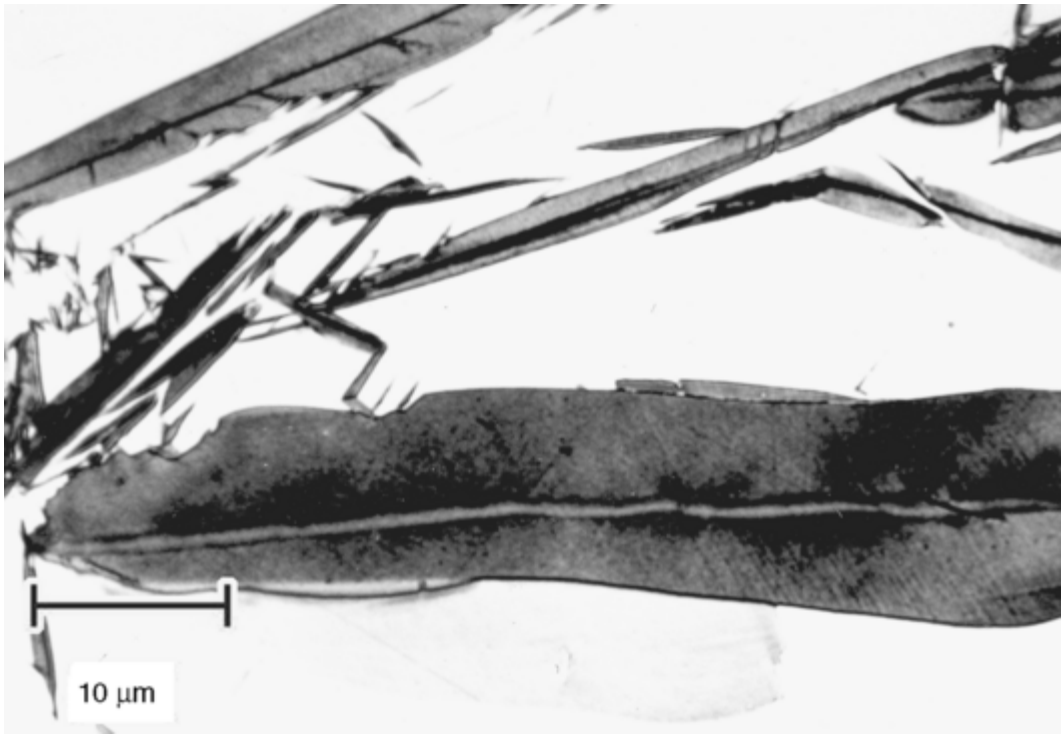

Fig. 21 Microstructure of plate martensite showing its midrib. The light region between the martensite plates is retained austenite. 2% nital etch. Original magnification 1000×

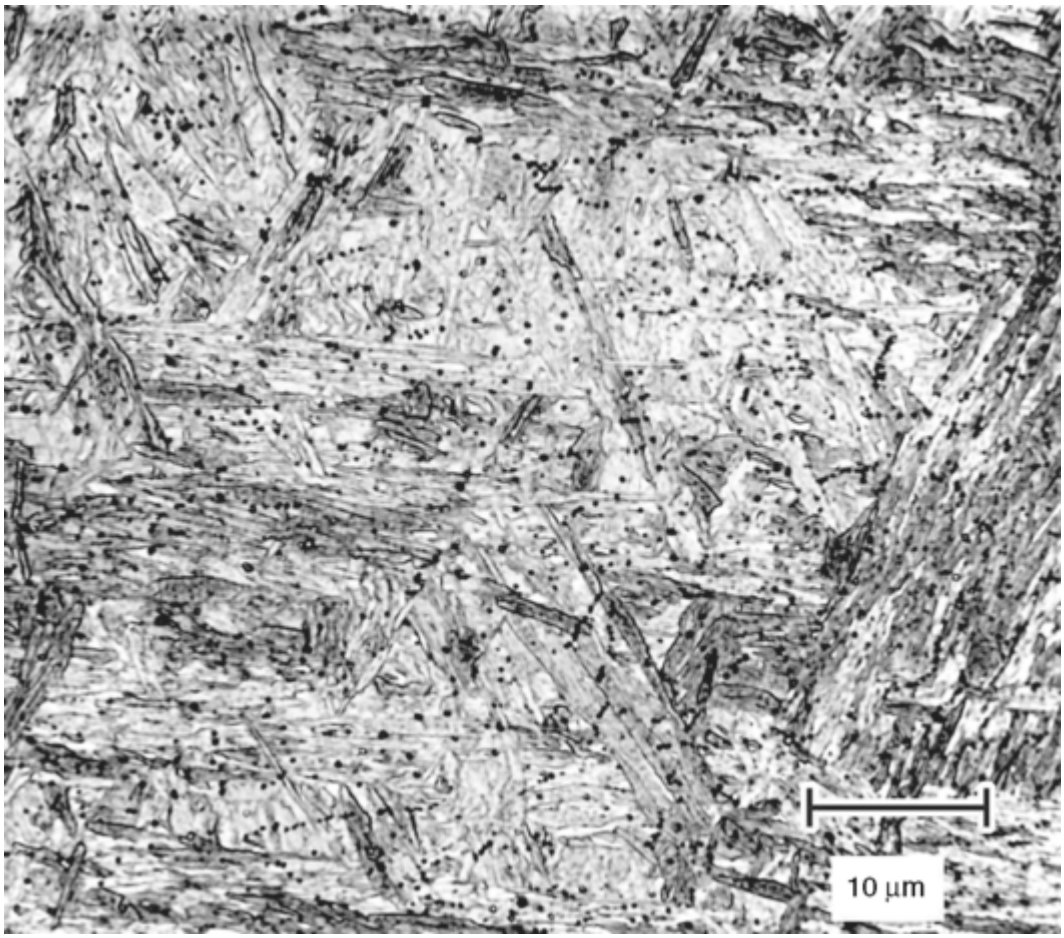

Fig. 22 Microstructure of tempered plate martensite showing small, rounded carbides that precipitated during the tempering treatment. 4% picral + 2% nital etch. Original magnification 1000×

Austenite. In plain carbon and low-alloy steels, austenite is the phase that exists at equilibrium above approximately 727 °C (1341 °F). It is the prior phase to the formation of ferrite, cementite, pearlite, bainite, and martensite on cooling. Although austenite is a high-temperature phase, it is sometimes retained at room temperature. This simply means that the austenite phase did not have a chance to completely transform into a lower transformation product (e.g., martensite). The result is a partially reacted microstructure. The white-appearing regions between the martensite plates in Fig. 20 are retained austenite. Retained austenite is usually avoided in plain carbon and low-alloy steels. However, recent high-strength sheet steels are designed with certain percentages of retained austenite. These steels are the dual-phase and transformation-induced plasticity (TRIP) steels now being used by the automotive industry. The austenite improves ductility and crash-worthiness of steel components (e.g., automobile bumper brackets/supports).

References cited in this section

2. G. Krauss, Steels: Heat Treatment and Processing Principles, ASM International, 1990

3. C.R. Brooks, Principles of the Heat Treatment of Plain Carbon and Low-Alloy Steels, ASM International, 1996

4. B.L. Bramfitt, Annealing of Steel, Heat Treating, Vol 4, ASM Handbook, ASM International, 1991, p 43

5. B.L. Bramfitt and A.O. Benscoter, Metallographer's Guide: Practices and Procedures for Irons and Steels, ASM International, 2002

B.L. Bramfitt and S.J. Lawrence, Metallography and Microstructures of Carbon and Low-Alloy Steels, Metallography and Microstructures, Vol 9, ASM Handbook, ASM International, 2004, p. 608–626

Metallography and Microstructures of Carbon and Low-Alloy Steels

Bruce L. Bramfitt and Samuel J. Lawrence, International Steel Group, Inc.

Metallographic Procedures

This section describes how to reveal the various constituents using proven metallographic procedures. The key is to use proven procedures and not to introduce a false microstructure (artifact) from sloppy or improper metallographic preparation.

The procedures used in this section are described in more detail elsewhere (Ref 5). Although other procedures can be used in specimen preparation and etching of metallographic specimens, the procedures described here are the conventional proven methods that have been developed through the years. The bulk of metallographic specimen preparation involves grinding, polishing, and etching a specimen, but sometimes, the metallographer can examine the structural features of a specimen with the naked eye. This applies to very coarse features, such as dendrites in a casting or flow lines in a forging. In these cases, the metallographer is observing the macrostructure rather than the microstructure seen in a microscope. Thus, macrostructural examination is discussed first.

Preparing Specimens for Macrostructural Examination

A macrostructure is a view of the structure of a material at low magnification, usually by the naked eye or a magnifier. One is observing the bulk structure and not the individual components described previously. Macrostructure includes such features as flow lines in forged, welded, or extruded products and dendritic

structure in cast products. An example of the flow lines in a flash-butt weld is shown in Fig. 23. These flow lines (dark streaks) define how the steel deformed when the two hot pieces of sheet were pushed together (the excess material was removed). The flow lines themselves are actually regions of segregation (higher concentration of manganese, phosphorus, carbon, etc.) in the steel that follow the contours of deformation in producing the product. These flow lines are an internal fingerprint of how the part was manufactured. Figure 24 shows a macrograph of the cross section of a steel casting. The structure shows the columnar nature of the grains. Each columnar grain is a dendrite. Each dendrite represents the growth of a single crystal of iron. These crystals grow parallel to but in the opposite direction of the source of heat extraction. The word dendrite is derived from the Greek and means treelike. This is evident in Fig. 25, an SEM image of dendrites in a shrinkage cavity of a UNS G10200 steel casting. The dendrites show the primary dendritic arms, with secondary and tertiary dendritic arms growing in orthogonal (90°) directions. The columnar grains in Fig. 24 are filled-in dendrites; that is, the primary, secondary, and tertiary dendritic arms have grown to completion during final solidification. In Fig. 25, the solidification is incomplete, because the liquid phase disappeared around the dendrites due to shrinkage of the liquid in the riser of the casting.

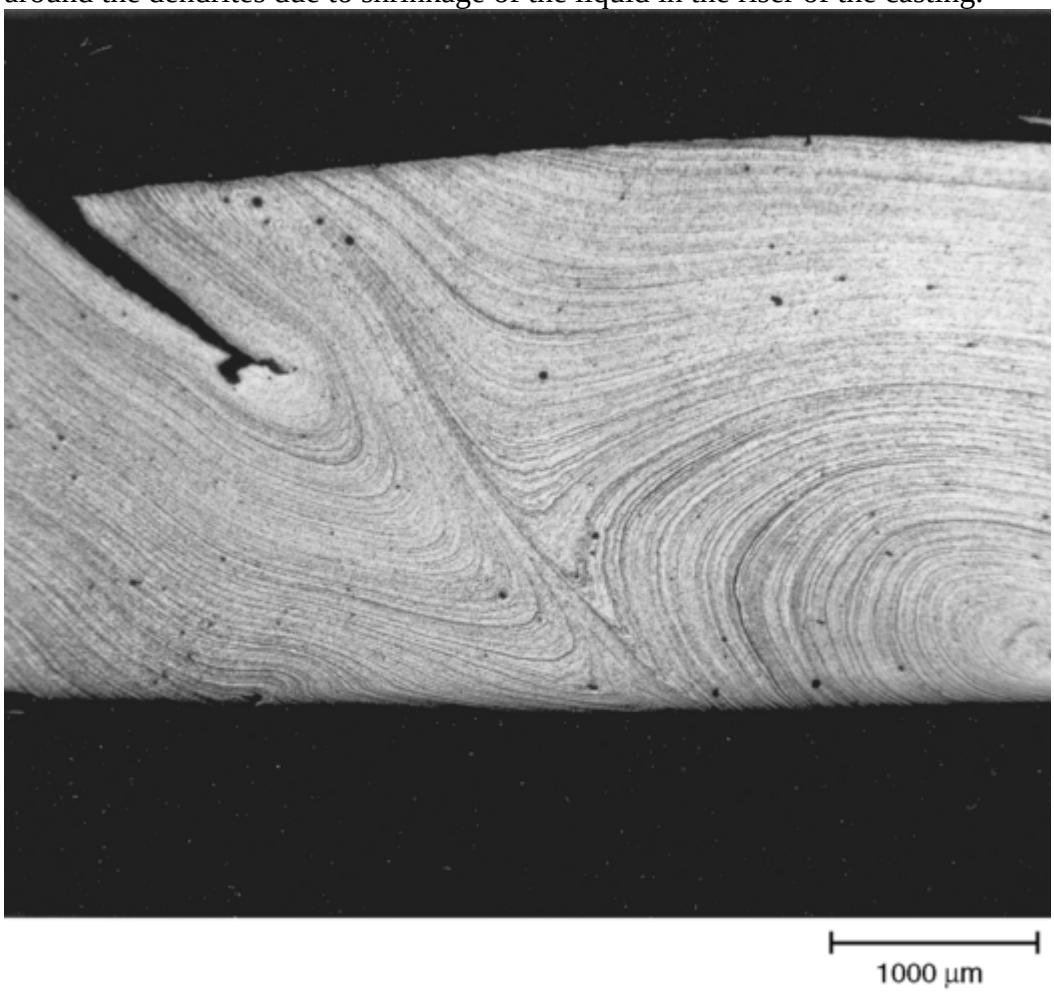

Fig. 23 Macrograph of flash-butt-welded sheet showing flow lines. Modified Winsteard's reagent. Original magnification 20×

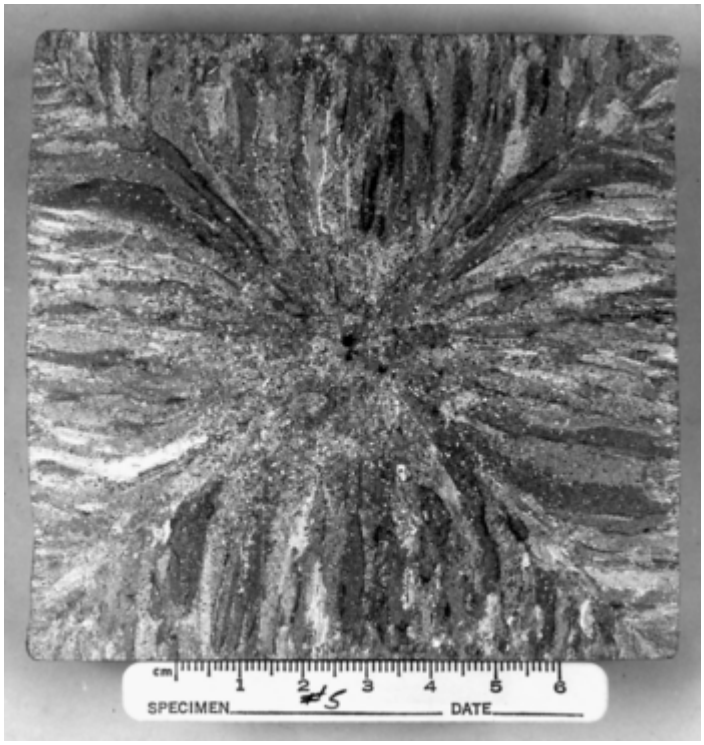

Fig. 24 Macrograph of the cross section of a steel casting showing columnar grains. Etched in hot 50% HCl + 50% water. Scale is 6 cm.

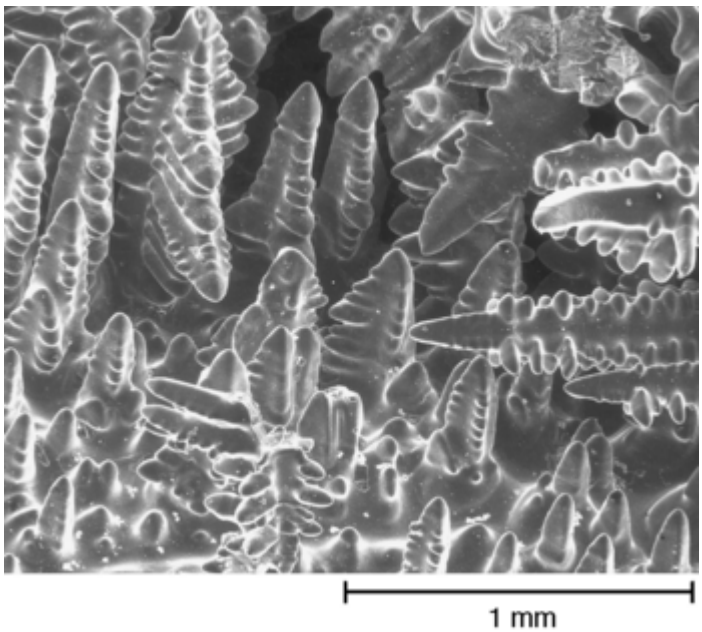

Fig. 25 SEM macrograph of dendrites in the shrinkage region of a steel casting. Original magnification 42×

Another example of a macrostructure of a steel component is seen in Fig. 26, where a used railroad rail was cross sectioned, surface ground, and etched in a solution of hot hydrochloric acid (HCl) (50%) in water (50%). Figure 26, representing the head of the rail, reveals two main features: the remains of a dendritic pattern and a large crack at the centerline of the rail. The primary and secondary dendrite arms appear as the light etching constituent. The crack appears to have initiated at the primary dendritic arms due to the compressive loads of train wheels exerted at the top of the rail head. This case illustrates the danger of not eliminating the dendritic (cast) structure by hot working the steel. Generally, a minimum reduction ratio of 4 to 1 (i.e., 4 in. of the cast form to 1 in. in the rolled or forged form) is required to break up the dendritic structure. In this rail, a ratio of only 2 to 1 was employed. Another macroetched sample is shown in Fig. 27. This cast steel was etched in

Oberhoffer's reagent to reveal the dendritic structure. Descriptions of other macroetchants can be found in Ref 5, 6, and 7.

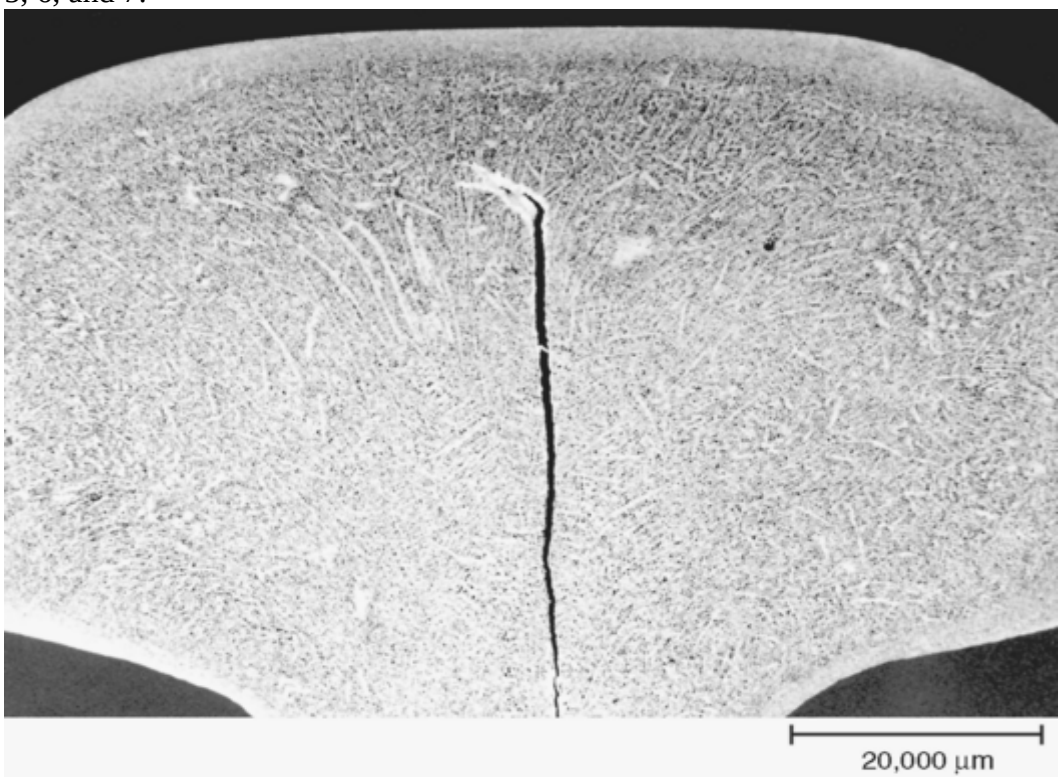

Fig. 26 Macrograph of a crack in the cross section of a rail head. The hot-acid-etched structure reveals the dendrites in the steel. Etched in hot 50% HCl in water. Original magnification 1.25×

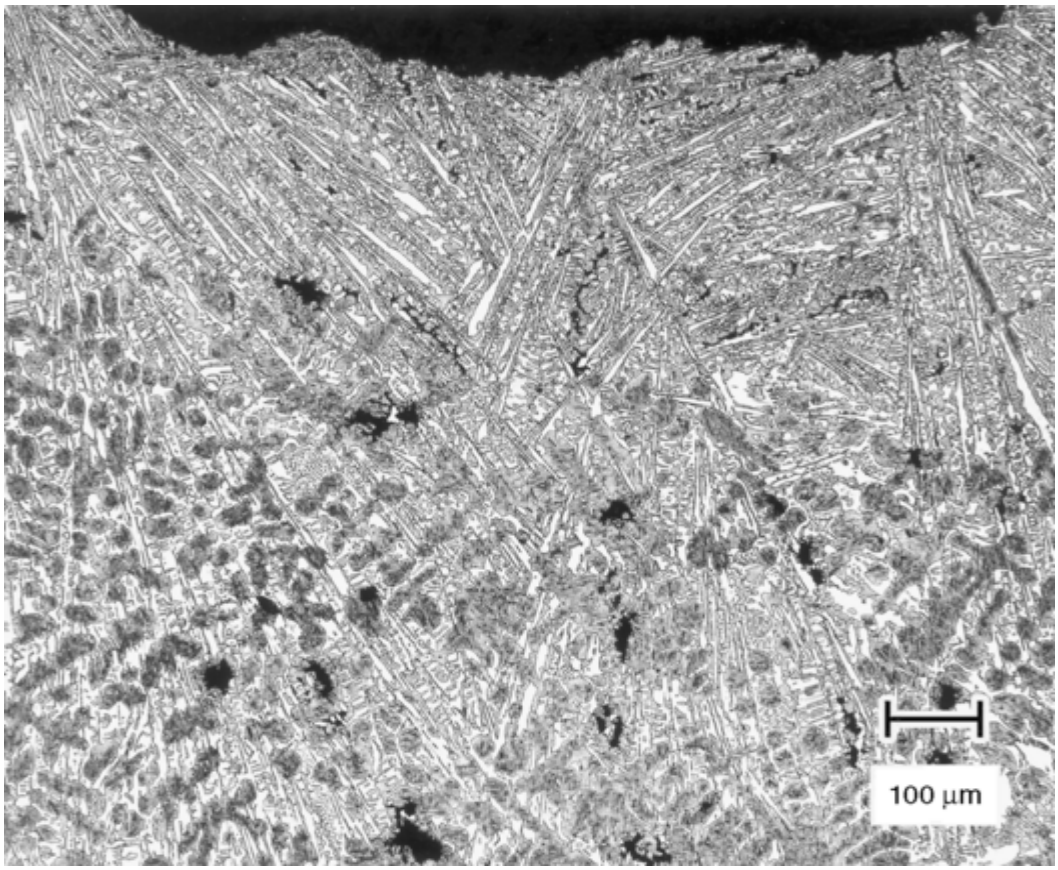

Fig. 27 Macrograph of dendrites in a steel casting. Etched in Oberhoffer's reagent. Original magnification 50×

With respect to specimen preparation for macrography, the specimen with the dendrites (Fig. 25) required no preparation other that obtaining a small enough section to observe directly in the SEM. However, in the cases of the flash-butt weld with the flow lines (Fig. 23) and the columnar grains (Fig. 24), cross sections were prepared by sectioning the component and surface grinding to provide a flat and smooth surface. The smoother the surface, the better the definition of the underlying structure (in some cases, smooth polishing may be required). The ground surface was etched in a macroetchant to reveal the structure. The features shown in the flow lines of the flash-butt-weld example were revealed because the acid in the etching solution selectively attacked specific regions in the steel. These regions include grain boundaries, regions of carbon and alloy segregation, and areas with populations of nonmetallic inclusions, such as manganese sulfides (MnS).

One special form of macrostructural examination, called sulfur printing, depends on the presence of MnS inclusions. Standard procedures for sulfur printing can be found in ASTM E 1180 (Ref 8). Figure 28 shows a sulfur print of the dendritic structure at the center of a strand-cast steel slab. The dark regions represent areas where sulfur (mainly MnS inclusions) was present in the steel. Note that the dendritic structure in this macrograph resembles the dendritic structure in the hot-acid-etched example (Fig. 26). This is because the hot HCl solution used for the rail head (Fig. 26) also attacked the MnS (and segregated material between the dendritic branches). To produce a sulfur print, the steel should be surface ground to provide an oil-free flat surface. A piece of bromide-type print paper (e.g., Kodak AZO) is soaked in a 2% solution of sulfuric acid. The print paper is then placed emulsion side down on top of the steel, surface. The acid attacks the MnS inclusions in the steel, which release hydrogen sulfide gas. This in turn reacts with the silver bromide crystals in the print paper to form silver sulfide. The dark pattern (the actual color is brown) on the sulfur print in Fig. 28 is actually a pattern of silver sulfide, which indirectly represents the distribution of sulfur in the original piece. The original sulfides are much smaller than those on the sulfur print, because the hydrogen sulfide gas expands and reacts with more silver bromide than necessary. One caution in performing this process is to avoid using your fingers to remove the air bubbles that become trapped between the print paper and the workpiece. The best technique is to use a roller while holding the edge of the paper to prevent it from moving. Finger pressure disturbs the sulfide image in the emulsion on the print paper. The blurred regions in Fig. 28 were caused by using fingers to remove bubbles. Macroetching and sulfur printing are important in examining certain products such as railroad rails.



Fig. 28 Sulfur print of strand-cast steel slab showing the dendritic pattern and some porosity (shrinkage) at the center of the slab. Original magnification 1×

Preparing Specimens for Microstructural Examination

The vast majority of metallographic procedures are aimed at preparing specimens to reveal the fine details contained in the microstructure of the material. These methods differ from those previously mentioned for macroetching. In the light microscope, magnifications of 50 to 1000× are typically used to observe the fine microstructural features of the material. For higher magnification, an electron microscope is employed.

Background Information. It is important to know the processing history and chemical composition of the steel that is being prepared. Documenting this will add value to the micrograph, and knowing the material composition will aid in the proper selection of sectioning, grinding, polishing, and etching procedures to be used. Different steel alloys may have different responses to chemical etching, so knowing the composition beforehand will allow the metallographer to choose the correct etching solution for optimal results. Also, it is important to know the type of microstructure in the sample beforehand. For example, if the steel is as-quenched martensite, it is crucial to avoid heating the specimen in a thermosetting plastic mount, because the process will temper the martensite and alter the original microstructure. The hardness of the material will also dictate the type of sectioning procedure. Soft steels require a different cutting method than hard steels. It is also very important to know which plane of polish to use. For example, in a rolled steel plate, should the metallographic specimen be polished on the transverse or longitudinal planes or planar? What information is being sought? Nonmetallic inclusions and grains will have a different morphology in the three different planes of polish. Thus, as a rule, the metallographer must always know how the plane of polish relates to the original object being evaluated. For example, what is the rolling direction? Generally, specimens are prepared on the longitudinal

plane parallel to the rolling direction. This plane will show the orientation and anisotropy of the grains and inclusions.

Other questions need to be addressed before starting. For example, in a hot-rolled steel sheet or plate, it may be important to prepare the specimen with the original top and bottom surface oxide (scale) layers intact. Figure 29 shows an oxide scale layer on a steel plate surface. Note the microstructural detail in the scale layer itself. In iron oxide scale, there are often three oxide phases: wustite (FeO), magnetite (Fe_3O_4), and hematite (Fe_2O_3). In this case, the oxide scale is not removed beforehand, and, in many cases, the top and bottom surfaces are coated with an epoxy mixture to retain the scale layers during sectioning of the specimen. Some steel components are rusted. Is it important to retain the rusted surface on the specimen? It may be important to determine the extent of rusting on the steel surface and to determine the composition of the oxide or hydrated compounds in the rust. It may also be important to maintain excellent edge retention in order to determine the extent of carbon removal (decarburization) on the surface of the steel. Figure 30 shows a decarburized surface of UNS G10800 steel. Note the gradual loss of carbon moving from the interior toward the surface of the specimen. In the interior, the carbon is leaving (diffusing) along the original prior-austenite grain boundaries.

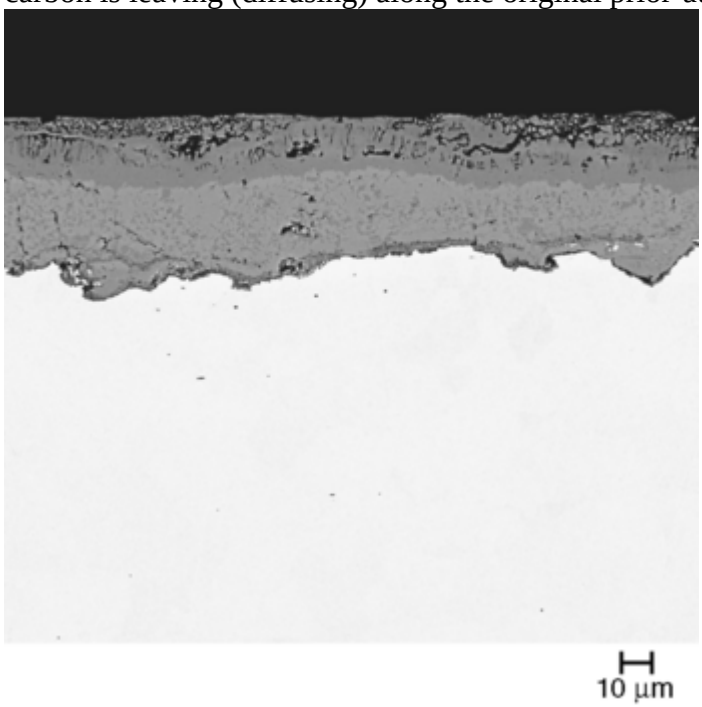

Fig. 29 Backscattered electron image of oxide scale layer on steel. Note the phases in the layer. Unetched. Original magnification 360×

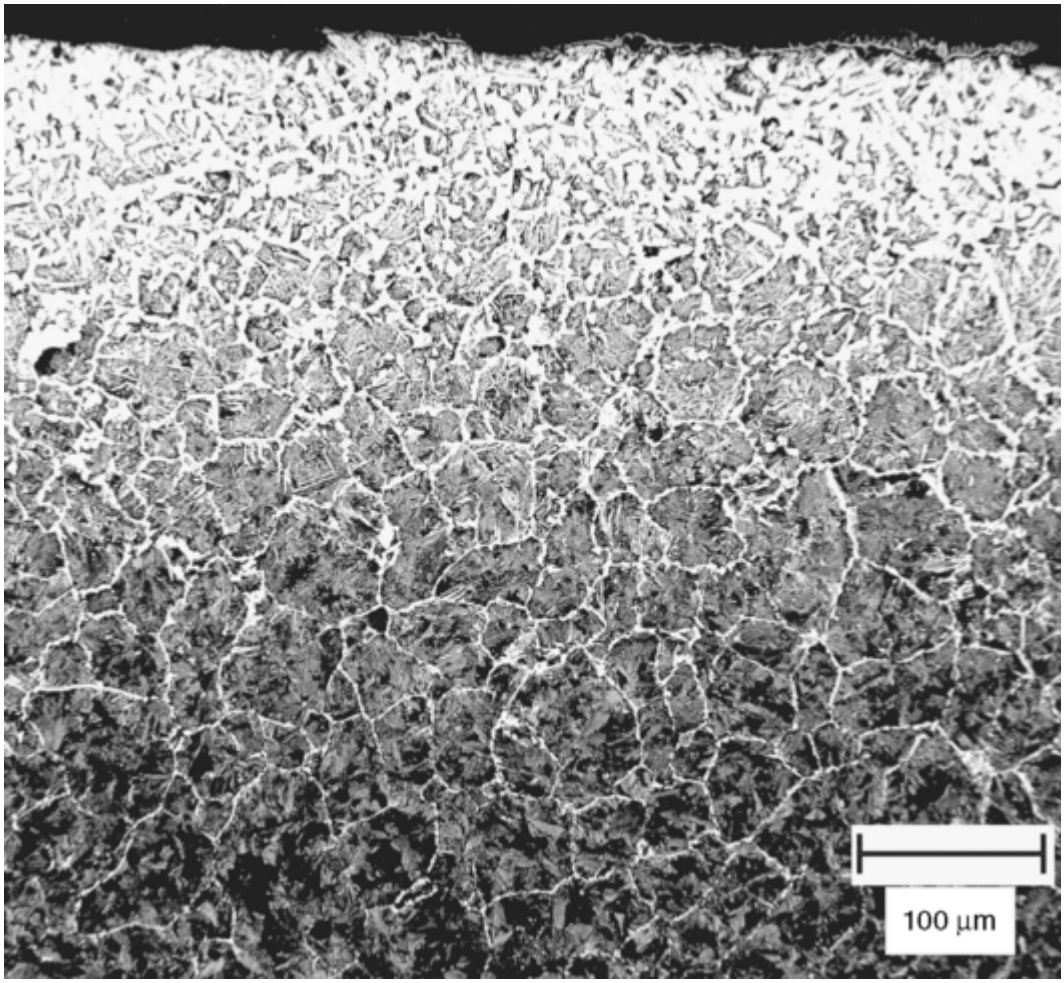

Fig. 30 Microstructure of UNS G10800 steel bar with decarburization at the surface. 4% picral etch. Original magnification 100×

Another important consideration is whether the specimen will be further analyzed in the electron probe microanalyzer (EMPA). If so, it is advisable not to use oxide-containing grinding/polishing materials (alumina or silica), because they may contaminate the specimen, especially if one is analyzing the specimen for silicate or alumina inclusions. Some special conductive mounting materials contain copper, aluminum, or iron, which will also contaminate the specimen and give erroneous results (an artifact) during compositional analysis in the EMPA or SEM. The main point here is to think ahead before starting any metallographic procedure. Think about the specimen-cutting method, specimen size, mounting, grinding, and polishing procedures. Think about what chemical analysis procedures may take place after preparation. This will save extra work later and prevent costly mistakes.

Sectioning. Once the plane of polish has been determined, the specimen must be sectioned properly to avoid distortion and heating of the steel. It is important not to introduce anything that will alter the original microstructure. If a specimen is cut from a steel plate or sheet by a shear, there will be a shear burr. The shear burr consists of a region of cold work and is not representative of the original structure (Fig. 31). Also, cutting a specimen with an abrasive wheel without water will heat the specimen and alter its microstructure. This is particularly true in a martensitic microstructure, where heat from the cutting procedure can heavily temper the structure near the cut surface.

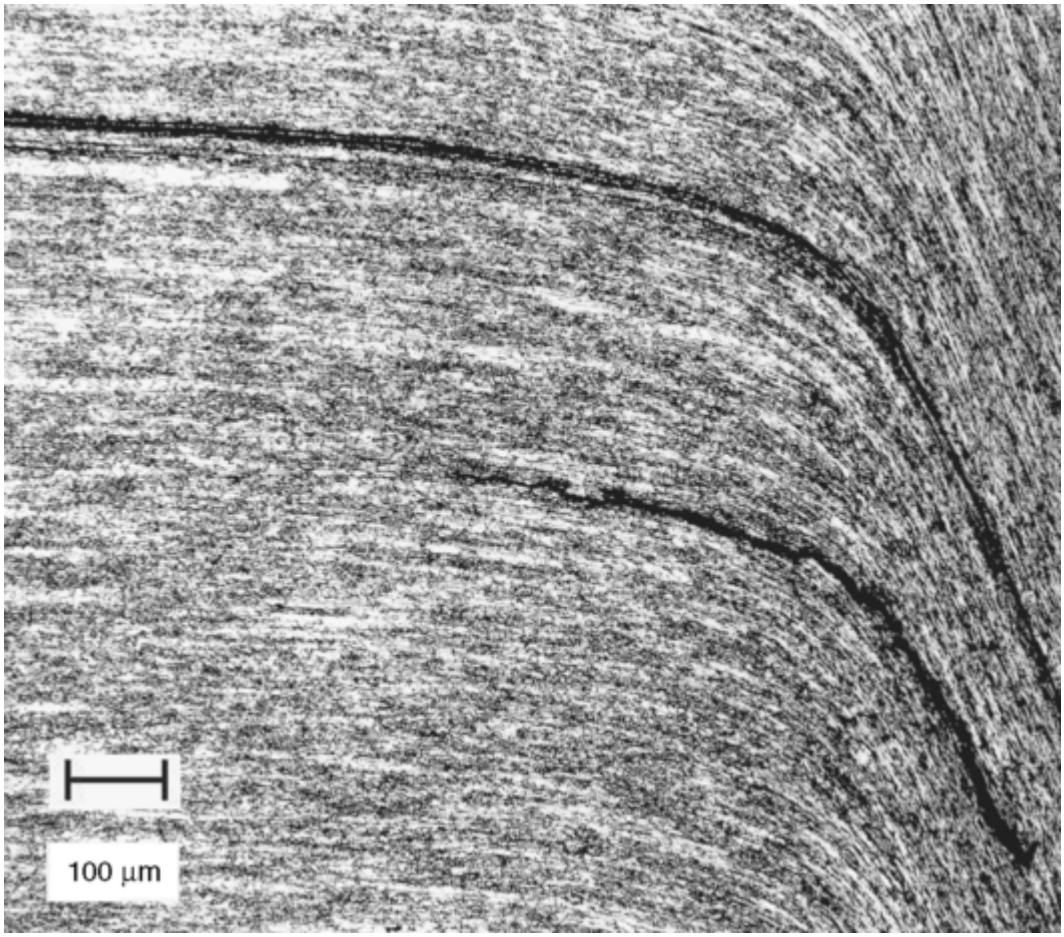

Fig. 31 Damage created by shearing a steel sample. 4% picral + 2% nital etch. Original magnification 50×

In some metallographic investigations, it is important to preserve the material at the surface. Oxide layers (scale) or other coatings may need to be evaluated and their thickness measured. Cutting a specimen may cause a brittle surface coating to mechanically spall from the surface. In this case, it is advisable to coat the surface with an epoxy liquid that will cure to retain the oxide layer during cutting. For brittle coatings, the specimen can be electroplated with electroless nickel to protect the coating.

Once the surface of the specimen is prepared, there are numerous sectioning techniques available to the metallographer (Ref 5). Some of these are described as follows.

Abrasive Cutoff Saw. A very common technique is to remove a metallographic specimen from a bulk object by cutting with an abrasive saw. Most metallographic supply houses provide this type of equipment. The cutting tool is actually a flat, thin disk or wheel of abrasive particles embedded in a resin, rubber, or rubber-resin bond. For plain carbon and low-alloy steel, medium-hardness aluminum oxide wheels are recommended. The metallographer simply maintains pressure on the specimen or disk as it is being cut. It is important to maintain the correct amount of pressure. Too much pressure will heat the specimen and alter its microstructure. In most cases, a water-based coolant must flow over the specimen at the region of cutting to prevent heating.

Shear. In many metallographic laboratories, a shear is used to remove specimens from a steel sheet or thin plate. As mentioned previously, this practice creates a shear burr that must be removed during subsequent grinding steps, as described in the section “Grinding.” Note the severe deformation at the cut surface (Fig. 31).

Band Saw. In many cases, a simple band saw can be used to cut a specimen from a bulk object. While feeding the specimen against the saw blade, it is important not to heat the specimen. A light lubricating oil can be used to minimize heating. Remember to remove the oil from the specimen before mounting. Different blades are used for hard and soft steels. Generally, a blade with fine teeth (16 to 20 teeth/in.) is used for hard steel, and a coarser-toothed blade (10 to 16 teeth/in.) is used for soft steel. Special blades impregnated with tungsten carbide particles are available for very hard steels such as tool steel.

Hacksaw. A hand-held hacksaw can be used, in some cases, to remove a specimen from a bulk object. This technique usually produces a very rough-cut surface that will require extra steps in specimen preparation.

Torch. Cutting a metallographic specimen with an oxyacetylene torch is not recommended. There is far too much damage at the cut surface. However, a torch-cut specimen can be recut on an abrasive saw into a smaller specimen far away (at least 50 mm, or 2 in.) from the original torch-cut surface. A plasma torch is much better than an oxyacetylene torch for cutting metallographic specimens. The damage zone (heat-affected area) of a plasma torch cut will be approximately one-tenth that of an oxyacetylene torch. Figure 32 shows the microstructure at a plasma-torch-cut surface. The microstructural damage zone is approximately 0.5 mm (0.02 in.) deep. A cut from a laser can be even less damaging.

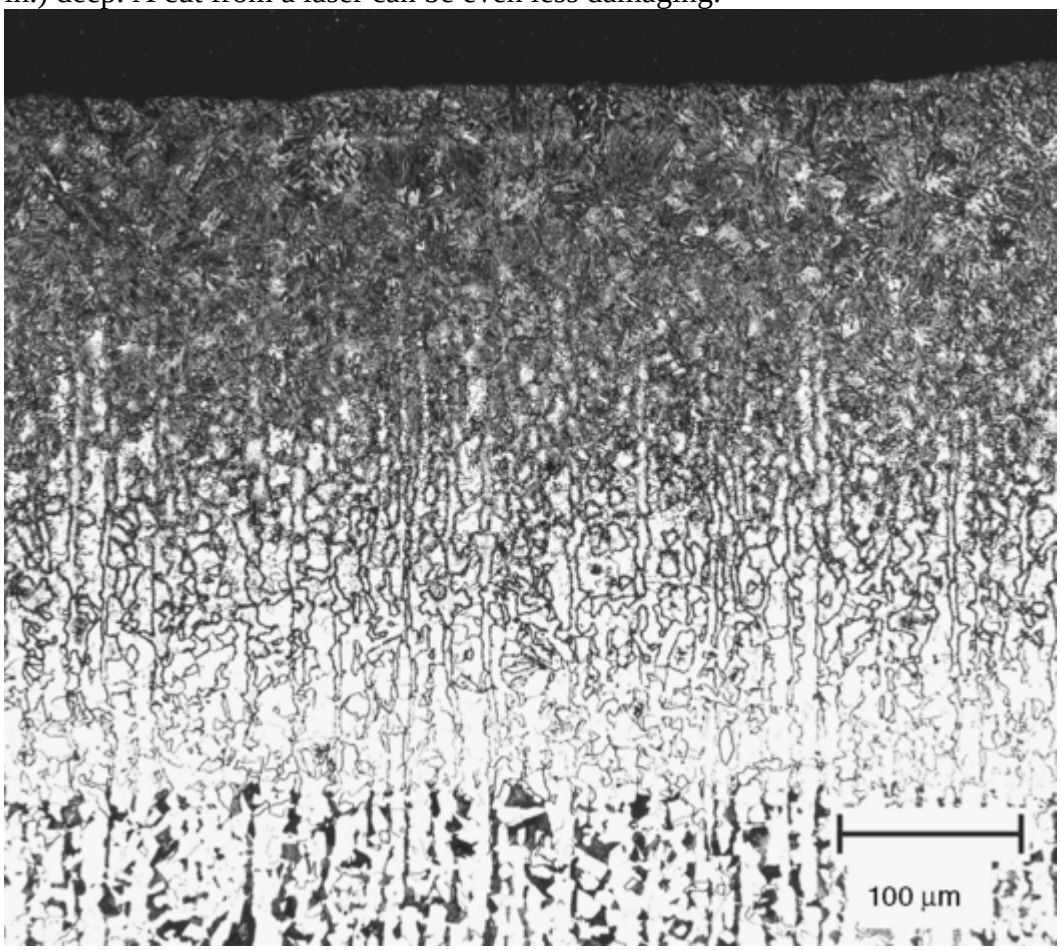

Fig. 32 Damage created by a plasma torch cut (top 80% of micrograph). Microstructure was originally a banded pearlite and ferrite. 4% picral etch. Original magnification 100×

Electric discharge machining (EDM) is an accurate but expensive and slow cutting process that is not generally recommended for cutting metallographic specimens. The process works by an electric discharge literally melting away the steel in the cutting zone. The area at the cut surface is melted and resolidified, and the material next to it has been heated and the microstructure altered. These changes make the EDM process unusable for a metallographic specimen.

Precision Saw (Slow-Speed Saw). For special care in minimizing damage, a constant force or constant feed precision saw can be used to remove a specimen from a larger object. These saws use thin, circular disks (wheels). Aluminum oxide blades are commonly used for steel. However, silica-, diamond-, or boron-nitride-impregnated steel blades are available. The process is slow, but a practically damage-free surface is produced. These saws are particularly useful as the first step in producing thin wafers to prepare thin foils for the TEM and scanning transmission electron microscope (STEM). These saws can also be used to precisely cut samples from coated material and samples with defects.

Wire Saw. Like the precision saw mentioned previously, the wire saw is used to remove practically damage-free specimens from a component. The cut is produced with a wire that is continuously drawn across the steel surface. The wire can be impregnated with diamonds or can be drawn through a slurry of abrasive particles. Although these saws remove material at a very slow rate, they are useful for preparing TEM and STEM specimens.

Fracturing in Liquid Nitrogen. Sometimes, cooling the steel in liquid nitrogen and applying an impact blow to remove a specimen is the only way to remove a metallographic specimen. A notch (shallow cut) aids the process and allows the fracture to proceed where one wants it to proceed. This method is especially useful in exposing a crack, hydrogen flake, or void inside a component. It is important to immediately immerse the broken steel specimen in ethyl alcohol (200 proof) to prevent water from condensing on its surface, which would promote rusting.

Mounting. In most cases, a steel specimen is mounted in a substance to preserve the flatness and edge retention of the specimen. However, before selecting a mounting method, the metallographer must think ahead to answer some questions. Can the specimen be heated? If not, avoid thermosetting and thermoplastic mounting methods. In what solution will the final polished specimen be etched? It must be remembered that certain acids will attack and swell the mounting material (e.g., phenolic resins). Is edge retention of utmost importance? If the edge must be preserved, the specimen edge may be mounted next to a “dummy” steel specimen to avoid rounding of the edge. The steel specimen may be electroplated with nickel to preserve the edge before mounting. Electroless nickel plating is useful for this purpose. As in sectioning the specimen, the metallographer must always think ahead before mounting the specimen. Several different mounting techniques can be found in Ref 5.

Mechanical Clamp. One simple and effective way to mount sheet or plate specimens is to clamp the material between two steel plates, as shown in Fig. 33. The steel clamp material should closely match the steel being mounted, so that it grinds and polishes away at a rate similar to the specimen itself. Figure 34 shows the edge retention at the junction of three steel sheet specimens in a clamp.

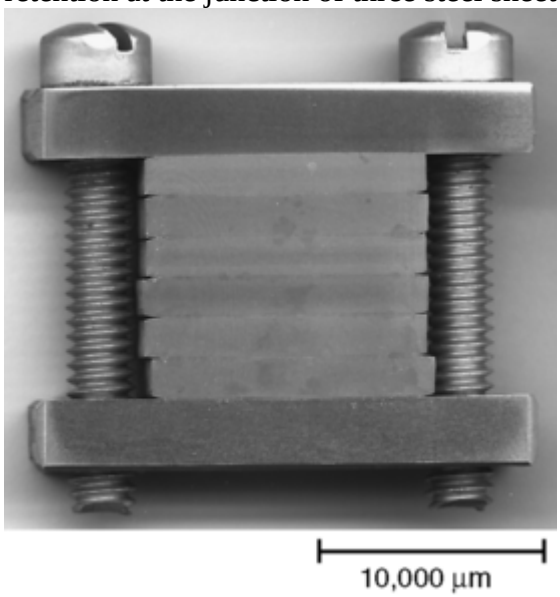

Fig. 33 Six specimens mounted in a steel clamp. Original magnification 2×

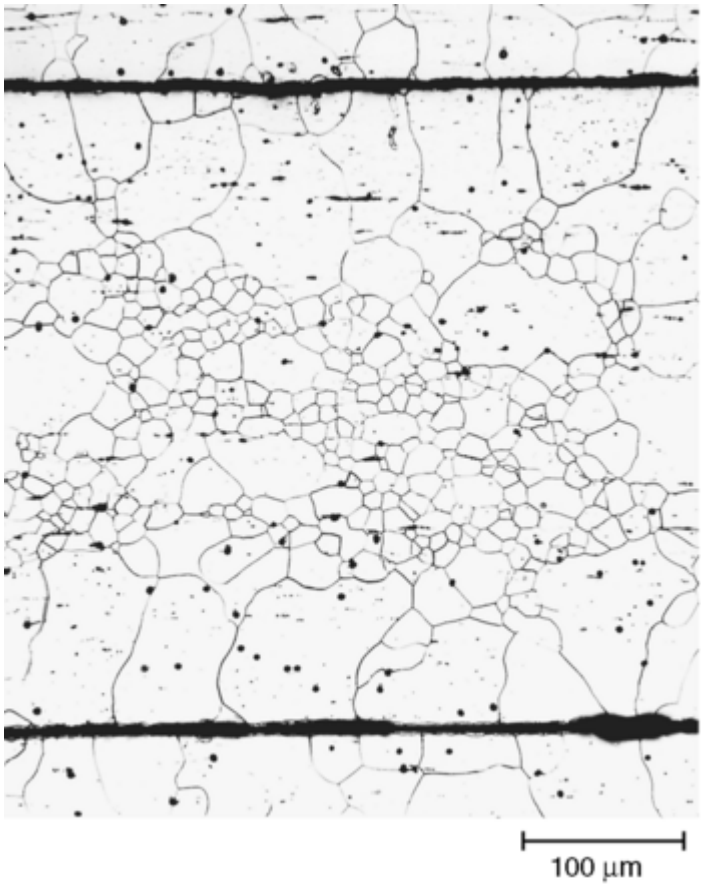

Fig. 34 Microstructure of the interfaces between specimens mounted, polished, and etched in a steel clamp. Note the excellent edge retention. 2% nital etch. Original magnification 100×

Thermal-Compression Mounting. Many metallographic laboratories are equipped with mounting presses that produce thermosetting or thermoplastic mounts. The specimen is placed on a steel piston within a thick-walled steel cylinder. The granular mounting material (or preform) is poured around the specimen, and another steel piston is placed at the top of the material in the cylinder. Heat and pressure are applied to melt the mounting material around the specimen. The assembly is allowed to cool, and the specimen is removed. Thermosetting resins such as Bakelite (Georgia-Pacific Corp.), Epomet (Buehler, Ltd.), DuroFast, and Plastimet are commonly used. These are phenolic resins that are relatively inexpensive and provide an adequate mount for most plain carbon and low-alloy steels. It must be remembered that boiling sodium alkaline picrate, an etchant used to darken cementite, will attack a phenolic mount. Another thermosetting resin is diallyl phthalate. Copper-filled diallyl phthalate mounts are electrically conductive and can be used in the SEM and EMPA. However, the copper in these mounts can contaminate a polishing cloth and the specimen itself and can produce erroneous results in a chemical analysis in the SEM or EMPA. To avoid copper contamination, other conductive mounting materials containing iron or aluminum can be used. Thermoplastic resins such as Lucite (an acrylic-methyl methacryalate, INEDS Acrylics, Inc.) are also used for mounting materials. An advantage of an acrylic mount is that it is transparent. This means that the specimen identification or code can be embedded within the mount. However, as a mounting material, acrylics have several disadvantages, because they have poor resistance to solvents (alcohol, acetone, etc.), shrink away from the steel specimen, require longer curing times, are much softer than steel, and provide poor edge retention. This type of mounting material is not recommended for steel specimens.

Castable Mounting Materials. One of the most popular castable mounting materials for plain carbon and low-alloy steel is epoxy (e.g., Epoxicure and EpoFix). This mounting medium is preferred when edge retention is necessary, such as for coated, painted steels and steels with surface oxides. Epoxy is also excellent for filling voids and cracks. Epoxy is more chemically inert for performing chemical analysis in the SEM or EMPA. This material is mixed in two parts: a liquid resin and a hardener (catalyst). The mixture is poured around the specimen, which is contained in a mold, usually an open-ended, precut phenolic cylinder. Air bubbles can be removed by curing the mount in a vacuum bell jar. Sometimes, evacuation is used to remove air bubbles,

immediately followed by pressure to force the liquid epoxy into cracks and voids. There is a low-viscosity form of epoxy that can be used to better fill cracks. A major advantage of mounting with epoxy is that many mounts can be made at one time, and the technique does not require a mounting press.

Fillers and Dyes. It may be desired to increase the hardness of a mounting material by adding commercially available aluminum oxide particles. This will minimize rounding at the edge of the specimen and provide excellent edge retention. Dyes can also be added to distinguish the mounting material from oxide scale or corrosion layers on the specimen surface. Some mounting dyes fluoresce in the light microscope (a fluorescence attachment is needed) and can be used to enhance the appearance and location of coatings, cracks, and voids.

Standard mount diameters are 19, 32, and 38 mm (0.75, 1.25, and 1.5 in.). It is important to use a standard-sized mount in order to use automatic grinding and polishing equipment and to use the specimen in other equipment, such as the EMPA.

Grinding. Once the steel specimen is mounted or is in sufficient shape to prepare without a mount, it must be planar. Grinding takes place on a series of progressively finer silicon carbide grinding papers, usually 120-, 240-, 320-, 400-, and 600-grit papers. More details on grinding papers and the standard grit sizes are listed in Ref 5. Finer-grit papers (1 to 10 μm particle size) can be used if special care is needed for inclusion retention and for coating/steel edge flatness.

Abrasive-coated grinding paper discs are commonly used for preparing steel metallographic specimens. These papers are either pressure-sensitive-adhesive (PSA) backed or magnetically backed. The papers are placed adhesive or magnetic face down on a flat metallic wheel. Once used, the paper is discarded. There are also metal-backed grinding discs available. These discs are bonded with abrasive particles (e.g., diamonds) and can be used many times. However, for steels, silicon carbide papers outperform these impregnated disks.

Manual (Hand-Held) Grinding Technique. For plain carbon and low-alloy steels, standard practice is to hold the specimen between the thumb and fingers. Keep the fingers as close to the paper as possible to prevent wobbling of the specimen. A constant pressure must be applied to each point of contact. This comes with experience. A firm amount of pressure should be used. The specimen should not be rotated counter to the rotation of the wheel but held in place at a fixed position, usually, the three o'clock position. However, the specimen should be moved sideways to expose newer abrasive particles for effective metal removal. The specimen and grinding paper are flooded with water to remove any debris. After grinding on a paper, usually 10 to 30 s, the paper is discarded, and a new paper of finer grit is used. A short grinding time is necessary, because long times tend to burnish the surface of the specimen and damage the surface. A uniform set of parallel scratches is produced with each paper. Always rotate the specimen 90° to the direction of the grinding scratches from each paper. This method allows the metallographer to observe if the previous set of parallel scratches is removed. It is also advisable to rinse the specimen in flowing water between grinding steps to remove grinding debris. Do not allow water to sit on the specimen surface after grinding steps, because this may cause pitting on the surface.

Automatic Grinding Technique. Many metallographic laboratories employ automatic grinding and polishing machines to prepare specimens. Although expensive, these machines can prepare multiple specimens. Mounted specimens are placed in specimen holders that can hold up to six mounts. As with hand grinding, the holder and specimens should be rinsed in flowing water to remove grinding debris between grinding steps.

Polishing. Once the specimen is properly prepared to at least 600 grit, it is almost ready for polishing to achieve a scratch-free mirror finish. The specimen must be cleaned thoroughly in running water to remove all grinding debris, and it can also be etched in 2% nital to remove the disturbed metal layer on the surface. The disturbed metal layer is actually cold work (plastic deformation) induced by grinding. This is especially true in soft ferrite microstructures. Removing the layer at this point assures an almost perfect, artifact-free polished sample. Etching the specimen after the last grinding step and the first coarse polishing step is recommended. However, if it is important to retain all the nonmetallic inclusions on the prepared surface, then these etching steps should be avoided.

Polishing takes place on cloth material impregnated with fine abrasive particles. For rough polishing, a long-nap cloth such as canvas is generally used. For fine polishing, a low-nap cloth is used. Details on polishing cloths can be found in Ref 5. These cloths are mounted on a rotating metallic wheel. For convenience, the cloth should have a PSA backing. Some cloths or polishing media have a magnetic backing to hold onto the wheel (the wheel must have a flat magnetic surface).

Various polishing abrasives can be used in the polishing process. Polishing abrasives for plain carbon and low-alloy steels include:

- Diamond particles: The diamond particles can be suspended in a thick water-based or oil-based paste or in a slurry or suspension of oil or ethyl alcohol or other water-free extender. They can also be sprayed on the surface of the polishing cloth by petroleum-based or alcohol-based aerosol spray. For most steels, 6, 3, and 1 μm diamond particles are used for the initial stages of polishing.
- Aluminum oxide (alumina) particles: These particles are usually suspended in water. Generally, a 0.3 μm (deagglomerated) alumina slurry is used for the near-final polish.
- Silicon dioxide (silica) particles: These particles are suspended as a colloidal aqueous liquid. For the final polish, a 0.05 μm silica suspension is used.

The diamond abrasives mentioned previously are more expensive but have superior cutting capability than the oxide abrasives. Diamonds work because they are friable and break into smaller particles, exposing more surfaces for cutting. Diamond is also a harder substance than the oxides. However, oxide particles are of a precise size and are more economical to use. All of these polishing materials are available from vendors of metallographic supplies.
Manual Hand-Held Polishing Technique. For plain carbon and low-alloy steels, a proven method of polishing a metallographic sample of steel is as follows:

1. After completely cleaning the specimen to remove grinding debris, use a long-nap cloth such as canvas impregnated with 6 μm (or 3 μm) diamond particles (paste, suspension/slurry, or aerosol spray). The cloth is mounted on a rotating polishing wheel. With the wheel rotating clockwise at approximately 150 revolutions per minute, rotate the specimen with heavy hand pressure in the opposite direction. Move the specimen in a counterclockwise direction on the wheel in order to expose newly fragmented diamond particles. Moving the specimen in this manner minimizes comet tailing of inclusions. This step will continue until the grinding scratches from the 600-grit paper are removed. This usually takes approximately 60 to 90 s.
2. Clean the polishing debris from the specimen by ethyl alcohol swabbing. Always swab in a unidirectional manner. Dry the specimen with a warm air blower. For soft ferritic steels, it is advisable to etch the specimen in 2% nital to remove the disturbed layer. Repeat step 1 except on a low-nap cloth with 1 μm diamond particles (paste or aerosol spray) or a 0.3 μm alumina slurry.
3. Clean the debris from the specimen by rinsing in running water and by swabbing with ethyl alcohol. Dry with a warm air blower. For the final polish, use a 0.05 μm colloidal silica slurry on a low-nap cloth. Clean the specimen by rinsing in water and swabbing in alcohol, then dry. Do not rinse in warm or hot water, because it will stain inclusions in the sample. As a warning, never allow water to rest on the specimen surface because of the potential for pitting. Be careful in using water on coated steels (hot dipped galvanized and electroplated), because a galvanic reaction can take place that will stain the specimen. Also because of staining, use caution when using water on steel samples polished for inclusion examination.

Automatic Polishing Technique. As mentioned in the section “Automatic Grinding Technique,” the same machines that automatically grind specimens also are used for polishing. Many metallographic laboratories use automatic grinding and polishing equipment when multiple samples are being prepared. Basically, the polishing cloths and abrasives used for manual polishing are the same as for automatic polishing.

Examination of As-Polished Specimens

For some investigations, the examination of the as-polished specimen is required. For example, the metallographer may want to measure and evaluate the microcleanliness of the steel. This means that constituents such as ferrite and pearlite are not important, but the inclusions need to be revealed. The inclusions in plain carbon and low-alloy steels are MnS, silicates, nitrides, and oxides. An example of MnS is shown in Fig. 35. They appear as elongated particles (called stringers) in the longitudinal plane of polish and as oval-shaped particles in the transverse plane of polish. Figure 35 shows MnS in the longitudinal plane of polish. The color of MnS inclusions is medium-gray in the light microscope. These inclusions are smooth and have rounded edges. An example of a silicate inclusion is seen in Fig. 36 (also appears gray). Sometimes, silicate inclusions appear iridescent in the light microscope due to the translucent nature of the material in the inclusions. Figure

37 shows aluminum oxide (alumina) inclusions. Alumina or oxide inclusions are gray and appear as small, chunky, angular particles, sometimes with multicomponents. Many times during rolling, large oxides break up into a line or stringer of smaller particles, as seen in Fig. 37. An unusual case of MnS inclusions in a lead-treated (leaded) free-machining steel is shown in Fig. 38. In this micrograph, the metallic lead appears as a white layer on the gray MnS inclusions. Titanium nitride (TiN) inclusions are seen in Fig. 39. When examined in the microscope, they appear angular, often cuboidal, and are yellowish or amber in color. The numerous TiN inclusions shown in Fig. 39 were found in a highly segregated region of a steel plate.

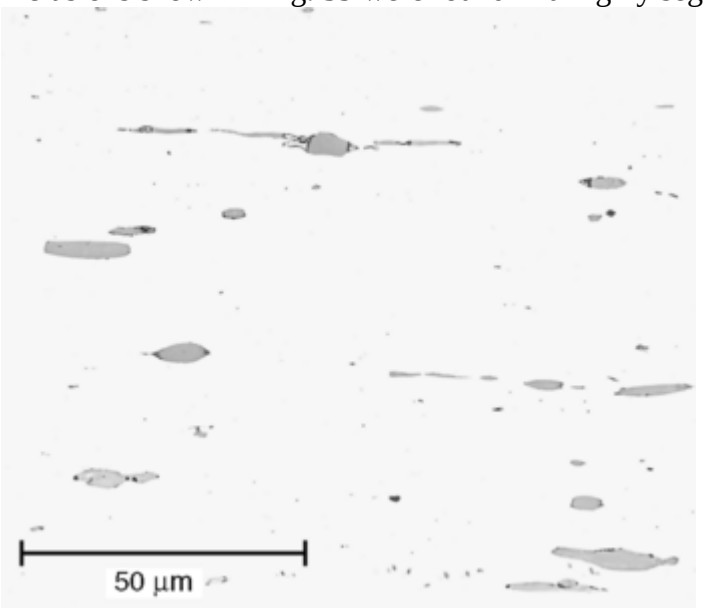

Fig. 35 Manganese sulfide inclusions in resulfurized free-machining steel. Unetched (as-polished). Original magnification 500×



Fig. 36 Silicate inclusions in steel. Unetched (as-polished). Original magnification 1000×

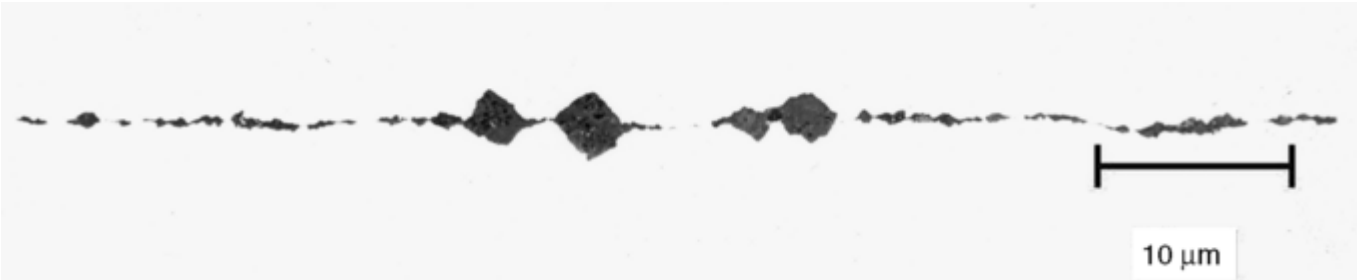

Fig. 37 Aluminum oxide inclusions in steel. Note how the particles break up during rolling. Unetched (as-polished). Original magnification 1000×

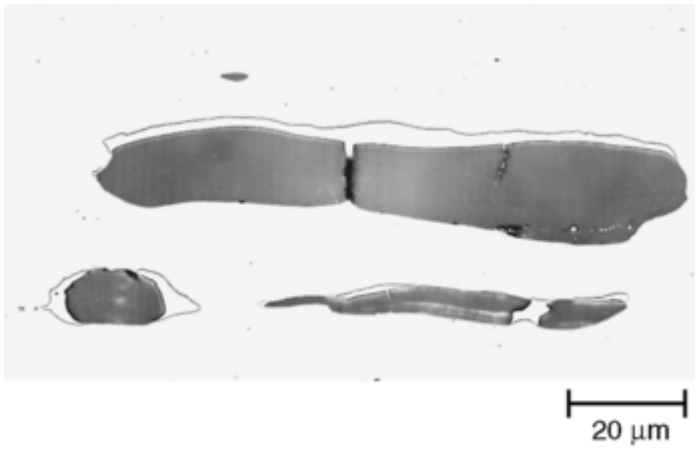

Fig. 38 Manganese sulfide inclusions coated with metallic lead (light-appearing layer on the sulfides) in free-machining steel. Unetched (as-polished). Original magnification 500×

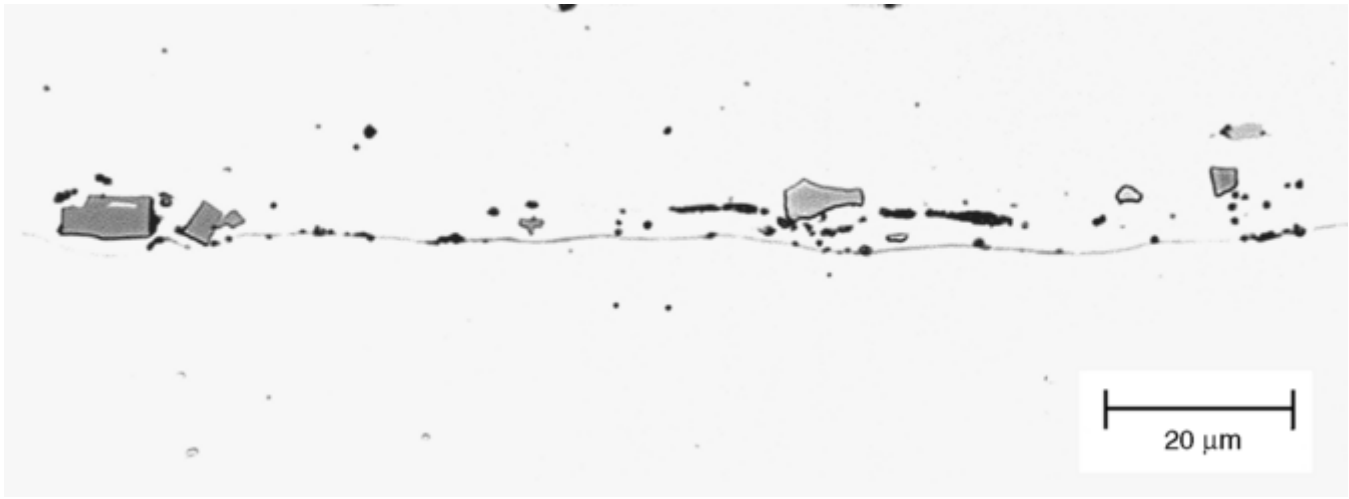

Fig. 39 Titanium nitride inclusions in steel. Unetched (as-polished). Original magnification 500×

The reason that inclusions are observed and measured in the as-polished condition is that etching will reveal other constituents that can obscure and complicate the examination. Etching may also disturb the inclusion-steel interface. For example, an acid etch will attack and destroy the lead layer in the free-machining steel in Fig. 38. Therefore, it is good metallographic practice to examine the specimen in the as-polished condition before etching the specimen.

Etching

One of the interesting and challenging aspects of the metallographer's job is the selection of suitable etching medium to reveal the underlying microstructure of a polished specimen. For plain carbon and low-alloy steels, the metallographer has a wide choice of etchants, depending on the constituents in the microstructure Ref 5, 6, and 7. For example, a sample that is mostly ferrite will be etched differently than a specimen that is mostly pearlite. Sometimes, combinations of etchants are used for multicomponent microstructures. This section illustrates the use of proven etching techniques for plain carbon and low-alloy steels. Some of these etchants are attack etchants that chemically attack the surface of the specimen, and some of the etchants are tint etchants that simply deposit a chemical layer selectively on various constituents in the microstructure. Lists of the useful attack and tint etchants for plain carbon and low-alloy steels can be found in Ref 5, 6, and 7. Table 1 is a list of some common etchants for carbon and low-alloy steels.

Table 1 Common etchants for carbon and low-alloy steels

Name	Ingredients	Applications
2% nital	2 mL nitric acid (concentrated) 98 mL ethyl alcohol	Common etchant for carbon and low-alloy steels. Reveals ferrite grain boundaries and constituents
Marshall's reagent	Mix equal amounts of part A and part B: Part A: 5 mL of sulfuric acid (concentrated) 8 g of oxalic acid 100 mL water Part B: 30% solution of hydrogen peroxide	Hold sample vertical to reduce pitting. Etch either statically or in ultrasonic bath. Can pre-etch in 2% nital for better results Uniform ferrite grain-boundary etch. Colors cementite and attacks inclusions. Reveals prior-austenite grain boundaries in martensitic low-carbon steels
Modified Marshall's reagent	Mix equal amounts of part A and part B; then add part C: Part A: 5 mL of sulfuric acid (concentrated) 8 g of oxalic acid 100 mL water Part B: 30% solution of hydrogen peroxide Part C: 4 drops hydrofluoric acid	Hold sample vertical to reduce pitting. Etch either statically or in ultrasonic bath. Can pre-etch in 2% nital for better results
4% picral	4 g picric acid 96 mL ethyl alcohol 5 mL zephiran chloride (wetting agent)	For structures consisting of ferrite and carbides. Does not reveal ferrite grain boundaries. Addition of zephiran chloride improves etch rate and uniformity.
Picral + hydrochloric acid	4 g picric acid 96 mL ethyl alcohol 5 drops hydrochloric acid	Hydrochloric acid improves etch rate.

	5 mL zephiran chloride (wetting agent)	
Hot saturated aqueous picric acid (superpicral)	10 g picric acid 100 mL water 1 g sodium dodecylbenzene sulfanate (wetting agent) Above saturation limit of picric acid: heat the solution for better dissolution of picric acid.	Typically used with high-alloy steels, tool steels, and stainless steels
Vilella's reagent	1 g picric acid 5 mL hydrochloric acid (concentrated) 95 mL ethyl alcohol	Good for ferrite-carbide structures. Produces grain contrast for estimating prior-austenite grain size. Results best on martensite tempered at 300–500 °C (570–930 °F). Occasionally reveals prior-austenite grain boundaries in high-alloy steels
Winsteard's reagent (modified)	Part A: 2 g picric acid 10 mL ethyl alcohol Part B: 200 mL water 5 mL sodium dodecylbenzene sulfunate (40% solution) 5 drops hydrochloric acid	To delineate prior austenite grain boundaries
4% picral + 2% nital	Same ingredients as listed above. Etch first in pical then in nital.	For ferrite + pearlite microstructures
Sodium metabisulfite	8 to 20 g of sodium metabisulfite dilute to 100 mL water	Tint etch
Oberhoffer's reagent	500 mL water 500 mL alcohol 30 g $FeCl_3$ 0.5 g $SnCl_3$ 1.9 g $CuCl_2$ 40 mL hydrochloric acid (concentrated)	Macroetch. Use at room temperature and immerse for approximately 20 s.

Attack Etching Techniques. There are basically three attack etchant families for plain carbon and low-alloy steels: variations of nitric acid solutions (nital), picric acid solutions (picral), and oxidizing-type solutions (Marshall's reagent). The various etching solutions important to revealing the microstructure of these steels are illustrated as follows, along with their advantages and disadvantages.

Nitric-Acid-Based Solutions (Nital). The most common nitric-acid-based solution is a simple mixture of 2 mL of concentrated nitric acid in 98 mL of ethyl alcohol and called 2% nital. The acronym nital is derived from the mixture of nitric acid and alcohol. It is one of the oldest etchants used for steel, dating back to the mid-19th century. Ethyl alcohol is preferred over methyl alcohol because of the toxicity of methyl alcohol. The historic use of nital has been in revealing ferrite grains and highlighting the features in martensitic microstructures. For example, 2% nital was used to delineate the ferrite grain boundaries in the low-carbon steel shown in Fig. 40. Note that most of the ferrite grains are delineated (there are some missing grain boundaries). Figure 41 shows low-alloy steel with lath martensite etched in 2% nital. Note that the prior-austenite grain boundaries are highlighted as well as the individual lath martensite packets. Figure 42 shows the use of 2% nital for plate martensite, and Fig. 43 shows a mixed martensite/bainite microstructure. Note the excellent delineation of prior-austenite grain boundaries in the latter micrograph. The grain boundaries of ferrite and martensite appear dark because the nitric acid chemically attacks each grain, which has a different crystallographic orientation (each grain of ferrite is a single crystal). The deeper the step at the grain boundary, the more evident (or darker) the boundary will appear in the reflected light of a light microscope. This is because there is more scattering of light, which means that less light is reflected back into the objective lens of the light microscope. However, 2% nital does not always delineate all the grain boundaries, because the grains at that particular boundary have a similar orientation or etching response. This means that grain size measurements may be in error because of the missing boundaries. Marshall's reagent is replacing nital for ferrite grain size measurements, especially for image analysis, because it does a much better job in attacking all the ferrite grain boundaries.

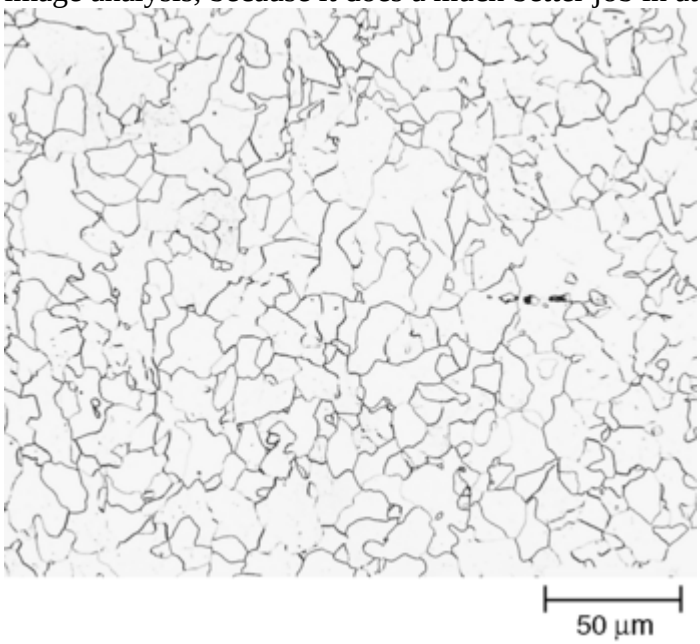

Fig. 40 Microstructure of low-carbon steel showing ferrite grain boundaries. 2% nital etch. Original magnification 200×

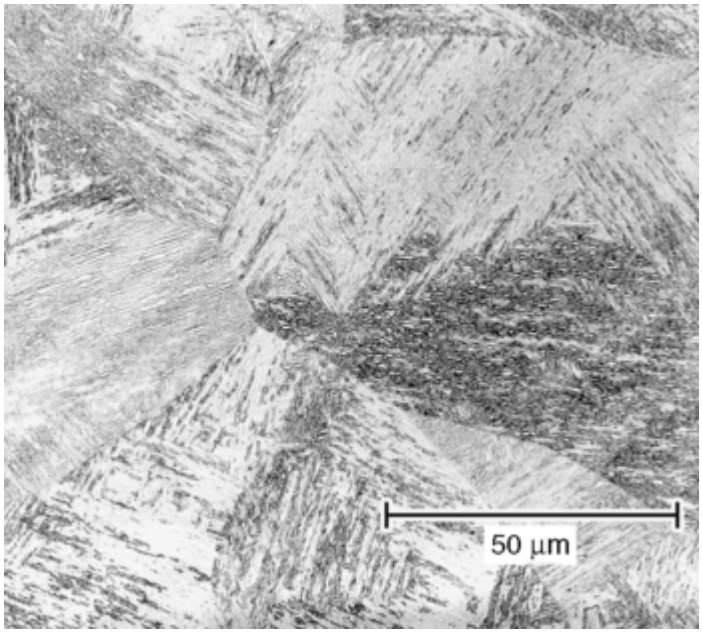

Fig. 41 Microstructure of quenched low-alloy steel showing delineation of the prior-austenite grain boundaries and lath martensite packets. 2% nital etch. Original magnification 500×

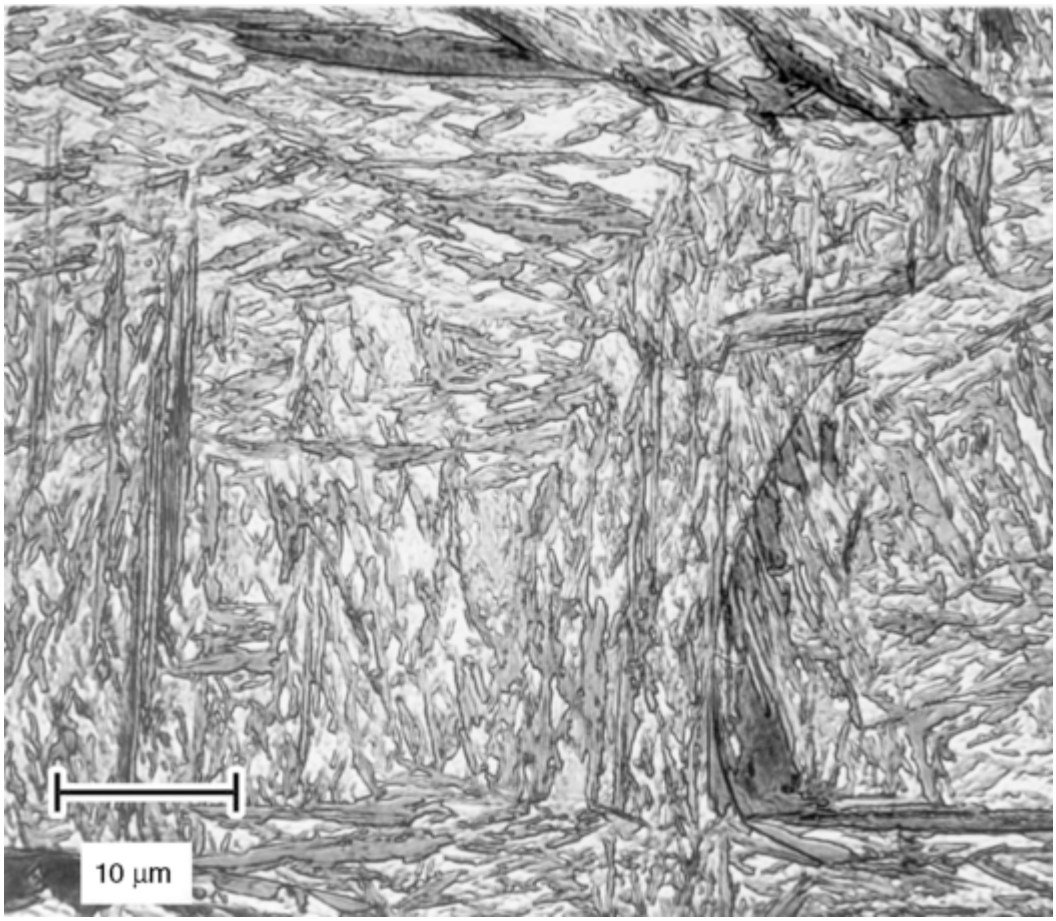

Fig. 42 Microstructure of quenched low-alloy steel showing plate martensite. 2% nital etch. Original magnification 1000×

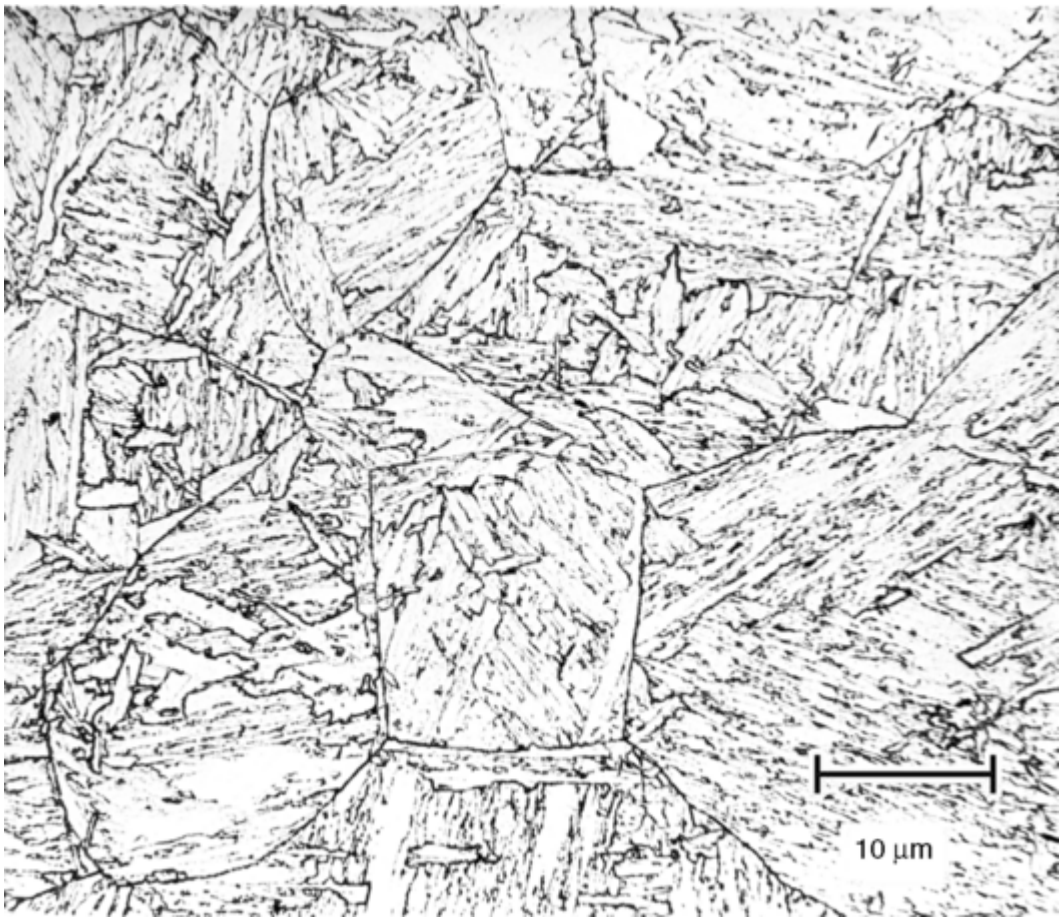

Fig. 43 Microstructure of quenched low-alloy steel showing mixed bainite and martensite. 2% nital etch. Original magnification 1000×

Oxidizing-Type Solutions (Marshall's Reagent). One of the more recent etchants developed for plain carbon and low-alloy steels is Marshall's reagent. Marshall's reagent is a little more complicated to prepare than nital, and it must be used fresh to obtain the optimal effect. It consists of two parts: part A is a mixture of 5 mL concentrated sulfuric acid and 8 g of oxalic acid crystals in 100 mL water, and part B is a 30% solution of hydrogen peroxide (the ingredient that makes this an oxidizing solution). It is replacing nital in many applications. An example of low-carbon steel that was etched in Marshall's reagent can be seen in Fig. 44. Note the sharpness and the completeness of the ferrite grain boundaries in the specimen etched with Marshall's reagent. However, Marshall's reagent can stain carbides (cementite), as seen in this micrograph.

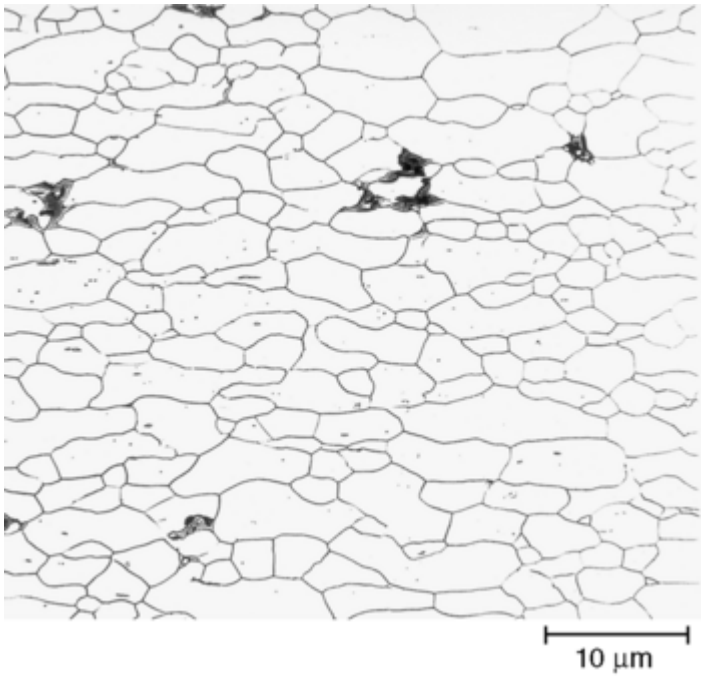

Fig. 44 Microstructure of low-carbon steel showing delineation of the ferrite grain boundaries. Note that the cementite particles are stained. Marshall's reagent. Original magnification 1000×

There is also a modified version of Marshall's reagent that contains an additional few drops of hydrofluoric acid (HF). When using this modified form, it must be kept in mind that HF is extremely corrosive and can quickly attack human skin, causing severe acid burns. Always use latex gloves and plastic containers when using HF, which attacks glass. Modified Marshall's reagent is used to sharpen ferrite grain boundaries, as seen in Fig. 45. Therefore, to accurately measure ferrite grain size using image analysis, the modified version of Marshall's reagent is the best choice.

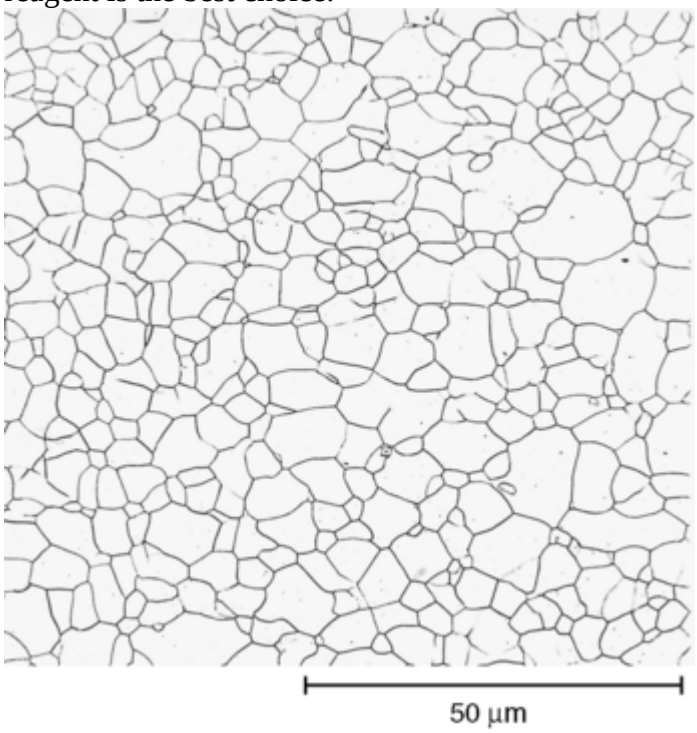

Fig. 45 Microstructure of low-carbon interstitial-free steel showing delineation of the ferrite grain boundaries. Modified Marshall's reagent (with hydrofluoric acid). Original magnification 500×

Marshall's reagent can also be used for delineating grain boundaries in martensite if the boundaries consist of allotriomorphs of ferrite or bainite. An example is shown in Fig. 46. This image was taken in dark-field

illumination, as opposed to the conventional bright-field illumination used for the other micrographs in this article. In dark-field illumination, the ferrite/bainite allotriomorphs appear dark.

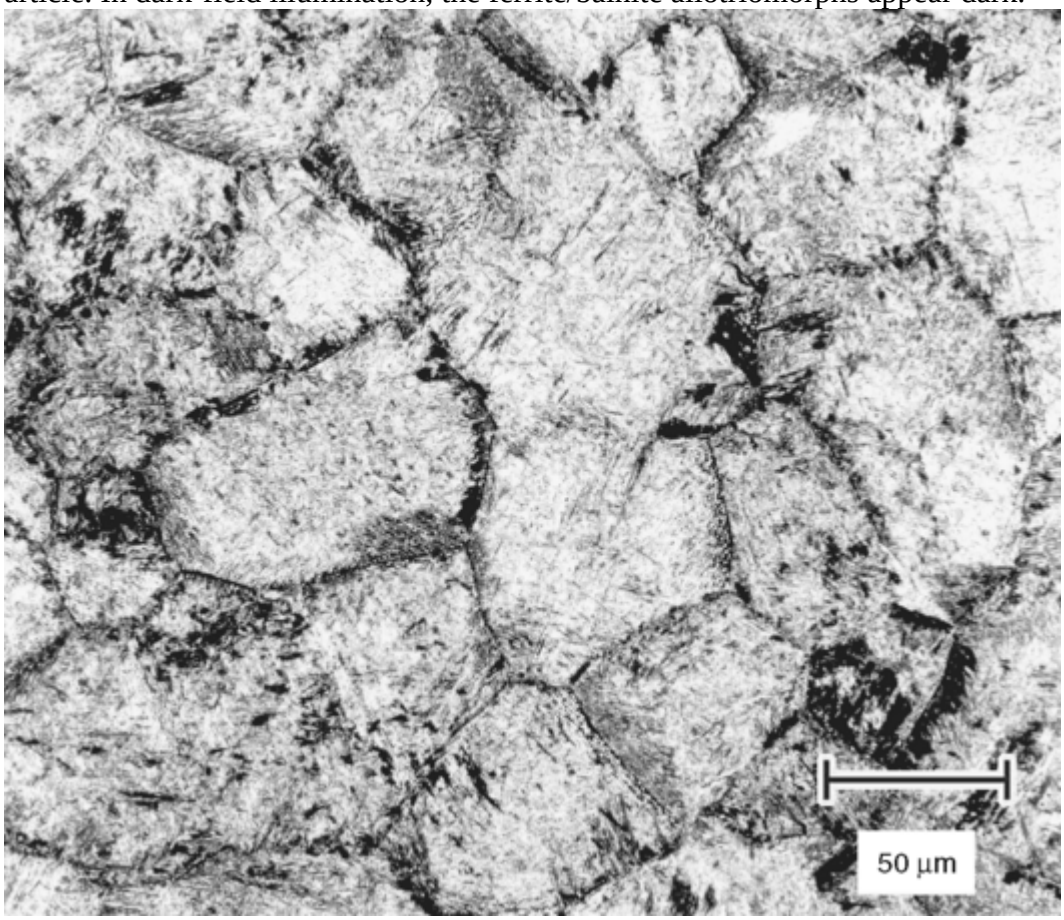

Fig. 46 Microstructure of quenched and tempered low-alloy steel showing ferrite and bainite at the prior-austenite grain boundaries. Taken in dark-field illumination. Marshall's reagent. Original magnification 200×

Picric-Acid-Based Solutions (Picral). One of the most versatile etchants for plain carbon and low-alloy steels is 4% picral and the numerous variations of picral. Picral has been a standard etchant for steel for decades. The common formulation is a mixture of 4 g picric acid crystals in 96 mL of ethyl alcohol. For optimal results, 5 drops of wetting agent zephiran chloride are added. As with nital, picral is an acronym for picric acid and alcohol. It must be noted that picric acid is a dangerous explosive in the dry crystal form. Thus, picric acid crystals are always stored wet (picric acid is practically insoluble in water). The yellow crystals should never be allowed to dry out. Because of the potential danger, many locations prohibit the use of picric acid in the metallographic laboratory. However, if properly handled and stored, the danger of explosion is nonexistent. It has been used in the author's laboratory for decades without incident.

Picral is used as a general etchant for pearlite, bainite, tempered martensite, cementite, and other carbides. Picral attacks interfaces between ferrite and a carbide phase, as opposed to nital, which attacks the entire ferrite grain. Picral is a standard etchant for pearlite (Fig. 47). Numerous specimens shown in previous figures in this article were etched with 4% picral. One peculiar aspect of 4% picral is that it develops a faster etching response with repeated use. This is an advantage, but it can also be a disadvantage, because the etching characteristics change from a freshly made solution to the same solution used later that day.

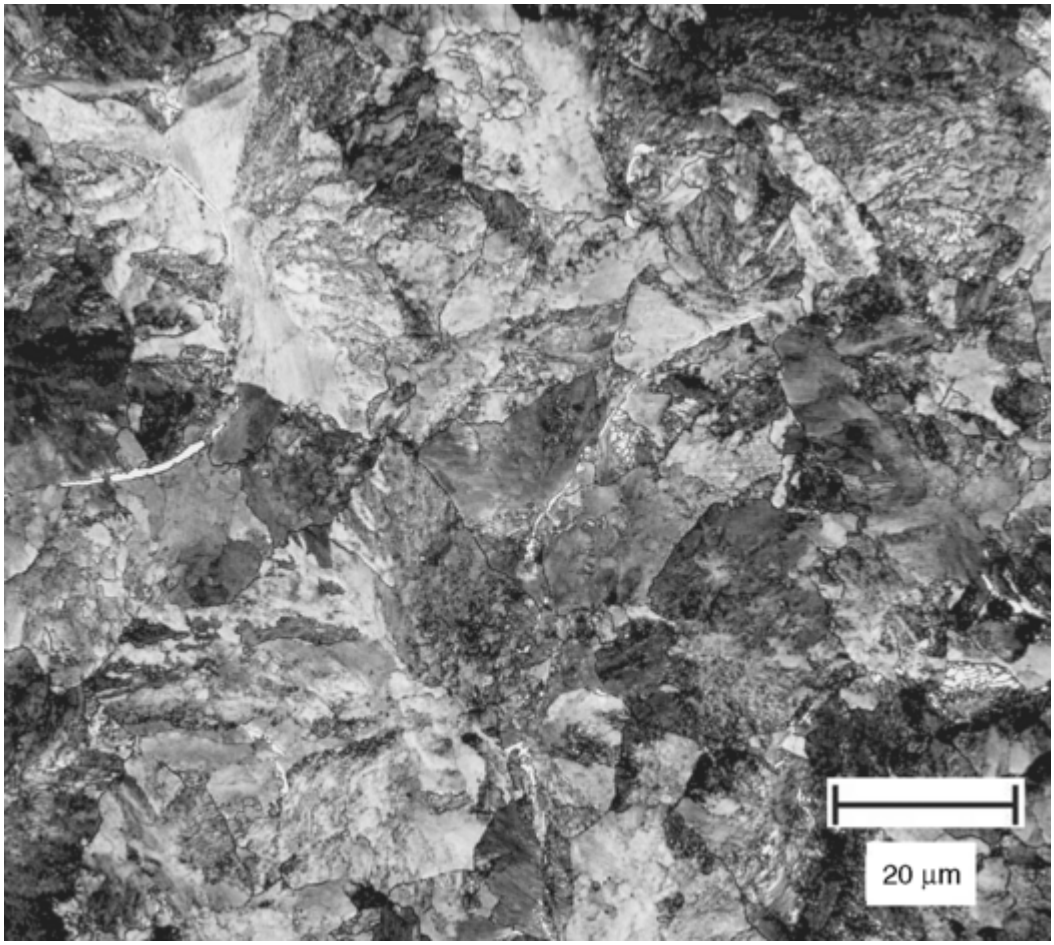

Fig. 47 Microstructure of UNS G10800 steel with a fully pearlitic microstructure. 4% picral etch. Original magnification 500×

One modification of picral is to add 5 drops of HCl. This sharpens features in low-alloy steels, particularly steels containing chromium. Another modification is Vilella's reagent, which is composed of only 1 g picric acid in 5 mL concentrated HCl and 100 mL water. Vilella's reagent is used to delineate prior-austenite grain boundaries and carbides in quenched and tempered low-alloy and alloy steel martensitic microstructures.

Winsteard's reagent is another important variation of picral. This reagent is a two-part mixture. Part A is 2 g of picric acid dissolved in 10 mL of ethyl alcohol. Part B is 5 mL of a 40% solution of sodium dodecylbenzene sulfonate (a surfactant) in 200 mL of water. A simple hair shampoo can also be used if it contains sodium lauryl sulfate. Alcohol is used in part A because picric acid dissolves easily in alcohol but not in water. Thus, once dissolved in alcohol, the picric acid solution will easily mix with the water-based part B. An example of the use of Winsteard's reagent in revealing prior-austenite grain boundaries can be seen in Fig. 48. To sharpen the effect of this reagent, 5 drops of HCl should be added to the final mixture. This modified Winsteard's reagent (with 5 drops of HCl) was used for Fig. 49 to highlight prior-austenite grain boundaries and carbides. Hot (70 °C, or 160 °F) modified Winsteard's reagent can be used to enhance regions of segregation, as seen in Fig. 50 and Fig. 51. The segregated elements include manganese, phosphorus, carbon, and sulfur. The specimens in these two figures are flash-butt welds of steel hot band, where both pieces of sheet are pushed together while hot. The regions of segregation indicate the metal flow as the material deformed. The vertical line in the center of each photo represents the original end of each sheet. This centerline can contain oxide scale from the original sheet.

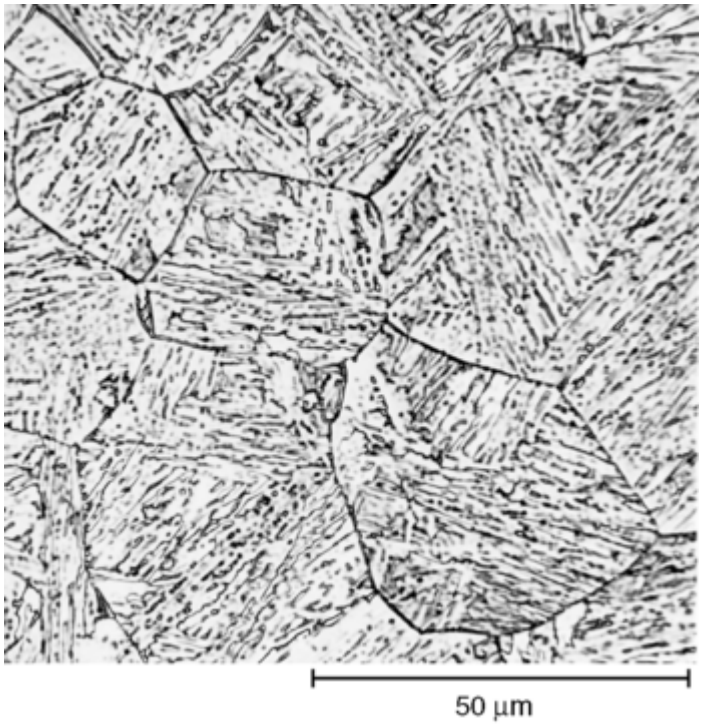

Fig. 48 Microstructure of quenched low-alloy steel showing delineation of the prior-austenite grain boundaries. The individual laths of bainite/martensite are also delineated. Winsteard's reagent. Original magnification 500×

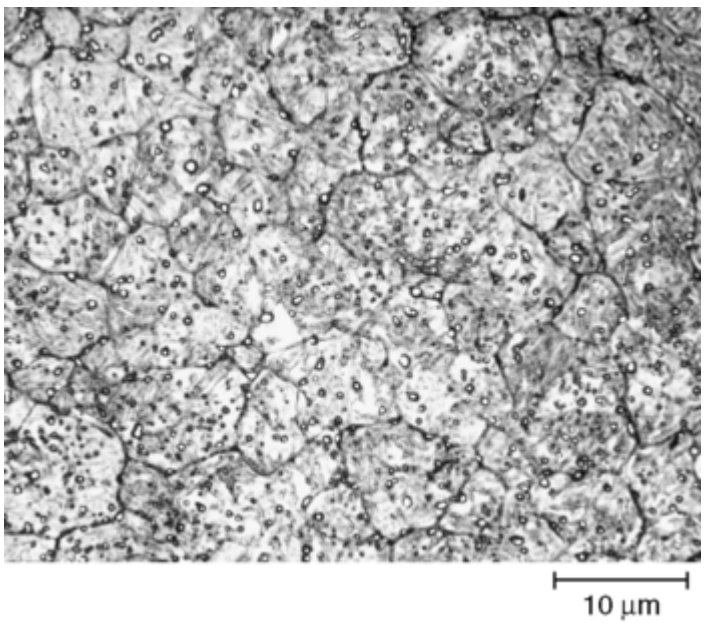

Fig. 49 Microstructure of quenched and tempered low-alloy steel showing delineation of the prior-austenite grain boundaries. The individual carbides are also delineated. Modified Winsteard's reagent. Original magnification 1000×

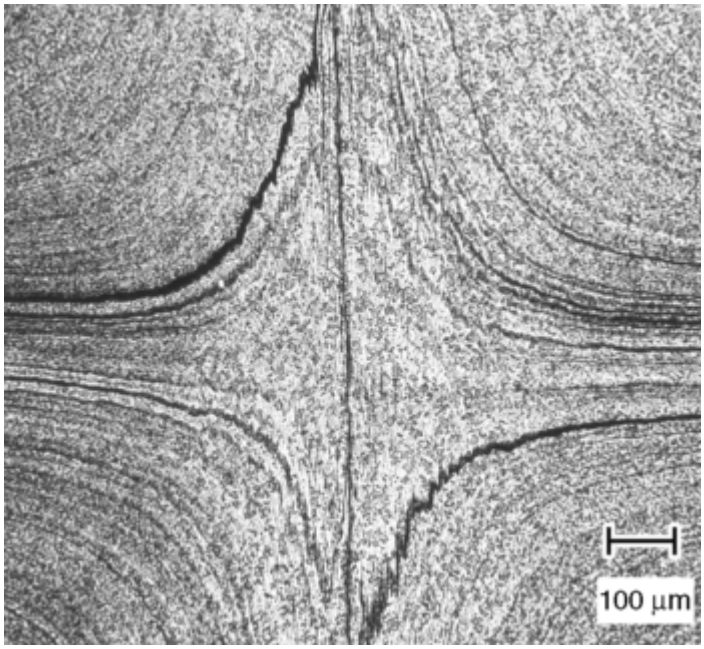

Fig. 50 Microstructure of flash-butt weld showing segregation bands representing the metal flow during deformation. Hot modified Winsteard's reagent. Original magnification 50×

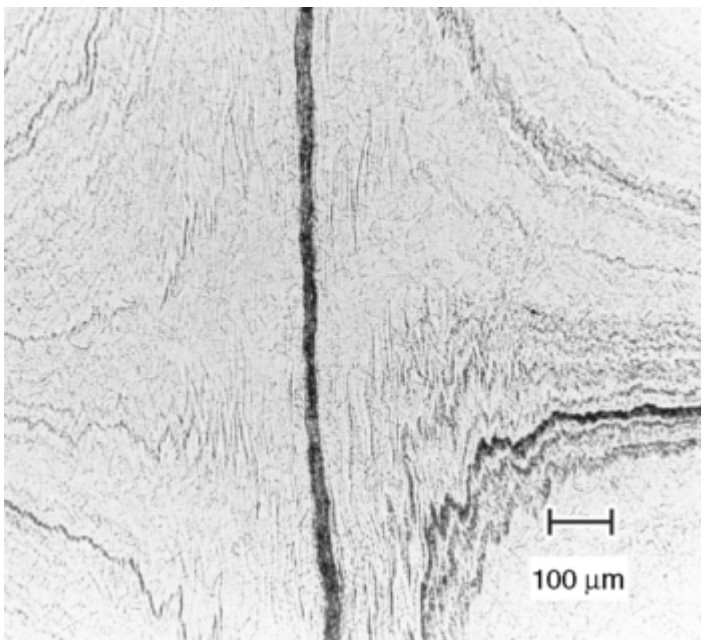

Fig. 51 Microstructure of flash-butt weld showing segregation bands representing the metal flow during deformation. Hot modified Winsteard's reagent. Original magnification 50×

Saturated aqueous picric acid is a water-based solution instead of an alcohol-based picric acid solution. However, as mentioned previously, only a small amount of picric acid will dissolve in water at room temperature (approximately 1%). Thus, mixing 10 g of picric acid in 100 mL water will saturate the water with approximately 1% picric acid. To be effective, 1 g of the wetting agent sodium dodecylbenzene sulfonate (surfactant) must be added. This is a water-soluble wetting agent, as opposed to zephiran chloride, which is an alcohol-soluble wetting agent. Saturated aqueous picric acid is used to highlight prior-austenite grain boundaries in a fully martensitic microstructure, as seen in Fig. 52. In this case, the solution was heated to 82 °C (180 °F) to accelerate the effect. To enhance the effectiveness, 5 drops of HCl can be added. The prior-austenite grain boundaries in Fig. 53 were revealed with this modified hot saturated picric acid (and wetting agent).

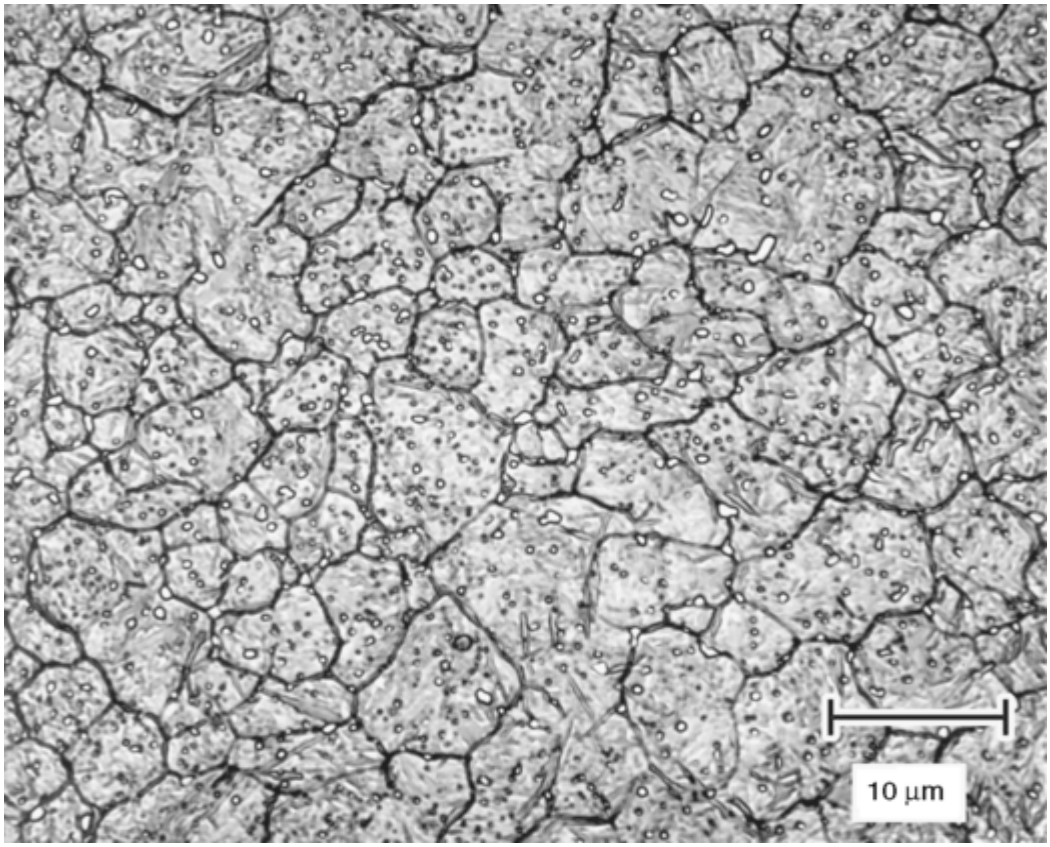

Fig. 52 Microstructure of quenched and tempered low-alloy steel showing delineation of the prior-austenite grain boundaries. The individual carbides are also delineated. Hot saturated aqueous picric acid etch. Original magnification 1000×

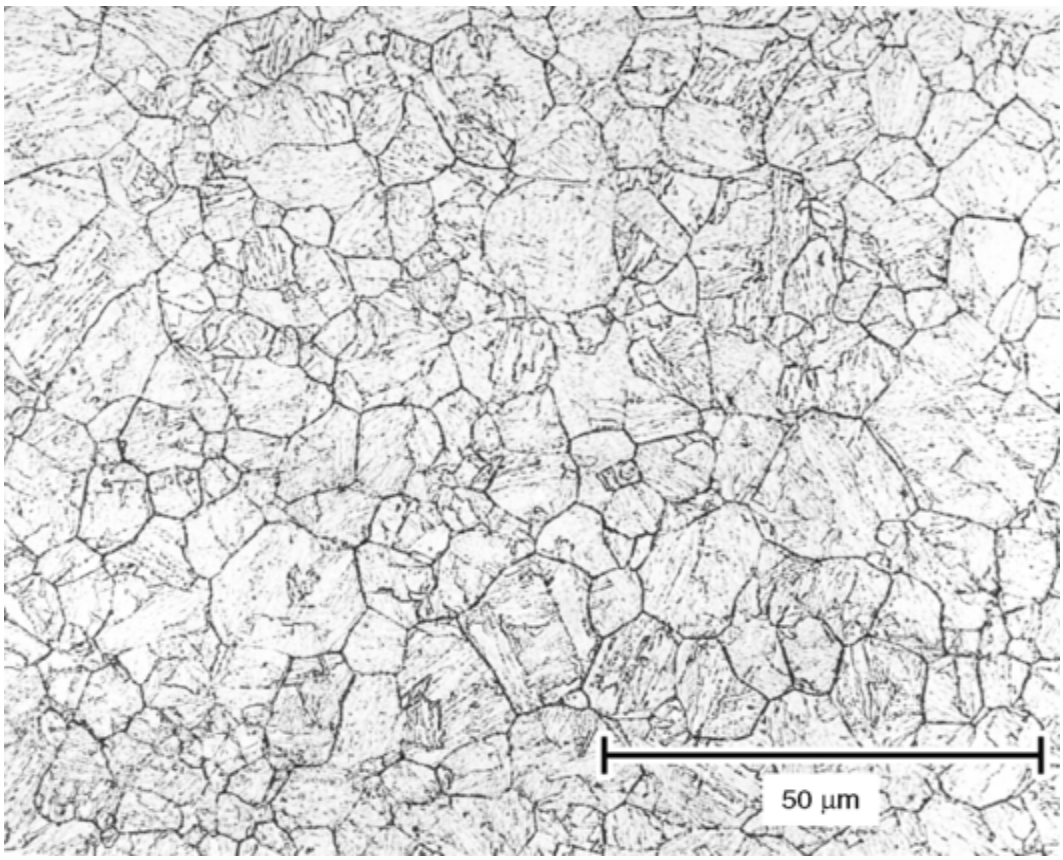

Fig. 53 Microstructure of quenched and tempered low-alloy steel showing delineation of the prior-austenite grain boundaries. Modified hot saturated aqueous picric acid etch. Original magnification 500×

Boiling alkaline sodium picrate is another water-based variation of picric acid and consists of 2 g picric acid, 25 g sodium hydroxide, and 100 mL water. The sodium hydroxide must be dissolved in the water first before adding the picric acid crystals. The exothermic reaction of the sodium hydroxide in water provides enough elevated temperature to dissolve the picric acid. Before using this etchant, it must be heated to boiling and held for 5 to 10 min. The specimen is etched in the boiling solution. This etchant can be particularly useful in darkening cementite and carbides. Thus, this etchant is used to selectively etch a microstructure to identify which constituents are cementite.

Sometimes, both 4% picral and 2% nital are used. First, the specimen is etched in 4% picral, then rinsed, and etched in 2% nital. This combination etchant is used for ferritic-pearlitic steels to delineate both the ferrite grains (the nital etch) and the boundaries between the ferrite and pearlite (the picric etch). Figure 54 shows an as-rolled microalloyed steel plate etched in 4% picral + 2% nital. The combination of these two etchants works well with bainitic steels, as seen in Fig. 55. Figure 56 shows a mixed martensite and bainite microstructure.

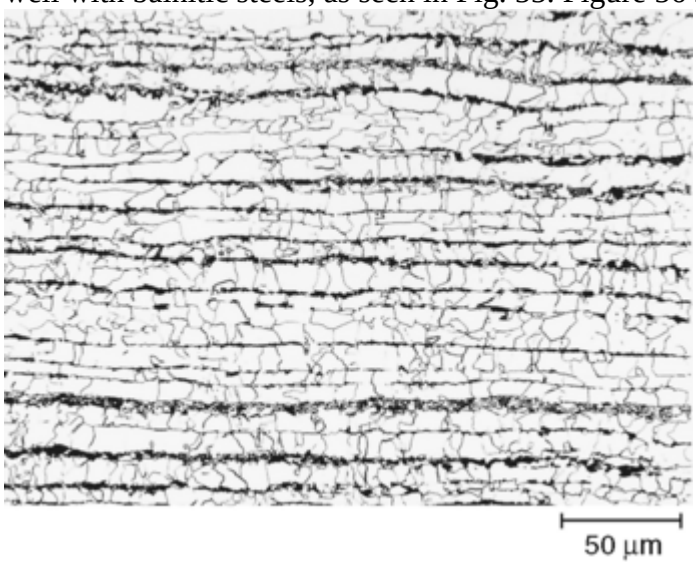

Fig. 54 Microstructure of as-rolled microalloyed steel showing ferrite grains and pearlite banding. Note that both the ferrite grains and pearlite bands are revealed. 4% picral + 2% nital. Original magnification 200×



Fig. 55 Microstructure of quenched low-alloy steel showing a bainitic structure (granular bainite). 4% picral + 2% nital. Original magnification 1000×

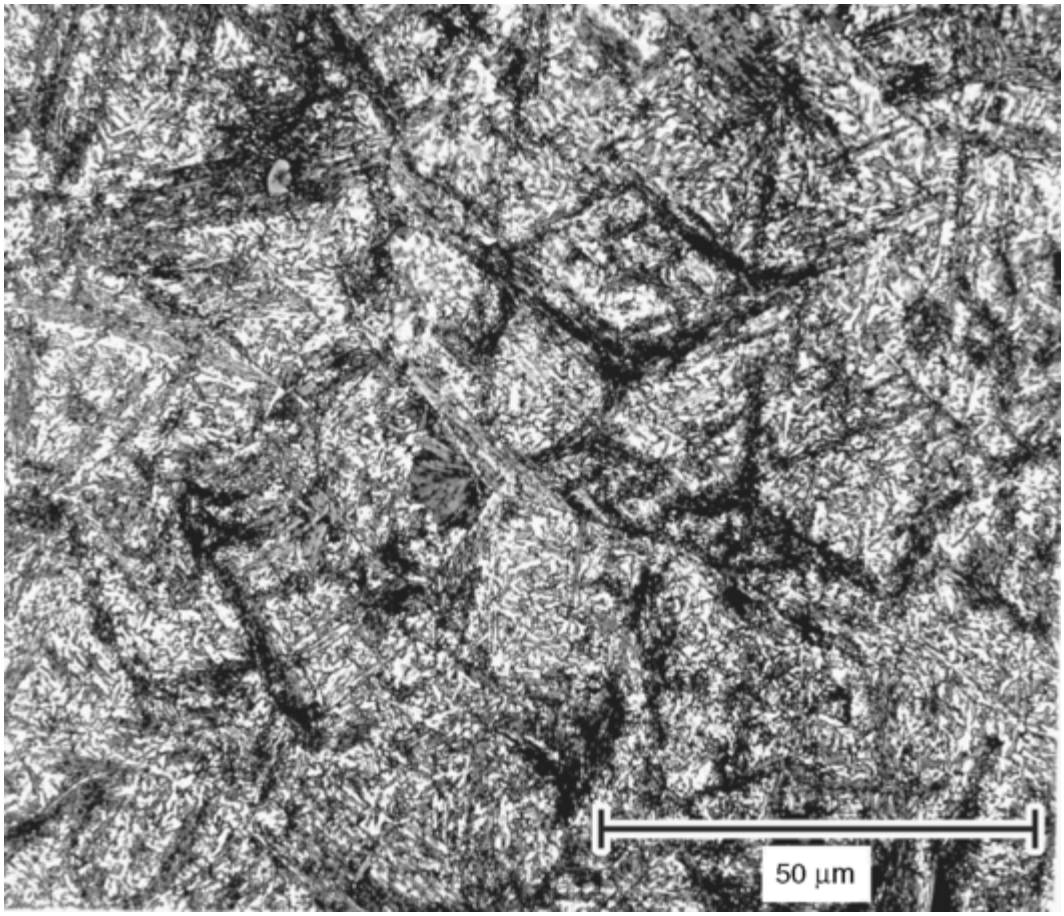

Fig. 56 Microstructure of quenched and tempered UNS G43400 steel showing a mixed bainite (dark-appearing constituent) and martensite structure. 4% picral + 2% nital. Original magnification 500×

Tint Etching Techniques. Another very important family of etchants is the tint etchants. These etchants do not chemically attack the steel but deposit chemical films selectively on constituents on the specimen surface. They are particularly important in color metallography. The most common tint etchants contain either a metabisulfite ion or a thiosulfate ion. The chemical compositions of these etchants are listed in Ref 5, 6, 7 and 9.

Sodium Metabisulfite Reagent. A general-purpose tint etchant for plain carbon and low-alloy steel is sodium metabisulfite (SMB). This etchant can be mixed in a range of concentrations of SMB from 8 to 20 g in 100 mL water, depending on the intensity of the tint and brown color desired. One popular use of the SMB tint etch is to darken martensite. For example, in some dual-phase steels and most transformation-induced plasticity steels, the microstructure consists of martensite and austenite islands in a matrix of ferrite. The SMB tint etch can be used to distinguish the martensite islands from the austenite islands by darkening (tinting) the martensite while leaving the ferrite and austenite untouched. Figure 57 shows an example of a dual-phase steel etched with a 10% solution of SMB. By careful examination of the islands in this micrograph, one can see that some islands are dark (actually tan/brown) and some islands are clear. The dark islands are martensite, and the clear islands are austenite. There are also very dark regions of pearlite. The martensite in these steels is usually autotempered (self-tempered). As-quenched martensite does not respond to the 10% SMB tint etch. Thus, SMB can be a powerful way to distinguish tempered martensite regions in mixed microstructures.

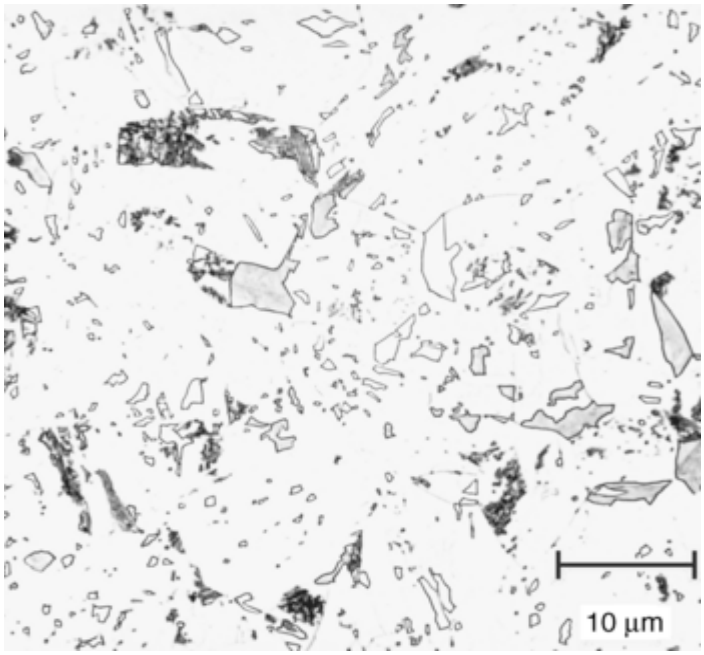

Fig. 57 Microstructure of dual-phase steel showing tint-etched martensite (light-gray islands) and unetched austenite (white islands). Pearlite shown as dark regions. 10% sodium metabisulfite tint etch. Original magnification 1000×

Beraha's Reagent. A variation of the simple SMB etchant described previously is a mixture of potassium metabisulfite (3 g) and SMB (10 g) in 100 mL water (Ref 7). This tint etchant has a behavior similar to SMB.

Klemm's Reagent. This tint etching reagent is mixed in two parts: part A is a saturated solution of sodium thiosulfate in water (50 mL), and part B is 1 g of potassium metabisulfite. This is not a common tint etchant for plain carbon steel but can be used to provide a blue and red color to ferrite.

Using the Microscope to Enhance Microstructure. Today's metallurgical microscopes are equipped with many optical features that can be used to enhance the microstructural features in a specimen. For plain carbon and low-alloy steel, differential interference contrast (DIC), also called Nomarksi illumination, can be used to reveal topographic or texture features in a specimen. Figure 58 and Figure 59 show grain-boundary carbides examined in DIC illumination. This specimen is in the unetched condition, and the carbides, because of their hardness, protrude from the ferritic matrix after polishing.

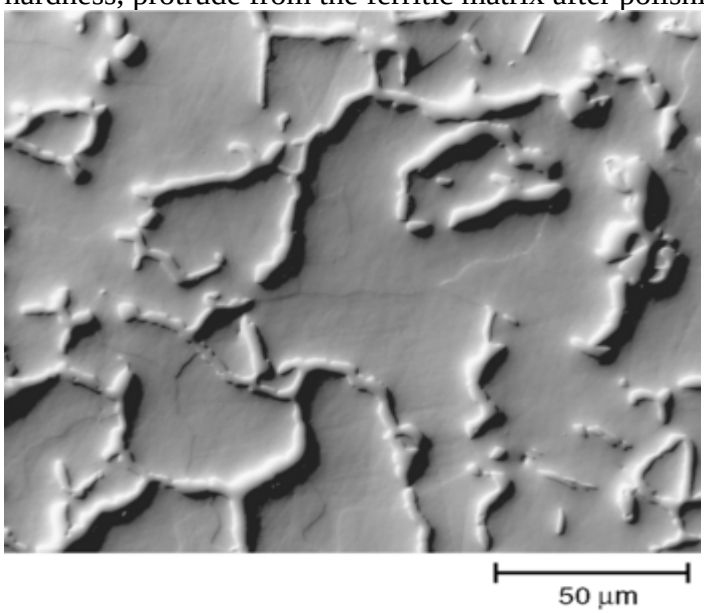

Fig. 58 Microstructure of ferritic steel with grain-boundary carbides. Note that the carbides are standing above the ferrite. Unetched (as-polished). Observed in differential interference contrast. Original magnification 200×

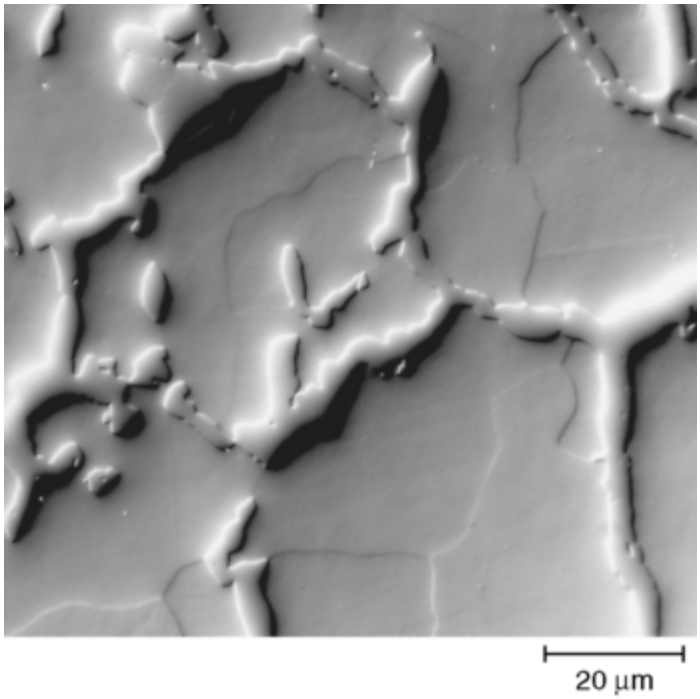

Fig. 59 Higher-magnification view of the microstructure in Fig. 58. Unetched (as-polished). Observed in differential interference contrast. 500×

Other features on the metallurgical microscope that can be used to enhance an image are dark-field illumination and polarized light. Compare Fig. 60, taken with dark-field illumination, with Fig. 48, taken with normal bright-field illumination. Note that the prior-austenite grain boundaries are white in Fig. 60, rather than dark as in Fig. 48. Additional information is provided in the article “Light Microscopy” in this Volume.

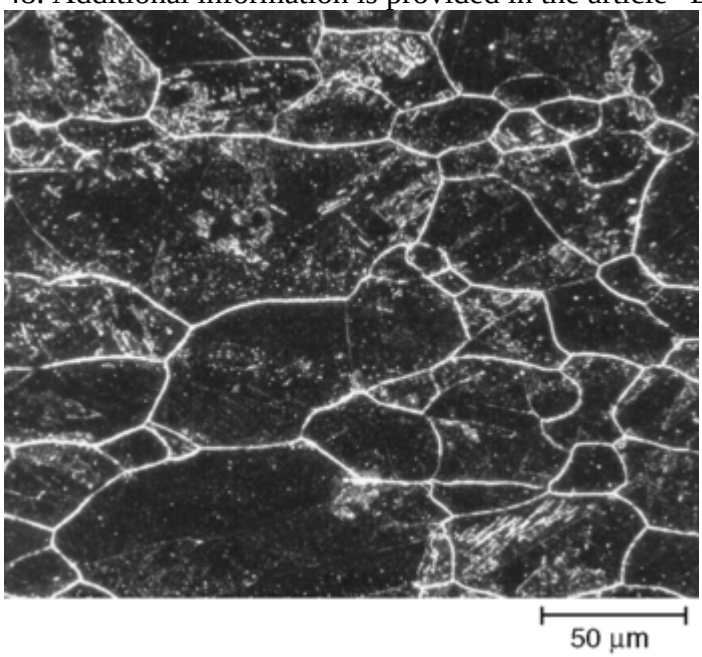

Fig. 60 Microstructure of quenched and tempered low-alloy steel showing prior-austenite grain boundaries. Taken in dark-field illumination. Hot saturated aqueous picric acid etch. 200×

References cited in this section

5. B.L. Bramfitt and A.O. Benscoter, Metallographer's Guide: Practices and Procedures for Irons and Steels, ASM International, 2002

6. G.F. Vander Voort, Metallography: Principles and Practice, McGraw Hill, 1984; reprinted by ASM International, 1999

7. L.E. Samuels, Light Microscopy of Carbon Steels, ASM International, 1999

8. “Practice for Preparing Sulfur Prints for Macrostructural Examination,” E 1180, Annual Book of ASTM Standards, ASTM, 1998

9. E. Beraha and B. Shpigler, Color Metallography, American Society for Metals, 1977

B.L. Bramfitt and S.J. Lawrence, Metallography and Microstructures of Carbon and Low-Alloy Steels, Metallography and Microstructures, Vol 9, ASM Handbook, ASM International, 2004, p. 608–626

Metallography and Microstructures of Carbon and Low-Alloy Steels

Bruce L. Bramfitt and Samuel J. Lawrence, International Steel Group, Inc.

References

1. Properties and Selection: Irons, Steels, and High-Performance Alloys, Vol 1, ASM Handbook, ASM International, 1990

2. G. Krauss, Steels: Heat Treatment and Processing Principles, ASM International, 1990

3. C.R. Brooks, Principles of the Heat Treatment of Plain Carbon and Low-Alloy Steels, ASM International, 1996

4. B.L. Bramfitt, Annealing of Steel, Heat Treating, Vol 4, ASM Handbook, ASM International, 1991, p 43

5. B.L. Bramfitt and A.O. Benscoter, Metallographer's Guide: Practices and Procedures for Irons and Steels, ASM International, 2002

6. G.F. Vander Voort, Metallography: Principles and Practice, McGraw Hill, 1984; reprinted by ASM International, 1999

7. L.E. Samuels, Light Microscopy of Carbon Steels, ASM International, 1999

8. “Practice for Preparing Sulfur Prints for Macrostructural Examination,” E 1180, Annual Book of ASTM Standards, ASTM, 1998

9. E. Beraha and B. Shpigler, Color Metallography, American Society for Metals, 1977

Metallography and Microstructures of Case-Hardening Steel, *Metallography and Microstructures*, Vol 9, *ASM Handbook*, ASM International, 2004, p. 627–643

Metallography and Microstructures of Case-Hardening Steel

Introduction

DIFFUSION of alloying elements for surface hardening of steels includes various thermochemical treatments (Table 1), of which carburizing and carbonitriding are the most widely used. Nitriding and nitrocarburizing are also widely used. In general, the steels best suited to these processes are low-carbon steels that rely on a surface layer, or case, of high hardness to provide a level of strength and wear resistance not obtainable from the core metal. Steels for nitriding—whether specially formulated for this purpose or adopted because of satisfactory performance in processing and in service—are usually medium-carbon low-alloy steels of high hardenability; stainless and tool steels can also be nitrided. Compositions of some typical case-hardening steels are given in Table 2. Types of diffusion methods for various types of steels are listed in Fig. 1(a).

Table 1 Typical characteristics of diffusion treatments

Process	Process temperature, °C (°F)	Typical case depth	Case hardness, HRC	Typical base metals	Process characteristics
Carburizing					
Pack	815–1090 (1500–2000)	125 μm–1.5 mm (5–60 mils)	50–63	Low-carbon steels, low-carbon alloy steels	Low equipment costs, difficult to control case depth accurately
Gas	815–980 (1500–1800)	75 μm–1.5 mm (3–60 mils)	50–63	Low-carbon steels, low-carbon alloy steels	Good control of case depth, suitable for continuous operation, good gas controls required, can be dangerous
Liquid	815–980 (1500–1800)	50 μm–1.5 mm (2–60 mils)	50–65	Low-carbon steels, low-carbon alloy steels	Faster than pack and gas processes, can pose salt disposal problem, salt baths require frequent maintenance
Vacuum	815–1090 (1500–2000)	75 μm–1.5 mm (3–60 mils)	50–63	Low-carbon steels, low-carbon alloy steels	Excellent process control, bright parts, faster than gas carburizing, high equipment costs
Nitriding					
Gas	480–590 (900–1100)	125 μm–0.75 mm (5–30 mils)	50–70	Alloy steels, nitriding steels, stainless steels	Hardest cases from nitriding steels, quenching not required, low distortion, process is slow, is usually a batch process
Salt	510–565 (950–1050)	2.5 μm–0.75 mm	50–70	Most ferrous metals,	Usually used for thin, hard cases <25 μm (1 mil), no

Process	Process temperature, °C (°F)	Typical case depth	Case hardness, HRC	Typical base metals	Process characteristics
		(0.1–30 mils)		including cast irons	white layer, most are proprietary processes
Ion	340–565 (650–1050)	75 μm–0.75 mm (3–30 mils)	50–70	Alloy steels, nitriding steels, stainless steels	Faster than gas nitriding, no white layer, high equipment costs, close case control
Carbonitriding					
Gas	760–870 (1400–1600)	75 μm–0.75 mm (3–30 mils)	50–65	Low-carbon steels, low-carbon alloy steels, stainless steel	Lower temperature than carburizing (less distortion), slightly harder case than carburizing, gas control critical
Liquid (cyaniding)	760–870 (1400–1600)	2.5–125 μm (0.1–5 mils)	50–65	Low-carbon steels	Good for thin cases on noncritical parts, batch process, salt disposal problems
Ferritic nitrocarburizing	565–675 (1050–1250)	2.5–25 μm (0.1–1 mil)	40–60	Low-carbon steels	Low-distortion process for thin case on low-carbon steel, most processes are proprietary
Other					
Aluminizing (pack)	870–980 (1600–1800)	25 μm–1 mm (1–40 mils)	<20	Low-carbon steels	Diffused coating used for oxidation resistance at elevated temperatures
Siliconizing by chemical vapor deposition	925–1040 (1700–1900)	25 μm–1 mm (1–40 mils)	30–50	Low-carbon steels	For corrosion and wear resistance, atmosphere control is critical
Chromizing by chemical vapor deposition	980–1090 (1800–2000)	25–50 μm (1–2 mils)	Low-carbon steel, <30; high-carbon steel, 50–60	High- and low-carbon steels	Chromized low-carbon steels yield a low-cost stainless steel, high-carbon steels develop a hard corrosion-resistant case
Titanium carbide	900–1010 (1650–1850)	2.5–12.5 μm (0.1–0.5 mil)	>70	Alloy steels, tool steels	Produces a thin carbide (TiC) case for resistance to wear, high temperature may cause distortion
Boriding	400–1150 (750–2100)	12.5–50 μm (0.5–2 mils)	40–>70	Alloy steels, tool steels, cobalt and nickel alloys	Produces a hard compound layer, mostly applied over hardened tool steels, high process temperature can cause distortion

Table 2 Compositions of case-hardening steels

Steel	Composition, %							
	C	**Mn**	**P**	**S**	**Si**	**Ni**	**Cr**	**Mo**
Carbon steels								
1010	0.08–0.13	0.30–0.60	0.040 max	0.050 max	…	…	…	…
1012 mod	0.10–0.15	0.30–0.60	0.040 max	0.050 max	…	0.30	0.30	…
1018	0.15–0.20	0.60–0.90	0.040 max	0.050 max	…	…	…	…
1020	0.17–0.23	0.30–0.60	0.040 max	0.050 max	…	…	…	…
1039	0.37–0.44	0.70–1.00	0.040 max	0.050 max	…	…	…	…
Resulfurized steels								
1113	0.13 max	0.70–1.00	0.07–0.12	0.24–0.33	…	…	…	…
1117	0.14–0.20	1.00–1.30	0.040 max	0.08–0.13	…	…	…	…
Alloy steels								
3310	0.08–0.13	0.45–0.60	0.025 max	0.025 max	0.20–0.35	3.25–3.75	1.40–1.75	…
4118	0.18–0.23	0.70–0.90	0.035 max	0.040 max	0.20–0.35	…	0.40–0.60	0.08–0.15
4140	0.38–0.43	0.75–1.00	0.035 max	0.040 max	0.20–0.35	…	0.80–1.10	0.15–0.25
4320	0.17–0.22	0.45–0.65	0.035 max	0.040 max	0.20–0.35	1.65–2.00	0.40–0.60	0.20–0.30
4620	0.17–0.22	0.45–0.65	0.035 max	0.040 max	0.20–0.35	1.65–2.00	…	0.20–0.30
8617	0.15–0.20	0.70–0.90	0.035 max	0.040 max	0.20–0.35	0.40–0.70	0.40–0.60	0.15–0.25
8620	0.18–0.23	0.70–0.90	0.035 max	0.040 max	0.20–0.35	0.40–0.70	0.40–0.60	0.15–0.25
8720	0.18–0.23	0.70–0.90	0.035 max	0.040 max	0.20–0.35	0.40–0.70	0.40–0.60	0.20–0.30
8822	0.20–0.25	0.75–1.00	0.035 max	0.040 max	0.20–0.35	0.40–0.70	0.40–0.60	0.30–0.40
9310	0.08–0.13	0.45–0.65	0.025 max	0.025 max	0.20–0.35	3.00–3.50	1.00–1.40	0.08–0.15
AMS 6470[a]	0.38–0.43	0.50–0.70	0.040 max	0.040 max	0.20–0.40	…	1.40–1.80	0.30–0.40
Nitralloy 125[b]	0.20–0.30	0.40–0.70	…	…	0.20–0.40	…	0.90–1.40	0.15–0.25
Nitralloy 1.35[b]	0.30–0.40	0.40–0.70	…	…	0.20–0.40	…	0.90–1.40	0.15–0.25
Nitralloy N[b]	0.20–0.27	0.40–0.70	…	…	0.20–0.40	3.25–3.75	1.00–1.50	0.20–0.30
Tool steel								
H13[c]	0.35	…	…	…	…	…	5.0	1.50
Maraging steel								
18% Ni (300	0.03	0.10	0.010	0.010	0.10	18.5	…	4.8

CVM)[d]	max	max	max	max	max

(a) AMS 6470 also contains 0.90 to 1.35% Al.
(b) These steels also contain 0.85 to 1.20% Al.
(c) H13 steel also contains 1.0% V.
(d) This steel also contains 0.10% Al, 0.60% Ti, 9.0% Co, 0.003% B, 0.02% Zr, and 0.05% Ca.

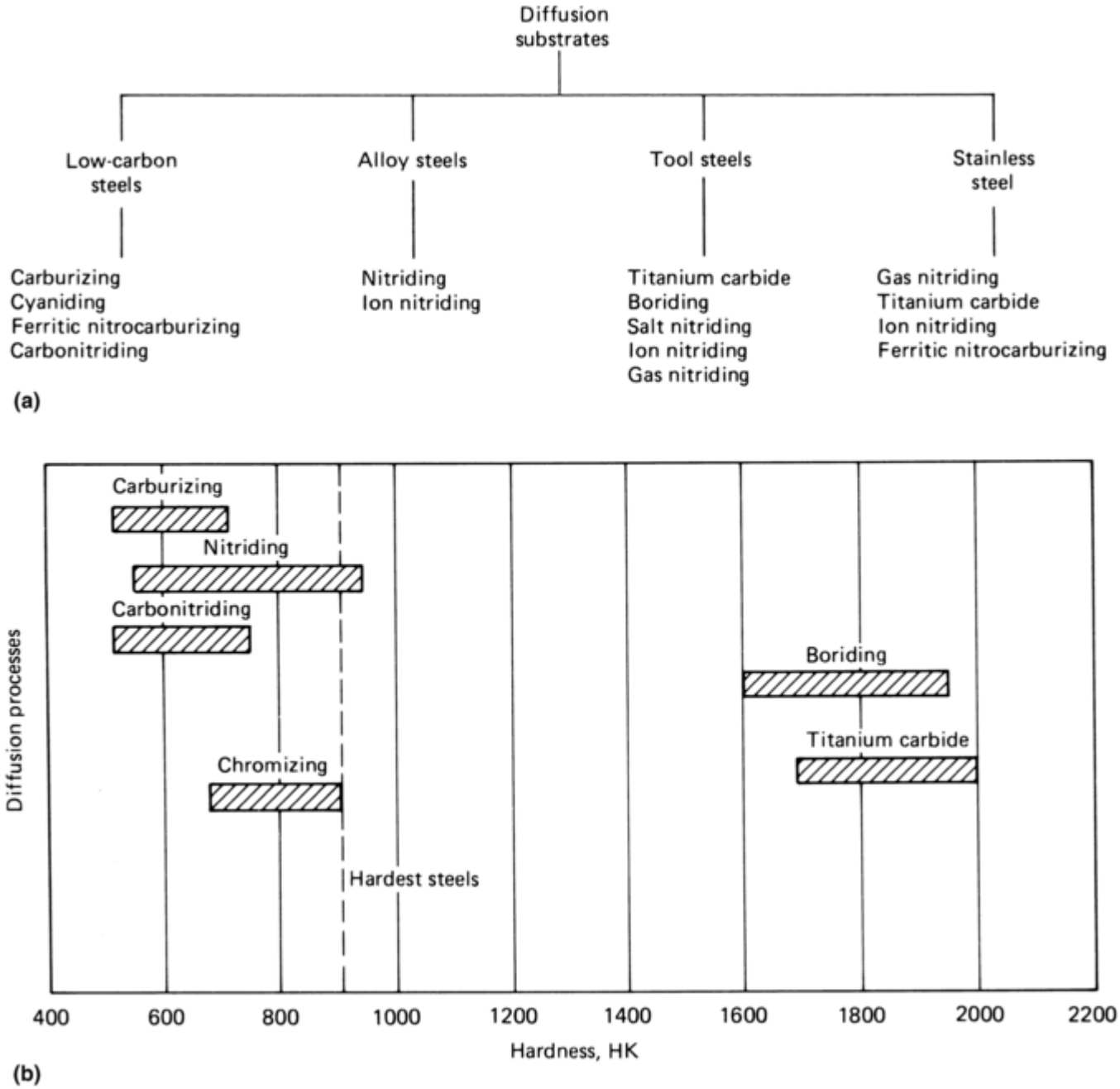

Fig. 1 Diffusion processes for case hardening of steel. (a) Processes applicable for different steel composition types. (b) Spectrum of hardness obtainable with selected diffusion processes of steel

This article covers the metallographic techniques and microstructures of carburized and carbonitrided steels. The special procedures required for nitrided steels, which can obtain high hardness (Fig. 1b), are also included. The microstructure of the case and of the underlying core metal serves as a fundamental guide in the quality control of case-hardening processes and a dependable method for detecting abnormalities that may affect performance and service life. This article describes metallographic techniques and microstructural features of carburized, carbonitrided, and nitrided steels. The division “Surface Hardening of Steel” in *Heat Treating*, Volume 4 of *ASM Handbook*, describes case-hardening processes in more detail.

Metallography and Microstructures of Case-Hardening Steel, *Metallography and Microstructures*, Vol 9, *ASM Handbook*, ASM International, 2004, p. 627–643

Carburized and Carbonitrided Steels

Most steels used for carburizing and carbonitriding have an initial carbon content of 0.10 to 0.30%. Medium-carbon steels (0.30 to 0.50% C) are sometimes carburized to satisfy special requirements. Because the carbon content of a carburized steel may range from 0.10 to 0.30% C in the uncarburized core to as much as 1.20% in the case, specimens are difficult to extract and prepare. In the metallographic study of carburized steel, the structure of the high-carbon case is usually very important.

The intended microstructure of carburized steel is essentially a lightly tempered high-carbon martensite case with decreasing martensite and carbon content as a function of distance from the surface. The depth of the martensitic case depends on how much carbon is allowed to diffuse into the interior of the part. This depends on the carbon content at the surface and the time-temperature exposure during carburization. An example is shown in Fig. 2 (Ref 1) for a 0.15 wt% C steel that was pack carburized at 940 °C (1725 °F) for various times.

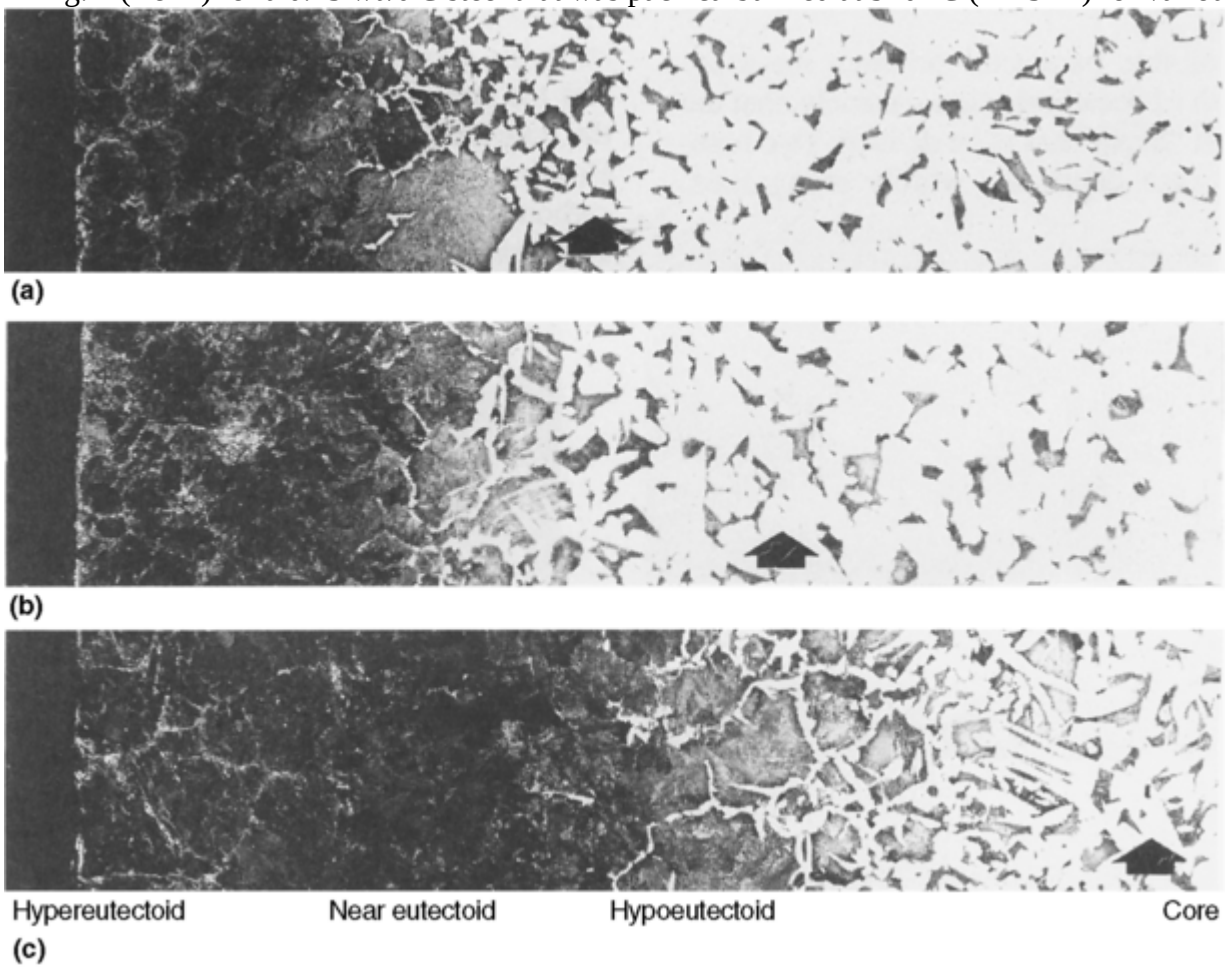

Fig. 2 Effect of carburizing time on case in 0.15% C steel (0.17C-0.5Si-0.64Mn, wt%) after slow cooling from pack carburization at 940 °C (1725 °F) for (a) 1 h, (b) 2 h, and (c) 4 h. Arrows indicate total case depth estimated from variation in carbon content of turnings removed from successive layers either 0.1 or 0.2 mm (0.004 or 0.008 in.) thick. All picral etch, 500×. Source: Ref 1

After high-temperature exposure in a carbonaceous environment, the carburized steel is then hardened, either by direct quenching (from the austenitizing temperature during carburization) or by reheating and quenching. Generally, lean grades of steel are direct quenched, while more-alloy grades are reheat quenched. The amount

and morphology of martensite in the case depends on the carbon content and the transformation kinetics. Other microstructural constituents (e.g., retained austenite, nonmartensitic transformation products, carbides, inclusions) also may be present and influence properties and performance. Microstructural features are described in more detail in the section “Carburized Case Microstructures” in this article.

Specimen Preparation

Metallographic preparation of specimens from case-carburized and carbonitrided steels generally follow procedures similar to carbon and low-alloy steels, as described in the article “Metallography and Microstructures of Carbon and Low-Alloy Steels” in this Volume. Metallography of case-hardening steels may also involve preparations for measurement of case depth, as described in more detail in the article “Methods of Measuring Case Depth in Steels” in *Heat Treating,* Volume 4 of *ASM Handbook.*

Sectioning. Small, separate testpieces are often used in order to minimize the amount of sectioning. They are treated along with the production parts being carburized and hardened. If the production parts are very small, one or more of them may be sectioned for metallographic study. As always, sectioning must be done with meticulous care, as described in the article “Metallographic Sectioning and Specimen Extraction” in this Volume. When a very thin surface layer is being examined, a taper section may be done.

Mounting. The mounting techniques and precautions used for specimens of high-carbon steels apply to those of carburized steels. Compression-mounting plastics can be used for routine examination, but cold mounting is required to examine for retained austenite.

Edge retention of the polished specimen is very important for a case-hardened surface, and good edge retention can be achieved by proper selection of a mounting material or by nickel plating of the specimen prior to mounting. Thermosetting epoxies with fillers (such as silica or alumina particles) closely match the polishing rates of steel and thus can provide good edge retention. Silica-filled thermosetting epoxies can provide excellent edge retention without nickel plating.

On unmounted specimens, total prevention of edge rounding is virtually impossible. However, it is possible to obtain acceptable flatness by clamping together two specimens with their carburized edges abutting at the center of the two-specimen arrangement. It is preferable to place a thin strip of copper, plastic, or other material between the specimens. For maximum edge retention, the spacer material should have abrasion and polishing rates similar to those of the specimens.

Grinding and polishing techniques are the same as those described for specimens of carbon and low-alloy steels. Carburized and hardened cases are extremely susceptible to alteration by overheating from grinding. Consequently, grinding must be performed carefully.

It is highly desirable to minimize the amount of polishing. Because of the wide differences in hardness within a single specimen, some constituents will polish in relief, and flatness of the specimen will be destroyed. Specimens that have been overpolished must be completely reworked to regain flatness. Use of napless polishing cloths also helps to minimize polishing in relief.

Etching. Specimens of carburized steel and carbonitrided steel are often etched with nital, which is a general-purpose etchant for routine metallography. Nital can contain 1 to 5% nitric acid (HNO_3). At a constant temperature, higher acid concentrations in the solution yield shorter etching times. In addition, etching time or acid concentration should be decreased when the specimen is to be examined at higher magnifications.

Nital is well suited to revealing case depth (Fig. 3), retained austenite (Fig. 4), carbide networks (Fig. 5), and surface decarburization (Fig. 6). Picral is equivalent to nital for revealing the characteristics noted previously. In addition, picral (usually 2 to 4% picric acid) or 4% picral to which 0.01% hydrochloric acid (HCl) has been added will produce sharper definition of carbide structures than nital (Fig. 7).

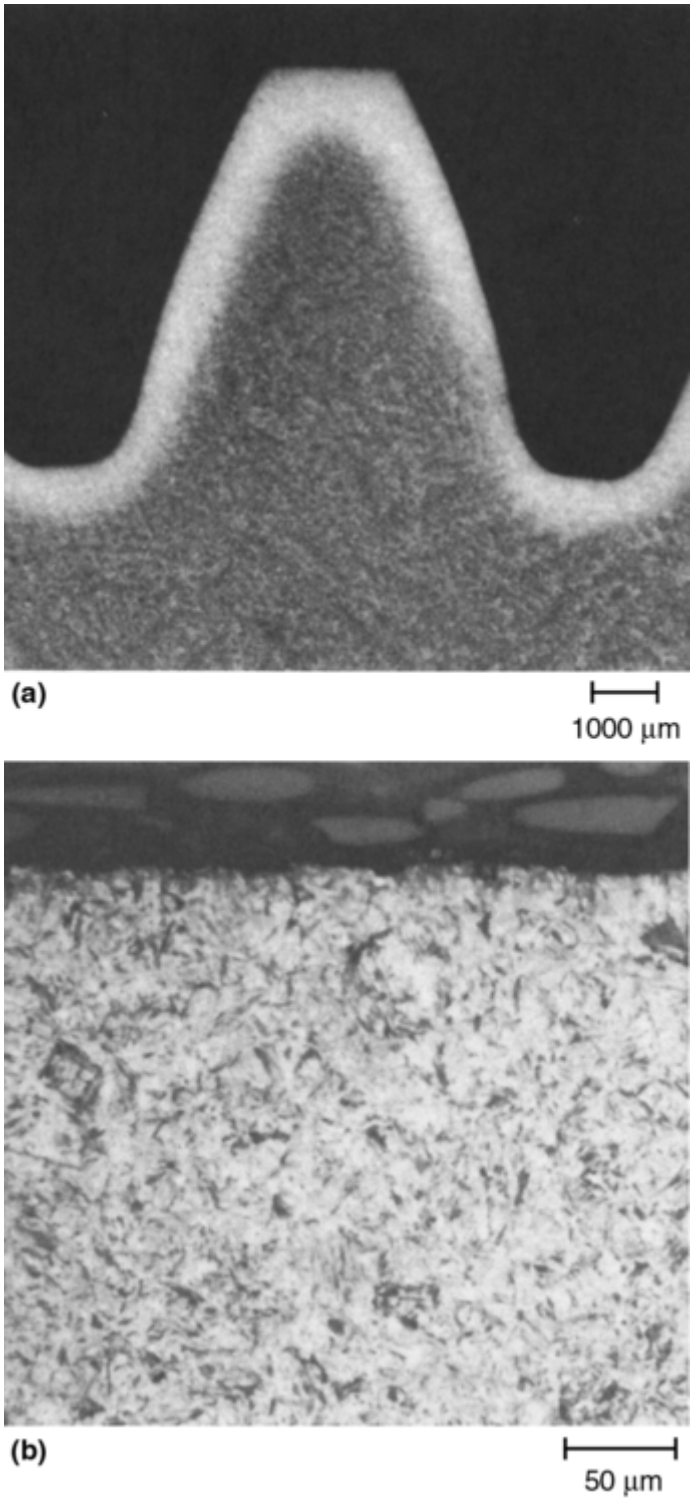

Fig. 3 Ion carburized 2H2N4A steel with uniform case depth on a 40-tooth gear. Effective case depth was 0.8 to 1.0 mm (0.03 to 0.04 in.). Composition limits (maximums) of 2H2N4A steel: 0.16% C, 0.6% Mn, 0.37% Si, 0.03% P, 0.025% S, 1.65% Cr, and 3.65% Ni. Ion carburization and diffusion at 920 °C (1690 °F), austenitized at 830 °C (1525 °F), oil quenched, and tempered at 150 °C (300 °F). (a) 6× image of case. (b) 200× magnification of microstructure of tempered martensite without evidence of carbide or retained austenite. Both nital etch

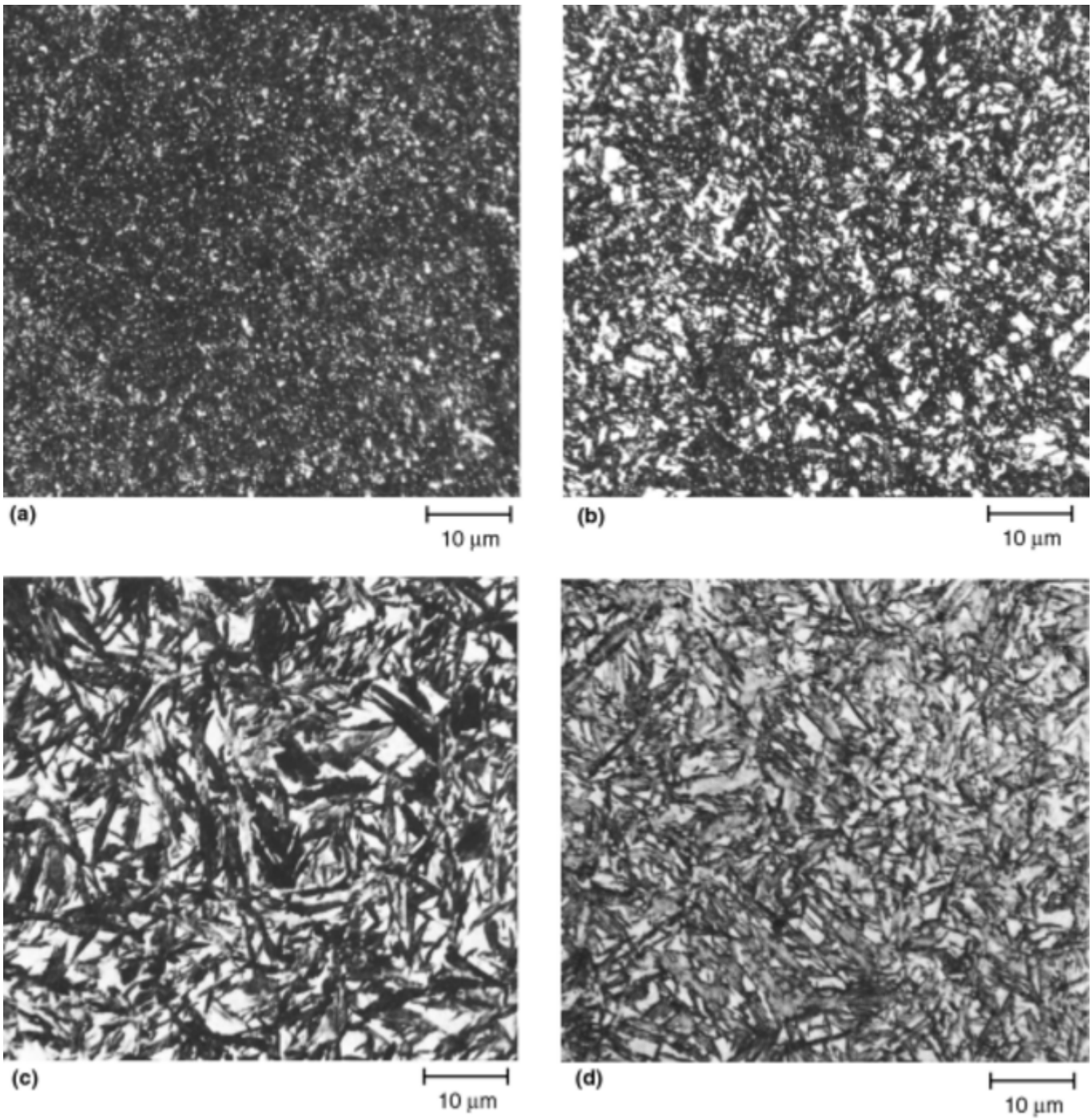

Fig. 4 Levels of retained austenite in gas-carburized and heat treated 4620 steel. All specimens carburized at 1.00% C potential for indicated time and temperatures. (a) 0% retained austenite (by x-ray) in matrix of tempered martensite with lower bainite and carbide. Carburized 8 h at 940 °C (1725 °F), oil quenched, tempered 1 h at 180 °C (360 °F), and retempered 2 h at 260 °C (500 °F). (b) Same processing as for (a) but retempered 2 h at 230 °C (450 °F). Structure is tempered martensite, lower bainite, dispersed carbide, and 10% retained austenite (by x-ray). (c) Carburized 4 h at 940 °C (1725 °F), oil quenched, and tempered 1 h at 180 °C (360 °F). Microstructure (0.90% C) is tempered martensite and 35% retained austenite (by x-ray). (d) Untempered martensite with 25% retained austenite (by x-ray). Gas carburized 4 h at 955 °C (1750 °F), austenitized 30 min at 820 °C (1510 °F), and oil quenched. All nital etch, 1000×

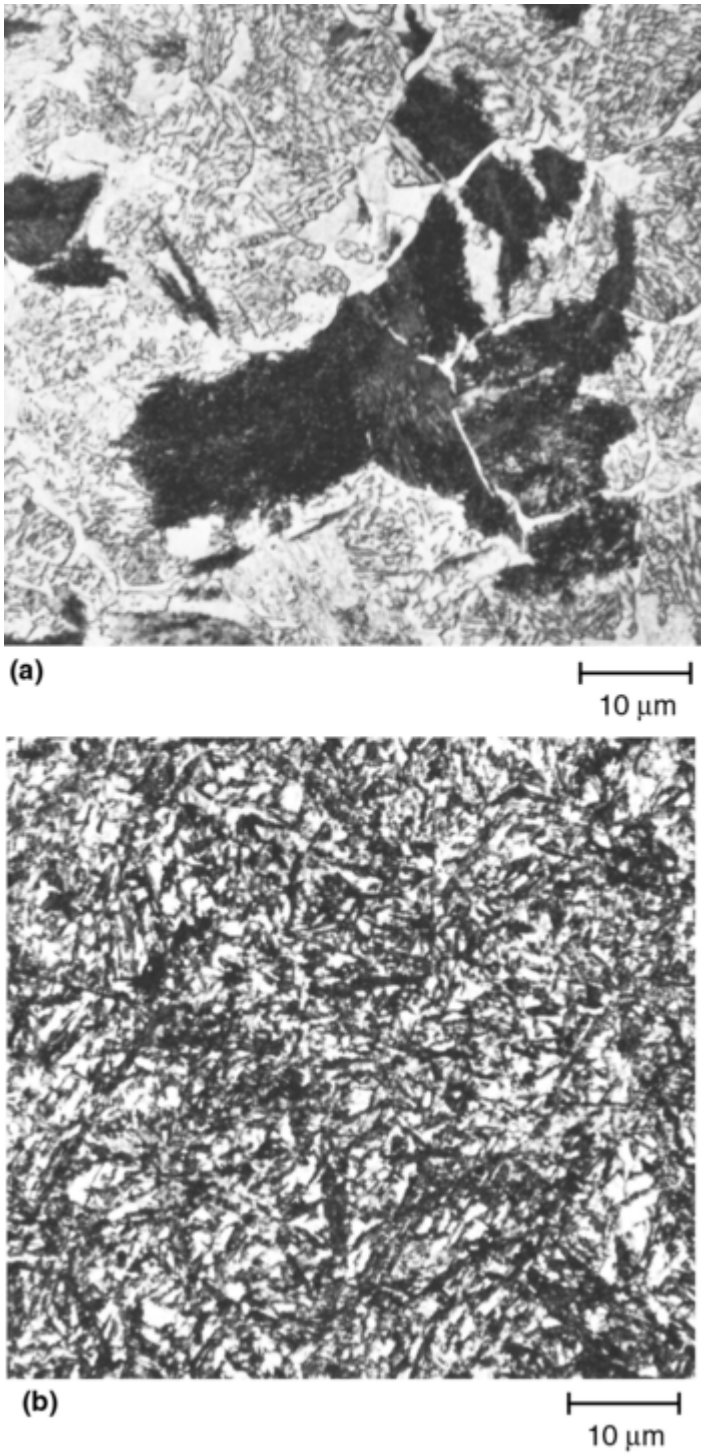

Fig. 5 Pack carburized 3310 steel. (a) Carburized 16 h at 940 °C (1725 °F) and cooled in the pot. Structure is fine pearlite (dark) and carbide envelopes at prior-austenite grain boundaries in a matrix of ferrite and dispersed alloy carbide. (b) Same carburizing conditions but tempered 13 h at 595 °C (1100 °F), air cooled, heated to 795 °C (1460 °F), oil quenched, and tempered 1 h at 180 °C (360 °F). Structure is tempered martensite, retained austenite (30% by x-ray), and carbide. Both nital etch, 1000×

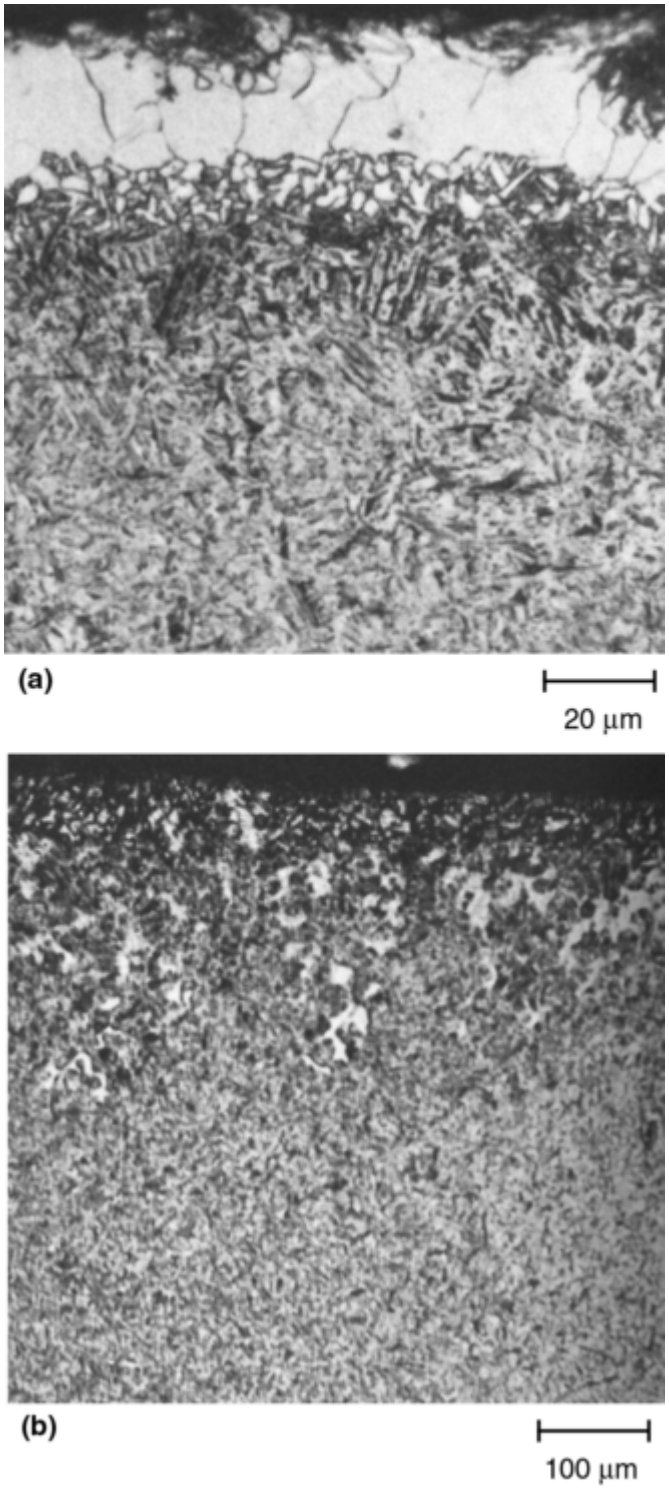

Fig. 6 Decarburization in 4118H steel bar, gas carburized 8 h at 925 °C (1700 °F), oil quenched, heated to 845 °C (1550 °F) and held 15 min, oil quenched, and tempered 1 h at 170 °C (340 °F). (a) Completely decarburized surface layer (white), a transition zone of ferrite and low-carbon martensite, and a matrix of tempered martensite and retained austenite. 4% nital etch. 500×. (b) Same material and heat treating conditions as in (a), but the surface is only partially decarburized. Decarburization was less severe, because the specimen contained precipitated, intergranular carbide particles before treatment. 4% nital etch. 100×

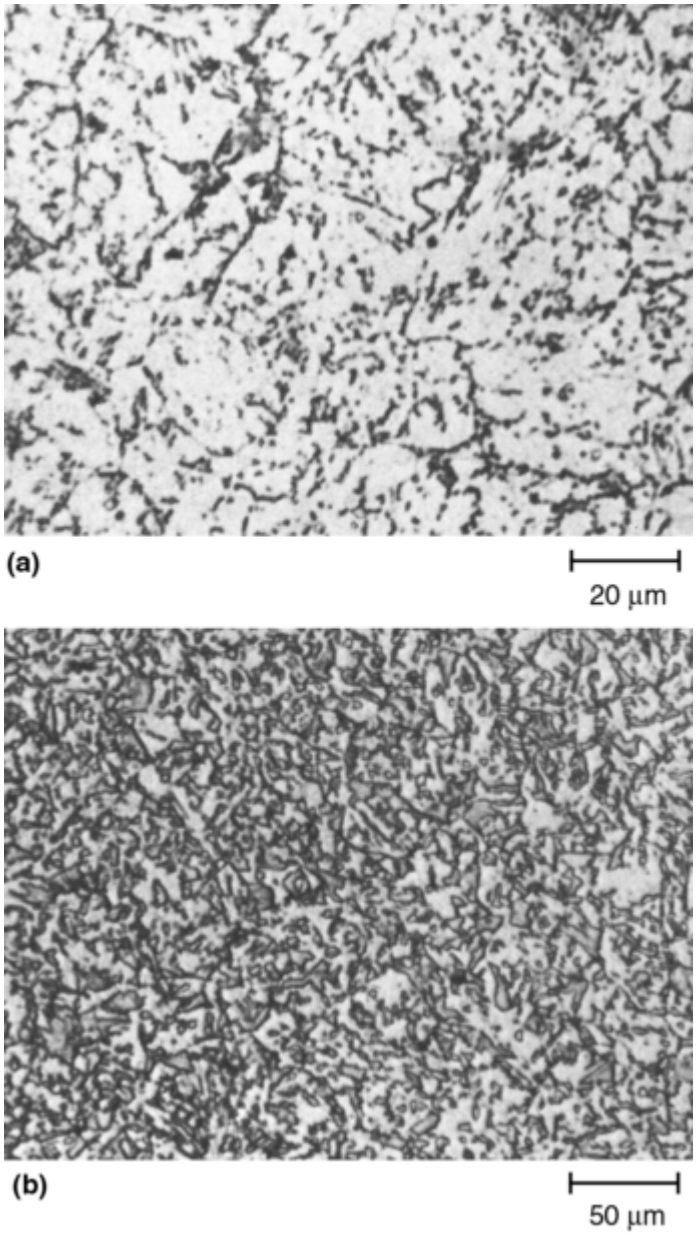

Fig. 7 Carbide appearance with nital and picral etchants. (a) 9310 steel normalized by austenitizing 2 h at 885 °C (1625 °F) and cooled slowly in the furnace. Structure consists of scattered carbide particles (dark) in a ferrite matrix (light). 3% nital etch. 500×. (b) Same steel and normalization as in (a) but cooled in still air. Structure is scattered carbide particles and unresolved pearlite in a matrix of ferrite (light). Picral etch. 200×

Electron Microscopy. Scanning electron microscopy (SEM) is useful in examining fracture surfaces and evaluating possible fracture mechanisms. For example, Fig. 8 and Fig. 9 are SEM images of fracture surfaces of fatigue cracks that initiated at the surface of carburized steels. Figure 8 is an example of intergranular fatigue initiation at the austenite grain boundaries with phosphorus-carbide structures (Ref 2). Figure 9 is an example of transgranular fatigue crack initiation, which is dependent on slip mechanisms during cyclic loading.

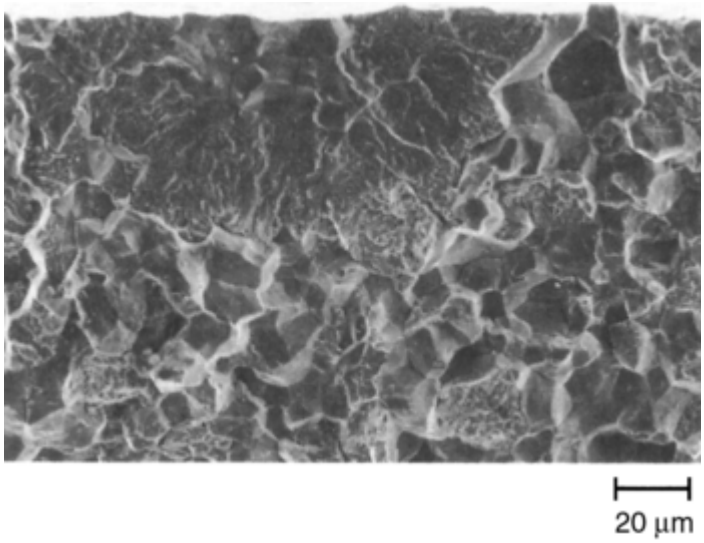

Fig. 8 Intergranular crack initiation site from bending fatigue of plasma-carburized steel containing 1.06% Mn, 0.52% Cr, 0.30% Ni, and 0.1% Mo. Source: Ref 2

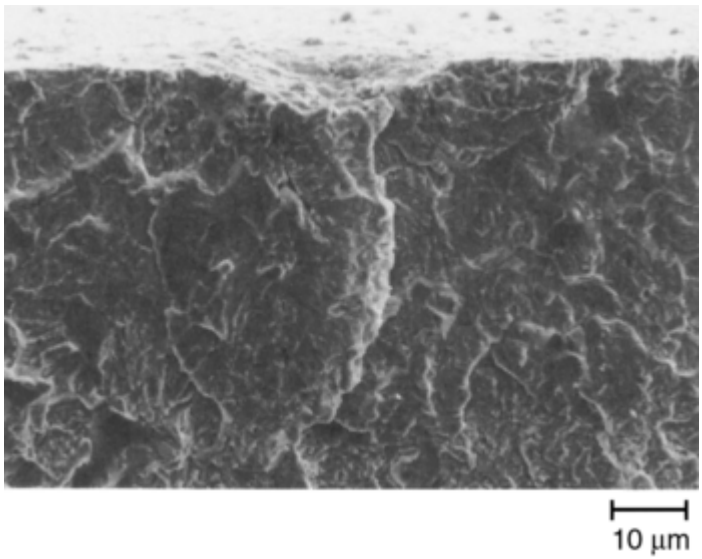

Fig. 9 Transgranular initiation and propagation from bending fatigue of gas-carburized 8719 steel. Source: Ref 2

Transmission electron microscopy, replica or thin-foil, can also be used for case-hardened parts, in some cases. Transmission electron microscopy is used to relate fine microstructure (traces of ferrite and bainite).

Carburized Case Microstructures

The depth and amount of carbon diffusion depends on the source of surface carbon and the processing time at temperature. The most common method is gas carburization in an endothermic furnace at temperatures in the range of approximately 815 to 980 °C (1500 to 1800 °F). Microstructures of a 1018 steel after gas carburization at 925 °C (1700 °F) are shown in Fig. 10 for various exposure times in a leaktight furnace (Fig. 10a–d) and in furnaces with some leaking (Fig. 10e, f). Carbon content at the surface can be qualitatively compared in terms of the eutectoid constituent (i.e., pearlite) and the proeutectoid constituents.

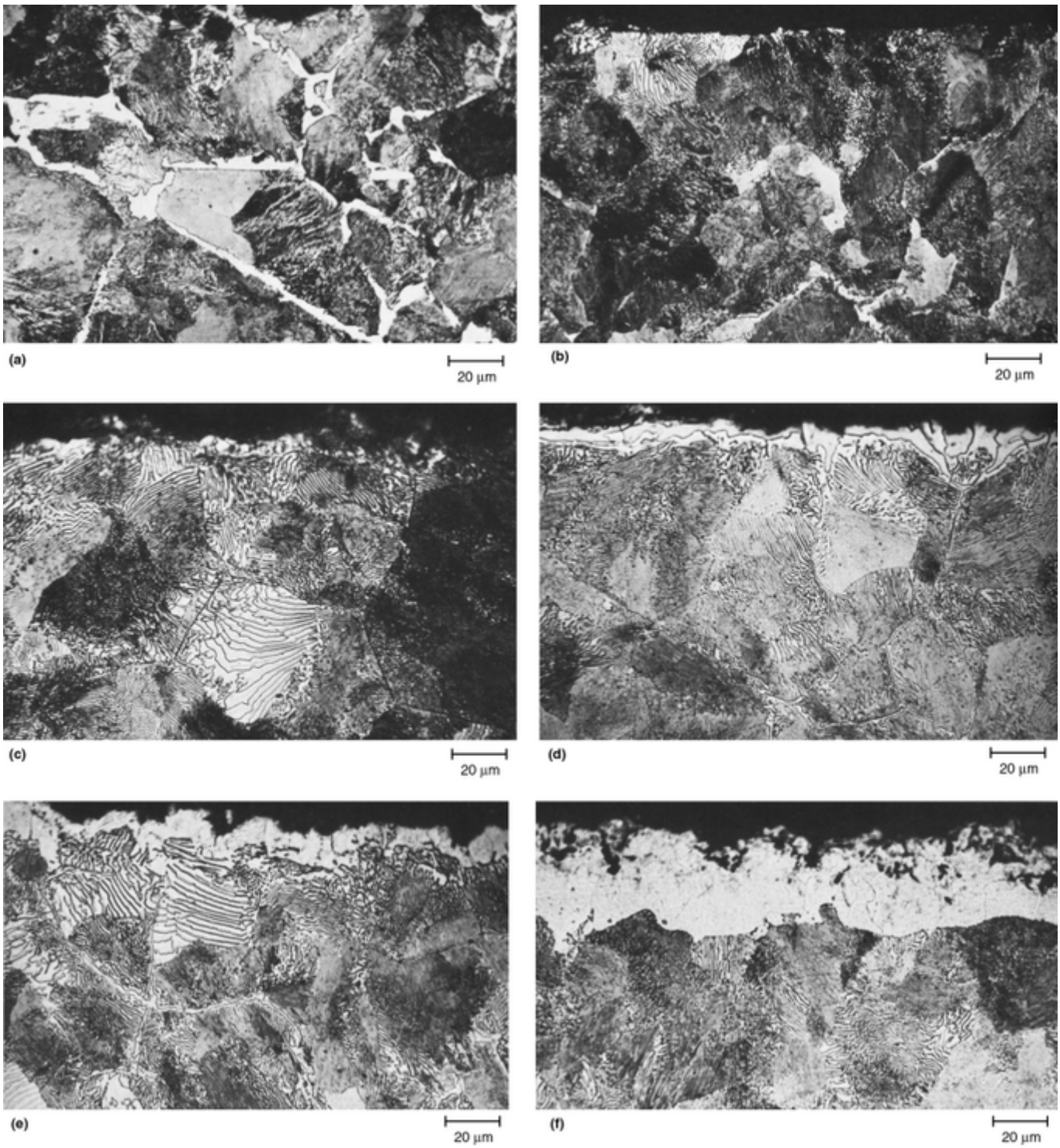

Fig. 10 Effect of carburization time on surface carbon content and microstructure of a carbon steel (type 1018). Gas carburized at 925 °C (1700 °F) for indicated times, furnace cooled to 540 °C (1000 °F) in 130 min, then air cooled to room temperature. Carburization was done in leaktight furnaces (pit type), except for last two examples. (a) Carburized for 2 h, with resulting surface carbon content between 0.60 to 0.70%. The structure is pearlite with proeutectoid ferrite (light) outlining prior-austenite grain boundaries. (b) Carburized for 4 h, with surface carbon content between 0.70 to 0.80% C. Some areas of ferrite outline prior-austenite grain boundaries, but the remaining structure is almost wholly pearlite. (c) Carburized for 6 h, with a resulting surface carbon content between 0.90 to 1.00%. A thin film of proeutectoid carbide (cementite) outlines prior-austenite grain boundaries; matrix is pearlite. (d) Carburized for 16 h, with resulting surface carbon between 1.00 to 1.10% C. The structure is identical to that in (c), but there is a surface layer (light) of carbide. (e) Carburized for 5 h in a furnace with an air leak, furnace cooled to 535 °C (1000 °F), then air cooled to room temperature. A thin decarburized layer (ferrite) caused by the air leak covers the surface; below the surface, the structure is pearlite and carbide

in prior-austenite grain boundaries. (f) Same conditions as in (e), but the air leak was more severe. The decarburized surface layer is thicker. All etched in 1% nital. 500×

In gas carburization, the presence of oxygen (from $H_2O \leftrightarrow H_2$ and $CO_2 \leftrightarrow CO$ reactions) may cause internal oxidation (Fig. 11, 12). Some oxidation during gas carburization is inevitable, but the extent must be controlled with appropriate carburizing temperatures and conditions. Oxidation can be completely eliminated in an oxygen-free chamber used for vacuum carburizing and plasma (or ion) carburizing. The higher processing temperatures of vacuum or plasma carburization (approximately 1040 °C, or 1900 °F) also allow higher diffusion rates and the additional benefit of increased solubility of carbon in austenite at a higher temperature. At a higher temperature, the surface of the hot steel part can become saturated to a higher carbon content, which thus increases the diffusivity (and hence the carburizing rate).

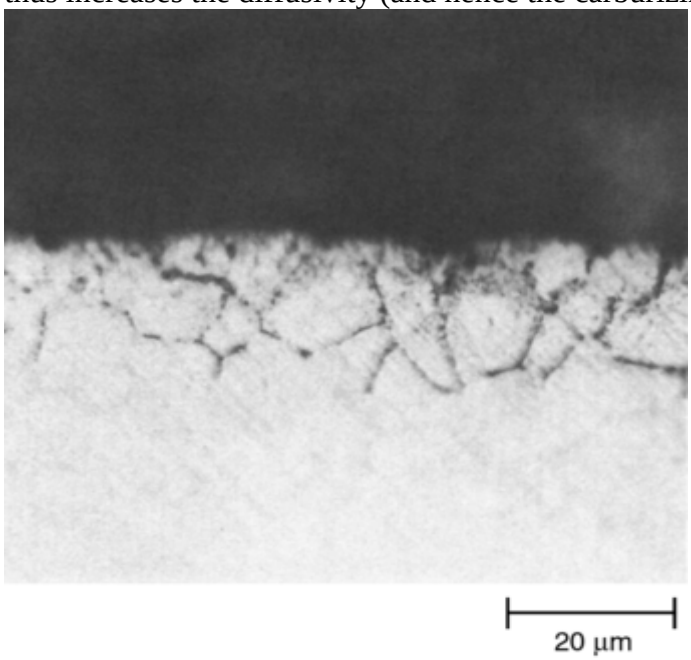

Fig. 11 Grain-boundary oxidation to a depth of approximately 0.02 mm (0.0008 in.) in gas-carburized 8620 steel; carburized at 955 °C (1750 °F). 1% nital etch. 750×

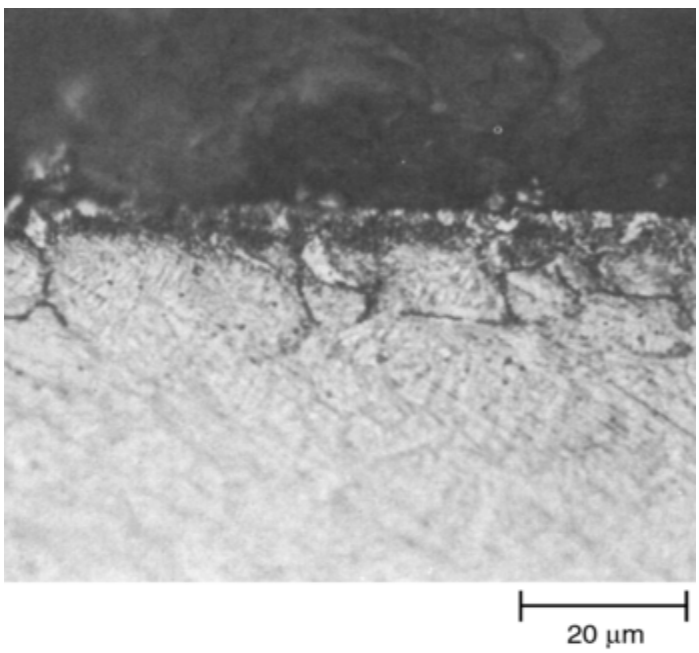

Fig. 12 Grain-boundary oxidation to a depth of approximately 0.02 mm (0.0008 in.) in 4118 steel gas carburized at 955 °C (1750 °F). As polished. 750×

Once the case is carburized, the hardening stage involves rapid quenching from austenite and subsequent tempering of the martensitic case. A typical case of tempered martensite is shown in Fig. 13 for gas-carburized 9310 steel. In addition to the tempered martensite, other possible constituents include retained austenite, carbides, and internal/surface oxidation. Microcracking is also possible.

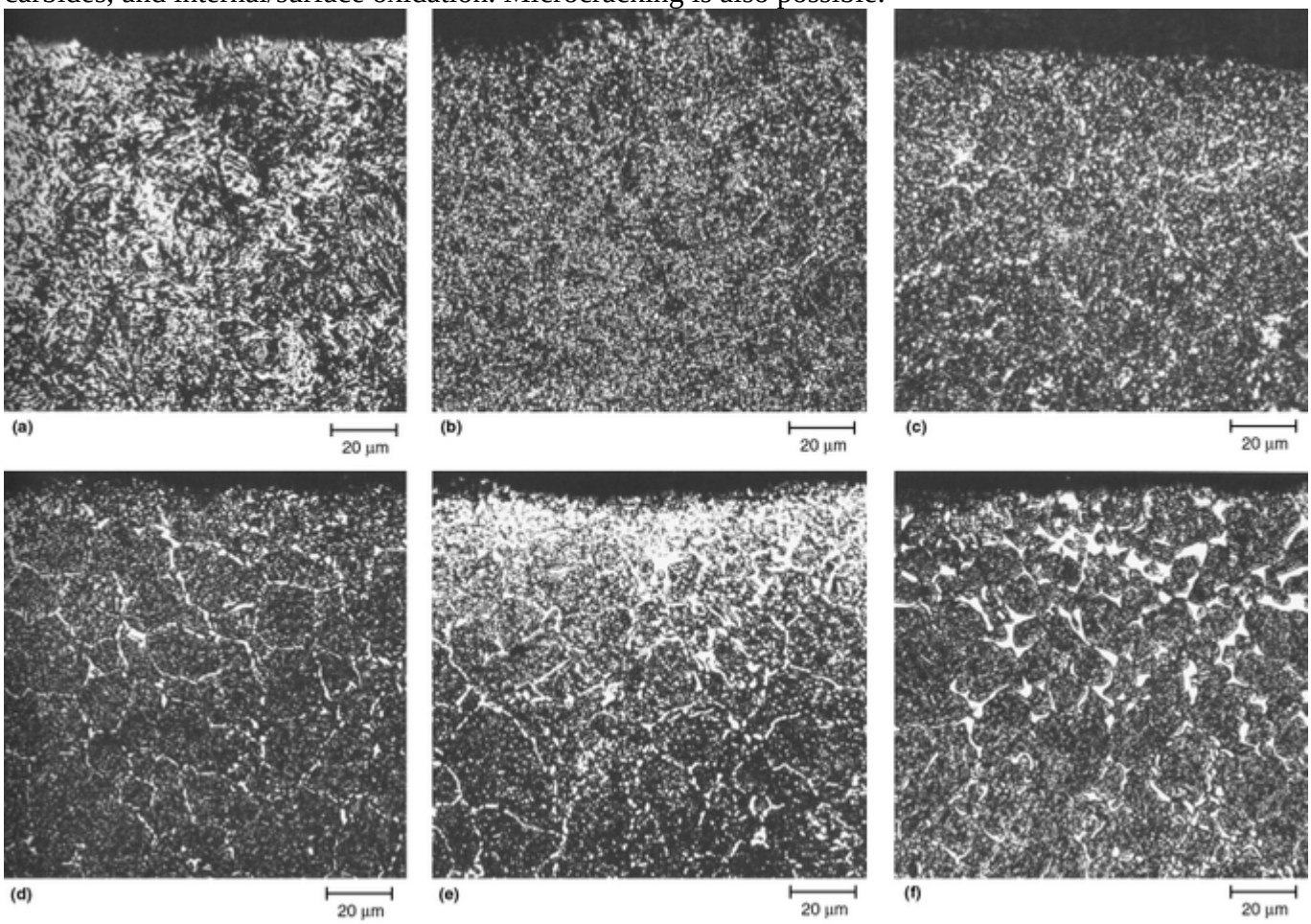

Fig. 13 Tempered martensite in gas-carburized 9310 steel. Specimens have different surface carbon contents because of variations in the carbon potential of the furnace atmosphere. Case carbon content is as follows. (a) 0.60% C. (b) 0.85% C. (c) 0.95% C. (d) 1.05% C. (e) 1.10% C. (f) 1.20% C. Processing and heat treatment are the same for all, as follows: gas carburized for 4 h at 925 to 940 °C (1700 to 1725 °F), furnace cooled, austenitized at 815 to 830 °C (1500 to 1525 °F), oil quenched, and tempered 4 h at 150 °C (300 °F). All etched in 2% nital. 500×

Surface/Internal Oxidation. In gas carburizing atmospheres, the presence of oxygen (from $H_2O \leftrightarrow H_2$ and $CO_2 \leftrightarrow CO$ reactions) can result in the internal oxidation of certain alloying elements in carburizing steels. Chromium, silicon, and manganese, all commonly found in carburizing steels, oxidize readily, while molybdenum, nickel, and iron are not oxidized. The oxidation is diffusion dependent, and therefore, the depth and extent of oxide formation is a function of carburizing time and temperature. The oxides may form on austenite grain boundaries or within austenite grains.

Internal oxidation is unavoidable in conventional gas carburization but can be eliminated in oxygen-free furnace atmospheres or in vacuum or plasma carburizing furnaces. Nitrogen-base atmospheres are also said to reduce it. However, internal oxidation remains an important concern, because conventional carburization with an endothermic carrier is still a common method for case hardening. Internal oxidation has important consequences of properties, and the composition gradients that develop during oxidation can influence the transformation behavior. Thus, nonmartensitic constituents may form in the regions adjacent to the oxides (Fig. 14) (Ref 3).

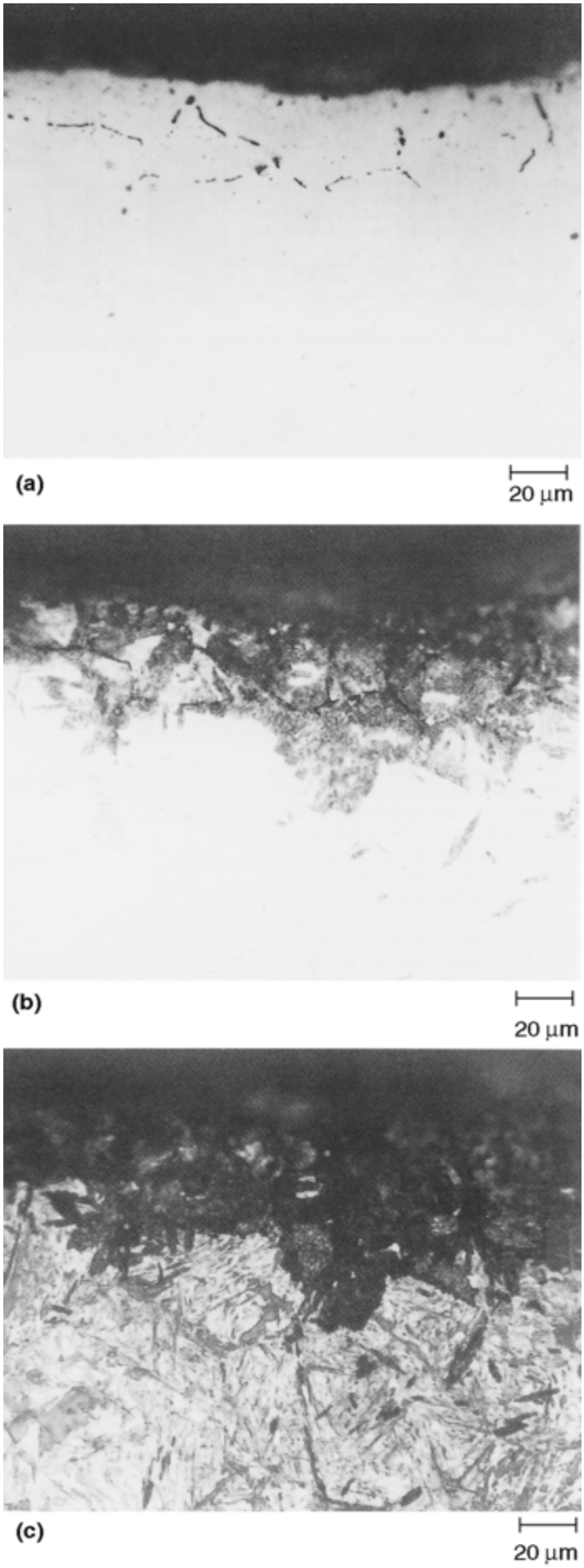

Fig. 14 High-temperature transformation products associated with internal oxidation. (a) Unetched specimen. (b) Lightly etched in 2% nital. (c) Medium etched in 2% nital. All 500×. Source: Ref 3

Retained Austenite. Moderate amounts of retained austenite are proper and unavoidable in the high-carbon case microstructure of carburized steels (Fig. 15a). However, excessive amounts of retained austenite (Fig. 15b) can lower hardness to unacceptable levels. Excess retained austenite also can lead to grinding problems.

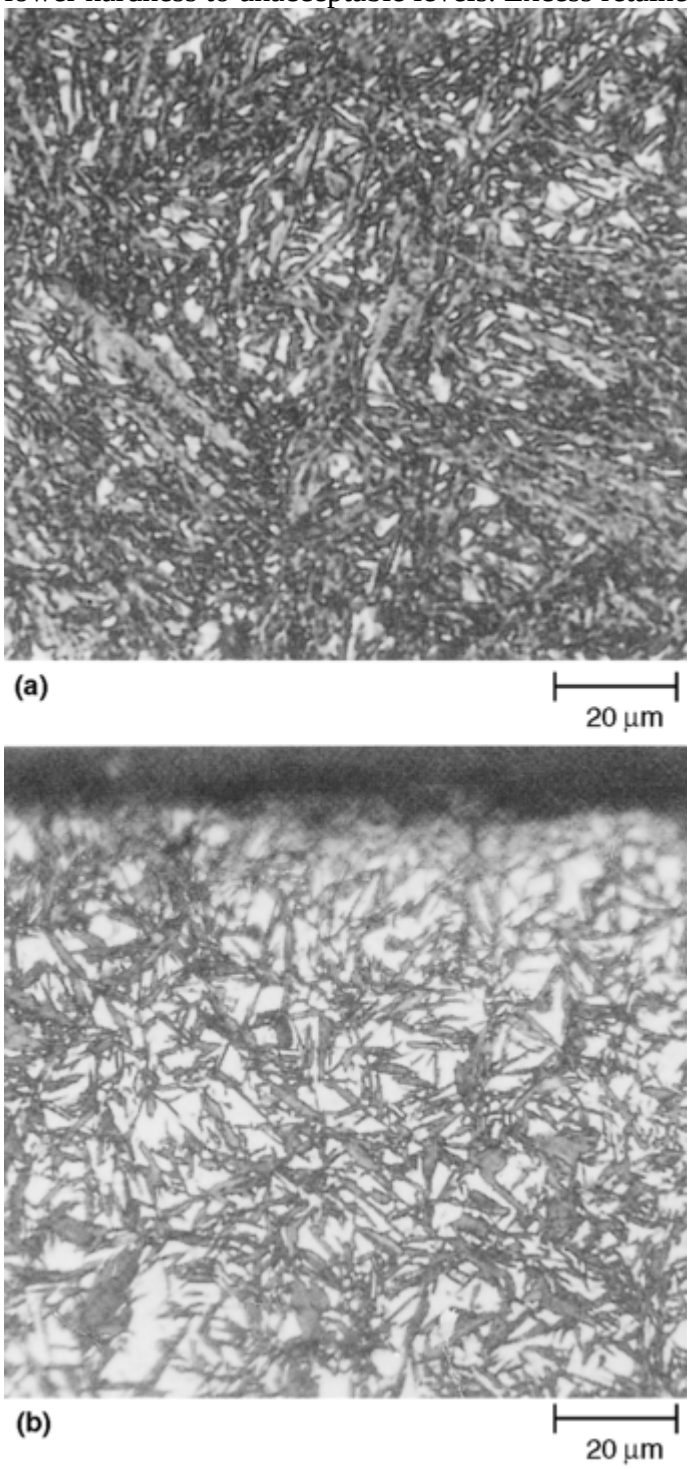

Fig. 15 Retained austenite (light) and martensite in the surface of carburized and hardened nickel-chromium steel. (a) ~15% austenite. (b) ~40% austenite. Both 550×

The most important cause of excessive amounts of retained austenite is too high a surface carbon content. This condition drives martensite start (M_s) temperatures down, causes the formation of plate martensite (Fig. 16), and can shift the balance of the temperature range for martensite transformation to well below room temperature. High alloy content also lowers M_s temperatures. Common locations of excessive surface carbon concentration are specimen corners at which the austenite is saturated with carbon during the first part of a carburizing cycle (see the article “Microstructures and Properties of Carburized Steels” in *Heat Treating*, Volume 4 of *ASM Handbook*).

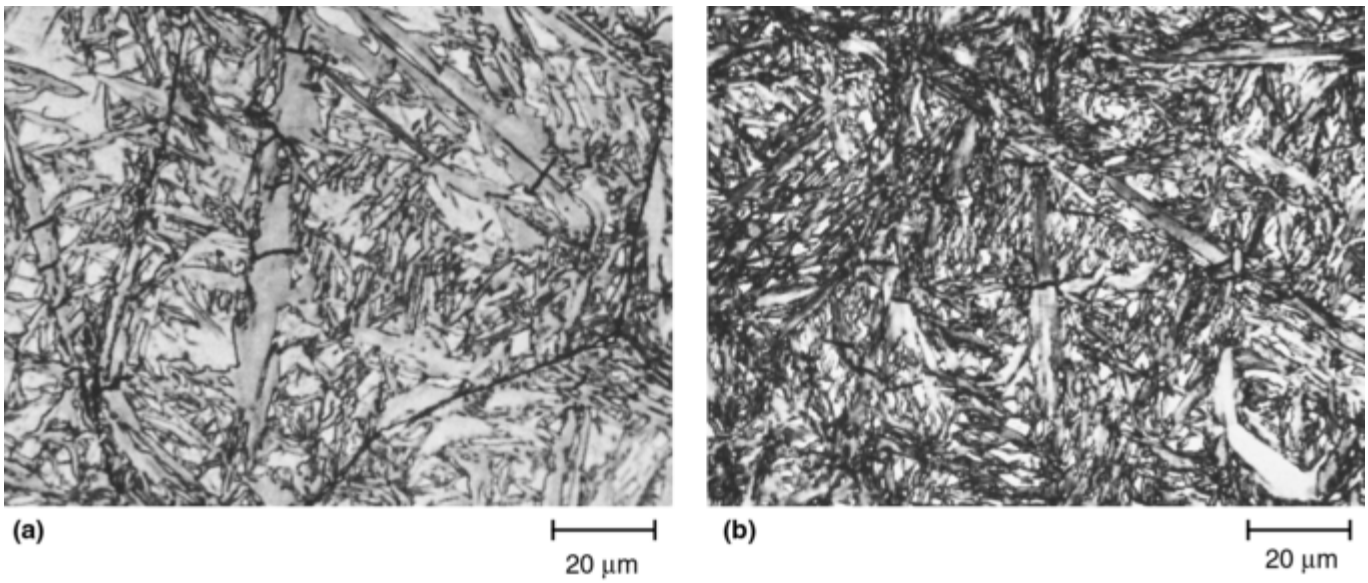

Fig. 16 Plate martensite with microcracks in a matrix of retained austenite. Type 3310H steel, gas carburized 12 h at 925 °C (1700 °F), furnace cooled to 535 °C (1000 °F), and air cooled. (a) 4% picral etch with 0.01% HCl. (b) More heavily etched specimen improves contrast of details in the structure, but the microcracks in the martensite plates have been obscured by the darker etch. 4% picral etch with 0.01% HCl. Both 500×

Carbon potential control and quenching methods are means of controlling the austenite content. Generally, lean grades of steel are direct quenched, and the more-alloy grades are reheat quenched. If retained austenite is unacceptably high, requenching from a lower temperature (watching for distortion) may be considered. Retained austenite also can be reduced by low-temperature treatment in order to allow for more transformation due to the lower M_s caused by high carbon content. This is shown in Fig. 17. The micrograph in Fig. 17(a) is from a surface region of the carburized case, quench hardened from 940 °C (1725 °F) and tempered; the section has been etched in nital on this occasion to show the microcracks more clearly. Figure 17(b) is of a similar region of the same bar after it had been cooled to -183 °C (-300 °F), by immersion in liquid nitrogen, and retempered. Most, but not all, of the retained austenite in the material transformed to martensite during cooling to the subzero temperature.

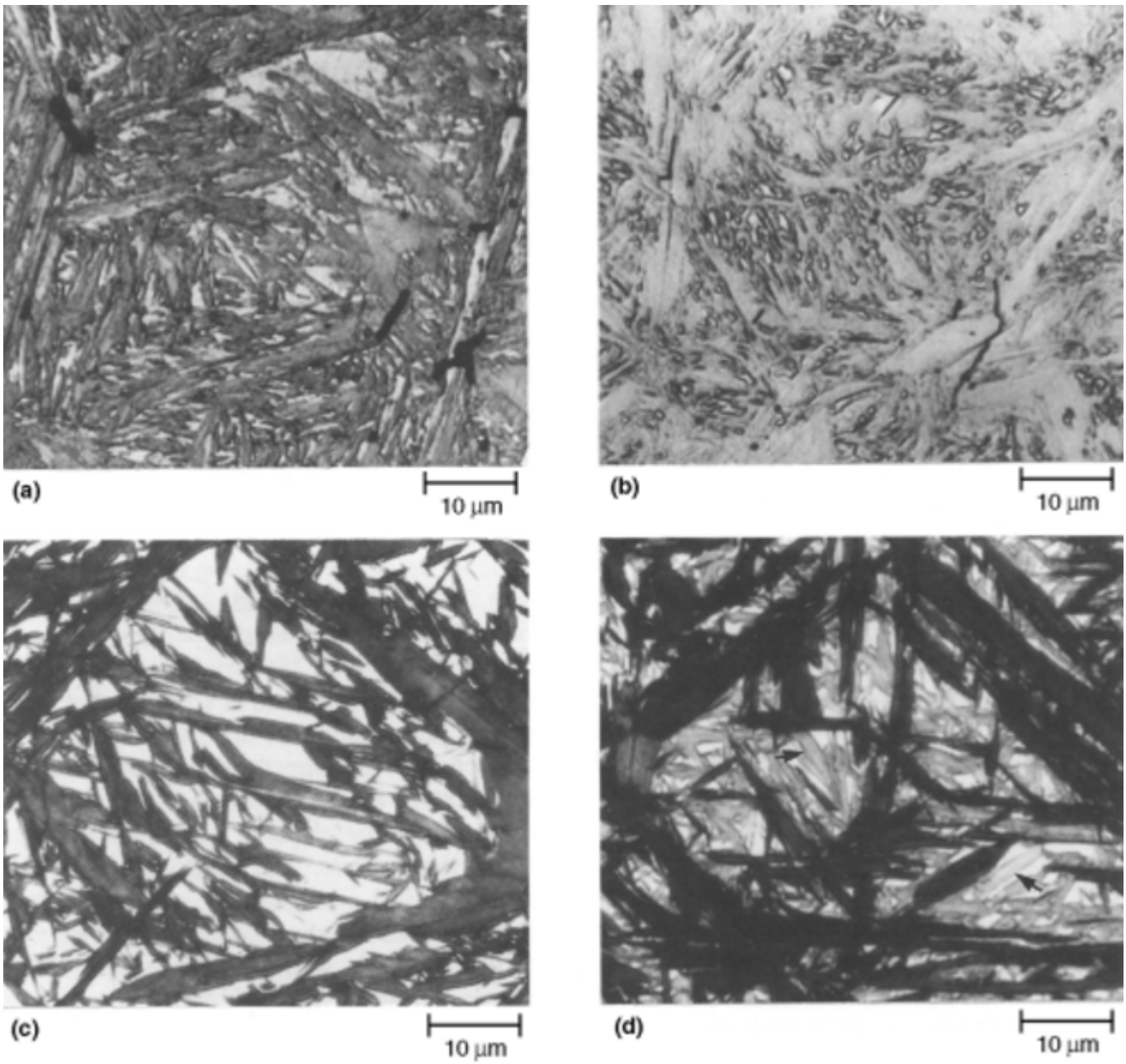

Fig. 17 Effect of subzero-temperature treatment on retained austenite in carburized 0.15% C steel (0.17C-0.05Si-0.64Mn, wt%). (a) Carburized at 940 °C (1725 °F) for 2 h, cooled slowly to room temperature, and single quenched from 940 °C (1725 °F). 1% nital etch. (b) Carburized at 940 °C (1725 °F) for 2 h, cooled slowly to room temperature, single quenched from 940 °C (1725 °F), cooled to -183 °C (-300 °F), and tempered at 150 °C (300 °F). 1% nital etch. (c) Gas carburized at 900 °C (1650 °F) and direct quenched in oil. Bisulfite etch. (d) Gas carburized at 900 °C (1650 °F), direct quenched in oil cooled to -183 °C (-300 °F), and tempered at 150 °C (300 °F). Bisulfite etch. All 1000×. Source: Ref 1

This example does not illustrate the effect particularly clearly, because only a comparatively small volume fraction of retained austenite was present in the first place. It is better illustrated in Fig. 17(c) and (d), which are micrographs of the immediate surface regions of a gas-carburized case that had been direct quenched from 900 °C (1650 °F). The case initially contained a large volume fraction of retained austenite (Fig. 17c), but most of it had transformed to martensite after cooling to -183 °C (-300 °F) (Fig. 17d). The martensite formed during the subzero treatment etches lighter than the martensite formed during cooling to room temperature, because it has not been subjected to as much autotempering, and so the two can be distinguished from one another in Fig. 17(d).

Carbides. Other than dispersed carbides, carbide formation can be either intergranular or, less commonly, intragranular. The latter type forms on planes within grains and thus has an orientation tendency. They also may

have a smooth, gently spiraling surface (Ref 3). Intergranular carbides are of two types: massive carbides and film carbides. They may have some similarity in appearance, but the mechanism of formation is distinct.

Massive carbides form isothermally in the carbon-supersaturated austenite at the junctions of austenite grains. These large-carbide grain-boundary allotriomorphs require considerable diffusion to grow, and therefore, they form during the high-temperature stages of carburizing or when the temperature of the part is lowered to approximately 845 °C (1550 °F) just prior to quenching. Such carbides often can readily form in three directions and have a blocky appearance (Fig. 18). However, depending on the alloy, massive carbides also may form as long, thin constituent (Fig. 19). Massive carbides at grain boundaries in the outer 0.05 mm (0.002 in.) at corners and edges may be detrimental.

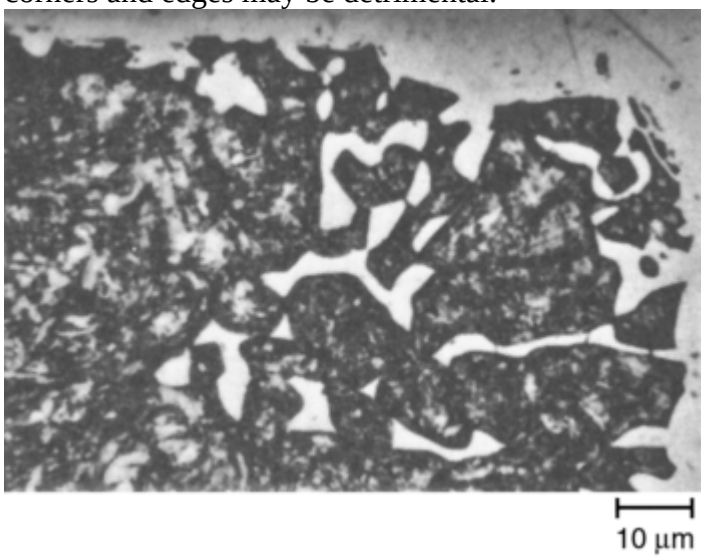

Fig. 18 Blocky shape of massive carbides at the specimen corners of carburized 8620 steel. Source: Ref 4

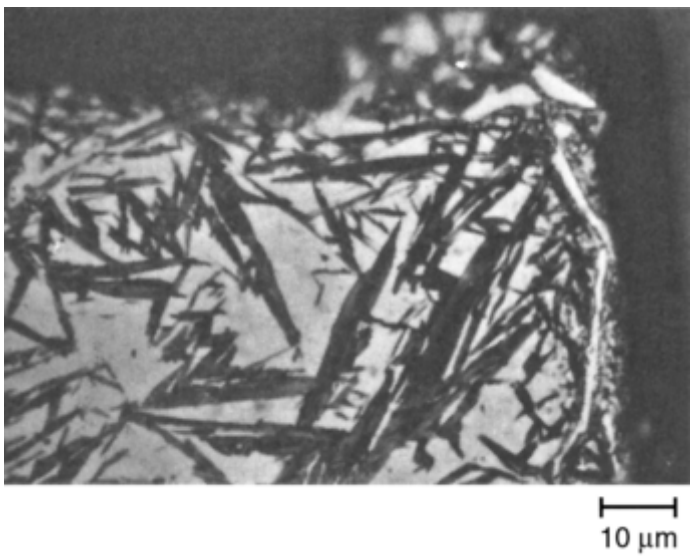

Fig. 19 Thin, continuous grain-boundary massive carbides in SAE 4121 steel. Source: Ref 4

Film, or network, carbides form during cooling below the A_{cm}. The excess carbon migrates to the austenite grain boundaries, where it is deposited as small, thin platelets that make contact and form a grain-boundary film. An example is shown in Fig. 20. Network carbides can be detrimental to properties and troublesome during posthardening manufacturing processes. Lean-alloy grades with high manganese contents may be more prone to developing network carbides.

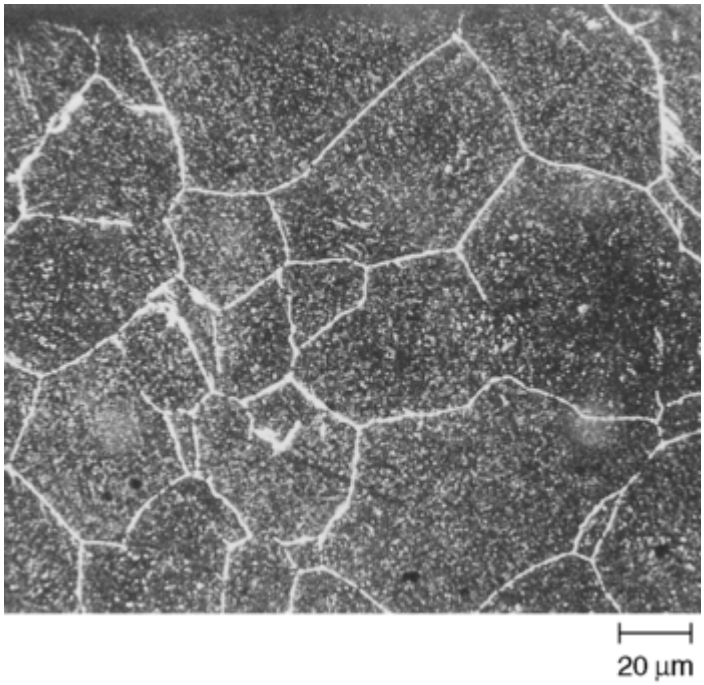

Fig. 20 Example of film network carbides in direct-quenched 3% Ni-Cr carburized steel. 500×. Source: Ref 3

Microcracks frequently form in martensite plates of high-carbon steels (Fig. 16a), especially with larger-grain austenite. Plain carbon and very lean alloy grades of steel are more prone to microcracking during case hardening. The effect of microcracking on properties depends on many other variables, such as load condition and the mode of crack propagation. For example, the influence of microcracks in martensite plates on transgranular crack propagation would be expected, while microcracks may have only a very secondary effect on fatigue when many fatigue cracks initiate at embrittled austenite grain boundaries (see the article "Microstructures and Properties of Carburized Steels" in *Heat Treating,* Volume 4 of *ASM Handbook*). In rolling-contact fatigue, subsurface alterations (referred to as "butterflies") can develop at microcracks (Fig. 21).

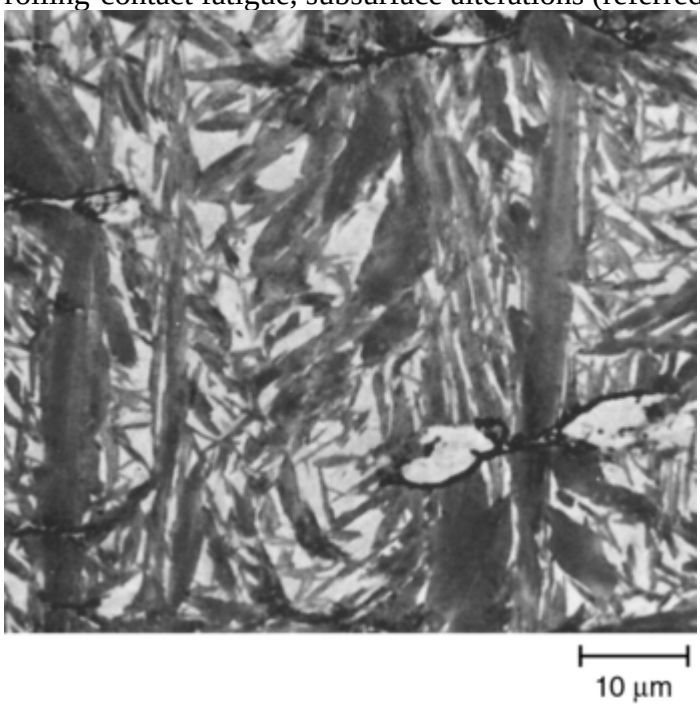

Fig. 21 "Butterfly" structural alterations at microcracks in gas-carburized 8620 steel subjected to contact-fatigue loading. Specimen was gas carburized 11 h at 925 °C (1700 °F), furnace cooled to 845 °C (1550 °F), oil quenched, and tempered 2 h at 195 °C (380 °F). Specimen was subjected to maximum

compressive stress of 4135 MPa (600 ksi) for 11.4 million cycles in a contact-fatigue test. Picral etch. 1000×

Microstructural Alterations from Contact Fatigue. Contact fatigue is the cracking of a surface subjected to alternating stresses produced under combined rolling and sliding loading conditions. In addition to cracking, contact fatigue can result in microstructural alterations, including changes in retained austenite, residual stress, and martensite morphology. Cyclic contact stresses cause microstructural changes, which are important because they are related to stress levels and the number of cycles. The microstructural changes usually observed in martensitic microstructures from contact fatigue are known as dark-etching areas, butterflies, and white bands, as described in more detail in the article “Contact Fatigue of Hardened Steels” in *Fatigue and Fracture*, Volume 19 of *ASM Handbook*. The development of these structural changes depends on the local magnitude of the applied shear stresses and the number of cycles, such that, below a certain stress limit or number of cycles, these structural changes are not observed. For example, of these three microstructural changes, the so-called white bands occur from many cycles (approximately 100 million total) after dark etching and butterfly formation.

Examples of microstructural alterations from contact fatigue of carburized steels are shown in Fig. 21, 22, 23, 24, and 25. It is also important to note the distinction between through-hardened and carburized steels. Microstructural alterations are different for 52100-type steels than for carburized steels. The undissolved carbides in 52100 and the higher level of retained austenite in the carburized steels contribute to these differences. Additional differences, such as hardness/strength and residual stress gradients found in carburized steels, may influence the type and location of the microstructural alterations with respect to load levels and stress cycles.

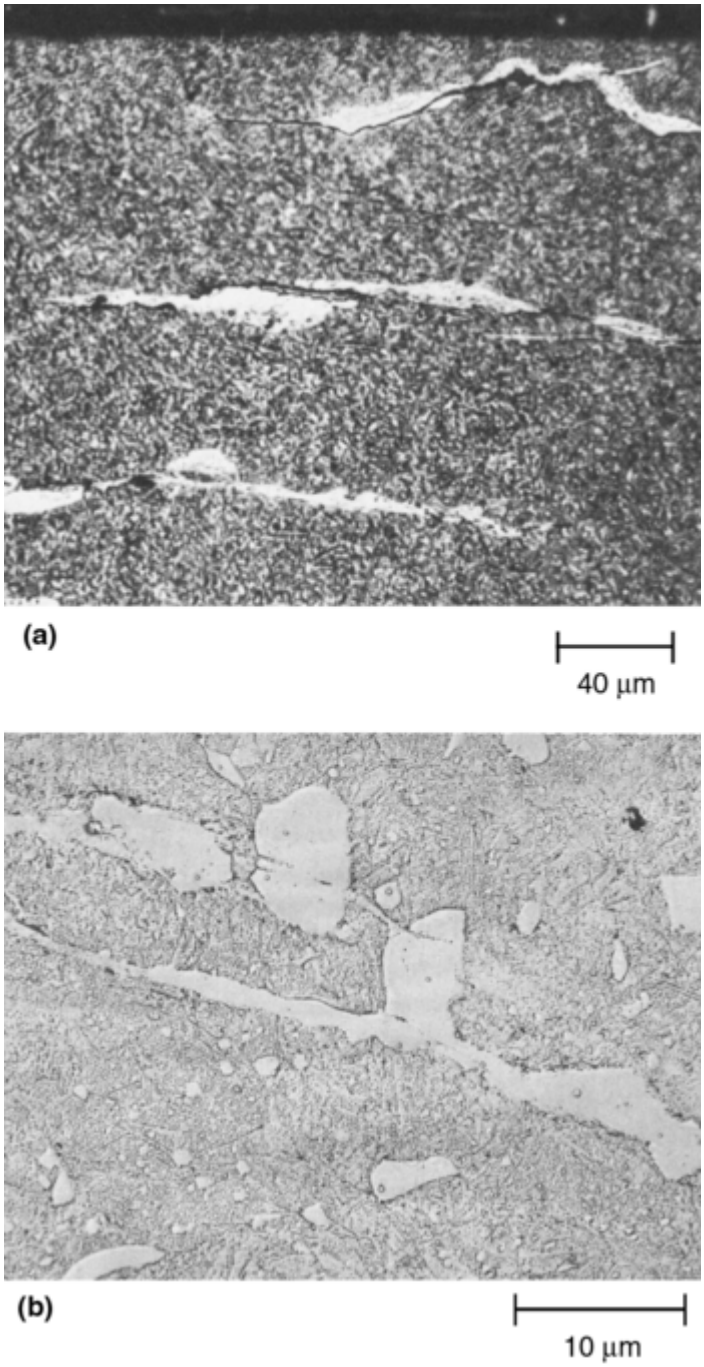

Fig. 22 Structural and "butterfly" alterations in a carburized 8822H steel roller after contact-fatigue testing Gas carburized 15 h at 925 °C (1700 °F), furnace cooled, heated to 805 °C (1480 °F) and held 1 h, oil quenched, and tempered 1 h at 175 °C (350 °F). (a) Structural alterations developed at subsurface cracks. 1% nital etch. 275×. (b) Replica electron micrograph revealing structural butterfly alterations that formed at inclusions. 4% picral etch. 1600×.

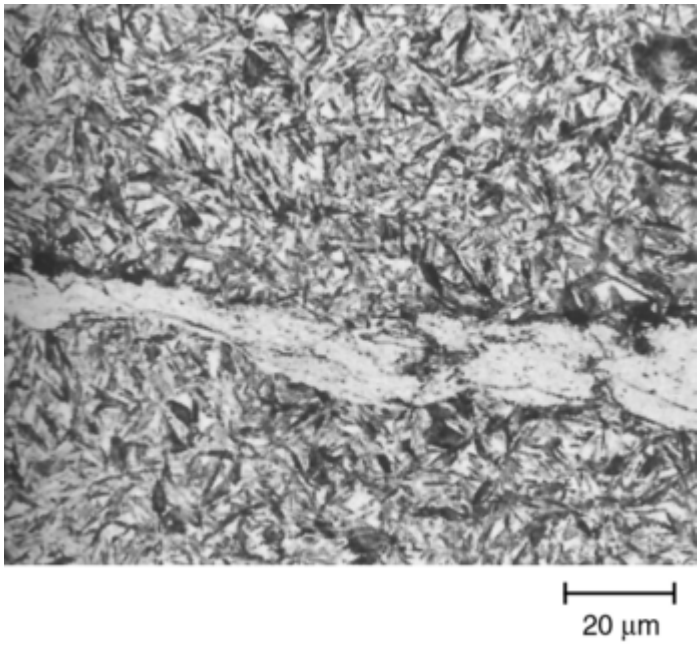

Fig. 23 Stress-induced microstructural alteration (light-gray streak) from contact fatigue on gas-carburized and hardened 4620 steel. The alteration formed at an Al_2O_3 stringer inclusion and is approximately 0.25 mm (0.01 in.) from the rolling-contact surface. Nital etch. 500×

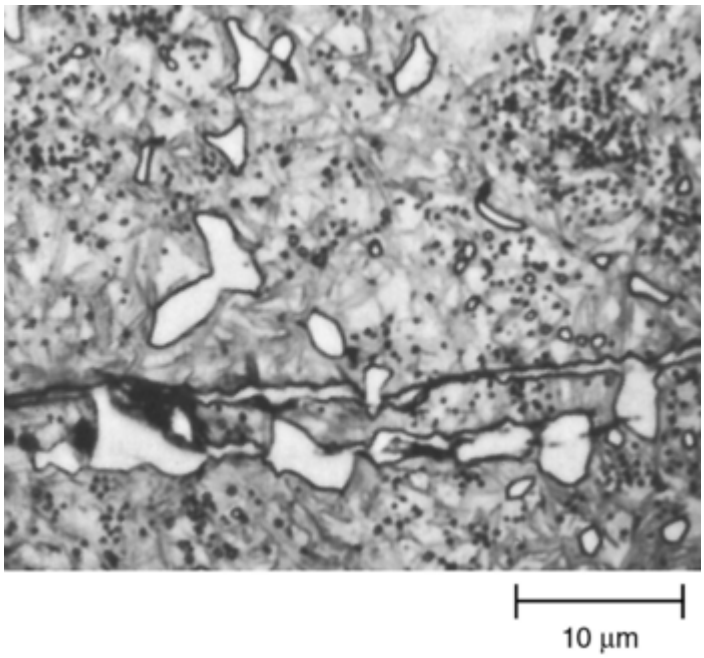

Fig. 24 Microstructural alteration associated with the carbide phase in a gas-carburized 8822H steel roller subjected to a contact-fatigue test. The roller was carburized, furnace cooled, reheated, oil quenched, and tempered. The structure consists of retained austenite, martensite, and carbide. 4% picral etch. 1500×

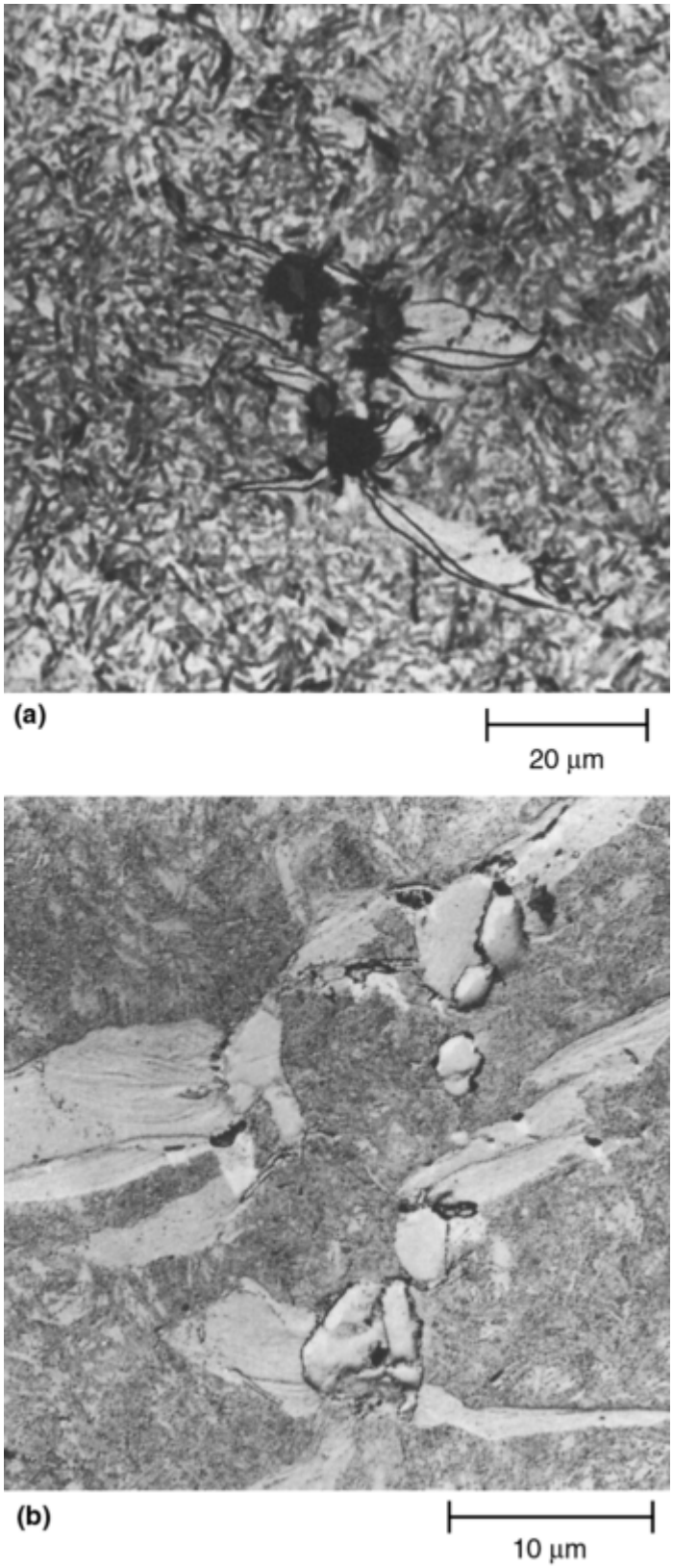

Fig. 25 “Butterfly” alterations at inclusions in gas-carburized 1039 roller steel after contact-fatigue testing. (a) Alterations in the center are approximately 0.1 mm (0.004 in.) below the contact surface. 1% nital etch. 750×. (b) Replica electron micrograph of butterfly alterations at inclusions. 2% picral etch. 1950×

Carbonitrided Steels

Carbonitriding is a modified form of gas carburizing rather than a form of nitriding. The modification consists of introducing ammonia into the gas carburizing atmosphere to add nitrogen to the carburized case as it is being

produced. Nascent nitrogen forms at the work surface by the dissociation of ammonia in the furnace atmosphere; the nitrogen diffuses into the steel simultaneously with carbon. Typically, carbonitriding is carried out at a lower temperature and for a shorter time than gas carburizing, producing a shallower case than is usual in production carburizing.

Carbonitrided cases have a martensitic structure (Fig. 26) with better hardenability than a carburized case (because nitrogen increases the hardenability of steel). Nitrogen is also an austenite stabilizer, and it thus lowers the martensite start and finish transformation temperatures of austenite. Therefore, a carbonitrided case usually contains more retained austenite than a carburized case of the same carbon content, particularly in alloy steels. Examples of retained austenite are shown in Fig. 27 and 28 for two carbonitrided cases. Too much retained austenite degrades properties in the same way as a carburized case. It also can be extremely detrimental in components of close-fitting assemblies, such as a rotating shaft in a sleeve, where the delayed transformation of austenite to martensite at ambient temperature results in a volume increase that may cause moving parts to bind or “freeze” in service.

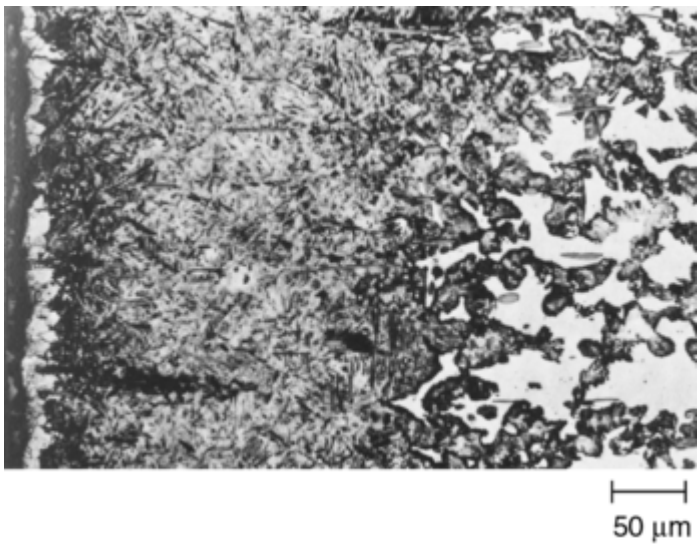

Fig. 26 Carbonitrided and oil-quenched 1117 steel with a surface layer of decarburized ferrite (left) superimposed on a normal case structure of martensite. The core (right) contains patches of ferrite (white). Nital etch. 200×

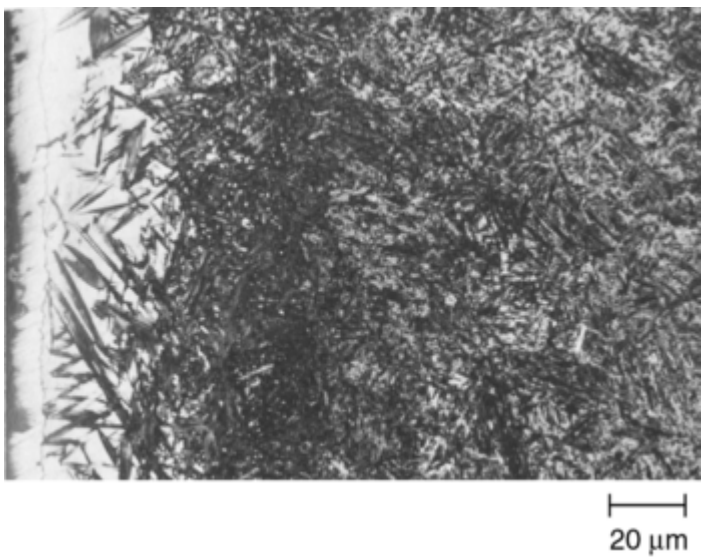

Fig. 27 Effects of too high a carbon potential on the microstructure of a carbonitrided and oil-quenched 1020 steel. The outer surface (left) has a white layer of cementite, and the subsurface consists of retained austenite interlaced with martensite needles and a martensite matrix (right). Nital etch. 500×

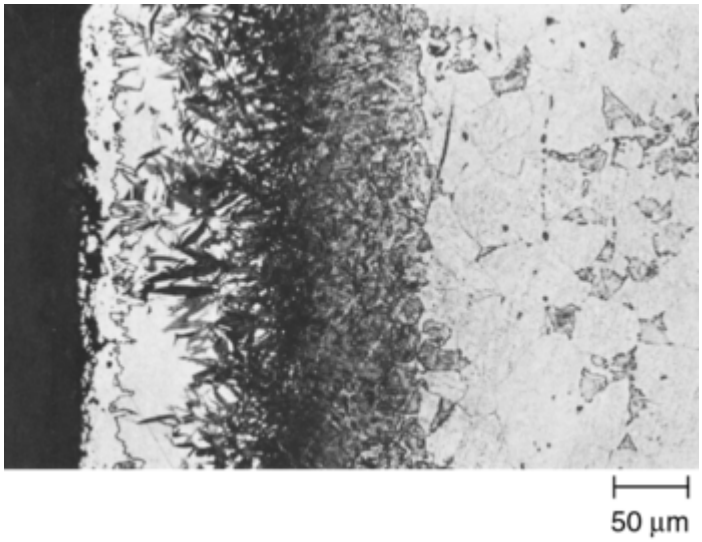

Fig. 28 Case microstructure of 1010 steel, carbonitrided at 790 °C (1450 °F) and oil quenched. The high-carbon case (left) is similar to that in Fig. 27, but the core (right) is predominantly ferrite. Nital etch. 200×

Retained austenite is normally at a maximum near the steel surface, where it can be removed from symmetrical contours by grinding (although care must be exercised in grinding high retained-austenite surfaces because of the increased possibility of grinding burn or checking). Grinding also may be considered an expensive operation, if it is not required for any reason other than to remove retained austenite. The preferred way to minimize retained austenite is by selection of steels and control of the carbonitriding process. The amount of retained austenite also can be significantly decreased by subzero-temperature treatments that allow lower-temperature martensitic transformation. This involves cooling the quenched parts to -40 to -100 °C (-40 to -150 °F). Examples are shown in Fig. 29.

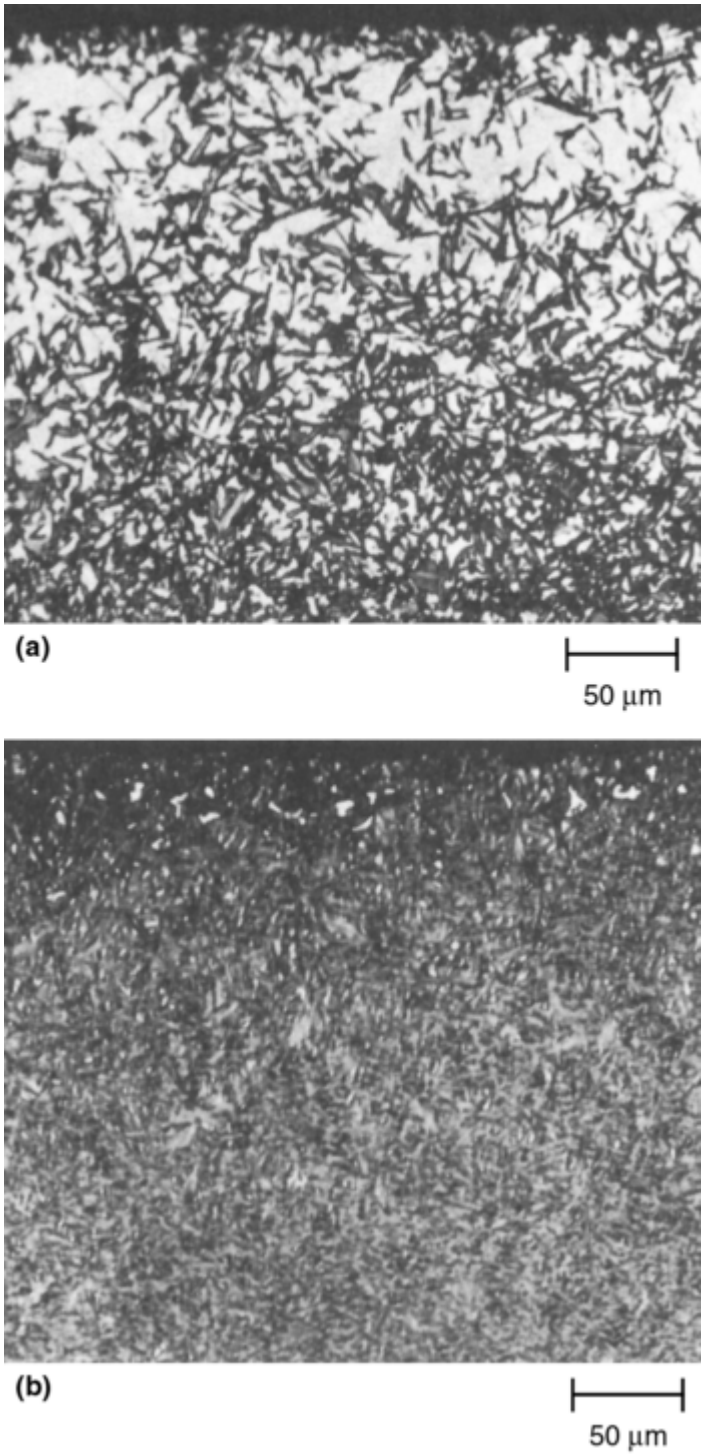

Fig. 29 Effect of low-temperature hold on retained austenite in carbonitrided 8617 steel bar. (a) Carbonitrided 4 h at 845 °C (1550 °F) in 8% ammonia, 8% propane, and remainder endothermic gas. Oil quenched and tempered 1.5 h at 150 °C (300 °F). Structure is tempered martensite (dark) and retained austenite. (b) Carbonitrided and tempered 8617 bar as in (a), except held 2 h at -75 °C (-100 °F) between quench and tempering. The structure is scattered carbide in a matrix of tempered martensite. Most of the retained austenite was transformed during low-temperature hold. Both 3% nital etch. 200×

Subsurface voids or porosity in the case structure (Fig. 30) may occur in carbonitrided parts if the processing conditions are not adjusted properly. Although details of the mechanism of void formation are not completely understood, the problem has been related to excessive ammonia additions. It should also be noted that the reprocessing of previously carbonitrided parts can, in many instances, lead to void formation.

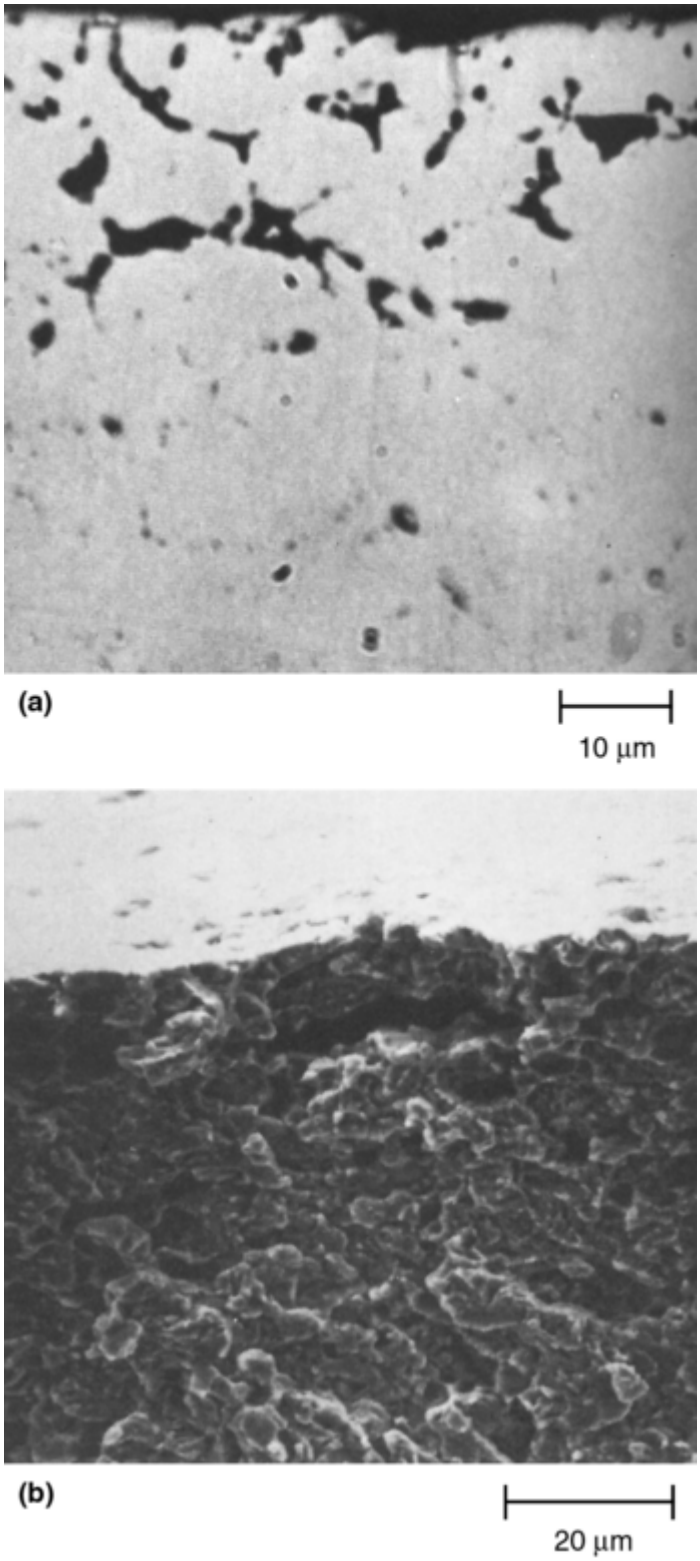

Fig. 30 Networks of subsurface grain-boundary voids in modified 1012 (0.03% Ni, 0.30% Cr) steel after carbonitriding and quenching. Cold-rolled strip, carbonitrided 1 h at 845 °C (1550 °F), and oil quenched. The formation of grain-boundary voids can occur with carbonitriding temperatures near 850 °C (1560 °F) and by total carbon and nitrogen potentials above 1%. (a) As-polished specimen. 1000×. (b) Scanning electron micrograph of a fracture surface. Void formation appears to involve the formation of diatomic gas molecules (probably nitrogen) at prior-austenite grain boundaries. Not polished, not etched. 750×

References cited in this section

1. L. Samuels, Chapter 12: Surface Oxidation, Decarburization, and Carburization, *Light Microscopy of Carbon Steels*, ASM International, 1999

2. J.L. Pacheco and G. Krauss, Microstructure and High Bending Fatigue Strength in Carburized Steel, *J. Heat Treat.*, Vol 7, 1989, p 77–86; *Härt.-Tech. Mitt.*, Vol 45, 1990, p 77–84

3. G. Parrish, *Carburizing: Microstructures and Properties,* ASM International, 1999

4. K.D. Jones and G. Krauss, Effects of High-Carbon Specimen Corners on Microstructure and Fatigue of Partial Pressure Carburized Steels, *Heat Treatment '79,* The Metals Society, 1980, p 188–193

Metallography and Microstructures of Case-Hardening Steel, *Metallography and Microstructures*, Vol 9, *ASM Handbook*, ASM International, 2004, p. 627–643

Nitrided Steels

Nitriding is a surface-hardening heat that introduces nitrogen into the surface of steel at a temperature range (500 to 550 °C, or 930 to 1020 °F), while it is in the ferritic condition. Because nitriding does not involve quenching from the austenite phase field to form martensite, nitriding can reduce distortion and provide excellent dimensional control. Nitriding is also used to surface harden austenitic stainless steels, although with more difficulty than martensitic stainless steels. All hardenable steels must be hardened and tempered before nitriding. The tempering temperature must be high enough to ensure stability at the nitriding temperature.

Process methods for nitriding include gas (box furnace or fluidized bed), liquid (salt bath), and plasma (ion) nitriding. Plasma nitriding allows faster nitriding times than for gas nitriding, which can take 10 to 20 h or even days, depending on the application. The mechanism of generating nascent nitrogen at the surface of the workpiece also affects the case structure, as described subsequently for gas and plasma (ion) nitriding.

Nitrided Case Structure

The case structure of a nitrided steel contains a diffusion zone, either with a compound zone (Fig. 31) or without (Fig. 32). The formation of the compound zone depends on the type and concentration of alloying elements and the processing environment, as briefly described here. The microstructure also influences nitridability. Ferrite favors the diffusion of nitrogen, and a low carbide content favors both diffusion and case hardness. Heat treated (quenched and tempered) alloy steels are usually used for nitriding, and the high surface hardness is obtained with nitriding steels that contain strong nitride-forming elements, such as aluminum, chromium, vanadium, and molybdenum. A general comparison of hardness profiles is shown in Fig. 33 (Ref 5).

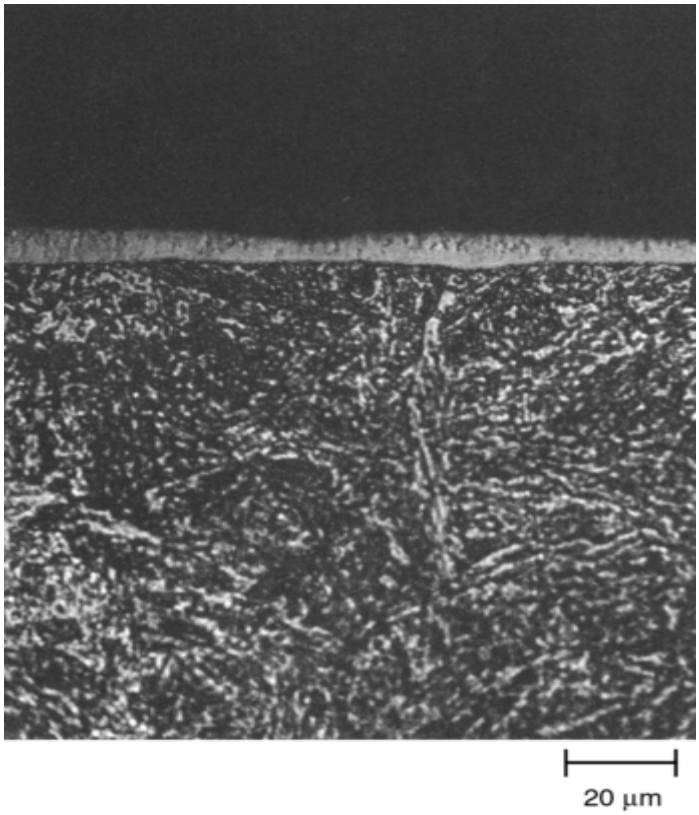

Fig. 31 Compound layer of γ′(Fe_4N) on the ion-nitrided surface of quenched and tempered 4140 steel. The γ′ compound layer is supported by a diffused case, which is not observable in this micrograph. Nital etch. 500×

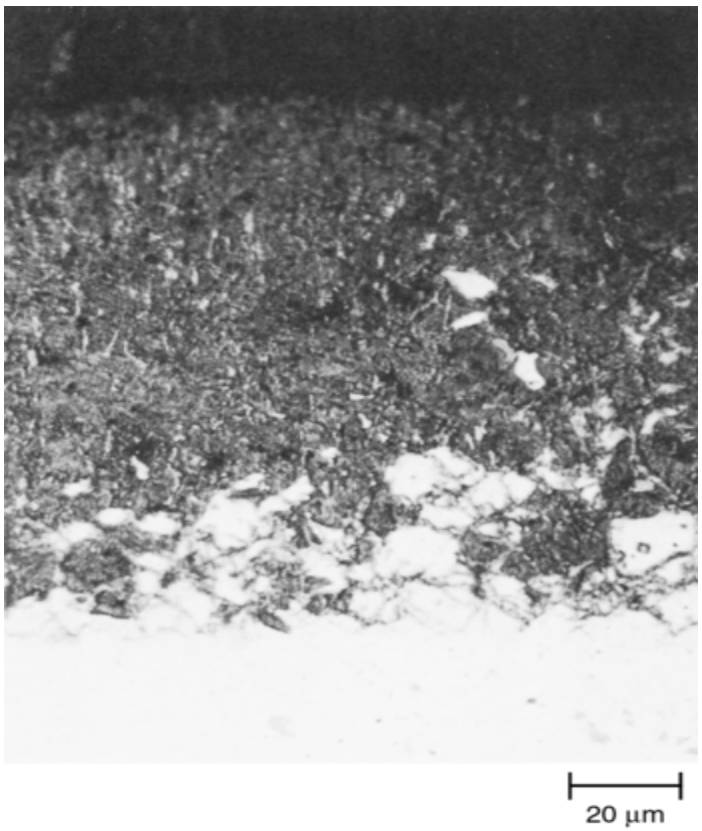

Fig. 32 Observable diffusion zone on the unetched (white) portion of an ion-nitrided 416 stainless steel. Nital etch. 500×

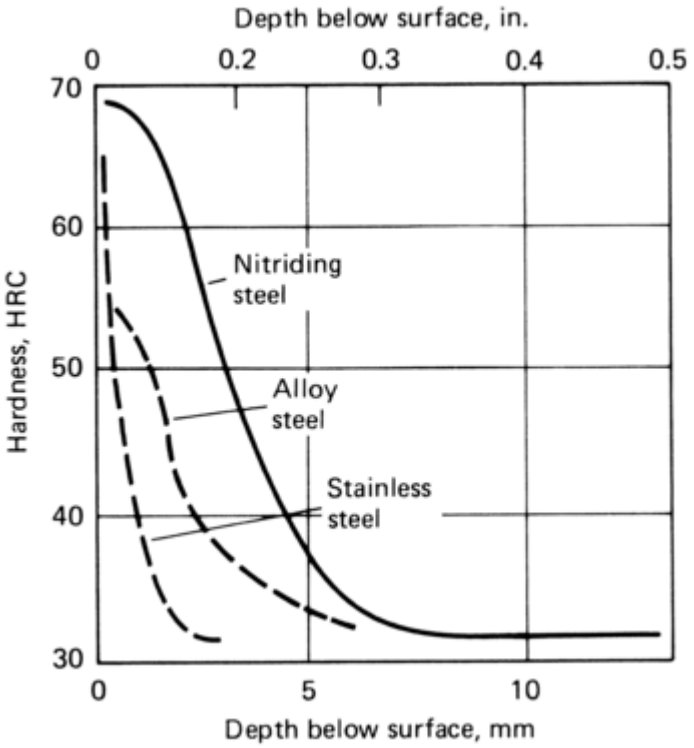

Fig. 33 Nitride case profiles in various steels

The diffusion zone of a nitrided case is essentially the original core microstructure with some solid-solution and precipitation strengthening. The depth of the diffusion zone depends on the nitrogen concentration gradient, time at a given temperature, and the chemistry of the workpiece. The deepest regions of the diffusion zone have the lowest nitrogen concentrations, where dissolved nitrogen provides some solid-solution strengthening of the iron lattice. This area of solid-solution strengthening is only slightly harder than the core. As the nitrogen concentration increases toward the surface, the solid-solubility limit of nitrogen in iron (~0.1 wt% N at 592 °C, or 1098 °F) is exceeded, and a second-phase (Fe_4N) precipitate begins to form. Depending on the alloy, other phases may also precipitate from nitride-forming elements, such as aluminum, chromium, molybdenum, vanadium, tungsten, titanium, and niobium.

The extent of precipitation strengthening in the diffusion zone depends on the alloy. In iron, when the solubility limit of nitrogen is exceeded, very fine, coherent precipitates form. The precipitates can exist both in the grain boundaries and within the lattice structure of the grains themselves. These precipitates, nitrides of iron or other metals, distort the lattice and substantially increase the hardness of the material. In most ferrous alloys, the diffusion zone formed by nitriding cannot be seen in a metallograph, because the coherent precipitates are generally not large enough to resolve. In Fig. 31, for example, martensite in the diffusion zone cannot be visually distinguished from that in the core. In some materials, however, the nitride precipitate is so extensive that it can be seen in an etched cross section. Such is the case with stainless steel (Fig. 32), in which the chromium level is high enough for extensive nitride formation.

When nitrogen concentration increases further at the surface, the outermost surface can be all γ′ (Fe_4N). The γ′ intermetallic is the equilibrium reaction product when nitrogen concentrations are approximately 6 wt% in iron (Fig. 34). This layer of γ′ is referred to as the white layer, because it etches white in metallographic preparation. If nitriding results in further increases of nitrogen, a compound layer begins to form with γ′ and an ε-phase constituent ($Fe_{2-3}N$). In iron, the ε phase begins to form at approximately 6.1 wt% N at 450 °C (840 °F) (Fig. 34). The formation of the ε phase involves several factors. Carbon content promotes ε formation. Hydrogen also tends to catalyze Fe_2N formation. Thus, the ε phase can occur in conjunction with the γ′ phase, resulting in a so-called compound layer. This compound layer is also referred to as a white layer, because it etches white.

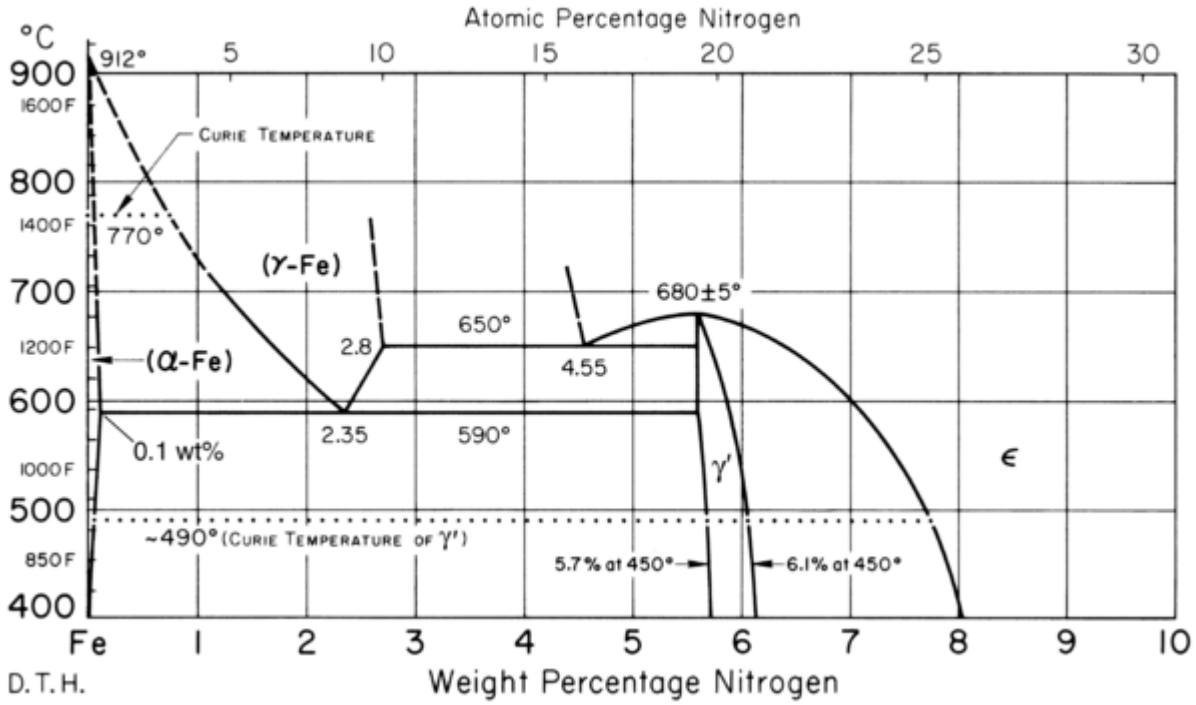

Fig. 34 Iron-nitrogen phase diagram

In steels, carbon content influences the amount of γ′ and ε formed within the surface structure. In a typical nitriding steel with a carbon content of approximately 0.4 wt%, the formation of γ′ to ε will be roughly equal, using the gas nitriding process. The thickness of the compound zone is a function of time, temperature, and pressure. The amount of carbon in the steel has a small effect on the thickness. The thickness of the compound layer is controlled, to a large extent, by the manipulation of the process techniques, such as dilution, the two-stage (Floe) process, or ion nitriding. Composition of the compound layer can also be controlled in the ion nitriding process.

Whether the compound zone is detrimental to the formed case depends on the application and the nitriding method (gas or ion, as described subsequently). See also the article “Nitriding and Nitrocarburizing” in *Friction, Lubrication, and Wear Technology,*” Volume 18 of *ASM Handbook.* This article includes 33 references that describe the influence of compound layer thickness, phase composition, chemical composition, and microstructure on the behavior of nitrided steels.

Case Structures with Ion-Nitrided Steel. In the ion nitriding process, nitrogen gas (N_2) is dissociated to form nascent nitrogen under the influence of the glow discharge. Therefore, the nitriding potential can be precisely controlled by the regulation of the N_2 content in the process gas. This control allows precise determination of the composition of the entire nitrided case and selection of a monophase layer of either ε or γ′, or total prevention of white-layer formation. Typical gas compositions and resulting metallurgical configurations are sketched in Fig. 35. Examples are shown in Fig. 36.

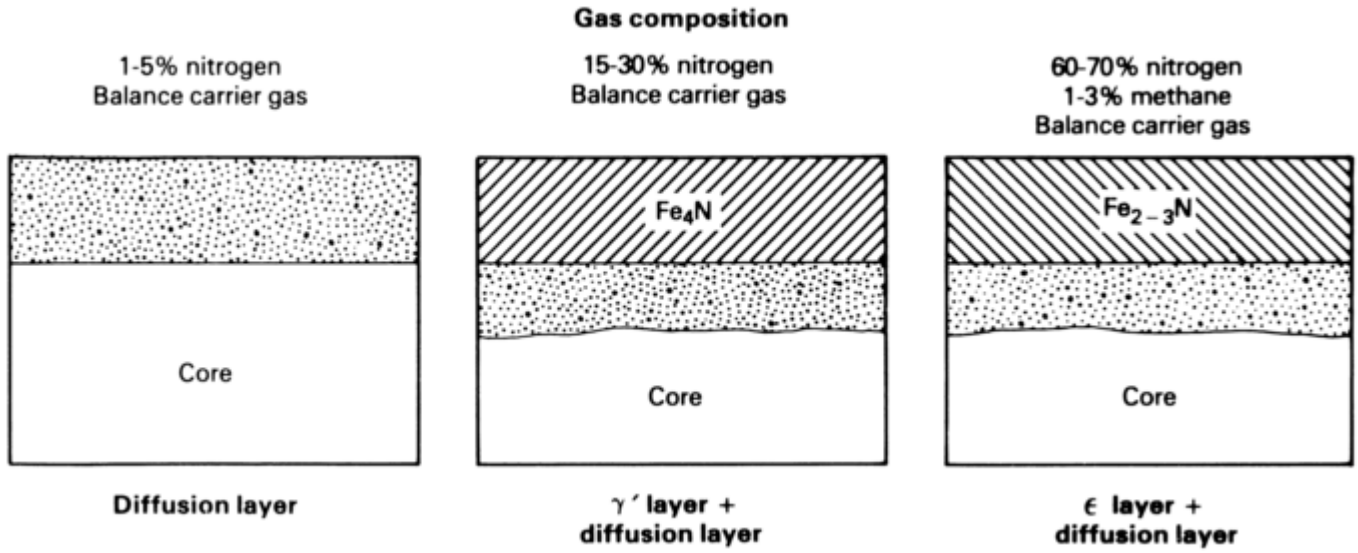

Fig. 35 Typical gas compositions and the resulting metallurgical configurations of ion-nitrided steel

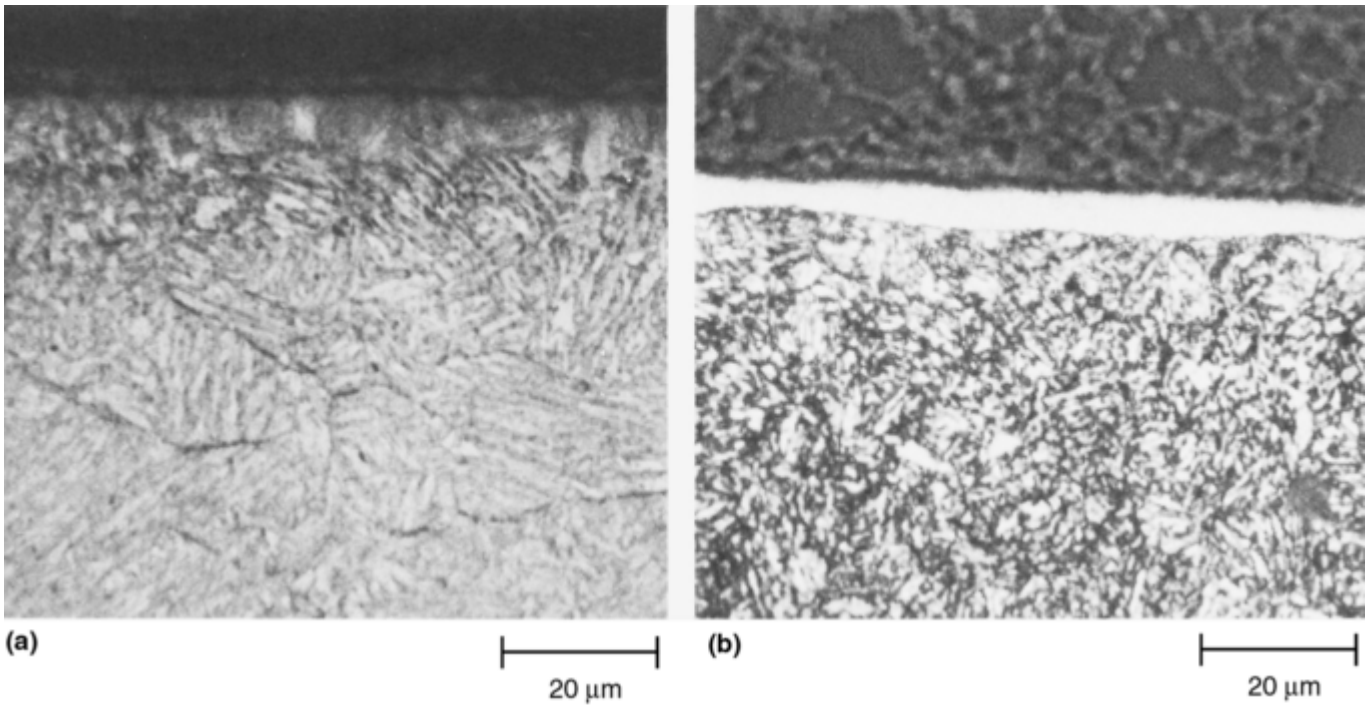

Fig. 36 Pure diffusion and monophase layers on ion-nitrided steel. (a) Pure diffusion zone with no white layer on Fe-0.31C-2.50Cr-0.2Mo-0.15V steel that was ion nitrided for 36 h at 525 °C (975 °F). Tempered before nitriding to 35 HRC. 2% nital etch. 750×. (b) Monophase surface layer of Fe_4N on a diffusion zone of nitride containing tempered martensite in 4140 steel. Quenched and tempered to 30 HRC, then ion nitrided for 24 h at 510 °C (950 °F). Nital etch. 750×

In many ion nitriding applications, a shallow γ′ compound zone with an underlying diffusion zone is the desired structure, particularly where good fatigue properties are important. Depth of the γ′ compound zone is inherently process-limited to approximately 10 μm (0.0004 in.) maximum. Steels with alloy contents greater than 6 to 8% inherently form compound zones with only trace thickness. Process-gas mixtures free of carbonaceous material are required to form compound zones having the γ′ structure. In the limiting condition, a diffusion zone is formed without an overlying compound zone. Gas compositions with less than the commonly used 25% N can completely suppress compound zone formation.

Single-phase ε iron-nitride compound zones having an Fe_2N-Fe_3N structure are formed when the process gas includes a carbonaceous component such as methane. The $Fe_{2–3}(N, C)$ ε structure is slightly harder and less ductile than γ′. The thickness of the ε compound zone is not process-limited; a zone 50 μm (2 mil) deep can be

formed. Industrially, zones 10 to 20 μm (0.4 to 0.8 mil) deep are applied to carbon steels and cast irons, where core hardness is usually low. Applications with light loads or broad area contact predominate. In addition to providing increased mechanical strength, the thicker compound zone is a good barrier against corrosion. Treatment time is typically 2 to 4 h at 570 °C (1060 °F), similar to other short-cycle nitrocarburizing processes. The compound zone is, however, pore-free, with low surface roughness.

Case Structure of Gas-Nitrided Steel. Gas nitriding with ammonia produces a compound zone that is a mixture of the γ′ and ε compounds; the mixture is due to the variability of ammonia dissociation, and therefore of nitriding potential, as the compound layer is formed. In conventional gas nitriding, the nascent nitrogen is produced by introducing ammonia (NH_3) to a work surface that is heated to at least 480 °C (900 °F). Under these conditions, the ammonia, catalyzed by the metal surface, dissociates to release nascent nitrogen into the work and hydrogen gas into the atmosphere of the furnace. The nitriding potential, which determines the rate of introduction of nitrogen to the surface, is determined by the NH_3 concentration at the work surface and its rate of dissociation. This nitriding potential, which can vary significantly in the gas process, is responsible for the limited control of microstructure in the nitrided case.

X-ray diffraction has shown that, from the outer surface to the beginning of the diffusion zone, the dominant compound changes from ε to γ′. However, both phases exist throughout the entire white layer, which is referred to as a dual-phase layer. The dual-phase layer has two characteristics that make it susceptible to fracture:

- Weak bonding at the interface between phases
- Different thermal expansion coefficients in the two phases

Layers that are particularly thick or that are subjected to temperature fluctuation in service are prone to failure. Another mechanical weakness in the gas-nitrided white layer is porosity in the outer region of the layer. As the compound zone builds, ammonia dissociation becomes more sluggish without the catalytic action of the steel surface, and gas bubbles begin to form in the layer.

Single-Stage and Double-Stage Gas Nitriding. Either a single- or double-stage process may be employed when nitriding with anhydrous ammonia. In the single-stage process, a temperature in the range of approximately 495 to 525 °C (925 to 975 °F) is used, and the dissociation rate ranges from 15 to 30%. This process produces the brittle, nitrogen-rich white layer. The double-stage process, known also as the Floe process (U.S. Patent 2,437,249), has the advantage of reducing the thickness of the white nitrided layer (Fig. 37).

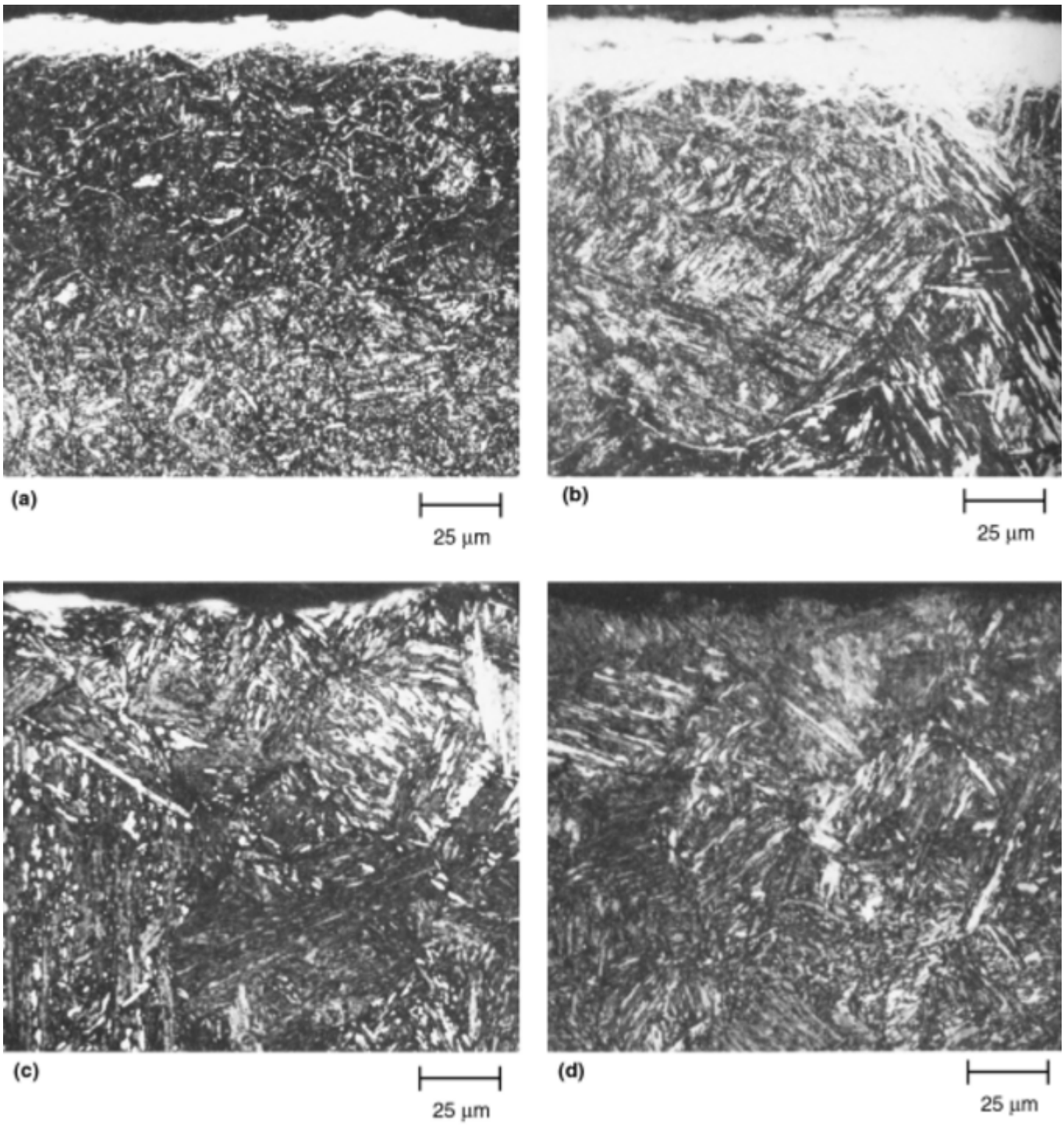

Fig. 37 Effect of single-stage and double-stage gas nitriding on formation of a compound layer in AMS 6470 steel (with 0.15 to 0.35% Pb added). Oil quenched from 900 °C (1650 °F), tempered 2 h at 605 °C (1125 °F), surface activated in manganese phosphate. (a) Gas nitrided 30 h at 525 °C (975 °F). Structure is a white layer (~0.01 to 0.13 mm, or 0.0004 to 0.005 in., thick) of Fe_2N and a matrix of tempered martensite. (b) Same material and heat treating conditions, except nitrided 36 h. The depth of the nitride layer has increased (~0.023 to 0.025 mm, or 0.0009 to 0.0010 in.), and platelets of iron nitride can be seen in the case. (c) Same steel and prenitriding conditions but double-stage nitrided: 5 h at 525 °C (975 °F), followed by 20 h at 565 °C (1050 °F). The white nitride layer has been eliminated by dissociation in the second stage of nitriding. (d) Same steel and processing as in (a), but the surface was heavily burnished and not chemically activated before nitriding. The lack of surface activation retarded diffusion into the case. All 2% nital etch, 400×

The first stage of the double-stage process is, except for time, a duplication of the single-stage process. The second stage may proceed at the nitriding temperature employed for the first stage, or the temperature may be

increased from 550 to 565 °C (1025 to 1050 °F); however, at either temperature, the rate of dissociation in the second stage is increased to 65 to 80% (preferably, 75 to 80%). Generally, an external ammonia dissociator is necessary for obtaining the required higher second-stage dissociation.

The principal purpose of double-stage nitriding is to reduce the depth of the white layer produced on the surface of the case. Except for a reduction in the amount of ammonia consumed per hour, there is no advantage in using the double-stage process, unless the amount of white layer produced in single-stage nitriding cannot be tolerated on the finished part, or unless the amount of finishing required after nitriding is substantially reduced.

Ferritic nitrocarburizing involves the diffusion of carbon and nitrogen into the ferrite phase and the formation of a thin white layer of a stable ε carbonitride phase. The case depths are thin (Table 1), but the treatment reduces spalling and scuffing. The introduction of carbon and nitrogen into a steel produces a compound white layer of iron carbonitrides/nitrides. The compound layer may contain varying amounts of γ′, ε phase, cementite, and various alloy carbides and nitrides. The exact composition is a function of the nitride-forming elements in the material and the composition of the atmosphere (see the article “Gaseous and Plasma Nitrocarburizing of Steels” in *Heat Treating,* Volume 4 of *ASM Handbook.* Gaseous nitrocarburizing is performed near 570 °C (1060 °F), a temperature just below the austenite range for the iron-nitrogen system. Treatment times generally range from 1 to 3 h.

Specimen Preparation

Preparation techniques for nitrided steel specimens must be even more exacting than those normally required. The extreme hardness differential between the case and the core causes problems. The case is often 1000 HK or more. In addition, the nitride concentration at the surface (white layer), which often is the primary subject of metallographic examination, is invariably partly or entirely destroyed by ordinary preparation techniques.

Testpieces. The principal use of metallography for nitrided steels is quality control of production nitriding. The workpieces being nitrided are often too valuable to permit destructive testing; therefore, separate testpieces of the same steels and heat treatment as the workpieces are prepared.

Two or more of these testpieces are placed in different parts of the nitriding furnace when it is loaded, for example, one near the top, one in the center, and one near the bottom. They can be placed at other locations as well, depending on the size and design of the furnace. The testpieces are identified so that they can be correlated with their location in the furnace. In addition to serving as specimens for metallographic examination, the testpieces serve for immediate visual inspection (by color), for superficial hardness testing (such as the Rockwell 15N), and for later microhardness surveys. Sizes and shapes of testpieces are not standardized, but the simplest design is a button 38 mm (1.5 in.) in diameter and 6 mm (0.25 in.) thick.

Care must be taken to ensure that testpieces are treated exactly the same as the load. Bars of convenient length and 40 mm (1.6 in.) in diameter are quenched and tempered, unless they are already in the heat treated condition, then turned and ground to a diameter of 38 mm (1.5 in.) to remove any decarburization or carburization that may have occurred in the preliminary heat treatment. The ground surface should be no rougher than 0.125 μm (5 μin.). Next, the turned and ground bars are cut into slices approximately 6 mm (0.25 in.) thick. This is preferably carried out on a lathe, but an abrasive cutoff machine can be used if abundant coolant is supplied to prevent burning. A hole can be drilled in the completed testpiece so it can be hung in the basket or from the workpiece to prevent its being lost during nitriding.

Plating of nitrided testpieces before sectioning is essential for protection of the edges and preservation of the white layer. Plating must be performed without blasting or severe etching. Nickel plating has proved best. The thickness of the deposit is not critical; 0.05 mm (0.002 in.) is usually sufficient, but a greater thickness is not harmful. Chromium plating is unsatisfactory, because the plate does not adhere well to nitrided surfaces without an unacceptable amount of surface preparation. Copper, zinc, and cadmium plates are too soft.

Surface preparation of a testpiece for nickel plating can be accomplished by two methods, neither of which will impair the surface to be examined. One method is to clean the testpiece in a detergent solution, preferably by the ultrasonic method. The other is to etch the testpiece for a few seconds in a metallographic etchant, such as nital.

Cutting and Mounting Test Specimens. The plated test specimens are clamped in the vise of a cutoff machine and cut so that one half of the testpiece remains (the width of cut is taken from the discard side). The half testpiece is then halved again by a cut perpendicular to the first cut, and the rounded portion is cut off. The size of the specimen facilitates positioning in the mold.

Various cutoff wheels have proved satisfactory for cutting testpieces, but 54-grit rubberbonded alumina (Al_2O_3) wheels are generally recommended. The use of copious coolant on the specimen is essential; water, synthetic compounds, or soluble-oil emulsions are satisfactory.

Phenolic (Bakelite, Georgia-Pacific Corp.) is suitable for mounting specimens of nitrided steel. The high mounting temperature of Bakelite, which is critical for some steels, does not affect nitrided steels. Use of hard, filled mounting materials is recommended for preserving flatness of the specimen during grinding and polishing. Filled epoxy mounts provide good edge retention.

Sectioning Nitrided Parts. When the workpieces being nitrided are very small, it is simpler and more economical to section actual parts for examination. The parts to be examined are completely nickel plated, then cut and mounted using the procedure described previously for specially prepared testpieces.

The procedure for extracting specimens from completed parts (service failures, for example) may vary, depending primarily on surface condition—whether the surface to be examined has been finished by grinding, honing, or lapping or is in the original nitrided condition. Finishing by grinding, honing, or lapping will have removed the white layer, and specimens can be extracted normally. However, unfinished surfaces should be nickel plated before sectioning to preserve the white layer.

Grinding and polishing of nitrided steel specimens is the same as grinding and polishing of other steel specimens. As is true for other case-hardened steels, which have large hardness variations in the same specimen, it is highly desirable to minimize grinding and polishing. Excessive grinding and polishing often produce out-of-flat specimens that must be reworked.

Etching. The optimal procedure is to etch the polished specimen, immediately repolish very lightly (just enough to remove evidence of etching), then etch again. This procedure may be repeated two or more times to ensure that all disturbed metal is removed and that the true structure is revealed.

For routine examination, nitrided steel specimens are most often etched in nital—2% nital for microscopic examination and up to 5% nital for case-depth measurements at low magnification. Nital reveals the white layer, the depth of case, and the structure of nitrided alloy steels and nitrided carbon steels.

Several other etchants are used for specific nitrided steels and for clearer resolution of certain microconstituents. Picral or a mixture of picral and nital (10 parts 4% picral and 1 part 4% nital) is often used as an alternative to nital. This mixture serves the same purpose as nital but often is preferred for revealing the structure of the nitrided case, especially at high magnification (Fig. 38). Other etching recipes include:

- Marble's reagent, consisting of 4 g cupric sulfate ($CuSO_4$), 20 mL HCl, and 20 mL H_2O, is used and often preferred for revealing total depth of nitrided case.
- A mixture of 1.25 g $CuSO_4$, 2 mL cupric chloride ($CuCl_2$), 10 g magnesium chloride ($MgCl_2$), 2 mL HCl, and 100 mL H_2O diluted to 1000 mL with 95% ethanol is sometimes used for etching high-chromium, vanadium-containing steels that have been nitrided.
- A solution of 1 to 4 g potassium ferricyanide ($K_3Fe(CN)_6$), 10 g potassium hydroxide (KOH), and 100 mL H_2O (modified Murakami's reagent) has also been used for etching specimens of nitrided steels to increase contrast between nitrides and carbides.
- Ferric chloride ($FeCl_3$) and modified Fry's reagent are also used to etch some steels, such as maraging steels (Fig. 39).

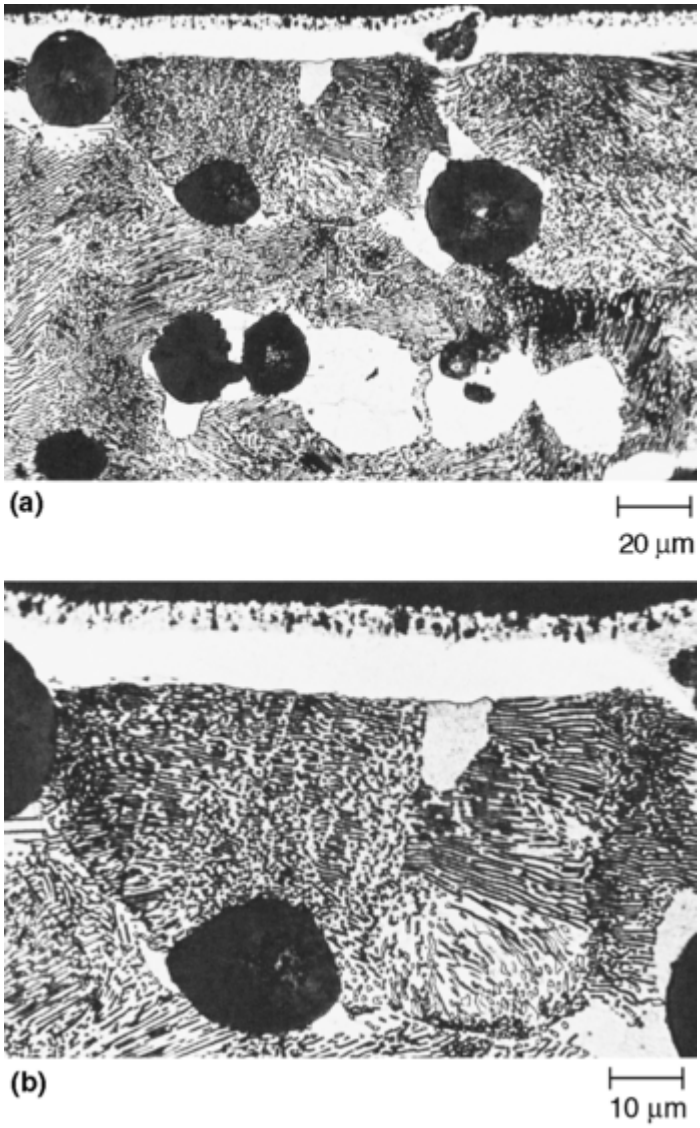

Fig. 38 Nitride layer etched with 3% picral on ductile iron specimen (grade 80-55-06). Liquid nitrided for 3 h in a salt bath at 570 °C (1060 °F) and water quenched. (a) 500×. (b) 1000×

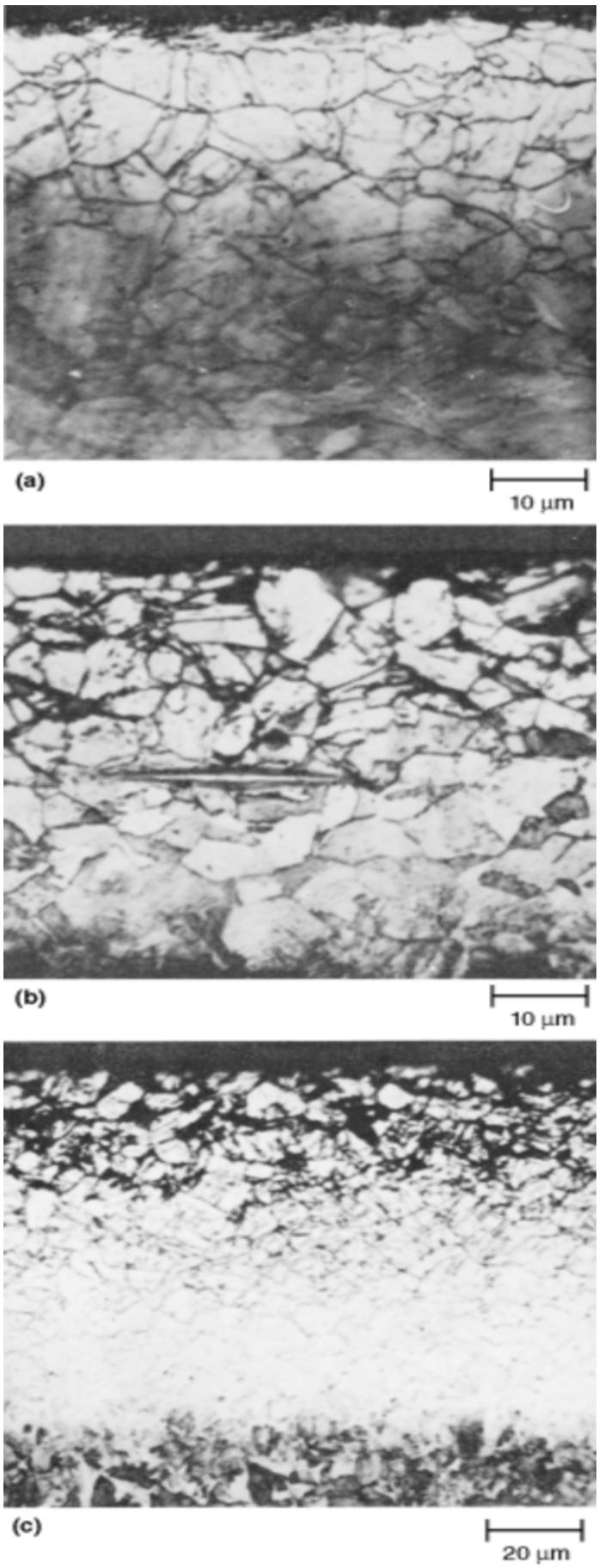

Fig. 39 Results from different etchants in specimen preparation of 18% Ni maraging steel (300 CVM). Solution treated 1 h at 815 °C (1500 °F), surface activated, and gas nitrided 24 h at 440 °C (825 °F). (a) Etched with nital, but this etchant does not clearly reveal the nitrided microstructure. 1000×. (b) Etching with modified Fry's reagent made the nitride surface layer and grain-boundary nitrides appear black.

1000×. (c) Etching with $FeCl_3$ makes the iron nitride appear as a black layer, similar to the specimen etched with modified Fry's reagent. 500×

Reference cited in this section

5. K.G. Budinski, *Surface Engineering for Wear Resistance,* Prentice-Hall, 1988

Metallography and Microstructures of Case-Hardening Steel, *Metallography and Microstructures,* Vol 9, *ASM Handbook,* ASM International, 2004, p. 627–643

References

1. L. Samuels, Chapter 12: Surface Oxidation, Decarburization, and Carburization, *Light Microscopy of Carbon Steels,* ASM International, 1999

2. J.L. Pacheco and G. Krauss, Microstructure and High Bending Fatigue Strength in Carburized Steel, *J. Heat Treat.,* Vol 7, 1989, p 77–86; *Härt.-Tech. Mitt.,* Vol 45, 1990, p 77–84

3. G. Parrish, *Carburizing: Microstructures and Properties,* ASM International, 1999

4. K.D. Jones and G. Krauss, Effects of High-Carbon Specimen Corners on Microstructure and Fatigue of Partial Pressure Carburized Steels, *Heat Treatment '79,* The Metals Society, 1980, p 188–193

5. K.G. Budinski, *Surface Engineering for Wear Resistance,* Prentice-Hall, 1988

G.F. Vander Voort, Metallographic Techniques for Tool Steels, *Metallography and Microstructures,* Vol 9, *ASM Handbook,* ASM International, 2004, p. 644–669

Metallographic Techniques for Tool Steels

George F. Vander Voort, Buehler Ltd.

Introduction

TOOL STEELS can be prepared for macroscopic and microscopic examination using the same basic procedures used for carbon and alloys steels. However, because many tool steels are highly alloyed and are generally heat treated to much higher hardness than most carbon and alloy steels, specific aspects of their preparation differ slightly. The reasons for these differences and the required procedural modifications are discussed in the following sections. Also covered are the effects of hot working, composition, austenitizing, and tempering on microstructure.

G.F. Vander Voort, Metallographic Techniques for Tool Steels, *Metallography and Microstructures,* Vol 9, *ASM Handbook,* ASM International, 2004, p. 644–669

Metallographic Techniques for Tool Steels

George F. Vander Voort, Buehler Ltd.

Macroexamination

Specimen selection is generally based on the original ingot locations. Sampling is usually performed after primary hot working to billet or bloom shapes. Disks 12 to 25 mm (0.5 to 1.0 in.) thick are most often cut from billet or bloom locations corresponding to the top and bottom of the ingot. They are sometimes cut from the middle location. The hardness of these products can be rather high, unless the billet or bloom was subjected to a full annealing cycle. Thus, sectioning of such specimens may be more difficult than for carbon or alloy steels. For most work, transversely oriented disks (perpendicular to the hot working axis) are preferred. However, longitudinal disks are better suited to studying deformation fiber or segregation. Transverse disks are preferred for general-quality evaluations. If very hard, the disks should be tempered before etching. For routine-quality studies, a saw-cut surface is adequate. If better resolution of detail is required or if photography is to be conducted, surface grinding is performed after cutting.

Macroetching. The macroetchant most widely used to evaluate macrostructural quality of tool steels is the standard immersion solution of equal parts of hydrochloric acid (HCl) and water at 70 to 80 °C (160 to 180 °F) for 15 to 45 min. Such etching will reveal segregation, cracks, porosity, inclusions (manganese sulfides, for example), flow lines, surface decarburization or carburization, and hardness variations. Interpretation of results is aided by referring to standard charts (Ref 1, 2, 3, 4). Figure 1 illustrates the use of the 50% hot HCl macroetch to reveal the case depth in different sized brine-quenched and tempered specimens of W1 tool steel with three levels of hardenability. Note that there is excellent contrast between the hardened case and the nonhardened core.

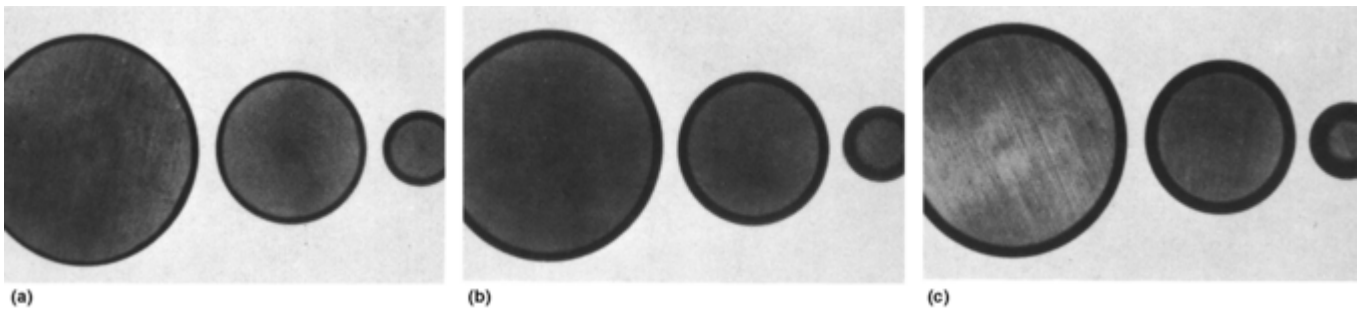

Fig. 1 AISI W1 tool steel austenitized at 800 °C (1475 °F), brine quenched, and tempered 2 h at 150 °C (300 °F). Black rings are hardened zones in 75, 50, and 25 mm (3, 2, and 1 in.) diameter bars. Core hardness decreases with increasing bar diameter (all one-half actual size). (a) Shallow-hardening grade. Case, 65 HRC; core, 34 to 43 HRC. (b) Medium-hardening grade. Case, 64.5 HRC; core, 36 to 41 HRC. (c) Deep-hardening grade. Case, 65 HRC; core, 36.5 to 45 HRC. Hot 50% HCl

This etching procedure can be used to evaluate disks cut from sections smaller than billets or disks cut from failed components; however, room-temperature macroetching, which is also quite common, often uses a 10% aqueous nitric acid (HNO_3) solution. Smooth-ground specimens are immersed for up to a few minutes in this solution to reveal such surface conditions as decarburization, carburization, nitriding, hardened layers, and grinding damage. Internal quality problems, such as segregation, are revealed but usually less effectively than by hot-acid etching. After etching, the surface is washed, scrubbed to remove etching smut, and dried. Etching of small polished sections in 2 to 5% nital will also bring out surface conditions that cannot be as clearly revealed by the cold 10% aqueous HNO_3 solution. However, nital is less effective on a smooth, ground surface. Figure 2 shows the carbide distribution on longitudinal planes of M2 and T1 high-speed steels revealed by

macroetching discs of varying diameter with 10% nital. Figure 3 and Figure 4 show the carbide segregation by light microscopy examination in three of the sizes for the M2 and T1 discs.

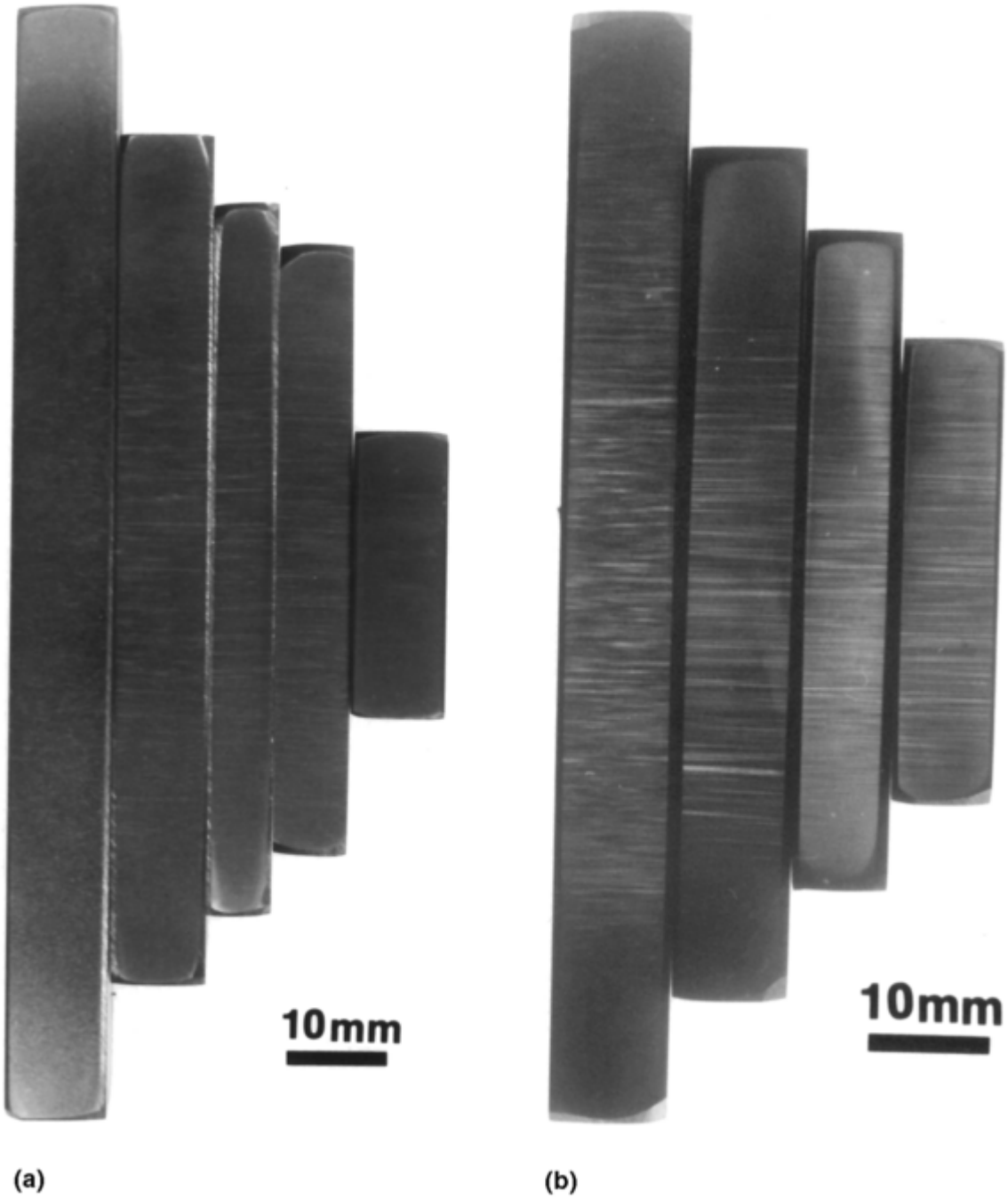

Fig. 2 Carbide distribution on longitudinal planes of high-speed steels revealed by macroetching discs of varying diameter with 10% nital. (a) M2 tool steel. (b) T1 tool steel. Both ~1×

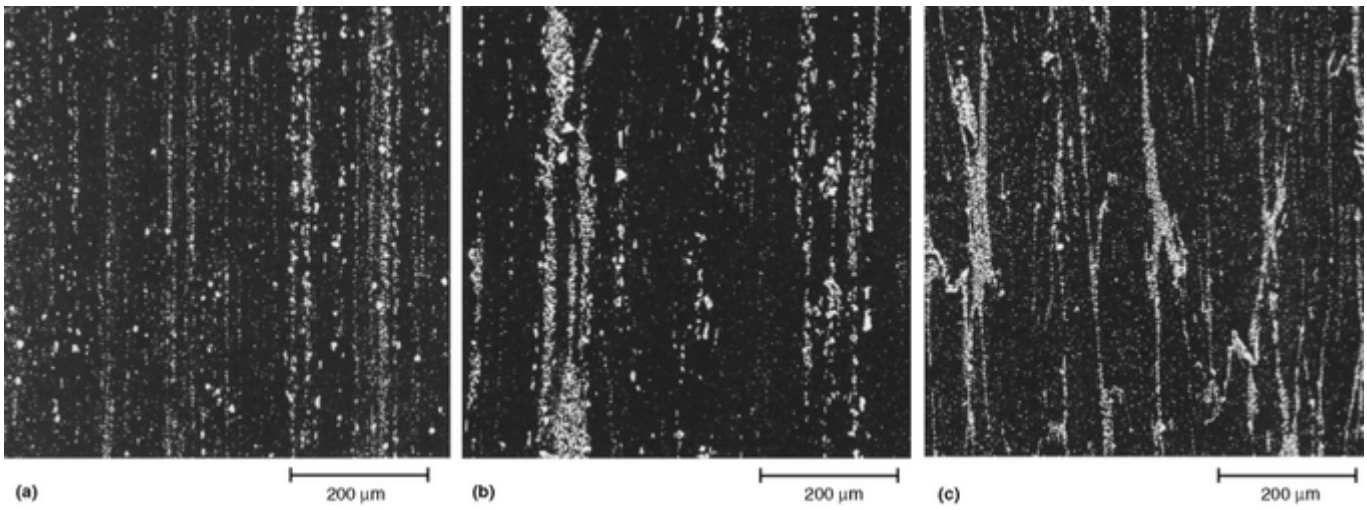

Fig. 3 AISI M2 round bars. Carbide segregation at the center of round bars of different diameters. (a) 27 mm (1 1/16 in.) diam. (b) 67 mm (2 5/8 in.) diam. (c) 105 mm (4 1/8 in.) diam. 10% nital. 100×

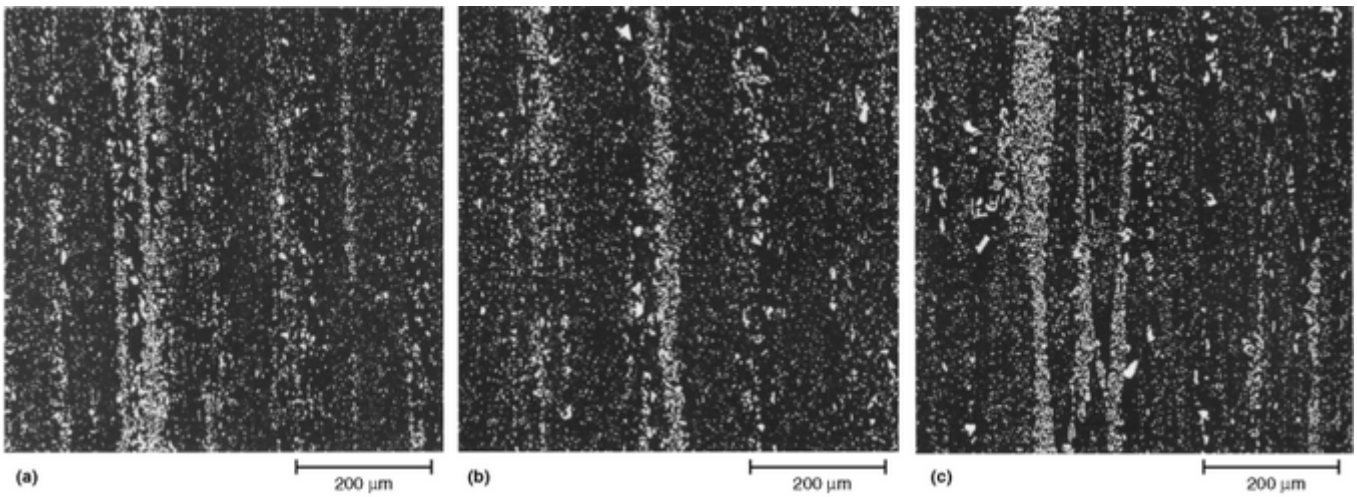

Fig. 4 AISI T1 round bars. Carbide segregation at the center of round bars of different diameters. (a) 35 mm (1 3/8 in.) diam. (b) 64 mm (2 1/2 in.) diam. (c) 83 mm (3 1/4 in.) diam. 10% nital. 100×

The sulfur print test (Ref 5, 6), another prevalent technique, is used to evaluate the distribution of manganese sulfides. Fracturing of hardened transverse etch disks is also performed to detect oxide inclusion stringers or graphite on the longitudinally oriented fracture. The fracture surface is often heated to produce a blue temper color, because the uncolored oxides exhibit strong contrast against the dark fracture.

References cited in this section

1. "Recommended Practice for Macroetch Testing of Tool Steel Bars," A 561, *Annual Book of ASTM Standards,* Vol 01.05, ASTM, 2003, p 335–341

2. "Macroetch Testing of Consumable Electrode Remelted Steel Bars and Billets," A 604, *Annual Book of ASTM Standards,* Vol 01.05, ASTM, 2003, p 371–384

3. "Standard Method of Macroetch Testing Steel Bars, Billets, Blooms and Forgings," E 381, *Annual Book of ASTM Standards,* Vol 03.01, ASTM, 1984, p 895–899

4. "Macrograph Standards for Steel Bars, Billets and Blooms," MIL-STD 430A, Department of Defense, 30 June 1966

5. G.F. Vander Voort, *Metallography: Principles and Practice,* McGraw-Hill, 1984; reprinted by ASM International, 1999

6. "Standard Practice for Preparing Sulfur Prints for Macrostructural Examination," E 1180, *Annual Book of ASTM Standards,* Vol 01.03, ASTM, 2003, p 787–789

G.F. Vander Voort, Metallographic Techniques for Tool Steels, *Metallography and Microstructures,* Vol 9, *ASM Handbook,* ASM International, 2004, p. 644–669

Metallographic Techniques for Tool Steels

George F. Vander Voort, Buehler Ltd.

Microexamination

Sectioning. Relatively soft specimens (less than 35 HRC) can be cut using band saws or hacksaws. However, such operations produce a substantial zone of deformation beneath the cut and rather rough surfaces. Thus, the initial rough grinding with a coarse abrasive (80- to 120-grit silicon carbide, for example) must remove this damage. However, such coarse abrasives generate large amounts of damage. Sectioning with an abrasive wheel developed for metallography is recommended, because it produces less damage and yields a better surface finish, so that damaging, coarse abrasive grinding can be minimized or eliminated. Then, a somewhat finer abrasive, which generates less damage, can be used for the first step (often called planar grinding with automated, multispecimen preparation systems). This procedure facilitates generation of a correctly prepared surface so that the true microstructure can be observed.

Higher-hardness specimens must be cut using water-cooled abrasive cutoff wheels. The blade should have a "soft" bond (that is, it breaks down readily, exposing fresh abrasive to the cut) for effective cutting and avoidance of burning. Effective water cooling limits heat generation but is inadequate by itself if the wrong blade is used, that is, a blade that does not break down at the proper rate. Dull abrasives generate excessive heat and damage in cutting. Cutting as-quenched specimens is very difficult without introducing some damaging heat that may cause burning or cracking. Cutting quenched and lightly tempered tool steels is much easier but still requires use of a wheel designed for such steels. Heat generated by improper technique can produce a highly tempered appearance in the martensite and, if heating is excessive, can re-austenitize the surface. In extreme cases, melting can occur at the surface, with an extensive heat-affected zone below this area. Subsequent grinding steps cannot easily remove such damage without introducing more damage.

When working with as-quenched high-alloy tool steels, it may be helpful to fracture the specimen. This will produce a flat, damage-free surface due to the extreme brittleness of such steels. The fractured surface can then be carefully ground, with adequate cooling, and polished for examination.

For high-hardness, high-alloy steels, sectioning with a low-speed saw or with a linear-precision saw at higher rotational speeds, with alumina wafering blades, diamond, or cubic boron nitride non-consumable blades, can provide high-quality surfaces with minimum cutting-induced damage. Although the cutting rate is slower than with an abrasive cutoff saw, such surfaces are smooth, damage is minimal, and grinding can begin with rather fine grits (320- or 400-grit silicon carbide, for example). Sectioning is a violent process, and excessive damage introduced in sectioning rarely is removed fully by the preparation method.

Mounting. Bulk samples frequently can be polished without mounting. Coding of unmounted specimens is generally limited to a few stamp marks (if the steel is soft enough to stamp), such as a job number. Vibratory scribers can be used, but subsequent corrosion may make these marks hard to read. Most modern automated grinding/polishing devices can handle unmounted specimens. If edge retention is important, mounting is recommended. Plating the surface prior to mounting (Ref 5) produces excellent results but is not always necessary. Compression-mounting epoxy resins with fillers provide excellent edge retention, even with nonplated specimens. Automated grinding/polishing devices, rather than hand polishing, yield much better edge

retention. Modern practices using napless polishing cloths provide excellent edge retention. Rigid grinding disks produce superb edge retention.

For small or oddly shaped specimens, mounting is preferred. If the edge is not of particular interest, most mounting media are satisfactory. However, some mounts have poor resistance to solvents such as alcohol, and most polymeric mounts are badly degraded if heated etchants are required. The compression-mounting epoxies prevent these problems. If a transparent mount is required to control grinding to a specific feature, transparent methyl methacrylate compression-mounting thermoplastic material can be used. Somewhat better results can be obtained using cast, "cold"-mounting epoxy resins.

Casting epoxies are the only materials that produce true adhesive bonding to the sample. When used correctly, they produce the lowest heat during polymerization and are useful when the specimen cannot tolerate the higher heat used in compression mounting. However, considerable heat can be generated during polymerization of epoxy resins if the process is not controlled properly. Cast acrylic resins generate substantial heat, because they polymerize in less than 10 min. When edge retention is not required and heat degradation is not anticipated, low-cost phenolic compression-molding materials can be used, although they are badly degraded by boiling etchants. Identification marks are easier to add on the back of a mounted specimen than on a nonmounted specimen. Nonmounted specimens degrade polishing cloths faster than mounted specimens.

Grinding is performed in the same manner as for carbon and alloy steels. Various manual or automated devices may be used. Water-cooled silicon carbide paper (200 to 300 mm, or 8 to 12 in., diameter) is used, although alumina-coated paper is preferred for ferrous alloys (but is not as readily available). The initial grit size selected depends on the technique used to generate the cut surface. Historically, the usual grit sequence is 120-, 240-, 320-, 400-, and 600-grit with the American National Standards Institute/Coated Abrasives Manufacturers Institute scale (P120, P280, P400, P600, and P1200 for the Federation of European Producers of Abrasives scale). Modern preparation procedures (Table 1, 2, 3 use a single SiC (or alternative surface) grinding step. Grinding pressure should be moderate to heavy, and grinding times of 1 to 2 min are typical to remove the scratches and deformation from the previous step. Fresh paper should be used; worn or loaded paper will produce deformation. Wheel speeds in grinding are generally in the range of 240 to 300 rpm.

Table 1 Five-step preparation practice for tool steels

Surface	Abrasive/size	Load		Speed, rpm/direction	Time, min
		N	**lbf**		
Waterproof grinding paper (or equivalent)	120/P120- to 240/P280-grit SiC, water cooled	22–27	5–6	Comp	Until plane
Silk cloth or rigid grinding disk	9 μm diamond (with lubricant)	22–27	5–6	Comp	5
Woven (napless) or pressed cloths	3 μm diamond (with lubricant)	22–27	5–6	Comp	3
Woven or pressed cloths	1 μm diamond (with lubricant)	22–27	5–6	Comp	2
Medium-nap cloth	~0.05 μm colloidal silica or sol-gel-type alumina suspensions	22–27	5–6	Contra	1.5–2

Table 2 Four-step preparation practice for tool steels

Surface	Abrasive/size	Load		Speed, rpm/direction	Time, min
		N	**lbf**		
Waterproof grinding paper (or equivalent)	120/P120- to 240/P280-grit SiC, water cooled	27	6	240–300 Comp	Until plane
Rigid grinding disk (or woven cloth)	9 μm diamond suspension (with lubricant)	27	6	120–150 Comp	5
Woven (napless) or pressed	3 μm diamond (with lubricant)	27	6	120–150	3

cloths				Comp	
Medium-nap cloth	~0.05 μm colloidal silica or sol-gel-type alumina suspensions	27	6	120–150 Contra	2

Table 3 Three-step preparation practice for tool steels

Surface	Abrasive/size	Load		Speed, rpm/direction	Time, min
		N	**lbf**		
Waterproof paper (or equivalent)	120/P120- to 320/P400-grit SiC, water cooled	27	6	240–300 Comp	Until plane
Hard or soft rigid grinding disks	3 μm diamond suspension	27	6	120–150 Comp	5
Medium-nap cloth	~0.05 μm colloidal silica or sol-gel-type alumina suspensions	27	6	120–150 Contra	5

Polishing is most commonly performed using one or more diamond abrasive stages, followed by one or more final abrasive stages. For routine work, polishing with 9 and 3 μm diamond abrasives is generally adequate. The diamond abrasive may be applied to the polishing cloth in paste, slurry, or aerosol form. Charging a new cloth with paste, however, is most effective, because the removal rate is high as soon as polishing starts. For the diamond abrasives, low-nap or napless cloths are preferred. A lubricant, or extender, compatible with the diamond abrasive should be added to moisten the cloth and minimize drag. Wheel speeds of 100 to 150 rpm and moderate pressure should be used. Polishing times depend on the number of steps in the procedure and the nature of the alloy (composition and heat treatment condition).

Final polishing can be conducted manually or automatically, using various devices. Alumina abrasives, generally 0.3 μm alumina ($A1_2O_3$) and 0.05 μm γ-Al_2O_3, have been widely employed with medium-nap cloths for final polishing. Colloidal silica (SiO_2, with a particle size range of 0.02 to 0.06 μm) is also very effective (Ref 5). Wheel speeds, pressure, and times are the same as for rough polishing with diamond abrasives. In general, tool steels are relatively easy to polish to scratch-free and artifact-free condition due to their relatively high hardnesses. Table 1 lists a contemporary five-step practice for preparing tool steels; Table 2 lists a contemporary four-step practice using a rigid grinding disk; and Table 3 lists a three-step practice using a rigid grinding disk. All methods produce excellent results.

In these methods, the cloth is first charged with diamond paste of the specified size, and then the appropriate lubricant is added. During the polishing cycle, diamond of the same size is added periodically in suspension form to keep the cutting rate high. *Comp* stands for complementary and means that the head (specimen holder) and base (platen) are both rotating in the same direction, counterclockwise (usually). *Contra* means that the head is rotating clockwise while the base is rotating counterclockwise. Contra is more aggressive than complementary. If the head rotates at less than 100 rpm, the slurries stay on the surface reasonably well. However, if the head rotational speed is greater than 100 rpm, the abrasive will be thrown off the platen onto the user and the walls. In complementary mode, the centrifugal force throws the abrasive off the platen surface and down the drain. Therefore, the amount of abrasive that must be added during a cycle depends on the surface being used, the head speed, and the rotational directions. When grinding, especially with cast polymeric mounts, complementary rotation may produce chatter and vibration, which is eliminated when using contra rotation. In certain specimens that have very hard or very soft (relative to the matrix) particles that are poorly bonded to the matrix, one may see excessive relief around these particles after the last step. If this happens, and it is specimen-specific and not frequent, simply repeat the last step in complementary rotation, and this problem will be eliminated.

Microetching. The etchant most widely used for tool steels is 2 to 5% nital. Stock solutions exceeding 3% HNO_3 in ethanol should not be stored in pressure-tight bottles. If higher concentrations are desired as a stock reagent, a bottle with a pressure-relief valve should be used. Methanol also may be substituted for ethanol,

although methanol poses health risks and thus may not be recommended. (See the article “Laboratory Safety in Metallography” in this Volume.)

Nital is generally used for tool steels regardless of the anticipated microstructural constituents. Although nital is superior to picral (4% picric acid in ethanol) for etching martensitic structures, picral produces better results for examining annealed samples. When examining spheroidize-annealed tool steels (the most common annealed condition), picral reveals only the interfaces between carbide and ferrite. Nital also reveals the ferrite grain boundaries that generally obscure the carbide shape. Also, because nital is orientation sensitive, carbides within some of the ferrite grains will be poorly delineated, making spheroidization ratings more difficult. Figure 5(a) and (b) illustrate the difference in etching response between nital and picral with spheroidize-annealed W2 tool steel. Note that within some grains, nital did not clearly reveal the cementite.

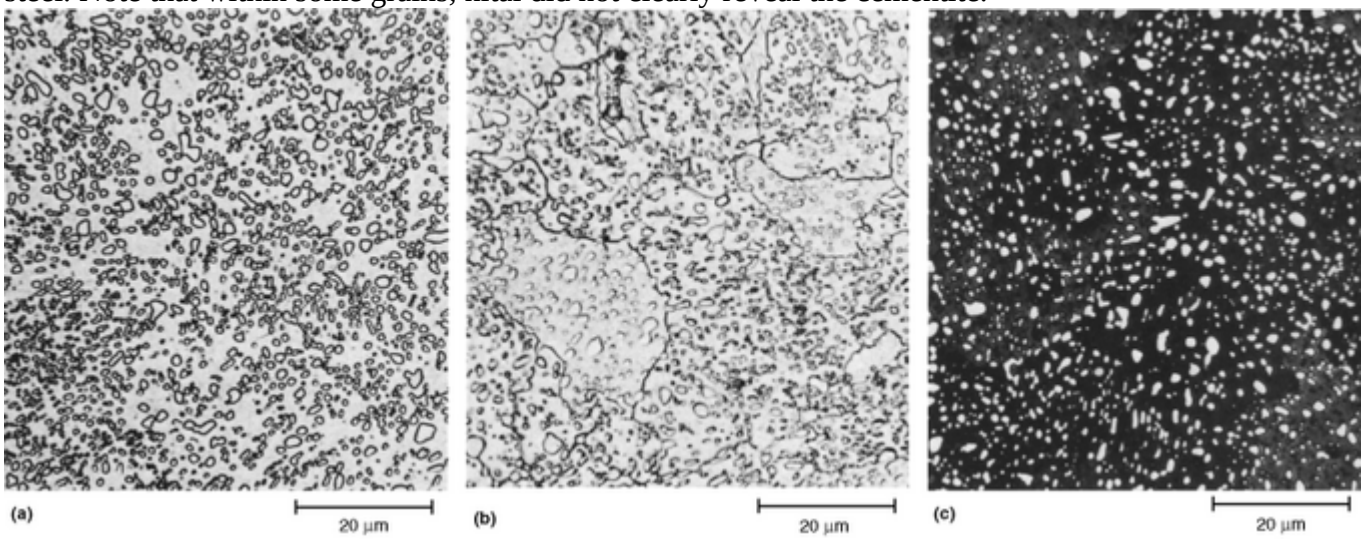

Fig. 5 AISI W2 (1.05% C), spheroidize annealed. (a) Etched with 4% picral to outline only cementite (uniform dissolution of the ferrite matrix). (b) Etched with 2% nital, which reveals ferrite grain boundaries and outlines cementite. Note that the ferrite in some grains is weakly attacked, and the carbides within these grains are barely visible. (c) Etched lightly with 4% picral, then tint-etched with Klemm's I reagent to color the ferrite (blue and red). 1000×

A 2% nital solution is usually preferred. Stronger concentrations increase the speed of etching, making it more difficult to control. Etching of martensitic high-alloy tool steels, such as the high-speed steels, may require a 5 or 10% concentration solution. Mix this solution fresh using ethanol; do not store the solution in a tightly stoppered bottle. Etching with nital or picral is usually performed by immersion. If swabbing is used, pressures should be light. Etching times are difficult to generalize because of the wide range of tool steel compositions and because heat treatment can markedly alter etch response. Trial and error will determine the degree of surface dulling necessary to obtain the correct degree of etching.

Other etchants, although less frequently used, can be of great value. Table 4 lists compositions of a number of specialized reagents for achieving selective etching or enhancing contrast among microconstituents. As examples of the use of various etchants, Fig. 5(c) and 6 show the same W2 specimen as in Fig. 5(a) and (b) but etched with four alternate reagents to evaluate the spheroidized cementite. Figure 7 shows the microstructure of D2 tool steel, in the quenched and tempered condition, revealed using three different etchants and by heat tinting, while Fig. 8 demonstrates the effect of four different etchants used to examine the structure of an improperly heat treated specimen of W1 (1% C) water-hardening tool steel.

Table 4 Microstructural etchants for tool steels

Etchant	Comments
1–10 mL HNO_3 and 99–90 mL alcohol	Nital. Most commonly used etchant. Do not store solutions with more than 3% HNO_3 in ethanol. Reveals ferrite grain boundaries and ferrite-carbide interfaces in annealed sample. Preferred etchant for martensite. Reveals prior-austenite grain boundaries in as-quenched and lightly tempered high-alloy tool steels. 2–3% nital most common; 5–10% nital used for high-alloy grades. Use by immersion.
4 g picric acid and 100 mL ethanol	Picral. Recommended for annealed structures or those containing pearlite or bainite. Does not reveal ferrite grain boundaries in annealed specimens. Etching response improved by adding 10–20 drops zephiran chloride. For high-alloy grades, add 1–5 mL HCl to improve etching response. Use by immersion.
1 g picric acid, 5 mL HCl, and 100 mL ethanol	Vilella's reagent. Used in the same manner as picral or picral plus HCl
10 g picric acid and 100 mL ethanol	Superpicral. Must be heated to dissolve picric acid. Use by immersion, up to 1 min or more. A few drops of HCl may be added to increase etch rate.
2 g picric acid, 25 g NaOH, and 100 mL H_2O	Alkaline sodium picrate. Immerse sample in boiling solution for 1–15 min or use electrolytically at 6 V dc, 20 °C (68 °F), 30–120 s, stainless steel cathode. Colors cementite and Fe_4W_2C
10 g $K_3Fe(CN)_6$ (potassium ferricyanide), 10 g KOH or NaOH, and 100 mL H_2O	Murakami's reagent. Use by immersion, fresh solution, hot or cold, up to 10 min. Cold darkens chromium carbides and tungstides; cementite not attacked. Hot attacks cementite.
1 g CrO_3 and 100 mL H_2O	Electrolytic etch, 2–3 V dc, 20 °C (68 °F), 30 s, stainless steel cathode. MC and M_7C_3 darkened; Mo_2C outlined
10 mL H_2O_2 (30%) and 20 mL 10% aqueous NaOH	Immerse 10 s at 20 °C (68 °F). Fe_2MoC, Mo_2C, and M_6C outlined (latter also colored)
4 g $KMnO_4$ (potassium permanganate), 4 g NaOH, and 100 mL H_2O	Groesbeck's reagent. Immerse at 20 °C (68 °F). Fe_2MoC and M_4C outlined and colored (blue and brown, respectively), Mo_2C colored brown, $(Fe,Cr)_{23}C_6$ attacked but $(Fe,Mo)_{23}Q$ not attacked
4 g NaOH and 100 mL saturated aqueous $KMnO_4$	Immerse at 20 °C (68 °F). Mo_2C and M_7C_3 attacked; M_6C outlined and colored brown
Saturated aqueous picric acid plus small amount of wetting agent	Prior-austenite grain-boundary etch for hardened steels. Many wetting agents can be used; sodium tridecylbenzene sulfonate most commonly used. Use at 20 to 100 °C (68 to 212 °F) by immersion for 2 to 60 min. Addition of approximately 1% HCl useful for higher-alloy grades. Room-temperature etching most common. Etching with solution in a beaker in an ultrasonic cleaner works well. Lightly backpolish to remove surface smut.
50 mL cold saturated aqueous $Na_2S_2O_3$ (sodium thiosulfate) and 1 g $K_2S_2O_5$ (potassium metabisulfite)	Klemm's I (tint etch) reagent. Immerse (never swab) at 20 °C (68 °F) for 40–100 s to color ferrite (blue or red) and martensite (brown). Cementite and austenite unaffected
1 g Na_2MoO_4 (sodium molybdate) and 100 mL H_2O	Beraha's tint etch for cementite. Add 0.2–0.3 g $NH_4F{\cdot}HF$ (ammonium bifluoride). Add HNO_3 to produce a pH of 2.5–3.0. Preetch sample with picral. Colors Fe_3C yellow-orange. Immerse up to 60 s; never swab.
3 g $K_2S_2O_5$, 10 g anhydrous $Na_2S_2O_3$, and 100 mL H_2O	Beraha's tint etch. Immerse (never swab) until surface is colored red-violet. Colors ferrite, martensite, bainite, and pearlite. Cementite unaffected

Note: When water is specified, use distilled water.

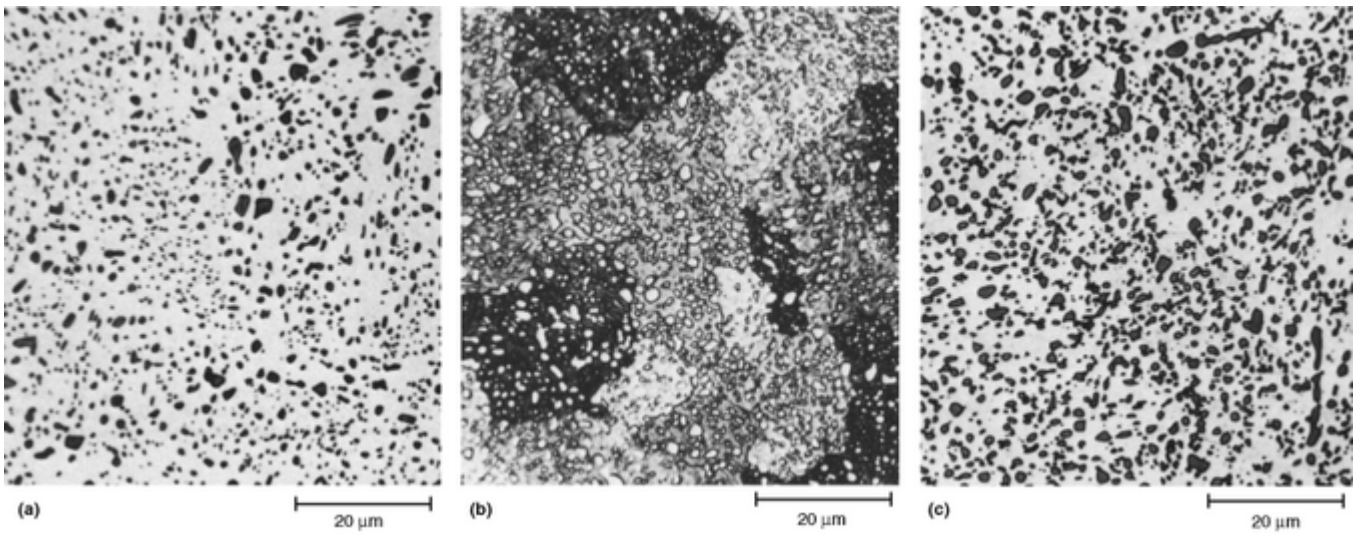

Fig. 6 AISI W2 (1.05% C), spheroidize annealed. (a) Etched with boiling alkaline sodium picrate for 60 s to color the cementite brown. (b) Etched lightly with 4% picral and tint etched with Beraha's $Na_2S_2O_3/K_2S_2O_5$ reagent to color the ferrite (wide range of colors). (c) Etched lightly with 4% picral and tint etched with Beraha's Na_2MoO_4 reagent to color the cementite dark orange. 1000×

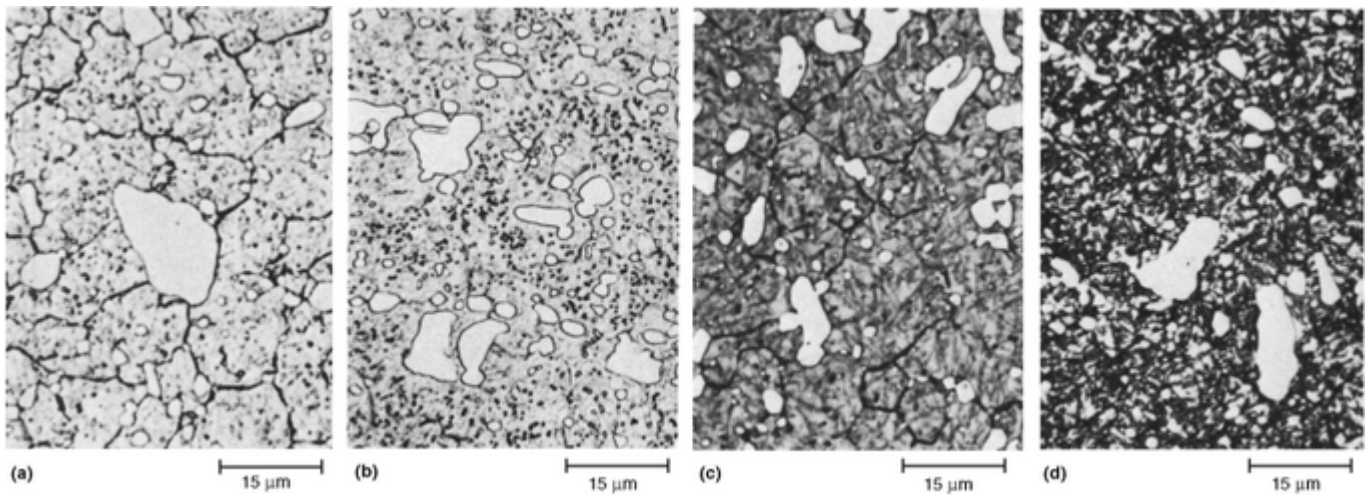

Fig. 7 AISI D2 austenitized at 1040 °C (1900 °F), air quenched, and tempered at 200 °C (400 °F). Influence of etchant on revealing martensite. (a) 10% nital etch reveals grain boundaries, carbides, and martensite (light). (b) 4% picral plus HCl etch reveals carbides and martensite (light). (c) Heat tinted at 540 °C (1000 °F) for 5 min after 10% nital etch to produce greater contrast and reveal the retained austenite. (d) Superpicral etch reveals retained austenite as white, but carbide also appears white. 1000×

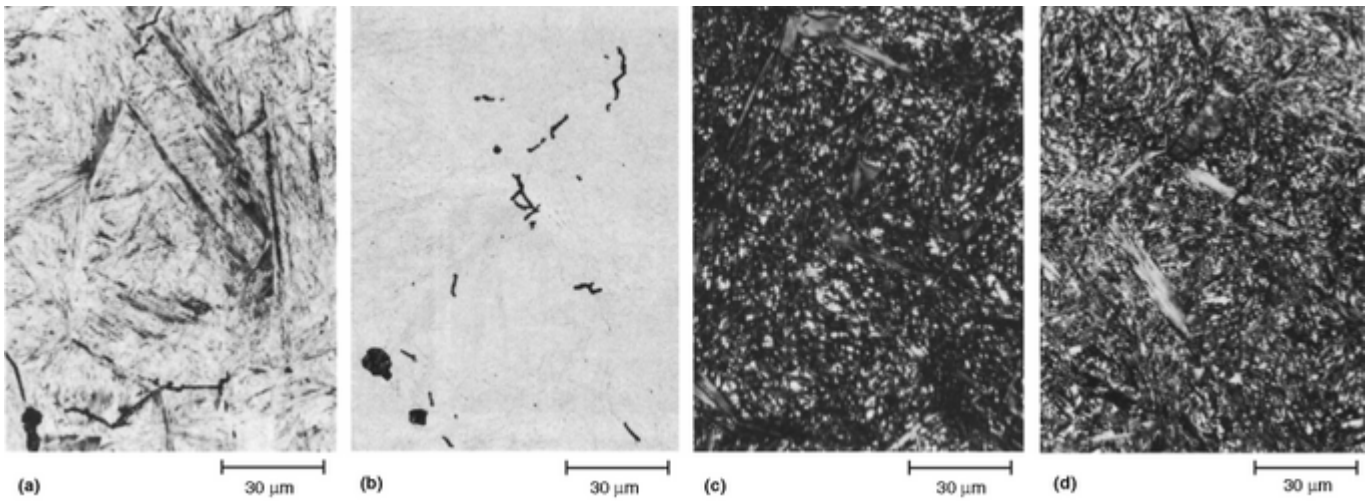

Fig. 8 AISI W1 (1% C) overaustenitized at 925 °C (1700 °F) and water quenched, producing martensite, retained austenite, and small patches of pearlite. Influence of etchant on revealing quenched martensite. (a) 2% nital etch reveals martensite and pearlite (black). (b) 4% picral etch reveals pearlite but only faintly reveals martensite. (c) 5% aqueous sodium metabisulfite etch produces a strong contrast between the martensite and retained austenite (white). (d) Beraha's $Na_2S_2O_3/K_2S_2O_5$ reagent produces similar results to (c), but pearlite is more visible. 500×

Pepperhoff interference film technique also improves contrast among constituents. A thin layer of a dielectric compound, such as zinc selenide (ZnSe), is vapor deposited onto the surface of the sample in a bell jar (Ref 5). As the thickness of this layer increases above 400 nm, colors are observed. First-order red to violet produces the best results. An example of this method, and a comparison to a standard etchant, is given in Fig. 9.

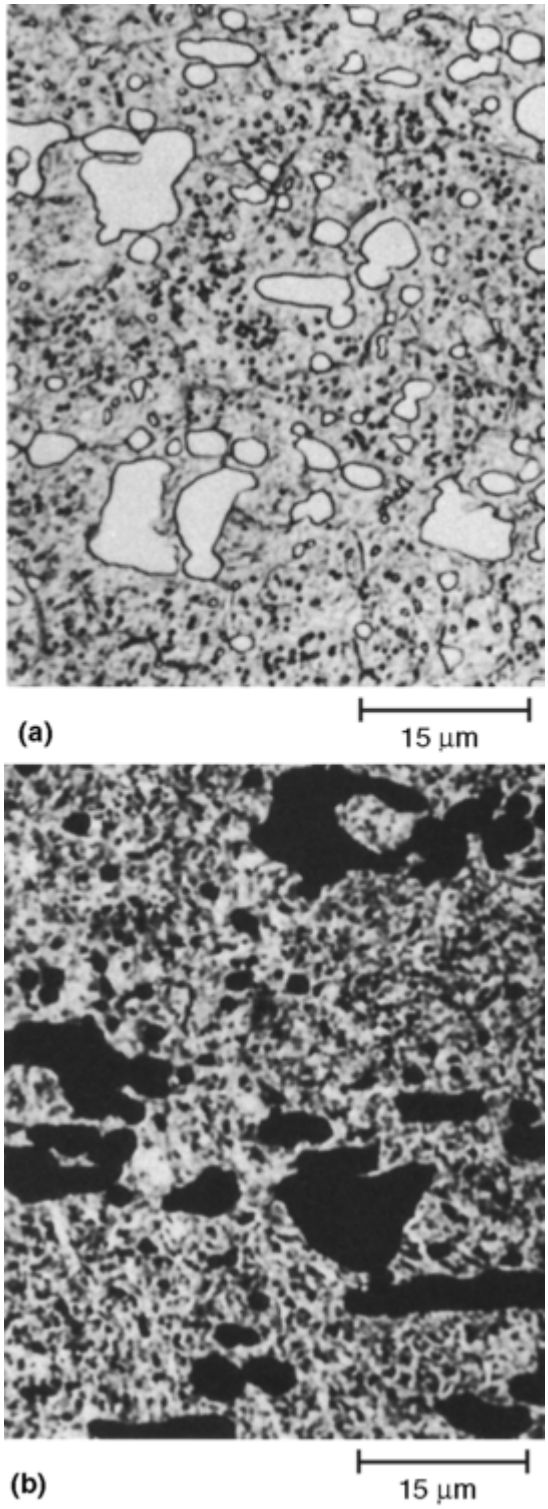

Fig. 9 AISI D2, quenched and tempered. Use of vapor-deposited zinc selenide to accentuate carbide detection and retained austenite. Samples were etched first with 4% picral plus HCl (a) to outline the carbides, then coated with a thin layer of zinc selenide (b) to reveal the carbides (dark violet), retained austenite (white), and martensite (dark). 1000×

Prior-Austenite Grain Size. Many tool steels can be etched with nital to reveal the prior-austenite grain boundaries. The high-speed steels and the D-type cold work tool steels (Fig. 7) can be handled in this way as long as the tempering temperature used is not too high. Etching techniques that reveal the prior-austenite grain boundaries are employed but can be difficult to implement successfully; therefore, a fracture grain size method is widely used. The Shepherd fracture grain size technique is simple, quick, and accurate, as long as the sample is martensitic—retained austenite may be present in substantial amounts—and not tempered to such an extent that reasonably flat, brittle (macroscopic) fractures cannot be obtained (Ref 5).

Reference cited in this section

5. G.F. Vander Voort, *Metallography: Principles and Practice*, McGraw-Hill, 1984; reprinted by ASM International, 1999

G.F. Vander Voort, Metallographic Techniques for Tool Steels, *Metallography and Microstructures*, Vol 9, *ASM Handbook*, ASM International, 2004, p. 644–669

Metallographic Techniques for Tool Steels

George F. Vander Voort, Buehler Ltd.

Microstructures of Tool Steels

A wide range of microstructures is observed in tool steels because of variations in composition and heat treatment. The mill metallurgist is generally most concerned with annealed microstructures and undesired surface decarburization. The failure analyst sees a broad spectrum of microstructures, both normal and abnormal.

Hot-Worked Microstructures. The structure produced after hot working can have a marked influence on the distribution and morphology of carbides after the subsequent spheroidize anneal. The micrographs in Fig. 10, 11, 12, 13, 14, 15, 16, and 17 illustrate the complex microstructures that are often present in the as-hot-worked condition prior to annealing and the influence of this structure on the annealed microstructure. In general, the cooling after hot working must be controlled to produce as uniform a carbon distribution as possible, so that the annealed carbide distribution does not vary.



Fig. 10 AISI W1 (1.3% C), as-rolled, containing pearlite and acicular cementite. 4% picral. 500×

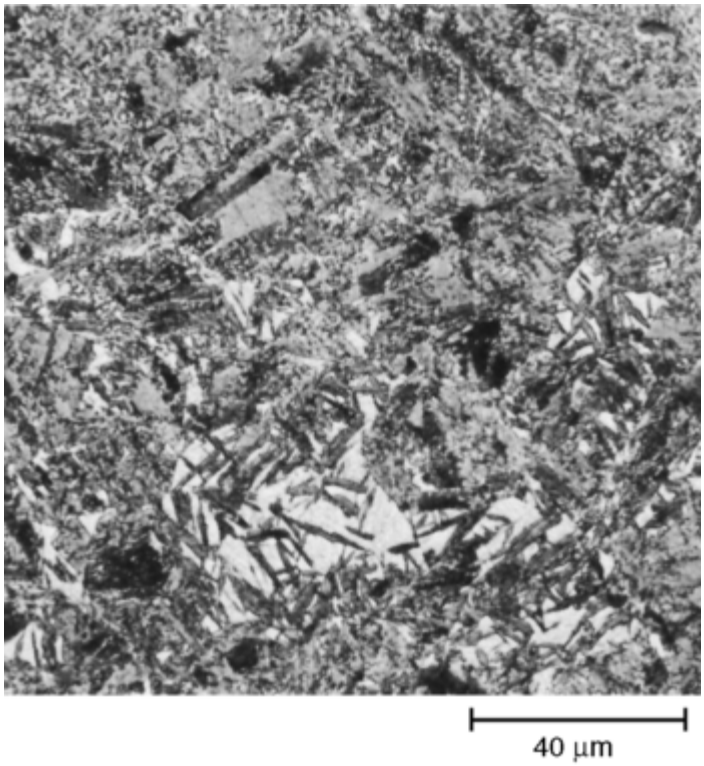

Fig. 11 AISI L6, as-rolled, containing bainite and martensite (white). 2% nital. 500×

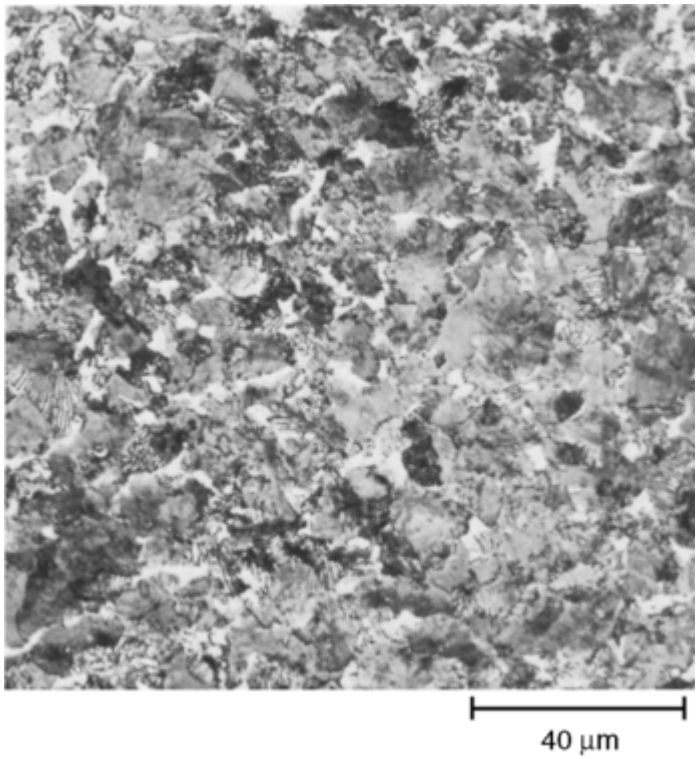

Fig. 12 AISI S4, as-rolled, containing ferrite (white) and pearlite. 4% picral. 500×

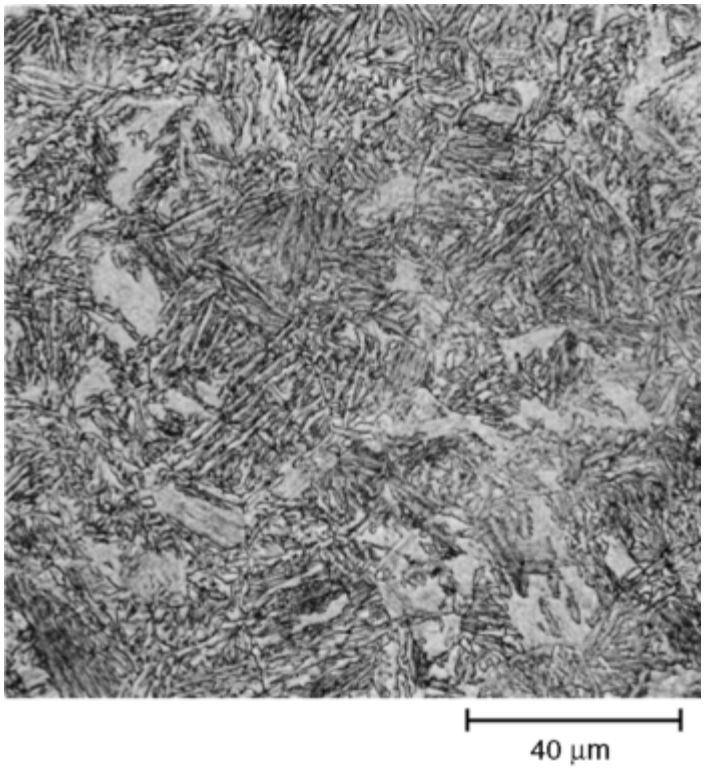

Fig. 13 AISI S4, as-rolled, containing bainite and martensite (featureless patches). This bar was cooled at a faster rate after rolling than the one in Figure 12 4% picral. 500×

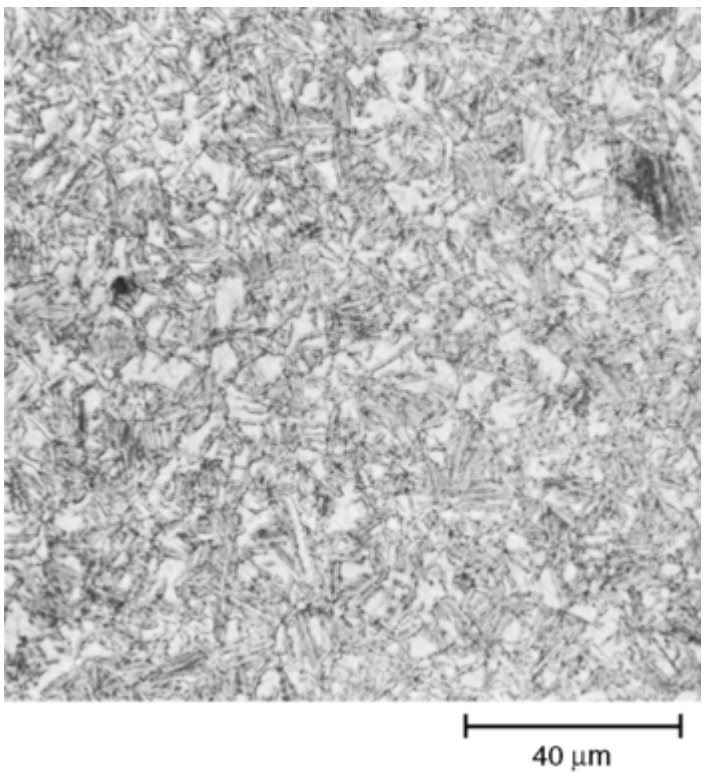

Fig. 14 AISI S5, as-rolled, containing bainite and martensite (white). 2% nital. 500×

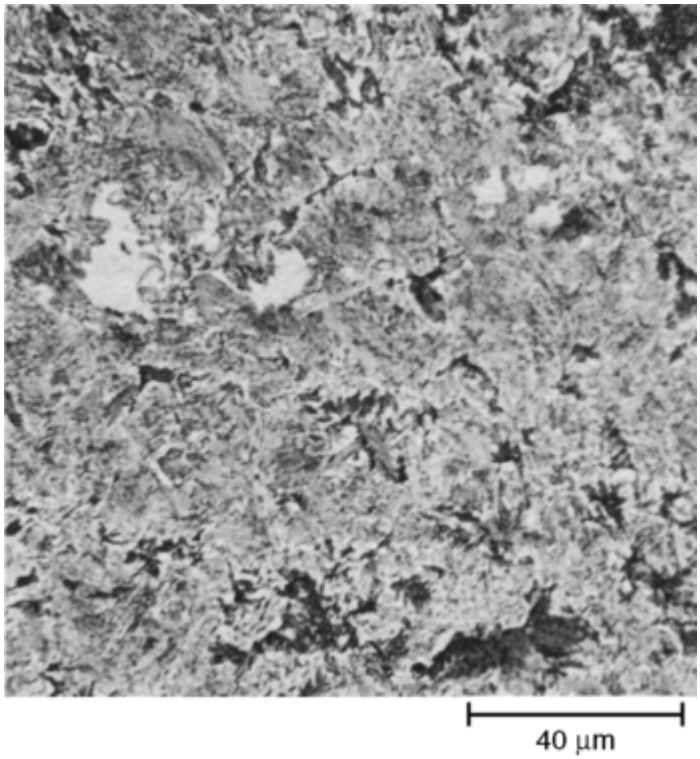

Fig. 15 AISI O1, as-rolled, containing bainite and martensite (white patches). The dark patches are pearlite. 4% picral. 500×

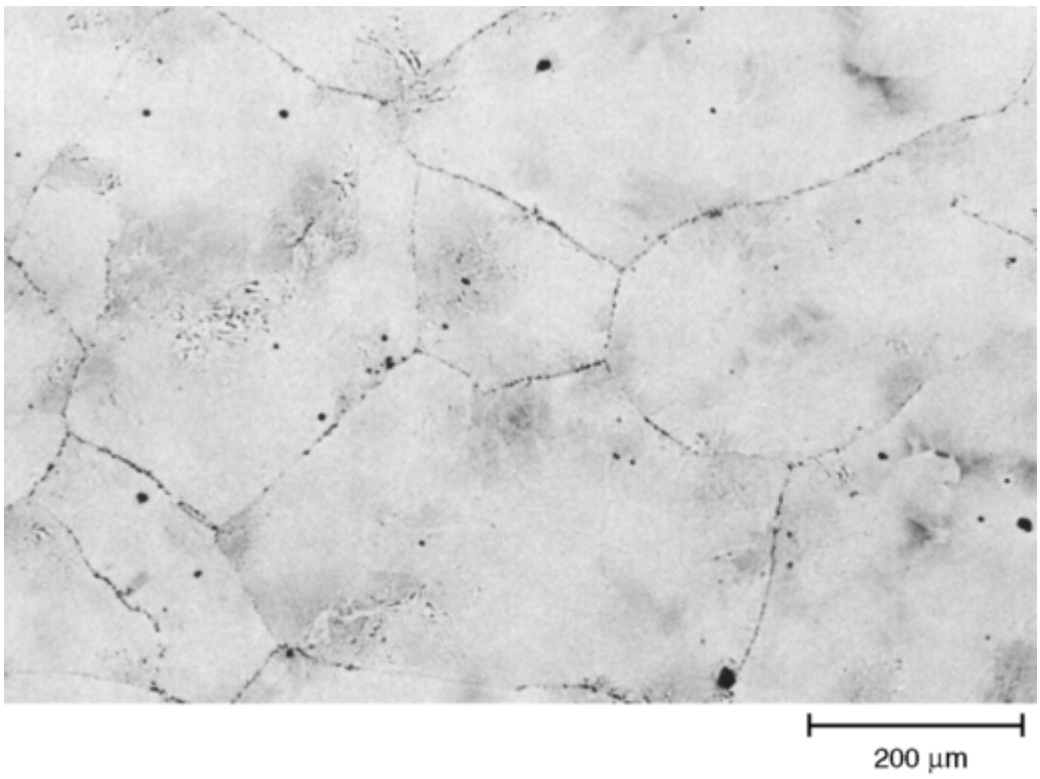

Fig. 16 AISI L1, as-rolled, containing pearlite and a grain-boundary cementite network. Boiling alkaline sodium picrate. 100×



Fig. 17 AISI A2, as-rolled, containing plate martensite (black) and retained austenite (white). 2% nital. 500×

Some tool steels, such as the 5% Cr hot work grades and the 12% Cr plastic molding steels, tend to form carbide networks at the prior-austenite grain boundaries present at the end of the hot working operation. Such networks can be difficult to remove during annealing and can degrade tensile ductility and toughness, even if they are semicontinuous. Figure 18 illustrates grain-boundary carbide networks in type 420 stainless steel used for plastic molding. The high-carbon, water-hardening grades may develop grain-boundary carbide networks after cooling from the hot rolling temperature, as shown in Fig. 19. Stringers of complex alloy carbides may be observed in certain grades, and these are often harmful. Figure 20 shows an example in H13 tool steel.

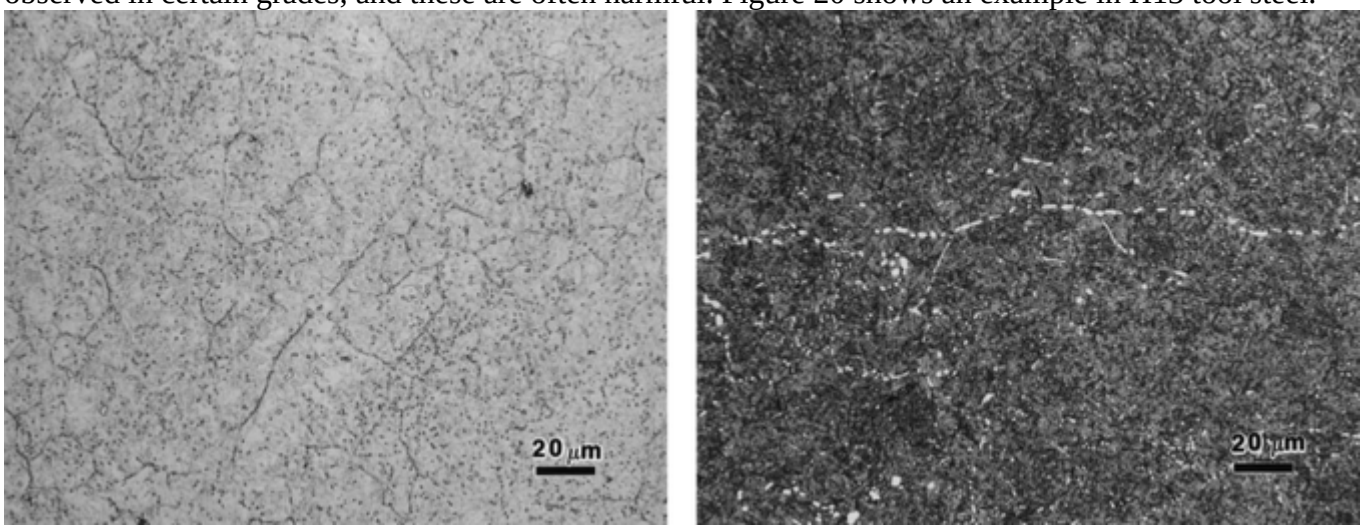

Fig. 18 Grain-boundary carbide networks in type 420 martensitic stainless steel (Fe-0.35%C-0.4%Mn-13%Cr) with two different etchants. (a) Vilella's reagent. (b) Beraha's sulfamic acid tint etch. Heat treatment: 1038 °C (1900 °F). Air quench: 177 °C (350 °F) temper. 500×

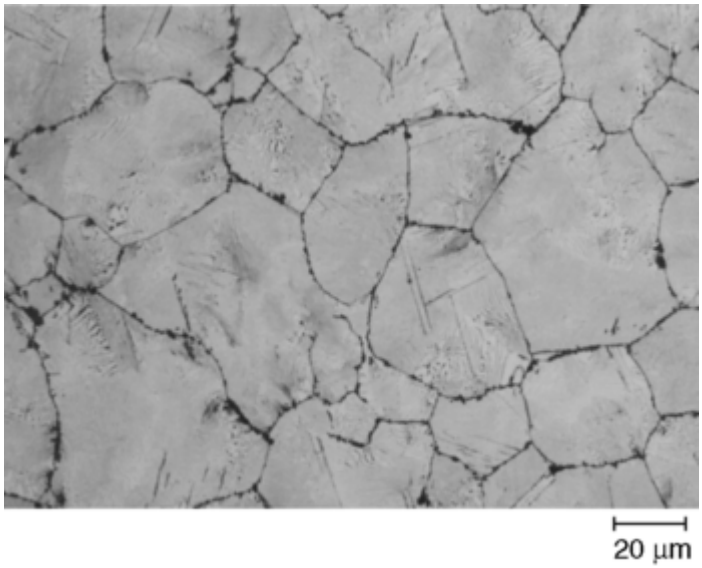

Fig. 19 Grain-boundary carbide networks after cooling from the hot rolling temperature of high-carbon, water-hardening grade (Fe-1.31%C-0.35%Mn-0.25%Si, as-rolled). Alkaline sodium picrate etch: 90 °C (195 °F), 60 s. 500×

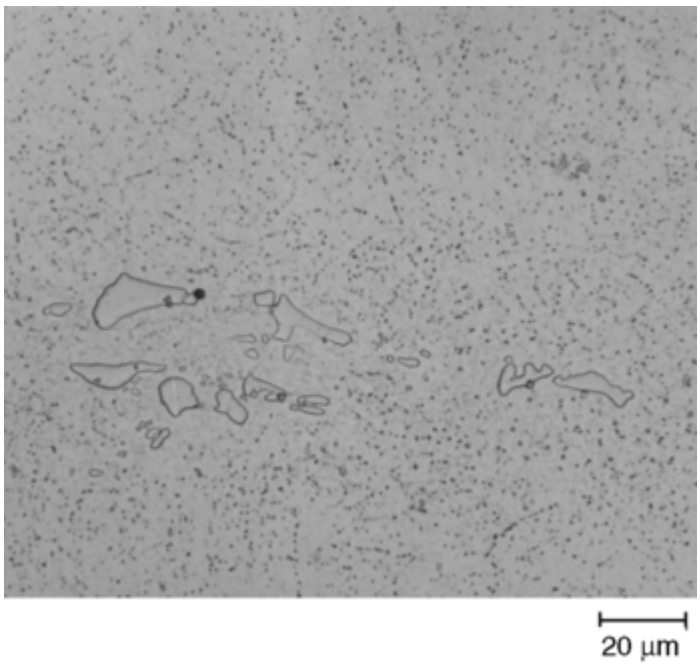

Fig. 20 Carbides in light-etching segregation band of AISI H13 hot work die steel (Fe-0.40%C-0.8%Si-5.25%Cr-1%V-1.35%Mo). 2% nital. 500×

Annealed Microstructures. Because most tool steels are relatively hard, even when annealed, it is usually necessary to control carbide morphology during annealing to maximize machinability and formability. For most tool steels, a spheroidal carbide shape is the desired condition, although for a few of the low-alloy tool steels, certain machining operations are improved when the structure is partially pearlitic.

Most tool steels and all high-alloy grades are spheroidize annealed at the mill. Control of annealed microstructures is discussed in the article “Introduction to Heat Treating of Tool Steels” in *Heat Treating*, Volume 4 of *Metals Handbook*, 9th ed. (1981). For a given grade, the hardness decreases as the degree of spheroidization increases. Once spheroidization has been obtained, growth of the carbides, which produces fewer carbides per unit volume and a greater apparent spacing, further reduces hardness. However, if the carbide structure is too coarse, dissolving the required amount of carbon during austenitization will be more difficult. In addition, many tool steels require a fine, uniform distribution of undissolved carbides to resist grain growth during austenitization.

Control of the spheroidization annealing process is important for good machinability and good formability, such as in hobbing. The more uniform the starting microstructure (the as-rolled microstructure), the more uniform the spheroidization and the softer the annealed hardness, all other conditions being the same. The as-rolled microstructures shown in Fig. 10, Fig. 10, Fig. 10, Fig. 10, Fig. 10, Fig. 10, Fig. 10, Fig. 10demonstrate varying degrees of non-uniformity and variability in the starting microstructure. Figure 21 shows the influence of the starting microstructure on the spheroidization of W1 tool steel. The as-rolled pearlite (Fig. 21a) is coarser in interlamellar spacing than the normalized specimen (Fig. 21c), and the annealed structure, although similar, is lower in hardness, with larger, more widely spaced carbides for the normalized and annealed specimen than for the as-rolled and annealed specimen. Of course, if the specimen contained grain-boundary carbide networks after rolling, they would still be present after spheroidize annealing, unless it was normalized before annealing. Figure 22, Figure 23, Figure 24, Figure 25, Figure 26, Figure 27, Figure 28, Figure 29, Figure 30, Figure 31, Figure 32, Figure 33, Figure 34, Figure 35, Figure 36 illustrate the wide range of annealed microstructures that can be observed in a variety of tool steel grades.

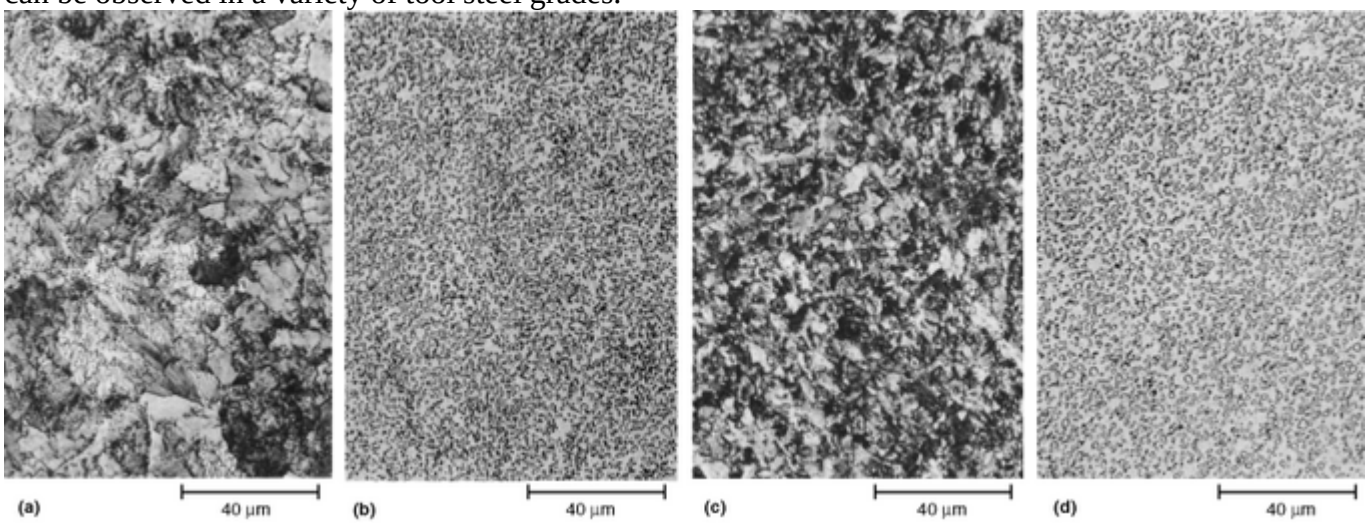

Fig. 21 AISI W1 (1.05% C). Influence of starting structure on spheroidization. (a) As-rolled; contains coarse and fine pearlite. (b) After spheroidization (heat to 760 °C, or 1400 °F; cool at a rate of 11 °C/h, or 20 °F/h, to 595 °C, or 1100 °F; air cool). (c) Austenitized at 870 °C (1600 °F) and oil quenched to produce fine pearlite. (d) Austenitized as in (c); annealed as in (b). Note the more uniform spherical carbide shape compared to (b). 4% picral. 500×

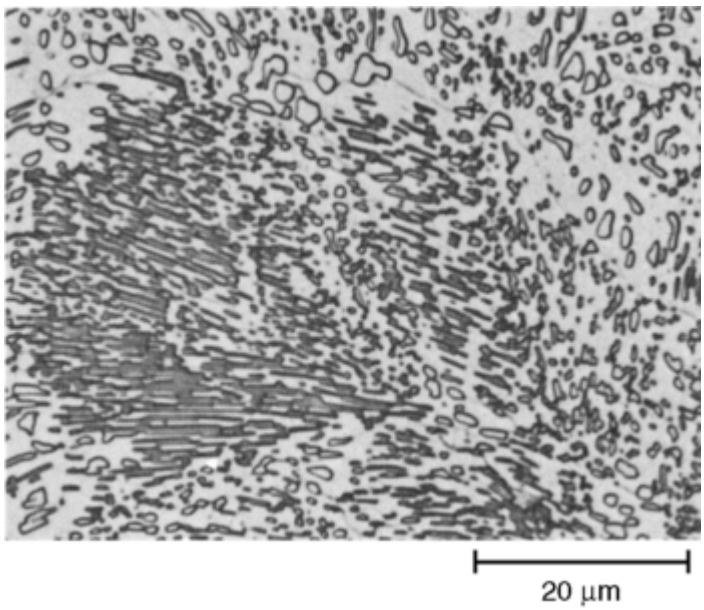

Fig. 22 AISI W4 water-hardening tool steel (0.98C-0.74Mn-0.14Cr-0.19Ni), as-received (mill annealed). 187 HB. Spheroidal cementite in a matrix of ferrite; a considerable amount of lamellar pearlite is also present. 4% picral. 1000×

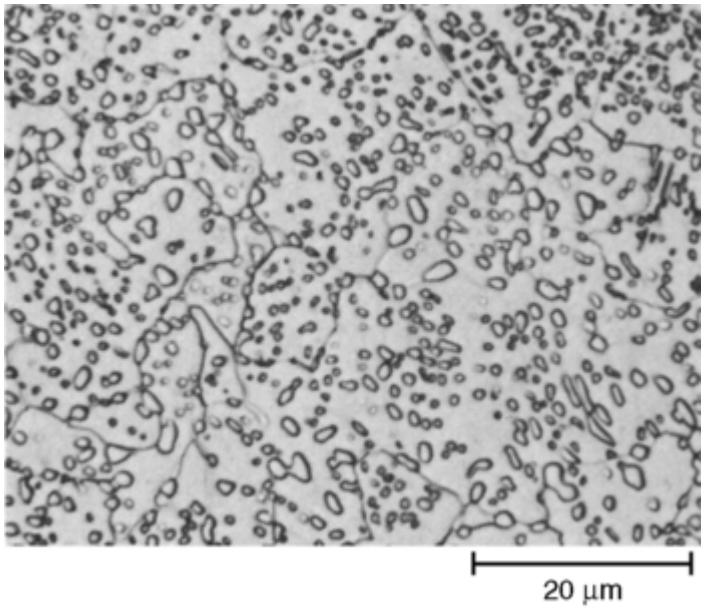

Fig. 23 AISI W4 water-hardening tool steel (0.96C-0.66Mn-0.23Cr), as-received (full annealed). 170 HB. Structure consists of spheroidal cementite in a ferrite matrix; no lamellar constituent is present. Compare with Figure 22 4% picral. 1000×

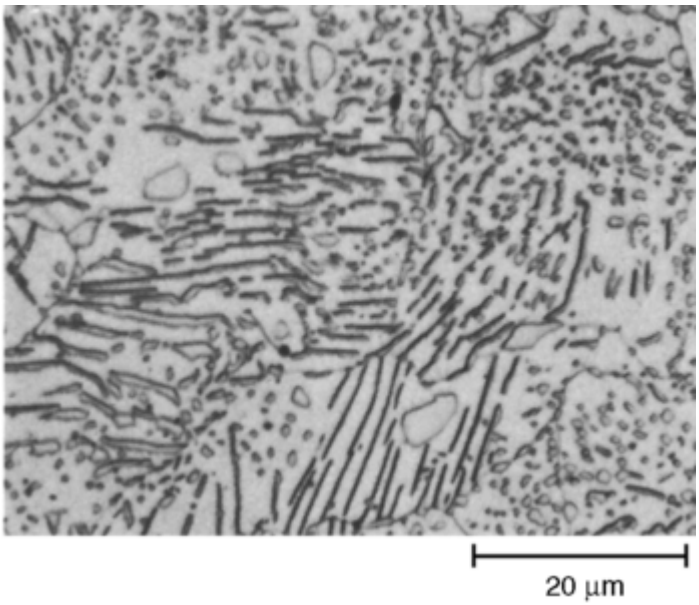

Fig. 24 AISI W1 water-hardening tool steel (0.94C-0.21Mn), as-received (mill annealed). 170 HB. Structure: mixture of lamellar pearlite and spheroidal cementite in a matrix of ferrite, with a few large, globular carbide particles. 3% nital. 1000×

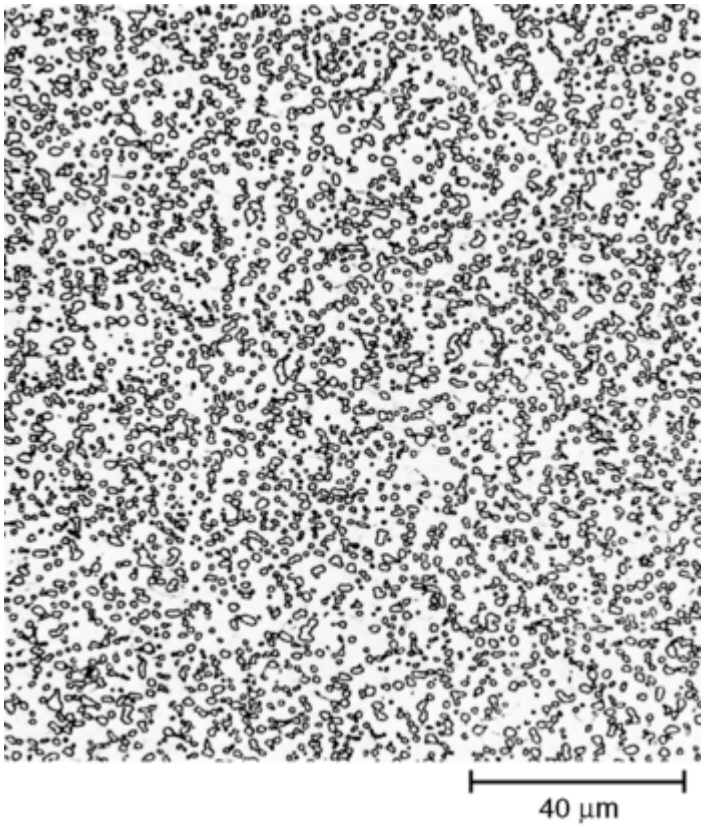

Fig. 25 AISI L1, spheroidize annealed. Note the very-well-formed spheroidal carbides. 4% picral. 500×

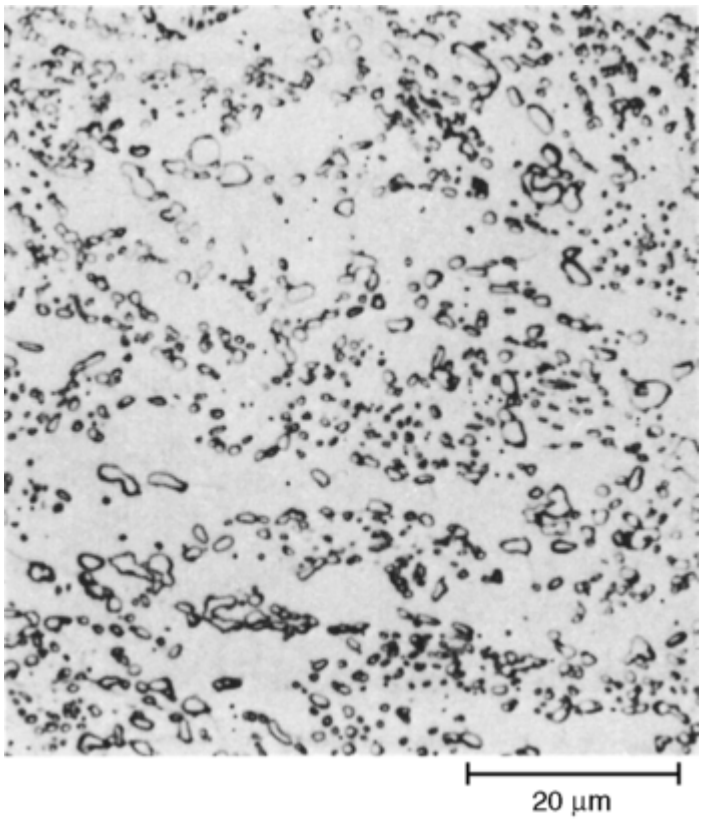

Fig. 26 AISI S2, spheroidize annealed. 4% picral. 1000×

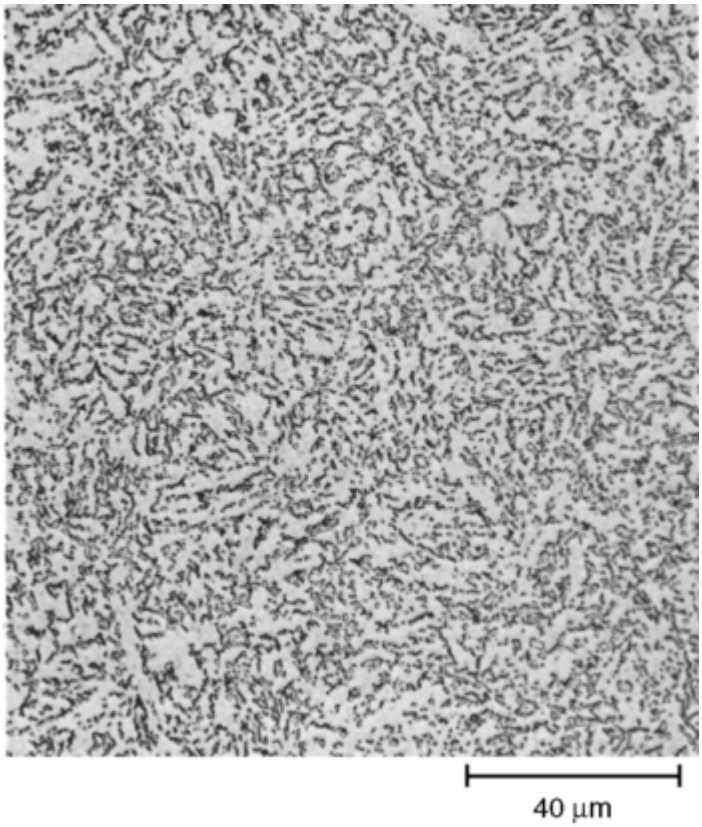

Fig. 27 AISI S5, spheroidize annealed. 4% picral. 500×

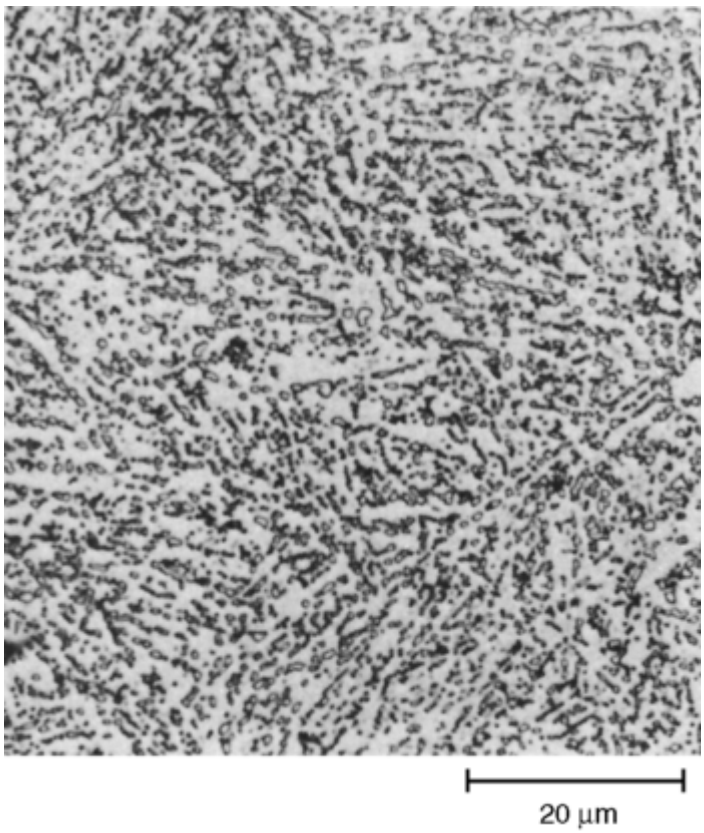

Fig. 28 AISI S7, spheroidize annealed. 4% picral. 1000×

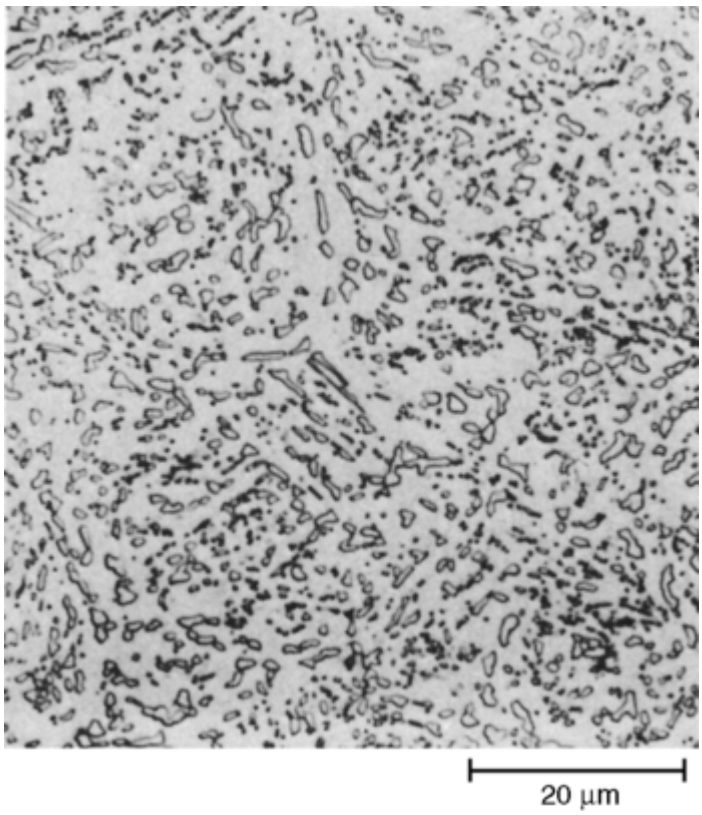

Fig. 29 AISI A6, spheroidize annealed. 4% picral. 1000×

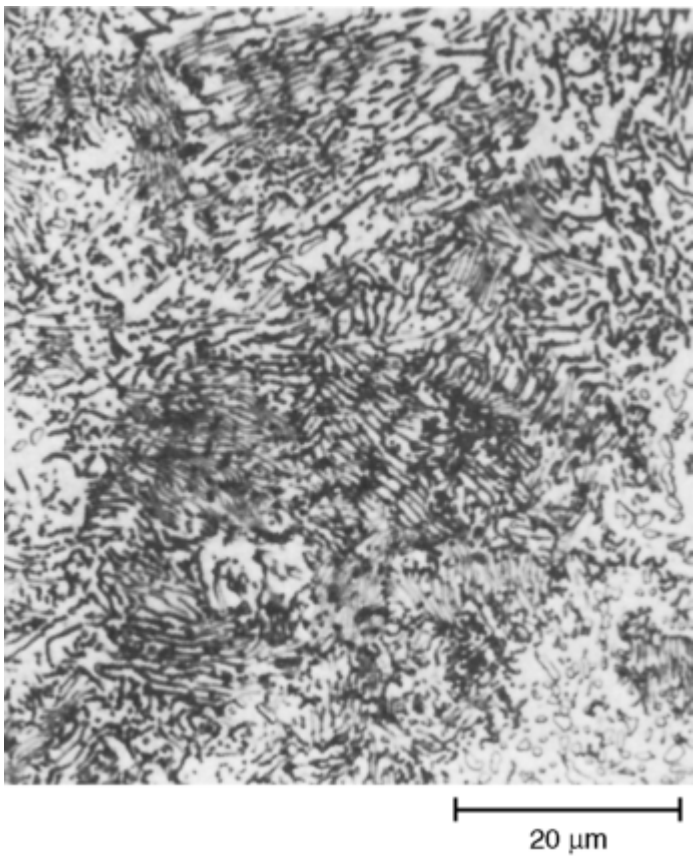

Fig. 30 AISI A6, partially spheroidized. Note lamellar pearlite. 4% picral. 1000×

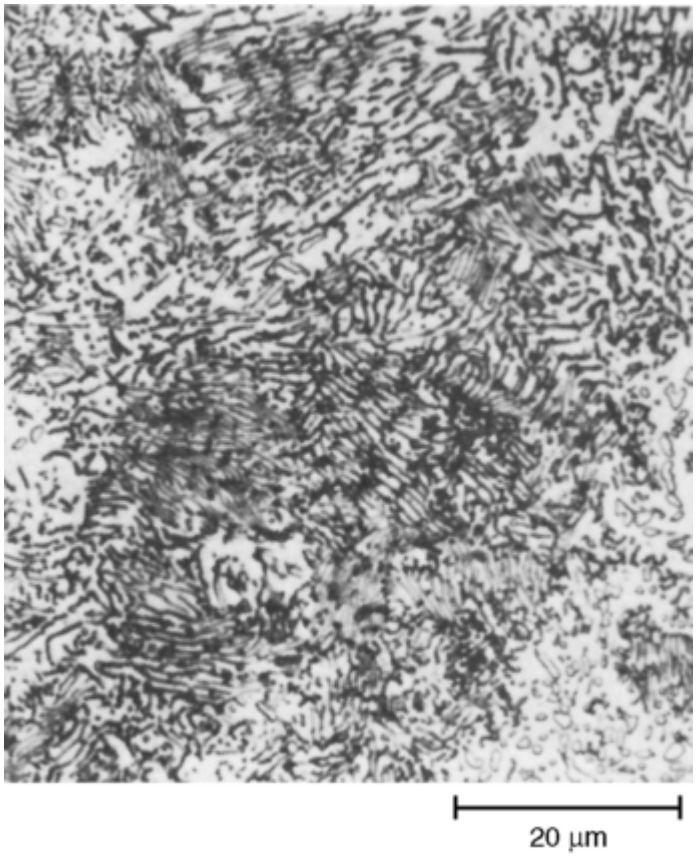

Fig. 30 AISI A6, partially spheroidized. Note lamellar pearlite. 4% picral. 1000×

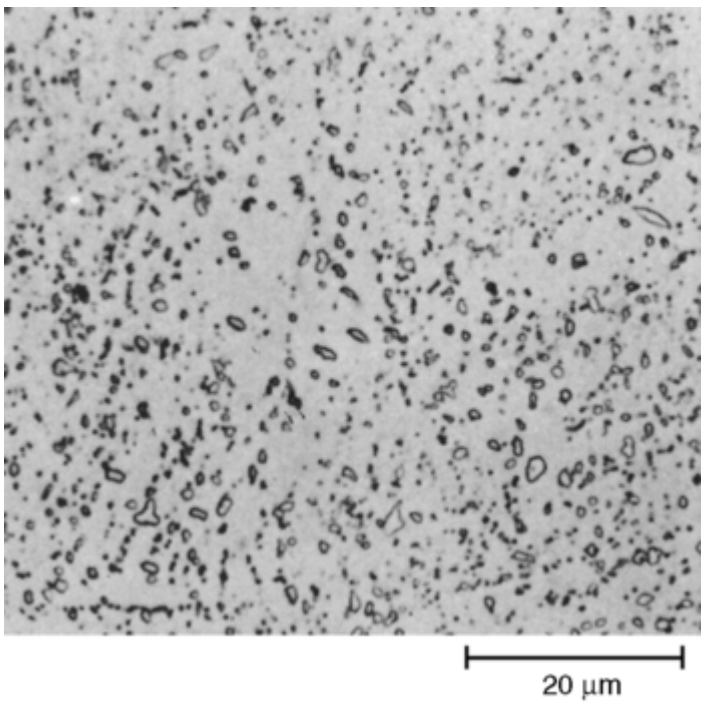

Fig. 31 AISI H13 chromium hot-worked tool steel, spheroidize annealed. 4% picral. 1000×

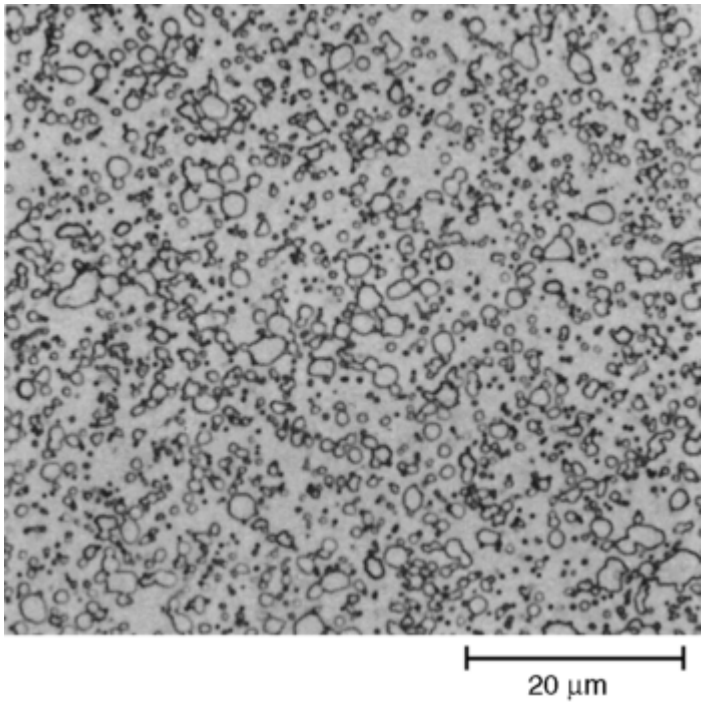

Fig. 32 AISI M2 molybdenum high-speed tool steel, spheroidize annealed. 4% picral. 1000×

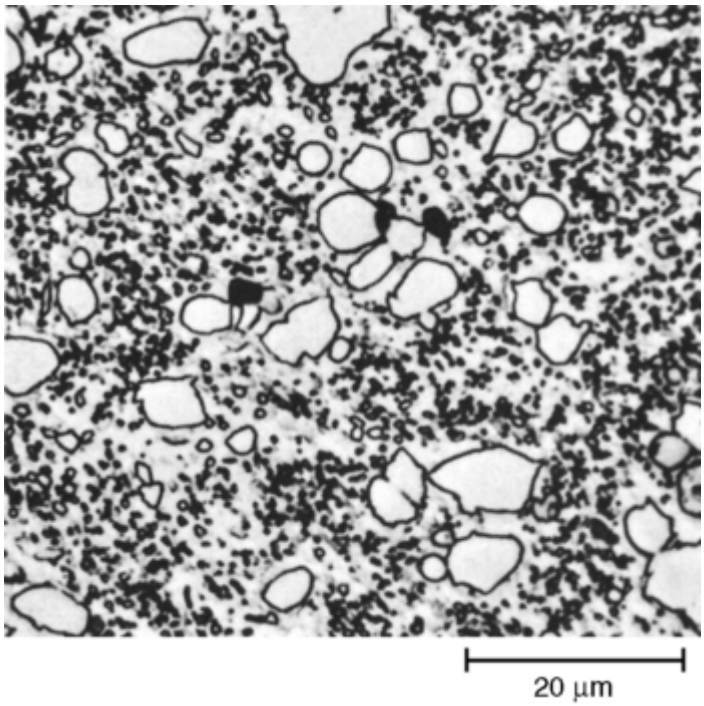

Fig. 33 AISI A7 tool steel, box annealed at 900 °C (1650 °F) for 1 h per 25 mm (1.0 in.) of container thickness and cooled at no more than 28 °C/h (50 °F/h). Massive alloy carbide and spheroidal carbide in a ferrite matrix. 4% nital. 1000×

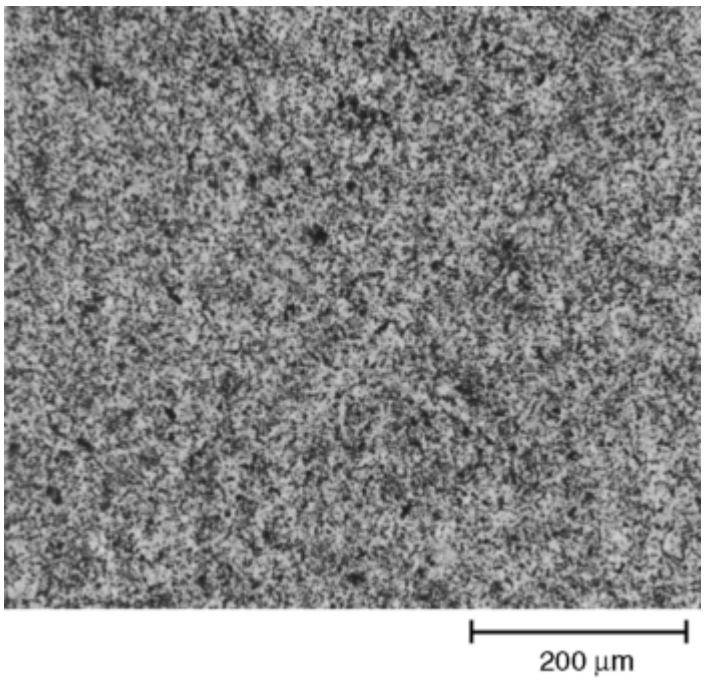

Fig. 34 AISI A10 tool steel, as-received (mill annealed). Section transverse to rolling direction. At the magnification used, the structure is poorly resolved. Nital. 100×

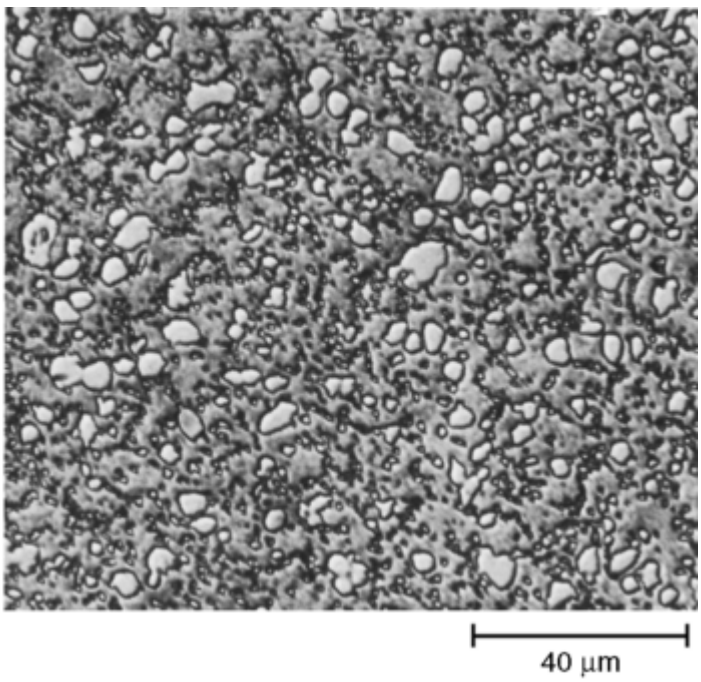

Fig. 35 AISI H23 tool steel, annealed by austenitizing at 870 °C (1600 °F) for 2 h and cooling at 28 °C/h (50 °F/h) to 540 °C (1000 °F), then air cooling. 98 HRB. Structure consists of tiny spheroidal and some larger alloy carbide particles in a matrix of ferrite. Kalling's reagent. 500×

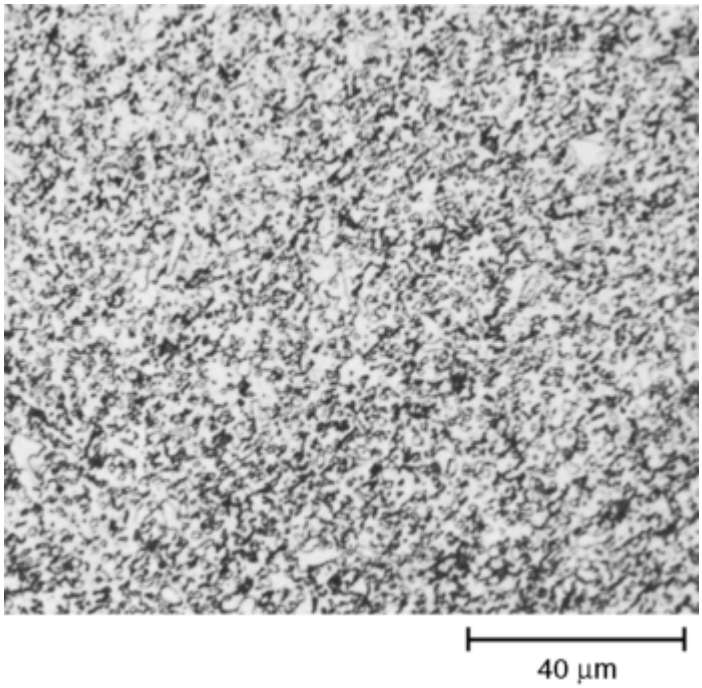

Fig. 36 AISI H26 tool steel, annealed by austenitizing at 900 °C (1650 °F), cooling at 8.5 °C/h (15 °F/h) to 650 °C (1200 °F), then air cooling. 22 to 23 HRC. Structure consists of a dispersion of fine particles of alloy carbide in a matrix of ferrite. Picral with HCl, 10 s. 500×

Carbides in Tool Steels. The amount and type of carbides present depend on the bulk carbon content and the quantity of carbide-forming elements (chromium, molybdenum, vanadium, and tungsten, for example) in the grade. Cementite is present in the carbon and low-alloy grades; more complex carbide types are found in the highly alloyed grades. The hardness of carbides varies with their composition, from approximately 800 HV for pure Fe_3C to approximately 1400 HV when other elements, such as chromium, are substituted for a portion of the iron. The high wear resistance of heat treated tool steels is attributable to the hardness of the matrix phase, chiefly martensite, and the amount and type of carbides remaining undissolved in the matrix.

Cementite (M_3C) is an iron-rich carbide with an orthorhombic crystal structure. In annealed tool steels, it will be very low in tungsten, molybdenum, or vanadium content and relatively low in chromium content, while the manganese content can be high. Cementite is found in all carbon tool steels and in alloy tool steels quenched and tempered below 538 °C (1000 °F). M_7C_3 is a chromium-rich carbide with a hexagonal crystal structure that is observed in steels with medium-to-high chromium contents and only moderate amounts of other carbide-forming alloy elements. It dissolves very slowly in austenite during the hardening process. This carbide is present in the D-type cold work grades in high-speed steels in the annealed or highly tempered conditions. $M_{23}C_6$ is a chromium-rich carbide with a face-centered cubic (fcc) crystal structure with a high solubility for iron, but much less for other strong carbide formers, such as molybdenum or tungsten. It is observed in type 420 stainless steel and in annealed high-speed steels. Figure 37 shows a portion of the isothermal section of the Fe-Cr-C system at 870 °C (1600 °F), illustrating the location of the various chromium-rich carbides observed in several chromium-bearing tool steels.

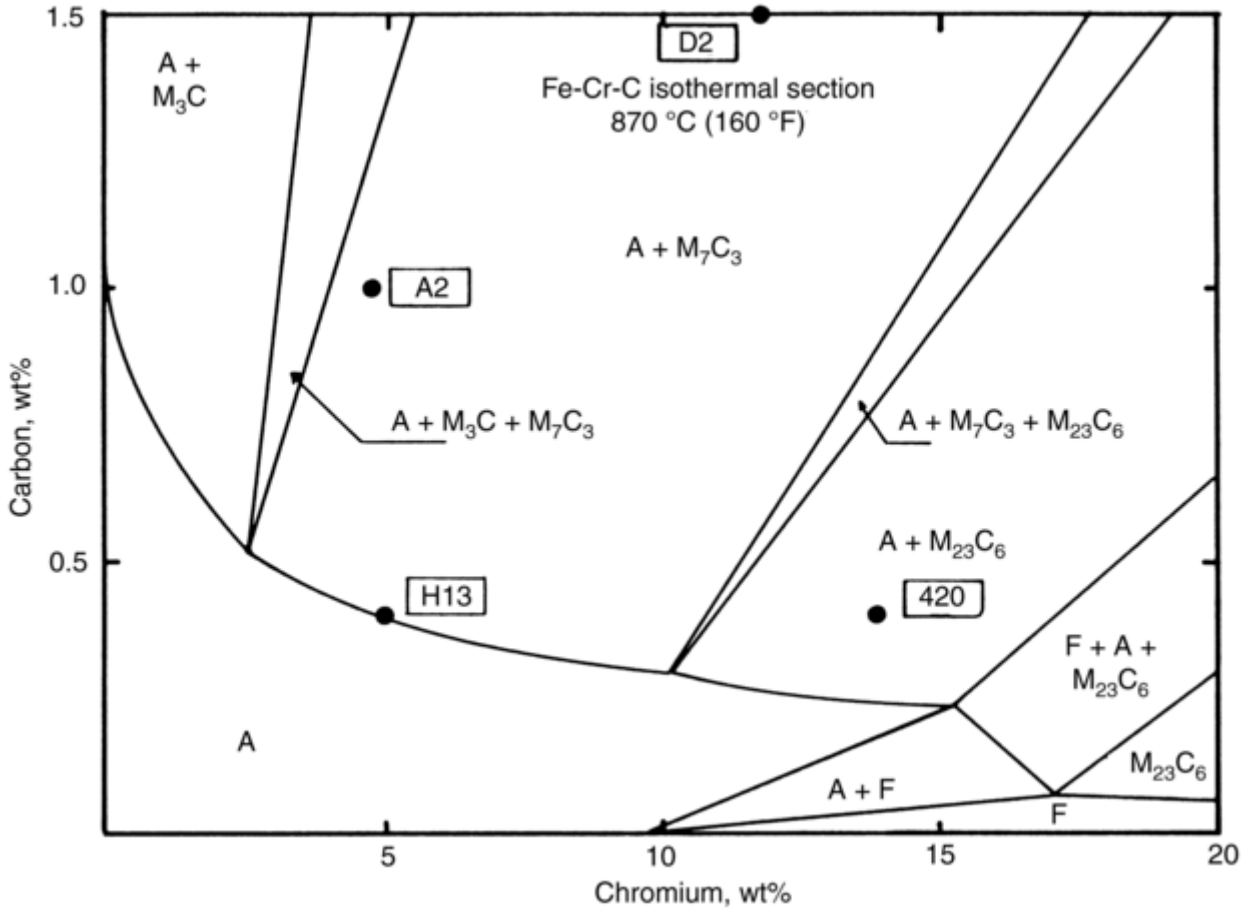

Fig. 37 Portion of the 870 °C (1600 °F) isothermal section of the Fe-Cr-C system with approximate compositions of AISI H13, A2, D2, and type 420 steels indicated. Source: Ref 7

M_6C is either a molybdenum- or a tungsten-rich carbide with a fcc crystal structure, such as Fe_4Mo_2C-Fe_3Mo_3C. A fair amount of chromium or vanadium can be present in the carbide. It is commonly seen in high-speed steels and dissolves slowly during austenization. Figure 38 shows an isothermal section in the Fe-W-C system at 1200 °C (2190 °F), illustrating the location of M_6C carbides and the composition of several hot work die steels. M_2C is a molybdenum- or tungsten-rich carbide with a hexagonal crystal structure. It is not frequently seen in tool steels, except for certain grades in the annealed condition. MC is most frequently a vanadium-rich carbide with a fcc NaCl-type crystal structure. Other strong carbide-forming elements, such as titanium, niobium, tantalum, and zirconium, can form MC carbides, but these elements are not common in tool steels. MC is observed in steels with moderate-to-high vanadium contents, chiefly high-speed tool steels. It has very strong bonds and is the hardest carbide. It resists dissolution during austenization.

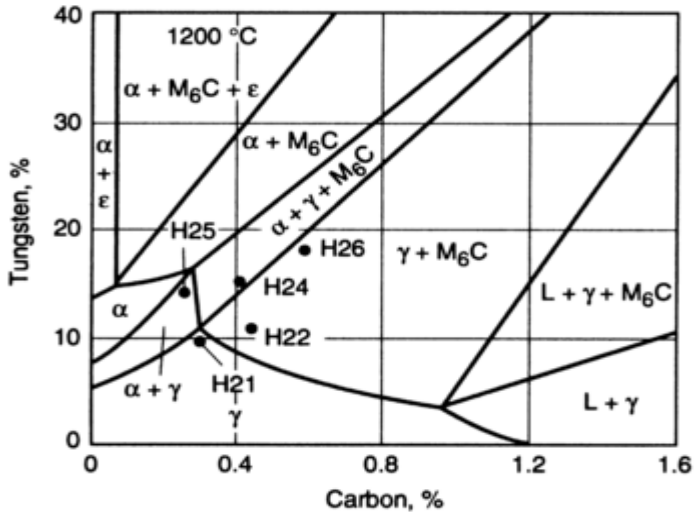

Fig. 38 Isothermal section of Fe-W-C diagram at 1200 °C (2190 °F). Nominal compositions of tungsten, carbon, and iron for some tungsten hot work steels are plotted. Source: Ref 8

The amount of carbides present in tool steels is greater in the annealed condition than after austenitizing and quenching, because the carbides supply the austenite with the carbon necessary to achieve high hardness levels. The type of carbides obtained also varies as a function of composition. As an example, Fig. 39 shows the composition and amount of carbides observed in different high-speed steels in the annealed and in the hardened conditions.

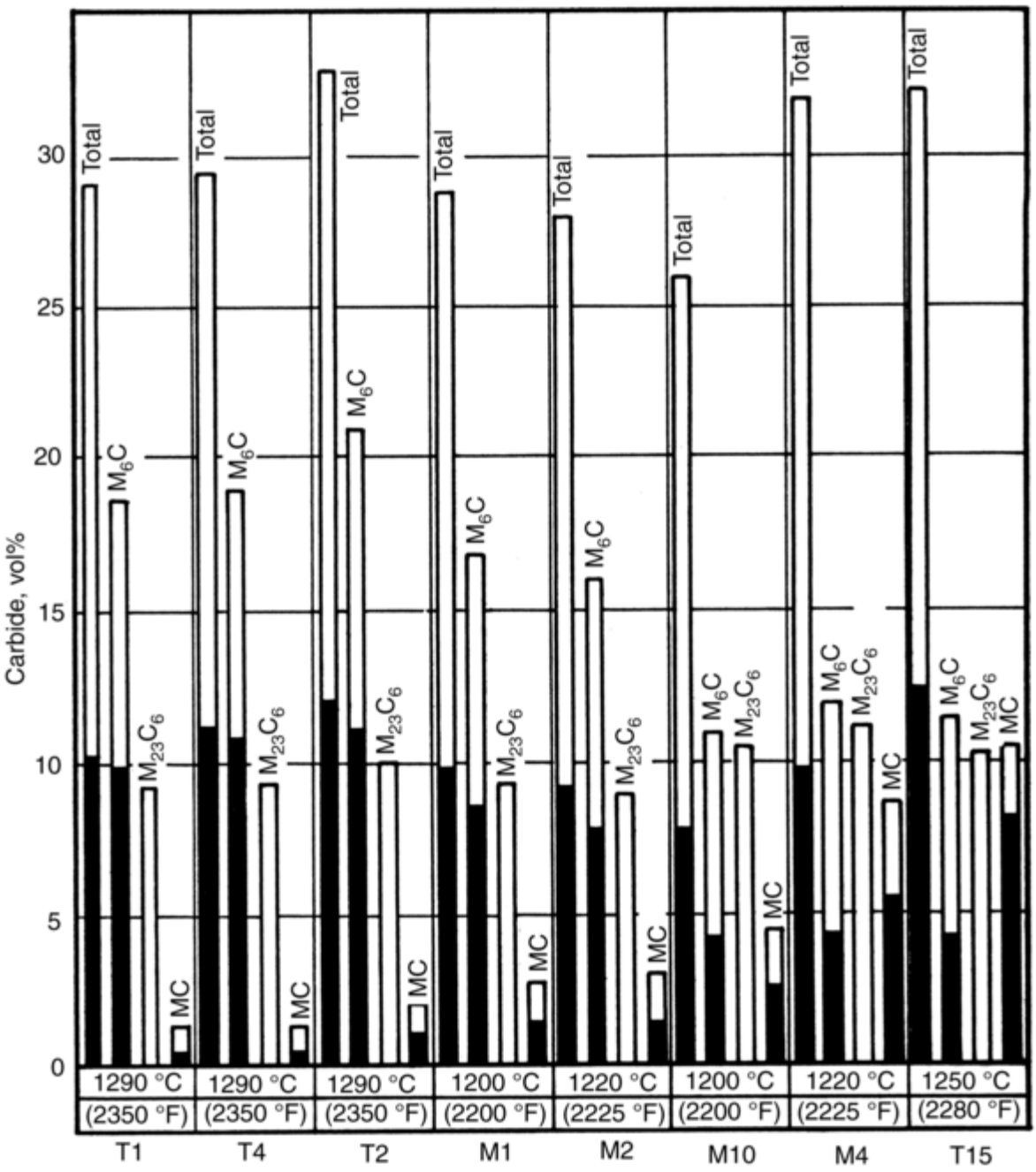

Fig. 39 Carbides in various high-speed steels, both in annealed conditions and after being heated to normal austenitizing temperatures. Open bars represent quantities in annealed steels. Solid bars indicate amounts after austenitizing at hardening temperatures indicated.

Effect of Composition on Microstructure. Because tool steels are somewhat more difficult to machine than carbon and alloy steels, the compositions of some grades are adjusted by increasing the silicon content to retain a certain amount of the carbon present as graphite. When viewed on a transverse plane (Fig. 40), the graphite appears as small, globular particles, but they are not nodular in shape as in ductile cast iron. On the longitudinal plane (Fig. 41), the graphite particles are shown to be elongated, although their aspect ratios are not excessively

high. The most commonly used graphitic tool steel is AISI O6, which typically contains approximately 0.3 to 0.5% of the total carbon content as graphite. The amount of carbon as graphite must be controlled carefully to ensure uniform hardening response. The presence of graphite improves machining and wear characteristics.

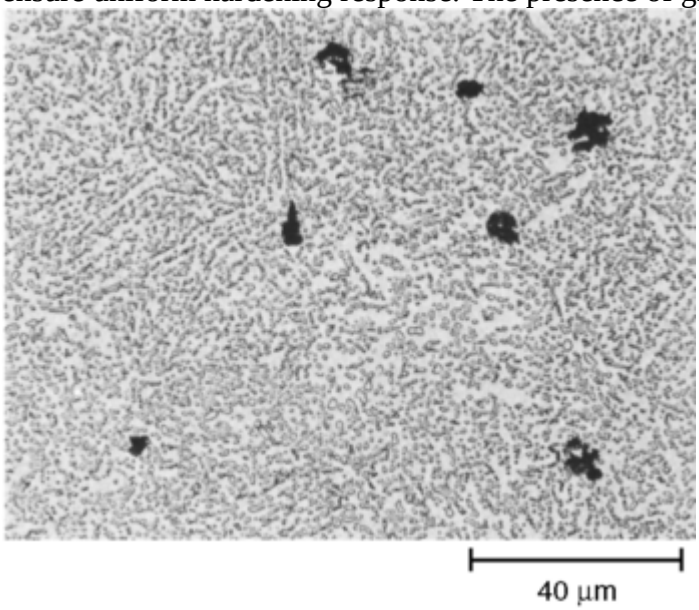

Fig. 40 AISI O6, spheroidize annealed, transverse section. Note the globular appearance of the graphite (black). 4% picral. 500×

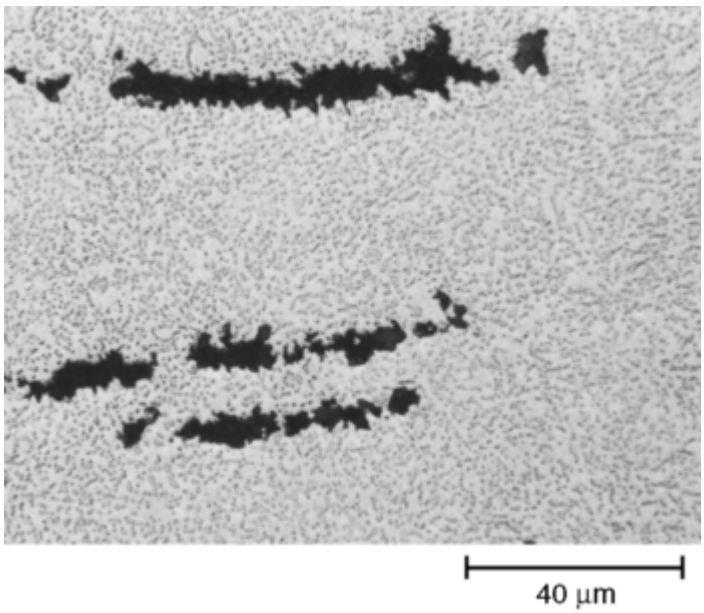

Fig. 41 AISI O6, spheroidize annealed, longitudinal section. Note that the graphite is elongated in the rolling direction. 4% picral. 500×

Undesired graphitization can occur in high-carbon tool steels if those elements that promote graphitization are not controlled. Processing procedures can also affect graphitization; therefore, in carbon tool steels with more than approximately 1.1% C, processing must also be carefully controlled.

Sulfur is added to several tool steel grades to improve machinability. Generally, the amount of sulfur added to tool steels is less than that added to free-machining carbon steels. Because manganese sulfide inclusions degrade toughness, certain tool steel grades are made with very low sulfur contents, often less than 0.003%, for critical applications. Although this practice enhances mechanical properties, these tool steels can be more difficult to machine.

Hobbing steels must be quite soft to permit optimal cold workability and maximum life of the master hob. Such steels are very low in carbon, although some medium-carbon alloy grades, such as AISI S5, are hobbed. The low-carbon hobbing steels, such as AISI P2, must be carburized after hobbing and before hardening. These

low-carbon grades are rather soft as-annealed and are designed to minimize work hardening during forming. Medium-carbon AISI S5 must be very carefully spheroidize annealed to as low a hardness as possible to enhance hobbability. Achieving a low annealed hardness with this grade is difficult, however, because its high silicon content substantially strengthens the ferrite.

Heat Treated Microstructures. Tool steel compositions range from carbon tool steels with no alloy additions to high-speed steels containing 20% or more alloying elements. Consequently, hardenabilities vary widely, producing quenching requirements that vary from brine to air. Each tool steel grade has been studied to determine the proper quench media, as a function of section size, to permit hardening to martensite. Although the carbon tool steels are usually not through hardened, most of the other grades are. Another exception is the low-carbon hobbing grades that are carburized and surface hardened. Figure 42 shows the surface of a poorly carburized specimen of P5 tool steel with an extensive intergranular carbide network and a carbide film on the surface. This mold failed prematurely in service as a result. A few grades are also nitrided or carbonitrided for special applications. Figure 43 shows the microstructure of gas nitrided H13 tool steel, while Fig. 44 shows an ion-nitrided H13 specimen. Note the (brittle) white-etching iron nitride layer at the extreme surface.

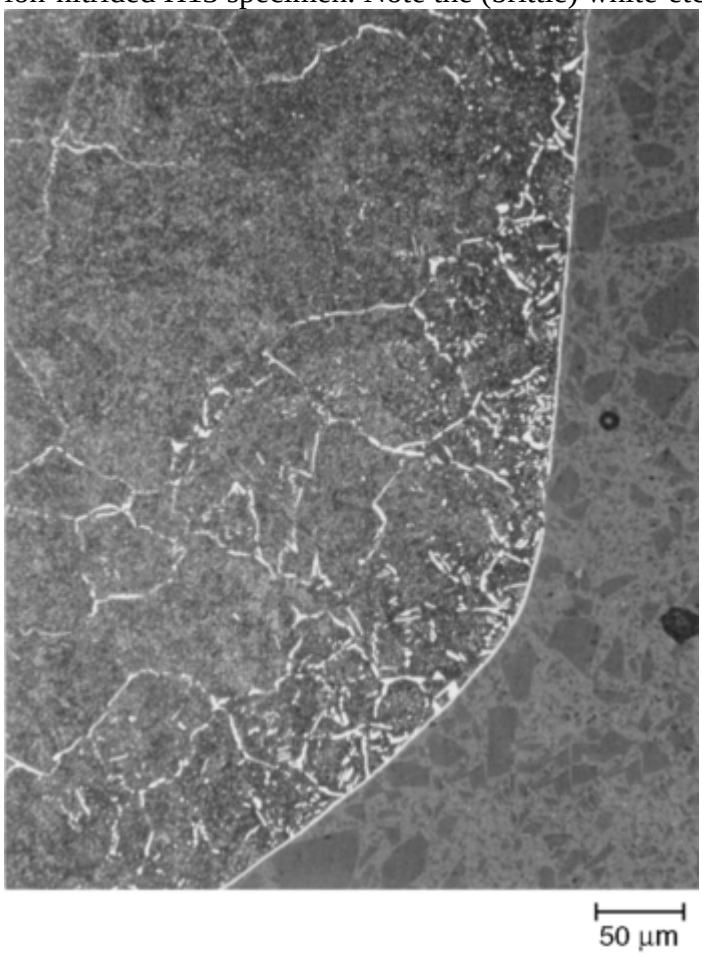

Fig. 42 Poorly carburized AISI P5 plastic-mold tool steel with an extensive intergranular carbide network and a carbide film on the surface. Three steps with a pressed synthetic chemical-textile pad; 10 min on step 3. Nital. 200×

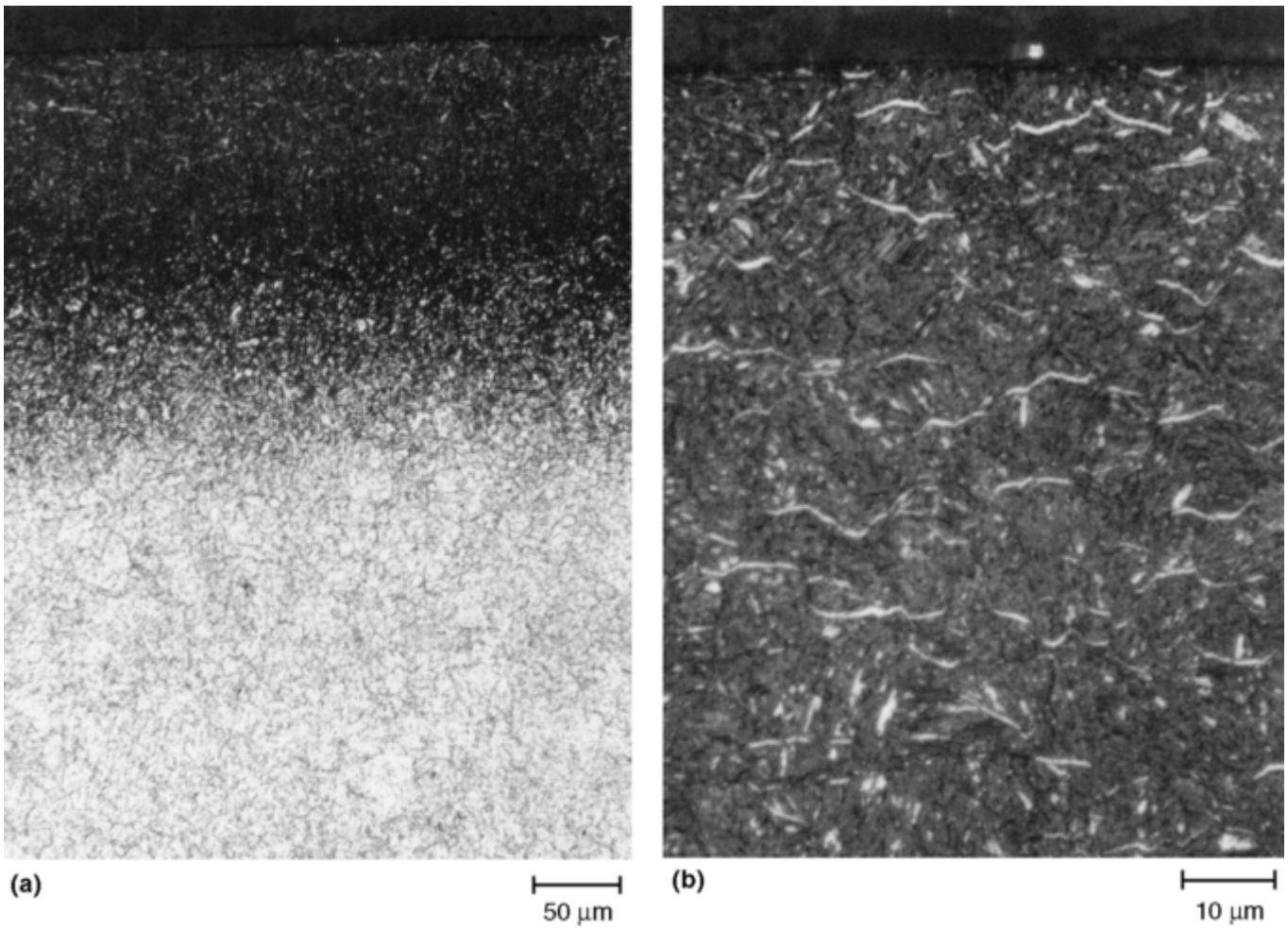

Fig. 43 Gas nitrided AISI H13 tool steel. Four steps with a rigid grinding disk. Nital. (a) 200×. (b) 1000×

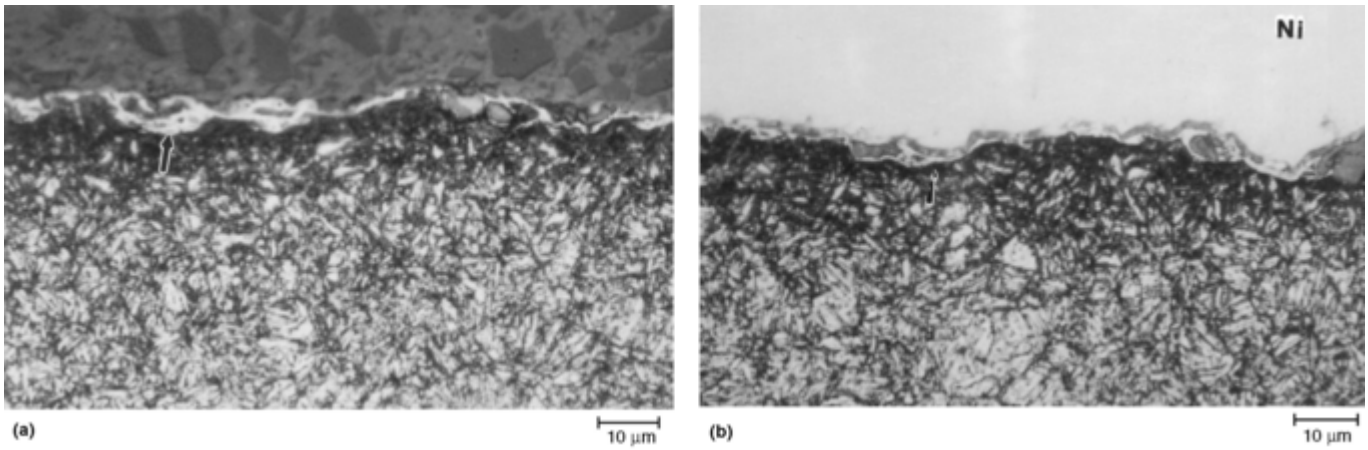

Fig. 44 Ion nitrided AISI H13 tool steel with a brittle white-etching iron nitride layer at the extreme surface. (a) Mounted with silica-filled epoxy. (b) Nickel plated and mounted with silica-filled epoxy. Vilella's reagent. Note that in (b) the iron nitride layer may be easily missed due to the similar color of it on the plating. 1000×

Most tool steels are hardened and tempered to rather high hardnesses (generally, ~58 HRC or greater) to obtain good wear resistance. Exceptions are the hot work tool steels that are quenched and tempered to hardnesses from approximately 42 to 55 HRC and prehardened plastic molding steels, such as AISI P20, that are sold in the heat treated condition at approximately 32 HRC. The prehardened tool steels are machined and used in this condition without subsequent heat treatment except, perhaps, for a stress-relief temper.

The correct austenitizing temperature for each grade has been determined experimentally by using an austenitizing series. Samples are heated to various temperatures and quenched at a rate consistent with the

anticipated hardenability. Each as-quenched sample is fractured to rate the prior-austenite grain size by the Shepherd comparison method. Next, the samples are carefully ground on one of the fracture faces and tested for hardness. As the austenitizing temperature increases, hardness will increase, level off, then decrease. The fracture grain size will remain relatively constant, usually up to the austenitizing temperature where the as-quenched hardness levels out, then will decrease due to grain growth. The optimal austenitizing temperature is that temperature or range where the hardness is highest and the grain size is finest. Dilatometry is generally conducted before such tests to establish the optimal temperature range.

To illustrate the effect of varying the austenitizing temperature on the microstructure of tool steels, it is necessary to examine grades with varying carbon content and carbide types. Figure 45 shows the microstructure of air-hardened S7 tool steel with a carbon content of approximately 0.5%. The preferred austenitizing temperature for S7 is 940 °C (1725 °F), and the grade is rather sensitive to under- and overaustenitization. Underaustenitization does not dissolve enough carbide to get full hardness. Overaustenitization results in grain growth, because all of the carbide is put in solution and it is not aluminum-killed, so there is no AlN to inhibit grain growth. Figure 46 shows the microstructure of O1 tool steel, an oil-hardening grade with approximately 0.9% C. The preferred austenitizing temperature is 800 °C (1475 °F), so this series compares the correct quenched microstructure to overaustenitized microstructures. It demonstrates how increasing the carbon content of the austenite depresses the martensite start temperature, resulting in increasing retained austenite. A more dramatic effect on the microstructure is observed when a high-carbon, high-alloy tool steel, such as type D2, is examined in the overaustenitized condition. Figure 47 shows D2 after air quenching from various temperatures, from 1010 to 1230 °C (1850 to 2250 °F). The recommended austenitizing temperature is 1010 °C (1850 °F). Note that retained austenite, which is present even at the correct austenitizing temperature, cannot be observed by light microscopy until a substantial amount is present; certainly, more than 10% is required before it can be seen.

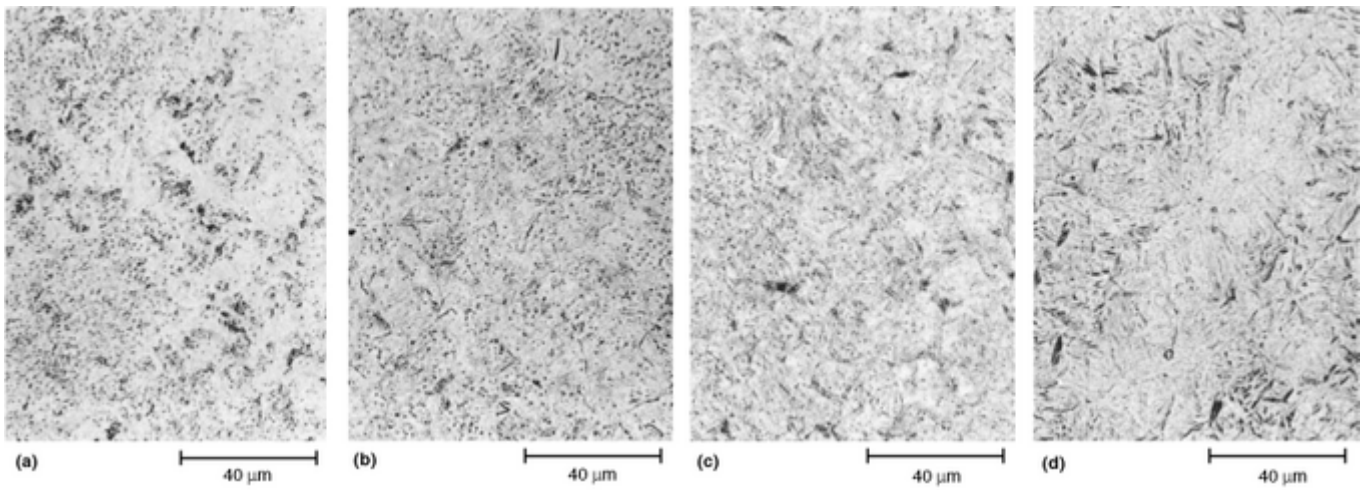

Fig. 45 AISI S7 (0.5% C). Influence of austenitizing temperature. (a) Austenitized at 915 °C (1675 °F) 1 h for every 25 mm (1.0 in.) of thickness and air quenched. Sample is underaustenitized. (b) Austenitized at 925 °C (1700 °F). Slightly underaustenitized. (c) Austenitized at the preferred temperature of 940 °C (1725 °F). (d) Austenitized at 955 °C (1750 °F). Slightly overaustenitized; note coarsening, no visible carbide. 4% picral. 500×

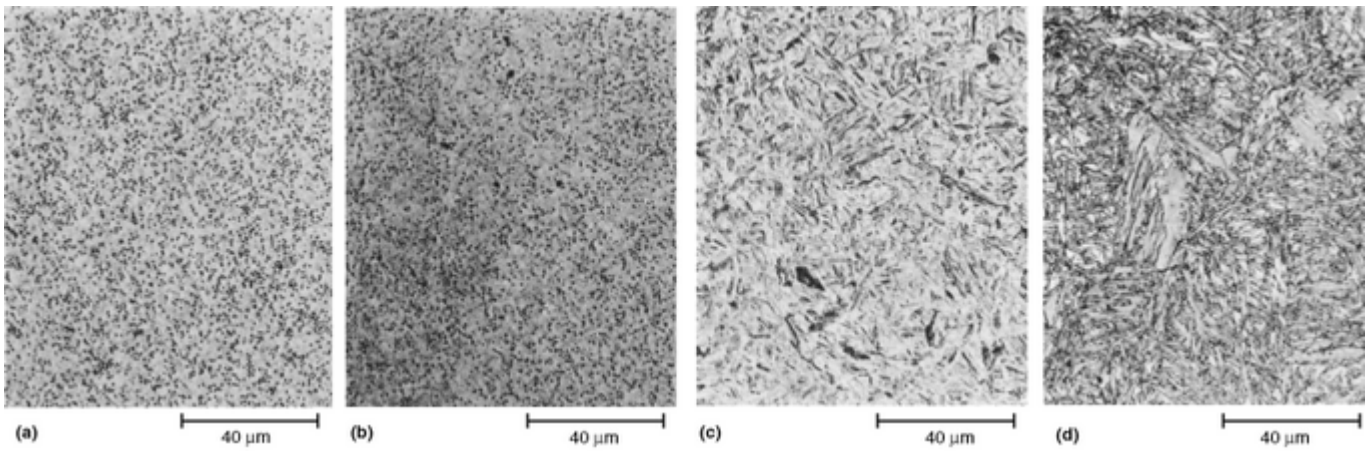

Fig. 46 AISI O1. Influence of austenitizing temperature on microstructure. (a) Austenitized at 800 °C (1475 °F) 1 h for every 25 mm (1.0 in.) of thickness. 65 HRC, grain size 9.5. Specimen properly austenitized. (b) Austenitized at 870 °C (1600 °F). 65 HRC, grain size 9. Overaustenitized. (c) Austenitized at 980 °C (1800 °F). 64 HRC, grain size 7. Very overaustenitized; all carbide dissolved. (d) Austenitized at 1100 °C (2010 °F). 64 HRC, grain size 3. Severely overaustenitized; note retained austenite (white). 4% picral. 500×

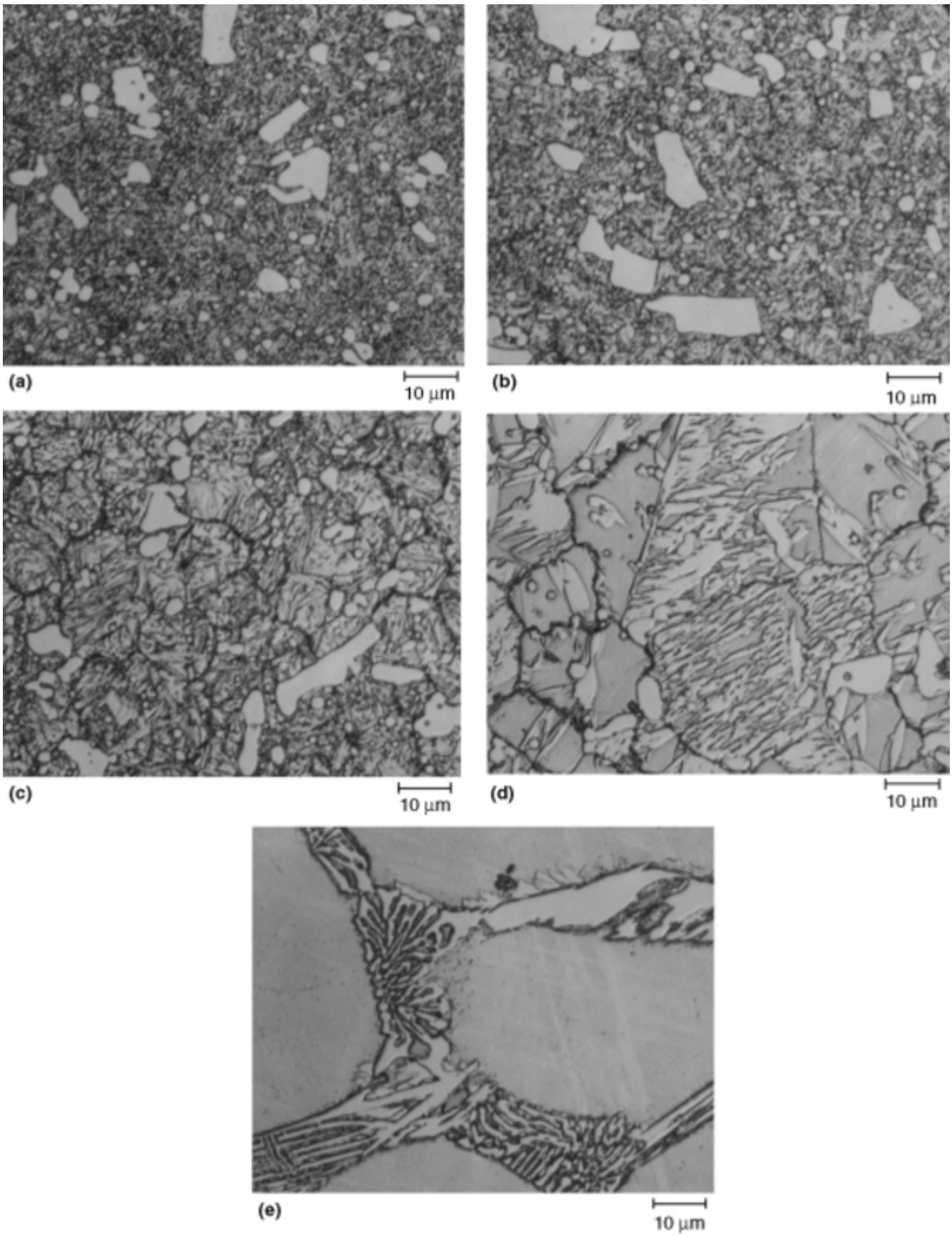

Fig. 47 AISI D2 tool steel microstructure (Vilella's etch, 1000×) after air quenching from various austenitizing temperatures. Note that retained austenite, which is present even at the correct austenitizing temperature (1010 °C, or 1850 °F), cannot be observed by light microscopy until a substantial amount is present. (a) 1010 °C (1850 °F) air quenched. (b) 1065 °C (1950 °F) air quenched. (c) 1120 °C (2050 °F) air quenched. (d) 1175 °C (2150 °F) air quenched. (e) 1230 °C (2250 °F) air quenched

Carbon tool steels are hypereutectoid and contain only cementite, which is easily dissolved. The iron-carbon equilibrium diagram is a good starting point for establishing the correct austenitizing temperature. For these steels, maximum hardness results when approximately 0.60 to 0.65% C is put into solution. Therefore, the as-quenched structure will consist of martensite and residual cementite, that is, the carbides not put into solution. A small amount of retained austenite will also be present, but it will not be detectable with a light microscope if the proper austenitizing temperature is used. Figure 48 shows the microstructure of W1 tool steel in the hardened case, the transition zone, and the unhardened core after brine quenching a 19 mm (0.75 in.) diameter bar. The case is high-carbon martensite, and the core is very fine pearlite. Not all of the cementite should be put into solution, so residual cementite should be present at all locations. Quenched and tempered microstructures of a variety of other low-alloy grades with medium levels of carbon are shown in Fig. 49, 50, 51, 52, 53, and 54 while the microstructure of higher-alloy tool steels are shown in Fig. 55, 56, 57, 58, 59, 60, 61, 62, 63, 64, 65, and 66

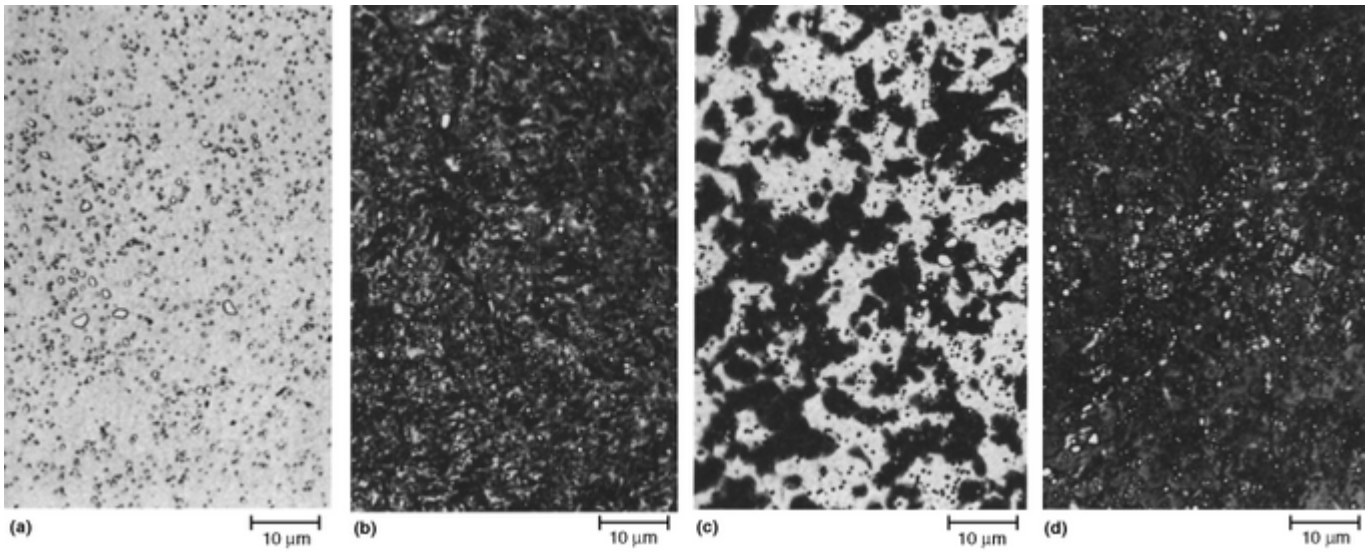

Fig. 48 AISI W1 (1.05% C), 19 mm (0.75 in.) diam bars, brine quenched. (a) Hardened case microstructure. 64 HRC. Case contains as-quenched martensite and undissolved carbides. 4% picral. (b) 2% nital etch reveals martensite as dark rather than light. (c) Transition zone. 55 HRC. Martensite is light and undissolved, carbide is outlined, and pearlite is dark. 4% picral. (d) Core microstructure. 42 to 44 HRC. 4% picral etch reveals fine pearlite matrix (black) containing some patches of martensite (white) and undissolved carbides (outlined white particles). 1000×

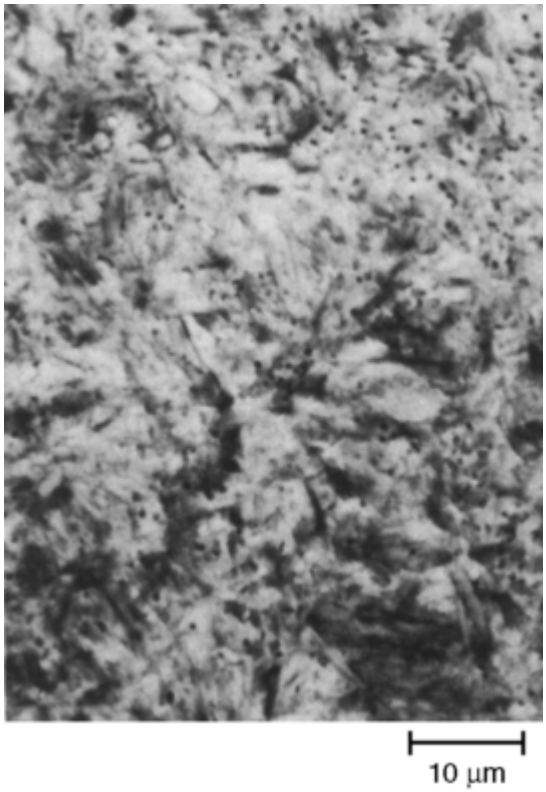

Fig. 49 AISI S2, heated to 845 °C (1550 °F), water quenched, and tempered at 150 °C (300 °F). 59.5 HRC. Structure consists of martensite and some very fine undissolved carbide. 2% nital. 1000×

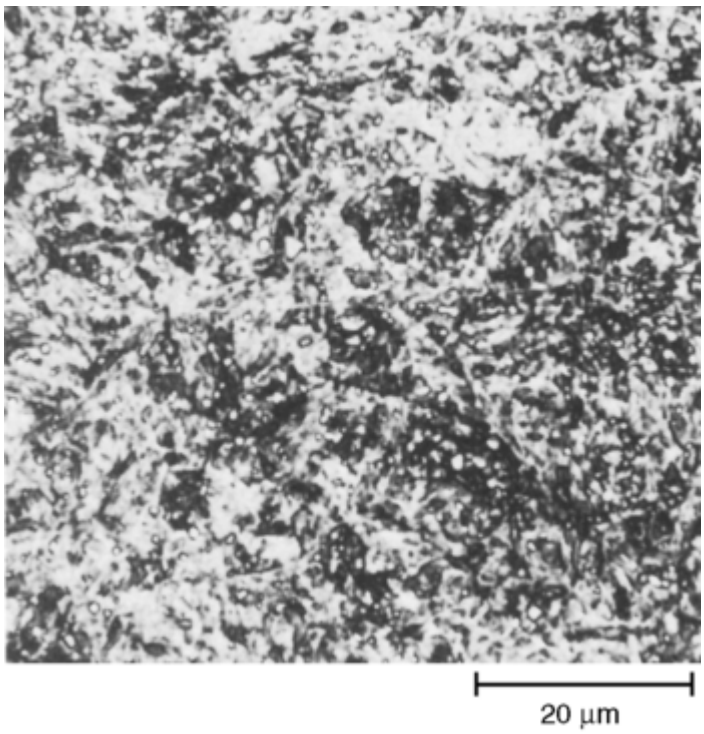

Fig. 50 AISI L6, heated to 840 °C (1550 °F), oil quenched, and tempered at 150 °C (300 °F). 61 HRC. Martensite and undissolved carbides are revealed. 2% nital. 1000×

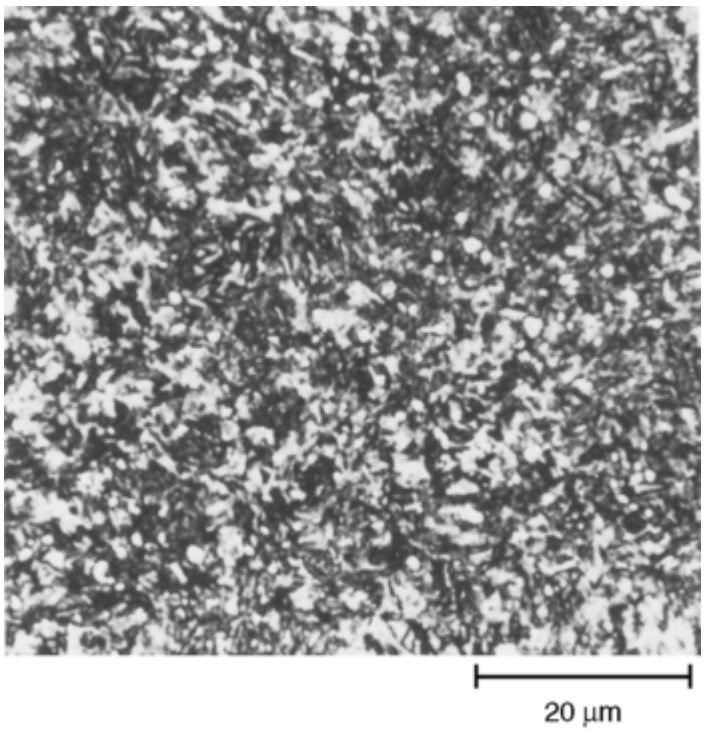

Fig. 51 AISI O2, heated to 850 °C (1560 °F), oil quenched, and tempered at 175 °C (350 °F). 61 HRC. Martensite and a small amount of undissolved carbide are revealed. 2% nital. 1000×

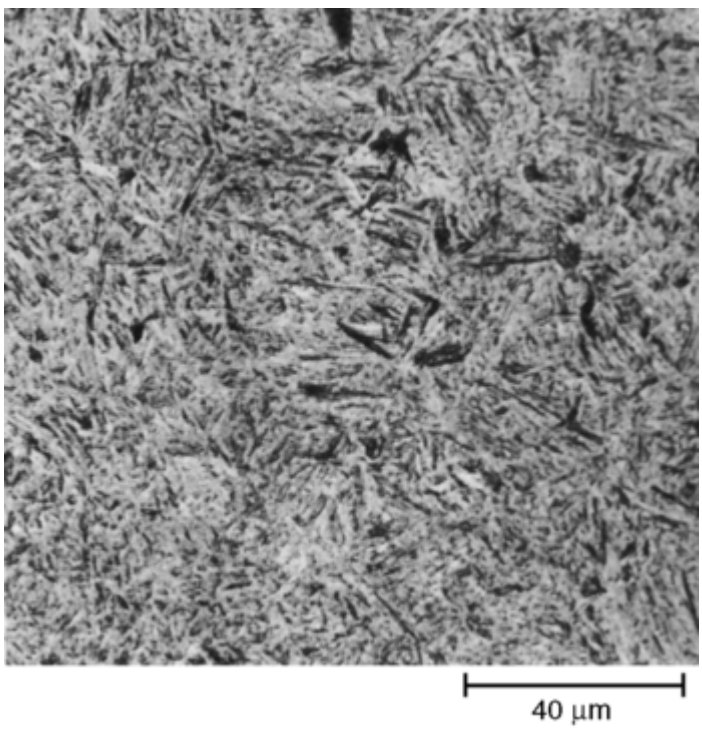

Fig. 52 AISI S1, heated to 955 °C (1750 °F), oil quenched, and tempered at 150 °C (300 °F). 58 to 59 HRC. Only martensite is visible. 2% nital. 500×

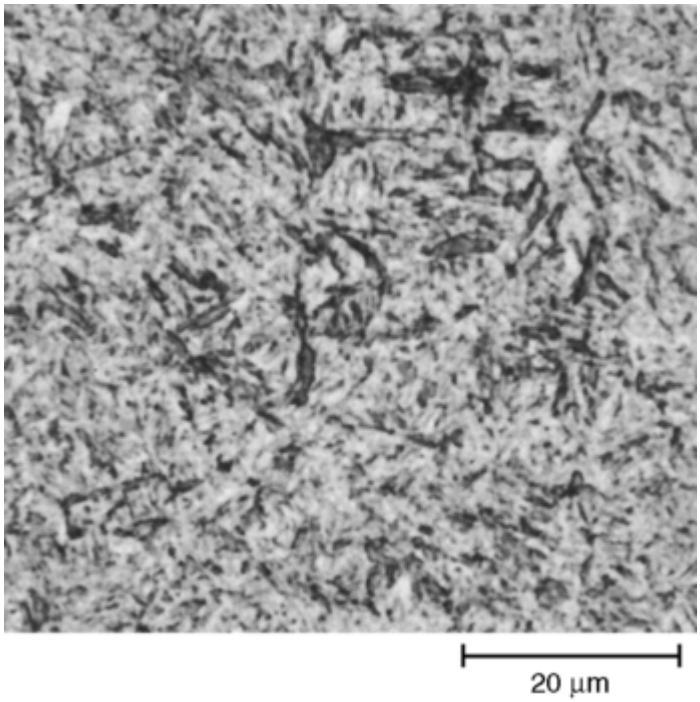

Fig. 53 AISI S5, heated to 870 °C (1600 °F), oil quenched, and tempered at 175 °C (350 °F). 60 HRC. Only martensite is visible. 2% nital. 1000×

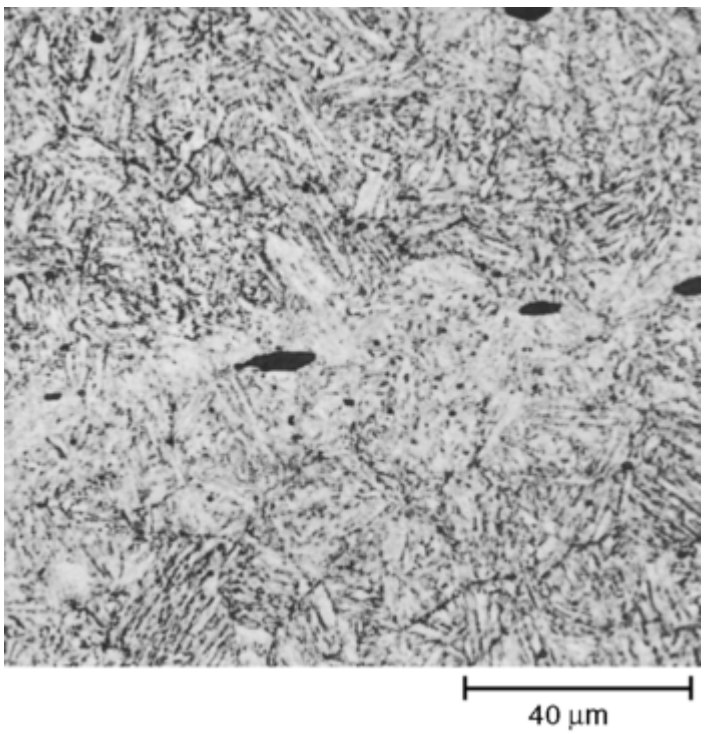

Fig. 54 AISI P20, heated to 900 °C (1650 °F), water quenched, and tempered at 525 °C (975 °F). 32 HRC. Matrix is martensite. Dark particles are manganese sulfides. Contrast process orthochromatic film. 2% nital. 500×

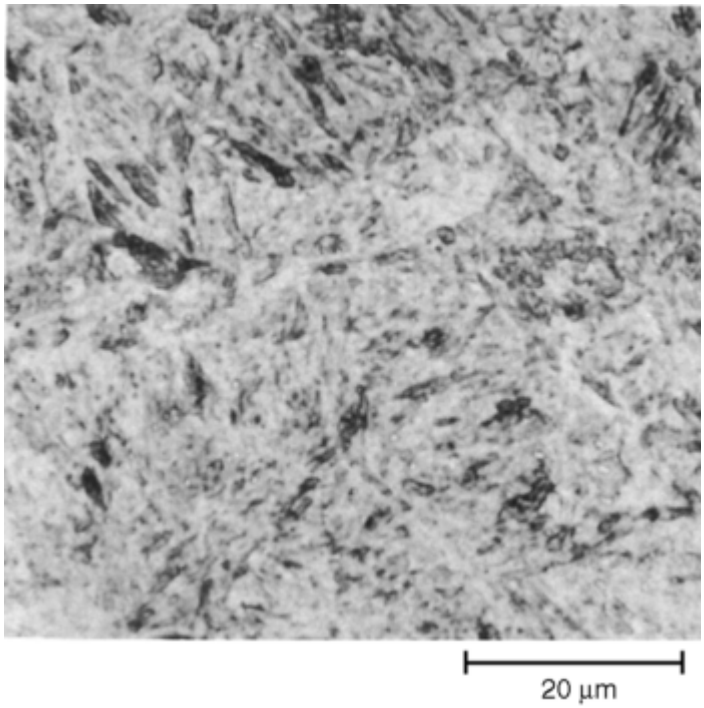

Fig. 55 AISI S7, heated to 940 °C (1725 °F), air quenched, and tempered at 200 °C (400 °F). 58 HRC. Martensite and a small amount of undissolved carbides are observed. Vilella's reagent. 1000×

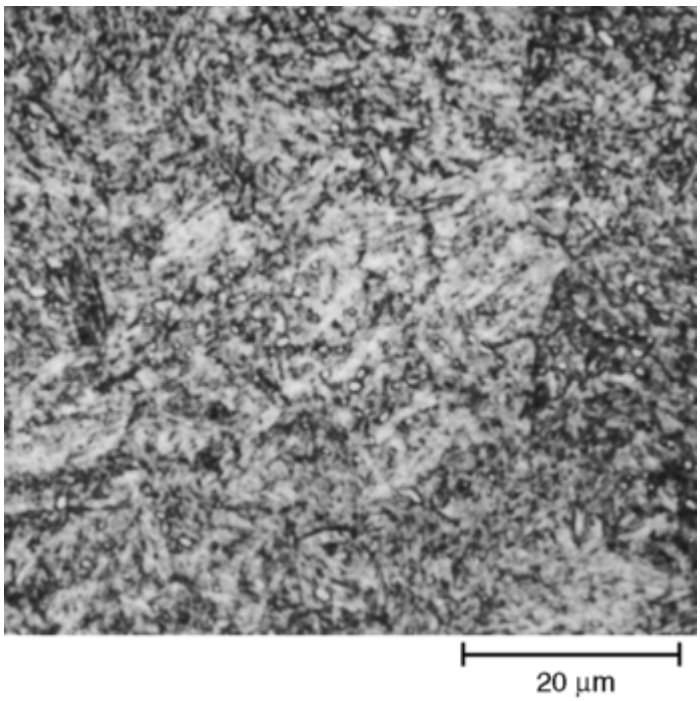

Fig. 56 AISI S7, heated to 940 °C (1725 °F), air quenched, and tempered at 495 °C (925 °F). 52 HRC. Martensite and a small amount of undissolved carbide are observed. Vilella's reagent. 1000×

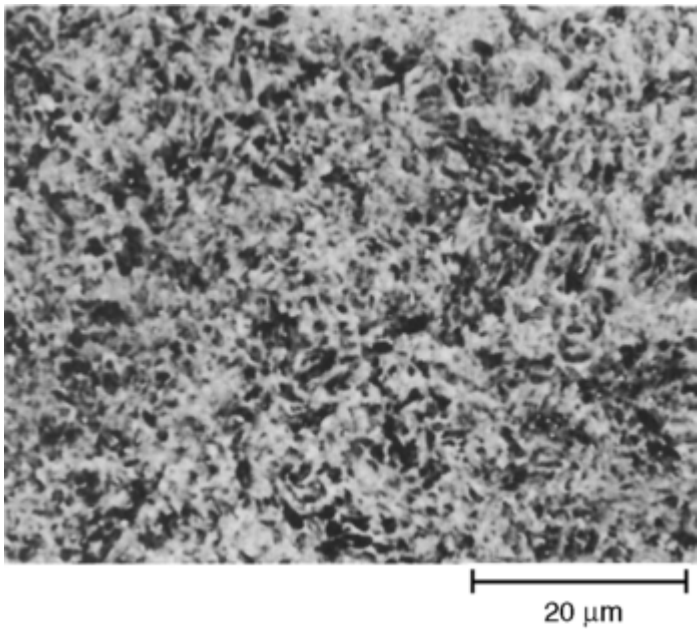

Fig. 57 AISI A6, heated to 840 °C (1550 °F), air quenched, and tempered at 150 °C (300 °F). 61.5 HRC. Martensite plus a small amount of undissolved carbide are observed. 2% nital. 1000×

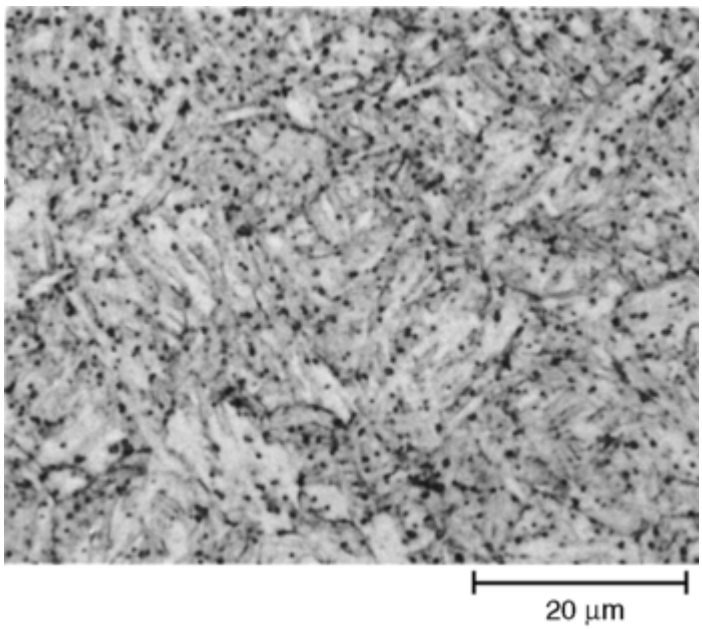

Fig. 58 AISI H11, heated to 1010 °C (1850 °F), air quenched, and double tempered at 510 °C (950 °F). 52 HRC. Martensite plus a small amount of very fine carbide are visible. Vilella's reagent. 1000×

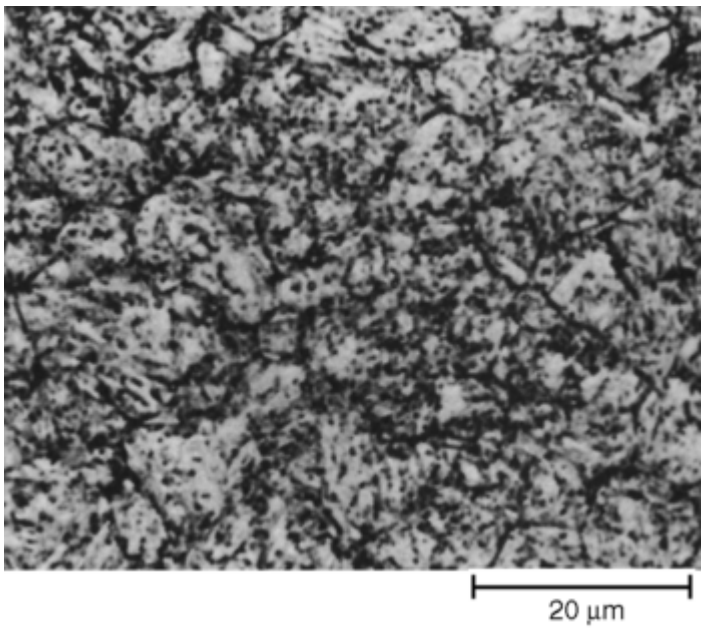

Fig. 59 AISI H13, heated to 1025 °C (1875 °F), air quenched, and double tempered at 595 °C (1100 °F). 42 HRC. All martensite plus a small amount of very fine undissolved carbide. 2% nital. 1000×

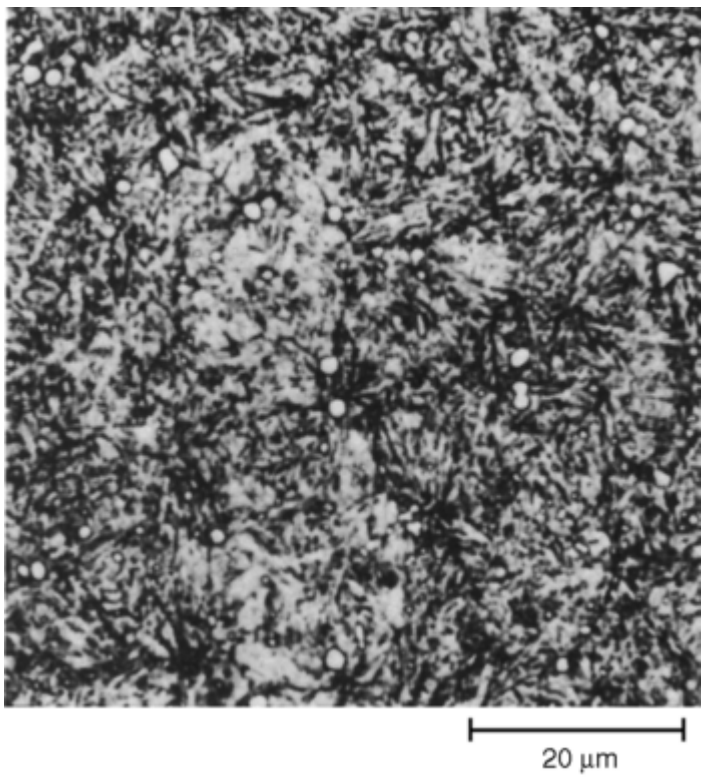

Fig. 60 AISI H21, heated to 1200 °C (2200 °F), oil quenched, and tempered at 595 °C (1100 °F). 53.5 HRC. Martensite and undissolved carbide are observed. 2% nital/Vilella's reagent. 1000×

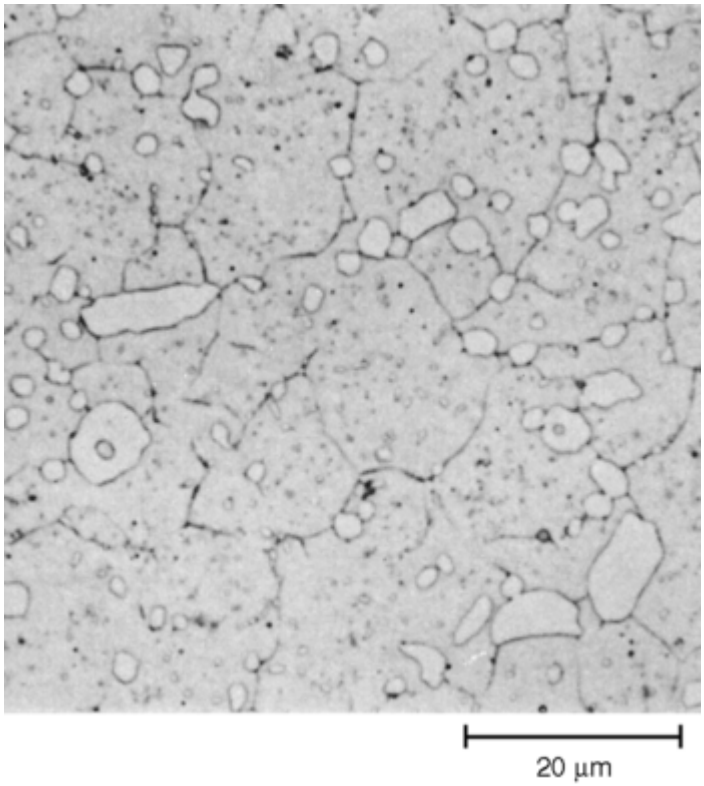

Fig. 61 AISI D2, heated to 1010 °C (1850 °F), air quenched, and tempered at 200 °C (400 °F). 59.5 HRC. Martensite plus substantial undissolved carbide; note the prior-austenite grain boundaries. 2% nital. 1000×

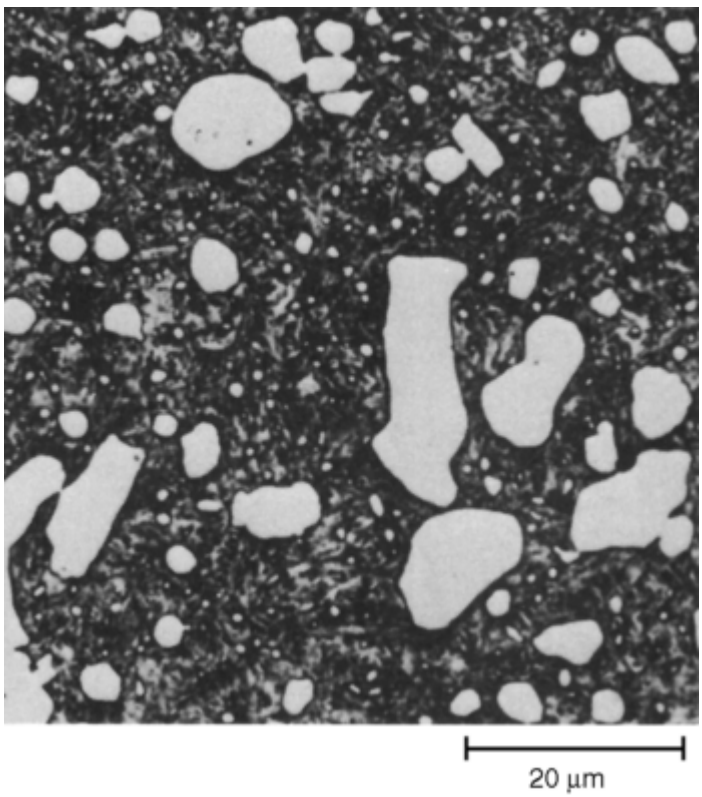

Fig. 62 AISI D3, heated to 980 °C (1800 °F), oil quenched, and tempered at 200 °C (400 °F). 60.5 HRC. Martensite plus substantial undissolved carbide are visible. 2% nital/Vilella's reagent. 1000×

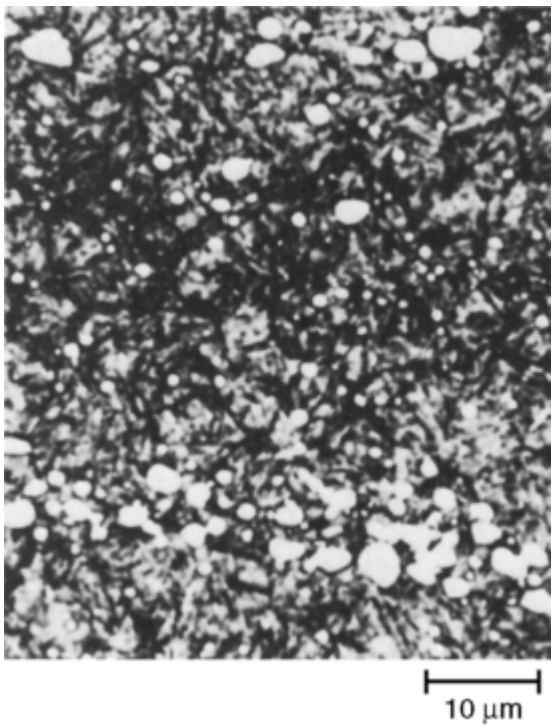

Fig. 63 AISI M1, heated to 1175 °C (2150 °F), oil quenched, and triple tempered at 480 °C (900 °F). 62 HRC. Martensite plus undissolved carbide are revealed. 2% nital. 1000×

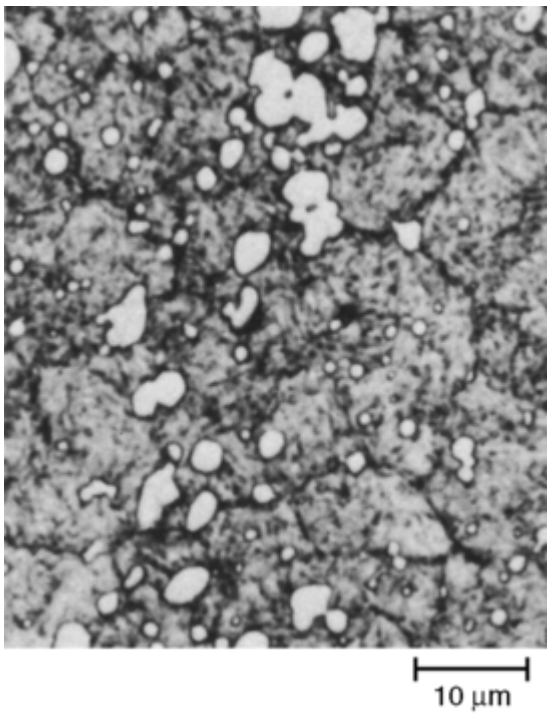

Fig. 64 AISI M2, heated to 1120 °C (2050 °F), oil quenched, and double tempered at 480 °C (900 °F). 62 HRC. Martensite plus undissolved carbide are revealed. Vilella's reagent. 1000×

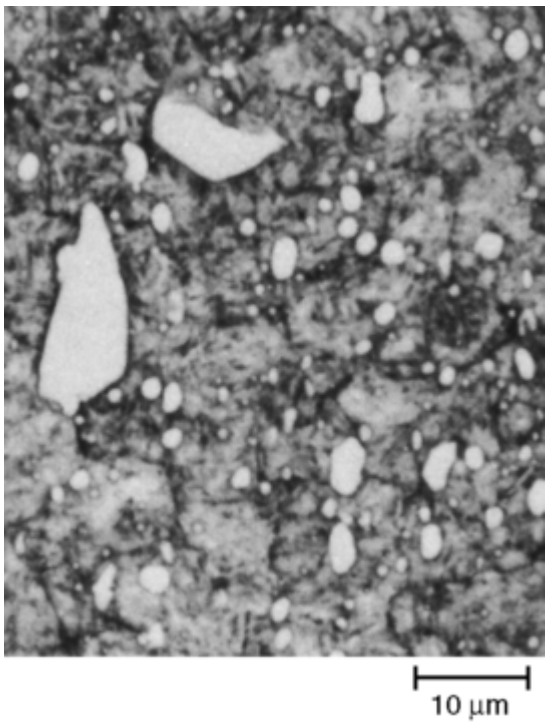

Fig. 65 AISI M4, heated to 1220 °C (2225 °F), oil quenched, and double tempered at 480 °C (900 °F). 62 HRC. Martensite plus undissolved carbide are revealed. Vilella's reagent. 1000×

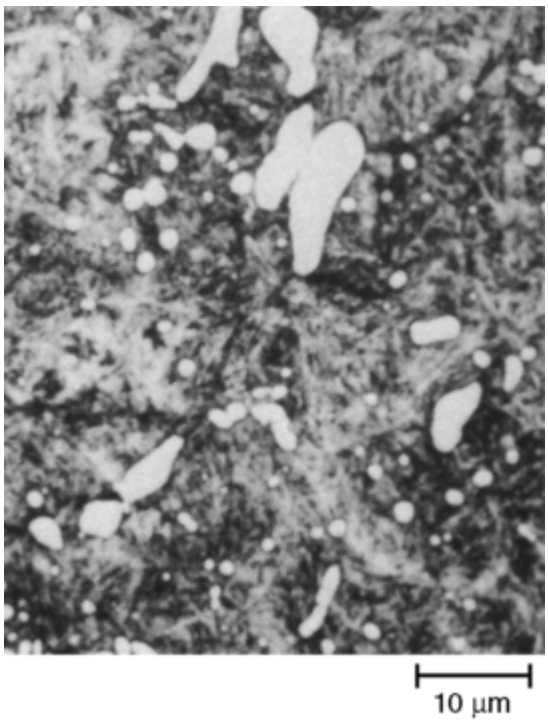

Fig. 66 AISI M42, heated to 1175 °C (2150 °F), oil quenched, and triple tempered at 565 °C (1050 °F). 65 HRC. Martensite plus undissolved carbide are observed. Vilella's reagent. 1000×

If a sufficiently high austenitizing temperature is used, the carbon content of the austenite will be raised to such an extent that the martensite finish temperature is well below room temperature. Because retained austenite is relatively soft compared to martensite, the bulk hardness will be lower. The microstructure will exhibit coarse plate (acicular) martensite and retained austenite. As the austenitizing temperature exceeds the optimal temperature, the amount of residual cementite decreases, the amount of retained austenite increases, the hardness decreases, and the grain size increases.

In general, if the amount of retained austenite is high enough to be observed with a light microscope, the steel has been overaustenitized. Tempering will not convert high levels of retained austenite to martensite or bainite unless the tempering temperature is rather high. Moreover, the retained austenite will not be stable enough to withstand shock-induced transformation to martensite during service. When such transformation occurs, the high-hardness matrix lacks enough ductility to accommodate the transformation stresses, and cracking results.

Low heat treated hardnesses may also result if the section size and quench rate are selected incorrectly for a particular grade. When the hardenability is inadequate to permit full hardening, pearlite or bainite will be observed in the microstructure. Ferrite may also be visible in the few tool steels that are hypoeutectoid, although this is less common. Brine- and water-quenching grades are also susceptible to formation of soft spots within the case, caused by localized slow cooling from tongs holding the sample or by inadequate agitation (failure to break up vapor pockets due to localized boiling of the quench media).

After quenching, tool steels must be immediately tempered to reduce the very high transformation stresses, or quench cracking may occur. Quench cracking is more likely to occur as the quench rate increases and if the geometry of the specimen exhibits stress raisers. Air-hardenable steels are less susceptible to quench cracking, because the slow rate of cooling helps to relieve some of the transformation stresses.

Many tool steels are often tempered at 175 to 230 °C (350 to 450 °F). These low tempering temperatures do little to the structure except relieve quenching stresses. Hot work and high-speed steels are usually tempered at relatively high temperatures. Due to their high alloy content, these grades can resist softening during tempering to rather high levels. These higher-alloy steels are often tempered hot enough to cause secondary hardening and to change the nature of the carbides present. These changes, however, can be detected only by methods more sophisticated than light microscopy. In general, the lowest-alloy tool steels receive a single temper, typically 2 h for every 25 mm (1 in.) of thickness. Higher-alloy tool steels are usually tempered twice; high-speed steels may be tempered three times. Double and triple tempering is required to condition and stabilize the microstructure.

When a substantial amount of strong carbide-forming elements are present, tempering at high temperatures, where secondary hardening occurs, results in a change in carbide composition and type. To illustrate this, Fig. 67 shows the effect of time and temperature on the type of carbide present in a 12% Cr martensitic steel, more highly alloyed than type 420. At low tempering temperatures, M_3C will be present. However, with higher temperatures and longer times, M_3C is replaced by M_7C_3 and $M_{23}C_6$, only the latter being present at still higher temperatures and longer times. This steel contained a somewhat high nitrogen content, and M_2N nitrides were observed as well. Figure 68 shows the sequence of carbide formation in two tungsten-type high-speed steels as a function of tempering temperature. Both exhibit strong secondary hardening at approximately 600 °C (1110 °F).

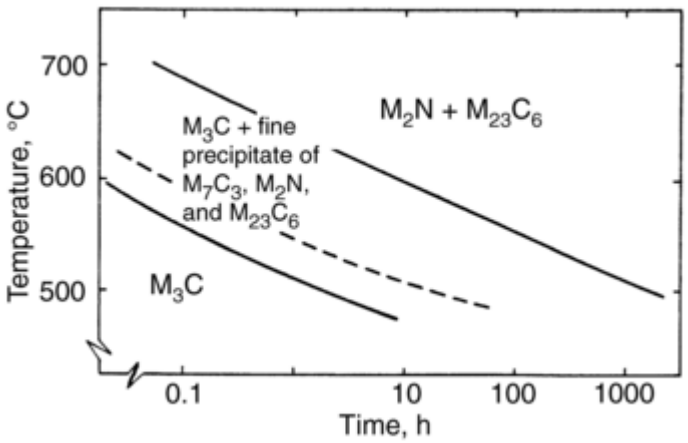

Fig. 67 Time-temperature diagram of carbides present in two 12% Cr martensitic stainless steels after tempering. Solid lines (for alloy A) and broken lines (for alloy B) show when fine precipitates are first observed. Alloy A composition: 0.21% C, 13.2% Cr, and 0.24% N. Alloy B composition: 0.18% C, 0.58% Mn, 0.31% Si, 0.18% Ni, 11.7% Cr, 0.49% Mo, 0.01% Al, 0.38% V, 0.20% Nb, and 0.033% N. This diagram is based on observations of specimens subjected to more than 30 different tempering treatments in the temperature interval of 500 to 700 °C (930 to 1290 °F). Source: Ref 9

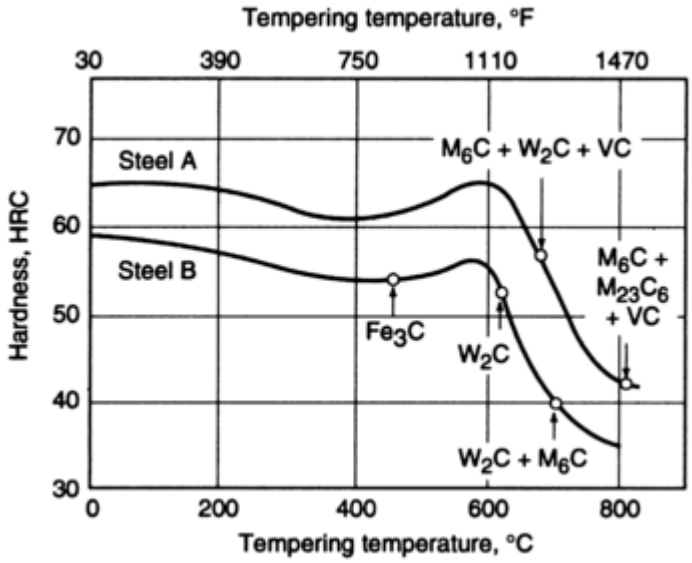

Fig. 68 Sequence of alloy carbide formation in two tungsten-type high-speed steels as a function of tempering temperature. Steel A contains 0.8% C, 18% W, 4% Cr, 2% V, and 10% Co; steel B contains 0.8% C, 9% W, 3% Cr, and 3% Co. Source: Ref 10

For many tool steels, tempering to approximately 540 °C (1000 °F) produces only subtle differences in the microstructure viewed optically, as shown in Fig. 69. The speed at which etching occurs and the darkness of the matrix will change with tempering. Tempering just below the lower critical temperature is required to produce pronounced microstructural changes, but such high tempers have no practical applications for tools and dies, except as an anneal.

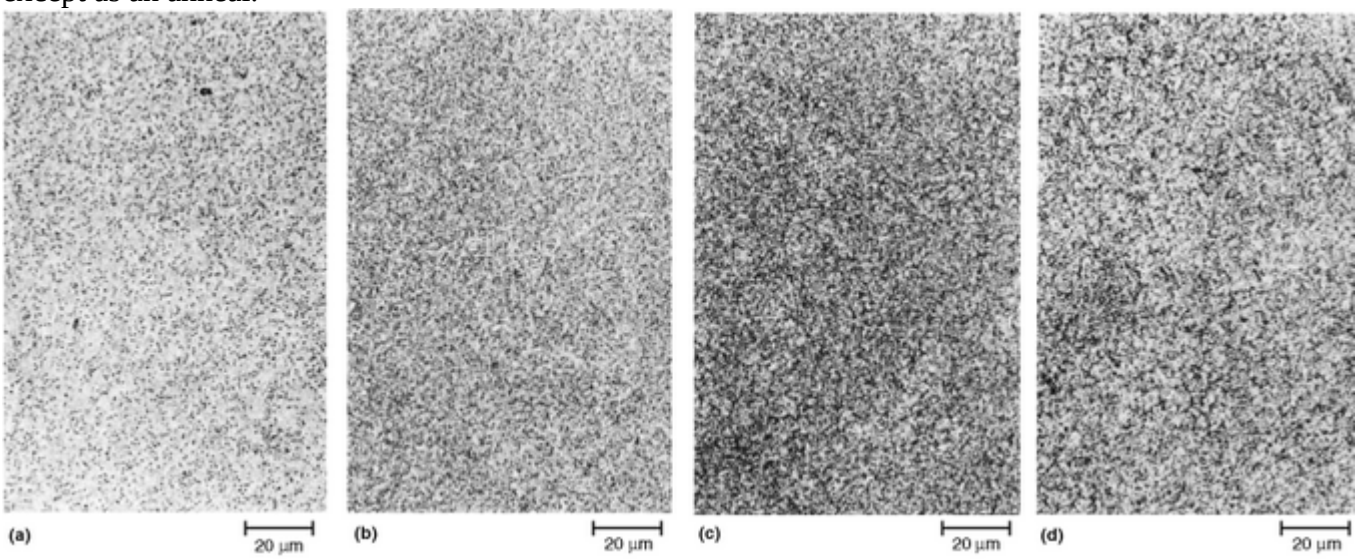

Fig. 69 Influence of tempering temperature on microstructure of AISI O1 (all: 4% picral, 500×). All specimens austenitized at 800 °C (1475 °F), oil quenched, and tempered at different temperatures. (a) 200 °C (400 °F). 60 HRC. (b) 315 °C (600 °F). 55 HRC. (c) 425 °C (800 °F). 49 HRC. (d) 540 °C (1000 °F). 43 HRC

Heat treated tool steel microstructures are similar in appearance when the grades are properly heat treated. The primary differences are the amount and type of the residual, undissolved carbides that will influence the coarseness of the plate martensite. In many tool steels, the martensite phase is so fine that little detail is observed. This is not the case for grades that exhibit very little residual carbides, for example, AISI S1, S5, and S7. These shock-resisting tool steels have lower carbon contents, and nearly all of the carbon is dissolved in the austenite. Consequently, the martensite is coarser, with more detail observable by light microscopy.

In some cases, quenching does not produce a fully martensitic structure. This occurs mainly when the hardenability is inadequate for through hardening for the section size and quench medium chosen. The

continuous cooling transformation (CCT) diagram is a good tool for the metallurgist when evaluating heat treatment problems. Unfortunately, diagrams do not exist for all standard grades. Figure 70 shows a CCT diagram for S7 tool steel. Figure 71 and 72 illustrate the microstructural variations in S7 produced by varying the quench rate from 2780 to 28 °C/h (5000 to 50 °F/h). Isothermal transformation (IT) diagrams (also called time-temperature-transformation or S-curves) have often been used when diagnosing heat treatment problems, but they cannot be used with most tool steels, because the transformations depicted by the IT diagram are much different than those shown in the corresponding CCT diagram. As an example, compare the CCT diagram for S7 shown in Fig. 70 with the IT diagram for S7 shown in Fig. 73. There is some similarity here, but with higher-alloyed tool steels, the similarity is less. The IT diagrams are very useful for developing annealing cycles and for isothermal treatments such as ausforming. Figure 74 shows the microstructure of S7 held at 704 °C (1300 °F) for 30 min (only a small amount of transformation before quenching) and for 4 h (almost complete transformation to pearlite). A wide range of isothermally formed microstructures is shown in Fig. 75, 76, 77, and 78 for S5 tool steel.

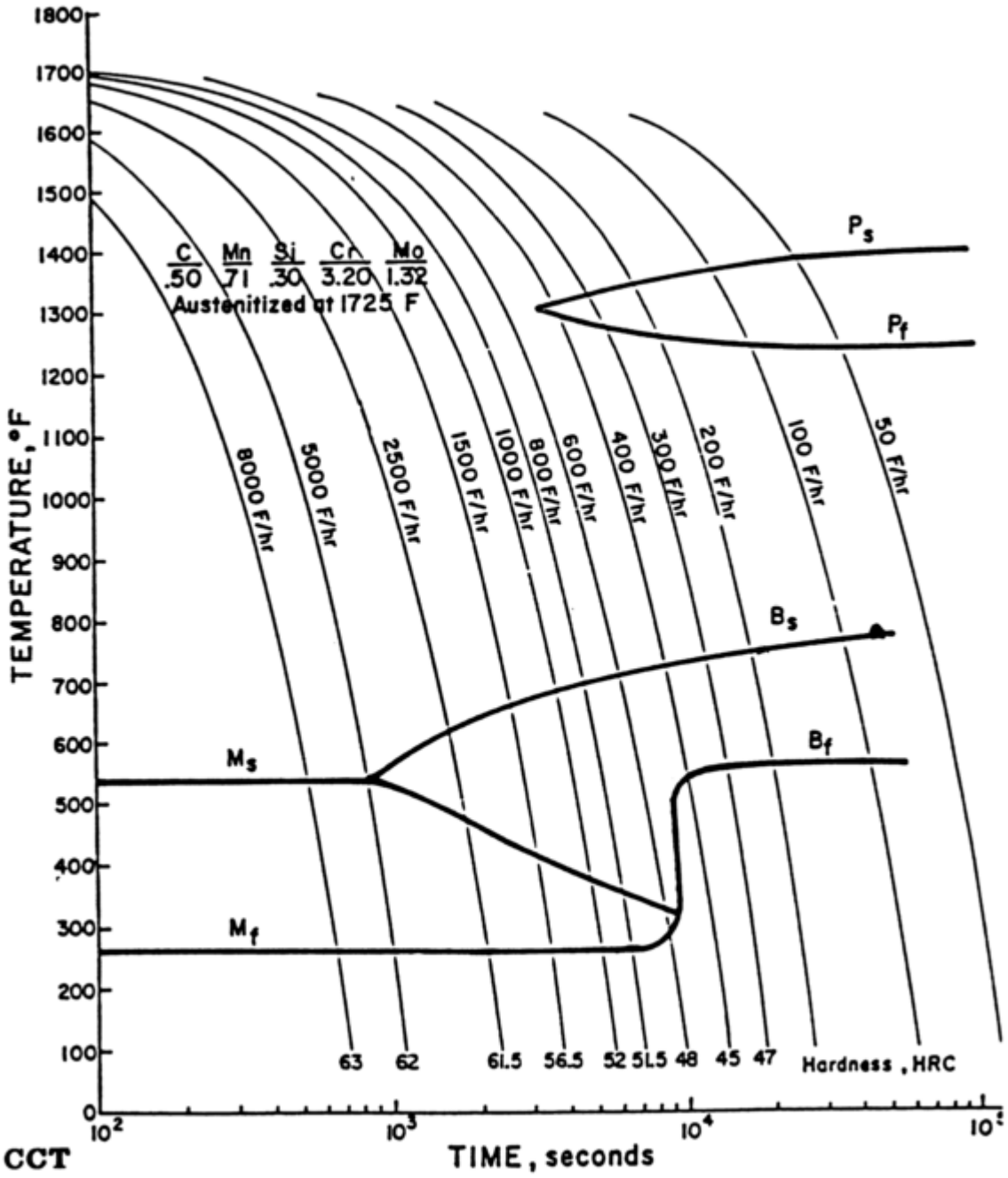

Fig. 70 Continuous coding transformation diagram for AISI S7 tool steel. M_s, martensite start; M_f, martensite finish; B_s, bainite start; B_f, bainite finish; P_s, pearlite start; P_f, pearlite finish. Source: *Atlas of Time-Temperature Diagrams,* ASM International

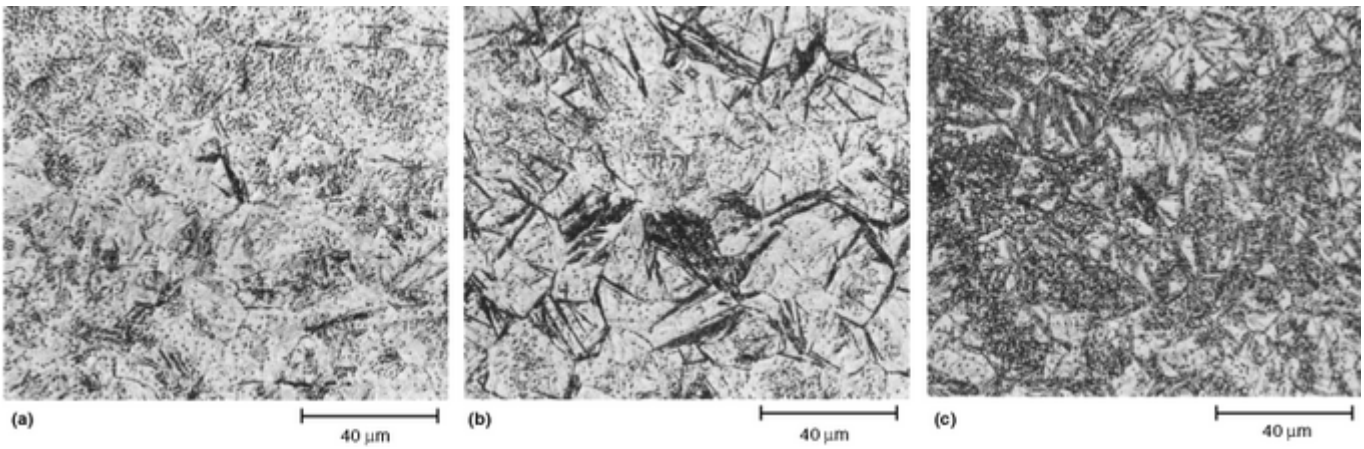

Fig. 71 AISI S7 continuous cooling transformations. Some very fine undissolved carbide is present in all specimens in this series. (a) Austenitized at 940 °C (1725 °F) and cooled at 2780 °C/h (5000 °F/h). 62 HRC. Structure is martensite plus a small amount of bainite. (b) Cooled at 1390 °C/h (2500 °F/h) to produce a greater amount of bainite. 61.5 HRC. (c) Cooled at 830 °C/h (1500 °F/h). 56.5 HRC. Structure is mostly bainite plus some martensite (light). 4% picral. 500×

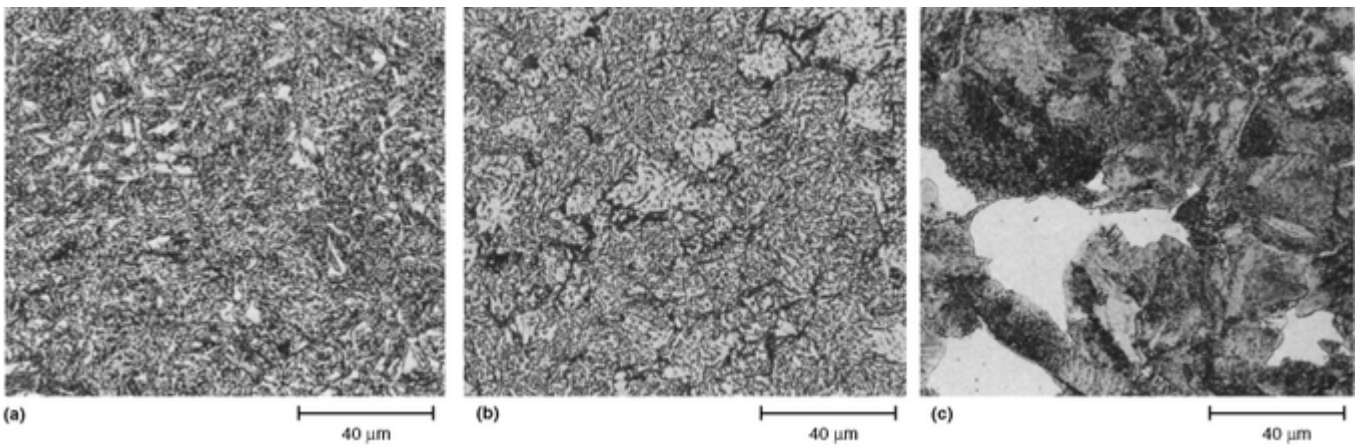

Fig. 72 AISI S7 continuous cooling transformations. Some very fine carbide is present in all specimens in this series. (a) Austenitized at 940 °C (1725 °F) and cooled at 445 °C/h (800 °F/h). 51.5 HRC. Structure is nearly all bainite with some small patches of martensite (white). (b) Cooled at 220 °C/h (400 °F/h). 45 HRC. Structure is mostly bainite with fine pearlite at the prior-austenite grain boundaries. (c) Cooled at 28 °C/h (50 °F/h) to 620 °C (1150 °F), then water quenched. Austenite present at 620 °C (1150 °F) was transformed to martensite. Structure is mostly fine pearlite with patches of martensite (white). See also Figure 71 4% picral. 500×

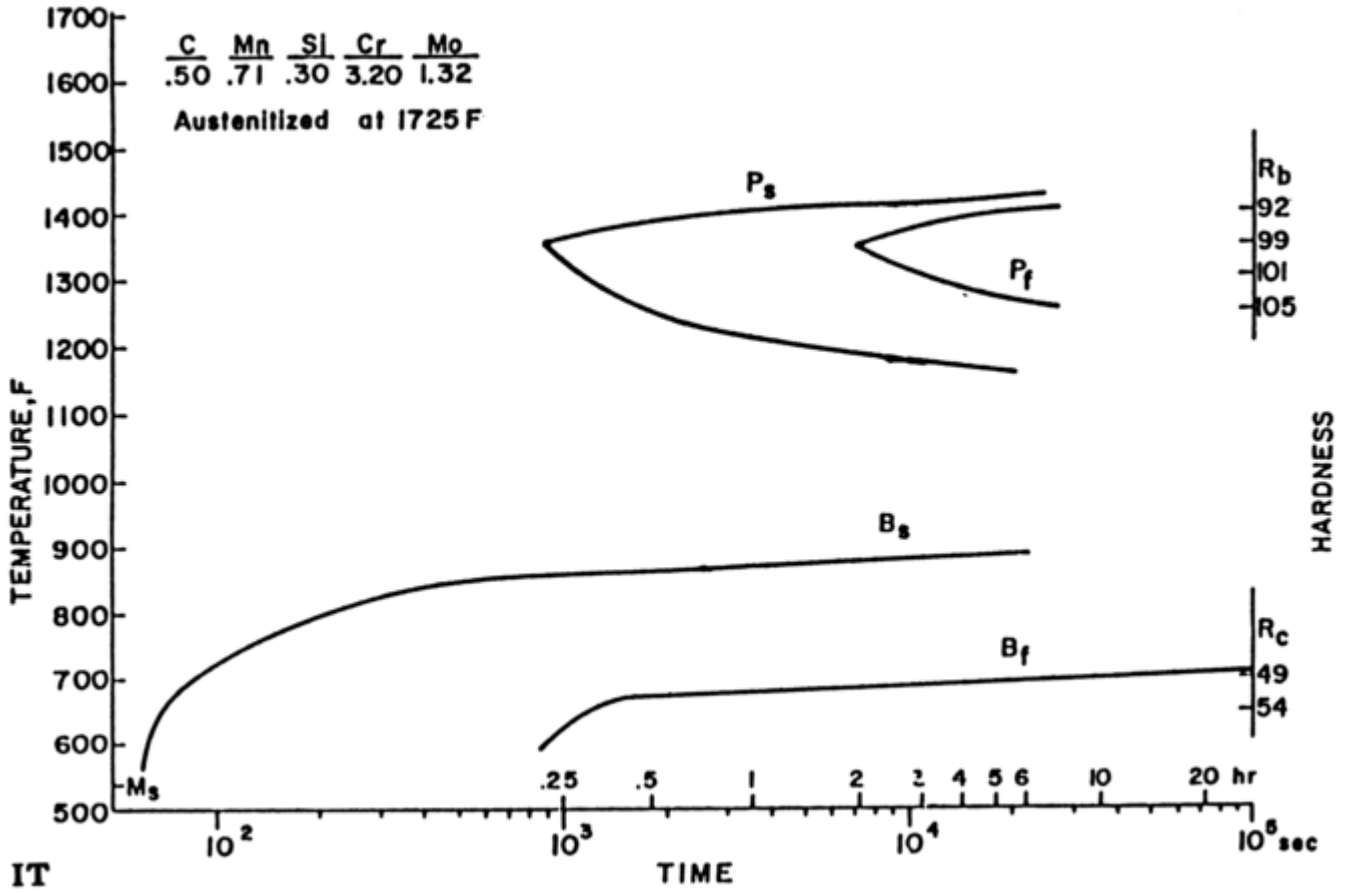

Fig. 73 Isothermal transformation diagram for AISI S7 tool steel. Composition: 0.50% C, 0.71% Mn, 0.30% Si, 3.20% Cr, and 1.32% Mo. Austenitized at 940 °C (1725 °F). M_s, martensite start; B_s bainite start; B_f, bainite finish; P_s, pearlite start; P_f, pearlite finish. Source: *Atlas of Time-Temperature Diagrams,* ASM International

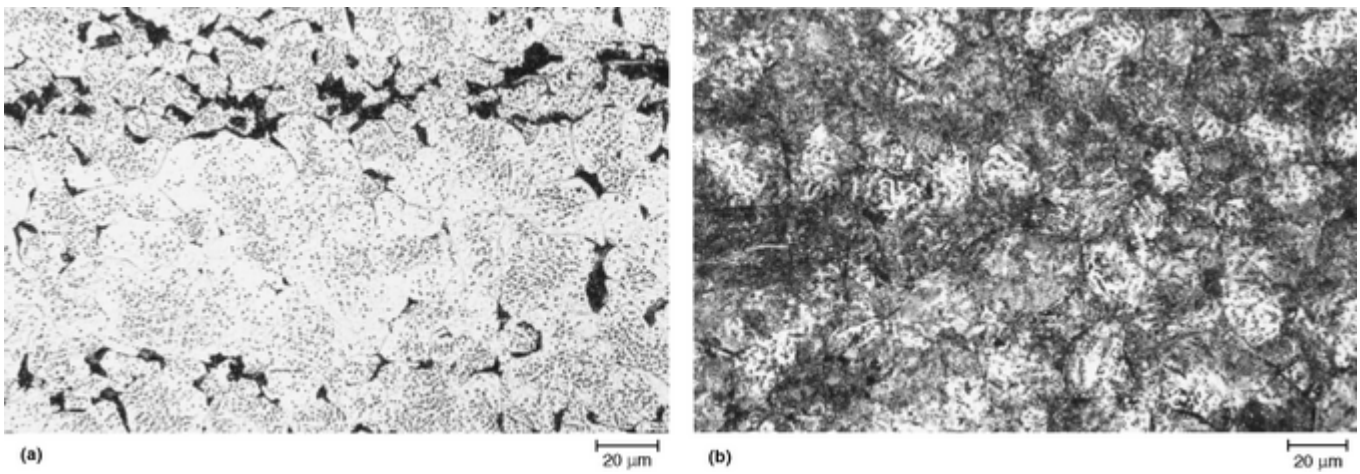

Fig. 74 Microstructure (picral etch, 500×) of AISI S7 tool steels with isothermal heat treatments. (a) Held at 704 °C (1300 °F) for 30 min (only a small amount of transformation before quenching). (b) Held at 704 °C (1300 °F) for 4 h (almost complete transformation to pearlite)

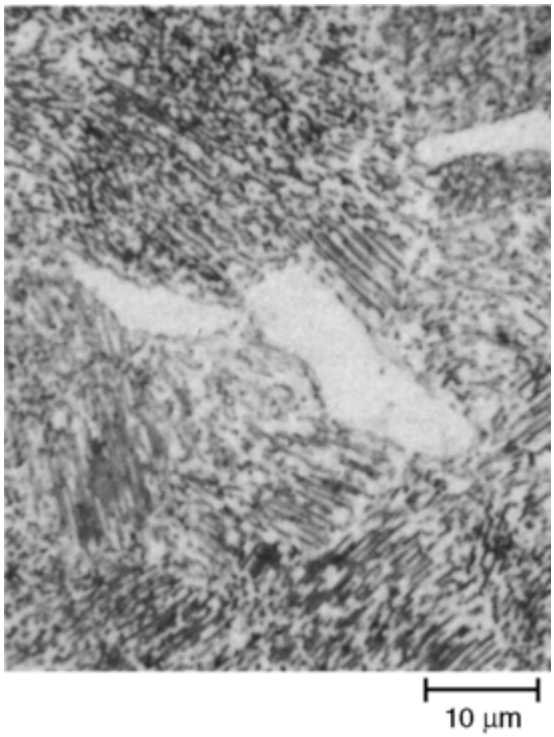

Fig. 75 AISI S5 austenitized and isothermally transformed at 650 °C (1200 °F) for 4 h (air cooled) to form ferrite and coarse pearlite. 23 to 24 HRC. 4% picral. 1000×

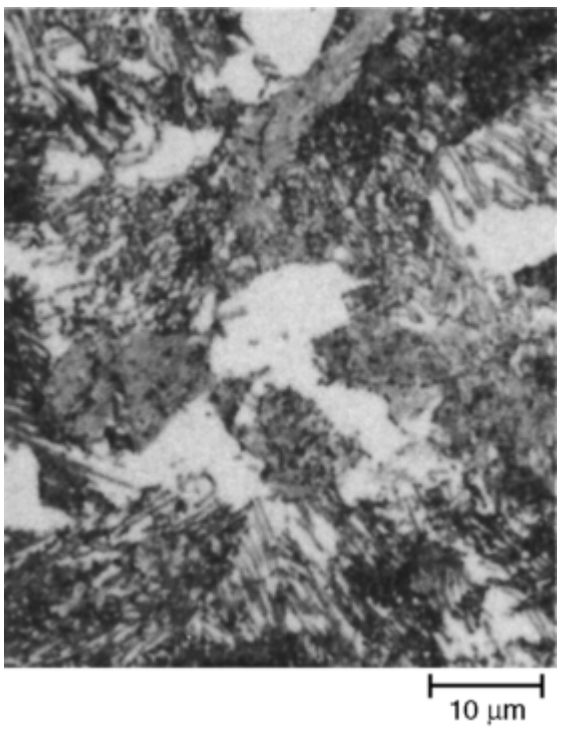

Fig. 76 AISI S5 austenitized, isothermally transformed at 595 °C (1100 °F) for 8 h, and air cooled to form ferrite and fine pearlite. 36 HRC. 4% picral. 1000×



Fig. 77 AISI S5 austenitized, isothermally transformed (partially) at 540 °C (1000 °F) for 8 h, and water quenched to form upper bainite (dark); balance of austenite formed martensite. 4% picral/2% nital. 1000×

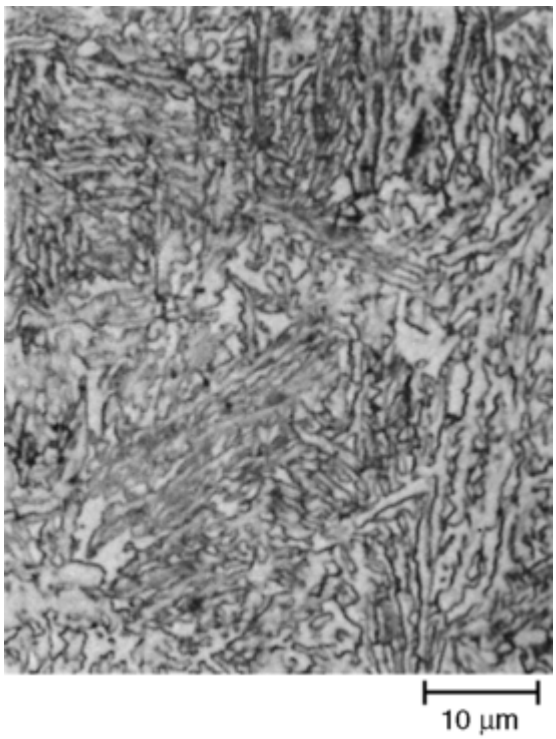

Fig. 78 AISI S5 austenitized, isothermally transformed at 400 °C (750 °F) for 1 h, and air cooled to form lower bainite. 37 to 38 HRC. 4% picral/2% nital. 1000×

Powder Metallurgy Products. Highly alloyed grades, such as the high-speed steels, are difficult to manufacture by ingot-making technology, because they are plagued by alloy and carbide segregation and poor ingot-to-finished product yields. Consequently, the powder metallurgy process now makes many of these grades routinely. Indeed, there are some grades that have been developed that can only be made by powder metallurgy, and these grades exhibit outstanding resistance to the high temperatures experienced by cutting tools. Figure 79, 80, 81, and 82 illustrate T15 high-speed steel made by powder metallurgy, showing the microstructure after hot

isostatic pressing, after it was spheroidize annealed, and after it was hardened. The carbides are fine and evenly distributed, without any apparent segregation.

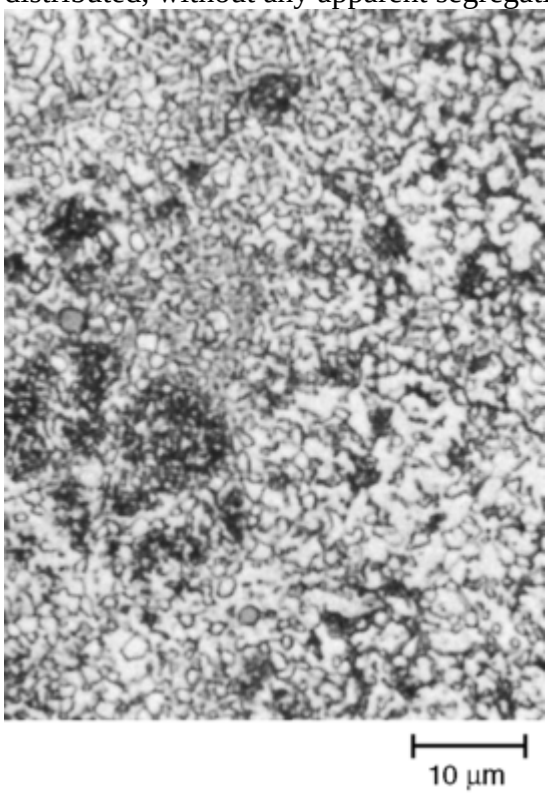

Fig. 79 AISI T15, powder-made. Sample was slow cooled after hot isostatic pressing. 28 HRC. Structure is partially annealed. 3% nital. 1000×

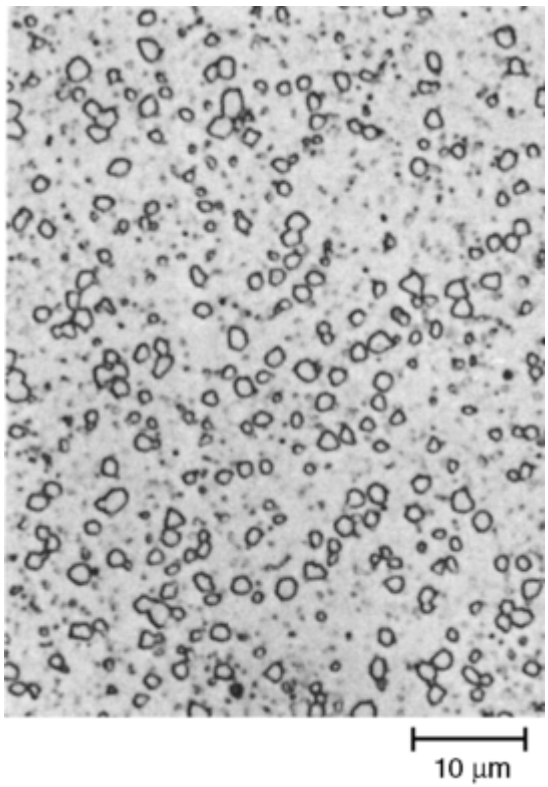

Fig. 80 AISI T15, powder-made. Sample was hot isostatically pressed, forged, and annealed. 24 HRC. Structure is fully annealed. 3% nital. 1000×

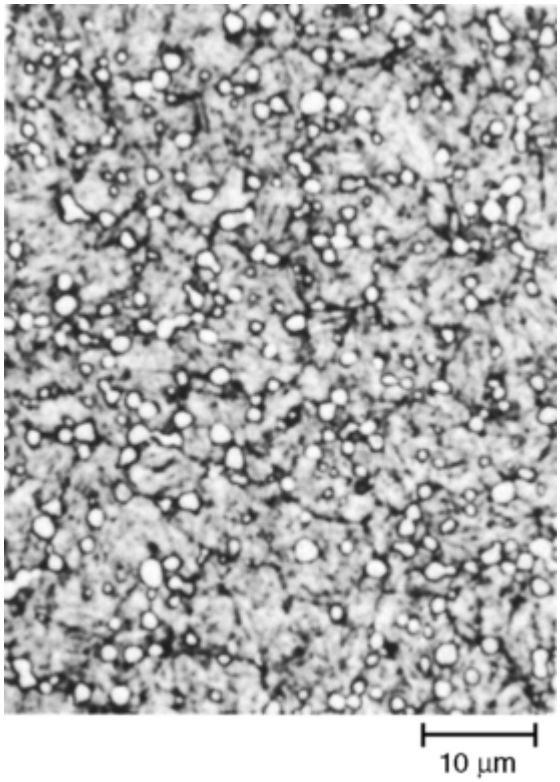

Fig. 81 AISI T15, powder-made. Processed as in Figure 80 then hardened; heated to 1230 °C (2250 °F) for 5 min in salt, oil quenched, triple tempered 2 h each at 540 °C (1000 °F). 65 HRC. 3% nital. 1000×

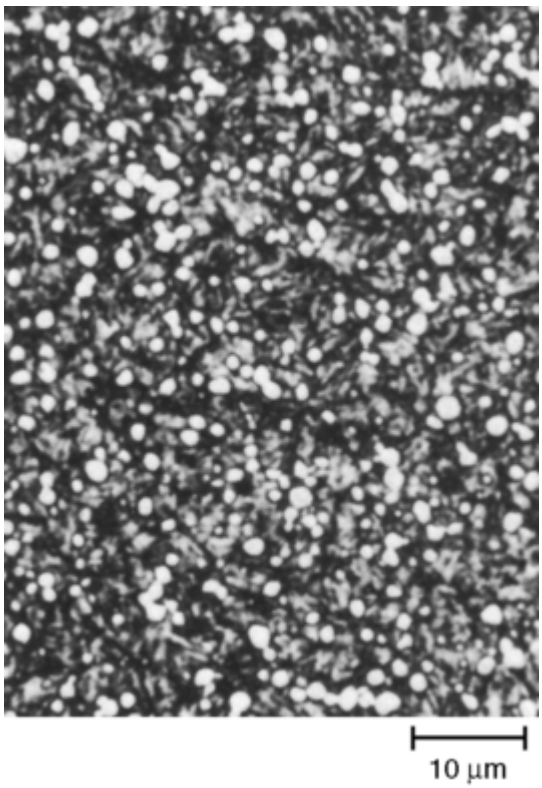

Fig. 82 AISI T15, powder-made. Same sample as in Figure 81 but etched in 100 mL H_2O, 1 mL HCl, 1 g $K_2S_2O_5$, and 1 g NH_4·HF. 1000×

Compositions for the tool steels illustrated in this article are listed in Table 5. Information on properties, tempers, designations, and applications of tool steels can be found in the articles “Wrought Tool Steels” and “P/M Tool Steels” in *Properties and Selection: Irons, Steels, and High-Performance Alloys,* Volume 1 of *ASM Handbook* (1990) and in Ref 11.

Table 5 Nominal compositions of illustrated tool steel grades

AISI type	Composition, %									
	C	**Mn[a]**	**Si[b]**	**Cr**	**Ni**	**V**	**W**	**Mo**	**Co**	**Ti**
W1	0.6–1.4	…	…	…	…	0.25	…	…	…	…
W2	0.6–1.4	…	…	…	…	…	…	…	…	…
S1	0.5	…	0.75	1.5	…	0.2[c]	2.5	…	…	…
S2	0.5	0.4	1.0	…	…	…	…	0.5	…	…
S4	0.55	0.8	2.0	…	…	…	…	…	…	…
S5	0.55	0.8	1.9	0.25[c]	…	0.2[c]	…	0.4	…	…
S7	0.5	0.7	…	3.25	…	…	…	1.40	…	…
O1	0.9	1.0	…	0.5	…	0.2[c]	0.5	…	…	…
O2	0.9	1.6	…	…	…	…	…	…	…	…
O6	1.45	0.8	1.1	…	…	…	…	0.25	…	…
A2	1.0	0.7	…	5.25	…	0.2[c]	…	1.1	…	…
A6	0.7	2.0	…	1.0	…	…	…	1.35	…	…
A7	2.00–2.85	0.8	0.5	5.0–5.75	0.3	3.9–5.15	0.5–1.5	0.90–1.40	…	…
A10	1.25–1.50	1.6–2.1	1.0–1.5	…	1.55–2.05	…	…	1.25–1.75	…	…
D2	1.5	0.5	…	12.0	…	0.2–0.9[c]	…	0.8	…	…
D3	2.1	…	…	12.0	0.5[c]	…	…	…	…	…
H11	0.35	…	0.9	5.0	…	0.4	…	1.5	…	…
H13	0.35	…	1.0	5.25	…	1.0	…	1.3	…	…
H21	0.35	…	…	3.5	…	0.4[c]	9.0	…	…	…
H23	0.25–0.35	0.15–0.40	0.15–0.60	11.0–12.75	0.3	0.75–1.25	11.0–12.75	…	…	…
H26	0.45–0.55	0.15–0.40	0.15–0.40	3.75–4.5	0.3	0.75–1.25	17.25–19.0	…	…	…
T1	0.7	…	…	4.0	…	1.0	18.0	…	…	…
T15	1.5	…	…	4.0	…	5.0	12.0	…	5.0	…
M1	0.8	…	…	4.0	…	1.1	1.5	8.5	…	…
M2	0.85	…	…	4.0	…	2.0	6.0	5.0	…	…
M4	1.3	…	…	4.5	…	4.0	5.5	4.5	…	…
M42	1.1	…	…	3.75	…	1.15	1.5	9.5	8.0	…
L1	1.0	…	…	1.4	…	…	…	…	…	…
L6	0.75	0.75	…	0.9	1.75	…	…	0.35	…	…
F2	1.25	0.75	…	…	…	…	0.35	…	…	…
P5	0.1	…	…	2.25	…	…	…	…	…	…
P20	0.35	…	…	1.25	…	…	…	0.4	…	…
AHT	1.0	…	…	3.0	…	0.25	1.05	1.1	…	1.0

(a) All tool steels contain some manganese, generally 0.2–0.4% when not listed.
(b) Tool steels usually contain 0.2–0.35% Si unless listed otherwise.
(c) Optional addition at discretion of manufacturer

References cited in this section

7. L.R. Woodyatt and G. Krauss, Iron-Chromium-Carbon System at 870 °C, *Metall. Trans. A,* Vol 7, 1976, p 983–989

8. S. Takeda, Metallographic Investigation of the Ternary Alloys of the Iron-Tungsten-Carbon System, *Tech. Rep. Sendai,* Vol 9, 1930, p 483; Vol 10, 1931, p 42

9. A. Hede and B. Aronsson, Microstructure and Creep Properties of Some 12% Chromium Martensitic Steels, *J. Iron Steel Inst.,* Vol 207, Sept 1969, p 124

10. H.W. Rayson, Tool Steels, *Constitution and Properties of Steels,* F.B. Pickering, Ed., VCH Publishing, 1992, p 581–640

11. G. Roberts, G. Krauss, and R. Kennedy, *Tool Steels,* 5th ed., ASM International, 1998

G.F. Vander Voort, Metallographic Techniques for Tool Steels, *Metallography and Microstructures,* Vol 9, *ASM Handbook,* ASM International, 2004, p. 644–669

Metallographic Techniques for Tool Steels

George F. Vander Voort, Buehler Ltd.

References

1. "Recommended Practice for Macroetch Testing of Tool Steel Bars," A 561, *Annual Book of ASTM Standards,* Vol 01.05, ASTM, 2003, p 335–341

2. "Macroetch Testing of Consumable Electrode Remelted Steel Bars and Billets," A 604, *Annual Book of ASTM Standards,* Vol 01.05, ASTM, 2003, p 371–384

3. "Standard Method of Macroetch Testing Steel Bars, Billets, Blooms and Forgings," E 381, *Annual Book of ASTM Standards,* Vol 03.01, ASTM, 1984, p 895–899

4. "Macrograph Standards for Steel Bars, Billets and Blooms," MIL-STD 430A, Department of Defense, 30 June 1966

5. G.F. Vander Voort, *Metallography: Principles and Practice,* McGraw-Hill, 1984; reprinted by ASM International, 1999

6. "Standard Practice for Preparing Sulfur Prints for Macrostructural Examination," E 1180, *Annual Book of ASTM Standards,* Vol 01.03, ASTM, 2003, p 787–789

7. L.R. Woodyatt and G. Krauss, Iron-Chromium-Carbon System at 870 °C, *Metall. Trans. A,* Vol 7, 1976, p 983–989

8. S. Takeda, Metallographic Investigation of the Ternary Alloys of the Iron-Tungsten-Carbon System, *Tech. Rep. Sendai,* Vol 9, 1930, p 483; Vol 10, 1931, p 42

9. A. Hede and B. Aronsson, Microstructure and Creep Properties of Some 12% Chromium Martensitic Steels, *J. Iron Steel Inst.,* Vol 207, Sept 1969, p 124

10. H.W. Rayson, Tool Steels, *Constitution and Properties of Steels,* F.B. Pickering, Ed., VCH Publishing, 1992, p 581–640

11. G. Roberts, G. Krauss, and R. Kennedy, *Tool Steels,* 5th ed., ASM International, 1998

G.F. Vander Voort, G.M. Lucas, and E.P. Manilova, Metallography and Microstructures of Stainless Steels and Maraging Steels, *Metallography and Microstructures,* Vol 9, *ASM Handbook,* ASM International, 2004, p. 670–700

Metallography and Microstructures of Stainless Steels and Maraging Steels

George F. Vander Voort and Gabriel M. Lucas, Buehler Ltd.; Elena P. Manilova, Polzunov Central Boiler and Turbine Institute, St. Petersburg, Russia

Introduction

STAINLESS STEELS are complex alloys containing a minimum of 11% Cr plus other elements to produce ferritic, martensitic, austenitic, duplex, or precipitation-hardenable grades. Procedures used to prepare stainless steels for macroscopic and microscopic examination are similar to those used for carbon, alloy, and tool steels. However, certain types require careful attention to prevent artifacts. Because the austenitic grades work harden readily, cutting and grinding must be carefully executed to minimize deformation. The high-hardness martensitic grades that contain substantial undissolved chromium carbide are difficult to polish while fully retaining the carbides. The most difficult to such grades to prepare is AISI 440C. For the most part, preparation of stainless steels is reasonably simple if the basic rules for metallographic preparation are followed. However, unlike carbon, alloy, and tool steels, etching techniques are more difficult due to the high corrosion resistance of stainless steels and the various second phases that may be encountered. Nominal compositions of standard wrought grades illustrated in this article are given in Table 1. Compositions of some nonstandard alloys mentioned in this article are given in Table 2. Nominal compositions of cast stainless steel, in accordance with designations of the Alloy Casting Institute, are given in Table 3 and 4 for corrosion-resistant and heat-resistant grades, respectively. Heat-resistant grades tend to have higher carbon contents for strengthening relative to corrosion-resistant grades of steel castings.

Table 1 Compositions of standard wrought stainless steels

Type	UNS designation	Composition[(a)], %							
		C	**Mn**	**Si**	**Cr**	**Ni**	**P**	**S**	**Other**
Austenitic types									
201	S20100	0.15	5.5–7.5	1.00	16.0–18.0	3.5–5.5	0.06	0.03	0.25 N
202	S20200	0.15	7.5–10.0	1.00	17.0–19.0	4.0–6.0	0.06	0.03	0.25 N
205	S20500	0.12–0.25	14.0–15.5	1.00	16.5–18.0	1.0–1.75	0.06	0.03	0.32–0.40 N
301	S30100	0.15	2.00	1.00	16.0–18.0	6.0–8.0	0.045	0.03	…
302	S30200	0.15	2.00	1.00	17.0–19.0	8.0–10.0	0.045	0.03	…
302B	S30215	0.15	2.00	2.0–3.0	17.0–19.0	8.0–10.0	0.045	0.03	…

303	S30300	0.15	2.00	1.00	17.0–19.0	8.0–10.0	0.20	0.15 min	0.6 Mo[(b)]
303Se	S30323	0.15	2.00	1.00	17.0–19.0	8.0–10.0	0.20	0.06	0.15 min Se
304	S30400	0.08	2.00	1.00	18.0–20.0	8.0–10.5	0.045	0.03	…
304H	S30409	0.04–0.10	2.00	1.00	18.0–20.0	8.0–10.5	0.045	0.03	…
304L	S30403	0.03	2.00	1.00	18.0–20.0	8.0–12.0	0.045	0.03	…
304LN	S30453	0.03	2.00	1.00	18.0–20.0	8.0–12.0	0.045	0.03	0.10–0.16 N
302Cu	S30430	0.08	2.00	1.00	17.0–19.0	8.0–10.0	0.045	0.03	3.0–4.0 Cu
304N	S30451	0.08	2.00	1.00	18.0–20.0	8.0–10.5	0.045	0.03	0.10–0.16 N
305	S30500	0.12	2.00	1.00	17.0–19.0	10.5–13.0	0.045	0.03	…
308	S30800	0.08	2.00	1.00	19.0–21.0	10.0–12.0	0.045	0.03	…
309	S30900	0.20	2.00	1.00	22.0–24.0	12.0–15.0	0.045	0.03	…
309S	S30908	0.08	2.00	1.00	22.0–24.0	12.0–15.0	0.045	0.03	…
310	S31000	0.25	2.00	1.50	24.0–26.0	19.0–22.0	0.045	0.03	…
310S	S31008	0.08	2.00	1.50	24.0–26.0	19.0–22.0	0.045	0.03	…
314	S31400	0.25	2.00	1.5–3.0	23.0–26.0	19.0–22.0	0.045	0.03	…
316	S31600	0.08	2.00	1.00	16.0–18.0	10.0–14.0	0.045	0.03	2.0–3.0 Mo
316F	S31620	0.08	2.00	1.00	16.0–18.0	10.0–14.0	0.20	0.10 min	1.75–2.5 Mo
316H	S31609	0.04–0.10	2.00	1.00	16.0–18.0	10.0–14.0	0.045	0.03	2.0–3.0 Mo
316L	S31603	0.03	2.00	1.00	16.0–18.0	10.0–14.0	0.045	0.03	2.0–3.0 Mo
316LN	S31653	0.03	2.00	1.00	16.0–18.0	10.0–14.0	0.045	0.03	2.0–3.0 Mo; 0.10–0.16 N
316N	S31651	0.08	2.00	1.00	16.0–18.0	10.0–14.0	0.045	0.03	2.0–3.0 Mo; 0.10–0.16 N
317	S31700	0.08	2.00	1.00	18.0–20.0	11.0–15.0	0.045	0.03	3.0–4.0 Mo
317L	S31703	0.03	2.00	1.00	18.0–20.0	11.0–15.0	0.045	0.03	3.0–4.0 Mo
321	S32100	0.08	2.00	1.00	17.0–19.0	9.0–12.0	0.045	0.03	5 × %C min Ti
321H	S32109	0.04–0.10	2.00	1.00	17.0–19.0	9.0–12.0	0.045	0.03	5 × %C min Ti
330	N08330	0.08	2.00	0.75–1.5	17.0–20.0	34.0–37.0	0.04	0.03	…
347	S34700	0.08	2.00	1.00	17.0–	9.0–	0.045	0.03	10 × %C min Nb

					19.0	13.0			
347H	S34709	0.04–0.10	2.00	1.00	17.0–19.0	9.0–13.0	0.045	0.03	8 × %C min–1.0 max Nb
348	S34800	0.08	2.00	1.00	17.0–19.0	9.0–13.0	0.045	0.03	0.2 Co; 10 × %C min Nb; 0.10 Ta
348H	S34809	0.04–0.10	2.00	1.00	17.0–19.0	9.0–13.0	0.045	0.03	0.2 Co; 8 × %C min–1.0 max Nb; 0.10 Ta
384	S38400	0.08	2.00	1.00	15.0–17.0	17.0–19.0	0.045	0.03	…
Ferritic types									
405	S40500	0.08	1.00	1.00	11.5–14.5	…	0.04	0.03	0.10–0.30 Al
409	S40900	0.08	1.00	1.00	10.5–11.75	0.50	0.045	0.045	6 × %C min–0.75 max Ti
429	S42900	0.12	1.00	1.00	14.0–16.0	…	0.04	0.03	…
430	S43000	0.12	1.00	1.00	16.0–18.0	…	0.04	0.03	…
430F	S43020	0.12	1.25	1.00	16.0–18.0	…	0.06	0.15 min	0.6 Mo[(b)]
430FSe	S43023	0.12	1.25	1.00	16.0–18.0	…	0.06	0.06	0.15 min Se
434	S43400	0.12	1.00	1.00	16.0–18.0	…	0.04	0.03	0.75–1.25 Mo
436	S43600	0.12	1.00	1.00	16.0–18.0	…	0.04	0.03	0.75–1.25 Mo; 5 × %C min–0.70 max Nb
439	S43035	0.07	1.00	1.00	17.0–19.0	0.50	0.04	0.03	0.15 Al; 12 × %C min–1.10 Ti
442	S44200	0.20	1.00	1.00	18.0–23.0	…	0.04	0.03	…
444	S44400	0.025	1.00	1.00	17.5–19.5	1.00	0.04	0.03	1.75–2.50 Mo; 0.025 N; 0.2 + 4 (%C + %N) min–0.8 max (Ti + Nb)
446	S44600	0.20	1.50	1.00	23.0–27.0	…	0.04	0.03	0.25 N
Duplex (ferritic-austenitic) type									
329	S32900	0.20	1.00	0.75	23.0–28.0	2.50–5.00	0.040	0.030	1.00–2.00 Mo
Martensitic types									
403	S40300	0.15	1.00	0.50	11.5–13.0	…	0.04	0.03	…
410	S41000	0.15	1.00	1.00	11.5–13.5	…	0.04	0.03	…
414	S41400	0.15	1.00	1.00	11.5–13.5	1.25–2.50	0.04	0.03	…
416	S41600	0.15	1.25	1.00	12.0–14.0	…	0.06	0.15 min	0.6 Mo[(b)]
416Se	S41623	0.15	1.25	1.00	12.0–14.0	…	0.06	0.06	0.15 min Se
420	S42000	0.15 min	1.00	1.00	12.0–14.0	…	0.04	0.03	…
420F	S42020	0.15	1.25	1.00	12.0–	…	0.06	0.15	0.6 Mo[(b)]

		min			14.0			min	
422	S42200	0.20–0.25	1.00	0.75	11.5–13.5	0.5–1.0	0.04	0.03	0.75–1.25 Mo; 0.75–1.25 W; 0.15–0.3 V
431	S43100	0.20	1.00	1.00	15.0–17.0	1.25–2.50	0.04	0.03	…
440A	S44002	0.60–0.75	1.00	1.00	16.0–18.0	…	0.04	0.03	0.75 Mo
440B	S44003	0.75–0.95	1.00	1.00	16.0–18.0	…	0.04	0.03	0.75 Mo
440C	S44004	0.95–1.20	1.00	1.00	16.0–18.0	…	0.04	0.03	0.75 Mo
Precipitation-hardening types									
PH 13-8 Mo	S13800	0.05	0.20	0.10	12.25–13.25	7.5–8.5	0.01	0.008	2.0–2.5 Mo; 0.90–1.35 Al; 0.01 N
15-5 PH	S15500	0.07	1.00	1.00	14.0–15.5	3.5–5.5	0.04	0.03	2.5–4.5 Cu; 0.15–0.45 Nb
17-4 PH	S17400	0.07	1.00	1.00	15.5–17.5	3.0–5.0	0.04	0.03	3.0–5.0 Cu; 0.15–0.45 Nb
17-7 PH	S17700	0.09	1.00	1.00	16.0–18.0	6.5–7.75	0.04	0.04	0.75–1.5 Al

(a) Single values are maximum values unless otherwise indicated.
(b) Optional

Table 2 Compositions of nonstandard wrought stainless steels

Grade	UNS No.	Composition, wt%								
		C	**Mn**	**Si**	**Cr**	**Ni**	**Mo**	**Cu**	**N**	**Other**
Austenitic types										
Nitronic 50[(a)]	…	<0.06	5.0	…	22	13	2.25	…	0.3	0.2 Nb, 0.2 V
20 Mo-6 HS	NO8036	<0.06	<1.0	…	24	35	5.75	2	0.3	…
AL-6XN	NO8067	<0.03	<2	<1	21	24.5	6.5	<0.75	0.2	…
SCF-23	…	0.02	4.25	0.45	22.75	17.75	5.5	…	0.4	…
NeutraSorb PLUS	…	<0.08	<2	<0.75	19	13.5	…	…	<0.1	≤2.25 B
18-18 PLUS	…	<0.15	18	<1	18	…	1	1	0.5	…
Ferritic types										
Monit	44635	<0.025	<1	<0.75	25	4	4	…	<0.035	Nb + Ta = 0.2 + 4(C + N)
Seacure	44660	<0.025	0.5	…	27.5	1.2	3.5	…	0.025	0.5 Ti
Martensitic types										
EP 428	…	0.2	0.6	<0.4	11.5	0.65	0.6	…	…	0.9 W, 0.22 V
Trimrite	S42012	0.02	…	…	14.25	0.6	0.7	…	…	…
5F[(b)]	S41600	<0.1	…	…	13.25	…	…	…	…	>0.3 S
Maraging types										
Vascomax T-250 (cobalt-free grade)	…	<0.03	<0.1	<0.1	…	18.5	3	…	…	0.1 Al, 1.4 Ti

(a) Trade name for 22-13-5 (generic name).
(b) Modified 416

Table 3 Compositions and typical microstructures of Alloy Casting Institute (ACI) corrosion-resistant cast stainless steels

ACI type	Wrought alloy type[a]	ASTM specifications	Most common end-use microstructure	Composition[b], %					
				C	**Mn**	**Si**	**Cr**	**Ni**	**Others[c]**
Chromium steels									
CA-15	410	A 743, A 217, A 487	Martensite	0.15	1.00	1.50	11.5–14.0	1.0	0.50 Mo[d]
CA-15M	…	A 743	Martensite	0.15	1.00	0.65	11.5–14.0	1.0	0.15–1.00 Mo
CA-40	420	A 743	Martensite	0.40	1.00	1.50	11.5–14.0	1.0	0.5 Mo[d]
CA-40F	…	A 743	Martensite	0.2–0.4	1.00	1.50	11.5–14.0	1.0	…
CB-30	431, 442	A 743	Ferrite and carbides	0.30	1.00	1.50	18.0–22.0	2.0	…
CC-50	446	A 743	Ferrite and carbides	0.30	1.00	1.50	26.0–30.0	4.0	…
Chromium-nickel steels									
CA-6N	…	A 743	Martensite	0.06	0.50	1.00	10.5–12.5	6.0–8.0	…
CA-6NM	…	A 743, A 487	Martensite	0.06	1.00	1.00	11.5–14.0	3.5–4.5	0.4–1.0 Mo
CA-28MWV	…	A 743	Martensite	0.20–0.28	0.50–1.00	1.00	11.0–12.5	0.50–1.00	0.9–1.25 Mo; 0.9–1.25 W; 0.2–0.3 V
CB-7Cu-1	…	A 747	Martensite, age hardenable	0.07	0.70	1.00	15.5–17.7	3.6–4.6	2.5–3.2 Cu; 0.20–0.35 Nb; 0.05 N max
CB-7Cu-2	…	A 747	Martensite, age hardenable	0.07	0.70	1.00	14.0–15.5	4.5–5.5	2.5–3.2 Cu; 0.20–0.35 Nb; 0.05 N max
CD-4MCu	…	A 351, A 743, A 744, A 890	Austenite in ferrite, age hardenable	0.04	1.00	1.00	25.0–26.5	4.75–6.0	1.75–2.25 Mo; 2.75–3.25 Cu
CE-30	312	A 743	Ferrite in austenite	0.30	1.50	2.00	26.0–30.0	8.0–11.0	…
CF-3[e]	304L	A 351, A 743, A 744	Ferrite in austenite	0.03	1.50	2.00	17.0–21.0	8.0–12.0	…
CF-3M[e]	316L	A 351, A 743, A 744	Ferrite in austenite	0.03	1.50	2.00	17.0–21.0	8.0–12.0	2.0–3.0 Mo
CF-3MN	…	A 743	Ferrite in austenite	0.03	1.50	1.50	17.0–21.0	9.0–13.0	2.0–3.0 Mo; 0.10–0.20 N
CF-8[e]	304	A 351, A 743, A 744	Ferrite in austenite	0.08	1.50	2.00	18.0–21.0	8.0–11.0	…
CF-8C	347	A 351, A 743, A 744	Ferrite in austenite	0.08	1.50	2.00	18.0–21.0	9.0–12.0	Nb[f]
CF-8M	316	A 351, A 743, A 744	Ferrite in austenite	0.08	1.50	2.00	18.0–21.0	9.0–12.0	2.0–3.0 Mo
CF-10	…	A 351	Ferrite in austenite	0.04–0.10	1.50	2.00	18.0–21.0	8.0–11.0	…

CF-10M	…	A 351	Ferrite in austenite		0.04–0.10	1.50	1.50	18.0–21.0	9.0–12.0	2.0–3.0 Mo
CF-10MC	…	A 351	Ferrite in austenite		0.10	1.50	1.50	15.0–18.0	13.0–16.0	1.75–2.25 Mo
CF-10SMnN	…	A 351, A 743	Ferrite in austenite		0.10	7.00–9.00	3.50–4.50	16.0–18.0	8.0–9.0	0.08–0.18 N
CF-12M	316	…	Ferrite austenite austenite	in or	0.12	1.50	2.00	18.0–21.0	9.0–12.0	2.0–3.0 Mo
CF-16F	303	A 743	Austenite		0.16	1.50	2.00	18.0–21.0	9.0–12.0	1.50 Mo max; 0.20–0.35 Se
CF-20	302	A 743	Austenite		0.20	1.50	2.00	18.0–21.0	8.0–11.0	…
CG-6MMN	…	A 351, A 743	Ferrite in austenite		0.06	4.00–6.00	1.00	20.5–23.5	11.5–13.5	1.50–3.00 Mo; 0.10–0.30 Nb; 0.10–30 V; 0.20–40 N
CG-8M	317	A 351, A 743, A 744	Ferrite in austenite		0.08	1.50	1.50	18.0–21.0	9.0–13.0	3.0–4.0 Mo
CG-12	…	A 743	Ferrite in austenite		0.12	1.50	2.00	20.0–23.0	10.0–13.0	…
CH-8	…	A 351	Ferrite in austenite		0.08	1.50	1.50	22.0–26.0	12.0–15.0	…
CH-10	…	A 351	Ferrite in austenite		0.04–0.10	1.50	2.00	22.0–26.0	12.0–15.0	…
CH-20	309	A 351, A 743	Austenite		0.20	1.50	2.00	22.0–26.0	12.0–15.0	…
CK-3MCuN	…	A 351, A 743, A 744	Ferrite in austenite		0.025	1.20	1.00	19.5–20.5	17.5–19.5	6.0–7.0 V; 0.18–0.24 N; 0.50–1.00 Cu
CK-20	310	A 743	Austenite		0.20	2.00	2.00	23.0–27.0	19.0–22.0	…
Nickel-chromium steel										
CN-3M	…	A 743	Austenite		0.03	2.00	1.00	20.0–22.0	23.0–27.0	4.5–5.5 Mo
CN-7M	…	A 351, A 743, A 744	Austenite		0.07	1.50	1.50	19.0–22.0	27.5–30.5	2.0–3.0 Mo; 3.0–4.0 Cu
CN-7MS	…	A 743, A 744	Austenite		0.07	1.50	3.50[g]	18.0–20.0	22.0–25.0	2.5–3.0 Mo; 1.5–2.0 Cu
CT-15C	…	A 351	Austenite		0.05–0.15	0.15–1.50	0.50–1.50	19.0–21.0	31.0–34.0	0.5–1.5 V

(a) Type numbers of wrought alloys are listed only for nominal identification of corresponding wrought and cast grades. Composition ranges of cast alloys are not the same as for corresponding wrought alloys; cast alloy designations should be used for castings only.

(b) Maximum unless a range is given. The balance of all compositions is iron.

(c) Sulfur content is 0.04% in all grades except: CG-6MMN, 0.030% S (max); CF-10SMnN, 0.03% S (max); CT-15C, 0.03% S (max); CK-3MCuN, 0.010% S (max); CN-3M, 0.030% S (max), CA-6N, 0.020% S (max); CA-28MWV, 0.030% S (max); CA-40F, 0.20–0.40% S; CB-7Cu-1 and -2, 0.03% S (max). Phosphorus content

is 0.04% (max) in all grades except: CF-16F, 0.17% P (max); CF-10SMnN, 0.060% P (max); CT-15C, 0.030% P (max); CK-3MCuN, 0.045% P (max); CN-3M, 0.030% P (max); CA-6N, 0.020% P (max); CA-28MWV, 0.030% P (max); CB-7Cu-1 and -2, 0.035% P (max).
(d) Molybdenum not intentionally added.
(e) CF-3A, CF-3MA, and CF-8A have the same composition ranges as CF-3, CF-3M, and CF-8, respectively, but have balanced compositions so that ferrite contents are at levels that permit higher mechanical property specifications than those for related grades. They are covered by ASTM A 351.
(f) (f) Nb, 8 × %C min (1.0% max); or Nb + Ta × %C (1.1% max).
(g) For CN-7MS, silicon ranges from 2.50 to 3.50%.

Table 4 Compositions of Alloy Casting Institute (ACI) heat-resistant casting alloys

ACI designation	UNS number	ASTM specifications[a]	Composition[b], %			
			C	**Cr**	**Ni**	**Si (max)**
HA	…	A 217	0.20 max	8–10	…	1.00
HC	J92605	A 297, A 608	0.50 max	26–30	4 max	2.00
HD	J93005	A 297, A 608	0.50 max	26–30	4–7	2.00
HE	J93403	A 297, A 608	0.20–0.50	26–30	8–11	2.00
HF	J92603	A 297, A 608	0.20–0.40	19–23	9–12	2.00
HH	J93503	A 297, A 608, A 447	0.20–0.50	24–28	11–14	2.00
HI	J94003	A 297, A 567, A 608	0.20–0.50	26–30	14–18	2.00
HK	J94224	A 297, A 351, A 567, A 608	0.20–0.60	24–28	18–22	2.00
HK30	…	A 351	0.25–0.35	23.0–27.0	19.0–22.0	1.75
HK40	…	A 351	0.35–0.45	23.0–27.0	19.0–22.0	1.75
HL	J94604	A 297, A 608	0.20–0.60	28–32	18–22	2.00
HN	J94213	A 297, A 608	0.20–0.50	19–23	23–27	2.00
HP	…	A 297	0.35–0.75	24–28	33–37	2.00
HP-50WZ[c]	…	…	0.45–0.55	24–28	33–37	2.50
HT	J94605	A 297, A 351, A 567, A 608	0.35–0.75	13–17	33–37	2.50
HT30	…	A 351	0.25–0.35	13.0–17.0	33.0–37.0	2.50
HU	…	A 297, A 608	0.35–0.75	17–21	37–41	2.50
HW	…	A 297, A 608	0.35–0.75	10–14	58–62	2.50
HX	…	A 297, A 608	0.35–0.75	15–19	64–68	2.50

(a) ASTM designations are the same as ACI designations.
(b) Bal Fe in all compositions. Manganese content: 0.35 to 0.65% for HA, 1% for HC, 1.5% for HD, and 2% for the other alloys. Phosphorus and sulfur contents: 0.04% (max) for all but HP-50WZ. Molybdenum is intentionally added only to HA, which has 0.90 to 1.20% Mo; maximum for other alloys is set at 0.5% Mo. HH also contains 0.2% N (max).
(c) Also contains 4 to 6% W, 0.1 to 1.0% Zr, and 0.035% S (max) and P (max)

G.F. Vander Voort, G.M. Lucas, and E.P. Manilova, Metallography and Microstructures of Stainless Steels and Maraging Steels, *Metallography and Microstructures,* Vol 9, *ASM Handbook,* ASM International, 2004, p. 670–700

Metallography and Microstructures of Stainless Steels and Maraging Steels

George F. Vander Voort and Gabriel M. Lucas, Buehler Ltd.; Elena P. Manilova, Polzunov Central Boiler and Turbine Institute, St. Petersburg, Russia

Macroexamination

The procedures used to select and prepare stainless steel disks for macroetching are identical to those used for carbon, alloy, and tool steels. Because these grades are more difficult to etch, however, all surfaces to be etched must be smooth ground or polished. Saw-cut surfaces will yield little useful information if they are macroetched.

Macroetchants for stainless steels are listed in Table 5. Heated macroetchants are used with stainless steels in the same manner as carbon, alloy, or tool steels. Etchant compositions are often more complex and more aggressive. In the study of weld macrostructures, it is quite common to polish the section and use one of the general-purpose microetchants.

Table 5 Macroetchants for stainless steels

Etchant	Comments
1. 50 mL HCl, 10 g $CuSO_4$ (copper sulfate), 50 mL H_2O[(a)]	Marble's reagent. General-purpose macroetch; can be heated
2. 50 mL HCl, 50 mL H_2O, 20 mL 30% H_2O_2	Mix HCl and H_2O, heat to 70–75 °C (160–170 °F). Immerse specimen and add H_2O_2 in steps when foaming stops; do not mix
3. [(a)] 15 g $(NH_4)_2S_2O_8$ (ammonium persulfate) and 75 mL H_2O **(b) 250 g $FeCl_3$ and 100 mL H_2O** **(c) 30 mL HNO_3**	Lepito's No. 1 etch. Combine [(a)] and (b), then add (c); immerse specimen at room temperature; use fresh
4. 1 part HCl and 1 part H_2O	Standard hot etch. Use at 70–80 °C (160–180 °F), 15–45 min; desmut by dipping in warm 20% aqueous HNO_3 solution to produce a bright surface
5. 10–40 mL HNO_3, 3–10 mL 48% HF, 25–50 mL H_2O	Use at 70–80 °C (160–180 °F); immerse until the desired degree of contrast is obtained
6. 50 mL HCl and 25 mL saturated $CuSO_4$ in H_2O	Use at 75 °C (170 °F); immerse until the desired degree of contrast is obtained

(a) When water is specified, use distilled water.

The standard sulfur print technique (Ref 1) can be used to reveal the distribution of manganese sulfide (MnS) inclusions in stainless steels. However, if the manganese content of the grade is low, chromium will substitute for manganese in the sulfides, and the sulfur print intensity will decrease. As the manganese content decreases below approximately 0.60%, chromium substitutes for manganese. At manganese contents below approximately 0.20%, pure chromium sulfides will form. These produce no image in the sulfur print test.

Reference cited in this section

1. G.F. Vander Voort, *Metallography: Principles and Practice,* McGraw-Hill, 1984. Reprinted by ASM International, 1999

G.F. Vander Voort, G.M. Lucas, and E.P. Manilova, Metallography and Microstructures of Stainless Steels and Maraging Steels, *Metallography and Microstructures,* Vol 9, *ASM Handbook,* ASM International, 2004, p. 670–700

Metallography and Microstructures of Stainless Steels and Maraging Steels

George F. Vander Voort and Gabriel M. Lucas, Buehler Ltd.; Elena P. Manilova, Polzunov Central Boiler and Turbine Institute, St. Petersburg, Russia

Microexamination

Sectioning techniques for stainless steels are identical to those used for carbon, alloy, or tool steels. Grades softer than approximately 35 HRC can be cut using a band saw or power hacksaw. However, such cutting produces substantial deformation and should be avoided, especially for the deformation-sensitive austenitic grades. Deformation will be greatly reduced if cutting is performed using abrasive cutoff wheels with the proper degree of bonding. Shearing can be used with the ferritic grades but should be avoided with the austenitic grades. Shearing does produce substantial damage, and the plane-of-polish may be within this layer at the end of the preparation cycle. If this happens, the true microstructure will not be observed. Metallographic preparation is more successful, and easier, if an abrasive cutoff wheel designed for metallographic work with stainless steels is used. Figure 1 illustrates the damage that results when an austenitic stainless steel is sectioned using different procedures. Figure 2 shows sectioning damage in a 26Cr-1Mo ferritic stainless steel.

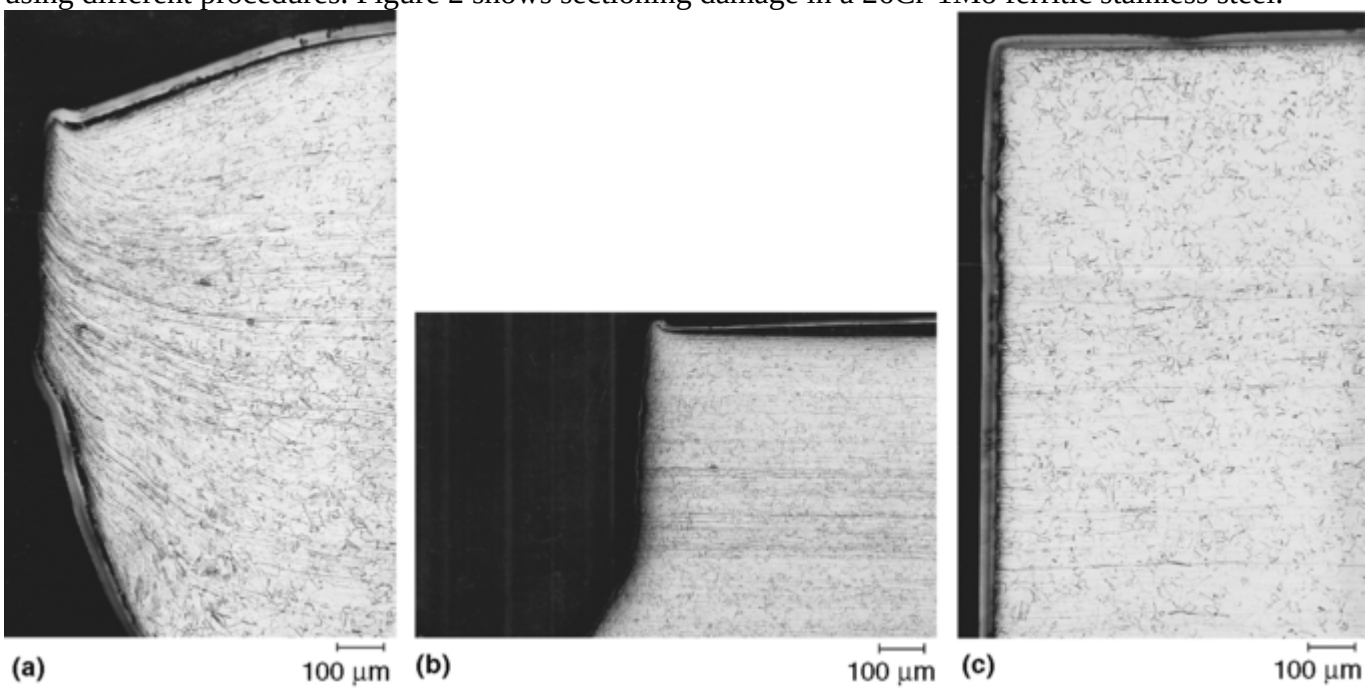

Fig. 1 Damage produced in sectioning austenitic 304 stainless steel using (a) metal shear, (b) band saw, and (c) abrasive cutoff saw. Glyceregia etch (electroless nickel plating used for the sheared and abrasive cutoff specimens)

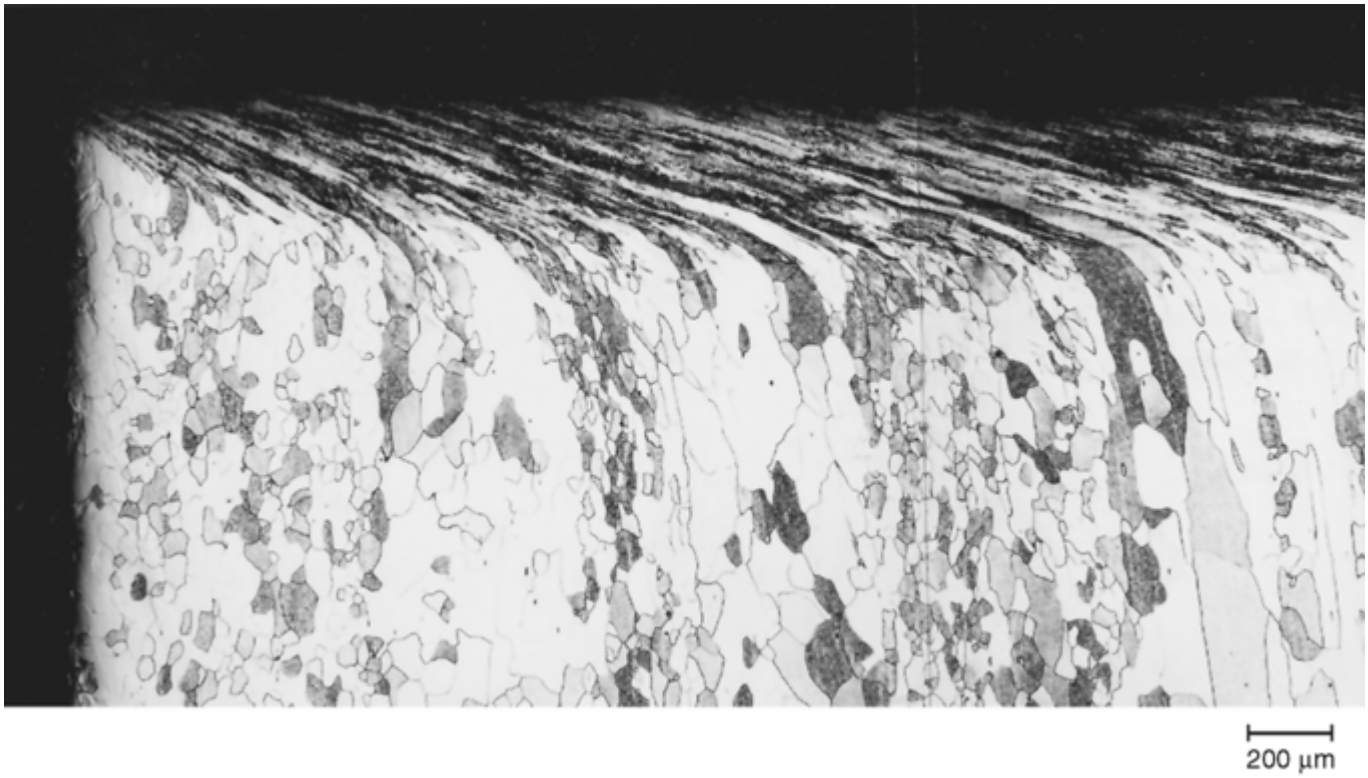

Fig. 2 Damage produced when 26Cr-1Mo ferritic stainless steel was cut with a band saw. Acetic glyceregia etch

Mounting procedures, when required, are also identical to those used for carbon, alloy, and tool steels. If edge preservation is required for near-surface examination, compression-mounting epoxy can be used, or specimens can be plated with electroless nickel. For specimens with surface cracks, it may be useful to vacuum impregnate the specimen in cold-setting epoxy; epoxy will be drawn into the cracks, minimizing bleed-out problems after etching.

Grinding has traditionally been performed using 120-, 240-, 320-, 400-, then 600-grit (P120-, P280-, P400-, P600-, and P1200-grit) water-cooled silicon carbide (SiC) papers. Care must be taken, particularly when grinding austenitic grades, to remove the cold work from cutting and from each grinding step. In general, speeds of 240 to 300 rpm and moderate, firm pressure are used. Grinding times are 1 to 2 min per step. If grinding is carried out by hand, the specimen should be rotated 45 to 90° between each step. Automatic grinding devices produce omnidirectional grinding patterns.

Polishing. After grinding, in the traditional method, specimens were usually rough polished using 6 or 3 μm diamond as a paste, spray, or slurry on napless, low-nap, or medium-nap cloths. Edge flatness and inclusion retention are improved by using napless cloths, although scratch removal may not be as complete as with medium-nap cloths. A lubricant extender compatible with the diamond abrasive should be used to moisten the cloth and reduce drag. A wheel speed of 120 to 150 rpm is usually adequate. Pressure should be moderate and firm; specimen rocking should be avoided if polishing is carried out by hand.

For hand polishing, rotate the specimen around the wheel in the direction opposite to the wheel rotation direction (contra rotation) while moving from center to edge. Automatic devices produce better edge flatness than hand polishing. After this step, the specimen may be polished using 1 μm diamond abrasive on a medium-nap cloth. For routine examination, a 1 μm diamond finish may be adequate, particularly for the hardened grades.

To produce high-quality, scratch-free surfaces suitable for photomicroscopy, specimens should be final polished using one or more fine abrasives. The most commonly used final abrasives are 0.3 μm α-alumina (Al_2O_3) or 0.05 μm γ-Al_2O_3. Medium-nap cloths are usually used. Polishing with these abrasives, mixed as a water slurry, is performed in the same manner as diamond polishing. Specimens should be carefully cleaned between each rough and final polishing step to avoid contamination at the next step. Colloidal silica is a highly suitable final abrasive for stainless steels. However, its use is more complicated, because cleaning is more difficult. Also, if colloidal silica is used, and the etchant contains Cl^- ions, such as Vilella's reagent or

glyceregia, an unusual etch reaction often occurs as soon as the etch touches the specimen surface. Examination reveals a heavy scratch pattern that can only be removed by going back to SiC paper. This problem has been called flashing and is illustrated in Fig. 3. Consequently, many metallographers avoid using colloidal silica. Electrolytic reagents do not flash, even if colloidal silica is used. The alumina powders and suspensions do exhibit agglomeration of particles, even in the deagglomerated grades (better, but still has agglomerates). Sol-gel processed alumina suspensions are free from this problem and produce excellent polished surfaces without staining or flashing problems.

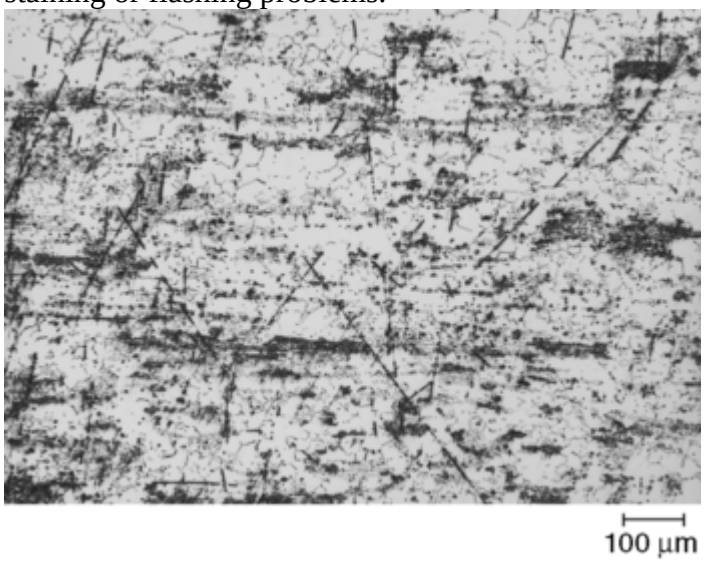

Fig. 3 Example of flashing when a stainless steel (duplex stainless steel in this case), polished with colloidal silica, is etched with a reagent containing chlorine ions. Glyceregia etch

Modern preparation procedures use only one grinding step and fewer overall steps. Further, they employ napless surfaces in all but the final step. This yields more efficient procedures, better edge retention, better flatness and relief control, and fewer artifact problems. Table 6 lists a contemporary procedure excellent for all stainless steels and maraging steels. Some substitution can be made at each step, depending on personal preference.

Table 6 Contemporary procedure for preparing stainless steels and maraging alloys

Step	Surface	Abrasive/size	Load per specimen		Base speed, rpm Direction	Time, min
			N	**lbf**		
1.	Waterproof abrasive paper	120–320 grit (P120–P400), water cooled	27	6	240–300 Complementary	Until planar
2.	Silk	9 μm diamond with lubricant	27	6	120–150 Complementary or contra	5
3.	Silk, polyester, or synthetic chemotextile	3 μm diamond with lubricant	27	6	120–150 Complementary or contra	4
4.	Silk, polyester, or synthetic chemotextile	1 μm diamond with lubricant	27	6	120–150 Complementary or contra	3
5.	Medium-nap synthetic rayon or polyurethane	0.05 μm sol-gel alumina suspension	27	6	100–150	1–3

	Complementary or contra

Notes: 1) Step 4 is optional and is used for the more difficult grades and heat treatment conditions. 2) Use a sectioning technique that produces minimal damage. Then, choose the finest possible SiC grit size that will remove this damage in a short time. Surfaces cut with band saws and power hacksaws, or that are sheared, will exhibit substantial damage depths that must be removed. 3) Use pressure-sensitive adhesive-backed surfaces for best results, especially when using automated equipment. 4) In step 1, do not use one sheet of SiC paper longer than 60 s when preparing several specimens in a holder. Use more than one sheet, if needed. Other types of abrasive surfaces with a similar abrasive particle size may be substituted but should be evaluated to be sure that they do not produce excessive damage. 5) Complementary rotation means that the head and platen both rotate in the same (counterclockwise) direction. Contra means that the head rotates clockwise, opposite the platen direction, which is slightly more aggressive. If the head speed is <100 rpm, one can use contra, and liquid abrasives will stay on the polishing surface longer. If the head speed is >100 rpm, the abrasive will be splattered all over the operator and the walls. Contra rotation in step 5 may cause excessive relief around MnS particles. If that happens, repeat step 5 using complementary rotation. 6) Colloidal silica can lead to the flashing problem, as described in text, when using etchings containing chlorine ions. 7) In step 5, when polyurethane is used, increase the load to 31 or 36 N (7 or 8 lbf). 8) When using diamond abrasive, charge the cloth with paste and press the paste into the cloth surface. Then, add the appropriate lubricant. During the cycle, add diamond of the same size in slurry form to maintain a high cutting rate.

Stainless steels, particularly the austenitic grades, are often polished electrolytically. In most cases, electropolishing is performed after grinding to a 600-grit silicon carbide finish. Table 7 lists recommended procedures. Electropolishing usually produces high-quality, deformation-free surfaces; however, inclusion attack is encountered, and second phases, cracks, and edges may be attacked preferentially.

Table 7 Electropolishing procedures for stainless steels

Electrolyte composition	Comments
1. 50 mL $HClO_4$ (perchloric acid), 750 mL ethanol, 140 mL H_2O[(a)]	Add $HClO_4$ last, with care. Use at 8–20 V dc, 0.3–1.3 A/cm^2 (1.9–8.4 A/in.^{2}), 20 °C (70 °F), 20–60 s. Rinse immediately after polishing
2. 78 mL $HClO_4$, 90 mL H_2O, 730 mL ethanol, 100 mL butyl cellusolve	Add $HClO_4$ last, with care. Use at 0.5–1.5 A/cm^2 (3.2–9.7 A/in.^{2}), 20 °C (70 °F) max
3. 62 mL $HClO_4$, 700 mL ethanol, 100 mL butyl cellusolve, 137 mL H_2O	Add $HClO_4$ last, with care. Use at 1.2 A/cm^2 (7.7 A/in.^{2}), 20 °C (70 °F), 20–25 s
4. 25 g CrO_3, 133 mL acetic acid, 7 mL H_2O	Use at 20 V dc, 0.09–0.22 A/cm^2 (0.58–1.4 A/in.^{2}), 17–19 °C (63–66 °F), 6 min. Dissolve CrO_3 in solution heated to 60–70 °C (140–160 °F)
5. 37 mL H_3PO_4, 56 mL glycerol, 7 mL H_2O	Use at 0.78 A/cm^2 (5.0 A/in.^{2}), 100–120 °C (210–250 °F), 5–10 min
6. 6 mL $HClO_4$ and 94 mL ethanol	Use at 35–40 V dc, 24 °C (75 °F), 15–60 s

(a) When water is specified, use distilled water.

Etching. For inclusion examination, etching is not required, although it is necessary for examining the microstructure. Figure 4, 5, 6, 7 illustrate sulfide inclusions in several common stainless steels designed for improved machinability. Although the stainless steels are reasonably easy to polish, etching is generally a more difficult step. The corrosion resistance of stainless steels and the potential microstructural complexity of these alloys make selection of the best etchant a more difficult problem than for carbon and alloy steels. In general, no one etchant will be suitable for a wide range of compositions. As the corrosion resistance of the alloys increases, stronger and stronger etchants must be used. Many of these etchants will attack the sulfide inclusions in resulfurized steels with improved machinability.

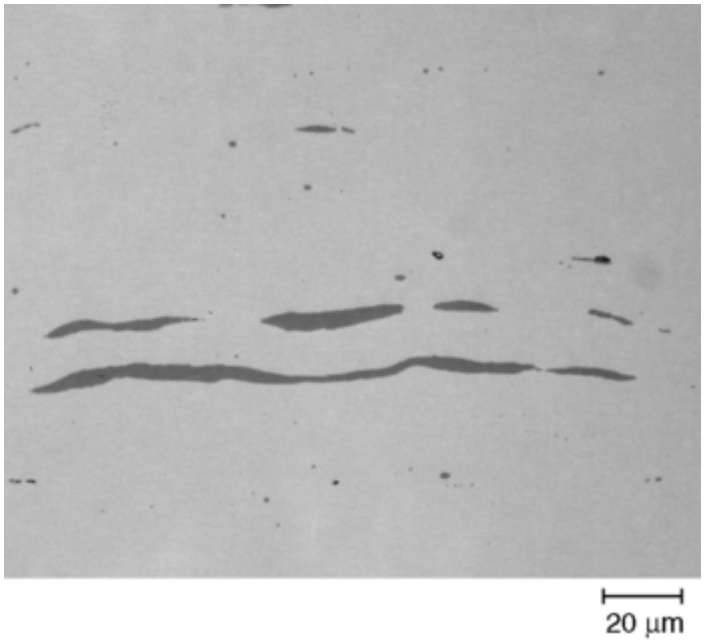

Fig. 4 Manganese sulfides (some chromium substitutes for manganese) in type 416 stainless steel

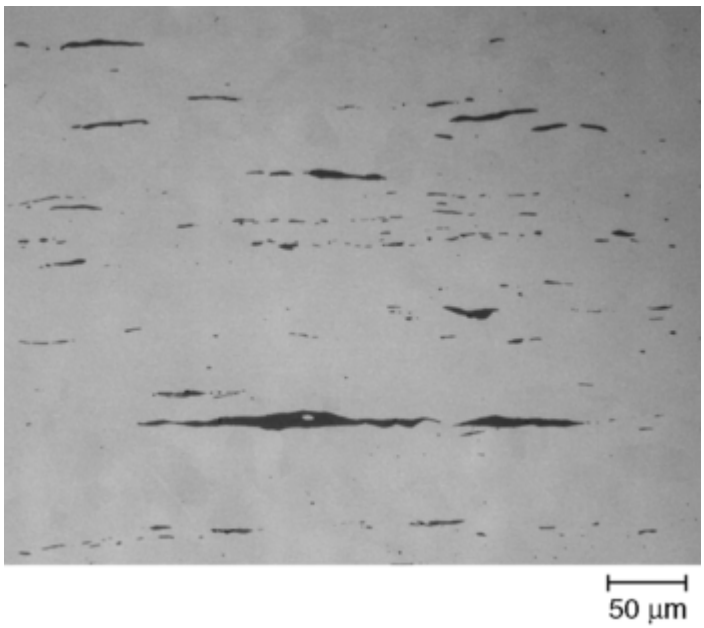

Fig. 5 Manganese sulfides in type 203 stainless steel

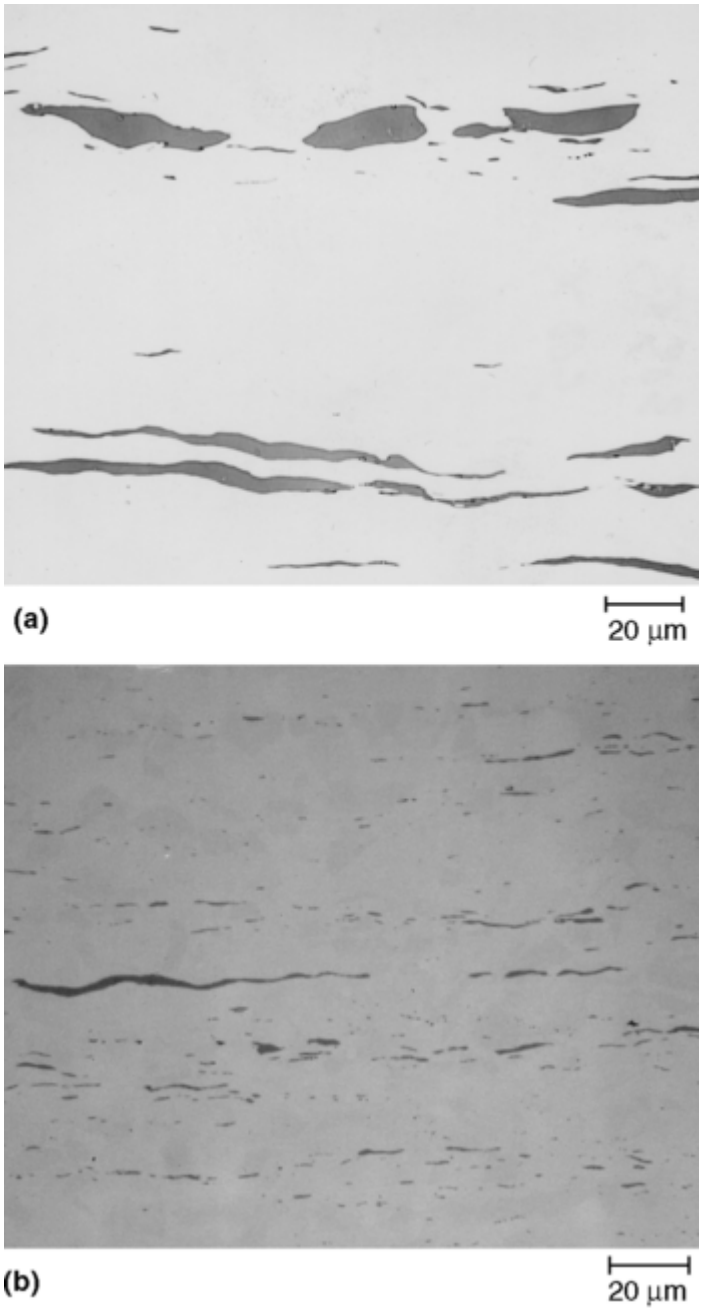

Fig. 6 Manganese sulfides in (a) a billet of ingot-cast type 303 stainless steel and (b) a bar of continuously cast 303 stainless steel

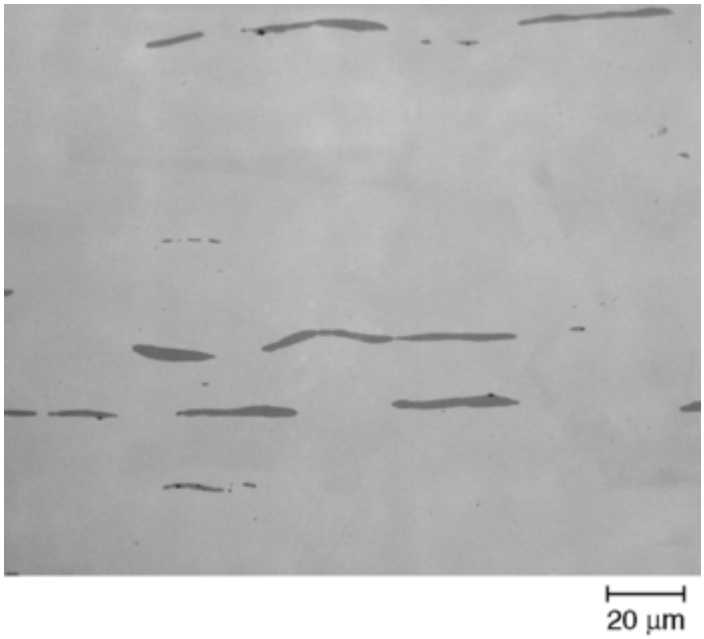

Fig. 7 Manganese selenides in type 303Se stainless steel

Stainless steel etchant ingredients are dissolved in water, methanol or ethanol, glycerol, or a mixture of these solvents. Reagents with alcohol or glycerol as the solvent provide better wetting of the surface than water-based reagents and generally provide more uniform etching. Because alcohol reduces dissociation, alcohol-based reagents can be made more concentrated without becoming too powerful for controlled etching. Stainless steel surfaces passivate; therefore, reducing conditions are preferred to oxidizing conditions that promote passivity. Consequently, stainless steel etchants often contain hydrochloric (HCl), sulfuric (H_2SO_4), or hydrofluoric (HF) acid, although nitric acid (HNO_3) may be used alone or mixed with HCl to produce aqua regia or a modified aqua regia. Swabbing, instead of immersion, may be desired to obtain more uniform etch results. Electrolytic etching is also very popular, because it produces uniform etching, is easier to control, and gives reproducible results. Numerous etchants have been proposed for stainless steels; each has advantages and disadvantages.

Etching the 400-series ferritic or martensitic grades is simpler than the 200- or 300-series austenitic grades or the 600-series precipitation-hardenable grades. Vilella's reagent (or 4% picral + HCl), superpicral, modified Fry's reagent, or Ralph's reagent (does not attack sulfide inclusions) are commonly used with ferritic, martensitic, and precipitation-hardenable stainless steels and maraging steel grades. However, these reagents will not be suitable for the most corrosion-resistant precipitation-hardenable grades, and a stronger etch must be used, such as glyceregia or waterless Kalling's. Etching of the extra low-interstitial-content ferritic grades to observe the grain boundaries, however, is much more difficult than the ordinary ferritic grades. The best etchant for ferritic grades is electrolytic 60% HNO_3, as illustrated in Fig. 8. Additional examples are given elsewhere in this article. Microetchants for stainless steels are listed in Table 8.

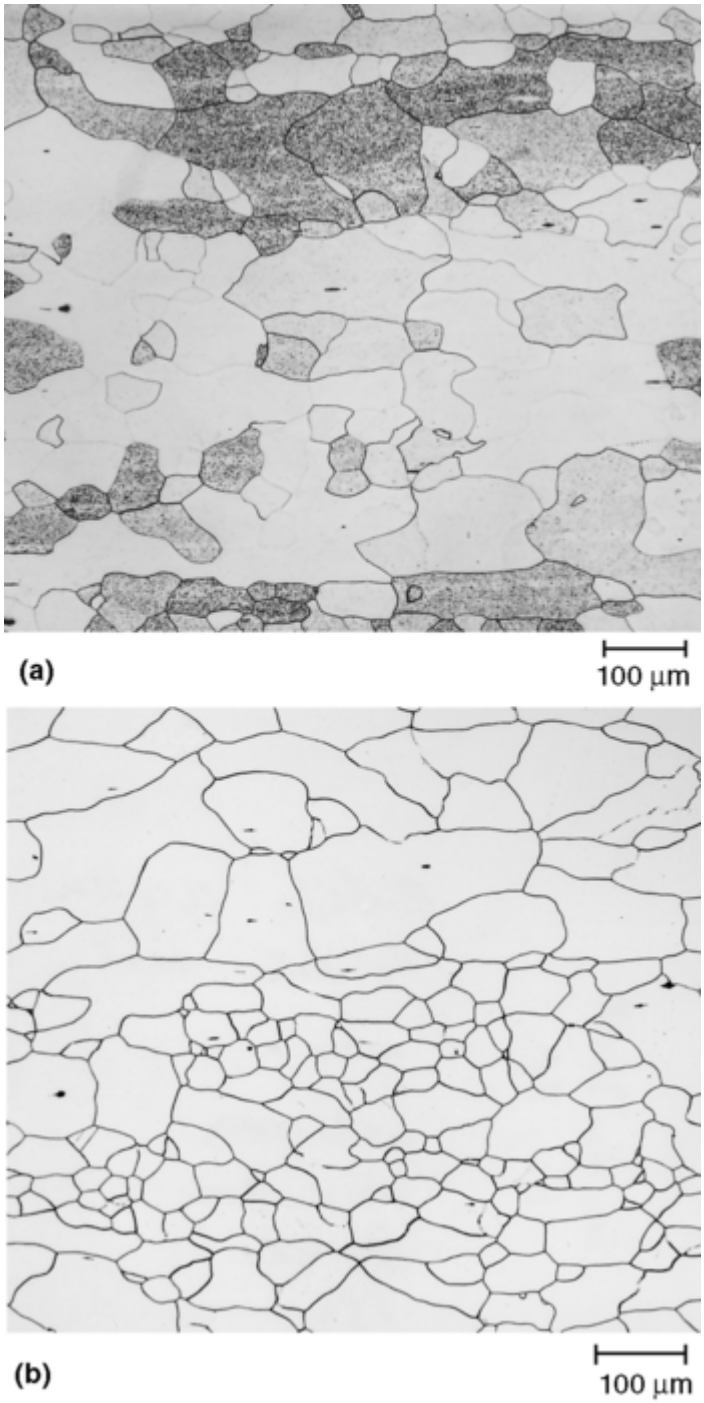

Fig. 8 Microstructure of annealed 26Cr-1Mo E-Brite ferritic stainless steel, revealed using (a) acetic glyceregia and (b) aqueous 60% HNO_3 at 1.2 V dc for 120 s

Table 8 Microetchants for stainless steel

Etchants	Comments
1. 1 g picric acid, 5 mL HCl, 100 mL ethanol	Vilella's reagent. Use at room temperature to 1 min. Outlines second-phase particles (carbides, σ phase, δ-ferrite); etches martensite. Can be stored
2. 1.5 g $CuCl_2$ (cupric chloride), 33 mL HCl, 33 mL ethanol, 33 mL H_2O[(a)]	Kalling's No. 1 reagent for martensitic stainless steels. Use at room temperature. Martensite dark, ferrite colored, austenite not attacked. Can be stored
3. 5 g $CuCl_2$, 100 mL HCl, 100 mL ethanol	Kalling's No. 2 reagent. Use at room temperature. Ferrite attacked rapidly, austenite slightly attacked, carbides not attacked. Can be stored
4. 5 g $CuCl_2$, 40 mL HCl, 30 mL H_2O, 25 mL ethanol	Fry's reagent. For martensitic and precipitation-hardenable grades. Use at room temperature. Can be stored

5. 1 g $CuCl_2$, 50 mL HCl, 150 mL H_2O, 50 mL HNO_3	Modified Fry's (Spaeder) for martensitic stainless steels, precipitation-hardenable stainless steels, and maraging steels. Use at room temperature. Can be stored
6. 4 g $CuSO_4$, 20 mL HCl, 20 mL H_2O	Marble's reagent. Used primarily with austenitic grades. Use at room temperature to 10 s. Attacks σ phase
7. 3 parts HCl, 2 parts glycerol, 1 part HNO_3	Glyceregia. Popular etch for all stainless grades. Use fresh; never store. Discard when reagent is orange colored. Use with care under a hood. Add HNO_3 last. Swab a few seconds to a few minutes. Attacks σ phase, outlines carbides. Substitution of water for glycerol increases attack rate.
8. 3 parts HCl, 2 parts acetic acid, 1 part HNO_3, 2 drops glycerol	Acetic glyceregia. Use as glyceregia (stronger).
9. 3 parts HCl, 2 parts acetic acid, 2 parts HNO_3	15-10-10 reagent. Use as glyceregia (more aggressive). Good for grades such as alloy 625 that are difficult to etch
10. 45 mL HCl, 15 mL HNO_3, 20 mL methanol	Methanolic aqua regia. Used with austenitic grades to reveal grain structure, outline ferrite and σ phase
11. 15 mL HCl, 5 mL HNO_3, 100 mL H_2O	Dilute aqua regia for austenitic grades. Uniform etching of austenite; outlines carbides, σ phase, and ferrite (sometimes attacked)
12. 4 g $KMnO_4$ (potassium permanganate), 4 g NaOH, 100 mL H_2O	Groesbeck's reagent. Use at 60–90 °C (140–195 °F) to 10 min. Colors carbides dark, σ phase gray, ferrite and austenite not affected
13. 30 g $KMnO_4$, 30 g NaOH, 100 mL H_2O	Modified Groesbeck's reagent. Use at 90–100 °C (195–210 °F) for 20 s to 10 min to color ferrite dark in duplex alloys. Austenite not affected
14. 10 g $K_3Fe(CN)_6$, 10 g KOH or NaOH, 100 mL H_2O	Murakami's reagent. Use at room temperature to 60 s to reveal carbides; σ phase faintly revealed by etching to 3 min. Use at 80 °C (175 °F) to boiling up to 60 min to darken carbides. Sigma may be colored blue, ferrite yellow to yellow-brown, austenite not attacked. Use under a hood.
15. 30 g KOH (or NaOH), 30 g $K_3Fe(CN)_6$, 100 mL H_2O; or **20 g KOH (or NaOH), 20 g $K_3Fe(CN)_6$, 100 mL H_2O**	Two modifications of Murakami's reagent. Use at 95 °C (205 °F). Second modification etches faster than the first modification, and it etches faster than etch 14. Colors σ phase reddish-brown, ferrite dark-gray, austenite not attacked, carbide black. Use under a hood.
16. 10 g oxalic acid and 100 mL H_2O	Popular electrolytic etch; 6 V dc, 25 mm (1.0 in.) spacing. 15–30 s reveals carbides; grain boundaries revealed after 45–60 s; σ phase outlined after 6 s. Lower voltages (1–3 V dc) can be used. Dissolves carbides. Sigma strongly attacked, austenite moderately attacked, ferrite not attacked
17. 10 g NaCN (sodium cyanide) and 100 mL H_2O	Electrolytic etch at 6 V dc, 25 mm (1.0 in.) spacing, 5 min, platinum cathode. Sigma darkened, carbides light, ferrite outlined, austenite not attacked. Good for revealing carbides. Use with care under a hood. Dangerous!
18. 10 mL HCl and 90 mL methanol	Electrolytic etch at 1.5 V dc, 20 °C (70 °F) to attack σ phase. Use at 6 V dc for 3–5 s to reveal structure.
19. 60 mL HNO_3 and 40 mL H_2O	Electrolytic etch to reveal austenite grain boundaries (but not twins) in austenitic grades. With stainless steel cathode, use at 1.1 V dc, 0.075–0.14 A/cm^2 (0.48–0.90 $A/in.^2$), 120 s. With platinum cathode, use at 0.4 V dc, 0.055–0.066 A/cm^2 (0.35–0.43 $A/in.^2$), 45 s. Will reveal prior-austenite grain boundaries in solution-treated (but not aged) martensitic precipitation-hardenable alloys and maraging steels
20. 50 g NaOH and 100 mL H_2O	Electrolytic etch at 2–6 V dc, 5–10 s to reveal σ phase in austenitic grades
21. 56 g KOH and 100 mL H_2O	Electrolytic etch at 1.5–3 V dc for 3 s to reveal σ phase (red-brown) and ferrite (bluish). Chi colored same as sigma
22. 20 g NaOH and 100 mL	Electrolytic etch at 20 V dc for 5–20 s to outline and color δ-ferrite tan

H_2O	
23. NH_4OH (conc)	Electrolytic etch at 1.5–6 V dc for 10–60 s. Very selective. At 1.5 V, carbide completely etched in 40 s; sigma unaffected after 180 s. At 6 V, σ phase etched after 40 s
24. 10 g $(NH_4)_2S_2O_8$ and 100 mL H_2O	Use at 6 V dc for 10 s to color $M_{23}C_6$ carbide dark brown
25. 200 mL HCl and 1000 mL H_2O	Beraha's tint etch for austenitic, duplex, and precipitation-hardenable grades. Add 0.5–1.0 g $K_2S_20_5$ per 100 mL of solution (if etching is too rapid, use a 10% aqueous HCl solution). Immerse at room temperature (never swab) for 30–120 s until surface is reddish. Austenite colored, carbides not colored. Longer immersion colors ferrite lightly. If coloration is inadequate, add 24 g $NH_4F{\cdot}HF$ (ammonium bifluoride) to stock reagent at left.
26. 20 g picric acid and 100 mL HCl	Etch by immersion. Develops grain boundaries in austenite and δ-ferrite in duplex alloys
27. Saturated aqueous $Ba(OH)_2$ (barium hydroxide)	Attacks carbides well before σ phase in austenitic grades when used at 1.5 V dc, but attacks both equally when used at 3–6 V dc. Has been used to differentiate χ phase and Laves phase (use at 4.3 V dc, platinum cathode, 20 s). Chi is stained mottled-purple, Laves is not colored, ferrite is stained tan.
28. 50 mL each H_2O, ethanol, methanol, and HCl; plus 1 g $CuCl_2$, 3.5 g $FeCl_3$, 2.5 mL HNO_3	Ralph's reagent. Use by swabbing. Can be stored. General-purpose etch for most stainless steels. Does not attack sulfides in free-machining grades
29. 150 mL HCl, 50 mL lactic acid, 3 g oxalic acid	Lucas's reagent. Etches less corrosion-resistant grades by immersion, more corrosion-resistant grades electrolytically, at 0.3 to 1.2 V dc for 10–30 s. The reagent can be stored.
30. 15 mL HCl, 85 mL ethanol	Immerse for 15–45 min to reveal all phase/grain boundaries in duplex stainless steel.

(a) When water is specified, use distilled water.

Etching of the austenitic grades to examine the grain structure is difficult with most standard reagents. As shown in the illustrations, most of the standard reagents reveal only a portion of the grain and twin boundaries. Tint etching, which requires a high-quality polish for good results, reveals all of the grains by color contrast. Figure 9(a) shows the grain structure of 316L austenitic stainless steel etched with waterless Kalling's (Kalling's No. 2) reagent, where many, but not all, of the grain boundaries and twin boundaries are revealed. This is inadequate for an actual measurement of grain size. Figure 9(b) shows the same specimen after tint etching with a Beraha reagent that colors all of the grains (shown in black and white). Additional examples of tint-etched stainless steels, but in color, can be found in the article “Color Metallography” in this Volume. To measure the grain size when a more accurate value is required than can be obtained by a comparison chart rating, all the boundaries must be revealed. Twin boundaries are ignored.

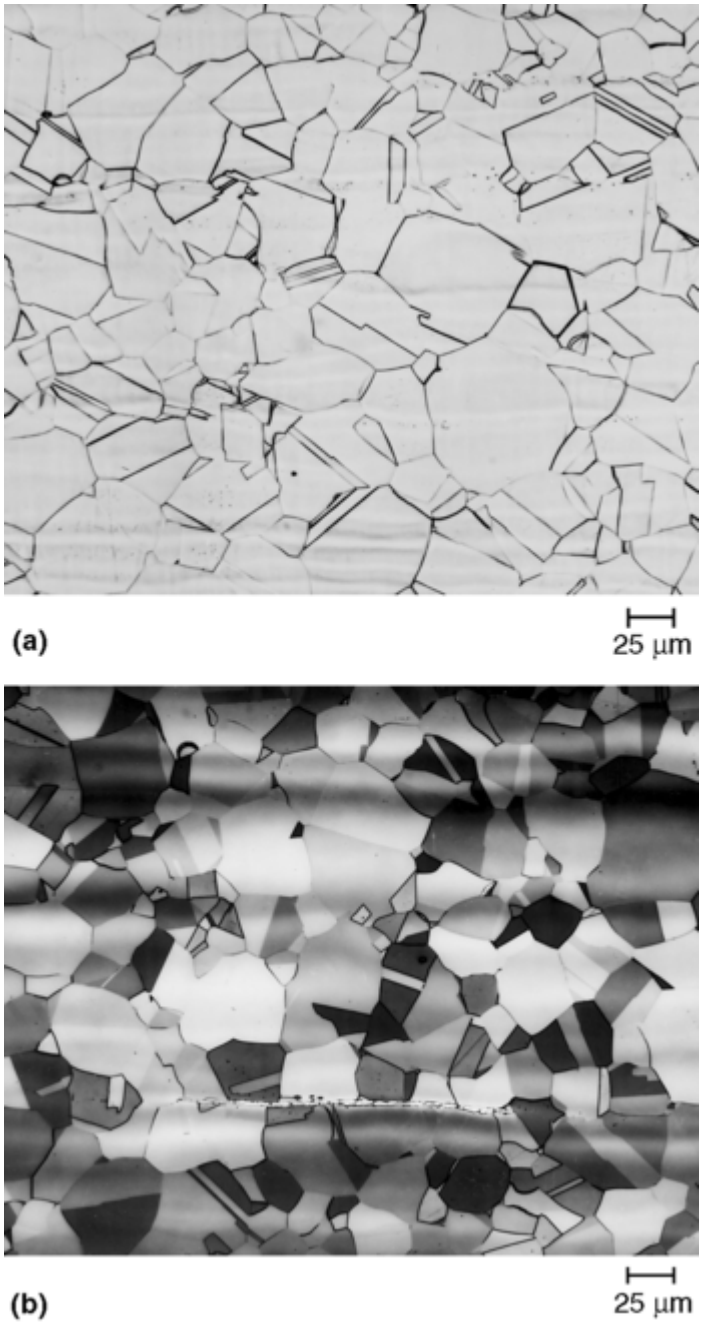

Fig. 9 Grain structure of austenitic type 316L, solution annealed at 954 °C (1750 °F) and etched with (a) waterless Kalling's and (b) Beraha's tint etch

Sensitizing the specimen by heating it for 1 to 6 h at 650 °C (1200 °F) will facilitate revealing the grain boundaries. However, the carbon content must be >0.03% to develop enough grain-boundary carbides to reveal the grains. Examples are shown in Fig. 10 and Fig. 11. Electrolytic 10% ammonium persulfate is an excellent etchant for sensitized stainless steels, because it colors the chromium carbides brown. Today, most steelmakers are melting to the L-carbon requirement, regardless of whether the grade being purchased is the standard carbon level or the L version for weldability, to save inventory costs. This method is not as successful for the low-carbon versions, because less $M_{23}C_6$ carbide can be precipitated at the grain boundaries.

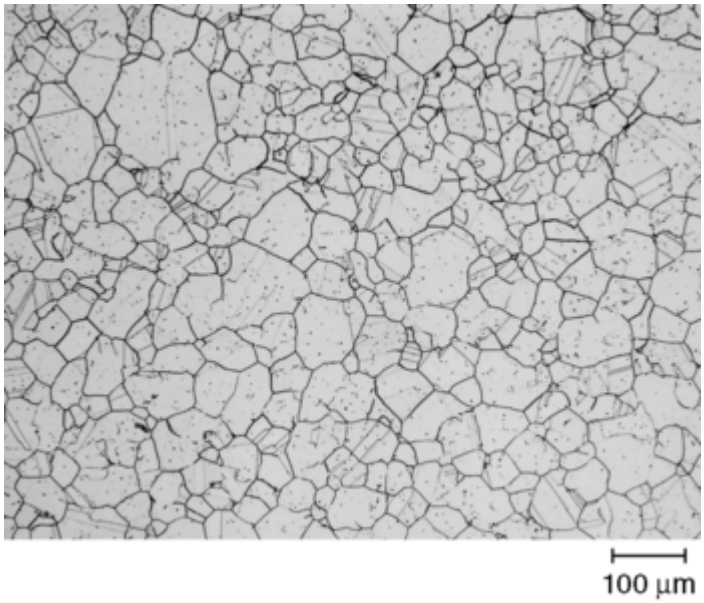

Fig. 10 Solution-annealed and sensitized (1038 °C, or 1900 °F, for 1 h, water quenched, aged at 650 °C, or 1200 °F, for 2 h, air cooled) type 304 stainless steel etched with aqueous 10% ammonium persulfate at 6 V dc for 10 s to color the $M_{23}C_6$ grain-boundary carbides

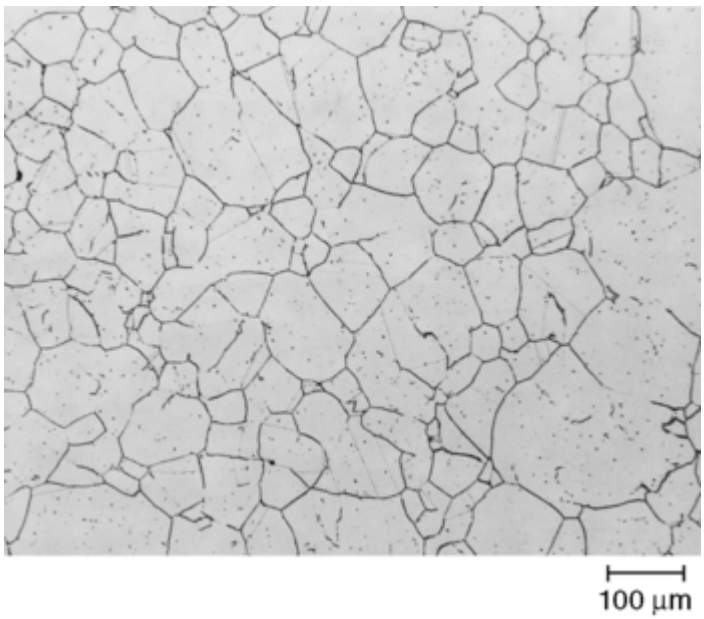

Fig. 11 Solution-annealed and sensitized type 316 stainless steel etched with waterless Kalling's reagent to reveal the $M_{23}C_6$ grain-boundary carbides

An alternate technique (Ref 2, 3) that does not depend on the carbon content involves electrolytically etching the solution-annealed specimen with aqueous 60% HNO_3 (Table 8). With this procedure, twin boundaries are not revealed as long as the voltage is kept low. Figure 12 shows the 316L specimen previously shown in Fig. 9 after electrolytic etching with 60% nitric acid in water. Note that virtually all of the grain boundaries are revealed. A few minor problems can be seen within certain grains, but these can be removed with image-editing techniques and are easily ignored in manual measurements. Figure 13 shows an additional example where a solution-annealed specimen of 316 grade has been etched with three standard reagents and two electrolytic reagents, including 60% nitric acid in water. The clear superiority of this etchant is evident in these micrographs. This etchant will also bring out prior-austenite grain boundaries in solution-annealed, but not aged, precipitation-hardened grades, including maraging grades. For structure-property correlations, the mean lineal intercept value for grain and twin boundaries should be measured, because the twin boundaries also contribute to strengthening. Such a measurement should not be converted to a grain size value.

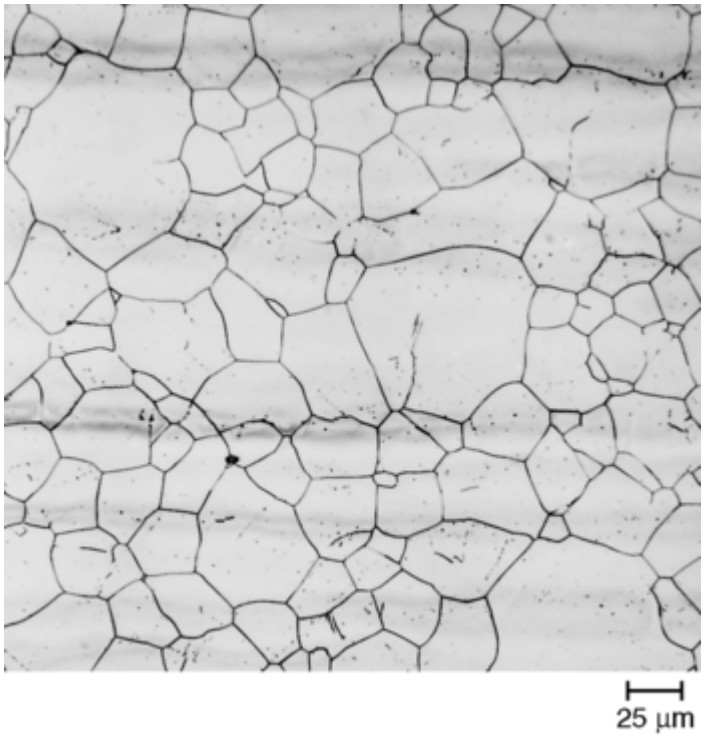

Fig. 12 Austenitic grain boundaries in solution-annealed (954 °C, or 1750 °F, water quenched) type 316L, revealed by electrolytic etching with aqueous 60% HNO_3 at 1 V dc for 120 s

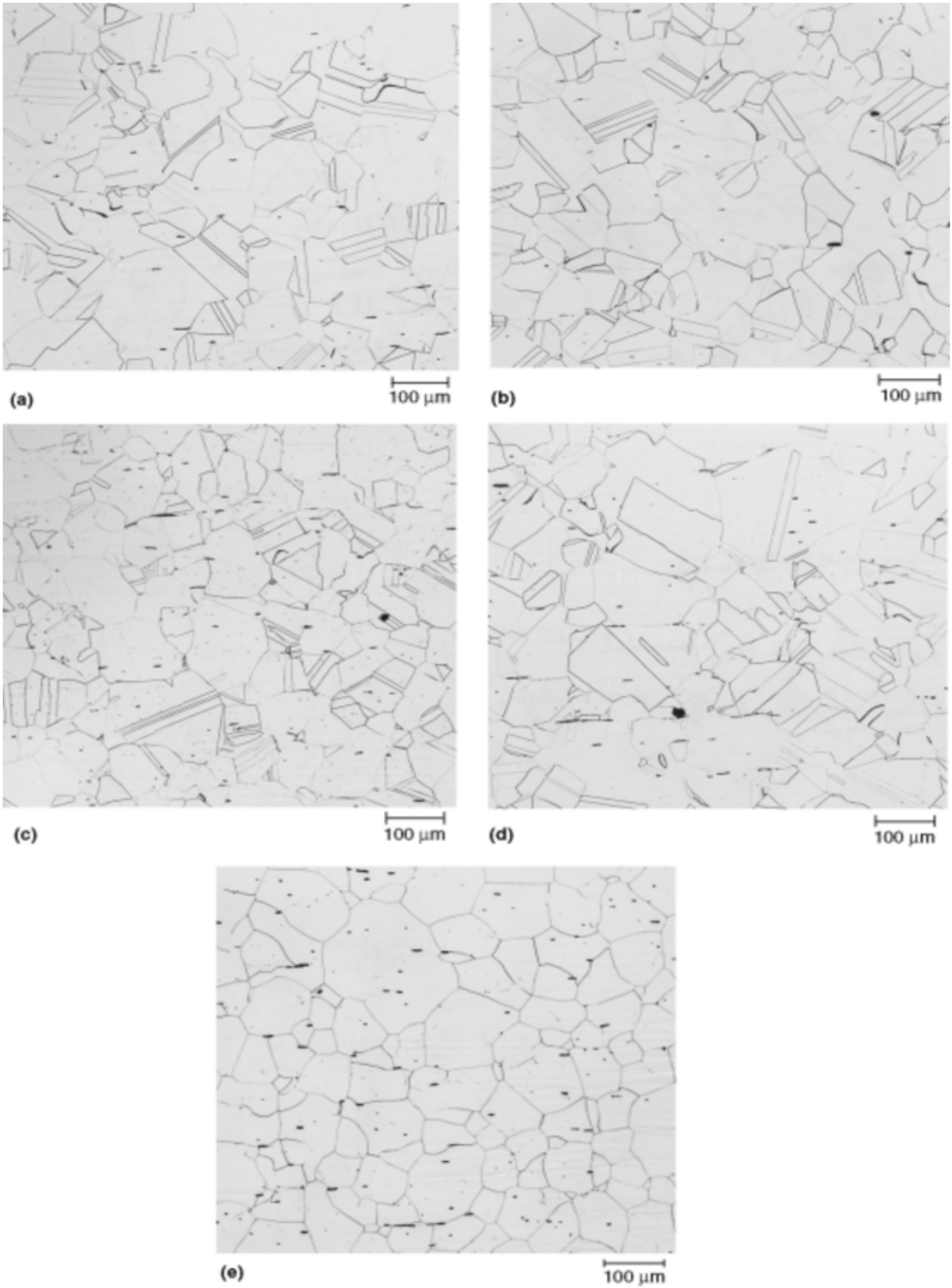

Fig. 13 Austenitic grain boundaries in solution-annealed type 316 stainless steel, revealed by (a) acetic glyceregia, (b) Marble's reagent, (c) equal parts HCl, HNO_3, and water, (d) aqueous 10% oxalic acid at 6 V dc, and (e) aqueous 60% HNO_3 at 0.6 V dc for 90 s

Various alkaline ferricyanide reagents, such as Murakami's reagent and its numerous modifications, have been widely used to etch austenitic stainless steels for phase identification. The colors produced by these etchants vary with etchant composition, temperature, time, and phase orientation. When using a particular reagent in the prescribed manner, the colors obtained may differ from those reported in the literature. However, the etch response, that is, what is attacked and what is not attacked at either room temperature or with a boiling solution, is highly reproducible.

When using the standard formulation of Murakami's reagent at room temperature, for example, the carbides will be attacked in 7 to 15 s, and σ phase will be only lightly attacked after 3 min. If higher concentrations of potassium hydroxide (KOH) or sodium hydroxide (NaOH) and potassium ferricyanide ($K_3Fe(CN)_6$) are used at room temperature, σ phase will be attacked instead of the carbides. Used boiling, the standard formulation attacks ferrite, carbide, and σ phase, although some evidence indicates that σ will not be attacked. Therefore, when using this reagent or one of its numerous modifications, directions should be followed carefully. Experimentation with specimens of known constitution is also recommended.

In some etchant compilations, the standard version of Murakami's reagent is listed as 10 g KOH (or 7 g NaOH) and 10 g $K_3Fe(CN)_6$ (potassium ferricyanide). Murakami's original publication in 1918 gave the formula as 10 g NaOH, 10 g $K_3Fe(CN)_6$, and 100 mL water and does not mention KOH. There are numerous modifications to this reagent, and several are quite useful. Useful modifications include 20 g NaOH (or KOH), 20 g $K_3Fe(CN)_6$, and 100 mL water, or 30 g NaOH (or KOH), 30 g $K_3Fe(CN)_6$, and 100 mL water. There is a slight variant of this last modification using only 60 mL water, but this solution is difficult to mix, because there is inadequate water to dissolve the two chemicals. In general, as the concentration of NaOH (or KOH) and $K_3Fe(CN)_6$ increases, etch time is reduced, which is very helpful when using a boiling reagent. The end results are the same, and there is little difference between using NaOH or KOH, although the authors prefer to use NaOH. Figure 14 shows how ferrite in a cast ASTM A 890, grade 5A, duplex stainless steel was revealed using the three versions of Murakami's reagent. Murakami's reagent etches carbides when used at room temperature but not ferrite or sigma. Figure 15 shows an example of the use of Murakami's at room temperature to reveal carbides in type 312 weld metal that was aged 160 h at 816 °C (1500 °F). There is σ in the weld also, but it was not darkened or colored. To color ferrite and sigma, Murakami's must be used between approximately 80 and 100 °C (180 and 210 °F). Sigma is colored more readily than ferrite. For example, when coloring ferrite in type 312 weld metal (as-welded), the standard grade was used boiling for 180 s, while the 20-20-100 version required 60 s, and the 30-30-100 version required 10 s (Fig. 16). To color σ in the aged 312 weld metal (Fig. 15), the 10-10-100 (Fig. 17) version required immersion in the boiling solution for 60 s, while the 30-30-100 version required <10 s.

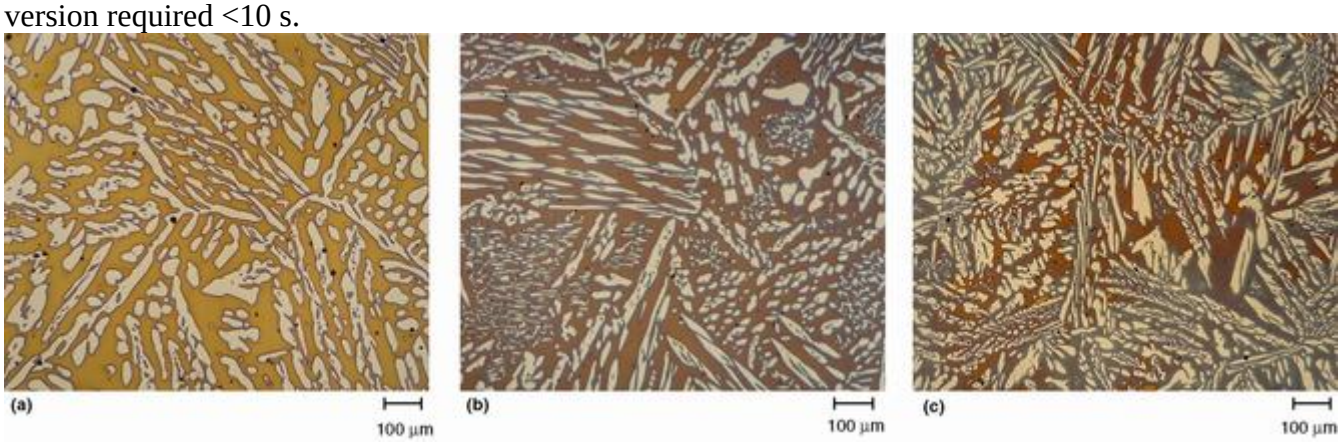

Fig. 14 Ferrite is colored preferentially when as-cast ASTM A 890, grade 5A, is etched with boiling Murakami's reagent using (a) 10 g NaOH 10 g $K_3Fe(CN)_6$ in 100 mL water for 90 s, (b) 20 g NaOH 20 g $K_3Fe(CN)_6$ in 100 mL water for 50 s, and (c) 30 g NaOH 30 g $K_3Fe(CN)_6$ in 100 mL water for 10 s

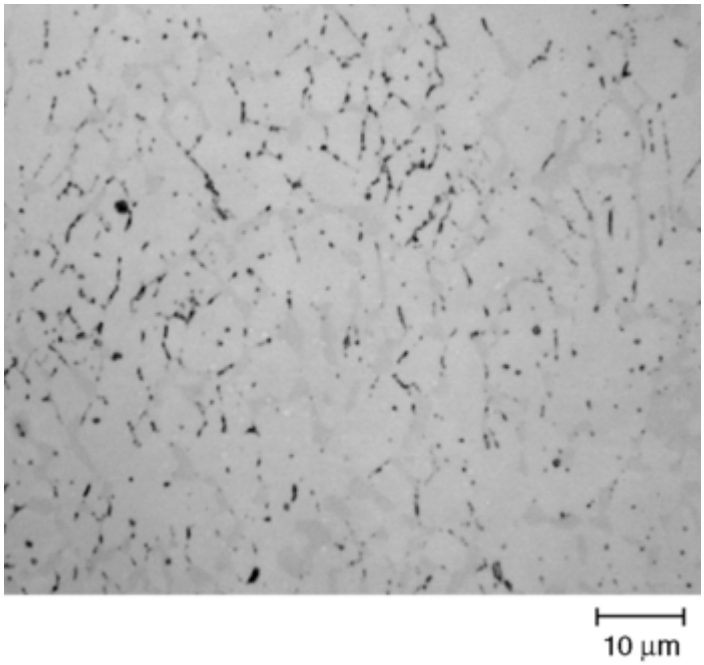

Fig. 15 Carbides in type 312 weld metal, aged at 816 °C (1500 °F) for 160 h, were revealed using standard Murakami's reagent at room temperature for 60 s.

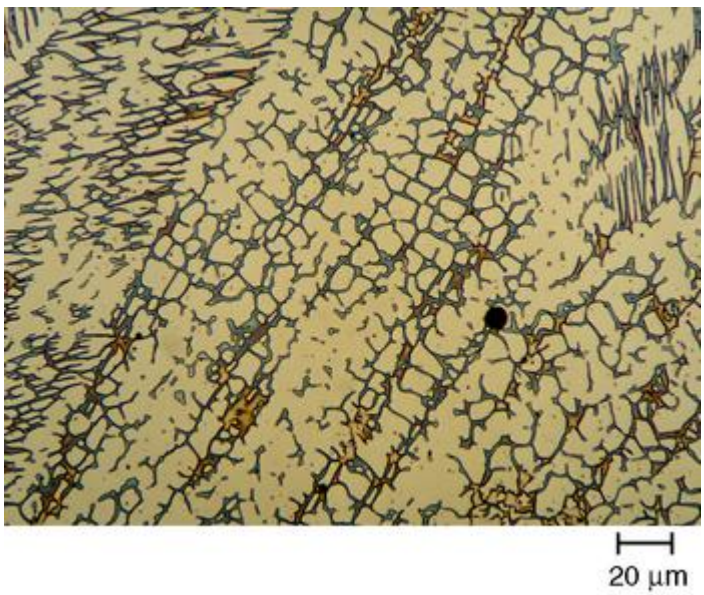

Fig. 16 Delta ferrite in type 312 weld metal revealed using modified Murakami's (30 g NaOH, 30 g $K_3Fe(CN)_6$, and 100 mL water) at 100 °C (210 °F) for 10 s

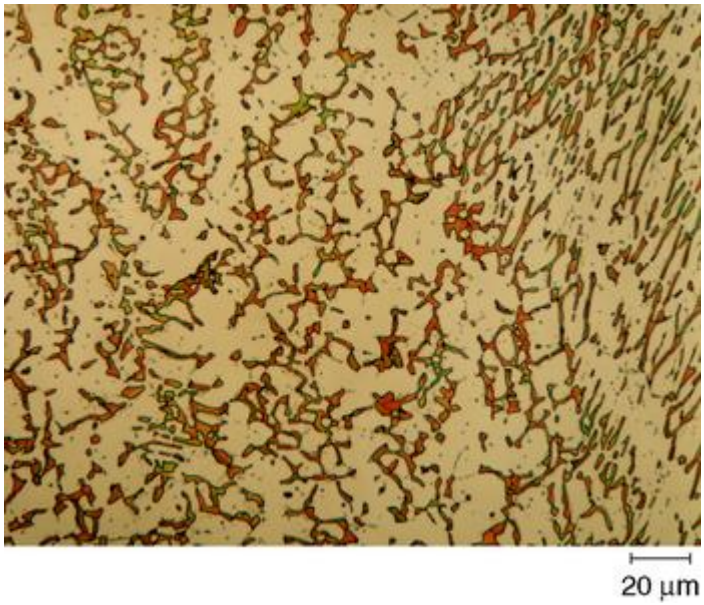

Fig. 17 Sigma phase in 312 weld metal, aged at 816 °C (1500 °F) for 160 h, was revealed using standard Murakami's reagent at 80 °C (175 °F) for 60 s.

Electrolytic reagents, which are used often with austenitic and duplex grades, provide greater control of the etching process and are highly reproducible. One of the most commonly used electrolytic reagents is 10% aqueous oxalic acid, which will reveal carbides after a short etch, if they are present (Table 7). When carbides are not present, the austenite grain boundaries will be revealed in 15 to 60 s (Fig. 13d). If ferrite is present, it will be outlined after 10 to 15 s. Electrolytic 10% ammonium persulfate is highly reliable for coloring $Cr_{23}C_6$ carbides in stainless steels (6 V dc, 10 s) (Fig. 10).

Electrolytic reagents are generally quite simple in composition. The selectivity of electrolytic reagents based on various hydroxide solutions has been demonstrated (Ref 4). Strong hydroxide solutions attack σ phase preferentially to carbides; weak hydroxide solutions attack carbides much more readily than σ phase. Therefore, to reveal σ phase, 10 *N* KOH or 20% NaOH is employed, and to reveal carbides, concentrated ammonium hydroxide (NH_4OH) is used. For intermediate-strength hydroxide solutions, etching response is altered by a change in the applied potential. Strong hydroxides also darken ferrite and σ when used electrolytically but do not affect austenite.

Figure 18 shows the 316L specimen illustrated in Fig. 9 and 12 etched electrolytically, this time with 20% NaOH to color the fine δ-ferrite stringers and subsequently with concentrated ammonium hydroxide (NH_4OH) to color carbides not dissolved in solution annealing (954 °C or 1750 °F, was used—lower than normal to minimize grain growth). Figure 19 shows 20% NaOH used electrolytically to darken the σ phase in the aged 312 weld metal (compare with Fig. 17). Figure 20 shows ferrite and σ in a modified type 329 (experimental) alloy that was aged 48 h at 816 °C (1500 °F), revealed by electrolytic etching with 20% NaOH. The austenite was unaffected, the ferrite was colored light brown, and the σ was colored orange. Figure 21 compares the use of electrolytic 10% ammonium persulfate with concentrated ammonium hydroxide to reveal grain-boundary carbide precipitation (sensitization) in the heat-affected zone of a 316 weld.

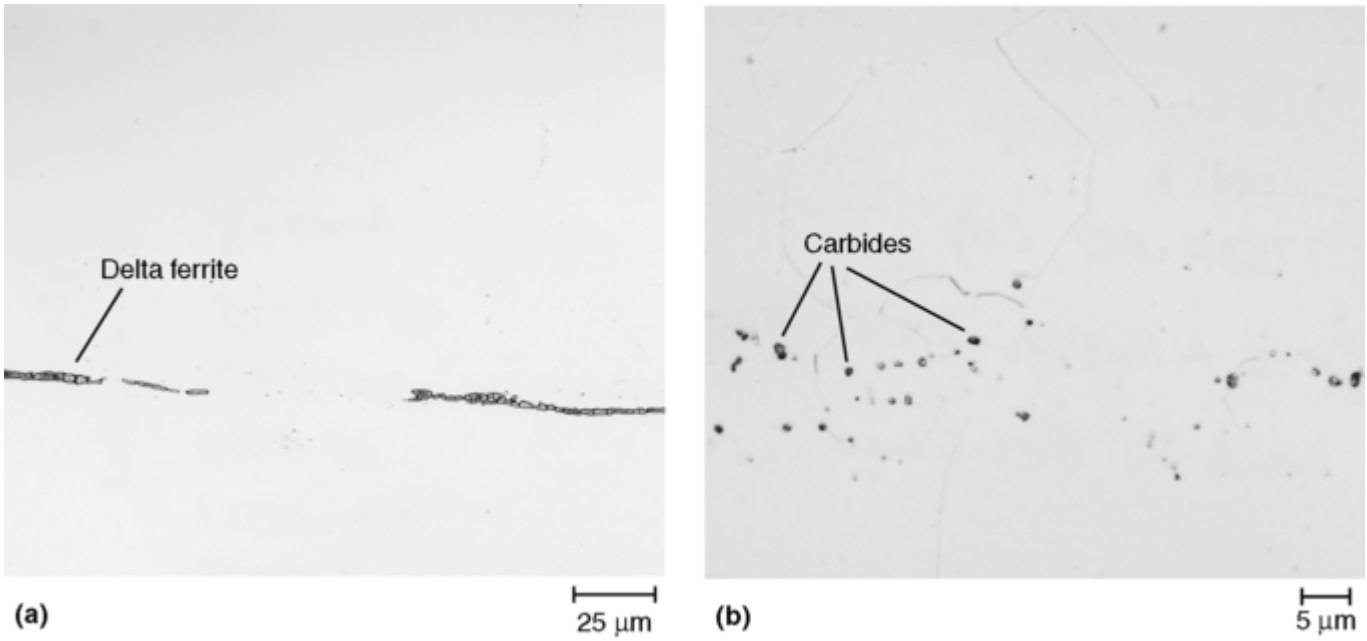

Fig. 18 Delta-ferrite stringer and carbides along the centerline in solution-annealed (954 °C, or 1750 °F, water quenched) type 316L were revealed using (a) aqueous 20% NaOH and (b) concentrated ammonium hydroxide (NH_4OH) at 5 V dc for 10 s.

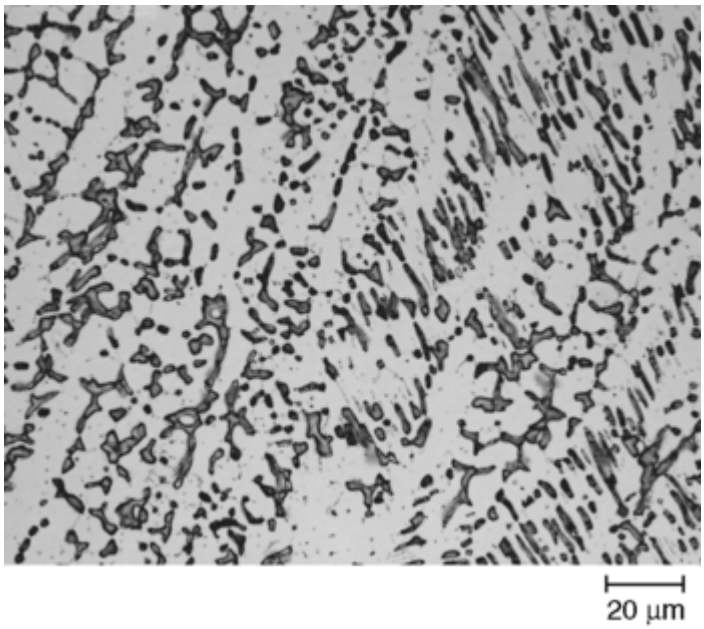

Fig. 19 Sigma phase in 312 weld metal, aged at 816 °C (1500 °F) for 160 h, was revealed using aqueous 20% NaOH at 3 V dc for 10 s.

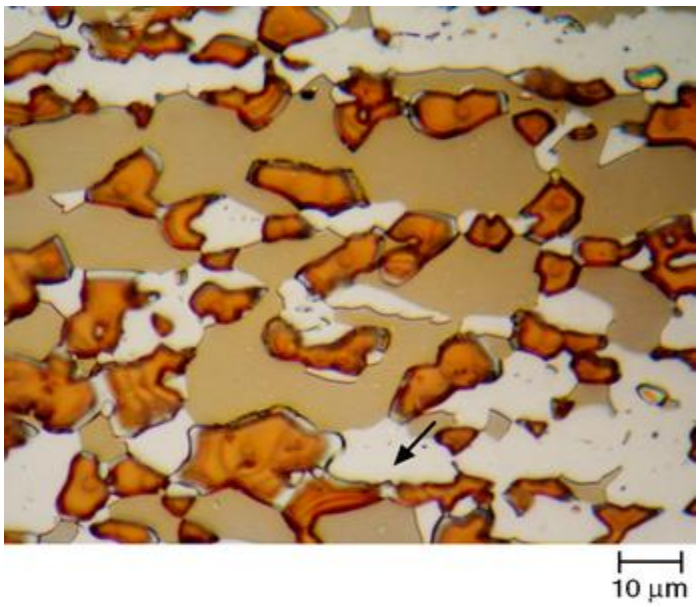

Fig. 20 Delta-ferrite and σ phase revealed in a modified type 329 duplex stainless steel, aged 48 h at 816 °C (1500 °F), using aqueous 20% NaOH at 3 V dc for 10 s. Austenite is not colored, ferrite is tan, and σ is orange. As the σ forms, new austenite (arrow) is also formed and can be seen around the σ particles.

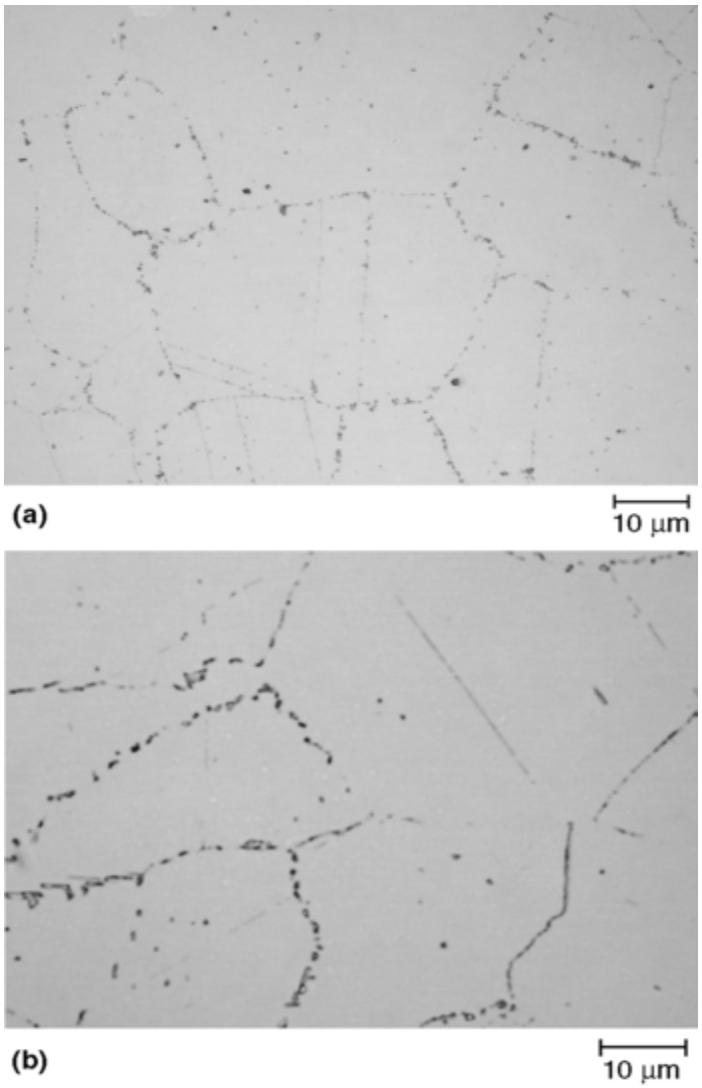

Fig. 21 Grain-boundary carbides in the heat-affected zone of a sensitized 316 stainless steel, revealed using (a) concentrated NH_4OH at 6 V dc for 60 s and (b) aqueous 10% ammonium persulfate at 6 V dc for 10 s

Several sequential etching procedures have been suggested for phase identification in austenitic stainless steels. One procedure (Ref 4) involves etching first with Vilella's reagent to outline the phases present. Next, the specimen is electrolytically etched with 10 *N* KOH at 3 V dc for 0.4 s to color σ phase, if present, but not carbides. The specimen is then electrolytically etched with concentrated NH_4OH at 6 V dc for 30 s to color any carbides present. Another procedure (Ref 5) also begins with Vilella's reagent to reveal the constituents. Next, Murakami's reagent is used at room temperature to stain the carbides present. Any σ phase or δ-ferrite present is unaffected. Finally, the specimen is electrolytically etched with aqueous chromium trioxide (CrO_3), which will attack carbides and σ phase but not δ-ferrite. Murakami's reagent does not attack carbides in titanium- or niobium-stabilized stainless steels. These carbides are attacked slowly in electrolytic CrO_3.

Delta-ferrite in martensitic, austenitic, or precipitation-hardenable grades can be preferentially colored by electrolytic etching with 20% aqueous NaOH at 3 V dc for 5 to 20 s. This procedure outlines and uniformly colors tan the δ-ferrite. Although the color varies with orientation, 10 *N* KOH also colors δ-ferrite. Figure 22 illustrates the use of five different etchants to reveal δ-ferrite in solution-annealed and aged 17-4 PH stainless. Note that 10 *N* KOH produced color variations from grain to grain (orientation sensitivity), while 20% NaOH colored the δ-ferrite uniformly and generally exhibits sharper phase boundaries. Figure 23 shows δ-ferrite revealed in a different specimen of 17-4 PH, using boiling Murakami's reagent. Figure 24 shows 20% NaOH used to reveal δ-ferrite in AM 350 and 15-7 PH stainless steels. Figure 25 shows the microstructure of 7-Mo PLUS duplex stainless steel etched with two standard reagents: a Beraha tint etch (colors the ferrite) and three electrolytic reagents. Although glyceregia (Fig. 25a) is a popular general-purpose etchant for stainless steels, it is orientation-sensitive and did not reveal the structure well. Ethanolic 15% HCl (developed at Carpenter Technology Corp.) is a very interesting etchant. It is used by immersion, but the time is not too critical. Usually, specimens are immersed from 15 to 45 min; long times do not seem to cause overetching problems. However, while it reveals the phase boundaries very well and uniformly (Fig. 25b), one cannot tell ferrite from austenite. The tint etch (Fig. 25c) does a great job coloring the ferrite, but it is more challenging to get this quality of results than by using electrolytic 20% NaOH. The very useful electrolytic aqueous 60% nitric acid etch also reveals the phase boundaries very well (Fig. 25d) and gives a slight gray color to the ferrite. Much stronger contrast, however, is obtained using electrolytic aqueous 20% NaOH or 10 *N* KOH (56%), as shown in Fig. 25(e) and (f). Note that the uniformity of the color and the sharpness of the phase boundaries are better with NaOH than with KOH.

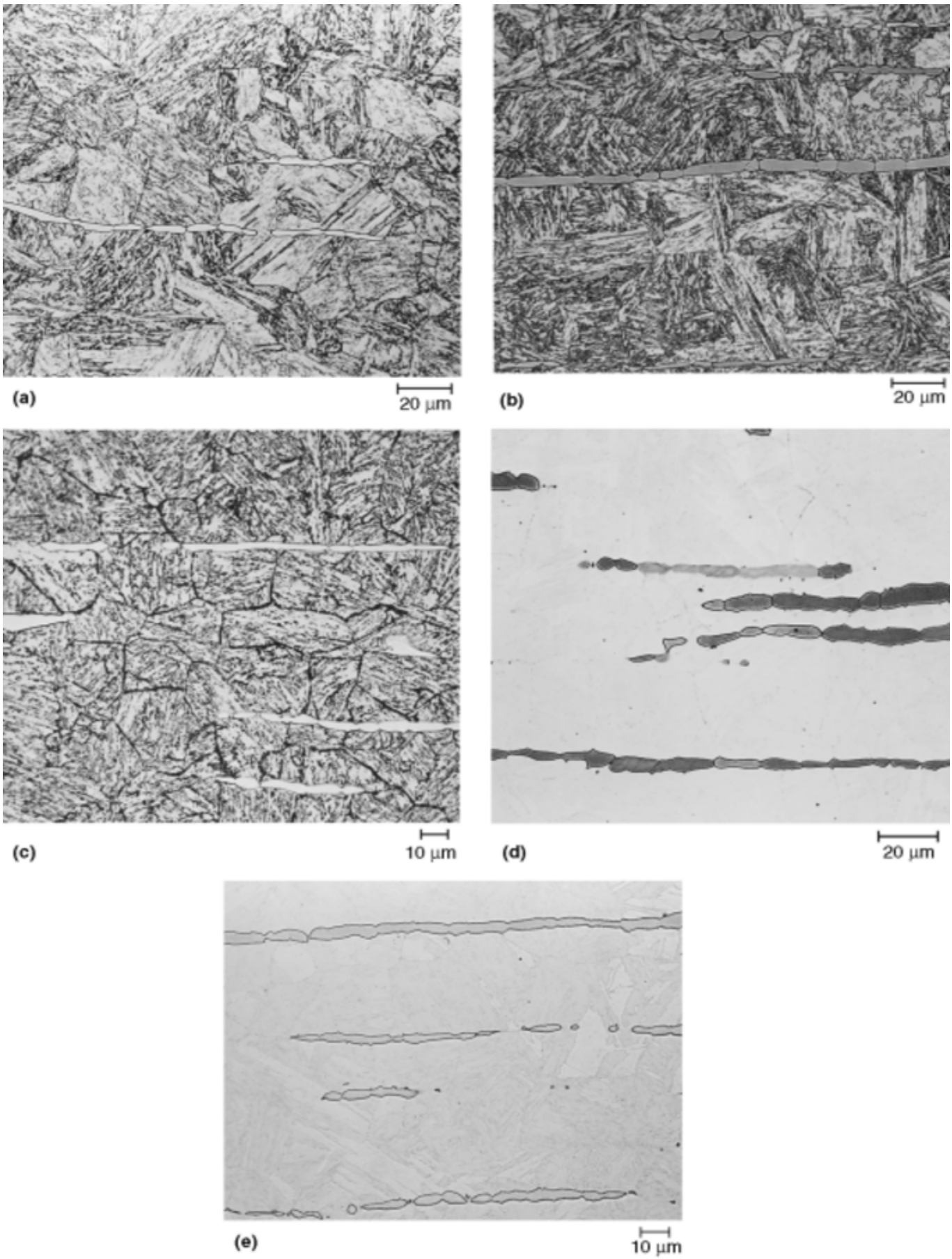

Fig. 22 Delta-ferrite in the martensitic matrix of solution-annealed and aged 17-4 PH stainless steel, revealed using (a) Fry's reagent, (b) Marble's reagent, (c) superpicral (which brought out the prior-austenite grain boundaries better than Fry's), (d) aqueous 10 *N* KOH at 2.5 V dc for 10 s, and (e) aqueous 20% NaOH at 20 V dc for 20 s

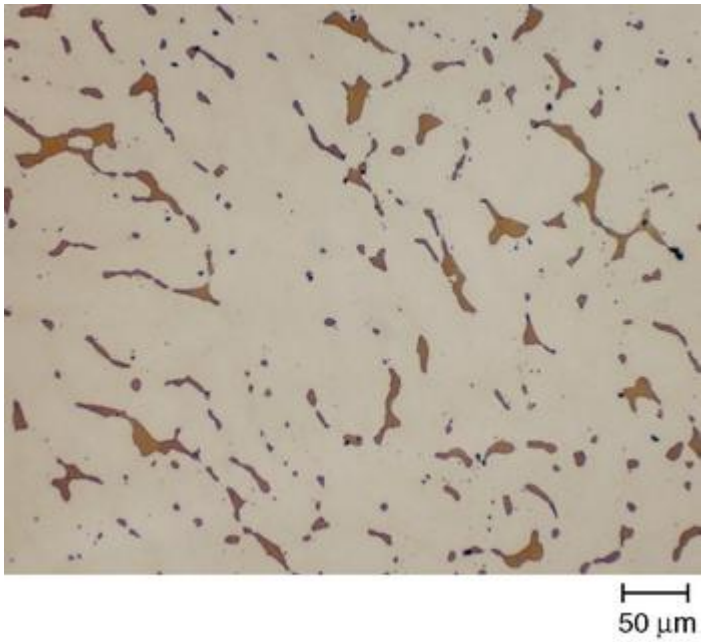

Fig. 23 Delta ferrite, colored brown in solution-annealed and aged (H900 temper) 17-4 PH stainless steel, revealed using the standard Murakami's reagent at 100 °C (210 °F) for 60 s

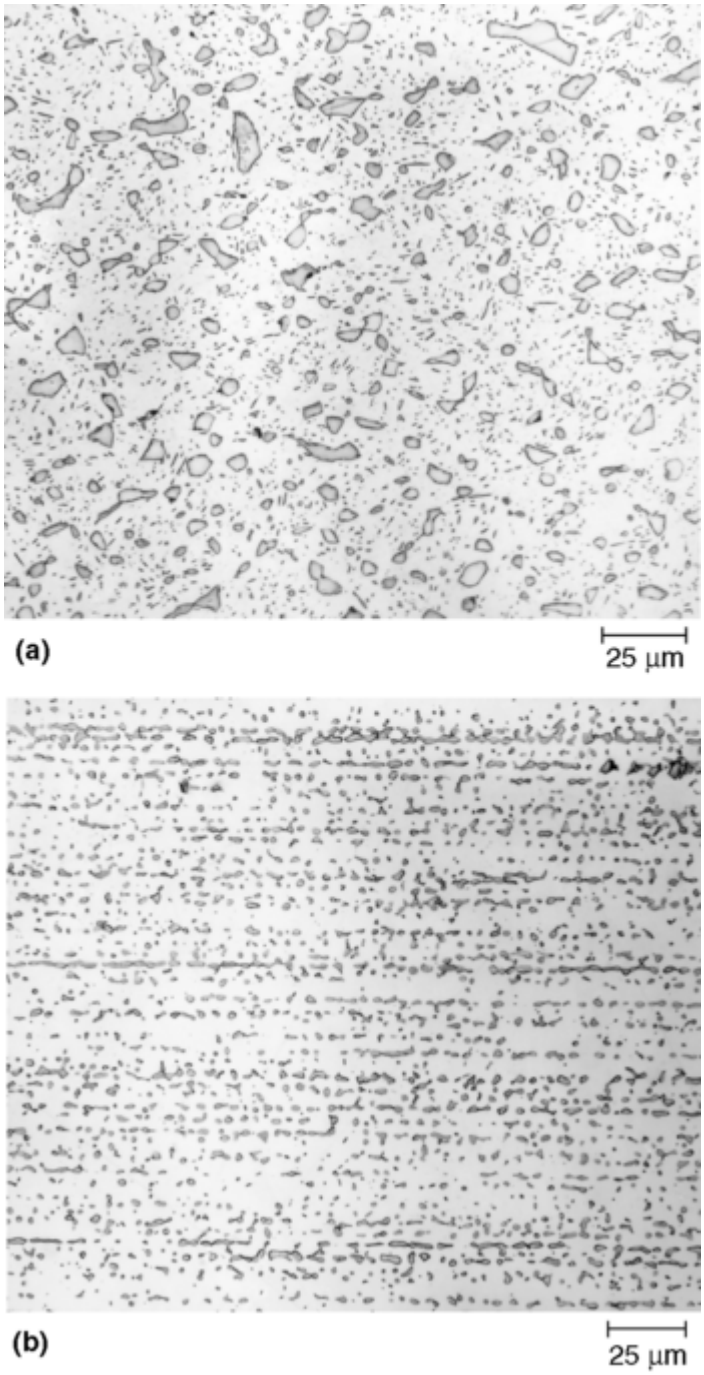

Fig. 24 Delta-ferrite revealed in (a) AM 350 and (b) PH 15-7 Mo stainless steels, using aqueous 20% NaOH at 3 V dc for 10 s

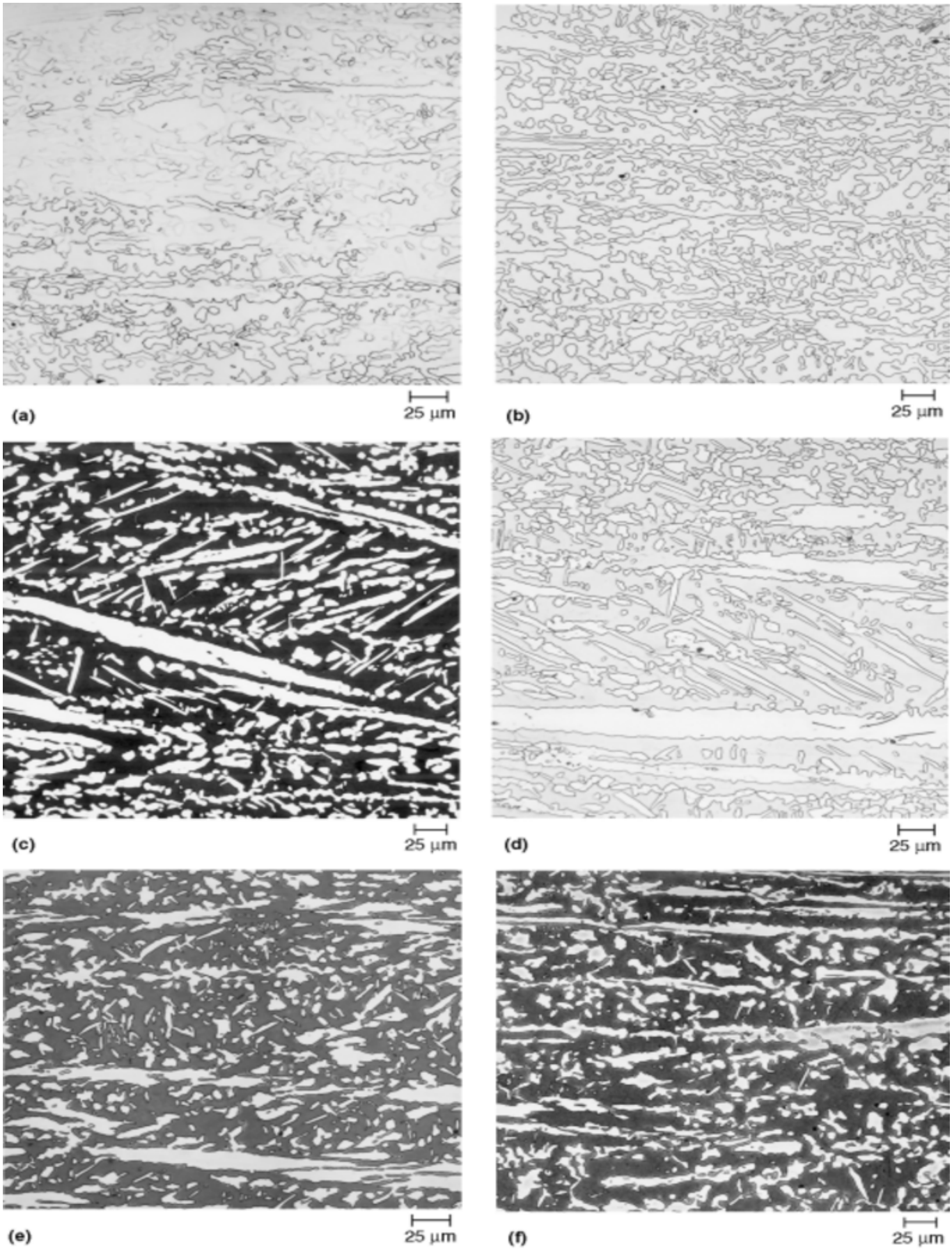

Fig. 25 Ferrite-austenite phase boundaries revealed in 7-Mo PLUS duplex stainless steel plate, using (a) glyceregia (poor results), (b) ethanol 15% HCl, (c) Beraha's tint etch, (d) aqueous 60% HNO_3 at 1 V dc for 60 s, (e) aqueous 20% NaOH at 4 V dc for 10 s, and (f) 10 *N* KOH at 3 V dc for 10 s

Potentiostatic etching (Ref 1) is frequently used for selective etching of constituents in stainless steels. This technique is similar to electrolytic etching, except a third electrode is included to monitor the etch potential, which is controlled using a potentiostat. This technique affords the greatest possible control over etching.

Heat tinting is a useful technique with austenitic stainless steels. Phase delineation is improved by first etching with a general-purpose reagent, such as Vilella's. The specimen is then heated in air at 500 to 700 °C (930 to 1290 °F); 650 °C (1200 °F) has been most commonly used, with times to 20 min. Austenite is colored more readily than ferrite (Fig. 19), and carbides resist coloration longest. After 20 min at 650 °C (1200 °F), austenite is blue-green, σ phase is orange, ferrite is light cream, and carbides are uncolored.

Magnetic colloids have also been used to detect ferromagnetic constituents in austenitic stainless steels. This technique has been extensively applied using a ferromagnetic colloid solution containing very fine magnetic particles (Ref 6). Delta-ferrite and strain-induced martensite are readily identified by this method.

Electron Microscopy. Scanning electron microscopy and transmission electron microscopy are used to examine the fine structure of stainless steels and for phase identification. Scanning electron microscopy examination uses the same specimens as light optical microscopy. As-polished specimens often can be examined, although etching is more common. Many second-phase constituents can be observed using backscattered electron detectors, due to the adequate atomic number contrast between these phases and the matrix. However, secondary electron images produced from topographic contrast and atomic number contrast are most often used. Energy-dispersive x-ray analysis (EDXA) is prevalent for chemical analysis of second phases, although lightweight elements, such as carbon and nitrogen, cannot be detected unless thin-window or windowless EDXA detectors or wavelength-dispersive detectors are used.

Transmission electron microscopy requires preparation of replica or thin-foil specimens. Replicas may be made to reveal the outline and topography of the phases, or, if the specimen is deeply etched, second-phase particles may be extracted. Extraction replicas permit analysis of second phases by electron diffraction and by EDXA. Thin-foil specimens can also be analyzed by these methods, although interference from the matrix is possible. Table 9 lists electropolishing procedures for producing stainless steel thin foils.

Table 9 Electropolishing procedures for preparing thin-foil stainless steel specimens

Solution composition	Comments
1. 5 or 10 mL $HClO_4$ and 95 or 90 mL acetic acid at 20 V dc	Popular electropolish for stainless steels. Used for window technique or for perforation of disk specimens. Keep solution cool
2. [(a)] 10 mL HNO_3 and 90 mL H_2O[(a)] at 50 V dc **(b) 10 mL, $HClO_4$, 20 mL glycerol, 70 mL ethanol at 65 V dc**	Popular procedures for austenitic grades. Use [(a)] to electrodish specimens, then (b) for perforation.
3. 10 mL $HClO_4$ and 90 mL ethanol at 12 V dc, 0 °C (32 °F)	Popular electropolish for stainless steels. Use for perforation.
4. 40 mL H_2SO_4 and 60 mL H_3PO_4 at 35 V dc, 0.3 A/cm^2 (1.9 A/in.^{2})	Electropolish for stainless steels for perforation
5. 25 g CrO_3, 133 mL acetic acid, 7 mL H_2O at 20 °C (70 °F)	Electropolish for stainless solution makes it difficult to use for jet perforation
6. [(a)] 40 mL acetic acid, 30 mL H_3PO_4, 20 mL HNO_3, 10 mL H_2O at 80–120 V dc, 0.1 A/cm^2 (0.65 A/in.^{2}) **(b) 54 mL H_3PO_4, 36 mL H_2SO_4, 10 mL ethanol at 6 V dc**	Procedure for austenitic grades. Jet electrodish disks with [(a)] prior to final thinning with (b) to perforation
7. 45 mL H_3PO_4, 30 mL H_2SO_4, 25 mL H_2O at 6 V dc	Procedure for austenitic grades for perforation

(a) When water is specified, use distilled water.

Bulk Extractions. Although bulk samples can be directly analyzed by x-ray diffraction for phase identification, it is quite common to extract the second phases chemically and analyze the extracted particles. This eliminates the matrix and concentrates the second phase, facilitating identification of small amounts of the second-phase

constituents. Bulk extraction of phases from stainless steels is performed using the same procedures as for heat-resistant grades (see the article “Metallography and Microstructures of Heat-Resistant Alloys” in this Volume).

References cited in this section

1. G.F. Vander Voort, *Metallography: Principles and Practice*, McGraw-Hill, 1984. Reprinted by ASM International, 1999

2. F.C. Bell and D.E. Sonon, Improved Metallographic Etching Techniques for Stainless Steel and for Stainless Steel to Carbon Steel Weldments, *Metallography*, Vol 9, 1976, p 91–107

3. J.M. Stephenson and B.M. Patchett, Grain-Boundary Etches for Austenitic and Ferritic Ni-Cr-Mo Corrosion-Resistant Alloys, *Sheet Met. Ind.*, Vol 56, 1979, p 45–50, 57

4. J.J. Gilman, Electrolytic Etching—The Sigma Phase Steels, *Trans. ASM*, Vol 44, 1952, p 566–600

5. E.J. Dulis and G.V. Smith, Identification and Modes of Formation and Re-Solution of Sigma Phase in Austenitic Chromium-Nickel Steels, in STP 110, ASTM, 1951, p 3–37

6. R.J. Gray, Magnetic Etching with Ferrofluid, *Metallographic Specimen Preparation*, Plenum Press, 1974, p 155–177

G.F. Vander Voort, G.M. Lucas, and E.P. Manilova, Metallography and Microstructures of Stainless Steels and Maraging Steels, *Metallography and Microstructures,* Vol 9, *ASM Handbook,* ASM International, 2004, p. 670–700

Metallography and Microstructures of Stainless Steels and Maraging Steels

George F. Vander Voort and Gabriel M. Lucas, Buehler Ltd.; Elena P. Manilova, Polzunov Central Boiler and Turbine Institute, St. Petersburg, Russia

Microstructures of Stainless Steels

The microstructures of stainless steels can be quite complex. Matrix structures vary according to the type of steel, such as ferritic, austenitic, martensitic, precipitation hardenable, or duplex. A wide range of second-phase constituents (Table 10) can be observed; welding or high-temperature exposure increases the complexity. Additional information is available in Ref 7.

Table 10 Second-phase constituents observed in stainless steels

Phase	Crystal structure	Lattice parameters, nm	Reported compositions	Comments
$M_{23}C_6$	Face-centered cubic	a_0 = 1.057–1.068	$(Cr_{16}Fe_5Mo_2)C_6$ $(Cr_{17}Fe_{4.5}Mo_{1.5})C_6$ $(Fe,Cr)_{23}C_6$	Most commonly observed carbide in austenitic stainless steels. Precipitates from 500–950 °C (930–1740 °F), fastest at 650–700 °C (1200–1290 °F)
M_6C	Face-centered cubic	a_0 = 1.085–1.111	$(Cr,Co,Mo,Ni)_6C$ $(Fe_3Mo_3)C$ Fe_3Nb_3C $(Fe,Cr)_3Nb_3C$	Observed in austenitic grades containing substantial molybdenum or niobium after long time exposure
M_7C_3	Hexagonal	a_0 = 1.398 c_0 = 0.4523	Cr_7C_3	Observed in martensitic grades
MC	Cubic	a_0 = 0.430–0.470	TiC NbC	Observed in alloys with additions of titanium or niobium. Very stable carbide. Will usually contain some nitrogen
Sigma (σ)	Tetragonal	a_0 = 0.8799–0.9188 c_0 = 0.4544–0.4599	FeCr FeMo Fe(Cr,Mo) $(Fe,Ni)_x(Cr,Mo)_y$	Formation from δ-ferrite is much more rapid than from austenite. Potent embrittler below 595 °C (1105 °F). Forms with long time exposure from 650–900 °C (1200–1650 °F)
Chi (χ)	Body-centered cubic: (α-Mn structure)	a_0 = 0.8862–0.892	$Fe_{36}Cr_{12}Mo_{10}$ $(FeNi)_{36}Cr_{18}Mo_4$ $M_{18}C$	Observed in alloys containing substantial molybdenum. Chi precipitates with exposure to 730–1010 °C (1345–1850 °F) (varies with alloy composition).
Laves	Hexagonal	a_0 = 0.470–	Fe_2Mo	Forms in austenitic alloys with substantial

(η)	0.4744		amounts of molybdenum, titanium, or
		($Ti_{21}Mo_9$)	niobium after long time exposure from 600–1100 °C (1110–2010 °F)
	c_0 = 0.772–0.7725	($Fe_{50}Cr_5Si_5$)	

Austenitic Stainless Steels. The most commonly used stainless steels are the austenitic grades, of which AISI 302, 304, and 316 are the most popular wrought grades, and CF-8 and CF-8M are the most popular cast grades. These grades contain 16% or more chromium, a ferrite-stabilizing element, and sufficient austenite-stabilizing elements, such as carbon, nitrogen, nickel, and manganese, to render austenite stable at room temperature. The grades containing silicon, molybdenum, titanium, or niobium—AISI 302B, 316, 317, 321, and 347, for example—will sometimes include a minor amount of δ-ferrite because of the ferrite-stabilizing influence of these elements. Alloys with substantial nickel are fully austenitic, for example, AISI 310 or 330. For alloys susceptible to δ-ferrite stabilization, the amount present will depend on the composition, chemical homogeneity, and hot working. Alloys with especially low carbon contents to minimize susceptibility to sensitization during welding (AISI 304L, 316L, or 317L, for example) will have a greater tendency toward δ-ferrite stabilization. Figure 26 shows examples of δ-ferrite stringers in wrought 203, 302-HQ, 304, and 316L stainless steels.

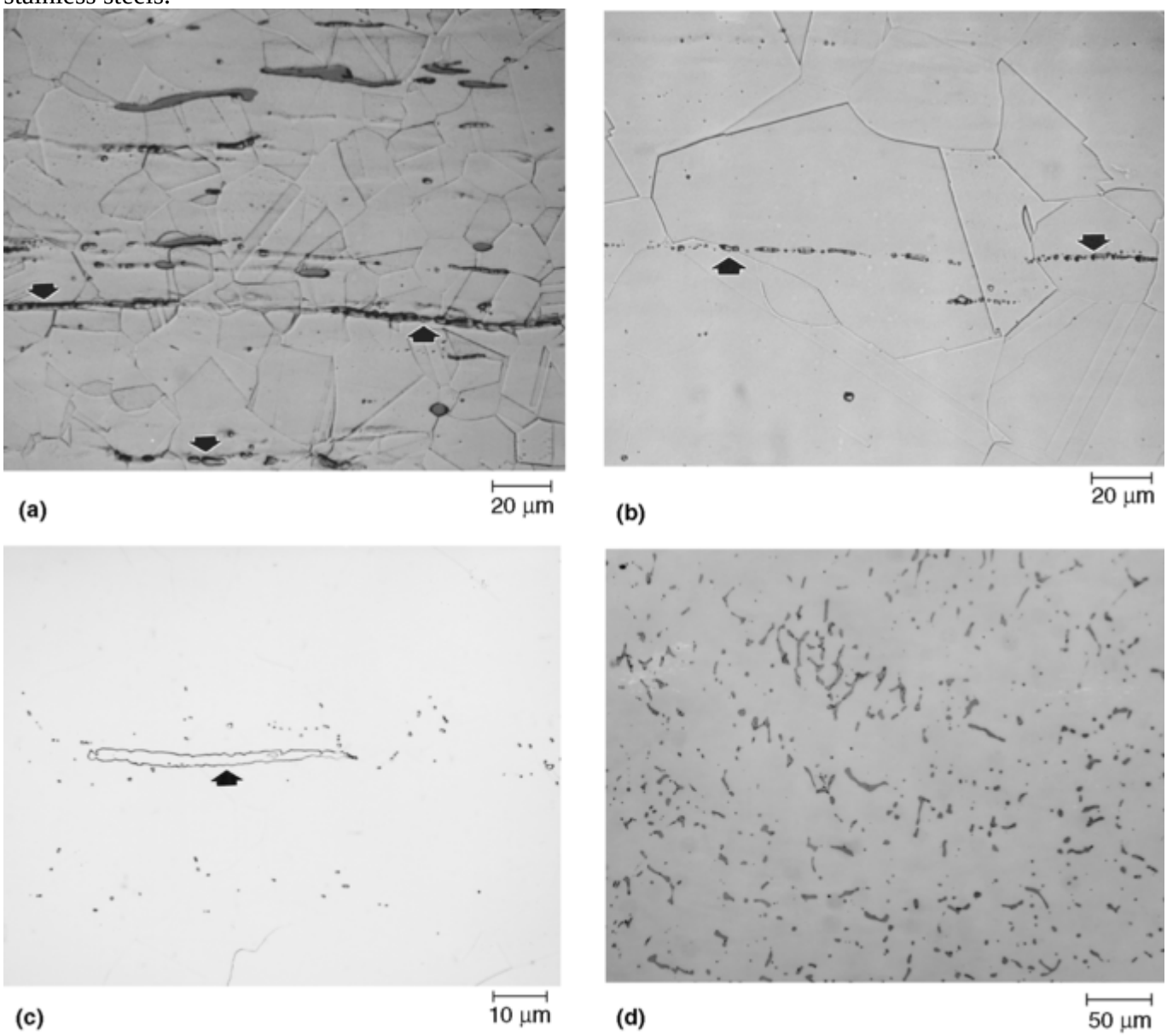

Fig. 26 Examples of δ-ferrite stringers (arrows) in austenitic stainless steels. (a) 203 etched with Ralph's reagent. (b) 302-HQ etched with waterless Kalling's reagent. (c) 316L etched with glyceregia. (d) 304 etched with aqueous 20% NaOH at 3 V dc for 20 s

Alloys CF-3 through CF-16F in Table 3 are austenitic, with limited amounts of ferrite; alloys CF-20, CK-20, and CN-7M are completely austenitic. They exhibit maximum corrosion resistance in the solution-treated condition. The corrosion resistance of certain alloys is enhanced by extralow carbon content (as in CF-3), a molybdenum addition (as in CF-3M and CF-8M), or the addition of niobium (as in CF-8C). Alloy CF-16F contains 0.20 to 0.35% Se for improved machinability. Figure 27 shows the microstructure of as-cast and as-cast and solution-annealed CF-8M. Figure 28 shows the microstructure of as-cast type 301, and Fig. 29 shows the microstructure of as-cast 316 stainless steel (wrought grades before hot working). Note that in the as-cast condition, both contain substantial ferrite. However, after hot working, they will be free or nearly free of ferrite.

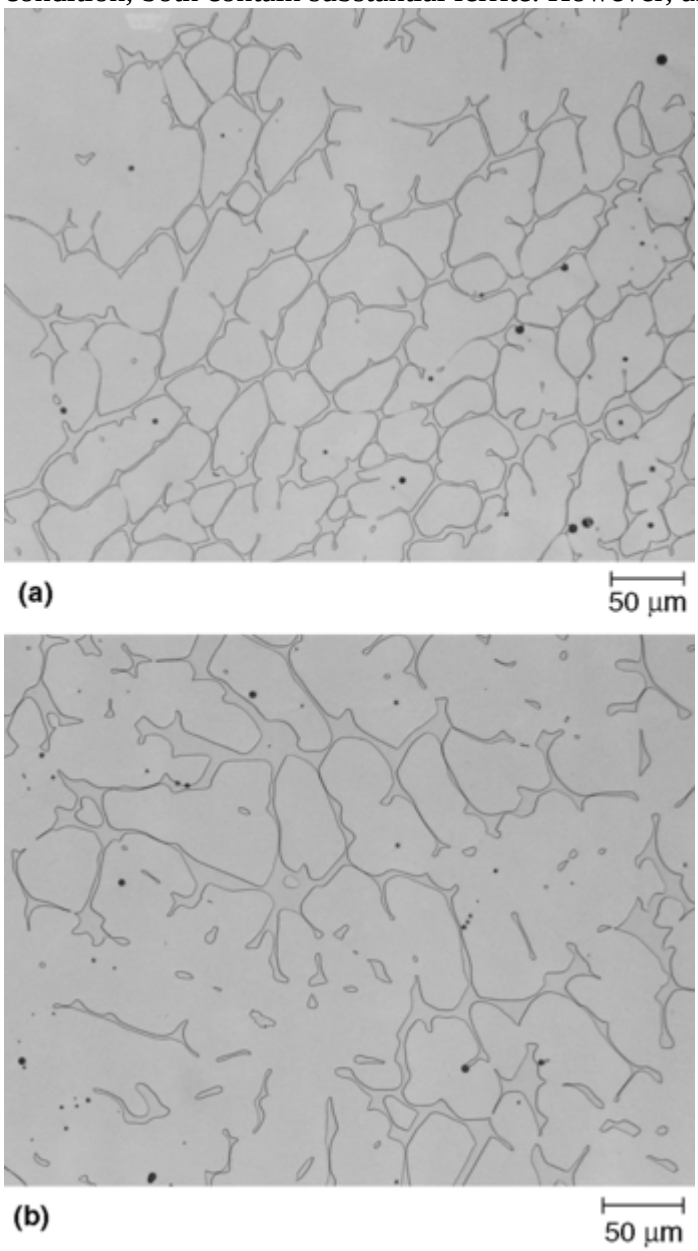

Fig. 27 Ferrite in CF-8M stainless steel in the (a) as-cast condition and (b) after solution annealing. Revealed using glyceregia

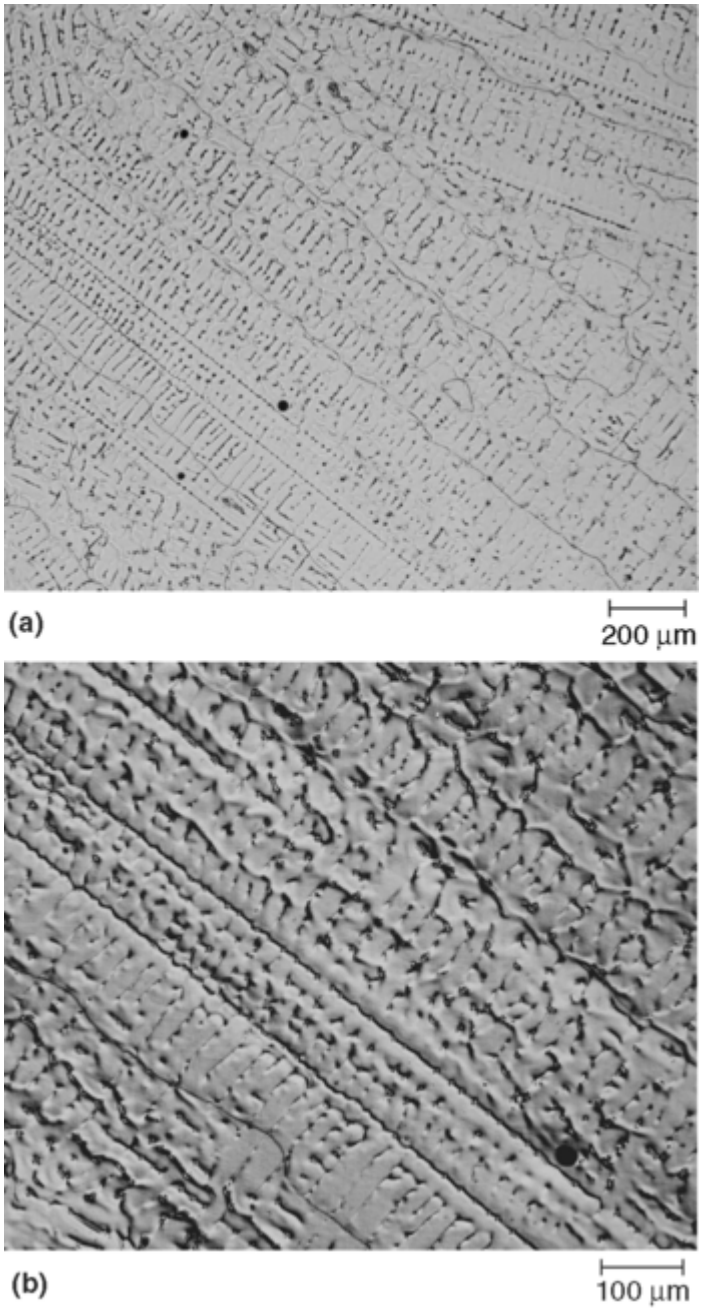

Fig. 28 As-cast microstructure of type 301 stainless steel, revealed using Ralph's reagent. (a) Bright field. (b) Nomarski differential interference contrast

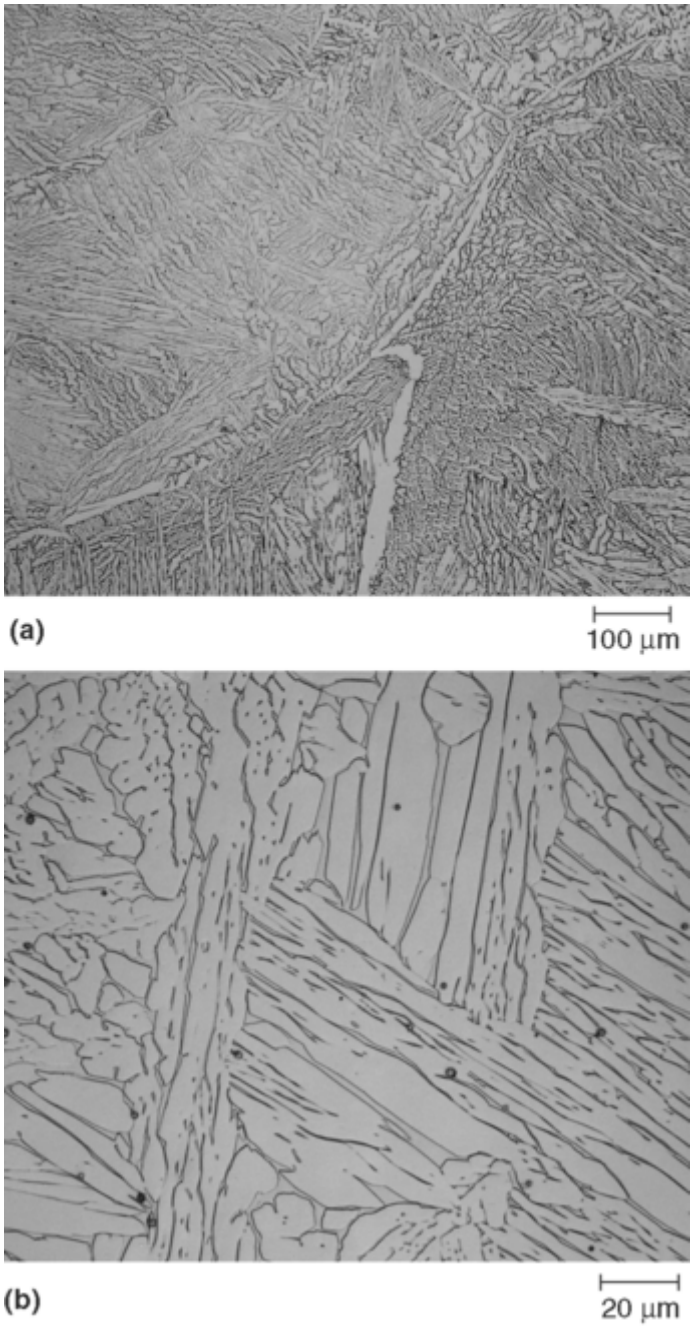

Fig. 29 As-cast microstructure of 316 stainless steel contains considerable δ-ferrite. Revealed using glyceregia.

Numerous studies have been conducted to predict matrix phases based on chemical composition. Most of these studies have concentrated on predicting weldment microstructures (Ref 8, 9, 10, 11, 12, 13, 14, 15); others have concentrated on predicting cast microstructures (Ref 16, 17, 18) or predicting structures at the hot-working temperature (Ref 19) or after hot working (Ref 20). Measurement of the δ-ferrite content of stainless steels, particularly weldments, has been widely studied (Ref 21, 22, 23, 24).

The austenite in these grades is not stable but metastable. Martensite can be formed, particularly in the leaner grades, by cooling specimens to very low temperatures or by extensive plastic deformation. Nonmagnetic, hexagonal close-packed ε-martensite and magnetic, body-centered cubic (bcc) α′-martensite have been observed. Empirical relationships have been developed to show how composition influences the resistance of such steel to deformation-induced martensite (Ref 25, 26). Figure 30 shows examples of martensite formed in cold-worked specimens of 203, 303, 303Se, and 304 stainless steels. In alloys where the austenite is more stable, cold working does not produce martensite. Because austenitic alloys are face-centered cubic, they have twelve well-developed slip systems, and only slip lines are observed, as shown in the examples for 302-HQ and 316L in Fig. 31. Figure 32 shows the slip in type 347 stainless steel, cold drawn with 5, 10, 15, and 30%

reductions. Cold drawing affects the metal at the surface far more than in the interior; thus, the slip line density will be highest at the surface and lowest at the center.

Fig. 30 Martensite (arrows) produced by cold working austenitic stainless steels. (a) 203 etched with Ralph's reagent. (b) 303 etched with Ralph's reagent. (c) 303 etched with Lucas reagent. (d) 303Se etched with waterless Kalling's reagent. (e) 304 etched with Vilella's reagent. (f) Same specimen as in (e) but higher magnification

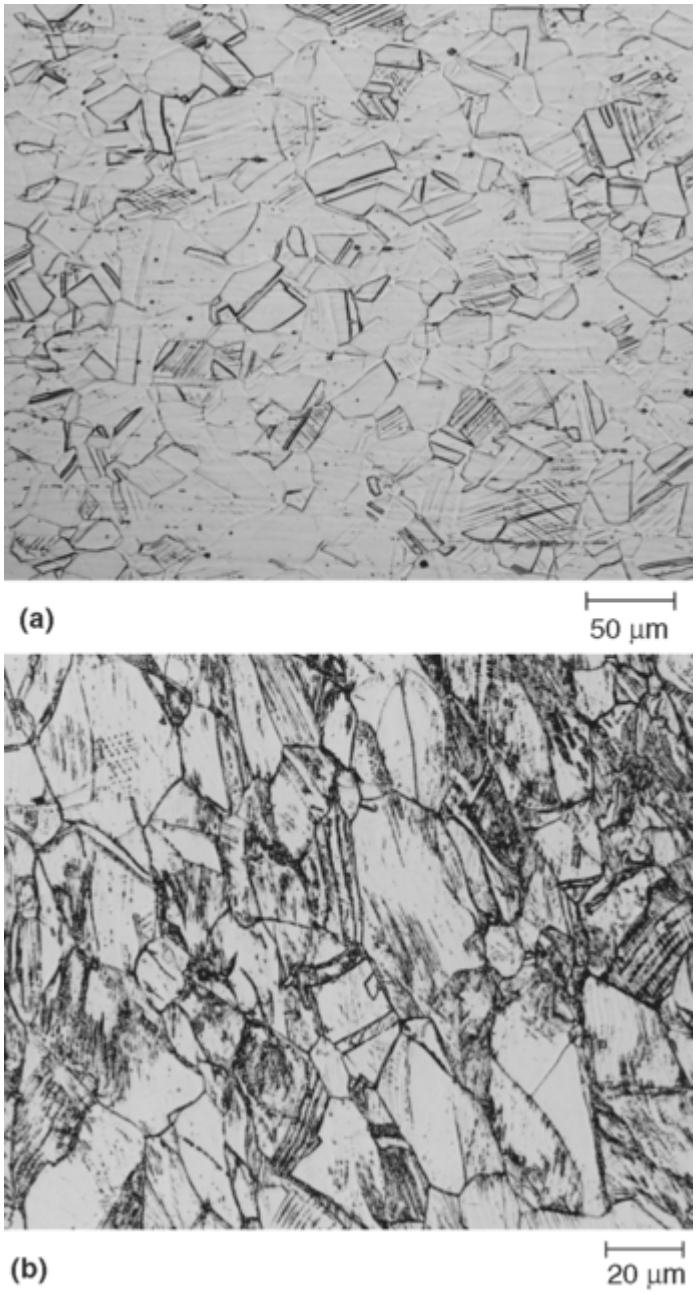

Fig. 31 Slip produced by cold working. (a) 302-HQ etched with waterless Kalling's reagent. (b) 316L stainless steel etched with glyceregia

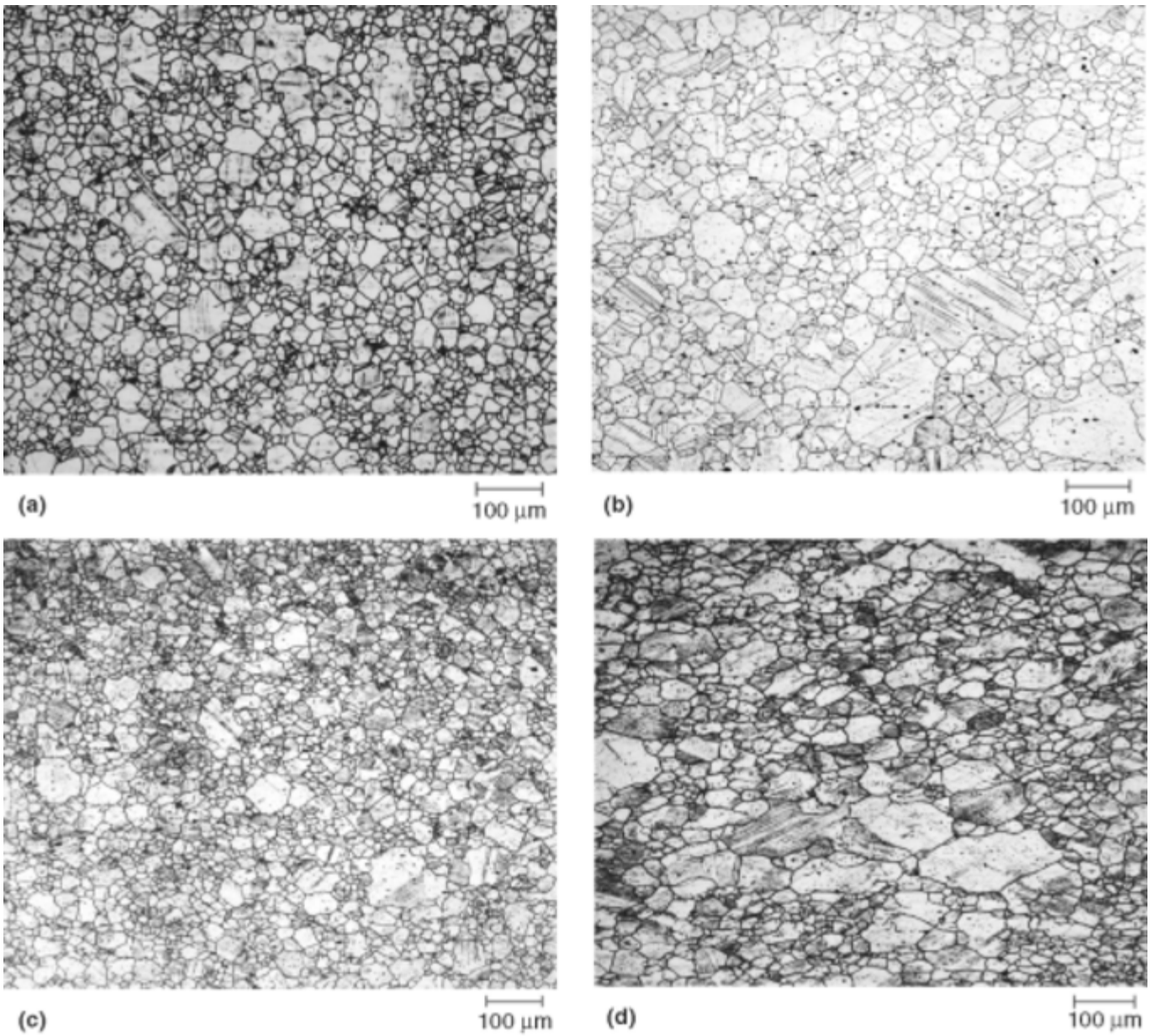

Fig. 32 Slip near the surface of cold-drawn 347 stainless steel reduced (a) 5%, (b) 10%, (c) 15%, and (d) 30% in diameter. Revealed using aqueous 60% HNO_3 at 4 V dc

Carbon content limits are generally 0.03, 0.08, or 0.15% in the austenitic grades. Solution annealing will usually dissolve all, or most of, the carbides present after hot rolling. Rapid quenching from the solution-annealing temperature of generally 1010 to 1065 °C (1850 to 1950 °F) will retain the carbon in solution, producing a strain-free, carbide-free austenitic microstructure. Some of these grades are water quenched from the hot working temperature. When properly performed, the solution-annealed structure should exhibit a single grain size distribution, with equiaxed grains containing annealing twins. Examples for a number of alloys are given in Fig. 33. The more highly alloyed grades can be quite difficult to etch and obtain full delineation of the grain structure. In such cases, use of Nomarski differential interference contrast illumination is very helpful in bringing out the grain structure as well as the alloy segregation, as shown in Fig. 33(i) to (l). However, grain structures are not always equiaxed and unimodal, especially in as-hot-worked specimens. Figure 34 shows examples of bimodal grain size distributions in austenitic stainless steels.

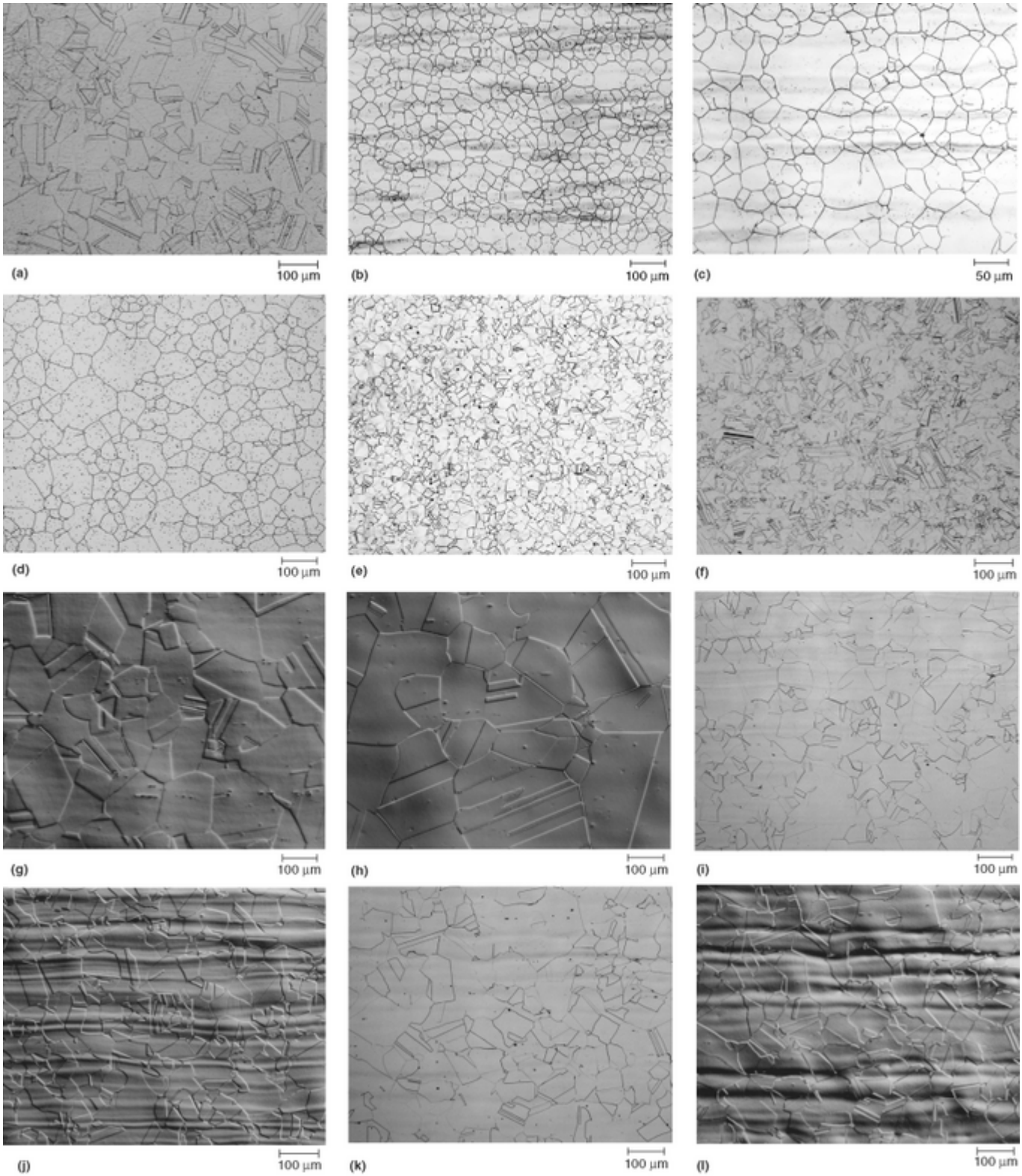

Fig. 33 Austenitic grain boundaries revealed in (a) 302-HQ etched with waterless Kalling's, (b) 304 Modified etched with aqueous 60% HNO_3 at 1 V dc for 90 s, (c) 316L etched as in (b) but for 20 s, (d) concast 316 etched with aqueous 60% HNO_3 at 1.5 V dc for 60 s, (e) 330 etched as in (d), (f) Nitronic 50 etched with glyceregia, (g) 18-18 PLUS etched with 15 HCl-10 HNO_3-10 acetic acid, (h) 20 Mo-6 etched as for (g), (i) AL-6XN plate etched as in (g), (j) same field as (i) but viewed with Nomarski differential interference contrast, (k) SCF-23 etched as in (g), and (l) same field as (k) but viewed with Nomarski differential interference contrast. (g) and (h) also viewed with Nomarski DIC.

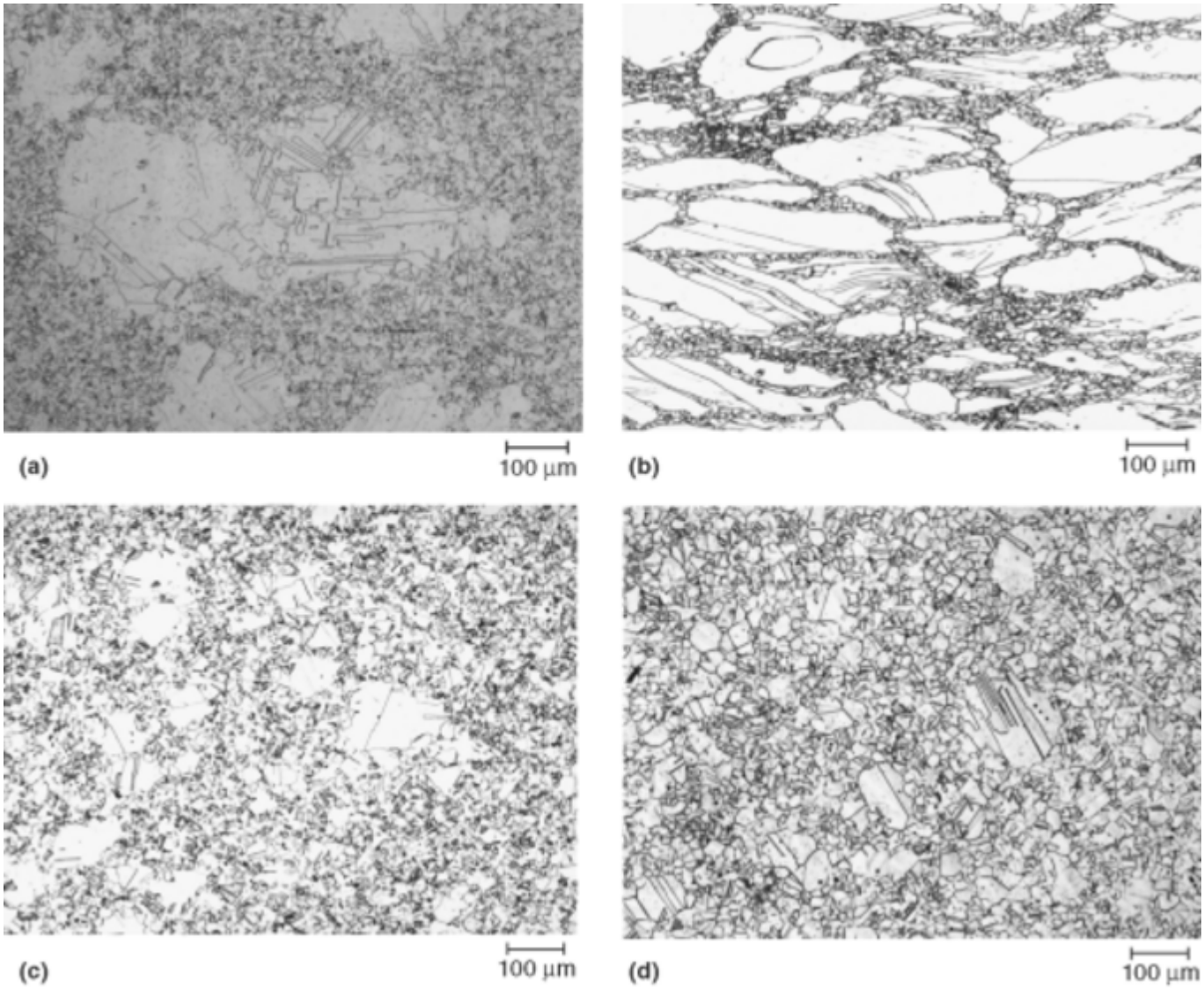

Fig. 34 Duplex grain structures observed in (a) Nitronic 50 etched with glyceregia, (b) SCF-19 etched with aqueous 60% HNO_3 at 1 V dc for 60 s ("necklace"-type condition), (c) 22-13-5 etched with waterless Kalling's reagent, and (d) 330 etched as in (b) but at 1.5 V dc

The most widely observed carbide type in austenitic stainless steels is $M_{23}C_6$, which is often referred to as $Cr_{23}C_6$, but more properly is $(Cr, Fe)_{23}C_6$ or $(Cr, Fe, Mo)_{23}C_6$. The precipitation of this carbide at grain boundaries during welding produces intergranular corrosion. To counter sensitization during welding, carbon contents are reduced or strong carbide formers are added, as in AISI 321 and 347.

Precipitation of $M_{23}C_6$ carbide occurs as a result of heating solution-annealed grades to 500 to 950 °C (930 to 1740 °F); the fastest rate of precipitation takes place from 650 to 700 °C (1200 to 1290 °F). Precipitation occurs first at austenite/δ-ferrite phase boundaries, when present, followed by precipitation at other noncoherent interfaces (grain and twin boundaries), and finally by precipitation at coherent twin boundaries. In addition, $M_{23}C_6$ may precipitate at inclusion/matrix-phase boundaries.

The appearance of $M_{23}C_6$ varies with the precipitation temperature and time. It is most easily studied using extraction replicas. At the lower precipitation temperatures, $M_{23}C_6$ has a thin, continuous, sheetlike morphology. When the precipitation temperature is 600 to 700 °C (1110 to 1290 °F), feathery dendritic particles form at boundary intersections. With time, these precipitates coarsen and thicken. At still higher precipitation temperatures, $M_{23}C_6$ forms at grain boundaries as discrete globular particles whose shape is influenced by the boundary orientation, degree of misfit, and temperature (Ref 27). The $M_{23}C_6$ that precipitates at noncoherent twin boundaries is lamellar or rodlike; that which precipitates at coherent twin boundaries is platelike. The $M_{23}C_6$ that forms at the lower precipitation temperatures is most detrimental to intergranular corrosion resistance. Examples of sensitized grain structures are shown in Fig. 35.

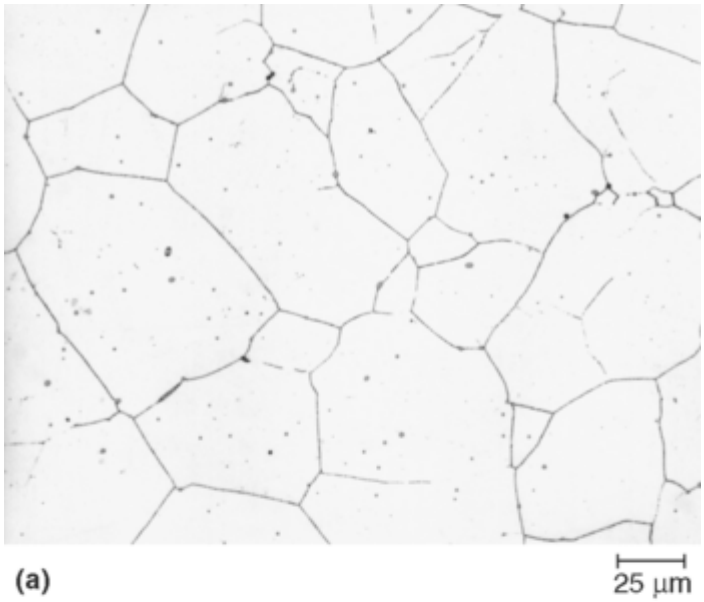

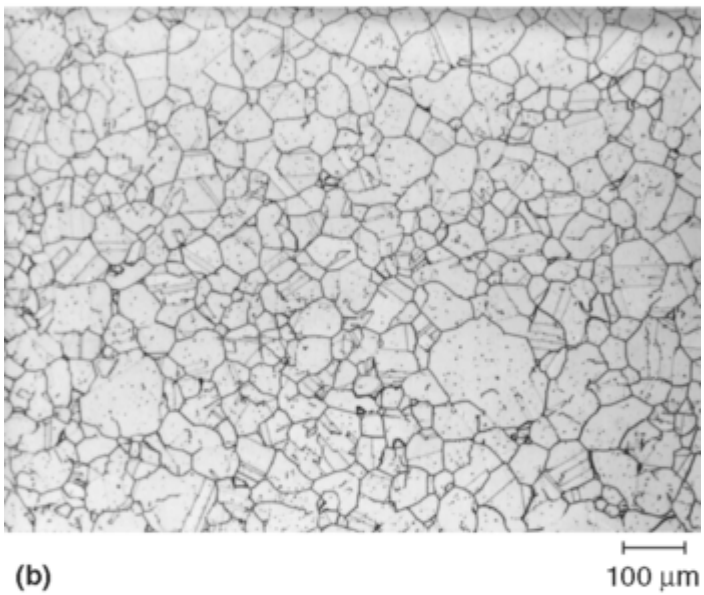

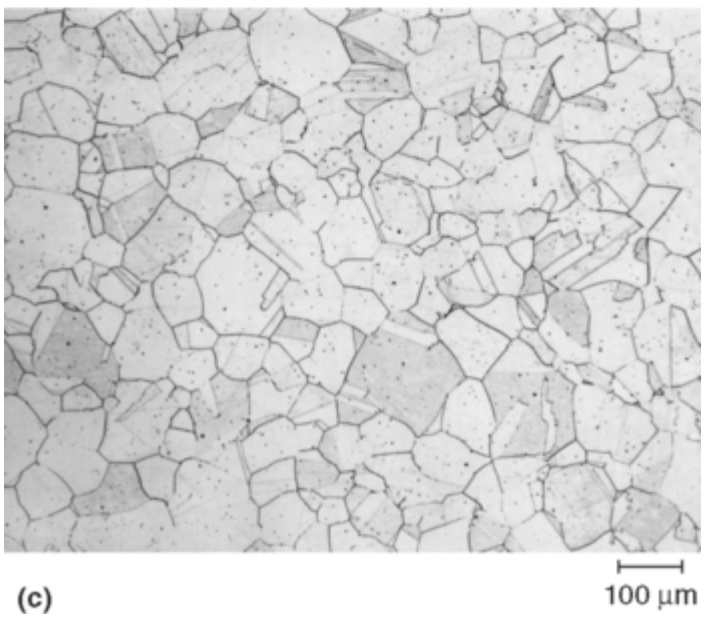

Fig. 35 Grain-boundary carbides in sensitized (a) 304 etched with Ralph's reagent, (b) 304 etched with aqueous 10% ammonium persulfate at 6 V dc for 10 s, and (c) 316 etched as in (a)

Alloys given deliberate minor additions of titanium or niobium—AISI 321 and 347, for example—form titanium or niobium carbides, rather than $M_{23}C_6$. To take full advantage of these additions, solution-annealed specimens are subjected to a stabilizing heat treatment to precipitate the excess carbon as titanium or niobium carbides. This treatment is commonly used with AISI 321 and involves holding the specimen several hours at 845 to 900 °C (1550 to 1650 °F). These MC-type carbides will precipitate intragranularly at dislocations or stacking faults within the matrix. Some may also precipitate on grain boundaries.

Additions of titanium or niobium must be carefully controlled to neutralize the carbon in solution. In practice, titanium and niobium carbides can contain some nitrogen, and both can form rather pure nitrides. Titanium nitrides usually appear as distinct, bright-yellow cubic particles. Titanium carbide is grayish, with a less regular shape. Titanium carbonitride will have an intermediate appearance that varies with the carbon/nitrogen ratio. Chromium nitrides are not usually observed in the austenitic grades, unless the service environment causes substantial nitrogen surface enrichment or they are nitrogen strengthened.

Carbides of the M_6C type are observed in austenitic grades containing substantial molybdenum or niobium additions. It usually precipitates intragranularly. For example, in AISI 316 with 2 to 3% Mo, M_6C will form after approximately 1500 h at 650 °C (1200 °F). Several types of M_6C have been observed, including Fe_3Mo_3C, Fe_3Nb_3C, and $(Fe, Cr)_3Nb_3C$.

Several types of sulfides have been observed in austenitic grades. The most common form is MnS. However, if the manganese content is low, chromium will replace some of the manganese in the sulfide. At manganese contents less than approximately 0.20%, pure chromium sulfides will form. Because these are quite hard, machinability (tool life) will be poor. Figure 36 shows manganese sulfides in types 203 and 303 resulfurized austenitic grades. Some free-machining grades have additions of selenium and sulfur to form manganese selenides as well as manganese sulfides. Figure 30(d) shows the manganese selenides in 303Se. In grades with substantial titanium, several forms of titanium sulfides have been observed, including Ti_2S, Ti_2SC, and $Ti_4C_2S_2$.

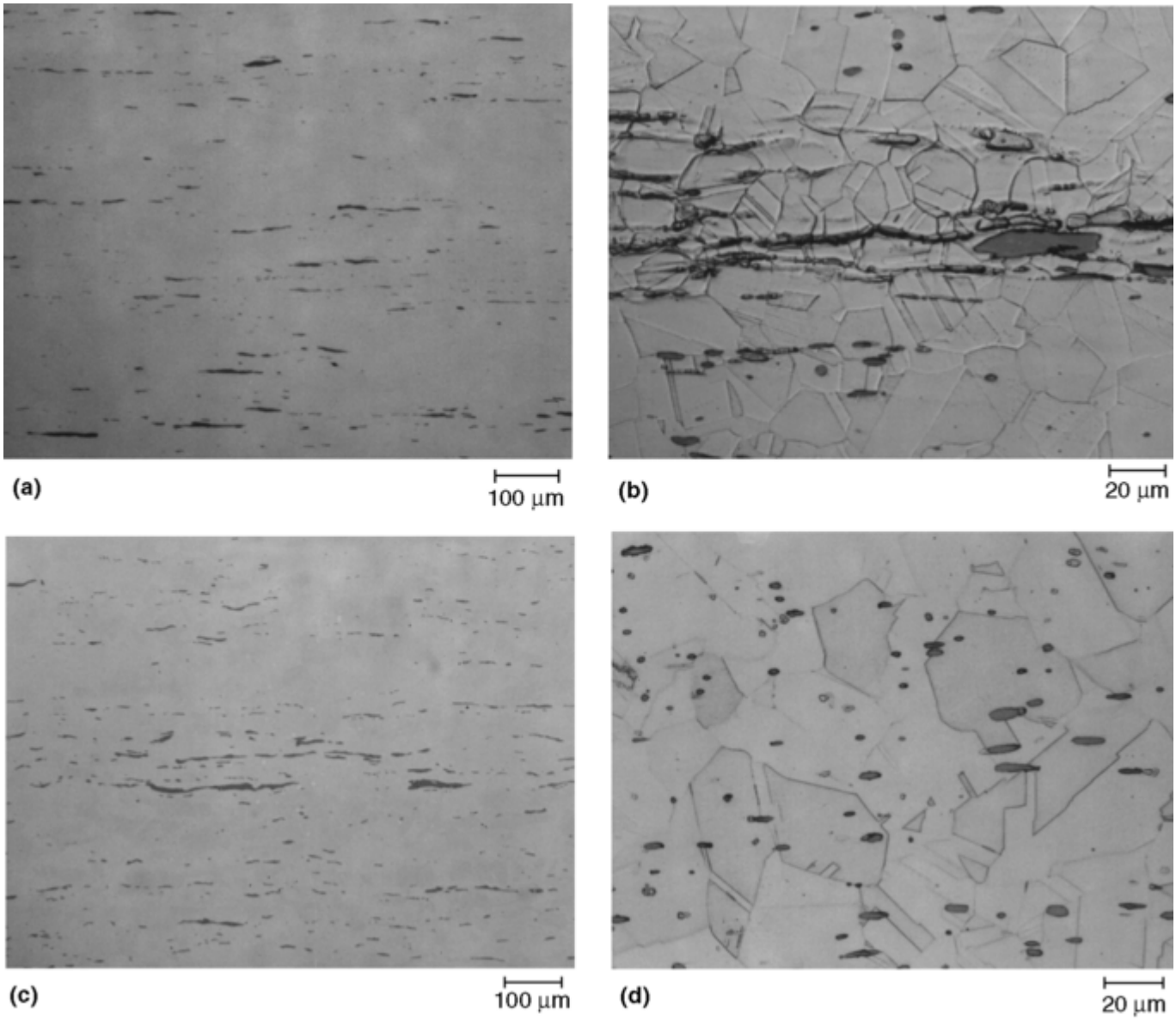

Fig. 36 Examples of the grain structures of resulfurized stainless steels revealed using Ralph's reagent. (a) and (b) 203. (c) and (d) 303

Several intermetallic phases may be formed by high-temperature exposure. These phases form from titanium, vanadium, and chromium (“A” elements) and from manganese, iron, cobalt, and nickel (“B” elements). Some of these phases are stoichiometric compounds. Probably the most important is σ phase, first observed in 1927. The leaner austenitic grades free of δ-ferrite are relatively immune to σ-phase formation, but the higher alloy grades and those containing δ-ferrite are prone to its formation. Sigma is frequently described as FeCr, although its composition can be quite complex and variable, ranging from B_4A to BA_4.

Certain elements, such as silicon, promote σ-phase formation. Cold working also enhances subsequent σ-phase formation. Empirical equations based on composition have been developed to predict the tendency toward σ-phase formation (Ref 28, 29). Sigma is a very potent embrittler whose effects are observable at temperatures below approximately 595 °C (1100 °F). Sigma also reduces resistance to strong oxidizers. The morphology of σ phase varies substantially. Etching techniques (Ref 5, 30, 31, 32) have been widely used to identify σ phase in stainless steels (Fig. 19), but x-ray diffraction is more definitive. Although its crystal structure is tetragonal, σ phase does not respond to crossed-polarized light.

Chi phase (Ref 33, 34, 35, 36, 37, 38) is observed in alloys containing substantial additions of molybdenum subjected to high-temperature exposure. Chi can dissolve carbon and exist as an intermetallic compound or as a carbide ($M_{18}C$). It is often observed in alloys susceptible to σ-phase formation and has a bcc, α-manganese-type crystal structure. Several forms of the intermetallic phase have been identified, as shown in Table 10. Chi

nucleates first at grain boundaries, then at incoherent twin boundaries, and finally intragranularly (Ref 38). Chi varies in shape from rodlike to globular. As with σ phase, cold work accelerates nucleation of χ phase.

Laves phase (η phase) can also form in austenitic stainless steels after long-term high-temperature exposure (Ref 37, 38). Alloys containing molybdenum, titanium, and niobium are most susceptible to Laves formation. Precipitation occurs from 650 to 950 °C (1200 to 1740 °F). Laves is a hexagonal intermetallic compound of AB_2 form. Several types have been observed, as shown in Table 10. Laves phase precipitates intragranularly and exists as globular particles.

Other phases have been observed in stainless steels but less often than those discussed previously. Among these is R phase (Ref 39, 40, 41), which has been observed in an Fe-12Cr-CoMo alloy and in welded AISI 316. A globular nickel-titanium silicide, G phase, was observed in a 26Ni-15Cr heat-resistant A-286-type alloy and was attributed to grain-boundary segregation (Ref 42). A chromium-iron-niobide phase, Z phase (Ref 43), was detected in an 18Cr-12Ni-1Nb alloy after creep testing at 850 °C (1560 °F). Table 10 summarizes the more common second-phase constituents observed in stainless steels. Austenitic grades, chiefly 304, have been modified with additions of boron to produce chromium borides. These steels have been used as control rods (using boron enriched in the B^{10} isotope, Fig. 37), and for nuclear waste containment (Fig. 38). Etching with waterless Kalling's reagent will outline the borides, and a deeper etch will bring up the austenite grain structure.

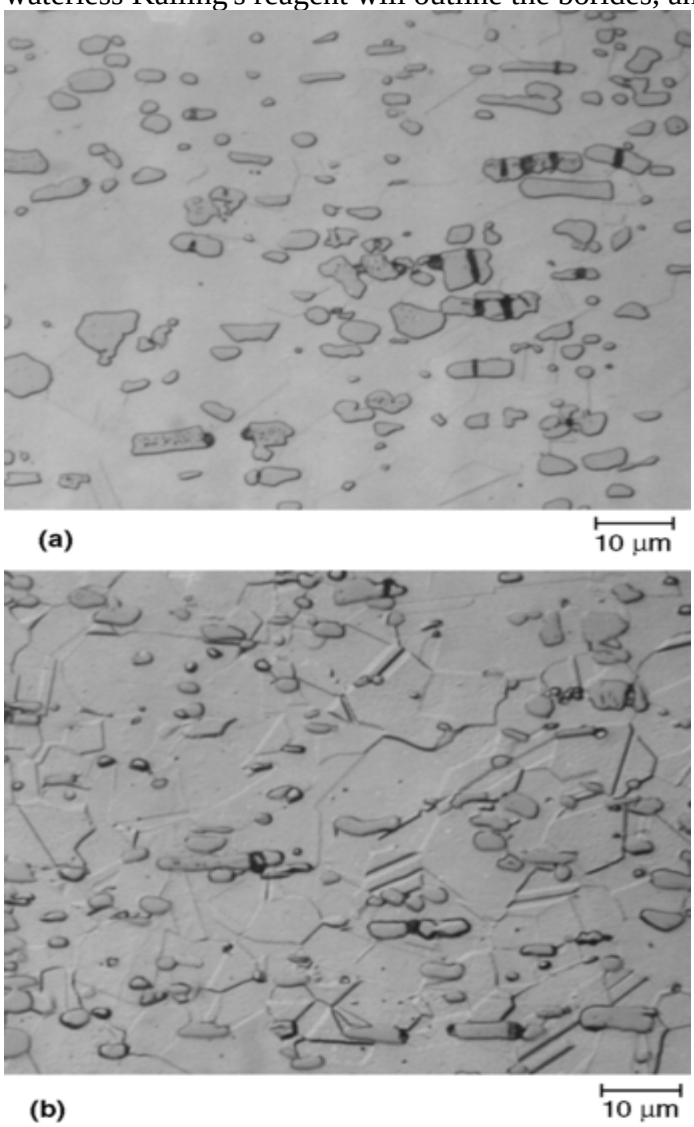

Fig. 37 The microstructure of 304 stainless steel plus boron enriched in the B^{10} isotope for nuclear reactors (Nautilus-class submarines). (a) Etched with waterless Kalling's reagent. (b) Etched with waterless Kalling's reagent but heavier than (a) to reveal the grain boundaries

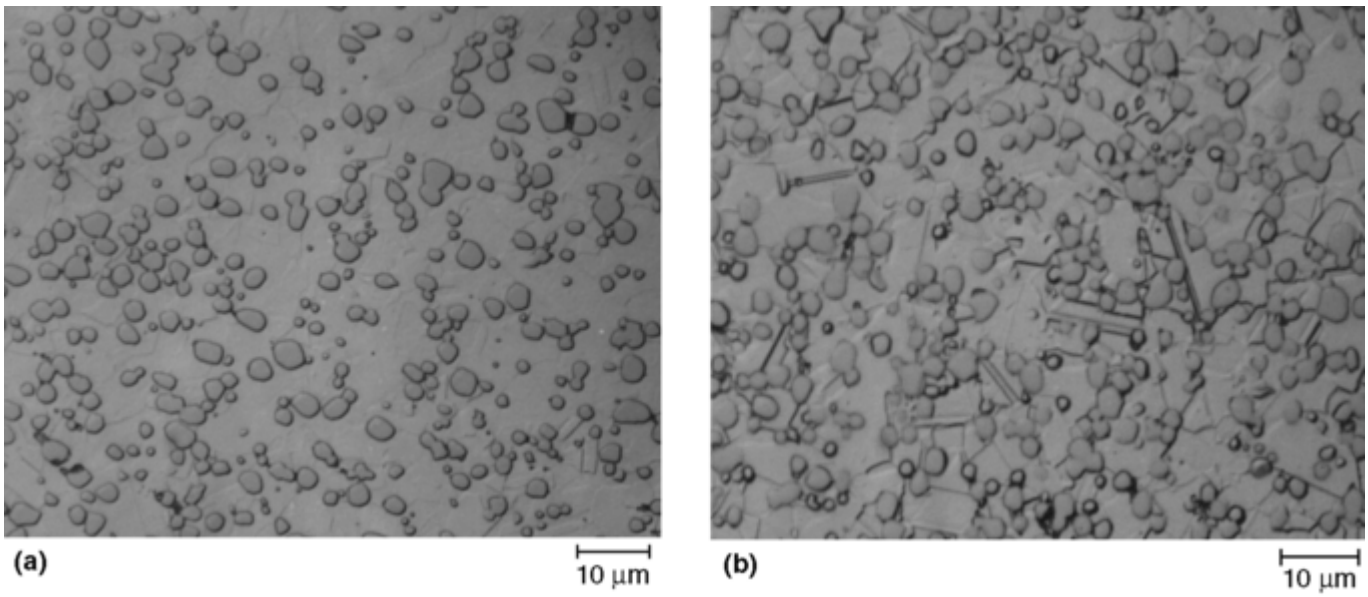

Fig. 38 The microstructure of powder metallurgy 304 stainless steel plus 1.75% B for nuclear waste containment. (a) Etched with waterless Kalling's reagent. (b) Etched with waterless Kaling's reagent but heavier than (a) to reveal the grain boundaries

The ferritic stainless steels (Ref 44) are basically iron-chromium alloys with enough chromium and other elements to stabilize bcc ferrite at all temperatures. Carbon and nitrogen contents must be minimized. The microstructure of these alloys consists of ferrite plus small amounts of finely dispersed $M_{23}C_6$, but other phases may form due to high-temperature exposure. However, because of severe embrittlement problems, these alloys are generally not used for elevated-temperature service.

The ferritic grades depend on solid-solution strengthening, because heat treatment cannot be used to harden the alloys or produce grain refinement. Quenching ferritic alloys from high temperatures produces only very slight increases in hardness. However, because many users desire higher strengths, steelmakers often make type 430 with a carbon content high in the allowable range (<0.12% C is specified), rather than keeping carbon as low as possible. This results in a duplex ferrite-martensite grade that can be heat treated to higher strength levels. Figure 39 illustrates the microstructure of a duplex 430 grade. Type 430 is also made with high sulfur for improved machinability (Fig. 40). However, the classic ferritic stainless steel contains only ferrite grains, as illustrated by the examples in Fig. 8 and 41. Figure 42 shows the microstructure of a weld in 29-4 ferritic stainless steel.

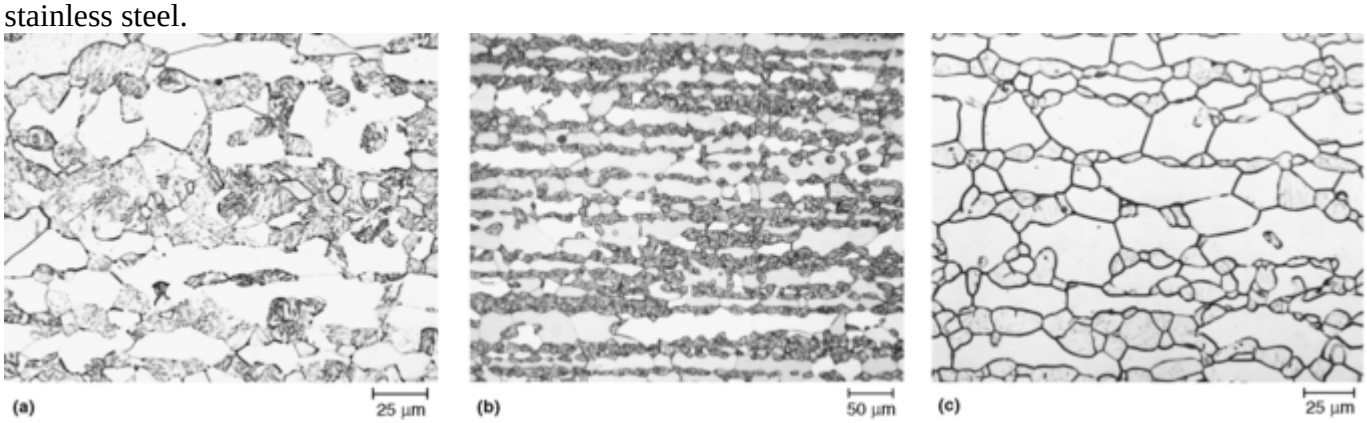

Fig. 39 Microstructure of high-carbon type 430 stainless steel with a duplex martensite-ferrite grain structure, revealed using (a) glyceregia, (b) Beraha's tint etch, and (c) aqueous 60% HNO_3 at 1 V dc for 60 s

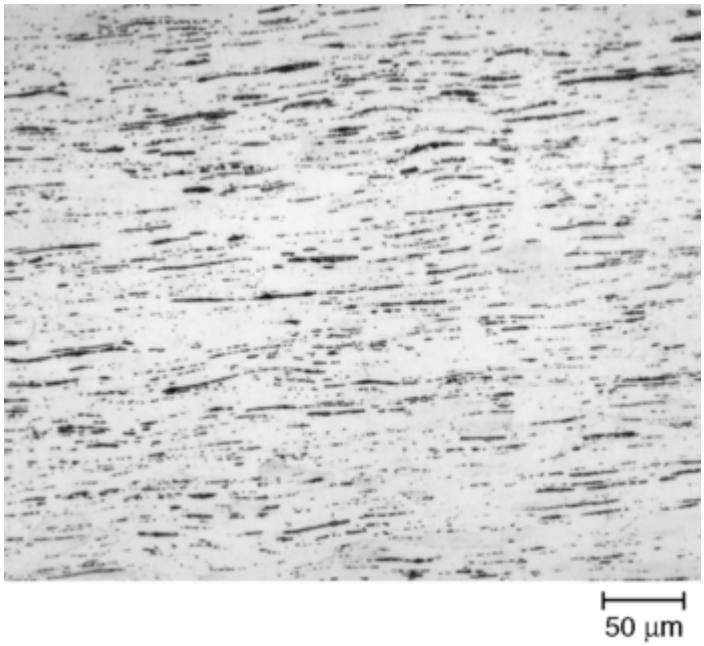

Fig. 40 Microstructure of 430F resulfurized steel etched lightly with Ralph's reagent

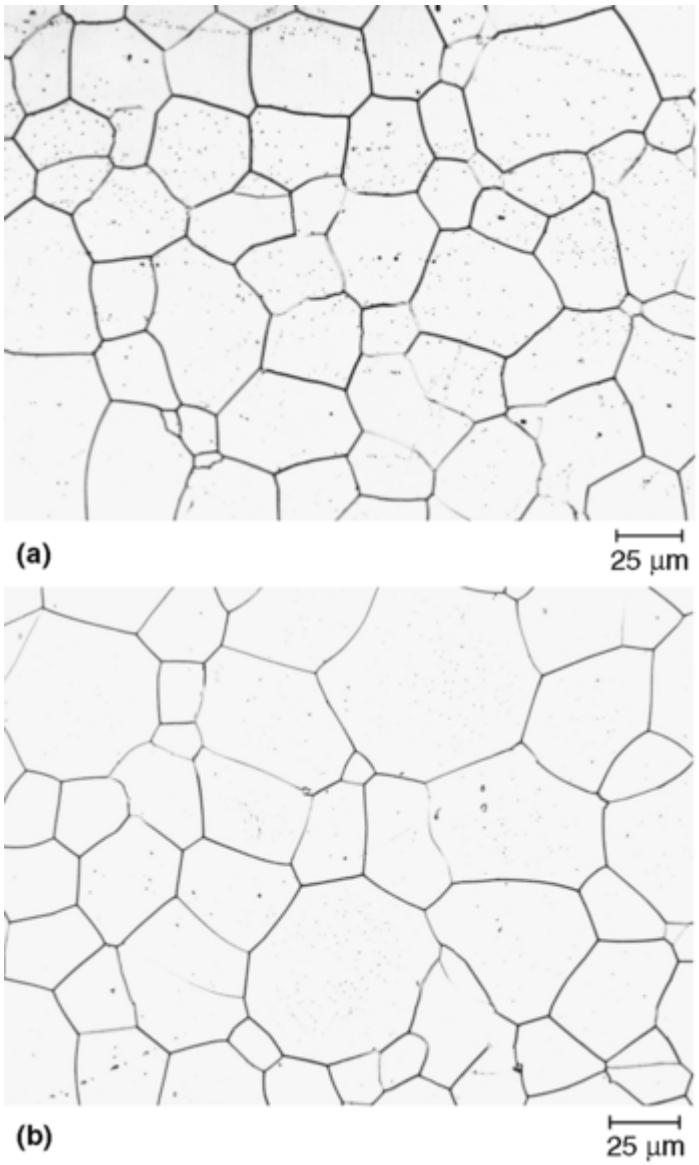

Fig. 41 Ferritic grain structure of (a) Monit and (b) Seacure stainless steels etched with aqueous 60% HNO_3 at 1.5 V dc for 120 s

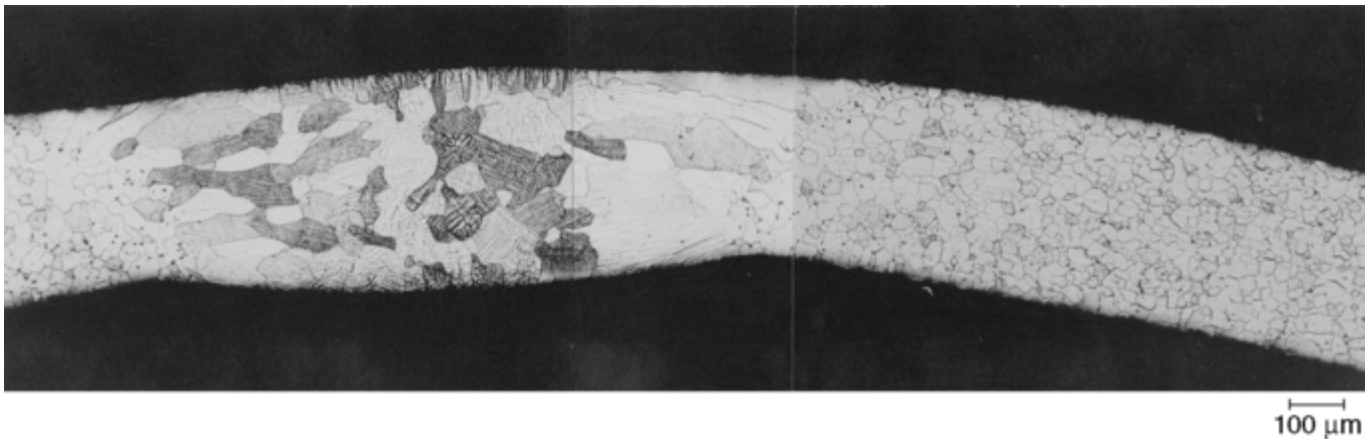

Fig. 42 Ferritic grain structure of a welded 29-4 ferritic tube etched with aqueous 60% HNO_3 at 1.5 V dc

Three forms of embrittlement can occur in ferritic stainless steels: σ-phase embrittlement, 475 °C (885 °F) embrittlement, and high-temperature embrittlement. Sigma is difficult to form in alloys with less than 20% Cr but forms readily in alloys with 25 to 30% Cr when heated between 500 and 800 °C (930 and 1470 °F). Molybdenum, silicon, nickel, and manganese additions shift the σ-forming tendency to lower chromium contents. As with the austenitic grades, σ phase severely reduces ductility and toughness below approximately 600 °C (1110 °F). Sigma can be redissolved by holding for a few hours above 800 °C (1470 °F).

Ferritic stainless steels are susceptible to embrittlement when heated from 400 to 540 °C (750 to 1005 °F), a condition referred to as 475 °C (885 °F) embrittlement. Embrittlement, which increases with time at temperature, is caused by production of chromium-rich and iron-rich ferrites but can be removed by heating above approximately 550 °C (1020 °F). Under identical aging conditions, embrittlement increases with increasing chromium content.

High-temperature embrittlement occurs in alloys with moderate to high interstitial carbon and nitrogen contents heated above 950 °C (1740 °F) and cooled to room temperature, resulting in severe embrittlement and loss of corrosion resistance. This has been attributed to chromium depletion adjacent to precipitated carbides and nitrides. The properties of such a sensitized specimen can be improved by heating to 700 to 950 °C (1290 to 1740 °F), which allows chromium to diffuse to the depleted areas. A better procedure, however, is to reduce the carbon and nitrogen contents to very low levels, which also improves toughness and weldability. Strong carbide-forming elements, such as titanium and niobium, may also be added.

Martensitic Stainless Steels. The hardenable martensitic stainless steels contain more than 10.5% Cr plus other austenite-stabilizing elements, such as carbon, nitrogen, nickel, and manganese, to expand the austenite phase field and permit heat treatment. The composition must be carefully balanced to prevent δ-ferrite formation at the austenitizing temperature. Delta-ferrite in the hardened structure should be avoided to attain the best mechanical properties. Empirical formulas have been developed to predict δ-ferrite formation based on the composition (Ref 45, 46). Temperature control during austenitization is also important for preventing δ-ferrite formation. To enhance the machinability of type 416 stainless steel, steelmakers deliberately form δ-ferrite, as shown in Fig. 43. The martensitic grades are generally immune from σ-phase formation.

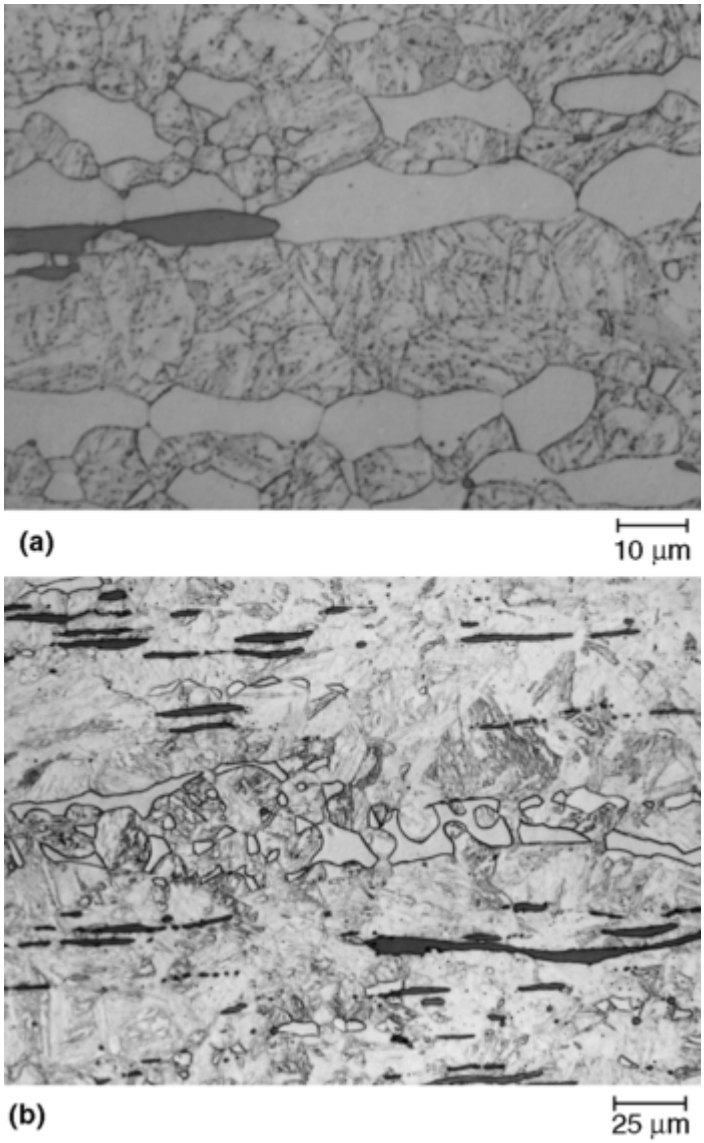

Fig. 43 Delta-ferrite and manganese sulfides in martensitic matrix of (a) 416 stainless steel etched with modified Fry's reagent and (b) 5F (modified 416) stainless steel etched with Ralph's reagent

Increases in strength when martensitic stainless steels are heat treated depend primarily on the carbon content, which can vary widely in these grades, and on the stability of δ-ferrite at the austenitizing temperature. The hardenability of these grades is very high due to the high chromium content. All these grades can be martempered to reduce the risk of quench cracking in complex shapes. The heat treatment of these grades is very similar to that of highly alloyed tool steels.

The appearance of martensite in these grades varies with carbon content. With increasing carbon content, the martensite becomes finer, changing from lath to plate morphology, and the amount of residual retained austenite increases but will not cause problems unless excessively high austenitizing temperatures are used. Figure 44 shows tempered martensite in martensitic stainless steels over the range of carbon contents encountered. This series also shows the structure of powder metallurgy (P/M) alloys versus ingot technology alloys of the same grade. The difference is more noticeable when comparing the P/M versus ingot technology 440C (Fig. 44f and g) than for the 422 grade (Fig. 44d and e), due to the marked difference in carbide size and segregation in P/M 440C versus the conventional product. In most cases, martensitic stainless steels are sold in the annealed condition. It is very important to control the carbide size and distribution in these alloys. If carbide is precipitated in the grain boundaries (Fig. 45), they will be present in the part after quenching and tempering (Fig. 46), which will drastically reduce toughness and ductility. Figure 47 shows examples of annealed martensitic stainless steel microstructures. A uniform dispersion of carbides in ferrite is desired. Coarse carbides in type 440C, made by conventional technology, have been a problem, because this limits cold formability and toughness. Figure 48 shows cracked primary carbides in 440B and 440C grades (compare Fig.

48b to Fig. 47e, which has large, noncracked primary carbides). Segregation can be a problem in any stainless grade. Figure 49 shows an example of alloy segregation that apparently caused δ-ferrite formation and then carbide precipitation at the δ-ferrite phase boundaries. Subsequent processing removed the δ-ferrite but not the carbides. Control of the austenitizing temperature is vitally important in martensitic stainless steels to avoid grain growth. In 440C, excessive austenitizing temperatures will dissolve more carbide, thus lowering the martensite start and finish temperatures, resulting in incomplete transformation of austenite to martensite during quenching, as illustrated in Fig. 50. Figure 51 shows the microstructure of EP 428, an alloy similar to type 422, used for turbine blades and disks in electric power-generation systems. Figure 51(a) shows the microstructure after the standard heat treatment, while Fig. 51(b) and (c) show the alloy after 100,000 h service at 350 and 500 °C (660 and 930 °F). The microstructure appears to be coarser after extended service. The carbide composition has changed with service exposure, but this cannot be detected by light microscopy.

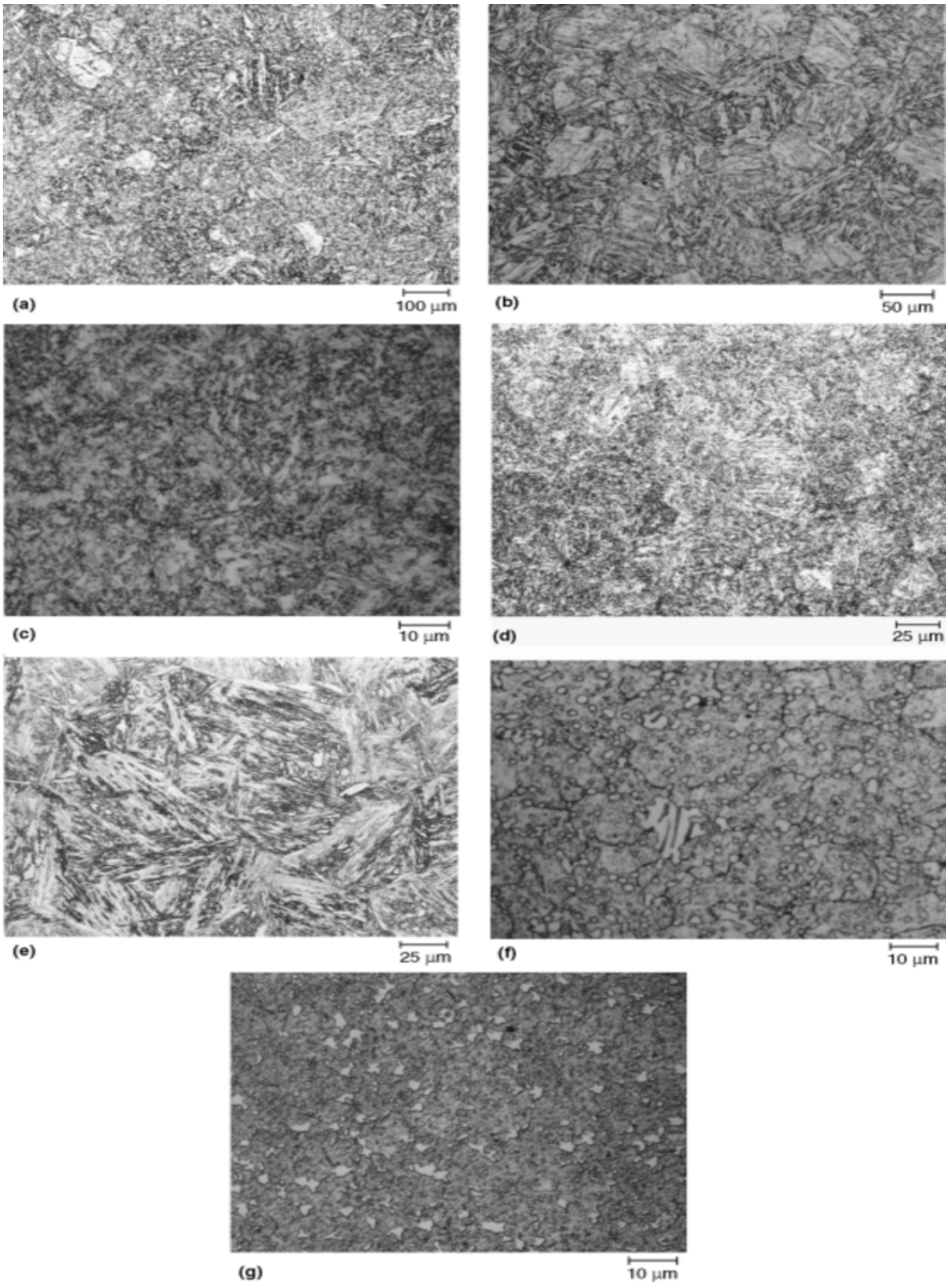

Fig. 44 Examples of the appearance of martensite in quenched and tempered martensitic stainless steels. (a) 403 etched with 4% picral plus HCl. (b) 410 etched with Vilella's reagent. (c) 420 etched with Ralph's reagent. (d) Powder metallurgy 422 etched with Ralph's reagent. (e) EF-AOD/ESR 422 etched with

Ralph's reagent. (f) Ingot technology 440C etched with Vilella's reagent. (g) Powder metallurgy 440C etched with Ralph's reagent

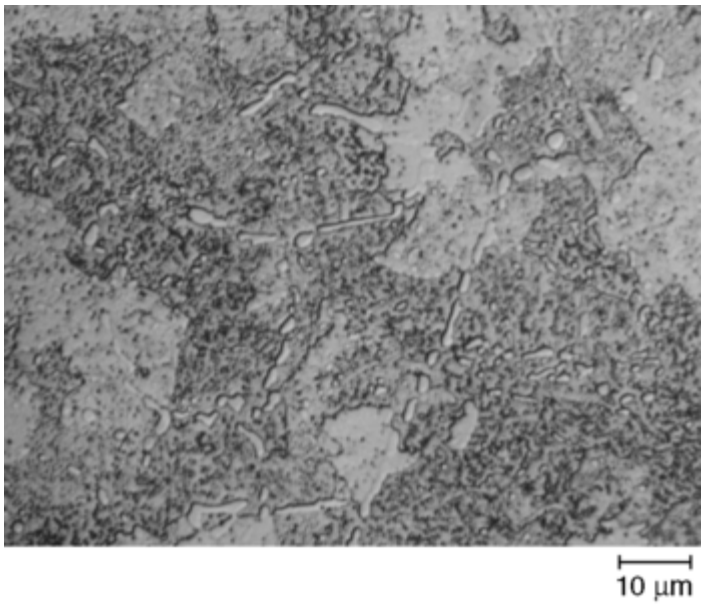

Fig. 45 Grain-boundary carbide networks in annealed 420 stainless steel etched with Ralph's reagent

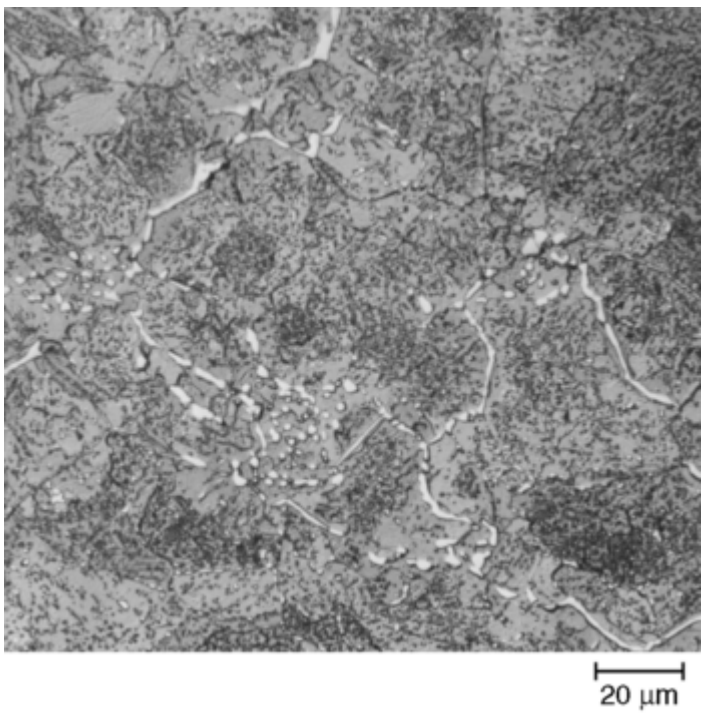

Fig. 46 Grain-boundary carbides in annealed 420 stainless steel tint etched with Beraha's sulfamic acid etch (No. 4)

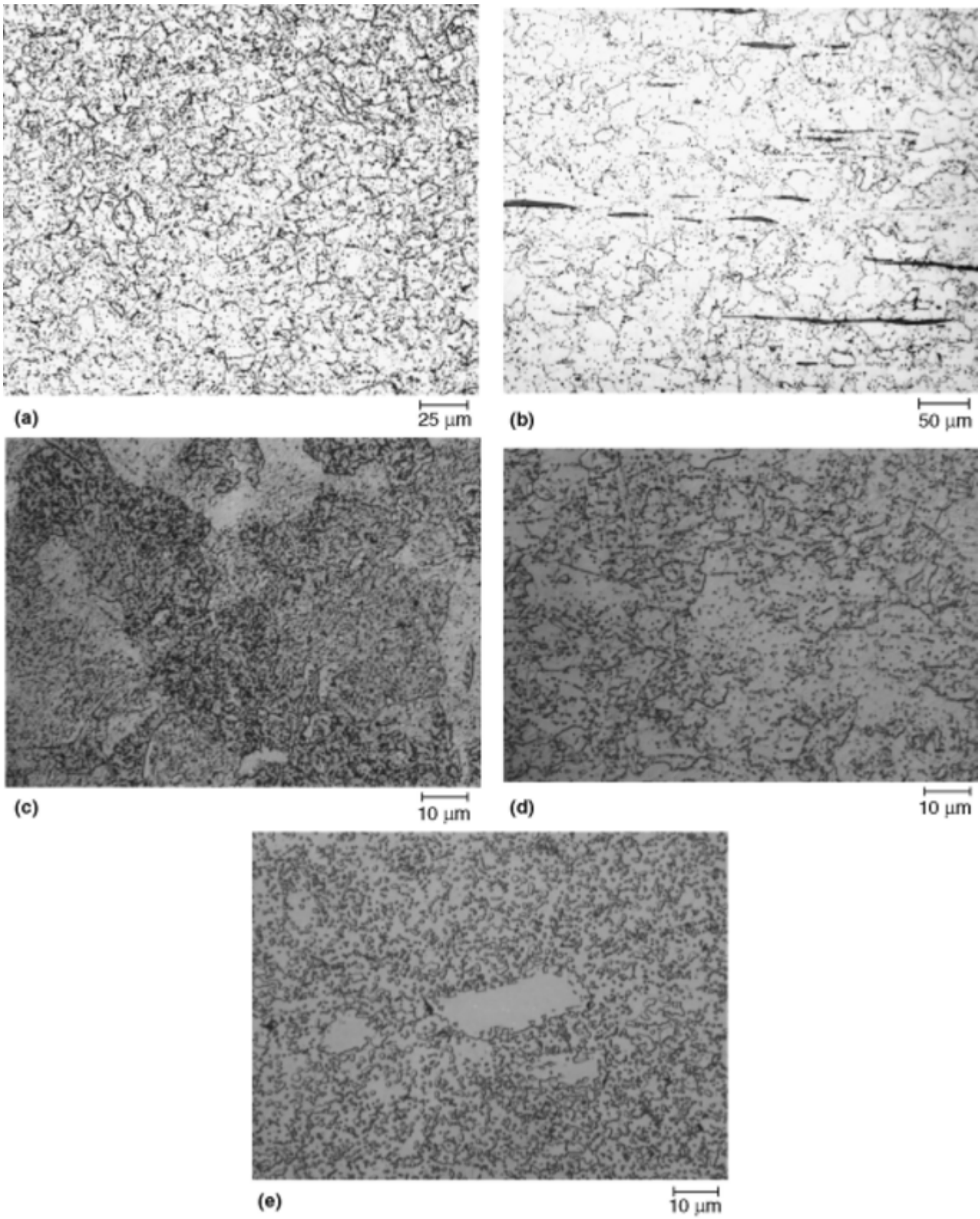

Fig. 47 Examples of annealed martensitic stainless steel microstructures. (a) 403 etched with 4% picral plus HCl. (b) Bushing-quality 416 etched with Vilella's reagent. (c) 420 etched with Ralph's reagent. (d) Trimrite etched with Vilella's reagent. (e) 440C etched with modified Fry's reagent

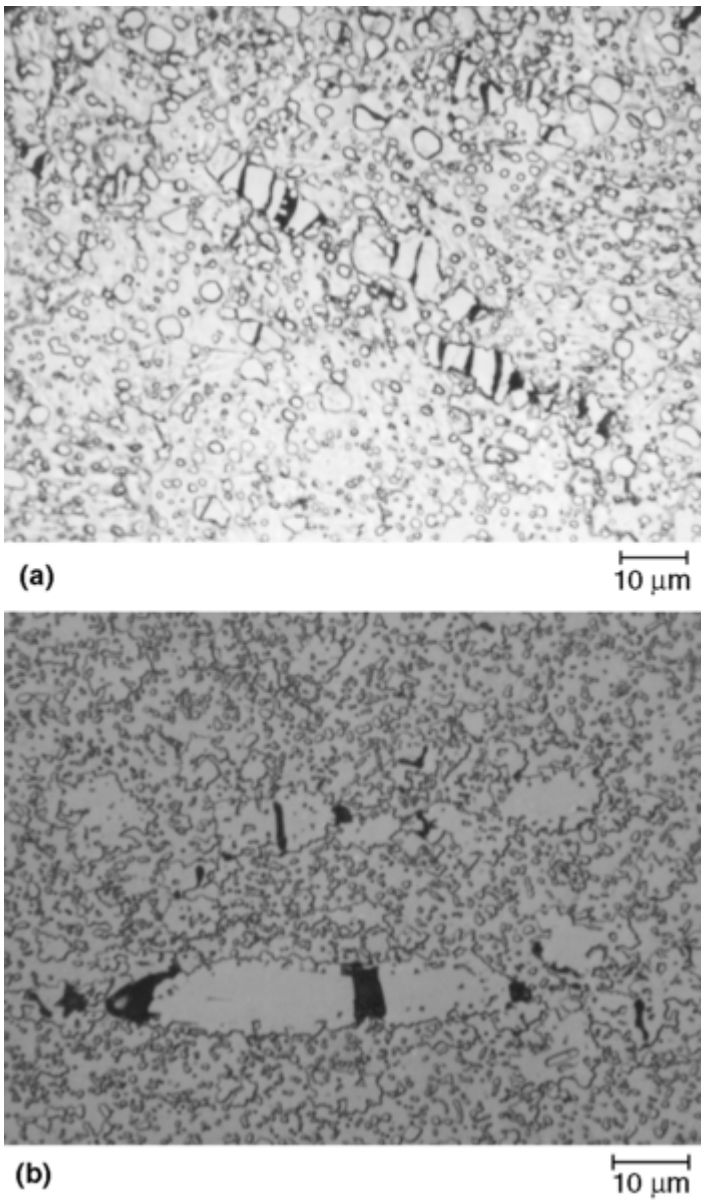

Fig. 48 Carbides cracked due to excessive cold deformation in (a) 440B etched with Vilella's reagent and (b) 440C martensitic stainless steel etched with modified Fry's reagent

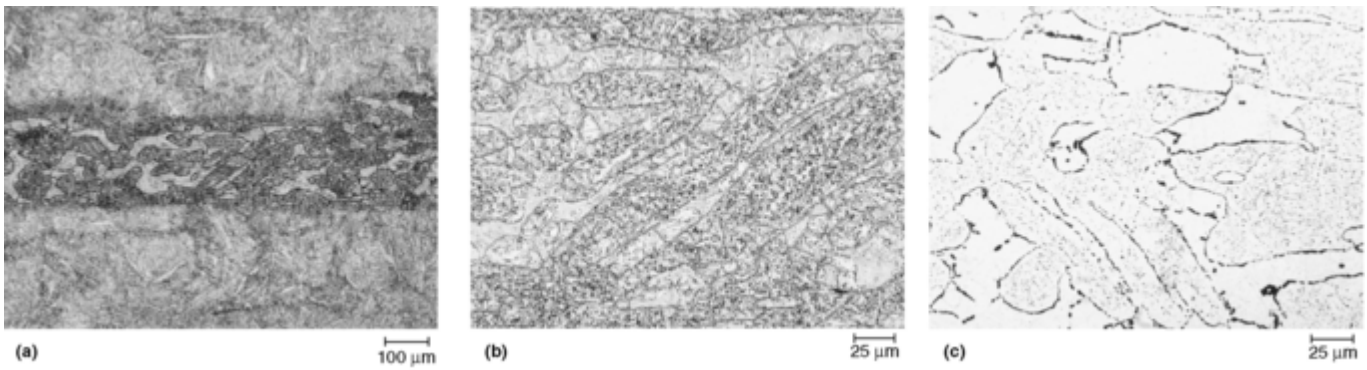

Fig. 49 Carbide segregation in a segregation streak in 422 martensitic stainless steel. (a) and (b) Etched with glyceregia. (c) Etched 30 s with Murakami's at room temperature to darken the carbides

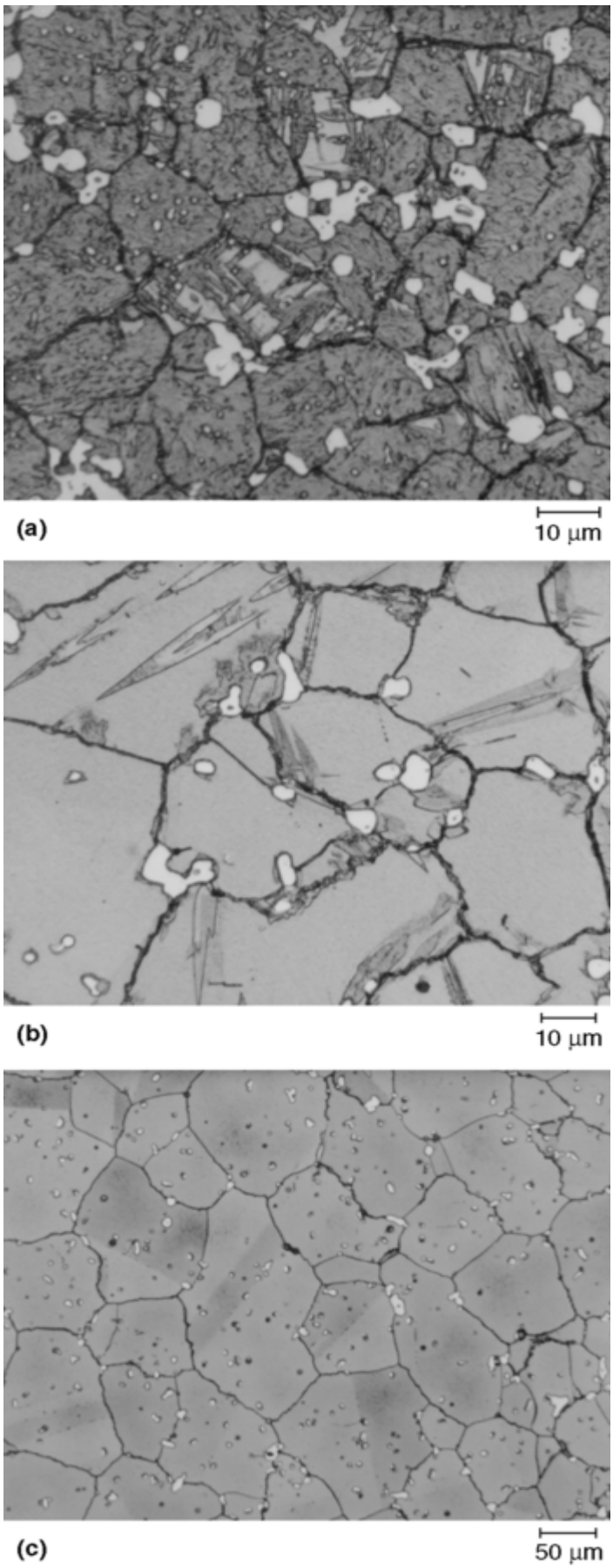

Fig. 50 Raising the austenitizing temperature during the heat treatment of type 440C stainless steel from (a) 1150 °C (2100 °F) to (b) 1204 °C (2200 °F) to (c) 1260 °C (2300 °F) caused the as-quenched microstructure to go from mainly martensite with some retained austenite (a) to mostly retained

austenite with a few martensite plates (b) to nearly all retained austenite (c). Note that the carbide content also decreases and the grain size increases. Revealed using Beraha's sulfamic acid No. 4 tint etch

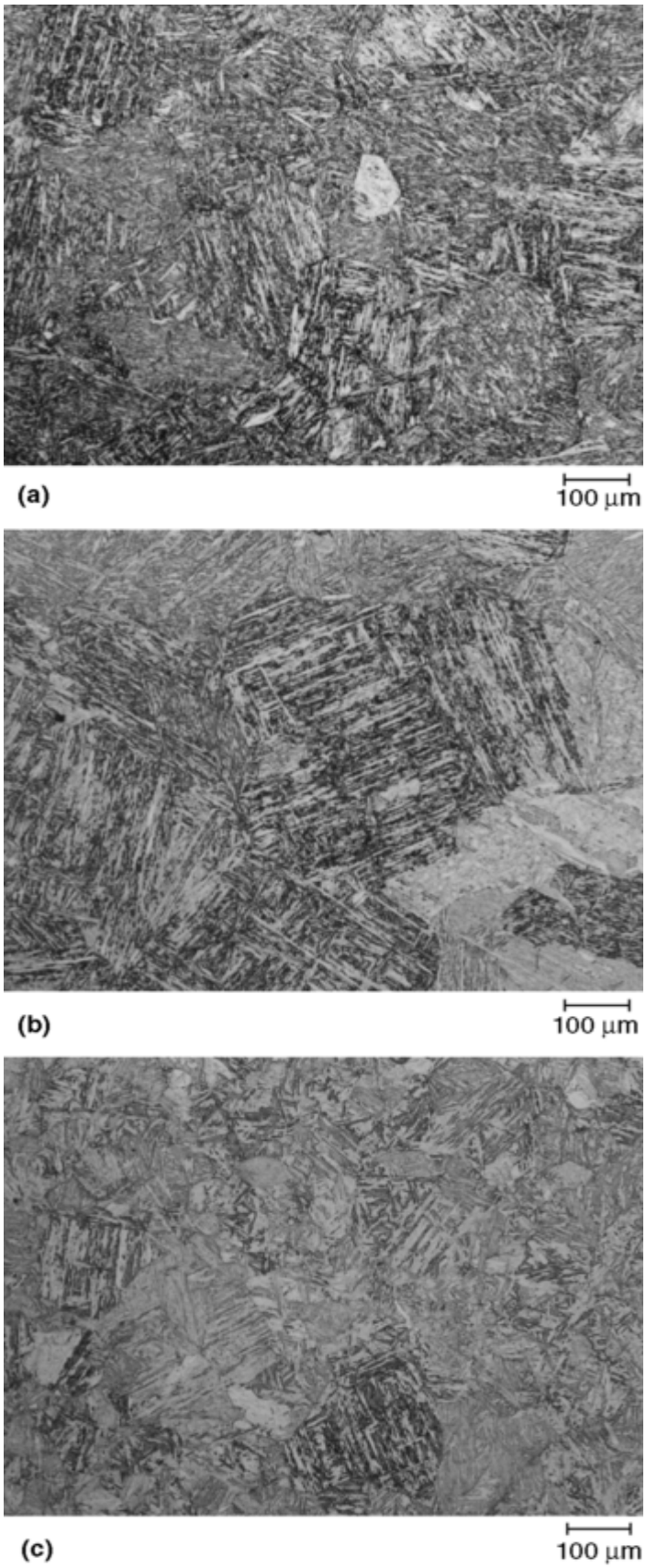

Fig. 51 Martensitic microstructure of EP 428 (revealed using Vilella's reagent) in the (a) as-heat-treated condition, and after 100,000 h at (b) 350 °C (660 °F) and (c) 500 °C (930 °F) service. Used as blades in electric power generators in Russia

Tempering reactions are similar to those observed in the high-alloy tool steels. For example, when as-quenched AISI 410 is tempered, M_3C is present at tempering temperatures to approximately 480 °C (900 °F) but is not present at approximately 650 °C (1200 °F). At approximately 480 °C (900 °F), $M_{23}C_6$ forms. It becomes the predominant carbide at 540 °C (1005 °F) and above. At approximately 480 °C (900 °F), M_7C_3 also forms but decreases in quantity with higher tempers. Because M_7C_3 seriously degrades corrosion resistance, its presence at tempering temperatures of 480 to 650 °C (900 to 1200 °F) precludes using this tempering range. Tempers below approximately 480 °C (900 °F) are also avoided due to low toughness. Overtempering must be avoided, particularly in those grades containing nickel, because of formation of reverted austenite.

Martensitic stainless steels are also susceptible to surface decarburization during heat treatment if the furnace atmosphere is not properly controlled. However, with their high chromium content, they are less susceptible than many of the low-alloy tool steels.

Of the cast alloys listed in Table 3, CA-6NM and CA-15 are essentially martensitic when cooled from the austenitizing temperature (approximately 980 °C, or 1800 °F). The martensitic structure of CA-6NM depends on a proper balance of low carbon content (0.06% maximum) and nickel content (nominally 4%). These alloys develop maximum strength and corrosion resistance in the hardened and tempered condition. They are normally tempered at a temperature safely above the maximum recommended service temperature—approximately 540 °C (1005 °F). Figure 52 shows the martensitic structure of cast CA-6NM (341 HV) etched with Ralph's reagent (note the small amount of δ-ferrite in Fig. 52b) and with 15 mL HCl-10 mL acetic acid-10 mL HNO_3. The latter etch, although quite strong, did not reveal the structure fully, but by going to Nomarski differential interference contrast (Fig. 52d), details can be better revealed. Figure 53 shows the martensitic microstructure of as-cast CD-4MCu (295 HV), with ferrite in the interdendritic boundaries. Figure 54 shows the microstructure of cast high-carbon, high-chromium martensitic white cast irons. Note the substantial amount of primary carbide, mostly Cr_7C_3, in these alloys. Beraha's sulfamic acid (No. 4) tint etch (see the article “Color Metallography” in this Volume) did a much better job of revealing the carbide distribution than standard etchants, such as Vilella's reagent. Figure 55 shows the martensitic structure of as-cast 410 stainless steel, which contained patches of δ-ferrite, while Fig. 56 shows the microstructure of as-cast 440C, with segregation and primary carbide eutectics in the interdendritic region.

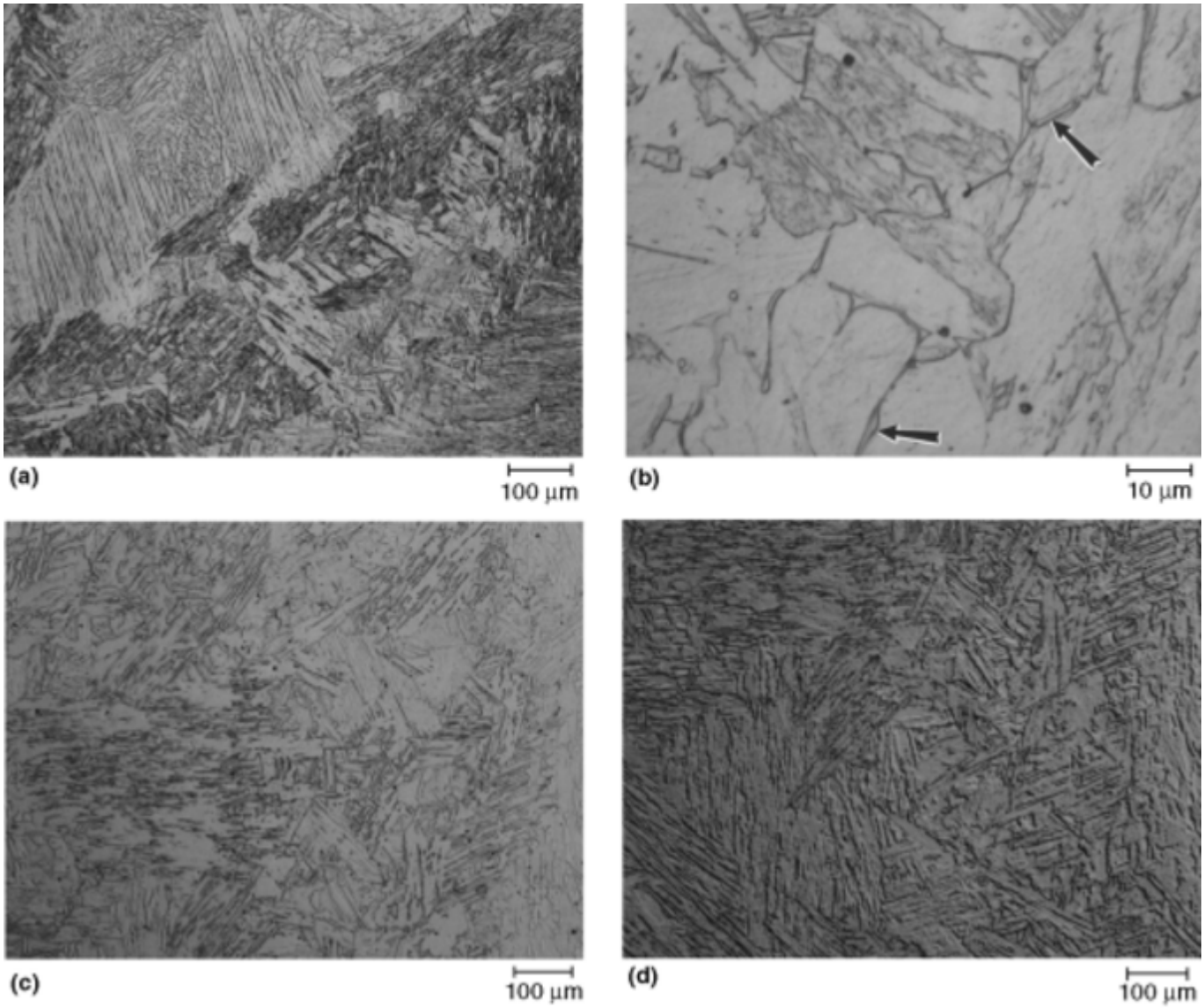

Fig. 52 Martensitic structure of as-cast CA-6NM stainless steel containing some δ-ferrite (see arrows in b). (a) and (b) Etched with Ralph's reagent. (c) and (d) Etched with 15 HCl-10 acetic acid-10 HNO_3. (d) Same field as (c) but viewed with Nomarski differential interference contrast

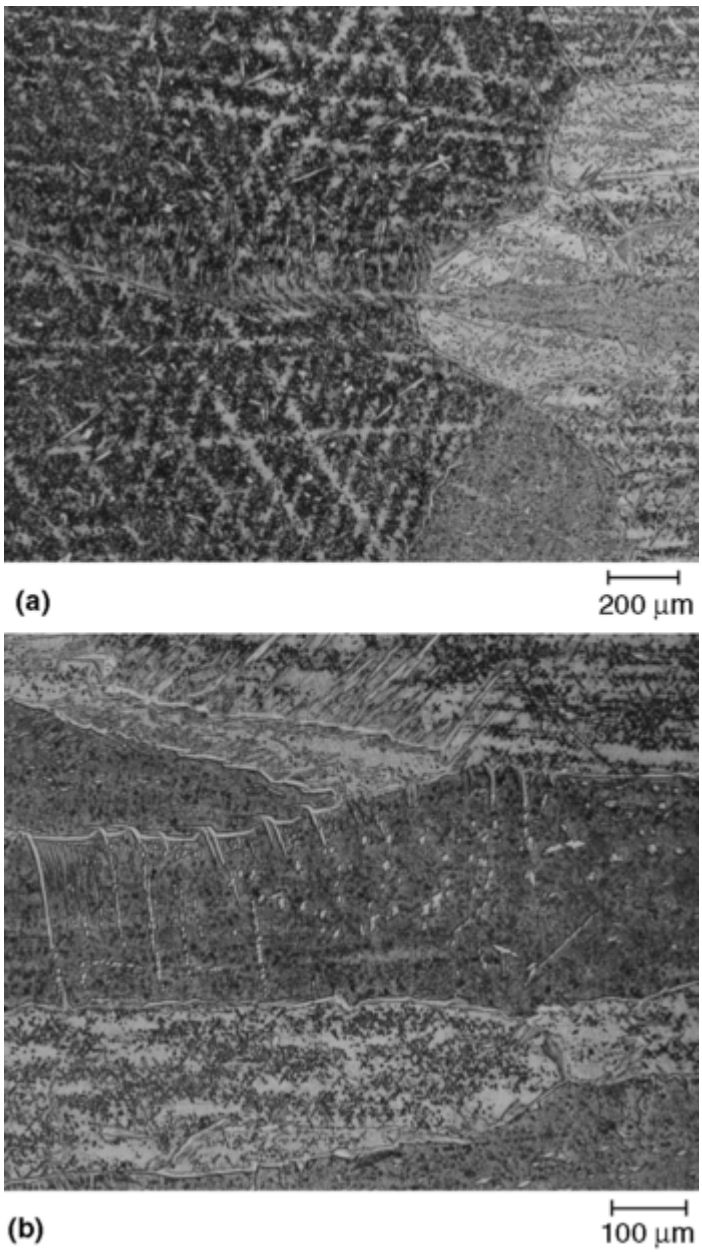

Fig. 53 Martensitic structure of as-cast CD-4MCu (295 HV) etched with waterless Kalling's reagent. There appears to be ferrite in the interdendritic boundaries.

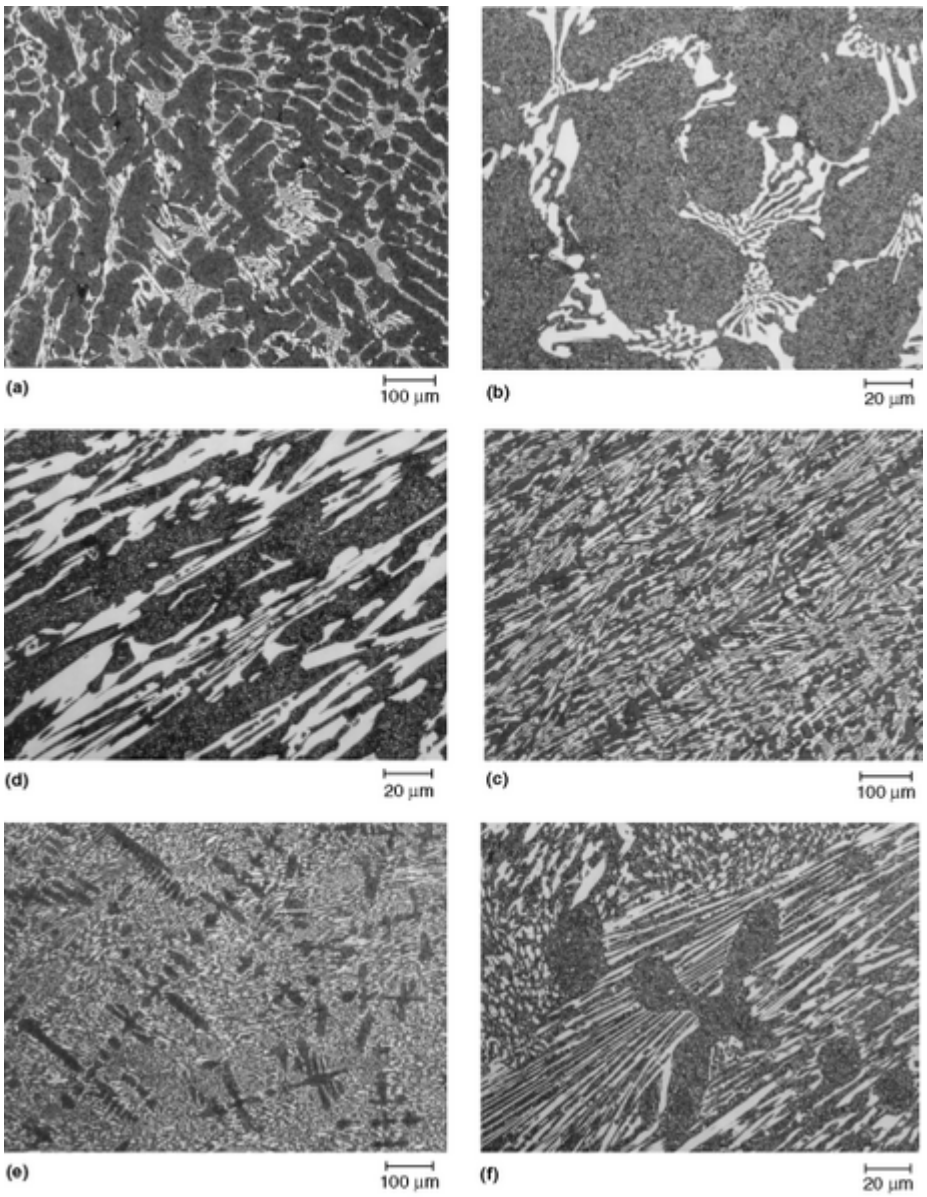

Fig. 54 Martensitic microstructure of Spanish cast high-chromium white irons. (a) and (b) Fe-2.21C-0.92Mn-0.54Si-12.65Cr-0.3Ni-0.70Mo-0.11V at 670 HV. (c) and (d) Fe-3.10C-0.75Mn-1.03Si-18.59Cr-0.22Ni-1.96Mo at 657 HV. (e) and (f) Fe-2.84C-0.67Mn-0.48Si-25.92Cr-0.21Ni-0.14Mo at 643 HV. All etched with Beraha's sulfamic acid (No. 4) reagent

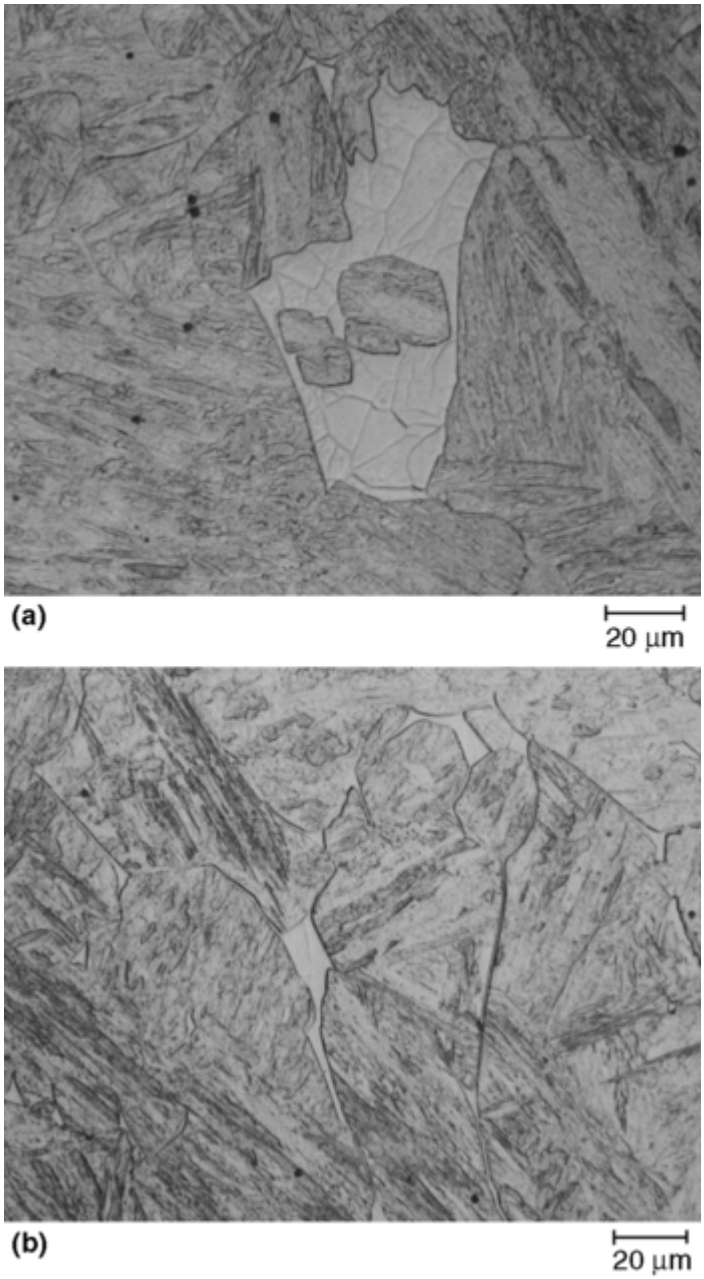

Fig. 55 Martensitic microstructure, with δ-ferrite, in as-cast 410 stainless steel (441 HV). Etched with Vilella's reagent

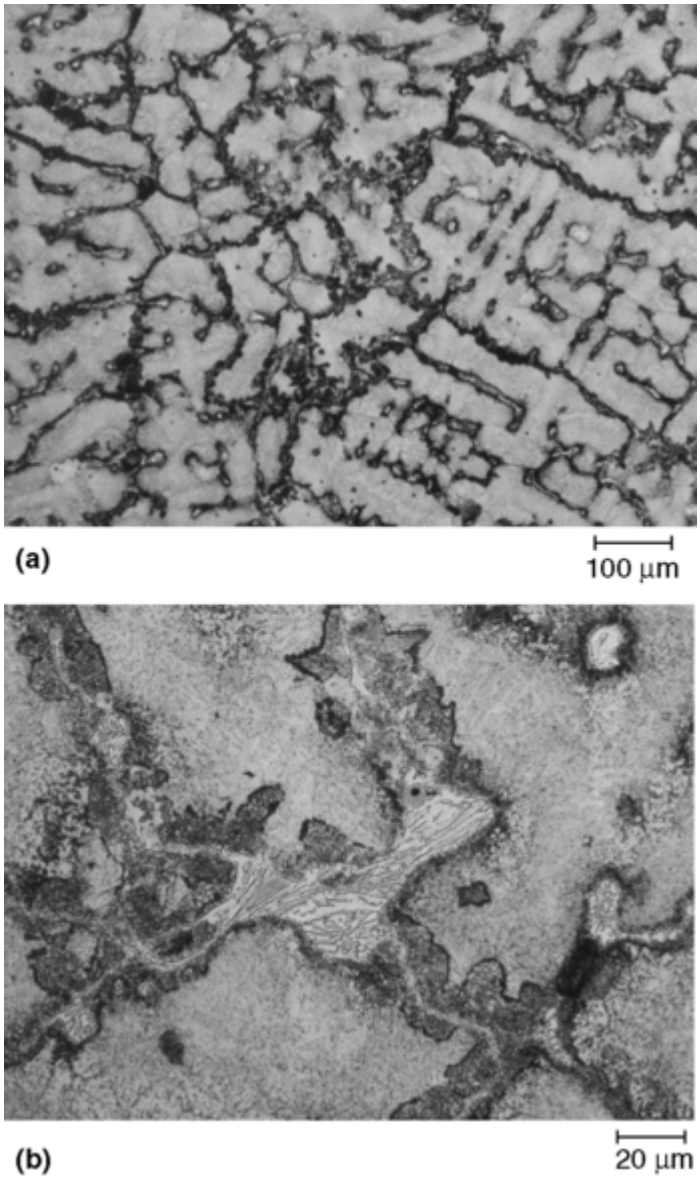

Fig. 56 As-cast microstructure of 440C (560 HV), with a martensitic matrix and a eutectic carbide constituent in the interdendritic regions. Revealed using Ralph's reagent

Precipitation-Hardenable Grades. The precipitation-hardenable stainless steels (Ref 47, 48, 49, 50) were developed in the 1940s when the first alloy of this type, Stainless W, was introduced. Three types of precipitation-hardenable grades have been developed: austenitic, semiaustenitic, and martensitic. All are hardened by a final aging treatment that precipitates very fine second-phase particles from a supersaturated solid solution. Precipitation introduces strain into the lattice, which produces the strengthening. Maximum strengthening occurs well before visible precipitates are produced. Increasing the aging temperature reduces the aging time for maximum strength, but a lower strength is obtained. As shown in Table 1, precipitation-hardenable grades contain additions of aluminum, copper, titanium, and, occasionally, molybdenum and niobium to produce the precipitates.

The semiaustenitic grades have an austenitic matrix with up to 20% δ-ferrite that persists throughout heat treatment. These grades are austenitic (plus δ-ferrite) in the solution-annealed condition but can be transformed to martensite by a series of thermal or thermomechanical treatments. Because they are complex alloys, the chemical composition must be carefully balanced.

Heat treatment of the semiaustenitic grades requires conditioning of the austenite matrix, transformation to martensite, then precipitation hardening. The austenite conditioning treatment removes carbon from solution as $Cr_{23}C_6$, beginning at the austenite/δ-ferrite interfaces. This is accomplished by heating to between 705 and 815 °C (1300 and 1500 °F). The austenite is unstable and transforms to martensite on cooling. The martensite start temperature, M_s, is approximately 65 to 93 °C (150 to 200 °F); the martensite finish temperature, M_f, is

approximately 15 °C (60 °F). The alloy is then aged, usually between 480 and 650 °C (900 and 1200 °F), to relieve stress produced during martensite formation and to increase toughness, ductility, and corrosion resistance. Aging at 565 °C (1050 °F) or above results in overaging, with the occurrence of precipitation of the strengthening intermetallic second phase, tempering of the martensite, and partial reversion of martensite to austenite (reverted austenite). Cold working can also be used to produce martensite, which is followed by aging.

Commercial examples of semiaustenitic precipitation-hardenable stainless steels include types 17-7 PH, PH 15-7 Mo, and PH 14-8 Mo. Also classed as semiaustenitic precipitation-hardenable grades are AM 350 and AM 355, but they do not have true precipitation reactions. These grades are embrittled by long-term exposure above approximately 550 °C (1020 °F), due to continued precipitation of the intermetallic-strengthening phase. Figure 57(a) shows nitrides in 17-7 PH, while Fig. 57(b) shows the etched microstructure of this specimen with isolated patches of ferrite. Figure 57(c) shows heavier δ-ferrite stringers in a different specimen of 17-7 PH. Figure 58(a) shows δ-ferrite stringers in PH 15-7 Mo. Etching longer with waterless Kalling's reagent brought up the martensitic matrix, but the δ-ferrite does not stand out as well. Figure 59 shows the appearance of δ-ferrite on transverse and longitudinal planes in AM 350. Figure 60 shows the microstructure of AM 355, revealing reverted austenite and ferrite stringers.

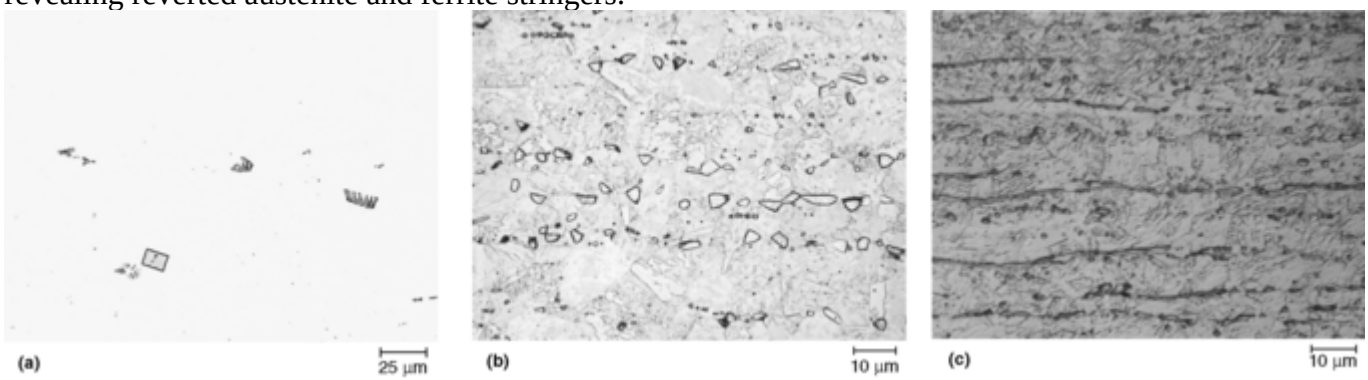

Fig. 57 Microstructure of 17-7 PH stainless steel (193 HV). (a) Nitrides viewed on an as-polished surface. (b) Delta-ferrite and martensitic matrix in specimen shown in (a). Etched with Vilella's reagent. (c) Delta-ferrite stringers and martensitic matrix of a different specimen. Etched with modified Fry's reagent

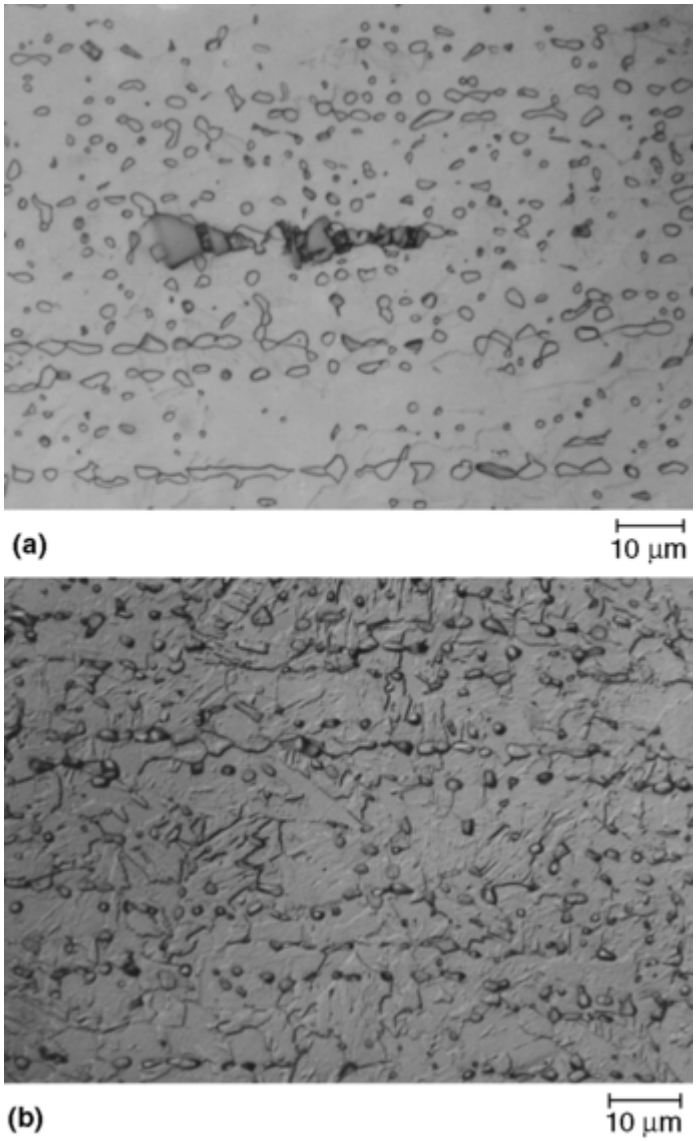

Fig. 58 Microstructure of PH 15-7 Mo stainless steel (360 HV) etched with waterless Kalling's reagent. (a) Light etch showing the δ-ferrite stringers and a nitride stringer. (b) Heavier etch to reveal the martensitic matrix

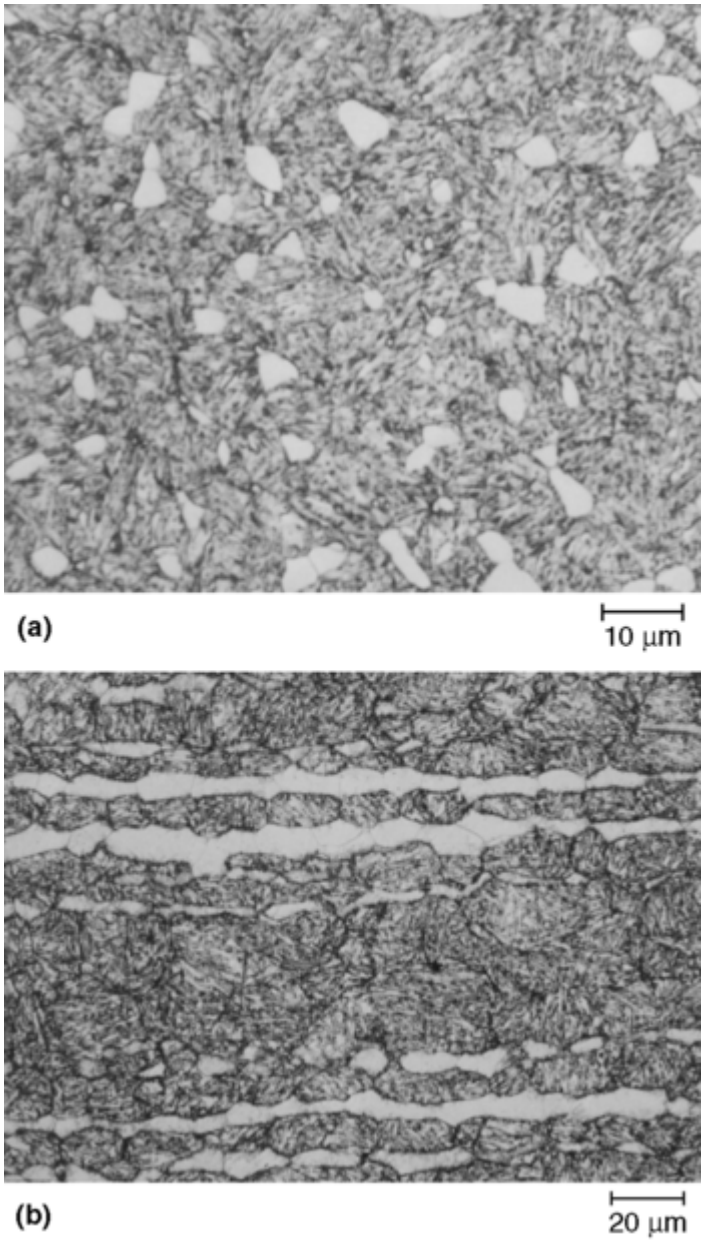

Fig. 59 Microstructure of AM 350 stainless steel etched with modified Fry's reagent, showing the difference in appearance of δ-ferrite in a martensitic matrix on (a) transverse and (b) longitudinal planes

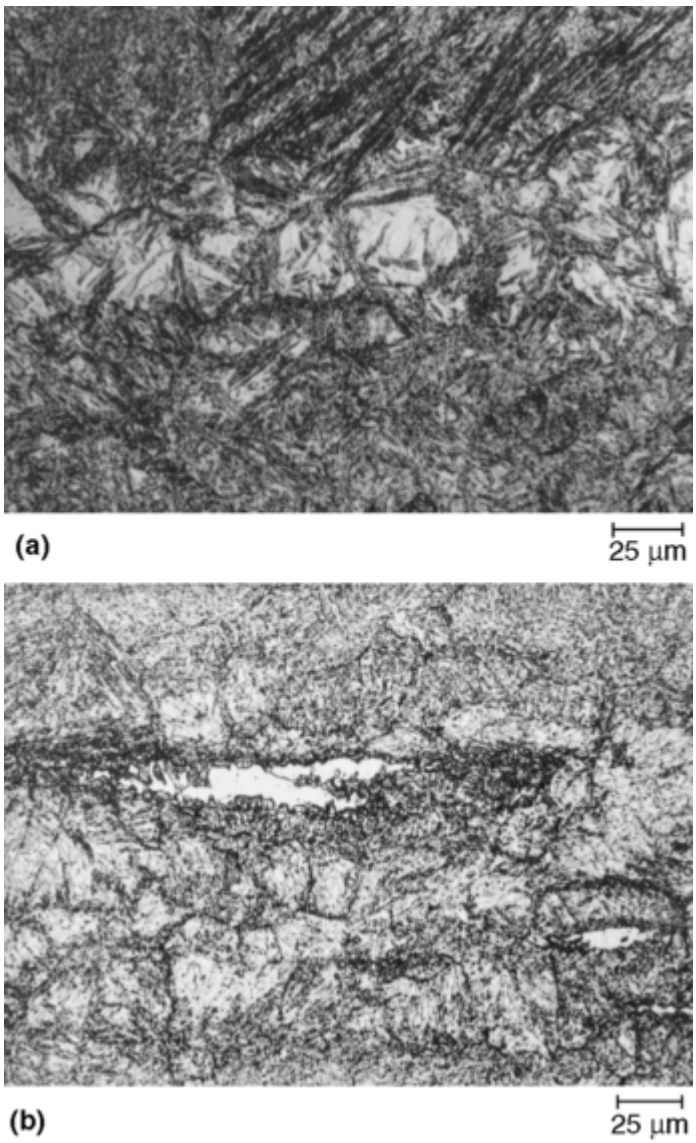

Fig. 60 Microstructure of as-hot-worked AM 355 stainless steel etched with glyceregia, showing (a) reverted austenite in a segregated area and (b) delta-ferrite in a martensitic matrix

The martensitic grades are the most popular precipitation-hardenable stainless grades. They are martensitic after solution annealing and do not retain austenite. Stainless W is a martensitic precipitation-hardenable type. Other more recently developed martensitic precipitation-hardenable grades are 17-4 PH, 15-5 PH, PH 13-8 Mo, Custom 450, and Custom 455, which are capable of strengths to 1380 MPa (200 ksi) or above. Figure 61(a) shows δ-ferrite (5.6%) in a 16.5 cm (6.5 in.) square billet after etching with Murakami's reagent. Figure 61(b) to (g) show 17-4 PH in the solution-annealed condition and after H900, H1025, H1075, H1100, and H1150M tempers (aging treatments). Figure 62(a) shows δ-ferrite in a 20 cm (8 in.) square billet (transverse plane, near the surface) after etching with Murakami's reagent. Figure 62(b) shows a fine δ-ferrite stringer in a smaller wrought bar. The specimen is in the H925 temper condition. Figure 62(c) shows a ferrite-free specimen with a martensitic structure after an H900 temper (41 HRC). Figure 63 shows the microstructure of PH 13-8 Mo in the solution-annealed and aged condition, with a fine martensitic structure. Figure 64(a) shows the structure of Custom 450 in the H1050 temper, while Fig. 64(b) shows it in the H1150 temper condition. Figure 65(a) shows Custom 455 in the solution-annealed condition, while Fig. 65(b) to (f) show it in the H850, H950, H1000, H1050, and H1100 temper conditions.

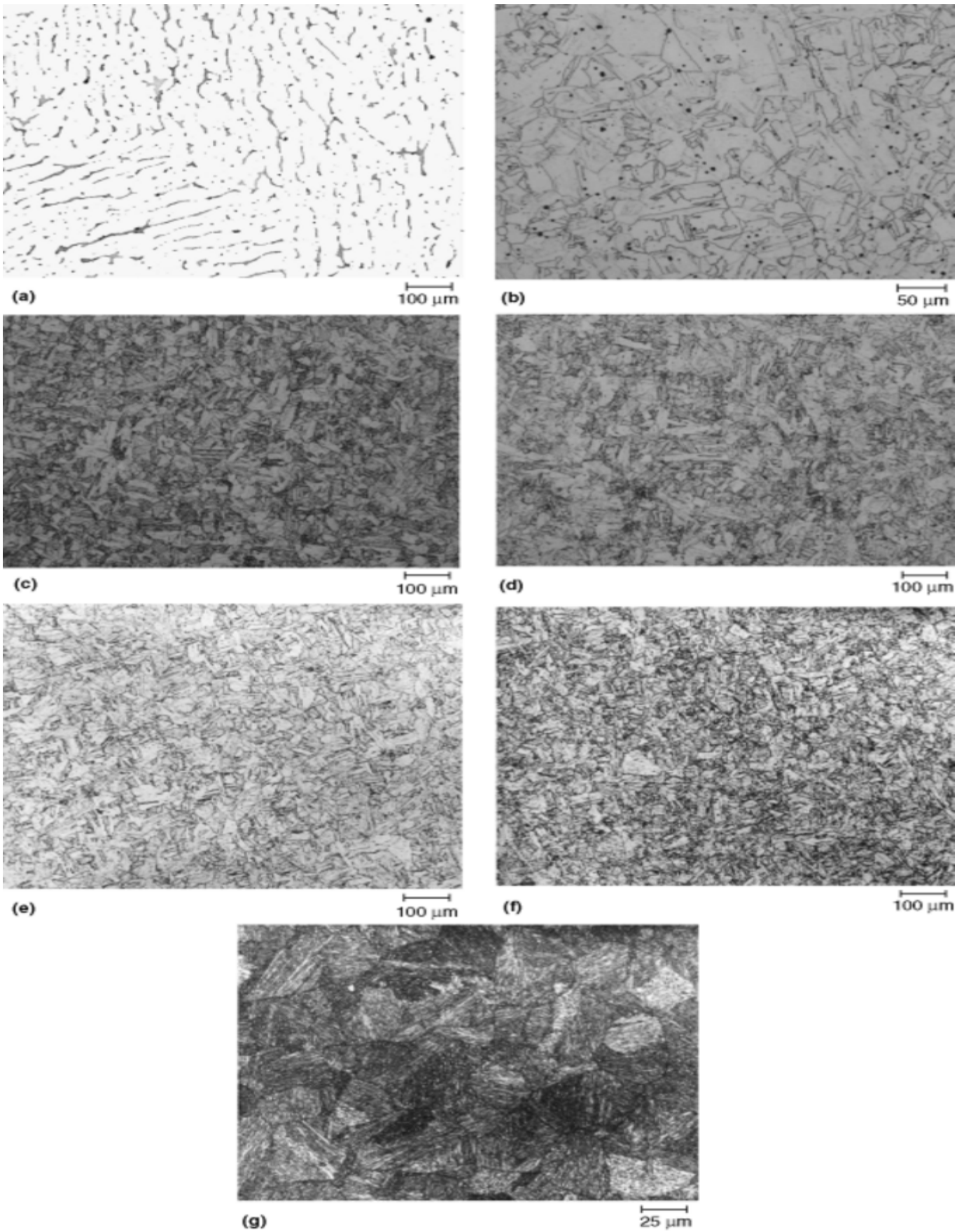

Fig. 61 Microstructure of 17-4 PH stainless steel. (a) Delta-ferrite (5.6%) revealed using Murakami's reagent (2 min at 100 °C, or 210 °F) on a transverse plane from a 16.5 cm (6.5 in.) square billet. (b) Martensitic matrix of a solution-annealed specimen. (c) H900 temper (430 HV). (d) H1025 temper (383 HV). (e) H1075 temper (359 HV). (f) H1100 temper (333 HV). (g) H1150 temper containing martensite and reverted austenite. (b) to (d) Etched with modified Fry's reagent. (e) to (g) Etched with Ralph's reagent

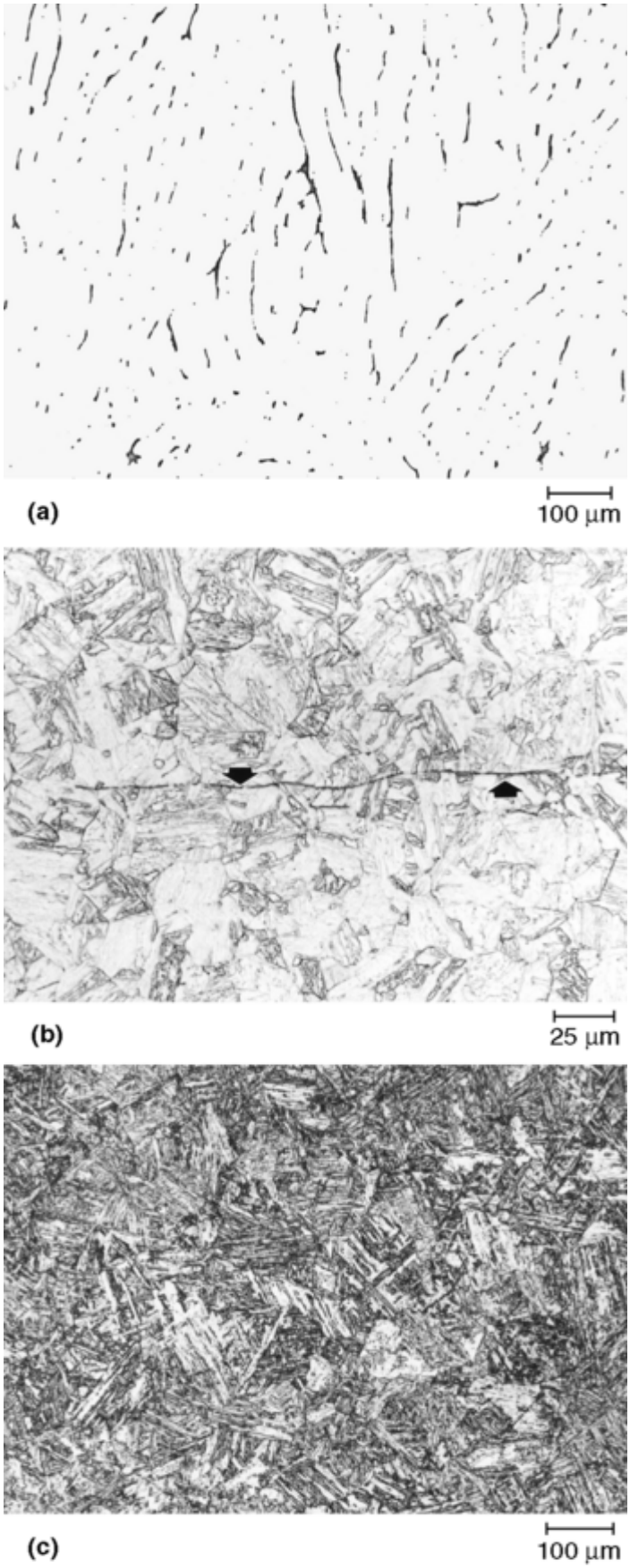

Fig. 62 Microstructure of 15-5 PH stainless steel. (a) Delta-ferrite on a transverse plane from a 20 cm (8 in.) square billet, near the surface. Revealed using Murakami's reagent (2 min at 100 °C, or 210 °F). (b) Delta-ferrite stringer (arrows) in a martensitic matrix on a bar (longitudinal plane) after solution annealing and aging (H925 temper). Revealed using modified Fry's reagent. (c) Martensitic matrix (41 HRC) of a solution-annealed and aged (H900 temper) bar etched with Vilella's reagent

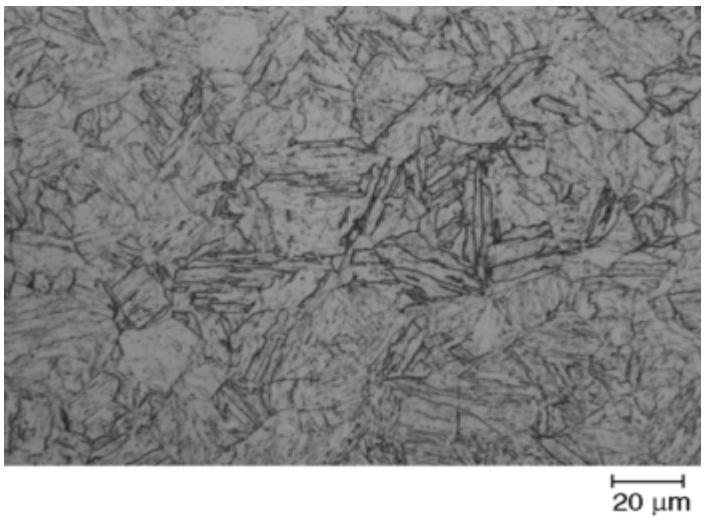

Fig. 63 Martensitic microstructure of PH 13-8 Mo stainless steel etched with modified Fry's reagent

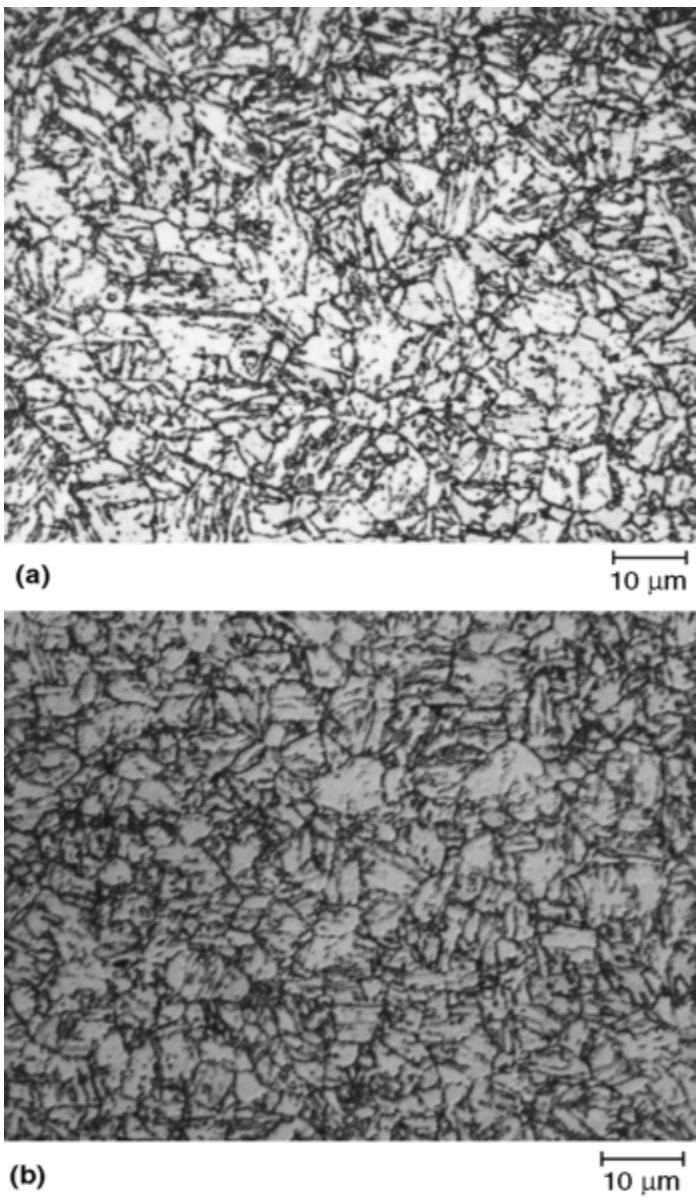

Fig. 64 Martensitic microstructure of Custom 450 stainless steel in the solution-annealed and aged condition. (a) H1050 temper. Etched with modified Fry's reagent. (b) H1150 temper. Etched with waterless Kalling's reagent

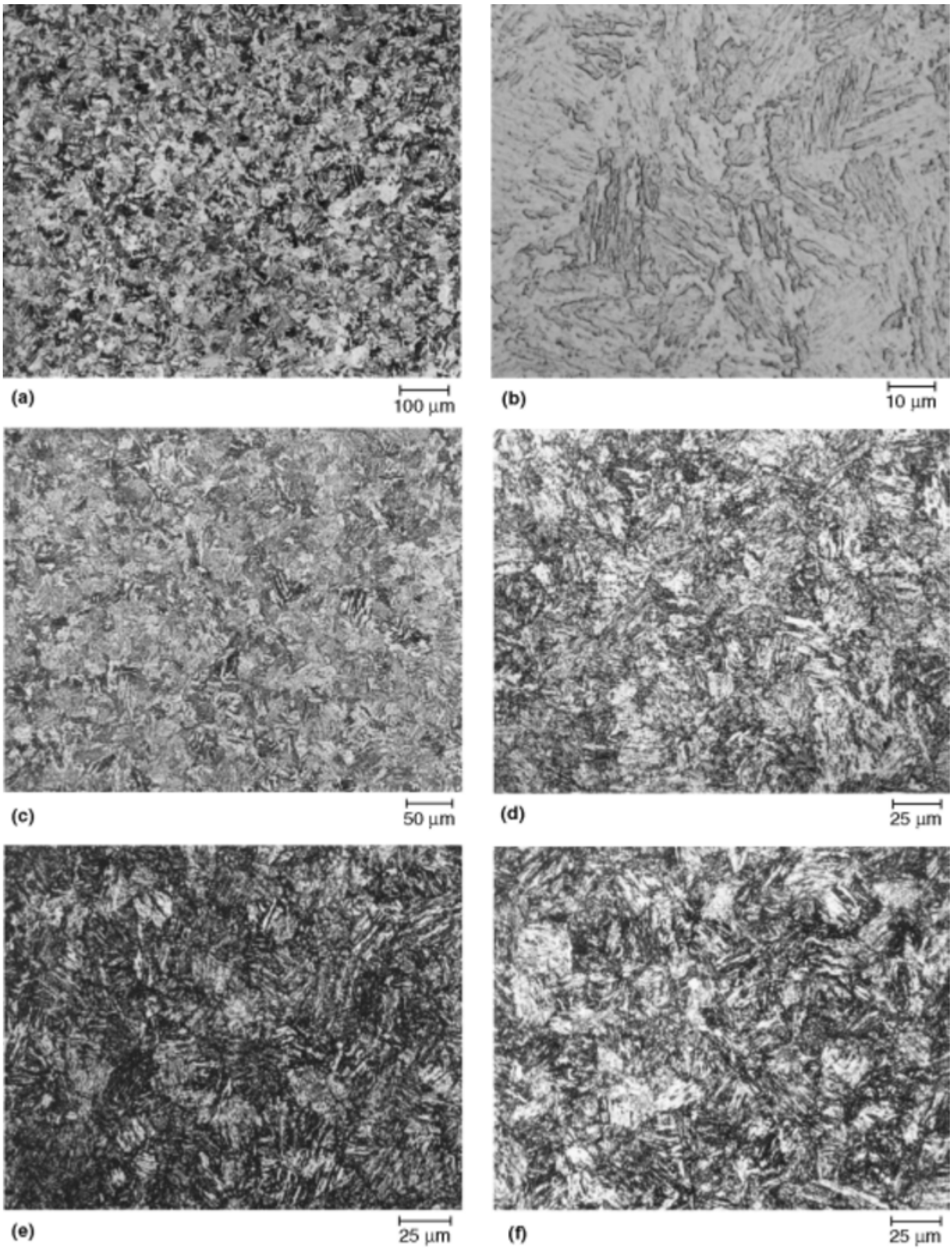

Fig. 65 Martensitic microstructure of Custom 455 stainless steel in the (a) solution-annealed condition (281 HV), etched with Vilella's reagent, and in the solution-annealed and aged conditions. (b) 900 temper (530 HV). Etched with modified Fry's reagent. (c) H950 temper (451 HV). (d) H1000 temper (446 HV). (e) H1050 temper (436 HV). (f) H1100 temper (396 HV). (c) to (f) Etched with Ralph's reagent

Stainless W and 17-4 PH contain δ-ferrite stringers in the martensitic matrix (17-4 PH can be made free of ferrite); the other grades are essentially free of δ-ferrite and so have better through-thickness properties. After solution annealing, they are aged at 425 to 455 °C (795 to 850 °F) or at 675 °C (1250 °F). High aging temperatures will produce reaustenitization, which transforms to untempered martensite on cooling to room temperature. Figure 22, Figure 23, and Figure 61(a) show δ-ferrite in 17-4 PH, while Fig. 24 and Fig. 59 show δ-ferrite in AM 350.

The austenitic precipitation-hardenable grades have the lowest usage. The austenite matrix in these alloys is very stable, even after substantial cold working. These grades are the forerunners of superalloys. The most common austenitic precipitation-hardenable grade is A-286 (illustrated in the article “Metallography and Microstructures of Heat-Resistant Alloys” in this Volume).

Alloy CB-7Cu-1 (Table 3) is a cast precipitation-hardening alloy similar to wrought 17-4 PH (Table 1). It is essentially martensitic in the solution-treated and aged conditions. It is generally solution treated at approximately 1040 °C (1900 °F) and aged at 480 to 620 °C (900 to 1150 °F) for maximum strength and resistance to corrosion.

The duplex stainless steels (Ref 51, 52, 53 were developed as a result of studies of superplasticity. They are usually very fine-grained microduplex structures with a composition centered on 26Cr-6.5Ni (IN-744). The very fine grain size improves strength and toughness, and their superplastic nature promotes hot workability. They exhibit good strength and corrosion resistance.

Thermomechanical processing is required to produce the fine duplex structure. During soaking for hot working, the second phase is dissolved. During hot working, it precipitates and stabilizes the grain size of the recrystallized matrix. The microduplex structure results only when second-phase precipitation precedes or occurs during recrystallization.

Service exposure at 370 to 540 °C (700 to 1005 °F) results in an increase in strength but loss of toughness. Sigma phase will form in IN-744 from exposure to temperatures between 550 and 800 °C (1020 and 1470 °F). Cold working enhances subsequent σ-phase formation. Other examples of duplex stainless steels include AISI 329, alloy 2205, 7-Mo PLUS, Ferralium alloy 255, and 44LN. Figure 66(a) and (b) show the microstructure of type 312 stainless steel in the annealed condition, while Fig. 66(c) to (e) show a bar after being removed from high-temperature exposure that broke because of embrittlement due to σ formation. Figure 67(a) shows the microstructure of solution-annealed alloy 2205 duplex stainless steel, while Fig. 67(b) and (c) show the precipitation of σ phase after 2 and 8 h at 800 °C (1470 °F). Figure 68 shows the microstructure of alloy 255 (Ferralium) in the annealed condition. The microstructure of 7-Mo PLUS duplex stainless steel is illustrated in Fig. 25.

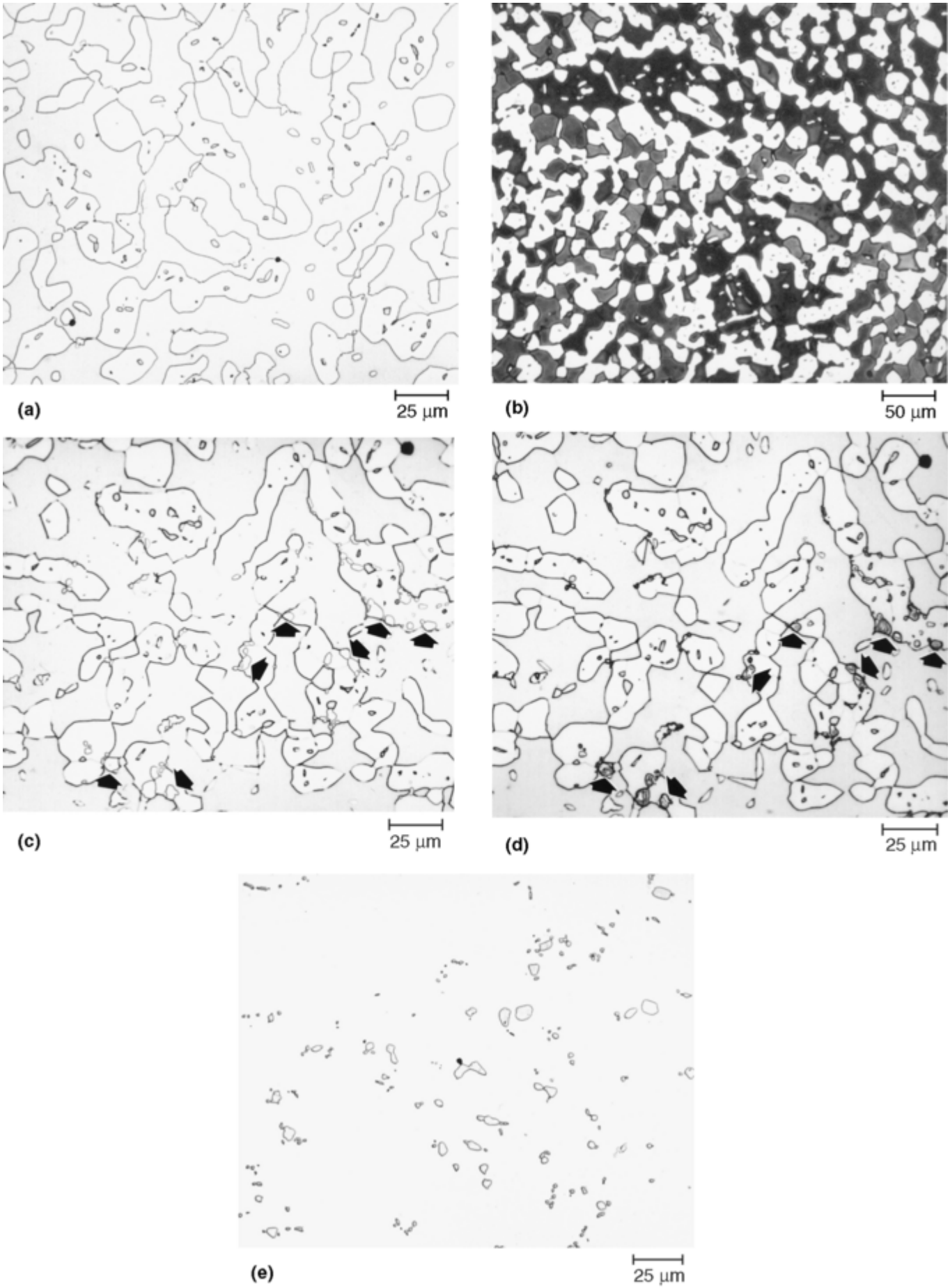

Fig. 66 Ferrite-austenite microstructure of type 312 stainless steel used for welding. (a) and (b) show a solution-annealed bar etched with (a) ethanolic 15% HCl, which reveals the phase boundaries, and (b) Beraha's tint etch, which colors the ferrite. (c) to (e) show the structure of a bar after high-temperature

exposure, where σ phase has precipitated. (c) Etched with aqueous 60% HNO_3 at 1 V dc to reveal the phase boundaries (arrows point to particles of σ). (d) Specimen etched as in (c) and given a second electrolytic etch with aqueous 20% NaOH at 2 V dc to color the σ particles. (e) The specimen repolished and etched with concentrated NH_4OH at 6 V dc to color the σ blue

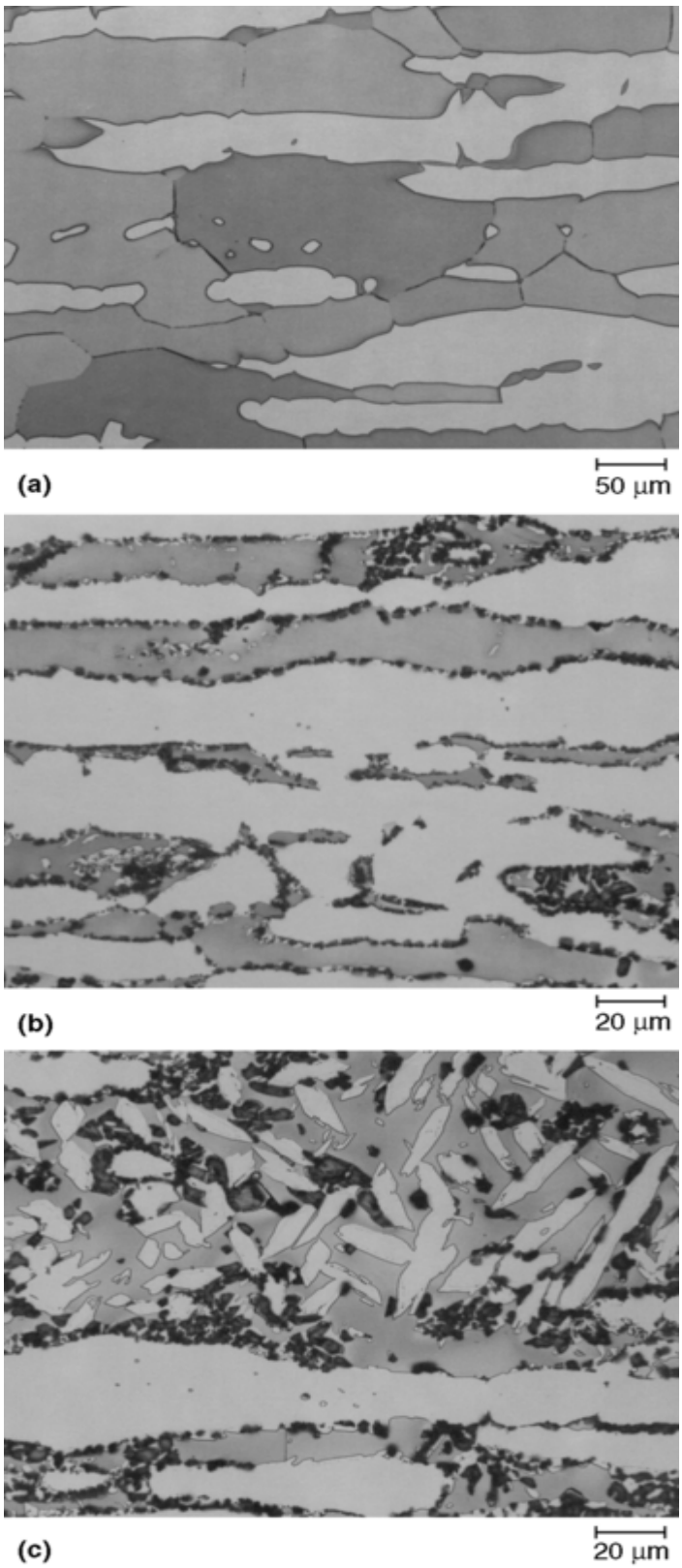

Fig. 67 Ferrite-austenite grain structure of 2205 duplex stainless steel etched with aqueous 20% NaOH at 3 V dc for 15 s to color ferrite. (a) Solution annealed at 1200 °C (2190 °F). (b) After high-temperature exposure at 800 °C (1470 °F) for 2 h, producing σ phase (dark spots). (c) After 8 h at the same temperature

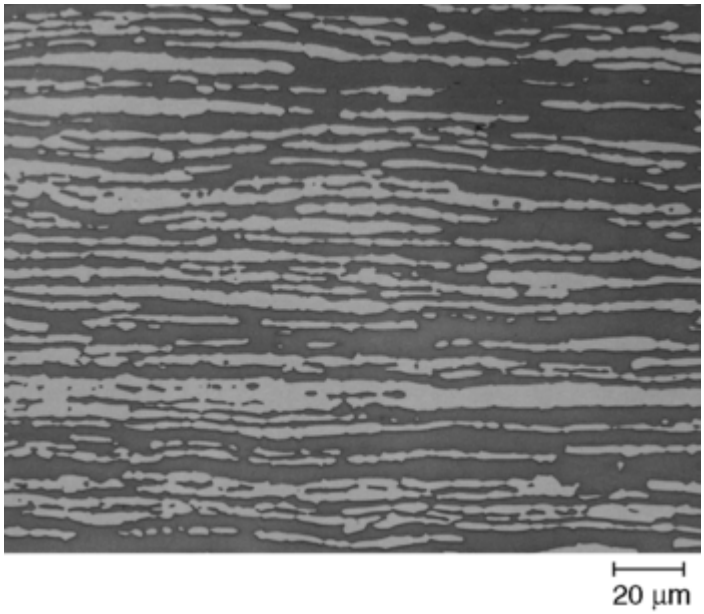

Fig. 68 Ferrite (dark) and austenite in alloy 255 (Ferralium) duplex stainless steel etched with aqueous 20% NaOH at 3 V dc for 3 s

Alloy CD-4MCu is a cast duplex-phase alloy that, in the solution-treated condition, consists of up to 65% ferrite and 35% austenite. It contains molybdenum and copper. It is normally used only in the solution-treated condition. After solution treating at temperatures above 1040 °C (1900 °F) and quenching in water, oil, or air (depending on casting shape and intended service), it has excellent corrosion resistance and approximately twice the strength of CF-8, an austenitic alloy that normally contains less than 15% ferrite. Other cast duplex stainless steels, as well as CD-7MCuN, are covered in ASTM A 890. The microstructure of cast duplex stainless steel is shown in Fig. 1.

Maraging Steels. Maraging steels do not contain chromium and do not have stainless characteristics (Table 11). However, they are strengthened by precipitation hardening and have microstructures somewhat similar to precipitation-hardened stainless steels, as discussed in this article. These alloys are nearly free of carbon and form a soft, substitutional type of lath martensite with a high dislocation density when solution annealed. Aging precipitates rod-shaped orthorhombic Ni_3Mo and spherical tetragonal FeTi. Naturally, these precipitates are exceptionally small and can only be observed with the transmission electron microscope. These alloys contain approximately 18% Ni, which depresses the M_s temperature to approximately 150 °C (300 °F). The standard alloys contain 8 to 12.55% Co, which appears to contribute strengthening by short-range ordering. Nickel is rejected from the ordered iron-cobalt regions, and this apparently alters the size of the Ni_3Mo precipitates. The nickel-depleted regions are sites for FeTi formation. If the impurity content is kept low, maraging steels will exhibit exceptionally good toughness at very high strength levels. Formation of Ti(C,N) or TiN and Ti_2S in the grain boundaries embrittles these alloys. Several low-cobalt and cobalt-free maraging grades have also been developed.

Table 11 Nominal compositions of commercial maraging steels

Grade	Composition[a], %					
	Ni	**Mo**	**Co**	**Ti**	**Al**	**Nb**
Standard grades						
18Ni(200)	18	3.3	8.5	0.2	0.1	…
18Ni(250)	18	5.0	8.5	0.4	0.1	…
18Ni(300)	18	5.0	9.0	0.7	0.1	…
18Ni(350)	18	4.2[b]	12.5	1.6	0.1	…
18Ni(Cast)	17	4.6	10.0	0.3	0.1	…
12-5-3(180)[c]	12	3	…	0.2	0.3	…
Cobalt-free and low-cobalt bearing grades						

Cobalt-free 18Ni(200)	18.5	3.0	…	0.7	0.1	…
Cobalt-free 18Ni(250)	18.5	3.0	…	1.4	0.1	…
Low-cobalt 18Ni(250)	18.5	2.6	2.0	1.2	0.1	0.1
Cobalt-free 18Ni(300)	18.5	4.0	…	1.85	0.1	…

(a) All grades contain no more than 0.03% C.

(b) Some producers use a combination of 4.8% Mo and 1.4% Ti, nominal.

(c) Contains 5% Cr

Figure 69(a) and (b) show the microstructure of 18Ni250 maraging steel in the solution-annealed and the solution-annealed and aged conditions. Figure 70(a) and (b) show the microstructure of low-residual 18Ni250 maraging steel in the solution-annealed and the solution-annealed and aged conditions. Figure 71 shows the microstructure of solution-annealed and aged 18Ni300 maraging steel. In each case, the lath martensitic structure is more visible after aging. Figure 72 shows the microstructure of solution-annealed and aged T-250 maraging steel, a cobalt-free grade. The prior-austenite grain boundaries can be revealed in the solution-annealed condition but not after aging. The precipitation-hardenable stainless steels act in a similar manner. The best etchant is electrolytic aqueous 60% nitric acid, but electrolytic aqueous 10% CrO_3 also works.

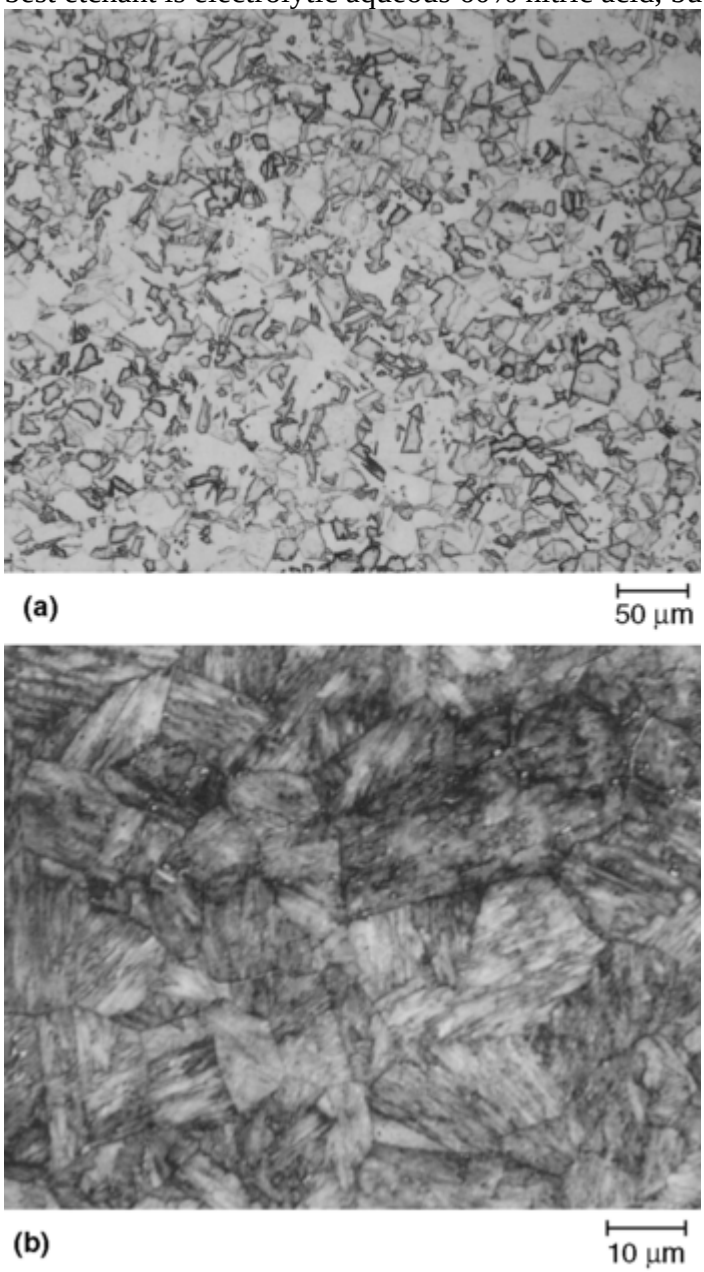

Fig. 69 Martensitic microstructure of 18Ni(250) maraging steel in the (a) solution-annealed condition (305 HV) and the (b) solution-annealed and aged condition (523 HV). Revealed using modified Fry's reagent

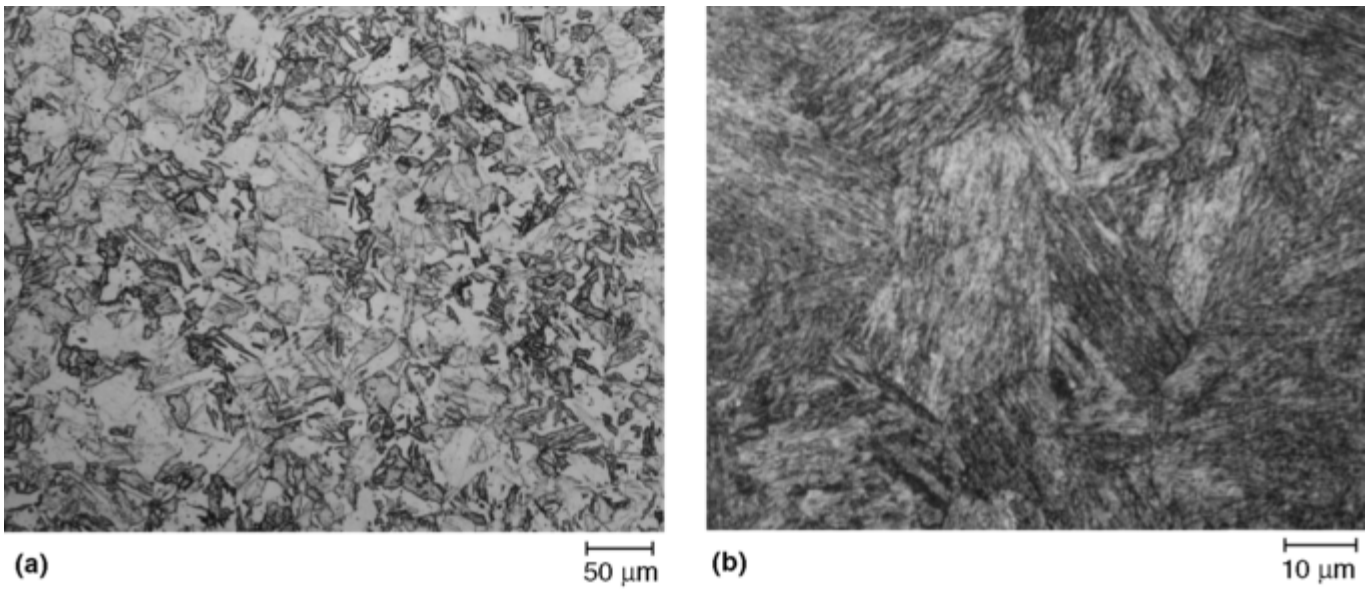

Fig. 70 Martensitic microstructure of low-residual 18Ni(250) maraging steel in the (a) solution-annealed condition (319 HV) and the (b) solution-annealed and aged condition (565 HV). Revealed using modified Fry's reagent

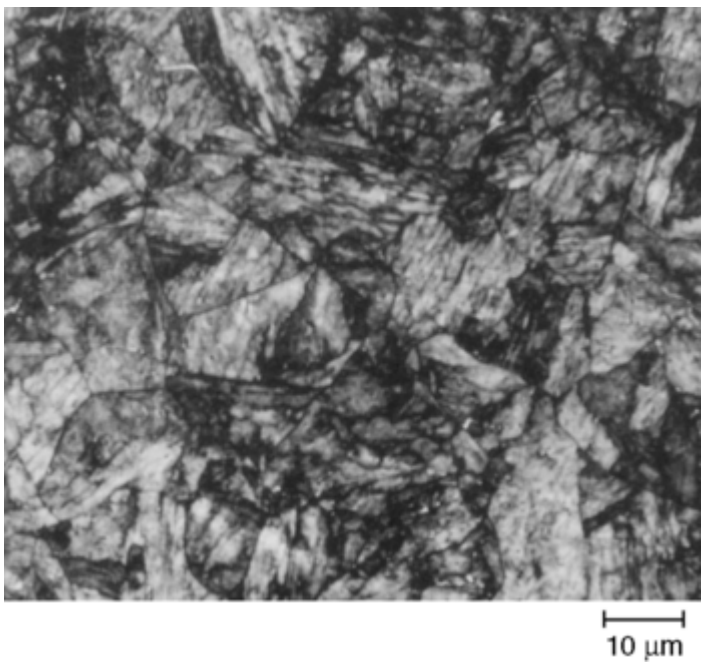

Fig. 71 Martensitic microstructure of solution-annealed and aged 18Ni(300) maraging steel (596 HV). Etched with modified Fry's reagent

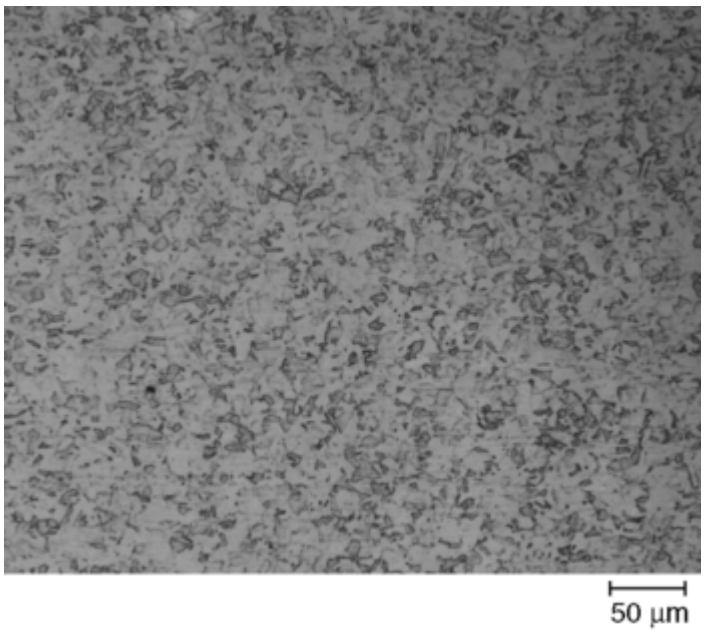

Fig. 72 Martensitic microstructure of solution-annealed and aged cobalt-free Vascomax T-250 maraging steel (535 HV). Etched with modified Fry's reagent

References cited in this section

5. E.J. Dulis and G.V. Smith, Identification and Modes of Formation and Re-Solution of Sigma Phase in Austenitic Chromium-Nickel Steels, in STP 110, ASTM, 1951, p 3–37

7. D. Peckner and I.M. Bernstein, Ed., *Handbook of Stainless Steels*, McGraw-Hill, 1977

8. A.L. Schaeffler, Constitution Diagram for Stainless Steel Weld Metal, *Met. Prog.*, Vol 56 (No. 11), Nov 1949, p 680–688

9. W.T. DeLong et al., Measurement and Calculation of Ferrite in Stainless Steel Weld Metal, *Weld. J.*, Vol 35 (No. 11), Nov 1956, p 521s–528s

10. W.T. DeLong, A Modified Phase Diagram for Stainless Steel Weld Metals, *Met. Prog.*, Vol 77, Feb 1960, p 98–100B

11. H.F. Reid and W.T. DeLong, Making Sense out of Ferrite Requirements in Welding Stainless Steels, *Met. Prog.*, Vol 103, June 1973, p 73–77

12. C.J. Long and W.T. DeLong, The Ferrite Content of Austenitic Stainless Steel Weld Metal, *Weld. J.*, Vol 52, July 1973, p 281s–297s

13. S. Mayerhofer and H. Kohl, Statistical Analysis of the Delta Ferrite Content of Austenitic Steels, *Berg Hüttenmänn. Monatsh.*, Vol III (No. 9), BISI 5304, 1966, p 443–453

14. W.T. DeLong, Ferrite in Austenitic Stainless Steel Weld Metal, *Weld. J.*, Vol 53, July 1974, p 273s–286s

15. H.A. Meijer, Quantitative Analysis of Ferrite in Austenitic Stainless Steel, *Br. Weld. J.*, Vol 13, Jan 1966, p 12–17

16. F.C. Hull, Delta Ferrite and Martensite Formation in Stainless Steels, *Weld. J.*, Vol 42 (No. 5), May 1973, p 193s–203s

17. L.S. Aubrey et al., Ferrite Measurement and Control in Cast Duplex Stainless Steels, in STP 756, ASTM, 1982, p 126–164

18. M.T. Leger, Predicting and Evaluating Ferrite Content in Austenitic Stainless Steel Castings, in STP 756, ASTM, 1982, p 105–125

19. L. Pryce and K.W. Andrews, Practical Estimation of Composition Balance and Ferrite Content in Stainless Steels, *J. Iron Steel Inst.,* Vol 195, Aug 1960, p 415–417

20. C.M. Hammond, The Development of New High-Strength Stainless Steels, in STP 369, ASTM, 1965, p 47–53

21. R.B. Gunia and G.A. Ratz, The Measurement of Delta Ferrite in Austenitic Stainless Steel, *Weld. Res. Counc. Bull.,* No. 132, Aug 1968

22. L.A. Brough, The Effects of Processing on Delta Ferrite Measurement, *J. Mater. Energy Syst.,* Vol 5 (No. 1), June 1983, p 36–42

23. W.L. Johns et al., Percent Delta Ferrite Determination in Type 304 Stainless Steel Weldments, *Microstruct. Sci.,* Vol 2, 1974, p 13–22

24. G.M. Goodwin et al., A Study of Ferrite Morphology in Austenitic Stainless Steel Weldments, *Weld. J.,* Vol 51, Sept 1972, p 425s–429s

25. C.B. Post and W.S. Eberly, Stability of Austenite in Stainless Steels, *Trans. ASM,* Vol 39, 1947, p 868–890

26. A.J. Griffiths and J.C. Wright, "Mechanical Properties of Austenitic and Metastable Stainless Steel Sheet and Their Relationships with Pressforming Behaviour," Publication 117, Iron and Steel Institute, 1969, p 51–65

27. R. Stickler and A. Vinckier, Morphology of Grain-Boundary Carbides and Its Influence on Intergranular Corrosion of 304 Stainless Steel, *Trans. ASM,* Vol 54, 1961, p 362–380

28. J.T. Gow and O.E. Harder, Balancing the Composition of Cast 25 Per Cent Chromium-12 Per Cent Nickel Type Alloys, *Trans. ASM,* Vol 30, 1942, p 855–935

29. F.C. Hull, Effects of Composition on Embrittlement of Austenitic Stainless Steels, *Weld. J.,* Vol 52, 1973, p 104s–113s

30. R. Franks et al., Experiments on Etching Procedures for the Identification of the Sigma Phase in Austenitic Chromium-Nickel Stainless Steels, *Proc. ASTM,* Vol 53, 1953, p 143–169, 177–180

31. A.J. Lena, Sigma Phase—A Review, *Met. Prog.,* Vol 66, Sept 1954, p 122–128

32. W.E. White and I. LeMay, Metallographic Observations on the Formation and Occurrence of Ferrite, Sigma Phase, and Carbides in Austenitic Stainless Steels, *Metallography,* Vol 3, 1970, p 35–50, 51–60

33. K.W. Andrews and P.E. Brookes, Chi Phase in Alloy Steels, *Met. Treatment Drop Forg.,* July 1951, p 301–311

34. P.K. Koh, Occurrence of Chi Phase in Molybdenum-Bearing Stainless Steels, *Trans. AIME,* Vol 197, 1953, p 339–343

35. J.S. Kasper, The Ordering of Atoms in the Chi-Phase of the Iron-Chromium-Molybdenum System, *Acta Metall.,* Vol 2, May 1954, p 456–461

36. J.G. McMullin et al., Equilibrium Structure in Fe-Cr-Mo Alloys, *Trans. ASM,* Vol 46, 1954, p 799–811

37. F.L. Ver Snyder and H.J. Beattie, The Laves and Chi Phases in a Modified 12Cr Stainless Alloy, *Trans. ASM,* Vol 47, 1955, p 211–230

38. B. Weiss and R. Stickler, Phase Instabilities during High Temperature Exposure of 316 Austenitic Stainless Steel, *Met. Trans.,* Vol 3, April 1972, p 851–866

39. H. Hughes and S.R. Keown, Precipitation of a Transition Intermetallic Compound (R-Phase) in Steels, *J. Iron Steel Inst.,* Vol 206, March 1968, p 275–277

40. D.J. Dyson and S.R. Keown, A Study of Precipitation in a 12% Cr-Co-Mo Steel, *Acta Metall.,* Vol 17, 1969, p 1095–1107

41. J.K. Lai and J.R. Haigh, Delta-Ferrite Transformation in a Type 316 Weld Metal, *Weld. J.,* Vol 58, Jan 1979, p 1s–6s

42. H.T. Beattie and W.C. Hagel, Intermetallic Compounds in Titanium-Hardened Alloys, *Trans. AIME,* Vol 209, July 1957, p 911–917

43. K.W. Andrews and H. Hughes, discussion of paper "Aging Reaction in Certain Superalloys," *Trans. ASM,* Vol 49, 1957, p 999

44. J.J. Demo, *Structure, Constitution, and General Characteristics of Wrought Ferritic Stainless Steels,* STP 619, ASTM, 1977

45. R.H. Thielemann, Some Effects of Composition and Heat Treatment on the High Temperature Rupture Properties of Ferrous Alloys, *Proc. ASTM,* Vol 40, 1940, p 788–804

46. K.J. Irvine et al., The Physical Metallurgy of 12% Chromium Steels, *J. Iron Steel Inst.,* Vol 195, Aug 1960, p 386–405

47. K.J. Irvine et al., Controlled-Transformation Stainless Steels, *J. Iron Steel Inst.,* Vol 192, July 1959, p 218–238

48. A. Kasak et al., Development of Precipitation Hardening Cr-Mo-Co Stainless Steels, *Trans. ASM,* Vol 56, 1963, p 455–467

49. B.R. Banerjee et al., Structure and Properties of PH15-7Mo Stainless, *Trans. ASM,* Vol 57, 1964, p 856–873

50. H.L. Marcus et al., Precipitation in 17-7PH Stainless Steel, *Trans. ASM,* Vol 58, 1965, p 176–182

51. R.C. Gibson et al., Properties of Stainless Steels with a Microduplex Structure, *Trans. ASM,* Vol 61, 1968, p 85–93

52. S. Floreen and H.W. Hayden, The Influence of Austenite and Ferrite on the Mechanical Properties of Two-Phase Stainless Steels Having Microduplex Structures, *Trans. ASM,* Vol 61, 1968, p 489–499

53. H.D. Solomon and T.M. Devine, "Duplex Stainless Steels—A Tale of Two Phases," paper 8201-089, presented at the 1982 ASM Metals Congress (St. Louis, MO), 1982

G.F. Vander Voort, G.M. Lucas, and E.P. Manilova, Metallography and Microstructures of Stainless Steels and Maraging Steels, *Metallography and Microstructures,* Vol 9, *ASM Handbook,* ASM International, 2004, p. 670–700

Metallography and Microstructures of Stainless Steels and Maraging Steels

George F. Vander Voort and Gabriel M. Lucas, Buehler Ltd.; Elena P. Manilova, Polzunov Central Boiler and Turbine Institute, St. Petersburg, Russia

References

1. G.F. Vander Voort, *Metallography: Principles and Practice,* McGraw-Hill, 1984. Reprinted by ASM International, 1999

2. F.C. Bell and D.E. Sonon, Improved Metallographic Etching Techniques for Stainless Steel and for Stainless Steel to Carbon Steel Weldments, *Metallography,* Vol 9, 1976, p 91–107

3. J.M. Stephenson and B.M. Patchett, Grain-Boundary Etches for Austenitic and Ferritic Ni-Cr-Mo Corrosion-Resistant Alloys, *Sheet Met. Ind.,* Vol 56, 1979, p 45–50, 57

4. J.J. Gilman, Electrolytic Etching—The Sigma Phase Steels, *Trans. ASM,* Vol 44, 1952, p 566–600

5. E.J. Dulis and G.V. Smith, Identification and Modes of Formation and Re-Solution of Sigma Phase in Austenitic Chromium-Nickel Steels, in STP 110, ASTM, 1951, p 3–37

6. R.J. Gray, Magnetic Etching with Ferrofluid, *Metallographic Specimen Preparation,* Plenum Press, 1974, p 155–177

7. D. Peckner and I.M. Bernstein, Ed., *Handbook of Stainless Steels,* McGraw-Hill, 1977

8. A.L. Schaeffler, Constitution Diagram for Stainless Steel Weld Metal, *Met. Prog.,* Vol 56 (No. 11), Nov 1949, p 680–688

9. W.T. DeLong et al., Measurement and Calculation of Ferrite in Stainless Steel Weld Metal, *Weld. J.,* Vol 35 (No. 11), Nov 1956, p 521s–528s

10. W.T. DeLong, A Modified Phase Diagram for Stainless Steel Weld Metals, *Met. Prog.,* Vol 77, Feb 1960, p 98–100B

11. H.F. Reid and W.T. DeLong, Making Sense out of Ferrite Requirements in Welding Stainless Steels, *Met. Prog.,* Vol 103, June 1973, p 73–77

12. C.J. Long and W.T. DeLong, The Ferrite Content of Austenitic Stainless Steel Weld Metal, *Weld. J.,* Vol 52, July 1973, p 281s–297s

13. S. Mayerhofer and H. Kohl, Statistical Analysis of the Delta Ferrite Content of Austenitic Steels, *Berg Hüttenmänn. Monatsh.,* Vol III (No. 9), BISI 5304, 1966, p 443–453

14. W.T. DeLong, Ferrite in Austenitic Stainless Steel Weld Metal, *Weld. J.,* Vol 53, July 1974, p 273s–286s

15. H.A. Meijer, Quantitative Analysis of Ferrite in Austenitic Stainless Steel, *Br. Weld. J.,* Vol 13, Jan 1966, p 12–17

16. F.C. Hull, Delta Ferrite and Martensite Formation in Stainless Steels, *Weld. J.,* Vol 42 (No. 5), May 1973, p 193s–203s

17. L.S. Aubrey et al., Ferrite Measurement and Control in Cast Duplex Stainless Steels, in STP 756, ASTM, 1982, p 126–164

18. M.T. Leger, Predicting and Evaluating Ferrite Content in Austenitic Stainless Steel Castings, in STP 756, ASTM, 1982, p 105–125

19. L. Pryce and K.W. Andrews, Practical Estimation of Composition Balance and Ferrite Content in Stainless Steels, *J. Iron Steel Inst.,* Vol 195, Aug 1960, p 415–417

20. C.M. Hammond, The Development of New High-Strength Stainless Steels, in STP 369, ASTM, 1965, p 47–53

21. R.B. Gunia and G.A. Ratz, The Measurement of Delta Ferrite in Austenitic Stainless Steel, *Weld. Res. Counc. Bull.,* No. 132, Aug 1968

22. L.A. Brough, The Effects of Processing on Delta Ferrite Measurement, *J. Mater. Energy Syst.,* Vol 5 (No. 1), June 1983, p 36–42

23. W.L. Johns et al., Percent Delta Ferrite Determination in Type 304 Stainless Steel Weldments, *Microstruct. Sci.,* Vol 2, 1974, p 13–22

24. G.M. Goodwin et al., A Study of Ferrite Morphology in Austenitic Stainless Steel Weldments, *Weld. J.,* Vol 51, Sept 1972, p 425s–429s

25. C.B. Post and W.S. Eberly, Stability of Austenite in Stainless Steels, *Trans. ASM,* Vol 39, 1947, p 868–890

26. A.J. Griffiths and J.C. Wright, "Mechanical Properties of Austenitic and Metastable Stainless Steel Sheet and Their Relationships with Pressforming Behaviour," Publication 117, Iron and Steel Institute, 1969, p 51–65

27. R. Stickler and A. Vinckier, Morphology of Grain-Boundary Carbides and Its Influence on Intergranular Corrosion of 304 Stainless Steel, *Trans. ASM,* Vol 54, 1961, p 362–380

28. J.T. Gow and O.E. Harder, Balancing the Composition of Cast 25 Per Cent Chromium-12 Per Cent Nickel Type Alloys, *Trans. ASM,* Vol 30, 1942, p 855–935

29. F.C. Hull, Effects of Composition on Embrittlement of Austenitic Stainless Steels, *Weld. J.,* Vol 52, 1973, p 104s–113s

30. R. Franks et al., Experiments on Etching Procedures for the Identification of the Sigma Phase in Austenitic Chromium-Nickel Stainless Steels, *Proc. ASTM,* Vol 53, 1953, p 143–169, 177–180

31. A.J. Lena, Sigma Phase—A Review, *Met. Prog.,* Vol 66, Sept 1954, p 122–128

32. W.E. White and I. LeMay, Metallographic Observations on the Formation and Occurrence of Ferrite, Sigma Phase, and Carbides in Austenitic Stainless Steels, *Metallography,* Vol 3, 1970, p 35–50, 51–60

33. K.W. Andrews and P.E. Brookes, Chi Phase in Alloy Steels, *Met. Treatment Drop Forg.,* July 1951, p 301–311

34. P.K. Koh, Occurrence of Chi Phase in Molybdenum-Bearing Stainless Steels, *Trans. AIME,* Vol 197, 1953, p 339–343

35. J.S. Kasper, The Ordering of Atoms in the Chi-Phase of the Iron-Chromium-Molybdenum System, *Acta Metall.,* Vol 2, May 1954, p 456–461

36. J.G. McMullin et al., Equilibrium Structure in Fe-Cr-Mo Alloys, *Trans. ASM,* Vol 46, 1954, p 799–811

37. F.L. Ver Snyder and H.J. Beattie, The Laves and Chi Phases in a Modified 12Cr Stainless Alloy, *Trans. ASM,* Vol 47, 1955, p 211–230

38. B. Weiss and R. Stickler, Phase Instabilities during High Temperature Exposure of 316 Austenitic Stainless Steel, *Met. Trans.,* Vol 3, April 1972, p 851–866

39. H. Hughes and S.R. Keown, Precipitation of a Transition Intermetallic Compound (R-Phase) in Steels, *J. Iron Steel Inst.,* Vol 206, March 1968, p 275–277

40. D.J. Dyson and S.R. Keown, A Study of Precipitation in a 12% Cr-Co-Mo Steel, *Acta Metall.,* Vol 17, 1969, p 1095–1107

41. J.K. Lai and J.R. Haigh, Delta-Ferrite Transformation in a Type 316 Weld Metal, *Weld. J.,* Vol 58, Jan 1979, p 1s–6s

42. H.T. Beattie and W.C. Hagel, Intermetallic Compounds in Titanium-Hardened Alloys, *Trans. AIME,* Vol 209, July 1957, p 911–917

43. K.W. Andrews and H. Hughes, discussion of paper "Aging Reaction in Certain Superalloys," *Trans. ASM,* Vol 49, 1957, p 999

44. J.J. Demo, *Structure, Constitution, and General Characteristics of Wrought Ferritic Stainless Steels,* STP 619, ASTM, 1977

45. R.H. Thielemann, Some Effects of Composition and Heat Treatment on the High Temperature Rupture Properties of Ferrous Alloys, *Proc. ASTM,* Vol 40, 1940, p 788–804

46. K.J. Irvine et al., The Physical Metallurgy of 12% Chromium Steels, *J. Iron Steel Inst.,* Vol 195, Aug 1960, p 386–405

47. K.J. Irvine et al., Controlled-Transformation Stainless Steels, *J. Iron Steel Inst.,* Vol 192, July 1959, p 218–238

48. A. Kasak et al., Development of Precipitation Hardening Cr-Mo-Co Stainless Steels, *Trans. ASM,* Vol 56, 1963, p 455–467

49. B.R. Banerjee et al., Structure and Properties of PH15-7Mo Stainless, *Trans. ASM,* Vol 57, 1964, p 856–873

50. H.L. Marcus et al., Precipitation in 17-7PH Stainless Steel, *Trans. ASM,* Vol 58, 1965, p 176–182

51. R.C. Gibson et al., Properties of Stainless Steels with a Microduplex Structure, *Trans. ASM,* Vol 61, 1968, p 85–93

52. S. Floreen and H.W. Hayden, The Influence of Austenite and Ferrite on the Mechanical Properties of Two-Phase Stainless Steels Having Microduplex Structures, *Trans. ASM*, Vol 61, 1968, p 489–499

53. H.D. Solomon and T.M. Devine, "Duplex Stainless Steels—A Tale of Two Phases," paper 8201-089, presented at the 1982 ASM Metals Congress (St. Louis, MO), 1982

Revised by S.Kuyucak, Austenitic Manganese Steel Castings, *Metallography and Microstructures*, Vol 9, *ASM Handbook*, ASM International, 2004, p. 701–708

Austenitic Manganese Steel Castings

Revised by Selçuk Kuyucak, CANMET, Department of Natural Resources Canada

Introduction

AUSTENITIC MANGANESE STEELS are retained austenites. Their high carbon and manganese contents delay pearlite formation and lower the martensite start temperature to typically far below room temperature. The first decomposition product from austenite, hypereutectoid cementite, however, forms rapidly at 550 to 750 °C (1020 to 1380 °F) as intergranular and interdendritic carbides and can embrittle the steel. Figure 1 shows a pseudobinary phase diagram of the Fe-Mn-C system at 13 wt% Mn. The desirable metastable austenitic structure is obtained by solution annealing in the equilibrium austenite phase field above 1000 °C (1830 °F) and rapidly quenching the steel to avoid any carbide formation. However, in heavier section-size castings, which are not uncommon for this grade of steel, the thermal conductivity of the metal, which is relatively poor, determines cooling rate. Thus, the microstructure is extremely sensitive to section size and the heaviest section should be included in examination.

Normalizing heat treatments are not applicable to grain refine austenitic manganese steel castings. Their grain size is determined during solidification and can vary widely depending on the amount of superheat in the liquid metal, section size, and the presence of nucleation agents. Consequently, to determine representative grain size and distribution, it may be useful to macroetch an entire cross section if one is available. This procedure is discussed in a subsequent section. Additional information on the properties and selection of austenitic manganese steels can be found in the article "Austenitic Manganese Steels" in Volume 1 of the *ASM Handbook.*

Austenitic Manganese Steel Castings

Revised by Selçuk Kuyucak, CANMET, Department of Natural Resources Canada

Revised by S.Kuyucak, Austenitic Manganese Steel Castings, *Metallography and Microstructures*, Vol 9, *ASM Handbook*, ASM International, 2004, p. 701–708

Specimen Preparation

Sectioning. After suitable locations of specimens to be examined are decided upon, the next step is to extract them without excessive thermal or mechanical damage. Depending on the size of the original casting, various

sectioning methods can be used. For example, flame or arc cutting can be used to isolate the sections of interest in very large castings. However, sufficient stock should be allowed to minimize thermal damage to the area of interest. Dry abrasive-wheel cutting can also be used with the same precautions.

The next series of cuts to reduce the specimen to metallographic dimensions should be performed using a "soft" silicon carbide abrasive wheel with flood cooling and a slow feed rate. Immersion electric discharge cutting is also suitable, because the associated heat-affected zones are fairly narrow. However, care should be taken subsequently to grind the specimen below the heat-affected zone before metallographic examination. Laboratory-sized diamond-edge cutting wheels are appropriate for thin specimen preparation for electron microscopy. Metal saw cutting is not recommended because of the work-hardening property of this alloy.

Mounting. Specimens can be mounted using conventional metallographic mounting materials. For edge preservation, electrolytic or electroless coatings can be applied before grinding. Another useful method involves simultaneously mounting hardened-steel ball bearings or similar guards around the specimen to facilitate flat, even grinding.

Grinding. Automatic and manual grinding methods may be used. Manual grinding is carried out wet using 80-, 180-, 320-, then 600- or 1000-grit waterproof silicon carbide abrasive papers. The specimen should be thoroughly cleaned, rinsed, and rotated 90° between grindings. The abrasive paper should be replaced often, because dull abrasive can cause light surface deformation and work hardening. Moderate pressure will minimize work hardening. Automated grinding equipment may also be used, and precautions should be taken to minimize surface deformation and contamination. Additional information is available in the article "Mechanical Grinding and Polishing" in this Volume.

Polishing is usually a two-step process. Rough polishing can be performed using 6 μm diamond paste on a napless nylon cloth, which enhances edge retention, followed by 1 μm diamond paste on a medium-nap rayon cloth. Use of diamond extender fluid is recommended in both cases. Fine polishing is carried out using a 0.06 μm colloidal silica or alumina (Al_2O_3) suspension and a medium-nap cloth.

The specimen should always be rotated in a direction opposite that of the polishing wheel. Moderate pressure is recommended. Between polishings, the specimen should be washed with soap and running water, rinsed with alcohol, and dried in a blast of warm air. After fine polishing, however, the specimen should be rinsed in alcohol to prevent staining by water. Alternate light etching and additional polishing can be used to minimize the effects of surface deformation resulting from specimen preparation.

Electrolytic polishing also yields satisfactory results. A solution of 80 g sodium chromate (Na_2CrO_4) in 420 mL glacial acetic acid is used as the electrolyte. The solution is prepared by slowly adding Na_2CrO_4 crystals to acetic acid with simultaneous stirring to prevent settling. Current densities should approximate 1 A/cm^2 (6.5 A/in.^{2}) at 30 to 50 V for 6 to 8 min. However, depending on the type of polishing apparatus used and the nature of the specimen and the mount, some experimentation may be necessary for optimal results. Copper-containing conductive specimen mounts are preferable.

Because electrolytic polishing can often magnify any microporosity in a cast specimen into larger "pits," polishing time should be kept to a minimum.

Revised by S.Kuyucak, Austenitic Manganese Steel Castings, *Metallography and Microstructures,* Vol 9, *ASM Handbook*, ASM International, 2004, p. 701–708

Austenitic Manganese Steel Castings

Revised by Selçuk Kuyucak, CANMET, Department of Natural Resources Canada

---

Macroexamination

Examination of a fracture surface can provide information on grain size, mode of failure, hot tears, and casting soundness. Tensile fractures can be dimpled or fibrous. The relative coarseness of the "orange peel" appearance on gage surfaces of broken tensile specimen stubs can sometimes indicate grain size, because very little necking occurs during tensile testing. Failures that occur from exposure to temperatures above 315 °C (600 °F) are

usually intergranular because of grain-boundary embrittlement by precipitated carbide. Poor heat treatment can also contribute to intergranular fracture.

Hot tears are usually caused by high levels of phosphorus in the steel, and macroshrinkage invariably results from pouring a casting with very low superheat (less than 20 °C, or 40 °F, above liquidus) or poor casting design (improper gating, risering, and so on). The presence of this kind of shrinkage can result in low ductility and rapid wear in service. Gas-related porosity in the form of pinholes or blowholes are caused by excessive nitrogen, hydrogen, and/or carbon monoxide generated by inadequate deoxidation of steel.

Austenitic manganese steels exhibit freezing ranges as wide as 200 °C (360 °F), making them susceptible to microporosity. Distribution of this porosity is best examined on as-polished surfaces at low magnification. Microporosity appears at interdendritic and intergranular areas, often concentrated in random pockets (Fig. 2, Ref 1). Compositions of alloys depicted in many of the micrographs in this article are given in Table 1.

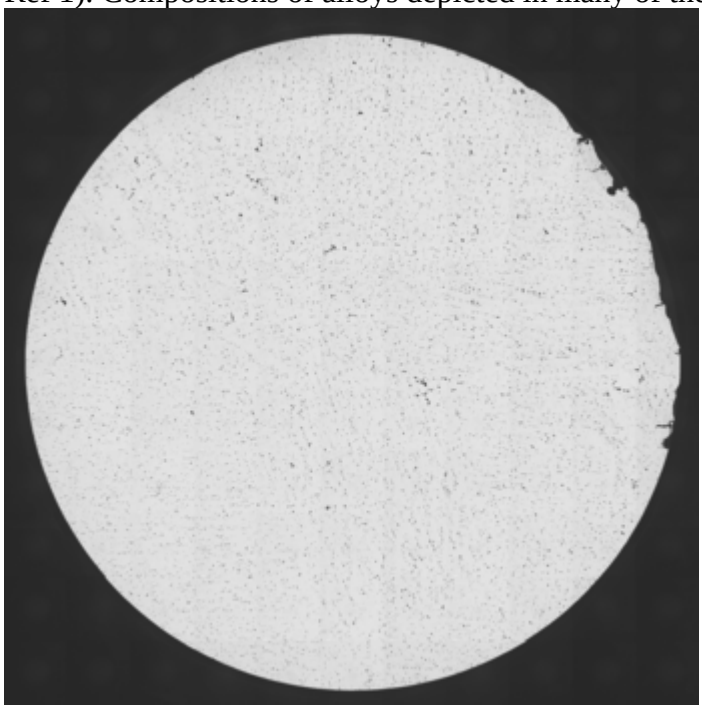

Fig. 2 Steel 2 in Table 1 (grade B3). Microporosity in a 25 mm (1 in.) diam coupon taken from a 500 mm (20 in.) long, 375 mm (15 in.) wide, 100–200 (4–8 in.) thick wedge-block. The coupon was taken from the center of the casting and measured 0.48% porosity. The block average was 0.41%. As-polished

Table 1 Chemical compositions of austenitic manganese steels shown in the micrographs

Steel[(a)]		Chemical composition, %										
		C	**Mn**	**Si**	**Cr**	**Mo**	**Ni**	**Al**	**Ti**	**P**	**S**	**N**
1	Grade B2	1.11	12.8	0.20	…	0.54	…	0.025	…	0.05	0.006	…
2	Grade B3	1.19	13.7	0.61	0.62	0.31	0.12	0.04	…	0.05	0.004	0.0265
3	Grade B4	1.27	12.7	0.43	0.63	<0.08	…	0.029	…	0.031	0.013	0.0160
4	Grade C	1.20	12.5	0.50	1.95	<0.08	…	0.042	…	0.013	0.014	0.0156
5	Grade C	1.35	13.0	0.28	2.06	…	…	0.025	…	…	…	…
6	Grade E1	1.18	12.4	0.66	0.72	1.0	0.23	0.035	0.05	0.031	0.006	…
7	Proprietary steel	1.10	13.2	0.64	0.68	1.7	0.09	0.035	0.042	0.042	0.004	
8	Grade E2	1.09	13.9	0.67	…	2.0	…	0.055	…	0.032	…	…
9	Grade F	1.06	7.6	0.50	0.54	1.1	0.05	0.07	0.03	0.025	0.004	…
10	Experimental steel	1.76	10.5	0.55	0.70	…	…	2.5	…	0.016	…	…

(a) ASTM A 128 grades (except Steels 7 and 10)

Macroetching. A smooth, unburned surface produced by wet abrasive cutting is most often adequate for macroetching. Special grinding is not required. For larger specimens, the grinding can be performed using a standard wet-grinding machine, taking precautions to ensure minimum surface deformation. Because of the nonmagnetic nature of manganese steel, a special holder or vise is usually required during grinding. Safety

precautions during macroetching are also necessary, because macroetching typically involves significant amounts of chemicals and vapors. Proper ventilation in the immediate area of the specimen is required.

Macroetchants are commonly used to reveal grain size and shape and other features, such as the presence of weld-metal repair, in austenitic manganese steel. A general-purpose etch is a 5 to 10% nital (5 to 10% concentrated nitric acid, or HNO_3, in ethanol). The preferred method is by immersion and scrubbing the surface while in contact with the etchant, with a soft-bristle brush or a cotton swab, to continuously remove a black surface film that forms. This procedure allows viewing the etched structure as it develops, which can take 15 min or more. Once the etch is completed, the specimen should be placed under running water, scrubbed lightly, and preferably cleaned with a solution of disodium salt of ethylenediamine tetraacetic acid (EDTA). Next, the specimen is well rinsed with alcohol, dried in a blast of warm air, and immediately sprayed with a thin, protective coating of a fast-drying clear lacquer, which also sometimes improves overall contrast. If overetching occurs, the specimen could be given a light regrind or polish and reetched. For large specimens, macroetch could be applied by swabbing with cotton.

Another common etchant is a 50% aqueous solution (by volume) of concentrated hydrochloric acid (HCl) applied at 60 to 70 °C (140 to 160 °F). The sample is periodically scrubbed under running water. Etching could take from 30 min to several hours. It is followed by scrubbing in water, treating with EDTA, rinsing in alcohol, drying, and protective spraying.

The above etchant could be made faster by the addition of one part hydrogen peroxide (30% H_2O_2 solution) to four to five parts of the HCl solution. The etch can be applied at room temperature or warm (up to 60 °C, or 140 °F) for a still faster reaction. If a warm etch is desired, the HCl solution is brought to temperature first, the sample is immersed, and the H_2O_2 solution is added gradually, waiting for any foaming to stop, especially when added to a warm solution. Etching should proceed for 15 to 25 s. Almost immediately, a black film forms, which should be scrubbed off under running water with a soft brush. This must be done without delay to prevent staining the etched surface. If the etch is too light, the specimen can be immersed for 5 to 10 s and scrubbed again. This procedure is repeated until a satisfactory etch is achieved. Then, the specimen is rinsed with alcohol, dried, and sprayed with a protective coat. This etchant produces a brilliant etch. Macroetching with the above etchants can be carried out in the as-cast or heat treated condition. No significant grain growth occurs during heat treatment, and better grain definition is often obtained after this operation.

Grain Size Measurements. Grain size in these steels is primarily a function of the pouring temperature of the casting and section size, and it is not unusual to encounter grain sizes larger than can be measured by the standard ASTM microscale (G-00 to G-10). The recommended procedure for grain sizes larger than 0.5 mm is to use the ASTM macrograin size number (MG-00 to MG-10). Both the G scale viewed at 100× and the MG scale at 1× have the same average intercept lengths that start at 32 mm for G-0 and MG-0. Thus, the two scales are displaced from each other by a factor of 100. ASTM numbers are based on a binary cycle where each number is separated by a factor of $\sqrt{2}$, and 6.64 size numbers make up one decimal cycle. Therefore, the micrograin size number can be converted to macrograin size number by adding 13.3 size numbers. The relationship between ASTM grain size number n and the average grain size d (in inches) is:

$$n(\text{G scale}) = -6.64(1.8 + \log d)$$

$$n(\text{MG scale}) = +6.64(0.2 - \log d)$$

Both procedures are detailed in ASTM E 112 “Standard Method for Determining Grain Size.”

An example macroetch is shown in Fig. 3 for a 165 mm ($6\frac{1}{2}$ in.) section (Ref 2). Low superheat resulted in a highly asymmetric structure between the cope and drag sides. Relatively fine grains exist in a 15 mm (0.6 in.) chill zone (1 to 2 mm, or 0.04 to 0.08 in., in size), but interior of the section has coarse columnar (4 to 30 mm, or 0.16 to 1.2 in., in size) and equiaxed grains (4 to 10 mm, or 0.16 to 04 in., in size).

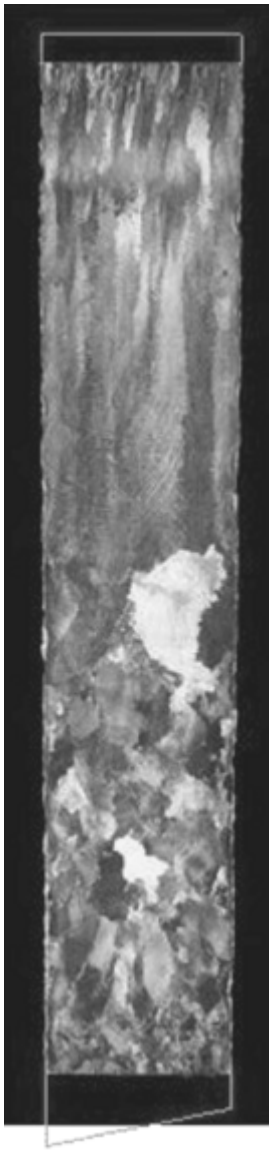

Fig. 3 Same steel as in Fig. 2 heat treated at 1120 °C (2050 °F), and water quenched. Macroetch of a 25 mm (1 in.) diam core taken across a 165 mm (6.5 in.) section and cut longitudinally, showing cope- and drag-side chill, columnar, and equiaxed zones. 3% nital

References cited in this section

1. S. Kuyucak, R. Zavadil, and G. Ouellet, On the Heat-Treatment of Hadfield's Austenitic Manganese Steels; Part VII: Casting Soundness and Microporosity in Large Wedge-Block Castings, Paper No. 03-134, *AFS Trans.*, 2003

2. S. Kuyucak and R. Zavadil, On the Heat-Treatment of Hadfield's Austenitic Manganese Steels; Part VI: Impact Toughness, Microstructure, Macro- and Micro-Segregation in Large Wedge-Block Castings, Paper No. 03-133, *AFS Trans.*, 2003

Revised by S.Kuyucak, Austenitic Manganese Steel Castings, *Metallography and Microstructures,* Vol 9, *ASM Handbook,* ASM International, 2004, p. 701–708

Austenitic Manganese Steel Castings

Revised by Selçuk Kuyucak, CANMET, Department of Natural Resources Canada

Microexamination

Table 2 summarizes etchants and procedures that are commonly used for austenitic manganese steels, including weld metal. The cyclic procedures based on nital and HCl often yield a clean etched surface. Nital, picral, and Vilella's reagent are also useful for quick results on as-cast and heat treated steels. However, these solutions sometimes produce a thin, irregular, yellowish brown film on the surface of the specimen that can obscure subsequent microscopic interpretation. This film can be removed by immersion in a 10% solution of HCl in water or alcohol. Cementite is usually better defined by using the 4% picral etch.

Table 2 Selected etching reagents for microscopic examination

Etchant	Procedure	Comments
Picral: 4–5 g picric acid, 100 mL alcohol[(a)] (95% grade)	Immerse 20 s or more if necessary. Rinse thoroughly in alcohol and dry.	Shows general structure, grain contrast, and coloration. Etches grain boundaries where carbide is present. Also reveals pearlite colonies if present
Glyceregia: 1 part concentrated HNO_3, 3 parts concentrated HCl, 3 parts glycerin (Ref 3)	Immerse 15 s or more if necessary. Rinse thoroughly in alcohol and dry.	Shows general structure, grain contrast, and coloration. Etches grain boundaries where carbide is present. Also reveals pearlite colonies if present
Short cyclic etch: (1) 3–6% nital[(b)], (2) 10–15% concentrated HCl in alcohol[(a)]	Immerse in (1) for a few seconds. Rinse thoroughly in alcohol and dry. Remove light yellowish-brown film by immersion in (2). Rinse in alcohol and dry. Repeat two to three times.	Shows general structure, grain contrast, and coloration. Etches grain boundaries where carbide is present. Also reveals pearlite colonies if present
Cyclic etch: (1) 3% nital[(b)], (2) 10% concentrated HCl in alcohol[(a)], (3) 2% NH_4OH (ammonium hydroxide) in alcohol[(a)] (Ref 3)	Alternate immersions in (1) and (2) for 15 s each. Rinse specimen in alcohol and dry between solutions. Repeat two to three times, then immerse in (3) for 15 s. Rinse in alcohol and dry.	Shows general structure, grain contrast, and coloration. Etches grain boundaries where carbide is present. Also reveals pearlite colonies if present
Villela's reagent: 1 g picric acid, 5 mL concentrated HCl, 100 mL ethanol	Swab with cotton. Rinse in alcohol and dry. Use 10% HCl solution to remove surface film if present.	Shows general structure, grain contrast, and coloration. Etches grain boundaries where carbide is present. Also reveals pearlite colonies if present
Equal part dilute aqua regia. Equal parts of concentrated HNO_3, concentrated HCl and H_2O (Ref 3)	Immerse 5–10 s if carbides are present, or up to 30–40 s if not. Clean in ultrasonic bath with 2% EDTA. Rinse in water, alcohol, and dry.	General-purpose etch to reveal grain boundaries in heat treated steels. Sensitive to grain orientation, some boundaries are heavily attacked while others are not.
Color-tint etch: (1) 2%	Swab (with cotton) or immerse in (1) for a	Produces excellent grain

nital, (2) 20% aqueous $Na_2S_2O_5$ (sodium metabisulfite) (Ref 4)	few seconds. Rinse thoroughly in alcohol and dry. If surface is colored with a light yellowish brown film, remove by swabbing or immersing in 10% HCl solution. Rinse again in alcohol and dry. Apply color tint by 20 s immersion in (2).	contrast. Reveals extent of decarburization near steel surface; deformation-induced ε martensite
Boiling alkaline sodium picrate: 2 g picric acid, 25 g NaOH (sodium hydroxide), and 100 mL H_2O	Immerse for 5–10 min. Rinse well and dry.	Reveals as-cast austenite grain boundaries in the presence of a pearlitic microstructure
Electrolytic etch (1): 80 g Na_2CrO_4 dissolved in 420 mL of glacial acetic acid	0.03–0.05 A/cm^2 (0.2–0.3 A/in.^{2}) at 5–10 V for 5–10 min. Higher current densities can be used to shorten etching time if surface rippling or waviness is a problem. Note: This same solution can be used to polish specimens electrolytically (see section on specimen preparation).	Reveals grain boundaries and annealing and deformation twins
Electrolytic etch (2): 20% HCl solution in methanol	0.25–0.5 A/cm^2 (1.6–3.2 A/in.^{2}) at 4–6 V for 30 s. For polishing, current densities of 0.6–0.8 A/cm^2 (3.9–5.2 A/in.^{2}) have given satisfactory results in some cases.	Reveals deformation in twinned structure

(a) Alcohol is ethanol or methanol.

(b) 3% nital is 3% concentrated HNO_3 (nitric acid) in alcohol.

Insufficient grain-boundary contrast, which is due to the virtual absence of carbide precipitates along the austenite grain boundaries, can often be compensated for by electrolytic etching or color tinting. Techniques that improve contrast in the microscope, such as oblique lighting, dark-field, or differential interference contrast, also may be helpful. Electrolytic etching can be used as well to reveal the presence of deformation and annealing twins in the austenite grains. Alcohol rinsing is again recommended to minimize staining of the specimen surface.

Deep immersion etching, that is, longer etching times, can be used to reveal the solute segregation pattern within the austenite grains. In addition, when a large volume fraction of pearlite in the microstructure obscures the as-cast austenite grain size, the grain boundaries can be revealed by an immersion etch in boiling alkaline sodium picrate, which preferentially colors the cementite.

References cited in this section

3. G.F. Vander Voort, *Metallography: Principles and Practice,* McGraw-Hill, 1984, p. 215, 634

4. A.J. Sedriks and T.O. Mulhearn, Austenitic Manganese Steel: Structure and Properties of Decarburized Layer, *J. Iron Steel Inst.,* Vol 202, Nov 1964, p 907–911

Revised by S.Kuyucak, Austenitic Manganese Steel Castings, *Metallography and Microstructures,* Vol 9, *ASM Handbook,* ASM International, 2004, p. 701–708

Austenitic Manganese Steel Castings

Revised by Selçuk Kuyucak, CANMET, Department of Natural Resources Canada

Microstructure

With the exception of vanadium-containing precipitation-hardened alloys and some molybdenum-containing alloys, the desirable microstructure in austenitic manganese steels is a single-phase austenitic solid solution.
In the as-cast state, the microstructure consists of an austenite matrix with massive intergranular and interdendritic carbides that start forming at triple points and are usually surrounded by pearlitelike lamellar carbide colonies. At their center, these usually contain a carbide-phosphide eutectic, distinguished by their mottled appearance (Fig. 4, 5). Silicon plays a role in carbide formation as it raises the carbon activity. At high silicon contents (>0.8%), cementite forms rapidly; steel behaves like a higher carbon grade. At low silicon contents (<0.3%), cementite formation occurs at lower temperatures and tends to be acicular (Ref 5). Typically, the alloy is given a “toughening” heat treatment, which consists of heating gradually from about 300 °C (600 °F) to avoid thermal cracking in the brittle as-cast alloy, solution annealing at a temperature high enough to dissolve the carbides, and rapid quenching in agitated water at room temperature to avoid carbide reprecipitation.

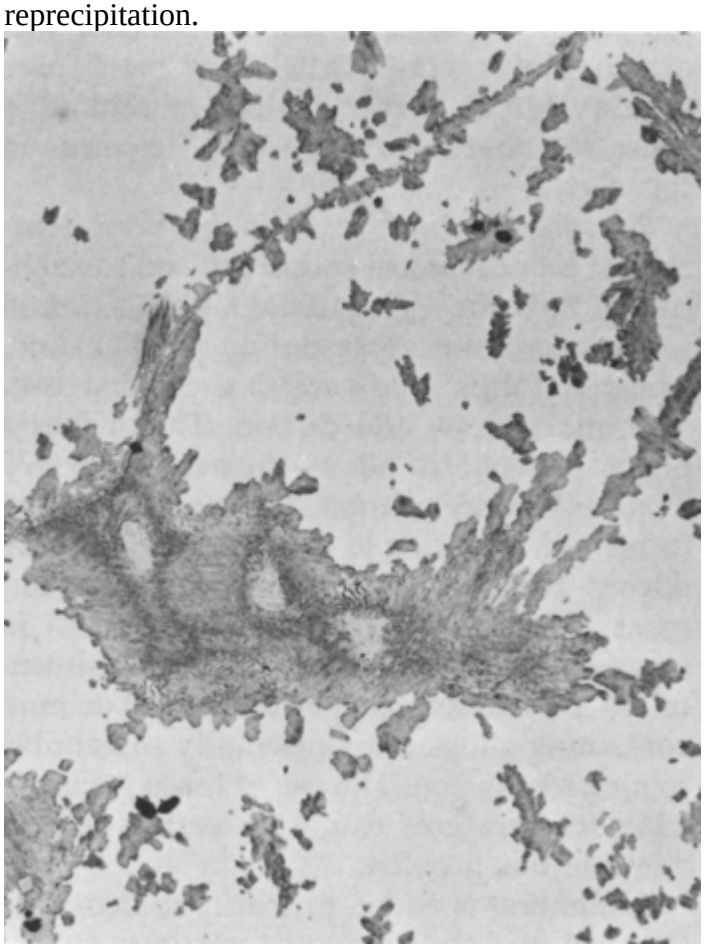

Fig. 4 Composition similar to steel 3 in Table 1 (grade B4), as-cast. Microstructure consists of austenite grains with intergranular and interdendritic carbides. The mottled phase in the centers of lamellar carbides is phosphide eutectic. 4% picral. 100×

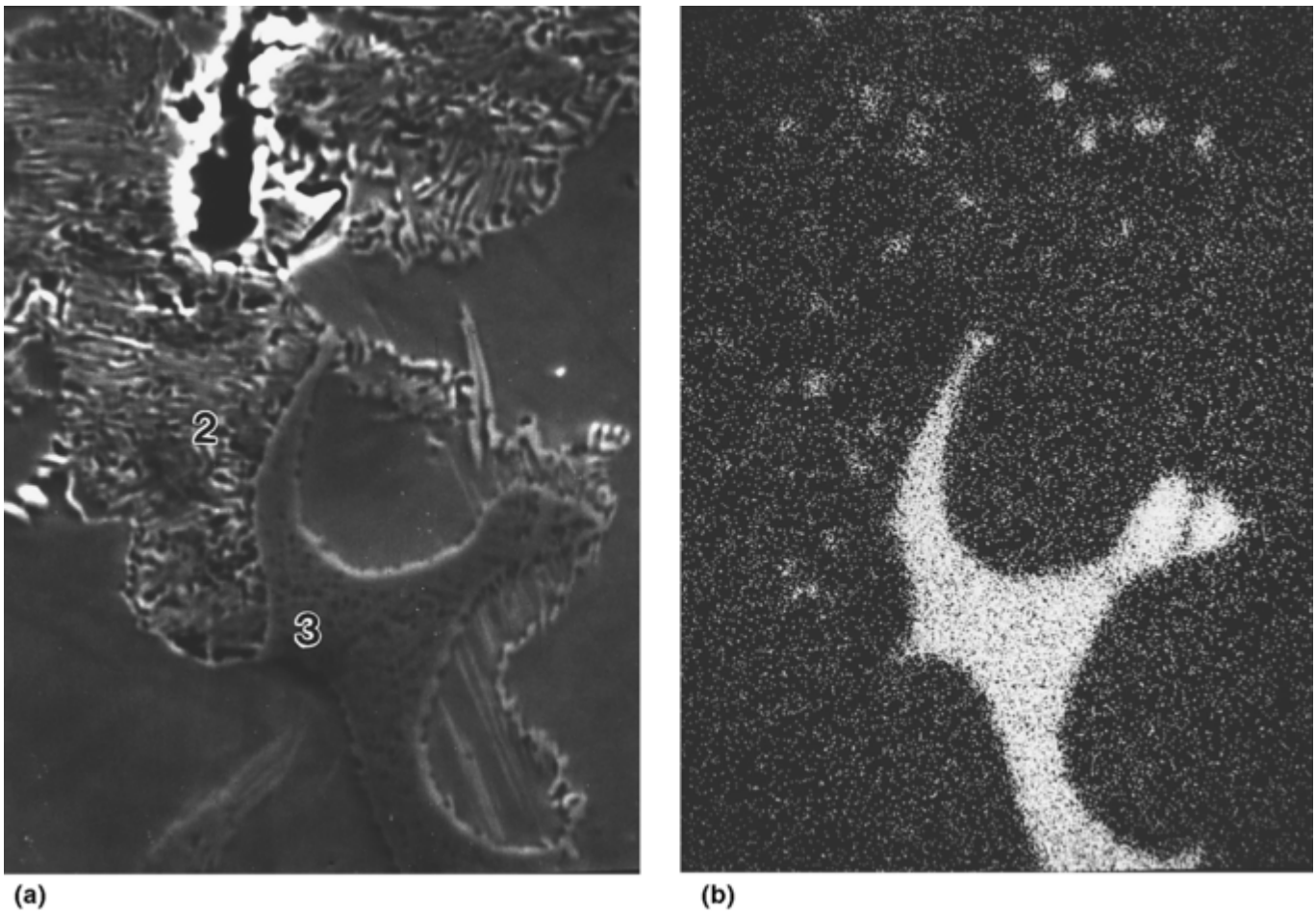

Fig. 5 Composition similar to steel 2 in Table 1 (grade B3), as-cast. (a) Secondary electron image by electron microprobe of lamellar carbides (area 2) with phosphide eutectic (area 3). (b) P-map of the same area as in (a)

In practice, the presence of some grain-boundary carbide is typical, especially in heavier sections. In regular manganese steel, first a thin carbide delineation forms and rapidly envelops the grain boundaries (Ref 6, 7). Maratray interpreted these delineations also as widening of grain boundaries (Ref 8). Then, thick carbides (>1 μm, or 40 μin., thick) nucleate at grain-boundary edges and corners and primarily grow intergranularly with little further thickening. The latter carbide is distinguished from the former by the appearance of clear carbide/austenite phase boundaries, resolved by a light microscope at 200× magnification (Fig. 6). The carbide delineations are not detrimental to impact toughness with any significance, whereas the thick carbides decrease impact toughness in proportion to their grain-boundary coverage.

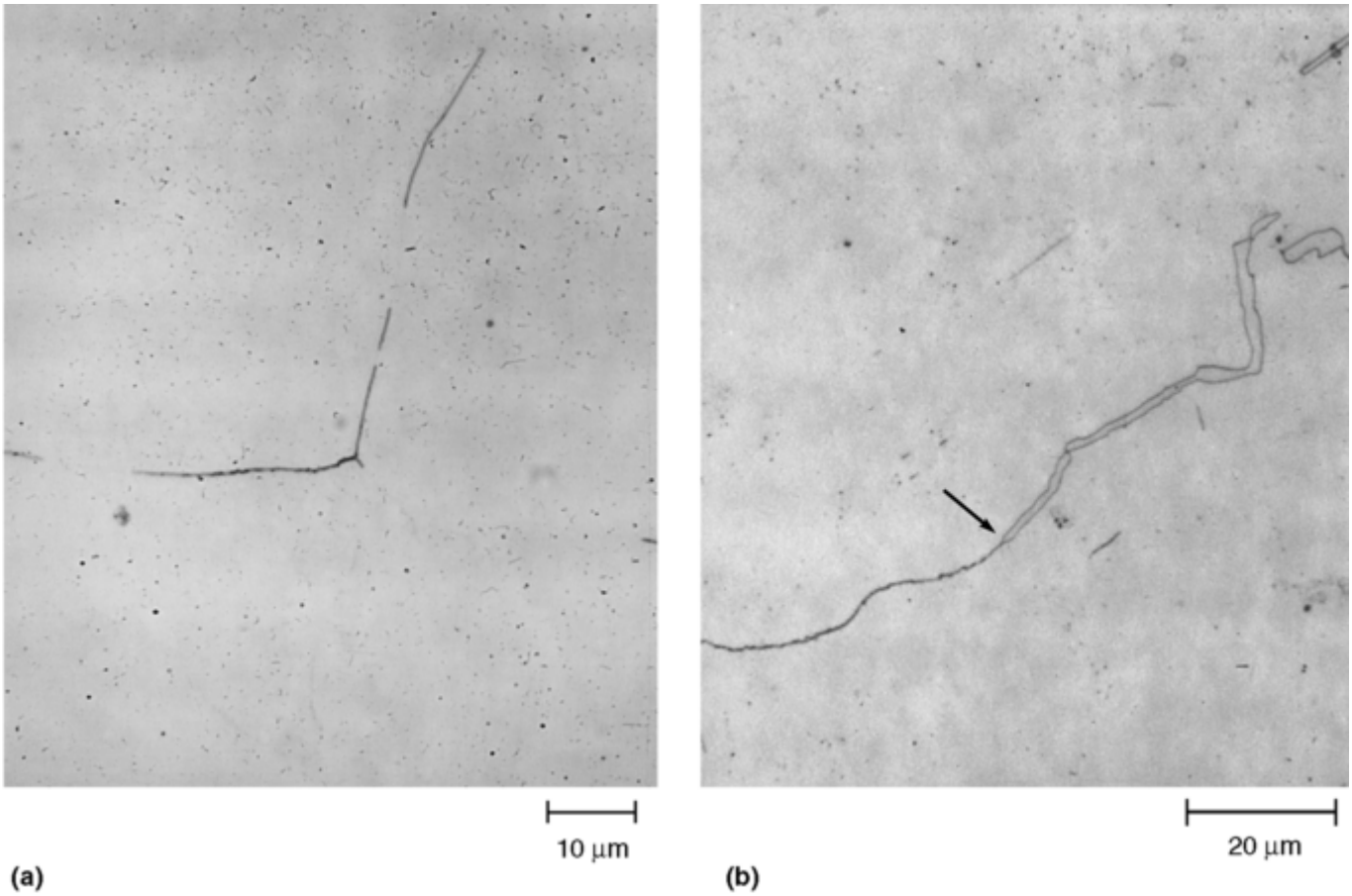

Fig. 6 Steel 3 in Table 1 (grade B4). Solution annealed at 1060 °C (1940 °F), stepped down to 950 °C (1740 °F) and water quenched. (a) 25 mm (1 in.) section, Charpy toughness was 196 J (145 ft · lbf). (b) 75 mm (3 in. section), Charpy toughness was 76 J (56 ft · lbf). Arrow indicates the change from a "thin" to a "thick" carbide. Etchant: equal part dilute aqua regia (see Table 2 for composition)

Alloying Elements. The regular elements, such as, carbon, manganese, and silicon, as well as other alloying elements, enhance specific properties in various applications. Raising carbon content increases wear resistance but it becomes increasingly difficult to prevent carbide reprecipitation during quenching. Therefore, in thick sections, lower carbon grades are preferred.

Chromium additions give some corrosion resistance and raise the yield strength, but also increase the high-temperature stability of the carbides, making it necessary to raise the solution-annealing temperature; otherwise, incomplete carbide dissolution may result (Fig. 7). It is customary to raise the solution-annealing temperature of grade C steels from 1060 to 1140 °C (1940 to 2080 °F) for complete dissolution of carbides. Small amounts of chromium (0.2 to 0.8%) are usually present as residual in other grades coming from the melting scrap. At a 2% Cr level, carbide delineations can thicken without displaying a clear phase boundary (Fig. 8). These thickened carbides are somewhat detrimental to impact toughness (Ref 9). Figure 9 shows transmission electron micrographs (TEMs) of replicas from a thin carbide delineation and a thick carbide film in grade B3 steel, and a thickened carbide delineation in grade C steel.

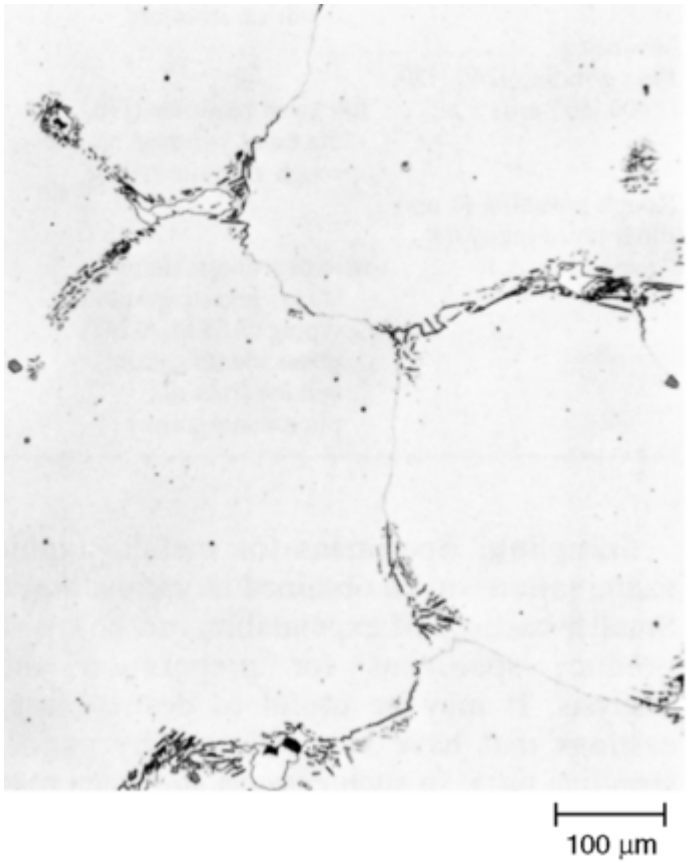

Fig. 7 Steel 5 in Table 1 (grade C), cast, heat treated at 1095 °C (2000 °F) for 2 h, and water quenched. Microstructure consists of austenite grains, with undissolved carbides at interdendritic areas and grain boundaries. The high carbon content of this steel also contributed to a large fraction of undissolved carbides. This is an undesirable microstructure. Cyclic etch (see Table 2 for composition and method). 100×

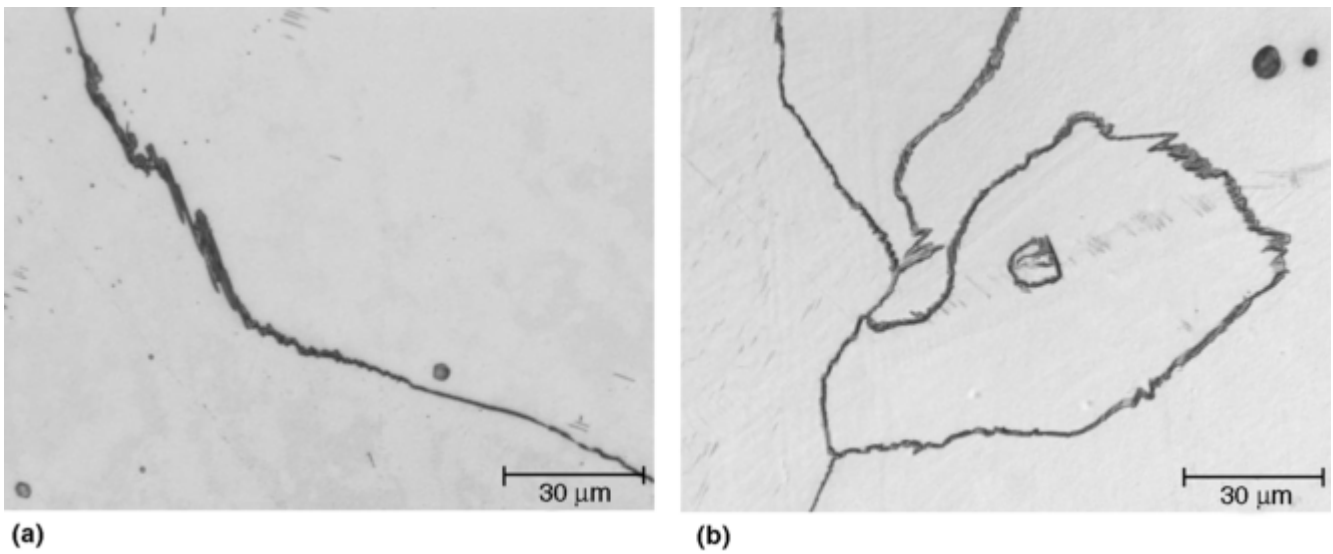

Fig. 8 Steel 4 in Table 1 (grade C), 125 mm (5 in.) Y-block. Solution annealed at 1140 °C (2080 °F) and water quenched. Microstructures show examples of regular and "thickened" carbide delineations. Charpy toughness was 130 and 73 J (96 and 54 ft · lbf). Same etch as Fig. 6(a)

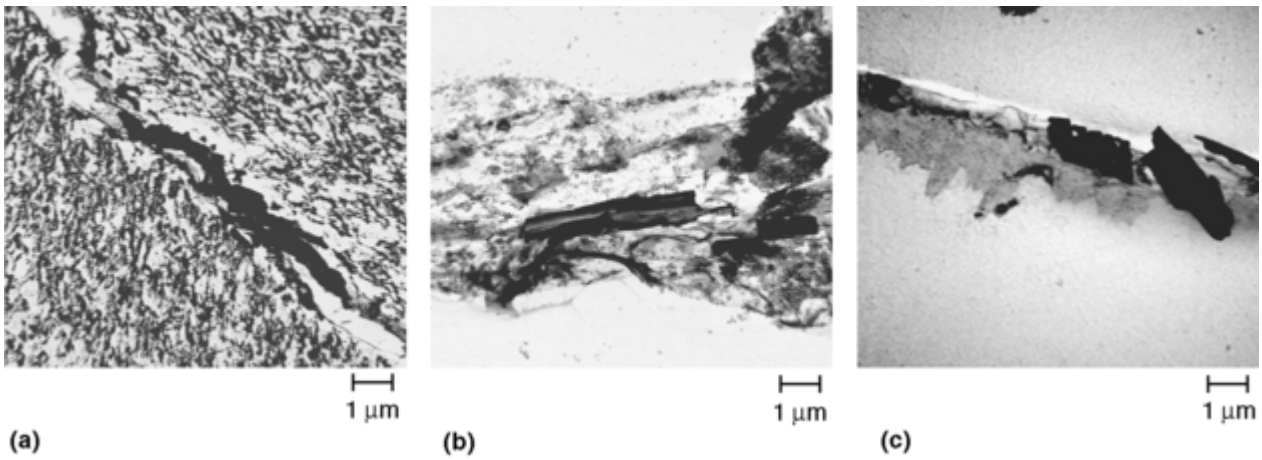

Fig. 9 Transmission electron micrographs from carbon replicas of thin, thick, and "thickened" carbides. (a) and (b) Same steel as in Fig. 2 (grade B3). (c) Same steel as in Fig. 8(a) (grade C)

Carbide formers attract carbon atoms in solution and decrease their mobility. This aspect lowers the rate of carbide precipitation and is beneficial. However, carbide formers also increase carbide stability and carbide reprecipitation starts at a higher temperature; this aspect increases the rate of carbide formation because of higher thermal activation. In the case of chromium (a strong carbide former), the resultant effect is to increase the overall precipitation rate during quenching. As a result, grade C steels are more difficult to produce in thick sections and are less weldable. However, molybdenum (a milder carbide former) significantly slows down the carbide reprecipitation. Its addition is beneficial in thick sections and in components where thermal resistance and weldability are desirable. Molybdenum also tends to break up the filmlike nature of the intergranular carbides, greatly improving the as-cast toughness (Fig. 10). A fast quench produces a structure similar to regular manganese steels (Fig. 6a). In a slower quench, molybdenum encourages a less harmful carbide precipitation in the form of nodules rather than a continuous film at the grain boundaries (Fig. 11). A special heat treatment is given to the 2% Mo (grade E2) steels where the metal is pearlitized at 595 °C (1100 °F) and solution annealed at 980 °C (1800 °F). The carbide does not completely dissolve at this temperature, but because of the nodularizing effect of molybdenum, it appears as a dispersed phase within the matrix (Fig. 12), imparting wear resistance at the expense of some toughness. The lower solution annealing temperature prevents steel from phosphide eutectic embrittlement, as described later in this article.

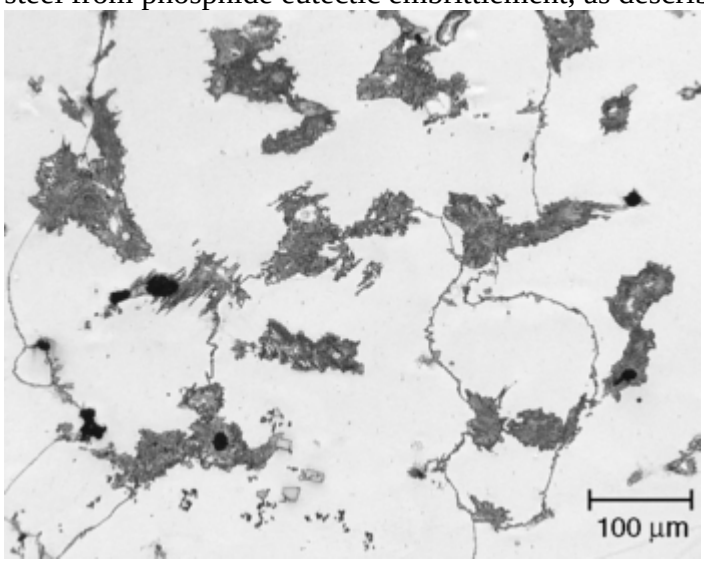

Fig. 10 Steel 6 in Table 1 (grade E1), as-cast. In molybdenum-bearing grades, carbides tend to be broken up into colonies. Same etch as Fig. 6 (a). Courtesy of P. Belding, Columbia Steel

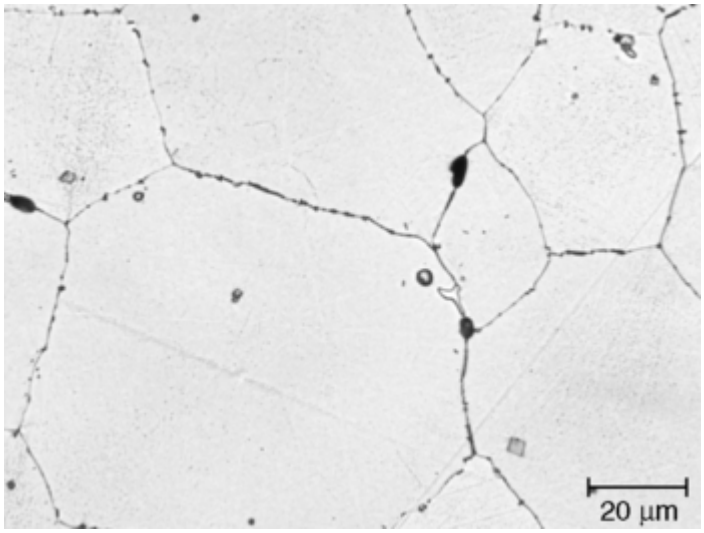

Fig. 11 Steel 7 in Table 1 (proprietary steel), cast, heat treated at 1090 °C (1990 °F), and water quenched. Slack quench resulted in some carbide precipitation. The intergranular carbide film is broken up into less harmful nodules because of the effect of molybdenum. Same etch as Fig. 6 (a)

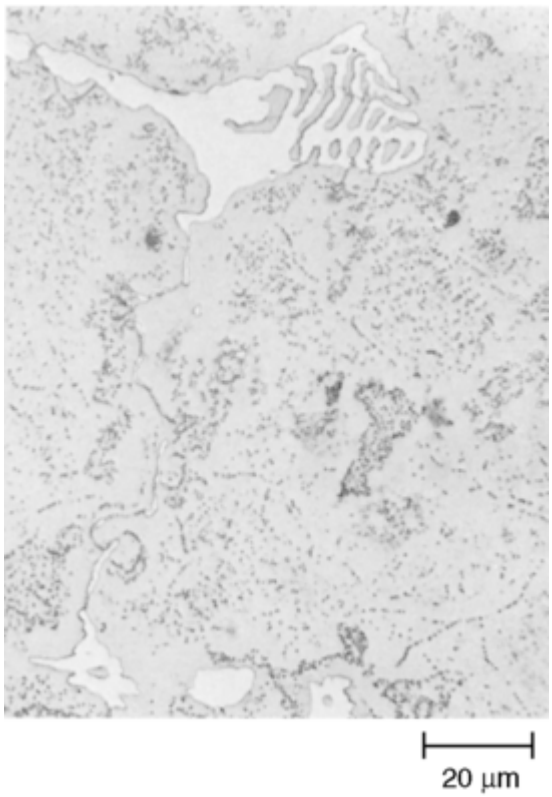

Fig. 12 Steel 8 in Table 1 (grade E2), pearlitized at 595 °C (1100 °F) for 12 h, air cooled, then partially solutionized at 980 °C (1800 °F) for 2 h and water quenched. Microstructure consists of austenite grains with dispersions of undissolved carbide. This is the so-called "dispersion-hardened" grade of austenitic manganese steel. 4% picral. 500×

Sulfur in austenitic manganese steels appears as globular, gray particles of manganese sulfide (MnS). Because of their compact shape, sulfur is seldom a cause for concern as a "tramp" element in these alloys.

Phosphorus, however, can be very detrimental to mechanical properties and castability. Phosphorus segregates along with carbon to interdendritic areas during solidification, where it forms a low-melting-point eutectic with iron, manganese, and carbon. This makes a higher phosphorus alloy—greater than 0.06% P in bulk concentration, for example—more prone to hot tearing in the mold. The phosphide eutectic is usually visible as a globular, mottled phase in the centers of carbide colonies in the as-cast structure (Fig. 4). During heat treatment, it dissolves into austenite along with the carbides. However, if the heat treatment temperature or the

phosphorus content is high, incipient melting can start at the grain-boundary triple points (Fig. 13). If more phosphide eutectic forms, with time at temperature, it tends to wet and spread along the grain boundaries. The resulting intergranular film that freezes upon quenching can be very detrimental to mechanical properties (Fig. 14). If a steel embrittled by overheating is reaustenitized again at an appropriate lower temperature, the eutectic film redissolves and the mechanical properties become largely restored. Such steels, however, often exhibit intergranular voids at the prior-phosphide eutectic sites (Fig. 15). Molybdenum-containing alloys are particularly susceptible to incipient melting. The use of lower solution-annealing temperatures can, to a certain extent, alleviate this problem.

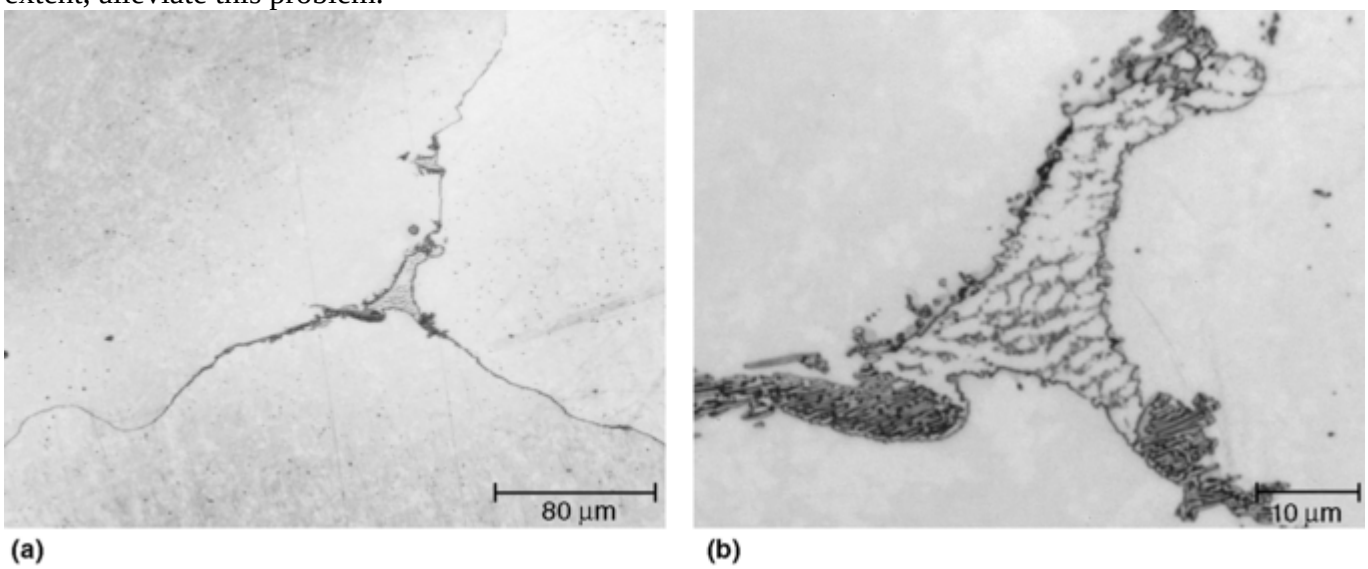

Fig. 13 Same steel as in Fig. 2. Phosphide eutectic at triple grain boundaries. Embrittlement depends on the fraction of grain-boundary coverage. In this steel, it was only 5%; Charpy toughness was 132 J (97 ft · lbf). Same etch as Fig. 6 (a)

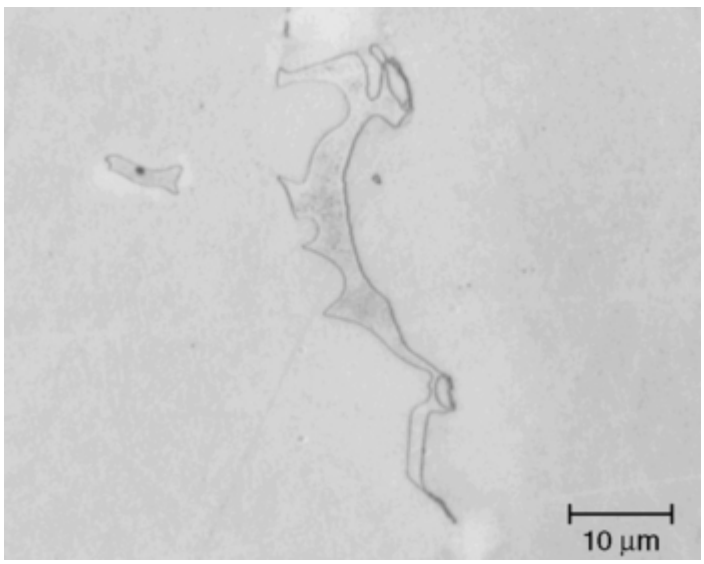

Fig. 14 Composition similar to steel 2 in Table 1, but having 0.076% P (grade B3), cast into 25 mm (1 in.) thick section. When solution annealed at 1050 °C (1920 °F) and water quenched, the structure was similar to that in Fig. 6 (a), phosphide eutectic rarely present; Charpy toughness was 182 J (134 ft · lbf). Same steel, solution annealed at 1250 °C (2280 °F) and water quenched. Extensive phosphide eutectic formed as a result of incipient melting. The micrograph shows a filmlike eutectic that has spread along the grain boundary. Charpy toughness dropped to 9 J (7 ft · lbf). Same etch as Fig. 6 (a)

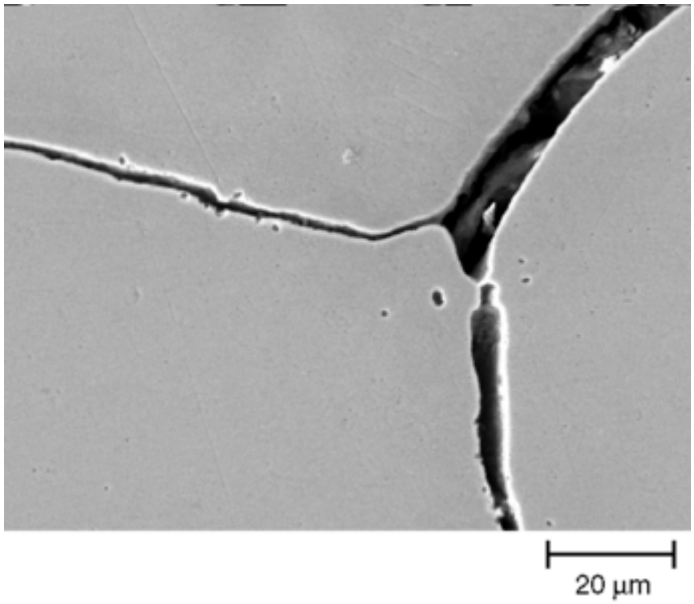

Fig. 15 Same steel as in Fig. 14 re-solution annealed at 1050 °C (1920 °F) and water quenched. The phosphide eutectic dissolved into the austenite matrix, but left behind intergranular cavities and voids. Charpy toughness improved to 137 J (101 ft · lbf). Secondary electron image by scanning electron microscopy

The degree of embrittlement of austenitic manganese steels is, therefore, related to the degree of grain-boundary coverage by the different embrittling phases. Figure 16 shows a weighted grain-boundary coverage by the embrittling constituents versus Charpy toughness (Ref 9). Different constituents give different degrees of decohesion at the grain boundary; the following weights were assigned in calculating the weighted total coverage in Fig. 16:

Porosity	**100%**
Thick carbides and phosphide eutectic	90%
Thickened carbides (chromium-bearing steels)	50%
Thin carbides	10%

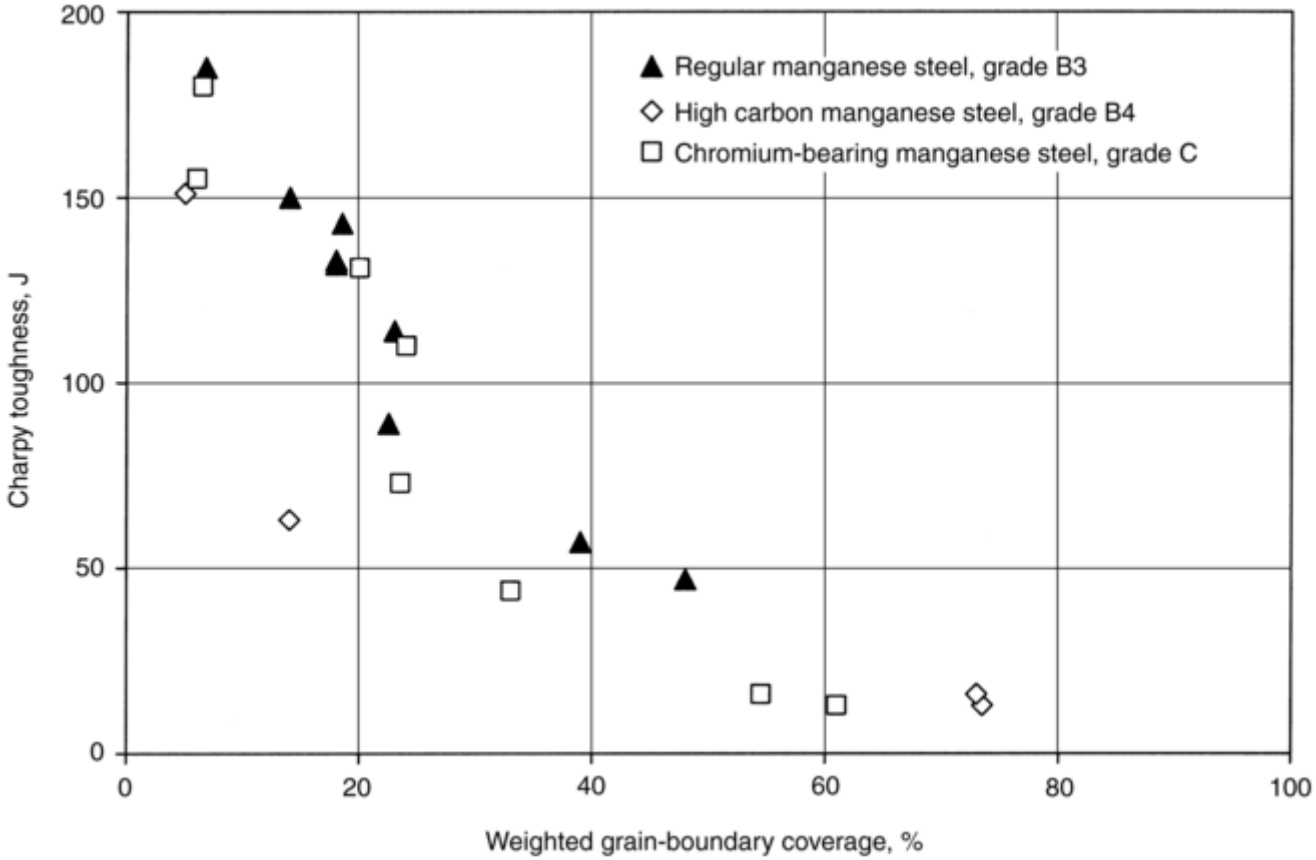

Fig. 16 Correlation between weighted grain-boundary coverage by the embrittling constituents and impact toughness, which decreases by 3.5 J per % grain boundary coverage from a nominal value of 185 J. The grain-boundary coverage was estimated for each embrittling constituent by examining 100 mm^2 (0.15 in.^{2}) area at 200× magnification.

The 200× magnification was chosen to comfortably distinguish between thin and thick carbides, and a large sample size of 100 mm^2 (0.15 in.^{2}) area ensured adequate averaging of the variable microstructure that is typical of these steels. Generally, when the weighted grain-boundary coverage was less than 20%, the Charpy toughness was excellent (>100 J, or 135 ft · lbf); less than 40%, good (>50 J, or 68 ft · lbf); and more than 50% coverage resulted in poor toughness (<20 J, or 27 ft · lbf). This method might provide a quantitative assessment of mechanical properties from microstructure, although more results may be needed to confirm its repeatability.

Titanium, zirconium, and vanadium additions form nitrides. Depending on the nature of charged scrap and melting practice employed, the nitrogen content in the alloy can range from 100 to 400 ppm. In the unetched condition, both titanium and zirconium nitrides appear shiny, faceted, and golden yellow when viewed with a light microscope.

In precipitation-hardening austenitic manganese steels containing vanadium, the small, relatively rounded vanadium nitrides present after solidification are first partially redissolved by a very high-temperature solution-annealing treatment (Ref 10). The steel is water quenched and aged at a suitable temperature to precipitate fine vanadium carbonitrides. These precipitates are not resolved by light microscopy.

Aluminum is added primarily to deoxidize the steel, and the products sometimes appear as clusters of (interconnected) alumina (Al_2O_3) and aluminate inclusions. The oxide inclusion content is related to the total oxygen content, which tends to be low in this steel; typically, 20 to 30 ppm, corresponding to 100 to 150 ppm oxide inclusions by volume. When the aluminum content in austenitic manganese steels exceeds approximately 5%, it becomes increasingly difficult to prevent carbide precipitation during quenching.

Special Features. Austenitic manganese steels are nonmagnetic. However, because of the loss of carbon and some manganese from the surface during solidification within a mold and during heat treatment, there sometimes exists a thin “skin” of magnetic (martensite) metal on the surface of the casting (Fig. 17).

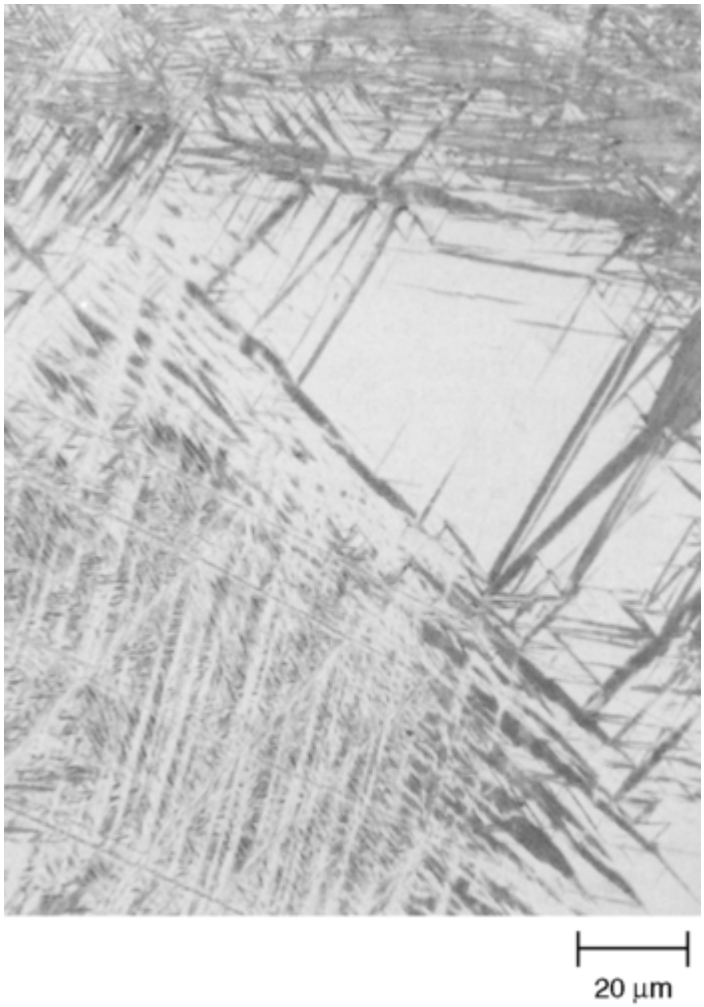

Fig. 17 Steel 1 in Table 1 (grade B2), heat treated at 1065 °C (1950 °F), and water quenched. Structure near the casting wear surface shows martensite formed during deformation as a result of decarburization of the austenite (light phase). 4% picral. 500×

These steels deform first by twinning and then by slip, mostly in the matrix, but also in the twinned regions (Ref 11). A large work-hardening capacity is one of the primary features of this steel; a typical yield strength at 350 MPa (50 ksi) usually rises to twice this value prior to failure. Deformation twins are easily visible in an etched sample under a light microscope and should not be mistaken for slip bands (Fig. 18, 19) (Ref 12, 13).

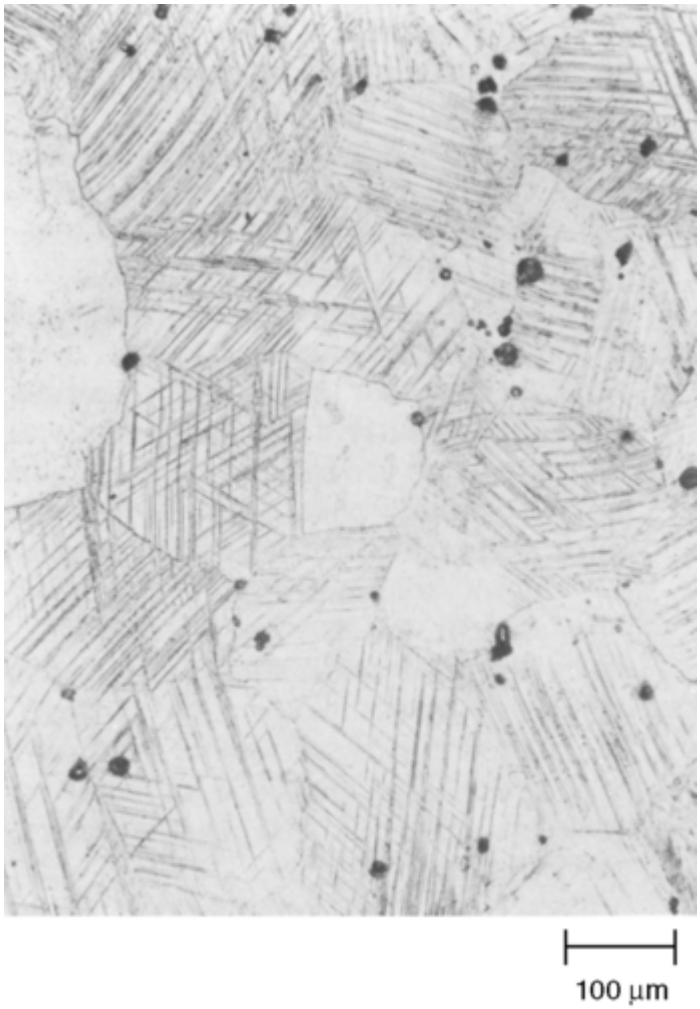

Fig. 18 Steel 1 in Table 1 (grade B2), cast and heat treated at 1065 °C (1950 °F), water quenched, machined into tensile specimen, and tested. Austenite grains show different amounts of twinning, depending on individual grain orientation. Sodium chromate in glacial acetic acid (see Table 2 for composition). 100×

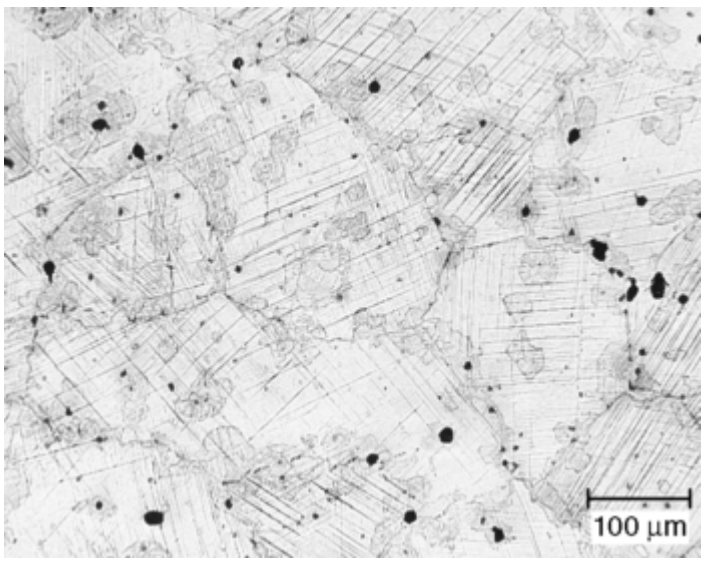

Fig. 19 Steel 9 in Table 1 (grade F), cast and heat treated at 1065 °C (1950 °F), water quenched. Sample was extracted from a failed component that was in service. Work hardening caused mostly "primary" deformation twins. Same etch as Fig. 6 (a). Courtesy of P. Belding, Columbia Steel

When solution-annealed austenitic manganese steel is not quenched fast enough through the 550 to 750 °C (1000 to 1400 °F) interval or a properly heat treated steel is reheated (by accident or intent) to this temperature range, carbide precipitates appear along the austenite grain boundaries. At temperatures of 480 to 705 °C (900 to 1300 °F) and longer times, conditions are also favorable for pearlite formation. When a steel containing a large volume fraction of pearlite is heat treated, the new austenite grains that nucleate from the pearlite colonies frequently contain annealing twins (Fig. 20, 21). Annealing twins are also observed in hot-rolled or cold-worked manganese steels that have been reheated above their recrystallization temperatures.

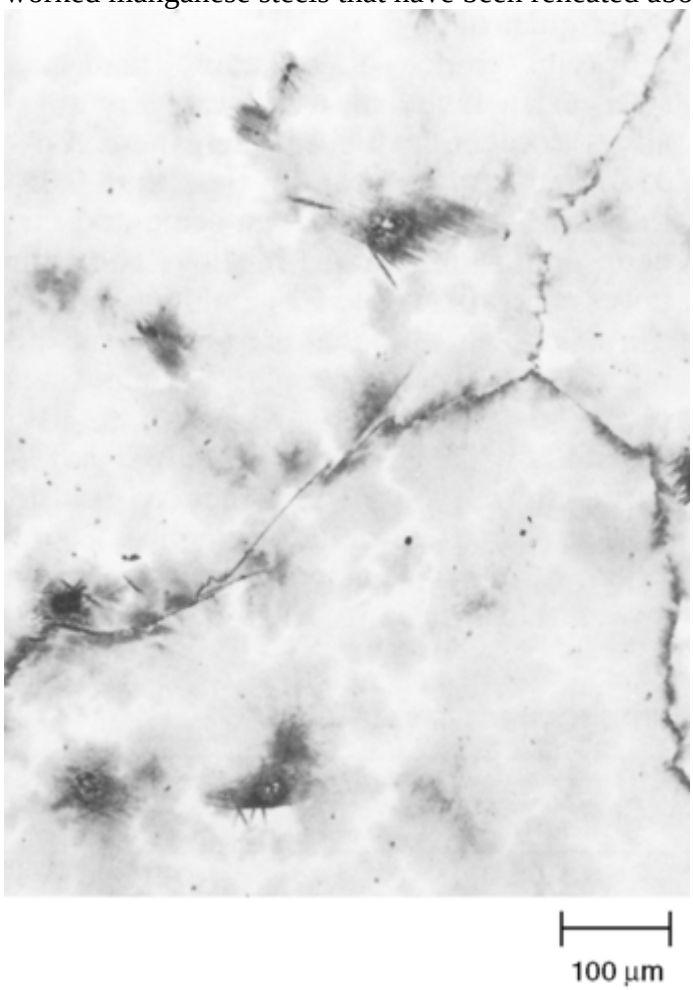

Fig. 20 Steel 10 in Table 1 (experimental steel), as-cast. Microstructure shows intergranular carbide, along with the interdendritic, acicular carbide, and outlines of pearlite colonies (grayish areas). Boiling alkaline sodium picrate (see Table 2 for composition). 100×

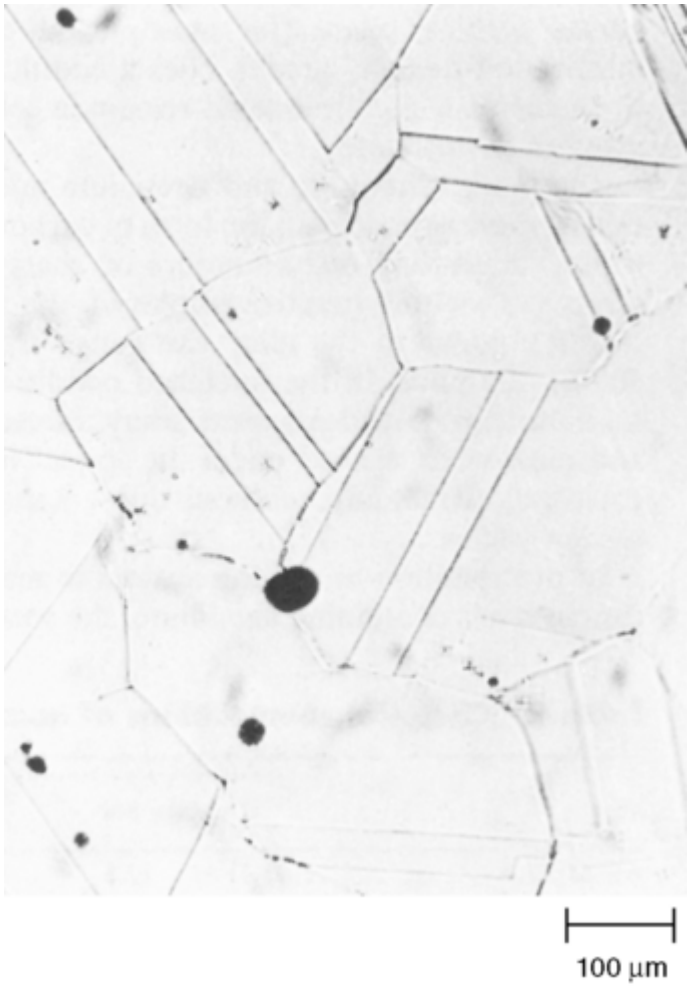

Fig. 21 Steel 10 in Table 1 (experimental steel), heat treated at 1120 °C (2050 °F) for 3 h and water quenched. Austenite grains show wide twins formed during transformation from as-cast pearlite. Only traces of grain-boundary carbides are visible. This microstructure is acceptable. Same etch as Fig. 18 100×

Special grades of austenitic manganese steels exist. Included in this category are (1) alloys containing higher manganese (up to 35%) and very low carbon (less than 0.05 %) that are used mostly in cryogenic and magnetic applications and (2) alloys containing lower manganese (7 to 9%) and higher carbon (for example, 1.3%) that are used in the mining industry. The former alloys are fully austenitic (retained austenite); the latter are initially austenitic, but for hardening rely on a strain-induced transformation to martensite during service.

References cited in this section

5. J. Beech and P. Scrichan, Influence of Casting Parameters on the As-Cast Structure of Hadfield's Steel, *Br. Foundryman,* Vol 78 (No. 9), 1985, p 453–458

6. S. Kuyucak and R. Zavadil, On the Heat-Treatment Processing of Austenitic Manganese Steels, *Proc. 21st Heat Treat Conf.,* 5–8 Nov 2001, ASM International

7. C-Y. Hung, et al., Three-Dimensional Observations of Proeutectoid Cementite Precipitates at Short Isothermal Transformation Times, *Acta Mater.,* Vol 50, 2002, p 3781–3788

8. F. Maratray, in *High Carbon Manganese Austenitic Steels,* International Manganese Institute, Paris, France, 1995, p 7

9. S. Kuyucak and R. Zavadil, On the Heat-Treatment of Hadfield's Austenitic Manganese Steels, Part IV: Microstructure vs. Impact Toughness Relationship, Paper No. 02-116, *AFS Trans.,* 2002

10. A. Atasoy, Effect of Alloying Elements and Heat Treatment on the Structure and Properties of Hadfield's Austenitic Manganese Steel, *Z. Metallkd.,* Vol 75 (No. 6), 1984, p 463–471

11. I. Karaman, et al., Modeling the Deformation Behavior of Hadfield Steel Single and Polycrystals Due to Twinning and Slip, *Acta Mater.,* Vol 48, 2000, p 2031–2047

12. Y.N. Dastur and W.C. Leslie, Mechanism of Work Hardening in Hadfield Management Steel, *Met. Trans. A,* Vol 12, May 1981, p 749

13. L. Rémy, The Interaction between Slip and Twinning Systems, and the Influence of Twinning on the Mechanical Behavior of fcc Metals and Alloys, *Met. Trans. A,* Vol 12, March 1981, p 387

Revised by S.Kuyucak, Austenitic Manganese Steel Castings, *Metallography and Microstructures,* Vol 9, *ASM Handbook,* ASM International, 2004, p. 701–708

Austenitic Manganese Steel Castings

Revised by Selçuk Kuyucak, CANMET, Department of Natural Resources Canada

---

References

1. S. Kuyucak, R. Zavadil, and G. Ouellet, On the Heat-Treatment of Hadfield's Austenitic Manganese Steels; Part VII: Casting Soundness and Microporosity in Large Wedge-Block Castings, Paper No. 03-134, *AFS Trans.,* 2003

2. S. Kuyucak and R. Zavadil, On the Heat-Treatment of Hadfield's Austenitic Manganese Steels; Part VI: Impact Toughness, Microstructure, Macro- and Micro-Segregation in Large Wedge-Block Castings, Paper No. 03-133, *AFS Trans.,* 2003

3. G.F. Vander Voort, *Metallography: Principles and Practice,* McGraw-Hill, 1984, p. 215, 634

4. A.J. Sedriks and T.O. Mulhearn, Austenitic Manganese Steel: Structure and Properties of Decarburized Layer, *J. Iron Steel Inst.,* Vol 202, Nov 1964, p 907–911

5. J. Beech and P. Scrichan, Influence of Casting Parameters on the As-Cast Structure of Hadfield's Steel, *Br. Foundryman,* Vol 78 (No. 9), 1985, p 453–458

6. S. Kuyucak and R. Zavadil, On the Heat-Treatment Processing of Austenitic Manganese Steels, *Proc. 21st Heat Treat Conf.,* 5–8 Nov 2001, ASM International

7. C-Y. Hung, et al., Three-Dimensional Observations of Proeutectoid Cementite Precipitates at Short Isothermal Transformation Times, *Acta Mater.,* Vol 50, 2002, p 3781–3788

8. F. Maratray, in *High Carbon Manganese Austenitic Steels,* International Manganese Institute, Paris, France, 1995, p 7

9. S. Kuyucak and R. Zavadil, On the Heat-Treatment of Hadfield's Austenitic Manganese Steels, Part IV: Microstructure vs. Impact Toughness Relationship, Paper No. 02-116, *AFS Trans.,* 2002

10. A. Atasoy, Effect of Alloying Elements and Heat Treatment on the Structure and Properties of Hadfield's Austenitic Manganese Steel, *Z. Metallkd.,* Vol 75 (No. 6), 1984, p 463–471

11. I. Karaman, et al., Modeling the Deformation Behavior of Hadfield Steel Single and Polycrystals Due to Twinning and Slip, *Acta Mater.,* Vol 48, 2000, p 2031–2047

12. Y.N. Dastur and W.C. Leslie, Mechanism of Work Hardening in Hadfield Management Steel, *Met. Trans. A,* Vol 12, May 1981, p 749

13. L. Rémy, The Interaction between Slip and Twinning Systems, and the Influence of Twinning on the Mechanical Behavior of fcc Metals and Alloys, *Met. Trans. A,* Vol 12, March 1981, p 387

M. Warmuzek, Metallographic Techniques for Aluminum and Its Alloys, *Metallography and Microstructures,* Vol 9, *ASM Handbook,* ASM International, 2004, p. 711–751

Metallographic Techniques for Aluminum and Its Alloys

Małgorzata Warmuzek, Foundry Research Institute, Kraków, Poland

Introduction

ALUMINUM ALLOYS encompass a wide range of chemical compositions and product forms that can be manufactured by all available metalworking techniques and standard casting processes. Manufactured forms of aluminum and aluminum alloys include standard mill products (e.g., sheet, plate, foil, rod, bar, wire, tube, pipe, and structural forms) and engineered forms for specific applications produced by extrusion, forging, stamping, powder metallurgy, semisolid processing, and machining. Aluminum products also include metal-matrix composites with either particulate or fiber reinforcement. This article focuses primarily on the metallography and microstructures of wrought and cast forms. Powder metallurgy, semisolid processing, and composite forms are discussed in other articles of this Volume.

Metallographic preparation of aluminum alloys may vary considerably due to the wide range of chemical compositions and resulting hardness. Softer alloys generally are more difficult to prepare by mechanical polishing, because:

- Deformation caused by cutting and grinding extends to a greater depth.
- The embedding of abrasive particles in the metal during polishing is more likely.
- Relief between the matrix and second-phase particles, which are considerably harder than the matrix, develops more readily during polishing.

Harder alloys, although easier to prepare, present a greater variety of phases and complexities of structure. In all cases, the procedures for sample collection and preparation must consider specific mechanical and structural properties, such as the high difference of hardness between matrix and other phase constituents and the relatively low temperature of the precipitation processes in the solid state.

Information taken from the structural images allows the formation of a qualitative or quantitative description of bulk (average) structure or specific local features in terms of spatial distribution, dispersion, morphology, and volume fraction of all the phase constituents. The interpretation of aluminum alloy microstructures requires an understanding of the various morphological forms and the simultaneous presence of the stable and metastable constituents, isomorphous compounds, and arrays of different continuous solid solutions. The following section briefly describes the function of major alloying elements, phase formation, and the morphologies of constituents formed by liquid-solid or solid-state transformations. Structure and properties of aluminum alloys are also described in more detail in Ref 1, 2, and 3.

References cited in this section

1. J.E. Hatch, *Aluminum: Properties and Physical Metallurgy,* American Society for Metals, 1984

2. J.R. Davis, Ed., *Aluminum and Aluminum Alloys,* ASM Specialty Handbook, ASM International, 1993

3. L.F. Mondolfo, *Aluminum Alloys: Structure and Properties,* Butterworths, 1976

M. Warmuzek, Metallographic Techniques for Aluminum and Its Alloys, *Metallography and Microstructures,* Vol 9, *ASM Handbook,* ASM International, 2004, p. 711–751

Metallographic Techniques for Aluminum and Its Alloys

Małgorzata Warmuzek, Foundry Research Institute, Kraków, Poland

Composition and Phases

Aluminum alloys encompass more than three hundred commonly recognized alloy compositions and many additional variations developed in supplier/consumer relationships. All commercial aluminum alloys contain some iron and silicon as well as two or more elements intentionally added to enhance properties. The main groups of commercial aluminum alloys of different chemical composition are presented in Table 1. The principal types of aluminum alloys achieve strengthening by the alloying effects of copper, magnesium, manganese, silicon, and zinc (Fig. 1) in conjunction with strain hardening, heat treatment, or both.

Table 1 Alloy composition range for major groupings of commercial aluminum alloys

Alloy group	Nominal chemical composition[(a)], wt%										
	Mg	**Si**	**Ti**	**Cr**	**Mn**	**Fe**	**Ni**	**Cu**	**Zn**	**Zr**	**Other**
Wrought alloys											
1*xxx* (Al > 99.00%)	0.006–0.25	0.006–0.7	0.002–0.06	0.01–0.03	0.002–0.05	0.006–0.6	…	0.006–0.35	0.006–0.05	…	…
2*xxx* (Cu)	0.02–0.8	0.10–1.3	0.02–0.3	0.05–0.2	0.05–1.3	0.12–1.3	0.05–2.3	0.8–6.8	0.10–0.80	0.05–0.5	…
3*xxx* (Mn)	0.05–1.3	0.3–1.8	0.05–0.10	0.05–0.40	0.05–1.8	0.1–1.0	0.05	0.05–0.50	0.05–1.0	0.1–0.5	…
4*xxx* (Si)	0.05–2.0	0.8–13.5	0.04–0.30	0.05–0.25	0.03–1.5	0.20–1.0	0.15–1.3	0.05–1.5	0.05–0.25	…	…
5*xxx* (Mg)	0.2–5.6	0.08–0.7	0.05–0.20	0.05–0.35	0.03–1.4	0.10–0.7	0.03–0.05	0.03–0.35	0.05–2.8	…	…
6*xxx* (Mg + Si)	0.05–1.5	0.20–1.8	0.08–0.20	0.03–0.035	0.03–1.0	0.08–1.0	0.2	0.10–1.2	0.05–2.4	0.05–0.20	…
7*xxx* (Zn)	0.10–3.7	0.10–0.50	0.03–0.15	0.04–0.35	0.02–1.5	0.10–0.70	0.10	0.05–2.6	0.8–8.7	0.05–0.18	…
8*xxx* (other element)	0.02–1.4	0.10–1.0	0.08–0.2	0.01–0.2	0.02–1.0	0.10–2.0	0.2–1.3	0.03–2.2	0.03–1.8	0.04–0.16	Li, B, Sn, Ga
Cast alloys											
1*xx.x* (Al > 99.00%)	…	0.10–0.15	0.15–0.35	…	…	0.25–0.8	…	0.05–0.10	0.05	…	…
2*xx.x* (Cu)	0.03–2.3	0.05–3.5	0.06–0.35	0.15–0.40	0.05–0.7	0.04–1.5	0.03–2.3	3.5–10.7	0.05–2.5	…	…
3*xx.x* (Si + Cu/Mg)	0.03–1.5	4.5–23.0	0.04–0.25	0.05–0.35	0.03–0.8	0.06–1.5	0.10–3.0	0.03–5.0	0.03–4.5	…	…
4*xx.x* (Si)	0.05–0.10	3.3–13	0.20–0.25	0.25	0.05–0.5	0.12–1.3	0.05–0.5	0.05–1.0	0.05–0.5	…	…
5*xx.x* (Mg)	1.4–10.6	0.10–2.2	0.10–0.25	0.25	0.05–0.6	0.10–1.3	0.05–0.4	0.05–0.30	0.05–0.20	…	…

7*xx.x* (Zn)	0.2–2.4	0.10–0.30	0.10–0.25	0.06–0.6	0.05–0.6	0.10–1.4	0.15	0.1–1.0	2.0–7.8	…	…
8*xx.x* (Sn)	0.1–0.9	0.4–6.5	0.2	…	0.1–0.5	0.5–0.7	0.3–1.5	0.7–4.0	Sn, 5.5–7.0	…	…

(a) bal aluminum. Source: Ref 1, Ref 2

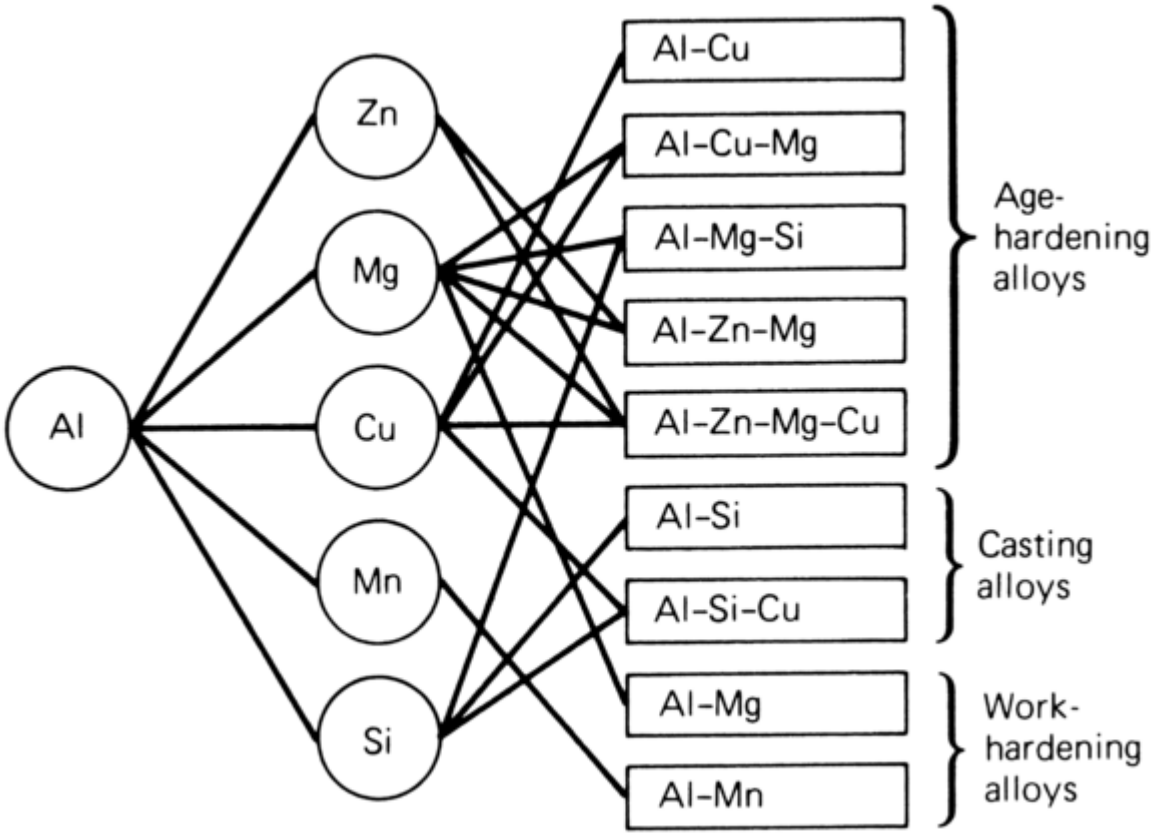

Fig. 1 The principal alloying elements of aluminum alloys. Source: Ref 2

Phase Formation and Morphology

Some common phase constituents present in the numerous commercial aluminum alloys are shown in Table 2 and 3 (Ref 2, 3, 4, 5, 6). In general, the phases may develop various morphologies with resulting microstructures that can range from a simple monophase (solid-solution) structure to various polyphase morphologies (Fig. 2). The occurrence of these various morphologies, which can have a strong influence on properties, depends on alloy concentration and solubility and how the phases form during solidification and/or solid-state heat treatment.

Table 2 Phase constituents present in commercial aluminum alloys

Alloy	Phase constituents [(a)]	
	Rough state	**Treated state**
Wrought alloys		
1*xxx* (Al > 99.00%), Al-Fe-Si, Al-Cu	Al_3Fe, α-Al(FeSi)	Al_6Mn, α-Al(FeSi)
2*xxx* (Cu), Al-Si-Cu-Mn-Mg, Al-Si-Cu-Mn, Al-Cu-Mg, Al-Cu-Mg-Ni, Al-Cu-Mn-Ti-V-Zr, Al-Cu-Mg-Ni-Fe-Ti	Al_2Cu, Al_2CuMg, $Al_{20}Cu_2Mn_3$, α-Al(FeMnSi), Al_3FeMn, Al_6MnFe, Al_7Cu_2Fe, Mg_2Si, $Al_5Cu_2Mg_8Si_6$	Al_2Cu, Al_2CuMg, $Al_{20}Cu_2Mn_3$, α-Al(FeMnSi), Al_7Cu_2Fe, $Al_{12}Mn_3Si$
3*xxx* (Mn), Al-Cu-Mn, Al-Fe-Si-Mg-Mn, Al-Si-Mn- Fe	α-Al(FeMnSi), Al_6MnFe	α-Al(FeMnSi), Al_6MnFe

4*xxx* (Si)	β-AlFeSi	…
5*xxx* (Mg), Al-Mn-Mg-Cr, Al-Mn-Mg-Cr, Al-Mn-Mg, Al-Mg	Mg_2Si, $Al_{18}Mg_3Cr_2$, Al_6Mn	Mg_2Si, Al_3Ni
6*xxx* (Mg, Si), Al-Si-Cu-Mg-Cr, Al-Si-Mg, Al-Si-Mg-Cr, Al-Si-Mn-Mg	β-AlFeSi, Mg_2Si, α-Al(FeSi)	Mg_2Si
7*xxx* (Zn), Al-Mn-Mg-Zn-Zr, Al-Mn-Mg-Cr-Zn, Al-Zn, Al-Cu-Mg-Cr-Zn, Al-Cu-Mn-Mg-Cr-Zn, Al-Cu-Mg-Cr-Zn	α-Al(FeCrSi), $Al_2CuMgZn$, Al_7Cu_2Fe	Al_2CuMg, Mg_2Si, Al_7Cu_2Fe, α-Al(FeCrSi), $Al_{18}Mg_3Cr_2$
8*xxx* (other element), Al-Li-Mg-Cu	…	…
Cast alloys		
1*xx.x* (Al > 99.00%), 7*xxx*(Zn)	Si, β-AlFeSi, α-Al(FeSi)	…
2*xx.x* (Cu), Al-Cu-Mg, Al-Cu-Mn, Al-Cu-Si-Mg, Al-Cu-Mn-Mg-Ni, Al-Cu-Mg-Ni, Al-Cu-Si	Si, Al_2Cu, Al_2CuMg, Al_7Cu_2Fe, $Al_5Cu_2Mg_8Si_6$, β-AlFeSi α-Al(FeMnSi), AlCuFeNi, Al_6Cu_3Ni	Al_2Cu, Al_2CuMg, $Al_{20}Cu_2Mn_3$, Al_7Cu_2Fe, AlCuFeNi, Al_6Cu_3Ni, Al_3Ni
3*xx.x* (Si + Cu/Mg), Al-Cu-Si, Al-Si-Cu-Mg-Ni, Al-Si-Cu-Mg, Al-Si-Mg, Al-Si-Mg-Fe, Al-Si-Mg-Ti, Al-Si-Mn-Mg-Cu	Si, Al_2Cu, Al_2CuMg, Al_7Cu_2Fe, $Al_5Cu_2Mg_8Si_6$, β-AlFeSi α-Al(FeMnSi), AlCuFeNi, Al_6Cu_3Ni, Mg_2Si, Al_3Ni, Al_9NiFe, $Al_8Mg_3FeSi_2$	Si, Al_2Cu, Al_2CuMg, Al_7Cu_2Fe, AlCuFeNi, Al_6Cu_3Ni, $Al_{20}Cu_2Mn_3$, Al_3Ni, $Al_8Mg_3FeSi_2$, $Al_5Cu_2Mg_8Si_6$, β-AlFeSi, α-Al(FeMnSi)
4*xx.x* (Si), Al-Si, Al-Si-Cu, Al-Si-Fe	Si, Al_2Cu, β-AlFeSi, α-Al(FeMnSi)	Si, Al_2Cu, β-AlFeSi, α-Al(FeMnSi)
5*xx.x* (Mg), Al-Mg	Mg_2Si, $Al_6(FeMn)$, Al_3Mg_2, $Al_{18}Mg_3Cr_2$	Mg_2Si, $Al_6(FeMn)$, Al_3Mg_2, $Al_{18}Mg_3Cr_2$
7*xx.x* (Zn)	$Al_{18}Mg_3Cr_2$, Al_3Fe, Al_7FeCr, $MgZn_2$	…
8*xx.x* (Sn)	Si, Sn, Cu_6Sn_5, Al_3Ni	Si, Sn, Cu_6Sn_5, Al_3Ni, Al_6Cu_3Ni

(a) α-Al(other) = solid solution.
Source: Ref 2, 3, 4, 5, 6

Table 3 Characteristics of phase constituents in aluminum-rich aluminum alloys

Phase	Crystal lattice		Chemical composition[(a)]		Morphology of precipitates
	System, space group	**Cell parameters, Angstroms**	**wt%**	**at.%**	
Si	Cubic, A4	a = 5.43054	100	100	Polyhedra, branched platelets, or rods
Sn	Tetragonal, Fd3m	a = 5.8318 c = 3.1819	100	100	Irregular, compact particles
Al	Cubic, fcc	a = 4.0333	100	100	Matrix of alloy grains, dendrites
$AlAg_2$	Hexagonal, P6/mmc	a = 2.885 c = 4.582	88.9% Ag	66.6% Ag	Dispersed particles
Al_9Co_2	Monoclinic, $P2_1/c$	a = 6.213	32.7% Co	18.2% Co	Irregular plates

		b = 6.29 c = 8.556 β = 94° 76′			
Al_2Cu	Tetragonal, I4/mcm	a = 6.066 c = 4.874	52.5–53.9% Cu	33.3% Cu	Round or irregular particles, dispersed particles
$Al_7(CrFe)$	Orthorhombic	a = 24.8 b = 24.7 c = 30.2	21.6% Cr	12.5% (Fe,Cr)	Irregular, faceted polyhedra, needles
$Al_{12}(CrMn)$	Cubic, bcc, Im3	a = 7.507	2–4% Cr, 10–12% Mn	7.7% (CrMn)	Irregular, compact particles
Al_3Fe	Monoclinic, C2/m	a = 15.520 b = 8.099 c = 12.051 β = 107°	40.8% Fe	25% Fe	Needles or rosettes
Al_6Fe	Orthorhombic, Ccmm	a = 6.464 b = 7.440 c = 8.779	25.65% Fe	14.3% Fe	Platelets or rods
α(FeCu)	$Ccm2_1$		7–8% Cu, 22–25% Fe		Platelets
Al_3Mg_2	Cubic, fcc, Fd3m	a = 28.16	34.8–37.1% Mg	40% Mg	Compact, rounded particles, outlining grains
AlLi	Cubic, bcc, Fd3m	a = 6.38	20.5% Li	50% Li	Dispersed particles at grain boundaries
Al_6Mn, $Al_6(MnFe)$	Orthorhombic, Cmcm	a = 6.498 b = 7.552 c = 8.870	25.34% Mn	14.3% Mn	Parallelograms, more or less elongated
Al_3Ni	Orthorhombic	a = 6.611 b = 7.366 c = 4.812	42% Ni	25% Ni	Branched polyhedra
Al_3Ti	Tetragonal, I4/mmm	a = 3.848 c = 8.596	36.5–37.5% Ti	25% Ti	Platelets
AlSb	Cubic, F43m	a = 6.096	81.9% Sb	50% Sb	Compact particles
Al_6V	Hexagonal, $P6_3/mmc$	a = 7.718 c = 17.15	23.8% V	14.3% V	Dispersed particles
$Al_{11}V$	Cubic, Im3	a = 14.586	15.1–15.9% V	8.3% V	Dispersed particles
Al_3Zr	Tetragonal, I4/mmm	a = 4.018 c = 17.320	53.0% Zr	25% Zr, bal Al	Compact particles

Mg_2Si	Cubic, fcc, Fm3m	a = 6.351	63.2% Mg, 36.8% Si	66.6% Mg, 33.3% Si	Fine Chinese script, dispersed particles
	Hexagonal, β′	a = 7.05 c = 4.05			
$MgZn_2$, AlCuMg	Hexagonal, $P6_3/mmc$	a = 5.18 c = 8.517	15.68% Mg, 84.32% Zn	33.3% Mg, 66.6% Zn	Irregular round particles, dispersed particles
		a = 5.07 c = 8.29	55.7% Cu, 20.8% Mg	33.3% Mg, 33.3% Cu	
Mg_2Zn_{11}- $Al_5Mg_2Cu_6$	Cubic, Pm3	a = 8.552 c = 8.311	56.4% Cu, 9.2% Mg	15.4% Mg, 74.6% Zn 46.2% Cu, 6.67% Mg	Irregular round particles, dispersed particles
TiB_2	Hexagonal, P6/mmm	a = 3.028 c = 3.228	68.9% Ti, 31.1% B	33.3% Ti, 66.7% B	Irregular particles
$Al_{18}Cr_2Mg_3$	Cubic, Fd3m	a = 14.53–14.65	15.7(11–13)% Cr, 11.1(8–12)% Mg	8.7% Cr, 13.0% Mg	Chinese script
Al_7Cu_2Fe	Tetragonal, P4/mnc	a = 6.33 c = 14.81	36.9% Cu, 16.2% Fe	10% Fe, 20% Cu	Thin needles
Al_2CuLi	Hexagonal	a = 4.96 c = 9.35	52.8% Cu, 5.4% Li	25% Cu, 25% Li	Dispersed particles
Al_6CuMg_4, $Al_2Mg_3Zn_3$	Cubic, bcc, Im3	a = 14.15	22–27% Cu, 27.5–30% Mg	9.1% Cu, 36.4% Mg	Irregular, round particles
$Al_{20}Cu_2Mn_3$	Orthorhombic, Cmcm	a = 24.11 b = 12.51 c = 7.71	12.8–19% Cu, 19.8–24% Mn	…	Irregular, compact particles
Al_7Cu_4Ni	Varied with composition	…	47–50.6% Cu, 12.1–12.5% Ni	…	Irregular, elongated particles, skeleton-like
Al_9FeNi	Monoclinic, $P2_1/c$	a = 6.2 b = 6.3 c = 8.6 α = 95°	4.5–14% Fe, 18–28% Ni	…	Branched, elongated polyhedra
β-AlFeSi	Monoclinic	a = 6.12 b = 6.12 c = 41.48 α = 91°	25–30% Fe, 12–15% Si	14.3% Fe, 14.3% Si	Needles
α-AlFeSi	Hexagonal, P6/mmc	a = 12.3	30–33% Fe, 6–12% Si	9.1% Si, 18.2% Fe	Chinese script

		c = 26.3			
γ-AlFeSi	Monoclinic, Cfc	a = 17.8 b = 10.25 c = 8.90 β = 132°	33.9% Fe, 16.9% Si, bal Al	20% Fe, 20% Si	Platelets or needles
δ-AlFeSi	Tetragonal	a = 6.16 c = 9.49	25.4% Fe, 25.5% Si	14.3% Fe, 28.6% Si	Platelets
α-AlMnSi	Cubic, Pm3	a = 12.652	26.3% Mn, 8.9% Si	15% Mn, 10% Si	Chinese script, polyhedra
α-AlFeMnSi	Cubic, Im3	a = 12.50	33% (FeMnCr), 5.97% Si	19.2% (FeMnCr), 7.7% Si	Polyhedra, Chinese script
$Al_4CuMg_5Si_4$	bcC	a = 12.63			
$Al_5Cu_2Mg_8Si_6$	Hexagonal	a = 10.32 c = 4.05	10.16% Cu, 31.1% Mg, 17.7% Si	28.5% Si, 38.1% Mg, 9.5% Cu	Round or irregular particles
$Al_8Mg_3FeSi_2$	Hexagonal, P62m	a = 6.63 c = 7.94	18.2% Mg, 13.9% Fe, 14.1% Si	14.3% Si, 21.4% Mg, 7.1% Fe	Chinese script

Note: fcc, face-centered cubic; bcc, body-centered cubic.
(a) Bal aluminum. Source: Ref 3, 4, 5

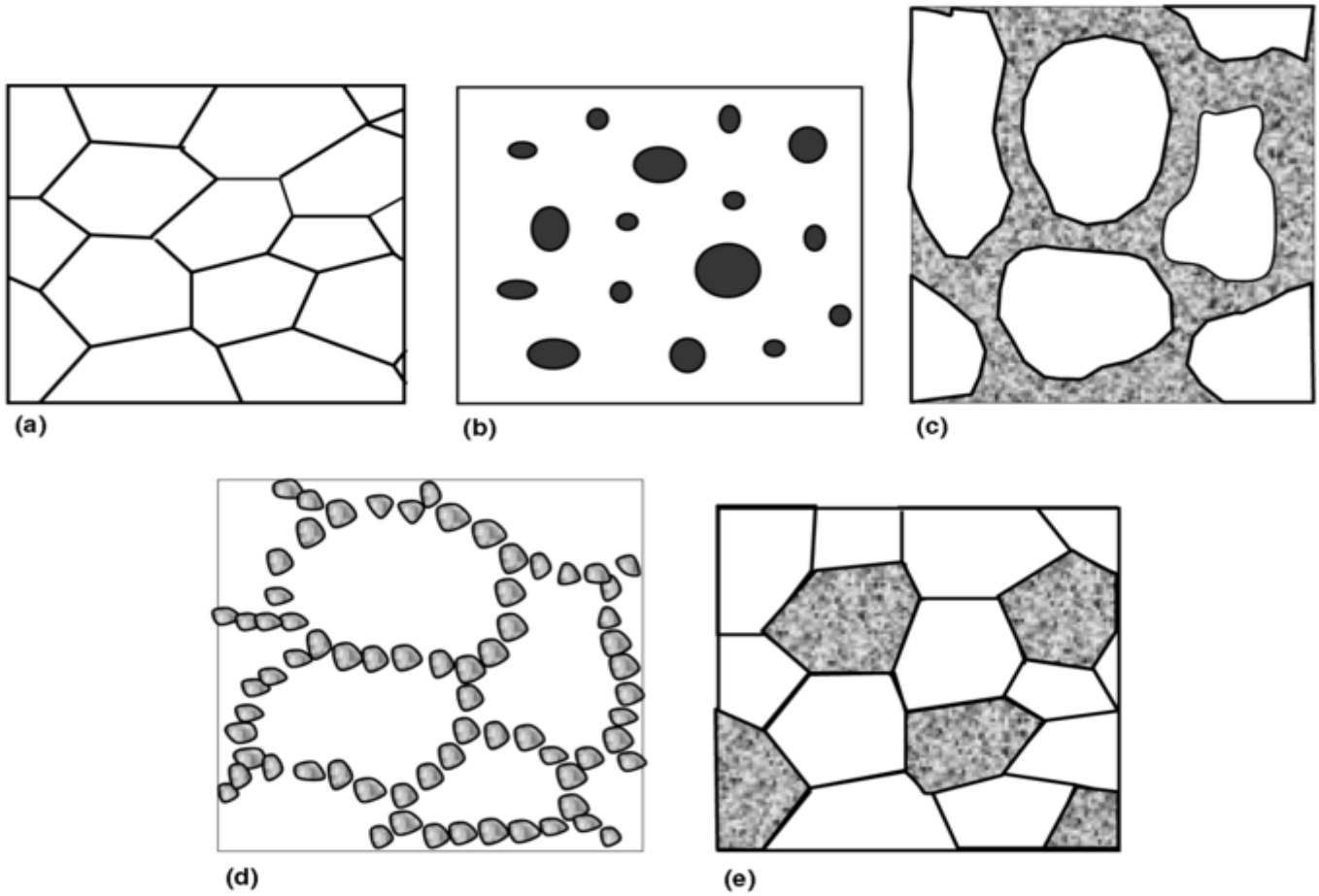

Fig. 2 Typical microstructure morphologies. (a) Solid-solution monophase typical of commercially pure (1*xxx* and 1*xx.x*) aluminum alloys. (b) Dispersed second phase typical of deformed and heat treated wrought aluminum alloys. (c) Continuous network of second phases typical of alloys in an as-cast

condition. (d) Discontinuous network of second-phase particles in heat treated cast or wrought alloys. (e) Duplex microstructure

The aluminum-copper phase diagram (Fig. 3), which includes the commercially important class of 2*xxx* aluminum alloys, can illustrate the basic alloying regions of phase formation. The three important regions of phase formation are:

- The solid-solution (α) region (below 0.1 wt% Cu), where the alloying atoms remain dissolved by substituting aluminum atoms in the aluminum/face-centered cubic (fcc) lattice. In this alloying region, the terminal (room-temperature) solid-state condition is essentially a monophase structure (Fig. 4).
- The solid-state region below the solvus line, where dispersed particles of the θ (Al_2Cu) intermetallic precipitate in a supersaturated aluminum-copper solid
- The region to the right of the maximum solid-solubility point (5.65 wt% Cu), where the θ(Al_2Cu) phase precipitates during solidification and thus forms a network of second-phase particles around the previously solidified α grains in the L + α region

The latter two reactions have an important influence on the morphology of the second-phase particles. When phase precipitation occurs during a liquid-solid transformation (such as for eutectic reactions described subsequently), the precipitates form a networklike morphology by solidifying around the α grains. In contrast, solid-state processes tend to produce a more dispersed second phase, such as those shown in Fig. 5 at various levels of magnification.

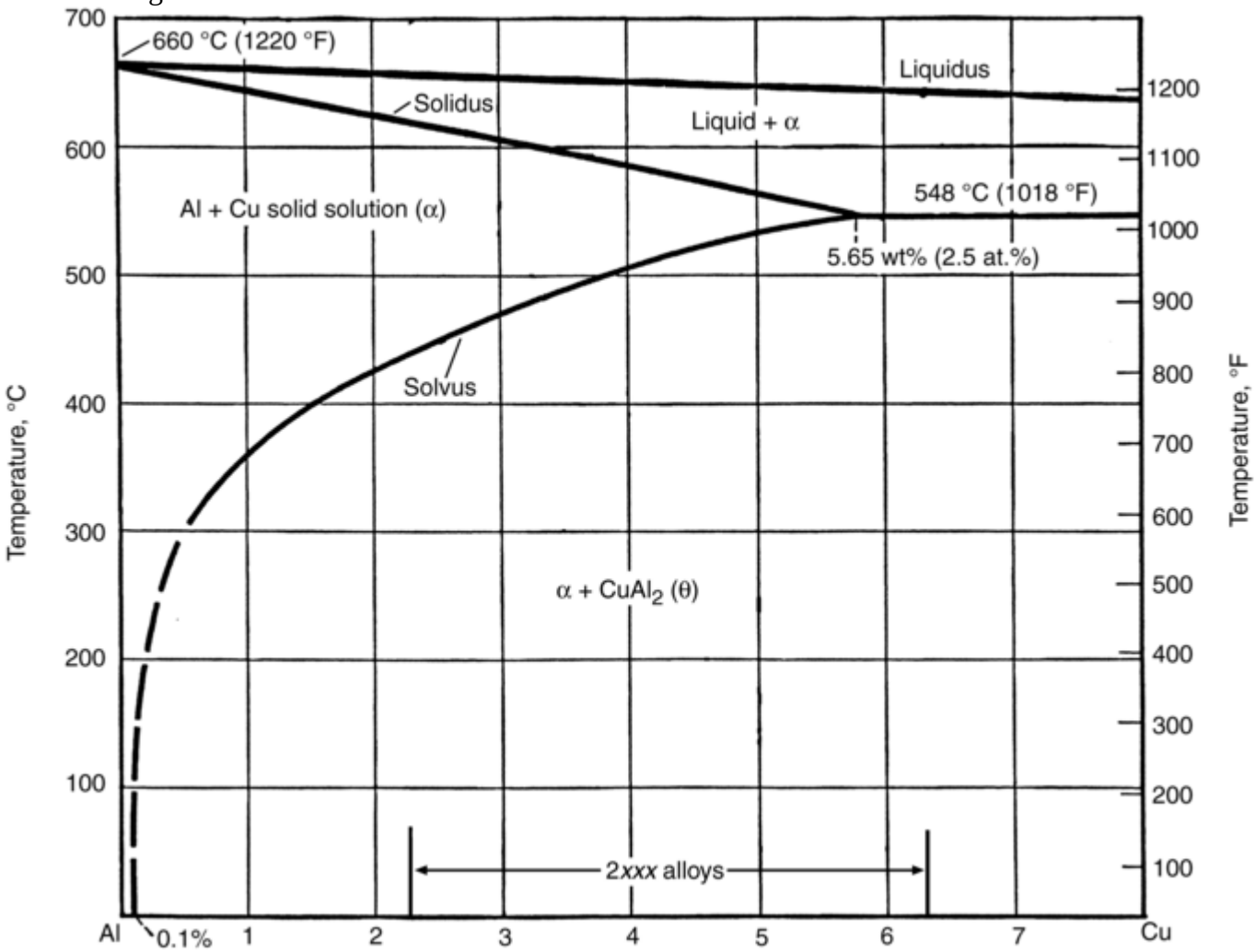

Fig. 3 Aluminum corner of the aluminum-copper phase diagram. Eutectic composition (not shown) is at 33 wt% (17 at.%) Cu.

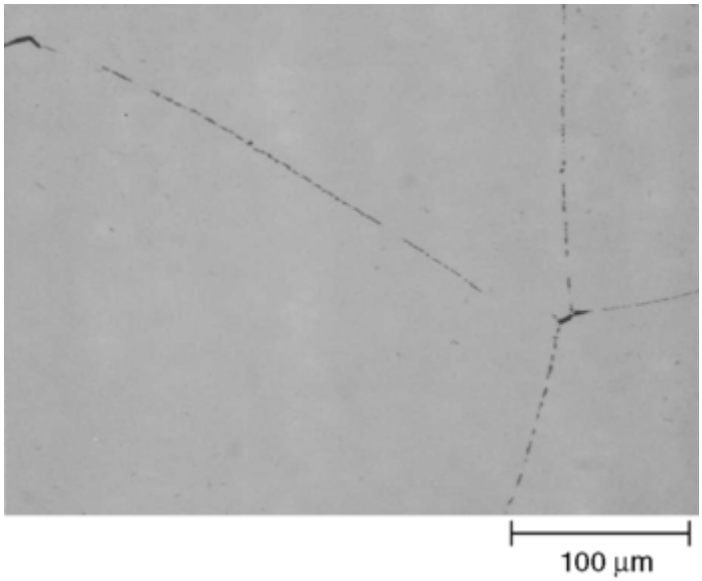

Fig. 4 Monophase structure of etched commercially pure aluminum (1*xx.x*) at 200× magnification. HF etchant (5m in Table 4)

Table 4 Reagents for chemical microetching

No.	Chemical composition	Etching mode	Purpose or application	Ref
1m	25 mL HNO_3 (70%) 75 mL distilled H_2O	70 °C (160 °F), 40 s	Phase identification, especially in Al-Cu alloys	Ref 7, 8, 9, 10
2m	20 mL H_2SO_4 (98%) 80 mL distilled H_2O	70 °C (160 °F), 30 s 30 s–3 min	Phase identification, Al-Cu, Mn, Mg, Fe, Be, Ti alloys	Ref 7, 8, 9, 10 11
3m	1 g NaOH 100 mL distilled H_2O	50 °C (120 °F), 5–15 s Clean in 5% HNO_3, rinse in cold water, prepare fresh before use	Phase identification; AlCuMgZn alloys need 2–3 min etching.	Ref 8, 9, 10
	1 g NaOH 100 mL distilled H_2O	Swab 5–10 s		Ref 7
4m	10 g NaOH 100 mL distilled H_2O	70 °C (160 °F), 5 s Prepare fresh before use	Phase identification	Ref 8, 11
5m	0.5 mL HF (40%) 100 mL distilled H_2O (The HF concentration can be increased up to 10 mL). Toxic!	At ambient temp., 5–60 s to alternately polish and etch several times	Phase identification; reveals grain boundaries, slip lines in pure Al	Ref 5, 8, 9, 10, 11
6m	5 mL HF (40%) 15 mL HCl (38%)	At ambient temperature, 5–60 s	Phase identification	Ref 8, 11

	25 HNO_3 (70%) 955 mL distilled H_2O			
7m	A) 2(4) mL HF (40%) 3(6) mL HCl (38%) 5(10) mL HNO_3 (70%) 190 mL distilled H_2O (concentration variable) Toxic!	At ambient temperature, 10–30 s Prepare fresh before use	Al and Al alloys (Al-Si cast alloys)	Ref 9, 10
	20 mL reagent 7m + 80 mL H_2O	5–10 s	…	Ref 7
	B) 2 mL HF (40%) 3 mL HCl (38%) 20 mL HNO_3 (70%) 175 mL distilled H_2O (Modifed 7m)	10–60 s Rinse in stream of warm water	Form thin layer of etching products on the specimen surface	Ref 7
8m	0.5–25 g NaOH 1 g $ZnCl_2$ 100 mL distilled H_2O	A few seconds–1 min	Al and Al alloys	Ref 9
10m	1 drop HF (40%) 25(30) mL HCl (38%) 25(20) mL HNO_3 (70%) 25(50) mL CH_3OH	20–25 °C (70–75 °F) 10–60 s Toxic!	Pure Al and Al-Mg, Al-Mg-Si alloys (etching figures)	Ref 9
11m	2 mL HCl (38%) 8 mL HNO_3 (70%) 45 mL H_2O 45 mL CH_3OH	10 s	All kinds of Al alloys	Ref 7
12m	10 g NaOH 5 g $K_4[Fe(CN)_6]$ 100 mL distilled H_2O	2 min	Grain boundaries, Al-Si, Al-Cu alloys	Ref 9
13m	4 g $KMnO_4$	At ambient temperature, 7–45 s	Microsegregation in Al alloys	Ref 14

	Distilled H_2O After dissolution, add 1 g NaOH			
14m	4 g $KMnO_4$ 2 g Na_2CO_3 94 mL distilled H_2O Add a few drops of wetting agent	Specimen surface must be well polished and precleaned in 20% H_3PO_4 at 95 °C (205 °F) for uniform wettability; after precleaning, rinse in cold water and immediately immerse in etchant for 30 s.	Chemical inhomogeneity and microsegregation in Al alloys	Ref 7
15m	A) 5 mL HF 95 mL distilled H_2O At boiling temperature, add MoO_3 until saturation	At ambient temperature, a few seconds	A) Phase identification	Ref 14
	B) 10 mL HF 90 mL distilled H_2O At boiling temperature, add MoO_3 until saturation		B) Grain boundaries revealed	
16m	2–2.5 g $(NH_4)MoO_4$ + 10 mL HNO_3 After dissolution, add 190 mL ethyl alcohol (stirring intensively)	20 °C (70 °F) 30–40 s	Phase identification	Ref 15
17m	1 g $(NH_4)MoO_4$ 200 mL distilled H_2O Add 6 g NH_4Cl	20 °C (70 °F), 30 s–3 min	Phase identification in Al-Si alloys	Ref 16
18m	1–2 g $(NH_4)HF_2$ 2–3 g $Na_2MoO_4 \times 2H_2O$ 5 mL HCl 100 mL distilled H_2O	20 °C (70 °F) 30–60 s	Phase identification	Ref 11, 12
19m	Stock solution: 3 g $(NH_4)MoO_4$ 20 mL HNO_3 20 mL distilled H_2O Use reagent:	20 °C (70 °F) 30–40 s	Phase identification	Ref 17

	1 p. stock solution + 4 p. ethyl alcohol			
20m	1.44 g $(NH)_4NO_3$ 9.4 mL HNO_3 100 mL distilled H_2O Add MoO_3 in excess	Before use, dilute 1:1 with water, 15–30 s	Phase identification	Ref 13
21m	5 mL HCl 10 mL H_2SO_4 85 mL distilled H_2O	30 s	All kinds of Al alloys	Ref 7
22m	2 g NaOH 5 g NaF 93 mL distilled H_2O	2–3 min	All kinds of Al alloys	Ref 7
23m	5 mL CH_3COOH (glacial) 1 mL HNO_3 (70%) 94 mL distilled H_2O	20–30 min	All kinds of Al alloys	Ref 7
24m	15.5 mL HNO_3 (70%) 0.5 mL HF (48%) 3 g CrO_3 84 mL distilled H_2O (Graff-Sargent reagent)	At ambient temperature, immerse 20–60 s, agitating mildly; second etching in Keller's reagent may reveal further details of the microstructure.	All kinds of Al alloys	Ref 7
25m	200 g CrO_3 20 g Na_2SO_4 17 mL HCl (35%) 1000 mL H_2O	Pre-etch: 4m, next, 50% HNO_3 in water, rinse in water, and immediately put in 25m	All kinds of Al alloys	Ref 11
26m	200 g CrO_3 200 g H_2SO_4 50 g NH_4HF_2 1000 mL H_2O	At ambient temperature, 5–30 s	All kinds of Al alloys	Ref 11
27m	1–2 mL HNO_3 98–99% ethyl alcohol	A few seconds–15 min	Al-Mg alloys	Ref 17

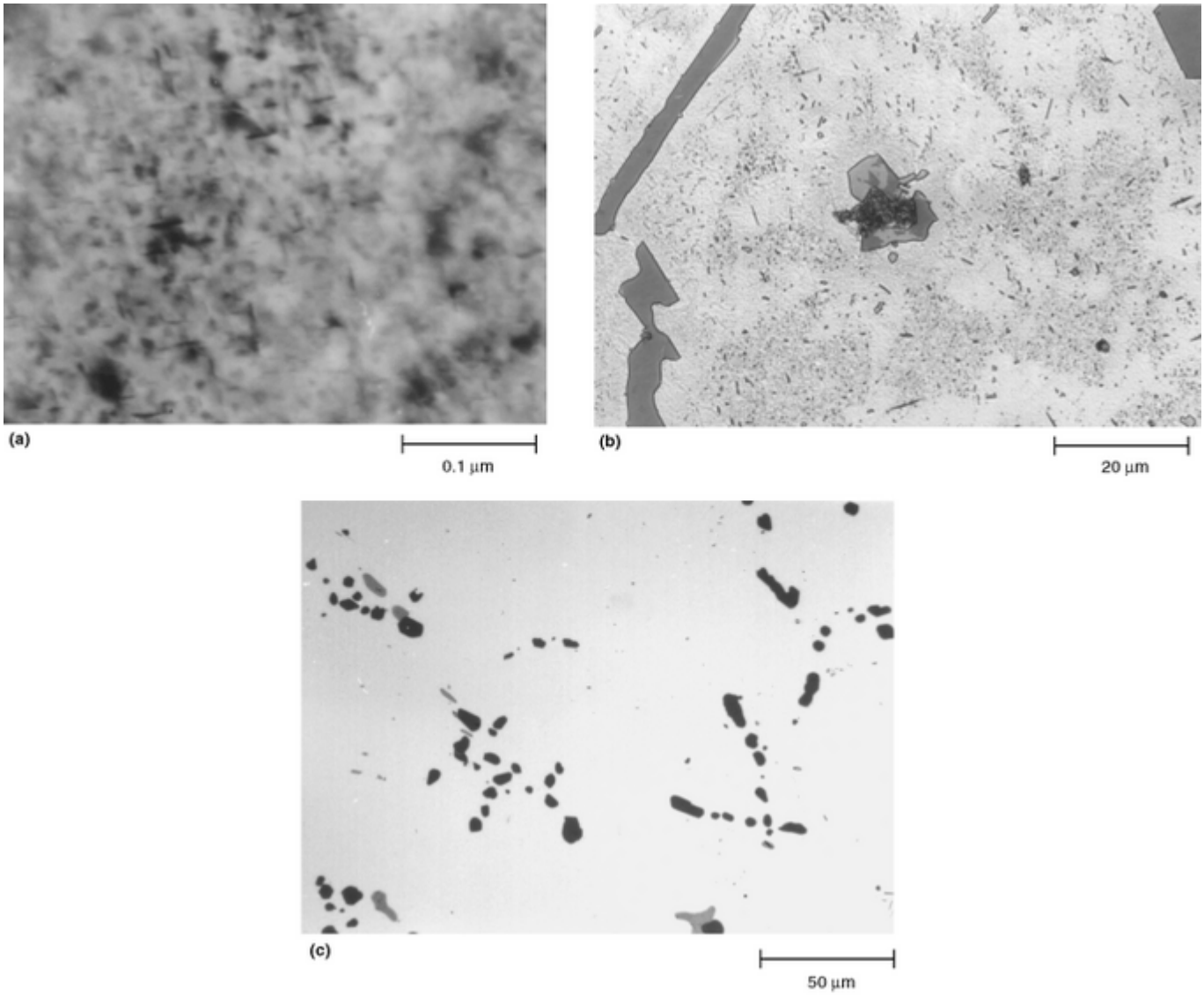

Fig. 5 Examples of dispersed precipitates shown at various magnifications. (a) Transmission electron microscopy image (at 200,000×) of η′ phase in thin foil of 7050-T6 alloy. (b) Micrograph (at 1000×) of heat treated (T6) 418 alloy etched with 0.5% HF (etchant 5m in Table 4). (c) Micrograph (at 400×) of heat treated 7050-T6 alloy etched with 0.5% HF (etchant 5m in Table 4)

Solid-state precipitation occurs when element concentrations exceed their solid solubility during cooling. The solubility limits of alloying elements in solid aluminum are very low (Table 5), and no element is known to have complete miscibility with aluminum in the solid state. Commercially pure aluminum is a pure solid-solution (monophase) material (Fig. 4). Among the commercial alloys, only the bright-finishing alloys such as 5657 and 5252, which contain 0.8 and 2.5% Mg (nominal), respectively, with very low limits on all impurities, may be regarded as nearly pure solid solutions. When the content of an alloying element exceeds the solid-solubility limit, the alloying element produces second-phase microstructural constituents. Second-phase constituents may consist of pure element precipitates or mainly intermetallic phases. In the first group are silicon, tin, and beryllium. If the alloy is a ternary or higher-order alloy, however, silicon or tin may form intermetallic-compound phases.

Table 5 Solubility limits of various binary aluminum alloys

Element	Temperature [a]		Liquid solubility		Solid solubility	
	°C	**°F**	**wt%**	**at.%**	**wt%**	**at.%**
Ag	570	1060	72.0	60.9	55.6	23.8
Au	640	1180	5	0.7	0.36	0.049
B	660	1220	0.022	0.054	<0.001	<0.002
Be	645	1190	0.87	2.56	0.063	0.188
Bi	660[b]	1220[b]	3.4	0.45	<0.1	<0.01
Ca	620	1150	7.6	5.25	<0.1	<0.05
Cd	650[b]	1200[b]	6.7	1.69	0.47	0.11
Co	660	1220	1.0	0.46	<0.02	<0.01
Cr	660[c]	1220[c]	0.41	0.21	0.77	0.40
Cu	550	1020	33.15	17.39	5.67	2.48
Fe	655	1210	1.87	0.91	0.052	0.025
Ga	30	80	98.9	97.2	20.0	8.82
Gd	640	1180	11.5	2.18	<0.1	<0.01
Ge	425	800	53.0	29.5	6.0	2.30
Hf	660[c]	1220[c]	0.49	0.074	1.22	0.186
In	640	1180	17.5	4.65	0.17	0.04
Li	600	1110	9.9	30.0	4.0	13.9
Mg	450	840	35.0	37.34	14.9	16.26
Mn	660	1220	1.95	0.97	1.25	0.62
Mo	660[c]	1220[c]	0.1	0.03	0.25	0.056
Na	660[b]	1220[b]	0.18	0.21	<0.003	<0.003
Nb	660[c]	1220[c]	0.01	0.003	0.22	0.064
Ni	640	1180	6.12	2.91	0.05	0.023
Pb	660	1220	1.52	0.20	0.15	0.02
Pd	615	1140	24.2	7.5	<0.1	<0.02
Rh	660	1220	1.09	0.29	<0.1	<0.02
Ru	660	1220	0.69	0.185	<0.1	<0.02
Sb	660	1220	1.1	0.25	<0.1	<0.02
Sc	660	1220	0.52	0.31	0.38	0.23
Si	580	1080	12.6	12.16	1.65	1.59
Sn	230	450	99.5	97.83	<0.01	<0.002
Sr	655	1210	…	…	…	…
Th	635	1180	25.0	3.73	<0.1	<0.01
Ti	665[c]	1230[c]	0.15	0.084	1.00	0.57
Tm	645	1190	10.0	1.74	<0.1	<0.01
U	640	1180	13.0	1.67	<0.1	<0.01
V	665[c]	1230[c]	0.25	0.133	0.6	0.32
Y	645	1190	7.7	2.47	<0.1	<0.03
Zn	380	720	95.0	88.7	82.8	66.4
Zr	660[c]	1220[c]	0.11	0.033	0.28	0.085

(a) Eutectic reactions unless designated otherwise.

(b) Monotectic reaction.

(c) Peritectic reaction.

Source: Ref 3, 4

Most of the other alloying elements form such intermetallic compounds with aluminum in binary alloys and more complex phases in ternary or higher-order alloys. In the aluminum-copper system, for example, when the α solid-solution phase is cooled below the solvus line, dispersed Al_2Cu particles precipitate, depleting copper from the α solid solution. When cooled to room temperature under near-equilibrium (slow) conditions, the α

solid solution contains little copper, so strength is low. To increase strength, the material must be solution heat treated, quenched, and aged to develop metastable precipitates. During fast cooling, the α solid solution is supersaturated, and then, as a result of its tendency to achieve thermodynamic equilibrium, the Al_2Cu intermetallic precipitates as dispersed particles.
Among the intermetallic phases, several groups can be mentioned:

- Electron compounds (Hume Rothery phases)
- Laves phases
- Intermediate solid-solution phases

The morphology and thermophysical properties of the intermetallic phase particles can influence the properties of the alloy at different steps of production or processing. Essentially, the intermediate solid-solution phases occur when the crystal lattice of the base metal cannot accommodate any more atoms of the alloying element. When this occurs, a new phase forms with a different crystal structure that can more easily accommodate the undissolved alloying atoms.
Liquid-Solid Transformations. The eutectic and peritectic reactions are the two major forms of liquid-solid transformation in aluminum alloys, and examples of each are briefly described in terms of equilibrium phase diagrams and phase morphology. Although few products are sold and used in their equilibrium condition, equilibrium phase diagrams are essential in understanding the effects of composition and both solidification and solid-state thermal processing on microstructure. For aluminum alloys, phase diagrams are used to determine solidification and melting temperatures, the solidification path, and the equilibrium phases that form and their dissolution temperatures. In addition to determining appropriate temperatures for casting and thermal treatments, phase diagrams are used to determine the maximum levels for ancillary element additions of certain elements to prevent the crystallization of coarse primary particles.
Eutectic Reaction. The aluminum-copper diagram (Fig. 3) and the aluminum-silicon diagram (Fig. 6) are two examples of simple eutectic systems. Using the aluminum-copper system as an example, the basic process of solidification and morphology formation is as follows. When the temperature goes below the liquidus line, the solid-solution phase (α) solidifies first, while most of the copper remains in liquid form. As the temperature approaches the solidus, the α solid phase becomes more enriched with copper. When the temperature falls below the solidus temperature in alloys containing less than the maximum solubility (5.65 wt% Cu), solidification is complete to the solid-solution phase condition (α). In alloys containing more than 5.65 wt% (2.5 at.%) Cu, some liquid remains when the eutectic temperature (548 °C, or 1018 °F) is reached. In this case, two terminal solid-solution phases (α and θ) separate out simultaneously from the molten liquid. On cooling below the eutectic temperature, a network of eutectic forms in the residual liquid surrounding the dendrites or grains of primary α.

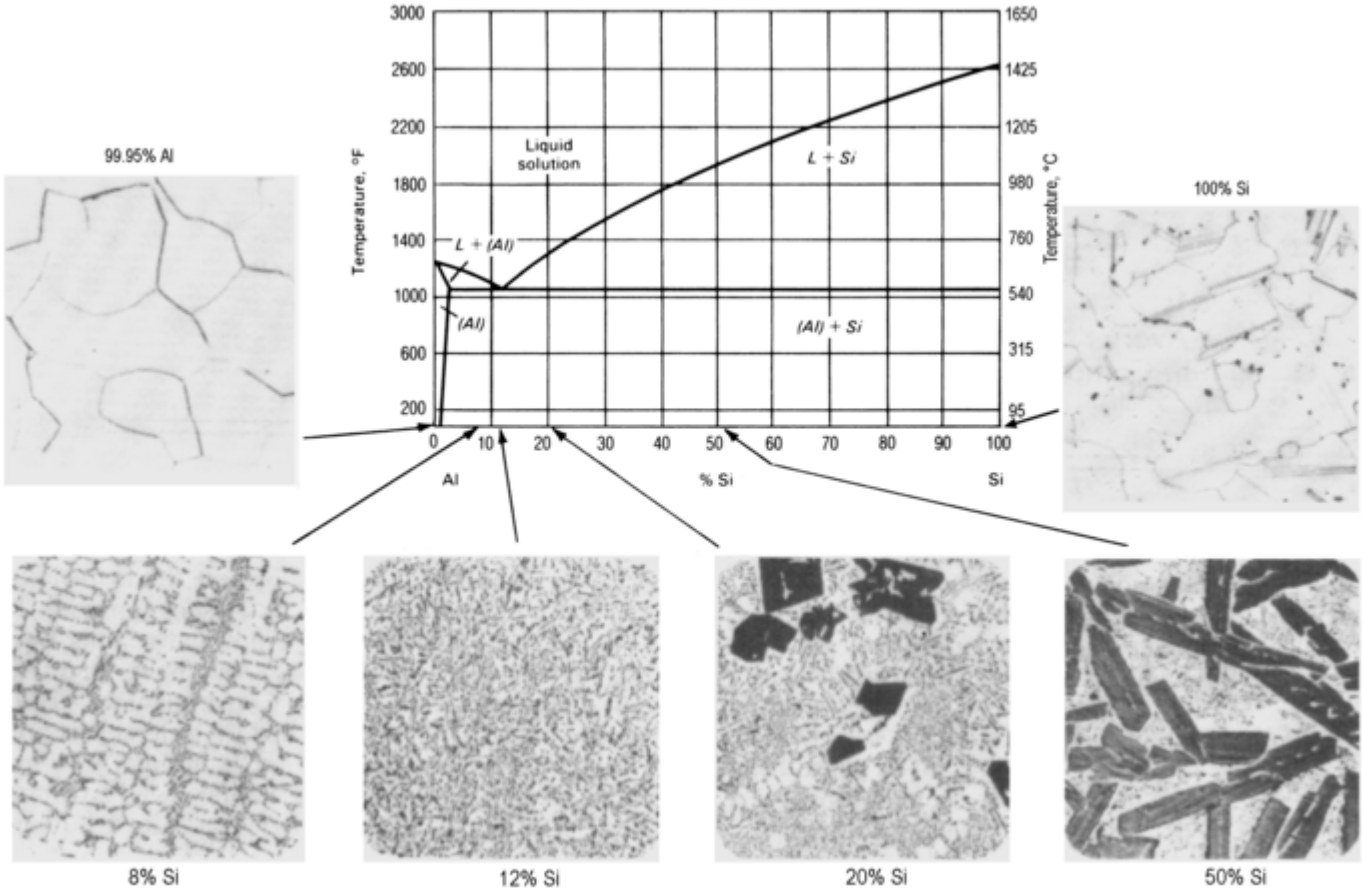

Fig. 6 Aluminum-silicon phase diagram and cast microstructures of hypoeutectic compositions (<12% Si), hypereutectic compositions (>12% Si), and one close to the eutectic composition of 12% Si

In the aluminum-copper system, a network of the Al_2Cu intermetallic can be detrimental, depending on the extent and coarseness of the Al_2Cu particles. In addition, it is also important to realize that the eutectic reaction can occur in alloys containing less than the maximum solid solubility under commercial casting conditions, even though the equilibrium phase diagram does not predict that. Consequently, Al_2Cu particles form during solidification of most aluminum alloy ingots and shaped castings. Therefore, they are preheated or homogenized to dissolve the intermetallic particles.

Various types of as-cast morphologies are obtained, depending on whether the alloy content is above, below, or near the eutectic composition. This is shown for the aluminum-silicon system (Fig. 6). Hypoeutectic aluminum-silicon alloys (i.e., those with alloying contents below the eutectic composition of 12.6 wt% Si) have a network structure of a second phase (gray) that surrounds grains of solid-solution aluminum (light). Similar as-cast structures are shown in Fig. 7 for two other hypoeutectic alloys. In the case of eutectic and hypereutectic compositions, the as-cast structure may have mixed morphologies of both networklike and dispersed second phases. In these cases, a dispersed second phase may occur as a primary product during solidification above the eutectic temperature. These types of mixed as-cast morphologies are shown in Fig. 8and Fig. 9 for some eutectic and hypereutectic alloys, respectively. Phase morphologies also can be modified either during the solidification process or by solid-state processing (such as bulk working and/or heat treatment). For example, Fig. 10 is the as-cast structure of aluminum-silicon eutectic with and without alloy modification during liquid processing. Modification of morphology by heat treatment is shown in Fig. 11 and Fig. 12.

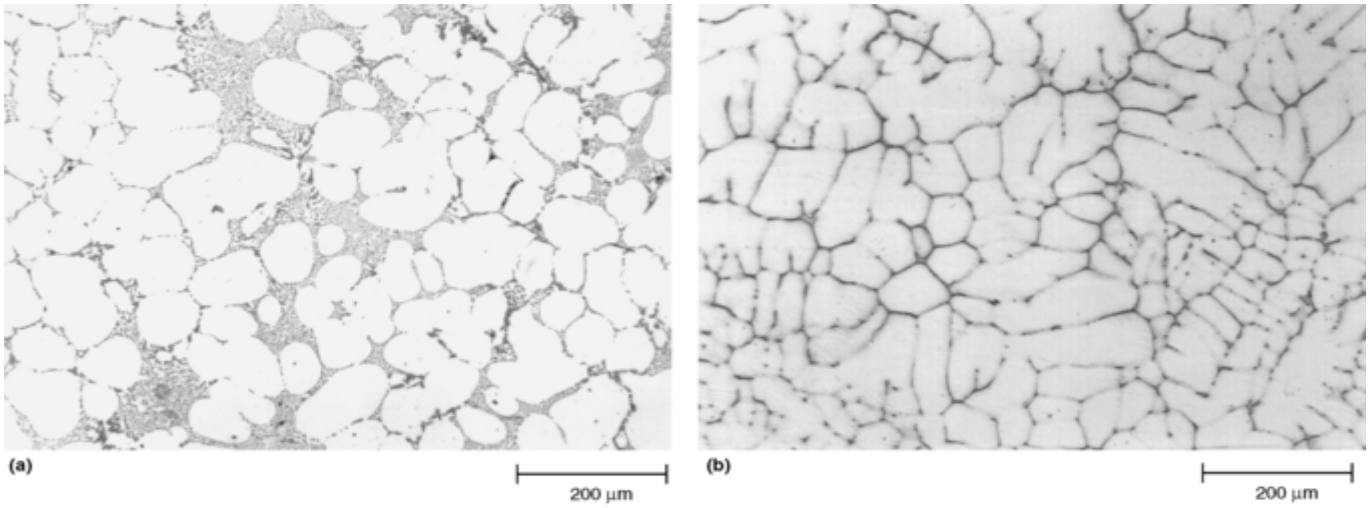

Fig. 7 Networklike morphology of second-phase structure in two hypoeutectic alloys. (a) As-cast 356 alloy. (b) As-cast 7050 alloy. Both etched with 0.5% HF (5m in Table 4) and magnified by 100×

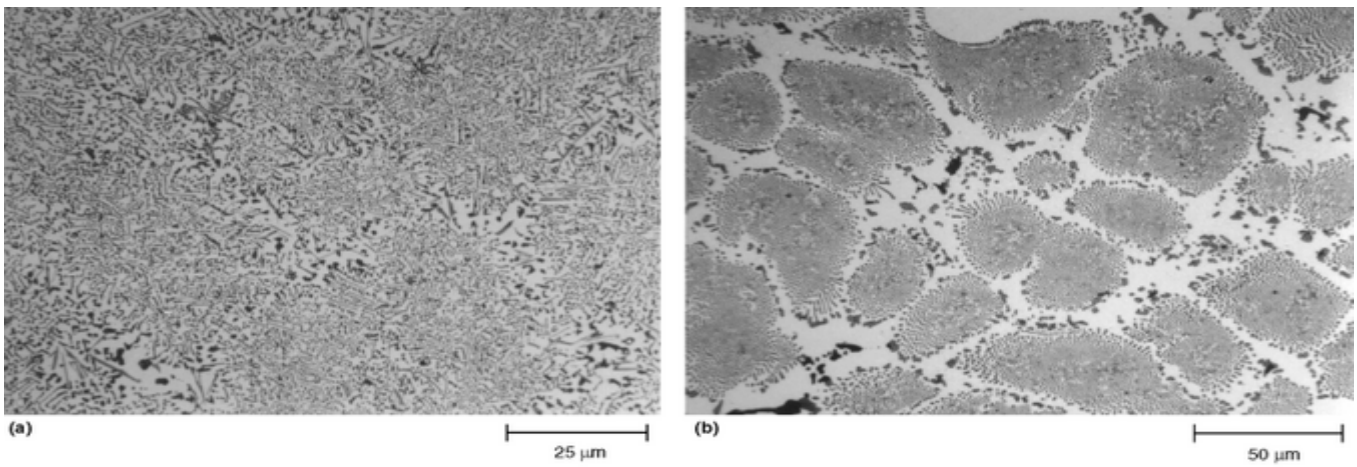

Fig. 8 Dispersed phase and networklike morphology of second-phase structure in two eutectic alloys. (a) As-cast 413 alloy at 750×. (b) As-cast aluminum-copper alloy at 400×. Both etched with 0.5% HF (5m in Table 4)

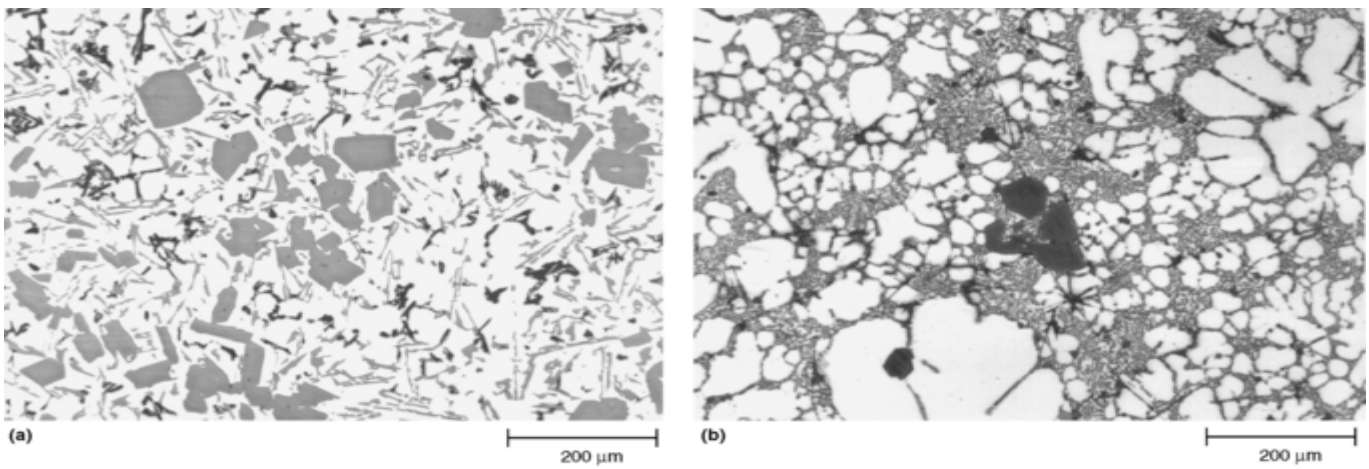

Fig. 9 Dispersed phase and networklike morphology of second-phase structure in two hypereutectic alloys. (a) As-cast 390 alloy with primary precipitates of silicon (light gray). (b) As-cast 384.0 alloy with primary precipitates of Al-Fe-Si. Both etched with 0.5% HF (5m in Table 4) and magnified by 100×

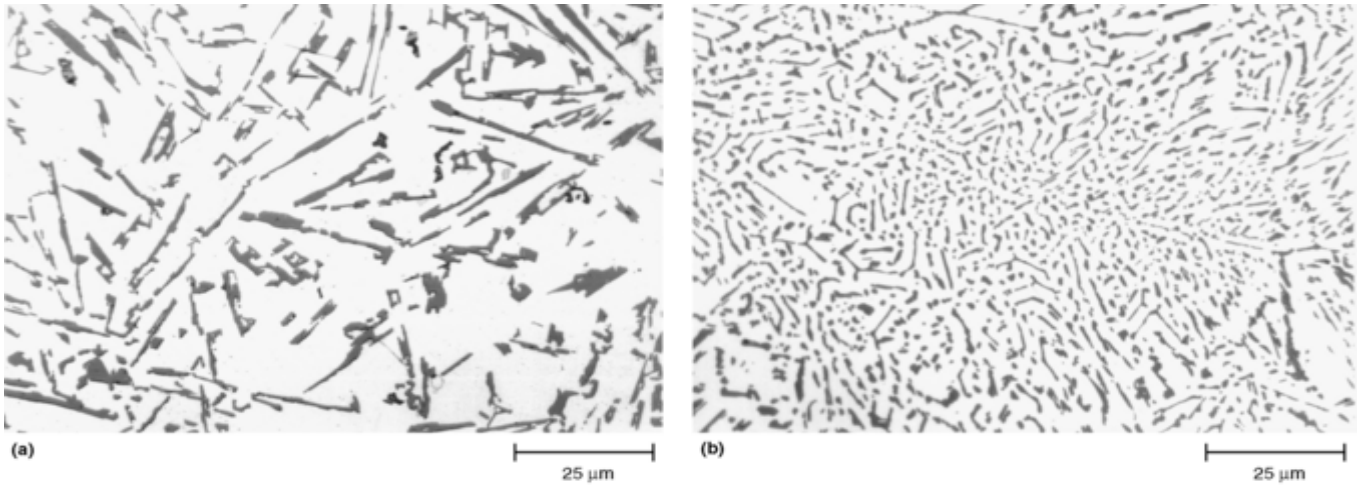

Fig. 10 As-cast morphologies in a eutectic aluminum-silicon alloy. (a) Unmodified alloy with coarse silicon precipitates formed during solidification. (b) Modified alloy with solidification of finer silicon precipitates. Both etched with 0.5% HF (5m in Table 4) and magnified by 750×

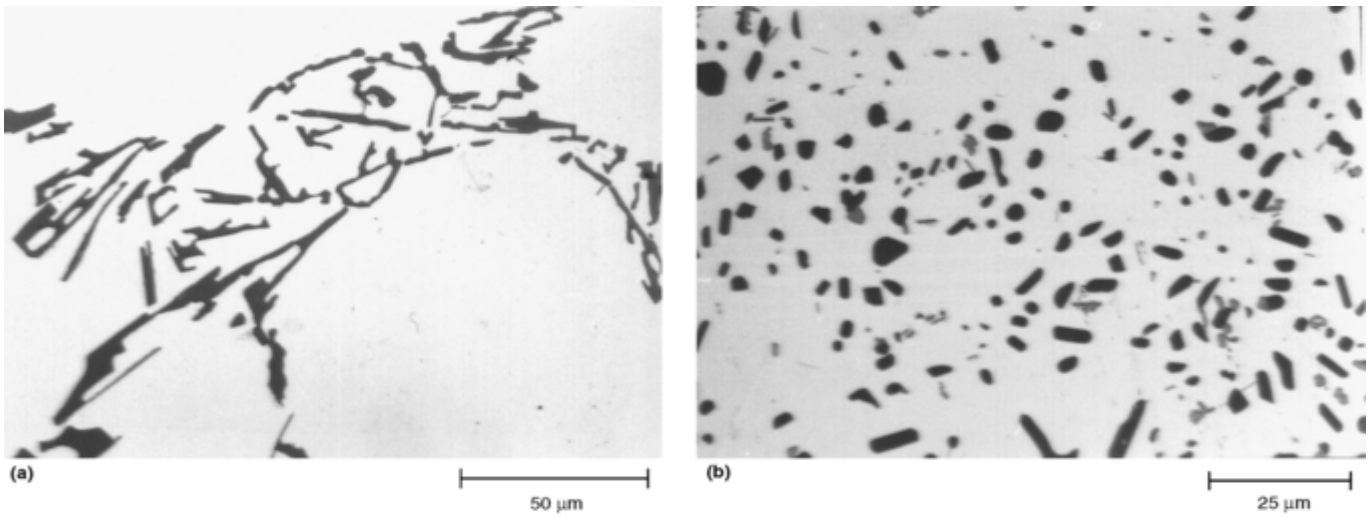

Fig. 11 Effect of heat treatment on phase morphology in a hypoeutectic alloy (alloy 355). (a) As-cast structure (at 500× magnification) with a continuous network of interdendritic precipitates of eutectic silicon. (b) Heat treated condition (T6) of same alloy with globular eutectic silicon precipitates shown at 750×. Both etched with 0.5% HF (5m in Table 4)

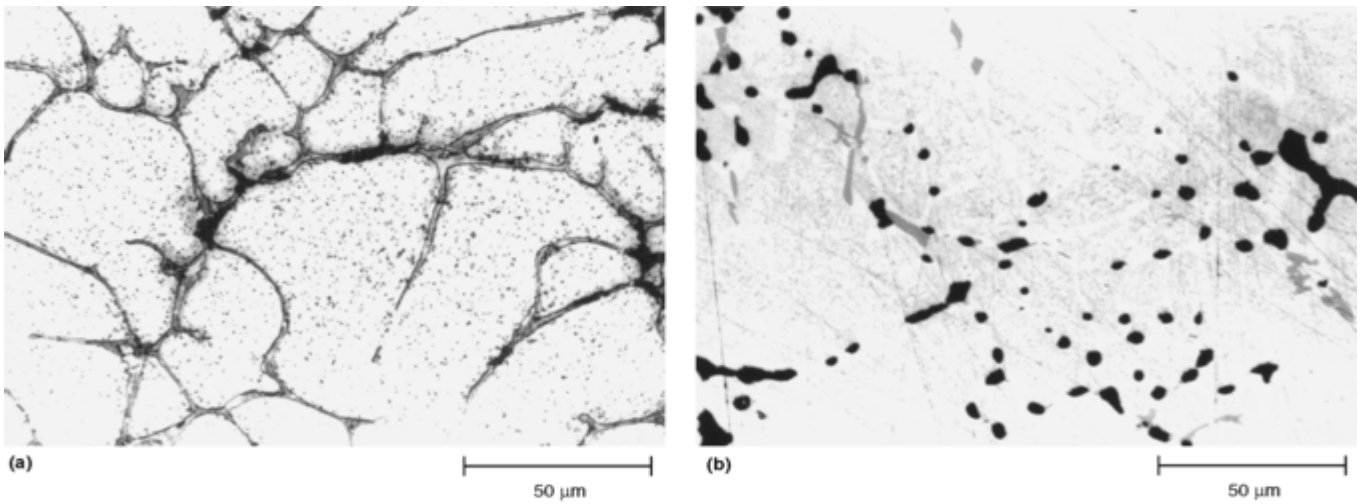

Fig. 12 Effect of heat treatment on phase morphology in alloy 7050. (a) As-cast structure with network of Al + M($MgZn_2$) eutectic and $Al_2Mg_3Zn_3$(T) precipitates. (b) Heat treated (T6) condition with globular

morphology of M($MgZn_2$) eutectic and $Al_2Mg_3Zn_3$(T) precipitates. Both etched with 0.5% HF (5m in Table 4) and magnified by 500×

Peritectic Reaction. The aluminum-chromium system (Fig. 13) is an example of a peritectic system. During equilibrium solidification of alloys containing more than the peritectic composition (0.41% Cr but less than the maximum solid solubility of 0.77%), an intermetallic compound, Al_7Cr, forms when the liquidus temperature is reached. When the temperature falls to the peritectic temperature, 661 °C (1222 °F), the remaining liquid along with the Al_7Cr transforms to α-aluminum. Under commercial solidification conditions, however, the primary particles of Al_7Cr would not have the opportunity to transform to α solid solution, so they would remain. Consequently, maximum chromium limits are established so that all of the chromium remains in supersaturated solid solution in the ingot. It precipitates as chromium-bearing dispersoids during ingot preheat. Micrographs of two other peritectic structures in Al-Fe(Mn)-Si and Al-Fe-Cu-Ni systems are shown in Fig. 14.

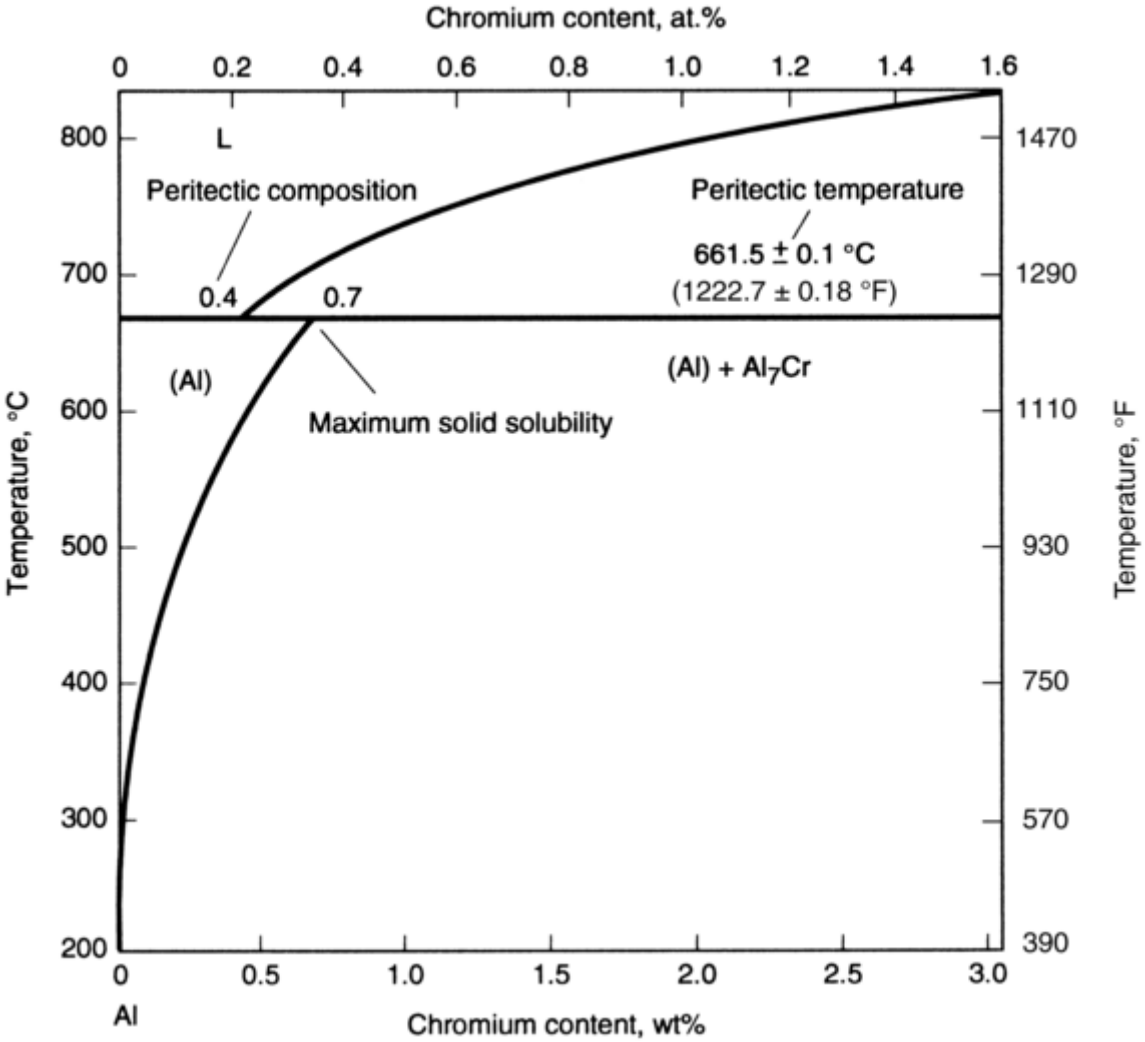

Fig. 13 Aluminum-chromium phase diagram illustrating the peritectic reaction

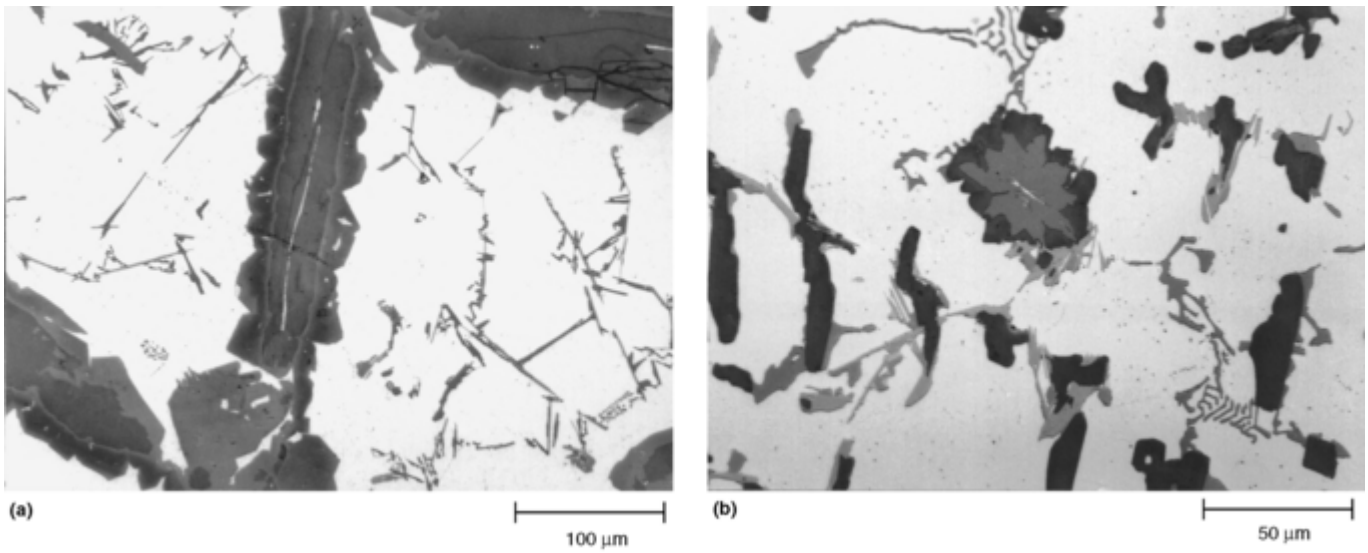

Fig. 14 Micrographs of peritectic structures. (a) Al-Fe-Mn-Si alloy (at 200×) with primary phase of $Al_3Fe(Mn)$ and peritectic phase of α-AlFeMnSi. (b) Al-Fe-Cu-Ni alloy (at 400×) with Al_3Ni primary phase and an Al_9FeNi peritectic phase. Both etched with 0.5% HF

Second-phase particles are divided into four classes, based on their mode of formation and their ability to be dissolved: primary particles, constituents, dispersoids, and precipitates.

Primary particles refer to the solid phase that separates first from the melt. For example, primary silicon particles form first in the L + Si phase of hypereutectic aluminum-silicon alloys (Fig. 6). The coarse, faceted primary silicon particles are refined to a fine, spherulitic structure using additives containing phosphorus. In certain casting alloys and 8*xxx* wrought alloys, primary iron-bearing constituents can form if the alloying content is such that the alloy is hypereutectic. In wrought alloys, macroscopically large, undesirable primary particles of Al_7Cr, Al_3Ti, or Al_3Zr can form by a peritectic reaction if chemical composition is not closely controlled.

Constituents. These particles may be either intermetallic compounds or metal crystals that form during solidification of hypoeutectic alloys. They range in size from a few micrometers to tens of micrometers. Constituents can be classified either as virtually insoluble or soluble. Most of these soluble constituents dissolve either during ingot preheating prior to deformation processing or during the solution heat treatment of cast shapes or wrought products. Constituent size decreases with increasing solidification rate. In hypoeutectic 3*xx.0* and 4*xx.0* castings, modification by elements such as strontium significantly refine the flake structure of the silicon particles to a finer fibrous morphology. Constituent particles are generally not beneficial.

Dispersoids form by solid-state precipitation, either during ingot preheating or during the thermal heat treatment of cast shapes of slow-diffusing supersaturated elements that are soluble in molten aluminum but that have limited solubility in solid aluminum. Manganese, chromium, or zirconium are typical dispersoid-forming elements. Unlike the precipitates that confer precipitation hardening, dispersoids are virtually impossible to dissolve completely, once precipitated. In addition to providing dispersion strengthening, the size distribution of dispersoids in wrought alloys is a key factor in controlling degree of recrystallization, recrystallized grain size, and crystallographic texture. Dispersoids in non-heat-treatable alloys also stabilize the deformation substructure during elevated-temperature exposures, for example, during paint baking.

In contrast to the commercially significant dispersion strengthening provided by dispersoids in 3*xxx* and 5*xxx* alloys, the level of dispersion strengthening afforded by dispersoids in wrought heat treatable alloys is trivial. In 2*x24* alloys, $Al_{20}Cu_2Mn_3$ dispersoids nucleate dislocations at the particle-matrix interface during the quench. These dislocations serve as nucleation sites for subsequent precipitation. The newer 7*xxx* alloys contain zirconium, which forms coherent Al_3Zr dispersoids, while most of the older 7*xxx* alloys contain $Al_{12}Mg_2Cr$ dispersoids, which exhibit incoherent interfaces. The incoherent interfaces serve to nucleate $MgZn_2$ precipitates during the quench, so alloys containing these precipitates lose a great deal of their potential to develop high strength after slow quenching (quench sensitivity). Nucleation is difficult on coherent interfaces, so the newer alloys are less quench sensitive. A number of casting alloys, and some wrought alloys, contain elements that can form either constituents or dispersoids, depending on the solidification rate.

Precipitates can form during any thermal operation below the solvus. In properly solution-heat-treated products, all precipitates dissolve during the solution-heat-treatment operation. Depending on quench rate and alloy, precipitates can form during the quench from the solution-heat-treatment temperature at grain and subgrain boundaries and at particle-matrix interfaces. These coarse precipitates do not contribute to age hardening and can serve to reduce properties such as ductility, fracture toughness, and resistance to intergranular corrosion. After the quench, Guinier-Preston (GP) zones form at ambient temperature (natural aging). These are agglomerates of atoms of the major solute elements with a diffuse, coherent boundary between the GP zone and the matrix. During elevated-temperature precipitation heat treatments (artificial aging), GP zones may either nucleate metastable precipitates or they may dissolve, and metastable precipitates nucleate separately. Cold working subsequent to quenching introduces dislocations that may serve to nucleate metastable or equilibrium precipitates. With prolonged artificial aging, equilibrium precipitates may form. Coarse equilibrium precipitates form during annealing treatments of heat treatable alloy products (O temper). They also form during most thermomechanical treatments prior to solution heat treatment.

Alloying Elements and Impurities

Solid solubility of the major alloying elements in aluminum as a function of temperature is plotted in the graph in Fig. 15. Of all the elements, zinc has the greatest solid solubility in aluminum, with a maximum of 82.8 wt% (66.4 at.%) listed in Table 5. In addition to zinc, the solid solubilities of silver, magnesium, and lithium are greater than 10 at.% (in order of decreasing maximum solubility). Gallium, germanium, copper, and silicon (in decreasing order) have maximum solubilities of less than 10 at.% but greater than 1 at.%. All other elements are less soluble. With the one known exception of tin (which shows a retrograde solid solubility between the melting point of aluminum and the eutectic temperature, 228.3 °C, or 442.9 °F, with a maximum of 0.10% at approximately 660 °C, or 1220 °F), the maximum solid solubility in aluminum alloys occurs at the eutectic, peritectic, or monotectic temperature. With decreasing temperature, the solubility limits decrease. This decrease from appreciable concentrations at elevated temperatures to relatively low concentrations at low temperatures is one fundamental characteristic that provides the basis for substantially increasing the hardness and strength of aluminum alloys by solution heat treatment and subsequent precipitation-aging operations.

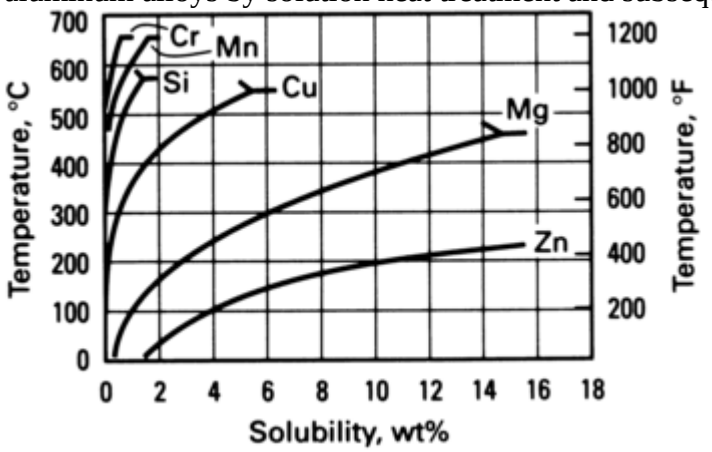

Fig. 15 Equilibrium binary solid solubility for common alloying elements of aluminum

Iron. Virtually all aluminum alloys contain some iron that is an impurity remaining after refining bauxite and smelting. The eutectic composition of the aluminum-iron system is 1.8 wt% Fe, and the maximum solid solubility is 0.05 wt% Fe at the eutectic temperature of 655 °C (1211 °F). Solid solubility of iron in aluminum is reduced by other alloying elements, and maximum solid solubility of iron is as low as or lower than 0.01 wt% Fe in most structural aluminum alloys. The equilibrium constituent above the solid solubility limit is Al_3Fe (θ), although other phases may be present. Depending on solidification rate and the presence of other elements such as manganese, metastable constituents may occur, such as $FeAl_6$ with moderate quenching and Fe_2Al_9 with rapid quenching (Ref 18). In most cases, the effects of iron in aluminum are considered in terms of ternary or quartenary phase diagrams, because some iron is always present in aluminum alloys.

Silicon is the other ubiquitous impurity in commercial aluminum alloys. Because iron and silicon are common impurities in commercially pure aluminum, the aluminum corner of the Al-Fe-Si ternary system is a subject of

interest (Ref 19). The presence of iron greatly reduces the solubility of silicon in aluminum (Ref 19). At low silicon contents, almost all of the iron is present as Al_3Fe. With increasing silicon contents, two ternary phases appear. A hexagonal α phase (Al_8Fe_2Si) and then a monoclinic β phase (of apparent stoichiometry noticed Al_5FeSi or $Al_9Fe_2Si_2$) form initially by peritectic and at the end of solidification by eutectic transformations. Phases in commercial products may not be those predicted by the equilibrium phase diagrams because of the long times at high temperatures required to approach equilibrium.

Aluminum-silicon alloys that do not contain copper additions are used when good castability and good corrosion resistance are needed. The binary aluminum-silicon system (Fig. 6) is a simple eutectic system with a eutectic composition of 12.6 wt% Si and a maximum solid solubility of 1.65 wt% Si (1.5 at.%) at the eutectic temperature of 577 °C (1071 °F). In the binary aluminum-silicon system, under the nonequilibrium conditions of casting, the volume fraction of α-Al + Si eutectic increases linearly from approximately 0 to 1 as silicon content increases from 1 to 12%. In large amounts, silicon improves castability and fluidity. Consequently, it is used in 4*xxx* brazing sheet and in 3*xx.x* and 4*xx.x* casting alloys. Alloys with silicon contents as low as 2% have been used for casting, but silicon content usually is between 5 and 13% or up to 20% Si in hypereutectic casting alloys. Hypereutectic alloys (>12% Si) are used for engine blocks, because the primary silicon particles are wear resistant.

Metallographic structures of the pure components and of several intermediate compositions are shown in Fig. 6. The intermediate compositions are mixtures of aluminum containing approximately 1% Si in solid solution as the continuous phase, with particles of essentially pure silicon. Hypereutectic alloys show angular primary crystals of silicon in eutectic (Fig. 6). The use of modifiers and refiners is also an important example of how microstructures and macrostructures can be optimized in foundry operations by influencing eutectic and hypereutectic structures in aluminum-silicon alloys. Strength and ductility of these alloys, especially those with higher silicon, can be substantially improved by modification of the aluminum-silicon eutectic. No elements are known that beneficially affect both eutectic and hypereutectic phases.

Modification of hypoeutectic alloys (<12% Si) is particularly advantageous in sand castings and can be effectively achieved through the addition of a controlled amount of sodium or strontium, which refines the eutectic phase. Modification is commonly used for those aluminum alloys with 5% or more silicon. Figure 16 shows alloy 356 before and after modification with sodium. Calcium and antimony additions are also used. Pseudomodification, in which the fineness of the eutectic but not the structure is affected, may be achieved by control of solidification rates.

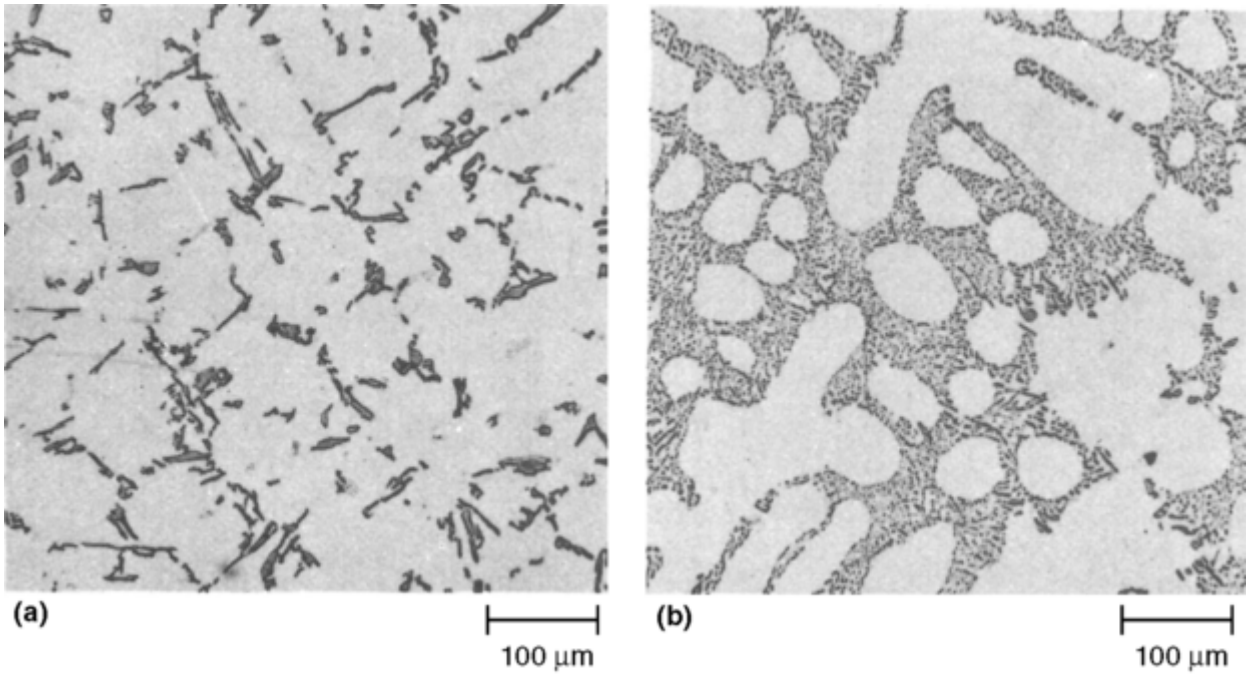

Fig. 16 Effect of sodium modification on microstructure of sand-cast aluminum-silicon hypoeutectic alloy 356-F. Both specimens were etched in 0.5% hydrofluoric acid and are shown at 100×. (a) As-cast structure in unmodified alloy consists of a network of silicon particles (sharp gray), which formed in the interdendritic aluminum-silicon eutectic. (b) Modified alloy by addition of 0.025% Na to the melt. Constituents are the same as in (a), but the particles of silicon are smaller and less angular

In hypereutectic aluminum-silicon alloys, refinement of the proeutectic silicon phase by phosphorus additions is essential for casting and product performance. The coarse primary silicon crystals are harmful in the casting and machining of hypereutectic silicon alloy compositions, and the function of phosphorus additions is to refine the primary silicon. Figure 17 shows the microstructural differences between refined and unrefined structures. Phosphorus also reacts with sodium, and probably with strontium and calcium, to form phosphides that nullify the effects of modification additions. Therefore, use low-phosphorus metal when modification is a process objective. Trace concentrations as low as 0.0015 through 0.03% P are effective in achieving the refined structure.

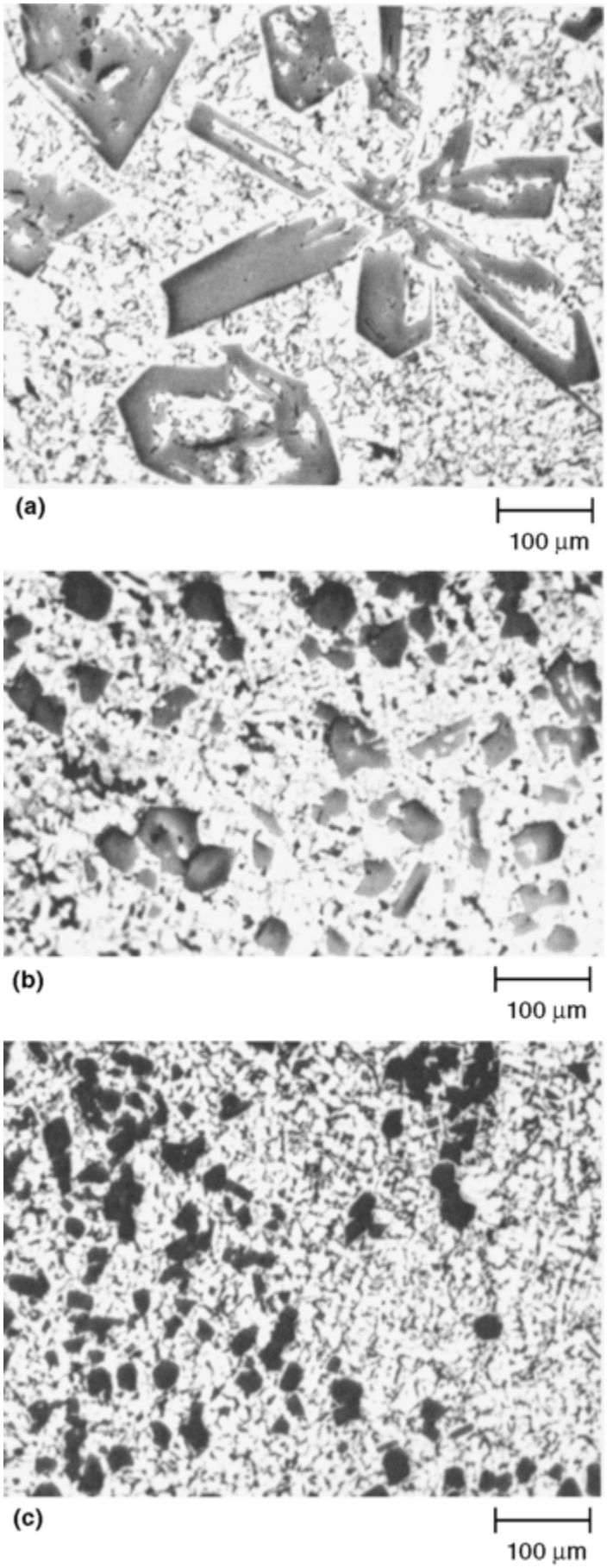

Fig. 17 Effect of phosphorus refinement on the microstructure of Al-22Si-1Ni-1Cu alloy. (a) Unrefined. (b) Phosphorus-refined. (c) Refined and fluxed. All 100×

Al-Si-Mg Alloys. If high strength and hardness are needed, magnesium additions make these alloys heat treatable. Ternary alloys are strengthened by precipitation of metastable precursors to Mg_2Si. The quasi-binary section for Al-Mg_2Si is shown in Fig. 18 (Ref 20) for the Al-Mg-Si system. Some 3*xx.x* casting alloys contain small additions of magnesium to render them capable of being age hardened. The Al-Mg-Si system also is the basis for the 6*xxx* alloys containing magnesium to provide precipitation hardening. Solidus and solvus projections of the ternary system are shown in Fig. 19 (Ref 21). At low magnesium contents, elemental silicon may be present as second-phase particles. As magnesium increases, both silicon particles and equilibrium hexagonal Mg_2Si constituents may be present. At higher magnesium contents, only Mg_2Si is present. With the addition of copper, a complex quaternary $Al_4CuMg_5Si_4$ Q phase can form. A precursor to this quaternary phase strengthens Al-Cu-Mg-Si alloys.

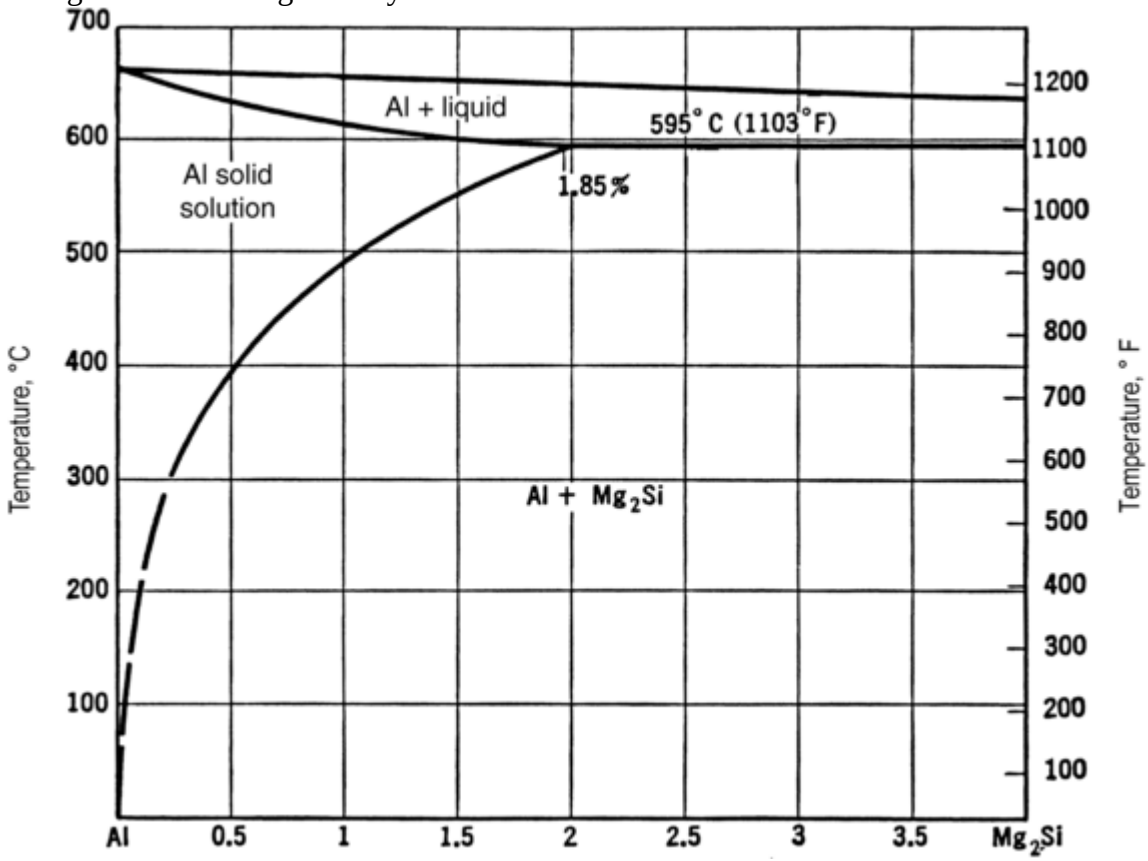

Fig. 18 Quasi-binary section showing the solid solubility of Mg_2Si in aluminum for the Al-Mg-Si ternary. Source: Ref 20

Constituent	Solubility limits, wt%. at:				
	559 °C (1038 °F)	**550 °C (1022 °F)**	**500 °C (932 °F)**	**400 °C (752 °F)**	**200 °C (392 °F)**
Mg	0.68	0.66	0.54	0.28	0.05
Si	1.16	1.04	0.60	0.24	0.04

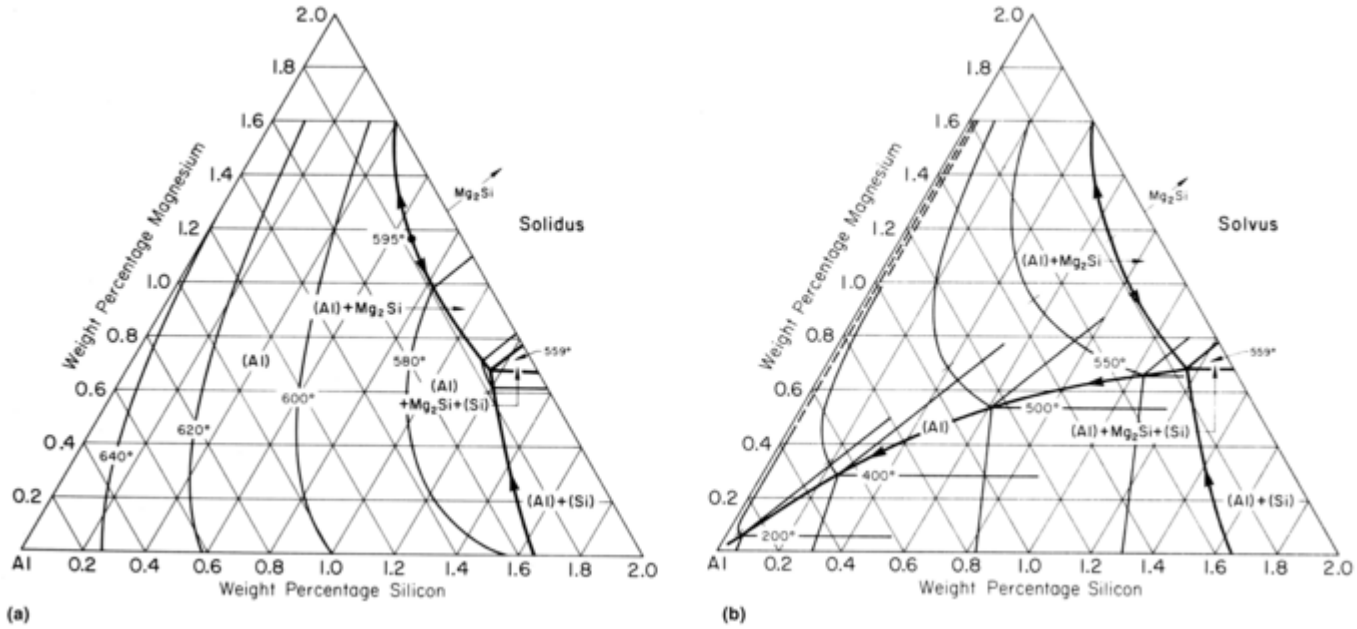

Fig. 19 Al-Mg-Si ternary diagrams. (a) Solidus projection. (b) Solvus projection. Solid-solubility limits along the locus for the aluminum-rich apex of the (Al) + Mg_2Si + (Si) phase field are given in the table. Source: Ref 21

Manganese. The aluminum-manganese system (Fig. 20, Ref 22) is the basis for the oldest aluminum alloys. Manganese is an important alloying element in wrought compositions but is normally considered an impurity in casting compositions and is controlled to low levels in most gravity-cast compositions. Manganese offers no significant benefits in cast aluminum alloys, but some evidence exists that a high volume fraction of $MnAl_6$ in alloys containing more than 0.5% Mn may be beneficial for internal casting soundness.

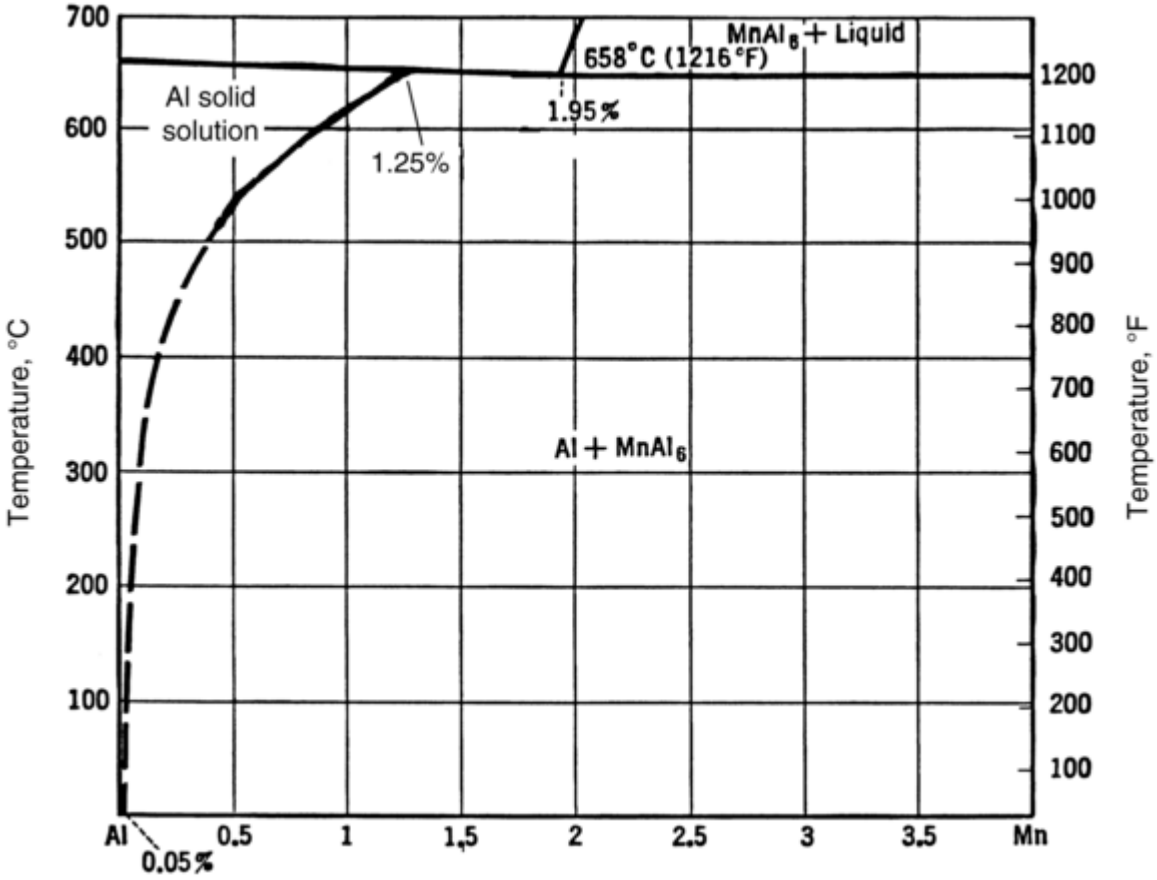

Fig. 20 Aluminum corner of aluminum-manganese phase diagram. Adapted from Ref 20 and 22

In the straight aluminum-manganese wrought alloys (3*xxx* series), manganese increases strength without reduction in corrosion resistance. They are the most widely used wrought alloys because of their excellent formability and resistance to corrosion. During solidification of commercial-sized ingots, some of the manganese forms initially orthorhombic $Al_6(FeMn)$ by eutectic reaction, then cubic $Al_{15}(FeMn)_3Si_2$ by peritectic, and in the residual liquid by eutectic transformations. The remaining manganese remains in solution and is precipitated during the ingot preheat as α-$Al_{15}(FeMn)_3Si_2$ or $Al_6(Mn,Fe)$ dispersoids. These dispersoids strengthen the material and control recrystallized grain size. Because only a limited percentage of manganese (up to approximately 1.5%) can be effectively added to aluminum, manganese is used as a major element in only a few alloys.

Manganese also is used as a minor alloying element. In aluminum-magnesium alloys, manganese acts as a grain refiner and probably hinders the formation of the Al-Fe-Mg-Si phase. In alloys containing copper, manganese precipitates as $Al_{20}Cu_2Mn_3$ dispersoid particles. Effects on strength are minor, but the dispersoids aid in grain size control after solution heat treatment. In silicon alloys, manganese counteracts the damaging effects of high iron content in aluminum-silicon alloys by the formation of α-$Al_{15}(FeMn)_3Si_2$ phase (in form of Chinese script) at the expense of β-$Al_9Fe_2Si_2$ (in form of sharp needles).

Magnesium. The aluminum-magnesium system (Fig. 21) is the basis for the wrought 5*xxx* and cast 5*xx.x* non-heat-treatable aluminum alloys, which provide excellent combinations of strength and corrosion resistance by solid-solution strengthening and work hardening. The aluminum-magnesium phase diagram has a positively sloping solvus, which is a necessary condition for a precipitation-hardening system such as aluminum-copper. However, the difficulty in nucleating the fcc Al_3Mg_2 precipitates in the aluminum-magnesium system has precluded commercialization of heat treatable aluminum-magnesium alloys, unless they contain enough silicon, copper, or zinc to form Mg_2Si, Al_2CuMg or $Al_2Mg_3Zn_3$ precipitates. Binary aluminum-magnesium alloys are widely used in applications requiring a bright surface finish and corrosion resistance, as well as attractive combinations of strength and ductility. Common compositions range from 4 to 10% Mg, and compositions containing more than 7% Mg are heat treatable. Instability and room-temperature aging characteristics at higher magnesium concentrations encourage heat treatment.

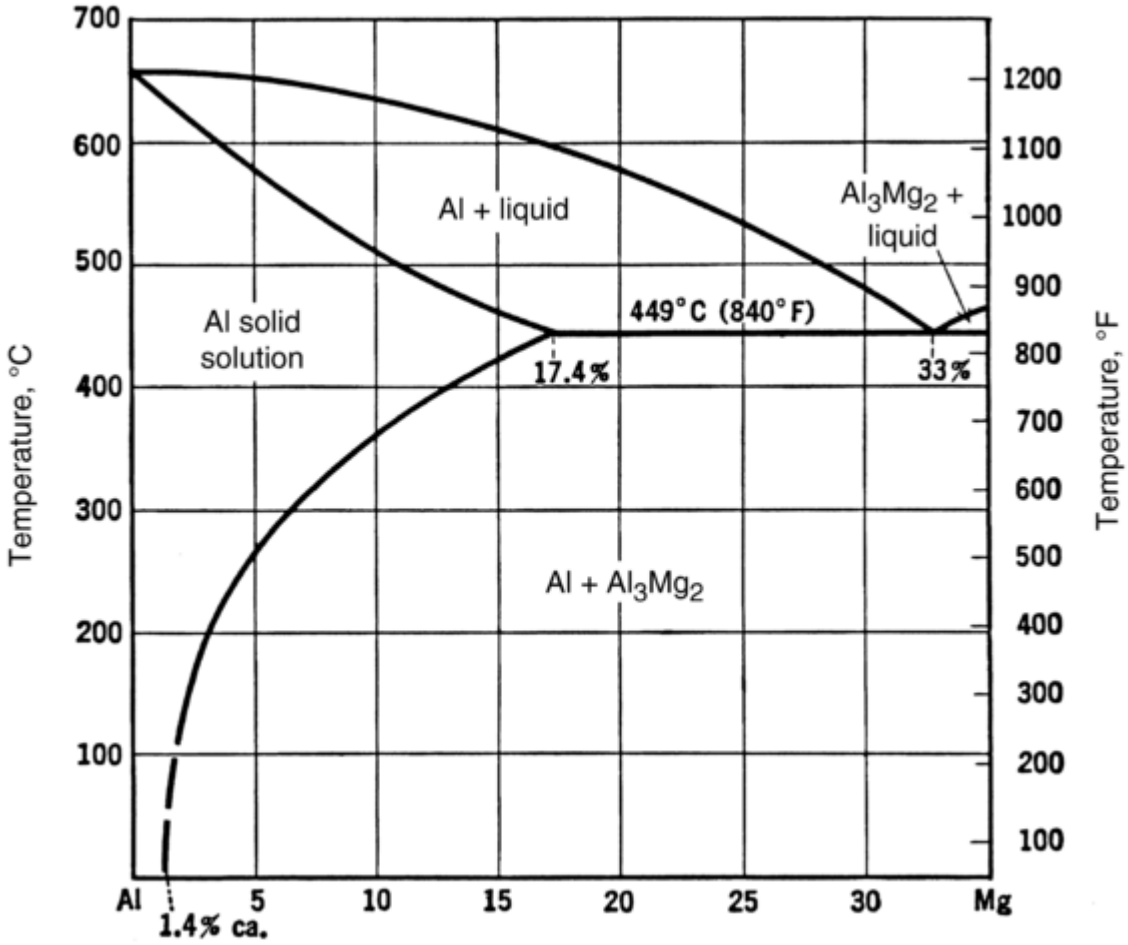

Fig. 21 Aluminum end of the the aluminum-magnesium phase diagram. Adapted from Ref 18 and 20

Alloys in the 6*xxx* series contain silicon and magnesium in the approximate proportions required for formation of magnesium silicide (Mg_2Si), thus making them heat treatable. Although not as strong as most 2*xxx* and 7*xxx* alloys, 6*xxx*-series alloys have good formability, weldability, machinability, and corrosion resistance, with medium strength. Magnesium also is the basis for strength and hardness development in heat treated aluminum-silicon alloys and is commonly used for the same purpose in more complex aluminum-silicon alloys containing copper, nickel, and other elements. The hardening phase of Mg_2Si displays a useful solubility limit corresponding to approximately 0.70% Mg, beyond which either no further strengthening occurs or matrix softening takes place. Common premium-strength casting compositions in the aluminum-silicon family employ magnesium in the range of 0.40 to 0.070%.

Copper. The aluminum-copper system is the basis for the wrought 2*xxx* and cast 2*xx.x* alloys, and many other heat treatable alloys contain copper. Alloys containing 4 to 6% Cu respond most strongly to thermal treatment. Heat treatable aluminum-copper alloys can reach quite high strengths with good ductility, especially if prepared from ingot containing less than 0.15% Fe. In commercial aluminum-copper alloys, some of the copper chemically combines with aluminum and iron to form either tetragonal Al_7Cu_2Fe or orthorhombic α(Al,Cu,Fe) constituent particles during solidification. These constituents cannot be dissolved during subsequent thermal treatments, but one can transform to the other during thermal treatments of ingots or castings. During heat treatment of aluminum-copper alloys containing little magnesium, Al_2Cu precipitates as the strengthening phase.

Adding magnesium to aluminum-rich aluminum-copper alloys results in the formation of the Al_2CuMg phase by eutectic decomposition. Metastable precursors to face-centered orthorhombic Al_2CuMg precipitates are used to strengthen several structural alloys used in the aerospace industry, because they confer a desirable combination of strength, fracture toughness, and resistance to the growth of fatigue cracks.

Al-Cu-Si Casting Alloys. Aluminum-copper alloys with somewhat higher copper contents (7 to 8%), formerly the most commonly used aluminum casting alloys, have steadily been replaced by Al-Si-Cu/Mg (3*xx.x*) alloys. Aluminum-copper-silicon alloys are the most widely used aluminum casting alloys. The amounts of both additions vary widely, so that the copper predominates in some alloys and the silicon in others. In these alloys, the copper contributes to strength, and the silicon improves castability and reduces hot shortness. Aluminum-copper-silicon alloys with more than 3 to 4% Cu are heat treatable, but usually heat treatment is used only with those alloys that also contain magnesium, which enhances their response to heat treatment.

Zinc. This element confers little solid-solution strengthening or work hardening to aluminum. No significant technical benefits are obtained by the addition of just zinc to aluminum, but the addition of copper and/or magnesium with zinc results in attractive compositions for heat treating or natural aging. Usually, other elements, such as chromium, are also added in small quantities.

The Al-Zn-Mg precipitates provide the basis for the 7*xxx* wrought alloys and the 7*xx.x* cast alloys. Two phases can form by eutectic decomposition in commercial Al-Zn-Mg alloys: hexagonal $MgZn_2$ and body-centered cubic $Al_2Mg_3Zn_3$. Depending on the zinc/magnesium ratio, copper-free alloys are strengthened by metastable precursors to either $MgZn_2$ or $Al_2Mg_3Zn_3$. In Al-Zn-Mg-Cu alloys, copper and aluminum substitute for zinc in $MgZn_2$ to form $Mg(Zn,Cu,Al)_2$. Particles of Al_2CuMg can also form in these alloys by eutectic decomposition and solid-state precipitation. Figure 22 shows solid solubilities of various phases in the aluminum corner.

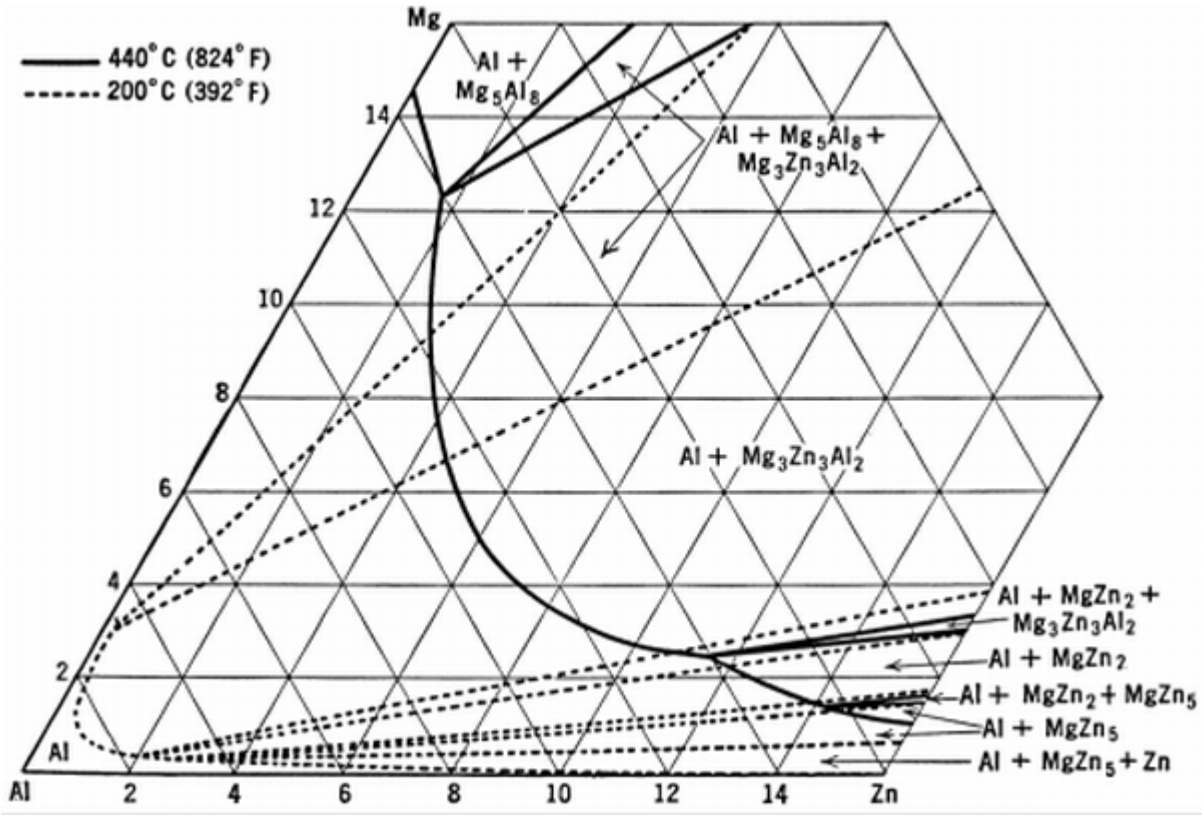

Fig. 22 Aluminum corner of the Al-Mg-Zn system showing solid solubilities of various phases. Source: Ref 20

The high-temperature solution heat treatment and drastic quenching required by other alloys (Al-Cu and Al-Si-Mg alloys, for example) are not necessary for optimal properties in most Al-Zn-Mg alloy castings. However, microsegregation of magnesium-zinc phases can occur in these alloys, which reverses the accepted rule that faster solidification results in higher as-cast properties. When it is found in an Al-Zn-Mg alloy casting that the strength of the thin or highly chilled sections are lower than the thick or slowly cooled sections, the weaker sections can be strengthened to the required level by solution heat treatment and quenching, followed by natural or artificial (furnace) aging.

Chromium. In commercial alloys, the solubility can be reduced to such an extent that Al_7Cr primary particles can form by a peritectic reaction at chromium contents lower than that indicated by the binary aluminum-chromium phase diagram. Because coarse primary particles are harmful to ductility, fatigue, and fracture toughness, the upper limits of chromium depend on the amount and nature of the other alloying and impurity elements. In 5*xxx* alloys, fcc cubic $Al_{18}Mg_3Cr_2$ dispersoids precipitate during ingot preheating. In 7*xxx* alloys, the composition of the dispersoids is closer to $Al_{12}Mg_2Cr$. Chromium dispersoids contribute to strength in non-heat-treatable alloys and control grain size and degree of recrystallization in heat treatable alloy products.

Zirconium also forms a peritectic with aluminum. The phase diagram predicts that the equilibrium Al_3Zr phase is tetragonal, but fine dispersoids of metastable cubic Al_3Zr form during ingot preheating treatments. Most 7*xxx* and some 6*xxx* and 5*xxx* alloys developed since the 1960s contain small amounts of zirconium, usually less than 0.15%, to form Al_3Zr dispersoids for recrystallization control.

Lithium. This element reduces the density and increases the modulus of aluminum alloys. In binary alloys, it forms metastable Al_3Li precipitates and combines with aluminum and copper in Al-Cu-Li alloys to form a large number of Al-Cu-Li phases. Because of its high cost relative to other alloying elements, lithium alloys have been found to be cost-effective thus far only in space and military applications.

Tin. Aluminum-tin alloys that contain approximately 6% Sn (and small amounts of copper and nickel for strengthening) are used for cast bearings because of the excellent lubricity imparted by tin. These tin-containing alloys were developed for bearing applications.

References cited in this section

1. J.E. Hatch, *Aluminum: Properties and Physical Metallurgy,* American Society for Metals, 1984

2. J.R. Davis, Ed., *Aluminum and Aluminum Alloys,* ASM Specialty Handbook, ASM International, 1993

3. L.F. Mondolfo, *Aluminum Alloys: Structure and Properties,* Butterworths, 1976

4. J.E. Hatch, *Aluminum—Properties and Physical Metallurgy*, American Society for Metals, 1984, p 30–31

5. E. di Russo, *The Atlas of Microstructures of Aluminum Casting Alloys,* Edimet, Brescia, 1993

6. *Struers—The Best of Structure 1–12,* Copenhagen, 1988, p 101–104

7. *Metallography and Microstructures,* Vol 9, *Metals Handbook,* 9th ed., American Society for Metals, 1985, p 351–388

8. M. Orman, *Metalografia Aluminium (Metallography of Aluminum),* Wyd. Śląsk, Katowice, 1957

9. G. Petzow, *Metallographic Etching,* 2nd ed., ASM International, 1999

10. "Standard Methods for Microetching Metals and Alloys," E 407–70, American National Standard Institute/ASTM, reapproved 1976

11. E. Beraha and B. Shpigler, *Color Metallography,* American Society for Metals, 1977

12. E. Beraha, Metallographic Reagents Based on Molybdate Solutions, *Prakt. Metallogr.,* Vol 11 (No. 5), 1974, p 271–275

13. R. Poganitsch, R. Sigl, and F. Jeglitsch, Sequential Etching for the Identification of Phases in Technical AlZnMgCu Alloys, *Prakt. Metallogr.,* Vol 21 (No. 5), 1984, p 258–268

14. E. Weck and E. Leistner, *Metallographic Instructions for Colour Etching by Immersion, Part III,* Deutscher Verlag fur Schweisstechnik-GmbH, Dusseldorf, 1986

15. M. Richard, Reactif Micrographic pour Colorer le Silicium Dans les Alliages d'Al (Metallographic Reagent for Coloration of the Silicon Precipitates in Aluminum Alloys), *Fonderie,* Vol 28 (No. 326), 1973, p 289–290

16. P. Lienard and C. Pacque, New Metallographic Etching Method for Aluminium Alloys Used in Foundries, *Struers—The best of structure 1–12,* Copenhagen, 1988, p 101–104

17. G. Vander Voort, Ed., *Applied Metallography,* Van Vostrand R., 1986

18. U.R. Kattner, Al-Fe (Aluminum-Iron), *Binary Alloy Phase Diagrams,* 2nd ed., T.B. Massalski, Ed., ASM International, 1990, p 149

19. G. Ghosh, Aluminum-Iron-Silicon, *Ternary Alloys: A Comprehensive Compendium of Evaluated Constitutional Data and Phase Diagrams,* Vol 5, G. Petzow and G. Effenberg, Ed., VCH (Germany), 1992, p 394–438

20. L.F. Mondolfo, *Metallography of Aluminum Alloys,* John Wiley & Sons, 1943, p 29, 106

21. *Metallography, Structures, and Phase Diagrams,* Vol 8, *Metals Handbook,* 8th ed., American Society for Metals, 1973, p 397

22. H. Okamoto, *Phase Diagrams of Dilute Binary Alloys,* ASM International, 2002, p 23

M. Warmuzek, Metallographic Techniques for Aluminum and Its Alloys, *Metallography and Microstructures,* Vol 9, *ASM Handbook,* ASM International, 2004, p. 711–751

Metallographic Techniques for Aluminum and Its Alloys

Małgorzata Warmuzek, Foundry Research Institute, Kraków, Poland

Examination of Macrostructure (Ref 1, 8, 9, 23, 24, 25)

Examination of macrostructure is done at low magnification of approximately 10× or less. Macroscopic examination is usually a preliminary procedure prior to microstructural examination. In addition, macroscopic examination is often used in the inspection and quality control of finished or semi-finished products such as castings, wrought forms, and welds. In wrought forms, macroscopic examination can help identify, for example, discontinuities (such as cracks), inhomogeneous features (such as deformation anisotropy, inclusions distribution), and grain-flow patterns. Macroscopic examination can also reveal various features in castings, such as:

- Casting discontinuities, such as shrinkage, gas pores, and freezing cracks
- Grain size and its morphology and distribution, dendrite morphology and dispersion degree, and results of the cooling-rate changes on the primary cast part structure morphology
- Chemical or structural heterogeneity of cast material
- Segregation of the contaminants and inclusions during alloy solidification

Macrostructure can be examined from a part surface, a fracture surface, or a prepared macrosection. Examination of a part surface can reveal the presence of some defects (scratches, bubbles, inclusions, cracks, and deposit extruded section). In all cases, the results of a macroexamination can be influenced by the conditions of observation and especially by the strength and orientation of the illumination relative to the specimen surface and the observer. Specimen rotation relative to the lighting source is very often used to reveal the true macrostructure image and to obtain satisfactory results. However, the light reflection from some planes of the examined surfaces can sometimes be incorrectly interpreted. Thus, macroscopic observation (and photography for purposes of documentation) demands some skill.

Of course, macroscopic observation of fracture surfaces is also an important and useful step in failure analysis. Several kinds of surface markings or topological features may help identify the crack origin and the mechanism of crack propagation. Other features that may be visible on a fracture surface include:

- Different kinds of inclusions
- Porosity, shrinkage, and other discontinuities
- Grain size heterogeneity
- Zones of solidification
- Overheating (eutectic melting)
- Oxide stringers
- Bright and dark flakes

Visual or low-magnification examination of a fracture surface does not involve special preparation other than cleaning and degreasing the sample. However, care of evidence is a critical factor in failure analysis investigations, and the method demands skill from the investigator, because the objective criteria of the result interpretation are not established or not repeatable in many cases. Lightening is also important, especially when

in the photography of fracture surfaces (e.g., see the article “Photography in Failure Analysis” in *Failure Analysis and Prevention,* Volume 11 of *ASM Handbook,* 2002).

Preparation and Examination of Macrosections (Ref 1, 2, 8, 9, 25). Preparation procedures (cutting and machining) of aluminium-alloy macrosections should be carried out with regard to the same general rules for preparation of specimens for microstructural examination. The relatively soft matrix makes the specimen very susceptible to superficial deformation. In such case, the grain and dendrite morphology can be distorted. Discontinuities such as shrinkage, gas porosity, and cracks also can be smoothed or deformed, thus making it impossible to reveal these defects by dye penetrants or other aids. A machined surface of the specimen can be acceptable for macroscopic etching. Nevertheless, the tools used for cutting and machining should be sharp with a suitable choice of feed and adjustment to a favorable cutting speed. A shaper or milling machine is preferred for securing the constant cutting speed.

The preliminary preparation of the specimen surface is important. Smoother specimen surfaces without deformation allow better examination of details and good repeatability of results after macroetching. The risk of loss of the some structure details during intensive and/or prolonged macroetching (to remove the initial surface roughness) can be avoided by good preliminary preparation. Degreasing or special precleaning of the specimen surface is not necessary but can be helpful for obtaining uniform and clear results of revealing the macrostructure. The best degreaser is a caustic reagent (Table 6). Its use is recommended before porosity observation on macrosections. In case of unclear results, the surface can be slightly rubbed with a pencil eraser to improve the contrast. A light pre-etching with a caustic reagent before the dye penetrant application removes some sealing of the porosity by smeared metal. The etching of the macrosections reveals the details of the structure, enabling an observation and description of its features (Table 7).

Table 6 Reagents for chemical macroetching

No. of reagent	Chemical composition [(a)]	Etching mode	Purpose or application	Ref
1M caustic etchant	100 mL distilled H_2O 10–20 g NaOH 90 mL distilled H_2O 10 g NaOH	5–15 min 60–70 °C (140–160 °F) 5–15 min 60–70 °C (140–160 °F) Rinse in water, then clean by fast dip in 50% HNO_3	Commercial Al and Al alloys	Ref 9 Ref 7
2M	75 mL HCl, (38%) 25 mL HNO_3, (70%) 5 mL HF, (40%) (+25 mL distilled H_2O)	Seconds to minutes Use freshly prepared reagent; rinse specimen with warm water	Cast Al-Si alloys, Al-Cu, Al-Mn, Al-Mg, Al-Ti	Ref 9
3M Flick's reagent	90 mL distilled H_2O 15 mL HCl 10 mL HF, (40%)	5 s–3 min	Pure Al, wrought parts	Ref 9

4M Keller's reagent	20(50) mL distilled H_2O 20(25) mL HNO_3, (70%) 20(15) mL HCl, (38%) 5(10) mL HF, 40%	1–3 min	All kinds of Al alloys; reveals grain size, rolling direction, welding zone	Ref 9
5M Tucker's reagent	25 mL distilled H_2O 45 mL HCl, (38%) 15 mL HNO_3, (70%) 15 mL HF, 40%	Seconds to minutes Use freshly prepared reagent	Pure Al	Ref 9
	27 mL distilled H_2O (warm) 16 mL HNO_3, (70%) 42 mL HCl, (38%) 15 mL HF, (40%)	6 min	Higher HNO_3 concentration can improve contrast	Ref 8
	25 mL distilled H_2O 45 mL HCl, (38%) 15 mL HNO_3, (70%) 15 mL HF, (48%)	Freshly prepared before using. Etching time until desired result is observed; repeat every 10–15 s; rinse in warm water	…	Ref 7
6M	100 mL distilled H_2O 5.5 mL H_2SO_4, (98%)	Seconds to minutes	Superficial defects of pure Al	Ref 9
7M Dix-Keller's reagent	950 mL distilled H_2O 25 mL HNO_3, (70%)	5–20 s at ambient temp. Rinse with warm water, next with alcohol	Al-Zn-Mg-Cu. Grains are tinted depending on crystal orientation	Ref 8

	15 mL HCl, 1.19 (38%) 10 mL HF, 40%			
8M	9 g H_3PO_4 100 mL distilled H_2O	30 min at ambient temp.	Reveals intergranular corrosion and flow lines in Al-Mg alloys	Ref 8
9M Zeerleder's reagent	10 g $FeCl_3$ 100 mL distilled H_2O 0.5 mL HF, 40%	At ambient temperature, time according to observation	Pure Al	Ref 8
10M Poulton's reagent	12 mL HCl, (38%) 6 mL HNO_3, (70%) 1 mL HF, (48%) 1 mL H_2O	May be prepared and stored. Avoid both specimen and reagent heating during etching; rinse in cold water	All kinds of Al alloys	Ref 7
11M	1 mL HF, (48%) 9 mL distilled H_2O	Used on prepared surfaces. Time of immersion until expected effect is observed; rinse in hot water	All kinds of Al alloys	Ref 7
12M	50 mL HCl 15 mL HNO_3, (70%) 3 mL HF, (8%) 5 mL $FeCl_3$ (conc. solution)	Prepare fresh before using. 10–15 °C (50–60 °F). In cold water bath, time of immersion until expected effect is observed	All kinds of Al alloys	Ref 7
13M	60 mL HCl 40 mL HNO_3 (70%)	Prepare fresh before using. Immerse for a few seconds, repeat until expected effect is observed	All kinds of Al alloys	Ref 7
14M	20 g $CuCl_2$ 100 mL H_2O	Etching time a few seconds; repeat until expected result is observed, cleaning each time in cleaning mixture: 6 p. HNO_3 (70%) 1 p. HF Rinse in water between steps	All kinds of Al alloys	Ref 7

15M	10 mL HCl 30 mL HNO_3 (70%) 20 mL H_2O 5 g $FeCl_3$	Mix before use; add HCl last. At ambient temp., immerse a few seconds, rinse in cold water, repeat until desired effect is observed	All kinds of Al alloys	Ref 7

(a) Always add an acid into water.

Table 7 Applicability of the reagents for macroexaminations

Alloy	Reagent	Effect of etching	Ref
Pure Al	3M	Macrostructure	Ref 7, 8, 9
	5M (higher HNO_3 concentration can improve the contrast)		
	6M	Superficial defects	
	9M	Macrostructure	
	10M, 12M		
Commercial-purity Al	1M, 5M, 10M	Macrostructure	Ref 7, 9
Al-Cu	1M, 2M, 4M, 13M, 15M	Reveals grain size, rolling direction, welding zone	Ref 9
Al-Mn	1M, 2M, 4M, 5M, 10M, 16M	Macrostructure	Ref 9
Al-Si	2M (cast alloys)	Macrostructure	Ref 9
	4M, 5M, 10M, 11M, 14M		
Al-Mg	1M, 2M, 4M	Macrostructure	Ref 7, 8, 9
	8M	Reveals intergranular corrosion and flow lines	
	5M, 10M, 15M		
Al-Mg-Si	4M	Macrostructure	Ref 7, 8, 9
	7M	Reveals grains, depending on the crystal orientation	
	1M, 5M, 10M, 15M	Macrostructure	
Al-Cu-Mg-Zn	4M	Macrostructure	Ref 7, 9
	1M, 15M		
Al-Ti	2M	Macrostructure	Ref 9

The following effects of the macroetching procedure should be observed:

- Surface smoothing
- Structure defects revealed: cracks, porosity, superficial defects, intergranular corrosion
- Structure features revealed: macrosegregation, grain size, rolling direction, welding zone

Reagents used for macroetching are very concentrated and have a strong action. Special precautions that are recommended for handling and storage should be followed. Cooling ventilation (in case of the effects of an exothermic reaction with a sample or during the mixing of the components) is necessary because many of the components, as concentrated acid vapors, are volatile and can irritate the respiratory tract. Gloves, glasses, and

aprons should be the default equipment of the laboratory. Some reagents (e.g., HF) should be stored in special containers made of materials that are resistant to reaction with their contents.

References cited in this section

1. J.E. Hatch, *Aluminum: Properties and Physical Metallurgy,* American Society for Metals, 1984

2. J.R. Davis, Ed., *Aluminum and Aluminum Alloys,* ASM Specialty Handbook, ASM International, 1993

7. *Metallography and Microstructures,* Vol 9, *Metals Handbook,* 9th ed., American Society for Metals, 1985, p 351–388

8. M. Orman, *Metalografia Aluminium (Metallography of Aluminum),* Wyd. Śląsk, Katowice, 1957

9. G. Petzow, *Metallographic Etching,* 2nd ed., ASM International, 1999

23. W.J.M. McTegart, *The Electrollytic and Chemical Polishing of Metals,* Pergamon Press Ltd., England, 1959, Wyd. N.-T. Warszawa, 1961

24. *Fractography and Atlas of Fractographs,* Vol 9, *Metals Handbook,* 8th ed., American Society for Metals, 1974

25. I. Lukac and S. Michna, *Colour Contrast, Structure and Defects in Aluminium and Aluminium Alloys,* Cambridge International Science Publishing, Cambridge, 2001

M. Warmuzek, Metallographic Techniques for Aluminum and Its Alloys, *Metallography and Microstructures,* Vol 9, *ASM Handbook,* ASM International, 2004, p. 711–751

Metallographic Techniques for Aluminum and Its Alloys

Małgorzata Warmuzek, Foundry Research Institute, Kraków, Poland

---

Examination of Microstructure (Ref 1, 2, 3, 4, 5, 6, 8, 9, 10, 11, 12, 13, 14, 15, 16, 17, 23, 25, 26, 27, 28, 29, 30, 31, 32, 33, 34, 35, 36, 37, 38, 39, 40)

Microscopic examination is carried out on metallographic microsections with prepared surfaces. The process involves four basic steps:

1. Preparation of specimens with a flat and smooth surface
2. Intensification of contrast between phase or structure constituents
3. Microscopic observation
4. Description and interpretation of the observed microstructure

The first step is specimen preparation, which consists of several processes to obtain microsections with smooth, mirrorlike surfaces. This is followed by various techniques to enhance contrast between structure or phase constituents. The initial preparation involves cutting of specimens, mounting, and smoothing of the surface.

Specimen Cutting

The following properties of aluminum alloys should be taken into account at the specimen cutting stage:

- The softness and ductility of the aluminum solid-solution (α) matrix
- The presence of a hard and brittle microstructure component—as silicon in the cast alloys or as intermetallic phases in both cast and wrought alloys in either the rough or treated state (Table 2)
- The low temperature of the phase transformation in the solid state (Table 8) and the disperse precipitation during heating of the particle-hardened alloys

Table 8 Typical temperature range of the heat treatment used for aluminum alloys

Alloy	Temperature range			
	Solution annealing		**Aging**	
	°C	**°F**	**°C**	**°F**
Cast alloys				
2*xx.x* (Cu)	490–530	915–985	Room temp., 155–355	310–670
3*xx.x* (Si + Cu/Mg)	505–540	940–1005	Room temp., 155–260	310–500
4*xx.x* (Si)	540	1005	…	…
5*xx.x* (Mg)	400–430	750–805	…	…
7*xx.x* (Zn)	430–590	805–1095	Room temp., 120–205	250–400
8*xx.x* (Sn)	480	895	220	445
Wrought alloys				
2*xxx* (Cu)	495–530	925–985	160–205	320–400
3*xxx* (Mn)	…		…	…
4*xx.x* (Si)	…		…	…
5*xx.x* (Mg)	…		…	…
6*xx.x* (Mg + Si)	515–570	960–1060	160–205	320–400
7*xx.x* (Zn)	465–515	870–960	120	250

8*xx.x* (other elements)	530–540	985–1005	190		375

Source: Ref 2

During cutting of the specimen, deformation of the alloy matrix can be introduced, which is very important. For this reason, the cut plane should be situated as far as possible from the examined region. This assures that the deformed material is eliminated during the next stage of preparation.

The hard phase constituents need the higher load and longer cutting time that increase the risk of fracture or pullout of certain microstructure constituents and the embedding of its parts into the matrix, making a false image of the microstructure and creating additional problems during the next specimen preparation steps.

Dispersion-strengthened material is much harder than the pure aluminum matrix. A temperature comparable with the temperature of the structure process in the solid state (precipitation, solid-solution decomposition, recovery, and recrystallization) can be easily achieved during the cutting operation (Table 8). From this point of view, the most appropriate method of sample sectioning is abrasive wet cutting.

Another important problem is the choice of the zone in obtaining a representative material specimen of the manufactured part. In the case of morphological anisotropy of the microstructure (especially in the wrought alloys), the microsection plane should be oriented in relation to the rolling direction (parallel or perpendicular).

Mounting (Ref 1, 6)

Usually, the examined specimen is mounted in a thermoset plastic material (e.g., Bakelite, duracryl) hardened under temperature or chemical action. Specimens are mounted in resin to make the preparation easier or faster (in the case of using an automated grinding-polishing machine). Specimen mounting is also necessary for edge retention with samples of fracture profiles, coating layers, perpendicular cross sections of very thin samples (such as rolled sheet, foils, and wire ends), and materials with surface inhomogeneity. Mounting is also necessary when discontinuities involve material porosity or internal cracks. The mounting of the specimen also facilitates handling and allows for more consistent planeness between the opposite sides of the specimen. This is important when performing microhardness measurements.

Specimen cleaning (with organic solvents in an ultrasonic cleaner) is recommended before embedding into resin to guarantee a good adhesion of the resin to the specimen surface. The standard available materials for sample mounting can be divided into two groups:

- Hot-mounting resins
- Cold-mounting resins

Although hot-mounting resins are less expensive, a mounting press is required for their use. They cure at elevated temperature (even as high as 180 °C, or 355 °F), which could be inadvisable for aluminum alloys. However, some hot-mounting resins are conducting resins, which may be very useful when samples are intended for scanning elctron microscopy (SEM) examination and x-ray microanalysis. Nevertheless, for aluminum alloys, the cold-mounting resins should be recommended. Vacuum impregnation of the porous materials (porosity is a very frequent defect of cast parts) can be used to improve the filling of internal pores and for revealing their microprofile.

Specimen Smoothing (Ref 1, 6)

Specimens with a flat, mirrorlike surface on a microscopic scale are prepared by various grinding and polishing procedures. Mechanical abrasion is the most common method of smoothing and polishing the surface of a metallographic microsection so that the specimen is suitable for examination at high magnification with the small depth of field of a light microscope. When the polished microsection is properly prepared, the high-quality surface should be devoid of imperfections such as those shown in Fig. 23and 24. The objectives of a properly polished specimen are:

- No deformation from cutting
- No scratches from grinding or polishing
- No pullouts of the brittle structure constituents
- No introduction of foreign particles
- Retained, flat edges
- No thermal modification of the microstructure

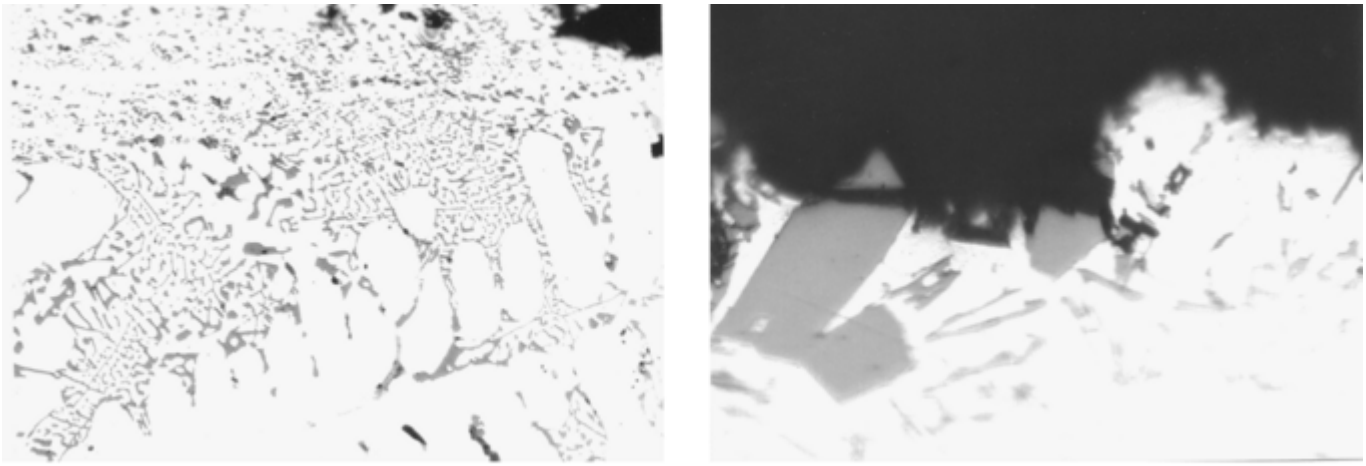

(a) (b)

Fig. 23 Defects of the metallographic microsection preparation from cutting and mounting. (a) Overheated and deformed material during specimen cutting 400×. (b) Badly retained fracture profile 500×

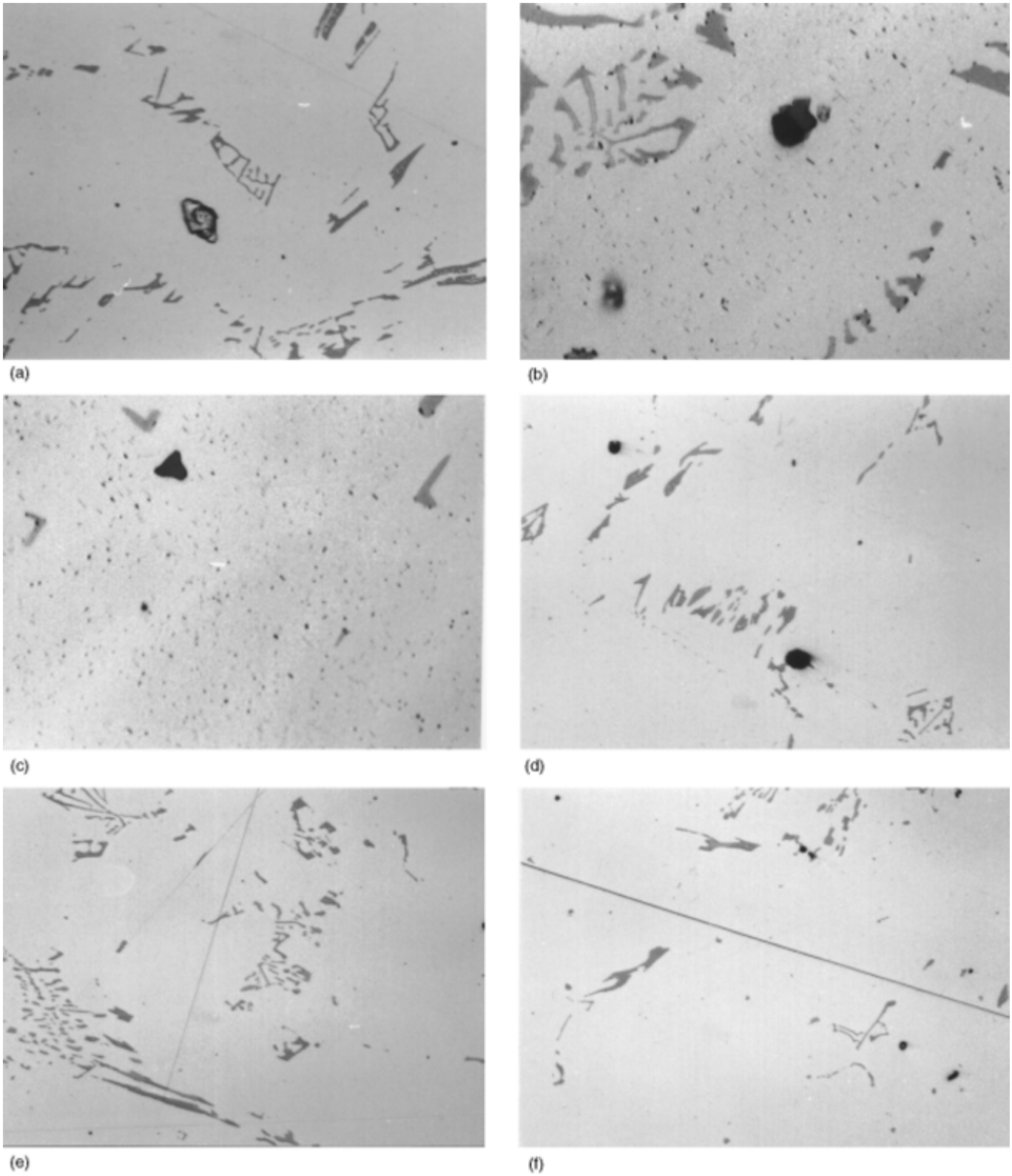

Fig. 24 Defects of the metallographic microsection preparation from grinding and polishing. (a) Pullouts of brittle particles 250×. (b) Embedding of SiC abrasive particles 400×. (c) Embedding of diamond abrasives 400×. (d) Effect of coma 250×. (e) Scratches from the previous step of polishing 250×. (f) Scratches because of a dirty disc 250×

Grinding (Ref 1, 6). The main aims of grinding are:

- To remove material deformed during cutting (rough, plane grinding)
- To remove the superficial layer of the specimen that covers the material destined for examination (rough, plane grinding)
- To prepare a flat surface while introducing only some residual or superficial deformation that can be eliminated during polishing (fine grinding)

For relatively soft materials such as aluminum alloys, the most useful abrasive for grinding is silicon carbide. Commercial papers with relatively coarse SiC abrasive particles are used for rough grinding. Abrasive papers with gradations of SiC particles are used in subsequent steps for fine grinding with reduced SiC particle size.
With a typical automated grinding-polishing machine, the grinding operation can be divided into two steps:

- Rough grinding (for planeness) with the commercial SiC wet grinding papers of decreasing grain size, starting from 120-grit paper, with water lubricant
- Fine grinding (to remove scratches from previous paper gradation) with commercial SiC wet grinding papers, starting from 500-grit paper, with water lubricant

The loading and time of process should be established individually, depending on the initial state of the samples. A typical procedure for the recommended fine grinding of aluminum alloys is shown in Table 9.

Table 9 Procedure for fine grinding

Step	Abrasive	Gradation	Lubricant	Rotational speed, rev/min	Force for specimen, N	Time, min
1	SiC	500	H_2O	200	50/30	1–5
2	SiC	1000	H_2O	200	40/15	1
3[(a)]	SiC	2400	H_2O	200	40/10	2.5

(a) Step 3 is optional to reduce the number of subsequent polishing steps or time.

Recently designed grinding-polishing machines also feature magnetic platens for quick substitution of steel-backed grinding papers. The use of magnetic discs and steel-backed paper/cloth reduces time in the removal and replacement of worn grinding paper. When automated grinding-polishing machines are used in smoothing mounted or unmounted specimens, holders are also needed to maintain planeness and the flat surface of the specimens. Various commercial holders are available, depending on the needs. Sometimes, the holders can be adjusted for the different mechanical preparation steps without removal from the machine and can be equipped with special clamps (for small-wire ends, plates, or untypical-shaped specimens).

Polishing (Ref 1, 6). The two most common methods for polishing metallographic microsections are by mechanical or electrochemical means. The main objective of polishing is to remove material deformation introduced by previous grinding and to obtain a flat, mirrorlike surface on a microscopic scale.

Mechanical Polishing. Table 10 lists a typical procedure recommended for the polishing of aluminum alloys. During successive steps of mechanical polishing, finer and finer abrasive particles are used. Two main groups of abrasive materials are usually used for polishing aluminum alloys:

- Diamond abrasive
- Oxide abrasive materials

Table 10 Procedure for mechanical polishing

Step	Cloth	Abrasive	Gradation, μm	Lubricant	Rotational speed, Rev/min	Force for specimen, N	Time, min
1	Napless	DP (spray or paste)	3	Alcohol based	150	40/20	1
2	With nap	DP (spray or paste)	1	Alcohol based	150	40/15	1.5

3a	With nap	DP (spray or paste)	$\frac{1}{4}$	Alcohol based	150	40–50/10	3
3b	With nap	Colloidal silica suspension	…	…	150	10	0.5

Note: DP, diamond abrasive

Diamond polishing is the fastest way to obtain a flat specimen surface without scratches and artifacts. Because of its very high hardness, diamond is able to cut almost all phase constituents of the aluminum alloys. The diamond materials for metallographic microsections are used in the form of polycrystalline sprays, suspensions, and paste. The optimal polishing results are achieved when the homogeneity of the grain size and the shape of the diamond particle are controlled. The following gradations of diamond abrasives are recommended: 3, 1, and 0.25 μm, successively.

Aluminum alloys characterized by a soft and ductile matrix can often require final polishing. Good results are obtained by using oxide-abrasive media. Colloidal dispersions of silica (SiO_2) particles with 0.04 μm particle size are used for final polishing to produce aluminum alloy microsections without any scratches, deformation, or surface artifacts. Because of its low alkalinity (pH 9.8), this polishing medium also can simultaneously act as an etchant, especially in the case of grain boundaries and some intermetallic phases present in aluminum alloys. The polishing is carried out by using special polishing cloths wet with lubricants. A water-free diamond suspension or spray with a carefully controlled narrow range of diamond particle grain size and shape is used to ensure a high level of reproducibility.

Electrolytic polishing can be a fast and clear way to reveal microstructural features without introducing any superficial deformation and changes in the material caused by local heating during mechanical treatment (Ref 1, 23, 25). Nevertheless, this procedure needs special reagents (Table 11) and equipment. A variable shape and size of the specimen is acceptable with this method. The main principle is that a specimen is an anode in an electrochemical cell, where the conditions of the process are adjusted to uniformly dissolve the superficial layer of the specimen material. This is very difficult to reach in the case of a polyphase material. The following are negative aspects of this method for aluminum alloys:

- The quality (flat and uniform) of the polished surface may be susceptibile to chemical and structural inhomogeneities of the alloy.
- Continuous and precise control of the current density or voltage conditions is needed, depending on the chemical composition and structural state of the alloy.
- Local electrochemical cell formation (interface dissolution) (e.g., Table 12) may cause the intermetallic inclusion to crumble away.

A material containing numerous nonmetallic inclusions (aluminum oxides) should be polished mechanically with special precaution.

Table 11 Reagents for electrolytic polishing and process conditions

No.	Electrolyte	Cathode	Current density, A/dcm^2	Voltage, V	Time of polishing	Circle	Temperature		Ref
							°C	**°F**	
1p	820 mL H_3PO_4 160 g CrO_3 135 mL H_2SO_4 100 mL distilled H_2O (for all Al alloys, except Si-Al)	Al	0.8–2.5	50–70 22–30	5–8 min	Potentiometer	<35	<95	Ref 8, 23

2p	400 mL H_3PO_4 380 mL ethanol 850 mL distilled H_2O	Al	35	…	4–6 min	Array	42–45	108–115	Ref 9, 23
3p	200 mL $HClO_4$ 800 mL ethanol	Stainless steel	100–400	110–220 35–70	10–25 s	Array	<35	<95	Ref 23
	200 mL $HClO_4$ 1000 mL ethanol	Graphite, Al	30	50–60 20	2 min	Potentiometer	<35	<95	
4p	50 mL $HClO_4$ 1000 mL CH_3COOH (glacial)	Al, stainless steel	50–55 25–30	10–15	10–25 s	Array	<35	<95	Ref 8, 9, 23
5p	62 mL $HClO_4$ (70%) 700 mL ethanol 10 mL 2-butoxyethanol 137 mL distilled H_2O	…	3.85 A/cm^2	…	20 s	…	Rinse in warm water, prevent overheating, use 10 s steps, cool specimen		Ref 7

Table 12 Electrochemical potential of aluminum and some intermetallic phases in 3% NaCl

Phase	Potential, mV
Al4N	-750
Mg_2Si	-1250
Al_3Mg_2	-930
$MgZn_2$	-790
Al_6Mn	-607
Al_2Cu	-370

Al_3Ni	-210
Al_3Fe	-140

Source: Ref 25

Chemical polishing reagents (Table 13) sometimes are used. Chemical polishing is rather rare, because continual improvements have made mechanical polishing more effective and easier. Mechanical methods are also less toxic.

Table 13 Reagents for chemical polishing

No.	Chemical composition	Time of polishing	Temperature		Remarks, Ref
			°C	°F	
1ch	80 mL H_3PO_4 35 mL HNO_3 160 mL distilled H_2O	1–5 min, depending on flatness of surface	80	175	Al and Al alloys, Ref 23
2ch	700 mL H_3PO_4 30 mL HNO_3 120 mL CH_3COOH (glacial) 160 mL distilled H_2O	2–6 min	100–120	210–250	Al alloys, Ref 23
3ch	100–170 mL HNO_3 100–200 g NH_4HF 0.08–0.8 g $PbSO_4$ 1000 mL distilled H_2O	15–30 s	50–80	120–175	Pure Al, 9, Ref 23
	10–20 mL HNO_3 10–20 mL saturated water solution of NH_4HF 0.08–0.8 g $PbSO_4$ 65–80 mL distilled H_2O	5–30 s	50–60	120–140	
4ch	1 p. HNO_3 1 p. ethanol 1% or less H_2O_2 (optimum depends	10–30 min After finish, mechanical grinding on paper of gradation 600	0	32	Al alloys, Ref 7

	on alloy polished)	Mechanical stirring			
5ch	25 mL H_2SO_4 70 mL H_3PO_4 5 mL HNO_3 160 mL distilled H_2O	30 s–2 min	85	185	Al alloys, Ref 9

Contrast Enhancement of Phases (Ref 1, 5, 6, 8, 9, 10, 11, 12, 13, 14, 15, 16, 17, 23, 25, 26)

Most of the phase constituents are visible after the fine-polishing step, but very often, the visible contrast under a microscope is too light either to identify the phases or to measure their stereological parameters. Two main techniques for improving contrast to reveal constituents in light microscopy are:

- Special illumination of the microsection during microscopic observation
- Chemical, physical, and electrochemical treatments of the metallographic microsection

Contrast enhancement is also achieved in scanning electron microscopy by detection of secondary electrons (typical topographic contrast of a SEM) or by detection of back-scattered electrons (composition and topographic contrast).

Illumination with a Light Microscope. Illumination of the specimen with a light microscope can be done with:

- Polarized light
- Phase contrast, Nomarski contrast
- Bright or dark field

These methods enhance contrast and improve microscopic observation of phases, as shown in the examples in Fig. 25 and 26. Most metallographic light microscopes are equipped with a cross-poles mode of observation, where two Nicol prisms are used as polarizer and analyzer. Their mutual rotation allows the choice of the optimal position to reveal some phase constituents or differentiate the contrast between some microregions, such as the grains or dendrites of an anisotropic material.

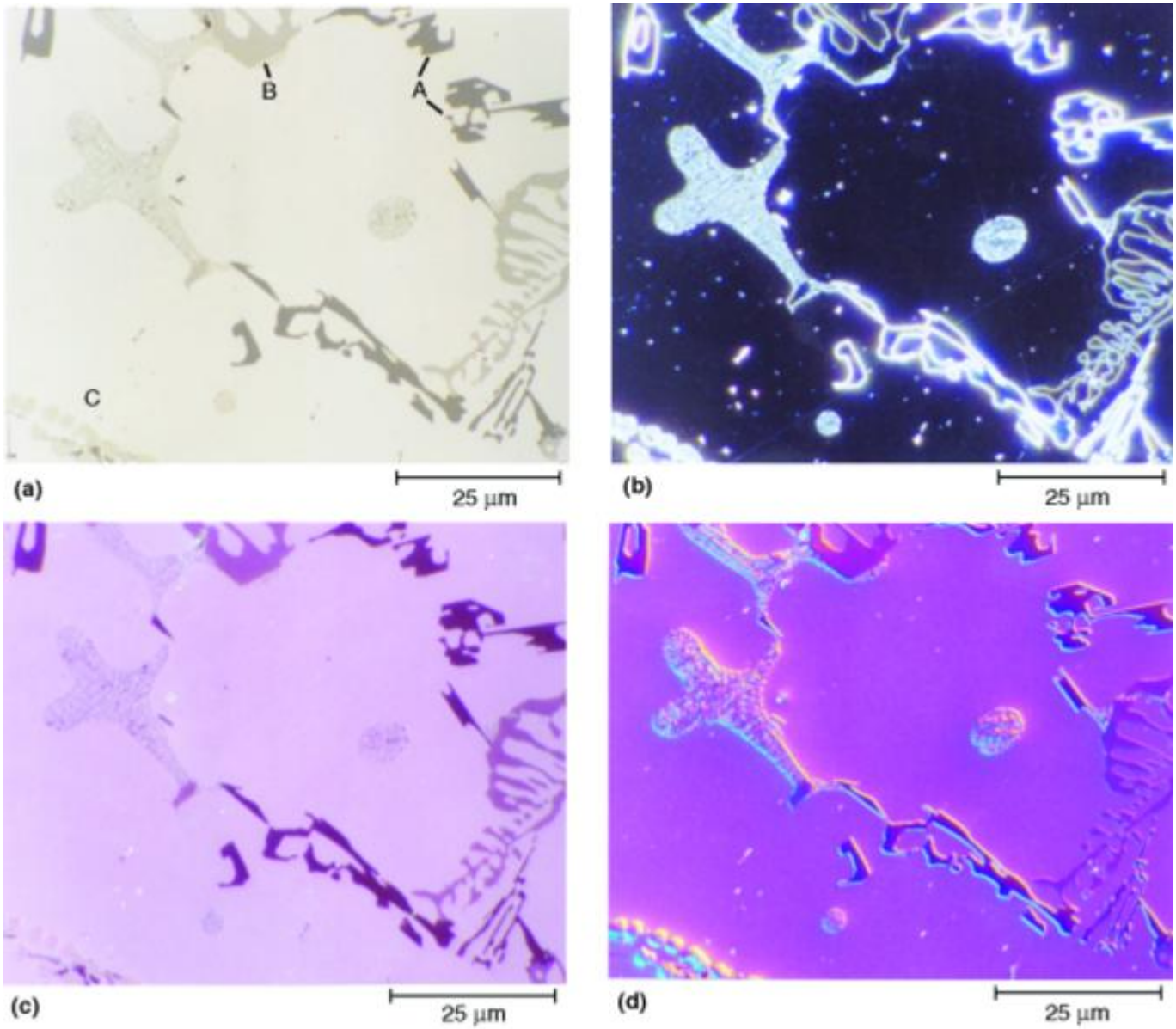

Fig. 25 Lighting effects to enhance contrast between phase constituents in an unetched specimen of Al-Si-Cu-Ni alloy. (a) Bright-field illumination with silicon (A, dark gray), α-Al(FeMn)Si (B, light gray), and Al_2Cu (C, beige). (b) Dark-field illumination with phase boundaries revealed. (c) Cross-pole mode of observation with silicon (dark violet), α-Al(FeMn)Si (light violet), and Al_2Cu (light pink). (d) Phase contrast with silicon (dark violet), α-Al(FeMn)Si (dark pink), and Al_2Cu (pink-yellow with blue contrast on the interfaces). All at 1000×.

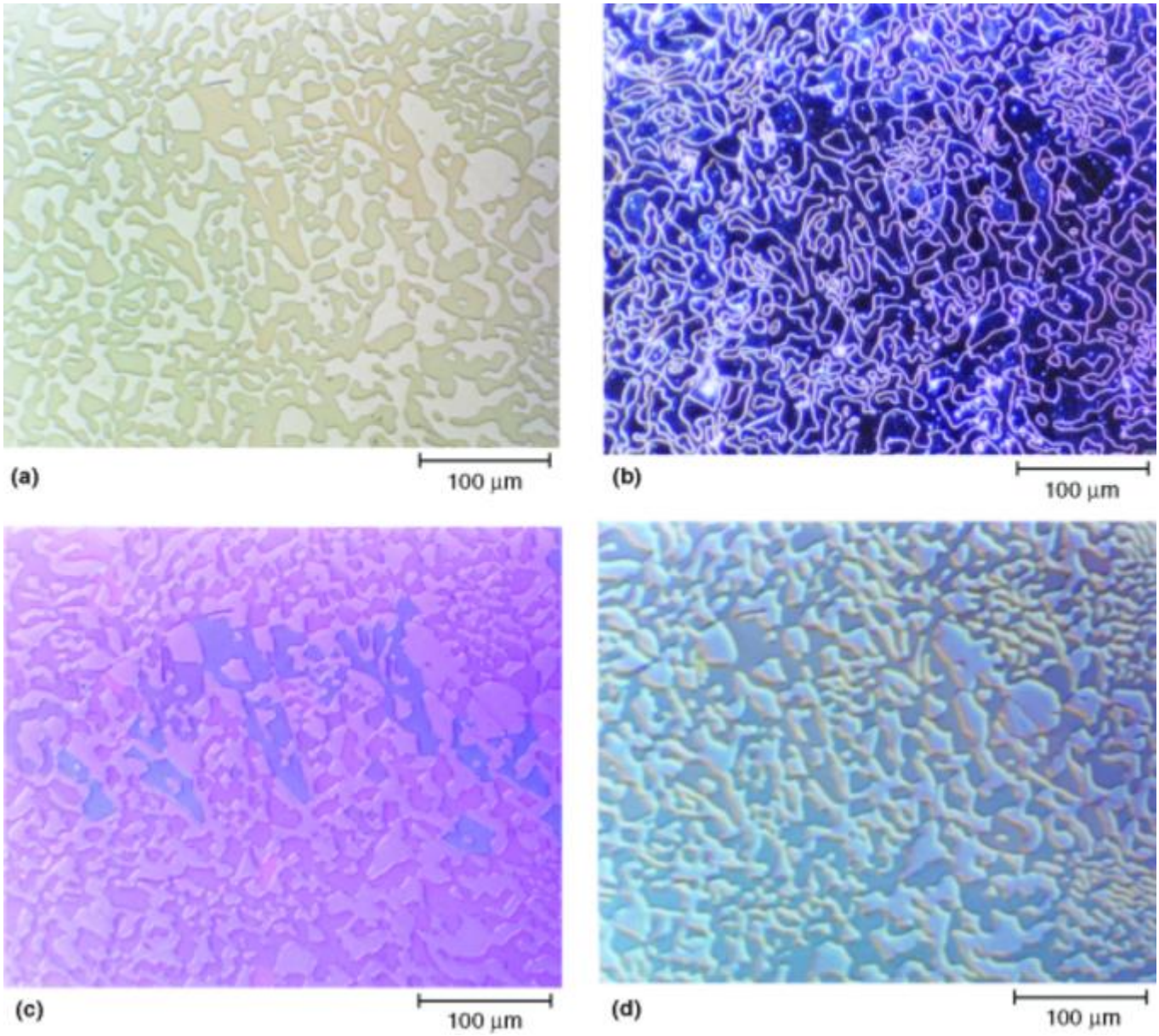

Fig. 26 Lighting effects to reveal contrast of crystal orientation in an etched aluminum-copper specimen. (a) Bright-field illumination with α-Al (light gray) and Al_2Cu (gray). (b) Dark-field illumination with phase boundaries revealed. (c) Cross-pole mode of observation revealing Al_2Cu crystal orientation in color image. (d) Phase contrast in color image. All etched with 0.5% HF. All at 200×.

Chemical and Physical Treatments of the Metallographic Microsection. Contrast between phases or microstructural constituents of a polished microsection can be improved by additional surface treatments. This includes chemical or electrochemical etching and physical surface treatments that deposit an interference layer on the specimen.

Chemical and Electrochemical Etching. Electrochemical and chemical reagents for etching aluminum alloys are shown in Table 14 and 15, respectively. The three main objectives of etching are:

- Attack and reveal the grain boundaries and the interface regions between the matrix and phase constituents
- Cover selected phase constituent surface with a thin film of chemical reaction products that improve or reveal contrast between different structure components (visible in black-and-white mode)
- Cover selected phase areas with a thin film of chemical reaction products that die/color the phase in a specific manner to allow phase identification (visible in a color mode)

Table 14 Reagents for electrolytic microetching

No.	Electrolyte	Cathode	Current density, A/dcm^2	Voltage, V	Time of etching	Remarks, Ref
1me	4–5 mL HBF_4 200 mL H_2O (Barker's reagent)	Al, stainless steel, lead	Anodize: 0.2 A/cm^2 Etch:	20 V/dc 20–40 V/dc	40–80 s Al-4N: 1–2 min Al-Mn1: 1–1.5 min Al-Mg-Si0.5: 1.5–2.0 min Al-Cu-Zn-Mg: 2–2.5 min Al-Mg: 2.5–3.0 min Al-Mg-Si: 3–3.5 min	Check results on microscope with cross poles; reveals grain structure or general structure in most series of wrought alloys Ref 7, 9, 10
2me	10 mL H_3PO_4 90 mL distilled H_2O	Stainless steel	…	1–8 V/dc	5–10 s	Reveals grain structure or general structure in most series of wrought alloys Ref 7, 9, 10

Table 15 Applicability of the reagents for chemical microetching, commonly recommended

Alloy group	Grain boundaries, interfaces, size and shape of phase constituents	Microsegregation of alloy components	Phase constituent identification	Deformation effects	Recrystallization effects	Heat treatment effects
1*xxx* (wrought)	5m, 7mB	…	…	…	…	…
2*xxx* (wrought)	4m, 5m, 7mA, B, 22m, 24m	7mA, B, 22m	1m, 2m, 10m	7m, 22m	7m, 22m, 24m	1m
3*xxx* (wrought)	5m, 7mB	14m	1m, 2m, 10m	…	…	…

4*xxx* (wrought)	5m, 7mA, B	…	…	…	…	…
5*xxx* (wrought)	1m, 4m, 5m, 7mA, B, 9m, 10m	14m	…	10mB > 3% Mg	…	…
6*xxx* (wrought)	1m, 4m, 5m, 7mB, 10m	…	1m, 2m, 4m, 5m, 10m	…	19m, 24m	7m, 22m
7*xxx* (wrought)	4m, 5m, 7m	…	1m, 2m, 5m, 7mA, 20m	7m, 22m	10mB, 23m, 24m	7mB
Cast alloys	7mA, B, 9m, 15mB, 11m, 12m, 22m, 24m	13m, 14m (Al-Mg)	1m (Al-Cu), 2m, 3m, 4m, 5m, 6m, 7mA (Al-Si), 9m, 10mB (Al-Cu, Al-Mg, Al-Mg-Si), 15m, 16m, 17m, 18m, 19m, 20m	…	…	…

Source: Ref 5, 7, 8, 9, 10, 11, 12, 13, 14, 15, 16, 17, 23, 26

The micrographs in Fig. 27 and 28 are examples of etching effects to reveal grain boundaries and phase boundaries, respectively. Etchant effect in revealing phase constituents is shown in Fig. 29. Both chemical and electrolytic etching achieve best results when freshly polished specimens are etched, because aluminum and its alloys tend to be covered with passivating oxide film. If necessary, the specimen surface should be degreased before etching. Sometimes, successive polishing and etching are repeated for best results.

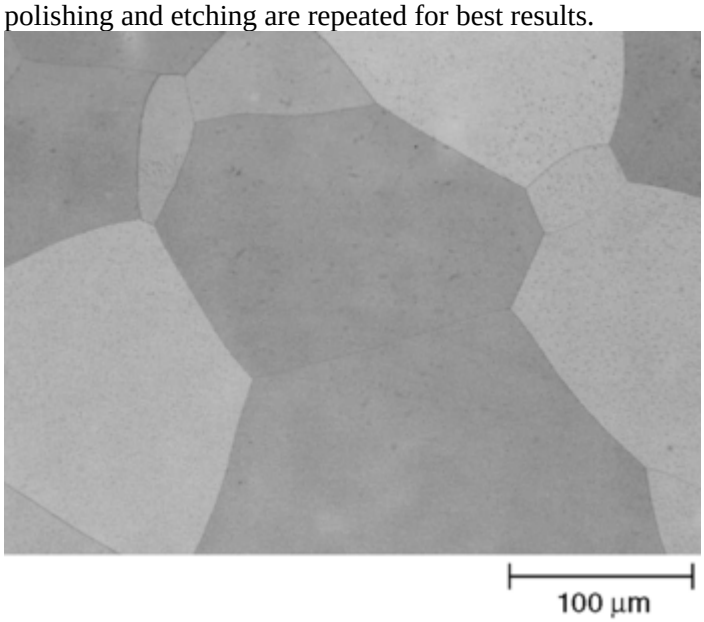

Fig. 27 Effect of etching in revealing grain boundaries of solution annealed (552 °C, or 1025 °F, for 1 h, water quenched) Al-4%Cu alloy. Keller's reagent (7m in Table 4). 200×

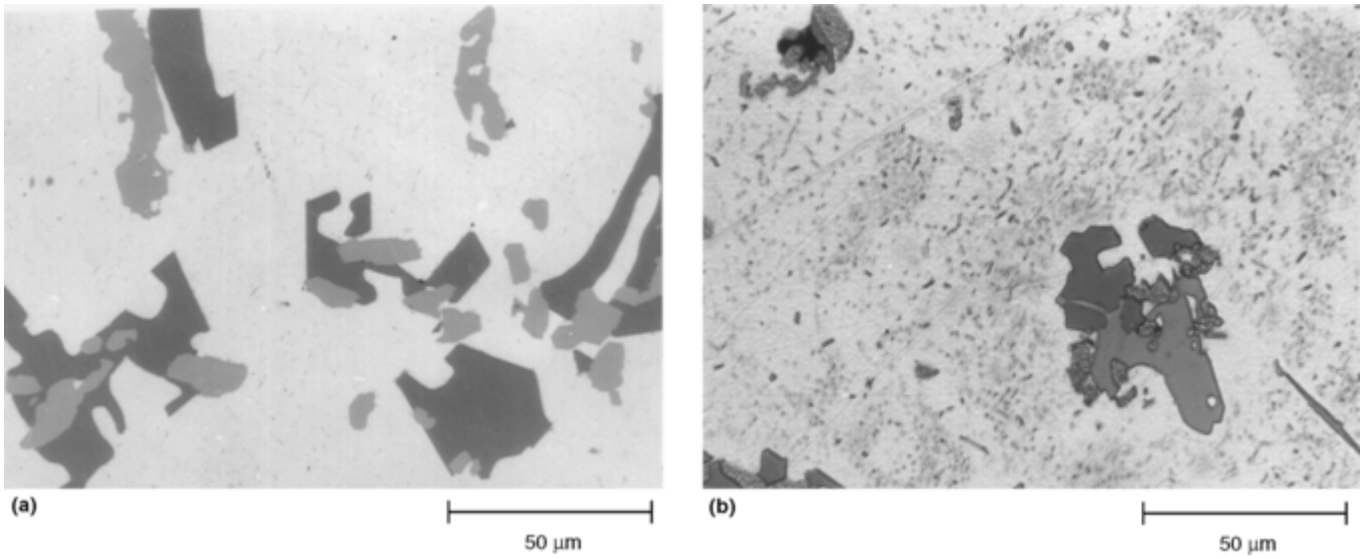

Fig. 28 Effect of etching in revealing phase boundaries of an Al-Si-Zn-Cu alloy at 500×. (a) Unetched. (b) Etched with 5m + 15m (solution B) reagents (Table 4)

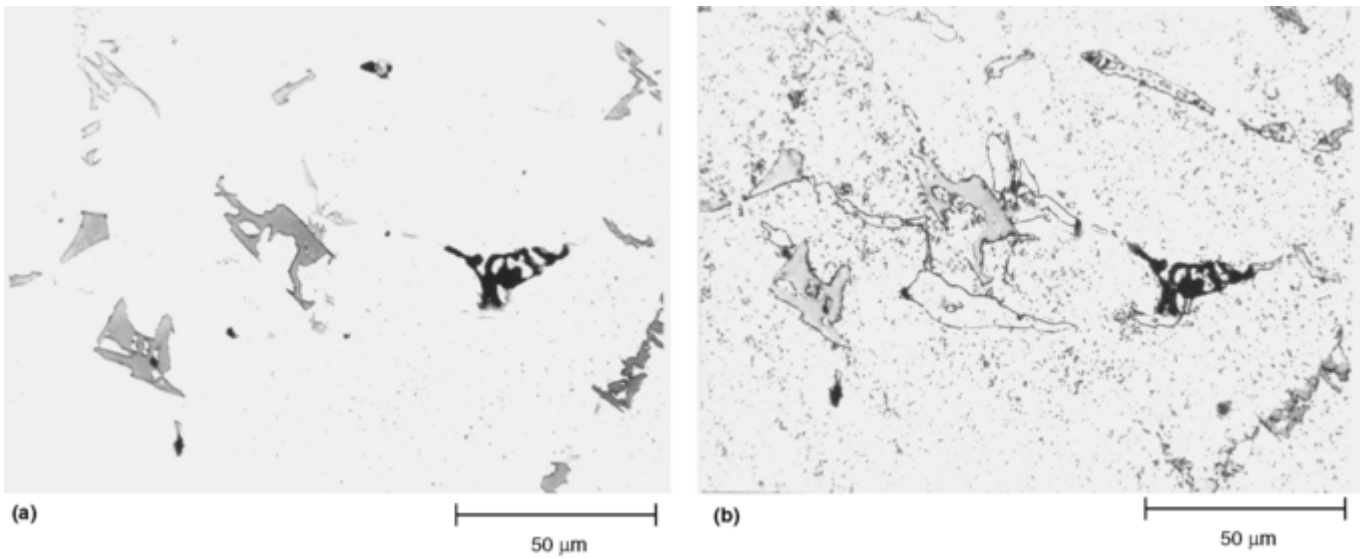

Fig. 29 Effect of etching in revealing phase constituents of alloy 390 etched with reagent 5m (Table 4). (a) Etched for 1 s. (b) Etched for 10 s. Both at 500×

Applications of the various chemical etchants are listed in Table 15. Electrolytic etching, which is often called an anodic oxidation (because the specimen is an anode), is especially useful for deformed and recrystallized wrought alloy as well. During etching, the grain boundaries are attacked and the grains covered with the oxide layer. The specimen observed in polarized light reveals the grain structure and their crystallographic orientation; that is, the grains of the different crystal orientation have the different color.

Physical Deposition of Interference Layer (Ref 16, 25). Microstructural phases can be revealed by covering the specimen surface with the interference layer formed during vacuum deposition of the evaporated (sublimated) or sputtered medium. The resultant color contrast is very dependent on the interference layer thickness. A very thin layer absorbs all the wavelengths and gives a gray contrast. If a thicker layer is applied, selective interference of one wavelength and the intensification of another causes the color contrast to appear. These methods can be used for phase identification only when strict control of the interference layer thickness is possible.

Observation and Description of Microstructure

Table 16 summarizes the observation characteristics for the three most common types of microscopes used in metallography. The choice of a microscopic technique depends on the required resolution, the methods of specimen preparation, and the microstructural constituents in terms of their chemical composition, morphology, and degree of dispersion. As noted, specimens should be examined immediately after preparation because of the very fast surface oxidation of aluminum alloys. This is especially important with SEM or x-ray microanalysis. In transmission electron

microscopy (TEM), specially prepared specimens (thin foils or replicas) are required. Interpretation of the contrast from thin foils under a TEM is difficult and related to the local crystal structure of the material.

Table 16 Microscopic techniques for metallographic examination of the alloy microstructure

Structure type, concentration range of alloying element	Microscopic technique		
	Light microscope Resolution: <300 nm	**Transmission electron microscope Resolution: 2–3 nm**	**Scanning electron microscope Resolution: 4–9 nm**
Pure solid solution (commercial-purity Al)	Grain size Anisotropy Material defects Inclusions	Dislocation structure Stacking faults	Fracture morphology Material defects
Dispersed precipitates with alloy concentration less than the maximum limit of solid solubility	Grain size Anisotropy Material defects—chemical or structural heterogeneity Inclusions Disperse particles distribution PFZ	Dislocation structure Disperse precipitates morphology and distribution PFZ Stacking faults	Fracture morphology Material defects Disperse precipitates morphology and distribution of PFZ on fracture surface or deep-etched section
Eutectic or peritectic solidification with alloy concentration greater than the maximum limit of solid solubility	Grain size Structure anisotropy Dendrite morphology Structure defects Chemical or structural heterogeneity Inclusions Phase precipitates morphology and distribution PFZ	Dislocation structure Disperse precipitates morphology and distribution PFZ Interface morphology Stacking faults	Fracture morphology Material defects Phase precipitates morphology and distribution on deep-etched section

Note: PFZ, precipitate-free zones

Interpretation of microstructural images requires the attribution of microstructural features by phase identification, phase composition estimation, and phase morphology formalization. The homogeneity and anisotropy of the structure parameters also should be taken into account. The description can be realized by qualitative or quantitative analysis of images from light microscopes. The second one includes stereological analysis—estimation of the degree of the constituent interfaces and grain boundaries, of the number and size of the alloy structure constituents, and of the shape of the particles, their three-dimensional (3-D) morphology, size, and spatial distribution.

Fracture Analysis with the Light Microscope (Ref 24, 32, 40, 41). The light microscope has a limited application for observation and identification of the fracture surface because of its small depth of field and resolution, in comparison with the electron microscope. Nevertheless, the light microscope is a very useful tool for the fracture profile observation of the metallographic microsection perpendicular to the average fracture surface. The metallographic problem is to prepare the microsection in such a manner that the profile line will not be deformed during the preparation procedure. Thus, as previously mentioned, special mounting materials should be used for edge retention. Another recommended method to protect the profile line from deformation is to cover the fracture surface with a protective layer before cross-section preparation (Fig. 30).

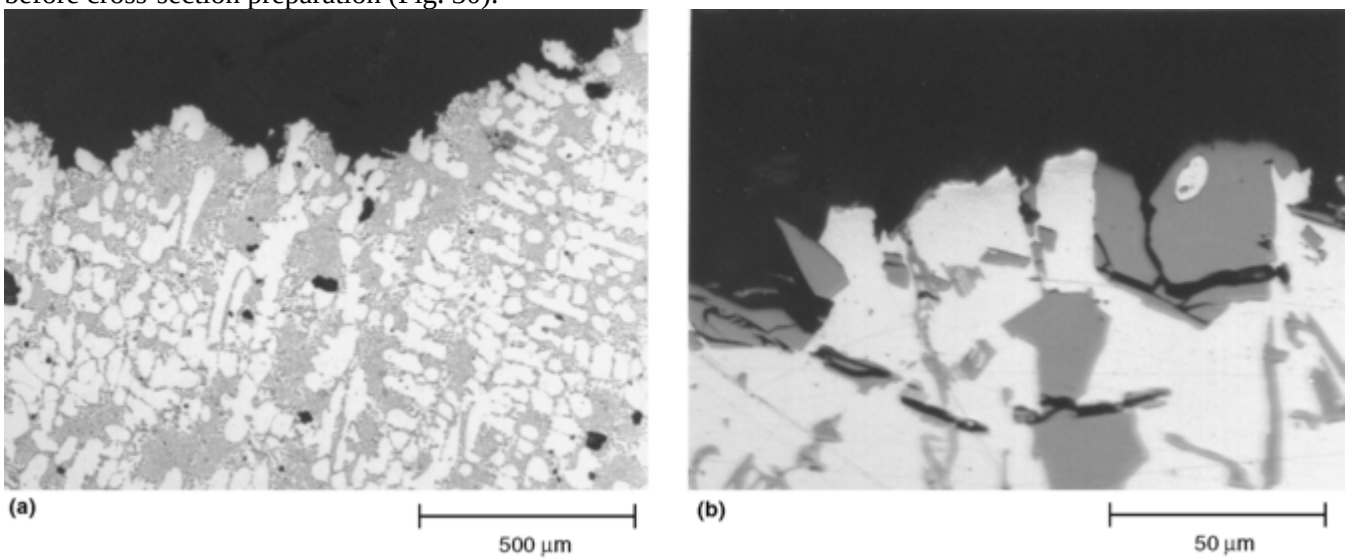

Fig. 30 Fracture profile from etched transverse microsection of two aluminum-silicon alloys. (a) Alloy 356.0 alloy at a magnification of 50×. (b) Alloy 390.0 at a magnification of 500×. Both etched with reagent 5m (Table 4)

Qualitative Microstructure Description and Identification of Phase Constituents. Microscopic observation of the metallographic microsection reveals the constituents of alloy microstructure. The classical comparative method of phase identification is by using an atlas of micrographs from alloys of similar chemical composition and structure. Very often, this allows identification of the phase microconstituents. The first step may be the identification of precipitate morphology and color (Table 17) from a polished (unetched) microsection. Sometimes, examination of an as-polished section is enough to know the alloy phase constituents. The next steps may involve microscopic observation with cross poles and etching of the microsection. If doubts remain after this second step, the use of selective etching may be done for phase identification (Table 18). Selective etching is usually complicated and time-consuming, but in most cases, it gives complete phase identification of the material.

Table 17 Example of the most common phase constituents identification procedure in commercial aluminum alloys

Morphology	Phase	Color of precipitates under light microscope	Identification	
			Birefringes	**Other methods[a]**
Needles	β-AlFeSi	Gray	Moderate, light to dark gray	Selective etching, EDS
	Al_7Cu_2Fe	Light gray, outlined	Moderate, light to dark	Selective etching,

			gray	EDS
	Al_3Fe	Gray	…	Selective etching, EDS
Polyhedra	Si	Blue-gray	None	Selective etching, EDS
	Al_6Mn, $Al_6(FeMn)$	Gray	Strong, light to dark gray	Selective etching, EDS
	Primary Al_6CuMg_4	Light yellow, white	…	Selective etching, EDS, BSED
	Primary α-Al(TM)Si[(b)]	Light gray	…	Selective etching, EDS, BSED
Chinese script	Si	Blue-gray	None	Selective etching, EDS
	Mg_2Si	Blue	None	Selective etching, EDS
	α-AlMnSi	Gray	…	Selective etching, EDS, BSED
	AlCuFeMn	Light gray	…	Selective etching, EDS, BSED
	α-AlFeSi	Light gray	None	Selective etching, EDS, BSED
	α-Al(TM)Si[(b)]	Gray-brown, depending on Mn, Cr contents	None	Selective etching, EDS, BSED
	$Al_8FeMg_3Si_6$	Light gray, not outlined	Strong, from yellow to blue	Selective etching, EDS
	Al_3Ni	Light gray, outlined	…	Selective etching, EDS, BSED
	Al_7Cu_4Ni	Light gray	…	Selective etching, EDS, BSED

Plates, irregular	Si	Blue-gray	None	Selective etching, EDS
	Al_9FeNi	Gray, outlined	…	Selective etching, EDS, BSED
	Al_4FeSi_2	Gray, outlined	…	Selective etching, EDS, BSED
	Al_3FeSi	Gray	…	Selective etching, EDS, BSED
Rounded, irregular particles	Al_2Cu	Pink-yellow, outlined	Strong, orange-greenish-blue	Selective etching, EDS
	Al_2CuMg	Darker than Al_2Cu	Very strong, yellowish-red, green-blue	Selective etching, EDS, BSED
	Al_3Mg_2	White, brighter than matrix	None	Selective etching, EDS
	AlCuMg-$MgZn_2$	Light, slightly outlined	Slight change from light to dark gray	Selective etching, EDS, BSED
	Al_6CuMg_4-$Al_2Mg_3Zn_3$	Light yellow, white	None	Selective etching, EDS, BSED
	$Al_5Cu_6Mg_2$-Mg_2Zn_{11}	Light, slightly outlined	…	…
	$Al_5Cu_2Mg_8Si_6$	Bright yellow, outlined	Strong, from orange to blue	Selective etching, EDS, BSED
Rosettes	Al_3Fe	Gray	Slightly visible	EDS

(a) EDS, energy-dispersive spectroscopy; BSED, backscattered electron diffraction.
(b) TM, transition metal.
Source: Ref 5, 7, 8, 9, 10, 11, 12, 13, 14, 15, 16, 17, 26

Table 18 Phase identification by selective microetching procedure

Phase	Reagent (Table 4) and effects												
	1m	2m	3m	4m	5m	6m	9m	13m	15m	17m	18m	19m	27m
Si	…	Not attacked (Ref 8)	…	…	Outlined (Ref 5)	…	Outlined (Ref 5)	…	Dark blue, brown (Ref 14)	Dark blue, 30 s; violet, 150 s (Ref 16)	…	…	…
α-Al	…	…	…	…	Grain boundaries (Ref 8)	…	Grain boundaries (Ref 8)	Microsegregation (Ref 14)	Grain boundaries (Ref 14)	…	…	…	…
Al_9Co_2	Not attacked (Ref 8)	Etched (Ref 8)	Dark (Ref 8)	Dark (Ref 8)	Brown (Ref 8)	Brown (Ref 8)	…	…	…	…	…	…	…
Al_2Cu	Red (Ref 8, Ref 26 Dark (Ref 2)	Not attacked (Ref 8)	Dark (Ref 8)	Dark (Ref 8, Ref 26 Brown (Ref 11)	Pink (Ref 26) Not attacked (Ref 8)	Not attacked (Ref 8)	…	…	…	Yellow, 30 s Green 150 s (Ref 16)	Slightly tinted (Ref 11, Ref 12	Blue (Ref 17)	…
$Al_7(CrFe)$	Not attacked (Ref 8)	Not attacked (Ref 8)	Blue (Ref 8)	Blue (Ref 8)	Pale brown (Ref 5)	Not attacked (Ref 8)	Outlined (Ref 5)	…	…	…	…	…	…

Phase	Reagent (Table 4) and effects												
	1m	2m	3m	4m	5m	6m	9m	13m	15m	17m	18m	19m	27m
Al_3Fe	…	Black (Ref 5) Etched (Ref 4)	Dark (Ref 8)	Dark (Ref 8, Ref 26	Etched (Ref 17) Not etched (Ref 7)	…	Dark brown/dark blue (Ref 2)	…	…	…	…	…	…
Al_3Mg_2	Etched (Ref 8)	Etched (Ref 8)	Not attacked (Ref 8)	Not attacked (Ref 8)	Outlined (Ref 17) Light blue (Ref 5) Slightly etched (Ref 8)	Slightly etched (Ref 8)	Outlined (Ref 5)	…	…	…	…	…	Brown (Ref 17)
Al_6Mn	Not attacked (Ref 8)	Not attacked (Ref 7)	Bright blue (Ref 8)	Brown (Ref 8)	Slightly etched (Ref 8)	Not attacked (Ref 8)	Not attacked (Ref 5)	…	…	…	…	…	…
Al_6(MnFe)	…	Not attacked (Ref 8)	Slightly etched (Ref 8)	Dark (Ref 8)	Dark gray (Ref 17) Unetched (Ref 4)	Black (Ref 8)	Etched (Ref 2)	…	…	…	…	…	…
Al_3Ni	Not attacked (Ref 8)	Slightly etched (Ref 8)	Bright brown (Ref 8)	Dark (Ref 8), outlined brown-blue	Dark (Ref 8)	Brown (Ref 11)	Not outlined, darkened (Ref 5)	…	…	…	Brown (Ref 11, Ref 12	…	…

Phase	Reagent (Table 4) and effects												
	1m	2m	3m	4m	5m	6m	9m	13m	15m	17m	18m	19m	27m
				(Ref 5)									
Al_3Ti	Not attacked (Ref 8)	Not attacked (Ref 8)	Not attacked (Ref 8)	Dark (Ref 8)	Outlined, darkened (Ref 5)	Not attacked (Ref 8)	Light gray (Ref 5)	…	…	…	…	…	…
$CaSi_2$	…	…	…	…	Dark blue (Ref 13)	…	Outlined, darkened (Ref 5)	…	…	…	…	…	…
Mg_2Si	Attacked dissoluted (Ref 26)	Etched (Ref 7) Darkened (Ref 11)	Not attacked (Ref 8)	Brown (Ref 11)	Blue (Ref 5, Ref 26 Unetched (Ref 8)	Darkened (Ref 11)	Blue-brown (Ref 5)	…	…	…	…	…	…
$MgZn_2$-AlCuMg	Etched (Ref 8)	Etched (Ref 8)	Not attacked (Ref 8)	Not attacked (Ref 8)	Outlined (Ref 13, Ref 17 Brown (Ref 5)	Brown (Ref 8)	Outlined, black (Ref 5)	…	…	…	…	…	…
$Al_{18}Cr_2Mg_3$	Etched (Ref 8)	Etched (Ref 8)	Not attacked (Ref 8)	Not attacked (Ref 8)	Not attacked (Ref 8)	Not attacked (Ref 8)	Outlined (Ref 5)	…	…	…	…	…	…
Al_7Cu_2Fe	Darkened (Ref 8)	Black (Ref 8)	Dark (Ref 8)	Dark (Ref 8)	Outlined (Ref 5)	Dark (Ref 8)	Not attacked	…	…	…	…	…	…

Phase	Reagent (Table 4) and effects												
	1m	2m	3m	4m	5m	6m	9m	13m	15m	17m	18m	19m	27m
					Not attacked (Ref 8)		(Ref 5)						
Al_6CuMg_4-$Al_2Mg_3Zn_3$	Dark, red-brown (Ref 8)	Black	Dark (Ref 8)	Dark (Ref 8)	Black (Ref 13) Etched (Ref 8)	Etched (Ref 8)	…	…	…	…	…	…	…
A_2CuMg	Outlined (Ref 5) Dark (Ref 4)	Not attacked (Ref 8)	Not attacked (Ref 8)	…	Unetched, gray (Ref 13) Black (Ref 5)	Dark (Ref 2, Ref 8	Dark (Ref 5)	…	…	…	…	…	…
$Al_{20}Cu_2Mn_3$	Not attacked (Ref 8)	Not attacked (Ref 8)	Not attacked (Ref 8)	Not attacked (Ref 8)	Brown-blue (Ref 5) Not attacked (Ref 8)	Not attacked (Ref 8)	Dark brown (Ref 5)	…	…	…	Blue (Ref 11)	…	…
Al_7Cu_4Ni	…	…	Not attacked (Ref 8)	…	Darkened (Ref 5)	…	Not attacked (Ref 5)	…	…	…	…	…	…
Al_9FeNi	Not attacked	Not attacked	Dark	Dark	Outlined (Ref 5,	Brown (Ref 8)	Outlined, darkened	…	…	…	Dark (Ref	…	…

Phase	Reagent (Table 4) and effects												
	1m	2m	3m	4m	5m	6m	9m	13m	15m	17m	18m	19m	27m
	(Ref 8)	(Ref 8)	(Ref 8)	(Ref 8)	Ref 17 Dark brown (Ref 8)	 Blue-violet (Ref 11)	(Ref 5)				11, Ref 12		
β-AlFeSi	Slightly etched (Ref 26) Unetched (Ref 8)	Etched (Ref 8, Ref 26	…	Etched (Ref 8, Ref 26	Light brown (Ref 26) Dark (Ref 8) Darkened (Ref 7)	…	…	…	…	…	Brown-blue (Ref 11, Ref 12	…	…
α-AlFeSi	Slightly etched (Ref 8)	Slightly etched (Ref 8)	Not attacked (Ref 8)	Not attacked (Ref 8)	Outlined (Ref 5) Not attacked (Ref 8)	Not attacked (Ref 8)	Outlined, darkened (Ref 5)	…	…	…	…	…	…
α-AlMnSi	Not attacked (Ref 8)	Not attacked (Ref 8)	Not attacked (Ref 8)	Pale brown (Ref 8)	Outlined (Ref 5) Not attacked (Ref 8)	Not attacked (Ref 8)	Outlined (Ref 5)	…	…	…	…	…	…
α-AlFeMnSi	Slightly etched	Etched (Ref 7,	…	…	Light brown	…	Brown/1 min (Ref	…	Gray (Ref	…	…	…	…

Phase	Reagent (Table 4) and effects												
	1m	2m	3m	4m	5m	6m	9m	13m	15m	17m	18m	19m	27m
	(Ref 8, Ref 26	Ref 8, Ref 26			(Ref 26) Unetched (Ref 8)		5)		14)				
$Al_{18}Mg_3Mn_2$	…	…	…	Not attacked (Ref 8)	Outlined (Ref 5)	…	Outlined (Ref 5)	…	…	…	…	…	…
$Al_5Cu_2Mg_8Si_6$	Blue (Ref 26)	Dark (Ref 16)	…	Dark (Ref 26)	Brown-black (Ref 5)	…	Not attacked (Ref 5)	…	…	…	…	…	…
$Al_8Mg_3FeSi_2$	Brown (Ref 26)	Etched (Ref 26)	…	Slightly etched (Ref 26)	Bright gray, outlined (Ref 26)	…	Slightly etched (Ref 26) Not attacked (Ref 5)	…	…	…	…	…	…

The selective etching procedure is very sensitive to the process conditions of time, temperature, and small differences in chemical composition of the reagents. Another very important factor is the influence of chemical composition of the specimen and chemical composition of the phase constituents on the results. Their apparent stoichiometry is usually established on the basis of the average chemical composition. The range of possible composition is rather wide; sometimes, an array of the continuous solid solutions may exist between two equilibrium systems (Al-Zn-Mg and Al-Cu-Mg, Al-Fe-Si and Al-Mn-Si). Figures 31, 32, 33, 34, 35, 36, 37, 38 and 39 show the results of selective etching in various reagents. As noted there, the results are not always exactly the same as suggested in Table 18. Nevertheless, they should be considered as examples of the results and as a guide for using this method in aluminum alloy metallography.





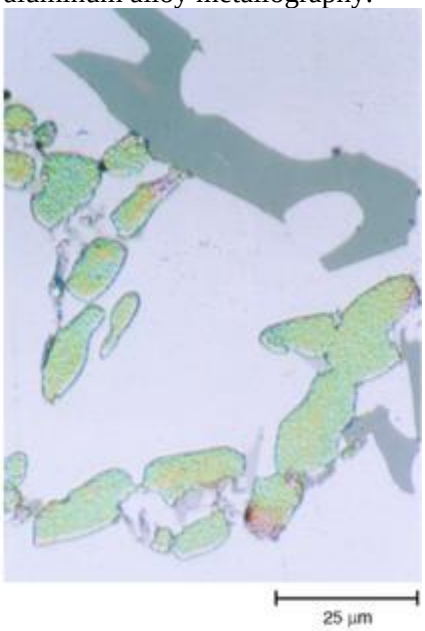



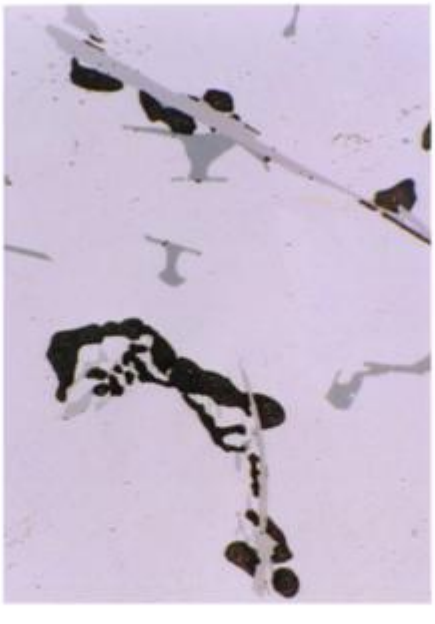



Fig. 31 Phase constituent identification in various aluminum alloys by means of selective etching with reagent 1m (Table 4). Compare with Table 18. (Małgorzata Warmuzek, Foundry Research Institute, Kraków, Poland)

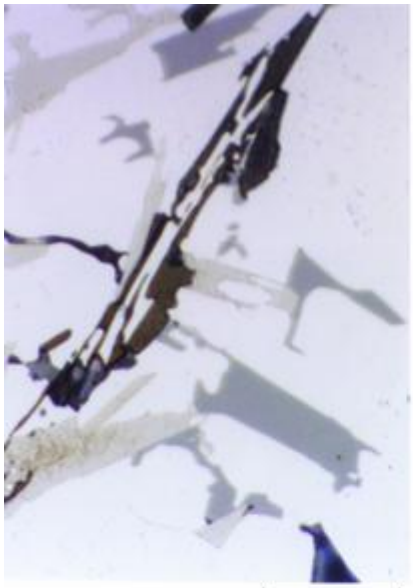

Magnification: 800×
Alloy: 413.0
Phase constituents: Si, gray; Al_9FeNi, black irregular plates; Mg_2Si, black partially dissolved Chinese script; Al_3Ni, tarnished beige irregular plates
Time of attack: 35 s

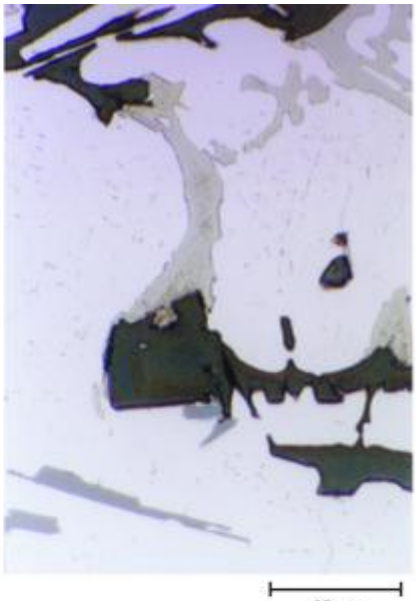

Magnification: 750×
Alloy: 413.0
Phase constituents: Si, gray; Al_9FeNi, black irregular plates; Al_3Ni, tarnished beige irregular plates; Al_7Cu_4Ni, outlined Chinese script
Time of attack: 50 s

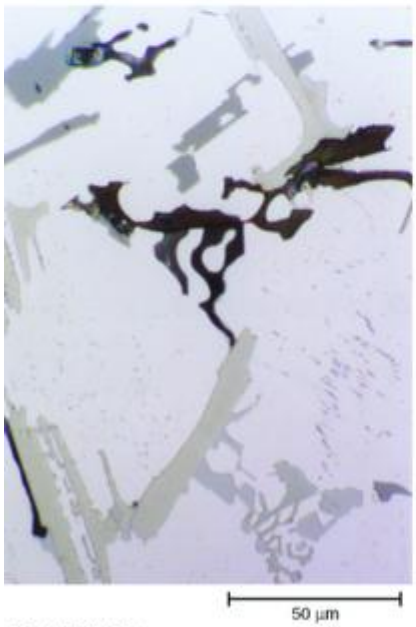

Magnification: 500×
Alloy: 413.0
Phase constituents: Si, gray; Al_9FeNi, black irregular plates; Mg_2Si, black partially dissolved Chinese script; Al_3Ni, tarnished beige irregular plates; α-Al(FeMnCu)Si, gray not etched Chinese script
Time of attack: 10 s

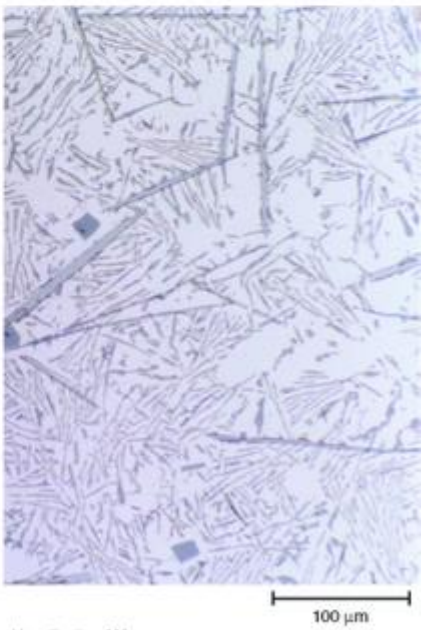

Magnification: 200×
Alloy: 380.0
Phase constituents: Si, gray; β-AlFeSi, outlined needles like particles
Time of attack: 20 s

Fig. 32 Phase constituent identification in various aluminum alloys by means of selective etching with reagent 2m (Table 4). Compare with Table 18. (Małgorzata Warmuzek, Foundry Research Institute, Kraków, Poland)



Magnification: 500x
Alloy: 356.0
Phase constituents: Si, gray; β-AlFeSi, brown needles
Time of attack: 10s



Magnification: 800x
Alloy: 356.0
Phase constituents: Si, dark gray; β-AlFeSi, light-gray needles; α-AlFeSi, light-gray Chinese script
Time of attack: 10 s

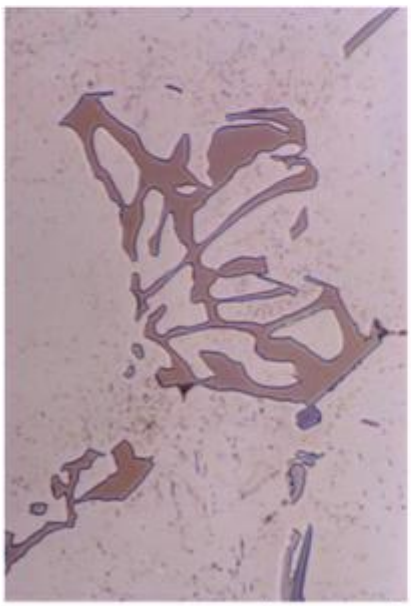

Magnification: 400x
Alloy: 355.0
Phase constituents: Si, gray; a-Al(FeMn)Si, brown Chinese script (Fe > Mn)
Time of attack: 15 s



Magnification: 200x
Alloy: 319.0
Phase constituents: Si, gray; Al_2Cu, black round particles; α-Al(F_3Mn)Si, brown Chinese script (Mn > Fe)
Time of attack: 15 s

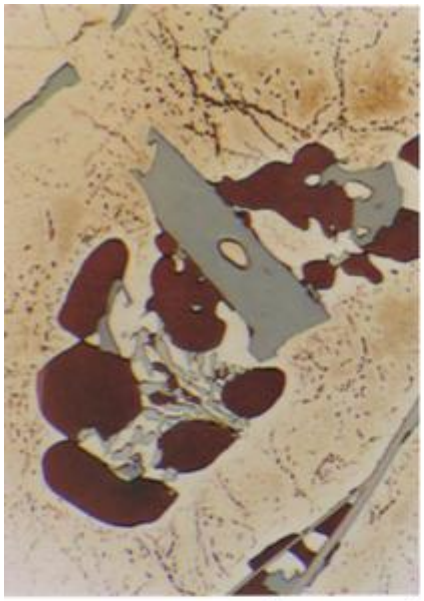

Magnification: 750x
Alloy: 319.0
Phase constituents: si, gray; Al2Cu, brown round particles; $Al_5Cu_2Mg_8Si_6$, light-brown round particles; β-AlFeSi, bright-gray needles
Time of attack: 15 s

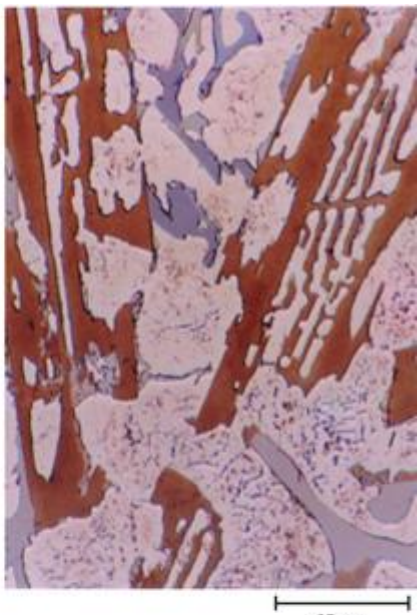

Magnification: 750x
Alloy: 390.0
Phase constituents: Si, dark gray; Al_9FeNi, brown plates; $Al_8Mg_3FeSi_2$, light-gray particles
Time of attack: 15 s

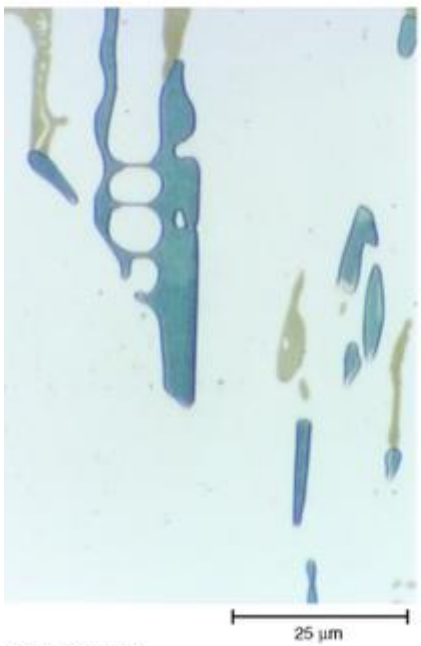

Magnification: 1000x
Alloy: 3004
Phase constituents: $Al_6(MnFe)$, blue rods or filigrees; α-Al(FeMn)Si, pale-brown irregular particles
Time of attack: 15 s



Magnification: 1000x
Alloy: 3004
Phase constituents: $Al_6(MnFe)$, blue rods or filigrees
Time of attack: 15 s

Fig. 33 Phase constituent identification in various aluminum alloys by means of selective etching with reagent 3m (Table 4). Compare with Table 18. (Małgorzata Warmuzek, Foundry Research Institute, Kraków, Poland)

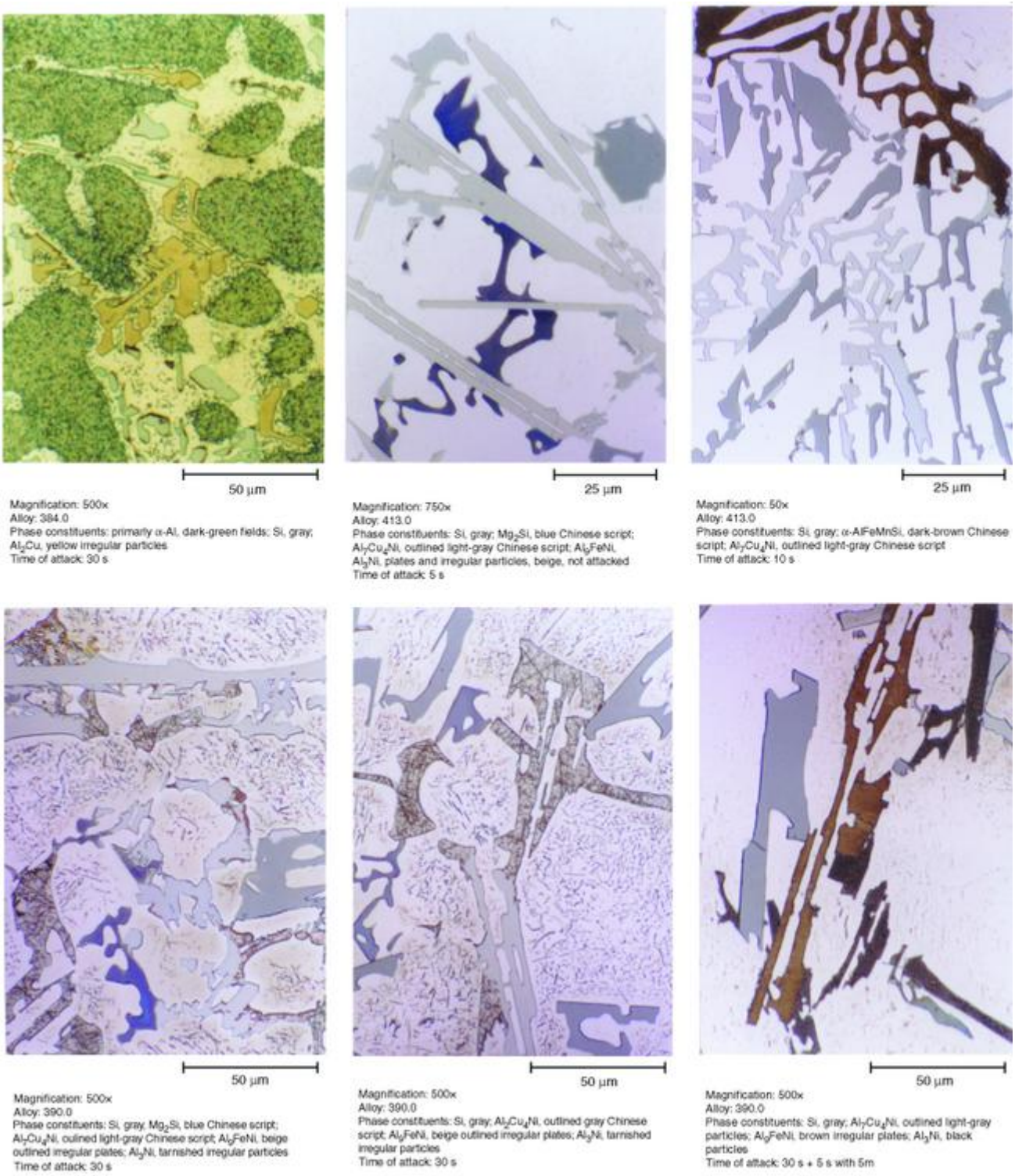

Fig. 34 Phase constituent identification in various aluminum alloys by means of selective etching with reagent 4m (Table 4). Compare with Table 18. (Małgorzata Warmuzek, Foundry Research Institute, Kraków, Poland)

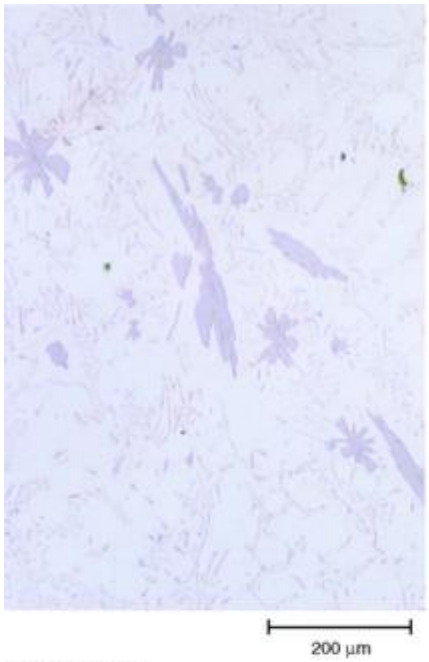

Magnification: 100x
Alloy: AlFe15
Phase constituents: Al_3Fe, rosettes, plates, and needles in eutectic
Time of attack: 5 s

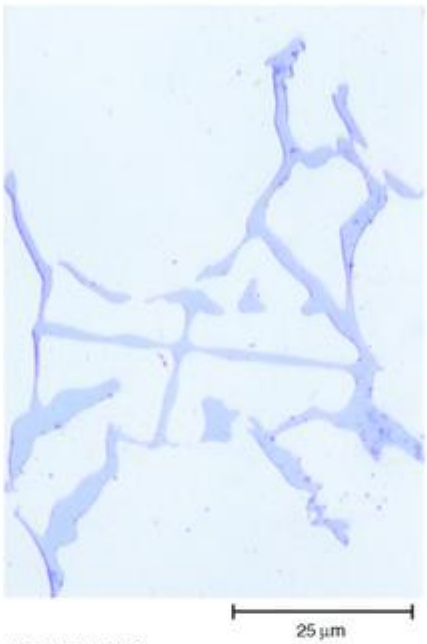

Magnification: 1000x
Alloy: 535.0
Phase constituents: Mg_2Si, gray-blue Chinese script
Time of attack: 3 s

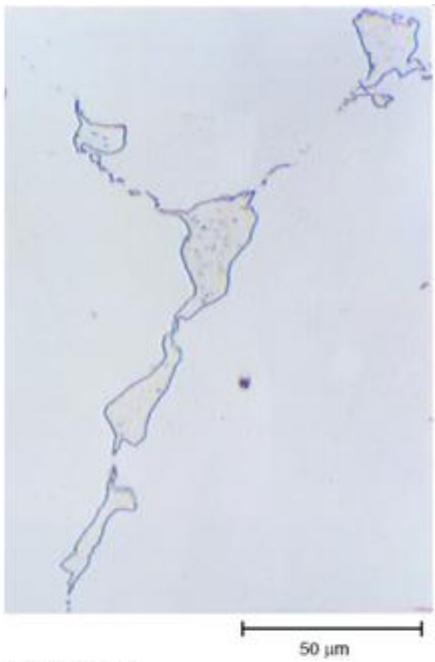

Magnification: 500x
Alloy: 535.0
Phase constituents: Al_8Mg_5, bright, outlined particles
Time of attack: 3 s

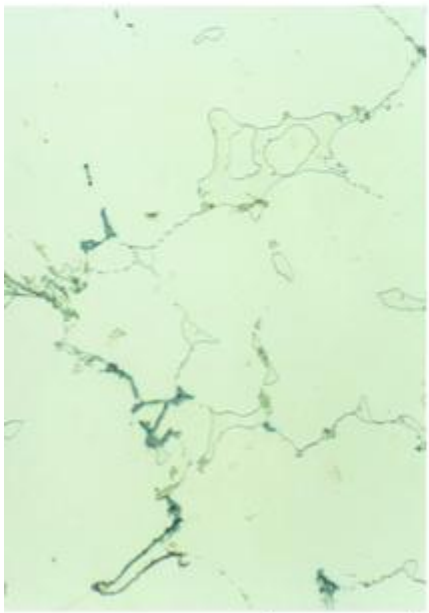

Magnification: 200x
Alloy: 535.0
Phase constituents: Al_8Mg_5, bright, outlined particles; Mg_2Si, gray-blue Chinese script
Time of attack: 3 s

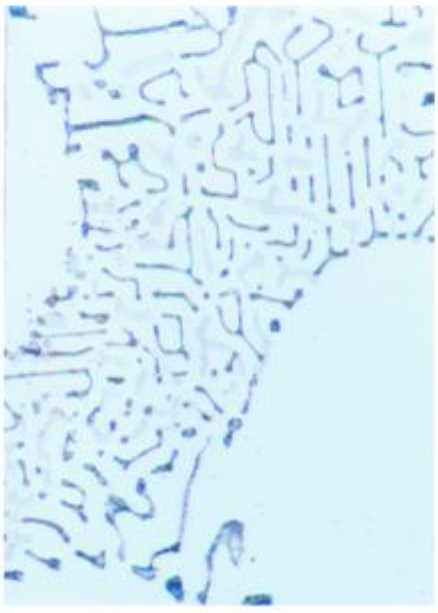

Magnification: 1000x
Alloy: 5083
Phase constituents: Mg_2Si, blue + α-AlFeMnSi gray precipitates in eutectic
Time of attack: 5 s

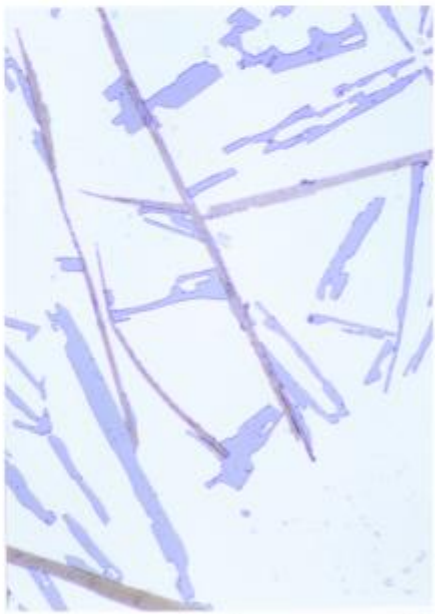

Magnification: 500x
Alloy: 380.0
Phase constituents: Si, dark gray; β-AlFeSi, brown needles
Time of attack: 5 s

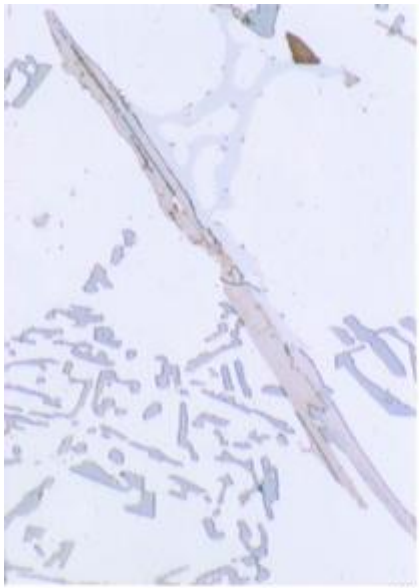

Magnification: 750x
Alloy: 380.0
Phase constituents: Si, dark gray; β-AlFeSi light-brown needles; $Al_8Mg_2FeSi_2$, light-gray, not attacked Chinese script
Time of attack: 5 s



Magnification: 450x
Alloy: 380.0
Phase constituents: Si, dark gray; α-Al(FeMn)Si, brown Chinese script
Time of attack: 5 s

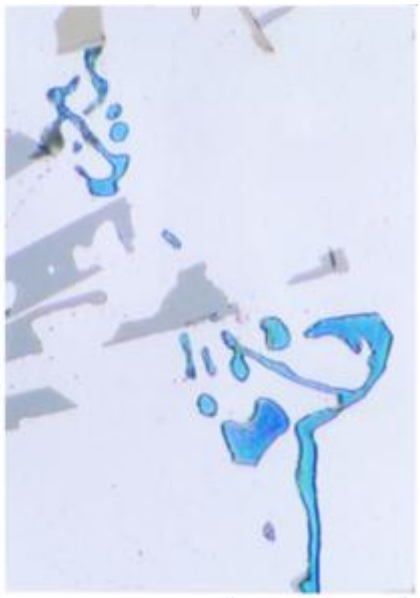

Magnification: 1000x
Alloy: 380.0
Phase constituents: Si, dark gray; A-AlFeSi, light brown; Mg_2Si, blue Chinese script
Time of attack: 5 s

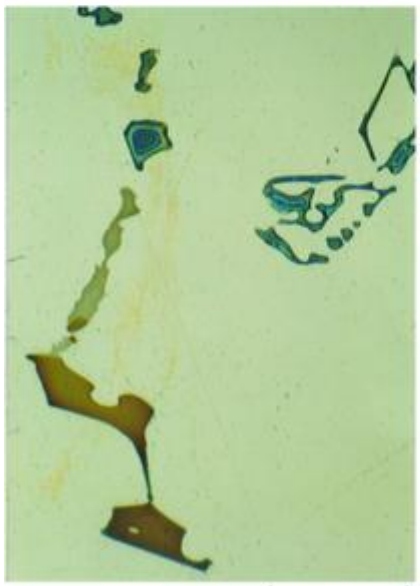

Magnification: 800x
Alloy: 3004
Phase constituents: Mg_2Si, blue Chinese script; $Al_6(FeMn)$, brown irregular polyhedra
Time of attack: 5 s



Magnification: 800x
Alloy: 355.0
Phase constituents: Si, gray; α-Al(FeMn)Si, brown precipitates; Al_2Cu, round, pink particles
Time of attack: 5 s



Magnification: 500x
Alloy: 390.0
Phase constituents: Si, gray; Al_2Cu, round, pink particles; Al_3Ni, dark-brown irregular precipitates; Al_9FeNi, brown irregular plates; $Al_9Mg_3FeSi_2$, light-gray not attacked Chinese script
Time of attack: 5 s



Magnification: 800x
Alloy: 413.0
Phase constituents: Si, dark gray; Mg_2Si, Blue Chinese script; Al_7Fe_2Cu, blue needles; $Al_9Mg_3FeSi_2$, light gray, not attacked Chinese script; $CaSi_2$, blue tarnished, hollow trapezoid
Time of attack: 5 s



Magnification: 1000x
Alloy: 7050, as-cast
Phase constituents: $M_{(AlZnMgCu)}$ + $T_{(AlZnMgCu)}$ + α-Al intergranular eutectic, blue-brown fine particles
Time of attack: 5 s



Magnification: 1000x
Alloy: 7050, as-cast
Phase constituents: $M_{(AlZnMgCu)}$ + (light brown)+$T_{(AlZnMgCu)}$ + (dark blue) + α-Al intergranular eutectic
Time of attack: 5 s

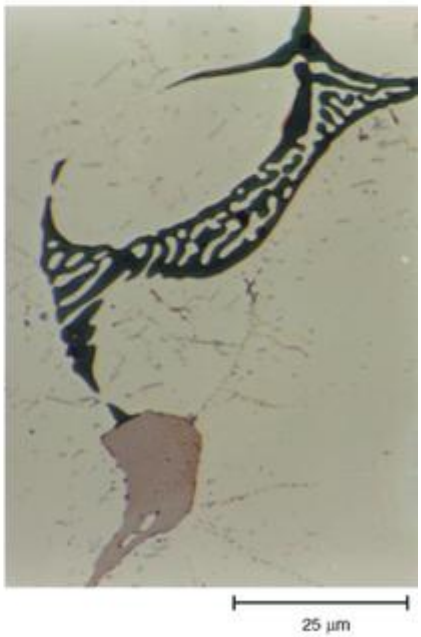

Magnification: 1000x
Alloy: 7050, as-cast
Phase constituents: $T_{(AlZnMgCu)}$ + (dark blue) + S (Al_2CuMg) (gray) + α-Al intergranular eutectic
Time of attack: 5 s

Fig. 35 Phase constituent identification in various aluminum alloys by means of selective etching with reagent 5m (Table 4). Compare with Table 18. (Małgorzata Warmuzek, Foundry Research Institute, Kraków, Poland)

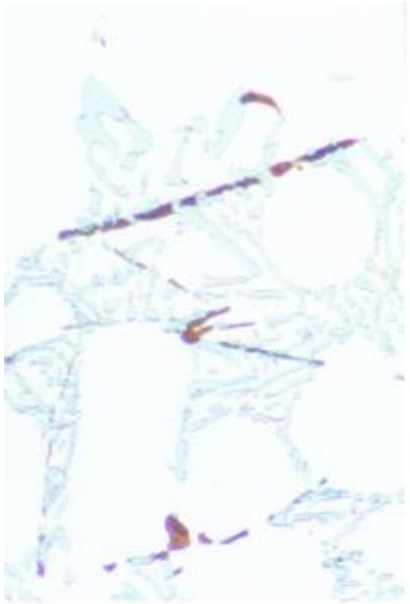

Magnification: 1000x
Alloy: 380.0
Phase constituents: Si, dark gray; β-AlFeSi, brwon needles; α-AlFeMnSi, brown polyhedra;
Time of attack: 5 s

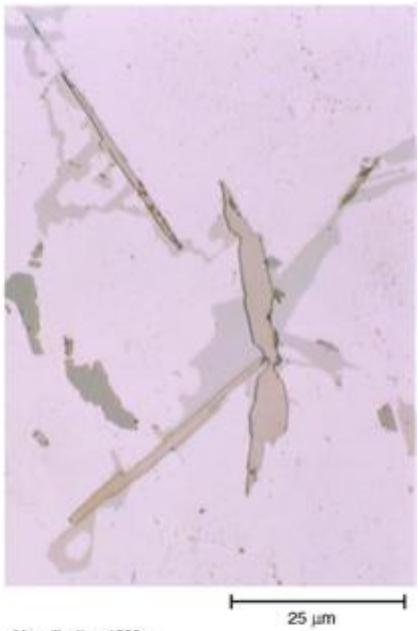

Magnification: 1000x
Alloy: 356.0
Phase constituents: Si, dark gray; $Al_8Mg_3FeSi_2$, light-gray not attacked Chinese script; β-AlFeSi, brown needles;
Time of attack: 5 s

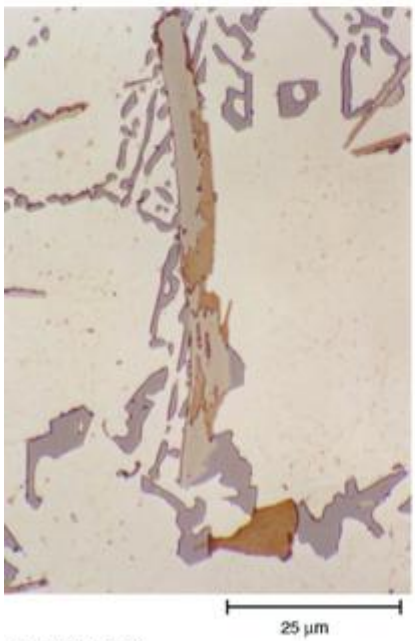

Magnificiation: 1000x
Alloy: 328.0
Phase constituents: Si, dark gray; Mg_2Si, blue Chinese script; Al_7Cu_2Fe, blue needles; α-alFeMnSi, brown polyhedra
Time of attack: 5 s

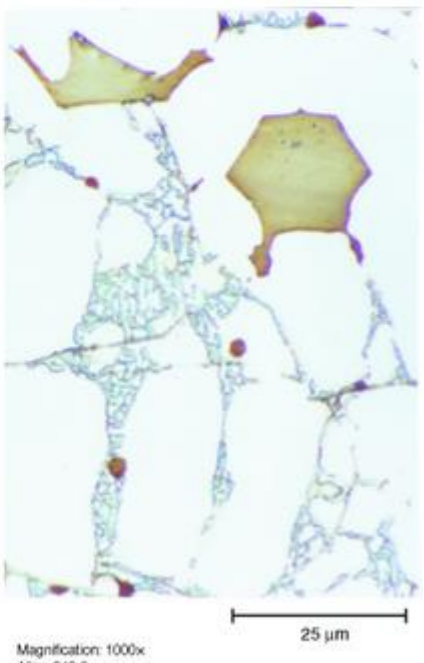

Magnification: 1000x
Alloy: 319.0
Phase constituents: Si, dark gray; β-AlFeSi, brown needles; primary α-AlFeMnSi, brown polyhedra
Time of attack: 5 s

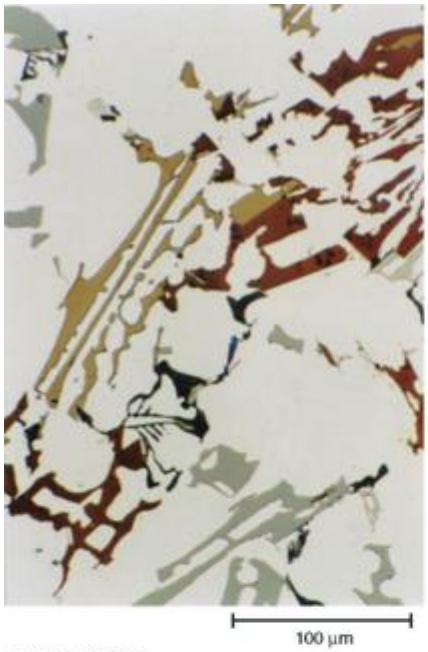

Magnification: 250×
Alloy: 413.0
Phase constituents: Si, gray; Mg_2Si, black Chinese script; α-Al(FeM)Si, brown plates; Al_2Cu, beige precipitates
Time of attack: 10 s

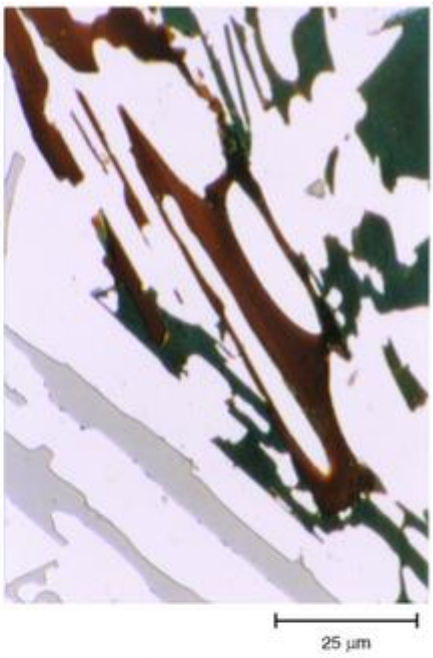

Magnification: 800×
Alloy: 390.0
Phase constituents: Si, gray; Mg_2Si, black Chinese script; Al_3Ni, black precipitates; Al_9FeNi, brown irregular plates
Time of attack: 20 s



Magnification: 800×
Alloy: 390.0
Phase constituents: Si, dark gray; Al_3Ni, dark blue; Mg_2Si, blue; Al_2Cu, yellow-pink round particles
Time of attack: 15 s

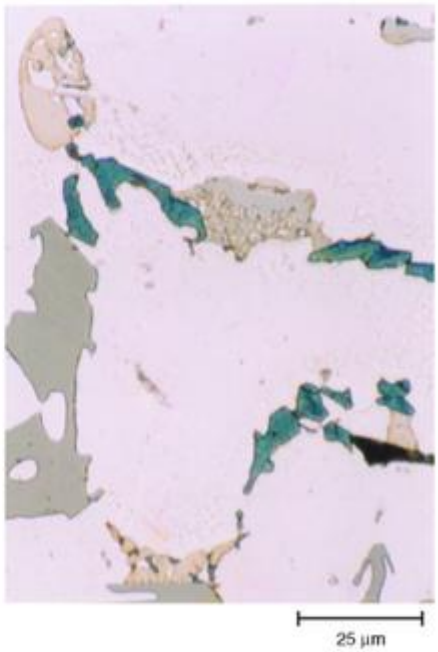

Magnification: 700×
Alloy: 319.0
Phase constituents: Si, dark gray; Mg_2Si, blue; Al_2Cu, yellow-pink round particles; $Al_5Cu_2Mg_8Si_6$, gray particles in eutectic
Time of attack: 15 s

Fig. 36 Phase constituent identification in various aluminum alloys by means of selective etching with reagent 6m (Table 4). Compare with Table 18. (Małgorzata Warmuzek, Foundry Research Institute, Kraków, Poland)

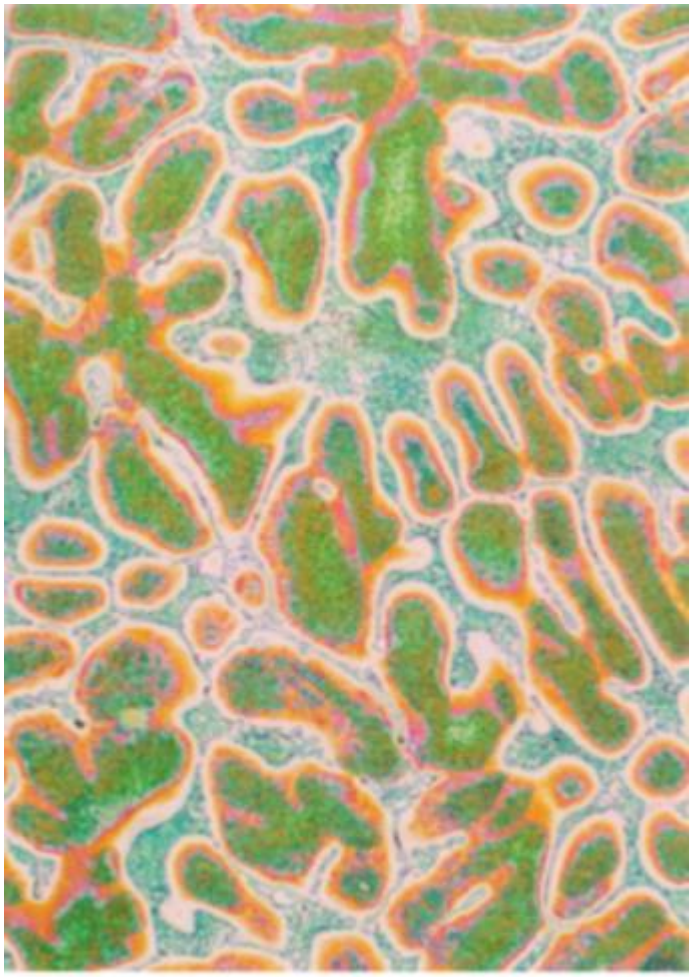

Fig. 37 Phase constituent identification in alloy 356.0 with reagent 13m (Table 4). Time of attack: 5 s. Orange-green fields are primary dendritic microsegregation regions with α-Al (solid solution). Blue fields are interdendritic eutectic (α-Al + Si). 800×. Compare with Table 18. (Małgorzata Warmuzek, Foundry Research Institute, Kraków, Poland)

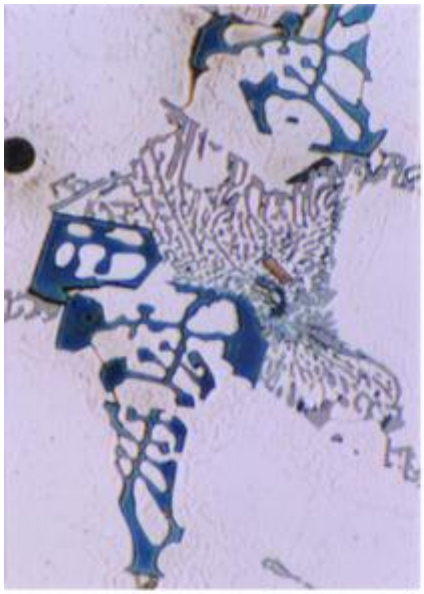

Magnification: 400x
Alloy: 319.0
Phase constituents: Si, dark gray; α-AlFeMnSi, dark blue Chinese script
Time of attack: 5 s

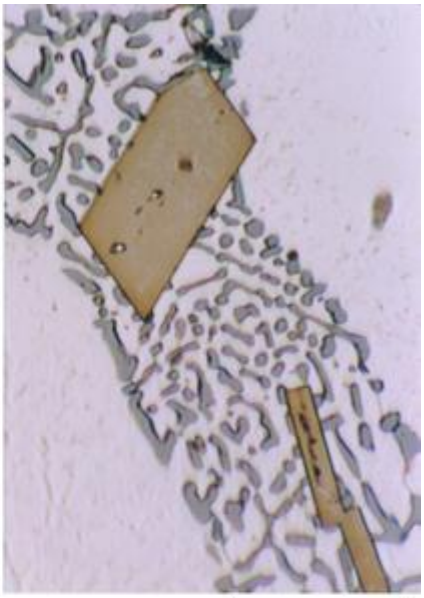

Magnification: 1000x
Alloy: 356.0
Phase constituents: Si, dark gray; $CaSi_2$, brown polygons
Time of attack: 5 s

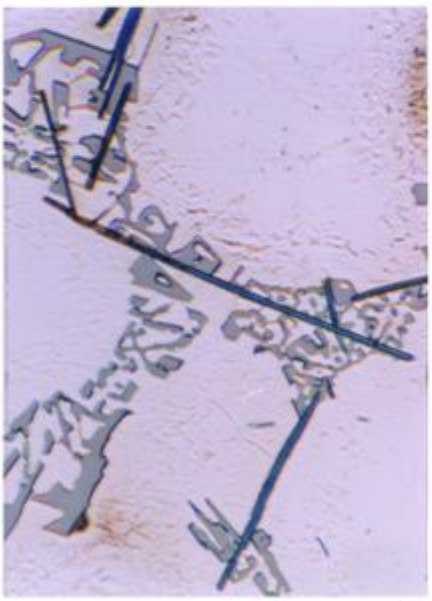

Magnification: 400x
Alloy: 319.0
Phase constituents: Si, dark gray; Al-Cu_2Fe, dark-blue needles
Time of attack: 5 s

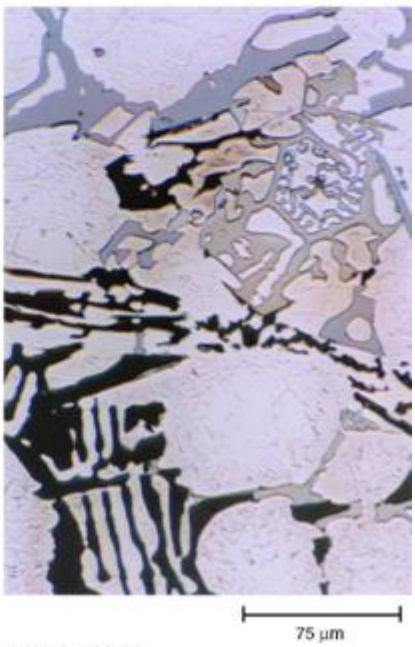

Magnification: 300x
Alloy: 413.0
Phase constituents: Si, gray; Al_3Ni, blue-black; Al_9FeNi, black-brown irregular plates; α-AlFeSi, beige outlined Chinese script
Time of attack: 5 s

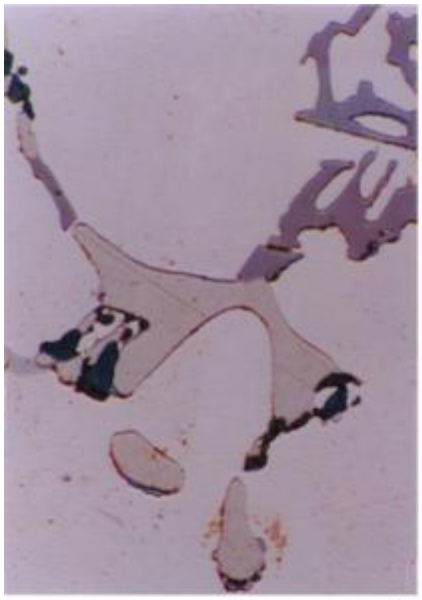

Magnification: 1000x
Alloy: 319.0
Phase constituents: Si, gray; eutectic: $Al_5Cu_2Mg_8Si_6$, dark-blue precipitates + Al_2Cu, round, gray-pink particles
Time of attack: 5 s

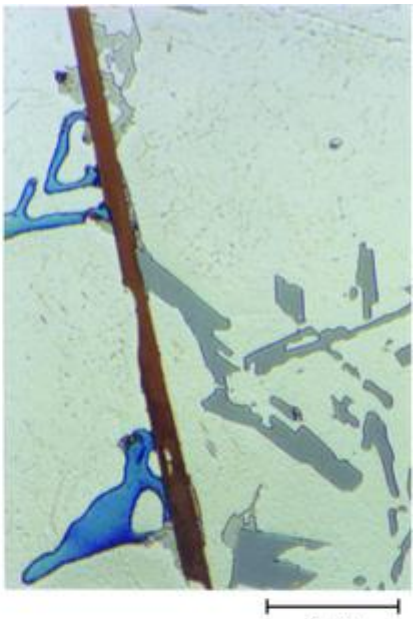

Magnification: 750x
Alloy: 356.0
Phase constituents: Si, gray; β-AlFeSi, brown needles; Mg_2Si, blue Chinese script; α-AlFeSi, outlined gray Chinese script
Time of attack: 5 s



Magnification: 400x
Alloy: 319.0
Phase constituents: Si, dark gray; α-Al(FeMn)Si, blue; Al_2Cu+Si+$Al_5Cu_2Mg_8Si_6$ + α-Al eutectic
Time of attack: 5 s

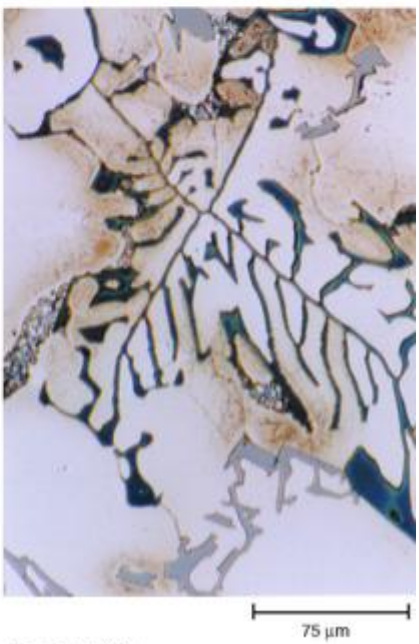

Magnification: 300x
Alloy: 356.0
Phase constituents: Si, gray; α-Al(FeMn)Si, blue Chinese script; Al_2Cu+Si+α-Al eutectic
Time of attack: 5 s

Fig. 38 Phase constituent identification in various aluminum alloys by means of selective etching with reagent 15m (Table 4). Compare with Table 18. (Małgorzata Warmuzek, Foundry Research Institute, Kraków, Poland)

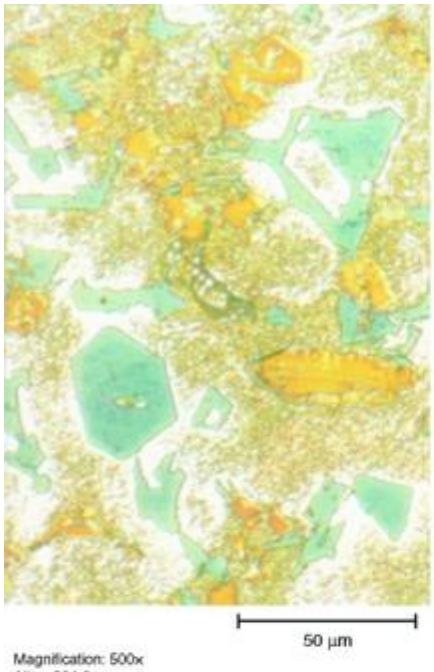

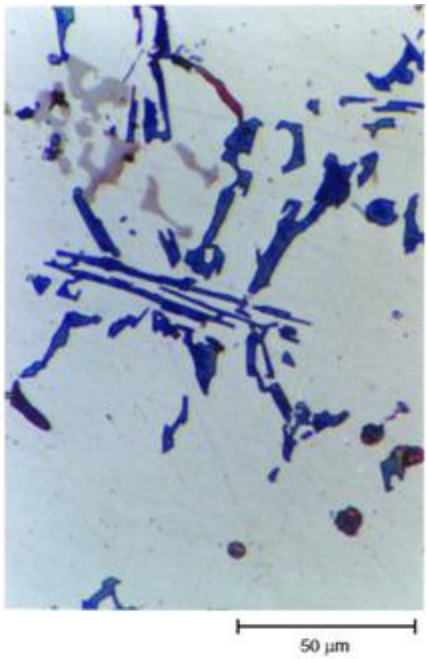

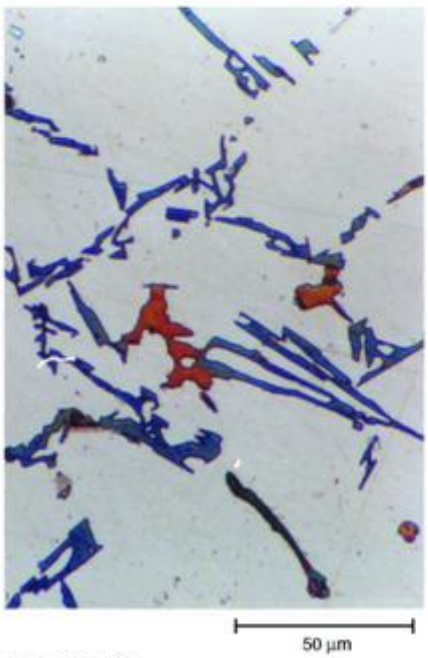

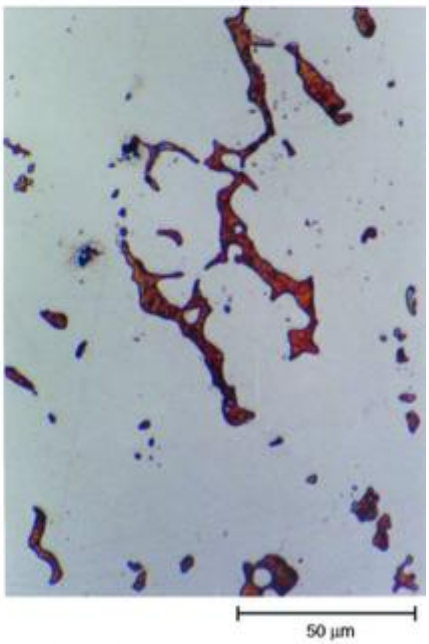

Fig. 39 Phase constituent identification in various aluminum alloys by means of selective etching with reagent 20m (Table 4). Compare with Table 18. (Małgorzata Warmuzek, Foundry Research Institute, Kraków, Poland)

Sometimes, in situ identification also is performed by x-ray microanalysis (energy-dispersive spectroscopy, wavelength-dispersive spectroscopy), and even x-ray diffraction phase analysis can be necessary. Detection of backscattered electrons in a SEM is a very useful but seldom used method. This method provides another alternative when phase attribution by morphology, color, and/or chemical composition is not successful. This last method allows the crystal structure identification in situ and sometimes eliminates the last doubts. Measurements of phase microhardness values (Table 19) may also allow some additional confirmation in attributing a phase structure with an observed precipitate.

Table 19 Hardness of chosen intermetallic phases in aluminum alloys

Phase	Microhardness, HV (MN/m^2)
Al	1200–1400
Al_2Cu	4000–6000
Al_9Co_2	6500–7500
Al_8Mg_5	2000–3400
Al_2CuLi	4250–5200
Al_6Cu_3Ni	10,000
Mg_2Si	4500
Al_3Fe	9600–11,500
β-AlFeSi	5800
α-AlFeSi	9580
Al_6FeMn	7040
α-AlFeMnSi	8000–9000
$MgZn_2$	2500
Si	8700–13,500
Al_6Mn	5400–5600
Al_9FeNi	6900–7400
Al_3Ni	7000–7700
Al_7Cr	5000–7000

Al_3Ti	4000–7000
Al_3Zr	4270–7400
$Al_{20}Cu_2Mn$	4200
$Al_8FeMg_3Si_6$	2700
$Al_5Cu_2Mg_8Si_6$	4500
$Al_{18}Cr_2Mg_3$	4600–5000

Source: Ref 3

Quantitative Microstructure Description (Ref 25, 27, 28, 29, 30, 31, 32, 33, 34, 35, 36, 37, 38, 39). Very often, the semiquantitative description of the microstructure is adequate by comparative methods (according to the special demands). Different microstructure standards also can be used to describe the alloy microstructure. Nonetheless, standardized quantitative methods are demanded by customers. For example, standard test methods are used in determining the average grain size (e.g., ASTM E 112) and the description of the dual grain size (ASTM E 1181).

Estimation of 3-D microstructural features involves analysis of images from random flats of two-dimensional (2D) section (Ref 27, 28). Primarily, two kinds of parameters are measured:

- Local (statistical) stereological parameters of a microstructural element/particle represent an average value of a geometrical feature of the particle, such as mean volume (V), mean chord (I) of the particle, mean perimeter (L) of the particle, or mean surface of the particle section A.
- Integral (global) stereological parameters represent the digitized characteristics of structure elements (volume, area, line length) in terms of measured units, such as specific volume fraction (V_v), specific surface of the interfaces (S_v), specific length of the interfaces (P_L), and number of particles on the unit area (N_a).

Topological parameters are not estimated very often and are seldom used during standard laboratory examinations. Quantitative description of microstructure more often involves measured or calculated value of parameters concerning phase composition and the morphology, distribution or dispersion of phase constituents. Examples of quantitative microstructure descriptions used in estimating material properties are listed in Table 21.

Table 20 Temperature of the eutectic transformation in multicomponent aluminum alloys

No.	System	Temperature		Eutectic phases
		°C	**°F**	
1	Al-Cu	548	1018	α-Al + Al_2Cu
2	Al-Mg	450	840	α-Al + Al_3Mg_2
3	Al-Li	180	355	α-Al + Al_4Li_9
4	Al-Si	577	1006	α-Al + Si

5	Al-Sn	231	448	α-Al + Sn
6	Al-Zn	277	531	α-Al + Zn(Al)
7	Al-Cu-Mg	449	840	α-Al + Al_6CuMg_4 + Al_8Mg_5
8	Al-Cu-Si	495	925	α-Al + Al_2Cu + Si
9	Al-Cu-Fe	545	1015	α-Al + Al_2Cu + Al_7Cu_2Fe
10	Al-Fe-Si	576	1069	α-Al + Al_5FeSi + Si
11	Al-Mg-Si	448	838	α-Al + Mg_2Si + Al_8Mg_5
12	Al-Mg-Zn	447	837	α-Al + $Al_2Mg_3Zn_3$ + Al_8Mg_5
13	Al-Mn-Si	547	1017	α-Al + α-AlMnSi + Si
14	Al-Cu-Mg-Si	444	831	α-Al + Al_6CuMg_4 + Al_8Mg_5 + Mg_2Si

Table 21 Some examples of quantitative descriptions of microstructure for material properties examination

Microstructure factor	Microstructure feature	Method of estimation [(a)]	Structure criterion [(b)]	Ref
Phase composition	V_v (phase volume fraction) for solid solution (V_v^{α}) or separate phases (V_v^{sp})	Measured directly	$\sigma = \sigma_\alpha V_v^{\alpha} + \sigma_\beta V_v^{\beta}$	Ref 29
			P_z (Zener drag) = $3\gamma V_v/d$	Ref 40, 41
Dispersion factors	*d* (grain diameter) DAS (dendrite arm size) δ (interlamellar space in eutectic) *r* (precipitates radius)	Measured directly or calculated by using measured parameters: DAS = $1/N_l$ $I = V_v/N_l$ *I* = mean intercept length N_l = linear number density	$R_e = kd^{-1/2}$	Ref 31
			UTS = $k + k_1\delta^{-1/2} + k_2 DAS^{-1/2}$	Ref 32, 33
			$R_{0.2} = k + k_3\delta^{-1/2} + k_4 DAS^{-1/2}$	Ref 32, 33

			DAS = $K\theta^n$	Ref 34, 41
			$\sigma = \Omega\{P(r < r_c)V_v^{1/2} + P(r > r_c)1.5 V_v^{1/2}/r\}$	Ref 35
Shape factors	*e* (particle elongation)	Calculated by using measured parameters (e.g., Feret diameter, *F*): $e = F_a/F_b$ F_a = maximum (Feret) diam. F_b = diam. orthogonal to F_a	$K_n = F_a/F_b$ K_n = stress concentration factor	Ref 31, 36
	DE (equivalent round particle diameter)	Calculated by using measured parameters: $DE = (4A/\pi)^{1/2}$, with A = mean surface of particle section $DE = 2(V_v/\pi N_a)^{1/2}$, with N_a = number of particles on unit area	VGP = $\sigma\gamma/DE$	Ref 30
	Roundness (C)	$C_L = \pi P_L/2A_A$ P_L = number of intersections of surfaces with unit test line A_A = area fraction		
Distribution	*l* = mean particle spacing	Calculated by using measured parameters: $l = 1/N_l$	$\tau = G \cdot b/l$	Ref 31
	λ = mean free path	Calculated by using measured parameters: $\lambda = (1 - V_v)/N_l$		Ref 36

(a) Source: Ref 13, 15, 27, 30, 32, 36, 37.

(b) σ, stress; γ, grain boundary energy; P_z, Zener drag; γ, strengthening of solid solution; R_e, yield stress; UTS, ultimate tensile strength; $R_{0.2}$, yield strength; θ, local solidification time; Ω, strengthening constant; K_n, stress concentration factor; VGP, void growth propagation rate; τ, shear stress; G, shear modulus; **b**, Burgers vector. *k*, k_1, k_2, k_3, k_4, and *K* are empirical coefficients, σ_α and σ_β stress in α phase and β phase, respectively.

(a) Source: Ref 13, 15, 27, 30, 32, 36, 37.

(b) σ, stress; γ, grain boundary energy; P_z, Zener drag; γ, strengthening of solid solution; R_e, yield stress; UTS, ultimate tensile strength; $R_{0.2}$, yield strength; θ, local solidification time; Ω, strengthening constant; K_n, stress concentration factor; VGP, void growth propagation rate; τ, shear stress; G, shear modulus; **b**, Burgers vector. k, k_1, k_2, k_3, k_4, and K are empirical coefficients, σ_α and σ_β stress in α phase and β phase, respectively.

Table 22 Reagents used for deep etching of aluminum alloys

No.	Chemical composition	Etching mode	Purpose or application	Ref
1s	A) 10 mL HCl 90 mL distilled H_2O B) 2.5 mL HCl 2 mL HNO_3 0.75 mL HF 40 mL distilled H_2O	24 h in reagent A, then 1 h in reagent B	Dissolves Al matrix and reveals Si	Ref 17
2s	A) 15 mL HCl 10 mL HF 90 mL distilled H_2O B) 25 mL HNO_3 90 mL distilled H_2O	30–60 min with A, then 2–4 min with B, 15–30 °C (60–85 °F), 20 min	Dissolves Al matrix; reveals eutectic Si morphology	Ref 42
3s	10 mL HCl 90 mL distilled H_2O	Approximately 60 min	Dissolves Al matrix; reveals Si morphology	Ref 17
	25 mL HCl 75 mL distilled H_2O	15–30 min		
4s	2 g K1	1) Electrolytic etch at 2–5 V, 5–20 min., wash in methanol 2) Raise in 30 s voltage 0–30 V, 30 s, stirring, 0.3 A/mm^2, clean ultrasonically in methanol for 30 s	Dissolves Al	Ref 17
5s	0.25–0.5 N solution of $HgCl_2$ in distilled water	5–15 min	Dissolves Al matrix; reveals details of Si crystal morphology	Ref 42
6s	30% solution of NaOH in distilled water	3–20 min, 70 °C	Dissolves Al matrix; reveals details of Si eutectic, intermetallic phase morphology	Ref 42

7s	3 g NaOH 3 g Na_2CO_3 100 mL distilled H_2O	3 min–2 h	Dissolves Al matrix; reveals details of Si eutectic, intermetallic phase morphology	Ref 42
8s	10 mL H_3PO_4 90 mL distilled H_2O	13 min–1 h, 50 °C (120 °F)	Dissolves Al matrix; reveals primary Si morphology	Ref 42

Phase Composition. The volume fraction of phase or structure constituents is the stereological parameter expressing the phase composition of the alloy. Phase volume fraction can be estimated by means of the area, line, or point fraction of this phase constituent carried out on the flat random microsections. The automatic analyzer of the microscope image or the special grid on the focusing screen of the microscope can be used as well as the point counting in the microscope ocular. The measurement conditions are established depending on the microstructure morphology and expected accuracy of estimation. From a metallographic point of view, the analyzed image of the microstructure should be a true representation of the material from a specimen without any defects or artifacts (scratches, pullouts) that can change the measurement results. Preparation procedures, which are intended to enhance contrast between phase constituents, are especially important in automatic image analysis. Contrast must allow the proper establishment of the detection threshold. The difference of gray level of the measured phase components must be higher than the minimum detection threshold. The homogeneous gray level, that is, the quality of the microsection surface, is also important from the point of view of the measurements results. The described selective etching procedure of the phase components can improve the contrast between them.

Phase Constituent Morphology, Distribution, and Degree of Dispersion. The polyphase aluminum alloys are characterized by the variety of morphological forms—shape of precipitates, dispersion degree, and distribution of their phase or structure constituents. A uniform quantitative description is difficult and must be regarded individually in dependence on the examined alloy. All the remarks concerning microsection quality for the volume fraction measurements are valid in the case of other morphological feature descriptions. The functions of the mathematical morphology allow the microstructure image modification and often can be used to improve and facilitate the establishment of the detection threshold establishing (Ref 34).

Specific Microstructural Problems of Al-Alloy Metallography

Qualitative Description. Eutectic melted zones in the microstructure of the aluminum alloy may appear in the following cases:

- In an alloy of composition $C_o > C_s$ when the eutectic is the equilibrium constituent of the microstructure (Fig. 40)
- In an alloy of composition $C_o < C_s$ when the eutectic is the nonquilibrium constituent of the microstructure (Fig. 40)

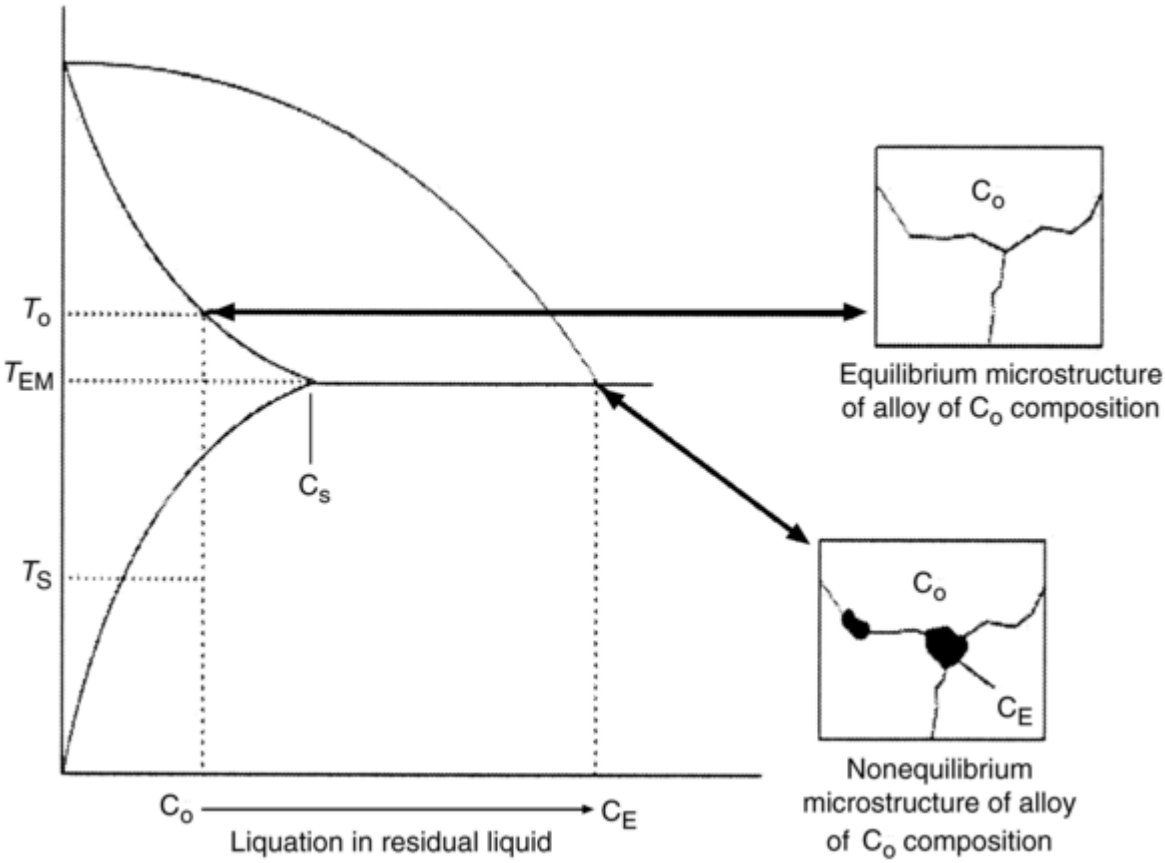

Fig. 40 Schematic of microstructure constituents formed with alloying variations in eutectic melting zones. C_o, average alloy composition; C_E, eutectic composition achieved by liquation into residual liquid during nonequilibrium solidification; C_s, limit of solid solubility in the aluminum-solid solution; T_o, solidus temperature for average alloy composition; T_{EM}, local solidus temperature for eutectic composition, or temperature of eutectic melting; T_S, solvus temperature

The nonequilibrium microstructure constituents can result from a liquation of the alloy components (both additional or impurities) of high partition ratio (between liquid and solid state) and low diffusivity during solidification (Fig. 40). In the residual liquid of high concentration of the segregated alloy components achieving eutectic composition (C_E), the multicomponent eutectic could form at the end stage of the solidification process, that is, at lower temperature (T_{EM}) than aluminum solid-solution solidified (T_o) (Table 20).

The risk of accidental melting of the fusible microstructure constituents (multicomponent eutectic) should be considered by a technologist for a particular alloy or process on the basis of the industrial practice, experiments, or literature data. The possibility of eutectic melting especially should be taken into account during heat treatment and welding, as shown schematically in Fig. 41. This undesirable phenomenon is a potential source of decrease in the material properties and can be difficult to control or repair.

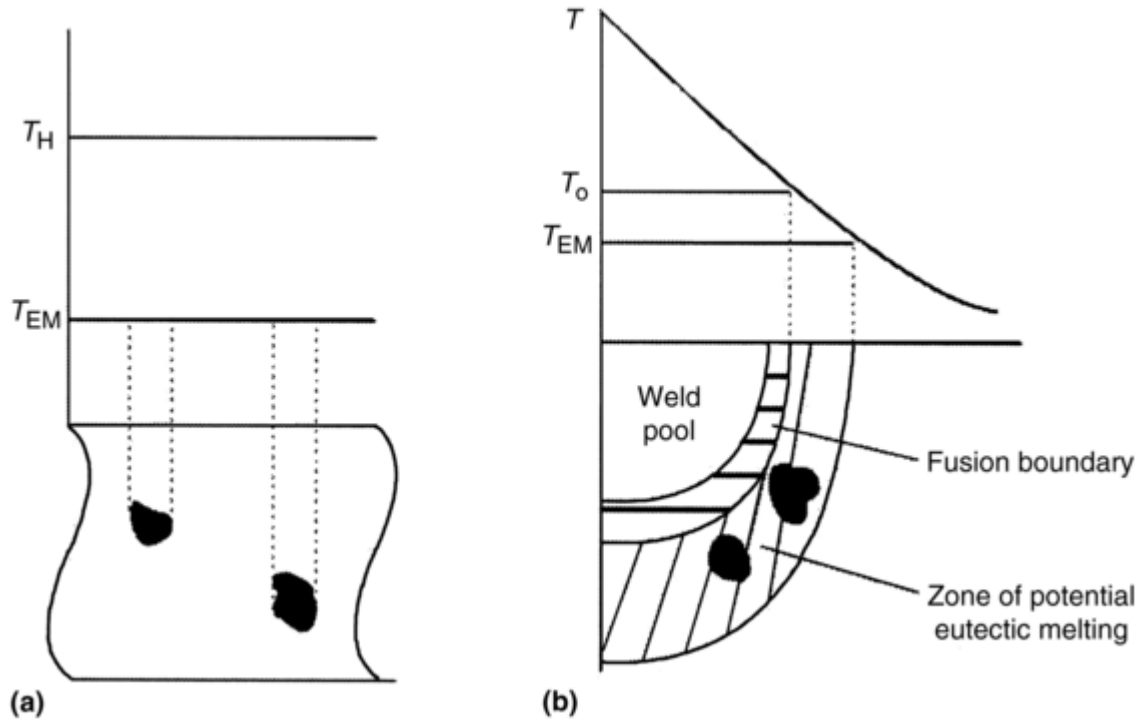

Fig. 41 Schematic of eutectic melting regions during (a) heat treatment and (b) welding. T_H, temperature of annealing; T_{EM}, temperature of eutectic melting; T_o, alloy solidus temperature. Dark areas represent regions of eutectic melting.

Eutectic Melted Zones. The following are metallographic problems concerning eutectic melting:

- Specimen preparation
- Eutectic melted zone recognition on the metallographic microsection

During cutting or mounting of the specimen in hot-mounting resins, preheating the specimen above T_{EM} should be avoided. Nevertheless, because the solvus temperature (T_S) is the limit on the precipitation process in the solid state at a temperature lower than T_{EM}, it is common not to exceed the solvus temperature during preparatory procedures.
The eutectic melted zone on the metallographic microsection may be visible as either oval or round pools filled with very dispersed particles of the eutectic phases (Fig. 42, Fig. 43).

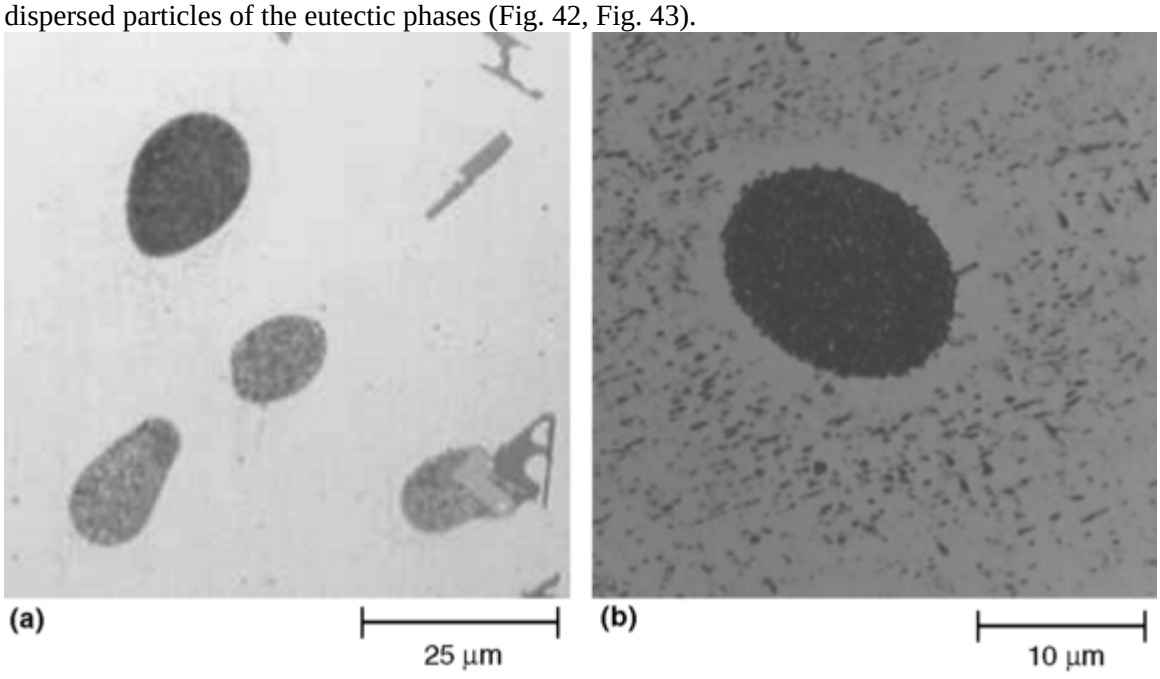

Fig. 42 Round islands of nonequilibrium eutectic in micrograph of 355 alloy at (a) 700× and (b) 1500×

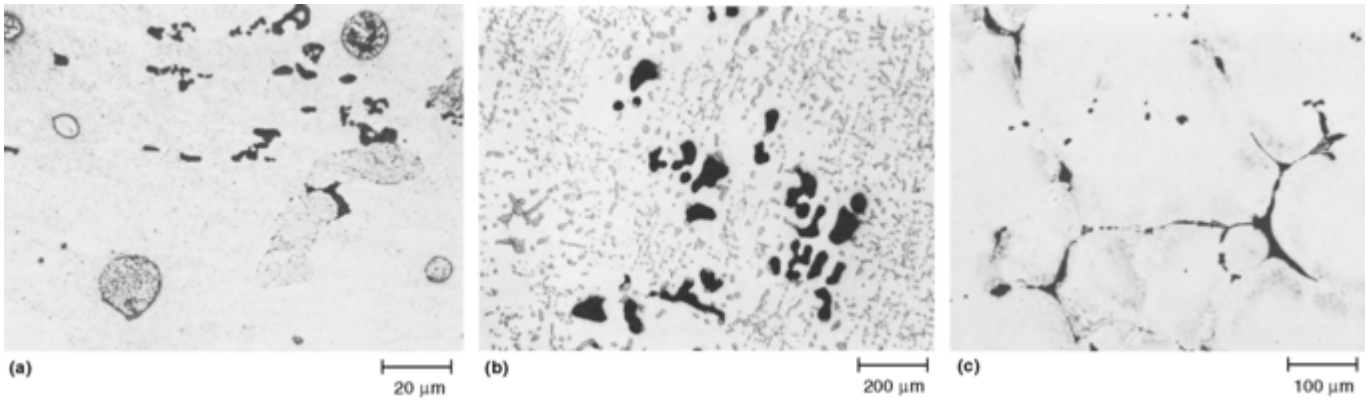

Fig. 43 Examples of eutectic melting microstructures (a) Alloy 2014-T6 closed-die forging, showing rosettes formed by eutectic melting when the solidus temperature (510 °C, or 950 °F) was exceeded during solution heat treating. Other constituents are particles of $CuAl_2$ (white, outlined) and insoluble $(Fe, Mn)_3SiAl_{12}$ (dark). Keller's reagent. 500× (b) A354-T4 investment casting with fusion voids (black) caused by eutectic melting when solidus was exceeded in solution heat treatment. Surface of casting is blistered. Gray particles are eutectic silicon. 0.1% HF. 50× (c) As-cast alloy D712-F with intergranular fusion voids (black) caused by eutectic melting as a result of exceeding the solidus temperature during dip brazing, Keller's reagent. 100×

Quantitative metallography of the aluminum alloys meets some specific problems concerning aluminum alloy microstructure regarding both cast and wrought alloys.

Dispersed Porosity in Castings (Ref 34, 37). Dispersed porosity can be regarded as a type of microstructural constituent from the point of view of image analysis and material performance. In cast alloys, dispersed porosity is generally of two types: gas porosity and shrinkage porosity. Gas porosity tends to be more convex or rounded in shape, while shrinkage porosity has more irregular (concave) features (Fig. 44). Dispersed pores also form clusters, such as the one shown in Fig. 44(c). At least two pores form a cluster. The dispersion of pores in a shrinkage-pore cluster may be different than the pore dispersion of a gas-pore cluster. The objects visible on the metallographic microsection are considered similar to other microstructure constituents and are measured.

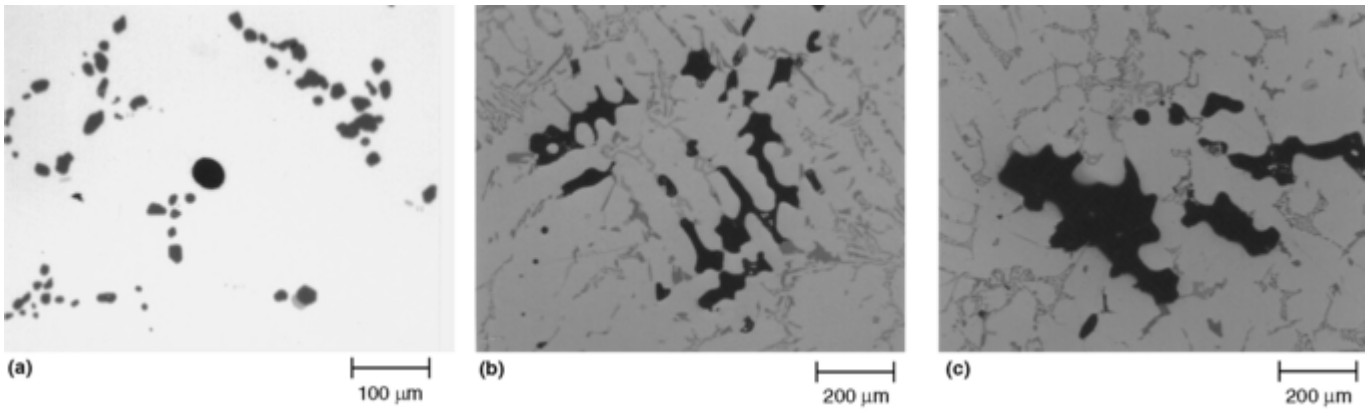

Fig. 44 Micrographs of porosity in a cast aluminum-silicon alloy. (a) Gaseous porosity. 100×. (b) Dispersed shrinkage porosity. 50×. (c) Cluster of shrinkage pores. 50×. Source: Ref 38

Despite the differences in morphology, the distinction of the two kinds of porosity on the metallographic section can be difficult, especially when porosity is in the form of many dispersed clusters. Taking into account the spatial morphology of the two kinds of porosity, one can assume that the objects include isolated pores and clusters from either shrinkage or gaseous porosity. The quantitative criterion to distinguish the isolated and gaseous pores is their distribution, described using the method of the nearest-neighbor distance (NND) (Ref 37). Pores that have a distance less than an established critical NND belong to a cluster of two pores or more; those with a greater NND are isolated.

Because of the small value of the volume fraction of the pores (<1% in good-quality aluminum cast parts) and the large range of possible sizes (from a few micrometers up to a few hundred micrometers), the following problems should be taken into account:

- The specimen surface destined for porosity measurement must be well prepared to retain pore profile and section contrast to establish a good detection threshold.
- The number of measurements must be quite large to achieve a good statistic (accuracy and repeatability) of the results.

- The microscope magnification must be adjusted for detection of both small and large pores.

The global stereological parameters of the isolated convex pores can be estimated by one of the quantitative parameters, such as volume fraction (V_v), specific surface of the pore/matrix interface (S_v), or number of pores per unit area on the metallographic microsection. These are the various methods for porosity characterization.
Quantitative metallography is used in the description of porosity with the assumption that a single 3-D entity results in one 2-D image on a random section of a metallographic flat. Volume fraction of the isolated pores is then estimated. The quantitative description of dispersed porosity from shrinkage should be carried out in two steps:

- Characteristics of shrinkage clusters (one cluster is regarded as an individual entity) by the number of clusters on a measured area unit
- Characteristics of individual pores by means of global or local stereological parameters

Dendrite Arm Size (Ref 34, 39). Dendrite arm size (DAS) measurement is very useful, because this parameter can be considered the microstructure criterion in the Hall-Petch equation for the cast alloys. Dendrite arm size is also an estimator of the local solidification time θ (Ref 34). Local solidification time is a very important parameter from the point of view of the numerical modelling and simulation of the casting processes. Daimler-Chrysler and General Motors specifications for A356-T6 automotive castings include the method for determination of Dendritic Arm Spacing of hypoeutectic aluminum-silicon alloys with reference to the American Foundry Society's chart “Microstructure Control in Hypoeutectic Aluminum-Silicon Alloys.”
The problem is to reveal on the metallographic microsection the image of the dendrites in such contrast (Fig. 45) that the automatic image analyzer may be used. Very often, the dendrites of the α-aluminum solid solutions are outlined with interdendritic eutectic, but sometimes, the eutectic constituents have similar and too small a contrast in regard to the matrix, and their interface does not form a continuous line. In this case, revealing the dendritic segregation can improve the image quality. The mathematical morphology functions application for improving detection threshold is a method used very often in quantitative metallography.
The problem is to reveal on the metallographic microsection the image of the dendrites in such contrast (Fig. 45) that the automatic image analyzer may be used. Very often, the dendrites of the α-aluminum solid solutions are outlined with interdendritic eutectic, but sometimes, the eutectic constituents have similar and too small a contrast in regard to the matrix, and their interface does not form a continuous line. In this case, revealing the dendritic segregation can improve the image quality. The mathematical morphology functions application for improving detection threshold is a method used very often in quantitative metallography.

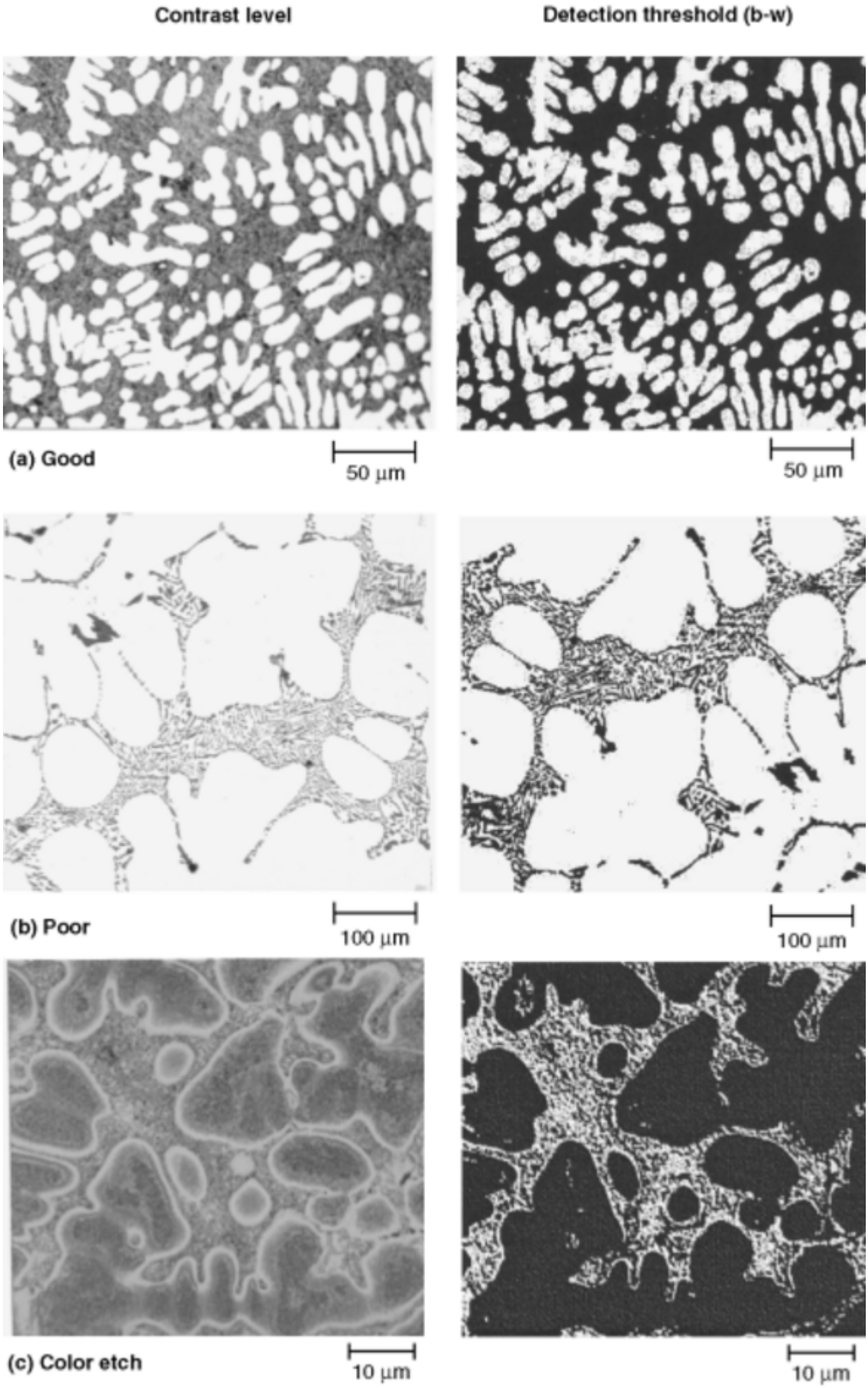

Fig. 45 Image contrast (left) and corresponding black-and-white (b-w) detection thresholds (right) for automatic image analysis of dendrite arm size in hypoeutectic aluminum-silicon cast alloys. (a) Good contrast for automatic image analysis of dendrite outlined with α-Al + Si eutectic. 200×. (b)

Poor contrast for automatic image analysis of dendrite outlined with α-Al + Si eutectic. 100×. (c) Dendrite revealed by color etching (shown here in black and white) with Weck I reagent (13m in Table 4) with detection in black-and-white mode. 800×

The true dendrite arm size of the *n*-th order measured on the metallographic microsection is:

$$DAS_n = L/n_n$$

where L is the true length of the measured line, and n_n is the number of arms of the *n*-th order intersected by a measured line (Fig. 46a). The distance between dendrite cross-section centers can be chosen as a measure of the DAS because of the close correlation between these parameters (Fig. 46b). The close correlation was also stated between DAS and a mean chord length of the dendrite cross sections. These stereological parameters can be measured automatically by means of the image analyzer (Fig. 46c).

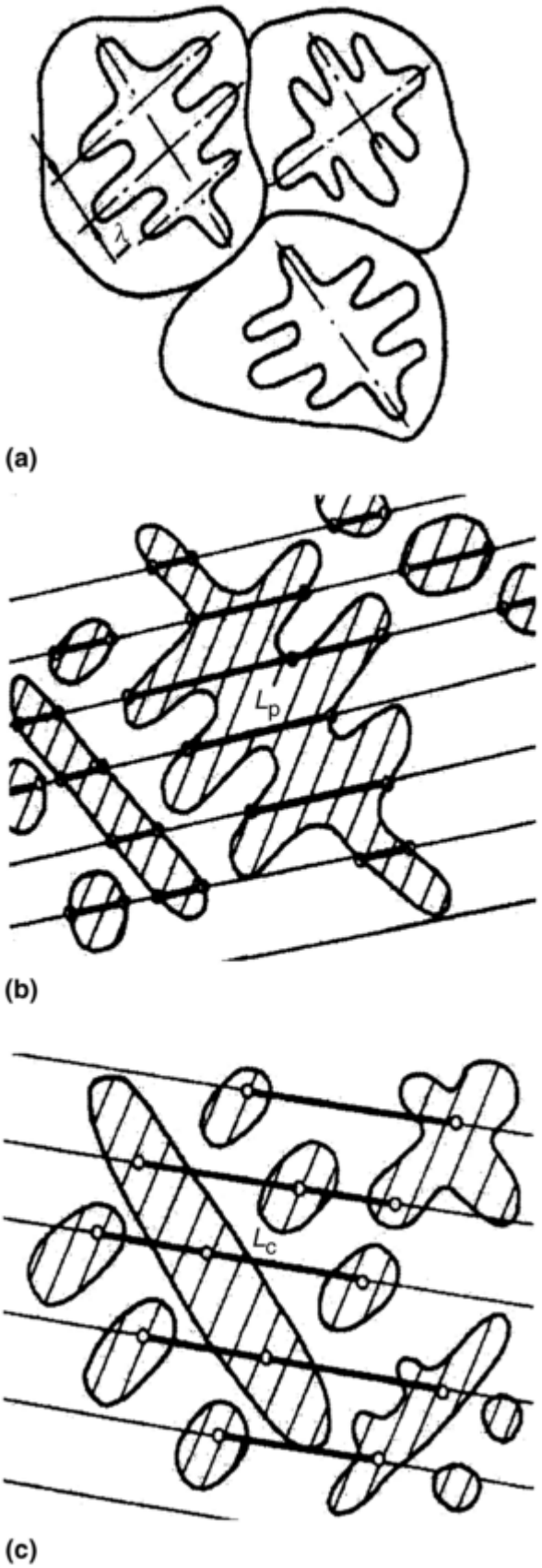

Fig. 46 Measure methods of dendrite arm size (DAS). (a) True DAS (λ). (b) Mean distance between dendrite cross-section centers (L_p). (c) Mean chord length of dendrite cross sections (L_c). Source: Ref 34, 39

Microstructure Anisotropy. Wrought alloy microstructure is often characterized by an anisotropy that results from plastic deformation. The grains of the alloy are nonequiaxed. Special attention must be given to the position of the microsections in relation to the deformation direction. The true results of the volume fraction of the phase constituents can be estimated on the cross sections perpendicular either to the axis of rotational symmetry or to the plane of the planar symmetry (Fig. 47).

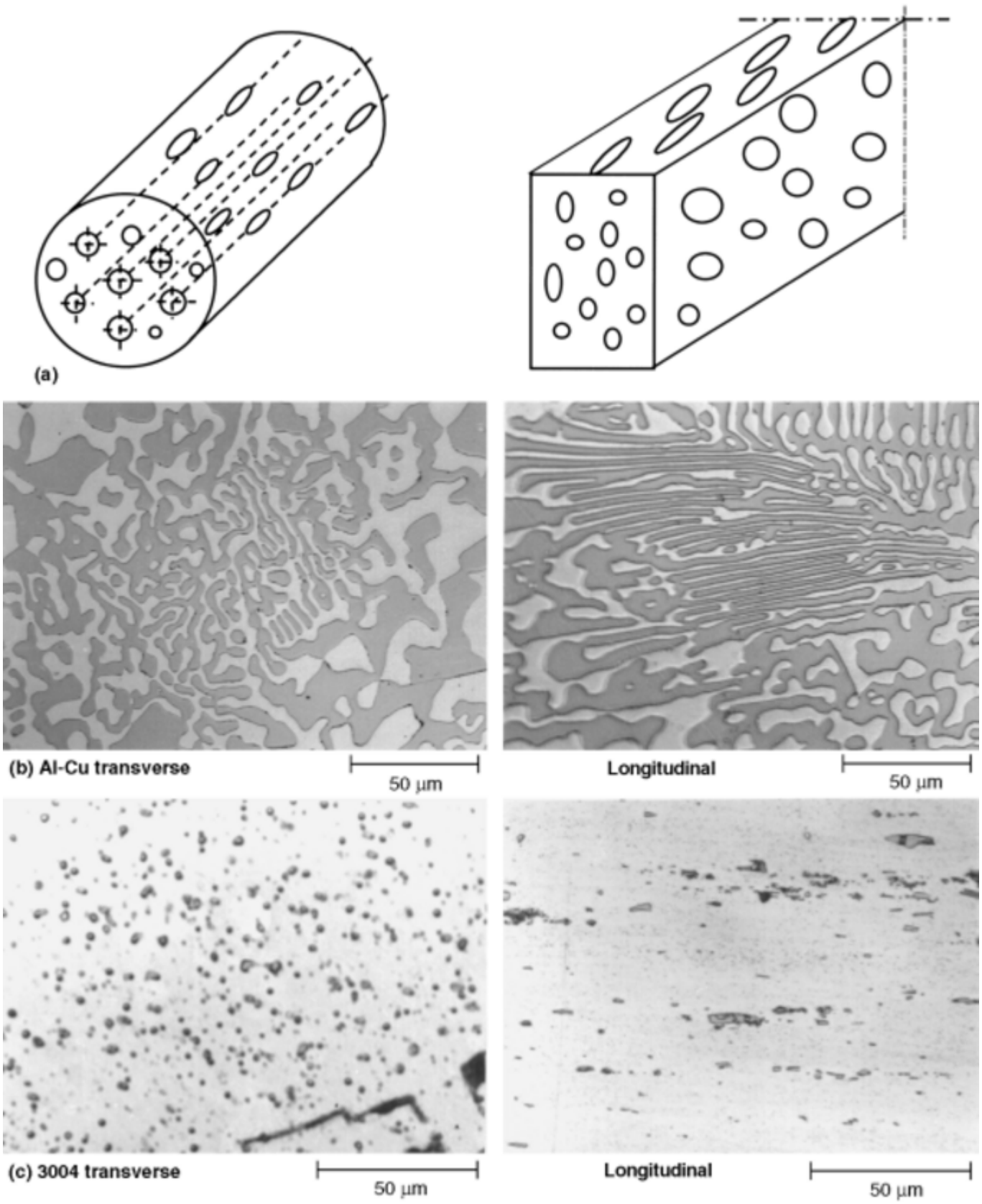

Fig. 47 Microstructure anisotropy. (a) Schematic views of microstructural anisotropy in cylindrical and rectangular sections. (b) Transverse (left) and longitudinal (right) view of anisotropy in solidification microstructure from directional cooling of aluminum-copper eutectic alloy. 400×. (c) Transverse (left) and longitudinal (right) view of anisotropy from plastic deformation of hot-rolled 3004 alloy. 500×. Etched with 0.5% HF (5m in Table 4)

The complete microstructure description demands two (in the case of a rotational microstructure symmetry) or even three (in the case of a planar microstructure symmetry) oriented microsections to be prepared and analyzed. The precautions that were mentioned in the section “Specimen Cutting” in this article must be respected. In the recrystallized alloys, the grains may have asymmetric or even bimodal grain size distributions, so the microscope magnification must be chosen in

such a manner that both large and small grains may be revealed, detected, and measured. The shape of the grain size distribution is influenced by the measure conditions; for example, the length of the measure line.

References cited in this section

1. J.E. Hatch, *Aluminum: Properties and Physical Metallurgy,* American Society for Metals, 1984
2. J.R. Davis, Ed., *Aluminum and Aluminum Alloys,* ASM Specialty Handbook, ASM International, 1993
3. L.F. Mondolfo, *Aluminum Alloys: Structure and Properties,* Butterworths, 1976
4. J.E. Hatch, *Aluminum—Properties and Physical Metallurgy,* American Society for Metals, 1984, p 30–31
5. E. di Russo, *The Atlas of Microstructures of Aluminum Casting Alloys,* Edimet, Brescia, 1993
6. *Struers—The Best of Structure 1–12,* Copenhagen, 1988, p 101–104
7. *Metallography and Microstructures,* Vol 9, *Metals Handbook,* 9th ed., American Society for Metals, 1985, p 351–388
8. M. Orman, *Metalografia Aluminium (Metallography of Aluminum),* Wyd. Śląsk, Katowice, 1957
9. G. Petzow, *Metallographic Etching,* 2nd ed., ASM International, 1999
10. "Standard Methods for Microetching Metals and Alloys," E 407–70, American National Standard Institute/ASTM, reapproved 1976
11. E. Beraha and B. Shpigler, *Color Metallography,* American Society for Metals, 1977
12. E. Beraha, Metallographic Reagents Based on Molybdate Solutions, *Prakt. Metallogr.,* Vol 11 (No. 5), 1974, p 271–275
13. R. Poganitsch, R. Sigl, and F. Jeglitsch, Sequential Etching for the Identification of Phases in Technical AlZnMgCu Alloys, *Prakt. Metallogr.,* Vol 21 (No. 5), 1984, p 258–268
14. E. Weck and E. Leistner, *Metallographic Instructions for Colour Etching by Immersion, Part III,* Deutscher Verlag fur Schweisstechnik-GmbH, Dusseldorf, 1986
15. M. Richard, Reactif Micrographic pour Colorer le Silicium Dans les Alliages d'Al (Metallographic Reagent for Coloration of the Silicon Precipitates in Aluminum Alloys), *Fonderie,* Vol 28 (No. 326), 1973, p 289–290
16. P. Lienard and C. Pacque, New Metallographic Etching Method for Aluminium Alloys Used in Foundries, *Struers—The best of structure 1–12,* Copenhagen, 1988, p 101–104
17. G. Vander Voort, Ed., *Applied Metallography,* Van Vostrand R., 1986
23. W.J.M. McTegart, *The Electrollytic and Chemical Polishing of Metals,* Pergamon Press Ltd., England, 1959, Wyd. N.-T. Warszawa, 1961
24. *Fractography and Atlas of Fractographs,* Vol 9, *Metals Handbook,* 8th ed., American Society for Metals, 1974
25. I. Lukac and S. Michna, *Colour Contrast, Structure and Defects in Aluminium and Aluminium Alloys,* Cambridge International Science Publishing, Cambridge, 2001
26. R. Kovacheva, Metallographic Investigation of Al-Si-Mg and Al-Si-Cu Alloys, *Prakt. Metallogr.,* Vol 30 (No. 2), 1993, p 68–77

27. J. Ryś, *Stereologia Materiałów (Stereology of Materials),* Fotobit Design, Kraków, 1995

28. E.E. Underwood, *Quantitative Stereology,* Adison-Wesley Publishing Company, 1970

29. M.L. Bernsztejn and W.A. Zajmowskij, *Struktura i Własności Mechaniczne Metali (Structure and Properties of Metals),* Wyd. Naukowo-Techniczne, Warszawa, 1973

30. M. Hafiz and T. Kobayashi, Metallurgical Factors Affecting Impact Toughness of Eutectic Al-Si Alloy, *Z. Metallkd.,* Vol 89, 1998, p 445–449

31. R.W. Hertzberg, *Deformation and Fracture Mechanics of Engineering Materials,* John Wiley and Sons, New York, 1989

32. M. Warmuzek, *Aluminum-Silicon Casting Alloys: Atlas of Microfractographs,* ASM International, 2004

33. P.N. Crepeau and S.D. Antolovich, Structure Property Relationships in Aluminum Alloy 339-T5: Tensile Behavior at Room and Elevated Temperature, *Trans. Am. Foundry Soc.,* Vol. 98, 1990, p 813–822

34. J.C. Jaquet and W. Hotz, Quantitative Description of the Microstructure of Aluminum Foundry Alloys, *Cast Met.,* Vol 4, (No. 4), 1992, p 200–225

35. C. Sigli, H. Vichery, and B. Grange, Computer Assisted Metallurgy Non Heat Treatable Aluminum Alloys, *Mater. Sci. Forum,* Vol 217–222, 1996, p 391–396

36. W.R. Cribb, Quantitative Metallography of Poly-Phase Microstructures, *Scr. Metall.,* Vol 12 (No. 10), 1978, p 893–898

37. J.P. Anson and J.E. Gruzleski, Effect of Hydrogen Content on Relative Shrinkage and Gas Microporosity in Al-7%Si Casting, *Trans. Am. Foundry. Soc.,* Vol 108, 2000, p 135–142

38. M. Biel-Gołaska, J. Piekło, and R. Żuczek, Analiza Rozwoju Uszkodzeń w Stopach Odlewniczych na Podstawie Mechaniki Pękania (Analysis of Failure Development in Cast Alloys Based on Fracture Mechanics), *Praca Naukowo—Badawcza Instytutu Odlewnictwa,* 2001, p 9051/01

39. M. Warmuzek, Dendritic Microstructures in Cast Al-Si Alloys—An Analysis of Dispersion Factors, *Proc. Foundry Res. Inst.,* Vol 48, (No. 102), 1998, p 56–73

40. H.-E. Ekstrom, J. Hagstrom, and L. Ostensson, Particle Size Distribution in a DC-Cast and Rolled AA3104 Alloy, *Mater. Sci. Forum,* Vol 331–337, 2000, p 391–396

41. H.M. Tensi and J. Hogerl, Metallographische Gefuge Untersuchung zur Qualitatssicherung von AlSi-Gussbautailen (Metallographic Investigation of Microstructure for Quality Assurance of Aluminum-Silicon Castings), *Metall,* Vol 48, 1994, p 776–781

42. M. Warmuzek, Zastosowanie Mikroanalizy Rentgenowskiej w Badaniach Mikrostruktury Stopów Metali (Application of X-ray Microanalysis for Examination of the Microstructure of the Metal Alloys), *Biuletyn IO,* Vol 3 (No. 3), 2000, p 3–24

M. Warmuzek, Metallographic Techniques for Aluminum and Its Alloys, *Metallography and Microstructures,* Vol 9, *ASM Handbook,* ASM International, 2004, p. 711–751

Metallographic Techniques for Aluminum and Its Alloys

Małgorzata Warmuzek, Foundry Research Institute, Kraków, Poland

SEM Examination

X-Ray Microanalysis (Ref 42). As noted, x-ray microanalysis of the chemical composition with modern SEM systems is a very useful technique in microstructural analysis of selected microregions of the specimen. Most SEMs in modern metallographic laboratories are equipped with x-ray analyzers of either the energy-dispersion spectrum (EDS) or, less widely, the wavelength-dispersion spectrum (WDS). Due to the strictly localized interference of the electron beam and specimen material, the identification of the chosen particular phase precipitates may be carried out. This facility is of great importance in the case of multiphase aluminum-alloys, when the phase constituent precipitates very often have similar morphology and color during observation under the metallographic light microscope. In this situation, x-ray microanalysis is an easy and repeatable method to unequivocally verify the phase composition of the alloy. The EDS mode of x-ray microanalysis gives fast measurements of the local chemical composition results, comparable with WDS from the point of view of accuracy and detection limit for elements of $Z > 11$.

The complementary use of classical metallography and x-ray microanalysis helps resolve the following problems (Fig. 48, 49, 50).

- Phase identification in a multiphase alloy (Fig. 48) or verification of the selective etching results
- Verification of structure observations using cross poles (Fig. 49)
- Key for phase designation: phase identification by means of its qualitative or quantitative chemical composition estimation in the microregions (Fig. 50)

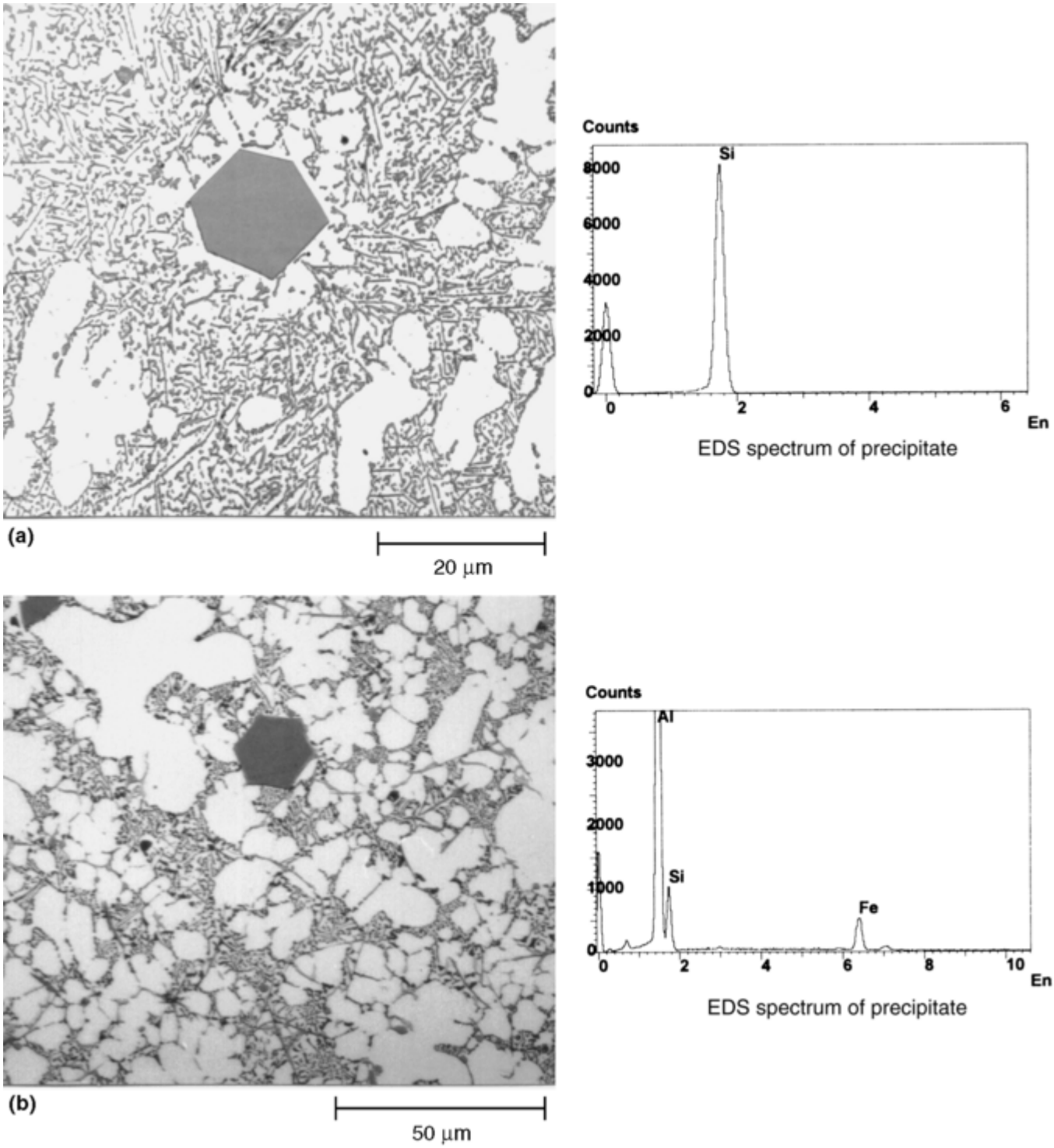

Fig. 48 Example of energy-dispersion spectrum (EDS)-aided metallography for phase identification of (a) a silicon primary precipitate in an unetched specimen of aluminum-silicon cast alloy at 1000×, and (b) an AlFeSi primary precipitate in an etched (0.5% HF) specimen of AlSiFe cast alloy at 500×

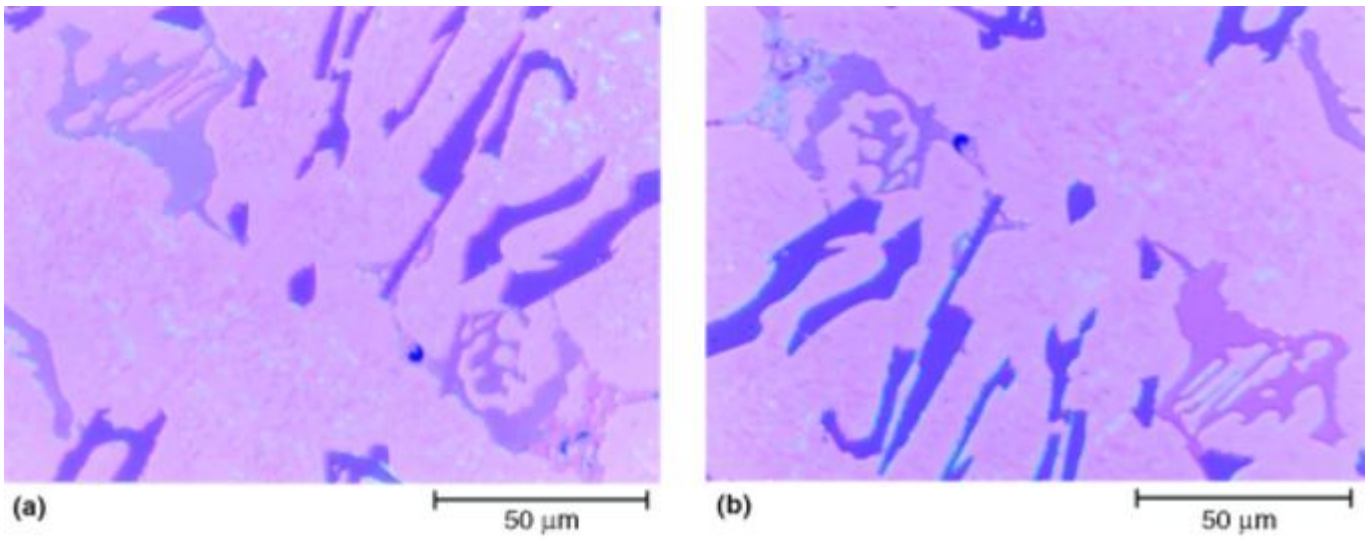

Fig. 49 Example of energy-dispersive spectroscopy (EDS)-aided metallography in interpretation of color images in polarized light. The Π phase ($Al_8FeMg_3Si_6$) in an Al-Si-Cu-Ni alloy is indicated by EDS for micrographs with (a) first position of cross poles and (b) second position of cross poles. Etched with 0.5% HF. 500×.

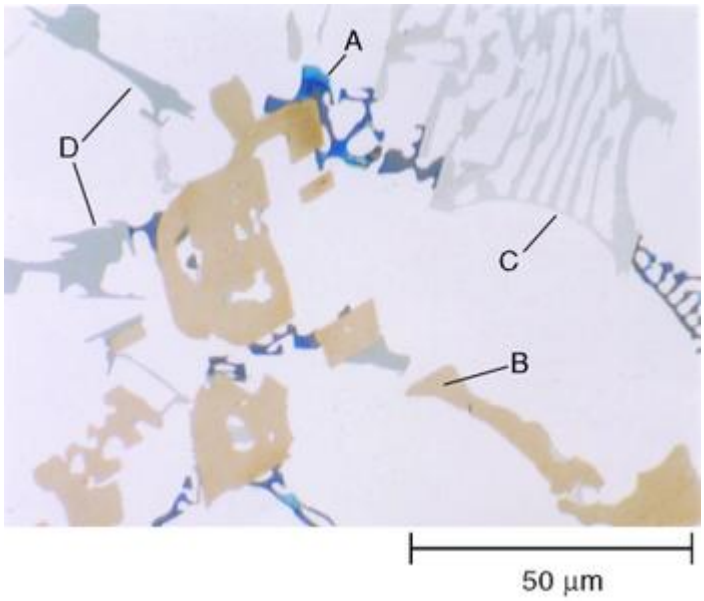

Fig. 50 Phases in an Al-Si-Cu-Ni alloy: Mg_2Si (blue precipitate), Al_3NiCu (light-brown precipitate), $Al_8Fe(Ni)Mg_3Si_6$ (gray precipitate), α-Al matrix (light-gray field), and eutectic silicon (dark gray).

In most cases, the qualitative results (EDS spectrum with identified peaks of a characteristic line) show the local chemical composition of chosen particles or microregions and are sufficient to solve these problems.

One of the demands of x-ray spectrum acquisition is a flat and clean sample surface. In the case of aluminum alloys, it is rather difficult because of their strong tendency for oxidation. To improve the contrast of the matrix/phase interface, slight etching is acceptable.

SEM Observation of Deep-Etched Microsections (Ref 2, 43). The polyphase structure formed during alloy solidification is characterized by 3-D morphology, which is often difficult to reconstruct on the basis of 2-D cross-section images. The SEM makes it possible to reveal the 3-D morphology of polyphase regions as interdendritic eutectic or intermetallic phase precipitates. The specimen preparation procedure consists of dissolving the aluminum matrix in a reagent that will not attack the eutectic components or intermetallic phase precipitates. The residuals of the etching products should be removed by intensive rinsing in tap water (in the case of alcohol-based reagents, alcohol for rinsing is recommended). Short rinsing in the ultrasonic cleaner gives very good results. The preliminary preparation of the specimen is not necessary, but removing the superficial deformed or contaminated layer can shorten the process.

Scanning electron examination of deep-etched specimens is a method often used in the analysis of modification effects on aluminum-silicon eutectic or primary silicon precipitates in aluminum-silicon cast alloys. The process of nucleation of the secondary phases on the matrix/primary phase interfaces also may be investigated with this method (Fig. 51, Fig. 52).

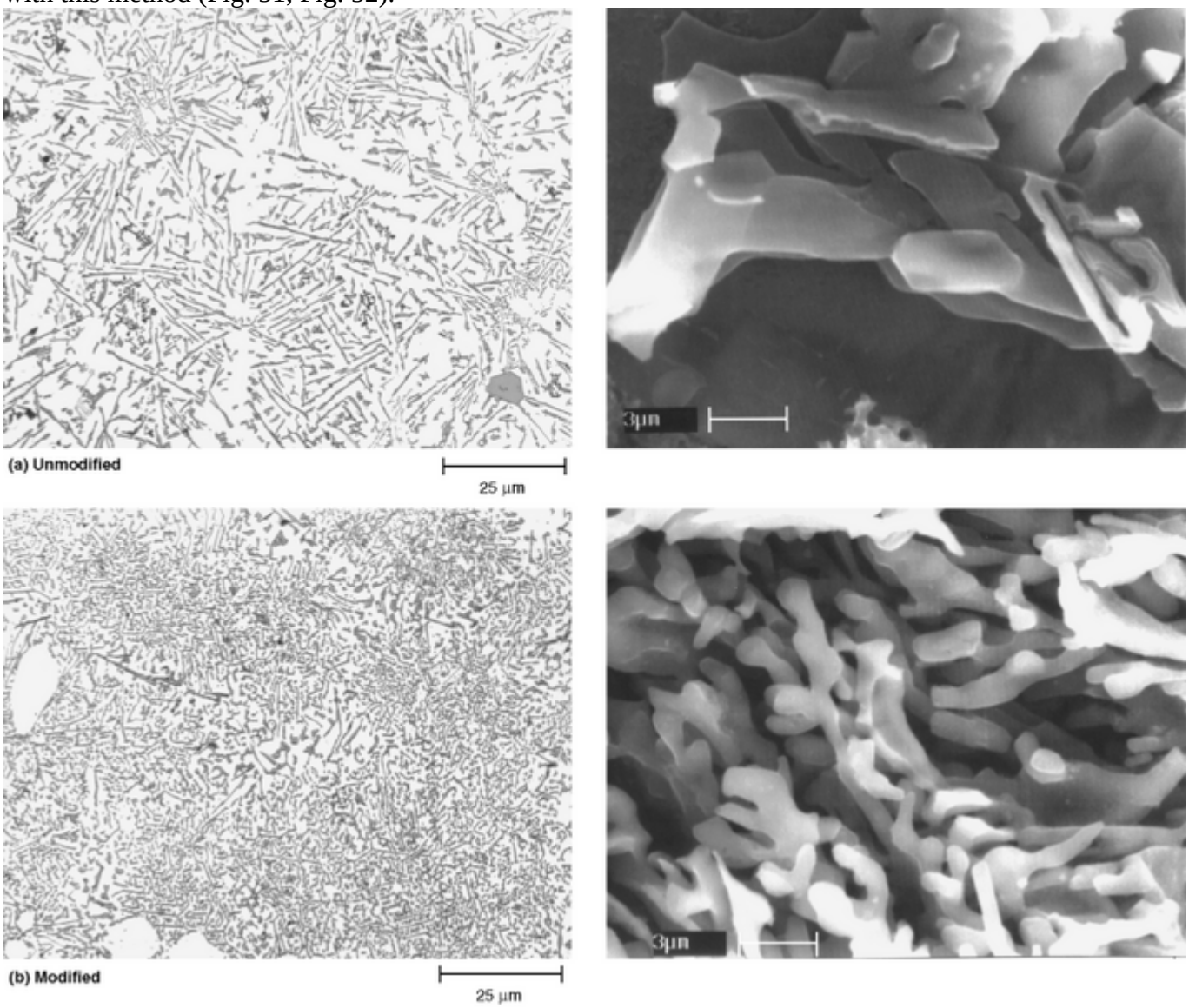

Fig. 51 Modified and unmodified phase morphology of a eutectic aluminum-silicon alloy from examination by light microscopy (left, at 750×) of etched specimens (0.5% HF) and by SEM imaging (right, at 4000×) of specimens deep etched with procedure 2s in Table 22 [Solution A (Flick's reagent) + Solution B]. (a) Unmodified alloy. (b) Modified alloy

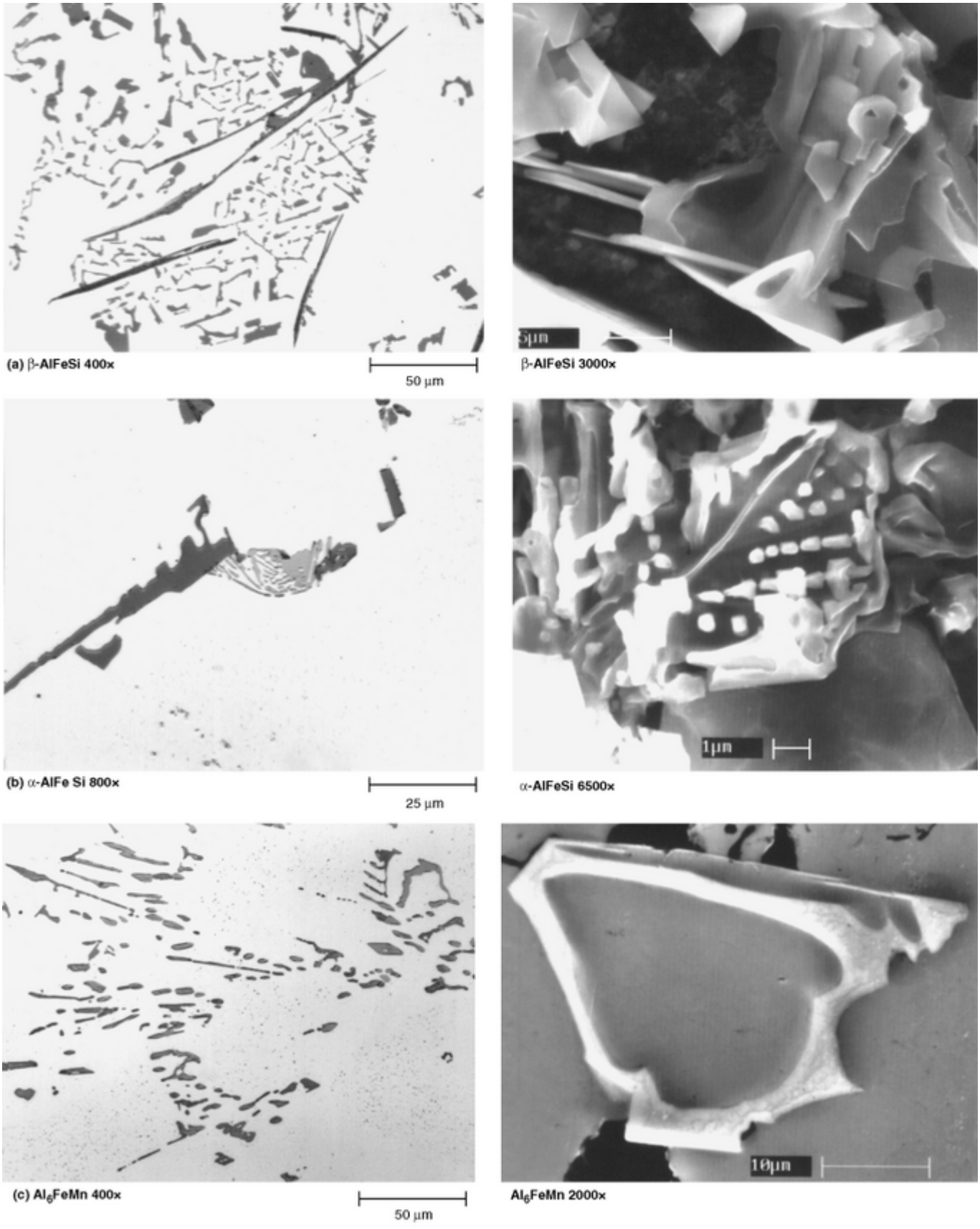

Fig. 52 Morphology of intermetallic phases examined by light microscopy (left) of etched specimens (0.5% HF) and by SEM imaging (right) of specimens deep etched with Flick's reagent. (a) β-AlFeSi phase particles in the interdendritic region of an unmodified hypoeutectic aluminum-silicon alloy. (b) Chinese script particles of α-AlFeSi phase in the interdendritic region of a modified hypoeutectic aluminum-silicon alloy. (c) Al_6FeMn phase particles in the interdendritic region of alloy 3004

SEM Observation of the Fracture Surface (Ref 24, 32, 44). Topography of fracture surfaces is commonly examined by SEM. The large depth of field is a very important advantage for fractographic investigations (Fig. 53). Fracture surfaces can be observed by means of SEM without almost any special preparation; nevertheless, if it is possible, the specimens should be examined immediately after failure because of the very fast superificial oxidation of aluminum and its alloys. In some cases, for example, after a catastrophic crack, the specimen should be cleaned mechanically by rinsing in ultrasonic cleaner, chemical reagents, or electrolytes.

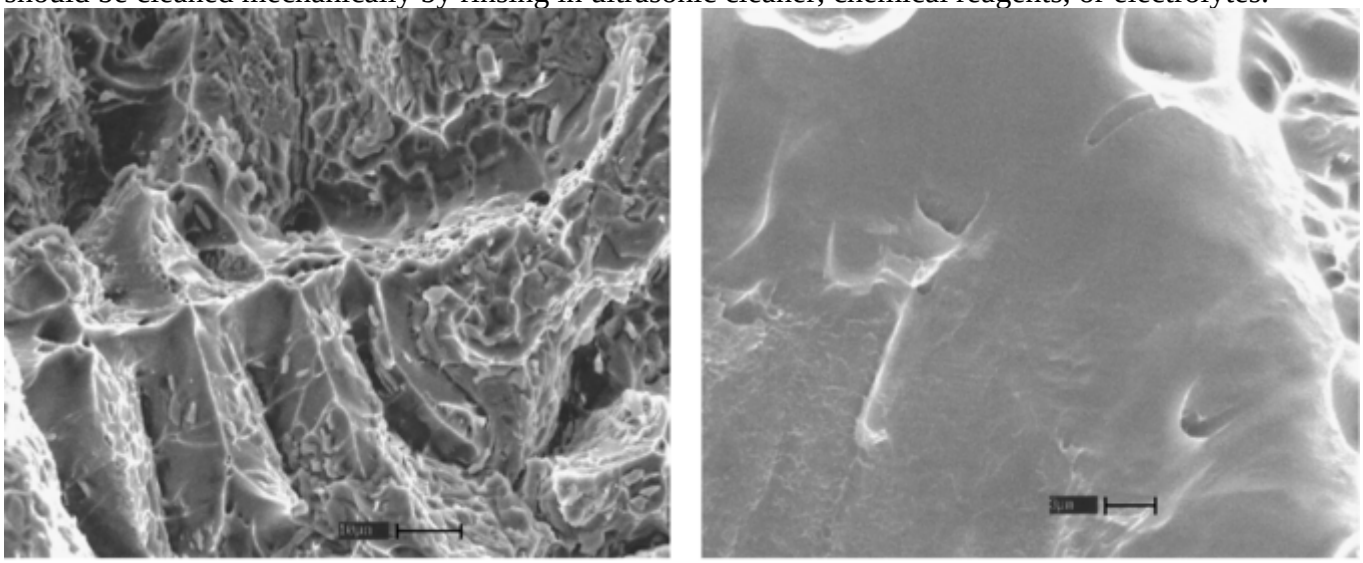

Fig. 53 SEM images, at two magnifications, of transgranular ductile (microvoid coalescence) fracture surface in hot-rolled 7050 alloy after T6 heat treatment. At the higher magnification (b), the oval shear dimples on the tear ridges indicate an inhomogeneous stress state.

Analysis of the SEM fracture images helps in the identification of:

- The specific failure mechanism
- The fracture path in structure constituents
- The microregion of crack initiation
- The areas of local inhomogeneous strain state
- The morphological features of the observed fracture area

Examples are shown in Fig. 53 and 54. Figure 53 is an example of a transgranular ductile fracture. The crack developed through aluminum solid solution hardened with the dispersed particles of the intermetallic phase $\eta(MgZn_2)$. The dimpled microvoids in the deformed material arose round these particles, and the first stage of the decohesion took place on the α-aluminum/$\eta(MgZn_2)$. The very elongated, large hollows were produced by a coalescence of the arrays of smaller voids, and they were separated with the long tear ridges on the top of the shear microregions. On the walls of the tear ridges, the oval shear dimples are visible (Fig. 53b). Such fracture morphology testifies to the inhomogeneous stress state.

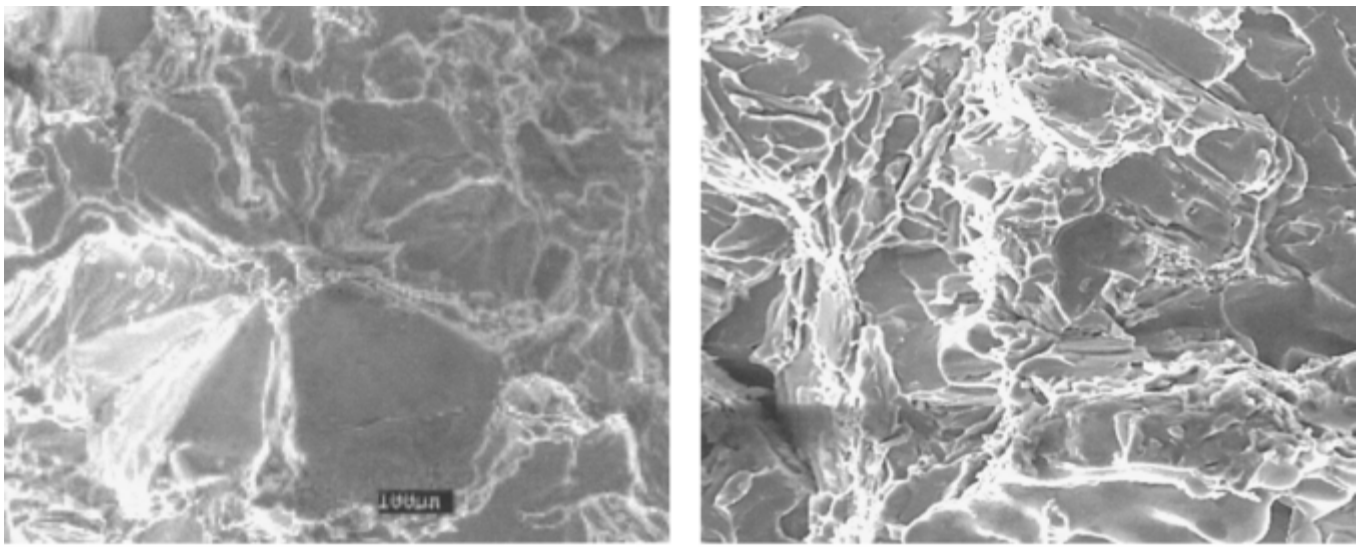

Fig. 54 SEM images of a mixed-mode fracture surface with indications of transgranular brittle and ductile cracking from an as-cast state 356 alloy tensile-test specimen. The area of the crack initiation is visible in the center of (a), and fracture went through the cleavage planes in the silicon particles. In the bottom part of (b), the dendrites of aluminum solid solution are visible in the shrinkage microarea.

An example of a mixed-mode fracture surface (with indications of brittle and ductile cracking on a microscopic scale) from the surface of an as-cast state 356 alloy tensile-test specimen is shown in Fig. 54. The morphology from transgranular brittle fracture (cleavage) is mainly visible, but some degree of plastic deformation in the aluminum solid solution also may be noticed in the form of shallow dimples. The first decohesion took place in the precipitates of the eutectic silicon. The area of the crack initiation is visible in the center of Fig. 54(a). The fracture then went through the cleavage planes in the silicon particles. In the bottom part of Fig. 54(b), the dendrites of aluminum solid solution were visible in the shrinkage microarea.

References cited in this section

2. J.R. Davis, Ed., *Aluminum and Aluminum Alloys*, ASM Specialty Handbook, ASM International, 1993

24. *Fractography and Atlas of Fractographs*, Vol 9, *Metals Handbook*, 8th ed., American Society for Metals, 1974

32. M. Warmuzek, *Aluminum-Silicon Casting Alloys: Atlas of Microfractographs*, ASM International, 2004

42. M. Warmuzek, Zastosowanie Mikroanalizy Rentgenowskiej w Badaniach Mikrostruktury Stopów Metali (Application of X-ray Microanalysis for Examination of the Microstructure of the Metal Alloys), *Biuletyn IO*, Vol 3 (No. 3), 2000, p 3–24

43. J.M. Guillemany and J.M. Virgili, Metalografia SEM en Aleaciones Al-Si- Reactivos Especificos (y2), *Fundición*, Vol 3–4, 1986, p 23–29

44. M. Warmuzek and K. Rabczak, "Microscopic Analysis of the Microstructure Aspects of Multiphase Al-Si Alloys Failure," Euromat 2001, Seventh European Conference on Advanced Materials and Processes, 10–14 June 2001 (Rimini, Italy)

M. Warmuzek, Metallographic Techniques for Aluminum and Its Alloys, *Metallography and Microstructures,* Vol 9, *ASM Handbook,* ASM International, 2004, p. 711–751

Metallographic Techniques for Aluminum and Its Alloys

Małgorzata Warmuzek, Foundry Research Institute, Kraków, Poland

References

1. J.E. Hatch, *Aluminum: Properties and Physical Metallurgy,* American Society for Metals, 1984
2. J.R. Davis, Ed., *Aluminum and Aluminum Alloys,* ASM Specialty Handbook, ASM International, 1993
3. L.F. Mondolfo, *Aluminum Alloys: Structure and Properties,* Butterworths, 1976
4. J.E. Hatch, *Aluminum—Properties and Physical Metallurgy,* American Society for Metals, 1984, p 30–31
5. E. di Russo, *The Atlas of Microstructures of Aluminum Casting Alloys,* Edimet, Brescia, 1993
6. *Struers—The Best of Structure 1–12,* Copenhagen, 1988, p 101–104
7. *Metallography and Microstructures,* Vol 9, *Metals Handbook,* 9th ed., American Society for Metals, 1985, p 351–388
8. M. Orman, *Metalografia Aluminium (Metallography of Aluminum),* Wyd. Śląsk, Katowice, 1957
9. G. Petzow, *Metallographic Etching,* 2nd ed., ASM International, 1999
10. "Standard Methods for Microetching Metals and Alloys," E 407–70, American National Standard Institute/ASTM, reapproved 1976
11. E. Beraha and B. Shpigler, *Color Metallography,* American Society for Metals, 1977
12. E. Beraha, Metallographic Reagents Based on Molybdate Solutions, *Prakt. Metallogr.,* Vol 11 (No. 5), 1974, p 271–275
13. R. Poganitsch, R. Sigl, and F. Jeglitsch, Sequential Etching for the Identification of Phases in Technical AlZnMgCu Alloys, *Prakt. Metallogr.,* Vol 21 (No. 5), 1984, p 258–268
14. E. Weck and E. Leistner, *Metallographic Instructions for Colour Etching by Immersion, Part III,* Deutscher Verlag fur Schweisstechnik-GmbH, Dusseldorf, 1986
15. M. Richard, Reactif Micrographic pour Colorer le Silicium Dans les Alliages d'Al (Metallographic Reagent for Coloration of the Silicon Precipitates in Aluminum Alloys), *Fonderie,* Vol 28 (No. 326), 1973, p 289–290
16. P. Lienard and C. Pacque, New Metallographic Etching Method for Aluminium Alloys Used in Foundries, *Struers—The best of structure 1–12,* Copenhagen, 1988, p 101–104
17. G. Vander Voort, Ed., *Applied Metallography,* Van Vostrand R., 1986

18. U.R. Kattner, Al-Fe (Aluminum-Iron), *Binary Alloy Phase Diagrams,* 2nd ed., T.B. Massalski, Ed., ASM International, 1990, p 149

19. G. Ghosh, Aluminum-Iron-Silicon, *Ternary Alloys: A Comprehensive Compendium of Evaluated Constitutional Data and Phase Diagrams,* Vol 5, G. Petzow and G. Effenberg, Ed., VCH (Germany), 1992, p 394–438

20. L.F. Mondolfo, *Metallography of Aluminum Alloys,* John Wiley & Sons, 1943, p 29, 106

21. *Metallography, Structures, and Phase Diagrams,* Vol 8, *Metals Handbook,* 8th ed., American Society for Metals, 1973, p 397

22. H. Okamoto, *Phase Diagrams of Dilute Binary Alloys,* ASM International, 2002, p 23

23. W.J.M. McTegart, *The Electrollytic and Chemical Polishing of Metals,* Pergamon Press Ltd., England, 1959, Wyd. N.-T. Warszawa, 1961

24. *Fractography and Atlas of Fractographs,* Vol 9, *Metals Handbook,* 8th ed., American Society for Metals, 1974

25. I. Lukac and S. Michna, *Colour Contrast, Structure and Defects in Aluminium and Aluminium Alloys,* Cambridge International Science Publishing, Cambridge, 2001

26. R. Kovacheva, Metallographic Investigation of Al-Si-Mg and Al-Si-Cu Alloys, *Prakt. Metallogr.,* Vol 30 (No. 2), 1993, p 68–77

27. J. Ryś, *Stereologia Materiałów (Stereology of Materials),* Fotobit Design, Kraków, 1995

28. E.E. Underwood, *Quantitative Stereology,* Adison-Wesley Publishing Company, 1970

29. M.L. Bernsztejn and W.A. Zajmowskij, *Struktura i Własności Mechaniczne Metali (Structure and Properties of Metals),* Wyd. Naukowo-Techniczne, Warszawa, 1973

30. M. Hafiz and T. Kobayashi, Metallurgical Factors Affecting Impact Toughness of Eutectic Al-Si Alloy, *Z. Metallkd.,* Vol 89, 1998, p 445–449

31. R.W. Hertzberg, *Deformation and Fracture Mechanics of Engineering Materials,* John Wiley and Sons, New York, 1989

32. M. Warmuzek, *Aluminum-Silicon Casting Alloys: Atlas of Microfractographs,* ASM International, 2004

33. P.N. Crepeau and S.D. Antolovich, Structure Property Relationships in Aluminum Alloy 339-T5: Tensile Behavior at Room and Elevated Temperature, *Trans. Am. Foundry Soc.,* Vol. 98, 1990, p 813–822

34. J.C. Jaquet and W. Hotz, Quantitative Description of the Microstructure of Aluminum Foundry Alloys, *Cast Met.,* Vol 4, (No. 4), 1992, p 200–225

35. C. Sigli, H. Vichery, and B. Grange, Computer Assisted Metallurgy Non Heat Treatable Aluminum Alloys, *Mater. Sci. Forum,* Vol 217–222, 1996, p 391–396

36. W.R. Cribb, Quantitative Metallography of Poly-Phase Microstructures, *Scr. Metall.,* Vol 12 (No. 10), 1978, p 893–898

37. J.P. Anson and J.E. Gruzleski, Effect of Hydrogen Content on Relative Shrinkage and Gas Microporosity in Al-7%Si Casting, *Trans. Am. Foundry. Soc.,* Vol 108, 2000, p 135–142

38. M. Biel-Gołaska, J. Piekło, and R. Żuczek, Analiza Rozwoju Uszkodzeń w Stopach Odlewniczych na Podstawie Mechaniki Pękania (Analysis of Failure Development in Cast Alloys Based on Fracture Mechanics), *Praca Naukowo—Badawcza Instytutu Odlewnictwa,* 2001, p 9051/01

39. M. Warmuzek, Dendritic Microstructures in Cast Al-Si Alloys—An Analysis of Dispersion Factors, *Proc. Foundry Res. Inst.,* Vol 48, (No. 102), 1998, p 56–73

40. H.-E. Ekstrom, J. Hagstrom, and L. Ostensson, Particle Size Distribution in a DC-Cast and Rolled AA3104 Alloy, *Mater. Sci. Forum,* Vol 331–337, 2000, p 391–396

41. H.M. Tensi and J. Hogerl, Metallographische Gefuge Untersuchung zur Qualitatssicherung von AlSi-Gussbautailen (Metallographic Investigation of Microstructure for Quality Assurance of Aluminum-Silicon Castings), *Metall,* Vol 48, 1994, p 776–781

42. M. Warmuzek, Zastosowanie Mikroanalizy Rentgenowskiej w Badaniach Mikrostruktury Stopów Metali (Application of X-ray Microanalysis for Examination of the Microstructure of the Metal Alloys), *Biuletyn IO,* Vol 3 (No. 3), 2000, p 3–24

43. J.M. Guillemany and J.M. Virgili, Metalografia SEM en Aleaciones Al-Si- Reactivos Especificos (y2), *Fundición,* Vol 3–4, 1986, p 23–29

44. M. Warmuzek and K. Rabczak, "Microscopic Analysis of the Microstructure Aspects of Multiphase Al-Si Alloys Failure," Euromat 2001, Seventh European Conference on Advanced Materials and Processes, 10–14 June 2001 (Rimini, Italy)

J.C. Harkness and A. Guha, Metallography and Microstructures of Beryllium, Copper-Beryllium, and Nickel-Beryllium Alloys, *Metallography and Microstructures,* Vol 9, *ASM Handbook*, ASM International, 2004, p. 752–761

Metallography and Microstructures of Beryllium, Copper-Beryllium, and Nickel-Beryllium Alloys

John C. Harkness, Brush Wellman Inc.; Amitava Guha

Introduction

THE TWO MAJOR TYPES of beryllium-containing alloys are copper-berylliums and nickel-berylliums. Beryllium additions, up to approximately 2 wt%, produce age-hardening effects in copper and nickel. Beryllium is also added to aluminum and magnesium to achieve grain refinement, oxidation resistance, castability, and workability. Other advantages are produced in gold, zinc, and other base metals. Unalloyed beryllium is used in weapons, spacecraft, nuclear reactor reflector segments, neutron sources, windows for x-ray tubes and radiation detection devices, rocket nozzles, aircraft brake discs, precision instruments, and mirrors. Beryllium has a close-packed hexagonal (α phase) arrangement at room temperature and a body-centered cubic (β phase) arrangement at 1270 °C (2320 °F). Metallography of beryllium is discussed at the end of this article.

The most widely used beryllium-containing alloys are wrought copper-berylliums, which provide good strength while retaining useful levels of electrical and thermal conductivity. Strengthening of copper-beryllium alloys is achieved by precipitation hardening based on the decreasing solid solubility of beryllium in a matrix of copper solid solution (α) as temperature is lowered (Fig. 1). Heat treatment typically consists of solution annealing followed by precipitation treatment, or age hardening. Cold work can be performed on wrought products between annealing and age hardening to enhance the magnitude of the age-hardening response. The β phase is a $BeCu_2$ compound, and the equilibrium γ phase in copper-beryllium alloys is BeCu. Commercial copper-beryllium alloys may also contain a third element addition, either of cobalt or of nickel. This addition to the binary alloy system restricts grain growth during annealing by establishing a dispersion of beryllide particles in the matrix. The addition also enhances the magnitude of the age-hardening response and retards the tendency to overage or soften at extended aging times and higher aging temperatures. In C17500 and C17200 (Table 1), the beryllides are (Cu,Co)Be with an ordered body-centered cubic CsCl (B2) superlattice. The beryllides in C17510 are (Cu,Ni)Be; they also display the B2 superlattice.

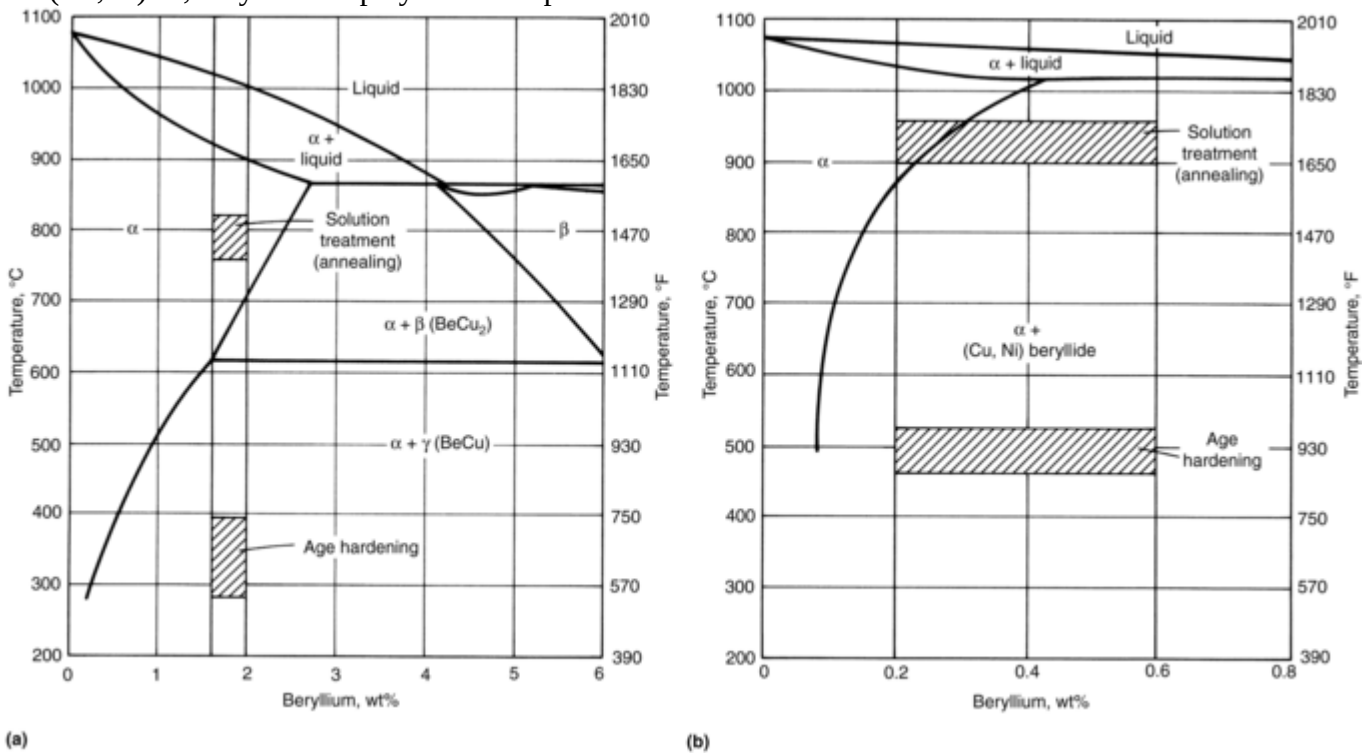

Fig. 1 Phase diagrams for copper-beryllium alloys. (a) Binary composition for high-strength alloys such as C17200. (b) Pseudobinary composition for C17510, a high-conductivity alloy

Table 1 Chemical compositions of copper-beryllium alloys

Composition, wt%						
UNS No.	**Be**	**Co**	**Ni**	**Pb**	**Other**	**Cu**
Wrought high-strength alloys						
C17000	1.60–1.79	[a]	[a]	…	…	bal
C17200	1.80–2.00	[a]	[a]	…	…	bal
C17300	1.80–2.00	[a]	[a]	0.20–0.6	…	bal
Wrought high-conductivity alloys						
C17410	0.15–0.50	0.35–0.6	…	…	…	bal
C17460	0.15–0.50	…	1.0–1.4	…	0.25 Sn max, 0.5 Zr max	bal
C17500	0.40–0.7	2.4–2.7	…	…	…	bal
C17510	0.20–0.6	0.3[b]	1.4–2.2	…	…	bal
Cast alloys						
C82000	0.45–0.8	2.4–2.7	0.20	…	0.15 Si	bal
C82200	0.35–0.8	…	1.0–2.0	…	…	bal

C84000	1.65–1.75	0.20–0.40	0.10	…	0.2 Fe	bal
C82500	1.90–2.15	0.35–0.7	0.20	…	0.20–0.35 Si, 0.20 Fe	bal
C85210	1.90–2.5	1.0–1.2	0.20	…	0.20–0.35 Si, 0.25 Fe	bal
C82600	2.25–2.45	0.35–0.7	0.20	…	0.20–0.35 Si, 0.25 Fe	bal
C82800	2.50–2.75	0.35–0.7	0.20	…	0.20–0.35 Si, 0.25 Fe	bal

(a) Nickel + cobalt, 0.20 min; nickel + cobalt + iron, 0.60 max.

(b) Maximum if no range given

The metallurgy of nickel-beryllium alloys is analogous to that of the high-strength copper-beryllium alloys. The alloys (Table 2) are solution annealed at a temperature high in the nickel solid-solution region to dissolve a maximum amount of beryllium, then rapidly quenched to room temperature to create a supersaturated solid solution. Precipitation hardening involves heating the alloy to a temperature below the equilibrium solvus to nucleate and grow metastable phase precipitates, which harden the matrix. In the high-strength copper-berylliums, the BeCu (γ) equilibrium precipitates form at grain boundaries only at higher age-hardening temperatures. On the other hand, the equilibrium γ phase (BeNi) in commercial nickel-beryllium alloys may precipitate in the grain boundaries at all temperatures in the age-hardening range.

Table 2 Chemical compositions of nickel-beryllium alloys

Alloy	Composition, wt%			
	Be	**Cr**	**Other**	**Ni**
Wrought alloy				
UNS N03360	1.85–2.05	…	0.4–0.6 Ti	bal[(a)]
Cast alloys				
M220C	2.0	…	0.5 C	bal
41C	2.75	0.5	0.1 C max	bal
42C	2.75	12.0	0.1 C max	bal
43C	2.75	6.0	0.1 C max	bal
44C	2.0	0.5	0.1 C max	bal
46C	2.0	12.0	0.1 C max	bal
Master	6[(b)]	…	0.1 C max	bal

(a) 99.4 Ni + Be + Ti + Cu min, 0.25 Cu max.

(b) Master alloys with 10, 25, and 50 wt% Be are also available.

Copper-beryllium and nickel-beryllium alloys are selected as representative metallographic specimens, depending on product form. Edge and interior samples are important in castings, forgings, and hot- or cold-finished rod, bar, tube, and plate. Longitudinal and transverse sections, which should be examined in strip and wire, are equally important in heavy-section wrought products. Strip may also be examined by electropolishing and etching a small spot on the rolled surface, although this approach is generally not used by domestic commercial suppliers. Care should be taken when examining components manufactured from these alloys to select sections that reveal the microstructural effects of the parts fabrication process (stamping and forming, machining, plating) and the undisturbed structure of the raw material. Age hardening of these beryllium-containing alloys by the parts fabricator can produce distinct changes in matrix etching response but does not alter the grain size or intermetallic compound particle distribution that is characteristic of the mill production process. Components should be examined before and after fabricator heat treatment.

J.C. Harkness and A. Guha, Metallography and Microstructures of Beryllium, Copper-Beryllium, and Nickel-Beryllium Alloys, *Metallography and Microstructures*, Vol 9, *ASM Handbook*, ASM International, 2004, p. 752–761

Metallography and Microstructures of Beryllium, Copper-Beryllium, and Nickel-Beryllium Alloys

John C. Harkness, Brush Wellman Inc.; Amitava Guha

Health and Safety

Despite low concentrations of beryllium in commercial copper-beryllium and nickel-beryllium alloys (nominally, 2% Be by weight or less), these materials can be hazardous to health if excessive quantities of dust, mist, or fume containing particles of alloy small enough to enter the lungs (typically, 10 μm or less) are inhaled. Standard precautions are required for metallographic sectioning, grinding, or polishing performed wet or for shearing of clean, thin-section strip or wire. Additional engineering controls, such as a local exhaust ventilation, and work practice controls, such as wet methods, personal protective equipment, and housekeeping, are required for sectioning, grinding, or polishing operations that produce dust or fume. Metallographic preparation equipment and laboratory work surfaces should be damp wiped periodically to remove the accumulation of dry alloy particles. See the manufacturer's Material Safety Data Sheet (MSDS) for detailed environmental, health, and safety information and guidance.

J.C. Harkness and A. Guha, Metallography and Microstructures of Beryllium, Copper-Beryllium, and Nickel-Beryllium Alloys, *Metallography and Microstructures*, Vol 9, *ASM Handbook*, ASM International, 2004, p. 752–761

Metallography and Microstructures of Beryllium, Copper-Beryllium, and Nickel-Beryllium Alloys

John C. Harkness, Brush Wellman Inc.; Amitava Guha

Specimen Preparation

Metallographic equipment and procedures for beryllium-containing alloys are much the same as those recommended for general metallurgical laboratory use.

Sectioning of specimens is typically carried out by sawing, abrasive cutting, or shearing, depending on section thickness and strength. Abrasive wheels formulated for nonferrous or medium-hardness materials and general-purpose use are satisfactory for copper-beryllium. Wheels formulated for hard materials and heavy sections are better for nickel-beryllium. Abrasive cutting should be performed wet to avoid thermal damage to the specimen and to guard health and safety. Sufficient surface metal is then removed from the sectioned face of the specimen by wet rough grinding to eliminate any deformed material introduced during sectioning. Wire electrical discharge machine cutting may generate a thin heat-affected layer on the sectioned surface that should be removed in the same manner as the disturbed material created by the mechanical sectioning methods mentioned previously.

Mounting is usually required for specimens too small to be hand held while polishing or for those requiring edge protection. Flat strip or transverse sections of small-diameter rod and wire may be stacked and gripped in reusable metal screw clamps for unembedded preparation. Alternatively, samples may be embedded with cold-mounting or compression-molding resins; commercial metal or plastic sample clips are used to stand the sample upright in the mold. Transparent mounting resins are preferred for delicate fabricated parts, such as electrical contacts, to help position features of interest in the final plane of polish. When distortion of the sample under pressure is to be avoided, cold mounting is preferred over compression molding.

Edge protection may be enhanced by nickel plating prior to mounting or by using hard compression-molding resins formulated for edge protection. Glass beads or alumina (Al_2O_3) granules added to cold-mounting resins for the same purpose will likely contaminate the polishing wheel and cause undesirable specimen scratching, particularly in the softer forms of copper-beryllium.

Grinding. Coarse grinding is performed wet on a belt or disk grinder using 120- or 180-grit abrasive paper to remove any deformed metal layer. Fine grinding is also performed wet, either by hand on strips of abrasive paper or mechanically on 300 revolutions per minute (rpm) or faster disks using 240-, 320-, 400-, then 600-grit abrasives. The sample is rotated 90° between each grinding. Silicon carbide or Al_2O_3 abrasives may be used.

Mechanical polishing is usually accomplished in rough and final stages. Rough polishing is performed using a 6 μm diamond on a wheel covered with a hard, napless chemotextile cloth. Extender oil is applied sparingly, and the wheel is rotated at approximately 300 rpm or less. The specimen is initially positioned so that the direction of polishing is perpendicular to the 600-grit grinding scratches. Maintaining this orientation, it is moved radially back and forth between center and edge of the polishing wheel under moderate pressure until these scratches are removed. The specimen is then briefly rotated counter to the rotation of the wheel to distribute the rough polishing scratches randomly.

Final polishing is performed using 0.05 μm Al_2O_3 in a distilled water suspension and a wheel covered with low-nap rayon cloth. Speeds are the same as those used for coarse polishing. The wheel is kept moderately saturated with polishing suspension, and the specimen is counterrotated to vary the direction of final polishing. An exception to this procedure is the case of the softer annealed or lightly cold-worked tempers of copper-beryllium, in which unidirectional final polishing, parallel to the specimen long axis, helps to minimize scratching. The specimen is washed under running water after each polishing step with mild soap and a cotton swab, then rinsed with alcohol and dried under a warm air blast.

Automatic Grinding and Polishing. Automatic metallographic preparation is appropriate for high-volume sample production intended for general microstructure examination. Techniques vary according to the type of machine used and the materials being prepared, but the following procedures have been successfully used for beryllium-containing alloys and can be adapted to any automatic system.

Holders containing mounted specimens or relatively square-cut, unembedded specimens are rough ground on 120- or 240-grit silicon carbide paper and fine ground on 240-, 320-, 400-, then 600-grit papers. Very uneven, unembedded specimens may require coarse 60- or 80-grit stone or paper grinding to bring all the samples in a holder to a common plane of polish. A copious flow of water-based coolant is applied to the work wheel during each grinding step. Wheel speeds of 150 rpm, pressures of 150 N (35 lbf), and times of approximately 30 s per grinding are usually sufficient. Zirconia (ZrO_2) abrasive papers will last longer than silicon carbide or Al_2O_3 under these grinding conditions. The loaded sample holder is then ultrasonically cleaned in alcohol, dried in an air blast, and returned to the machine for polishing.

Two or three polishing steps may be employed. One approach, which applies primarily to holders containing up to six 30 mm (1.25 in.) diameter mounts, begins with 6 μm diamond on a hard, napless chemotextile, proceeds to 3 μm diamond on a low-nap cloth, and finishes with 1 μm diamond on a soft, high-nap cloth. Wheel speed in each case is 150 rpm. The first and second polishing steps use a pressure of 150 N (35 lbf) for 2 min per step, and the final polishing uses 100 N (25 lbf) pressure for 35 s. Polishing extender is dripped sparingly on the wheels during each step, and the sample holder and work wheels should rotate in the same direction in each step.

Another approach, useful for high-volume production of embedded and unembedded samples, is to use a 9 μm diamond slurry on a lapping disk, followed by a 0.3 μm Al_2O_3 suspension on a low-nap rayon cloth, with an optional intermediate step of 3 μm Al_2O_3 suspension on a hard chemotextile. Times and pressures are varied to suit the size and number of samples.

The sample holder is ultrasonically cleaned and dried after each polishing step, and the samples are then removed from the holder for etching and final examination. Specimens of different alloys and hardnesses usually may be mixed in a single holder without harming the prepared surfaces of the softer samples.

Electropolishing. Clean, as-rolled strip surfaces or sectioned sample faces of copper-beryllium alloys prepared through 400- to 600-grit grinding paper may be electropolished. A satisfactory all-purpose electrolyte for copper-beryllium alloys is a mixture of 1 part nitric acid (HNO_3) and 2 parts methanol used at a temperature of -30 °C (-20 °F), with a voltage of 25 V direct current (dc) and a platinum cathode. An electrolyte of 40 mL phosphoric acid (H_3PO_4), 60 mL hydrogen peroxide (H_2O_2), 40 mL methanol, and 20 mL H_2O may also be used for copper-beryllium in conjunction with a stainless steel cathode, a mask of 0.5 to 1 cm^2 (0.08 to 0.16

in.^{2}) area, 20 to 30 V dc, and approximately 0.2 A. This technique is applicable to general polishing but is particularly suited to examining intermetallic phases in copper-beryllium, which can be rendered in high relief. Polishing is accomplished in a few seconds to a few minutes, using a moderately pumped electrolyte.

J.C. Harkness and A. Guha, Metallography and Microstructures of Beryllium, Copper-Beryllium, and Nickel-Beryllium Alloys, *Metallography and Microstructures,* Vol 9, *ASM Handbook*, ASM International, 2004, p. 752–761

Metallography and Microstructures of Beryllium, Copper-Beryllium, and Nickel-Beryllium Alloys

John C. Harkness, Brush Wellman Inc.; Amitava Guha

Macroexamination

Castings, forgings, billet, hot-rolled plate, and hot-extruded rod, bar, and tube forms of beryllium-containing alloys are frequently subjected to low-magnification macroexamination. Fracture surfaces of failed components or mechanical test specimens of these product forms may also be examined at low magnification. One purpose of macroexamination is to evaluate grain structure and/or metal flow patterns indicating casting or thermomechanical processing history. The technique also applies to documentation of differential heat treatment, weld penetration, or localized structural damage due to environmental attack. Fracture surfaces indicate the relative ductility of the material and the mode of failure.

Fracture Surface Characteristics. Tensile fracture surfaces of wrought copper-beryllium appear macroscopically ductile. Tensile fractures of annealed material typically exhibit macrocup/cone ductile behavior. Alloys heat treated at temperatures and/or times less than or equal to those required to achieve maximum precipitation-hardened strength are underaged or peak aged and exhibit blocky, transgranular fractures. Alloys heat treated at higher temperatures and longer times than those required to produce maximum strength are overaged, have a ductile appearance, and show grain facets.

Fatigue fracture features in wrought copper-beryllium depend on stress intensity and bending mode. Low stress intensity tends to produce ductile fracture surfaces with a mixed-mode character. Higher levels of stress intensity cause a trend toward transgranular fracture. Copper-beryllium resists corrosion in many environments but can stress-corrosion crack in the presence of ammonia. Such cracks are transgranular and intergranular and typically incorporate a corrosion product.

Macroetching. Once ground to at least 320 or 400 grit, copper-beryllium is macroetched by an initial, brief immersion in concentrated HNO_3, followed by immersion in or flooding with dilute HNO_3 (1 part concentrated HNO_3 to 2 parts distilled H_2O). The etchant attack is stopped by rinsing in running water. After the etched sample is rinsed in alcohol and dried in a warm air blast, the macrostructure can be preserved by spraying on a coat of clear lacquer. Nickel-beryllium can be macroetched by the same procedure, omitting the concentrated HNO_3 presoak.

In addition to grain structure and flow patterns, macroetched samples of copper-berylliums with 1.6 wt% or more beryllium reveal locally heat-affected zones as light etched areas if reannealed or unaged and as dark etched areas if aged. Light etched or reddish-colored areas adjacent to exterior or crack surfaces in uniformly aged materials usually signal environmental attack leading to local depletion of beryllium and lack of aging response. Matrix darkening on etching is not as pronounced in aged nickel-beryllium and is absent in copper-berylliums containing less than 0.6 wt% Be, essentially limiting the information revealed by macroetching of these alloys to matters of grain morphology. Castings and cast billet exhibit columnar dendritic grain growth from solidification. Hot-finished, large-section forms of the beryllium-containing alloys occasionally exhibit individual large grains, elongated in the direction of working, in the macrostructure.

J.C. Harkness and A. Guha, Metallography and Microstructures of Beryllium, Copper-Beryllium, and Nickel-Beryllium Alloys, *Metallography and Microstructures*, Vol 9, *ASM Handbook*, ASM International, 2004, p. 752–761

Metallography and Microstructures of Beryllium, Copper-Beryllium, and Nickel-Beryllium Alloys

John C. Harkness, Brush Wellman Inc.; Amitava Guha

Microexamination

Etching procedures for beryllium-containing alloys vary with alloy type and condition or temper. Particularly for copper-berylliums with less than 0.6 wt% Be, general microstructures are more difficult to reveal in the age-hardened conditions than in the hot-finished, solution-annealed, or cold-worked conditions.

Microetchants for copper-beryllium and nickel-beryllium are listed in Table 3, along with their compositions, etching procedures, uses, and precautions. Nitric acid and water (etchant 10, Table 3) is a good, general-purpose etchant for all forms and tempers of nickel-beryllium. Modified Marble's etchant (etchant 11, Table 3), which is especially suited to hot-worked or annealed nickel-beryllium, provides dramatic grain-structure detail with sensitive tint polarized light illumination.

Table 3 Etching reagents for copper-beryllium and nickel-beryllium alloys

Etchant	Composition	Comments
1. Ammonium persulfate-hydroxide	1 part NH_4OH (conc) and 2 parts $(NH_4)_2S_2O_6$ (ammonium persulfate) 2.5% in H_2O	All copper-beryllium alloys. General structure. Preheat sample in hot water (optional); swab etch 2–20 s; use fresh.
2. Ammonium persulfate-hydroxide (variation)	2 parts 10% $(NH_4)_2S_2O_6$, 3 parts NH_4OH (conc), 1 part 3% H_2O_2, and 5–7 parts H_2O[(a)]	All copper-beryllium alloys. Offers improved grain-boundary delineation in unaged material. A, $\frac{1}{4}$H, $\frac{1}{2}$ H, H tempers (unaged, use less H_2O. AT through HT and aged, use more H_2O). Use fresh; swab or immerse 5–60 s. Preheat specimen in hot H_2O if etching rate is slow.
3. Dichromate	2 g $K_2Cr_2O_7$ (postassium dichromate), 8 mL H_2SO_4 (conc), 1 drop HCl per 25 mL of solution, and 100 mL H_2O[(a)]	Grain structure of wrought C17000, C17200, C17300. Use for AT through HT and mill hardened (aged). Etch first with ammonium persulfate-hydroxide (No. 1 or 2); wipe dichromate 1–2 times over specimen to remove dark etch color. Do not overetch; sample may pit. May be used with laboratory aging of annealed or as-rolled material at 370 °C (700 °F) for 15–20 min to enhance grain-boundary delineation for grain-size determination.
4. Hydroxide/peroxide	5 parts NH_4OH (conc), 2–5 parts 3% H_2O_2, and 5 parts H_2O	Common etchant for copper and brass; also applicable to copper-beryllium alloys. Use fresh.
5. Ferric chloride	5 g $FeCl_3$ (ferric chloride), 50 mL HCl, and 100 mL H_2O	Common etchant for copper alloys; also applicable to cold-rolled tempers of copper-beryllium alloys C17500 and C17510 to show grain structure. Immerse 3–12 s.
6. Cyanide	1 g KCN (potassium cyanide) and 100 mL H_2O	General structure of copper-beryllium alloys C17500, C17510. Immerse 1–5 min; stir slowly while etching; use etchant 7 if others are too weak

		to bring out structure. A two-step technique for improved results on C17510 includes immersion in etchant 6 followed by swabbing with etchant 8. *Caution!* Poisonous fumes! Use fume hood. Do not dispose of used solutions directly into drains. Pour used solution into beaker containing chlorine bleach. Let stand 1 h, then flush down drain with plenty of water.
7. Persulfate-hydroxide-cyanide	4 parts ammonium persulfate-hydroxide etchant (etchant 1 or 2) and 1 part cyanide etchant (etchant 6)	Nickel-beryllium, all tempers. General structure. Swab etch.
8. Cyanide-peroxide-hydroxide	20 mL KCN, 5 mL H_2O_2, and 1–2 mL NH_4OH	Nickel-beryllium, all tempers. General structure. Swab etch. May also be used with sensitive tint illumination to reveal grain structure of hot-worked or annealed material
9. Cyanide-peroxide	4 parts 1% KCN (etchant 6) and 1 part 3% H_2O_2	Copper-beryllium alloys C17500, C17510, C17410, and C17460. Enhances grain boundaries and reduces twinning while maintaining the integrity of primary beryllides. Swab etch.
10. Nitric acid and water	30 mL HNO_3 (conc) and 70 mL H_2O	Nickel-beryllium alloys: Use for observation of the general structure of all tempers of nickel-beryllium. Swab etch.
11. Modified Marble's etchant	4 g $CuSO_4$ (copper sulfate), 20 mL HCl (conc), and 20 mL H_2O	Used for observation of the general structure of all tempers of nickel-beryllium. Swab etch. Can also be used with sensitive tint illumination to reveal the grain structure of hot-worked or annealed material
12. Phosphoric acid electrolyte	20 mL H_2O (tap, not distilled), 58 mL 3% H_2O_2, 48 mL H_3PO_4, and 48 mL ethyl alcohol	For deep etching of copper-beryllium. Polish specimen through 1 μm or finer Al_2O_3. Use 0.5–1 cm^2 (0.08–0.16 $in.^2$) mask, 0.1 A to etch (higher amperes to polish). Low to moderate flow rate. 3 to 6 s to etch; up to 60 s to polish
13. Nitric and acetic acids	50 mL HNO_3 (conc) and 50 mL glacial CH_3COOH (acetic acid), optionally diluted with 25–50 mL CH_3COCH_3 (acetone)	Used for observation of the general structure of nickel-beryllium casting alloys. Swab etch.

(a) Use distilled water unless otherwise noted.

Ammonium persulfate-hydroxide (etchant 1, Table 3) is a general-purpose etchant for copper-berylliums. It reveals grain structure in unaged material, although twinning may be present to complicate grain-size measurement. A variation of this etchant that contains H_2O_2 (etchant 2, Table 3) offers improved grain-boundary delineation in unaged material. In the case of alloys with 1.6 wt% or more beryllium, etchant 2 darkens the matrix of age-hardened material; the degree of coloration varies with the extent of precipitation in the alloy and may be used, but only as a general guide, to roughly estimate the aging history of the material as follows:

- In the underaging regime of 260 to 300 °C (500 to 575 °F), metallographic specimens exhibit a very slow to slow etching response rate, with color ranging from light golden-brown through yellow-gold to pink with hints of yellow and green and grain boundaries ranging from faint and indistinct to light but distinct with increasing aging temperature.
- In the peak aging regime at approximately 315 to 345 °C (600 to 650 °F), the etch rate is moderate to moderately fast; color ranges from red with highlights of blue or green to mostly blue with some red, and grain boundaries become very distinct.

- Overaging at 372 to 482 °C (700 to 900 °F) induces a fast to very fast etch rate. Purple color with some blue through light brown changes to dull gray-brown, with grain boundaries changing from distinctly thick and dark to displaying an increasing volume fraction of grain-boundary precipitate.
- Material severely overaged at 540 °C (1000 °F) etches very rapidly. It presents a dull gray-brown color and displays mainly gamma precipitate with no distinct grain boundaries.

Actual results will differ depending on beryllium content, individual technique, and personal judgment of color. Grains in aged, concentrated copper-beryllium alloys (beryllium > 0.8 wt%) may be highlighted by etching with ammonium persulfate-hydroxide, followed by brief swabbing with dichromate (etchant 3, Table 3) to lighten the matrix. Another reliable way to enhance grain boundaries in unaged alloys of these compositions is to age the samples for 15 to 20 min at 370 °C (700 °F), then follow with the two-stage etching procedure described previously. This technique eliminates twinning, and grain size can be accurately determined from the decoration of the grain boundaries with dark etching γ precipitate. Required microhardness measurements on the as-received specimen must be made prior to applying the previously mentioned heat treatment, because the resultant precipitation will harden the material.

Lean copper-beryllium alloys (beryllium < 0.8 wt%) exhibit little microstructural difference between the aged and unaged conditions. The lean copper-berylliums do not exhibit lamellar grain-boundary γ precipitation like the richer alloys. Hence, the short-time aging treatment described previously cannot be used to better delineate grain boundaries. In lean copper-beryllium alloys, grain structure is frequently obscured by twinning if ammonium persulfate-hydroxide is used. To enhance the general microstructure in these situations, the following etchants (Table 3) are used:

- Cyanide (etchant 6), Fig. 2, 3, and 4
- Persulfate-hydroxide-cyanide (etchant 7)
- Two-step etch with cyanide (etchant 6) and cyanide-peroxide-hydroxide (etchant 8), Fig. 5

Enhanced grain-boundary delineation and suppression of twinning may sometimes be achieved with the cyanide-peroxide solution (etchant 9, Table 3). For these toxic solutions, care must be taken to observe all established lab safety procedures (MSDS, etc.) and local waste disposal regulations regarding safe handling/disposal of cyanide-containing etchants.

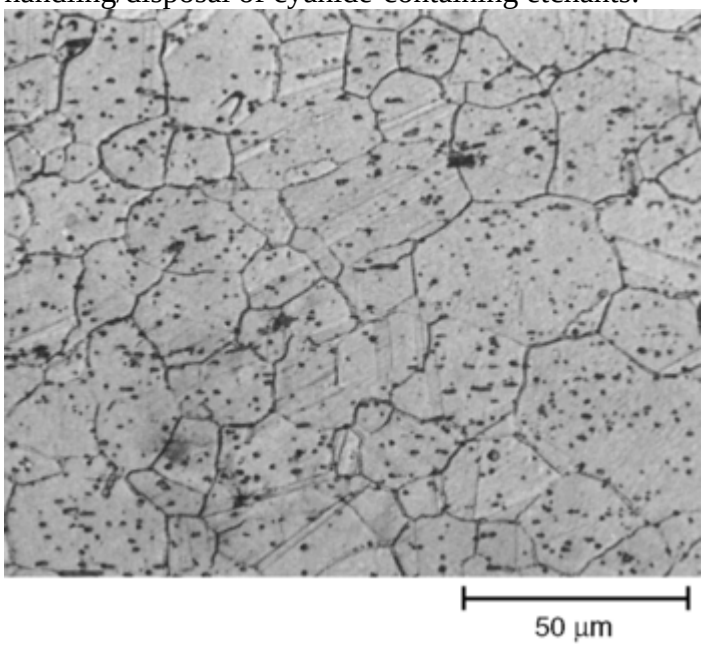

Fig. 2 C17510 alloy strip, solution annealed at 900 °C (1650 °F), quenched rapidly to room temperature, and precipitation hardened at 480 °C (900 °F) for 3 h to achieve maximum hardness. Equiaxed grains of supersaturated solution of beryllium and nickel in copper are shown. Etchant 6 (Table 3). 400×

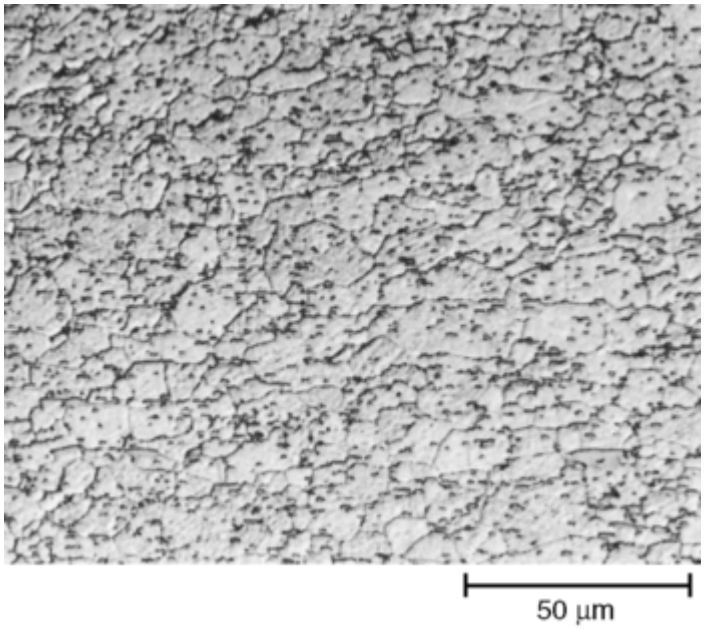

Fig. 3 C17500 alloy strip, solution annealed at 900 °C (l650 °F), quenched rapidly to room temperature, and precipitation hardened at 480 °C (900 °F) for 3 h to achieve maximum hardness. Microstructure shows equiaxed grains of supersaturated solution of beryllium and cobalt in copper. The cobalt-beryllide phase is uniformly distributed, and metastable hardening precipitates are not resolved. Etchant 6 (Table 3). 400×

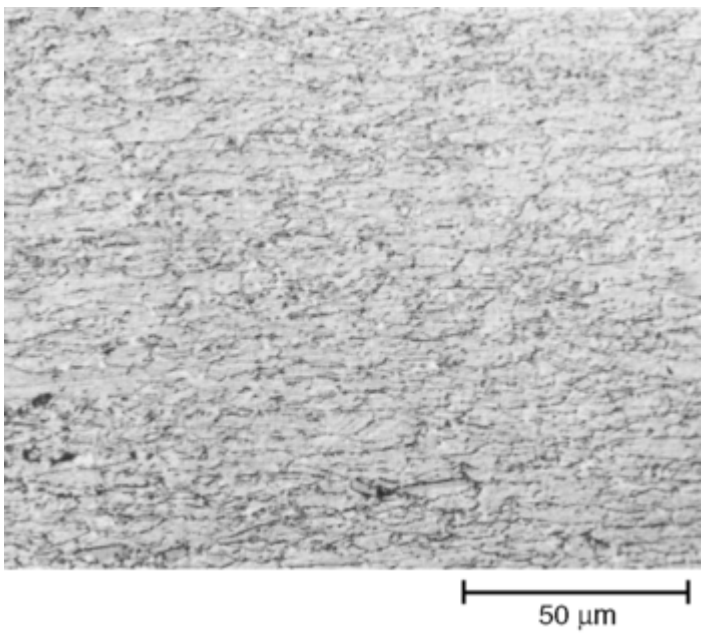

Fig. 4 Cl7500 alloy strip, solution annealed, cold rolled, and precipitation hardened at 480 °C (900 °F) for 2 h to achieve maximum hardness. Structure consists of the α phase and a uniform distribution of the beryllide phase. Elongated grains are the result of cold work, and metastable hardening precipitates are not resolved. Etchant 6 (Table 3). 400×

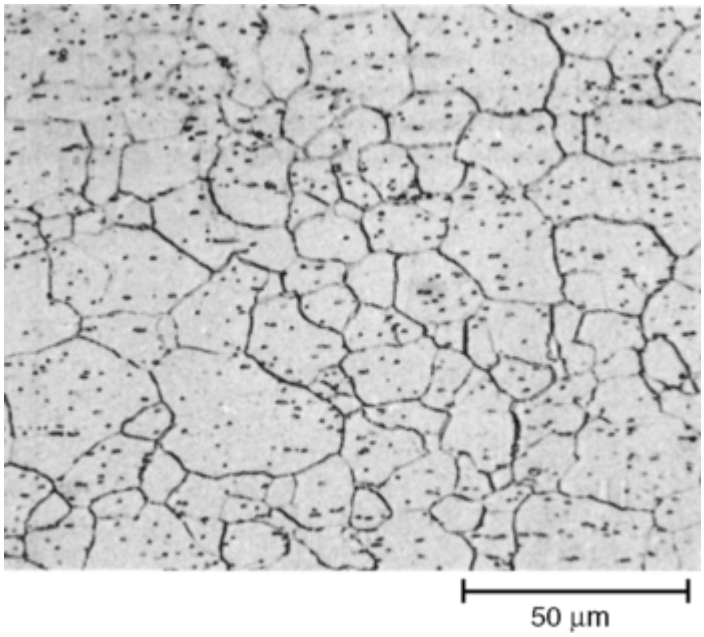

Fig. 5 Cl7510 alloy strip, solution annealed, cold rolled, and precipitation hardened at 480 °C (900 °F) for 2 h to achieve maximum hardness. Structure consists of α phase and a uniform distribution of the nickel-beryllide phase. Elongated grains are the result of cold work. Metastable precipitates are not resolved. Etchant 6, followed by swabbing with etchant 8 (Table 3). 400×

None of the etchants listed differentially attack intermetallic compounds in copper-beryllium—to distinguish cobalt or nickel beryllides from β phase, for example. This distinction must be made on the basis of appearance in the as-polished condition. Beryllides are blue-gray; β phase is creamy white and surrounded by a thin, dark outline.

Any of the etchants listed, which are intended for bright-field light optical microscopy, may be used for scanning electron microscopy examination to reveal fine structural detail that was not resolvable. One such application is the resolution of the lamellar structure of grain-boundary γ precipitate in high-temperature-aged copper-berylliums containing 1.60 to 2.00 wt% Be.

J.C. Harkness and A. Guha, Metallography and Microstructures of Beryllium, Copper-Beryllium, and Nickel-Beryllium Alloys, *Metallography and Microstructures*, Vol 9, *ASM Handbook*, ASM International, 2004, p. 752–761

Metallography and Microstructures of Beryllium, Copper-Beryllium, and Nickel-Beryllium Alloys

John C. Harkness, Brush Wellman Inc.; Amitava Guha

Microstructures of Copper-Beryllium Alloys

The two general categories of copper-beryllium alloys are the high-strength and the high-conductivity alloys. The wrought high-strength alloys contain 1.60 to 2.00 wt% Be, with approximately 0.25 wt% Co. The addition of cobalt promotes finer grain size in the cast form, lessens grain growth during annealing, and reduces the rapid softening of the alloy due to overaging. Solution annealing at temperatures of 760 to 790 °C (1400 to 1450 °F) in a protective atmosphere is followed by rapid quenching to retain the beryllium in solid solution at room temperature. Precipitation hardening can be accomplished by aging for 0.1 to 4 h at 260 to 400 °C (500 to 750 °F). Internal oxidation occurs from solution annealing without a protective atmosphere (Fig. 6), but is confined to the copper-beryllium alloys with less than 0.7 wt% Be.

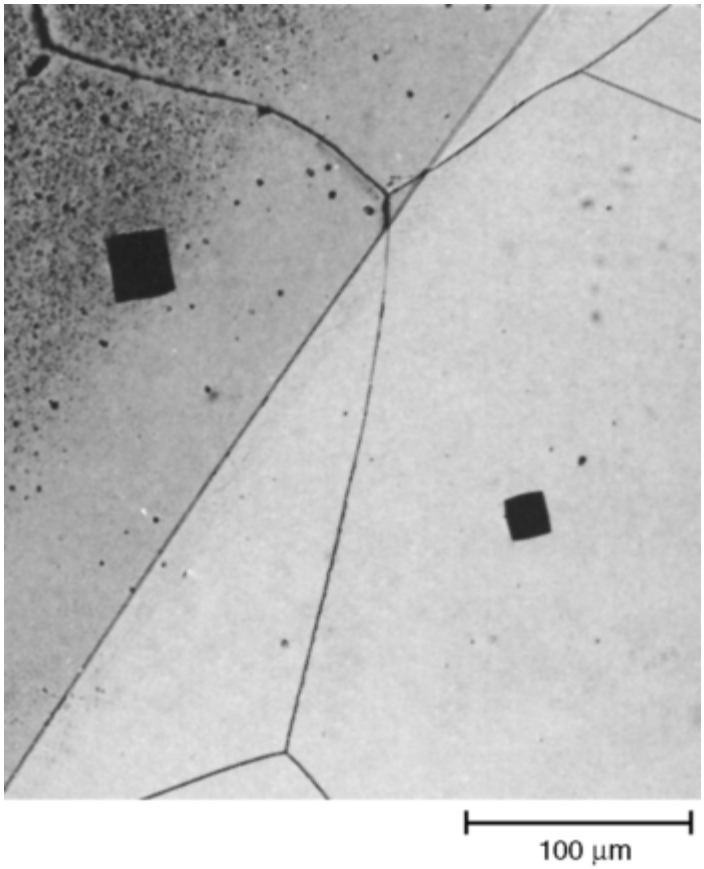

Fig. 6 C17510 alloy rod, solution annealed in air at 980 °C (1800 °F) for 3 h, then aged at 480 °C (900 °F) for 3 h. The microstructure shows internal oxidation resulting from solution annealing without a protective atmosphere. Note the loss in hardness (as indicated by the microhardness indentations) within the internal oxidation zone. Etchant 6 (Table 3). 200×

The aging time and temperature depend on the composition, amount of cold work, and strength levels desired. Cold working just prior to aging results in faster age hardening and higher strengths. Nonuniform distribution of grain size is typical of a hot-worked product (Fig. 7), and greater uniformity is achieved by successive cold-working and annealing operations.

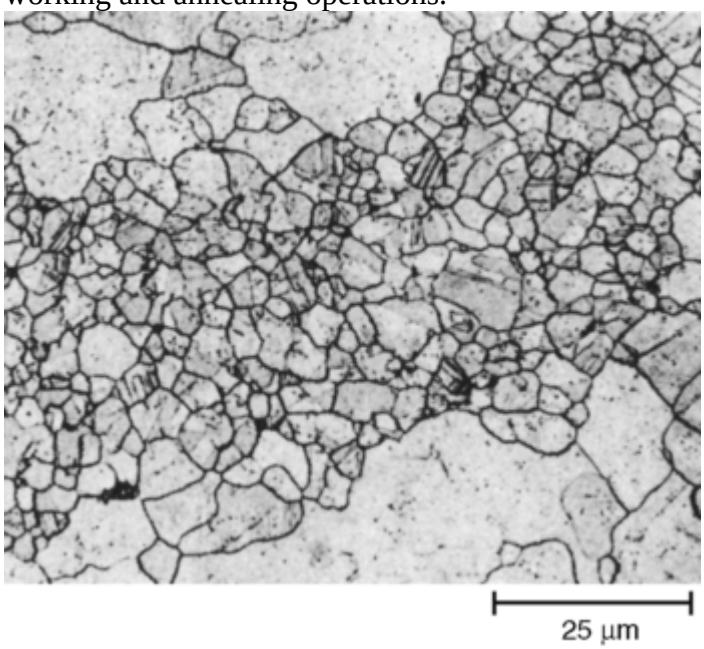

Fig. 7 C17200 alloy plate, cast, homogenized, and hot worked. The microstructure shows nonuniform distribution of grain sizes, which is typical of a hot-worked product. Greater uniformity in grain-size

distribution may be achieved in the finished product by successive cold-working and annealing operations. Etchant 1 (Table 3). 700×

The most commercially important of the high-strength compositions is C17200 (Table 1), which contains 1.80 to 2.00 wt% Be. This is the strongest of the copper-beryllium alloys; tensile strengths range to 1520 MPa (220 ksi) in the fully age-hardened condition. A leaded version of this alloy, C17300, exhibits improved machinability. A composition slightly lower in cost, C17000, with 1.60 to 1.79 wt% Be, has tensile properties in the age-hardened condition approximately 10% lower than those of C17200.

The high-strength alloys are also produced as casting alloys, designated C82400, C82500, C82510, C82600, and C82800. The beryllium content is higher (up to approximately 2.75 wt%) than in wrought alloys, but the general microstructural characteristics are similar. These alloys are produced as cast ingots that can be remelted and cast by foundries using any conventional molding technique.

The traditional high-conductivity alloys have low beryllium levels (0.20 to 0.7 wt%) and high cobalt and nickel levels. The wrought version of the alloy containing 2.4 to 2.7 wt% Co is designated C17500. The cast version is designated C82000. The wrought version containing 1.4 to 2.2 wt% Ni instead of cobalt is designated C17510, and the corresponding casting alloy is C82200. The properties of the nickel-containing alloys are very similar to the cobalt-containing alloys. The solution-annealing temperature range for the high-conductivity alloys is 900 to 955 °C (1650 to 1750 °F). Aging is performed at 425 to 565 °C (800 to 1050 °F) for 3 to 8 h, depending on the amount of cold work and the combination of properties sought. In recent years, even leaner high-conductivity alloys have been commercialized. The alloy with 0.15 to 0.50 wt% Be and 0.35 to 0.6 wt% Co is designated C17410. The alloy with similar low beryllium content and 1.0 to 1.4 wt% Ni is designated C17460. Both of these lean alloys are available only in wrought form, with proprietary mill-applied age-hardening treatments to establish specific ranges of as-shipped properties. Microconstituents in these lean alloys are consistent with those of their slightly richer cobalt- and nickel-containing counterparts, C17500 and C17510, respectively.

The compositional limits of various commercial copper-beryllium alloys are listed in Table 1. Data sheets published by the alloy producers may be consulted for detailed information, such as physical and mechanical properties and typical applications. The phases and constituents resulting from alloying elements and various heat treatments are discussed as follows.

The Beryllide Phase. Commercial copper-beryllium alloys contain cobalt or nickel or both. These alloying elements are normally in solution in the liquid metal. Because of their strong affinity for beryllium, they combine with it and separate during solidification as particles that are approximately 10 μm in the longest dimension. These constituent particles are termed beryllides. During subsequent thermomechanical processing, the beryllides are broken up somewhat but are not completely dissolved into solid solution during normal solution annealing. The primary beryllide phase is best observed in the as-polished condition as blue-gray Chinese script in castings. The secondary beryllides forming after solidification of the major phase can have a rodlike morphology with preferred crystallographic orientation with the matrix. In wrought products, the beryllides appear as roughly spherical, blue-gray particles. Examples of beryllides revealed in etched specimens are shown in Fig. 8, 9, 10, . 11, 12, 13, 14, and 15.

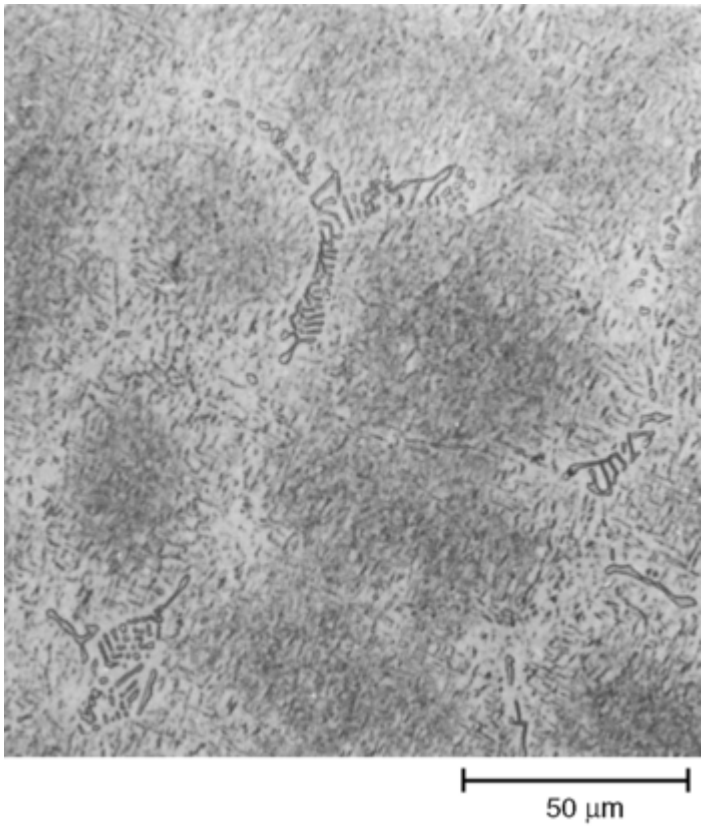

Fig. 8 C82200 alloy casting. As-cast microstructure shows interdendritic networks of large primary beryllide phase in a matrix of α solid solution. Preferred orientation of small secondary beryllides is observed with the matrix. Etchant 6 (Table 3). 400×



Fig. 9 C82500 alloy casting, solution annealed at 790 °C (1450 °F) and aged to peak hardness at 315 °C (600 °F) for 3 h. Microstructure consists of Chinese-script beryllides in a copper-rich α solid-solution matrix, with angular β phase transformed to a lamellar aggregate of α and γ phases. Striations are the result of metastable precipitation in the alloy. Etchant 1 (Table 3). 400×

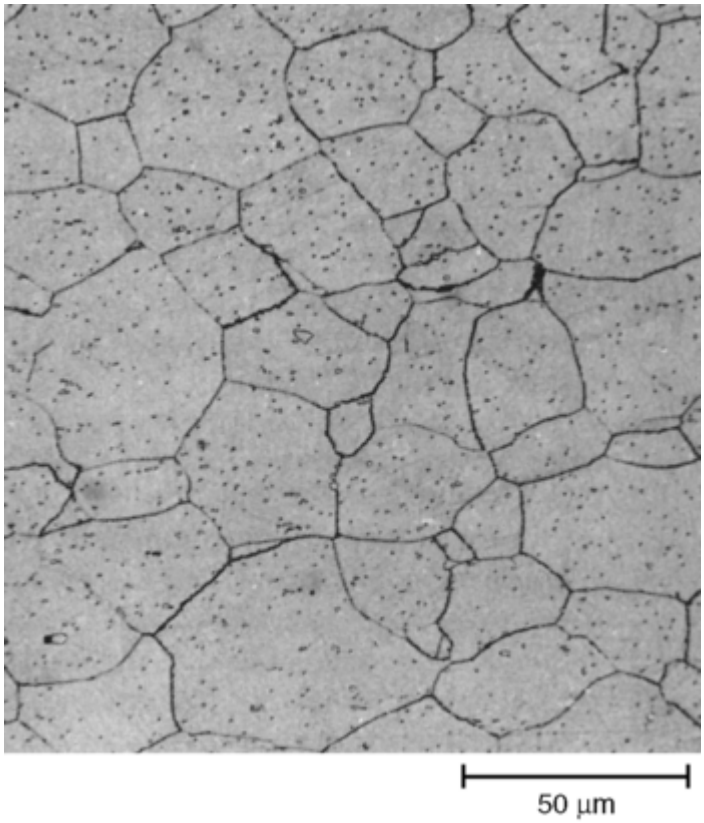

Fig. 10 C17200 alloy strip, mill hardened to AM (TM00) temper to achieve maximum formability at moderate strength. Longitudinal section shows roughly equiaxed grains of α phase and cobalt beryllides. Metastable precipitates that form during hardening and increase strength and hardness are not resolved. Etchant 1 (Table 3). 400×

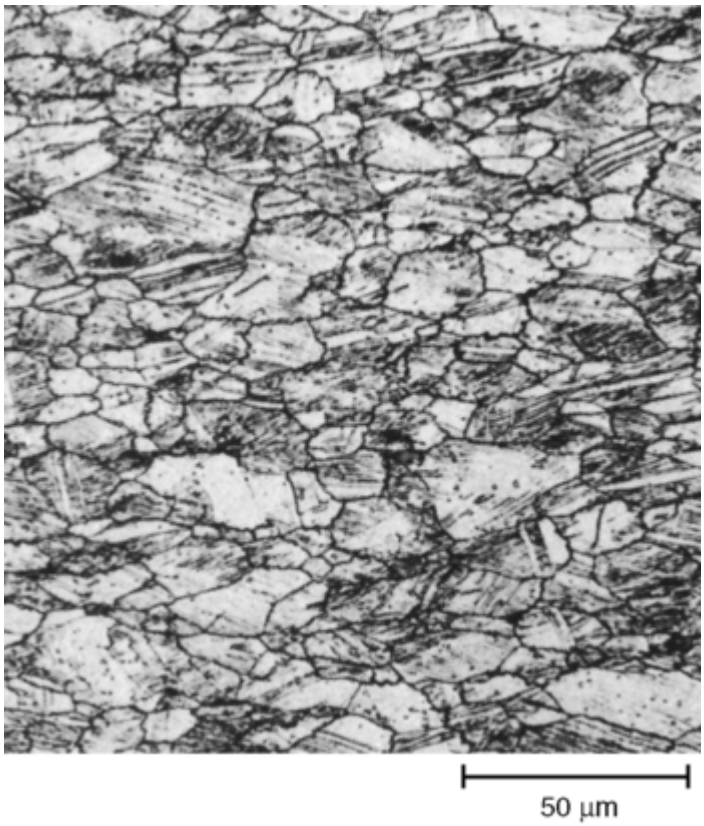

Fig. 11 C17200 alloy strip, mill hardened to XHMS (TM08) temper for high strength and limited formability. Longitudinal section shows elongated grains of the α phase and cobalt beryllides. Striations

result from precipitation of metastable phases not resolved by optical microscopy. Etchant 1 (Table 3). 400×

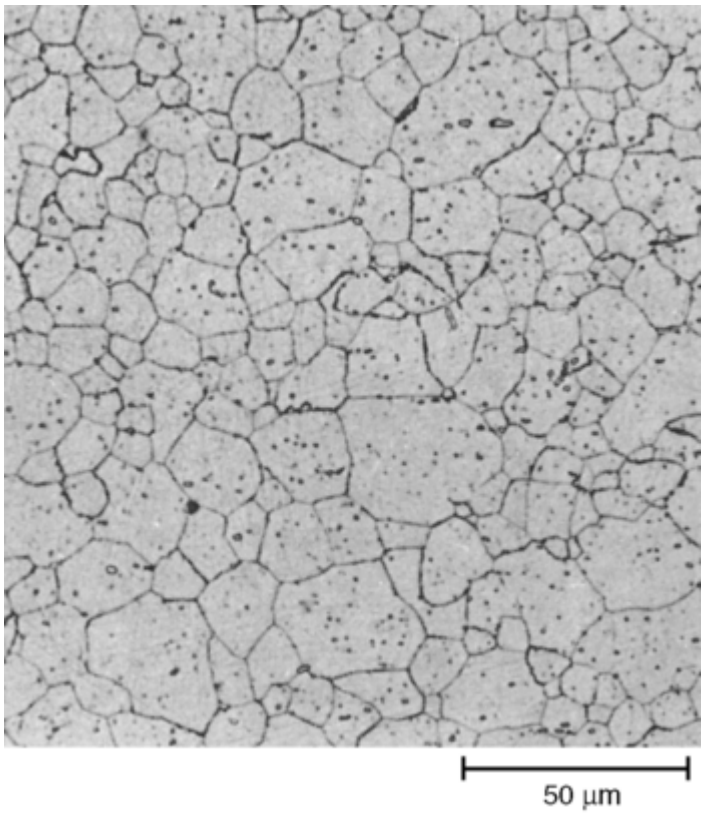

Fig. 12 C17200 alloy strip, solution annealed at 790 °C (1450 °F) and water quenched. Longitudinal section shows equiaxed grains of supersaturated α-phase solid solution of beryllium in copper. Cobalt beryllide particles are uniformly dispersed throughout the structure. Etchant 2 (Table 3) was probably used, but either etchant 1 or 2 would give similar structural detail, to a first approximation. Any visual difference between the two etchants would be only a matter of degree. The actual history of etching is not explicitly documented, but the etchant is either 1 or 2 (Table 3), because the grain boundaries are well delineated. 400×

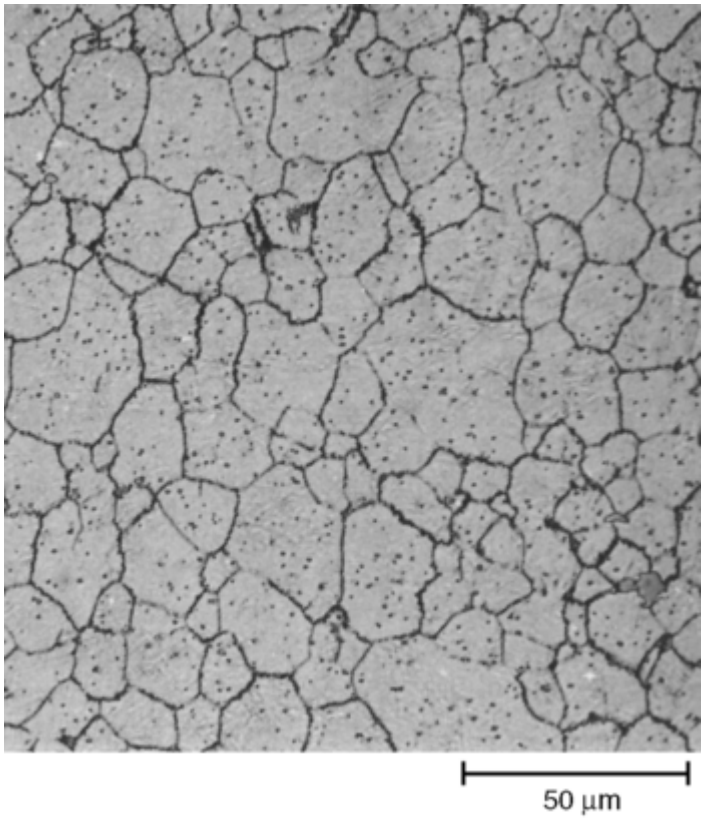

Fig. 13 Cl7200 alloy strip, solution annealed at 790 °C (1450 °F), quenched rapidly to room temperature, and precipitation hardened at 315 °C (600 °F) for 3 h to achieve maximum hardness. Longitudinal section shows equiaxed α grains and the cobalt-beryllide phase uniformly dispersed. Metastable phases are not resolved, but small quantities of equilibrium γ phase are present in the grain boundaries. Etchant 1 (Table 3). 400×

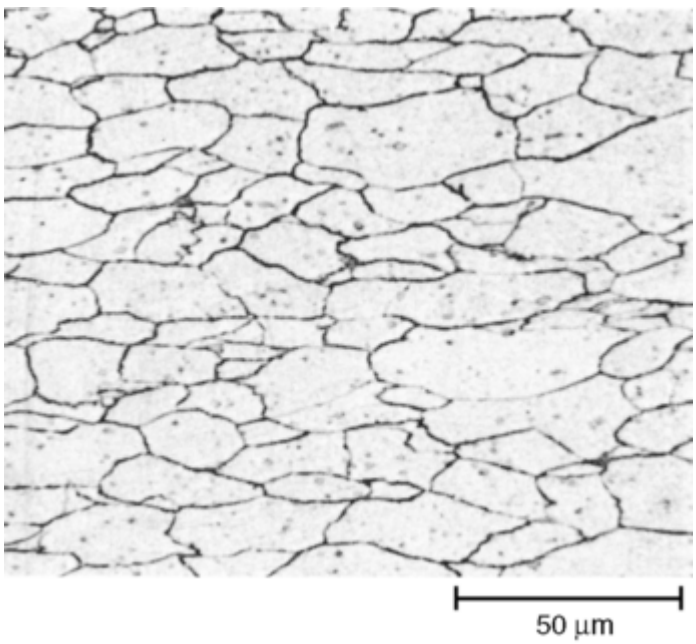

Fig. 14 Cl7200 alloy strip, solution annealed at 790 °C (1450 °F) and cold rolled at 37% to full hard temper. Longitudinal section shows elongated grains of α phase and cobalt beryllides. Etchant 2 (Table 3) was probably used, but either etchant 1 or 2 would give similar structural detail, to a first approximation. Any visual difference between the two etchants would be only a matter of degree. The actual history of etching is not explicitly documented, but the etchant is either 1 or 2 (Table 3), because the grain boundaries are well delineated. 400×

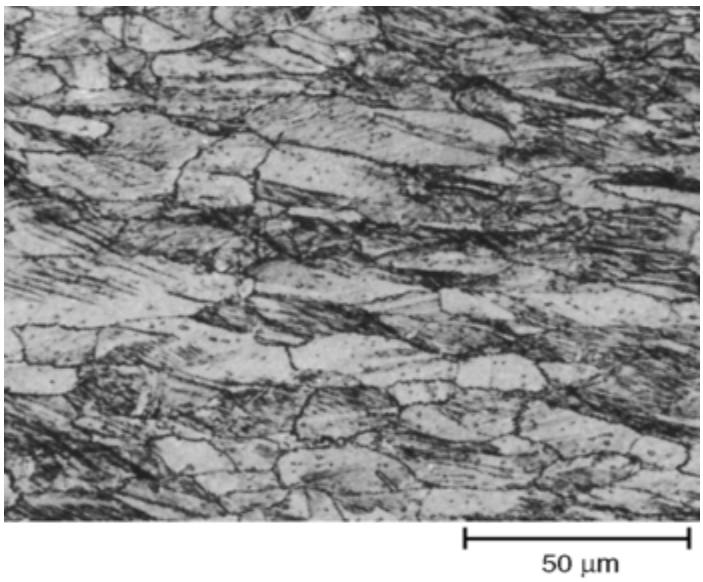

Fig. 15 C17200 alloy strip, solution annealed, cold rolled full hard, and precipitation hardened at 315 °C (600 °F) for 2 h to achieve maximum hardness. Longitudinal section shows elongated grains of α phase and cobalt beryllides. Striations are caused by metastable precipitates not resolved by optical microscopy. Etchant 1 (Table 3). 400×

The Beta Phase. The β phase ($BeCu_2$) forms peritectically from the liquid metal (Fig. 1). It is observed in high-strength alloy castings as an interdendritic network surrounding the primary copper-rich α phase. Experiments have shown that the β phase cannot be retained at room temperature, because it decomposes into α and γ phases by a eutectoid transformation. The (transformed) β phase stands out in relief in the as-polished state as white angular patches. In wrought metal containing 1.8 to 2.0 wt% Be, long (transformed) β stringers may exist due to insufficient homogenization before hot working (Fig. 16). When the solution-anneal temperature is excessive, partial melting at grain boundaries may resolidify as β phase (Fig. 17). The β phase is not observed in the high-conductivity copper-berylliums with less than 0.7 wt% Be.

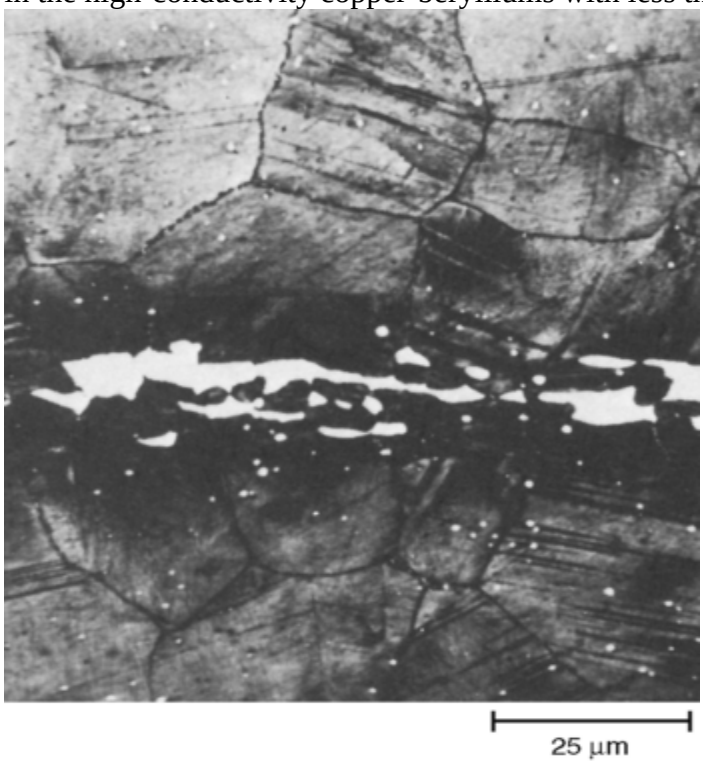

Fig. 16 C17200 alloy strip, solution annealed and age hardened. The white constituents of the structure are β stringers. These zones of beryllium segregation are carried through from billet casting and homogenization. Etchant 1 (Table 3). 700×

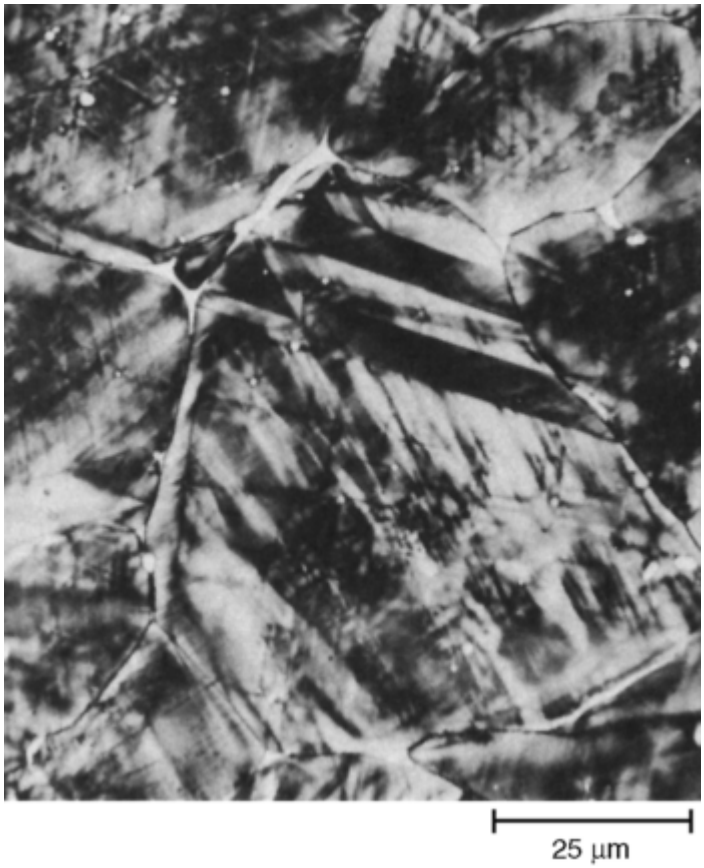

Fig. 17 C17200 alloy strip heated to 885 °C (1625 °F) and water quenched. The microstructure shows "burned metal" caused by solution annealing at too high a temperature. Partial melting at the grain boundaries, caused by extreme temperatures, resolidifies as β phase. Etchant 1 (Table 3). 700×

The Gamma Phase. The γ phase forms in overaged copper-beryllium alloys as an equilibrium precipitate. In concentrated alloys of copper-beryllium (such as C17200), the γ-phase precipitation starts at the grain boundaries and advances into the adjoining grains, consuming the fine, metastable precipitates. This type of precipitation is termed discontinuous precipitation or cellular precipitation. The γ precipitates formed by this mechanism have a characteristic platelike lamellar morphology. In the age-hardened state, the grain boundary containing the γ precipitate is soft compared to the hardened matrix.

Precipitation of the γ phase can also occur in the grain boundaries in high-strength copper-beryllium alloys if the rate of quenching from the solution-annealing temperature is not fast enough to retain beryllium in solid solution. In metallographically polished specimens etched using standard procedures, the γ phase stands out at the grain boundaries as dark nodules on a bright matrix (Fig. 18). The lamellar morphology of the γ phase is resolved by scanning or transmission electron microscopy. On the other hand, increased overaging causes discrete particles of equilibrium γ phase to appear in the grain boundaries of the high-conductivity copper-beryllium alloys (Fig. 18).

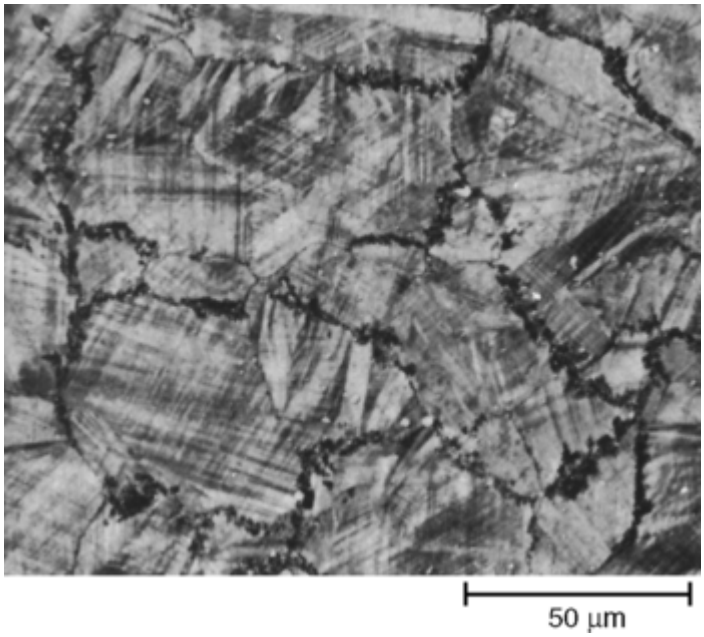

Fig. 18 C17200 alloy strip, solution annealed and aged at 370 °C (700 °F) for 6 h to attain an overaged condition. The structure shows γ precipitates in the grain boundaries, which appear as dark nodules in a light matrix. Etchant 1 (Table 3). 400×

Hardening Precipitates. Excellent room-temperature mechanical properties of copper-beryllium alloys are derived from the formation of a series of metastable precipitates during aging. Several such metastable phases form before the equilibrium γ phase is observed. The precipitation sequence from supersaturated solid solution is Guinier-Preston zones → γ″ → γ′ → and finally the equilibrium γ phase, BeCu. Guinier-Preston zones are the first precipitates to form and are coherent with the matrix. They are nucleated in large densities. The coherency strain fields set up due to the misfit of the zones and the matrix strengthen the alloy. With continued aging, Guinier-Preston zones transform to more stable precipitates.

The metastable precipitates can be detected by transmission electron microscopy. They are identified by the characteristic features observed in the electron diffraction pattern. The presence of hardening precipitates can be recognized only indirectly by light microscopy as striations on the surface of a polished and etched alloy that result from the overlap of coherency strains. No such striations are observed in the optical microstructure of the high-conductivity alloys.

J.C. Harkness and A. Guha, Metallography and Microstructures of Beryllium, Copper-Beryllium, and Nickel-Beryllium Alloys, *Metallography and Microstructures*, Vol 9, *ASM Handbook*, ASM International, 2004, p. 752–761

Metallography and Microstructures of Beryllium, Copper-Beryllium, and Nickel-Beryllium Alloys

John C. Harkness, Brush Wellman Inc.; Amitava Guha

Microstructures of Nickel-Beryllium Alloys

Wrought and cast nickel-beryllium alloys respond to processing and age-hardening heat treatments as readily as the copper-beryllium alloys but offer higher strength with better resistance to thermal softening and stress relaxation. Precipitation hardening is similar to copper-beryllium alloys by solution annealing, quenching, optional cold working, and aging. Precipitation in the nickel-beryllium system is similar to the copper-beryllium system regarding the sequence and the structure of the metastable phases formed during aging. The equilibrium γ phase (NiBe) is formed by a discontinuous reaction consuming the hardening precipitates.

Nickel-beryllium compound particles containing titanium exist in the wrought alloy and assist grain refinement. Graphite nodules are present in the cast alloys containing carbon and contribute to improved machinability.

These alloys usually contain 1.80 to 2.70 wt% Be; titanium, chromium, or carbon, among others, are added for grain-size control, corrosion resistance, hot workability, or machinability. Typical chemical compositions of the alloys are listed in Table 2. Solution annealing of these alloys is performed at approximately 980 to 1065 °C (1800 to 1950 °F). After quenching, tensile strengths approaching 2068 MPa (300 ksi) are obtained by aging at approximately 510 °C (950 °F) for 1 to 3 h. Metallographic sample preparation of nickel-beryllium is identical to the technique used for copper-beryllium. Descriptions of the swab etchants suitable for revealing the microstructure of all tempers of wrought and cast nickel-beryllium alloys are given in Table 3.

Wrought unaged nickel-beryllium microstructures exhibit nickel-beryllide intermetallic compound particles containing titanium in a nickel-rich matrix of equiaxed or deformed grains, depending on whether the alloy is in the solution-annealed or a cold-worked temper. After age hardening, a small volume fraction of equilibrium nickel-beryllium phase is generally observed at the grain boundaries (Fig. 19). In other respects, unaged and aged nickel-beryllium microstructures are essentially indistinguishable when viewed in an optical microscope.

Cast nickel-beryllium alloys containing carbon exhibit graphite nodules in a matrix of nickel-rich dendrites with an interdendritic nickel-beryllium phase. Cast chromium-containing alloys exhibit primary dendrites of nickel-chromium-beryllium solid solution and an interdendritic nickel-beryllium phase. Solution annealing cast nickel-beryllium partially spheroidizes but does not appreciably dissolve the interdendritic nickel-beryllium phase.

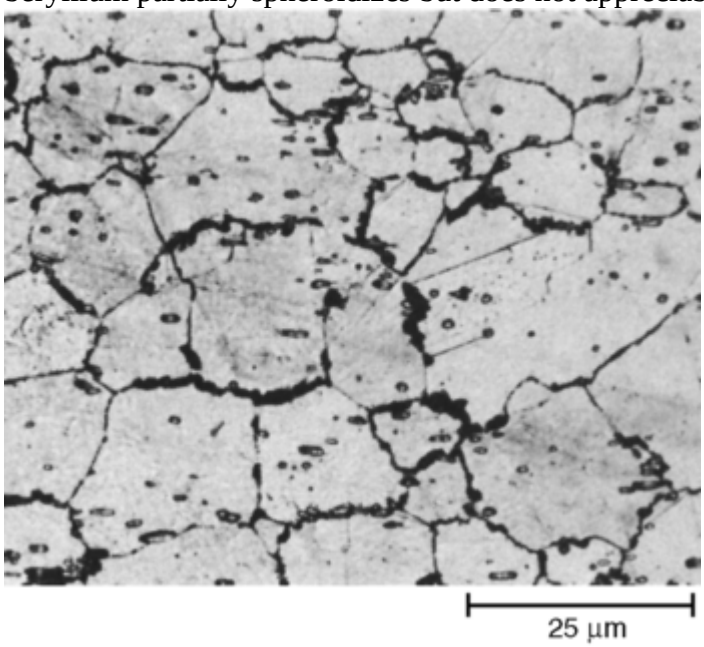

Fig. 19 Nickel-beryllium alloy strip (UNS N03360), solution annealed at 990 °C (1800 °F), water quenched, and aged at 510 °C (950 °F) for 1.5 h. The structure shows nickel-beryllium compound particles dispersed uniformly through the nickel-rich matrix. Hardening precipitates are not resolved, but equilibrium γ (NiBe) precipitates are present in grain boundaries. Etchant 11 (Table 3). 800×

J.C. Harkness and A. Guha, Metallography and Microstructures of Beryllium, Copper-Beryllium, and Nickel-Beryllium Alloys, *Metallography and Microstructures*, Vol 9, *ASM Handbook*, ASM International, 2004, p. 752–761

Metallography and Microstructures of Beryllium, Copper-Beryllium, and Nickel-Beryllium Alloys

John C. Harkness, Brush Wellman Inc.; Amitava Guha

Beryllium

Beryllium is prepared and examined metallographically in much the same way as other more common metals; however, the toxicity of beryllium necessitates the use of extreme care. Procedures and equipment must be designed to contain the harmful dust that can be produced during metallographic preparation. Examination usually is performed to determine grain size, distribution of second-phase oxide particles, voids, inclusions, the presence of machine-damaged surfaces, and, in the case of rolled sheet, the state of cold work. These microstructural characteristics can be important in determining the performance of a beryllium component.

Polarized light is generally used for metallographic examination instead of chemical etchants, although grain-boundary etchants have been used in some investigations. The fine grain size of the most common commercial forms of beryllium (vacuum hot-pressed block and rolled sheet) limits the value of magnifications less than 250×.

Specimen Preparation. Metallographic preparation begins with standard sectioning and mounting techniques. Wet rough grinding contains and carries away dust generated during this operation. Disks of waterproof silicon carbide grinding paper are mounted on a wheel rotating at approximately 1150 rpm. Grit sizes of 120, 240, 320, 400, and 600 are used. Care must be taken to prevent deformation twinning, and ample time must be allowed at each grinding step to remove damage caused by previous operations.

Another mechanical grinding procedure that has proved successful for beryllium uses 120-, 240-, and 400-grit silicon carbide papers on a wheel rotating at 1750 rpm. Kerosene is used as the lubricant. Grinding pressures should be extremely light. Fresh papers are used to minimize surface deformation and chipping. More information on this and other grinding techniques can be found in Ref 1.

Rough polishing is performed using a 550 rpm wheel, a chemotextile cloth with adhesive backing, and a medium-light concentration of 8 to 22 μm diamond compound. The specimen should be frequently rotated counter to the direction of wheel rotation. Heavy pressure is used to maximize material removal. Polishing time is approximately 2 min.

Fine polishing is carried out using a 550 rpm wheel, an adhesive-backed rayon cloth, and a medium-light concentration of 1 to 5 μm diamond compound. The mount should be frequently rotated counter to the direction of wheel rotation. Heavy to medium hand pressure is used to maximize removal of material. Polishing time is approximately 3 min.

The final fine polishing is performed using a 550 rpm wheel, an adhesive-backed rayon cloth, and a 0.05 μm deagglomerated γ-Al_2O_3 and water slurry. Final polishing takes approximately 3 to 5 min. The specimen should appear flat and free of most scratches.

An attack-polish procedure may also be used. Initial polishing is performed using Al_2O_3 abrasive on a short-nap cloth at 1750 rpm. A 5 to 10% aqueous oxalic acid solution is used with the Al_2O_3 to achieve a simultaneous chemical attack and mechanical polish. Final polishing is then performed using γ-Al_2O_3 and the aqueous oxalic acid solution on a medium-nap cloth at 1750 rpm. Water, instead of oxalic acid solution, is used to keep the wheel moist during the last few seconds of final polishing. Care must be taken to maintain the proper balance between chemical attack and abrasive action to achieve optimal polishing conditions. Polishing times are approximately 1 min for each wheel. Vibratory polishing and electrolytic polishing of beryllium have also been used (Ref 1).

Macroexamination. Commercially available beryllium is predominantly a powder metallurgy (P/M) product. Structural castings have poor strength and ductility because of their coarse grain size, and forgings tend to be highly anisotropic. Therefore, macroexamination is seldom used for beryllium, because vacuum hot pressing does not produce substantial flow, and the grain size is too small for macroexamination to be a valuable tool.

For additional information on production of beryllium powders and properties and applications of beryllium P/M parts, see the article "Powder Metallurgy Beryllium" in *Powder Metal Technologies and Applications,* Volume 7 of *ASM Handbook.*

Microexamination of beryllium is generally carried out using polarized light. Polarized light techniques cause color differences between grains as a result of crystallographic orientation differences. Polarized light also shows the positions from which oxide particles have been "pulled out" of the structure during polishing. These locations generally appear bright white.

An etchant that is sometimes used, known as 2-2-2 etch, consists of 2% concentrated sulfuric acid (H_2SO_4), 2% diluted (48%) hydrofluoric acid (HF), 2% concentrated nitric acid (HNO_3), and the balance distilled water. The specimen should be swabbed 5 to 10 s at (preferably) 20 °C (70 °F). Although strongly temperature dependent and not as widely used as the polarized light observation mode, this method can reveal grain boundaries and oxides. Other etchants used for beryllium are listed in Table 4.

Table 4 Etchants used for beryllium

Etchant	Remarks
Chemical etchants	
90 mL ethanol, 10 mL HF	Immerse specimen 10–30 s; increases contrast between inclusions or constituent particles and the matrix
100 mL H_2O, 0.5–2 mL HF	Same as above; HF can also be used in glycerol
95 mL H_2O, 5 mL H_2SO_4	Immerse 1–15 s to reveal grain boundaries
100 mL H_2O, 3–20 g oxalic acid	Use boiling; immerse specimen 2 min to reveal precipitates, up to 16 min to reveal grain boundaries
Electrolytic etchants	
2 mL HCl, 2 mL HNO_3, 2 mL $HClO_4$ (perchloric acid), 94 mL ethylene glycol	Etch at 5 V dc for 5–7 s, stainless steel cathode; solution can be used for electropolishing at 10–16 V dc, 0.1 A/cm^2 (0.65 A/$in.^2$)
2 mL HCl, 98 mL ethylene glycol	Etch at ~70 V dc, 1–4 min, stainless steel cathode at 10–15 °C (50–60 °F); if structure not etched, reduce to 6–8 V dc for 3–5 s; stir solution, wash specimen in boiling water, specimen can be examined under bright-field illumination
100 mL H_3PO_4, 30 mL glycerol, 30 mL ethanol, 2.5 mL H_2SO_4	Grain-boundary etch; cathode covered with cotton, and specimen swabbed lightly in a circular pattern; use stainless steel cathode, 25 V dc for 1–3 min (30s cycles) at 10 °C (50 °F); polarized light improves contrast

dc, direct current.

Source: Ref 1

Microstructures of Beryllium. Beryllium microstructures are shown in Fig. 20, 21, 22, 23, and 24. The microstructure of vacuum hot-pressed beryllium has grains of beryllium and particles of beryllium oxide (BeO) as major constituents. The microstructural differences between grades are subtle; grain size and oxide content are the only distinguishing characteristics.

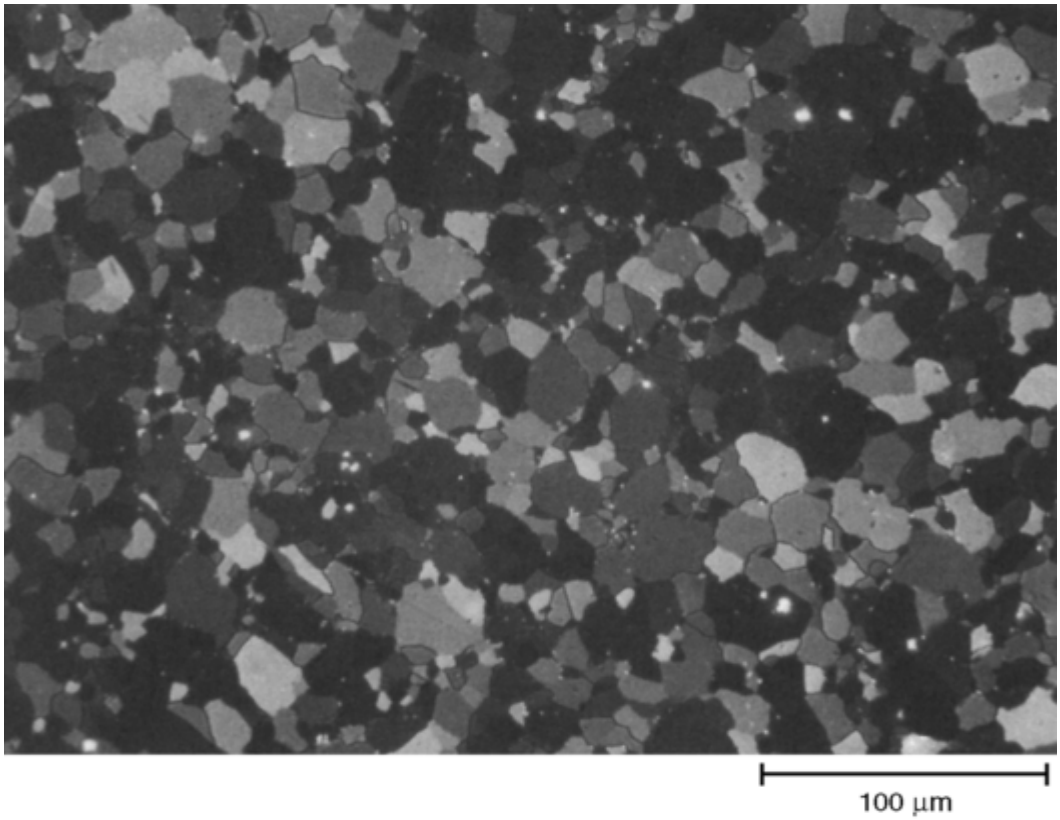

Fig. 20 S-65B vacuum hot-pressed block; billet consolidated from impact-ground powder. Polarized light micrograph shows substantially equiaxed grains with particles of BeO. Bright areas are locations where BeO has been "pulled out" during metallographic preparation. As-polished. 250×

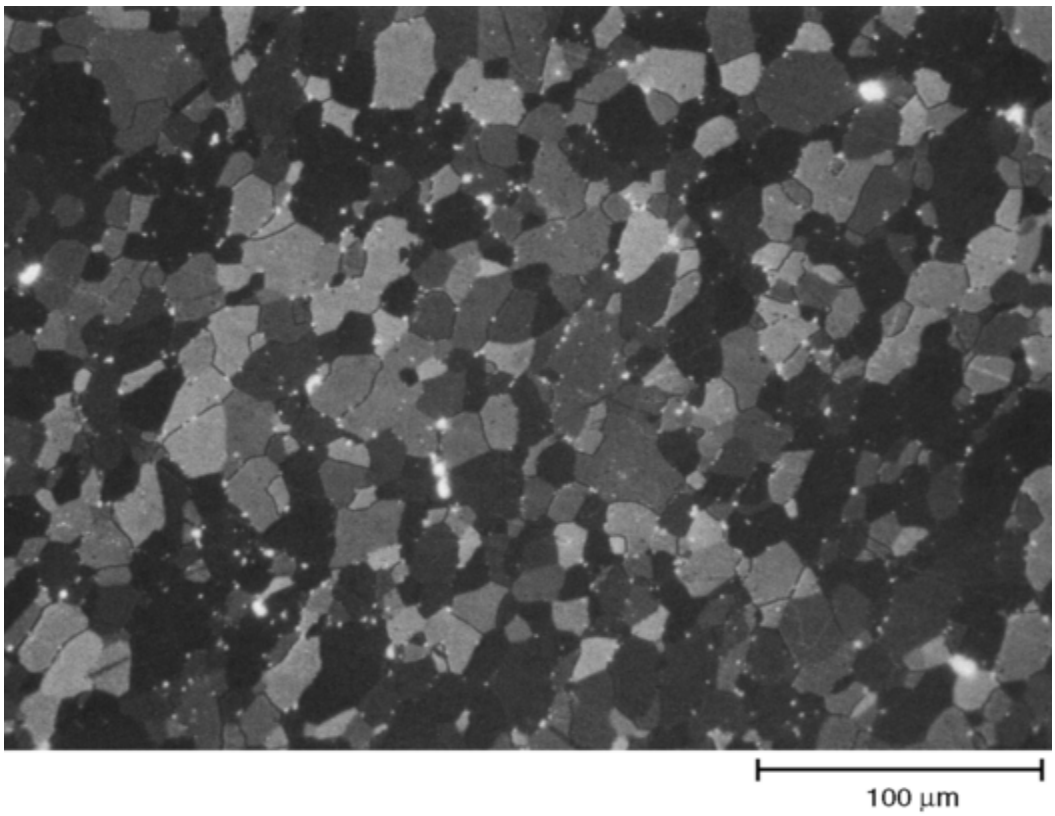

Fig. 21 S-200F vacuum hot-pressed block; billet consolidated from impact-ground powder. Seen under polarized light, the microstructure consists of equiaxed grains with particles of BeO. Average grain size is 8 to 10 μm; bright areas show where oxide has been "pulled out" during preparation. As-polished. 250×

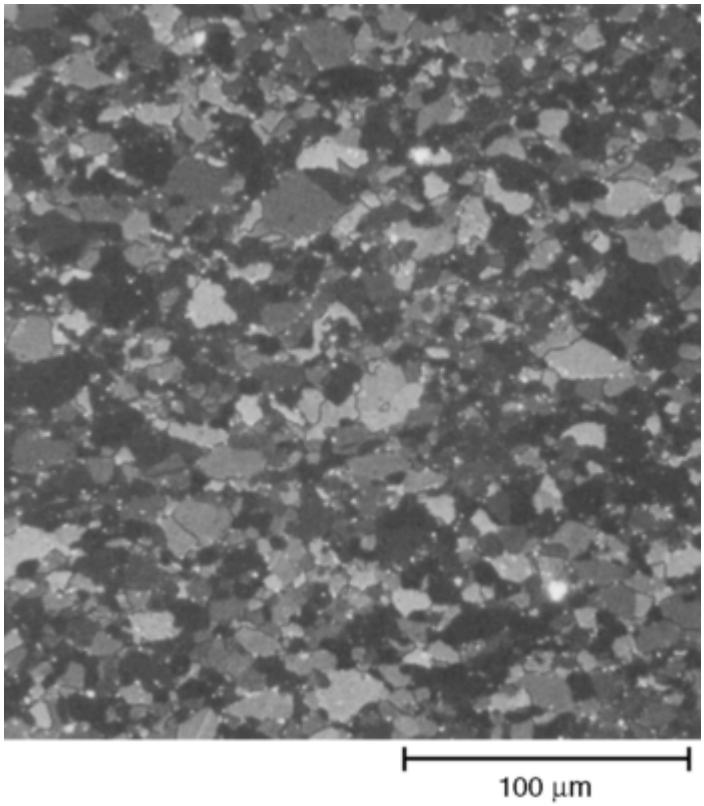

Fig. 22 I-220 vacuum hot-pressed block; billet consolidated from impact-ground powder. Polarized light micrograph shows substantially equiaxed grains with BeO particles. Average grain size is 8 to 9 μm; bright areas are locations where BeO was "pulled out" during preparation. The relatively high oxide content of I-220 produces the greater number of oxide particles present. As-polished. 250×

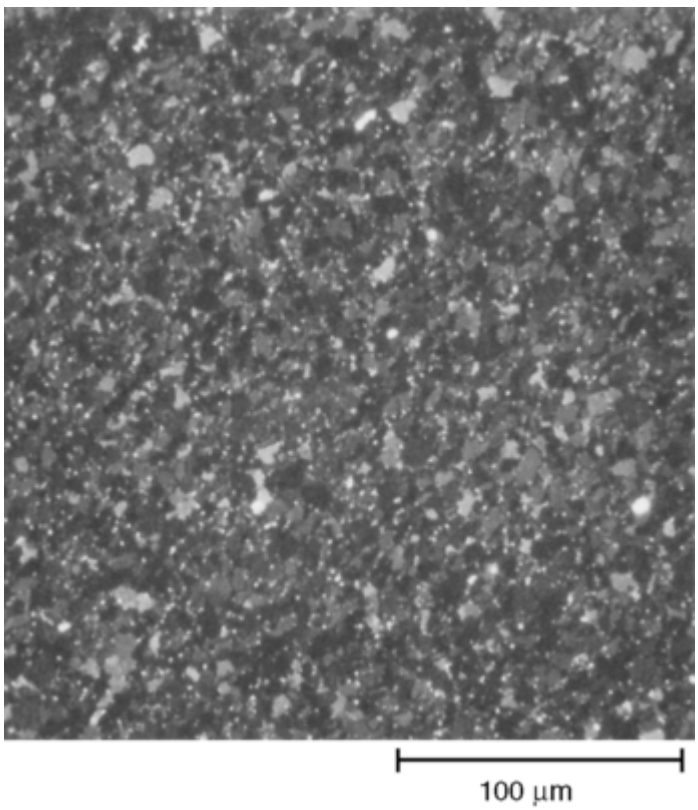

Fig. 23 I-400 vacuum hot-pressed block; billet consolidated from ball-milled powder. Under polarized light, microstructure shows substantially equiaxed grains with particles of BeO, along with bright areas where BeO was "pulled out" during preparation. Average grain size is 5 μm or less. The relatively high (4.2% min) BeO content of I-400 is apparent in this micrograph. As-polished. 250×

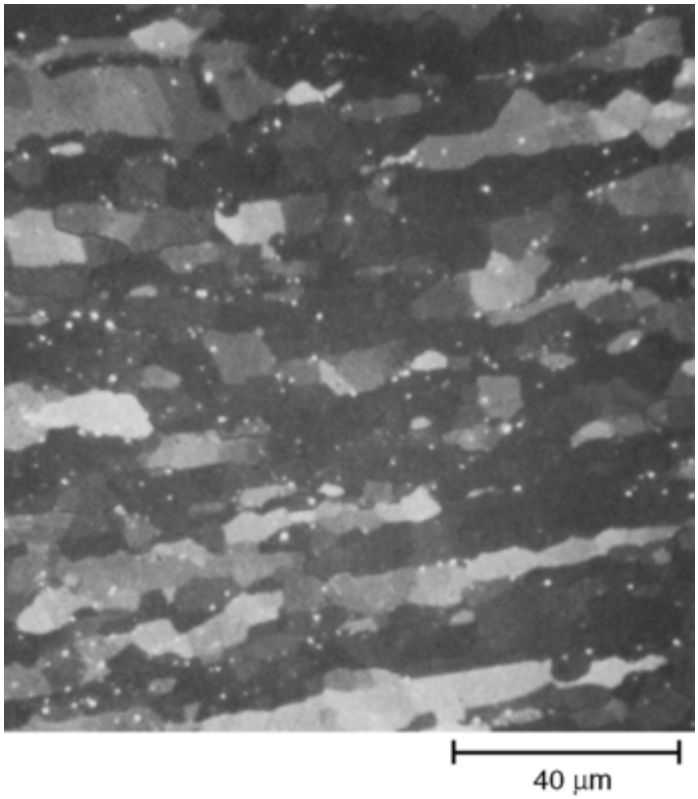

Fig. 24 SR-200 sheet, rolled at elevated temperature from S-200E vacuum hot-pressed block. Under polarized light, longitudinal section shows grains elongated in the rolling direction. This structure is typical of beryllium sheet, which often has reduced ductility if it is recrystallized after rolling. As-polished. 500×

Rolled beryllium sheet begins as a hot-pressed block, which is subsequently subjected to warm rolling. The final microstructure consists of the usual elongated grains; aspect ratios depend on the actual reduction performed.

Intentional alloying does not occur in the production of pure beryllium, because beryllium has low solubility for most elements, and the introduction of alloying elements generally compromises the desirable density and modulus of this metal. Microalloying, which is essentially performed by controlling the proportions of iron and aluminum, is used primarily to prevent the formation of grain-boundary films.

The predominant second-phase constituent is BeO, which has the hexagonal close-packed crystal structure and acts as a grain-boundary pinning agent. Because the strength of beryllium is strongly dependent on grain size, there is a strong correlation among oxide content, grain size, and strength.

The amount of oxide also correlates inversely with ductility. Therefore, a high-strength, low-ductility grade, such as I-400, has a high oxide level of 4.2% minimum. High-ductility structural grades, such as S-65 and S-200F, have oxide levels of 1 and 1.5%, respectively. Particles of BeO appear in polarized light micrographs as bright spots, which are actually locations from which the particles have “pulled out” during metallographic preparation.

The typical commercial grades of vacuum hot-pressed beryllium fall into two categories. Instrument grades are designated “I” and structural grades, “S.” Instrument grades typically find application in gyroscopes, inertial navigation systems, and as precision satellite and airborne optical components. Typical structural-grade applications are satellite superstructures, antenna booms, and optical support structures. The microstructures of four grades of vacuum hot-pressed beryllium and an example of rolled sheet are illustrated in the micrographs in Fig. 20, 21, 22, 23, and 24. The chemical compositions of these materials are given in Table 5.

Table 5 Grades of vacuum hot-pressed beryllium

Chemical composition	S-65B	S-200F	I-220A	I-400
Be, % (min)	99.0	98.5	98.0	94.0
BeO, % (max)	1.0	1.5	2.2	4.2[(a)]
Al, ppm (max)	600	1000	1000	1600
C, ppm (max)	1000	1500	1500	2500
Fe, ppm (max)	800	1300	1500	2500
Mg, ppm (max)	600	800	800	800
Si, ppm (max)	600	600	800	800
Other, ppm (max)	400	400	400	1000

ppm, parts per million.
(a) BeO specified is minimum in this instance.

Reference cited in this section

1. C.W. Price and J.L. McCall, "A Review of Metallographic Preparation Procedures for Beryllium and Beryllium Alloys," DMIC Memorandum 237, Defense Metals Information Center, Batelle Memorial Institute, Columbus, OH, 1968

J.C. Harkness and A. Guha, Metallography and Microstructures of Beryllium, Copper-Beryllium, and Nickel-Beryllium Alloys, *Metallography and Microstructures,* Vol 9, *ASM Handbook*, ASM International, 2004, p. 752–761

Acknowledgment

The section on beryllium was adapted from J.M. Marder and R. Batich, Beryllium, *Metallography and Microstructures,* Volume 9, *ASM Handbook,* American Society for Metals, 1985, p 389 to 391.

J.C. Harkness and A. Guha, Metallography and Microstructures of Beryllium, Copper-Beryllium, and Nickel-Beryllium Alloys, *Metallography and Microstructures,* Vol 9, *ASM Handbook*, ASM International, 2004, p. 752–761

Metallography and Microstructures of Beryllium, Copper-Beryllium, and Nickel-Beryllium Alloys

John C. Harkness, Brush Wellman Inc.; Amitava Guha

References

1. C.W. Price and J.L. McCall, “A Review of Metallographic Preparation Procedures for Beryllium and Beryllium Alloys,” DMIC Memorandum 237, Defense Metals Information Center, Batelle Memorial Institute, Columbus, OH, 1968

Revised by D. Klarstrom, P. Crook, and J. Wu, Metallography and Microstructures of Cobalt and Cobalt Alloys, *Metallography and Microstructures,* Vol 9, *ASM Handbook,* ASM International, 2004, p. 762–774

Metallography and Microstructures of Cobalt and Cobalt Alloys

Revised by D. Klarstrom, Haynes International, Inc.; P. Crook, Haynes International, Inc; and J. Wu, Deloro Stellite Group Limited

Introduction

COBALT is used as an alloying element in alloys for various applications such as:

- Permanent and soft magnetic materials
- Superalloys for creep resistance at high-temperature
- Hardfacing and wear-resistant alloys
- Corrosion-resistant alloys
- High-speed steels, tool steels, and other steels
- Cobalt-base tool materials (e.g., the matrix of cemented carbides)
- Electrical-resistance alloys
- High-temperature spring and bearing alloys
- Magnetostrictive alloys
- Special expansion and constant-modulus alloys
- Biocompatible materials for use as orthopedic implants or dental materials

Historically, many of the commercial cobalt-base alloys are derived from the Co-Cr-W and Co-Cr-Mo ternaries first investigated in the early twentieth century by Elwood Haynes. He discovered the high strength and stainless nature of binary cobalt-chromium alloys and first patented cobalt-chromium alloys in 1907. He later identified tungsten and molybdenum as powerful strengthening agents within the cobalt-chromium system. These developments led to various cobalt-base alloys for corrosion and high-temperature applications in the 1930s and early 1940s. Of the corrosion-resistant alloys, a Co-Cr-Mo alloy with a moderately low carbon content was developed to satisfy the need for a suitable investment cast dental material. This biocompatible material, which has the tradename Vitallium, is in use today for surgical implants. In the 1940s, this same alloy also underwent investment casting trials for World War II aircraft turbocharger blades, and, with modifications to enhance structural stability, was used successfully for many years in this and other elevated-temperature applications. This early high-temperature material, Stellite alloy 21, is still in use today, but predominantly as an alloy for wear resistance.

A current overview on cobalt-base alloys is in Ref 1. This article describes the metallurgy, metallography, and microstructures of cobalt alloys used for applications that require wear resistance, high-temperature strength, or corrosion resistance. Cobalt-base alloys designed for wear service typically have higher carbon content than cobalt alloys designed for high-temperature strength and/or corrosion resistance. The basic metallurgy and representative microstructures for these three major categories of cobalt-base alloys are described in this article. Typical compositions of present-day cobalt-base alloys are listed in Table 1(a) and (b) for these three

application areas. This article does not address cobalt-base materials in applications such as cemented carbides, biomedical devices, or magnetic/electrical devices.

Table 1(a) Compositions of various wear-resistant cobalt-base alloys

Alloy tradename[(a)]	UNS No.	Nominal composition, wt%									
		Co	**Cr**	**W**	**Mo**	**C**	**Fe**	**Ni**	**Si**	**Mn**	**Others**
Cast, P/M, and weld overlay wear-resistant alloys											
Stellite 1	R30001	bal	30	13	0.5	2.5	3	1.5	1.3	0.5	…
Stellite 3 (P/M)	R30103	bal	30.5	12.5	…	2.4	5 (max)	3.5 (max)	2 (max)	2 (max)	1 B (max)
Stellite 4	R30404	bal	30	14	1 (max)	0.57	3 (max)	3 (max)	2 (max)	1 (max)	…
Stellite 6	R30006	bal	29	4.5	1.5 (max)	1.2	3 (max)	3 (max)	1.5 (max)	1 (max)	…
Stellite 6 (P/M)	R30106	bal	28.5	4.5	1.5 (max)	1	5 (max)	3 (max)	2 (max)	2 (max)	1 B (max)
Stellite 12	R30012	bal	30	8.3	…	1.4	3 (min)	1.5	0.7	2.5	…
Stellite 21	R30021	bal	27	…	5.5	0.25	3 (max)	2.75	1 (max)	1 (max)	0.007 B (max)
Stellite 98M2 (P/M)	…	bal	30	18.5	0.8 (max)	2	5 (max)	3.5	1 (max)	1 (max)	4.2 V. 1 B (max)
Stellite 190	R30014	bal	27	14	1.0 (max)	3.5	3 (max)	4.0 (max)	2 (max)	1 (max)	…
Stellite 703	…	bal	32	…	12	2.4	3 (max)	3 (max)	1.5 (max)	1.5 (max)	…
Stellite 704	…	bal	30	…	14	1.0	2 (max)	3 (max)	1 (max)	0.5 (max)	…
Stellite 706	…	bal	29	…	5	1.2	3 (max)	3 (max)	1.5 (max)	1.5 (max)	…
Stellite 712	…	bal	29	…	8.5	2	3 (max)	3 (max)	1.5 (max)	1.5 (max)	…
Stellite 720	…	bal	33	…	18	2.5	3 (max)	3 (max)	1.5 (max)	1.5 (max)	0.3 B
Stellite F	R30002	bal	25	12.3	1 (max)	1.75	3 (max)	22	2 (max)	1 (max)	…
Stellite Star J (P/M)	R30102	bal	32.5	17.5	…	2.5	3 (max)	2.5 (max)	2 (max)	2 (max)	1 B (max)
Stellite Star J	R31001	bal	32.5	17.5	…	2.5	3 (max)	2.5 (max)	2 (max)	2 (max)	…
Tantung G	…	bal	29.5	16.5	…	3	3.5	7 (max)	…	2 (max)	4.5 Ta/Nb
Tantung 144	…	bal	27.5	18.5	…	3	3.5	7 (max)	…	2 (max)	5.5 Ta/Nb
Laves-phase wear-resistant alloys											
Tribaloy T-400	R30400	bal	9	…	28	…	…	…	2.6	…	…
Tribaloy T-400C	…	bal	14	…	27	…	…	…	2.6	…	…
Tribaloy T-800	…	bal	18	…	28	…	…	…	3.9	…	…
Tribaloy T-	…	bal	31	…	4.3	1.6	3.0	3.0	2.0	2.0	…

900							(max)	(max)	(max)	(max)	
Wrought wear-resistant alloys											
Stellite 6B	R30016	bal	30	4	1.5 max	1	3 (max)	2.5	0.7	1.4	…
Stellite 6K	…	bal	30	4.5	1.5 max	1.6	3 (max)	3 (max)	2 (max)	2 (max)	…
Stellite 706K	…	bal	31	…	4.3	1.6	3 (max)	3 (max)	2 (max)	2 (max)	…

(a) Stellite and Tribaloy are registered trademarks of Deloro Stellite, Inc.; Tantung is a registered trademark of Asteg Sales Pty Ltd.

Table 1(b) Compositions of various heat-resistant cobalt-base alloys

Alloy tradename[(a)]	UNS No.	Nominal composition, wt%									
		Co	**Cr**	**W**	**Mo**	**C**	**Fe**	**Ni**	**Si**	**Mn**	**Others**
Wrought heat resistant alloys											
Haynes 25 (L605)	R30605	bal	20	15	…	0.1	3 (max)	10	0.4 (max)	1.5	…
Haynes 188	R30188	bal	22	14	…	0.1	3 (max)	22	0.35	1.25	0.03 La
Inconel 783	R30783	bal	3	…	…	0.03 (max)	25.5	28	0.5 (max)	0.5 (max)	5.5 Al, 3 Nb, 3.4 Ti (max)
S-816	R30816	40 (min)	20	4	4	0.37	5 (max)	20	1 (max)	1.5	4 Nb
Haynes alloy 6B[(c)]	…	bal	30	4	1.5 (max)	1.0	3 (max)	2.5	0.7	1.4	…
Haynes alloy 31	…	bal	25.5	7.5	…	0.50	2 (max)	10.5	1 (max)	1 (max)	…
Haynes alloy 150	…	bal	28	…	…	0.05 (max)	2 (max)	…	1 (max)	1 (max)	…
Wrought corrosion-resistant alloys											
MP35N® alloy	R30035	35	20	…	10	…	…	35	…	…	…
MP159® alloy	R30159	bal	19	…	7	…	9	25.5	…	…	0.2 Al, 0.6 Nb, 3 Ti
Corrosion resistant alloys											
Ultimet (1233)	R31233	bal	26	2	5	0.06	3	9	0.3	0.8	0.08 N
Duratherm 600	R30600	41.5	12	3.9	4	0.05 (max)	8.7	bal	0.4	0.75	2 Ti, 0.7 Al, 0.05 Be
Elgiloy	R30003	40	20	…	7	0.15 (max)	bal	15.5	…	2	1 Be (max)
Havar	R30004	42.5	20	2.8	2.4	0.2	bal	13	…	1.6	0.06 Be (max)
Cast superalloys											
AiResist 13	…	62	21	11	…	0.45	…	…	…	…	0.1 Y, 3.4 Al, 2 Ta
AiResist 213	…	64	20	4.5	…	0.20	0.5	0.5	…	…	0.1 Y, 3.5 Al, 6.5 Ta, 0.1 Zr
AiResist 215	…	63	19	4.5	…	0.35	0.5	0.5	…	…	0.1 Y, 4.3 Al, 7.5 Ta,

											0.1 Zr
FSX-414	…	52.5	29	7.5	…	0.25	1	10	…	…	0.010 B
J-1650	…	36	19	12	…	0.20	…	27	…	…	0.02 B, 3.8 Ti, 2 Ta
MAR-M 302	…	58	21.5	10	…	0.85	0.5	…	…	…	0.005 B, 9 Ta, 0.2 Zr
MAR-M 322	…	60.5	21.5	9	…	1.0	0.5	…	…	…	0.75 Ti, 4.5 Ta, 2 Zr
MAR-M 509	…	54.5	23.5	7	…	0.6	…	10	…	…	0.2 Ti, 3.5 Ta, 0.5 Zr
NASA Co-W-Re	…	67.5	3	25	…	0.40	…	…	…	…	2 Re, 1 Ti, 1 Zr
S-816	R30816	42	20	4	4	0.4	4	20	0.4	1.2	4 Nb
V-36	…	42	25	2	4	0.27	3	20	0.4	1	2 Nb
WI-52	…	63.5	21	11	…	0.45	2	…	…	…	2 Nb + Ta
Stellite 23	R30023	65.5	24	5	…	0.40	1	2	0.6	0.3	…
Stellite 27	R30027	35	25	…	5.5	0.40	1	32	0.6	0.3	…
Stellite 30	R30030	50.5	26	…	6	0.45	1	15	0.6	0.6	…
Stellite 31 (X-40)	R30031	57.5	22	7.5	…	0.50	1.5	10	0.5	0.5	…

(a) Haynes is a registered trademark of Haynes International, Inc.; MP35N and MP159 are registered trademarks of SPS Technologies, Inc. Elgiloy is a registered trademark of Elgiloy Specialty Metals; MAR-M is a registered trademark of Martin Marietta Corp.; Stellite is a registered trademark of Deloro Stellite, Inc.; (b) Maximum. (c) Haynes 6B is currently known as Stellite 6B.

Reference cited in this section

1. D. Klarstrom and P. Crook, Cobalt Alloys: Alloy Designation System, Cobalt Alloys: Alloying and Thermomechanical Processing, and Cobalt Alloys: Properties and Applications, *Encyclopedia of Materials: Science and Technology*, Elsevier Science, 2001, p 1279–1288

Revised by D. Klarstrom, P. Crook, and J. Wu, Metallography and Microstructures of Cobalt and Cobalt Alloys, *Metallography and Microstructures,* Vol 9, *ASM Handbook*, ASM International, 2004, p. 762–774

Metallography and Microstructures of Cobalt and Cobalt Alloys

Revised by D. Klarstrom, Haynes International, Inc.; P. Crook, Haynes International, Inc; and J. Wu, Deloro Stellite Group Limited

---

Cobalt Alloy Metallurgy

Many of the properties of the alloys arise from the crystallographic nature of cobalt. Cobalt provides a unique alloy base because of its allotropic face-centered cubic (fcc) to hexagonal close-packed (hcp) phase transformation, which occurs at a temperature of approximately 422 °C (792 °F) (Ref 2). Alloying elements such as iron, manganese, nickel, and carbon tend to stabilize the fcc structure and increase stacking-fault energy, whereas elements such as chromium, molybdenum, tungsten, and silicon tend to stabilize the hcp structure and decrease stacking-fault energy (Ref 3). The fcc to hcp transformation reaction is quite sluggish even for pure cobalt. However, in metastable compositions, it can be promoted by cold work via a mechanism involving the coalescence of stacking faults (Ref 4). This phenomenon provides a practical limit in the design of wrought cobalt-base alloys in terms of the manufacturing methods that can be used to produce various

product forms. Those involving hot-working operations such as plate, bar, and hot-rolled sheet do not present obstacles, because the working temperatures typically are well within the stable fcc range. However, those products that require extensive cold-working sessions, such as cold-rolled sheet, cold-drawn tubulars, and cold-drawn bar and wire products, must possess adequate levels of matrix stability to be economically viable. Such stability usually is imparted through additions of nickel.

For imparting resistance to oxidizing and sulfidizing types of environments, chromium is the preferred alloying element. Attempts to incorporate aluminum in amounts sufficient to provide protective alumina scales have not been commercially successful, because the formation of the brittle intermetallic compound β-CoAl significantly reduced fabricability. In addition to chromium, small amounts of elements such as manganese, silicon, and rare-earth elements (e.g., lanthanum) can be used to enhance the formation of protective oxide scales at elevated temperatures.

Strengthening of cobalt-base alloys is accomplished by solid-solution alloying (e.g., molybdenum, tungsten, tantalum, and niobium) in combination with carbon to promote carbide precipitation. Compared to the wrought alloys, cast cobalt-base superalloys are characterized by higher contents of high-melting metals (chromium, tungsten, tantalum, titanium, and zirconium) and by higher carbon contents. The solid-solution alloying decreases stacking-fault energy, thereby making the cross slip and climb of glide dislocations more difficult. Carbide precipitation (especially $M_{23}C_6$ carbides) also can be quite effective in pinning glide dislocations, and both wrought and cast alloys depend on the dispersion of complex carbides for strength. However, the use of high levels of carbon will limit manufacturing operations to hot-working processes. Compositions intended for cold-working processes usually contain carbon at levels of 0.15% or less. For service temperatures of 700 °C (1300 °F) or less, special alloy compositions have been developed that exploit the fcc to hcp transformation in products that are mechanically worked and aged (Ref 5).

The various carbide phases that form depend on chemical composition, heat treatment, and cooling. The carbides also may be different sizes and somewhat varying shapes, even for the same phase. In Co-Cr-C, M_7C_3 and $M_{23}C_6$ are common. In the as-cast condition, the MC phase is predominant, because it is the first formed upon cooling from the molten state. Cast alloys invariably have M_7C_3 carbides located within the grains, although M_7C_3 may be found at grain boundaries as well. Subsequent heat treatments (intentional or from service exposure) modify the morphology, amounts, and types of carbides found in the grains of superalloys. Some secondary carbides within grains can be formed by precipitation on dislocations located near large primary carbides.

The carbides are seldom binary compositions; chromium, tungsten, tantalum, silicon, zirconium, nickel and cobalt may all be present in a single particle or carbide. In more complex alloy systems, cobalt, tungsten, and molybdenum replace some of the chromium in the carbide phases. Niobium and tantalum (8 to 10%), and titanium and zirconium (less than 0.5%) form carbides of the MC type. Molybdenum and tungsten form M_6C in the Co-Cr-C alloys when the content of either element is great enough so that it will no longer substitute for chromium in $M_{23}C_6$. Molybdenum, although used extensively in nickel-base superalloys, is used only sparingly in cobalt-base superalloys. In cobalt-base superalloys, tungsten is more effective and less detrimental than molybdenum. However, corrosion-resistant grades of cobalt alloys rely on molybdenum instead of tungsten for corrosion resistance. In addition, molybdenum has been found to enhance wear resistance in cobalt-base wear resistant alloys (Ref 6).

Another important aspect in the physical metallurgy of cobalt-base alloys is the occurrence of intermetallic compounds such as σ, μ, and Laves phases. These phases are deleterious in high-temperature applications, but Laves-phase alloys are used for wear-resistance applications (see the section “Laves-Phase Alloys” in this article). The σ and μ intermetallic compounds are classified as electron compounds, and they are often referred to as topologically closed-packed (tcp) phases. The Laves phase is formed mainly on the basis of atomic size factors. Some examples of these compounds in terms of general composition and crystal structure are given in Table 2. Specific data for Haynes alloy 25 are listed in Table 3 (Ref 7). In addition to the gross chemistry factors responsible for the formation of these compounds, it has also been recognized that minor elements, notably silicon, can play important roles (Ref 8, 9). The precipitation of these intermetallic phases can cause embrittlement, especially at low temperatures. Some success in retarding the formation of the Laves phase was achieved in the development of Haynes alloy 188 by control of the chemistry (Ref 10, 11). On the other hand, precipitation of Laves phase can impart wear resistance, especially at high temperatures.

Table 2 Deleterious intermetallic compounds in cobalt-base superalloys

Compound	Structure
Co_2 (Mo, W, Ta, Nb)	Hexagonal Laves phase
Co_2 $(Mo, W)_6$	Rhombohedral, hexagonal μ phase
Co_2 (Ta, Nb, Ti)	Cubic Laves phase
Co_2 $(Mo, W)_3$	σ phase

Table 3 Phases present in Haynes alloy 25

Phase	Crystal structure	Lattice parameters, nm
M_7C_3	Hexagonal (trigonal)	a = 1.398, c = 0.053, c/a = 0.0324
$M_{23}C_6$	fcc	a = 1.055 to 1.068
M_6C	fcc	a = 1.099 to 1.102
Co_2W	Hexagonal	a = 0.4730, c = 0.7700, c/a = 0.1628
α-Co_3W	Ordered fcc	a = 0.3569
β-Co_3W	Ordered hexagonal	a = 0.5569, c = 0.410, c/a = 0.0802
Co_7W_6	Hexagonal (rhombohedral)	a = 0.473, c = 2.55, c/a = 0.539
Matrix	fcc	a = 0.3569
	hcp	a = 0.2524, c = 0.4099, c/a = 0.1624

References cited in this section

2. T.B. Massalski, H. Okamoto, P.R. Subramanian, and L. Kacprzak, Ed., *Binary Alloy Phase Diagrams,* Vol 2, 2nd ed., ASM International, 1990, p 1214–1215

3. C.T. Sims and W.C. Hagel, Ed., *The Superalloys,* John Wiley & Sons, 1972, p 145–174

4. H.M. Tawancy, V.R. Ishwar, and B.E. Lewis, On the fcc-hcp Transformation in a Cobalt-Base Superalloy (Haynes Alloy 25), *J. Mater. Sci. Lett.,* Vol 5, 1986, p 336–341

5. F.C. Hagen et al., Mechanical Properties of New Higher Temperature Multiphase Superalloy, *Superalloys 1984,* Metallurgical Society of AIME, 1984, p 621–630

6. D. Raghu and J.B.C. Wu, Alloy Solutions to Combat Synergistic Wear and Corrosion in Demanding Process Environments, *Proc. EPRI Corrosion and Degradation Conference,* 2–4 June 1999, Electric Power Research Institute

7. S. Takeda and N. Yukawa, *Nippon Kinz. Gakkai-ho,* Vol 6 (No. 11, 12), 1967, p 784–802, 850–855

8. D.I. Bardos, K.P. Gupta, and P.A. Beck, Ternary Laves Phases with Transition Elements and Silicon, *Trans. AIME,* Vol 221, Oct 1961, p 1087–1088

9. S.T. Wlodek, Embrittlement of a Co-Cr-W (L-605 Alloy), *Trans. ASM,* Vol 56 1963, p 287–303

10. C.T. Sims, The Occurrence of Topologically Close-Packed Phases, *The Superalloys,* John Wiley, 1972

11. R.B. Herchenroeder, S.J. Matthews, J.W. Tackett, and S.T. Wlodek, Haynes Alloy No. 188, *Cobalt,* Vol 54, March 1972, p 3–13

Revised by D. Klarstrom, P. Crook, and J. Wu, Metallography and Microstructures of Cobalt and Cobalt Alloys, *Metallography and Microstructures*, Vol 9, *ASM Handbook*, ASM International, 2004, p. 762–774

Metallography and Microstructures of Cobalt and Cobalt Alloys

Revised by D. Klarstrom, Haynes International, Inc.; P. Crook, Haynes International, Inc; and J. Wu, Deloro Stellite Group Limited

Metallographic Preparation

Cobalt-base alloys are relatively easy to polish and nearly any mounting procedure can be employed unless edge retention is required. Polishing techniques may be similar to those for nickel-base alloys, but cobalt and its alloys are more difficult to prepare than nickel and its alloys. Cobalt and its alloys work harden rapidly (due to the fcc-to-hcp transformation), and some twin readily. Consequently, grinding and polishing rates are lower for cobalt than for nickel, copper, or iron. Preparation of cobalt and its alloys is somewhat similar to that of refractory metals.

The following general practice (see Table 4, Ref 12) is for preparing cobalt and its alloys. Two steps of SiC paper may be needed to get the specimens coplanar. If the cut surface is of good quality, start with 320-grit paper. Cobalt and its alloys are more difficult to cut than most steels, regardless of their hardness, and abrasive cutting wheels are recommended. Attack polishing has been used after mechanical polishing. Morral (Ref 13) has recommended two chemical polishing solutions: equal parts of acetic and nitric acids (immerse) or 40 mL lactic acid, 30 mL hydrochloric acid, and 5 mL nitric acid (immerse). A wide variety of cobalt-base alloys has been prepared with the previously described method without need for chemical polishing. The 1-μm diamond step could be eliminated for routine work.

Table 4 Five-step procedure for cobalt

Surface	Abrasive/size	Load		Base speed (rpm)/direction[(b)]	Time (min:s)
		N	**lb**		
Abrasive disks (waterproof paper)	220–320 (P240–P400) grit SiC water cooled	27	6	250–300 contra	Until plane
Cloth or rigid grinding disk	9 μm diamond suspension[(a)]	27	6	100–150 contra	5:00
Pad	3 μm diamond suspension[(a)]	27	6	100–150 contra	5:00
	1 μm diamond suspension[(a)]	27	6	100–150 contra	3:00
Cloth or pad	~0.05 μm colloidal silica or alumina suspensions	27	6	80–120 contra	2:00–3:00

(a) Plus fluid extender as desired. (b) Contra: platen and specimen rotate in opposite directions

Polishing procedures for different categories of cobalt alloys are summarized below (Ref 14):

Pure Cobalt. Cold working from cutting and grinding can be troublesome with purer metals. Pure cobalt tends to form smear and deformation layers. Grinding is done wet on SiC paper (down to 1200 grit) with light pressure. Polishing methods include:

- Initial polishing with 6, 3, and 1 μm diamond and final polishing with 0.3 and 0.05 μm alumina slurry, with if necessary, etching between polishing steps with 3% nitric acid in alcohol
- Initial polishing with 6 μm diamond particle size, then for 2 to 3 h on a vibratory polisher charged with 0.3 μm alumina slurry or chromium oxide. Final polishing in a 10% aqueous SiO_2 suspension
- Electrolytic polishing with EP2 recipe (see Table 5).

Table 5 Electrochemical polishing recipes for cobalt alloys

No.	Recipe	Conditions
Electrolytic polishing		
EP1	600 mL methanol 99.8%	10–60 s
	330 mL nitric acid 65%	40–70 V dc Stainless steel cathode. Do not store!
EP2	Phosphoric acid 85%	3–5 min. 1.5 V dc Stainless steel cathode
EP3	600 mL distilled water	1–15 min. 1–2 V dc
	400 mL phosphoric acid 85%	Stainless steel or Co cathode. Rinsing will remove black deposit.
EP4	900 mL distilled water	Seconds to minutes. 6 or 4 V dc
	100 mL sulfuric acid 95–97%	Stainless steel cathode
EP5	200 mL perchloric acid 60%	Seconds to minutes. 30–60 V dc
	700 mL ethanol 96% 100 mL butyl glycol 99%	Stainless steel cathode
EP6	15 mL sulfuric acid 95–98% 85 mL methanol	25 V dc, 3–10 s
Chemical polishing		
CP1	40 mL lactic acid 90% 30 mL hydrochloric acid 32% 5 mL nitric acid 65%	Seconds to minutes
CP2	100 mL distilled water 5 g chromium (VI) oxide	Seconds to minutes
CP3	50 mL glacial acetic acid 50 mL nitric acid 65%	Seconds to minutes

Source: Ref 14

Magnetic Alloys. Cobalt alloys for magnetic applications are diverse and include:

- Cobalt-rich alloys (>50 wt% Co) such as Co-Ni, Co-Fe, Co-Pt, Co-V, and Co-Sm alloys
- Alloys with less than 50 wt% Co such as Alnico alloys (25 to 30 wt% Co with Al, Cu, Fe, Li, Ni) Reamalloy (12 wt% Co with Fe), Unico (29 wt% Co with Cu, Ni), and Fe-Ni-Co alloys

Preparation of these diverse alloys is not very difficult, although preparation has to be adjusted accordingly for the mechanical behavior that may range from ductile to hard brittle. Wet grinding on SiC paper down to 1200 grit is done. Polishing techniques include:

- For hard and brittle alloys, rough polishing with 6, 3, 1, and 0.25 μm diamond particle size, and final polishing with 0.05 μm alumina slurry
- For ductile alloys, rough polishing with 6 to 1 μm diamond particle size, and shock polishing with the electrolyte recipes EP1 or EP5 (Table 5)
- Electrolytic polishing of Alnico with recipe EP2; intermetallic alloy with EP5 (cobalt alloys tarnish easily and should only be rinsed with alcohol)

Cobalt-Base Superalloys. Preparation of wrought and cast cobalt-base superalloys is similar to nickel-base superalloys. Preparation recommended in Ref 14 is:

- Wet grinding on SiC papers down to 1200 grit
- Grinding on SiC papers down to 320 grit, then lapping on a synthetic-bonded lapping disk with 6 μm diamond particle size
- Polishing with 3 and 1 μm diamond particle size on a hard synthetic cloth. Final polishing with 0.05 μm alumina on a hard silk cloth
- Electrolytic polishing with EP4 (Table 5)

A more detailed description of metallographic preparation of Hastelloy and Haynes superalloys is in the section "Heat-Resistant Cobalt Alloys"in this article.
Wear-resistance alloys such as the Stellite alloys can be prepared as follows:

- Wet grinding on SiC papers down to 320 grit, then lapping on a synthetic-bonded lapping disk with 6 μm diamond particle size
- Grinding on a diamond disk with 20 μm particle size
- Polishing with 6 μm diamond particle size on a hard synthetic cloth. Final polishing with 1 μm diamond particle size on a cotton cloth

Etching. Cobalt is attacked readily by dilute nitric acid and less rapidly by hydrochloric or sulfuric acids, but not caustic solutions. Pitting is commonly encountered with many etchants. Morral has compiled an extensive list of reagents for cobalt and its alloys (Ref 13). Young has described etching methods delineating oxide and sulfide phases in cobalt (Ref 15). These etchants color the matrix phases, but do not affect the oxides and sulfides. Weeton and Signorelli (Ref 16) have described different procedures for identifying sigma phases and carbides in wrought Stellite 21 (Table 6, Ref 16). Etchants for cobalt and cobalt alloys are listed in Table 7. Macroetchants are listed in Table 8.

Table 6 Staining and heat tinting procedures for identification of sigma phase and carbides in Stellite 21, wrought cobalt alloy

Coloring process	Method	Purpose	First etchant		Staining method		Colors of minor phases obtained by previous investigators
			Solution	**Method**	**Solution**	**Method**	
1	Etch	To stain sigma phase	8% oxalic acid 92% water	Electrolytic etch 8–10 s 6 V Room temperature	5 g $KMnO_4$ 5 g NaOH 90 mL water	Immerse 10–20 s Room temperature	Sigma: bright green or red to purple
2	Etch	To differentiate between carbides and sigma phase	10% NaCN 90% water	Electrolytic etch 10–20 s 1.5 V	Murakami's 10 g $K_3Fe(CN)_6$ 10 g KOH 100 mL water	Immerse 2–4 s Room temperature	Carbides: straw to yellow-brown or buff Gamma (sigma): gray to blue or greenish gray
3	Etch	To identify carbides	2% chromic	Light electrolytic	1 part (20% $KMnO_4$,	Immerse 7 s	$Cr_{23}C_6$: brown

			acid 98% water	etch	80% water) 1 part (8% NaOH, 92% water)	Room temperature	Cr_7C_3: pale yellow to light tan M_6C: red, green, yellow, blue (also reticulation)
4	Heat tint	To identify carbides and sigma phase	5% HCl 95% water	Light electrolytic etch 1 s 5 V		Heat polished specimen to dull red Held at temperature until surface becomes colored Air cooled or Hg quenched	Sigma: dark medium brown $Cr_{23}C_6$: white M_6C: dark Note M_6C and sigma cannot be differentiated in same structure

Source: From Ref 16

Table 7 Etchants for cobalt alloys

No.	Material	Etchant	Condition and comments
General			
m1	Pure Fe Co-Fe alloys	100 mL methanol 99.8% 10 mL HNO_3 65%	For Co and Co-Fe alloys. Immerse sample for up to 30 s. 1–50% nital has been used with varying immersion times from seconds to minutes. Do not store; neutralize after use.
m2	Pure and low-alloy Co Co-B, Co-Ti, and Co-Mn alloys WC-TiC-TaC-Co hardmetals Grain-boundary etchant	15 mL distilled water 15 mL glacial acetic acid 60 mL HCl 32% 15 mL HNO_3 65%	Age 1 h before use. Immerse sample from 5 s up to 30 s.
m3	Co and alloys, general etch	7.5 mL HF 2.5 mL HNO_3 200 mL methanol	Immerse sample for 2–4 min
m4	Co alloys	25 mL water 25 mL acetic acid 50 mL HNO_3	
m5	Co alloys (Battelle)	80 mL lactic acid 10 mL H_2O_2 (30%)	

		10 mL HNO_3	
m6	Pure Co Color etchant	98 mL distilled water 2 mL hydrofluoric acid 40%, boiling, add molybdic acid to saturate	Seconds to minutes Room temperature
m7	Co-base casting material and rolling stock Stellite Color etchant	100 mL stock solution Beraha III 1 g potassium disulfite	30 s to 5 min Wet etching Keep only for 1–2 h.
m8	Stock solution, Beraha III	600 mL distilled water 400 mL HCl 32% 50 mL ammonium hydrogen difluoride	*Caution: stock solution must be stored in plastic bottle.*
m9	Hardfacing alloys and superalloys	100 mL HCl 5 mL H_2O_2 (30%)	Use under a hood. Use fresh. Immerse sample a few seconds.
Etchants for specific alloys/phases			
m10	Co superalloys	200 mL HCl 32% 5 mL nitric acid 65% 65 g $FeCl_3$	Immerse sample a few seconds. Use under a head.
m11	Co superalloys	50 mL distilled water 50 mL HCl 32% 10 g copper (II) sulfate (Marble's etch)	Seconds to minutes Immersion or swabbing Add few drops of sulfuric acid to increase activity.
m12	Magnetic alloys Co-Fe alloys	100 mL distilled water 100 mL HCl 32% 200 mL methanol 99.8% 5 mL HNO_3 65% 7 g $FeCl_3$ 2 g copper (II) chloride	10–15 s Immersion or swab etching
m13	Co-Sm alloys	100 mL distilled water 1 mL glacial acetic acid 1 mL nitric acid 65%	Immerse sample a few seconds.
m14	So-Sm alloys Color etchant	100 mL distilled water 2 mL HCl 32%	10 s

		20 g potassium disulfite	
m15	Co-Sm alloys Grain-boundary etchant	100 mL distilled water 8 g chromium (VI) oxide 2 g sodium sulfate	5–10 s Rinse in hot water and remove smudge layer with 20% aqueous chromium (VI) oxide solution
m16	Co-Ti alloys	100 mL water 2 mL Hf 5 mL H_2O_2 (30%)	
m17	Co-Pt alloys (48–54 at.% Co)	3 parts HNO_3 1 part HCl	
m18	Co-Pt alloys WC-TiC-NbC-Co hardmetals	75 mL HCl 32% 25 mL HNO_3 65%	Up to 5 min Use fresh mixture only.
m19	Co borides	30 mL distilled water 10 mL HCl 32% 10 mL HNO_3 65%	Seconds to minutes
m20	Co silicide	100 mL distilled water 15 g CrO_3	Seconds to minutes Add few drops of hydrochloric acid before use.
m21	Co and Co-Al alloys	25 mL distilled water 50 mL HCl 32% 15 g $FeCl_3$ 3 g ammonium tetrachlorocuprate (II) (Adler's reagent)	Seconds to minutes
m22	Co-base superalloys Color etchant	50 mL distilled water 50 mL HCl 32% 2 g potassium disulfite	Seconds to minutes; carbides remain white
m23	Alloy C73 (Co, 40Cr, 2.4C)	95 mL water 1 g KOH 4 g $KMnO_4$	Colors M_7C_3 gray and $M_{23}C_6$ black
m24	Co, cobalt oxides, and sulfides	Solution 1: 1 g mercuric chloride 99 mL water Solution 2:	Etch with solution 1 for 30 s or with solution 2 for 2 min to distinguish between Co metal, cobalt oxide, and sulfides. Both stain the Co matrix brown, oxide remains dark gray, cobalt sulfide remains yellowish, and MnS remains bluish gray.

		35 g sodium bisulfite 100 mL water	
Tint etch			
m19	Beraha's tint etch for Co alloys	Solution 1: HCl and water (1:1) (stock solution) Ingredient 2: 0.6–1 g potassium metabisulfite Ingredient 3: 1–1.5 g $FeCl_3$	Add ingredient 2 to 100 mL of stock solution 1, then add ingredient 3. Immerse sample at 20 °C for 60–150 s, agitate sample. Matrix is colored, carbides and nitrides are unaffected.
Electrolytic etching			
Em1	Pure Co and Co-Al alloys	100 mL distilled water 5 mL HCl 32% 10 g $FeCl_3$	Several seconds 6 V dc Use stainless steel cathode.
Em2	Stellites up to 70% Co and Co-base superalloys	100 mL distilled water 5–10 mL HCl 32% 2–10 g CrO_3	2–20 s 3 V dc Stainless steel cathode
Em3	Pure Co and Co-base superalloys	100 mL distilled water 5–10 mL HCl 32%	2–10 s 3 V dc Graphite cathode; pitting sometimes occurs
Em4	Co-base abrasion-resistant alloys and tool materials, superalloys	100 mL HCl 32% 5 mL hydrogen peroxide 30%	3–5 s 4 V dc Stainless steel cathode
Em5	Co-base superalloys	95 mL HCl 32% 5 g oxalic acid	2–3 V dc, pointed stainless steel contact anode, graphite cathode, 1–5 s
Em6	Hardfacing alloys and superalloys	Solution 1: 100 mL water 2 g CrO_3 Solution 2: 85 mL water 4 g NaOH 10 g $KMnO_4$	Use solution 1 at 3 V dc for 2 s. Rinse in water and immerse sample in solution 2 for 5–10 s. Use solution 2 fresh.
Em7	Co superalloys	140 mL HCl	Use at 3 V dc for 2–10 s.

		1 g CrO_3	
Em8	Cobalt	940 mL water 45 mL HNO_3 15 mL HCl	Use stainless steel cathode, 3.5 V dc, 0.75 A/cm^2, 15 s, 20 °C

Adapted from Ref 14, 17

Table 8 Macroetchants for cobalt and cobalt alloys

Material	Etch composition	Remarks and conditions
49%Co-49%Fe-V alloy and some Stellites	50 mL HCl (32%) 50 mL H_2O	Good for general structure. Immerse sample in hot (60–80°C) solution for 30 min. Rinse in hot water.
Co-25Cr-10Ni-8W, Co-21Cr-20Ni, Co-3Cr-3Mo-1Nb, Stellite	50 mL HCl (32%) 10 mL HNO_3 (65%) 10 g $FeCl_3$ 100 mL H_2O	Good for general structure and grain size. Swab sample until desired contrast is obtained.
HA-36	2 g cupric ammonium chloride 5 g $FeCl_3$ 5 mL HNO_3 50 mL HCl 80 mL H_2O	Good for general structure and grain size. Swab sample until desired contrast is obtained.
Co, Co alloys	Solution 1 Saturated solution of $FeCl_3$ in HCl Solution 2 Add 5% HNO_3 to solution 1 prior to use.	Use at room temperature. After etching dip sample in 1:1 solution of HCl and H_2O.
Co, Co alloys	Solution 1 21 mL H_2SO_4 15 mL HCl 21 mL HNO_3 21 mL HF 22 mL H_2O	Etch sample 5 min in solution 1 and then 5 min in solution 2.

	Solution 2 40 mL of a solution of 1 g $CuCl_2 \cdot 2H_2O$ and 5 mL H_2O 40 mL HCl 20 mL HF	
Nimonic, Ni-Cr-Co alloys, Ni-Cr-Co-Mo alloys	5 mL HF 3 mL HCl 50 mL alcohol “pinch” of sodium hyposulfite	Use boiling.
Co-Ni-Fe high-temperature alloys	25 mL H_2O 50 mL HCl (32%) 25 mL HNO_3 (65%)	Immerse sample at room temperature for 10–30 min.

Source: Ref 14, 17

References cited in this section

12. *Buehler's Guide to Materials Preparation,* Buehler, Ltd., 2002, p 46

13. F.R. Morral, Metallography of Cobalt-Base and Cobalt-Containing Alloys, *Prakt. Metallogr.,* Vol 10, 1973, p 398–413

14. G. Petzow, *Metallographic Etching,* 2nd ed., ASM International, 1999, p 75–77

15. R.S. Young, Metallographic Differentiation of Cobalt Metal, Oxide and Sulphide, *Metallurgia,* Vol 59, April 1959, p 210

16. J.W. Weeton and R.A. Signorelli, Effects of Heat Treatment upon Microstructures, Microconstituents, and Hardness of a Wrought Cobalt Base Alloys, *Trans. ASM,* Vol 47, 1955, p 815–852

17. G.F. Vander Voort, *Metallography Principles and Practice,* McGraw-Hill, 1984 (reprinted by ASM International, 1999), p 207

Revised by D. Klarstrom, P. Crook, and J. Wu, Metallography and Microstructures of Cobalt and Cobalt Alloys, *Metallography and Microstructures*, Vol 9, *ASM Handbook*, ASM International, 2004, p. 762–774

Metallography and Microstructures of Cobalt and Cobalt Alloys

Revised by D. Klarstrom, Haynes International, Inc.; P. Crook, Haynes International, Inc; and J. Wu, Deloro Stellite Group Limited

Wear-Resistant Cobalt Alloys

The Stellite alloys listed in Table 1(a) are most commonly used in the form of castings or weld overlays (hardfacing alloys). Only a few of them can be made into hot-worked plates, sheets, or bars. Powder metallurgy techniques as well as hot isostatic pressing can be used to consolidate Stellite alloy powders into solid components. Some alloys (e.g., Stellite alloys 1, 6, and 12) are derivatives of the original Co-Cr-W alloys developed by Haynes. These alloys are characterized by their carbon and tungsten/molybdenum contents (Ref 18). Their microstructures (in weld overlay form) are presented in Fig. 1(a) to (c) and illustrate the extent of carbide precipitation.

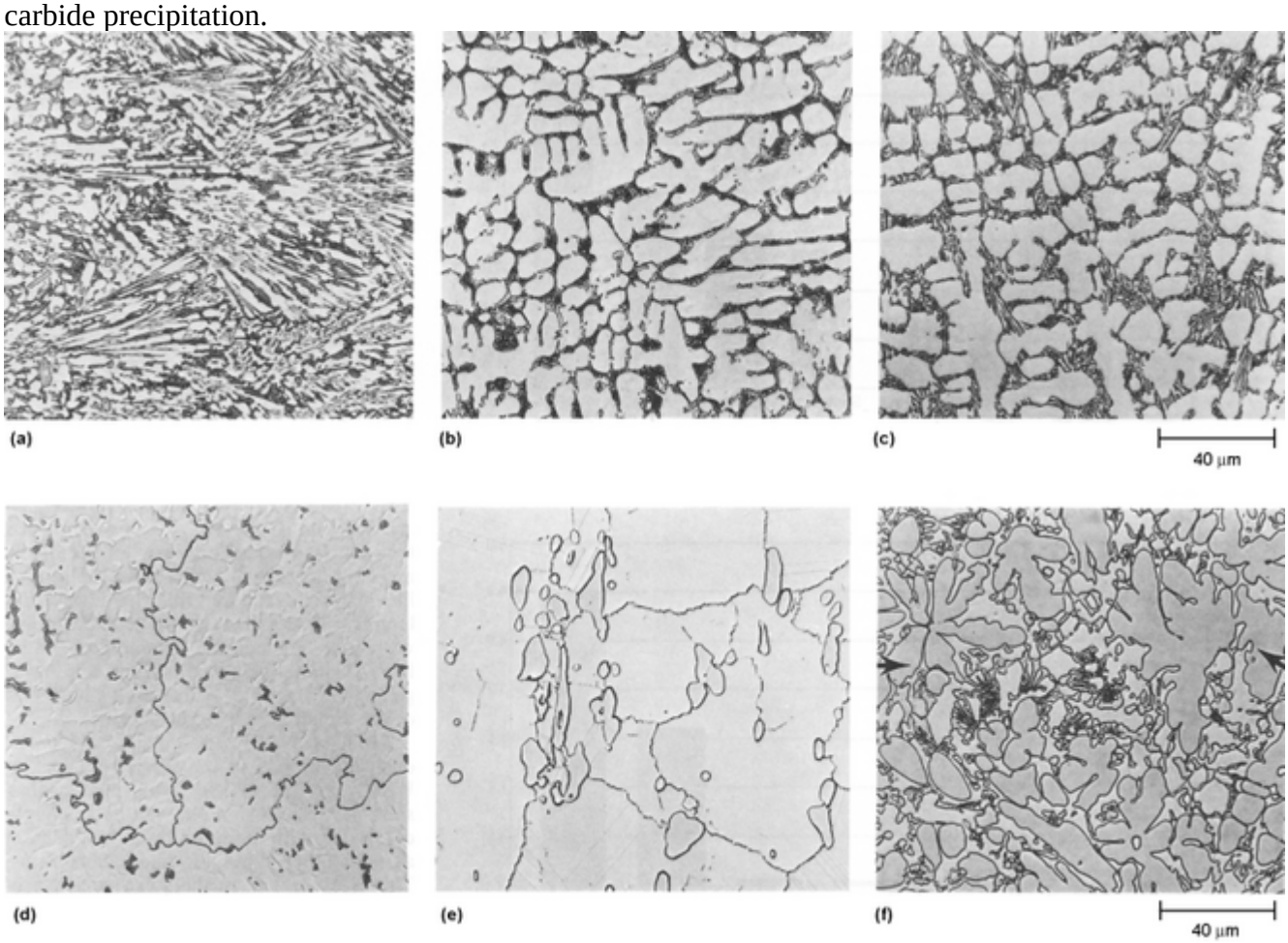

Fig. 1 Microstructures of various cobalt-base wear-resistant alloys. (a) Stellite 1, two-layer gas tungsten arc deposit. (b) Stellite 6, two-layer gas tungsten arc deposit. (c) Stellite 12, two-layer gas tungsten arc deposit. (d) Stellite 21, two-layer gas tungsten arc deposit. (e) Haynes alloy 6B, 13 mm (0.5 in.) plate. (f) Tribaloy alloy (T-800) showing the Laves precipitates (the largest continuous precipitates some of which are indicated with arrows). All 500×

The most common carbide in the hypereutectic high-carbon alloys is a chromium-rich M_7C_3 type, although chromium-rich $M_{23}C_6$ carbides are abundant in the hypoeutectic low-carbon alloys such as Stellite alloy 21. In high-tungsten alloys (such as Stellite alloy 1) tungsten-rich M_6C carbides also are usually present. Tungsten and molybdenum participate in the formation of M_6C carbides during alloy solidification. Stellite alloy 21 employs

molybdenum, rather than tungsten, to strengthen the solid solution. Stellite alloy 21 also contains considerably less carbon. This alloy is more resistant to corrosion than Stellite alloys 1, 6, and 12, because of the high molybdenum content and because most of the chromium is in solution (rather being tied up in carbides). The most recently developed alloys in the Stellite family are those in the 700 series (alloys 703, 704, 706, 712, and 720 in Table 1(a)). As with Stellite alloy 21, the tungsten in these alloys has been replaced by molybdenum (molybdenum contents range from 5 to 18%).

The microstructures of these alloys are characterized by the separation of chromium-rich and molybdenum-rich eutectic regions, as shown in the scanning electron micrograph (SEM) of Stellite 712 in Fig. 2, where the light areas are molybdenum rich and dark areas chromium rich. It is likely that $M_{23}C_6$ carbides are in the chromium-rich areas and the M_6C or M_2C carbides are in the molybdenum-rich areas.

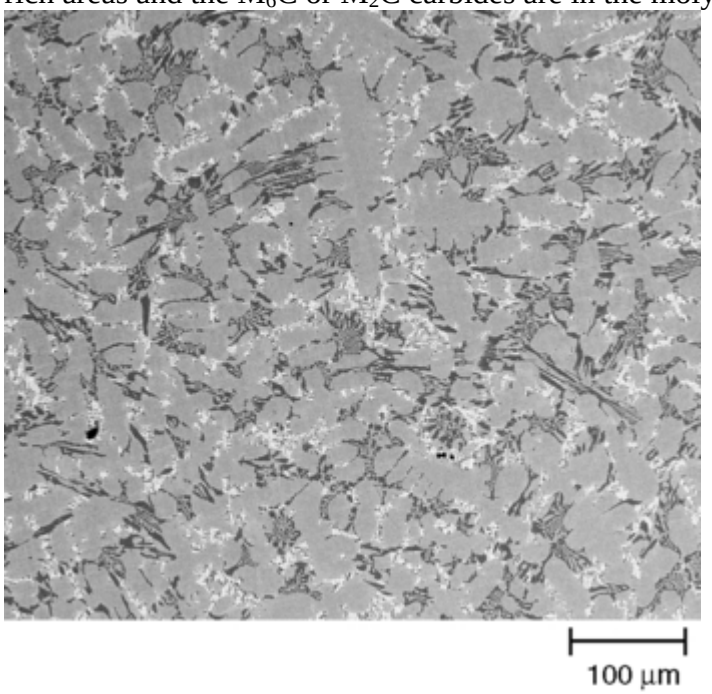

Fig. 2 Scanning electron micrograph from as-cast Stellite 712 alloy characterized by the separation of chromium-rich regions (dark) and molybdenum-rich eutectic regions (light). Original magnification at 1000×. Courtesy of J. Wu, Deloro Stellite Group Limited

The size and shape of the carbide particles within the Stellite alloys are strongly influenced by cooling rate and subtle chemistry changes. For example, typical overlay microstructures as applied by different welding processes are shown in Fig. 3 and 4. Such changes markedly affect abrasion resistance, because there is a distinct relationship among the size of abrading species, the size of the structural hard particles, and the abrasive wear rate. The fraction of carbides is also influenced by cooling rate, carbon contents, and alloying. For example, at a carbon level of 2.4 wt% (Stellite 3), the carbides constitute about 30 wt% of the material. These are of the M_7C_3 (chromium-rich primary) and M_6C (tungsten-rich eutectic) types. At 1 wt% carbon (Stellite 6B alloy), the carbides constitute approximately 13 wt% of the material.

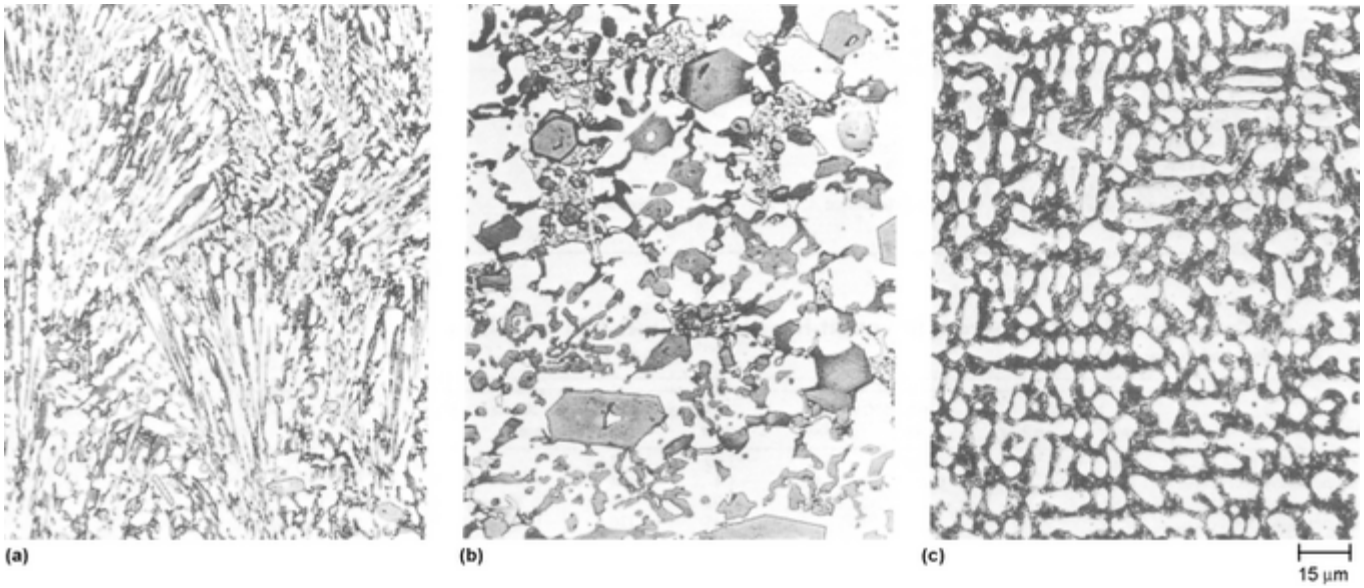

Fig. 3 Typical overlay microstructures of Stellite 1 alloy applied by different weld processes. (a) Three-layer gas tungsten arc. (b) Three-layer oxyacetylene. (c) Three-layer shielded metal arc. All 500×

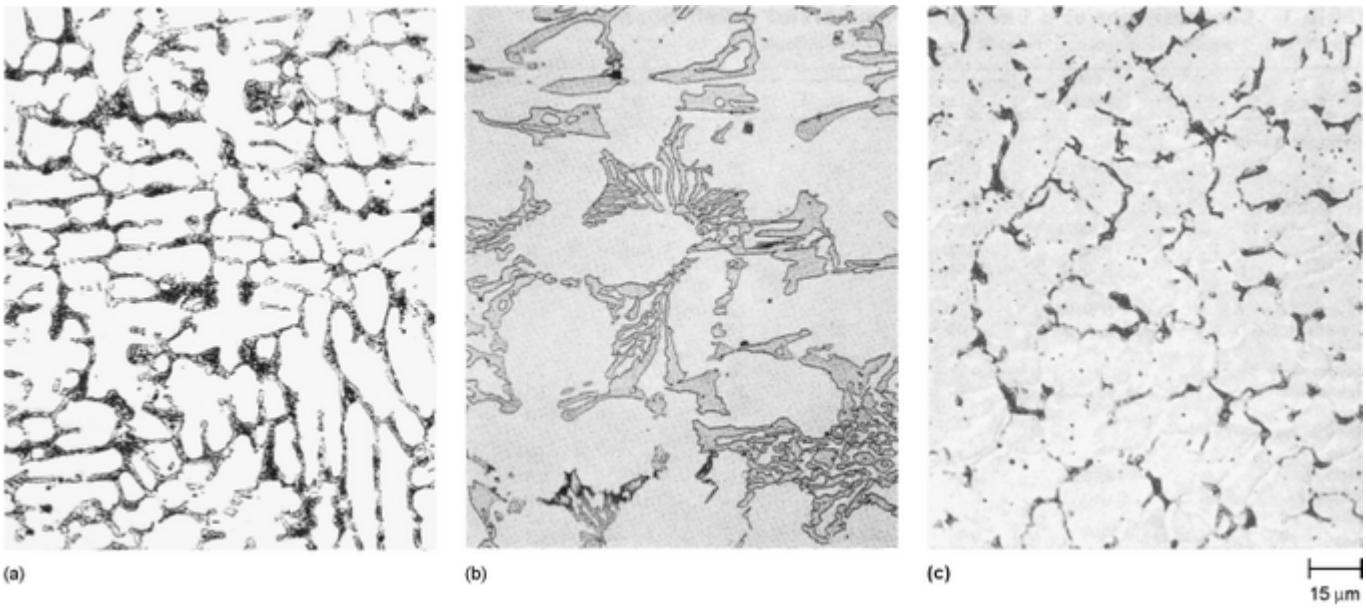

Fig. 4 Typical overlay microstructures of Stellite 6 alloy applied by different weld processes. (a) Three-layer gas tungsten arc. (b) Three-layer oxyacetylene. (c) Three-layer shielded metal arc. See alsoFig. 1 All 500×

Powder metallurgy (P/M) versions of several Stellite alloys (typically containing low levels of boron—1.0% max as listed in Table 1(a)—to enhance sintering) are available for applications where the P/M process is cost effective (e.g., high-volume production of small simple shapes). The microstructure of P/M Stellite alloys contains complex combinations of M_7C_3, M_6C, and $M_{23}C_6$ carbides that are embedded in a Co-Cr-W matrix. Boron is expected to replace some of the carbon atoms in these carbides to form borocarbides.

Laves-phase alloys include the Tribaloy family of wear-resistant materials. Four cobalt-base Laves-type alloy compositions (T-400, T-400C, T-800, and T-900) are listed in Table 1(a). In these materials, molybdenum and silicon are added at levels in excess of their solubility limit with the objective of inducing the precipitation of the hard (and corrosion-resistant) Laves phase (CoMoSi or Co_3Mo_2Si). Carbon is held as low as possible in these alloys to discourage carbide formation. An example is shown in Fig. 1(f) and 5.

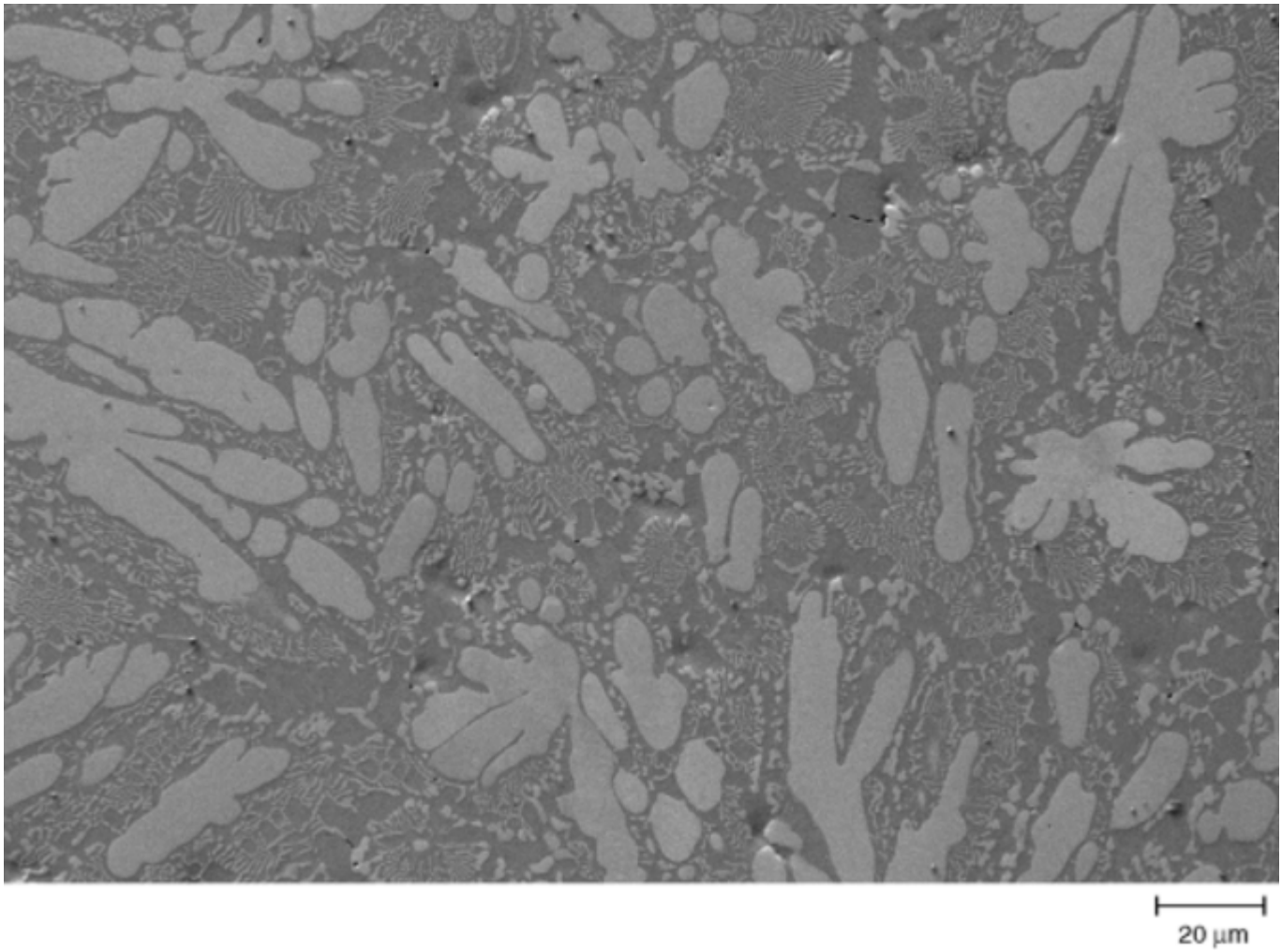

Fig. 5 Electron backscattered image of as-cast Tribaloy T-400C. The white areas are the Laves phase. Original magnification at 500×. Courtesy of J. Wu, Deloro Stellite Group Ltd.

Because the Laves intermetallic phase is so abundant in these alloys (35 to 70 vol%), its presence governs all the material properties. Accordingly, the effects of the matrix composition in these alloys are less pronounced than in the case for the cobalt-base carbide-type Stellite alloys, for example. The Laves phase is specifically responsible for outstanding abrasion resistance, but it severely limits the material ductility and the impact strength. In fact, it is difficult to attain crack-free overlays on all but the smallest components given adequate preheat. In recent years, with the advanced manufacturing technologies, crack-free cast or P/M components have been made and used widely in applications where high performance is required.

Wrought Alloys. The high-carbon alloys, such as Stellite alloys 6B, 6K, and 706K in Table 1(a), are essentially wrought versions of the hardfacing alloys described previously. Wrought processing improves chemical homogeneity (important in a corrosion sense), markedly increases ductility, and modifies substantially the geometry of the carbide precipitates within the alloys (blocky carbides within the microstructure enhance abrasion resistance). In terms of composition, the alloys are essentially Co-Cr-W/Mo-C quaternaries with chromium providing strength and corrosion resistance to the solid solution in addition to functioning as the chief carbide former (during alloy solidification). Tungsten or molybdenum provides additional solid-solution strength. Alloy 6B contains approximately 12.5 wt% carbides of the M_7C_3 and $M_{23}C_6$ types in the ratio 9 to 1. Alloys 6K and 706K exhibit an even greater carbide volume fraction, again with the M_7C_3 as the predominant type. Alloy 706K may also contain M_6C or M_2C due to the presence of molybdenum.

Reference cited in this section

18. J.B.C. Wu and J.E. Redman, Hardfacing with Cobalt and Nickel Alloys, *Weld. J.*, Sept 1994, p 63–68

Revised by D. Klarstrom, P. Crook, and J. Wu, Metallography and Microstructures of Cobalt and Cobalt Alloys, *Metallography and Microstructures*, Vol 9, *ASM Handbook*, ASM International, 2004, p. 762–774

Metallography and Microstructures of Cobalt and Cobalt Alloys

Revised by D. Klarstrom, Haynes International, Inc.; P. Crook, Haynes International, Inc; and J. Wu, Deloro Stellite Group Limited

Heat-Resistant Cobalt Alloys

Cobalt-base superalloys for aircraft engines were among the first true members of the superalloy family. An historical perspective of these materials is given in Table 9. The initial applications involved cast compositions for use as blades in turbo superchargers for piston engines in the 1930s, then as blades and vanes in the first gas turbine engines of the 1940s. The use of cast cobalt-base alloys continues in current gas turbine engines, mainly as nozzle guide vanes and stator blades. Wrought cobalt-base superalloys did not enjoy extensive use until the 1950s for such components as forged turbine blades, combustor liners, and afterburner tailpipes. Their development and use has been greatly over-shadowed by the advent of nickel-base superalloys, but cobalt-base superalloys still play an important role, by virtue of their excellent resistance to sulfidation and their strength at temperatures exceeding those at which the gamma-prime (γ') and gamma-double-prime (γ'') precipitates dissolve in the nickel and nickel-iron alloys.

Table 9 Cobalt-base superalloys: historical perspective

Co-Cr alloys first patented by Elwood Haynes	**1907**
Haynes alloy 6B	1913
Stellite alloy 21 (Vitallium supercharger buckets)	1936–1943
Stellite alloy 31 (X-40) buckets	1941–1943
S816 alloy wrought buckets	1946–1953
Haynes alloy 25 afterburner components	1948–1955
MAR-M 302 vanes	1958
Airesist vanes	1964
Haynes alloy 188 combustor, afterburner components	1966–1968

Note: Haynes is a registered trademark of Haynes International, Inc.; Stellite is a registered trademark of Deloro Stellite, Inc.; MAR-M is a registered trademark of Martin Marietta Corp.; Airesist is a registered trademark of Allied Signal Aerospace Co.; and Vitallium is a registered trademark of Pfizer Hospital Products Group, Inc.
Source: Ref 19

Since the early use of Stellite 21 (which is now used primarily for wear resistance), cobalt-base superalloys have gone through various stages of development to increase their high-temperature capability. The use of tungsten rather than molybdenum, moderate nickel contents, lower carbon contents, and rare-earth additions typify current cobalt-base superalloys. For many years, the predominant user of heat-resistant alloys was the gas turbine industry. In the case of aircraft gas turbine power plants, the chief material requirements were elevated-temperature strength, resistance to thermal fatigue, and oxidation resistance. For land-base gas turbines, which typically burn lower grade fuels and operate at lower temperatures, sulfidation resistance was the major concern. Today, the use of heat-resistant alloys is more diversified, as more efficiency is sought from the burning of fossil fuels and waste, and as new chemical processing techniques are developed.

The roles of alloying elements in cobalt-base superalloys are summarized in Table 10. The addition of nickel helps to stabilize the desired fcc matrix, while tungsten provides solid-solution strengthening and promotes carbide formation. For high-temperature applications, strengthening relies on the solid-solution alloying and carbide precipitation typical of cobalt-base alloys. In addition, the diffusion of substitutional alloying elements tends to be slower in cobalt than in nickel (Ref 20), which gives the cobalt base an inherent advantage in high-temperature creep. Carbide precipitation, especially $M_{23}C_6$ carbides, is the other important key to the strengthening of cobalt-base alloys, as noted. Carbide precipitation is quite effective in pinning glide dislocations, and both wrought and cast superalloys alloys depend on the dispersion of complex carbides for

strength. Carbides within grains act to impede basic dislocation movement, with an attendant increase in strength. Carbide formation is not uniform and regular, as is that of γ′ precipitation. Thus, the strength increase obtained from carbide dispersion in grains is less than that of the typical hardening caused by γ′ precipitation but still may be significant.

Table 10 Role of various alloying elements in cobalt-base superalloys

Element	Effect
Chromium	Improves oxidation and hot corrosion resistance; produces strengthening by formation of M_7C_3 and $M_{23}C_6$ carbides
Nickel	Stabilizes fcc form of matrix; produces strengthening by formation of intermetallic compound Ni_3Ti; improves forgeability
Molybdenum, tungsten	Solid-solution strengtheners; produces strengthening by formation of intermetallic compound Co_3M; formation of M_6C carbide
Tantalum, niobium	Solid-solution strengtheners; produces strengthening by formation of intermetallic compound Co_3M and MC carbide; formation of M_6C carbide
Carbon	Produces strengthening by formation of carbides MC, M_7C_3, $M_{23}C_6$, and possibly M_6C
Aluminum	Improves oxidation resistance; formation of intermetallic compound CoAl
Titanium	Produces strengthening by formation of MC carbide and intermetallic compound Co_3Ti with sufficient nickel produces strengthening by formation of intermetallic compound Ni_3Ti
Boron, zirconium	Produces strengthening by effect on grain boundaries and by precipitate formation; zirconium produces strengthening by formation of MC carbides
Yttrium, lanthanum	Increase oxidation resistance

These alloys also contain significant levels of both nickel and tungsten. Other alloying elements contributing to the solid-solution and/or carbide formation are tantalum, niobium, zirconium, vanadium, and titanium. Yttrium is also added to some alloys for improved oxidation resistance. Attempts have been made to develop age-hardenable alloys based on Co_3Ti- and Co_3Ta-type precipitates. However, problems with the thermal stability of the precipitates and the fact that the strength levels attained were easily matched or exceeded by the γ′-strengthened nickel-base alloys precluded their commercial introduction (Ref 21).

In the as-cast condition, MC carbides are particularly evident in cast superalloys, as they form first from the molten state. Numerous MC carbides may develop within the grains and at the grain boundaries and may have a script-form appearance, as shown Fig. 6. More complex carbides may also be present in either eutectic or precipitate form. For example, Fig. 6 and 7 are as-cast microstructures from two Co-Cr-W-Ta superalloys with MC carbides and more complex carbides such as $M_{23}C_6$ (Fig. 6) and M_6C (Fig. 7). As-cast microstructures of Haynes 31 alloy with and without subsequent aging are shown in Fig. 8. Subsequent heat treatments and/or wrought processing will modify the morphology, amounts, and types of carbides found in the grains of superalloys. Examples are shown in Fig. 9 and 10 for Haynes 25 and 188 alloys, respectively. Carbide distributions in wrought alloys result from the mill anneal after final working. Properties are largely a result of grain size, refractory-metal content, and carbon level. Some secondary carbides within grains can be formed by precipitation on dislocations located near large primary carbides.

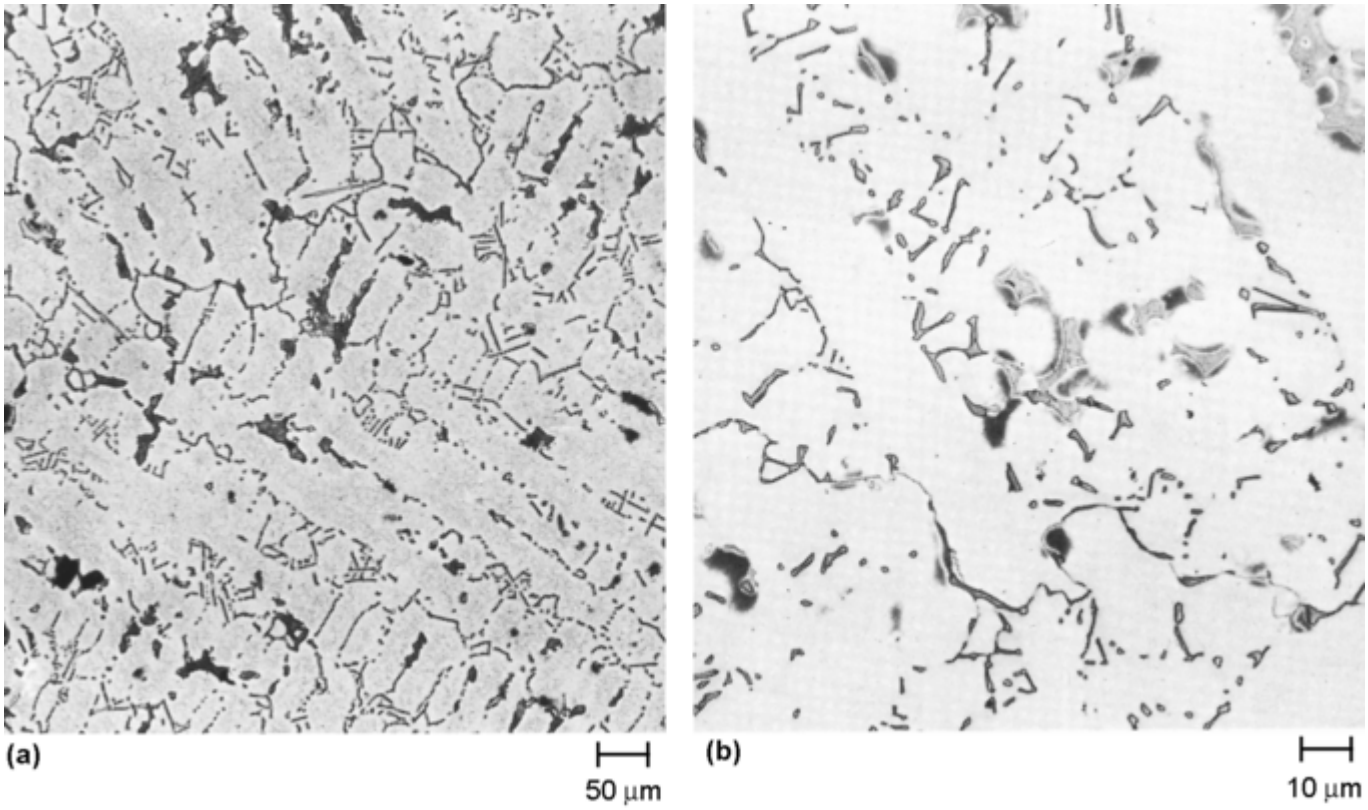

Fig. 6 As-cast structure of Co-Cr-W-Ta superalloy (MAR-M 509). (a) The structure consists of metal carbide (MC) particles in script form and $M_{23}C_6$ particles in eutectic form (gray areas) and precipitate form in the dendritic alpha solid-solution matrix. (b) Higher magnification reveals morphology of the MC script particles, primary eutectic particles, and precipitated $M_{23}C_6$ (shadowy constituent). (a) Kalling's reagent. 1000×. (b) Electrolytic: 5% phosphoric acid, 500×

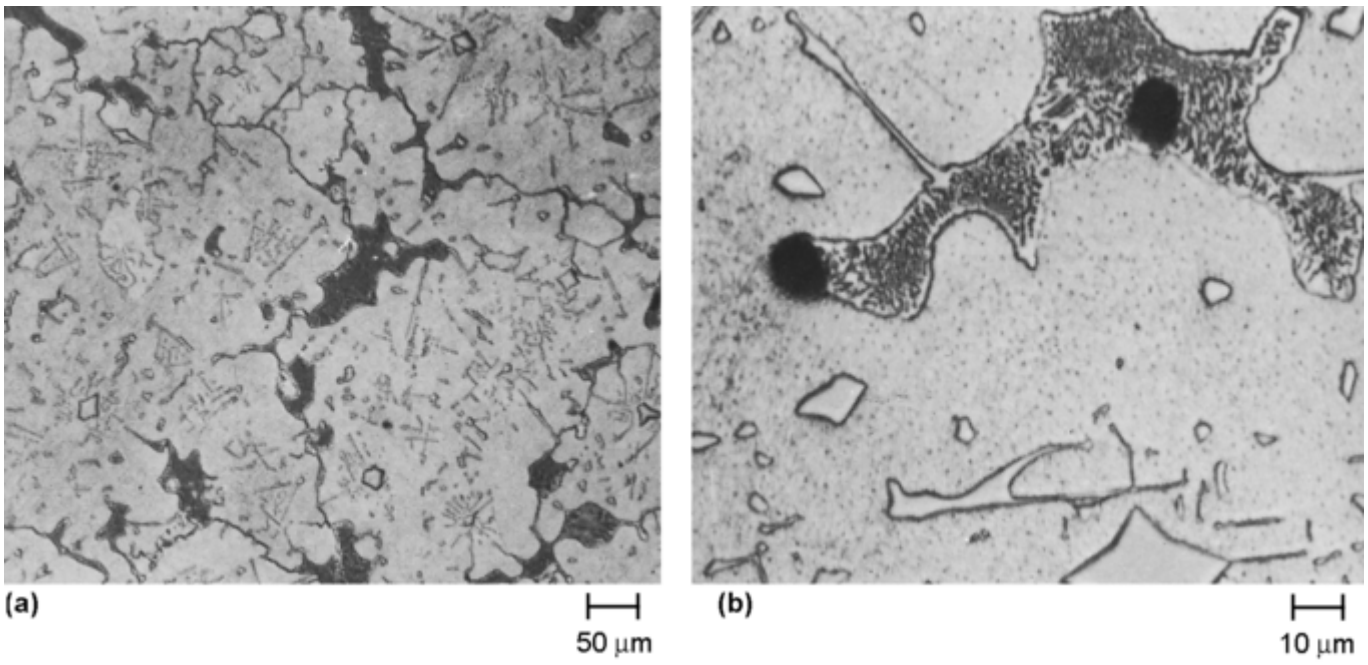

Fig. 7 As-cast microstructure of Co-Cr-W-Ta superalloy (MAR-M 302). (a) Structure at 100× reveals primary or, eutectic, M_6C carbides (dark gray) and MC particles (small white crystals in the solid-solution matrix). (b) At higher magnification (500×), the mottled gray islands are primary eutectic carbide; the light crystals are MC particles; the peppery constitutes within grains is $M_{23}C_6$. Kalling's reagent

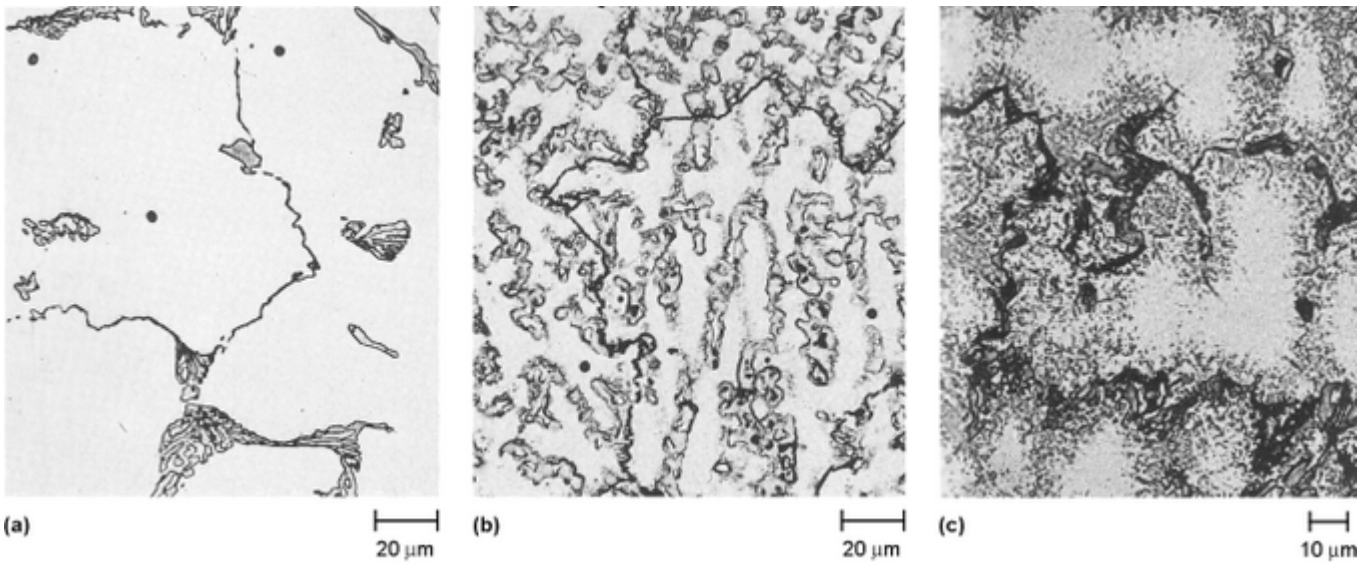

Fig. 8 Haynes 31 casting microstructures. (a) As-cast structure consisting of large primary M_7C_3 particles and grain-boundary $M_{23}C_6$ in an fcc matrix. 400×. (b) As-cast thin section, aged 22 h at 730 °C (1350 °F) with precipitated $M_{23}C_6$ at grain boundaries and adjacent to primary (M_7C_3) particles. 400×. (c) As-cast thick section aged 22 h at 730 °C (1350 °F); large particles are M_7C_3; grain boundary and mottled dispersions are $M_{23}C_6$ in fcc matrix. Electrolytic: 2% chromic acid. 500×

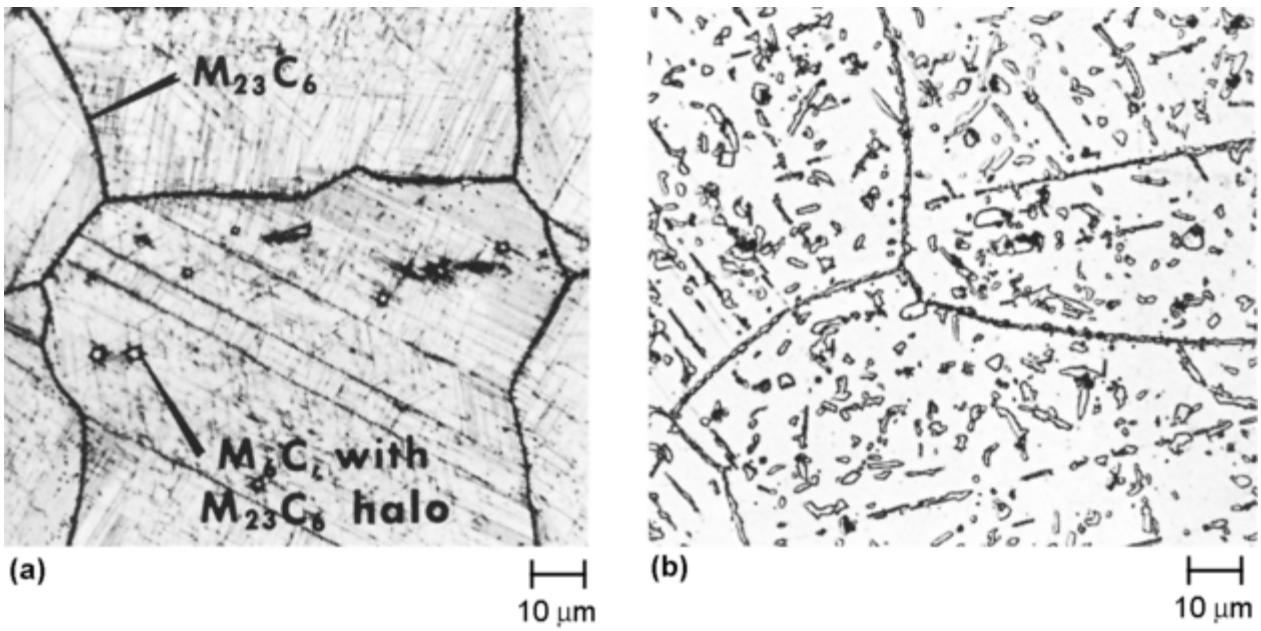

Fig. 9 Haynes 25 solution annealed at 1205 °C (2200 °F) and aged. (a) Aged at 650 °C (1200 °F) for 3400 h; constituents are M_6C and $M_{23}C_6$ in a mixed hcp and fcc matrix. (b) Aged at 870 °C (1600 °F) for 3400 h; structure consists of precipitates of M_6C and "Co_2W" intermetallic compound in fcc matrix. Electrolytic: HCl. H_2O_2. Both 500×

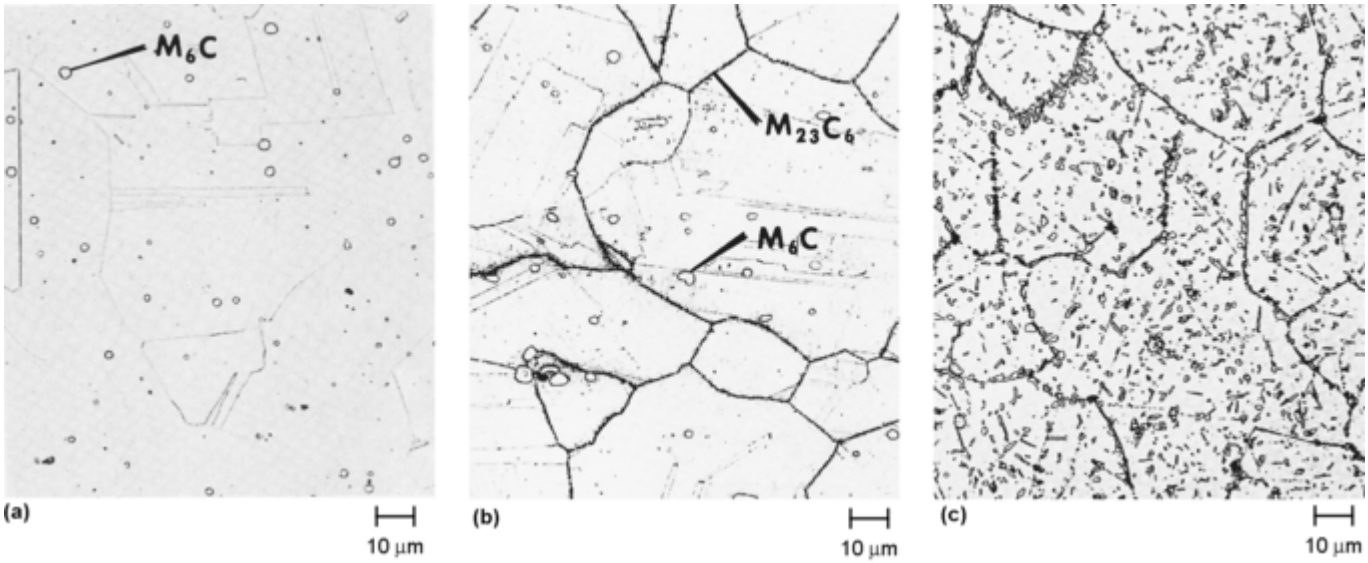

Fig. 10 Microstructures of aged Haynes 188 alloys. (a) Cold-rolled 20% and fully annealed structure with M_6C particles in an fcc matrix; solution anneal was 1177 °C (2150 °F) for 10 min, water quenched. (b) Solution anneal (at 1177 °C) with aging at 650 °C (1200 °F) for 3400 h. (c) Solution annealed (at 1177 °C) and aged at 870 °C (1600 °F) for 6244 h. Structure consists of $M_{23}C_6$, Laves phase, and probably M_6C in fcc matrix. Electrolytic HCl, H_2O_2. All 500×

Complete solution treatments, in which all minor constituents are dissolved, is not possible in most cobalt-base superalloys, because melting often occurs before all the carbides are dissolved. Some enhancement of creep-rupture behavior has been achieved by heat treatment where some carbides are dissolved for reprecipitation. Although some aging of a cobalt-base superalloy may lead to strength improvement, solution treating and aging is not suitable for producing stable cobalt-base superalloys for use above 815 °C (1500 °F) because of subsequent carbide dissolution or overaging during service exposure.

Typical wrought and cast cobalt alloy compositions developed for high-temperature use are presented in Table 1(b). Haynes alloy 25 (also known as L605) and 188 are wrought alloys available in the form of sheets, plates, bars, pipes, and tubes (together with a range of matching welding products for joining purposes). Alloys 25 and 188 are considerably more ductile, oxidation resistant, and microstructurally stable than the wear-resistant wrought cobalt alloys. Both alloys contain approximately 0.1 wt% C (about one-tenth of that in wrought, wear-resistant alloy 6B), which is sufficient to provide carbide strengthening, yet low enough to maintain ductility. Carbide precipitation, which is predominately of the M_6C type, is important to the high-temperature properties of these materials, partially because it restricts grain growth during heat treatment and service. Structural stability is enhanced in these alloys by nickel, which decreases the fcc/hcp transformation temperature in cobalt-base alloys.

Cast heat-resistant alloys, such as alloys MAR-509 and FSX-414, are designed around a cobalt-chromium matrix with chromium contents ranging from approximately 18 to 30%. The high chromium content contributes to oxidation resistance, hot corrosion resistance, and sulfidation resistance, but also participates in carbide formation (Cr_7C_3 and $M_{23}C_6$) and solid-solution strengthening. Carbon content generally ranges from 0.25 to 1.0%, with nitrogen occasionally substituting for carbon. MAR-M alloy 509 is an alloy designed for vacuum investment casting. Compared to the wrought alloys, cast cobalt-base superalloys are characterized by higher contents of high-melting metals (chromium, tungsten, tantalum, titanium, and zirconium) and by higher carbon contents.

Metallographic Preparation of Hastelloy and Haynes Alloys (Ref 22). The following are guidelines for etching to produce satisfactory samples. It is the responsibility of individuals to follow safe practices and to use protective equipment in accordance with all appropriate local, municipal, state, and federal regulations covering safety and health.

Sectioning. Cut the specimen to a convenient size using any of various types of SiC cutoff blades. Deformation damage can be minimized by using thin cutoff wheels ($\frac{1}{32}$ in. thick as opposed to $\frac{1}{16}$in.). This is especially beneficial if the sectioning is to be done dry. Adequate water coolant is desired to reduce the amount of disturbed metal created, in part, from frictional heat during this phase of preparation. The original

microstructure of a specimen may also be radically altered, at least superficially, on the cut surface due to metallurgical changes if an excessive amount of frictional heat is generated.

Coarse Grinding. Use a 120 grit silicon carbide (SiC), wet-belt grinder and light contact pressure to obtain a plane surface free from deep grooves. In addition to producing a flat surface, this procedure removes burred edges or other mechanical abuses that may have occurred during sectioning.

Mounting. To ensure flatness and facilitate handling, it is recommended that specimens be mounted in phenolic, acrylic, or cold-setting epoxy resins. Epoxy resins involve the blending of a liquid or powder resin in a suitable hardener to initiate an exothermic reaction to promote hardening and curing at room temperature. This usually requires an overnight operation. However, an advantage of epoxy is that the mount is semitransparent and permits observation of all sides of the specimen during each phase of the preparation.

Compression molding techniques may be used with phenolic powders to produce the standard 1.25 in. (~32 mm) diam mounts. Phenolic mounts are convenient when time constraints do not permit an overnight cold-setting operation.

Fine Grinding. Rotating disks flushed with running water are recommended with successively finer grit papers of 220, 320, 400, and 600 grit SiC. (A light to medium amount of pressure is exerted on the specimen to minimize the depth of deformation). Best results are obtained on the 600 SiC paper by grinding the specimen twice. Specimens are rotated 90° after each step until the abrasive scratches from the preceding grit have been removed. In each step, the grinding time should be increased to twice as long as that required to remove previous scratches. This ensures removal of disturbed metal from the previous step. Considerable care should be used in the fine grinding state to prevent the formation of artifacts.

Rough Polishing. The specimen should be hand washed and, preferably, ultrasonically cleaned to ensure the complete removal of SiC carryover from the fine-grinding stage. A pellon pan-W type cloth should be charged with 9 μm diamond paste, and water should be used as the lubricant. The specimen is moved counter to the direction of the rotating polishing wheel from the center to the outer periphery around the entire lapping surface. Extremely heavy pressure is used with diamond abrasive techniques to gain the maximum cutting rate. At the conclusion of this stage, the specimen should again be ultrasonically cleaned to remove any diamond polishing residue remaining in pinholes, cracks, and cavities.

Vibratory Polishing. Semifinal and final polishing operations on a major portion of metallographic specimens can be completed on vibratory polishing units such as the Syntron units. A nylon polishing cloth using a slurry of 30 g of Linde type “A” alumina polishing abrasive and 500 mL of distilled water are recommended for this operation. Additional weight in the form of a stainless steel cap must be placed on the specimen. The suggested weight to achieve a satisfactory polish in 20 to 30 min on a standard 1.25 in. (~32 mm) diam mount is 350 g.

Samples should be cleaned with a cotton swab under running water to remove type “A” alumina film, placed on a short-nap microcloth with a slurry of 30 g of Linde type “B” alumina abrasive and 500 mL of distilled water and polished until a scratch-free surface is obtained. Again, a 350 g weight is used to augment polishing. Specimens usually require 25 to 30 min to produce a satisfactory final polish. The specimen can usually be polished an additional 10 to 15 min without producing harmful overpolishing effects, but too much time may create relief on thin samples.

Surface Preparation. The surface, prior to etching, should:

- Be free from scratches, stains, and other imperfections that mar the surface
- Contain all nonmetallic inclusions intact
- Not exhibit any appreciable relief effect between microconstituents

Immediately prior to etching, specimens should be lightly polished (Linde type “B” wheel) and swabbed with cotton under running water to remove any air-formed oxide film to reduce chances of staining.

Electrolytic Etching. Place the specimen face up in the etching reagent. The cathode is placed approximately 25 mm (1 in.) from the specimen, and the anode is put in contact with the sample. During etching, the cathode is moved to ensure a uniform action of the etching reagent on the specimen. The sample is then washed and repolished lightly, if needed, to remove any traces of disturbed metal on the surface and then reetched.

The following etchant is used for most Hastelloy and Haynes alloys, with the exception of Hastelloy alloys B, B-2, N, and W (see the following section “Immersion Etching”):

- 5 g oxalic acid mixed with 95 mL HCl (reagent grade)

- Electrolytic—6 V dc
- Carbon cathode
- Stainless anode probe
- 1 to 5 s, depending on heat treated condition and size of samples

The procedure is:

- Sample must have a fresh polish. If surface has been dry, even for a few seconds, give sample 6 to 10 laps on final 0.05 μm alumina (Linde "B") cloth then directly under running water and swab with a cotton pad. *It is important that the sample surface be kept wet.*
- Put sample face up in etchant. Then, with good overhead light to visually see sample surface, make contact at end or corner of sample with anode probe, dip carbon cathode into etchant, watch to see any surface change, break contact.
- Before removing sample from etchant, it is important to agitate to remove any film on surface, then pull sample and put under running water, next rinse with methanol, then place sample under hair dryer until it is thoroughly dry.
- If etch is too light and needs to be heavier, *do not* take sample back to running water and then into etchant. Instead, it must go back to the final cloth for 6 to 10 laps, making sure that no part of surface dries; *failure to do this can, and most likely will, result in staining.* If the sample does stain, do not try to remove stain on final cloth. Rather, go back to the papers, at least to the 400 and 600 grit, then 9 μm diamond and then to 0.05 alumina, and again, *keeping sample surface wet, repeat as described before.*

Immersion etching techniques are usually used for the high-molybdenum alloys, namely Hastelloy alloys B, B-2, N, and W. The preferred etchant for this family of alloys is chrome-regia (one part chromic acid to three parts reagent grade HCl). Stock chromic acid is made by mixing 300 g chromic acid with 300 mL of hot water. For immersion etching, it is equally important to work with a wet, freshly polished surface (i.e., follow procedure steps above for electrolytic etching). The wet sample is then immersed face up into the chrome regia for 1 to 3 s, depending on heat treated condition and sample size. Then pull sample and put under running water, rinse with methanol, and blow dry. If etch is too light, follow the last step of electrolytic procedures.

References cited in this section

19. D.L. Klarstrom, Wrought Cobalt-Base Alloys, *J. Mater. Eng. Perform.,* Vol 2 (No. 4), Aug 1993, p 523

20. A Davin et al., *Cobalt,* Vol 19, June 1963, p 51–56

21. C.P Sullivan. M.J. Donachie, Jr., and F.R. Morral, *Cobalt-Base Superalloys-1979,* Cobalt Information Center, Brussels, Belgium

22. *Metallographic Preparation of Hastelloy and Haynes Alloys,* Haynes International, Inc., 2003

Revised by D. Klarstrom, P. Crook, and J. Wu, Metallography and Microstructures of Cobalt and Cobalt Alloys, *Metallography and Microstructures,* Vol 9, *ASM Handbook*, ASM International, 2004, p. 762–774

Metallography and Microstructures of Cobalt and Cobalt Alloys

Revised by D. Klarstrom, Haynes International, Inc.; P. Crook, Haynes International, Inc; and J. Wu, Deloro Stellite Group Limited

---

Cobalt-Base Corrosion Resistant Alloys

Several low-carbon, wrought cobalt alloys are used to satisfy applications that require corrosion resistance with the attributes of cobalt as an alloy base (resistance to various forms of wear and high strength over a wide range of temperatures). The cobalt-base wear-resistant alloys possess some resistance to aqueous corrosion, but they are limited by grain-boundary carbide precipitation. Wrought cobalt superalloys (which typically contain tungsten rather than molybdenum) are even more resistant to aqueous corrosion than the Stellite alloys, but they still fall well short of the Ni-Cr-Mo alloys in corrosion performance.

Compositions of several cobalt alloys for corrosion-resistant applications are listed in Table 1(b). They include implant Co-Ni-Cr-Mo alloys (such as MP35N) and the Co-Cr-Mo alloys (such as Vitallium) for prosthetic devices and implants on account of their excellent compatibility with body fluids and tissues. Cobalt-chromium-molybdenum alloys are still used for biomedical applications, while the use of MP35N alloy has declined partially due to concerns about nickel release from the alloys, which can cause metal-sensitivity reactions in some patients. The Ultimet alloy (UNS R31233) combines excellent corrosion resistance to pitting (especially in oxidizing acids) with very high wear resistance (cavitation erosion, galling, and abrasion).

These alloys are provided in various wrought forms, in the work-hardened or work-plus-age-hardened condition. The alloys work harden rapidly due to strain-induced transformation, which provide a dispersion of fine hcp platelets. Higher-strength, fine-grained Co-Cr-Mo alloys for implant devices also have been made by forging of nitrogen-strengthened bar stock or by hot isostatic pressing (HIP) of carbide-strengthened powders. Microstructures of these materials are compared with a cast microstructure (Fig. 11).

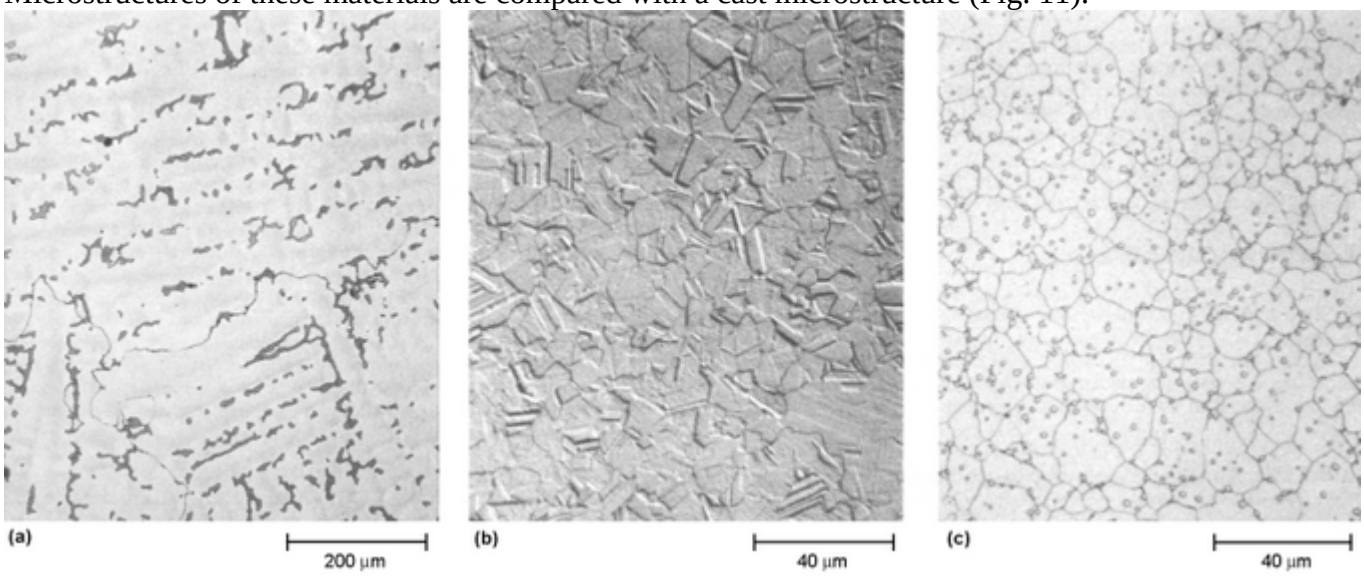

Fig. 11 Microstructures of Co-Cr-Mo alloys. (a) Investment cast with relatively coarse carbides and the large grain size (ASTM macrograin size 7.5). (b) High-strength fine-grain forging from nitrogen-strengthened bar stock. (c) Hot isostatically pressed from powder

---

Revised by D. Klarstrom, P. Crook, and J. Wu, Metallography and Microstructures of Cobalt and Cobalt Alloys, *Metallography and Microstructures,* Vol 9, *ASM Handbook*, ASM International, 2004, p. 762–774

Metallography and Microstructures of Cobalt and Cobalt Alloys

Revised by D. Klarstrom, Haynes International, Inc.; P. Crook, Haynes International, Inc; and J. Wu, Deloro Stellite Group Limited

---

References

1. D. Klarstrom and P. Crook, Cobalt Alloys: Alloy Designation System, Cobalt Alloys: Alloying and Thermomechanical Processing, and Cobalt Alloys: Properties and Applications, *Encyclopedia of Materials: Science and Technology,* Elsevier Science, 2001, p 1279–1288

2. T.B. Massalski, H. Okamoto, P.R. Subramanian, and L. Kacprzak, Ed., *Binary Alloy Phase Diagrams,* Vol 2, 2nd ed., ASM International, 1990, p 1214–1215

3. C.T. Sims and W.C. Hagel, Ed., *The Superalloys,* John Wiley & Sons, 1972, p 145–174

4. H.M. Tawancy, V.R. Ishwar, and B.E. Lewis, On the fcc-hcp Transformation in a Cobalt-Base Superalloy (Haynes Alloy 25), *J. Mater. Sci. Lett.,* Vol 5, 1986, p 336–341

5. F.C. Hagen et al., Mechanical Properties of New Higher Temperature Multiphase Superalloy, *Superalloys 1984,* Metallurgical Society of AIME, 1984, p 621–630

6. D. Raghu and J.B.C. Wu, Alloy Solutions to Combat Synergistic Wear and Corrosion in Demanding Process Environments, *Proc. EPRI Corrosion and Degradation Conference,* 2–4 June 1999, Electric Power Research Institute

7. S. Takeda and N. Yukawa, *Nippon Kinz. Gakkai-ho,* Vol 6 (No. 11, 12), 1967, p 784–802, 850–855

8. D.I. Bardos, K.P. Gupta, and P.A. Beck, Ternary Laves Phases with Transition Elements and Silicon, *Trans. AIME,* Vol 221, Oct 1961, p 1087–1088

9. S.T. Wlodek, Embrittlement of a Co-Cr-W (L-605 Alloy), *Trans. ASM,* Vol 56 1963, p 287–303

10. C.T. Sims, The Occurrence of Topologically Close-Packed Phases, *The Superalloys,* John Wiley, 1972

11. R.B. Herchenroeder, S.J. Matthews, J.W. Tackett, and S.T. Wlodek, Haynes Alloy No. 188, *Cobalt,* Vol 54, March 1972, p 3–13

12. *Buehler's Guide to Materials Preparation,* Buehler, Ltd., 2002, p 46

13. F.R. Morral, Metallography of Cobalt-Base and Cobalt-Containing Alloys, *Prakt. Metallogr.,* Vol 10, 1973, p 398–413

14. G. Petzow, *Metallographic Etching,* 2nd ed., ASM International, 1999, p 75–77

15. R.S. Young, Metallographic Differentiation of Cobalt Metal, Oxide and Sulphide, *Metallurgia,* Vol 59, April 1959, p 210

16. J.W. Weeton and R.A. Signorelli, Effects of Heat Treatment upon Microstructures, Microconstituents, and Hardness of a Wrought Cobalt Base Alloys, *Trans. ASM,* Vol 47, 1955, p 815–852

17. G.F. Vander Voort, *Metallography Principles and Practice,* McGraw-Hill, 1984 (reprinted by ASM International, 1999), p 207

18. J.B.C. Wu and J.E. Redman, Hardfacing with Cobalt and Nickel Alloys, *Weld. J.,* Sept 1994, p 63–68

19. D.L. Klarstrom, Wrought Cobalt-Base Alloys, *J. Mater. Eng. Perform.,* Vol 2 (No. 4), Aug 1993, p 523

20. A Davin et al., *Cobalt,* Vol 19, June 1963, p 51–56

21. C.P Sullivan. M.J. Donachie, Jr., and F.R. Morral, *Cobalt-Base Superalloys-1979,* Cobalt Information Center, Brussels, Belgium

22. *Metallographic Preparation of Hastelloy and Haynes Alloys,* Haynes International, Inc., 2003

Revised by R.N. Caron, R.G. Barth, and D.E. Tyler, Metallography and Microstructures of Copper and Its Alloys, *Metallography and Microstructures*, Vol 9, *ASM Handbook*, ASM International, 2004, p. 775–788

Metallography and Microstructures of Copper and Its Alloys

Revised by R.N. Caron, R.G. Barth, and D.E. Tyler, Olin Brass, Division of Olin Corporation

Introduction

COPPER AND COPPER ALLOYS have played an integral role in human technological progress since antiquity. Native copper and then bronze alloys were fashioned into the first metal tools and decorations. The combination of electrical and thermal conductivity, workability, corrosion resistance, strength, and its abundance makes this family of metals important to all industry.

Revised by R.N. Caron, R.G. Barth, and D.E. Tyler, Metallography and Microstructures of Copper and Its Alloys, *Metallography and Microstructures,* Vol 9, *ASM Handbook*, ASM International, 2004, p. 775–788

Metallography and Microstructures of Copper and Its Alloys

>Revised by R.N. Caron, R.G. Barth, and D.E. Tyler, Olin Brass, Division of Olin Corporation

Alloying Systems

Copper alloys have traditionally been classified by composition and as wrought or cast in the groups show in Table 1. The alloys are listed by UNS designation that is administered by the Copper Development Association. Selected alloys are listed for each group. Similar compositional grouping is present in international designation systems.

Table 1 Nominal compositions of copper and copper alloys

UNS No.	Name	Nominal composition, %
Wrought copper		
C10100	Oxygen-free electronic copper (OFE)	99.99 (min) Cu
C10200	Oxygen-free copper (OF)	99.95 (min) Cu
C11000	Electrolytic tough pitch copper (ETP)	99.90 (min) Cu
C12200	Phosphorus-deoxidized copper, high-residual phosphorus (DHP)	99.90 (min) Cu, 0.028 P
C12500	Fire-refined tough pitch copper (FRTP)	99.88 (min) Cu
C14520	Phosphorus-deoxidized copper, tellurium bearing	99.90 (min) Cu, 0.010 P, 0.55 Te
C14700	Sulfur-bearing copper	99.90 (min) Cu, 0.35 S
C15000	Zirconium copper	99.80 (min) Cu, 0.15 Zr
C15720	Dispersion-strengthened copper	99.52 (min) Cu, 0.2 Al, 0.2 O_2 (O_2 present as CuO_2)
Wrought high-copper alloys		

C17200	Beryllium-copper	Bal Cu, 1.90 Be, 0.40 Co
C18200	Chromium-copper	Bal Cu, 0.9 Cr
C18700	Leaded copper	Bal Cu, 1 Pb, 0.05 P
C19400	Iron-bearing copper	97 (min) Cu, 2.35 Fe, 0.125 Zn, 0.05 P
Wrought brasses		
C26000	Cartridge brass, 70%	70 Cu, 30 Zn
C26800	Yellow brass, 66%	66 Cu, 34 Zn
C28000	Muntz metal, 60%	60 Cu, 40 Zn
C31600	Leaded commercial bronze, nickel bearing	89 Cu, 2 Pb, 1 Ni, 8 Zn
C33500	Low-leaded brass	63.5 Cu, 0.5 Pb, 36 Zn
C36000	Free-cutting brass	62 Cu, 3 Pb, 35 Zn
C44300	Admiralty, arsenical	71.5 Cu, 27.5 Zn, 1 Sn, (0.04 As)
C44400	Admiralty, antimonial	71.5 Cu, 27.5 Zn, 1 Sn, (0.06 Sb)
C44500	Admiralty, phosphorized	71.5 Cu, 27.5 Zn, 1 Sn, (0.06 P)
C46400	Uninhibited naval brass	61 Cu, 38 Zn, 1 Sn
C48500	High-leaded naval brass	60.5 Cu, 1.75 Pb, 0.75 Sn, 37 Zn
Wrought bronzes		
C51000	Phosphor bronze, 5% A	Bal Cu, 5.0 Sn, 0.2 P
C52100	Phosphor bronze, 8% C	Bal Cu, 8.0 Sn, 0.2 P
C63000	Aluminum bronze, 10%	82.2 Cu, 10 Al, 3 Fe, 4.8 Ni
C64700	Silicon-nickel bronze	Bal Cu, 1.9 Ni, 0.6 Si
C67500	Manganese bronze A	58.5 Cu, 1 Sn, 38.7 Zn, 1.5 Fe, 0.3 Mn
C68700	Arsenical aluminum brass	77.5 Cu, 20.3 Zn, 2.2 Al, (0.04 As)
Wrought copper-nickel alloys and nickel silvers		
C70600	Copper-nickel, 10%	88.6 Cu, 10 Ni, 1.4 Fe
C71300	Copper-nickel, 25%	75 Cu, 25 Ni
C71500	Copper-nickel, 30%	68.5 Cu, 31 Ni, 0.50 Fe
C71900	Copper-nickel	Bal Cu, 30.5 Ni, 2.6 Cr
C74500	Nickel silver, 65-10	65 Cu, 10 Ni, 25 Zn
C75200	Nickel silver, 65-18	65 Cu, 18 Ni, 17 Zn
Cast high-copper alloy		
C81500	Chromium-copper	98 (min) Cu, 1.0 Cr
Cast brasses, bronzes, and nickel silver		
C83600	Leaded red brass	85 Cu, 5 Sn, 5 Zn, 5 Pb
C86200	Manganese bronze	64 Cu, 26 Zn, 4 Al, 3 Fe, 3 Mn
C86300	Manganese bronze	63 Cu, 25 Zn, 3 Fe, 6 Al, 3 Mn
C90300	Tin bronze	88 Cu, 8 Sn, 4 Zn
C92600	Leaded tin bronze	87 Cu, 10 Sn, 2 Zn, 1 Pb
C94100	High-leaded tin bronze	74 Cu, 20 Pb, 6 Sn
C95300	Aluminum bronze	89 Cu, 10 Al, 1 Fe
C95400	Aluminum bronze	85 Cu, 11 Al, 4 Fe
C95500	Nickel-aluminum bronze	81 Cu, 11 Al, 4 Fe, 4 Ni
C95600	Silicon-aluminum bronze	91 Cu, 7 Al, 2 Si
C97800	Nickel silver	66 Cu, 25 Ni, 5 Sn, 2 Zn, 2 Pb
Brazing alloys		
C55284	BCuP-5 brazing alloy	80 Cu, 15 Ag, 5 P

Coppers. The alloys designated as coppers contain 99.3% or more copper. These have the highest electrical and thermal conductivity. Impurities such as phosphorus, tin, selenium, tellurium, and arsenic are detrimental to properties such as electrical conductivity and recrystallization temperature (Ref 1). If deliberately added, however, these alloying elements can enhance other desirable properties. Silver is the only impurity that does not significantly lower the conductivity of pure copper, so it is included in the percent weight of copper when calculating the minimum percent weight of an alloy.

High-copper alloys contain between 96 and 99.3% Cu in wrought products that do not fall into any other special categories. For cast alloys, copper content above 94% is included. The chief alloying elements are cadmium, beryllium, and chromium.

Copper-zinc alloys (brasses) have zinc as the prime alloying element. Wrought alloys are subdivided into Cu-Zn alloys, Cu-Zn-Pb (leaded brasses), and Cu-Zn-Sn alloys (tin brasses). Cast brasses have four subdivisions: Cu-Zn-Sn and Cu-Zn-Sn-Pb alloys (red and leaded red, semired and leaded semi-red, and yellow and leaded yellow brass); Cu-Mn-Zn and Cu-Mn-Zn-Pb (high-strength and leaded high-strength brass, also called manganese bronze and leaded manganese bronze); and Cu-Si (silicon brasses and bronzes); and Cu-Bi and Cu-Bi-Se (copper-bismuth and copper-bismuth-selenium alloys).

Bronzes include copper alloys that do not have zinc or nickel as the major alloying element. The four subgroups of wrought alloys are: Cu-Sn-P (phosphor bronze), Cu-Sn-P-Pb (leaded phosphor bronze), Cu-Al (aluminum bronze), and Cu-Si (silicon bronze). Although called bronzes, the manganese bronzes that have zinc as the major alloying element are classed with the brasses. The cast bronzes are called Cu-Sn (tin bronze), Cu-Sn-Pb (leaded and high-leaded tin bronze), Cu-Sn-Ni (nickel-tin bronze), and Cu-Al-Fe and Cu-Al-Fe-Ni (aluminum bronze).

Copper-nickels are available as wrought and cast alloys.

Copper-nickel-zinc alloys, wrought and cast, are known as nickel silvers. This name is based on their luster, not their composition, because they do not have silver as an intentional alloying element.

Other alloys include specialty alloys, copper leads, and brazing alloys.

Gas Solubility. Hydrogen and oxygen are quite soluble in liquid copper, but the solubility in solid copper is very small. The metal therefore rejects a considerable amount of these (and other) gases on solidification. Oxygen content must be carefully controlled so that detrimental quantities of Cu_2O, which decreases workability, are not formed. In molten copper, oxygen can react with dissolved hydrogen to form water vapor, which evolves as voids during solidification, called hydrogen illness. The voids cause hairline cracks that can lead to fracture during hot rolling and produce a variety of defects on the surface of wire rods (Ref 2).

Oxygen and hydrogen interfere with conductivity; however, small and controlled amounts of oxygen are actually beneficial to conductivity in that they combine with and remove from solution impurities such as iron that are far more detrimental. A copper-oxygen phase diagram would show a eutectic at 0.4 wt% O (or 3.4 wt% Cu_2O). Figure 1, 2, 3, and 4 show hypoeutectic copper-oxygen alloys, where the primary dendrites (light color) are copper. Figure 5, 6, 7, and 8 are hypereutectic, where the structure consists of particles or dendrites of Cu_2O (dark colored) and eutectic.

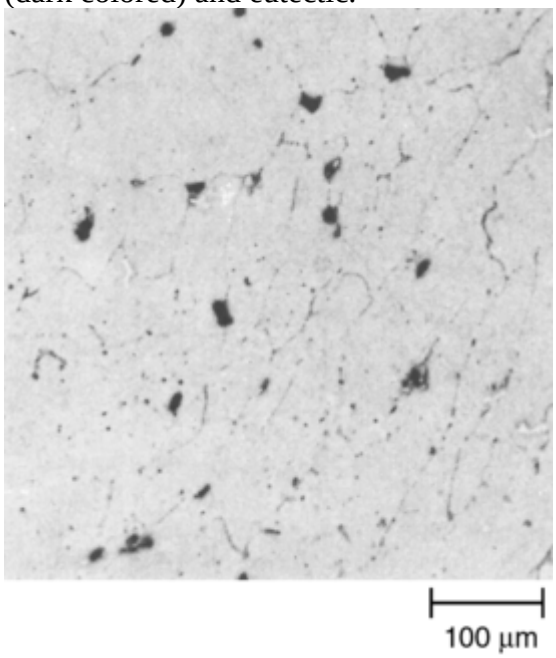

Fig. 1 The effect of oxygen content on the microstructure of a hypoeutectic as-cast copper-oxygen alloy. Oxygen content of 0.024% results in primary dendrites of copper (light) plus eutectic (mottled areas of small, round oxide in copper). As-polished. 100×

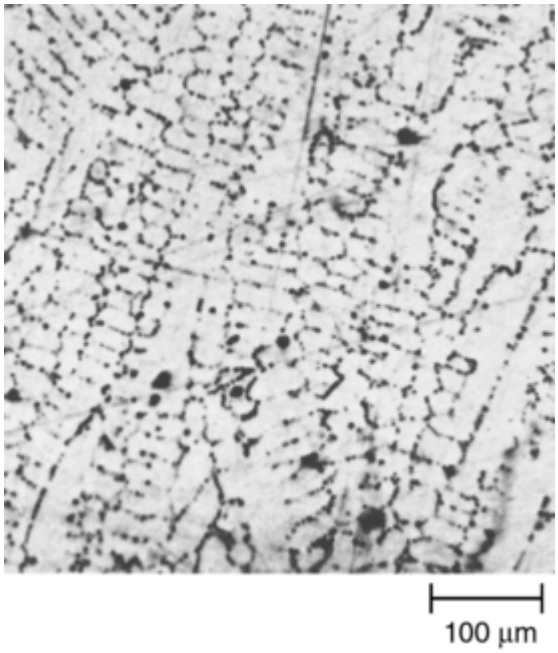

Fig. 2 The effect of oxygen content on the microstructure of a hypoeutectic as-cast copper-oxygen alloy. Oxygen content of 0.09% results in primary dendrites of copper (light) plus eutectic (mottled areas of small, round oxide in copper). As-polished. 100×

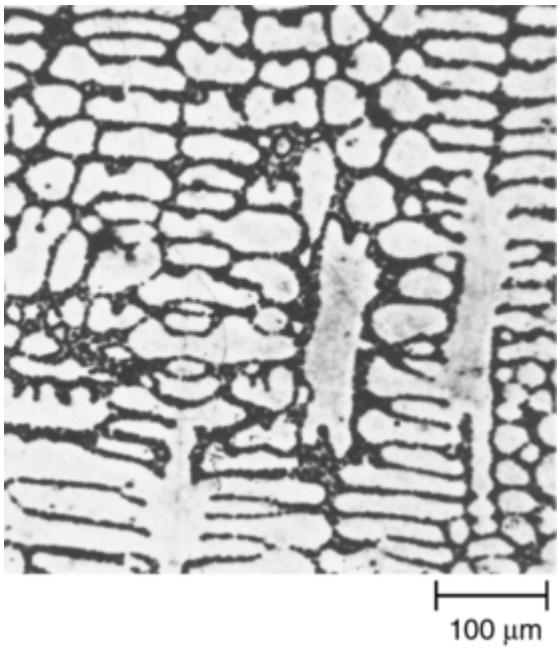

Fig. 3 The effect of oxygen content on the microstructure of a hypoeutectic as-cast copper-oxygen alloy. Oxygen content of 0.18% results in primary dendrites of copper (light) plus a more connected area of eutectic than in Figure 2 As-polished. 100×

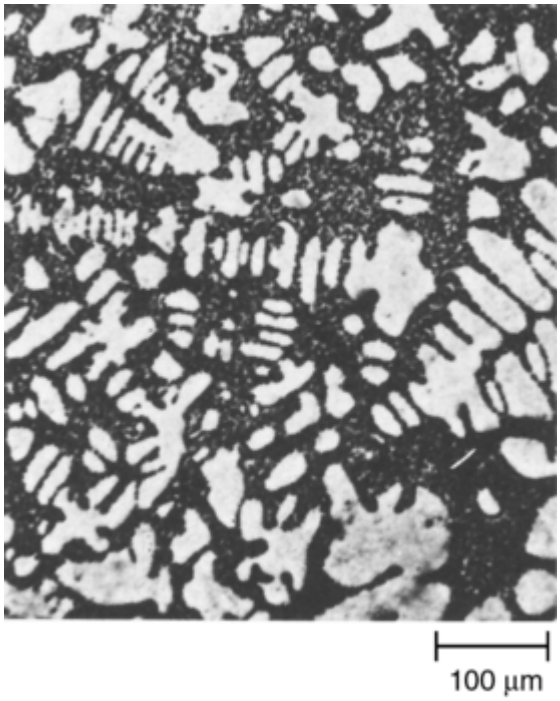

Fig. 4 The effect of oxygen content on the microstructure of a hypoeutectic as-cast copper-oxygen alloy. Oxygen content of 0.23% results in less primary dendrites of copper (light) plus more connected areas of eutectic than in Figure 3 As-polished. 100×

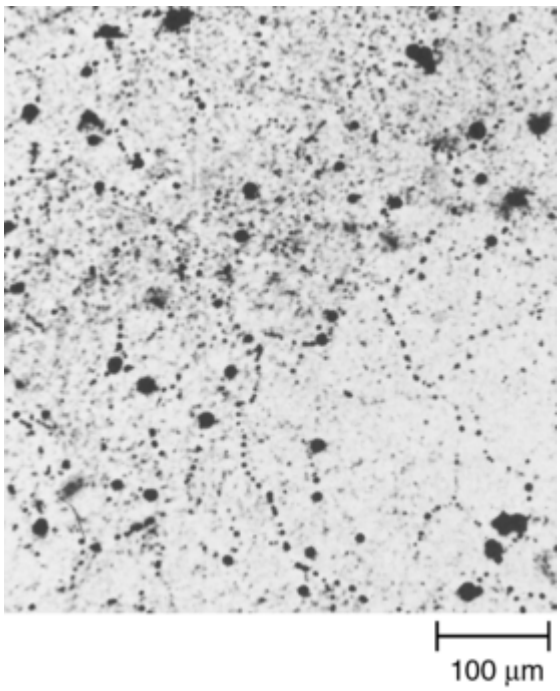

Fig. 5 The effect of oxygen content on the microstructure of a hypereutectic as-cast copper-oxygen alloy. Oxygen content of 0.44% results in particles or dendrites of oxide (dark) and light eutectic. As-polished. 100×

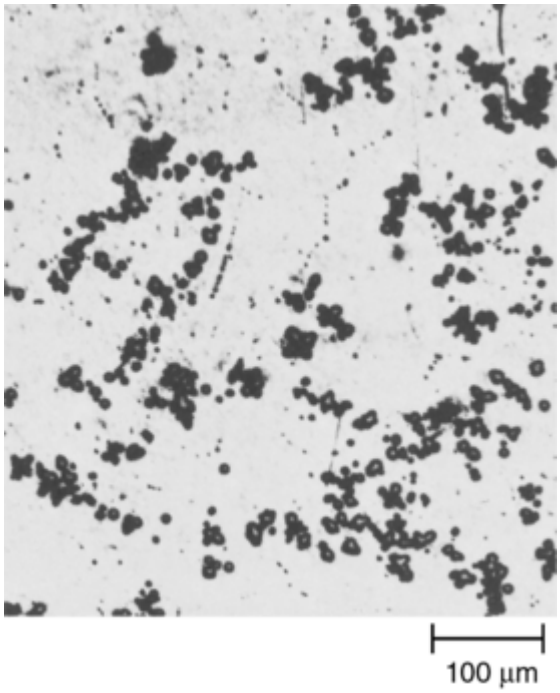

Fig. 6 The effect of oxygen content on the microstructure of a hypereutectic as-cast copper-oxygen alloy. Oxygen content of 0.50% results in the increased amount of particles or dendrites of oxide (dark) in the light eutectic, as compared to Figure 5 As-polished. 100×

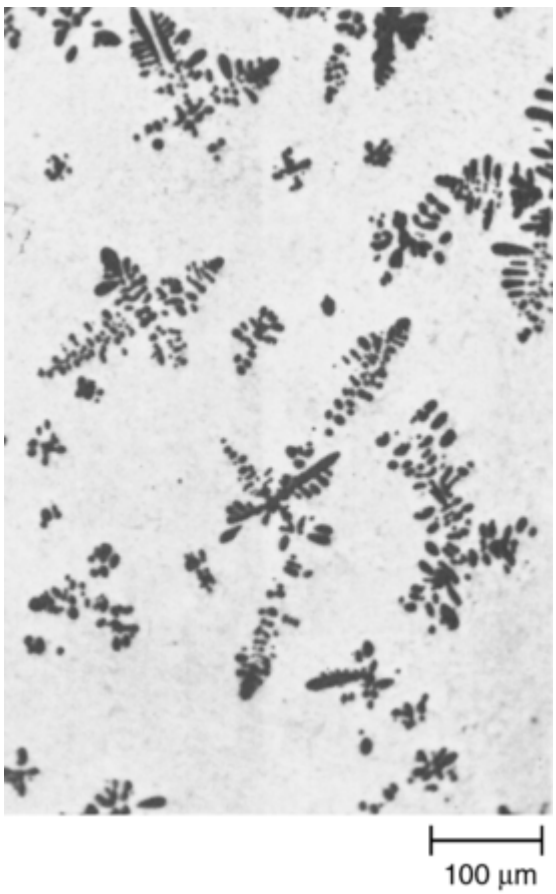

Fig. 7 The effect of oxygen content on the microstructure of a hypereutectic as-cast copper-oxygen alloy. Oxygen content of 0.70% results in the increase of dendritic structure of oxide (dark) in the light eutectic matrix, as compared to Figure 6 As-polished. 100×

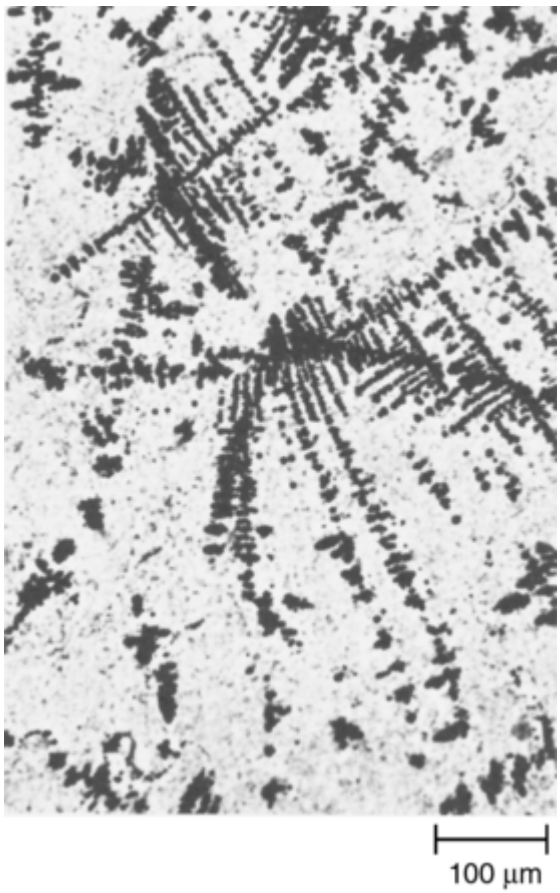

Fig. 8 The effect of oxygen content on the microstructure of a hypereutectic as-cast copper-oxygen alloy. Oxygen content of 0.91% results in the increase of dendritic structure of oxide (dark) in the light eutectic matrix, as compared to Figure 7 As-polished. 100×

References cited in this section

1. G. Joseph, *Copper, Its Trade, Manufacture, Use, and Environmental Status,* ASM International, 1999

2. M. Tisza, *Physical Metallurgy for Engineers,* ASM International and Freund Publishing House, Ltd., 2001

Revised by R.N. Caron, R.G. Barth, and D.E. Tyler, Metallography and Microstructures of Copper and Its Alloys, *Metallography and Microstructures,* Vol 9, *ASM Handbook*, ASM International, 2004, p. 775–788

Metallography and Microstructures of Copper and Its Alloys

>Revised by R.N. Caron, R.G. Barth, and D.E. Tyler, Olin Brass, Division of Olin Corporation

---

Microstructures of Copper and Copper Alloys

Coppers and High-Copper Alloys. The pure coppers are commercially significant because they have the highest conductivity. The effect of hot and cold working and heat treatment of oxygen-free coppers is shown in Fig. 9, 10, and 11. Note in Fig. 11 that oxygen has been reintroduced into the previously oxygen-free metal by heating in a noninert atmosphere. The dendritic structure of electrolytic tough pitch copper is seen in the cast ingot of C11000 (Fig. 12). A macrograph of C12200, phosphorus-deoxidized copper (Fig. 13), reveals a typical

solidification pattern of grains in a 102 mm (4 in.) continuously cast ingot. As is typical with relatively pure copper, the grain boundaries are well defined. The transverse and longitudinal sections of the ingot show that the grains grow perpendicular to the wall. Grain boundaries are parallel to the direction of heat flow. At the core, a columnar grain is along the axis of the ingot. Sections taken normal to the direction of heat flow near the wall (Fig. 14) and near the center (Fig. 15) show how the grain structure gets finer near the center. These images (Fig. 13, 14, and 15 illustrate the significance that the orientation of a specimen section has in determining the appearance of the grain structure.

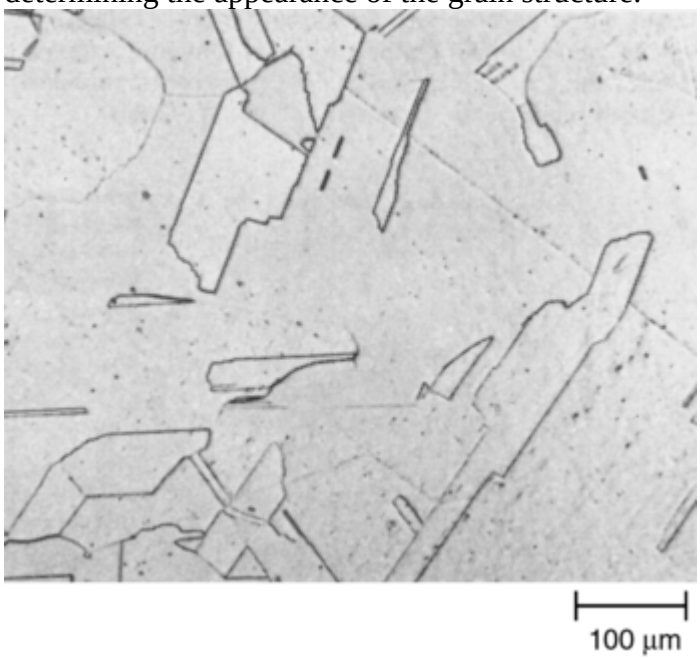

Fig. 9 Copper C10200 (oxygen-free copper), hot-rolled bar. Large, equiaxed, twinned grains. Etchant 1, Table 2. 100×

Table 2 Etchants and procedures for microetching of coppers and copper alloys

Composition[a]		Procedure	Copper or copper alloy
1.	20 mL NH_4OH, 0–20 mL H_2O, 8–20 mL 3% H_2O_2	Immersion or swabbing 1 min; H_2O_2 content varies with copper content of alloy to be etched; use fresh H_2O_2 for best results[b]	Use fresh for coppers and copper alloys; film on etched aluminum bronze can be removed using weak Grard's solution, preferred for brasses
2.	1 g $Fe(NO_3)_3$ and 100 mL H_2O	Immersion	Etching and attack polishing of coppers and alloys
3.	25 mL NH_4OH, 25 mL H_2O, 50 mL 2.5% $(NH_4)_2S_2O_8$	Immersion	Attack polishing of coppers and some copper alloys
4.	2 g $K_2Cr_2O_7$, 8 mL H_2SO_4, 4 mL NaCl (saturated solution), 100 mL H_2O	Immersion; NaCl replaceable by 1 drop HCl per 25 mL solution; add just before using; follow with $FeCl_3$ or other contrast etch	Coppers; copper alloys of beryllium, manganese, and silicon; nickel silver, bronzes, chromium-copper; preferred for all coppers to reveal grain boundaries, grain contrast, and cold deformation
5.	CrO_3 (saturated aqueous solution)	Immersion or swabbing	Coppers, brasses, bronzes, nickel silver
6.	50 mL 10–15% CrO_3 and 1–2 drops HCl	Immersion; add HCl at time of use	Same as above; color by electrolytic etching or with $FeCl_3$ etchants
7.	8 g CrO_3, 10 mL HNO_3, 10 mL H_2SO_4, 200 mL H_2O	Immersion or swabbing	Grain contrast etch for electrolytic tough pitch copper; does not dissolve Cu_2O; use after etchant 3 when etching deoxidized high-phosphorus copper for

				microstructure
8.	10 g $(NH_4)_2S_2O_3$ and 90 mL H_2O			Immersion; use cold or boiling	Coppers, brasses, bronzes, nickel silver, and aluminum bronze
9.	10% aqueous copper ammonium chloride plus NH_4OH to neutrality or alkalinity			Immersion; wash specimen thoroughly	Coppers, brasses, nickel silver; darkens β in α-β brass.
10.	$FeCl_3$, g	HCl, mL	H_2O, mL	Immersion or swabbing; etch lightly or by successive light etches to required results	Coppers, brasses, bronzes, aluminum bronze; darkens β phase in brass; gives contrast following dichromate and other etches
	5	50	100		
	20	5	100[(c)(d)]		
	25	25	100		
	1	20	100		
	8	25	100		
	5	10	100[(e)(f)]		
11.	5 g $FeCl_3$, 100 mL ethanol, 5–30 mL HCl			Immersion or swabbing for 1 s to several minutes	Coppers and copper alloys; darkens β phase in α-β brasses and aluminum brass
12.	HNO_3 (various concentrations)			Immersion or swabbing; 0.15–0.3% $AgNO_3$ added to 1:1 solution gives a brilliant, deep etch	Coppers and copper alloys
13.	NH_4OH (dilute solutions)			Immersion	Attack polishing of brasses and bronzes
14.	50 mL HNO_3, 20 g CrO_3, 75 mL H_2O			Immersion	Aluminum bronze, free-cutting brass; film from polishing can be removed with 10% HF
15.	5 mL HNO_3, 20 g CrO_3, 75 mL H_2O			Immersion	Same as above
16.	59 g $FeCl_3$ and 96 mL ethanol			Immersion; heat sample first in hot H_2O	Macro- and microetch for annealed copper-nickel alloys
17.	16 g CrO_3, 1.8 g NH_4Cl (ammonium chloride), 10 mL HNO_3, 200 mL H_2O			Immersion	Preferred etch for copper-nickel; preferential attack of copper-rich phase in castings
18.	5 parts HNO_3, 5 parts acetic acid, 1 part H_3PO_4			Immersion, 3 s	Coppers, brasses
19.	Equal parts NH_4Cl and H_2O			Immersion	Coppers and alloys
20.	60 g $FeCl_3$, 20 g $Fe(NO_3)_3$, 2000 mL H_2O			Immersion	Copper-nickel alloys
21.	1 part acetic acid, 1 part HNO_3, 2 parts acetone			Immersion	Copper-nickel alloys

(a) The use of concentrated etchants is intended unless otherwise specified.
(b) This etchant may be alternated with $FeCl_3$.
(c) Grard's No. 1 etchant.
(d) Plus 1 g CrO_3.
(e) Grard's No. 2 etchant.
(f) (f) Plus 1 g $CuCl_2$ and 0.03 g $SnCl_2$ (tin chloride)

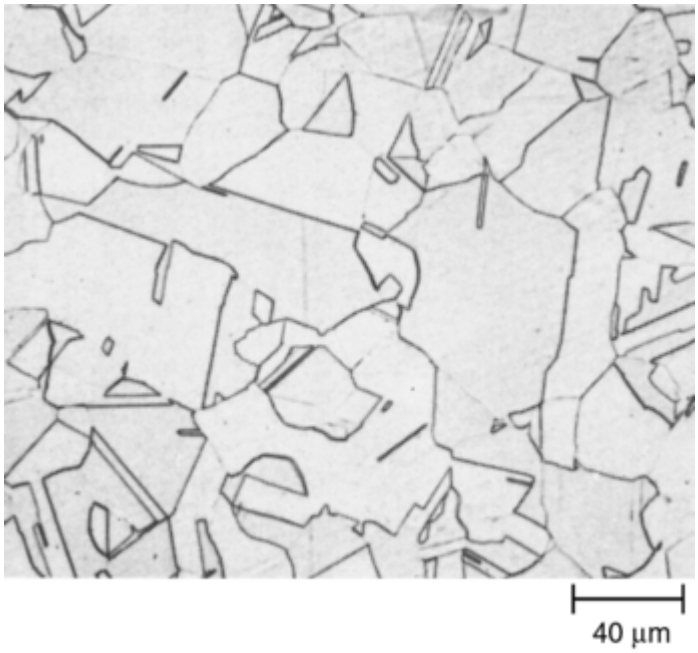

Fig. 10 Copper C10200 (oxygen-free copper), cold worked, annealed 30 min at 850 °C (1560 °F). Equiaxed, recrystallized grains containing twinned areas. Etchant 4, Table 2. 250×

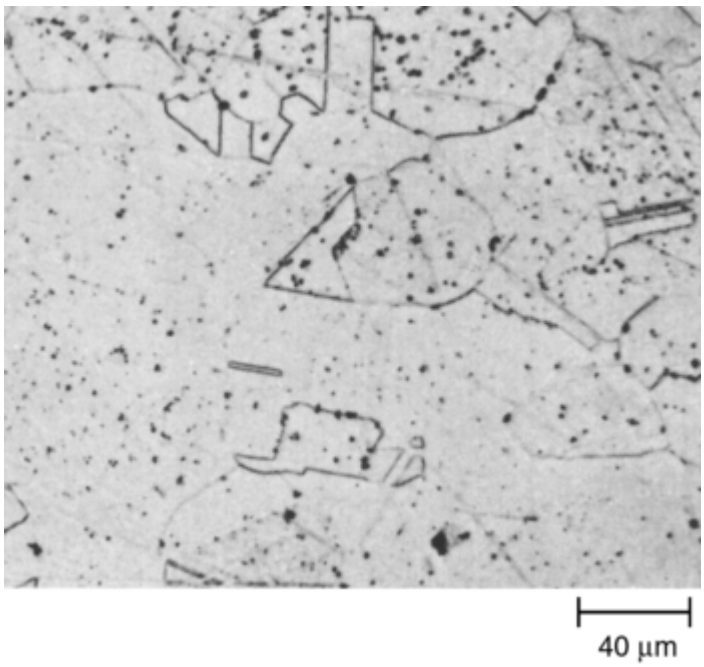

Fig. 11 Copper C10200 (oxygen-free copper), hot-rolled bar, heated 1 h in air to 665 °C (1225 °F). Specimen taken from near the bar surface shows Cu_2O (dark dots) caused by oxygen penetration during heating. Etchant 1, Table 2. 250×



Fig. 12 Alloy C11000 (electrolytic tough pitch copper), static cast. Excellent definition of dendritic structure. Etchant 10, Table 2. 5×

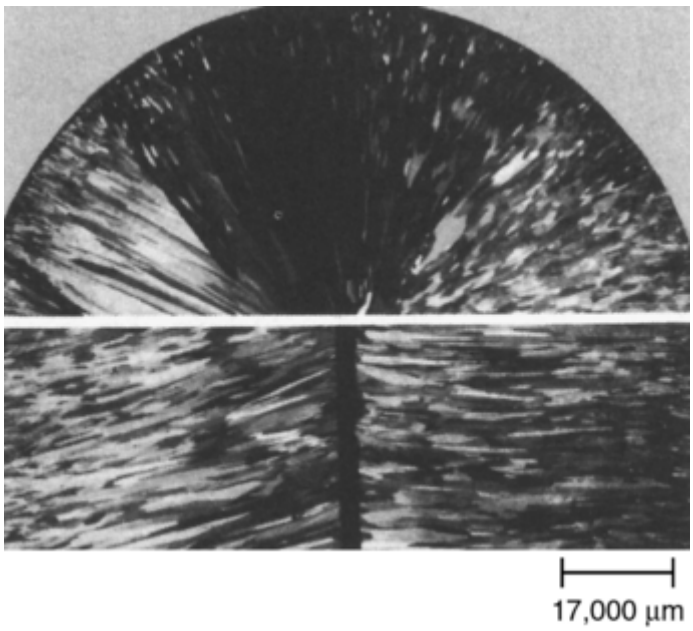

Fig. 13 Alloy C12200 (deoxidized high-phosphorus copper), continuously cast in a 102 mm (4 in.) diameter ingot. Top, transverse section showing radial grain growth. Bottom, longitudinal section. Dark center is columnar grains oriented along the axis of the ingot. Waterbury reagent was used, which has same constituents as etchant 7, Table 3. 0.6×

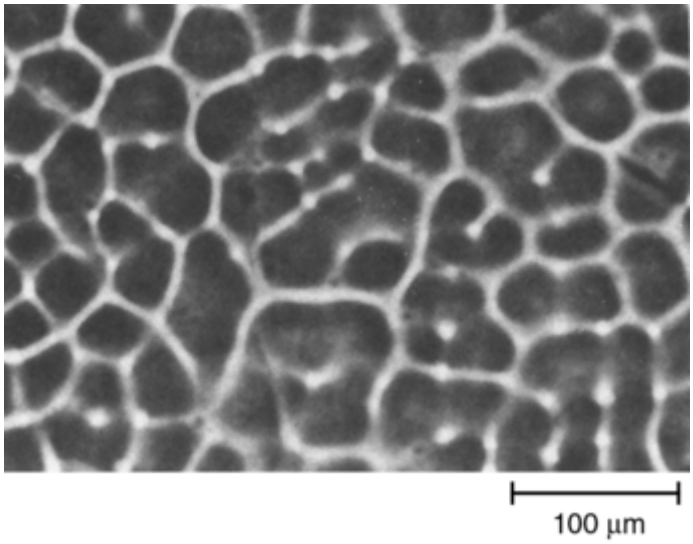

Fig. 14 The same C12200 (deoxidized high-phosphorus copper) continuously cast alloy in a 102 mm (4 in.) diameter ingot as in Figure 13 Section taken near the ingot surface normal to the radial grain growth. The structure is coarse, unbranched dendrites. Waterbury reagent was used, which has the same constituents as etchant 7, Table 3. 150×

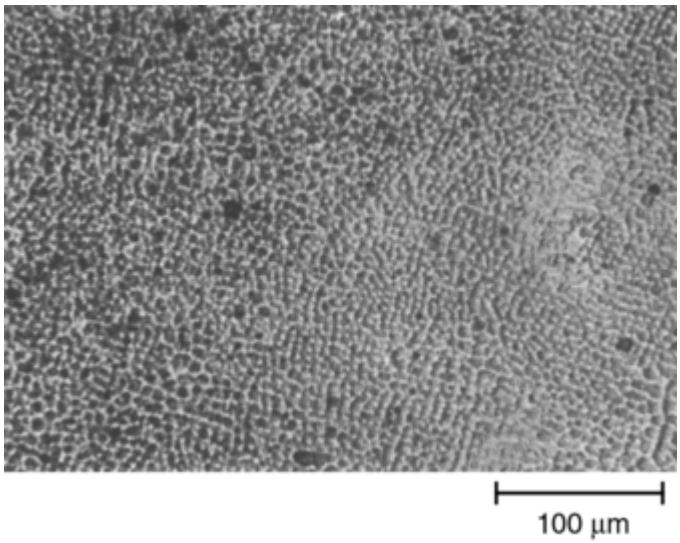

Fig. 15 The same C12200 (deoxidized high-phosphorus copper) continuously cast alloy in a 102 mm (4 in.) diameter ingot as in Fig. 14 Section taken near the ingot core normal to the radial grain growth. The dendrite structure is much finer than in Fig. 14. Waterbury reagent was used, which has the same constituents as etchant 7, Table 3. 150×

Alloy C12200 (deoxidized high-phosphorus copper) contains high-residual phosphorus, a common deoxidizer, that improves weldability. The micrograph (Fig. 16) shows the presence of P_2O_5. The addition of tellurium to copper-phosphorus alloy improves machinability. Figure 17, a micrograph of C14520, designated DPTE, shows the effect of hot working. The copper-telluride is present in the dark particles. The addition of sulfur likewise improves machinability. A cold-worked sample of C14700 is given in Fig. 18.

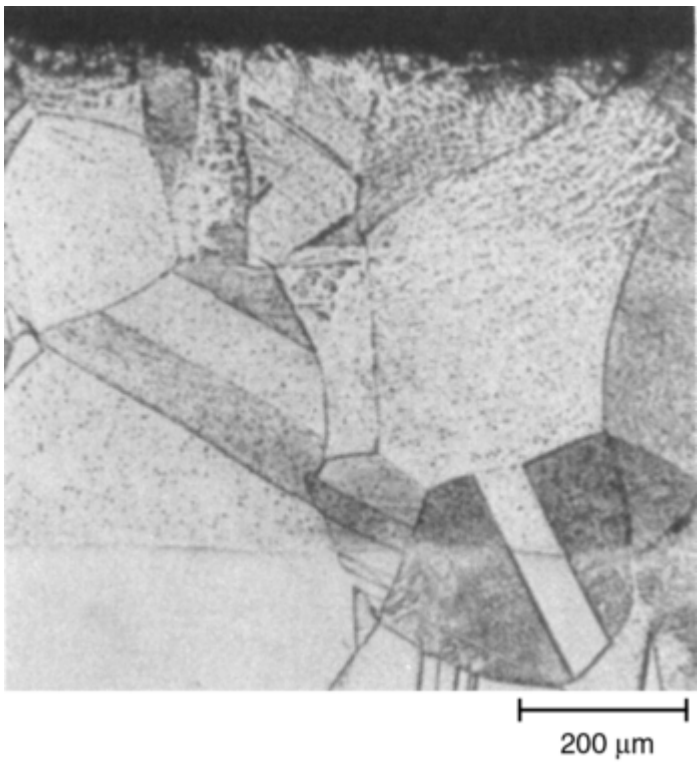

Fig. 16 Copper C12200 (deoxidized high-phosphorus copper). Internal oxidation (presence of dark dots of P_2O_5). Etchant 4, Table 2. 75×

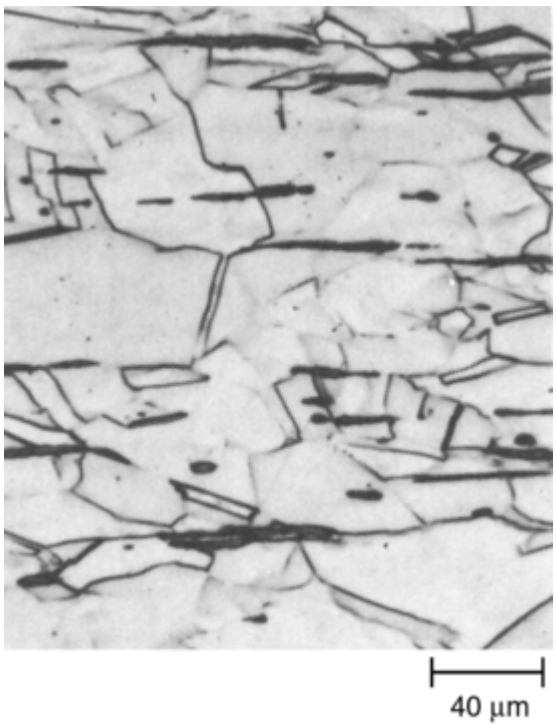

Fig. 17 Copper C14520 (DPTE), hot-rolled and drawn rod. Dark particles elongated in the rolling direction are copper telluride, which improves machinability. Etchant 7, Table 3. 250×

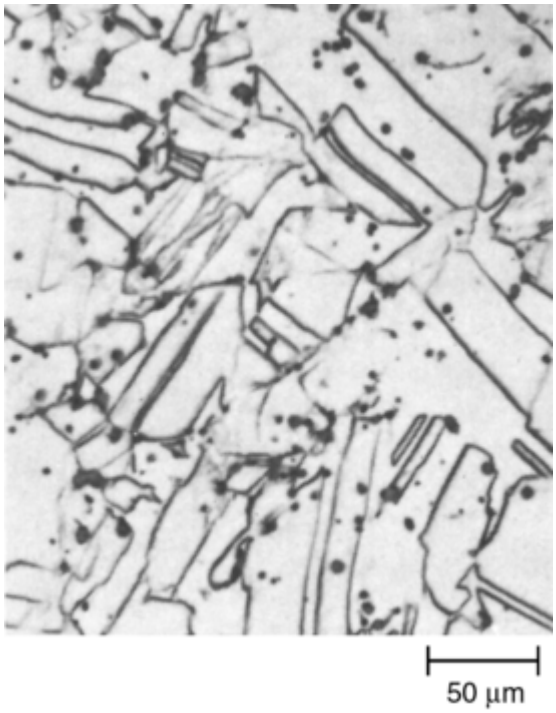

Fig. 18 Copper C14700 (sulfur-bearing copper) rod, cold worked to 50% reduction. Transverse section shows dispersion of round particles of CuS, which improves machinability. Etchant 7, Table 3. 200×

The greatest tonnage of copper alloys are those consisting of solid solutions. The high-copper alloys, copper-beryllium, copper-chromium, and copper-zirconium, have limited solid solubility, however. These systems can be precipitation hardened. The phenomenon, which is also called precipitation strengthening and age hardening, is possible because the limit of solid solubility contracts with decreasing temperature, a condition known as retrograde solubility (Ref 1). Copper-beryllium alloys (Fig. 19, 20, and 21can be heat treated to remarkably high strengths, as evidenced by their hardnesses. The precipitation process increases the copper content of the surrounding matrix and improves the conductivity of the alloy. This combination of strength and conductivity makes these alloys useful as electrical contact components.

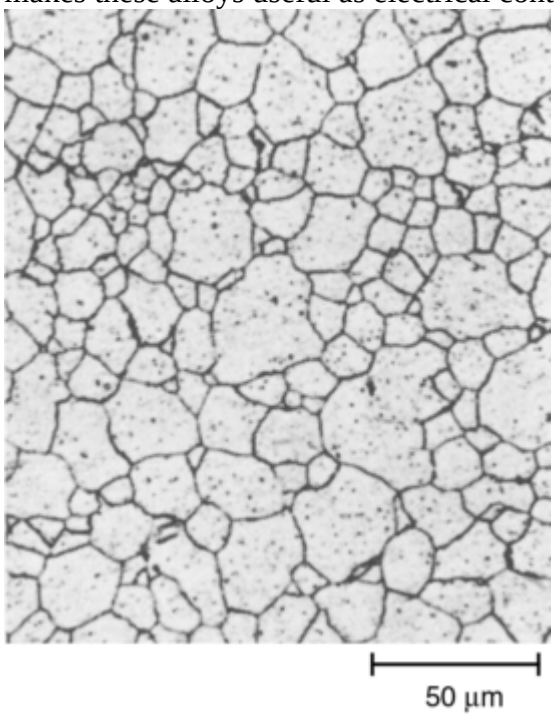

Fig. 19 Alloy C17200 (beryllium-copper), solution treated 10 min at 790 °C (1450 °F) and water quenched. Typical hardness is 62 HRB. Structure is equiaxed grains of supersaturated solid solution of beryllium in copper. Etchant 3, Table 2. 300×

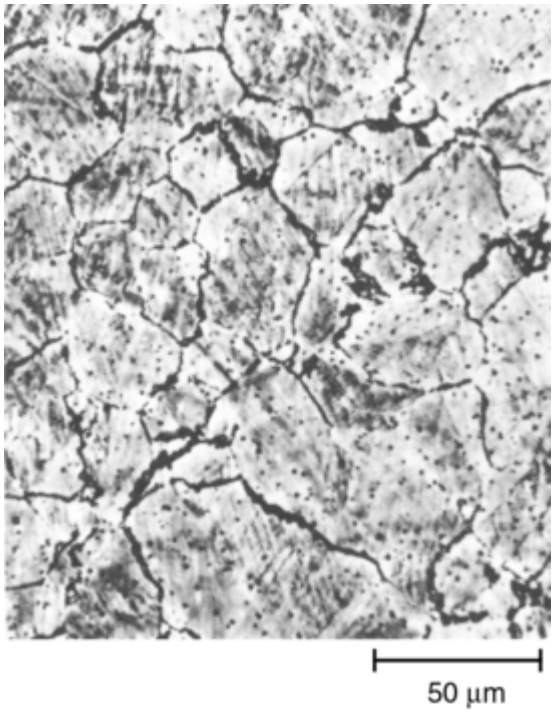

Fig. 20 Same alloy (C17200) and processing as in Figure 19 but aged 3 h at 360 °C (680 °F) after solution treatment. Typical hardness is 37 HRC. Copper-beryllium precipitates at grain boundaries and within α grains. Etchant 3, Table 2. 300×

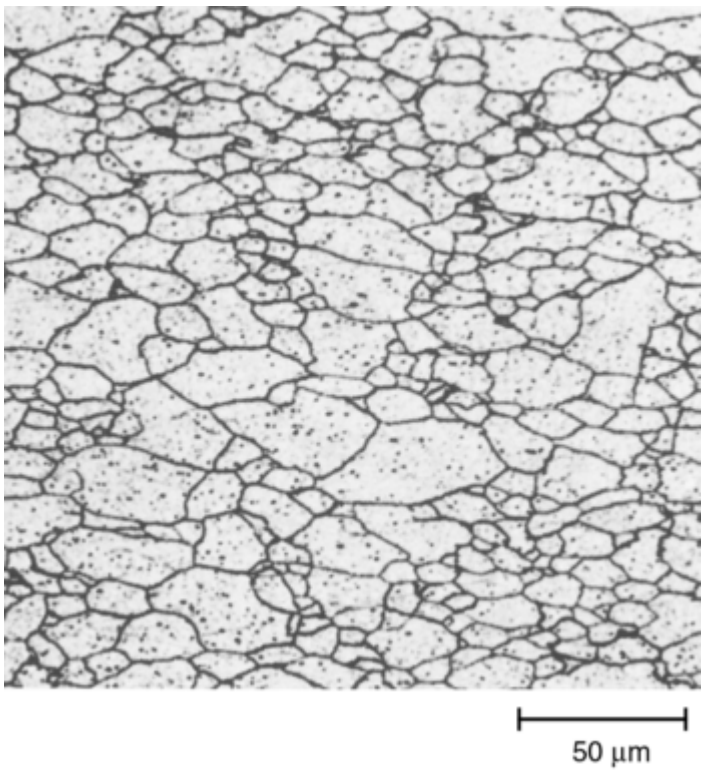

Fig. 21 Same alloy and processing as in Figure 19 except reduced 11% by cold rolling to quarter-hard temper. Typical hardness is 79 HRB. Alpha grains are elongated in the direction of rolling. Etchant 3, Table 2. 300×

Brasses. The phase diagram of the copper-zinc system (Fig. 22) has the compositional ranges of five common brasses superimposed. It is seen that the α-solid-solution region extends to 32.5 wt% Zn and includes red brasses (C23000), low brass (C24000), and cartridge brass (C26000). These have formability similar to pure copper. The dendritic structure of C26000 (Fig. 23, 24) and the annealed grains of Fig. 24 are similar to the

coppers. The effect of grain size on formability is illustrated with C26000 in Fig. 25, 26, 27, and 28 Processing combinations of hot and cold working and various annealing temperatures alter the grain size and shape. Hot-rolled and annealed, transverse and short longitudinal samples (Fig. 29, 30) are compared to the same alloy cold rolled (Fig. 31, 32). Cartridge brass that had been hot rolled, annealed, cold rolled, annealed, cold rolled to a 70% reduction, and then annealed at various temperatures yielded the grain sizes seen in Fig. 33, 34, 35, and 36

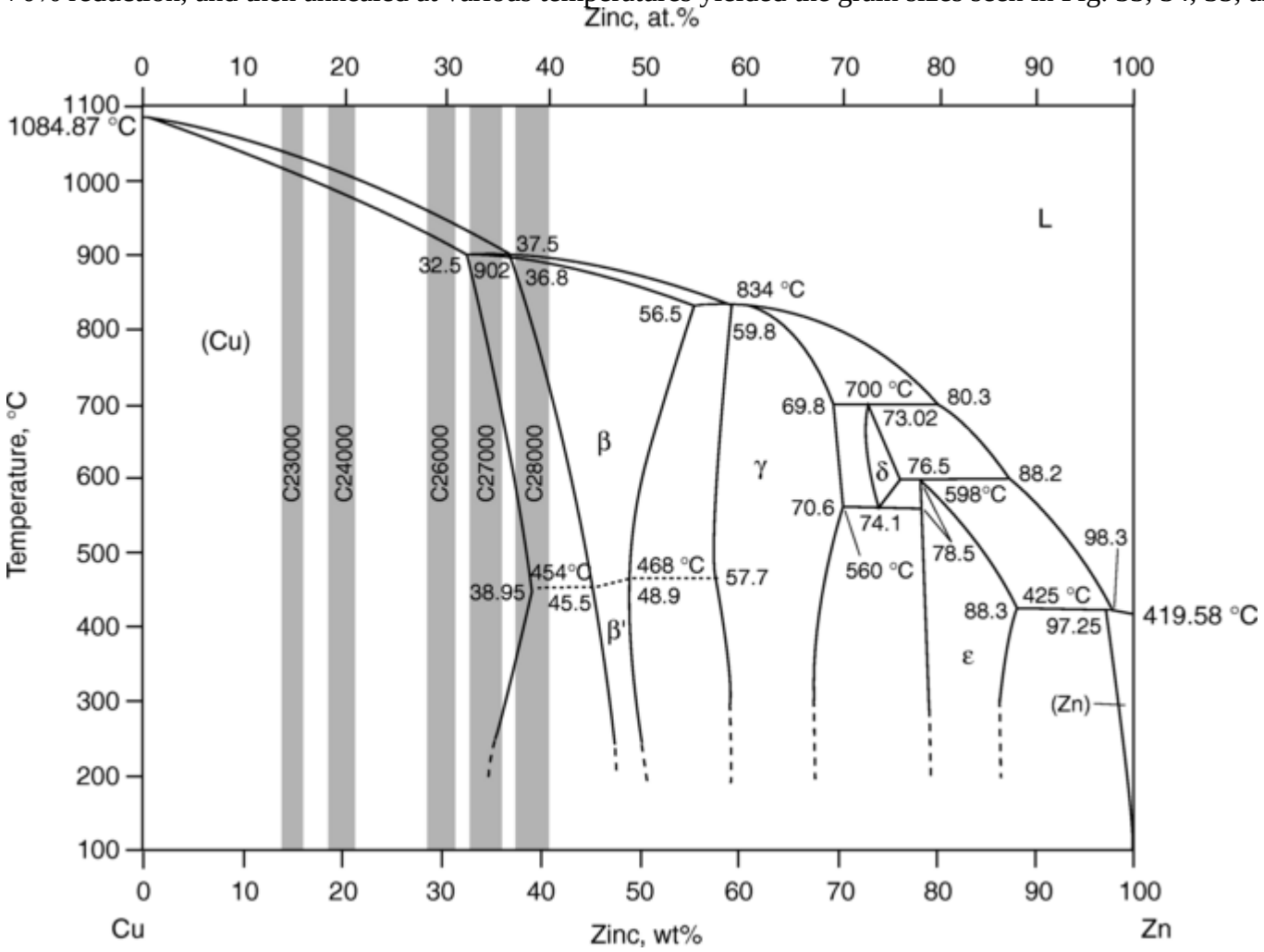

Fig. 22 A copper-zinc phase diagram with the compositional ranges of five common brasses (UNS designation) superimposed on it. Adapted from Ref 3



Fig. 23 Alloy C26000 (cartridge brass), cast, slowly cooled, and quenched. Primary dendrites aligned in 〈100〉 crystallographic directions. The fine, quenched structure has the same orientation as the coarse dendrites. Etchant 1, Table 2, then electropolished with electrolyte 1, Table 4. 30×

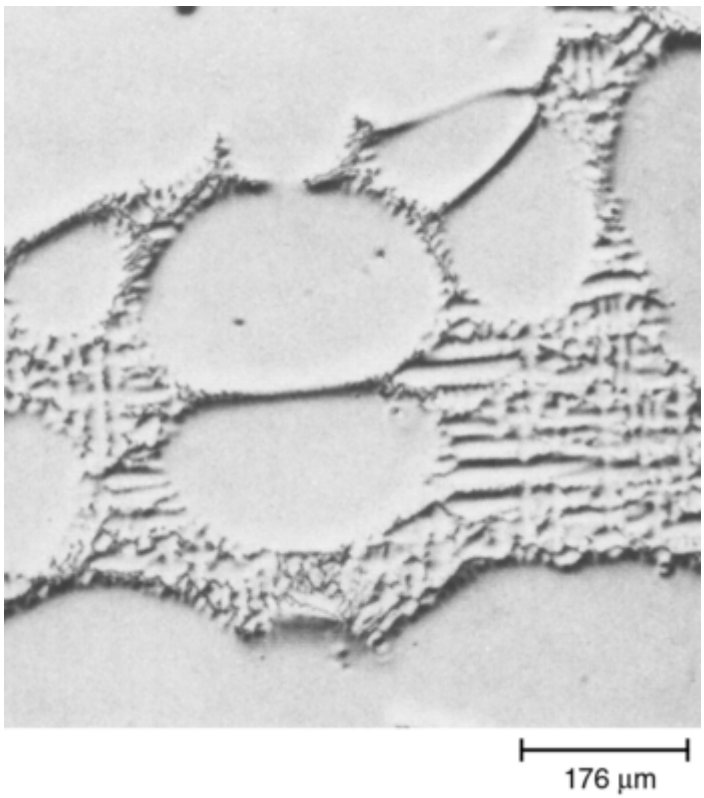

Fig. 24 Alloy C26000 (cartridge brass), same processing as in Fig. 23. Higher magnification shows that fine dendrites originate in the coarse ones and have the same orientation. Dendrites starting in directions that are not 〈100〉 do not grow very far. Same etchant and electrolyte as in Fig. 23. 85×

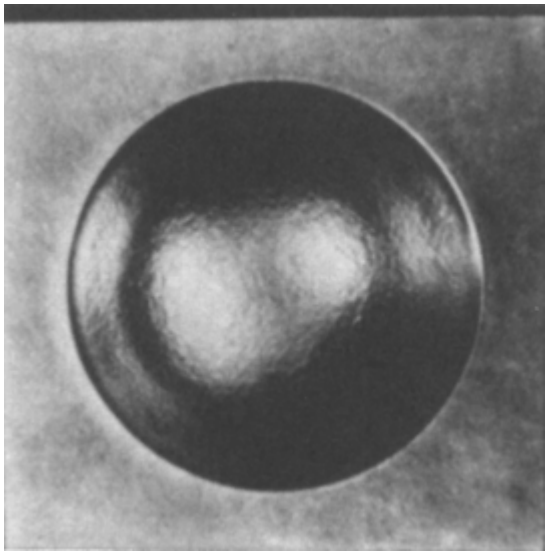

Fig. 25 Alloy C26000 (cartridge brass) drawn cup, showing “orange peel” (rough surface). See Figure 27 for grain structure. Etchant 1, Table 2. Actual size

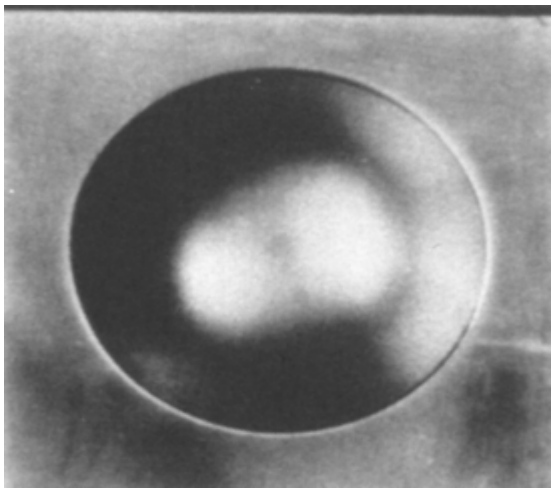

Fig. 26 Alloy C26000 (cartridge brass) drawn cup, with a smooth surface. See Figure 28 for structural details. Etchant 1, Table 2. Actual size

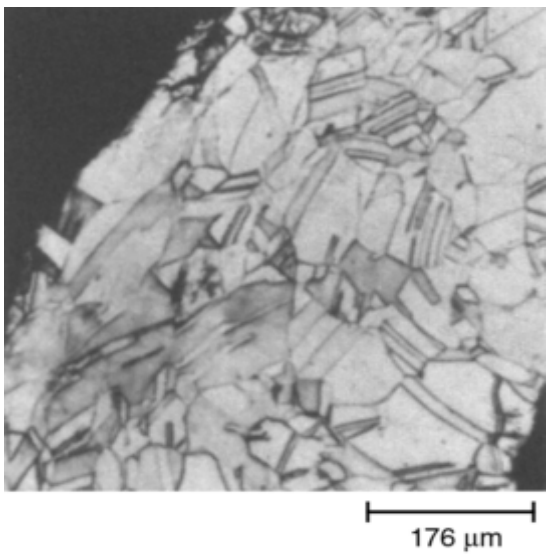

Fig. 27 Grain structure of drawn cup in Figure 25 The rough surface of the cup was caused by the large grain size. Etchant 1, Table 2. 85×

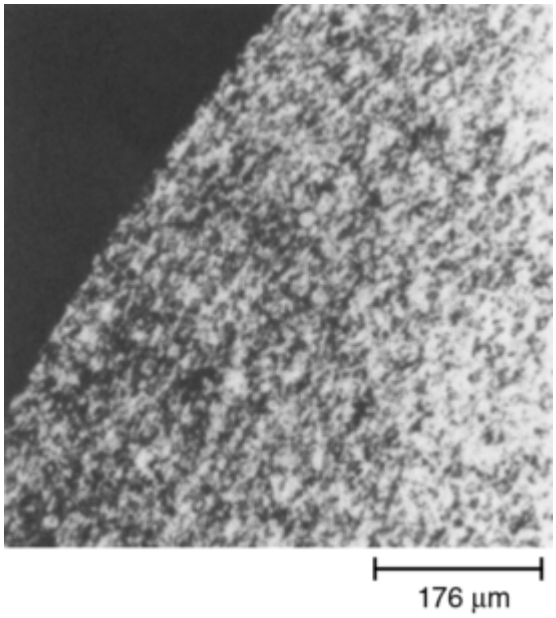

Fig. 28 Structure of the drawn cup in Figure 26 Because grains are small, the cup has a smooth surface. Etchant 1, Table 2. 85×



Fig. 29 Alloy C26000 (cartridge brass), hot rolled to 10 mm (0.4 in.) thick, annealed to a grain size of 15 µm, cold rolled to 40% to 6 mm (0.24 in.) thick, and annealed to a grain size of 120 µm. Diagram in lower left corner of micrograph indicates the view relative to the rolling plane of the sheet. Nominal tensile strength of 296 MPa (43,000 psi). Etchant 1, Table 2. 75×

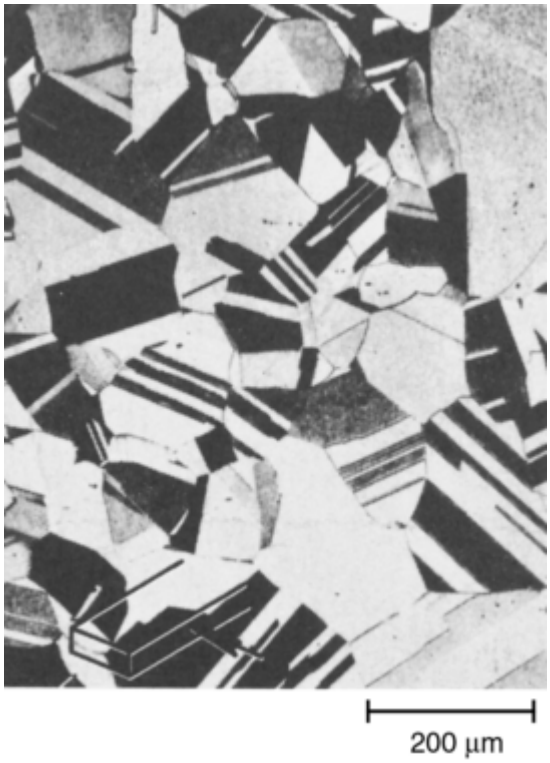

Fig. 30 Alloy C26000 (cartridge brass), hot rolled to 10 mm (0.4 in.) thick, annealed to a grain size of 15 µm, cold rolled to 40% to 6 mm (0.24 in.) thick, and annealed to a grain size of 120 µm. Diagram in lower left corner of micrograph indicates the view relative to the rolling plane of the sheet. Nominal tensile strength of 296 MPa (43,000 psi). Etchant 1, Table 2. 75×



Fig. 31 Alloy C26000 (cartridge brass), hot rolled to 10 mm (0.4 in.) thick, annealed to a grain size of 15 µm, cold rolled to 40% to 6.1 mm (0.24 in.) thick, and annealed to a grain size of 120 µm. Further reduced 37% by cold rolling from 6.1 to 3.8 mm (0.24 to 0.15 in.) thick, hard temper, nominal tensile strength of 524 MPa (76,000 psi). Diagram in lower left corner of micrograph indicates the view relative to the rolling plane of the sheet. Etchant 1, Table 2. 75×



Fig. 32 Alloy C26000 (cartridge brass), hot rolled to 10 mm (0.4 in.) thick, annealed to a grain size of 15 µm, cold rolled to 40% to 6.1 mm (0.24 in.) thick, and annealed to a grain size of 120 µm. Further reduced 37% by cold rolling from 6.1 to 3.8 mm (0.24 to 0.15 in.) thick, hard temper, nominal tensile strength of 524 MPa (76,000 psi). Diagram in lower left corner of micrograph indicates the view relative to the rolling plane of the sheet. Etchant 1, Table 2. 75×

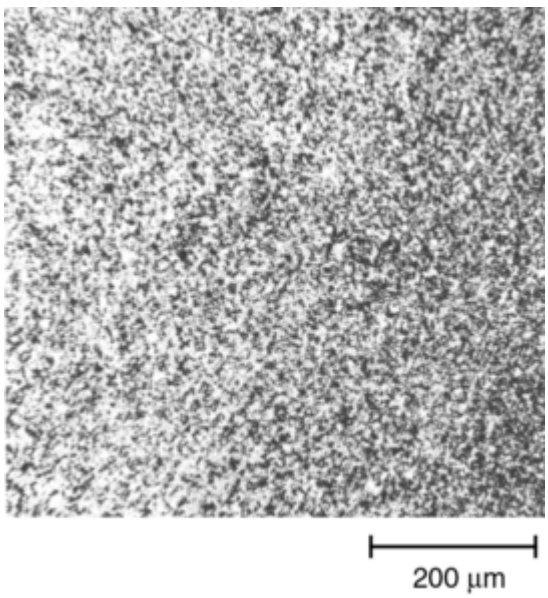

Fig. 33 Alloy C26000 (cartridge brass), processed to obtain specific grain size. Preliminarily hot rolled, annealed, cold rolled, annealed to a grain size of 25 µm, cold rolled to 70% reduction. Final anneal at 330 °C (625 °F) for 5 µm grain size. Etchant 1, Table 2. 75×

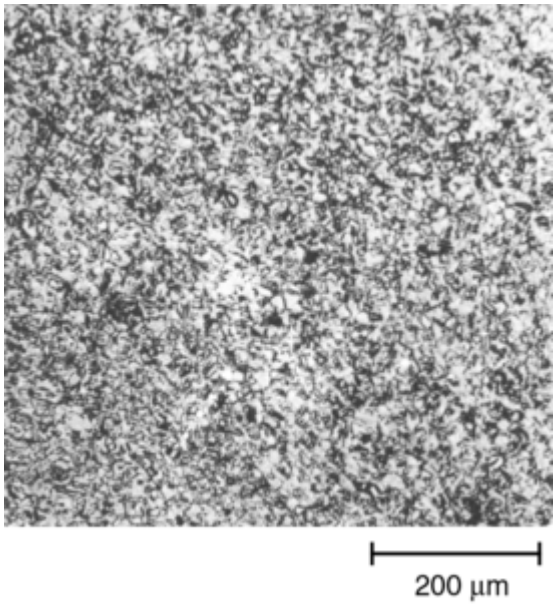

Fig. 34 Alloy C26000 (cartridge brass), processed to obtain specific grain size. Preliminarily hot rolled, annealed, cold rolled, annealed to a grain size of 25 µm, cold rolled to 70% reduction. Final anneal at 370 °C (700 °F) for 10 µm grain size. Etchant 1, Table 2. 75×

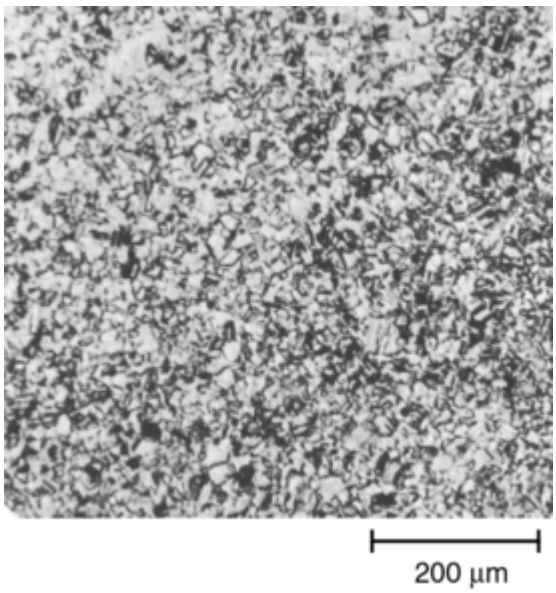

Fig. 35 Alloy C26000 (cartridge brass), processed to obtain specific grain size. Preliminarily hot rolled, annealed, cold rolled, annealed to a grain size of 25 µm, cold rolled to 70% reduction. Final anneal at 405 °C (760 °F) for 15 µm grain size. Etchant 1, Table 2. 75×

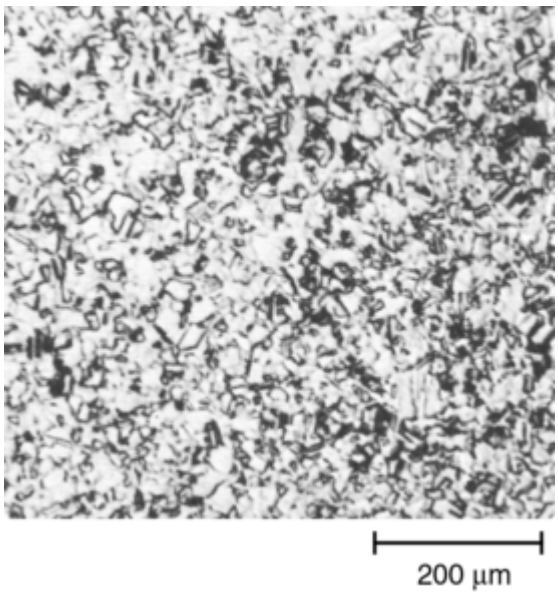

Fig. 36 Alloy C26000 (cartridge brass), processed to obtain specific grain size. Preliminarily hot rolled, annealed, cold rolled, annealed to a grain size of 25 µm, cold rolled to 70% reduction. Final anneal at 425 °C (800 °F) for 20 µm grain size. Etchant 1, Table 2. 75×

Above 37.5% Zn, the β phase crystallizes. Along the vertical solubility limit line of the α phase, note that the α-phase solubility increases with a decrease in temperature. The structure of brass containing α and β phases, such as the C36000 free-cutting brass alloy, is seen in Fig. 37, 38, 39, and 40

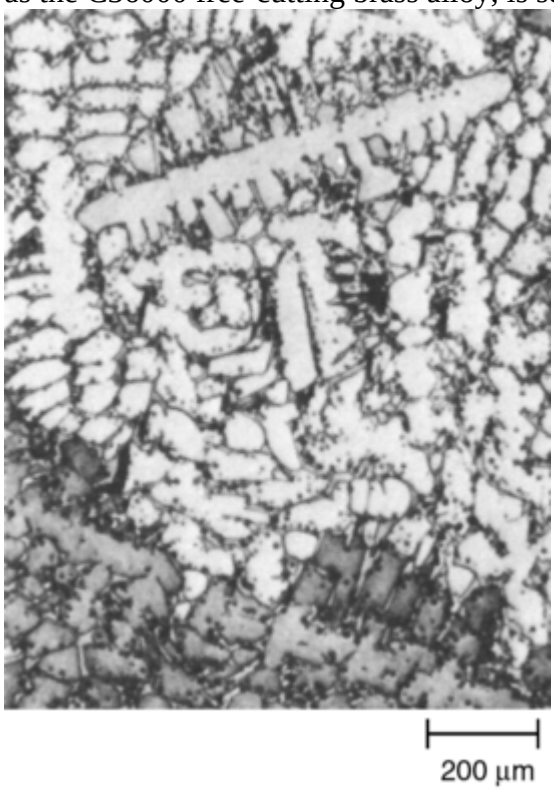

Fig. 37 Alloy C36000 (free-cutting brass), with primary dendrites of α phase darkened. Lead appears as small spheroids. Etchant 1, Table 2. 50×

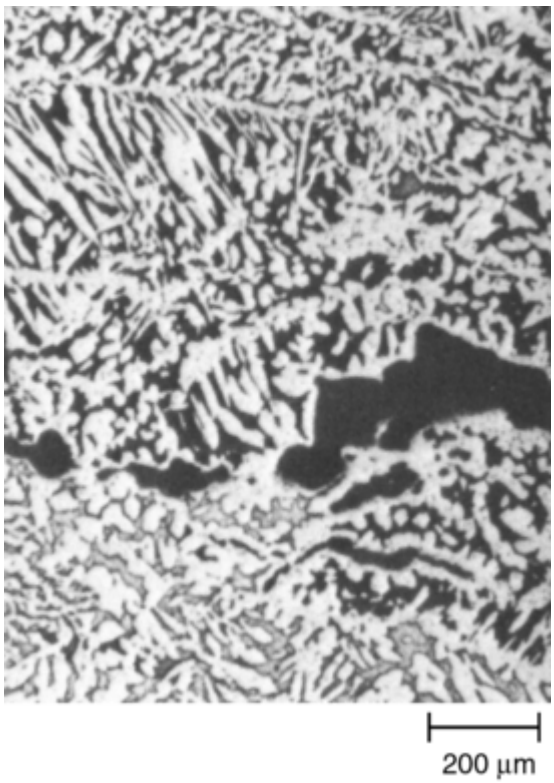

Fig. 38 Alloy C36000 (free-cutting brass), with β phase darkened by preferential attack of the etchant. In this case, α phase is formed in the solid state during cooling. Etchant 16, Table 2. 50×



Fig. 39 Alloy C36000 (free-cutting brass), semicontinuous cast. Alpha-phase dendrites in the columnar zone near the outside edge of the ingot. Etchant 1, Table 2. 30×. Source: Ref 4

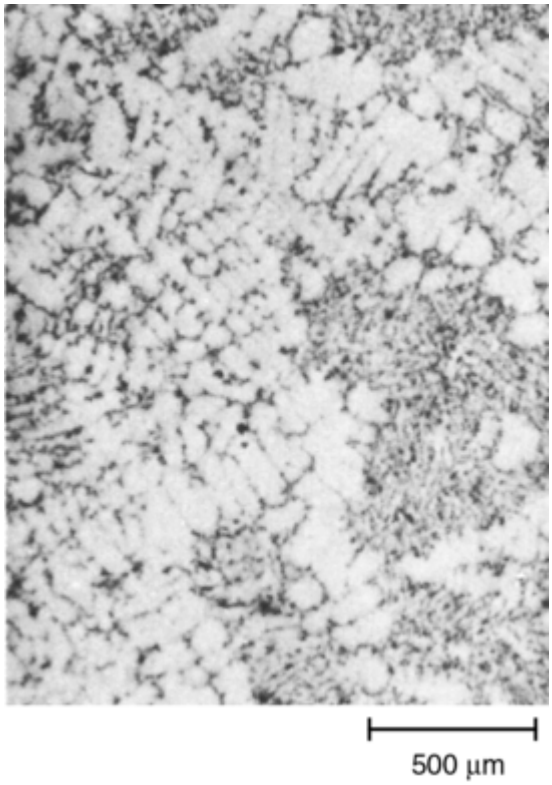

Fig. 40 Alloy C36000 (free-cutting brass), mixed α- and β-phase dendrites near the center of the ingot. Etchant 1, Table 2. 30×. Source Ref 4

Muntz metal, C28000, has higher zinc content than the C36000 alloy. The α and β phases are again evident in the as-cast and processed samples (Fig. 41, 42, and 43). Alloys with higher zinc content have increased strength but are prone to dezincification corrosion, as seen in Fig. 43.

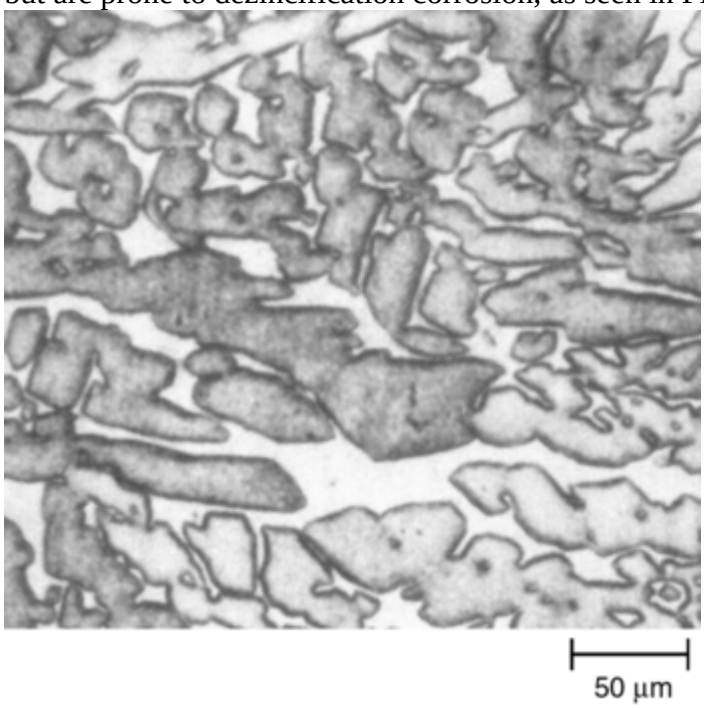

Fig. 41 Alloy C28000 (Muntz metal) ingot, as-cast. Structure is dendrites of α phase in a matrix of β phase. Etchant 1, Table 2. 210×

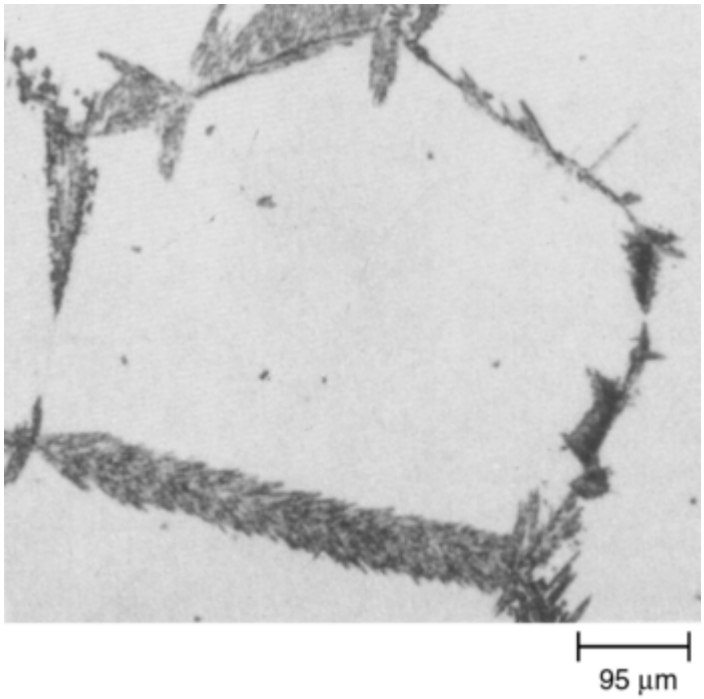

Fig. 42 Alloy C28000 (Muntz metal) ingot, as-cast, showing α feathers that formed at β grain boundaries during quenching of the all-β structure. Etchant 1, Table 2. 105×

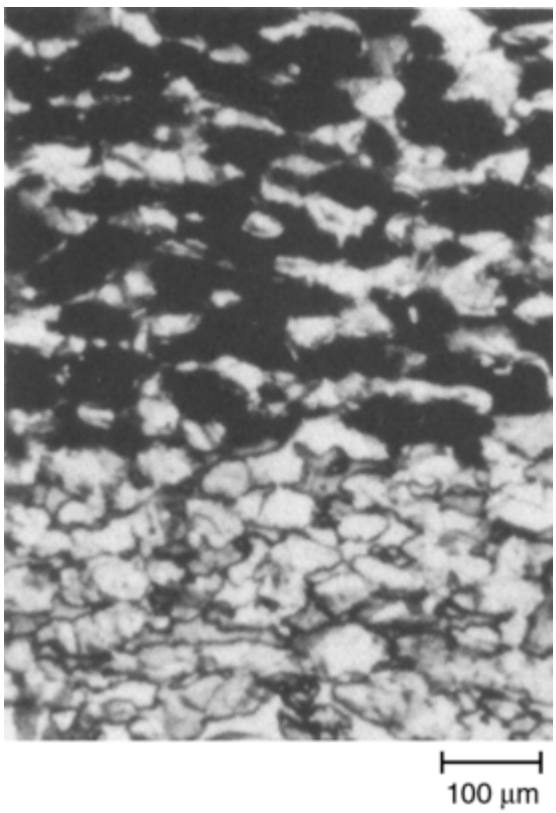

Fig. 43 Alloy C28000 (Muntz metal) ingot, hot-rolled plate. Uniform (layer) dezincification. Alpha grains remain in the corroded area (top). Etchant 1, Table 2. 90×

Bronzes. The copper-tin system equilibrium diagram (Ref 5) indicates a larger range of temperatures in the first sections of the liquidus and solidus curves than exists in the copper-zinc system. The tin bronzes, also called phosphor bronzes, form alpha solid solutions with copper extending to 15.8% Sn at temperatures between 520 and 586 °C (968 and 1087 °F). This extended freezing range causes tin bronzes to pass through a semisolid or "mushy" stage during solidification. Casting molds must be designed to take this weak structure into account. The extended liquidus-solidus gap is also responsible for the dendritic segregation, or coring, found in tin

bronze castings (Ref 1). This segregation is seen in Fig. 44 and 45. Figure 46 is C51000 containing 5% Sn, where processing has produced recrystallized α-phase grains with annealing twins.

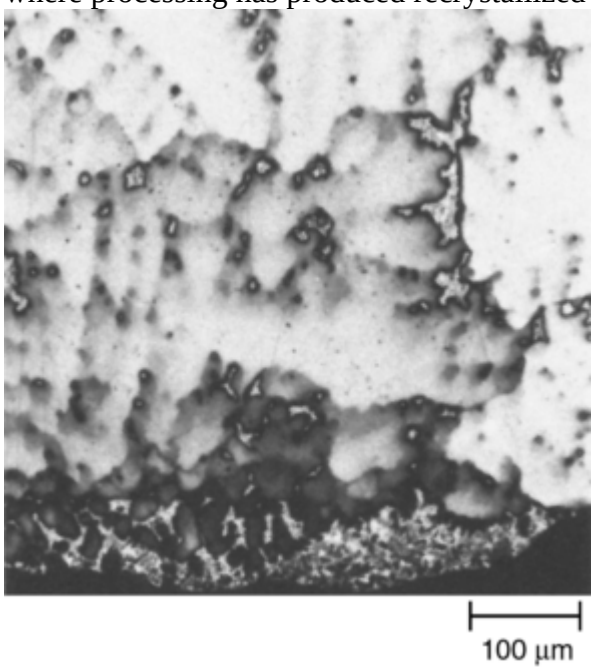

Fig. 44 Horizontal cast strip of tin bronze (5% Sn), showing inverse segregation at the bottom surface of the casting. The bottom is nearly pure tin. Etchant: 40 mL HNO_3, 25 g CrO_3, 35 mL H_2O. 100×. Source: Ref 6

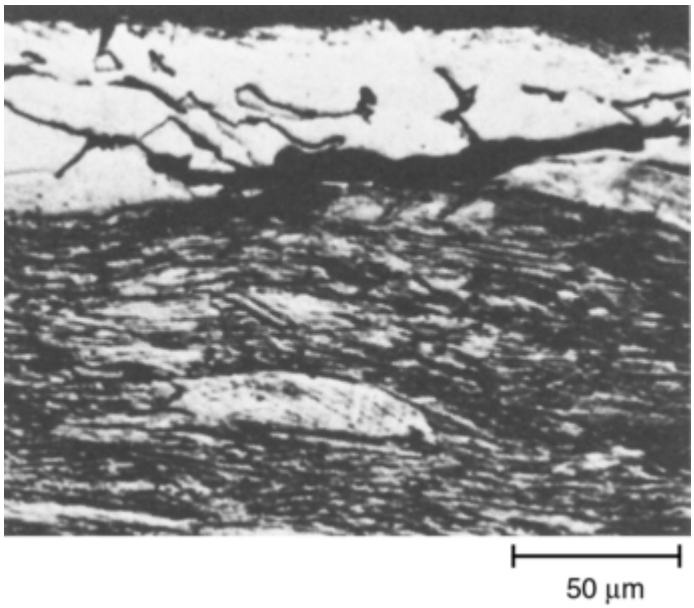

Fig. 45 Phosphor bronze strip rolled from a static cast ingot, showing gross tin sweat on the top surface. This illustrates how segregation caused by exudation persists in the fabricated structure. Etchant not reported. 300×. Source: Ref 7

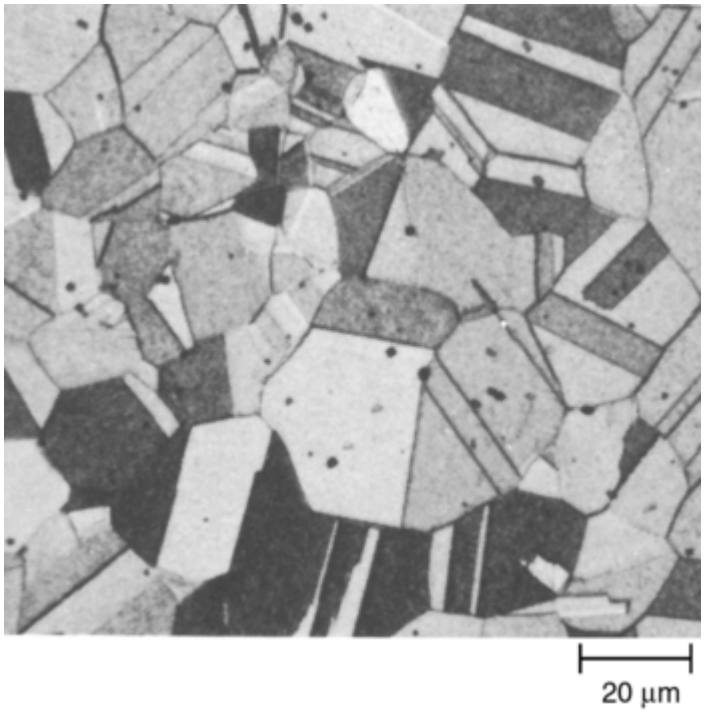

Fig. 46 Alloy C51000 (phosphor bronze, 5% Sn) rod, extruded, cold drawn, and annealed 30 min at 565 °C (1050 °F). Structure consists of recrystallized α grains with annealing twins. Etchant 4, Table 2. 500×

Aluminum bronzes are copper-aluminum alloys that generally have aluminum between 5 and 15%. Cast alloys are show in Fig. 47, 48, and 49. Alloys less than 8.5 wt% Al are a single α-phase solid solution. Numerous intermetallic phases exist with higher aluminum content. At approximately 12% Al, the alloy will solidify as a eutectic and undergo eutectoid transformation on slow cooling (Fig. 50). Under faster cooling, a martensitic transformation occurs analogous to that in heat treated steels, and martensitic needles result (Fig. 47, 51, and 52) (Ref 8). It should be realized that the copper-aluminum bronzes are not just binary alloys but are multicomponent and multiphased systems that can contain combinations of iron, manganese, nickel, or silicon as well. In the Cu-Zn-Al and Cu-Al-Ni systems, the martensitic transformation is reversible and responsible for the shape memory effect (Ref 1).

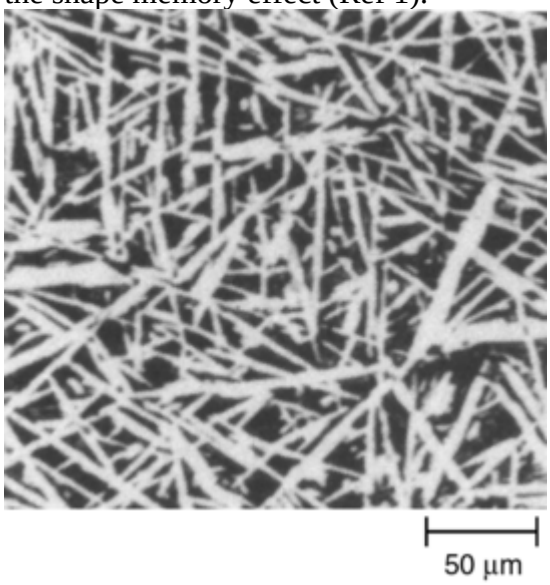

Fig. 47 Alloy C95400 (aluminum bronze), solution treated 2 h at 900 °C (1650 °F), water quenched, tempered 2 h at 650 °C (1200 °F), and water quenched. Alpha grains (white martensitic needles) are smaller than in the as-cast condition. Etchant 4, Table 2. 200×

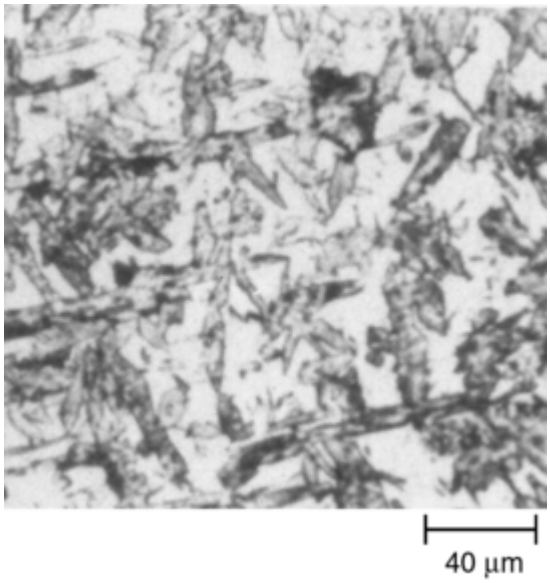

Fig. 48 Alloy C95500 (aluminum bronze with 11.5% Al), as sand cast. Small α grains (light gray, mottled) in matrix of retained β phase (white), with same eutectoid decomposed β phase (dark gray). Compare with Figure 49. Electrolytically etched in electrolyte 5, Table 5. 250×

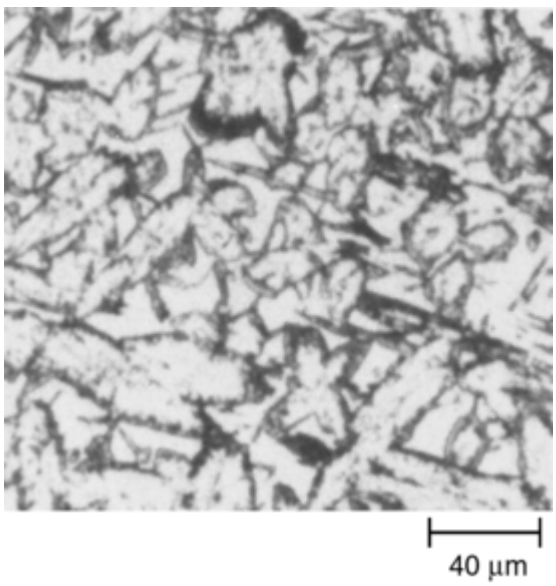

Fig. 49 Alloy C95500 (aluminum bronze with 11.0% Al), with larger α grains and a greater amount of eutectoid decomposed β phase in the matrix than Figure 48. Electrolytically etched in electrolyte 5, Table 5. 250×

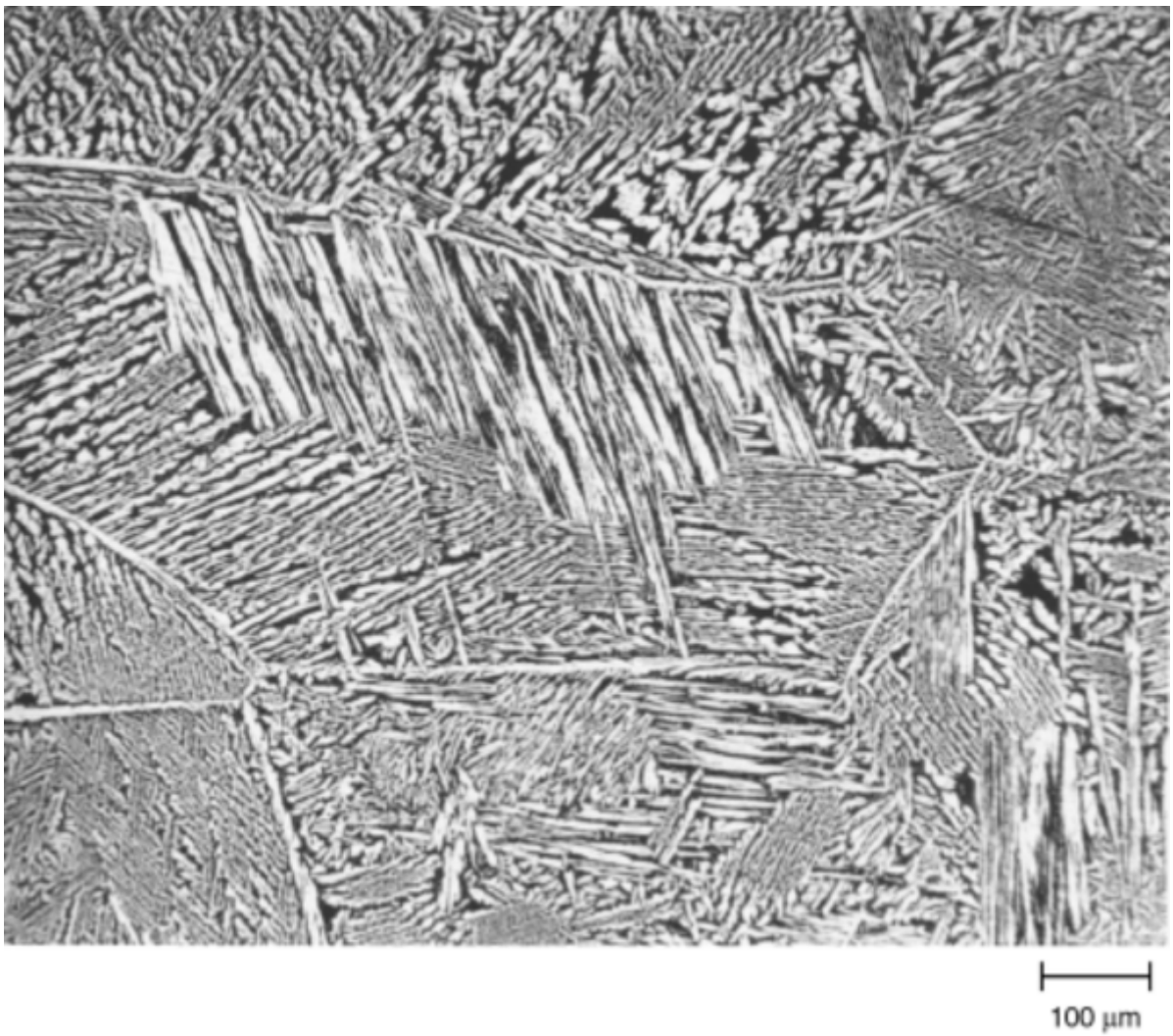

Fig. 50 Metal mold cast aluminum bronze casting. Alloy contains 5% Ni and 5% Fe (similar to C95500). Under slow cooling, the laminar Widmänstatten structure (light) is visible on a background of fine martensitic structure (dark). Etchant not reported. 100×. Source: Ref 8



Fig. 51 Cast aluminum bronze (11.8% Al). Under faster cooling than Figure 50 specimen, the structure has been transformed, with the formation of martensitic needles mixed with pearlite (trostite). Etchant not reported. 50×. Source: Ref 8

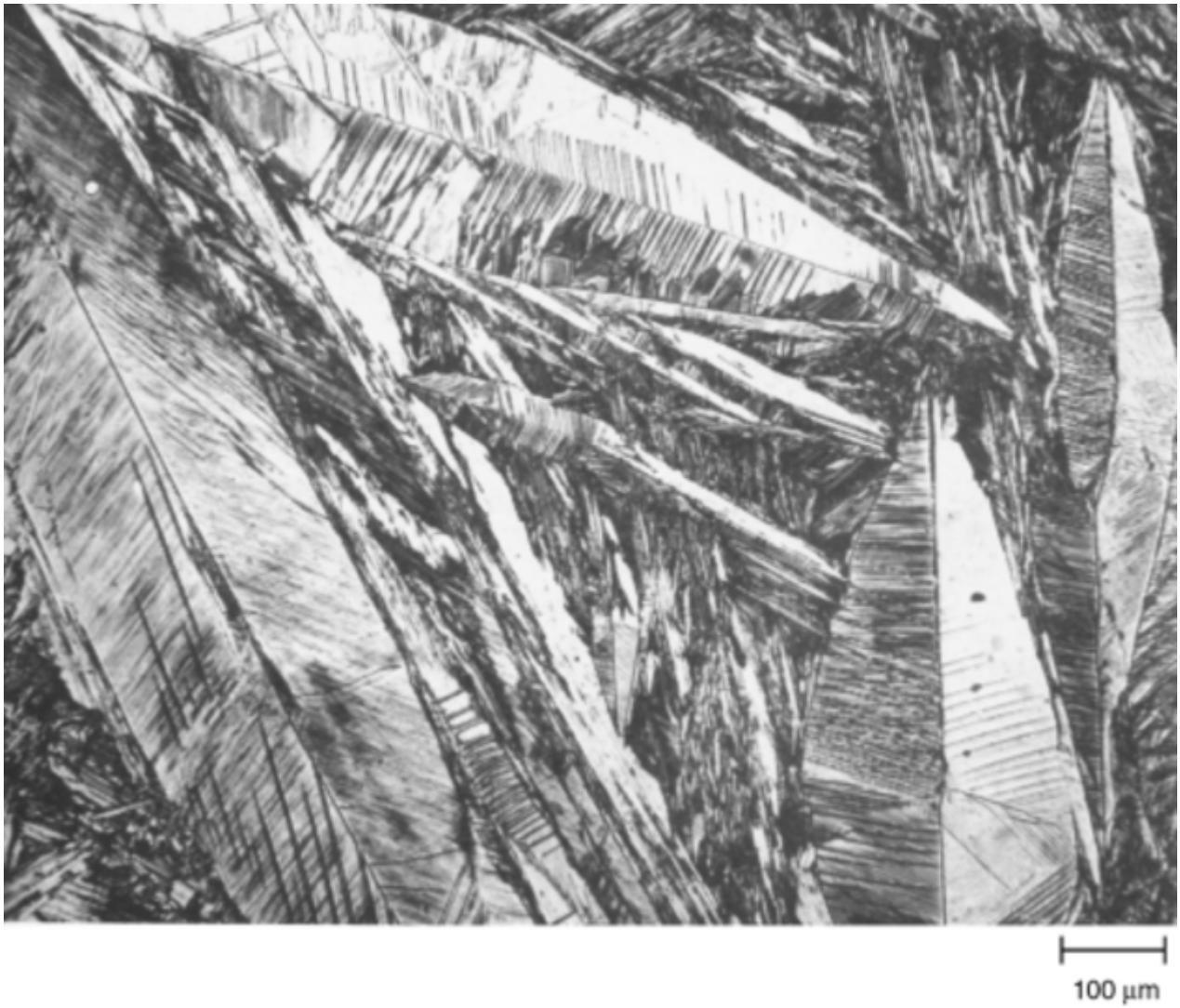

Fig. 52 Detail of cast Cu-Al-Ni alloy. Under fast cooling, the structure of martensitic needles forms. Etchant not reported. 100×. Source: Ref 8

Copper-nickel alloys form a continuous series of solid solutions over their entire binary composition range, because copper and nickel atoms differ by only 2.5% in volume and both exhibit the face-centered cubic structure. When atoms of different elements can occupy equivalent sites randomly on a crystal lattice, such elements form what are known as substitutional solid solutions (Ref 1). The C71500 wrought alloy seen in its as-cast state at the core of a billet is 30% Ni (Fig. 53). The nickel silver C74500 (65Cu-10Ni, balance zinc) exhibits the equiaxed grains and twinning found in pure copper (Fig. 54).

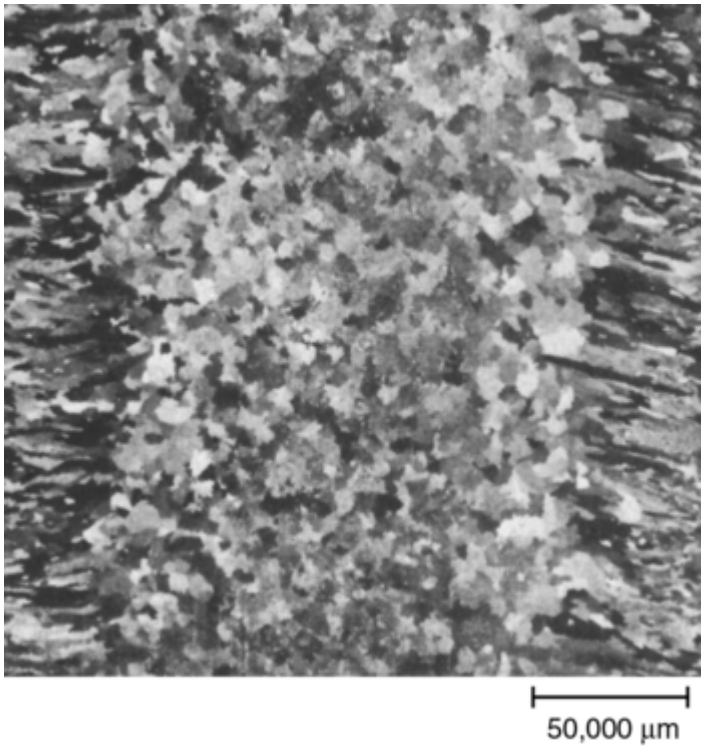

Fig. 53 Alloy C71500 (copper-nickel, 30% Ni), as-cast. Longitudinal section showing columnar structure near the surface of the billet. The grains are inclined upward from horizontal by up to 30° due to convection in the initial state of freezing. Etchant 18, then etchant 16, Table 2. 0.3×

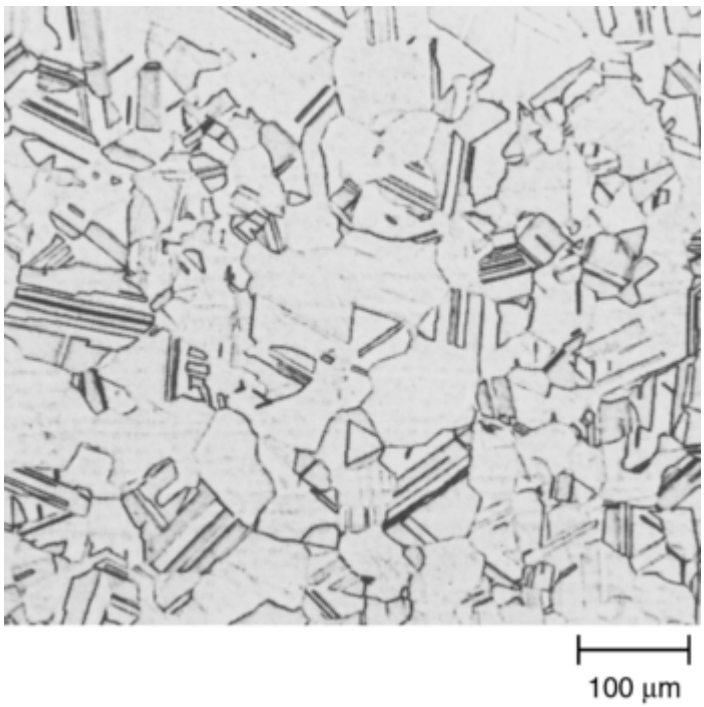

Fig. 54 Alloy C74500 (nickel silver, 65-10) cold-rolled sheet, 2.5 mm (0.10 in.) thick, annealed at 650 to 700 °C (1200 to 1290 °F). Longitudinal section shows equiaxed crystallized grains of a solid solution containing twin bands. Etchant 20, Table 2. 100×

References cited in this section

1. G. Joseph, *Copper, Its Trade, Manufacture, Use, and Environmental Status,* ASM International, 1999

3. T.B. Malssalski, Ed., *Binary Phase Diagrams,* ASM International, 1990

4. T.F. Bower and D.A. Granger, "Copper and Copper Alloy Ingot Structure—A Preliminary Survey," Report 70-34, The Casting Laboratory, Cleveland, 1970

5. *Alloy Phase Diagrams,* Vol 3, *ASM Handbook,* ASM International, 1992, p 2, 178

6. A. Cibula, "Review of Metallurgical Factors Influencing the Quality of Copper and Copper Alloy Casting," BNFRMRA International Conference on the Control of the Composition and Quality of Copper and Copper Alloy Casting for Fabrication, Oct 1967 (Düsseldorf)

7. G.L. Bailey and W.A. Baker, "Melting and Casting of Non-Ferrous Metals," Monograph and Report Series 6, Institute of Metals, London, 1949

8. A. Tomer, *Structure of Metals through Optical Microscopy,* ASM International, 1991

Revised by R.N. Caron, R.G. Barth, and D.E. Tyler, Metallography and Microstructures of Copper and Its Alloys, *Metallography and Microstructures,* Vol 9, *ASM Handbook,* ASM International, 2004, p. 775–788

Metallography and Microstructures of Copper and Its Alloys

>Revised by R.N. Caron, R.G. Barth, and D.E. Tyler, Olin Brass, Division of Olin Corporation

---

Metallographic Examination

Common applications of metallographic examination for quality control, material evaluation, and alloy development include (Ref 1):

- *Measurement of grain size:* Grain size has a strong influence on properties and formability in cold-worked and annealed products. Qualitative estimates of grain size in sheet and strip products also can be obtained by cup testing.
- *Evaluation of the dispersion of second phases:* This is particularly useful for lead and other additives that promote machinability.
- *A check on heat treating conditions:* Complex alloys, such as aluminum bronzes and high-tensile brasses, rely on the development of proper microstructures for mechanical properties and optimal corrosion resistance.
- *Failure analysis:* Metallographic examination readily reveals stress-corrosion cracking, dezincification, dealuminification, and other common corrosion mechanisms. The technique can also uncover defects in wrought, cast, and welded structures.

Both macrographic and micrographic examination are of use in these applications.

Macroscopic Examination

Specimens for macroscopic examination are extracted from larger masses using common cutting tools. The tools must be kept sharp to minimize cold working of the specimens and cooled to avoid over-heating (recrystallizing) the samples. The article "Metallographic Sectioning and Specimen Extraction" in this Volume provides insight into the specimen selection method as well as processing advice.

Surface Preparation. Surfaces suitable for macroetching usually can be obtained in two machining operations. In the first operation, a heavy cut is taken to remove the metal that was cold worked during sectioning; in the second, a light cut is taken, using a V-shaped tool, to remove the remaining effects of cold work.

The need for further surface preparation depends on the amount of detail required. The surface detail revealed by etching increases as the degree of surface irregularity decreases. The machined surface is often ground using 180-grit or finer abrasive and sometimes as fine as 600-grit, which is especially useful for revealing fine defects or cracks.

Etching. Deep etching removes the effects of cold work but produces a rough surface; therefore, it is common practice to deep etch the machined or rough-ground surface and regrind it lightly, followed by a light etch.

Selection of an etchant for a macrospecimen depends primarily on the alloy to be etched and the features to be examined. Because the capabilities of two or more etchants often overlap or are the same, selection of a specific etchant is arbitrary. Table 3 lists compositions of the more commonly used macroetchants, along with etching procedures, purposes of the etchants or characteristics revealed, and alloys for which they are ordinarily used. Any etchant used for macroetching should not remove second-phase particles, lest they appear as defects, such as porosity or grain-boundary cracks.

Table 3 Etchants for macroscopic examination of coppers and copper alloys

Procedure for use: Immerse at room temperature, rinse in warm water, dry

Composition	Copper or copper alloy	Comments
1. 50 mL HNO_3, 0.5 g $AgNO_3$ (silver nitrate), 50 mL H_2O	All coppers and copper alloys	Produces a brilliant, deep etch
2. 10 mL HNO_3 and 90 mL H_2O	Coppers and all brasses	Grains, cracks, and other defects
3. 50 mL HNO_3 and 50 mL H_2O[(a)]	Coppers, all brasses, aluminum bronze[(b)]	Same as above; reveals grain by contrast
4. 30 mL HCl, 10 mL $FeCl_3$, 120 mL H_2O or methanol	Coppers and all brasses	Same as etchant above[(c)]
5. 20 mL acetic acid, 10 mL 5% CrO_3, 5 mL 10% $FeCl_3$, 100 mL H_2O[(d)]	All brasses	Produces a brilliant, deep etch
6. 2 g $K_2Cr_2O_7$, 4 mL saturated solution of NaCl, 8 mL H_2SO_4, 100 mL H_2O[(e)]	Coppers, high-copper alloys, phosphor bronze	Grain boundaries, oxide inclusions
7. 40 g CrO_3, 7.5 g NH_4Cl (ammonium chloride), 50 mL HNO_3, 8 mL H_2SO_4, 100 mL H_2O	Silicon brass, silicon bronze	General macrostructure
8. 45 mL acetic acid and 45 mL HNO_3	Copper	Grain boundary and macroetch by polish attack
9. Saturated $(NH_4)_2S_2O_8$ (ammonium persulfate)	Copper and copper alloys	Use after the acetic acid listed above; increases contrast of brass
10. 40 mL HNO_3, 20 mL acetic acid, 40 mL H_2O	Copper and copper alloys	Macroetch 90-10, 70-30, and leaded brass

(a) Solution should be agitated during etching to prevent pitting of some alloys.
(b) Aluminum bronzes may form smut, which can be removed by brief immersion in concentrated HNO_3.
(c) Excellent for grain contrast.
(d) Amount of water can be varied as desired.
(e) Immerse specimen 15–30 min, then swab with fresh solution.

Microscopic Examination

Specimens of copper and copper alloys for microscopic examination are extracted from larger masses by sawing, shearing, filing, hollow boring, or abrasive-wheel and low-speed diamond saw cutting. Use sharp tools and care to avoid deep cold work, and adequate cooling to prevent recrystallizing of cold-worked lean alloys. The use of an abrasive cutoff wheel or precision low-speed diamond saw is recommended for sectioning, depending on the size and specimen material. The as-cut surface is generally free of damage and distortion and is ready for encapsulation with minimal grinding and polishing.

Mounting. In general, the procedures for mounting copper and copper alloy specimens are the same as those for other metals. Coppers and copper alloys are extremely susceptible to work hardening; therefore, when possible, the face used for examination should be the one that has been subjected to the least cutting damage.

Phenolic is the mounting material most often used. Diallyl phthalate, glass or fiber filled, is a suitable alternative. The transparency offered by mounts made of acrylic thermoplastic mounting resins, such as methyl methacrylate, is often advantageous. However, these materials are softer than Bakelite (Georgia-Pacific Corp.) and are not as good for edge preservation of the sample. Heat generated during thermosetting can cause heavily cold-worked coppers to recrystallize.

The combination of heat and pressure needed for compression-mounting materials will sometimes crush or adversely affect specimens, especially those of thin sheet or strip. Under these conditions, one of the epoxies or some other castable mounting material must be used. Edge preservation of copper and copper alloy specimens can be accomplished by the same methods used for specimens of other metals (see the article “Mounting of Specimens” in this Volume). It can also be done by plating with a hard metal or by the use of co-mounted samples of similar composition.

Grinding. Wet grinding is preferred for all coppers and copper alloys. Common practice involves rough grinding the specimen surface to remove metal that has been cold worked, then finish grinding to obtain a suitable surface. Finish grinding is performed using flat wheels and silicon carbide papers of progressively finer grit—usually 240, 320, 400, and 600. Ultrafine 800- and 1200-grit papers are sometimes used.

Rough Polishing. Most coppers and copper alloys are relatively soft and thus require cutting with minimum rubbing. Rough polishing should be performed using diamond-impregnated nylon cloth. Duck canvas, wool broadcloth, and cotton (listed in order of decreasing preference) are also used for polishing.

The preferred abrasive for rough polishing on any of the cloths mentioned previously is 1 to 9 μm diamond paste. A wheel speed of approximately 200 rpm is generally recommended.

Fine Polishing. Generally, napped cloths are preferred for fine polishing. The abrasive is usually 0.3 μm α-Al_2O_3 or 0.05 μm γ-Al_2O_3; both abrasives are used with water as a vehicle. Other abrasives that have proved satisfactory for fine polishing are colloidal silica (SiO_2) and fine diamond paste. Recommended wheel speed is 120 to 150 rpm.

Specimen rotation during polishing elicits numerous opinions. Hand polishing necessitates developing a personal technique that may require a degree of manual dexterity; mechanical polishing gives more reproducible results and is preferred. Examples of different methods of hand polishing that produce artifact-free or nearly artifact-free results are given in Fig. 55(a) to (d) (Ref 9).

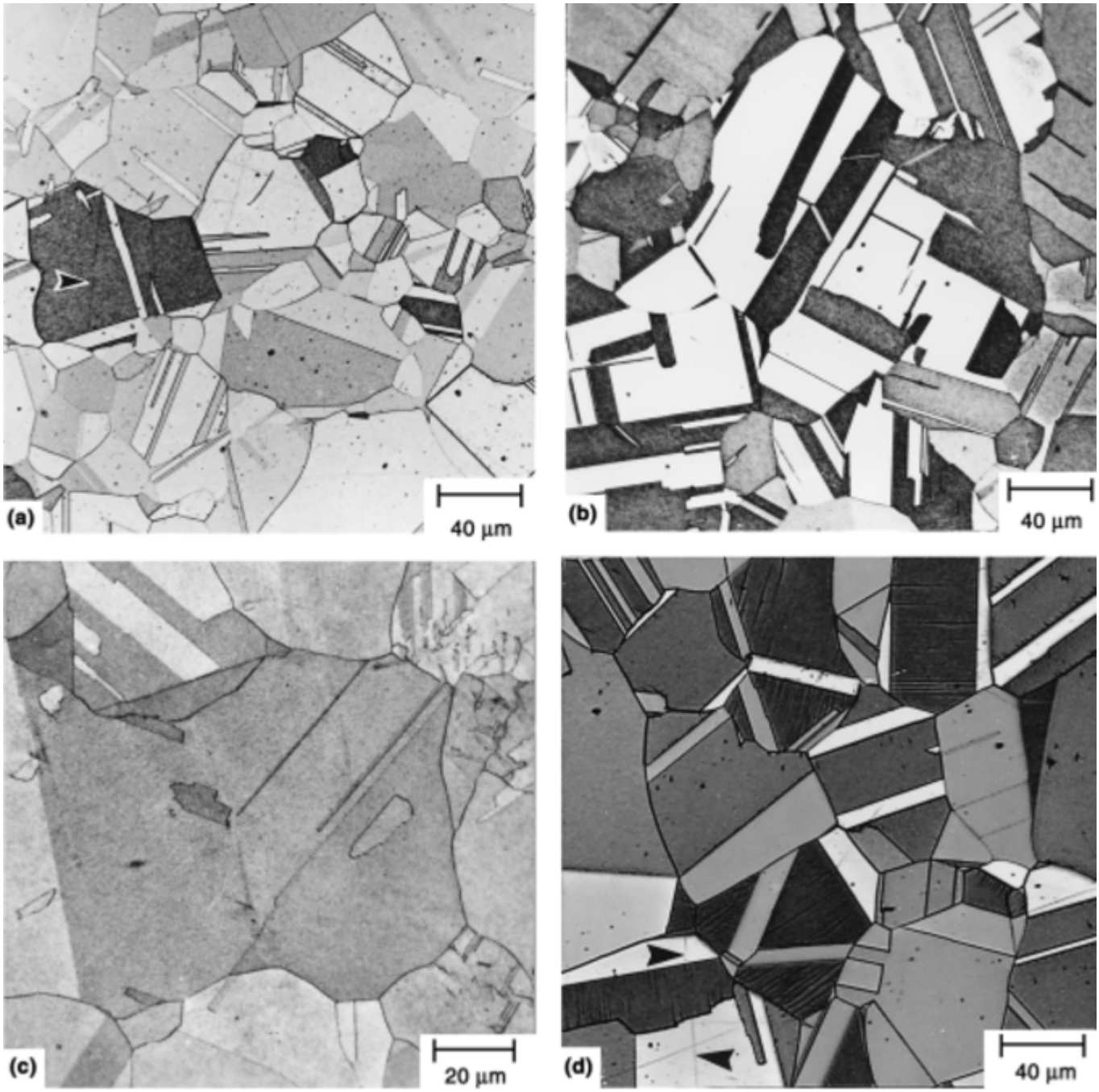

Fig. 55 Examples of artifact-free or nearly artifact-free surfaces produced by different manual final polishing methods on 30% Zn annealed brass (similar to C26000). (a) Polished manually using 0.1 µm grade polycrystalline diamond abrasive. Etched in a ferric chloride reagent. (b) Polished manually by skidding on a thick slurry of magnesium oxide abrasive. Etched in a ferric chloride reagent. (c) Polished as for (b); etched in a high-sensitivity sodium thiosulfate reagent. (d) Manually polished with colloidal silica (1% ferric nitrate solution added) using repeated polish-etch cycles. Etched in Klemm's No. 1 reagent. The arrows in (a) and (d) indicate scratch-trace etch markings. (d) Courtesy of G.F. Vander Voort, Buehler Ltd. Source: Ref 9

After polishing, the specimen is rinsed in water and dried with warm air. Automated polishing (usually vibratory) is efficient for polishing copper alloys, especially when a large number of specimens must be prepared. Attack polishing (combined polishing and etching) using ferric nitrate ($Fe(NO_3)_3$) or ammonium hydroxide/ammonium persulfate (NH_4OH and $(NH_4)_2S_2O_8$) solution can be more safely performed using automatic equipment than by hand. An example of the grain relief that is created if the time duration of the etch-polish cycle is not properly rationed is given in Fig. 56 (Ref 9).

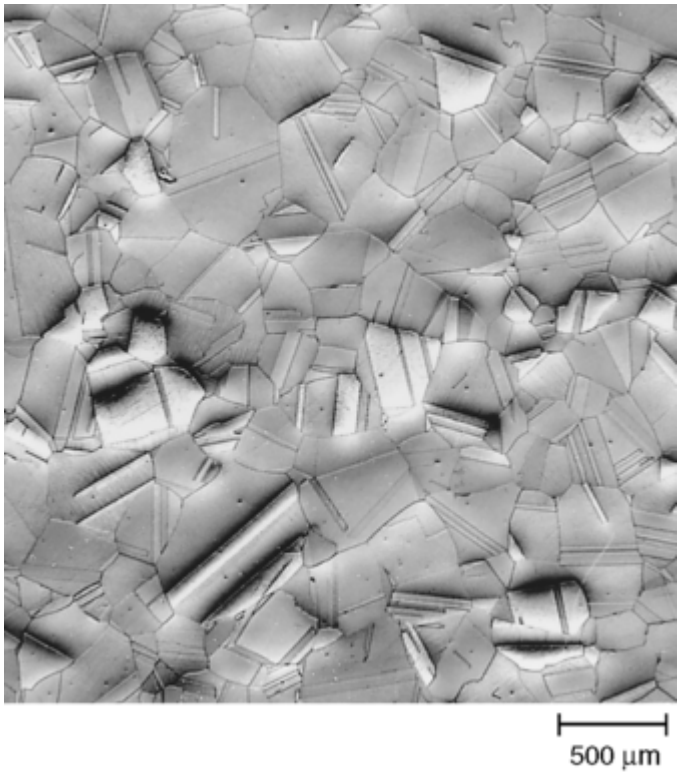

Fig. 56 An example of the manual polish-etch technique as used in Figure 55(d) on 30% Zn annealed brass (similar to C26000) but with inadequate time for polishing, as compared to etch time during each cycle. An excessive degree of relief has developed between the grains. This effect is enhanced by oblique illumination. 20×. Courtesy of G.F. Vander Voort, Buehler Ltd. Source: Ref 9

Electrolyte polishing of coppers and copper alloys alleviates many of the difficulties encountered in mechanical polishing. Additional information is available in the article “Chemical and Electrolytic Polishing” in this Volume.

Apart from offering the usual advantages over mechanical polishing of saving time, minimizing the human variable, and minimizing artifacts resulting from disturbed metal, electrolytic polishing offers some advantages for copper and copper alloys:

- It is excellent for revealing grain size and shape on all sides of specimens.
- It is especially well adapted to use on single-phase copper alloys.
- It reveals true microstructure with less difficulty than mechanical polishing.

Disadvantages of electrolytic polishing for copper and copper alloys include:

- Different rates of attack cause some phases of multiphase alloys to stand out in relief.
- The edge effect of electrolytic polishing, whereby edges of specimens are attacked and polished more than other areas, limits application of the process to examination of surfaces in from the edges.
- It will round edges of cracks and pores.
- Attack around nonmetallic particles, voids, and inclusions in the specimen may occur at a more rapid rate than attack of the matrix, and so the size of voids or inclusions may be exaggerated.
- Because it changes surface topography, it should not be used for failure analysis or image analysis.

Table 4 lists compositions of some electropolishing solutions, together with electropolishing conditions that have proved satisfactory for the coppers and copper alloys shown in the last column in the table. The durations listed in Table 4 are generally based on conditions where electrolytic polishing completely replaces mechanical polishing. Useful results may be obtained when mechanical polishing is followed by electrolytic polishing. Durations for electrolytic polishing are then always under 1 min.

Table 4 Electrolytes and conditions for electrolytic polishing of copper and copper alloys

Composition	Voltage, V_{dc}	Current density		Cathode	Duration	Copper or copper alloy
		A/cm^2	**A/in.^{2}**			
1. 825 mL H_3PO_4 and 175 mL H_2O	1.0–1.5	0.02–0.1	0.13–0.65	Copper	10–40 min	Unalloyed copper
2. 250 mL H_3PO_4, 250 mL ethanol, 50 mL propanol, 500 mL distilled H_2O, 3 g urea	3–6	0.4–0.8	2.6–5.2	Stainless steel	50 s	Coppers and copper alloys
3. 700 mL H_3PO_4 and 350 mL H_2O	1.2–2.0	0.06–0.1	0.39–0.64	Copper	15–30 min	Coppers; α, β, and α-β brasses; aluminum; silicon; tin; phosphor bronzes; beryllium; iron-lead; or chromium
4. 580 g $H_4P_2O_7$ and 1000 mL H_2O	1.2–1.9	0.08–0.12	0.05–0.77	Copper	10–15 min	Coppers, brasses
5. 300 mL HNO_3 and 600 mL methanol	20–70	0.65–3.1	4.2–20.0	Stainless steel	10–60 s	Coppers, brasses
	30–50	2.5–3.1	16.1–51.0	Stainless steel	5–10 s	Silicon bronze, phosphor bronze
6. 170 g CrO_3 and 830 mL H_2O	1.5–12	0.95–2.2	6.1–14.2	Stainless steel	10–60 s	Brasses
7. 400 mL H_3PO_4 and 600 mL H_2O	1.0–2.0	0.06–0.15	0.39–0.97	Copper or stainless steel	1–15 min	α, α-β brasses, copper-iron, copper-chromium
8. 30 mL HNO_3, 900 mL methanol, 300 g $Cu(NO_3)_2$ (cupric nitrate)	45–50	1.05–1.25	6.77–8.1	Stainless steel	15 s	Bronzes (have tendency to etch)
9. 670 mL H_3PO_4, 100 mL H_2SO_4, 300 mL distilled H_2O	2–3	0.1	0.64	Copper	15 min	Copper; copper-tin containing up to 6% Sn
10. 470 mL H_3PO_4, 200 mL H_2SO_4, 400 mL distilled H_2O	2–2.3	0.1	0.64	Copper	15 min	Copper-tin up to 9% Sn
11. 350 mL H_3PO_4 and 650 mL ethanol	2–5	0.02–0.07	0.13–0.45	Copper	10–15 min	Copper alloys with high lead (to 30%)
12. 540 mL H_3PO_4 and 460 mL H_2O	2	0.065–0.075	0.4–0.5	Copper	5–15 min	Copper
	2–2.2	0.1–0.15	0.64–0.97	Copper	15 min	Nickel silver

Reference 10 contains extensive appendixes of macroetchants, microetchants, and polishing solutions.

Examination of As-Polished Specimens. As-polished specimens of coppers and copper alloys are frequently examined metallographically. Characteristics revealed include the presence of oxide in copper, lead particles in leaded brass and bronze, intermetallic phases in the precipitation-hardened alloys, oxides, phosphides, sulfides, and corrosion products. Specimens are also examined under polarized light to differentiate cuprous oxide (Cu_2O) inclusions from other inclusions. Under polarized light, only the Cu_2O inclusions appear ruby red; under white light, copper oxide and other inclusions appear blue-gray. Oxides of arsenic and antimony also are optically active under polarized light. As-polished specimens are used also for scanning electron microscopic examination.

Chemical Etching. Table 2 lists chemical etchants that are used for coppers and copper alloys and includes etching procedures and the alloys to which each etchant is commonly applied. The ammonium

hydroxide/hydrogen peroxide/water solution (etchant 1, Table 2) is by far the most widely used etchant. It is probably optimal for routine work and applies to most coppers and copper alloys. This etchant was used for many of the specimens shown in the micrographs in this article. This etchant is also widely used for determining the inclusion content of brass and bronze strip.

The potassium dichromate/sulfuric acid/sodium chloride/water etchant (usually referred to simply as potassium dichromate, $K_2Cr_2O_7$; see etchant 4 in Table 2) is also used extensively, especially for revealing structures of welded and brazed joints.

Chromic acid (H_2CrO_4, etchant 5 in Table 2) is also prevalent. It is formed when chromium trioxide (CrO_3) is dissolved in water. The other etchants listed in Table 2 have limited uses, although some are used for the same alloys and structures as the etchants discussed previously.

Electrolytic etching reveals cold-worked structures of brasses, gives contrast to β phase in brass, and, in copper-nickel alloys, reduces the contrast due to coring that usually appears with chemical etching. It is also used to bring out the general structure of beryllium-copper, cartridge brass, free-cutting brass, aluminum bronze, nickel silver, and admiralty metal. Table 5 lists five electrolytes that have proved successful for electrolytic etching.

Table 5 Electrolytes and operating conditions for electrolytic etching of copper and copper alloys

Composition	Operating conditions[(a)]	Copper or copper alloy
1. 5–14% H_3PO_4 (8%) and bal H_2O	Voltage range, 1–8; etching time, 5–10 s	Coppers, cartridge brass, free-cutting brass, admiralty, gilding metal
2. 250 mL 85% H_3PO_4, 250 mL 95% ethanol, 500 mL H_2O, 2 mL wetting agent	Voltage range, 1–3; current density, 0.1–0.15 A/cm^2 (0.64–0.97 A/in.^{2}); etching time, 30–60 s	Coppers
3. 30 g $FeSO_4$ (ferrous sulfate), 4 g NaOH, 100 mL H_2SO_4, 1900 mL H_2O	0.1 A at 8–10 V for 15 s; do not swab surface after etching	Darkens β phase in brasses and gives contrast after H_2O_2-NH_4OH etch; also for nickel silver and bronzes
4. 1 mL CrO_3 and 99 mL H_2O	6 V; aluminum cathode; etching time, 3–6 s	Beryllium-copper and aluminum bronze
5. 5 mL acetic acid (glacial), 10 mL HNO_3, 30 mL H_2O	Voltage range, 0.5–1; current density, 0.2–0.5 A/cm^2 (1.3–1.9 A/in.^{2}); etching time, 5–15 s	Copper-nickel alloys; avoiding contrast associated with coring

(a) Voltages are direct current

Examination for Inclusions. Microscopic examination has become increasingly valuable for evaluating the fabrication characteristics of certain copper alloys, particularly brass and bronze sheet and strip. A correlation exists between the number of inclusions present, as well as their length and distribution, and fabrication characteristics, especially formability. Inclusions are best revealed by swabbing the specimen quickly with NH_4OH/H_2O_2 (etchant 1, Table 2), then washing it in running water and drying with an air blast. In Fig. 57, the C26800 yellow brass with abnormally high sulfur content (0.02%) in (a) is lightly etched to reveal the zinc sulfide stringers. The image of a normally etched specimen is seen in (b), which is appropriate to develop the contrast required for grain size and constituent volume fraction measurements.

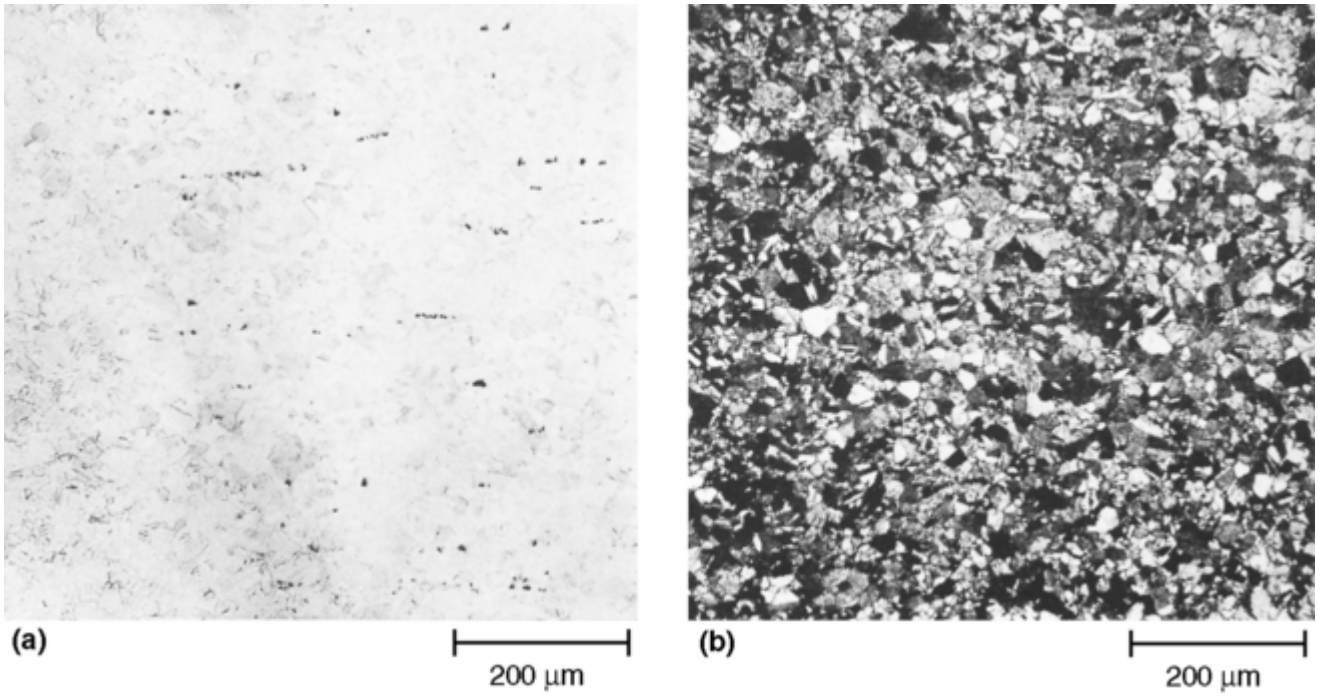

Fig. 57 Alloy C26800 with abnormally high sulfur content (0.02%). (a) Specimen is lightly etched with NH_4OH/H_2O_2 (etchant 1, Table 2) to expose the zinc sulfide stringers. (b) Same specimen is etched in the normal manner to reveal grain contrast, but the zinc sulfide stringers are then concealed. Etchant 1, Table 2. 75×

Sources of Micrographs. The Copper Development Association has a collection of micrographs of copper alloys at their Web site. The ASM Micrograph Center Web site contains a compendium of micrographs that supplements those illustrated in this article. The Copper Development Association has provided a number of micrographs in this collection.

References cited in this section

1. G. Joseph, *Copper, Its Trade, Manufacture, Use, and Environmental Status,* ASM International, 1999

9. L.E. Samuels, *Metallographic Polishing by Mechanical Methods,* 4th ed., ASM International, 2003

10. G.F. Vander Voort, *Metallography: Principles and Practice,* McGraw-Hill, 1984, reprinted by ASM International, 1999

Revised by R.N. Caron, R.G. Barth, and D.E. Tyler, Metallography and Microstructures of Copper and Its Alloys, *Metallography and Microstructures,* Vol 9, *ASM Handbook,* ASM International, 2004, p. 775–788

Metallography and Microstructures of Copper and Its Alloys

>Revised by R.N. Caron, R.G. Barth, and D.E. Tyler, Olin Brass, Division of Olin Corporation

---

References

1. G. Joseph, *Copper, Its Trade, Manufacture, Use, and Environmental Status,* ASM International, 1999

2. M. Tisza, *Physical Metallurgy for Engineers,* ASM International and Freund Publishing House, Ltd., 2001

3. T.B. Malssalski, Ed., *Binary Phase Diagrams,* ASM International, 1990

4. T.F. Bower and D.A. Granger, "Copper and Copper Alloy Ingot Structure—A Preliminary Survey," Report 70-34, The Casting Laboratory, Cleveland, 1970

5. *Alloy Phase Diagrams,* Vol 3, *ASM Handbook,* ASM International, 1992, p 2, 178

6. A. Cibula, "Review of Metallurgical Factors Influencing the Quality of Copper and Copper Alloy Casting," BNFRMRA International Conference on the Control of the Composition and Quality of Copper and Copper Alloy Casting for Fabrication, Oct 1967 (Düsseldorf)

7. G.L. Bailey and W.A. Baker, "Melting and Casting of Non-Ferrous Metals," Monograph and Report Series 6, Institute of Metals, London, 1949

8. A. Tomer, *Structure of Metals through Optical Microscopy,* ASM International, 1991

9. L.E. Samuels, *Metallographic Polishing by Mechanical Methods,* 4th ed., ASM International, 2003

10. G.F. Vander Voort, *Metallography: Principles and Practice,* McGraw-Hill, 1984, reprinted by ASM International, 1999

Metallography and Microstructures of Lead and Its Alloys, *Metallography and Microstructures,* Vol 9, *ASM Handbook,* ASM International, 2004, p. 789–800

Metallography and Microstructures of Lead and Its Alloys

Introduction

LEAD AND LEAD ALLOY specimens are prepared for metallographic examination in a similar fashion as other metals (see the Section "Metallographic Techniques" in this Volume), but the softness of the material presents challenges. Lead and lead alloys are so soft (25 to 40 HV hardness) that considerable surface flow or distortion occurs during grinding and polishing. If not removed, the distorted layer obscures the true structure of the specimen. In addition, the deformation and heating caused by the preparation can be sufficient to develop a pseudostructure (recrystallization) in the specimen. Abrasives used for polishing are easily embedded into the lead. It is essential, therefore, to employ techniques that minimize these effects in sample preparation.

Metallography and Microstructures of Lead and Its Alloys, *Metallography and Microstructures,* Vol 9*, ASM Handbook,* ASM International, 2004, p. 789–800

Specimen Preparation

Sectioning. Because lead and lead alloys are so soft, specimens can be extracted from large masses by any of several processes, including cutting with a knife or with a microtome, sawing, shearing, and machining. If specimens are cut by manual or power sawing, a coolant, such as water or methanol, should be used to minimize buildup of frictional heat.

A conventional metallurgical cutoff machine is the preferred means of extracting specimens from the larger mass of material. Liquid coolants minimize the possibility of overheating. The cutoff wheels in such machines produce specimens with surfaces that often are smooth enough to require only light grinding and polishing prior to microexamination.

Lead storage batteries account for approximately 75% of lead alloy use (Ref 1). In order to study lead in this application, with corrosion products preserved as in Fig. 1, embedding the sample in resin prior to polishing is recommended (Ref 2). Encapsulating the sample prior to sectioning is suggested in Ref 3.

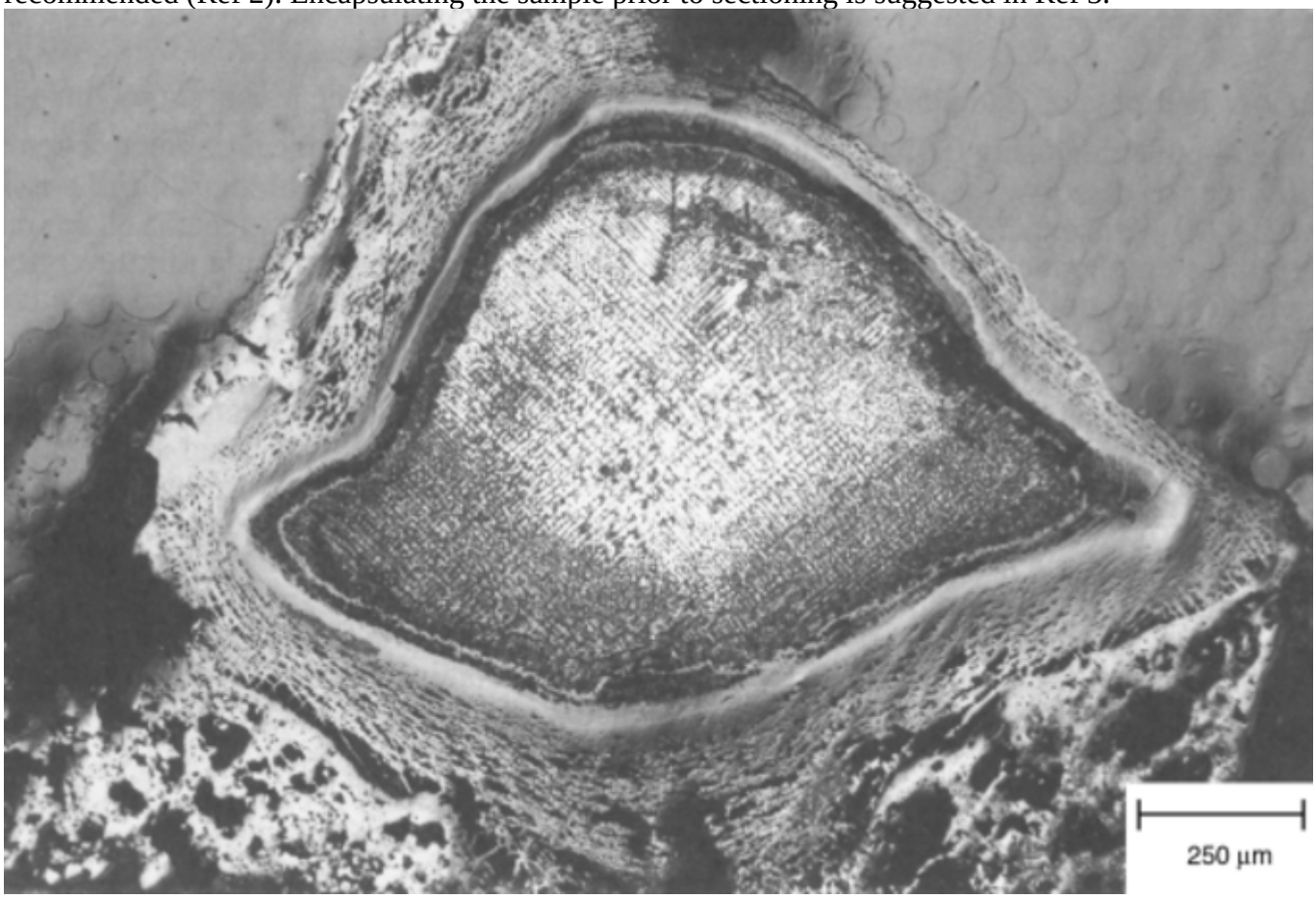

Fig. 1 Corroded Pb-3Sb battery grid. To preserve oxides and sulfate layers, the grid was embedded in resin prior to polishing. Classical etching would reveal the metal structure but destroy corrosion. A very long final mechanical polish, with 0.05 µm alumina and chemical etching for just 1 s using acetic acid/hydrogen peroxide, distinguishes the dark oxide from the clear, nonattacked sulfate. Source: Ref 2

Mounting. Specimens can be ground and polished unmounted, but usually it is more convenient to mount them. Mounting techniques using thermoplastic or thermosetting resins are not suitable for mounting lead and lead alloys, because these mounting materials require heat and pressure. The required mounting pressure deforms

the specimen, and the heat will cause recrystallization. Therefore, the specimen should be mounted in materials that can be cast and subsequently cured at room temperature. The materials and the techniques for using them are described in the article “Mounting of Specimens” in this Volume.

Grinding. If the specimen to be examined has been extracted with an abrasive cutoff wheel or by turning on a lathe, grinding prior to polishing and etching may not be necessary. Lathe turning using cryogenically treated and then polished cemented carbide inserts allows lead samples to be immediately polished either chemically or mechanically. Immediate polishing is recommended to prevent recrystallization from turning into induced strains (Ref 4).

Grinding is also not necessary for specimens that have been cut on a microtome. Using a sharp microtome and the proper technique, it is possible to remove from the specimen several layers (shavings) of material approximately 1 to 5 μm thick. The smooth cut obtained with a microtome leaves a surface that has minimum distortion and that can be polished without having been ground. Specimens with uneven and severely distorted surfaces, such as those produced by sawing, usually require grinding, which can be done automatically, by machine or by hand.

Automatic grinding of lead and lead alloys is accomplished using mounted specimens, which are loaded into a ring sample holder. These holders accommodate several specimens at once, and each specimen in the ring receives identical treatment. Specimens are wet ground using 320-, 400-, and 600-grit silicon carbide papers in sequence, with water as the lubricant. Grinding times are usually 3 min per step for this method. The specimens and the ring holder should be thoroughly cleaned—preferably ultrasonically—between each grinding step.

In machine grinding, fresh abrasive and abundant liquid (usually water) on the grinding belt or wheel, especially during grinding with finer abrasives, must be used to prevent abrasive particles from becoming embedded in the lead specimen. Machine grinding can be done with a belt-type machine or with a disk grinder using 120-grit silicon carbide paper as the abrasive. Then the specimen should be wet ground (preferably on a disk grinder) using silicon carbide papers of progressively finer sizes through approximately 400 grit.

Hand grinding can be performed on abrasive papers lubricated with a saturated solution of paraffin in kerosene and backed by a glass plate. Water is sometimes used as a lubricant instead of paraffin in kerosene. With proper technique, hand grinding is less likely to embed abrasive particles in the specimen surface than is machine grinding.

In hand grinding, the specimen is held with firm pressure and drawn with an even, smooth stroke from the top to the bottom of the abrasive paper. At the completion of the stroke, the specimen is lifted, replaced at the top of the abrasive paper, and again drawn down the length of the paper. It is important not to use a back-and-forth motion, which will smear the specimen surface excessively and increase the probability that abrasive particles will become embedded in the specimen and that the specimen surface will have a high center. During grinding, it is essential that the specimen and the paper be cleaned frequently to remove loose particles of abrasive that may become embedded in the specimen.

Polishing. Specimens that have been ground on automatic equipment may be polished using a similar technique. The specimens, loaded in a ring holder, are rough polished using 9 μm diamond on a canvas cloth, then 1 μm alumina on a rayon cloth. Final polishing is performed with 0.5 μm cerium oxide (CeO_2) on a rayon cloth, followed by colloidal silica on a rayon cloth. Times of approximately 3 min per step are sufficient, and the specimens should be cleaned between each step. After polishing with colloidal silica, specimens are removed from the ring holder and vibratory polished using colloidal silica on rayon cloth for 20 min. If a layer of disturbed metal has formed on the specimen surface during grinding, it can be removed by deep chemical etching using a mixture of glacial acetic acid and 30% hydrogen peroxide (H_2O_2) or a mixture of aqueous solutions of ammonium molybdate [$(NH_4)_2MoO_4$] and nitric acid (HNO_3) (see etchants 3 and 4 in Table 1). The specimen is usually etched to remove the deformed metal before polishing.

Table 1 Recommended etchants and procedures for macroscopic and microscopic examination of lead and lead alloys

Etchant	Composition (parts are by volume)	Procedure	Use
1	1 part acetic acid (glacial) 1 part nitric acid (conc) 4 parts glycerol	Use freshly prepared solution at 80 °C (176 °F); discard after use. For macroetching: etch several minutes, rinse in water. For microetching: etch several seconds. For best results, alternate etching with polishing.	Macroetching of lead; development of microstructures and grain boundaries in lead, and in lead-calcium, lead-antimony, and lead-tin (low-tin) alloys
2	100 parts acetic acid (glacial) 10 parts H_2O_2 (30%)	Etch for 10–30 min, depending on the depth of the disturbed layer. Dry and clean with concentrated nitric acid if required.	Microetching of lead-antimony alloys containing up to 2% Sb
3	3 parts acetic acid (glacial) 1 part H_2O_2 (30%)	Etch by immersing specimen in solution for 6–15 s. Dry with alcohol.	Microetching of lead, lead-calcium alloys, and lead-antimony alloys containing more than 2% Sb. Also removes disturbed metal
4	Solution A: 15 g $(NH_4)_2MoO_4$ 100 mL distilled H_2O Solution B: 6 parts nitric acid (conc) 4 parts distilled H_2O	Mix equal quantities of solutions A and B. Etch by alternately swabbing specimen and washing in running water.	Macroetching of lead. A very rapid etchant; well suited for removing thick layers of disturbed metal from specimens
5	3 parts acetic acid (glacial) 4 parts nitric acid (conc) 16 parts distilled H_2O	Use freshly prepared solution at 40–42 °C (104–108 °F). Immerse specimen for 4–30 min until disturbed layer is removed. Clean with cotton in running water.	Microetching of unalloyed lead, and lead-tin alloys containing up to 3% tin
6	2 parts acetic acid (glacial) 2 parts nitric acid (conc) 2 parts H_2O_2 (30%)	Etch for 2–10 s by swabbing. Rinse specimen in running water and dry with alcohol.	Macroetching of unalloyed lead, and of lead-bismuth, lead-tellurium, and lead-nickel alloys

	5 parts distilled H_2O		
7	1 part nitric acid (conc) 1 part distilled H_2O	Etch for 5–10 min by immersion. If thick layer of disturbed metal is to be removed, solution can be heated to boiling. Rinse in running water, rinse in alcohol, and dry.	Developing macrostructure of welds and laminations in lead products
8	Solution A: 10% aqueous solution of $(NH_4)_2S_2O_8$ Solution B: 30% aqueous solution of tartaric acid	Mix 5 mL of solution A with 2 mL of solution B. Swab specimen for 5–10 s. Rinse in running water.	Microetching to distinguish cuboidal antimony-tin phase from antimony-rich phases in lead-antimony-tin alloys such as bearing alloys or type metals. Solution A blackens antimony-tin phase; solution B etches antimony-rich phases.
9	6 parts $HClO_4$ (70%) 4 parts H_2O	Immerse specimen (anode) in electrolyte; cathode is platinum spiral. Etch 45–90 s at 6 V, 4 A.	Electrolytic etching of lead-antimony alloys containing more than 2% Sb
10	1 part HCl (conc) 9 parts H_2O	Same as for etchant 9	Same as for etchant 9
11	1 part $(NH_4)_2MoO_4$ (ammonium molybdate) 1 part citric acid 10 parts distilled H_2O	…	…

For mechanical polishing, a felt wheel using a water suspension of 0.3 μm alumina (Al_2O_3) as the abrasive is adequate. Polishing must be done with light pressure, using clean polishing cloths to prevent extraneous materials from becoming embedded in the soft lead surface. Final polishing, if required, is generally done on a 120 rpm wheel using 0.05 μm Al_2O_3 suspended in water as the abrasive.

Etch-polishing is recommended for all lead and lead alloy specimens, especially for the softer lead-base metals such as unalloyed lead and low alloys of tin, bismuth, and antimony. Etch-polishing consists of alternately etching and polishing until a bright, lustrous, scratch-free surface is obtained. The specimen is then rinsed in water, dipped in a warm solvent such as ethanol, methanol, or acetone, and dried in forced air.

Electropolishing produces good results, especially for unalloyed lead. It is not used if the mircosections contain porosity or corrosion (Ref 3).

The use of an electrolyte consisting of 3 parts glacial acetic acid and 1 part 60% perchloric acid ($HClO_4$) with a copper cathode and a current density of 100 to 200 A/cm^2 (650 to 1300 A/in.^{2}) for 3 to 5 min is recommended in Ref 2. To avoid the hazard of using this electrolyte (mixtures of $HClO_4$ and acetic acid can be explosive), 60% $HClO_4$ without the acetic acid can be used; however, $HClO_4$ is a very strong acid, and precautions should be taken in its use.

Another method uses a mixture of perchloric acid and ethanol at -50 °C (-58 °F), 20 V, and 0.1 to 0.2 A/cm^2 (0.6 to 1.3 A/in.^{2}) (Ref 2). This is followed by etching at room temperature.

Etching. Table 1 lists compositions of the etchants most often used for macroetching and microetching of lead and lead alloy specimens. Etching procedures and specific uses for the various etchants are also included in Table 1. All but two of these etchants are used by immersing or swabbing the specimen; only etchants 9 and 10 are used for electrolytic etching.

Primarily because lead and lead alloys smear so easily, etch-polishing alternated with examination under the microscope is required. Sometimes, several cycles of polishing, etching, and examination are necessary, requiring much skill and patience. In addition to smearing, lead and lead alloys are susceptible to tarnishing (or blackening) during etching. One or two light turns on the final polishing wheel, followed by flushing of the specimen with water, rinsing in warm ethanol or methanol, and drying in warm air, will often remove this tarnish and reveal the true structure. Discoloration from overetching or oxidation or both can sometimes be removed by lightly swabbing the specimen with a 2 to 3% aqueous solution of ethylenediamine tetraacetic acid disodium salt.

The tarnishing of the lead in the polishing operation can be used to differentiate between various phases in such commercially important alloy systems as antimonial lead and lead-tin solders. With such alloys, polishing often causes the lead matrix to blacken, whereas the secondary antimony or tin-rich phases remain bright.

References cited in this section

1. Lead Development Association International, web site, London, U.K., 2004

2. J.P. Hilger, Developments in Metallography of Lead and Lead Alloys, *MC95 International Metallography Conference Proceedings,* ASM International, 1996, p 229

3. K.H. Ednie, Metallographic Preparation of Soft Materials-Lead Alloys, *MC95 International Metallography Conference Proceedings,* ASM International, 1996, p 193

4. J. Yewko and D. Marshall, Lead Metallography Made Easy, *Adv. Mater. Process.,* Vol 153 (No. 2), 1998, p 22–23

Metallography and Microstructures of Lead and Its Alloys, *Metallography and Microstructures,* Vol 9, *ASM Handbook*, ASM International, 2004, p. 789–800

Microscopic Examination

Microscopic examination of lead and lead alloys is normally done by conventional reflected-light techniques using bright-field illumination. Polarized light can be used for contrasting phases in lead alloys (Fig. 2), particularly when the specimen contains particles of hard intermediate phases such as antimony-tin, tin-arsenic, or lead-tellurium. However, these phases can be easily identified by bright-field microscopy. No particular use is made of dark-field illumination.



Fig. 2 High-purity lead (99.99% Pb), as-cast. Transverse section through a pig showing large equiaxed and columnar grains. Large grains result from the absence of grain-nucleating impurities and alloying elements (such as copper). Ammonium molybdate reagent. Actual size

If the need exists, specialized microscopic techniques can be used to advantage for studying the structure of lead alloys. For example, replica electron microscopy has been used to study the nucleation of precipitates that occurs during aging of the supersaturated solid solutions of antimony in lead.

The scanning electron microscope and the microprobe microanalyzer have proved to be valuable tools in the structural analysis of lead alloys. The microprobe, because it can quantitatively describe constituents, is particularly helpful in identifying the phases that occur in complex alloys such as Pb-Sn-Sb-As and Pb-Bi-Sn-Cd.

Metallography and Microstructures of Lead and Its Alloys, *Metallography and Microstructures,* Vol 9, *ASM Handbook,* ASM International, 2004, p. 789–800

Microstructures of Lead and Lead Alloys

Lead alloys for which micrographs are shown in this section can be grouped into five alloy systems: lead-calcium (with and without tin), lead-copper, lead-tin (with and without silver), lead-antimony, and lead-antimony-tin (with and without arsenic or copper). For information on the uses and properties of these alloys,

see the article “Lead and Lead Alloys” in *Properties and Selection: Nonferrous Alloys and Special-Purpose Materials*, Volume 2 of *ASM Handbook*, formerly 10th edition *Metals Handbook*, 1990.

Lead-Calcium. An alloy with approximately 0.04% Ca is shown in Fig. 3 and 4. At 300 °C (570 °F), approximately 0.06% Ca is soluble in lead, but at room temperature, the solubility drops to approximately 0.01%, causing intragranular precipitation of rods of Pb_3Ca (Fig. 5). If solidified slowly enough, lead alloys containing more than approximately 0.07% Ca also show primary Pb_3Ca, which appears as cubes or star-shaped dendrites (Fig. 6, 7a and b). Small additions of tin to dilute lead-calcium alloys cause the formation of a Pb-Ca-Sn phase, which precipitates as acicular particles at grain boundaries (Fig. 8a and b, 9a and b).

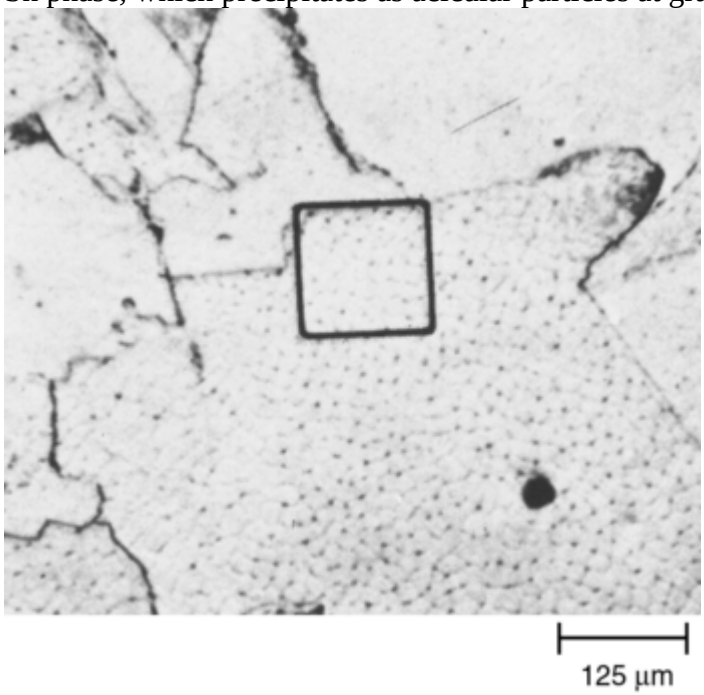

Fig. 3 Pb-0.044Ca, etched in 5 parts acetic acid, 1 part 30% H_2O_2, then in ammonium molybdate reagent. See Fig. 4 for a close-up view of area in square. Original magnification 92×

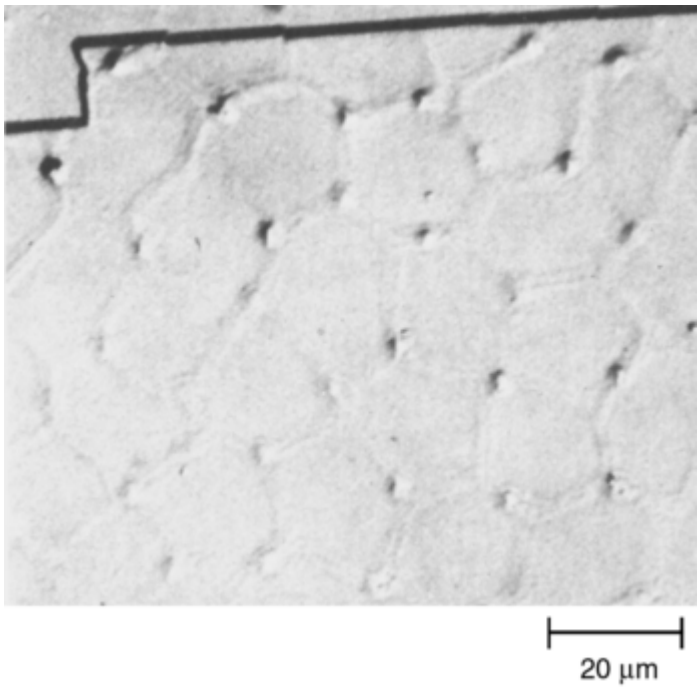

Fig. 4 Magnified view of area outlined by square in Fig. 3. The mosaic pattern and the pits in the grains resulted from overetching with the ammonium molybdate reagent used in Fig. 3. Original magnification 600×

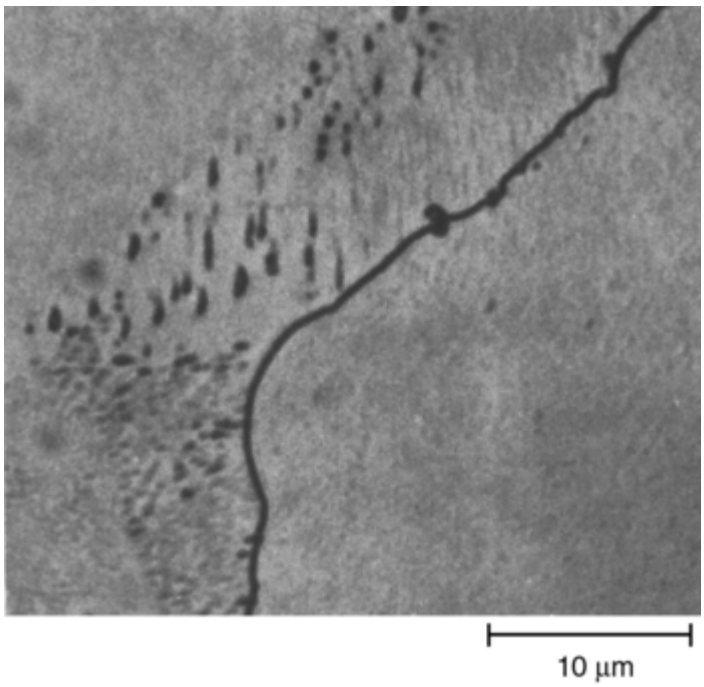

Fig. 5 Pb-0.058Ca. Small particles of Pb_3Ca phase (dark) that precipitated near a grain boundary. 5 parts acetic acid, 1 part 30% H_2O_2, then in ammonium molybdate reagent. Original magnification 1825×

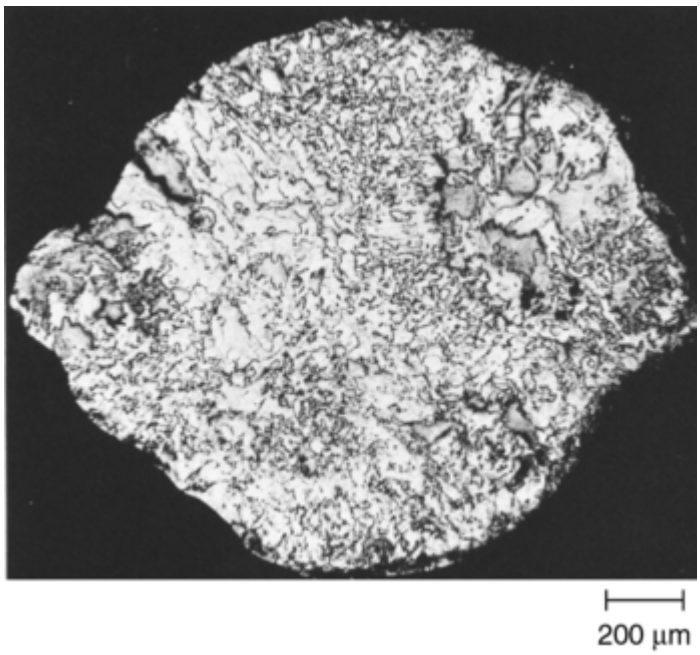

Fig. 6 Pb-0.08Ca, as-cast. Section through a cross-member wire of a battery grid (parting line horizontal) showing fine grain structure. See Fig. 7(a) and (b) for details of the structure in a similar lead alloy. 15 g citric acid + 9 g ammonium molybdate in 80 mL H_2O. Original magnification 50×

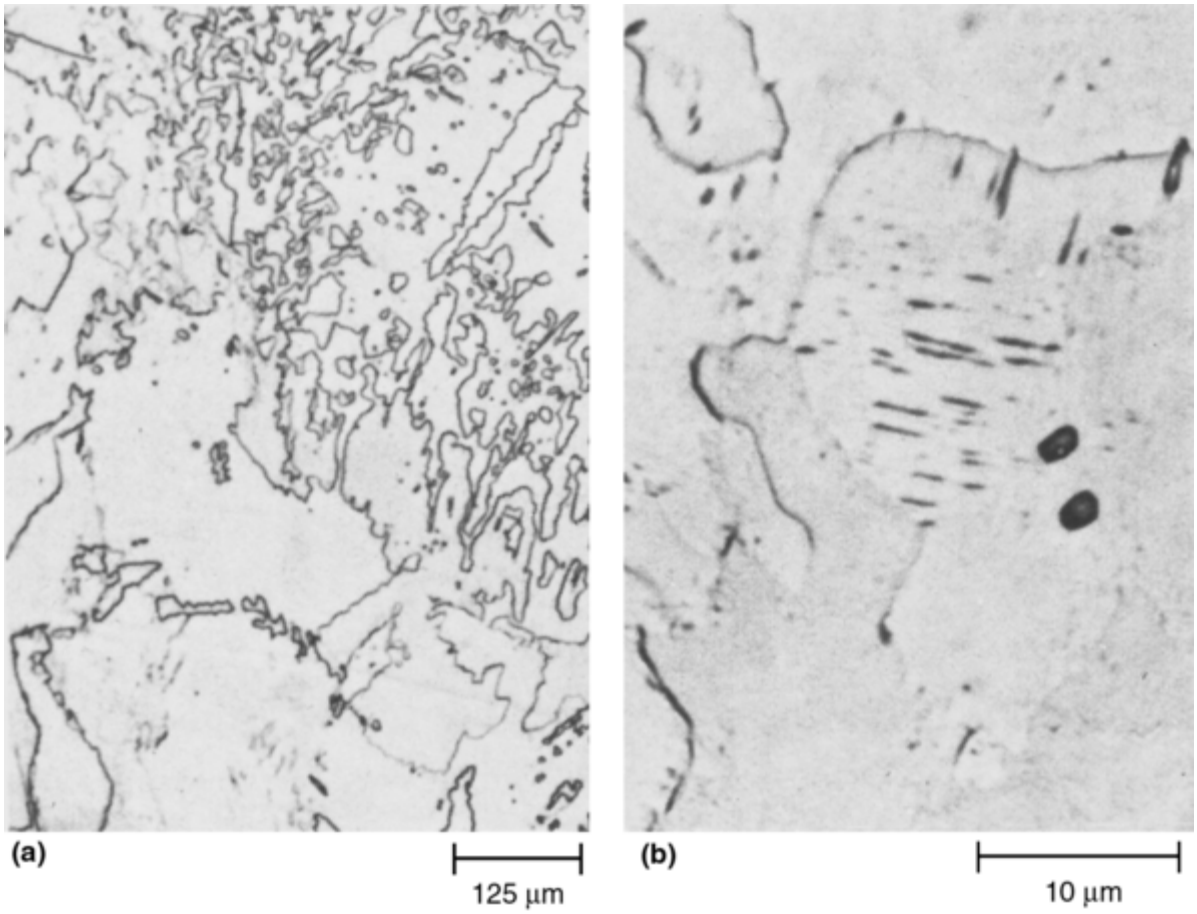

Fig. 7 Pb-0.083Ca. A higher calcium content than in Fig. 6 results in smaller grains. Fine Pb_3Ca precipitate (dark) is recognizable in (b). 15 g citric acid + 9 g ammonium molybdate in 80 mL H_2O. (a) Original magnification 92×. (b) Original magnification 1825×

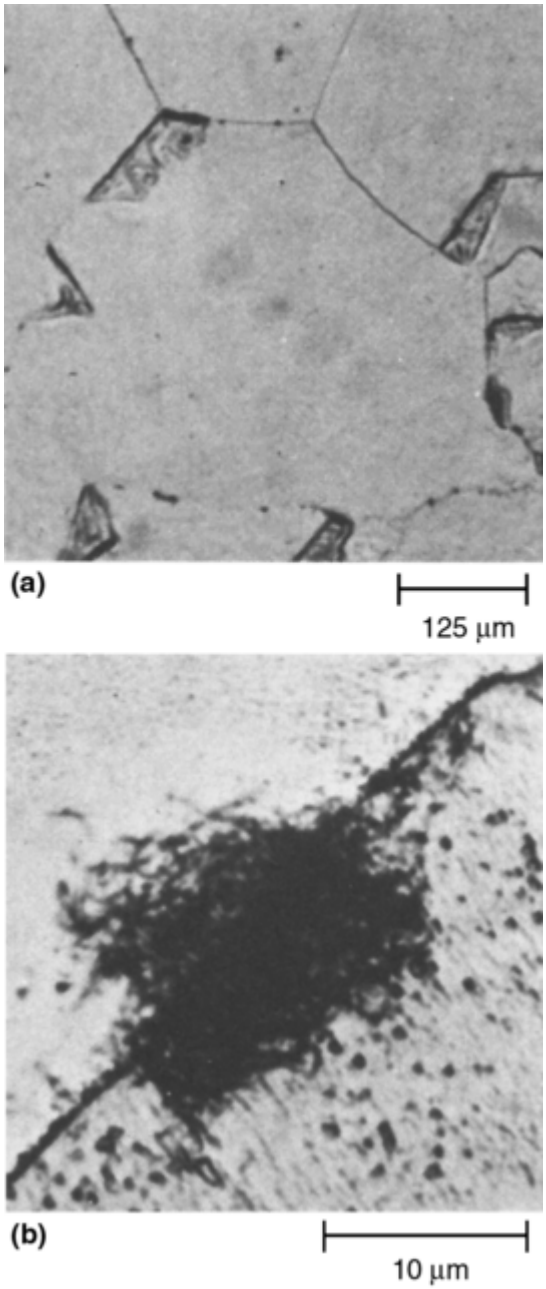

Fig. 8 Pb-0.045Ca-0.46Sn. Large grains, similar in size to those of the lead-calcium alloy shown in Fig. 3. 5 parts acetic acid, 1 part 30% H_2O_2, then in ammonium molybdate reagent. (a) Original magnification 92×. (b) A clump of dark acicular precipitate of Pb-Ca-Sn intermetallic phase is revealed at higher magnification. Original magnification 1825×

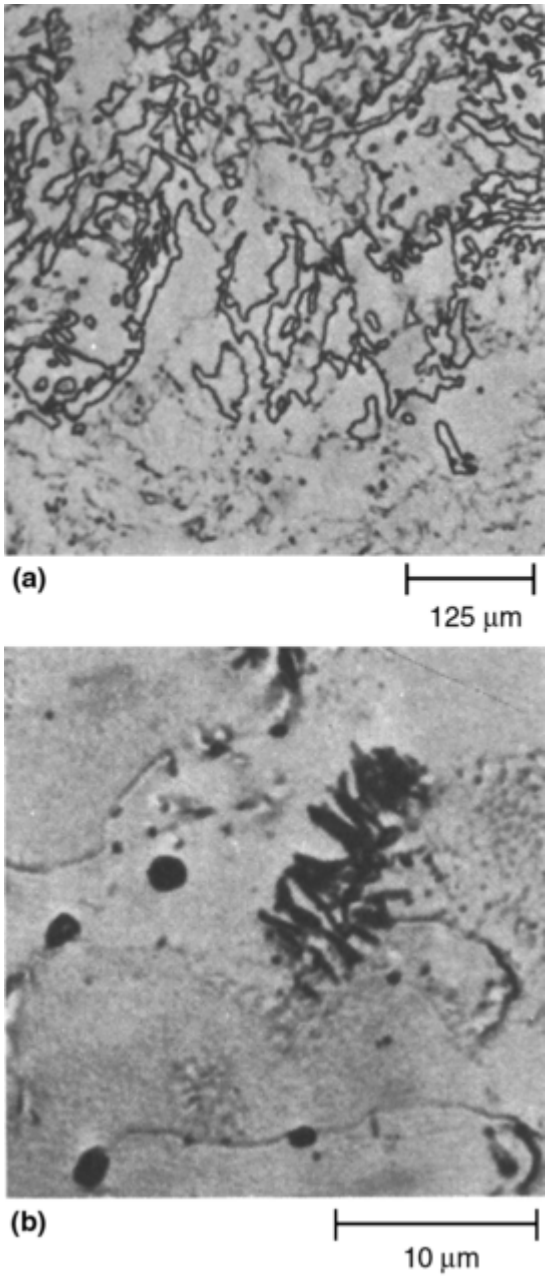

Fig. 9 Pb-0.083Ca-0.49Sn. 5 parts acetic acid, 1 part 30% H_2O_2, then in ammonium molybdate reagent. (a) Small grains, similar in size to those of the lead-calcium alloy shown in Fig. 7(a). Original magnification 92×. (b) View at higher magnification, showing large primary particles and a clump of acicular precipitate of Pb-Ca-Sn phase (dark). Original magnification 1825×

Lead-Copper. Copper and lead, which are essentially insoluble in the solid state, form a eutectic at 0.06% Cu. The eutectic structure appears as small discrete particles of copper in a matrix of lead, which blends into any primary lead that is also present. Additions of copper up to the eutectic composition result in grain refinement as well as improvement in fatigue properties (Fig. 10, 11).

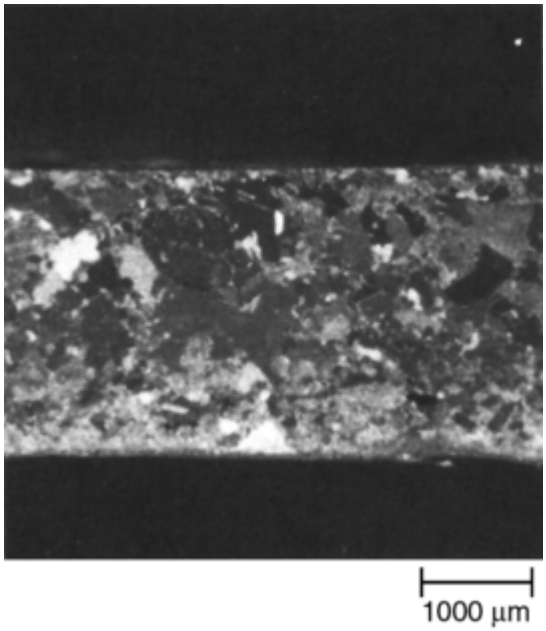

Fig. 10 Copper-bearing lead (0.04 to 0.08% Cu); cross section of cable sheath with 2.7 mm (0.105 in.) wall thickness. The grains contain lead-copper eutectic, which forms at a copper content of 0.06%. $(NH_4)_2MoO_4$, then acetic-nitric acid. Original magnification 10×

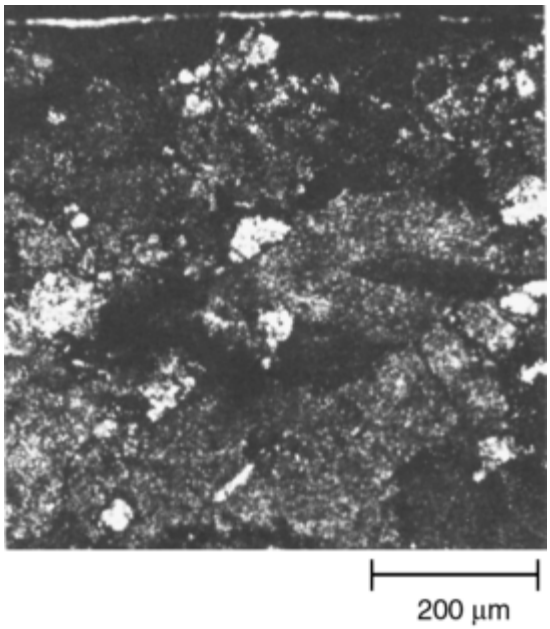

Fig. 11 Copper-bearing lead (0.15% Cu); section through wall of cable sheath showing intergranular cracks (black areas in center) that resulted from creep. $(NH_4)_2MoO_4$, then acetic-nitric acid. Original magnification 75×

Lead-Tin. A eutectic forms between tin and lead at 183 °C (361 °F). Because the eutectic composition is 61.9Sn-38.1Pb, all of the lead-base alloys in the system contain primary grains of lead-rich solid solution. Alloys that have more than 19% Sn contain some eutectic, which consists of lamellae or globules of lead-rich solid solution in a tin-rich matrix (Fig. 12). A low solidification rate favors formation of the lamellar type of eutectic (Fig. 13); a high rate, as in most soldering applications, favors the globular type (Fig. 14).

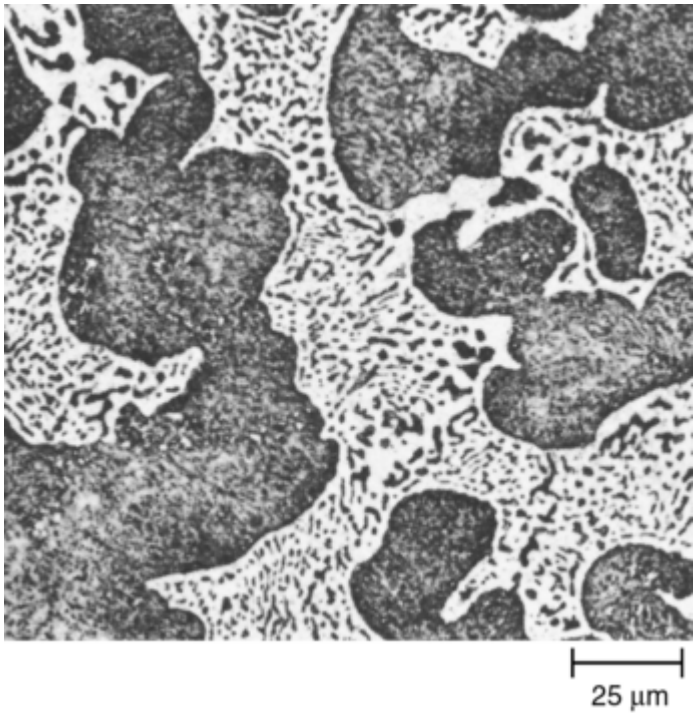

Fig. 12 Plumber's wiping solder (Pb-40Sn), slowly solidified. Dark dendritic grains of lead-rich solid solution in a lamellar eutectic matrix of tin-rich solid solution (white) and lead-rich solid solution (dark). 1 part acetic acid, 1 part HNO_3, 8 parts glyercol. Original magnification 400×

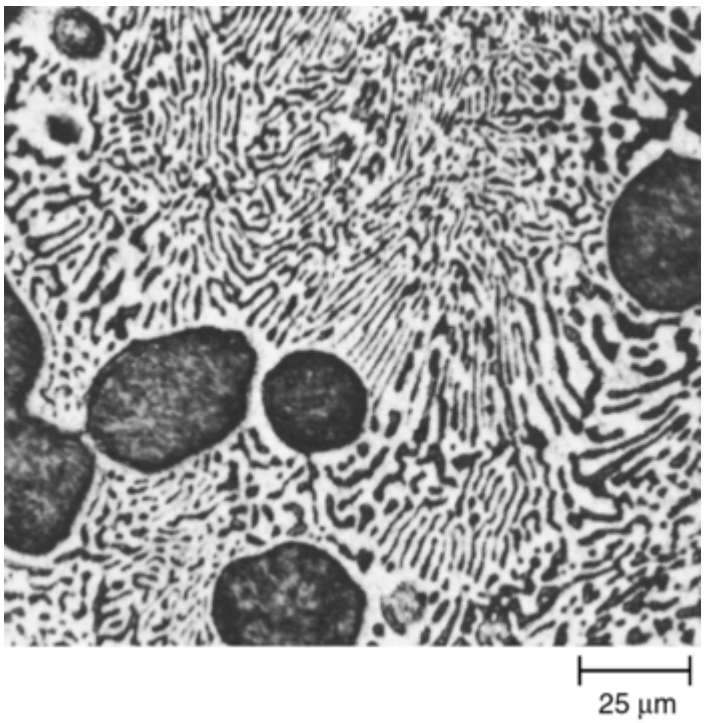

Fig. 13 Half-and-half solder (Pb-50Sn), slowly solidified. Dark dendritic grains of lead-rich solid solution in lamellar eutectic matrix of tin-rich solid solution (white) and lead-rich solid solution (dark). 1 part acetic acid, 1 part HNO_3, 8 parts glyercol. Original magnification 400×

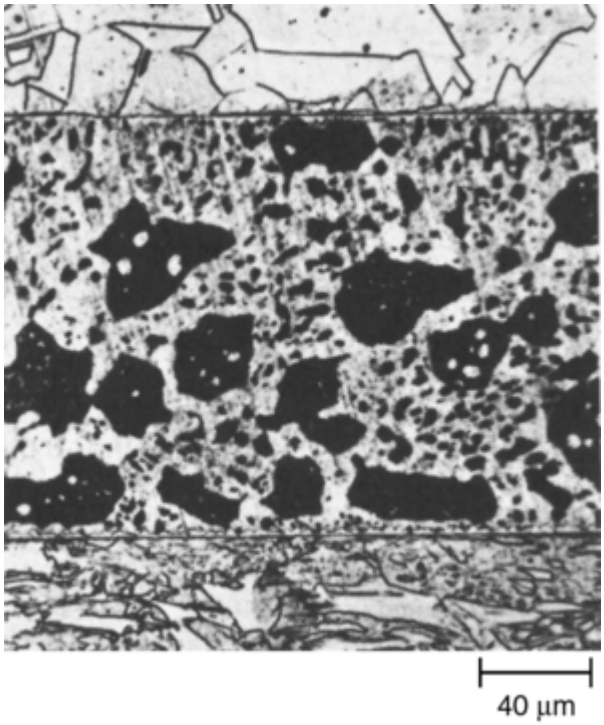

Fig. 14 Copper parts (top and bottom) soldered with Pb-50Sn. The eutectic is globular because of faster solidification than in Fig. 13. 1 part NH_4OH, 1 part 3% H_2O_2, 1 part H_2O. Original magnification 250×

Although the solubility of tin in lead at the eutectic temperature is 19%, at room temperature it is reduced to approximately 2%, causing considerable precipitation of tin-rich solid solution, which appears as granules and needles within the grains of lead-rich solid solution (Fig. 15).

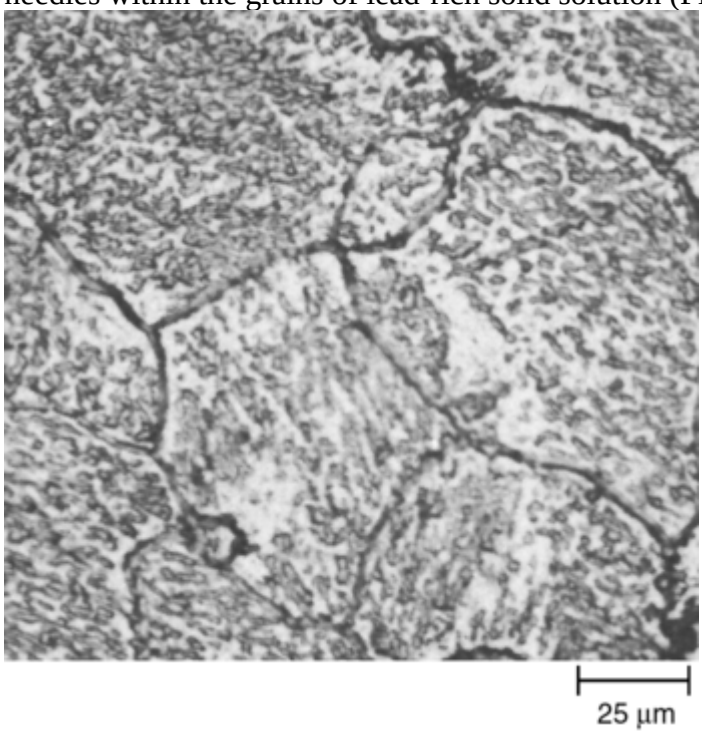

Fig. 15 Can solder (Pb-2Sn), slowly solidified. Light-gray lead-rich grains with dark-gray tin precipitate in grain boundaries and within grains. 1 part acetic acid, 1 part HNO_3, 8 parts glycerol. Original magnification 400×

When silver is added to lead-tin alloys, it combines with tin to form Ag_3Sn, which then forms a pseudobinary eutectic with lead at 1.75% Ag and 0.7% Sn. At the eutectic temperature of 309 °C (589 °F), the solubility of Ag_3Sn in lead is approximately 0.1%. Therefore, most silver-lead solders, which contain 0.5 to 1.5% Ag and 1

to 2% Sn, have cast microstructures comprising dendrites of lead-rich solid solution and interdendritic eutectic that consists of Ag_3Sn in lead-rich solid solution (Fig. 16). At higher tin contents, some tin-rich solid solution may also appear in the eutectic.

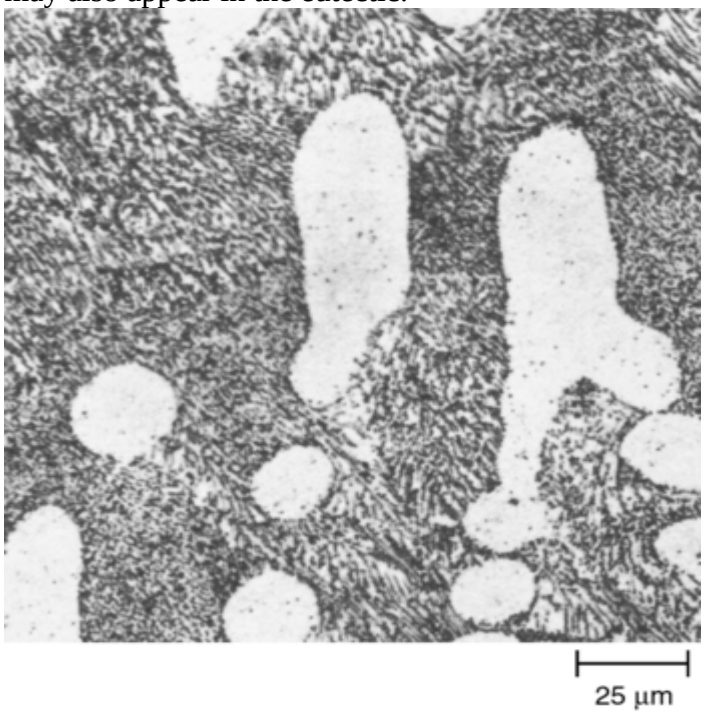

Fig. 16 Silver-lead solder (Pb-1Sn-1.5Ag), as-solidified. Light dendritic grains of lead-rich solid solution in lamellar eutectic matrix of lead-rich solid solution (light) and Ag_3Sn intermetallic phase (dark). 1 part acetic acid, 1 part HNO_3, 8 parts glycerol. Original magnification 400×

Lead-Antimony. At the eutectic temperature of 251 °C (484 °F), 3.5% Sb is soluble in lead. At room temperature, only 0.44% Sb is soluble in lead, and after cooling at a rate lower than that of air cooling, small rods of antimony precipitate from solid solution. After furnace cooling, the rods appear at the grain boundaries; after even slower cooling, they also appear within the grains. After air cooling, the antimony often is retained in solution, permitting subsequent age hardening (Fig. 17, Fig. 18, Fig. 19, Fig. 20).

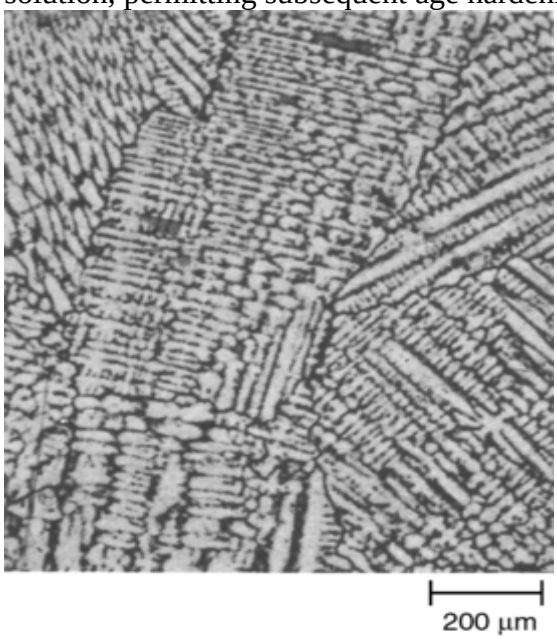

Fig. 17 Pb-5Sb, as-cast. Section through wire of battery grid showing larger grains than in Fig. 6. 15 g citric acid + 9 g ammonium molybdate in 80 mL H_2O_2. Original magnification 50×



Fig. 18 Pb-5Sb, as-cast. Section through the connection tab of a battery grid showing dendritic grains. 15 g citric acid + 9 g ammonium molybdate in 80 mL H_2O_2. Original magnification 100×

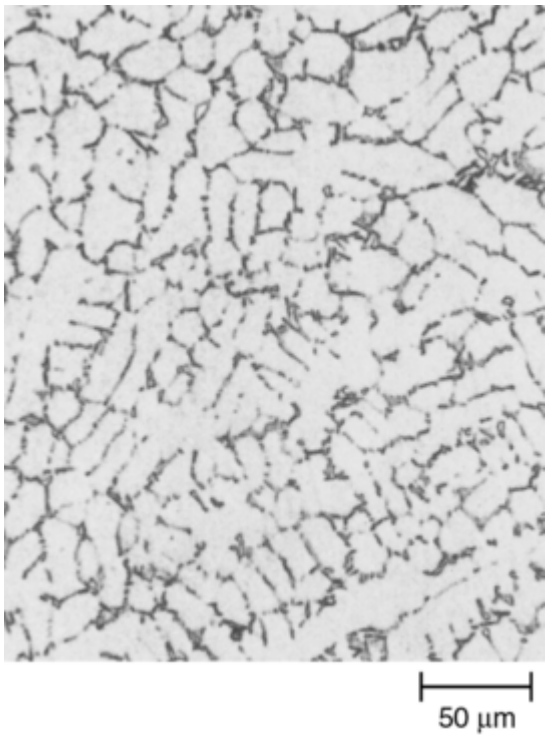

Fig. 19 Same as Fig. 18, except not etched. Higher magnification shows dendrites of lead-rich solid solution. As-polished. Original magnification 200×

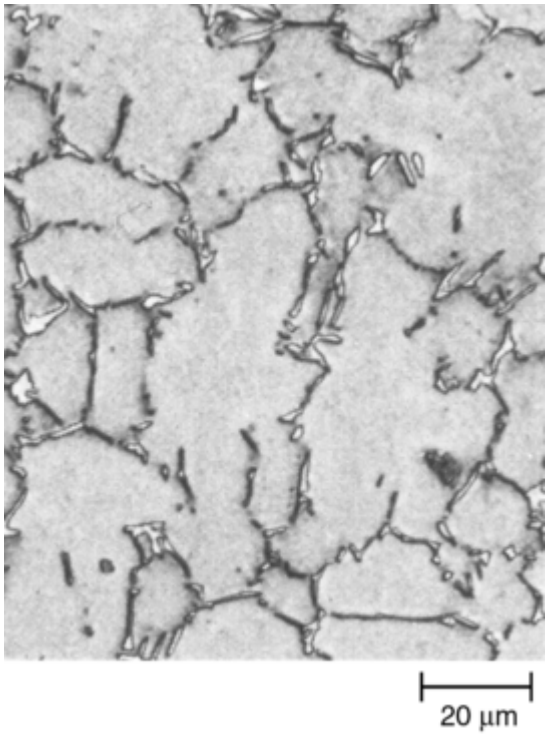

Fig. 20 Same as Fig. 19, except at higher magnification, which shows interdendritic network of antimony (light). As-polished. Original magnification 500×

The eutectic mixture has a lamellar form, with particles of antimony in a matrix of lead-rich solid solution. In hypoeutectic alloys (below 11.2% Sb), the lead-rich phase of the eutectic blends into the primary lead-rich phase that is also present, giving the eutectic a divorced appearance (Fig. 21). Hypereutectic alloys show angular primary crystals of antimony in eutectic (Fig. 22).

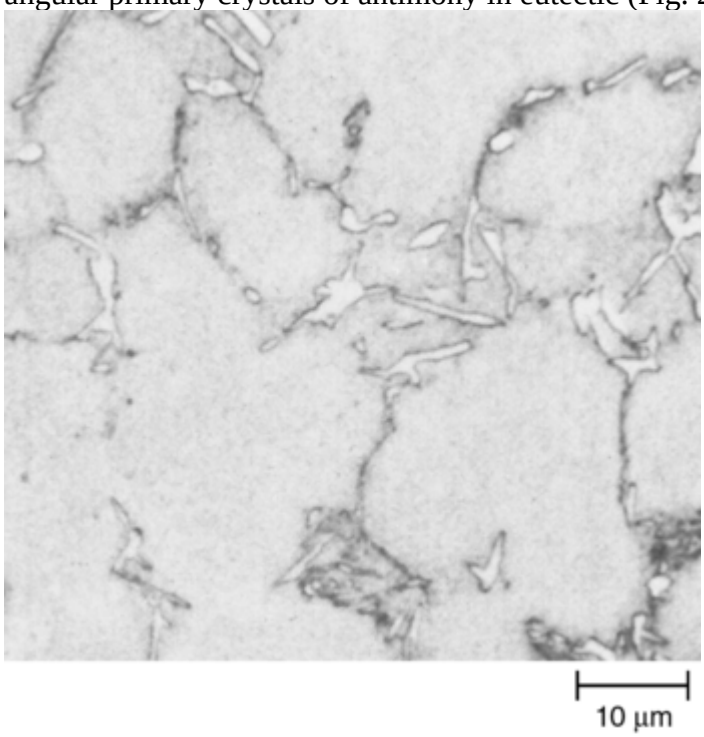

Fig. 21 Same as Fig. 20, except at higher magnification, which shows that the eutectic in the interdendritic area (discrete particles of antimony in matrix of lead-rich solid solution) is of the divorced type. As-polished. Original magnification 1000×

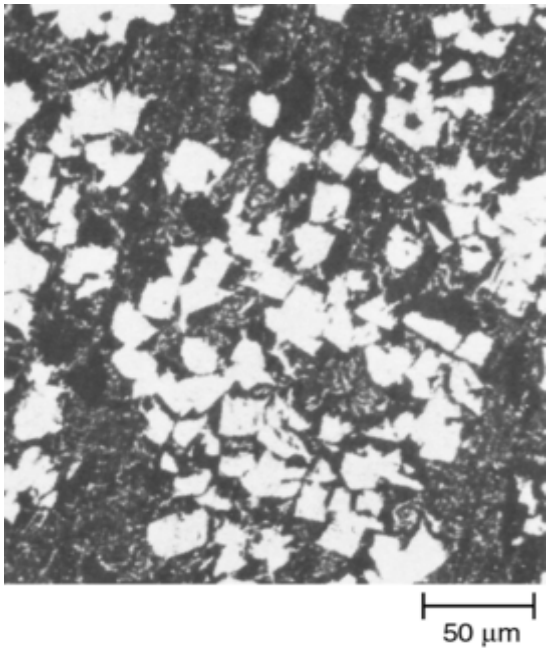

Fig. 22 Pb-20Sb. Primary crystals of antimony (light) in a fine eutectic matrix of antimony in lead-rich solid solution. Acetic-nitric acid. Original magnification 200×

Lead-Antimony-Tin. One of the two peritectics in the antimony-tin system occurs at 425 °C (797 °F), where molten metal reacts with antimony-rich solid solution to form SbSn. Both antimony and tin are moderately soluble in SbSn, resulting in a phase field extending at room temperature approximately from 44 to 59% Sn.

At approximately 10% Sb, 10% Sn, and 247 °C (476 °F), the Pb-SbSn pseudobinary system contains a eutectic that has a lamellar form, with particles of SbSn-rich phase in a matrix of lead-rich solid solution. The eutectic point lies on a eutectic trough in the liquidus surface of the ternary diagram. This trough, which defines the limit for the formation of primary lead crystals, connects the lead-antimony and lead-tin eutectic points. The trough also passes through a ternary eutectic point at 11.5% Sb, 3.5% Sn, and 240 °C (464 °F). The form of the ternary eutectic mixture is also lamellar, with particles of both SbSn-rich phase and antimony-rich solid solution in a matrix of lead-rich solid solution (Fig. 23).

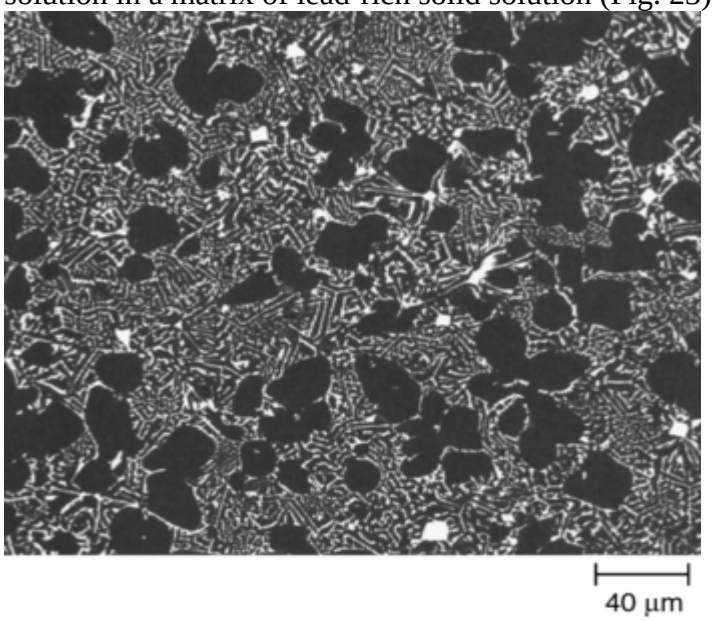

Fig. 23 Lead-base babbitt, SAE alloy 13 (Pb-10Sb-5Sn-0.5Cu). Dendritic grains of lead-rich solid solution (black) and primary cuboids of antimony-tin intermetallic phase (white) in matrix of ternary eutectic (filigreed) consisting of antimony-rich solid solution (white), antimony-tin phase (also white), and lead-rich solid solution (black). 15 mL acetic acid, 20 mL HNO_3, 80 mL H_2O; at 42 °C (108 °F). Original magnification 250×

A line from the lead-antimony eutectic point through the ternary eutectic point and terminating at the SbSn peritectic defines the limit for the formation of primary antimony crystals. Lines leading from the ternary eutectic point to both peritectics in the antimony-tin system define the limits for the formation of primary SbSn crystals. Because the antimony-rich side of the SbSn phase field can dissolve approximately 13% Pb, the boundary between the Pb-SbSn field and the Pb-Sb-SbSn field lies at an antimony-to-lead ratio of 2 to 1. The boundary between the lead-antimony field and the Pb-Sb-SbSn field lies at approximately 2% Sb.

Antimony-rich solid solution and SbSn-rich phase can often be distinguished by etching with a mixture of 5 mL ammonium persulfate [$(NH_4)_2S_2O_8$] solution (10 g in 100 mL H_2O) and 2 mL tartaric acid solution (30 g in 100 mL H_2O). The antimony-rich phase is white and remains so during etching; the SbSn-rich phase is light gray but becomes yellowish during etching and may develop etch pits. In a fine eutectic structure, the lamellae of antimony-rich phase are unchanged by etching, but the lamellae of SbSn-rich phase develop dark edges. Primary crystals of antimony-rich phase are angular but are usually somewhat elongated; primary crystals of SbSn-rich phase are cuboidal.

Additions of copper to Pb-Sb-Sn alloys usually combine with tin to form creamy-white needles of Cu_6Sn_5 (Fig. 24). However, the copper occasionally combines with antimony to form rods of Cu_2Sb that have a purple or violet color (light gray in micrographs). Additions of arsenic dissolve in the lead, antimony, and SbSn phases and therefore are not visible in the microstructure.

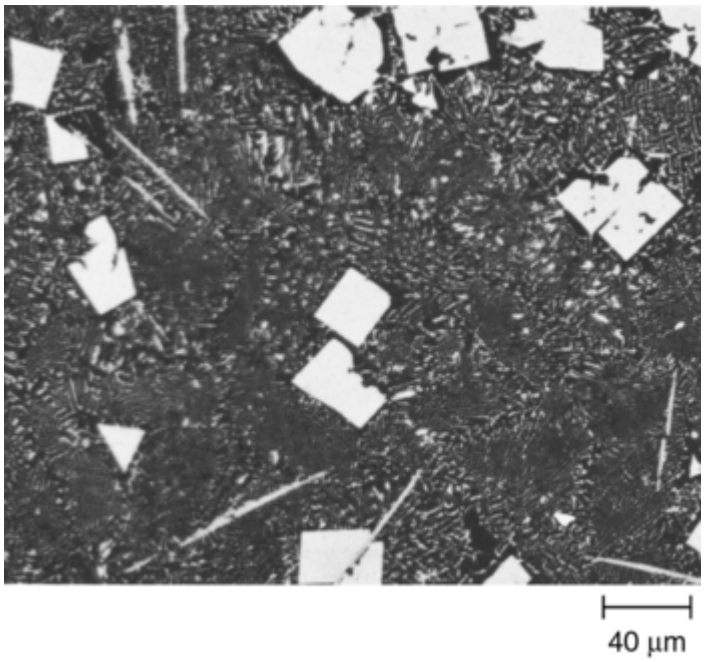

Fig. 24 Lead-base babbitt, SAE alloy 14 (Pb-15Sb-10Sn-0.5Cu). Primary needles of Cu_6Sn_5 phase and primary cuboids of antimony-tin intermetallic phase (both white) in a matrix of fine pseudobinary eutectic (filigreed) made up of lead-rich solid solution (dark) and antimony-tin phase (light). 15 mL acetic acid, 20 mL HNO_3, 80 mL H_2O; at 42 °C (108 °F). Original magnification 250×

Metallography and Microstructures of Lead and Its Alloys, *Metallography and Microstructures,* Vol 9*, ASM Handbook,* ASM International, 2004, p. 789–800

Lead Alloys in Sleeve Bearings

As already stated, the primary use of lead is in batteries. The use of lead in solders has diminished in recent years as public and manufacturers' concern over the disposal of electronic devices has risen. Lead alloys, along with other materials, are used in sleeve bearings. This application often requires the use of metallographic investigation. The following procedures are applicable to lead alloys as well as other soft metals.

Specimen Preparation

Sleeve bearings usually consist of one or more layers of a comparatively soft bearing alloy(s), or liners, bonded to a relatively thick steel backing. Therefore, they require metallographic preparation techniques that differ somewhat from those used for singular metals and alloys.

Sectioning. Small specimens for metallographic preparation reduce polishing time. A recommended length is 19 mm ($\frac{3}{4}$ in.); the width should be equal to the thickness of the bearing alloy wall for thin-wall liners or a maximum of 6.4 mm ($\frac{1}{4}$ in.) for heavy-wall liners.

When sampling a piece of bearing material to produce a specimen, the thickness of the steel backing should be minimized in proportion to that of the bearing alloy. A thick steel layer increases the probability that a relief will be produced during polishing, because the softer bearing liner will be polished away more rapidly. As a result, the bearing alloy and the steel will not be viewed in the same plane, and part of the structure shown will appear out of focus.

Initial cutting can be performed with a handsaw, power saw, or cutoff wheel. Cutting should begin at the bearing alloy and proceed through the steel, or it should begin with the bearing alloy/steel interface parallel to the plane of cutting and proceed through the sleeve bearing. Cutting should never take place from the steel into the bearing alloy. If the initial cutting severely distorts the bearing alloy, the disturbed metal should be removed by wet abrasive belt grinding. The finishing cut should also proceed from the bearing alloy into the steel backing.

Mounting. Specimens of sleeve bearing materials are mounted in much the same way as specimens of other metals. For additional information, see the article “Mounting of Specimens” in this Volume. It is often convenient to mount several small specimens together. Each specimen should then be positioned so that the bearing liner faces the same direction.

Thermosetting polymers are frequently used as mounting materials. They are unsuitable, however, for examining a bearing alloy for internal voids, which would likely be collapsed by the time-temperature-pressure combination used. Such examinations require a cold-mounting material, such as a self-curing acrylic or an epoxy liquid. A short vacuum treatment applied immediately after pouring the mounting liquid over the specimen will eliminate as much of the trapped air as possible and will improve penetration of the cold-mounting liquid.

Grinding is performed first on an abrasive belt flooded with water or on a low-speed disk grinder (approximately 500 rpm) using water-cooled 180-grit silicon carbide abrasive. The mount is ground next with 240-, 320-, 400-, then 600-grit silicon carbide papers placed on a flat marble pedestal, a plate-glass surface, or a rotating wheel. The grinding is preferably performed wet, with thorough washings of the mount between abrasives. As an alternative, grinding may be performed successively with grades 1, 0, 00, and 000 alumina (Al_2O_3) paper, using frequent applications of kerosene as a lubricant; the mount should be thoroughly rinsed with kerosene between grindings.

Grinding should begin at the bearing alloy and proceed toward the steel backing, or it should begin with the bearing alloy/steel interface parallel to the direction of grinding and proceed along the specimen. Frequent

washings of the abrasive paper with water or kerosene minimize contamination of the bearing alloy by abrasive particles or other debris.

Polishing usually begins on a 500 to 600 rpm wheel covered with nylon, to which a coating of 6 to 10 μm diamond paste has been applied. Polishing should continue with firm pressure for approximately 5 min or until the scratches and disturbed metal from grinding have been removed. The mount should then be thoroughly washed to remove all the diamond abrasive.

Intermediate polishing is performed on a 300 rpm wheel using 0.3 μm Al_2O_3 abrasive and a medium-nap cloth. The abrasive is mixed with distilled water before polishing to form a suspension that should be applied frequently to the cloth during polishing. The mount should be polished for 1 min using light pressure. Additional distilled water is then added to remove most of the Al_2O_3 abrasive. After the mount is removed from the wheel, the polished surface should be thoroughly and alternately rinsed in cold and hot water. Excess water should be wiped away with a damp cotton square while the surface is exposed to a dry air blast.

The intermediate polish often yields a surface that is suitable for routine examination. However, a final step using a 300 rpm wheel with a medium-nap cloth will produce a perfect polish. The cloth is moistened with distilled water, then dusted with magnesium oxide abrasive, which is worked into a paste. The mount should be polished for several minutes using heavy pressure. The wheel is then flooded with distilled water, and the pressure is reduced to complete the polish. The mount should be thoroughly rinsed with cold, then hot, water and wiped with a moist cotton square while the surface is exposed to a dry air blast.

Certain polishing techniques that are standard for most singular materials are not always suited to bimetal or trimetal sleeve bearing structures. For sleeve bearing materials, a circular rotation of the mount should be avoided. Instead, the mount should be moved laterally across the wheel with the specimen oriented such that polishing proceeds from the steel toward the bearing alloy (the opposite of the orientation used in grinding). This procedure lessens the tendency of the bearing alloy to polish away at a faster rate than the steel, producing a relief or step at the interface between the two layers.

A relief, if produced, is visible under low magnification as a dark line at the interface between the steel backing and the bearing alloy. This line could easily be misinterpreted as a bond defect. However, examination at high magnification will reveal the true nature of the bond line. Minimizing the ratio of steel backing to bearing alloy, keeping the specimen size small, and following the instructions on mount orientation during polishing will help minimize bond-line relief.

Etching of sleeve bearing materials for metallographic examination is usually performed by immersion, although it is sometimes desirable to swab the surface with a cotton square saturated with the etchant just before the rinse. Immediately following removal from the etching reagent, the mount should be thoroughly rinsed in cold, then hot, water, and excess moisture should be removed with a damp cotton square while the surface is exposed to a dry air blast. Rinsing or wiping the surface of a mount with alcohol will promote staining, especially on aluminum bearing alloys. The most common etchants and some of the sleeve bearing alloys to which they best apply are listed in Table 2.

Table 2 Etchants for microscopic examination of sleeve bearing materials

Etchant	Bearing material
NH_4OH and H_2O_2[(a)]	Commercial bronze liner
	Copper-lead alloy liner
	Copper-lead-tin alloy liner
	High-leaded tin bronze liner
	Leaded tin bronze liner
	Lead-tin-copper overlay on copper-lead alloy liner
	Nickel bronze infiltrated with lead-base babbitt

	Nickel-tin bronze infiltrated with lead-base babbitt Silver electroplate on steel Silver-lead alloy electroplate on steel Tin-base babbitt overlay on copper-lead-tin alloy liner Tin bronze infiltrated with lead-base babbitt Tin bronze infiltrated with synthetic fluorine-containing resin Trimetal bearing: lead-tin-copper electroplated overlay, brass electroplated barrier, copper-lead alloy
0.5% HF	Aluminum alloy clad to steel Aluminum-silicon alloy clad to steel High-tin aluminum alloy clad with unalloyed aluminum Lead-tin-copper overlay on aluminum alloy liner Low-tin aluminum alloy clad to steel Trimetal bearing: lead-tin-copper electroplated overlay, copper electroplated barrier, aluminum-silicon-cadmium alloy
5% nital	High-tin aluminum alloy clad to nickel-plated steel Lead-base babbitt liner Tin-base babbitt liner Steel backing of any bearing alloy
Keller's reagent	Lead-tin-copper overlay on aluminum-cadmium alloy

(a) Equal parts of concentrated NH_4OH and water with 2–4 drops of H_2O_2 (30%) per 10 mL of solution

Microstructures of Sleeve Bearing Materials

Tin- and lead-base sleeve bearing materials depicted in micrographs in this article are identified, and nominal compositions of the materials are given in Table 3. Tin-base alloys are shown in Fig. 25, 26, and 27; lead-base alloys in Fig. 23, 24, 28, 29, 30, 31, 32, 33, 34, 35, 36, and 37; plated overlay alloys in Fig. 38, 39, 40, 41, 42, 43, 44, 45 46, 47, and 48; copper-lead alloys in Fig. 49, 50, 51, 52, 53, and 54; some of the copper-lead alloys provide the underlayer for the plated overlays, so some figures are listed twice.

Table 3 Chemical compositions of sleeve bearing alloys

Fig.	Alloy designation		Composition[a], %									
	SAE	**ISO**	**Sn**	**Sb**	**Pb**	**Cu**	**Fe**	**As**	**Bi**	**Zn**	**Al**	**Others (total)**
Tin base												
25–27	12	SnSb8Cu4	88.0	7.0–8.0	0.50[b]	3.0–4.0	0.10	0.10	0.08	0.005	0.005	0.02
Fig.	Alloy designation		Composition[a], %									

	SAE	ISO	Pb	Sn	Sb	Cu	As	Bi	Zn	Al	Cd	Others (total)
Lead base												
23, 28–30	13	PbSb10Sn6	bal	5.0–7.0	9.0–11.0	0.7	0.25	0.10	0.005	0.005	0.05	0.02
24, 31–33	14	PbSb15Sn10	bal	9.0–11.0	14.0–16.0	0.7	0.6	0.10	0.005	0.005	0.05	0.02
34–36	15	PbSb1As	bal	0.9–1.7	13.5–15.5	0.7	0.8–1.2	0.10	0.005	0.005	0.02	0.02
37	16[c]	…	bal	3.5–4.7	3.0–4.0	0.10	0.05	0.10	0.005	0.005	0.005	0.40

Fig.	Alloy designation		Composition[a], %				
	SAE	ISO	Pb	Sn	Cu	In	Others (total)
Plated overlay							
38, 39	191	PbSn10	bal	8.0–12.0	…	…	0.5
40–44	192	PbSn10Cu2	bal	8.0–12.0	1.0–3.0	…	0.5
45, 46	193	…	bal	16.0–20.0	2.0–3.0	…	0.5
47, 48	194	PbIn7	bal	…	…	5.0–10.0	0.5

Fig.	Alloy designation		Composition[a], %								
	SAE	ISO	Cu	Pb	Sn	Ag	Zn	P	Fe	Others (total)	Others (each)
Copper-lead[d]											
44, 49, 50	48	CuPb30	67.0–74.0	26.0–33.0	0.5	1.5	0.10	0.02	0.7	0.15	…
40, 41, 47, 48, 51, 52	49	CuPb24Sn	73.0–79.0	21.0–27.0	0.6–2.0	…	…	…	0.7	0.45	…
53, 54	485	…	bal	44.0–58.0	1.0–5.0	…	…	…	0.35	0.45	0.15

(a) All values not given as ranges are maximum except as shown otherwise.
(b) ISO SnSb8Cu4 has 0.35 max Pb.
(c) SAE 16 is cast into and on a porous sintered matrix (usually copper-nickel bonded to steel). The surface layer is 0.025 to 0.13 mm (0.001 to 0.005 in.) thick.
(d) A corrosion-resistant overlay, such as SAE alloys 191 to 194, may be used with SAE alloys 48, 480, and 481 and is recommended for SAE 49.

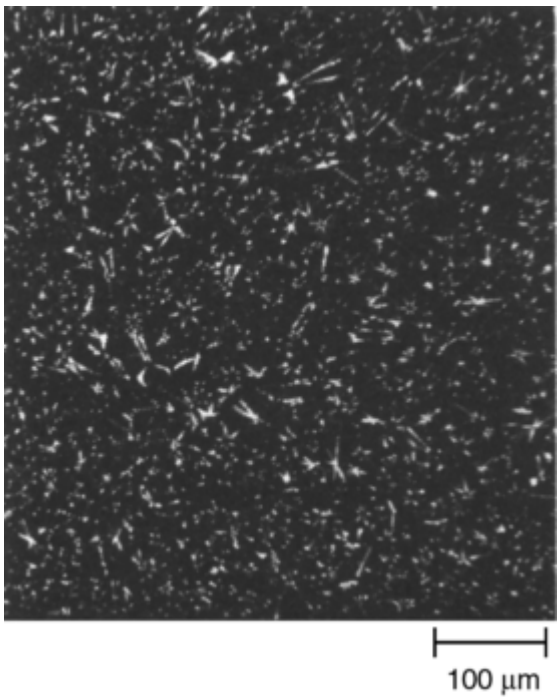

Fig. 25 Tin-base babbitt liner (SAE 12), continuously cast on steel backing strip (bottom). White second-phase particles (see Fig. 26); matrix of tin saturated with copper and antimony. Nital. Original magnification 100×

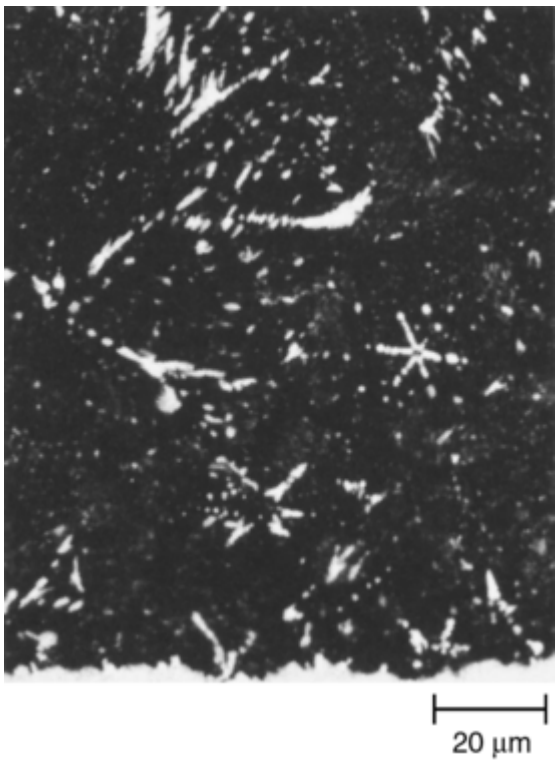

Fig. 26 Same as Fig. 25, except at higher magnification, which reveals starlike arrays of needles of copper-rich constituent and small, round particles of precipitated antimony-tin. Nital. 500×

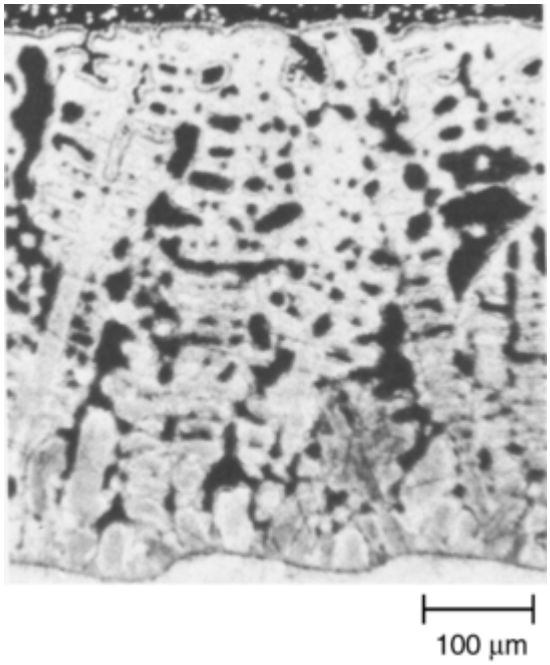

Fig. 27 Overlay of tin-base babbitt (SAE 12), centrifugally cast on the cast 75Cu-24Pb-1Sn liner; steel backing at bottom. $NH_4OH + H_2O_2$. Original magnification 100×

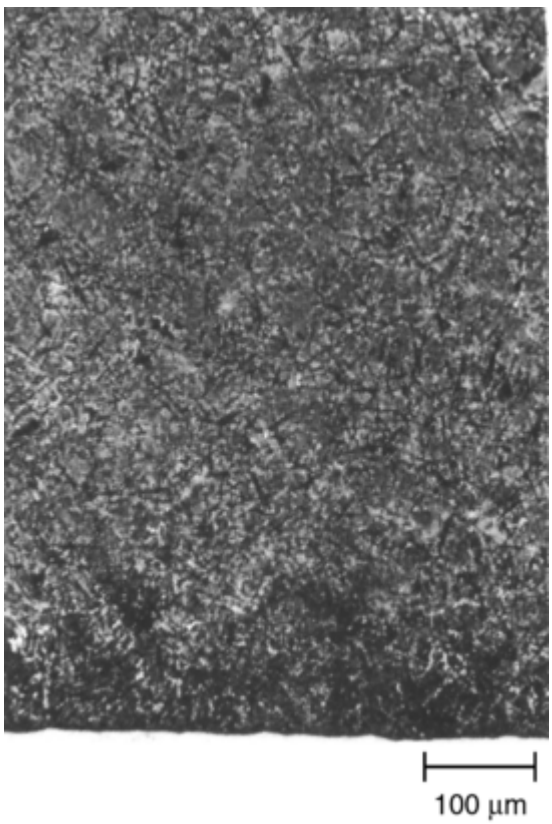

Fig. 28 Lead-base babbitt liner (SAE 13), continuously cast on steel backing strip (bottom). Dark primary crystals of lead in a light matrix of antimony-tin and lead. See also Fig. 29. Nital. Original magnification 100×

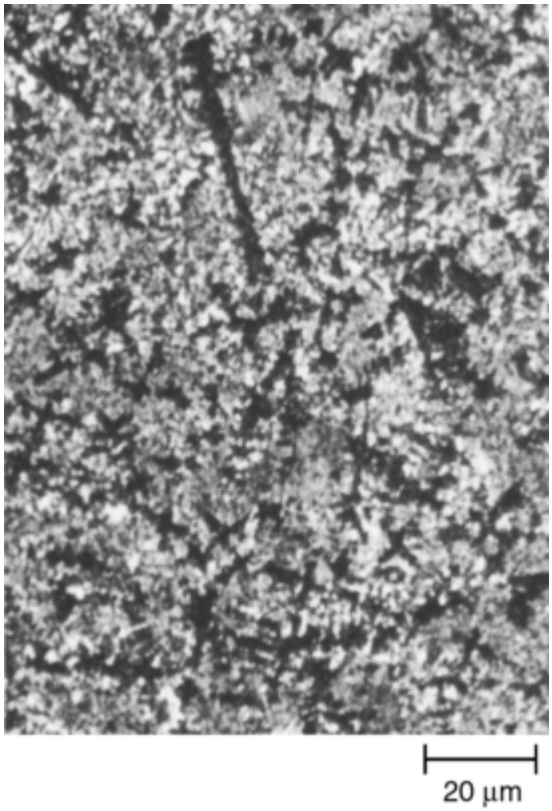

Fig. 29 Same as Fig. 28, except at higher magnification, which reveals the configuration of the lead dendrites and the structure of the eutectic-like matrix of antimony-tin and lead. Compare with Fig. 30. Nital. Original magnification 500×

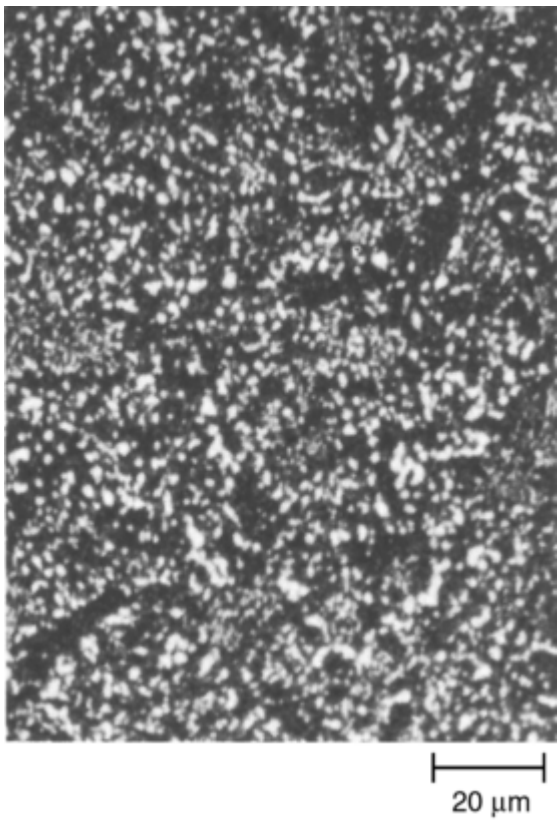

Fig. 30 Same as Fig. 29, except annealed to increase formability, which changed the microstructure to white crystals of eutectic antimony-tin in a dark matrix of lead-rich solid solution. Nital. Original magnification 500×

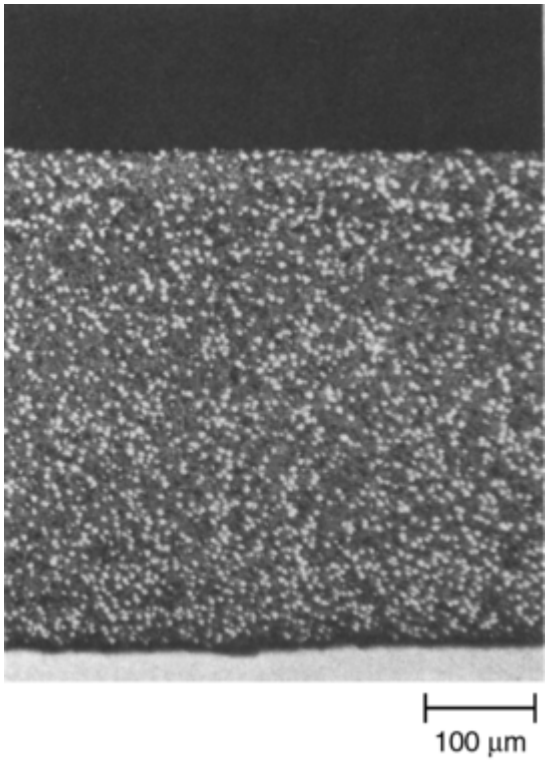

Fig. 31 Lead-base babbitt liner (SAE 14), continuously cast on steel backing strip (bottom). White particles of antimony-tin in a dark matrix of lead-rich solid solution. See also Fig. 32. Nital. Original magnification 100×

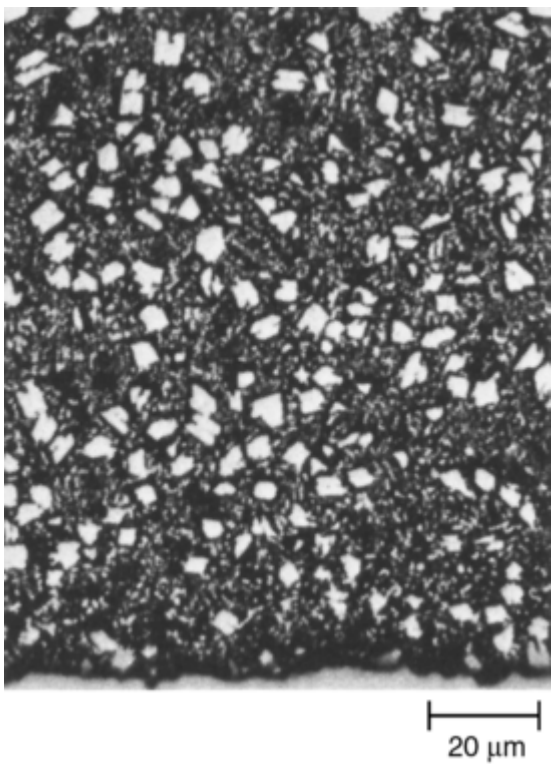

Fig. 32 Same as Fig. 31, except at higher magnification, which reveals that the white antimony-tin compound is in the form of cuboid-shaped primary crystals and small eutectic particles. Compare with Fig. 33. Nital. Original magnification 500×

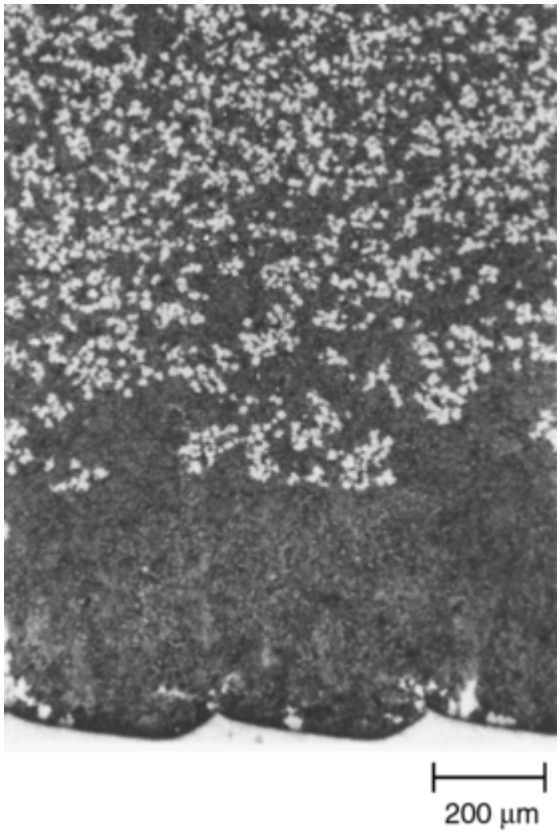

Fig. 33 Same as Fig. 31, but centrifugally cast against inside wall of cylindrical steel shell (bottom). Primary crystals of antimony-tin segregated away from bond between babbitt and steel backing. Nital. Original magnification 50×

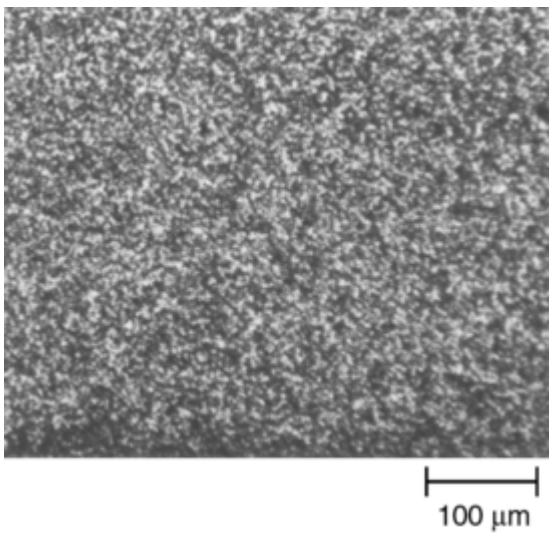

Fig. 34 Lead-base babbitt liner (SAE 15), continuously cast on steel backing strip (bottom). Antimony-arsenic phase (white) in dark matrix of lead-rich solid solution. See also Fig. 35. Nital. Original magnification 100×

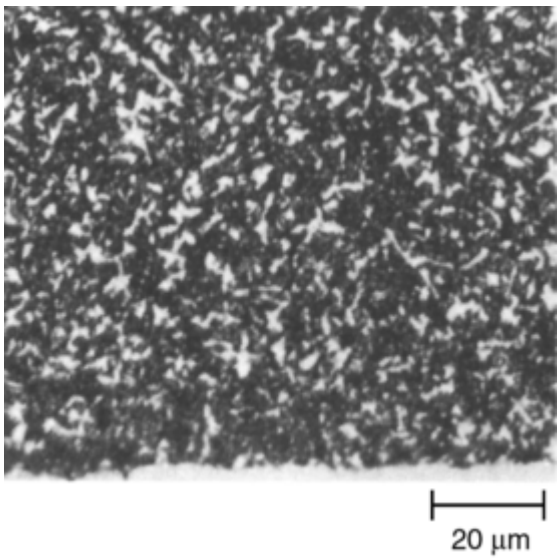

Fig. 35 Same as Fig. 34, except at higher magnification, showing the white particles of antimony-arsenic phase to be of two types: small eutectic particles and large primary crystals. Compare with Fig. 36. Nital. Original magnification 500×

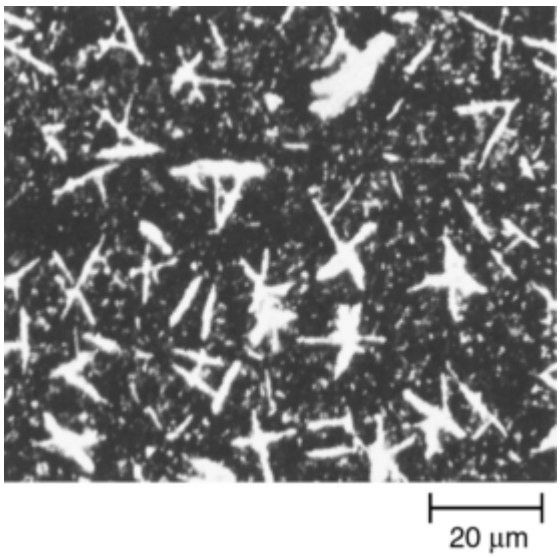

Fig. 36 Same as Fig. 35, except that improper casting conditions have caused the primary antimony-arsenic crystals to form undesirable starlike patterns of needles, causing a decrease in formability. Nital. Original magnification 500×

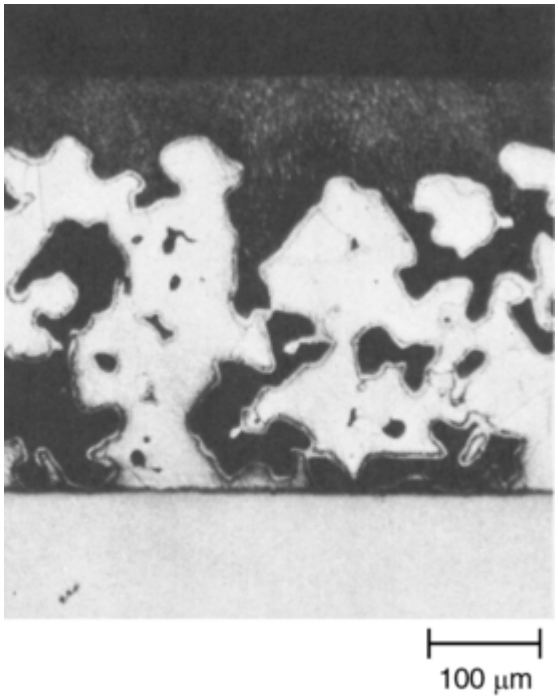

Fig. 37 Liner that was made by infiltrating an open grid of tin bronze (98Cu-2Sn) with molten lead-base babbitt (SAE 16). The grid was made by sintering a mixture of copper and copper-tin alloy powders on a steel backing strip. The excess babbitt formed an overlay. $NH_4OH + H_2O_2$. Original magnification 100×

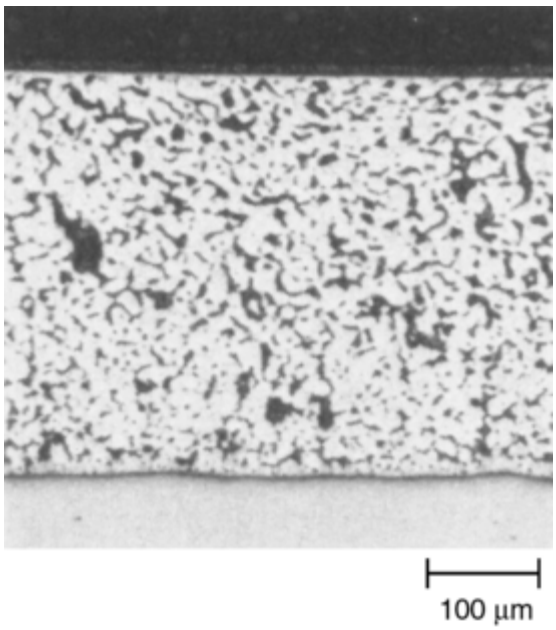

Fig. 38 From top: electroplated 0.013 mm (0.0005 in.) overlay of lead-tin alloy (SAE 191), sintered copper-lead alloy (SAE 49) liner, and steel backing. See also Fig. 39. $NH_4OH + H_2O_2$. Original magnification 100×

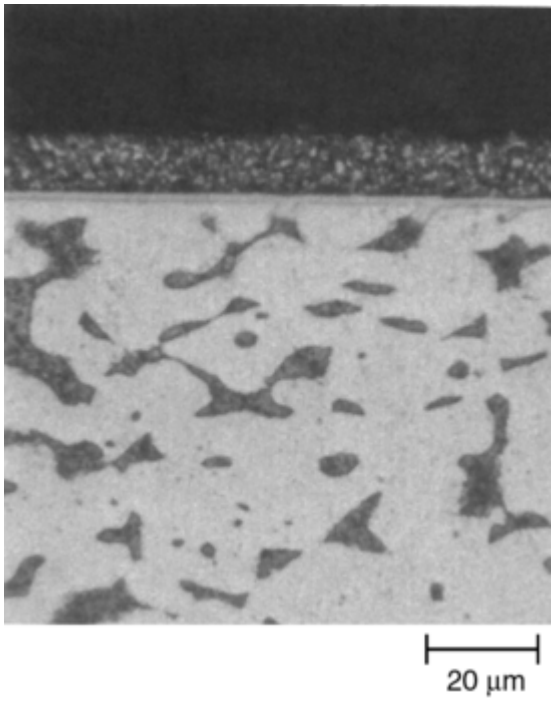

Fig. 39 Higher-magnification view of Fig. 38, showing SAE 191 overlay at top of micrograph separated from sintered SAE 49 bearing liner by flashed 0.001 mm (0.00004 in.) nickel diffusion barrier (gray band below overlay). Light areas in overlay are tin-rich phase; dark areas, lead-rich phase. $NH_4OH + H_2O_2$. Original magnification 500×

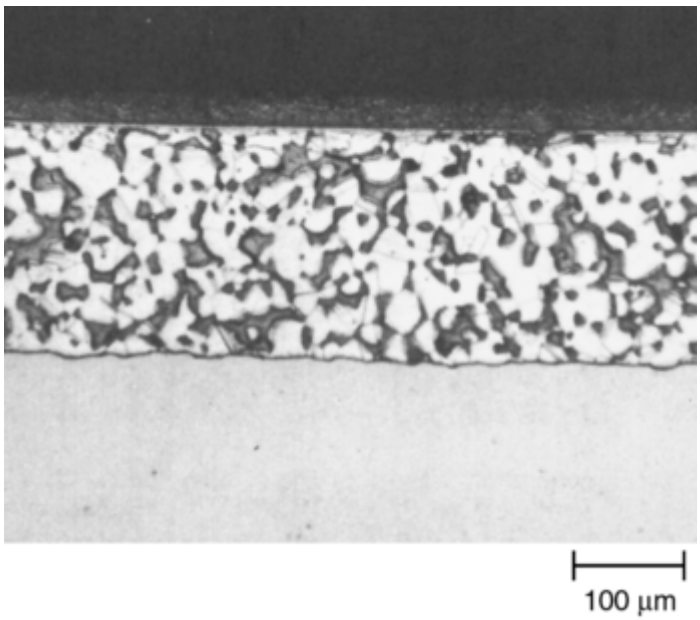

Fig. 40 From top: electroplated overlay of lead-tin-copper alloy (SAE 192), electroplated brass barrier layer (see Fig. 41 for better detail), sintered copper-lead alloy liner (SAE 49), and steel backing strip (bottom). $NH_4OH + H_2O_2$. Original magnification 100×

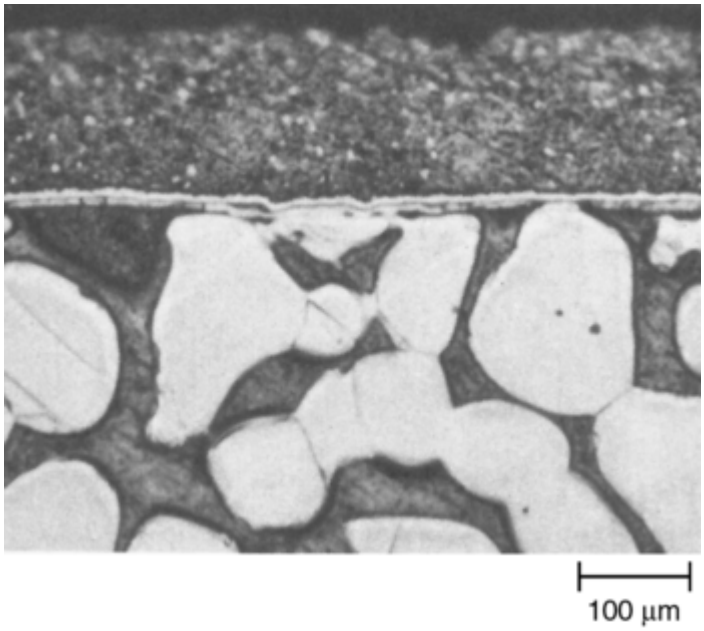

Fig. 41 Upper part of Fig. 40 at higher magnification. Light bands are the brass plated between overlay (top) and liner (bottom) to prevent diffusion of tin from overlay into liner during operation. Duplex brass layer resulted when tin diffused into upper part of the brass. $NH_4OH + H_2O_2$. Original magnification 500×

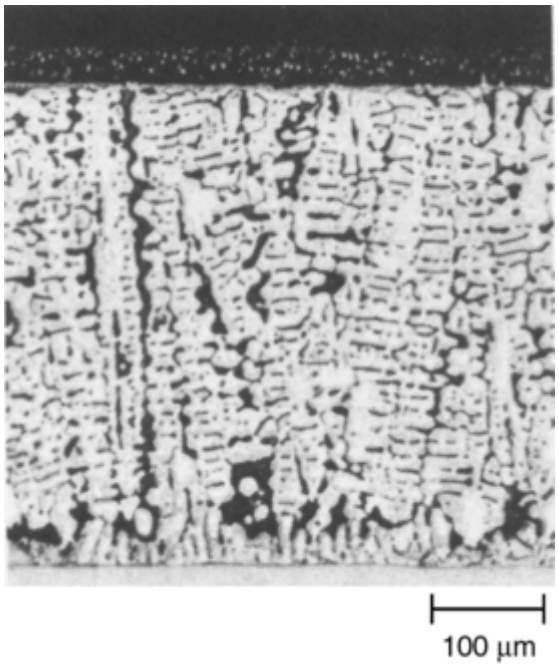

Fig. 42 Electroplated overlay of SAE 192 on the cast 75Cu-25Pb alloy liner that first had been nickel plated; steel backing strip is at bottom. See also Fig. 43. $NH_4OH + H_2O_2$. Original magnification 100×

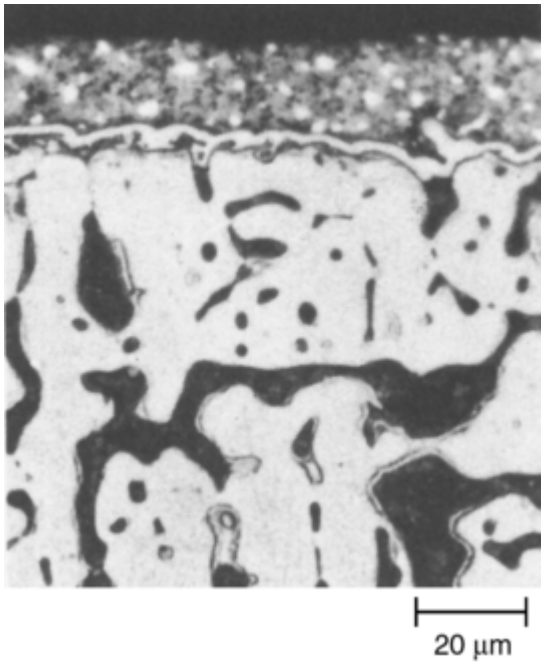

Fig. 43 Higher-magnification view of Fig. 42 (without steel), showing the nickel (light band) plated on the liner to prevent diffusion of tin from the overlay into the copper-lead alloy liner. $NH_4OH + H_2O_2$. Original magnification 500×



Fig. 44 Similar to Fig. 42, except the lead-tin-copper alloy overlay was electroplated on the copper-lead alloy liner (SAE 48) shown in Fig. 50, which first had been nickel electroplated. $NH_4OH + H_2O_2$. Original magnification 100×

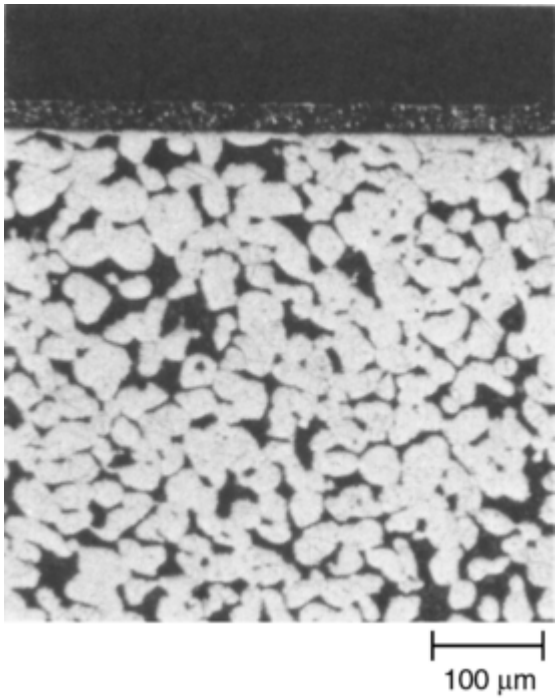

Fig. 45 From top: electroplated 0.02 mm (0.0008 in.) overlay of lead-tin-copper alloy (SAE 193) and sintered copper-lead alloy (SAE 49) liner. See also Fig. 46, which shows both tin and nickel diffusion barriers not resolvable at lower magnifications. $NH_4OH + H_2O_2$. Original magnification 100×

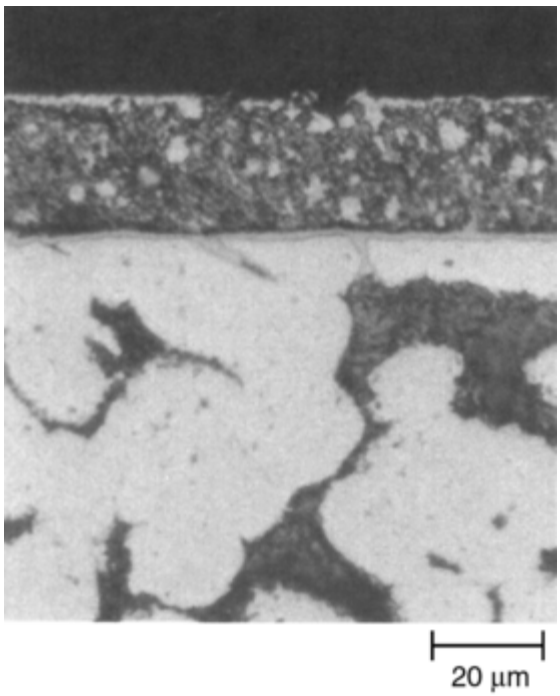

Fig. 46 Higher-magnification view of Fig. 45, showing from top: tin flash (thin white band along upper edge of overlay), SAE 193 overlay, 0.001 mm (0.00004 in.) nickel flash (gray band below overlay) to prevent diffusion of tin into the liner alloy, and SAE 49 liner. Light areas in overlay are tin-rich phase; dark areas, lead-rich phase. $NH_4OH + H_2O_2$. Original magnification 500×

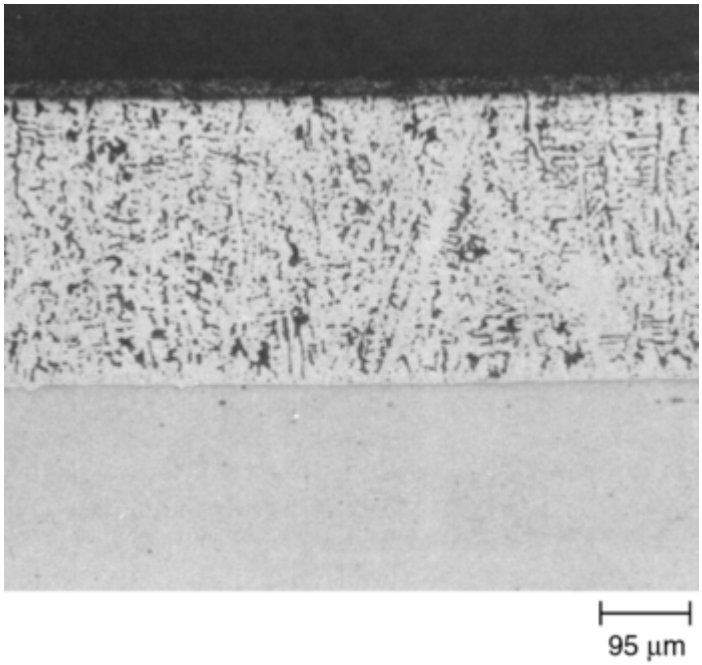

Fig. 47 From top: electroplated 0.02 mm (0.0008 in.) overlay of lead-indium alloy (SAE 194), cast copper-lead alloy (SAE 49) liner, and steel backing. See also Fig. 48. $NH_4OH + H_2O_2$. Original magnification 105×

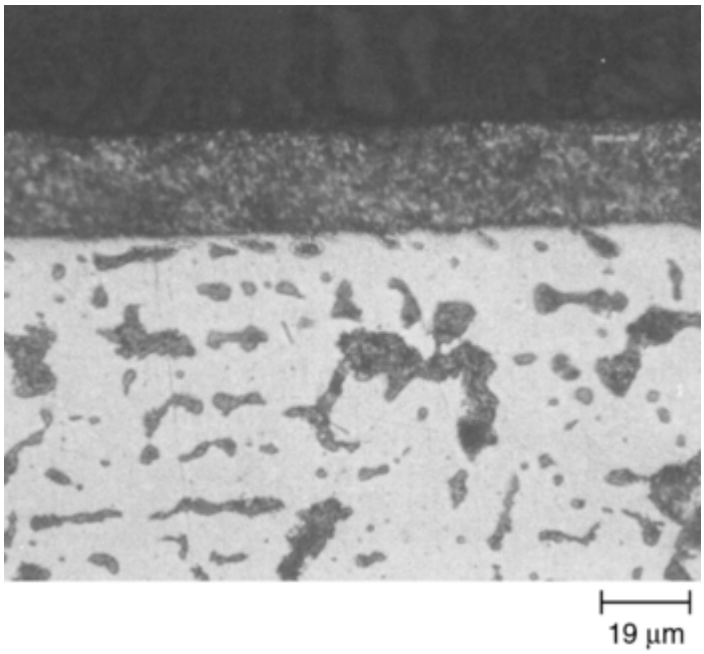

Fig. 48 Higher-magnification view of Fig. 47 (steel not shown). Light areas in the overlay are indium-rich phase; dark areas, lead-rich phase. $NH_4OH + H_2O_2$. Original magnification 525×

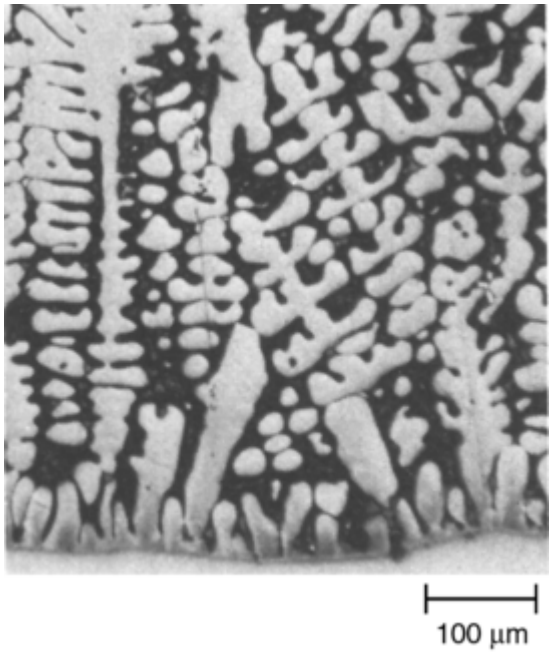

Fig. 49 Copper-lead alloy liner (SAE 48), gravity cast against inner wall of cylindrical steel shell (bottom). Coarse copper dendrites, blunted by addition of silver, in a continuous matrix of lead. Compare with Fig. 50. $NH_4OH + H_2O_2$. Original magnification 100×

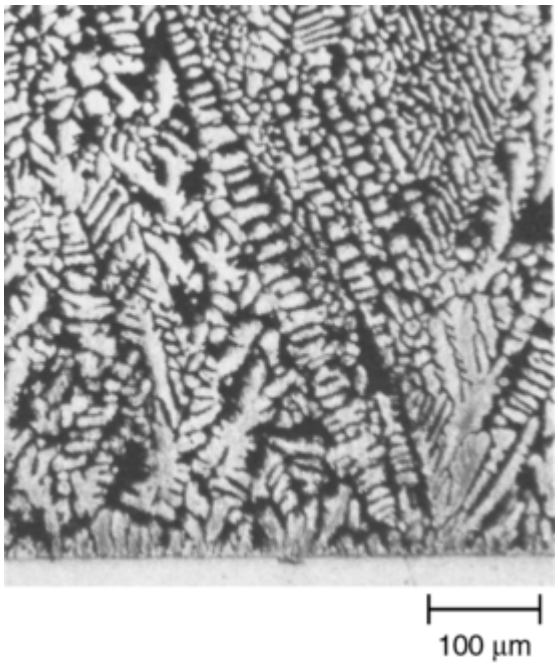

Fig. 50 Same as Fig. 49, except the copper-lead alloy liner was continuously cast on a steel backing strip (bottom of micrograph), which resulted in a faster cooling rate and thus produced finer dendrites of copper. $NH_4OH + H_2O_2$. Original magnification 100×

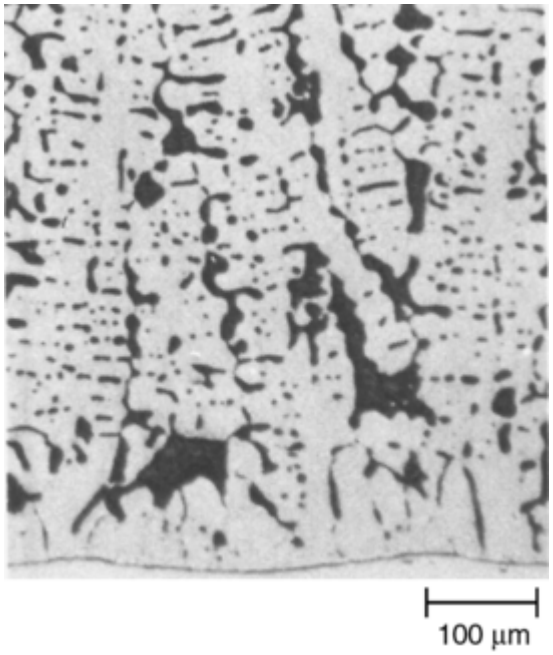

Fig. 51 Copper-lead alloy liner (SAE 49), gravity cast against inside wall of cylindrical steel shell (bottom). Coarse copper dendrites (light) in a matrix of lead (dark). Compare with Fig. 52. $NH_4OH + H_2O_2$. Original magnification 100×

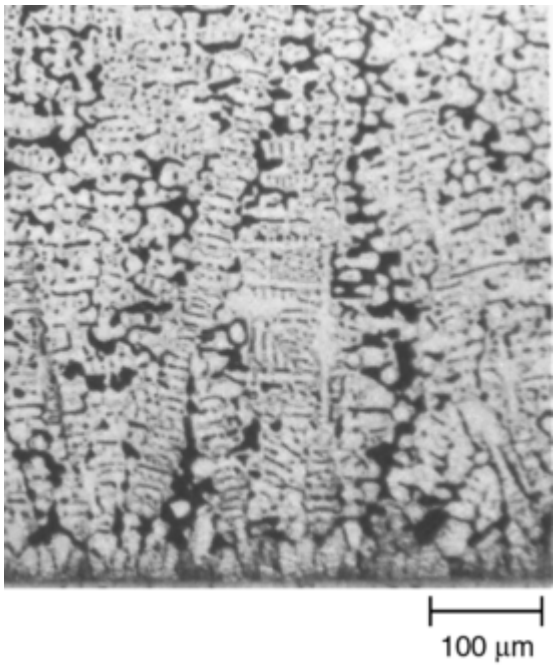

Fig. 52 Same as Fig. 51, except the copper-lead alloy was continuously cast on a steel backing strip (bottom), which resulted in faster cooling and thus produced finer dendrites of copper. $NH_4OH + H_2O_2$. Original magnification 100×

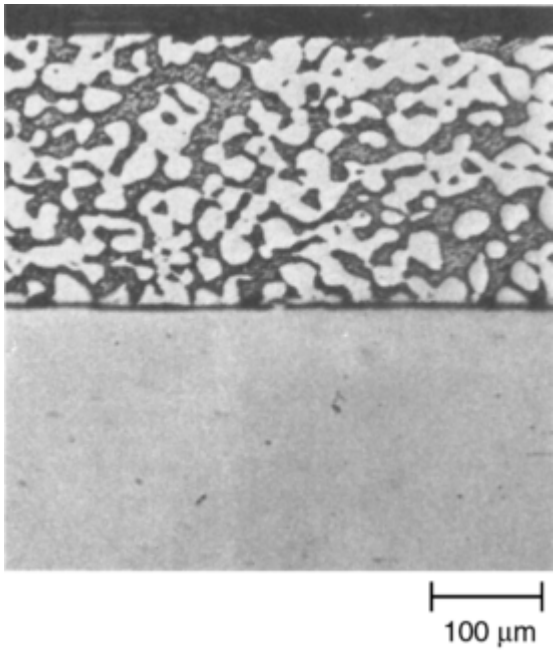

Fig. 53 High-leaded tin bronze liner (SAE 485); prealloyed powder, sintered on a steel backing strip (bottom), cold rolled, resintered. Copper grains; intergranular lead (black). See also Fig. 54. $NH_4OH + H_2O_2$. Original magnification 100×

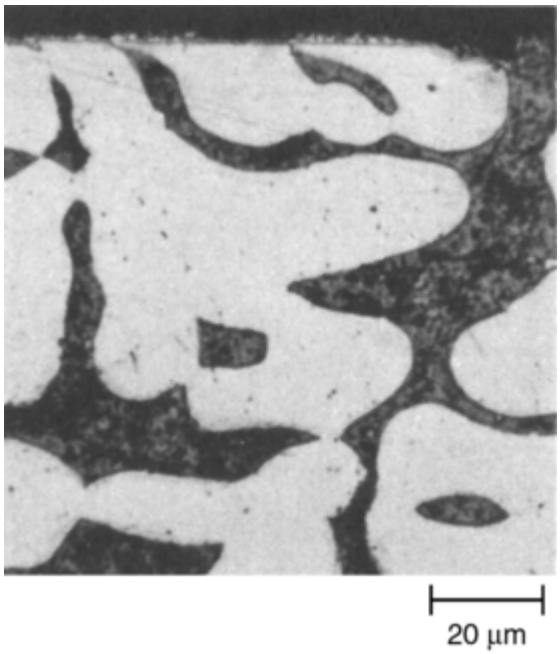

Fig. 54 Same as Fig. 53, but higher magnification reveals the details of the structure, which shows the dark intergranular matrix of lead is almost continuous. $NH_4OH + H_2O_2$. Original magnification 500×

Bimetal Bearings. Bearing materials are often bonded to a backing of stronger material such as steel to form a bimetal bearing with increased load-carrying capacity. The bonded layer of the bearing material can be thinner than 0.13 mm (0.005 in.). Babbitts, copper-lead alloys, and leaded tin bronzes are often bonded to steel backing by such processes as continuous gravity casting onto a steel strip (Fig. 25, 28, 31, 34) as well as static gravity and centrifugal casting (Fig. 37, 33) against the inside surface of a cylindrical shell.

Aluminum alloys are generally clad to a steel backing by warm rolling. To facilitate bonding, the steel is roughened by belt sanding or grit blasting and is sometimes electroplated with a thin layer of nickel before being clad with the aluminum alloy (the resulting bearing is still referred to as bimetal).

Other aluminum bearing alloy liners are bonded using an unalloyed aluminum layer. This layer may be formed as part of the bearing alloy fabrication process (as is the case with the powder-rolled Al-8Pb-4Si-1Sn-1Cu

alloy), or it may be established during fabrication of the bearing alloy strip prior to its cladding to steel (as is often true for SAE 783 alloy).

Silver and silver alloy liners can also be deposited onto a steel backing. A layer of unalloyed silver is deposited by electroplating, followed by a layer of alloyed silver.

Sintered liners for sleeve bearings are made from prealloyed powders of copper-lead alloys or high-leaded tin bronzes by spreading the powder uniformly on a continuously moving steel strip that passes through a sintering furnace with a reducing atmosphere. The particles of powder become sintered together, forming an open grid bonded to the steel strip. This bimetal is then rolled to compact the liner and resintered to improve the bond strength. However, aluminum alloy powder for liners is usually roll compacted and sintered before being roll clad to the steel backing strip.

Liners are also made by infiltration of a lower-melting material into a layer of sintered copper or copper alloy powder. The powder layer, usually a copper alloy, is not compacted after sintering; the open grid of the sintered powder layer is infiltrated with molten material having a lower melting temperature than that of the grid alloy. This infiltrant is often lead or a lead alloy, but it may be a nonmetallic material such as a synthetic fluorine-containing resin. Detailed information on sintering, infiltration, and roll compaction of metal powders can be found in *Powder Metal Technologies and Applications,* Volume 7 of *ASM Handbook,* 1998.

Trimetal Bearings. The fatigue strength of babbitt or lead-tin alloy can be increased significantly by reducing the thickness of the material to 0.013 to 0.05 mm (0.0005 to 0.0020 in.). Such layers are typically produced by electrodeposition. Under severe operating conditions, these layers may easily wear through; if the backing is steel, seizure can result. To avoid seizure, an interlayer of strong bearing material is placed between the steel backing and the babbitt surface layer.

During the operation of some trimetal bearings, the temperature may rise enough to cause the diffusion of tin from overlays of lead-tin alloys into the intermediate liners of copper alloy, with resulting deterioration of the bearings. To prevent this diffusion, the liner material of such bearings is first electroplated with a thin barrier layer of brass or nickel (the resulting bearing is still referred to as trimetal). Aluminum alloy liners are given a zinc immersion coating (zincate), then a thin electroplated layer of copper or nickel in preparation for electrodeposition of the overlay. Thin overlays can also be cast in place by using an excess amount of the lower-melting material when infiltrating sintered liners, as described previously.

Metallography and Microstructures of Lead and Its Alloys, *Metallography and Microstructures,* Vol 9, *ASM Handbook,* ASM International, 2004, p. 789–800

Lead Alloys in Sleeve Bearings

As already stated, the primary use of lead is in batteries. The use of lead in solders has diminished in recent years as public and manufacturers' concern over the disposal of electronic devices has risen. Lead alloys, along with other materials, are used in sleeve bearings. This application often requires the use of metallographic investigation. The following procedures are applicable to lead alloys as well as other soft metals.

Specimen Preparation

Sleeve bearings usually consist of one or more layers of a comparatively soft bearing alloy(s), or liners, bonded to a relatively thick steel backing. Therefore, they require metallographic preparation techniques that differ somewhat from those used for singular metals and alloys.

Sectioning. Small specimens for metallographic preparation reduce polishing time. A recommended length is 19 mm ($\frac{3}{4}$ in.); the width should be equal to the thickness of the bearing alloy wall for thin-wall liners or a maximum of 6.4 mm ($\frac{1}{4}$ in.) for heavy-wall liners.

When sampling a piece of bearing material to produce a specimen, the thickness of the steel backing should be minimized in proportion to that of the bearing alloy. A thick steel layer increases the probability that a relief will be produced during polishing, because the softer bearing liner will be polished away more rapidly. As a result, the bearing alloy and the steel will not be viewed in the same plane, and part of the structure shown will appear out of focus.

Initial cutting can be performed with a handsaw, power saw, or cutoff wheel. Cutting should begin at the bearing alloy and proceed through the steel, or it should begin with the bearing alloy/steel interface parallel to the plane of cutting and proceed through the sleeve bearing. Cutting should never take place from the steel into the bearing alloy. If the initial cutting severely distorts the bearing alloy, the disturbed metal should be removed by wet abrasive belt grinding. The finishing cut should also proceed from the bearing alloy into the steel backing.

Mounting. Specimens of sleeve bearing materials are mounted in much the same way as specimens of other metals. For additional information, see the article “Mounting of Specimens” in this Volume. It is often convenient to mount several small specimens together. Each specimen should then be positioned so that the bearing liner faces the same direction.

Thermosetting polymers are frequently used as mounting materials. They are unsuitable, however, for examining a bearing alloy for internal voids, which would likely be collapsed by the time-temperature-pressure combination used. Such examinations require a cold-mounting material, such as a self-curing acrylic or an epoxy liquid. A short vacuum treatment applied immediately after pouring the mounting liquid over the specimen will eliminate as much of the trapped air as possible and will improve penetration of the cold-mounting liquid.

Grinding is performed first on an abrasive belt flooded with water or on a low-speed disk grinder (approximately 500 rpm) using water-cooled 180-grit silicon carbide abrasive. The mount is ground next with 240-, 320-, 400-, then 600-grit silicon carbide papers placed on a flat marble pedestal, a plate-glass surface, or a rotating wheel. The grinding is preferably performed wet, with thorough washings of the mount between abrasives. As an alternative, grinding may be performed successively with grades 1, 0, 00, and 000 alumina (Al_2O_3) paper, using frequent applications of kerosene as a lubricant; the mount should be thoroughly rinsed with kerosene between grindings.

Grinding should begin at the bearing alloy and proceed toward the steel backing, or it should begin with the bearing alloy/steel interface parallel to the direction of grinding and proceed along the specimen. Frequent washings of the abrasive paper with water or kerosene minimize contamination of the bearing alloy by abrasive particles or other debris.

Polishing usually begins on a 500 to 600 rpm wheel covered with nylon, to which a coating of 6 to 10 μm diamond paste has been applied. Polishing should continue with firm pressure for approximately 5 min or until the scratches and disturbed metal from grinding have been removed. The mount should then be thoroughly washed to remove all the diamond abrasive.

Intermediate polishing is performed on a 300 rpm wheel using 0.3 μm Al_2O_3 abrasive and a medium-nap cloth. The abrasive is mixed with distilled water before polishing to form a suspension that should be applied frequently to the cloth during polishing. The mount should be polished for 1 min using light pressure. Additional distilled water is then added to remove most of the Al_2O_3 abrasive. After the mount is removed from the wheel, the polished surface should be thoroughly and alternately rinsed in cold and hot water. Excess water should be wiped away with a damp cotton square while the surface is exposed to a dry air blast.

The intermediate polish often yields a surface that is suitable for routine examination. However, a final step using a 300 rpm wheel with a medium-nap cloth will produce a perfect polish. The cloth is moistened with distilled water, then dusted with magnesium oxide abrasive, which is worked into a paste. The mount should be polished for several minutes using heavy pressure. The wheel is then flooded with distilled water, and the pressure is reduced to complete the polish. The mount should be thoroughly rinsed with cold, then hot, water and wiped with a moist cotton square while the surface is exposed to a dry air blast.

Certain polishing techniques that are standard for most singular materials are not always suited to bimetal or trimetal sleeve bearing structures. For sleeve bearing materials, a circular rotation of the mount should be avoided. Instead, the mount should be moved laterally across the wheel with the specimen oriented such that polishing proceeds from the steel toward the bearing alloy (the opposite of the orientation used in grinding). This procedure lessens the tendency of the bearing alloy to polish away at a faster rate than the steel, producing a relief or step at the interface between the two layers.

A relief, if produced, is visible under low magnification as a dark line at the interface between the steel backing and the bearing alloy. This line could easily be misinterpreted as a bond defect. However, examination at high magnification will reveal the true nature of the bond line. Minimizing the ratio of steel backing to bearing alloy, keeping the specimen size small, and following the instructions on mount orientation during polishing will help minimize bond-line relief.

Etching of sleeve bearing materials for metallographic examination is usually performed by immersion, although it is sometimes desirable to swab the surface with a cotton square saturated with the etchant just before the rinse. Immediately following removal from the etching reagent, the mount should be thoroughly rinsed in cold, then hot, water, and excess moisture should be removed with a damp cotton square while the surface is exposed to a dry air blast. Rinsing or wiping the surface of a mount with alcohol will promote staining, especially on aluminum bearing alloys. The most common etchants and some of the sleeve bearing alloys to which they best apply are listed in Table 2.

Table 2 Etchants for microscopic examination of sleeve bearing materials

Etchant	Bearing material
NH_4OH and H_2O_2[(a)]	Commercial bronze liner
	Copper-lead alloy liner
	Copper-lead-tin alloy liner
	High-leaded tin bronze liner
	Leaded tin bronze liner
	Lead-tin-copper overlay on copper-lead alloy liner
	Nickel bronze infiltrated with lead-base babbitt
	Nickel-tin bronze infiltrated with lead-base babbitt
	Silver electroplate on steel
	Silver-lead alloy electroplate on steel
	Tin-base babbitt overlay on copper-lead-tin alloy liner
	Tin bronze infiltrated with lead-base babbitt
	Tin bronze infiltrated with synthetic fluorine-containing resin
	Trimetal bearing: lead-tin-copper electroplated overlay, brass electroplated barrier, copper-lead alloy
0.5% HF	Aluminum alloy clad to steel
	Aluminum-silicon alloy clad to steel
	High-tin aluminum alloy clad with unalloyed aluminum
	Lead-tin-copper overlay on aluminum alloy liner
	Low-tin aluminum alloy clad to steel

	Trimetal bearing: lead-tin-copper electroplated overlay, copper electroplated barrier, aluminum-silicon-cadmium alloy
5% nital	High-tin aluminum alloy clad to nickel-plated steel Lead-base babbitt liner Tin-base babbitt liner Steel backing of any bearing alloy
Keller's reagent	Lead-tin-copper overlay on aluminum-cadmium alloy

(a) Equal parts of concentrated NH_4OH and water with 2–4 drops of H_2O_2 (30%) per 10 mL of solution

Microstructures of Sleeve Bearing Materials

Tin- and lead-base sleeve bearing materials depicted in micrographs in this article are identified, and nominal compositions of the materials are given in Table 3. Tin-base alloys are shown in Fig. 25, 26, and 27; lead-base alloys in Fig. 23, 24, 28, 29, 30, 31, 32, 33, 34, 35, 36, and 37; plated overlay alloys in Fig. 38, 39, 40, 41, 42, 43, 44, 45 46, 47, and 48; copper-lead alloys in Fig. 49, 50, 51, 52, 53, and 54; some of the copper-lead alloys provide the underlayer for the plated overlays, so some figures are listed twice.

Table 3 Chemical compositions of sleeve bearing alloys

Fig.	Alloy designation		Composition[a], %									
	SAE	**ISO**	**Sn**	**Sb**	**Pb**	**Cu**	**Fe**	**As**	**Bi**	**Zn**	**Al**	**Others (total)**
Tin base												
25–27	12	SnSb8Cu4	88.0	7.0–8.0	0.50[b]	3.0–4.0	0.10	0.10	0.08	0.005	0.005	0.02

Fig.	Alloy designation		Composition[a], %									
	SAE	**ISO**	**Pb**	**Sn**	**Sb**	**Cu**	**As**	**Bi**	**Zn**	**Al**	**Cd**	**Others (total)**
Lead base												
23, 28–30	13	PbSb10Sn6	bal	5.0–7.0	9.0–11.0	0.7	0.25	0.10	0.005	0.005	0.05	0.02
24, 31–33	14	PbSb15Sn10	bal	9.0–11.0	14.0–16.0	0.7	0.6	0.10	0.005	0.005	0.05	0.02
34–36	15	PbSb1As	bal	0.9–1.7	13.5–15.5	0.7	0.8–1.2	0.10	0.005	0.005	0.02	0.02
37	16[c]	…	bal	3.5–4.7	3.0–4.0	0.10	0.05	0.10	0.005	0.005	0.005	0.40

Fig.	Alloy designation		Composition[a], %				
	SAE	**ISO**	**Pb**	**Sn**	**Cu**	**In**	**Others (total)**
Plated overlay							
38, 39	191	PbSn10	bal	8.0–12.0	…	…	0.5
40–44	192	PbSn10Cu2	bal	8.0–12.0	1.0–3.0	…	0.5
45, 46	193	…	bal	16.0–20.0	2.0–3.0	…	0.5
47, 48	194	PbIn7	bal	…	…	5.0–10.0	0.5

Fig.	Alloy designation		Composition[(a)], %								
	SAE	**ISO**	**Cu**	**Pb**	**Sn**	**Ag**	**Zn**	**P**	**Fe**	**Others (total)**	**Others (each)**
Copper-lead[(d)]											
44, 49, 50	48	CuPb30	67.0–74.0	26.0–33.0	0.5	1.5	0.10	0.02	0.7	0.15	…
40, 41, 47, 48, 51, 52	49	CuPb24Sn	73.0–79.0	21.0–27.0	0.6–2.0	…	…	…	0.7	0.45	…
53, 54	485	…	bal	44.0–58.0	1.0–5.0	…	…	…	0.35	0.45	0.15

(a) All values not given as ranges are maximum except as shown otherwise.
(b) ISO SnSb8Cu4 has 0.35 max Pb.
(c) SAE 16 is cast into and on a porous sintered matrix (usually copper-nickel bonded to steel). The surface layer is 0.025 to 0.13 mm (0.001 to 0.005 in.) thick.
(d) A corrosion-resistant overlay, such as SAE alloys 191 to 194, may be used with SAE alloys 48, 480, and 481 and is recommended for SAE 49.

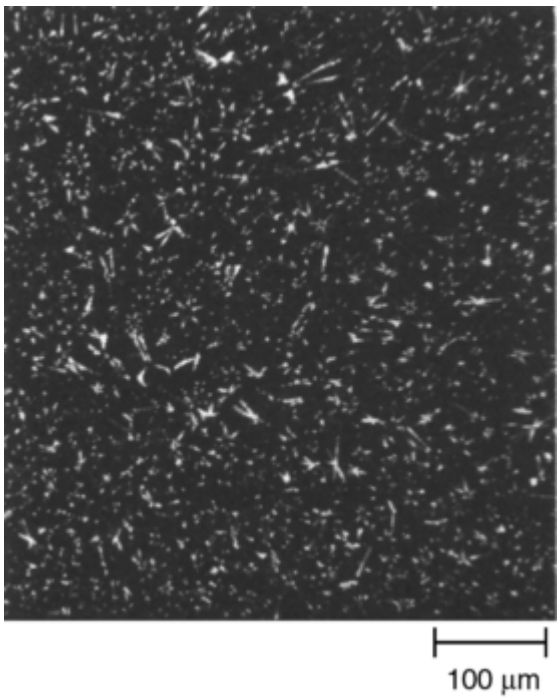

Fig. 25 Tin-base babbitt liner (SAE 12), continuously cast on steel backing strip (bottom). White second-phase particles (see Fig. 26); matrix of tin saturated with copper and antimony. Nital. Original magnification 100×

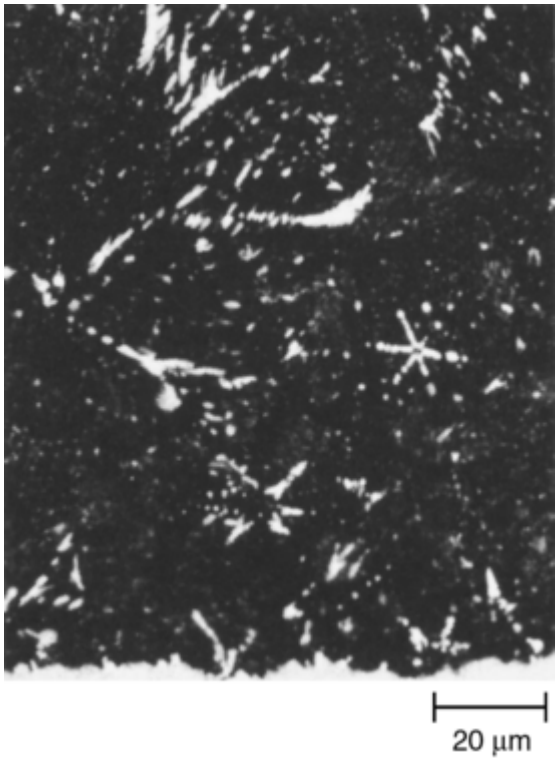

Fig. 26 Same as Fig. 25, except at higher magnification, which reveals starlike arrays of needles of copper-rich constituent and small, round particles of precipitated antimony-tin. Nital. 500×

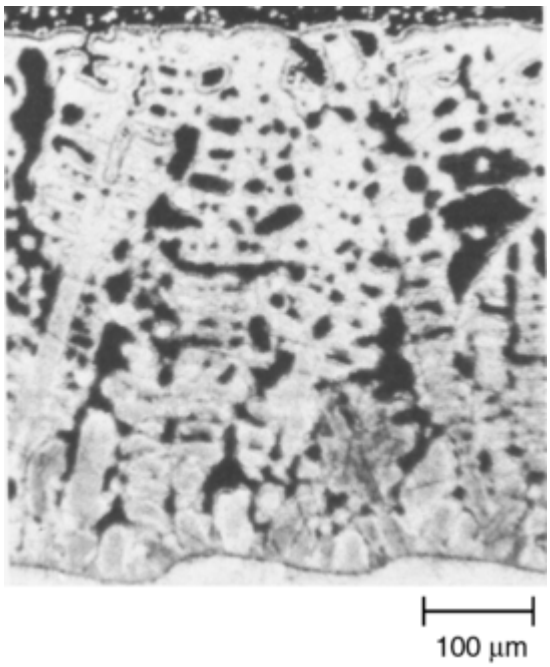

Fig. 27 Overlay of tin-base babbitt (SAE 12), centrifugally cast on the cast 75Cu-24Pb-1Sn liner; steel backing at bottom. $NH_4OH + H_2O_2$. Original magnification 100×

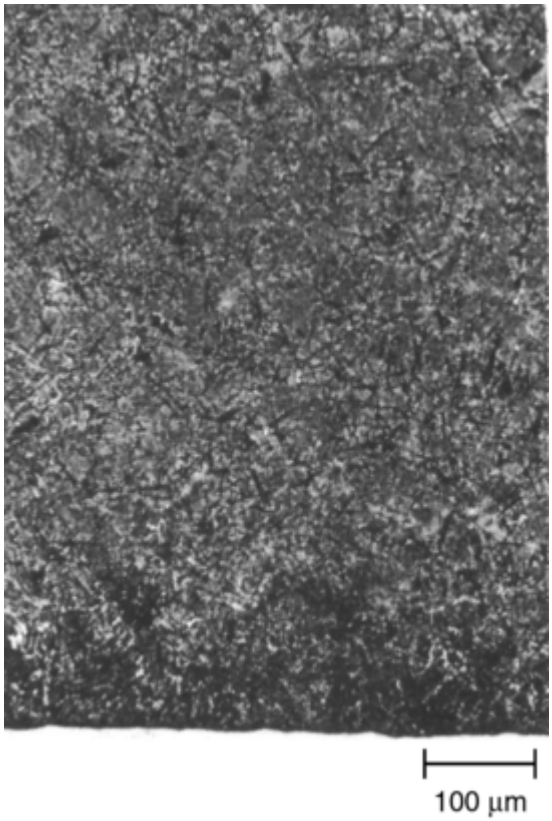

Fig. 28 Lead-base babbitt liner (SAE 13), continuously cast on steel backing strip (bottom). Dark primary crystals of lead in a light matrix of antimony-tin and lead. See also Fig. 29. Nital. Original magnification 100×

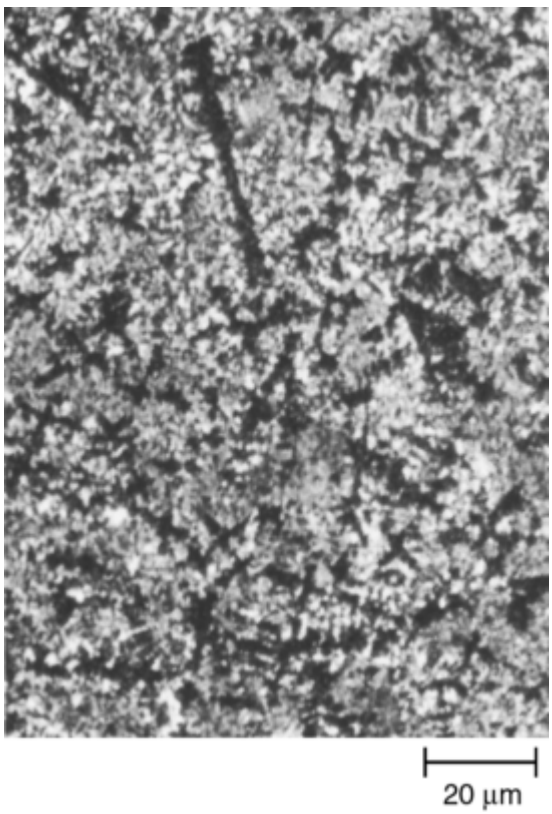

Fig. 29 Same as Fig. 28, except at higher magnification, which reveals the configuration of the lead dendrites and the structure of the eutectic-like matrix of antimony-tin and lead. Compare with Fig. 30. Nital. Original magnification 500×

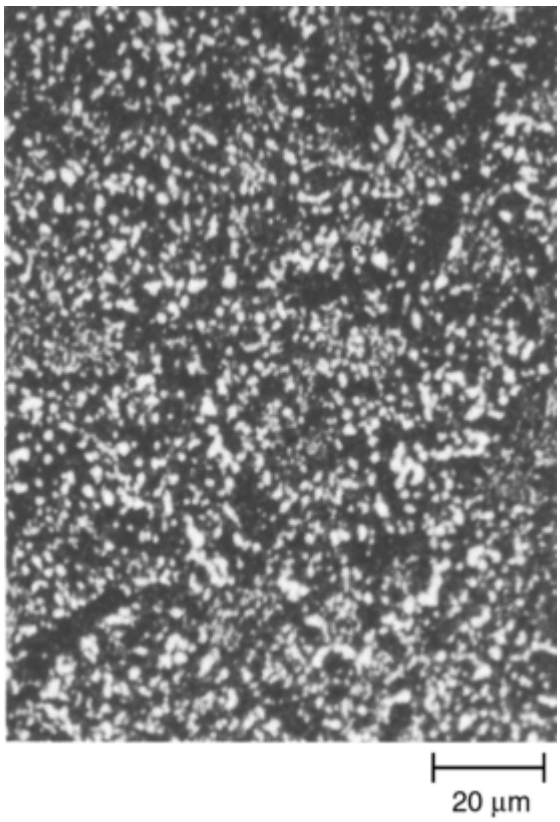

Fig. 30 Same as Fig. 29, except annealed to increase formability, which changed the microstructure to white crystals of eutectic antimony-tin in a dark matrix of lead-rich solid solution. Nital. Original magnification 500×

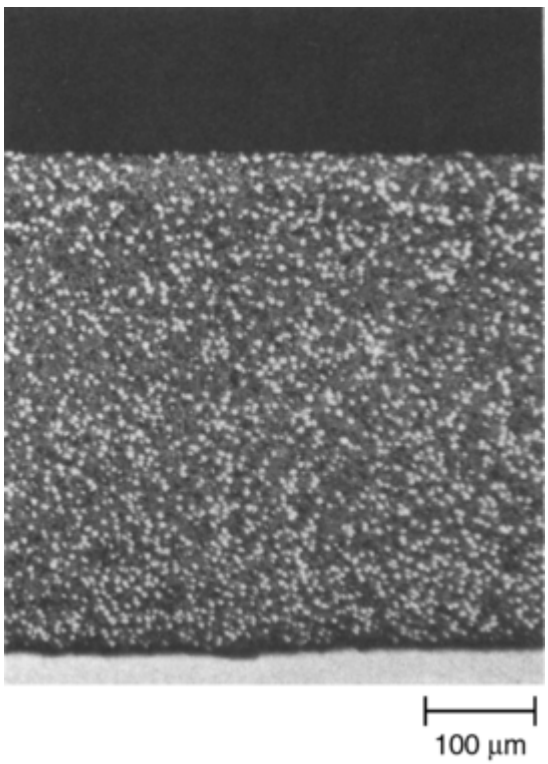

Fig. 31 Lead-base babbitt liner (SAE 14), continuously cast on steel backing strip (bottom). White particles of antimony-tin in a dark matrix of lead-rich solid solution. See also Fig. 32. Nital. Original magnification 100×

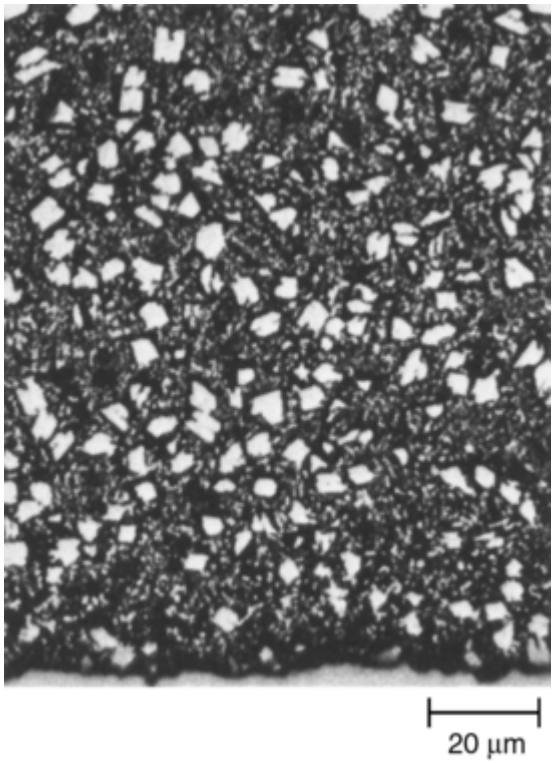

Fig. 32 Same as Fig. 31, except at higher magnification, which reveals that the white antimony-tin compound is in the form of cuboid-shaped primary crystals and small eutectic particles. Compare with Fig. 33. Nital. Original magnification 500×

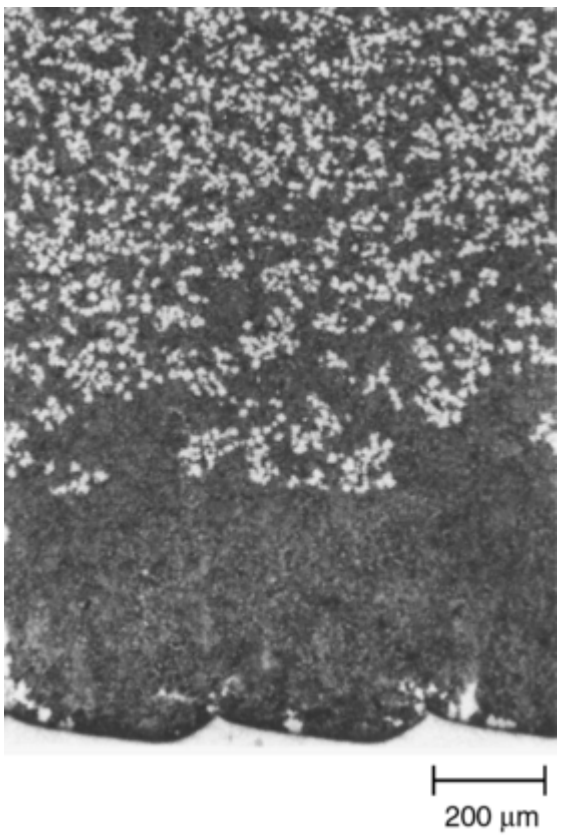

Fig. 33 Same as Fig. 31, but centrifugally cast against inside wall of cylindrical steel shell (bottom). Primary crystals of antimony-tin segregated away from bond between babbitt and steel backing. Nital. Original magnification 50×

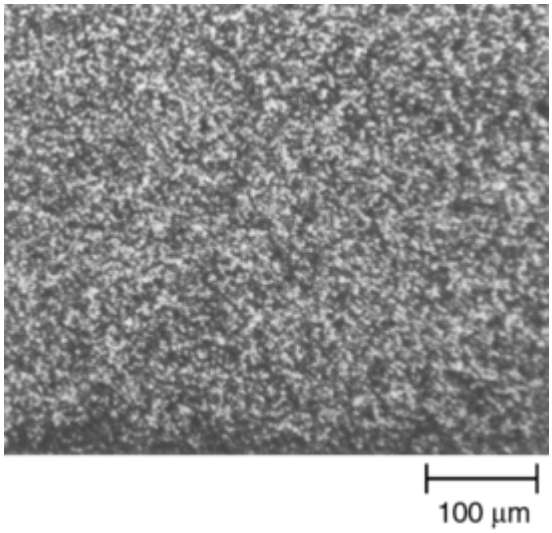

Fig. 34 Lead-base babbitt liner (SAE 15), continuously cast on steel backing strip (bottom). Antimony-arsenic phase (white) in dark matrix of lead-rich solid solution. See also Fig. 35. Nital. Original magnification 100×

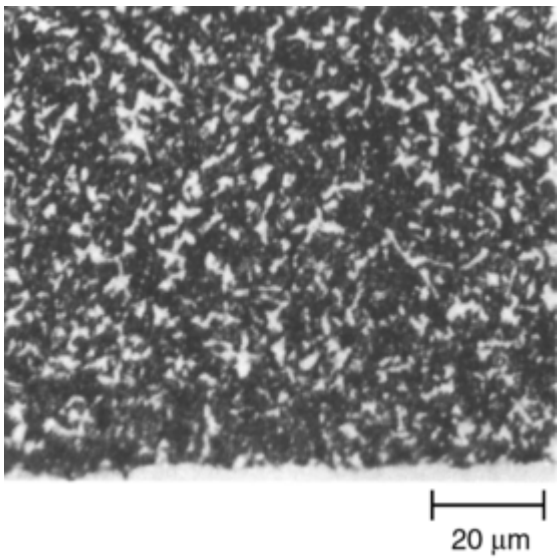

Fig. 35 Same as Fig. 34, except at higher magnification, showing the white particles of antimony-arsenic phase to be of two types: small eutectic particles and large primary crystals. Compare with Fig. 36. Nital. Original magnification 500×

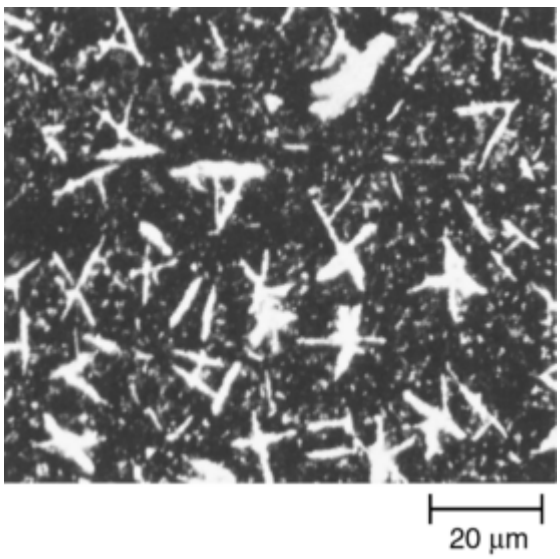

Fig. 36 Same as Fig. 35, except that improper casting conditions have caused the primary antimony-arsenic crystals to form undesirable starlike patterns of needles, causing a decrease in formability. Nital. Original magnification 500×

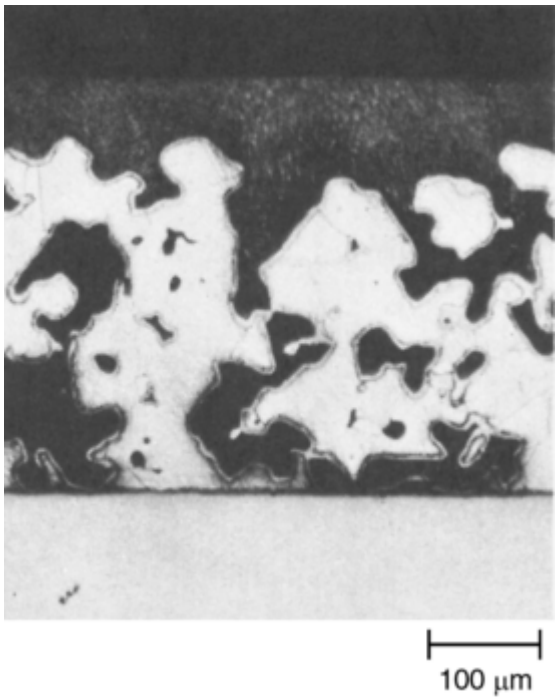

Fig. 37 Liner that was made by infiltrating an open grid of tin bronze (98Cu-2Sn) with molten lead-base babbitt (SAE 16). The grid was made by sintering a mixture of copper and copper-tin alloy powders on a steel backing strip. The excess babbitt formed an overlay. $NH_4OH + H_2O_2$. Original magnification 100×

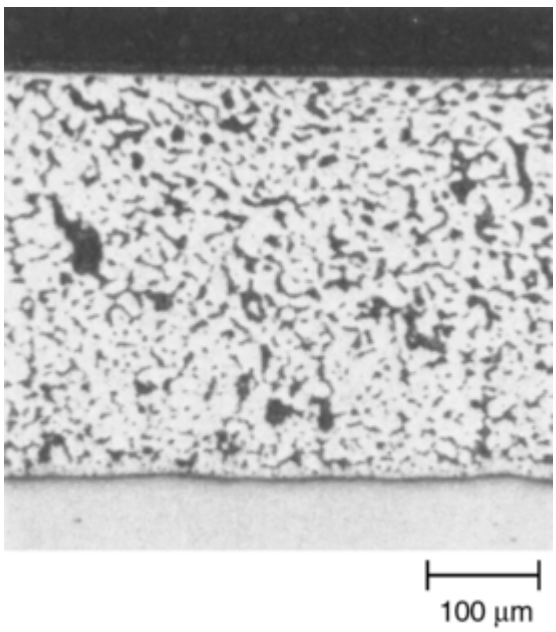

Fig. 38 From top: electroplated 0.013 mm (0.0005 in.) overlay of lead-tin alloy (SAE 191), sintered copper-lead alloy (SAE 49) liner, and steel backing. See also Fig. 39. $NH_4OH + H_2O_2$. Original magnification 100×

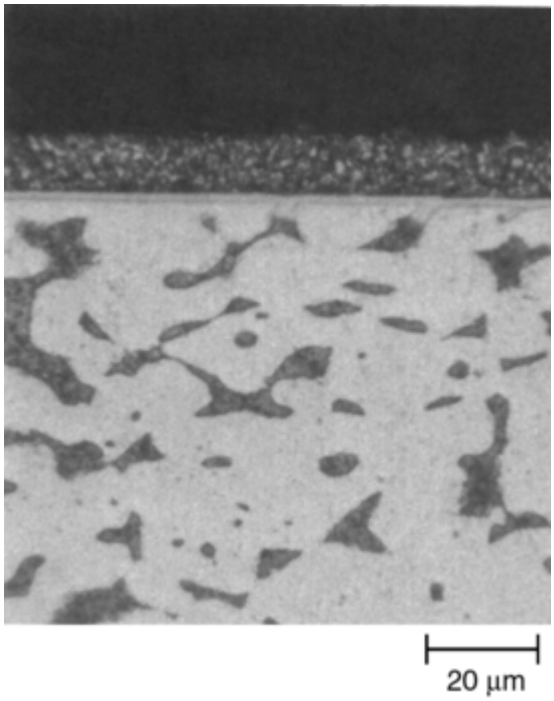

Fig. 39 Higher-magnification view of Fig. 38, showing SAE 191 overlay at top of micrograph separated from sintered SAE 49 bearing liner by flashed 0.001 mm (0.00004 in.) nickel diffusion barrier (gray band below overlay). Light areas in overlay are tin-rich phase; dark areas, lead-rich phase. $NH_4OH + H_2O_2$. Original magnification 500×

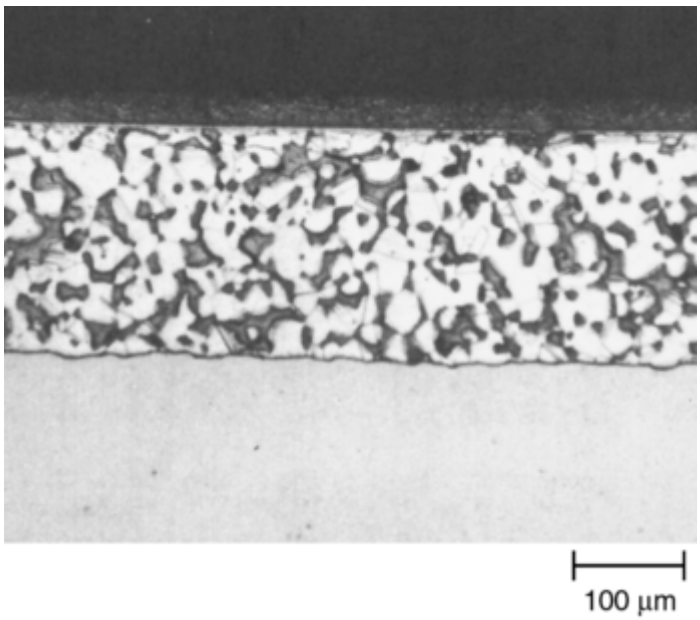

Fig. 40 From top: electroplated overlay of lead-tin-copper alloy (SAE 192), electroplated brass barrier layer (see Fig. 41 for better detail), sintered copper-lead alloy liner (SAE 49), and steel backing strip (bottom). $NH_4OH + H_2O_2$. Original magnification 100×

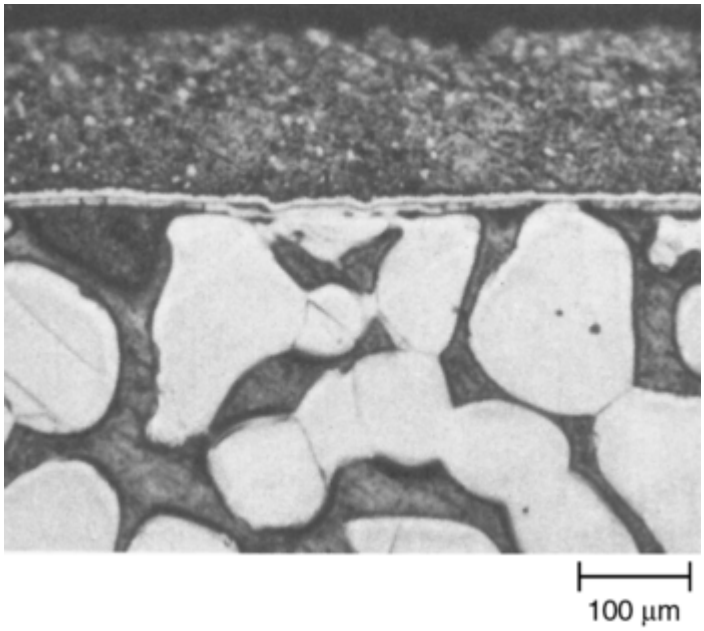

Fig. 41 Upper part of Fig. 40 at higher magnification. Light bands are the brass plated between overlay (top) and liner (bottom) to prevent diffusion of tin from overlay into liner during operation. Duplex brass layer resulted when tin diffused into upper part of the brass. $NH_4OH + H_2O_2$. Original magnification 500×

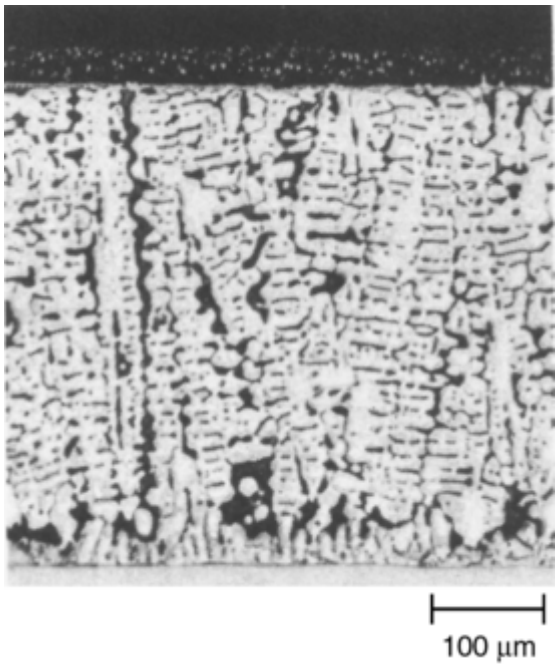

Fig. 42 Electroplated overlay of SAE 192 on the cast 75Cu-25Pb alloy liner that first had been nickel plated; steel backing strip is at bottom. See also Fig. 43. $NH_4OH + H_2O_2$. Original magnification 100×

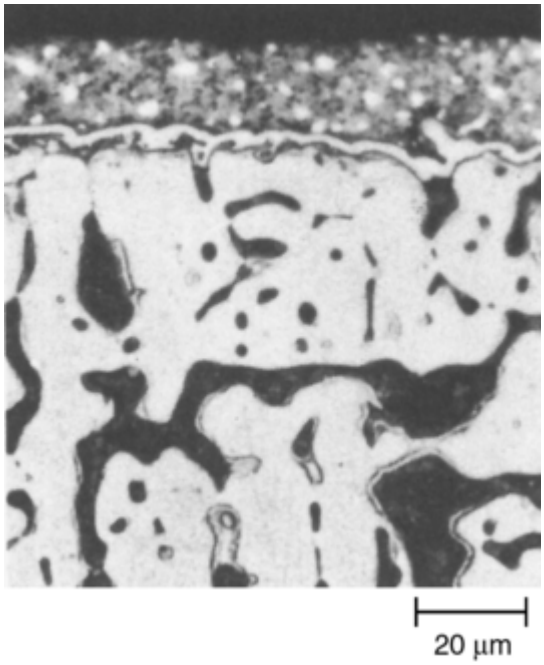

Fig. 43 Higher-magnification view of Fig. 42 (without steel), showing the nickel (light band) plated on the liner to prevent diffusion of tin from the overlay into the copper-lead alloy liner. $NH_4OH + H_2O_2$. Original magnification 500×



Fig. 44 Similar to Fig. 42, except the lead-tin-copper alloy overlay was electroplated on the copper-lead alloy liner (SAE 48) shown in Fig. 50, which first had been nickel electroplated. $NH_4OH + H_2O_2$. Original magnification 100×

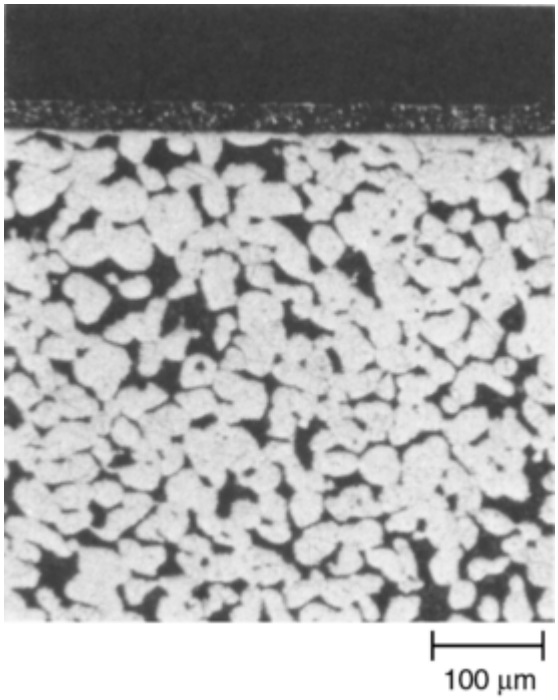

Fig. 45 From top: electroplated 0.02 mm (0.0008 in.) overlay of lead-tin-copper alloy (SAE 193) and sintered copper-lead alloy (SAE 49) liner. See also Fig. 46, which shows both tin and nickel diffusion barriers not resolvable at lower magnifications. $NH_4OH + H_2O_2$. Original magnification 100×

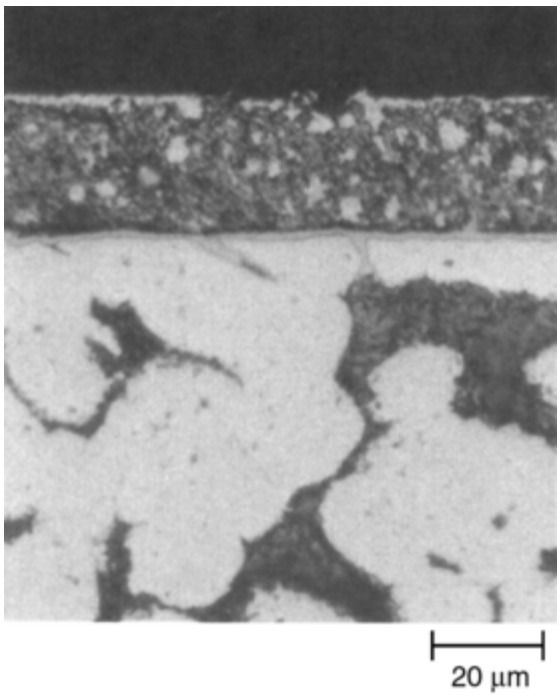

Fig. 46 Higher-magnification view of Fig. 45, showing from top: tin flash (thin white band along upper edge of overlay), SAE 193 overlay, 0.001 mm (0.00004 in.) nickel flash (gray band below overlay) to prevent diffusion of tin into the liner alloy, and SAE 49 liner. Light areas in overlay are tin-rich phase; dark areas, lead-rich phase. $NH_4OH + H_2O_2$. Original magnification 500×

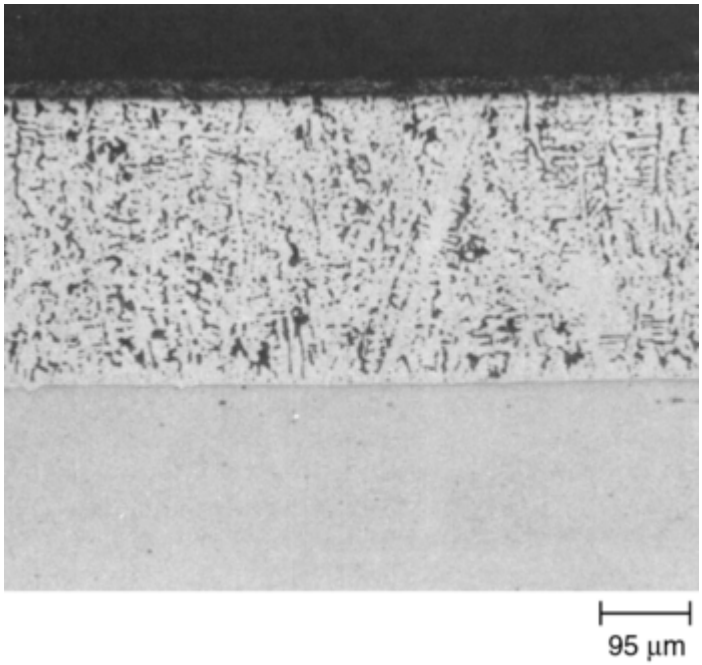

Fig. 47 From top: electroplated 0.02 mm (0.0008 in.) overlay of lead-indium alloy (SAE 194), cast copper-lead alloy (SAE 49) liner, and steel backing. See also Fig. 48. $NH_4OH + H_2O_2$. Original magnification 105×

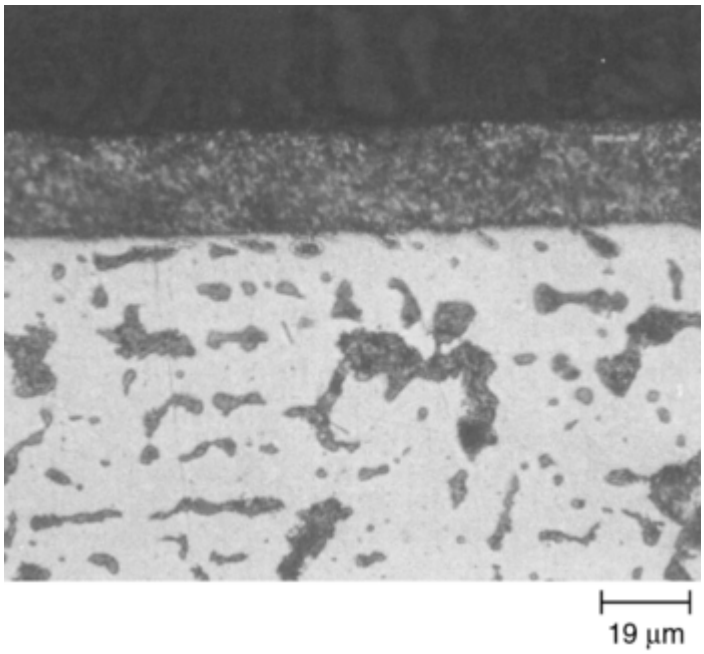

Fig. 48 Higher-magnification view of Fig. 47 (steel not shown). Light areas in the overlay are indium-rich phase; dark areas, lead-rich phase. $NH_4OH + H_2O_2$. Original magnification 525×

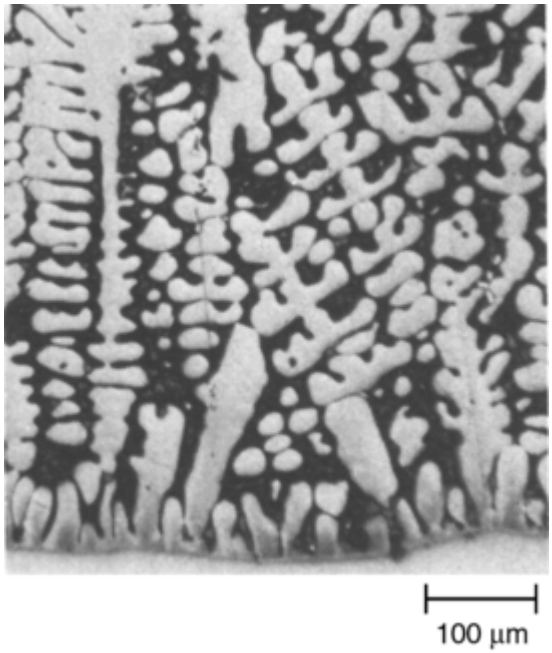

Fig. 49 Copper-lead alloy liner (SAE 48), gravity cast against inner wall of cylindrical steel shell (bottom). Coarse copper dendrites, blunted by addition of silver, in a continuous matrix of lead. Compare with Fig. 50. $NH_4OH + H_2O_2$. Original magnification 100×

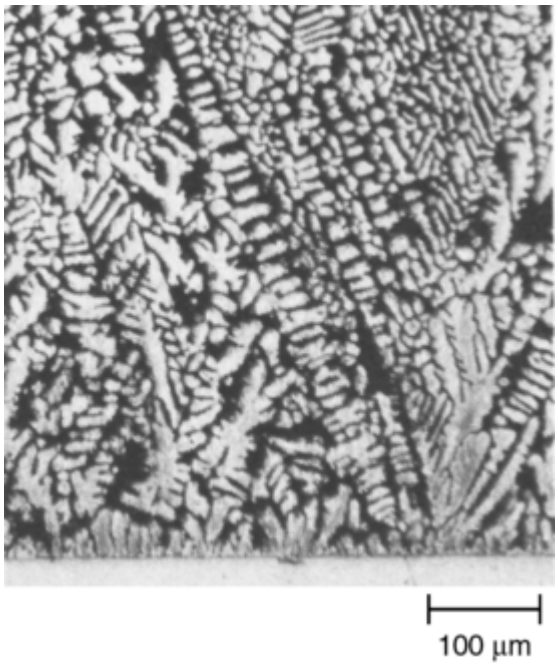

Fig. 50 Same as Fig. 49, except the copper-lead alloy liner was continuously cast on a steel backing strip (bottom of micrograph), which resulted in a faster cooling rate and thus produced finer dendrites of copper. $NH_4OH + H_2O_2$. Original magnification 100×

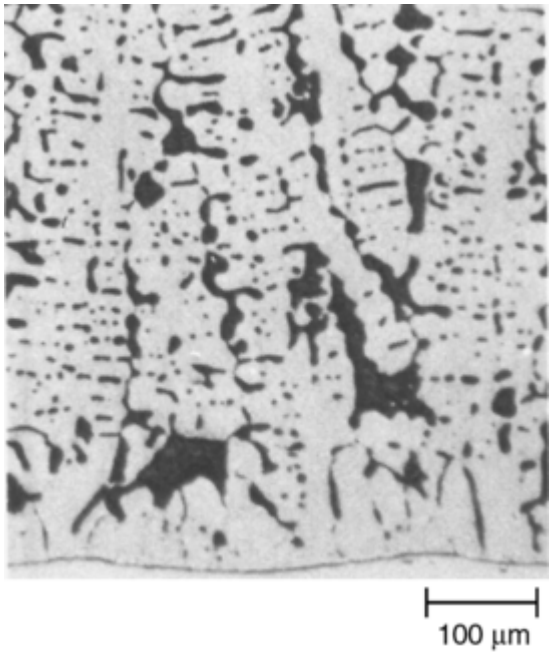

Fig. 51 Copper-lead alloy liner (SAE 49), gravity cast against inside wall of cylindrical steel shell (bottom). Coarse copper dendrites (light) in a matrix of lead (dark). Compare with Fig. 52. $NH_4OH + H_2O_2$. Original magnification 100×

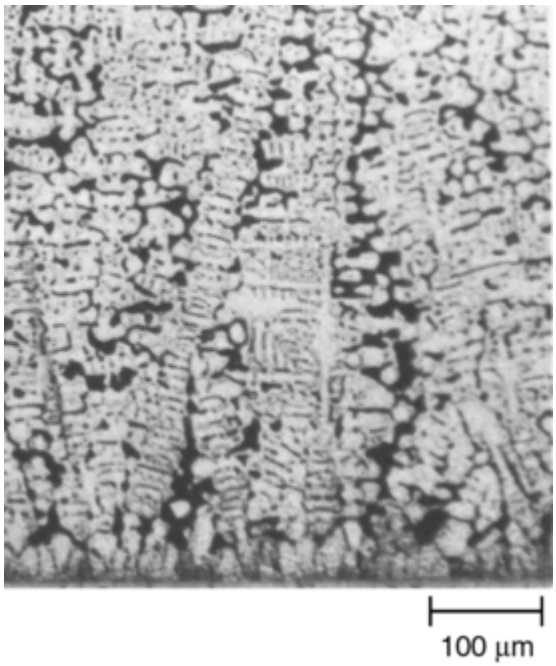

Fig. 52 Same as Fig. 51, except the copper-lead alloy was continuously cast on a steel backing strip (bottom), which resulted in faster cooling and thus produced finer dendrites of copper. $NH_4OH + H_2O_2$. Original magnification 100×

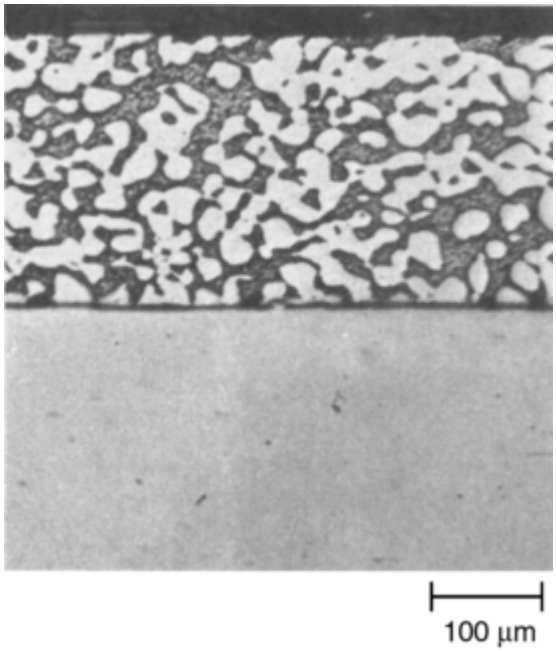

Fig. 53 High-leaded tin bronze liner (SAE 485); prealloyed powder, sintered on a steel backing strip (bottom), cold rolled, resintered. Copper grains; intergranular lead (black). See also Fig. 54. $NH_4OH + H_2O_2$. Original magnification 100×

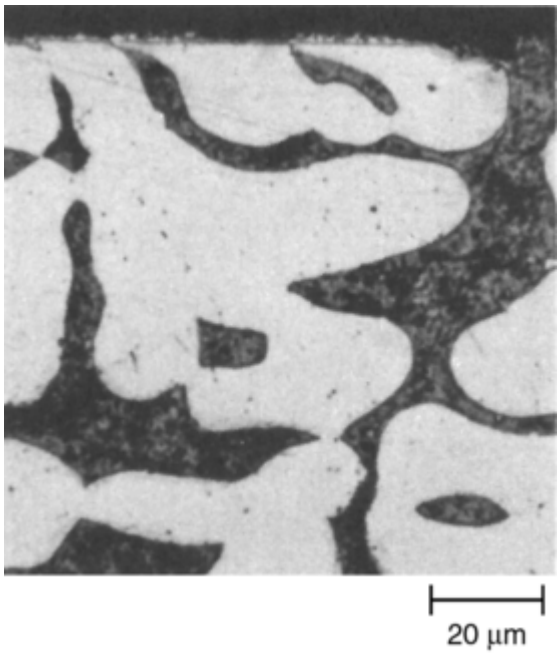

Fig. 54 Same as Fig. 53, but higher magnification reveals the details of the structure, which shows the dark intergranular matrix of lead is almost continuous. $NH_4OH + H_2O_2$. Original magnification 500×

Bimetal Bearings. Bearing materials are often bonded to a backing of stronger material such as steel to form a bimetal bearing with increased load-carrying capacity. The bonded layer of the bearing material can be thinner than 0.13 mm (0.005 in.). Babbitts, copper-lead alloys, and leaded tin bronzes are often bonded to steel backing by such processes as continuous gravity casting onto a steel strip (Fig. 25, 28, 31, 34) as well as static gravity and centrifugal casting (Fig. 37, 33) against the inside surface of a cylindrical shell.

Aluminum alloys are generally clad to a steel backing by warm rolling. To facilitate bonding, the steel is roughened by belt sanding or grit blasting and is sometimes electroplated with a thin layer of nickel before being clad with the aluminum alloy (the resulting bearing is still referred to as bimetal).

Other aluminum bearing alloy liners are bonded using an unalloyed aluminum layer. This layer may be formed as part of the bearing alloy fabrication process (as is the case with the powder-rolled Al-8Pb-4Si-1Sn-1Cu

alloy), or it may be established during fabrication of the bearing alloy strip prior to its cladding to steel (as is often true for SAE 783 alloy).

Silver and silver alloy liners can also be deposited onto a steel backing. A layer of unalloyed silver is deposited by electroplating, followed by a layer of alloyed silver.

Sintered liners for sleeve bearings are made from prealloyed powders of copper-lead alloys or high-leaded tin bronzes by spreading the powder uniformly on a continuously moving steel strip that passes through a sintering furnace with a reducing atmosphere. The particles of powder become sintered together, forming an open grid bonded to the steel strip. This bimetal is then rolled to compact the liner and resintered to improve the bond strength. However, aluminum alloy powder for liners is usually roll compacted and sintered before being roll clad to the steel backing strip.

Liners are also made by infiltration of a lower-melting material into a layer of sintered copper or copper alloy powder. The powder layer, usually a copper alloy, is not compacted after sintering; the open grid of the sintered powder layer is infiltrated with molten material having a lower melting temperature than that of the grid alloy. This infiltrant is often lead or a lead alloy, but it may be a nonmetallic material such as a synthetic fluorine-containing resin. Detailed information on sintering, infiltration, and roll compaction of metal powders can be found in *Powder Metal Technologies and Applications,* Volume 7 of *ASM Handbook,* 1998.

Trimetal Bearings. The fatigue strength of babbitt or lead-tin alloy can be increased significantly by reducing the thickness of the material to 0.013 to 0.05 mm (0.0005 to 0.0020 in.). Such layers are typically produced by electrodeposition. Under severe operating conditions, these layers may easily wear through; if the backing is steel, seizure can result. To avoid seizure, an interlayer of strong bearing material is placed between the steel backing and the babbitt surface layer.

During the operation of some trimetal bearings, the temperature may rise enough to cause the diffusion of tin from overlays of lead-tin alloys into the intermediate liners of copper alloy, with resulting deterioration of the bearings. To prevent this diffusion, the liner material of such bearings is first electroplated with a thin barrier layer of brass or nickel (the resulting bearing is still referred to as trimetal). Aluminum alloy liners are given a zinc immersion coating (zincate), then a thin electroplated layer of copper or nickel in preparation for electrodeposition of the overlay. Thin overlays can also be cast in place by using an excess amount of the lower-melting material when infiltrating sintered liners, as described previously.

Metallography and Microstructures of Lead and Its Alloys, *Metallography and Microstructures,* Vol 9, *ASM Handbook*, ASM International, 2004, p. 789–800

Acknowledgment

This article is adapted from the articles by “Lead and Lead Alloys,” Carl DiMartini, and “Sleeve Bearing Materials,” by Milton W. Toaz, *Metallography and Microstructures,* Volume 9 of *ASM Handbook,* 1985.

Metallography and Microstructures of Lead and Its Alloys, *Metallography and Microstructures,* Vol 9, *ASM Handbook*, ASM International, 2004, p. 789–800

Metallography and Microstructures of Lead and Its Alloys

References

1. Lead Development Association International, web site, London, U.K., 2004

2. J.P. Hilger, Developments in Metallography of Lead and Lead Alloys, *MC95 International Metallography Conference Proceedings,* ASM International, 1996, p 229

3. K.H. Ednie, Metallographic Preparation of Soft Materials-Lead Alloys, *MC95 International Metallography Conference Proceedings,* ASM International, 1996, p 193

4. J. Yewko and D. Marshall, Lead Metallography Made Easy, *Adv. Mater. Process.,* Vol 153 (No. 2), 1998, p 22–23

5. G. Kehl, *Metallurgical Laboratory Practices,* McGraw-Hill, 1949

T.V. Padfield, Metallography and Microstructures of Magnesium and Its Alloys, *Metallography and Microstructures,* Vol 9, *ASM Handbook,* ASM International, 2004, p. 801–815

Metallography and Microstructures of Magnesium and Its Alloys

Toby V. Padfield, ZF Sachs Automotive of America

Introduction

FIVE BASIC MAGNESIUM ALLOY SYSTEMS are currently in commercial production, and these can be classified by the major alloying elements: aluminum, manganese, zinc, zirconium, and rare earths. In the past, thorium also was used in alloys requiring creep strength at elevated temperatures. However, the radioactive nature of this element now generally precludes its use in most applications.

Magnesium alloys also can be classified broadly into three categories depending on the type of processing to which they will be subjected: sand and gravity or low-pressure die (permanent mold) casting alloys; high-pressure die casting alloys; and wrought alloys. The nominal compositions and processing routes for these alloys are summarized in Table 1.

Table 1 Magnesium alloys, nominal composition

Alloy	Nominal composition, mass%					
	Al	**Mn**	**Th**	**Zn**	**Zr**	**Other[(a)]**
Sand and low-pressure die (permanent mold) casting alloys						
AM100A	10.0	0.10	3.3	3.0	0.7	1.5 Ag, 2.1 Di
AZ63A	6.0	0.15				
AZ81A	7.6	0.13		0.7		
AZ91C & E	8.7	0.13		0.7		
AZ92A	9.0	0.1		2.0		
EQ21A						
EZ33A				2.7	0.6	3.3 RE
HK31A					0.7	
HZ32A			3.3	2.1	0.7	
K1A					0.7	
QE22A					0.7	2.5 Ag, 2.1 Di
QH21A			1.0		0.7	2.5 Ag, 1.0 Th
WE43A					0.7	4.0 Y, 3.4 RE
WE54A					0.7	5.2 Y, 3.0 RE
ZC63A		0.25		6.0		2.7 Cu
ZE41A				4.2	0.7	1.2 RE
ZE63A				5.8	0.7	2.6 RE
ZH62A			1.8	5.7	0.7	
ZK51A				4.6	0.7	
ZK61A				6.0	0.7	
High-pressure die casting alloys						
AE42	4.0	0.1				2.5 RE
AM20	2.1	0.1				
AM50A	4.9	0.26				

AM60A & B	6.0	0.13				
AS21	2.2	0.1				1.0 Si
AS41A	4.2	0.2		1.0 Si		
AZ91A, B & D	9.0	0.13				0.7
Wrought alloys						
AZ10A	1.2	0.2				0.4
AZ31B & C	3.0	0.20				1.0
AZ61A	6.5	0.15				1.0
AZ80A	8.5	0.12				0.5
M1A		1.2				
ZC71		0.5		6.5	1.25 Cu	
ZK21A				2.3		0.45
ZK31				3.0		0.6
ZK40A				4.0		0.45
ZK60A				5.5		0.45
ZK61			6.0	0.8		
ZM21		0.5	2.0			

(a) RE, rare earth metals in the form of cerium-base mischmetal (nominal composition: 50 mass % Ce, 25 mass% La, 15 mass% Nd, 8 mass% Pr, balance other); Di, didymium, a neodymium-base mischmetal (nominal composition: 80 mass% Nd, 16 mass% Pr, 2 mass% Gd, 2 mass% other).

Source: Ref 1

Although there is no universally used system for designating magnesium alloys, there is a trend toward using the ASTM International nomenclature (Ref 2, 3). This four-part system of alloy and temper designations is explained in Table 2. The first code letters, generally two, indicate the principal alloying elements in order of decreasing concentration. The number part of the code indicates the mass percent of the major alloying elements rounded to the nearest whole number. The third code letter indicates the sequence when that particular alloy composition was registered relative to other alloys having the same nominal composition. The last part is the temper designation.

Table 2 Standard four-part ASTM system of alloy and temper designations for magnesium alloys

See text for discussion.

First part	Second part	Third part	Fourth part
Indicates the two principal alloying elements	Indicates the amount of the two principal alloying elements	Distinguishes between different alloys with the same percentages of the two principal alloying elements	Indicates condition (temper)
Consists of two code letters representing the two main alloying elements arranged in order of decreasing concentration (or alphabetically if concentrations are equal)	Consists of two numbers corresponding to rounded-off percentages of the two main alloying elements and arranged in same order as alloy designations in first part	Consists of a letter of the alphabet assigned in order as compositions become standard	Consists of a letter followed by a number (separated from the third part of the designation by a hyphen)
A—aluminum **B—bismuth** **C—copper** **D—cadmium**	Whole numbers	Letters of alphabet except I and O	F—as fabricated O—annealed H10 and H11—slightly strain hardened

E—rare earth **F—iron** **G—magnesium** **H—thorium** **J—strontium** **K—zirconium** **L—lithium** **M—manganese** **N—nickel** **P—lead** **Q—silver** **R—chromium** **S—silicon** **T—tin** **W—yttrium** **X—calcium** **Y—antimony** **Z—zinc**	H23, H24, and H26—strain hardened and partially annealed T4—solution heat treated T5—artificially aged only T6—solution heat treated and artificially aged T8—solution heat treated, cold worked, and artificially aged

For example, AZ91D-F is a magnesium alloy comprising approximately 9% Al and 1% Zn and is the fourth alloy to be registered with this nominal composition. The -F indicates that this die casting is used in the as-fabricated condition. High-pressure die castings often are identified without the temper designation. Other designation systems used include UNS (Ref 4), EN (Ref 5), and ISO (Ref 6, Ref 7).

Although a large number of alloys are listed in Table 1, many of these have limited or no commercial usage. Due to a significant increase in automotive applications using high-pressure die castings beginning in the mid-1990s, the most frequently used alloys are AZ91D, AM50A, and AM60B (Ref 8, 9). This increased automotive usage has also spurred considerable research into new alloy development, particularly casting alloys that can provide improved strength and creep resistance on a cost-effective basis (similar price to AZ91D) (Ref 10). Although the compositions of many of these new alloys have not been disclosed fully, they are based on either magnesium-aluminum alloys with the addition of alkaline earth metals strontium or calcium, or on magnesium/rare-earth alloys. In either case, enhanced creep resistance is provided by the precipitation of intermetallic compounds along the primary magnesium grain boundaries. Some of these alloys, the casting process used, the nominal composition, and the developers/suppliers are listed in Table 3 (Ref 11).

Table 3 New magnesium alloy development for automotive applications

Alloy	Process	Nominal composition	Developer
AJ52	HPDC	5Al, 2Sr	Noranda (Ref 12, 13)
AJ62	HPDC	6 Al, 2Sr	Noranda (Ref 12, 13)
AXJ530	HPDC	5Al, 3Ca, 0.15Sr	GM (Ref 14, 15)
AEX522	HPDC	5Al, 2Ca, 2RE	Honda (Ref 16, 17)
MRI-153M	HPDC	7Al, 0.7Zn, 0.3Mn, Ca, RE, Sr	Dead Sea & VW (Ref 18, 19)
MRI-230D	HPDC	5Al, 6Zn, 0.3Mn, 0.7Ca, RE, Sr	Dead Sea & VW (Ref 18, 19)
ASE210	HPDC	2Al, 1Si, 0.15RE	Hydro (Ref 20)
ML10	SC or LPDC	2.5Nd, 0.7Zr, 0.4Zn	Solikamsk
MRI-201S, MRI-202S	SC or LPDC	6Al, 0.4Mn, 0.4 Zn, 2.5 Ca, Sn, Sr	Dead Sea & VW (Ref 21, 22)
AMC SC1	SC or LPDC	1.7Nd, 1RE, 0.5Zr, 0.5Zn	AMC & CSIRO (Ref 23, 24)

HPDC, high-pressure die casting; SC, sand casting; LPDC, low-pressure die casting (permanent mold casting).
Source: Ref 11

References cited in this section

1. L. Gaines et al., *Analysis of the Potential for New Automotive Uses of Wrought Magnesium,* Center for Transportation Research National Laboratory, United States Department of Energy, 1996 (available to the public from National Technical Information Service, U.S. Department of Commerce)

2. "Practice for Codification of Certain Nonferrous Metals and Alloys, Cast and Wrought," B 275, *Annual Book of ASTM Standards,* ASTM International

3. "Practice for Temper Designation of Magnesium Alloys, Cast and Wrought," B 296, *Annual Book of ASTM Standards,* ASTM International

4. "Standard Practice for Numbering Metals and Alloy (UNS)," E 527, *Annual Book of ASTM Standards,* ASTM International

5. "Magnesium and Magnesium Alloys—Magnesium and Magnesium Alloy Anodes, Ingots and Castings—Designation System," EN 1754, European Committee for Standardization

6. "Magnesium and Magnesium Alloys—Magnesium Alloy Ingots and Castings," ISO 16220, International Organization for Standardization

7. "Magnesium and Magnesium Alloys—Magnesium Alloy—Wrought Magnesium Alloys," ISO 3116, International Organization for Standardization

8. D. Webb, "Magnesium Supply and Demand," Proc. 60th Annual World Magnesium Conference, International Magnesium Association, 2003

9. D. Kramer, Magnesium, *Minerals Yearbook,* Vol I, Metals and Minerals, U.S. Government Printing Office, 2002

10. M.O. Pekguleryuz et al., Creep Resistant Magnesium Alloys for Powertrain Applications, *Adv. Eng. Mater.,* Vol 5 (No. 12), 2003, p 866–878

11. B.R. Powell et al., "Progress Toward a Magnesium-Intensive Engine: The USAMP Magnesium Powertrain Cast Components Project," Technical Paper Series 2004-01-0654, SAE International

12. M.O. Pekguleryuz et al., “Magnesium-Based Casting Alloys Having Improved Elevated Temperature Performance,” United States Patent 6,322,644

13. M.O. Pekguleryuz et al., Development of Creep Resistant Mg-Al-Sr Alloys, *Magnesium Technology 2001*, TMS (The Minerals, Metals, & Materials Society) 2001, p 119–125

14. B.R. Powell et al., “Creep-Resistant Magnesium Alloy Die Castings,” United States Patent 6,264,763

15. B.R. Powell et al., Creep and Microstructure of Magnesium-Aluminum-Calcium Based Alloys, *Metall. Mater. Trans. A*, Vol 33A, March 2002, p 567–574

16. T. Baba et al., “Heat-Resistant Magnesium Alloy,” United States Patent 5,811,058

17. S. Koike et al., “Development of Lightweight Oil Pans Made of a Heat-Resistant Magnesium Alloy for Hybrid Engines,” Technical Paper Series 2000-01-1117, SAE International

18. B. Bronfin et al., “Magnesium Alloy for High Temperature Applications,” United States Patent 6,139,651

19. B. Bronfin et al., Development of New Magnesium Alloys for Advanced Applications, *Magnesium—Alloys and Technologies*, Wiley-VCH, 2003

20. P. Bakke et al., “Die Cast Magnesium Alloys for High Temperature Applications,” Technical Paper Series 2003-01-0189, SAE International

21. B. Bronfin et al., “High Strength Creep Resistant Magnesium Alloys,” United States Patent Application US 2003/0084968 A1

22. B. Bronfin et al., “High Temperature Mg Alloys for Sand and Permanent Mold Casting Applications,” Technical Paper Series 2004-01-0656, SAE International

23. C.J. Bettles et al., “Creep Resistant Magnesium Alloy,” International Publication Number WO 2004/001087 A1, World Intellectual Property Organization

24. C.J. Bettles et al., “AMC-SC1: A New Mg Alloy Suitable for Powertrain Applications,” Technical Paper Series 2003-01-1365, SAE International

---

T.V. Padfield, Metallography and Microstructures of Magnesium and Its Alloys, *Metallography and Microstructures*, Vol 9, *ASM Handbook*, ASM International, 2004, p. 801–815

Metallography and Microstructures of Magnesium and Its Alloys

Toby V. Padfield, ZF Sachs Automotive of America

Specimen Preparation

Magnesium and its alloys are among the most difficult metallic specimens to prepare for macrostructural and microstructural examination (Ref 25, 26). Relief is an issue due to the differences in hardness between the matrix and the precipitate phases. The low matrix hardness also contributes to problems with persistent

scratches and surface deformation, usually in the form of mechanical twinning. Also, the high reactivity of magnesium restricts the use of water during final polishing and the types of etchants that can be used.

Specimens chosen for metallographic examination should be representative. The edge and center of large ingots should be examined; longitudinal and transverse sections should be taken from sheet, extrusions, and forgings. When sectioning high-pressure die castings, it is necessary to take into account that the microstructure of the skin (near surface) is usually significantly different from that of the interior of the casting. Subsurface banded defects are also a common feature of magnesium alloy die castings.

Sectioning. Specimens can be obtained by using a hack saw, band saw, or an abrasive cut-off wheel. Always use the cutting method that produces the least amount of damage. The use of a coolant during sectioning is recommended in order to minimize the thermal effects generated during sectioning.

Care should be exercised to prevent cold working of the metal, which can alter the microstructure and complicate interpretation of constituents. Specimens that have been severely cold worked by rough sawing, squeezing in a vise, or heavy deformation are likely to be mechanically twinned close to the worked surface. The cold-worked surface can be removed by extending the time of each grinding and polishing step up to twice the time required for removing scratches from the preceding stage. Metal should be removed to a depth of approximately 1 mm (0.040 in.) during preparation of the specimen. Cold deformation introduced in the surface layers by grinding and polishing has little detrimental effect on the microstructure, unless the prepared specimen is subsequently heated above the recrystallization temperature. In general, the methods and equipment for specimen preparation discussed in the article “Metallographic Sectioning and Specimen Extraction” in this Volume apply to magnesium alloy specimens.

Mounting. Specimens that are too small to be held conveniently for grinding and polishing or that have an edge that is to be studied can be mounted in one of the common plastic mounting materials. Cold-mounting materials are preferred, but hot compression mounting can be used. When examining alloys in the solution-annealed condition, it is advisable to use a cold castable resin such as epoxy to minimize heat generated during polymerization. Use of a conductive molding arrangement rather than an insulative mold (rubber or plastic molds) can minimize the exothermic temperature increase to less than 10 °C (18 °F) above ambient even when using slow-curing epoxy. One method employs an aluminum foil wrapped steel block with a phenolic cylinder bonded to the foil to create a conductive heat path.

The pressure used in hot compression mounting can also induce mechanical twinning in pure magnesium. Sheet specimens can be clamped together to form packs. Clamping or bolting must be done carefully to prevent cold working. More information is available in the article “Mounting of Specimens” in this Volume.

Grinding. Dry grinding of magnesium should be avoided due to the potential fire hazard associated with magnesium dust. Dry grinding may also result in excessive heating, which can lead to modification of the microstructure and separation of the sample from the plastic mount. If dry grinding cannot be avoided, then the dust should be trapped in an oil bath.

Wet grinding is preferred because it prevents overheating of the specimen and maintains exposure of the sharp edges of the abrasive. Conventional horizontal wheels (200 to 300 mm, or 8 to 10 in. diam) rotating at 250 to 300 rpm using silicon carbide (SiC) paper can be used for plane grinding. Traditional approaches recommend four or more grinding steps, starting with 180 or 240 grit (P180 to P280) and proceeding to 600 grit (P1200) or finer (Ref 25, 26, 27, 28, 29).

A small stream of water directed at the disks during grinding flushes away the abraded fragments. The force applied to each 30 mm (1.25 in.) diam mounted specimen should be 20 to 25 N (4.5 to 5.6 lbf), with grinding time of 2 to 3 min per step. If a sample holder is used, the rotation should be complementary to the platen, otherwise samples should be rotated 90° between steps. Thorough cleaning should be performed after each step using soap and water. A short immersion in an ultrasonic bath can be done also. The surface finish after grinding will be 6 to 14 μm (0.2 to 0.6 mils), which is suitable for macroexamination. Microexamination requires a polished surface.

If the initial surface finish is already sufficient, such as that obtained from high-pressure die casting, grinding may require only a short 1 min step using 35 N (7.9 lbf) per sample on a 1200 grit (P4000) SiC paper rotating at 150 rpm (Ref 30). When using this type of procedure, it is best to use the same lubricant that will be used in the subsequent polishing steps.

Use of rigid-disk grinding can significantly reduce the preparation time, while also improving flatness and edge retention (Ref 31, 32). The disk must be one designed for low hardness metals (40 to 75 HV), as the disks suitable for higher-hardness materials are too aggressive. An initial grinding step using water-lubricated 240

(P280) or 320 grit (P400) SiC may be used depending on the surface quality obtained from sectioning. This is followed by rigid-disk grinding for 3 min using 25 N (5.6 lbf) of force per sample and wheel rotation of 300 rpm. A less aggressive procedure calls for 5 min using 30 N (6.7 lbf) per sample and wheel rotation of 150 rpm. The lubricant used for rigid-disk grinding can be either water or alcohol based.

Mechanical Polishing. Polishing usually entails two or three steps of diamond polishing followed by a final oxide polishing step (Ref 25, 26, 29, 30, 31, 32). Diamond polishing is performed on a woven cloth or napless, flat pads. Napped cloths should be avoided as they can introduce problems with excessive relief and drag/pullout. Lubricants may be water, oil, or alcohol based, with oil-based solutions usually providing a better surface with fewer, shallower scratches.

A typical sequence would be 9 μm (0.4 mils) diamond polishing for 3 to 6 min using 20 to 30 N (4.5 to 6.7 lbf) per sample and wheel rotation of 150 rpm followed by 3 μm (0.12 mils) diamond polishing for 3 to 5 min using 20 to 30 N per sample and wheel rotation of 150 rpm. Wheel rotation can be either complementary or counter to the specimen holder.

A combination of soap and ethanol is recommended for cleaning the oil-based diamond lubricants from the specimens and any holders or fixtures used in automated polishers. The surface may be scrubbed using cotton saturated with ethanol. A quick rinse under water can be used provided it is followed by an ethanol rinse. Compressed air should be used for drying instead of hot air.

Final polishing is performed using synthetic, short nap pads or napless elastomer pads (neoprene or polyurethane). Colloidal silica (SiO_2) with a particle size of 0.02 to 0.04 μm (0.8 to 1.6 μin.), 0.05 μm (2 μin.) alumina, or proprietary solutions that contain both abrasives can be used. Polishing is performed for 1 to 3 min using 10 to 13 N (2.2 to 2.9 lbf) per sample and wheel rotation of 120 to 150 rpm. Longer polishing times in conjunction with SiO_2 may result in slight etching.

The use of water is not recommended during final polishing, even though this complicates cleaning. A mixture of soap and ethanol or glycerol and ethanol can usually clean the specimen adequately. Holding the sample under running water for approximately 1 s can improve the cleaning process with minimal impact to the microstructure. The use of cotton after final polishing can introduce new scratches.

Chemical polishing of magnesium and its alloys is generally not as effective as mechanical polishing, and a rather rough surface results. Samples are first ground down through 600 grit (P1200) SiC and then subjected to chemical polishing using one of the following procedures:

- 10% nital (10 mL HNO_3 in 100 mL anhydrous ethanol or methanol)—swab for 30 to 60 s
- 1% HNO_3 in ethylene glycol—immerse sample face up and swab—a rather slow-acting chemical polish

Following chemical polishing, samples may be etched using one of the appropriate magnesium etchants.

Electrolytic polishing is a relatively slow process, but it is useful when a scratch-free surface is desired for critical examination without etching. It is also useful for polishing large pieces; whole test bars can be polished in 4 to 8 h. For electrolytic polishing of magnesium alloys, a conventional setup and a stainless steel cathode are used. The electrolyte consists of three parts 85% phosphoric acid (H_3PO_4) and five parts 95% ethanol; both are cooled to approximately 2 °C (35 °F) before mixing. Specimens should be polished through 600 grit SiC paper using a kerosene and paraffin mixture as a lubricant and then solvent cleaned before electrolytic polishing.

The cathode and specimen are spaced 20 mm (0.8 in.) apart in a quiescent bath. A current of 3 V direct current (dc) is applied for 30 s, then reduced to 1.5 V, and maintained until the desired finish is produced. While the current is on, the specimen is removed from the electrolyte and rinsed quickly in rapidly running tap water. If the current is shut off while the specimen is in the electrolyte, chemical etching and roughening result.

More rapid electrolytic polishing is obtained with an electrolyte consisting of 10% hydrochloric acid (HCl) in butyl cellosolve (2-butoxyethanol). This electrolyte must be kept below 4 °C (40 °F) during polishing.

Transmission Electron Microscopy (TEM) Preparation Procedures. The thin foils required for TEM examination can be prepared in one of three ways: ion beam milling, electropolishing, or ultramicrotomy.

Ion Beam Milling. Samples for ion beam milling are initially prepared as 3 mm (0.12 in.) diam disks, which are then ground to a thickness of about 0.1 mm (0.004 in.). Some practitioners also dimple the disk to achieve a center disk thickness of 25 to 40 μm (1 to 1.6 mils) before ion beam milling.

Ion beam milling generally is carried out with argon ions at 5 to 8 keV, a current of 0.5 to 1.0 mA, and an incident angle between 5° and 15° (Ref 33, 34, 35, 36, 37, 38).

Electropolishing. Twin-jet electropolishing is carried out on samples that are ground initially to a thickness of 0.15 mm (0.006 in.) or less. The composition and operating parameters for two electrolytes are shown in Table 4.

Table 4 Transmission electron microscopy sample preparation by electropolishing

Electrolyte	Operating parameters	Comments	Ref
87.5 g sodium thiocyanate **15 mL phosphoric acid** **500 mL butyl cellosolve** **500 mL ethanol**	22 V dc 3–5 °C	Initial sample size: 3 mm diameter 50 μm thick	Ref 39
5.3 g lithium chloride **11.1 g magnesium perchlorate** **100 mL 2-butoxyethanol** **500 mL methanol**	90 V dc 100 mA -60 °C	Initial sample size: 3 mm diameter <150 μm thick	Ref 40, 41, 42, 43
1 part nitric acid **2 parts ethanol**	30 V dc -10 °C		Ref 44

Ultramicrotomy. The ultramicrotome has also been used for preparing thin foils of magnesium alloys for TEM examination (Ref 13, 45).

References cited in this section

13. M.O. Pekguleryuz et al., Development of Creep Resistant Mg-Al-Sr Alloys, *Magnesium Technology 2001*, TMS (The Minerals, Metals, & Materials Society) 2001, p 119–125

25. G.F. Vander Voort, Metallography of Magnesium and its Alloys, *Tech-Notes*, Vol 4 (No. 2), Buehler Ltd., 2004

26. Light Metals, *Buehler SUM-MET—The Science Behind Materials Preparation*, Buehler Ltd., 2004

27. K.J. Clark, Magnesium Alloys, *Metallography and Microstructures*, Vol 9, *ASM Handbook*, American Society for Metals, 1985, p 425–434

28. J.M. Tartaglia et al., Magnesium Alloy Ingots: Chemical and Metallographic Analyses, *JOM*, Nov 2001, p 16–19

29. E. Schaberger et al., Development of a Metallographic Microstructure Characterization for the High-Purity Magnesium Alloy, *Pract. Metallogr.*, Vol 35 (No. 6), 1998, p 306–315

30. Metalog Method 350, *e-Metalog*, Struers A/S, Rødovre, Denmark

31. E. Schaberger et al., The Development of an Electrolytic Etching Process for Examining the Microstructure of Thixocast Magnesium Alloy AZ91 hp, *Pract. Metallogr.*, Vol 37 (No. 3), 2000, p 140–149

32. Metalog Method A, *Struers Metalog Guide,* Struers A/S, Rødovre, Denmark, 2000

33. L.-Y. Wei et al., Characterisation of Manganese Containing Intermetallic Particles and Corrosion Behaviour of Die Cast Mg-Al Based Alloys, *Magnesium Technology 2000,* TMS (The Minerals, Metals, & Materials Society), 2000, p 153–160

34. T. Mitchell et al., Microstructure Property Studies of In Situ Worked PVD Mg-Ti Alloys, *Magnesium Technology 2000,* TMS (The Minerals, Metals, & Materials Society), 2000, p 169–174

35. M. Cabibbo et al., Microstructural Study and Mechanical Properties of Thixoformed AZ91, *Magnesium Technology 2000,* TMS (The Minerals, Metals, & Materials Society), 2000, p 301–307

36. E.A. Nyberg et al., Microstructure and Microchemistry of Creep Resistant Magnesium Alloys, *Magnesium Technology 2001,* TMS (The Minerals, Metals, & Materials Society), 2001, p 169–1173

37. L. Shepeleva et al., TEM Study of the As-Cast and Aged Microstructures of Mg-Al-Zn Alloys and the Influence of Zn Content on Precipitation, *Magnesium Technology 2001,* TMS (The Minerals, Metals, & Materials Society), 2001, p 189–194

38. M. Cabibbo et al, Microstructural Study After Solution Treatments of a Thixocast AZ91, *Magnesium Technology 2001,* TMS (The Minerals, Metals, & Materials Society), 2001, p 211–216

39. T. Horie et al., Development of High Creep-Resistant Magnesium Alloy Strengthened by Ca Addition, *Magnesium Technology 2000,* TMS (The Minerals, Metals, & Materials Society), 2000, p 261–269

40. R.V. Allen et al., Magnesium Alloy Sheet Produced by Twin-Roll Casting, *Magnesium Technology 2001,* TMS (The Minerals, Metals, & Materials Society), 2001, p 75–79

41. I.P. Moreno et al., Microstructure and Creep Behavior of a Die Cast Magnesium Rare Earth Alloy, *Magnesium Technology 2002,* TMS (The Minerals, Metals, & Materials Society), 2002, p 111–116

42. G. S. Song et al., Enhancement of the Properties of Mg-Li Alloys by Small Alloying Additions, *Magnesium Technology 2003,* TMS (The Minerals, Metals, & Materials Society), 2003, p 77–79

43. C. Mendis et al., Effects of Ca Additions on Microstructures, Age Hardening Response and Creep Behavior of Mg-8Zn-4Al Casting Alloy, *Magnesium Technology 2003,* TMS (The Minerals, Metals, & Materials Society), 2003, p 183–188

44. F. Czerwinski et al., Correlating the Microstructure and Tensile Properties of a Thixomolded AZ91D Alloy, *Acta Mater.,* Vol 49, 2001, p 1225–1235

45. B.R. Powell et al., The Relationship Between Microstructure and Creep Behavior in AE42 Magnesium Die Casting Alloy, *Magnesium Technology 2001,* TMS (The Minerals, Metals, & Materials Society), 2001, p 175–181

T.V. Padfield, Metallography and Microstructures of Magnesium and Its Alloys, *Metallography and Microstructures,* Vol 9, *ASM Handbook*, ASM International, 2004, p. 801–815

Toby V. Padfield, ZF Sachs Automotive of America

Macroexamination

Macroexamination of magnesium alloys is accomplished using techniques similar to those used for other metals. Much can be learned from low-magnification examination of component surfaces, fracture surfaces, and prepared cross sections, especially with the use of macroetching. Macroexamination is used often for inspection and quality control of finished or semifinished articles such as castings, weldments, and wrought products (forgings, extrusions, etc.).

General Examination. Visual inspection of some fabricated surfaces can be performed without sectioning or mounting, while others may require one or the other. Examination should be performed in high ambient lighting conditions. The use of low-magnification optical microscopy is also helpful for identifying various defects, aesthetic problems such as stains or blemishes, and issues related to surface roughness (machining marks, shot peening indications, etc.). Cross sections that have been prepared suitably (see above) likewise are examined visually and with the aid of a stereomicroscope.

Table 5 presents some of the common defects that occur in castings, including billets and ingots (Ref 46, 47, 48, 49). Examples of misruns, cold shuts, cracks, hot tears, and die soldering appear in Fig. 1, 2, and 3 (Ref 50).

Table 5 International classification of common casting defects

Seven basic categories of defects	Examples
Metallic projections	Flash, fins, heat checking, scabs, veins
Cavities	Entrapped gas, shrinkage porosity
Discontinuities	Cold shuts, hot tears, cold cracks
Defective surface	Folds, soldering, flow marks, stains, sinks
Incomplete casting	Misruns, short shots
Incorrect dimensions or shape	Shift, mismatch
Inclusions or structural anomalies	Slag, dross, oxide skin

Source: Ref 47

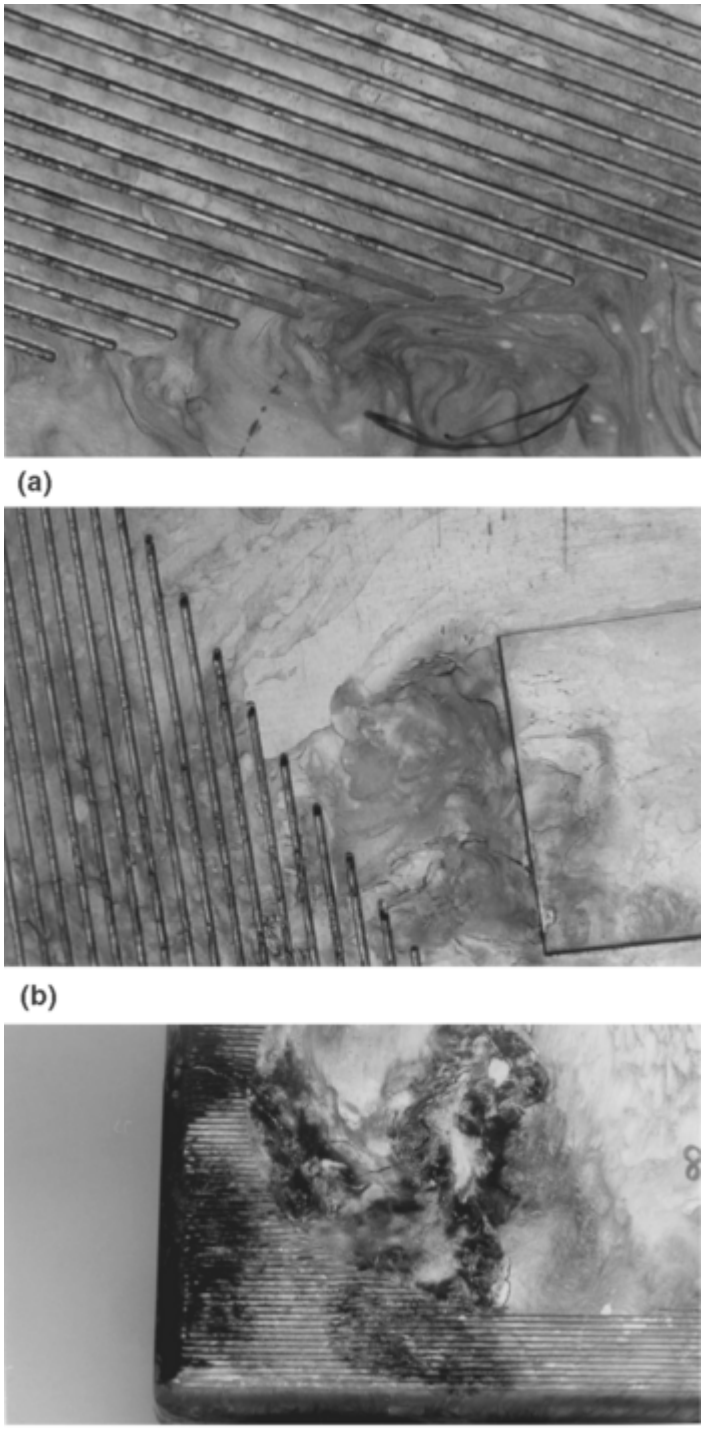

Fig. 1 Casting defects in a Mg-Al-Ca-Sr alloy die cast computer housing. Defects are associated with filling the die cavity. (a) Misruns in decorative ribbing. (b) Swirl-like cold shuts. (c) Surface stains. Courtesy of B.R. Powell, General Motors Corporation

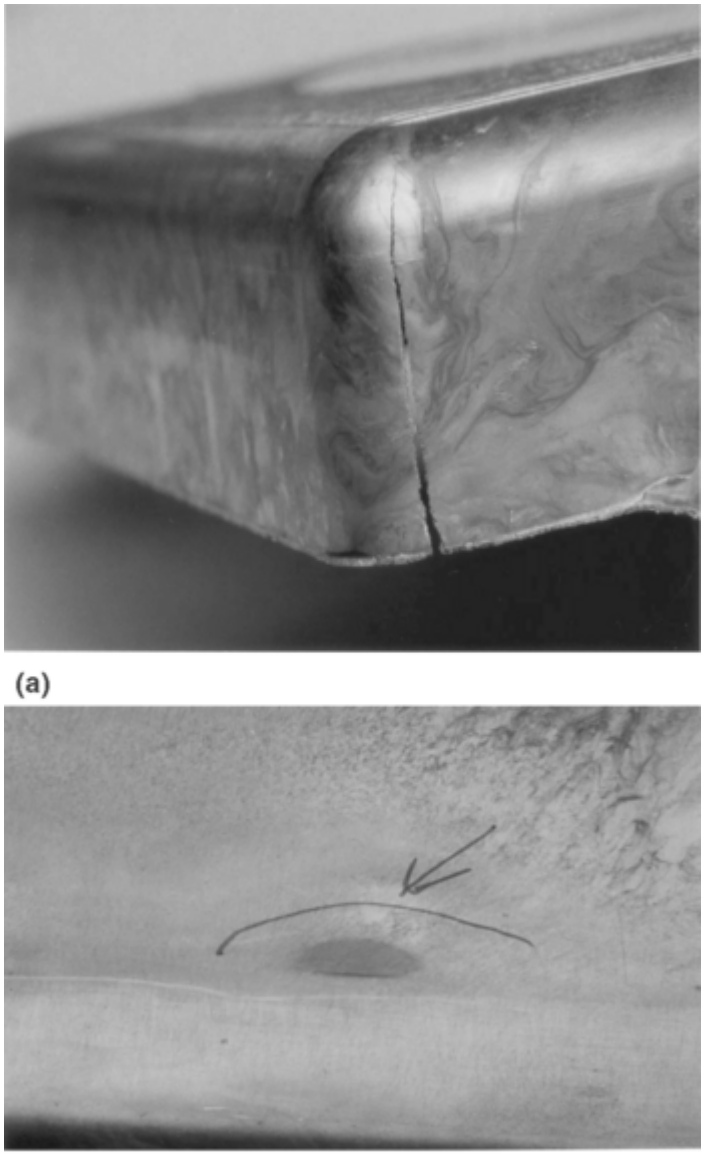

Fig. 2 Casting defects in a Mg-Al-Ca-Sr alloy die cast computer housing. Defects are associated with solidification. (a) Hot cracking (tearing). (b) Sink associated with solidification shrinkage. Courtesy of B.R. Powell, General Motors Corporation

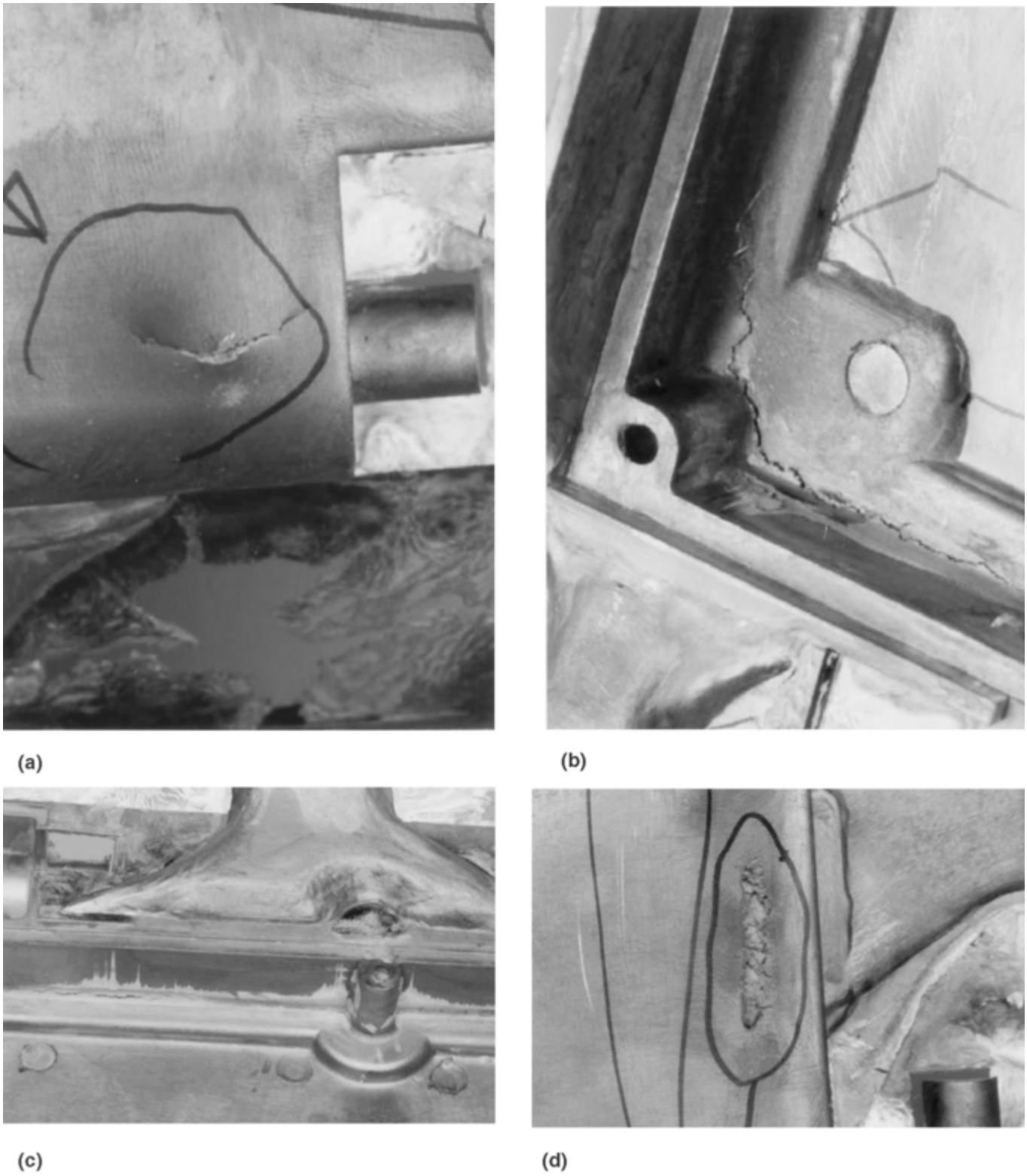

Fig. 3 Casting defects in a Mg-Al-Ca-Sr alloy die cast computer housing. Defects are associated with ejection. (a) Cold or hot cracking (tearing) through the outside of the casting opposite the ejector pin. (b) Cracking on the same side as the ejector pin. (c) Drag or scoring along vertical walls and boss. (d) Soldering in which a portion of the casting is torn due to bonding with the die. Courtesy of B.R. Powell, General Motors Corporation

More information on macroexamination of castings and semisolid molded components is available in the article "Metallography and Microstructures of Semisolid Formed Alloys" in this Volume.

Similar to castings, macroscopic examination of welds is performed with the unaided eye or with additional magnification, both on external surfaces as well as on metallographically prepared cross sections. A number of macrocharacterization parameters can be assessed by visual inspection, such as weld location, size, shape, and

general uniformity. In many cases, the presence of gross defects such as hot cracking (hot tearing) or porosity also may be detected by visual inspection. Additional examples of factors included in overall weld bead appearance include distortion, discoloration due to inadequate shielding or excessive heat, undercut, excessive crater size, cracks (crater cracks, toe cracks, etc.), poor bead shape (excessive convexity or concavity), and uneven bead width (Ref 51).

Defects that can be observed on cross-sectioned welds include subsurface porosity (linear, cluster, wormhole, etc.), inclusions (nonmetallic, tungsten particles from gas tungsten arc welding), and geometric discontinuities such as excessive sheet separation in spot welds or toe overlap in fusion welds (Ref 52). More information about weld defects is available in the article "Metallography and Microstructures of Weldments" in this Volume and in Ref 53, 54, and 55.

Wrought products such as extrusions and forgings are commonly evaluated for surface defects such as laps and folds using nondestructive examination (NDE) methods such as dye-penetrant inspection. The item normally is etched in sulfuric or nitric acid (or a combination of the two) followed by hot-water rinsing and visual inspection using ambient light or ultraviolet light (Ref 56, 57). Surface and subsurface flaws such as laps, cracks, flow-through defects, and extrusion defects also are evaluated on cross sections (Ref 58). Macroetching can aid further in identification and interpretation of defects (see the section "Macroetching" in this article).

Fracture-Surface Characteristics. Cast forms, such as slabs, ingots, and sand castings, are fractured and examined for grain-size variations, porosity, hot tears, oxide inclusions, phases that have limited solubility in the matrix, coring, and approximate degree of solution of massive compounds. Similarly, extrusions and forgings are fractured to show flow patterns, grain-size variations, oxide stringers, phases that have limited solubility in the matrix, laps, and variations in amount of plastic deformation. Fractured surfaces are sometimes placed in controlled cabinets and exposed to high humidity to look for "salt bloom," indicating the presence of chlorides and fluorides.

The fracture brightness technique (light reflectance) is used especially for evaluating the melt cleanliness of recycled metal (Ref 59, 60). Fracture brightness results have been compared with other methods (fast neutron activation analysis, image analysis, scanning electron microscopy/energy dispersive spectroscopy, or SEM/EDS) and correlates well in terms of oxide concentration. Die casting alloys in the AM series should have a minimum brightness of 53 to 54 to indicate appropriate cleanliness; the minimum values are 48 for AZ alloys and 40 to 42 for AJ alloys (Ref 60).

Fractures resulting from tensile and fatigue failures and from stress corrosion exhibit distinct features. Tensile or tensile-impact failures are transcrystalline and leave a rough, striated surface contour. Failure is likely to occur along basal crystallographic planes; under these conditions, the striations change from grain to grain. If tensile failure occurs at an elevated temperature, commonly greater than 230 °C (450 °F), intercrystalline grain-boundary surfaces with geometrical facets are exposed. However, this temperature can vary depending on the alloy content and the strain rate.

Fatigue fractures are transcrystalline but relatively smooth. Fan-shape striations radiate from one or more point origins. Stress-corrosion failures are characterized by cracks with many branches.

Macroetching is used to reveal the heterogeneity of metals and alloys (Ref 61). This technique can provide information on variations in structure and chemical composition, as well as defects and discontinuities. Variations in structure that can be characterized include grain size and grain size distribution, columnar structure, dendrites, and recrystallization. Macroetching can provide a qualitative evaluation of compositional variations by highlighting segregation and coring. Examples of discontinuities that can be detected include seams, laps, porosity, bursts, and cracks. Table 6 lists selected macroetchants for magnesium alloys. Less frequently used etchants are also described in Ref 61. For general information on macroetching, refer to the article "Macroetching" in this Volume.

Table 6 Macroetchants for magnesium and magnesium alloys

Etchant	Composition	Etching procedure	Comments
1	5–20 mL acetic acid 80–95 mL H_2O	Immerse or swab specimen in solution at room temperature for 10 s to 3 min until desired contrast is obtained.	Reveals grain size; also reveals flow lines in forgings and discontinuities in castings
2	5 mL acetic acid 6 g picric acid 10 mL H_2O 100 mL ethanol	As above for 30 s to 3 min	Grain size and flow patterns in both cast and wrought forms
3	10 mL acetic acid 4.2 g picric acid 20 mL H_2O 50 mL ethanol	As above	As above. Better than etchant 2 for dilute alloys like AZ31
4	20 mL acetic acid 80 mL H_2O 5g $NaNO_3$	Immerse face up with gentle agitation. Rinse quickly (1–10 s) with water followed by ethanol and blow dry	Shows general structure and grain boundaries. Useful for alloys containing Zn, no black deposit is formed
5	2.1 g oxalic acid 100 mL water	Immerse 5 s to 1 min. until desired contrast is obtained.	A universal etchant. Shows general structure and texture of wrought alloys

Welds frequently are sectioned and macroetched to reveal weld structure, depth of fusion, penetration, porosity, and cracks. Figure 4, 5, 6, and 7 show several examples of weld defects in gas tungsten arc welded AZ31.

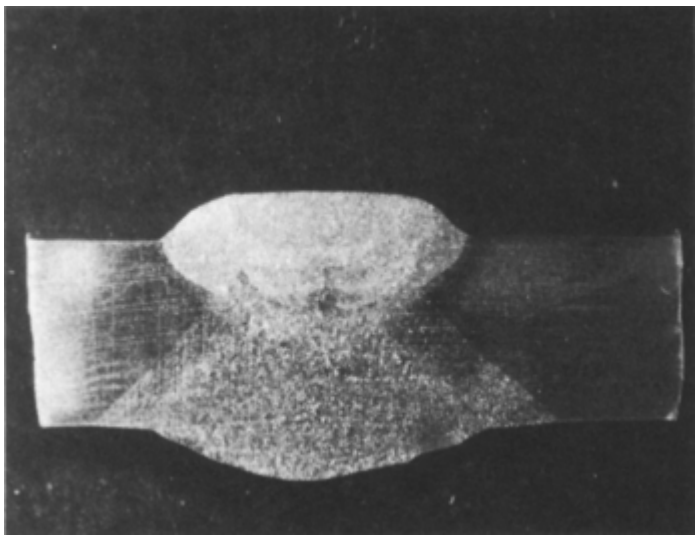

Fig. 4 Incomplete fusion in a two-pass gas tungsten arc butt weld in 4 mm (0.160 in.) thick AZ31B-H24 sheet. Weld was made with alloy ER AZ61A filler metal. Note the unfused area at the root of the second pass (top). Etchant 2, Table 6. 3.8×

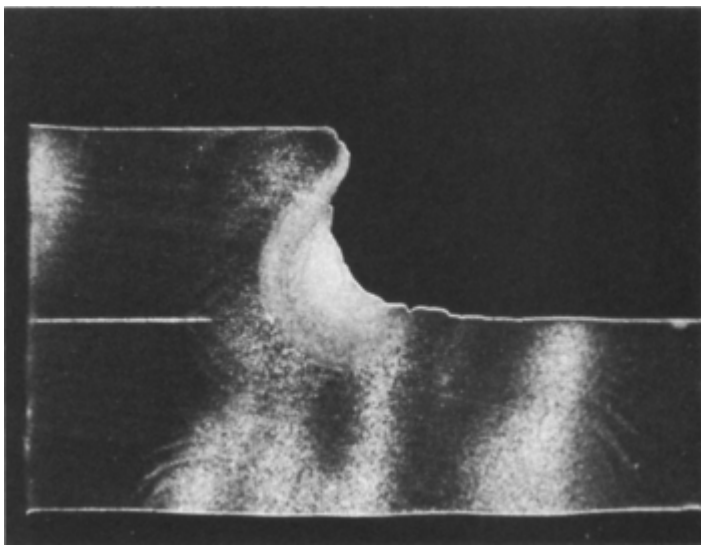

Fig. 5 Undercutting in a gas tungsten arc fillet weld in 4 mm (0.160 in.) thick AZ31B-H24 sheet. Weld was made with alloy ER AZ61A filler metal. Note the undercut area in the edge of the top sheet of the lap joint. Etchant 2, Table 6. 3.8×

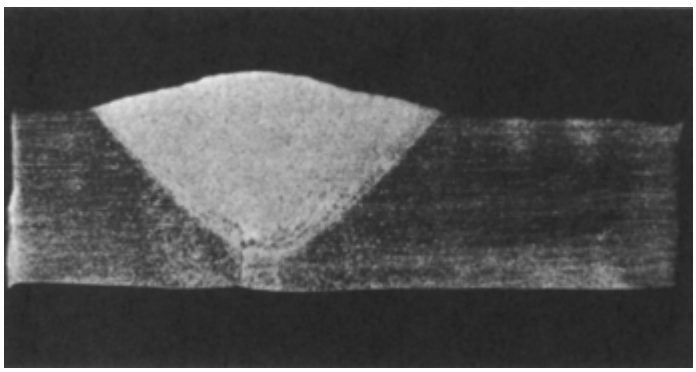

Fig. 6 Incomplete joint penetration of a gas tungsten arc weld in a butt weld in 4 mm (0.160 in.) thick AZ31B-H24 sheet. Weld was made with alloy ER AZ61A filler metal. Note the unfused joint at the root of the weld. Etchant 2, Table 6. 3.8×

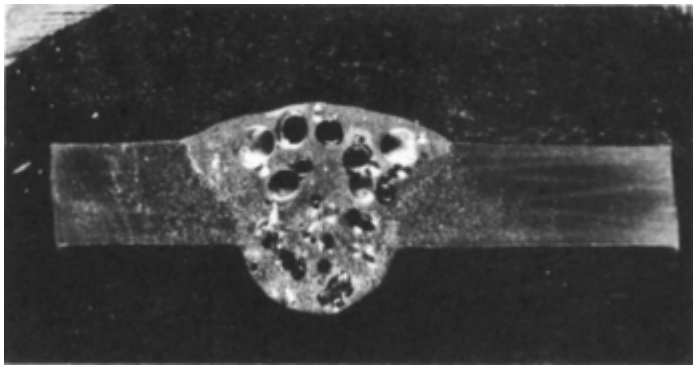

Fig. 7 Gross porosity in gas tungsten arc weld joining 5 mm (0.190 in.) thick AZ31B-H24 sheets. ER AZ61A filler metal. Causes include dirty base metal and filler metal, inadequate coverage by shielding gas, and moisture in gas. Etchant 2, Table 6. 3.8×

The macroetchant most often used for showing discontinuities in castings and flow lines in forgings is an aqueous solution containing 5 to 20% acetic acid (etchant 1 in Table 6). The prepared surface is immersed or swabbed for 10 s to 3 min, then washed away in running water and air-blast dried.

The dense, black deposit encountered when alloys containing appreciable amounts of zinc are etched in acetic acid solutions can be removed by immersion, immediately after rinsing, in an aqueous solution of 10 to 100% of 48% hydrofluoric acid (HF). The reactivity of this etchant is proportional to the concentration of HF. With some structures, it may be advantageous to retain the black deposit, especially if it is thin. An acetic-nitrate pickle (etchant 4 in Table 6) is often preferred for macroetching magnesium alloys containing zinc, because no black deposit is formed. The part is immersed for 1 to 5 min for etching in an aqueous solution of 20% acetic acid plus 5% sodium nitrate ($NaNO_3$), rinsed quickly in water and ethanol, and air-blast dried.

One of the acetic-picral etchants listed in Table 6 should be used for castings and to show the grain structure of impact extruded or forged parts that have a homogeneous recrystallized structure and a minimum of alloy gradients. The part is immersed in the etchant for 10 s to 3 min, transferred to a pan of ethanol to rinse the etched surface uniformly, rinsed in warm flowing ethanol, and then air-blast dried. Another etchant for general macroexamination (structure, texture, defects) is oxalic acid (etchant 5, Table 6). Figure 8 is an example of how macroetching can be used to augment defect analysis. Cracks in direct chill cast AZ31 billets are shown to be mostly intergranular, with no evidence of macroporosity or gross segregation.

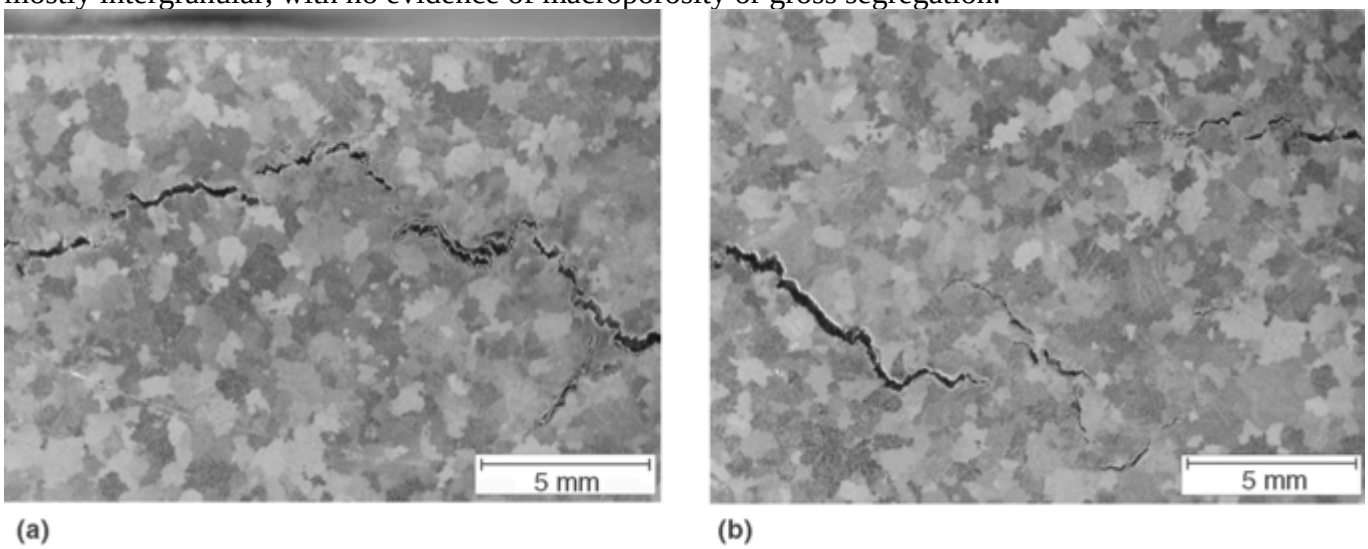

Fig. 8 Macroetched sections of AZ31 direct chill cast billets showing large cracks. The cracks are mostly intergranular in nature. Etchant 5, Table 6. Courtesy of F. Pravdic, ARC Leichtmetallkompetenzzentrum Ranshofen

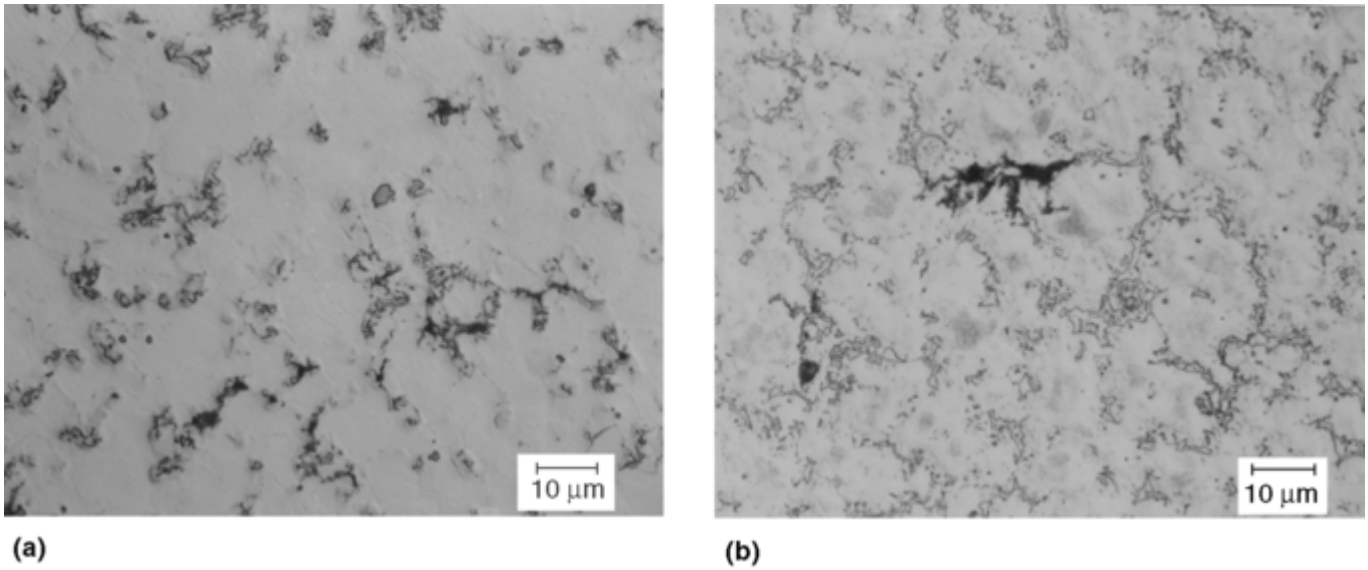

Fig. 9 Microstructures of (a) AM60 and (b) AZ91D high-pressure die cast specimens after etching with the glycol etchant (etchant 2, Table 7). The microstructures consist of small, cored grains of primary α-solid solution in which the aluminum content increases toward the grain boundaries. The grain-boundary phase is a divorced eutectic comprising supersaturated α-Mg plus $Al_{12}Mg_{17}$. Courtesy of G.F. Vander Voort, Buehler Ltd.

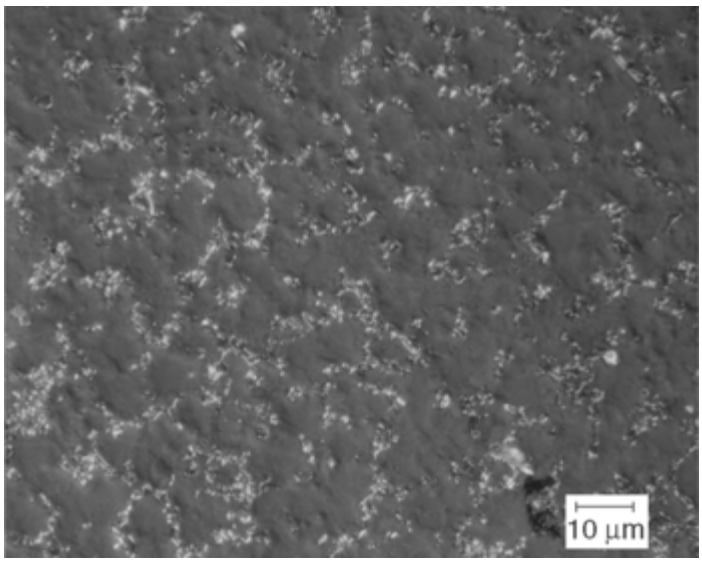

Fig. 10 Microstructure of high-pressure die cast AZ91D after etching with glycol and viewing with polarized light plus a sensitive tint filter. Courtesy of G.F. Vander Voort, Buehler Ltd.

References cited in this section

46. M.T. Rowley, Ed., *International Atlas of Casting Defects,* American Foundry Society, 1993

47. Testing and Inspection of Casting Defects, *Casting,* Vol 15, *ASM Handbook,* ASM International, 1988, p 544–561

48. W.G. Walkington, *Die Casting Defects—Causes and Solutions,* North American Die Casting Association, 1997

49. *Castings, Classification and Inspection of,* MIL-STD-2175, Department of Defense Single Stock Point for Military Specifications and Standards, Document Automation and Production Service

50. B.R. Powell et al., The Die Castability of Calcium-Containing Magnesium Alloys: Thin-Wall Computer Case, *Magnesium Technology 2002*, TMS (The Minerals, Metals, & Materials Society, 2002, p 123–129

51. C.R. Dallam et al., Characterization of Welds, *Welding, Brazing, and Soldering,* Vol 6, *ASM Handbook,* ASM International, 1993, p 97–106

52. Overview of Weld Discontinuities, *Welding, Brazing, and Soldering,* Vol 6, *ASM Handbook,* ASM International, 1993, p 1073–1080

53. *Guide for the Visual Examination of Welds,* AWS B1.11,

54. "Welding and Allied Processes—Classification of Geometric Imperfections in Metallic Materials—Part 1: Fusion Welding," ISO 6520-1, International Organization for Standardization

55. "Welding and Allied Processes—Classification of Geometric Imperfections in Metallic Materials—Part 2: Welding with Pressure," ISO 6520-2, International Organization for Standardization

56. *SAE Magnesium Alloys AMS Handbook,* AHB-002, SAE International, 1997

57. P. Chaudhury et al., Forging of Magnesium Alloys, *Forming and Forging,* Vol 14, *ASM Handbook,* ASM International, 1988

58. G. Dieter, Workability Tests, *Forming and Forging,* Vol 14, *ASM Handbook,* ASM International, 1988

59. J.C. Grebetz et al., Measuring the Cleanliness of Recycled Magnesium for Automotive Applications: A Detailed Examination of the Fracture Brightness Technique, *Light Metal Age,* Aug 1997, p 60–69

60. D. Argo et al., Chemical Composition and Cleanliness During Recycling of the AJ52 Magnesium Strontium Alloy, *Magnesium Technology 2003,* TMS (The Minerals, Metals, & Materials Society), 2002, p 33–37

61. "Standard Test Method for Macroetching Metals and Alloys," E 340, *Annual Book of ASTM Standards,* ASTM International

---

T.V. Padfield, Metallography and Microstructures of Magnesium and Its Alloys, *Metallography and Microstructures,* Vol 9, *ASM Handbook,* ASM International, 2004, p. 801–815

Metallography and Microstructures of Magnesium and Its Alloys

Toby V. Padfield, ZF Sachs Automotive of America

Microexamination

The etchants and etching times used for microexamination depend on the composition, physical condition, and temper of the specimen. Time may vary from 5 to 10 s for a specimen of an alloy in the as-cast or aged condition to 60 s for one in the solution heat treated condition. Etchants used for specimens of magnesium alloys are listed in Table 7, along with their compositions, etching procedures, characteristics, and uses.

Table 7 Selected etchants for microscopic examination of magnesium alloys

Etchant	Composition	Etching procedure	Characteristics and use
1	Nital: 1–5 mL HNO_3 (conc), 100 mL ethanol (95%) or methanol (95%)	Swab or immerse specimen for a few seconds to 1 min. Wash in water, then alcohol and dry.	Shows general structure
2	Glycol: 1 mL HNO_3 (conc), 24 mL water, 75 mL ethylene glycol	Immerse specimen face up and swab with cotton for 3–5 s for as-cast or aged metal and up to 1 min for heat treated metal. Wash in water, then alcohol and dry.	Shows general structure. Reveals constituents in magnesium/rare earth and magnesium-thorium alloys
3	Acetic glycol: 20 mL acetic acid, 1 mL HNO_3 (conc), 60 mL ethylene glycol, 20 mL water	Immerse specimen face up with gentle agitation for 1–3 s for as-cast or aged metal and up to 10 s for solution-heat-treated metal. Wash in water, then alcohol and dry.	Shows general structure and grain boundaries in heat treated castings. Shows grain boundaries in magnesium/rare earth and magnesium-thorium alloys
4	10 mL HF (48%) 90 mL H_2O	Immerse specimen face up for 1–2 s. Wash in water, then alcohol and dry.	Darkens $Al_{12}Mg_{17}$ phase and leaves $(Al,Zn)_{49}Mg_{32}$ phase unetched and white
5	Phospho-picral: 0.7 mL H_3PO_4, 4 to 6 g picric acid, 100 mL ethanol (95%)	Immerse specimen face up for about 10–20 s or until polished surface is darkened. Wash in alcohol and dry.	For estimating the amount of massive phase. Stains matrix and leaves phase white. Staining improves as magnesium-ion content increases with use.
6	Acetic-picral: 5 mL acetic acid, 6 g picric acid, 10 mL H_2O, 100 mL ethanol (95%)	Immerse specimen face up with gentle agitation until face turns brown. Wash in a stream of alcohol; dry with a blast of air.	A universal etchant. Defines grain boundaries in most alloys and tempers by etch rate and color of stain. Reveals cold work and twinning readily
7	Acetic-picral: 20 mL acetic acid, 3 g picric acid, 20 mL H_2O, 50 mL ethanol (95%)	Same as for etchant 6 but etch for at least 15 s to develop a heavy film.	Orientation of crackled film is parallel to trace of basal plane. Film crackles in high-alloy areas. Distinguishes between fusion voids surrounded by normal level of alloy and microshrinkage with low alloy content
8	Acetic-picral: 10 mL acetic acid, 4.2 g picric acid, 10 mL H_2O, 70 mL ethanol (95%)	Same as for etchant 6	Reveals grain boundaries more readily than etchant 6, especially in dilute alloys
9	0.6 g picric acid 10 mL ethanol (95%) 90 mL H_2O	Immerse specimen face up for 15–30 s. Wash in alcohol and dry.	Used after HF etchant to darken matrix to give better contrast between matrix and white ternary phase
10	2 mL HF (48%) 2 mL HNO_3 (conc) 96 mL H_2O	Immerse specimen face up with gentle agitation. Do not swab.	Grain structure and coring in Mg-Zn-Zr alloys
11	Citric: 5 g citric acid, 95 mL H_2O	Immerse specimen face up for 10–60 s. Wash in water then alcohol and dry.	Reveals grain boundaries readily, particularly in alloys with >5% Al content. Suitable for solution heat treated alloys

12	5 mL acetic acid 95 mL ethanol	Immerse specimen face up for 50–60 s. Wash in alcohol and dry.	General structure
13	2.1 g oxalic acid 100 mL water	Immerse 3–5 s. Wash in water, then alcohol and dry.	General structure
14	4–5 mL HBF_4 200 mL H_2O	Electrolytic: use stainless steel cathode; specimen is anode. Use minimum etching time and voltage (less than 40 s and 20 V dc respectively).	When viewed with polarized light, grains with the same orientation are colored similarly. Shows general structure, intergranular phases

For sand, low-pressure die cast, and high-pressure die cast alloys in the as-cast condition and for virtually all the alloys in the aged condition, the glycol etchant is used; it is especially useful for the magnesium/rare-earth alloys and magnesium-thorium alloys. Figure 9 and 10 show examples of high-pressure die cast alloys that have been etched with glycol. Etching affects the magnesium solid solution, causing the β phase to stand out in relief. Polarized light with or without the addition of a sensitive tint filter aids in distinguishing the primary magnesium grains from the eutectic phase (Fig. 10). Etching with acetic-glycol is similar to etching with glycol (Fig. 11). Acetic-picral etchants are used to stain the grains selectively (Fig. 12).

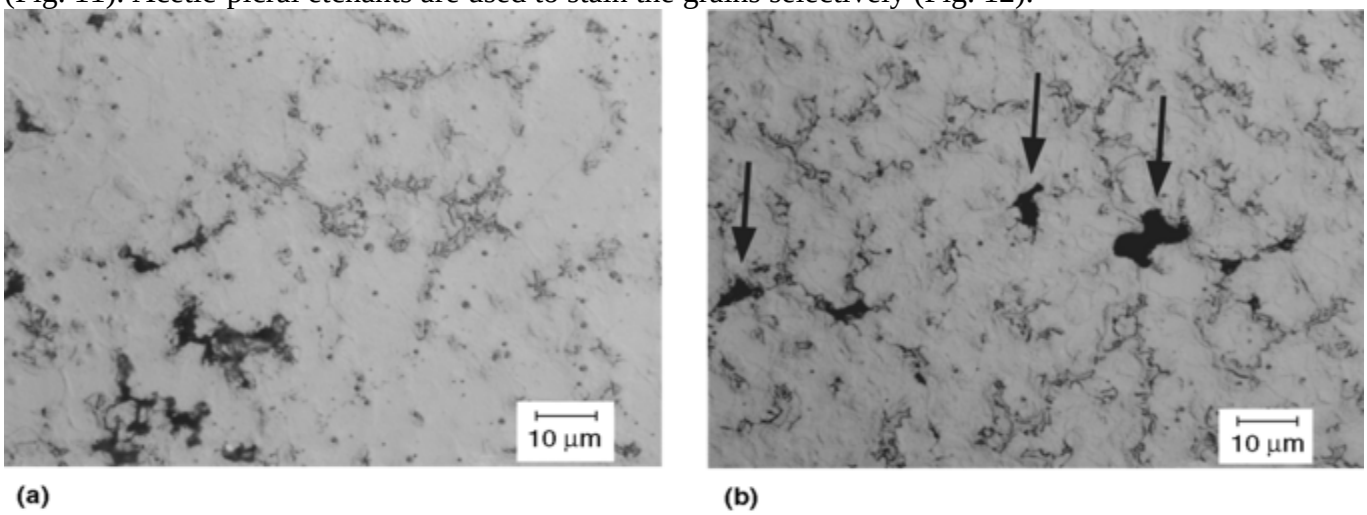

Fig. 11 Microstructures of (a) AM60 and (b) AZ91D high-pressure die cast specimens after etching with acetic-glycol. The matrix appears light, with the eutectic phase slightly darker. The large black areas (arrows) are microporosity due to entrapped gas and solidification shrinkage. Courtesy of G.F. Vander Voort, Buehler Ltd.

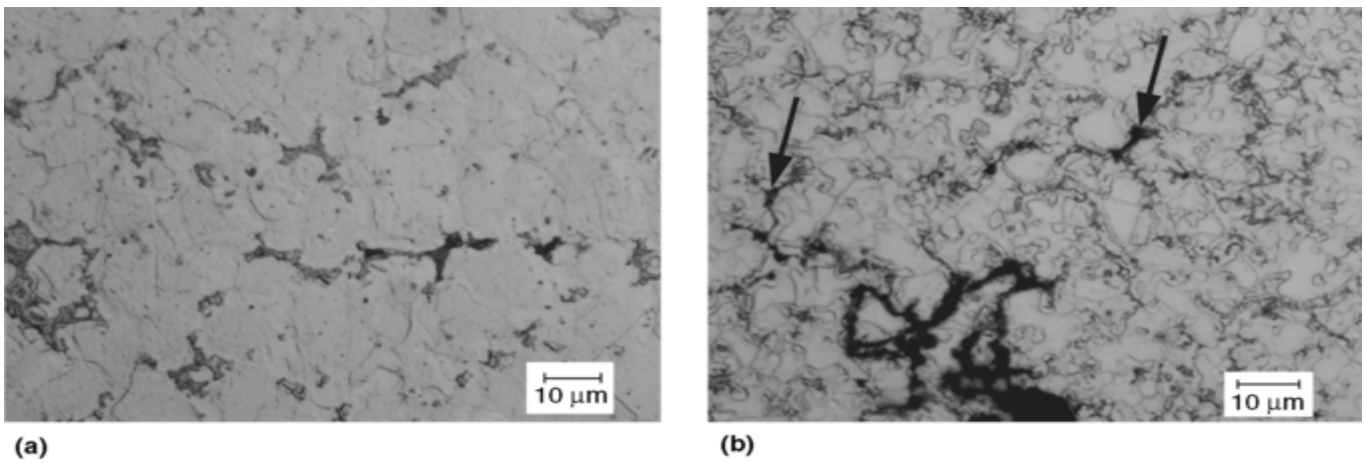

Fig. 12 Microstructures of (a) AM60 and (b) AZ91D high-pressure die cast specimens after etching with acetic-picral. The matrix appears light, with the eutectic phase slightly darker. Areas of interdendritic microporosity due to solidification shrinkage are indicated with arrows. The large irregular feature in

the lower portion of the image is an oxide film that formed due to reaction with air. Courtesy of G.F. Vander Voort, Buehler Ltd.

For cast metal in the as-cast or solution heat treated condition and for most wrought alloys, the glycol, acetic-glycol, and acetic-picral etchants in Table 7 are satisfactory. Etchants containing HF darken $Al_{12}Mg_{17}$ and are therefore useful for alloys containing zinc (Fig. 13). Etchant 10 in Table 7 reveals the grain structure of alloys containing zinc and zirconium.

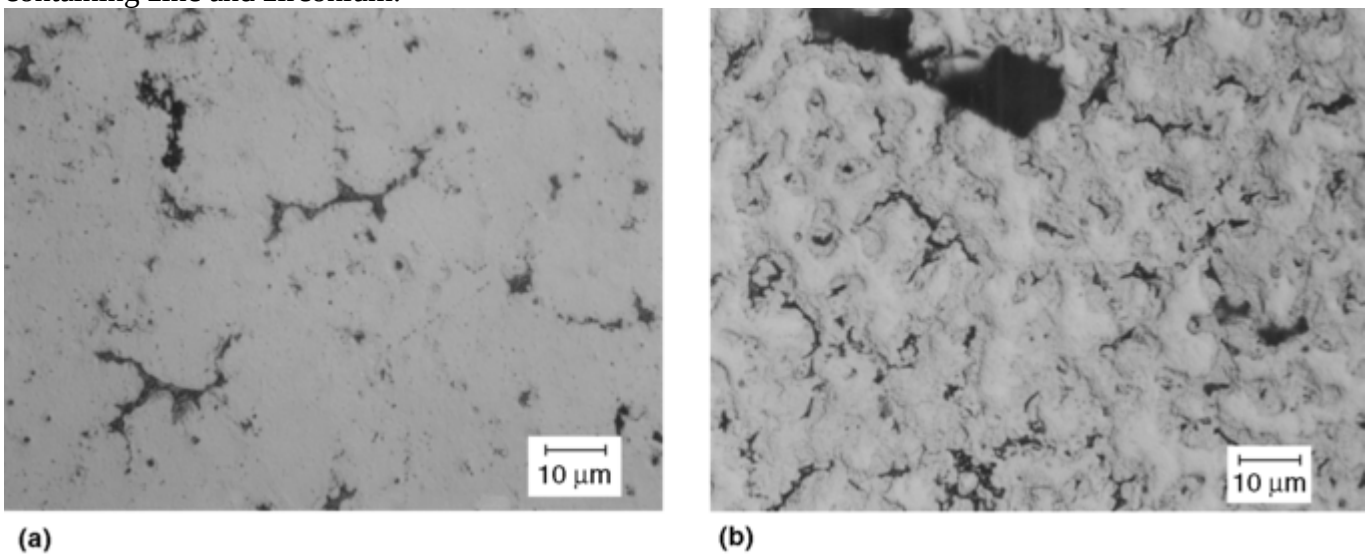

Fig. 13 Microstructures of (a) AM60 and (b) AZ91D high-pressure die cast specimens after etching with aqueous 10% HF. Note that this etchant darkened the $Al_{12}Mg_{17}$ intermetallic β phase. The matrix appears light, while the aluminum-enriched solid solution is darker gray. The aluminum concentration is higher near the grain boundaries and the β phase. Courtesy of G.F. Vander Voort, Buehler Ltd.

Phospho-picral with 6% picral (etchant 5 in Table 7) darkens the magnesium solid solution and leaves the other phases unchanged. The amount of staining is a function of the saturation of the solid solution. This etchant is particularly useful for quickly estimating the amount of undissolved second phase in solution heat treated metal, because of the extreme contrast it produces between the darkened matrix and the unetched second phase. In high-pressure die cast alloys, the primary magnesium is lightly stained, with the aluminum-enriched eutectic stained dark (Fig. 14). The $Al_{12}Mg_{17}$ phase remains uncolored and stands in relief.

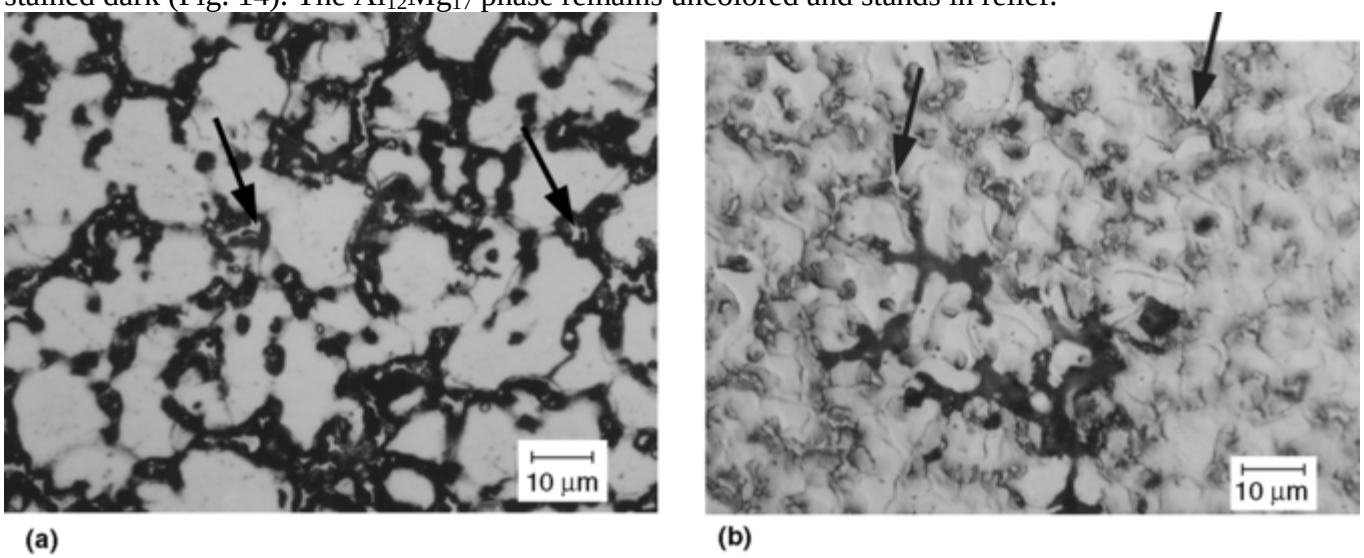

Fig. 14 Microstructures of (a) AM60 and (b) AZ91D high-pressure die cast specimens after etching with phospho-picral. Primary magnesium grains are not heavily etched, with the aluminum-enriched eutectic phase (intergranular) being darkened. Arrows identify the uncolored β phase. Courtesy of G.F. Vander Voort, Buehler Ltd.

In etching with phospho-picral, the specimen is immersed face up for 10 to 20 s or until the polished surface darkens. Next, it is washed in ethanol and dried or washed in ethanol, then water, then ethanol and dried. Washing directly in water lightens the stain and lessens the contrast. Staining can be accelerated by immersing the specimen in the etchant, then withdrawing it into the air. The phospho-picral etchant is also useful for resolving grain boundaries and lamellar precipitate.

When alloy AZ31B and other dilute alloys normally fabricated in wrought form do not respond well to the acetic-picral etchant 6 in Table 7, the slightly different acetic-picral etchants 7 or 8 are recommended. Figure 15 shows the microstructure of AZ31B sheet in both the strain-hardened and annealed conditions. A microstructure from a sample of AZ31B extrusion is shown in Fig. 16 for a specimen prepared with etchant 8 in Table 7.

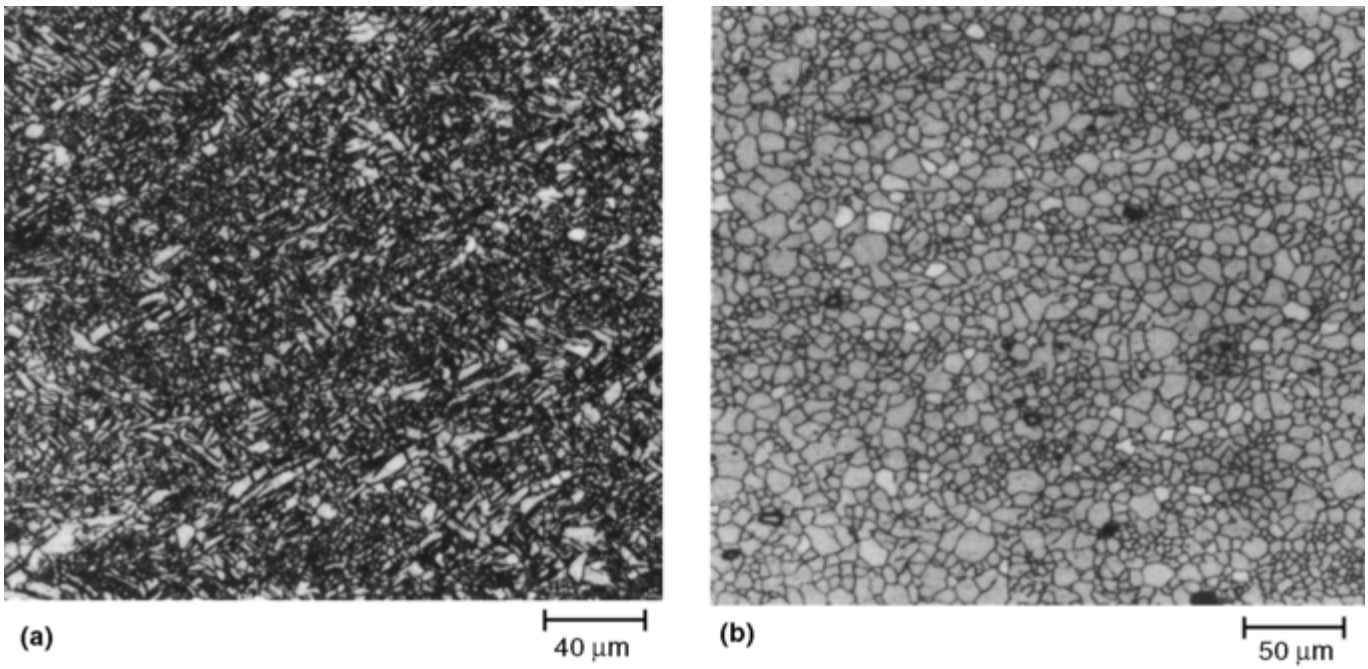

Fig. 15 (a) AZ31B-H24 sheet. Longitudinal edge view of worked structure, showing elongated grains and mechanical twins, which resulted from warm rolling of the sheet. Etchant 8, Table 7. 250×. (b) AZ31B-O sheet. Longitudinal edge view of structure recrystallized by annealing. Particles of manganese-aluminum compound (dark gray) and fragmented $Al_{12}Mg_{17}$ (outlined). Etchant 8, Table 7. 200×.

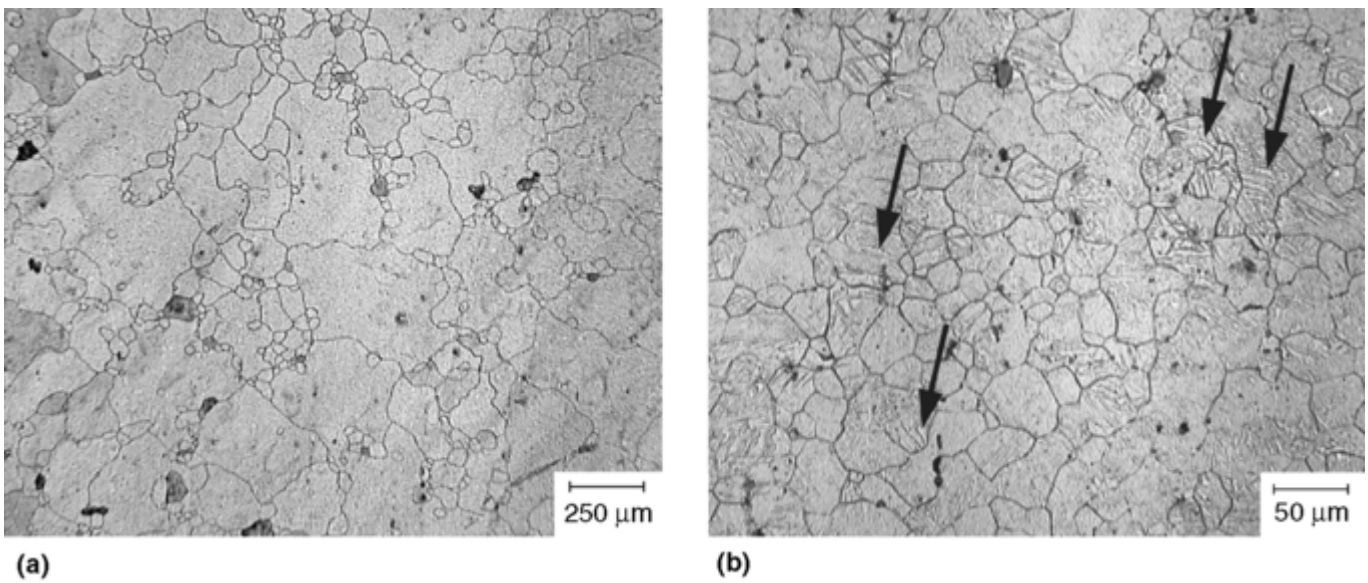

Fig. 16 Longitudinal view (lt plane) of an AZ31B-F extrusion. (a) Microstructure in a relatively thick section (~20 mm) showing a partially recrystallized structure of equiaxed grain with some manganese-aluminum particles (dark). Large differences in grain size exist among individual grains. Etchant 8, Table 7. (b) Microstructure in a relatively thin section (<5 mm) showing a fully recrystallized structure of

equiaxed grain with some manganese-aluminum particles (dark). Considerable twinning (arrows) is also visible, due to the greater deformation induced in the thin section. Note the difference in scale between the two images. Etchant 8, Table 7. Courtesy of C.J. Padfield

When etchants do not delineate grain boundaries, polarized light may be used, or the specimen may be pinched in a vise to produce twins. Grain boundaries in the AZ81 alloys are best seen after solution heat treatment. In dilute magnesium-zirconium alloys containing rare earth (RE) metals or thorium, care must be taken not to confuse cells surrounded by interdendritic β phase with grains.

Color Etching. As previously mentioned, magnesium alloys will respond to polarized light, and this can produce color on suitable etched samples. The glycol and acetic-picral etchants work best, especially when using a sensitive tint. Figure 17 shows the microstructure of an as-cast Mg-RE-Zn-Zr alloy without the use of polarized light. While the general structure is represented quite well in Fig. 17, alloy segregation (coring) and especially the grain boundaries are identified more clearly when viewed in color with polarized light (see Fig. 18).

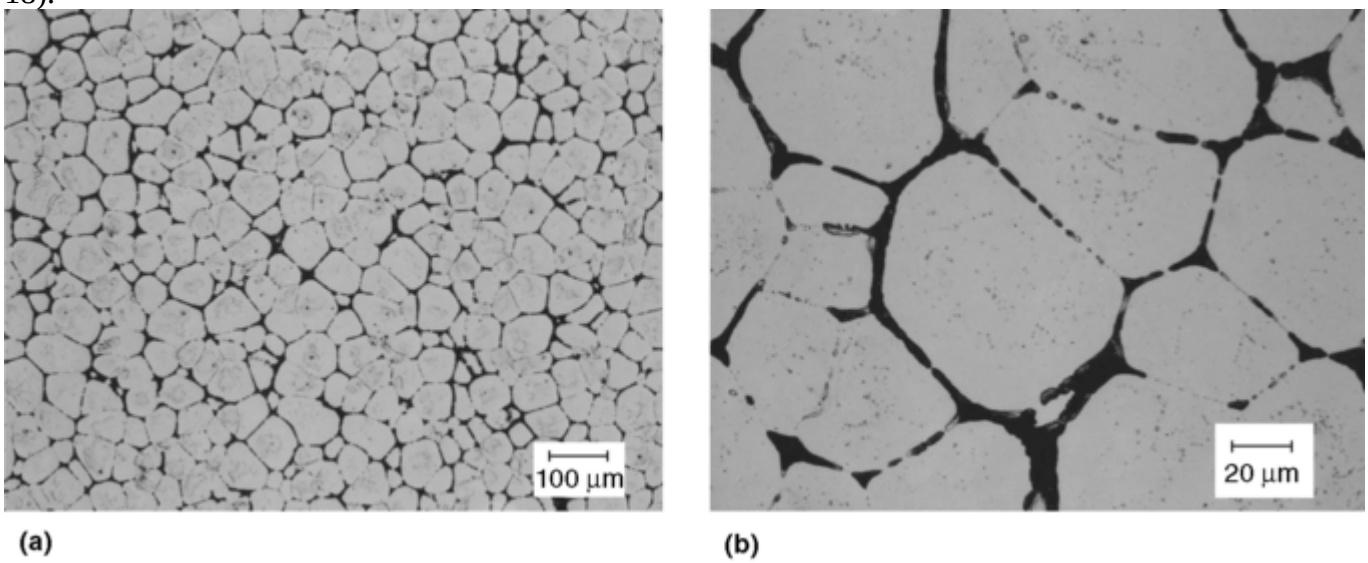

Fig. 17 Microstructure of as-cast Mg-2.5% RE-2.11%Zn-0.64%Zr revealed using acetic-glycol. See also Fig. 18 for a color version with polarized light plus a sensitive tint filter. Courtesy of G.F. Vander Voort, Buehler Ltd.

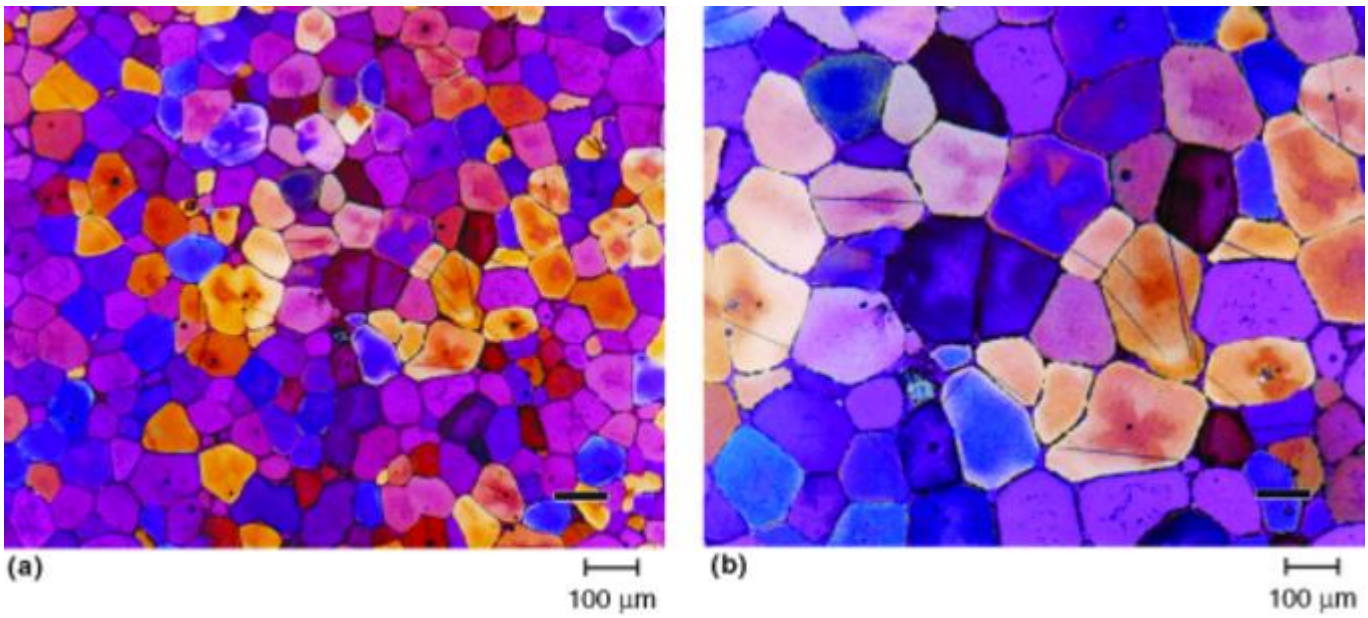

Fig. 18 Microstructure of as-cast Mg-2.5% rare earth elements-2.11%Zn-0.64%Zr revealed using the acetic-picral etch and viewed with polarized light illumination plus a sensitive tint filter. Alloy

segregation (coring) and grain boundaries are well depicted in these images, as are the mechanical twins present. (G.F. Vander Voort, Buehler Ltd.)

Additional examples of color etching are shown by Fig. 19 and 20. Figure 19 shows an as-cast zinc-zirconium alloy etched with acetic-picral and viewed with polarized light and a sensitive tint. The color is useful for interpreting the grain shape and size, as well as the grain size distribution. Figure 20 illustrates how color etching can be used in conjunction with normal brightfield examination to better understand different features. Color etching reveals the extensive twinning near the surface in far better detail than would be possible using conventional etching.

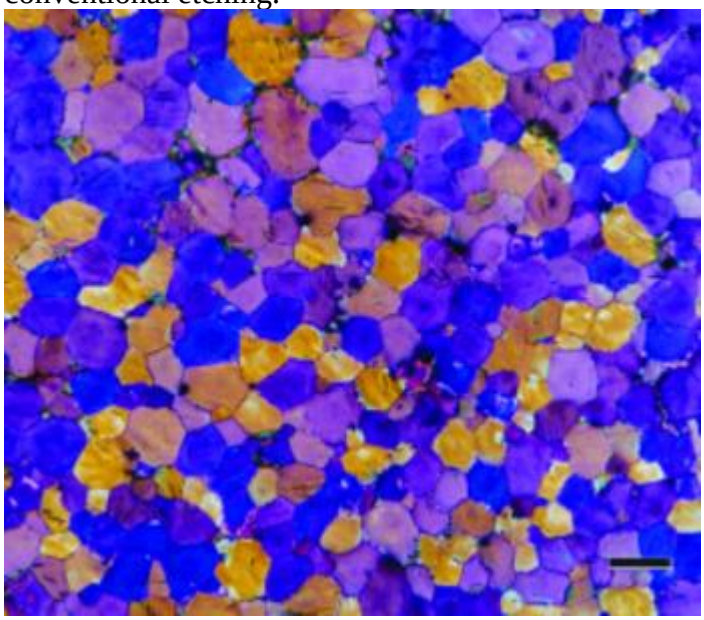

Fig. 19 Microstructure of as-cast Mg-4.6%Zn-0.76%Zr revealed using acetic-picral etch and viewed with polarized light illumination plus a sensitive tint filter. (G.F. Vander Voort, Buehler Ltd.)

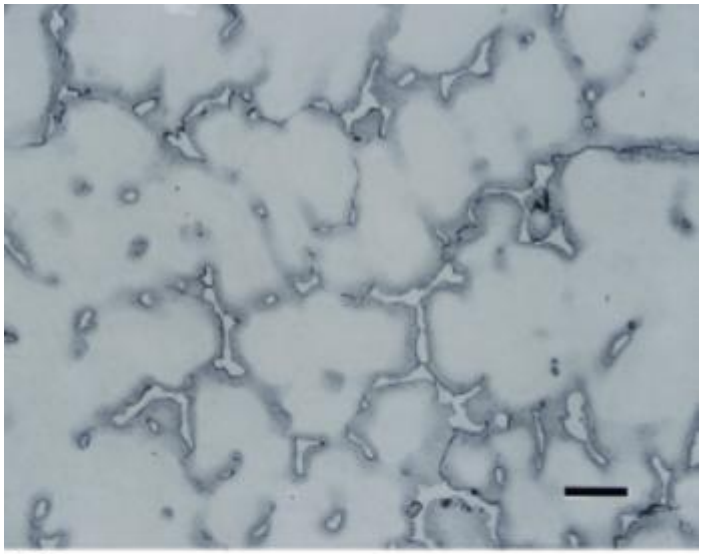

(a)

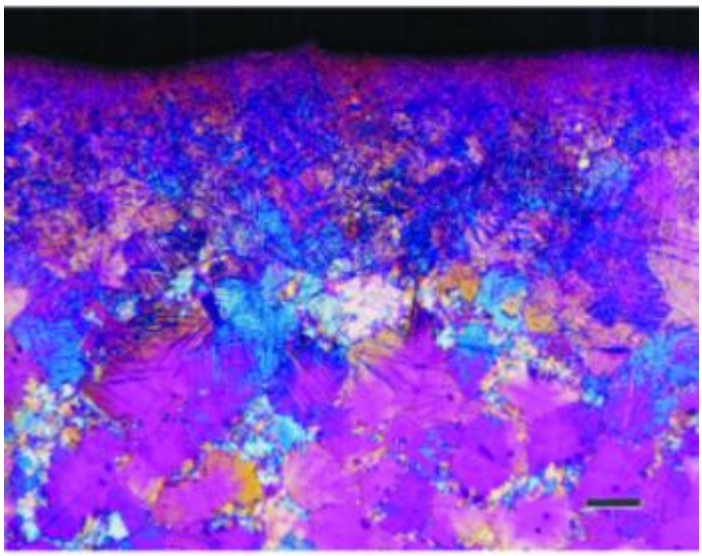

(b)

Fig. 20 Microstructure of sand-cast AZ91C (Mg-9%Al-0.25%Mn-0.7%Zn-0.0008%Be) revealed (a) using acetic-glycol etch and viewed in bright-field illumination and (b) after etching with glycol and viewed with polarized light illumination plus a sensitive tint filter. Part (a) shows the general structure (primary α-Mg grains, intergranular eutectic phase) after etching with acetic glycol. Part (b) is a lower-magnification view of the near-surface microstructure. Note the mechanical twins at the surface. (G.F. Vander Voort, Buehler Ltd.)

An electrolytic etching process also has been developed for magnesium based on the anodic oxidation process used for aluminum (Ref 31). Due to the high reactivity of magnesium with oxygen, electrolytic etching must take place quickly after final polishing. Preetching with 5% acetic acid is also helpful. The key parameters for the electrolytic etching process are the electrolyte flow rate, the applied voltage, and the etching time. All three must be minimized in order to produce acceptable results.

During electrolytic etching, the sample is the anode, which leads to a thin oxide layer forming on the grains, as well as some attack at the grain boundaries. This oxide layer is optically anisotropic, with the thickness dependent on the crystallographic orientation of the individual grains. When viewed with polarized light, grains with the same orientation are colored similarly (see Fig. 21). Even after etching the surface will oxidize rapidly, leading to a decrease in the color contrast between the grains. Therefore, imaging and analysis should be performed as soon as possible after etching. Additional information on color etching of magnesium and magnesium alloys can be found in the article “Color Metallography” in this Volume.

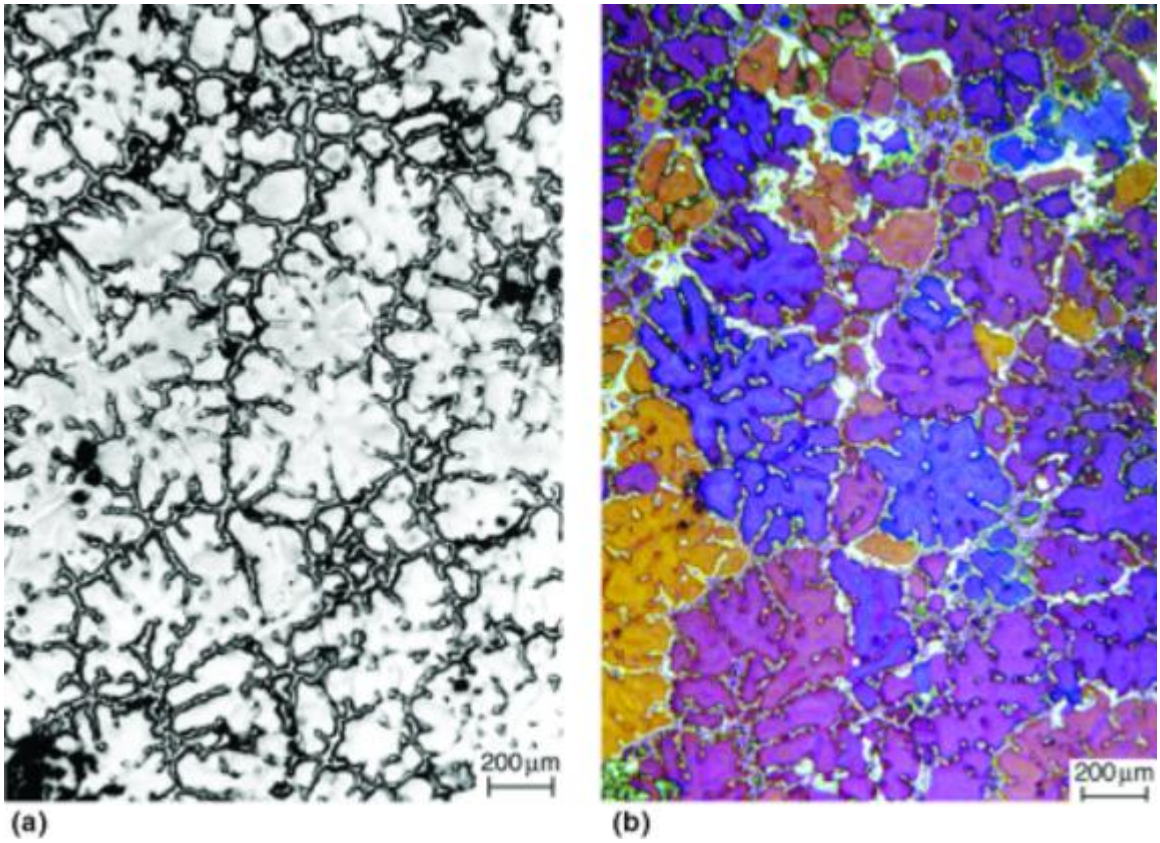

Fig. 21 Comparison of (a) conventional etching and bright-field illumination with (b) electrolytic etching and polarized light illumination. Specimen is thixocast (semisolid process) AZ91. Electrolytic etching reveals individual grains by the coloration while retaining good contrast at the grain boundaries. The addition of color allows for identification of orientation of the grains, in addition to parameters such as shape factor, the ratio of minimum to maximum grain diameters, and so on. (E. Schaberger, Gießerei-Institut, RWTH Aachen)

Reference cited in this section

31. E. Schaberger et al., The Development of an Electrolytic Etching Process for Examining the Microstructure of Thixocast Magnesium Alloy AZ91 hp, *Pract. Metallogr.*, Vol 37 (No. 3), 2000, p 140–149

T.V. Padfield, Metallography and Microstructures of Magnesium and Its Alloys, *Metallography and Microstructures,* Vol 9, *ASM Handbook*, ASM International, 2004, p. 801–815

Metallography and Microstructures of Magnesium and Its Alloys

Toby V. Padfield, ZF Sachs Automotive of America

Metallurgy and Microstructures

Most magnesium alloys can be classified into five groups: (1) Mg-Al-Mn (with or without zinc or silicon), (2) Mg-Zn-Zr (with or without thorium), (3) Mg/RE/Zr (with or without zinc or silver), (4) Mg-Th-Zr (with or without zinc), and (5) Mg-Li-Al. Table 8 is a list of probable precipitation processes in the various alloy systems (Ref 62).

Table 8 Probable precipitation processes in magnesium alloys

Alloy system	Precipitation processes			
Mg-Al	SSSS → $Al_{12}Mg_{17}$ equilibrium precipitate nucleated on $(0001)_{Mg}$ (incoherent)			
Mg-Zn(-Cu)	SSSS →	GP zones →	$MgZn_2$ →	$MgZn_2$ →	Mg_2Zn_3
		Discs	Rods	Discs	Trigonal
		$\parallel \{0001\}_{Mg}$	$\perp (0001)_{Mg}$	$\parallel \{0001\}$	a = 1.724 nm
		(coherent)	hcp	$(11\bar{2}0)_{MgZn2} \parallel$	b = 1.445 nm
			a = 0.52 nm	$(10\bar{1}0)_{Mg}$	c = 0.52 nm
			c = 0.85 nm	hcp	γ = 138°
				a = 0.52 nm	(incoherent)
				c = 0.848 nm	
				(semicoherent)	
Mg-RE (Nd)	SSSS →	GP zones →	β″ →	β′ →	β
		(Mg-Nd)	$(Mg_3Nd?)$	(Mg_3Nd)	$Mg_{12}Nd$
		Plates	hcp	fcc	bct
		$\parallel \{10\bar{1}0\}_{Mg}$	$D0_{19}$ superlattice	plates	a = 1.03 nm
		(coherent)	Plates $(0001)_{β″} \parallel (0001)_{Mg}$	a = 0.736 nm	c = 0.593 nm
			$\{1010\}_{Mg} \parallel \{10\bar{1}0\}_{Mg}$	$(001)_{β′} \parallel (0001)_{Mg}$	(incoherent)
				$(\bar{1}1\bar{1}) . \{\bar{2}110\}_{Mg}$	
				(semicoherent)	
Mg-Y-Nd	SSSS →	β′ →	$β_1$ →	β
		$Mg_{12}NdY$	Mg_3X (X = Nd, Ce, etc.)	$Mg_{14}Nd_2Y$
		bco	fcc	fcc
		a = 0.640 nm	a = 0.74 nm	a = 2.223 nm
		b = 2.223 nm	Plates $\parallel (1\bar{1}00)_{Mg}$	$(\bar{1}12)_β \parallel (1\bar{1}00)_{Mg}$
		c = 0.521 nm	$(\bar{1}12)_{β1} \parallel (1\bar{1}00)_{Mg}$	$[110]_β \parallel [0001]_{Mg}$
		$(100)_{β′} \parallel (1\bar{2}10)_{Mg}$	$[110]_{β1} \parallel [0001]_{Mg}$	
		$[001]_{β′} \parallel [0001]_{Mg}$		
Mg-Th	SSSS →	β″ →	β′ →	β

		Mg_3Th	Mg_2Th	$Mg_{23}Th_6$
		hcp	(i) $\beta_1$hexagonal	fcc
		$D0_{19}$ superlattice	(ii) $\beta_2$fcc	a = 1.43 nm
		Discs	(both semicoherent)	(incoherent)
		$\parallel \{10\bar{1}0\}_{Mg}$		
		(coherent)		
Mg-Ag-RE	SSSS	Rod-like	γ	
		GP zones	hexagonal rods	
		$\perp (0001)_{Mg}$	a = 0.963 nm	
		(coherent)	c = 1.024 nm	
			|| to [0001]Mg	
			(coherent)	
			↓	
		Ellipsoidal	β →	$Mg_{12}Nd_2Ag$
		GP zones	hexagonal	complex
		$\parallel (0001)_{Mg}$	equiaxed	hexagonal laths
		(coherent)	a = 0.556 nm	(incoherent)
			c = 0.521 nm	
			$(0001)_\beta \parallel (0001)Mg$	
			$(11\bar{2}0)_\beta \parallel (10\bar{1}0)Mg$	
			(semicoherent)	

SSSS, supersaturated solid solution; hcp, hexagonal close packed; fcc, face-centered cubic; bct, body-centered tetragonal; bco, body-centered orthogonal; GP, Guinier-Preston. Source: Ref 62

Magnesium alloys deform plastically by slip and twinning. As in other metals, slip lines are visible only when a polished surface is deformed or when a deformed specimen has been given a subsequent heat treatment to cause precipitation along the slip planes. Twins, however, are not destroyed by polishing; they may be recognized by their lenticular shape after etching (Fig. 22).

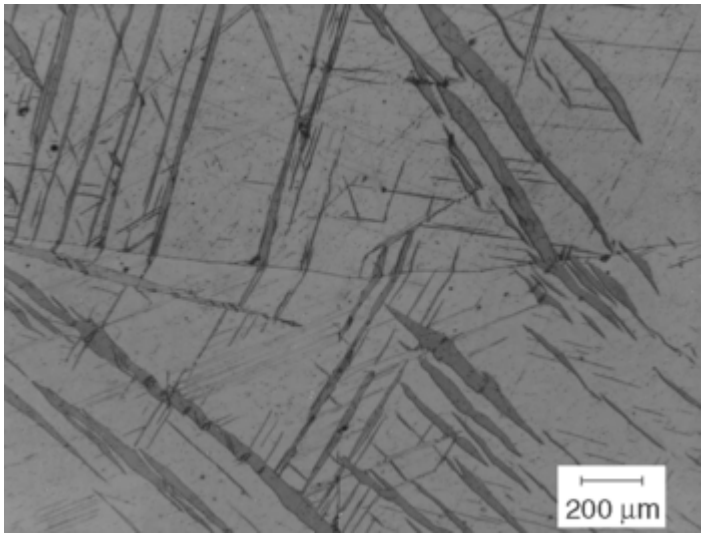

Fig. 22 Microstructure of wrought pure magnesium in the as-polished condition viewed in cross polarized light using a microscope with a Foster prism and a sensitive tint plate. Note the change in direction of the mechanical twins at the grain boundary. Courtesy of G.F. Vander Voort, Buehler Ltd.

Magnesium alloys are processed most frequently by casting processes such as high-pressure die casting or semisolid molding. Porosity is a consequence of these processes, both macroscopic (gross porosity) and microscopic (entrapped gas, solidification shrinkage). Figure 23 shows examples of solidification shrinkage and entrapped gas porosity, as well as gross porosity (Fig. 23b) on as-polished cross sections of high-pressure die castings. Figure 24 is an electron micrograph that demonstrates the three-dimensional character of solidification shrinkage. Large-scale cast billets are also subject to porosity, as shown in Fig. 25.

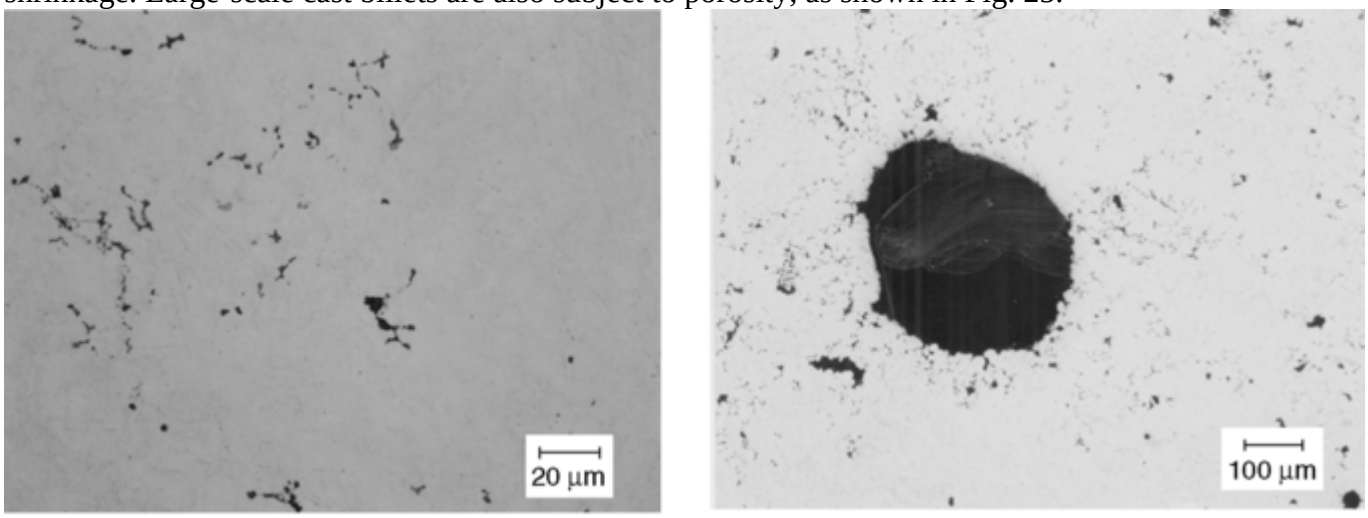

Fig. 23 As-polished surfaces of (a) AM60 and AZ91D pressure die cast specimens prepared using Masterprep alumina for the final step. Courtesy of G.F. Vander Voort, Buehler Ltd.

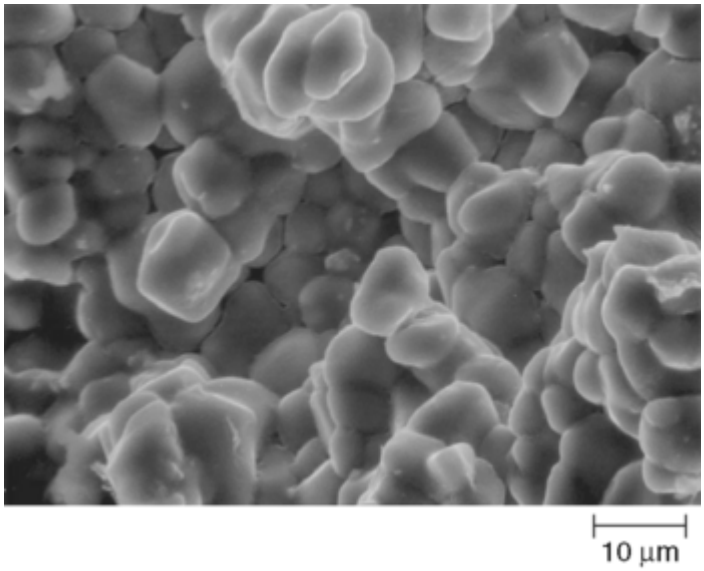

Fig. 24 Scanning electron micrograph of the interdendritic microporosity associated with solidification defect shown in Figure 2 (b). Note the rounded appearance of the grains that solidified without proper metal feeding. Courtesy of B.R. Powell, General Motors Corporation

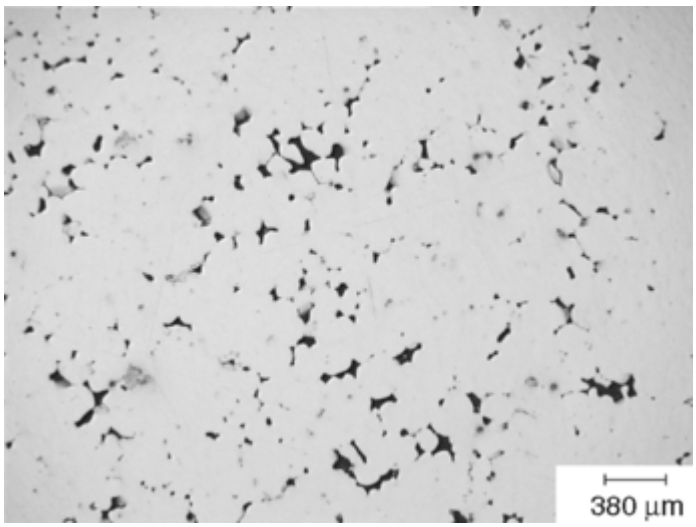

Fig. 25 As-polished section of AZ31 direct chill cast billet showing solidification shrinkage. Courtesy of F. Pravdic, ARC Leichtmetallkompetenzzentrum Ranshofen

Another feature of high-pressure die castings is the so-called skin effect. The use of metallic dies results in rapid cooling, producing a surface layer characterized by an extremely fine grain size and no porosity. Figure 26 shows two sections of an AM50A high-pressure die casting, one near the surface and one near the center of the section. The extremely fine grain size of the skin can be clearly seen.

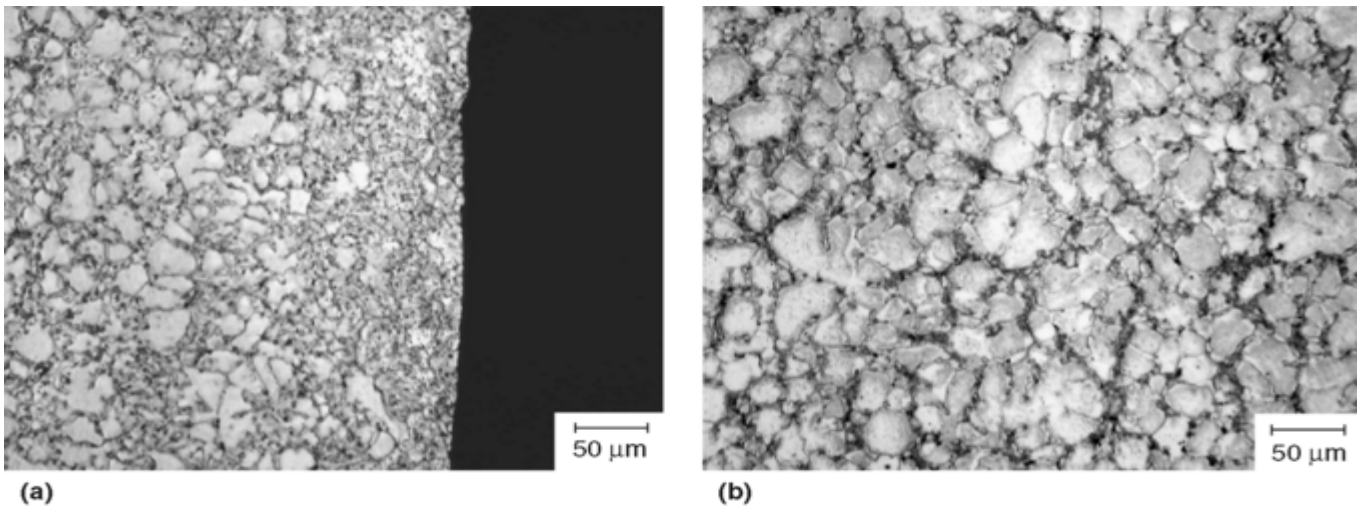

Fig. 26 Microstructure of high-pressure die cast AM50A. (a) Near the surface. (b) Near the center of the section. The skin effect can be clearly seen in (a) where a high-integrity layer has formed, characterized by an extremely fine grain size and no porosity. (b) Due to a section thickness of ~4 mm (~0.16 in.), the center section also cooled rapidly, resulting in a uniform distribution of fine grains. Etchant 5, Table 7. Courtesy of C.J. Padfield

Magnesium alloys are solution heat treated in a protective atmosphere—usually 0.5% sulfur dioxide or 3 to 5% carbon dioxide. Without the protective atmosphere, "high-temperature oxidation" or "burning" occurs. The eutectic deposits near the surface of the metal are attacked preferentially. This high-temperature oxidation is particularly rapid if eutectic melting is present concurrently. Eutectic melting is recognizable under a microscope as small shrinkage voids, chiefly intergranular, that are similar in appearance to microporosity, which is generally more irregular in outline.

Voids of doubtful origin in magnesium-aluminum alloys can be identified after solution heat treatment by the distribution of the precipitated $Al_{12}Mg_{17}$ constituent. If little or no precipitate is formed in the immediate vicinity of the voids, the voids are definitely attributable to microporosity. The presence of more precipitate in this location than in the surrounding area is proof that the voids are caused by eutectic melting during heat treatment.

Oxide films are found occasionally as thin, dark irregular lines in the microstructure of castings. Films formed in the crucible are usually thick and clustered and may contain entrapped manganese-rich particles. Films are thin and extended when produced by the breaking of the oxide "tube" in pouring or by turbulence in filling the mold (Fig. 27a). Oxides also appear as clusters or loosely connected agglomerates (Fig. 27b). Other common contaminants in magnesium melts include organic particles (from paint, oil) and salts (Na-, Ca-, or K-base chlorides carried over from electrolysis).

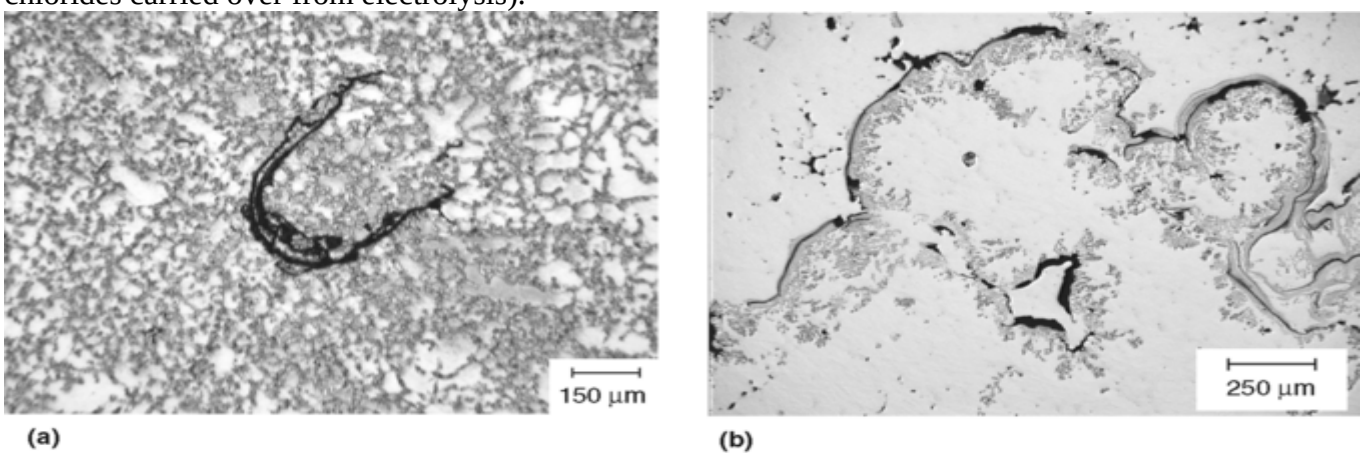

Fig. 27 (a) Example of an oxide film in an AM60B high-pressure die casting. Etchant 5, Table 7. Courtesy of C.J. Padfield. (b) An oxide cluster in a direct chill cast AZ31 billet. As-polished (unetched). Courtesy of F. Pravdic, ARC Leichtmetallkompetenzzentrum Ranshofen

For information on the mechanical and other properties of magnesium alloys, see the articles “Selection and Application of Magnesium and Magnesium Alloys” (Ref 63) and “Properties of Magnesium Alloys” (Ref 64) in *Properties and Selection: Nonferrous Alloys and Special-Purpose Materials,* Volume 2 of the *ASM Handbook.* Reference 62, 65, 66, 67, 68, and 69 discuss the physical metallurgy of magnesium and magnesium alloys in more detail.

Effects of Alloying Elements

Aluminum. A eutectic forms between the solid solution of aluminum in magnesium and the intermetallic compound $Al_{12}Mg_{17}$ (β phase). With normal air cooling of castings, this eutectic takes either of two forms, depending on whether or not the alloy contains zinc. In an alloy without zinc, the eutectic forms as a massive compound, which contains islands of magnesium solid solution; in an alloy that contains zinc, it takes a completely divorced form—particles of compound in solid solution whose appearance blends into that of the adjacent primary solid solution.

The precipitation of $Al_{12}Mg_{17}$ from solid solution can be continuous or discontinuous. At aging temperatures above approximately 205 °C (400 °F), it appears in a continuous Widmanstätten pattern (Fig. 28). Discontinuous precipitation, which starts at grain boundaries and has a lamellar form, is favored by lower aging temperatures and aluminum content above 8%. At approximately 290 °C (550 °F), the lamellar precipitate begins to coalesce, and at approximately 370 °C (700 °F) it redissolves in the matrix.

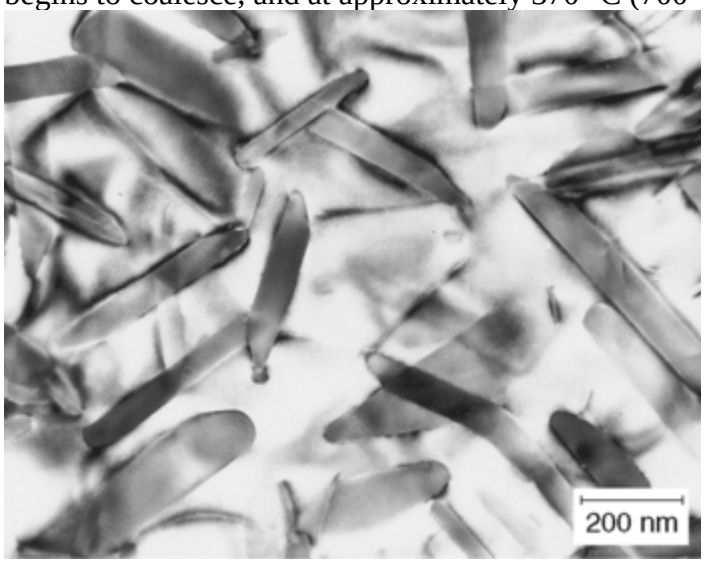

Fig. 28 Transmission electron micrograph of AZ91 showing continuous (Widmanstätten) precipitation of $Al_{12}Mg_{17}$ after 8 h at 200 °C (390 °F). Courtesy of J.-F. Nie, Monash University

Aluminum forms a number of other intermetallic phases such as $Al_{49}Mg_{32}$, Al_4RE, Al_4Sr, $Al_{11}RE_3$, Al_9Ca, Al_2Ca, and Al_2Nd.

Beryllium. Although only slightly soluble in magnesium, adding up to about 0.001 mass%, beryllium decreases the tendency for the surface of the molten metal to oxidize during melting, casting, and welding. It can be used successfully in die cast and wrought alloys, but must be used judiciously in sand casting alloys because of its grain-coarsening effect.

Calcium has a number of effects on magnesium alloys. Similar to beryllium, it is added to casting alloys prior to pouring to reduce oxidation and burning of the melt, as well as during subsequent heat treating. When present in amounts greater than ~0.1%, it forms the intermetallic phase $CaMg_2$. If aluminum is also present in the alloy, Al_2Ca is favored, but only when the calcium-to-aluminum ratio is below ~0.8; when this ratio is >0.8, $CaMg_2$ and Al_2Ca both form or a hybrid $(Al,Mg)_2Ca$ forms (Fig. 29). Both precipitates form along grain boundaries.

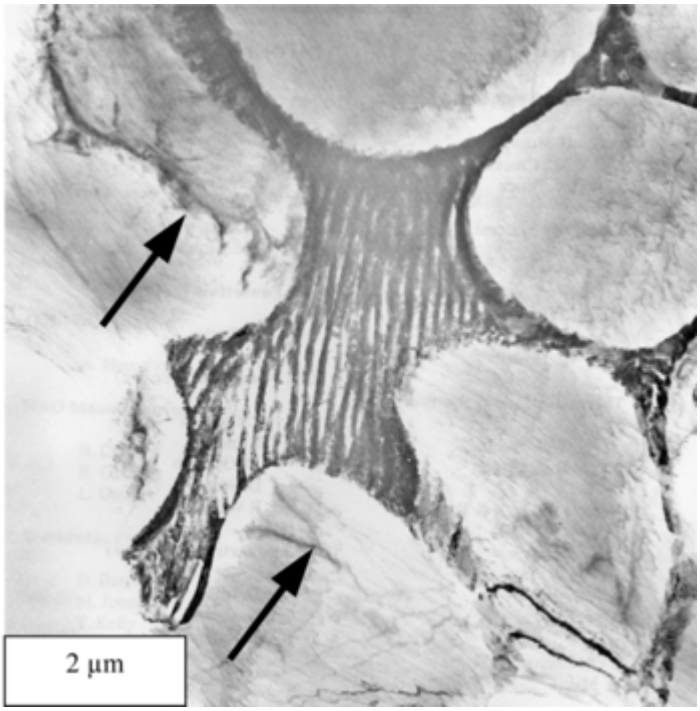

Fig. 29 Brightfield transmission electron micrograph of AXJ530. The microstructure consists of primary magnesium with aluminum in solid solution surrounded by a grain-boundary eutectic phase. The eutectic phase has a lamellar structure consisting of alternating layers of magnesium and the intermetallic $(Al,Mg)_2Ca$. Note the dislocation networks within the primary magnesium grains (arrows). Courtesy of B.R. Powell, General Motors Corporation

The Al_2Ca compound has stability at high temperatures, contributing to increased creep resistance, while also suppressing the formation of β-$Al_{12}Mg_{17}$ (Ref 10). At aluminum concentrations below 5%, calcium additions make die castings prone to hot cracking and die soldering. Calcium also substitutes in a number of other precipitates: $(Al,Zn,Ca,Sr)_{49}Mg_{32}$, $Al_2(Ca,Sr)$, $Al_2(Ca,Zn)$, and $(Al,Zn)_{11}(RE,Ca)_3$.

Copper. The addition of copper to magnesium-zinc alloys induces a relatively large age-hardening response, due to the formation of $Mg(Cu,Zn)_2$. The structure of the eutectic is also changed from being completely divorced in binary magnesium-zinc alloys, with the magnesium-zinc compound distributed around grain boundaries and between dendrite arms, to truly lamellar in the ternary copper-containing alloys (Ref 65). While copper normally has a significantly negative effect on corrosion resistance of magnesium alloys, its incorporation into the eutectic phase as $Mg(Cu,Zn)_2$ appears to prevent this in Mg-Zn-Cu alloys.

Iron is one of the most harmful impurities in magnesium alloys with regard to corrosion resistance. It combines with aluminum, manganese, rare earths, and zirconium to form complex intermetallic particles. Particle morphologies range from blocky to needlelike.

Lithium. The solid solubility of lithium is relatively high in hexagonal close-packed (hcp) α-magnesium: 5.5 mass%, 17.0 at.%. Moreover, only 11 mass% Li is needed to form the body-centered cubic (bcc) β phase. When added to magnesium-aluminum alloys, equilibrium phases such as AlLi, Al_2Li_3, and Al_4Li_9 form.

Manganese. In magnesium alloys that contain manganese but no aluminum, the manganese appears as bluish-grey, primary elemental particles. Manganese combines with aluminum, when present, to form the compounds AlMn, Al_4Mn, or Al_6Mn. These compounds may be contained in a single particle, with the ratio of aluminum to manganese increasing from the center to the surface of the particle. Solution heat treatment transforms the particle to Al_6Mn. The presence of sufficient iron modifies the manganese-aluminum compounds to very hard manganese-aluminum-iron compounds.

Particles of manganese-aluminum compound often occur in the form of chunks and needles. The particles sometimes have irregular, sawtooth surfaces, which result from growth in the mushy and the early solid stages.

Rare Earth Metals. Because of the low solubility of rare earth metals in magnesium, there is usually an excess of Mg_9RE compound at the grain boundaries of magnesium-mischmetal and magnesium-didymium alloys. In Mg-Y-Nd alloys, the precipitation sequence ends with the equilibrium β phase, which has a composition of

$Mg_{14}Nd_2Y$ (Ref 70). Figure 30 is an electron micrograph showing the precipitate structure after 48 h aging at 250 °C. In Mg-Ag-RE alloys, the equilibrium phase is $Mg_{12}Nd_2Ag$.

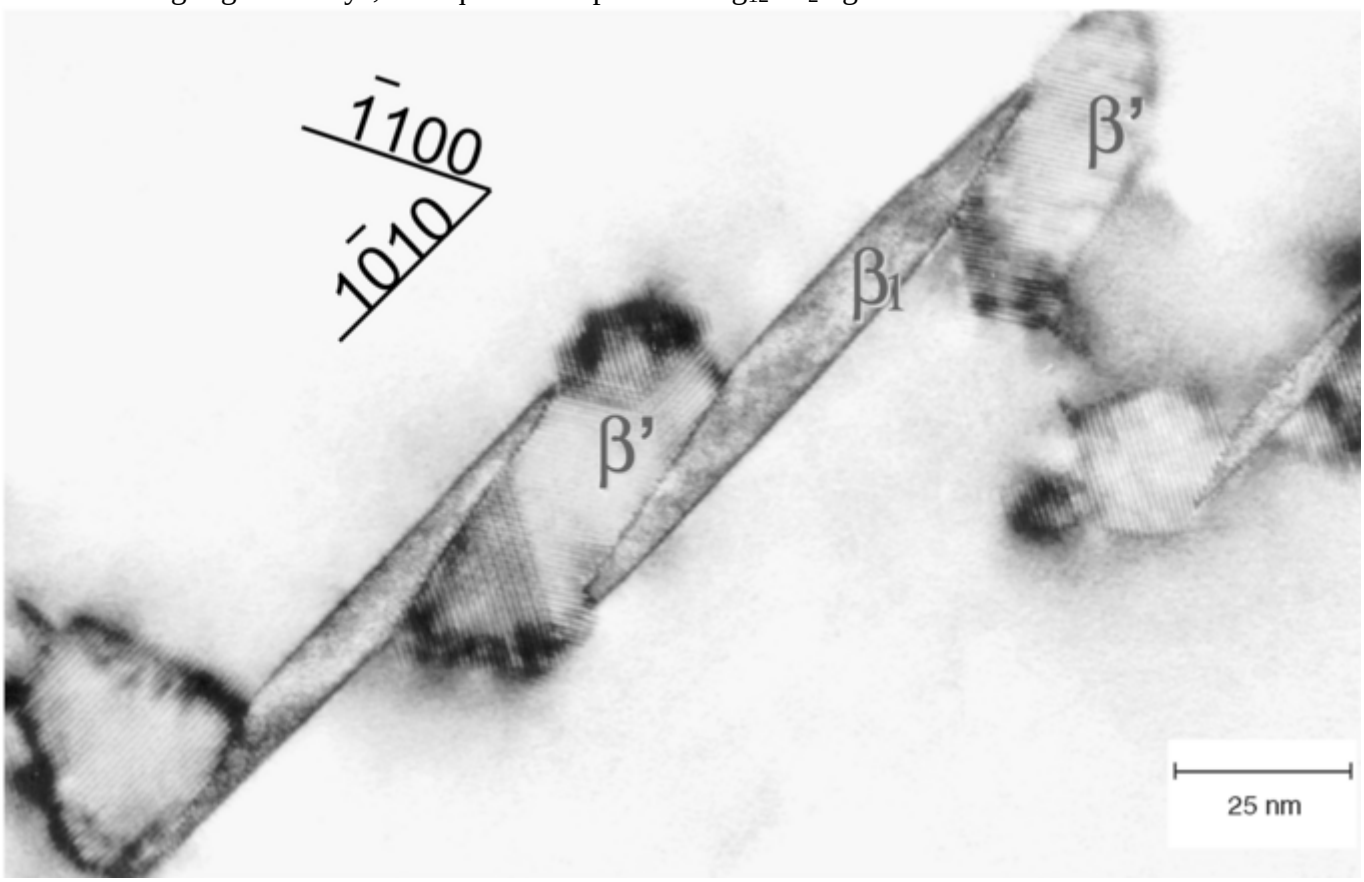

Fig. 30 Brightfield electron micrograph of sand cast WE54 after aging for 48 h at 250 °C (480 °F). The image shows assemblies of plate-shaped and irregular globular precipitates. With extended aging, the β′ phase decomposes, and the β_1 plates transform in situ to the equilibrium phase, although the peak-aged microstructure contains all three phases. Courtesy of J.-F. Nie, Monash University

When added to magnesium-aluminum alloys, a lamellar interdendritic phase forms with the composition $Al_{11}RE_3$ (~Al_4RE). A minor particulate interdendritic phase also forms with the composition Al_2RE (Ref 45). The microstructure of AE42 is described in Fig. 31.

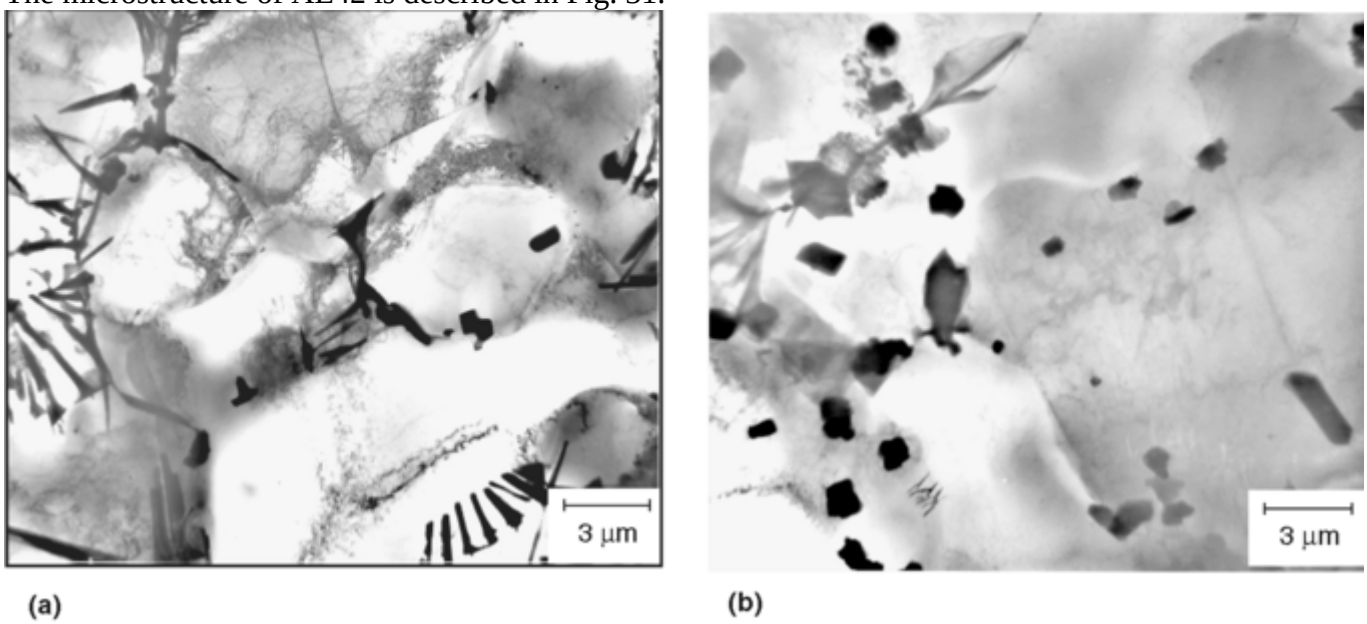

Fig. 31 Brightfield transmission electron micrograph of high-pressure die cast AE42. (a) Primary magnesium with aluminum in solid solution surrounded by the lamellar phase $Al_{11}RE_3$ and the

particulate phase Al_2RE. (b) After exposure to temperature above 175 °C (345 °F), the presence of the lamellar phase is reduced and the particulate phase dominates. This may help to explain the loss in creep resistance of this alloy at these temperatures. B.R. Powell, General Motors Corporation

Silicon is present in magnesium alloys as particles of Mg_2Si. These particles are distinguished by their angular outline, smooth edges, and light-blue color.

Silver. Silver contributes to precipitation hardening by forming incoherent precipitates with the composition $Mg_{12}Nd_2Ag$. These precipitates contribute to increased strength and creep resistance.

Strontium. Alloying with strontium results in different microstructures depending on the strontium-to-aluminum ratio. For strontium-to-aluminum ratio ~0.3, Al_4Sr is the only intermetallic phase present (Fig. 32). The strontium-to-aluminum ratio controls the formation of $Al_{12}Mg_{17}$—at very low ratios there is insufficient strontium to tie up all of the available aluminum, and $Al_{12}Mg_{17}$ can form (Ref 10). At higher ratios, a ternary phase Mg-Al-Sr phase is also observed (Fig. 33). Figure 34 shows the lamellar structure of the eutectic phase.

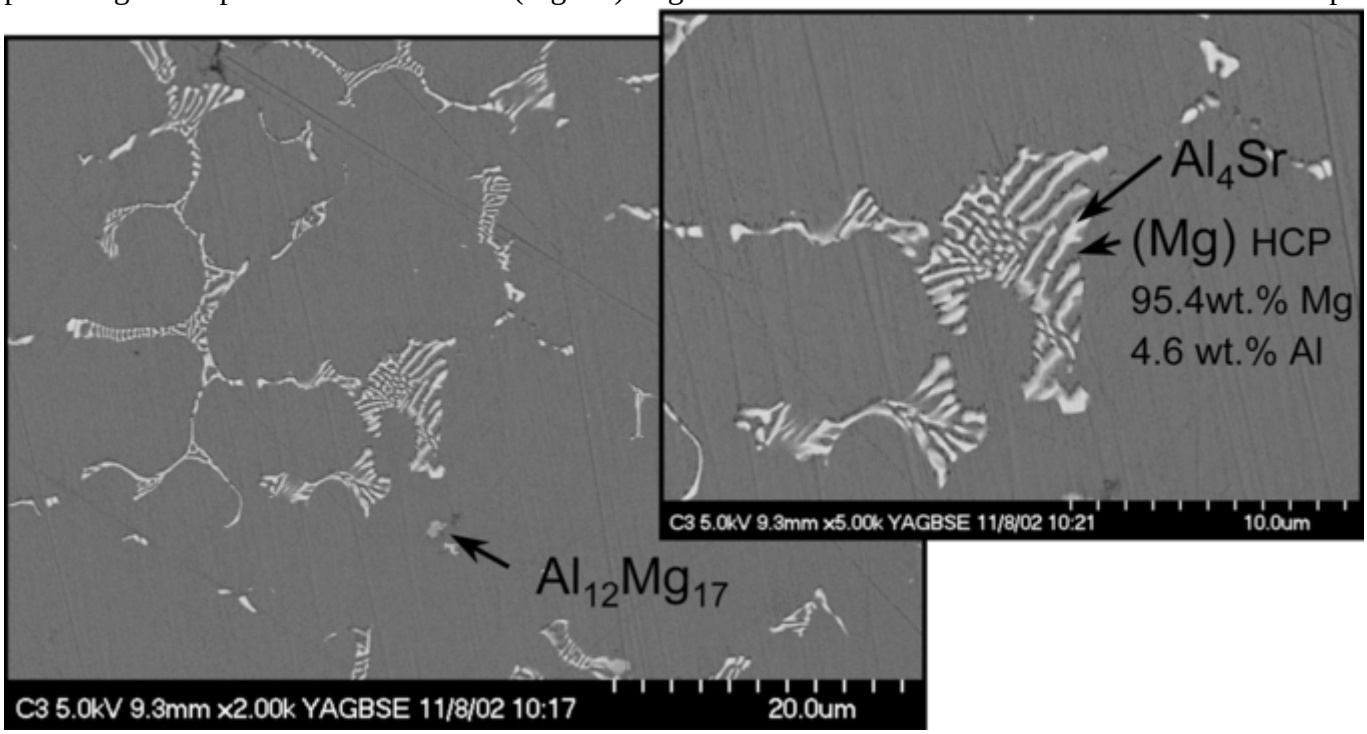

Fig. 32 Backscattered electron micrograph (FEG-SEM) of high-pressure die cast AJ62L (low strontium). Microstructure consists of primary magnesium grains surrounded by grain-boundary eutectic phase. Al_4Sr is the main intermetallic phase present, but due to the low strontium content, some $Al_{12}Mg_{17}$ also forms. Courtesy of Éric Baril, Noranda

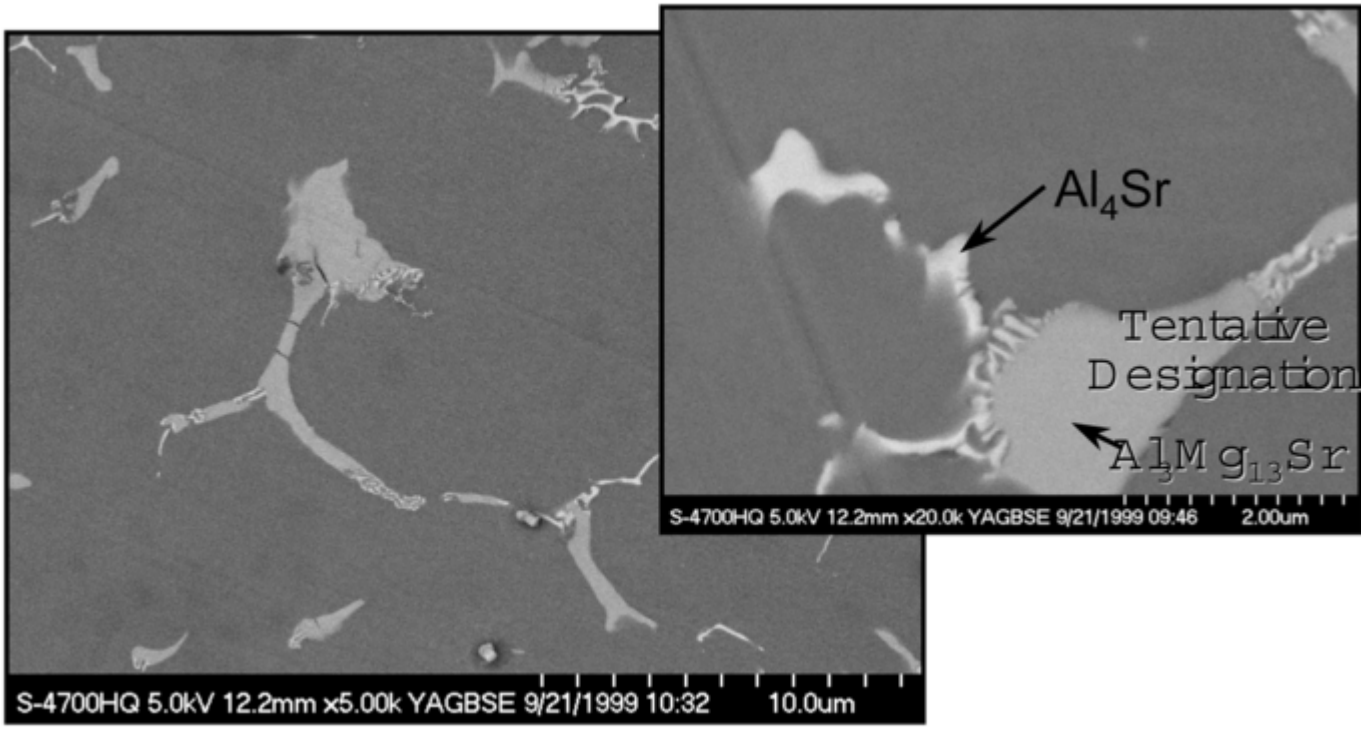

Fig. 33 Backscattered electron micrograph (FEG-SEM) of high-pressure die cast AJ52. Microstructure consists of primary magnesium grains surrounded by grain-boundary eutectic phase. Two intermetallic phases are present: Al_4Sr and a ternary Al-Mg-Sr phase. Courtesy of Éric Baril, Noranda

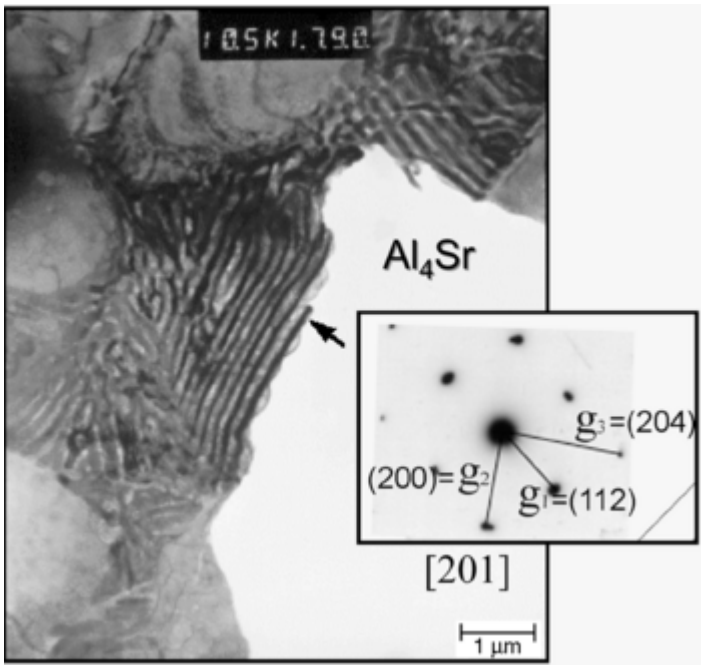

Fig. 34 Transmission electron micrograph and diffraction pattern of high-pressure die cast AJ52. The eutectic phase has a lamellar structure consisting of alternating layers of magnesium and Al_4Sr. The lamellar structure is similar to that of AE42 and AXJ530. Courtesy of Éric Baril, Noranda

Thorium. At the eutectic temperature of 589 °C (1092 °F), 4.5% Th is soluble in magnesium; however, because of alloy segregation, magnesium alloys containing as little as 2% Th often contain a divorced eutectic and show massive magnesium-thorium compound at the grain boundaries. At temperatures below the eutectic, this compound is also precipitated from solid solution. In castings, the precipitate forms within grains and is seldom visible. In worked structures, the precipitate is often clearly visible at grain boundaries.

The addition of thorium to magnesium-zinc alloys changes the degenerate eutectic, which contains magnesium-zinc compound, to a lamellar eutectic, which contains a Mg-Th-Zn compound.

Tin is useful when alloyed with magnesium in combination with small amounts of aluminum. It substitutes in several intermetallic phases including $Al_9(Ca,Sn)$ and $Al_2(Ca,Sn,Sr)$.

Zinc. At the eutectic temperature of 340 °C (644 °F), 6.2% Zn is soluble in magnesium, but at lower temperatures there is general precipitation of magnesium-zinc compound whose particles are not clearly resolvable by optical or electron microscopy until the alloy is overaged (see Fig. 35 and 36).

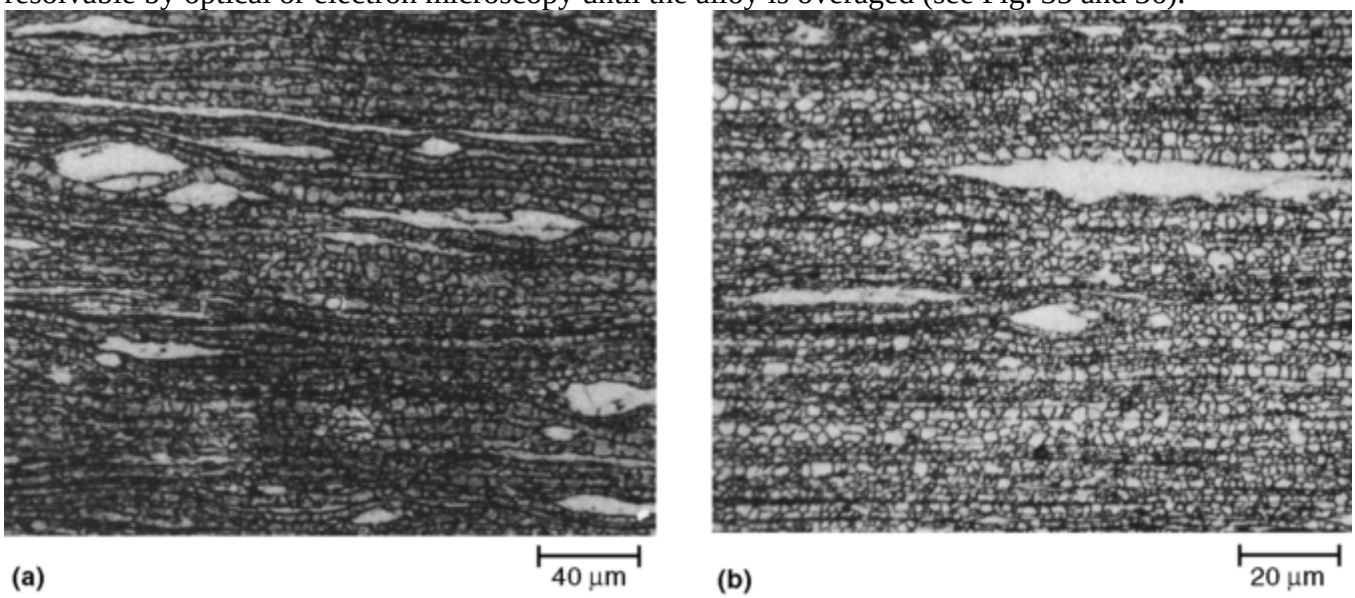

Fig. 35 ZK60A-F extrusion. (a) Longitudinal view of banded hot-worked structure. Small, recrystallized grains. Light islands are solid-solution deficient in zinc and zirconium (due to alloy segregation) and so more resistant to hot working. Etchant 6, then etchant 4 (Table 7). 250×. (b) Artificially aged to the T5 temper. Despite the higher magnification, structure appears the same as in (a) (precipitate formed during aging is irresolvable by microscopy). Etchant 7 for 7 s, then etchant 6, 1 s (Table 7). 500×

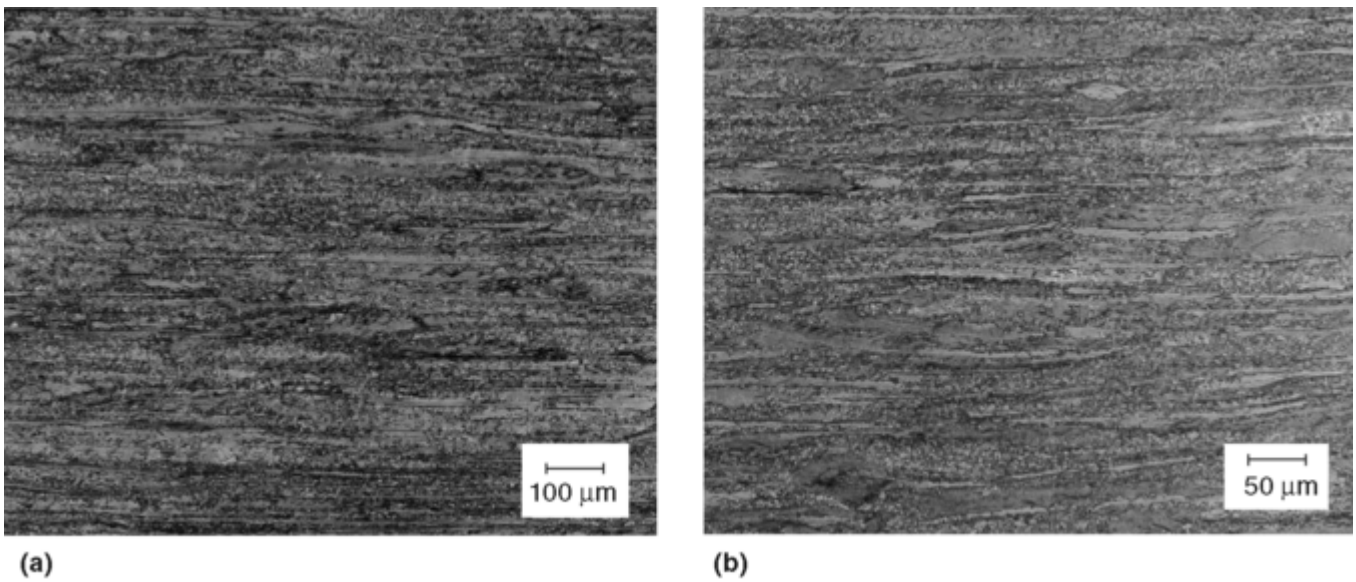

Fig. 36 Two views of the microstructure of wrought Mg-2.8%Zn-0.62%Zr etched with acetic-picral and viewed with polarized light plus a sensitive tint filter. Etching clearly depicts the deformation anisotropy, as well as alloy segregation leading to grain size variation. The grain structure is not recrystallized after working. Courtesy of G.F. Vander Voort, Buehler Ltd.

When zinc is added to magnesium-aluminum alloys, the magnesium-aluminum eutectic takes a completely divorced form, in which massive particles of $Al_{12}Mg_{17}$ compound—or of $(Al,Zn)_{49}Mg_{32}$ compound, if the ratio of zinc to aluminum exceeds 1 to 3—are surrounded by magnesium solid solution. Additions of zinc to magnesium/rare-earth metal alloys increase the amount and continuity of the compound at the grain boundaries. Zinc additions also promote the change of the magnesium/rare-earth eutectic to the divorced form. By adding

approximately 2% Zn to magnesium alloys containing at least 2% Th, an acicular, or platelet, form of compound develops. The acicular form entirely replaces the massive form when the zinc content is increased to approximately 3%, but it again disappears when the zinc content is further increased to above 5%.

Zirconium, in amounts less than 1%, is alloyed with magnesium and added to magnesium alloys containing zinc, rare earth metals, or thorium. The remarkable effectiveness of zirconium in grain-refining magnesium has been explained by the similarities in crystal structure and lattice parameters of the two elements. The lattice parameters of zirconium (a = 0.323 nm, c = 0.514 nm) are very similar to those of magnesium (a = 0.320 nm, c = 0.520 nm). Magnesium grains nucleate epitaxially on the (0001) basal planes of hcp α-zirconium phase crystals, which are first to separate during cooling.

In binary magnesium-zirconium alloys, zirconium-rich particles can be seen within grains and near grain boundaries. Zirconium-rich cores generally appear as either elliptical or nearly circular form on polished sections. Electron microscopy using backscatter detection shows the particles to be bright points within a highly cored primary magnesium grain (Ref 71). In the more complex alloys, zirconium may form compounds with zinc and with certain elements that are impurities in those alloys, such as aluminum, iron, silicon, and hydrogen.

References cited in this section

10. M.O. Pekguleryuz et al., Creep Resistant Magnesium Alloys for Powertrain Applications, *Adv. Eng. Mater.,* Vol 5 (No. 12), 2003, p 866–878

45. B.R. Powell et al., The Relationship Between Microstructure and Creep Behavior in AE42 Magnesium Die Casting Alloy, *Magnesium Technology 2001,* TMS (The Minerals, Metals, & Materials Society), 2001, p 175–181

62. I.J. Polmear, *Metallurgy of the Light Metals,* Halstead Press (John Wiley & Sons, Ltd.), 1996

63. S. Housh et al., Selection and Application of Magnesium and Magnesium Alloys, *Properties and Selection: Nonferrous Alloys and Special-Purpose Materials,* Vol 2, *ASM Handbook,* ASM International, 1990

64. Properties of Magnesium Alloys, *Properties and Selection: Nonferrous Alloys and Special-Purpose Materials,* Vol 2, *ASM Handbook,* ASM International, 1990

65. C.S. Roberts, *Magnesium and Its Alloys,* John Wiley and Sons, 1960

66. E.F. Emley, *Principles of Magnesium Technology,* Pergamon Press Ltd., 1966

67. G.V. Raynor, *The Physical Metallurgy of Magnesium and Its Alloys,* Pergamon Press, 1959

68. A. Beck, *The Technology of Magnesium and Its Alloys,* F.A. Hughes and Co., Ltd., 1943

69. B.E. Carlson, "Influence of Processing Variables and Aluminum Content on the Microstructure and Mechanical Properties of Cast Mg-Al Alloy," Ph.D. dissertation, University of Michigan—Ann Arbor, 1997

70. J.-F. Nie et al., Characterisation of Strengthening Precipitate Phases in a Mg-Y-Nd Alloy, *Acta Mater.,* Vol 48, 2000, p 1691–1703

71. M. Qian et al., Characteristic Zirconium-Rich Coring Structures in Mg-Zr Alloys, *Scr. Mater.,* Vol 46, 2002, p 649–654

T.V. Padfield, Metallography and Microstructures of Magnesium and Its Alloys, *Metallography and Microstructures,* Vol 9, *ASM Handbook,* ASM International, 2004, p. 801–815

Acknowledgment

The author would like to thank the following individuals for contributing images to this article: Éric Baril of Noranda, Jian-Feng Nie of Monash University, Cory Padfield of Hyundai America, Bob Powell of GM, Franka Pravdic of ARC Leichtmetallkompetenzzentrum Ranshofen, Elke Schaberger of Gießerei-Institut, RWTH Aachen, and George Vander Voort of Buehler Ltd. Also, the author is extremely grateful for the thorough review and helpful discussions provided by Cory Padfield during this project.

T.V. Padfield, Metallography and Microstructures of Magnesium and Its Alloys, *Metallography and Microstructures,* Vol 9, *ASM Handbook,* ASM International, 2004, p. 801–815

Metallography and Microstructures of Magnesium and Its Alloys

Toby V. Padfield, ZF Sachs Automotive of America

References

1. L. Gaines et al., *Analysis of the Potential for New Automotive Uses of Wrought Magnesium,* Center for Transportation Research National Laboratory, United States Department of Energy, 1996 (available to the public from National Technical Information Service, U.S. Department of Commerce)

2. "Practice for Codification of Certain Nonferrous Metals and Alloys, Cast and Wrought," B 275, *Annual Book of ASTM Standards,* ASTM International

3. "Practice for Temper Designation of Magnesium Alloys, Cast and Wrought," B 296, *Annual Book of ASTM Standards,* ASTM International

4. "Standard Practice for Numbering Metals and Alloy (UNS)," E 527, *Annual Book of ASTM Standards,* ASTM International

5. "Magnesium and Magnesium Alloys—Magnesium and Magnesium Alloy Anodes, Ingots and Castings—Designation System," EN 1754, European Committee for Standardization

6. "Magnesium and Magnesium Alloys—Magnesium Alloy Ingots and Castings," ISO 16220, International Organization for Standardization

7. "Magnesium and Magnesium Alloys—Magnesium Alloy—Wrought Magnesium Alloys," ISO 3116, International Organization for Standardization

8. D. Webb, "Magnesium Supply and Demand," Proc. 60th Annual World Magnesium Conference, International Magnesium Association, 2003

9. D. Kramer, Magnesium, *Minerals Yearbook,* Vol I, Metals and Minerals, U.S. Government Printing Office, 2002

10. M.O. Pekguleryuz et al., Creep Resistant Magnesium Alloys for Powertrain Applications, *Adv. Eng. Mater.,* Vol 5 (No. 12), 2003, p 866–878

11. B.R. Powell et al., "Progress Toward a Magnesium-Intensive Engine: The USAMP Magnesium Powertrain Cast Components Project," Technical Paper Series 2004-01-0654, SAE International

12. M.O. Pekguleryuz et al., "Magnesium-Based Casting Alloys Having Improved Elevated Temperature Performance," United States Patent 6,322,644

13. M.O. Pekguleryuz et al., Development of Creep Resistant Mg-Al-Sr Alloys, *Magnesium Technology 2001,* TMS (The Minerals, Metals, & Materials Society) 2001, p 119–125

14. B.R. Powell et al., "Creep-Resistant Magnesium Alloy Die Castings," United States Patent 6,264,763

15. B.R. Powell et al., Creep and Microstructure of Magnesium-Aluminum-Calcium Based Alloys, *Metall. Mater. Trans. A,* Vol 33A, March 2002, p 567–574

16. T. Baba et al., "Heat-Resistant Magnesium Alloy," United States Patent 5,811,058

17. S. Koike et al., "Development of Lightweight Oil Pans Made of a Heat-Resistant Magnesium Alloy for Hybrid Engines," Technical Paper Series 2000-01-1117, SAE International

18. B. Bronfin et al., "Magnesium Alloy for High Temperature Applications," United States Patent 6,139,651

19. B. Bronfin et al., Development of New Magnesium Alloys for Advanced Applications, *Magnesium—Alloys and Technologies,* Wiley-VCH, 2003

20. P. Bakke et al., "Die Cast Magnesium Alloys for High Temperature Applications," Technical Paper Series 2003-01-0189, SAE International

21. B. Bronfin et al., "High Strength Creep Resistant Magnesium Alloys," United States Patent Application US 2003/0084968 A1

22. B. Bronfin et al., "High Temperature Mg Alloys for Sand and Permanent Mold Casting Applications," Technical Paper Series 2004-01-0656, SAE International

23. C.J. Bettles et al., "Creep Resistant Magnesium Alloy," International Publication Number WO 2004/001087 A1, World Intellectual Property Organization

24. C.J. Bettles et al., "AMC-SC1: A New Mg Alloy Suitable for Powertrain Applications," Technical Paper Series 2003-01-1365, SAE International

25. G.F. Vander Voort, Metallography of Magnesium and its Alloys, *Tech-Notes,* Vol 4 (No. 2), Buehler Ltd., 2004

26. Light Metals, *Buehler SUM-MET—The Science Behind Materials Preparation,* Buehler Ltd., 2004

27. K.J. Clark, Magnesium Alloys, *Metallography and Microstructures,* Vol 9, *ASM Handbook,* American Society for Metals, 1985, p 425–434

28. J.M. Tartaglia et al., Magnesium Alloy Ingots: Chemical and Metallographic Analyses, *JOM,* Nov 2001, p 16–19

29. E. Schaberger et al., Development of a Metallographic Microstructure Characterization for the High-Purity Magnesium Alloy, *Pract. Metallogr.,* Vol 35 (No. 6), 1998, p 306–315

30. Metalog Method 350, *e-Metalog,* Struers A/S, Rødovre, Denmark

31. E. Schaberger et al., The Development of an Electrolytic Etching Process for Examining the Microstructure of Thixocast Magnesium Alloy AZ91 hp, *Pract. Metallogr.,* Vol 37 (No. 3), 2000, p 140–149

32. Metalog Method A, *Struers Metalog Guide*, Struers A/S, Rødovre, Denmark, 2000

33. L.-Y. Wei et al., Characterisation of Manganese Containing Intermetallic Particles and Corrosion Behaviour of Die Cast Mg-Al Based Alloys, *Magnesium Technology 2000,* TMS (The Minerals, Metals, & Materials Society), 2000, p 153–160

34. T. Mitchell et al., Microstructure Property Studies of In Situ Worked PVD Mg-Ti Alloys, *Magnesium Technology 2000,* TMS (The Minerals, Metals, & Materials Society), 2000, p 169–174

35. M. Cabibbo et al., Microstructural Study and Mechanical Properties of Thixoformed AZ91, *Magnesium Technology 2000,* TMS (The Minerals, Metals, & Materials Society), 2000, p 301–307

36. E.A. Nyberg et al., Microstructure and Microchemistry of Creep Resistant Magnesium Alloys, *Magnesium Technology 2001,* TMS (The Minerals, Metals, & Materials Society), 2001, p 169–1173

37. L. Shepeleva et al., TEM Study of the As-Cast and Aged Microstructures of Mg-Al-Zn Alloys and the Influence of Zn Content on Precipitation, *Magnesium Technology 2001,* TMS (The Minerals, Metals, & Materials Society), 2001, p 189–194

38. M. Cabibbo et al, Microstructural Study After Solution Treatments of a Thixocast AZ91, *Magnesium Technology 2001,* TMS (The Minerals, Metals, & Materials Society), 2001, p 211–216

39. T. Horie et al., Development of High Creep-Resistant Magnesium Alloy Strengthened by Ca Addition, *Magnesium Technology 2000,* TMS (The Minerals, Metals, & Materials Society), 2000, p 261–269

40. R.V. Allen et al., Magnesium Alloy Sheet Produced by Twin-Roll Casting, *Magnesium Technology 2001,* TMS (The Minerals, Metals, & Materials Society), 2001, p 75–79

41. I.P. Moreno et al., Microstructure and Creep Behavior of a Die Cast Magnesium Rare Earth Alloy, *Magnesium Technology 2002,* TMS (The Minerals, Metals, & Materials Society), 2002, p 111–116

42. G. S. Song et al., Enhancement of the Properties of Mg-Li Alloys by Small Alloying Additions, *Magnesium Technology 2003,* TMS (The Minerals, Metals, & Materials Society), 2003, p 77–79

43. C. Mendis et al., Effects of Ca Additions on Microstructures, Age Hardening Response and Creep Behavior of Mg-8Zn-4Al Casting Alloy, *Magnesium Technology 2003,* TMS (The Minerals, Metals, & Materials Society), 2003, p 183–188

44. F. Czerwinski et al., Correlating the Microstructure and Tensile Properties of a Thixomolded AZ91D Alloy, *Acta Mater.,* Vol 49, 2001, p 1225–1235

45. B.R. Powell et al., The Relationship Between Microstructure and Creep Behavior in AE42 Magnesium Die Casting Alloy, *Magnesium Technology 2001,* TMS (The Minerals, Metals, & Materials Society), 2001, p 175–181

46. M.T. Rowley, Ed., *International Atlas of Casting Defects,* American Foundry Society, 1993

47. Testing and Inspection of Casting Defects, *Casting,* Vol 15, *ASM Handbook,* ASM International, 1988, p 544–561

48. W.G. Walkington, *Die Casting Defects—Causes and Solutions,* North American Die Casting Association, 1997

49. *Castings, Classification and Inspection of,* MIL-STD-2175, Department of Defense Single Stock Point for Military Specifications and Standards, Document Automation and Production Service

50. B.R. Powell et al., The Die Castability of Calcium-Containing Magnesium Alloys: Thin-Wall Computer Case, *Magnesium Technology 2002,* TMS (The Minerals, Metals, & Materials Society, 2002, p 123–129

51. C.R. Dallam et al., Characterization of Welds, *Welding, Brazing, and Soldering,* Vol 6, *ASM Handbook,* ASM International, 1993, p 97–106

52. Overview of Weld Discontinuities, *Welding, Brazing, and Soldering,* Vol 6, *ASM Handbook,* ASM International, 1993, p 1073–1080

53. *Guide for the Visual Examination of Welds,* AWS B1.11,

54. "Welding and Allied Processes—Classification of Geometric Imperfections in Metallic Materials—Part 1: Fusion Welding," ISO 6520-1, International Organization for Standardization

55. "Welding and Allied Processes—Classification of Geometric Imperfections in Metallic Materials—Part 2: Welding with Pressure," ISO 6520-2, International Organization for Standardization

56. *SAE Magnesium Alloys AMS Handbook,* AHB-002, SAE International, 1997

57. P. Chaudhury et al., Forging of Magnesium Alloys, *Forming and Forging,* Vol 14, *ASM Handbook,* ASM International, 1988

58. G. Dieter, Workability Tests, *Forming and Forging,* Vol 14, *ASM Handbook,* ASM International, 1988

59. J.C. Grebetz et al., Measuring the Cleanliness of Recycled Magnesium for Automotive Applications: A Detailed Examination of the Fracture Brightness Technique, *Light Metal Age,* Aug 1997, p 60–69

60. D. Argo et al., Chemical Composition and Cleanliness During Recycling of the AJ52 Magnesium Strontium Alloy, *Magnesium Technology 2003,* TMS (The Minerals, Metals, & Materials Society), 2002, p 33–37

61. "Standard Test Method for Macroetching Metals and Alloys," E 340, *Annual Book of ASTM Standards,* ASTM International

62. I.J. Polmear, *Metallurgy of the Light Metals,* Halstead Press (John Wiley & Sons, Ltd.), 1996

63. S. Housh et al., Selection and Application of Magnesium and Magnesium Alloys, *Properties and Selection: Nonferrous Alloys and Special-Purpose Materials,* Vol 2, *ASM Handbook,* ASM International, 1990

64. Properties of Magnesium Alloys, *Properties and Selection: Nonferrous Alloys and Special-Purpose Materials,* Vol 2, *ASM Handbook,* ASM International, 1990

65. C.S. Roberts, *Magnesium and Its Alloys,* John Wiley and Sons, 1960

66. E.F. Emley, *Principles of Magnesium Technology,* Pergamon Press Ltd., 1966

67. G.V. Raynor, *The Physical Metallurgy of Magnesium and Its Alloys,* Pergamon Press, 1959

68. A. Beck, *The Technology of Magnesium and Its Alloys,* F.A. Hughes and Co., Ltd., 1943

69. B.E. Carlson, "Influence of Processing Variables and Aluminum Content on the Microstructure and Mechanical Properties of Cast Mg-Al Alloy," Ph.D. dissertation, University of Michigan—Ann Arbor, 1997

70. J.-F. Nie et al., Characterisation of Strengthening Precipitate Phases in a Mg-Y-Nd Alloy, *Acta Mater.,* Vol 48, 2000, p 1691–1703

71. M. Qian et al., Characteristic Zirconium-Rich Coring Structures in Mg-Zr Alloys, *Scr. Mater.,* Vol 46, 2002, p 649–654

W.L. Mankins, Metallography and Microstructures of Nickel and Nickel-Copper Alloys , *Metallography and Microstructures,* Vol 9, *ASM Handbook,* ASM International, 2004, p. 816–819

Metallography and Microstructures of Nickel and Nickel-Copper Alloys

William L. Mankins, Metallurgical Services, Inc.

Introduction

THE PREPARATION of metallographic specimens and the microstructures of alloys containing 96% or more nickel (Nickel 200, Nickel 270, and Duranickel 301) and nickel-copper alloys (Monel 400, Monel R-405, and Monel K-500) are considered in this article. Micrographs of these alloys are shown in Fig. 1, 2, 3, 4, 5, 6, 7, 8, 9, 10, 11, 12, 13, 14 and 15.

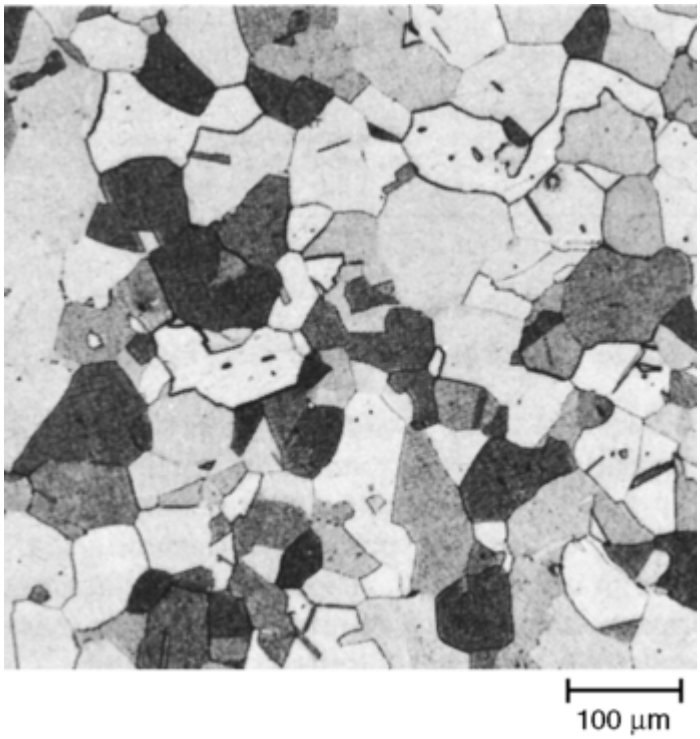

Fig. 1 Nickel 200, cold drawn and annealed in a continuous process at 830 °C (1525 °F). Structure: nickel solid solution. See also Fig. 2. NaCN, $(NH_4)2S_2O_8$. 100×

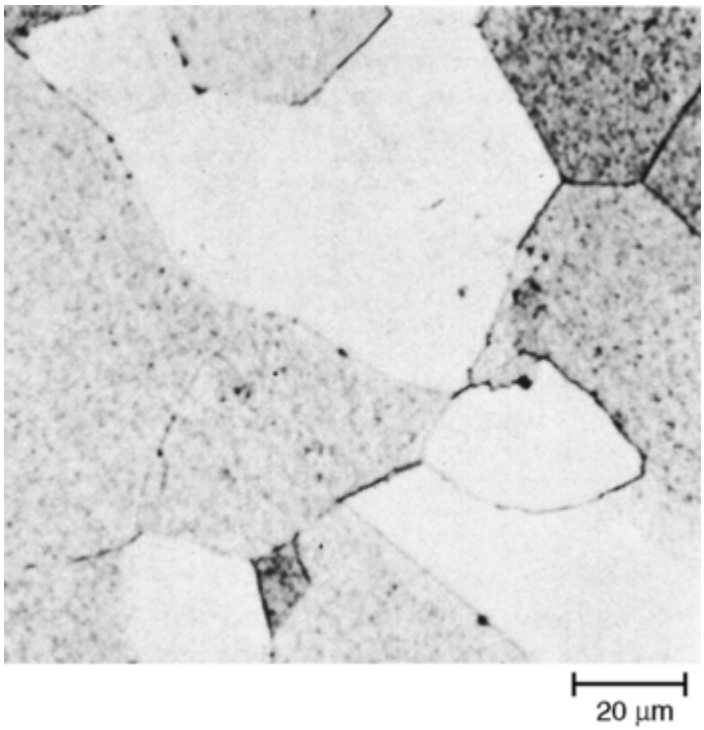

Fig. 2 Same as Fig. 1 but at higher magnification. Variation in shade of grains is caused by variation in grain orientation. NaCN, $(NH_4)_2S_2O_8$. 500×

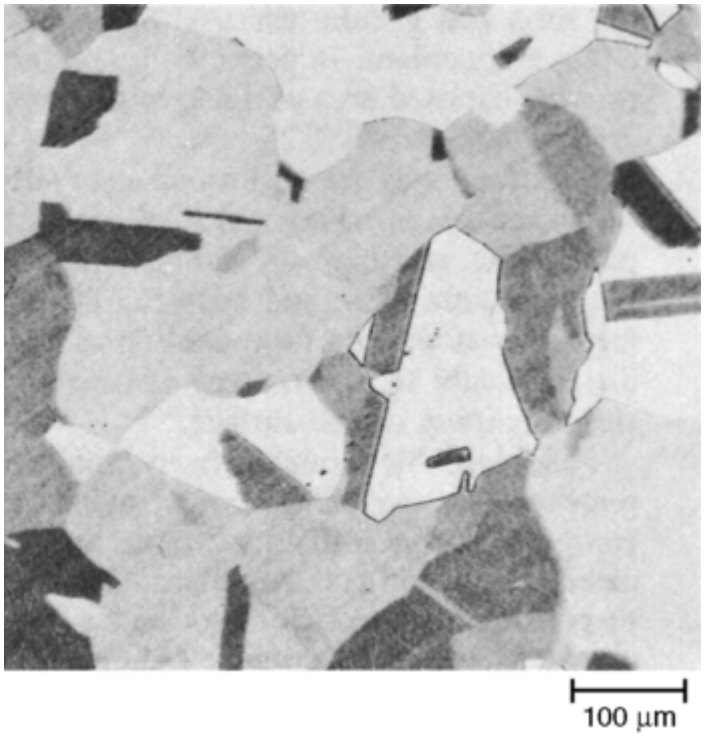

Fig. 3 Nickel 270, hot rolled and annealed in a continuous process at 830 °C (1525 °F). Structure: nickel solid solution. See also Fig. 4. NaCN, $(NH_4)_2S_2O_8$. 100×

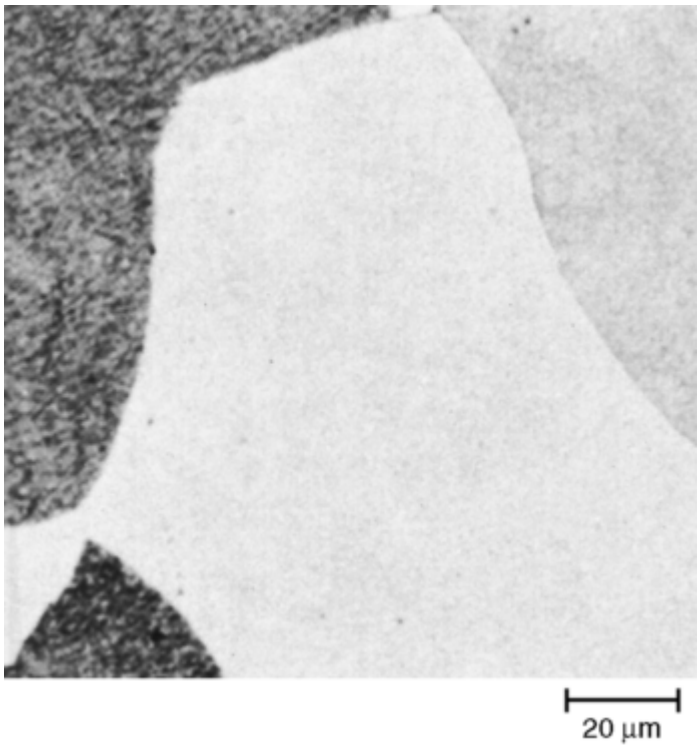

Fig. 4 Same alloy and same processing as in Fig. 3 but shown at a higher magnification. The variation in shade of the grains (dark, gray, and white) is the result of variation in grain orientation. NaCN, $(NH_4)_2S_2O_8$. 500×

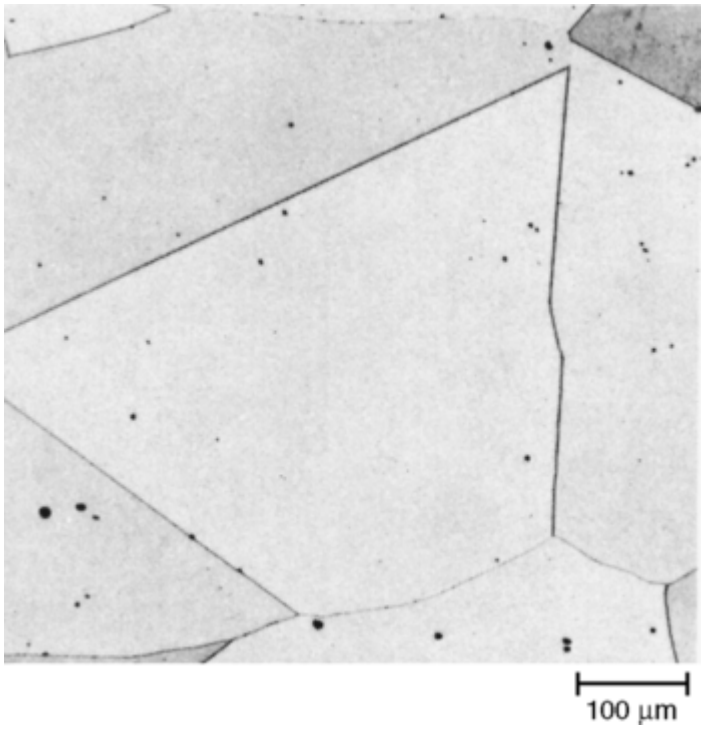

Fig. 5 Permanickel 300, solution annealed 1 h at 1205 °C (2200 °F) and water quenched, aged 10 h at 480 °C (900 °F) and water quenched. Dispersed particles of TiN and graphite (black dots) in nickel solid solution. NaCN, $(NH_4)_2S_2O_8$. 100×

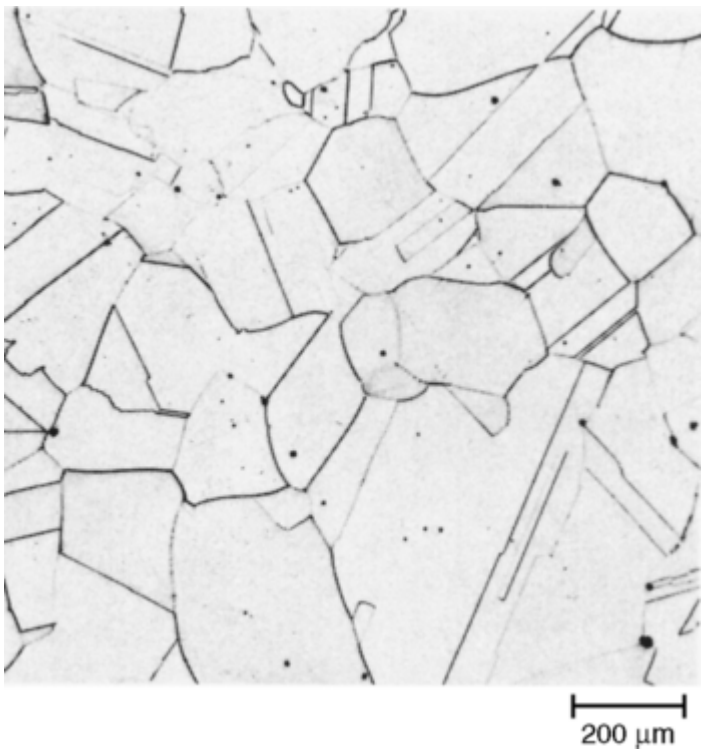

Fig. 6 Duranickel 301, solution annealed for 30 min at 980 °C (1800 °F) and water quenched, aged for 20 h at 480 °C (900 °F) and water quenched. Microstructure: nickel solid solution; graphite particles (black dots). NaCN, $(NH_4)_2S_2O_8$. 50×

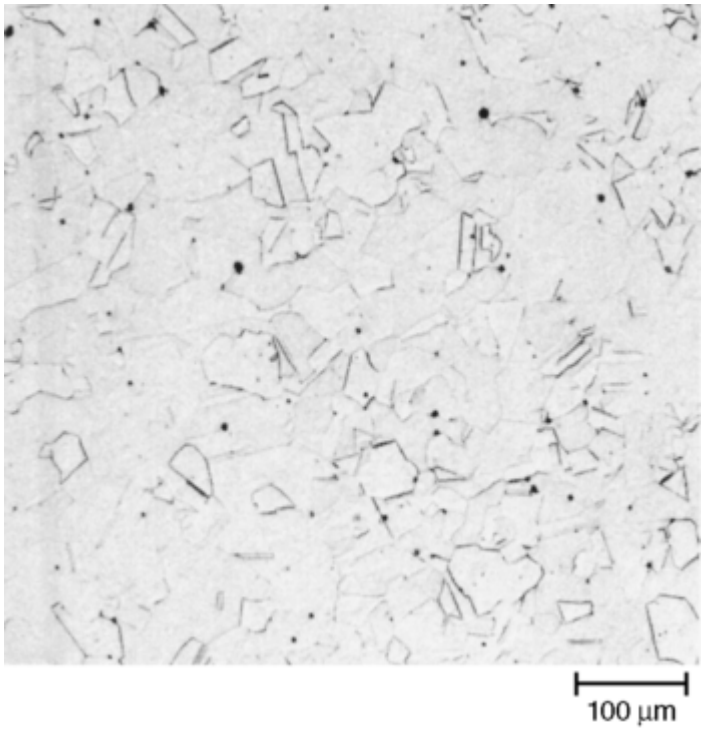

Fig. 7 Monel 400, cold drawn and annealed in a continuous process at 830 °C (1525 °F). Nickel-copper solid solution with a few unidentified nonmetallic inclusions (black). NaCN, $(NH_4)_2S_2O_8$. 100×

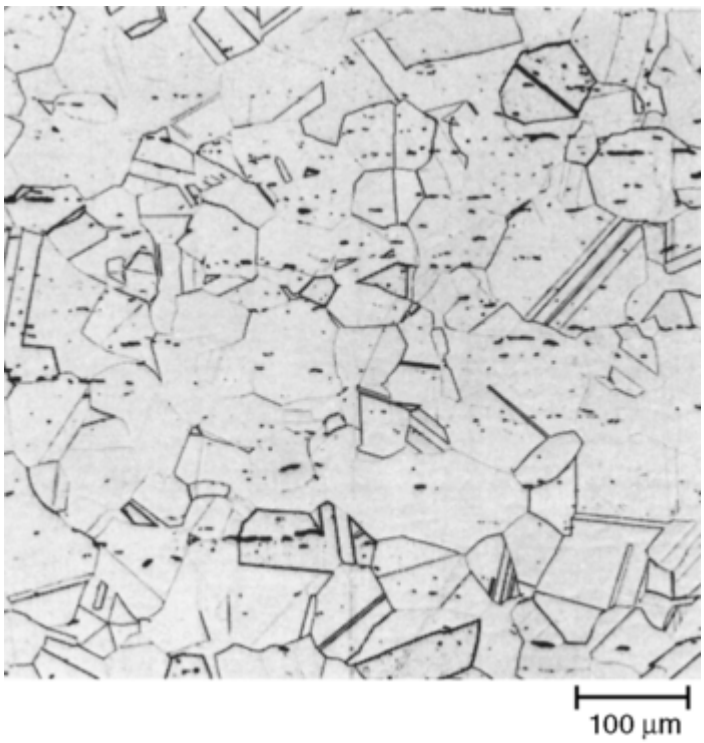

Fig. 8 Monel R-405, cold drawn, and annealed in a continuous process at 830 °C (1525 °F). Microstructure: nickel-copper solid solution with sulfide stringers (black constituent). NaCN, $(NH_4)_2S_2O_8$. 100×

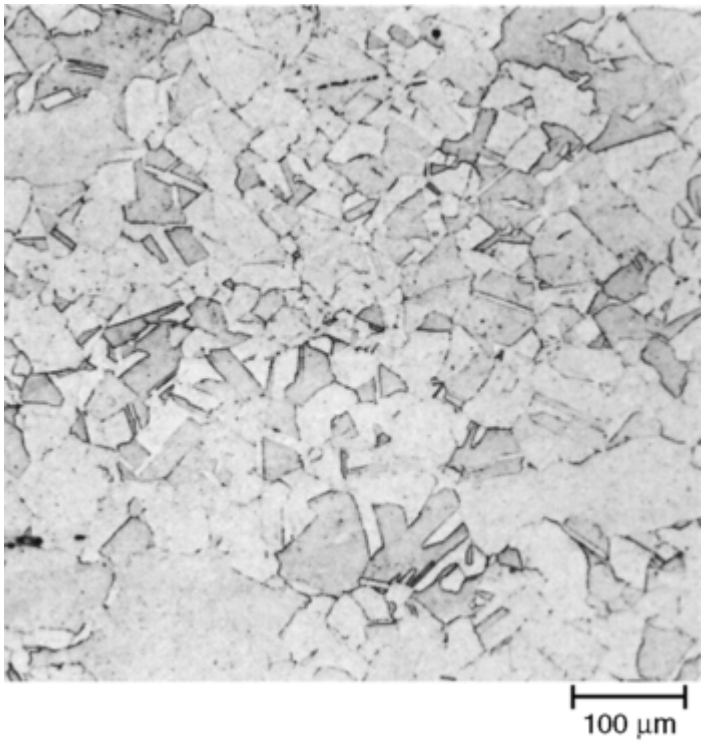

Fig. 9 Monel K-500 in the hot rolled condition. Structure: nickel-copper solid solution. Variation in shade of grains is the result of variation in grain orientation. Glyceregia. 100×

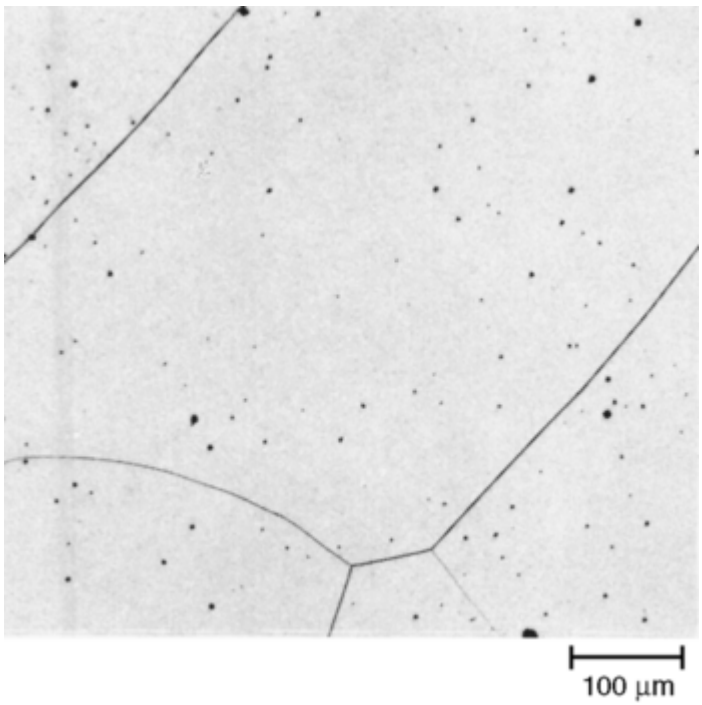

Fig. 10 Monel K-500, solution annealed for 1 h at 1205 °C (2200 °F) and quenched in water. Nickel-copper solid-solution matrix. See also Fig. 11, 12, 13, 14 and 15. NaCN, $(NH_4)_2S_2O_8$. 100×

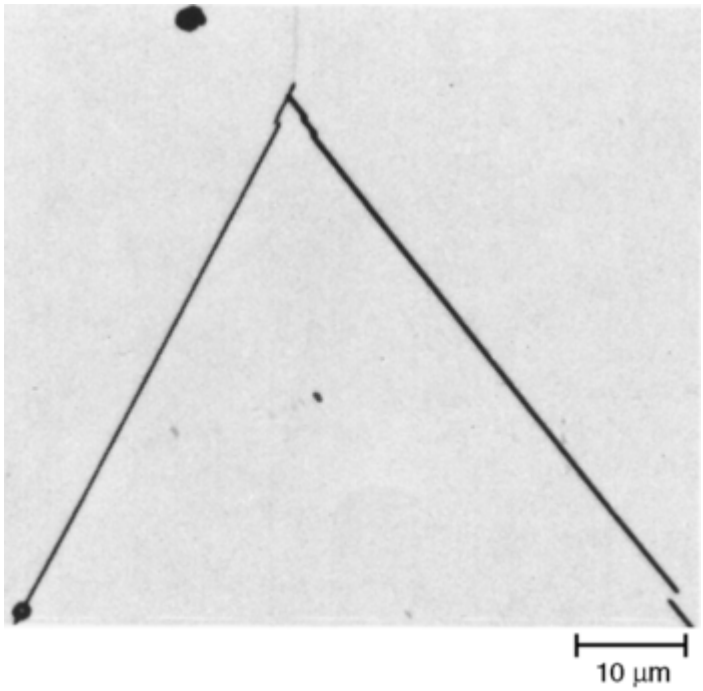

Fig. 11 Same as Fig. 10 but at higher magnification. Portions of only three grains are visible. The black dots are nitride particles. See also Fig. 10 and 12, 13, 14, 15, Monel K-500, solution to 15. NaCN, $(NH_4)_2S_2O_8$. 1000×

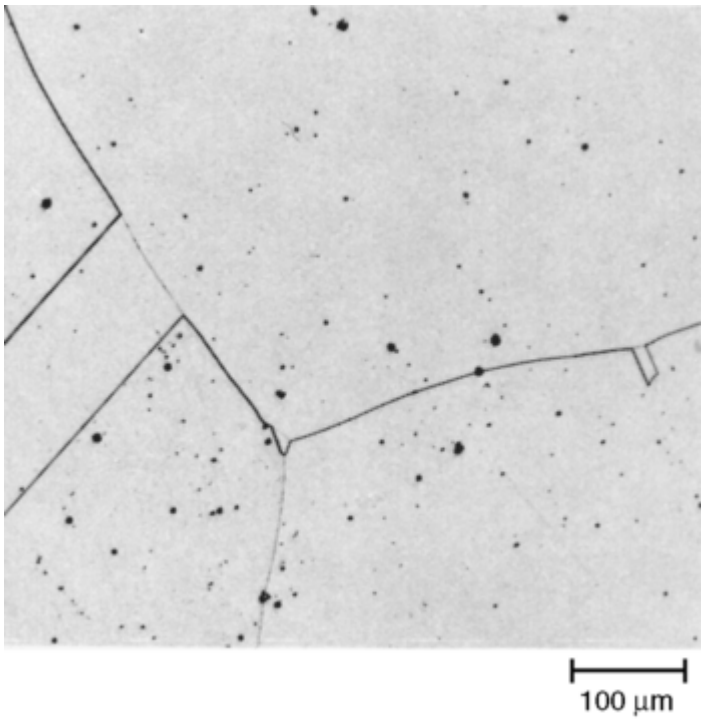

Fig. 12 Monel K-500, held 1 h at 1205 °C (2200 °F), transferred to a furnace at 595 °C (1100 °F) and aged 4 h, water quenched. Solid-solution matrix; nitride particles. See also Fig. 10, 11, and 13, 14 and 15 NaCN, $(NH_4)_2S_2O_8$. 100×

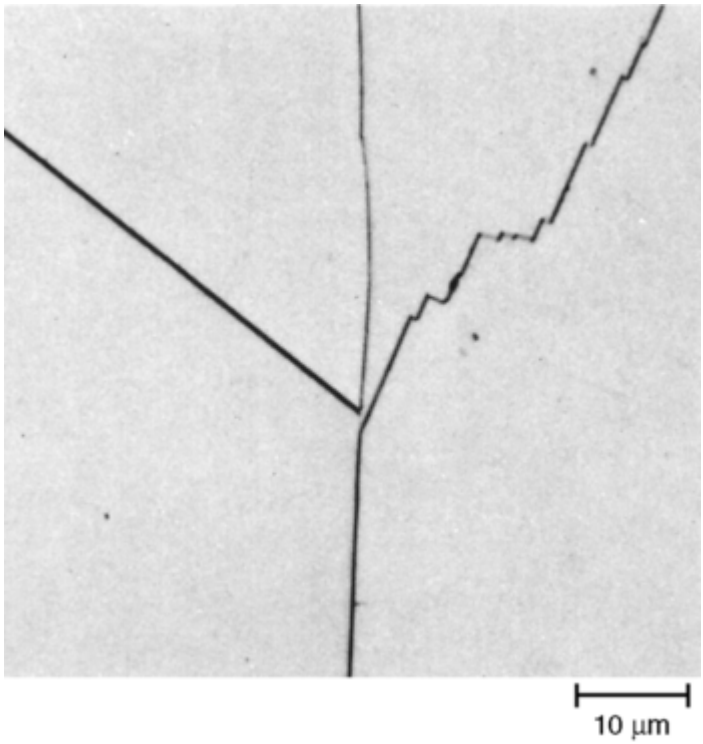

Fig. 13 Same as Fig. 12 but at higher magnification. Structure contains precipitated $Ni_3(Al,Ti)$, resolvable only by electron microscopy unless aging temperature is higher than 595 °C (1100 °F). See also Fig. 10, 11, 12, 14 and 15. NaCN, $(NH_4)_2S_2O_8$. 1000×

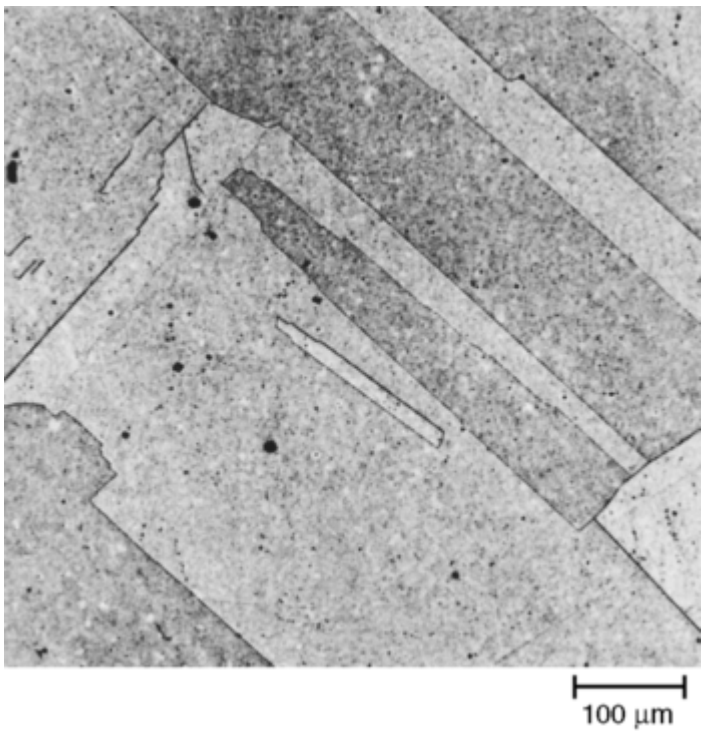

Fig. 14 Monel K-500, held 1 h at 1205 °C (2200 °F), transferred to a furnace at 705 °C (1300 °F) and aged 4 h, water quenched. Precipitated $Ni_3(Al,Ti)$ appears as tiny particles dispersed in the matrix solid solution. See also Fig. 10, 11, 12, 13 and 15. NaCN, $(NH_4)_2S_2O_8$. 100×

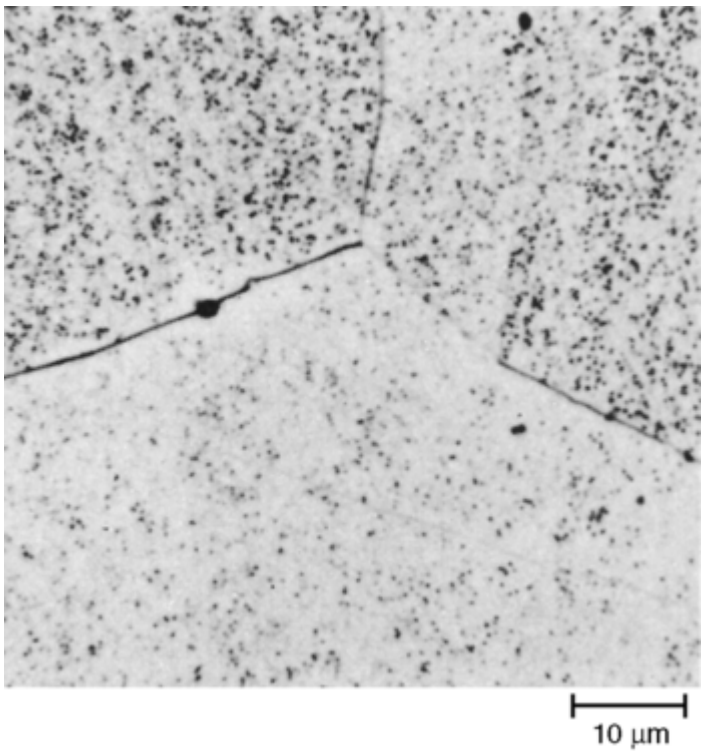

Fig. 15 Same as Fig. 14 except at a higher magnification. The $Ni_3(Al,Ti)$ precipitate is better resolved. When this precipitate is resolvable by optical microscopy, overaging is indicated. See also Fig. 10, 11, 12, 13 and 14. NaCN, $(NH_4)_2S_2O_8$. 1000×

The procedures and materials for sectioning, mounting, grinding, and polishing specimens are essentially the same for all nickel alloys regardless of specimen size or sophistication of laboratory facilities. In preparing specimens for metallographic examination, it is important to prevent cold working of the surface during grinding/polishing steps.

W.L. Mankins, Metallography and Microstructures of Nickel and Nickel-Copper Alloys , *Metallography and Microstructures,* Vol 9, *ASM Handbook,* ASM International, 2004, p. 816–819

Metallography and Microstructures of Nickel and Nickel-Copper Alloys

William L. Mankins, Metallurgical Services, Inc.

Preparation for Microscopic Examination

The specimen to be examined is cut to a convenient size with a silicon carbide water-cooled abrasive cutoff wheel, then mounted in a hard plastic, such as Bakelite (Georgia-Pacific) or a hard epoxy resin. Next, the mounted specimen is ground flat on a belt grinder using 120-grit abrasive and water coolant. In general, it is preferable that the exposed area of the specimen not exceed approximately 1.6 cm^2 (0.25 $in.^2$).

Grinding may be performed manually or on power-driven wheels using silicon carbide paper disks, starting with 220-grit and following with 320-, 400-, and 600-grit abrasives. The specimen is then washed thoroughly between grind steps and cleaned ultrasonically after final grinding to remove any abrasive particles remaining on the surface.

Polishing. All scratches from grinding are removed by polishing on a nylon cloth charged with 6 μm diamond paste and lubricated with lapping oil. An alternate method is to polish on a broadcloth-covered wheel using 5 μm levigated alumina (Al_2O_3) powder suspended in water.

Final polishing may be performed in one or two stages with a polishing wheel or vibratory polisher. If a polishing wheel is used, microcloth and γ-Al_2O_3 powder (<0.1 μm particle size) suspended in water are recommended. An alternative requires semifinal and final polishing using a vibratory polisher. Semifinal polishing employs a nylon polishing cloth and a slurry of 0.3 μm Al_2O_3 and distilled water. A 350 g (12 oz)

weight is placed on the specimen throughout the polishing cycle. At the conclusion of each polishing cycle, the specimen is cleaned ultrasonically. Final polishing employs a short-nap microcloth and a slurry of 0.05 μm Al_2O_3 and distilled water. Polishing continues until the surface is free of scratches.

Electropolishing. Nickel and nickel-copper alloys can be electropolished satisfactorily, although best results are generally obtained with specimens that first have been polished mechanically through 600-grit abrasive. Recommended electrolytes and current densities for electropolishing these alloys are given in Table 1. A platinum cathode is suggested, and the electrolyte should be water cooled and continuously stirred.

Table 1 Electrolytes and current densities for electropolishing of nickel and nickel-copper alloys

Electrolyte composition	Applicable alloys	Current density	
		A/cm^2	**A/in.^{2}**
37 mL H_3PO_4 (conc), 56 mL glycerol, 7 mL H_2O	Nickel 200	1.4–1.5	9–10
	Nickel 270	1.5–1.8	10–12
	Duranickel 301	1.25–1.5	8–10
	Monel 400	0.9–1	6–7
33 mL HNO_3 (conc), 66 mL methanol	Monel 400, R-405, K-500	1.5–2.3	10–15

Etching. The solutions and conditions for etching nickel alloys for microscopic examination are described in Table 2. The acids used should be concentrated; when water is indicated, use distilled water only.

Table 2 Etchants for microscopic examination of nickel and nickel-copper alloys for grain boundaries and general structure

Composition of etchant	Conditions for use
Etchants for Nickel 200 and 270; Permanickel; Duranickel 301; and Monel 400, R-450, and K-500	
1 part 10% aqueous solution of NaCN (sodium cyanide), 1 part 10% aqueous solution of $(NH_4)_2S_2O_8$ (ammonium persulfate). Mix solutions when ready to use.	Immerse or swab specimen for 5–90 s.[(a)]
1 part HNO_3 (conc), 1 part acetic acid (glacial). Use fresh solution.	For revealing grain boundaries. Immerse or swab specimen for 5–20 s.
7.5 mL HF, 2.5 mL HNO_3, 200 mL methanol	Immerse sample 2–4 min.
5 g $FeCl_3$, 50 mL HCl, 100 mL H_2O	Immerse or swab specimen up to a few minutes.
Alternate etchant for Monel K-500	
Glyceregia: 10 mL HNO_3 (conc), 20 mL HCl (conc), 30–40 mL glycerol	Etch by immersing or swabbing the specimen for 30 s to 5 min.

(a) This cyanide-containing etchant is very hazardous in its preparation and use. Cyanide, even in small quantities, as dust, solution, or fumes may be fatal when taken into the body. A fume hood must be used with this etchant.

W.L. Mankins, Metallography and Microstructures of Nickel and Nickel-Copper Alloys , *Metallography and Microstructures,* Vol 9, *ASM Handbook*, ASM International, 2004, p. 816–819

Metallography and Microstructures of Nickel and Nickel-Copper Alloys

William L. Mankins, Metallurgical Services, Inc.

Microstructures of Nickel and Nickel-Copper Alloys

Nickel-base alloys are widely used as high-temperature materials. Micrographs of such alloys are presented in the article “Metallography and Microstructures of Heat Resistant Alloys” in this Volume. The micrographs in this article show structures of nickel alloys that are used primarily for their resistance to corrosion and for other specialized applications. As shown in Table 3, these alloys range in nickel content from 66.5 to 99.98%.

Table 3 Nominal compositions of nickel and nickel-copper alloys

Alloy	Composition
Nickel 200	99.5Ni-0.08C-0.18Mn-0.20Fe
Nickel 270	99.98Ni-0.01C
Permanickel 300	98.5Ni-0.20C-0.25Mn-0.30Fe-0.35Mg-0.40Ti
Duranickel 301	96.5Ni-0.15C-0.25Mn-0.30Fe-0.63Ti-4.38Al
Monel 400	66.5Ni-31.5Cu-0.15C-1.0Mn-1.25Fe
Monel R-405	66.5Ni-31.5Cu-0.15C-1.0Mn-1.25Fe-0.043S
Monel K-500	66.5Ni-29.5Cu-0.13C-0.75Mn-1.0Fe-0.60Ti-2.73Al

The microstructure of Nickel 200 typically contains some nonmetallic inclusions (principally oxide). Prolonged exposure to temperatures from 425 to 650 °C (800 to 1200 °F) results in the precipitation of graphite from the nickel solid solution.

Although Nickel 270 (99.98% Ni) is less likely than Nickel 200 to contain nonmetallic inclusions, their structures are similar, assuming that mechanical working and thermal treatments are similar (compare Fig. 1 and 2 to Fig. 3 and 4). The very low carbon in Nickel 270 (≤0.01%) assumes the absence of graphite after long time exposures at elevated temperatures (425 to 650 °C, or 800 to 1200 °F).

Permanickel 300 is an age-hardening alloy that, in the solution-annealed condition, shows randomly dispersed particles of titanium nitride (TiN) and graphite when observed through an optical microscope. When subsequently age hardened, the alloy has a similar appearance (Fig. 5), but it also contains a fine granular precipitate. This phase is not resolvable by optical microscopy in material aged at a normal aging temperature (480 °C, or 900 °F) but is visible in overaged material. The phase or phases responsible for the age hardening of this alloy have not been positively identified. The mechanism appears to be a complex precipitate. It has been observed that in addition to nickel, carbon, magnesium, and titanium are required for full hardness. Precipitation of a compound such as $Ni_3(Mg,Ti)C_x$ seems likely during age hardening.

Duranickel 301, an age-hardening alloy, combines the corrosion resistance of unalloyed nickel with increased strength and hardness. After solution annealing, this alloy is age hardened by holding in the temperature range of 425 to 705 °C (800 to 1300 °F), which precipitates the phase $Ni_3(Al,Ti)$ throughout the structure. In the solution-annealed and properly aged condition (Fig. 6), the precipitated phase is not resolved by an optical microscope, but hardness effects are easily measured. Some particles of graphite, however, are usually visible.

Nickel-Copper Alloys. Monel 400 is a widely used stable solid-solution alloy of nickel and copper. Nonmetallic inclusions often appear in the microstructure (Fig. 7).

Monel R-405 is a free-machining grade of Monel 400 produced with an intentional addition of sulfur (0.025 to 0.050%). The microstructures of these two alloys are similar for the same hot/cold working history of mechanical and thermal treatment, except for the sulfide particles in Monel R-405, which improve its machinability (Fig. 8).

Monel K-500 is produced by adding aluminum and titanium to the basic nickel-copper composition. Solution annealing and aging produce a γ' precipitate throughout the matrix. In material aged at the normal temperature

of 595 °C (1100 °F), this precipitate is not resolvable by an optical microscope (Fig. 12, 13). However, in material that is overaged—by holding at 705 °C (1300 °F), for example—the precipitate is visible by optical microscopy (Fig. 14, 15). In addition to the precipitate, particles of TiN are usually present in the microstructure.

G.F. Vander Voort, G.M. Lucas, and E.P. Manilova, Metallography and Microstructures of Heat-Resistant Alloys, *Metallography and Microstructures*, Vol 9, *ASM Handbook*, ASM International, 2004, p. 820–859

Metallography and Microstructures of Heat-Resistant Alloys

George F. Vander Voort and Gabriel M. Lucas, Buehler Ltd.; Elena P. Manilova, Polzunov Central Boiler and Turbine Institute, St. Petersburg, Russia

Introduction

HEAT-RESISTANT ALLOYS cover a wide range of chemical compositions, microstructural constituents, and mechanical properties. This article summarizes metallographic techniques and microstructural constituents for three types of cast and wrought heat-resistant alloys: iron-base, nickel-base, and cobalt-base. The metallographic methods discussed also are suitable for preparing both cast and wrought heat-resistant alloys; microstructural constituents are quite similar except for obvious differences in homogeneity and porosity.

The procedures used to prepare metallographic specimens of cast or wrought heat-resistant grades are quite similar to those for iron-base alloys, especially stainless steels (see the Section “Metallographic Techniques” in this Volume). Aspects particularly significant to the preparation of cast or wrought heat-resistant alloys are emphasized. Table 1, 2, and 3 list the nominal compositions of Fe-Ni-Cr Alloy Casting Institute H-series alloys and other iron-nickel, nickel-, and cobalt-base cast and wrought heat-resistant alloys, respectively.

Table 1 Compositions of Fe-Cr-Ni heat-resistant casting alloys

Grade	Type	Composition, %							
		C	**Mn, max**	**Si, max**	**P, max**	**S, max**	**Cr**	**Ni**	**Mo, max** [(a)]
HF	19 chromium, 9 nickel	0.20–0.40	2.00	2.00	0.04	0.04	18.0–23.0	8.0–12.0	0.50
HH	25 chromium, 12 nickel	0.20–0.50	2.00	2.00	0.04	0.04	24.0–28.0	11.0–14.0	0.50
HI	28 chromium, 15 nickel	0.20–0.50	2.00	2.00	0.04	0.04	26.0–30.0	14.0–18.0	0.50
HK	25 chromium, 20 nickel	0.20–0.60	2.00	2.00	0.04	0.04	24.0–28.0	18.0–22.0	0.50
HE	29 chromium, 9 nickel	0.20–0.50	2.00	2.00	0.04	0.04	26.0–30.0	8.0–11.0	0.50
HT	15 chromium, 35 nickel	0.35–0.75	2.00	2.50	0.04	0.04	17.0–21.0	33.0–37.0	0.50
HU	19 chromium, 39 nickel	0.35–0.75	2.00	2.50	0.04	0.04	17.0–21.0	37.0–41.0	0.50
HW	12 chromium, 60 nickel	0.35–0.75	2.00	2.50	0.04	0.04	10.0–14.0	58.0–62.0	0.50
HX	17 chromium, 66 nickel	0.35–0.75	2.00	2.50	0.04	0.04	10.0–14.0	58.0–62.0	0.50
HC	28 chromium	0.50 max	1.00	2.00	0.04	0.04	26.0–30.0	4.0 max	0.50
HD	28 chromium, 5 nickel	0.50 max	1.50	2.00	0.04	0.04	26.0–30.0	4.0–7.0	0.50

HL	29 chromium, 20 nickel		0.20–0.60	2.00	2.00	0.04	0.04	28.0–32.0	18.0–22.0	0.50
HN	20 chromium, 25 nickel		0.20–0.50	2.00	2.00	0.04	0.04	19.0–23.0	23.0–27.0	0.50
HP	26 chromium, 35 nickel		0.35–0.75	2.00	2.50	0.04	0.04	24.0–28.0	33.0–37.0	0.50

(a) Castings having a specified molybdenum range agreed on by the manufacturer and the purchaser may also be furnished under these specifications. Source: ASTM A 297

Table 2 Nominal compositions of nickel- and cobalt-base heat-resistant casting alloys

Alloy	Composition, %															
	C	**Cr**	**Mo**	**Nb**	**Ti**	**Al**	**B**	**Zr**	**Fe**	**W**	**V**	**Ta**	**Re**	**Hf**	**Ni**	**Co**
Nickel-base alloys																
Alloy 713 C	0.12	12.5	4.2	2	0.80	6.1	0.012	0.10	2.5	…	…	…	…	…	bal	…
Alloy 718	0.04	19	3.05	5.13 + Ta	0.90	0.50	…	…	18.5	…	…	…	…	…	bal	…
B-1900	0.10	8	6	0.1 max	1	6	0.015	0.08	0.35	0.1	…	4.3	…	…	bal	10
Hastelloy B	0.10	0.6	28	…	…	…	…	…	5	…	0.30	…	…	…	bal	2.5 max
Hastelloy C	0.07	16	17	…	…	…	…	…	5	4	…	…	…	…	bal	2.5 max
IN-100	0.15	10	3	…	4.7	5.5	0.015	0.06	…	…	1	…	…	…	bal	15
IN-738	0.17	16	1.75	0.9	3.4	3.4	0.01	0.10	0.50 max	2.6	…	1.75	…	…	bal	8.5
MAR-M 246	0.15	9	2.5	…	1.5	5.5	0.015	0.05	…	10	…	1.5	…	…	bal	10
TRW-NASA VI A	0.13	6.1	2	0.5	1	5.4	0.02	0.13	333	5.5	333	9	0.2	0.43	bal	7.5
U-700	0.15 max	15	5.2	…	3.5	4.25	0.05 max	…	1 max	…	…	…	…	…	bal	18.5
Cobalt-base alloys																
Haynes 21	0.25	27	5	…	…	…	…	…	1	…	…	…	…	…	3	bal
Haynes 31	0.50	25.5	…	…	…	…	0.01	…	2	7.5	…	…	…	…	10.5	bal
Haynes 151	0.50	20	…	…	…	…	0.05	…	…	12.7	…	…	…	…	…	bal
MAR-M 302	0.85	21.5	…	…	…	…	0.005	0.20	…	10	…	9	…	…	…	bal
MAR-M 509	0.30	24	…	…	0.20	…	…	0.50	…	7	…	3.5	…	…	10	bal
Wi-52	0.45	21	…	2	…	…	…	…	2	11	…	…	…	…	1.0 max	bal

Table 3 Nominal compositions of wrought heat-resistant alloys

Alloy	Composition, %							
	C	**Fe**	**Ni**	**Co**	**Cr**	**Ti**	**Mo**	**Others**
Iron-nickel-base alloys								
A-286 (AISI 660)	0.05	bal	26.0	…	15.0	2.15	1.25	0.3 V, 0.2 Al, 0.003 B
Greek Ascoloy	0.18	bal	2.0	…	13.0	…	0.50 max	3.0 W
Moly Ascoloy	0.12	bal	2.5	…	12.0	…	1.75	0.70 Mn, 0.32 V, 0.025 N
Incoloy 800	0.05	bal	32.5	…	21.0	0.38	…	0.38 Al
Incoloy 901	0.05	bal	42.7	…	13.5	2.5	6.2	0.25 Al
AISI 330	0.05	bal	36.0	…	19.0	…	…	…
Hastelloy X (AISI 680)	0.10 max	18.5	bal	1.5	22.0	…	9.0	0.6 W
Pyromet 31	0.04	bal	55.5	…	22.7	2.5	2.0	1.5 Al, 1.1 Nb, 0.005 B
Alloy 718	0.04	18.5	bal	…	19.0	0.9	3.05	5.13 Nb + Ta, 0.5 Al
Nickel-base alloys								
Astroloy	0.06	…	bal	17.0	15.0	3.5	5.25	4.0 Al, 0.03 B
Hastelloy B	…	5.0	bal	2.5 max	1.0 max	…	28.0	…
Hastelloy C	0.07	5.0	bal	2.5 max	16.0	…	…	4.0 W
Hastelloy C-276	0.02	5.5	bal	2.5 max	15.5	…	16.0	3.75 W, 0.35 V
Hastelloy G30	0.03 max	15	bal	5.0 max	30	…	5.0	1.0 Nb + Ta
Hastelloy W	0.12 max	5.5	bal	2.5	5.0	…	24.5	0.6 V
Alloy 600	0.1 max	8.0	bal	…	15.5	…	…	…
Alloy 617	0.07	…	bal	12.5	22	…	9.0	1.0 Al
Alloy 625	0.1 max	5.0 max	bal	1.0 max	21.5	0.4 max	9.0	3.65 Nb + Ta, 0.4 Al max
Alloy X-750	0.04	7.0	bal	…	15.5	2.5	…	0.95 Nb + Ta, 0.7 Al
ZMI-3U	0.08	…	bal	5.5	13	5.0	1.2	5.0 W, 3.0 Al, 0.015 B
CNK7	0.08	…	bal	9.0	14.8	4.2	0.4	7.0 W, 0.01 B, 0.02 Ce
René 41	0.09	…	bal	11.0	19.0	3.1	10.0	1.5 Al, 0.010 B max
René 95	0.15	…	bal	8.0	14.0	2.5	3.5	3.5 Al, 3.5 W, 3.5 Nb
U-520	0.05	…	bal	12.0	19.0	3.0	6.0	1.0 W, 2.0 Al, 0.005 B
U-700	0.15 max	1.0 max	bal	18.5	15.0	3.5	5.2	4.25 Al, 0.05 B
U-710	0.07	…	bal	15.0	18.0	5.0	3.0	2.5 Al, 1.5 W, 0.02 B
U-720	0.035	…	bal	14.7	18.0	5.0	3.0	1.25 W, 2.5 Al, 0.035 B
Waspaloy	0.07	…	bal	13.5	19.5	3.0	4.3	1.4 Al, 0.07 Zr,

								0.006 B
Haynes HR-160	0.05	2.0	37.0	29.0	28.0	…	…	0.5 Mn
Cobalt-base alloys								
Haynes 25 (L-605)	0.10	…	10.0	bal	20.0	…	…	15.0 W, 1.5 Mn, 0.55 Si
Haynes 188	0.10	1.5	22.0	bal	22.0	…	…	14.0 W, 0.08 La
Stellite 6B	1.1	3.0 max	3.0 max	bal	30.0	…	…	4.5 W
S-816	0.38	4.0	20.0	bal	20.0	…	4.0	4.0 W, 4.0 Nb
MP35N	0.025 max	1.0 max	35.0	bal	20.0	1.0 max	10.0	0.010 B max

G.F. Vander Voort, G.M. Lucas, and E.P. Manilova, Metallography and Microstructures of Heat-Resistant Alloys, *Metallography and Microstructures,* Vol 9, *ASM Handbook*, ASM International, 2004, p. 820–859

Metallography and Microstructures of Heat-Resistant Alloys

George F. Vander Voort and Gabriel M. Lucas, Buehler Ltd.; Elena P. Manilova, Polzunov Central Boiler and Turbine Institute, St. Petersburg, Russia

Macroetching

Cast and wrought heat-resistant alloys are examined for macrostructure in the same manner as tool steels and stainless steels. Macroetching of cast specimens is generally performed as a research tool to study the solidification characteristics; macroetching of wrought specimens can be performed as part of a research study but is more commonly performed as a required test by product specifications and is, therefore, a routine production test. To evaluate castings, the disk is generally removed so that the etched surface (ground smooth before etching for best results) is parallel to the solidification direction. For wrought alloys, disks are cut (usually from wrought billet samples) at representative locations, such as the top and bottom of ingots or remelted (electroslag remelted or vacuum arc remelted) stock, and are ground before macroetching. Macroetchants for the cast or wrought austenitic Fe-Ni-Cr heat-resistant alloys are the same as those recommended for cast and wrought austenitic stainless steels (see the article “Metallography and Microstructures of Stainless Steels and Maraging Steels” in this Volume). Macroetchants for cast and wrought iron-nickel-, nickel-, and cobalt-base heat-resistant alloys are given in Table 4.

Table 4 Macroetchants for wrought heat-resistant alloys

Composition[(a)]	Comments
1. 1 part 30% H_2O_2, 2 parts HCl, 2 or 3 parts H_2O	Recommended for nickel-chromium alloys; use fresh solution; reveals grain structure; if the surface is stained, remove with 50% aqueous HNO_3; etch approximately 2 min
2. (a) 15 g $(NH_4)_2S_2O_8$ (ammonium persulfate) and 75 mL H_2O **(b) 250 g $FeCl_3$ and 100 mL HCl** **(c) 30 mL HNO_3**	Lepito's macroetch for general macrostructure and weldments; mix a and b, add c; immerse 30–120 s at room temperature
3. 200 g $FeCl_3$, 200 mL HCl, H_2O to 1000 mL	For nickel-base superalloys; etch to 90 min at 100 °C (212 °F)
4. HCl saturated with $FeCl_3$	For cobalt-base superalloys; add 5% HNO_3 before use at room

	temperature; clean surface by dipping in 50% aqueous HCl
5. (a) 21 mL H_2SO_4, 15 mL HCl, 21 mL HNO_3, 21 mL HF, 22 mL H_2O **(b) 40 mL 20% aqueous $CuCl_2$ (copper chloride), 40 mL HCl, 20 mL HF**	For cobalt-base superalloys; etch 5 min in a, then 5 min in b
6. 50 mL saturated aqueous $CuSO_4$ (copper sulfate) and 50 mL HCl	For iron-nickel- and nickel-base alloys; swab or immerse, room temperature

(a) Whenever water is specified, use distilled water.

Features observed on the macroetched cast disks depict the results of solidification. Near the surface, the grain structure will be finer than elsewhere. Dendrites will be visible, with the primary axis in the solidification direction. Segregation and shrinkage cavities may also be observed. Porosity due to gas evolution is unlikely to be seen. Macroetch features on disks from consumable-electrode remelted superalloys are different from those observed in ingot cast steels. Unique macroetch features observed in these remelted alloys include freckles, radial segregation, and ring patterns (Ref 1, 2, 3, 4, 5, 6, 7). Freckles are dark-etching spots due to localized segregation or to enrichment in carbides or Laves phase. They are detrimental to material quality. The microstructure of a freckle in René 41 is shown in Fig. 1. Radial segregation appears as dark-etching elongated spots in a radial or spiral pattern. Ring patterns are concentric rings that etch lighter (usually) or darker than the matrix. They are revealed only by macroetching. The nature of ring patterns remains obscure. Examination has revealed little difference between ring and matrix areas and no measurable influence on mechanical properties.

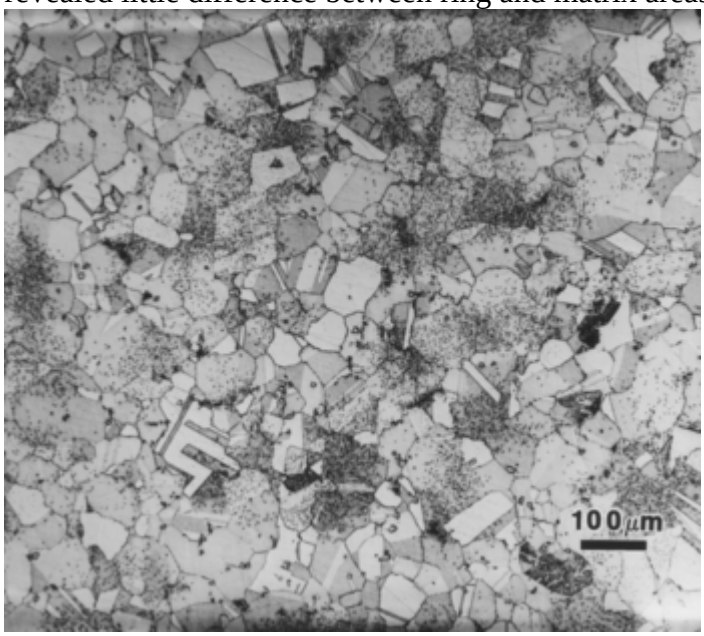

Fig. 1 Microstructure of a freckle in as-rolled René 41 (15 mL HCl, 10 mL acetic acid, 10 mL HNO_3)

References cited in this section

1. G.F. Vander Voort, *Metallography: Principles and Practice,* McGraw-Hill, 1984; reprinted by ASM International, 1999

2. C.E. Smeltzer, Solve Steel “Freckle” Mystery, *Iron Age,* Vol 184, 10 Sept 1959, p 188–189

3. G.C. Gould, Freckle Segregation in Vacuum Consumable-Electrode Ingots, *Trans. AIME,* Vol 233, July 1965, p 1345–1351

4. J. Preston, Segregation in Vacuum-Arc-Melted Alloy Steel Ingots, *Int. Trans. Vacuum Metallurgy Conf. 1967*, American Vacuum Society, 1968, p 569–588

5. R.C. Buehl and J.K. McCauley, Processing Improvement in Vacuum-Arc Remelting of Ingots, *Int. Trans. Vacuum Metallurgy Conf. 1967*, American Vacuum Society, 1968, p 695–709

6. A.F. Giamei and B.H. Kear, On the Nature of Freckles in Nickel Base Superalloys, *Met. Trans.*, Vol 1, Aug 1970, p 2185–2192

7. R. Schlatter, Electrical and Magnetic Interactions in Vacuum-Arc Remelting and Their Effect on the Metallurgical Quality of Specialty Steels, *J. Vac. Sci. Technol.*, Vol 11, Nov/Dec 1974, p 1047–1054

G.F. Vander Voort, G.M. Lucas, and E.P. Manilova, Metallography and Microstructures of Heat-Resistant Alloys, *Metallography and Microstructures*, Vol 9, *ASM Handbook*, ASM International, 2004, p. 820–859

Metallography and Microstructures of Heat-Resistant Alloys

George F. Vander Voort and Gabriel M. Lucas, Buehler Ltd.; Elena P. Manilova, Polzunov Central Boiler and Turbine Institute, St. Petersburg, Russia

Specimen Preparation

Sectioning. Various sectioning devices have been used with heat-resistant alloys. The usual precautions regarding excessive heating should be followed. For austenitic grades, which are sensitive to deformation, the more vigorous sectioning techniques, such as band sawing or power hacksawing, will introduce excessive distortion or work hardening, depending on the alloy and heat treatment condition. Such methods are suitable for initial sectioning of large pieces, but final cutting of specimens should be performed using abrasive cutoff machines with abrasive blades designed for metallographic work (blades designed for production cutting introduce too much damage and should not be used for metallography). Heavy deformation introduced by sawing may be difficult, if not impossible, to remove by subsequent grinding and polishing steps. Abrasive cutoff wheels used are usually the consumable type. Coolant flow must be adequate and uniformly distributed to minimize heat-induced damage. Sectioning of cast nickel alloys and all cobalt-base alloys requires use of an abrasive blade that breaks down at a high rate, exposing fresh, sharp particles in the cutting zone. These are the most difficult grades to section of the heat-resistant alloys.

Mounting. Many bulk specimens can be ground and polished without mounting, although specimen identification is generally limited to stamp marks, such as a job number and a specimen number. Some automatic grinding and polishing devices require a mounted specimen, usually 25, 32, or 38 mm (1, $1\frac{1}{4}$, or $1\frac{1}{2}$ in.) in diameter; others do not. Mounting facilitates polishing of small or irregularly shaped specimens.

When it is necessary to view the microstructure at the extreme edge of a specimen, it must be mounted. Edge retention of nonmounted specimens is inferior, and examination above 100× magnification may be impossible. Optimal results are obtained when the edge of interest is plated with electroless or electrolytic nickel before mounting (see the article “Mounting of Specimens” in this Volume). However, excellent results can be obtained without plating if the specimen is mounted using a compression-molded thermosetting epoxy resin containing a filler material, such as Epomet (Buchler Ltd.) resin. This resin provides near-freedom from shrinkage gaps between specimen and mount that lead to edge rounding and bleed-out problems. Edge retention is much better when automated grinding-polishing devices are used. Rigid grinding disks provide superb edge flatness, and napless, woven cloths or pressed pads preserve that flatness through to the final step. A medium-nap cloth can be used for the final polishing step without problems, unless shrinkage gaps are present between specimen and mounting material. When shrinkage gaps are present, use a polyurethane pad for the final step.

When edge retention is not a primary requirement, specimens can be mounted using any of the popular compression-mounting materials or castable resins. Most produce acceptable results; each resin has advantages and disadvantages. The selection of a particular resin is often based on familiarity or cost.

Grinding of specimens takes place by hand or by use of automatic devices. Hand grinding should be avoided, if at all possible, because the specimens cannot be kept perfectly flat during grinding. Grinding is most commonly performed using water-cooled silicon carbide (SiC) paper at 240 to 300 rpm. Today, a variety of other grinding formats are available, although SiC remains very popular. Historically, the usual grit-size sequence was 120, 240, 320, 400, and 600 grit (P120, P280, P400, P600, and P1200 in the Federation of European Producers of Abrasives, or FEPA, scale); finer grits were occasionally used. Today, preparation procedures employ only one grinding step before switching to diamond abrasives on a napless woven cloth or a pressed pad. When proper metallographic abrasive blades have been used to section the specimens, so that cutting damage is minimal and the surface finish is optimal, grinding should commence with the finest possible abrasive, such as 180-, 240-, or 320-grit SiC (P180, P280 or P400 in the FEPA scale). The coarser the abrasive, the greater the damage introduced by grinding. Thus, when cutting damage is minimal, a finer-size abrasive can be used for the grinding step. This removes the damage from cutting while imparting less damage than a coarser grit size grinding abrasive.

Moderately heavy pressure is used for hand grinding. The specimen must be held flat against the paper. After each grinding, the specimen is rinsed, wiped clean, and rotated 45 to 90° before grinding with the next paper. Grinding should proceed for approximately twice as long as needed to remove all the scratches from the previous step; 1 to 2 min per step is usually adequate. Automated grinding devices produce omni-directional scratch patterns. Heat-resistant alloys are not susceptible to embedding of silicon carbide from the grinding paper, but if the specimen contains cracks or pores, it may be advisable to clean ultrasonically after each step. For most specimens, a simple wash under running water will remove any loose abrasive or grinding debris. Specimens should be rinsed in alcohol (preferably ethanol) and dried with hot air.

Rough polishing, historically, often began with 6 or 3 μm diamond abrasive, generally as a paste, although aerosols or slurries were also used. Diamond abrasives have largely replaced use of 5 μm alumina (Al_2O_3) for rough polishing, except where economic considerations do not permit use of diamond abrasives. In modern procedures, the grinding step is usually followed by 9 or 6 μm diamond on a napless, woven cloth or pressed pad. This step is followed by one or two more diamond abrasive steps, depending on the difficulty in preparing the alloy, or on the degree of perfection desired by the metallographer. People in production laboratories often believe that they save time and money by preparing specimens “just good enough” for their work. However, one does not know that “just good enough” is really good enough until the specimen has been properly prepared. If the metallographer is simply asked to rate the grain size of a specimen according to a chart method, then some degree of imperfection can be tolerated. However, in failure analysis, research and many quality studies, important information will be missed if the specimen is not prepared properly so that the true structure can be seen.

Although a wide range of cloths is available, low-nap or napless cloths are preferred for rough polishing, although canvas, which was quite popular, provides economical durability. Today, woven, napless cloths, such as natural silk or synthetic nylon or polyester, are recommended, because they provide good cutting rates, excellent surface flatness, and good surface finishes for each abrasive size used. Synthetic, napless chemo-textile pads are also used. Billiard cloth and red felt have been used, but they can cause excessive relief, poor edge retention, pull-outs, and other artifact problems, especially if the lubrication level is not correct. A lubricant/extender fluid, compatible with the diamond abrasive, should always be added to reduce friction and drag and to promote more efficient cutting. Wheel speeds for polishing are 100 to 150 rpm, in most work. Moderate pressure is applied.

During hand polishing, the specimen should be rotated counter to wheel rotation while it is moved slowly from center to edge. Again, the specimen must be held firmly against the wheel to avoid rocking. Polishing should continue until grinding scratches are removed; 1 to 2 min is usually adequate. With an automated machine, the specimen rotates in either the same direction or the opposite direction to the platen (complementary or contra rotation, respectively). Contra rotation is slightly more aggressive. It is best used when the specimen holder rotates at <90 rpm. If the head operates at a higher speed, the abrasive may be thrown off the platen surface onto the operator and the walls. When the head rotates at <90 rpm, it stays on the platen surface nicely during the cycle. When the head rotates in the same direction as the platen (complementary), the abrasive is thrown off the platen, into the surrounding bowl, and down the drain due to centrifugal force, regardless of the head speed.

Of course, the faster the platen and head speed, the greater the centrifugal force, and the faster the abrasive goes down the drain.

A second diamond-polishing step, generally using 3 or 1 μm diamond, is usually performed in modern methods but was optional in the former "traditional" methods. A synthetic suede medium-nap cloth was commonly used, but other cloths may also yield good results. This step is carried out in the same manner as the initial diamond polishing. After each diamond polishing step, the specimen should be carefully cleaned to remove abrasive, extender oil, and polishing debris. Ultrasonic cleaning produces excellent results but is not always required, especially with wrought specimens. With a cast specimen that contains voids, it may be best to ultrasonically clean after each preparation step. Today, medium-nap cloths are no longer recommended for use with diamond abrasives in most polishing routines. Instead, woven, napless cloths or pressed chemo-textile pads are promoted, because flatness and edge retention are better.

Final polishing, historically, involved one or more steps, depending on the need to remove all scratches. For routine examination, polishing to a 1 μm diamond finish may be adequate. When photomicroscopy is anticipated, additional steps are usually required. A wide range of final polishing abrasives may be used. Alumina slurries are quite common, using 0.3 and/or 0.05 μm Al_2O_3. Nearly all alumina abrasives are produced by the calcination process, and agglomerates are always present, even in the deagglomerated abrasives. However, alumina is now available in the 0.05 μm size, made by the sol-gel process where the particles are grown from a solution. This abrasive, called MasterPrep (Buehler Ltd.) alumina, produces superior results compared to ordinary aluminas and is free of the problems associated with the use of colloidal silica.

Colloidal silica (Ref 1) produces excellent results with these alloys but is more difficult to use. The amorphous silica particles will crystallize if the solution evaporates. This ruins the cloth. Specimens must be carefully cleaned, because a whitish film may be present that will alter etch response. To clean the surface, stop adding abrasive with approximately 20 s left in the cycle (using an automated polisher). With approximately 10 s left in the cycle, direct the water jet onto the cloth surface. The specimen and the cloth will be cleaned simultaneously. When the machine stops, rinse the sample holder under running water, scrub the surfaces with ethanol, and blow dry. However, even with this precaution, strange etch results can occur. For example, when swab etching with reagents such as glyceregia, it usually takes approximately 60 to 120 s to bring up etch detail and make the surface appear to be etched to the proper level by eye. However, after using colloidal silica, sometimes when etching with reagents that contain Cl^- ions, the surface immediately turns dull gray as soon as the etchant touches the specimen (called "flashing"). This produces a heavy craze-crack appearance when viewed microscopically (Fig. 2). This false structure cannot be removed by simply repeating the last preparation step. Instead, one must go back to approximately a 240-grit (P280) SiC abrasive to remove the affected layer. Interestingly, electrolytic etchants never produce this problem. To avoid this problem, start the final step with colloidal silica, flush it off with water, and complete the cycle using the sol-gel alumina slurry. One can split the total time equally between the two abrasives or use any desired percentage of time with each, as long as approximately 10 s are dedicated at the end of the cycle to the sol-gel alumina abrasive. Again, use the previously mentioned cleaning procedure to clean both the cloth and specimen before the cycle ends, or use only the sol-gel alumina suspension.

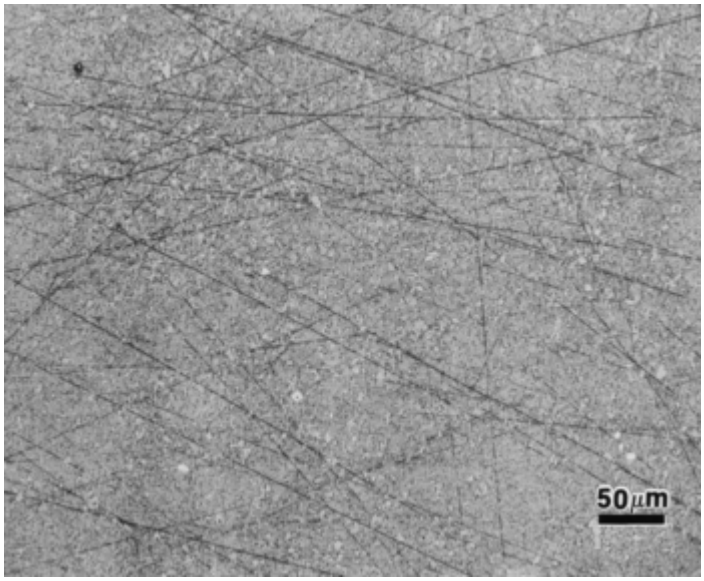

Fig. 2 Example of flashing, a strange etching response that occurs frequently on nickel-base alloys final polished with colloidal silica and etched with reagents containing Cl^- ions (glyceregia etch of alloy 718)

Cleaning between steps is important, because contamination can occur. In many cases, the holder can be simply rinsed under running water to remove the debris. However, it is often necessary to scrub the surfaces with ethanol to remove adherent debris. If this falls down onto the cloth in the next step, the cloth will be contaminated, and the results will be poor. The operator's hands must also be cleaned after each step, because contamination can result if this is not done. Cleanliness is important in metallography, and this extends to the entire laboratory.

Final polishing is generally performed using a synthetic suede medium-nap cloth or a polyurethane pad at 100 to 150 rpm. During hand polishing, the specimen should be rotated counter to the wheel rotation direction while it is moved from center to edge. The slurry is added periodically to the cloth during polishing. Moderate pressure is used, and care must be taken to avoid rocking the specimen. A polishing time of 1 to 2 min is usually adequate. After polishing, the specimen should be carefully cleaned and dried to avoid staining, and the operator's hands must be cleaned after each rough and final polishing step to prevent contamination.

Automatic polishing machines are quite useful for final polishing. A wide variety of devices is available. The time required using these units ranges from a few minutes to approximately 30 min for vibratory polishing. Vibratory polishing will remove any minor damage that might be present and will yield crisper images of the structure after etching. Table 5 and 6 present automated procedures for preparing Fe-Ni-Cr-, nickel-, and cobalt-base heat-resisting alloys.

Table 5 Preparation method for Fe-Ni-Cr- and nickel-base heat-resisting alloys

Surface	Abrasive/size	Load/specimen		Base speed, rpm/direction	Time, min
		N	**lbf**		
Waterproof paper (water cooled)	220–240-grit (P240–P280) SiC	27	6	240–300 Complementary or contra	Until plane
Silk cloth (PSA backing)	9 μm diamond with lubricant	27	6	120–150 Complementary or contra	5
Polyester cloth	3 μm diamond with lubricant	27	6	120–150 Complementary or contra	4

Polyester cloth	1 μm diamond with lubricant	27	6	120–150 Complementary or contra	3
Synthetic rayon medium-nap cloth	0.05 μm alumina suspension	27	6	100–150 Complementary or contra	3

Note: PSA, pressure-sensitive adhesive. Other surfaces can be substituted in step 1, as long as the abrasive size is similar (for example, a diamond grinding disc or a rigid grinding disc could be used). In step 1, remove the damage from sectioning and get all of the specimens in the holder to a common plane. In steps 2 to 4, charge the cloth first with diamond in paste form. With a clean fingertip, press the paste into the cloth. Apply lubricant. During the cycle, periodically add diamond of the same size as a suspension to keep the cutting rate high. Step 4 is optional. Use it for the most difficult specimens. Use contra rotation if the specimen holder motor rotates at <100 rpm. At higher speeds, the suspensions, particularly the alumina, will be splattered all over the walls. Contra rotation is slightly more aggressive and gives better flatness. If the head rotates <100 rpm, the suspension will stay on the cloth better (in complementary rotation, the centrifugal forces shoot the suspensions off the platen and down the drain).

Table 6 Preparation method for cobalt-base heat-resisting alloys

Surface	Abrasive/size	Load/specimen		Base speed, rpm/direction	Time, min
		N	**lbf**		
Waterproof paper (water cooled)	220–320-grit (P240–P400) SiC	27	6	240–300 Complementary or contra	Until plane
Silk cloth (PSA backing)	9 μm diamond with lubricant	27	6	100–150 Complementary or contra	5
Polyester cloth	3 μm diamond with lubricant	27	6	100–150 Complementary or contra	5
Polyester cloth	1 μm diamond with lubricant	27	6	100–150 Complementary or contra	4
Synthetic rayon medium-nap cloth	0.05 μm colloidal silica or alumina suspension	27	6	80–120 Complementary or contra	3

Note: PSA, pressure-sensitive adhesive. It is vitally important to use the best possible abrasive cutoff blade, designed for metallography, when working with cobalt and its alloys. More aggressive surfaces are not recommended when preparing cobalt alloys (steps 1 and 2). Step 4 is not optional. Final polishing is improved by attack polishing. Mix one part H_2O_2 (30% conc) with 5 parts of abrasive suspension. Avoid skin contact. For step 5, stop adding abrasive with 20 s left in the cycle. With 10 s left in the cycle, direct the water jet onto the cloth surface to wash both the specimen and the cloth. This simplifies cleaning.

Mechanical polishing is sometimes followed with a brief electropolish to remove any smeared or flowed metal without introducing preferential attack of the second-phase constituents. Extended electropolishing should be avoided. This procedure has been promoted for scanning electron microscopy examination of second-phase particles in superalloys, because they stand above the matrix, and their shape can be easily assessed. However, such an image is unsuitable for quantitative metallography unless the results are corrected to account for the

etch depth. Table 7 lists appropriate electropolishing solutions for nickel- and cobalt-base heat-resistant alloys. Electropolishing solutions for Fe-Ni-Cr austenitic alloys are the same as those used for wrought austenitic stainless steels.

Table 7 Electropolishing techniques for wrought heat-resistant alloys

Electrolyte composition	Comments
1. 37 mL H_3PO_4, 56 mL glycerol, 7 mL H_2O	For Inconel 625, use 1.2–1.6 A/cm_2 (8–10 A/in.^{2}); for Incoloy 800, use 3.1 A/cm^2 (20 A/in.^{2}); platinum cathode
2. 25 mL H_3PO_4, 25 mL HNO_3, 50 mL H_2O	For Inconel 600 and X-750, use 17.8 A/cm^2 (115 A/in.^{2}), 5–10 s; platinum cathode
3. 144 mL ethanol, 10 g $AlCl_3$ (anhydrous aluminum chloride), 45 g $ZnCl_2$ (anhydrous zinc chloride), 16 mL N-butyl alcohol, 32 mL H_2O	For cobalt-base superalloys, use 23–25 V dc at room temperature with successive 1 min periods
4. 40 mL $HClO_4$ (perchloric acid), 450 mL acetic acid, 15 mL H_2O	For Nimonic alloys, use 15 V dc, 0.1 A/cm^2 (0.65 A/in.^{2}), below 25 °C (77 °F)
5. 10 mL $HClO_4$ and 90 mL acetic acid	For nickel-base alloys, use at 0.5–0.9 A/cm^2 (3–6 A/in.^{2}), 30 s for aged specimens, longer for solution-annealed ones; keep cool (10-15 °C, or 50-60°F); best results by polishing in 5 s intervals
6. 70 mL methanol and 10 mL H_2SO_4	For nickel-base superalloys, use at 20–25 V dc, 0.3–0.8 A/cm^2 (2–5 A/in.^{2}), room temperature; 10–15 s after a 600-grit finish or 5 s after a 0.3 μm Al_2O_3 finish; γ′ slightly etched, carbides in relief
7. 60 mL methanol, 10 mL H_2SO_4, 5 mL HCl	Use same as No. 6; produces more etching of γ′ phase; if HNO_3 is substituted for HCl, the surface will be smooth without relief or attack.
8. 7 mL ethanol, 20 mL $HClO_4$, 10 mL glycerol	Use same as No. 6; mix carefully, keep cool; produces smooth surfaces
9. 15 mL HCl and 85 mL methanol	For nickel-base superalloys, use at 30–40 V dc, 0.3–1.2 A/cm^2 (2–8 A/in.^{2}), at room temperature for 5–10 s after a 600-grit silicon carbide finish or 2–5 s after a 0.3 μm Al_2O_3 finish; produces strong carbide relief, etches γ′; very good for SEM examination

Etching. Some minor phases in heat-resisting alloys can be observed easily in the as-polished condition. Light relief can be introduced during final polishing to accentuate these particles by hand polishing the specimen using a figure-eight motion and light pressure for approximately 10 to 20 s on a stationary platen, using either alumina or colloidal silica. This makes the particles easier to see, even without etching. A brief electropolish can also be used for this purpose. If image analysis measurements are to be performed, relief must be minimized, or the stereological rules, unless corrected to account for the etch depth, are invalid, and measurement bias will result. The particles can be observed in bright-field illumination by color contrast, which is useful for phase identification. Carbides, nitrides, carbonitrides, and borides are readily observed without etching. Viewing with differential interference contrast illumination will bring out height differences between the particle and the matrix. Generally, nitrides show less relief than carbides relative to the matrix.

The cast or wrought Fe-Ni-Cr heat-resistant alloys are basically austenitic stainless steels (the wrought alloys are usually called iron-nickel-base alloys even though they all contain more than 12% Cr). The techniques for etching and identifying phases in wrought austenitic stainless steels apply to these alloys (see the article "Metallography and Microstructures of Stainless Steels and Maraging Steels" in this Volume). Preparation practices are identical.

Glyceregia is one of the most prevalent reagents for revealing the general structure of Fe-Ni-Cr- and nickel-base heat-resistant alloys. It should always be mixed fresh and discarded carefully when it turns orange. Glyceregia will etch all the heat-resistant grades, except some of the high-cobalt-content superalloys. Glyceregia will reveal grain and twin boundaries and second phases in the leaner alloys but will be less effective, or ineffective, in revealing the grain structure in the higher nickel and chromium alloys, although second-phase particles will generally be outlined. For etching solution-annealed nickel-base alloys, the glycerol content is often decreased, and the nitric acid (HNO_3) content is often increased. The standard composition is

ideal for solution-annealed and aged specimens, which are easier to etch. Specimens etched with reagents containing Cl^- ions may exhibit erratic etch behavior (called flashing) after polishing with colloidal silica. As soon as etching begins, the surface becomes dull. When viewed with the microscope, a heavy craze-crack pattern is observed that can be quite deep. The problem seems to be due to passivation effects. To counter this problem, follow the colloidal silica polish with a short polish with alumina. Electrolytic etchants do not have this problem, even after using colloidal silica.

The mixture of hydrochloric acid, sulfuric acid, and nitric acid (HCl-H_2SO_4-HNO_3) (95-5-3) is also quite popular for these alloys and is used similarly. For grain size examination in aged specimens, etching with waterless Kalling's reagent (Kalling's number 2) or Marble's reagent is quite common. These reagents can be made and stocked in reasonable quantities. Several electrolytic reagents are also commonly used. Color etchants, although not widely used for these alloys, can produce good results (see the article "Color Metallography" in this Volume).

Table 8 lists some of the more commonly used reagents for etching Fe-Ni-Cr-, nickel-, and cobalt-base heat-resistant alloys. Additional information regarding the etching of wrought heat-resistant alloys can be found in Ref 1, 8, 9, 10, 11, 12, 13, 14, 15.

Table 8 Microetchants for wrought heat-resistant alloys

Composition	Comments
1. 2 parts glycerol, 3 parts HCl, 1 part HNO_3	Glyceregia; mix fresh, do not store; discard when solution is orange; use by immersion or swabbing 5–60 s; very popular general etch for structure of iron- and nickel-base superalloys; γ′ in relief
2. 5 mL HF, 10 mL glycerol, 85 mL ethanol	Electrolytic etch at 0.04–0.15 A/cm^2 (0.25–1.0 A/in.^{2}), 6–12 V dc; for nickel-base alloys, γ′ in relief; stop etch when edges are brownish; excellent etch for transmission electron microscopy (TEM) replica work
3. 12 mL H_3PO_4, 47 mL H_2SO_4, 41 mL HNO_3	Electrolytic etch at 6 V dc, 0.12–0.15 A/cm^2 (0.75–1.0 A/in.^{2}), a few seconds; add to 100 mL H_2O to slow etch; for nickel-base alloys; use under hood; mix H_3PO_4 and HNO_3, then add H_2SO_4; stains matrix when γ′ is present; good for revealing segregation and for examining γ′ with TEM replicas; attacks Bakelite (Georgia-Pacific Corp.); stop etch when edge of specimen is brownish
4. 30 mL lactic acid, 20 mL HCl, 10 mL HNO_3	For nickel-base superalloys
5. 5g $CuCl_2$, 100 mL HCl, 100 mL ethanol	Waterless Kalling's reagent; immerse or swab to a few minutes; for iron- and nickel-base superalloys
6. 10 g $CuSO_4$, 50 mL HCl, 50 mL H_2O[(a)]	Marble's reagent for iron-nickel- and cobalt-base superalloys; immerse or swab 5–60 s; a few drops of H_2SO_4 will increase etch activity; reveals grain boundaries and second-phase particles
7. 5 mL H_2SO_4, 3 mL HNO_3, 92 mL HCl	For iron- and nickel-base alloys; add H_2SO_4 to HCl, stir, allow to cool, add HNO_3; discard when orange; swab 10–30 s; use under hood; do not store
8. 20 mL HNO_3 and 60 mL HCl	Aqua regia; for iron- and nickel-base superalloys; use under hood, do not store; immerse or swab 5–60 s; attacks σ phase, outlines carbides, reveals grain boundaries
9. 50 mL HCl and 1–2 mL 30% H_2O_2	For nickel-base alloys; attacks γ′ phase; immerse 10–15 s
10. 5 mL H_2SO_4, 8 g CrO_3, 85 mL H_3PO_4	Electrolytic etch at 10 V dc, 0.2 A/cm^2 (1.3 A/in.^{2}), 5–30 s; reveals inhomogeneities in nickel-base alloys
11. 10 mL HNO_3, 10 mL acetic acid, 15 mL HCl, 2–5 drops glycerol	Acetic glyceregia; use fresh, same precautions as glyceregia; used for hard-to-etch solution-treated nickel-base alloys
12. 15 mL HCl, 10 mL acetic acid, 10 mL HNO_3	15-10-10 etch; use in same manner as glycerregia or acetic-glyceregia; use for more difficult to etch grades, such as alloy 625
13. [(a)] 33 mL HCl and 67 mL H_2O	Beraha's tint etch for nickel-base alloys; add 0.6–1 g $K_2S_2O_5$ (potassium metabisulfite) to 100 mL stock solution a; immerse (never swab) 60–150 s,

(b) 50 mL HCl and 50 mL H_2O	slowly agitate; if colors are not developed, add 1–1.5 g $FeCl_3$ or 2–10 g NH_4F-HF (ammonium bifluoride) to 100 mL stock solution b; immerse 60–150 s, agitate gently; colors matrix
14. 10 g $K_3Fe(CN)_6$ (potassium ferricyanide), 10 g KOH, 100 mL H_2O	Murakami's reagent; for iron- and nickel-base superalloys; use hot (75 °C, or 170 °F) to darken a phase; use at room temperature to darken carbides; better results may be obtained if the specimen is first etched in 50% aqueous HNO_3 at 8 V dc; use under a hood
15. 10 g CrO_3 and 100 mL H_2O	Electrolytic etch at 6 V dc, 10–30 s; for iron- and nickel-base superalloys; σ attacked, carbides outlined or attacked
16. 80 mL H_3PO_4 and 10 mL H_2O	Electrolytic etch for nickel-base superalloys at 3 V dc (closed circuit), 0.11–0.12 A/cm^2 (0.7–0.8 A/in.^{2}), 7–9 s; if the surface is stained, swab with the electrolyte; use fresh solution; used to determine the degree of carbide continuity at the grain boundaries
17. 25 g CrO_3, 130 mL acetic acid, 7 mL H_2O	Electrolytic etch for nickel-base superalloys at 10 V dc (closed circuit) for 2 min; the current density will drop during the first 20 s; use fresh; used to reveal prior grain boundaries
18. 30 mL HCl, 7 mL H_2O, 3 mL 30% H_2O_2	Popular etch for cobalt-base superalloys
19. 100 mL HCl and 5 mL 30% H_2O_2	Popular etch for cobalt-base superalloys; up to 20% H_2O_2 has been used; mix fresh; immerse 1–10 s
20. 5–10 mL HCl and 95–90 mL H_2O	Electrolytic etch for cobalt-base superalloys; use at 3 V dc, 1–5 s, carbon cathode
21. 2 mL H_2SO_4 and 98 mL H_2O	Etch first with glyceregia to dissolve matrix uniformly, then etch electrolytically at 6–12 V dc, 0.12–0.15 A/cm^2 (0.75–1.0 A/in.^{2}) until edge of specimen is brownish; good for TEM replica studies
22. 5 mL HF, 10 mL glycerol, 10–50 mL ethanol, H_2O to 100 mL total volume	Etch first with glyceregia to dissolve matrix uniformly, then etch with solution at left to dissolve γ′; use at 6–12 V dc, 0.12–0.15 A/cm^2 (0.75–1.0 A/in.^{2}) for less than 1 s; good for TEM replica work or SEM examination
23. 100 mL water, 100 mL HCl, 100 mL HNO;i3, 3 g molybdic acid	Molybdic acid etch; mix and let stand for 1 h minimum. Immerse for several seconds. Etch can be stored after use. Excellent for as-cast dendritic structures
24. 150 mL HCl, 50 mL lactic acid, 3 g oxalic acid	Lucas' reagent; use at 1–2 V dc for 10–20 s to reveal the structure of iron-nickel-, nickel-, and cobalt-base superalloys

(a) When water is specified, use distilled water.

The effects of 19 etchants on 11 Fe-Cr-Ni alloys containing 0.02 to 0.18% C have been documented (Ref 8). Vilella's reagent proved superior for removing disturbed metal (using several etch and polish cycles) and for outlining σ phase, carbide particles, and ferrite. Etching for 1 min at room temperature was recommended. Staining etchants form films of reaction products on the surface of the specimen. These etchants are generally aqueous solutions of potassium hydroxide (KOH) or sodium hydroxide (NaOH) with an oxidizing agent added. Picrates, potassium permanganate ($KMnO_4$), hydrogen peroxide (H_2O_2), and ferricyanides are used as oxidizing agents. These reagents are used to color carbides, delta ferrite, and sigma and chi phases.

Murakami's reagent, which contains NaOH with potassium ferricyanide [$K_3Fe(CN)_6$] as the oxidizing agent, is a versatile staining etchant. At least four variations of the original composition have been reported in the literature. Murakami's permits differentiation between several types of carbide and sigma phase. Certain phases are colored only when it is used at room temperature or when used boiling. Reliance on production of specific colors to identify phases is less reliable than whether the phase is colored when used either at room temperature or boiling. Murakami's reagent has been used cold, warm, or boiling to obtain various effects, but it must be used with care. It is best to check its results with control specimens of the same or similar composition where the thermal history is known and other more definitive characterization methods have been used (e.g., x-ray diffraction, convergent-beam electron diffraction, etc.).

Electrolytic etching, when the time is controlled, offers precision and reproducibility. The specimen to be etched is usually made the anode; stainless steel is often used as the cathode (ideally, the cathode should be more noble than the anode). The current can be supplied by a variable voltage direct current (dc) power supply,

although ordinary dry-cell batteries wired in series to provide outputs of 1.5, 3.0, 4.5, and 6.0 V can be used. Current density will range from less than 0.16 to 2 A/cm^2 (1 to 13 A/in.^{2}) or more.

A wide variety of methods have been developed to electrolytically etch either mounted or unmounted specimens (Ref 1). Unmounted specimens are held with stainless steel tongs. If the specimen is mounted in a nonconducting material, the electrical connection can be conveniently made using a brass machine screw that contacts the underside of the specimen through a tapped hole. The electric current at the anode surface promotes oxidation and therefore serves in place of the oxidizing agents that are added to hydroxide solutions.

Some electropolishing procedures are useful for microstructural examination using scanning electron microscopy (SEM) or transmission electron microscopy (TEM) using replicas. The electropolishing solution removes the γ′ phase but not the matrix (or more slowly), and subsequent etching is unnecessary. Backscattered electron imaging with the SEM can be very useful for viewing the second-phase particles without etching. For replica examination, it is often helpful to use a reagent or an electropolish that attacks γ′ so that this phase is readily distinguished from other phases (Ref 16, 17, 18). In such cases, γ′ is recessed, but other second phases are in relief.

Selective etchants and heat tinting have been commonly used to differentiate various carbide types and to identify phases. Borides, which are similar in appearance to metal carbides, can be discriminated by selective etching. Metal carbides are selectively colored; borides are unaffected (Ref 19).

There are differences in how etchants bring up the microstructure of alloys and this can only be learned by experimentation. A few examples of the effect of different etchants in revealing the dendritic structure of cast alloys follow to illustrate this. Figure 3 shows the microstructure of IN-738, a nickel-base cast alloy, etched with four different etchants. The color etch (Fig. 3d), which is usually very sensitive to chemistry variations, did the best job revealing the dendrites. Figure 4 shows the dendritic structure of cast MAR-M 247, a nickel-base alloy, etched with glyceregia, the Lucas electrolytic reagent, and the ammonium molybdate reagent. All three revealed the dendrites well, but the latter gave the strongest contrast. Figure 5 shows the dendritic structure of CNK7, a cast Russian nickel-base alloy, etched with four different, etchants. The Lucas reagent (Fig. 5c) and the color etch (Fig. 5d) gave the strongest contrast. Figure 6 shows the dendritic structure of MAR-M 509 revealed by using three different etchants.

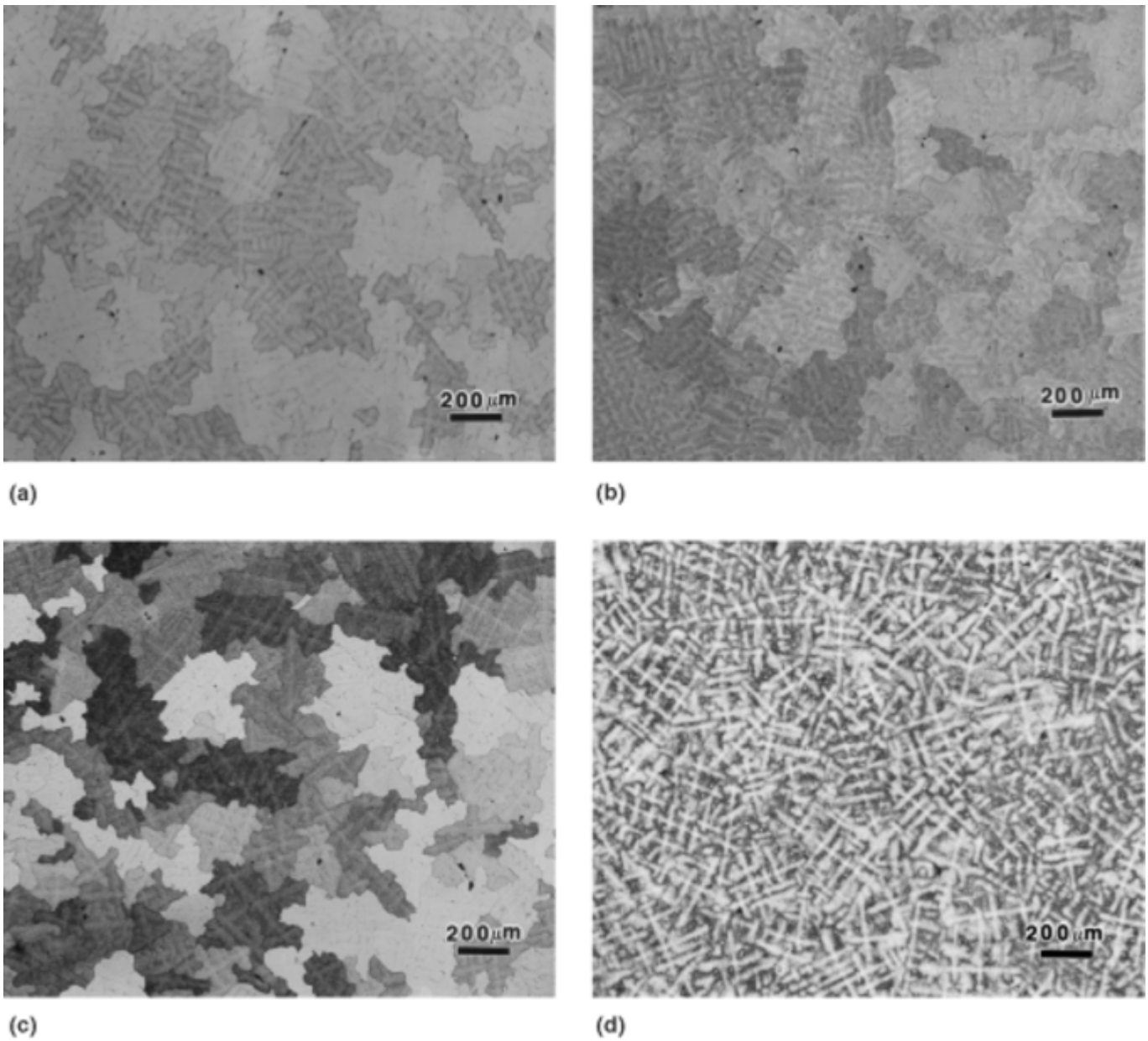

Fig. 3 Cast dendritic structure of IN-738 revealed using (a) Kalling's No. 2, (b) 15 mL HCl, 10 mL acetic acid, and 10 mL HNO_3, (c) the Lucas electrolytic reagent (2 V dc, 10 s), and (d) Beraha's tint etch (50 mL HCl, 50 mL water, 0.8 g $K_2S_2O_5$, 4 g $NH_4F{\cdot}HF$, 1 g $FeCl_3$

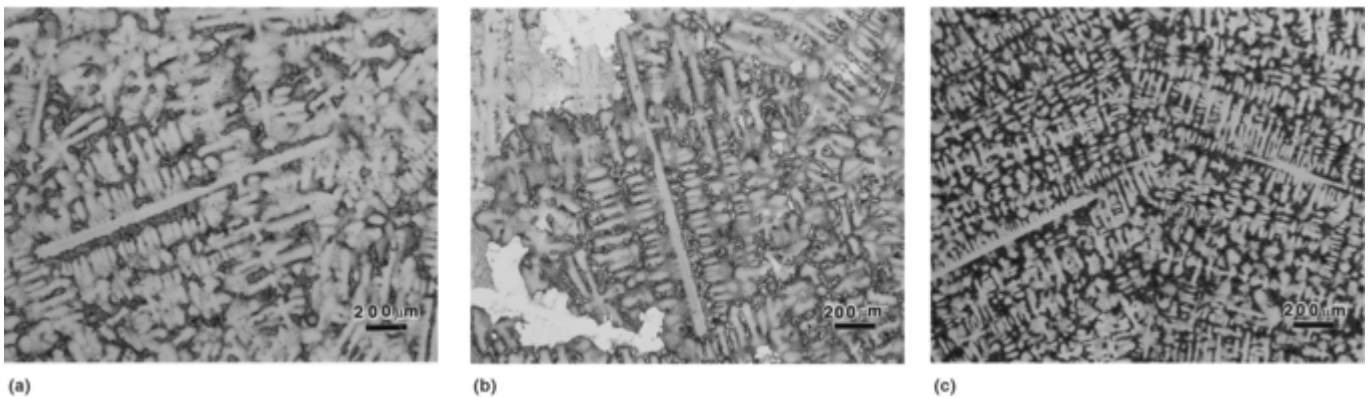

Fig. 4 Cast dendritic structure of MAR-M 247 revealed using (a) glyceregia, (b) the Lucas electrolytic reagent (2 V dc, 10 s), and (c) the molybdic acid reagent

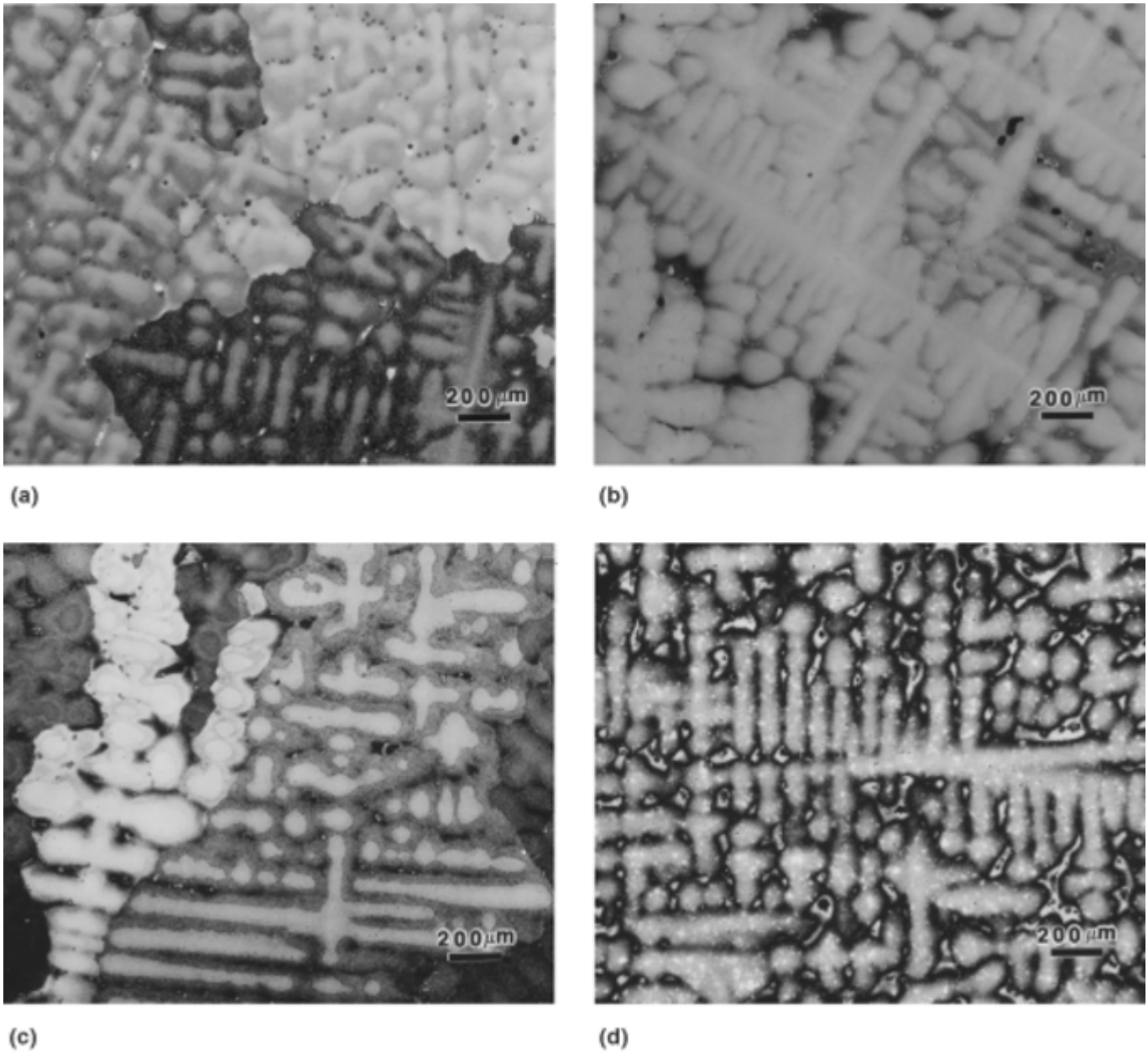

Fig. 5 Cast dendritic structure of Russian nickel-base alloy CNK7 revealed using (a) glyceregia, (b) Kalling's No. 2, (c) the Lucas electrolytic reagent (2 V dc, 10 s), and (d) Beraha's tint etch (50 mL HCl, 50 mL water, 0.8 g $K_2S_2O_5$, 4 g $NH_4F{\cdot}HF$, 1 g $FeCl_3$

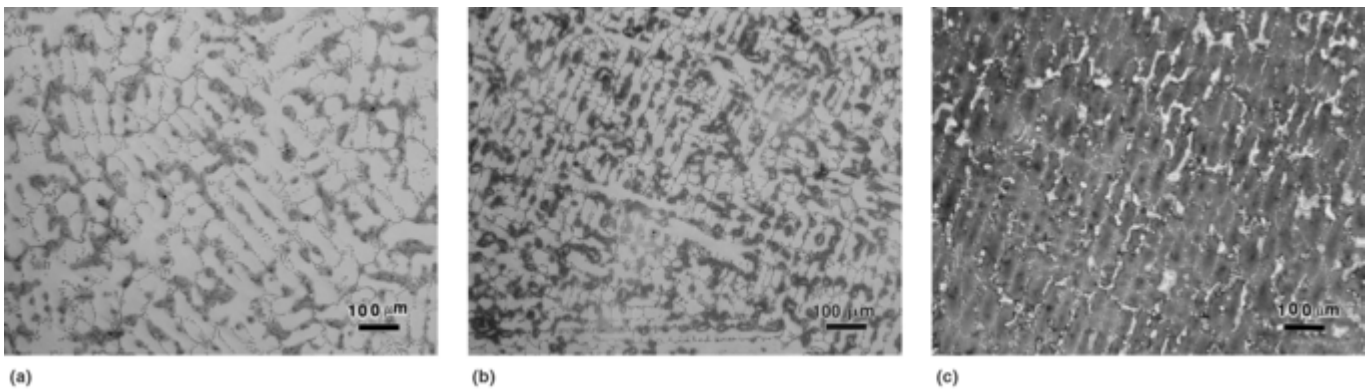

Fig. 6 Cast dendritic structure of MAR-M 509 cobalt-base superalloy revealed using (a) 15 mL HCl, 10 mL acetic acid, and 10 mL HNO_3, (b) the Lucas electrolytic reagent (2 V dc, 20 s), and (c) Beraha's tint etch (50 mL HCl, 50 mL water, 0.8 g $K_2S_2O_5$, 4 g $NH_4F{\cdot}HF$

Different etchants can reveal the structure of wrought alloys with different results, as demonstrated by Fig. 7, 8, 9 and 10 where alloy A-286 is shown in different heat treatment conditions and different locations, etched with glyceregia versus a Beraha-type color etch (20 mL HCl, 100 mL water, 0.5 g $K_2S_2O_5$, 1 g $NH_4F{\cdot}HF$). Figure 11 shows the grain structure of solution annealed and aged Pyromet 31, an iron-nickel superalloy etched with waterless Kalling's and with a Beraha-type color etch (66 mL HCl, 33 mL water, 1 g $K_2S_2O_5$). Figure 12 shows the grain structure of alloy X-750, a nickel-base superalloy in the solution annealed and aged condition etched with glyceregia, waterless Kalling's, Marble's reagent, aqua regia, HCl + 1% Na_2O_2, and a Beraha tint etch (50 mL HCl, 50 mL water, 1 g $K_2S_2O_5$). Figure 13, 14 and 15 show the grain structure of Waspaloy, a nickel-base superalloy, in the solution annealed (1010, 1035, and 1065 °C, or 1850, 1900, and 1950 °F) and aged conditions, etched with glyceregia and with a Beraha-type color etchant (50 mL HCl, 50 mL water, 1 g $K_2S_2O_5$). In each of these examples, the color etch revealed the grain structure with strong contrast.

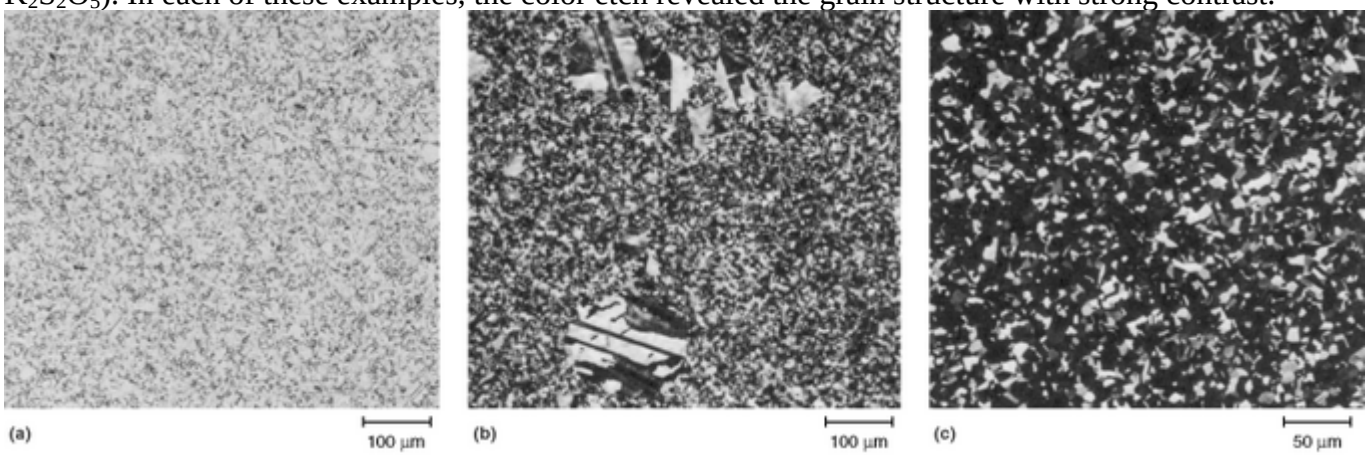

Fig. 7 Alloy A-286 (AISI 660, 195 HV), solution annealed 2 h at 900 °C (1650 °F) and oil quenched. (a) View showing very fine austenite grain size. Glyceregia. Original magnification 100×. (b) View showing area near the surface of the specimen with a duplex grain structure. Tint etch: 20 mL HCl, 100 mL H_2O, 2.4 g $NH_4F{\cdot}HF$, and 0.8 g $K_2S_2O_5$. Original magnification 100×. (c) View showing the very fine austenite matrix grains. Tint etch: 20 mL HCl, 100 mL H_2O, 1 g $NH_4F{\cdot}HF$, 0.5 g $K_2S_2O_5$. Original magnification 200×

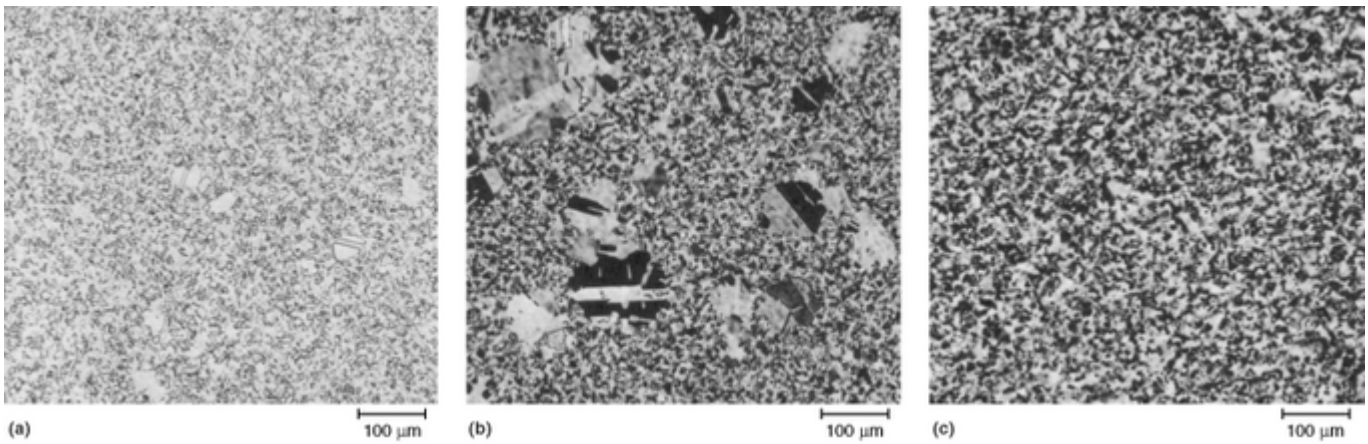

Fig. 8 Alloy A-286 (AISI 660, 357 HV), solution annealed 2 h at 900 °C (1650 °F), oil quenched, and held 16 h at 720 °C (1325 °F). (a) View showing very fine-grained structure similar to that shown in Fig. 7(a). Glyceregia. (b) View showing a region near the surface of the specimen with a duplex grain structure. Tint etched some as Fig. 7(b). (c) View showing the very fine matrix grain structure. Tint etched same as Fig. 7(b). All original magnification 100×

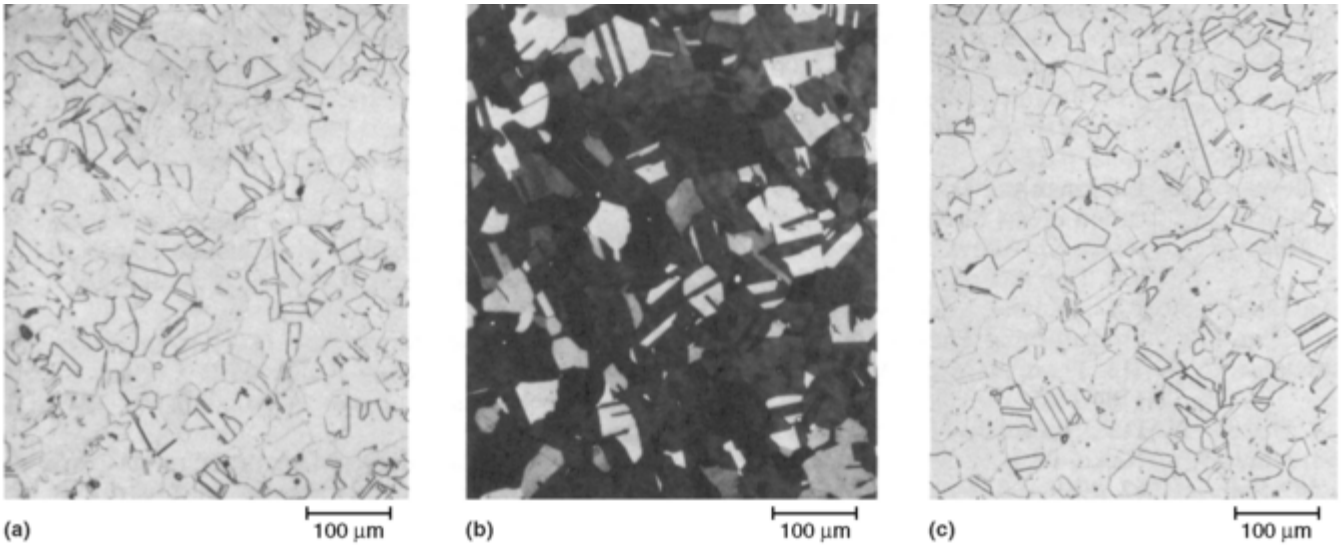

Fig. 9 Alloy A-286 (AISI 660, 150 HV), solution annealed 1 h at 980 °C (1800 °F) and oil quenched. (a) View showing a coarser grain structure than in Fig. 7 and 8 due to the higher solutionizing temperature. Glyceregia. (b) Tint etched using 20 mL HCl, 100 mL H_2O, 1 g $NH_4F{\cdot}HF$, and 0.5 g $K_2S_2O_5$. (c) Alloy A-286 (AISI 660, 318 HV), solution annealed 1 h at 980 °C (1800 °F), oil quenched, aged 16 h at 720 °C (1325 °F), and air cooled. Glyceregia. All original magnification 100×

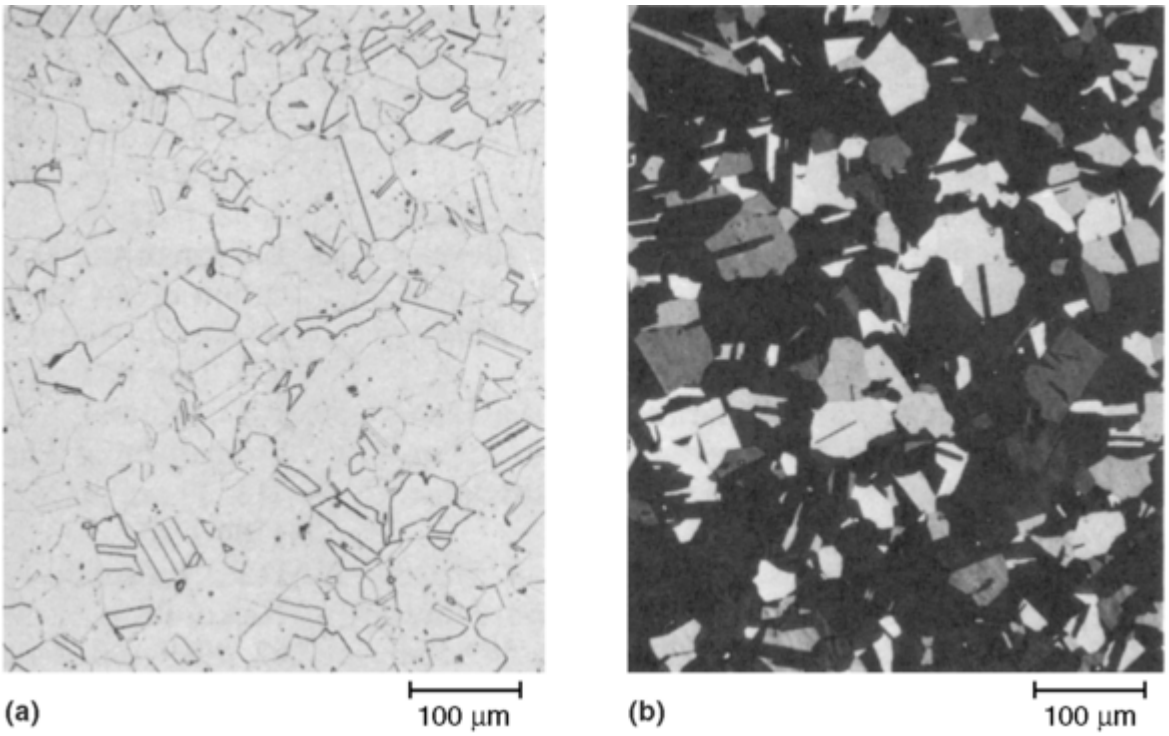

Fig. 10 Alloy A-286 (AISI 660, 318 HV), solution annealed 1 h at 980 °C (1800 °F), oil quenched, aged 16 h at 720 °C (1325 °F), and air cooled. (a) Glyceregia. (b) Tint etched. Only the matrix phase has been colored. 20 mL HCl, 100 mL H_2O, 1 g $NH_4F{\cdot}HF$, and 0.5 g $K_2S_2O_5$. Original magnification, both 100×

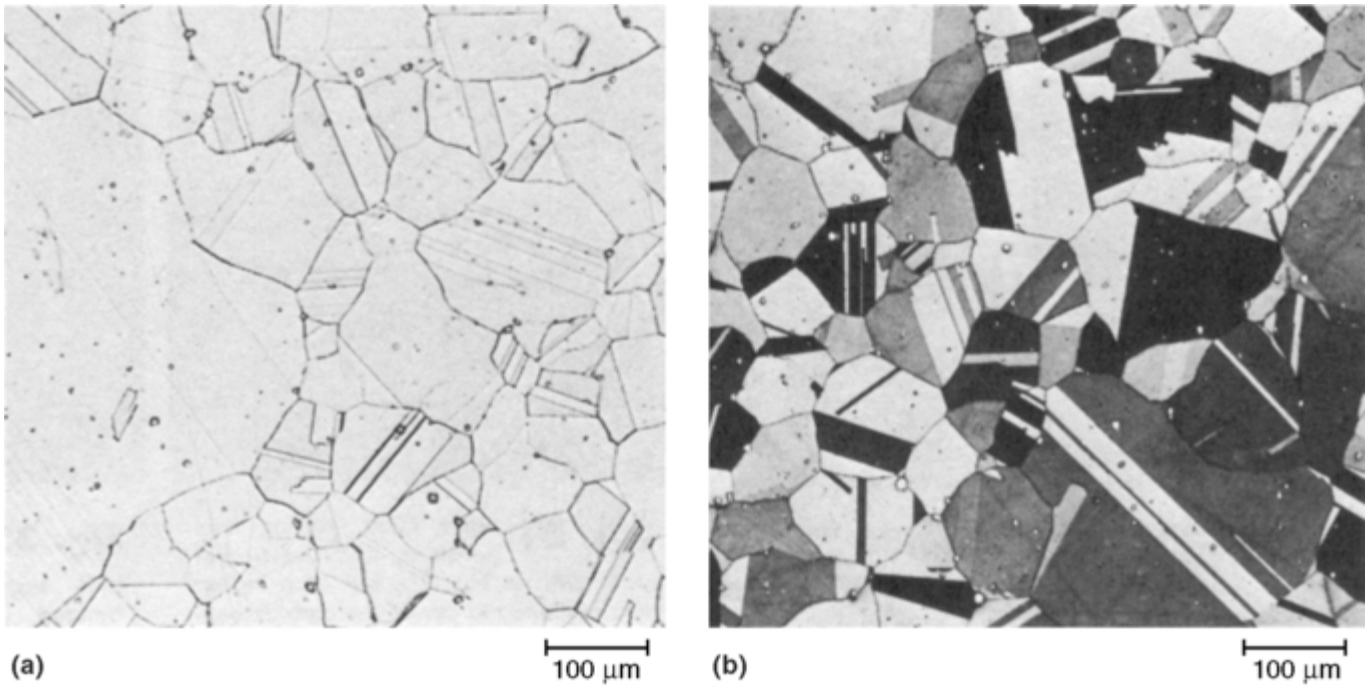

Fig. 11 Pyromet 31 (40 HRC), solution annealed and aged. (a) Etched using Kalling's reagent 2 (waterless Kalling's). (b) Tint etched with 66 mL HCl, 33 mL H_2O, and 1 g $K_2S_2O_5$. Original magnification, both 100×

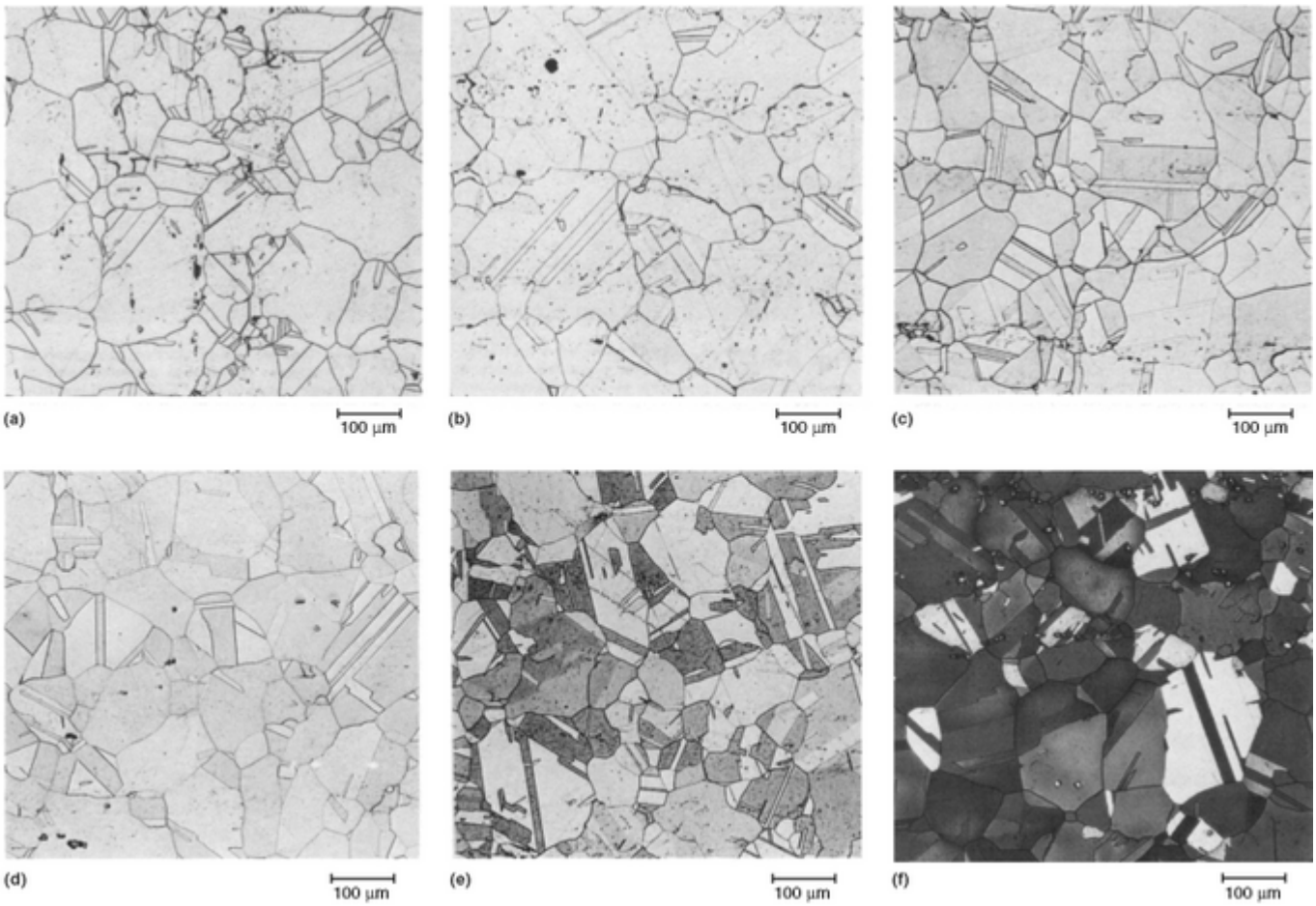

Fig. 12 The effects of different etchants on solution-annealed and aged alloy X-750. (a) Etched using glyceregia. Original magnification 100×. (b) Etched using Kalling's reagent 2. Original magnification 100×. (c) Etched using Marble's reagent. 100×. (d) Etched using aqua regia. 100× (e) Etched using HCl + 1% Na_2O_2. Original magnification 100×. (f) Tint etched in 50 mL HCl, 50 mL H_2O, and 1 g $K_2S_2O_5$

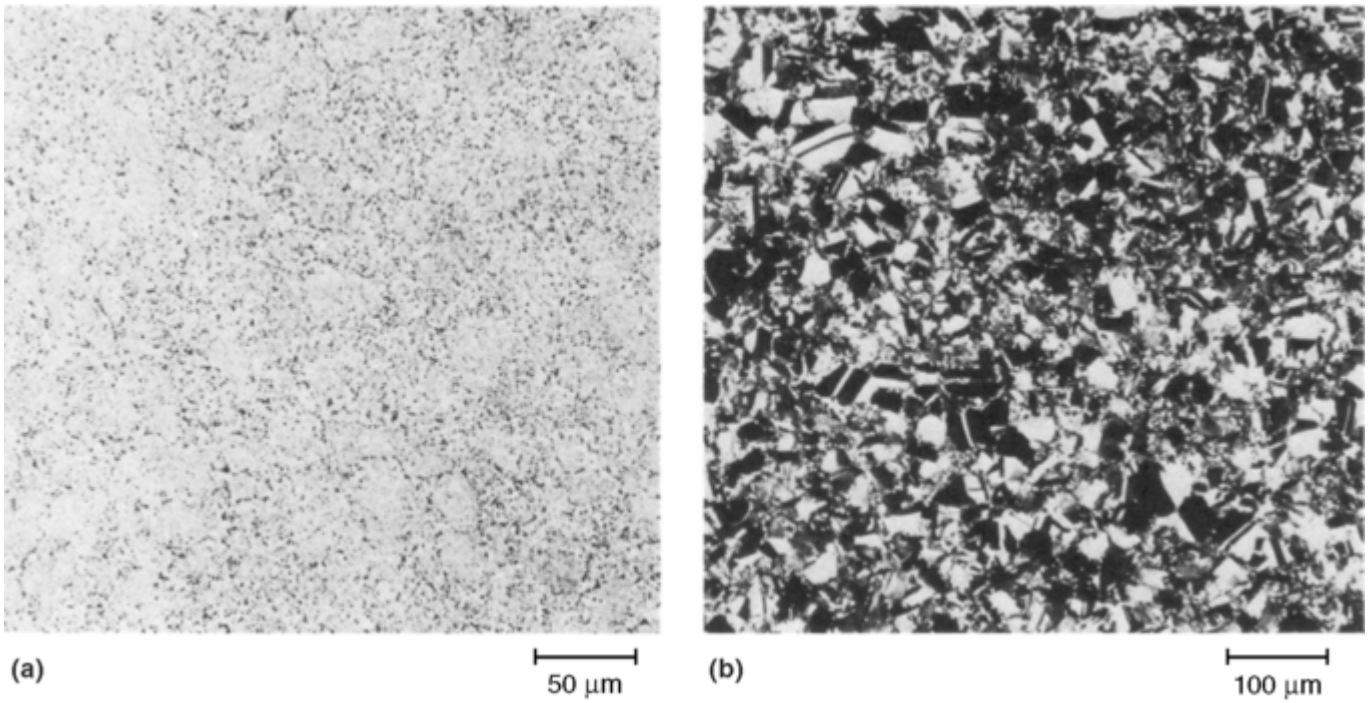

Fig. 13 Waspaloy (42 HRC), solution annealed 4 h at 1010 °C (1850 °F), water quenched, aged 4 h at 845 °C (1550 °F), air cooled, aged 16 h at 760 °C (1400 °F), and air cooled. (a) Glyceregia. Original magnification 200×. (b) Tint etched to color matrix phase. 50 mL HCl, 50 mL H_2O, and 1 g $K_2S_2O_5$. Original magnification 100×

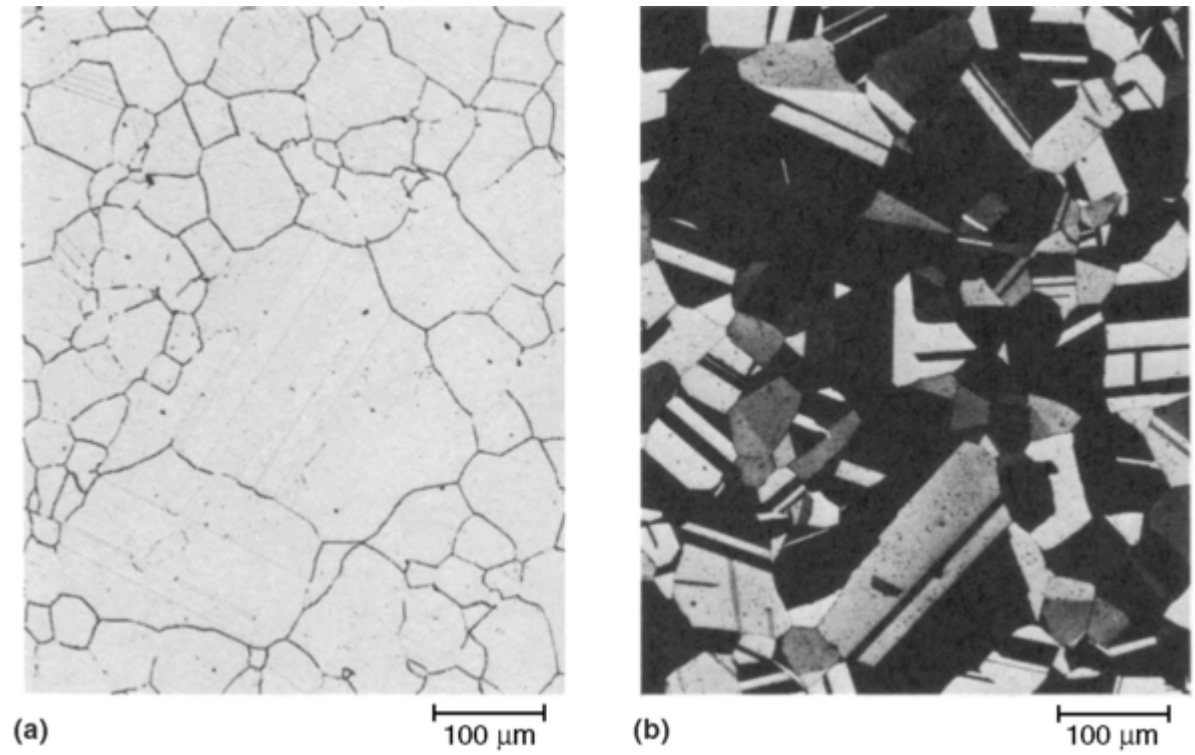

Fig. 14 Waspaloy (37 HRC), solution annealed 4 h at 1035 °C (1900 °F), water quenched, aged 4 h at 845 °C (1550 °F), air cooled, aged 16 h at 760 °C (1400 °F), and air cooled. (a) Etched in glyceregia. (b) Tint etched in 50 mL HCl, 50 mL H_2O, and 1 g $K_2S_2O_5$. Original magnification, both 100×

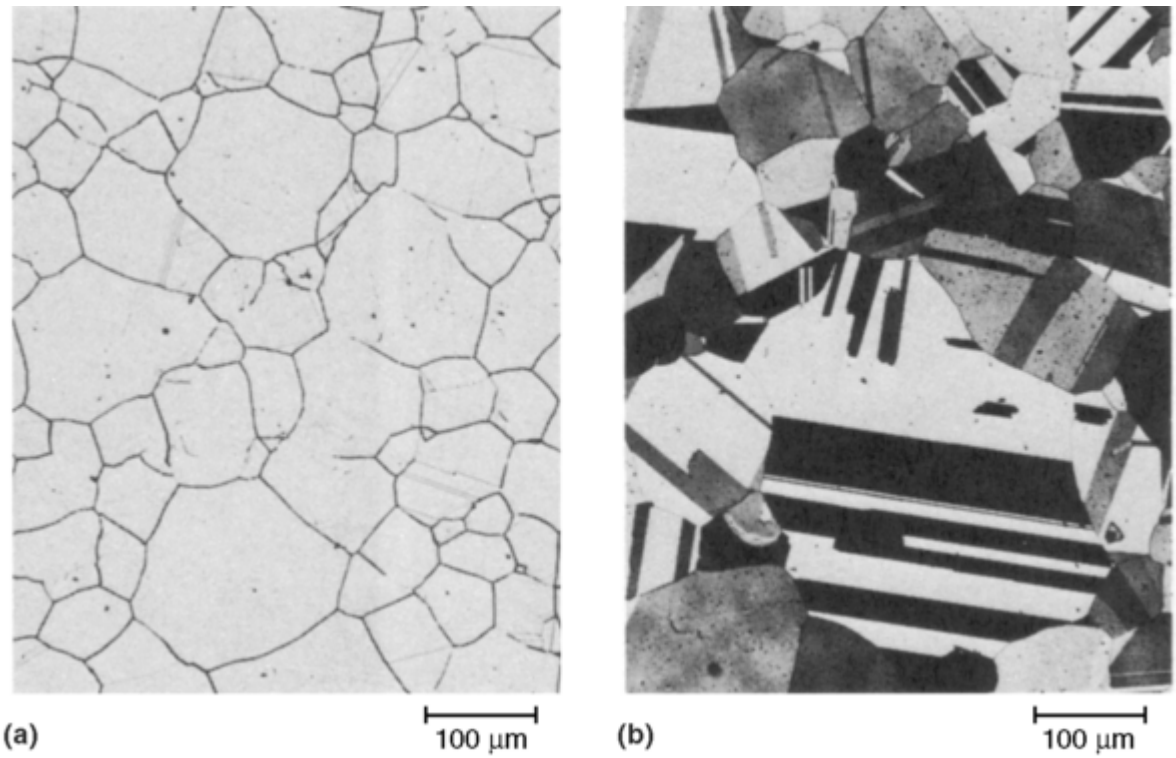

Fig. 15 Waspaloy (35 to 36 HRC), solution annealed 4 h at 1065 °C 1950 °F), water quenched, aged 4 h at 845 °C (1550 °F), air cooled, aged 16 h at 760 °C (1400 °F), and air cooled. (a) Etched in glyceregia. (b) Tint etched using 50 mL HCl, 50 mL H_2O, 3 g $NH_4F{\cdot}HF$, and 1.5 g $K_2S_2O_5$. Original magnification, both 100×

Identification of Ferrite by Magnetic Etching. Because of the low contrast, or lack of contrast, after etching, it is sometimes difficult to differentiate ferrite contained in an austenite matrix. A technique using a magnetic field and magnetic particles (smaller than 30 nm) in an organic or an aqueous colloidal suspension can be used in conjunction with the light optical microscope to identify ferrite positively (Ref 20, 21, 22, 23, 24). Details of the magnetic technique are described as follows. Additional information can be found in the article “Contrast Enhancement and Etching” in this Volume.

A drop (5 μL measured in a micropipette) of the suspension is deposited on the surface of a specimen that has been polished and lightly etched with HCl. A thin cover is placed over the suspension. If the specimen is contained in a 25 mm (1 in.) diameter plastic mount, a cover glass of the same diameter is ideal. The specimen is placed on an inverted metallographic microscope. When the specimen is face down, its weight plus the spring pressure applied will press on the suspension under the glass, keeping it thin and relatively uniform in thickness.

An electromagnet or a permanent magnet can be used to apply a magnetic field to the specimen. If an electromagnet is used for applying the magnetic field, it is a solenoid placed around the specimen, as shown in Fig. 16. It has a winding of 2300 A turn and operates on batteries or on direct current rectified from alternating current. The field can be cut off or reversed readily using switches. A variable autotransformer between the line and rectifier input or a rheostat in series with a battery source controls the intensity of the magnetizing field. The magnetic field will cause a visible concentration of the colloid particles over the magnetic areas. Figure 17(b) shows the magnetic pattern produced. Comparison of Fig. 17(b) with Fig. 17(a) shows that the magnetic pattern identifies the ferrite in the specimen.

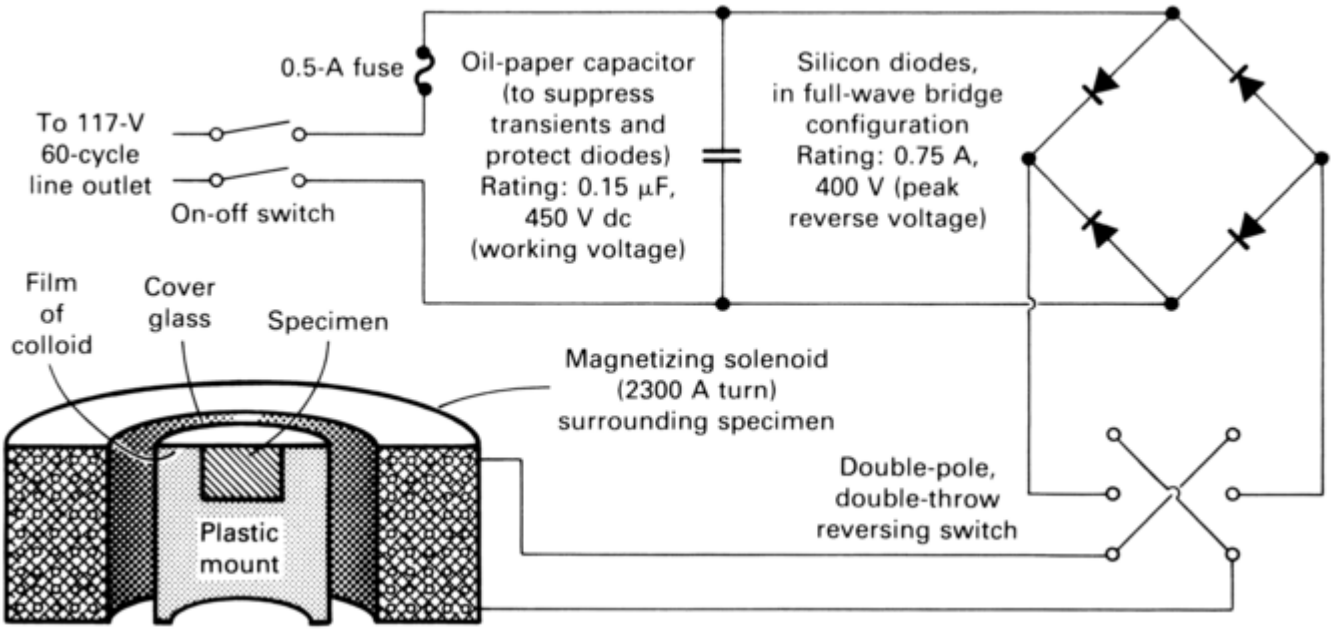

Fig. 16 Electromagnet setup for identification of ferrite in Fe-Cr-Ni alloys

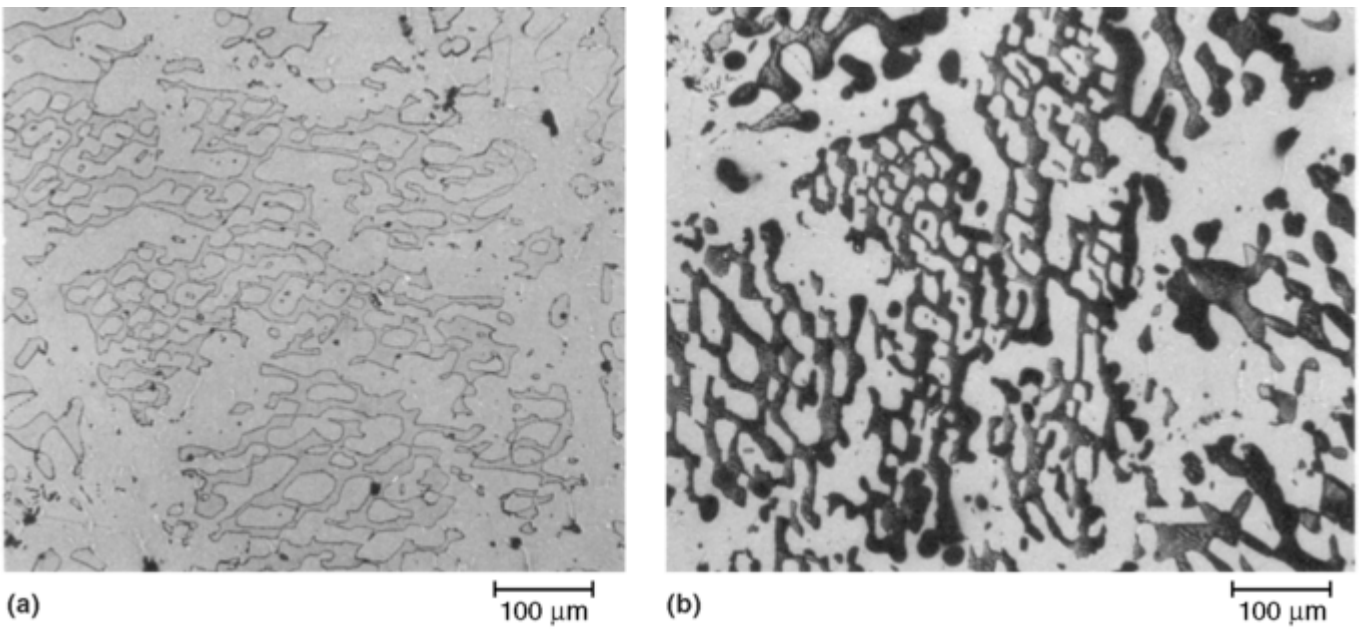

Fig. 17 (a) HE-14 alloy, creep tested at 4.5 MPa (650 psi) and 980 °C (1800 °F) for 336 h. Structure: islands of ferrite (darker gray) in an austenite matrix (lighter gray). White constituent is carbide particles. Compare appearance of ferrite in (b). (b) Same alloy and condition as in (a), showing the magnetic pattern (dark) on ferrite as influenced by a vertical magnetic field from a concentric solenoid. Dark areas with diffuse edges and no mosaic pattern indicate subsurface ferrite. Striped pattern shows magnetic domains. 50% HCl. Original magnification, both 100×

For cursory ferrite identification, it is simpler to use a permanent magnet. Various shapes are available. A cylindrical Alnico permanent magnet can be placed on top of the inverted specimen, as shown in Fig. 18(a) and (b), or an Alnico horseshoe magnet can be placed alongside, as shown in Fig. 18(c). The horseshoe magnet provides a horizontal and a vertical field. The field is most intense through that part of the specimen closest to the pole pieces of the magnet.

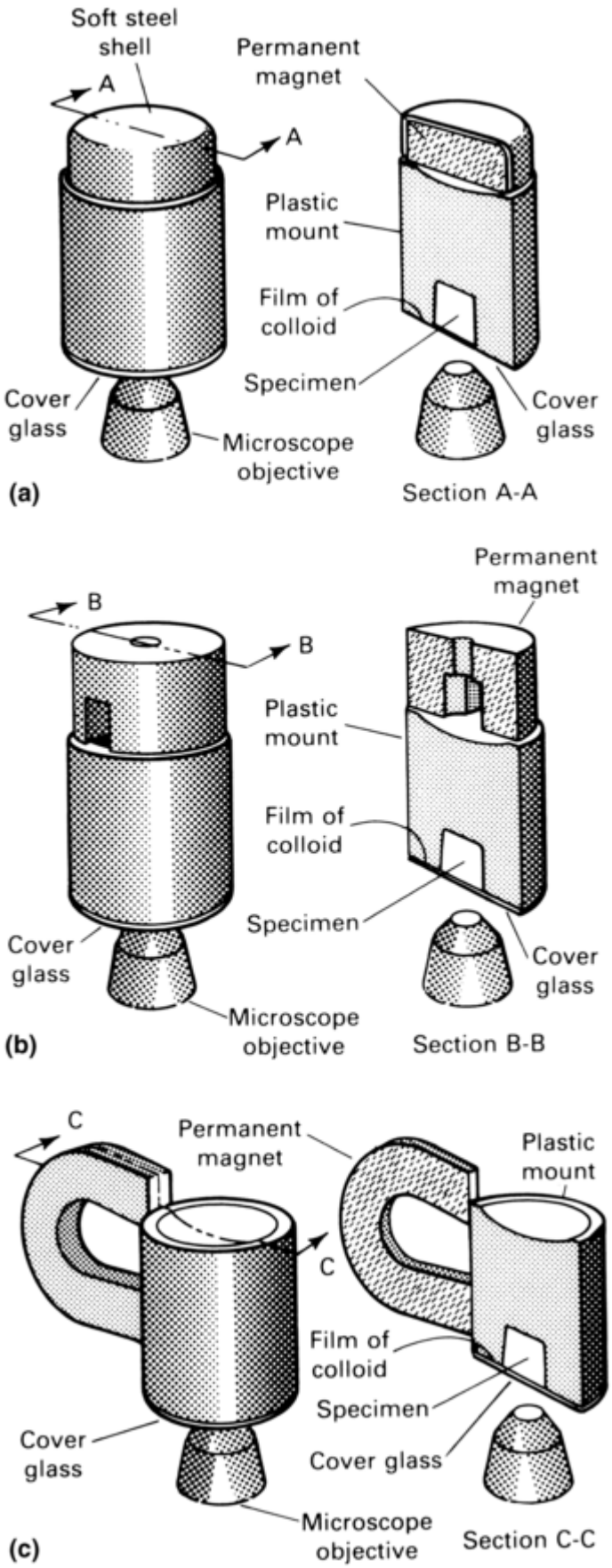

Fig. 18 Permanent-magnet setups for identification of ferrite in an austenite matrix. (a) and (b) Use of cylindrical magnets. (c) Use of horseshoe magnet

Transmission Electron Microscopy. Because some of the important constituents in wrought heat-resistant alloys, such as γ′ phase, are generally too small to observe using the light optical microscope, considerable use

has been made of TEM. Besides affording greater resolution and higher magnification, TEM provides means for phase identification by electron diffraction and, when equipped with x-ray detectors, can provide chemical analysis data. Such analytical procedures are necessary to understand the strengthening mechanisms for heat-resistant alloys. Today, field emission SEMs provide enough resolution to examine the γ′ particles in nearly all wrought superalloys. The γ′ in cast heat-resistant alloys is coarser than in wrought alloys and easier to study. Electron-backscattered diffraction can provide a useful alternative to the more tedious convergent-beam electron diffraction with the TEM for identification of the crystal structure of phases. Energy-dispersive spectroscopy provides chemical information and can be used with either the SEM or the TEM.

Several types of specimens can be prepared for TEM examination; each type has advantages and disadvantages. The replica method, which had been prevalent, is being replaced by use of the SEM (Ref 17, 18). A well-polished and properly etched specimen can be examined with a standard SEM at magnifications of 50,000× or more. Therefore, much of the structural examination role of TEM replicas can be accomplished without replica preparation and the complication of replica interpretation or artifact control.

In addition, the contrast mechanisms operable in the SEM are valuable for structural examination. Because chemical analysis using SEM is limited to features larger than a few microns, TEM examination and analysis of extracted constituents remains an important procedure. Procedures for preparing structural and extraction replicas are discussed in Ref 25, 26, 27, 28, 29, 30, 31, 32, and 33. Direct examination of the fine structure of heat-resistant alloys is also performed by TEM examination of thin foils. As with extraction replicas, electron diffraction and chemical analysis can be performed.

Because the beam size in a transmission electron microscope or a scanning transmission microscope is much smaller than in a scanning electron microscope, much finer particles can be analyzed using thin foils without interference from the surrounding matrix. Extremely small particles are difficult to analyze even with a transmission electron microscope. Extraction replicas are useful, because matrix effects can be eliminated. In addition, using a transmission electron microscope, microdiffraction patterns are obtainable from individual particles rather than many particles. The microdiffraction pattern is of great value in basic structural studies of the constituents.

Thin foils are prepared by the window method or the disk method described in Ref 25, 26, 27, 33, 34, 35 and 36. These methods involve careful sectioning to obtain a relatively thin slice of the material free of artifacts, followed by mechanical, chemical, or electrolytic thinning until a small area is thin enough for electron transmission. Table 9 lists several popular electropolishing procedures for preparing thin foils of heat-resistant alloys.

Table 9 Electropolishing solutions for transmission electron microscopy thin foils of wrought heat-resistant alloys

Composition	Comments
1. 950 mL acetic acid and 50 mL $HClO_4$	Popular electropolish for wrought superalloys for perforation; use at 70–80 V dc, 100–120 mA, 15 °C (60 °F)
2. 133 mL acetic acid, 25 g CrO_3, 7 mL H_2O	Best for window method; opacity makes jet thinning difficult; use at 10–12 V dc, 20 °C (70 °F)
3. 77 mL acetic acid and 23 mL $HClO_4$	For cobalt-base superalloys; keep temperature below 30 °C (85 °F), stainless steel cathode; used with the window method; use at 22 V dc, 0.08 A/cm^2 (0.5 A/in.^{2})
4. 600 mL methanol, 250 mL butanol, 60 mL $HClO_4$	Two step procedure: (a) 0.13 mm (0.005 in.) disk, polished 15–30 min at 30 V. (b) Final thinning at 16–24 V; use at -60 to -70 °C (-75 to -95 °F)

Figure 19 shows the microstructure of cast B-1900 nickel-base alloy containing carbides and coarse γ′ precipitates in a γ matrix revealed by light microscopy and with a replica viewed with the TEM. The large angular particle in the center of Fig. 19(c) is an MC carbide, while the γ′ is finer in size and in high concentration. Similar examples are given in Fig. 20 and 21 for cast IN-100 and in Fig. 22 for alloy 713C, both nickel-base alloys. Figure 23 shows coarse γ′ in cast IN-738 alloy where the shape is basically cubical. However, after solution annealing (1120 °C, or 2050 °F, for 2 h) and aging 24 h at 845 °C (1550 °F), the γ′ is finer and spherical in shape with two different sizes, as shown in Fig. 24. If an IN-738 casting is aged at 815 °C (1500 °F) for 1000 h, the γ′ is spherical with a single size distribution (Fig. 25). Other shapes and phases can be observed in cast superalloys, as illustrated in Fig. 26. This shows light optical and TEM views of a MAR-M

246 casting held at 980 °C (1800 °F) for 5000 h. There is needlelike M_6C carbide and γ′ in the matrix. In this case, the γ′ is not uniform in shape. Figure 27 shows an example of the structural changes in cast MAR-M 246 heated above 980 °C (1800 °F). Compare these micrographs to those in Fig. 26.

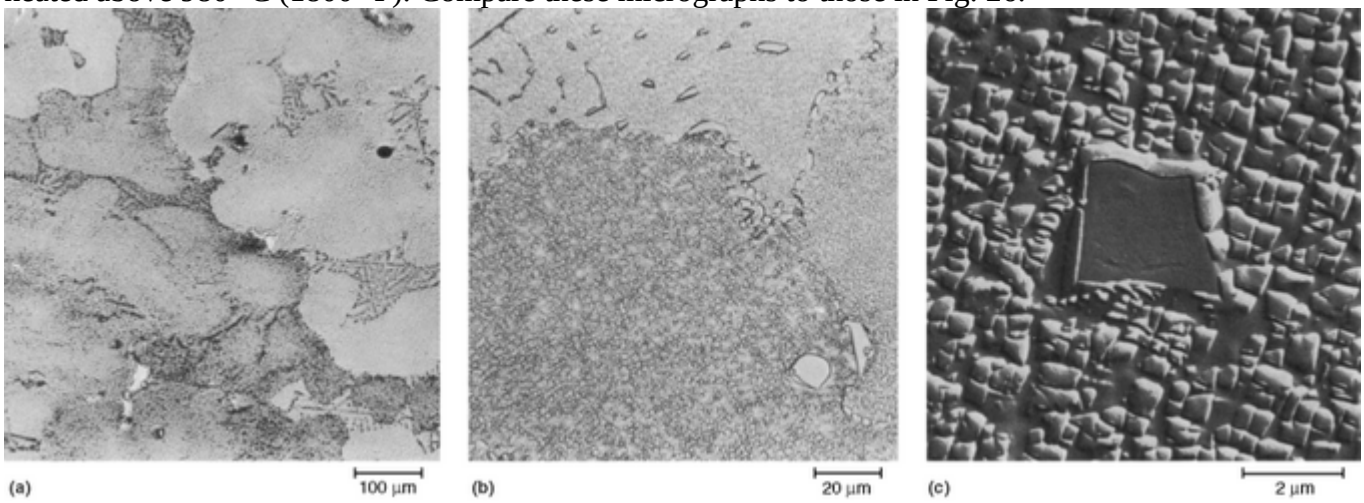

Fig. 19 B-1900 nickel-base alloy, as-cast. (a) Structure consists of nickel-rich γ solid-solution matrix containing a few light-etching carbide particles and dispersed γ′. Kalling's reagent. Original magnification 100× (b) Higher magnification. The light-etching carbide particles are dispersed and at grain boundaries. The fine constituent within grains is γ′. Kalling's reagent 2. Original magnification 500×. (c) Higher magnification and a replica electron micrograph showing details of a large MC carbide particle and particles of γ′ in the γ matrix. HCl, ethanol, $CuCl_2$, and H_2O_2. Original magnification 7500×

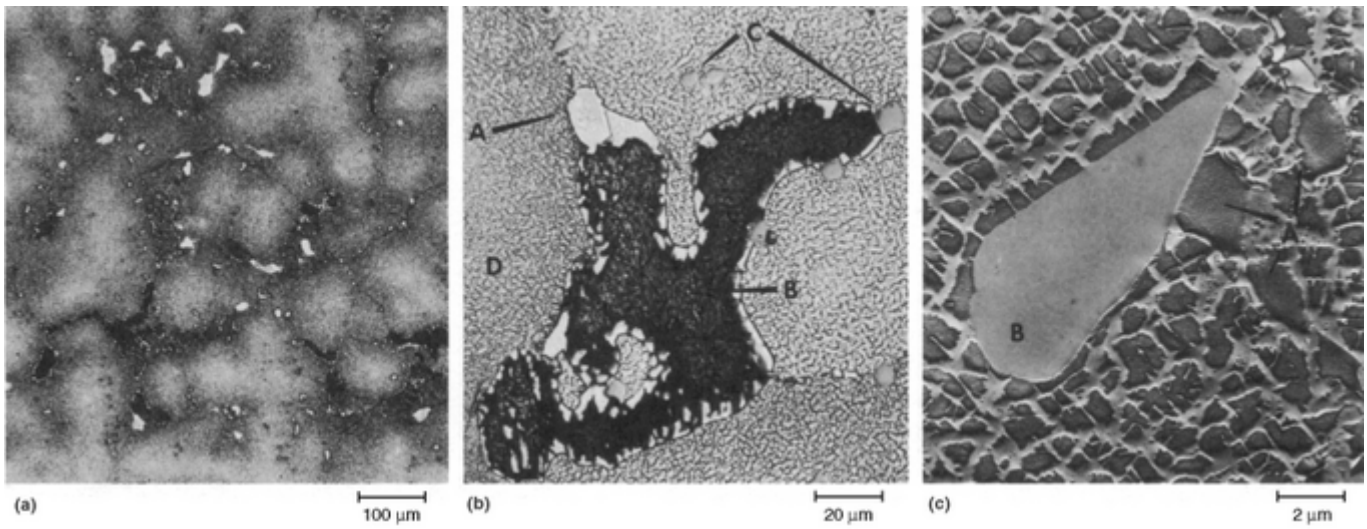

Fig. 20 IN-100, as-cast. (a) Small, white islands are primary (eutectic) γ′; peppery gray constituent is precipitated γ′; black constituent is probably perovskite, a complex carbide. $Ni_3(Al,Ti)C$; matrix is nickel-rich γ. Marble's reagent. Original magnification 100×. (b) Higher magnification. Light constituent (A) is primary (eutectic) γ′; dark (B), probably perovskite, $Ni_3(Al,Ti)C$. Dispersed carbide particles are shown at C. Gamma matrix contains precipitated γ′ (D). Marble's reagent. Original magnification 500×. (c) Higher magnification and a replica electron micrograph showing islands of primary γ′ (A), a large particle of primary carbide (B), and dispersed particles of precipitated γ′ in γ matrix. Marble's reagent. Original magnification 5000×

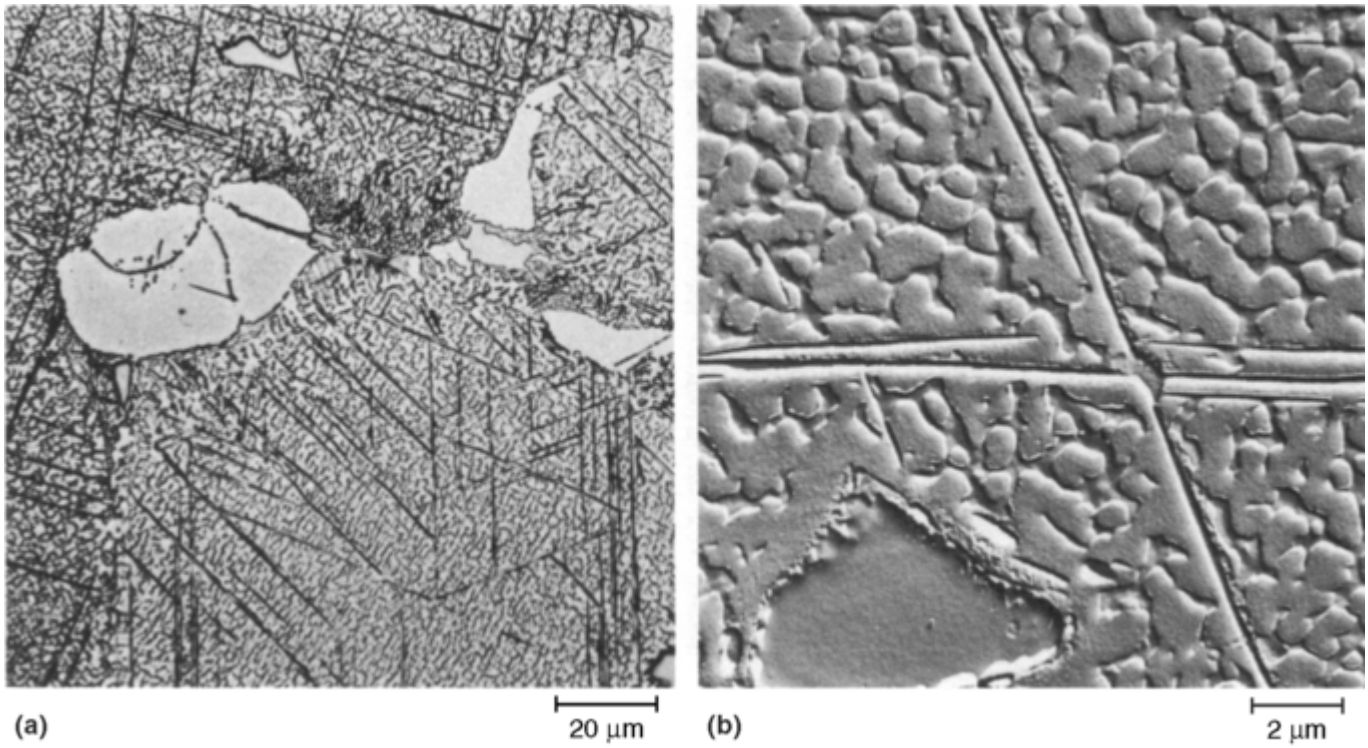

Fig. 21 IN-100 casting, held at 815 °C (1500 °F) for 5000 h. (a) Structure consists of massive MC particles, platelets of σ phase, and primary and precipitated γ′ in the γ matrix. HCl, ethanol, and H_2O_2. Original magnification 500× (b) Replica electron shows a massive particle of MC, Widmanstätten platelets of σ phase, and γ′ in the γ matrix. HCl, ethanol, and H_2O_2. Original magnification 4500×

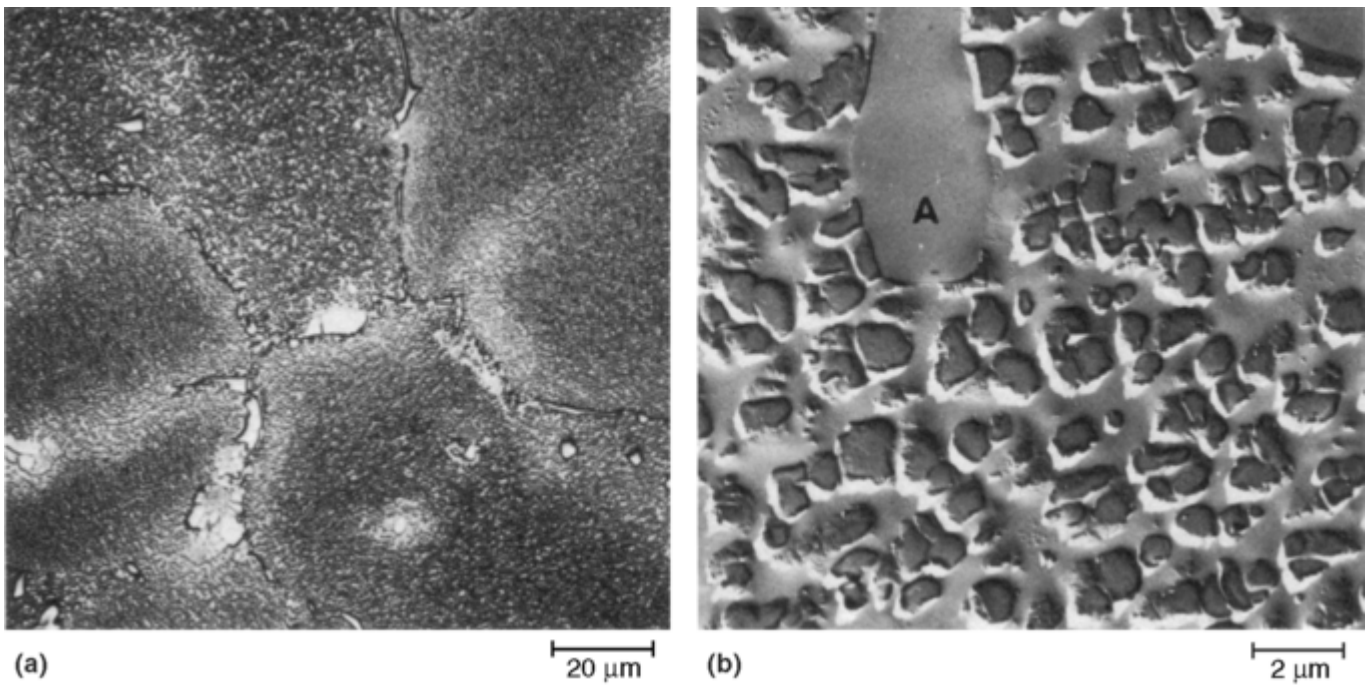

Fig. 22 Alloy 713C, as-cast. (a) The massive white particles are primary γ′; the grain-boundary film is MC particles. Gamma matrix contains γ′. Glyceregia. Original magnification 500×. (b) Replica electron micrograph. Structure shown consists of large particles of carbide (A) and γ′ in the matrix of γ solid solution. Marble's reagent. Original magnification 5000×

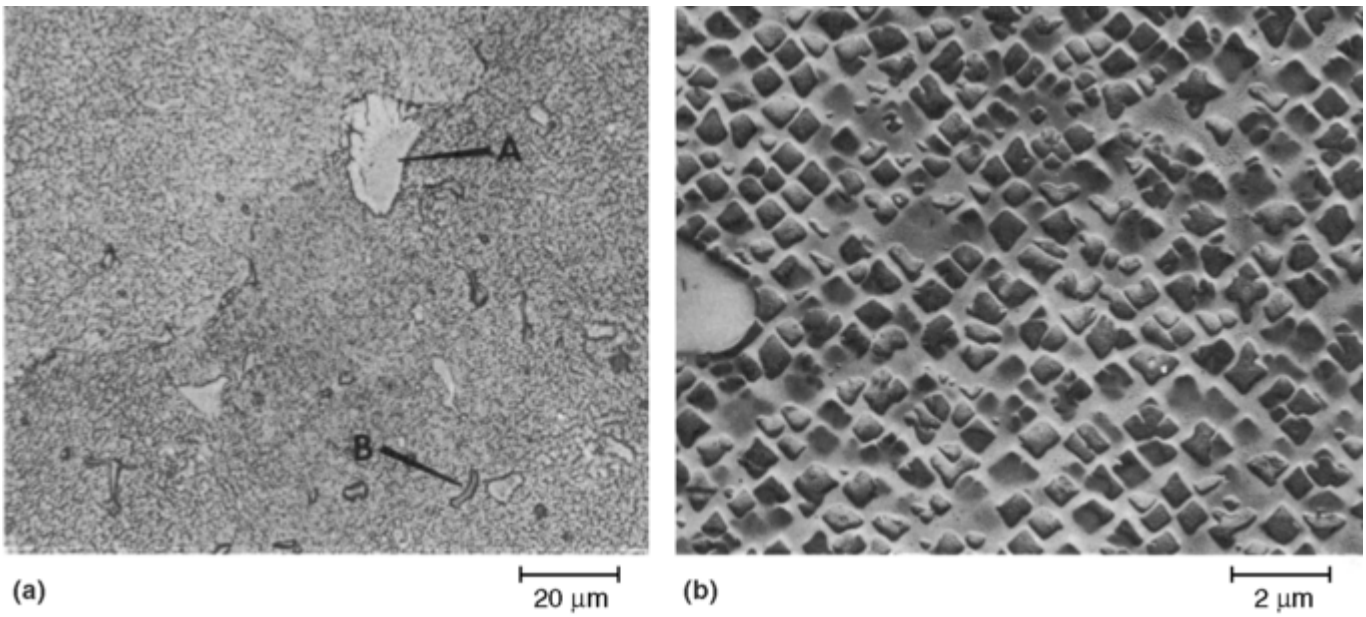

Fig. 23 IN-738, as-cast. (a) The structure consists of primary, or eutectic, γ′ islands (shown at A), dispersed carbide particles (shown at B), and precipitated γ′ in the matrix of γ solid solution. Marble's reagent. Original magnification 500×. (b) Higher magnification and a replica electron micrograph showing randomly distributed precipitated γ′ Ni_3(Al,Ti) and a carbide particle (at right edge) in matrix of γ solid solution. Marble's reagent. Original magnification 5000×

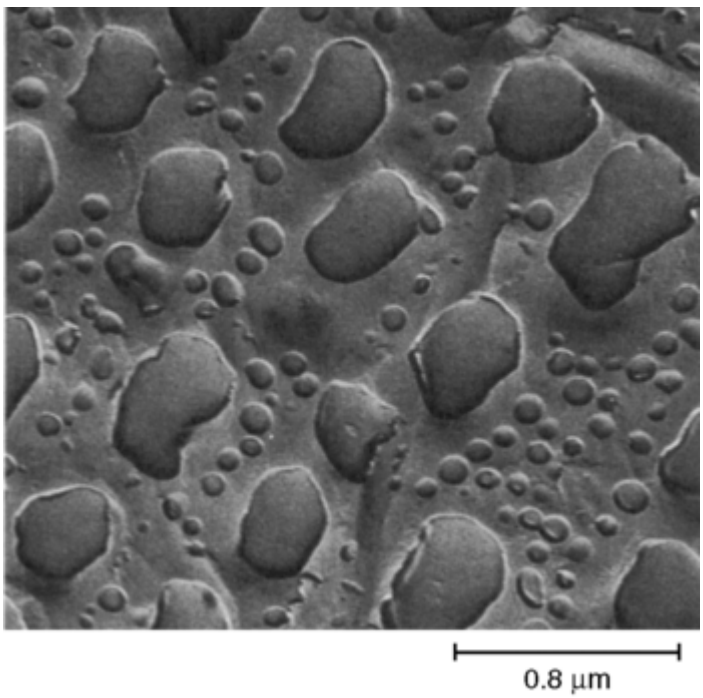

Fig. 24 IN-738 solution annealed 2 h at 1120 °C (2050 °F), held 24 h at 845 °C (1550 °F), replica electron micrograph. Gamma-prime particles in γ; the smaller particles formed in cooling. Electrolytic etch: H_2SO_4 and methanol. Original magnification 25,000×

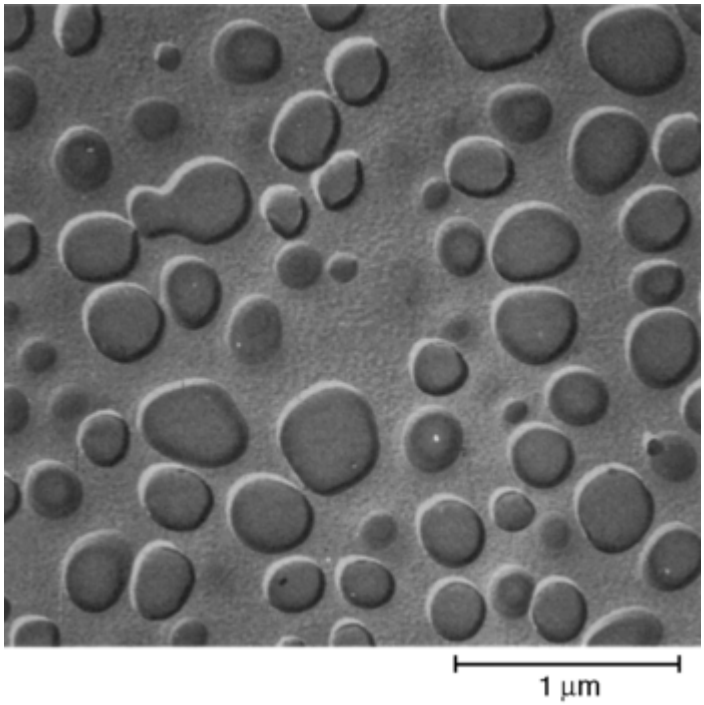

Fig. 25 IN-738 casting, after holding at 815 °C (1500 °F) for 1000 h. A replica electron micrograph. Structure consists of rounded γ′ particles in γ matrix. Compare with Fig. 24. Electrolytic etch: H_2SO_4 and methanol. Original magnification 20,000×

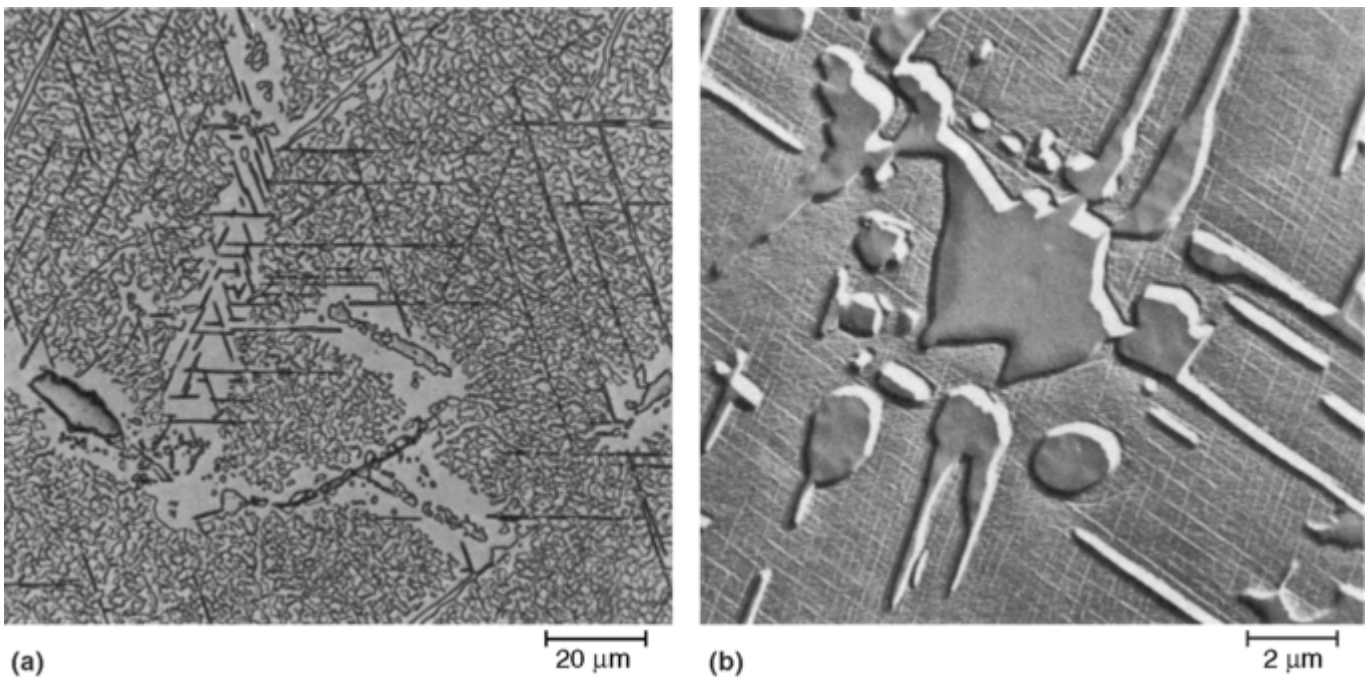

Fig. 26 MAR-M 246 casting, held at 980 °C (1800 °F) for 5000 h. (a) The structure consists of needlelike particles of M_6C and γ′ in the γ matrix. HCl, ethanol, and H_2O_2. Original magnification 500×. (b) Higher magnification. A replica transmission electron micrograph. Structure consists of needlelike particles of M_6C, and γ′ in the γ matrix. HCl, ethanol, and H_2O_2. Original magnification 4500×

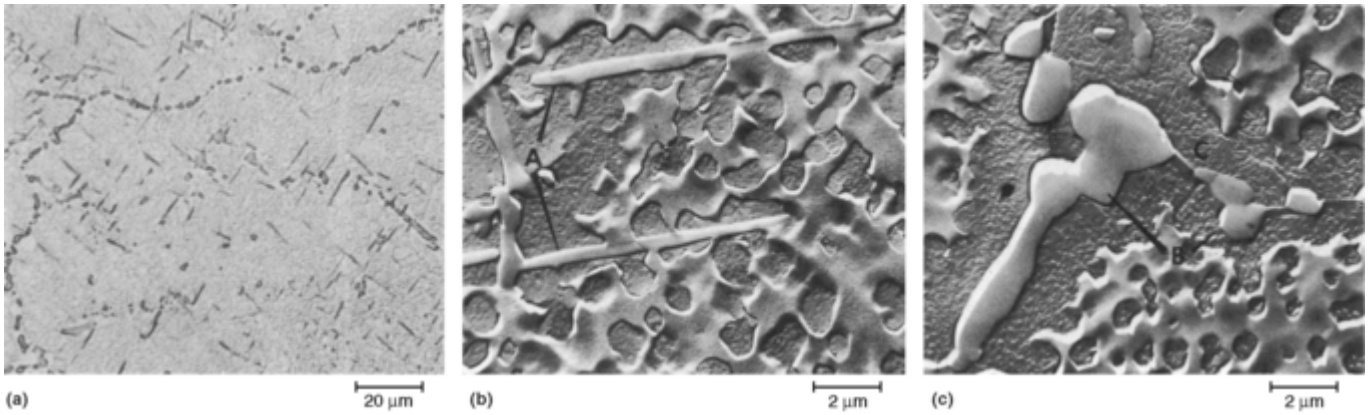

Fig. 27 MAR-M 246 casting, exposed to temperatures above 980 °C (1800 °F). (a) Chainlike $M_{23}C_6$ particles at grain boundaries and needlelike M_6C within grains. Matrix is γ. Marble's reagent. Original magnification 500×. (b) Replica electron micrograph. Needles of M_6C (A), $M_{23}C_6$ at grain boundaries, and γ′ $Ni_3(Al,Ti)$. Original magnification 5000×. (c) Replica electron micrograph. A large particle of $M_{23}C_6$ and a connecting carbide (B), and a γ′ envelope (C). The matrix is γ. Marble's reagent. Original magnification 5000×

Transmission electron microscopy examination is also crucial in the examination of the fine strengthening phases in wrought alloys. Figure 28 shows light optical and TEM views of the grain structure of Astroloy and γ′ in a specimen solution annealed 1 h at 1150 °C (2100 °F). The γ′ is fine and spherical. Figure 29 shows the same nickel-base alloy, Astroloy, solution annealed 4 h at 1150 °C (2100 °F), air cooled, aged 4 h at 1080 °C (1975 °F), oil quenched, aged 4 h at 845 °C (1550 °F), air cooled, aged 16 h at 760 °C (1400 °F), and air cooled. Light microscopy reveals grain-boundary MC carbides and coarse γ′, while the TEM replica reveals irregularly shaped γ′ in the grain boundaries and two sizes of γ′ from the aging treatments at 845 and 760 °C (1550 and 1400 °F). Figure 30 shows differences in γ′ precipitation in alloy X-750. In Fig. 30(a), the specimen was solution annealed at 1150 °C (2100 °F) for 2 h, air cooled, then aged 24 h at 815 °C (1500 °F). The γ′ is small and uniformly dispersed. $M_{23}C_6$ carbide can be seen in the grain boundary. In Fig. 30(b), the specimen was given the same solution anneal, but it was double aged, first at 845 °C (1550 °F) for 24 h and then at 705 °C (1300 °F) for 24 h. The grain-boundary $M_{23}C_6$ carbide is stabilized, and there is a denser precipitation of γ′ in the matrix.

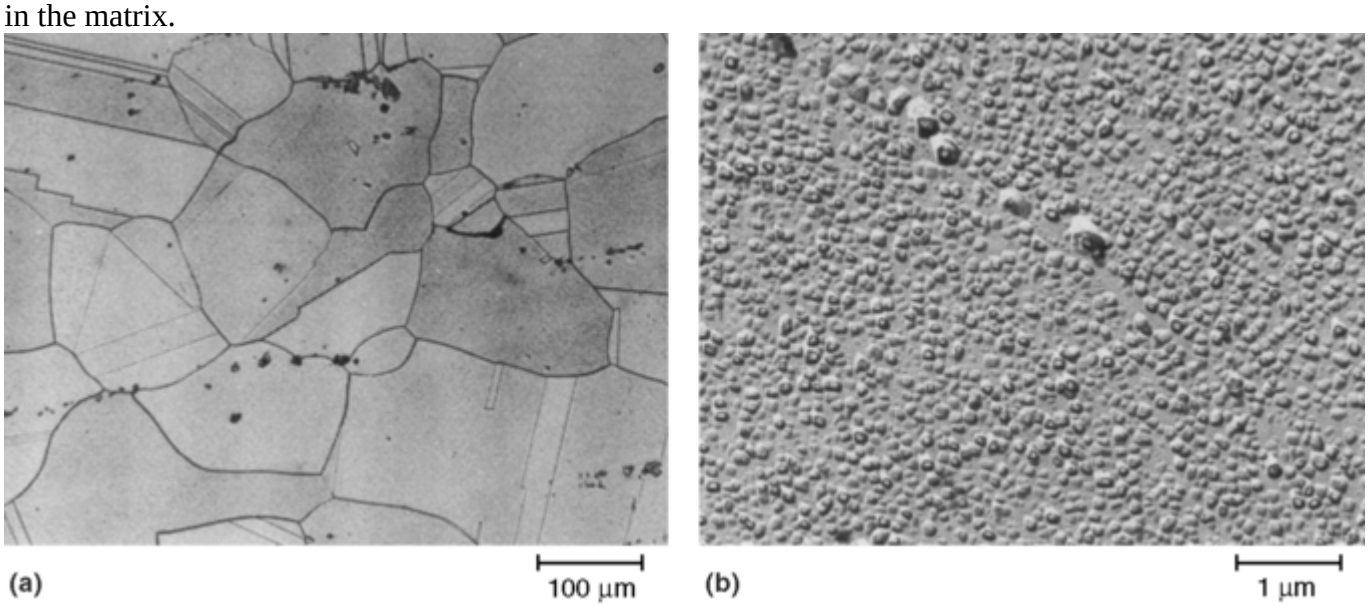

Fig. 28 Astroloy forging, solution annealed 1 h at 1150 °C (2100 °F) and air cooled. (a) View showing grain boundaries and fine MC carbides in a γ-phase matrix. Kalling's reagent 2. Original magnification 100×. (b) Replica electron micrograph showing a clean grain boundary (diagonal). γ′ precipitate is visible in the γ matrix. Electrolytic: H_2SO_4, H_3PO_4, and HNO_3. Original magnification 10,000×

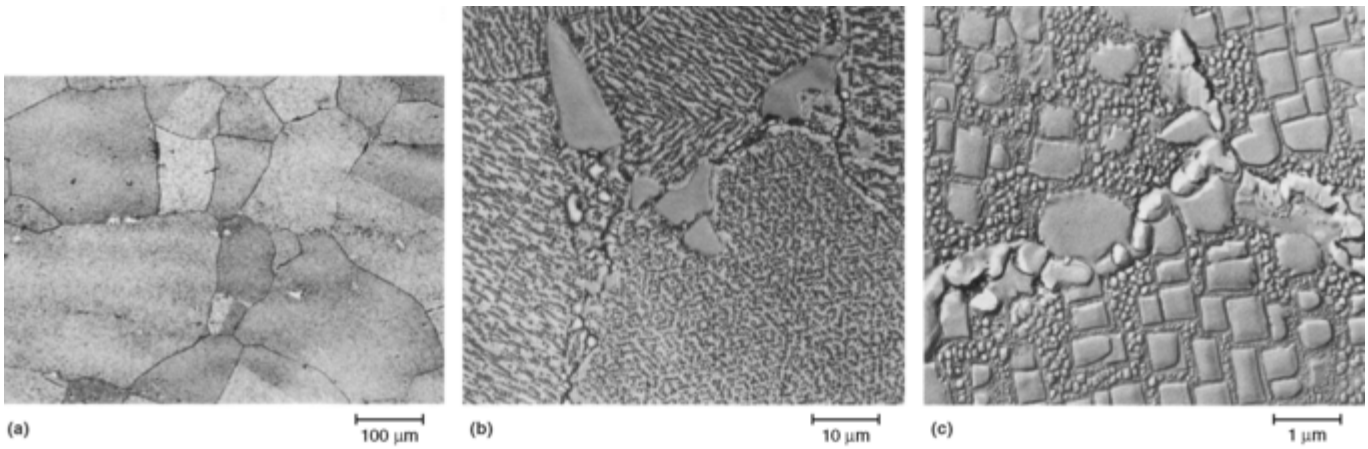

Fig. 29 Astroloy forging, solution annealed 4 h at 1150 °C (2100 °F), air cooled, aged 4 h at 1080 °C (1975 °F), oil quenched, aged 4 h at 845 °C (1550 °F), air cooled, aged 16 h at 760 °C (1400 °F), and air cooled. (a) Kalling's reagent 2. Original magnification 100×. (b) Higher magnification. MC carbides are precipitated at grain boundaries; the solid-solution matrix contains γ′ particles. Kalling's reagent 2. Original magnification 1000×. (c) Replica electron micrograph showing intergranular γ′ precipitated at 1080 °C (1975 °F) as well as fine γ′ precipitated at 845 °C (1550 °F) and 760 °C (1400 °F). Carbide particles are visible at grain boundaries. Electrolytic: H_2SO_4, H_3PO_4, and HNO_3. Original magnification 10,000×

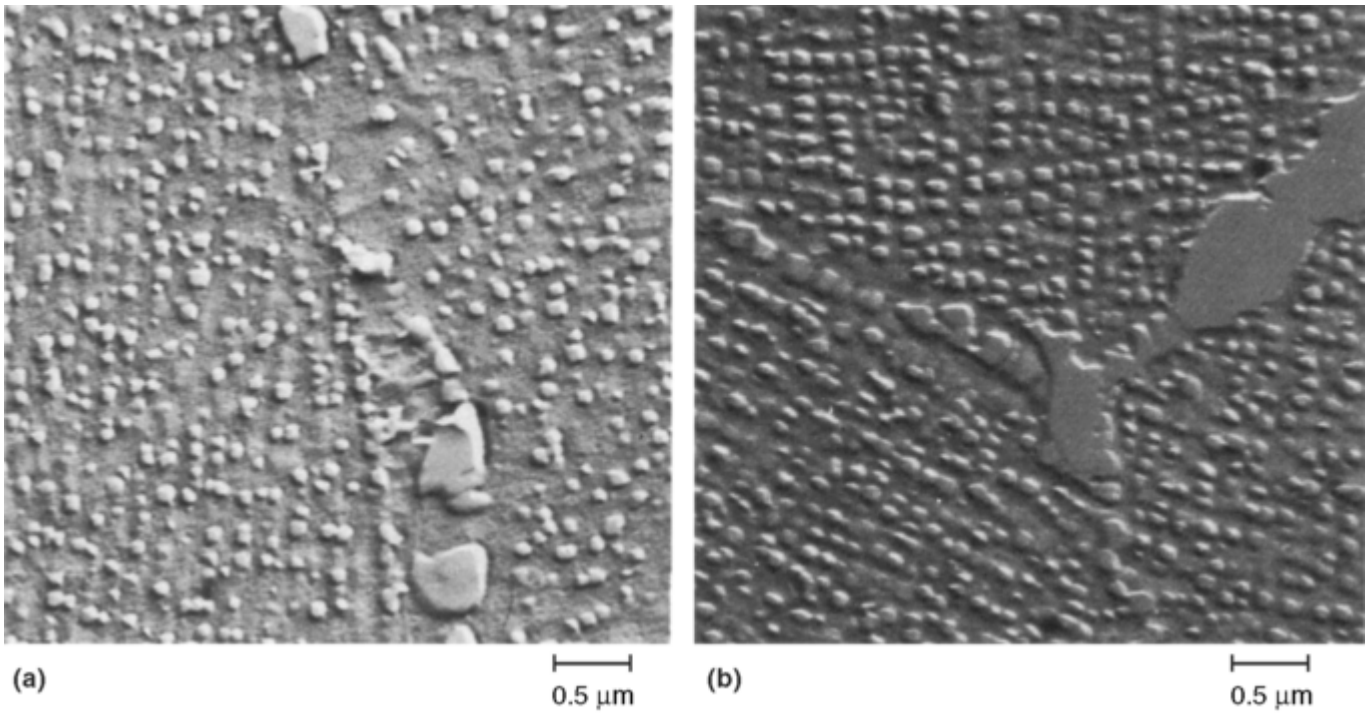

Fig. 30 Replica electron micrograph of Inconel X-750, solution annealed 2 h at 1150 °C (2100 °F) and air cooled. (a) Aged 24 h at 815 °C (1500 °F). Structure is small, uniformly dispersed γ′ precipitate and large, discontinuous $M_{23}C_6$ carbide at the grain boundary. (b) Aged 24 h at 845 °C (1550 °F), then 24 h at 705 °C (1300 °F). Grain-boundary $M_{23}C_6$ carbide is stabilized, and precipitation of fine γ′ particles has increased. Both glyceregia. Original magnification, both 15,000×

Bulk Extractions. X-ray diffraction studies of phases extracted electrolytically are widely practiced. X-ray diffraction is an important tool for phase identification in heat-resistant alloys (Ref 37, 38, 39, 40, 41, 42, 43, 44, 45). Because of the complex nature of these alloys, such techniques must be carefully controlled to ensure good results. Qualitative identification of the phases by this method is considerably easier than quantitative evaluations. The extraction method must be designed to permit separation of the carbides, nitrides, γ′, and

topologically close-packed (tcp) phases. Once separated, the phases can be analyzed using x-ray diffraction, chemical analysis (elemental), and light and electron microscopy procedures.

Considerable research has been conducted to establish reliable procedures for bulk extraction in heat-resistant alloys (Ref 37, 38, 39, 40, 41, 42, 43, 44, and 45). Anodic dissolution using 10% HCl in methanol, which dissolves γ′ and the austenitic matrix, is implemented to extract carbides, borides, nitrides, and tcp phases. If the alloy to be digested contains substantial amounts of tungsten, tantalum, or niobium, 1% tartaric acid is added to prevent contamination of the residue.

To extract γ′ from nickel-base alloys, two electrolytes have been used: 20% aqueous phosphoric acid (H_3PO_4), or an aqueous solution containing 1% ammonium sulfate [$(NH_4)_2SO_4$] and 1% citric acid or tartaric acid. The latter electrolyte produces better recovery of γ′. When the ammonium sulfate/citric or tartaric acid electrolyte is used, the residue will also contain carbides, nitrides, and borides (if present in the alloy). All the γ′ morphologies are extracted using this electrolyte. Details concerning the use of these electrolytes and others are given in Table 10 and provided in Ref 37, 38, 39, 40, 41, 42, 43, 44 and 45.

Table 10 Techniques for bulk electrolytic extractions

Solution	Comments
1. 10% HCl in methanol	For extraction of carbides, borides, topologically close-packed phases, and geometrically close-packed phases from nickel- and iron-nickel-base alloys; solution may dissolve Ni_3Ti; maintain bath at 0–30 °C (32–85 °F); for alloys containing tungsten, niobium, tantalum, or hafnium, add 1% tartaric acid; use 0.05–0.1 A/cm^2 (0.33–0.65 A/in.^{2}) for 4 h or longer (additional details in ASTM E 963)
2. 0.5–2% citric acid and $(NH_4)_2SO_4$ in H_2O (1% of each is most common)	Used to extract γ′ phase in nickel-base Udimet 700; use at 0.03 A/cm^2 (0.2 A/in.^{2}) for 3 h at room temperature; minor amounts of carbides and borides will also be extracted (additional details in Ref 35, 36, 37, 38)
3. 10 or 20% H_3PO_4 in H_2O	Used to extract γ′ in nickel-base alloys; may etch the γ′ phase, although results have been contradictory
4. 50 mL HNO_3, 20 mL $HClO_4$, 1000 mL H_2O	For extraction of γ′ and η in nickel-base superalloys; use at 0.1 A/cm^2 (0.65 A/in.^{2}), 25 °C (75 °F)
5. 300 g KCl (potassium chloride), 30 g citric acid, 50 mL HCl, 1000 mL H_2O	For extraction of carbides from nickel-base superalloys; use at 0.1 A/cm^2 (0.65 A/in.^{2}), 25 °C (75 °F)

References cited in this section

1. G.F. Vander Voort, *Metallography: Principles and Practice,* McGraw-Hill, 1984; reprinted by ASM International, 1999

8. E.J. Dulis and G.V. Smith, Identification and Mode of Formation and Re-Solution of Sigma Phase in Austenitic Chromium-Nickel Steels, *Symposium on the Nature, Occurrence and Effects of Sigma Phase,* STP 110, ASTM, 1951

9. G. Petzow, *Metallographic Etching,* 2nd ed., ASM International, 1999

10. C.H. Lund and H.J. Wagner, "Identification of Microconstituents in Superalloys," DMIC Memorandum 160, Battelle Memorial Institute, Columbus, OH, 15 Nov 1962

11. H.J. Beattie and F.L. Ver Snyder, Microconstituents in High Temperature Alloys, *Trans. ASM,* Vol 45, 1953, p 397–428

12. J.W. Weeton and R.A. Signorelli, Effect of Heat Treatment upon Microstructures, Microconstituents, and Hardness of Wrought Cobalt Base Alloy, *Trans. ASM,* Vol 47, 1955, p 815–852

13. H. Meisel et al., Metallographic Development of the Structure of Nickel Based Alloys, *Pract. Metallogr.,* Vol 17, 1980, p 261–272

14. F.R. Morral, Metallography of Cobalt-Base and Cobalt-Containing Alloys, *Pract. Metallogr.,* Vol 10, 1973, p 398–413

15. E. Kohlhaas and A. Fischer, The Metallography of Superalloys, *Pract. Metallogr.,* Vol 8, Jan 1971, p 3–25

16. W.C. Bigelow et al., Electron Microscopic Identification of the γ′ Phase of Nickel-Base Alloys, *Proc. ASTM,* Vol 56, 1956, p 945–953

17. L. Bartosiewicz, Preferential Electrolytic Etching Technique to Reveal the γ′ Phase in Nickel Base Alloys, *Pract. Metallogr.,* Vol 10, 1973, p 450–461

18. P.K. Footner and B.P. Richards, A Rapid Method for Measurement of γ′ Size Distribution in Nickel-Base Superalloys, *Pract. Metallogr.,* Vol 17, 1980, p 489–496

19. C.P. Sullivan, The Metallographic Identification of Borides in Udimet 700, *Trans. ASM,* Vol 58, 1965, p 702–705

20. H.S. Avery, V.O. Homerberg, and E. Cook, Metallographic Identification of Ferro Magnetic Phases, *Met. Alloys,* Vol 10, 1939, p 353–355

21. H.S. Avery, "Cast Heat-Resistant Alloys for High-Temperature Weldments," Bulletin 143, Welding Research Council, Aug 1969

22. A New Way to Reveal Magnetic Domains at High Magnifications, *Met. Prog.,* Vol 100, Dec 1971, p 82

23. W.C. Elmore, Ferromagnetic Colloid for Studying Magnetic Structures, *Phys. Rev.,* Vol 54, 1938, p 309–310

24. Gray, "Revealing Ferromagnetic Microstructures with Ferrofluid," Report RNL-TM-3681, Oak Ridge National Laboratory, March 1972

25. G.N. Maniar and A. Szirmae, Ed., *Manual on Electron Metallography Techniques,* STP 547, ASTM, 1973

26. I.S. Brammar and M.A.P. Dewey, *Specimen Preparation for Electron Metallography,* Blackwell Scientific, 1966

27. G. Thomas, *Transmission Electron Microscopy of Metals,* John Wiley & Sons, 1964

28. J.R. Mihalisin, The Selective Identification of Constituents in Nimonic 80 by Extraction-Replica Technique, *Trans. AIME,* Vol 212, June 1958, p 349–350

29. E. Kohlhaas and A. Fischer, The Use of the Carbon-Extraction Technique in Investigations of Superalloys, *Pract. Metallogr.,* Vol 6, 1969, p 291–298

30. R.J. Seher and G.N. Maniar, Analytical Preshadowed Extraction Replica Technique, *Metallography,* Vol 5, 1972, p 409–414

31. W.L. Mankins, Chromic Acid as an Electrolytic Etchant and Electrolyte for the Extraction of γ′ in Nickel-Base Superalloys, *Metallography,* Vol 9, 1976, p 227–232

32. A.J. Portner and B. Ralph, A Technique for the Replication of γ′ in Nickel-Base Superalloys, *Pract. Metallogr.,* Vol 16, 1979, p 592–601

33. K.C. Thompson-Russell and J.W. Edington, Electron Microscope Specimen Preparation Techniques in Materials Science, Part 5, *Practical Electron Microscopy in Materials Science,* Philips Electronic Instruments, 1977

34. L. Bartosiewicz, Improved Techniques of Thin Foil Preparation of Ni Base Alloys for Electron Microscopy, *Pract. Metallogr.,* Vol 9, 1972, p 525–534

35. C. Hays and D.A. Nail, Transmission Electron Microscopy of Incoloy Alloy 901, *Metallography,* Vol 7, 1974, p 59–68

36. R.E. Schafrik and M. Henry, Transmission Electron Microscopy Foil Preparation and Results for Incoloy 901, *Metallography,* Vol 13, 1980, p 157–165

37. T.P. Hoar and K.W.J. Bowen, The Electrolytic Separation and Some Properties of Austenite and Sigma in 18-8-3-1 Chromium-Nickel Molybdenum-Titanium Steel, *Trans. ASM,* Vol 45, 1953, p 443–474

38. J.F. Brown et al., The Extraction of Minor Phases from Austenitic Steel, *Metallurgia,* Vol 56, Nov 1957, p 215–223

39. K.W. Andrews and H. Hughes, The Isolation, Separation, and Identification of Microconstituents in Steels, in STP 393, ASTM, 1966, p 3–21

40. O.H. Kriege and C.P. Sullivan, The Separation of Gamma Prime from Udimet 700, *Trans. ASM,* Vol 61, 1968, p 278–282

41. O.H. Kriege and J.M. Baris, The Chemical Partitioning of Elements in Gamma Prime Separated from Precipitation-Hardened, High-Temperature Nickel-Base Alloys, *Trans. ASM,* Vol 62, 1969, p 195–200

42. M.J. Donachie and O.H. Kriege, Phase Extraction and Analysis in Superalloys Summary of Investigations by ASTM Committee E-4 Task Group 1, *J. Mater.,* Vol 7, Sept 1972, p 269–278

43. O.H. Kriege, Phase Separation as a Technique for the Characterization of Superalloys, in STP 557, ASTM, 1974, p 220–234

44. E. Kny, On the Methodology of Phase Extraction in Ni-Base Superalloys, *Pract. Metallogr.,* Vol 13, Nov 1976, p 549–564

45. "Practice for Electrolytic Extraction of Phases from Ni and Ni-Fe Base Superalloys Using a Hydrochloric-Methanol Electrolyte," E 963, *Annual Book of ASTM Standards,* ASTM, 1984

G.F. Vander Voort, G.M. Lucas, and E.P. Manilova, Metallography and Microstructures of Heat-Resistant Alloys, *Metallography and Microstructures*, Vol 9, *ASM Handbook*, ASM International, 2004, p. 820–859

Metallography and Microstructures of Heat-Resistant Alloys

George F. Vander Voort and Gabriel M. Lucas, Buehler Ltd.; Elena P. Manilova, Polzunov Central Boiler and Turbine Institute, St. Petersburg, Russia

Phases in Wrought Heat-Resistant Alloys

The microconstituents observed in iron-nickel and nickel-base wrought heat-resistant superalloys are identical, with a few exceptions. The cobalt-base alloys are not strengthened by precipitated intermetallics but share many common features. All the alloys have an austenitic (γ-phase) matrix that is strengthened by solid-solution alloying and by carbide precipitation. Most of the phases discussed subsequently have some degree of solubility for other elements; therefore, their true compositions will vary from alloy to alloy and may be altered by heat treatment and thermal exposure. Not all phases permit substitution, however. Eta phase (Ni_3Ti) has no significant solubility for other elements. Table 12 summarizes data on the commonly encountered second-phase constituents in heat-resistant alloys.

Table 12 Constituents observed in wrought heat-resistant alloys

Phase	Crystal structure[(a)]	Lattice parameter[(b)], nm	Formula	Comments
γ′	fcc (ordered, $L1_2$)	0.3561 for pure Ni_3Al to 0.3568 for $Ni_3(Al_{0.5}Ti_{0.5})$	NiAl $Ni_3(Al,Ti)$	Principal strengthening phase in many nickel- and nickel-iron-base superalloys; crystal lattice varies slightly in size (0 to 0.5%) from that of austenite matrix; shape varies from spherical to cubic; size varies with exposure time and temperature
η	hcp (DO_{24})	a_0 = 0.5093 c_0 = 0.8276	Ni_3Ti (no solubility for other elements)	Found in iron-, cobalt-, and nickel-base superalloys with high titanium/aluminum ratios after extended exposure; may form intergranularly in a cellular form or intragranularly as acicular platelets in a Widmanstätten pattern
γ″	bct (ordered DO_{22})	a_0 = 0.3624 c_0 = 0.7406	Ni_3Nb	Principal strengthening phase in Inconel 718; γ″ precipitates are coherent disk-shaped particles that form on the (100) planes (average diam, approximately 600 Å; thickness, approximately 50–90 Å); metastable phase
Ni_3Nb (δ)	Orthorhombic (ordered Cu_3Ti)	a_0 = 0.5106–0.511 b_0 = 0.421–0.4251 c_0 = 0.452–0.4556	Ni_3Nb	Observed in overaged Inconel 718; has an acicular shape when formed between 815 and 980 °C (1500 and 1800 °F); forms by cellular reaction at low aging temperatures and by intragranular precipitation at high aging temperatures
MC	Cubic	a_0 = 0.430–	TiC	Titanium carbide has some solubility

		0.470	NbC HfC	for nitrogen, zirconium, and molybdenum; composition is variable; appears as globular, irregularly shaped particles that are gray to lavender; “M” elements can be titanium, tantalum, niobium, hafnium, thorium, or zirconium
$M_{23}C_6$	fcc	a_0 = 1.050–1.070 (varies with composition)	$Cr_{23}C_6$ $(Cr,Fe,W,Mo)_{23}C_6$	Form of precipitation is important; it can precipitate as films, globules, platelets, lamellae, and cells; usually forms at grain boundaries; “M” element is usually chromium, but nickel-cobalt, iron, molybdenum, and tungsten can substitute.
M_6C	fcc	a_0 = 1.085–1.175	Fe_3Mo_3C Fe_3W_3C-Fe_4W_2C Fe_3Nb_3C-Nb_3CO_3C Ta_3Co_3C-Cr_7C_3	Randomly distributed carbide; may appear pinkish; “M” elements are generally molybdenum or tungsten; there is some solubility for chromium, nickel-niobium, tantalum, and cobalt.
M_7C_3	Hexagonal	a_0 = 1.398 c_0 = 0.4523	Cr_7C_3	Generally observed as a blocky intergranular shape; observed only in alloys such as Nimonic 80A after exposure above 1000 °C (1830 °F) and in some cobalt-base alloys
M_3B_2	Tetragonal	a_0 = 0.560–0.620 c_0 = 0.300–0.330	Ta_3B_2 V_3B_2-Nb_3B_2 $(Mo,Ti,Cr,Ni,Fe)_3B_2$ Mo_2FeB_2	Observed in iron-nickel- and nickel-base alloys with approx. 0.03% B or greater; borides appear similar to carbides but are not attacked by preferential carbide etchants; “M” elements can be molybdenum, tantalum, niobium, nickel, iron, or vanadium.
MN	Cubic	a_0 = 0.4240	TiN (Ti,Nb,Zr)N (Ti,Nb,Zr)(C,N) ZrN NbN	Nitrides are observed in alloys containing titanium, niobium, or zirconium; they are insoluble at temperatures below the melting point; easily recognized as-polished, having square to rectangular shapes and ranging from yellow to orange
μ	Rhombohedral	a_0 = 0.0475 c_0 = 2.577	Co_7W_6 $(Fe,Co)_7(Mo,W)_6$	Generally observed in alloys with high levels of molybdenum or tungsten; appears as coarse, irregular Widmanstätten platelets; forms at high temperatures
Laves	Hexagonal	a_0 = 0.475–0.495 c_0 = 0.770–0.815	Fe_2Nb Fe_2Ti Fe_2Mo Co_2Ta	Most common in iron- and cobalt-base superalloys; usually appears as irregularly shaped globules, often elongated, or as platelets after extended high-temperature exposure

				Co_2Ti	
σ	Tetragonal	a_0 = 0.880–0.910		FeCr	Most often observed in iron- and cobalt-base superalloys, less commonly in nickel-base alloys; appears as irregularly shaped globules, often elongated; forms after extended exposure between 540 and 980 °C (1005 to 1795 °F)
				FeCrMo	
		c_0 = 0.450–0.480		CrFeMoNi	
				CrCo	
				CrNiMo	

Note: For more information on this subject, see the article “Crystal Structure” in this Volume.
(a) fcc, face-centered cubic; hcp, hexagonal close-packed; bct, body-centered tetragonal.
(b) 1 nm = 10Å

Gamma prime, a geometrically close-packed phase, has an ordered face-centered cubic $L1_2$ crystal structure and is Ni_3Al or $Ni_3(Al,Ti)$, although considerable elemental substitution occurs. For example, cobalt and chromium will replace some of the nickel, and titanium will replace part of the aluminum. Iron can replace nickel or aluminum. The lattice parameters of γ and γ′ are similar, resulting in coherency, which accounts for the value of γ′ as the principal strengthening agent in Fe-Ni-Cr- and nickel-base superalloys.

Gamma prime is spherical in Fe-Ni-Cr-base alloys and in some of the older nickel-base alloys, such as Nimonic 80A and Waspaloy. In the more recently developed nickel-base alloys, γ′ is generally cuboidal. Experiments have shown that variations in molybdenum content and in the aluminum/titanium ratio can change the morphology of γ′. With increasing γ/γ′ mismatch, the shape changes in the following order: spherical, globular, blocky, cuboidal (Ref 58). When the γ/γ′ lattice mismatch is high, extended exposure above 700 °C (1290 °F) causes undesirable η (Ni_3Ti) or δ (Ni_3Nb) phases to form.

The volume fraction, size, and distribution of γ′ are important parameters for control of properties. The volume fraction of γ′ increases with the addition of aluminum and titanium, but the amounts of each must be carefully controlled. Gamma prime contents above approximately 45% render the alloy difficult to deform by hot or cold working. This is not a restriction, of course, in cast alloys, where the γ′ content can reach 70%. In the Fe-Ni-Cr-base alloys, the volume fraction of γ′ phase is less than 20%, and it is usually spherical. Optimal strength results when γ′ is in the size range of 0.01 to 0.05 μm, much too small to be seen using the light optical microscope. If the aluminum/titanium ratio is equal to or greater than 1, extended high-temperature exposure results in replacement of γ′ by Ni_2AlTi, NiAl, or Ni(Al,Ti). These phases overage rapidly at moderately high temperatures, forming massive platelike precipitates.

Alloys with γ′ contents below 20%, such as Nimonic 80A, are heat treated using a simple two-step process of solution annealing and aging. The solution anneal recrystallizes the austenitic matrix and dissolves any γ′ and $M_{23}C_6$ carbides present. Aging precipitates γ′ uniformly throughout the matrix and precipitates $M_{23}C_6$ carbides at grain and twin boundaries. Alloys with γ′ contents of approximately 30%, such as Waspaloy or Udimet 500, are solution treated and then given two aging treatments. Alloys with 40 to 45% γ′, such as Udimet 700, are solution treated and then given three aging treatments.

Positive identification of γ′ is usually performed by x-ray diffraction of the residue of bulk extractions or by electron diffraction using extraction replicas. Some of the electrolytes that selectively attack γ′ can be quite useful, because the γ′ will be recessed below the matrix, and the other second phases will be in relief or plane with the surface, depending on the preparation procedure.

Gamma double prime has an ordered body-centered tetragonal (bct) DO_{22} crystal structure with an Ni_3Nb composition and is found in iron-nickel-base alloys containing niobium. It gained prominence as the strengthening phase with the introduction of Inconel 718 (Ref 59). Early studies of the strengthening mechanism produced conflicting results until the precise details of γ″-phase formation, composition, crystallography, and stability were determined (Ref 60, 61, 62, 63, 64, 65).

Gamma double prime has a disk-shaped morphology and precipitates with a well-defined relationship to the austenite matrix: $[001]_{\gamma''} \parallel \langle 001 \rangle_{\gamma}$ and $\{100\}_{\gamma''} \parallel \{100\}_{\gamma}$. Strengthening is due to the coherency strains produced by the low degree of γ/γ″ lattice mismatch. Although γ″ and γ′ are present in Inconel 718 after aging, the amount of γ′ is much less, and γ″ is the primary strengthening agent. Other alloys strengthened by γ″ include Inconel 706 and Udimet 630.

Because γ″ is not a stable phase, application of alloys such as Inconel 718 is restricted to below 700 °C (1290 °F). Above this temperature, extended exposure produces a loss of strength due to rapid coarsening of γ″, solutioning of γ″ and γ′, and formation of the stable orthorhombic form of Ni_3Nb, which has an acicular, platelike shape.

Positive identification of bct γ″ is more difficult than γ′, because x-ray diffraction of bulk extraction residues will not detect γ″. The failure to detect bct γ″ is attributed to line broadening due to the very fine particle size that obscures the peaks of interest (Ref 62). Electron diffraction will, however, detect the superlattice lines of bct γ″. Bright-field TEM examination is unsatisfactory for resolving γ″, due to the high density of the precipitates and the strong contrast from the coherency strain field around the precipitates. However, dark-field TEM examination provides excellent imaging of the γ″ by selective imaging of precipitates that produce specific superlattice reflections (Ref 62). In addition, γ″ can be separated from γ′ using the dark-field mode, because the γ″ dark-field image is substantially brighter than that of γ′ (Ref 62).

Eta phase has a hexagonal DO_{24} crystal structure with a Ni_3Ti composition. Eta can form in Fe-Ni-Cr-, nickel-, and cobalt-base superalloys, especially in grades with high titanium/aluminum ratios that have had extended high-temperature exposure. Eta phase has no solubility for other elements and will grow more rapidly and form larger particles than γ′, although it precipitates slowly. Coarse η can be observed using the light optical microscope.

Two forms of η may be encountered. The first develops at grain boundaries as a cellular constituent similar to pearlite, with alternate lamellae of γ and η; the second develops intragranularly as platelets with a Widmanstätten pattern (Ref 66, Ref 67, 68). The cellular form is detrimental to notched stress-rupture strength and creep ductility, and the Widmanstätten pattern impairs stress-rupture strength but not ductility. Eta phase is relatively easy to identify, due to its characteristic appearance. Most of the general-purpose reagents will reveal η, as will x-ray diffraction of bulk-extracted residues.

Carbides, which are important constituents, are present in all the cast and wrought heat-resistant alloys. Four basic types are encountered: MC, $M_{23}C_6$, M_6C, and M_7C_3 (where “M” represents one or more metallic elements). Carbides in these alloys serve three principal functions. First, grain-boundary carbides, when properly formed, strengthen the grain boundary, prevent or retard grain-boundary sliding, and permit stress relaxation. Second, if fine carbides are precipitated in the matrix, strengthening results. This is important in cobalt-base alloys that cannot be strengthened by γ′. Third, carbides can tie up certain elements that would otherwise promote phase instability during service. Carbide precipitation in nickel-base alloys has a stronger tendency to form at grain boundaries than in Fe-Ni-Cr- or cobalt-base alloys. Although grain-boundary carbides, depending on their morphology, can degrade properties, reducing carbon content to low levels substantially reduces creep life and ductility in nickel-base alloys.

Aging of Fe-Ni-Cr- and nickel-base superalloys causes $M_{23}C_6$ to form at the grain boundaries. The optimal situation is a chain of discrete globular $M_{23}C_6$ particles at the grain boundaries. This form benefits creep-rupture life. However, if the carbides precipitate as a continuous grain-boundary film, properties will be seriously degraded. It is not uncommon to observe zones around the grain boundaries that are devoid of γ′. Such precipitate-free zones can significantly influence stress-rupture life, depending on the width of the zones (Ref 69).

In these alloys, the MC-type carbide is most frequently titanium carbide; other types, such as niobium carbide, tantalum carbide, or hafnium carbide, are less common. Titanium carbide has some solubility for other elements, such as nitrogen, zirconium, and molybdenum. They are large, globular particles observable on the as-polished surface, particularly if some relief is introduced during final polishing. Metal carbides usually are irregular in shape or cubic. They can be preferentially colored by certain etchants.

The most important carbide in superalloys is $M_{23}C_6$, because it forms at the grain boundaries during aging and, when properly formed, increases the strength of the grain boundaries to balance the matrix strength. Although chromium is the primary “M” element, other metallic elements, such as nickel, cobalt, iron, molybdenum, and tungsten, can substitute for it. The discrete globular form is the most desirable morphology; films, platelets, lamellae, and cells have also been observed.

The M_6C carbide is generally rich in molybdenum or tungsten, but other elements, such as chromium, nickel, or cobalt, may substitute for it to some degree. It is the most commonly observed carbide in the cobalt-base superalloys and in nickel-base alloys with high molybdenum and/or tungsten contents. In these alloys, M_6C is often observed in the as-cast condition randomly distributed throughout the matrix. In wrought alloys, it will

usually be dissolved during heating before hot working. It may precipitate at the grain boundaries in a blocky form or intragranularly in a Widmanstätten pattern and can be preferentially stained by certain etchants.

The Cr_7C_3 carbide is likely to appear in the higher-carbon Fe-Cr-Ni cast alloys as spinelike crystals of roughly hexagonal cross section, frequently with a hole in the center. It can be easily stained with Murakami's reagent. In the alloys with 0.20 to 0.75% C, the Cr_7C_3 carbide is likely to be the eutectic carbide. Although M_7C_3 is not widely observed in wrought superalloys, it is present in some cobalt-base alloys and in Nimonic 80A, a Ni-Cr-Ti-Al superalloy, when heated above 1000 °C (1830 °F). Additions of such elements as cobalt, molybdenum, tungsten, or niobium to nickel-base alloys prevent formation of M_7C_3. Massive Cr_7C_3 is formed in Nimonic 80A in the grain boundaries after heating to 1080 °C (1975 °F). Subsequent aging at 700 °C (1290 °F) to precipitate γ′ impedes precipitation of $M_{23}C_6$ due to the previously formed Cr_7C_3, which generally exhibits a blocky shape when present at grain boundaries.

Borides. Boron is added in small amounts to many heat-resistant alloys to improve stress-rupture and creep properties or to retard formation of η phase, which would impair creep strength. Boron retards formation of the cellular grain-boundary form of η but has no influence on the intragranular Widmanstätten η. Consequently, boron influences grain-boundary structures. Boron also reduces the solubility of carbon in austenite, which increases precipitation of finer-sized MC and $M_{23}C_6$ carbides. If the boron addition is sufficiently high, detrimental borides will form. Borides are hard and brittle and precipitate at the grain boundaries. Borides are generally of M_3B_2 composition with a tetragonal structure (Ref 70). Molybdenum, tantalum, niobium, nickel, iron, or vanadium can be “M” elements. The identification of borides in Udimet 700 has been documented (Ref 70).

Laves phase, a tcp phase, has a $MgZn_2$ hexagonal crystal structure with a composition of the AB_2 type. Typical examples include Fe_2Ti, Fe_2Nb, and Fe_2Mo, but a more general formula is $(Fe,Cr,Mn,Si)_2(Mo,Ti,Nb)$. They are most commonly observed in the iron-nickel-base alloys as coarse intergranular particles; intragranular precipitation may also occur. Silicon and niobium promote formation of Laves phase in alloy 718. Excessive amounts will impair room-temperature tensile ductility; creep properties are not significantly affected. Laves phases have been observed in certain cobalt-base alloys and have been identified as Co_2W, Co_2Ti, or Co_2Ta.

Sigma phase is a tetragonal intermetallic tcp phase that forms with a wide range of compositions. Sigma is a hard, brittle compound usually formed from ferrite (but sometimes directly from austenite) between approximately 650 °C (1200 °F) and slightly above 870 °C (1600 °F). It develops most rapidly near 870 °C (1600 °F). The classic sigma-phase compound has an approximate FeCr composition, but in the alloys discussed in this article, it has a more complex, variable composition. The addition of silicon promotes the formation of σ, and a ternary composition of 43Fe43Cr-14Si (at.%) has been suggested. Because σ imparts ambient-temperature brittleness and a loss of creep-rupture strength, its presence is generally undesirable. Various morphologies may be encountered, some of which are quite detrimental to properties. However, the presence of σ in superalloys is not necessarily damaging to properties. Sigma, in the form of plate precipitation, can improve creep properties.

Considerable effort has been devoted to determining how composition influences σ-phase formation, particularly in nickel-base superalloys. Reference 71, 72e 73, 74, and 75 present examples of the many studies that have been conducted. This work has substantially influenced alloy development.

Sigma can be preferentially attacked or stained by a number of reagents. However, because of the wide range of alloy compositions that may contain σ and the variable nature of its composition, positive identification by etching is not always possible. X-ray diffraction of bulk extraction residues is a more reliable technique. Etching procedures are best applied when they can be tested for response on specimens of the alloy known to contain σ phase.

Mu phase is a rhombohedral (triagonal) intermetallic tcp phase with a W_6Fe_7 structure (Ref 76). In general, it has little influence on properties. Mu precipitates as coarse, irregularly shaped platelets in a Widmanstätten pattern. A general formula for μ is $(Fe,Co)_7(Mo,W)_6$. Nickel can substitute for part of the iron or the cobalt.

Nitrides are commonly observed in heat-resistant alloys containing titanium or niobium as titanium nitride (most common) or niobium nitride. Nitrides are not influenced by heat treatment and are insoluble to the melting point. Nitrides are easily identified in the as-polished condition or after etching due to their regular, angular shapes and distinct yellow-to-orange color. Nitrides are quite hard and will appear in relief after polishing. They have some solubility for carbon and may be referred to as Ti(C,N), Nb(C,N), and so on. They should not be confused with carbonitrides, which are much richer in carbon and lower in nitrogen. Nitrides, often duplex, include an embedded phase or a surrounding film; this second phase is generally a darker colored

nitride containing considerable carbon. The usual amounts present in superalloys generally have little influence on properties.

The acicular constituent that occurs near creep fractures in cast Fe-Ni-Cr alloys is likely to be chromium nitride, which originates by diffusion of nitrogen from the atmosphere. The acicular pattern is the result of precipitation on crystallographic planes. However, nitrides are not always acicular, and acicular platelets are not necessarily nitrides; σ phase, and even carbides, can exhibit an acicular pattern. A frequently encountered lamellar constituent that resembles pearlite has been identified as an aggregate of austenite with carbonitrides, chromium nitride, or chromium carbide. Etching in Murakami's reagent at room temperature for approximately 10 s will stain the carbide but not the nitrides or carbonitrides.

Chi phase may be encountered in Fe-Cr-Ni heat-resistant casting alloys containing molybdenum. Chi phase has a composition similar to that of σ phase, coexists with σ (Ref 8), and is hard and brittle. Ternary diagrams have been developed at 815 and 900 °C (1500 and 1650 °F) for the Fe-Cr-Mo system that identify χ phase as containing approximately 18% Cr, 28% Mo, and 54% Fe by weight, approximating Fe_3CrMo. Chi phase can be revealed with a brief etch in Vilella's reagent, followed by electrolytic etching in concentrated NaOH at 1.5 V. Chi phase is first stained light brown, but after approximately 10 s, it develops a blue-gray tint, distinguishing it from sigma phase, which etched brown.

Other Phases. A few other phases are less frequently observed in wrought heat-resistant alloys. For example, a few cobalt-base alloys have been developed that attain some degree of strengthening by precipitation of intermetallic phases, such as CoAl, Co_3Mo, or Co_3Ti. In alloys similar to A-286, G phase (Ni_{18} Ti_8Si_6) has been observed (Ref 77, 78). This phase has a globular shape and precipitates in grain boundaries. It is detrimental to stress-rupture life. A chromium-iron niobide, Z phase, has been observed in an Fe-18Cr12Ni-1Nb alloy after creep testing at 850 °C (1560 °F) (Ref 79). Inclusions, some of which are similar to those found in steels, can also be found in these alloys. However, in the nickel-base alloys, titanium sulfides may be observed. Oxides, such as Al_2O_3 or magnesia, may also be present. Oxides and sulfides may be observed at the surface of components due to environmental effects. Coatings are also used on some alloys, and their microstructures may be of interest (Ref 80, 81).

References cited in this section

8. E.J. Dulis and G.V. Smith, Identification and Mode of Formation and Re-Solution of Sigma Phase in Austenitic Chromium-Nickel Steels, *Symposium on the Nature, Occurrence and Effects of Sigma Phase,* STP 110, ASTM, 1951

58. W.T. Loomis et al., The Influence of Molybdenum on the γ′ Phase in Experimental Nickel-Base Superalloys, *Met. Trans.,* Vol 3, April 1972, p 989–1000

59. J.F. Barker, A Superalloy for Medium Temperatures, *Met. Prog.,* Vol 81, May 1962, p 72–76

60. I. Kirman and D.K. Warrington, Identification of the Strengthening Phase in Fe-Ni-Cr-Nb Alloys, *J. Iron Steel Inst.,* Vol 205, Dec 1967, p 1264–1265

61. P.S. Kotval, Identification of the Strengthening Phase in “Inconel” Alloy 718, *Trans. AIME,* Vol 242, Aug 1968, p 1764–1765

62. D.F. Paulonis et al., Precipitation in Nickel-Base Alloy 718, *Trans. ASM,* Vol 62, 1969, p 611–622

63. W.J. Boesch and H.B. Canada, Precipitation Reactions and Stability of Ni_3Cb in Inconel Alloy 718, *J. Met.,* Vol 21, Oct 1969, p 34–38

64. I. Kirman and D.H. Warrington, The Precipitation of Ni_3Nb Phases in a Ni-Fe-Cr-Nb Alloy, *Met. Trans.,* Vol 1, Oct 1970, p 2667–2675

65. R. Cozar and A. Pineau, Morphology of γ′ and γ″ Precipitates and Thermal Stability of Inconel 718 Type Alloys, *Met. Trans.,* Vol 4, Jan 1973, p 47–59

66. J.R. Mihalisin and R.T. Decker, Phase Transformations in Nickel-Rich Nickel-Titanium-Aluminum Alloys, *Trans. AIME,* Vol 218, June 1960, p 507–515

67. B.R. Clark and F.B. Pickering, Precipitation Effects in Austenitic Stainless Steels Containing Titanium and Aluminum Additions, *J. Iron Steel Inst.,* Vol 205, Jan 1967, p 70–84

68. L.K. Singhal and J.W. Martin, Precipitation Processes in an Austenitic Stainless Steel Containing Titanium, *J. Iron Steel Inst.,* Vol 205, Sept 1967, p 947–952

69. E.L. Raymond, Effect of Grain Boundary Denudation of Gamma Prime on Notch-Rupture Ductility of Inconel Nickel-Chromium Alloys X750 and 718, *Trans. AIME,* Vol 239, Sept 1967, p 1415–1422

70. H.J. Beattie, The Crystal Structure of a M_3B_2 Type Double Boride, *Acta Crystallogr.,* Vol 11, 1958, p 607–609

71. L.R. Woodyatt et al., Prediction of Sigma-Type Phase Occurrence from Compositions in Austenitic Superalloys, *Trans. AIME,* Vol 236, 1966, p 519–527

72. E.O. Hall and S.H. Algie, The Sigma Phase, *Met. Rev.,* Vol 11, 1996, p 61–88

73. J.R. Mihalisin et al., Sigma—Its Occurrence, Effect, and Control in Nickel-Base Superalloys, *Trans. AIME,* Vol 242, Dec 1968, p 2399–2414

74. R.G. Barrows and J.B. Newkirk, A Modified System for Predicting a Formation, *Met. Trans.,* Vol 3, Nov 1972, p 2889–2893

75. E.S. Machlin and J. Shao, SIGMA-SAFE: A Phase Diagram Approach to the Sigma Phase Problem in Ni-Base Superalloys, *Met. Trans. A,* Vol 9, April 1978, p 561–568

76. A. Raman, The μ Phases, *Z. Metallkd.,* Vol 57, April 1966, p 301–305

77. H.J. Beattie and F.L. Ver Snyder, A New Complex Phase in a High-Temperature (Iron-Nickel-Chromium-Molybdenum) Alloy, *Nature,* Vol 178 (No. 4526), 1956, p 208–209

78. H.J. Beattie and W.C. Hagel, Intermetallic Compounds in Titanium-Hardened Alloys, *Trans. AIME,* Vol 209, July 1957, p 911–917

79. K.W. Andrews and H. Hughes, Discussion of Aging Reactions in Certain Superalloys, *Trans. ASM,* Vol 49, 1957, p 999

80. G.F. Slattery, Microstructural Aspects of Aluminized Coatings on Nickel-Base Alloys, *Met. Technol.,* Vol 10, Feb 1983, p 41–51

81. G.W. Goward et al., Formation and Degradation Mechanisms of Aluminide Coatings on Nickel-Base Superalloys, *Trans. ASM,* Vol 60, 1967, p 228–241

G.F. Vander Voort, G.M. Lucas, and E.P. Manilova, Metallography and Microstructures of Heat-Resistant Alloys, *Metallography and Microstructures*, Vol 9, *ASM Handbook*, ASM International, 2004, p. 820–859

Metallography and Microstructures of Heat-Resistant Alloys

George F. Vander Voort and Gabriel M. Lucas, Buehler Ltd.; Elena P. Manilova, Polzunov Central Boiler and Turbine Institute, St. Petersburg, Russia

References

1. G.F. Vander Voort, *Metallography: Principles and Practice,* McGraw-Hill, 1984; reprinted by ASM International, 1999

2. C.E. Smeltzer, Solve Steel "Freckle" Mystery, *Iron Age,* Vol 184, 10 Sept 1959, p 188–189

3. G.C. Gould, Freckle Segregation in Vacuum Consumable-Electrode Ingots, *Trans. AIME,* Vol 233, July 1965, p 1345–1351

4. J. Preston, Segregation in Vacuum-Arc-Melted Alloy Steel Ingots, *Int. Trans. Vacuum Metallurgy Conf. 1967,* American Vacuum Society, 1968, p 569–588

5. R.C. Buehl and J.K. McCauley, Processing Improvement in Vacuum-Arc Remelting of Ingots, *Int. Trans. Vacuum Metallurgy Conf. 1967,* American Vacuum Society, 1968, p 695–709

6. A.F. Giamei and B.H. Kear, On the Nature of Freckles in Nickel Base Superalloys, *Met. Trans.,* Vol 1, Aug 1970, p 2185–2192

7. R. Schlatter, Electrical and Magnetic Interactions in Vacuum-Arc Remelting and Their Effect on the Metallurgical Quality of Specialty Steels, *J. Vac. Sci. Technol.,* Vol 11, Nov/Dec 1974, p 1047–1054

8. E.J. Dulis and G.V. Smith, Identification and Mode of Formation and Re-Solution of Sigma Phase in Austenitic Chromium-Nickel Steels, *Symposium on the Nature, Occurrence and Effects of Sigma Phase,* STP 110, ASTM, 1951

9. G. Petzow, *Metallographic Etching,* 2nd ed., ASM International, 1999

10. C.H. Lund and H.J. Wagner, "Identification of Microconstituents in Superalloys," DMIC Memorandum 160, Battelle Memorial Institute, Columbus, OH, 15 Nov 1962

11. H.J. Beattie and F.L. Ver Snyder, Microconstituents in High Temperature Alloys, *Trans. ASM,* Vol 45, 1953, p 397–428

12. J.W. Weeton and R.A. Signorelli, Effect of Heat Treatment upon Microstructures, Microconstituents, and Hardness of Wrought Cobalt Base Alloy, *Trans. ASM,* Vol 47, 1955, p 815–852

13. H. Meisel et al., Metallographic Development of the Structure of Nickel Based Alloys, *Pract. Metallogr.,* Vol 17, 1980, p 261–272

14. F.R. Morral, Metallography of Cobalt-Base and Cobalt-Containing Alloys, *Pract. Metallogr.,* Vol 10, 1973, p 398–413

15. E. Kohlhaas and A. Fischer, The Metallography of Superalloys, *Pract. Metallogr.,* Vol 8, Jan 1971, p 3–25

16. W.C. Bigelow et al., Electron Microscopic Identification of the γ′ Phase of Nickel-Base Alloys, *Proc. ASTM,* Vol 56, 1956, p 945–953

17. L. Bartosiewicz, Preferential Electrolytic Etching Technique to Reveal the γ′ Phase in Nickel Base Alloys, *Pract. Metallogr.,* Vol 10, 1973, p 450–461

18. P.K. Footner and B.P. Richards, A Rapid Method for Measurement of γ′ Size Distribution in Nickel-Base Superalloys, *Pract. Metallogr.,* Vol 17, 1980, p 489–496

19. C.P. Sullivan, The Metallographic Identification of Borides in Udimet 700, *Trans. ASM,* Vol 58, 1965, p 702–705

20. H.S. Avery, V.O. Homerberg, and E. Cook, Metallographic Identification of Ferro Magnetic Phases, *Met. Alloys,* Vol 10, 1939, p 353–355

21. H.S. Avery, "Cast Heat-Resistant Alloys for High-Temperature Weldments," Bulletin 143, Welding Research Council, Aug 1969

22. A New Way to Reveal Magnetic Domains at High Magnifications, *Met. Prog.,* Vol 100, Dec 1971, p 82

23. W.C. Elmore, Ferromagnetic Colloid for Studying Magnetic Structures, *Phys. Rev.,* Vol 54, 1938, p 309–310

24. Gray, "Revealing Ferromagnetic Microstructures with Ferrofluid," Report RNL-TM-3681, Oak Ridge National Laboratory, March 1972

25. G.N. Maniar and A. Szirmae, Ed., *Manual on Electron Metallography Techniques,* STP 547, ASTM, 1973

26. I.S. Brammar and M.A.P. Dewey, *Specimen Preparation for Electron Metallography,* Blackwell Scientific, 1966

27. G. Thomas, *Transmission Electron Microscopy of Metals,* John Wiley & Sons, 1964

28. J.R. Mihalisin, The Selective Identification of Constituents in Nimonic 80 by Extraction-Replica Technique, *Trans. AIME,* Vol 212, June 1958, p 349–350

29. E. Kohlhaas and A. Fischer, The Use of the Carbon-Extraction Technique in Investigations of Superalloys, *Pract. Metallogr.,* Vol 6, 1969, p 291–298

30. R.J. Seher and G.N. Maniar, Analytical Preshadowed Extraction Replica Technique, *Metallography,* Vol 5, 1972, p 409–414

31. W.L. Mankins, Chromic Acid as an Electrolytic Etchant and Electrolyte for the Extraction of γ′ in Nickel-Base Superalloys, *Metallography,* Vol 9, 1976, p 227–232

32. A.J. Portner and B. Ralph, A Technique for the Replication of γ′ in Nickel-Base Superalloys, *Pract. Metallogr.,* Vol 16, 1979, p 592–601

33. K.C. Thompson-Russell and J.W. Edington, Electron Microscope Specimen Preparation Techniques in Materials Science, Part 5, *Practical Electron Microscopy in Materials Science,* Philips Electronic Instruments, 1977

34. L. Bartosiewicz, Improved Techniques of Thin Foil Preparation of Ni Base Alloys for Electron Microscopy, *Pract. Metallogr.,* Vol 9, 1972, p 525–534

35. C. Hays and D.A. Nail, Transmission Electron Microscopy of Incoloy Alloy 901, *Metallography,* Vol 7, 1974, p 59–68

36. R.E. Schafrik and M. Henry, Transmission Electron Microscopy Foil Preparation and Results for Incoloy 901, *Metallography,* Vol 13, 1980, p 157–165

37. T.P. Hoar and K.W.J. Bowen, The Electrolytic Separation and Some Properties of Austenite and Sigma in 18-8-3-1 Chromium-Nickel Molybdenum-Titanium Steel, *Trans. ASM,* Vol 45, 1953, p 443–474

38. J.F. Brown et al., The Extraction of Minor Phases from Austenitic Steel, *Metallurgia,* Vol 56, Nov 1957, p 215–223

39. K.W. Andrews and H. Hughes, The Isolation, Separation, and Identification of Microconstituents in Steels, in STP 393, ASTM, 1966, p 3–21

40. O.H. Kriege and C.P. Sullivan, The Separation of Gamma Prime from Udimet 700, *Trans. ASM,* Vol 61, 1968, p 278–282

41. O.H. Kriege and J.M. Baris, The Chemical Partitioning of Elements in Gamma Prime Separated from Precipitation-Hardened, High-Temperature Nickel-Base Alloys, *Trans. ASM,* Vol 62, 1969, p 195–200

42. M.J. Donachie and O.H. Kriege, Phase Extraction and Analysis in Superalloys Summary of Investigations by ASTM Committee E-4 Task Group 1, *J. Mater.,* Vol 7, Sept 1972, p 269–278

43. O.H. Kriege, Phase Separation as a Technique for the Characterization of Superalloys, in STP 557, ASTM, 1974, p 220–234

44. E. Kny, On the Methodology of Phase Extraction in Ni-Base Superalloys, *Pract. Metallogr.,* Vol 13, Nov 1976, p 549–564

45. "Practice for Electrolytic Extraction of Phases from Ni and Ni-Fe Base Superalloys Using a Hydrochloric-Methanol Electrolyte," E 963, *Annual Book of ASTM Standards,* ASTM, 1984

46. C. Razim, Metallography of Heat Resistant and High Temperature Alloys, *Pract. Metallogr.,* Vol 5, May 1968, p 225–241; June 1968, p 299–309

47. G.P. Sabol and R. Stickler, Microstructure of Nickel-Base Superalloys, *Phys. Status Solidi,* Vol 35 (No. 1), 1968, p 11–52

48. P.S. Kotval, The Microstructure of Superalloys, *Metallography,* Vol 1, 1969, p 251–285

49. F.R. Morral et al., Microstructure of Cobalt-Base High-Temperature Alloys, *ASM Met. Eng. Q.,* Vol 9, May 1969, p 1–16

50. J.F. Radavich and W.H. Couts, Metallography of the Superalloys, *Rev. High-Temp. Mater.,* Vol 1, Aug 1971, p 55–96

51. C.P. Sullivan and M.J. Donachie, Some Effects of Microstructure on the Mechanical Properties of Nickel-Base Superalloys, *ASM Met. Eng. Q.*, Vol 7, Feb 1967, p 36–45

52. R.F. Decker, Strengthening Mechanisms in Nickel-Base Superalloys, *Symposium: Steel-Strengthening Mechanisms,* 5–6 May 1969 (Zurich), 1970, p 147–170

53. C.T. Sims and W.C. Hagel, Ed., *The Superalloys,* John Wiley & Sons, 1972

54. C.P. Sullivan et al., Relationship of Properties to Microstructure in Cobalt-Base Superalloys, *ASM Met. Eng. Q.*, Vol 9, May 1969, p 16–29

55. C.P. Sullivan and M.J. Donachie, Microstructures and Mechanical Properties of Iron-Base (-Containing) Superalloys, *ASM Met. Eng. Q.*, Vol 11, Nov 1971, p 1–11

56. D.R. Muzyka, Controlling Microstructure and Properties of Superalloys via Use of Precipitated Phases, *ASM Met. Eng. Q.*, Vol 11, Nov 1971, p 12–20

57. D.R. Muzyka and G.N. Maniar, Microstructure Approach to Property Optimization in Wrought Superalloys, in STP 557, ASTM, 1974, p 198–219

58. W.T. Loomis et al., The Influence of Molybdenum on the γ' Phase in Experimental Nickel-Base Superalloys, *Met. Trans.*, Vol 3, April 1972, p 989–1000

59. J.F. Barker, A Superalloy for Medium Temperatures, *Met. Prog.*, Vol 81, May 1962, p 72–76

60. I. Kirman and D.K. Warrington, Identification of the Strengthening Phase in Fe-Ni-Cr-Nb Alloys, *J. Iron Steel Inst.*, Vol 205, Dec 1967, p 1264–1265

61. P.S. Kotval, Identification of the Strengthening Phase in "Inconel" Alloy 718, *Trans. AIME,* Vol 242, Aug 1968, p 1764–1765

62. D.F. Paulonis et al., Precipitation in Nickel-Base Alloy 718, *Trans. ASM,* Vol 62, 1969, p 611–622

63. W.J. Boesch and H.B. Canada, Precipitation Reactions and Stability of Ni_3Cb in Inconel Alloy 718, *J. Met.*, Vol 21, Oct 1969, p 34–38

64. I. Kirman and D.H. Warrington, The Precipitation of Ni_3Nb Phases in a Ni-Fe-Cr-Nb Alloy, *Met. Trans.*, Vol 1, Oct 1970, p 2667–2675

65. R. Cozar and A. Pineau, Morphology of γ' and γ'' Precipitates and Thermal Stability of Inconel 718 Type Alloys, *Met. Trans.*, Vol 4, Jan 1973, p 47–59

66. J.R. Mihalisin and R.T. Decker, Phase Transformations in Nickel-Rich Nickel-Titanium-Aluminum Alloys, *Trans. AIME,* Vol 218, June 1960, p 507–515

67. B.R. Clark and F.B. Pickering, Precipitation Effects in Austenitic Stainless Steels Containing Titanium and Aluminum Additions, *J. Iron Steel Inst.*, Vol 205, Jan 1967, p 70–84

68. L.K. Singhal and J.W. Martin, Precipitation Processes in an Austenitic Stainless Steel Containing Titanium, *J. Iron Steel Inst.*, Vol 205, Sept 1967, p 947–952

69. E.L. Raymond, Effect of Grain Boundary Denudation of Gamma Prime on Notch-Rupture Ductility of Inconel Nickel-Chromium Alloys X750 and 718, *Trans. AIME,* Vol 239, Sept 1967, p 1415–1422

70. H.J. Beattie, The Crystal Structure of a M_3B_2 Type Double Boride, *Acta Crystallogr.,* Vol 11, 1958, p 607–609

71. L.R. Woodyatt et al., Prediction of Sigma-Type Phase Occurrence from Compositions in Austenitic Superalloys, *Trans. AIME,* Vol 236, 1966, p 519–527

72. E.O. Hall and S.H. Algie, The Sigma Phase, *Met. Rev.,* Vol 11, 1996, p 61–88

73. J.R. Mihalisin et al., Sigma—Its Occurrence, Effect, and Control in Nickel-Base Superalloys, *Trans. AIME,* Vol 242, Dec 1968, p 2399–2414

74. R.G. Barrows and J.B. Newkirk, A Modified System for Predicting a Formation, *Met. Trans.,* Vol 3, Nov 1972, p 2889–2893

75. E.S. Machlin and J. Shao, SIGMA-SAFE: A Phase Diagram Approach to the Sigma Phase Problem in Ni-Base Superalloys, *Met. Trans. A,* Vol 9, April 1978, p 561–568

76. A. Raman, The μ Phases, *Z. Metallkd.,* Vol 57, April 1966, p 301–305

77. H.J. Beattie and F.L. Ver Snyder, A New Complex Phase in a High-Temperature (Iron-Nickel-Chromium-Molybdenum) Alloy, *Nature,* Vol 178 (No. 4526), 1956, p 208–209

78. H.J. Beattie and W.C. Hagel, Intermetallic Compounds in Titanium-Hardened Alloys, *Trans. AIME,* Vol 209, July 1957, p 911–917

79. K.W. Andrews and H. Hughes, Discussion of Aging Reactions in Certain Superalloys, *Trans. ASM,* Vol 49, 1957, p 999

80. G.F. Slattery, Microstructural Aspects of Aluminized Coatings on Nickel-Base Alloys, *Met. Technol.,* Vol 10, Feb 1983, p 41–51

81. G.W. Goward et al., Formation and Degradation Mechanisms of Aluminide Coatings on Nickel-Base Superalloys, *Trans. ASM,* Vol 60, 1967, p 228–241

E. van der Lingen, L. Cornish, S. Taylor, R. Süss, S. Grice, Metallography and Microstructures of Precious Metals and Precious Metal Alloys, *Metallography and Microstructures,* Vol 9, *ASM Handbook,* ASM International, 2004, p. 860–876

Metallography and Microstructures of Precious Metals and Precious Metal Alloys

Elma van der Lingen, Lesley Cornish, Stefanie Taylor, Rainer Süss, Physical Metallurgy Division, Mintek, South Africa; Stewart Grice, Hoover & Strong Inc.

Introduction

THE PRECIOUS METALS include the six platinum-group metals (platinum, palladium, rhodium, ruthenium, iridium, and osmium) as well as gold and silver. These elements share properties such as inert softness, crystal

structure, relatively high density, and good corrosion resistance, which directly influence their metallographic preparation. The crystal structure of both ruthenium and osmium is hexagonal close-packed (hcp), whereas the other precious metals have a face-centered cubic (fcc) structure. The hcp structure of ruthenium and osmium makes it possible to use polarized light for metallographic investigations. The fcc structure is generally relatively soft, and Vickers hardness values are under 50 for fine platinum, palladium, gold, and silver in the annealed condition. All the precious metals are relatively dense, with values varying between 10.5 g/cm^3 (0.379 lb/in.^{3}) for silver to 22.65 g/cm^3 (0.818 lb/in.^{3}) for iridium.

Precious metals are known primarily for their use in money and jewelry. However, they also have industrial applications, including catalysis, high-temperature applications, electrical contacts, electronics, corrosion resistance, and dental and medical uses.

E. van der Lingen, L. Cornish, S. Taylor, R. Süss, S. Grice, Metallography and Microstructures of Precious Metals and Precious Metal Alloys, *Metallography and Microstructures,* Vol 9, *ASM Handbook,* ASM International, 2004, p. 860–876

Metallography and Microstructures of Precious Metals and Precious Metal Alloys

Elma van der Lingen, Lesley Cornish, Stefanie Taylor, Rainer Süss, Physical Metallurgy Division, Mintek, South Africa; Stewart Grice, Hoover & Strong Inc.

Specimen Preparation

Due to the high cost of material, precious metals samples for metallographic investigations are usually small, which makes mounting of specimens exacting. The following steps are generally followed for preparing good metallographic samples (Ref 1, 2).

Cutting. Precious metals should be cut with sharp cutting tools. When cutting wheels are used, adequate coolant is required to prevent structural changes and smearing (Ref 1).

Mounting. Thermosetting epoxy resin is the main medium employed for mounting of precious metals. Precious metals are often used as coatings. To prevent damage to the coating during polishing, plating of specimens before mounting is recommended. Copper, nickel, or rhodium are most often used for plating (Ref 3). Lubricants for mount releasing should be omitted, because fine cracks form between the specimen and the mount, resulting in subsequent polishing and etching problems (Ref 2).

Grinding. Coarse grinding on 80- and 120-grit SiC paper is recommended to remove the deformation layer formed during sectioning. A specimen that has not been subjected to cutting can be ground on a succession of 240- to 2400-grit SiC paper. Moderate pressure is employed, with running water as a lubricant. Samples can be rinsed, but a short cycle of ultrasonic cleaning is recommended to remove any impurities after each paper. Ultrasonic cleaning should be limited to less than 30 s to avoid cavitation (Ref 2).

Polishing. Coarse polishing should be done with a napless cotton cloth with 6 μm polycrystalline diamond, odorless kerosene, or diamond extender lubricant and moderate pressure.

Fine polishing should be carried out using a short-napped synthetic velvet cloth with 1 μm polycrystalline diamond and deionized water lubricant, using moderate to light pressure. After polishing, the sample can be cleaned ultrasonically in detergent and rinsed with methanol to aid water evaporation and to minimize watermarks on the polished microsections, then air dried.

Because of the hardness range of precious metals, the polishing time varies from material to material. Microscopic investigation between polishing steps is recommended to determine when scratches from the previous step have been removed and to avoid overpolishing (Ref 2).

Etchants. The four etching techniques that are often used for precious metals include immersion, swab, etch polishing, and electrolytic etching. Due to the extreme corrosion resistance of precious metals, the etchants used are very corrosive and can be hazardous. In many cases, etchants need to be heated, which further increases the risks. The hazards of working with the relevant chemicals should be well understood, and appropriate safety precautions should be followed. For example, all etching should be conducted under a properly operating chemical fume hood, and inhalation of fumes from etchants should be avoided. Appropriate safety equipment,

such as an acid-protective apron, gloves, and face shield or goggles, should be used. Disposal of the spent etchant must be in accordance with local legal requirements (Ref 2).
A list of etchants for precious metals and their alloys is given in Table 1 (Ref 1, 2, 4).

Table 1 Etching reagents for precious metals

Precious metal or alloy	Etchant composition and use[(a)]	Method
100 Au **Au alloys (e.g., 60Au-40Pd, 75Au-12Ag-13Cu)**	Part A: 5% KCN (potassium cyanide) Part B: 5% $(NH_4)_2S_2O_8$ (ammonium persulfate)	Mix fresh, part A:B (1:1) Immersion: 1–5 min
Au alloys (>75 Au)	30 g KI (potassium iodide) 15 g I (iodide sublimed) 30 mL deionized water	Dilute stock solution 50% with water to use as a chemical polish/etch.
Au alloys (<75 Au)	Part A: 10% NaCN (sodium cyanide) Part B: H_2O_2 30% conc. (hydrogen peroxide)	Mix equal amounts of A and B directly on sample, either from droppers or with swabs. If swabbing, begin swabbing with NaCN, follow by swabbing with H_2O_2, using a clean swab. Reaction will cause foaming. Continue swabbing alternately with NaCN and H_2O_2, using clean swabs, until desired result is achieved (usually less than 1 min). If brown stain appears, it can be removed by swabbing with NaCN.
100 Ag	5 cm^3 NH_4OH (ammonium hydroxide) 25 cm^3 H_2O (deionized water) 25 cm^3 H_2O_2 (hydrogen peroxide)	Swab or etch polish To slow reaction, dilute with H_2O.
100 Ag	1 part (by volume) NH_4OH (conc. ammonium hydroxide) 1 part by volume (3%) H_2O_2 (hydrogen peroxide)	Solution must be prepared fresh each time. May be diluted with water. Recommended for etch-polish technique
100 Pt **Pt alloys (e.g., 90Pt-10Ir, 95Pt-**	100 cm^3 HCl (conc. hydrochloric acid) 10 g NaCl (sodium	Electrolytic: 3–6 V alternating current (ac)

Precious metal or alloy	Etchant composition and use[a]	Method
5Ru, 90Pt-10Rh, 77Pt-23Co, 98Pt-2W)	chloride)	
Pt and Pt alloys	30 mL HCl (conc. hydrochloric acid) 10 mL HNO_3 (nitric acid)	Immerse sample in boiling solution for 10–20 min.
Pt alloys (e.g., 77Pt-23Co)	20 cm^3 HCl (conc. hydrochloric acid) 80 cm^3 H_2O (deionized water) 4 g Fe_3O_2 (ferric oxide)	Electrolytic: 3–6 V ac or direct current (dc)
100 Pd **Pd alloys (e.g., 60Pd-40Cu, 93.5Pd-6.5Ru, 75Pd-25Ag)** **100 Au**	Part A: 10% KCN (potassium cyanide) Part B: 10% $(NH_4)_2S_2O_8$ (ammonium persulfate)	Mix fresh, part A:B (1:1) Immersion: 1–5 min To discard, neutralize with ammonia and flush with copious water.
100 Pd and Pd alloys	60 mL HCl (conc. hydrochloric acid) 40 mL HNO_3 (nitric acid)	Immerse specimen up to 60 s.
100 Ir **Pt/PGM alloys (e.g., 90Pt-10Ir, 95Pt-5Ru)(b)**	75 cm^3 HCl (conc. hydrochloric acid) 75 cm^3 H_2O (deionized water)	Electrolytic: 3 V ac
100 Ir **100 Rh**	1 part HCl (conc. hydrochloric acid) 2 parts H_2O (deionized water)	Electrolytic: 4–7 V ac
100 Ru	9 g NaOH (sodium hydroxide) 2.5 g $KFe(CN)_6$ (potassium ferricyanide) 380 cm^3 H_2O (deionized water)	Electrolytic: 3 V ac or Immersion: 0.5 min to 1 h
100 Ru **100 Rh**	40 cm^3 HCl (conc. hydrochloric acid)	Electrolytic: 3 V ac

Precious metal or alloy	Etchant composition and use[(a)]	Method
Pt-Ru alloys (e.g., 95Pt-5Ru)	60 cm^3 H_2O (deionized water) 20 cm^3 H_2O_2 (hydrogen peroxide)	
100 Os	100 cm^3 HCl (conc. hydrochloric acid) 25 g NaCl (sodium chloride)	Electrolytic: 4 V dc for 2–5 min
100 Ir **100 Pt** **100 Pd and Pd alloys**	90 mL ethanol 10 mL HCl (conc. hydrochloric acid)	Electrolytic: 10 V dc for 30 s
100 Pd **100 Pt**	30 mL H_2O (deionized water) 25 mL HCl (conc. hydrochloric acid) 5 mL HNO_3 (nitric acid)	Immerse sample in hot solution for 1–5 min.
Ir alloys	20 mL HCl (conc. hydrochloric acid) 25 g NaCl (sodium chloride) 65 mL H_2O (deionized water)	Electrolytic: 20 V ac for 1–2 min. Use graphite cathode and Pt lead wires.
Ru alloys	20 mL HCl (conc. hydrochloric acid) 25 g NaCl (sodium chloride) 65 mL H_2O (deionized water)	Electrolytic: 5–20 V ac for 1–2 min. Use graphite cathode and Pt lead wires.
Rh alloys	Part A: 40 g NaCl (sodium chloride), 100 mL water Part B: HCl (conc. hydrochloric acid)	Mix fresh, part A:B (4:1) Electrolytic: 10 V ac for 25 s After etching, remove film by reversing polarity.

(a) Compositions in weight percent. (b) PGM, platinum-group metals. Source: Ref 1, 2, 4

References cited in this section

1. T. Piotrowski and D.J. Accinno, Metallography of the Precious Metals, *Metallography*, Vol 10, Elsevier Publishing, 1977, 234–289

2. J. Stewart, *Tech-Notes*, Vol 2 (No. 5), G.F. Vander Voort, Ed., Buehler 1998

3. *Canning Handbook of Electroplating*, 23rd Edition, EFN Spon, 1982

4. G.F. Vander Voort, *Metallography, Principles and Practice*, McGraw-Hill Book Company, 1984

E. van der Lingen, L. Cornish, S. Taylor, R. Süss, S. Grice, Metallography and Microstructures of Precious Metals and Precious Metal Alloys, *Metallography and Microstructures*, Vol 9, *ASM Handbook*, ASM International, 2004, p. 860–876

Metallography and Microstructures of Precious Metals and Precious Metal Alloys

Elma van der Lingen, Lesley Cornish, Stefanie Taylor, Rainer Süss, Physical Metallurgy Division, Mintek, South Africa; Stewart Grice, Hoover & Strong Inc.

Microstructures of Gold and Gold Alloys

Pure Gold

Figures 1, 2 and 3 in this article show macrostructures of a sectioned 1kg 99.99% pure gold bar. The grain morphology in the gold bars varies due to the different cooling mechanisms after casting. The samples were etched in boiling aqua regia (HCl to HNO_3: 3 to 1) for 10 to 20 s. Several polishing/etching cycles were done to obtain a scratch-free and stress-free surface. A significant difference can be seen between two smaller cast gold bars, one of which shows equiaxed grains (Fig. 4), while a cold stamped bar reveals a very fine, disordered grain structure in a stamped bar (Fig. 5).



Fig. 1 A section of a 1 kg 99.99 Au bar casting. Etched with boiling aqua regia (HCl:HNO_3, 3:1) for 10 to 20 s

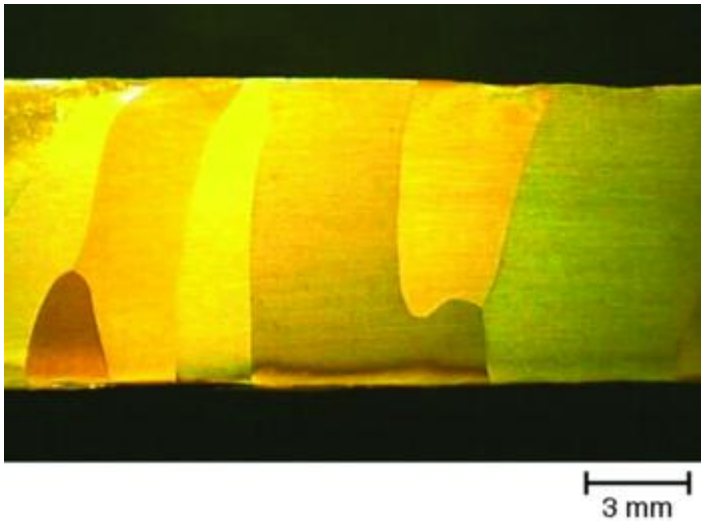

Fig. 2 This section of a 1 kg 99.99 Au bar casting has a slightly different grain structure than Fig. 3 due to a difference in cooling mechanism. Etched with boiling aqua regia ($HCl:HNO_3$, 3:1) for 10 to 20 s

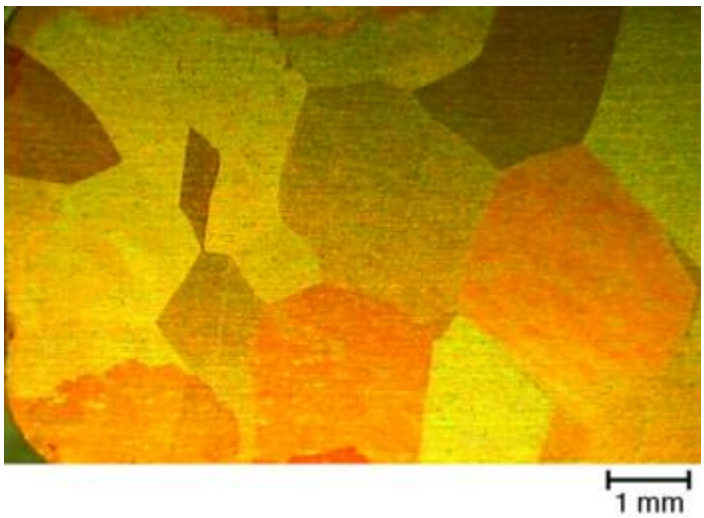

Fig. 3 A section of a 1 kg 99.99 Au bar casting. Etched with boiling aqua regia ($HCl:HNO_3$, 3:1) for 10 to 20 s

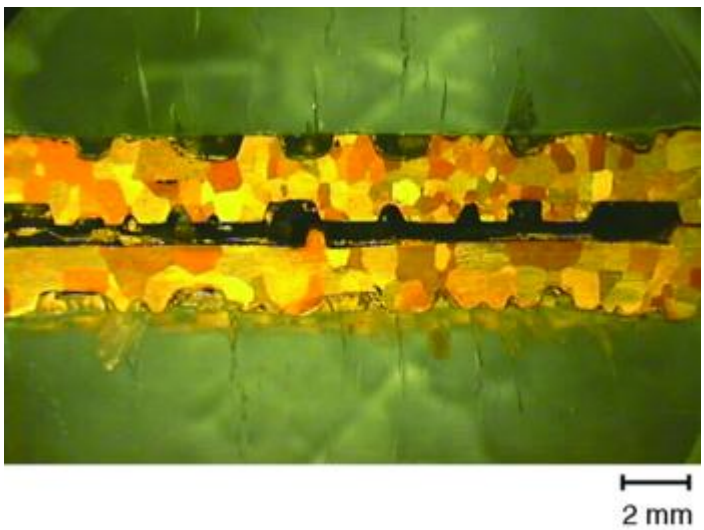

Fig. 4 Gold casting, smaller than those in Fig. 1, 2, 3 reveals equiaxed grains. Etched with boiling aqua regia ($HCl:HNO_3$, 3:1) for 10 to 20 s

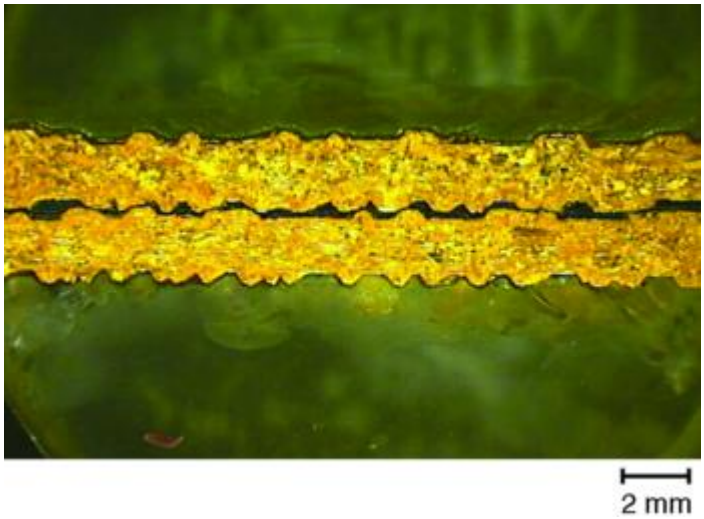

Fig. 5 A gold bar that was pressed, undergoing cold deformation, shows a very fine disordered grain structure. Etched with boiling aqua regia ($HCl:HNO_3$, 3:1) for 10 to 20 s

Gold Jewelry Alloys

Pure gold is very soft and is considered the most malleable of all metals. Jewelry items are produced mainly from gold alloy, because alloying additions improve the hardness and contribute to color variations. The Au-Ag-Cu system, which is the basis of most gold jewelry and dental alloys used today, dates back several millennia. The binary phase diagrams of silver-gold, silver-copper, and gold-copper can be found in Section 2, "Binary Alloy Phase Diagrams," in *Alloy Phase Diagrams*, Volume 3 of *ASM Handbook*. The general characteristics of the ternary Au-Ag-Cu system are much what might be expected from the binary systems. The solid-state immiscibility field in the copper-silver system intrudes into the ternary diagram (Fig. 6). In the same way, the gold-copper ordering regions (AuCu and $AuCu_3$) of the binary diagram also intrude into the ternary diagram (Ref 5). The alloys exist as homogeneous solid solutions at temperatures above the immiscibility gap, but if slowly cooled to room temperature, a second phase will form. On cooling below 410 °C (770 °F), the gold and copper atoms become rearranged and take up regularly spaced positions, forming a superlattice consisting of a layer of copper atoms on a layer of gold atoms. This structure is known as an ordered solid solution. The existence of the immiscibility field and the occurrence of AuCu ordering are important factors in determining the metallurgical properties of gold jewelry alloys, particularly their susceptibility to hardening.

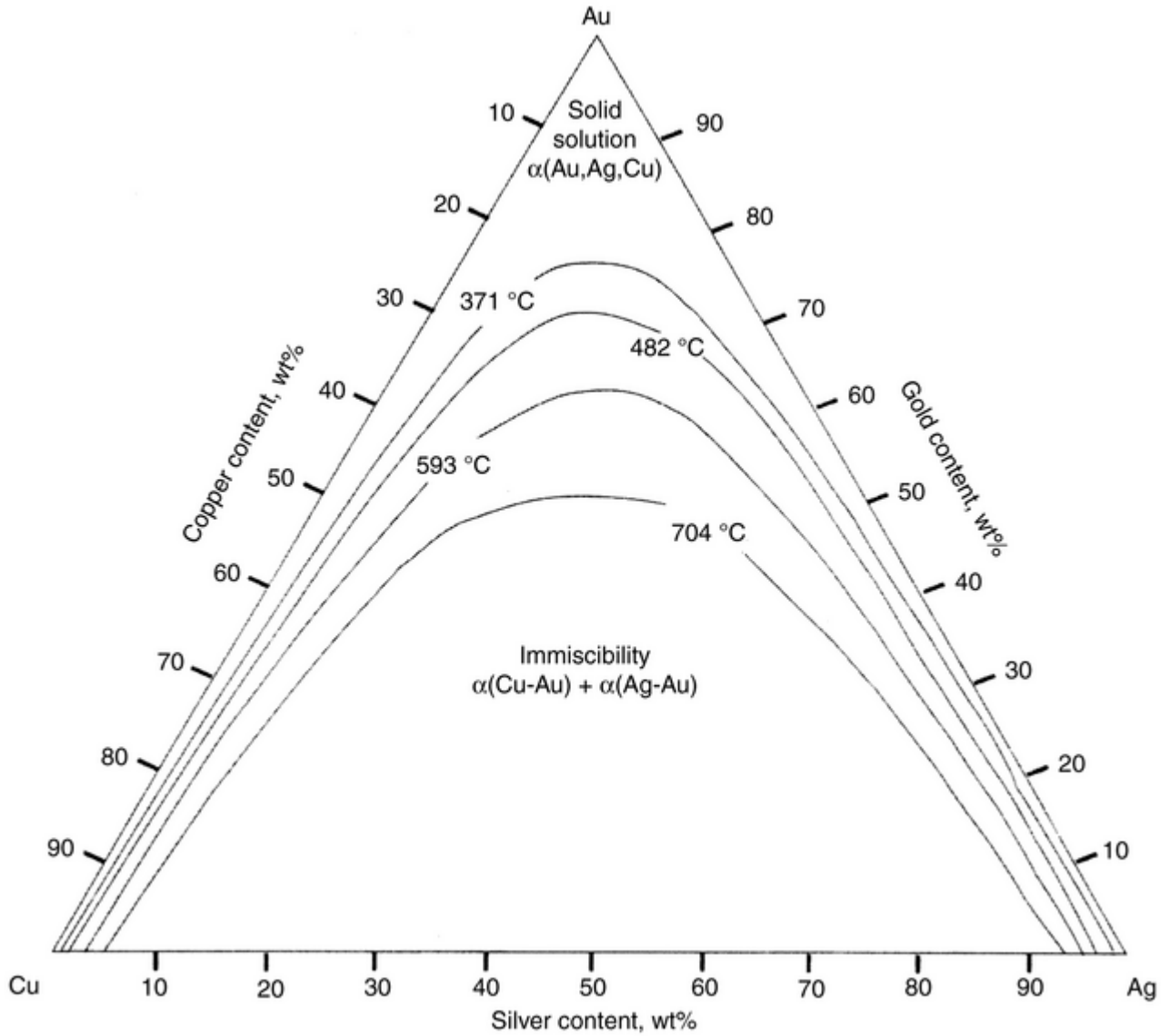

Fig. 6 Ternary Au-Ag-Cu phase diagram. Source: Ref 5

Hard 24 and 22 k Gold Alloys. The hardness of pure gold (~50 HV) can be increased by means of deformation (~70 HV at 80% deformation). Additional strengthening can be obtained by one or more of the following mechanisms: solid-solution strengthening, hardening by grain refining, and, usually more significantly, hardening through aging (precipitation hardening in particular). These hardening mechanisms are facilitated by the addition of one or more alloying elements, either through conventional alloying (where the alloying element is greater than 0.5 wt%) or microalloying (where the alloying element is less than 0.5 wt%). A number of microalloyed 99.5 to 99.9 wt% Au alloys have been developed (Ref 6).

The amount of gold in an alloy can be measured in karats (k) (in the United States and Germany; spelled "carats" elsewhere); 24 k is pure gold (99.9%), and 22 k is 22/24 or 91.60% Au (by definition). The purity is also measured by fineness; 916 fineness; is 91.6% Au content. By law in certain countries, only certain caratage of gold can be sold. In many countries, the law also requires that each piece of jewelry is tested—or assayed—and marked for gold content. This is known as Hallmarking when done by an independent laboratory (Ref 7).

The gold-antimony phase diagram (Section 2, "Binary Alloy Phase Diagrams," in Alloy Phase Diagrams, Volume 3 of *ASM Handbook*) predicts that up to ~1 wt% Sb can dissolve in gold at temperatures between 500 and 650 °C (930 and 1200 °F). The solubility of antimony in gold at temperatures below 300 °C (570 °F) is negligible. This is characteristic of a potential age-hardening system, although not much precipitation would be expected.

A low-temperature aging heat treatment given to a Au-0.2Co-0.3Sb (wt%) alloy after solution annealing at 750 °C (1380 °F) and quenching induces the precipitation of small (less than 20 nm in diameter) antimony-rich

particles in the matrix. Figure 7 (Ref 8, 9) is a transmission electron microscope micrograph showing these precipitates after such a heat treatment of 350 °C (660 °F) for 50 h. These particles, which become visible only after a long aging time, induce hardening. This alloy, which can be hallmarked as 24 k in many countries, can obtain a hardness of 123 HV through a combination of cold work and aging. This is higher than the hardness of pure gold, which cannot be aged and can obtain only ~75 HV after substantial cold working. The exact hardening mechanism for Au-0.2Co-0.3Sb has not been established, but it would be expected that it would be in agreement with the classic explanation for precipitation hardening.

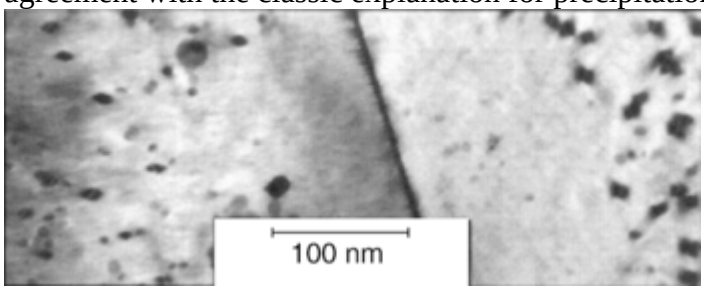

Fig. 7 Transmission electron microscope micrograph of an overaged sample of Au-0.2Co-0.3Sb (wt%) alloy showing small antimony-rich precipitates in the matrix. Source: Ref 8, 9

The binary gold-cobalt alloy phase diagram (Section 2, “Binary Alloy Phase Diagrams,” in Alloy Phase Diagrams, Volume 3 of *ASM Handbook*) indicates that small additions of cobalt could potentially induce a precipitation-hardening reaction. The solubility of cobalt in gold decreases from 8 wt% at the eutectic temperature down to almost zero below 450 °C (840 °F). A cobalt-rich ε-cobalt phase will precipitate from metastable gold-rich gold-cobalt solid solutions during aging at temperatures below ~422 °C (792 °F). It is also known that cobalt acts as a grain refiner in gold alloys, especially in the annealed and cold-worked state (Ref 10). The solubility of cobalt in gold is low and is even less in alloyed gold (because of the silver content), and only a concentration of cobalt exceeding its solubility in the alloy is necessary to induce a grain-refining effect (Ref 11).

A low-temperature aging heat treatment given to a 22 k alloy, Au-3.84Ag-1.96Cu-2.5Co (wt%), after solution annealing at 900 °C (1650 °F) and quenching induces the precipitation of cobalt-rich particles on the grain boundaries. Figure 8 is a light micrograph showing these precipitates after such a heat treatment of 350 °C (660 °F) for 15 min. The sample was polished to 0.25 μm finished, followed by etching in boiling aqua regia (HCl to HNO_3: 3 to 1) for 10 to 20 s.

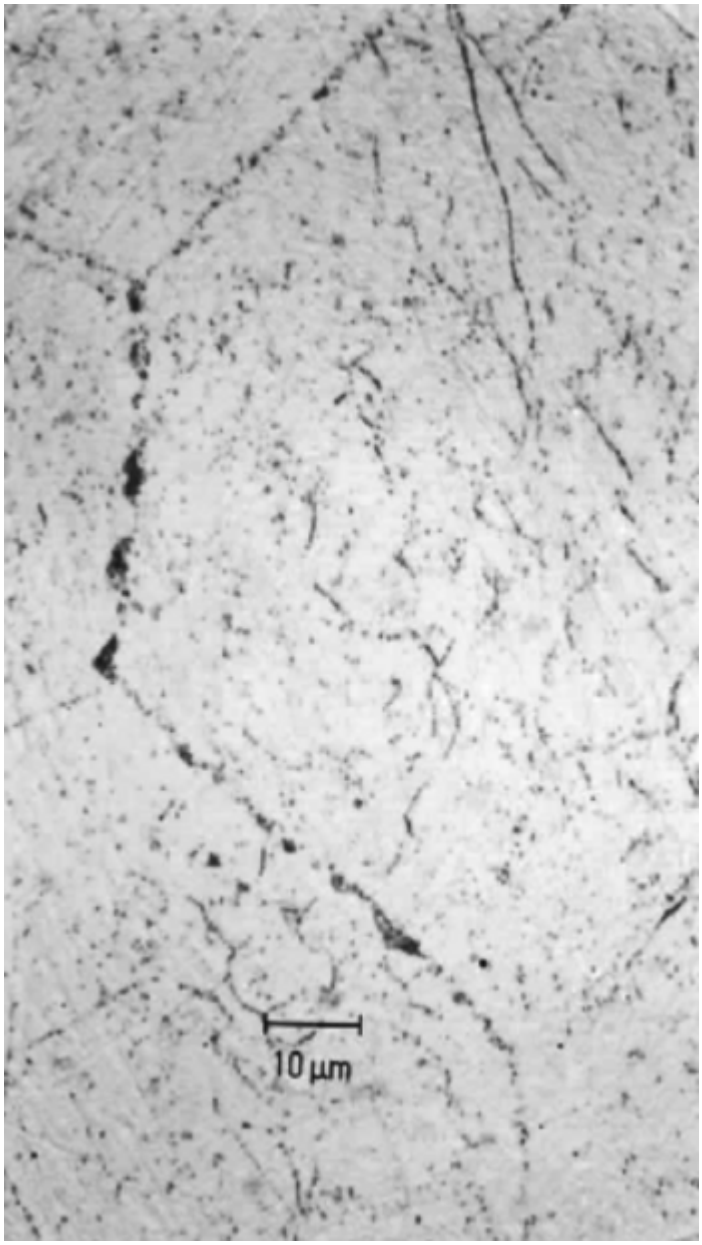

Fig. 8 Light micrograph of Au-3.84Ag-1.96Cu-2.5Co (wt%) alloy showing cobalt precipitates growing at the grain boundaries. Source: Ref 8

18, 14, 10, and 9 k Gold Alloys. Jewelry samples for metallographic analysis were set in the phenolic mounting compound using a compression mounting press. The setting parameters were 150 °C (300 °F) at 8 MPa (80 bar) pressure, heating for 60 s, and cooling for 180 s.

Initial grinding of the specimens used 180-grit paper at 35 N (7.9 lbf) force and a platen speed of 250 rpm. This was done until sufficient sample was exposed for analysis. This was followed by grinding through 400-, 800-, 1200-, and 2400-grit papers. The samples were then washed in detergent to ensure no residual SiC particles were remaining. Samples were then polished using identical machinery dedicated to polishing to prevent cross contamination. Parameters set were 20 N (4.5 lbf) force and a platen speed of 125 rpm. Samples were polished progressively with 9, 3, and 1 µm pads, again cleaning the samples with detergent between each grade to prevent cross contamination of the polycrystalline diamond suspensions. After completion of the polishing operation, the sample was washed in detergent and rinsed with methanol to aid water evaporation, minimizing watermarks on the polished microsections.

The Spangold alloys are 18 k gold jewelry alloys that use a martensitic-type transformation, following a complex heat treatment that induces a slight change in surface relief. After the transformation, the reflection of incident light from the parallel laths in differently orientated grains gives an attractive sparkle effect. The samples were prepared using normal metallographic techniques and were polished to a 0.25 µm finish using a

diamond suspension, followed by colloidal silica polishing. Figure 9 shows the microstructure of a 76Au-18Cu-6Al (wt%) alloy viewed using Nomarski interference.

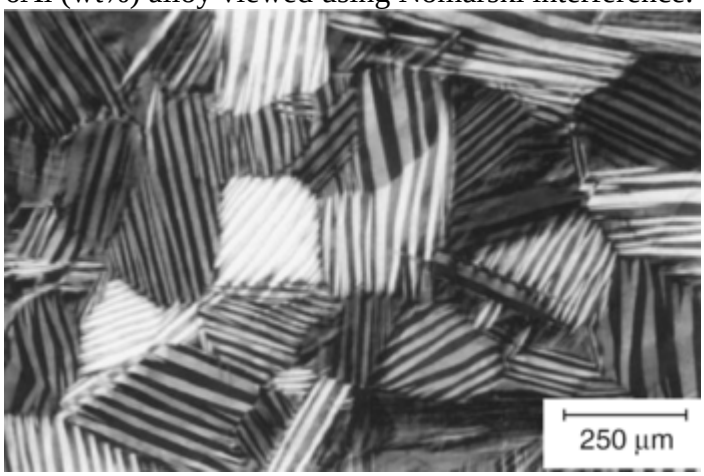

Fig. 9 Light image using Normaski interference of 76Au-18Cu-6Al (wt%) alloy, colloidal silica polished, showing martensite laths and tilted grains

18 k White Gold. Figure 10 is a palladium white 18 k gold investment casting. The severe shrinkage porosity that can be seen in the ring shank is a result of insufficient feeding, which caused premature freeze-off at the gate. Increasing the gate diameter and optimizing the casting parameters would solve this problem. The coring effect on solidification is also clearly visible with the dendritic morphology.

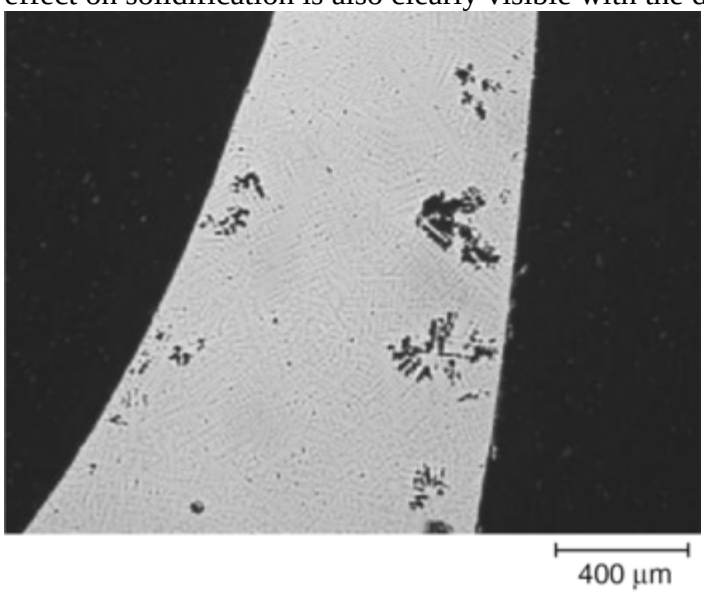

Fig. 10 An 18 k white-gold (75Au-10Cu-15Pd) casting showing shrinkage porosity. 50×

18 k Yellow Gold. Figure 11 is an example of an 18 k 3N yellow-gold investment casting (3N is a color designation). There is severe gas porosity near the surface. This through-section gas porosity differs from the defect caused by gas released from the investment during decomposition. Here, gas absorbed into the liquid metal, either from the pregraining or casting process, has evolved during solidification. The solidification process was completed before the gas had a chance to escape, resulting in the spherical pores seen in the sample. An alternative source of dissolved gas results from recycling unclean casting scrap that includes residual investment mold material. This can break down during the melting cycle and generate sulfur dioxide gas, leading to similar porosity defects. There are also sulfides in the microstructure resulting from the dissolution of the investment mold. These sulfides are not visible at magnifications less than 500×.

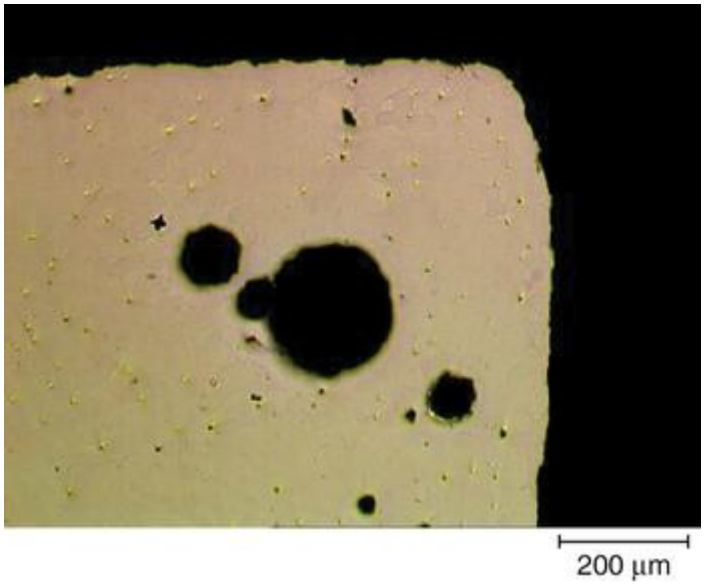

Fig. 11 An 18 k gold casting (75Au-12.5Ag-12.5Cu) showing gas porosity. 100×

Figure 12 shows the effect of adding 0.01% Ir as a grain refiner to an 18 k 2N (pale-yellow) alloy. The average grain size is reduced by a factor of more than a hundred.

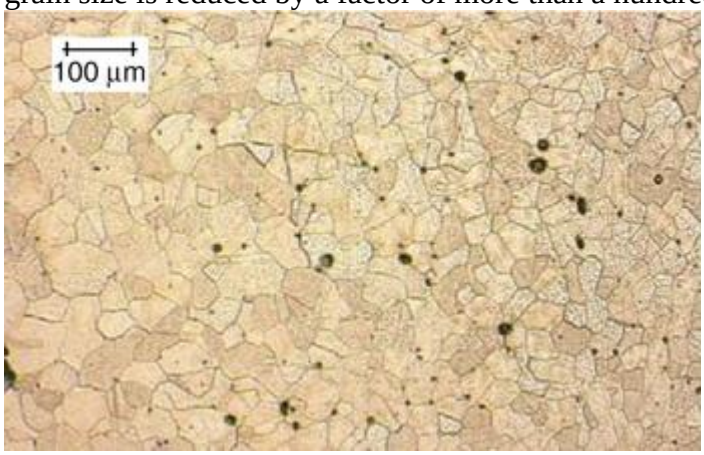

Fig. 12 18 k gold (75Au-15Ag-9Cu-1Zn) with 0.01% Ir added as a grain refiner. Etched for 45 s in a 1:1 mix of 10% potassium cyanide and 10% ammonium persulfate at room temperature. 50×

14 k White Gold. Figure 13 shows an example of metal/investment mold reaction in investment-cast 14 k palladium white-gold alloys. For the casting process, a regular sulfate-bonded investment mold with a final flask temperature of 650 °C (1200 °F) was used. The resulting castings had excessively rough surfaces. The micrograph clearly shows that a metal/investment mold reaction occurred during solidification. The high liquidus temperature of the alloy, 1185 °C (2165 °F), and therefore high superheat required for casting caused decomposition of the investment mold when in contact with the liquid charge. This resulted in the generation of sulfur dioxide from the coating, which has pushed the solidifying charge away from the mold, resulting in the rough surface seen. This problem could be resolved by using a higher-operating-temperature phosphate-bonded investment mold.

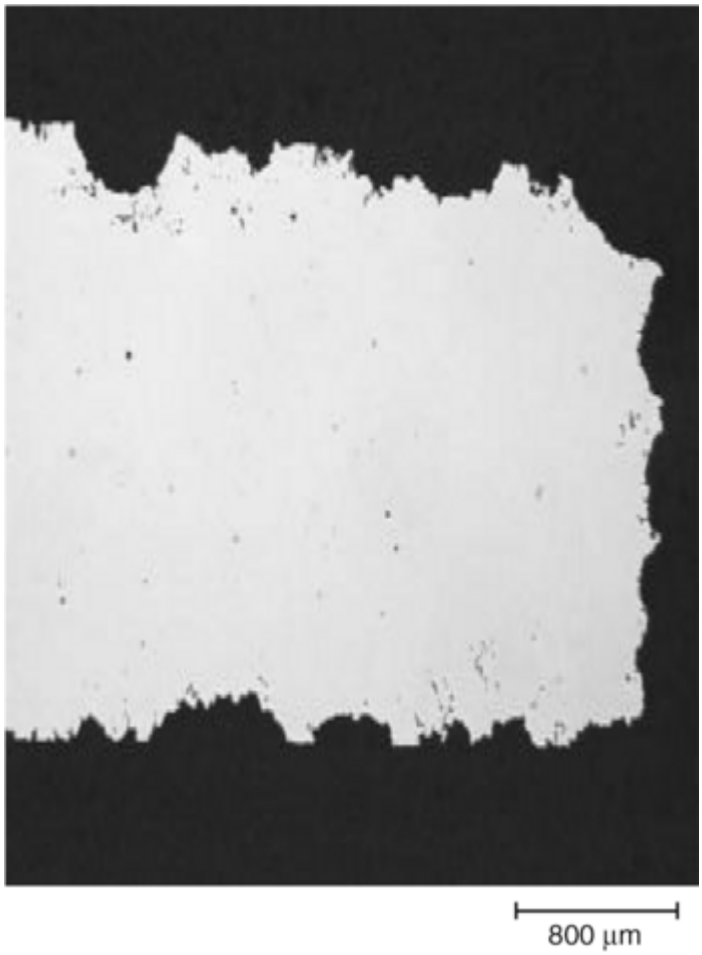

Fig. 13 Results of metal reaction with investment cast mold are seen in 14 k white gold (58.5Au 24.9Cu-7.6Zn-9Ni). 25×

The micrograph in Fig. 14 is that of a continuous-cast wire, drawn in minimum 50% reductions and annealed at 700 °C (1290 °F) to a diameter of 0.5 mm (0.02 in.). It was then reduced a further 10% by area, then the wire failed while in storage at a customer's workshop. The failure was determined to be stress-corrosion cracking, suggesting that at some point it was exposed to a corrosive element. The structure also shows slight deformation due to the 10% cold work. Stress-corrosion cracking is usually more predominant in lightly worked structures.

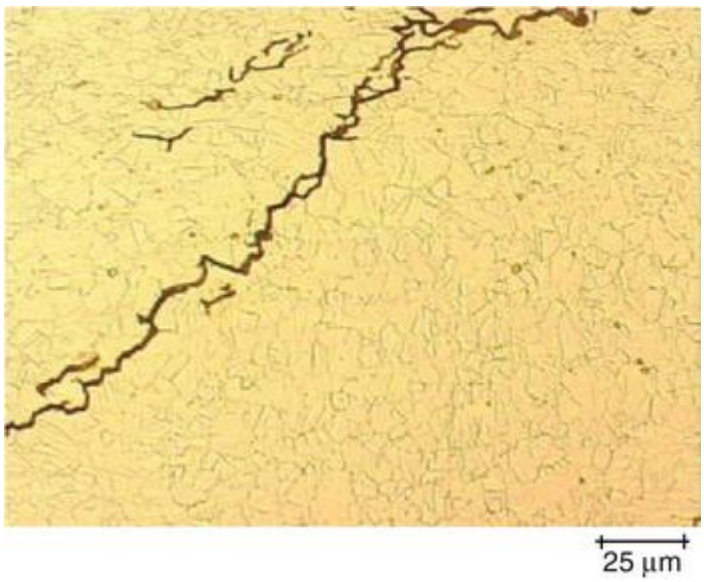

Fig. 14 A 14 k gold (58.5Au-24.9Cu-7.6Zn-9Ni) continuous-cast wire etched for 45 s in a 1:1 mix of 10% potassium cyanide and 10% ammonium persulfate at room temperature. 500×

Figure 15 shows a production ring blank in a 14 k nickel-white alloy that failed during processing. Continuous-cast sheet was processed to 3 mm (0.12 in.) thickness and then blanked into a washer using a hydraulic press. The washer was then annealed in a belt furnace at 700 °C (1290 °F) and formed into the blank and sized. This blank failed on sizing.



Fig. 15 Failed 14 k white-gold (58.5Au-24.9Cu-7.6Zn-9 Ni) ring blank

Working nickel-white alloys for certain applications can be complex. Insufficient work during processing—common with intrinsically hard nickel-white-gold alloys—can lead to internal tensile stresses that result in quench cracking if cooled too rapidly. However, if cooled too slowly, the alloy will age harden and will not process to such a high degree of cold work, which can lead to the initial problem of insufficient cold work. The blank shown in Fig. 16 developed internal intergranular cracking during processing, probably due to either fire cracking or quench cracking. The resulting blank did not have sufficient strength to withstand the sizing operation.

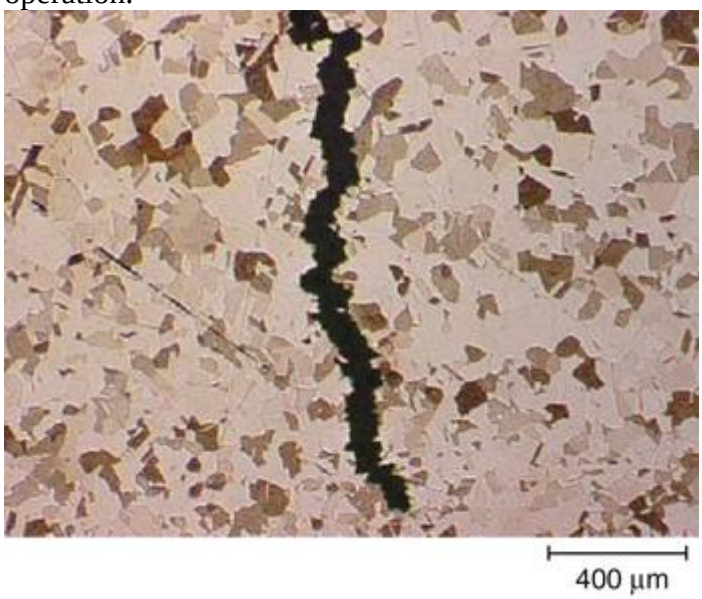

Fig. 16 Intergranular cracking in a 14 k white-gold ring blank (58.5Au-24.9Cu-7.6Zn-9Ni) etched for 45 s in a 1:1 mix of 10% potassium cyanide and 10% ammonium persulfate at room temperature. 50×

Another example of a production failure in a 14 k nickel-white-gold alloy (Ref 12) is shown in Fig. 17. These cup settings are manufactured from sheet that has been continuous cast and processed to 6 mm (0.24 in.) thickness (using 750 and 700 °C, or 1380 and 1290 °F, anneals and minimum 50% cold work). A suitably shaped blank is stamped from the sheet then inserted into a tool set and die struck to form the cup setting by

undergoing several deep-drawing operations. If the sheet does not have sufficient ductility, failure occurs at the base of the setting (Fig. 17a). From the micrograph of the failed setting, it is clear that the sample did not fully recrystallize prior to deep drawing and so failed where the wall of the setting underwent maximum deformation—at the base (Fig. 17b). In correctly processed mill stock that has undergone full recrystallization, even flow is seen in the base area, and a perfect setting is produced.

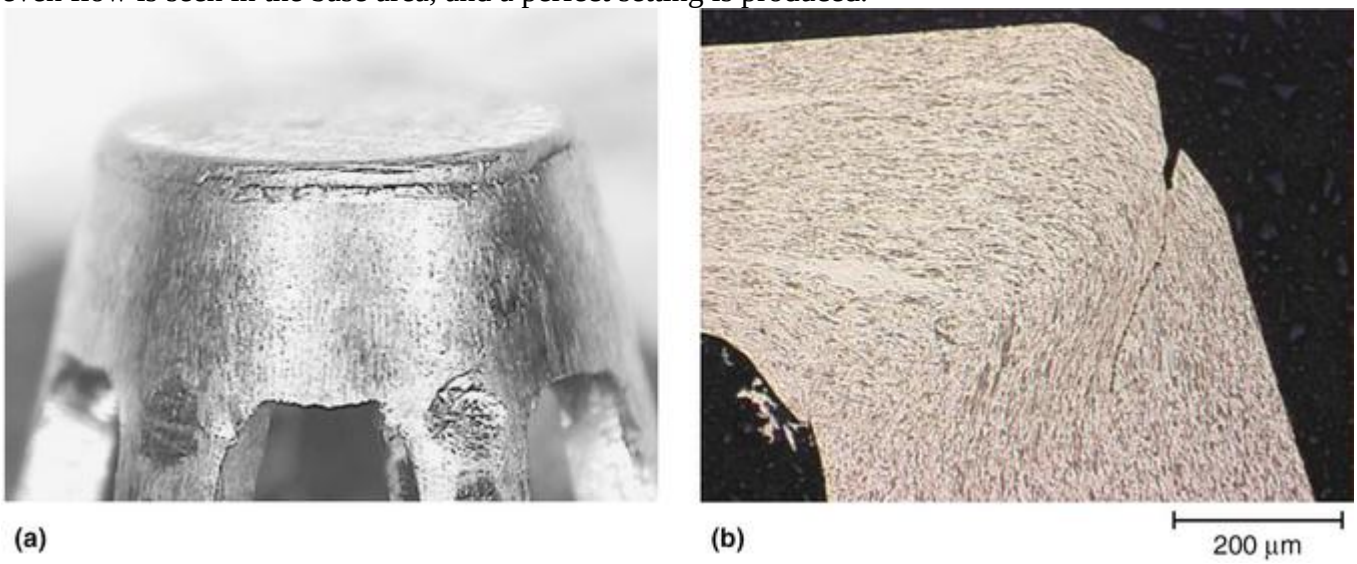

Fig. 17 A 14 k white-gold (58.5Au-24.9Cu-7.6Zn-9Ni) cup. (a) Failed cup setting. (b) Micrograph of cross section etched for 45 s in a 1:1 mix of 10% potassium cyanide and 10% ammonium persulfate at room temperature. 100×

Figure 18 is a micrograph of a 14 k nickel-white-gold alloy with a higher nickel content (Ref 13). This is a continuous-cast wire rod drawn in minimum 50% reductions and annealed at 760 °C (1400 °F) until 0.71 mm (0.028 in.) in diameter. The wire was then heat treated at 650 °C (1200 °F) for 30 min, followed by quenching in room-temperature water. To induce a stress-corrosion cracking failure, the wire was bent through 135°, had a static load applied, and was immersed in 1% FeCl. The failure occurred after approximately 200 s.

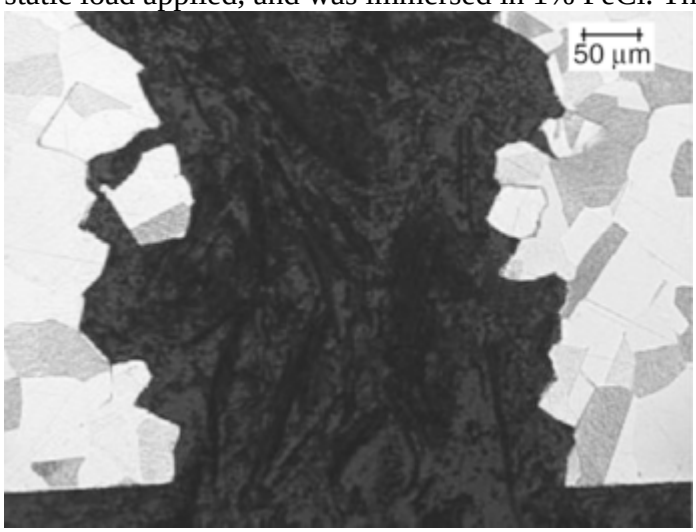

Fig. 18 A 14 k white-gold wire rod (58.5Au-21Cu-6.5Zn-14Ni) etched for 45 s in a 1:1 mix of 10% potassium cyanide and 10% ammonium persulfate at room temperature. 200×

Figure 19 is a micrograph of a very high-nickel- content 14 k white-gold alloy (Ref 13). This was continuous-cast wire rod drawn in minimum 50% reductions and annealed at 760 °C (1400 °F) until 0.7 mm (0.028 in.) in diameter. The wire was then heat treated at 480 °C (895 °F) for 30 min prior to quenching in room-temperature water. The dark lamellar phase was analyzed using electron dispersive x-ray and determined to be the α(Ni-Cu) phase precipitated as a result of the immiscibility boundary detailed in the Au-Cu-Ni ternary diagram (Fig. 20). The α(Au-Cu) and α(Ni-Cu) duplex solid solution in Au-Cu-Ni alloys is a direct result of the immiscibility

curves present in the gold-nickel and copper-nickel binary diagrams (Section 2, "Binary Alloy Phase Diagrams," in *Alloy Phase Diagrams,* Volume 3 of *ASM Handbook*).

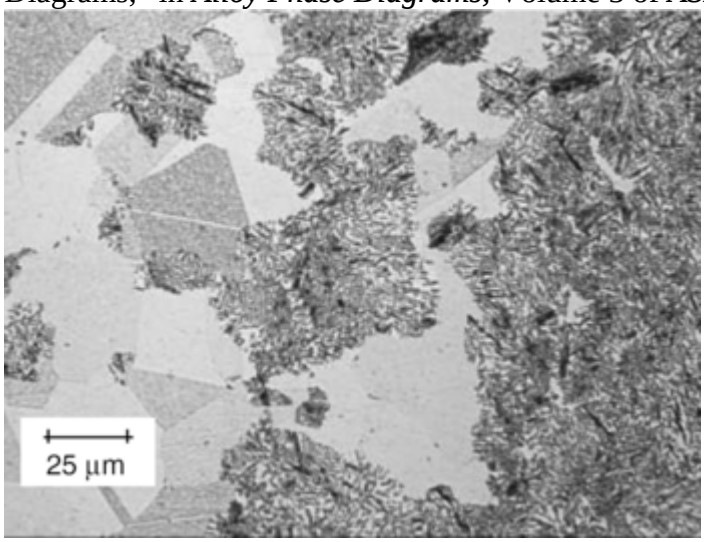

Fig. 19 A 14 k white-gold rod (58.5Au-14Cu-6.5Zn-21Ni) etched for 45 s in a 1:1 mix of 10% potassium cyanide and 10% ammonium persulfate at room temperature. 500×

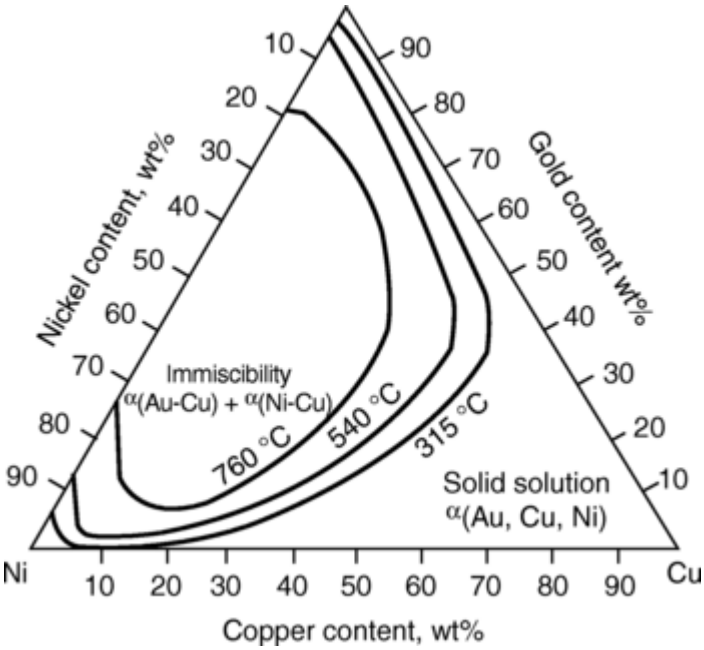

Fig. 20 Ternary Au-Ni-Cu phase diagram. Source: Ref 5

14 k Yellow Gold. Comparing the standard 14 k yellow-gold investment casting shown in Fig. 21 with that shown in Fig. 22 demonstrates the effect of adding 0.01% Ir to this alloy as a grain refiner.

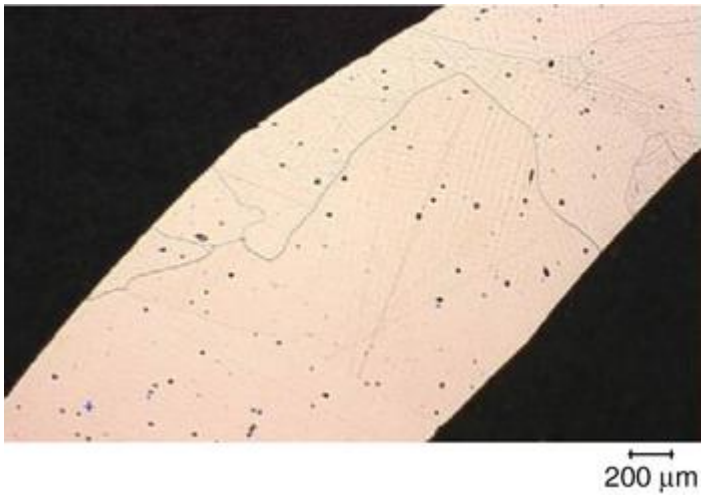

Fig. 21 A 14 k gold investment casting (58.5Au-12.5Ag-24Cu-5Zn) etched for 45 s in a 1:1 mix of 10% potassium cyanide and 10% ammonium persulfate at room temperature. 50×

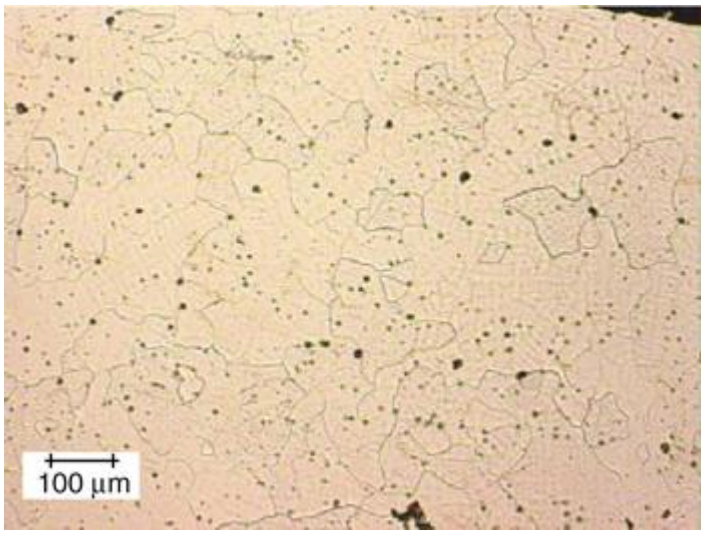

Fig. 22 A 14 k gold investment casting (58.5Au-12.5Ag-24Cu-5Zn-0.01Ir) with 0.01% Ir added as a grain refiner. Etched for 45 s in a 1:1 mix of 10% potassium cyanide and 10% ammonium persulfate at room temperature. 100×

10 k Yellow Gold. Figure 23 in this article shows an example of stress-corrosion failure. Continuous-cast bar stock was cold rolled using reductions of a minimum of 50% between annealing at 600 °C (1110 °F) to 1 mm (0.04 in.) flat stock. This was then formed and soldered into a wedding band. After several months of being worn by the customer, it was returned after it developed cracking. Microsections revealed intergranular cracking typical of stress-corrosion failure in low-karat alloys. Exposure of low-karat alloys to corrosive environments can result in stress-corrosion failure when there is a residual stress present in the workpiece. This has been documented as occurring after exposure to household detergents and chlorinated swimming pool water. In some cases, human sweat has been suggested as the corrosive medium.

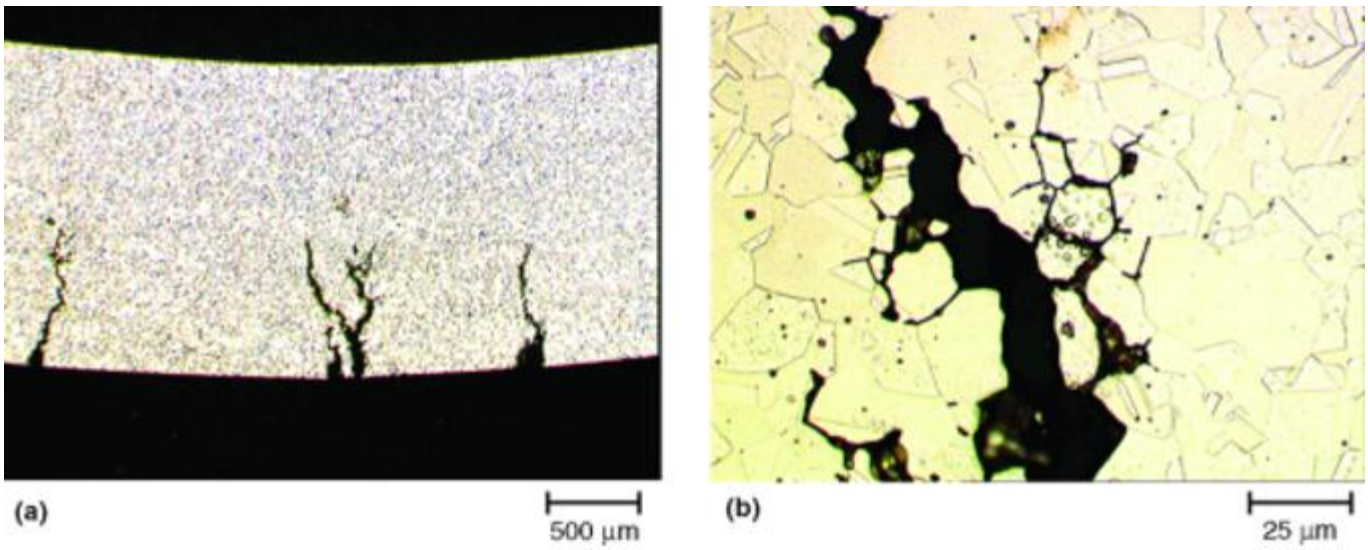

Fig. 23 Stress-corrosion failure in a 10 K gold ring (41.7Au-12Ag-41.3Cu-5Zn) etched for 45 s in a 1:1 mix of 10% potassium cyanide and 10% ammonium persulfate at room temperature. (a) 25×. (b) 500×

Figure 23(a) in this article is an example of stress-corrosion failure in a 10 k yellow alloy, photographed at lower magnification. Continuous-cast wire stock was cold rolled/drawn using reductions of a minimum of 50% between anneals to 2 mm (0.08 in.) in diameter. Note that cracking has initiated on the outer face, which is in tension—a common phenomenon in stress-corrosion failures.

The sample shown in Fig. 24 in this article was generated as part of an investigation into the precipitation characteristics of 10 k yellow silicon and nonsilicon-containing alloys. This nonsilicon-containing alloy was liquated and cooled to 400 °C (750 °F), where it was soaked for 2 h prior to quenching in water at room temperature. The etched sample demonstrates the decomposition of the solid solution α(Au,Ag,Cu,Zn) into α1(Ag-rich) + α2(Cu-rich) phases. This precipitation is a direct result of the superimposition of the immiscibility boundary in the silver-copper binary system (Section 2, “Binary Alloy Phase Diagrams,” in Alloy Phase Diagrams, Volume 3 of *ASM Handbook*) into the Au-Ag-Cu ternary system (Fig. 6).

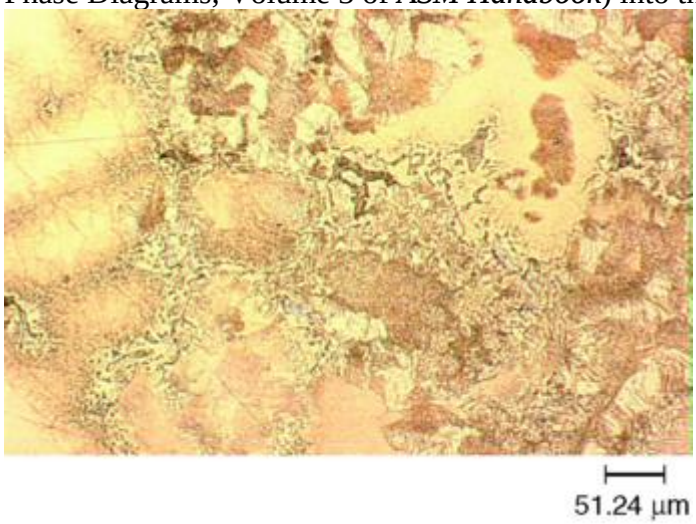

Fig. 24 Precipitation in a 10 K gold ring (41.7Au-12Ag-41.3Cu-5Zn) etched for 45 s in a 1:1 mix of 10% potassium cyanide and 10% ammonium persulfate at room temperature. 200×

The samples in Fig. 25 were part of the same investigation. Low-karat investment casting alloys with high silicon additions (>0.3 wt%) were noted to be brittle under certain processing conditions, with failures noted after devesting production flasks. Microsection analysis revealed the presence of several phases associated with failures. For ease of analysis and to determine under what processing conditions precipitation occurred, the parent 10 k yellow alloy was overdoped with 1.0 wt% Si (Fig. 25a), resulting in a higher volume fraction of the phases in microsection. This sample was liquated, then cooled to 700 °C (1290 °F), where it was soaked for 2 h

prior to quenching in water at room temperature. Precipitations of an interdendritic light-colored silver-rich, silicon-free phase and a dark-gray-colored brittle intermetallic (Cu,Au)5Si are noted. The intermetallic is a result of the increasing concentration of silicon in the residual liquid phase as solidification is approached. The same specimen at higher magnification (Fig. 25b) shows the relationship between the intermetallic $(Cu,Au)_5Si$ and the silver-rich, silicon-free phase, the latter appearing to exist with a eutectic-type morphology with the matrix phase. The hardness of the intermetallic was measured as >500 HV, with silicon additions as low as 0.25 wt% under certain processing conditions.

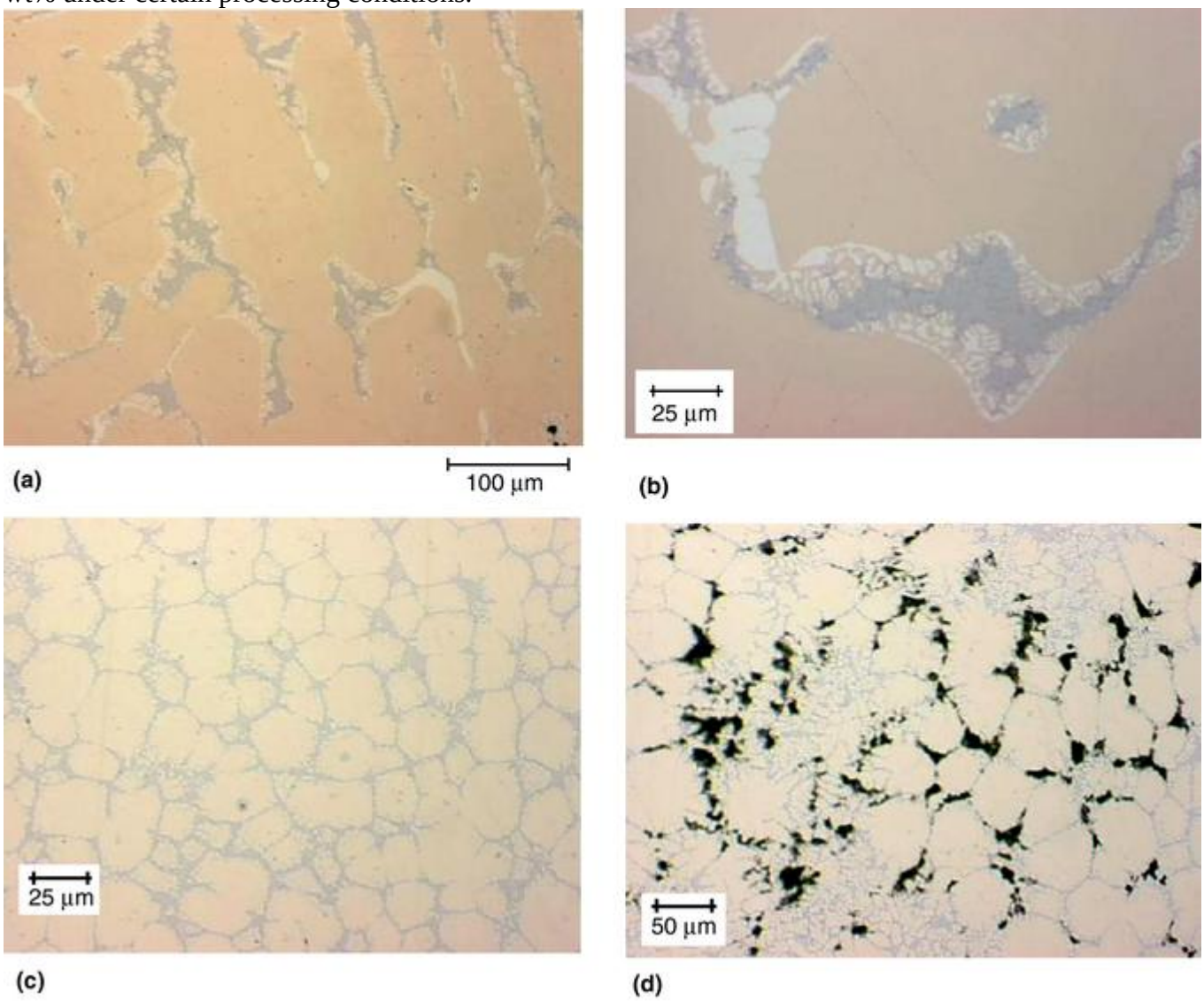

Fig. 25 A 10 k gold alloy showing precipitation phases (41.7Au-12Ag-40.3Cu-5Zn 1 Si). This sample was overdoped with 1% Si, and then processing was varied to determine conditions that led to failure. (a) Liquated, held at 700 °C (1290 °F) for 2 h, water quenched at room temperature. 200×. (b) Same process as (a) viewed at 500×. (c) Liquated, cooled to 300 °C (570 °F) for 2 h, water quenched at room temperature. 500×. (d) Same process as (c) but showing severe interdendritic porosity. 200×

The specimen in Fig. 25(c) is similar to that in Fig. 25(a) and (b), but it was heat treated by liquating and then cooling to 300 °C (570 °F) and soaking for 2 h prior to quenching in water at room temperature. The precipitation characteristics of the intermetallic (Cu,Au)5Si and the silver-rich/silicon-free phases show different morphologies. The latter phase is more dispersed throughout the matrix phase, and the intermetallic phase is more coherent.

The specimen in Fig. 25(d) is the same casting as in Fig. 25(c); however, the micrograph shows severe interdendritic porosity associated with the intermetallic phase $(Cu,Au)_5Si$. Because this phase will be the last to solidify during the cooling process, any porosity present is expected to be associated with it. The porosity will weaken the ring section, particularly if any deformation occurs, such as in a prong when stone setting. This, in

conjunction with the brittle nature of the intermetallic phase, gives the potential for failure. Cracks are initiated in the porous area and progress through the intermetallic phase.

The specimen in Fig. 26 is the parent 10 k yellow alloy over-doped with 2.0 wt% Si, resulting in a higher volume fraction of the intermetallic phases in microsection. This material was liquated, then cooled to 500 °C (930 °F), where it was soaked for 2 h prior to quenching in room-temperature water. Again, precipitation of the light-colored silver-rich, silicon-free phase and the dark-gray-colored brittle intermetallic $(Cu,Au)_5Si$ is noted. Also, note the increase in volume fraction of the intermetallic phase compared with the 1.0 wt% Si alloy shown in Fig. 25(a).

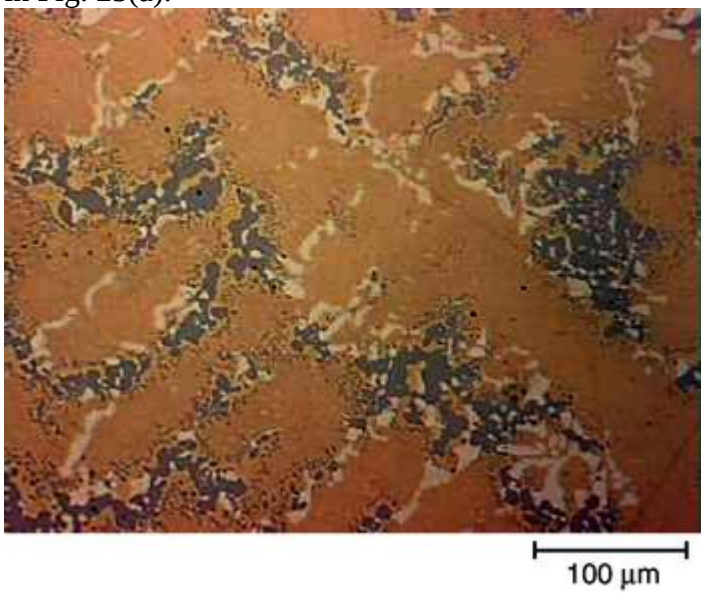

Fig. 26 A 10 k gold alloy (41.7Au-12Ag-39.3Cu-5Zn-2Si) overdoped with 2 wt% Si. 200×

9 k Yellow Gold. Figure 27 shows the effect of cobalt additions on the grain refining of a 9 k gold alloy. A fine grain structure in materials is generally considered to be beneficial, because it improves both strength and toughness and also prevents “wrinkling” or “orange-peel” effect during deformation.

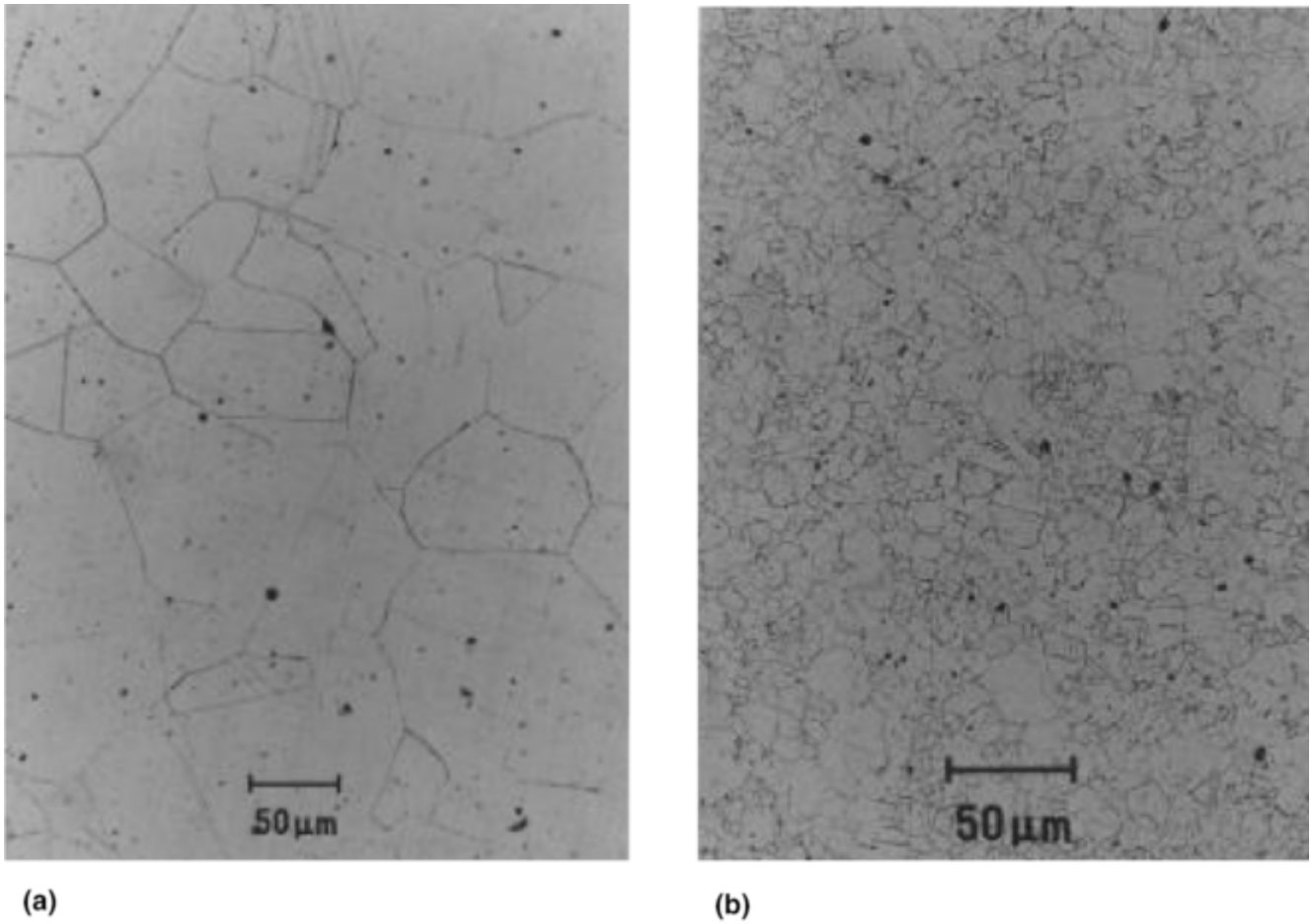

Fig. 27 The effect of 0.3% Co addition on the grain refining of a 9 k gold alloy. (a) Without cobalt. (b) With cobalt

Casting and Other Defects in Gold Jewelry Alloys (Ref 14). The polished surface of a flat jewelry item shows numerous, uniformly distributed round pores (Fig. 28, 29, 30). The pores are like pinholes and are randomly distributed on the surface. The type of porosity and its origin cannot be identified by its visual external appearance alone. Examination of a microsection is necessary. Typically, the gas pores are roughly spherical and are often situated in a discrete layer just beneath the surface, indicating their origin from reaction of the investment at casting. Alternatively, as in this case, they may be distributed across the entire cross section, indicating their likely origin as a reaction of contaminated (polluted) alloy. The gas pores are small but abundant. Only a few pores are exposed and visible on the surface. Obviously, attempting to remove these pinholes by polishing them away is unrewarding, because other, subsurface pores will then become exposed.

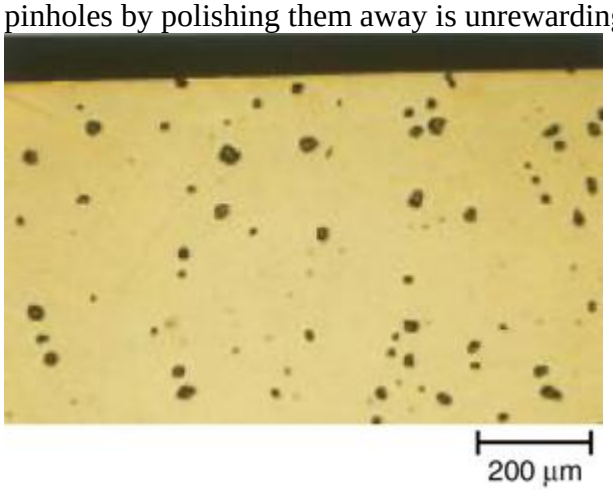

Fig. 28 Microsection through a piece of jewelry reveals gas porosity defect. 50×

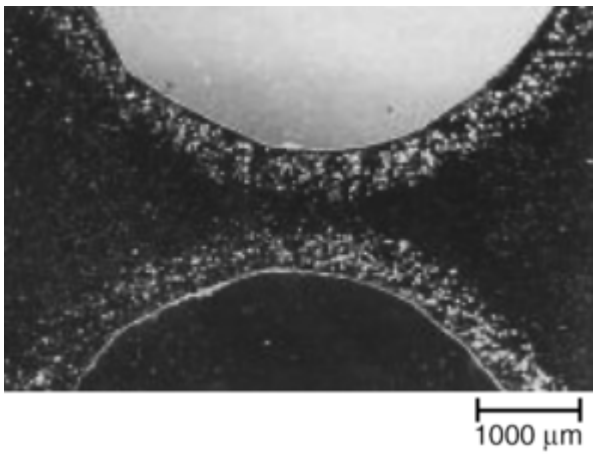

Fig. 29 Typical layer of gas pores just beneath the surface. 9×

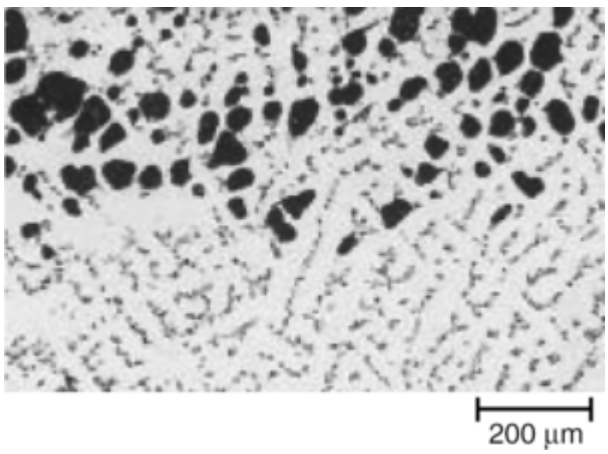

Fig. 30 Detail of Figure 29 gas pores at higher magnification. 50×

The sample in Fig. 31 and 32 shows severe porosity. The pores, which are near to the surface, are of two types: small, almost spherical gas pores and irregularly shaped larger pores. At higher magnification, small inclusions are visible, which are probably copper oxide (CuO). Most cases exhibiting a combination of spherical and irregular-shaped pores are the result of impurities.

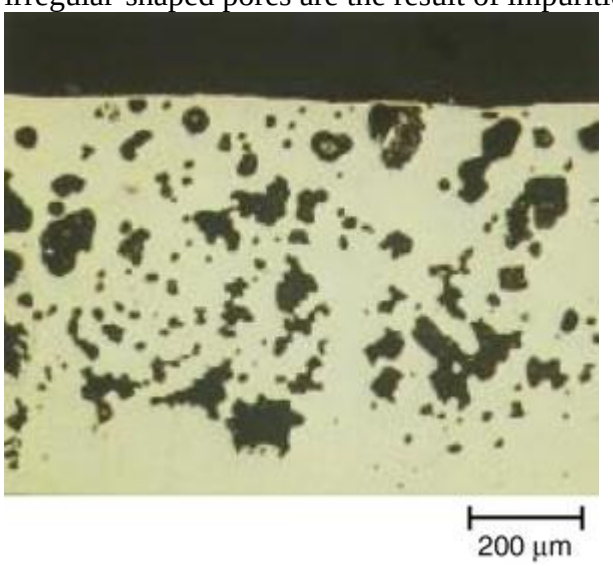

Fig. 31 Microstructure of a ring with a porous surface. 50×

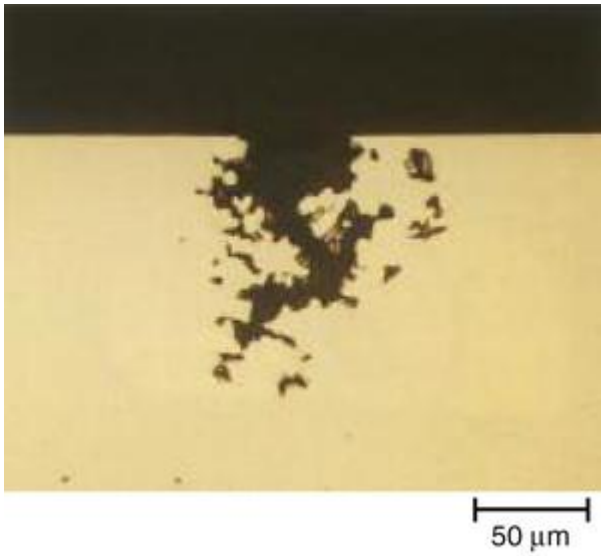

Fig. 32 Detail of surface porosity. 200×

The micrographs in Fig. 33 show the cross section of the shank of a ring at different magnifications. At low magnification, nests of dendritic pores are visible, randomly distributed over the cross section. Only a few of them reach the surface, causing dark spots on the polished shank. The microsection makes clear that further polishing would not improve the surface; on the contrary, more pores would be exposed. At higher magnification, some interesting detail is revealed: The pores are a mixture of roughly spherical, small gas pores and dendritic pores. Real shrinkage porosity can be excluded as a cause. More detailed examination leads to the conclusion that the main cause is impurities, probably copper oxide, introduced by use of dirty scrap material or improper melting methods.

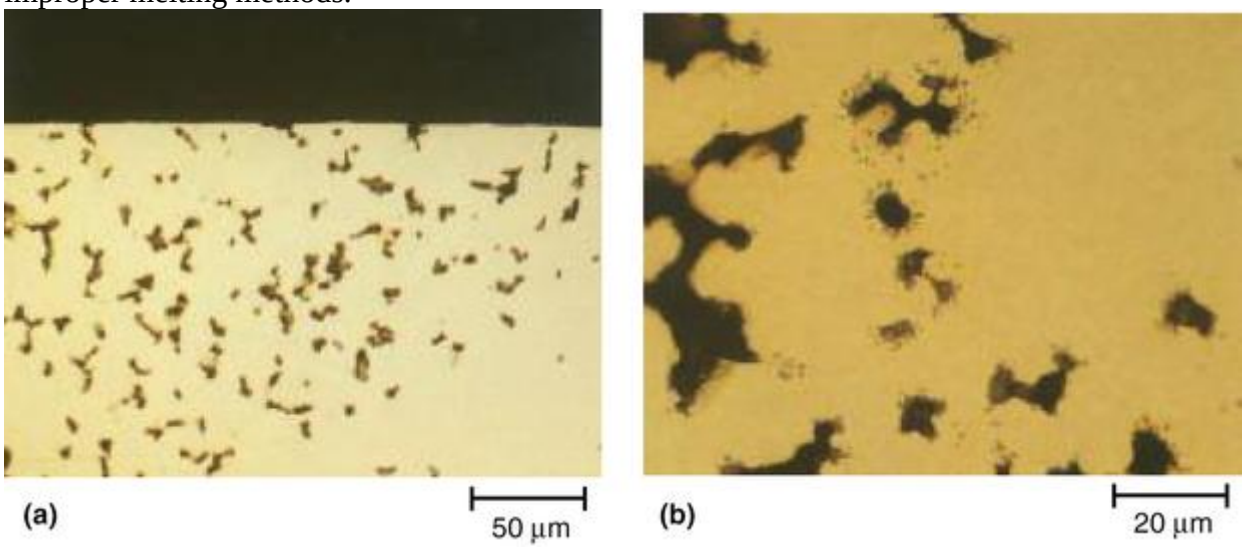

Fig. 33 Microstructure of porous gold specimen. (a) 200×. (b) 500×

A petal of a flowerlike jewelry item broke off after final polishing. A microstructure through the fracture of the petal discloses a morphology typical of interdendritic shrinkage porosity (Fig. 34). The petal, with a relatively thick cross section, is connected to the calyx of the flower by a thin neck. The fracture occurred at this neck, the thinnest part of the item, where the flow of liquid metal was restricted. In this region alone, a spongy structure of dendrites is formed, with voids in between.

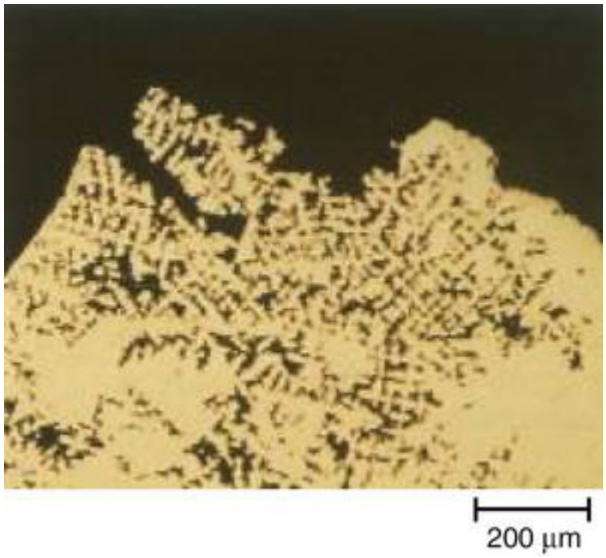

Fig. 34 Microstructure of dendrites on fractured petal of gold jewelry. 50×

A part of a tie clip shows small pores on the surface that are concentrated on the tapered end of the item. A microsection through the porous end of the clip, at the opposite end to the gate, discloses a typical dendritic appearance of the pores (Fig. 35), resulting in a spongy metal structure with dendritic pores. Such a pronounced dendritic porous structure drastically reduces the strength, and the part may break with little effort.

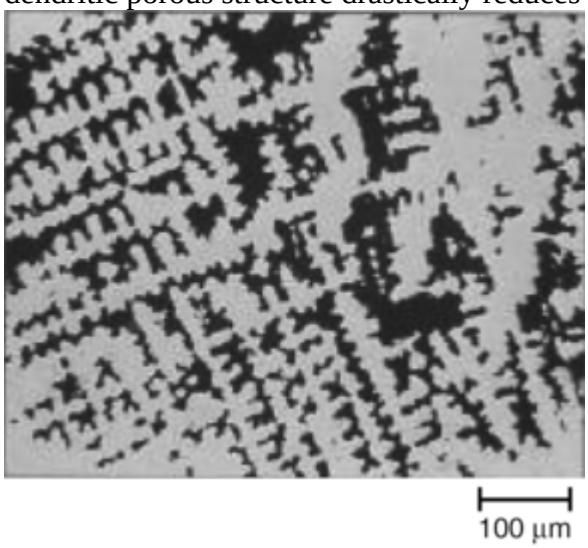

Fig. 35 Microstructure of clip showing shrinkage porosity. 80×

Usually, the defect is not visible until the jewelry is polished. Sometimes, an attempt to remove the defect by grinding or polishing may be successful. However, in other cases, the pores will be enlarged by this procedure. In Fig. 36(a), many pores are visible on and just beneath the surface. Inclusions are not apparent, but inclusions could have been removed by surface treatment or sample preparation. Figure 36(b) shows a pore at higher magnification. Only a small part of the defect volume reaches the surface, and more polishing would enlarge the defect.

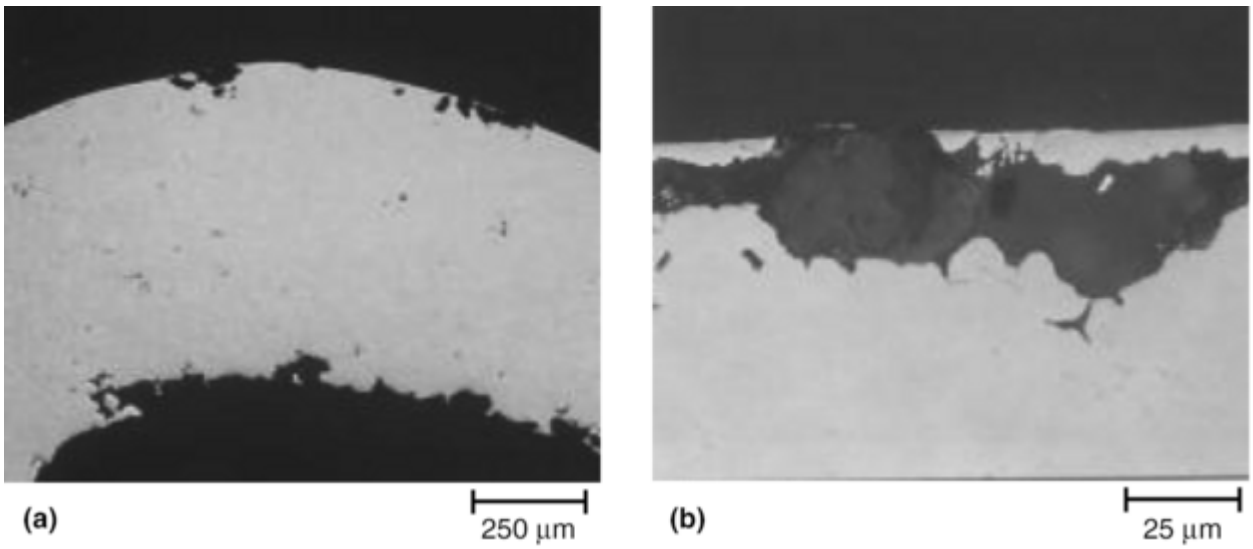

Fig. 36 Microstructure showing pores caused by investment casting. (a) 40× (b) 400×

Small cracks were visible on the surface of a ring and were apparently restricted to the surface. While fracture of the rings was not reported, it could occur if a ring is enlarged by stretching. Figure 37 shows the surface cracks. The cracks are not very deep, and there are no signs of embrittlement. The defects cannot be removed by polishing, because the cracks are too pronounced. The cause of the defects is probably a bad surface on the tube produced during continuous casting.

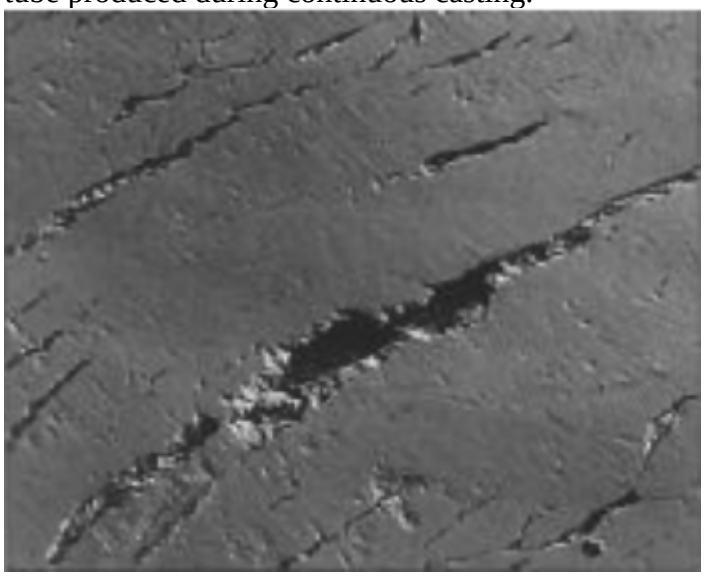

Fig. 37 Scanning electron microscope image of cracked surface

Intermetallic Gold Compounds

The intermetallic compounds are a special group of materials with properties very different from the individual metals that constitute them. An intermetallic compound is defined by an intermediate phase in an alloy system, having a narrow range of homogeneity and relatively simple stoichiometric proportions. Intermetallic compounds are usually brittle, which makes their use in traditional jewelry virtually impossible. They can, however, be faceted and used as gemstones or inlays.

The best known among these compounds is $AuAl_2$, which is formed at 79 wt% Au and 21 wt% Al (Ref 15) (Fig. 38). (For a version with the weight percent linear, see Section 2, "Binary Alloy Phase Diagrams," in *Alloy Phase Diagrams*, Volume 3 of *ASM Handbook*). The compound is characterized by its beautiful purple color. The crystal structure of $AuAl_2$ was determined in 1934 to be the simple cubic CaF_2 structure. Recent research (Ref 16) has revealed that the aluminum sublattice is incompletely occupied and that the actual composition of $AuAl_2$ is closer to $Al_{11}Au_6$.

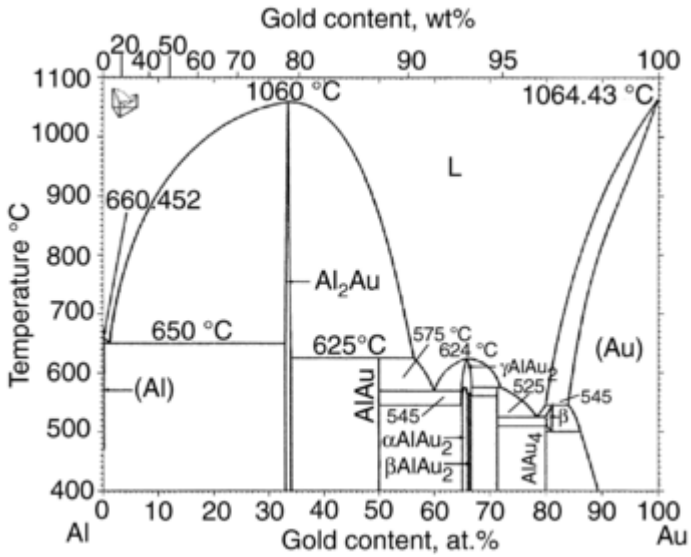

Fig. 38 Binary aluminum-gold phase diagram

Two other intermetallic compounds that are known to produce colors in gold alloys are $AuIn_2$, which has a clear blue color, and $AuGa_2$ (Ref 17), which displays a slightly bluish hue. The gold-indium intermetallic compound $AuIn_2$ forms at 46 wt% Au, and $AuGa_2$ forms at 58.5 wt% Au. Both have a crystal structure similar to the purple-gold compound, which is based on the CaF_2 prototype.

The purple-gold compound has received considerable attention from the microelectronics industry. If bonds between gold and aluminum in electronic devices are heat treated above 250 °C (480 °F), all five gold-aluminum intermetallic compounds (Au_4Al, Au_5Al_2, Au_2Al, AuAl, and $AuAl_2$) develop during diffusion of gold and aluminum (Ref 18). Studies conducted on bimetallic metal systems revealed that Au_2Al and Au_5Al_2 form first and that $AuAl_2$ is the final equilibrium phase (Ref 19, 20). Differential diffusion rates of aluminum and gold lead to formation of Kirkendall voids, causing porosity and eventual breakage of the aluminum-gold joint (Ref 21). This mechanical failure was nicknamed “purple plague.” However, although the purple-gold compound is brittle, it is stable and does not disintegrate with heat treatment (Ref 22).

The gold-aluminum phase diagram contains a number of intermetallic compounds formed at compositions situated close to the gold-rich end of the diagram. $AuAl_2$ has a gold content close to that of an 18 k alloy (75 wt% Au), which makes it possible to produce a hallmarkable 18 k purple alloy. The microstructure of an 18 k purple-gold alloy (75 wt% Au, 25 wt% Al) is shown in Fig. 39. The light-gray phase represents the purple intermetallic, and the dark phase represents aluminum (Ref 22). As the composition deviates from $AuAl_2$ toward the aluminum-rich side of the phase diagram, the color approaches that of aluminum. The volume percentage of the purple intermetallic phase decreases, with an increase in the second phase consisting of an aluminum-rich solid solution. The purple color is preserved until the aluminum content decreases to 15 wt% (Ref 23).

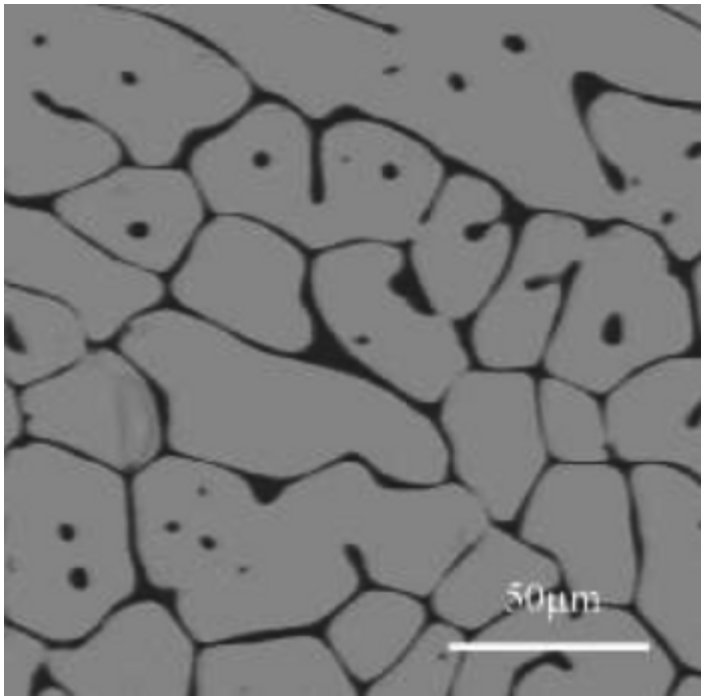

Fig. 39 Secondary electron image of 75Au-25Al (wt%) alloy, with the light phase representing $AuAl_2$ and the secondary phase representing aluminum

Gold catalysts can be produced from the Au_xAl_y intermetallic compounds (Ref 24, 25). Due to the brittleness of the Au_xAl_y precursor, the compound can be easily milled to fine powder. Subsequent leaching of the aluminum from the precursor Au_xAl_y powder results in a skeletal structure with good catalytic activity (Fig. 40).

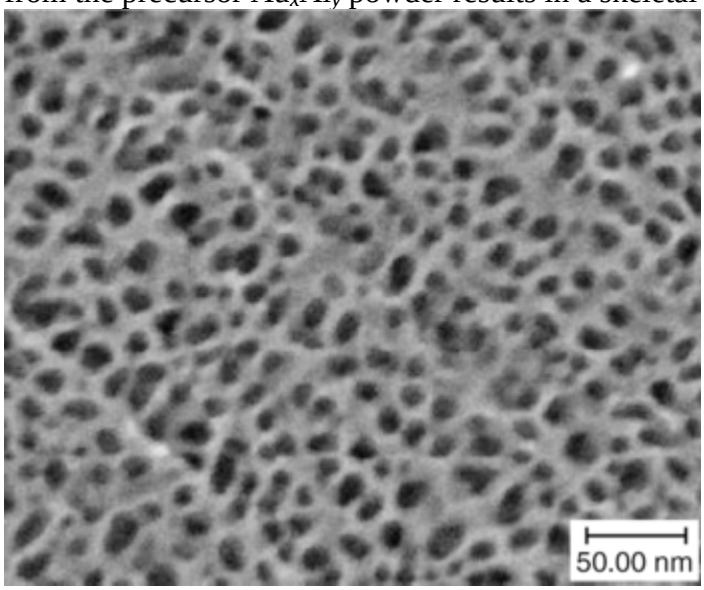

Fig. 40 High-resolution scanning electron micrograph of leached $AuAl_2$ revealing the skeletal gold mesoporous structure

Figure 41, 42 and 43 are backscattered electron images of $AuAl_2$ alloyed with 5 wt% Fe, Cr, and Mo, respectively. These alloying elements were added to investigate the effect of gold on catalytic activity for carbon monoxide oxidation. Various quantities of RuAl (50, 30, and 10%) were alloyed with $AuAl_2$ in Fig. 44, 45 and 46, respectively. All the micrographs of the AuRuAl alloys indicate that at least three to four phases are formed. All the phases consist of either gold with aluminum or ruthenium with aluminum, for example, AuAl, $AuAl_2$, and $RuAl_2$, which were confirmed by x-ray diffraction investigations.

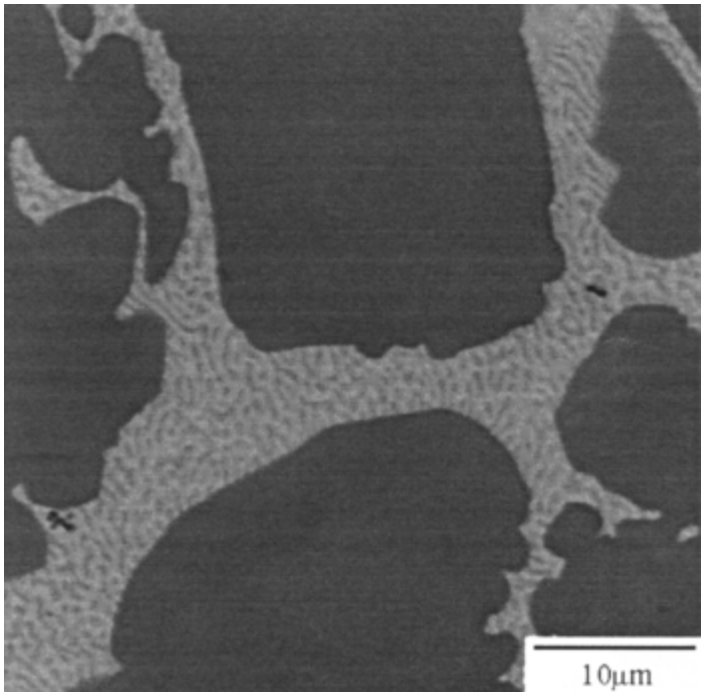

Fig. 41 Backscattered electron image of the $AuAl_2$ + 5 wt% Fe alloy. Iron is in solid solution in the matrix phase (74Au-21Al-5Fe), lowering the gold content in the $AuAl_2$ phase. The secondary phase consists of a eutectic mixture of AuAl and Au_2Al, with gold contents between 89 to 93 wt%.

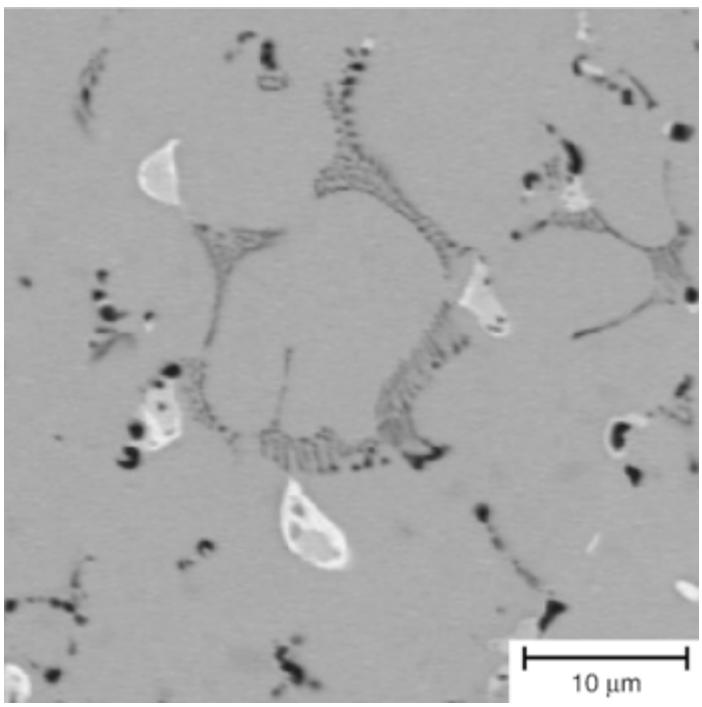

Fig. 42 Backscattered electron image of the $AuAl_2$ + 5 wt% Cr alloy. In the matrix (76.5Au-20.5Al-3Cr), the chromium has replaced some of the gold in the previous purple $AuAl_2$ phase. The secondary white phase appears to be a mixture of gold-rich intermetallic compounds (AuAl, Au_2Al, Au_4Al). A relatively large number of chromium-rich intermetallic compounds (black secondary phase) were present.

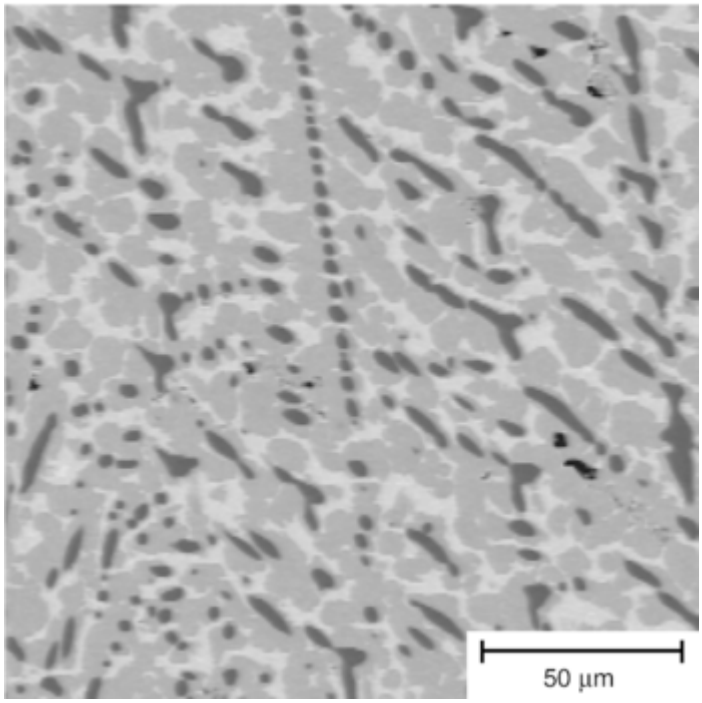

Fig. 43 Backscattered electron image of the $AuAl_2$ + 5 wt% Mo alloy. The ternary alloying element (molybdenum) can mainly be found in the secondary black phase, and the matrix consists of the purple $AuAl_2$ phase (dark gray). The secondary white phase consists of gold-rich intermetallic compounds and most likely AuAl and Au_2Al.

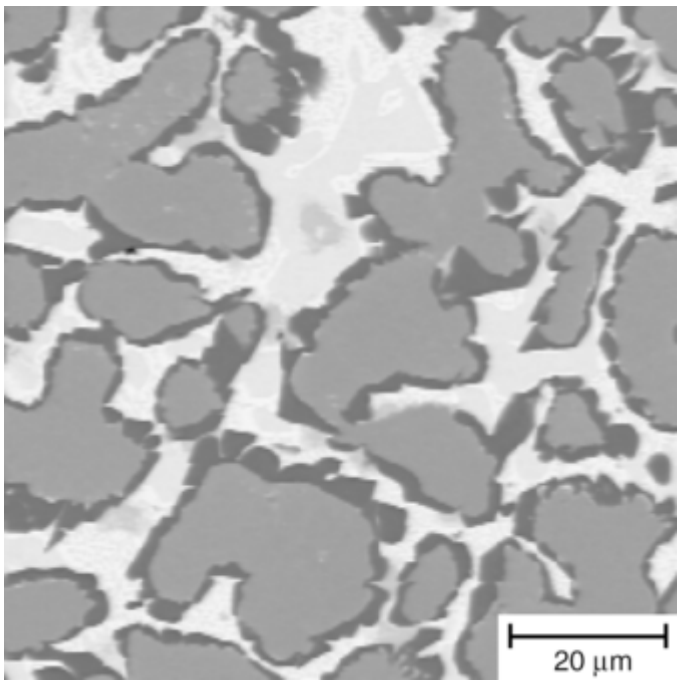

Fig. 44 Backscattered electron image of 50$AuAl_2$-50RuAl alloy. The white phase consists of ~6.4Al-92.5Au, the light-gray phase of ~12.2Al-87.8Ru, the gray phase of ~10.6Al-89.3Au, and the dark-gray phase of ~35.1Al-64.5Ru.

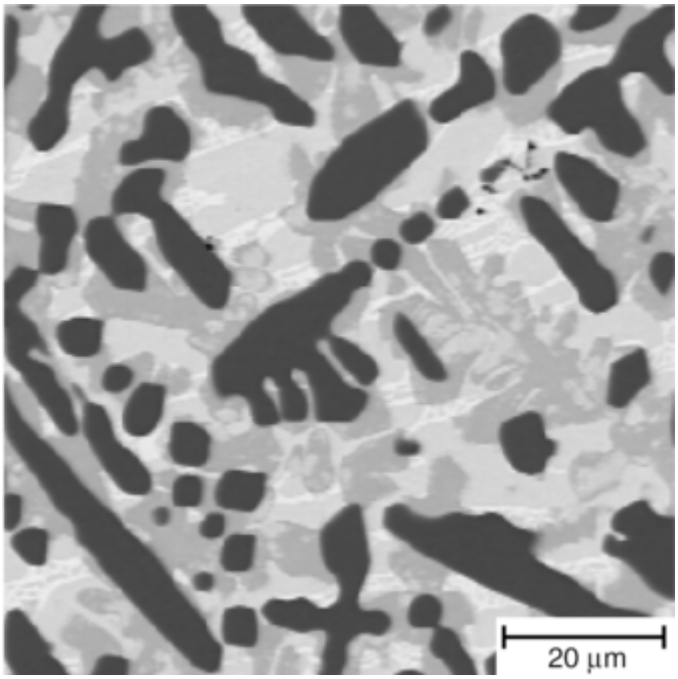

Fig. 45 Backscattered electron image of 70AuAl$_2$-30RuAl alloy. The white phase consists of ~6.8Al-93.2Au, the light-gray phase of ~12.2Al-87.8Ru, the gray phase of ~21.7Al-76.6Au, and the dark-gray phase of ~35.8Al-63.9Ru.

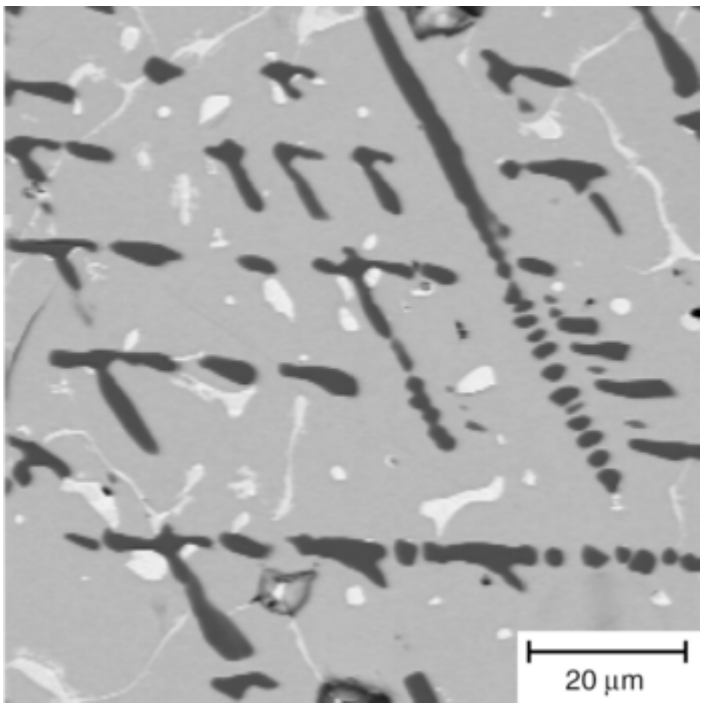

Fig. 46 Backscattered electron image of 90AuAl$_2$-10RuAl alloy. The white phase consists of ~8.3Al-91.7Au, the gray phase of ~21.4Al-77.1Au, and the dark-gray phase of ~35.6Al-63.8Ru.

References cited in this section

5. A.S. McDonald and G.H. Sistare, The Metallurgy of Some Carat Gold Jewelry Alloys, Part I, *Gold Bull.*, Vol 11 (No. 3), 1978, p 66–73

6. C.W. Corti, *Gold Bull.*, Vol 32 (No. 2), 1999, p 39

7. C.W. Corti, Assaying of Gold Jewelry-Choice of Technique, *Gold Technology,* No. 32, Summer 2001, p 20–30

8. M. du Toit, E. van der Lingen, L. Glaner, and R. Süss, *Gold Bull.,* Vol 35 (No. 2), 2002, p 46

9. R. Süss, E. van der Lingen, M. du Toit, C. Cretu, and L. Glaner Hard Gold Alloys *Gold Bull.,* in press, paper No. 985, Gold 2003 Conference; see www.gold.org

10. D. Ott, *Gold Technol.,* Vol 22, 1997, p 31

11. J.C. Chaston, *Gold Bull.,* Vol 4 (No. 4), 1971, p 70

12. F. Klotz and S. Grice, "Live and Let Die (Struck)," *Gold Technol.,* Vol 36, 2002, p 16

13. S. Grice, Failures in 14 kt Nickel White Gold Tiffany Head Settings, Proceedings of the 16th Santa Fe Symposium, Met-Chem Research, 2002, p 189–230

14. D. Ott, *Handbook on Casting and Other Defects in Gold Jewelry Manufacture,* World Gold Council, London, 1997

15. W.S. Rapson, *Gold Bull.,* Vol 29, 1996, p 141

16. H. Büchler and K.-J. Range, *J. Less-Common Met.,* Vol 160, 1990, p 143

17. K.E. Saeger and J. Rodies, *Gold Bull.,* Vol 10, 1977, p 10

18. W.S. Rapson, in *Intermetallic Compounds, Principles and Practice,* Vol 2, J.H. Westbrook and R.L. Fleischer, Ed., John Wiley & Sons, 1994, p 559

19. T. Inagaki, E.T. Arakawa, and T.A. Callcott, *J. Appl. Phys.,* Vol 52, 1981, p 5597

20. R. Pretorius, T.K. Marais, and C.C. Theron, *Materials Sci. Eng.,* Vol 10, 1993, p 1

21. T. Raymond, *Semicond. Int.,* Vol 12, 1989, p 152

22. R. Süss and C. Cretu, in *MSSA Proceedings,* Vol 28, M. McLean, J.A.A. Engelbrecht, J.H. Neethling, C. Dennison, D. Mycock, and R.H.M. Cross, Ed., (Johannesburg), Microscopy Society of Southern Africa 1998, p 20

23. S. Hori, K. Kurokawa, T. Shimizo, M. Steel, M. Tsuboi, and K. Yanagase, in *Precious Metals Science and Technology,* L.S. Benner, T. Suzuki, K. Meguro, and S. Tanaka, Ed., International Precious Metals Institute, 1991, p 430

24. E. van der Lingen, M.B. Cortie, H. Schwarzer, S.J. Roberts, and G. Pattrick, Gold Catalysts Prepared via Intermetallic Precursor Gold 2003 Conference, Paper No. 988 (Vancouver), 2003 World Gold Council, www.gold.org

25. G. Patrick, E. van der Lingen, H. Schwarzer, and S.J. Roberts, Development of Gold-Sponge Catalysts for Lean Buen De No_x Paper No. 993 Gold 2003 Conference, (Vancouver), 2003 World Gold Council, www.gold.org

E. van der Lingen, L. Cornish, S. Taylor, R. Süss, S. Grice, Metallography and Microstructures of Precious Metals and Precious Metal Alloys, *Metallography and Microstructures,* Vol 9, *ASM Handbook*, ASM International, 2004, p. 860–876

Metallography and Microstructures of Precious Metals and Precious Metal Alloys

Elma van der Lingen, Lesley Cornish, Stefanie Taylor, Rainer Süss, Physical Metallurgy Division, Mintek, South Africa; Stewart Grice, Hoover & Strong Inc.

Microstructures of Platinum and Platinum Alloys

Platinum Jewelry Alloys. Pure platinum is ductile, malleable, easily soldered, and takes a lustrous polish, but unless it is finished in a heavily cold-worked state, it is too soft for hardwearing jewelry. Small amounts of alloying elements can be added to platinum to improve its jewelry properties, such as castability and hardness.

The many platinum jewelry alloys in use around the world most generally conform to the international hallmarking standard of 950 Pt or 95 wt% Pt and 5 wt% other metal. Each country has its preferred platinum jewelry alloys, and often, there is no metallurgical reason for these choices, only tradition.

Historically, the common platinum alloys were PtRu, PtPd, and PtIr, but over the past 20 to 30 years, platinum alloys have been developed to meet specific needs. The high melting temperature of both platinum and the traditional platinum alloys, such as platinum-ruthenium, complicates the casting process. To address the problem, PtCo was developed as a casting alloy. This alloy has good fluidity when molten, thus resulting in better mold fill, and also gives castings with less porosity. The melting range is not significantly reduced, and the alloy has a good final hardness.

The platinum-ruthenium phase diagram (Section 2, “Binary Alloy Phase Diagrams,” in Alloy Phase Diagrams, Volume 3 of *ASM Handbook*) shows that at 5 wt% Ru, the platinum and ruthenium form a solid solution. The melting temperature of the alloy is more than 1800 °C (3270 °F), and a casting temperature of between 1995 and 2195 °C (3625 and 3985 °F) should be used, depending on the size of the casting (Ref 26). In comparison, an 18 k gold alloy can be cast at 950 °C (1740 °F). The addition of 5 wt% Ru increases the hardness of platinum from 50 to 130 HV.

Pt-5Pd is an alloy traditionally favored in Japan. The alloy is extremely soft (60 HV) and melts between 1755 and 1765 °C (3190 and 3210 °F), with casting temperatures the same as those for Pt-5Co. Platinum and palladium form an uninterrupted series of solid solutions, although the platinum-palladium phase diagram (Section 2, “Binary Alloy Phase Diagrams,” in the article “Au (Gold) Binary Alloy Phase Diagram” in *Alloy Phase Diagrams,* Volume 3 of *ASM Handbook*) indicates the existence of a decomposition transformation at approximately 770 °C (1420 °F) to form platinum-rich and palladium-rich phases.

Pt-5Ir is another of the traditional platinum jewelry alloys and is regarded as having high work hardenability for use in safety catches, springs, pins, chain, and mesh. At high temperatures, platinum and iridium form an unbroken series of solid solutions. However, at temperatures below approximately 975 °C (1785 °F), a miscibility gap forms, and the alloy decomposes into platinum-rich and iridium-rich phases (Section 2, “Binary Alloy Phase Diagrams,” in *Alloy Phase Diagrams,* Volume 3 of *ASM Handbook*). A 5 wt% Ir alloy may fall into this region of the phase diagram, thus explaining the increased hardness values and the hardening properties. The alloy hardness increases to 80 HV with an addition of 5 wt% Ir.

Platinum with 5 wt% Co melts between 1750 and 1765 °C (3180 and 3210 °F) and should be cast at temperatures between 1965 and 2165 °C (3570 and 3930 °F). The platinum-cobalt phase diagram (Section 2, “Binary Alloy Phase Diagrams,” in *Alloy Phase Diagrams,* Volume 3 of *ASM Handbook*) indicates that an order-disorder transformation (Pt_3Co) occurs at approximately 91 wt% Pt. However, in the region of 5 wt% Co addition, there is uncertainty regarding this transformation, and the alloy may well lie inside the Pt_3Co phase field. This could explain the large increase in alloy hardness from 50 HV for pure platinum to 135 HV for Pt-5Co in the annealed condition.

Many of the platinum jewelry alloys are single-phase material, and thus, a study of the microstructure can only be used to determine grain size, porosity, inclusions, and processing and/or heat treatment history.

Platinum alloys require aggressive etching solutions, including various mixtures of hot nitric acid and hydrochloric acid. Platinum and its alloys can also be immersed in a solution of potassium cyanide mixed with

ammonium persulfate. Electrolytic etchants include a solution of hydrochloric acid and sodium chloride, sodium cyanide solution, and concentrated hydrochloric acid. The latter is particularly useful as a grain contrast etch. Other electrolytic etching solutions include sulfuric acid, a mixture of sodium chloride solution and concentrated hydrochloric acid (for revealing grain boundaries), and excellent results are recorded for a mixture of hydrochloric acid and alcohol.

Figure 47 shows a 95Pt-5Ru investment casting and illustrates the effect of dissolved gas in the liquid metal being released on solidification. The casting freezes before the gas can escape, resulting in the spherical porosity noted.

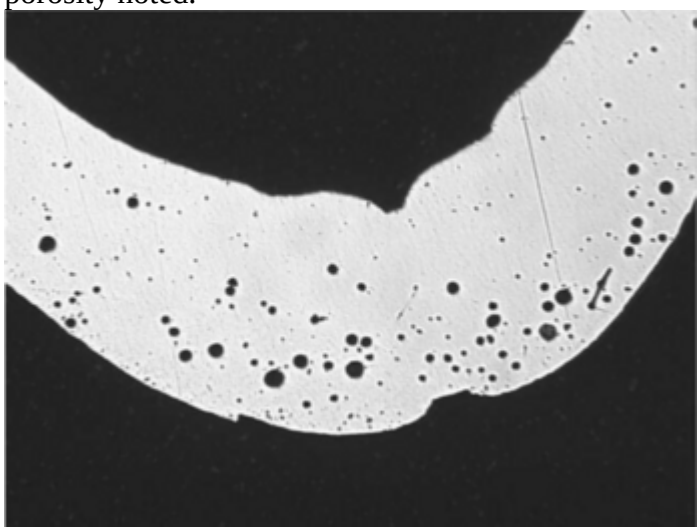

Fig. 47 A casting of a Pt-5Ru alloy showing the effect of dissolved gas in the liquid metal being released on solidification

Figure 48 is a 95Pt-5Ru investment casting and shows the effect of gas evolution from the investment mold, resulting in a rough, porous surface. The surface layer is approximately 100 to 150 μm deep. Note that the remainder of the section is completely porosity-free, a sure indication that an investment mold reaction has occurred. The platinum smith should be able to remove this surface layer mechanically and use the casting. These specimens were ground and polished in the conventional way, finishing with a 1 μm diamond polish.

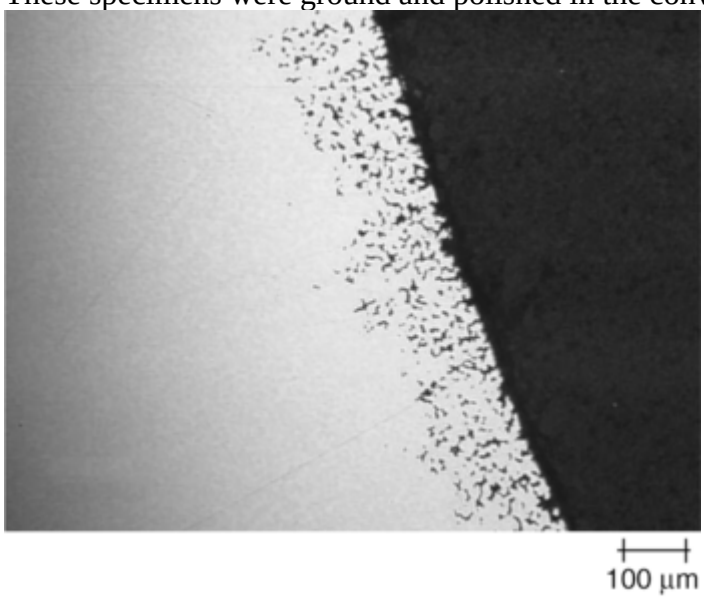

Fig. 48 A Pt-5Ru alloy showing the effect of gas evolution during investment casting

The samples in Fig. 49 were prepared with an etching solution using 25 g NaCl, 20 mL HCl, and 65 mL distilled water. Electrolytic etching was done with a graphite cathode. The specimen was partly coated with colloidal silver liquid, and a stainless steel clamp was used to connect the anode and the specimen. A 10 V

alternating current source was used, and the etching time varied between 40 s and 5 min. A fresh solution was used for etching.

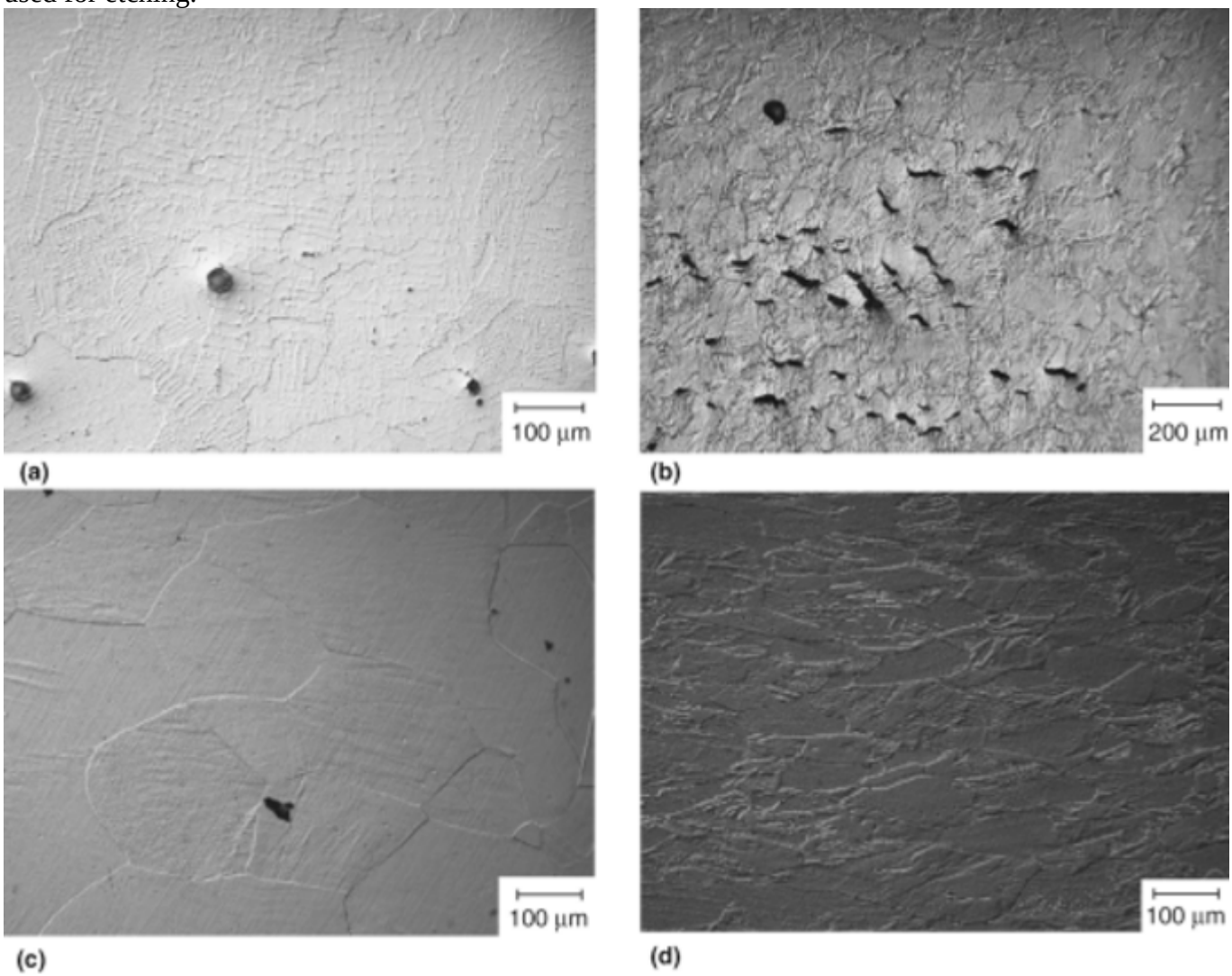

Fig. 49 Micrographs of Pt-5Cu alloy using interference contrast. (a) As cast. (b) Annealed. (c) Annealed. (d) With 50% cold deformation

A light microscope using interference contrast was used to make the micrographs of the Pt-5Cu alloy (Fig. 49), which show the effect of processing. In Fig. 49(a), the cast alloy was melted and cast in water. In Fig. 49(b) and (c), the annealed alloy was melted and cast into a mold, then cold rolled by approximately 50% reduction and annealed at temperatures of 1000 °C (1830 °F) for 2 to 3 min, then quenched into water. Figure 49(d) illustrates an alloy with 50% cold deformation.

The 95Pt-5Ru sample was prepared in the same way as the previously mentioned 95Pt-5Cu sample. The as-cast alloy using interference contrast is seen in Fig. 50.

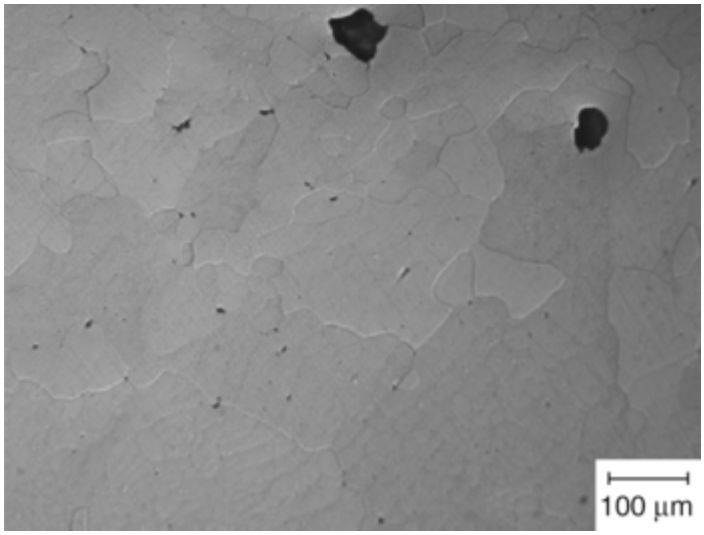

Fig. 50 Pt-5Ru alloy as cast. Interference contrast

Platigems—Pt-Al-Cu Alloys. $PtAl_2$ is an intermetallic compound, which, in contrast to the component elements, appears yellow to the naked eye. $PtAl_2$ forms by means of a peritectic reaction, so that cooling even a stoichiometric $PtAl_2$ liquid must result in initial formation of a $PtAl_2$ + Pt_2Al_3 mix (Section 2, "Binary Alloy Phase Diagrams," in *Alloy Phase Diagrams,* Volume 3 of *ASM Handbook.*) The alloy thus comprises two phases: one yellow ($PtAl_2$) and one blue (Pt_2Al_3). The latter phase has a needlelike morphology.

Preparation of the samples for scanning electron microscopy (SEM) was carried out using a colloidal silica polish. The method is ideal for viewing the two phases, either by light microscope or SEM. The specimen is mounted and polished to a 1 μm finish, then polished using a colloidal silica solution for 15 min, using light pressure.

Figure 51 shows needles of blue Pt_2Al_3 phase (light area) in a matrix of yellow $PtAl_2$. Another area of the sample, Fig. 52(a) at low magnification, shows a different morphology related to the cooling of the button-shaped sample. Figure 52(b) details the difference at the interface in the zones seen in Fig. 52(a).

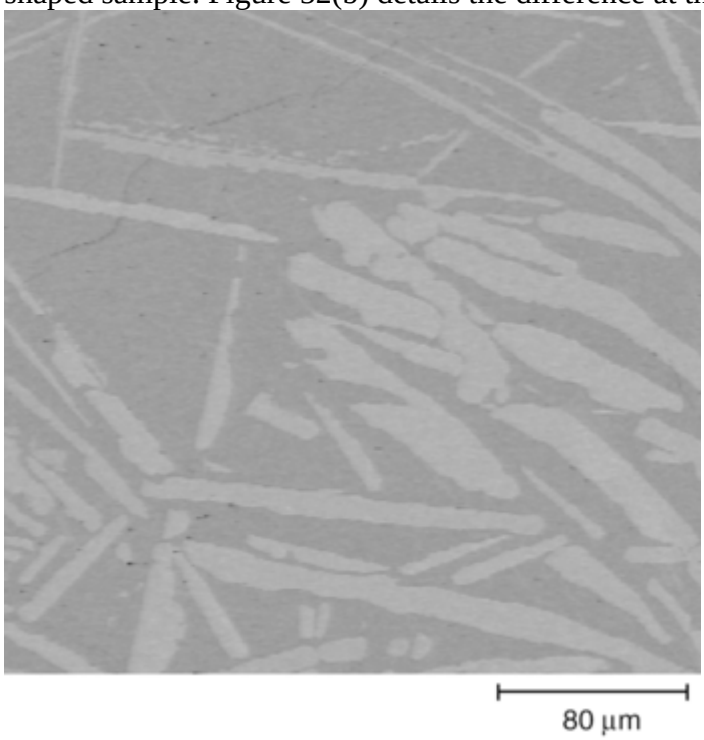

Fig. 51 Backscattered SEM image of two-phase platinum-aluminum alloy. The needlelike structures are Pt_2Al_3 in a matrix of $PtAl_2$. 300×

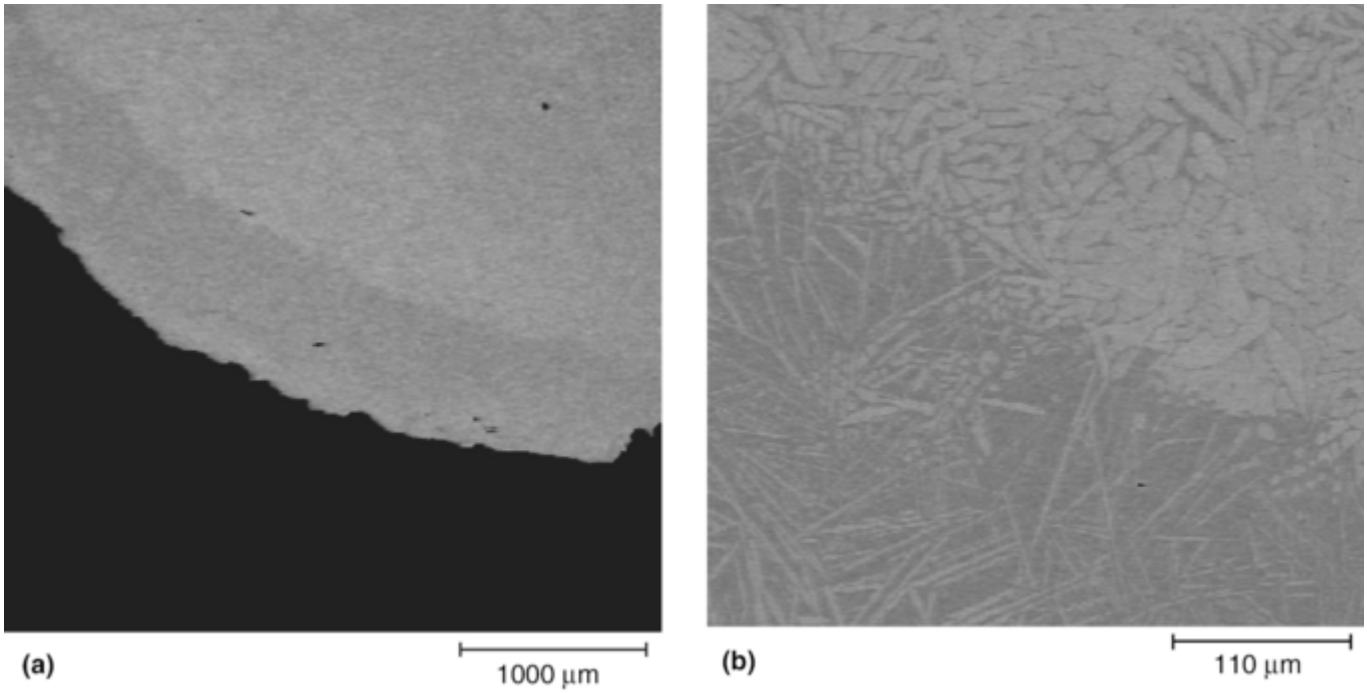

Fig. 52 Backscattered SEM image of the outer edge of the platinum-aluminum sample. (a) 25×. (b) The interface between the predominantly blue Pt_2Al_3 phase area (light gray) and the predominantly yellow $PtAl_2$ phase area (dark gray). 220×

When copper is added to the platinum-aluminum alloy (Ref 27, 28), the metal becomes a dusky-pink color. A composition of 64.5Pt-19Al-16.5Cu shows a two-phase structure (Fig. 53), with a predominant pink phase and a white grain-boundary phase. The more extensive pink phase (the light phase) has a composition of approximately 66Pt-19Al-15Cu, while the composition of the white grain-boundary phase (the dark phase in Fig. 53) is approximately 22Pt-17Al-61Cu. X-ray diffraction analysis indicates that the main pink phase is based on the PtA_{12} structure but with a slightly larger cubic lattice.

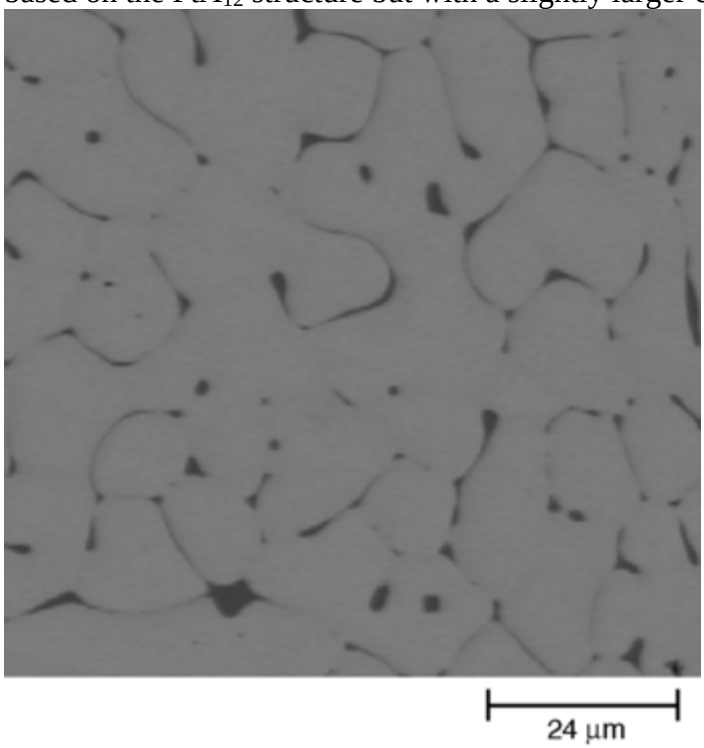

Fig. 53 Backscattered SEM image of pink 64.5Pt-19Al-16.5Cu alloy. 1000×

A shape memory alloy (SMA) is an alloy that can change shape, either through reaching a critical temperature or through reaching a critical stress. The SMAs can be one-way, returning to the starting (parent) shape on heating, or they can be trained by repeated cyclic deformation to be two-way SMAs, that is, to have two different shapes. These shapes would be one specific shape for the parent phase and one for the product phase. This works through a martensitic-type transformation between two different crystal structures that exist at different temperatures but are the same composition. The transformation allows the alloy to return to a previous shape after deformation, when heated to a specific temperature or when subjected to sufficient stress. Platinum-containing SMAs could be useful for applications demanding high temperatures or relative inertness. Shear transformations are those in which a shear is involved, and the shape change thus arises from the different crystal structures of the two phases: parent (high temperature) and product (lower temperature). Martensitic transformations are a special case of shear transformation and involve (among many other things) no diffusion of atoms, resulting in a change in shape. Many SMAs have a β electron compound as the high-temperature parent phase and a low-temperature martensite phase that is an ordered version of the parent high-temperature phase. These martensite phases are either internally twinned or internally faulted (Ref 29), and it is this feature that is easily seen when studying the microstructure. Platinum has been added to the SMA Nitinol (base composition 50 at.% Ti-Ni), and other potential alloys have been identified (Ref 30). In the platinum-aluminum system, the Pt_3Al phase has at least two forms, with a martensitic-like transformation between them. The transformation between the two phases has a very steep temperature-composition curve in binary platinum-aluminum, so ternary additions have been made in an attempt to make the transformation temperature less composition-dependent. The micrographs in Fig. 54 and 55 show Pt-Al-Ni alloys. Other additions, such as titanium, tantalum, and iridium, have been tried. Other alloys that showed potential, but with different phases, include Pt-Ti-Ni (Fig. 56) and Ti-Pt-Ru (Fig. 57). Other alloys exhibit martensitic-like transformations to ordered phases and could have potential, such as platinum-chromium (Fig. 58) and platinum-copper (Fig. 59).

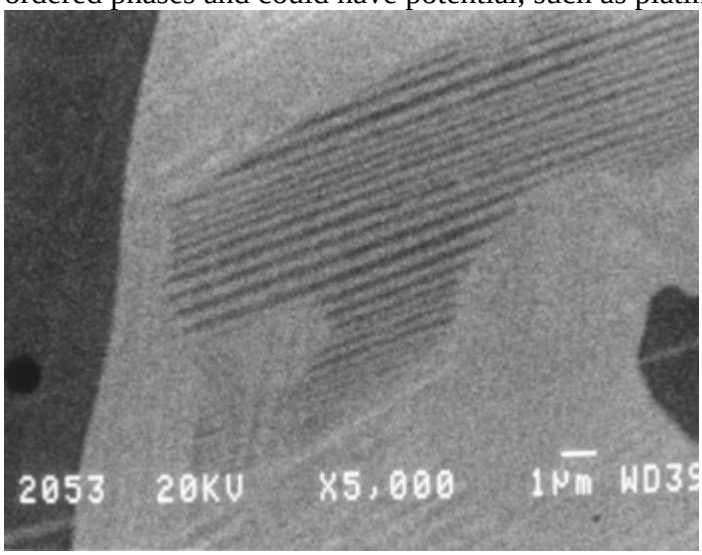

Fig. 54 Scanning electron microscope image in secondary electron mode of 56Pt-24Al-20Ni (at.%) alloy after arc melting and colloidal silica polishing, showing tetragonal ~Pt_3Al



Fig. 55 Optical micrograph of 64Pt-25Al-11Ni (at.%) alloy after heat treatment at 1350 °C (2460 °F) for 3 days, furnace cooling, and etching in aqua regia, showing martensitic laths of ~Pt_3Al

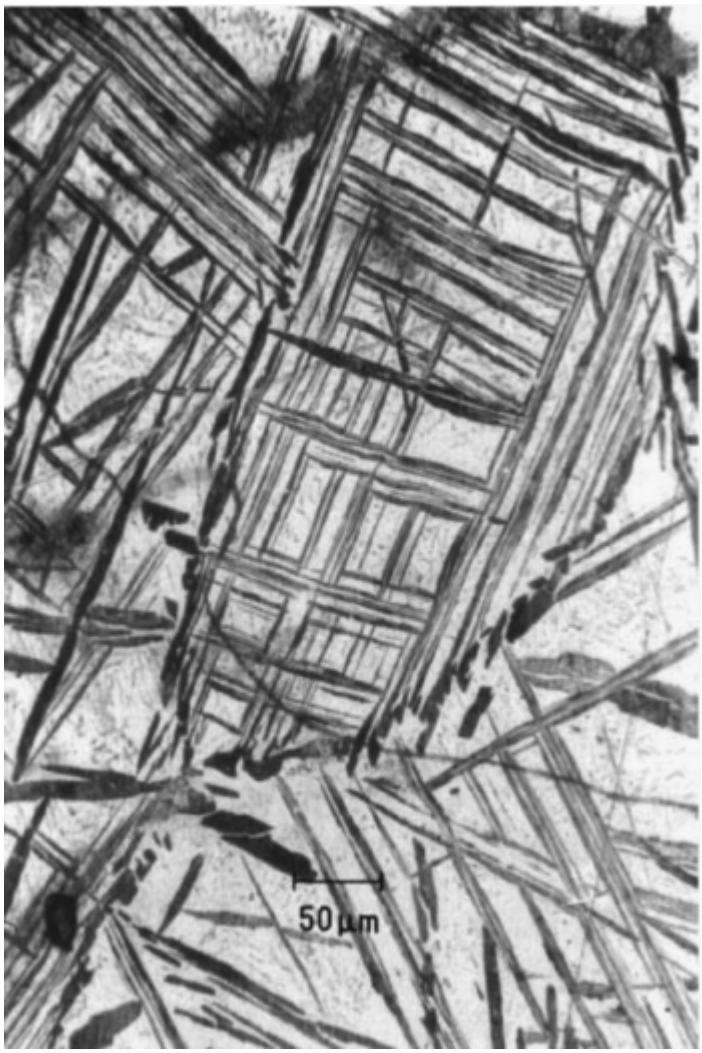

Fig. 56 Optical micrograph of 79.9Pt-20Ti-0.1Ni (wt%) alloy heat treated at 1200 °C (2190 °F), furnace cooled, and etched in aqua regia for 5 min, showing laths of αTiPt



Fig. 57 SEM image in backscattered mode of 46Pt-49Ti-5Ru (at.%) alloy heat treated at 1200 °C (2190 °F) and furnace cooled, showing laths of αTiPt



Fig. 58 Optical micrograph of 80Pt-20Cr (at.%) alloy after heat treatment at 1200 °C (2190 °F) for 3 days, furnace cooling, and etching in aqua regia, showing typical microstructure of α′ laths



Fig. 59 Scanning electron microscope image in backscattered mode of 81Pt-19Cu (wt%) alloy after heat treatment at 1200 °C (2190 °F) for 3 days, furnace cooling, and etching in aqua regia, showing laths of ordered PtCu

The samples were prepared by normal metallographic techniques, followed by colloidal silica polishing or etching in aqua regia. Colloidal silica polishing uses a combination of chemical and gentle abrasive action of the oxide (amorphous silica) suspension in colloidal silica (grain size, 0.04 μm; pH, 9.8). The method allows selective polishing of the softer phases and renders etching unnecessary. The aqua regia solution was usually warm and was 50% diluted with water (3 to 1 mixture of concentrated HCl to HNO_3).

Platinum-Base Alloys for High-Temperature Use. Nickel-base superalloys have virtually reached their temperature limit for operation in turbine engines. The operational temperatures of these engines need to be increased to achieve greater thrust, reduced fuel consumption, and lower pollution. Platinum has been selected as the base material for a suite of new-generation superalloys being developed, because of its similarity to nickel in fcc structure and chemistry. Platinum has a higher melting point (1769 °C, or 3216 °F, compared to 1455 °C, or 2651 °F, for nickel) and improved corrosion resistance. Although platinum-base alloys are unlikely to replace all nickel-base superalloys due to higher price and higher density, it is likely that they can be used for the components in the highest-temperature applications. Pt_3Al has two forms. The more desirable high-temperature $L1_2$ form can be stabilized by alloying additions such as ruthenium or chromium. These platinum-base alloys have the same microstructure as a standard nickel-base superalloy: ordered γ' precipitates in a γ (fcc) matrix. A number of ternary alloys, including Pt-Al-Cr (Fig. 60), have the required structure. A quaternary alloy composition has been optimized at 84Pt-11Al-2Ru-3Cr (at.%) for the best microstructure (Fig. 61) and hardness. These and similar alloys are prepared by conventional metallographic methods. Samples were prepared with colloidal silica for SEM.

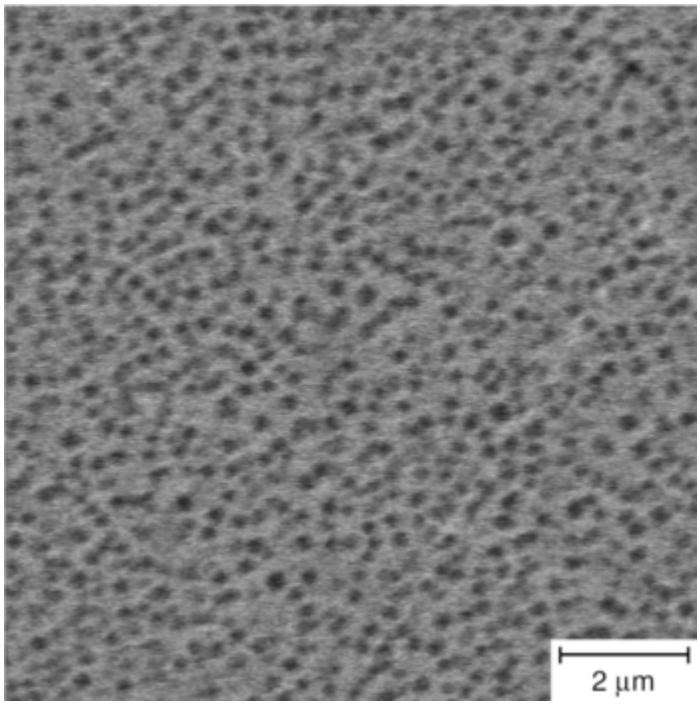

Fig. 60 Scanning electron microscope micrograph in backscattered electron mode of 86Pt-10Al-4Cr (at.%) alloy annealed at 1350 °C (2460 °F) for 96 h, showing a fine mixture of platinum-rich solid solution (light contrast) and ~Pt_3Al (dark contrast)

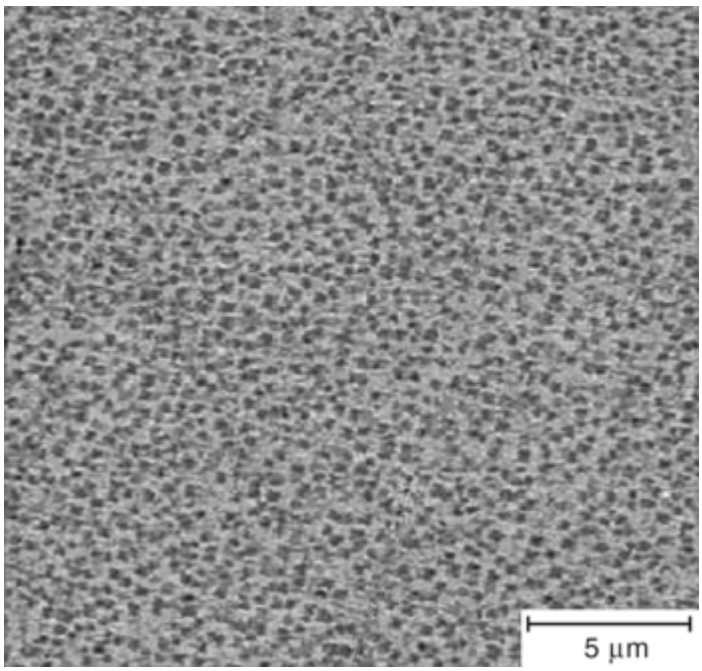

Fig. 61 Scanning electron microscope micrograph in backscattered electron mode of 84Pt-11Al-2Ru-3Cr alloy annealed at 1350 °C (2460 °F) for 96 h, showing a fine mixture of platinum-rich solid solution (light contrast) and ~Pt_3Al (dark contrast)

Miscellaneous Alloys Containing Platinum. Other platinum alloys with interesting microstructures include Pt-Ti-Re and Ru-Pt-Nb- (Ref 31) alloys. These were prepared metallographically in the normal way, then polished using an acidic alumina polish for 15 min at the lowest pressure possible and etched in boiling aqua regia. The samples are shown in Fig. 62 and Fig. 63.

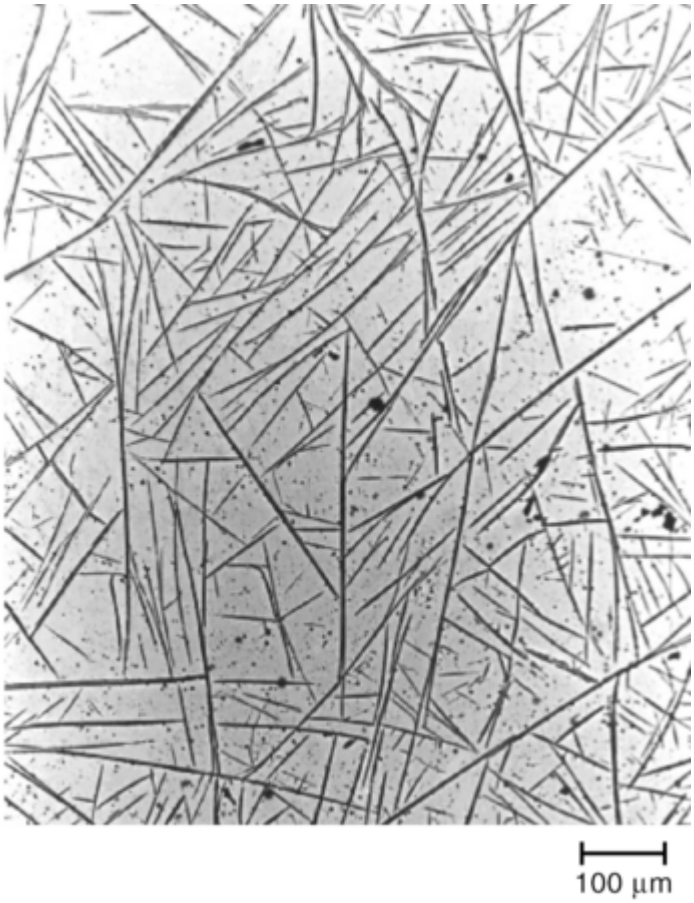

Fig. 62 Light micrograph of 73Pt-22Ti-4Re (wt%) alloy etched in boiling aqua regia, showing needles of rhenium solid solution (dark) in a matrix comprising γ (~Pt_3Ti) and platinum-rich solid solution (both light gray)

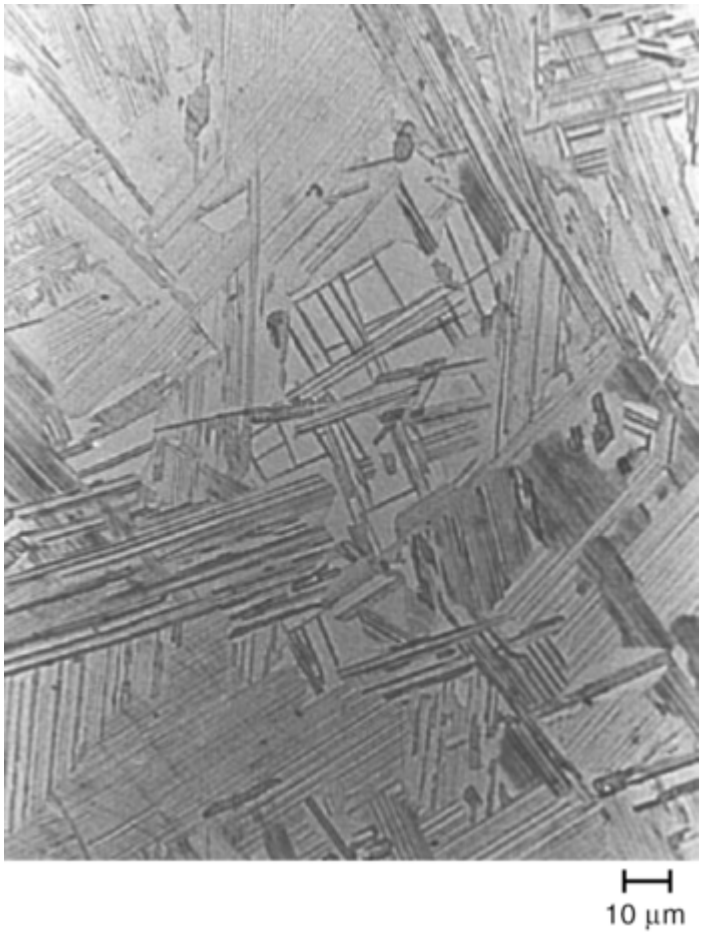

Fig. 63 Light micrograph of 72Pt-16Ru-12Nb (wt%) alloy etched in boiling aqua regia, showing laths of ~Pt_3Nb in a platinum solid-solution matrix

References cited in this section

26. "An Introduction to Platinum," Johnson Matthey 1990

27. J. Hurly, U.S. Patent 5,045,280; South Africa Patent 90/7777, 1989

28. J. Hurly and P.T. Wedepohl, Optical Properties of Colored Platinum Intermetallic Compounds, *J. Mater. Sci.,* Vol 28, 1993, p 5648–5653

29. C.M. Wayman, Thermoelastic Martensitic Transformations and the Shape Memory Effect, *Noble Metal Alloys,* T.B. Massalski et al., Ed., AIME, 1986, p 181–196

30. T. Biggs, M.B. Cortie, M.J. Witcomb, and L.A. Cornish, Platinum Alloys for Shape Memory Applications, *Platin. Met. Rev.,* Vol 47, 2003, p 142–156

31. P.J. Hill, "Superalloy Analogues Based on Platinum for Ultra-High Temperature Applications," Ph.D. dissertation, University of the Witwatersrand, Johannesburg, 2001

E. van der Lingen, L. Cornish, S. Taylor, R. Süss, S. Grice, Metallography and Microstructures of Precious Metals and Precious Metal Alloys, *Metallography and Microstructures*, Vol 9, *ASM Handbook*, ASM International, 2004, p. 860–876

Metallography and Microstructures of Precious Metals and Precious Metal Alloys

Elma van der Lingen, Lesley Cornish, Stefanie Taylor, Rainer Süss, Physical Metallurgy Division, Mintek, South Africa; Stewart Grice, Hoover & Strong Inc.

Other Precious Metals

Palladium has various uses, such as catalysts in catalytic converters, fuel cells, and as electrical contact material. It is very malleable and ductile and is used as a nonallergic addition to whiten gold alloys. Palladium is the least dense of the platinum-group metals (PGMs) and is an attractive jewelry metal, being commonly alloyed with silver or molybdenum as well as the other PGMs. The excellent ductility and good electrical conductivity mean that the alloys can also be used for wires and other electronic contacts. Palladium alloys are also used for thermocouples.

The micrographs in Fig. 64, 65, 66 and 67 show palladium alloys that were prepared metallographically in the conventional way. An electrolytic etch of 90 mL (96%) ethanol and 10 mL (1.19 specific gravity) HCl was used at 10 V direct current for 30 s. The final polish was undertaken using 0.25 μm diamond paste.

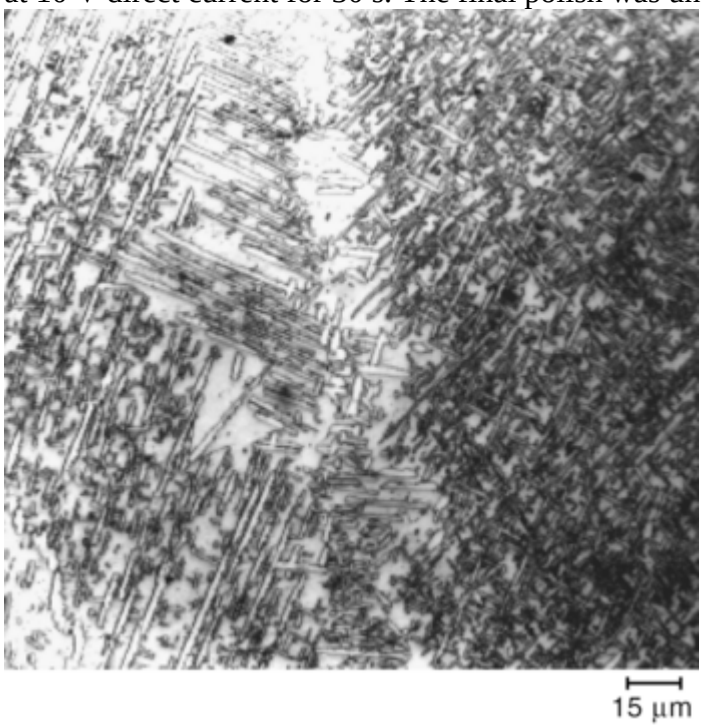

Fig. 64 Light micrograph of nominal 81Pd-19Ru (at.%) alloy annealed at 1150 °C (2100 °F) for 1406 h and 1200 °C (2190 °F) for 989 h, showing ruthenium-rich hexagonal close-packed needles in a palladium-rich face-centered cubic matrix. 400×

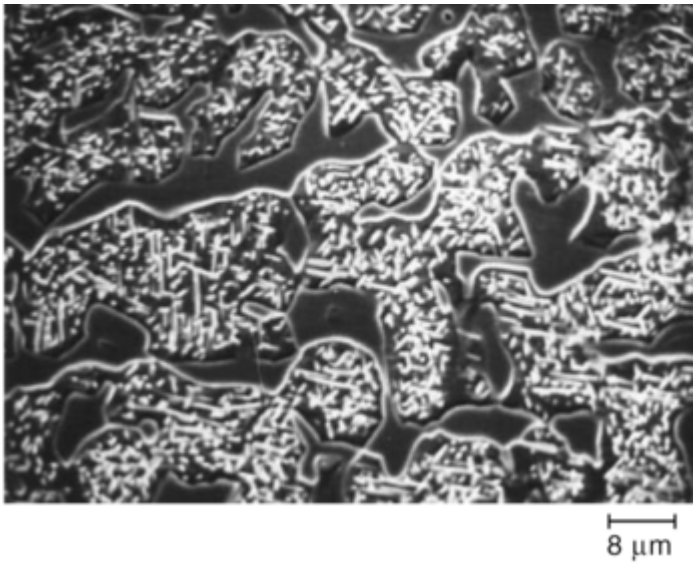

Fig. 65 Scanning electron microscope micrograph in secondary electron mode of nominal 20Pd-80Mo (at.%) alloy annealed at 1200 °C (2190 °F) for 1312 h, showing molybdenum-rich body-centered cubic dendrites with palladium-rich face-centered cubic needles (precipitated in the solid state) in a palladium-rich face-centered cubic matrix. 1250×

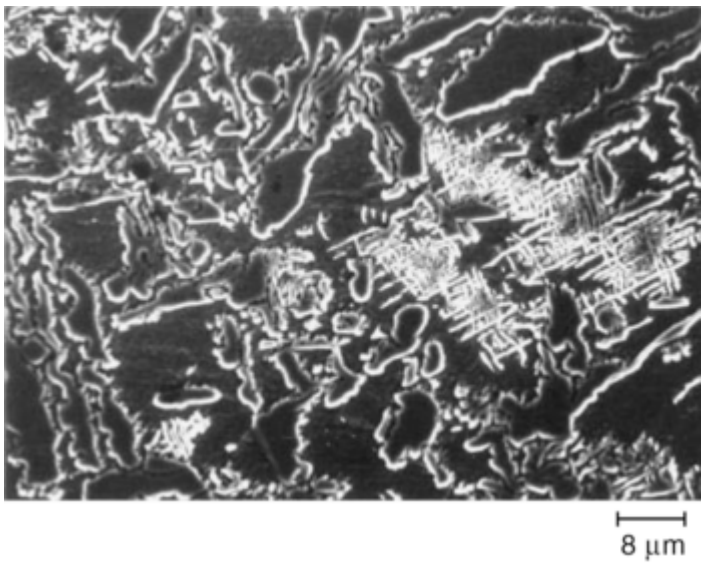

Fig. 66 Scanning electron microscope micrograph in secondary electron mode of nominal 60Pd-30Ru-10Mo (at.%) alloy annealed at 1200 °C (2190 °F) for 1345 h, showing ruthenium-rich hexagonal close-packed needles in a palladium-rich face-centered cubic matrix. The smaller needles were precipitated in the solid state. 1250×

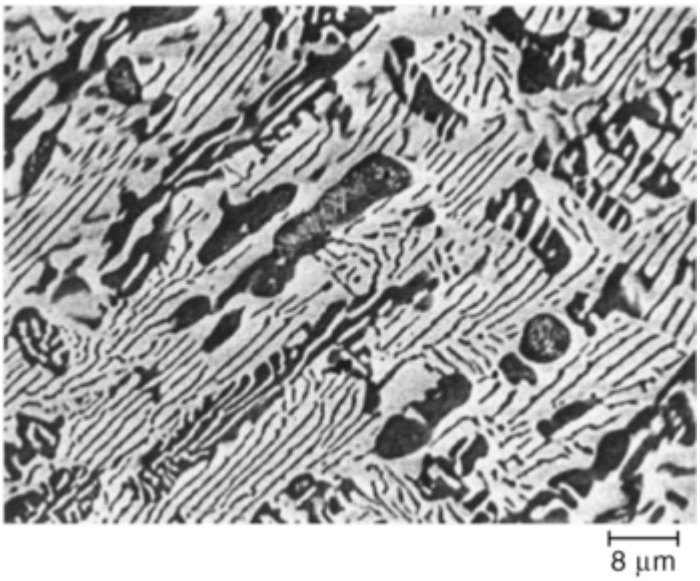

Fig. 67 Scanning electron microscope micrograph in backscattered electron mode of nominal 70Mo-20Pd-10Ru (at.%) alloy annealed at 1200 °C (2190 °F) for 840 h, showing molybdenum-rich body-centered cubic (dark contrast) and ruthenium-rich hexagonal close-packed (light contrast). 1250×

Iridium alloys are outstanding candidates for high-temperature applications, because they have a very high melting point (2433 °C, or 4411 °F), a high elastic modulus, high strength that is maintained at elevated temperatures, excellent creep resistance, and good resistance to oxidation and corrosion (Ref 32). Iridium has found application in environments such as coatings in combustion chambers that must withstand temperatures of up to 2260 °C (4100 °F) (Ref 33). It is, however, very brittle at room temperature (Ref 34). Ordered intermetallic compounds containing iridium have several favorable properties, such as good high-temperature strength and oxidation resistance. Much of the current research into intermetallic compounds is driven by the need for high-temperature structural materials for gas turbine engines. The major obstacle to the application of these materials is that they have low toughness and ductility at room temperature. It has been shown that AlRu intermetallic compounds have reasonable room-temperature toughness and ductility (Ref 35). The mechanical properties of IrAl intermetallic compounds have also been investigated to establish whether they may find useful applications (Ref 36, 37). It was found that the eutectic between iridium-rich solid solution and AlIr (Fig. 68) has a beneficial effect on the material toughness. Alloys based on AlIr with a stoichiometric excess of aluminum are more brittle due to the presence of $Al_{2.7}Ir$, which has a faceted structure (Fig. 69).

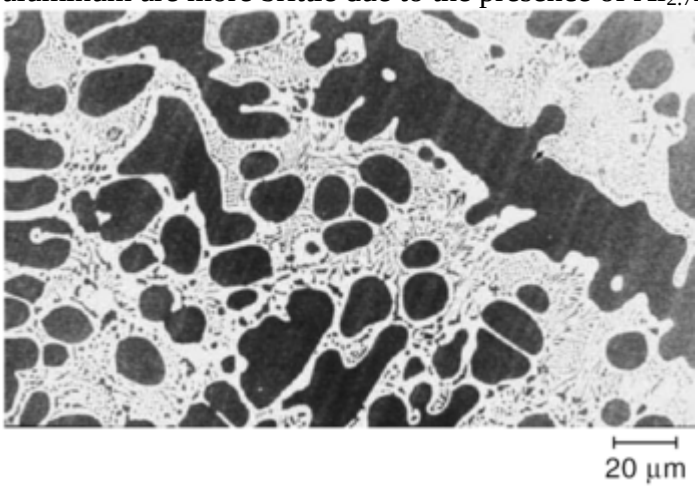

Fig. 68 Backscattered electron image of 38Al-62Ir (at.%) alloy showing dark AlIr and a eutectic mixture of dark AlIr and light iridium-rich solid solution

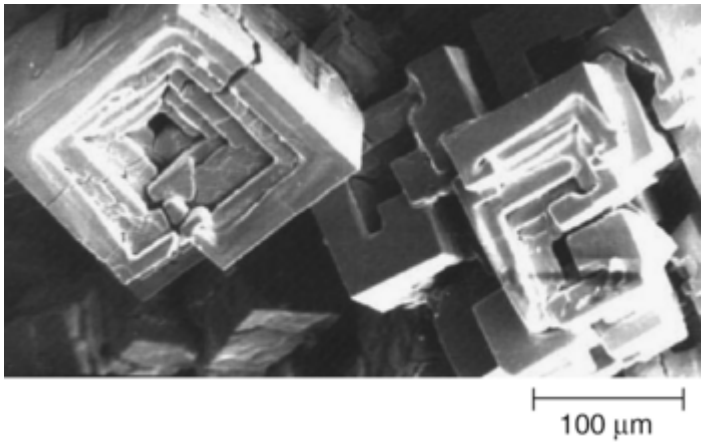

Fig. 69 Backscattered electron image showing cracks within $Al_{2.7}Ir$ crystals on nominal 77Al-23Ir (at.%) alloy

The specific specimens were ground using SiC grinding paper to a 1200-grit finish, then polished on a 1 μm diamond wheel. The etchant was Murakami's reagent (10 g $K_3Fe(CN)_6$, 10 g NaOH, 100 mL water).

Ruthenium Alloys. The intermetallic compound RuAl has been identified as having potential for high-temperature applications, due to its good strength at elevated temperatures as well as its relatively good ductility compared to other intermetallic compounds (Ref 38, 39). It also has very good corrosion resistance in strong acids (Ref 40), and its use as a corrosion-resistant coating has been demonstrated (Ref 41). The electronic conductivity is high, almost metallic, and it exhibits good work function attributes (Ref 42). These properties, as well as good thermal conductivity (Ref 43), make the RuAl compound a potential material for spark-plug electrodes (Ref 44). The material has a high melting point and can be processed using powder metallurgical techniques. The optimal microstructure contains primary RuAl with some eutectic RuAl + Ru-rich solid solution at the grain boundaries. The specimen shown in Fig. 70 was prepared by normal metallographic techniques, finishing at 1 μm. Etching is not necessary if SEM is used, although etching in Murakami's reagent (10 g $K_3Fe(CN)_6$, 10 g KOH, 100 mL water) is needed for light microscopy. Low-ruthenium-content alloys need only 10 s immersion, whereas the higher-ruthenium-content alloys (near 50 at.%) require up to 30 s. Figure 71 shows a lower-ruthenium-content alloy; these often have additional phases from the cascade of peritectic reactions in the aluminum-ruthenium system.

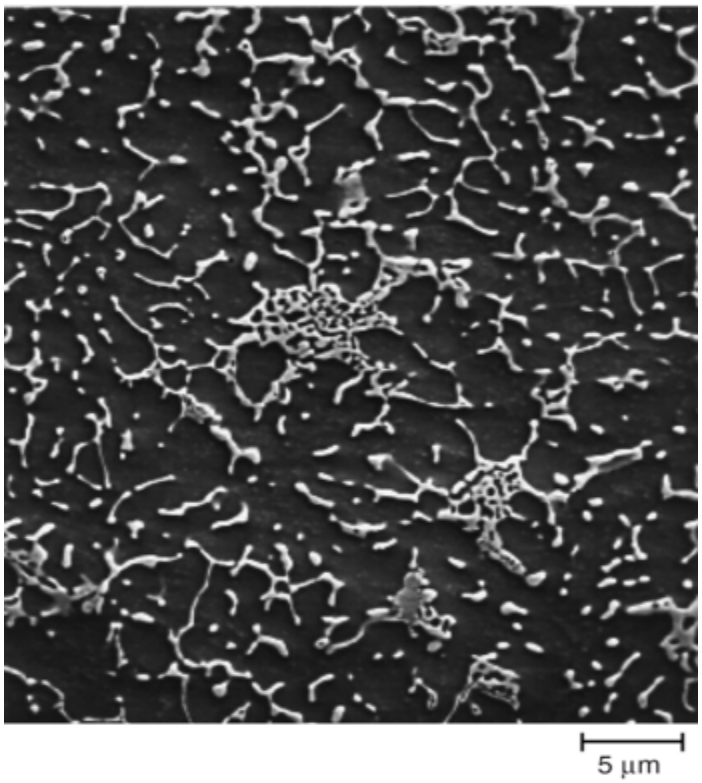

Fig. 70 Scanning electron microscope micrograph in secondary electron mode of nominal 28Ru-72Al (at.%) alloy annealed at 1300 °C (2370 °F) for 6.5 h, showing RuAl dendrites surrounded by eutectic comprising RuAl + Ru-rich solid solution



Fig. 71 Scanning electron microscope micrograph in secondary electron mode of nominal 4Ru-98Al (at.%) alloy as cast, showing primary $RuAl_6$ needles (light contrast) in a fine eutectic comprising $RuAl_6$ + Al-rich solid solution (dark contrast)

References cited in this section

32. “Iridium,” The International Nickel Company (MOND), Thames House, London, 1995

33. I.M. Wolff and G. Sauthoff, *Metall. Mater. Trans. A,* Vol 27, 1996, p 2642–2652

34. C.N. Reid and J.L. Routbort, *Metall. Trans. A,* Vol 3, 1972, p 2257–2259

35. R.L. Fleischer, R.D. Field, and C.L. Briant, *Metall. Trans. A,* Vol 24, 1991, p 403–413

36. P.J. Hill, “The Microstructure and Mechanical Properties of Al-Ru-Ir Alloys,” master's thesis, University of the Witwatersrand, Johannesburg, 1998

37. P.J. Hill, L.A. Cornish, and M.J. Witcomb, *Proc. Micros. Soc. South Afr.,* Vol 27, 1997, p 17

38. R.L. Fleischer, R.D. Field, and C.L. Briant, Mechanical Properties of High Temperature Alloys of AlRu, *Metall. Trans. A,* Vol 22, 1991, p 404–414

39. R.L. Fleischer and D.W. McKee, Mechanical and Oxidation Properties of AlRu-Based High-Temperature Alloys, *Metall. Trans. A,* Vol 24, 1993, p 759–763

40. W. Wopersnow and C.J. Raub, Eigenshaften Einiger Binärer Intermetallischen Phasen des Palladiums und Rutheniums mit Anderen Metallens, *Metall. Technik,* Vol 33, 1979, p 736–740

41. J.J. McEwan and T. Biggs, “Exploiting the Excellent Corrosion Resistance of a Precious Metal Aluminide,” Paper 096, 13th International Corrosion Congress (Melbourne, Australia), ACA Inc., 1996

42. E.G. Smith and C.I. Lang, High Temperature Resistivity and Thermo-emf of RuAl, *Scr. Metall. Mater.* Vol 33, 1995, p 1225–1229

43. S.A. Anderson and C.I. Lang, Thermal Conductivity of Ruthenium Aluminide (RuAl), *Scr. Metall. Mater.,* Vol 38, 1998, p 493–497

44. I.M. Wolff, Towards a Better Understanding of Ruthenium Aluminde, *J. Met.,* Jan 1977, p 34–39

E. van der Lingen, L. Cornish, S. Taylor, R. Süss, S. Grice, Metallography and Microstructures of Precious Metals and Precious Metal Alloys, *Metallography and Microstructures,* Vol 9, *ASM Handbook,* ASM International, 2004, p. 860–876

Metallography and Microstructures of Precious Metals and Precious Metal Alloys

Elma van der Lingen, Lesley Cornish, Stefanie Taylor, Rainer Süss, Physical Metallurgy Division, Mintek, South Africa; Stewart Grice, Hoover & Strong Inc.

References

1. T. Piotrowski and D.J. Accinno, Metallography of the Precious Metals, *Metallography,* Vol 10, Elsevier Publishing, 1977, 234–289

2. J. Stewart, *Tech-Notes,* Vol 2 (No. 5), G.F. Vander Voort, Ed., Buehler 1998

3. *Canning Handbook of Electroplating,* 23rd Edition, EFN Spon, 1982

4. G.F. Vander Voort, *Metallography, Principles and Practice,* McGraw-Hill Book Company, 1984

5. A.S. McDonald and G.H. Sistare, The Metallurgy of Some Carat Gold Jewelry Alloys, Part I, *Gold Bull.,* Vol 11 (No. 3), 1978, p 66–73

6. C.W. Corti, *Gold Bull.,* Vol 32 (No. 2), 1999, p 39

7. C.W. Corti, Assaying of Gold Jewelry-Choice of Technique, *Gold Technology,* No. 32, Summer 2001, p 20–30

8. M. du Toit, E. van der Lingen, L. Glaner, and R. Süss, *Gold Bull.,* Vol 35 (No. 2), 2002, p 46

9. R. Süss, E. van der Lingen, M. du Toit, C. Cretu, and L. Glaner Hard Gold Alloys *Gold Bull.,* in press, paper No. 985, Gold 2003 Conference; see www.gold.org

10. D. Ott, *Gold Technol.,* Vol 22, 1997, p 31

11. J.C. Chaston, *Gold Bull.,* Vol 4 (No. 4), 1971, p 70

12. F. Klotz and S. Grice, "Live and Let Die (Struck)," *Gold Technol.,* Vol 36, 2002, p 16

13. S. Grice, Failures in 14 kt Nickel White Gold Tiffany Head Settings, Proceedings of the 16th Santa Fe Symposium, Met-Chem Research, 2002, p 189–230

14. D. Ott, *Handbook on Casting and Other Defects in Gold Jewelry Manufacture,* World Gold Council, London, 1997

15. W.S. Rapson, *Gold Bull.,* Vol 29, 1996, p 141

16. H. Büchler and K.-J. Range, *J. Less-Common Met.,* Vol 160, 1990, p 143

17. K.E. Saeger and J. Rodies, *Gold Bull.,* Vol 10, 1977, p 10

18. W.S. Rapson, in *Intermetallic Compounds, Principles and Practice,* Vol 2, J.H. Westbrook and R.L. Fleischer, Ed., John Wiley & Sons, 1994, p 559

19. T. Inagaki, E.T. Arakawa, and T.A. Callcott, *J. Appl. Phys.,* Vol 52, 1981, p 5597

20. R. Pretorius, T.K. Marais, and C.C. Theron, *Materials Sci. Eng.,* Vol 10, 1993, p 1

21. T. Raymond, *Semicond. Int.,* Vol 12, 1989, p 152

22. R. Süss and C. Cretu, in *MSSA Proceedings,* Vol 28, M. McLean, J.A.A. Engelbrecht, J.H. Neethling, C. Dennison, D. Mycock, and R.H.M. Cross, Ed., (Johannesburg), Microscopy Society of Southern Africa 1998, p 20

23. S. Hori, K. Kurokawa, T. Shimizo, M. Steel, M. Tsuboi, and K. Yanagase, in *Precious Metals Science and Technology,* L.S. Benner, T. Suzuki, K. Meguro, and S. Tanaka, Ed., International Precious Metals Institute, 1991, p 430

24. E. van der Lingen, M.B. Cortie, H. Schwarzer, S.J. Roberts, and G. Pattrick, Gold Catalysts Prepared via Intermetallic Precursor Gold 2003 Conference, Paper No. 988 (Vancouver), 2003 World Gold Council, www.gold.org

25. G. Patrick, E. van der Lingen, H. Schwarzer, and S.J. Roberts, Development of Gold-Sponge Catalysts for Lean Buen De No_x Paper No. 993 Gold 2003 Conference, (Vancouver), 2003 World Gold Council, www.gold.org

26. "An Introduction to Platinum," Johnson Matthey 1990

27. J. Hurly, U.S. Patent 5,045,280; South Africa Patent 90/7777, 1989

28. J. Hurly and P.T. Wedepohl, Optical Properties of Colored Platinum Intermetallic Compounds, *J. Mater. Sci.,* Vol 28, 1993, p 5648–5653

29. C.M. Wayman, Thermoelastic Martensitic Transformations and the Shape Memory Effect, *Noble Metal Alloys,* T.B. Massalski et al., Ed., AIME, 1986, p 181–196

30. T. Biggs, M.B. Cortie, M.J. Witcomb, and L.A. Cornish, Platinum Alloys for Shape Memory Applications, *Platin. Met. Rev.,* Vol 47, 2003, p 142–156

31. P.J. Hill, "Superalloy Analogues Based on Platinum for Ultra-High Temperature Applications," Ph.D. dissertation, University of the Witwatersrand, Johannesburg, 2001

32. "Iridium," The International Nickel Company (MOND), Thames House, London, 1995

33. I.M. Wolff and G. Sauthoff, *Metall. Mater. Trans. A,* Vol 27, 1996, p 2642–2652

34. C.N. Reid and J.L. Routbort, *Metall. Trans. A,* Vol 3, 1972, p 2257–2259

35. R.L. Fleischer, R.D. Field, and C.L. Briant, *Metall. Trans. A,* Vol 24, 1991, p 403–413

36. P.J. Hill, "The Microstructure and Mechanical Properties of Al-Ru-Ir Alloys," master's thesis, University of the Witwatersrand, Johannesburg, 1998

37. P.J. Hill, L.A. Cornish, and M.J. Witcomb, *Proc. Micros. Soc. South Afr.,* Vol 27, 1997, p 17

38. R.L. Fleischer, R.D. Field, and C.L. Briant, Mechanical Properties of High Temperature Alloys of AlRu, *Metall. Trans. A,* Vol 22, 1991, p 404–414

39. R.L. Fleischer and D.W. McKee, Mechanical and Oxidation Properties of AlRu-Based High-Temperature Alloys, *Metall. Trans. A,* Vol 24, 1993, p 759–763

40. W. Wopersnow and C.J. Raub, Eigenshaften Einiger Binärer Intermetallischen Phasen des Palladiums und Rutheniums mit Anderen Metallens, *Metall. Technik,* Vol 33, 1979, p 736–740

41. J.J. McEwan and T. Biggs, "Exploiting the Excellent Corrosion Resistance of a Precious Metal Aluminide," Paper 096, 13th International Corrosion Congress (Melbourne, Australia), ACA Inc., 1996

42. E.G. Smith and C.I. Lang, High Temperature Resistivity and Thermo-emf of RuAl, *Scr. Metall. Mater.* Vol 33, 1995, p 1225–1229

43. S.A. Anderson and C.I. Lang, Thermal Conductivity of Ruthenium Aluminide (RuAl), *Scr. Metall. Mater.,* Vol 38, 1998, p 493–497

44. I.M. Wolff, Towards a Better Understanding of Ruthenium Aluminde, *J. Met.,* Jan 1977, p 34–39

Metallography and Microstructures of Refractory Metals and Alloys, *Metallography and Microstructures,* Vol 9, *ASM Handbook,* ASM International, 2004, p. 877–888

Metallography and Microstructures of Refractory Metals and Alloys

Introduction

REFRACTORY METALS and their alloys are prepared similarly for metallographic examination. Slight modifications in grinding, polishing, and etching times may be required for alloys, because they are generally harder than the unalloyed metals. Particular product forms, such as wire, may also necessitate special preparation techniques. Information on the properties and selection of refractory metals and their alloys can be found in *Properties and Selection: Nonferrous Alloys and Special-Purpose Materials,* Volume 2 of *ASM Handbook.* Powder production and powder metallurgy of refractory metals are described in *Powder Metal Technologies and Applications,* Volume 7 of *ASM Handbook.* This article focuses on the refractory metals of niobium, tantalum, molybdenum, tungsten, and rhenium. Other metals classified as refractory (i.e., zirconium, hafnium, and titanium) are discussed elsewhere in this Volume.

Metallography and Microstructures of Refractory Metals and Alloys, *Metallography and Microstructures,* Vol 9, *ASM Handbook,* ASM International, 2004, p. 877–888

Niobium, Tantalum, Molybdenum, Tungsten and Their Alloys

Revised by Ann Kelly, Los Alamos National Laboratory

This section describes procedures that can be applied to metallographic preparation of niobium (columbium), tantalum, molybdenum, tungsten, and their alloys. Alternate procedures that have been used for each of these materials are also described. Specific etchants for these metals and their alloys are listed in Table 1.

Table 1 Etchants for metallographic specimens of refractory metals

See also Table 2 for etchants suitable for refractory metals

Etchant	Composition	Comments
Etchants for niobium and tantalum and their alloys		
ASTM 66[(a)]	30 mL HF, 15 mL HNO_3, 30 mL HCl	Swab 3 to 10 s or immerse for 2 min
ASTM 158[(a)]	10 mL HF, 10 mL HNO_3, 20 mL glycerol	Swab 5 to 15 s
ASTM 159[(a)]	5 mL HF, 20 mL HNO_3, 50 mL acetic acid	Swab 10 to 30 s
ASTM 161[(a)]	25 mL HNO_3, 5 mL HF, 50 mL H_2O	Immerse 5 to 120 s
ASTM 163[(a)]	30 mL H_2SO_4, 30 mL	Immerse 5 to 60 s; use this solution for alternate etch and polishing.

	HF, 3–5 drops 30% H_2O_2, 30 mL H_2O	Adjust amount of H_2O_2 to obtain a reaction rate that will reveal the microstructure after etching for approximately 20–40 s.
ASTM 164	50 mL HNO_3, 30 g NH_4HF_2 (ammonium bifluoride), 20 mL H_2O	Swab 3 to 10 s; use fume hood
Additional etchants for niobium and niobium alloys		
ASTM 160[(a)]	20 mL HF, 15 mL H_2SO_4, 5 mL HNO_3, 50 mL H_2O	Immerse up to 5 min
ASTM 162B[(a)]	10 mL HNO_3, 10 mL HF, 30 mL lactic acid	Swab for 5 s; repeat if necessary
HNO_3 + HF + H_2O	25 mL HNO_3, 5 mL HF, 50 mL H_2O	Immerse up to 2 min
Solution A Solution B	50 mL lactic acid, 30 mL HNO_3, 2 mL HF 30 mL lactic acid, 10 mL HNO_3, 10 mL HF	Swab specimen 1 to 3 min with solution A, acts as a chemical polishing agent and etchant; then swab 5 s with solution B; repeat if necessary; HF content in solution B controls etch speed
Additional etchants for tantalum and tantalum alloys		
ASTM 177[(a)]	10 g NaOH, 100 mL H_2O	Swab or immerse 5 to 15 s
ASTM 178[(a)]	20 mL HF, 20 mL HNO_3, 60 mL lactic acid	Swab for 5 to 20 s
Solution C Solution D	10 mL HF, 10 mL HNO_3, 30 mL lactic acid 10 mL HF, 90 mL H_2SO_4	Swab specimen 2 or more min using solution C for desired surface; solution C is used as a chemical polish, though some etching will occur; if surface is not etched sufficiently, use solution D electrolytically at 0.08 to 0.16 V/cm^2 (0.5 to 1 V/in.^{2}) of specimen; solution D should be mixed very slowly; use carbon cathode and platinum connection to specimen; discard solution D after 1 h; use fume hood
ASTM 164[(a)]	50 mL HNO_3, 30 g NH_4HF_2, 20 mL H_2O	Swab 3 to 10 s; use fume hood
Etchants for tungsten and molybdenum and their alloys		
Murakami's reagent (ASTM 98C)	10 g $K_3Fe(CN)_6$ (potassium ferricyanide), 10 g KOH or NaOH, 100 mL H_2O	Swab 5 to 60 s; immersion will produce a stain etch; follow with water rinse, alcohol rinse, dry
Murakami's reagent (modified)	15 g $K_3Fe(CN)_6$, 2 g NaOH, 100 mL H_2O	
Murakami's reagent (modified A)	30 g $K_3Fe(CN)_6$, 10 g NaOH, 200 mL H_2O	
ASTM 131[(a)]	5 mL H_2SO_4, 1 mL HF, 100 mL 95% methanol	Electrolytic at 50 to 60 V for 10 to 20 s
ASTM 132[(a)]	5 mL HF, 10 mL HNO_3, 30 mL lactic acid	Swab with heavy pressure for 5 to 10 s; water rinse, alcohol rinse, dry, then swab etch using ASTM 98C for 5 to 30 s
ASTM 209[(a)]	15 mL HNO_3, 3 mL HF, 80 mL H_2O	Immerse for 5 to 60 s
Additional etchants for molybdenum and molybdenum alloys		

ASTM 129[(a)]	10 mL HF, 30 mL HNO_3, 60 mL lactic acid	Swab 10 to 20 s; vary HF content to increase/decrease etching activity
ASTM 130[(a)]	25 mL HCl, 10 mL H_2SO_4, 75 mL methanol	Electrolytic at 30 V for 30 s; Caution: keep below 24 °C (75 °F)

Caution: For all etchants that contain HF, immerse the specimen for the necessary time, rinse in water, and place in boiling 5% solution of ammonium pentaborate for 1 min. Cool the mount under cold running water, then wipe dry with a soft disposable tissue or rinse in hot water and blow dry. This procedure protects microscope optics from HF attack and minimizes stain.

(a) ASTM etchant numbers in ASTM E407.

This section describes procedures for mechanical processing of specimens that have been used and published in the previous edition of this Volume. However, it should be noted that lengthy mechanical-processing time is typically not needed with the chemical-polishing procedure described in Table 2. General-purpose etchants for refractory metals are also listed in Table 2. Application guidelines of these solutions are given in Table 3.

Table 2 Specimen preparation procedures for refractory metals

See Table 3 for application guidelines

Preparation step	Description	Figures in this article
Grinding/polishing (all)	All specimens were sequentially ground through 1200-grit SiC grinding papers, mechanically polished using 0.3 μm alumina slurry on napless cloth (Texmet, Buehler, Ltd.) for ~20 min, final mechanically polished on a napped cloth (Microcloth, Buehler, Ltd.) using a 0.3 μm alumina slurry for ~15–20 min, and chemically polished and etched using the following solutions.	Fig. 1, 2, 3, 4, 5, 6, 7, 8, 12, 13, 14, 15, 16, 17, 18, 19, 20, 21, 22, 23, 24 , 28, 32, 33
Chemical polish (solution A)[(a)]	Chemical-polish solution consists of[(b)]: • 25 mL lactic acid • 15 mL HNO_3 • 5 mL HF Limited shelf life, <5 days	Fig. 1, 2, 3, 7, 8, 12, 13, 14, 15, 16, 17, 18, 19, 20, 21, 22, 23, 24, 28, 32, 33
Etch solution B[(a)]	• 20 mL HNO_3 • 20 mL HF • 60 mL H_2SO_4 • Shelf life, ~3 mo • Recommend chilling solution during the addition of sulfuric acid	Fig. 1, 2, 3, 7, 12, 13, 14, 15, 16, 17, 18, 19, 20, 21, 22, 23, 24, 28, 32, 33
Etch solution C[(a)]	• 10 mL H_2O • 2 mL HNO_3 • 2 mL HF • 3 mL H_2SO_4	Fig. 4, 5, 6, 8

(a) Solution applied by swabbing.

(b) Listed as a macroetch for refractory metals in Ref 1

Table 3 Recommended chemical-polish and etching times of solutions in Table 2 for selected refractory metals and alloys

Material[(a)]	Chemical polish, s	Etchant, s	Comments
Tantalum (wrought)	90	30–60	…
Tantalum (P/M-HIP, 1600 °C, or 2910 °F)	60	20–30	Recommend chemical polish or etch but not both—prefer etch
Tantalum (P/M-CIP/sintered, 2400 °C, or 4350 °F)	30–45	5–15	Recommend chemical polish or etch but not both—prefer etch
Ta-(5–10%)W	90	30–60	…
Zirconium (crystal bar)	45	Not required	…
Zr-19Ti-17Co-14Ni	10	30	…
Zr-1.5%Ta	60–120	30	…
Zr-2V	90–120	30	…
Niobium	60	30	…
Ti-5%Ta	120–150	30	…
Ti-3V	90	30	…
Ti-37Ta-7Sc	90	30	…
Mo-0.5Ti-0.1Zr	Not recommended	30	Molybdenum tends to pit in the chemical-polishing solution
Fansteel 85	30	30	…
Ti-Al-V (Ti-6-4)	30	30	…
Molybdenum	Not recommended	20–30	Molybdenum tends to pit in the chemical-polishing solution
Ti-60Ta (as cast)	45	20–30	…
Rhenium	35–45	Not recommended	…
Fe-40Ni-20B	Not required	2	…
Nb-20Ti-10Hf-4Cr-1Al-7Si	Not required	20	…
Vanadium	60–90	Prefer Barker's electrolytic etch, 6 V for ~15 s	…

(a) P/M, powder metallurgy; HIP, hot isostatic pressed; CIP, cold isostatic pressed

Reference cited in this section

1. ASTM E340, Standard Method for Macroetching Metals and Alloys

Metallography and Microstructures of Refractory Metals and Alloys, *Metallography and Microstructures,* Vol , *ASM Handbook,* ASM International, 2004, p. 877–888

General Specimen Preparation

Sectioning. The following abrasive wheels have been found to be efficient regarding cutting quality, cutting speed, and wheel wear. Generally, abrasive cutting discs (Al_2O_3 or SiC) have been found more effective for sectioning refractory metals than diamond discs. This is due to the fact that abrasive blades wear with use, continuously exposing a fresh cutting surface, whereas diamond blades tend to load with smeared abraded material (except tungsten) hindering its cutting effectiveness.

- *Niobium and tantalum (all sizes):* A 180 PR rubber-bonded, 180-grit alumina, Al_2O_3 or SiC abrasive blades
- *Molybdenum (larger specimens):* A 180 PR or A 60 MR rubber-bonded, 60-grit Al_2O_3 or SiC abrasive blades, which cuts faster at the expense of wheel wear
- *Molybdenum (thin specimens):* A 180 PR or SiC abrasive blades
- *Tungsten (thicker than 3 mm, or* $\frac{1}{8}$ *in.):* A 90 KR (rubber-bonded, 90-grit Al_2O_3) or C 120 KR (rubber-bonded, 120-grit silicon carbide)
- *Tungsten (thinner than 3 mm, or* $\frac{1}{8}$ *in.):* A 180 PR (cut slowly)
- *Tungsten (general):* A 70 TB (resinoid-bonded, 70-grit Al_2O_3)

Tungsten products, such as wire, can be cut using wet or dry abrasive wheels, preferably after a heavy nickel plate has been applied to the wire. Nickel plating aids edge retention and helps keep wire sections flat during polishing. Because tungsten products can delaminate, they should not be cut with shears or wire cutters.

Initial Grinding. Irregularly shaped specimens that are not cut can be ground flat using a coarse grit grinding paper (80–120 grit) with either a belt sander or a grinding wheel. It is generally preferable to remove excess stock in this manner before mounting.

Mounting methods include (but are not limited to) an epoxy-based resin and phenolic resins, e.g. Bakelite (Georgia-Pacific Corp.). For Bakelite, a two-step process can be used. First, the resin is mounted in a heated press under 690 kPa (100 psi) pressure at 150 to 180 °C (300 to 355 °F) for 2 min. The pressure is then released and the press opened. Epoxy-based resins may be used successfully with a vacuum impregnation method, followed by curing under pressure in a dry nitrogen atmosphere. This process ensures excellent penetration of the resin to all surface-accessible porosity, making it easier to distinguish between porosity and pullout in relatively porous specimens.

Grinding. Wet grinding is performed using 120-, 320-, 600-, 800-, and 1200-grit silicon carbide paper on rotating grinding wheel with running water as the lubricant. Older machines had brass laps, which have been replaced by aluminum wheels on new grinding machines. Aluminum wheels are less reactive than brass when attack polishing.

Some materials, such as tantalum and niobium, may develop a dull film during the final grinding step; this is smeared material and must be removed before proceeding to the polishing step. Changing grinding papers often during this stage will alleviate this problem. Grinding time depends on specimen hardness and size but is usually twice the time required to remove scratches from the previous operation. A good rule of thumb is to rotate the specimen 45° between grinding steps. The purpose is twofold: to indicate when the abrasive scratches from the previous step have been removed and to avoid comet tails or faceting.

Polishing is carried out in two steps using rotating polishing wheels. Initial polishing is accomplished on a low napped cloth such as Texmet (Buehler) or Mol cloth (Struers) or equivalent, using 15–20N force, 0.3 μm alumina slurry with a (light) water lubricant. Polishing time varies from 5–15 minutes depending on the material type. Typical polishing time for tantalum, niobium, and molybdenum is approximately 5–7 min, whereas; tungsten requires a longer polishing time, approximately 15 min. Diamond abrasives are not

recommended as they seem to cause comet tails, which require extensive polishing time to remove. Specimens are rinsed thoroughly with water, rinsed with alcohol and air dried (canned or forced hot air such as hand driers) before proceeding to the final polishing step.

Final polishing is performed using a rotating polishing wheel covered with a bonded synthetic rayon polishing cloth, using 15N force, 0.3 μm alumina slurry with (light) water lubricant. Again, polishing time varies with each material, with tungsten having the longest polishing time of approximately 10 min, while tantalum, niobium, and molybdenum polish is approximately 3–5 minutes. The medium nap of the synthetic rayon polishing cloth (microcloth or equivalent) produces an excellent scratch-free finish; however, during grinding and polishing, some refractory metals (Ta, Nb, Zr, Hf) develop a disturbed surface layer that must be removed to observe the true structure. This layer may be removed by chemically polishing with a solution of 25 mL lactic acid, 15 mL HNO_3, and 5 mL HF by swabbing using firm pressure. The specimen will darken during the chemical-polishing step but changes to a bright metallic color (60 to 120 s) as the worked layer is removed. Microscopic examination at this point reveals some evidence (DIC lighting for tantalum and niobium) of grain boundary definition, similar in appearance to mechanical polish relief. To further enhance grain boundary definition, etching may be required. An etchant that works well on most refractory metals (using the mechanical and chemical polishing method described previously) is a swab etchant consisting of 20 mL HNO_3, 20 mL HF, and 20 mL H_2SO_4 using firm pressure for approximately 20–30 s. This solution should be cooled (place beaker in ice water) during the H_2SO_4 addition to prevent the solution from overheating. Other recommended etchants are listed in Table 1.

Vibratory polishing is an excellent alternative to the previously mentioned procedures. The polished mount is cleaned and placed in a 300 g (0.7 lb) holder for use in a vibratory lapping-polishing machine with a long-nap synthetic velvet (Rayvel, Buehler, Ltd.) and an aqueous suspension of 0.3 μm Al_2O_3. In a freshly cleaned machine, disturbed metal can be removed in approximately 18 h. As metal sludge accumulates over a few weeks, the time required may double. After a final etch, the true structure is revealed.

For molybdenum and tungsten, the standard specimens are ground through 1200 grit SiC grinding papers, coarse polished through a 30 μm diamond lap on Texmet, Mol, or equivalent. The mounts are then cleaned and placed in the vibratory lapping-polishing machine as for tantalum and niobium, except that nylon cloth is used. The remaining scratches are removed, and the specimen is polished without disturbing the metal. Depending on the cleanliness of the polishing apparatus, 6 to 15 h are required. The true structure appears after one etch.

Electropolishing. Unmounted larger specimens of molybdenum and tungsten can be electropolished adequately for routine examination. The cutting wheels previously listed yield a surface smooth enough for this operation. An excellent polish, particularly with difficult-to-polish alloys such as molybdenum alloys, TZM, and TZC, can be obtained using an electrolyte consisting of 12.5% sulfuric acid (H_2SO_4) in methanol, with nickel as the cathode and 8 to 50 V direct current (dc). Voltage is easily monitored by inspection; an intense blue layer forms on the surface of the specimen when the correct voltage is applied. Because alcohol has a relatively low boiling point, the electrolyte must be prepared carefully and must be cooled by a water bath during electrolytic polishing.

Electropolishing of higher quality can be obtained by first mounting the specimens, followed by grinding and rough polishing with 30 μm diamond. The power requirements in this case are approximately 3 A at a lower voltage, and the etching time is 30 to 40 s for a typical specimen.

Aqueous electrolytes containing 1 to 10% sodium hydroxide (NaOH) or potassium hydroxide (KOH) can be used successfully for electropolishing of tungsten and tungsten alloys. Best results are obtained if half the volume of water in the solution is replaced by glycerol and the NaOH content is approximately 5%. With a 4% NaOH aqueous solution, a satisfactory polish should be obtained in 20 s using a current density of 2.3 A/cm^2 (15 A/$in.^2$).

Excellent polishes can be obtained over a wide range of current densities. However, if the current density is too high, pitting will occur; if too low, the specimen will etch. Heat is generated at high current densities and, if excessive, may cause uneven polishing, etching, or both. Overheating can be minimized by frequently cooling the specimen in a stream of cold water. Electropolishing also can remove inclusions. Large sections often do not polish evenly.

Electrolytic Etching. Molybdenum and tungsten can be electroetched with the same equipment and electrolytes used for electropolishing. The power required is approximately 0.4 A for 8 s for molybdenum and 0.4 A for 5 s for tungsten. Large specimens will etch more evenly in a chemical etchant. The specimens should be cleaned prior to examination.

Etchants. ASTM etchant #163 (Table 1) in ASTM E407 is preferred for niobium and tantalum; Murakami's reagent (modified A) is preferred for molybdenum and tungsten.

Metallography and Microstructures of Refractory Metals and Alloys, *Metallography and Microstructures,* Vol 9, *ASM Handbook,* ASM International, 2004, p. 877–888

Alternate Preparation Procedures for Niobium and Tantalum

Polish-etching, also known as chemical-mechanical polishing or attack polishing, is suited to niobium, tantalum, and their alloys, but the procedure is different from that for polish-etching of tungsten and molybdenum. After grinding, the specimen is rough polished on a conventional corrosion-resistant horizontal polishing wheel covered with a chemotextile material (Texmet, Buehler; Mol cloth, Struers) using 0.3 μm Al_2O_3. The specimen is then polish-etched on synthetic velvet cloth using a slurry of 0.05 μm Al_2O_3 and a solution of hydrofluoric acid (HF) (2 mL for niobium, 5 mL for tantalum), 5 mL nitric acid (HNO_3), and 30 mL lactic acid. Because this mixture is hazardous and extremely corrosive, and because polish-etching is time-consuming, the specimen should be held in a mechanical holder rather than by hand. Initial polishing is performed for 1 to 4 h using a 160 rpm wheel and a 450 g (1 lb) weight on the holder. For final polish-etching, the weight on the holder is reduced to 225 g (0.5 lb) and held for 15 min.

Etchants used for metallographic specimens of niobium, tantalum, and their alloys are listed in Table 1.

Metallography and Microstructures of Refractory Metals and Alloys, *Metallography and Microstructures,* Vol 9, *ASM Handbook,* ASM International, 2004, p. 877–888

Metallography and Microstructures of Refractory Metals and Alloys

Alternate Preparation Procedures for Molybdenum

Because molybdenum is relatively soft, scratches and distorted metal that develop in mechanical polishing are difficult to eliminate; therefore, electropolishing, as previously described, and electromechanical polishing are often used for molybdenum.

Electromechanical polishing combines electrolytic and mechanical polishing. It is excellent for retention of second phases and inclusions, for providing the most realistic representation of porosity, and for obtaining specimen flatness. Polishing time is only slightly longer than for electropolishing.

Operating conditions for electromechanical polishing of molybdenum and molybdenum alloys are not critical. The following conditions are typical. The polishing wheel must be covered with a material that will resist the electrolyte used; synthetic velvet is suggested. Polishing wheel speed should range from 50 to 150 rpm. The abrasive/electrolyte is 0.05 μm Al_2O_3 dispersed in a small amount of a 30% $K_3Fe(CN)_6$ aqueous solution. Polishing time is 2 to 5 min.

Electromechanical polishing is generally preferred for final polishing of large specimens and often is used as an intermediate or final polish for wire specimens. Final polishing may also be performed electrolytically. The etchants used in this technique and in polish-etching can corrode brass laps, as can the metals being polished.

Attack Polishing. Although electropolishing and electromechanical polishing provide the most consistent results, polish-etching is also satisfactory for molybdenum specimens. Polish-etching substitutes chemical attack for the electrolytic action obtained in electromechanical polishing.

Polish-etching is recommended when the equipment required for electromechanical polishing is not available. The slurry used in polish-etching is prepared by adding 0.05 μm Al_2O_3 to a solution containing 3.5 g

$K_3Fe(CN)_6$, 1 g NaOH, and 300 mL H_2O or to a solution containing 1 g CrO_3 and 75 mL H_2O. Results are improved by chemical polishing using a solution of 30 mL lactic acid, 10 mL HNO_3, and 5 mL HF, then polish-etching. The solution is used fresh (it should not be stored) and is applied by swabbing with heavy pressure.

Etchants. A modified Murakami's reagent, which provides good grain-boundary contrast and minimizes etch pitting, is recommended for etching molybdenum. A typical mixture contains 15 g $K_3Fe(CN)_6$, 2 g NaOH, and 100 mL H_2O. Specimens are immersed 5 to 10 s. Other recommended etchants for molybdenum and its alloys are given in Table 1, 2 and 3.

Metallography and Microstructures of Refractory Metals and Alloys, *Metallography and Microstructures,* Vol 9, *ASM Handbook*, ASM International, 2004, p. 877–888

Alternate Preparation Procedures for Tungsten

Mounting. Most specimens of tungsten or tungsten alloys are mounted. In mounting wires, however, it is difficult to obtain sections that are parallel to the longitudinal axis, because wires are seldom perfectly straight. Several methods are available for mounting wire specimens. One method is to affix the wire to a small block of epoxy using a five-minute epoxy. Apply five-minute epoxy lightly to a flat epoxy blank, position specimens in the desired orientation, allow epoxy to fully cure before proceeding to the mounting step. Bear in mind that five-minute epoxy is generally softer than most mounting material, therefore should not be applied near the area of microstructural interest as this could serve as a collection point for grinding and polishing debris. For larger diameter wire, a small hole may be drilled into the epoxy block and the wire inserted to accommodate a specific orientation. An epoxy blank is recommended to eliminate complications which could occur during subsequent processing, such as smearing of material from metal such as lead blocks (which is also unacceptable from a health and environmental standpoint) and also to maintain equal or near equal hardness throughout mounted materials.

When mounting wires of any type, a double-mount technique is useful. First affix the samples into a molding cup using double-sided tape so they will not shift during the epoxy impregnation. Add epoxy into the molding cup ~$\frac{1}{4}$ in. deep. Pour enough clear epoxy resin to make a thin disk over the wires. To hasten curing, the mold then may be heated on a hotplate at 70 to 90 °C (160 to 190 °F) for 20 min (although this may cause bubbles to form as part of the exothermic reaction). When the epoxy resin hardens, the disk containing the wires is removed from the mold and is cut transversely to the axis of the wires. The transverse section is then placed upright in the mold (place in mounting clips to hold upright). More epoxy resin is poured in—this time to a substantial depth. The mold maybe again heated as described previously. When the epoxy resin has cured, the wires are held perpendicular to the plane of polish, and the section of the original epoxy-resin disk is completely fused into the new mount. While this method reduces curing time, it may compromise the quality of the mount, such as inducing shrinkage gaps around the wires or increased bubble formation. Grinding, polishing, and etching can now be performed as required.

Grinding. Rough and finish grinding of tungsten and tungsten alloys is performed with conventional procedures using wet Al_2O_3 laps or papers from 60 through 600 grit. Light pressure is recommended throughout grinding, and fresh abrasive laps or papers should be used during final grinding. However, fine wire requires a less coarse initial grinding, because the depth of cold work resulting from grinding may exceed the diameter of the wire. Wires less than 25 μm in diameter are polished using a cloth-covered lap and 0.05 μm Al_2O_3. Further mechanical polishing is not required if electropolishing or electromechanical polishing methods are to be used.

Electromechanical Polishing. Conditions for electromechanical polishing of tungsten are similar to those used for molybdenum. Voltage is increased to 5 to 15 V dc, and the speed of the polishing wheel is decreased to 160 to 550 rpm.

Polish-Etching. Tungsten is attack polished in the same manner as molybdenum.

Etchants. Murakami's reagent, conventional or modified, is used most often for etching tungsten and tungsten alloys, although other etchants are sometimes used. In addition to the etchants shown in Table 1, electrolytic

etching in an aqueous 4% NaOH solution with 10 to 50 A/cm^2 (65 to 325 A/in.^{2}) alternating current or 5 to 10 A/cm^2 (30 to 65 A/in.^{2}) direct current has been used to improve grain-boundary contrast. Additional recommendations are given in Table 2 and 3.

Metallography and Microstructures of Refractory Metals and Alloys, *Metallography and Microstructures*, Vol 9, *ASM Handbook*, ASM International, 2004, p. 877–888

Microstructures

Niobium alloys were developed to provide greater oxidation resistance and elevated-temperature strength than are obtainable with the commercially pure metal. Niobium oxidizes less rapidly than the other refractory metals. Although no single element can be added to niobium to make an oxidation-resistant alloy, combinations will produce various oxidation behaviors. Many of the alloying additions that improve oxidation resistance also benefit high-temperature strength.

Combinations of molybdenum, tantalum, tungsten, and titanium serve as solid-solution strengtheners when added to niobium; the ternary and quaternary solid-solution alloys exhibit complex strength-temperature responses. Second-phase strengthening is achieved by controlled additions of zirconium, hafnium, or both. These additions develop metal-nonmetal systems in which strengthening results from the formation of zirconium oxide (ZrO_2) or of zirconium or hafnium carbide. Micrograph examples of niobium and niobium-containing alloys are given in Fig. 1 , 2, 3, 4, 5, 6, 7, 8, 9, 10, 11 and 12.

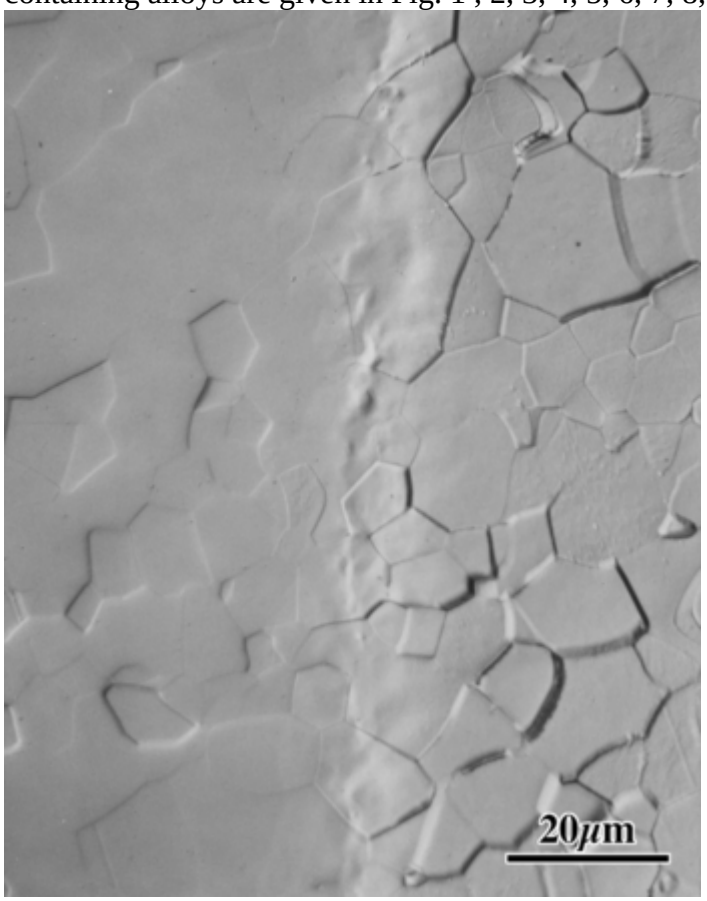

Fig. 1 Differential interference contrast light micrograph of unalloyed niobium showing microstructural characteristics in two different conditions. Left half of the specimen was chemically polished with solution A (Table 2) for 60 s, while the right shows refinement of structure after both chemical polishing and etching with solution B for 30 s. Source: Ref 2

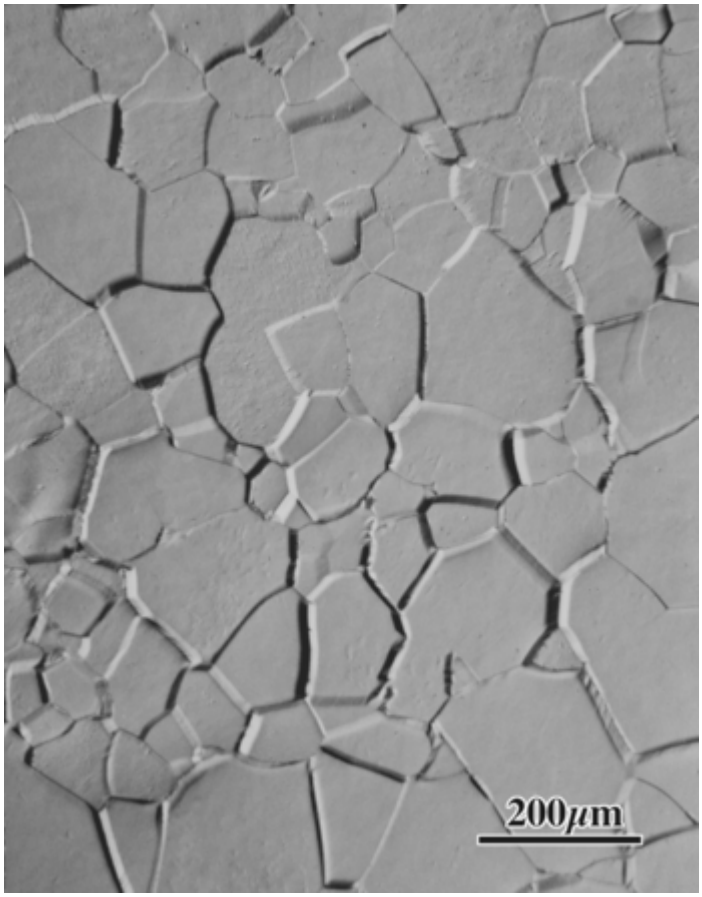

Fig. 2 Differential interference contrast light micrograph of unalloyed niobium showing a typically equiaxed grain structure. Chemically polished (solution A, Table 2), swabbed for ~90 s, and swab etched (solution B, Table 2) for ~90 s

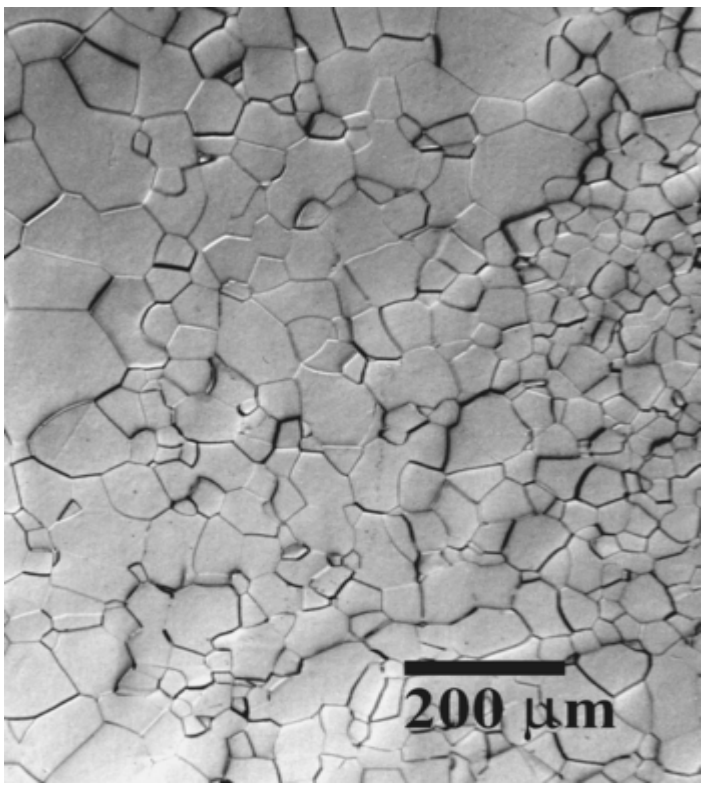

Fig. 3 Differential interference contrast light micrograph of unalloyed niobium bar stock showing equiaxed grain structure. Chemically polished (solution A, Table 2), swabbed for ~90 s, etched (solution B, Table 2), and swabbed for ~15 s. Source: Ref 2

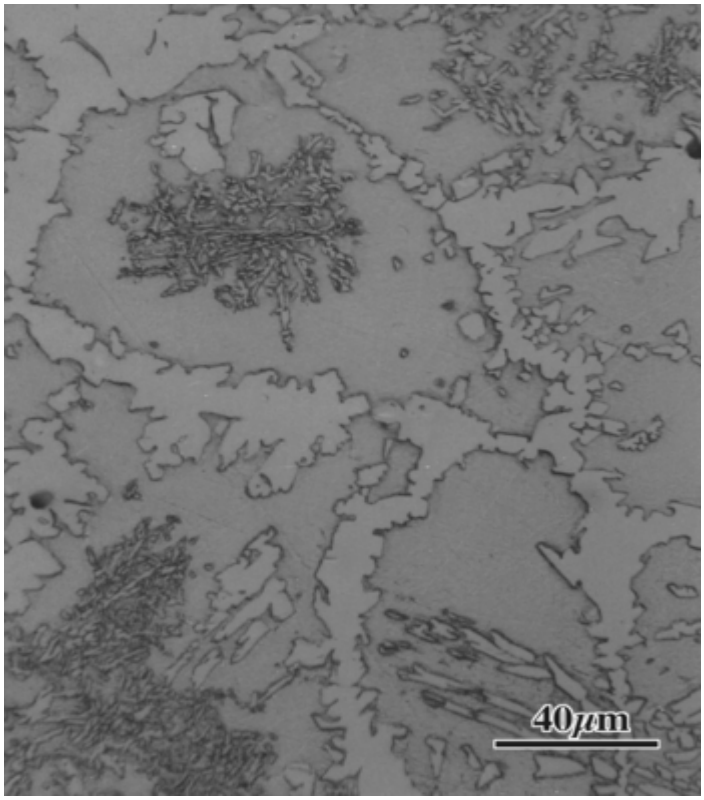

Fig. 4 Differential interference contrast light micrograph of cast 37Nb-36Cr-27Ti Laves phase deformed by vacuum compression at 1200 °C, showing faults resulting from G14 to G15 phase transformation. The coarse Laves phase resided at the grain boundaries after casting, and precipitation of the fine Laves phase evolved on the body-centered cubic grains while being tested at temperature. Etched (solution C, Table 2) for ~20 s. Courtesy of Dan J. Thoma, Los Alamos National Laboratory

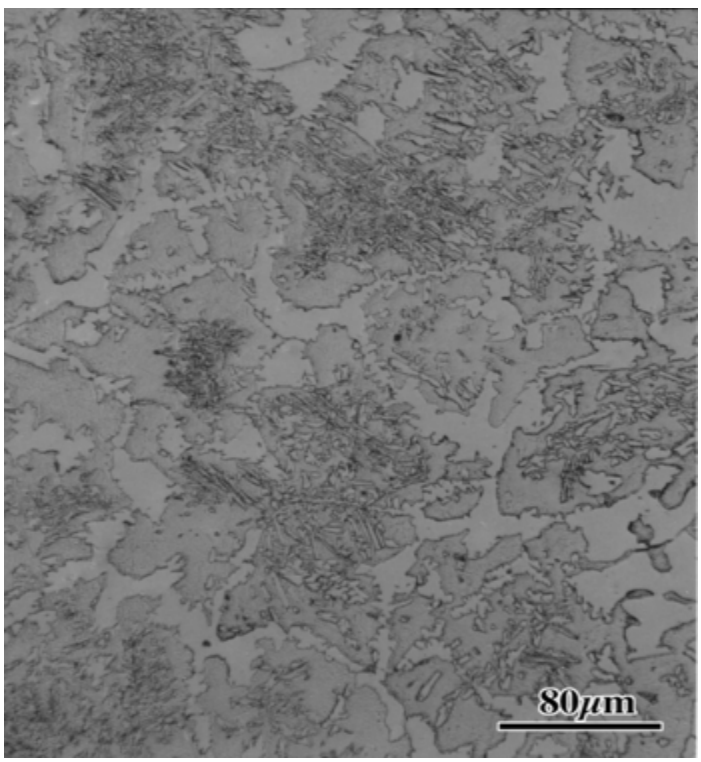

Fig. 5 Differential interference contrast light micrograph of cast 37Nb-36Cr-27Ti Laves phase deformed by vacuum compression at 1200 °C, showing faults resulting from G14 to G15 phase transformation. The coarse Laves phase resided at the grain boundaries after casting, and precipitation of the fine Laves

phase evolved on the body-centered cubic grains while being tested at temperature. Etched (solution C, Table 2) for ~20 s. Courtesy of Dan J. Thoma, Los Alamos National Laboratory

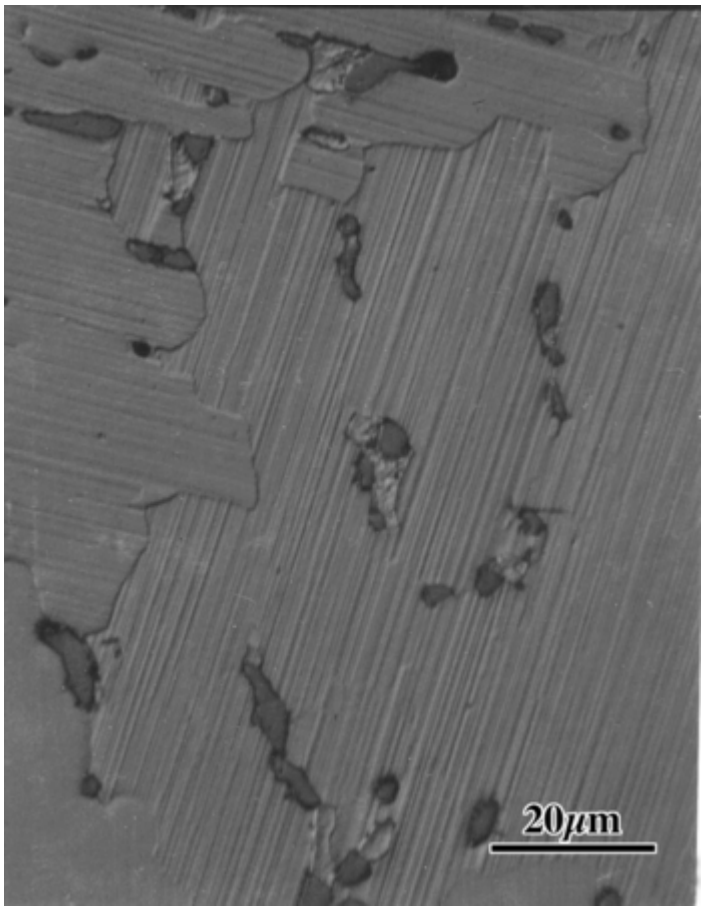

Fig. 6 Differential interference contrast light micrograph of cast 18Nb-15Ti-67Cr Laves phase showing titanium-rich second phase and faults resulting from C14 to C15 phase transformation. Etched (solution C, Table 2) for ~8 s. Courtesy of Dan J. Thoma, Los Alamos National Laboratory

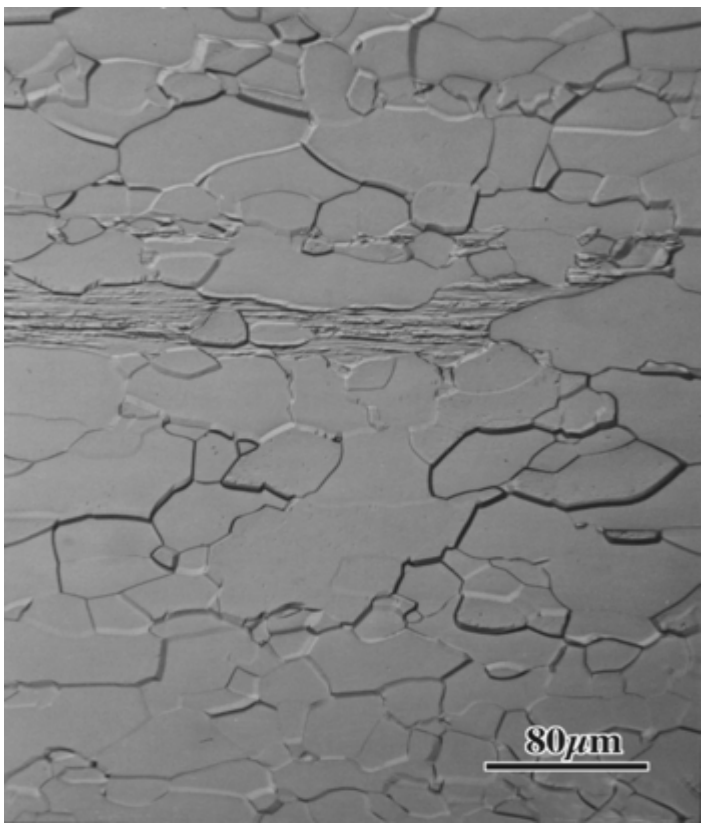

Fig. 7 Differential interference contrast light micrograph of high-purity niobium, rolled and annealed (for super-conductive applications), showing bands of unrecrystallized microstructure. Chemically polished (solution A, Table 2) for ~90 s and etched (solution B, Table 2) for ~30 s

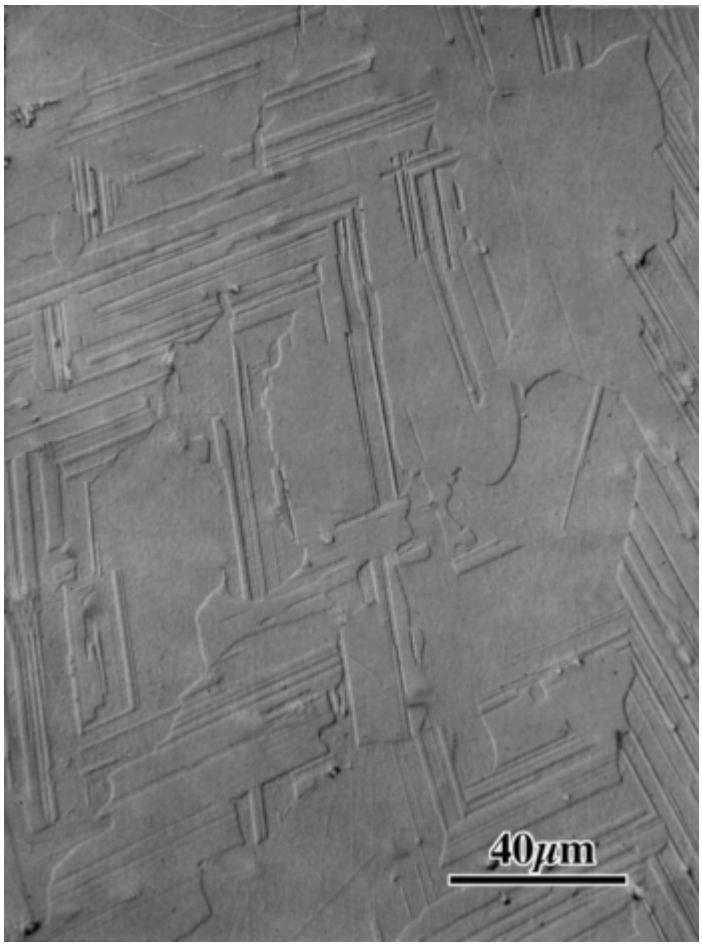

Fig. 8 Differential interference contrast light micrograph of $NbCr_2$ Laves phase. Chemically polished (solution A, Table 2) for ~30 s and etched (solution C, Table 2) for ~30 s

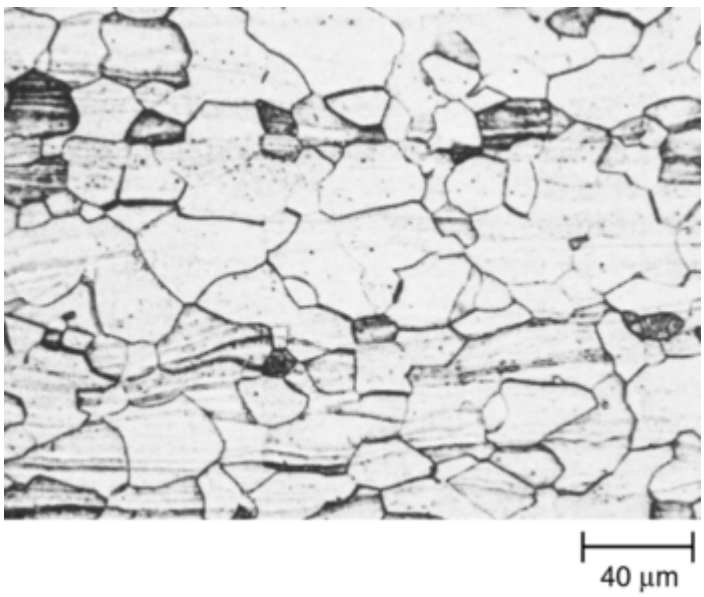

Fig. 9 Niobium alloy FS-85 (Nb-28Ta-11W-0.8Zr), 2.8 mm (0.110 in.) thick sheet. Arc melted, hot extruded, warm rolled at 705 °C (1300 °F), 50 to 75% reductions between anneals. Final anneal in vacuum at 1315 °C (2400 °F) for 1 h. Longitudinal section of fully recrystallized structure showing typical banding. ASTM grain size 7. Etchant: ASTM 163 (Table 1). 250×

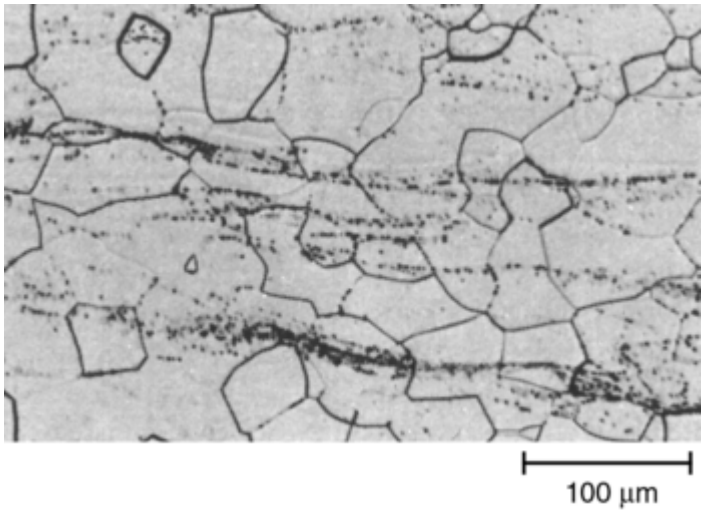

Fig. 10 Niobium alloy C-103 (Nb-10Hf-1Ti-0.5Zr), 6.4 mm (0.25 in.) thick plate, cold worked and annealed. The microstructure shows stringers, elongated in the rolling direction, of a dispersed phase consisting of HfO_2 and ZrO_2 compounds. Etchant: ASTM 163 (Table 1). 150×

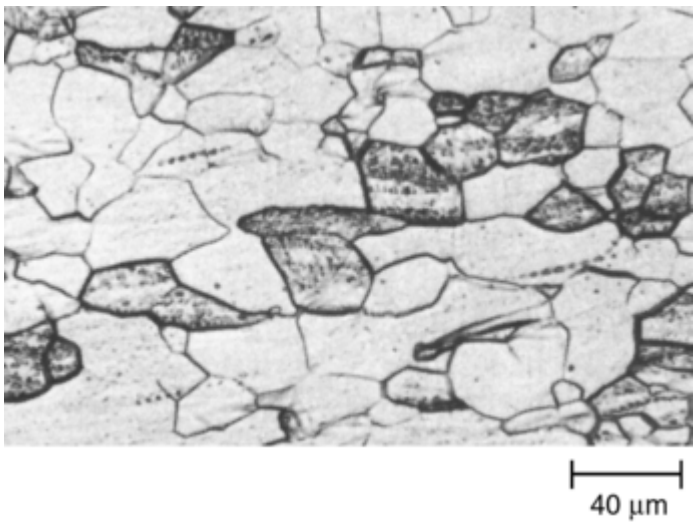

Fig. 11 Niobium alloy C-103 sheet, 1 mm (0.040 in.) thick. Arc melted, hot extruded, warm rolled, and annealed. Cold rolled to finished size. Final annealed in vacuum at 1290 °C (2350 °F) for 1 h. Longitudinal section showing fully recrystallized structure. ASTM grain size 7. Etchant: ASTM 163 (Table 1). 250×

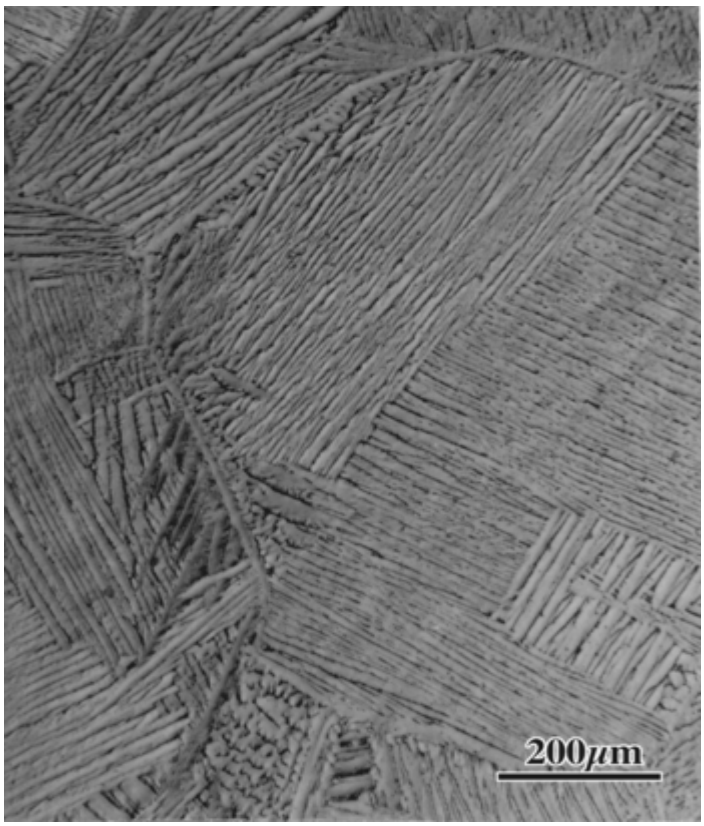

Fig. 12 Differential interference contrast light micrograph of arc-melted hafnium-niobium alloy (Hf-2 wt% Nb) buttons showing acicular α within prior-β grains. Chemically polished (solution A, Table 2), swabbed for ~45 s, and swab etched (solution B, Table 2) for ~20 s



Fig. 13 Differential interference contrast light micrograph of arc-melted hafnium-niobium alloy (Hf-3 wt% Nb) buttons showing acicular α within prior-β grains. Chemically polished (solution A, Table 2), swabbed for 60 to 90 s, and swab etched (solution B, Table 2) for ~20 to 30 s. Source: Ref 2

Tantalum. In industry, tantalum, which closely resembles niobium, is produced as a powder or sponge and is further purified in the solid or the liquid state. Solid-state purification occurs during sintering; liquid-state purification occurs during vacuum arc melting or electron beam melting in high vacuum. Consolidated high-purity tantalum has also been produced by the thermal decomposition of a halide, such as tantalum bromide ($TaBr_5$), on a hot wire. Unalloyed tantalum has limited usefulness in high-temperature applications, because it has relatively low hot strength and low resistance to oxidation, even at moderate temperatures.

The elevated-temperature strength of tantalum is significantly increased by alloying. Additions of up to 10% W or Mo are effective in solid solution. Additions of zirconium or hafnium to ternary alloys also contribute to solid-solution strengthening. Alloying, however, does not significantly increase oxidation resistance. Examples are given in Fig. 14, 15, 16, 17, 18, 19, 20, 21, 22, 23, 24, 25, 26, and 27.

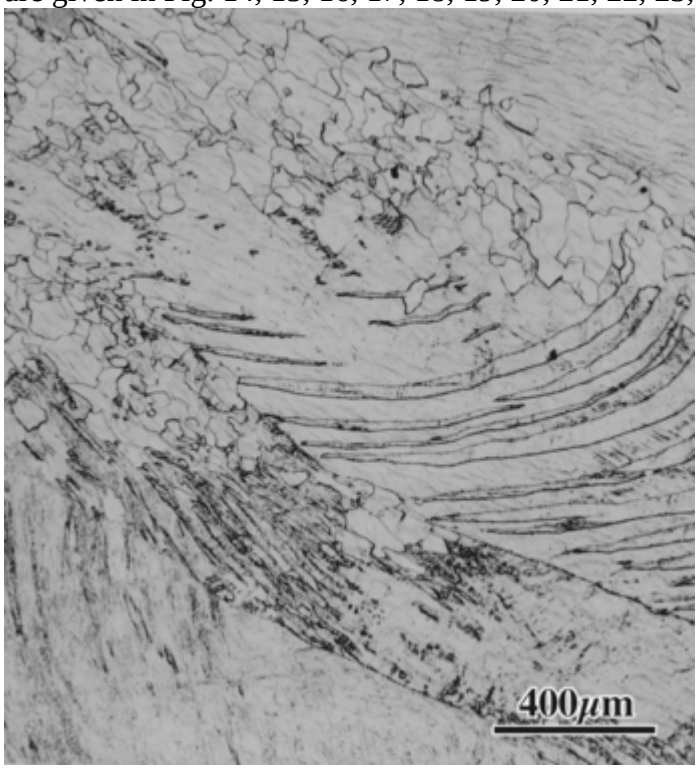

Fig. 14 Differential interference contrast light micrograph of Ta-2.5 wt% W wrought bar product showing partially recrystallized microstructure. Chemically polished (solution A, Table 2) for ~90 s and swab etched (solution B, Table 2) for ~30 s

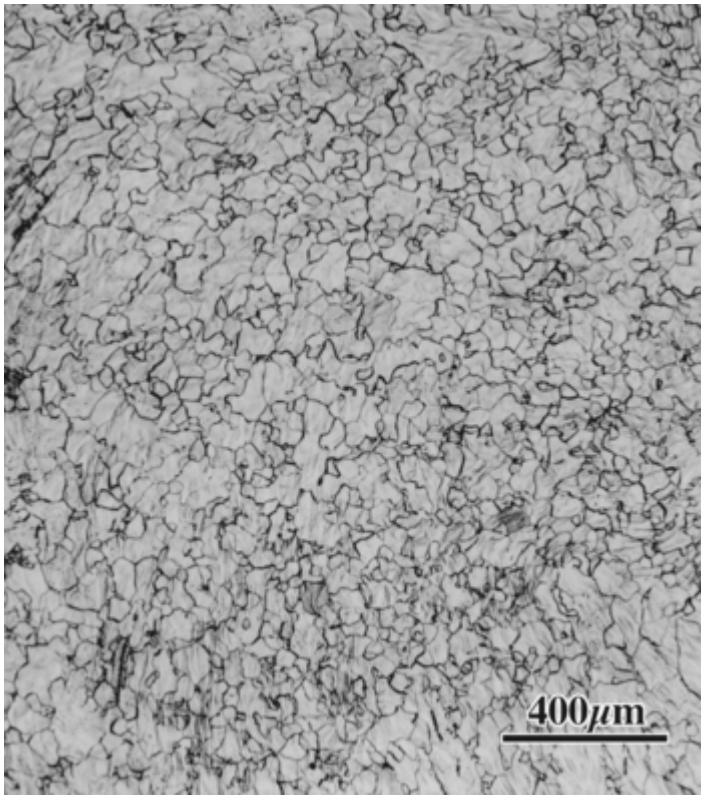

Fig. 15 Differential interference contrast light micrograph of Ta-2.5 wt% W wrought bar product showing a fully recrystallized microstructure. Chemically polished (solution A, Table 2) for ~90 s and swab etched (solution B, Table 2) for ~90 s

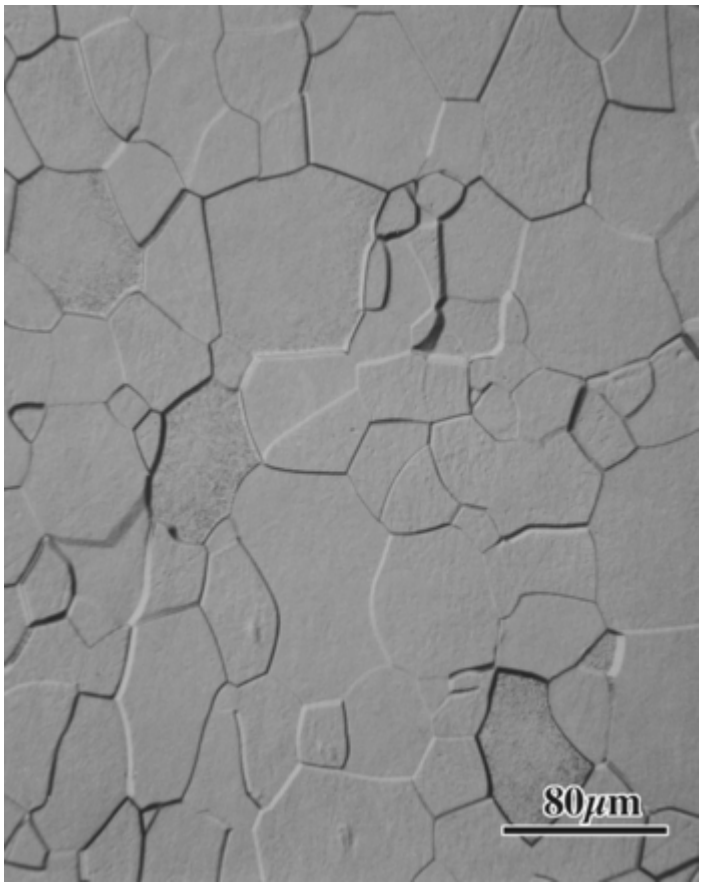

Fig. 16 Differential interference contrast light micrograph showing typical grain structure of wrought unalloyed tantalum. Chemically polished (solution A, Table 2), swabbed for ~120 s, and swab etched (solution B, Table 2) for ~90 s

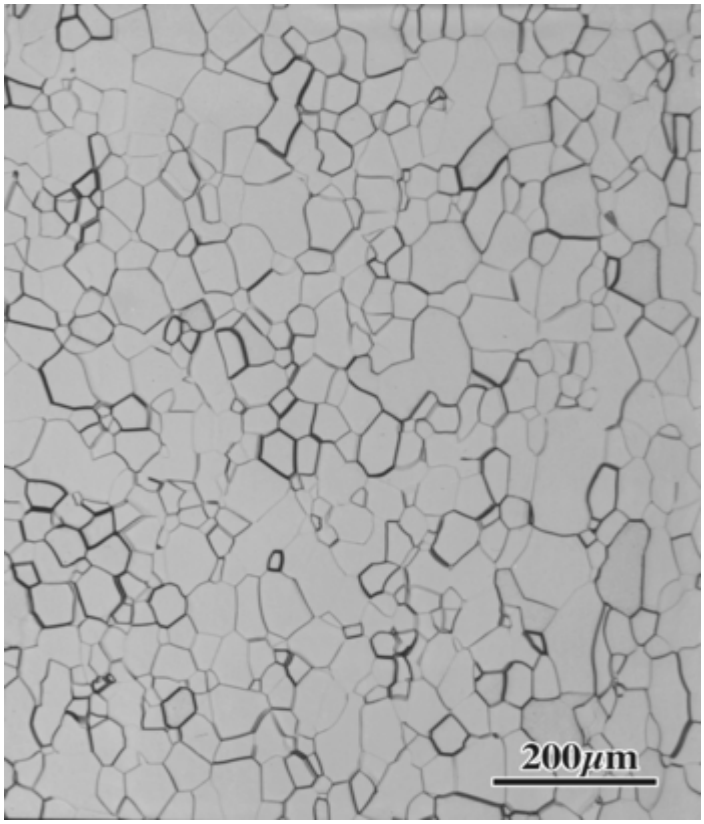

Fig. 17 Differential interference contrast light micrograph of wrought Ta-5 wt% W showing a typical equiaxed grain structure. Chemically polished (solution A, Table 2), swabbed for ~120 s, and swab etched (solution B, Table 2) for ~90 s

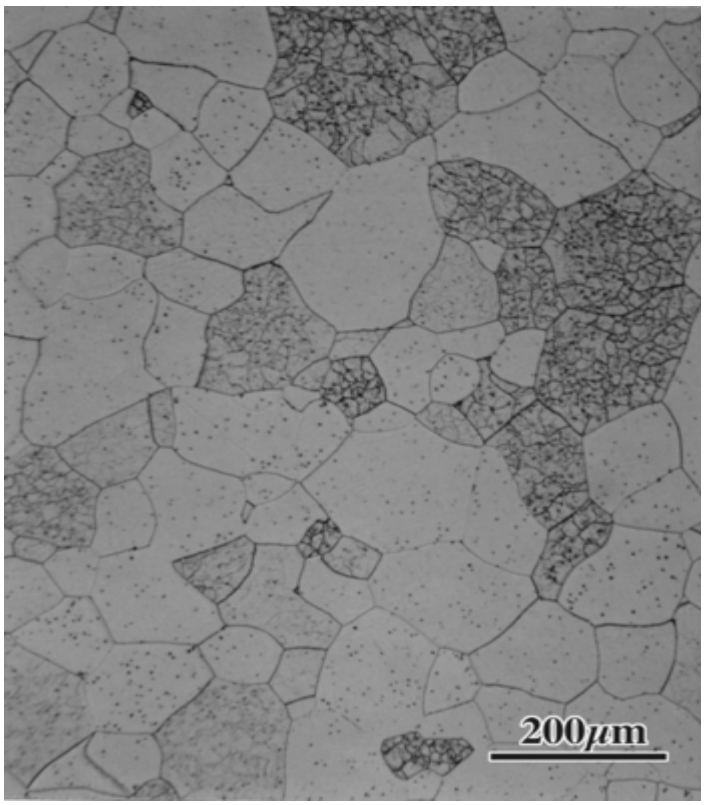

Fig. 18 Differential interference contrast light micrograph of powder metallurgy tantalum (hot isostatically pressed) showing equiaxed grains with substructure and fine porosity. Chemically polished (solution A, Table 2), swabbed for ~90 s, and swab etched (solution B, Table 2) for ~20 s. Source: Ref 3. Courtesy of Sherri R. Bingert, Los Alamos National Laboratory

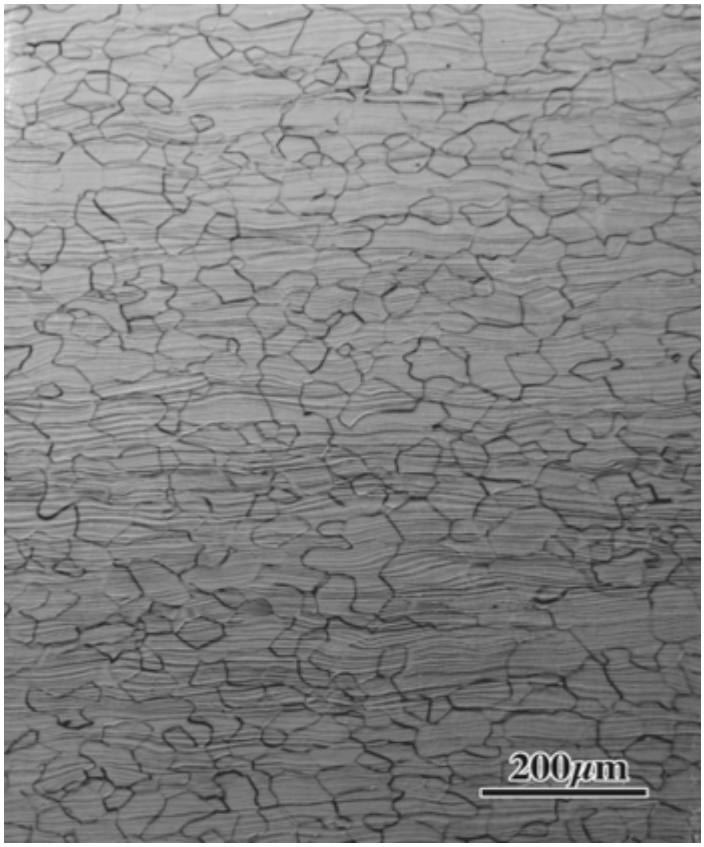

Fig. 19 Differential interference contrast light micrograph showing recrystallized grains and residual chemical banding in a longitudinal section of rolled Ta-10 wt% W. Chemically polished (solution A, Table 2) for ~90 s and etched (solution B, Table 2) for ~60 s. Source: Ref 3

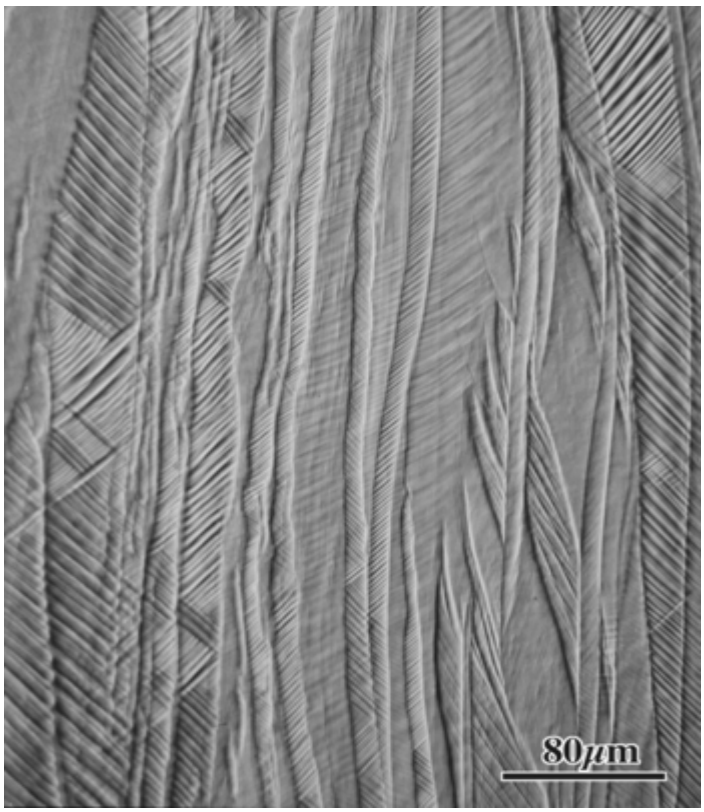

Fig. 20 Differential interference contrast light micrograph showing deformation structure (longitudinal view) of a Ti-60 wt% Ta tensile specimen. Chemically polished (solution A, Table 2), swabbed for ~90 s, and swab etched (solution B, Table 2) for ~45 to 60 s. Source: Ref 2

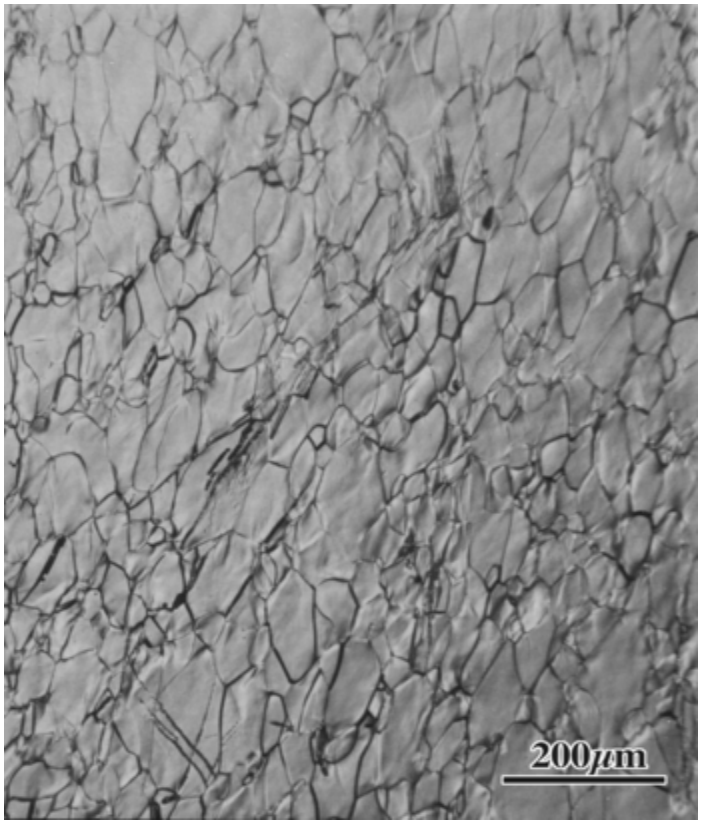

Fig. 21 Differential interference contrast light micrograph of unalloyed tantalum showing deformation structure resulting from Taylor cylinder testing. Chemically polished (solution A, Table 2), swabbed for ~90 s, and etched (solution B, Table 2) for ~20 s

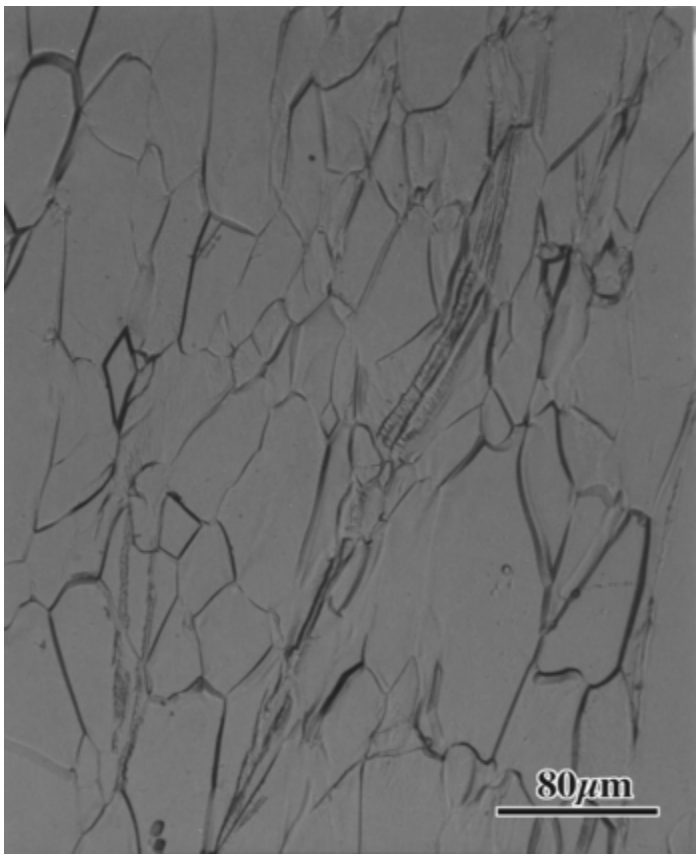

Fig. 22 Differential interference contrast light micrograph of unalloyed tantalum showing shear localization resulting from Taylor cylinder testing. Chemically polished (solution A, Table 2), swabbed for ~90 s, and etched (solution B, Table 2) for ~20 s

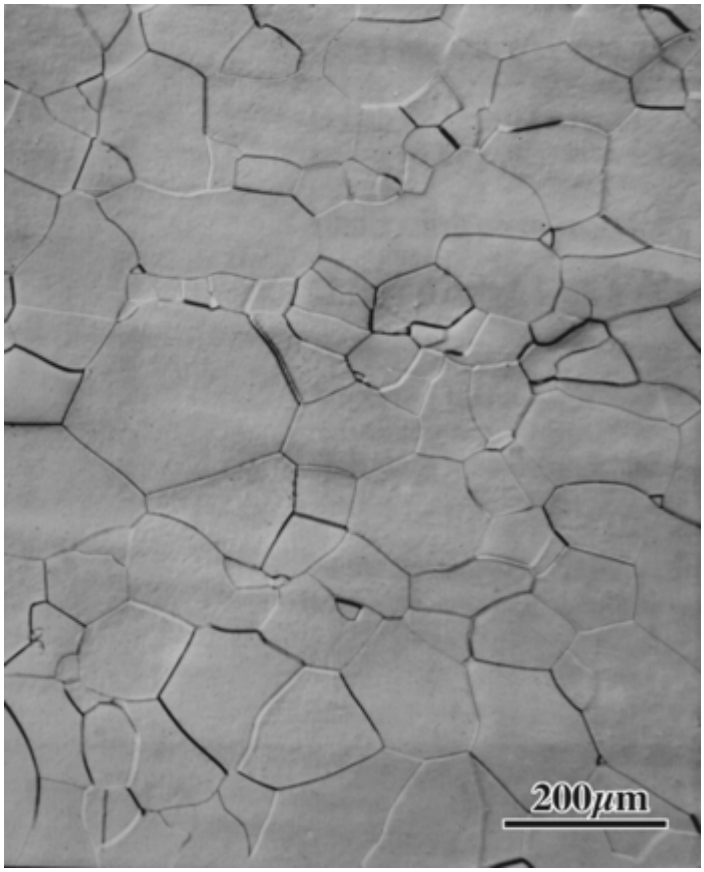

Fig. 23 Bright-field light micrograph of wrought unalloyed tantalum showing equiaxed grains. Chemically polished (solution A, Table 2) for ~120 s and etched (solution B, Table 2) for ~30 s. Source: Ref 3

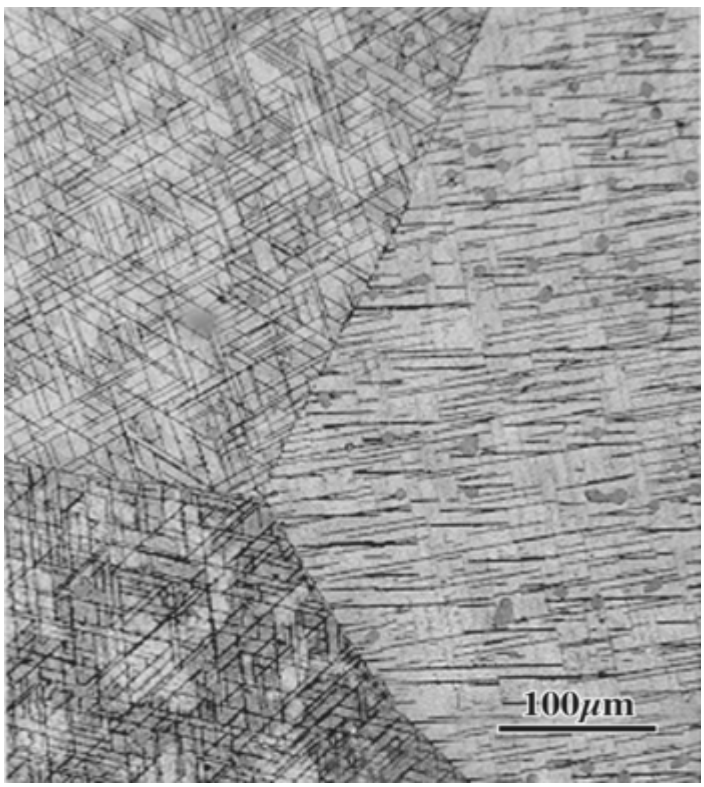

Fig. 24 Differential interference contrast light micrograph of as-cast plasma-melted tantalum showing a triple-point structure with Ta_2O_5 inclusions and TaN needles. Chemically polished (solution A, Table 2) for ~90 s and etched (solution B, Table 2) for ~30 s. Source: Ref 2

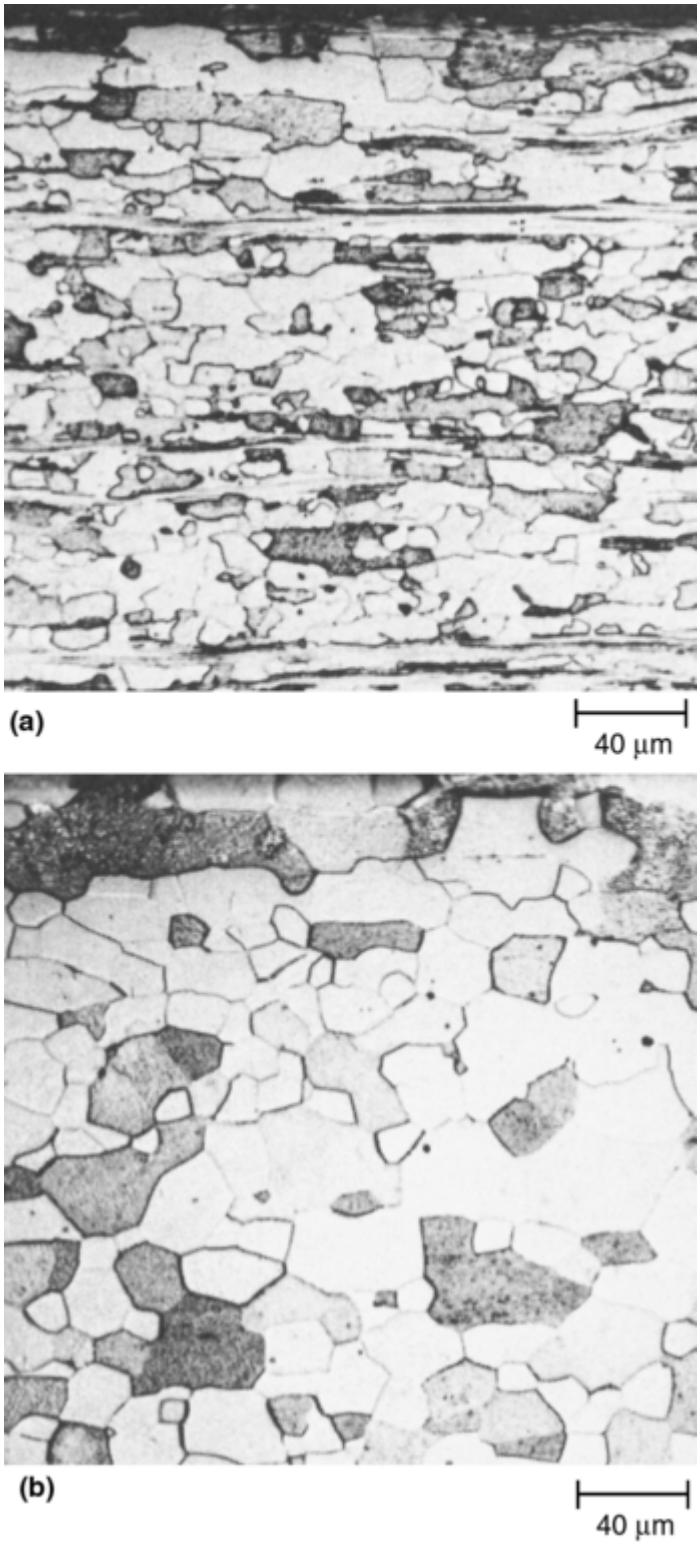

Fig. 25 Ta-250 ppm Y (added as Y_2O_3) powder metallurgy sheet. Bar cold rolled 85%, annealed, and finish rolled to 0.25 mm (0.010 in.) thick sheet. Final annealed in vacuum at 1260 °C (2300 °F) for 1 h. (a) Longitudinal cross section showing banding from residual cold work resulting from yttria stabilization. ASTM grain size 9. (b) Same processing, with added 30 min final anneal at 2000 °C (3630 °F). Longitudinal cross section. ASTM grain size 8. Etchant: ASTM 163 (Table 1). 250×

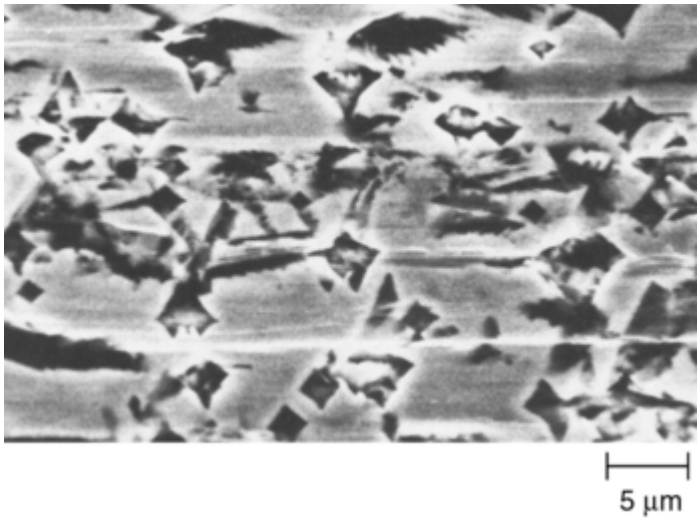

Fig. 26 Ta-100 ppm V (vanadium-doped) 25 μm (0.001 in.) thick powder metallurgy capacitor foil. Bar rolled to 60% reduction, annealed in vacuum 1 h, rolled to 0.45 mm (0.018 in.) thickness, final annealed, and finish rolled to final gage. Scanning electron micrograph showing the cold-worked through-surface structure after etching. Etched in electrolyte consisting of 30 g ammonium bromide, 5 g calcium chloride, and 18 mL deionized H_2O in 1000 mL methyl alcohol. Current density: 18 mA/cm^2 (118 mA/in.^{2}) for 20 min. 2000×

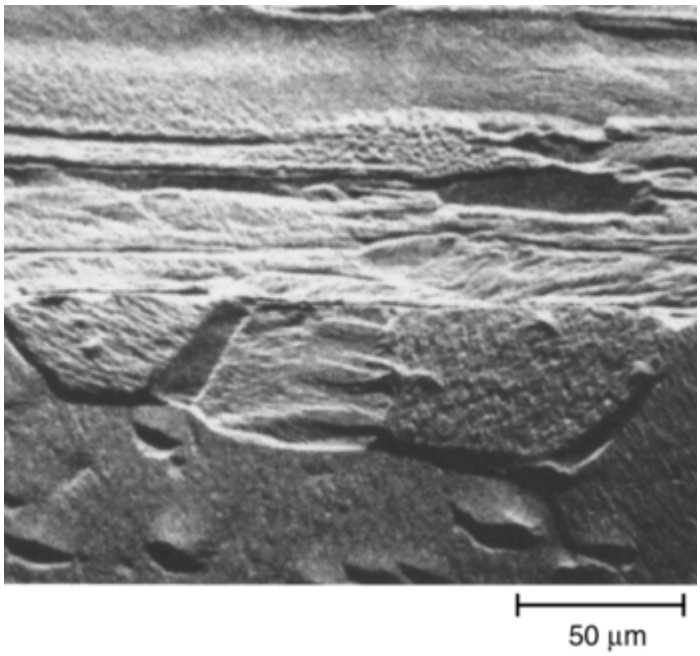

Fig. 27 Unalloyed tantalum/Nickel 201 explosively bonded bimetal; both materials 3.2 mm (0.125 in.) thick. Cold rolled to size and annealed. Scanning electron micrograph shows fully cold-worked tantalum (top) and fully recrystallized nickel (bottom). Etchant: ASTM 163 (Table 1), then ASTM 24. 300×

Molybdenum. Wrought products of molybdenum are developed from powders that are compacted and sintered. Sintered ingots can be fabricated directly. Purification of molybdenum is a major problem, however, and consolidation and purification are often achieved concurrently by vacuum arc melting, electron beam melting, zone refining, or levitation melting. Multiple melting to attain a desired level of purification is common.

The earliest alloys of molybdenum contained less than 2% alloying elements, providing higher recrystallization temperatures and higher mechanical properties at elevated temperature than could be obtained with unalloyed molybdenum. For several years, the development of molybdenum alloys with higher alloy content was limited by the inability of existing facilities to work the alloys. On an experimental basis, however, binary alloys of molybdenum and niobium, tantalum, titanium, tungsten, vanadium, hafnium, and zirconium were prepared as arc-cast ingots and studied primarily in the cast condition.

Binary alloys of molybdenum and tungsten have higher melting points than unalloyed molybdenum. As tungsten content increases, the melting point, hardness, and density of binary alloys increase almost linearly between those of pure molybdenum and pure tungsten; however, the workability and machinability of binary alloys decrease gradually.
Micrograph examples are given in Fig. 28, 29, 30 and 31.

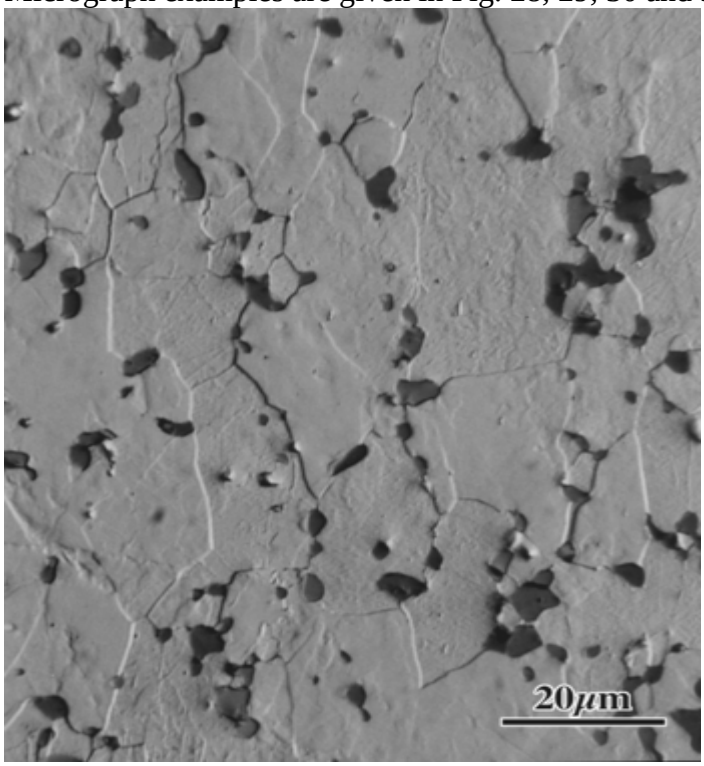

Fig. 28 Differential interference contrast light micrograph of mechanically alloyed Mo-1 wt% W powder dispersed in a molybdenum matrix by cold isopress/hot isopress powder metallurgy processes. Chemically polished (solution A, Table 2) for ~20 s and etched (solution B, Table 2) for ~30 s. Courtesy of Sherri R. Bingert, Los Alamos National Laboratory

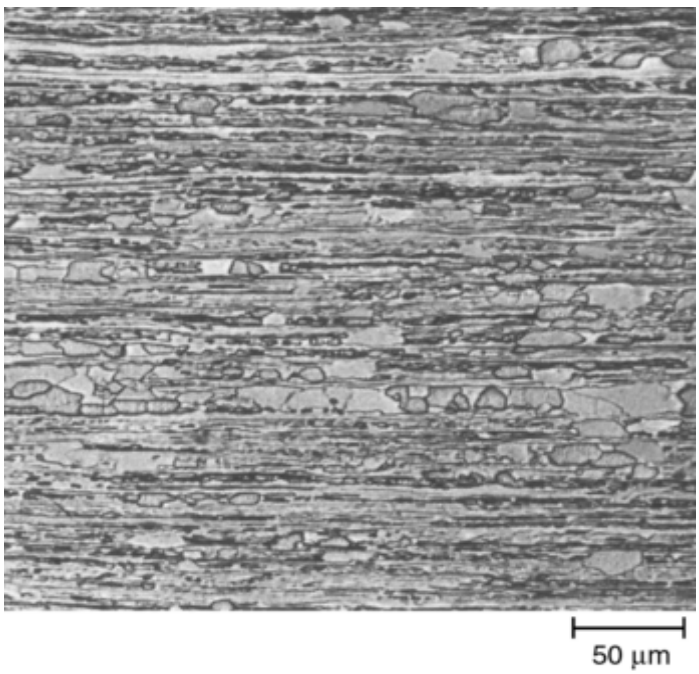

Fig. 29 Commercially pure molybdenum, rolled to 1.0 mm (0.040 in.) thick sheet, annealed at 900 °C (1650 °F) for 1 h. Longitudinal section. Partly recrystallized. See also Figure 30 Murakami's reagent (modified). 200×

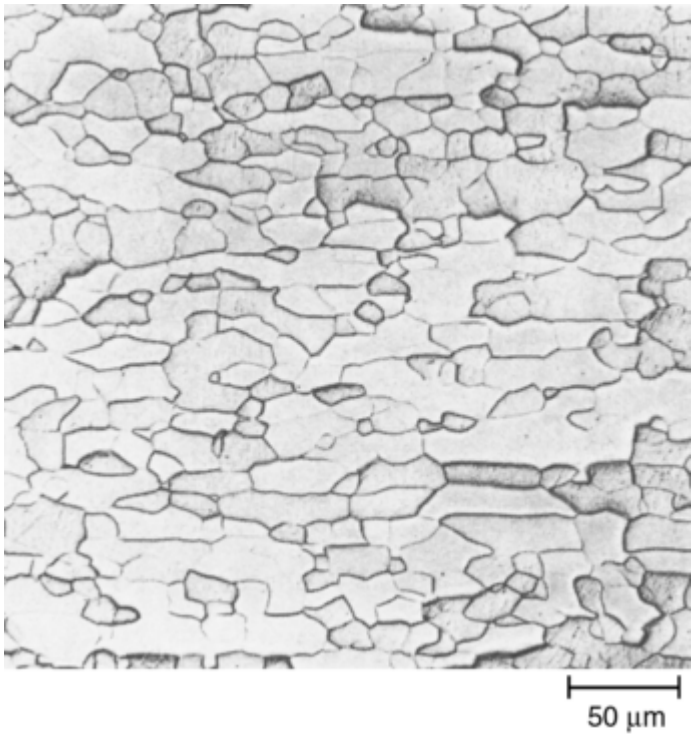

Fig. 30 Same sheet as in Figure 29 annealed 15 min at 1350 °C (2460 °F). Completely recrystallized. No voids are visible. Murakami's reagent (modified). 200×

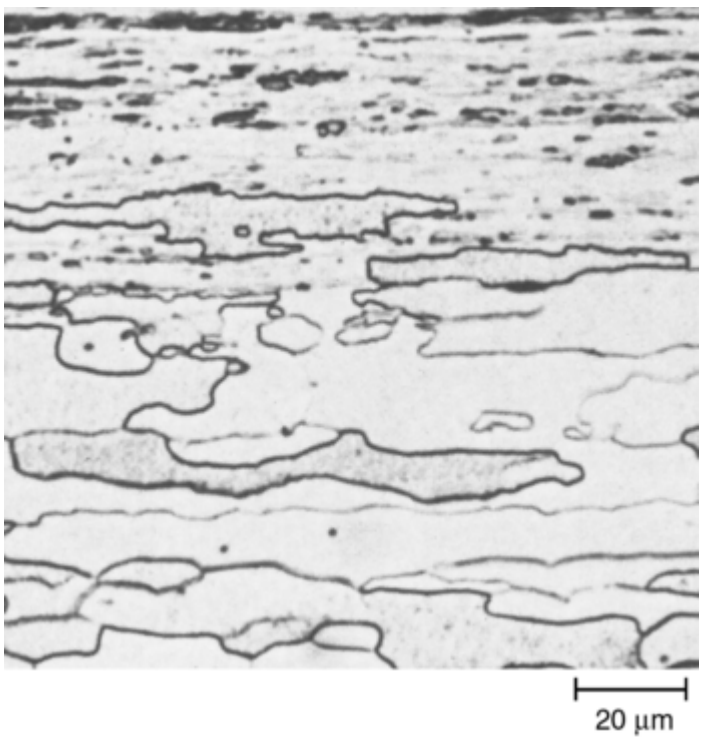

Fig. 31 Mo-0.5Ti alloy, cold rolled; recrystallized by annealing. Surface layer (top) is unrecrystallized because of nitrogen contamination. Etchant: ASTM 129 (Table 1). 500×

Tungsten. Wrought products of tungsten, such as wire and sheet, are developed initially from high-purity powder that is pressed to form a compact, then sintered. The sintered compact may be fabricated directly, which is the more common practice, or it may be used as an electrode in a melting process, such as consumable-electrode vacuum arc melting. Micrographs of sintered and wrought products are presented in this article.

Although prepared from commercially pure powders, most wrought tungsten products, especially those used in lamp and electronic-tube applications, contain one or more useful additives. Nonsag, doped tungsten is

prepared with a small amount of alkaline alummosilicate; most of the silicate evaporates in sintering, leaving a residue of approximately 100 ppm.

Doping increases the recrystallization temperatures of tungsten by approximately 415 °C (750 °F), changes the recrystallized grains from equiaxed to elongated, and improves resistance to creep and high-temperature deformation, properties that are essential for tungsten wire used in incandescent lamps. Thoriated tungsten, an alloy normally containing a dispersion of from 0.5 to 2.0% thorium dioxide, has greater resistance to impact and vibration in lamp filaments and improved thermionic emission in tungsten cathode electronic tubes than unalloyed tungsten. Perhaps the best known solid-solution alloys are those containing rhenium. The tungsten-rhenium alloys presented in this section exhibit higher electrical resistivity than unalloyed tungsten and are widely used in filaments for photographic flashbulbs.

Micrograph examples are given in Fig. 32, Fig. 33, Fig. 34, Fig. 35, Fig. 36.

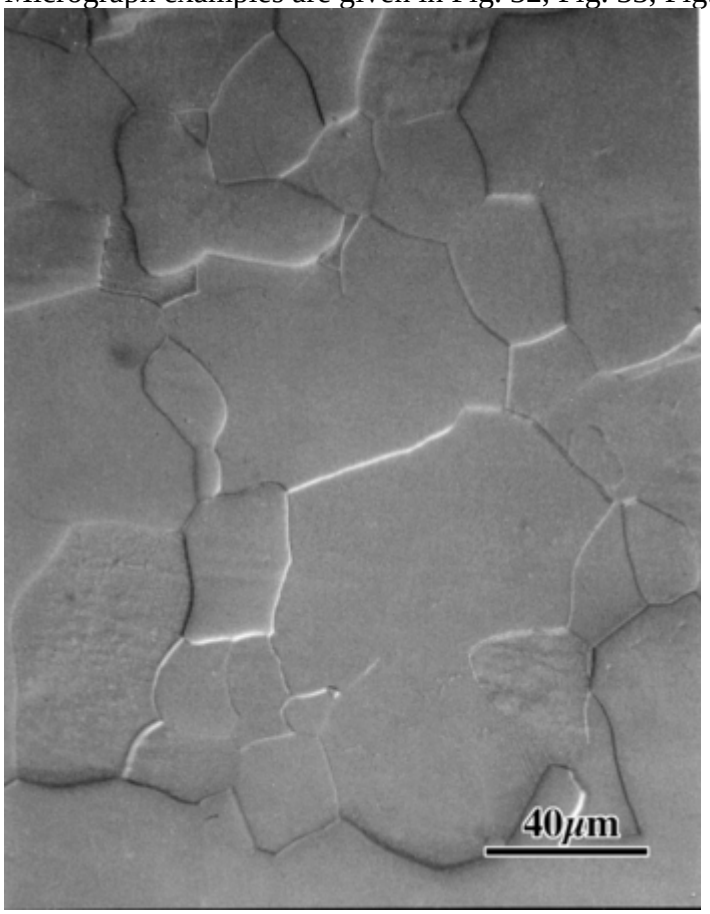

Fig. 32 Differential interference contrast light micrograph of tungsten plate material showing equiaxed grain structure. Chemically polished (solution A, Table 2), swabbed for ~30 s, and swab etched (solution B, Table 2) for ~40 s

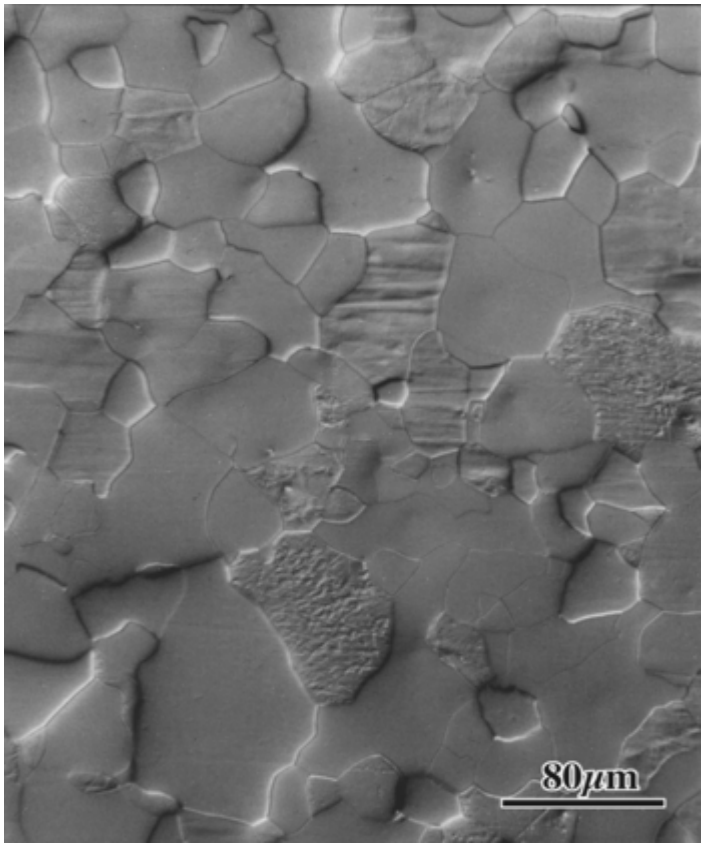

Fig. 33 Differential interference contrast light micrograph of tungsten plate showing equiaxed grain structure. Chemically polished (solution A, Table 2), swabbed for ~30 s, and swab etched (solution B, Table 2) for ~40 s

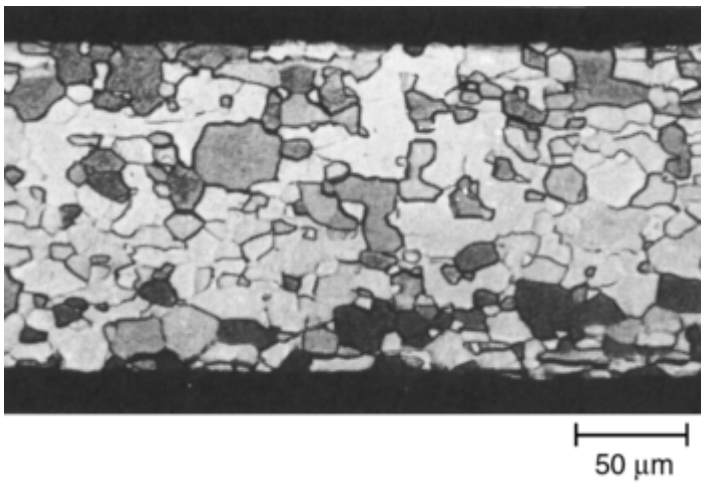

Fig. 34 Tungsten wire (not doped), 0.2 mm (0.007 in.) diameter, annealed at 2700 °C (4890 °F) for 5 min. Fully recrystallized, equiaxed grains. Murakami's reagent (modified). 200×

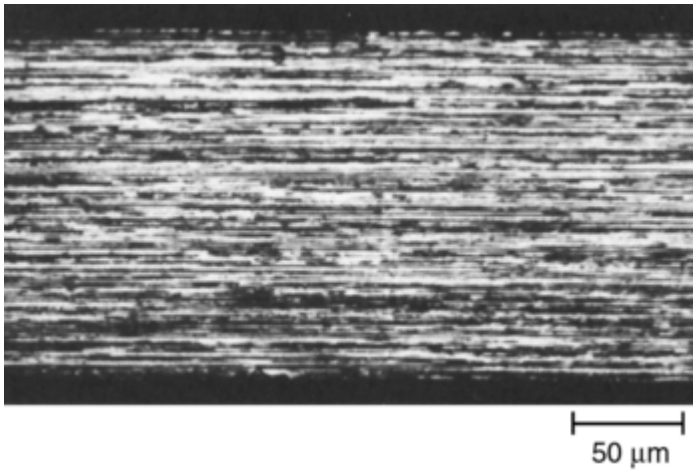

Fig. 35 Tungsten wire (nonsag, doped lamp grade), 0.2 mm (0.007 in.) diameter. As-drawn structure showing elongated grains. Murakami's reagent (modified). 200×

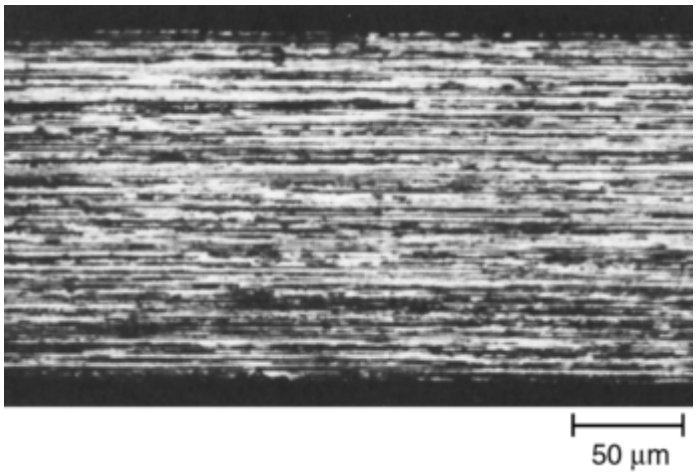

Fig. 36 Same grade and size of tungsten wire as for Figure 35 annealed 10 min at 1900 °C (3450 °F), showing start of recrystallization. Murakami's reagent (modified). 200×

References cited in this section

2. A.M. Kelly, S.R. Bingert, and D.J. Thoma, Application of New Tantalum Metallographic Preparation Techniques to Group IV and V Metals, *Microstruct. Sci.*, Vol 26, 1998, p 347–353

3. A.M. Kelly, S.R. Bingert, R.D. Reiswig, New Tantalum Metallographic Preparation Techniques for Tantalum and Tantalum Alloys, *Microstruct. Sci.*, Vol 23, 1996, p 185–195

Metallography and Microstructures of Refractory Metals and Alloys, *Metallography and Microstructures,* Vol 9, *ASM Handbook*, ASM International, 2004, p. 877–888

Rhenium and Its Alloys

Revised by Todd A. Leonhardt, Rhenium Alloys Inc., and John P. Sauer, Sauer Engineering

Rhenium, discovered in 1925 by Ida Tacke, Walter Noddak, and Otto Berg, was one of the last naturally occurring elements to be discovered and was named after the Rhine River in Germany. Only a few milligrams of rhenium were produced in 1927 and only one full gram in 1928. It was not until the 1960s that rhenium was produced in a full-scale manufacturing operation.

Rhenium is a heavy transition metal with a melting point of 3453 K. Even though rhenium does not form a carbide and is hexagonal close-packed, it is often referred to as a refractory metal. Rhenium is unique because of its high elastic modulus (420 GPa, or 61 × 10^6 psi), and it has a work-hardening rate of n = 0.5. Rhenium also possesses high electrical resistance across a wide temperature range. Additionally, rhenium consistently provides high yield and ultimate tensile strengths at both ambient and elevated temperatures while maintaining excellent ductility and exceptional creep qualities, as well as the low-cycle fatigue properties required by demanding high-temperature applications.

Another important property of rhenium is its ability to be alloyed with molybdenum and tungsten, thereby increasing the ductility of these alloys and decreasing the ductile-brittle transition temperatures of tungsten-rhenium and molybdenum-rhenium alloys. This property of rhenium is referred to as the rhenium effect. General alloys of molybdenum-rhenium range from 41.5 to 47.5% Re and tungsten-rhenium from 3 to 25 % Re. Commercially pure rhenium is available as wire, rod, foil, and sheet/plate. Rhenium-bearing alloys are available as:

- Foil of molybdenum-rhenium alloys with 41.5, 44.5, or 47.5% Re
- Rod for Mo-47.5% Re
- Wire tungsten-rhenium alloys with contents of 3.0, 5.0, 10, or 25 wt% Re

Rhenium and rhenium-containing alloys are typically produced via powder metallurgy (P/M), where powders are consolidated and then sintered at temperatures within approximately 80 to 90% of their melting point to a density of greater than 96%. The P/M process is used to produce wrought products that are formed into plate, sheet, foil, ingots, rods, and wire. Rhenium and some rhenium-containing alloys can be produced by chemical vapor deposition, electroforming, and spray forming. These methods make net- to near-net-shaped components. Additional information on the uses of rhenium and rhenium-bearing alloys, as well as the effects of alloying additions of rhenium on the ductility and tensile strength of refractory metals, is available in the article “Powder Metallurgy Refractory Metals” in *Powder Metal Technologies and Applications*, Volume 7 of *ASM Handbook.*

Commercially pure rhenium materials are usually analyzed to determine the degree of porosity. General microstructure analysis of materials shows that up to 48 wt% Re is soluble in molybdenum, and up to 26 wt% Re is soluble in tungsten. Optimal processing conditions require the use of high-purity powder blends, proper sintering times and temperatures, and careful annealing practices. Molybdenum-rhenium alloys are annealed in hydrogen above the recrystallization temperature (approximately 1600 °C, or 2910 °F); tungsten-rhenium alloys are stress-relief annealed below the recrystallization temperature. All rhenium-bearing alloys should be cooled rapidly on completion of the annealing hold time. The temperature should be dropped by 1000 °C (1800 °F) as quickly as possible in a water-jacketed cooling zone. Complete cooling takes approximately 5 to 10 min, depending on the thickness of the material. There are obviously many processing steps to achieve a final product, ranging from sintered and hot isostatic pressed to final form (wire to plate). The following microstructural examples will provide some representative conditions for the many product forms and alloys.

Molybdenum-rhenium alloys are prone, if process conditions are not optimal, to exhibit evidence of a second phase (σ phase) in the microstructure. Sigma phase is a rhenium-rich phase that is hard and brittle. During

polishing, it usually appears intergranularly and slightly raised from the solid solution surrounding it. Higher rhenium contents are difficult to fabricate; therefore, little work has been performed to observe the microstructure that may result.

Tungsten-rhenium alloys also can be prone, if process conditions are not optimal, to exhibit evidence of a second phase (σ phase) in the microstructure (Fig. 37, 38, 39). Evidence of σ phase in tungsten-rhenium alloys, when present, is similar to that exhibited in molybdenum-rhenium alloys.

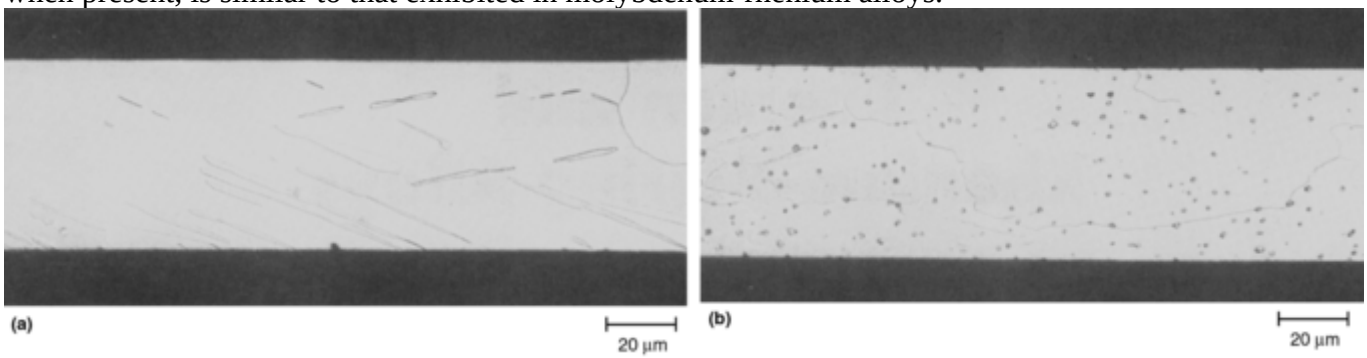

Fig. 37 Mo-48Re foil (longitudinal section). Warm worked from ingot, then cold worked to a 0.025 mm (0.001 in.) thickness. Hydrogen annealed at 1600 °C (2910 °F) and held at temperature for 2 min. (a) Lamellar-type σ phase. (b) Globular-type σ phase. Modified Murakami's reagent. 500×

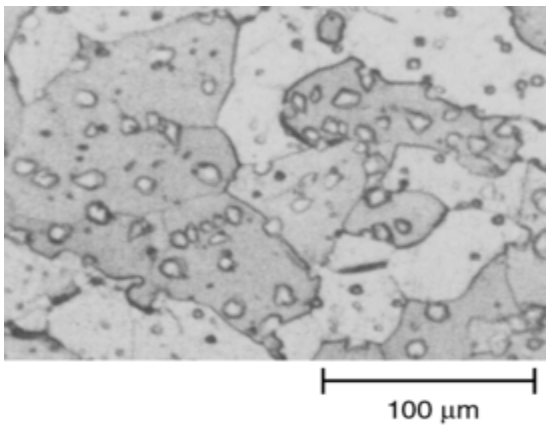

Fig. 38 Mo-47Re rod. Warm worked from 38 mm (1.5 in.) diameter ingot to 16 mm ($\frac{5}{8}$ in.) diameter. Hydrogen annealed 30 min at 1600 °C (2910 °F). Microstructure exhibits some σ phase. Modified Murakami's reagent. 190×

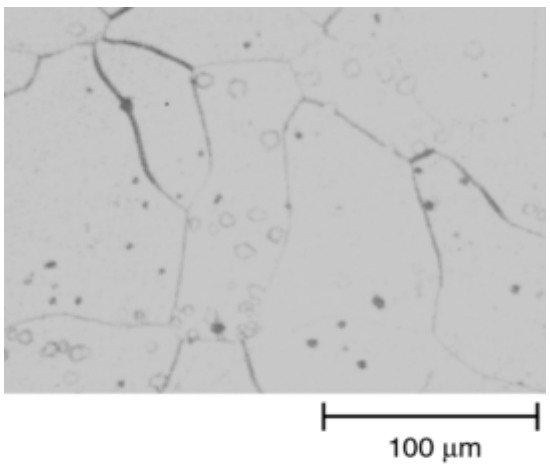

Fig. 39 Mo-41Re rod. Warm worked from 38 mm (1.5 in.) diameter ingot to 23 mm (0.90 in.) diameter. Hydrogen annealed 2 h at 1600 °C (2910 °F). Evidence of σ phase. Dark areas are porosity. Modified Murakami's reagent. 190×

Metallography and Microstructures of Refractory Metals and Alloys, *Metallography and Microstructures,* Vol 9, *ASM Handbook,* ASM International, 2004, p. 877–888

Specimen Preparation

The preparation of rhenium-containing materials can be categorized into two groups:

- Size of samples (foil and wire versus sheet/plate, etc.)
- Alloy composition (molybdenum-rhenium versus tungsten-rhenium and pure rhenium materials)

With molybdenum-rhenium materials and small sample sizes, more conventional metallurgical preparation techniques can be used. As sample size increases and alloy content changes, special techniques, as detailed in the subsequent sections, are required.

The procedures recommended are based on experience and techniques that have produced acceptable results. The logic for the preparation sequence is listed to help the laboratory technician better understand the need for each step. This allows for problem solving if issues with preparation are encountered or if new alloys not specifically listed are encountered.

Sectioning. With the high work-hardening rate of rhenium, care must be taken in sectioning samples. Molybdenum-rhenium alloys can be conventionally sectioned but with extra care. Sheet and plate can be sheared, but significant deformation or twinning will be evident in the microstructure, which is undesirable for evaluation purposes.

Pure rhenium and tungsten-rhenium can be sectioned using “soft”-bonded abrasive cutoff wheels; however, electrical discharge machining (EDM) is preferred, because of the deformation produced by the abrasive wheel. Single-point machining is not possible, because of the work-hardening rate mentioned earlier.

Mounting. Procedures for rhenium and rhenium-containing alloys depend on the sample size and configuration. Foil and wire samples should be cold mounted in an epoxy, so as not to induce deformation from compression mounting. Plate and sheet samples can be mounted via compression hot mounting.

Sample size is extremely important for pure rhenium and tungsten-rhenium-containing alloys. If the mount has a substantial cross-sectional area, grinding of the sample will be very difficult and time-consuming, due to the slow removal rate of these metals. When possible, specimens should be cut into smaller sections for mounting and subsequent preparation.

Grinding. With the high work-hardening rate of rhenium and rhenium-containing alloys, the grinding step is extremely important, so as not to induce microstructural artifacts from severe deformation. For this reason, semiautomated preparation is highly recommended. The key issue is the use of a system that provides a high removal rate with a continuous supply of sharp, fresh abrasive. This process results in less deformation and minimal work hardening. If high speeds and high removal rates are not maintained, edge rounding can also occur.

For foil/wire samples and smaller molybdenum-rhenium alloys, traditional grinding procedures using 320-, 400-, 600-, 800-, and 1200-grit silicon carbide papers can be performed (300 rpm for less than 30 s per paper). The newer grinding disc formats are also applicable if available.

For pure rhenium and tungsten-rhenium alloys, which have a higher work-hardening rate, a different approach is needed. Rough grinding should be performed with a 150-grit alumina wheel traveling at 1500 rpm, with a pressure of 300 N (67 lbf) force on the holder (assuming a holder with six mounts) and a high cooling rate to keep the sample cool during planar grinding or other high-removal-rate methods.

Due to the need for a uniform and high removal rate with fresh abrasive, as mentioned earlier, the use of grinding/lapping discs is recommended over the conventional grinding paper format. Therefore, after rough (planar) grinding, a grinding/lapping disc with a rotational speed of 150 rpm and 300 N (67 lbf) force with 9 μm polycrystalline diamond suspension is suggested for 7 to 10 min. This procedure should produce a flat, evenly scratched sample.

Intermediate Polishing. The polishing steps are again driven by the sample size and alloy combinations. If the traditional grinding paper format has been used for foil, wire, and small molybdenum-rhenium samples, then diamond/alcohol-based lubricant/silklike cloth combinations are suggested. Both 3 and 1 μm polycrystalline diamond steps for 3 to 5 min at 150 rpm and 300 N (67 lbf) force should be sufficient.

For larger molybdenum-rhenium samples and pure rhenium or tungsten-rhenium alloys, use a 6 μm polycrystalline diamond suspension on a nylon cloth for 10 min, with the same processing parameters as for 3 and 1 μm diamond steps. The 6 μm diamond step is recommended for a smooth transition from the 9 μm grinding/lapping step to the 3 and 1 μm fine polishing steps.

Final Polishing. Two methods of final polishing are suggested and are applicable to all size/alloy combinations. Again, with the high work-hardening rate and tendency toward deformed material, attack/etch polishing is a necessary last step to reveal the true microstructure.

Attack Polishing. The final polishing step can be performed with a fine abrasive 0.05 μm alumina or colloidal silica and an oxidizing or basic attack-polishing solution at 150 rpm and 200 N (45 lbf) force (assuming holder with six mounts). The polishing cloth used should be a chemical-resistant cloth designed for attack polishing. Times may vary, but a 1 to 2 min polish should be sufficient. Attack-polishing solutions are:

- Modified Murakami's reagent: 15 g potassium ferricyanide ($K_3Fe(CN)_6$), 2 g sodium hydroxide (NaOH), 100 mL H_2O, and equal part of polishing solution (colloidal silica or alumina)
- 20% solution of chromium trioxide, and equal part of polishing solution
- 150 mL H_2O, 150 mL colloidal silica, 30 mL H_2O_2, 3 mL HNO_3 (30% concentration), and 2 mL HF

Vibratory Polishing. Another method for final polishing is vibratory polishing. Polishing on a soft cloth for extended periods of time will produce a deformation-free microstructure with either 0.05 μm alumina or colloidal silica. A mixture of 75 mL of polishing solution with 25 mL of 30% H_2O_2 is recommended to reduce the time for polishing.

Macroexamination of rhenium and rhenium-bearing alloys is useful to determine the size, shape, and volume of porosity. Because rhenium and molybdenum-rhenium alloys are normally used in the recrystallized condition, mechanical working flow lines are almost nonexistent.

Macroexamination is also useful in observing fractured surfaces, seams, folds, and inclusions. As-polished or polish-etched specimens (see the etchants in the section “Microexamination” in this article) are best for macroexamination.

Microexamination of rhenium and rhenium-containing alloys is usually performed in the etched condition. As mentioned earlier, with the high work-hardening rate and tendency toward deformed material, an assessment must be made that the sample being reviewed is the true microstructure and does not contain artifacts from preparation. Additional attack polishing could be necessary and must be considered on a sample-to-sample basis.

Etching with modified Murakami's reagent is the preferred technique for microexamination of most rhenium and rhenium-bearing alloys. Grain boundaries and details of the structure usually appear within 15 to 60 s at room temperature. Longer times tend to produce etch pitting and do not provide a representative view of the microstructure. When porosity is present, care must be taken not to overly enlarge the size of the pores from the etching (or also the polishing method). Evidence of mechanical twinning, if present, will be observed during the same time span. Additional re-polishing and etching are necessary, at times, to confirm the true metallurgical condition of the specimen.

Etchants for microexamination include:

- Modified Murakami's reagent: 15 g potassium ferricyanide ($K_3Fe(CN)_6$), 2 g sodium hydroxide (NaOH), and 100 mL H_2O
- Modified Murakami's reagent: 10 g potassium ferricyanide ($K_3Fe(CN)_6$), 4 g sodium hydroxide (NaOH), and 200 mL H_2O
- 30 mL lactic acid, 15 mL HNO_3, and 5 mL HF
- Equal parts 30% H_2O_2 and HNO_3

All etchants should be mixed fresh for each usage and all etching should be performed at room temperature. The time required and selection of etchant is governed by the characteristics being evaluated.

Metallography and Microstructures of Refractory Metals and Alloys, *Metallography and Microstructures,* Vol 9, *ASM Handbook*, ASM International, 2004, p. 877–888

References

1. ASTM E340, Standard Method for Macroetching Metals and Alloys

2. A.M. Kelly, S.R. Bingert, and D.J. Thoma, Application of New Tantalum Metallographic Preparation Techniques to Group IV and V Metals, *Microstruct. Sci.,* Vol 26, 1998, p 347–353

3. A.M. Kelly, S.R. Bingert, R.D. Reiswig, New Tantalum Metallographic Preparation Techniques for Tantalum and Tantalum Alloys, *Microstruct. Sci.,* Vol 23, 1996, p 185–195

Metallography and Microstructures of Tin and Tin Alloys, *Metallography and Microstructures,* Vol 9, *ASM Handbook*, ASM International, 2004, p. 889–898

Metallography and Microstructures of Tin and Tin Alloys

Introduction

TIN AND TIN ALLOYS are extremely soft and have low recrystallization temperatures; therefore, the preparation of metallographic specimens from tin and tin alloys presents special problems. As with other very soft metals and alloys (with hardness less than about 25 HV), it is often difficult to obtain an unworked surface free from scratches for tin and other soft metals with low melting points (such as antimony, bismuth, cadmium, and zinc). In a pure or nearly pure condition, very soft metals also can deform under pressure used in compression mounting. This is especially true for pure tin (hardness of 6 HV with melting point of 231 °C, or 448 °F) and even more so for lead (hardness of 4 HV with melting point of 327 °C, or 621 °F). The low crystallization temperature of tin and lead can also result in a false structure if the distortion occurs during polishing.

To overcome these difficulties, it is necessary to take special precautions during both mounting and polishing of pure tin or nearly pure tin alloys. More concentrated alloys with higher hardness than the pure metals are easier to prepare and usually can be prepared by basic metallographic procedure (Ref 1). For example, results obtained with a solder alloy (63wt%Sn-37wt%Pb eutectic alloy) are shown in Fig. 1. Discrete areas of tin and lead are distributed as components of a globular eutectic in this alloy, and both the tin and lead phases of the eutectic are clearly delineated. No scratches are discernible in either phase. In another group of tin- or lead-base alloys, alloying elements such as bismuth and copper are added in substantial amounts. Comparatively hard, idiomorphic particles of intermetallic compounds of the alloying and base metals are then present in the microstructure, distributed in a matrix of the base metal. Examples, after preparation using the basic procedure, are shown in Fig. 1(c) to (f).

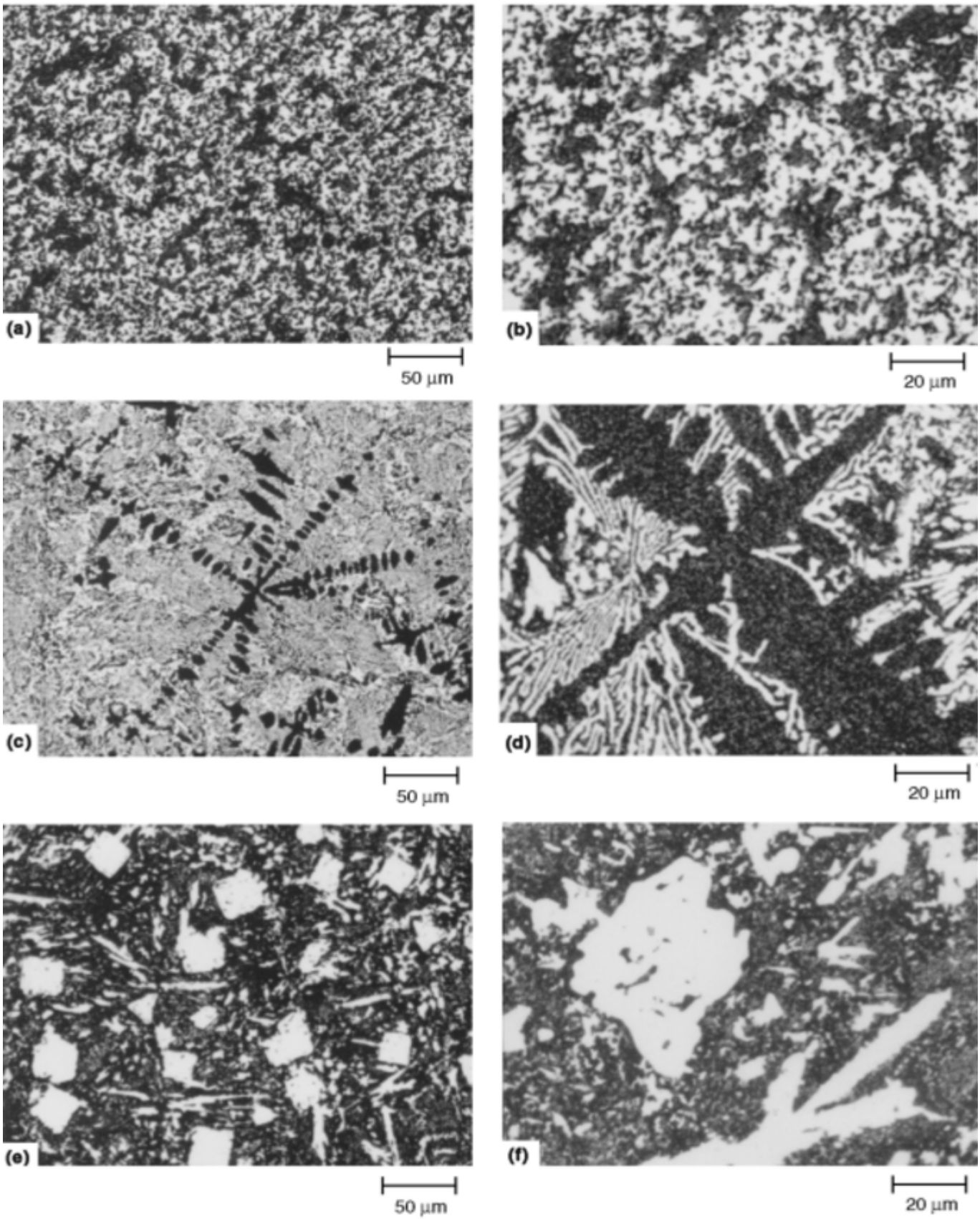

Fig. 1 Very soft metals; alloys of lead and tin. (a) and (b) A near-eutectic soft solder (63% Sn, 37% Pb; hardness, 9 HV). A globular eutectic of tin phase (light) and lead phase (dark). (c) and (d) A linotype metal (4% Sn, 12% Sb, 84% Pb; hardness, 26 HV). Primary lead dendrite in a ternary eutectic of tin and antimony compounds and a continuous lead phase. (e) and (f) A bearing metal (86% Sn, 4% Cu, 10% Sb; hardness, 21 HV). Large cuboids of a tin-antimony compound, needle-shaped particles of a copper-tin compound, and smaller particles of these compounds in a matrix of tin phase. All sections prepared

by the basic procedure and final polished with 0.1 μm diamond. All etched in 2% nital. (a), (c), and (e), 200×; (b), (d), and (f), 500×. Source: Ref 1

Reference cited in this section

1. L.E. Samuels, *Metallographic Polishing by Mechanical Methods*, ASM International, 2003, p 274, 276

Metallography and Microstructures of Tin and Tin Alloys, *Metallography and Microstructures*, Vol 9, *ASM Handbook*, ASM International, 2004, p. 889–898

Specimen Preparation

Sectioning. The use of an abrasive cutoff wheel is preferred for extracting specimens of tin and tin alloys from larger masses of material. Specimens may also be sawed. A coolant, such as water or alcohol, should be used to minimize the buildup of frictional heat. If distortion is difficult to avoid while a section is being cut from a component, it may be desirable to cast a complex-shaped component part. A resin that sets below about 40 °C (105 °F) needs to be used (Ref 1).

Mounting of tin and tin alloy specimens should be carried out at room temperature, because elevated temperatures can induce structural changes. Thermosetting mounting compounds are therefore unsuitable. Specimens can be mounted satisfactorily at room temperature using castable mounting materials, such as the polyesters and acrylics. Care should be taken to select a material with minimum temperature rise during curing.

When examination of the edges of a specimen is required, a supporting layer is deposited on the surface by electroplating or electroless plating before mounting. The coating should be harder than the specimen; copper and nickel coatings are most often used.

Grinding and Polishing. Distortion of the surface layers of tin and tin alloys may cause recrystallization, which will mask the true structure. For tin alloys in a metastable state, distortion of the surface regions as a result of working may cause such structural changes as precipitation from a supersaturated solid solution.

To avoid working the surface, extreme care must be exercised during grinding and polishing because of the susceptibility to distortion during those operations. The method described below is, with slight modifications, suitable for grinding and polishing of tin and all types of tin alloys with minimum distortion.

The specimen is flattened with a file or by careful turning in a lathe, then wet ground on silicon carbide papers of successively finer grit. The papers are maintained wet by a continuous stream of lubricant, usually water, that washes away the particles of metal cut from the specimen surface. This prevents clogging of the abrasive papers, which would lead to surface flowing of the metal instead of cutting. During grinding, new sheets of abrasive papers and excessive pressure should be avoided, because loose particles of silicon carbide can easily embed in many soft tin-base alloys. For alloys with zinc- and aluminum-rich phases, which may be stained by water, kerosene is used as the lubricant.

A light, positive pressure is preferred during polishing. Each polishing should continue for at least twice as long as required to remove the scratches from the previous polishing stage. Polishing is usually carried out using different grades of diamond suspended in an oil- or water-base lubricant. The polishing wheels and the pads used for diamond pastes should always be free of dust, grit, and the diamond particles from the previous polishing step. Coarse grinding and fine polishing should be carried out at different locations; fine polishing requires an environment free of corrosive fumes.

Scratches from the final abrasive papers are removed by polishing for several minutes on a wheel covered with a short-nap or napless cloth impregnated with 3 to 6 μm diamond paste. Next, the specimen is polished on a wheel covered with a short-nap cloth impregnated with 0.25 to 1 μm diamond paste; the duration depends on the microstructure of the specimen. Specimens should be polished thoroughly to remove deformation from the previous stage, but excess polishing can easily result in grain or phase relief. If grain-boundary relief appears

before a heavily worked layer from the previous polishing is completely removed, the diamond impregnation of the polishing cloth should be increased to maintain a rapid cutting rate. Polishing may continue using 0.25 and 0.1 μm diamond on wheels covered with short-nap cloth or may proceed to the final polishing. The commercially available lubricants may be used with all diamond polishings. After each polishing, the specimen should be thoroughly washed in a dilute solution of liquid detergent; rinsing in water and ethanol and drying in forced air is also suitable. An ultrasonic cleaner may be used, but care should be taken with specimens that may contain loose particles.

Further polishing, if necessary, is carried out by hand using a pad of long-nap cloth impregnated with γ-alumina (Al_2O_3) and a suitable lubricant (usually water). A plain long-nap cloth is recommended, because a dyed cloth may stain the freshly cut metal on polished surfaces. Vibratory polishing can also be employed.

Etching. Although the method of polishing is the same for all types of tin and tin alloys, different etchants are used for the various alloys (see Table 1 for etchant compositions).

Table 1 Etchants for tin and tin alloys

Etchant	Uses
1. 2 mL HCl, 5 mL HNO_3, 93 mL methanol	General use for tin and tin alloys
2. 2 mL HCl, 5 mL HNO_3, 93 mL H_2O	Grain-contrast etchant for tin and pewter
3. 5 mL HCl, 2 g $FeCl_3$, 30 mL H_2O, 60 mL 95% methanol or 95% ethanol	General use for tin and tin alloys
4. 2 mL HCl and 98 mL 95% methanol or 95% ethanol	Grain-boundary etchant for pure tin
5. 10 mL HNO_3, 10 mL acetic acid, 80 mL glycerol	Darkens the lead in the eutectic of tin-rich tin-lead alloys
6. 5% $AgNO_3$ in H_2O	Darkens primary and eutectic lead in lead-rich tin-lead alloys
7. 2% nital (2 mL HNO_3 in 98 mL 95% ethanol or 95% methanol)	Recommended for etching tin-antimony alloys; darkens tin-rich matrix, leaving intermetallics unattacked. Often used for etching specimens of babbitted bearings
8. Picral (4 g picric acid in 100 mL 95% methanol or 95% ethanol)	For etching tin-coated steel and tin-coated cast iron (see text)
9. 1 drop concentrated HNO_3, 2 drops HF[(a)], 25 mL glycerol; then picral	For etching tin-coated steel (see text)
10. 20 mL concentrated NH_4OH diluted with 80 mL distilled water, and a few drops of 30% H_2O_2	For etching tin-coated copper and copper alloys (polish attack)
11. 3 parts acetic acid, 4 parts HNO_3, 16 parts H_2O	General etchant for lead-tin alloys and for soldered joints

(a) Safety requirements should be strictly observed when handling HF.

Pure tin can be etched easily in an alcoholic ferric chloride ($FeCl_3$) solution or in a 2% solution of hydrochloric acid (HCl) in alcohol.

Tin-lead alloys have simple two-phase structures, with a eutectic occurring at 63% Sn. Primary tin phase and primary lead phase are present, respectively, in hypereutectic and hypoeutectic alloys. Alloys containing primary tin are best etched in a solution of (by volume) 1 part nitric acid (HNO_3), 1 part acetic acid, and 8 parts glycerol; a 5% solution of silver nitrate ($AgNO_3$) in water is most suitable for alloys containing the primary lead phase. Both etchants blacken the lead without attacking the tin.

Tin-antimony alloys are more difficult to etch than other tin-base alloys. Several of the etchants listed in Table 1 can be used, but 2% nital is considered optimal. Etching should be carried out as soon as possible after final polishing, because a thin, porous film forms on the surface if the specimen is left standing. This results in pitting when the specimen is immersed in the etchant. In Sn-Sb-Cu alloys, the Sn-Sb solid solution is supersaturated at room temperature and is therefore metastable. If deformation remains in the surface regions as a result of working during polishing, recrystallization and precipitation may occur, masking the true structure (compare Fig. 2 and 3).

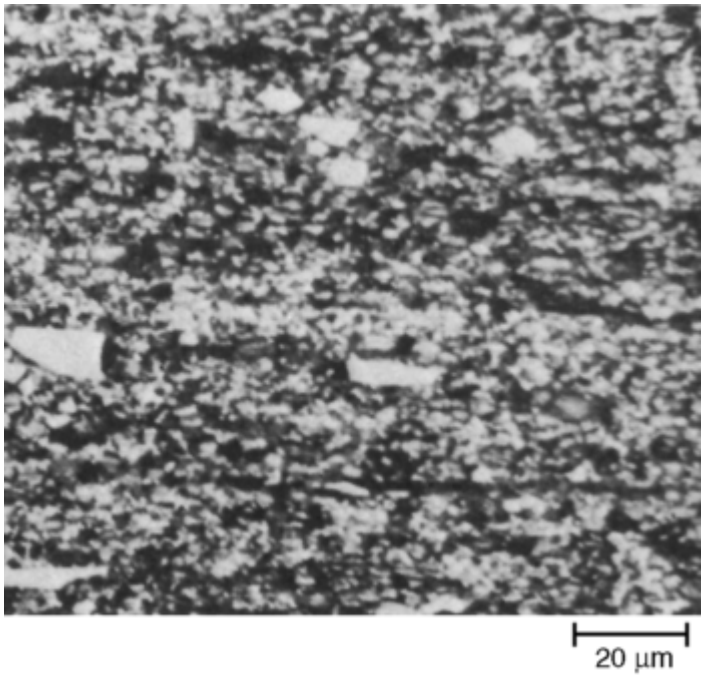

Fig. 2 Sn-6Sb-2Cu pewter, cold rolled. This specimen was poorly prepared; the surface is scratch-free, but deformation in the surface from previous polishings has masked the true structure. Compare with Figure 3 Etchant 2, Table 1. 500×

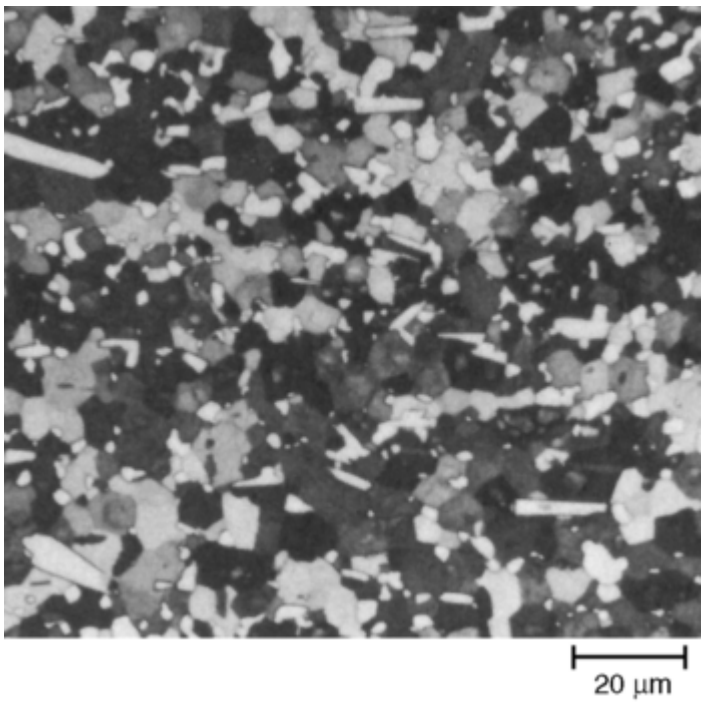

Fig. 3 Same alloy and etchant as Figure 2 correctly prepared so the true structure of the pewter is apparent. The tin-rich matrix is shown in contrast; SbSn and Cu_6Sn_5 intermetallic particles are unattacked. 500×

Reference cited in this section

1. L.E. Samuels, *Metallographic Polishing by Mechanical Methods*, ASM International, 2003, p 274, 276

Metallography and Microstructures of Tin and Tin Alloys, *Metallography and Microstructures,* Vol 9, *ASM Handbook,* ASM International, 2004, p. 889–898

Techniques for Tin and Tin Alloy Coatings

Whenever specimens of harder base metals coated with tin or tin alloys are prepared for microscopic examination, it is difficult to prevent a step from forming at the interface between the relatively soft coating and the base metal. With such coatings, it is imperative to deposit a supporting metal layer with a hardness similar to that of the base metal on top of the coating. When the base metal is copper or a copper alloy, the supporting layer should be copper; when the base metal is steel or cast iron, this layer usually is nickel. In examining the interface between a base metal and a thick coating, as in the study of bearings, using a supporting layer offers no advantage unless examination of the edge of the specimen is required.

Mounting. For reasons stated earlier in this article, specimens with tin or tin alloy coatings should be mounted at room temperature. In addition, thin sheet specimens may be crushed or deformed if mounted in a material that requires pressure and high temperature. Specimens usually are mounted so that a normal cross section of the coating is obtained. However, when an extremely thin coating, such as electroplated tin, is to be examined, an oblique section, called a taper section (Fig. 4), is often used. The use of taper sections increases the effective magnification in the direction normal to the interface and so offers information on small details that otherwise would not be visible. A true interface structure is obtained only along the edge adjacent to the acute angle (see Fig. 4).

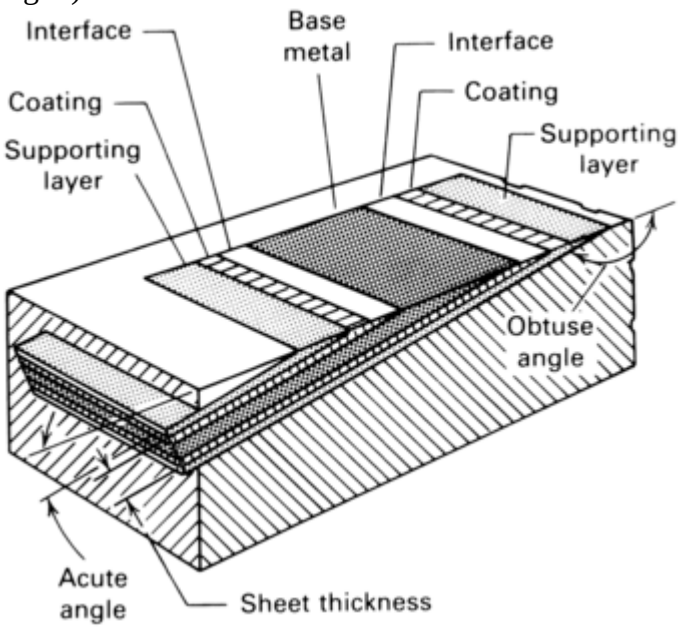

Fig. 4 Components of a taper section of tinplate. See text for a more complete discussion.

The linear enlargement obtained by using taper sections, termed the distortion ratio, is equal to the cosecant of the angle between the section plane and the specimen axis. Therefore, for a distortion ratio of 10, which is often the nominal aim, the angle, θ is 5° 44′ 21″. For accuracy, the actual distortion ratio should be determined directly from precise measurements of the thickness of the specimen before mounting and the thickness of the taper section after mounting.

Taper sections are obtained using the procedure shown in Fig. 5. First, the specimen, with the coated surface down, is mounted using an inclined-surface mounting plug, which has the face on which the specimen rests tapered to the desired angle θ (Fig. 5a). The tapered mount holding the specimen is extracted from the mounting die, and, if necessary, the back face of the mount is turned in a lathe to make it flat and normal to the axis of the mount.

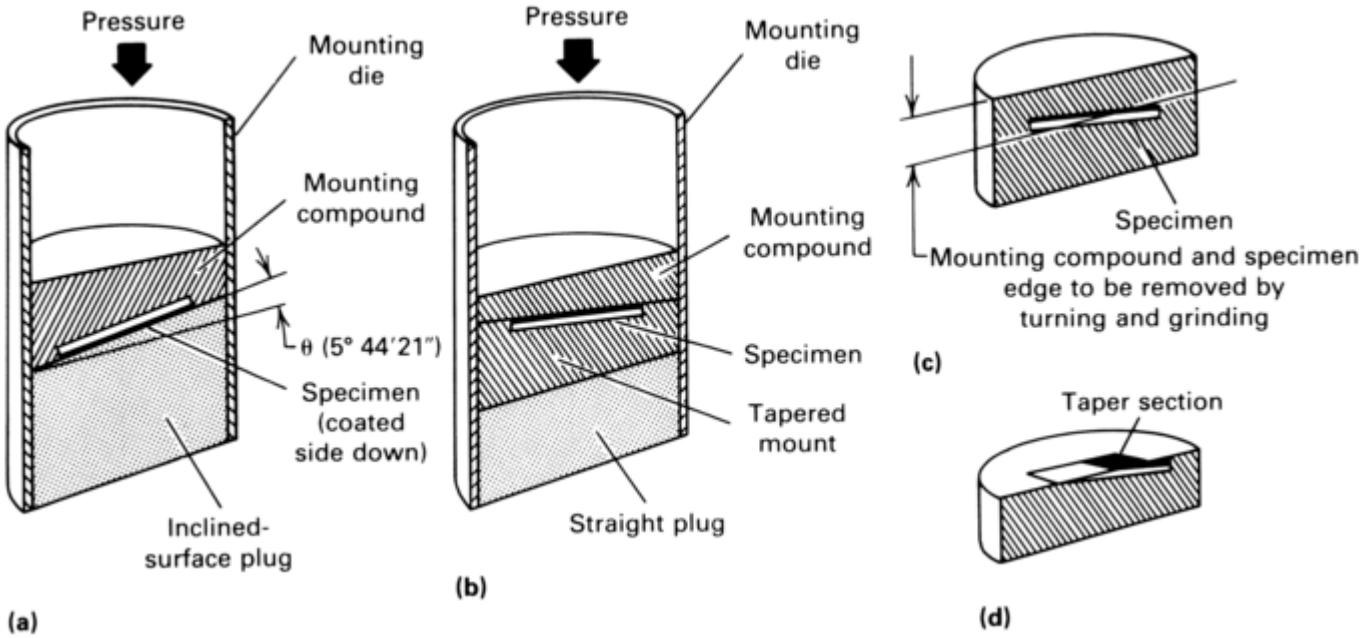

Fig. 5 Steps in the preparation of a taper section. (a) First mount, using an inclined-surface plug. (b) Second mount, using a straight plug. (c) Mounted specimen before turning and grinding. (d) Mounted taper section after turning and grinding. See text for more information.

The tapered mount is then inverted, placed on a straight mounting plug in the mounting die, and completely covered with an additional layer of mounting compound (Fig. 5b). After this layer has set and fused with the tapered mount and the mounted specimen has been removed from the die (Fig. 5c), the mount is carefully turned in a lathe until the edge of the specimen is exposed; that edge is then removed by grinding (Fig. 5d). The resulting exposed area is the taper section, which is subsequently polished, etched, and examined. The exposed taper section should be near the center of the mount.

Grinding and Polishing. In grinding and polishing tin and tin alloy coatings, the effect of differences in hardness between the coating and the base metal can be minimized and often (for thin coatings) almost eliminated by the following procedure. The specimen is carefully turned in a lathe; each cut should be shallower than the previous cut, finishing with five or six cuts 0.01 mm (0.0005 in.) deep. The specimen is then ground on successively finer grades of well-lubricated silicon carbide papers. Grinding is performed with the interface between the coating and the base metal oriented at an angle of 15° to 20° to the direction of grinding; this orientation is alternated from left to right with successive strokes, as shown in Fig. 6.

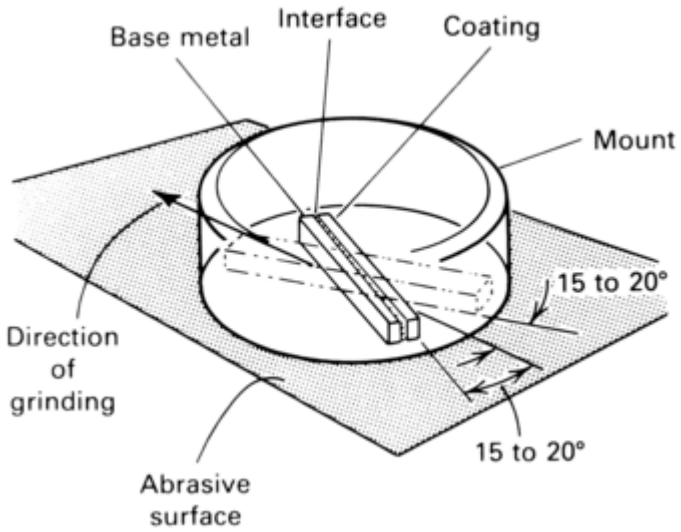

Fig. 6 Orientations of the interface regarding the direction of grinding. Specimens with tin and tin alloy coatings are alternated 15° to 20° on either side of the direction of grinding to minimize differences in hardness between the coating and the base.

Diamond paste should be used for polishing to obtain satisfactory final results. Use of any other polishing medium, such as Al_2O_3, results in the formation of a considerable step, which complicates examining the interface. Even when diamond paste is used, precautions must be taken to minimize the step. Fast cutting on the polishing wheel is necessary, and the specimen should be stationary, with the interface at an angle near 90° to the direction of motion during the final stages of polishing.

First the specimen is polished for up to several minutes on a wheel covered with a napless cloth impregnated with 3 to 6 μm diamond paste; the specimen is rotated on the cloth to remove the unidirectional scratches resulting from the finest abrasive paper. Napless cloth allows fast and uniform cutting of the base metal and the coating, which limits the depth of any step that might subsequently form. The next polishing is performed using a short-nap cloth and 0.25 to 1 μm diamond paste; the specimen is rotated for 30 to 40 s, then polished for an additional 30 s using light pressure while holding the specimen stationary. If necessary, this procedure is repeated using 0.25 and 0.1 μm pastes. Finally, if required, the specimen may be lightly rubbed on a pad of plain long-nap cloth impregnated with γ-Al_2O_3 or placed on a vibratory polisher for a short time. This last operation must be of short duration, because the specimen will rapidly develop steps at the interface. This is generally true for all stages of preparation—the longer the time spent at any stage, the more likely is the formation of a step—but is particularly true of final stages of polishing.

The harder tin alloy coatings, such as speculum metal (copper-tin) and tin-nickel, are generally deposited onto steel or copper-base alloys to provide corrosion resistance and to enhance appearance. Because of the hardness of these coatings, there is far less danger of a step forming at an interface. Such specimens may be satisfactorily polished using the methods described for bronzes. Sometimes in grinding tin-nickel coatings, particularly when the grinding papers are new, the extremely brittle tin-nickel compound will chip, and extensive cracks will form below the surface, which requires removing the coating to an appreciable depth to reach a truly representative region.

With thick tin alloy coatings, such as those on babbitted bearings, little can be gained by plating a supporting layer on top of the coating. The step formed during polishing is usually greater than that obtained with a thin coating. This can be minimized if grinding is carried out alternately in the directions shown in Fig. 6.

Etching. When tin and tin alloy coatings are examined, the interface between the coating and the base metal often is of primary interest, and the microstructure at this interface is usually revealed by etching. Hot dip and electrodeposited tin coatings on steel are best etched in picral, which also outlines the interface between the steel and the tin-iron alloy layer without etching the tin. Another procedure to reveal this layer involves etching in a solution of 1 drop concentrated HNO_3, 2 drops hydrofluoric acid (HF), and 25 mL glycerol to outline the interface between the tin and the $FeSn_2$, then etching in picral to outline the interface between the $FeSn_2$ and the steel. Safety procedures for handling HF should be strictly observed.

Picral is also used to etch cast iron having a tin coating, because it does not attack the tin. The microstructure of cast iron generally consists of graphite nodules and cementite (Fe_3C) in a pearlitic matrix. Because of the presence of Fe_3C, picral does not outline the Fe-$FeSn_2$ interface as it does with tin coatings on steel, but the $FeSn_2$ is still easily discerned (Fig. 7).

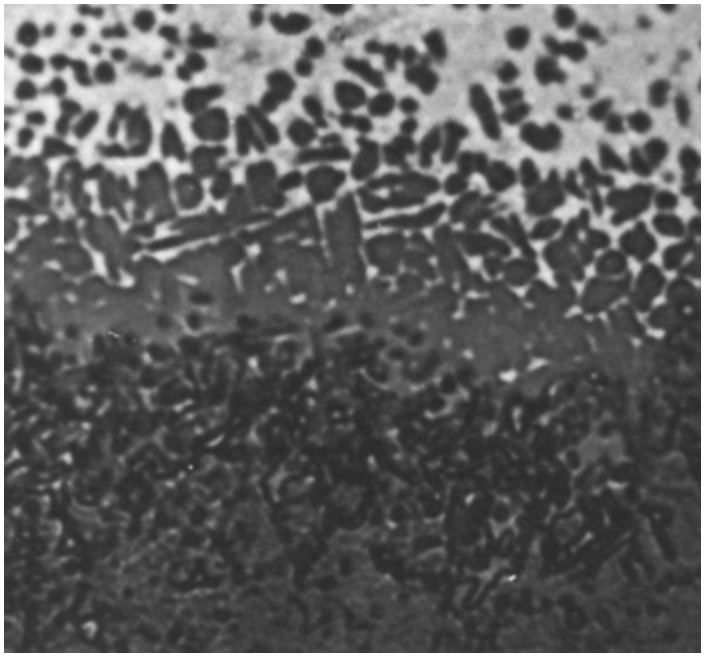

Fig. 7 Steel-tin interface of hot dip tinplate. A 6° taper section is shown. From bottom: steel substrate (dark gray), interface between steel and $FeSn_2$ (dark, mottled), gray crystals of $FeSn_2$ in tin, and bottom of tin coating (light). 2% picral. 22,500× vertical; 2250× horizontal

Electrodeposited or hot dip tin coatings on copper and copper alloys are readily etched by polish attack using a solution of 20 mL concentrated ammonium hydroxide (NH_4OH), 80 mL distilled H_2O, and a few drops of 30% hydrogen peroxide (H_2O_2). This solution etches the base metal and outlines the interface between the base metal and the alloy layer, but does not attack the tin (Fig. 8). Polish-attack etching in a solution of 10 g ammonium persulfate [$(NH_4)_2S_2O_8$], 45 mL concentrated NH_4OH, and 135 mL distilled H_2O yields similar results.

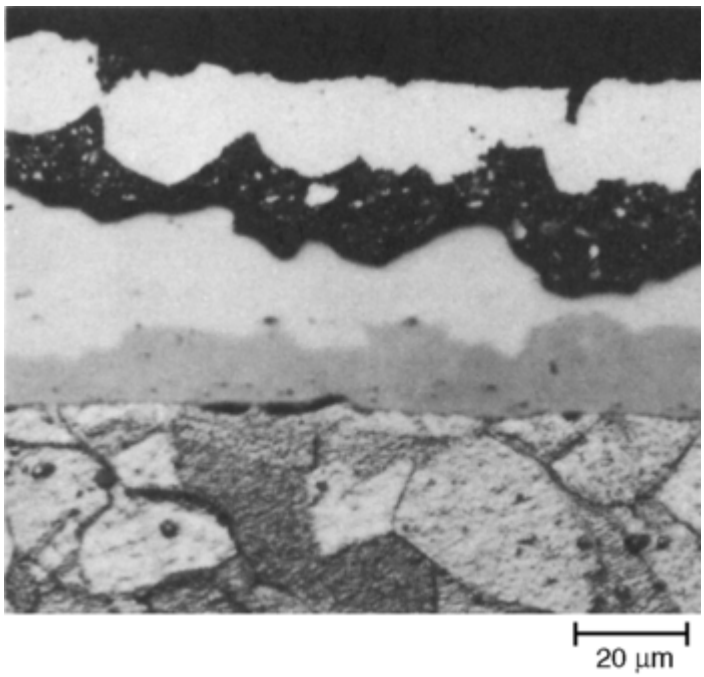

Fig. 8 Sn-40Pb coating electrodeposited on a copper substrate and stored 200 days at 170 °C (340 °F). A layer of Cu_3Sn has formed near the copper, and on top of that a layer of Cu_6Sn_5 has formed. Attack polished using etchant 10, Table 1, then exposed to HCl vapor. 500×

Specimens of steel-backed tin alloys, such as babbitted bearings, are best etched in 2% nital, which generally etches the steel and the tin alloy. With some specimens, however, the microstructure of the tin alloy is revealed before that of the steel. If this occurs, the specimen should be etched in picral, which reveals the structure of the

steel without affecting the tin alloy. If etching does not immediately follow final polishing, the surface of the specimen passivates and pitting occurs upon etching.

Specimens of steel-backed aluminum-tin bearings are etched in 2% nital, which outlines the particles of tin in the aluminum-tin alloy. If the steel backing is not etched within the time required for etching the aluminum-tin alloy, it can be emphasized by subsequent etching as described above for steel-backed tin alloy specimens.

Use of Electron Microscopy. The following procedure is recommended for electron microscopy to determine the nature of the intermetallic compound formed by the reaction between tin or tin-lead coatings on various substrates (Fig. 9, 10, 11). The overlying coating is removed using a solution of 10 parts sodium hydroxide (NaOH) plus 7 parts orthonitrophenol at 60 °C (140 °F). Thick or high-lead coatings require longer immersion times; gentle swabbing with cotton wool increases the dissolution rate of tin-lead coatings. After complete removal of the coating to expose the intermetallic surface (the surface usually appears a uniform matte gray), the specimen should be thoroughly washed in warm distilled water, then dried using acetone. The surface of the intermetallic should be examined in the light microscope to ensure that all tin-base coating has been removed before replicating for transmission electron microscopy or gold coating for scanning electron microscopy.

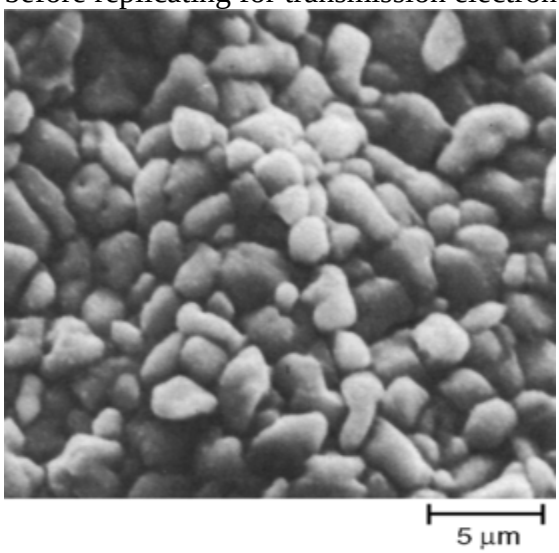

Fig. 9 Scanning electron micrograph of a Cu_6Sn_5 intermetallic formed beneath Sn-40Pb alloy coating. The coating was originally electrodeposited on a copper substrate and was reflowed in hot oil. Alkaline orthonitrophenol (10 parts NaOH and 7 parts orthonitrophenol) at 60 °C (140 °F) used to remove coating. 2000×

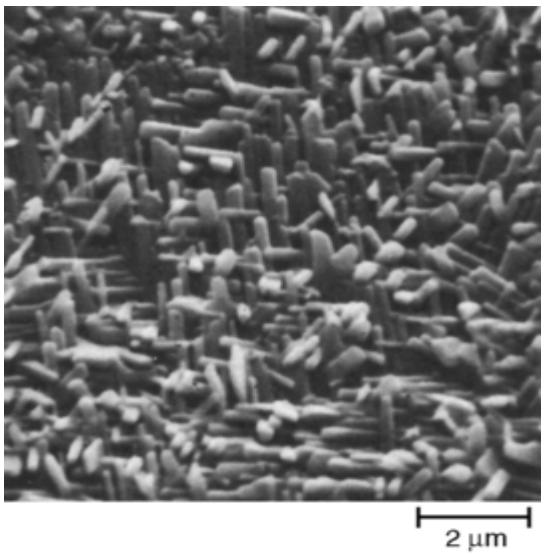

Fig. 10 Intermetallic layer of electrolytic tinplate, with electrodeposited tin reflowed, then removed with same solution used in Figure 9 $FeSn_2$ crystallites have formed at the coating/substrate interface. 5000×

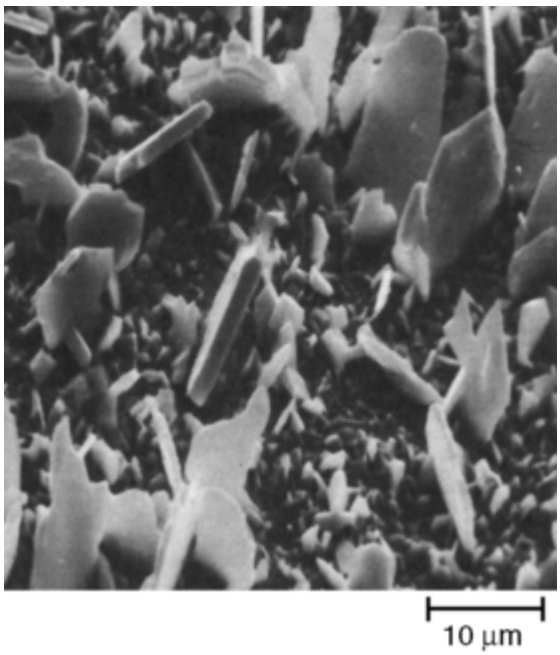

Fig. 11 Scanning electron micrograph of tin-plated nickel specimen that was stored 11 years at room temperature. The tin coating has been removed using the same solution as Figure 9 revealing the nickel-tin intermetallic compound formed by solid-state diffusion. 1000×

Electron microscopy can also be useful in examining surface conditions such as cracks in solder joints (Fig. 12) in conjunction with light metallography (Fig. 13). Backscattered electron imaging is also used in examination of surface microstructure and metallographically sectioned solder and solder joints.

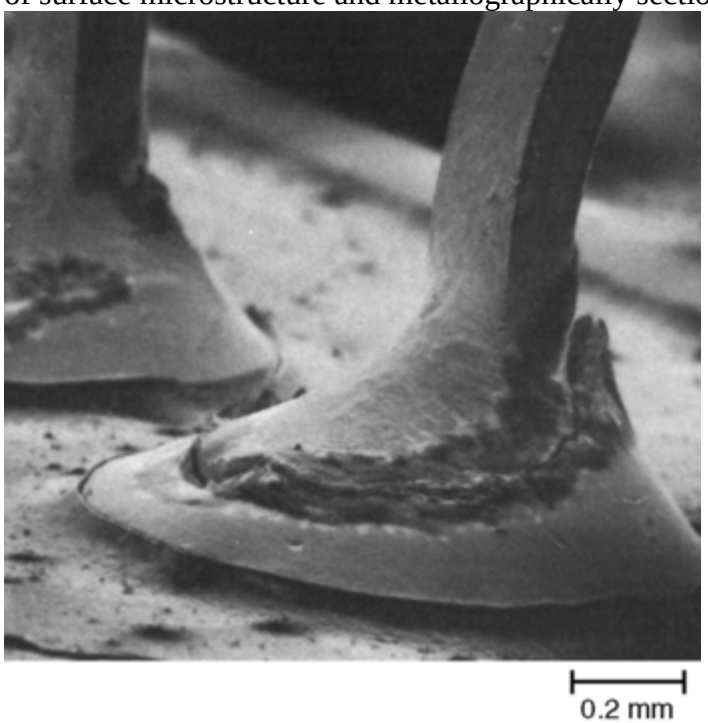

Fig. 12 Scanning electron micrograph of Sn-40Pb alloy wave-soldered printed circuit board joint that was thermally cycled. Micrograph shows a typical thermal fatigue crack in the joint. The crack is at a 45° angle to the circuit lead and totally encircles it. 50×

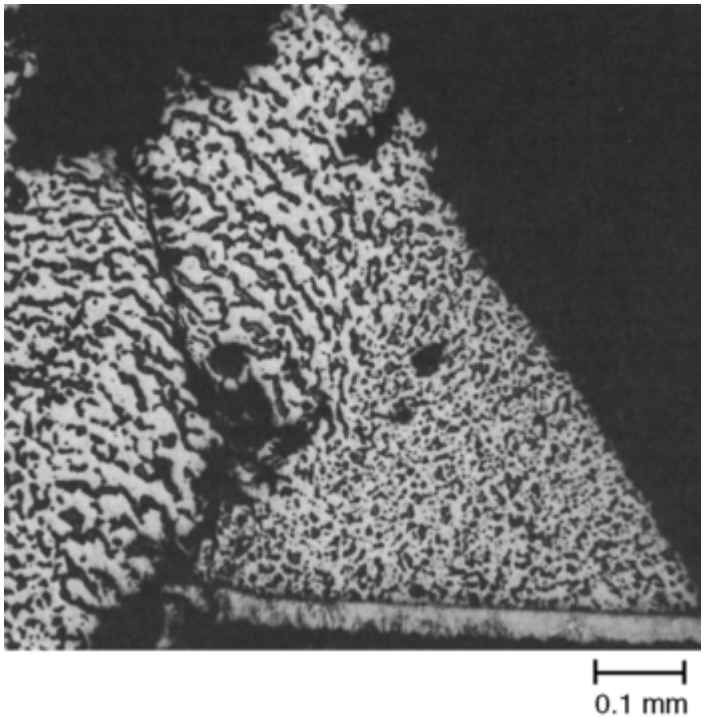

Fig. 13 Sn-40Pb alloy, section of a wave-soldered printed circuit board joint that was thermally cycled. Structure shows a thermal fatigue crack propagating through the tin-lead fillet. The tin-lead structure has coarsened in the highly stressed region near the crack. Etchant 7, Table 1. 80×

Metallography and Microstructures of Tin and Tin Alloys, *Metallography and Microstructures,* Vol 9, *ASM Handbook*, ASM International, 2004, p. 889–898

Microstructures of Tin and Tin Alloys

The more important tin-rich alloys depicted in this article are based on the following systems: Sn-Cu, Sn-Pb, Sn-Pb-Cd, Sn-Sb, Sn-Sb-Cu, Sn-Sb-Cu-Pb, Sn-Ag, Sn-In, Sn-Zn, and Sn-Zn-Cu.

Pure tin (Fig. 14, 15) is allotropic with a body-centered tetragonal crystal structure (β-phase) at room temperature and face-centered cubic structure (α-phase) below a transformation temperature of 13.2 °C (55.8 °F). Hardness of pure tin (6 HV) is slightly higher than lead (4 HV), and a scratchfree surface on pure tin can be achieved by a skidding technique with magnesium oxide abrasive (Fig. 16). Lead cannot be polished at all with magnesium oxide. Pure tin is less prone to twinning than zinc.

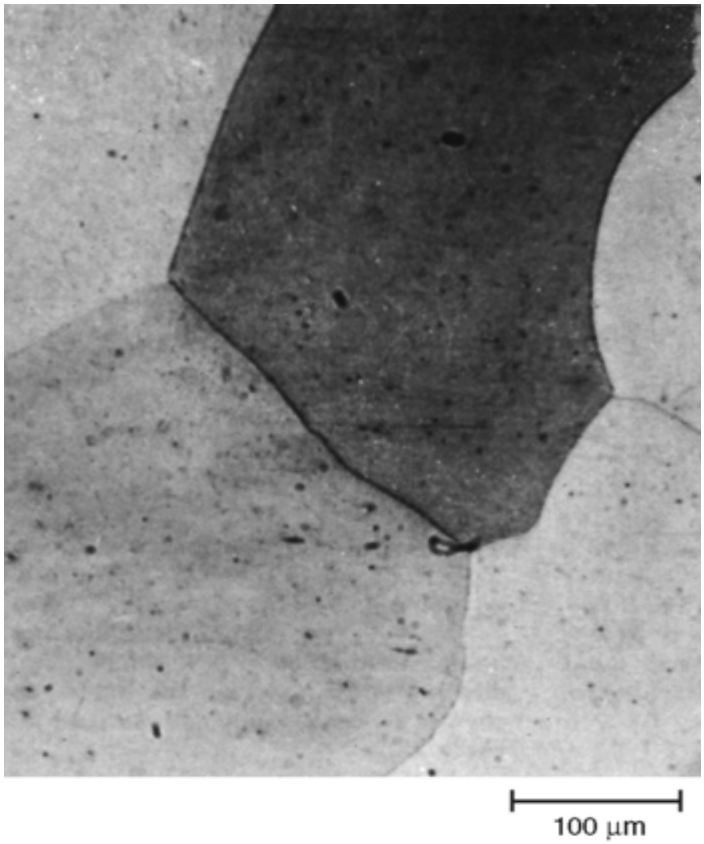

Fig. 14 High-purity tin. The structure consists of large, equiaxed grains that show no deformation from polishing. Etchant 1, Table 1. 150×



Fig. 15 Pure tin, showing twinned grains and recrystallized grains along original grain boundaries that result from working during polishing. Etchant 2, Table 1. 100×

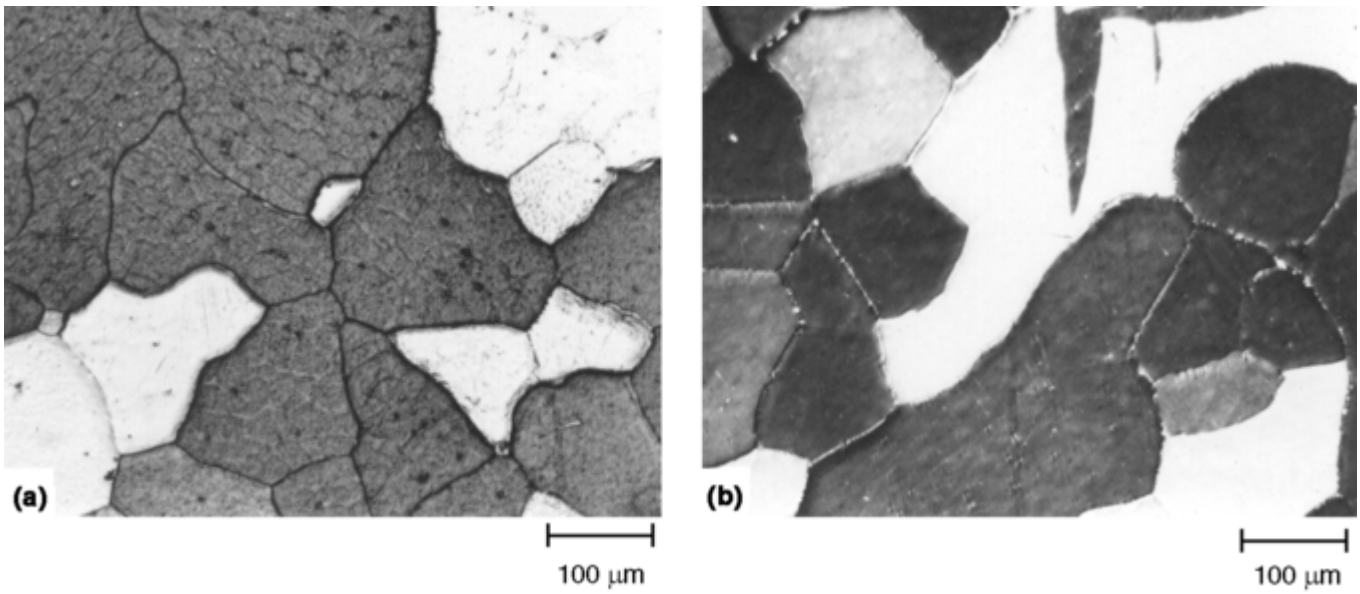

Fig. 16 Very soft metals; commercially pure tin (hardness, 6 HV). (a) Etched in 10% ammonium persulfate solution. Bright-field illumination. (b) Not etched. Polarized light illumination. A final polishing process incorporating a component of chemical solution is needed to achieve this standard of finish. The specimen illustrated was finish polished by skidding on magnesium oxide. 100×. Source: Ref 1

Tin-Copper. Tin and copper form a eutectic containing 0.9% Cu that consists of fine lamellae of Cu_6Sn_5 in a matrix of virtually pure tin. Hypoeutectic alloys (Fig. 17) of the tin-copper system are composed of primary tin with interdendritic eutectic. In tin-copper alloys that have copper contents above the eutectic composition, large acicular crystals of primary Cu_6Sn_5 are present in the Sn-Cu_6Sn_5 eutectic matrix.

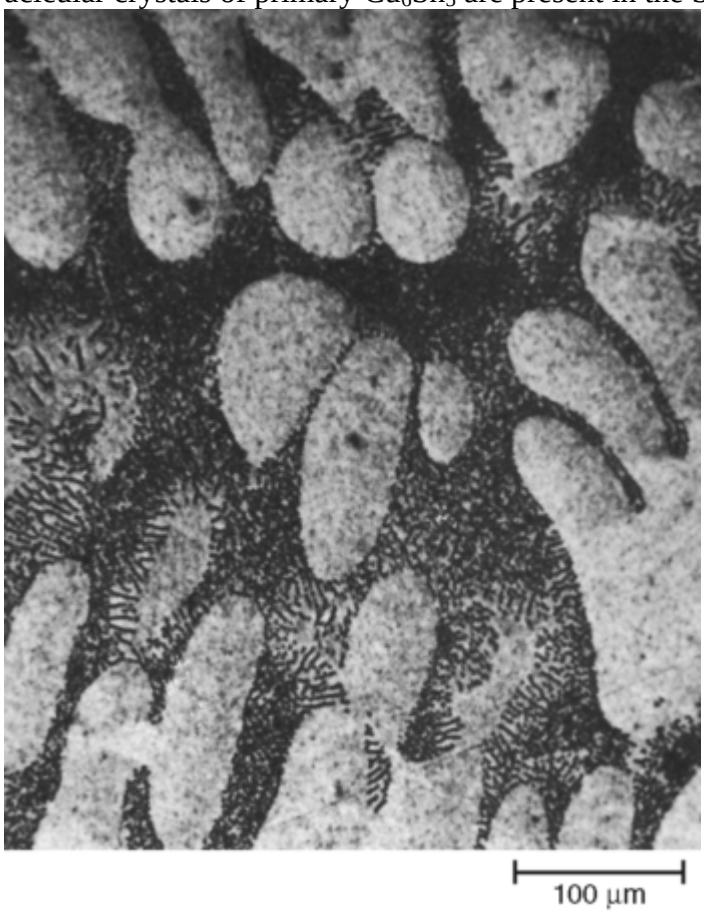

Fig. 17 Sn-0.4Cu alloy. Structure consists of dendritic grains of tin-rich solid solution in a eutectic matrix of Cu_6Sn_5 (dark) in tin-rich solid solution. Etchant 1, Table 1. 150×

Tin-Lead. Alloys of this simple eutectic system (Fig. 18, 19, 20, 21, 22, 23) are composed of primary dendrites of tin-rich or lead-rich solid solution surrounded by eutectic (e.g., Fig. 24). The eutectic, which occurs at 61.9% Sn, consists of the lead-rich and tin-rich phases as lamellae or globules, depending on the solidification rate. In general, a high solidification rate, as in most soldering applications, favors the formation of a globular eutectic. At the eutectic composition, chill casting also normally results in a globular eutectic. Slower solidification rates, such as from air cooling, lead to the formation of the characteristic lamellar eutectic structure. Heat treatment at a temperature approaching that of the eutectic converts the lamellar structure to the globular forms.

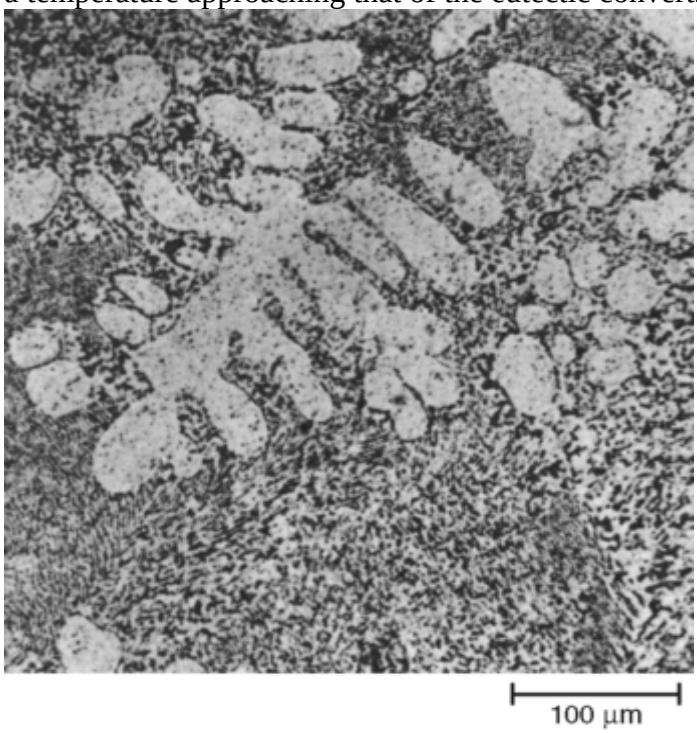

Fig. 18 Sn-30Pb alloy (soft solder). Dendrites of tin-rich solid solution (light) in a matrix of tin-lead eutectic. Figure 19 shows the structure of the eutectic. Etchant 2, Table 1. 150×

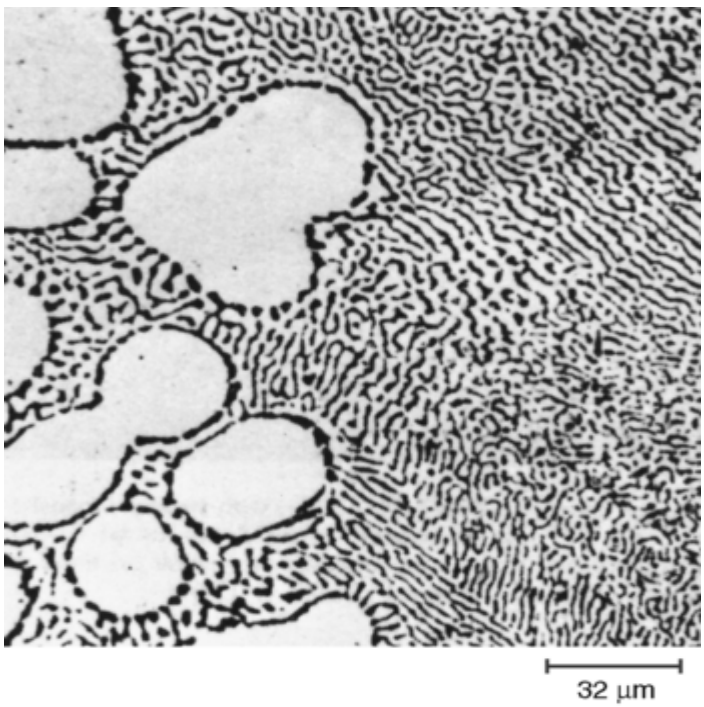

Fig. 19 Same structure and etchant as Figure 18 but at higher magnification to show structure of the tin-lead eutectic. Black outlines of the dendrites are formed by divorced eutectic. 375×

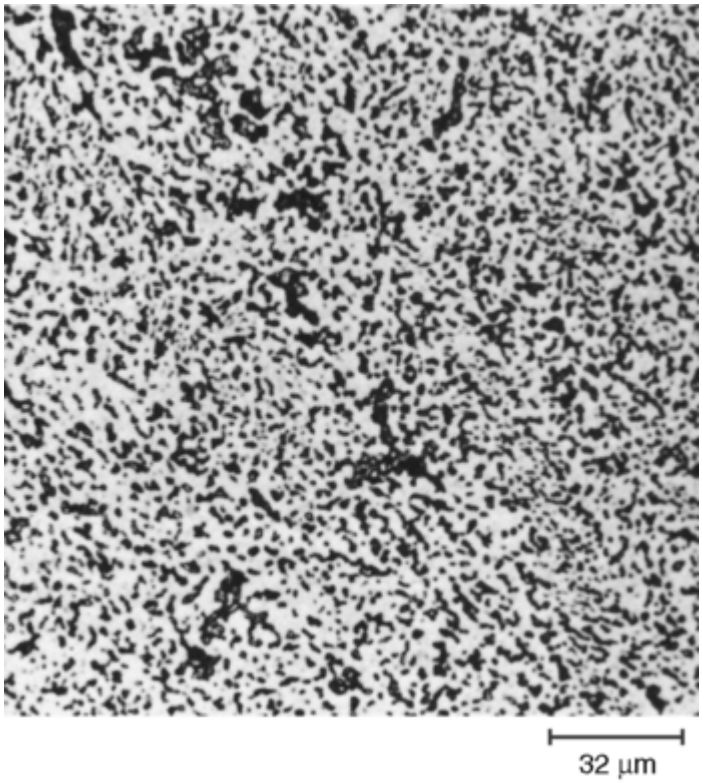

Fig. 20 Sn-37Pb alloy (eutectic soft solder). Structure shows globules of lead-rich solid solution (dark), some of which exhibit a slightly dendritic structure, in a matrix of tin. Etchant 7, Table 1. 375×

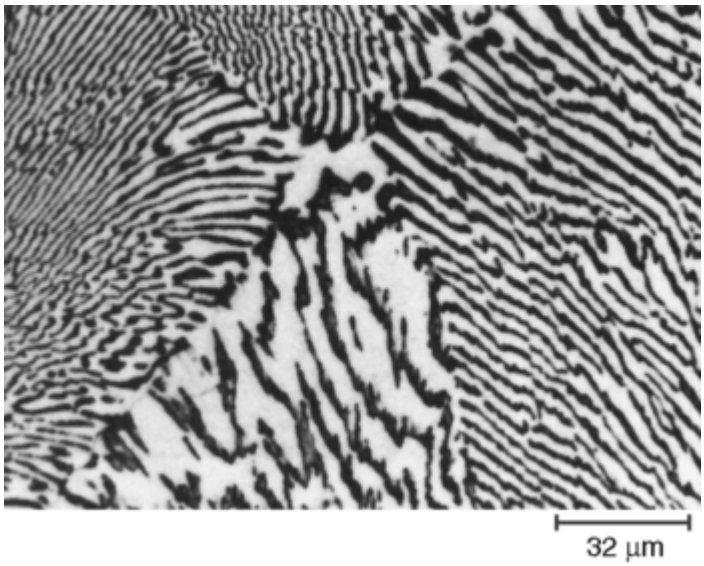

Fig. 21 Same alloy and etchant as Figure 20 except the mold was warmed to slow cooling. This resulted in the lamellar, rather than globular, structure of tin (light) and lead-rich solid solution (dark). 375×

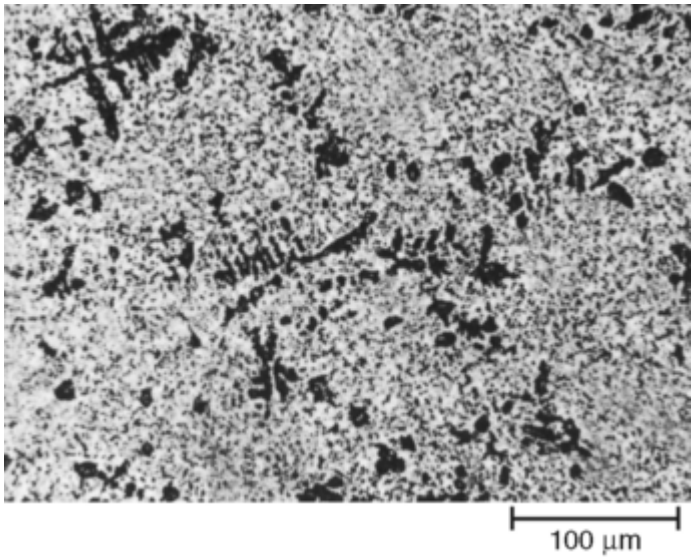

Fig. 22 Sn-40Pb alloy (soft solder). Structure consists of small dendrites of lead-rich solid solution (dark) in a fine matrix of globular tin-lead eutectic. Etchant 7, Table 1. 150×

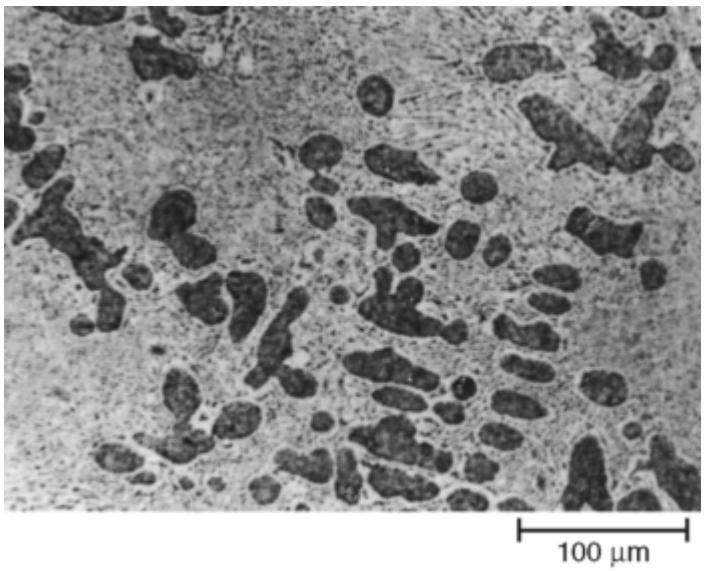

Fig. 23 Sn-50Pb alloy. Dendrites of lead-rich solid solution (dark) in a matrix of fine lamellar eutectic consisting of lead-rich solid solution (dark) and tin (light). Etchant 7, Table 1. 150×

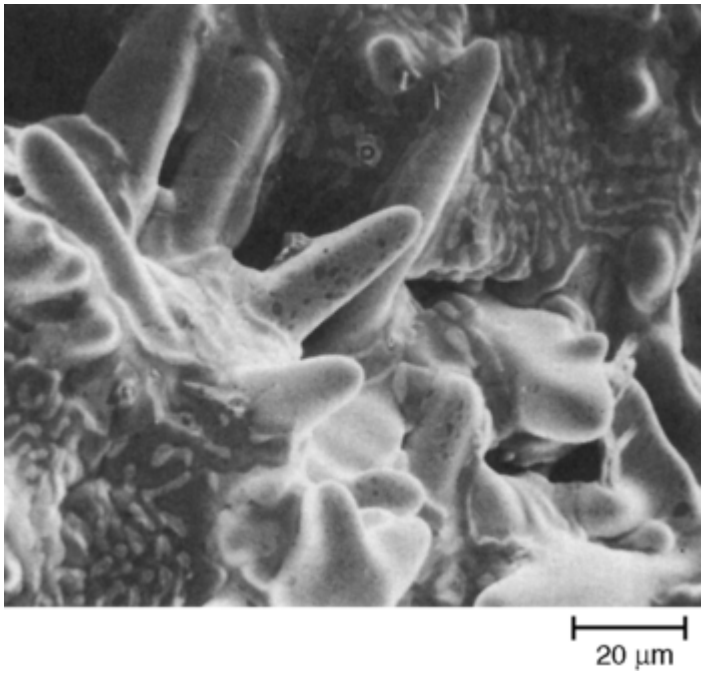

Fig. 24 Scanning electron micrograph of Sn-48Pb-2Sb cast alloy. Surface structure of a contraction cavity in the casting. Lead-rich dendrite arms (light phase) protrude from the eutectic matrix. As-polished. 500×

Tin-Lead-Cadmium. The composition of the most frequently used commercial Sn-Pb-Cd (Fig. 25) is close to that of the ternary eutectic, which contains approximately 52% Sn, 30% Pb, and 18% Cd. The eutectic consists of the three terminal solid solutions. In as-polished specimens, the tin-rich phase appears white, the lead-rich phase light gray, and the cadmium-rich phase nearly black.

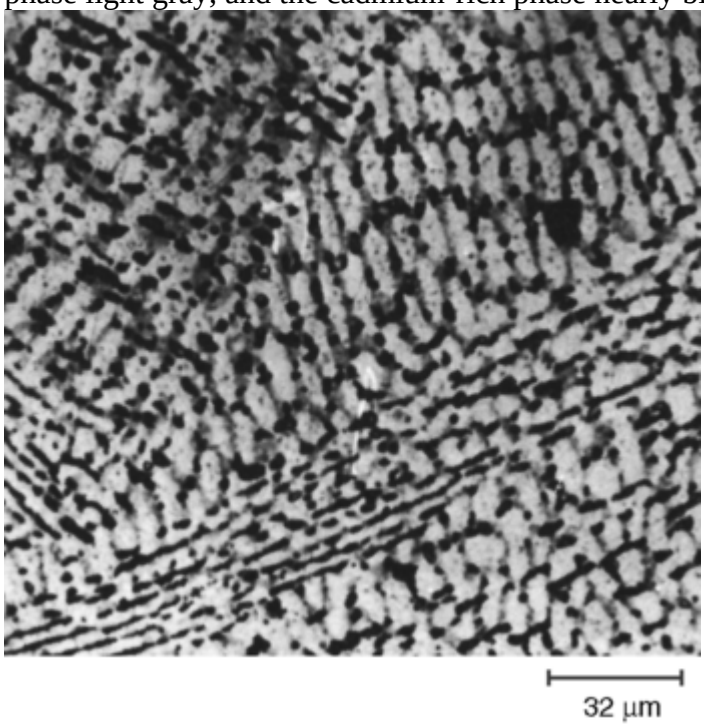

Fig. 25 Sn-31Pb-18Cd alloy. Structure is a lamellar ternary eutectic of solid solutions of cadmium in tin (light), tin in lead (gray), and cadmium in lead (dark). Etchant 7, Table 1. 375×

In some regions, the structure of the eutectic is lamellar, consisting of bands of the dark cadmium-rich phase bordered on either side with bands of the light gray lead-rich phase, which are in turn bordered along their outer edges by the tin-rich phase. In other regions, the phases are more globular and form a fine cellular pattern.

Tin-Antimony. The solid solubility of antimony in tin is appreciable at elevated temperature, but decreases rapidly as temperature decreases. Chill-cast alloys with antimony contents to 8% normally consist of a cored solid solution of antimony in tin. Slow cooling allows some precipitation of SbSn, which is evident as white particles between the tin-rich dendrites. The SbSn (β) intermetallic phase has a fairly wide phase field, extending from 41 to 56% Sb (Fig. 26). At antimony contents exceeding 8%, cuboids of primary SbSn (Fig. 27) are produced in a tin-rich matrix that is formed by a peritectic reaction between the melt and the primary SbSn.

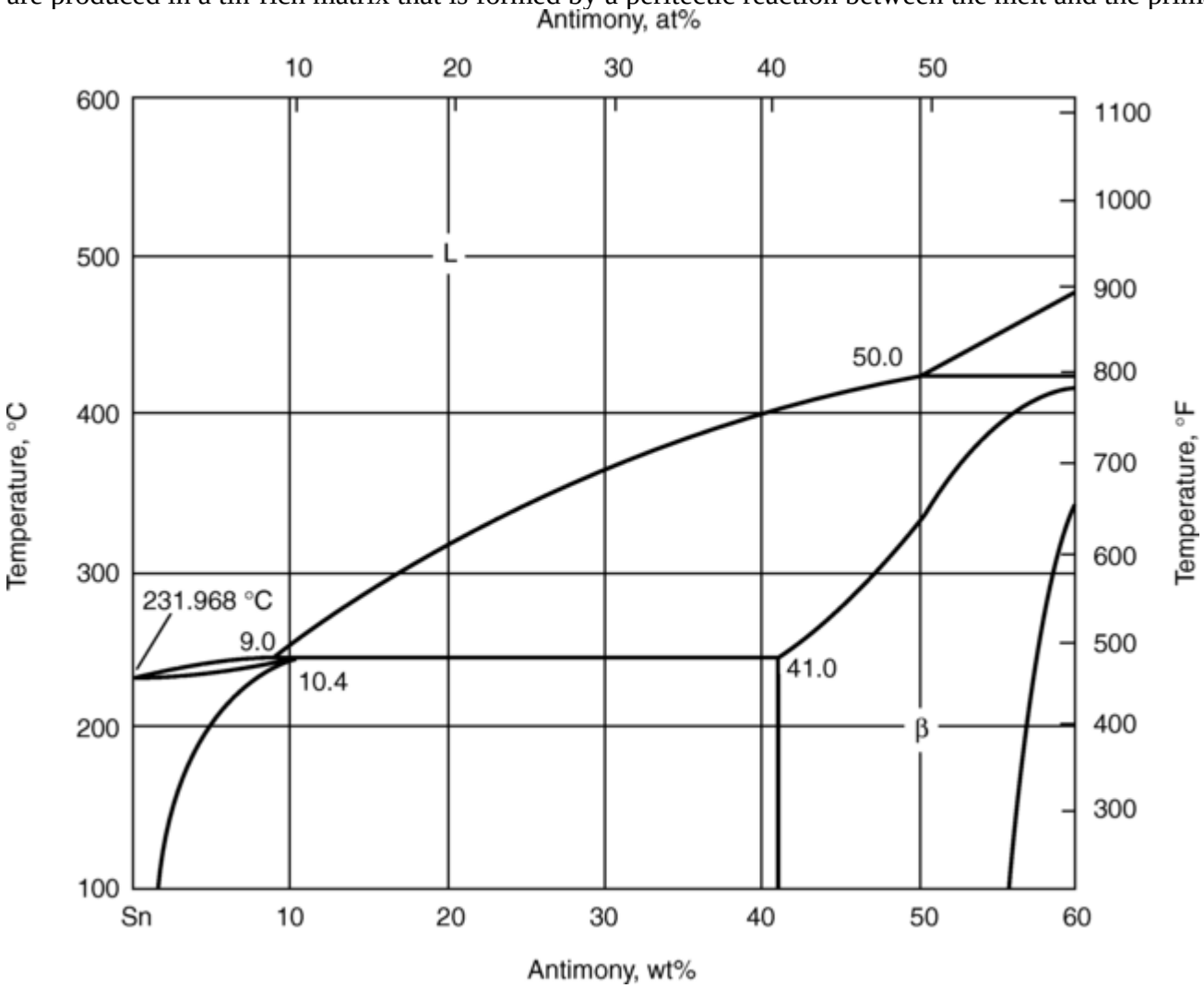

Fig. 26 Tin-rich side of Sn-Sb phase diagram

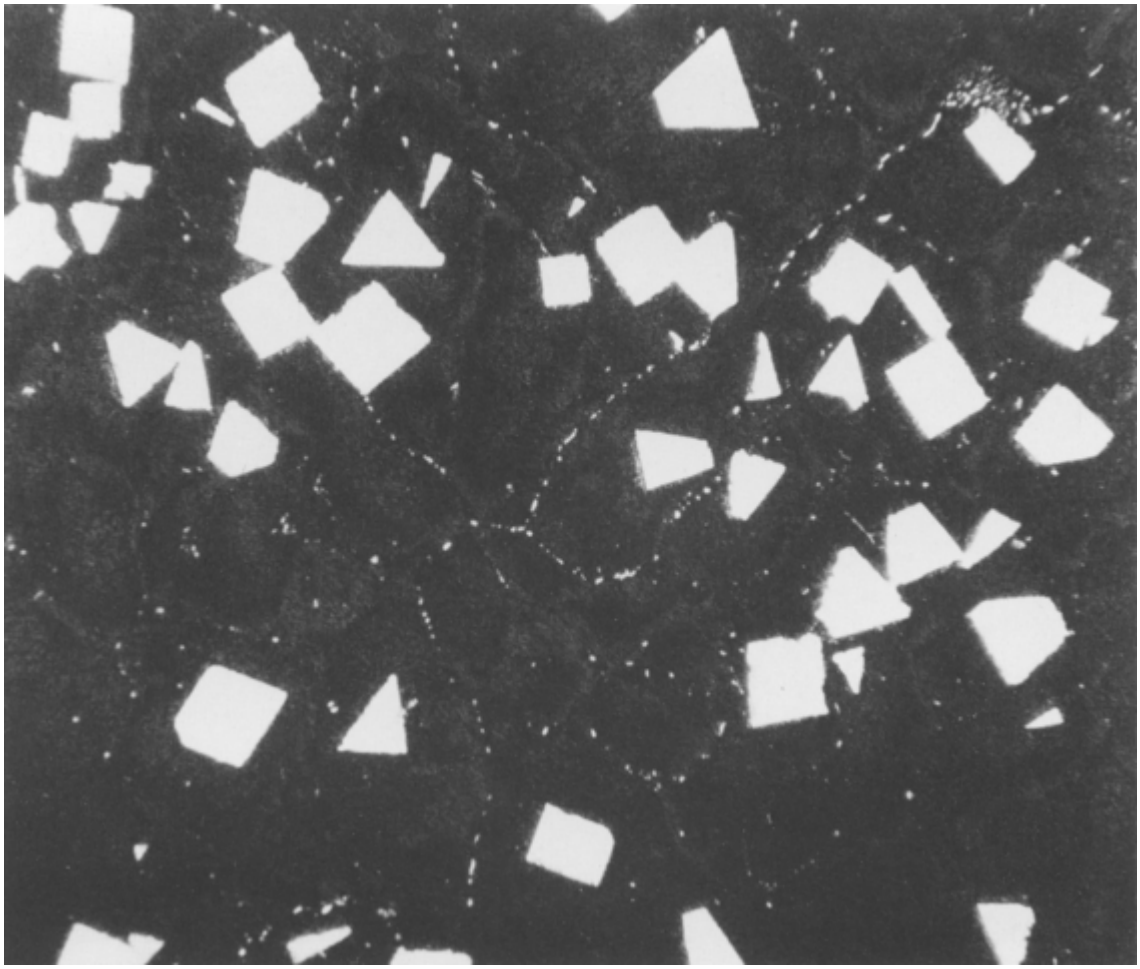

Fig. 27 Tin alloy with 10% Sb, cast in sand. Primary grains of a β-phase (white squares) on a background of a peritectic α-phase. At the boundaries, secondary β (SnSb) is prominent, which is formed because of a decrease in the solubility of antimony from solid solution. Source: Ref 2

Heat treatment or natural aging increases the amount of interdendritic SbSn; upon prolonged aging, an acicular precipitate of SbSn also appears within the dendrites. Finely divided particles of SbSn may again precipitate from the tin-rich matrix. Secondary β (SbSn) along grain boundaries is revealed in Fig. 27. At antimony contents of 30 to 40%, primary SbSn precipitates from the melt as irregularly shaped dendrites. Figure 28, Figure 29, Figure 30 show typical microstructures of tin-antimony alloys.

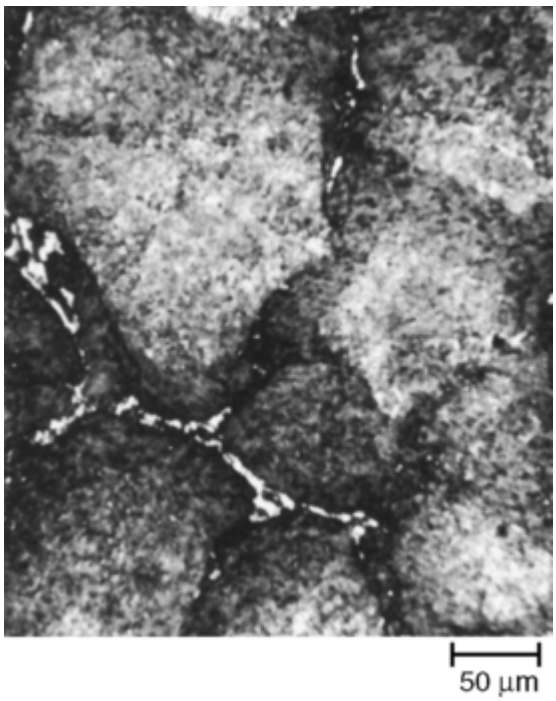

Fig. 28 Sn-5Sb alloy. Structure consists of coarse, cored dendrites of tin-rich solid solution and precipitated interdendritic SbSn phase (light). Etchant 7, Table 1. 150×



Fig. 29 Same alloy and etchant as Figure 28 except the casting mold was chilled for faster cooling. The structure consists of heavily cored dendrites with well-marked branches. 150×



Fig. 30 Sn-30Sb alloy. Structure consists primarily of crystals of SbSn (light) in fine peritectic matrix of SbSn and tin-rich solid solution. Etchant 7, Table 1. 375×

Tin-Antimony-Copper. Additions of up to 2% Cu to tin-antimony alloys containing up to 8% Sb (Fig. 31) result in the formation of needles of primary Cu_6Sn_5, with some finer interdendritic eutectic of Cu_6Sn_5 and a solid solution of antimony in tin. As copper content increases (Fig. 32, 33, 34), successively larger amounts of primary Cu_6Sn_5 crystals form. Copper contents in excess of 4 or 5% (Fig. 35, 36) often produce long needles of Cu_6Sn_5 that appear in cross section as hollow hexagons, H-shapes, or chevrons arranged in hexagonal or triangular patterns or as multiple-limbed starlike configurations.

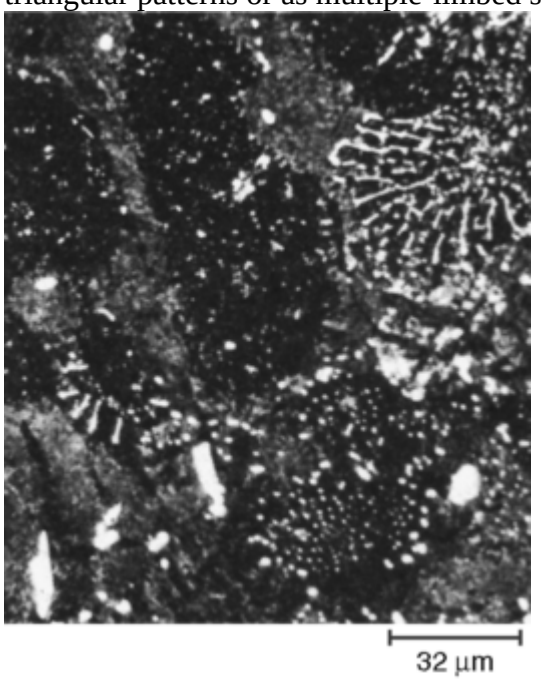

Fig. 31 Sn-6Sb-2Cu alloy (pewter). Cored dendrites are tin-rich solid solution that contain needles of white Cu_6Sn_5. The matrix is coarse Sn-Cu_6Sn_5 eutectic. Etchant 7, Table 1. 375×

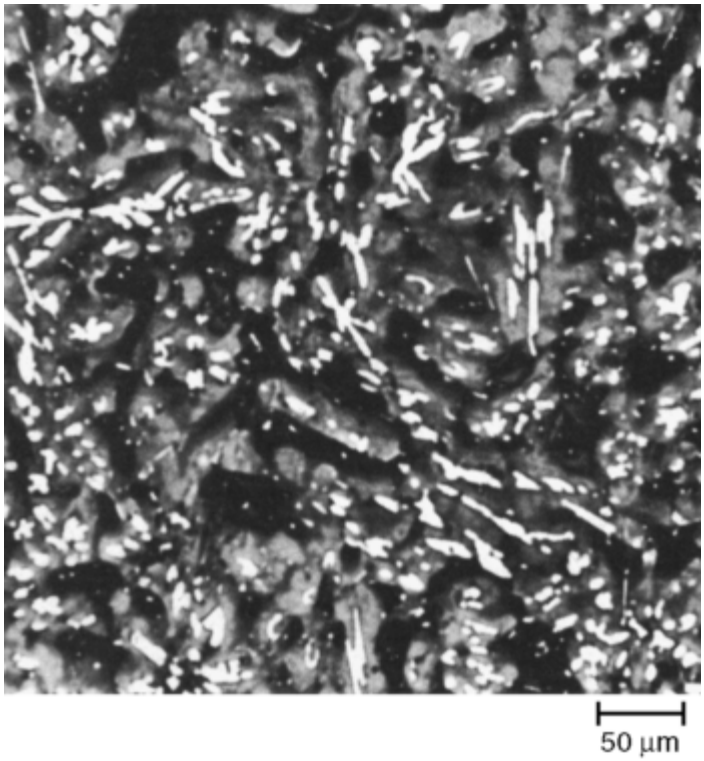

Fig. 32 Sn-4.5Sb-4.5Cu alloy. Structure consists of fine, cored dendrites of tin-rich solid solution containing needles and small particles of Cu_6Sn_5 (white). Etchant 7, Table 1. 150×

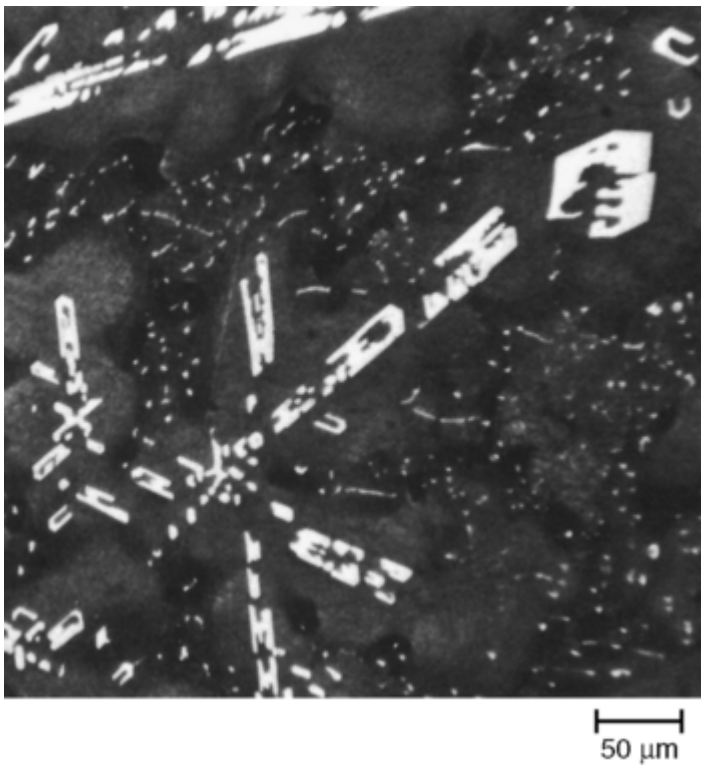

Fig. 33 Sn-7Sb-3.5Cu alloy, with structure consisting of coarse, cored dendrites of tin-rich solid solution containing needles and small particles of Cu_6Sn_5 (white). Etchant 7, Table 1. 150×

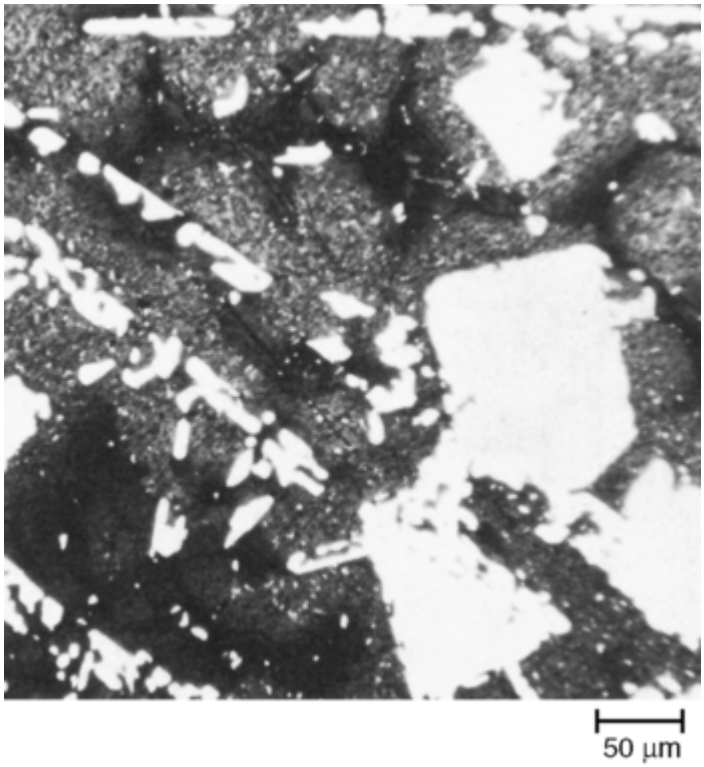

Fig. 34 Sn-9Sb-4Cu alloy. Structure consists of coarse, cored dendrites of tin-rich solid solution containing needles of Cu_6Sn_5 and cuboids of SbSn (both white). Etchant 7, Table 1. 150×

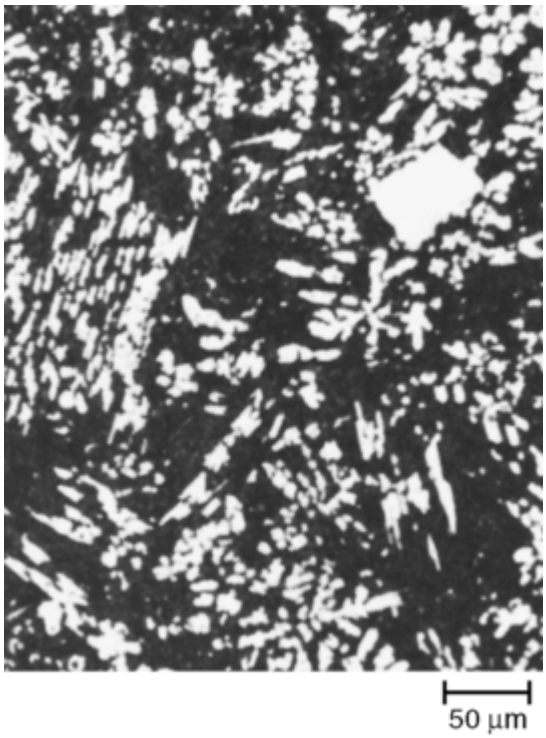

Fig. 35 Sn-8Sb-8Cu alloy. Needles of Cu_6Sn_5 and cubic particles of SbSn (both white) in a matrix of tin-rich solid solution. Etchant 7, Table 1. 150×

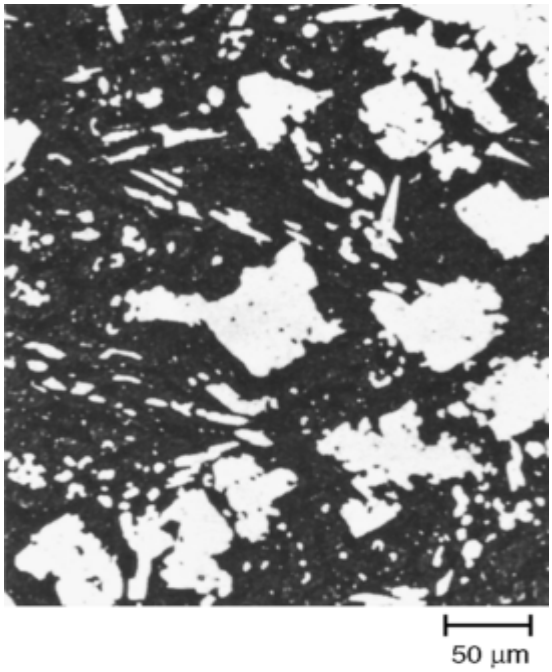

Fig. 36 Sn-13Sb-5Cu alloy. Microstructure similar to that of Figure 35 Etchant 7, Table 1. 150×

In alloys with antimony contents above 9% and copper contents of 2% or more, the SbSn cuboids that form are often nucleated by the primary Cu_6Sn_5 needles; the Cu_6Sn_5 needles then appear embedded within, or passing through, the SbSn cuboids.

After exposure to elevated temperature during service or heat treatment, the corners of the SbSn cuboids often become rounded, and irregular particles of SbSn are precipitated between the tin-rich dendrites and also on the sides of the primary Cu_6Sn_5 needles and SbSn cuboids.

Tin-Antimony-Copper-Lead. When lead is added to the Sn-Sb-Cu ternary system (Fig. 37, 38), the solubility of antimony in the tin-rich solid solution is reduced, and more cuboids of SbSn, possibly containing some lead, are observed. In addition, coring of the tin-rich dendrites is reduced, and interdendritic lakes of a ternary eutectic (probably composed of SbSn and of tin-rich and lead-rich solid solutions) appear. The primary Cu_6Sn_5 needles are unaffected by the presence of lead.

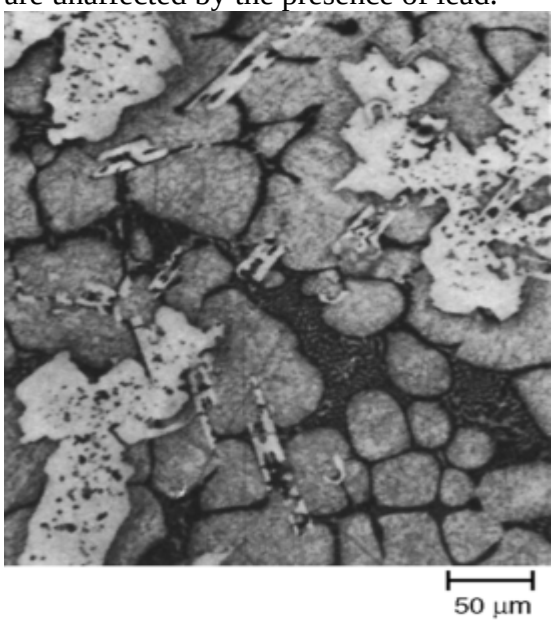

Fig. 37 Sn-12Sb-10Pb-3Cu alloy. Structure consists of Cu_6Sn_5 needles and SbSn crystals (both light) in dendrites of tin-rich solid solution, along with some interdendritic eutectic. Etchant 7, Table 1. 150×

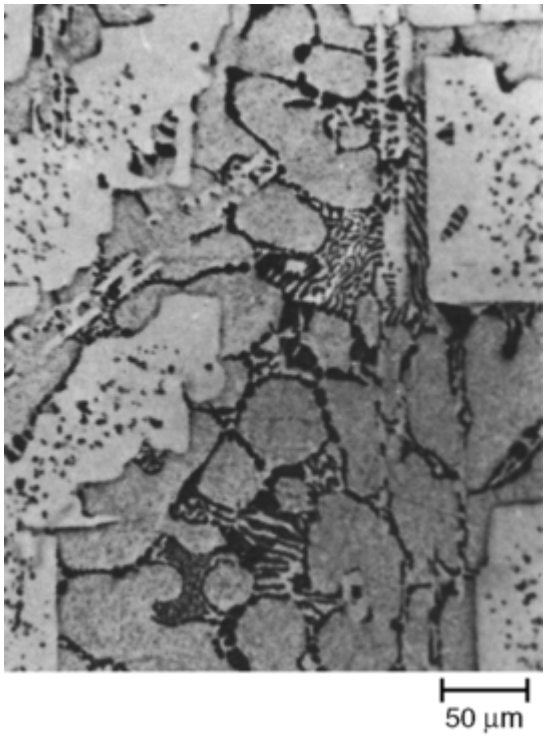

Fig. 38 Sn-15Sb-18Pb-2Cu alloy. Structure is similar to that in Figure 37 but contains more SbSn crystals and more, coarser interdendritic eutectic. Etchant 7, Table 1. 150×

Tin-Silver. A eutectic containing 3.5% Ag forms between nearly pure tin and Ag_3Sn. The eutectic consists of fine needles of Ag_3Sn in the tin-rich matrix. In hypereutectic alloys (Fig. 39), the primary Ag_3Sn appears as coarse needles in the eutectic matrix.

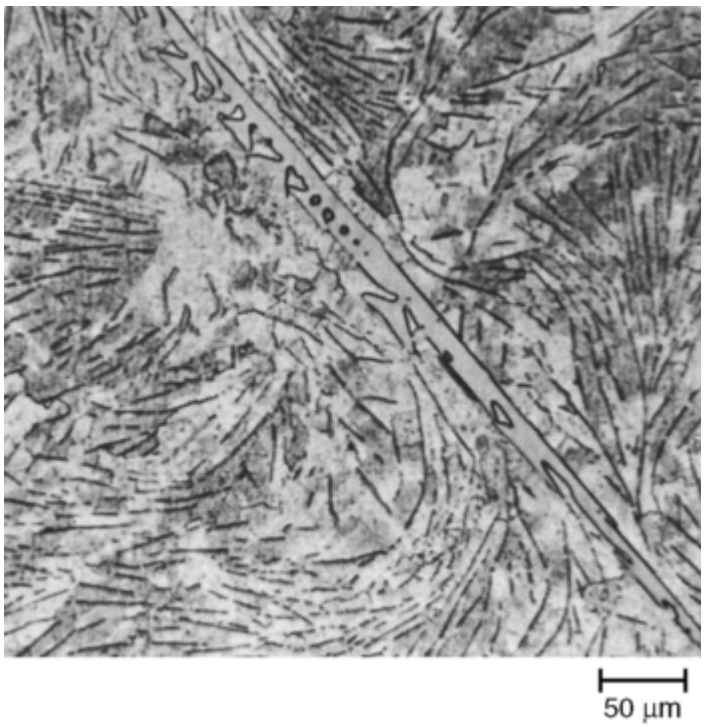

Fig. 39 Sn-5Ag alloy. Structure consists of a large, acicular, primary crystal of Ag_3Sn in a eutectic matrix of acicular Ag_3Sn in tin. Etchant 1, Table 1. 150×

Tin-Indium. At 50.9% In, the tin-indium system forms a eutectic consisting of two intermetallic phases: a light, tin-rich solid solution and a dark, indium-rich solid solution. Cast 50Sn-50In alloy (Fig. 40) shows mainly a eutectic structure of fairly coarse, rounded particles of the tin-rich phase in a matrix of the indium-rich phase.

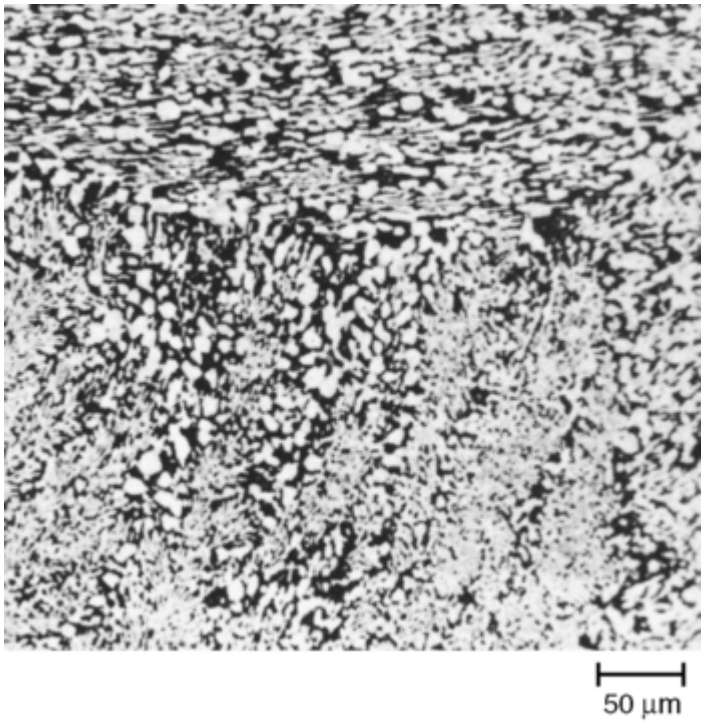

Fig. 40 50Sn-50In alloy. Structure is a eutectic of globular tin-rich intermetallic phase (light) in a matrix of dark indium-rich intermetallic. Etchant 1, Table 1. 150×

Tin-Zinc. Zinc and tin form a simple eutectic at 8.9% Zn that consists of a solid solution of zinc in tin and almost pure zinc. The eutectic consists of fine needles of zinc and a tin-rich solid solution. Alloys containing more than 8.9% Zn (Fig. 41) exhibit a network of acicular dendrites of primary zinc in a eutectic matrix.

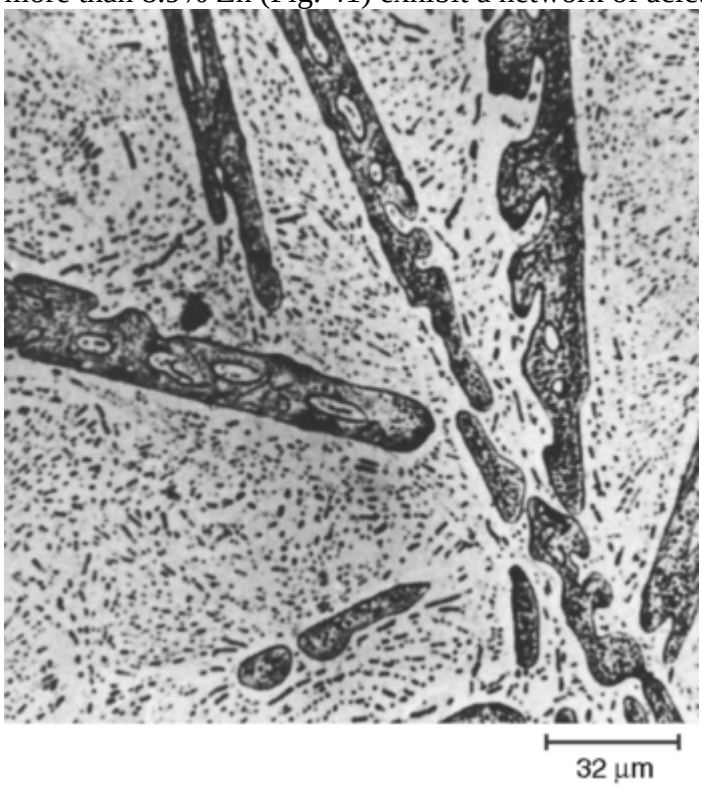

Fig. 41 Sn-30Zn alloy. Structure consists of acicular dendritic crystals of zinc (dark, mottled) in a eutectic matrix of zinc particles (dark) in tin (light), 1% nital. 375×

Tin-Zinc-Copper. The addition of a small amount of copper to an Sn-30Zn alloy causes the zinc-rich components of the eutectic to coarsen and the zinc to appear in the form of large plates. The copper combines with tin to form Cu_6Sn_5 and with zinc to form a compound described as Cu_5Zn_8 or $CuZn_3$. The copper-tin and

copper-zinc compounds occur in intimate contact, forming roughly hexagonal prisms. Prisms of Cu_6Sn_5 are often embedded in the copper-zinc compound, which accurately follows the original outline of the Cu_6Sn_5. Figure 42 and 43 show examples of microstructures of this ternary system.

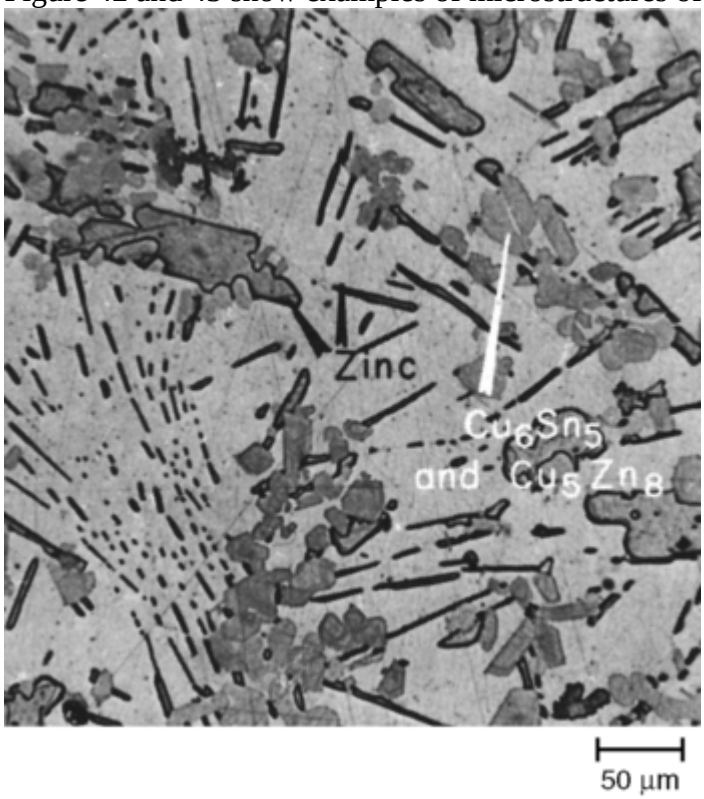

Fig. 42 Sn-28Zn-2Cu alloy. Large and small zinc needles (dark) are intermingled with particles of Cu_6Sn_5 and Cu_5Zn_8 in a tin matrix. Figure 43 for an enlarged view of this structure. 1% nital. 150×

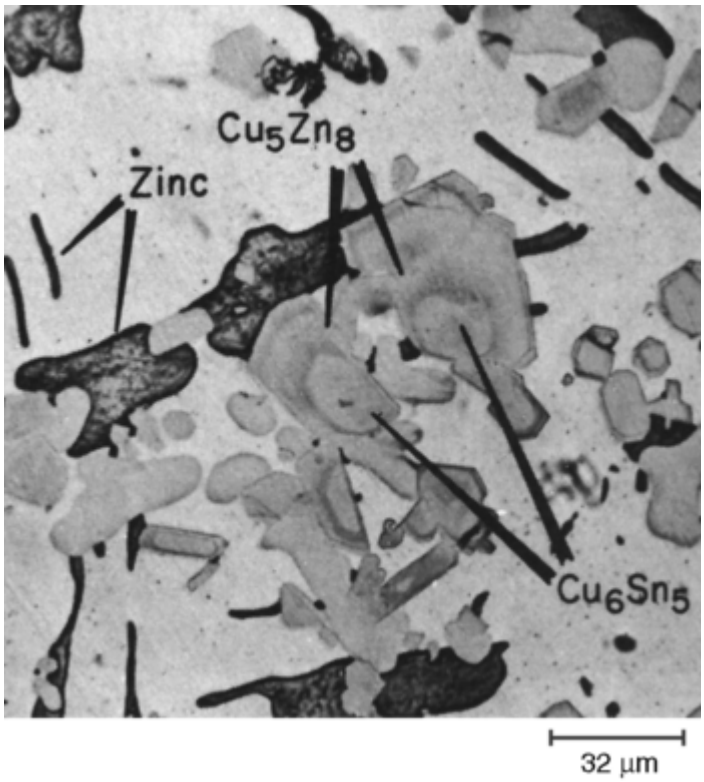

Fig. 43 Same alloy as Figure 42 Cu_5Zn_8 (yellow under bright-field illumination) often surrounds Cu_6Sn_5 (blue under bright-field illumination). The dark constituent is zinc. 1% nital. 375×

References cited in this section

1. L.E. Samuels, *Metallographic Polishing by Mechanical Methods,* ASM International, 2003, p 274, 276

2. A. Tomer, *Structure of Metals through Optical Microscopy,* ASM International, 1991, p 86

Metallography and Microstructures of Tin and Tin Alloys, *Metallography and Microstructures,* Vol 9, *ASM Handbook,* ASM International, 2004, p. 889–898

Acknowledgment

This article is adapted from C.J. Thwaites, M.E. Warwick, and Brian Scott, Tin and Tin Alloys, *Metallography and Microstructures,* Volume 9, *ASM Handbook,* ASM International, 1985, p 449 to 457.

Metallography and Microstructures of Tin and Tin Alloys, *Metallography and Microstructures,* Vol 9, *ASM Handbook,* ASM International, 2004, p. 889–898

Metallography and Microstructures of Tin and Tin Alloys

References

1. L.E. Samuels, *Metallographic Polishing by Mechanical Methods,* ASM International, 2003, p 274, 276

2. A. Tomer, *Structure of Metals through Optical Microscopy,* ASM International, 1991, p 86

L.M. Gammon, R.D. Briggs, J.M. Packard, K.W. Batson, R. Boyer, C.W. Domby, Metallography and Microstructures of Titanium and Its Alloys, *Metallography and Microstructures,* Vol 9, *ASM Handbook*, ASM International, 2004, p. 899–917

Metallography and Microstructures of Titanium and Its Alloys

Luther M. Gammon, Robert D. Briggs, John M. Packard, Kurt W. Batson, Rodney Boyer, and Charles W. Domby, The Boeing Company

Introduction

METALLOGRAPHY is a complex process with many variables that involve compromises between time, resources, and the end product or purpose of the investigation. For example, a research lab may benefit from the more time-consuming method of vibratory polishing, while a production quality-control lab may not require specimen preparation with a vibratory polisher. A lab for teaching also may benefit from the training experience of manual polishing, or polishing may be done with semiautomatic polishing machines.

With a little forethought and planning, excellent metallographic samples can be produced in a short time for light microscopy of titanium and its alloys. This article describes the fundamentals of titanium metallographic sample preparation. Representative micrographs are also presented for each class of titanium alloys, which include unalloyed titanium, alpha alloys, alpha-beta alloys, and beta titanium alloys. Metallography and metallographic sample preparation of titanium alloys are also described in more detail in Ref 1 and 2.

References cited in this section

1. G.F. Vander Voort, *Metallography: Principles and Practice,* McGraw-Hill, 1984, reprinted by ASM International, 1999

2. Struers Metallographic Application Guide: Titanium Alloys, Struers

L.M. Gammon, R.D. Briggs, J.M. Packard, K.W. Batson, R. Boyer, C.W. Domby, Metallography and Microstructures of Titanium and Its Alloys, *Metallography and Microstructures,* Vol 9, *ASM Handbook*, ASM International, 2004, p. 899–917

Metallography and Microstructures of Titanium and Its Alloys

Luther M. Gammon, Robert D. Briggs, John M. Packard, Kurt W. Batson, Rodney Boyer, and Charles W. Domby, The Boeing Company

Types of Titanium Alloys

Titanium is an allotropic element; that is, it exists in more than one crystallographic form. At room temperature, titanium has a hexagonal close-packed (hcp) crystal structure, which is referred to as “alpha” phase. This structure transforms to a body-centered cubic (bcc) crystal structure, called “beta” phase, at 883 °C (1621 °F).

Alloying elements generally can be classified as alpha or beta stabilizers. Alpha stabilizers, such as aluminum and oxygen, increase the temperature at which the alpha phase is stable. Beta stabilizers, such as vanadium and

molybdenum, result in stability of the beta phase at lower temperatures. This transformation temperature from an alpha-beta phase (or all-alpha phase) to all beta is known as the beta transus temperature. The beta transus is defined as the lowest equilibrium temperature at which the material is 100% beta.

Below the beta transus temperature, titanium will be a mixture of $\alpha + \beta$ if the material contains some beta stabilizers, or it will be all alpha if it contains no beta stabilizers. The beta transus is important, because processing and heat treatment are often carried out with reference to some incremental temperature above or below the beta transus. Alloying elements that favor the alpha crystal structure and stabilize it by raising the beta transus temperature include aluminum, gallium, germanium, carbon, oxygen, and nitrogen.

Two groups of elements stabilize the beta crystal structure by lowering the transformation temperature. The beta isomorphous group consists of elements that are miscible in the beta phase, including molybdenum, vanadium, tantalum, and niobium. The other group forms eutectoid systems with titanium, having eutectoid temperatures as much as 333 °C (600 °F) below the transformation temperature of unalloyed titanium. The eutectoid group includes manganese, iron, chromium, cobalt, nickel, copper, and silicon. Two other elements that often are alloyed in titanium are tin and zirconium. These elements have extensive solid solubilities in alpha and beta phases. Although they do not strongly promote phase stability, they retard the rates of transformation and are useful as strengthening agents.

Alloy Classes. Titanium alloys have generally been classified as alpha alloys, alpha-beta alloys, and beta alloys. Alpha alloys have essentially an all-alpha microstructure. Beta alloys are those alloys from which a small volume of material can be quenched into ice water from above its beta transus without martensitic decomposition of the beta phase. Alpha-beta alloys contain a mixture of alpha and beta phases at room temperature. Within the alpha-beta class, an alloy that contains less than 2 to 3% beta, such as Ti-8Al-1Mo-1V, may also be referred to as a “near-alpha” or “super-alpha” alloy.

The principal alloying element in alpha alloys is aluminum (oxygen is the principal alloying element in commercially pure titanium), but certain alpha alloys and most commercially pure (unalloyed) titanium contain small amounts of beta-stabilizing elements. Similarly, beta alloys contain small amounts of alpha-stabilizing elements as strengtheners in addition to the beta stabilizers.

The beta alloys can be further broken down into beta and “near-beta.” This distinction is necessary, because the phase transformations that occur, the reaction kinetics, and the processing could be different if the alloy is a near-beta (lean) alloy, such as Ti-10V-2Fe-3Al, or a rich beta alloy, such as Ti-13V-11Cr-3Al.

Further information on the metallurgy, selection, processing, and application of titanium alloys is contained in Ref 3 and in *Properties and Selection: Nonferrous Alloys and Special-Purpose Materials,* Volume 2 of the *ASM Handbook* (see, for example, the articles “Wrought Titanium and Titanium Alloys” and “Titanium and Titanium Alloy Castings”).

Reference cited in this section

3. M.J. Donachie, Jr., *Titanium: A Technical Guide,* 2nd ed., ASM International, 2000

L.M. Gammon, R.D. Briggs, J.M. Packard, K.W. Batson, R. Boyer, C.W. Domby, Metallography and Microstructures of Titanium and Its Alloys, *Metallography and Microstructures,* Vol 9, *ASM Handbook*, ASM International, 2004, p. 899–917

Metallography and Microstructures of Titanium and Its Alloys

Luther M. Gammon, Robert D. Briggs, John M. Packard, Kurt W. Batson, Rodney Boyer, and Charles W. Domby, The Boeing Company

---

Specimen Preparation

Specimen preparation comprises many detailed steps. The first stages of sample preparation are equipment dependant, while the final polish step is driven by the needs of the investigator. Sufficient attention must be paid to each step or the quality of the finished mount may be compromised.

The method chosen depends on two factors: the facilities and equipment present and the purpose of the investigation. There is a large difference between methods used in a research environment, where time may not be as pressing as in a production environment, or in a college instructional lab where the facilities may not be as elaborate.

Sectioning. Common methods for sectioning titanium metallographic samples include the band saw, abrasive cut-off wheel, and slow-speed wafering wheels. Band sawing titanium should be done with slow blade speed using a toothed blade and high pressure applied to the workpiece. If a high blade speed and low pressure are applied to the workpiece, damage in the form of cold work will be introduced into the sample, possibly preventing the true microstructure from being observed. With all three cutting methods, sufficient amounts of coolant should be used to prevent the introduction of heat damage into the sample. Abrasive cut-off wheels should be a soft rubber-bonded abrasive type. The erosion of the rubber-bonded wheel will continually provide a fresh cutting surface and prevent titanium debris from loading up on the blade. If a dull band saw blade is used or if an abrasive blade has loaded up with cutting debris, the sample will be damaged from overheating and cold work. Figure 1 shows the edge of a cross section cut with an abrasive cut-off wheel.

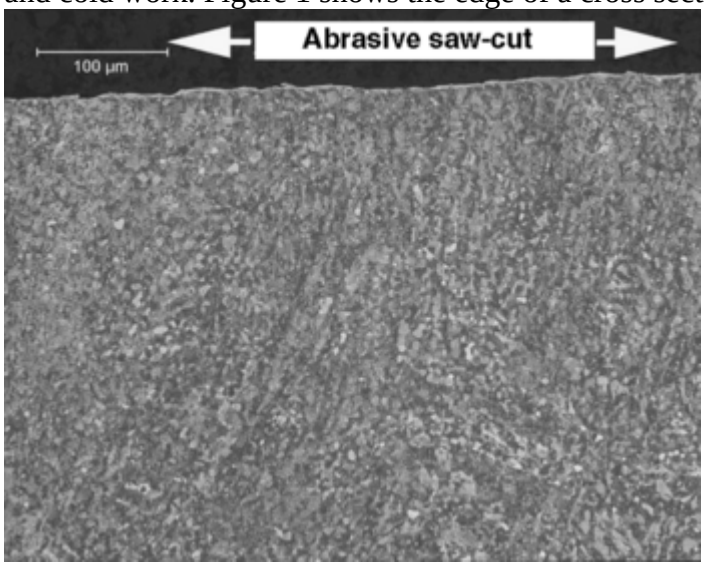

Fig. 1 Cross section through the abrasive saw-cut edge of a Ti-6Al-4V sample. Note there is less than 5 µm depth of disturbed material requiring removal for proper specimen preparation, seen as a thin layer at the surface. This layer would be deeper in commercially pure titanium and more difficult to discern.

Mounting. The sample should also be degreased and dried before mounting to ensure adequate adhesion of the mounting media. Careful consideration is also necessary for making a proper metallurgical mount.

The first consideration is choosing the most appropriate mounting medium. Titanium is a very abrasion-resistant material, and it is essential that the titanium be mounted correctly to produce a quality metallographic sample. The selection of mounting material has a significant impact on edge retention and the surface flatness of the mount. Failure to use the proper mounting media may cause rounding of the interface between the mount and sample, resulting in poor edge retention. It can also cause rounding or faceting of the overall mount surface. (See the article “Mounting of Specimens” in this Volume for more information on mounting and edge retention.)

In selecting a mounting material, it is recommended to use a mineral- or glass-filled hot-compression thermosetting resin. While the costs of the filled resins are higher than the traditional bakelite or epoxy resins, the performance of filled resins is superior, as the filler can allow close matching of the abrasive wear resistance of the specimen and the mount. The cost-to-benefit ratio makes filled resins a good choice when transparency is not needed. When transparency is needed or voids are present in a part with complex shape, it is necessary to use an alternative cold-setting material such as a clear epoxy. This can be vacuum impregnated into sample voids and irregularities such as the gap in Fig. 2.

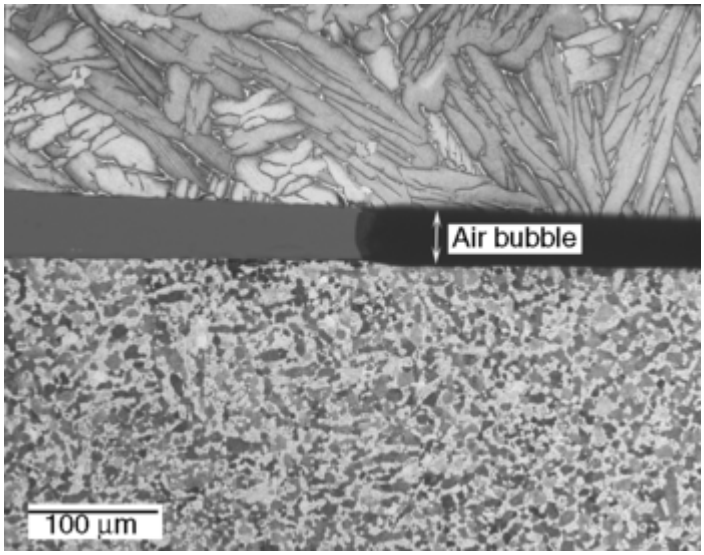

Fig. 2 This micrograph shows the impact of mounting defects on edge retention. Note the edge rounding near the air bubble and the sharp edge where the mounting material filled the gap. This shows the importance of good-quality mounting techniques and materials.

The second consideration is the sample configuration, which refers to the position and number of samples in a mount. The method of polishing can determine the sample configuration, as described in more detail in the article “Mounting of Specimens” in this Volume. In general, there are three types of polishing methods:

- Semiautomatic polishing machine with samples held in a “fixed” sample holder (Fig. 3a)
- Semiautomatic polishing machine with samples held in a “nonfixed” sample holder (Fig. 3b)
- Manual or hand polishing

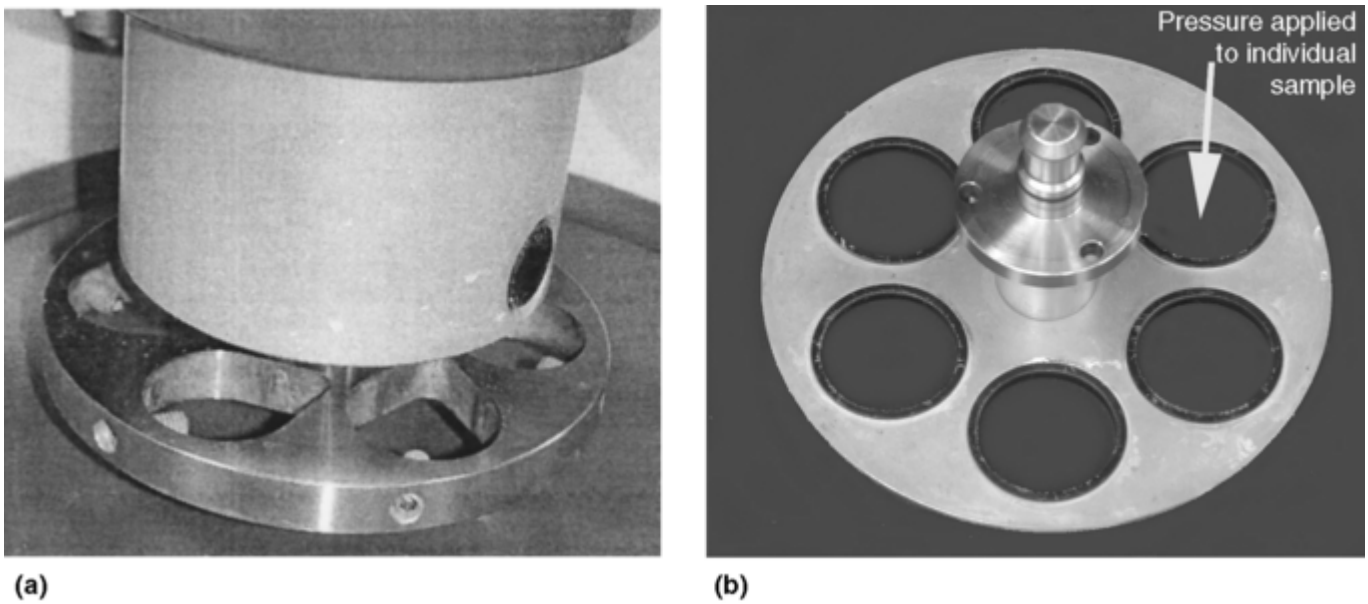

Fig. 3 Sample holders for semiautomated polishing machines. (a) Fixed-sample holder with load applied from a central column. (b) Nonfixed specimen mover plate with load applied over one mount

Polishing with a fixed-sample holder in a semiautomated machine is achieved by a powerhead that moves the sample holder around the polishing platen. In this method, mounted samples are fixed in place within a rigid sample holder, and central force loading is applied to all specimens in the holder through a centrally located column. In this method, three or six mounted samples must be symmetrically placed in the holder in order to ensure good flatness of the specimens after polishing. The mount surface thus remains flat, as the samples are held in-plane by the sample holder. This method provides optimal edge retention and flatness and is the

recommended sample preparation method for operators requiring larger volumes of throughput. With this method, each mount can contain only one specimen.

In the semiautomated nonfixed (or individual force) method, the specimens sit in a hole in a holder (a thin plate), and a piston comes down and presses each specimen against the working surface. In this case, two or more specimens should always be placed in each mount (Fig. 4). By centering them in each side of the mount, the specimens support the mount so it will not tend to rock back and forth. The result is a flatter sample with better edge retention. This is still not as good as the fixed method. A single specimen should never be mounted in the center of a mount. The result is usually a convex and/or faceted mount surface with poor edge retention. The mount will have the tendency to rock back and forth about the small, hard specimen, rounding the mount surface and degrading the quality of the edge. This convex surface will have an adverse effect on the appearance of the microstructure. A similar-sized mount with two small samples in the holders will reduce the rocking effect, making it possible to prepare a flatter sample.

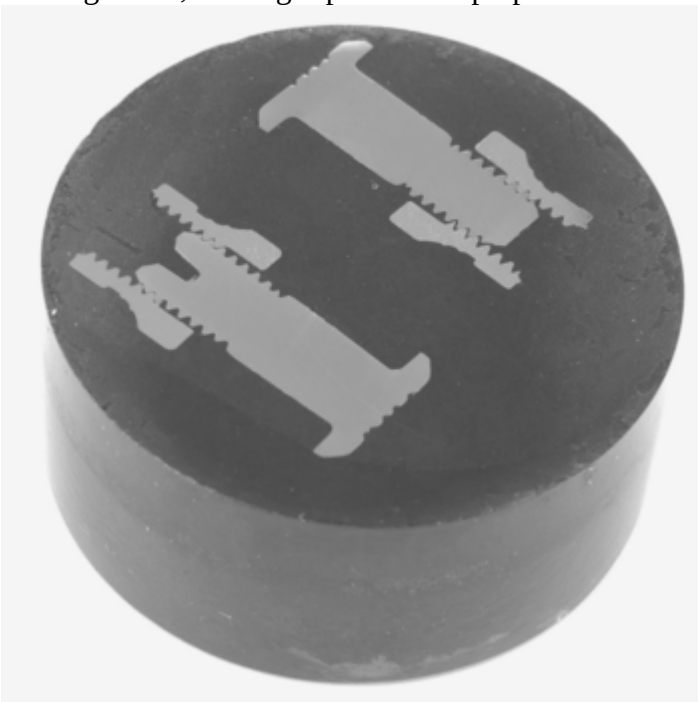

Fig. 4 Mount with two specimens for manual polishing or polishing on a semiautomated polisher with a non-fixed specimen mover plate

Manual or hand polishing is similar to the semiautomatic nonfixed method. Two or more specimens should always be mounted in each sample. The only difference is that the mass of titanium in the mount for hand preparation should be kept to a minimum to facilitate grinding and maintain a uniform applied pressure across the mount.

Grinding. The purpose of grinding is to remove the damage caused by the sectioning process. Sectioning methods, such as slow-speed wafering, that do not introduce much damage into the sample do not require extensive grinding and decrease sample preparation time.

Semiautomated grinding with a specimen mover plate or the fixed holder can be done with semiautomated polishers using diamond-embedded platens or platens with proprietary coatings designed for applied diamond suspensions. There is a wide assortment of diamond platens on the market to be used with automated grinding.

For a 20 to 30 cm (8 to 12 in.) diamond-embedded platen, the following parameters should be used. Keep in mind that there are many possible ways to accomplish a grinding operation depending on the complexity of the part, amount of material to be removed, and time available. Various combinations of these steps can be used:

- The speed should be <150 rpm (note: titanium machines work best at high pressure and low speed).
- The applied pressure should be 40 to 70 N (9 to 15 lbf) per 38 mm (1.5 in.) diam mount.
- Grinding step A uses 70 μm or 220 grit diamond.
- Grinding step B uses 1200 grit diamond.
- Always use a sufficient amount of coolant to prevent heat damage.

With proper sectioning most ordinary samples can be ground with a single 220 grit finish followed by a 9 μm diamond suspension on either a grinding platen with a proprietary coating or a woven non-nap silk cloth.
Grinding by hand usually involves the use of silicon-carbide papers. The following parameters should be observed:

- The speed should be kept to no more than 150 rpm.
- Always use new paper. The maximum paper lifetime is 15 s (or perhaps up to 60 s max in one-time manual grinding). Abrasives quickly lose their cutting ability and smear the sample and introduce cold-work damage.
- Apply as much pressure as can be controlled when holding the sample to the paper. High pressure and slow speed will produce favorable results.
- The common grit progression sequence is 120 (or 240), 320, and 600 grit. If the sectioning process produces a fine smooth face, it is possible to start the grinding process with 320 or 600 grit papers, but there must be sufficient material removal to eliminate all cutting damage.
- Always use sufficient amounts of coolant or water to prevent heat damage.

Polishing can be broken down into two phases, the intermediate polish and final polish. The purpose of polishing is to gradually remove the trace amounts of damage and the surface scratches introduced during the grinding operations. Again, there are numerous methods documented for intermediate and final polishing that may fit different operations. The list below discusses of a few of the procedures. An example of abusive polishing is shown in Fig. 5 after etching. Excessive etching cannot correct poor specimen preparation.

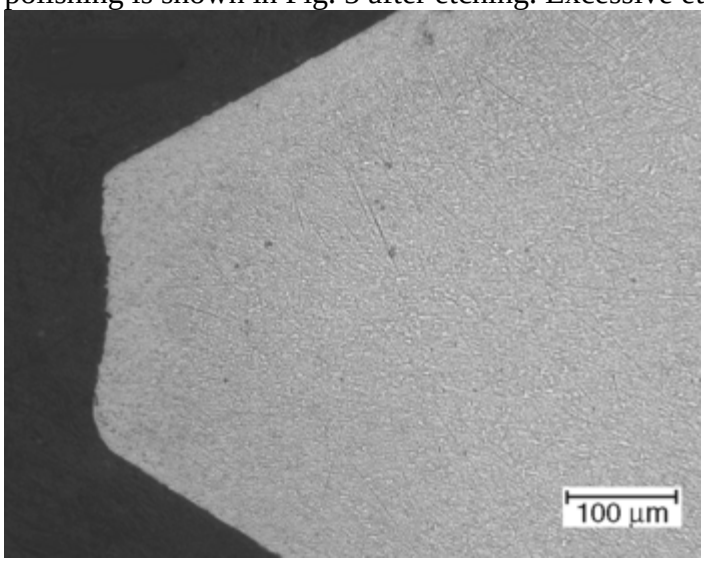

Fig. 5 Etched with Kroll's reagent for 45 s. Abusively polished example of a Ti-6Al-4V fastener resulting in a smeared and scratched surface. Excessive etching cannot correct poor specimen preparation. Note the severe distortion in microstructure and edge rounding.

Intermediate polishing is the bridge step or steps between grinding and <1 μm final step or steps. It can be done successfully by either the semiautomated or hand method. The semiautomated method is generally recommended because it is very effective with typical removal rates of 5 μm/min and as much as 25 μm/min with minimal cold work introduced into the sample. It can be utilized both as a fine grinding and a polishing step at the same time. Several semiautomated intermediate polishing parameters have been found effective:

- A 9 μm diamond suspension with an alcohol-based lubricant on a woven non-nap cloth such as silk or a proprietary platen designed for diamond suspension application is used.
- A 3 μm diamond suspension on a polyester cloth with an emulsified oil-based lubricant is used.
- Speed should be 120 to 150 rpm.
- Direction of specimen holder rotation should be complementary to the rotation of the platen.
- Applied force should be 40 to 80 N (9 to 18 lbf) per 38 mm (1.5 in.) diam mount.

There are two options for intermediate hand polishing; the beeswax platen and the traditional nap cloth diamond method. *The nap cloth and diamond option is not recommended* where edge retention is critical. The sequence used for hand polishing is typically:

1. A 6 μm diamond slurry on nap cloth is used.
2. A 3 μm diamond slurry on nap cloth is used.
3. Apply as much pressure as possible without rocking the specimen.

A recommended intermediate hand-polishing method using a beeswax wheel is an effective, inexpensive method that routinely produces quality samples. About 2.5 mm (0.10 in. of beeswax is cast on the platen into which relief grooves (Fig. 6) are cut at a spacing of 10 to 14 grooves per inch. Polishing is done with a paste made with 5 μm alumina and hydrogen peroxide. While polishing with the paste, drops of 3% hydrogen peroxide (or higher percentage with protective gloves) may be applied to the wheel. Higher percentages of hydrogen peroxide can be more effective. Another way is to polish with the alumina paste, followed by a Kroll's etch, repeating this cycle until a clean microstructure can be observed. A combination of these steps can prove effective as well. This method has proven very effective for labs without automated polishers. The beeswax wheel would be an excellent choice for the small lab or classroom.

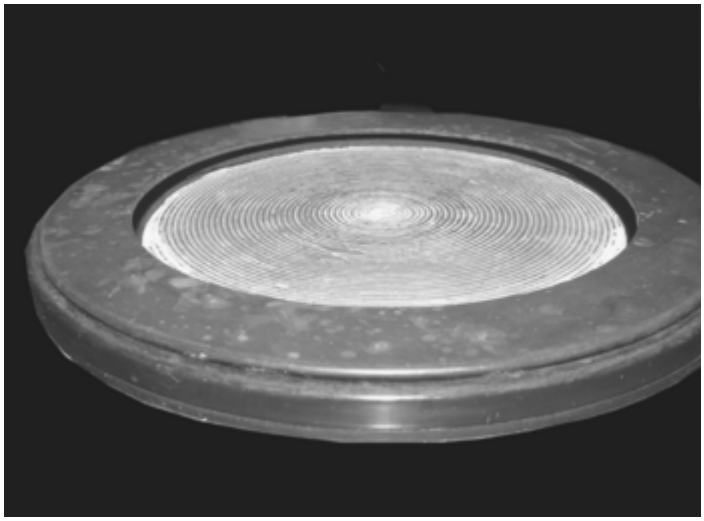

Fig. 6 A 200 cm (8 in.) wax wheel with relief grooves

Final Polishing. There are three methods for final polishing: hand polishing, semiautomated, and vibratory polishing. For hand polishing a 50/50 mix of 3% hydrogen peroxide and a 10% solution of a 0.05 μm premixed alumina suspension is used. These suspensions are available from several suppliers. A nap cloth or a closed-cell chemical-resistant foam pad is recommended. For increased edge retention a Dacron or polyester cloth is preferred.

A semiautomatic method is used for most titanium alloys as well as commercially pure (CP) titanium when not inspecting for hydrides. The same 50/50 mix of 3% hydrogen peroxide and a diluted 0.05 μm premixed alumina suspension is used on a closed-cell chemical-resistant foam pad (neoprene rubber cloth). The wheel speed should be 120 to 150 rpm and the force should be <15 N (3.4 lbf) per 38 mm (1.5 in.) diam mount. Head rotation should be in the complementary direction. For even better edge retention, a Dacron or polyester cloth may be used with the same parameters except the force should be 25 to 40 N (5.6 to 9.0 lbf) per 38 mm (1.5 in.) diam mount. The foam pad usually produces a clearer overall microstructure, but with slight edge rounding. Polishing times will vary, with much longer times required for CP titanium than the more highly alloyed materials.

The vibratory polisher set up with a short-nap woven synthetic cloth is the preferred method to produce a finish with the least amount of deformation to the microstructure. However, this process can take a considerable amount of time. A 10% solution of premixed 0.05 μm alumina on a short-nap synthetic cloth may be used. This will optimize removal of deformation from previous steps, but will yield slight edge rounding and require polishing for 8 to 16 h with a weight of only about 0.3 kg (11 oz). More weight will round the edges more.

The vibratory polisher set up with a non-nap polyester cloth is the preferred method to produce a microstructure that provides optimal edge retention and little or no deformation to the microstructure. The same suspension is used on a Dacron or polyester non-nap cloth. A weight of 1.0 to 1.5 kg (2.2 to 3.3 lb) is attached to a 38 to 50 mm (1.5 to 2 in.) mount with double-back tape. The polishing time is 1 h. This method works well on hybrid materials containing titanium as well as other materials. It optimizes edge retention.

Example: Comparison of Polishing Methods. Micrographs of a beta-annealed Ti-6Al-4V structure are shown in Fig. 7 for three different polishing preparations, as described below. Each procedure is designed for a different purpose.

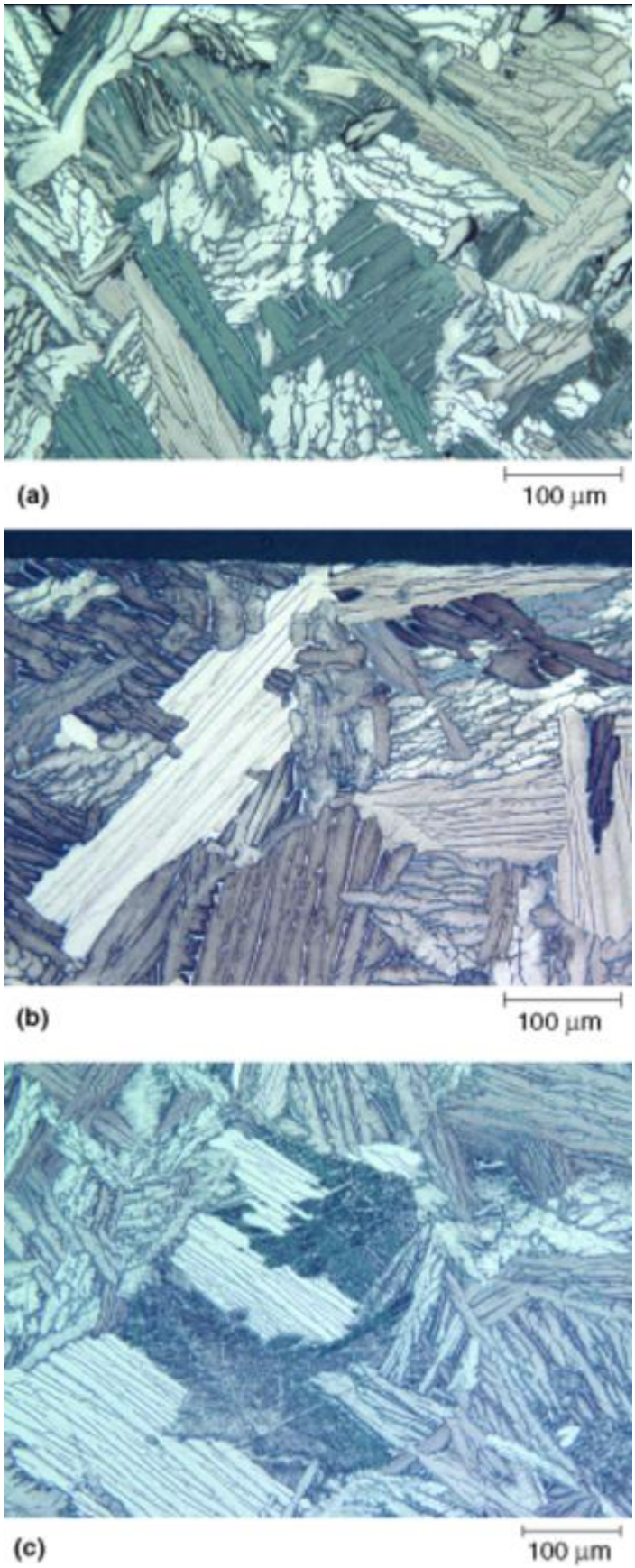

Fig. 7 Ti-6Al-4V alloy with Widmanstätten alpha in a beta matrix after furnace cooling from above the transus. Beta-anneal temperature was 1040 °C (1900 °F). Samples were etched with the oxalic tinting reagent for 15 s after polishing by (a) the four-step method for optimizing removal of deformed material, (b) the four-step method for optimizing edge retention, or (c) the three-step semiautomated method for optimizing preparation time (note the lack of detail in the dark regions). See text for description of polishing procedures.

Polishing to Optimize Removal of Deformed Material (Fig. 7a). In this example, polishing was accomplished with a four-step method for optimizing removal of deformed material. This method is best for overall polish quality:

1. 200 grit diamond-embedded platen
2. 9 μm proprietary grinding platen
3. 3 μm polyester cloth
4. 16 h on vibratory polisher with short-nap synthetic cloth and 10% solution of premixed 0.05 μm alumina suspension

Polishing to Optimize Edge Retention (Fig. 7b). In this example, the same material and etch is used, but polishing was accomplished by the following four-step method for optimizing edge retention:

1. 220 grit diamond-embedded platen
2. 9 μm proprietary grinding platen
3. 3 μm polyester cloth
4. 1 h on vibratory polisher with non-nap polyester cloth and 10% solution of premixed 0.05 μm alumina suspension

Another example is Fig. 8 from Ti-6Al-4V material solution treated at 925 °C (1700 °F) and aged. It was polished with the four-step method for edge retention. It was etched with the oxalic tint etch to reveal the deformed grain structure from drilling. Figure 8(a) shows the depth of the cold work as evidenced by the disturbed microstructure to a depth of 310 μm. Figure 8(b) shows the normal microstructure for comparison.

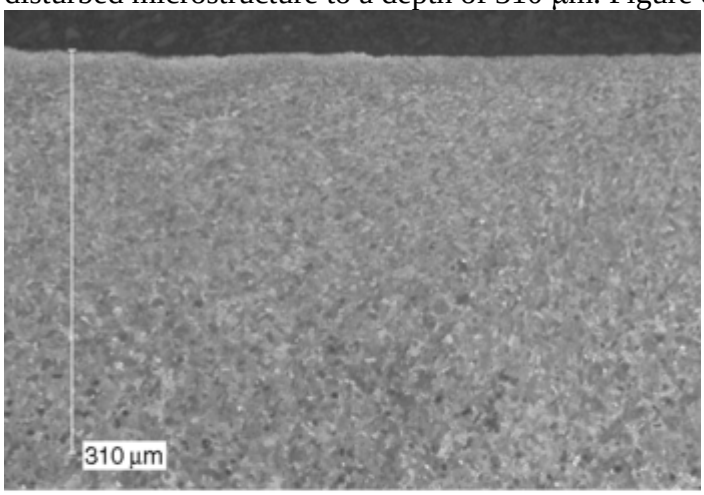

(a)

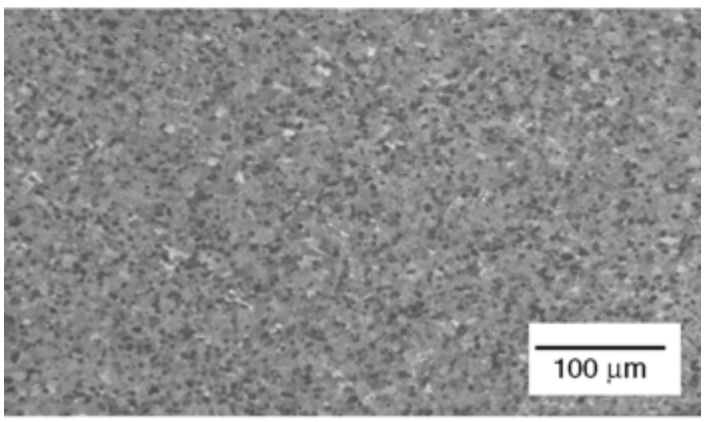

(b)

Fig. 8 Deformed grain structure from drilling in solution treated and aged Ti-6Al-4V. Solution treatment was at 925 °C (1700 °F) and aged. Polishing was the four-step method for edge retention, and it was etched with the oxalic tint etch to reveal the deformed grain structure from drilling. (a) Depth of

the cold work as evidenced by the disturbed microstructure to a depth of 310 μm. (b) Normal microstructure for comparison

Polishing to Optimize Preparation Time (Fig. 7c). In this example, the same material and etch is used. Polishing was accomplished with a three-step, semiautomated method for optimizing preparation time:

1. 220 grit diamond-embedded platen
2. 9 μm proprietary grinding platen
3. Closed-cell chemical-resistant foam pad with a 50/50 mix of 3% hydrogen peroxide and a 0.05 μm premixed alumina suspension

Total time to prepare sample is less than 20 min. Note that the addition of an intermediate 3 μm polyester cloth step will further improve this process. Also note the lack of detail in the dark regions in Fig. 7(c).
Etchants. There are numerous choices of etchants for revealing titanium alloy microstructure. Table 1 lists various etchants, and a more extensive listing is also contained in Ref 1. However, this article focuses on three types of etchants that can easily handle nearly all the needs in any laboratory. The three etchants are Kroll's reagent and two tint etches: an oxalic-acid tint etch and an ammonium bifluoride (ABF) tint etch (Table 2).

Table 1 Etchants for examination of titanium and titanium alloys

Etchant	Comments
Macroetchants	
50 mL HCl, 50 mL H_2O	General-purpose etch for α + β alloys
30 mL HNO_3, 3 mL HF, 67 mL H_2O (slow) to 10 mL HNO_3, 8 mL HF, 82 mL H_2O (fast)	Used at room temperature to 55 °C (130 °F) for 3–5 min. Reveals grain size and surface defects
15 mL HNO_3, 10 mL HF, 75 mL H_2O	Etch about 2 min. Reveals flow lines and defects
Two-stage etch[(a)] consisting of: (1) 8 mL HF, 10 mL HNO_3, 82 mL H_2O and (2) 18 g/L (2.4 oz/gal) of NH_4HF_2 (ammonium bifluoride) in H_2O	Reveals α and β segregation (aluminum segregation)
Microetchants	
1–3 mL HF, 10 mL HNO_3, 30 mL lactic acid	Reveals hydrides in unalloyed titanium
1 mL HF, 30 mL HNO_3, 30 mL lactic acid	Reveals hydrides in unalloyed titanium
Kroll's reagent: 1–3 mL HF, 2–6 mL HNO_3, H_2O to 1000 mL	General-purpose etch for most alloys
10 mL HF, 5 mL HNO_3, 85 mL H_2O	General-purpose etch for most alloys
1 mL HF, 2 mL HNO_3, 50 mL H_2O_2, 47 mL H_2O	Removes etchant stains for most alloys
10 mL HF, 10 mL HNO_3, 30 mL lactic acid	Chemical polish and etch for most alloys
2 mL HF, 98 mL H_2O	Reveals α case for most alloys
98 mL saturated oxalic acid in H_2O, 2 mL HF	Reveals α case (interstitial contamination) for most alloys
6 g NaOH, 60 mL H_2O, heat to 80 °C (180 °F), add 10 mL H_2O_2	Good α-β contrast, general microstructures for most alloys
2 mL HF, 98 mL H_2O, then 1 mL HF, 2 mL HNO_3, 97 mL H_2O	General-purpose etch for near-α alloys[(b)]
10 mL KOH (40%), 5 mL H_2O_2, 20 mL H_2O	Stains α, transformed β
18.5 g benzalkonium chloride, 33 mL ethanol, 40 mL glycerol, 25 mL HF	General-purpose etch for Ti-Al-Zr and Ti-Si alloys
2 mL HF, 4 mL HNO_3, 94 mL H_2	Reveals microstructure in aged Ti-13V-11Cr-3Al
50 mL 10% oxalic acid, 50 mL 0.5% HF with H_2O	Etch 12–20 s. General-purpose etch for β alloys

10 s with Kroll's, then 10–15 s with 50 mL 10% oxalic acid, 50 mL 0.5% HF with H_2O	Brings out aged structure in Ti-10V-2Fe-3Al

(a) Two-stage etch procedure: Degrease (if necessary) and clean, making sure the surface is water-break free. Immerse in solution (1) at 45–55 °C (110–135 °F) for 2–3 min and rinse thoroughly in clean cold water. Immerse in agitated bath of solution (2) at room temperature for 1–2 min. Rinse thoroughly in clean cold water, rinse thoroughly in clean hot water at 90–100 °C (190–210 °F), blow dry with clean compressed air. Solutions must be used fresh.
(b) First etchant stains α phase; second etchant removes stain.

Table 2 Typical compositions of microetchants suitable in most applications of titanium metallography

Name	Typical composition	Notes	Figures
Kroll's reagent	1.5 mL HF 4 mL HNO_3 94 mL H_2O	…	Fig. 5, 9, 10, 11, 13, 14, 16, 35, 37, 56
Oxalic reagent (tint etch)	20 mL HF 20 g oxalic 98 mL H_2O	15 s for Ti-6Al-4V. Do not remove etch products.	Fig. 9, 10, 11, 15, 28, 46, 50, 57, 58, 62, 64
Ammonium bifluoride (ABF)	1 g ammonium bifluoride (NH_4FHF) 99 mL H_2O	Do not remove etch products.	Fig. 9, 10, 11, 47, 48, 49, 61
Lactic hydride reagent	Mix fresh 5 mL lactic acid and 5 mL stock solution (3 mL HF, 97 mL HNO_3)	Commercially pure titanium hydrides	…

The etching time will vary depending on the alloy and heat treat condition of the sample. It is a good practice to document successful etching practices in the laboratory. When using the tint etchants, it is critical not to swab the specimen after etching. Just wash with warm tap water. Any swabbing or contact will disturb the surface. The etchant products highlight the grain orientation. The use of tint etchants on specimens where cold work (plastic and elastic deformation) is left from the sample preparation is not recommended. Kroll's reagent is more forgiving in that case.
Comparison of contrast developed by the three etchants is shown for three types of structures or conditions:

- Coarse lamellar structure after slow furnace cool of T-6Al-4V from beta anneal at 1035 °C (1900 °F) revealed by Kroll's reagent and tint etches (Fig. 9)
- Worked structure in Ti-6Al-4V plate air cooled after heat treatment at 885 °C (1625 °F) revealed by Kroll's reagent and tint etches (Fig. 10)
- Bimodal structure representative of an alpha/beta forging revealed by Kroll's reagent and tint etches (Fig. 11). The light phase in Fig. 11(b)—primary alpha in a matrix of transformed beta, a lamellar alpha/beta structure as clearly illustrated in the inset of Fig. 11(c)

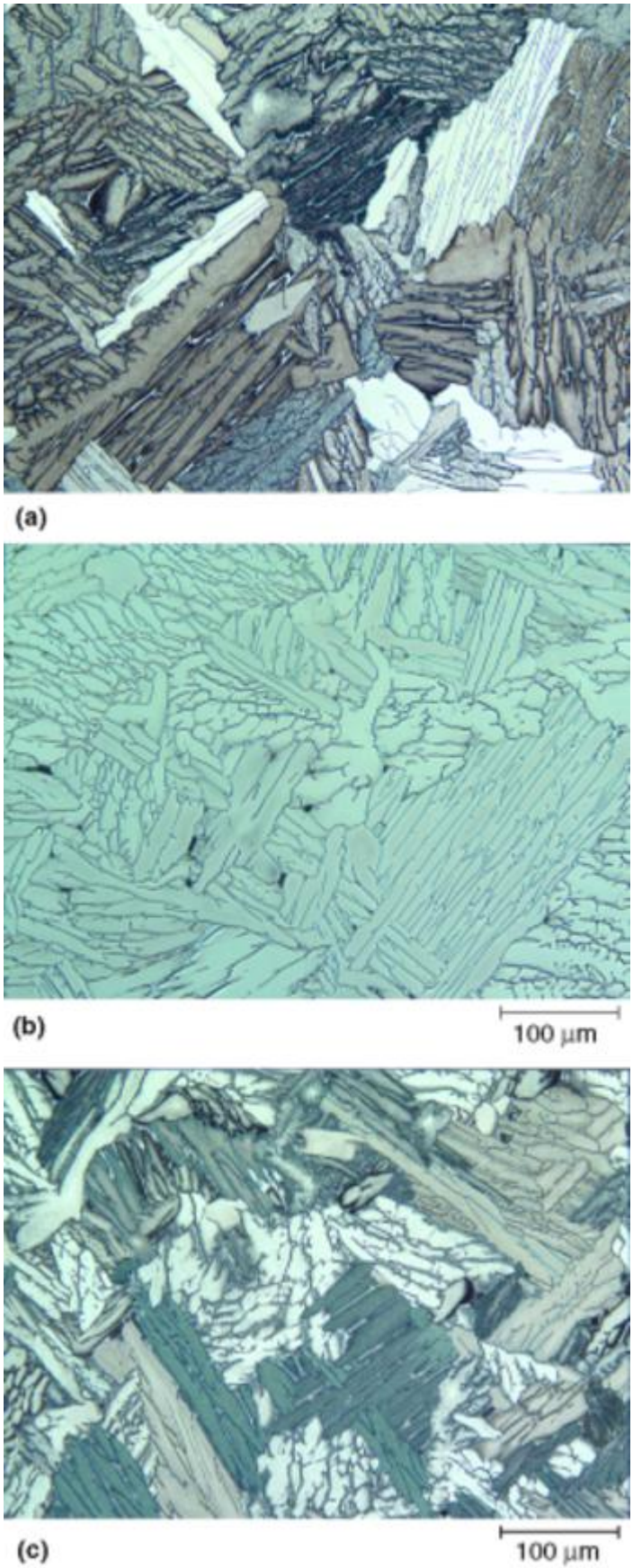

Fig. 9 Coarse lamellar alpha revealed by different etches in Ti-6Al-4V structure after beta anneal at 1040 °C (1900 °F) and furnace cooling. Preparation was four-step polishing, with final polish of 16 h on vibratory polisher and 10% alumina slurry. Slightly uncrossed polarized light illumination for all three etches. (a) Ammonium bifluoride tint etch, 60 s. (b) Kroll's reagent, 15 s. (c) Oxalic tint etch, 60 s.

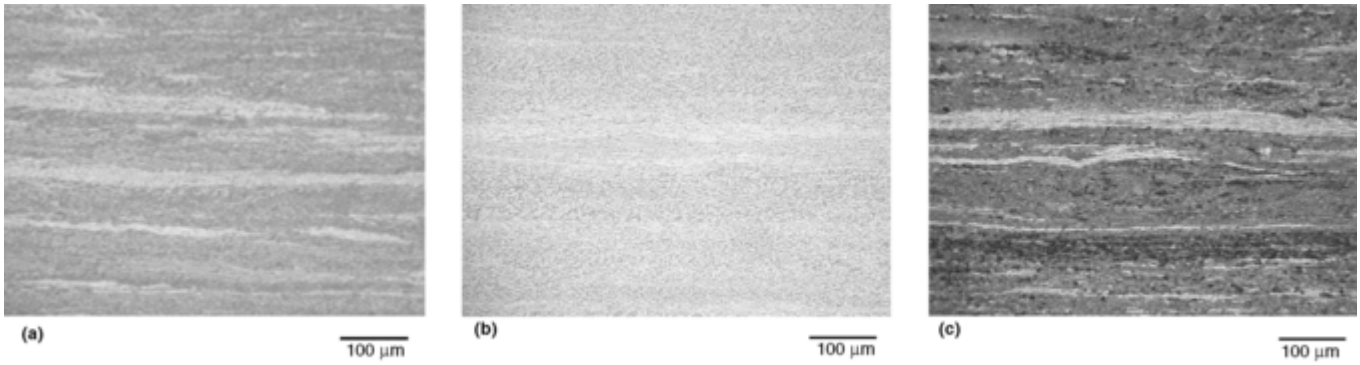

Fig. 10 Ti-6Al-4V plate heated at 885 °C (1625 °F) for 15 min, air cooled. (a) Ammonium bifluoride (ABF) tint etch, 60 s; slightly uncrossed polarized light. (b) Kroll's reagent, 15 s. (c) Oxalic tint etch, 15 s

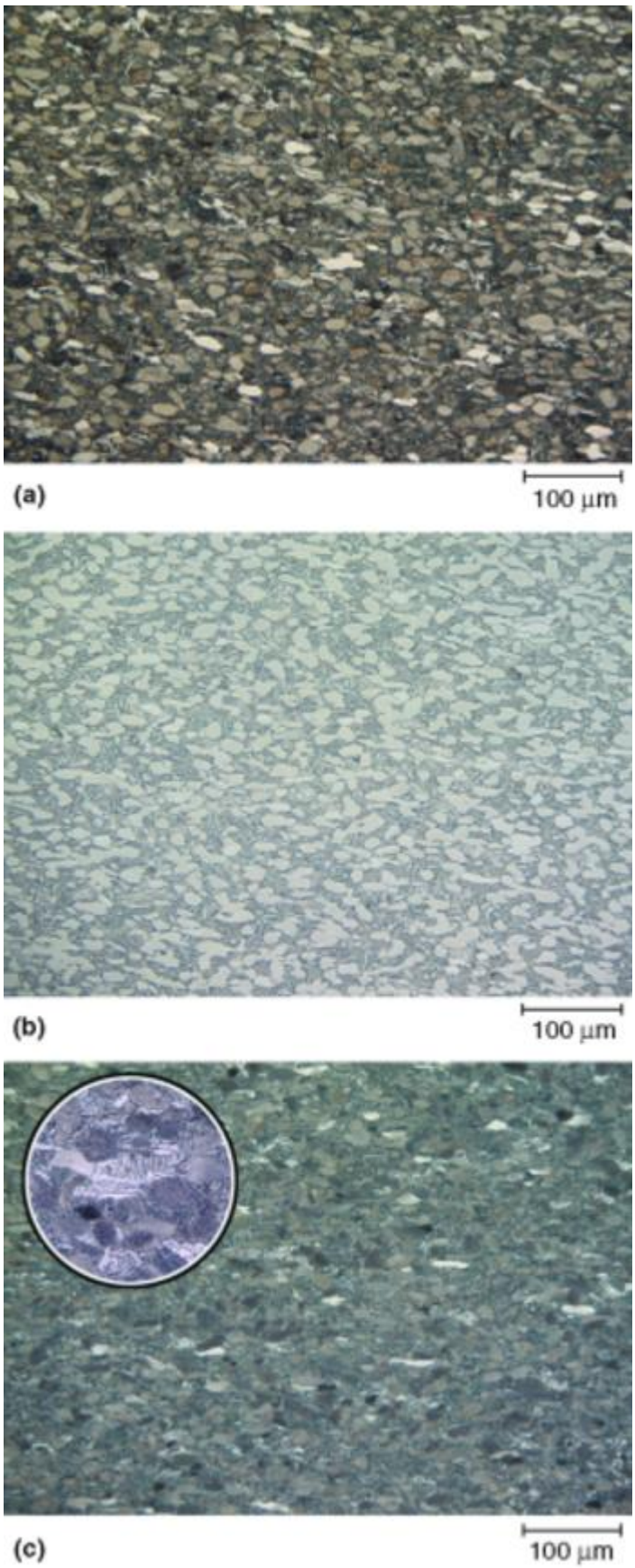

Fig. 11 Ti-6Al-4V die forging, mill-annealed. (a) Ammonium bifluoride tint etch, 60 s. Slightly uncrossed polarized light illumination. (b) Kroll's reagent, 15 s. Slightly uncrossed polarized light illumination. (c) Oxalic tint etch, 15 s. Slightly uncrossed polarized light illumination.

Figure 12, 13, 14 and 15 are all of a Ti-6Al-4V solution treated and aged fastener with rolled threads. Examples are shown etched with both oxalic acid and Kroll's reagent. Both etchants show the fine detail without

overetching. However, it is difficult to show etched microstructure in titanium alloy fasteners due to the cold work from rolling the threads. Figure 12 and 13 show the crest area of the thread. Note the lighter structure at the crest where the cold work is greatest.

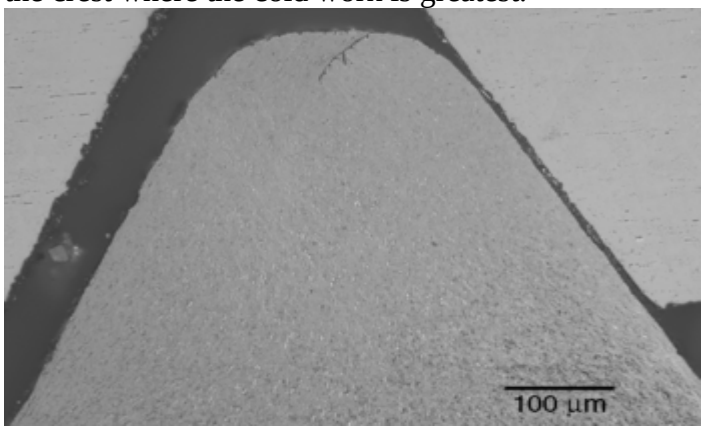

Fig. 12 Oxalic tint etch for 15 s. Ti-6Al-4V fastener solution treated and aged. 1 h vibratory polisher, non-nap polyester cloth and alumina. Note: the mounted parts were vacuum impregnated with hydrated rhodamine-dyed epoxy. Note the crest lap, which is typical for a rolled thread.

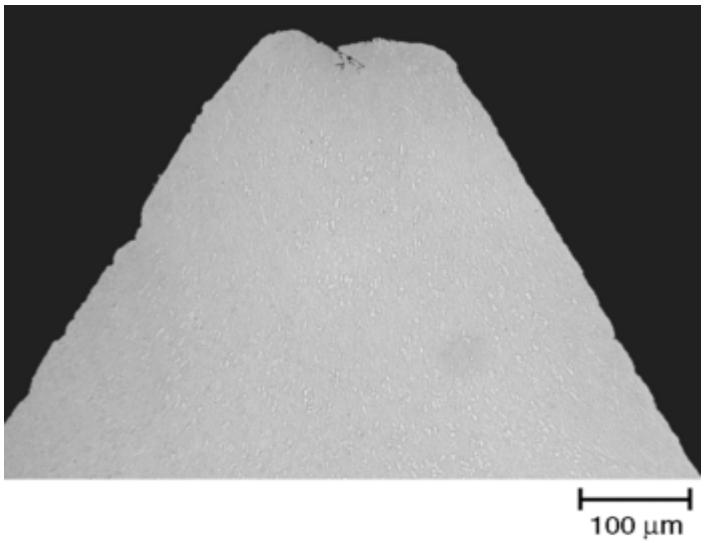

Fig. 13 Etched with Kroll's reagent for 15 s. Ti-6Al-4V fastener solution treated and aged. 1 h vibratory polisher, non-nap polyester cloth and alumina. Note the crest lap, which is typical for a rolled thread.

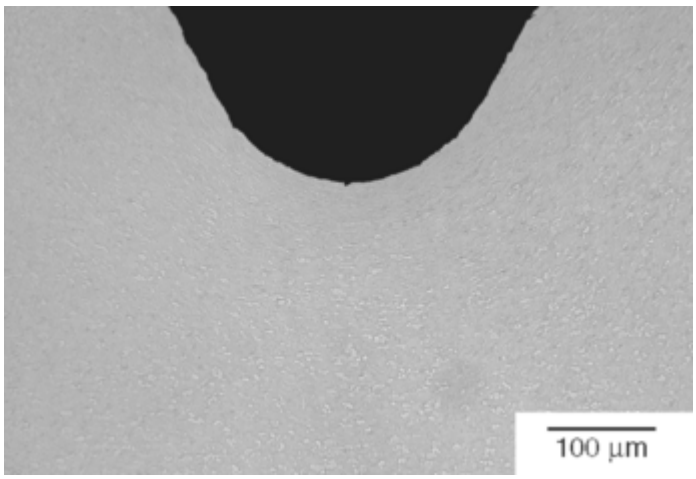

Fig. 14 Etched with Kroll's reagent for 15 s. Ti-6Al-4V fastener solution treated and aged. 1 h vibratory polisher, non-nap polyester cloth and alumina.

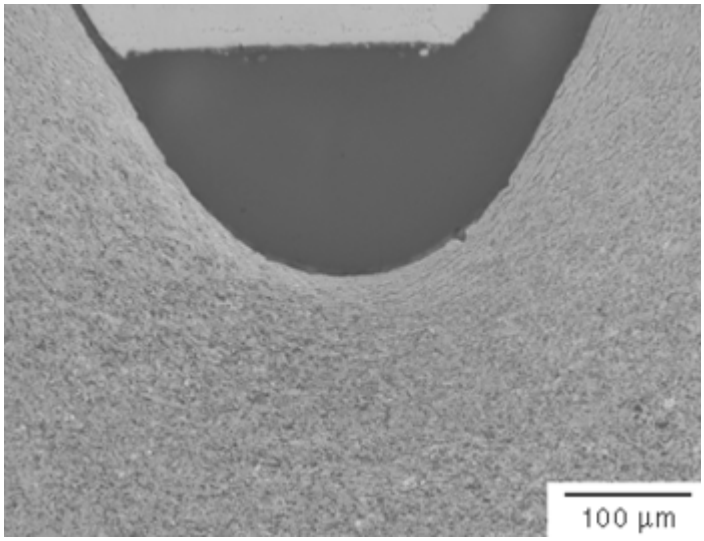

Fig. 15 Oxalic tint etch for 15 s. Ti-6Al-4V fastener solution treated and aged. 1 h vibratory polisher, non-nap polyester cloth and alumina. Note: This mount was vacuum impregnated with hydrated, rhodamine-dyed epoxy.

Kroll's reagent, the most common etchant or reagent used on titanium alloys (Table 2), is used for bringing out the general microstructure in alpha-beta alloys. It is a relatively low-contrast etchant. Figure 16 shows examples of etched microstructures from the same Ti-6Al-4V overaged plate with varying etch severity with (Kroll's) reagent. Etchant time is a compromise between detail and contrast. The shorter times reveal more detail, while longer etching times result in more contrast. As etching time increases, all detail is lost in the contrast (see Fig. 16d). It is better to underetch than overetch. Figure 16(a) is underetched; however, it has all the detail necessary to analyze the specimen correctly. Figure 16(b) is a good compromise at 15 s.

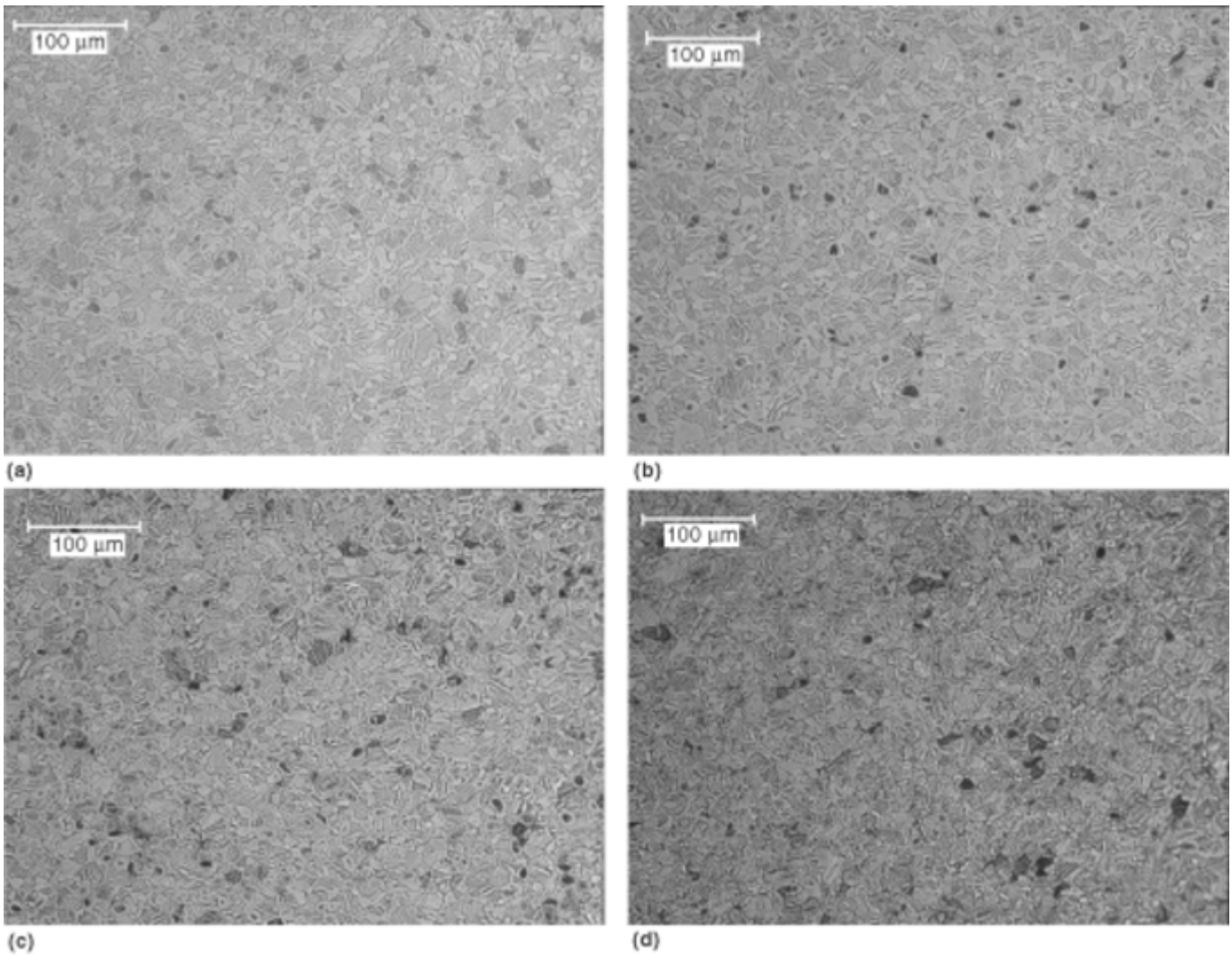

Fig. 16 Micrographs from solution treated and overaged Ti-6Al-4V plate after etching with Kroll's reagent for (a) 5 s, (b) 15 s, (c) 30 s, and (d) 60 s. All specimens polished for 1 h with vibratory polisher, non-nap polyester cloth and alumina. In the severe etch (d), note that fine detail is etched away and the relief is becoming excessive.

Oxalic acid is a tint etch that stains the microstructure and provides more contrast in the microstructure in alpha-beta alloys. Etching with oxalic acid requires a better quality polish. It is good for revealing grain orientation, heat effects, and alpha-rich regions formed by exposure to alpha stabilizers such as oxygen or nitrogen. *Note:* do not remove the etching products or swab during the procedure.

Ammonium bifluoride (ABF) is another tint etch. It is similar to oxalic acid and also provides more contrast in the microstructure of alpha-beta alloys. Both reagents will reveal grain orientation. It is most often used for investigating alpha case or alpha-enriched areas in the microstructure. *Note:* do not remove the etching products or swab during the procedure.

Reference cited in this section

1. G.F. Vander Voort, *Metallography: Principles and Practice*, McGraw-Hill, 1984, reprinted by ASM International, 1999

L.M. Gammon, R.D. Briggs, J.M. Packard, K.W. Batson, R. Boyer, C.W. Domby, Metallography and Microstructures of Titanium and Its Alloys, *Metallography and Microstructures,* Vol 9, *ASM Handbook*, ASM International, 2004, p. 899–917

Metallography and Microstructures of Titanium and Its Alloys

Luther M. Gammon, Robert D. Briggs, John M. Packard, Kurt W. Batson, Rodney Boyer, and Charles W. Domby, The Boeing Company

Macroexamination

Macrostructural examination of titanium alloys provides useful information about material processing, both melting and metalworking. It is used for detection of melting defects or anomalies, qualitative assessment of grain refinement and uniformity, as well as determination of grain flow in forged products. Macroetching of titanium alloys is discussed in the article "Macroetching" in this Volume.

Four principal defects are to be found in macrosections of ingot, forged billet, or other semifinished product forms. These include high-aluminum defects (HADs or type II defects), high interstitial defects (HIDs, also referred to as type I defects or low-density interstitial defects), beta flecks and high-density inclusions (HDI), High-aluminum defects are areas containing an abnormally high amount of aluminum. These are soft areas in the material (Fig. 17, 18) and are also referred to as "alpha segregation." Defects referred to as "beta segregation" are sometimes associated with alpha segregation. These are areas in which aluminum is depleted. The high interstitial defects (Fig. 19, 20) are normally high in oxygen and/or nitrogen, which stabilize the alpha phase. These defects are hard and brittle; they are normally associated with porosity, as shown in Fig. 21.



Fig. 17 Ti-6Al-4V alpha-beta processed billet illustrating the macroscopic appearance of a high-aluminum defect. See also Fig. 18 1.25×. Courtesy of C. Scholl

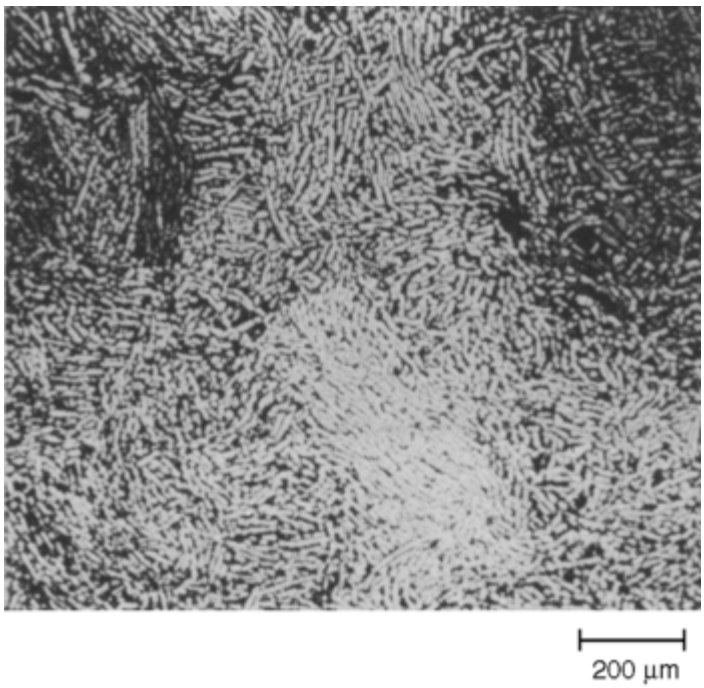

Fig. 18 Same as Figure 17 There is a higher volume fraction of more elongated alpha in the area of high aluminum content. 50×. Courtesy of C. Scholl

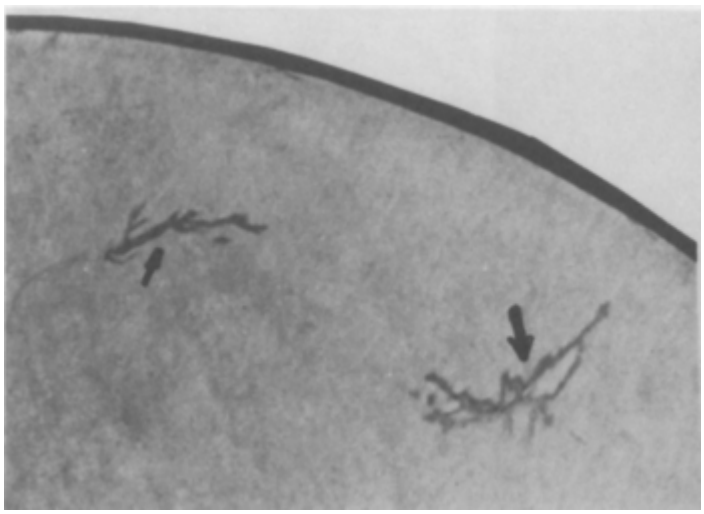

Fig. 19 Ti-6Al-4V alpha-beta processed billet illustrating macroscopic appearance of a high interstitial defect. See also Fig. 20 Actual size

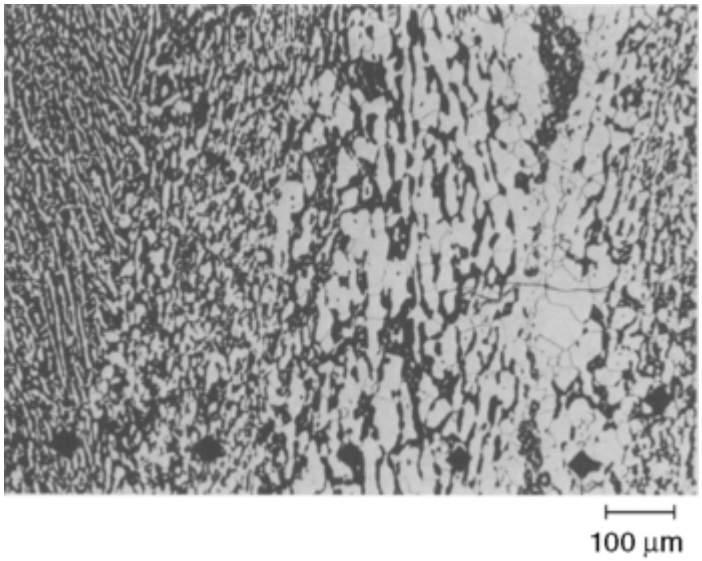

Fig. 20 Same as Figure 19 The high oxygen content results in a region of coarser and more brittle oxygen-stabilized alpha than observed in the bulk material. 100×

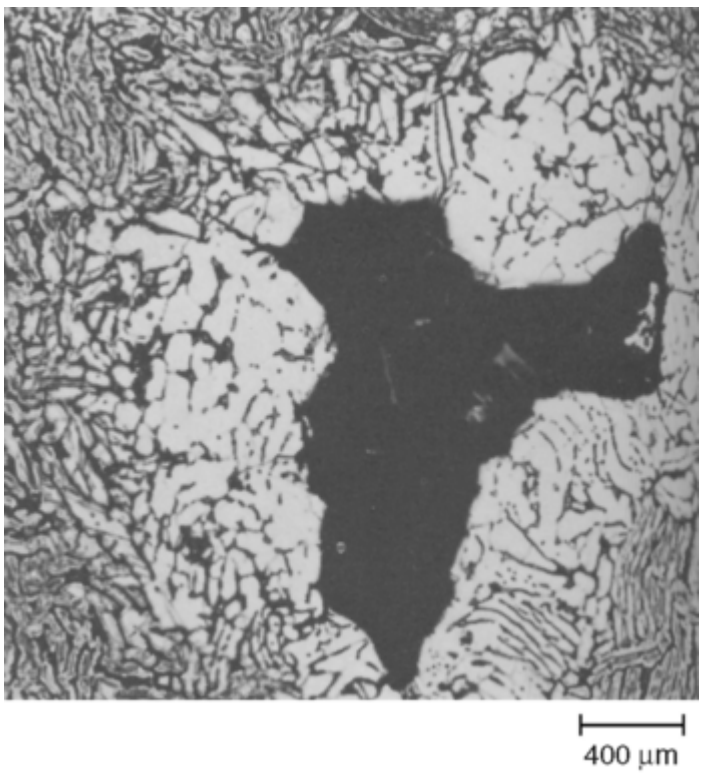

Fig. 21 Ti-8Al-1Mo-1V, as forged. Ingot void (black), surrounded by a layer of oxygen-stabilized alpha (light). The remaining structure consists of elongated alpha grains in a dark matrix of transformed beta. Etchant: Kroll's reagent (ASTM 192). 25×

Beta flecks are regions enriched in a beta-stabilizing element due to segregation during ingot solidification. Their occurrence in alpha-beta alloys is uncommon. Flecking becomes more of a problem with beta alloys, which have much higher amounts of beta-stabilizing additions. The problem is most prevalent in iron- and chromium-bearing alloys. This enrichment of a localized region with beta stabilizers lowers the beta transus, locally changing the microstructure and thereby enabling their detection.

This microstructural modification can take two forms. In alpha-beta alloys, such as Ti-6Al-6V-2Sn, vanadium enrichment lowers the beta transus, but is not sufficient to stabilize the beta to room temperature. When working or heat treating the material high in the $\alpha + \beta$ phase field, the microstructure observed (after cooling back to room temperature) will consist of primary alpha and transformed beta. The beta fleck is a result of the

local composition with a higher beta-stabilizer content that results in a local beta transus lower than that of the bulk material. Beta flecks occur if the temperature is above the transus in the “flecked” region. This condition is apparent in Fig. 22 and Fig. 23. A beta fleck could go undetected if the final processing and heat treatment are conducted at a temperature low enough that the beta transus suppression is not sufficient to cause a microstructural perturbation. The effects of beta flecks on properties in such alloys as Ti-6Al-4V and Ti-6Al-6V-2Sn are still in question, but the effect is not a major one.

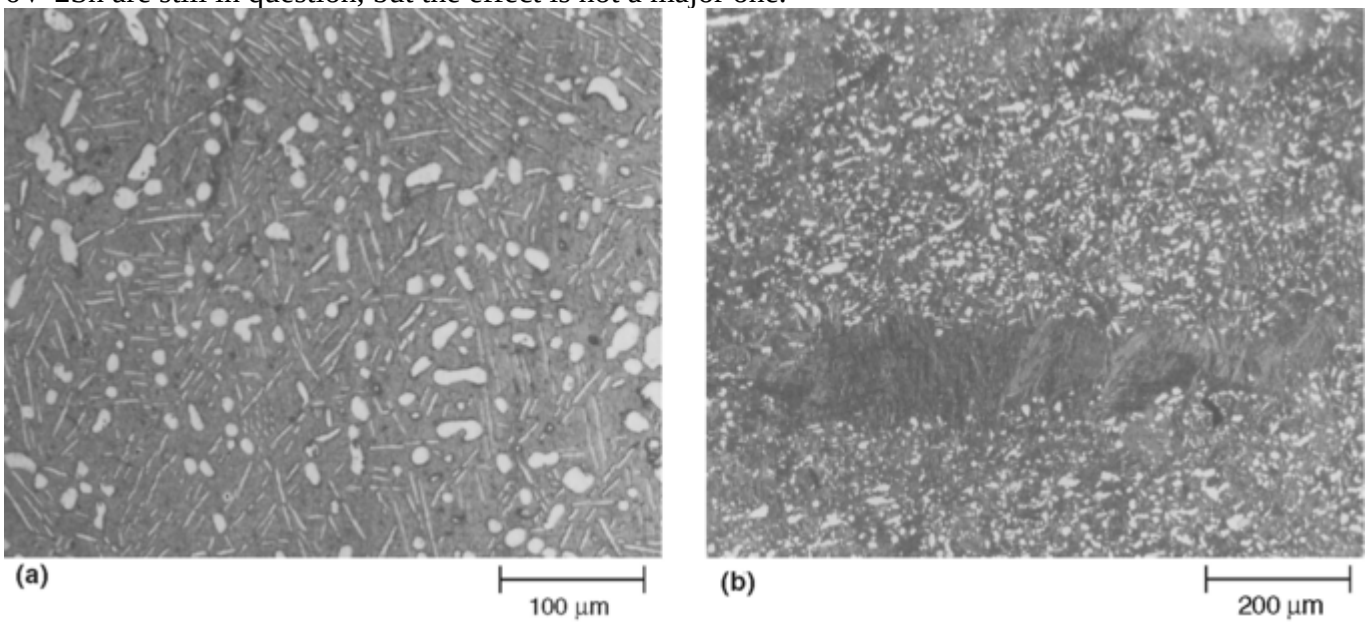

Fig. 22 Ti-6Al-6V-2Sn alpha-beta alloy forging, solution treated, quenched, and aged. Hand forging at 925 °C (1700 °F), solution treated for 2 h at 870 °C (1600 °F), water quenched, aged 4 h at 595 °C (1100 °F), and air cooled. (a) “Primary” alpha grains (light) in a matrix of transformed beta containing acicular alpha. Kroll's reagent (ASTM 192). 150×. (b) Same structure is the same as in (a), except that alloy segregation has resulted in a dark “beta fleck” (center of micrograph) that shows no light “primary” alpha. See also Fig. 23 and 24 Etchant: Kroll's reagent (ASTM 192). 75×

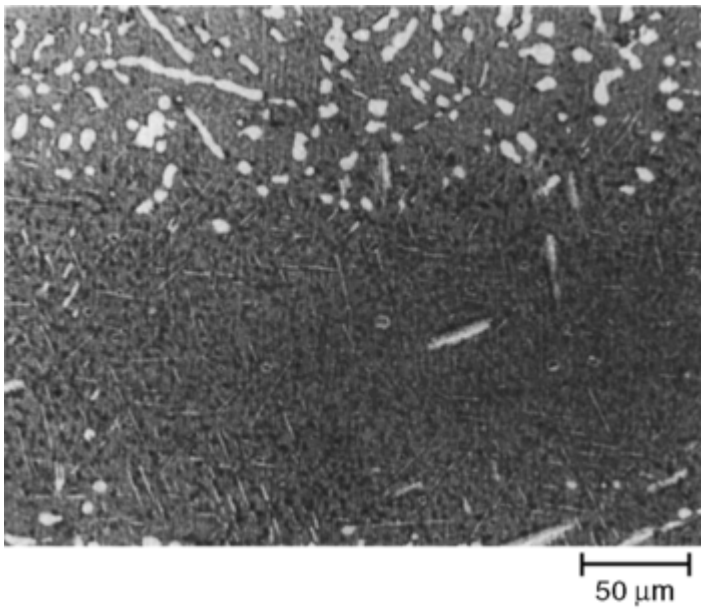

Fig. 23 Ti-6Al-6V-2Sn forging, solution treated for 1¼ h at 870 °C (1600 °F), water quenched, and aged 4 h at 575 °C (1070 °F). Structure: same as in Fig. 22(b), but higher magnification shows a small amount of light, acicular alpha in the dark “beta fleck.” See also Fig. 24. Etchant: 2 mL HF, 8 mL HNO_3, 90 mL H_2O. 200×

Beta flecks are more of a problem with near-beta alloys; they are observed macroscopically as shiny spots or flecks. Their appearance is similar in α + β alloys (Fig. 24). The beta-stabilizer enrichment in the flecked regions of beta alloys, however, is sufficient to stabilize the beta down to room temperature. To guarantee material that will be fleck-free, producers must solution treat samples at a certain temperature below the beta transus, assuring the user that the material will not form beta flecks if heat treated to a temperature up to or below the test temperature. The material will then form alpha, but beta fleck regions will be above or much nearer the transus. Therefore, they will be void of alpha or contain a significantly lower volume fraction of alpha upon cooling to room temperature, as shown in Fig. 25 and 26. These regions in beta alloys will be harder, will have higher strength and lower ductility, and will have lower low-cycle fatigue strength than the bulk material.

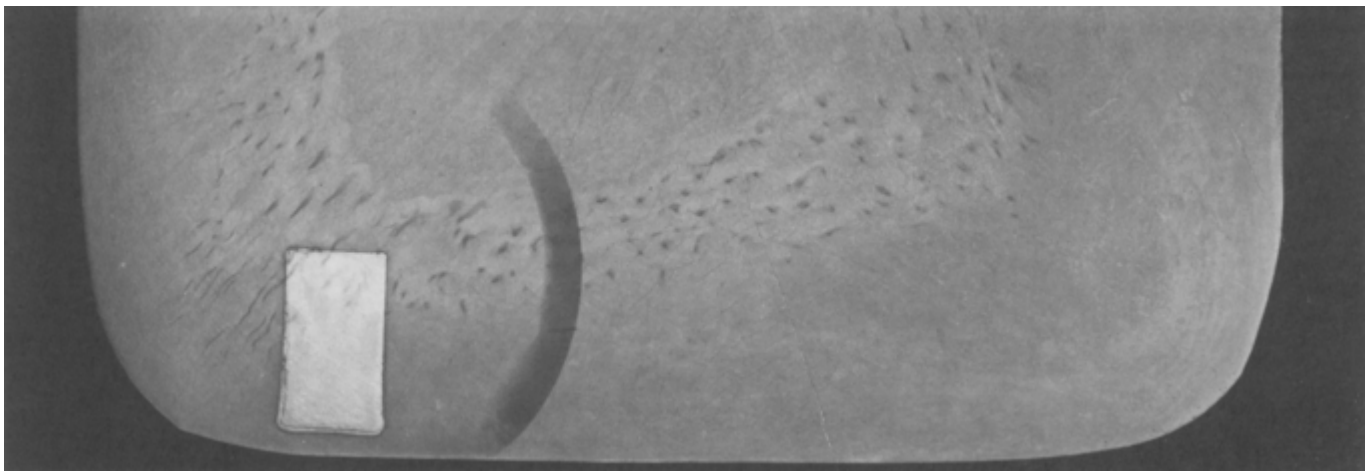

Fig. 24 Ti-6Al-6V-2Sn α + β forged billet illustrating macroscopic appearance of beta flecks that appear as dark spots. See also Fig. 22 and Fig. 23 Etchant: 8 mL HF, 10 mL HNO_3, 82 mL H_2O, then 18 g/L (2.4 oz/gal) of NH_4HF_2 in H_2O. Less than 1×. Courtesy of C. Scholl

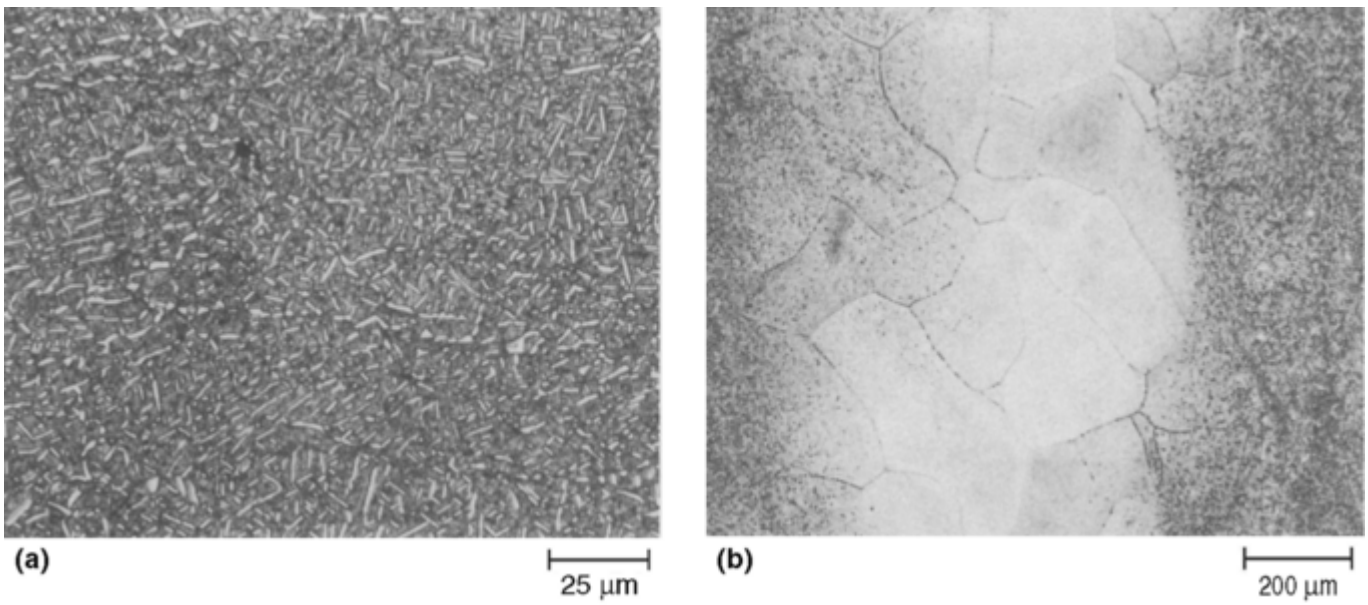

Fig. 25 Ti-10V-2Fe-3Al pancake forging. (a) Beta forged about 50% + alpha-beta finish forged about 5%, with heat treatment at 750 °C (1385 °F), 1 h, water quench, + 540 °C (1000 °F), 8 h. (a) Lamellar alpha with a small amount of equiaxed alpha in an aged beta matrix. Etched 10 s with Kroll's reagent, then 50 mL of 10% oxalic acid, 50 mL of 0.5% HF. 400×. Courtesy of R. Boyer. (b) Same as (a), but amount of α + β finish forging is 2%. Micrograph illustrates darkened aged beta surrounding a lighter etched beta fleck. See also Fig. 26 Same etch as (a). 50×. Courtesy of T. Long

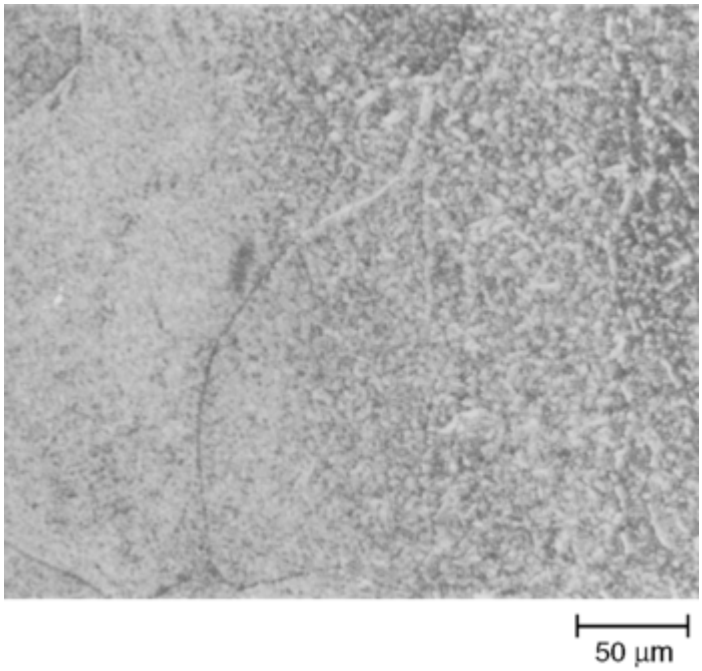

Fig. 26 Same as Fig. 25(b), but at higher magnification to demonstrate the reduced amount of alpha in the beta fleck. The alpha observed (light) is primary alpha; the alpha that forms upon aging is too fine to resolve. Same etch as Fig. 25(a). 200×. Courtesy of T. Long

Tree rings (Fig. 27) are another macrostructural anomaly observed in titanium alloy macrosections. This phenomenon represents very minor composition variations that occur during melting. The appearance of tree rings is normally only a cosmetic nuance, not a cause for concern.

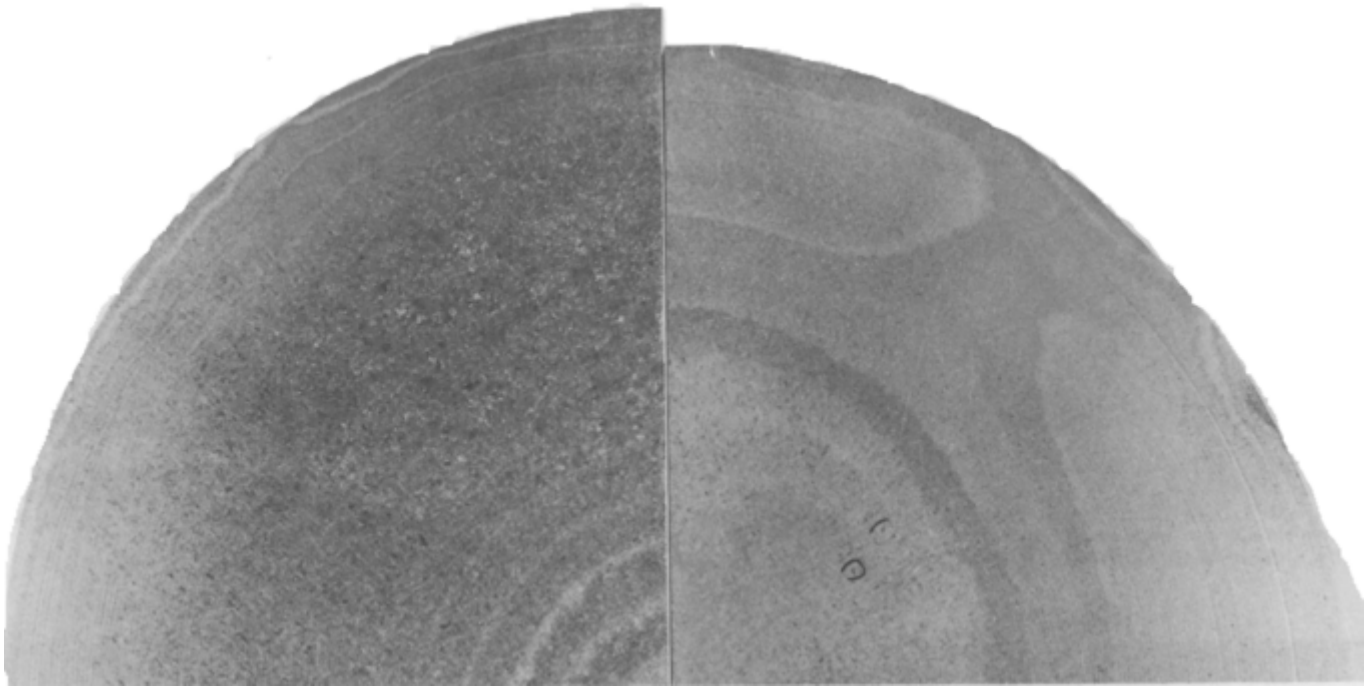

Fig. 27 Ti-6Al-2Sn-4Zr-2Mo alpha-beta forged billet macroslice illustrating "tree rings," which represent minor compositional fluctuations. The slices are from two ingot locations. Etchant unknown. 0.63×. Courtesy of W. Reinsch

Grain flow of forgings is useful for evaluating the forging process. For high-quality forgings, in general, the grain flow should conform to the general shape of the part. There should be no forging laps, seams, or areas of grain flow that appear as though they could produce forging laps in subsequent operations. In addition, the part should be uniformly recrystallized and sufficiently worked in all areas.

L.M. Gammon, R.D. Briggs, J.M. Packard, K.W. Batson, R. Boyer, C.W. Domby, Metallography and Microstructures of Titanium and Its Alloys, *Metallography and Microstructures*, Vol 9, *ASM Handbook*, ASM International, 2004, p. 899–917

Metallography and Microstructures of Titanium and Its Alloys

Luther M. Gammon, Robert D. Briggs, John M. Packard, Kurt W. Batson, Rodney Boyer, and Charles W. Domby, The Boeing Company

Microexamination

Bright-field illumination reveals microstructure of properly prepared specimens in most cases, but image enhancement can be achieved in nearly all cases by using just the polarizer (plane-polarized light) or using the analyzer for slightly uncrossed polarized light. This also acts as a neutral density filter for capturing the digital image. High-quality, strain-free objectives are desirable for any polarized light microscopy, while non-strain-free objectives or objectives with a long working distance will compromise the polarized light image. Figure 28 provides comparative micrographs from the examination of a Ti-6Al-4V specimen with different illumination modes.

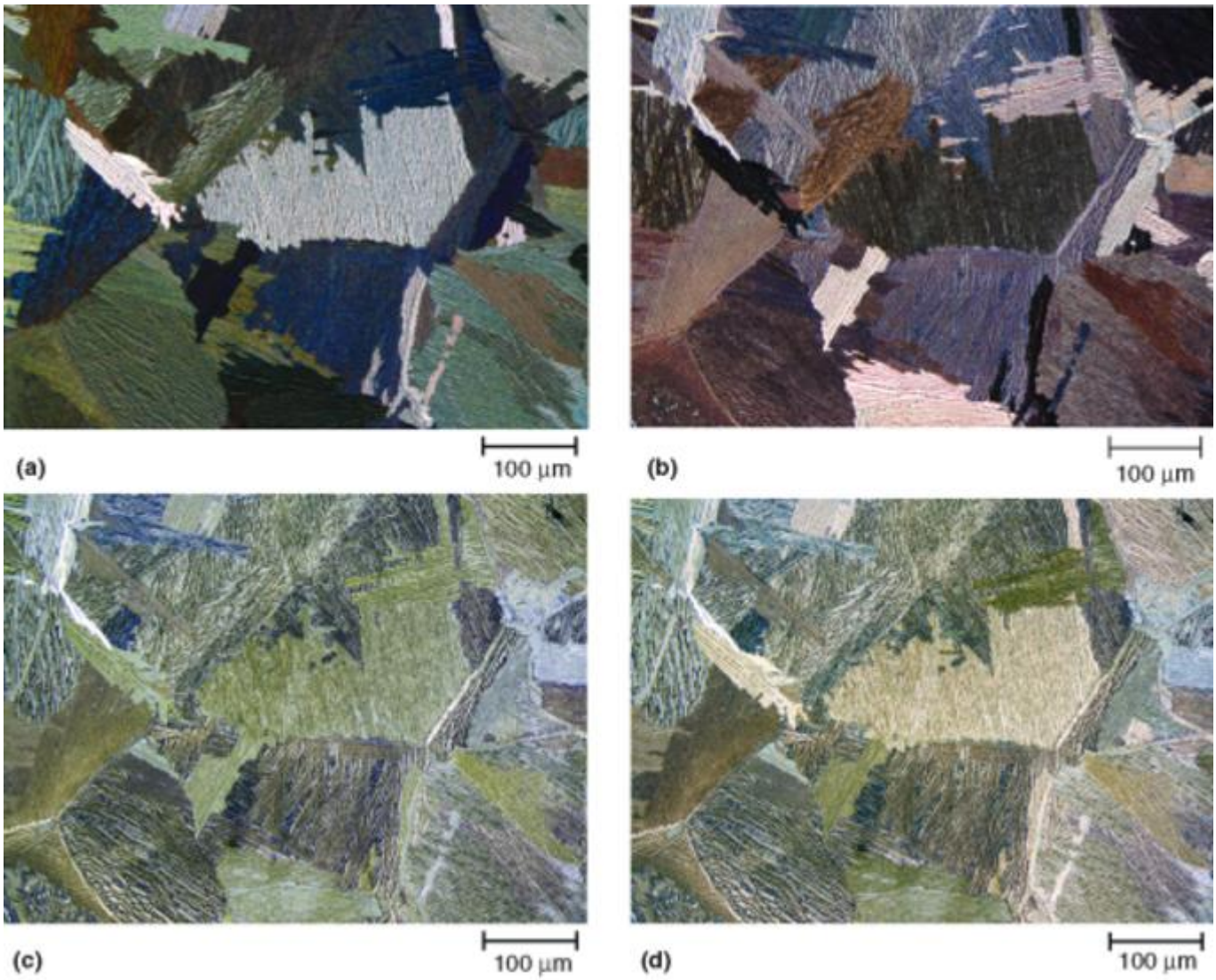

Fig. 28 Variation in appearance with changes in illumination of a Ti-6Al-4V specimen with oxalic tint etch (15 s). Material was beta annealed at 1050 °C (1925 °F) and furnace cooled. (a) Illuminated and examined with slightly uncrossed (45–129) polarized light. (b) Illuminated and examined with slightly uncrossed (45–139) polarized light. (c) Plane-polarized light illumination. (d) Bright-field illumination.

Alpha Structures

Generally, two types of alpha are present: primary alpha and secondary alpha or transformed beta (Fig. 29, 30). The primary alpha is that present during prior hot working, remnants of which persist through heat treatment. The secondary alpha is produced by transformation from beta. This may occur upon cooling from above the beta transus (Fig. 29d) or high within the alpha-beta phase field (Fig. 29b and c) by aging or by aging of the beta (Fig. 30d). The aged alpha is usually too fine to resolve using light (optical) microscopy. The alpha in these areas has different appearances and may be acicular or lamellar, platelike, serrated, or Widmanstätten.

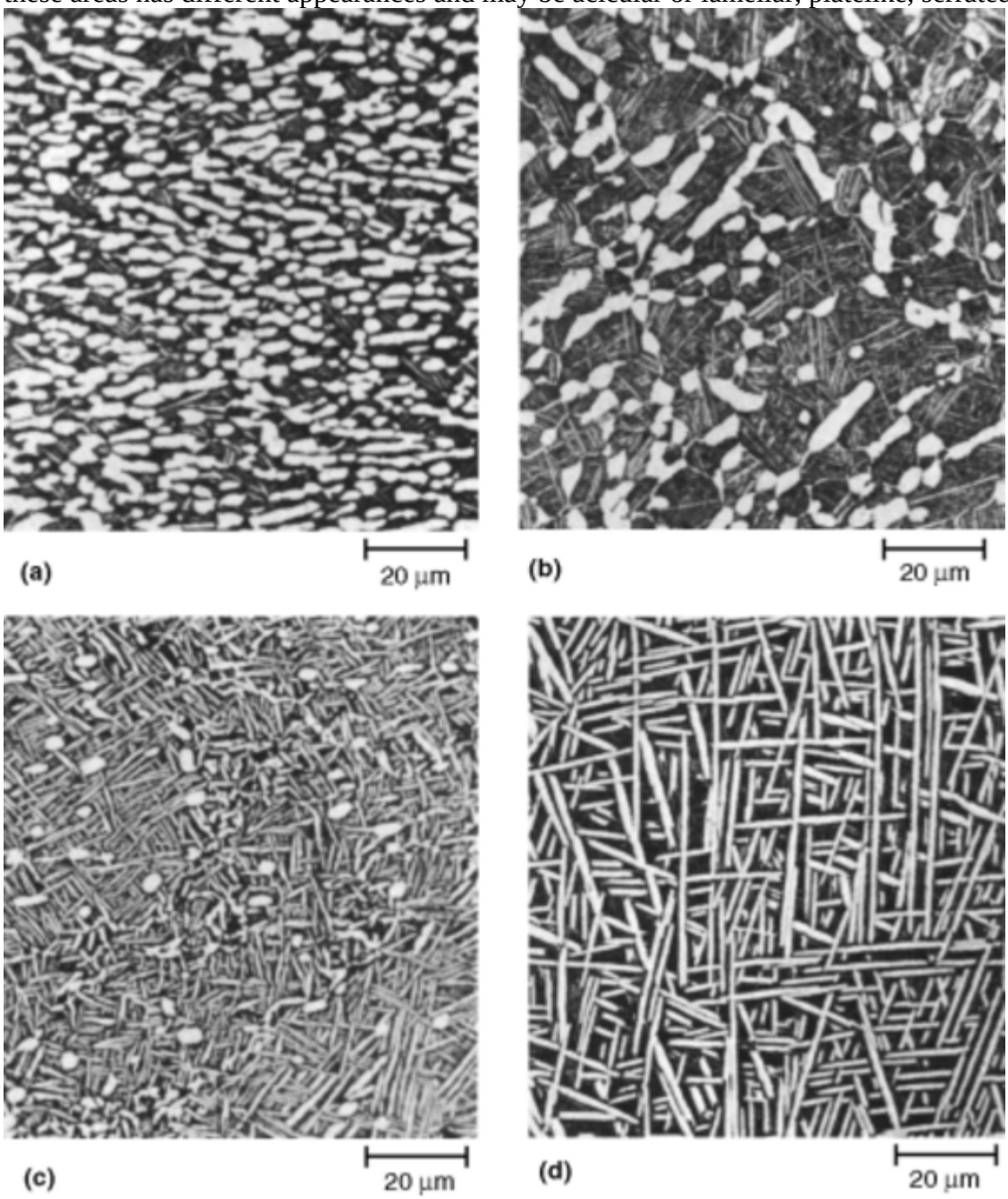

Fig. 29 Ti-6Al-2Sn-4Zr-6Mo, forged at 870 °C (1600 °F). (a) Solution treated 2 h at 870 °C (1600 °F), water quenched, and aged 8 h at 595 °C (1100 °F), and air cooled. Elongated "primary" alpha grains (light) in aged transformed beta matrix containing acicular alpha. (b) Solution treated at 915 °C (1675 °F) instead of at 870 °C (1600 °F), which reduced the amount of "primary" alpha grains in the α + β matrix. (c) Solution treated at 930 °C (1710 °F), which reduced the amount of alpha grains and coarsened the acicular alpha in the matrix. (d) Solution treated at 955 °C (1750 °F), which is above the beta transus. The resulting structure is coarse, acicular alpha (light) and aged transformed beta (dark). All etched with Kroll's reagent (ASTM 192). 500×

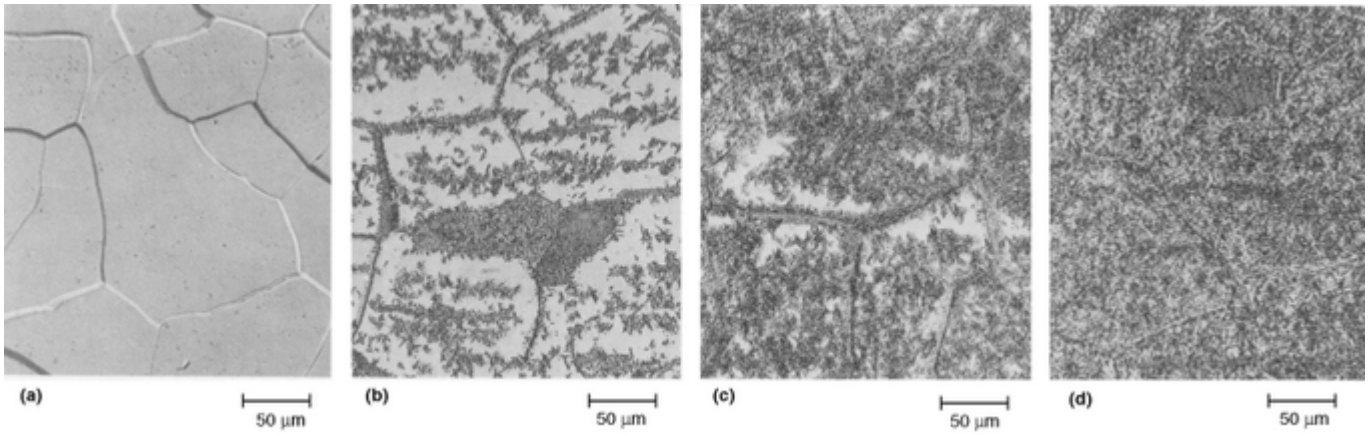

Fig. 30 Ti-15V-3Cr-3Al-3Sn cold-rolled strip that has been annealed at 790 °C (1450 °F) for 10 min and aged at various times to illustrate the progression of aging and what is termed "decorative aging," a technique used to determine the extent of recrystallization. (a) Not aged. (b) Aged 2 h at 540 °C (1000 °F). (c) Aged 4 h. (d) Aged 8 h. Grains in center are completely aged (uniform alpha precipitation throughout the grains). An 8 h age results in a fully aged structure. All etched with Kroll's reagent. All 200×. Courtesy of P. Bania

Equiaxed alpha grains, such as are shown in Fig. 31 and 32 are usually developed by annealing cold-worked alloys above the recrystallization temperature. Elongated alpha grains (Fig. 33, 34) result from unidirectional working of the metal and are commonly found in longitudinal sections of rolled or extruded alloys.

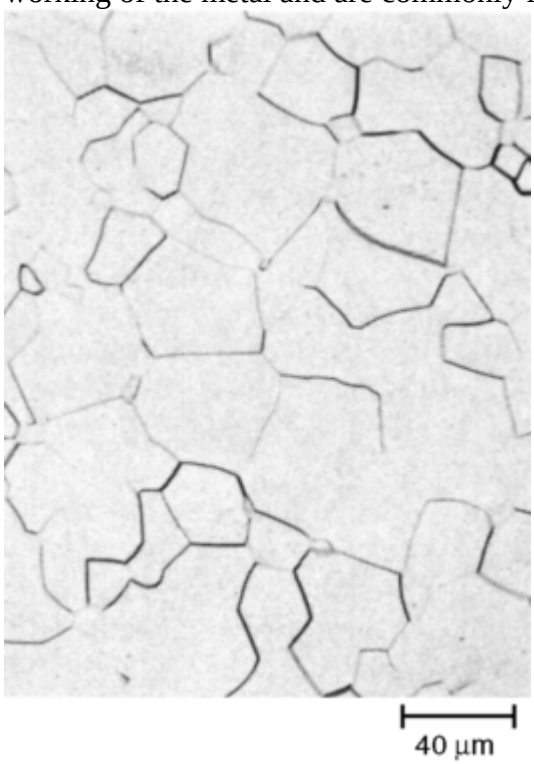

Fig. 31 High-purity (iodide-process) unalloyed titanium sheet, cold rolled, and annealed 1 h at 700 °C (1290 °F). Equiaxed, recrystallized grains of alpha. Etchant: Kroll's reagent (ASTM 192). 250×

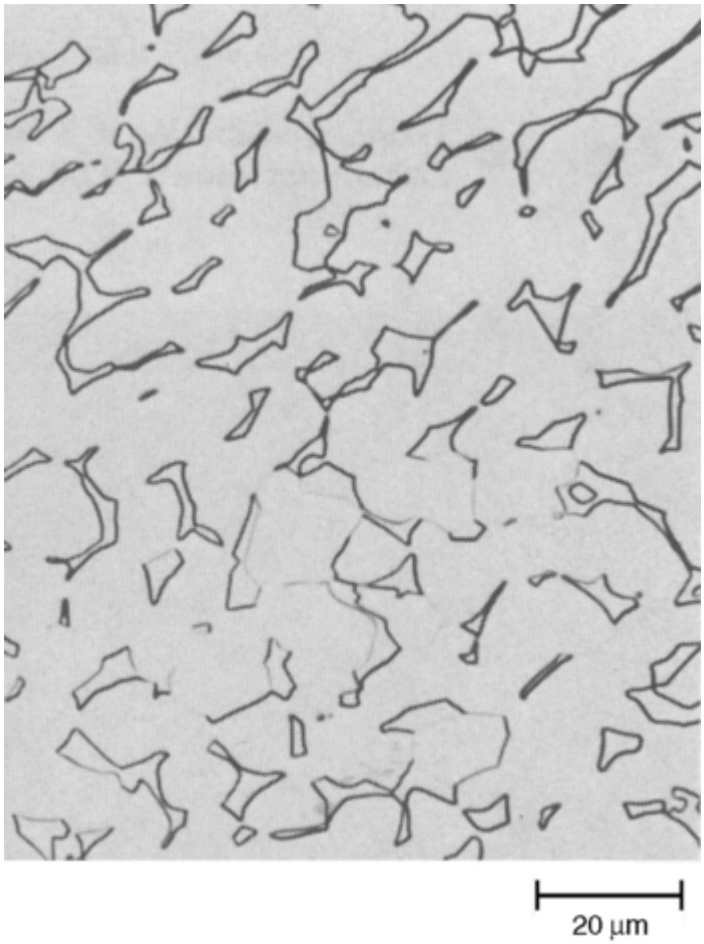

Fig. 32 Ti-6Al-4V plate, recrystallize annealed at 925 °C (1700 °F) 1 h, cooled to 760 °C (1400 °F) at 50 to 55 °C/h (90 to 100 °F/h), then air cooled. Equiaxed alpha with intergranular beta. The alpha-alpha boundaries are not defined. Etchant: 50 mL oxalic acid in H_2O, 50 mL 1% HF in H_2O. 500×. Courtesy of J.C. Chesnutt

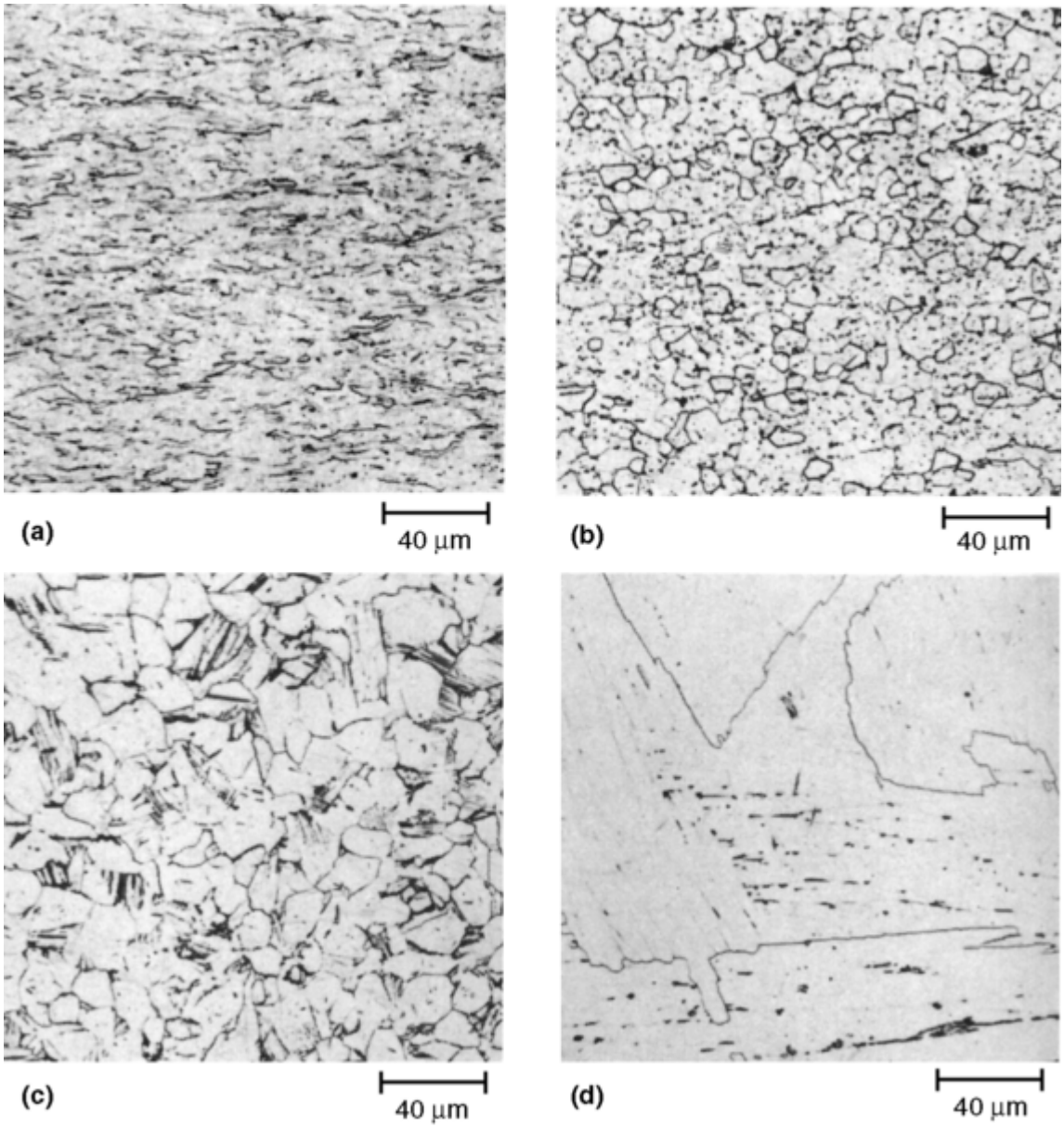

Fig. 33 Commercial-purity (99.0%) unalloyed titanium sheet. (a) As-rolled to 1.0 mm (0.040 in.) thick at 760 °C (1400 °F). Grains of alpha, which have been elongated by cold working. (b) Same as in (a), but annealed 2 h at 700 °C (1290 °F) and air cooled. Recrystallized alpha grains, particles of TiH (black), and particles of beta (also black) stabilized by impurities. (c) Same as in (a), but annealed 1 h at 900 °C (1650 °F)—just below the beta transus—and air cooled. Recrystallized grains of "primary" alpha and transformed beta containing acicular alpha. (d) Same as in (a), but annealed 2 h at 1000 °C (1830 °F) and air cooled. Colonies of serrated alpha plates; particles of TiH and retained beta (both black) between the plates of alpha. All etched with Kroll's reagent (ASTM 192). 250×

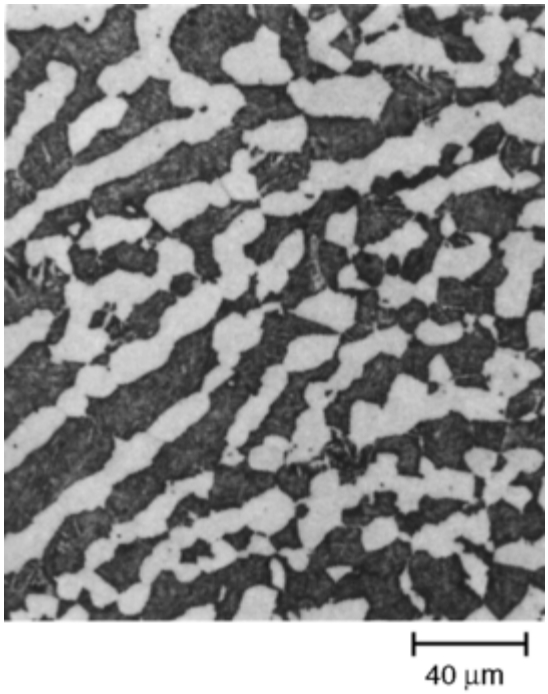

Fig. 34 Ti-6Al-4V, as-forged at 955 °C (1750 °F), below the beta transus. Elongated alpha (light), caused by low reduction (20%) of a billet that had coarse, platelike alpha, in a matrix of transformed beta containing acicular alpha. Etchant: Kroll's reagent (ASTM 192). 250×

The microstructure of titanium alloys is strongly influenced by the processing history and heat treatment. The effect of cooling rate on Ti-5Al-2.5Sn annealed above the beta transus can be seen in Fig. 35. This is also illustrated for Ti-6Al-4V in Fig. 36. As the cooling rate increases, the lamellar alpha (or martensite, depending on the alloy and cooling rate) becomes finer. Coarse and finer lamellar structures in alloy Ti-6Al-4V are also shown, respectively, in Fig. 9 and 28 after furnace cooling from different temperatures above the beta transus. The extent of lamellar alpha in the Ti-10V-2Fe-3Al lean beta alloy is shown in Fig. 37. The structure is completely lamellar alpha (Fig. 37a) when heat treatment is below the beta transus. When heat treated just below the beta transus, a beta structure develops with some residual alpha (Fig. 37b). When heated above the transus and cooled, the structure of Ti-10V-2Fe-3Al is completely beta.

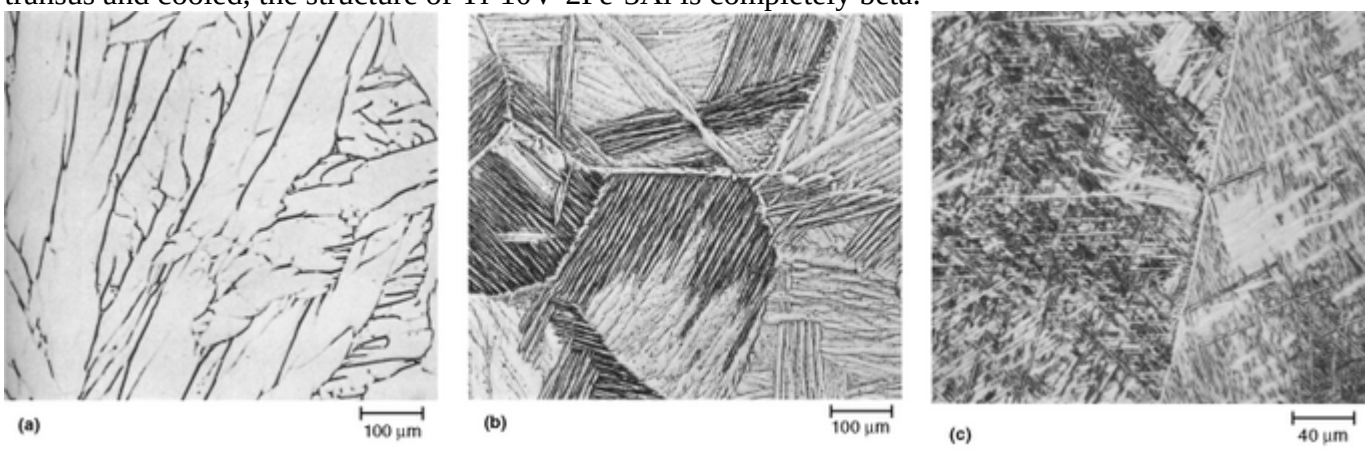

Fig. 35 Ti-5Al-2.5Sn, hot worked below the alpha transus, annealed 30 min at 1175 °C (2150 °F), which is above the beta transus. (a) Furnace cooled to 790 °C (1450 °F) in 6 h, and furnace cooled to room temperature in 2 h. Coarse, platelike alpha. Etchant: Kroll's reagent (ASTM 192). 100×. (b) Air cooled from the annealing temperature instead of furnace cooled. The faster cooling rate produced acicular alpha that is finer than the platelike alpha in (a). Prior beta grains are outlined by the alpha that was first to transform. Etchant: Kroll's reagent (ASTM 192). 100×. (c) Water quenched from the annealing temperature instead of furnace cooled and shown at a higher magnification. The rapid cooling produced fine acicular alpha. A prior beta grain boundary can be seen near the center of the micrograph. Etchant: Kroll's reagent (ASTM 192). 250×

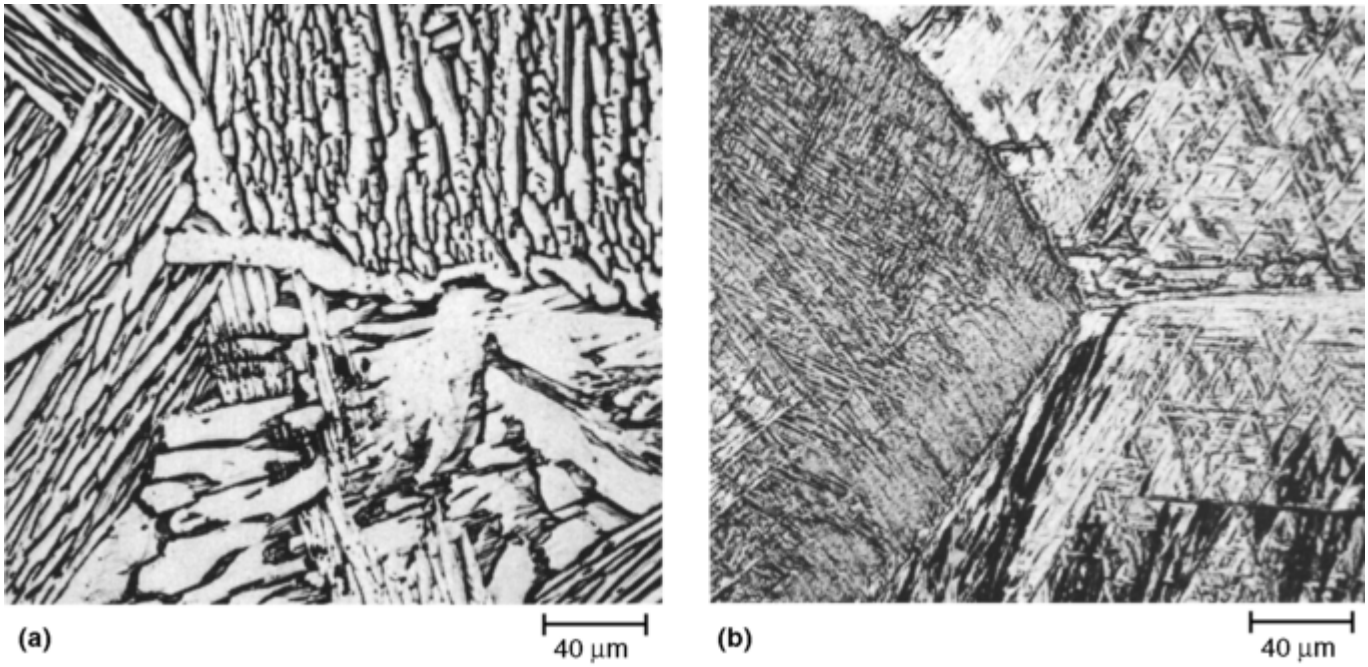

Fig. 36 Ti-6Al-4V bar, held for 1 h at 1065 °C (1950 °F), above the beta transus. (a) Furnace cooled. Platelike alpha (light) and intergranular beta (dark). (b) Air cooled. The structure consists of acicular alpha (transformed beta); prior beta grain boundaries. Etchant for both (a) and (b): 10 mL HF, 5 mL HNO_3, 85 mL H_2O. 250×

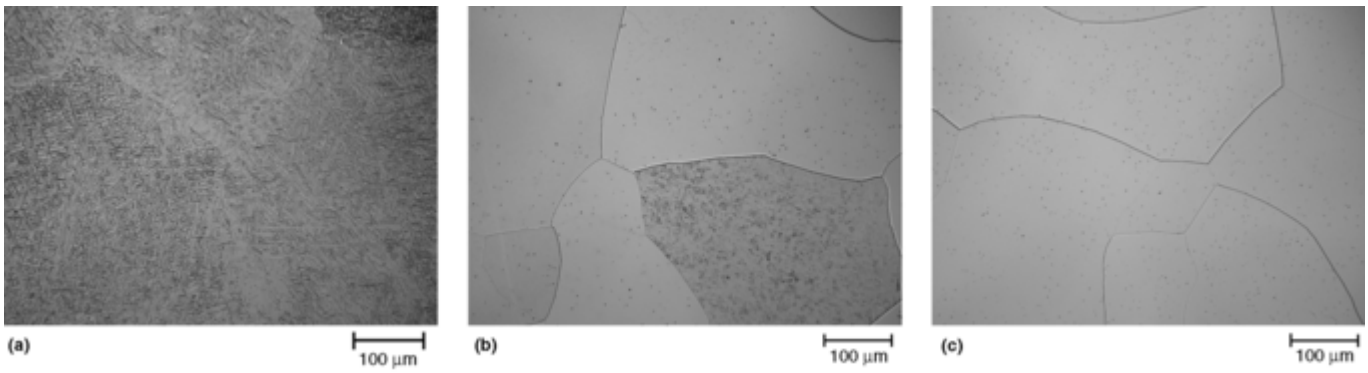

Fig. 37 Effect of heat treatment temperature below, near, and above the transus temperature on etched appearance of lean beta alloy Ti-10V-2Fe-3Al. All specimens were polished with four-step procedure ending up with 16 h on vibratory polisher (10% alumina slurry), etched with Kroll's reagent for duration noted, and examined under slightly uncrossed polarized light (a) lamellar alpha after air cool (AC) from temperature about 70 °C (130 °F) below beta transus (730 °C, or 1350 °F, for 2 h). (b) Heat treated just below the beta transus (788 °C, or 1450 °F, for 2 h, AC), where almost all of the alpha has gone back into solution. One grain in this view contains residual alpha. (c) All-beta structure from beta heat treatment. Duration of etching with Kroll's reagent: (a) 15 s, (b) and (c) 60 s

The effect of forging temperature is illustrated for Ti-8Al-1Mo-1V in Fig. 38. As the forging temperature increases, the amount of transformed beta increases until the forging temperature is above the beta transus, at which point the structure is 100% transformed beta. The effect of the amount of forging deformation is illustrated for Ti-6Al-2Sn-4Zr-2Mo and Ti-5Al-6Sn-2Zr-1Mo-2.5Si, respectively in Fig. 39 and 40. Sufficient working of the cast Widmanstätten structure at a temperature below the beta transus causes recrystallization of the lamellar structure to a more equiaxed structure. Sufficient working and proper heat treatment can produce a completely equiaxed crystal structure (Fig. 32). The microstructural behavior trends will be similar for all-alpha and $\alpha + \beta$ alloys.

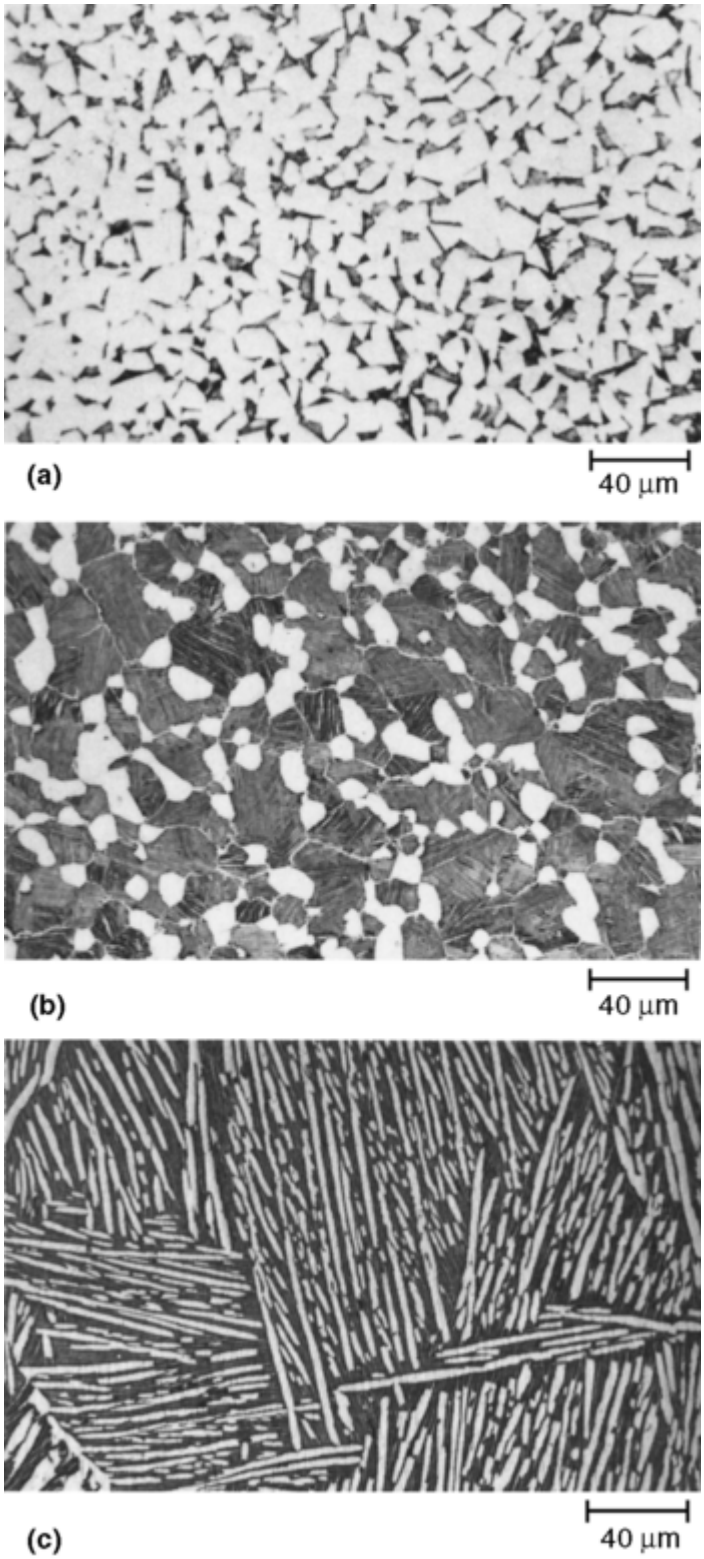

Fig. 38 Ti-8Al-1Mo-1V forging. (a) Forged with a starting temperature of 900 °C (1650 °F), which is below the normal temperature range for forging this alloy. Structure: equiaxed alpha grains (light) in a matrix of transformed beta (dark). (b) Forged with starting temperature of 1005 °C (1840 °F), which is within the normal range, and air cooled. Equiaxed grains of "primary" alpha (light) in a matrix of transformed beta (dark) containing fine acicular alpha. (c) Starting temperature for forging was 1095 °C (2000 °F), which is above the beta transus temperature, and the finished forging was rapidly air cooled. The structure consists of transformed beta containing coarse and fine acicular alpha (light). All etched with Kroll's reagent (ASTM 192). 250×

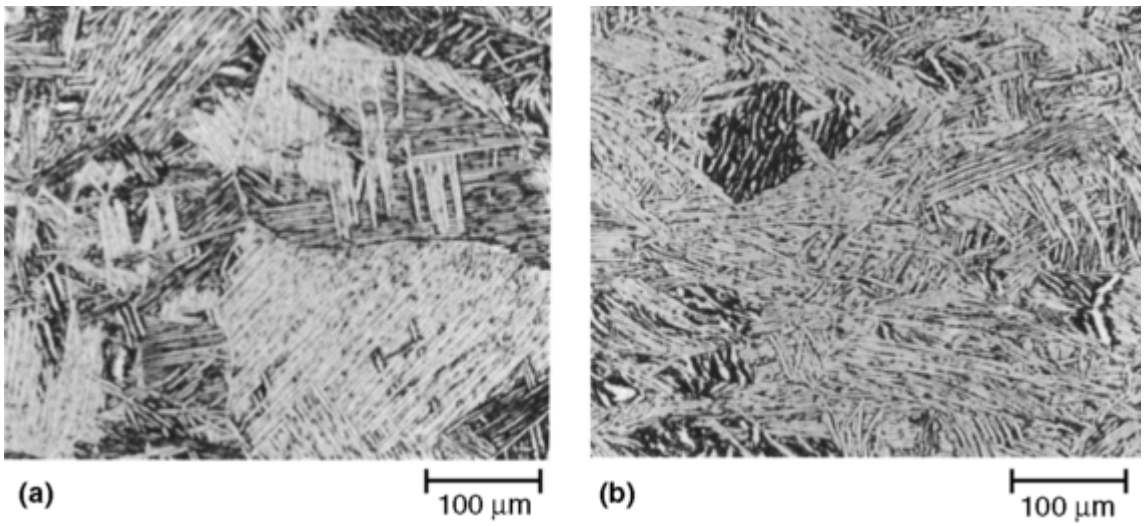

Fig. 39 Ti-6Al-2Sn-4Zr-2Mo forged ingot. (a) Forged and held 1 h at 1010 °C (1850 °F), air cooled, heated to 970 °C (1775 °F), and immediately air cooled. Acicular alpha (transformed beta); prior beta grain boundaries. (b) Same as (a), but reduced 15% by upset forging while at 970 °C (1775 °F). The structure consists of slightly deformed acicular alpha (transformed beta), boundaries of elongated prior beta grains. Both etched with Kroll's reagent (ASTM 192). 100×

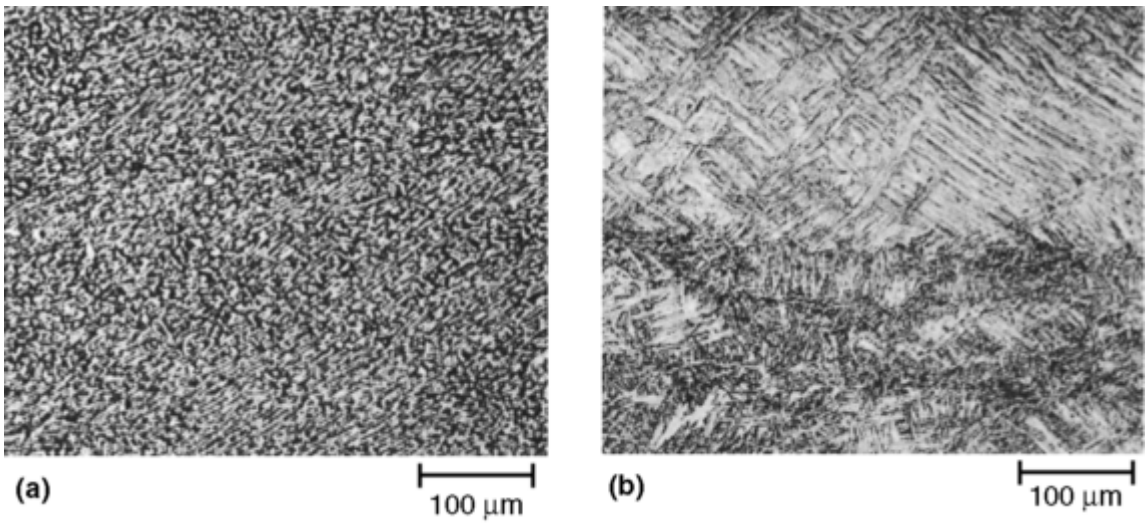

Fig. 40 Ti-5Al-6Sn-2Zr-1Mo-2.5Si forging. (a) Reduced 75% by upset forging starting at 980 °C (1800 °F), annealed 1 h at 980 °C (1800 °F), air cooled, and stabilized 2 h at 595 °C (1100 °F). Fine alpha grains (light); intergranular beta. (b) Same as (a), except upset forged starting at 1150 °C (2100 °F), which is above the beta transus temperature. Distorted acicular alpha (light constituent); intergranular beta; and boundaries of elongated prior beta grains. Both etched with HF, HNO_3, HCl, glycerol (ASTM 193). 100×

Acicular or lamellar alpha is the most common transformation product formed from beta during cooling. It is a result of nucleation and growth on crystallographic planes of the prior beta matrix. Precipitation normally occurs on multiple variants or orientations of this family of habit planes, as illustrated in Fig. 29(d) and 41. A packet or cluster of acicular alpha grains aligned in the same orientation is referred to as a “colony.” When correlating this type of microstructure with properties such as fatigue or fracture toughness, colony size is often regarded as an important microstructural feature. The multiple orientations of alpha have a basketweave appearance characteristic of alpha Widmanstätten structure. Lamellar alpha forming from small beta grains also may have a singular orientation (Fig. 42).

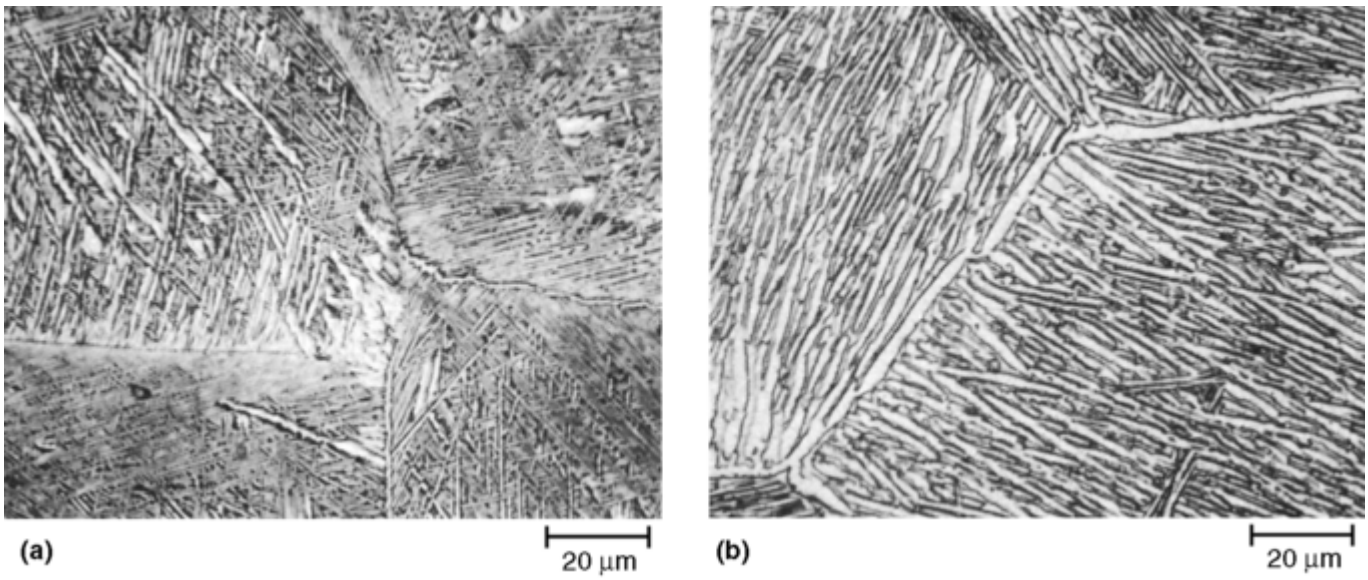

Fig. 41 Ti-6Al-5Zr-4Mo-1Cu-O.2Si casting. (a) As-cast. Microstructure: transformed beta containing acicular alpha (light platelets). A thin film of alpha phase (light) is evident at the prior beta grain boundaries. (b) Same as (a), but solution treated 1 h in argon at 845 °C (1550 °F), air cooled, and aged 24 h at 500 °C (930 °F). Acicular alpha (light) and aged beta; alpha platelets at prior beta grain boundaries. Both etched with 10 mL HF, 30 mL HNO_3, 50 mL H_2O (ASTM 187). 500×

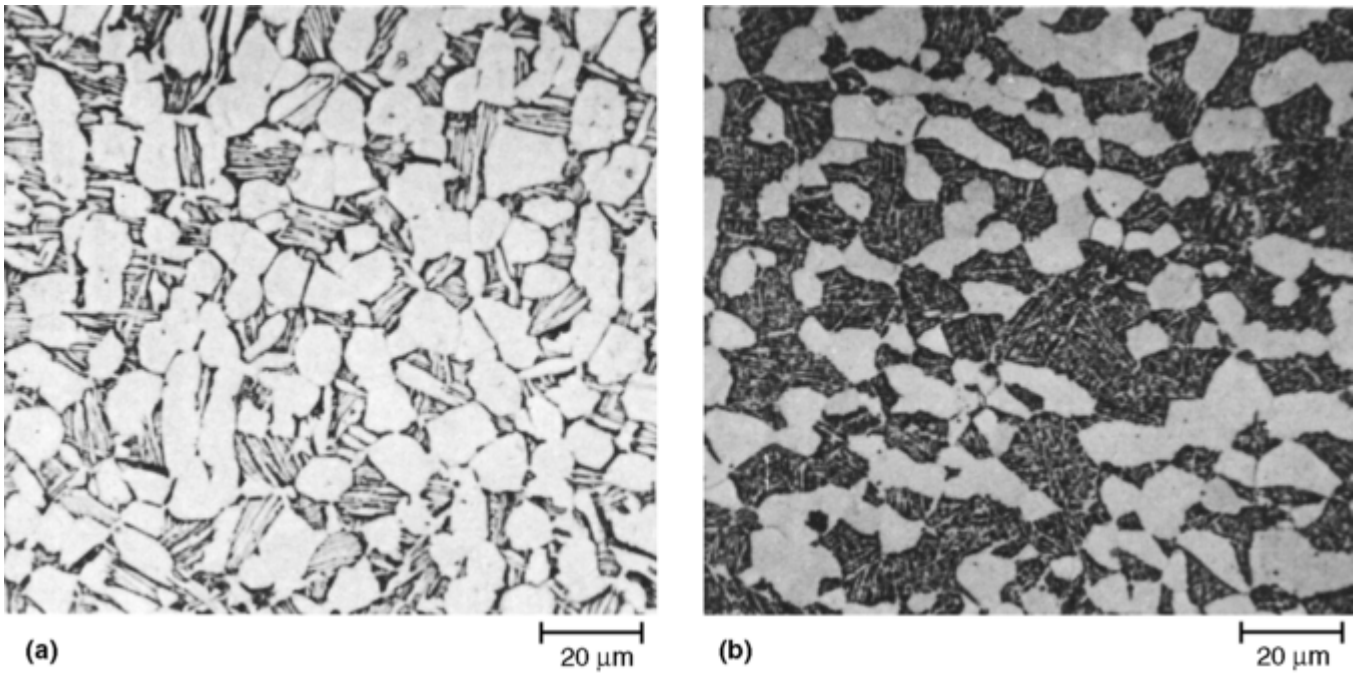

Fig. 42 Ti-6Al-4V forging. (a) Solution treated 1 h at 955 °C (1750 °F), air cooled, and annealed 2 h at 705 °C (1300 °F). Equiaxed alpha grains (light) in transformed beta matrix (dark) containing coarse, acicular alpha. (b) Same as in (a), except water quenched from the solution treatment (before the anneal) instead of air cooled. Structure is similar to that in (a), but the faster cooling resulted in finer acicular alpha in the transformed beta. Both etched with Kroll's reagent (ASTM 192). 500×

Under some conditions, the long grains of alpha produced along preferred planes in the beta matrix take on a wide, platelike appearance, as shown in Fig. 35(a). Under other conditions, grains of irregular size and with jagged boundaries, called “serrated alpha,” are produced (Fig. 43).

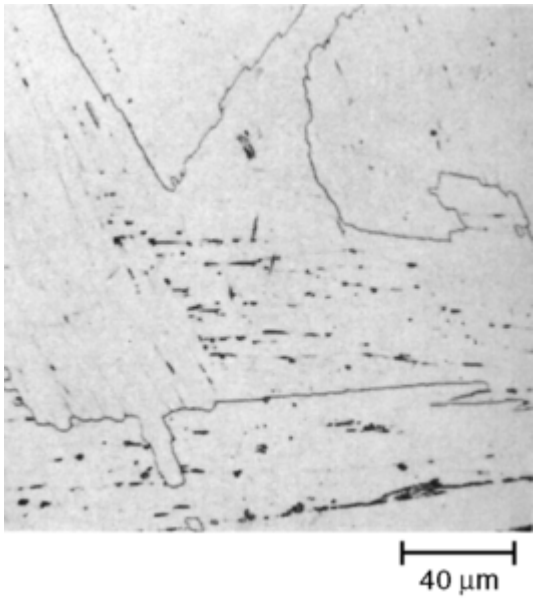

Fig. 43 Unalloyed titanium sheet. Same as Fig. 33 but annealed 2 h at 1000 °C (1830 °F) and air cooled. Colonies of serrated alpha plates; particles of TiH and retained beta (both black) between the plates of alpha. Etchant: Kroll's reagent (ASTM 192). 250×

Alpha Case. Unless heat treatments are performed in an inert atmosphere, oxygen and nitrogen will be absorbed at the surface, stabilize the alpha, and form a hard, brittle layer referred to as an “alpha case” (Fig. 44, 45). This case is normally removed by chemical milling or machining. A part should not be put into service unless this alpha case has been removed.

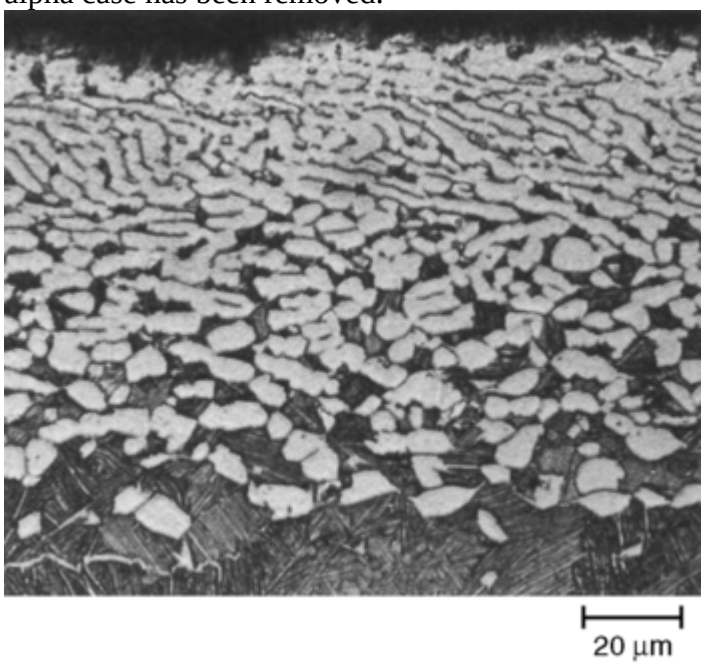

Fig. 44 Ti-7Al-2Mo-1V plate, heated to 1010 °C (1850 °F), which is above the beta transus. Surface layer of white, oxygen-stabilized alpha (alpha case); the remainder of the structure is acicular alpha (transformed beta). Etchant: 2 mL HF, 8 mL HNO_3, 90 mL H_2O. 450×

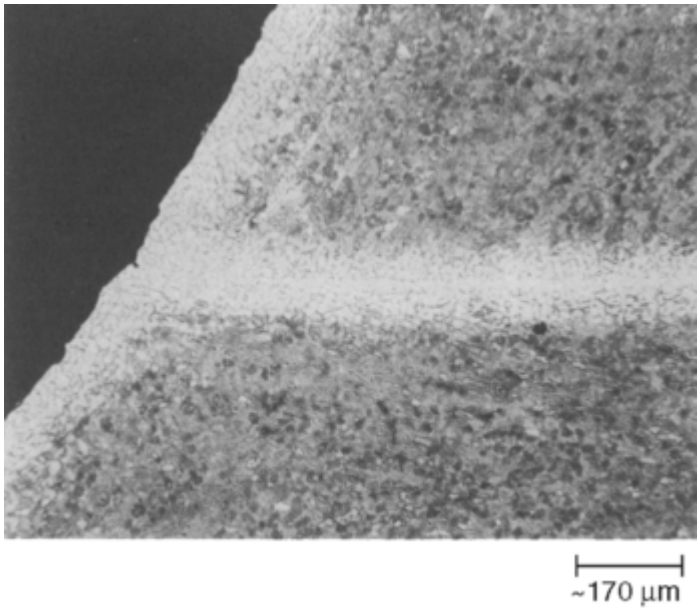

Fig. 45 Ti-6Al-4V plate diffusion-bonded joint (bonded at 925 °C, or 1700 °F) illustrating bond-line contamination. The white horizontal band is an area of O_2 and/or N_2 enrichment. An alpha case is also observable on the exterior surface. Etchant: 50 mL H_2O, 50 mL 10% oxalic acid, 1 mL HF. 58×. Courtesy of J.C. Chesnutt

Figure 46, 47, 48, 49, 50 show alpha case layers caused by interstitial oxygen migration through the surface. This illustrates the increase in alpha case thickness as the thermal exposure is increased with longer times or higher temperatures. The oxygen migration causes an increase in hardness beyond the visible depth of the alpha case layer.

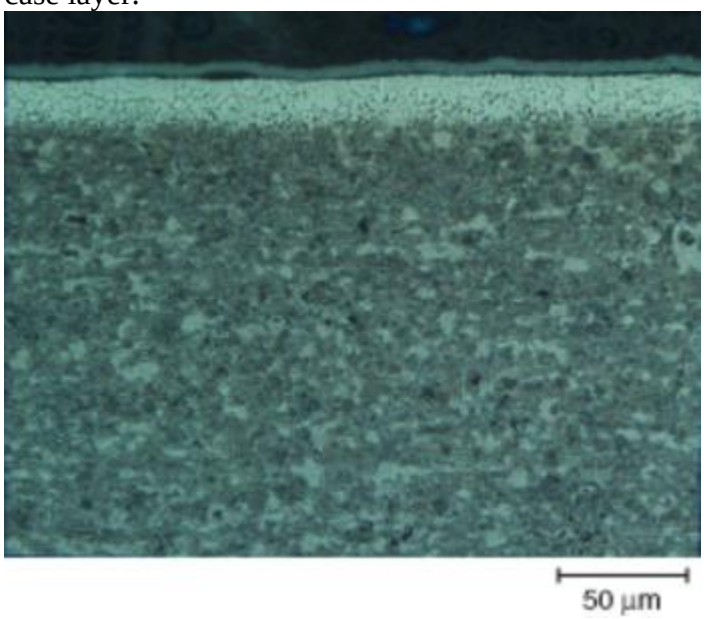

Fig. 46 Alpha case in Ti-6Al-4V after exposure to 760 °C (1400 °F) for 90 min. Preparation: oxalic tint etch for 60 s, and four-step edge-retention process ending with 1 h on vibratory polisher with a non-nap polyester cloth and alumina.

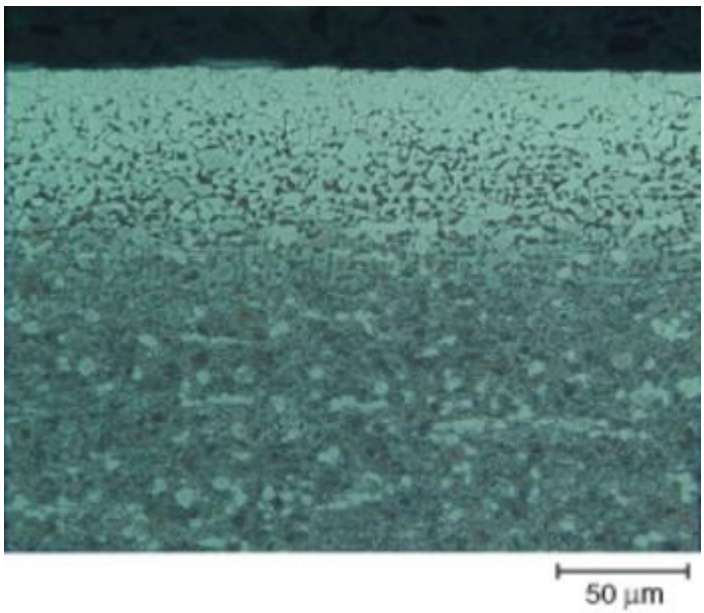

Fig. 47 Alpha case in Ti-6Al-4V after exposure to 885 °C (1625 °F) for 90 min. Preparation: ammonium bifluoride tint etch for 60 s and four-step edge-retention process, ending with 1 h on vibratory polisher with a non-nap polyester cloth and alumina.

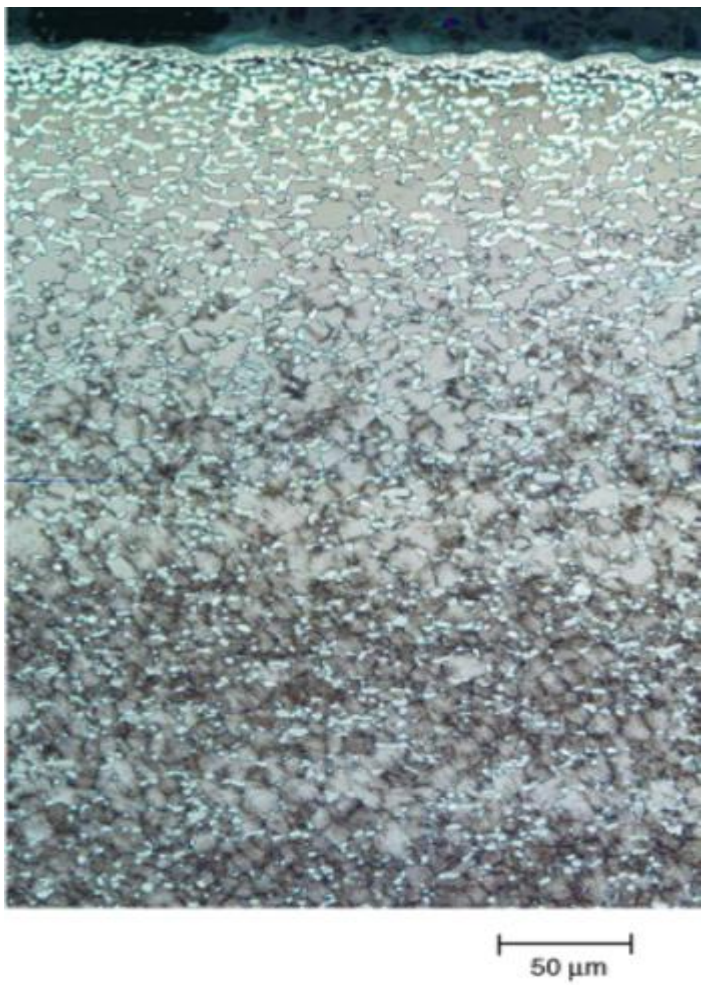

Fig. 48 Alpha case in Ti-SP 700 (Ti-4.5Al-3V-2Mo-2Fe) after exposure to 900 °C (1650 °F) for 90 min. Preparation: ammonium bifluoride tint etch for 60 s and four-step edge-retention process, ending with 1 h on vibratory polisher with a nonnap polyester cloth and alumina.

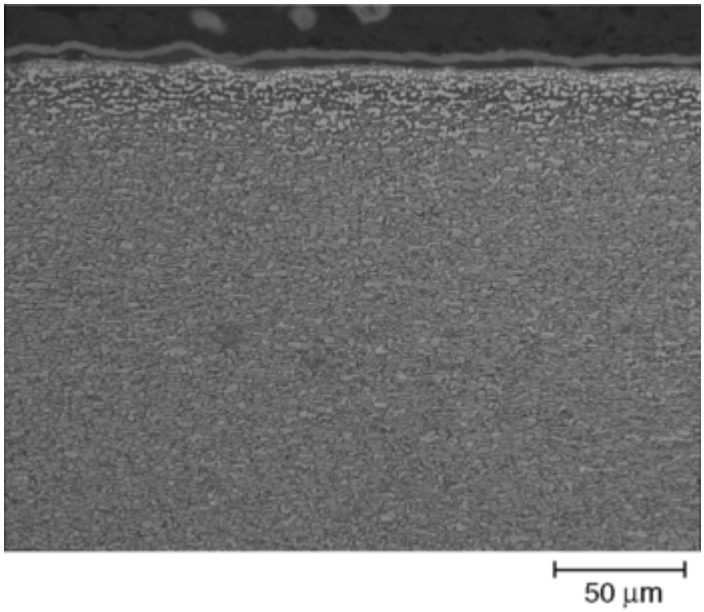

Fig. 49 Alpha case in Ti-SP 700 after exposure to 760 °C (1400 °F) for 90 min. Preparation: ammonium bifluoride tint etch for 60 s, and four-step edge-retention process ending with 1 h on vibratory polisher with a non-nap polyester cloth and alumina

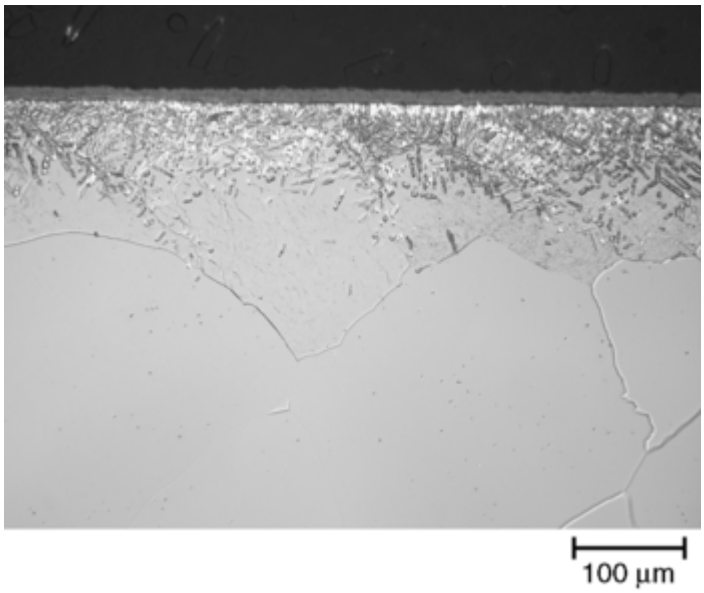

Fig. 50 Alpha case in Ti-10V-2Fe-3Al after exposure to 790 °C (1450 °F) for 2 h. Preparation: Oxalic tint etch for 60 s, and four-step edge-retention process ending with 1 h on vibratory polisher with a non-nap polyester cloth and alumina

Ti_3Al (Alpha-2) Ordered Phase. The alpha phase can decompose to α + Ti_3Al, an ordered phase, at compositions greater than about 6 wt% Al. This ordered phase is submicron in size and can be observed only by electron microscopy (Fig. 51).

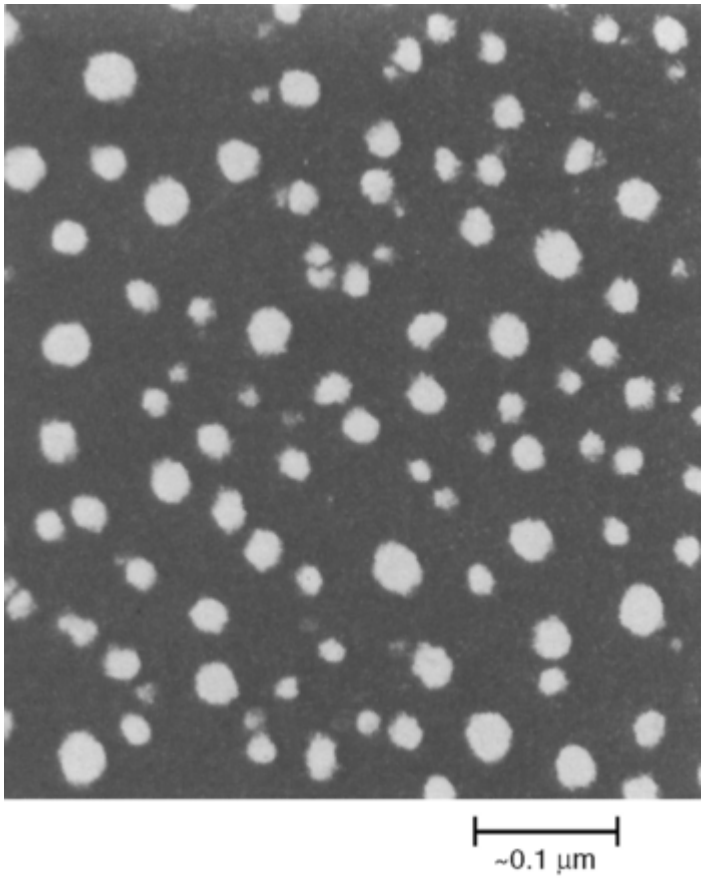

Fig. 51 Ti-8Al (with 1800 ppm O_2) sheet aged to precipitate the ordered alpha-2 (Ti_3Al) phase. The dark-field transmission electron micrograph illustrates α_2 precipitates (light) in an alpha matrix. 105,600×. Courtesy of J.C. Williams

Martensite

Martensite is a nonequilibrium supersaturated alpha-type structure produced by diffusionless (martensitic) transformation of the beta. There are two types of martensite: α′, which has a hexagonal crystal structure, and α″, which has an orthorhombic crystal structure. Martensite can be produced in titanium alloys by quenching (athermal martensite) or by applying external stress (stress-induced martensite). The α″ can be formed athermally or by a stress-assisted transformation (see Fig. 52, 53). However, α′ can be formed only by quenching. Examples of α′ structures are exhibited in Fig. 54 and 55. Aging of the martensite results in its decomposition to α + β.



Fig. 52 Ti-8.5Mo-0.5Si water quenched from 1000 °C (1830 °F). Thin-foil transmission electron micrograph illustrating heavily twinned athermal α″ martensite. 5000×. Courtesy of J.C. Williams

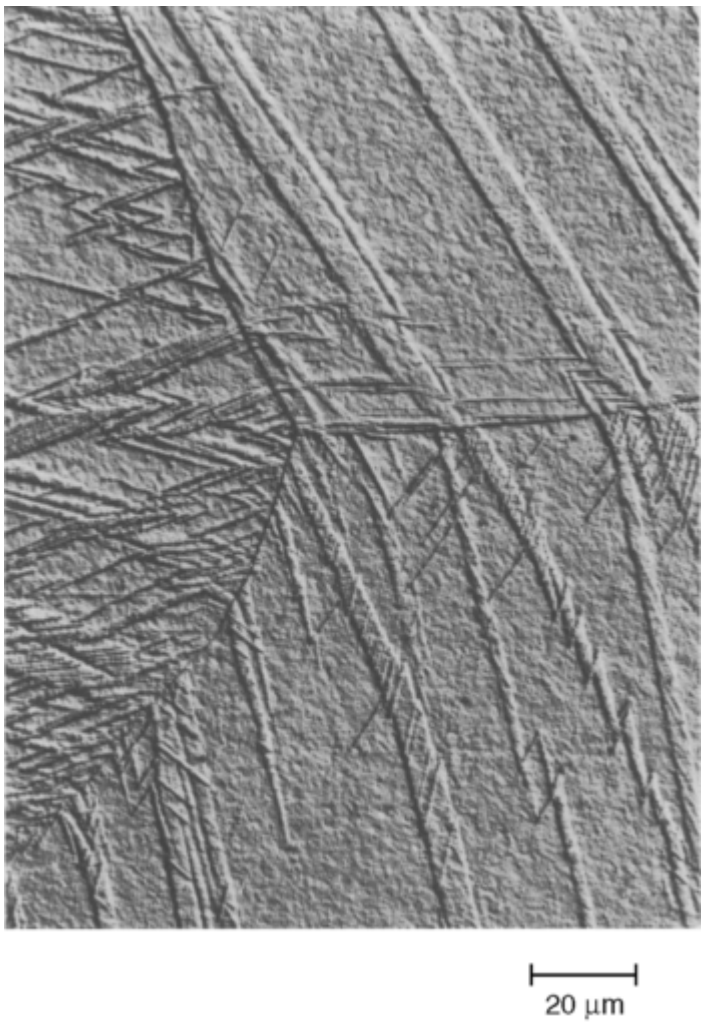

Fig. 53 Ti-10V-2Fe-3Al, beta solution treated, water quenched, and strained 5% at room temperature. This Nomarski interference micrograph illustrates deformation-induced α″ martensite in a beta matrix. No etch. 500×. Courtesy of J.E. Costa

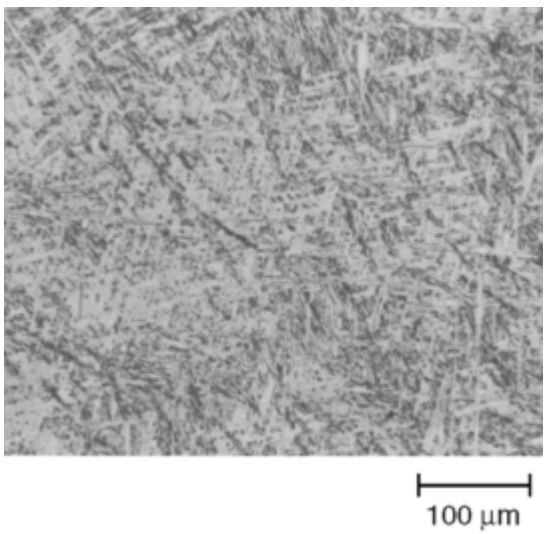

Fig. 54 Ti-6Al-2Sn-4Zr-2Mo forgings, finish forged starting at 970 °C (1775 °F), air cooled, machined to 13 mm (0.5 in.) diam test bars, reheated to 995 °C (1825 °F), the beta transus, held for 1 h, and air cooled. The microstructure is entirely α′. Etched with Kroll's reagent (ASTM 192). 100×

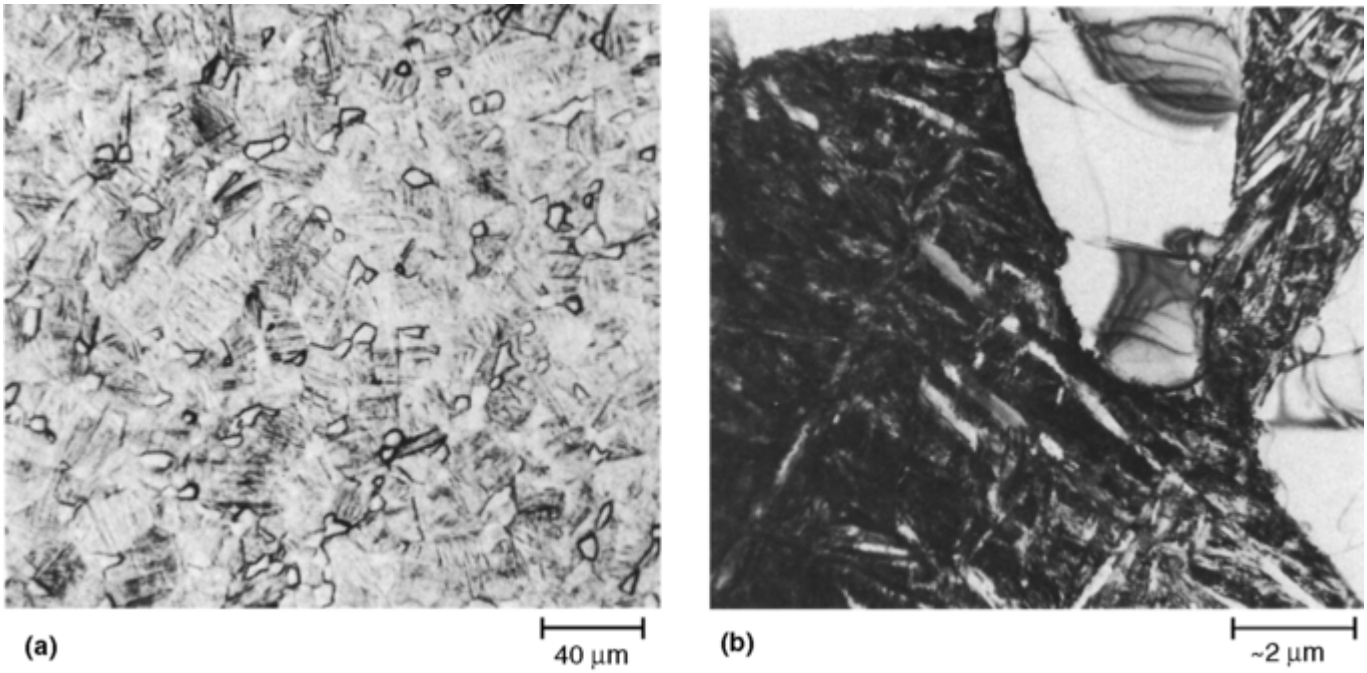

Fig. 55 α′ martensite in Ti-6Al-4V. (a) Light micrograph of bar, held for 1 h at 955 °C (1750 °F), which is below the beta transus, and water quenched. Equiaxed "primary" alpha grains (light) in a matrix of α′ (martensite). Etched with 10 mL HF, 5 mL HNO_3, 85 mL H_2O. 250×. (b) Thin foil transmission electron micrograph of the same microstructure as in (a), but at higher magnification. The large light grains are primary alpha; the darker region is acicular α′ martensite in a beta matrix. 5880×. Courtesy of J.C. Williams

Beta Structures

In alpha-beta and beta alloys, some equilibrium beta is present at room temperature. A nonequilibrium, or metastable, beta phase can be produced in alpha-beta alloys that contain enough beta-stabilizing elements to retain the beta phase at room temperature on rapid cooling from high in the α + β phase field. The composition of the alloy must be such that the temperature for the start of martensite formation is depressed to below room temperature. One hundred percent beta can be retained by air cooling beta alloys. The decomposition of this retained beta (or martensite, if it forms) is the basis for heat treating titanium alloys to higher strengths.

Aged Structures

The alpha that forms upon aging of retained beta is often too fine to be resolved by optical microscopy, particularly with beta and near-beta alloys. Aging of α′ martensite results in the formation of equilibrium α + β, but most aged martensite structures cannot be distinguished from unaged martensite by optical microscopy.
Unresolved alpha precipitation is shown in Fig. 56 for alloy Ti-10V-2Fe-3Al with Kroll's etch. Figure 57 and 58 are light micrographs of cold-rolled and aged Ti-15V-3Cr-3Al-3Sn foil. The white regions indicate there was less or no heat treatment response. Precipitation of alpha during aging of beta results in some darkening of the aged beta structure. The progression of aging response in alloy Ti-15V-3Cr-3Al-3Sn is shown in Fig. 30.

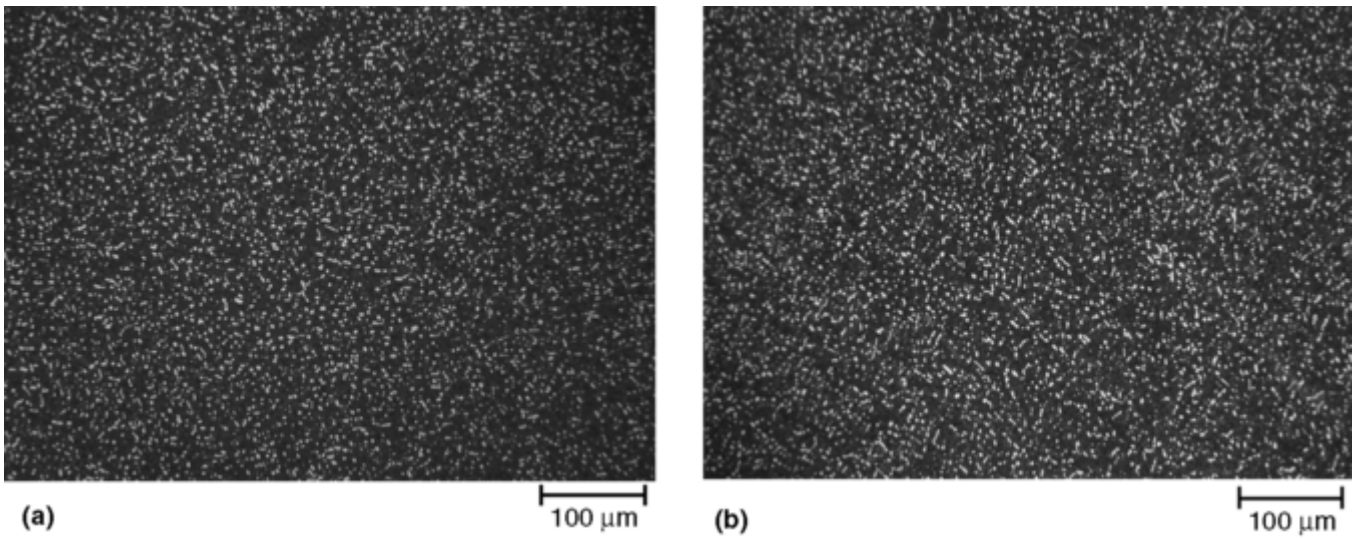

Fig. 56 Fine, unresolved alpha precipitation in light micrograph of aged Ti-10V-2Fe-3Al alloy. The white phase is primary alpha in an aged beta matrix, dark background. Slightly uncrossed polarized light, and a four-step polishing ending up with 16 h on vibratory polisher 10% alumina slurry. Etched with Kroll's reagent for 15 s (a) and 7 s (b)

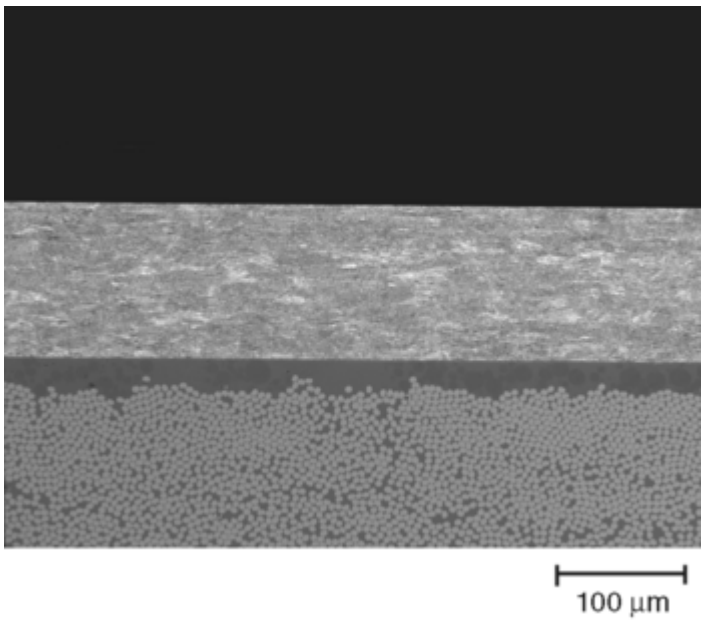

Fig. 57 Structure from cold-rolled and aged foil of beta alloy Ti-15V-3Cr-3Al-3Sn. Oxalic tint etch for 3 s, 1 h vibratory polisher, non-nap polyester cloth and alumina

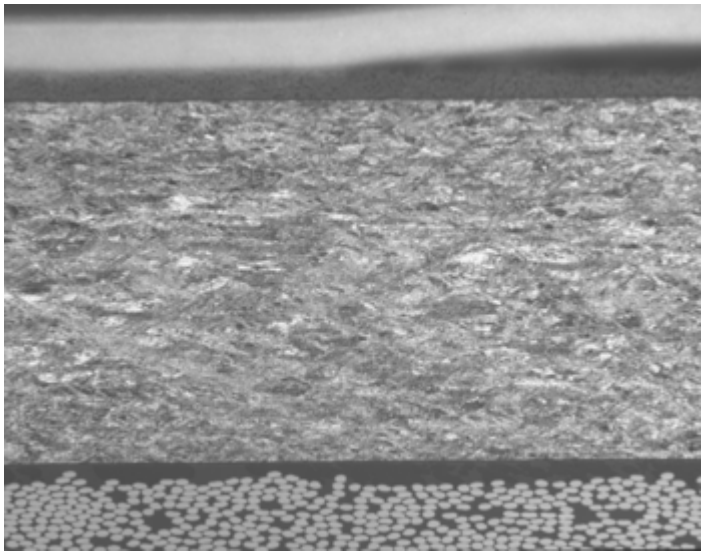

Fig. 58 Structure from cold-rolled and aged foil of beta alloy Ti-15V-3Cr-3Al-3Sn. Oxalic tint etch for 15 s, 1 h vibratory polisher, non-nap polyester cloth and alumina. The white regions indicate there was no or a lesser heat treat response (alpha precipitation).

Other precipitation products include:

- Eutectoid products
- ω phase (Fig. 59), which is a transition phase (potentially resulting in severe embrittlement)
- Phase splitting

Phase splitting, or phase separation only, occurs in the solute-rich beta alloys; $\beta \rightarrow \beta_r + \beta_1$ where β_r is solute-rich beta and β_1 is solute lean beta. The solute lean beta is designated β' (Fig. 60). This is not an important decomposition product from a practical standpoint, because it does not occur in commercial alloys with heat treatments that are used. The ω phase and phase splitting can only be observed using electron microscopy.

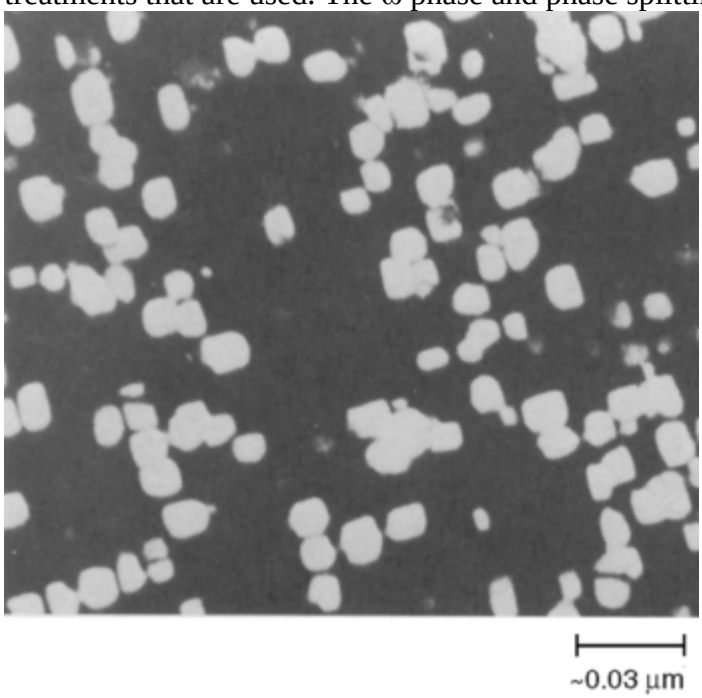

Fig. 59 A titanium-iron binary alloy, beta solution treated, water quenched, and aged to form ω. The ω is the light precipitate in this thin-foil transmission electron micrograph. In alloys where the ω has a high lattice misfit, the ω is cuboidal to minimize elastic strain in the matrix. 320,000×. Courtesy of J.C. Williams

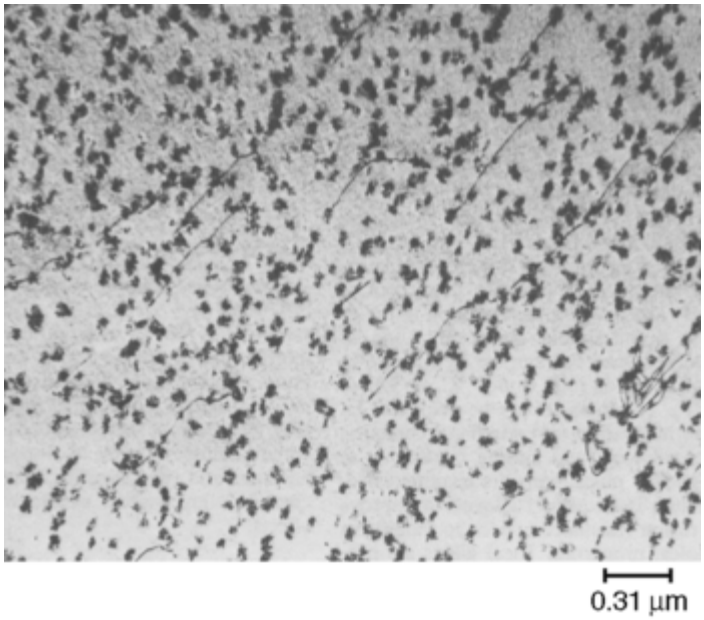

Fig. 60 Ti-40Nb (at.%), beta solution heat treated at 900 °C (1650 °F), water quenched, then aged at 400 °C (750 °F) for 24 h. The dark precipitate is β′ (solute lean beta phase) in a solute-enriched beta matrix. Thin-foil transmission electron micrograph. 31,000×. Courtesy of J.C. Williams

Other Structures

Hydrides. Figure 61 shows hydrides in commercially pure (CP) titanium sheet located at the weld heat-affected zone (HAZ). The black needles in this micrograph are a result of hydrogen migrating to high residual stress areas and forming a titanium hydride. In most cases, because of their brittle nature, hydrides will result in microcracks. Material with this extent of hydrides will be very brittle. Commercially pure titanium is more difficult to polish than more highly alloyed titanium alloys because it is softer and retains more cold work. The same polishing method used for titanium alloys will also work for CP titanium, but longer final polishing times may be needed. Do not use hydrogen peroxide or etch-polish to remove residual cold work induced by previous polishing steps. Etching will mask the hydrides. It is best just to add more time to the last two steps. If hand polishing with a 5 μm alumina and beeswax wheel, it can take 20 min.

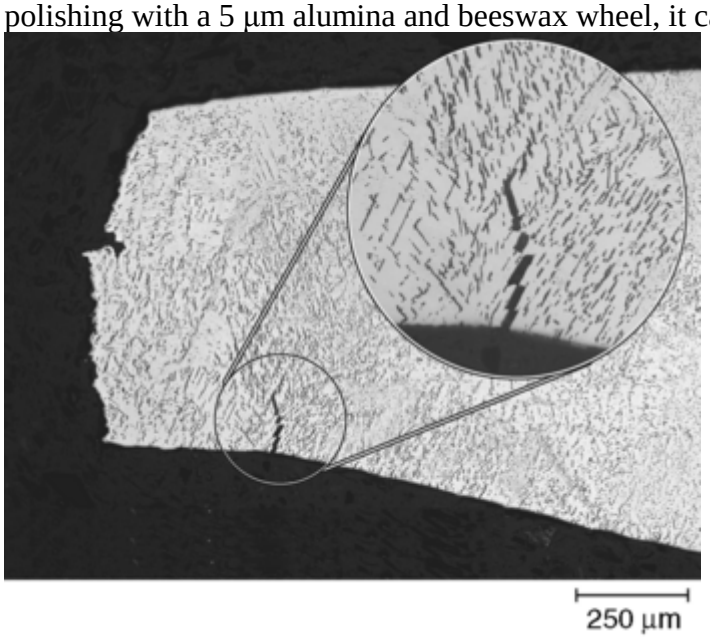

Fig. 61 Ammonium bifluoride tint etch for 10 s. Commercially pure titanium sheet. Four-step polishing ending up with 16 h on vibratory polisher, 10% alumina slurry

Revealing hydrides in CP titanium with an ABF etch (Fig. 61) requires a perfectly polished surface. The lactic hydride reagent (Table 2) may be more easily applied to reveal the presence of hydrides with etching times ranging from $1\frac{1}{2}$ to 3 min. A 3 min etch can provide good contrast to reveal hydrides with a light microscope. An etch of $1\frac{1}{2}$ min may provide subtle contrast under a light microscope, but examination in a scanning electron microscope can easily reveal microcracks associated with hydride cracking.

Heat-Affected Zones. Heat damage from machining, sample excision, or preparation is often confused with alpha case. The difference can be determined by making 10 g Knoop indents since the heat-damaged layer will be softer than the base material but would be harder in an alpha case area. Unlike heat damage from straight thermal exposure (which results in a harder surface), heat damage from mechanical sources during preparation results in a softer surface. In the example of Fig. 62, the layer is softer from heat damage, yielding a larger indent. Another example is shown in Fig. 63 of a heat-affected zone from a molten fine, which had a 50% knockdown factor on fatigue life.

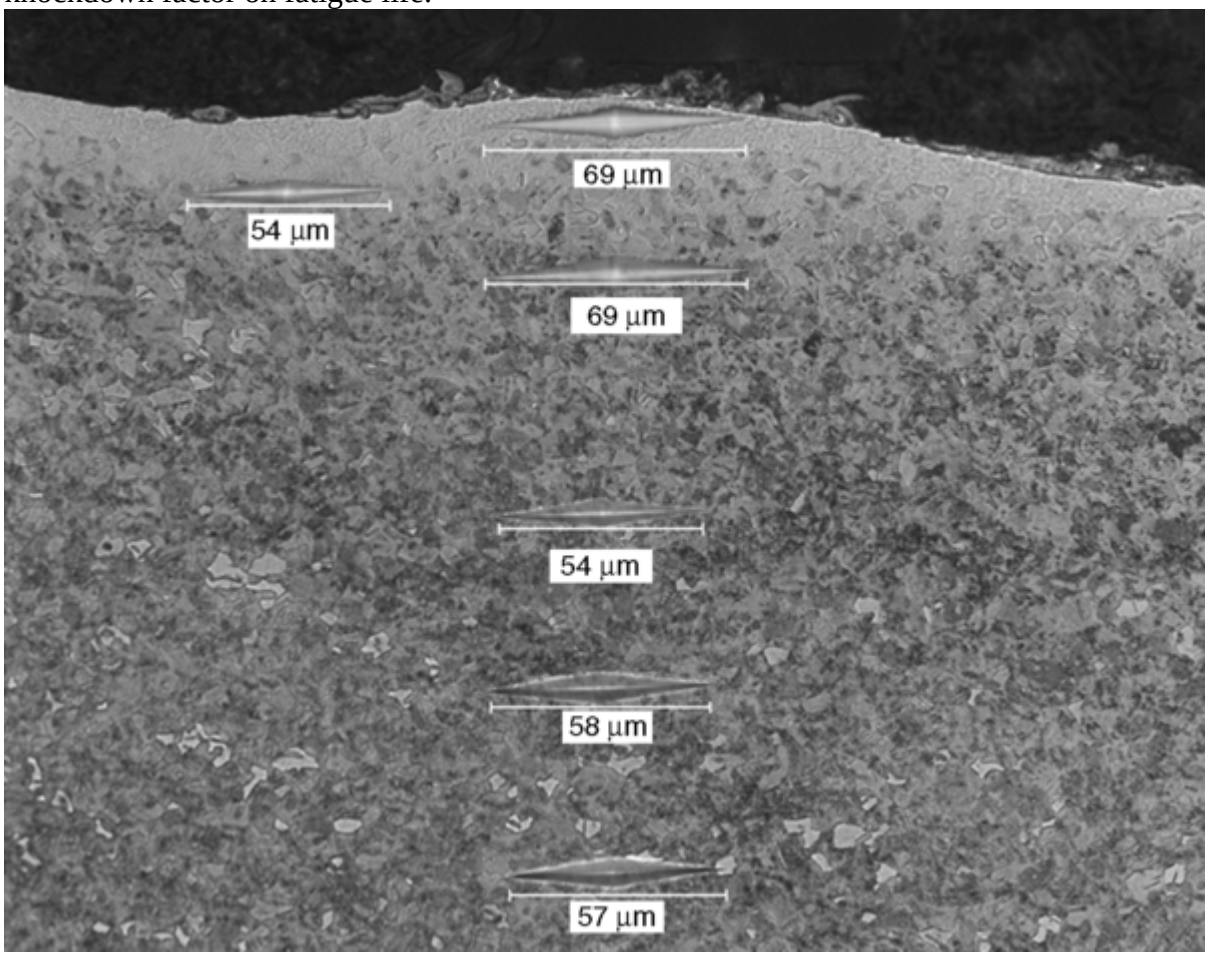

Fig. 62 Ti-6Al-4V heat damage. Oxalic tint etch for 15 s. Four-step edge retention process ending up with 1 h on a vibratory polisher and alumina

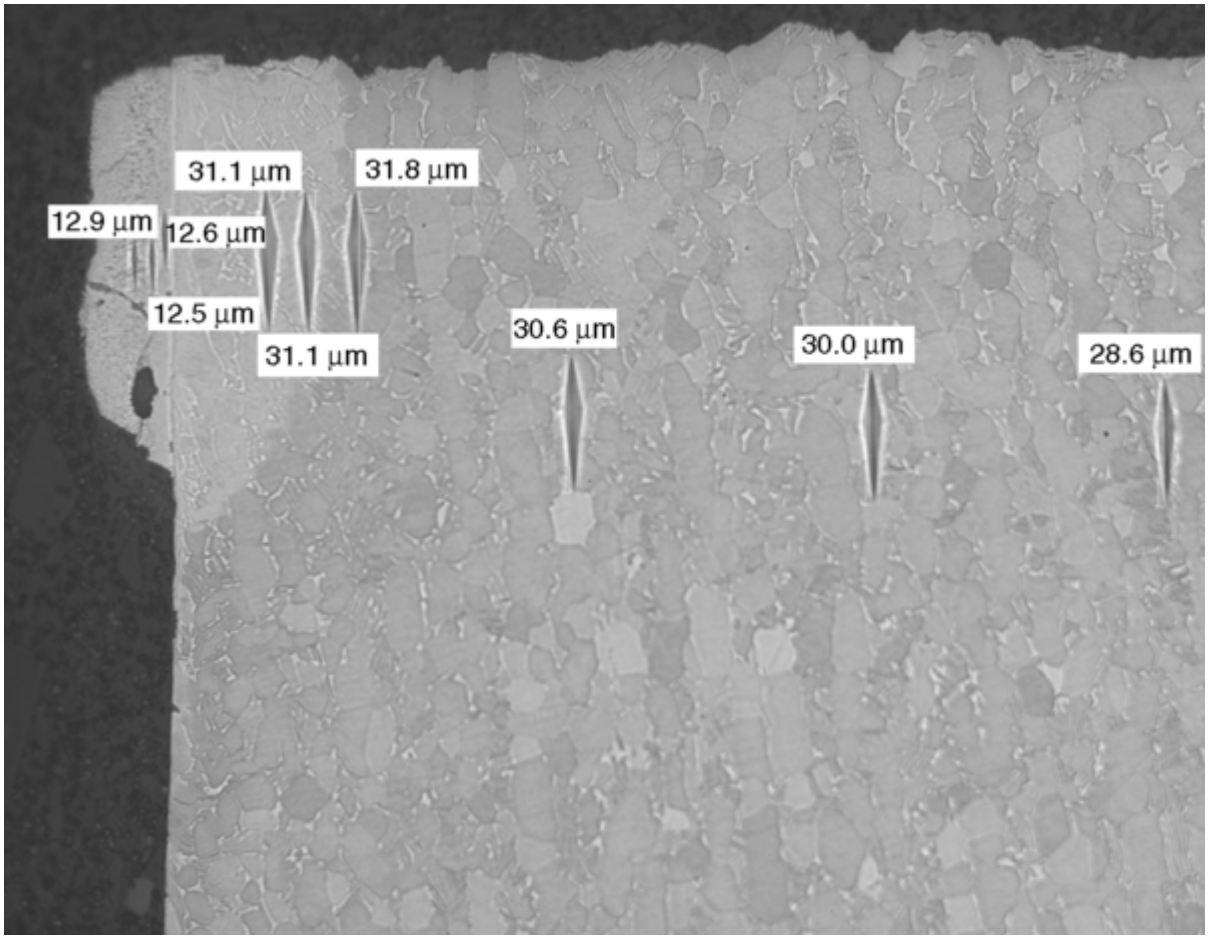

Fig. 63 Ti-6Al-4V plate fatigue specimen with molten fine and heat-affected zone 1 h vibratory polisher with non-nap polyester cloth and alumina

Figure 64 and 65 show heat damage from a lab-induced lightening strike. Note the compromise in etching time in Fig. 64, where the heat-affected zone is underetched, while the base material is overetched. Figure 65 shows the effects of intraply arcing and heat-affected zone from a lab-induced lightning strike.

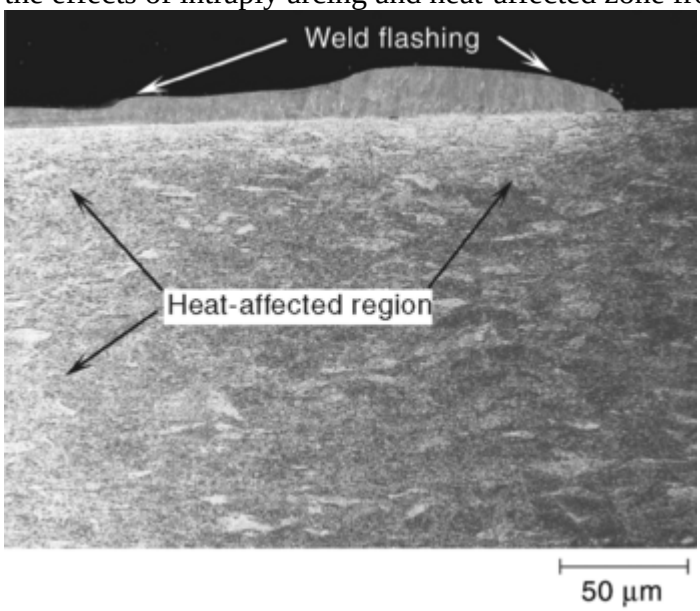

Fig. 64 Oxalic tint etch for 15 s. Ti-15V-3Cr-3Al-3Sn foil heat-affected zone. This is from a lab-induced lightning strike. Note the compromise in etching time. The heat-affected zone is underetched and the base material is overetched. 1 h vibratory polisher, non-nap polyester cloth and alumina

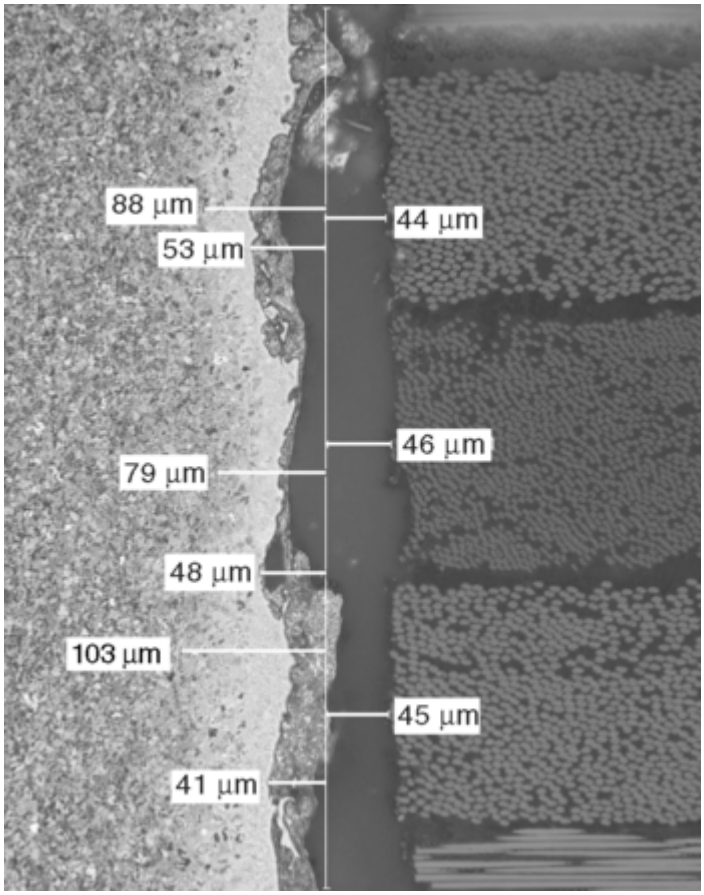

Fig. 65 Hybrid Ti-6Al-4V carbon-reinforced polymer composite with arcing and heat damage from a lab-induced lightning strike. Note the heat-affected zone. The vertical line shows the original surface of the titanium fastener and the extent of intraply arcing. Because of its complex shape, the specimen was vacuum impregnated with hydrated rhodamine-dyed two-part epoxy after sectioning on a wafering saw. This sample was prepared with a five-step edge retention process; 220 grit, 9 µm, 3 µm silk, 3 µm non-nap polyester and ending up with 1 h on a vibratory polisher with a non-nap polyester cloth and 10% alumina solution.

L.M. Gammon, R.D. Briggs, J.M. Packard, K.W. Batson, R. Boyer, C.W. Domby, Metallography and Microstructures of Titanium and Its Alloys, *Metallography and Microstructures,* Vol 9, *ASM Handbook,* ASM International, 2004, p. 899–917

Metallography and Microstructures of Titanium and Its Alloys

Luther M. Gammon, Robert D. Briggs, John M. Packard, Kurt W. Batson, Rodney Boyer, and Charles W. Domby, The Boeing Company

---

Other Techniques

Several metallographic techniques have been developed for specific purposes, including recrystallization studies and microstructure/fracture topography correlations. Decoration aging was developed to study the extent of recrystallization in beta alloys. After recrystallization annealing, the material is given a partial age at a time and temperature appropriate for the alloy of interest. The incompletely recrystallized grains retain some dislocation substructure (stored energy) that accelerates the aging process, resulting in a more rapidly aged grain. These grains then etch darker than the recrystallized ones, making it easy to identify the extent of recrystallization. This effect is illustrated in Fig. 30.

Another technique utilizes deep macroetching and thermal etching. The deformed specimen is polished, then subjected to overetching to produce deep grooves at the deformed grain boundaries. Next, the specimen is subjected to the recrystallization cycle of interest in a hard vacuum (10^{-6} torr), followed by oil quenching. The material recrystallizes and thermal etching occurs, which differentiates between different grains, because surface atoms evaporate or sublimate at different rates on different crystallographic planes. Different grains will have different crystallographic planes at the exposed surface.

The original grain boundaries are observable as ghost boundaries, due to the deep macroetching used previously. Therefore, the recrystallized and original microstructures can be observed simultaneously. This permits studying not only the recrystallized structure, but also the recrystallization nucleation sites. The ghost boundaries can be removed by repolishing and chemically etching. This technique is illustrated in Fig. 66. Figure 66(a) demonstrates the as-deformed structure that has been heavily etched. The specimen was recrystallized at 925 °C (1700 °F) for 1 h in a vacuum of 10^{-6} torr. Recrystallization in vacuum caused thermal etching of the recrystallized grains (Fig. 66b shows recrystallized structure). The prior unrecrystallized structure can still be observed as ghost boundaries remaining from the initial overetching.

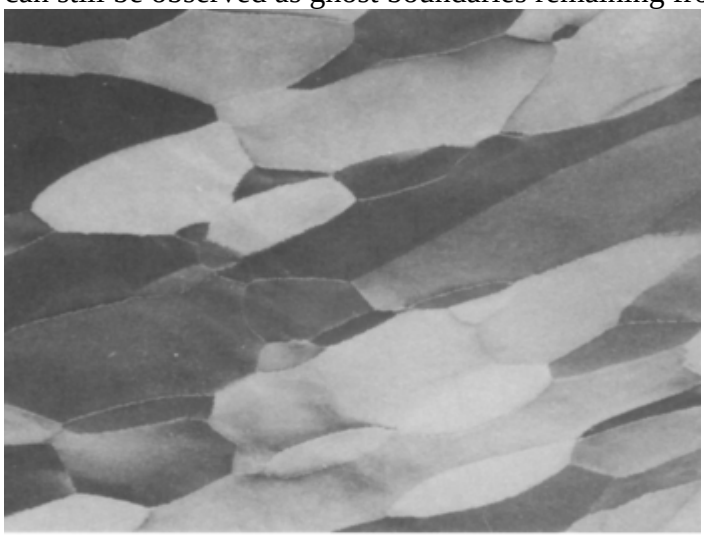

(a)

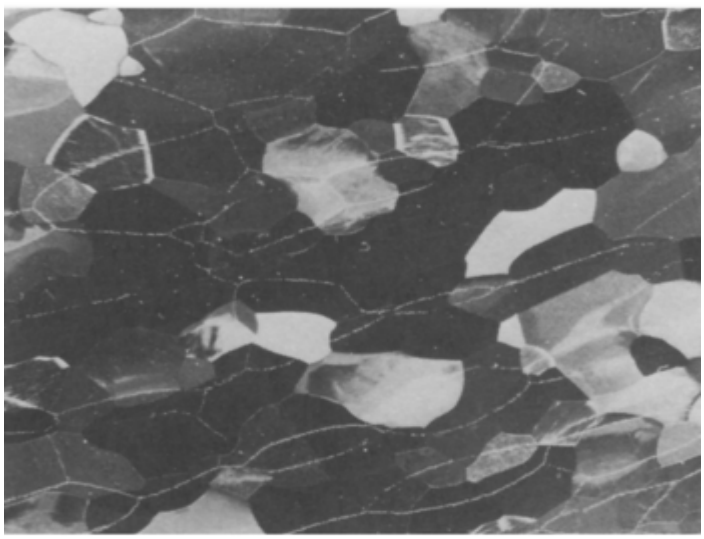

(b)

Fig. 66 Ti-10V-2Fe-3Al deformed at 1150 °C (2100 °F). (a) Etched with 60 mL H_2O, 40 mL HNO_3, 10 mL HF for 30 min. (b) Etched with 60 mL H_2O, 40 mL HNO_3, 10 mL HF for 30 min + thermally etched at 925 °C (1700 °F) for 1 h in vacuum (10^{-6} torr). Magnification not given. Courtesy of D. Eylon

Subgrain boundaries can be revealed using a relatively simple technique. The specimen is electropolished and viewed in the scanning electron microscope in the backscattered electron mode. The contrast and delineation of subgrains are due to differences in crystallographic orientation. Electropolishing occurs at different rates on different crystallographic planes, similar to the thermal etching phenomenon.

Several techniques have been developed to observe fracture topography and microstructure simultaneously in the scanning electron microscope using its large depth of field. A very simple method involves selective polishing and etching of the fracture face. The fracture face and machined surfaces are first masked with a suitable maskant, such as a stop-off lacquer, which can be applied with a small paint brush. Selected areas of the fracture face are left unmasked. The specimen is then electropolished, which will affect only the unmasked areas, and etched. Studying the interface between the polished and etched and the masked areas permits a correlation of microstructural features and fractographic details, as shown in Fig. 67. This technique is useful for correlating general microstructural details, but it may be difficult to pinpoint a specific area to study.

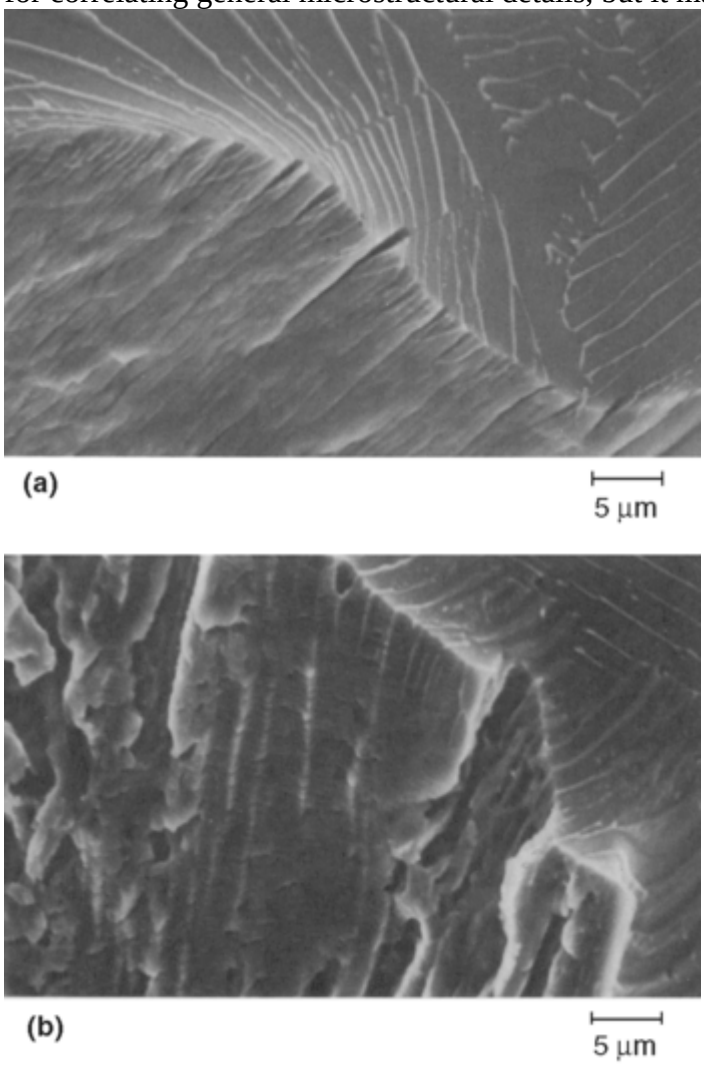

Fig. 67 Scanning electron micrograph (SEM) image from Ti-6Al-4V beta-annealed fatigued plate specimen. (a) SEM at the polished and etched/unetched fracture topography interface showing microstructure/fracture topography correlation. Secondary cracks are a result of intense slip bands. (b) SEM that illustrates “furrows” or “troughs” that are defined by the lamellar alpha plates. These furrows link up as the crack progresses. Kroll's reagent. 2000×. Courtesy of R. Boyer

Precision sectioning techniques have also been developed. The area of interest on the fracture face, such as crack origin, is first located. The specimen is then cut on a plane perpendicular to the fracture face close to the area of interest. The distance from the cut face to the area of interest is measured. Next, the specimen is placed in a metallurgical mount, then ground and polished the measured distance for metallurgical analysis of the precise area of interest and correlation of microstructure to fractographic features. An example of this technique is shown in Fig. 68. The microstructure and fracture face can be observed simultaneously using the scanning

electron microscope by carefully dissolving the mount material. This fatigue specimen had an internal origin at point A, which initiated at an iron inclusion, as determined in Fig. 68(b) by precision sectioning. The cleavage zone at point C in Fig. 68(a) is due to the $TiFe_2$ zone seen at point C in Fig. 68(b). Below the $TiFe_2$, the structure consists of transformed Widmanstätten alpha. The section (Fig. 68b) was taken at line AB in Fig. 68(a).

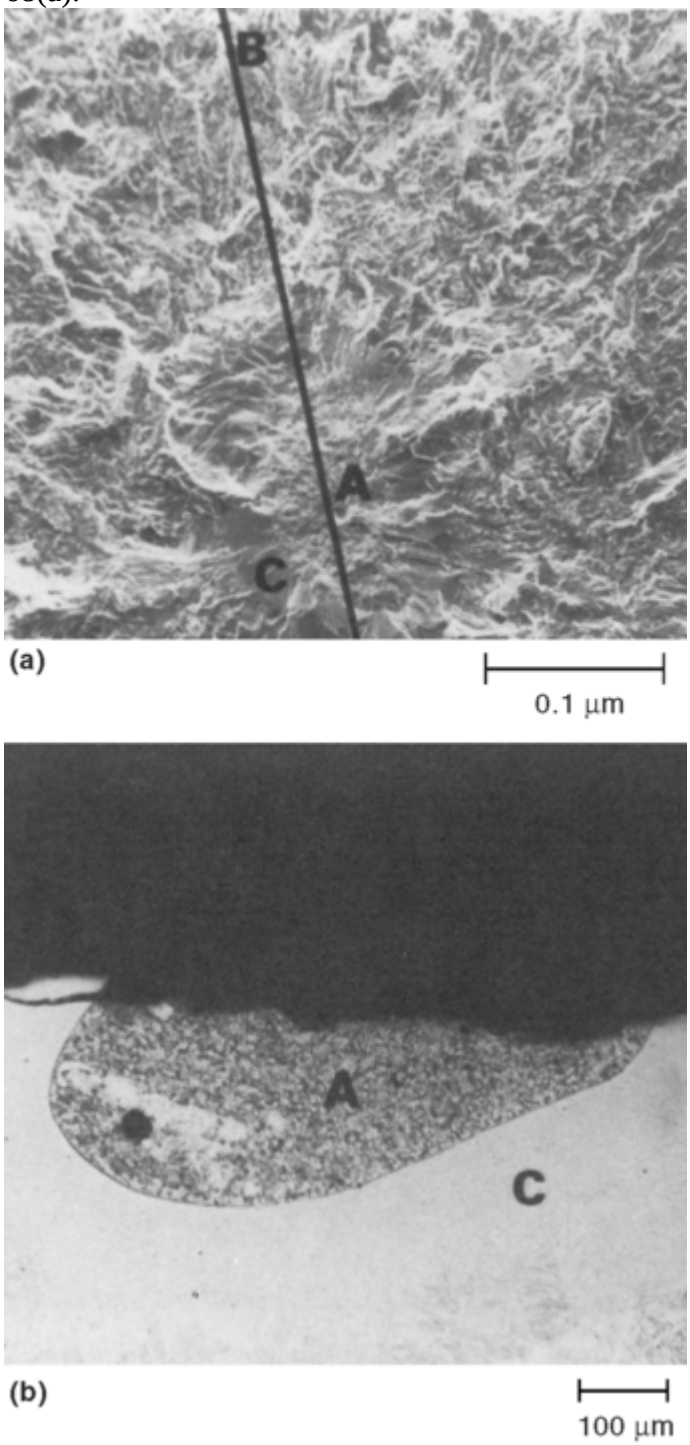

Fig. 68 Ti-6Al-4V powder metallurgy compact, hot isostatically pressed at 925 °C (1700 °F), 103 MPa (15 ksi), for 2 h. (a) Scanning electron micrograph. No etch. 80×. (b) Optical micrograph. Etchant: Kroll's reagent. 16×. Courtesy of D. Eylon

L.M. Gammon, R.D. Briggs, J.M. Packard, K.W. Batson, R. Boyer, C.W. Domby, Metallography and Microstructures of Titanium and Its Alloys, *Metallography and Microstructures,* Vol 9, *ASM Handbook*, ASM International, 2004, p. 899–917

Metallography and Microstructures of Titanium and Its Alloys

Luther M. Gammon, Robert D. Briggs, John M. Packard, Kurt W. Batson, Rodney Boyer, and Charles W. Domby, The Boeing Company

References

1. G.F. Vander Voort, *Metallography: Principles and Practice,* McGraw-Hill, 1984, reprinted by ASM International, 1999

2. Struers Metallographic Application Guide: Titanium Alloys, Struers

3. M.J. Donachie, Jr., *Titanium: A Technical Guide,* 2nd ed., ASM International, 2000

Revised by H.E. Fairman and A. Kelly, Metallography and Microstructures of Uranium and Its Alloys, *Metallography and Microstructures,* Vol 9, *ASM Handbook,* ASM International, 2004, p. 918–932

Metallography and Microstructures of Uranium and Its Alloys

Revised by Henry E. Fairman, Department of Energy Feed Materials Production Center (Retired) and Ann Kelly, Los Alamos National Laboratory

Introduction

URANIUM is used in a variety of applications for its high density (19 g/cm^3, 68% greater than lead) and/or its unique nuclear properties. Uranium and its alloys exhibit typical metallic ductility, can be fabricated by most standard hot- and cold-working techniques, and can be heat treated to hardnesses ranging from approximately 92 HRB to 55 HRC. Metallography is a useful tool for quality assurance, failure analysis, and understanding the effects of processing on the properties of uranium and its alloys.

Natural uranium consists of two primary isotopes: U^{235} (0.7%) and U^{238} (99.3%). Isotopic separation is carried out as one of the steps in converting the ore to metal, resulting in two grades of metallic uranium. Enriched uranium, sometimes termed “oralloy,” contains more than 0.7% U^{235} and is used primarily for its nuclear properties. Depleted uranium, sometimes termed “tuballoy,” DU, or D-38, contains only about 0.2% U^{235} and is used primarily for its high physical density along with its nuclear cross section. Although access to enriched uranium is controlled, depleted uranium is industrially available. Since the 1990s when commercial producers stopped production of aircraft counterweights and medical equipment shielding, the primary applications have been military, such as kinetic energy penetrators and armor plate. The major source of DU metal is the remaining inventory produced by the U.S. Department of Energy's (DOE's) Feed Materials Production Center, which ceased production in 1989 and is in the final process of being demolished. Large quantities of depleted UF_6 are still available, but no commercial or Department of Energy facility exists in 2004 to convert this to UF_4, which is the starting point for producing uranium metal. The remaining inventory of UF_4 at the DOE's Paducah's Enrichment Center was transferred to the Department of Defense for use in producing military kinetic energy penetrators. There is a sizeable inventory in Russia as a by-product of their enrichment process. This inventory, along with a portion of DOE's, is being used to convert U.S. and Russian bomb grade uranium to commercial reactor grade UO_2.

This article considers the physical metallurgy and metallography of depleted uranium. The metallurgy of enriched uranium is identical to that of depleted uranium, although additional measures are necessary during metallographic preparation to maintain material accountability and to avoid health hazards. Detailed information on uranium alloy metallurgy and microstructures is presented in subsequent sections of this article and in Ref 1, 2, 3, 4, 5, 6, 7, and 8.

References cited in this section

1. A.N. Holden, *Physical Metallurgy of Uranium,* Addison-Wesley, 1958

2. W. Lehmann and R.F. Hills, Proposed Nomenclature for Phases in Uranium Alloys, *J. Nucl. Mater.,* Vol 2, 1960, p 261

3. W.D. Wilkinson, *Uranium Metallurgy,* Vol 1 and 2, Interscience, 1962

4. J.J. Burke et al., Ed., *Physical Metallurgy of Uranium Alloys,* Brook Hill, 1976

5. K.H. Eckelmeyer, Microstructural Control in Dilute Uranium Alloys, *Microstruc. Sci.,* Vol 7, 1979, p 133

6. *Metallurgical Technology of Uranium and Uranium Alloys,* Vol 1, 2, and 3, American Society for Metals, 1982

7. J.G. Speer, "A Study of Solid-State Phase Transformations in Uranium Alloys," Ph.D. thesis, Oxford University, 1983

8. K.H. Eckelmeyer, A.D. Romig, and L.J. Weirick, The Effect of Quench Rate on the Microstructure, Mechanical Properties, and Corrosion Behavior of U-6 Wt. Pct. Nb, *Met. Trans. A,* Vol 15, 1984, p 1319

Revised by H.E. Fairman and A. Kelly, Metallography and Microstructures of Uranium and Its Alloys, *Metallography and Microstructures,* Vol 9, *ASM Handbook*, ASM International, 2004, p. 918–932

Metallography and Microstructures of Uranium and Its Alloys

Revised by Henry E. Fairman, Department of Energy Feed Materials Production Center (Retired) and Ann Kelly, Los Alamos National Laboratory

Principles of Uranium Alloy Metallurgy

Uranium ore is processed by mineral beneficiation and chemical procedures to produce enriched or depleted uranium tetrafluoride (UF_4). The UF_4 is then reduced with magnesium or calcium at elevated temperature, resulting in metallic uranium ingots that are known as "derbies." These derbies are vacuum induction remelted and cast into the shapes required for engineering components or for subsequent mechanical working. Crucibles and molds are usually made of graphite; a zirconia or yttria wash prevents or minimizes carbon pickup by the metal.

Solid elemental uranium exhibits three polymorphic forms: γ phase (body-centered cubic) above 771 °C (1420 °F), β phase (tetragonal) between 665 and 771 °C (1230 and 1420 °F), and α phase (orthorhombic) below 665 °C (1230 °F). Hot working (rolling, forging, extruding) is readily accomplished in the γ (800 to 840 °C, or 1470 to 1545 °F) or high α (600 to 640 °C, or 1110 to 1185 °F) temperature ranges, and cold or warm working (rolling, swaging) can be done from room temperature to about 400 °C (750 °F). Because of its relatively low ductility, deformation in the β phase is not desirable. Recrystallization of cold-worked material can be performed in the high α region (500 to 640 °C, or 930 to 1185 °F). The material can be machined by most normal cutting and grinding techniques, but special tools and cutting conditions as well as safety precautions are recommended due to the pyrophoric nature of its chips.

Uranium is frequently alloyed to improve its corrosion resistance and/or to modify its mechanical properties. These alloys are produced by vacuum induction or vacuum arc melting and, like unalloyed uranium, can be fabricated hot, warm, or cold. As shown in Fig. 1, the high-temperature γ phase can dissolve substantial amounts of several alloying elements, but these elements are less soluble in the intermediate- and low-temperature β and α phases. Uranium alloys are generally heat treated at approximately 800 °C (1470 °F) to get all the alloying additions into solid solution in the γ phase, then cooled at various rates to room temperature. Slow cooling permits the γ phase to decompose to two-phase structures morphologically similar to pearlite in steels. Rapid quenching suppresses these diffusional decomposition modes, resulting in various metastable phases.

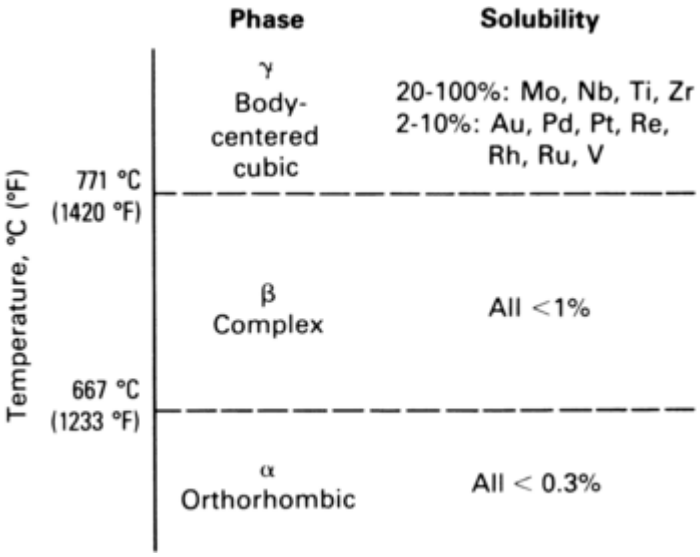

Fig. 1 Polymorphism and solubilities of alloying elements in uranium. Note that alloying elements are substantially less soluble in lower temperature phases.

The microstructures and hardnesses produced by quenching are summarized in Fig. 2. Very dilute alloys (see Fig. 3) exhibit supersaturated α phase with an irregular grain morphology similar to that of unalloyed uranium. Slightly more concentrated alloys exhibit acicular martensitic microstructures (Fig. 4). Both of these microconstituents are orthorhombic variants of α-uranium. Their hardness and yield strength increase with increasing alloy content due to solid-solution effects.

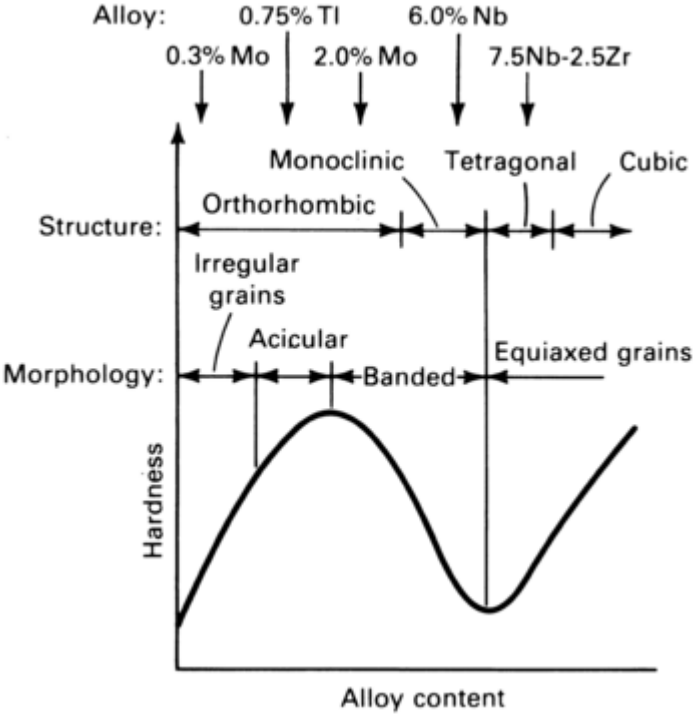

Fig. 2 Effects of alloy concentration on structure and properties of quenched alloys

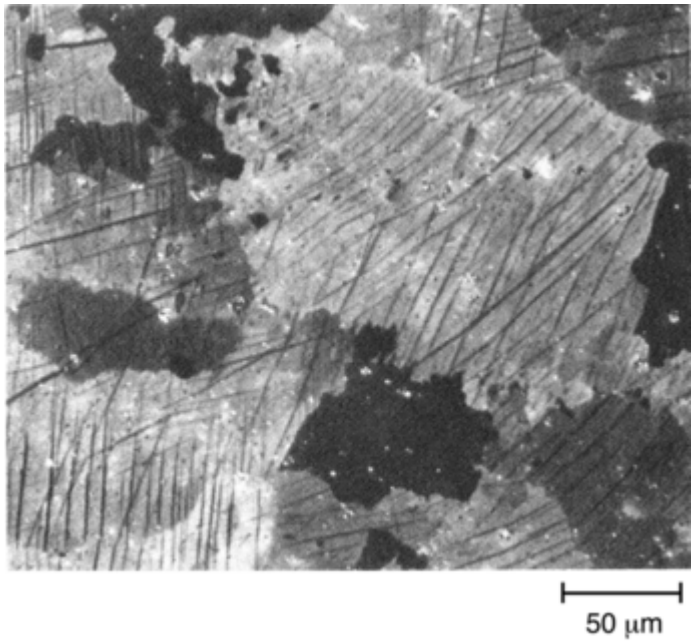

Fig. 3 Polarized light micrograph of U-0.3Mo quenched from 800 °C (1470 °F) showing highly twinned, irregular grains of supersaturated α phase. Electropolished using procedure 1 in Table 1 and anodized using procedure 2 in Table 4. 200×. Courtesy of M.M. Lappin

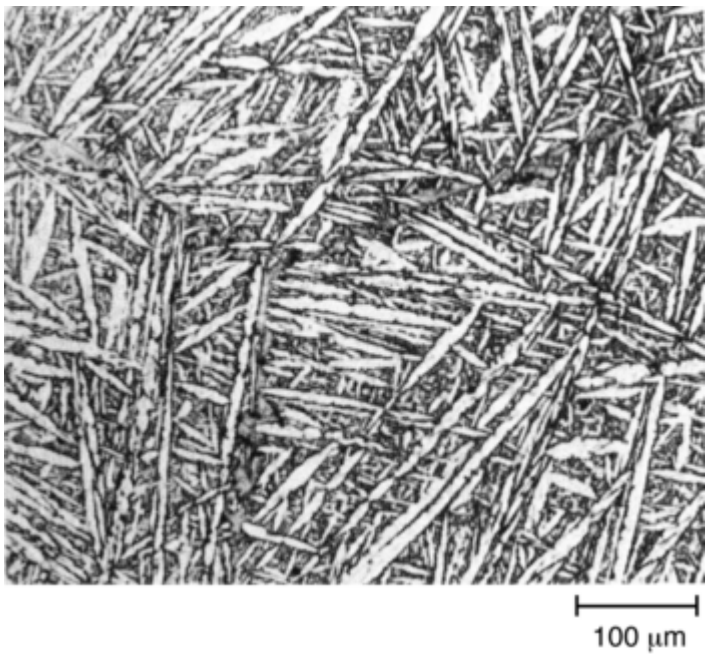

Fig. 4 Bright-field micrograph of U-0.75Ti cooled from 800 °C (1470 °F) at 75 °C/s (135 °F/s) showing light etching acicular martensite and darker etching α + U_2Ti produced by the γ → α + U_2Ti reaction in the interstices between the martensite plates. Etched using procedure 1 in Table 5. 100×. Courtesy of M.E. McAllaster

Further increases in alloy content cause a transition to a thermoelastic, or banded, martensite (see Fig. 5, 6, 7). The hardness and yield strength of the thermoelastic martensites decrease with increasing alloy content, apparently due to increasing mobilities of the boundaries of the many fine twins produced during the transformation. Midway in the thermoelastic martensite composition range, the crystal structure changes to monoclinic, as one lattice angle departs gradually from 90°. This change in crystal structure has little apparent effect on mechanical behavior. These martensitic variants of α-uranium are frequently termed α'_a, α'_b, and α_b; the subscripts a and b denote the acicular and banded morphologies, respectively, and the prime and double prime superscripts denote the orthorhombic and monoclinic crystal structures, respectively.

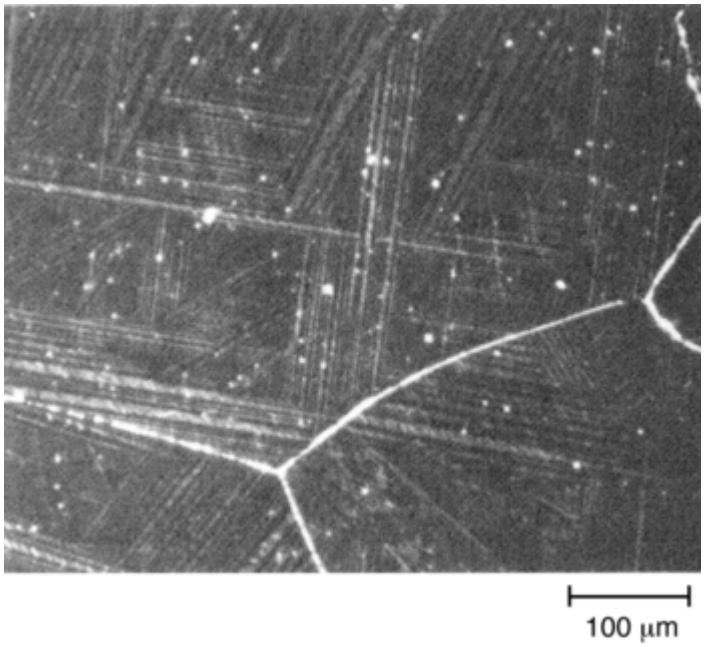

Fig. 5 Polarized light micrograph of U-2.0Mo cooled from 800 °C (1470 °F) at >100 °C/s (>180 °F/s) showing internally twinned thermoelastic martensite, α'_b. Electropolished using procedure 1 in Table 1 and anodized using procedure 2 in Table 4. 100×. Courtesy of M.E. McAllaster

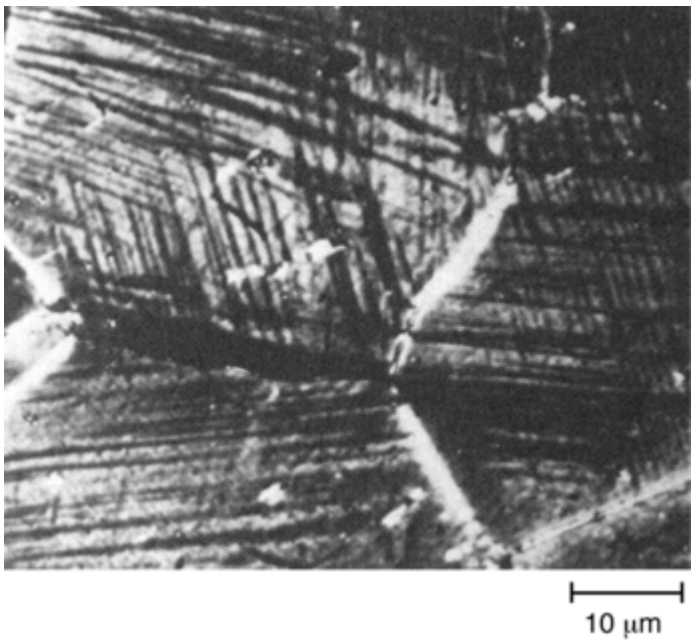

Fig. 6 Polarized light micrograph of U-6.0Nb quenched from 800 °C (1470 °F) showing $\alpha_b$thermoelastic martensite. Attack polished using 5 wt% CrO_3 in H_2O (etchant no longer recommended). 1000×. Courtesy of J.W. Koger

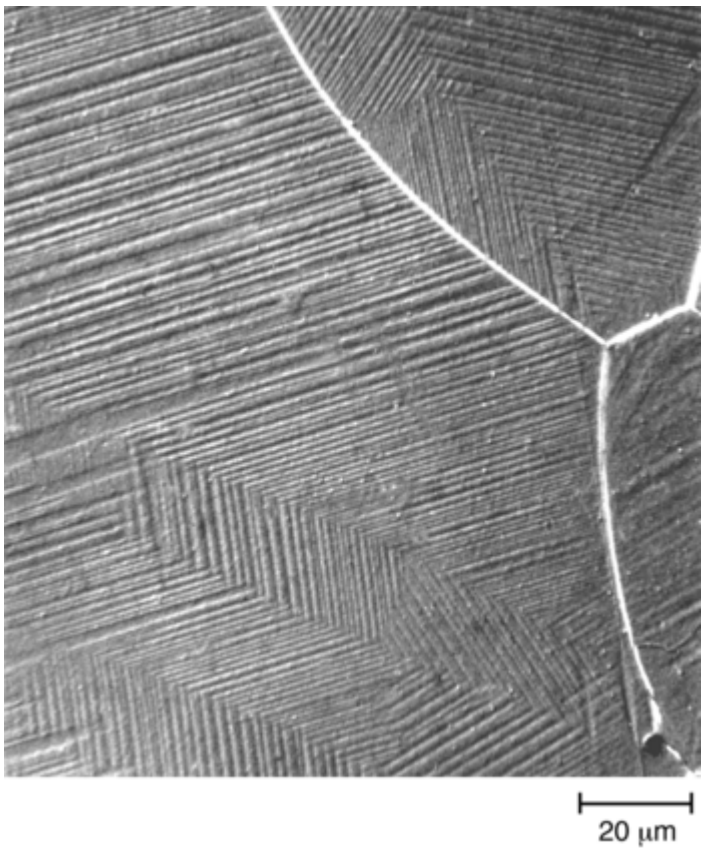

Fig. 7 Differential interference contrast (DIC) light micrograph of as quenched U-6.0Nb showing transformation twinning. Electropolished with 5% H_3PO_4, electroetched using procedure 2 in Table 5. 1000×. Courtesy of A. Kelly

Additional increases in alloy content produce a transition to γ°, an ordered tetragonal variant of elevated-temperature γ-uranium (Fig. 8). Further alloy additions cause retention of the cubic γ phase. These variants of the γ phase can be distinguished by x-ray diffraction, but not by metallography.

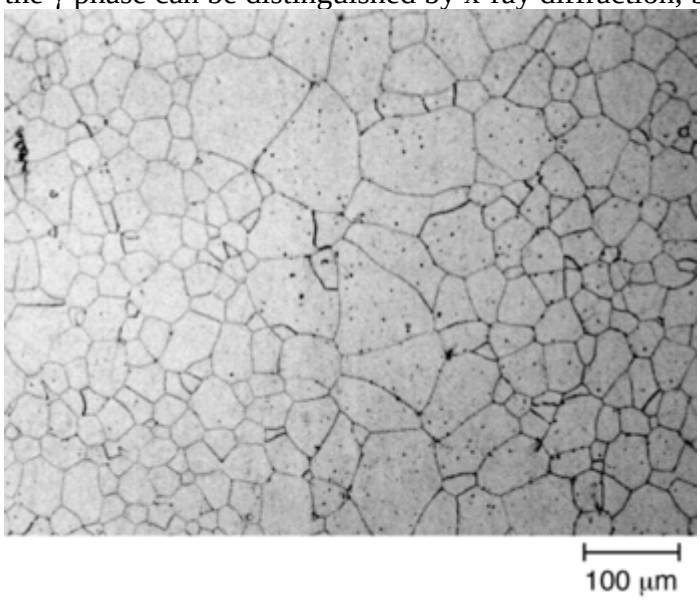

Fig. 8 Bright-field micrograph of U-7.5Nb-2.5Zr quenched from 800 °C (1470 °F) showing equiaxed grains of γ°. Etched using procedure 2 in Table 5. 100×. Courtesy of J.W. Koger, ORNL

The phases produced by quenching are metastable and supersaturated; therefore, they are amenable to subsequent heat treatment. As substitutional solid solutions, they are relatively soft (92 HRB to 35 HRC) and ductile (15 to 32% tensile elongation). Subsequent heat treatment increases their hardness and strength. Age

hardening occurs at temperatures below approximately 450 °C (840 °F) due to fine-scale microstructural changes observable only by transmission electron microscopy or other very high resolution techniques. Overaging occurs at higher temperatures or longer times by decomposition of the metastable structures. This decomposition, which commonly takes place by cellular or discontinuous precipitation, is revealed by optical metallography (Fig. 9, 10, 11, 12).

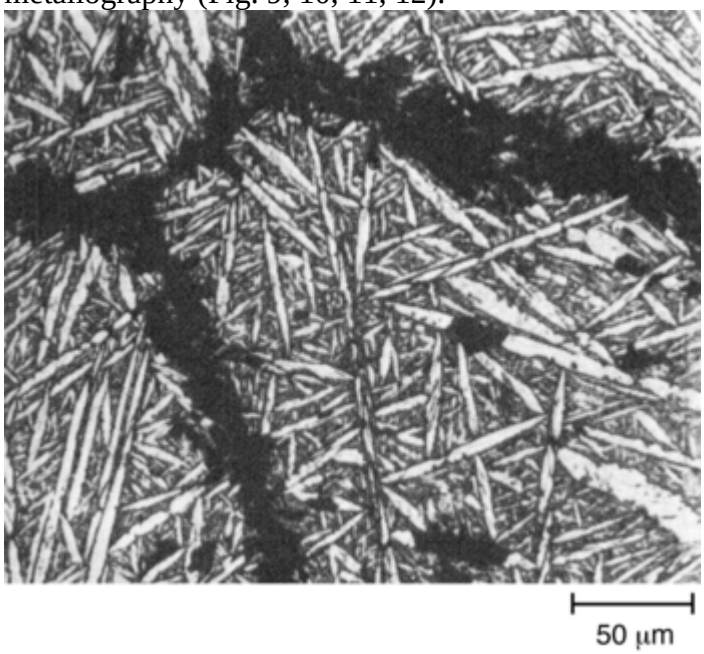

Fig. 9 Bright-field micrograph of U-0.75Ti quenched from 800 °C (1470 °F) and partially overaged at 450 °C (840 °F) for 42 h showing cellular decomposition of martensite nucleating along the prior γ grain boundaries. Etched using procedure 1 in Table 5. 200×. Courtesy of M.E. McAllaster

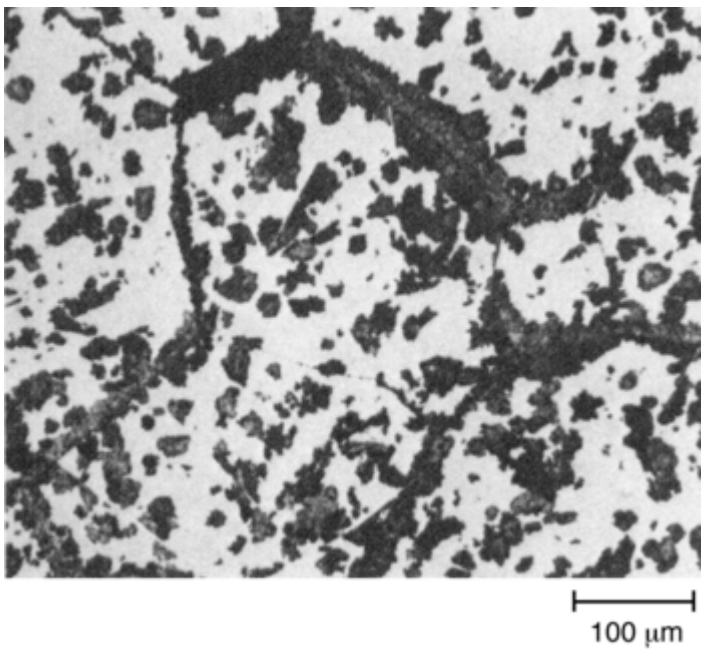

Fig. 10 Bright-field micrograph of U-2.0Mo quenched from 800 °C (1470 °F) and partially averaged at 400 °C (750 °F) for 5 h showing cellular decomposition of the thermoelastic martensite nucleating at inclusions and along prior γ grain boundaries. Etched using procedure 1 in Table 5. 100×. Courtesy of M.E. McAllaster



Fig. 11 Bright-field micrograph of U-6.0Nb quenched from 800 °C (1470 °F) and aged at 400 °C (750 °F) for 6 h showing cellular decomposition of $\alpha_b$martensite along prior γ grain boundaries. Etched using procedure 1 in Table 5. 500×. Courtesy of M.E. McAllaster

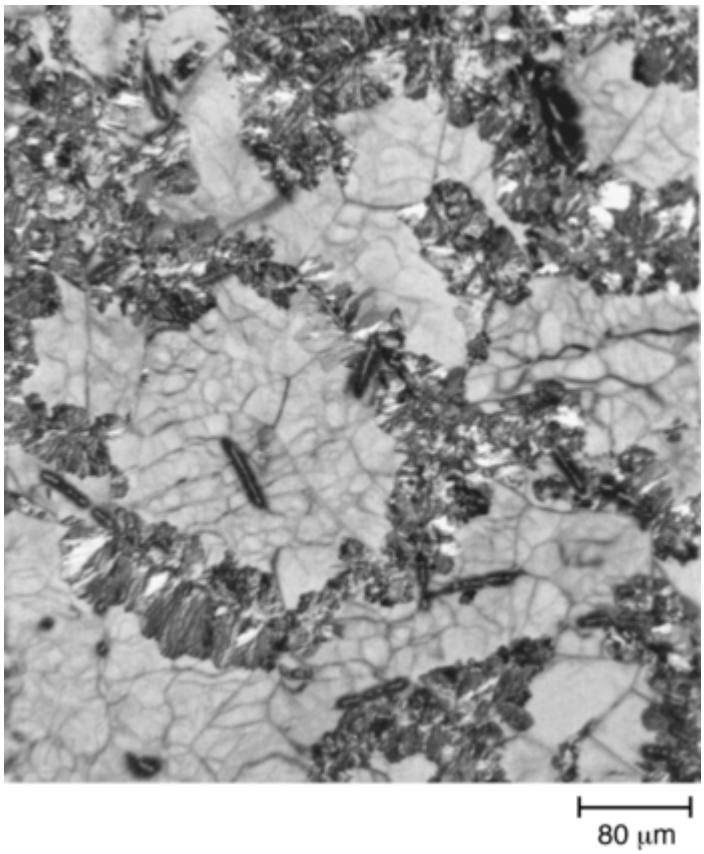

Fig. 12 Differential interference contrast (DIC) light micrograph of U-6.0Nb showing cellular decomposition of the thermoelastic martensite nucleating at inclusions and along prior γ grain boundaries. Electropolished with 5% H_3PO_4, electroetched using procedure 2 in Table 5. 250× Courtesy of A. Kelly

Although heat treatment is the primary method for controlling mechanical properties, ductility is also strongly influenced by the presence of impurities. Carbon, oxygen, and nitrogen are picked up in the melting process from the crucibles and molds (in the case of carbon), from contamination of the surfaces of the materials being melted, or from the furnace atmosphere. These elements cause inclusions to form in the metal. Metal fluorides can also be carried over from the metal reduction process. Other tramp elements, such as silicon and iron, can

form intermetallic compound inclusions with uranium. These impurities deleteriously affect ductility when present above various threshold levels.

Perhaps the most insidious impurity, however, is hydrogen, which can be introduced during melting or subsequent processing. (Salt baths for heating metal prior to working are notorious sources of hydrogen.) In some alloys, the presence of less than 1 ppm (by weight) hydrogen causes a 50% decrease in the reduction in area associated with tensile fracture. Hydrogen is commonly removed by vacuum heat treatment at 800 to 900 °C (1470 to 1650 °F).

Revised by H.E. Fairman and A. Kelly, Metallography and Microstructures of Uranium and Its Alloys, *Metallography and Microstructures*, Vol 9, *ASM Handbook*, ASM International, 2004, p. 918–932

Metallography and Microstructures of Uranium and Its Alloys

Revised by Henry E. Fairman, Department of Energy Feed Materials Production Center (Retired) and Ann Kelly, Los Alamos National Laboratory

Structures of Uranium and Uranium Alloys

Unalloyed uranium is generally vacuum induction melted and cast. Components are sometimes cast to final or near-final dimensions; in other cases, subsequent metalworking operations are employed. Primary metalworking operations such as ingot breakdown by extrusion, forging, and rolling are often carried out in the high α range (600 to 640 °C, or 1110 to 1185 °F), if sufficient tonnage equipment is available. Secondary forming operations, including rolling, swaging, and deep drawing, can be done at temperatures as low as 25 °C (75 °F). Cold- and warm-worked parts can be recrystallized at 500 to 650 °C (930 to 1200 °F).

Large uranium castings frequently contain coarse, columnar grain structures that can be revealed by macroetching (see Fig. 13). Heating to the β-phase field and quenching provides significant grain refinement (Fig. 14). The microstructure of as-cast uranium consists of large, irregular grains, each containing slightly misoriented subgrains and a substantial density of thin twins (Fig. 15, 16, 17, 18). The irregular grains and subgrains are produced by the γ to β and β to α phase transformations that occur during cooling. The twins are formed by localized deformation that takes place on cooling to accommodate the extremely anisotropic thermal contraction of the variously oriented α grains. These twins are often bent and deflected as they cross the low-angle subgrain boundaries. Heating into the β phase field and quenching produces a finer grain structure, but the grains are still extremely irregular and highly twinned (Fig. 19).

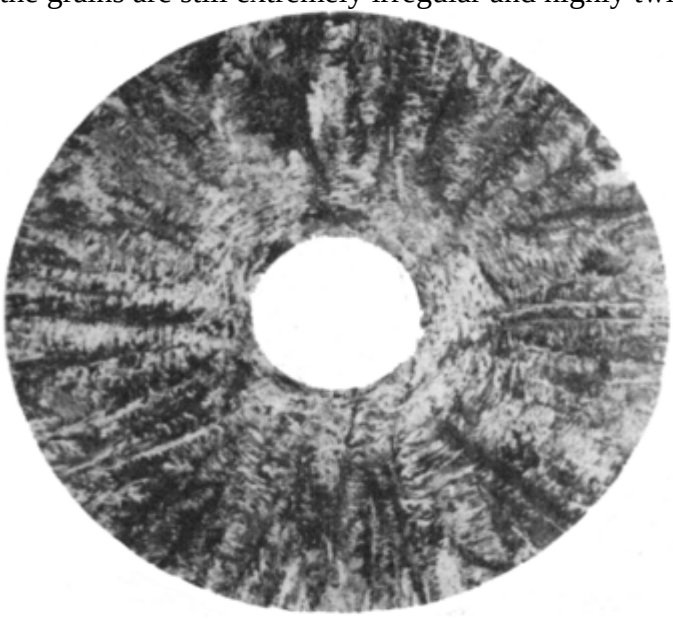

Fig. 13 Macrograph of cross section through as-cast unalloyed uranium ingot showing coarse columnar grain structure. Etched using procedure 1 in Table 2. One half actual size. Courtesy of M.H. Cornell and W.N. Wise, FMPC



Fig. 14 Macrograph of cross section through unalloyed uranium ingot showing refined grain structure produced by β quenching. Etched using procedure 1 in Table 2. One half actual size. Courtesy of M.H. Cornell and W.N. Wise, FMPC

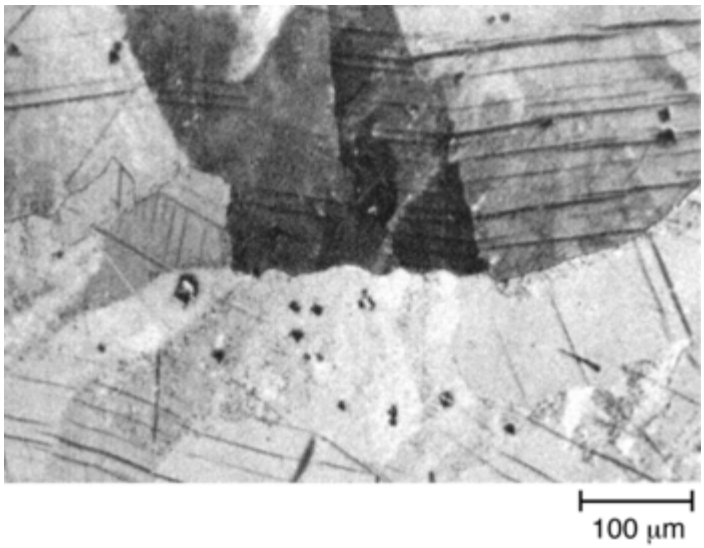

Fig. 15 Polarized light micrograph of as-cast unalloyed uranium showing large irregular grains, subgrains, and a substantial density of thermal contraction accommodation twins. Attack polished using 5 wt% CrO_3 in H_2O (etchant no longer recommended). 100×. Courtesy of J.W. Koger, ORNL

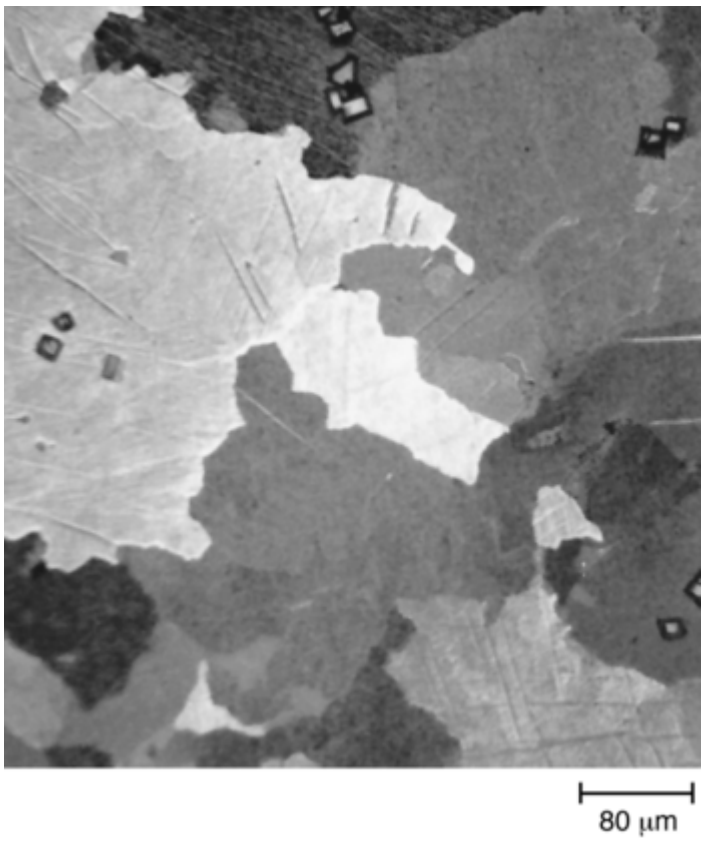

Fig. 16 Differential interference contrast (DIC) light micrograph of as-cast unalloyed uranium showing large irregular grains and well defined inclusions. Electropolished with 5% H_3PO_4, electroetched using procedure 2 in Table 5. Original magnification 250×. Courtesy of A. Kelly

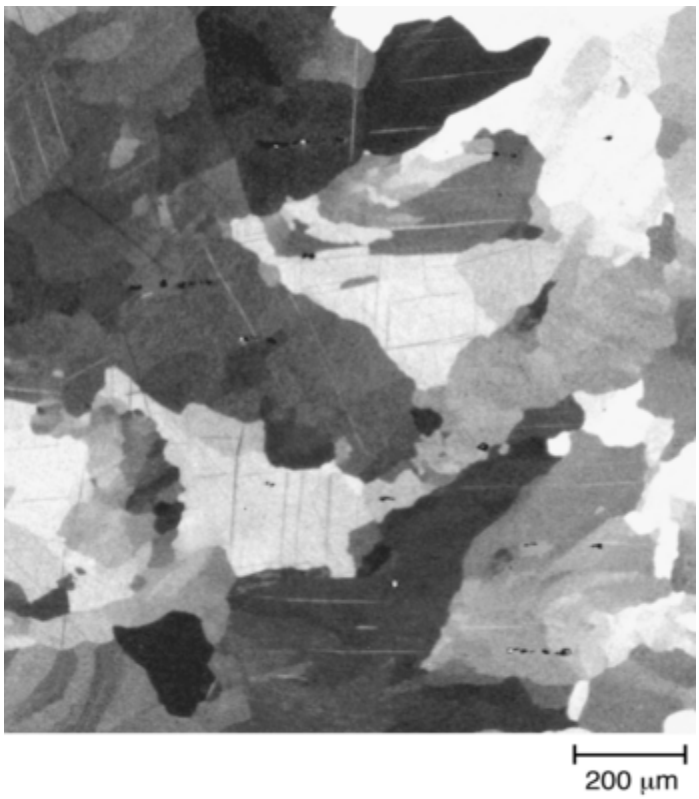

Fig. 17 Differential interference contrast (DIC) light micrograph showing typical as-cast structure in unalloyed uranium. Dark lines are uranium carbide stringers. Electropolished with 5% H_3PO_4, electroetched using procedure 2 in Table 5. 100×. Courtesy of A. Kelly

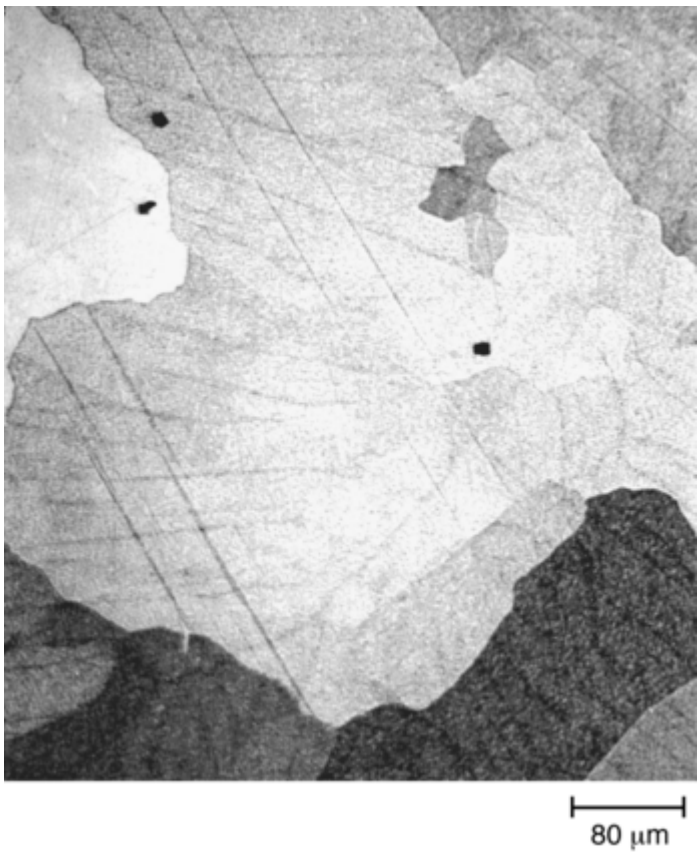

Fig. 18 Differential interference contrast (DIC) light micrograph of as-cast unalloyed uranium showing subgrain boundaries. Electropolished with 5% H_3PO_4, electroetched using procedure 2 in Table 5. 250×. Courtesy of A. Kelly

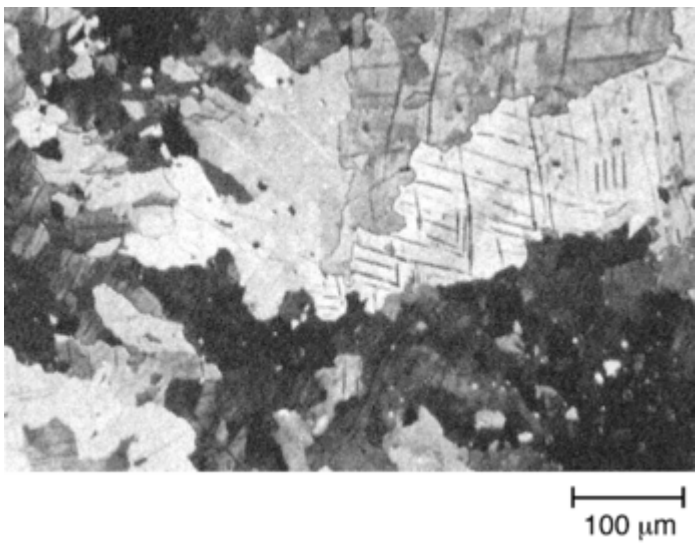

Fig. 19 Polarized light micrograph of cast and β-quenched unalloyed uranium showing irregular grains and thermal contraction accommodation twins. Attack polished using 5 wt% CrO_3 in H_2O (etchant no longer recommended). 100×. Courtesy of J.W. Koger, ORNL

Hot working of unalloyed uranium in the high α phase field (600 to 640 °C, or 1110 to 1185 °F) produces finer and more regularly shaped grains (Fig. 20). Recrystallization occurs during deformation, frequently resulting in a duplex grain structure with some grains substantially larger than others. Despite recrystallization, the grain shapes are usually somewhat elongated in the direction of working, particularly in relatively low-purity materials where grain boundaries are pinned by large numbers of inclusions.

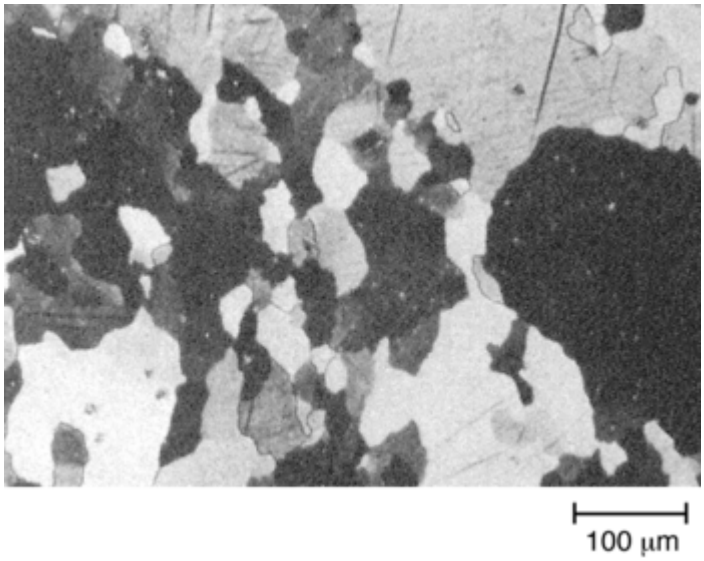

Fig. 20 Polarized light micrograph of unalloyed uranium rolled at 630 °C (1165 °F) showing duplex grain structure and few thermal contraction accommodation twins. Attack polished using 5 wt% CrO_3 in H_2O (etchant no longer recommended). 100×. Courtesy of J.W. Koger, ORNL

Cold and warm working at temperatures below 350 °C (660 °F) produce an elongated grain structure (Fig. 21, 22) containing a high density of deformation twins. The number of twins increases with decreasing deformation temperature. Warm working followed by recrystallization at 500 to 650 °C (930 to 1200 °F) results in the finest and most equiaxed grain structure (Fig. 23, 24). A partially recrystallized structure is shown in Fig. 25. Material in this condition also exhibits the lowest density of twins, apparently because the stresses that develop from anisotropic contraction during cooling are smaller and more easily accommodated in fine-grained material.

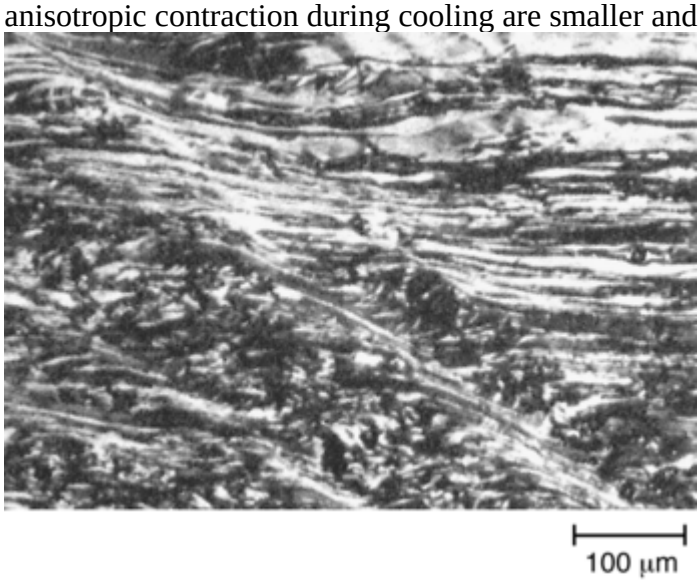

Fig. 21 Polarized light micrograph of unalloyed uranium hot rolled at 630 °C (1165 °F), then hydroformed at 300 °C (570 °F) showing highly elongated grains. Attack polished using 5 wt% CrO_3 in H_2O (etchant no longer recommended). 100×. Courtesy of J.W. Koger, ORNL



Fig. 22 Differential interference contrast (DIC) light micrograph of rolled unalloyed uranium showing elongated grains. Electropolished with 5% H_3PO_4, electroetched using procedure 2 in Table 5. Courtesy of A. Kelly

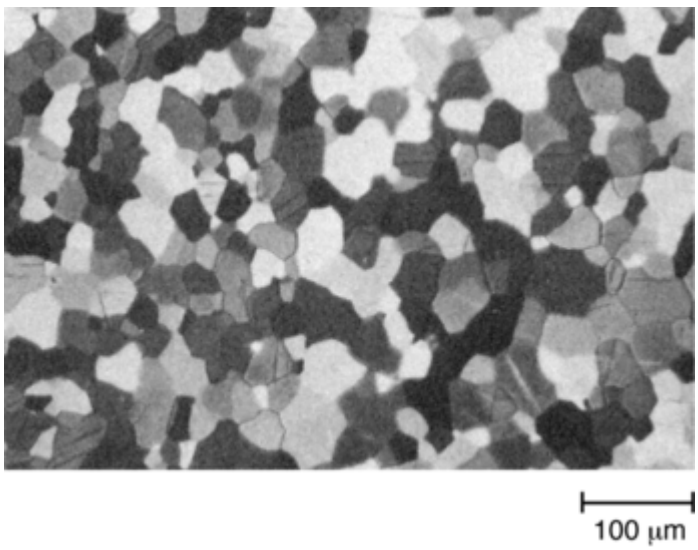

Fig. 23 Polarized light micrograph of unalloyed uranium hot rolled at 630 °C (1165 °F), then warm rolled at 325 °C (615 °F) showing fine equiaxed grains with few thermal contraction accommodation twins. Attack polished using 5 wt% CrO_3 in H_2O (etchant no longer recommended). 100×. Courtesy of J.W. Koger, ORNL



Fig. 24 Differential interference contrast (DIC) light micrograph of unalloyed uranium annealed at 550 °C (1020 °F) 2 h, slow cooled showing a fully recrystallized structure. Electropolished with 5% H_3PO_4 at 3 V for ~4 s. 250×. Courtesy of A. Kelly



Fig. 25 Differential interference contrast (DIC) light micrograph of rolled unalloyed uranium annealed at 450 °C (840 °F) for 1 h, showing partially recrystallized structure. Electropolished with 5% H_3PO_4, electroetched using procedure 2 in Table 5. 250×. Courtesy of A. Kelly

Twin artifacts are shown in Fig. 26. Examples of inclusions in uranium are shown in Fig. 27, 28, 29, 30, 31, 32, 33, 34.

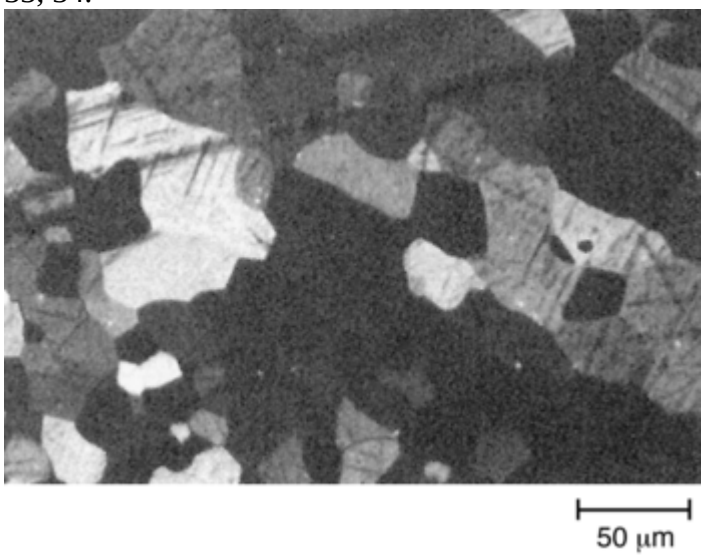

Fig. 26 Polarized light micrograph showing grinding artifacts in unalloyed uranium. Bands of fine twins are due to deformation from coarse grinding steps that was not removed by subsequent fine grinding and polishing. Electropolished using procedure 1 in Table 1 and anodized using procedure 2 in Table 4. 200×. Courtesy of M.E. McAllaster

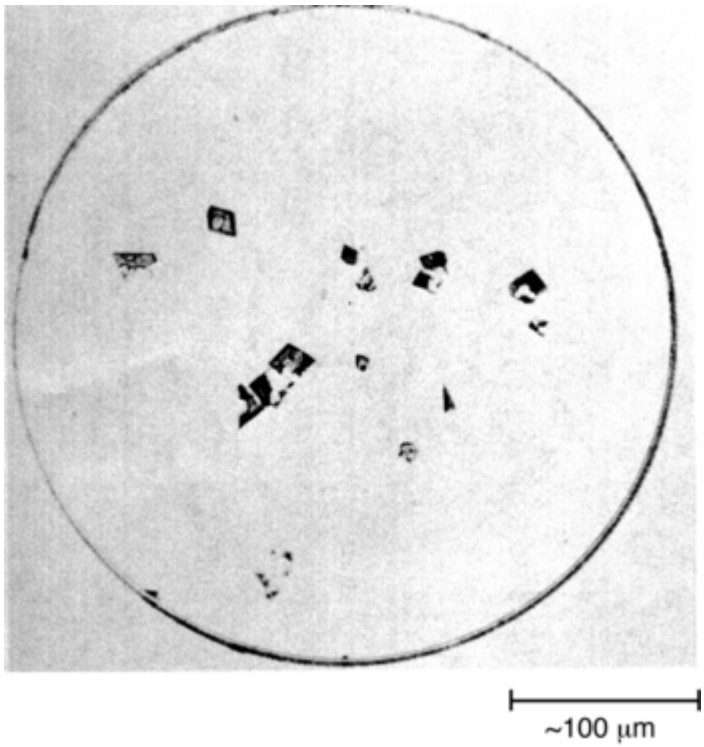

Fig. 27 Bright-field micrograph of angular uranium carbide inclusions in cast unalloyed uranium. Attack polished using procedure 11 in Table 5. 184×. Courtesy of W.N. Wise, FMPC

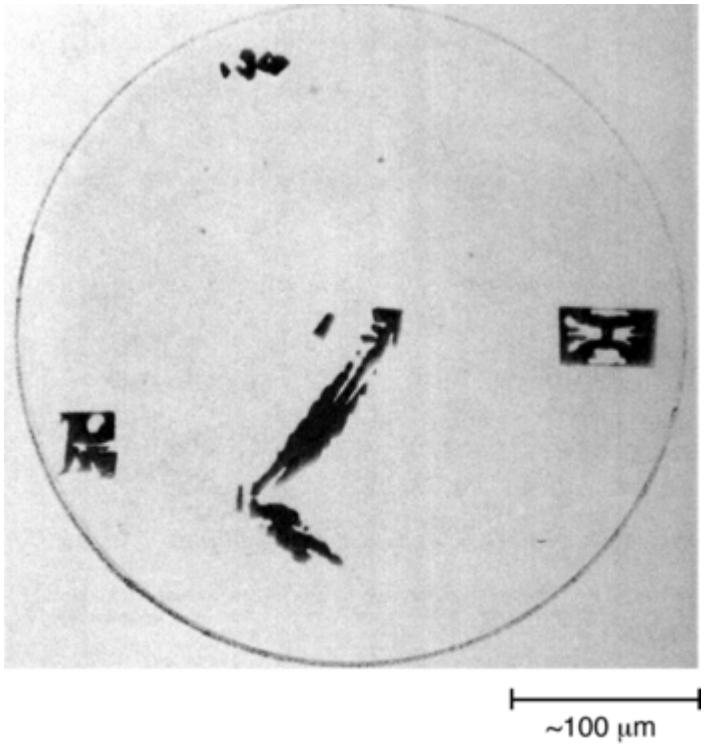

Fig. 28 Bright-field micrograph of U(CN) inclusions in cast unalloyed uranium. Attack polished using procedure 11 in Table 5. 184×. Courtesy of W.N. Wise, FMPC

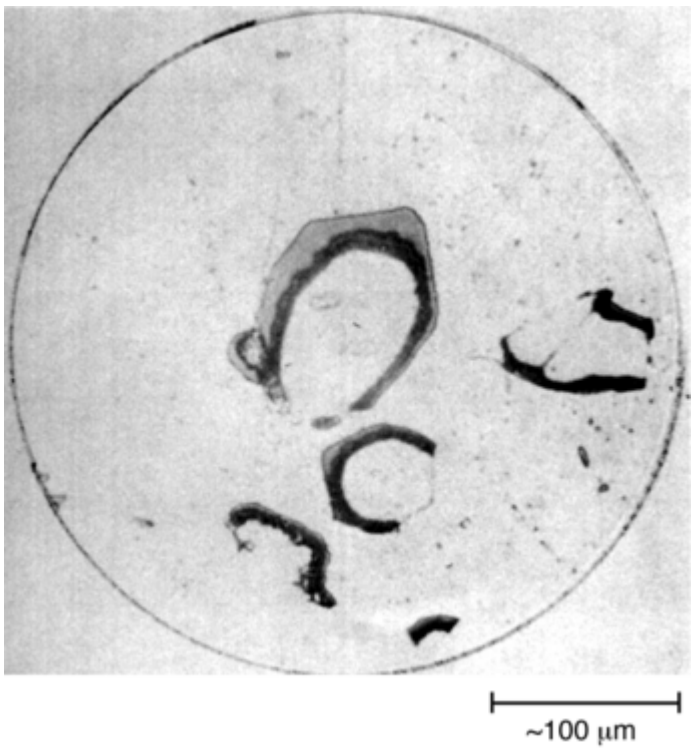

Fig. 29 Bright-field micrograph of U(CNO) inclusions in cast unalloyed uranium. Attack polished using procedure 11 in Table 5. 184×. Courtesy of W.N. Wise, FMPC

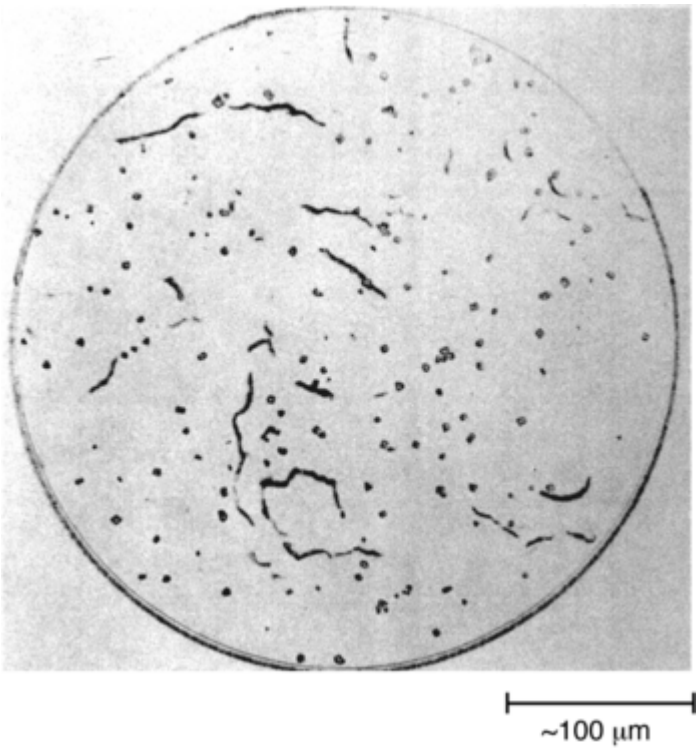

Fig. 30 Bright-field micrograph of uranium carbide (equiaxed) and UH_3 (elongated) in cast unalloyed uranium. Attack polished using procedure 11 in Table 5. 184×. Courtesy of W.N. Wise, FMPC

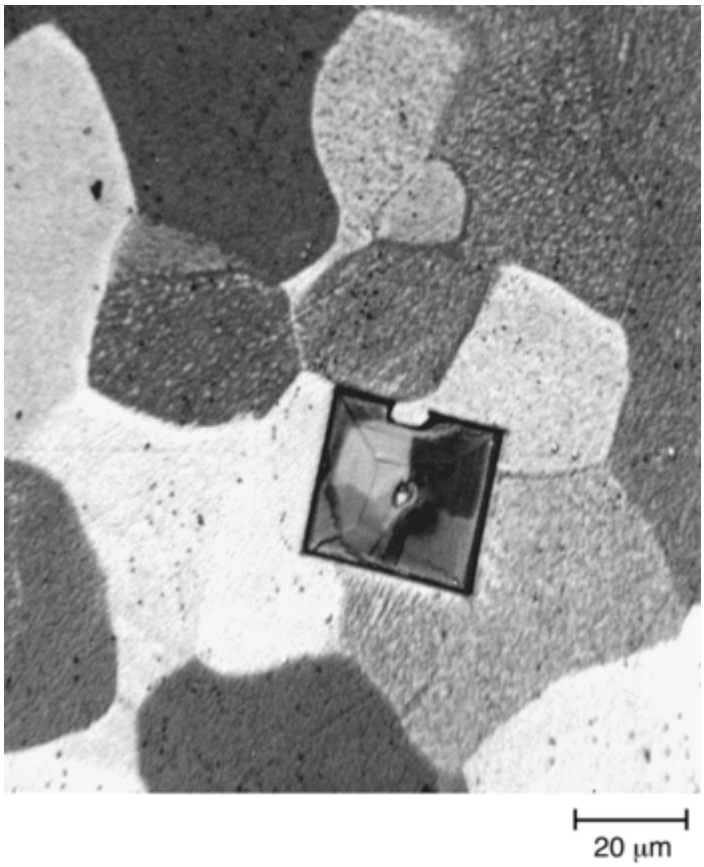

Fig. 31 Differential interference contrast (DIC) light micrograph of unalloyed uranium showing a typical uranium carbide inclusion. Electropolished with 5% H_3PO_4, electroetched using procedure 2 in Table 5. 1000×. Courtesy of A. Kelly

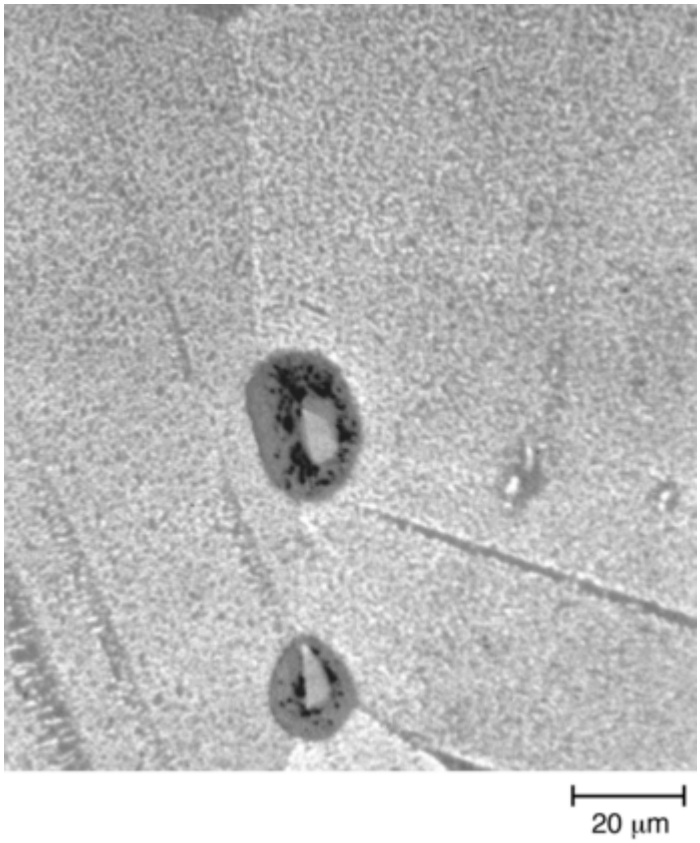

Fig. 32 Differential interference contrast (DIC) light micrograph of as cast unalloyed uranium showing large iron inclusions. Electropolished with 5% H_3PO_4, electroetched using procedure 2 in Table 5. 500×. Courtesy of A. Kelly

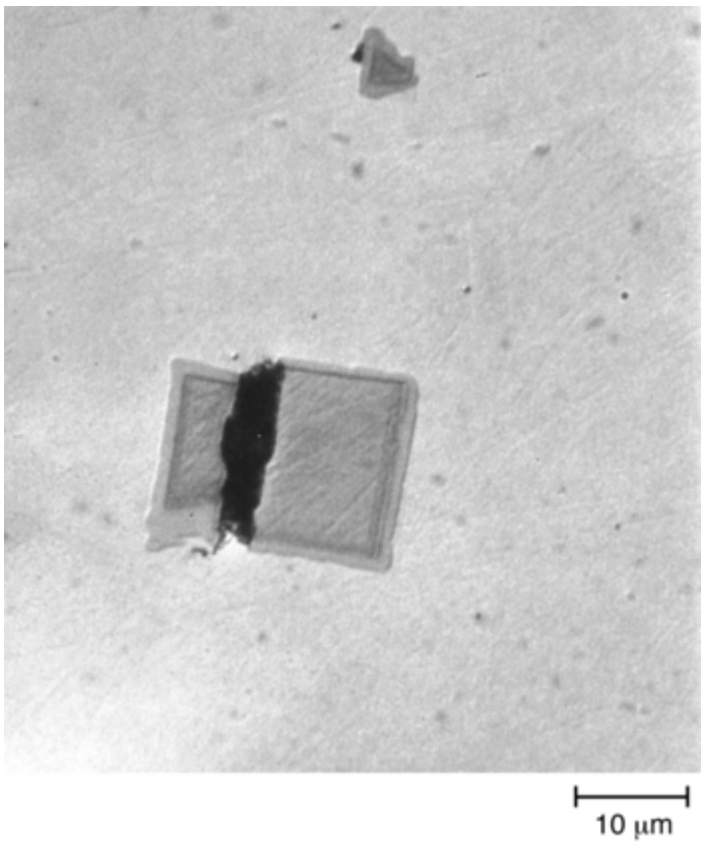

Fig. 33 Differential interference contrast (DIC) light micrograph of a broken oxycarbonitride inclusion in unalloyed uranium. Electropolished in 5% H_3PO_4 at 3 V for ~4 s. 1600×. Courtesy of A. Kelly

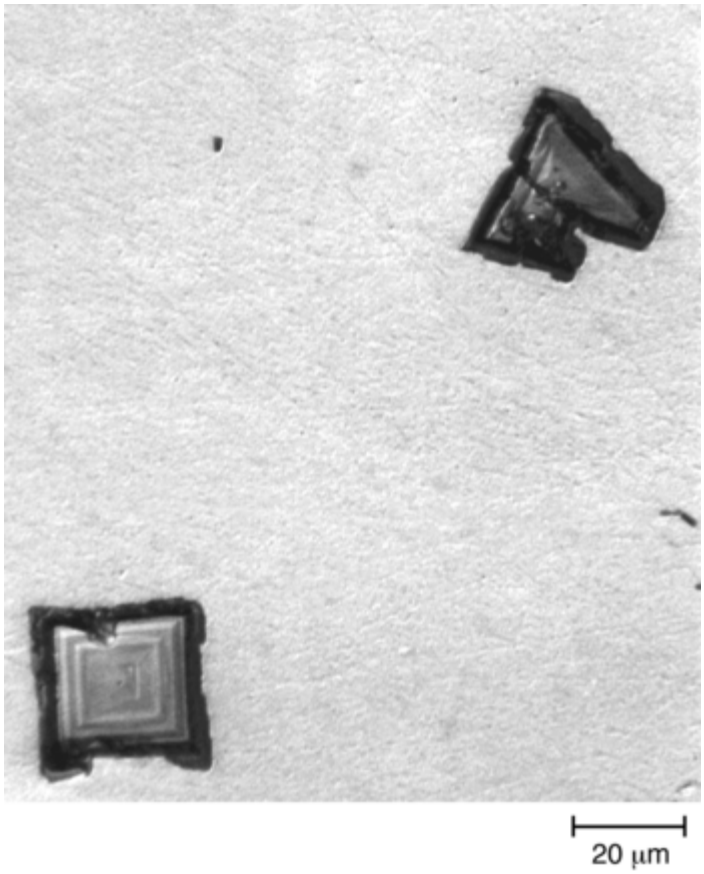

Fig. 34 Differential interference contrast (DIC) light micrograph of unalloyed uranium showing uranium carbide inclusions. Electropolished with 5% H_3PO_4, electroetched using procedure 2 in Table 5. 1000×. Courtesy of A. Kelly

U-0.3Mo is used for applications requiring a higher yield strength than that of unalloyed uranium. The material is usually vacuum induction melted, cast to near final shape, then used in the as-cast condition.

Low-magnification polarized light microscopy of as-cast U-0.3Mo reveals an irregular grain structure similar to that of cast unalloyed uranium, except that the grain size is finer (see Fig. 35). High-magnification bright-field microscopy reveals a fine, lamellar two-phase microstructure morphologically similar to pearlite in steels (Fig. 36). Apparently, this microstructure develops when the β phase, which dissolves the 0.3% Mo in solid solution, undergoes eutectoid decomposition to essentially pure α-uranium plus a molybdenum-enriched γ phase. Under some conditions, the γ phase may decompose at a lower temperature to a fine (probably optically unresolvable) mixture of α-uranium and U_2Mo.

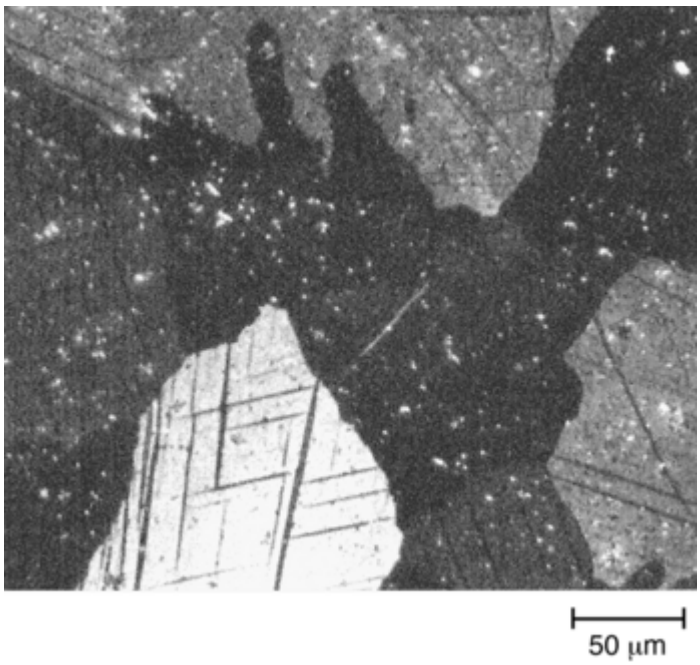

Fig. 35 Polarized light micrograph of cast U-0.3Mo showing irregular grain structure similar to that of unalloyed uranium. Electropolished using procedure 1 in Table 1and anodized using procedure 2 in Table 4. 200×. Courtesy of M.M. Lappin

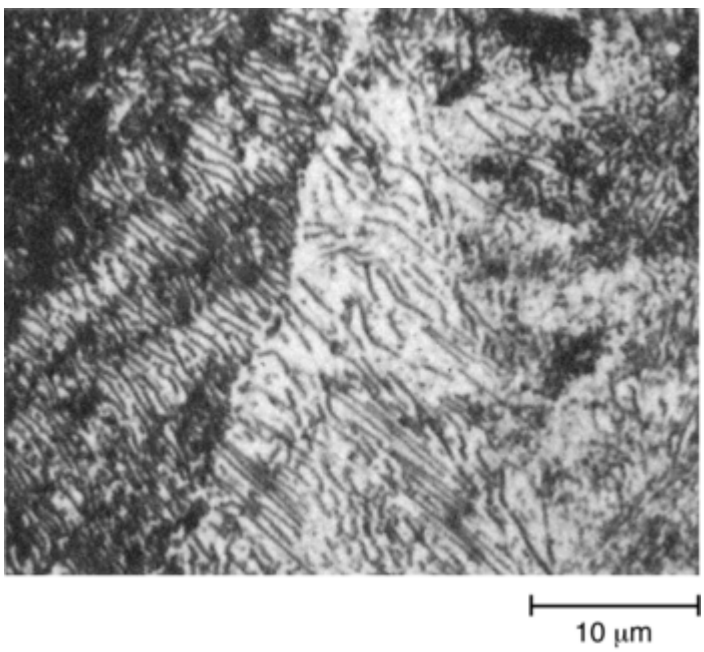

Fig. 36 Bright-field micrograph of cast U-0.3Mo showing two-phase lamellar structure resulting from eutectoid decomposition of β phase. Etched using procedure 1 in Table 5. 1500×. Courtesy of M.M. Lappin

Quenching of thin sections of U-0.3Mo from the α phase field suppresses the diffusional transformations that produce two-phase microstructures during slow cooling and results in a microstructure of supersaturated α phase (Fig. 3). The morphological similarities to unalloyed uranium suggest that the quenched material undergoes the γ to β to α transformation sequence of pure metal.

U-0.75Ti is used for applications requiring outstanding combinations of strength and ductility. Material is made by vacuum induction melting and casting. It is then mechanically worked in the high α range (600 to 640 °C, or 1110 to 1185 °F) by such processes as extrusion, rolling, and swaging, after which it is vacuum heat treated in the γ phase field to remove hydrogen, quenched to produce a supersaturated variant of α phase, and age hardened. This alloy is age hardenable to ~50 HRC, but its ductility and toughness are low in the fully aged

condition (elongation and reduction in area <3%, K_{Ic} ≈ 18 MPa$\sqrt{m}$, or 16 ksi $\sqrt{\text{in.}}$). Partial aging to • 44 HRC is more commonly used, resulting in a strong but ductile material with the following properties:

Yield strength, MPa (ksi)	**930 (135)**
Ultimate tensile strength, MPa (ksi)	1550 (225)
Elongation, %	20
Reduction in area, %	32
Plane-strain fracture toughness, MPa$\sqrt{m}$ (ksi$\sqrt{\text{in.}}$)	47 (43)

The microstructure of U-0.75Ti varies dramatically with cooling rate from the γ phase field and subsequent aging treatment. Slow cooling (<2 °C/s, or 3.6 °F/s) permits the equilibrium transformation sequence (γ → β + U_2Ti → α + U_2Ti) to occur and produces an optically resolvable two-phase microstructure that etches rapidly (see Fig. 37). Faster cooling suppresses formation of the β phase and results in direct decomposition of γ to α + U_2Ti. This microconstituent etches a uniform gray, because the individual phases are too fine to be resolved optically (Fig. 38). At cooling rates exceeding 10 °C/s (18 °F/s), the γ → α + U_2Ti reaction begins to be suppressed, resulting in partial transformation of the γ phase by a martensitic (diffusionless) reaction to a supersaturated variant of the α phase (Fig. 39). At cooling rates between 10 and 75 °C/s (18 and 135 °F/s), the α + U_2Ti microconstituent nucleates along the γ grain boundaries and proceeds inward, beginning to consume the γ phase. Before this reaction is complete, however, martensitic transformation begins and competes with α + U_2Ti formation for the remaining γ phase. The result is a microstructure with α + U_2Ti along the prior γ grain boundaries and α' martensite plus α + U_2Ti in the prior γ-grain interiors (Fig. 39).

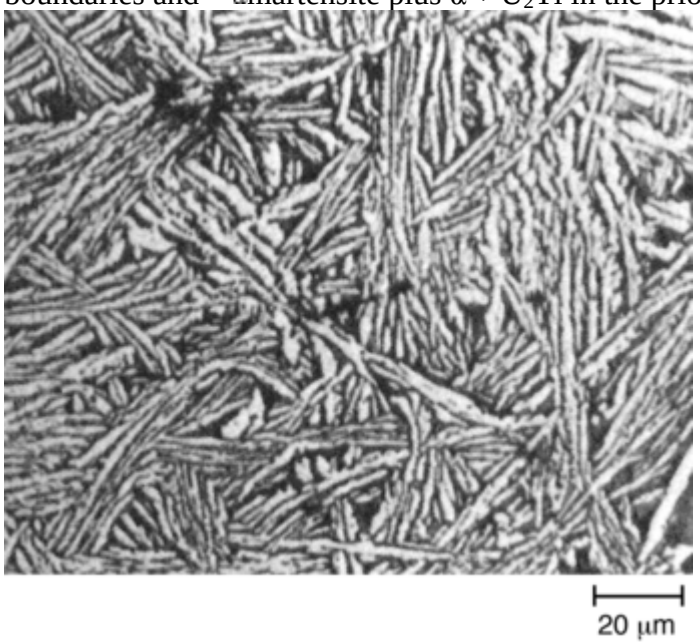

Fig. 37 Bright-field micrograph of U-0.75Ti cooled from 800 °C (1470 °F) at less than 1 °C/s (1.8 °F/s) showing coarse α + U_2Ti microstructure produced by the equilibrium γ → β + U_2Ti → α + U_2Ti transformation sequence. Etched using procedure 1 in Table 5. 400×. Courtesy of M.E. McAllaster

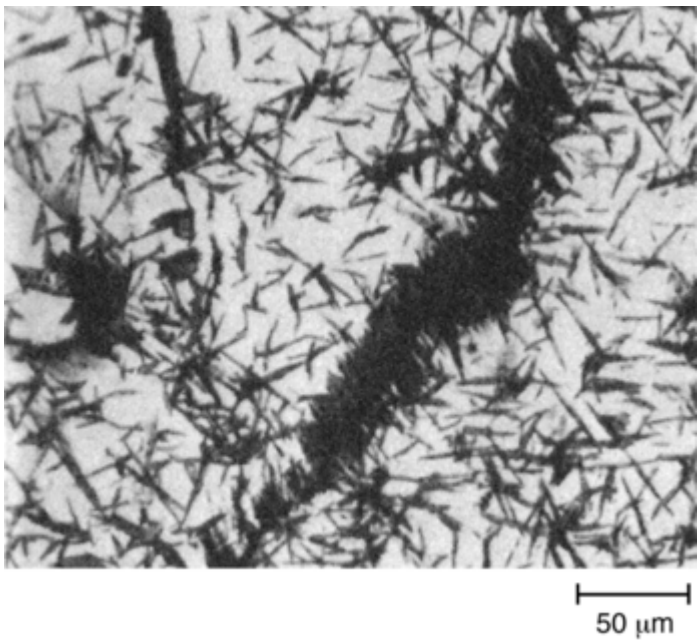

Fig. 38 Bright-field micrograph of U-0.75Ti cooled from 800 °C (1470 °F) at 5 °C/s (9 °F/s) showing dark-etching α + U_2Ti produced by the equilibrium γ → β + U_2Ti → α + U_2Ti transformation sequence and uniform gray α + U_2Ti produced by direct transformation of γ → α + U_2Ti. Etched using procedure 1 in Table 5. 200×. Courtesy of M.E. McAllaster

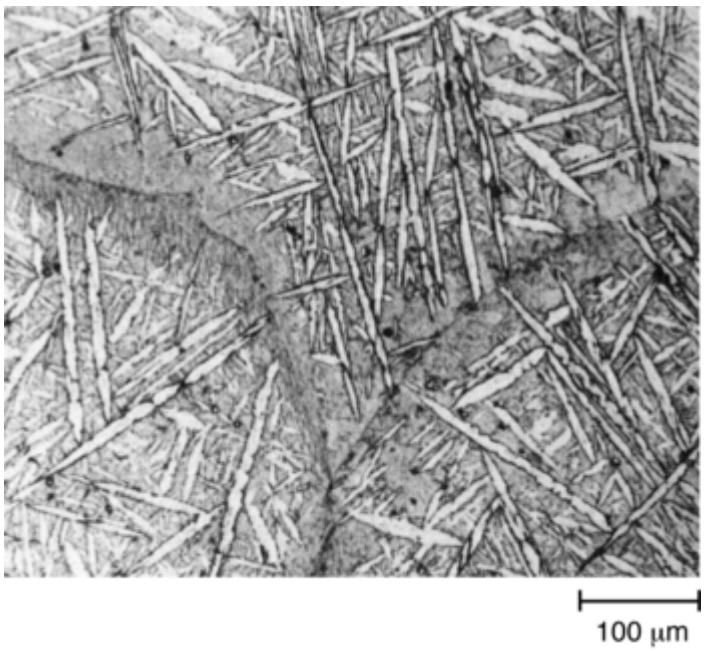

Fig. 39 Bright-field micrograph of U-0.75Ti cooled from 800 °C (1470 °F) at 25 °C/s (45 °F/s) showing light-etching acicular martensite and darker etching α + U_2Ti produced by the γ → α + U_2Ti reaction along the prior γ grain boundaries and in the interstices between the martensite plates. Etched using procedure 1 in Table 5. 100×. Courtesy of M.E. McAllaster

The amount of martensite in the microstructure increases with increasing cooling rate. At cooling rates greater than 75 °C/s (135 °F/s), decomposition of γ phase to α + U_2Ti no longer precedes the onset of the martensitic transformation; therefore, no α + U_2Ti is seen along the prior grain boundaries (the martensite start temperature is reached before α + U_2Ti can nucleate). Formation of α + U_2Ti, however, continues in the interstices between the martensite plates (nucleation of α + U_2Ti occurs before the martensite finish temperature is reached). This interplate α + U_2Ti forms a background against which the martensite can be revealed by etching and bright-field illumination (Fig. 4). At cooling rates greater than 200 °C/s (360 °F/s), diffusional decomposition is suppressed,

and the γ phase transforms to α' martensite. Because this is a single-phase microstructure, it is difficult to reveal by etching and bright-field microscopy (Fig. 40) and can be more easily observed with polarized light microscopy (Fig. 41).

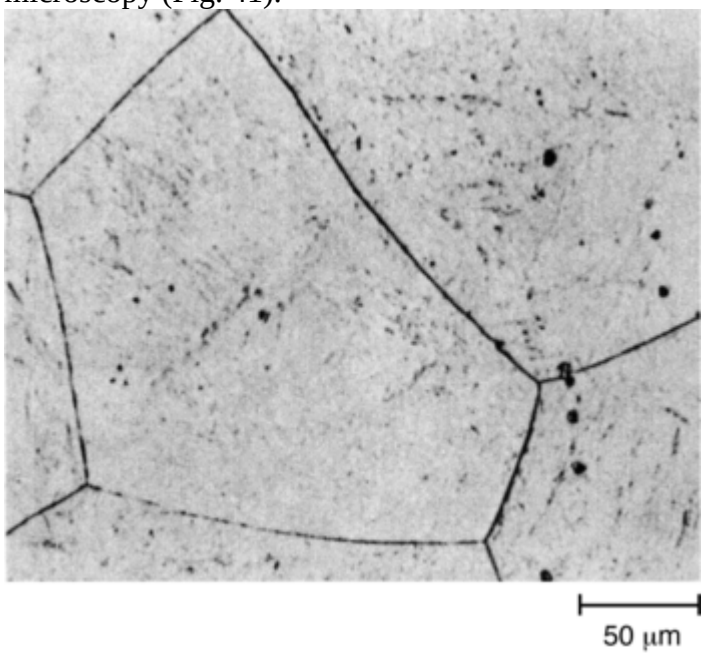

Fig. 40 Bright-field micrograph of U-0.75Ti cooled from 800 °C (1470 °F) at >200 °C/s (>360 °F/s) showing difficulty in revealing fully martensitic structure by etching and bright-field illumination. Etched using procedure 1 in Table 5. 200×. Courtesy of M.E. McAllaster

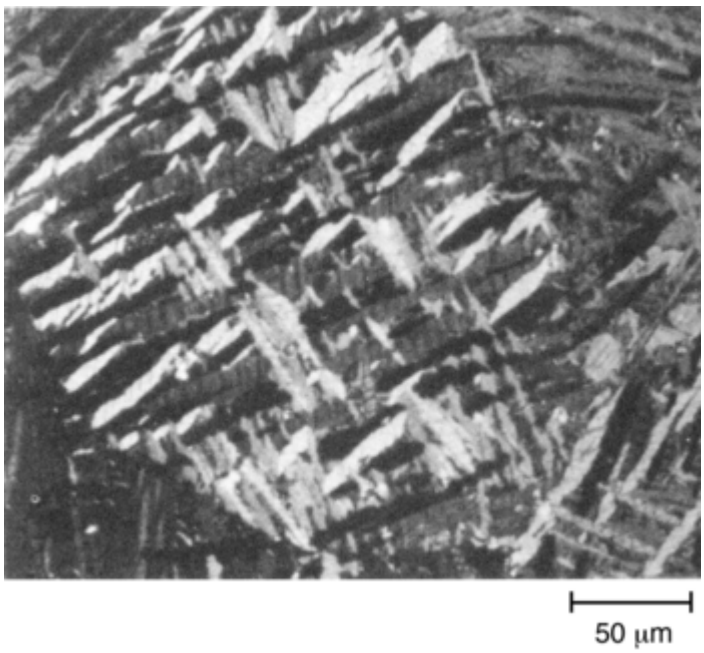

Fig. 41 Polarized light micrograph of U-0.75Ti cooled from 800 °C (1470 °F) at >200 °C/s (>360 °F/s) showing acicular martensite. Electropolished using procedure 1 in Table 1 and anodized using procedure 2 in Table 4. 200×. Courtesy of M.E. McAllaster

The rapid cooling required to suppress diffusional decomposition of the γ phase limits the section thicknesses in which martensite can be obtained. Water quenching produces fully martensitic microstructures with optimal ductility and age hardenability only in plates thinner than a few millimeters. The amount of martensite decreases with increasing plate thickness, but good mechanical properties can be obtained in plates as thick as at least 25 mm (1 in.). Plates thicker than about 30 mm (1.2 in.) exhibit predominantly nonmartensitic microstructures and substantially lower ductilities, even when quenched in severely agitated cold water. Severe

quenching of thick sections (25 mm, or 1 in., or more) may also cause centerbursting in bar stock due to the volume changes associated with phase transformations.

Material with a fully or predominantly martensitic microstructure can be age hardened at 325 to 450 °C (615 to 840 °F). The microstructural changes responsible for age hardening of the martensite are too fine to be resolved by light microscopy, but transmission electron microscopy has shown that strengthening occurs due to the formation of coherent precipitates of U_2Ti. Overaging occurs at temperatures above about 450 °C (840 °F) by cellular decomposition of the martensite to the equilibrium α and U_2Ti phases. This decomposition reaction nucleates preferentially along the prior γ grain boundaries, and its product etches much darker than the α_2' martensite (Fig. 9). The individual α and U_2Ti features are too fine to be resolved optically, except after extensive averaging, when the U_2Ti can be seen to form a semicontinuous, embrittling film along the prior martensite plate boundaries (Fig. 42).

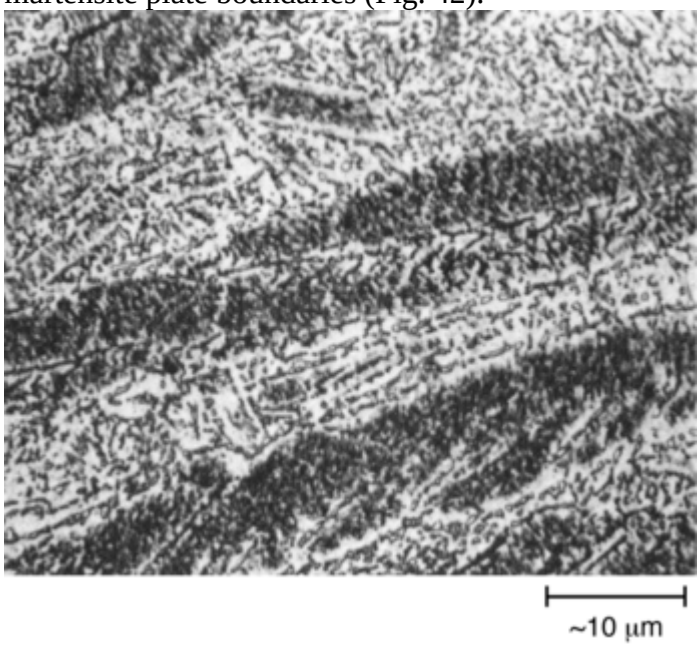

Fig. 42 Bright-field micrograph of U-0.75Ti quenched from 800 °C (1470 °F) and fully overaged at 600 °C (1110 °F) for 5 h showing decoration of prior martensite plate boundaries with brittle U_2Ti. Etched using procedure 1 in Table 5. 1250×. Courtesy of M.E. McAllaster

U-2.0Mo is used for applications requiring higher strength than unalloyed uranium and where section thickness or other constraints prevent the use of U-0.75Ti. The alloy is made by vacuum induction melting and casting. It is frequently used in the form of castings, but it can also be fabricated in the high α (600 to 640 °C, or 1110 to 1185 °F) or γ (800 to 840 °C, or 1470 to 1545 °F) temperature ranges. Thick components are usually used in the as-cast or annealed (slowly cooled) condition, while thinner parts are sometimes more rapidly cooled, then aged.

The microstructure of a slowly cooled, rapidly etched material consists of a coarse α + Mo-enriched-γ mixture (see Fig. 43) similar to that of slowly cooled U-0.75Ti. These phases become more finely divided with increasing cooling rate. At rates from about 2 to 10 °C/s (3.6 to 18 °F/s), the individual phases become difficult to resolve optically, and substantial morphological changes occur (Fig. 44). Although these have not been studied in detail, preliminary indications suggest that these microstructures may be analogous to bainite in steels (that is, fine two-phase microstructures produced by a combination of displacive and diffusional atom movements). Rapid quenching (>50 °C/s, or 90 °F/s) suppresses most diffusional transformations and produces a thermoelastic, or banded, martensite. Etching and bright-field examination reveal primarily the prior γ grain boundaries (Fig. 45), but the martensitic structure can be clearly seen by anodizing the sample and using polarized light illumination (Fig. 5).

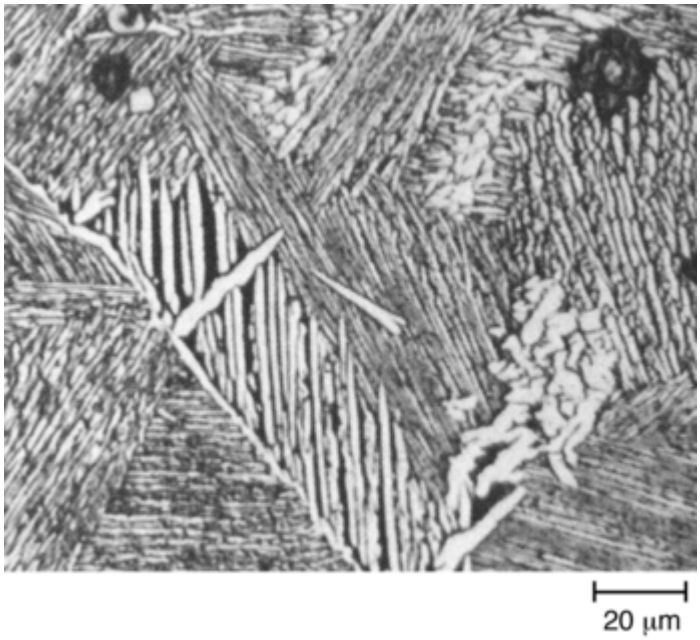

Fig. 43 Bright-field micrograph of as-cast U-2.0Mo showing coarse α + γ microstructure. Etched using procedure 1 in Table 5. 400×. Courtesy of M.E. McAllaster

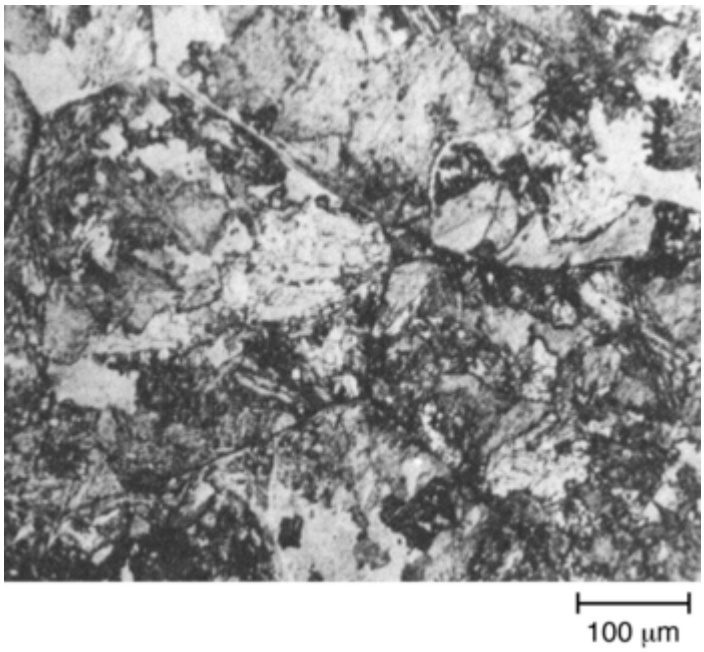

Fig. 44 Bright-field micrograph of U-2.0Mo cooled from 800 °C (1470 °F) at 4 °C/s (7 °F/s) showing microstructure typical of intermediate cooling rates. Etched using procedure 1 in Table 5. 100×. Courtesy of M.E. McAllaster

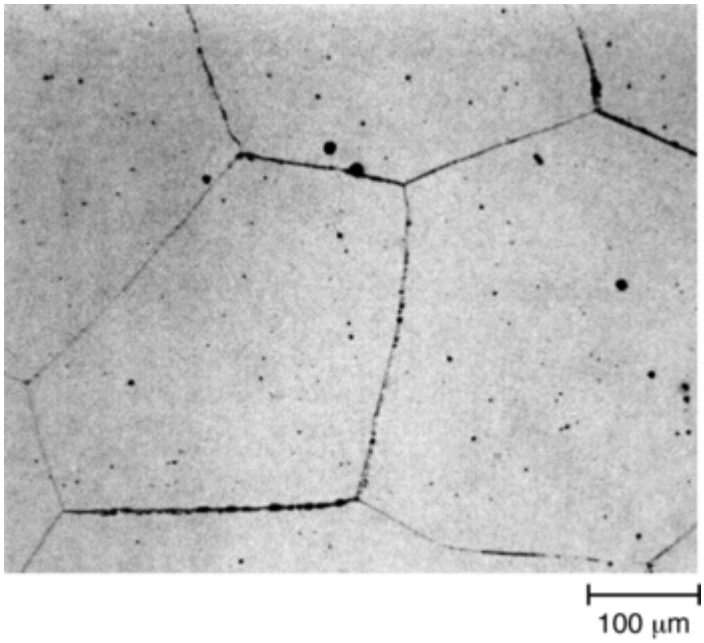

Fig. 45 Bright-field micrograph of U-2.0Mo cooled from 800 °C (1470 °F) at >100 °C/s (>180 °F/s) showing difficulty in revealing thermoelastic martensitic structure by etching and bright-field illumination. Etched using procedure 1 in Table 5. 100×. Courtesy of M.E. McAllaster

This martensite and, to a lesser extent, some structures produced by intermediate cooling rates can be age hardened, but the microstructural changes responsible for strengthening have not yet been resolved, even by transmission electron microscopy. Overaging occurs at temperatures above ~400 °C (~750 °F) by cellular decomposition of the martensite. Decomposition begins along the prior γ grain boundaries and at inclusions (Fig. 10), eventually consuming the martensite and resulting in what appears metallographically to be a network of fine irregular grains within each prior γ grain (Fig. 46). This rapid etching decomposition product consists of a very fine mixture of α phase and molybdenum-enriched γ phase that can be resolved only by transmission electron microscopy. Higher temperature or longer aging transforms this decomposition product, through a second discontinuous reaction, into a coarser two-phase mixture of α phase and U_2Mo. This reaction nucleates on small, persistent vestiges of the original martensite structure, and the crystallographic orientations of the α phase it produces are apparently related to, and perhaps identical to, those of the martensite. As a result, this reaction, when partially complete, gives the appearance that the original banded martensite is reappearing within the irregular grains of the first decomposition product (Fig. 47). When this reaction is complete, the microstructure observable by etching and bright-field microscopy consists of an optically resolvable lamellar mixture of α phase and U_2Mo (Fig. 48). Anodization and polarized light examination, however, reveal that the α phase is crystallographically oriented in parallel bands that span numerous lamellae and are reminiscent of the original martensite morphology (Fig. 49).

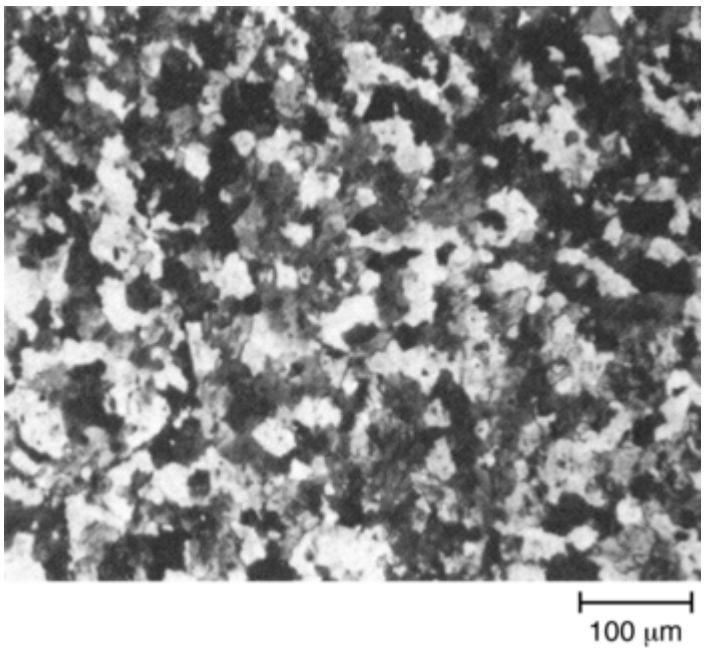

Fig. 46 Polarized light micrograph of U-2.0Mo quenched from 800 °C (1470 °F) and overaged at 400 °C (750 °F) for 90 h showing colonies of fine (optically unresolvable) α + γ produced by cellular decomposition of the thermoelastic martensite. Electropolished using procedure 1 in Table 1and anodized using procedure 2 in Table 4. 100×. Courtesy of M.E. McAllaster

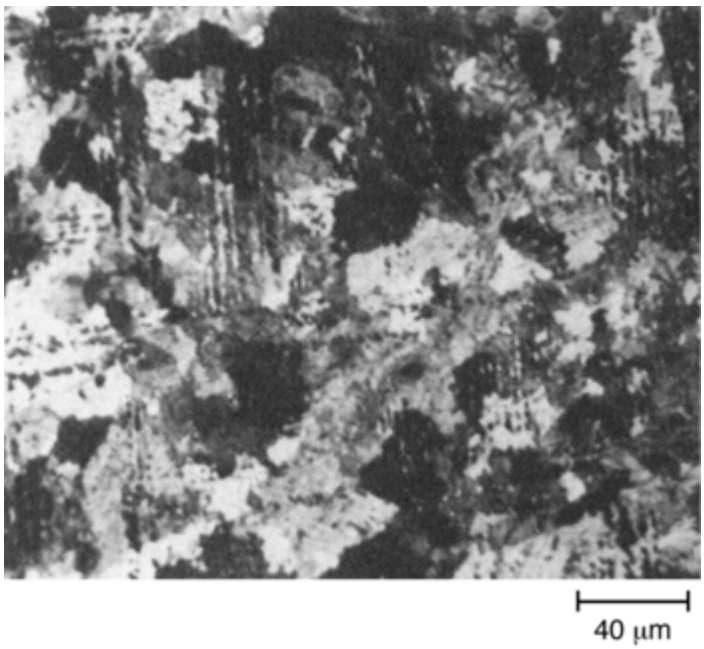

Fig. 47 Polarized light micrograph of U-2.0Mo quenched from 800 °C (1470 °F) and overaged at 450 °C (840 °F) for 5 h showing beginning of discontinuous transformation of α + γ (irregular equiaxed colonies) to α + U_2Mo (long, parallel features). Electropolished using procedure 1 in Table 1and anodized using procedure 2 in Table 4. 250×. Courtesy of M.E. McAllaster

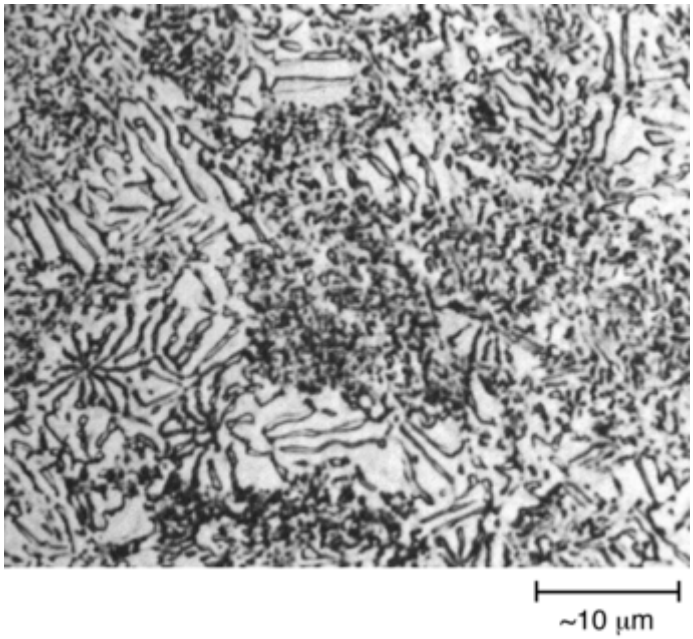

Fig. 48 Bright-field micrograph of U-2.0Mo quenched from 800 °C (1470 °F) and fully overaged at 500 °C (930 °F) for 90 h showing lamellar α + U_2Mo structure. Etched using procedure 1 in Table 5. 1250×. Courtesy of M.E. McAllaster

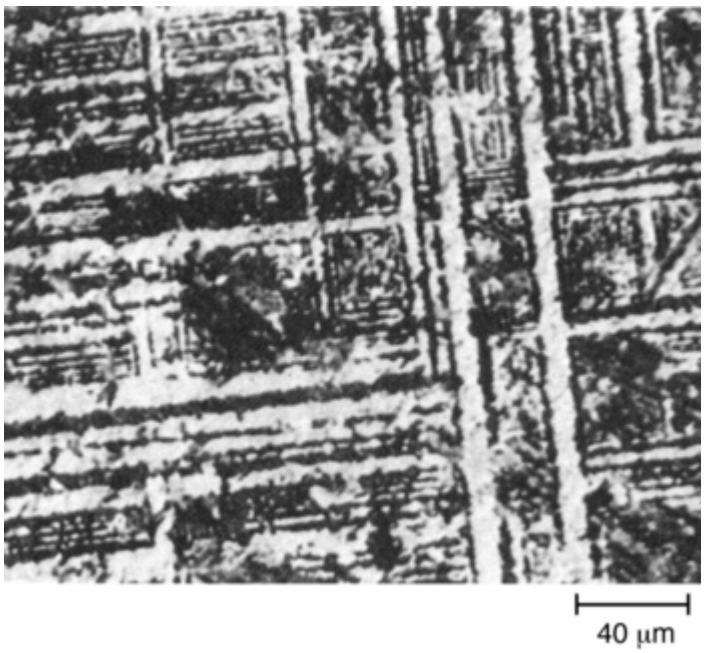

Fig. 49 Polarized light micrograph of U-2.0Mo quenched from 800 °C (1470 °F) and fully overaged at 500 °C (930 °F) for 90 h showing crystallographic orientation of the α phase in parallel bands reminiscent of the preexisting α'_bmartensite. Electropolished using procedure 1 in Table 1 and anodized using procedure 2 in Table 4. 250×. Courtesy of M.E. McAllaster

U-6.0Nb is used for applications requiring excellent corrosion resistance (for a uranium alloy) and outstanding ductility. The material is made by sub arc melting of DU with niobium plates followed by consumable electrode vacuum arc melting. This alloy is usually produced by the DOE's ORNL. The high amount of alloying element provides relatively high elevated-temperature strength; therefore, equipment tonnage limitations frequently force metalforming operations to be performed in the γ region (800 to 840 °C, or 1470 to 1545 °F). The alloy is solution treated in the γ phase field and quenched to room temperature, producing a soft and ductile thermoelastic martensite with the following properties:

Hardness, HRB	**92**
Yield strength, MPa (ksi)	170 (25)
Ultimate tensile strength, MPa (ksi)	895 (130)
Elongation, %	32
Reduction in area, %	36

This martensite can be aged to hardnesses as high as 54 HRC, but because ductility decreases substantially with increasing strength, age hardening is rarely used. The as-quenched martensite, however, is often given a very low temperature (~150 °C, or 300 °F) heat treatment to improve dimensional stability. The α_b to γ° reversible martensitic transformation that occurs slightly above room temperature produces a strong mechanical shape memory effect in this alloy. Because arc melting causes significant chemical inhomogeneity and the α_b to γ° transformation temperature is very sensitive to alloy content, the as-quenched material frequently undergoes dimensional instabilities that are related to normal fluctuations in ambient temperature. Very low temperature aging stabilizes the material to these temperature variations without appreciably altering its tensile properties.

U-6.0Nb is markedly less quench-rate sensitive than U-0.75Ti. Only at cooling rates well below 1 °C/s (1.8 °F/s) are rapid-etching two-phase lamellar microstructures produced (see Fig. 50, Fig. 51). As the cooling rate increases toward 1 °C/s (1.8 °F/s), these regions become confined to the prior γ grain boundaries (Fig. 52); polarized light examination reveals that the remainder of the microstructure consists of martensitic α_b. The martensite produced at cooling rates of 1 to 10 °C/s (1.8 to 18 °F/s), however, contains two features that are not completely understood. Bands parallel to the rolling direction consisting of apparent subgrain boundaries are visible with bright-field illumination (Fig. 52). A fine, modulated structure, which can be seen by transmission electron microscopy, substantially increases strength and decreases ductility. At cooling rates greater than 10 °C/s (18 °F/s), the modulated structure disappears, and the α_b martensite becomes more soft and ductile. The subgrain structure, which has no apparent effect on mechanical properties, becomes more uniformly distributed but less extensive with increasing cooling rate (Fig. 53).

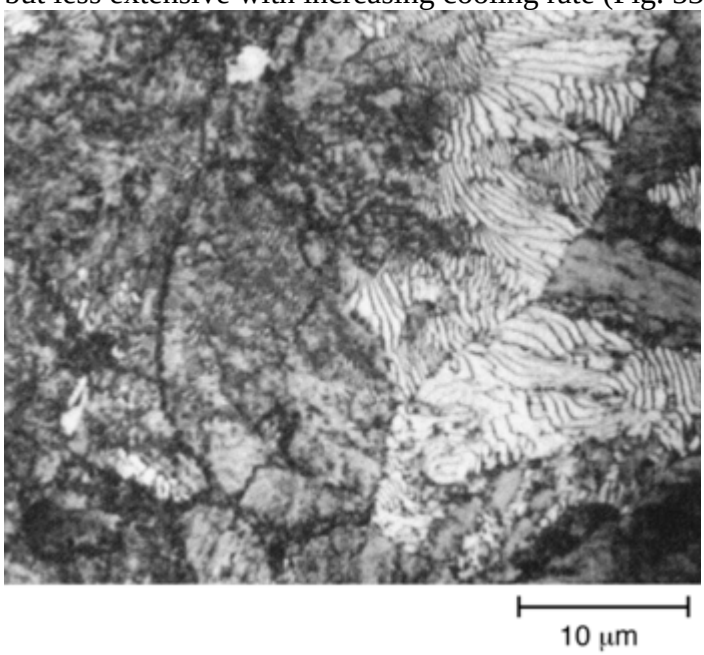

Fig. 50 Bright-field micrograph of U-6.0Nb cooled from 800 °C (1470 °F) at 0.04 °C/s (0.07 °F/s) showing lamellar two-phase structure. Etched using procedure 1 in Table 5. 1500×. Courtesy of M.E. McAllaster

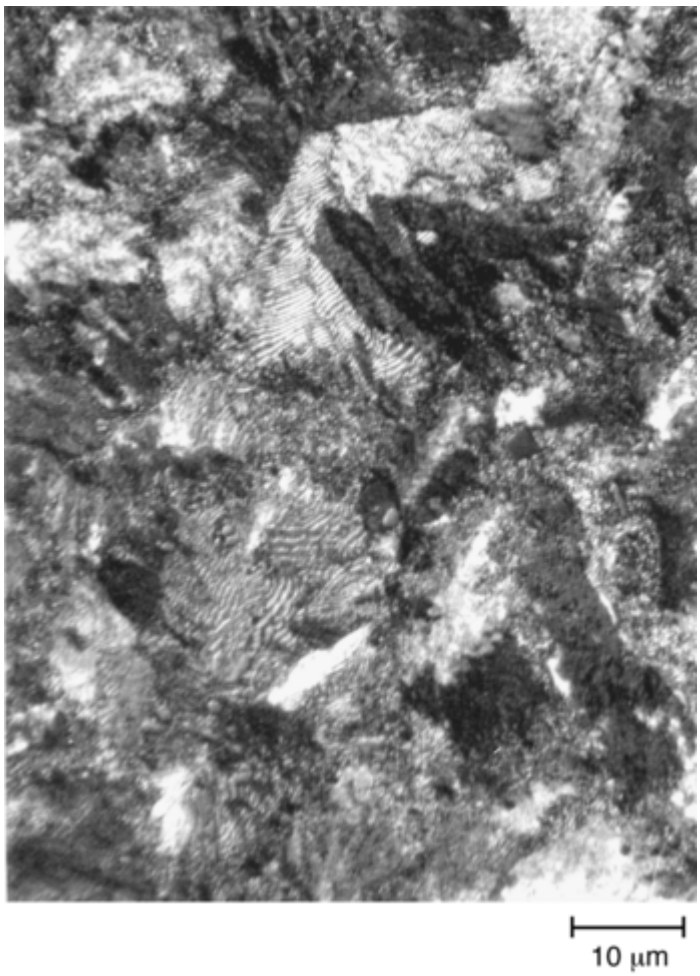

Fig. 51 Differential interference contrast (DIC) light micrograph of cast U-6.0Nb showing two-phase lamellar structure resulting from monotectoid decomposition of the α phase. Electropolished with 5% H_3PO_4, electroetched using procedure 2 in Table 5. 1000×. Courtesy of A. Kelly

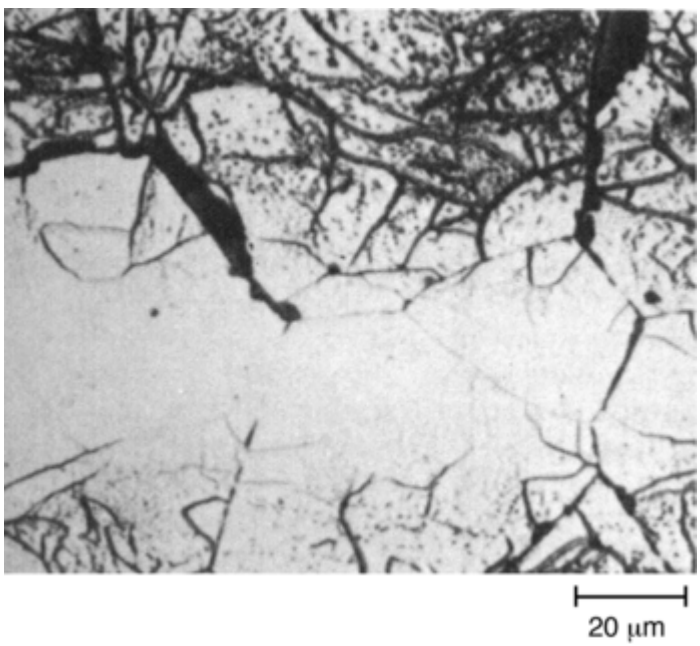

Fig. 52 Bright-field micrograph of U-6.0Nb cooled from 800 °C (1470 °F) at 0.08 °C/s (1.4 °F/s) showing diffusional decomposition product at some prior γ grain boundaries and bands of subgrain boundaries parallel to the rolling direction. Etched using procedure 1 in Table 5. 500×. Courtesy of M.E. McAllaster

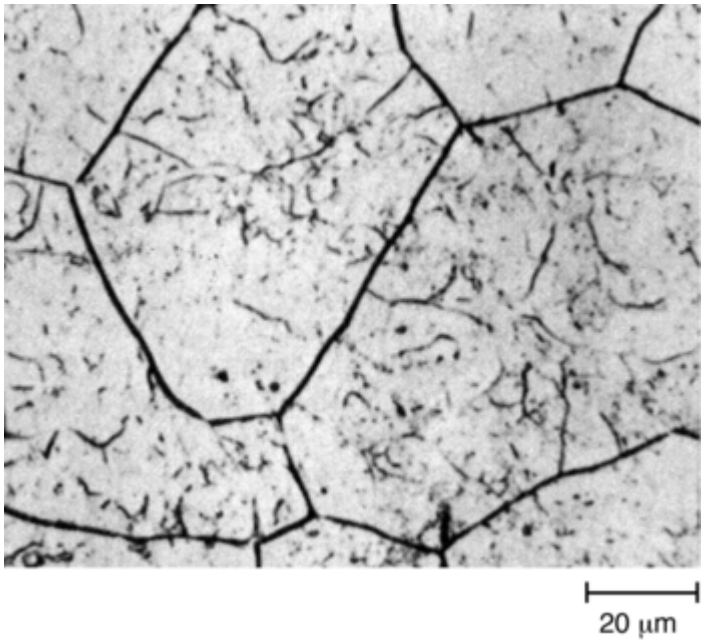

Fig. 53 Bright-field micrograph of U-6.0Nb cooled from 800 °C (1470 °F) at 20 °C/s (36 °F/s) showing prior γ grain boundaries and more uniformly distributed subgrain structure. Etched using procedure 1 in Table 5. 500×. Courtesy of M.E. McAllaster

The $\alpha_b$thermoelastic martensite within the prior γ grains are revealed by polarized light microscopy (Fig. 6) or by differential interference contrast illumination (DIC) (Fig. 7). Other examples of grain structure, twins, and inclusions revealed by DIC illumination are shown in Fig. 54, 55, 56, 57 and 58. Figure 58 also shows an example of chemical banding. Figure 59 shows a more pronounced example of chemical banding, which was verified by hardness data. The image also served as a map for electron microprobe analysis, which showed that the niobium composition varied from 4 to 7.5 wt% Nb.

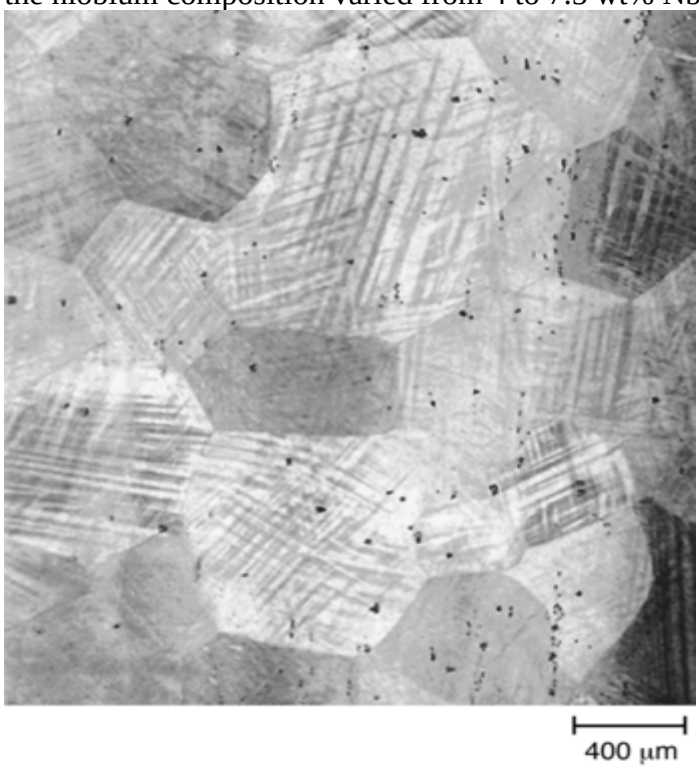

Fig. 54 Differential interference contrast (DIC) light micrograph of U-6.0Nb showing twinning, grain boundaries, and inclusions. Electropolished with 5% H_3PO_4, electroetched using procedure 2 in Table 5. Original magnification, 50×. Courtesy of A. Kelly

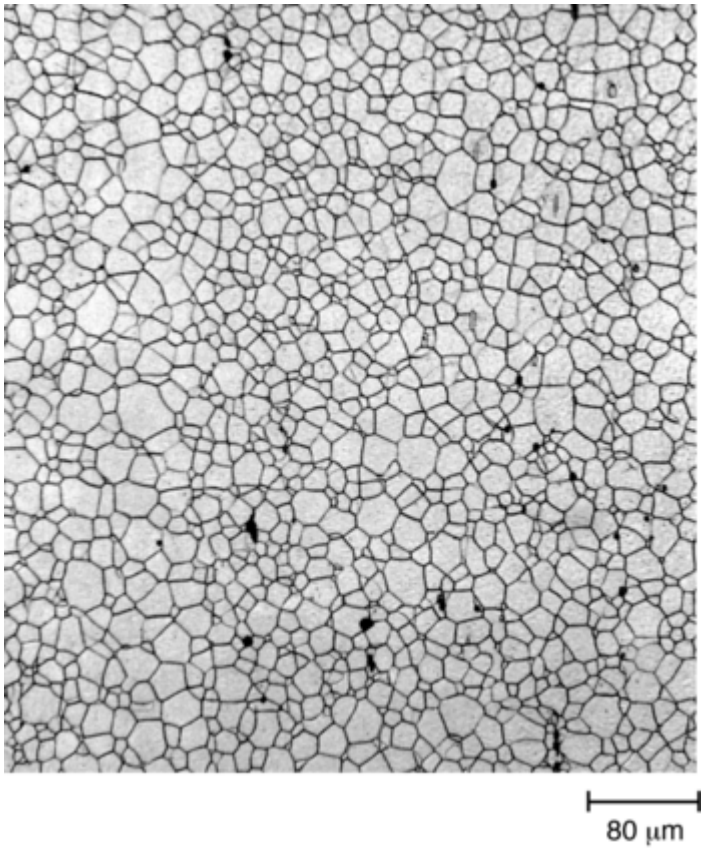

Fig. 55 Differential interference contrast (DIC) light micrograph of U-6.0Nb solution annealed material. Electropolished with 5% H_3PO_4, electroetched using procedure 2 in Table 5. 250×. Courtesy of A. Kelly

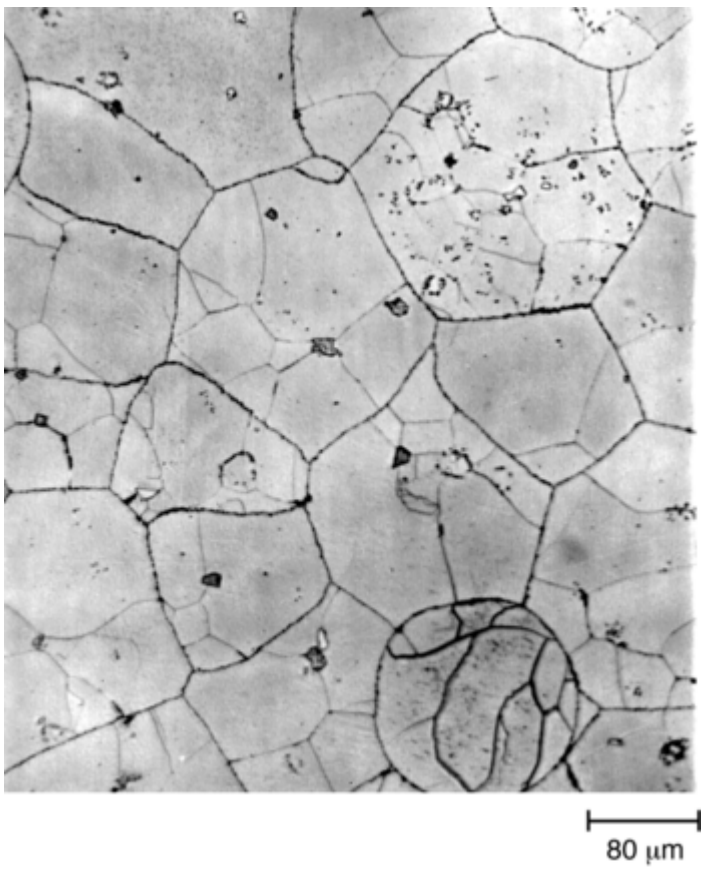

Fig. 56 Differential interference contrast (DIC) light micrograph of PM U-6.0Nb showing grain and inclusion definition. Specimen was electropolished with 5% H_3PO_4, at 5 V for ~3 s followed by electroetching with 10% oxalic at 6 V for ~4 s. 250×. Courtesy of A. Kelly



Fig. 57 Differential interference contrast (DIC) light micrograph of U-6.0Nb showing grain delination and twinning. Electropolished with 5% H_3PO_4, electroetched using procedure 2 in Table 5. 1000×. Courtesy of A. Kelly

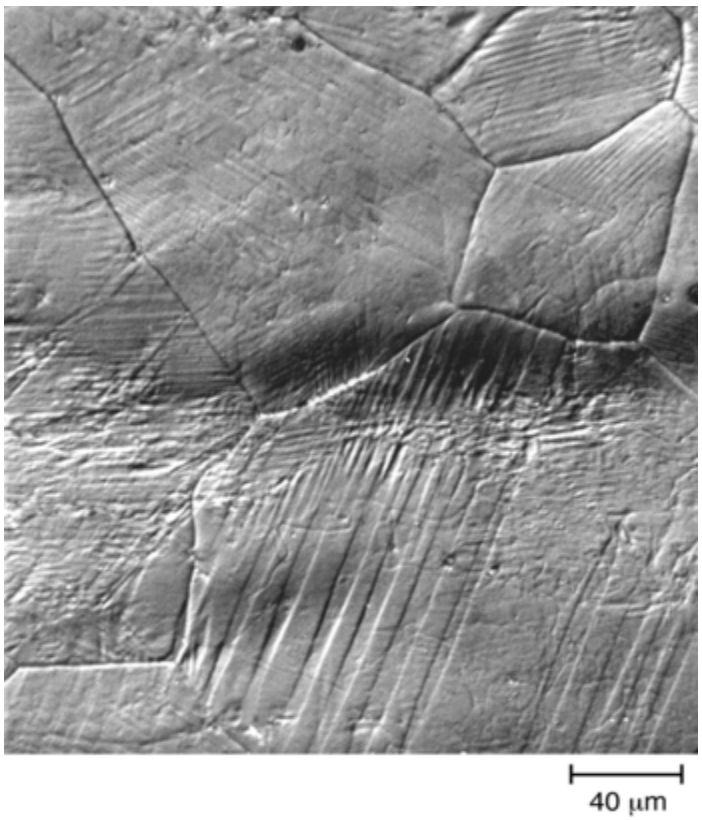

Fig. 58 Differential interference contrast (DIC) light micrograph of U-6.0Nb showing grain boundaries, chemical banding, twins and inclusions. Electropolished with 5% H_3PO_4, electroetched using procedure 2 in Table 5. Courtesy of A. Kelly

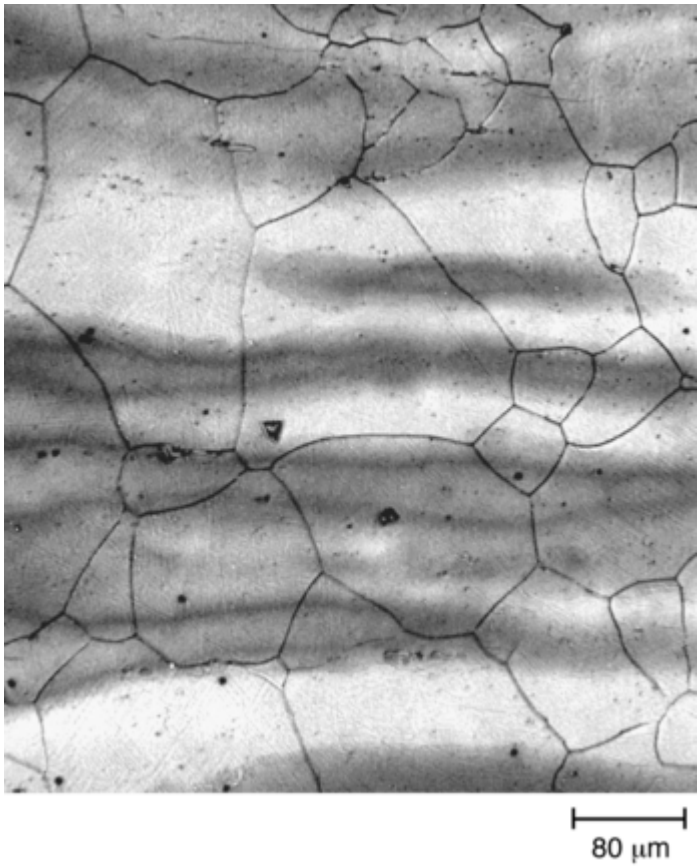

Fig. 59 Differential interference contrast (DIC) light micrograph of U-6.0Nb showing chemical banding. Electropolished using 5% H_3PO_4, electroetched using procedure 2 in Table 5. Followed by a second (as above) electropolish that defines chemical banding. 250×. Courtesy of A. Kelly

Age hardening produces no microstructural changes resolvable by optical microscopy. A fine, modulated structure, similar to that in higher-strength material cooled at about 1 °C/s (1.8 °F/s), can be detected by transmission electron microscopy in age-hardened material. Overaging occurs at temperatures in excess of about 400 °C (750 °F) via cellular decomposition of the martensite. As with other alloys, this decomposition nucleates along the prior γ grain boundaries, and the decomposition product etches more rapidly than the martensite (Fig. 11).

U-7.5Nb-2.5Zr, sometimes termed “mulberry,” is similar to U-6.0Nb. Its high alloy content, however, enables the γ° tetragonal distortion of the γ phase to be retained after quenching to room temperature. This microstructure appears as simple equiaxed grains with no internal substructure when viewed by optical microscopy (see Fig. 8), although transmission electron microscopy has revealed a fine, modulated substructure. The alloy can be age hardened at temperatures between 100 and 400 °C (210 and 750 °F), but is most frequently used in the as-quenched or quenched and thermally stabilized condition. Overaging occurs at temperatures above 400 °C (750 °F) due to grain boundary nucleated cellular decomposition, resulting in microstructures similar to those of U-6.0Nb.

Revised by H.E. Fairman and A. Kelly, Metallography and Microstructures of Uranium and Its Alloys, *Metallography and Microstructures,* Vol 9, *ASM Handbook,* ASM International, 2004, p. 918–932

Metallography and Microstructures of Uranium and Its Alloys

Revised by Henry E. Fairman, Department of Energy Feed Materials Production Center (Retired) and Ann Kelly, Los Alamos National Laboratory

Sample Preparation

Methods for preparation of metallographic samples of uranium have been thoroughly reviewed in Ref 1 and 9. This section draws heavily on these references and emphasizes current, successful techniques. Methods for preparation of thin foils for transmission electron microscopy are also described in the literature (Ref 6, 10), but are not reviewed in this article.

Health and Safety Considerations. Handling and metallographic preparation of depleted uranium is similar to that of most metals, although its mild radioactivity, chemical toxicity, and pyrophoricity require additional precautions. Although extreme measures such as shielded glove box handling are not required, a common-sense approach based on a realistic understanding of the hazards involved is essential. This section briefly outlines the principal hazards and necessary precautions associated with the metallographic preparation of depleted uranium. More complete information on the health and safety aspects of working with uranium can be found in Ref 11, 12 and 13. Organizations performing uranium metallography should have their procedures as well as the engineering designs of their cutting and grinding areas approved regularly by an occupational health and safety organization for compliance with the referenced guidelines and government regulations. Personnel and work areas should also be tested and inspected periodically.

Department of Energy Standard 1136, "Guide of Good Practices for Occupational Radiological Protection in Uranium Facilities," provides the current guidance for health and safety considerations along with requirements for compliance with the U.S. Clean Air and U.S. Clean Water acts.

The primary radiological hazards associated with depleted uranium are beta and alpha emission. The beta-ray dose rate at the surface of a uranium slug is 0.23 rad/h. This dose rate decreases dramatically with increasing distance from the source, due to absorption in the air and geometric effects. In addition, for specimens mounted in Bakelite or epoxy, virtually none of the beta radiation passes through the mount. Alpha radiation is also emitted, but is almost totally absorbed in 10 mm (0.4 in.) of air or in the 0.07 mm (0.003 in.) thick protective layer of skin and, therefore, presents no external health hazard. The gamma-radiation dose rate measured at a typical working distance of 400 mm (16 in.) from an unmounted 55 g (2 oz) sample is 1×10^{-6} R/h, or about one-tenth of the natural gamma background rate. (1 R, or roentgen, equals 2.58×10^{-4} coulomb/kg.) As a result, normal metallographic handling of depleted uranium virtually never causes exposures approaching the federal and state external exposure limits of 3 rem (roentgen equivalent man) per quarter/5 rem per year for whole body exposure or 25 rem per quarter/75 rem per year for extremity (e.g., finger) exposures. Undesirable exposure could result, however, from storing samples in clothes pockets or repeatedly wearing lab coats extensively soiled with fine debris from uranium cutting or grinding operations.

While alpha radiation poses essentially no external health hazard, it does require caution during sectioning and grinding to ensure that finely divided uranium particles do not become airborne, where they could be inhaled and result in alpha irradiation of delicate lung tissue. Methods for ensuring that airborne uranium concentrations remain below the U.S. Occupational Safety and Health Administration standard of 0.25 mg/m^3 of air are discussed later in this section.

Depleted uranium is about as chemically toxic as other heavy metals, such as lead. Although this does not dictate a need for extreme measures in handling, appropriate housekeeping and personal hygiene practices will minimize the possibility of ingesting uranium, which could damage the kidneys. For example, disposable gloves should be worn during cutting and grinding; hands should be washed thoroughly before eating; smoking, eating, or drinking should not be permitted in areas where cutting and grinding are performed; and tabletops and floors should be wet wiped or mopped daily. These measures are particularly important in areas where hot-worked parts are being handled, because the powdery oxide scale accentuates contamination of laboratory furniture and personnel.

Because finely divided uranium is also pyrophoric, sparks are frequently generated during cutting. The ignition temperature for 270-mesh (about 50 mm, or 2 in.) powder is only 20 °C (68 °F). Therefore, liberal amounts of cutting fluid should be used in cutting and grinding, and cleaning should be done regularly to avoid accumulation of finely divided waste in saws, cutoff wheels, or grinders. Extinguishers for metal fires should also be available. (Met-L-EX is recommended, as CO_2 and halon are ineffective).

Sectioning. Samples for metallographic preparation can be cut with a power saw or an abrasive cutoff wheel (see the article "Metallographic Sectioning and Specimen Extraction" in this Volume for additional information on these methods). Liberal amounts of nonflammable cutting fluid will minimize the generation of airborne material and the danger of fire. In addition, high-speed cutoff wheels that produce finely divided uranium particles should be enclosed and their interiors vented with negative-pressure high-efficiency particulate arrestance (HEPA) filtered units to prevent airborne material from escaping into the room and/or the atmosphere, where it could be directly inhaled or perhaps eventually ingested after settling on laboratory surfaces. Wearing disposable gloves during cutting as well as washing samples and hands after sectioning will further reduce laboratory contamination and health hazards. Finely divided metal residue should be removed regularly to minimize the danger of fire. Metal scraps, cutting residue, used cutting fluid, worn grinding papers, and so forth should be stored and discarded appropriately.

Excessive heat during sectioning can alter the hardness and microstructures of many uranium alloys. Cutting-induced temperature increases can be minimized with low cutting rates and large amounts of cutting fluid. The care required to avoid heating depends on the material being prepared and on the type of measurements planned. The most temperature-sensitive materials are as-quenched alloys (particularly those containing substantial amounts of alloying elements), such as U-6Nb. In these alloys, changes in hardness and fine microstructural features (sometimes resolvable by transmission electron microscopy and similar techniques, but not by light microscopy) can occur from short-time exposures to temperatures as low as 150 °C (300 °F), and gross microstructural changes (resolvable by light microscopy) can occur below 400 °C (750 °F). As-quenched alloys that contain lesser amounts of alloying elements, such as U-0.75Ti, are more stable, exhibiting fine and gross microstructural changes at approximately 350 °C (660 °F) and 500 °C (930 °F), respectively. Age-hardened materials are stable up to the temperature at which they had been heat treated, while annealed two-phase materials and unalloyed uranium are stable to greater than 600 °C (1110 °F).

Cutting-induced deformation can also result in microstructural artifacts. Sensitivity to deformation generally increases with decreasing hardness and is most acute in unalloyed uranium and as-quenched alloys near the α'' to γ° transition, such as U-6Nb. Sectioning deformation is best minimized with low cutting rates; when suspected, it can often be removed by careful grinding to below the depth of deformation damage.

Mounting. Uranium can be mounted in any of the common metallographic mounting materials, such as Bakelite, phenolic, and epoxy. Compression mounting may not be an acceptable mounting method for material that is fragile or susceptible to phase transformation at or near the molding temperature (180° C, or 360 °F). Therefore, the recommended mounting method is to vacuum impregnate the specimens with a slow curing epoxy. This is accomplished using a vacuum chamber designed to allow simultaneous evacuation of specimen and epoxy (mixed at a 10-to-1 ratio of Epon 815 resin and diethylenetriamine) and subsequent pouring of the epoxy into the mounting cups while under vacuum. Once impregnated, the specimens are pressure cured in a dry nitrogen atmosphere of 6 to 7 MPa (800 to 1000 psi), followed by a postcure (optional) of ~60 °C (~140 °F). If this method is not feasible, coating the specimens (nickel plating, spraying with epoxy paint, etc.) prior to mounting can prevent bubble formation. Nickel plating also can be used to avoid edge rounding during polishing—when a fracture profile is to be examined, for example. However, because uranium surfaces oxidize rapidly when exposed to air, the nickel plating may not adhere. This can be overcome by sputter depositing a thin layer of a conductive material, such as a gold-palladium alloy, onto the oxidized surface prior to nickel plating. Sputtering can usually be performed in a scanning electron microscopy laboratory, because nonconductive materials must be coated prior to examination by scanning electron microscopy.

An example of good edge retention is in Fig. 60 by showing twins at the very edge of the sample. Another fracture surface, where edge retention is secondary, is nonetheless interesting because it reveals shear bands near the fracture surface (Fig. 61).

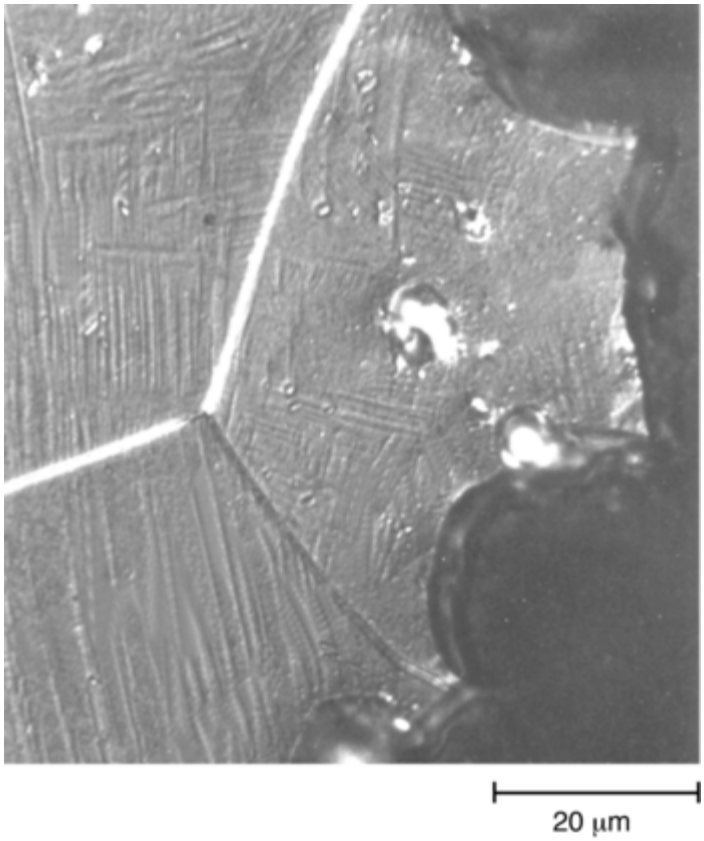

Fig. 60 Differential interference contrast (DIC) light micrograph of U-6.0Nb showing sample flatness and well-defined microstructure to the edge of fracture surface. Electropolished with 5% H_3PO_4, electroetched using procedure 2 in Table 5. Courtesy of A. Kelly

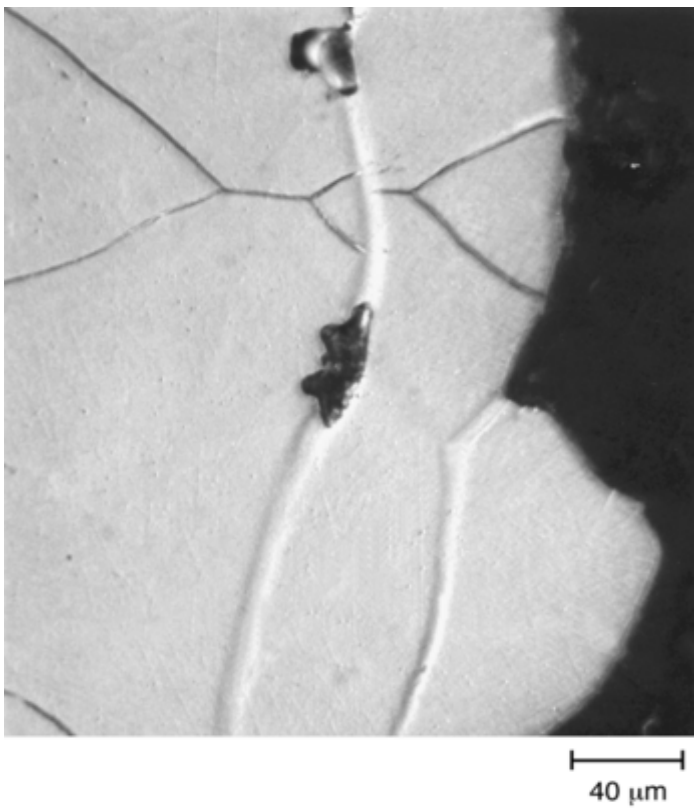

Fig. 61 Differential interference contrast (DIC) light micrograph of U-6.0Nb fracture specimen showing shear banded region near fracture surface. Electropolished with 5% H_3PO_4, electroetched using procedure 2 in Table 5. 500×. Courtesy of A. Kelly

Grinding. Uranium samples can be ground by various standard metallographic procedures. Fixed abrasive silicon carbide papers flushed with water work well. A uniform 800-grit finish is desired for subsequent polishing, as it will eliminate the need for rough polishing, thus reducing polishing time.

Sufficient material should be removed in each grinding step to eliminate the deformed material produced by the previous coarser grit. The depth of deformation damage increases with decreasing metal hardness; damage is most severe in soft materials, such as unalloyed uranium and as-quenched U-6Nb. Deformation-induced artifacts in unalloyed uranium are shown in Fig. 26.

The health and safety precautions listed in the previous discussion of uranium sample sectioning also apply to grinding. Dry grinding should always be avoided to minimize the possibility of producing hazardous airborne particulates and to prevent the possibility of excessive specimen heating.

Polishing. Uranium can be polished by standard mechanical and electrolytic techniques, as described in the articles “Mechanical Grinding and Polishing”and “Chemical and Electrolytic Polishing” in this Volume. Rough polishing is best done on a low-nap cloth, such as Texmet (Buehler) or DP Mol (Struers). The use of a 3 μm diamond abrasive with a commercial petroleum-base vehicle works best, but silicon carbide and aluminum oxide (Al_2O_3) abrasives with water vehicles are also satisfactory.

Final polishing can be accomplished mechanically or electrolytically. Mechanical polishing is most frequently used when the samples are to be etched and viewed using bright-field illumination. This is normally the case with multiphase specimens. Chemical differences between the phases cause them to respond differently to etchants, thus producing differential surface relief effects that make the various microstructural features discernible with bright-field illumination. Final mechanical polishing is best done on a high-nap cloth using a 1 μm diamond abrasive with a commercial petroleum-base vehicle. In some cases, this can be followed by a similar step using 0.05 μm diamond abrasive. These final polishing steps can be carried out on rotating wheels or vibratory polishers. Polishing on a rotating wheel requires less time and produces more than satisfactory results.

Electrolytic final polishing is frequently used to remove the last vestiges of surface deformation in preparation for polarized light examination. Electrolytic polishing and polarized light examination are usually applied to unalloyed uranium and single-phase alloys, where the primary distinctions between adjacent microstructural features are differences in crystallographic orientation. Electrolytic polishing solutions and the conditions for their use are given in Table 1. Orthophosphoric acid (ortho-H_3PO_4) and water (No. 1 in Table 1) works well with many alloys.

Table 1 Electropolishing solutions for uranium and uranium alloys

Solution		Comments
1.	1 part ortho-H_3PO_4 acid 1 part H_2O	30 V open circuit, stainless steel cathode
2.	1 part ortho-H_3PO_4 acid 1 part ethylene glycol 1–2 parts ethyl alcohol	10–30 A/cm^2 (65–195 A/in.^{2}), must be kept cold and free of water
3.	85 parts ortho-H_3PO_4 acid 13 parts H_2O 2 parts H_2SO_4	0.4 A/cm^2 (2.5 A/in.^{2}), stainless steel cathode
4.	1–2 parts ortho-H_3PO_4 acid 2 parts H_2SO_4 2 parts H_2O	0.5 A/cm^2 (3 A/in.^{2}), agitate solution
5.	1 part $HClO_4$ (perchloric	60 V, 0.6–0.8 A/cm^2 (4–5 A/in.^{2}), vigorous stirring

acid)[(a)] 20 parts glacial acetic acid

(a) Solutions containing substantial amounts of $HClO_4$ are potentially explosive, especially in contact with oxidizable materials, such as organics (Bakelite). Regular use of perchloric acid requires special fume hood with waterfall type of fume washer to remove perchlorate fumes before they can enter the exhaust hood or cooled (with liquid nitrogen) and kept below 0 °C (32 °F); therefore, fumes are not created. This solution should be prepared by slowly adding $HClO_4$ to acetic acid while stirring. Use of more concentrated solutions is also reported in the literature, but is not recommended because of safety considerations.

Pure ethyl alcohol and warm air drying is required for drying of final polished specimens as MEK, methyl alcohol, and denatured alcohol will attack the polished surface. Polished samples may also oxidize upon exposure to air, so etching needs to be done before final drying of the surface.

References cited in this section

1. A.N. Holden, *Physical Metallurgy of Uranium,* Addison-Wesley, 1958

6. *Metallurgical Technology of Uranium and Uranium Alloys,* Vol 1, 2, and 3, American Society for Metals, 1982

9. R.F. Dickerson, Metallography of Uranium, *Trans. ASM,* Vol 52, 1960, p 748

10. A.D. Romig, Jr. and W.R. Sorenson, Uranium Alloys: Sample Preparation for Transmission Electron Microscopy, *J. Microsc.,* Vol 132, 1983, p 203

11. *Radiological Health Handbook,* U.S. Department of Health, Education, and Welfare, Public Health Service, Food and Drug Administration, Bureau of Radiological Health, Rockville, MD, 1970

12. "Occupational Health Guideline for Uranium and Insoluble Compounds," U.S. Department of Health and Human Services, Washington, DC, 1978

13. "Hygienic Guide Series—Uranium," American Industrial Hygiene Association, Detroit, MI

Revised by H.E. Fairman and A. Kelly, Metallography and Microstructures of Uranium and Its Alloys, *Metallography and Microstructures,* Vol 9, *ASM Handbook,* ASM International, 2004, p. 918–932

Metallography and Microstructures of Uranium and Its Alloys

Revised by Henry E. Fairman, Department of Energy Feed Materials Production Center (Retired) and Ann Kelly, Los Alamos National Laboratory

---

Macroetching and Macroexamination

Macroetching and macroexamination are sometimes used to characterize the grain structures, segregation patterns, and metal flow geometries produced by solidification and mechanical working processes. Macroetching procedures are listed in Table 2. Contrast between regions of different chemical composition may be enhanced by heating the part to the γ-phase field, quenching, and slightly averaging; because decomposition of the martensite generally begins at lower temperatures in alloy-rich regions, the regions in which alloying elements are concentrated will preferentially overage and etch much darker. Flow lines in forged or extruded parts are often difficult to delineate unless segregation in the original ingot provides bands of varying alloy

content. It is sometimes useful to produce deliberately banded vacuum arc melted uranium alloy ingots for studying metal flow during subsequent forming operations.

Table 2 Macroetching procedures for uranium and uranium alloys

Procedure	Comments
1. Immerse 30 s to 1 min in HCl Rinse in cold water Rinse in HNO_3 1–5 s[(a)] Rinse in cold water	Macroetches unalloyed uranium
2. Immerse 30 min in: 1 part acetic acid 1 part HNO_3[(a)]	Macroetches unalloyed uranium
3. Electrolytically etch at 0.05 A/cm^2 (0.3 A/in.^{2}) in: 1 part trichloracetic acid 1 part H_2O Remove black film in 50% HNO_3[(a)]	Macroetches unalloyed uranium
4. Electrolytically etch at 0.05 A/cm^2 (0.3 A/in.^{2}) in: 5 g citric acid 5 mL H_2SO_4 450 mL H_2O	Macroetches unalloyed uranium
5. Heat tint at 200–400 °C (390–750 °F) for 3–5 min	Reveals chemical segregation in alloys. Surface must be clean and free of oxide prior to heat tinting.
6. Water quench from 800 °C (1470 °F) Age to just past peak hardness (temperature varies depending on alloy) Electroetch with H_3PO_4 or oxalic acid (see Table 3)	Reveals chemical segregation in alloys
7. Heat sample to 450 °C (840 °F) Cool Electroetch to 0.01 A/cm^2 (0.06 A/in.^{2}) in: 1 part 55 g CrO_3 in 50 mL H_2O 1 part saturated solution of Na_2CrO_4 (sodium chromate) in H_2O	Reveals chemical segregation and flow lines in uranium-niobium alloys

(a) Solutions containing HNO_3 are not recommended for use with uranium-niobium alloys due to the formation of an explosive surface layer.

Macroexamination and photography are carried out with low-magnification optical devices and techniques identical to those used with other alloy systems. Typical macrographs are shown in Fig. 13 and 14.

Revised by H.E. Fairman and A. Kelly, Metallography and Microstructures of Uranium and Its Alloys, *Metallography and Microstructures,* Vol 9, *ASM Handbook,* ASM International, 2004, p. 918–932

Metallography and Microstructures of Uranium and Its Alloys

Revised by Henry E. Fairman, Department of Energy Feed Materials Production Center (Retired) and Ann Kelly, Los Alamos National Laboratory

Microetching and Microexamination

Inclusions in uranium and uranium alloys are usually visible without etching. Metallographic techniques for inclusion identification include heat tinting, copper plating from a copper cyanide solution, and chemical etching in nitric acid. These methods are detailed in Table 3, along with descriptions of the typical morphologies of inclusions and intermetallic compounds associated with impurities in uranium. These indirect metallographic methods were widely used prior to the proliferation of electron beam microanalytical techniques in the 1960s and 1970s, and they continue to be useful for rapid analysis of heat-to-heat variations in microcleanliness, and so forth. More definitive inclusion identification can now be done on as-polished samples with electron probe microanalysis and/or scanning Auger microscopy.

Table 3 Metallographic identification of inclusions and intermetallic compounds in uranium and uranium alloys

			Appearance	
Inclusion	**Morphology**	**Sample condition**	**Bright field**	**Polarized light**
UC	Small and angular or large and dendritic	As-polished	White/gray	…
		Heat tinted	Orange/red	…
		Copper plated 1–2 min	Discontinuous deposit	…
		HNO_3 etched	Black	Black
UN	Angular, dendritic, or Chinese script	As-polished	Gray	Dark gray
		Copper plated 3–10 s	Continuous deposit	…
		HNO_3 etched	Gray	Dark gray
U(C,N)	Angular, dendritic, or Chinese script	As-polished	Gray	Dark gray
		Heat tinted	Yellow	…
		Copper plated 20 s	Continuous deposit	…
		HNO_3 etched	Dark gray	Dark gray
UO or U(O,C,N)	Spherical, rimmed with second phase, or irregular globules	As-polished	Light gray	Dark gray
		Heat tinted	Dark gray	…
		Copper plated 1–2 min	No deposit	…
UO_2	Globular or partly elongated	As-polished	Dark gray	Red, rust
		Heat tinted	Dark gray	…
		Copper plated 1–2 min	No deposit	…

UH_3	Needles or stringers	As polished	Tan, light brown	Gray
		Heat tinted	Silver halo	…
		HNO_3 etched	No attack	…
U_3Si_2	Globular, frequently rimmed with U_3Si	Attack polished with dilute HF-HNO_3	Gray	…
U_3Si	Globular, or rim around globular U_3Si_2	Attack polished with dilute HF-HNO_3	Brown	…
MgF_2 and CaF_2	Glassy, globular or partly elongated stringers	As-polished	Black	White
UF_3	Globular, elongated	As-polished	Black	Violet
U_6Fe	Decorates γ grain boundaries	Electropolished	Gray	…
		Copper plated 1 min	Continuous deposit	…
		HNO_3 etched	Gray	…
Nb_2C	Sharp, angular	As-polished	White	…
NbC	Sharp, angular	As-polished	Light gray	…

The microstructures of unalloyed uranium and single-phase uranium alloys are most frequently characterized with polarized light microscopy. Although such features as grain and twin boundaries are often difficult to delineate by etching and bright-field examination, the optical anisotropy of the orthorhombic crystal structure of uranium allows adjacent regions of differing crystallographic orientation to be defined by polarized light microscopy. Development of good polarized light contrast requires metallographic surfaces that are free from polishing deformation; therefore, final polishing is usually done by electropolishing (Fig. 62). Some metallographers perform polarized light microscopy on as-polished samples, but most employ various treatments to form a thin epitaxial oxide film on the polished surface prior to metallographic examination. This thin oxide frequently increases polarized light contrast. Heat tinting, incorporation of chemically active vehicles during final mechanical polishing, and electrolytic anodization are some of the ways epitaxial oxide films can be formed. These preparation treatments for polarized light microscopy are summarized in Table 4. Examples of the microstructures revealed by these techniques are shown in Fig. 5, 6, 8, 9, 10, 11, 20, 23, 35, 41, 43, 44, 46, and 50.

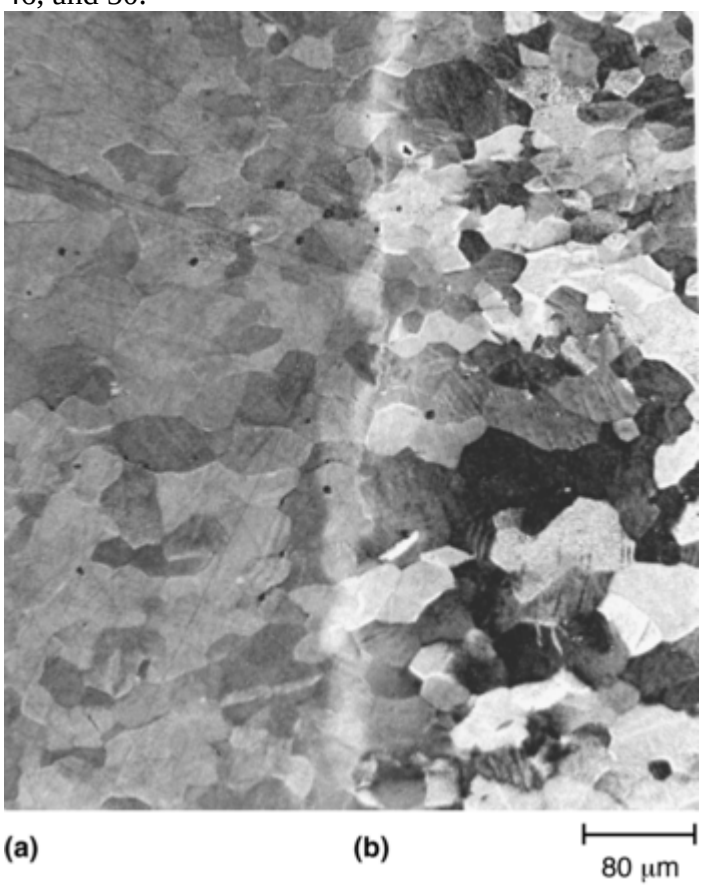

Fig. 62 Differential interference contrast (DIC) light micrograph of unalloyed uranium. (a) As-polished condition. (b) Electropolished in 5% H_3PO_4 solution for 3 s at 3 V, electroetched using procedure 2 in Table 5. 250×. Courtesy of A. Kelly

Table 4 Final preparation of uranium samples for polarized light microexamination

Solution	Comments
Attack polishing methods	
1. 1 part HF 1 part HNO_3 2 parts H_2O	A few drops on final polishing wheel. *Caution: Hydrofluoric acid solutions cause severe burns if allowed to contact skin.*
Anodizing solutions (electrolytic)[(a)]	
2. 1 part NH_4OH 30 parts ethylene glycol	60 V open circuit potential, 30 s to 2 min. Solution must be kept free of water.
3. 1 part NH_4OH 4 parts ethanol	
Chemical[(a)]	
4. 10% $FeCl_3$ in H_2O	Immerse sample in boiling solution.
Atmospheric oxidation[(a)]	
5. Air	Allow sample to oxidize in air at 25–300 °C (75–570 °F). Temperature and time vary strongly with alloy composition.

(a) Sample must have deformation-free polished surface prior to treatment; electropolishing is suggested as a means of producing this surface.

Uranium alloys with more than one phase are frequently etched and examined by bright-field microscopy. Etching is most often done electrolytically, although some chemical etchants are also used. Preparation treatments for bright-field microscopy are listed in Table 5, and examples of microstructures revealed by this method are shown in Fig. 26, 27, 28, 29, 30, 36, 37, 38, 39, 40, 42, 45, 47, 48, 49, 52, and 53.

Table 5 Final preparation of uranium samples for bright-field microexamination

Solution	Comments
Electrolytic etches	
1. 1 part ortho-H_3PO_4 acid 1 part H_2O	1–5 V open circuit[(a)], stainless steel cathode
2. 5 parts ortho-H_3PO_4 acid 100 parts H_2O	3–5 V open circuit, stainless steel cathode, use tantalum wire to complete connection between sample (anode) and power source.
3. 5–10% oxalic acid in H_2O	1–5 V open circuit[(a)], stainless steel cathode
4. 1 part ortho-H_3PO_4 acid 2 parts H_2SO_4 2 parts H_2O	1–10 V open circuit[(a)], stainless steel cathode

5.	85 parts ortho-H_3PO_4 acid 13 parts H_2O 2 parts H_2SO_4	1–10 V open circuit[a], stainless steel cathode
6.	1 part ortho-H_3PO_4 acid 1 part ethylene glycol 1–2 parts ethyl alcohol	1–5 V open circuit[a], stainless steel cathode
7.	10 g citric acid 215 mL HNO_3 490 mL H_2O	1–10 V open circuit[a], stainless steel cathode
8.	1 part $HClO_4$[b] 20 parts glacial acetic acid	1–10 V open circuit[a], stainless steel cathode
Chemical etches		
9.	1 part HF[c] 10 parts HNO_3 25 parts ortho-H_3PO_4 10 parts H_2O	Immerse.
10.	1 part HF[c] 1 part HNO_3 2 parts glycerol	Immerse, can also be used as electrolytic etch.
11.	1 part 0.3 μm Al_2O_3 2 parts saturated solution of $Na_2Cr_2O_7 \cdot 2H_2O$ (sodium dichromate) 12 parts H_2O	Used in final polish to sharpen edges of inclusions. **No longer recommended.**
Atmospheric oxidation		Allow sample to oxidize in air at 25–300 °C (75–570 °F). Temperature and time vary strongly with alloy composition.

(a) Voltage varies depending on alloy composition and heat treatment. Best practice is to start with low voltage while watching sample surface and increase voltage until visible etching begins.

(b) Caution: Solutions containing substantial amounts of $HClO_4$ are potentially explosive, especially when brought into contact with oxidizable material, such as organics. This solution should be prepared by slowly adding $HClO_4$ to acetic acid while stirring. Use of more concentrated solutions are also reported in the literature, but these are not recommend because of safety considerations.

(c) Caution: Hydrofluoric acid solutions cause severe burns if allowed to contact skin.

Differential interference contrast (DIC) illumination is also effective in revealing structure (see Fig. 7, 12, 16, 17, 18, 22, 24, 25, 31, 32, 33, 34, 51, 54, 55, 56, 57, 58, 59, 60, 61, 62).

Revised by H.E. Fairman and A. Kelly, Metallography and Microstructures of Uranium and Its Alloys, *Metallography and Microstructures,* Vol 9, *ASM Handbook*, ASM International, 2004, p. 918–932

Metallography and Microstructures of Uranium and Its Alloys

Revised by Henry E. Fairman, Department of Energy Feed Materials Production Center (Retired) and Ann Kelly, Los Alamos National Laboratory

Acknowledgment

This article (published in Volume 9 in the 9th Edition of the Metals Handbook series in 1985) was originally prepared by Kenneth H. Eckelmeyer, Division Supervisor, DOE's Sandia National Laboratories. In the original article, the following individuals are thanked for their assistance: T.N. Simmons, DOE's Sandia National Laboratories; A.G. Dobbins, Martin-Marietta (Operator of DOE's Oak Ridge National Laboratory; C.E. Polson, NLO, Inc. (DOE's Feed Materials Production Center); A.L. Geary, Nuclear Metals, Inc.; and A.D. Romig, Jr., DOE's Sandia National Laboratories.

Revised by H.E. Fairman and A. Kelly, Metallography and Microstructures of Uranium and Its Alloys, *Metallography and Microstructures,* Vol 9, *ASM Handbook*, ASM International, 2004, p. 918–932

Metallography and Microstructures of Uranium and Its Alloys

Revised by Henry E. Fairman, Department of Energy Feed Materials Production Center (Retired) and Ann Kelly, Los Alamos National Laboratory

References

1. A.N. Holden, *Physical Metallurgy of Uranium,* Addison-Wesley, 1958
2. W. Lehmann and R.F. Hills, Proposed Nomenclature for Phases in Uranium Alloys, *J. Nucl. Mater.,* Vol 2, 1960, p 261
3. W.D. Wilkinson, *Uranium Metallurgy,* Vol 1 and 2, Interscience, 1962
4. J.J. Burke et al., Ed., *Physical Metallurgy of Uranium Alloys,* Brook Hill, 1976
5. K.H. Eckelmeyer, Microstructural Control in Dilute Uranium Alloys, *Microstruc. Sci.,* Vol 7, 1979, p 133
6. *Metallurgical Technology of Uranium and Uranium Alloys,* Vol 1, 2, and 3, American Society for Metals, 1982
7. J.G. Speer, “A Study of Solid-State Phase Transformations in Uranium Alloys,” Ph.D. thesis, Oxford University, 1983
8. K.H. Eckelmeyer, A.D. Romig, and L.J. Weirick, The Effect of Quench Rate on the Microstructure, Mechanical Properties, and Corrosion Behavior of U-6 Wt. Pct. Nb, *Met. Trans. A,* Vol 15, 1984, p 1319
9. R.F. Dickerson, Metallography of Uranium, *Trans. ASM,* Vol 52, 1960, p 748

10. A.D. Romig, Jr. and W.R. Sorenson, Uranium Alloys: Sample Preparation for Transmission Electron Microscopy, *J. Microsc.*, Vol 132, 1983, p 203

11. *Radiological Health Handbook*, U.S. Department of Health, Education, and Welfare, Public Health Service, Food and Drug Administration, Bureau of Radiological Health, Rockville, MD, 1970

12. "Occupational Health Guideline for Uranium and Insoluble Compounds," U.S. Department of Health and Human Services, Washington, DC, 1978

13. "Hygienic Guide Series—Uranium," American Industrial Hygiene Association, Detroit, MI

Metallography and Microstructures of Zinc and Its Alloys, *Metallography and Microstructures*, Vol 9, *ASM Handbook*, ASM International, 2004, p. 933–941

Metallography and Microstructures of Zinc and Its Alloys

Introduction

ZINC AND ZINC ALLOY specimen preparation techniques are discussed in this article. Typical structures observed in these specimens are also covered, as is the effect of alloying elements and processes. The etchants used for many of the micrographs included in this article are listed in Table 1.

Table 1 Etchants for zinc and zinc alloys

Etchant	Composition
1[(a)]	200 g CrO_3, 15 g Na_2SO_4, 1000 mL H_2O
2[(b)]	50 g CrO_3, 4 g Na_2SO_4, 1000 mL H_2O
3	200 g CrO_3 and 1000 mL H_2O
4	5 mL HNO_3 and 100 mL H_2O
5	5 g $FeCl_3$, 10 mL HCl, 240 mL alcohol
6[(c)]	375 mL H_3PO_4, and 625 mL ethyl alcohol
7	1 drop HNO_3 and 10 mL amyl alcohol

(a) For rolled zinc-copper alloys, the Na_2SO_4 content can be reduced to 7.5 g. If desired, a smoothly etched surface can be obtained by increasing the Na_2SO_4 to 30 g.
(b) This etchant can be prepared by mixing one part (by volume) etchant 1 and three parts H_2O.
(c) Electrolytic; current density, 0.1 to 0.2 A/cm^2 (0.6 to 1.3 A/$in.^2$) for 3 to 8 s

Metallography and Microstructures of Zinc and Its Alloys, *Metallography and Microstructures,* Vol 9, *ASM Handbook,* ASM International, 2004, p. 933–941

Microstructures of Zinc and Zinc Alloys

The natural impurities, contaminants, and alloying additions present in commercial zinc materials have extremely limited solid solubility. They readily produce alterations in cast or wrought microstructures and changes in one or more properties. High-purity zinc, UNS Z13002, for example, is 99.99% Zn with maximum limits of 0.003% each on lead, iron, and cadmium and is almost free of mircosegregation (Fig. 1, 2). Nominal compositions of the alloys depicted in this article are noted in the captions.

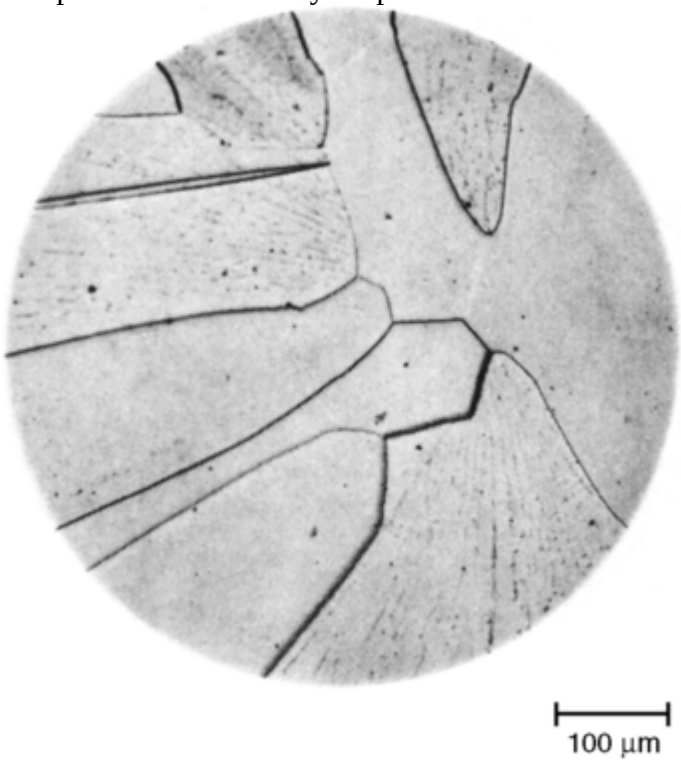

Fig. 1 Special high-grade zinc, UNS Z13002 [99.99% Zn (min), 0.003% Pb (max), 0.003% Fe (max), 0.003% Cd (max)], as-cast. Almost free of microsegregation. Etchant 1, Table 1. 100×

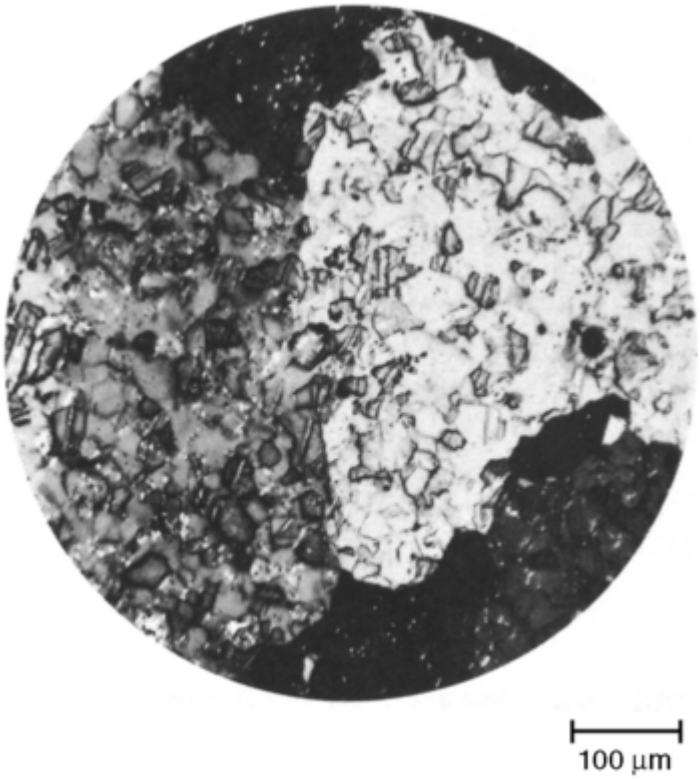

Fig. 2 Same alloy as Fig. 1 under polarized light illumination to show the extent of grain growth from original etched grain boundaries within large grains. Etchant 1, Table 1. 100×

The elements commonly found in zinc are lead, cadmium, iron, copper, aluminum, titanium, and tin. Lead, cadmium, tin, and iron are natural impurities in zinc and are also added to zinc to develop desired properties. Zinc casting alloys are primarily zinc-aluminum with small additions of other elements, such as copper and magnesium. Wrought zinc alloys for rolled products generally contain lead, iron, cadmium, copper, or titanium alone or in combination and usually in concentrations under 1%. The effects on microstructure produced by these elements are described as follows.

Zinc has a familiar role as a protective coating for steel in galvanizing processes. Pure zinc and zinc-aluminum alloys are used in continuous hot dip processes. The galvanneal process uses zinc-iron alloys (Ref 1). Batch process hot dip galvanizing uses high-grade zinc (UNS Z15001, with impurities less than 0.10%; UNS Z13001, with impurities less than 0.010%; and prime western zinc, UNS Z19001) (Ref 2). The interaction between base materials and coatings results in interesting profiles of microstructures (Ref 1, 3, 4, 5).

Lead. The solubility of lead in solid zinc is extremely limited. A monotectic is formed at 418 °C (784 °F) and a lead content of 0.9%, and zinc crystals and liquid exist in equilibrium down to the eutectic temperature of 318 °C (604 °F). As a result, lead appears in cast zinc and zinc alloys at the dendrite boundaries in the form of small, spherical droplets or surface films (Fig. 3). Because of their softness, the droplets can be easily pulled out during polishing, leaving holes that appear black in the microstructure. Special care in polishing is required to retain the lead particles.

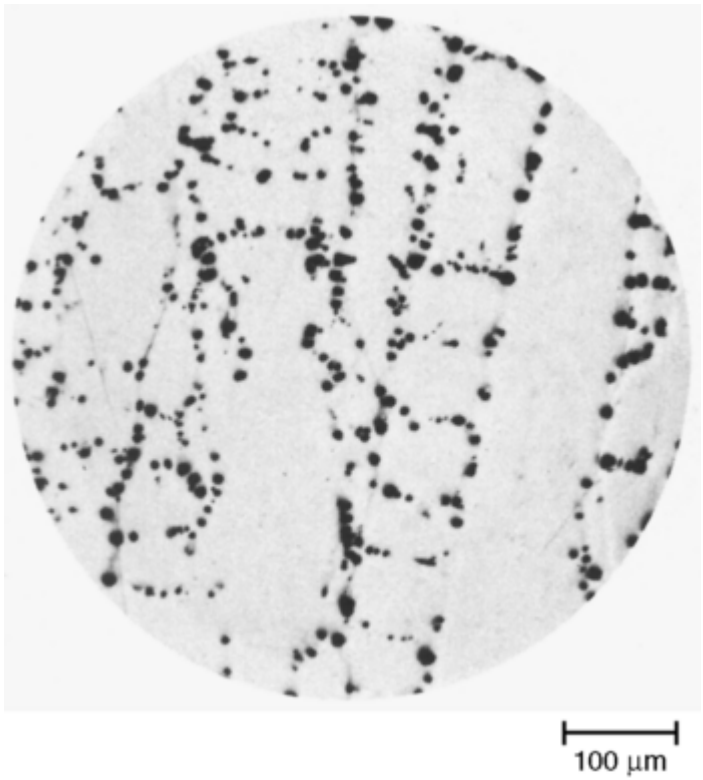

Fig. 3 Prime western zinc, UNS Z19001 [98% Zn (min), 1.4% Pb (max), 0.05% Fe (max), 0.20% Cd (max)], as cast. The dark spots are lead particles at the grain boundaries. Etchant 1, Table 1. 100×

When rolled, the particles of lead are elongated in the rolling direction and are not located preferentially at the recrystallized grain boundaries. In zinc-aluminum alloys, lead induces intergranular corrosion; concentrations must be maintained below 0.004%. Lead was added to UNS Z33520 to illustrate this effect in Fig. 4 and 5.

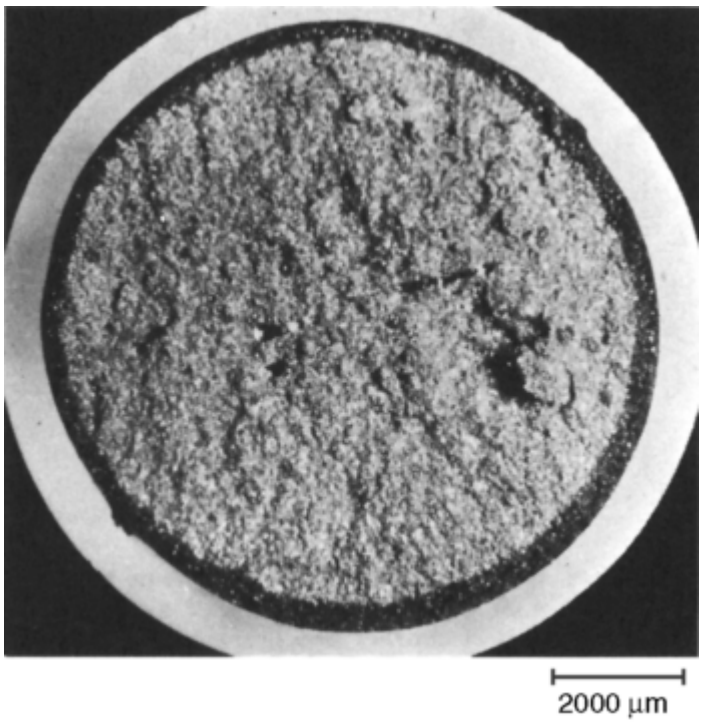

Fig. 4 Fracture surface of the 10 mm (0.375 in.) diameter end of a tension test bar die cast from alloy 3 (UNS Z33520) to which 0.018% Pb was added (0.005% Pb is allowed). Exposed 10 days to wet steam at 95 °C (205 °F). Dark ring is intergranular corrosion. See also Fig. 5 Not polished, not etched. 6×

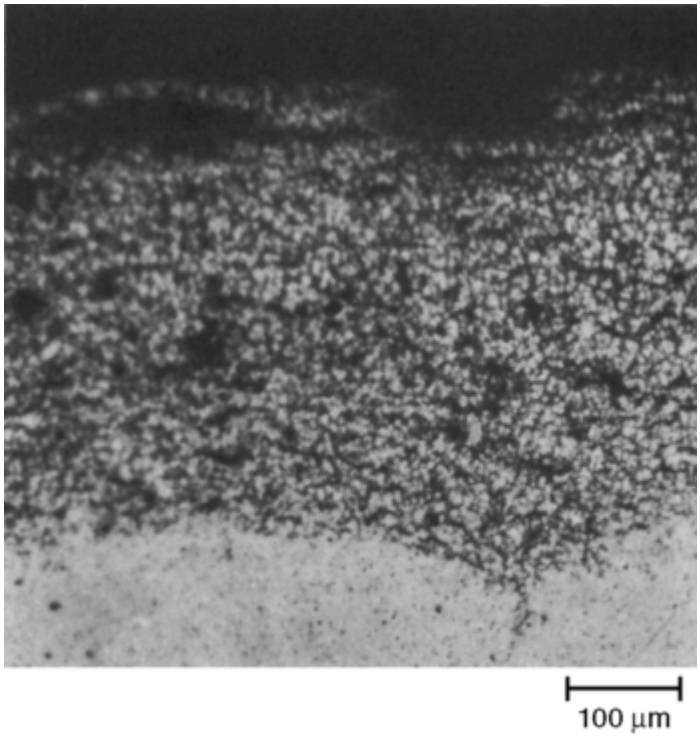

Fig. 5 Micrograph of edge of fracture surface in Fig. 4 Subsurface intergranular corrosion (top) causes swelling and decreases mechanical properties. Deliberate addition of 0.018% Pb to the alloy approximates the contamination that might occur from the use of remelted scrap. As-polished. 100×

The cadmium present in most commercial zinc products is in solid solution and produces no change in microstructure, except coring in the cast structure. In rolled zinc, the cadmium remains in solid solution, increasing strength, hardness, and creep resistance and raising the recrystallization temperature (Fig. 6, Fig. 7). In zinc-aluminum alloys, because cadmium lowers resistance to intergranular corrosion, concentrations must remain below 0.003%.

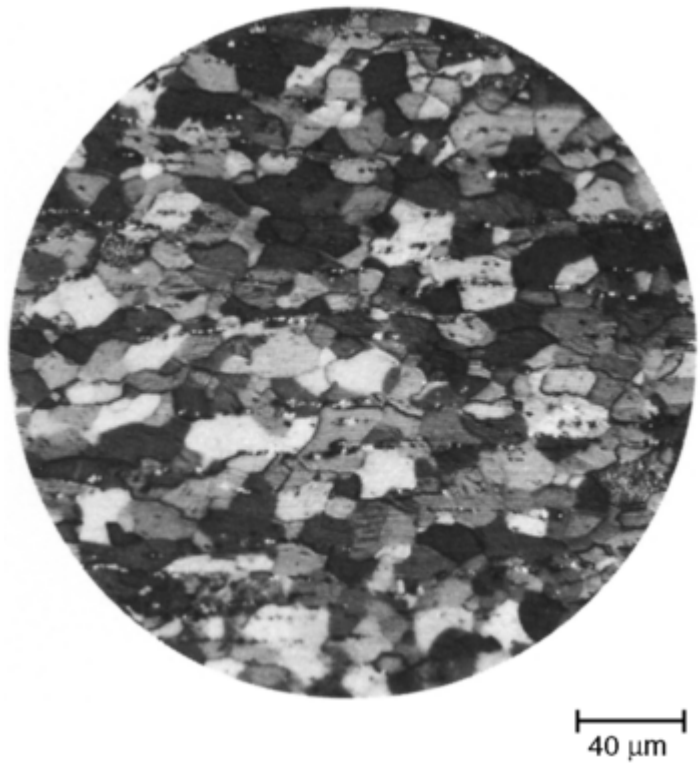

Fig. 6 Hot-rolled special zinc [99% Zn (min), 0.6% Pb (max), 0.03% Fe (max), 0.50% Cd (max)], under polarized light; grains are clearly defined. Etchant 1, Table 1. 250×

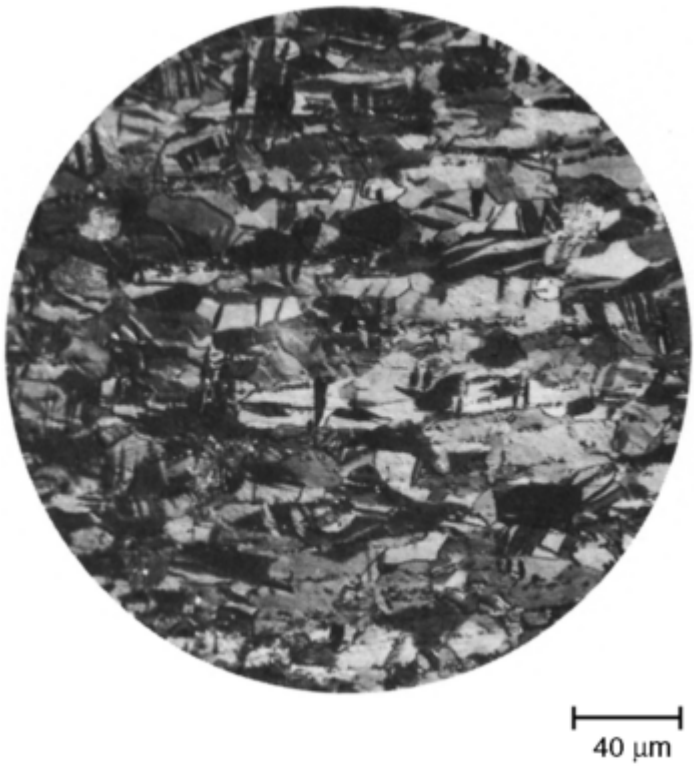

Fig. 7 Same alloy as Fig. 6 except cold rolled and photographed under polarized light. Note distortion of the grains caused by cold working. Etchant 1, Table 1. 250×

Iron, when present in zinc in amounts exceeding approximately 0.001%, appears in the microstructure as an intermetallic compound containing approximately 6% Fe. The particle size is controlled by the amount of iron present and the thermal history of the part. Fine particles in a casting can be coalesced to a coarser form by prolonged heating at 370 °C (700 °F).

Cast specimens with fast cooling (Fig. 8) and very slow cooling (Fig. 9) show the zeta-phase intermetallics. Four distinct phases are seen in the profiles of galvanized coating on steel (Ref 5, Fig. 1) and galvannealed coating (Ref 1, Fig. 7).

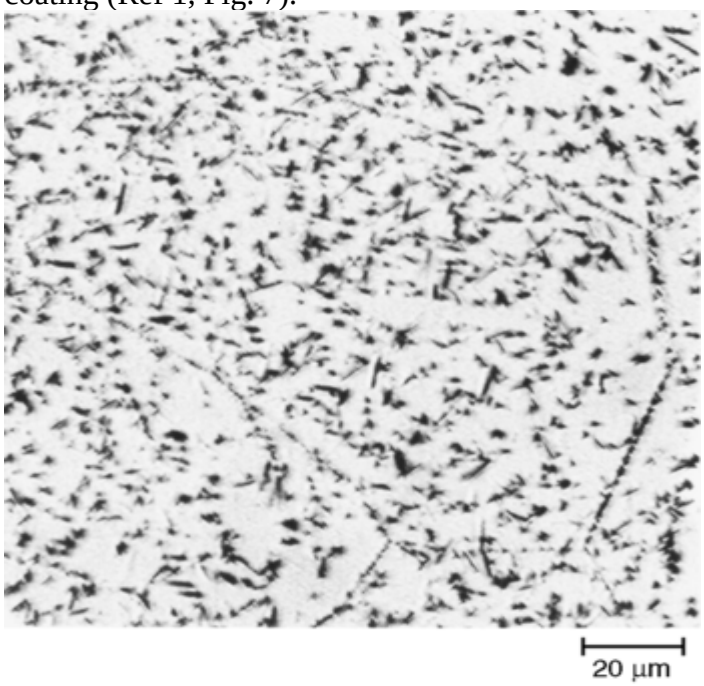

Fig. 8 Zn-0.025Fe alloy, permanent mold, rapid cooling, annealed 40 h at 380 °C (716 °F). Zeta-phase intermetallic compounds appear as fine precipitate through annealing. Electrolytic polish. Etchant: similar to etchant 1, Table 1 (but only 10 g Na_2SO_4). 500×

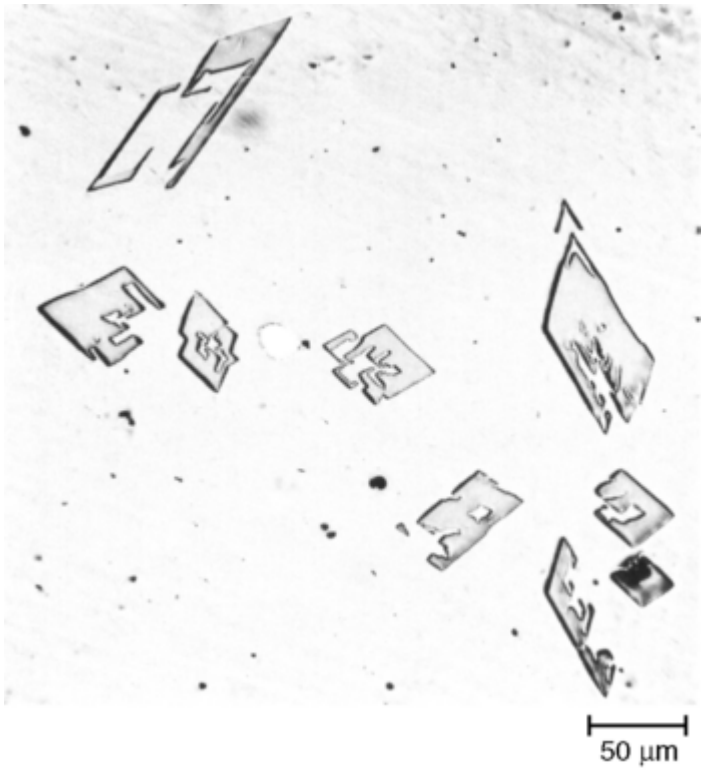

Fig. 9 Zn-0.025Fe alloy, hot graphite mold, slow cooling. Zeta-phase intermetallic compounds. Electrolytic polish. Electrolytic etch: etchant 6, Table 1 (short time). 200×

The iron-zinc compound, like lead, precipitates at dendrite boundaries. When a zinc casting is rolled, the iron-zinc particles are elongated in the rolling direction, along with any lead particles present. The presence of iron particles in the proper concentration and distribution in rolled zinc assists in control of grain size. Iron in zinc-aluminum alloys is present as $FeAl_3$ particles, which can significantly lower ductility. Alloy ZA-27, UNS Z35841, with 0.05% Fe added (Fig. 10) and with 0.013% Fe added (Fig. 11) results in an $FeAl_3$ intermetallic.

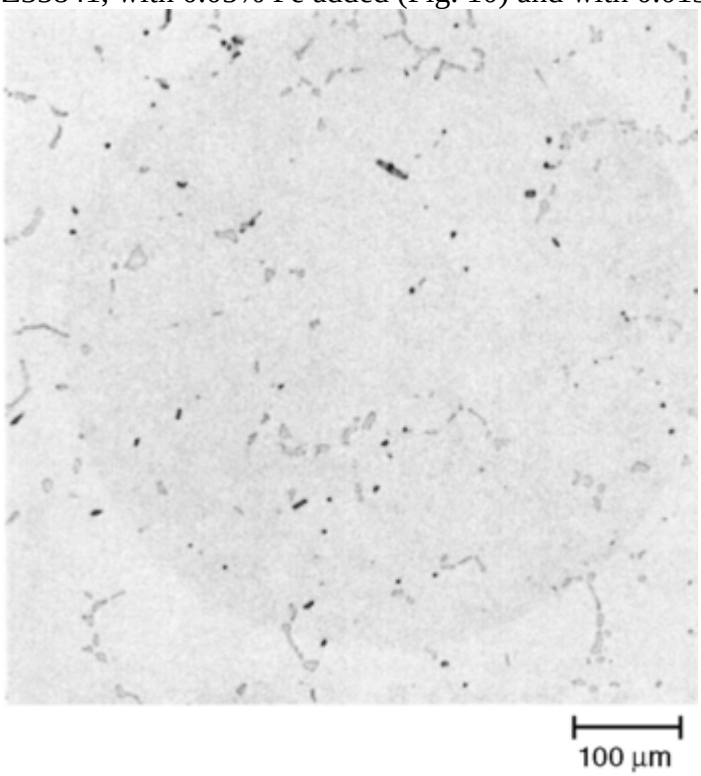

Fig. 10 ZA-27 alloy, UNS Z35841, with 0.05% Fe (0.075% Fe max allowed), as sand cast. Structure consists of intermetallic $FeAl_3$ particles (dark gray) in a matrix of α particles (light) and ε particles (light gray). As-polished. 100×

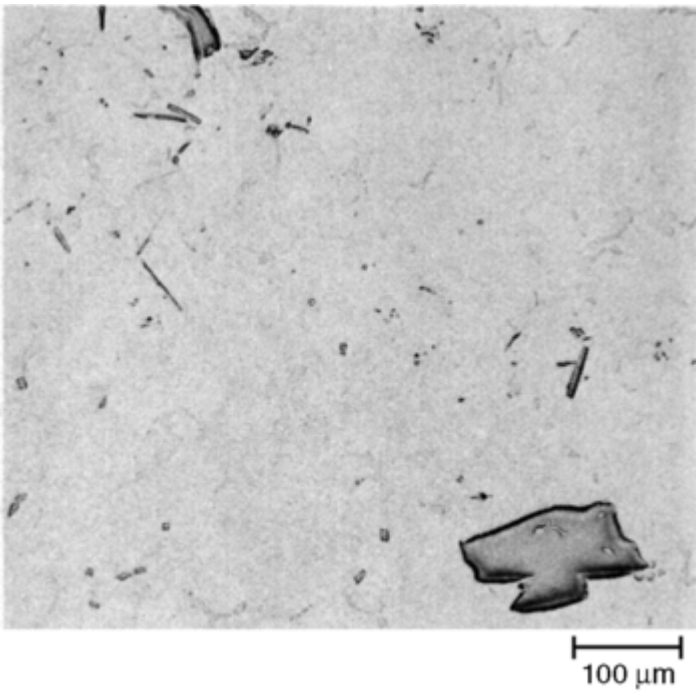

Fig. 11 ZA-27 alloy, UNS Z35841, with 0.13% Fe (excess, 0.075% Fe max allowed), as sand cast. Structure is intermetallic $FeAl_3$ particles (dark gray) in a matrix of α phase and ε phase. Structure is much coarser than in Fig. 10 As-polished. 100×

Copper, when present in zinc in amounts to approximately 1%, is in solid solution and results in a cored structure. During hot rolling at approximately 205 °C (400 °F), the copper is retained in supersaturated solid solution. On cooling, some of the zinc-copper ε phase precipitates at the final recrystallized grain boundaries (Fig. 12). During long exposures near room temperature, ε phase will continue to precipitate at grain boundaries and finally in the interior of the grains, ultimately forming T′ phase (ternary eutectic). When cold rolled, ε phase precipitates rapidly and abundantly in the cold-worked structure (Fig. 13). In concentrations beyond 1% in zinc-aluminum alloys, ε phase precipitates as an interdendritic phase.

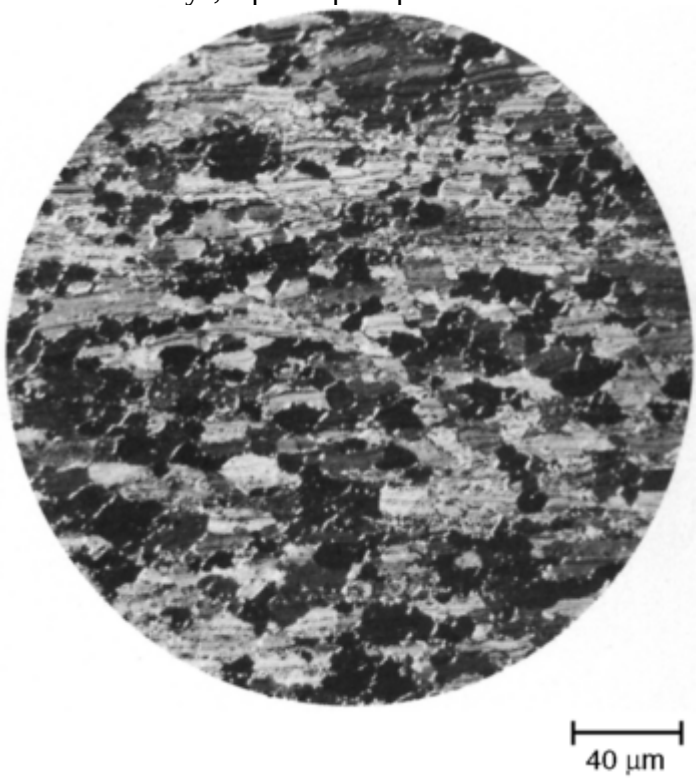

Fig. 12 Zinc containing 1% Cu, UNS Z44330, hot rolled. Polarized light illumination clearly defines the zinc-copper ε phase at grain boundaries. Etchant 1, Table 1. 250×

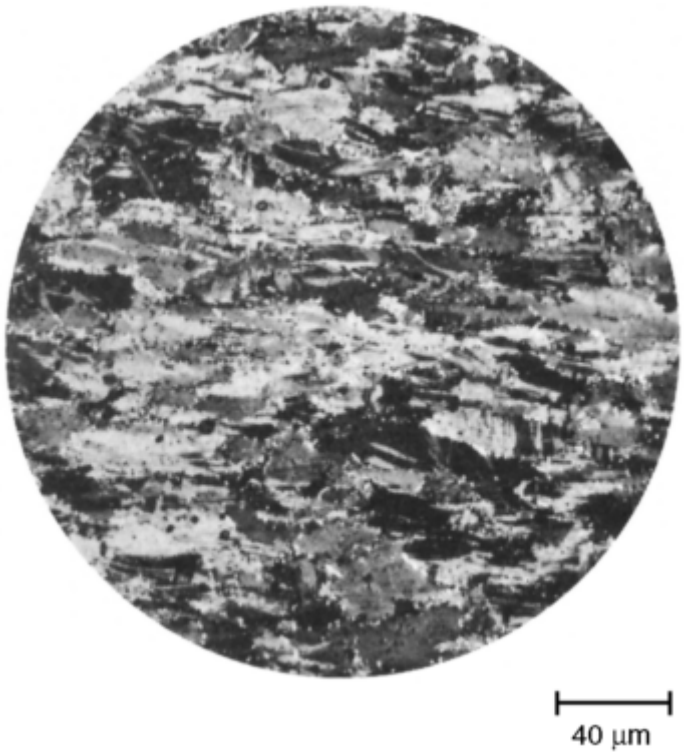

Fig. 13 Cold-rolled Zn-1Cu alloy, UNS Z44330, photographed under polarized light. Note the severe distortion of grains caused by cold working (compare with Fig 12). Etchant 1, Table 1. 250×

Die cast alloy UNS Z35531, alloy 5, containing 1% Cu is seen in Fig. 14. Aging for 10 days at 95 °C (205 °F) increases the amount of precipitation in the zinc solid solution (Fig. 15). An alloy with 0.9% Cu, UNS Z35841, ZA-27, shows primary cored aluminum-rich dendrites with peritectic α + η and white ε-phase particles (Fig. 16). The same alloy in a sand cast specimen that was treated 3 h at 360 °C (680 °F) shows course ε-phase particles at old dendritic boundaries (Fig. 17). With longer lower-temperature exposure, the ε phase is converted to a fine T′ phase (ternary eutectic) (Fig. 18). Continuously cast, the same alloy has a finer microstucture. The presence of the ε-phase particles varies with the size of the bar being cast (Fig. 19, 20).

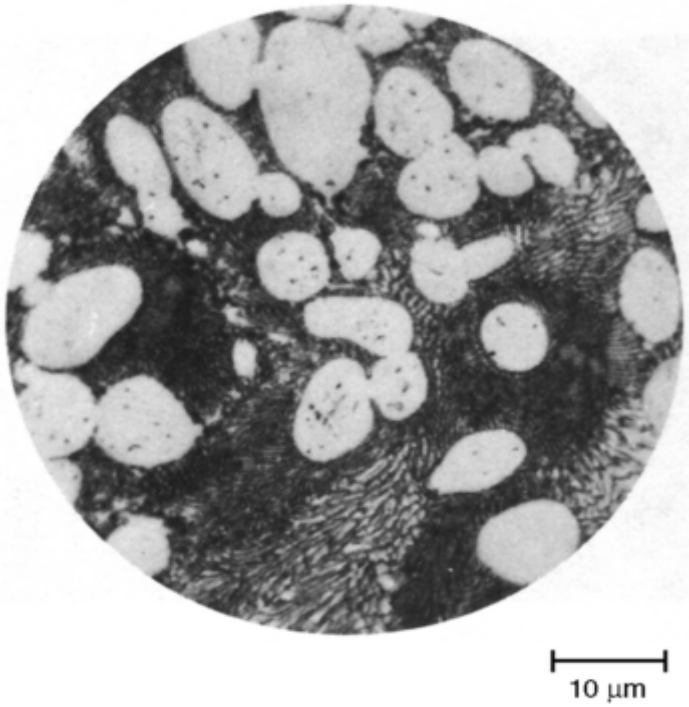

Fig. 14 Alloy 5 (UNS Z35531, ASTM AC41A, Zn-4.1Al-0.055Mg-1.0Cu), as die cast. Alloy 5 has more copper and magnesium and higher strength and hardness than alloy 3. Etchant 2, Table 1. 1000×

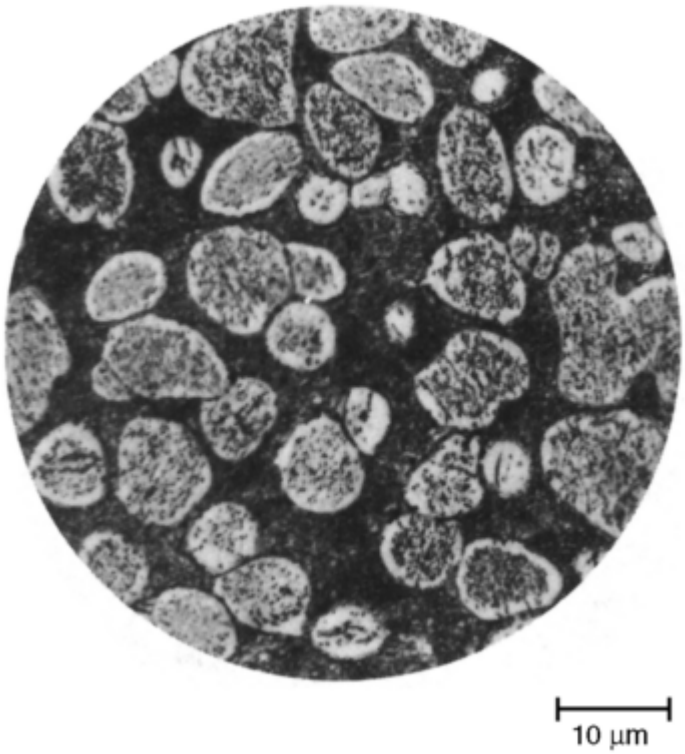

Fig. 15 Same as Fig. 14 except aged 10 days at 95 °C (205 °F). Aging had the same effect on the die cast structure as for alloy 3 (UNS Z33520) (Fig. 24b). Etchant 2, Table 1. 1000×

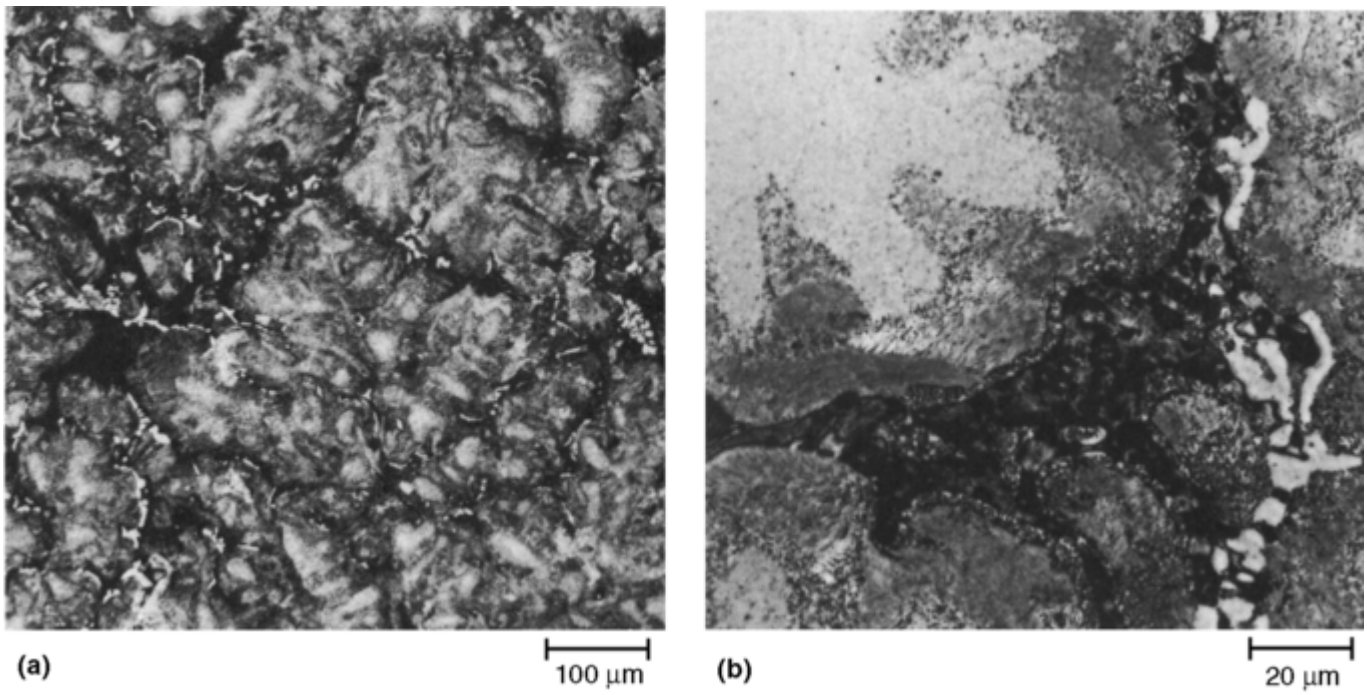

Fig. 16 ZA-27 alloy (UNS Z23841, Zn-11Al-0.9Cu-0.02Mg), as sand cast. Primary, cored aluminum-rich dendrites surrounded by peritectic α + η. White particles are ε phase. Less eutectic is apparent than in Fig. 1, 2, 23, 24 Etchant 1, Table 1. (a) 100×. (b) 500×

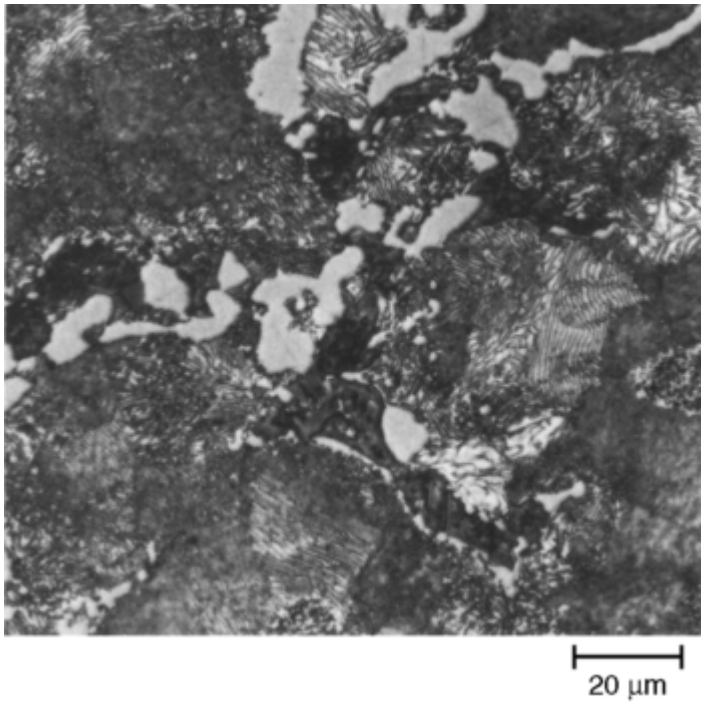

Fig. 17 Same alloy as Fig. 16 sand cast, homogenized 3 h at 360 °C (680 °F), and furnace cooled. Structure is fully stabilized β phase decomposed into α + η lamellar eutectoid. Coarse ε-phase particles are present at old dendritic boundaries. Etchant 1, Table 1. 500×

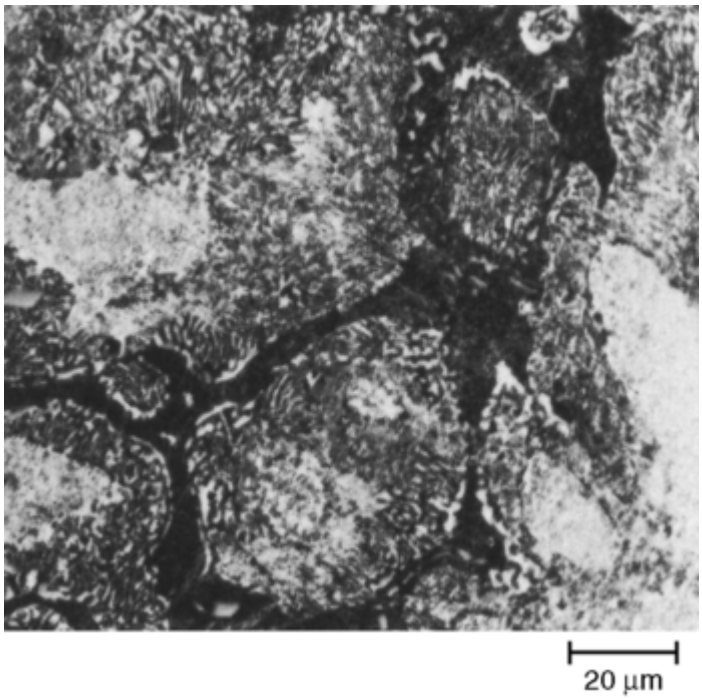

Fig. 18 Same alloy as Fig. 16 sand cast, heat treated 12 h at 250 °C (480 °F), and furnace cooled. Structure consists of coarse eutectoid α + η phase and eutectic. The metastable ε phase has been converted to fine T′ (ternary eutectic). Etchant 1, Table 1. 500×

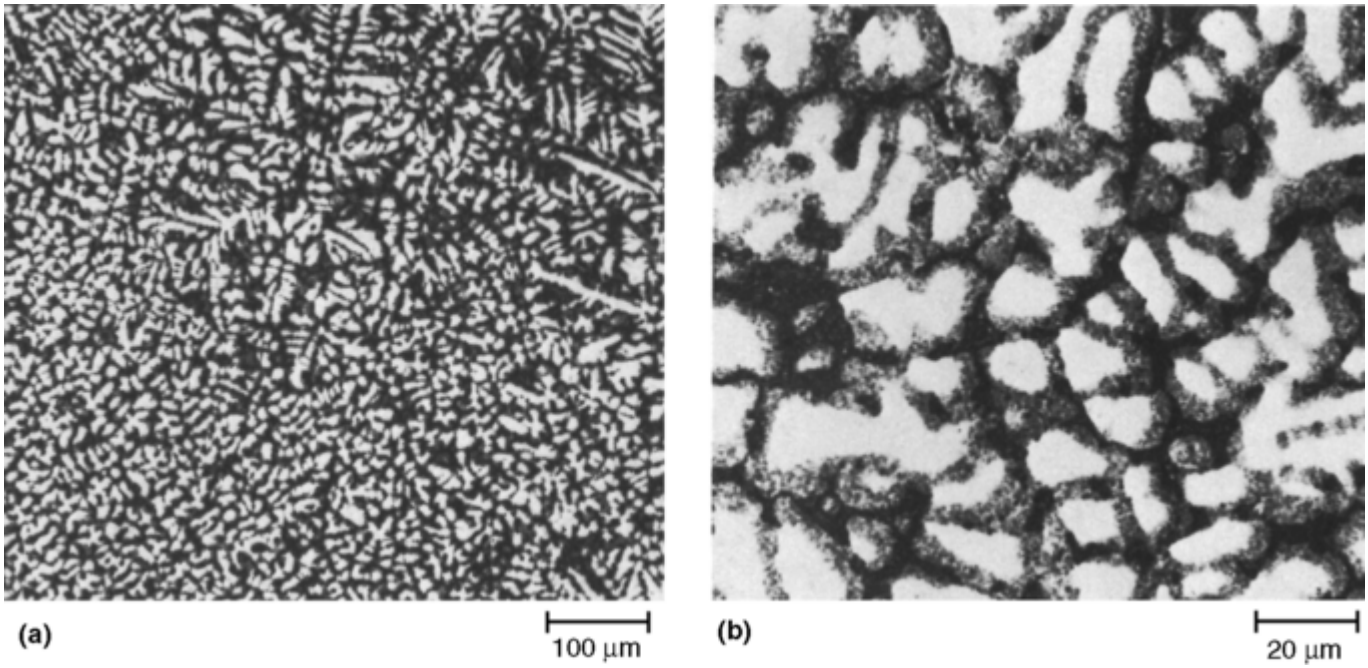

Fig. 19 Same alloy as Fig. 16 except continuous cast in a 25 mm (1 in.) diameter bar. There is a much finer microstructure, with more eutectic and no coarse ε-phase particles. Compare also with Fig. 20. Etchant 1, Table 1. (a) 100×. (b) 500×

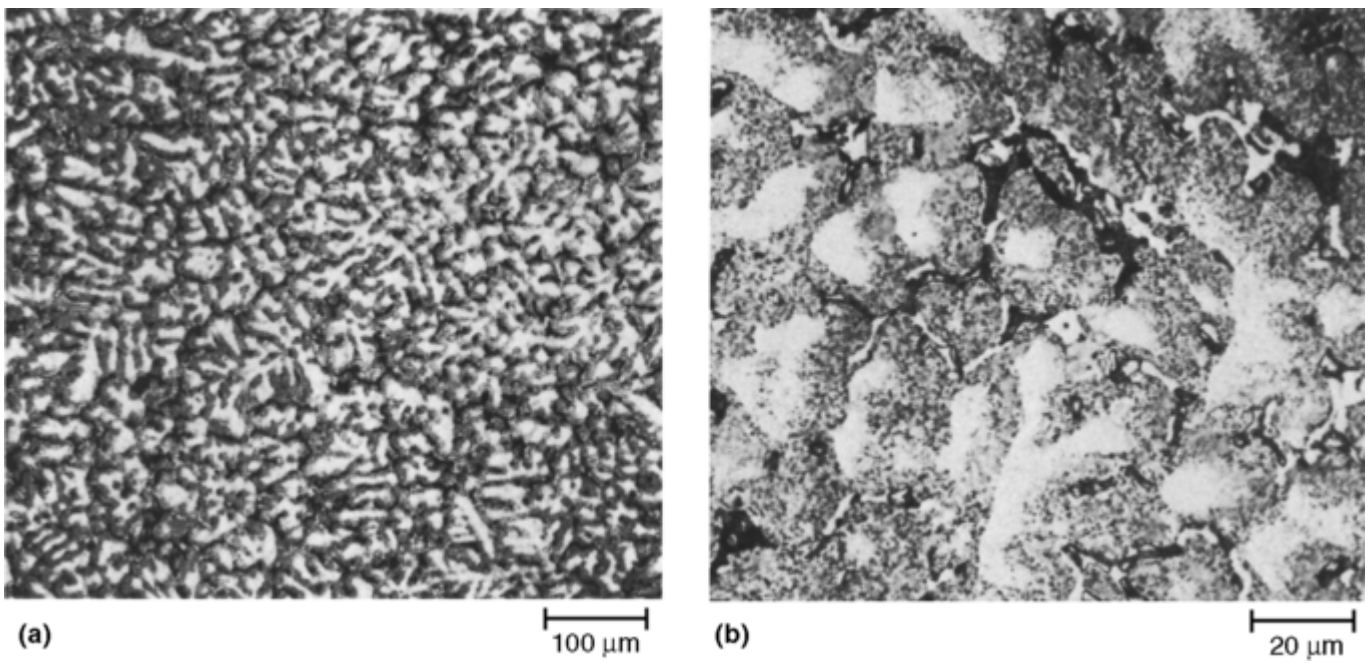

Fig. 20 Same alloy as Fig. 16 except continuously cast in a 150 mm (6 in.) diameter bar. Same constituents as Fig. 16, but a finer structure. Some coarse ε-phase particles (white) are evident. Compare with Fig. 19(a) and (b), which show the same alloy cast in a smaller section. Etchant 1, Table 1. (a) 100×. (b) 500×

Titanium. The solid solubility of titanium in zinc is very limited. At approximately 0.12% Ti, a lamellar eutectic of zinc and $TiZn_{15}$ (4.66% Ti) forms (Fig. 21). The eutectic forms at dendrite boundaries in a casting. The $TiZn_{15}$ compound decreases the cast grain size of zinc and restricts grain growth in hot-rolled zinc. In rolled strip, particles of the compound are elongated in the rolling direction. Zinc grain growth is limited to the spacing between the stringers of compound.

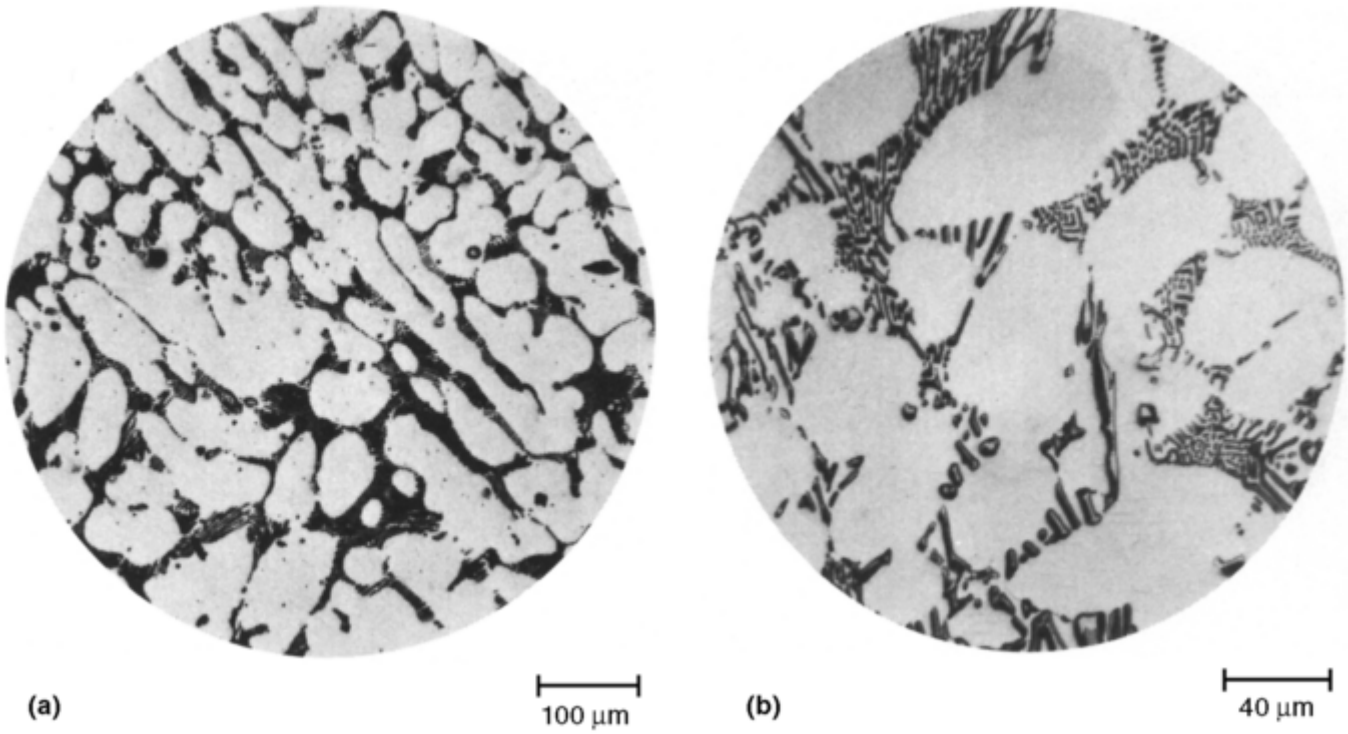

Fig. 21 Cast zinc with 0.6% Cu and 0.14% Ti. Eutectic (zinc and titanium-zinc phases) at grain boundaries. Both etched in etchant 1, Table 1. (a) 100×. (b) Showing the lamellar eutectic. Coarse needles of titanium-zinc phase are parallel to the polishing plane; fine needles, perpendicular. 250×

Aluminum. A lamellar eutectic forms at 5% Al between aluminum (α) and zinc (η) solid solution at 382 °C (720 °F). The α constituent of the eutectic is stable only above 275 °C (527 °F); at lower temperatures, it transforms eutectoidally into α and η phases (Fig. 22, 23). Although the solid solubility of aluminum in zinc at the eutectic temperature is approximately 1%, castings containing as little as 0.10% Al display the eutectic structure in interdendritic areas. At the normal aluminum concentration in standard zinc die-casting alloys (4.0% Al), the rate of attack by the melt on iron is sufficiently low to permit die casting in hot-chamber machines in which the operating mechanism is immersed continuously in the molten alloy.

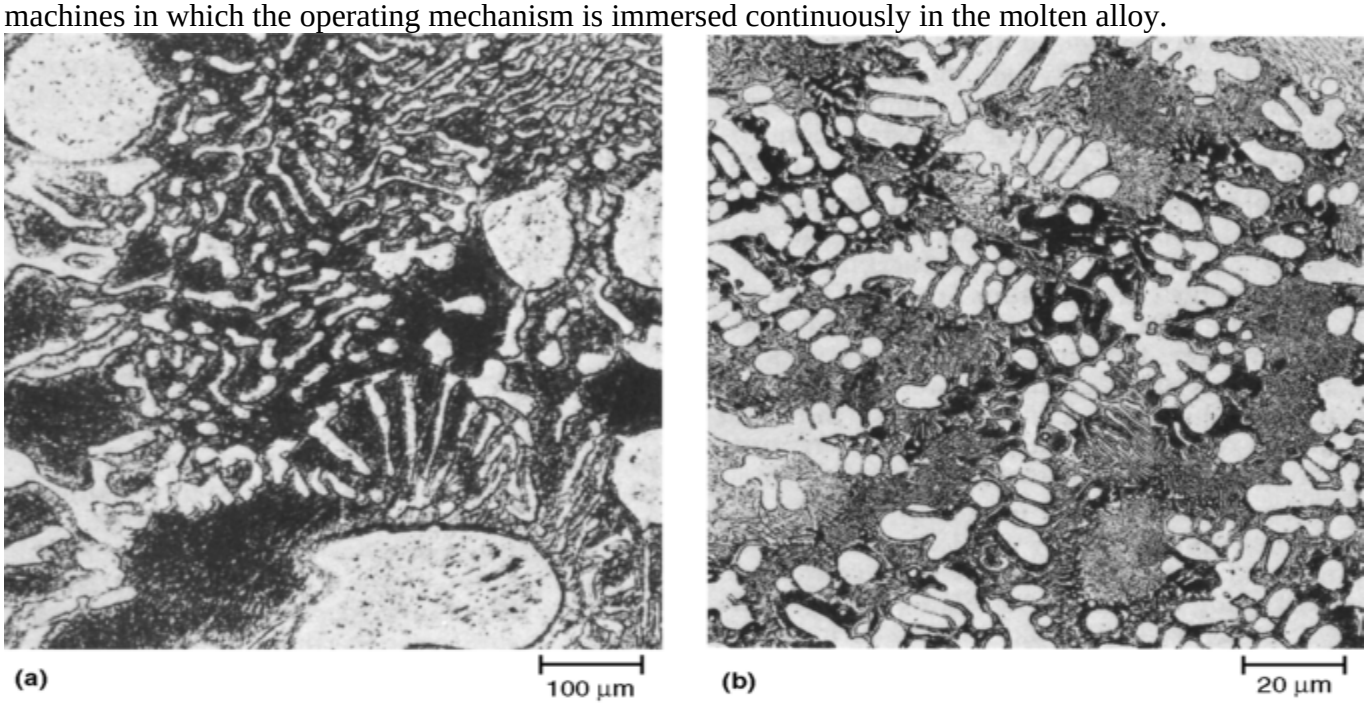

Fig. 22 ZA-8 alloy (UNS Z35636, Zn-8Al-1Cu-0.02Mg), as sand cast. Both etched in etchant 1, Table 1. (a) Dendrite structure at a lower magnification, 100×. (b) Coarse, zinc-rich dendrites in a matrix of α + η eutectic phase. 500×

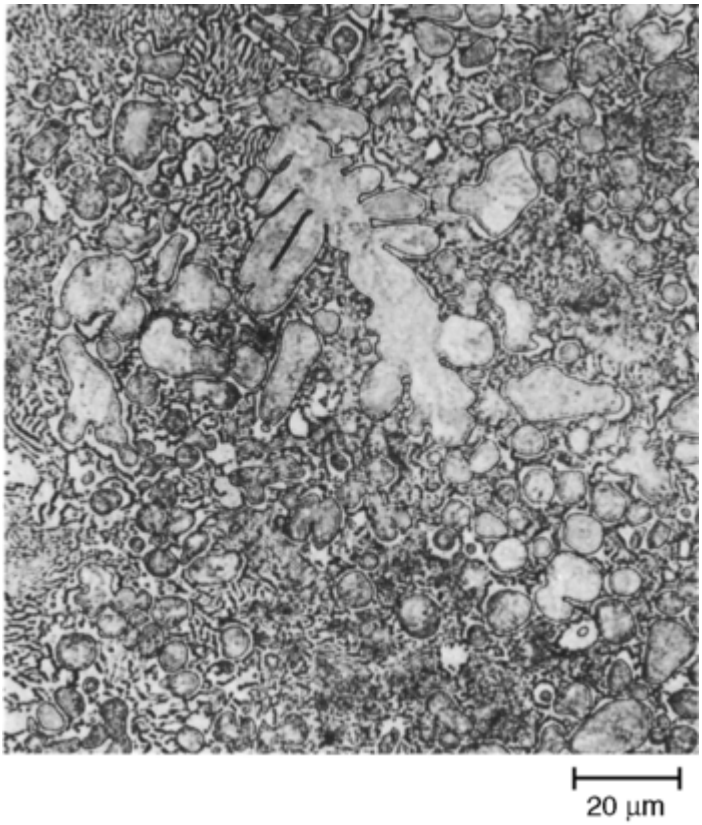

Fig. 23 Same alloy as Fig. 22 except as pressure die cast. Same constituents as Fig. 22, but pressure die casting has yielded a much finer microstructure. Etchant 2, Table 1. 500×

During solidification of hypoeutectic zinc die-casting alloys containing approximately 4% Al, such as alloy 3 in Fig. 24(a), the first material to freeze appears as primary particles of zinc-rich solid solution (η phase). Later, the remaining liquid solidifies as eutectic composed of η phase and the unstable high-temperature constituent α. Aluminum acts as a grain refiner in cast zinc; together with the high solidification rates of the die casting process, this results in a fairly fine equiaxed grain structure, which is primarily responsible for the strength, ductility, and toughness of zinc die castings.

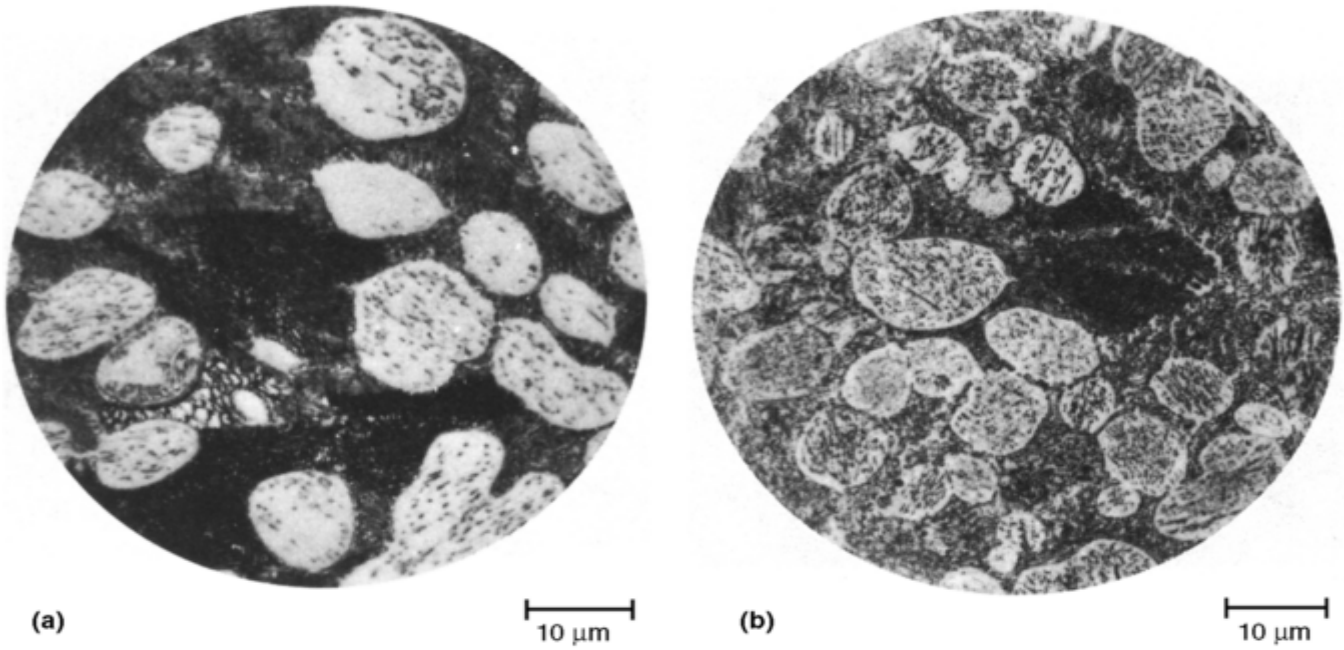

Fig. 24 Alloy 3 (ASTM AG40A, Zn-4.1Al-0.035Mg). (a) As die cast. Structure is zinc solid solution surrounded by eutectic. (b) Same as (a) except aged 10 days at 95 °C (205 °F). Aging increased the amount of precipitation in the zinc solid solution. Both etched in etchant 2, Table 1. 1000×

When die castings are aged at room temperature or a slightly elevated temperature, a precipitation reaction occurs in the zinc-rich η phase. In a freshly made die casting, η phase may contain approximately 0.35% Al in solution. During five weeks at room temperature, this will decrease to approximately 0.05%, the difference appearing as minute particles of α within the η-phase structure. Most of the aluminum can be precipitated in much less time by aging at a slightly elevated temperature (Fig. 24b). Similar aging effects are observed in alloys containing copper, which is added to increase tensile strength and hardness. Copper additions to 1.5% yield die castings with reasonably stable properties and dimensions. Low-temperature stabilization annealing is occasionally used to achieve maximum stability. The zinc-aluminum alloys extend the amount of primary phase; in the ZA-8 (Fig. 22) and ZA-12 (Fig. 25) alloys, this is η phase but is replaced by α in the ZA-27 alloy (Fig. 11).

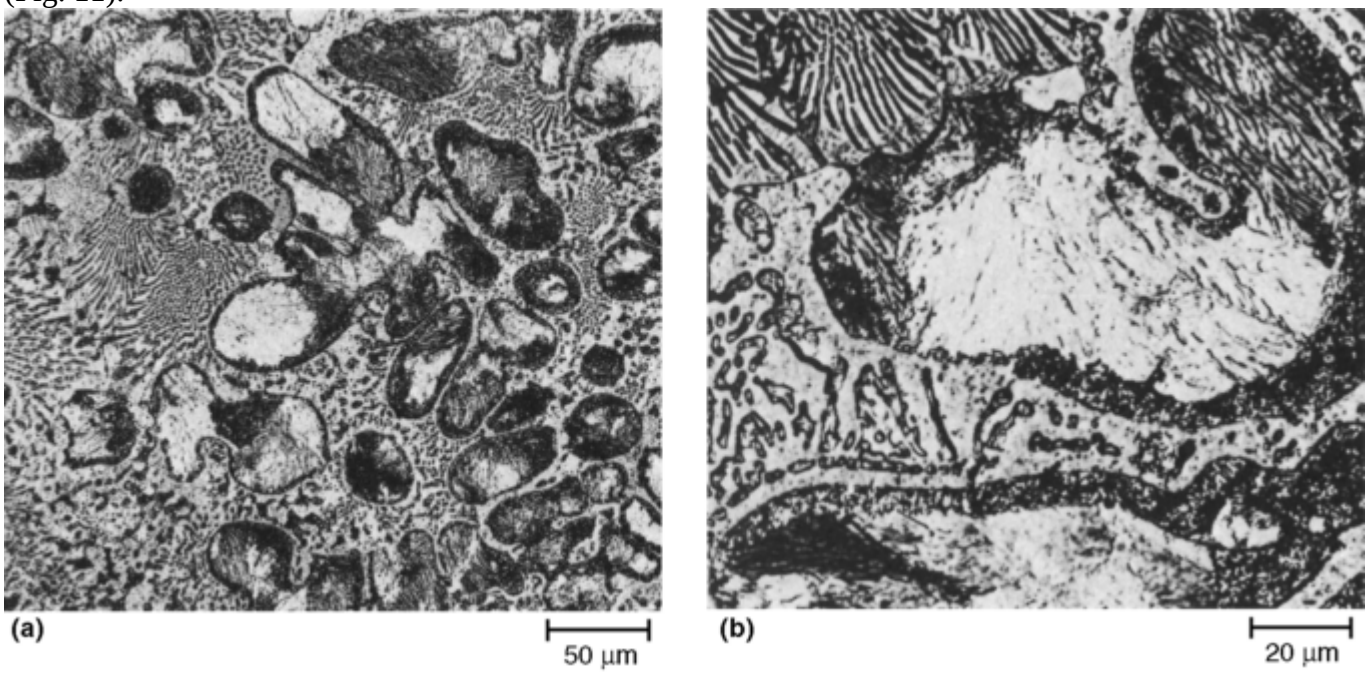

Fig. 25 ZA-12 alloy (UNS Z35631, Zn-11Al-0.9Cu-0.02Mg), as sand cast. Coarse, zinc-rich dendrites in a matrix of eutectic α + η phase. This alloy contains less of the eutectic than ZA-8 (Fig. 22, Fig. 23). Etchant 1, Table 1. (a) 200×. (b) 500×

The casting method will influence the cooling rate and the microstructure that results. Figure 26 shows permanent mold, pressure die cast, and continuous cast specimens of the same alloy that was sand cast in Fig. 25.

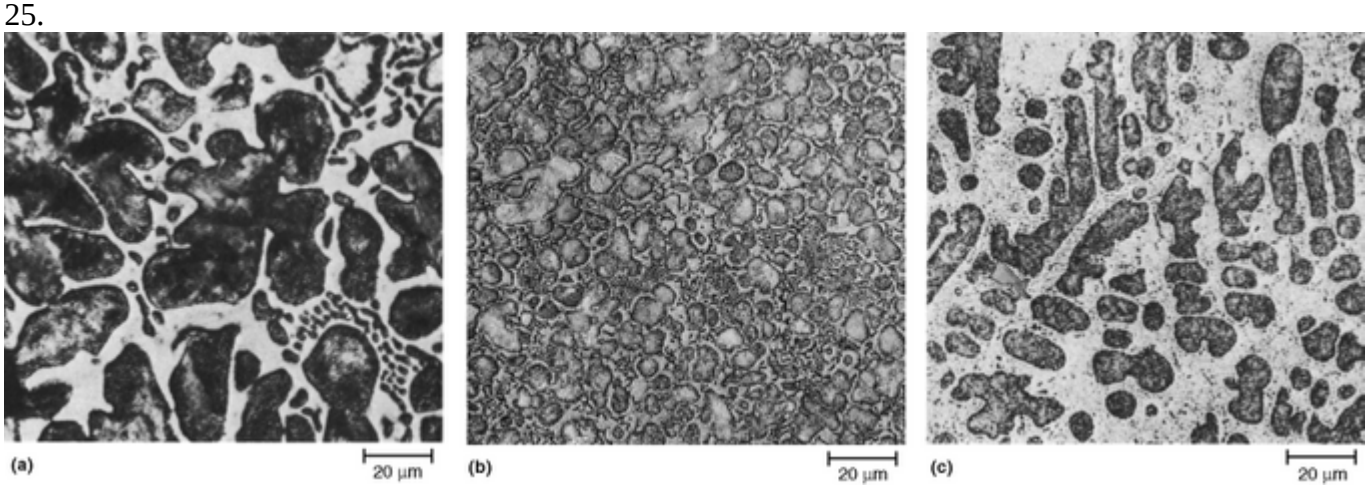

Fig. 26 Same alloy as Fig. 25 (a) As-cast in a permanent mold. Same constituents as Fig. 25, but permanent mold casting results in a finer microstructure. Etchant 1, Table 1. (b) Same constituents, but pressure die casting results in a much finer microstructure. Etchant 4, Table 1. (c) Continuous cast in an 80 mm (3.25 in.) diameter ingot results in finer structure than the sand casting. Etchant 1, Table 1. All: 500×

Wrought alloys based on the eutectoid composition of 78% Zn and 22% Al are of commercial interest because of their superplastic properties. Microstructures developed in this alloy depend on the heat treatment used (Fig. 27).

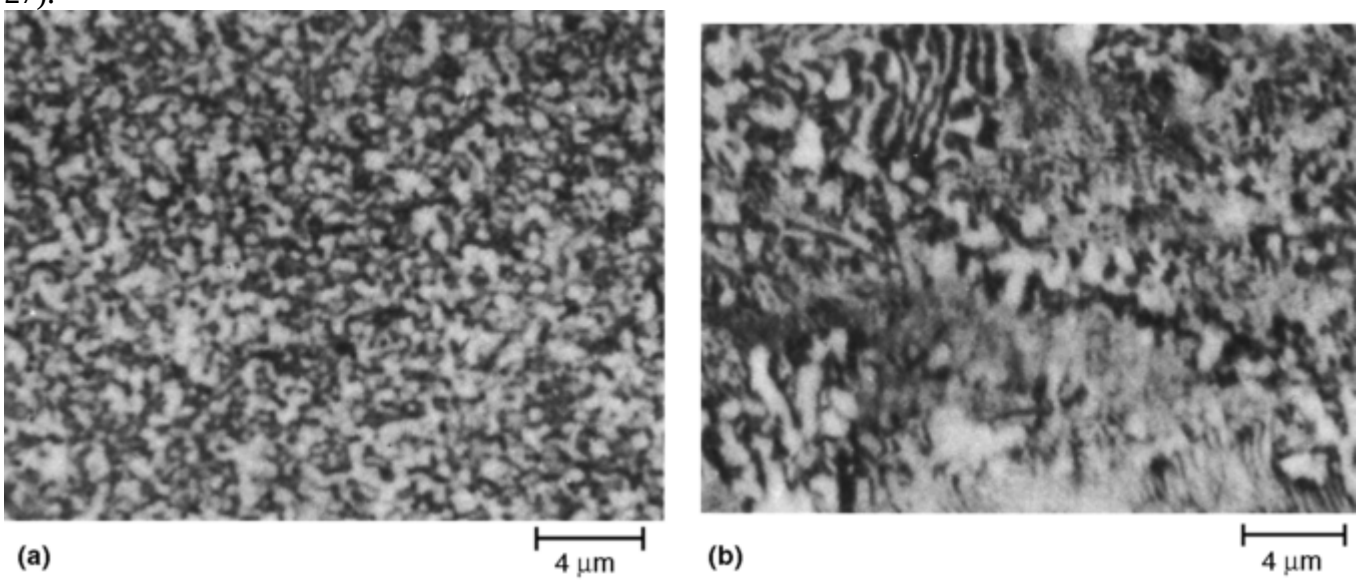

Fig. 27 Zn-22Al alloy (eutectoid composition). (a) Superplastic, fine-grained structure obtained by annealing at 350 °C (660 °F) and water quenching. (b) Same alloy held 1 h at 350 °C (660 °F) and air cooled. Structure consists of lamellar and granular α and η, both products of eutectoid transformation. Etchant 2, Table 1. 2500×

Magnesium additions in concentrations of 0.01 to 0.03% to the ZA-8, ZA-12, and ZA-27 alloys increase strength and hardness but decrease ductility.

Tin forms a low-melting eutectic with zinc at 91% Sn at 198 °C (388 °F). The solubility of tin in solid zinc is extremely restricted, and the zinc-tin eutectic appears in alloys containing as little as 0.001% Sn. Figure 28 shows the dendritic distribution of tin.

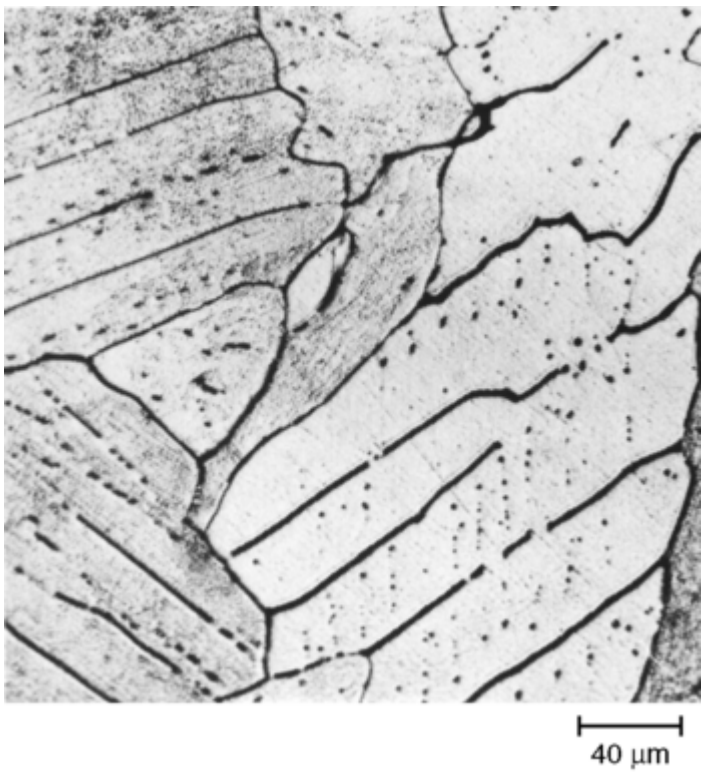

Fig. 28 Zn-1Sn permanent mold with rapid cooling. There is a dendritic distribution of tin. Mechanically polished. Etchant: similar to etchant 1, Table 1 (but only 10 g Na_2SO_4). 500×

The only deliberate use of tin additions to zinc is in certain hot dip galvanizing operations. In some galvanizing operations, tin additions are widely used to regulate the formation of bright, smooth, large white spangles in the coating. Tin present in hot-rolled zinc can cause hot shortness, the tendency of an alloy to separate along grain boundaries under stress near its melting point. In zinc-aluminum alloys, tin induces intergranular corrosion; concentrations must be maintained below 0.002%.

References cited in this section

1. R.W. Leonard, Continuous Hot Dip Coatings, *Corrosion: Fundamentals, Testing, and Protection,* Vol 13A, *ASM Handbook,* ASM International, 2003, p 786–793

2. T.J. Langgill, Batch Process Hot Dip Galvanizings, *Corrosion: Fundamentals, Testing, and Protection,* Vol 13A, *ASM Handbook,* ASM International, 2003, p 794–802

3. H.E. Townsend, Continuous Hot Dip Coatings, *Surface Engineering,* Vol 5, *ASM Handbook,* ASM International, 1994, p 339–348

4. S.G. Fountoulakis, Continuous Electrodeposited Coatings for Steel Strip, *Surface Engineering,* Vol 5, *ASM Handbook,* ASM International, 1994, p 349–359

5. D. Wetzel, Batch Hot Dip Galvanized Coatings, *Surface Engineering,* Vol 5, *ASM Handbook,* ASM International, 1994, p 360–371

Metallography and Microstructures of Zinc and Its Alloys, *Metallography and Microstructures,* Vol 9, *ASM Handbook,* ASM International, 2004, p. 933–941

Metallography and Microstructures of Zinc and Its Alloys

Specimen Preparation

Sectioning. The initial sample can be removed from a larger mass of material by sawing, breaking, or shearing (see the article “Metallographic Sectioning and Specimen Extraction” in this Volume). Because zinc alloys are comparatively soft, final sectioning of specimens is sometimes performed using special techniques. Either abrasive or diamond wheels are employed, because they produce less metal flow than sawing or shearing.

Mounting. Most specimens are mounted using conventional cold resin materials (see the article “Mounting of Specimens” in this Volume). Hot compression is not used, because the zinc will deform and recrystallize. Specimens of rolled zinc and zinc alloys can be secured by clamping. Several specimens are mounted together in a screw clamp using thin spacers of soft zinc between specimens and heavy strips of zinc between the clamp plates and the outermost specimens. The assembly is tightly clamped to prevent seepage of etchants between specimens. The zinc spacers are of known structure and serve as convenient standards of comparison for determining if the specimens have been prepared correctly.

Grinding and polishing of cast zinc can cause distortion to a depth 20 to 100 times as great as the deepest scratch. Therefore, in each stage of grinding and polishing, considerably more metal should be removed than the amount required for eliminating the scratches that remain from the previous stage. It is easier to prepare a distortion-free surface on specimens of fine-grained zinc than on specimens of coarse-grained, soft zinc.

Wet grinding on a belt grinding machine using 60- and 180-grit silicon carbide abrasives is suitable for zinc and zinc alloys. Local heating from grinding must be minimized using water cooling, because heat can cause structural changes too deep to remove by polishing.

Rough polishing is performed using 240-, 320-, 400-, and then 600-grit (65, 45, 35, and 20 μm) silicon carbide papers. These papers are less susceptible to loading than emery papers. Some authorities recommend applying

wax to the polishing papers so that they do not become embedded with zinc particles. Specimens should be rotated 90° relative to the direction of polishing after each polishing step. For soft (pure) zinc, polishing can be carried out by hand on papers supported on a flat surface. Zinc alloys are polished on a wheel using the same grades of paper. A low wheel speed (250 rpm maximum) during polishing will minimize overheating of the specimen, as will application of water to the silicon carbide papers and polishing in intervals of a few seconds, allowing the specimen to cool before polishing resumes.

Fine polishing is performed using magnesium oxide (MgO) or alumina (Al_2O_3). A method for preparing specially graded wet-polishing abrasives is described in Ref 6. In fine polishing, the first two wheels are covered with smooth canvas, the third wheel with felt or billiard cloth. A soft-nap polishing cloth is used for fine polishing. Hands as well as the specimen must be washed between polishing steps to prevent carryover of coarser grit from previous steps. Overpolishing and its consequences can be avoided by etching between polishing steps.

Zinc alloys that have intermetallic phases etch differently than unalloyed zinc. Because the intermetallic phases remain in relief, excessive polishing and etching should be avoided. Some of the steps listed previously can often be eliminated for alloys with intermetallic phases.

Polishing through all four wheels is necessary only for specimens with microstructures requiring high magnifications for resolution. Most low-magnification examinations can proceed after polishing on the third wheel. An ethanol powder mixture instead of water should be used when polishing galvanized steel. The specimen is then cleaned ultrasonically with alcohol and blown dry with warm air. Vibratory polishing of zinc and zinc alloys will produce surfaces with improved response to polarized light.

Macroetching. Use of concentrated hydrochloric acid (HCl) at room temperature, followed by rinsing and wiping off the resulting black deposit, produces satisfactory grain contrast on copper-free zinc and zinc alloys. Etchant 1 in Table 1 may be used for zinc containing 1% Cu or less, but with this etchant, grain contrast is not well defined. An etchant equal to HCl for producing grain contrast has not been found for the zinc alloys containing copper.

Microetching. The most useful etchants for microscopic examination of zinc and zinc alloys are aqueous solutions of chromic acid (CrO_3) to which sodium sulfate (Na_2SO_4) has been added. The grades of CrO_3 used for chromium plating are adequate. The compositions of etchants commonly used are given in Table 1. Any use of chromic acid and the other etchants must done with strict adherance to the safety and regulatory requirements. Chromic acid is toxic, may cause cancer by inhalation, and must not enter ground water, bodies of water, or sewage systems. See the Material Safety Data Sheets available from the supplier for conditions of use.

Etching should follow soon after final polishing. The specimen should be cleaned in alcohol, then running water, and etched while wet. To avoid staining, the use of etchant 1 or 2 in Table 1 should be followed immediately by a rinse in etchant 3. The specimen is then thoroughly washed in running water, dipped in alcohol, and dried with a stream of warm, clean air.

Table 2 lists recommendations for etchants and etching times for zinc and zinc die-casting alloys. The etching time may be longer or shorter for specific etching conditions; a minor difference in solution temperature may affect etching time. In addition, as indicated in Table 2 for cast or rolled zinc, etching time is often decreased as the magnification to be used is increased. Etchant 4 in Table 1 may also be used for etching zinc pressure die cast and galvanized specimens. Etching should proceed for 4 to 5 s, followed by rinsing in water and drying in warm air.

Table 2 Etchants and etching times for zinc and zinc die-casting alloys

Specimen metal[(a)]	Etchant (from Table 1)	Time, s, for examination at	
		250×	**1000×**
Cast or rolled zinc	1	5	1
Die cast alloy 3 (Z33520), 5 (Z35531), or 7 (Z33523)	2	1	1
Zinc-coated steel	7	1–30	1–30

(a) Selected die cast alloys given by common name (UNS)

Electrolytic etching has been used to differentiate two intermediate phases of the zinc-copper system (γ phase and ε phase). The electrolyte is a 17% aqueous solution of CrO_3. The polished specimen is the anode, and a small coil of platinum wire in the bottom of the dish or beaker holding the electrolyte serves as the cathode. The

specimen is connected to the current source before immersion in the electrolyte. At a current density of 0.2 A/cm^2 (1.5 $A/in.^2$), γ and ε phases are approximately equally attacked. At higher current densities, γ phase is preferentially attacked; at lower current densities, ε phase is preferentially attacked.

In a common procedure, the specimen is first etched at 0.78 A/cm^2 (5 $A/in.^2$). Gamma, if present, will be attacked; ε phase will not be attacked. The specimen is then repolished and etched at 0.15 A/cm^2 (1 $A/in.^2$), which will reveal any ε phase present. Further details on electrolytic etching of zinc alloys are available in Ref 7.

References cited in this section

6. J.L. Rodda, Preparation of Graded Abrasives for Metallographic Polishing, *Trans. AIME*, Vol 99, 1932, p 149–158

7. J.L. Rodda, Notes on Etching and Microscopical Identification of the Phases Present in the Copper-Zinc System, *Trans. AIME*, Vol 124, 1937, p 189–193

Metallography and Microstructures of Zinc and Its Alloys, *Metallography and Microstructures*, Vol 9, *ASM Handbook*, ASM International, 2004, p. 933–941

Preparation of Zinc Coating Specimens

The preparation of specimens of zinc coatings on steel presents several challenges due to the difference in mechanical and chemical properties of the materials. The electrochemical properties that make zinc coatings desirable as a cathodic protection will not cease while the sample is prepared.

Sectioning. Shearing sufficient to cut the base material may deform the coating. An abrasive cut-off wheel is recommended.

Mounting. Gaps around the specimen caused by resin shrinkage are to be avoided, because water, alcohol, or polishing materials could be trapped in the gap. Degrease the specimen with acetone before mounting. The cold mounting resins mentioned previously, such as slow-curing epoxies, generally have little shrinkage.

Grinding and Polishing. The previous general guide is applicable. Fine polishing with a diamond paste on a slow-speed wheel is recommended. Care must be taken to keep the surface of the entire specimen flat, because grinding will remove material of various constituents at different rates. Soft-nap cloth should not be used, because it may create more relief than is desired. Zinc reacts in water, causing stains, so alcohol rinses are recommended, followed by forced-air drying.

Etching. Amyl alcohol/nital, such as etchant 7, Table 1, is commonly used. The concentration of acid can vary from 0.5 to 2%, and etching time will vary with the type of coating. Amyl alcohol is a toxic substance; the etchant must be prepared under a hood, and skin contact must be avoided. Profiles of galvanized, galvannealed, and electrogalvanized steel are given in Fig. 29, 30 and 31.

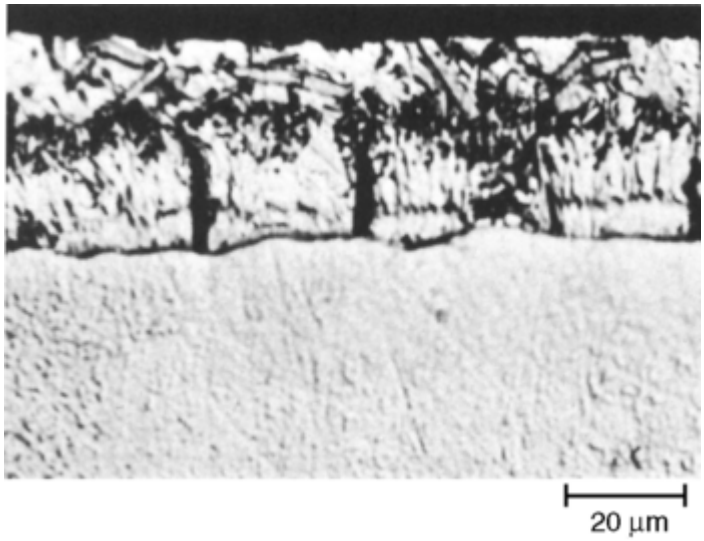

Fig. 29 Hot dip galvanized 1006, UNS G10060, steel. The galvannealed process produced a coating with no free zinc. Coating weight: 275 g/m^2 (0.9 oz/ft^2). Etchant: amyl-nital. 550×

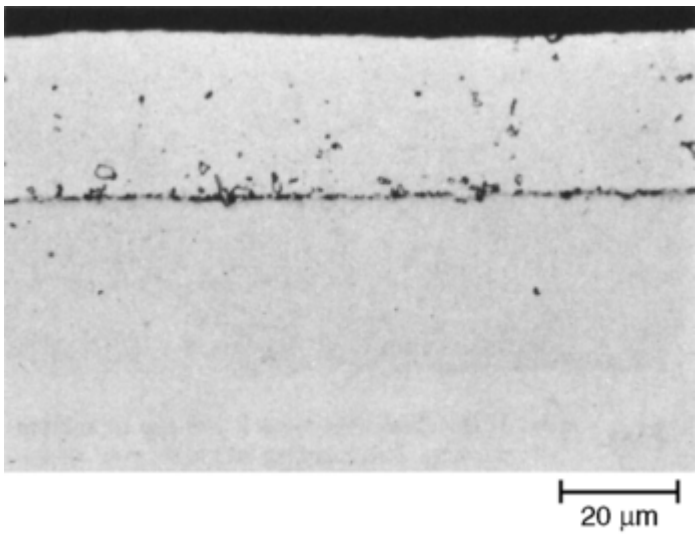

Fig. 30 Hot dip galvanized 1006, UNS G10060, steel, without annealing. Zinc-iron compounds are present at the interface, while the remainder of the coating is free zinc. Coating weight: 320 g/m^2 (1.05 oz/ft^2). Etchant: amyl-nital. 550×

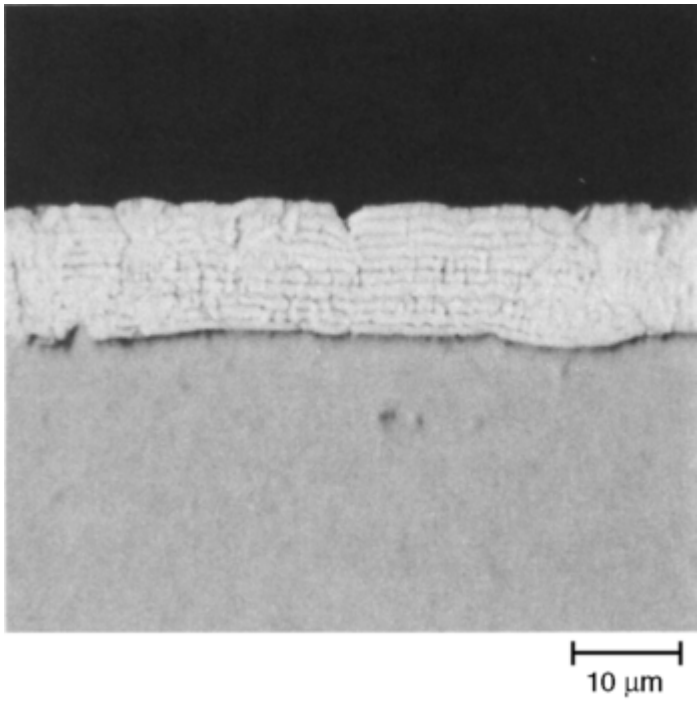

Fig. 31 Electrogalvanized 1006, UNS G10060, steel. Careful etching with a chromic acid/sodium sulfate etchant, with a concentration intermediate between etchant 1 and 2 in Table 1, reveals the interface between layers of zinc deposited in individual cells in a continuous multicell electrogalvanizing line. Note the absence of a zinc-iron alloy layer at the interface with the steel. Coating weight: 80 g/m^2 (0.26 oz/ft^2). Etchant: 8 to 10 g CrO_3, 1 g Na_2SO_4, 100 mL H_2O. 1000×

Examination. A collection of three-dimensional images depicting the surface morphology and the profile of coated steel produced using a scanning electron microscope can be found in Ref 7. Examination of the thickness of various intermetallic layers provides information on the formability and corrosion resistance of the coated sheet.

Reference cited in this section

7. J.L. Rodda, Notes on Etching and Microscopical Identification of the Phases Present in the Copper-Zinc System, *Trans. AIME,* Vol 124, 1937, p 189–193

Metallography and Microstructures of Zinc and Its Alloys, *Metallography and Microstructures,* Vol 9, *ASM Handbook,* ASM International, 2004, p. 933–941

Microexamination

Grain size is best determined under polarized light illumination, which displays each grain as a different shade, depending on orientation (Fig. 2, 6, 7, 32). Grain counts can be made with good accuracy. Grain boundaries are poorly defined under bright-field illumination.

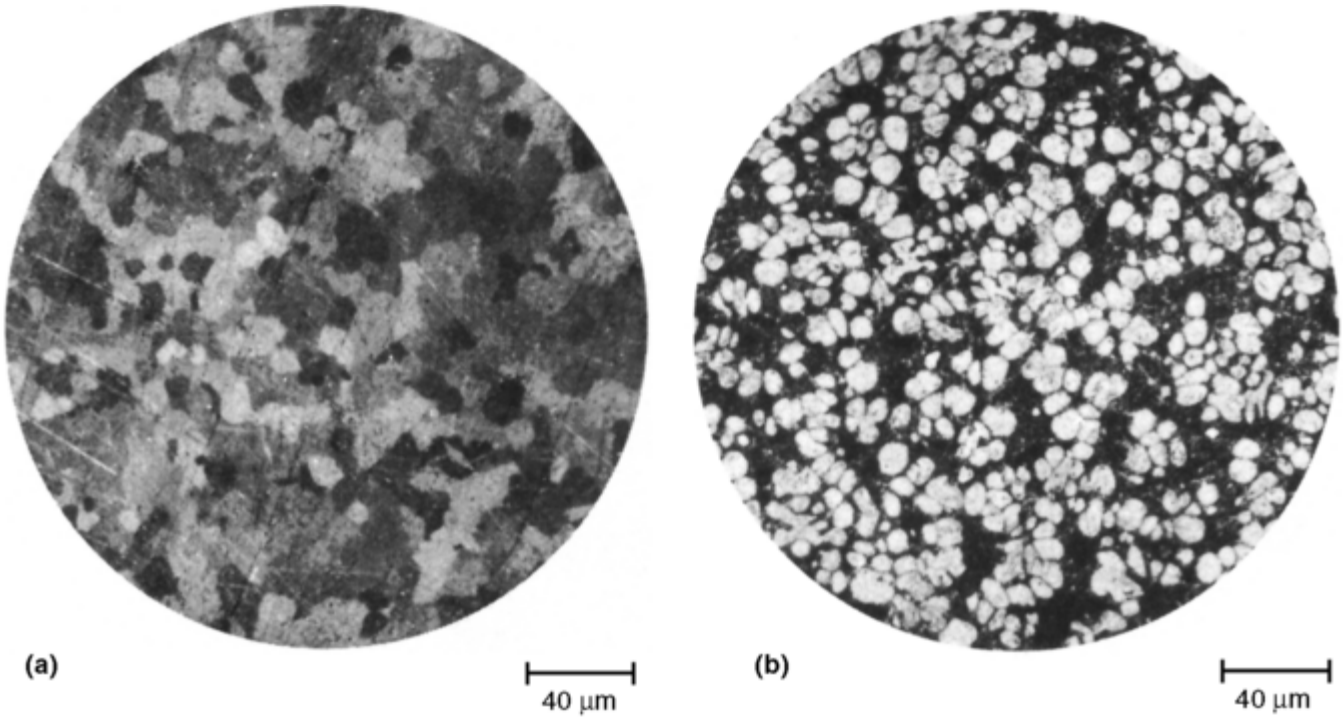

Fig. 32 Alloy 5, UNS Z35531, die cast with rapid freezing, unetched. (a) Polarized light illumination shows grain size but not alloy phases. Grains are larger than primary crystallites in (b), indicating that the zinc grains extend into the eutectic. (b) Fine primary crystallites of solid solution in fine lamellar eutectic. The fine structure imparts toughness and high strength to the alloy. Compare with Fig. 14 and 15 As-polished. Etchant 2, Table 1. 250×

Dendrite arm spacing can be measured on micrographs of selected areas using the linear intercept procedure in ASTM E 112 (Ref 8). Soundness values (porosity levels) can also be obtained in cast alloys by the use of quantitative analysis on a volume percent basis. Specimens to be examined for corrosion should be in the as-polished condition.

Reference cited in this section

8. "Test Methods for Determining the Average Grain Size," E 112, *Annual Book of ASTM Standards,* Vol 03.01, ASTM

Metallography and Microstructures of Zinc and Its Alloys, *Metallography and Microstructures,* Vol 9, *ASM Handbook,* ASM International, 2004, p. 933–941

Acknowledgment

This article is adapted from "Zinc and Zinc Alloys," *Metallography and Microstructures, ASM Handbook,* Volume 9, 1985, that had been revised for that edition by L. Mongeon and R.J. Barnhurst.

References

1. R.W. Leonard, Continuous Hot Dip Coatings, *Corrosion: Fundamentals, Testing, and Protection,* Vol 13A, *ASM Handbook,* ASM International, 2003, p 786–793

2. T.J. Langgill, Batch Process Hot Dip Galvanizings, *Corrosion: Fundamentals, Testing, and Protection,* Vol 13A, *ASM Handbook,* ASM International, 2003, p 794–802

3. H.E. Townsend, Continuous Hot Dip Coatings, *Surface Engineering,* Vol 5, *ASM Handbook,* ASM International, 1994, p 339–348

4. S.G. Fountoulakis, Continuous Electrodeposited Coatings for Steel Strip, *Surface Engineering,* Vol 5, *ASM Handbook,* ASM International, 1994, p 349–359

5. D. Wetzel, Batch Hot Dip Galvanized Coatings, *Surface Engineering,* Vol 5, *ASM Handbook,* ASM International, 1994, p 360–371

6. J.L. Rodda, Preparation of Graded Abrasives for Metallographic Polishing, *Trans. AIME,* Vol 99, 1932, p 149–158

7. J.L. Rodda, Notes on Etching and Microscopical Identification of the Phases Present in the Copper-Zinc System, *Trans. AIME,* Vol 124, 1937, p 189–193

8. "Test Methods for Determining the Average Grain Size," E 112, *Annual Book of ASTM Standards,* Vol 03.01, ASTM

P.E. Danielson and R.C. Sutherlin, Metallography and Microstructures of Zirconium, Hafnium, and Their Alloys, *Metallography and Microstructures*, Vol 9, *ASM Handbook*, ASM International, 2004, p. 942–958

Metallography and Microstructures of Zirconium, Hafnium, and Their Alloys

Paul E. Danielson, Albany Research Center, U.S. Department of Energy; Richard C. Sutherlin, Wah Chang, An Allegheny Technologies Company

Introduction

ZIRCONIUM, HAFNIUM, and their alloys are reactive metals used in a variety of nuclear and chemical processing applications. Zirconium alloys are primarily used for cladding of uranium fuel elements and for other internal components for nuclear power reactors due to their corrosion resistance and low neutron cross section. Because of the excellent resistance to chemical corrosion, the commercial grades of zirconium (UNS R60702, R60705) are commonly used in chemical equipment for processing of organic and mineral acids, as well as strong alkaline environments. Hafnium, with its high neutron cross section and corrosion resistance similar to zirconium in high-temperature water and steam environments, is used as nuclear reactor control rods and has been used for reprocessing of spent nuclear fuel. Zirconium also finds use in flashbulbs, incendiary devices, sputtering targets, and medical implants. Hafnium is frequently used as an alloying element for nickel-base superalloys and for some high-temperature alloys in turbojet and rocket engine parts. Hafnium is manufactured into sputtering targets and cutting tips for steel and was previously used in flashbulbs. Nominal compositions of the zirconium and hafnium grades discussed in the article are shown in Table 1.

Table 1 Chemical compositions of common zirconium and hafnium alloys

UNS No.	Common designation	Composition, %										
		Nb	**Sn**	**Fe**	**Cr**	**Ni**	**O, max**	**C, max**	**H, max**	**N, max**	**Hf, max**	**Zr + Hf, max**
R60702	Zirconium grade 702	…	…	Fe + Cr = 0.20		…	0.16	0.05	0.005	0.025	4.50%	99.20%
R60705	Zirconium grade 705	2.0–3.0	…	Fe + Cr = 0.20		…	0.18	0.05	0.005	0.025	4.50%	99.50%
R60802	Zircaloy 2	…	1.20–1.70	0.07–0.20	0.05–0.15	0.03–0.08	0.12	…	…	…	…	…
R60804	Zircaloy 4	…	1.20–1.70	0.18–0.24	0.07–0.13	…	0.12	…	…	…	…	…
R60901	Zr 2.5Nb	2.40–2.80	…	…	…	…	0.09–0.13	…	…	…	…	…
…	Low-oxygen Zr	…	…	…	…	…	0.10	0.05	0.005	0.025	4.50%	99.20%
…	Hafnium	…	…	0.04	…	…	0.05	…	…	…	…	4% max Zr

P.E. Danielson and R.C. Sutherlin, Metallography and Microstructures of Zirconium, Hafnium, and Their Alloys, *Metallography and Microstructures,* Vol 9, *ASM Handbook,* ASM International, 2004, p. 942–958

Metallography and Microstructures of Zirconium, Hafnium, and Their Alloys

Paul E. Danielson, Albany Research Center, U.S. Department of Energy; Richard C. Sutherlin, Wah Chang, An Allegheny Technologies Company

Metallurgy of Zirconium and Hafnium Alloys

Zirconium and hafnium both have hexagonal close-packed (hcp) crystal structures at room temperature. Pure forms of zirconium and hafnium exhibit allotropic transformations from the hcp alpha (α) structure to a body-centered cubic (bcc) beta (β) structure. The hcp structure responds well to polarized light due to the strong anisotropy. While the commercially pure alloys of Zr702, hafnium, and the Zircaloys are single-phase structures at room temperature, the niobium-containing zirconium alloys (Zr2.5Nb and Zr705 grades) exist as two-phase alloys. When the single-phase zirconium alloys cool from the β-phase to a temperature range of approximately 815 to 865 °C (1500 to 1590 °F), α-zirconium nucleates on small heterogeneities such as carbides, silicides, and chlorides. Normally, a high frequency of nucleation sites leads to a Widmanstätten or basketweave structure in the matrix. Intermetallic compounds or second-phase particles of Zr-Fe, Zr-Cr, or Zr-Ni will form as small precipitates in the metal structure (Ref 1). Beta quenching during the metallurgical processing will help to distribute these particles more uniformly.

Hafnium is similar to zirconium and has an hcp structure below 1760 °C (3200 °F) and a bcc structure above this temperature. Hafnium is essentially a single-phase alloy except for the presence of extremely fine iron-rich precipitates. Hafnium welds show a transformed β-structure with large grains. Because of the high purity of hafnium, the structure shows large prior β grain boundaries in the weld area with little delineation of the acicular α within these grains. Similar to zirconium, hafnium shows grain coarsening in the heat-affected zone (HAZ) where welding temperatures have exceeded the transformation temperature.

This article examines the methods for metallographic preparation and shows representative microstructures of zirconium, zirconium alloys, and hafnium.

Reference cited in this section

1. J. Haygarth and R. Graham, Zirconium and Hafnium, *Review of Extraction, Processing, Properties & Applications of Reactive Metals,* B. Mishra, Ed., TMS, 2002, p 1–71

P.E. Danielson and R.C. Sutherlin, Metallography and Microstructures of Zirconium, Hafnium, and Their Alloys, *Metallography and Microstructures,* Vol 9, *ASM Handbook,* ASM International, 2004, p. 942–958

Metallography and Microstructures of Zirconium, Hafnium, and Their Alloys

Paul E. Danielson, Albany Research Center, U.S. Department of Energy; Richard C. Sutherlin, Wah Chang, An Allegheny Technologies Company

History of Zirconium Metallography

Some of the early metallography performed and published on zirconium alloy structures was that of Vogel and Tonn in 1931. The zirconium samples were prepared using an electropolishing process in nitric acid and subsequent heat tinting revealing a β-quenched structure in zirconium (Ref 2). In 1948, Roth described a procedure involving mechanical polishing and hydrofluoric acid etching (Ref 3). Hydrofluoric acid, being one

of the few acids that will attack zirconium, has been used for more than 50 years and continues to be utilized in metallographic preparation processes for zirconium and hafnium. In the 1950s, Cain subsequently developed a metallographic preparation method consisting of a bright dip using hydrofluoric acid in combination with various diluents. This method was reported to be fast, simple, and effective. Electropolishing with perchloric acid baths was also reported to be used. Electropolishing employed hydrofluoric acid and in some cases an electrolyte containing ammonium bifluoride for metallographic preparation (Ref 4).

Since the 1930s, metallographic procedures have improved dramatically with the use of new polishing methods, advanced polishing cloths, better mounting materials, pressure-sensitive adhesives (PSAs), improved etchants, and other advanced equipment. Metallography imaging capabilities have improved significantly due to the use of lower-cost, high-speed computers. Digital cameras are currently being used with more than 12 megapixel resolution and extremely high light sensitivity, resulting in greater speed and flexibility.

References cited in this section

2. V.R. Vogel and W. Tonn, Über einen Umwantlungspunkt des Zirkons, *Z. Anorg.uallhem, Chem.,* Vol 202, 1931, p 292

3. H.P. Roth, "Metallography of Zirconium," Report MIT-1004, MIT Metallurgical Project Quarterly Technical Progress Report for the Period February through April, 1948, Massachusetts Institute of Technology, p 115–126

4. B. Lustman and F. Kerze, Jr., Ed., *The Metallurgy of Zirconium,* McGraw-Hill, 1955

P.E. Danielson and R.C. Sutherlin, Metallography and Microstructures of Zirconium, Hafnium, and Their Alloys, *Metallography and Microstructures,* Vol 9, *ASM Handbook,* ASM International, 2004, p. 942–958

Metallography and Microstructures of Zirconium, Hafnium, and Their Alloys

Paul E. Danielson, Albany Research Center, U.S. Department of Energy; Richard C. Sutherlin, Wah Chang, An Allegheny Technologies Company

---

Specimen Preparation

Specimens of zirconium and hafnium for metallographic examination should be selected exhibiting proper orientation so they are representative of the specific attributes to be studied in a particular product. A longitudinal section is generally used to examine grain size, recrystallization, grain directionality, preferred orientation, and second-phase particle uniformity in wrought products. A transverse section (full cross section, if possible) may be used to examine such defects as cracks, porosity, and centerburst in wrought products. In as-cast products, the structure is generally random and not conforming to a general specimen orientation is less critical.

Sectioning. Specimens can be sectioned using a variety of methods, including hacksawing, band sawing, and abrasive cutting. Band sawing and abrasive cutting generally utilize a water-soluble oil to keep the sample cool. Care should be taken during cutting to minimize mechanical deformation. This deformation, however, can be removed during subsequent grinding and polishing steps.

Mounting. Larger samples may be polished unmounted if they can be handled easily. Specimens that are too small to be handheld for grinding and polishing or have a surface that must be preserved may be mounted using hot- or cold-mounting methods. Cold mounting may be preferred if the material is to be studied for the presence of hydrides in order to avoid alteration due to high temperature encountered during the mounting process. Cold mounting is accomplished using room-temperature setting epoxy resins. It should be noted that some edge retention may be sacrificed if cold-mounting techniques are used. For hot mounts, thermosetting diallyl

phthalate or epoxy resins with fillers work well. Fillers help match the abrasion/polishing rates of mounting resins and the specimen (see the article “Mounting of Specimens” in this Volume). Bakelite is also used, but it does not provide the edge retention or resistance to acid corrosion offered by the other mounting materials mentioned. Some high-production facilities may use a combination of bakelite as a backer and a mineral-filled epoxy (adjacent to the sample). Although different colors of mounting materials are available (red, green, yellow, and black), black-colored mounting is preferred because of its ability to absorb light, especially if polarized light is to be used.

Grinding. Wet and dry grinding is performed using abrasive belts or rotating disks or may be ground by hand using abrasive paper. Abrasives used include silicon carbide and in some cases alumina (Al_2O_3). Wet grinding begins with a disk or belt sander using 120- to 180-grit paper with water being the preferred coolant. Fine grinding may be performed using wet or dry methods. If dry grinding is used, it is important to be aware of the hazards of fine metallic zirconium or hafnium particles generated during this operation. One should be especially cognizant of the accumulation of pyrophoric metallic fines in sumps and air-collection systems. These fines could ignite, causing severe burn injuries and property damage.

The standard grinding sequence of 180-grit through 600-grit papers may not be necessary because of the fast cutting rate of the subsequent rough-polishing step, which uses abrasives for metal removal. Hand emery papers with 2 grit through 00 grit may be substituted for the grinding stage. Care should be taken since heat generated during this grinding step can smear or swell the cold-mounting materials. Grinding wheel speeds range from 400 to 1200 rpm.

Manual Chemical-Mechanical (“Attack”) Polishing. Chemical-mechanical polishing, also known as “attack” polishing, can be used in both the rough and final preparation stages. It is important in the attack-polishing method that the sample is abraded and etched simultaneously. This will result in a true, undisturbed structure and prevent smeared metal from being created. Wheel speeds range from 400 to 1200 rpm for both rough and final polishing. Polishing wheels are commonly available in 8, 10, 12, and 14 in. (205, 255, 305, and 355 mm) diam sizes. It should also be noted that eye protection and lightweight, acid-proof gloves should be used while chemically polishing. Metal wheels, such as bronze or aluminum, if used, should be protected from acid attack by placing an acid-resistant material between the cloth and wheel. This also prevents an electrolytic reaction between the specimen and the metallic wheel. Advanced PSA polishing cloths have been developed to help provide that barrier.

Rough Polishing. There are three major components included in rough polishing: a soft nonwoven abrasive cloth, an acid solution, and the rough polishing suspension. The wheel should be predampened with water at a speed of 400 to 600 rpm. Approximately 2 to 4 mL of acid solution composed of 85 mL of water (H_2O), 5 mL nitric acid (70% HNO_3), 5 mL of hydrogen peroxide (30% H_2O_2), and 5 mL hydrofluoric acid (48 to 52% HF) is initially applied to the wheel. This is followed by the application of approximately 2 to 4 mL of a polishing suspension composed of 10 g of 1.0 μm α-Al_2O_3 in 100 mL of water. Both solutions are applied to the middle of the rotating wheel. The sample is then placed on the 400 to 600 rpm polishing wheel with roughly 7 to 35 kPa (1 to 5 lb) of pressure. Care should be taken to rotate the sample to achieve an even surface removal and eliminate comet tails (directional marks) on the sample surface. The sample is then rinsed with water. Before each polishing step, the wheel is flushed with water and a bristled brush (nailbrush) is used to remove any remaining abrasive and acid. One or two charges of the acid/slurry combination may be required to remove the previous grinding and polishing marks during rough polishing. This polishing step usually lasts 2 to 4 min.

If performed properly, the rough-polished specimen should have uniform 1.0 μm scratches and have all previous grinding media removed. Care should be taken during this rough polishing to ensure that all the embedded silicon carbide and/or Al_2O_3 is removed before proceeding to the next step.

When only the grain size or basic microstructural condition of the materials is to be examined, satisfactory results can be obtained with only a rough polish followed by a swab etch.

Final Polishing. For a more detailed examination of second-phase particles or contaminants, the goal of final polishing is to obtain a surface free of surface-deformation scratches. The components used for the final-polishing sequence are:

- A soft, fine-polishing cloth designed for attack polishing
- An acid solution of 85 mL water (H_2O), 5 mL of nitric acid (70% HNO_3), 5 mL of hydrogen peroxide (30% H_2O_2), and 5 mL of hydrofluoric acid (48 to 52% HF)
- An abrasive suspension (such as 0.6 μm colloidal silica)

An acid solution composed of 75 mL of water (H_2O), 10 g of oxalic acid, 10 mL of acetic acid (glacial), 3 mL of nitric acid (70% HNO_3), and 2 mL of hydrofluoric acid (48 to 52% HF) works equally as well in final polishing. The fine-polishing cloth designed for attack polishing is used for final-polishing processes. The wheel is first dampened with water. The spinning wheel is then charged at speeds ranging from 400 to 600 rpm with the acid/abrasive suspension. The ratio of the abrasive suspension depends on the specimen material, ranging from four parts of abrasive suspension to one part acid for the purer zirconium materials to equal amounts of solution for the Zircaloys and hafnium materials. The purer zirconium material tends to be more susceptible to hydrofluoric acid attack.

Charging at high speed may be beneficial to even out the acid/abrasive suspension, but may not be necessary. The specimen should be placed on the 400 to 600 rpm wheel for 45 to 60 s while applying light pressure. A absorbent paper wipe may also be used to smooth out the media during polishing to lessen the occurrence of scratches. This process can be repeated if needed after first cleaning the wheel with a nailbrush as explained in the rough-polishing section. Preparation of the specimen may require two to three charges of the acid/abrasive solution. This final-polishing step can last from 3 to 5 min. When polishing is complete, a slight indication of second-phase structure would be visible using bright field illumination. Polarized light also works well for checking the progress during final polishing, especially for scratches and flowed metal.

The final-polishing step is complete when using polarized light if the grain structure is easily seen and free of flowed metal and scratches. The purer or softer materials tend to be more difficult to polish to a flow or scratch-free condition.

When polishing is complete, additional microstructural enhancement techniques may be employed, such as anodization, heat tinting, or selective etching. Anodization and heat tinting can be used for identification of basic grain structure, inclusions, and second-phase or intermetallic compounds, as well as interstitial contamination. Specimens that are to be anodized after final polishing should be thoroughly cleaned prior to the anodization process. The anodization layer can greatly enhance any previous oxide films and stains on the polished surfaces. Selective etching can be used for hydride identification or alloy segregation.

Automatic Polishing. Automatic grinding and polishing (robotic or vibratory) as opposed to manual attack polishing will also provide good results on zirconium and hafnium. Automatic methods for standard metallographic preparation may have some advantages over manual polishing, such as better repeatability, higher production rates, and greater safety. Manual methods are more adaptable to dissimilar alloys or different material combinations on the individual mount.

Rough Polishing. As in manual preparation procedures, there are three major components included in automatic rough polishing: a soft, nonwoven abrasive cloth, an acid solution, and the rough-polishing suspension. The wheel should be predampened with water at a speed of 400 to 600 rpm. Approximately 2 to 4 mL of acid solution composed of 85 mL water (H_2O), 5 mL of nitric acid (70% HNO_3), 5 mL of hydrogen peroxide (30% H_2O_2), and 5 mL of hydrofluoric acid (HF) is initially applied to the wheel. This is followed by the application of approximately 2 to 4 mL of a polishing suspension composed of 10 g of 1.0 μm α-Al_2O_3 in 100 mL of water. Both solutions are applied to the middle of the rotating wheel. The sample fixture is then placed on the 400 to 600 rpm wheel with roughly 7 to 35 kPa (1 to 5 lb) of pressure per sample. The samples are then rinsed with water. The samples should not be removed from the fixture unless the sample fixture is designed so that the samples can be placed back in the identical position for further polishing. Ultrasonic cleaning should be used between the grinding and polishing steps. If a second rough-polishing step is required, the wheel is flushed with water, and a bristled brush (nailbrush) is used to remove any remaining polishing residue. One or two charges of the acid/slurry combination may be required to remove the grinding and polishing marks during rough polishing. This polishing step usually lasts 1 to 2 min.

Final Polishing. As in manual polishing, final polishing by automatic means is meant to obtain a surface free of surface deformation scratches for a more detailed examination of second-phase particles or contaminants. Final polishing is required for a more detailed examination of second-phase particles or contaminants. The goal is to obtain a flow-free, scratch-free polished surface. The components used for the final-polishing sequence are:

- A soft, fine polishing cloth designed for attack polishing
- An acid solution of 75 mL H_2O, 10 g of oxalic acid, 5 mL of acetic acid (glacial), 6 mL of nitric acid (70% HNO_3), 2 mL of hydrofluoric acid (48 to 52%HF)
- An abrasive suspension of colloidal silica

The suspension shall be added to the wheel in equal amounts of acid and abrasive media during a 1 to 2 min period. The fine-polishing cloth designed for attack polishing is used for final-polishing methods. The wheel is first dampened with water. The polishing wheel is then charged at speeds ranging from 400 to 600 rpm with the acid/abrasive suspension. The ratio of the suspension will vary depending on the material that is being prepared. The purer zirconium material tends to be more susceptible to acid attack. The appropriate pressure should be applied in this final-polishing step to achieve a shiny, bright polished finish.

This process can be repeated if needed after first cleaning the wheel with a nailbrush as explained in the rough-polishing section. Preparation of the specimen may require one or more charges of the acid/abrasive solution. This final-polishing step can last 1 to 5 min. When polishing is complete, a slight indication of second-phase structure would be visible using bright field illumination. Polarized light also works well for checking the progress during final polishing, especially for scratches and surface deformation. Specimens that are to be anodized after final polishing should be thoroughly cleaned prior to anodization. The anodization layer can greatly enhance any previous oxide films and stains on the polished surfaces.

Etching is used to show certain attributes of the macrostructure and microstructure in zirconium and hafnium alloys. Macroetching is performed using a pickle tank or a temporary container for immersion of the sample in the etch solution. Microetching is accomplished by using either swabbing or immersion. Table 2 shows the typical etchants used for macrostructural and microstructural examination of prepared samples.

Table 2 Selected etchants for macroscopic and microscopic examination of zirconium, hafnium, and their alloys

Procedure	Etchant	Procedure	Characteristics and use
1	4–5% HF (48–52%), 30–35% HNO_3 (70%), and balance H_2O	Immerse sample face up; etch 10–15 min, air dry	Shows general macrostructure in zirconium and hafnium
2	45 mL H_2O, 45 mL HNO_3 (70%), and 10 mL of HF (48–52%)	Rough polish, then swab etch 5–10 s; wash in water; air dry	Shows general microstructure in zirconium and hafnium
3	10 mL H_2O, 10 mL HNO_3 (70%), and 1 drop of HF (48–52%)	Final etching	Shows second phase in Zircaloys
4	25 mL of H_2O_2 (30%), 25 mL HNO_3 (70%) and 8–10 drops of HF (48–52%)	Rough polish, then swab etch 5–10 s; wash in water; air dry	Shows hydrides in zirconium and Zircaloys
5	45 mL of lactic acid, 45 mL of HNO_3 (70%), and 8 mL of HF (48–52%)	Rough polish, then swab etch 5–10 s; wash in water; air dry	Shows hydrides in zirconium-niobium alloys
6	97 mL ethanol (absolute), 2–3 mL HF (48–52%) followed by 250 mL H_2O, 22 mL HNO_3 (70%), and 3 mL HF (48–52%) solution[(a)]	Final polishing	Shows alloy variation

Note: Use fairly large swabs with all etching procedures.

(a) Dispose after using because the etchant may become unstable with time and a chemical reaction may occur.

Anodization is a metallographic-enhancement technique used for contrasting and identifying specific microstructural attributes, such as grain structure, secondary-phase boundaries, interstitial contamination, alloy segregation, and alloy variation. Anodization is an electrolytic process for depositing a thin oxide film on the surface of the specimen. The resulting interference colors are a function of the anodic film thickness, which depends on the anodization voltage and the anodizing solution.

Materials, when placed in an anodizing solution, will form an anodic layer by applying a direct-current (dc) potential between the sample and the solution. A 0 to 150 V dc power supply with low amperage (0.25 to 1.0 A) is required for anodization. The negative lead of the power supply should be attached to a stainless steel metal beaker, and the positive lead should contact the sample surface using a probe. The anode, in the form of a sharpened probe (approximately 66 mm, or 2.5 in., long) must be a material that can be anodized, such as zirconium, hafnium, niobium, or tungsten. Materials such as steels and coppers will not develop an anodized layer and therefore will not allow the specimen to anodize evenly.

The thickness of the anodization layer depends primarily on the voltage. The mounted specimen should be immersed face up in the proper anodizing solution inside a stainless steel beaker (which acts as the cathode) with approximately 6 mm (0.25 in.) of solution covering the top of the specimen. The polished surface of the specimen should be touched with the anode in an area that will not be conspicuous during examination. The power supply, which is set at 0 V, should be slowly adjusted to the desired voltage to control the anodization process. Best results will be achieved by taking 5 to 10 s to reach the appropriate voltage. Only the lower voltage layers (≤20 V) do not need this slower adjustment. Once the appropriate voltage is reached, the specimen should be held at the preferred voltage for 10 to 20 s. The sample should then be cleaned and dried. A cotton swab with soap and warm water works well for cleaning the sample.

Anodization achieved at 15 to 140 V works well for the preparation of zirconium, hafnium, and their alloys. The voltages used will depend on the microstructural attributes that are to be revealed. The anodizing solution (see Table 3) contains ethanol, which makes it flammable, so care must be taken to avoid electrical sparks. Moreover, ethanol and water will evaporate if left uncovered for several hours, which can affect the anodization results (Ref 5).

Table 3 Anodization techniques for microscopic examination of zirconium, hafnium, and their alloys

Procedure	Anodization procedure	Characteristics and use
1	15–20 V anodization layer (gold color in zirconium and hafnium)	Improves grain structure contrast under polarized lighting and prevents specimens for staining and oxidizing
2	110–115 V anodization layer (purple-blue color in zirconium)	Reveals intermetallic compounds, inclusions, and lighter element contamination in zirconium (bright field)
3	180 V anodization layer (light red color in zirconium)	Enhances second phase in Zircaloys (bright field)

Note: Anodization solution consists of 60 mL absolute ethanol, 35 mL H_2O, 20 mL glycerin, 10 mL lactic acid, 5 mL H_3PO_4 (85%) and 2 g citric acid.

Heat tinting is a complementary technique to anodization. Heat tinting enhances the visibility of grain structure, alloy variation, alloy segregation, and secondary phases. Heat tinting also improves polarized light capability. This technique must be done on an unmounted sample or one that has been broken out of the mount after polishing. This method uses the mechanism of surface oxide thickening of these reactive metals at elevated temperatures. While anodizing is relatively insensitive to variations in alloy distribution in the Zircaloys, heat tinting highlights those slight differences in alloy composition due to the variation of oxide-thickening rates that take place on the sample surface. These differences in oxide-film formation result in color variations when viewed in bright field. In some cases, the heat tinting can enhance the metallurgical attributes under polarized light or differential interference contrast (DIC). This is a result of the thin interference oxide film that will build up on the surface of the sample.

Heat tinting is generally accomplished on a prepared sample at approximately 300 to 370 °C (600 to 700 °F) using a small oven, hot plate, or even a small propane torch. If a furnace or hot plate is used, the sample(s) should be placed either on the metal floor in the furnace or on a metal hot plate to provide uniform heat distribution. The sample(s) will be heated at times ranging from 3 to 10 min depending on the alloy. It is very important that the heat tinting is done at a slow rate, or differences in the microstructural attributes may not be seen. Note that it is very important that the final step before heat tinting be a sample wash using distilled water.

Reference cited in this section

5. M.L. Picklesimer, Anodizing for Controlled Microstructural Contrast by Color, *Microscope,* Vol 15, Oct 1967

P.E. Danielson and R.C. Sutherlin, Metallography and Microstructures of Zirconium, Hafnium, and Their Alloys, *Metallography and Microstructures*, Vol 9, *ASM Handbook*, ASM International, 2004, p. 942–958

Metallography and Microstructures of Zirconium, Hafnium, and Their Alloys

Paul E. Danielson, Albany Research Center, U.S. Department of Energy; Richard C. Sutherlin, Wah Chang, An Allegheny Technologies Company

Examination and Interpretation

This section briefly reviews some examples of microstructure and examination for:

- Zircaloy alloys (Fig. 1, 2, 3, 4, 5, 6, 7, 8, 9, 10, 11)
- Zirconium (Fig. 12, 13, 14, 15, 16, 17, 18, 19, 20, 21, 22, 23, 24, 25, 26, 27, 28, 29, 30, 31, 32, 33, 34, 35, 36, 37, 38, 39)
- Hafnium (Fig. 40, Fig. 41, 42, 43, 44, 45, 46, 47, 48, 49)
- Bimetallic forms (Fig. 50, 51)

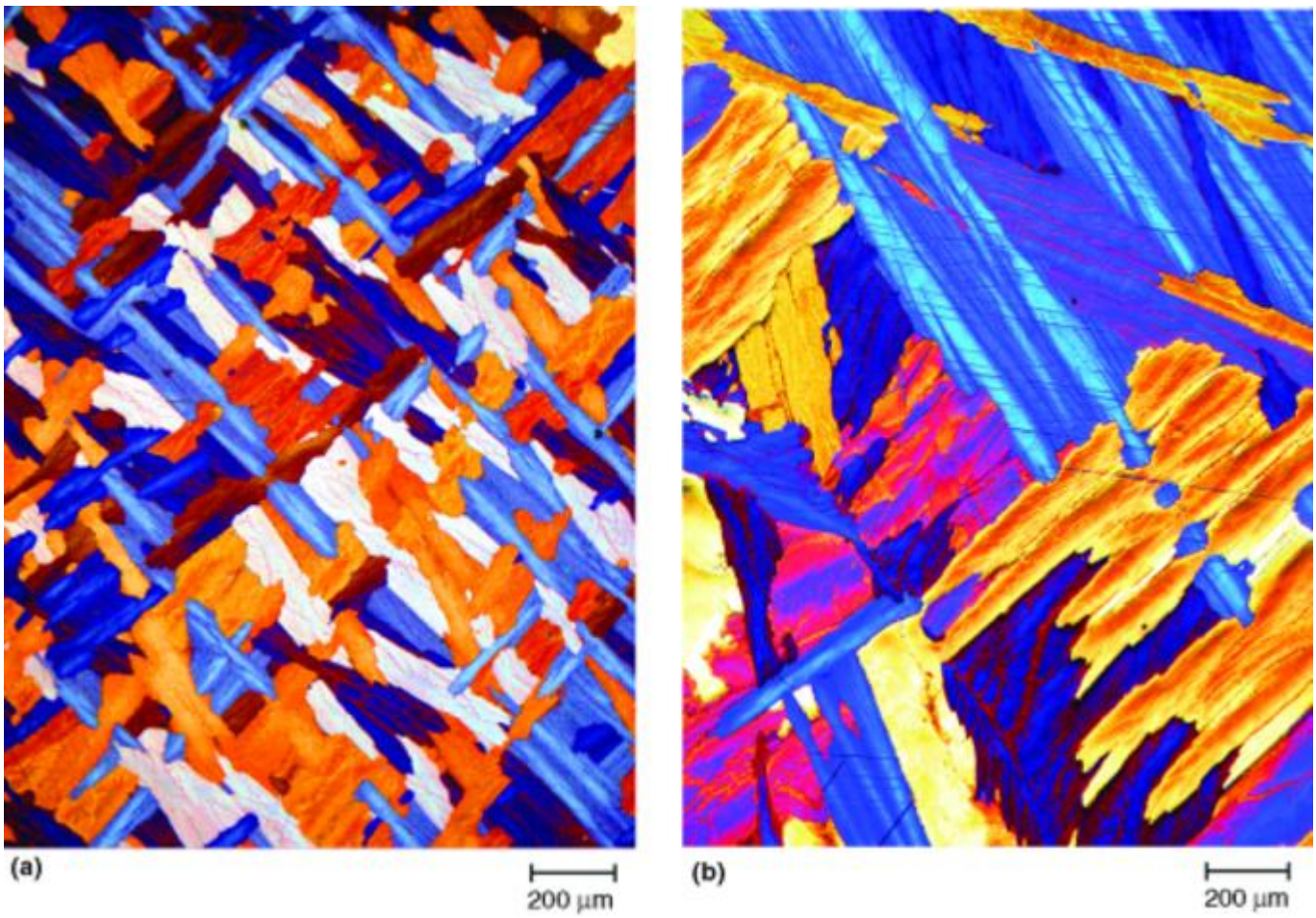

Fig. 1 Zircaloy 4 as-cast ingot. (a) Outside edge. (b) Center section. As-attack polished, heat tinted, and viewed with polarized light illumination. These micrographs show the effect of the cooling rate from the inside to the outside locations of the ingot. The outer surface shows a finer acicular structure due to the faster cooling rate. Original magnification: 50×.

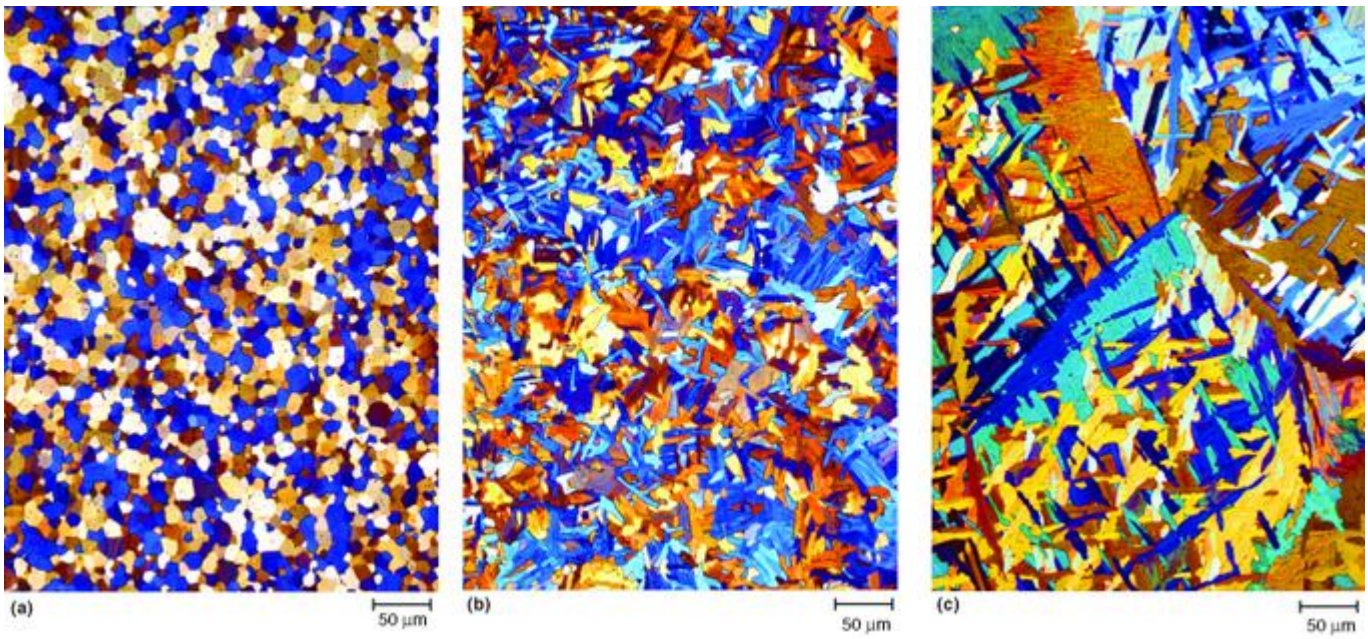

Fig. 2 Zircaloy 4 welded sheet. (a) Parent metal. (b) Heat-affected zone. (c) Weld metal. Attack polished, heat tinted, and viewed with polarized light illumination. The parent metal is an equiaxed alpha structure, an acicular alpha heat-affected zone, with a Widmanstätten structure in the weld zone. Original magnification: 200×.

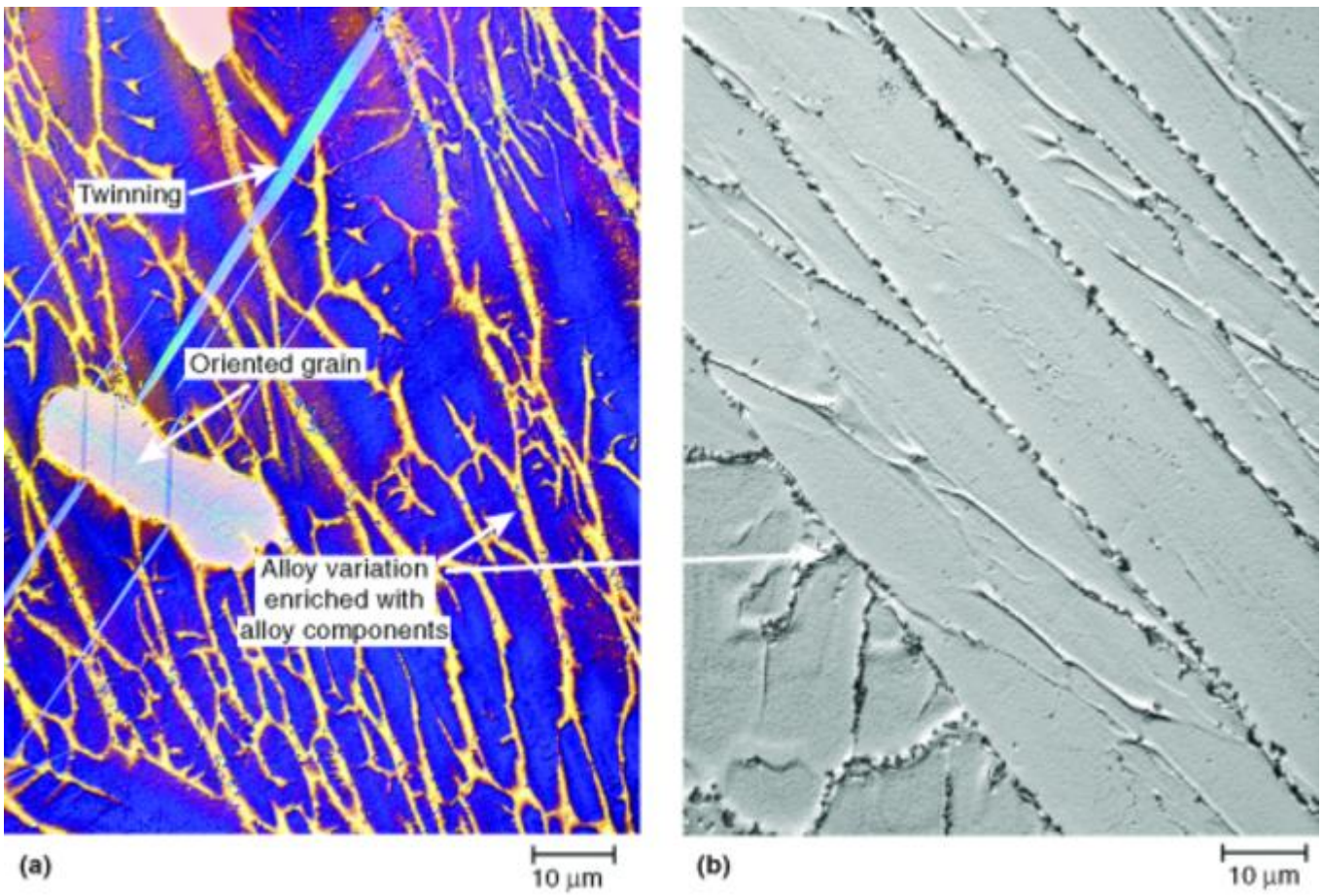

Fig. 3 Zircaloy 4 as-cast ingot. (a) Center section. Attack polished, heat tinted, etchant procedure No. 6, and viewed with differential interference contrast illumination. (b) Midthickness. Attack polished, heat tinted, and viewed with differential interference contrast illumination. The micrographs show a Zircaloy as-cast structure with twinning and alloy variation, as exhibited by different preparation methods. Original magnification: 1000×.

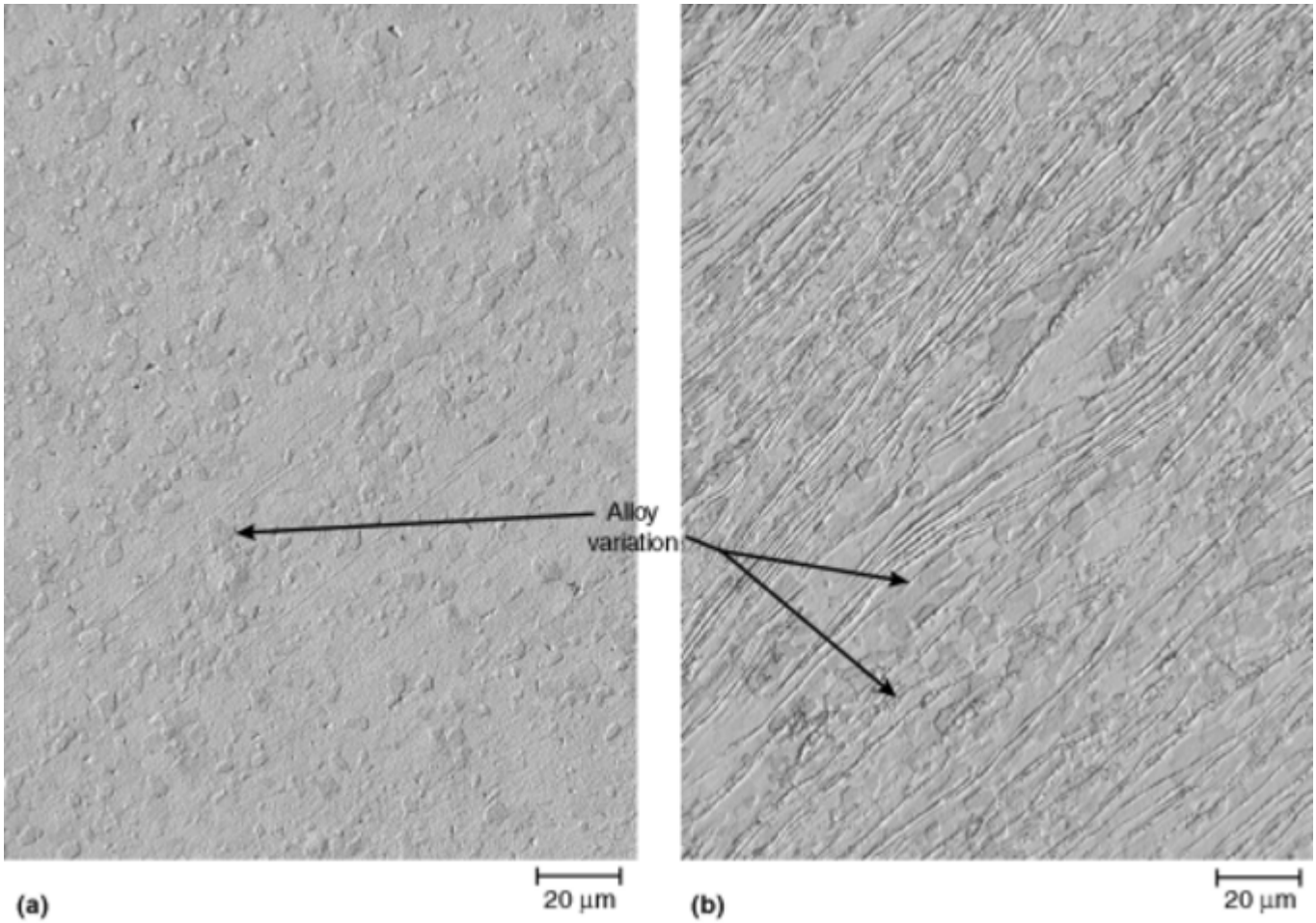

Fig. 4 Zircaloy 4 tube, longitudinal. (a) Mid-thickness. (b) Near surface, attack polished, etchant procedure No. 6 (Table 2), differential interference contrast. These micrographs show the difference in alloy variation between mid-thickness and near-surface locations. Original magnification: 500×



Fig. 5 Zircaloy 4 hot-worked plate, longitudinal. Attack polished, heat tinted, and viewed with polarized light illumination. This micrograph shows a hot-worked and annealed structure. Original magnification: 100×.

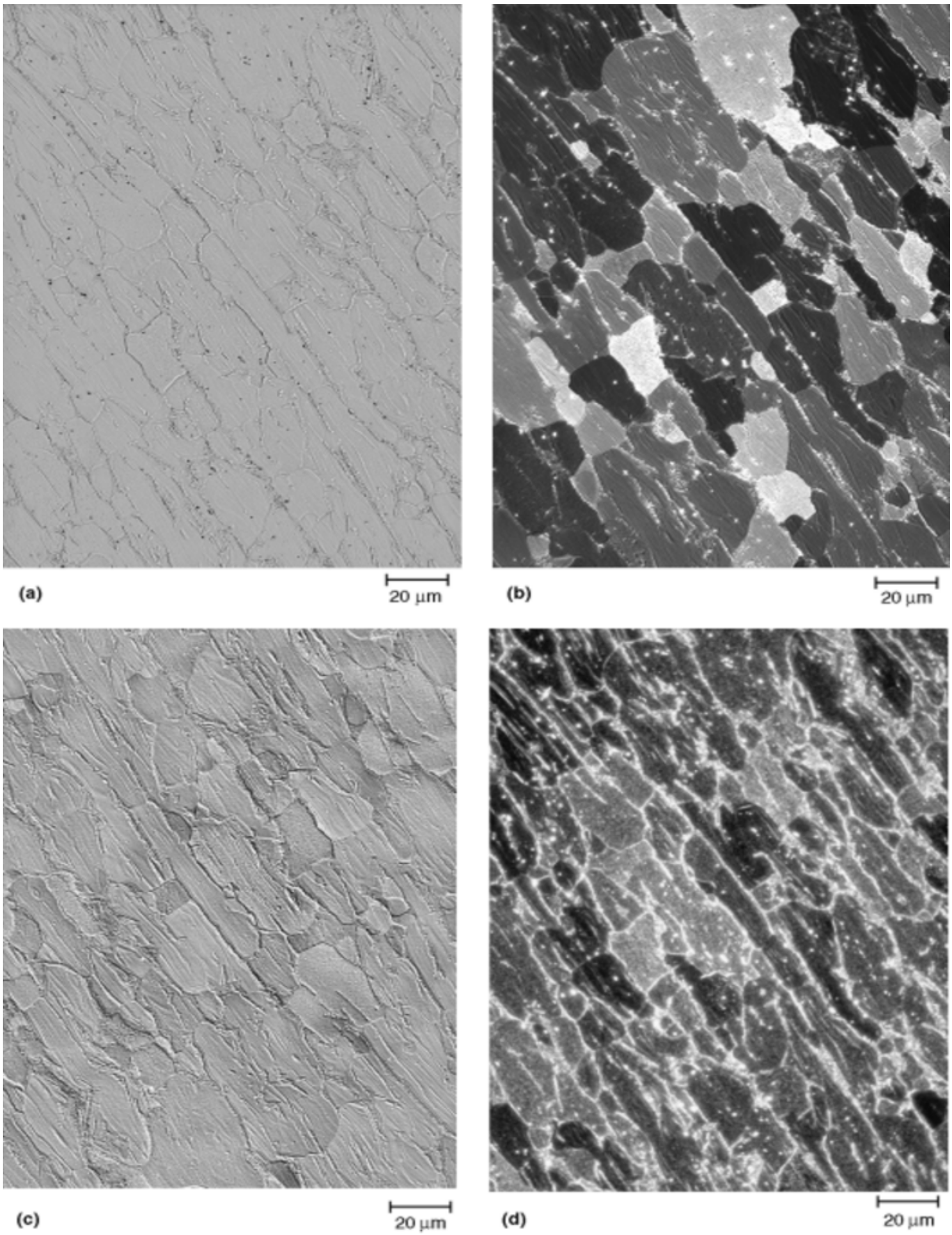

Fig. 6 Zircaloy 4 plate, longitudinal, attack polished, etchant procedure No. 3 (Table 2). (a) Bright field. (b) Polarized light. (c) Differential interference contrast. (d) Dark field. These micrographs compare four different lighting conditions used for metallurgical examination. Original magnification: 500×

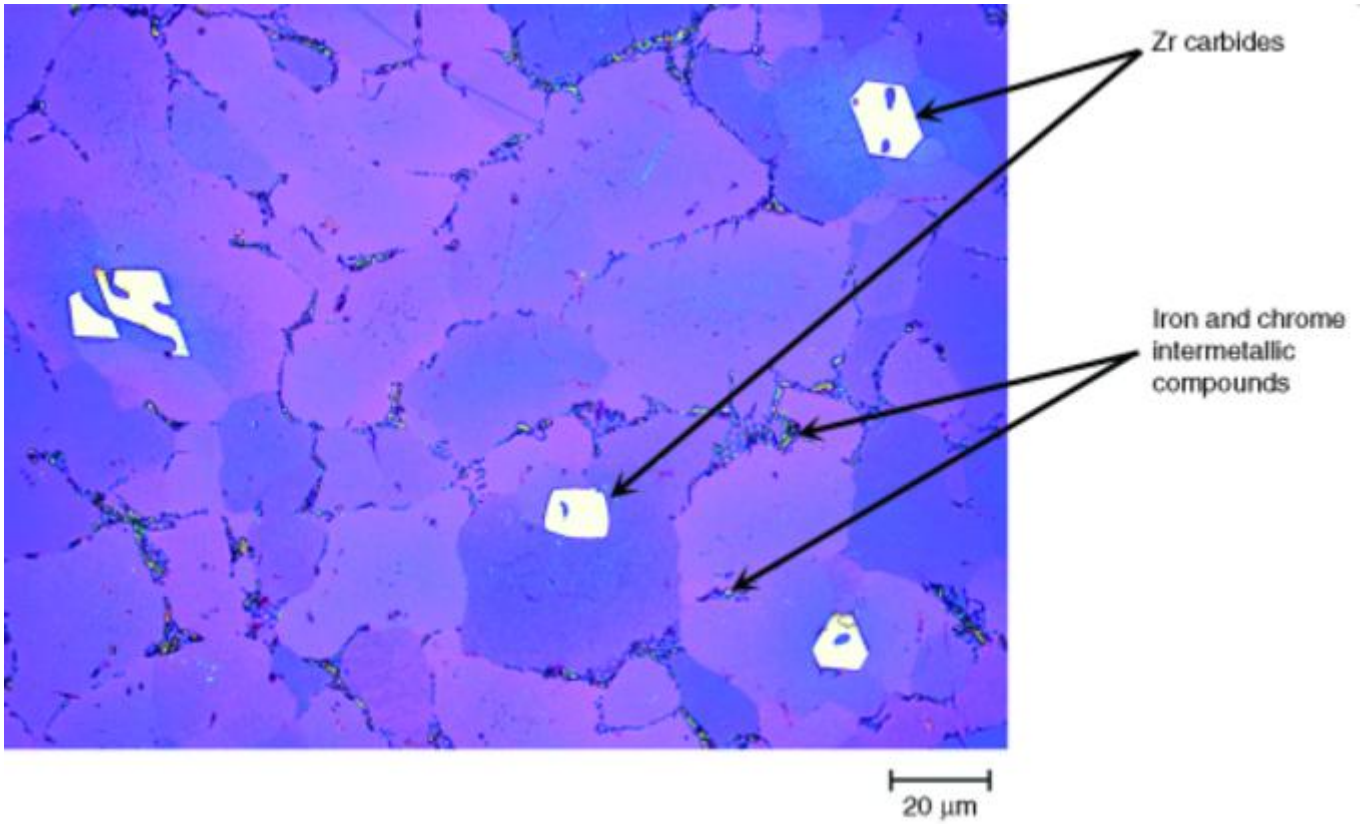

Fig. 7 Zircaloy 2 plate, transverse. Attack polished, anodized at 103 V, and viewed with bright-field illumination. This micrograph shows the presence of zirconium carbides, irregular in shape, in a Zircaloy matrix. Original magnification: 500×.

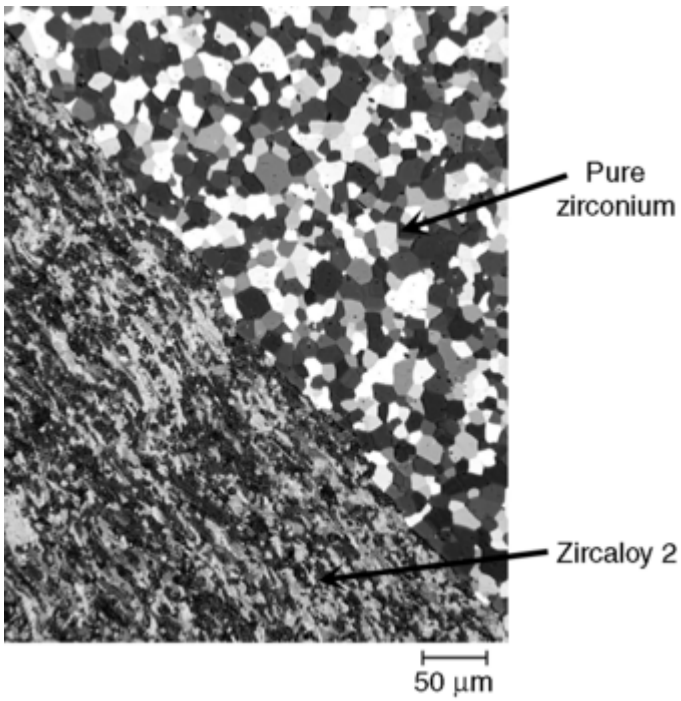

Fig. 8 Zircaloy 2/pure zirconium coextruded tubing, transverse, attack polished, etchant procedure No. 2 (Table 2), anodized at 15 V, polarized light. This area shows the interface region of the coextruded tube. Original magnification: 200×

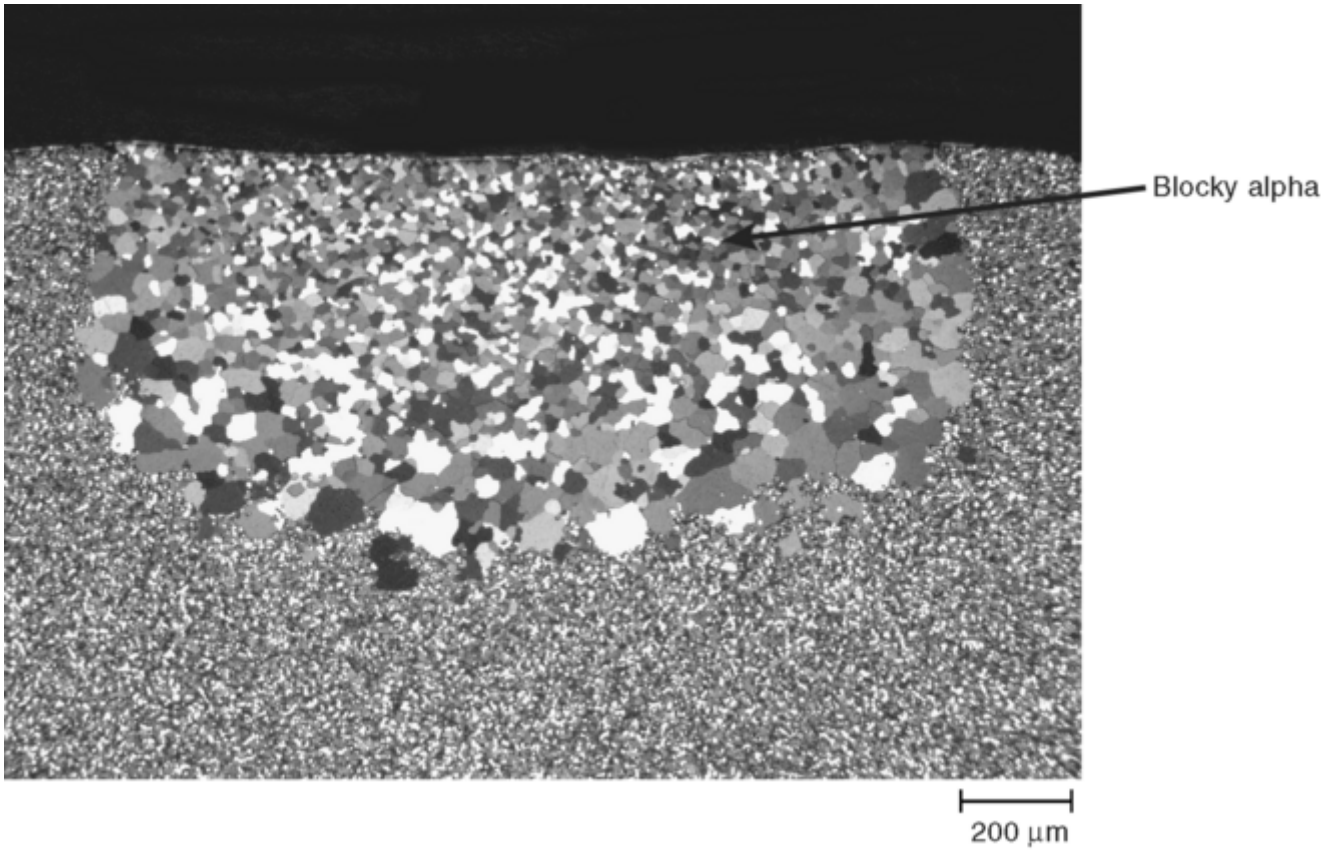

Fig. 9 Zircaloy 4 tube, attack polished, etchant procedure No. 2 (Table 2), anodized at 15 V, polarized light. This micrograph shows an area of blocky α caused by cold work or surface damage followed by a recrystallization anneal (675 to 790 °C, or 1230 to 1455 °F). Original magnification: 50×

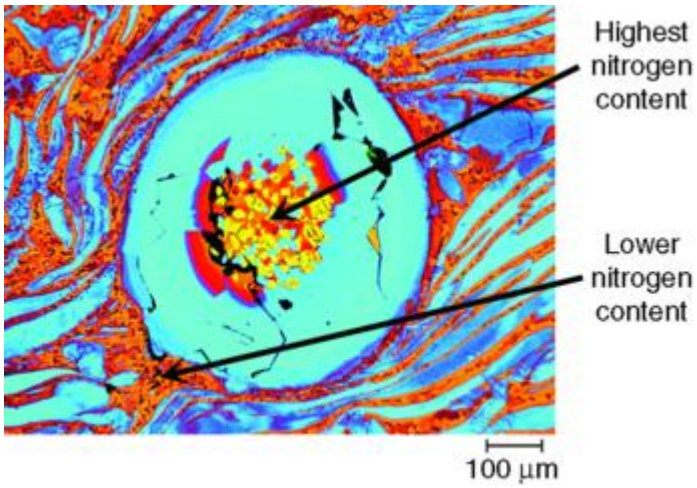

Fig. 10 Zircaloy 4 rod, longitudinal. Attack polished, anodized at 108 V, and viewed with bright-field illumination. This micrograph shows the presence of a large nitride in the zirconium matrix. Original magnification: 100×.

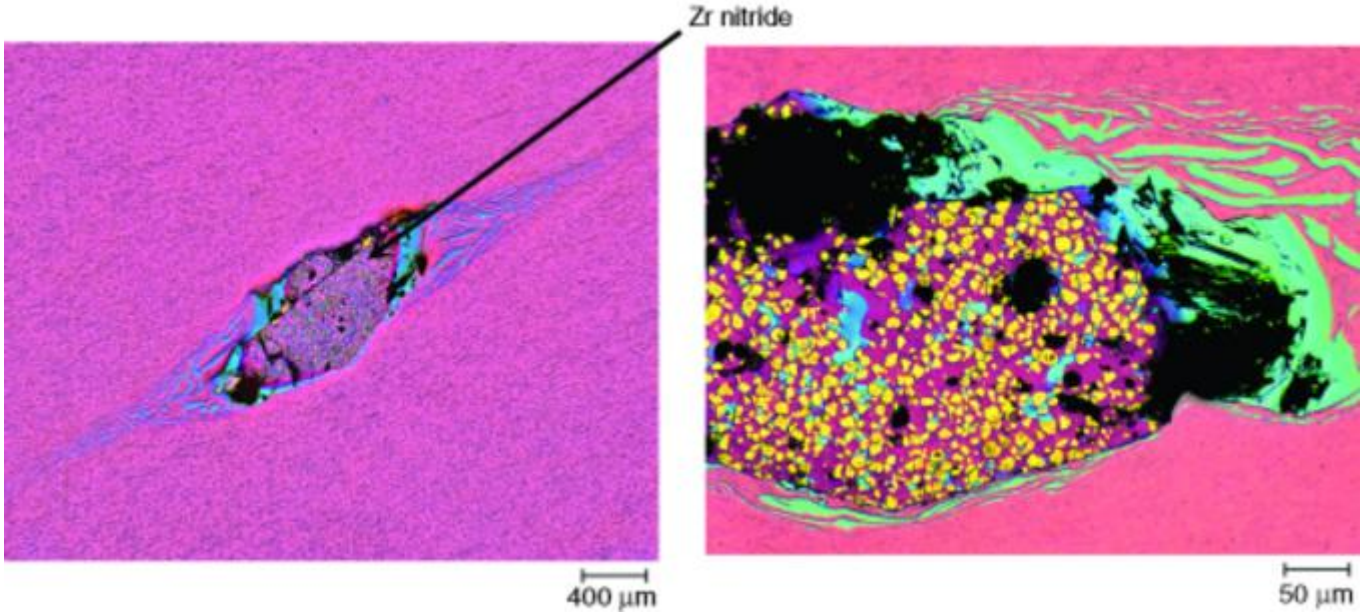

Fig. 11 Zircaloy 4 plate. Attack polished, anodized at 103 V, and viewed with bright-field illumination. These micrographs show a plate sample revealing a high-nitrogen area (bluish color) and a zirconium-nitride phase in the matrix. (a) Original magnification: 25×. (b) Original magnification: 200×.

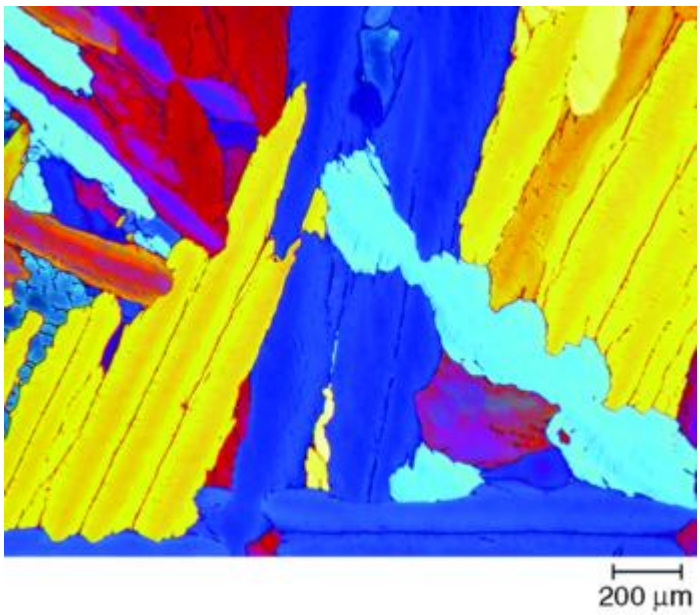

Fig. 12 Zirconium crystal bar. Attack polished, heat tinted, and viewed with polarized light illumination. This micrograph shows large as-cast grains in zirconium crystal bar. Original magnification: 50×.

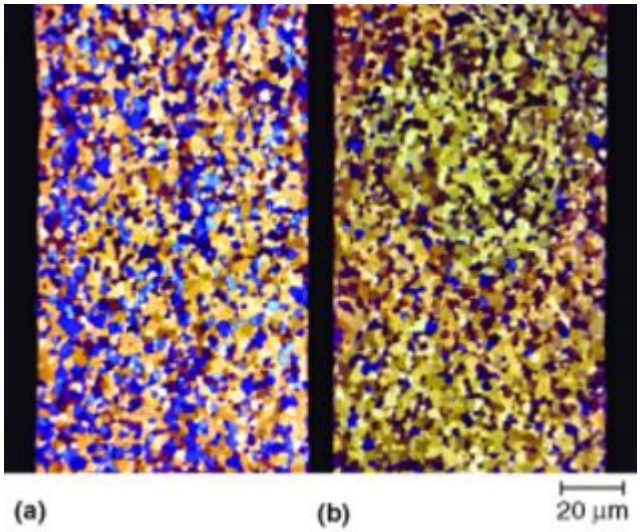

Fig. 13 Zr702 sheet. Attack polished, etchant procedure No. 2, anodized at 15 V, and viewed with polarized light illumination. These micrographs show the difference in overall grain orientation between the (a) transverse and (b) longitudinal directions. Original magnification: 500×.

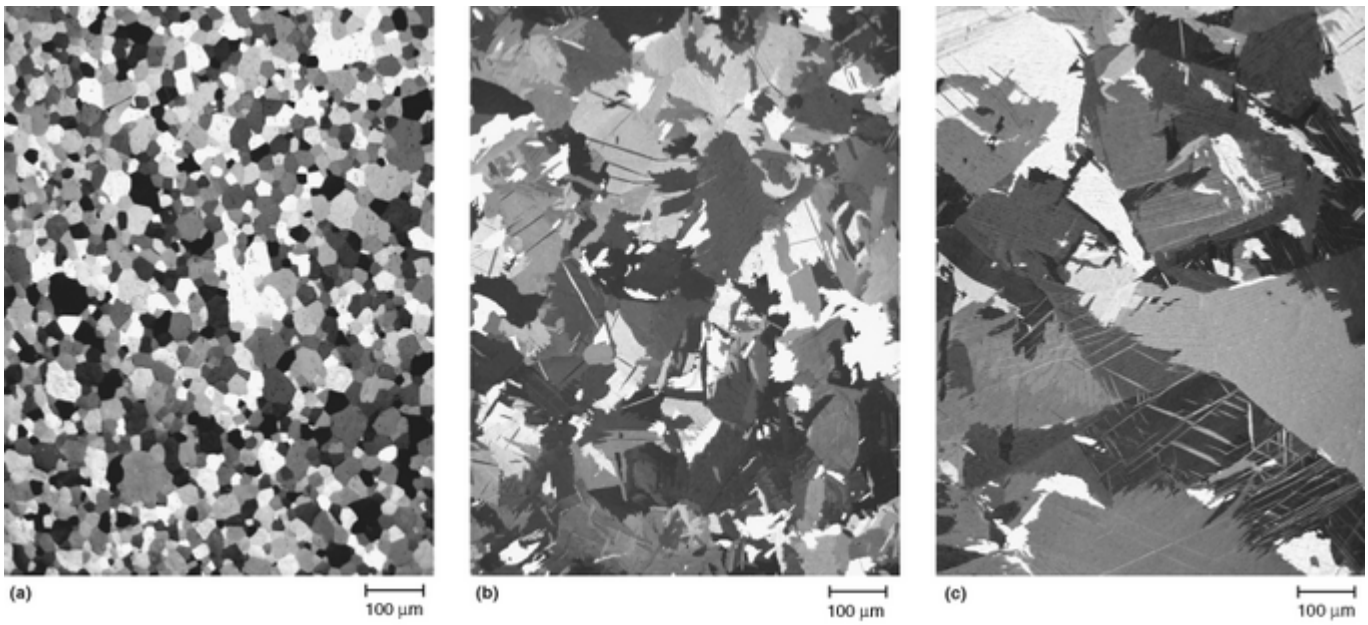

Fig. 14 Zr 702 Weld, transverse. (a) Parent metal. (b) Heat-affected zone. (c) Weld metal, attack polished, etchant procedure No. 2 (Table 2), anodized at 15 V, polarized light. These micrographs show an (a) equiaxed structure in the parent metal, (b) an acicular structure in the heat-affected zone, and (c) a Widmanstätten structure in the weld area. Original magnification: 100×

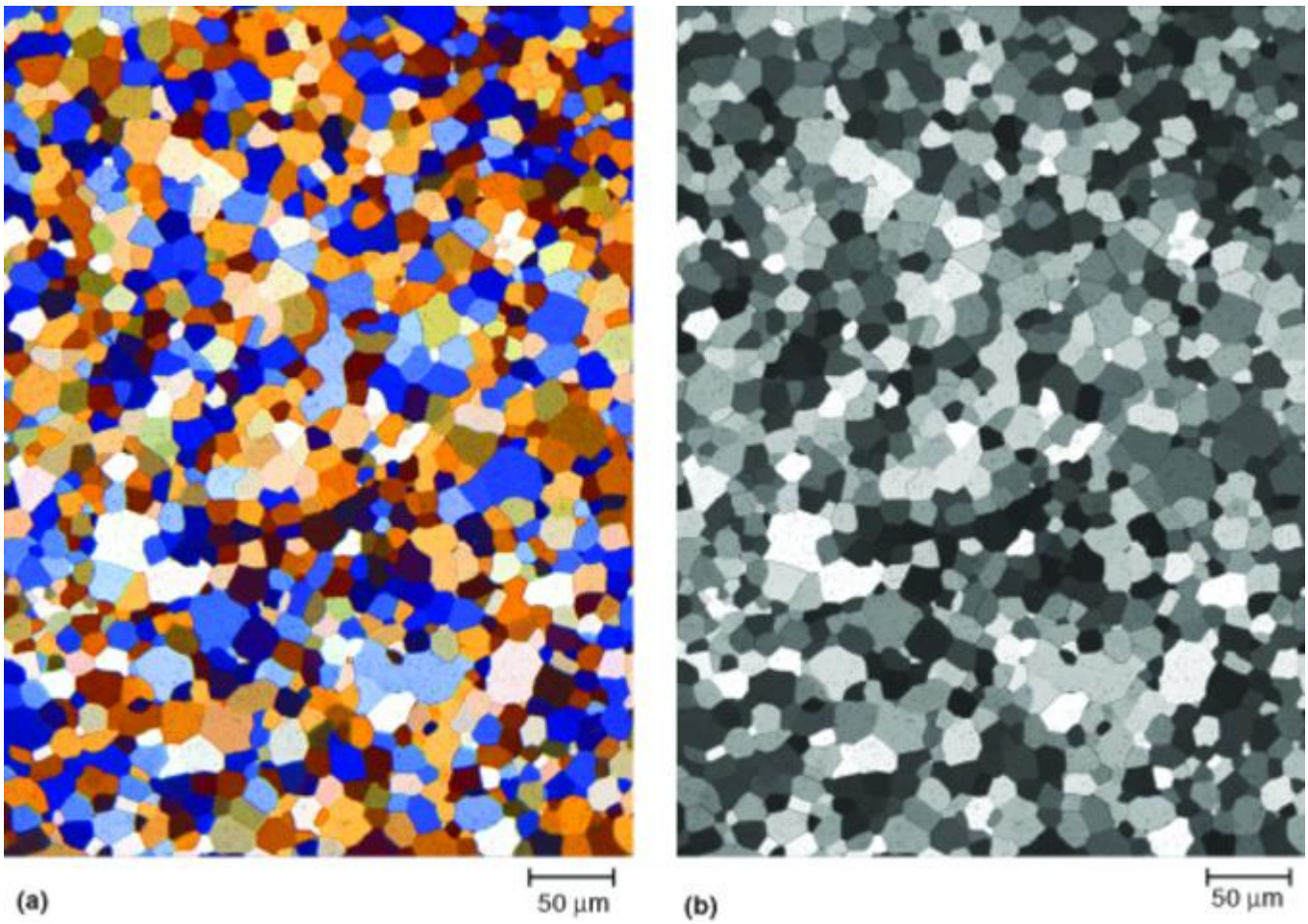

Fig. 15 Zr702 plate, transverse. Attack polished, heat tinted, and viewed with polarized light illumination. These micrographs show an equiaxed alpha structure comparing the difference as viewed in (a) color and (b) monochromatic. Original magnification: 200×.

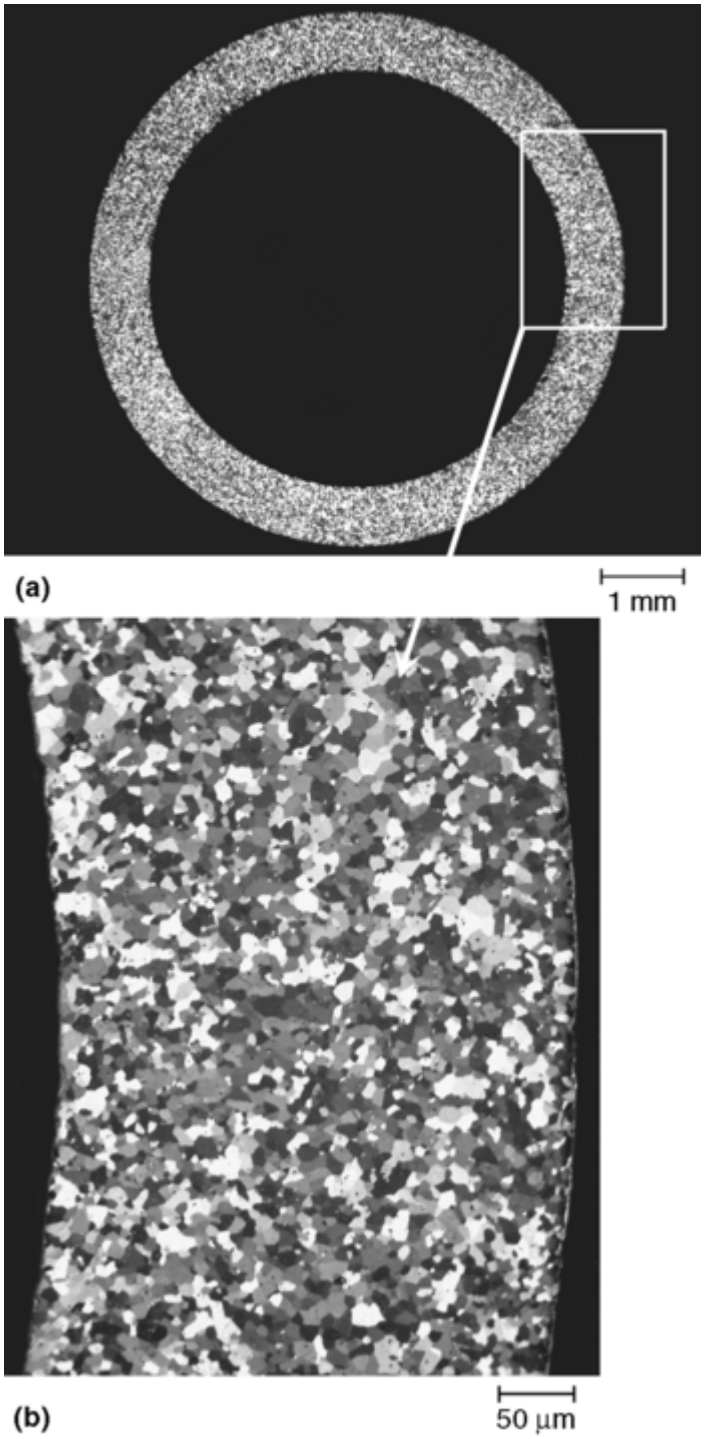

Fig. 16 Zr702 Tube, transverse. (a) Full cross section. (b) Section of wall, attack polished, etchant procedure No. 2 (Table 2), anodized at 15 V, polarized light. These photos illustrate lower magnification, full cross-section tube for macroscopic examination, with a higher magnification tube section for microscopic examination of the grain structure. (a) Original magnification: 12×. (b) Original magnification: 200×

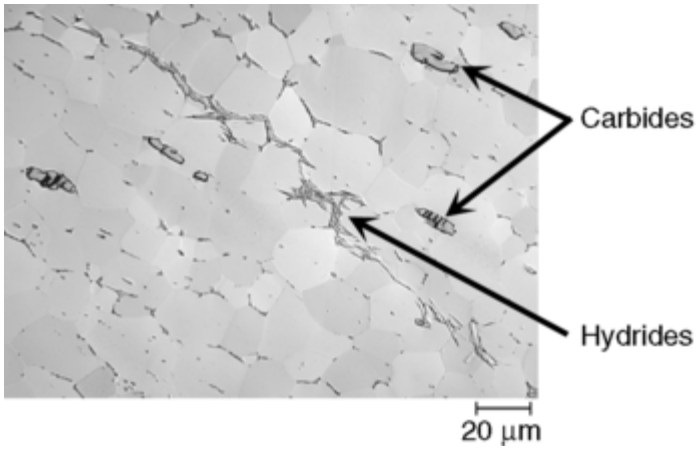

Fig. 17 Zr702 plate, longitudinal, attack polished, etchant procedure No. 4 (Table 2), bright field. The micrograph shows the presence of hydrides and carbides in a zirconium plate structure. Original magnification: 500×

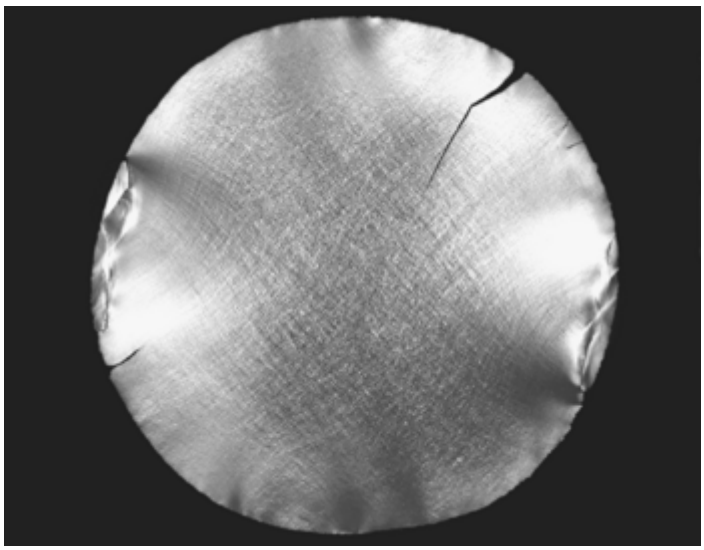

Fig. 18 Zirconium rod 12.5 mm (0.5 in.) diameter, attack polished, etchant procedure No. 2 (Table 2), anodized at 15 V, polarized light. This micrograph shows local surface areas with higher cold work and surface cracking. Original magnification: ~6×

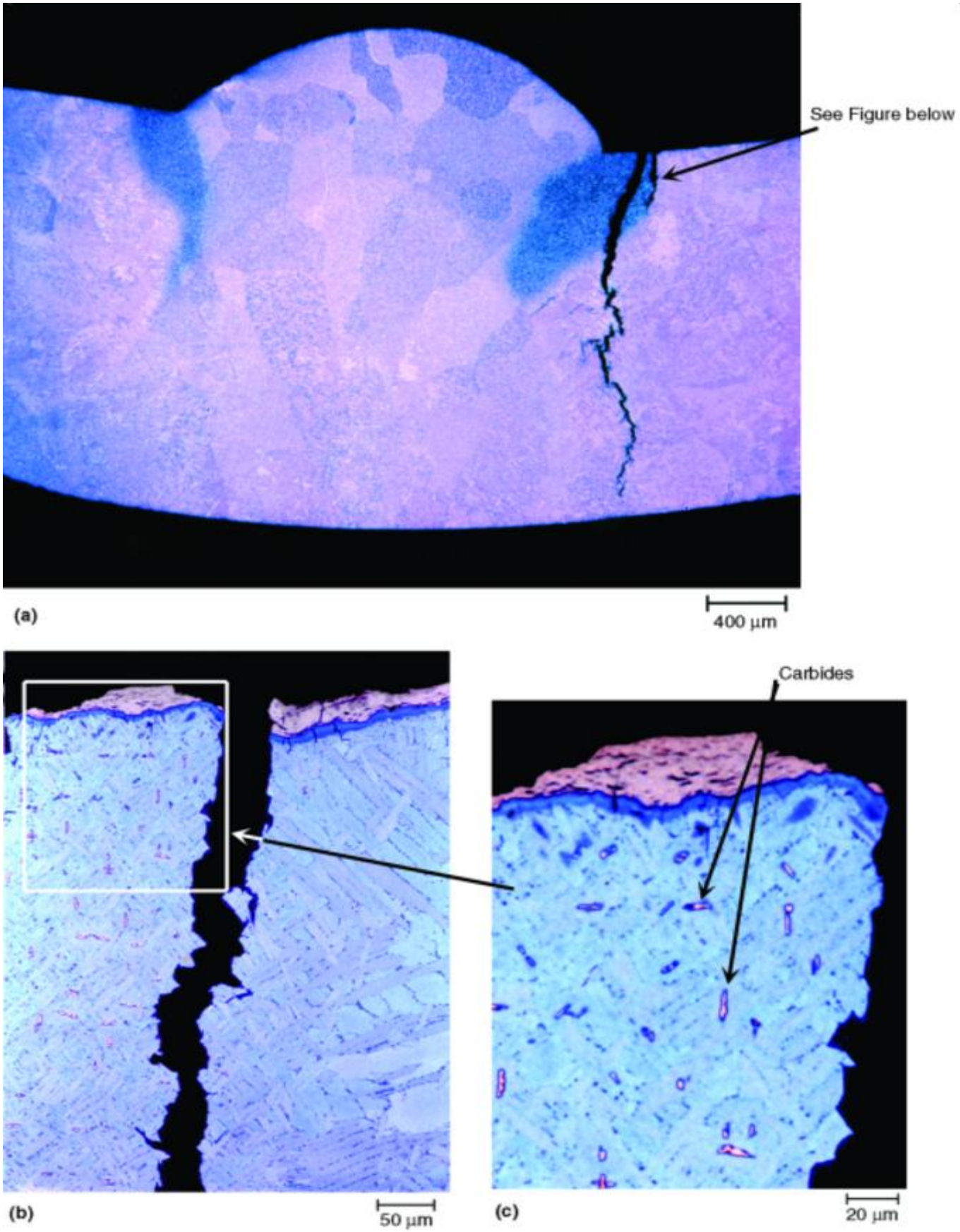

Fig. 19 Zr702 welded plate, transverse. Attack polished, anodized at 29 V, and viewed with bright-field illumination. This micrograph shows a crack in the area between the parent metal and the heat-affected zone. This also shows carbides along the area of crack propagation. (a) Original magnification: 25×. (b) Original magnification: 200×. (c) Original magnification: 500×.

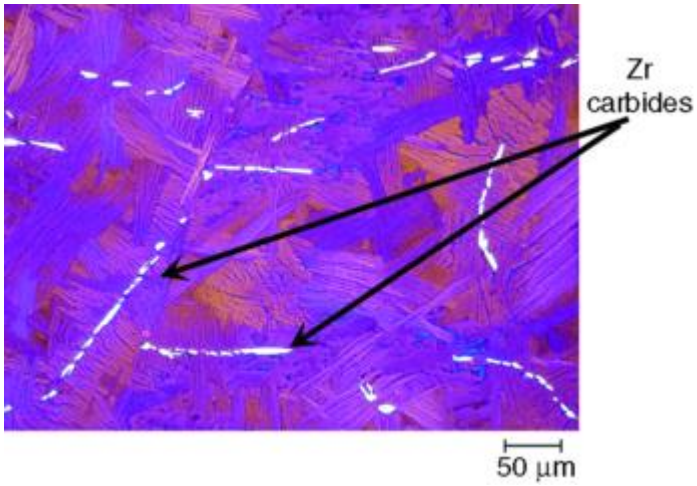

Fig. 20 Zr705 as-cast structure. Attack polished, anodized at 103 V, and viewed with bright-field illumination. This micrograph shows the presence of carbides in the cast structure. Original magnification: 200×.

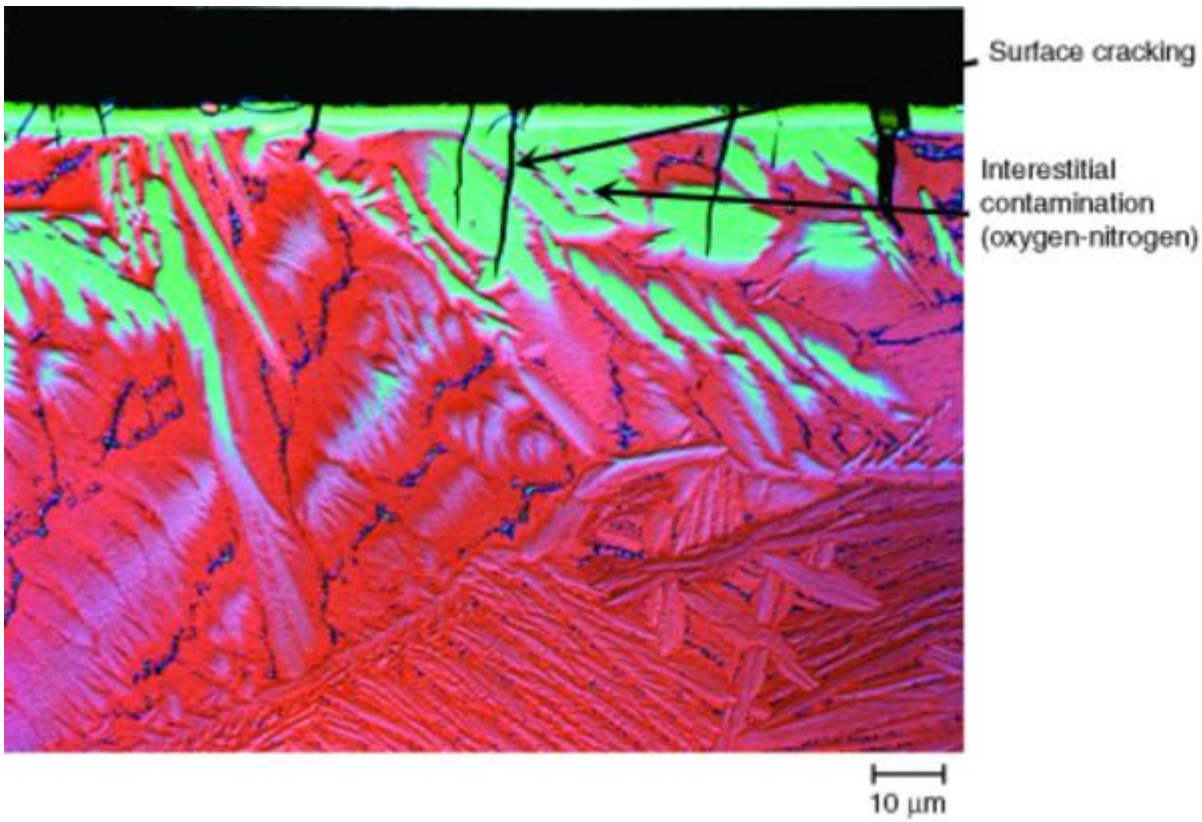

Fig. 21 Zr702 plate, transverse. Attack polished, anodized, and viewed with differential interference contrast illumination. This micrograph shows interstitial contamination in the weld area. Original magnification: 750×.

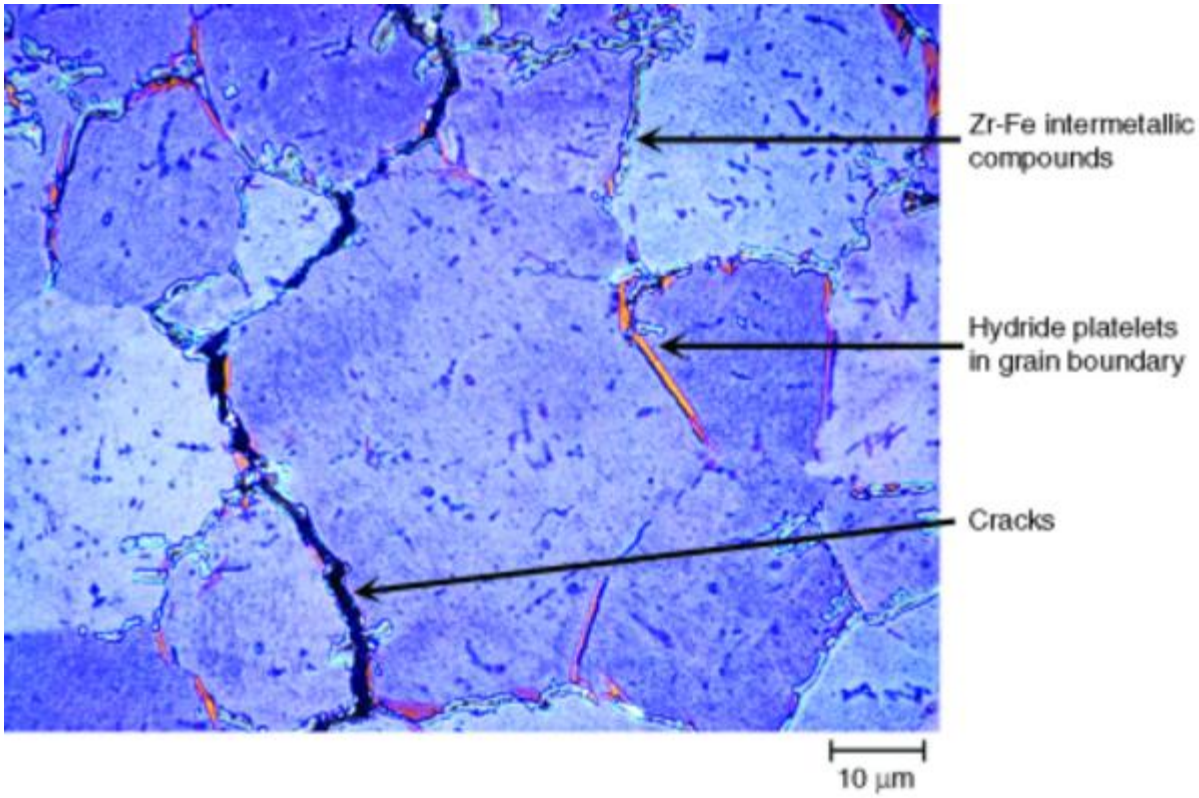

Fig. 22 Zr702 sheet, heat-affected zone of weld. Attack polished, anodized at 28 V, and viewed with bright-field illumination. This micrograph shows the presence of hydride platelets (gold) and intermetallic particles in the zirconium grain boundaries. Original magnification: 1000×.

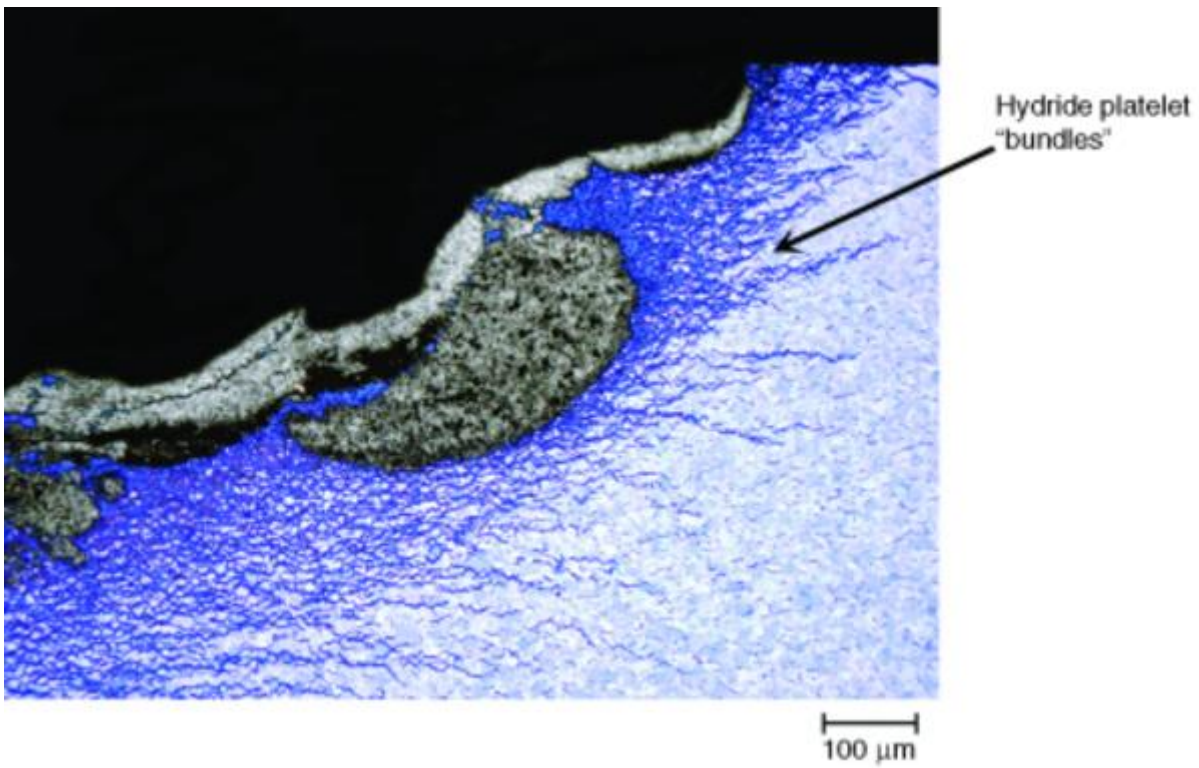

Fig. 23 Zr702 sheet, transverse. Attack polished, anodized at 28 V, and viewed with polarized light illumination. This micrograph shows the presence of massive hydrides caused by corrosion. Original magnification: 100×.

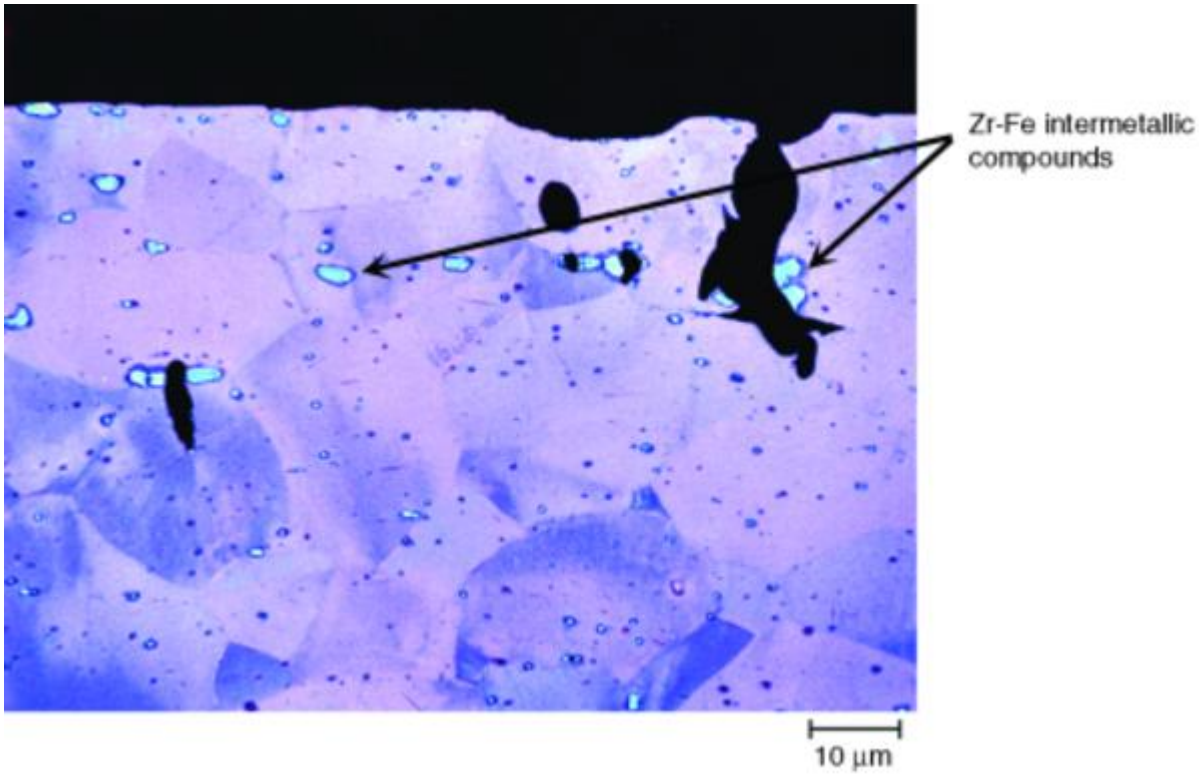

Fig. 24 Zr702 plate, transverse. Attack polished, anodized at 28 V, and viewed with bright-field illumination. This micrograph of a plate bend sample shows the effect of large second-phase particles (zirconium-iron) causing cracking during bending. These intermetallic compound particles are nonductile and will crack when stressed. Original magnification: 1000×.

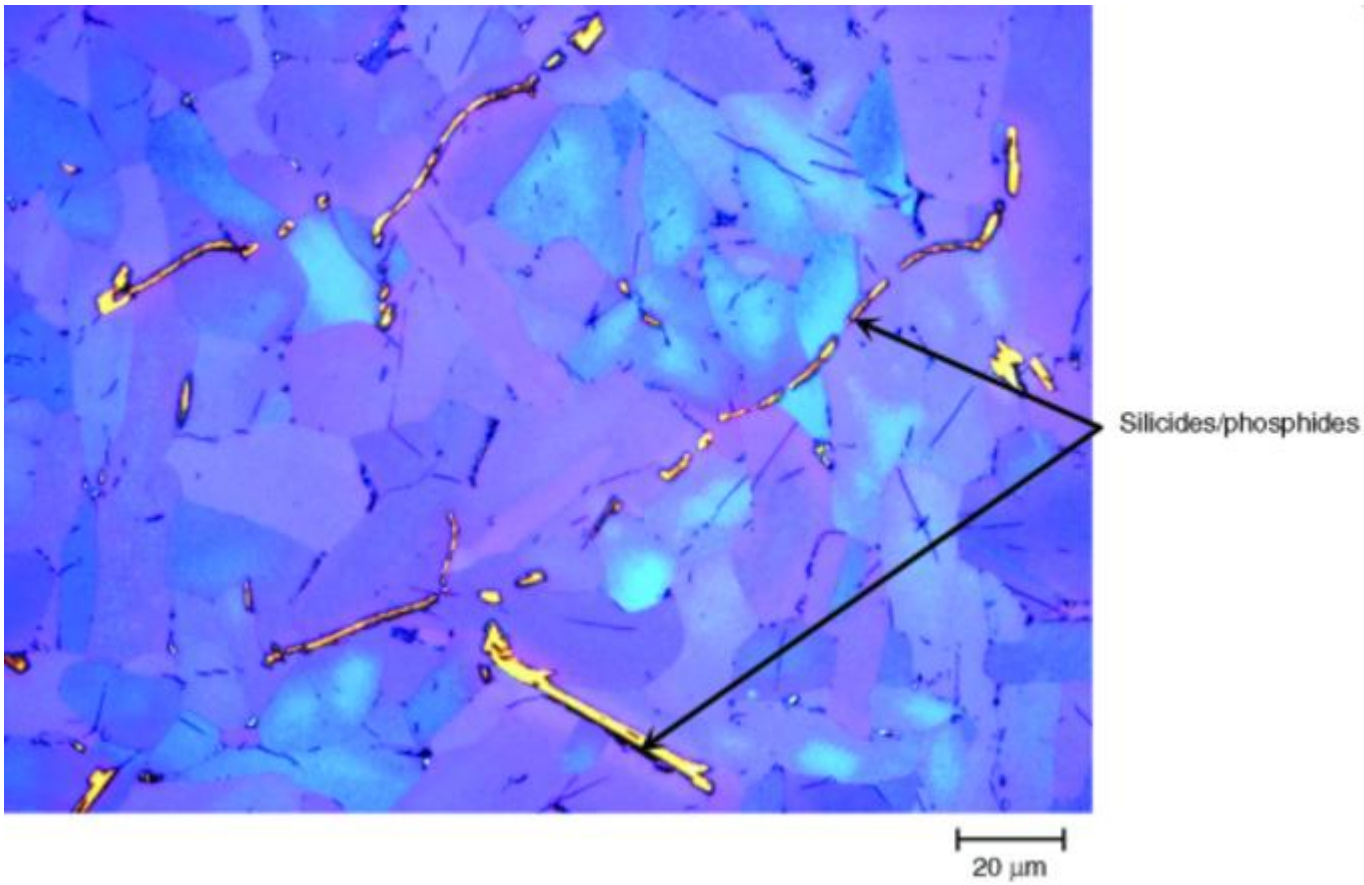

Fig. 25 Zr702. Attack polished, anodized at 108 V, and viewed with bright-field illumination. This micrograph shows the presence of silicide/phosphide inclusions. 500×.

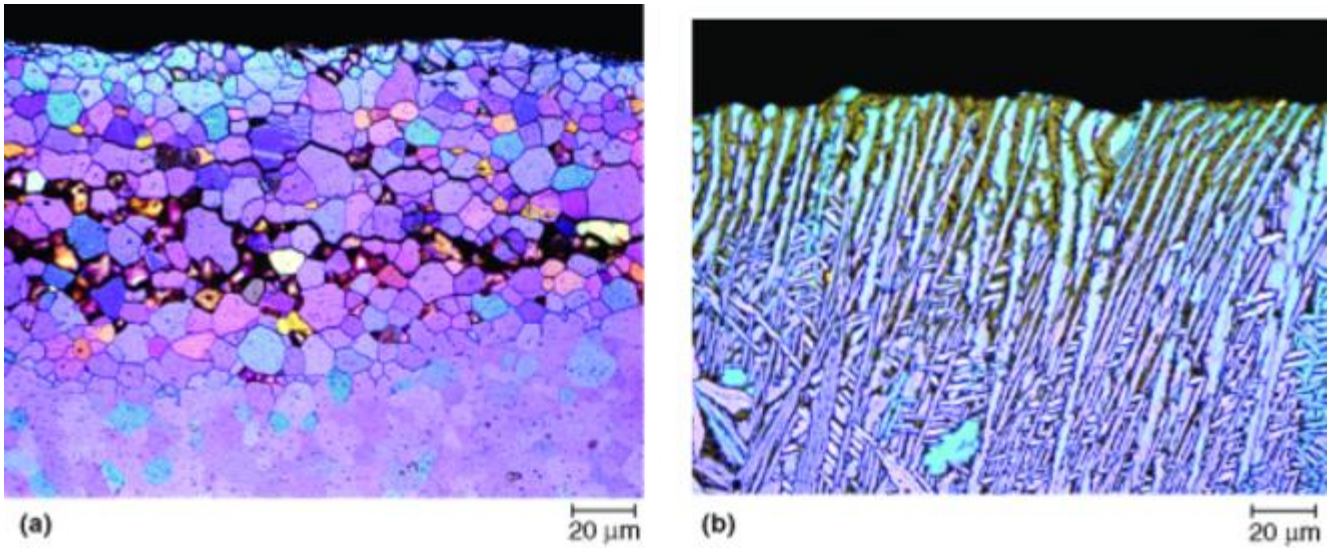

Fig. 26 Zr702 sheet, transverse. Attack polished, anodized at 108 V, and viewed with bright-field illumination. These micrographs show intergranular corrosion attack in the (a) parent metal and (b) weld metal. Original magnification: 500×.

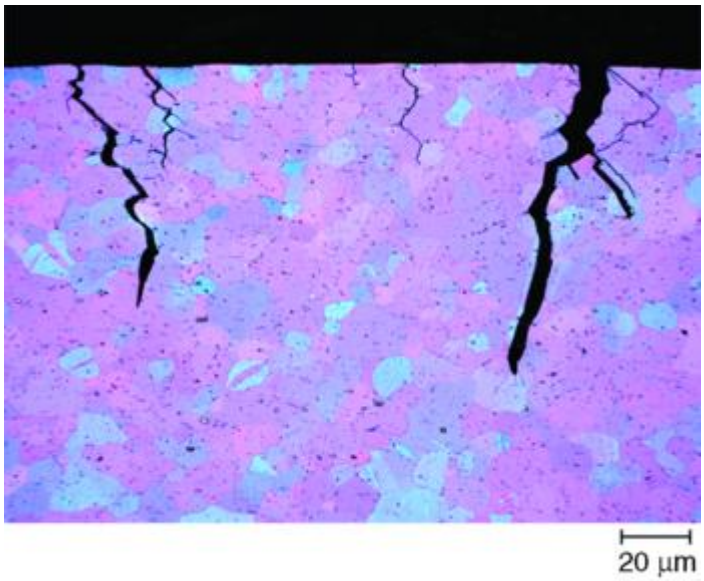

Fig. 27 Zr702 plate. Attack polished, anodized at 108 V, and viewed with bright-field illumination. This micrograph shows the presence of stress-corrosion cracking. Original magnification: 500×.



Fig. 28 Zr702 sheet. Attack polished, anodized at 15 V, polarized light. This micrograph shows the effect of forming annealed plate into pipe followed by a recrystallization anneal heat treatment. This can result in a blocky α structure on the outer and inner fibers of the pipe wall thickness, as shown here. Original magnification: 25×

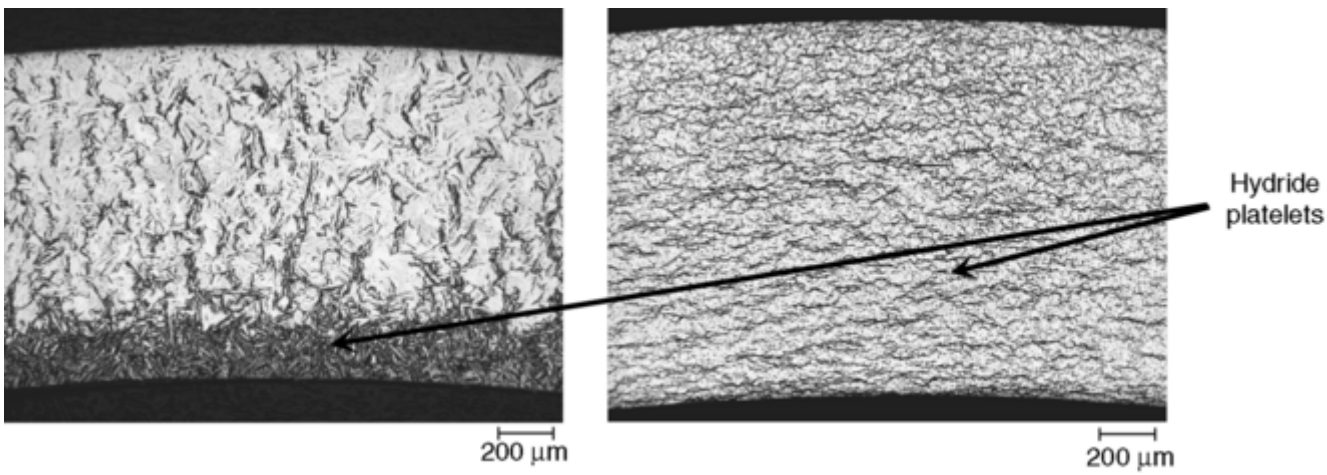

Fig. 29 Zr702 tube, transverse, attack polished, hydride etched No. 4 (Table 2), bright field. These micrographs show the presence of massive hydrides oriented in opposite directions. Original magnification: 50×

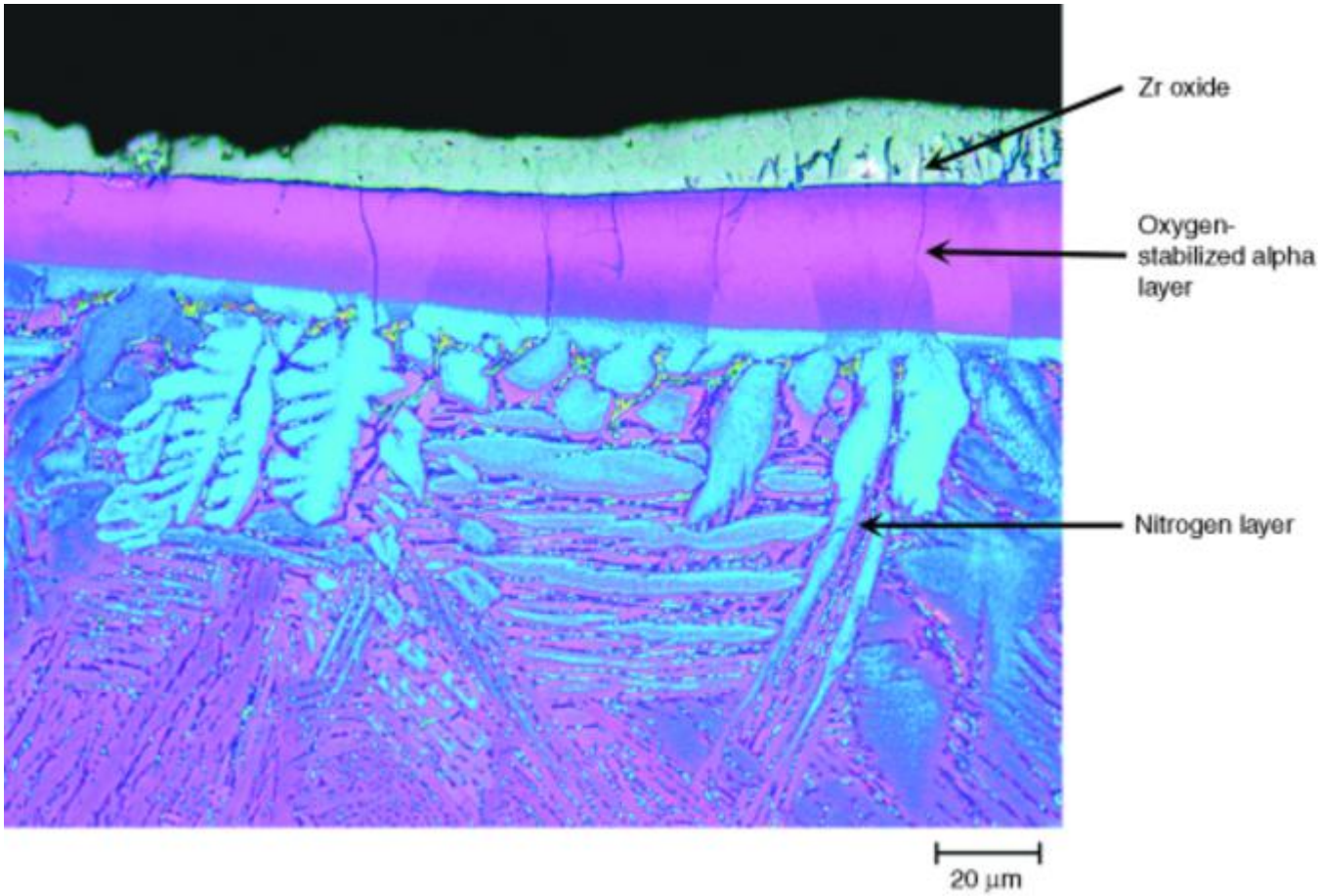

Fig. 30 Zr702 plate. Attack polished, anodized at 108 V, and viewed with bright-field illumination. This micrograph shows the edge of a zirconium plate that has been laser cut. The surface exhibits light element contamination caused by the heat generated during cutting. Original magnification: 500×.

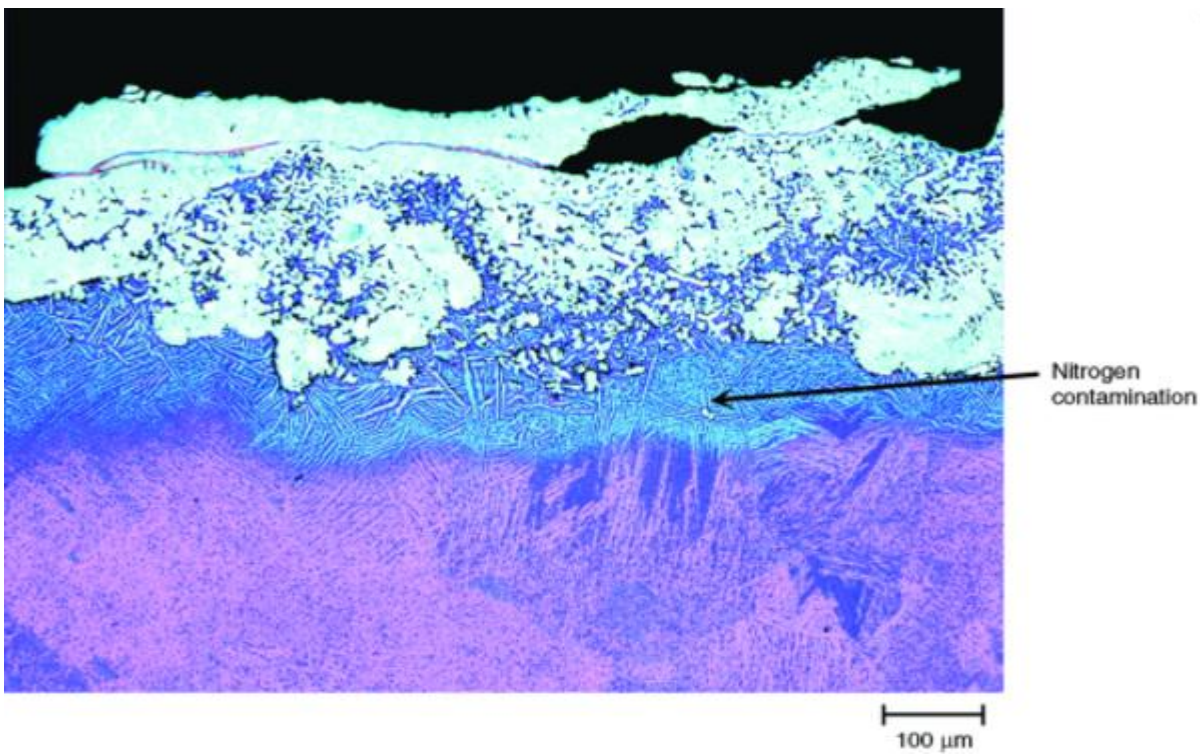

Fig. 31 Zr702 plate, transverse. Attack polished, anodized at 108 V, and viewed with bright-field illumination. This micrograph shows the edge of a zirconium plate plasma cut with nitrogen gas. Original magnification: 100×.

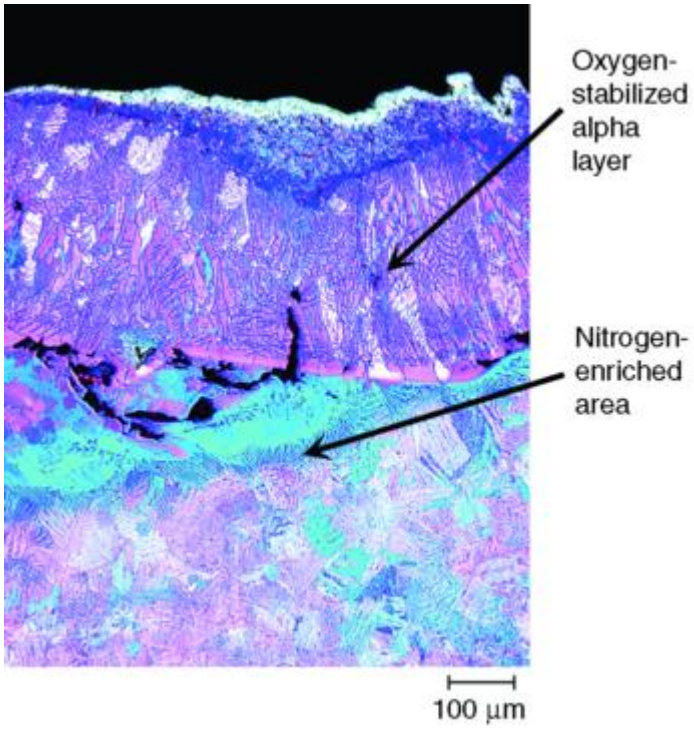

Fig. 32 Zr702 plate. Attack polished, anodized at 108 V, and viewed with bright-field illumination. This micrograph shows an edge of a zirconium plate that has been oxyacetylene cut. The sample exhibits severe light-element contamination on the surface, created during the cutting process. Original magnification: 100×.

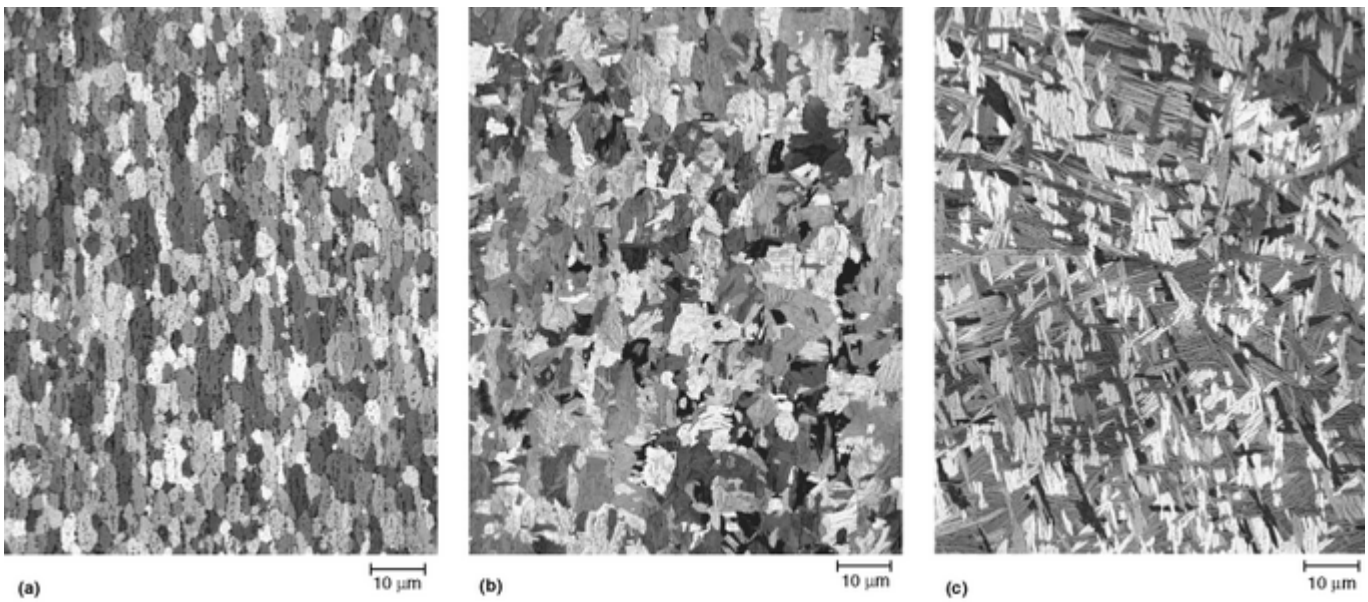

Fig. 33 Zr705 plate weld area, longitudinal. (a) Parent metal. (b) Heat-affected zone. (c) Weld metal, attack polished, heat tinted, polarized light. These micrographs show the appearance of the parent metal and weld zones. Original magnification: 1000×

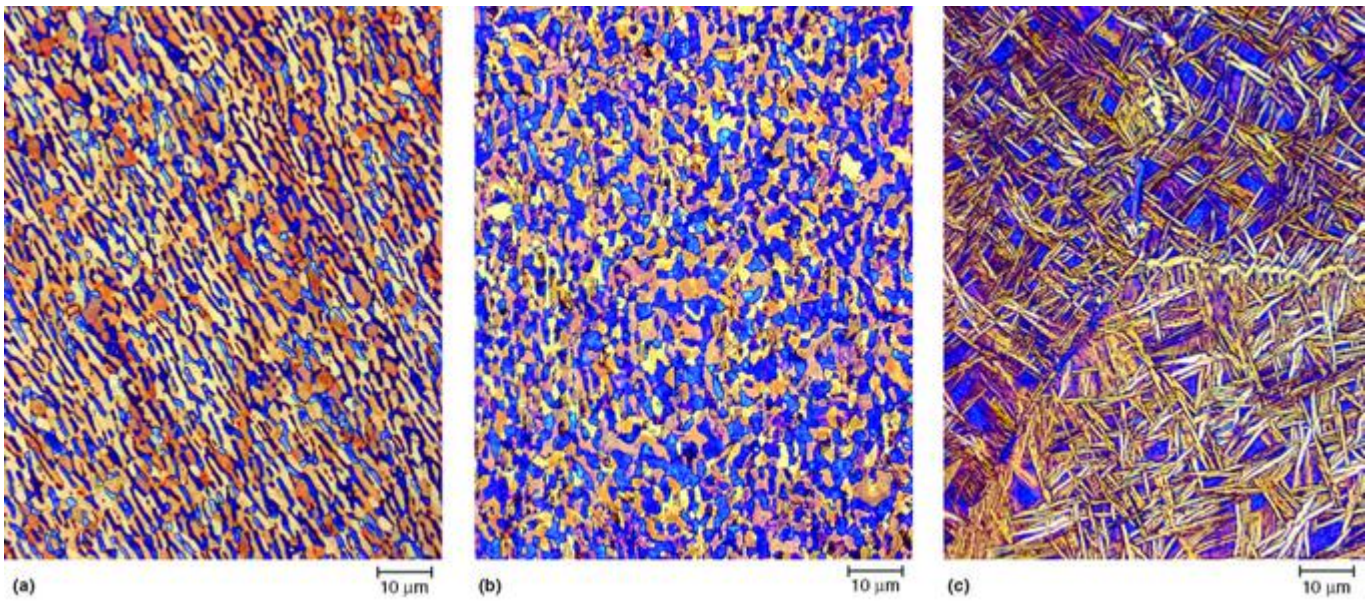

Fig. 34 Zr705 plate, weld area, longitudinal. (a) Parent metal. (b) Heat-affected zone. (c) Weld metal. Attack polished, heat tinted, and viewed with bright-field illumination. These micrographs show the appearance of the zirconium-niobium parent metal and weld zones. Original magnification: 1000×.

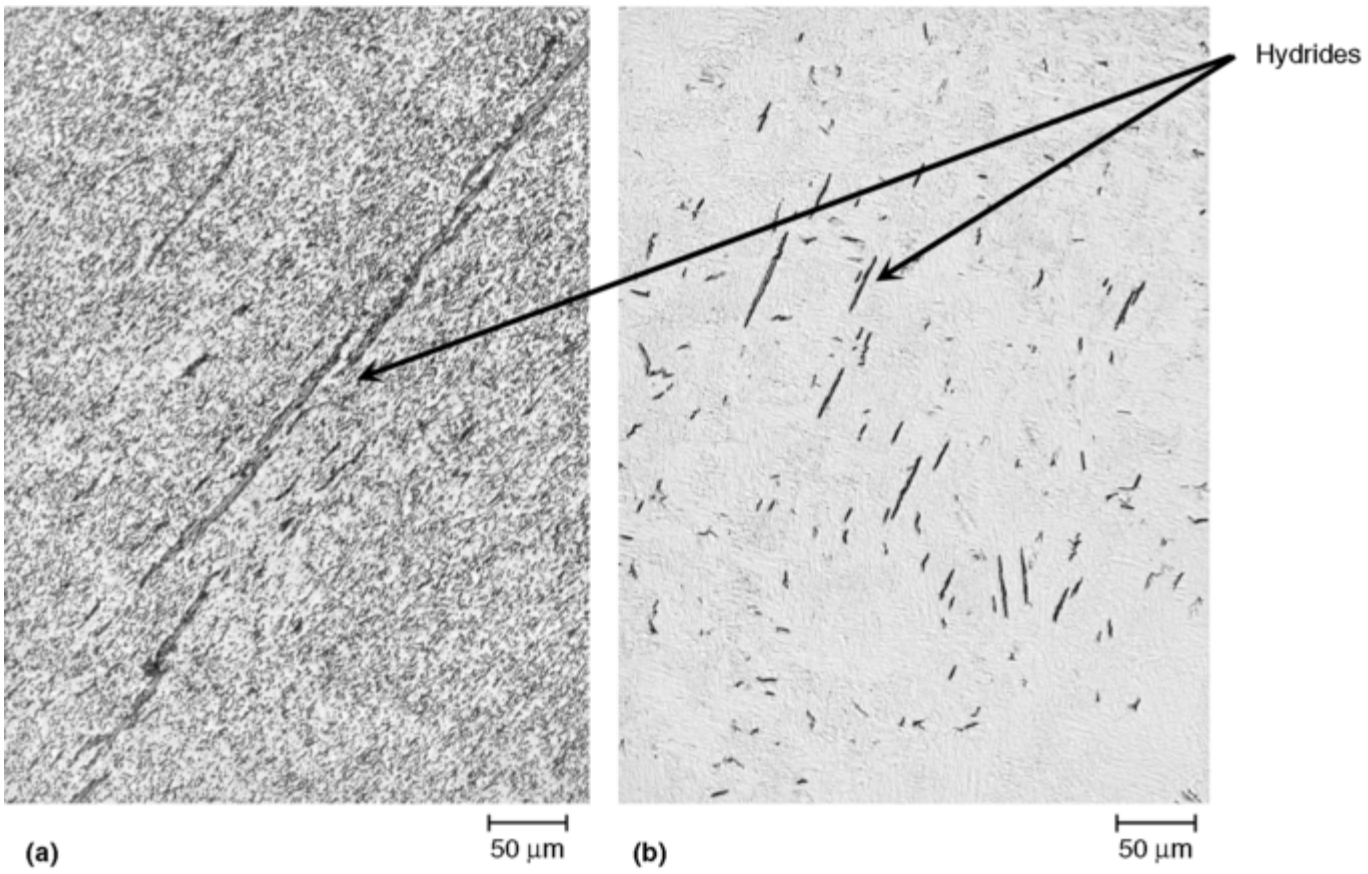

Fig. 35 Zr705 plate. (a) Transverse, parent metal. (b) Longitudinal, weld metal, attack polished, etchant procedure No. 5 (Table 2), bright field. These photos show the presence of hydride platelets in the metallurgical structure. Original magnification: 200×

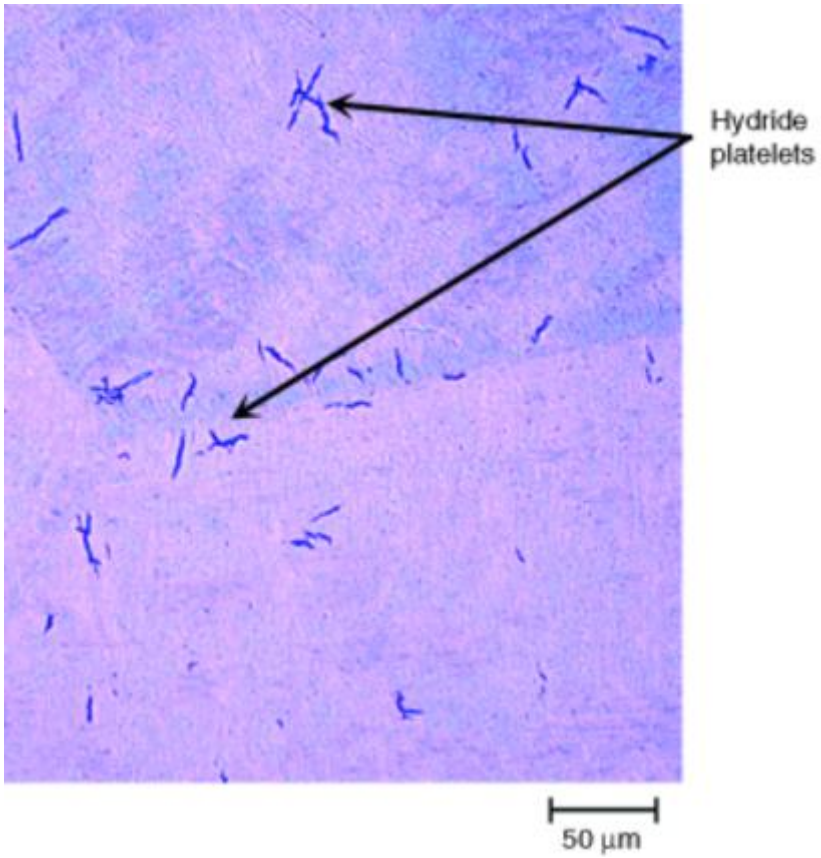

Fig. 36 Zr705 welded plate. Attack polished, anodized at 108 V, and viewed with bright-field illumination. The micrograph reveals hydrides in a zirconium grade 705 matrix. Original magnification: 200×.

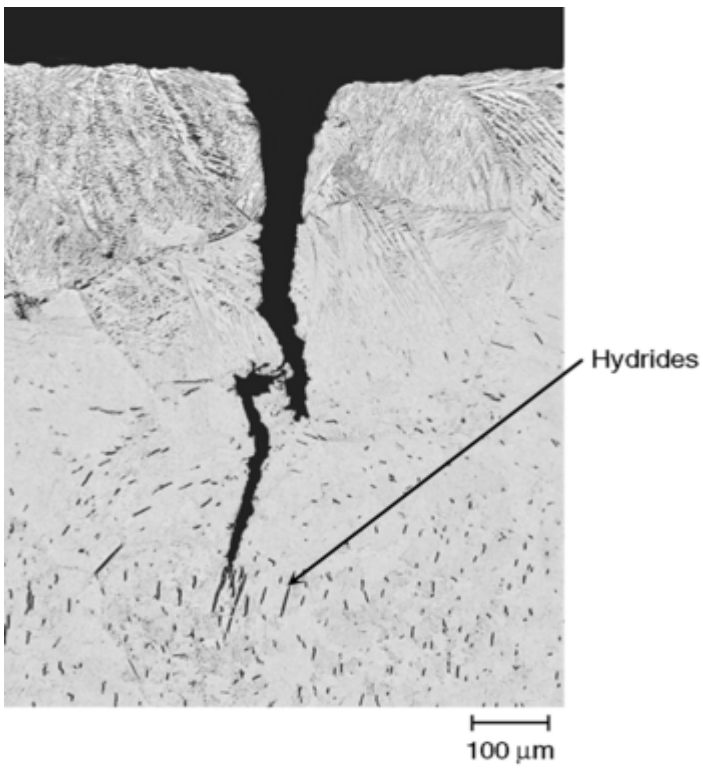

Fig. 37 Zr705 weld, attack polished, etchant procedure No. 5 (Table 2), bright field. This micrograph shows the presence of delayed hydride cracking in a Zr705 weld. This condition occurs in a non-stress-relieved welded structure. Original magnification: 100×

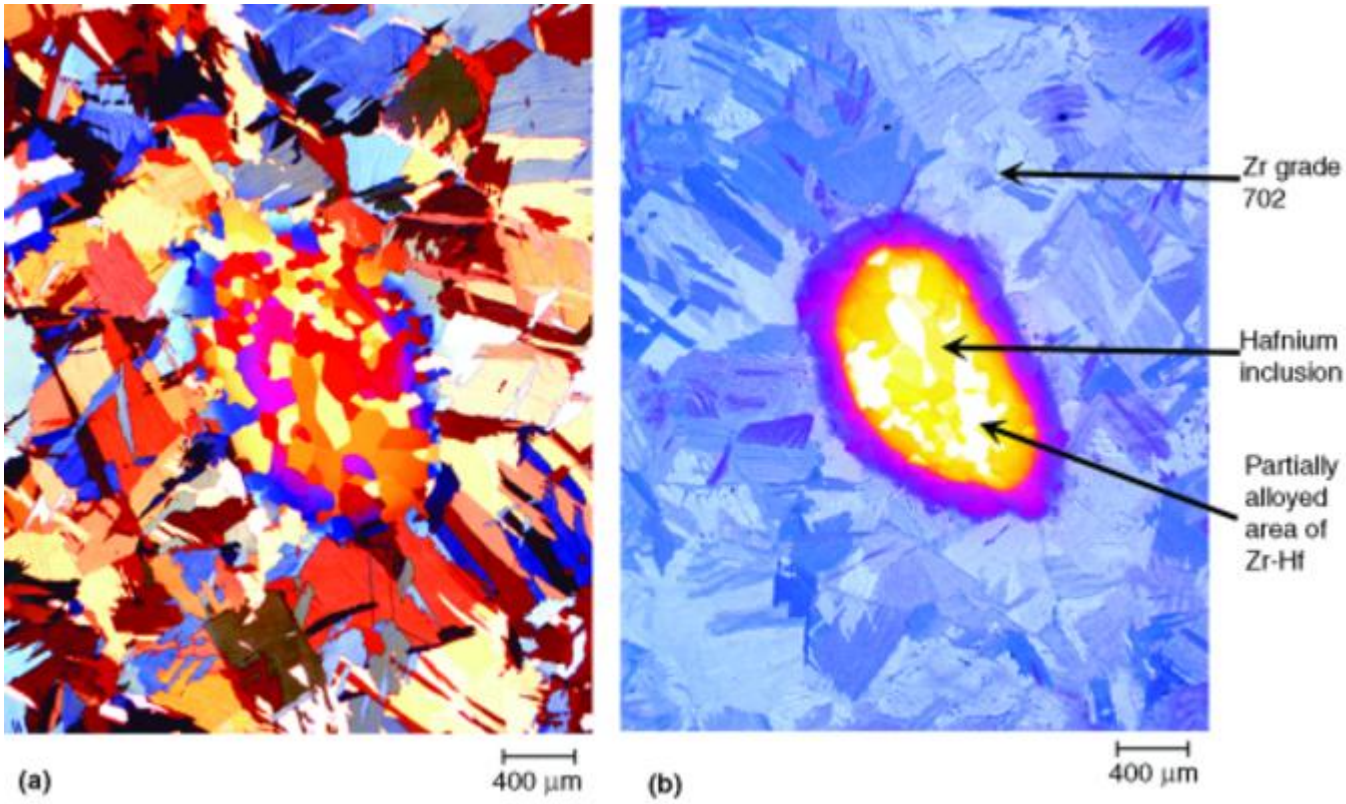

Fig. 38 Zirconium sheet. (a) Attack polished, heat tinted, and viewed with polarized light illumination. (b) Attack polished, etchant procedure No. 2, anodized at 108 V, and viewed with bright-field illumination. These micrographs show the advantages certain preparation procedures offer for the identification of a metallic inclusion in a zirconium matrix. Original magnification: 25×.

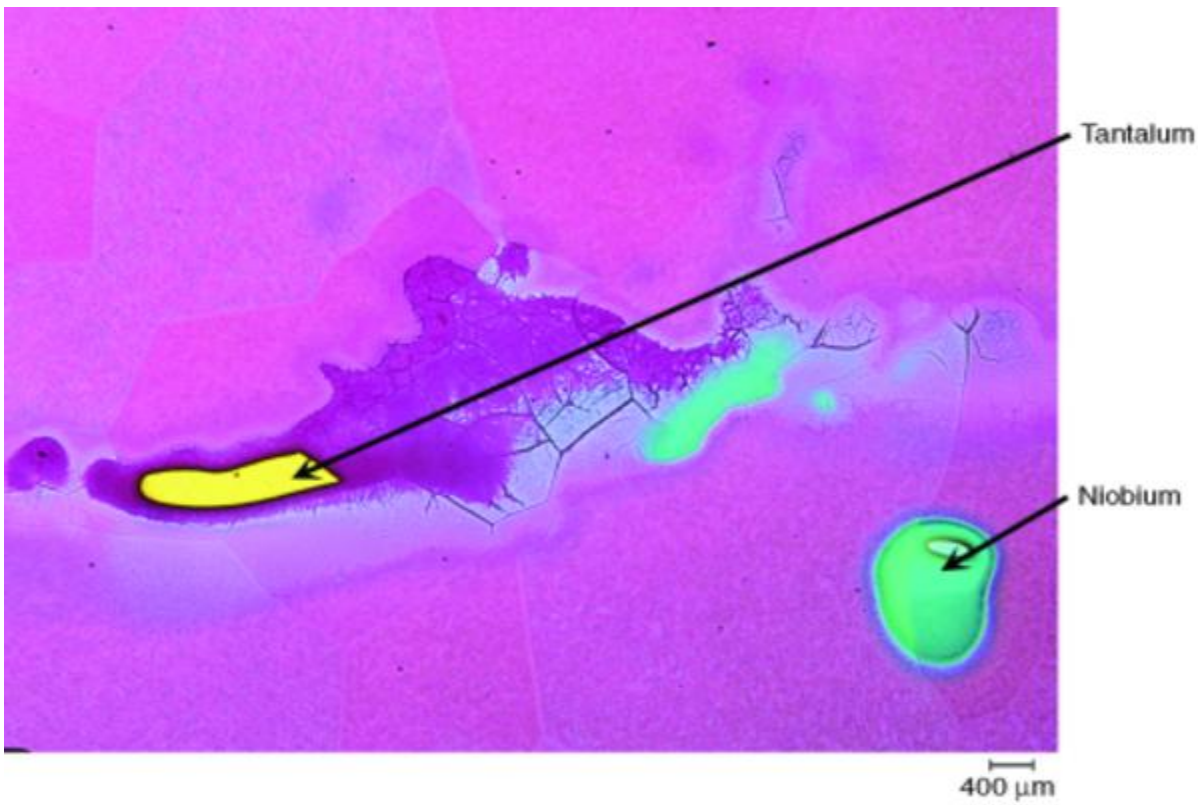

Fig. 39 Zr705 cast recycle. Attack polished, anodized at 108 V, and viewed with bright-field illumination. This micrograph shows the presence of tantalum (gold) and niobium (green) inclusions in the Zr705 matrix. Original magnification: 25×.

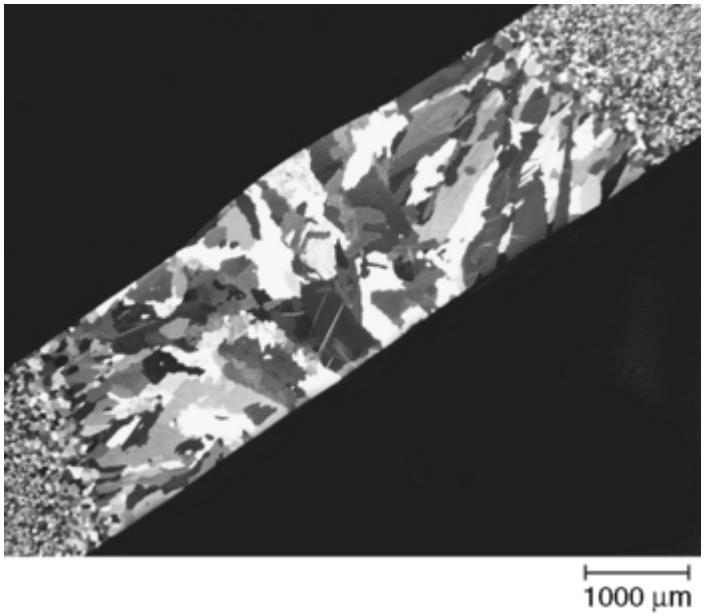

Fig. 40 Hafnium sheet, transverse, attack polished, etchant procedure No. 2 (Table 2), anodized at 15 V, polarized light. This micrograph shows the appearance of a hafnium weld structure. Original magnification: 15×

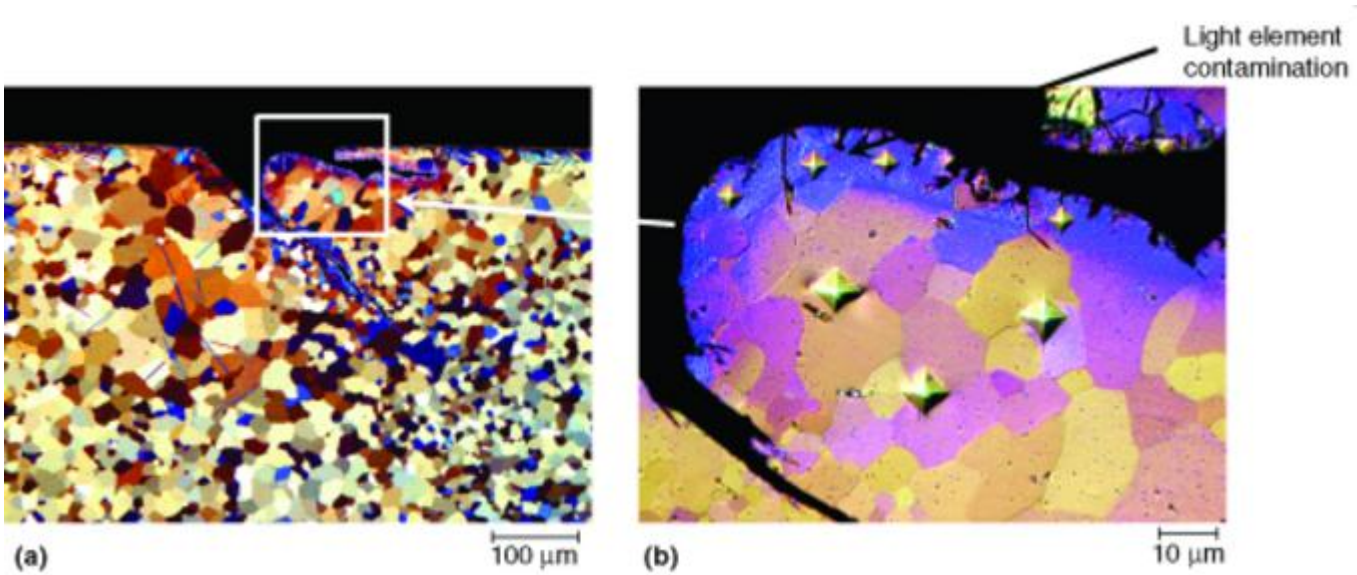

Fig. 41 Hafnium plate, wrought, longitudinal. (a) Plate surface viewed with polarized light illumination. (b) Contaminated area. Attack polished, etchant procedure No. 2, anodized at 118 V, and viewed with bright-field illumination. These micrographs show the hardness differences between the matrix of the hafnium and that of the oxygen/nitrogen contaminated layer. Anodization and hardness impressions illustrate the degree of contamination. (a) Original magnification: 150×. (b) Original magnification: 1000×.

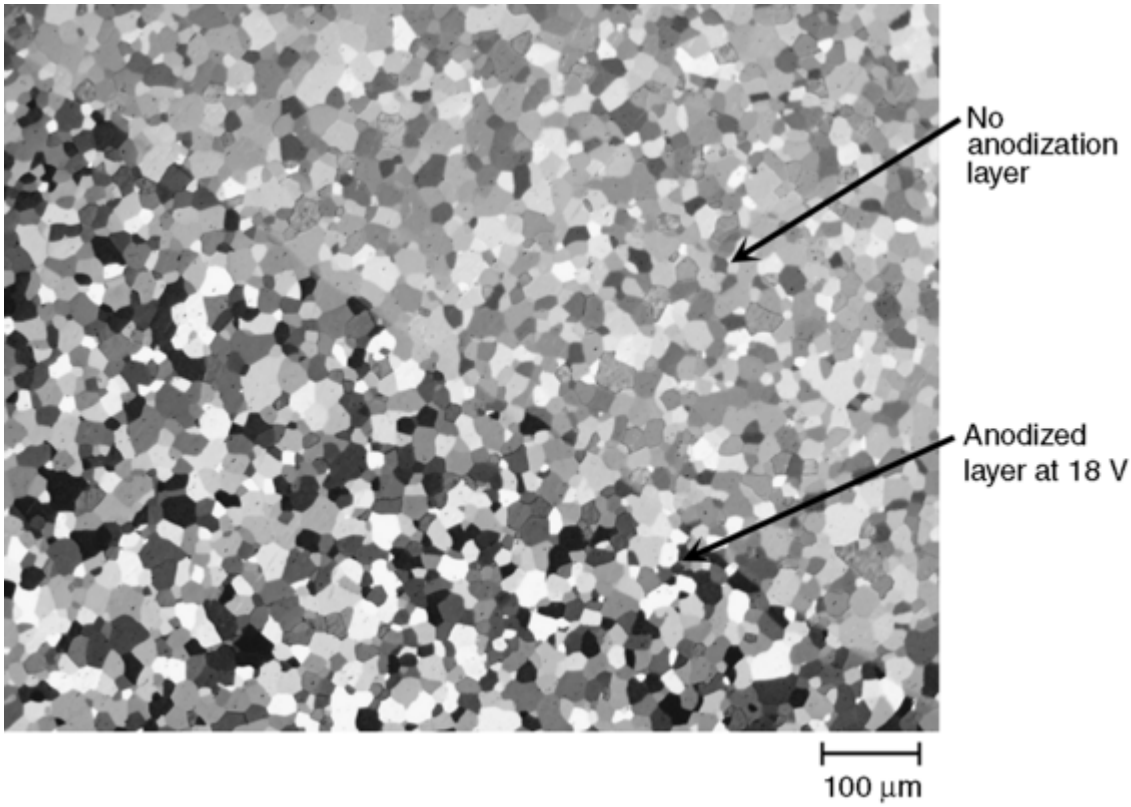

Fig. 42 Hafnium plate, longitudinal, attack polished, etchant procedure No. 2 (Table 2), polarized light. This microphotograph shows how anodization assists in delineation of the grain structure. Original magnification: 100×

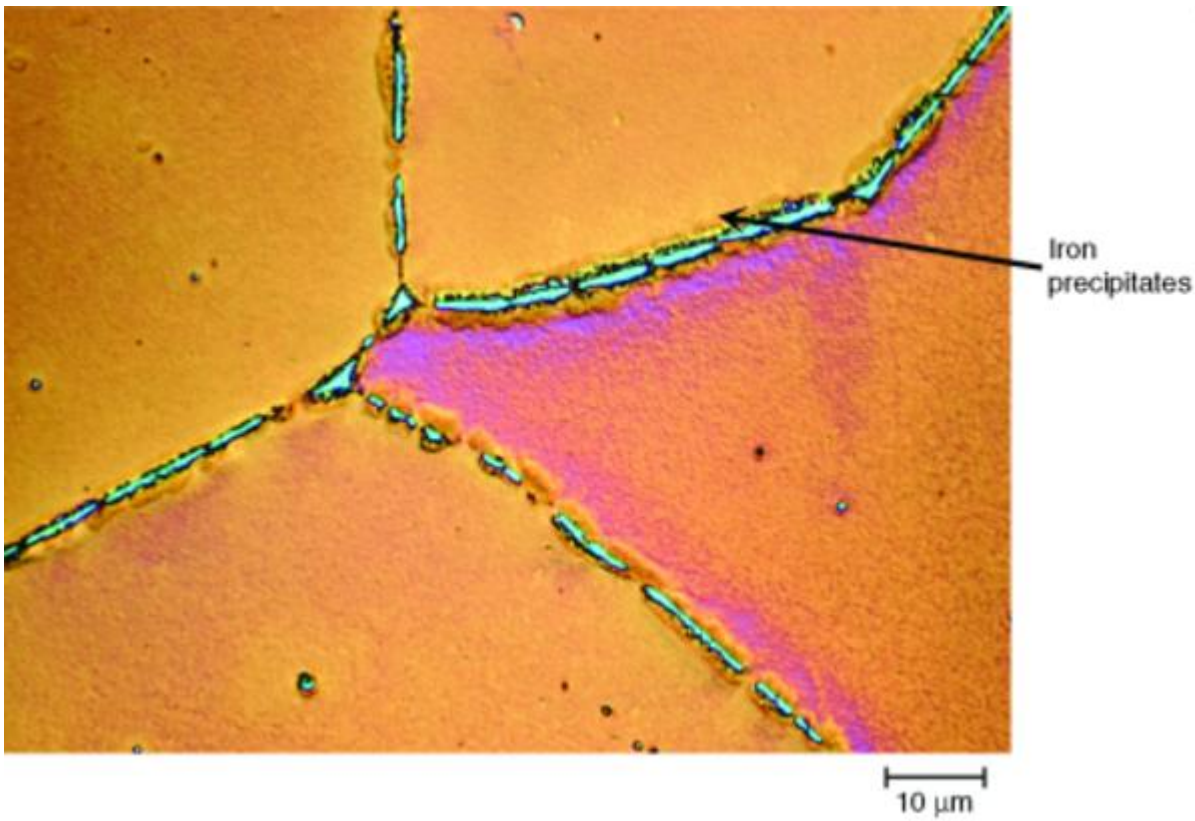

Fig. 43 Hafnium rod, powder metallurgy, transverse. Attack polished, etchant procedure No. 2, anodized at 118 V, and viewed with bright-field illumination. Transverse view of a hafnium grain structure with second phase (iron enriched) in the grain boundaries. Original magnification: 1000×.

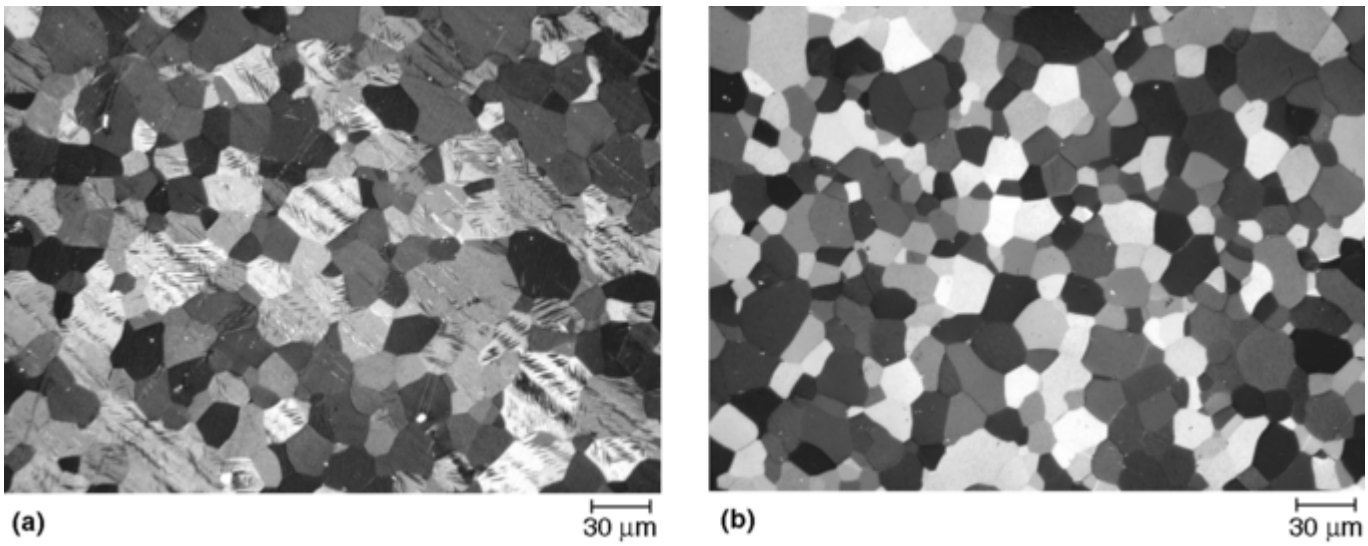

Fig. 44 Hafnium sheet, attack polished, etchant procedure No. 2 (Table 2), anodized at 115 V, polarized light. Softer materials may be more susceptible to artifacts caused during preparation. (a) Improper polishing caused what appear to be defects in the grains. (b) Properly prepared sample. Original magnification: 300×

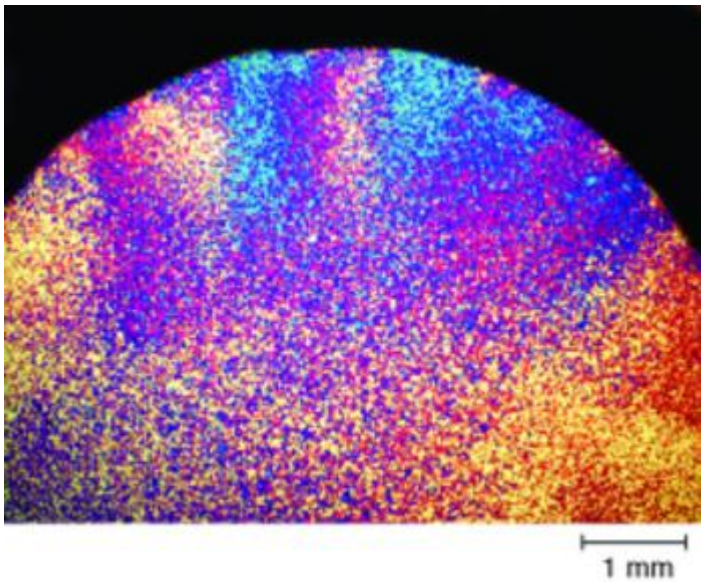

Fig. 45 Hafnium rod, 19 mm ($\frac{3}{4}$ in.) in diameter, transverse. Attack polished, etchant procedure No. 2, anodized at 115 V, and viewed with polarized light illumination. This micrograph shows texture "lobes" caused by localized deformation. Original magnification: 15×.

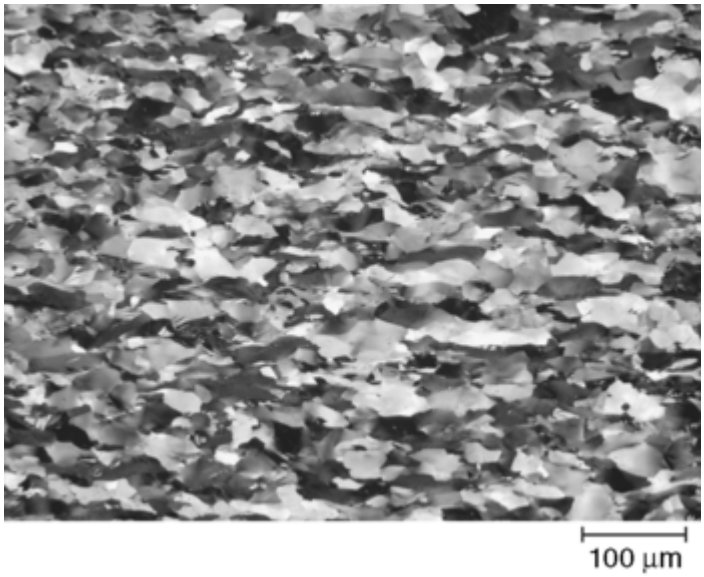

Fig. 46 Hafnium sheet, wrought, longitudinal, attack polished, etchant procedure No. 2 (Table 2), anodized at 15 V, polarized light. This micrograph shows the effect of cold work in a structure. Original magnification: 150×

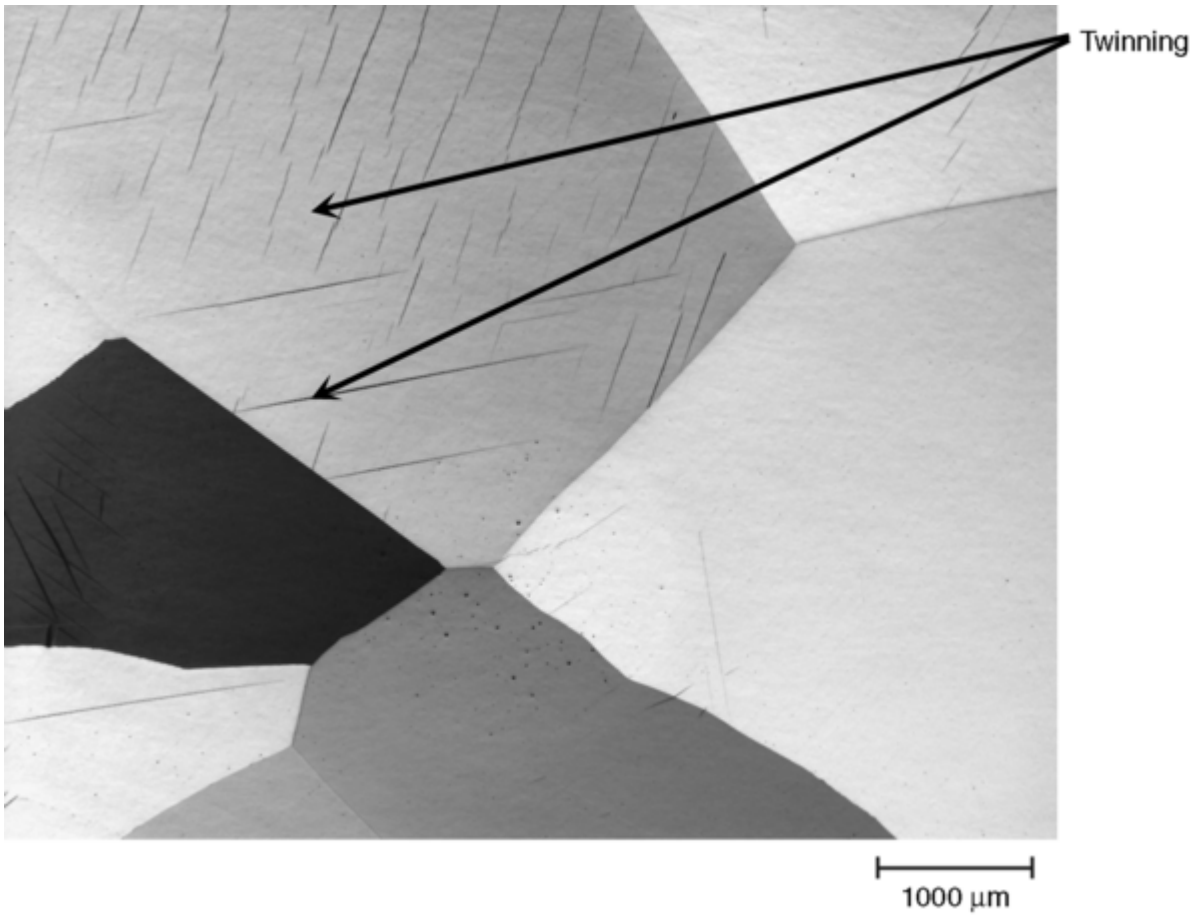

Fig. 47 Hafnium crystal bar, longitudinal, attack polished, etchant procedure No. 2 (Table 2), anodized at 15 V, polarized light. This hafnium grain structure exhibits very large grains due to high purity and shows twinning in the grains. Original magnification: 15×

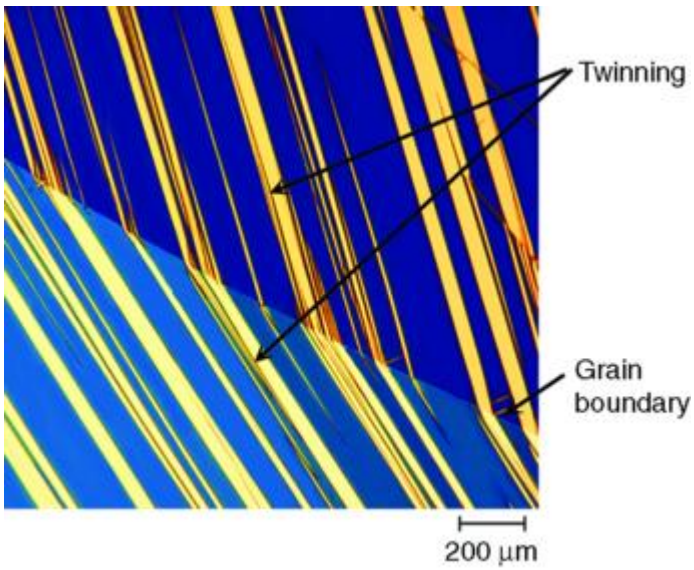

Fig. 48 Hafnium crystal bar, longitudinal. Attack polished, heat tinted, and viewed with polarized light illumination. This micrograph shows the twinning in hafnium grains. Original magnification: 50×.

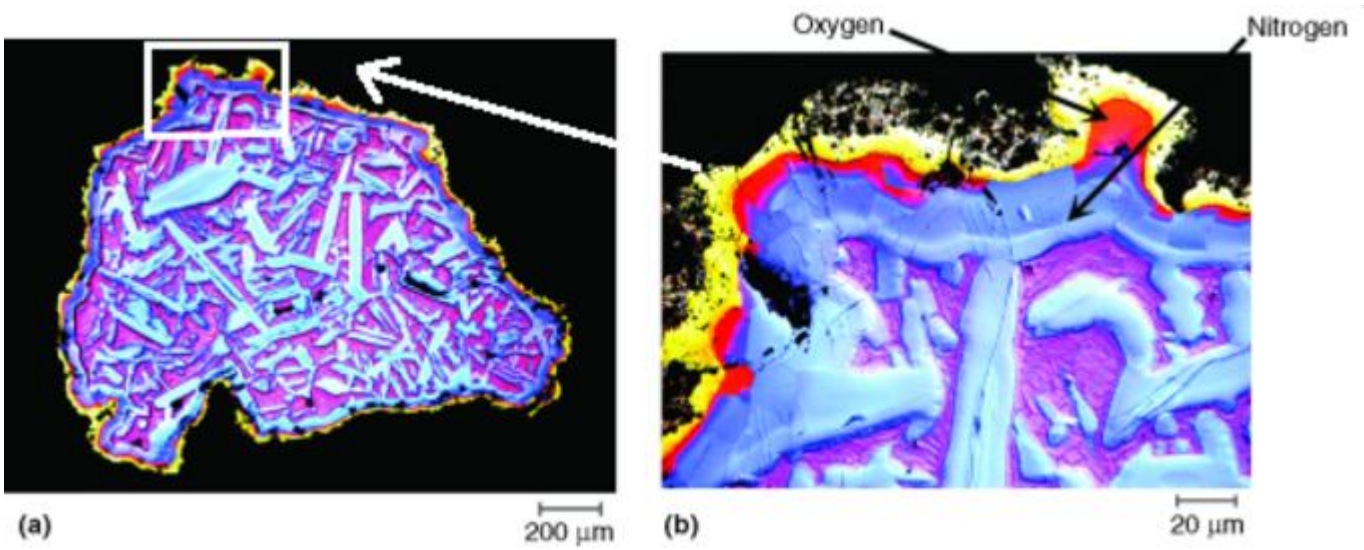

Fig. 49 Zirconium sponge. Attack polished, etchant procedure No. 3, anodized at 108 V, and viewed with differential interference contrast illumination. These micrographs show a contaminated zirconium sponge particle. The outer surface exhibits a surface layer with greater contamination. (a) Original magnification: 50×. (b) Original magnification: 500×.

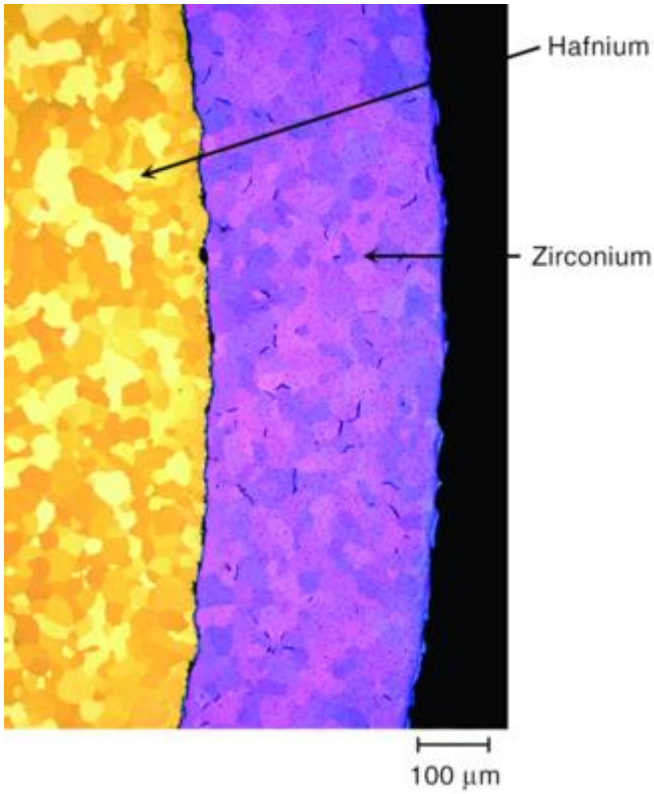

Fig. 50 Zircaloy 4/hafnium bimetallic tube. Attack polished, etchant procedure No. 2, anodized at 108 V, and viewed with bright-field illumination. This micrograph shows the difference in anodization color of zirconium as compared to hafnium. Original magnification: 100×

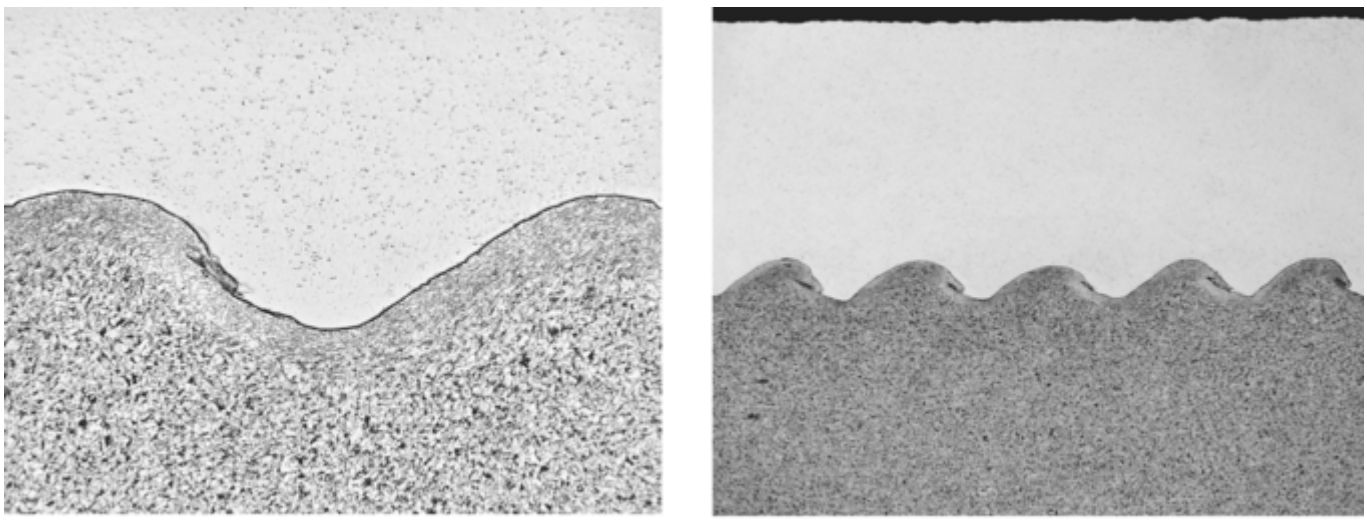

Fig. 51 Zirconium/steel explosive bonded area, attack polished, bright field. These micrographs show the zirconium/steel interface region of an explosive clad plate. (a) Original magnification: 50×. (b) Original magnification: 15×

Macrostructural Examination. Low-magnification examination (<25×) of macroetched cross sections often reveals considerable structural detail. Cast forms, such as ingot slices, extrusions, forgings, and other large parts, can be examined for grain-size variations, weld integrity, porosity, shrinkage, cavities, cracks, flow lines, and other macrostructural features.

In microstructural examination, the sample must be in the proper metallographically prepared condition, which includes both sample polishing and optical enhancement techniques. The materials must be appropriately

prepared to ensure a surface that is optically free of surface deformation and scratches for the fully contained microstructure. The sample must then be enhanced to reveal microstructural features. Microstructural enhancement techniques include light conditions such as bright field, dark field, DIC, and polarized light. It is important to choose the proper lighting conditions as shown in Fig. 6. Further enhancement techniques that should be considered include etching processes, anodization, and heat tinting. These tools will be applied in the appropriate manner to best reveal specific attributes in the microstructure.

Microstructural Considerations. Materials that are unalloyed or have low alloy content primarily exist as α-grain structures at room temperature. The structure is strongly influenced by the thermomechanical processing history. Unalloyed zirconium or hafnium will exhibit an equiaxed α-structure when cold worked and fully annealed. Figure 14(a), 15, and 42 show this structure. Material that is worked at temperatures exceeding 650 °C (1200 °F) will exhibit a hot-worked structure such as shown in Fig. 5. The Zircaloys have a structure with elongated α-grains and precipitates of iron- and chrome-containing intermetallic particles between the α-platelets. These second-phase particles can best be seen using an anodization layer with bright field illumination. Figure 7 shows a Zircaloy 2 structure with second-phase particles surrounding the α-grains. Zirconium grade 702 (unalloyed) structure will typically show an equiaxed α-structure with some fine, well-distributed second-phase particles (primarily zirconium-iron). The hot-worked structure will appear more elongated in the longitudinal direction.

Zirconium alloys of Zr2.5Nb and Zr705 exhibit a two-phase structure. Due to the nature of these two-phase alloys, they exhibit a much finer grain structure than that of the α-alloys. These alloys show the presence of the β-niobium and α-zirconium phase in the parent metal. Upon heating above the β-transus and subsequently cooling, the structure will have a fine acicular structure of α-zirconium and β-niobium. Figure 34(a) shows the β-niobium dispersed an α-zirconium structure.

As-cast zirconium has an acicular (needlelike) microstructure, which varies slightly in appearance depending on the composition and/or cooling rate. An example of this is shown in Fig. 1. Upon cooling, the high-temperature β-phase transforms to acicular α at approximately 865 °C (1590 °F) or about 980 °C (1800 °F) for typical Zircaloys. Welds will have three regions exhibiting different grain structures showing the parent metal, HAZ, and weld area. As the weld material is heated to a molten state, a phase transformation will take place going from the α-phase to the β-phase and then to the liquid state. Upon cooling, the weld will exhibit a transformed grain structure or acicular α-grains surrounded by prior β grain boundaries (Widmanstätten or basketweave structure). Figure 2(c) and 14(c) show this type of structure. An area adjacent to the weld metal will appear acicular, with finer needlelike α-grains. This grain structure is formed when the material not reaching the molten state is heated near to or above the β-transus, creating the HAZ (see Fig. 2b and 14b). When the material cools, it results in an acicular α-structure. Figure 2, 14, 33, 34, and 40 show the appearance of parent metal, HAZ, and weld areas in zirconium and hafnium alloys.

If a small amount of cold work (2 to 8%) is introduced into the fully annealed equiaxed α-material followed by an α-anneal (625 to 790 °C, or 1160 to 1455 °F) of more than 30 min at temperature, the grain structure of the worked area can create a critical grain growth condition known as “blocky α.” This structure is shown in Fig. 9 and 28.

Zirconium intermetallic compounds or second-phase particles are enriched in iron, chromium, and nickel. These $Zr(Fe,Cr)_2$ or Zr_2-Ni intermetallic compounds will precipitate between the α-platelets of the Zircaloys and zirconium grade 702 alloys. These intermetallic compounds are readily identified using less aggressive etching, heat tinting, and anodization techniques. Figure 3(a), (b), and 7 show the intermetallic compounds. Hafnium can also exhibit second-phase particles of hafnium-iron in the grain boundaries as shown in Fig. 43.

Zirconium and hafnium alloys also exhibit twins and slip lines in their microstructures when plastically deformed (see Fig. 3a, 47, and 48). Twins and slip lines are most prevalent in the softer, large α-type grain structures. These twins can be recognized by their lenticular shape. When they cross from one grain boundary to another, their direction usually changes.

Zirconium hydrides (Zr_2H_x) occur in thin platelets and appear as irregularly shaped needles. It is emphasized that care should be taken to select the proper anodization voltage to contrast the hydride platelets that are present. Figure 17, 22, 35, and 36 show examples of these hydride platelets. These can form in either grain boundaries or within specific grains. Hydrides are identified using a “hydride-etch” procedure as described in Table 2 as etchant procedure No. 5. These hydrides can exist primarily as distinct separate needles, but can also occur in some severe cases as “bundles of platelets” as shown in Fig. 23 and 29.

Intermetallic compounds in zirconium and hafnium can also be highlighted and identified using anodization techniques. This will result in a significant color contrast between the retained intermetallic compounds and the matrix. Slight color variations combined with other metallographic features, such as shape and location, will allow one to distinguish between the various intermetallic compounds. These intermetallic compounds can exist in zirconium as carbides (ZrC), silicides (Zr_3Si), and phosphides (Zr_3P) (Ref 6). The solubility of zirconium carbide, silicide, and phosphide intermetallic compounds decrease in that order for any given heat treatment. For this reason, these compounds have different shapes, which aid in their identification. Generally, carbides tend to be more idiomorphic or irregular in shape (see Fig. 7, 17, 19). The carbides do not generally form in the grain boundaries, but precipitate within the matrix. The color, size, shape, appearance, and location of the zirconium carbides make it easier to distinguish between the carbides and the phosphides and silicides. Silicides will also be located in grain boundaries or α-stabilized regions near the prior grain boundaries. Phosphides can also be sharp and needlelike in appearance or can vary in shape such as those shown in Fig. 25. The presence of silicides/phosphides in a zirconium matrix are shown in Fig. 25. The characteristics of each type of intermetallic compound are fairly independent of alloy composition.

Identification of Metallurgical Attributes in Reactive Metals. Metallography is commonly used during production to monitor product quality and to examine specific attributes or defects in the metallurgical structure. It is extremely important to use the proper metallographic techniques for identification of second-phase particles or intermetallic compounds, and inclusions, as well as other metal impurities. If a dissimilar metal alloy inclusion is found to exist in the metallurgical structure, for example, during a nondestructive test, preparation procedures are important for proper identification of this inclusion. Figure 38(a) and (b) show a hafnium inclusion in a zirconium matrix. In Fig. 38(a), using the heat tinting process, the contrast between the zirconium and hafnium inclusion is less dramatic than in Fig. 38(b). This is due to the use of polarized light illumination, which gives better grain structure delineation in both hafnium and zirconium. In Fig. 39, tantalum- and niobium-base inclusions are shown in the zirconium grade 705 structure. This is another instance where the proper anodization techniques contrast the differences in these materials.

When material is improperly processed, a high or uneven amount of work could be placed on the part being manufactured. This could result in the material cracking as shown in Fig. 18. Metallographic techniques, such as polarized light, can also be used to identify the higher strained or greater worked areas as shown in Fig. 45.

When reviewing a final explosive clad zirconium to steel plate, it is important to use a technique that will attack polish the zirconium but not overetch the steel. Figure 51 shows the zirconium to carbon steel interface region or a “wave bond zone” where the two materials are explosively joined together.

Metallography used for Failure Analysis. Metallography is commonly used as a technique for evaluation of mechanical and corrosion failures in reactive metals. Metallography can identify areas in a metallurgical structure that may cause a failure during bending, as shown in Fig. 24. This mechanical failure was a result of large (low-ductility) second-phase zirconium-iron particles in a zirconium plate that cracked during bending.

Metallography is also an excellent method to determine the presence of light element contamination in a reactive metal weld structure since anodization at ~108 V shows the presence of nitrogen as a bluish-green and oxygen as a reddish coloration. This is shown in heat-related failures (welding or cutting) in zirconium microstructures (Fig. 21, 30, 31, 32). If light element contamination exists in welds, it may also cause weld cracking due to localized nonductile areas. Figure 19 shows a crack that began in the contaminated HAZ of the weld. This particular weld and HAZ zone was decorated with zirconium carbides caused by inadequate cleaning of the weld area. Without proper metallographic techniques, the presence of carbides would not have been identified.

It should be noted that metallography, if not performed properly, will also show polishing artifacts that are not present. Figure 44(a) shows very soft hafnium sheet that appears to have defects in the grains, but which are only due to improper polishing. Figure 44(b) is the same sample prepared properly. It should be stressed that each stage of grinding and polishing needs to be done with care to remove the effects of the previous preparation step.

Some welds will exhibit cracking without showing any indication of weld contamination such as that in Fig. 37. This Zr705 weld failed due to the delayed hydride-cracking phenomenon that occurs in the higher-strength zirconium-niobium alloys. In this case, it is mandatory that the zirconium-niobium welds be stress relieved after welding to prevent the movement of hydrogen in the structure to the higher stress areas, eventually causing cracking.

Metallography is a common method for identification of corrosion failures and mechanisms. Corrosion failures such as intergranular attack, stress corrosion, and localized pitting attack can be identified using certain metallographic techniques. Figure 26(a), (b), and 27 show these types of corrosion failures.

Reference cited in this section

6. P.D. Kaufmann, P. Danielson, and E.F. Baroch, "Metallographic Preparation of Zirconium Alloys for Improved Contrast of Low-Solubility Intermetallic Compounds," Teledyne Wah Chang Albany, Aug 1972

P.E. Danielson and R.C. Sutherlin, Metallography and Microstructures of Zirconium, Hafnium, and Their Alloys, *Metallography and Microstructures,* Vol 9, *ASM Handbook,* ASM International, 2004, p. 942–958

Metallography and Microstructures of Zirconium, Hafnium, and Their Alloys

Paul E. Danielson, Albany Research Center, U.S. Department of Energy; Richard C. Sutherlin, Wah Chang, An Allegheny Technologies Company

---

References

1. J. Haygarth and R. Graham, Zirconium and Hafnium, *Review of Extraction, Processing, Properties & Applications of Reactive Metals,* B. Mishra, Ed., TMS, 2002, p 1–71

2. V.R. Vogel and W. Tonn, Über einen Umwantlungspunkt des Zirkons, *Z. Anorg.uallhem, Chem.,* Vol 202, 1931, p 292

3. H.P. Roth, "Metallography of Zirconium," Report MIT-1004, MIT Metallurgical Project Quarterly Technical Progress Report for the Period February through April, 1948, Massachusetts Institute of Technology, p 115–126

4. B. Lustman and F. Kerze, Jr., Ed., *The Metallurgy of Zirconium,* McGraw-Hill, 1955

5. M.L. Picklesimer, Anodizing for Controlled Microstructural Contrast by Color, *Microscope,* Vol 15, Oct 1967

6. P.D. Kaufmann, P. Danielson, and E.F. Baroch, "Metallographic Preparation of Zirconium Alloys for Improved Contrast of Low-Solubility Intermetallic Compounds," Teledyne Wah Chang Albany, Aug 1972

7. B.T. Buzalski and R.L. Gulbransen, Hafnium Fuel for Photoflash Lamps, *J. Illum. Eng. Soc.,* Vol 2, July 1973

8. D.E. Thomas and E.T. Hayes, Ed., "The Metallurgy of Hafnium, Naval Reactors," Division of Reactor Development, United States Atomic Energy Commission (ERDA), 1960

D.J. Medlin and R. Compton, Metallography of Biomedical Orthopedic Alloys, *Metallography and Microstructures,* Vol 9, *ASM Handbook*, ASM International, 2004, p. 961–968

Metallography of Biomedical Orthopedic Alloys

D.J. Medlin and R. Compton, Zimmer, Inc.

Introduction

METALS AND ALLOYS have a diverse application in the medical field, particularly as implantable internal (in vivo) structural, load-bearing materials in devices for partial and total joint replacement, fracture fixation, and instruments. The field of metallography plays a significant role in the quality control of metals and alloys used in the manufacture of implantable surgical devices. Metallographic examination of raw materials prior to fabrication of the devices and systematic examinations during specific processing steps helps to ensure that the devices will be safe and effective when used in patients. The field of orthopedic biomaterials research is continuing to grow and develop due to increased patient demographics (aging) and the increased expectations from both patients and surgeons for implant performance. The future development of new biomedical materials and the development of new manufacturing processes to improve the performance of traditional biomedical materials will increase the need for more materials science and metallurgical engineering research, including metallography and microstructural characterization. The continued used of metallic components for implant devices will require the use of metallography as a quality-assurance tool for both raw materials and manufacturing process evaluations. This paper focuses on the metallographic techniques and microstructures of implantable biomedical orthopedic metals and alloys.

D.J. Medlin and R. Compton, Metallography of Biomedical Orthopedic Alloys, *Metallography and Microstructures,* Vol 9, *ASM Handbook*, ASM International, 2004, p. 961–968

Metallography of Biomedical Orthopedic Alloys

D.J. Medlin and R. Compton, Zimmer, Inc.

Implant Devices

Implantable biomedical devices range the spectrum of design and materials selection consideration from relatively simple devices requiring one material, such as commercially pure titanium dental implants, to highly complex assemblies, such as cardiac pacemakers (Ref 1, 2). Total joint replacement is widely regarded as a major achievement in orthopedic surgery in the twentieth century. Arthroplasty, or the creation of a prosthetic joint, is the name given to the surgical treatment of degenerate joints with the goal of relieving pain and restoring mobility.

Figure 1(a) shows an illustration of the components that are typically assembled to create a prosthetic hip implant. A typical total hip implant system consists of a femoral stem (with or without a porous coating), a femoral head, a polymeric (ultrahigh molecular weight polyethylene, or UHMWPE) liner, and a metal acetabular shell. Figure 1(b) shows a typical total knee implant system that includes a tibial component, which is an upper extension of the tibia (shin bone) with a polymeric (UHMWPE) cushion, a femoral component that curves around the end of the femur (thigh bone), and a patellar component that replaces the kneecap. Bone structures can also be damaged by trauma and require surgical reduction in order to facilitate proper bone healing and alignment. Figure 1(c) shows some fracture fixation components that are used to stabilize bone fractures, including plates, screws, cables, and rods.

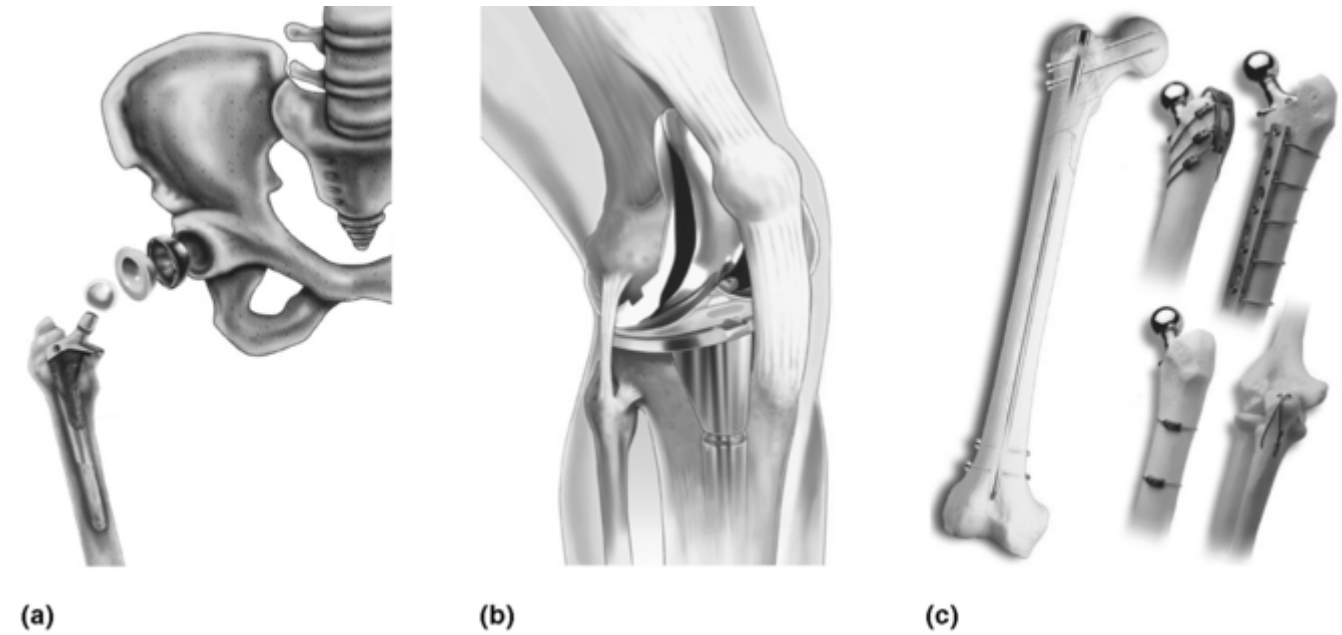

Fig. 1 Implant devices. (a) The components of a prosthetic total hip implant system. (b) The components for a prosthetic total knee implant system. (c) Examples of fracture fixation components such as plates, screws, cables, and rods

Metals and alloys have a successful history as implant materials in the human body because of their appropriate mechanical properties, corrosion resistance, biocompatibility, and manufacturability (Ref 2, 3, 4, 5). In order to optimize the performance of a medical device, the relationship between properties and microstructure must be understood. This requires a fundamental understanding of appropriate metallographic techniques and proper characterization of the microstructural features for these particular biomedical metals and alloys.

The field of metallography plays a significant role in the quality control of metals and alloys used to manufacture medical implants. In particular, the metallographic examination of raw materials (metals) prior to the fabrication of implant devices helps ensure that the devices will be safe and effective in the internal environment of the human body. While it is not possible to predict the clinical performance of metals by microstructural analysis alone, metallography does serve to relate the clinically observed performances of metals to the microstructural characteristics of the initial raw metals.

Compared to other materials, metals have high elastic moduli and useful yield strengths such that components may be manufactured that will sustain significant loads without large elastic deformations or any plastic deformations. Metals also possess enough ductility that, when excessively loaded above the yield point, they will plastically deform rather than exhibiting a sudden catastrophic brittle failure and incurring potentially more damage to the patient and additional surgeries. These metals also possess sufficient fatigue strength, making them suitable for cyclic load applications for joint replacements or fracture fixation plates. If properly fabricated, the fatigue strength of metal components is very predictable and can be designed using appropriate margins of safety (Ref 4, 5).

One restriction for implant metals is that they cannot have magnetic properties due to the use of magnetic resonance imaging (MRI) systems used as diagnostic tools in the medical field (Ref 4). The very high magnetic fields from MRI systems will induce heat and dynamic magnetic forces on a magnetized metal, and this could be unsafe for the patient. This limitation substantially restricts the metals and alloys available for implantation in the body.

The metals and alloys used for orthopedic medical device implantation are classified into the following groups: stainless steels, cobalt-base alloys, titanium and titanium alloys, porous coatings, and emerging materials.

References cited in this section

1. J.R. Davis, Ed., *Handbook of Materials for Medical Devices,* ASM International, 2003

2. C.R. Blanchard, D.J. Medlin, and R. Shetty, Advances in Metals, *Joint Replacements and Bone Resorption: Pathology and Clinical Practice,* Marcel Dekker, 2003

3. D.C. Mears, *Materials and Orthopaedic Surgery,* Williams and Wilkens Co., 1979, p 1–28

4. J. Black, *Orthopaedic Biomaterials in Research and Practice,* Churchhill Livingstone, 1988

5. D.J. Wise, D.J. Trantolo, and D.E. Altobelli, *Encyclopedic Handbook of Biomaterials and Bioengineering, Part-B: Applications,* Marcel-Dekker, 1995, p 509–539

D.J. Medlin and R. Compton, Metallography of Biomedical Orthopedic Alloys, *Metallography and Microstructures,* Vol 9, *ASM Handbook*, ASM International, 2004, p. 961–968

Metallography of Biomedical Orthopedic Alloys

D.J. Medlin and R. Compton, Zimmer, Inc.

Stainless Steels

In 1906 Leon Guillet developed an Fe-Cr-Ni alloy with a face-centered-cubic (fcc) microstructure, more commonly known today as austenitic stainless steel. Research showed that when these alloys had chromium contents in excess of 10.5%, the stainless characteristics of the alloy would result due to the formation of an invisible and adherent chromium-oxide film (<2 nm thick). The application of stainless steel in surgical applications began in the 1920s with the development of 18-8-Mo stainless steel, and today the most common implantable stainless steels for orthopedic applications are 316L, 22Cr-13Ni-5Mn, and REX-734 (Ref 2). Table 1 shows the chemistries and designations of some commonly implanted stainless steels. The austenitic microstructure of these stainless steels is very important due its superior corrosion resistance and nonmagnetic property. These alloys can be processed by forging, annealing, stress relieving, cold working, and welding to a variety of mechanical properties depending on the processing method used and the properties required for the application. Other references list the appropriate temperature ranges and times for heat treating these alloys (Ref 6, 7, 8). Care must be taken to avoid sensitization of the microstructure at certain temperature ranges and cooling rates that will decrease the corrosion resistance of these alloys and may be catastrophic for implant devices (Ref 7).

Table 1 Nominal compositions of stainless steels (SS) for medical implant applications

ASTM designation	ISO designation	Alloy group and condition	Composition, wt%												
			Fe	**Cr**	**Ni**	**Mo**	**Mn**	**Si**	**Cu**	**C**	**N**	**S**	**P**	**Nb**	**V**
F 138	5832-1	316L SS wrought	bal	17.00–19.00	13.00–15.00	2.25–3.00	2.00 max	0.75 max	0.50 max	0.030 max	0.10 max	0.010 max	0.025 max	…	…
F 621	5832-3	316L SS forging	bal	17.00–19.00	13.00–15.00	2.25–3.00	2.00 max	0.75 max	0.50 max	0.030 max	0.10 max	0.010 max	0.025 max	…	…
F 621	…	22-13-5 SS forging	bal	20.50–23.50	11.50–13.50	2.00–3.00	4.00–6.00	0.75 max	0.50 max	0.030 max	0.20–0.40	0.010 max	0.025 max	0.10–0.30	0.10–0.30
F 621	…	REX 734 forging	bal	19.50–22.00	9.00–11.00	2.00–3.00	2.00–4.25	0.75 max	0.25 max	0.08 max	0.25–0.50	0.010 max	0.025 max	0.25–0.80	…
F 1314	…	22-13-5-SS wrought	bal	20.50–23.50	11.50–13.50	2.00–3.00	4.00–6.00	0.75 max	0.50 max	0.030 max	0.20–0.40	0.010 max	0.025 max	0.10–0.30	0.10–0.30
F 1586	5832-9	REX 734 wrought	bal	19.50–22.00	9.00–11.00	2.00–3.00	2.00–4.25	0.75 max	0.25 max	0.08 max	0.20–0.50	0.010 max	0.025 max	0.25–0.80	…

Austenitic stainless steels can be prepared by standard metallographic techniques. The standard cutting, mounting, and polishing techniques described in ASTM E 3 will do an adequate job of producing quality metallographic specimens (Ref 9). Table 2 outlines a typical metallographic sample preparation methodology. Because these alloys are corrosion resistant, etching techniques are more difficult and meticulous than carbon steels. Table 3 lists several common etching methods used for austenitic stainless steels. The ammonium persulfate and water ($(NH_4)S_2O_8$ and H_2O) etchant, when applied at 3 to 5 V for 1 to 3 min, is a good general-purpose electrolytic etchant that reveals most of the important microstructural features needed for proper metallographic characterization (see Table 3). The nitric acid and water (HNO_3 and H_2O) etchant, when applied at 1 V for 30 to 90 s, reveals grain boundaries in cold-worked microstructures for distinct measurement of the grain size. A third etching method listed in Table 3 uses a potassium hydroxide and water etchant (KOH and H_2O) at 1 to 3 V and for 3 to 5 s. This etching process works well to reveal ferrite phase as a blue color and sigma phase as a red/brown color, depending on the etchant concentration and etching time. Unlike many ferrous-based alloys, these metallographic mounts store well in dust-free cabinets and the use of a desiccant is not necessary.

Table 2 Polishing schedule

Step	Surface	Abrasive	Lubricant	Force, N	Platen rpm	Time, s	Relative rotation[(a)]
Planar grinding	SiC paper	150 grit SiC	Water	20–30	200–300	15–45	Comp
Fine grinding	Rigid disc	6–15 μm diamond	Diamond lubricant	20–30	100–150	108–300	Comp
Rough polishing	No nap cloth	3–6 μm diamond	Diamond lubricant	20–30	100–150	120–300	Comp
Final polishing	Medium nap cloth	1 μm diamond	Diamond lubricant	10–20	100–150	60–120	Comp
Final polishing[(b)]	Synthetic suede	Colloidal silica	Water	10–20	100–150	30–60	Contra

(a) Comp, complementary rotation—platen and power head rotate in the same direction; contra, platen and power head rotate in opposite directions.
(b) This step may not be necessary for some applications.

Table 3 Etchants

Metal/alloy	Etchant	Instructions	Purpose
Stainless steels	10 $g(NH_4)S_2O_8$[(a)] 90 mL H_2O	Electrolytic 3–5 V, 1–3 min	General purpose
	60 mL HNO_3 40 mL H_2O	Electrolytic 1 V, 30–90 s	Shows grain boundaries in cold-worked material
	60 g KOH 100 mL H_2O	Electrolytic 1–3 V, 3–5 s	Reveals ferrite (blue) and sigma (red-brown); austenite not attacked
Cobalt alloys	10 $g(NH_4)S_2O_8$[(a)] 90 mL H_2O	Electrolytic 3–5 V, 5–10 s	Castings; not effective for wrought/forged material
	100 mL HCL 20 mL 3%	Etch immediately after polishing, immerse, and swab 2–4 min	Wrought/forged material

	H_2O_2		
Titanium and titanium alloys	10 mL HF 5 mL HNO_3 85 mL H_2O	Immerse 5–30 s	General purpose
	1 mL HF 200 mL H_2O	Immerse up to 5 s	Stains alpha phase, alpha case

(a) Ammonium persulfate

Figure 2 shows a typical unetched microstructure of 22Cr-13Ni-5Mn stainless steel alloy with small, dispersed inclusions in the microstructure. Figure 3 shows the same alloy electrolytically etched with an ammonium persulfate and water solution ($(NH_4)S_2O_8$ and H_2O) for approximately 1 min at 3 to 5 V. The very fine single-phase fcc microstructure is apparent. The recommended grain size for type 22Cr-13Ni-5Mn stainless steel for implant applications (ASTM F 1314) is ASTM No. 5 or finer when tested in accordance with ASTM E 112 for determining average grain size (Ref 10, 11). The same grain size restrictions apply to 316L stainless steel (ASTM F 138) and REX-734 (ASTM F 1586) (Ref 11). The grain size for these alloys should be relatively homogeneous throughout the specimen/device for uniform mechanical performance. The maximum corrosion resistance of these alloys is obtained when the carbon is in solution and there is a homogeneous single fcc phase microstructure. Proper heat treatments to obtain the optimal microstructures can be found in other references (Ref 6, Ref 7, 8).

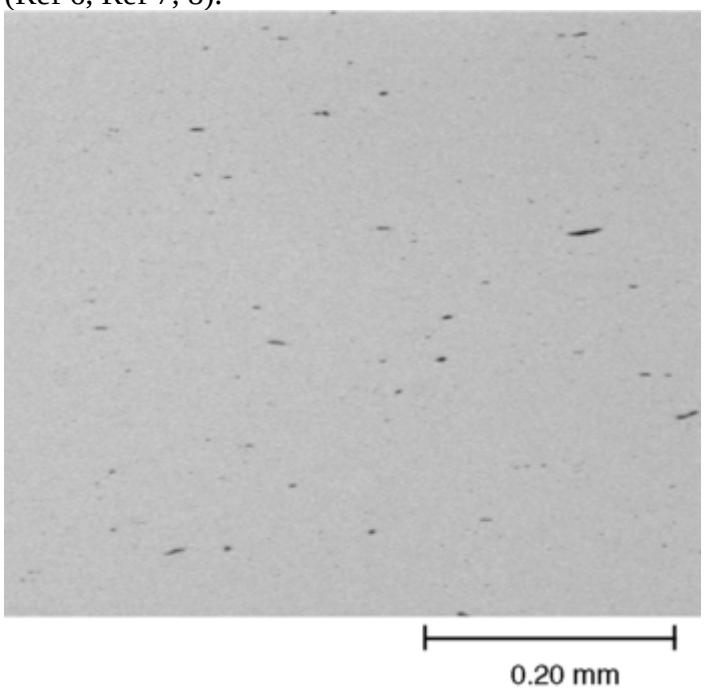

Fig. 2 A typical unetched microstructure of a 22Cr-13Ni-5Mn stainless steel alloy

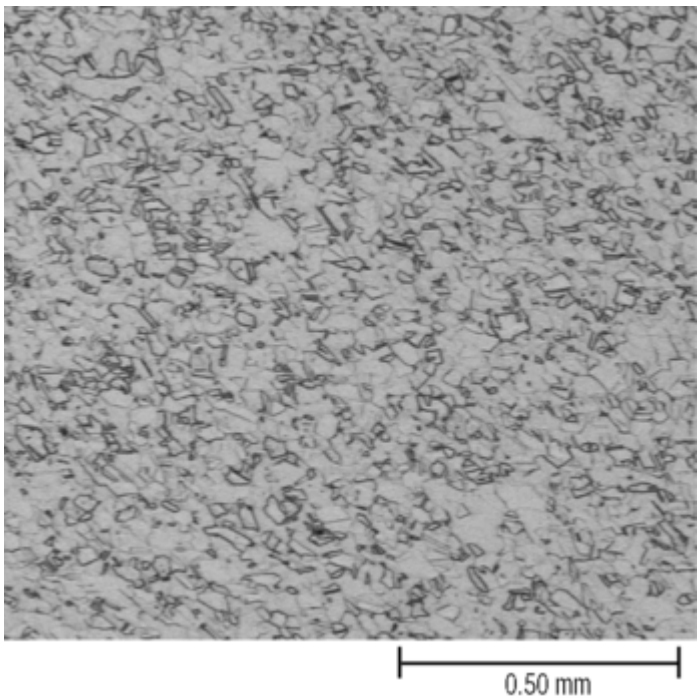

Fig. 3 A typical etched microstructure of a 22Cr-13Ni-5Mn stainless steel alloy. Electrolytically etched with a $(NH_4)S_2O_8$ and H_2O solution for approximately 1 min at 3–5 V

Austenitic stainless steels can be annealed for optimum ductility or cold worked to increase the yield and tensile strengths of the alloy. The fcc microstructure will readily plastically deform and twin when cold worked due to the multiple slip systems associated with this crystal structure. Figure 4 shows the dislocation structure and twin planes in a cold-worked 22Cr-13Ni-5Mn alloy. Figure 5 and Figure 6 compare the transverse and longitudinal orientations of a 316L sample after electrolytic etching in a nitric acid and water etchant at 1 V for approximately 1 min. The equiaxed grain shape of the transverse orientation (Fig. 5) is apparent when compared to the elongated grain structure of the longitudinal direction (Fig. 6).

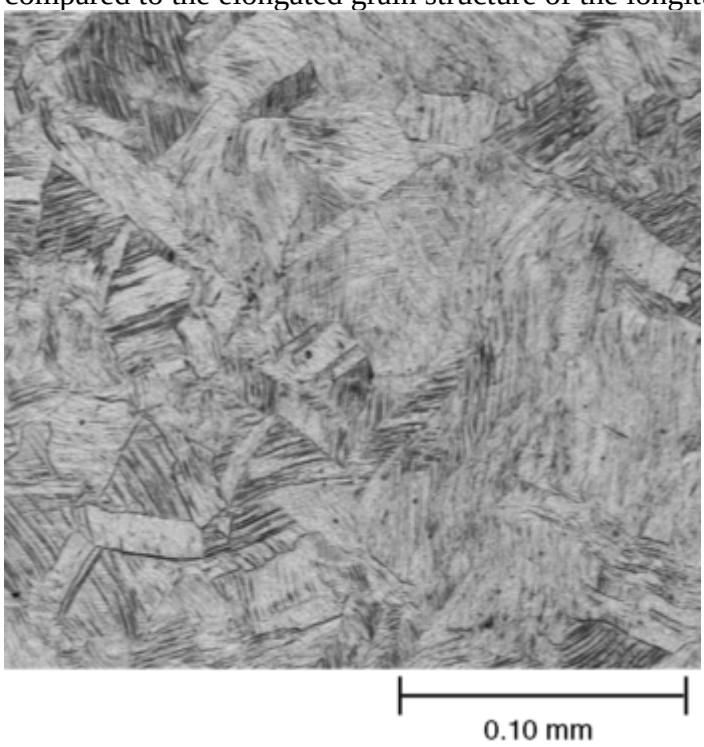

Fig. 4 The annealed and cold-worked microstructure of a 22Cr-13Ni-5Mn stainless steel alloy. Electrolytically etched with a $(NH_4)S_2O_8$ and H_2O solution for approximately 1 min at 3–5 V

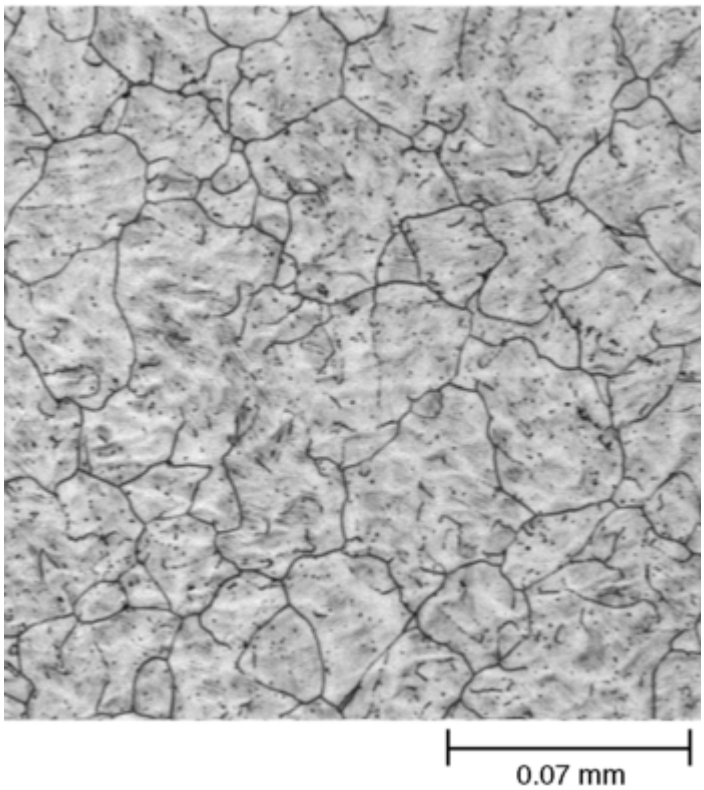

Fig. 5 A transverse view of a 316L stainless steel alloy showing the semispherical grain structure from a fracture fixation plate. Electrolytically etched in a nitric acid and water etchant at 1 V for approximately 1 min

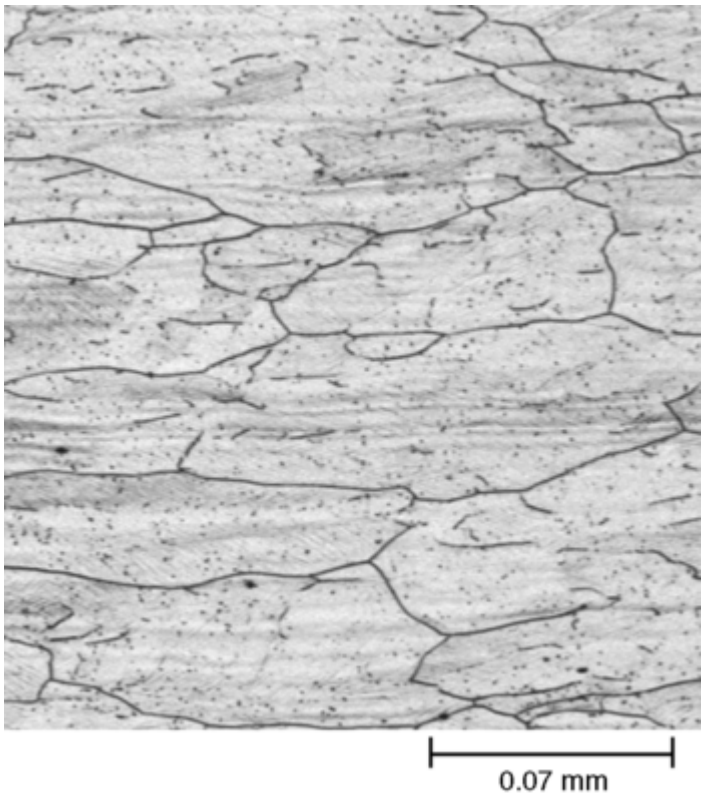

Fig. 6 A longitudinal view of a 316L stainless steel alloy showing the elongated grain structure from a fracture fixation plate. Electrolytically etched in a nitric acid and water etchant at 1 V for approximately 1 min

References cited in this section

2. C.R. Blanchard, D.J. Medlin, and R. Shetty, Advances in Metals, *Joint Replacements and Bone Resorption: Pathology and Clinical Practice,* Marcel Dekker, 2003

6. H. Chandler, Ed., *Heat Treater's Guide: Practices and Procedures for Irons and Steels,* ASM International, 1995

7. W.F. Smith, *Structures and Properties of Engineering Alloys,* 2nd ed., McGraw-Hill, 1993

8. *Properties and Selection: Irons, Steels, and High-Performance Alloys,* Vol 1, *ASM Handbook,* ASM International, 1990

9. "Standard Practice for Preparation of Metallographic Specimens," E 03-01, *Annual Book of ASTM Standards,* Vol 03.01, ASTM, 2003

10. "Standard Test Methods for Determining Average Grain Size," E 112–96, *Annual Book of ASTM Standards,* Vol 03.01, ASTM, 2003

11. *Annual Book of ASTM Standards,* Vol 13.01, ASTM, 2002

D.J. Medlin and R. Compton, Metallography of Biomedical Orthopedic Alloys, *Metallography and Microstructures,* Vol 9, *ASM Handbook,* ASM International, 2004, p. 961–968

Metallography of Biomedical Orthopedic Alloys

D.J. Medlin and R. Compton, Zimmer, Inc.

Cobalt-Base Alloys

The initial medical use of cobalt-base alloys was in the dental field (Ref 12). The successful application of these alloys in the very corrosive, high-impact, wear environment of the mouth was very attractive to orthopedic surgeons. Early evaluations of these alloys showed excellent wear resistance, corrosion resistance, biocompatibility, and mechanical properties when used in vivo as orthopedic implants (Ref 2, 3, 4). Early use of this alloy was limited to cast components; however, high-strength forged products with increased ductility were soon developed. The ability of this metal to work harden and experience transformation-induced plasticity made it very difficult to machine and limited its application as an implant metal (Ref 2). Eventually, successful machining techniques and machine tools were developed that made routine drilling and milling operations feasible. Today, cobalt-based alloys are a standard implant alloy in orthopedic applications and have an excellent history of successful implantation inside the human body.

The most common Co-Cr-Mo alloys in use today are the cast grade (ASTM F 75), the forged grade (ASTM F 799), and the wrought grade (ASTM F 1537), as shown in Table 4 (Ref 11). The main strengthening mechanism in the cast alloy is second-phase carbide precipitation, and the wrought alloy has additional solid-solution strengthening from the addition of nitrogen (Ref 2, 3, 4, 12). These alloys typically contain approximately 30% Cr and around 6% Mo, and cobalt forms solid solutions with these elements. The high corrosion resistance of these alloys is due to the formation of a thin chromium-oxide layer on the surface, similar to stainless steel. Other cobalt-base alloys that are less popular include wrought Co-Cr-W-Ni (L-605) and wrought Co-Ni-Cr-Mo (MP-35N), also shown in Table 4 (Ref 2).

Table 4 Nominal compositions of cobalt-base alloys for medical implant applications

ASTM designation	ISO designation	Trade-name	Alloy group and condition	Composition, wt%												
				Co	**Cr**	**Mo**	**W**	**C**	**Ni**	**Fe**	**Si**	**Mn**	**N**	**S**	**Ti**	**P**
F 75	5832–4	Haynes Stellite 21	Co/Cr/Mo castings	bal	27.00–30.00	5.00–7.00	0.20 max	0.35 max	1.00 max	0.75 max	1.00 max	1.00 max	0.25 max	0.01 max	…	0.02 max
F 799	…	Haynes Stellite 21	Co/Cr/Mo forgings	bal	26.00–30.00	5.00–7.00	…	0.35 max	1.00 max	0.75 max	1.00 max	1.00 max	0.25 max	…	…	…
F 1537	1532–12	Haynes Stellite 21	Co/Cr/Mo wrought	bal	26.00–30.00	5.00–7.00	…	0.35 max	1.00 max	0.75 max	1.00 max	1.00 max	0.25 max	…	…	…
F 90	5832–5	Haynes Stellite 21 L605	Co/Cr/W/Ni wrought	bal	19.00–21.00	…	14.00–16.00	0.05–0.15	9.00–11.00	3.00 max	0.40 max	1.00–2.00	…	0.03 max	…	0.04 max
F 562	5832–6	MP35N	Co/Ni/Cr/Mo wrought	bal	19.00–21.00	9.00–10.50	…	0.025 max	33.00–37.00	1.00 max	0.15 max	0.15 max	0.15 max	0.01 max	1.00 max	0.015 max
F 563	5832–8	…	Co/Ni/Cr/Mo/W/Fe wrought	bal	18.00–22.00	3.00–4.00	3.00–4.00	0.05 max	15.00–25.00	4.00–6.00	0.5 max	1.00 max	0.25 max	0.01 max	0.50–3.50	…

Metallographic sample preparation of these alloys can be accomplished with traditional cutting, mounting, and polishing techniques, as described in Table 2. Electrolytic etching is the best method to reveal the microstructure of the cast alloy, while standard chemical etching gives the most uniform microstructural contrast for the wrought alloys. The ammonium persulfate and water etchant, $(NH_4)S_2O_8$ and H_2O, listed in Table 3, is a good general-purpose electrolytic etchant when used at 3 to 5 V for 5 to 10 s on cast Co/Cr alloys. This electrolytic etching process is not as effective on wrought and forged alloys. Wrought and forged Co/Cr alloys are more effectively etched with a hydrochloric acid and peroxide (HCl and H_2O_2) etchant by immersing or swabbing the sample immediately after polishing. Delays between polishing and etching can cause nonuniform etching and/or ineffective etching. Similar to stainless steels, the good corrosion resistance of these alloys allows metallographic sample storage without the need for desiccant materials.

A typical microstructure from an as-cast Co/Cr/Mo alloy is shown in Fig. 7 after being electrolytically etched in ammonium persulfate and water. The large $M_{23}C_6$ interdendritic primary carbides are apparent in the microstructure of an fcc Co/Cr/Mo solid-solution matrix. In addition, the large grain size of the cast structure is also visible. The size and distribution of these primary carbides are a function of alloy and carbon content, metal pouring temperature, section thickness (cooling rate), and mold preheat temperature (Ref 12). The nominal mechanical properties of as-cast Co/Cr/Mo alloys can be improved by hot isostatic pressing (HIP) and annealing, as shown in Fig. 8. The HIP process reduces the solidification porosity and decohesion present between the carbides and the matrix material that are inherent with cast microstructures, and this significantly reduces fatigue cracking that could initiate from these sites (Ref 2, 12).

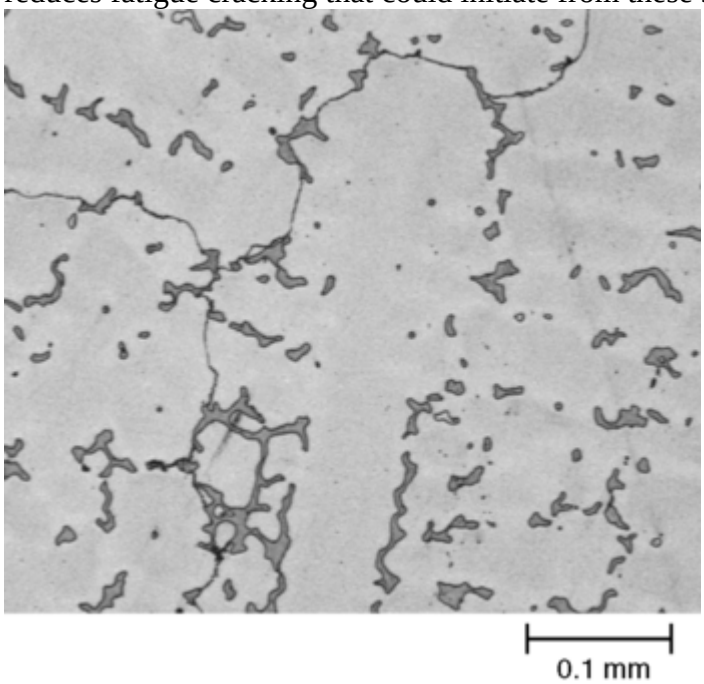

Fig. 7 The as-cast microstructure of a Co/Cr/Mo alloy electrolytically etched with an ammonium persulfate and water solution ($(NH_4)S_2O_8$ and H_2O) at 3–5 V for 5–10 s

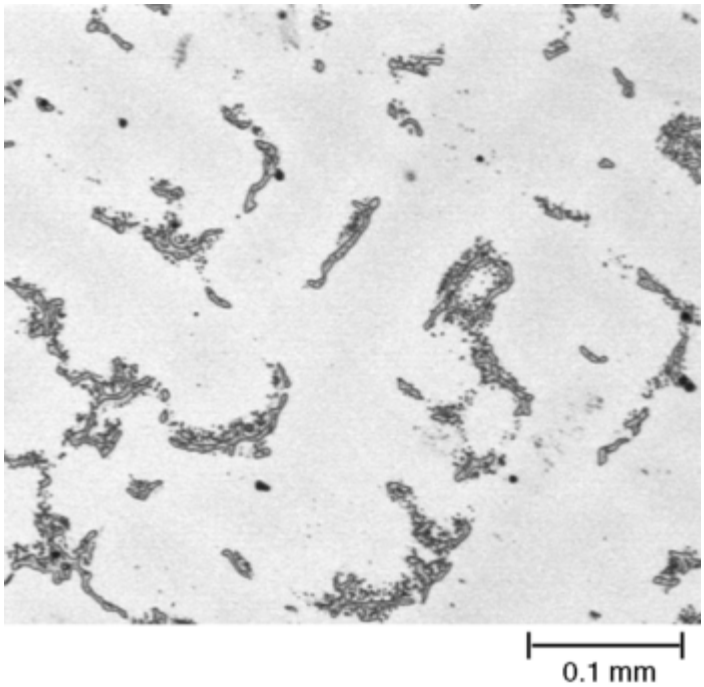

Fig. 8 The as-cast microstructure of a hot isostatically pressed and solution annealed Co/Cr/Mo alloy electrolytically etched with an ammonium persulfate and water solution ($(NH_4)S_2O_8$ and H_2O) at 3–5 V for 5–10 s

A typical etched microstructure of a wrought Co/Cr/Mo alloy is shown in Fig. 9. The ability of this alloy to work harden is apparent by the dark etching dislocation structures within the grains. Previous research has shown that increased hardness and strength of the wrought and forged alloys can be obtained by increasing the carbon content to form very fine dispersed carbides throughout the microstructure. Figure 10 shows the very hard and fine carbides scattered across the microstructure that increase strength by impeding dislocation motion when the material is stressed. Further increases in mechanical properties, particularly fatigue strength, are obtained by making the alloys with powder metallurgy (P/M) processing (Ref 13). The consolidated metal powders maintain a very fine grain structure after processing, as shown in Fig. 11.

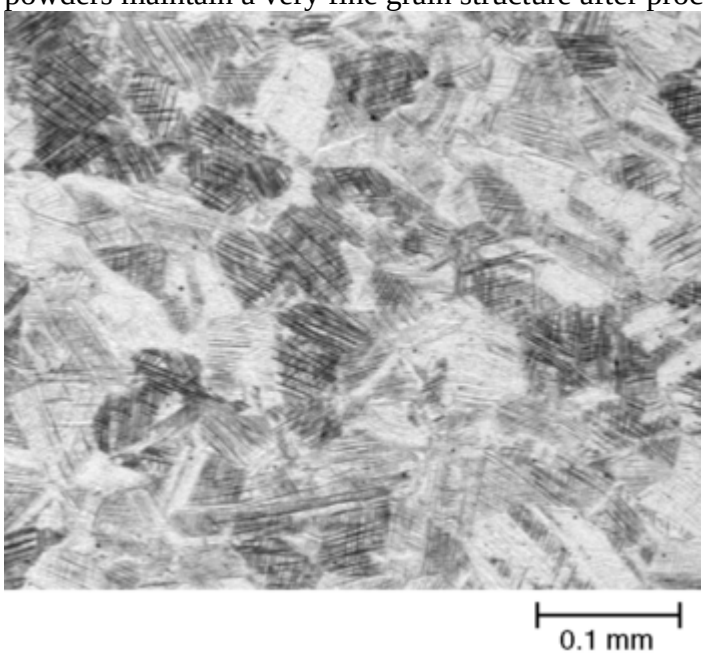

Fig. 9 The typical microstructure of a wrought Co/Cr/Mo alloy etched with a hydrochloric acid and peroxide solution

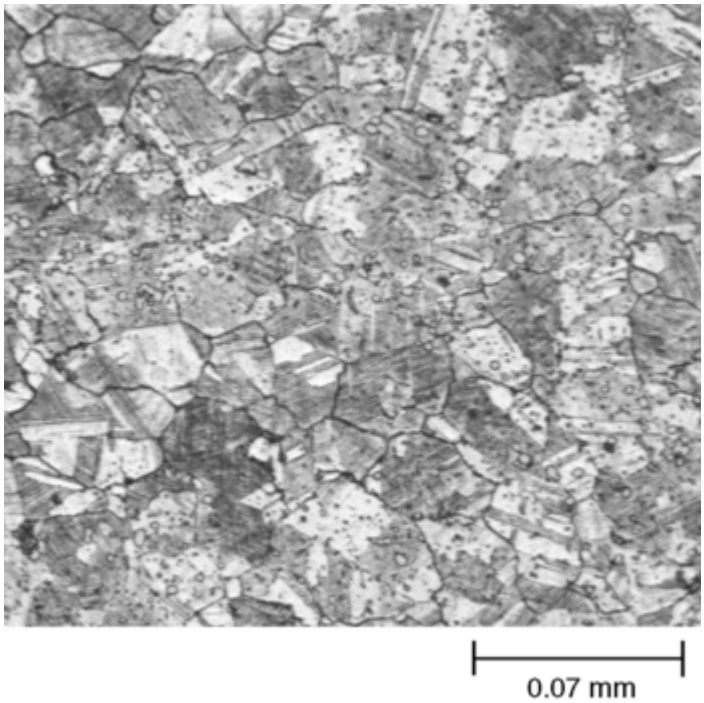

Fig. 10 The etched microstructure of a wrought/forged high-carbon Co/Cr/Mo alloy etched with a hydrochloric acid and peroxide solution. The very fine and evenly dispersed carbides can be seen throughout the microstructure.

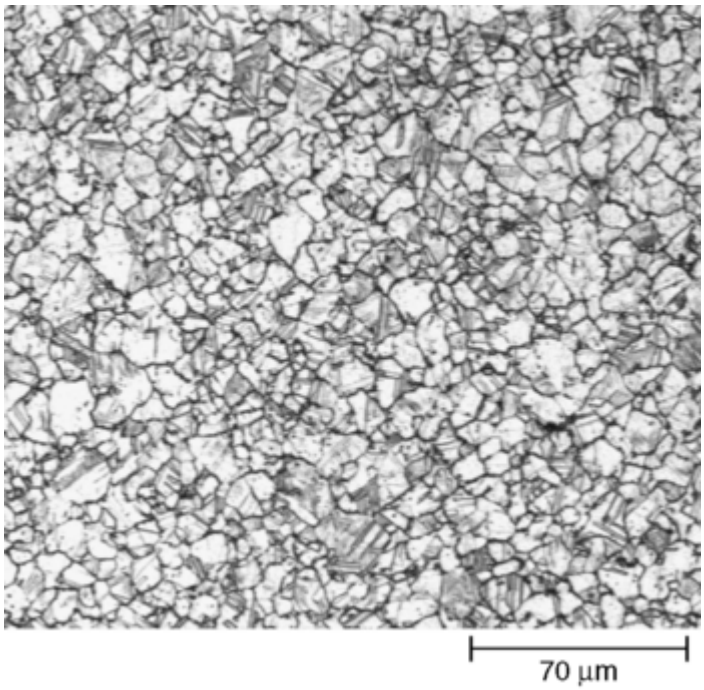

Fig. 11 A Co/Cr/Mo alloy that was originally processed from powder metallurgy (P/M) to form a very fine grain size. Etched with a hydrochloric acid and peroxide solution

References cited in this section

2. C.R. Blanchard, D.J. Medlin, and R. Shetty, Advances in Metals, *Joint Replacements and Bone Resorption: Pathology and Clinical Practice,* Marcel Dekker, 2003

3. D.C. Mears, *Materials and Orthopaedic Surgery,* Williams and Wilkens Co., 1979, p 1–28

4. J. Black, *Orthopaedic Biomaterials in Research and Practice,* Churchhill Livingstone, 1988

11. *Annual Book of ASTM Standards,* Vol 13.01, ASTM, 2002

12. P.J. Anderson, Medical and Dental Applications, *Powder Metallurgy,* Vol 7, *ASM Handbook,* ASM International, 1984, p 657–663

13. *Powder Metal Technologies and Applications,* Vol 7, *ASM Handbook,* 1998

D.J. Medlin and R. Compton, Metallography of Biomedical Orthopedic Alloys, *Metallography and Microstructures,* Vol 9, *ASM Handbook,* ASM International, 2004, p. 961–968

Metallography of Biomedical Orthopedic Alloys

D.J. Medlin and R. Compton, Zimmer, Inc.

Titanium and Titanium Alloys

Commercially pure (CP) titanium and titanium alloys are a relatively new group of materials used for medical devices when compared to stainless steels and cobalt-chromium alloys. The high strength-to-weight ratio and excellent corrosion resistance exhibited by these alloys led to years of government-sponsored research for aerospace applications. The utilization of these alloys in the medical field transpired quickly during the 1970s due to the vast amount of aerospace research data available and the unique properties such as corrosion resistance, low density, high strength, good ductility, biocompatibility, and lower modulus when compared to stainless steel and cobalt-chromium alloys (Ref 14, 15, 16). The outstanding corrosion resistance of titanium alloys is attributed to the formation of a thin, adherent, surface-oxide film (TiO) that is chemically resistant, especially in saline environments (Ref 14).

Four grades of CP titanium are used for implant devices; two of these grades are shown in Table 5. These alloys are classified according to their interstitial contents that included oxygen, nitrogen, and iron. Grade 1 has the lowest interstitial content and, subsequently, the lowest mechanical properties. Higher interstitial contents result in increased strength. Among all the titanium alloys, Ti-6Al-4V-ELI has been the most widely used alloy in the medical device industry largely due to its acceptable properties and convenient availability because of its extensive use in the aerospace industry. The “ELI” designation signifies the additional chemistry requirement for extra-low interstitials. Other alloys that are used to a lesser extent include Ti-3Al-2.5V, Ti-5Al-2.5Fe, and Ti-6Al-7Nb (Ref 14).

Table 5 Nominal compositions of titanium-base alloys for medical implant applications

ASTM designation	ISO designation	Alloy group and condition	Composition, wt%										
			Ti	**Al**	**V**	**Nb**	**O**	**N**	**C**	**H**	**Fe**	**Ta**	**Zr**
F 67	5832–2	CP Ti wrought grade 1	bal	…	…	…	0.18 max	0.03 max	0.08 max	0.015 max	0.20 max	…	…
F 136	5832–3	Ti-6A1-4V ELI wrought	bal	5.50–6.50	3.50–4.50	…	0.13 max	0.05 max	0.08 max	0.012 max	0.25 max	…	…
F 1108	…	Ti-6Al-4V casting	bal	5.50–6.75	3.50–4.50	…	0.20 max	0.05 max	0.10 max	0.015 max	0.30 max	…	…
F 1295	5832–11	Ti-6Al-7Nb	bal	5.50–6.50	…	6.50–7.50	0.20 max	0.05 max	0.08 max	0.009 max	0.25 max	0.50 max	…
F 1713	…	Ti-13Nb-13Zr wrought	bal	…	…	12.50–14.00	0.15 max	0.05 max	0.08 max	0.012 max	0.25 max	…	12.50–14.00

Titanium alloys are used in the cast, wrought, and forged conditions. The investment casting method has been widely used to produce complex shapes such as femoral knee components (Ref 12). Special process controls must be used when casting titanium due to its high reactivity with oxygen, and other references discuss these processing restrictions (Ref 14, 15, 16).

Titanium alloys typically have either a hexagonally close-packed (hcp) phase (alpha), a body-centered cubic (bcc) phase (beta), or a combination of both phases. The relative amounts of these two phases and their phase morphology in the alloy are usually determined by chemistry and thermomechanical treatments. For example, the addition of aluminum to the Ti-6Al-4V alloy stabilizes the alpha phase and the vanadium stabilizes the beta phase. More details concerning the thermomechanical treatments and chemistry effects are available in other references (Ref 7, 14, 15).

Metallographic specimen preparation of these alloys can be accomplished with traditional cutting, mounting, and polishing techniques, as described in Table 2. Etchants containing hydrofluoric acid (HF) are best for revealing the microstructure of the cast and wrought alloys; however, care must be taken when using HF-containing solutions because of the potential for serious acid burns. Several solutions that contain hydrofluoric acid, nitric acid, and water make good general-purpose etchants for CP titanium and titanium alloys when the samples are immersed or swabbed with the mixtures. Two of the more useful etchants are listed in Table 3. As with the two previous alloys systems, the good corrosion resistance of titanium alloys allows metallographic sample storage without the need for desiccant materials.

Figure 12 shows a forged and annealed microstructure from a Ti-6Al-4V-ELI specimen showing a fine-grained alpha matrix (white) with a fine dispersion of intergranular beta phase (dark). The forging process creates a fine equiaxed microstructure when compared to cast structures. This specimen was etched with a hrdrofluoric acid, nitric acid, and water solution. Figure 13 shows the cast and annealed microstructure of a Ti-6Al-4V alloy in which large prior beta grain boundaries are evident (white). Each grain is characterized by a transformed alpha-beta microstructure in the basketweave (acicular) appearance. The thin alpha phase present along the prior beta grain boundary is thought to reduce the mechanical performance when compared to the same alloy in the wrought and forged conditions (Ref 14). Figure 14 shows a higher-magnification image of the transformed alpha-beta (acicular) microstructure within each grain. Figure 15 shows a Widmanstätten microstructure from a forged alloy that has experienced a different thermomechanical treatment than the sample shown in Fig. 12. A typical microstructure from a wrought commercially pure titanium wire shows an equiaxed alpha structure due to the very low amount of beta stabilizers in the alloy (see Fig. 16).

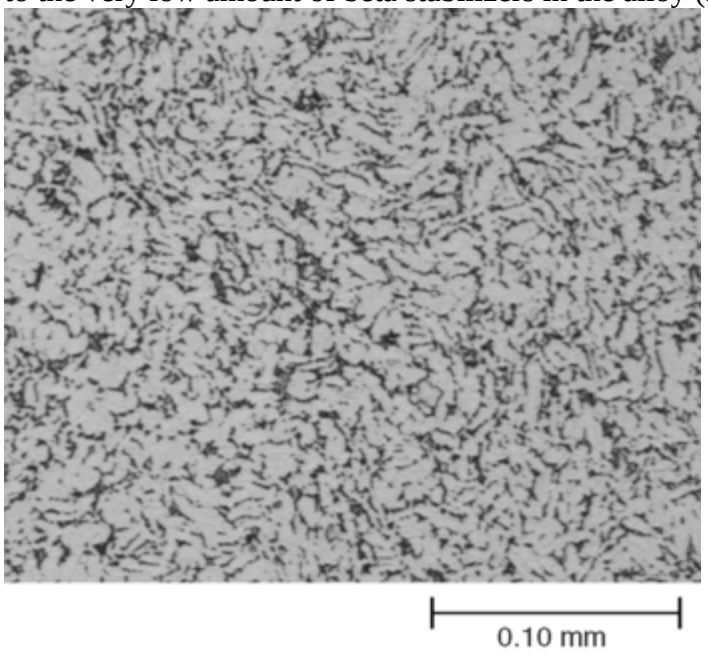

Fig. 12 The forged and annealed microstructure of a Ti-6Al-4V-ELI alloy showing a fine-grained alpha-matrix (white) with a fine dispersion of intergranular beta-phase (dark). Etched with a hydrofluoric acid, nitric acid, and water solution

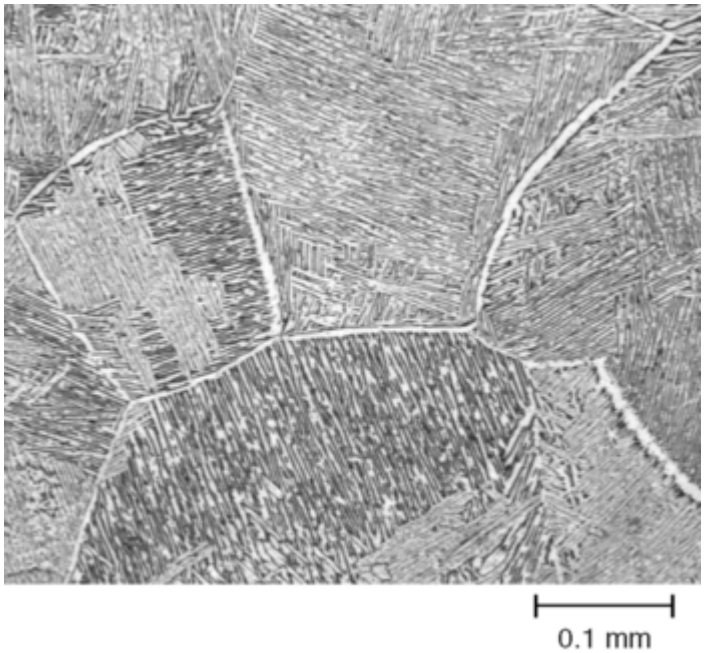

Fig. 13 The as-cast microstructure of a Ti-6Al-4V alloy showing the very large grain structure typical of cast metals. Etched with a hydrofluoric acid, nitric acid, and water solution (Table 3)

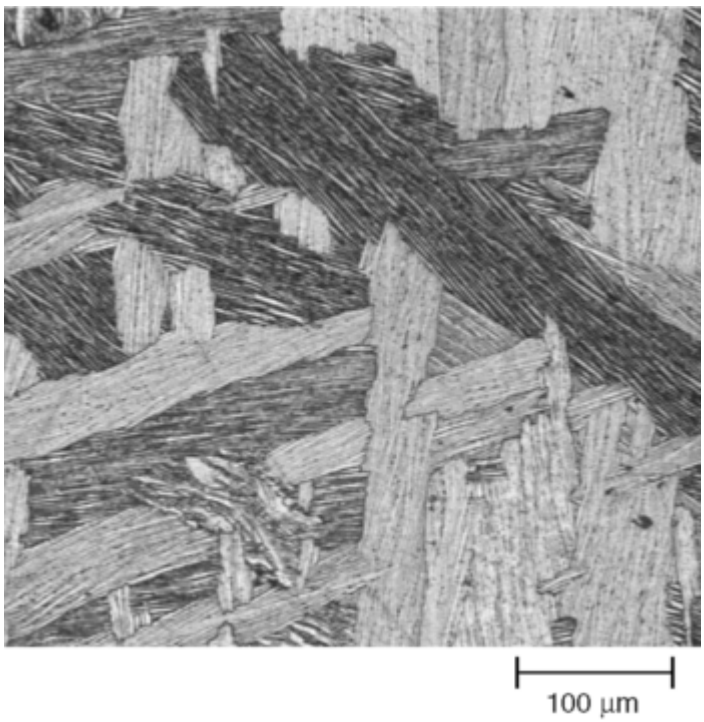

Fig. 14 A higher magnification of the basketweave (acicular) microstructure from a cast and annealed Ti-6Al-4V alloy. Etched with hydrofluoric acid, nitric acid, and water solution (Table 3)

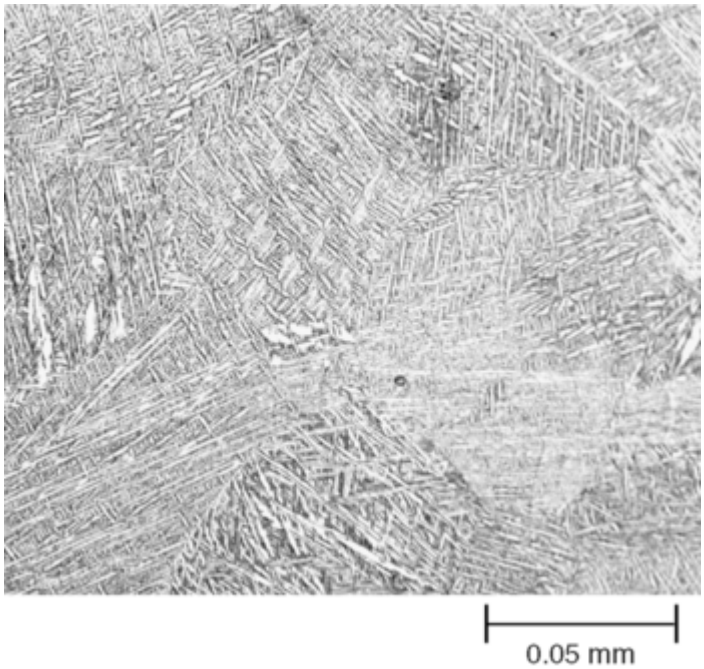

Fig. 15 A Widmanstätten (acicular alpha-beta) microstructure of a Ti-6Al-4V-ELI alloy etched with a hydrofluoric acid, nitric acid, and water solution (Table 3)

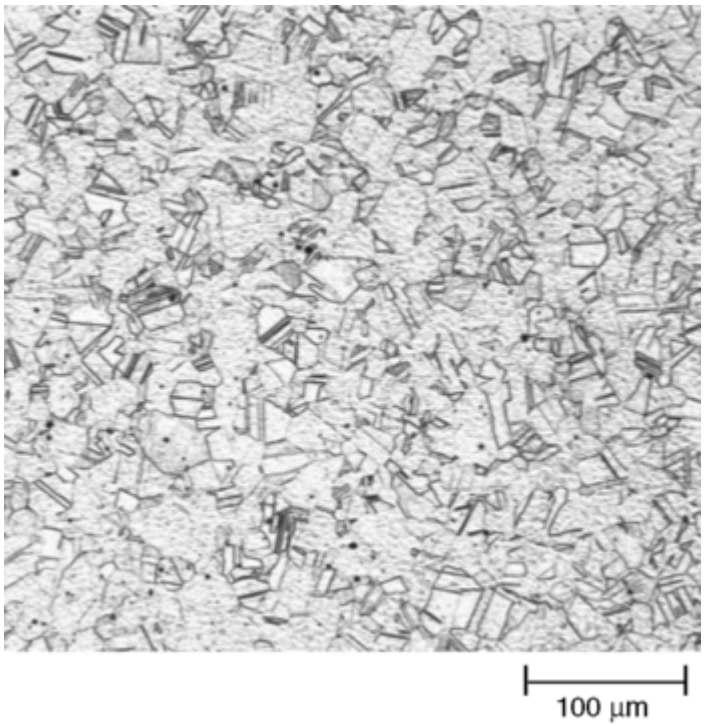

Fig. 16 An equiaxed alpha microstructure of wrought commercially pure titanium wire etched with a hydrofluoric acid, nitric acid, and water solution (Table 3)

References cited in this section

7. W.F. Smith, *Structures and Properties of Engineering Alloys*, 2nd ed., McGraw-Hill, 1993

12. P.J. Anderson, Medical and Dental Applications, *Powder Metallurgy,* Vol 7, *ASM Handbook,* ASM International, 1984, p 657–663

14. M.J. Donachie, *Titanium: A Technical Guide,* 2nd ed., ASM International, 2000

15. *Properties and Selection: Nonferrous Alloys and Special-Purpose Materials,* Vol 2, *ASM Handbook,* ASM International, 1990

16. B.D. Ratner, A.S. Hoffman, F.J. Schoen, and J.E. Lemons, *Biomaterials Science: An Introduction to Materials in Medicine,* Academic Press, 1996, p 37–50

D.J. Medlin and R. Compton, Metallography of Biomedical Orthopedic Alloys, *Metallography and Microstructures,* Vol 9, *ASM Handbook,* ASM International, 2004, p. 961–968

Metallography of Biomedical Orthopedic Alloys

D.J. Medlin and R. Compton, Zimmer, Inc.

Porous Coatings

The two general methods for implanting total joint arthroplasty devices are cementation and biologic fixation (Ref 1, 3, 4, 16). In the cementation method, bone cement (polymethyl methacrylate, or PMMA) is used as a grout to provide mechanical fixation between the cancellous bone structure and the small surface irregularities on the surface of the implant. The potential for decohesion among implant/cement/bone interfaces can lead to loosening of the implant and subsequent revision surgeries. For biologic fixation, porous coated implant devices are seated into the mechanically formed cavity of the bone with initial fixation accomplished by the interference fit between the bone cavity and the device. Long-term fixation is accomplished by bone in-growth into, or on-growth onto, the porous coating of the device. The porous coatings on the surface of the device range in porosity from 25 to 50%, depending on the type of coating and the manufacturing process (Ref 2). After implantation, bone tissues grow into the porous coating over a period of weeks/months, depending on the health of the patient, and achieve a biological attachment between the implant and bone (Ref 1, 3, 4, 16). The four general types of porous coatings include fiber metal, sintered beads, plasma spray, and calcium phosphate ceramic coatings.

Fiber metal coatings are made from randomly oriented titanium or Co/Cr/Mo wires that are mechanically pressed into a blanket (pad) and diffusion bonded to the surface of a device. Diffusion bonding involves elevated temperature, applied pressure, and time at temperature to form a solid-state metallurgical bond between the metallic fibers and the surface of the device. Depending on the wire diameter and processing variables, the porosity of the fiber metal coatings range from 35 to 50%. Figure 17 shows a scanning electron micrograph (SEM) image of a commercially pure titanium fiber metal coating on the surface of a hip implant. The random nature of the wire structure is evident, and this leads to the overall mechanical strength of the coating. Figure 18 shows the metallurgical bonding between the metallic wires and the titanium substrate on a transverse cross sectional sample.

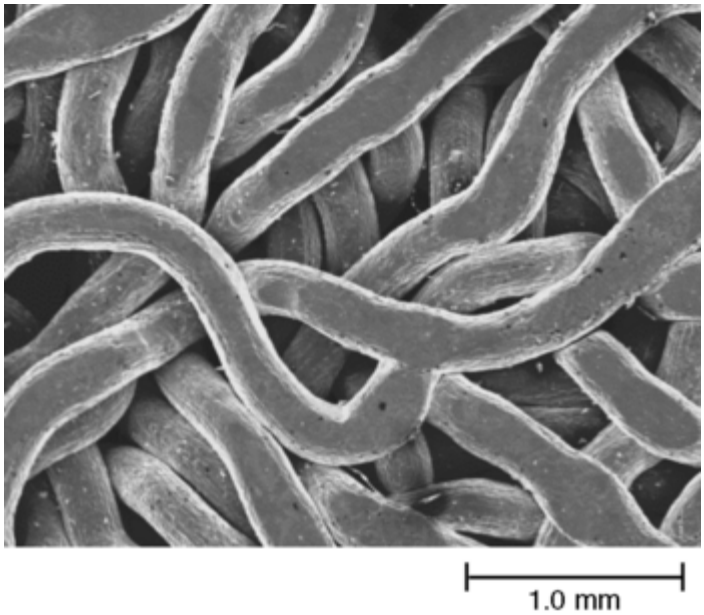

Fig. 17 A scanning electron microscope image of a commercially pure titanium fiber metal pad on the surface of a porous coated hip implant

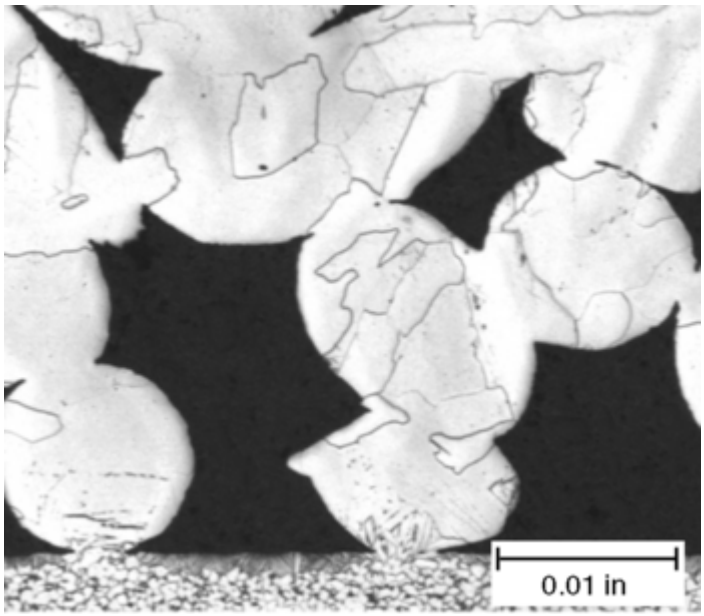

Fig. 18 A transverse view of a titanium fiber metal pad (commercially pure titanium) attached to a titanium hip implant (Ti-6Al-4V) showing the metallurgical bonds between the titanium wires and the substrate

Bead coatings are manufactured by attaching multiple layers of fine metallic beads made of titanium or Co/Cr/Mo to the surface of a substrate with a suitable binder and sintering the coated component to 90 to 95% of the substrate melting point. The binder is vaporized at these temperatures, the beads partially melt, and metallurgical bonds form between the beads and the substrate due to surface tension effects. After cooling, porous bead coatings typically have porosities ranging from 40 to 50%, depending on initial bead size and processing variables (Ref 2). In order to avoid the detrimental issues associated with intermetallic compounds, titanium beads are attached to titanium substrates and Co/Cr/Mo beads are attached to Co/Cr/Mo substrates. Figure 19 shows an SEM image of a porous beaded layer sintered to the surface of an orthopedic device. Figure 20 is a cross-sectional view showing the interface between the Co/Cr/Mo bead layer and the Co/Cr/Mo substrate. The partial melting, or necking, between the beads and the substrate can be seen.

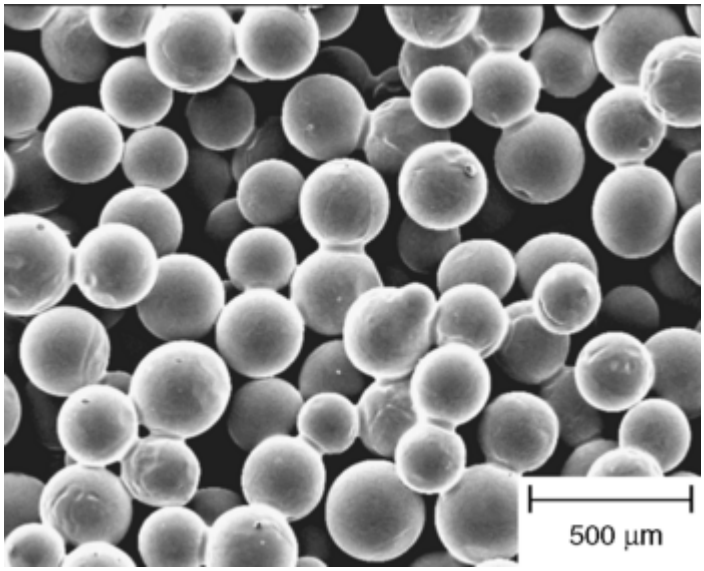

Fig. 19 A scanning electron microscope image of a sintered Co/Cr/Mo bead layer on the surface of a Co/Cr/Mo orthopedic implant device

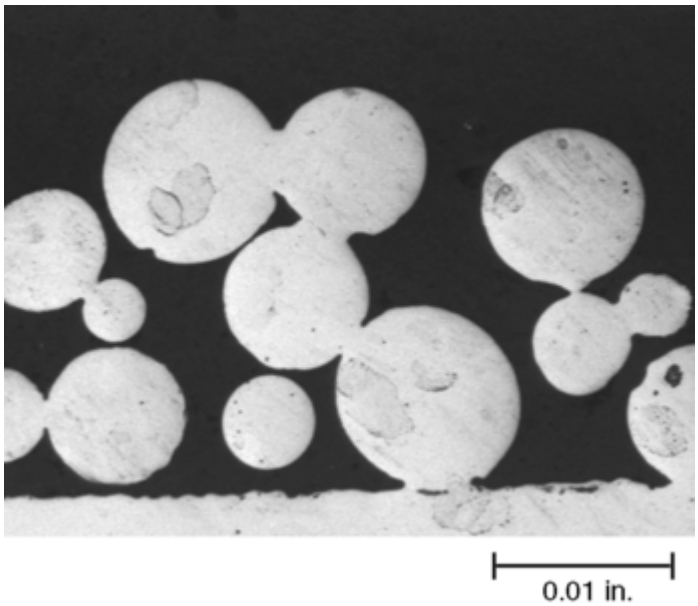

Fig. 20 A cross-sectional view of the interface between the Co/Cr/Mo bead layer and the Co/Cr/Mo substrate

Plasma spray coatings are manufactured by spraying a molten metal onto the surface of a metallic substrate causing the molten metal coating to instantaneously solidify and form a porous coating (Ref 1, 2, 4, 5). An electric arc ionizes a nonreactive gas forming a high-temperature plasma. Fine metallic powders are sprayed through the ionized plasma forming the molten metal spray. The plasma coatings attached to orthopedic implants are generally CP titanium and Ti-6Al-4V-ELI. The porosity of the coatings range from 25 to 35% depending on process variables such as plasma temperature, substrate temperature, plasma volume, metallic particle size, multiple spray layers, and so forth (Ref 14). Even though the porosity of the plasma spray layer is not as high as other porous coatings intended for bone in-growth, the rough surface is thought to have significant bone on-growth capabilities. Figure 21 shows an SEM image of a CP titanium plasma spray coating on the surface of a Ti-6Al-4V-ELI orthopedic implant device.

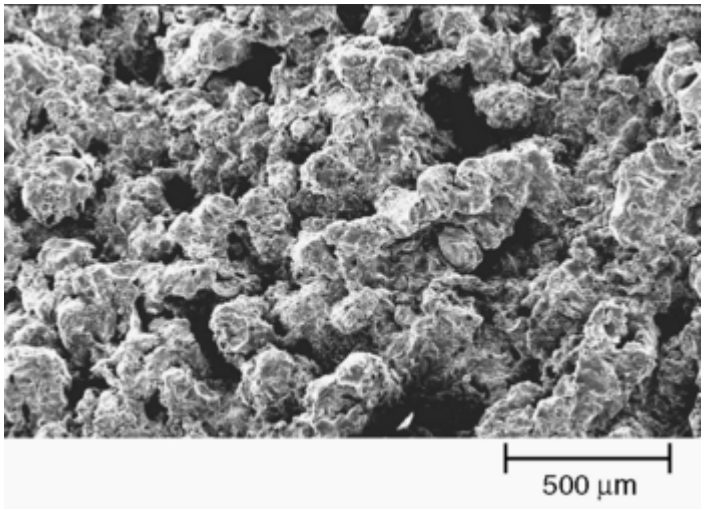

Fig. 21 A scanning electron microscope image of a commercially pure titanium plasma spray coating on the surface of a Ti-6Al-4V orthopedic device

References cited in this section

1. J.R. Davis, Ed., *Handbook of Materials for Medical Devices,* ASM International, 2003

2. C.R. Blanchard, D.J. Medlin, and R. Shetty, Advances in Metals, *Joint Replacements and Bone Resorption: Pathology and Clinical Practice,* Marcel Dekker, 2003

3. D.C. Mears, *Materials and Orthopaedic Surgery,* Williams and Wilkens Co., 1979, p 1–28

4. J. Black, *Orthopaedic Biomaterials in Research and Practice,* Churchhill Livingstone, 1988

5. D.J. Wise, D.J. Trantolo, and D.E. Altobelli, *Encyclopedic Handbook of Biomaterials and Bioengineering, Part-B: Applications,* Marcel-Dekker, 1995, p 509–539

14. M.J. Donachie, *Titanium: A Technical Guide,* 2nd ed., ASM International, 2000

16. B.D. Ratner, A.S. Hoffman, F.J. Schoen, and J.E. Lemons, *Biomaterials Science: An Introduction to Materials in Medicine,* Academic Press, 1996, p 37–50

D.J. Medlin and R. Compton, Metallography of Biomedical Orthopedic Alloys, *Metallography and Microstructures,* Vol 9, *ASM Handbook,* ASM International, 2004, p. 961–968

Metallography of Biomedical Orthopedic Alloys

D.J. Medlin and R. Compton, Zimmer, Inc.

Emerging Materials

Oxidized zirconium is a relatively new orthopedic material for implant applications and has shown increased use in components that need substantial wear resistance against polyethylene liners in total knee and hip assemblies (Fig. 1) (Ref 17). Historically, zirconium has not been used to manufacture implant devices due to its inferior mechanical properties when compared to titanium alloys, stainless steels, and cobalt alloys.

However, the addition of 2.5% Nb and controlled amounts of oxygen increase the properties, particularly ductility, of this material, making it suitable for some orthopedic applications. When the surface of the Zr-2.5Nb alloy is oxidized to form a thin zirconium-oxide ceramic surface coating, the wear resistance of the UHMWPE liner oscillating against the ceramic surface may be improved, while the brittle nature of a fully ceramic (oxide) component is avoided. The oxidized-zirconium alloy has been in clinical use since 2001 for knee and hip applications (Ref 2).

Trabecular metal is a three-dimensional, open-celled, porous metallic foam made primarily from tantalum (Ref 2). This metallic foam material is named after trabecular bone due to their similarities in structure and appearance. Figure 22 shows an SEM image of trabecular bone, and Fig. 23 shows an image of trabecular metal. Trabecular metal has two unique characteristics that distinguish it from other porous materials. First, it has a porosity of 75 to 85%, which is substantially higher than other porous coatings historically used for implants. This high porosity has been reported to have excellent bone in-growth characteristics that have resulted in high bone/implant interface strengths. Secondly, the modulus of elasticity is similar to bone tissues and this significantly reduces the potential risk associated with stress shielding (Ref 2, 4, 5). Trabecular metal has been in clinical use since 1995 for acetabular cups, tibial knee components, patella components, spinal devices, and more recently for soft tissue in-growth applications (Ref 2, 18).

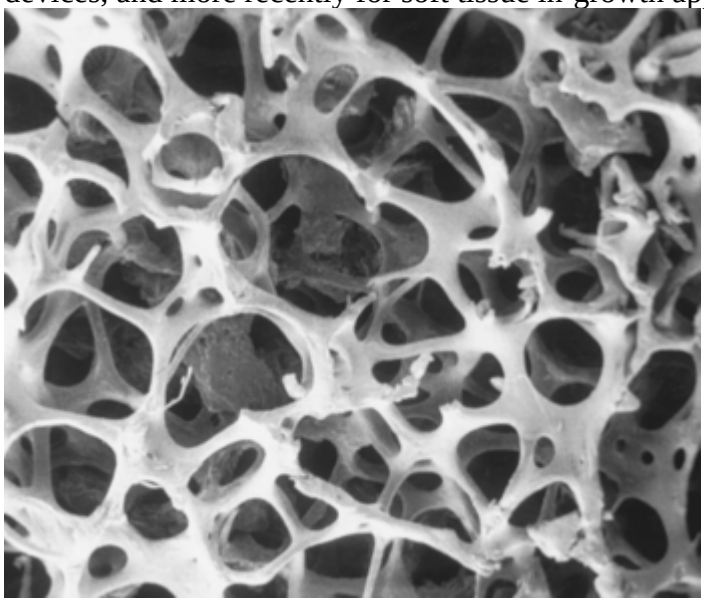

Fig. 22 A scanning electron microscope image showing the natural structure of trabecular bone. Source: Ref 18

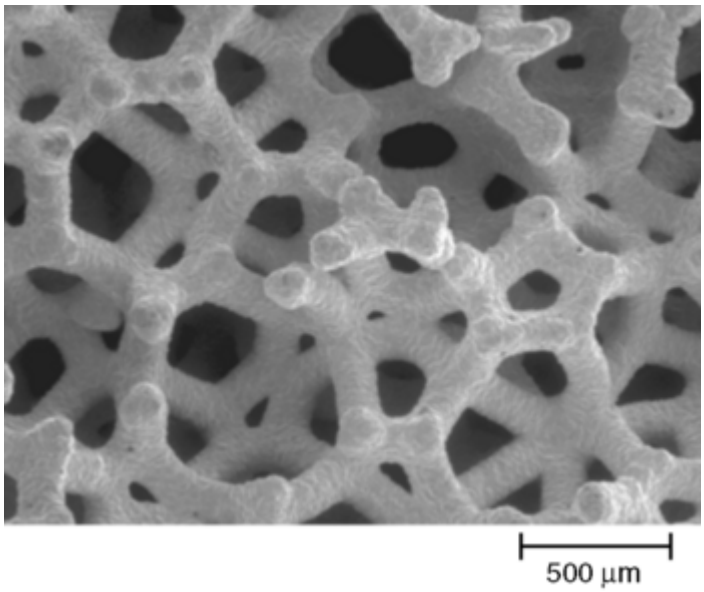

Fig. 23 A scanning electron microscope image of an open-celled, porous, tantalum foam called trabecular metal

References cited in this section

2. C.R. Blanchard, D.J. Medlin, and R. Shetty, Advances in Metals, *Joint Replacements and Bone Resorption: Pathology and Clinical Practice,* Marcel Dekker, 2003

4. J. Black, *Orthopaedic Biomaterials in Research and Practice,* Churchhill Livingstone, 1988

5. D.J. Wise, D.J. Trantolo, and D.E. Altobelli, *Encyclopedic Handbook of Biomaterials and Bioengineering, Part-B: Applications,* Marcel-Dekker, 1995, p 509–539

17. B.M. Spector, M.D. Reis, R.B. Bourne, W.A. Sauer, M. Long, and G. Hunter, Wear Performance of UHMWPE on Oxidized Zirconium Total Knee Femoral Components, *J. Bone Joint Surg.,* American Vol 83, 2001, p 80–86

18. D.J. Medlin, Processing Microstructure and Performance of Metallic Orthopaedic Medical Devices, *Proc. Microscopy and Microanalysis 2003,* D. Piston, J. Bruley, I.M. Anderson, and P. Kotula, Ed., Vol 9, Suppl. 2, Cambridge Press, 2003, p 542

D.J. Medlin and R. Compton, Metallography of Biomedical Orthopedic Alloys, *Metallography and Microstructures,* Vol 9, *ASM Handbook,* ASM International, 2004, p. 961–968

Acknowledgment

The authors would like to thank Katy Rettig, John Perkins, Kim England, and Jack Moon for their assistance with the manuscript.

D.J. Medlin and R. Compton, Metallography of Biomedical Orthopedic Alloys, *Metallography and Microstructures,* Vol 9, *ASM Handbook,* ASM International, 2004, p. 961–968

Metallography of Biomedical Orthopedic Alloys

D.J. Medlin and R. Compton, Zimmer, Inc.

References

1. J.R. Davis, Ed., *Handbook of Materials for Medical Devices,* ASM International, 2003

2. C.R. Blanchard, D.J. Medlin, and R. Shetty, Advances in Metals, *Joint Replacements and Bone Resorption: Pathology and Clinical Practice,* Marcel Dekker, 2003

3. D.C. Mears, *Materials and Orthopaedic Surgery,* Williams and Wilkens Co., 1979, p 1–28

4. J. Black, *Orthopaedic Biomaterials in Research and Practice,* Churchhill Livingstone, 1988

5. D.J. Wise, D.J. Trantolo, and D.E. Altobelli, *Encyclopedic Handbook of Biomaterials and Bioengineering, Part-B: Applications,* Marcel-Dekker, 1995, p 509–539

6. H. Chandler, Ed., *Heat Treater's Guide: Practices and Procedures for Irons and Steels,* ASM International, 1995

7. W.F. Smith, *Structures and Properties of Engineering Alloys,* 2nd ed., McGraw-Hill, 1993

8. *Properties and Selection: Irons, Steels, and High-Performance Alloys,* Vol 1, *ASM Handbook,* ASM International, 1990

9. "Standard Practice for Preparation of Metallographic Specimens," E 03-01, *Annual Book of ASTM Standards,* Vol 03.01, ASTM, 2003

10. "Standard Test Methods for Determining Average Grain Size," E 112–96, *Annual Book of ASTM Standards,* Vol 03.01, ASTM, 2003

11. *Annual Book of ASTM Standards,* Vol 13.01, ASTM, 2002

12. P.J. Anderson, Medical and Dental Applications, *Powder Metallurgy,* Vol 7, *ASM Handbook,* ASM International, 1984, p 657–663

13. *Powder Metal Technologies and Applications,* Vol 7, *ASM Handbook,* 1998

14. M.J. Donachie, *Titanium: A Technical Guide,* 2nd ed., ASM International, 2000

15. *Properties and Selection: Nonferrous Alloys and Special-Purpose Materials,* Vol 2, *ASM Handbook,* ASM International, 1990

16. B.D. Ratner, A.S. Hoffman, F.J. Schoen, and J.E. Lemons, *Biomaterials Science: An Introduction to Materials in Medicine,* Academic Press, 1996, p 37–50

17. B.M. Spector, M.D. Reis, R.B. Bourne, W.A. Sauer, M. Long, and G. Hunter, Wear Performance of UHMWPE on Oxidized Zirconium Total Knee Femoral Components, *J. Bone Joint Surg.,* American Vol 83, 2001, p 80–86

18. D.J. Medlin, Processing Microstructure and Performance of Metallic Orthopaedic Medical Devices, *Proc. Microscopy and Microanalysis 2003,* D. Piston, J. Bruley, I.M. Anderson, and P. Kotula, Ed., Vol 9, Suppl. 2, Cambridge Press, 2003, p 542

M.A. Willard and G.F. Vander Voort, Microstructure and Domain Imaging of Magnetic Materials, *Metallography and Microstructures,* Vol 9, *ASM Handbook,* ASM International, 2004, p. 969–993

Microstructure and Domain Imaging of Magnetic Materials

Matthew A. Willard, Naval Research Laboratory; George F. Vander Voort, Buehler Ltd.

Introduction

MAGNETIC MATERIAL MICROSTRUCTURES are studied using a wide range of metallographic techniques, both for conventional microscopy and imaging specific to magnetic domain visualization. The wide variety of specialized types of magnetic materials, involving diverse compositions, requires individual attention to metallographic sample preparation for each. A defining characteristic of magnetic materials is the formation of a magnetization, in the absence of an applied magnetic field (i.e., spontaneous magnetization). Additionally, magnetic materials possess hysteresis in the switching of magnetization from one direction to another when a magnetic field is applied. Magnetic domains explain the small magnetic fringing fields found in demagnetized samples, even though each domain possesses the full magnitude of the spontaneous magnetization. Magnetic domains can greatly influence the switching of the magnetization when a magnetic field is applied. For these reasons, an understanding of the microstructures and magnetic domain structure is essential to understanding the properties of magnetic materials.

Magnetic materials are classified as either magnetically soft or magnetically hard. Soft magnetic materials are typically used for applications where small, applied magnetic fields are used to switch the magnetization direction (i.e., transformer cores, filters, etc.). These materials typically have low coercivity, high permeability, and high magnetization. Magnetically soft materials include high-purity iron, low-carbon steels, nonoriented and oriented silicon-iron electrical steels, iron-nickel alloys, iron-cobalt alloys, ferritic stainless steels, spinel ferrites, and Ni-Fe-Co-base amorphous and nanocrystalline materials.

Hard magnetic materials, or permanent magnets, are used in applications where the magnetization does not change, unless relatively large magnetic fields are applied (i.e., speakers/microphones, cordless electronic devices, etc.). Characteristics desired for hard magnets include large coercivity and large remanent magnetization. Permanent magnet materials include hard magnetic steel alloys, Alnico alloys (Fe-Al-Ni-Co plus other elements), barium ferrites, Cunife (Cu-Fe-Ni), Cunico (Cu-Co-Ni), Vicalloy alloys (Fe-Co-V), Nd-Fe-B alloys, cobalt-rare earth alloys, Cr-Co-Fe, and Pt-Co alloys.

In the absence of an applied magnetic field, both hard and soft magnetic materials consist of multiple domains. Each domain consists of atoms with magnetic moments in a common direction, differing from the direction in the adjacent domains. The direction of the magnetization is determined by many effects, including terms dependent on the crystalline lattice, local strain, and the shape of the sample. The boundaries between domains, called domain walls, become mobile when a sufficiently large field is applied. This makes domains important for the properties of both hard and soft magnetic materials. For optimal soft magnetic properties, ease of domain switching is necessary; therefore, in many cases high domain wall mobility is beneficial. Hard magnetic materials, on the other hand, benefit from immobility of domain walls.

Although macrostructural examination is common for only a few of these materials, microstructural examination is used for most, with major emphasis on grain-structure analysis. Much of the microstructural analysis has centered on examination of optical, electron, and scanning probe metallographic techniques. This article reviews the methods pertaining to the microstructural examination of bulk magnetic materials, including microscopy techniques specific to magnetic materials (e.g., domain imaging), with specific examples where possible. Many texts are available for a more comprehensive overview of magnetic materials and their characteristics (Ref 1, 2, 3, 4, 5, 6, 7, 8, 9). Additional information is available in the articles “Magnetically Soft Materials” and “Permanent Magnet Materials” in *Properties and Selection: Nonferrous Alloys and Special-Purpose Materials,* Volume 2 of *ASM Handbook.* The following sections include metallographic sample

preparation procedures, followed by descriptions of microstructures of bulk magnetic materials. Finally, microscopy techniques unique to magnetic materials characterization are discussed.

References cited in this section

1. R.C. O'Handley, *Modern Magnetic Materials: Principles and Application,* John Wiley and Sons, 2000
2. S. Chikazumi, *Physics of Ferromagnetism,* 2nd ed., Clarendon Press, 1997
3. R.M. Bozorth, *Ferromagnetism,* IEEE Press, 1978
4. B.D. Cullity, *Introduction to Magnetic Materials,* Addison-Wesley, 1972
5. C. Heck, *Magnetic Materials and Their Applications,* Crane, Russak and Co., 1974
6. C.-W. Chen, *Magnetism and Metallurgy of Soft Magnetic Materials,* Dover Publications, 1986
7. R. Boll, Ed., *Soft Magnetic Materials,* Heyden & Son, Ltd., 1978
8. R.S. Tebble and D.J. Craik, *Magnetic Materials,* Wiley-Interscience, 1969
9. R. Skomski and J.M.D. Coey, *Permanent Magnetism,* Inst. of Physics Publ., 1999

M.A. Willard and G.F. Vander Voort, Microstructure and Domain Imaging of Magnetic Materials, *Metallography and Microstructures,* Vol 9, *ASM Handbook,* ASM International, 2004, p. 969–993

Microstructure and Domain Imaging of Magnetic Materials

Matthew A. Willard, Naval Research Laboratory; George F. Vander Voort, Buehler Ltd.

Specimen Preparation

Electrical Steels. The general procedures for sectioning, mounting, polishing, and etching electrical steels are essentially the same as those described for low-carbon steels. Silicon-iron electrical steels tend to stain, and the use of water in the final preparation steps and after etching is best avoided. Alcohol, typically ethanol, is usually an acceptable substitute.

Etching is most commonly performed using 2 to 3% nital (etchant 1, Table 1), which reveals the αFe grain boundaries. Because nital is orientation sensitive, a portion of the grain boundaries may not be well delineated, as indicated in Fig. 1(a). However, Marshall's reagent (etchant 5, Table 1) helps fully develop the grain structure in electrical steels (see Fig. 1b). Picral (etchant 2, Table 1) is preferred when the residual carbide (cementite) is of interest. Unlike nital, picral does not reveal ferrite grain boundaries; therefore, the residual carbide is easier to observe, particularly along grain boundaries (see Fig. 2).

Table 1 Etchants for microscopic examination of magnetic alloys

No.	Etchant composition[(a)]	Procedure for use
1	*Nital* 1–6 mL HNO_3	For Fe, Fe-Ni, Fe-Co, Alnico 5, Nd-Fe-B, and Sm-Co alloys; reveals grain structure; for $SmCo_5$, a pre-etch with 30% HNO_3 in glycerol may be needed, followed by nital etch for 2–3 min; for Fe-Co-V (2–3% V) alloys, etch 10–50 s;

	99-94 mL ethanol	examination in differential interference contrast shows α_2 in relief and α_1 recessed (Fig. 1a)
2	*Picral* 4 g picric acid 100 mL alcohol	For Fe and Fe-Si electrical steels; 0.5–1.0% zephiran chloride may be added; reveals cementite (Fig. 2)
3	(A) 10% picral plus zephiran chloride (B) 5% nital	For Fe and Fe-Si electrical steels; etch using (A) for 4 s, then (B) for 20 s; used to study progress of decarburization
4	10 mL HNO_3 20 mL HF 30 mL methanol 40 mL glycerol	For Fe-3Si; swab for 1 min at 20 °C (70 °F); line etches (100) planes completely and exclusively
5	*Marshall's reagent* (A) 5 mL H_2SO_4 8 g oxalic acid 10 mL H_2O (B) 30% solution H_2O_2	For Fe and Fe-Si electrical steels; mix equal parts (A) and (B); use fresh for 1–3 s; if no reaction occurs, pre-etch with nital for 3 s, then immerse in Marshall's; a post-etch in nital for 20 s increases etch attack; provides uniform grain boundary attack (Fig. 1b)
6	(A) 2 g picric acid 25 g NaOH 100 mL H_2O (B) 1–2% nital	Line-etching technique for grain-oriented Fe-Si electrical steels; sample must be well polished; immerse in (A) boiling for 20–30 min, then in (B) for 3–5 min
7	5 g $FeCl_3$ 15 mL HCl 60 mL alcohol	For Fe-Ni alloys; immerse or swab 5–10 s; good for replica work
8	50 mL HCl 2 mL 30% H_2O_2 50 mL H_2O	For Fe-Ni alloys; immerse 10–30 s; do not store
9	*Glyceregia* 60 mL HCl 20 mL HNO_3 40–60 mL glycerol	For Fe-Ni, Fe-Co, and Fe-Co-V (2–3% V) alloys; orientation sensitive etch; use fresh under a hood; do not store; swab up to 1 min; discard when solution turns dark yellow (Fig. 7a)
10	10 g $(NH_4)_2S_2O_8$ 90 ml H_2O	For Fe-Ni alloys, particularly 50Ni-50Fe; immerse 20–30 s (Fig. 3)

	(saturated aqueous)	
11	100 mL HCl 2 g $CuCl_2$ 7 g $FeCl_3$ 200 mL methanol 100 mL H_2O	For Fe-Ni and Fe-Co alloys; immerse or swab 10–15 s; general-purpose etch (Fig. 8, 9)
12	3 parts HCl 1 part HNO_3 saturate with $CuCl_2$	For high Ni and Co alloys, e.g., Moly-Permalloy; swab 2–3 s
13	*Marble's reagent* 50 mL HCl 10 g $CuSO_4$ 50 mL H_2O	For Fe-Ni, Fe-Co, Alnico alloys, and barium ferrite; good for grain structure (Fig. 7b, 14a)
14	*10% nital* 10 mL HNO_3 90 mL methanol	For Fe-Co alloys; immerse up to 30 s
15	*Double strength Rosenhain's etchant* 30 g $FeCl_3$ 1 g $CuCl_2$ 0.5 g $SnCl_2$ 100 mL HCl up to 500 mL H_2O	For Fe-Ni-Al alloys; darkens Fe-rich phases leaving Ni-rich phases unetched
16	10 mL HCl 90 mL ethanol	For Alnico 5; use by immersion
17	200 mL HCl 5 ml HNO_3 65 g $FeCl_3$	For Alnico alloys
18	1 part HNO_3 1 part acetic acid	For Alnico alloys. Swab.
19	*Ralph's reagent* 50 mL each of ethanol, methanol,	For ferritic stainless steels; use by swabbing (Fig. 5)

	HCl 1 g $CuCl_2$ 3.5 g $FeCl_3$ 2.5 mL HNO_3	
20	3 parts HNO_3 1 part HCl	For Co-Pt alloys
21	3 parts glycerol 1 part acetic acid 1 part HNO_3	For Sm-Co alloys
22	100 mL H_2O 1 ml acetic acid 1 mL HNO_3	For Sm-Co alloys; immerse a few seconds
23	10 g $(NH_4)_2S_2O_8$ 100 mL H_2O	For rare earth-cobalt alloys; use boiling, short immersion
24	(A) 2 mL HNO_3 98 mL ethanol (B) 4 g picric acid 100 mL alcohol 1 drop HCl	For Nd-Fe-B alloys
25	1 g picric acid 5 mL HCl 95 mL ethanol	For Nd-Fe-B alloys; 5–20 s at 20 °C (68 °F)
26	3 parts HCl 1 part ethanol	For (Mn,Zn)-ferrites
27	15 mL lactic acid 15 mL HNO_3 5 mL HF	For (Ni,Zn)-ferrite and Ni-ferrite; use at 65–80 °C (150–175 °F) for 20 min
28	10 mL HF 10 mL HNO_3 20 mL H_2O	For ferrites and garnets; use at 60–90 °C (140–195 °F) for a few seconds to 30 min
29	H_2SO_4 (conc)	For garnets; immerse up to 30 min at 115 °C (240 °F); use with care; a face shield is recommended
30	30 mL lactic acid 15 mL HNO_3	For $Y_3Fe_5O_{12}$; use at 65 °C (150 °F) for 10 min

	5 mL HF	
31	*Klemm's reagent* 50 mL cold-saturated aqueous $Na_2S_2O_3$ 1 g $K_2S_2O_3$	For Fe-Si electrical steels

(a) Parts are by volume

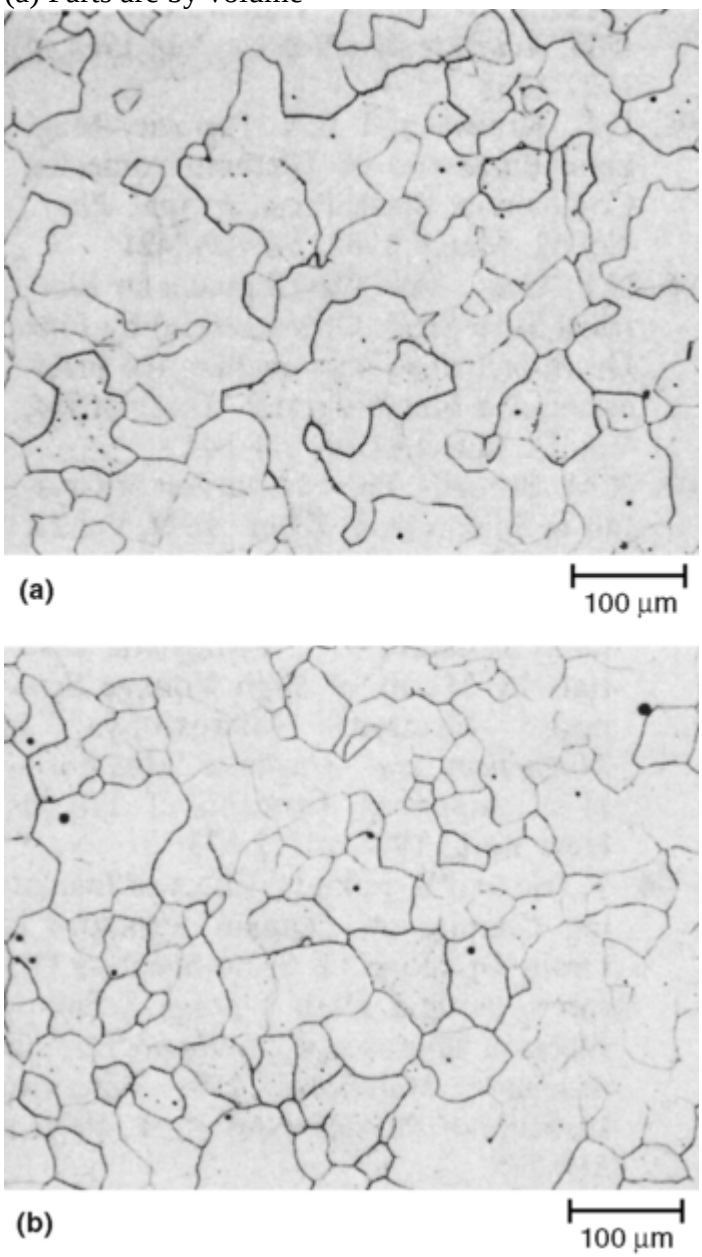

Fig. 1 Electrical iron (Fe-0.1Mn-0.1Si-0.2Cr-0.08Ni-0.05V-0.03Al) after decarburization annealing 4 h in wet hydrogen at 845 °C (1550 °F) and furnace cooling. (a) Etched using 2% nital (etchant 1, Table 1). (b) Etched 2 s using 2% nital, 3 s using Marshall's reagent (etchant 5, Table 1), then 20 s using 2% nital to develop more fully the ferrite grain boundaries. Both Original magnification 100×

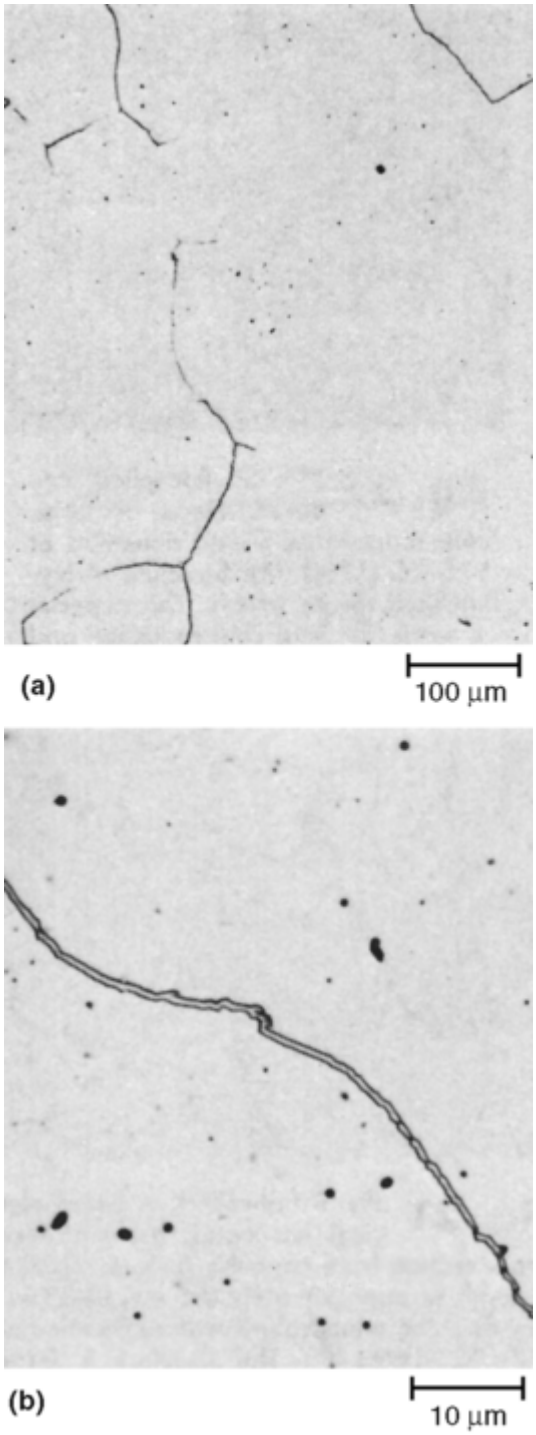

Fig. 2 Silicon core iron (Fe-0.4Mn-2.5Si-0.1P) bar, 13.5 mm (0.530 in.) in diameter, annealed 4 h in wet hydrogen at 845 °C (1550 °F) and furnace cooled. Specimen from near the surface of the bar shows thin grain-boundary films of cementite. Decarburization was incomplete. Both etched using 4% picral (etchant 2, Table 1). (a) Original magnification 100×. (b) Original magnification 1000×

The degree of grain orientation is often of interest in electrical steels, especially the oriented silicon-iron grades. Several approaches can be used to study the degree and type of crystallographic texture. X-ray procedures are used, as are metallographic approaches, particularly for the large-grain-oriented grades. One common approach involves use of dislocation etch pitting reagents, which require carefully polished specimens. Chemical polishing (Table 2) or electrolytic polishing (Table 3) is normally used as the final preparation step before etching. Solutions that produce etch pits are listed in Table 4. Many of these reagents pit grains with only certain orientations, usually those with low crystallographic indices. An optical goniometer is used to measure the orientation of the pits within etched grains. Grain-oriented silicon-iron electrical steels often do not require

polishing of the sheet surface before etch pitting, because the annealing furnace atmosphere provides a satisfactory surface condition if an insulating coating is not present.

Table 2 Chemical polishing solutions

Material	Solution	Comments
Fe-Si electrical steels	6 mL HF 94 mL 30%H_2O_2	Use at room temperature; keep cool; wash in successive baths of H_2O_2, H_2O, and ethanol.
Fe-Si electrical steels, Fe-Co, Fe-Co-V alloys (2–3% V)	100 mL H_3PO_4 100 mL 30% H_2O_2	Use at room temperature; keep cool; up to 10 min immersion

Table 3 Electropolishing solutions for metallographic specimens

No.	Material	Solution	Electropolishing conditions
1	Fe and Fe-Ni alloys	135 mL glacial acetic acid 25 g CrO_3 7 mL H_2O	For Fe: use at 20 V dc, 0.09–0.22 A/cm^2 (0.6–1.4 A/in.^{2}), 17–19 °C (63–66 °F), 6 min, stainless steel cathode. For Fe-Ni: use at 80 V dc, 0.8–1.6 A/cm^2 (5–10 A/in.^{2}), <7 °C (45 °F). Grind samples to 600 grit surface finish.
2	Fe-3Si and Ni alloys	185 mL H_3PO_4 765 mL acetic anhydride 50 mL H_2O	Age solution 24 h before use; use at 50 V dc (external), <30 °C (85 °F), 0.1 A/cm^2 (0.65 A/in.^{2}), 4–5 min; use large Fe or Al cathode.
3	Fe-Ni, Fe-Co, and Alnico alloys	10 mL $HClO_4$ 100 mL glacial acetic acid	Use at 45 V dc, 0.2 A/cm^2 (1.3 A/in.^{2}), 24 °C (75 °F), 3–4 min.
4	Fe-Si electrical steels	80 mL H_3PO_4 13 g CrO_3 7 mL H_2O	Use at 0.6 A/cm^2 (3.9 A/in.^{2}), 20 °C (68 °F).
5	Permanent magnet alloys	H_3PO_4 saturated with CrO_3	Use at approximately 1 A/cm^2 (6.5 A/in.^{2}) at approximately 75 °C (165 °F), for 30–120 s.
6	Fe-Co alloys	5–10 mL HCl 100 mL H_2O	Use 2–5 s at 0.25–0.50 A/cm^2 (1.6–3.2 A/in.^{2}).
7	Fe-Co alloys	2 g CrO_3 100 mL H_2O	Use 2–5 s at 0.10–0.20 A/cm^2 (0.65–1.3 A/in.^{2}).
8	*Jacquet's Solution* (for Fe-Si electrical steels)	300 mL acetic acid 27 mL $HClO_4$	Use at 40 V dc, 1.5 A/cm^2 (9.7 A/in.^{2}) for 5 min; use a stainless steel cathode.

Table 4 Dislocation etch-pitting solutions

Etchant composition[(a)]	Etchant use procedure	Effect of etchant
1 part HF **1 part HNO_3** **4 parts H_2O**	Immerse 10 s.	Exposes {100} crystallographic faces in (110) [001] (cube-on-edge) oriented 3.25% Si steel
2 parts HF **1 part HNO_3** **3 parts methanol** **4 parts glycerol**	Swab 1 min.	Same as for etchant 1
(A) 6 mL 30% H_2O_2 **0.1 mL HCl** **100 mL H_2O** **(B) 40 mL $FeCl_3$** **40 mL ethanol** **20 mL H_2O**	Immerse in (A) for 10 s, rinse and dry; then immerse in (B) for 3 s, rinse and dry.	Develops etch pits in (110) [001] (cube-on-edge) oriented 3.25% Si steel
10 g $Fe_2(SO_4)_3$ **10 mL H_2SO_4** **100 mL H_2O**	Immerse 15 s in solution heated to 80–90 °C (175–195 °F).	Develops etch pits in (100) [001] (cube-on-face) oriented 3.25% Si steel (Fig. 6)
(A) 5 mL HF **95 mL methanol** **(B) 100 mL 3% H_2O_2** **100 mL H_2O** **2 drops HCl** **(C) 5 mL HCl** **95 mL methanol**	Polish, etch heavily in nital; repolish, etch in nital to reveal grain boundaries; immerse 10 s in (A), rinse, dry; 2 s in (B), rinse, dry; 30 s in (C), rinse, dry.	Exposes {100} crystallographic faces in primary recrystallized 3.25% Si steel and nonoriented silicon steels

(a) Parts are by volume

Another approach includes line (“hatch”) etching procedures (Ref 10, 11, 12, 13, 14). In this technique, an opaque reaction layer is formed on the specimen surface during etching. This layer shrinks and cracks when dried to produce on the surface a lineal pattern that is related to the crystallographic orientation of the underlying grains. Grain-oriented silicon-iron electrical steels exhibit a parallel line pattern in which the lines are parallel to the direction of magnetization.

Two reagents have been used for silicon-iron alloys. Klemm's reagent (etchant 31, Table 1) is made fresh before etching for 2 h by immersion. Boiling alkaline sodium picrate (etchant 23, Table 1)—a 20 to 30 min etch—provides more pronounced line patterns. This is followed by a 3 to 5 min etch in 1 to 2% nital to improve contrast. The nital seeps into the cracks in the layer formed by the alkaline sodium picrate and attacks the underlying material to produce lines. The surface layer dissolves, leaving a bright surface with a linear etch pattern.

A parallel line pattern is obtained for silicon steels when the grains deviate only slightly from {110}. As the orientation deviates from {110}, intersecting lines form that are perpendicular for {100} grains. The growth of the surface layer during the alkaline sodium picrate etch has been documented (Ref 11). For best results, the specimen must be carefully polished; electropolishing is recommended (etchant 4, Table 3).

A procedure for detecting undesirably oriented grains in sheets of coarse-grained oriented silicon iron has been developed (Ref 15). This macroscopic approach is suitable for observing the grains on a large sheet surface. The sheet surface is swabbed 1 min at room temperature with an etchant containing nitric acid, hydrofluoric acid, methanol, and glycerol (etchant 4, Table 1). This produces a line etching pattern on the (100) planes. The grains are observed using an optical apparatus described in Ref 15.

An additional feature of interest in these steels and many other magnetic materials is grain size. In general, the final annealed or heat treated grain size is most important, but for some work the penultimate grain size (that prior to the final processing step) must be controlled to obtain the desired properties. Of the numerous methods for measuring grain size (Ref 16, 17), the intercept procedure is preferred. Grain size measurements in thin sheet may be complicated by the possibility of the sheet thickness direction restricting growth in that direction compared with that of the rolling direction.

The magnetic domain structure of oriented silicon irons has been studied extensively. The various techniques used for magnetic materials are described below. A metallographic approach for revealing the domain structure in ferrite has been developed using Jacquet's electropolishing solution (etchant 8, Table 3) (Ref 18).

Iron-nickel and iron-cobalt alloys require preparation procedures similar to those described for nickel and nickel-copper alloys (see the article “Metallography and Microstructures of Nickel and Nickel-Copper Alloys” in this Volume).

Sectioning and mounting of iron-nickel and iron-cobalt strip is performed in the same manner as most metals. Strip specimens may be bent into self-supporting shapes for mounting, or plastic clamps may be used to support the specimens. Most mounting resins can be used, but cold-setting resins should be used for thin sheets to avoid foldover during compression mounting. For edge protection, plating the surface prior to mounting may be beneficial.

Grinding and polishing procedures are basically the same as for low-carbon steel specimens. Wet grinding is recommended to minimize heating problems and abrasive embedment. Because they are rather mechanically soft, care must be taken during preparation to prevent distortion and smearing of grain boundaries. Vibratory final polishing and electropolishing are quite useful in elimination of fine polishing scratches. Silicon carbide of 120, 240, 320, 400, and 600 grit is used with 45 to 90° rotation of the specimen between grinding steps. Rough polishing is performed using 6 or 3 μm diamond abrasive (paste, spray, or slurry) on a napless or low-nap cloth. Rough polishing may be followed by a 1 μm diamond polish on a medium-nap cloth. Final polishing may involve one or two grades of alumina (Al_2O_3), for example, 0.3 and 0.05 μm Al_2O_3 on a medium-nap cloth. These procedures may be executed manually using a rotating polishing wheel or by automated devices. Final polishing using a vibratory polisher may be preferred for scratch removal. Reference 17 provides additional details on carrying out grinding and polishing.

Electropolishing is an alternative for obtaining high-quality surface finishes on these soft alloys and is especially useful for annealed vacuum-melted alloys. The specimen is usually ground to a 600 grit finish before electropolishing. Through-thickness specimens are difficult to handle; planar surfaces are easier to handle. Table 3 lists commonly used electrolytes and polishing conditions.

Macroetching of iron-nickel alloys is commonly performed by thermal etching. Cold-rolled strip specimens are annealed several hours in dry hydrogen at 1175 °C (2150 °F), followed by furnace cooling (see Fig. 3). Thermal

etching will reveal grain structures, and subsequent etching with Marble's reagent (etchant 13, Table 1) or other solutions will enhance grain contrast. Larger specimens are macroetched during manufacturing using standard hot-acid etching procedures described in the article “Metallography and Microstructures of Carbon and Low-Alloy Steels” in this Volume.

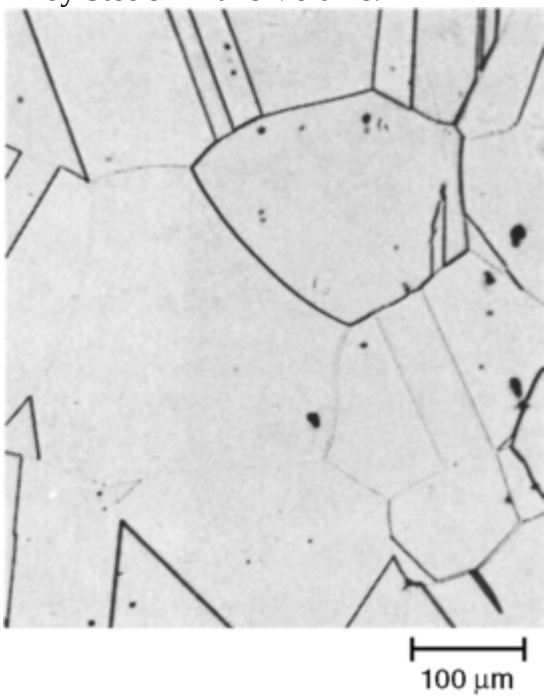

Fig. 3 Fe-50Ni cold-rolled 0.03 mm strip, annealed 4 h at 1175 °C (2150 °F) in dry H_2 and furnace cooled. Structure is nonoriented primary recrystallized grains. Saturated $(NH_4)_2S_2O_8$ (etchant 10, Table 1). Original magnification 100×

Etchants for iron-nickel and iron-cobalt alloys are usually more aggressive than for electrical steels, as shown in Fig. 4, although nital may be satisfactory for some specimens. Choice of etchants (Table 1) is often a matter of personal preference. Complete delineation of all the grains in iron-nickel alloys, such as stainless steels, can be difficult (see Fig. 5).

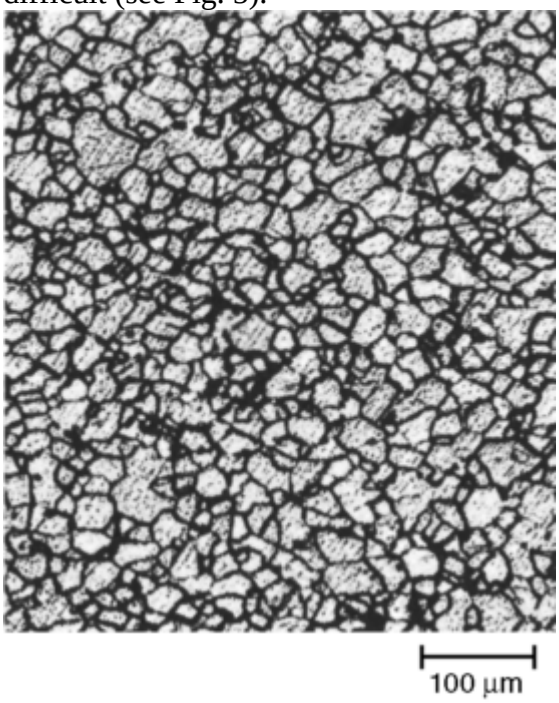

Fig. 4 Fe-50Ni cold-rolled 0.15 mm strip, annealed 2 h in H_2 at 900 °C and furnace cooled. Structure: primary recrystallized grains of austenite. 60 mL ethanol, 15 mL HCl, and 5 g anhydrous $FeCl_3$. Original magnification 100×

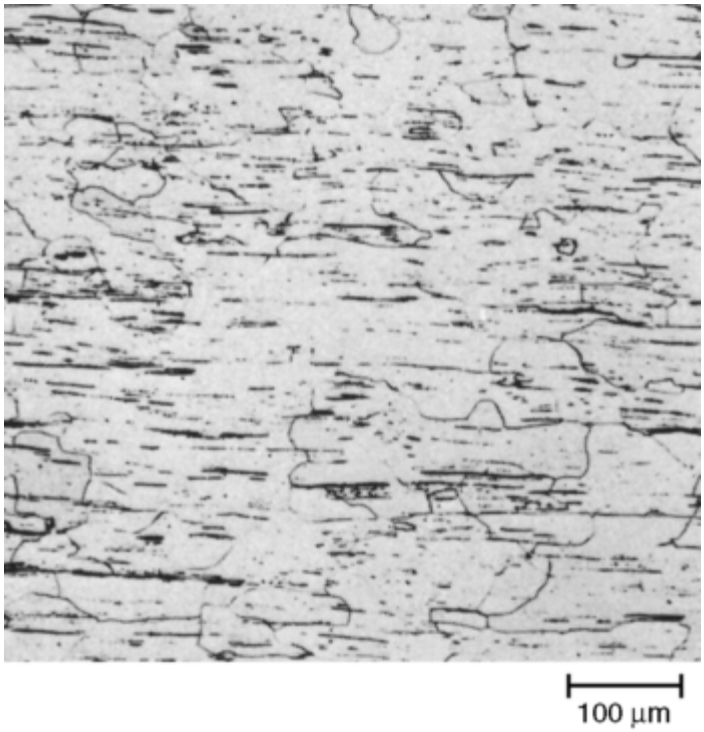

Fig. 5 Solenoid-quality type 430FR ferritic stainless steel. Note that some of the ferrite grain boundaries were not revealed. Ralph's reagent (etchant 19, Table 1). Original magnification 100×

Amorphous and Nanocrystalline Alloys. Most commercial amorphous and nanocrystalline alloys are produced by a rapid-solidification technique called melt spinning. The alloys are produced as ribbons, 20 to 50 μm thick, meters in length, and up to 10 cm wide. Sectioning of amorphous alloys is easily accomplished by shearing with scissors. Nanocrystalline specimens tend to be brittle. When scissors or shears are used to section these materials, the ribbons tend to shatter. A sharp edge or razor blade can be used for sectioning if the ribbon is not too wide for these samples. An alternative method for sectioning using a diamond saw requires mounting the ribbon on a support block.

When properly prepared, metallic glasses are entirely amorphous; therefore they do not provide particularly interesting metallographic images. However, if the processing conditions do not provide a high enough quench rate to avoid crystallization, some crystallites are formed on the surfaces of the ribbons. Depending on the composition of the metallic glass, the surface crystallites will typically have the cubic crystal structure of the element making up the majority of the alloy (e.g., body-centered cubic, or bcc, for iron-rich alloys; face-centered cubic, or fcc, for cobalt- and nickel-rich alloys). The crystallites may have fiber texture along the crystallite growth direction.

Since the crystallites formed in this way are located at the surface of the ribbon, cross-sectional methods of observation are required. Samples can be mounted in standard metallographic mounting epoxy, using clips to hold the sample upright, for observation by optical methods. Standard polishing for metallic samples should be used for these materials, as well. Etchants should be chosen depending on the crystal structure and composition of the phase to be imaged.

Nanocrystalline samples consist of randomly oriented crystallites up to 20 nm in diameter surrounded by an amorphous matrix less than 5 nm thick. Such small features require the use of transmission electron microscopy for metallographic imaging. Samples can be ion milled without prior grinding or chemical etching if the plan-view of the ribbon is desired. This is possible since the samples are typically 20 μm in thickness. For cross-sectional samples of either nanocrystalline or amorphous alloys, the ribbons can be mounted inside a 3 mm copper or stainless steel tube, using heated epoxy to mount the sample. The tube can then be sliced to make 3 mm diam section samples of the alloy ribbon. Standard grinding procedures are necessary (as discussed for iron-silicon electrical steels above), with caution used as the sample becomes nearly thin enough for ion milling.

Ferrites and Garnets. Preparation procedures for ferrites and garnets differ from those for the alloys previously described because of their brittle nature and chemical inertness. Also, their lack of significant electrical conductivity prohibits the use of electrolytic techniques.

Sectioning is best performed using a low-speed diamond saw. The high quality of the cut surface obviates the need for coarse grinding; that is, grinding can generally begin using 320 or 400 grit silicon carbide paper. Mounting can be performed using most materials, but cold-setting resins offer advantages compared to compression-mounting materials. Because ferrites and garnets are made by powder processing, some porosity can be expected. Vacuum impregnation of epoxy into the voids may be quite useful for some more porous specimens.

Grinding is performed up to 600 grit. This should be carried out wet with a high volume of water and somewhat higher downward force than that used for metal specimens. Automatic devices may be desired to reduce operator fatigue. Polishing is executed in the same manner as for metals; 6 and 1 μm diamond abrasives are frequently used. A 1 μm diamond finish is generally adequate, although finer abrasives may also be used.

Ferrites and garnets are examined in the as-polished condition to detect porosity and second phases. Etchants (Table 1) are usually mixtures of heated acids, requiring long etch times (10 to 30 min).

Alnico alloys are generally quite hard—to approximately 60 HRC—and their preparation is similar to that of hardened tool steels. Sectioning can be performed using wire saws, diamond saws, or abrasive cutoff saws. For the latter, a soft wheel must be selected. Cutting technique is critical for preventing cracking or burning; light pressure (slow feed) and copious coolant flow are required. Grinding and polishing rates are slow. Therefore, if manual procedures are used, relatively small sections are advisable. Automatic devices easily handle larger specimens. Small sections require mounting to facilitate handling. Most mounting materials can be used (see the article “Mounting of Specimens” in this Volume).

Grinding is performed in the usual manner. If the surface to be polished is cut using a low-speed diamond saw, grinding can begin using 320 or 400 grit silicon carbide. If an abrasive cutoff wheel is used, grinding must commence with a coarser grit, for example, 180 or 240 grit silicon carbide. Grinding should be carried out wet. Kerosene or a lightweight oil is sometimes used for grinding with abrasives finer than 400 grit.

Electropolishing is often used to polish Alnico alloys. Polishing is performed after grinding to a 600 grit silicon carbide finish. The primary difficulty in using electropolishing is obtaining electrical contact with the specimen. If the specimen is large enough to grind without mounting, it can be secured with a clamp. If mounting is necessary, a wire can be attached to the back of the specimen by spot welding or by use of a silver paste. The wire must extend through the mount; this is easily accomplished with cold-mounting materials. A suitable electrolyte for polishing is listed in Table 3 (etchant 3).

Many of these alloys are routinely examined in the as-polished condition before etching to detect porosity or microshrinkage cavities. Many can be etched using nital. Marble's reagent (etchant 13, Table 1) is also commonly used. Electrolytic etching is sometimes preferred.

Rare Earth Permanent Magnets. Similar to Alnico alloys, rare earth permanent magnets are mechanically hard. However, where the Alnico alloys can be sectioned with a slow cutting speed and plenty of cutting fluid, Nd-Fe-B type magnets are prone to oxidation under such conditions. A balance between using enough coolant to avoid a rough cut, yet not so much as to oxidize the sample is necessary for optimal sample preparation. Samarium-cobalt permanent magnets oxidize less readily and can be sectioned using the same procedure as Alnico alloys.

Although most mounting materials can be used for rare earth magnets, care should be taken when using automated mount processing machines since the samples are brittle enough to crack under sufficiently high pressures. Grinding procedures are the same as Alnico alloys, keeping in mind that Nd-Fe-B alloys may show signs of oxidation if polished for extended periods in an aqueous solution. After polishing the sample with 0.25 μm diamond paste, a picric/hydrochloric acid immersion (etchant 24, Solution B, Table 1, Ref 19) may be used to etch the sample.

The structure of permanent magnet alloys is often too fine to observe using optical microscopy. Therefore, transmission electron microscopy (TEM) using thin foils is frequently implemented (see Table 5 for chemical thinning solutions). Basic texts on specimen preparation and techniques for TEM are cited in Ref 20, 21, 22, 23, 24, 25, and additional information is provided in the article “Analytical Transmission Electron Microscopy” in *Materials Characterization,* Volume 10 of *ASM Handbook.*

Table 5 Electropolishing procedures for preparing TEM thin foils

Material	Solution	Conditions
Fe metal	5 mL $HClO_4$ 100 mL glacial acetic acid	Window method. Use stainless steel cathode, 35–45 V dc, 0.7 A/cm^2 (4.5 A/in.^{2}), <30 °C (85 °F).
Fe-Si electrical steel	19 mL, HNO_3 1 mL HCl 80 mL methanol	Jet polish, -50 °C (-60 °F), 30 V dc
Fe-Si electrical steels and 50Fe-50Co alloy	135 mL glacial acetic acid 27 g CrO_3 7 mL H_2O	Pointed stainless steel cathode, 25–30 V dc, 0.1–0.2 A/cm^2 (0.65–1.3 A/in.^{2}), <30 °C (85 °F)
Fe and Ni alloys	10 mL $HClO_4$ 90 mL glacial acetic acid	Jet polish. For iron use 12–13 V dc; for nickel alloys use 30 V dc.
Ni alloys	5 mL $HClO_4$ 95 mL ethanol	18–20 V dc, 0 °C (32 °F)
Fe-Ni alloys	40 mL H_3PO_4 35 mL H_2SO_4 24 mL H_2O	Pointed electrode or window method. Use 8–9 V dc, 30 °C (85 °F), stainless steel cathode.
Ni alloys	80 mL ethanol 25 mL iso-butanol 20 mL $HClO_4$	Jet polish. Use 0.15–0.35 A/cm^2 (0.97–2.3 A/in.^{2}).
High-Ni content alloys	23 mL $HClO_4$ 77 mL acetic acid	Window method. Use stainless steel cathode, 20–30 V dc, 0.7 A/cm^2 (4.5 A/in.^{2}), 30 °C (85 °F).
Alnico 5	20 mL $HClO_4$ 80 mL ethanol	Use pointed platinum wire cathode, -20 to -50 °C (-5 to -60 °F), 35 V dc, 0.2 A/cm^2 (1.5 A/in.^{2}).
Alnico 5	4 mL $HClO_4$ 96 mL glacial acetic acid	Use at 80 V dc, 0.6–1.2 A/cm^2 (4–8 A/in.^{2}).
Fe-Co-V (2–3% V)	22 mL $HClO_4$ 118 mL iso-butanol 390 mL methanol	Window method. Use at -20 °C (-5 °F), 20 V dc.
Fe-Co and Fe-Co-V alloys (2–3% V)	20 mL $HClO_4$ 80 mL methanol	Jet polish -20 to -30 °C (-5 to -20 °F).

Sm-Co alloys	(A) 10 mL HCl 90 mL H_2O (B) 15 mL $HClO_4$ 85 mL glacial acetic acid	Jet polish with (A) at 50 V dc. Electropolish to perforation with (B) at 10 V dc; ion bombardment around perforation
Nd-Fe-B alloys	6 mL $HClO_4$ 94 mL acetic acid	Use at 40–60 V dc for 2–15 s at 20 °C; Follow with Ar^+ ion beam milling (4–6 kV, 1 mA) for 1–4 h

References cited in this section

10. W. Schatt, Control of Textured Sheet by Means of Line Etching, *Pract. Metallog.*, Vol 4, Dec 1967, p 620–627

11. I. Friede, A Modification of Line Etching According to Sved Using Alkaline Sodium Picrate on Transformer Sheet, *Pract. Metallog.*, Vol 5, June 1968, p 325–333

12. L. Kosec et al., Production of Etch Figures on Transformer Sheet, *Pract. Metallog.*, Vol 5, June 1968, p 333–337

13. H. Klemm, Uses of Sodium Thiosulphate (Klemm's Reagent) as an Etchant, *Pract. Metallog.*, Vol 5, April 1968, p 163–177

14. W. Schatt, New Investigations on Hatch-Etching, *Radex Runschau,* No. 3/4, 1967, p 657–667

15. L.J. Regitz, Simultaneous Observation of Grain Structure and Orientation in Oriented Silicon Steel, *IEEE Trans. Magnetics*, MAG-6, Sept 1970, p 576–579

16. G.F. Vander Voort, Grain Size Measurement, *Practical Applications of Quantitative Metallography,* STP 839, ASTM, 1984, p 85–131

17. G.F. Vander Voort, *Metallography: Principles and Practice,* McGraw-Hill, 1984

18. A. Scortecci and E. Stagno, New Metallographic Method for Revealing Magnetic Patterns in Ferrite, *Mem. Sci. Rev. Met.,* BISI No. 5569, Vol 62, 1965, p 741–746

19. S.J. Lillywhite, A.J. Williams, B.E. Davies, and I.R. Harris, A Preliminary Electron Backscattered Diffraction Study of Sintered NdFeB-type Magnets, *J. Microsc.*, Vol 205, 2002, p 270–277

20. M. De Graef, *Introduction to Conventional Transmission Electron Microscopy,* Cambridge University Press, 2004

21. L.E. Murr, *Electron and Ion Microscopy and Microanalysis: Principles and Applications,* (Optical Engineering, No. 29) Marcel Dekker, 2nd ed., 1991

22. P.J. Goodhew, *Practical Methods in Electron Microscopy,* Vol 11, *Thin Foil Preparation for Electron Microscopy,* Elsevier Science Ltd., 1986

23. G. Thomas and M.J. Goringe, *Transmission Electron Microscopy of Materials,* John Wiley & Sons, 1987

24. M. Von Heimendahl and A. Norwick, *Electron Microscopy of Materials: An Introduction,* Academic Press, 1980

25. K.C. Thompson-Russell and J.W. Edington, *Electron Microscope Preparation Techniques in Materials Science,* Macmillan, Philips Technical Library, 1977

M.A. Willard and G.F. Vander Voort, Microstructure and Domain Imaging of Magnetic Materials, *Metallography and Microstructures,* Vol 9, *ASM Handbook,* ASM International, 2004, p. 969–993

Microstructure and Domain Imaging of Magnetic Materials

Matthew A. Willard, Naval Research Laboratory; George F. Vander Voort, Buehler Ltd.

Microstructures of Magnetically Soft Materials

The most commonly used soft magnetic materials are the low-carbon steels (for example, AISI 1006 or 1008), the silicon-iron electrical steels, iron-nickel and iron-cobalt alloys, spinel ferrites (manganese-zinc and nickel-zinc ferrites in particular), and garnets.

Electrical Steels. Low-carbon, magnetic-lamination-quality electrical steels have a randomly oriented grain structure, and their microstructures are identical to those of low-carbon sheet steels. These alloys are ferritic, containing minor amounts of cementite and inclusions.

Low-carbon (≤0.08%) electrical steels contain additions of phosphorus (0.03 to 0.15%) and manganese (0.25 to 0.75%) to increase electrical resistivity, which subsequently reduces eddy current losses. These steels are subjected to a decarburization anneal, which also increases grain size, lowering hysteretic losses due to domain wall pinning. Oxygen and sulfur increase core loss, but grain size and texture variations have only a small influence on the core loss of magnetic lamination steels (Ref 26).

Silicon-iron electrical steels are flat-rolled sheet with low carbon contents, frequently less then 0.005%. The nonoriented grades have low sulfur levels, often below 0.01%; the oriented grades use sulfides and/or nitrides to improve grain orientation by promoting secondary recrystallization.

Nonoriented silicon iron electrical steels, which are covered in ASTM A 677 (Ref 27) and A 683 (Ref 28), have silicon contents from 0.5 to 3.25%, with up to approximately 0.5% Al added to the highest quality grades. They are available in the semiprocessed (user performs the decarburization/recrystallization/grain growth anneal) or fully processed condition. Semiprocessed steels exhibit improved magnetic properties, because the anneal relieves stresses produced by shearing and punching the laminations.

The magnetic properties of nonoriented steels are improved by reducing the thickness, increasing the silicon and aluminum contents (increases resistivity), obtaining an optimal grain size, and reducing the impurity content. Increasing the grain size reduces core losses up to a critical grain size, but further grain growth produces no further improvement while reducing permeability (Ref 29). The optimal grain size for a 2.89% Si, 0.43% Al, nonoriented steel with relatively high impurity (sulfur, oxygen, and nitrogen) levels is approximately 50 μm (Ref 29).

A study of nonoriented silicon irons with very low impurity contents revealed that the optimal grain size for minimum core loss varies with silicon content (Ref 30). At 1.85% Si, the optimal grain size was approximately 100 μm; at 3.25% Si, it was approximately 150 μm. Low residual levels of sulfur (<30 ppm), oxygen (<20 ppm), and nitrogen (<30 ppm) were found to be necessary to obtain minimum core losses. For semiprocessed nonoriented silicon-iron electrical steels, additions of antimony (0.04%) produced strong (100) texture after processing.

In a similar study of high-quality nonoriented silicon-iron electrical steel, zirconium nitrides restricted grain growth, resulting in high core loss (Ref 31). They also encountered high core loss due to oxidation of the subsurface by the annealing atmosphere, which produced aluminum nitride (AlN) and Al_2O_3 and restricted grain growth at the surface.

For rotating machinery applications, development of an (001) [*uvw*] texture in low-carbon steel (commercial black plate) improves properties. In this texture, the cube plane is parallel to the sheet surface, but the cube edges are randomly oriented in the sheet surface (Ref 32, 33). Therefore, magnetic properties are better than in nonoriented irons.

The magnetocrystalline anisotropy of iron is reduced slightly by the addition of silicon, but the [100] direction remains the easy direction of magnetization. Although the benefits of adding silicon to iron have been known since 1900, it was not until 1933 that Goss (U.S. Patent No. 1,965,559) developed a procedure to align preferentially the [100] directions of the grains in the rolling direction (Ref 34). This texture, known as the cube-on-edge (COE) or Goss texture, is a (110) [001] texture that has been widely exploited commercially to produce high-permeability, low-loss silicon-iron electrical steels (Ref 35). Subsequent experimentation demonstrated the technical possibility of developing a texture having the [001] direction parallel to the rolling direction and orienting the (100) plane parallel to the rolling plane (Ref 36). This texture has been referred to as a cube texture, cubex, cube-on-face, or four-square texture (as seen in Fig. 6).

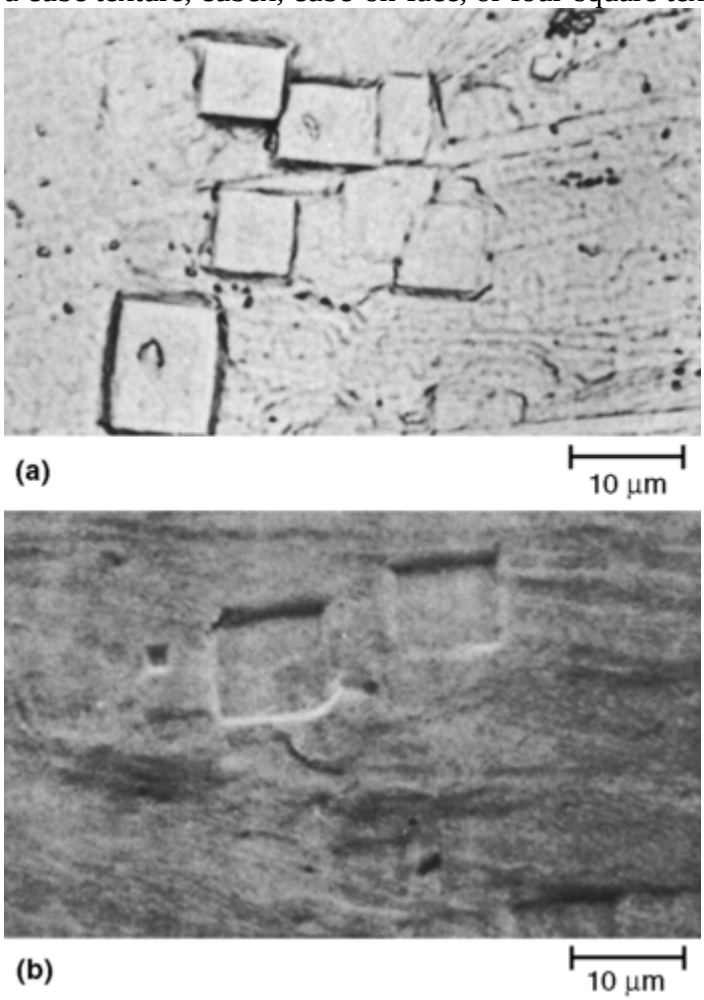

Fig. 6 Cubic etch pits in cube-on-face grain-oriented 3% Si steel. A solution of $Fe_2(SO_4)_3$ and sulfuric acid was used as an etchant (see Table 4). (a) Optical micrograph of a single αFe grain, obtained by annealing at 1175 °C (2150 °F) or higher. (b) Scanning electron micrograph of cubic etch pits in cube-on-face grain-oriented 3% Si steel. The area shown is a single grain of ferrite. Both original magnification 1000×

The COE silicon-iron electrical steels have been in commercial production since about 1940. These steels include manganese sulfide to inhibit primary grain growth and develop the COE texture by secondary recrystallization (Ref 37). Beginning in the mid-1960s, considerable progress was made in improving texture, reducing core losses, and raising permeability. The first development was the introduction of the HI-B process by Nippon Steel (U.S. Patent No. 3,287,183) to improve the Goss texture (Ref 38, 39, 40). This was achieved by use of AlN for normal grain growth inhibition prior to secondary recrystallization plus a high degree of cold reduction (typically 80 to 90%) in the final step before annealing. Such steels also contain a minor amount of

sulfur. Following the last hot-rolling step, the hot band is cooled to approximately 800 °C (1470 °F), then water quenched. This produces a fine dispersion of manganese sulfide (MnS) with sizes of 0.05 to 0.08 μm (Ref 41). Because of the high final cold reduction, grain growth cannot be inhibited by the MnS alone, but requires a second AlN addition.

The desired fine AlN particle size is also obtained by the final hot-band reduction. Texture is further improved if a hard second phase, such as martensite, is present in small amounts (1 to 10%) before the final cold-reduction step (Ref 42). If the martensite is tempered before the final cold-reduction step, the texture is not favorable. Following the cold-rolling step, the sheet is subjected to a decarburization anneal at approximately 800 °C (1470 °F), then is annealed in a hydrogen atmosphere at approximately 1200 °C (2190 °F) to produce secondary recrystallization, denitriding, and desulfurization (Ref 41). Grain sizes are generally 10 to 20 mm (0.4 to 0.8 in.).

Other improved grain-oriented silicon-iron electrical steels use additions of antimony or boron to inhibit primary recrystallization. These steels also contain MnS (the grain-growth inhibitor in the circa 1940 COE steels), and some also contain manganese selenides. Antimony and boron inhibit primary grain growth due to their segregation to the grain boundaries, which produces a solute drag influence. A wide range of sulfides, carbides, and nitrides have been evaluated for their influence in promoting COE texture during secondary recrystallization (Ref 43).

Streaks of poorly oriented grains in oriented silicon-iron electrical steels containing 3% Si can degrade magnetic properties (Ref 44). These streaks consist of smaller grains that do not have the usual (110) [001] orientation. The percentage of these fine, nonoriented grains increases with average core loss. The fine-grained regions contain approximately three times as many glassy silicate inclusions that are much longer than in the coarse-grained-oriented regions. These inclusions prevent the occurrence of recrystallization during the final process anneal, which results in small, poorly oriented grains after secondary recrystallization.

Grain-oriented silicon-iron electrical steels have also been the subject of many studies of domain structures. These studies have led to improved properties. Shilling and Houze have prepared a comprehensive survey of magnetic properties and domain structures in these materials (Ref 45). Core losses are influenced by domain-wall spacing and mobility, which depend on grain size, stress, and defect structure.

In general, a reduction of the domain size produces lower core losses. This can be accomplished by reducing grain size or by applying a tensile stress in the rolling direction. However, any applied coating must have a smooth surface, because a rough coating surface leads to decreased domain-wall mobility. In commercial COE silicon-iron electrical steels, the grain sizes are much larger than the sheet thickness, and the domains are large. Reduction of the grain size using secondary recrystallization processes, as described previously, is difficult. An alternate approach involves use of primary recrystallization to produce the COE texture with grain sizes about the same size as the sheet thickness (Ref 46, 47).

Nickel-Iron Alloys. The nickel-iron soft magnetic alloys are the most ductile and most versatile soft magnetic alloys currently in use. Compared with silicon-iron electrical steels, they exhibit much higher permeabilities and lower core losses. Their exceptional ductility permits production of thin foil or wire shapes. Additionally, a large number of elements can enter into solid solution, permitting tailoring of their magnetic and physical properties. Three ranges of nickel content are used as soft magnetic alloys: 36% Ni for maximum resistivity, 50% Ni for maximum saturation magnetization (see Fig. 7), and 80% Ni for highest initial and maximum permeabilities. Further iron-nickel alloys containing 6 to 12% Ni have been developed as substitutes for 2V-Permendur (49C-49Fe-2V) for telephone applications. Of the above alloys, the 50% and 80% Ni alloys are most widely used commercially.

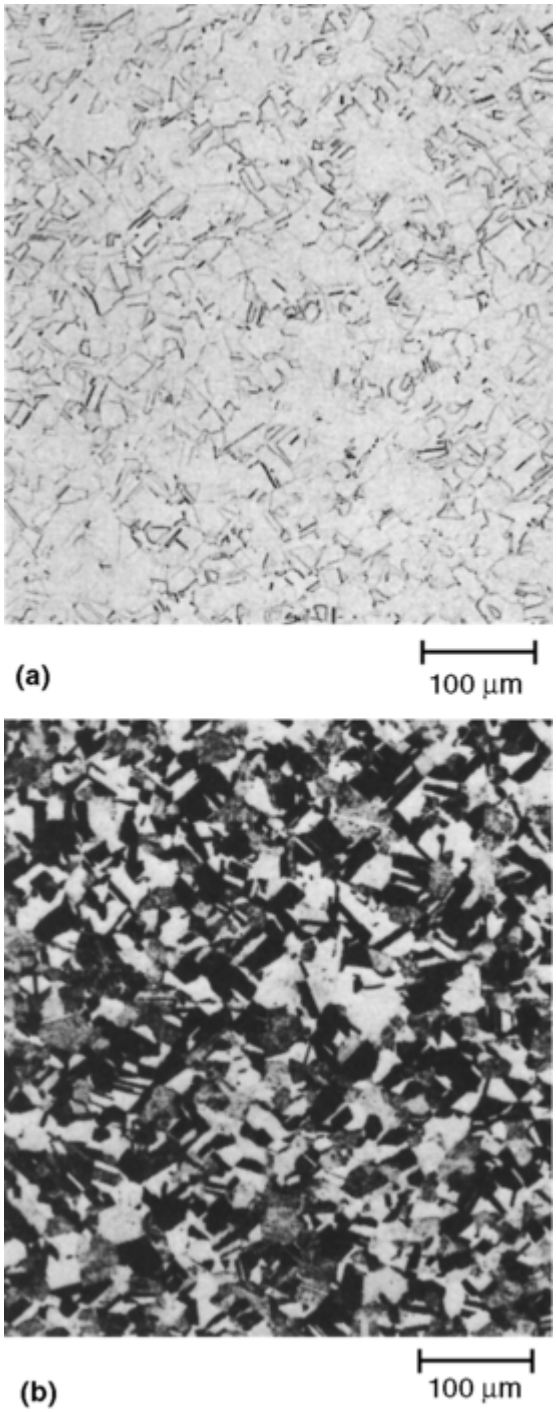

Fig. 7 Austenitic Fe-50.5Ni soft magnetic alloy, showing the effects of different etchants. (a) Etched using a flat etchant, glyceregia (etchant 9, Table 1). (b) Etched using a grain contrast etchant, Marble's reagent (etchant 13, Table 1). Both Original magnification 100×

Many of these alloys are modified using additions of molybdenum, silicon, manganese, copper, or chromium to produce specific magnetic properties. Alloys in the range of 50 to 80% Ni can be annealed in a magnetic field to produce an easy axis of magnetization and a substantial increase in permeability. Grain-oriented (001) [100] cube-texture Fe-50Ni alloys are also produced for applications requiring a square hysteresis loop. As with the silicon-iron electrical steels, high-temperature annealing in dry hydrogen is performed to reduce the carbon, sulfur, and oxygen contents, which greatly improves magnetic properties, especially permeability (see Fig. 8).

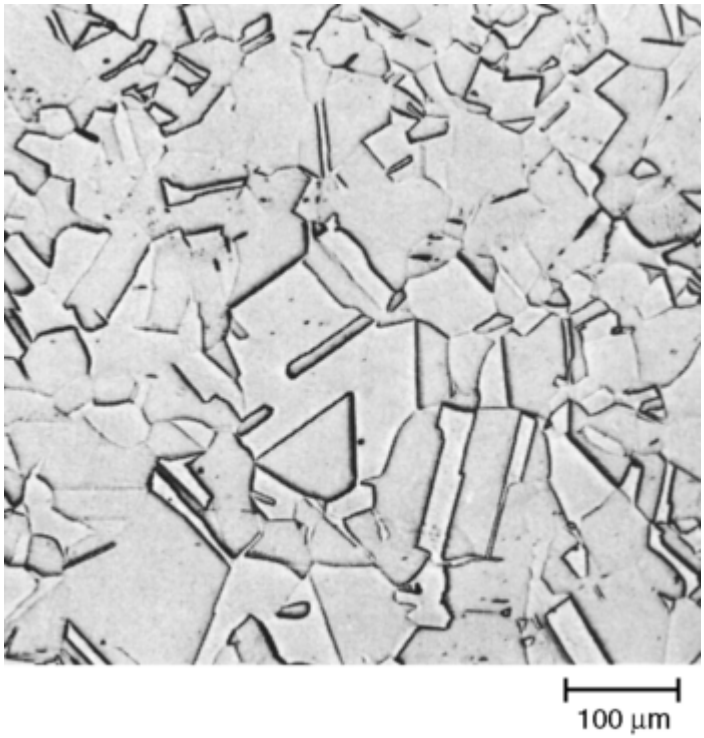

Fig. 8 Fe-30Ni cold-rolled strip, batch annealed 6 h at 950 °C (1740 °F) and furnace cooled in dry hydrogen. Grains are coarse because carbon content was low. A general purpose etchant consisting of HCl, $CuCl_2$, $FeCl_3$, HNO_3, methanol, and H_2O was used for contrast (etchant 11, Table 1). Both Original magnification 100×

The nickel-iron alloys with 36% or more Ni are austenitic single-phase alloys and exhibit numerous annealing twins due to low stacking-fault energies. Their microstructures are similar to those of austenitic stainless steels.
Iron-Cobalt and Iron-Cobalt-Vanadium Alloys. The soft magnetic iron-cobalt alloys exhibit the highest saturation magnetization, a high Curie temperature, and low crystalline anisotropy. Figure 9 shows the microstructure for a cold-rolled Fe-27Co alloy, an alloy with the highest magnetization of any alloy. Their use, however, has been limited due to the high cost of cobalt and the brittleness of alloys at 35 to 50% Co. These alloys order rapidly upon cooling below 730 °C (1345 °F), which induces extreme brittleness.

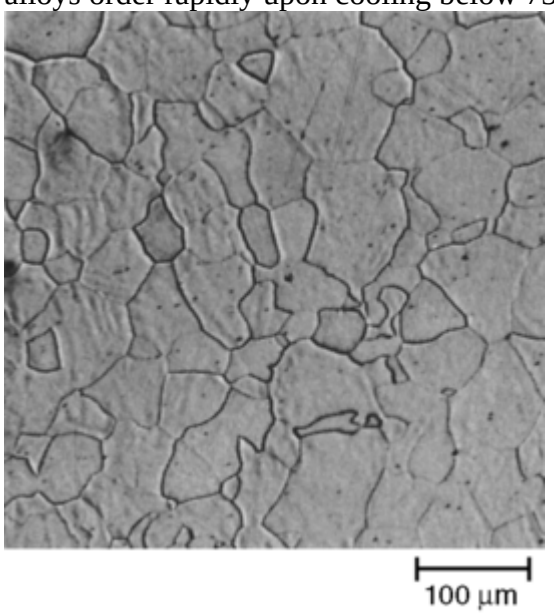

Fig. 9 Fe-27Co cold-rolled strip, annealed 2 h in dry H_2 at 925 °C (1700 °F) and furnace cooled. The microstructure is a body-centered cubic solid solution. An etchant made up of HCl, $CuCl_2$, $FeCl_3$, methanol, and H_2O was used for contrast (etchant 11, Table 1). Original magnification 100×

Iron-cobalt alloys containing 2 to 3% V have magnetic properties intermediate to those of the soft Fe-Co binary alloys and the hard Fe-Co-V alloys containing 14% V and are more properly classified as semihard magnetic alloys. Iron-cobalt alloys containing 2 to 3% V are much more ductile than the binary Fe-50Co alloy and possess higher resistivity. The embrittlement problems of these alloys have been reviewed (Ref 48).

The physical metallurgy of iron-cobalt alloys containing 2 to 3% V has been studied in depth (Ref 48, 49, 50, 51, 52, 53, 54). Heating at 900 to 950 °C (1650 to 1740 °F) produces a two-phase structure, bcc α_1, and fcc γ. Rapid cooling yields α_1, and supersaturated bcc α_2. Increasing the temperature in this range provides an increased amount of γ, which results in more α_2 upon quenching. Slow cooling from the all-γ region produces only α_2, which is brittle. The two-phase mixture of α_1, and α_2 is ductile enough to permit drawing. If the quench rate from the two-phase region is not fast enough, the α_1 bcc structure will order, forming α'_1, which is very brittle. Heating at 925 °C (1695 °F) produces approximately equal amounts of α_1 and α_2, which results in optimal magnetic properties after a subsequent precipitation anneal at 600 to 610 °C (1110 to 1130 °F). This anneal produces submicron-size particles of stable cobalt-rich and vanadium-rich fcc γ by the decomposition of supersaturated α_2 into ordered α'_1 and γ. This increases strength, but results in brittle cleavage fractures rather than ductile fractures that are produced prior to annealing. The favorable magnetic properties result from the fine dispersion of stable γ particles that impede domain-wall motion.

Amorphous and Nanocrystalline Alloys. Although they are not as widely used as silicon-iron electrical steels or spinel ferrites, amorphous and nanocrystalline soft magnetic materials have excellent magnetic properties. Both types of alloys are produced by melt spinning. During the processing, alloy ingots are induction melted in a crucible with an orifice in the bottom. The melt is ejected from the crucible onto a rapidly rotating wheel, which quenches the alloy at approximately 10^6 °C/s. This quench rate is sufficient to prevent crystallization of the alloy during optimal processing.

The basic composition of amorphous soft magnetic alloys consists of 75 to 80% magnetic transition metal (e.g., iron, cobalt, nickel) with the remainder being metalloid elements (e.g., silicon, boron, phosphorus, etc.). These compositions are near deep eutectics, a necessary requirement to avoid crystallization. Nanocrystalline soft magnetic alloys are similar in composition to amorphous alloys; however, they have small amounts (3–7%) of early transition metals (e.g., niobium, zirconium, hafnium) and sometimes 1% Cu. These alloys are annealed at a high enough temperature to provide primary crystallization of the alloy. The primary crystallites are typically high-symmetry solid solutions of the magnetic transition metals with small amounts of the early transition metals. The early transition metals act as diffusion barriers to grain growth, allowing the grains to remain less than 10 nm in diameter. The copper provides nucleation sites for crystallization during the early stages of annealing for some alloys. There is evidence for improved core losses by annealing in a magnetic field for both of these types of alloys.

Nanocrystalline soft magnetic alloys are similar to amorphous alloys in composition and processing method; both consist of long, continuous ribbons, approximately 20 μm in thickness, when optimally processed. Whereas amorphous alloys have very few features to observe by virtue of the nonperiodic atomic arrangement, nanocrystalline alloys possess ample features; however, they are primarily smaller than the diffraction limit of optical microscopes. Even high-resolution scanning electron microscopes do not have the resolution to reveal the 5 to 10 nm grains found in these alloys. Transmission electron microscopy is the preferred imaging method for these alloys.

Commercially, metallic glasses and nanocrystalline alloys are used for saturable core inductor and motor controller applications. The high resistivity of these alloys, compared with electrical steels allows them to be used at higher operation frequencies (10 to 100 kHz). Detailed information on nanocrystalline and amorphous alloys is provided in Ref 55.

Garnets and Ferrites. Ferrites are powder-made ceramic materials of the cubic spinel crystal structure, the cubic garnet type, or the hexagonal type (discussed in the section “Microstructures of Permanent Magnets” in this article). The cubic spinel types, also called ferrospinels, have the general formula $M^{2+}Fe_2^{3+}O_4$, where M is a divalent metal ion with an ionic radius between 0.055 and 0.085 nm (0.55 and 0.85 Å), (e.g., magnesium, iron, cobalt, nickel, manganese, copper, zinc, and cadmium). Commercial spinel ferrites partially populate both octahedral and tetrahedral sites with M^{2+} cation, due to their size similarity to the Fe^{3+} cations. An exception is lithium ferrite, with the formula $Li_{0.5}Fe_{2.5}O_4$. Commercially important materials include ferrite solid solutions with compositions, $(Mn,Zn)Fe_2O_4$ and $(Mn,Ni)Fe_2O_4$. The manganese-zinc ferrite is quite important due to its large resistivity, low losses, and relatively high Curie temperature at operation frequencies above 1 MHz.

Nickel-zinc ferrites possess even higher resistivity allowing them to operate at frequencies up to 1 GHz. Spinel ferrites suffer from low saturation magnetization compared to metallic alloys and poor mechanical strength.

The grain structure of ferrites is an important microstructural parameter. Optimal magnetic properties are obtained with very regular grain shapes of nearly equal size and sharply delineated grain boundaries. Therefore, control of the sintering temperature and time is critical. Control of the sintering atmosphere is also important. Silica is the chief impurity in manganese-zinc ferrites. As the amount of silica increases, the magnetic properties are improved, but amounts above approximately 0.04% impair magnetic properties due to discontinuous grain growth (Ref 56).

The cubic ferrites of the garnet type consist of mixed oxides, the most common being $Mn_3Al_2Si_3O_{12}$. Magnetic garnets have the general formula $3M_2O_3 \cdot 5Fe_2O_3$ or $2M_3$, where M is a rare earth element. Garnets are ferrimagnetic materials, as are spinel ferrites. This means that the magnetic moments are in different directions depending on the crystal lattice site. The most commonly discussed configuration fills some lattice sites with magnetic moments antiparallel to the remaining sites. As an example, the R^{3+} cations are found in dodecahedral sites and possess magnetic moments that are parallel to three-fifths of the Fe^{3+} cations (in the tetrahedral sites). The other two-fifths of the Fe^{3+} cations, occupying octahedral sites, are antiparallel to the previously mentioned cations. Due to the large size difference between the rare earth and iron cations, antisite disorder is not as common as in the case of spinel ferrites.

Specific types of garnets are referred to as gadolinium iron garnet (GdIG) or yttrium iron garnet (YIG), which have the formulas $Gd_3Fe_5O_{12}$ and $Y_3Fe_5O_{12}$, respectively. Both spinel ferrites and garnets are used for high-frequency applications (above 1 MHz) due to their low eddy current losses, made possible by their high resistivities. Reference 57 and 58 provide detailed information about the specific characteristics of these oxide magnets and their application as high-frequency soft magnets.

References cited in this section

26. E.T. Stephenson and M.R. Amann, Effects of Composition, Grain Size and Texture on the AC Core Loss of Magnetic Lamination Steel, in *Energy Efficient Electrical Steels,* American Institute of Mining, Metallurgical, and Petroleum Engineers, 1981, p 43–60

27. "Specification for Nonoriented Electrical Steel Fully Processed Types," A 677/A 677M, *Annual Book of ASTM Standards,* Vol 03.04, ASTM, 2003

28. "Specification for Nonoriented Electrical Steel, Semiprocessed Types," A 683/A 683M, *Annual Book of ASTM Standards,* Vol 03.04, ASTM, 2002

29. R.R. Judd and K.E. Blazek, Effect of High-Temperature Annealing on the Magnetic Properties of Fully Processed Nonoriented Silicon-Steel Sheets, in *Energy Efficient Electrical Steels,* American Institute of Mining, Metallurgical, and Petroleum Engineers, 1981, p 147–155

30. H. Shimanaka et al., Non-Oriented Si-Steels Useful for Energy Efficient Electrical Apparatus, in *Energy Efficient Electrical Steels,* American Institute of Mining, Metallurgical, and Petroleum Engineers, 1981, p 193–204.

31. Y. Shimoyama et al., Development of Non-Oriented Silicon Steel Sheet with Very Low Core Loss, *IEEE Trans. Magnetics,* MAG-19, Sept 1983, p 2013–2015

32. R.G. Aspden et al., Anisotropic and Heterogeneous Nucleation During the Gamma to Alpha Transformation in Iron, *Acta Metall.,* Vol 16, Aug 1968, p 1027–1035

33. R.F. Krause and B.A. Popovic, Magnetic Properties of Textured Annealed Commercial Black Plate, *J. Appl. Phys.,* Vol 52, March 1981, p 2419–2421

34. N.P. Goss, New Development in Electrical Strip Steels Characterized by Fine Grain Structure Approaching the Properties of a Single Crystal, *Trans. ASM,* Vol 23, June 1935, p 511–544

35. R.M. Bozorth, The Orientation of Crystals in Silicon Iron, *Trans. ASM,* Vol 23, Dec 1935, p 1107–1111

36. F. Assmus et al., Iron-Silicon Alloy With Cubic Structure, Parts I and II. *Z. Metallkde.,* Vol 48, June 1957, p 341–349

37. J.E. May and D. Turnbull, Secondary Recrystallization in Silicon Iron, *Trans. AIME,* Vol 212, Dec 1958, p 769–781

38. S. Taguchi and A. Sakakura, Characteristics of Magnetic Properties of Grain-Oriented Silicon Iron with High Permeability, *J. Appl. Phys.,* Vol 40, 1 March 1969, p 1539–1541

39. A. Sakakura et al., Recent Developments in Magnetic Properties of Grain-Oriented Silicon Steel with High Permeability, *Magnetism and Magnetic Materials—1974,* AIP Conference Proceedings No. 24, American Institute of Physics, 1975, p 714–715

40. S.M. Pegler, The Magnetic Properties of Japanese HI-B (110) [001] Grain-Oriented Silicon-Iron, *Magnetism and Magnetic Materials—1974,* AIP Conference Proceedings No. 24, American Institute of Physics, 1975, p 718–720

41. M. Barisoni and M. Candiotti, A New High Permeability Grain Oriented Fe-3% Si Steel, *IEEE Trans. Magnetics,* MAG-14, Sept 1978, p 345–349

42. M. Barisoni et al., Effect of Second Phase on the Primary and Secondary Recrystallization Texture of Grain Oriented Si-Fe Sheets, *IEEE Trans. Magnetics,* MAG-11, 1975, p 1361–1363

43. T. Matsuoka, Effect of Impurities on the Development of (110) [001] Secondary Recrystallization Texture in 3% Silicon Iron, *Trans. ISIJ,* Vol 7 (No. 1), 1967, p 19–28

44. L.J. Regitz, Origins of Streaks of Poorly Oriented Grains in Oriented Silicon Steel, *J. Met.,* Vol 23, Sept 1971, p 17–25

45. J.W. Shilling and G.L. Houze, Jr., Magnetic Properties and Domain Structure in Grain-Oriented 3% Si-Fe, *IEEE Trans. Magnetics,* MAG-10, No. 2, June 1974, p 195–223

46. G.C. Rauch et al., Development of (110) [001] Texture in Low-Alloy Iron by Primary Recrystallization and Normal Grain Growth, *Met. Trans.,* Vol 8A, Jan 1977, p 210–212, 510, 1835

47. D.R. Thornburg et al., The Effect of Manganese and Sulfur on the Development of Orientation (110) [001]-Oriented Low-Alloy Iron, *J. Appl. Phys.,* Vol 52, March 1981, p 2413–2415

48. C.W. Chen, Metallurgy and Magnetic Properties of an Fe-Co-V Alloy, *J. Appl. Phys.,* Vol 32, March 1961, p 348S–355S

49. D.R. Thornburg, High-Strength High-Ductility Cobalt-Iron Alloys, *J. Appl. Phys.,* Vol 40, 1 March 1969, p 1579–1580

50. M.R. Pinnel and J.E. Bennett, The Metallurgy of Remendur: Effects of Processing Variations, *Bell System Tech. J.,* Vol 52, Oct 1973, p 1325–1340

51. J.E. Bennett and M.R. Pinnel, Aspects of Phase Equilibria in Fe/Co/2.5 to 3.0% V. Alloys, *J. Mater. Sci.,* Vol 9, 1974, p 1083–1090

52. S. Mahajan, M.R. Permel, and J.E. Bennett, Influence of Heat Treatments on Microstructures in an Fe-Co-V Alloy, *Met. Trans.,* Vol 5, June 1974, p 1263–1272

53. M.R. Pinnel and J.E. Bennett, Correlation of Magnetic and Mechanical Properties with Microstructure in Fe/Co/2-3Pct V Alloys, *Met. Trans.,* Vol 5, June 1974, p 1273–1283

54. M.R. Pinnel, S. Mahajan, and J.E. Bennett, Influence of Thermal Treatments on the Mechanical Properties of an Fe-Co-V Alloy (Remendur), *Acta Metall.,* Vol 24, 1976, p 1095–1106

55. M.E. McHenry, M.A. Willard, and D.E. Laughlin, Amorphous and Nanocrystalline Materials for Applications as Soft Magnets, *Prog. Mater. Sci.,* Vol 44, 1999, p 291–434

56. G.C. Jain et al., On the Origin of Core Losses in a Manganese Zinc Ferrite with Appreciable Silica Content, *J. Appl. Phys.,* Vol 49, May 1978, p 2894–2897

57. G. Winkler, *Magnetic Garnets,* Vieweg, 1981

58. E.C. Snelling, *Soft Ferrites: Properties and Applications,* Iliffe, 1969

M.A. Willard and G.F. Vander Voort, Microstructure and Domain Imaging of Magnetic Materials, *Metallography and Microstructures,* Vol 9, *ASM Handbook,* ASM International, 2004, p. 969–993

Microstructure and Domain Imaging of Magnetic Materials

Matthew A. Willard, Naval Research Laboratory; George F. Vander Voort, Buehler Ltd.

Microstructures of Permanent Magnets

Permanent magnet materials differ from the soft magnetic materials in that the greatest possible coercivity and large hysteresis loops are desired. Coercivity is a structure-sensitive property obtained by controlling composition and microstructure (Ref 59). In general, permanent magnet materials are processed for maximum coercivity by controlling one or more of the following: grain size, degree of atomic order, texture, defects, and phase distribution (for multiphase materials). The pinning, or immobilization of domain walls, and suppression of reverse domain nucleation when a demagnetizing field is applied are the primary driving forces for the use of these coercivity control mechanisms.

Permanent magnets obtain their useful magnetic properties due to their domain structure, which is controlled by composition, phase distribution, particle size, and crystallographic orientation. Permanent magnets must exhibit good remanence and high coercivity with a high maximum energy product. The coercive force is increased if domain-boundary motion can be impeded or if single domain particles are created.

Domain boundary motion is impeded by four major types of anisotropy forces: crystalline, shape, strain, and exchange anisotropy. The crystalline anisotropy force orients the magnetization vector along a preferred easy crystallographic direction. Shape anisotropy forces cause the magnetization vector to be aligned along the major axis of elongated, single-domain particles.

The earliest permanent magnet alloys were martensitic carbon steels with up to 1.5% C. Alloys containing additions of manganese, tungsten, or chromium provided marginal improvements to performance. These were followed by high-cobalt steels containing tungsten and chromium, then by development of Fe-Co-Mo and Fe-Co-W alloys, such as Remalloy. The Fe-Co-Mo alloys were the first carbon-free alloys, and all subsequent work has centered on carbon-free compositions.

In 1931, Fe-Ni-Al alloys with high coercive forces were developed. This led to the development of the Alnico alloys, which were improved by additions of cobalt or copper and by advances in heat treatments. Next came the Fe-Ni-Cu (Cunife) and Fe-Co-V (Vicalloy) alloys. Further development of the Alnico alloys has produced popular grades such as Alnico 5, 8, and 9, which are still in use.

Research showed that cold work improves magnetic properties of certain alloys. For example, Vicalloy II (Fe-52Co-14V) is nearly nonmagnetic (austenitic) before cold working, but exhibits excellent hard magnetic properties after cold reduction (approximately 95%) and tempering at 600 °C (1110 °F). Permanent magnet properties can also be produced in various austenitic stainless steels by such processing as cold working, which produces ferromagnetic martensite from the paramagnetic austenite.

High coercivity is also obtained in certain binary alloys, for example, platinum-cobalt, platinum-iron, and palladium-cobalt. These alloys are precipitation hardened by an ordered tetragonal precipitate ($L1_0$ structure) in a disordered matrix (fcc). Very high coercivity is obtained in Pt-23.3Co (Platinax II) by oil quenching from 1250 °C (2280 °F), followed by aging at 650 °C (1200 °F). Although these materials have high coercivity, they are prohibitively expensive for most bulk magnet applications (being mainly considered for thin film magnetic recording media).

Development of powder-metallurgy magnetic materials began in 1931 with the OP magnets, a mixture of Fe_3O_4 and cobalt oxide. This was followed by a "Heusler" alloy containing manganese and bismuth. For manganese-bismuth alloys, the magnetic phase is Mn_3Bi_2. The powder is mixed with a small amount of resin and molded under pressure in a magnetic field at approximately 100 °C (212 °F). Coercivity increases as the powder particle size decreases to some critical size (near 3 μm).

Rare Earth Permanent Magnets. The technologically interesting intermetallic compounds of rare earth elements and transition metals, such as iron, nickel, and cobalt, possess high coercivity, uniaxial crystalline anisotropy, and magnetization larger than 1 Tesla at room temperature. The term rare earth permanent magnet applies to two classes of materials: rare earth-iron-boron alloys and rare earth-cobalt alloys. The rare earth-iron-boron alloys, based on the intermetallic compounds $R_2Fe_{14}B$, are processed by either powder-metallurgy techniques or melt spinning. Neodymium is the most common rare earth element used in these alloys. Typical rare earth (R)/cobalt intermetallic compounds include R_2Co_{17} and RCo_5.

Neodymium-iron-boron ($Nd_2Fe_{14}B$) magnets have become important for applications where small size and large coercivity are necessary. Being iron-base, these rare earth permanent magnets are much less expensive than samarium-cobalt alloys; however, they possess much lower Curie temperatures limiting their use to less than 150 °C. At room temperature, Nd-Fe-B alloys exceed all other commercial permanent magnets in their energy product (~360 kJ/m^3), a figure of merit for permanent magnets. Typical microstructures of Nd-Fe-B-type magnets are shown in Fig. 10 (Ref 60). These materials were produced by an inexpensive technique, called hydrogenation disproportionation desorption recombination (HDDR), which relies on a reversible incorporation of hydrogen into the material during processing for grain size reduction. Figure 10(a) shows a Nd-(Fe,Co,Ga)-B alloy prepared by solid-HDDR processing with grain size in the range from 200 to 800 nm. The corresponding domain structure, produced by Foucault magnetic contrast imaging, shows the domain walls following the grain boundaries of small grains and through the center of larger grains (Fig. 10c). Figure 10(b) shows an alloy with composition, Nd-(Fe,Co,Ga,Al)-B, processed by conventional HDDR followed by die upsetting. The grain size average is 310 × 670 nm^2 for this material, with the domain walls cutting across the short axis of the grains and in the direction of pressing (Fig. 10d).

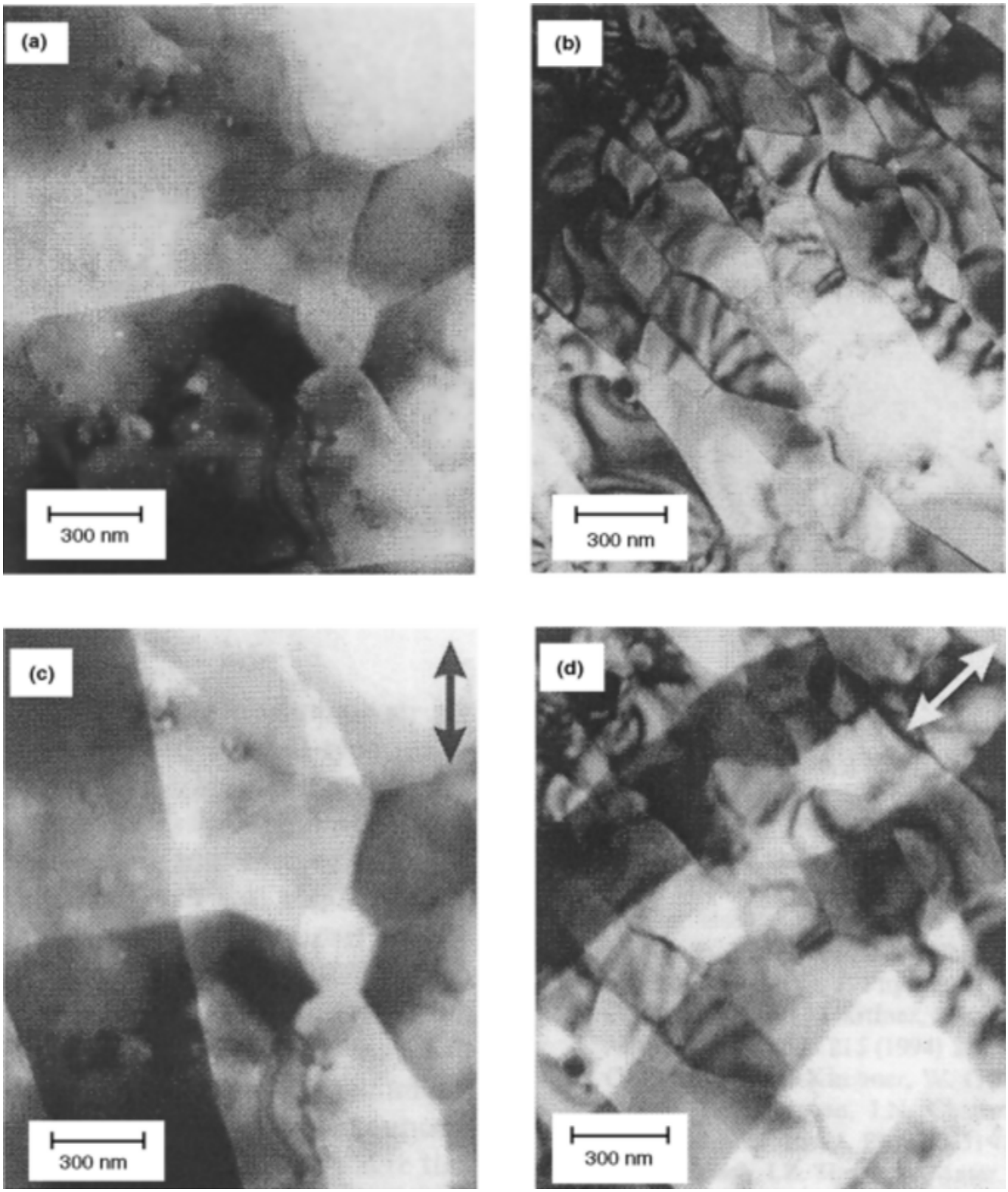

Fig. 10 Transmission electron micrographs of two different Nd-(Fe,Co,Ga)-B alloys prepared by hydrogenation disproportionation desorption recombination (HDDR) processing. The first sample was prepared by solid-HDDR processing shows an average grain size of 300 nm (a) and corresponding domains aligned with the *c*-axis of the $Nd_2Fe_{14}B$ grains (c) (the component of the magnetization examined by the Foucault method indicated by the double headed arrow). The second alloy was produced by conventional HDDR followed by die upsetting, having grain averaging 310 × 670 nm^2. In this case, the domains are aligned with the die-upset direction. The double-headed arrow in this case refers to both the die upset pressing direction and the component of the magnetization examined. Reproduced with permission from Ref 60

Neodymium-iron-boron alloys are produced as either sintered anisotropic or bonded isotropic magnets. Powder-metallurgy techniques are used to produce the magnets with best properties. However, great care must be taken during processing due to the large amount of easily oxidized rare earth in these alloys. The typical fracture surface of a fully dense sintered magnet with composition $Nd_{16}Fe_{76}B_8$ is shown in Fig. 11 (Ref 61).

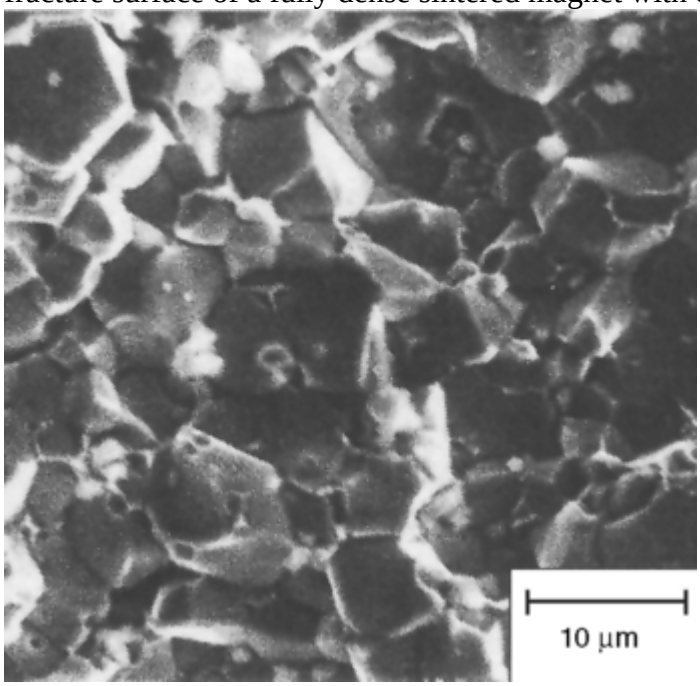

Fig. 11 Micrograph of the fracture surface of a fully dense sintered rare earth permanent magnet with composition $Nd_{16}Fe_{76}B_8$. A scanning electron microscope was used to image this sample, using secondary electrons. This image shows the typical grain size is uniform and about 5 to 10 μm in diameter. Reproduced with permission from Ref 61

The coercivity tends to increase as the grain size is reduced for Nd-Fe-B alloys. Typical microstructures for anisotropic magnets consist of uniform grains a few microns in diameter; however, reduction of grain size is a major research effort (Ref 61). Special processing by mechanical alloying, rapid solidification, or hydrogen processing are potential routes for improvements to the microstructures (Ref 61, 62). Additional information about rare earth permanent magnets, their microstructures, and applications are found in Ref 9, 63, and 64.

Magnetic properties of RCo_5 magnets (where R is Sm, Y, La, Ce, or Pr) have been discussed (Ref 65). Of these, $SmCo_5$ has exceptional properties, with energy densities nearly five times that of the best Alnico magnets. Production of $SmCo_5$ magnets, however, is rather challenging, and they are expensive. The hard magnetic properties of $Sm_2(Co,Cu,Zr,Fe)_{17}$ alloys are maintained to high temperatures, giving these alloys primary use for applications between 150 and 350°C (300 and 660 °F).

As shown in Fig. 12, the microstructure of $Sm(Co,Fe,Zr,Cu)_{7–9}$ alloy magnets is quite complex. Sintered anisotropic Sm_2Co_{17}-type magnets have additional alloying elements to produce a cellular microstructure, which helps to block domain wall motion, thereby increasing the energy product of the material. The rhombohedral 2:17 grains, as seen in Fig. 12(a), are surrounded by a crystallographically coherent copper-rich 1:5 phase at the grain boundaries. The *z*-phase, or platelet phase, is formed perpendicular to the *c*-axis of the 2:17 phase and traverses grain boundaries. The platelet microstructure improves the coercivity of these alloys and is produced in alloys with zirconium additions.

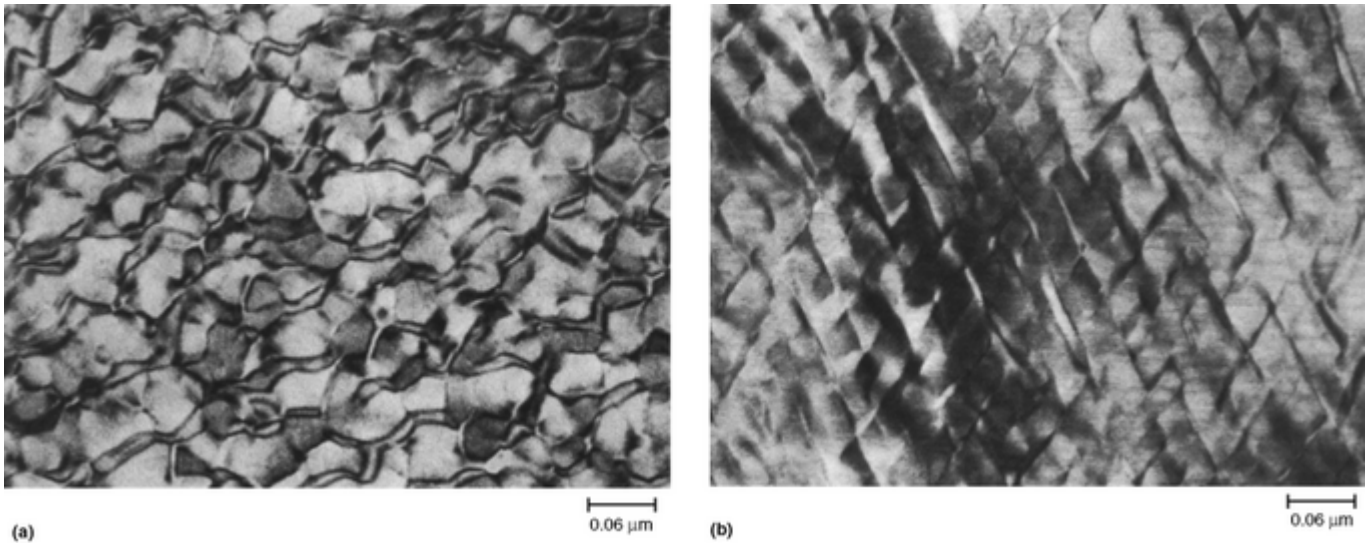

Fig. 12 Transmission electron micrographs showing the cellular microstructure of $Sm(Co_{0.8}Cu_{0.15}Fe_{0.05})_7$ permanent magnet in the peak-aged condition (aged 30 min at 850 °C, or 1560 °F). (a) A section normal to the magnetic alignment direction (*c*-axis), showing the diamond-shaped cells of Sm_2Co_{17} phase surrounded by a coherent $SmCo_5$ phase at the boundaries. (b) A section including the alignment direction (*c*-axis vertical). Cell interiors show the Sm_2Co_{17} structure; cell boundaries have the $SmCo_5$ structure with the phases fully coherent. The $SmCo_5$ phase at the cell boundaries helps to pin the domain walls providing improved coercivity. As-polished. Original magnification 160,000×. Reproduced with permission from Ref 66

Hexagonal Ferrite Magnets. Ceramic magnet materials, ferrites, have become very popular permanent magnet materials. Barium ferrite, $BaO{\cdot}6Fe_2O_3$ (M-type), has considerable commercial value. Related crystal structures based on stacking cubiclike and rhombohedrallike sequences of barium/iron planes is possible to produce a number of other hexagonal ferrite types (e.g., W, Y, Z). M-type barium ferrites, however, have the highest Curie temperature and largest room-temperature coercivity, making them more attractive for many applications. Ferrites are made by sintering blended powders (as seen in Fig. 13). Other useful ferrites include lead ferrite and strontium ferrite. Ferrites with a preferred magnetic direction can be produced using powders that will orient in a magnetic field.

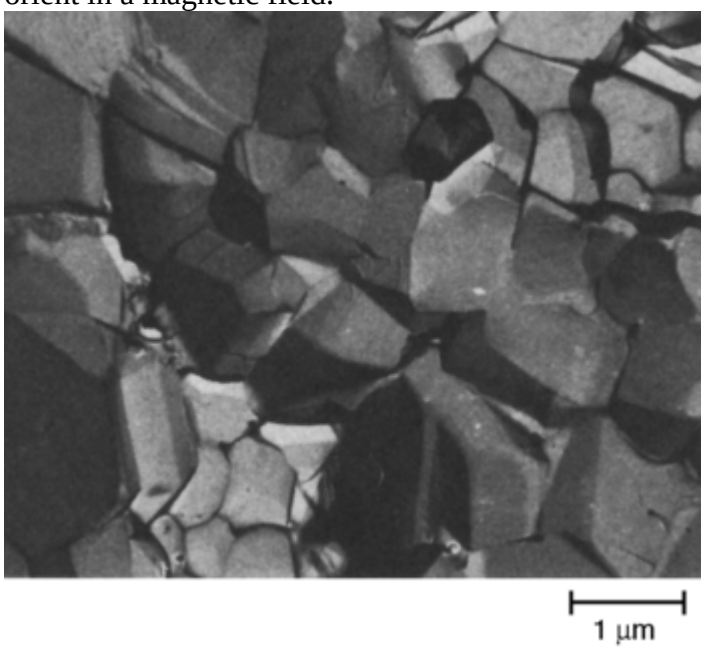

Fig. 13 Electron micrograph of a fracture surface of isotropic barium ferrite pressed from micron-size powder and sintered at 1205 °C (2200 °F) to obtain final magnetic properties. Crystals are ~1 μm in size, which approximates the dimensions of a single domain. As-polished. Original magnification 10,000×

Alnico Alloys. Precipitation-hardenable Alnico alloys in the cast conditions have a coarse-grained macrostructure that appears to be single phase using optical microscopy. Use of electron microscopy reveals that two phases are present, including fine, rod-shaped α′ precipitates of a bcc ferromagnetic phase in an α matrix, which is also bcc but weakly magnetic. The α′ precipitates grow in the three ⟨100⟩ directions. Optimal magnetic properties are obtained by homogenization followed by reprecipitation of the α′. For Alnico 5, the heat treatment is performed under a magnetic field aligned in the direction desired for the end use.

Homogenization of Alnico 5 has been conducted in the α solid-solution single-phase region at 930 °C (1705 °F) or 1300 °C (2370 °F). The former temperature must be carefully controlled; the latter is less critical, but oxidation is more of a problem. The cooling rate from the homogenization temperature must be carefully controlled in the magnetic field from either temperature down to approximately 600 °C (1110 °F). This is followed by aging from 550 to 650 °C (1020 to 1200 °F) to develop the magnetic properties. This aligns the α′ precipitates in the direction of the applied field, producing a periodic pattern (see Fig. 14). The precipitation arises from spinodal decomposition (see the article “Spinodal Transformation Structures” in this Volume). This transformation process in Alnico alloys has been reviewed (Ref 67).

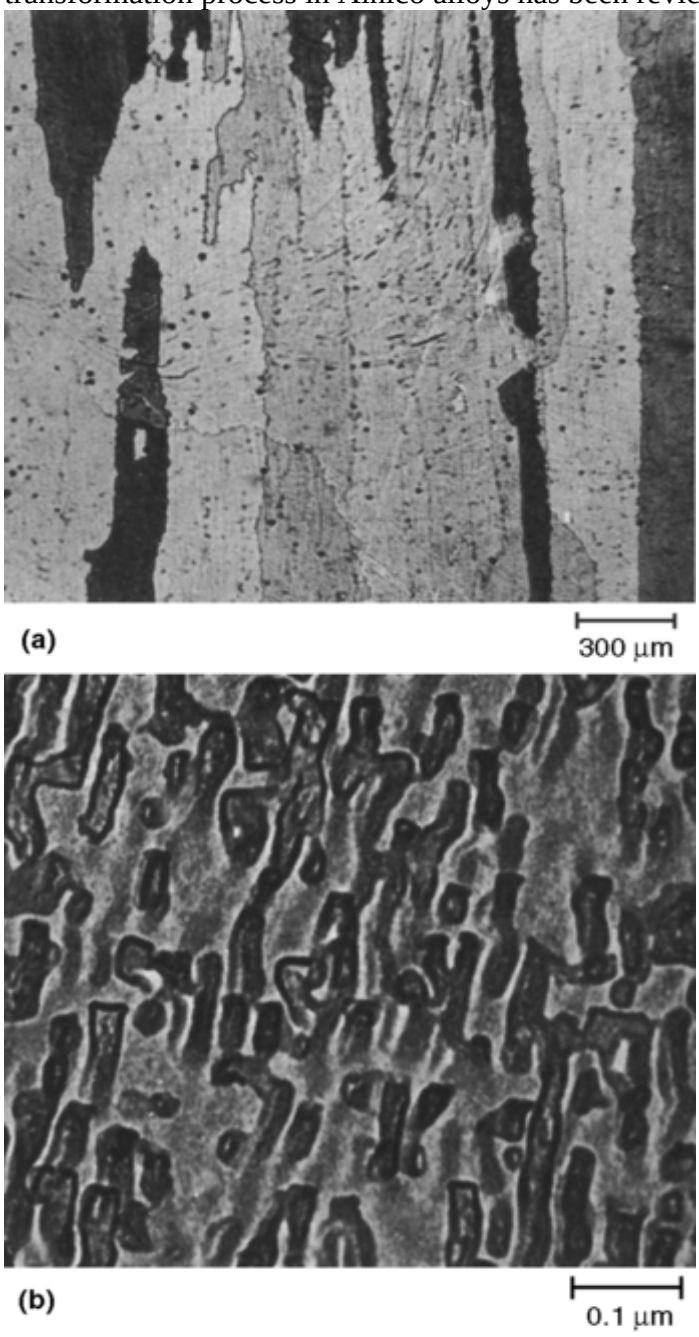

Fig. 14 Alnico 5, cast with random grains, annealed 30 min at 925 °C (1700 °F) in a magnetic field of 1000 Oe min, and aged 24 h at 550 °C (1020 °F). (a) Note pattern and boundaries of random equiaxed grains of the α-phase matrix. Marble's reagent (etchant 13, Table 1). 30×. (b) Transmission electron

micrograph of an Alnico 5 casting, solution annealed above the Curie temperature, cooled in a magnetic field, and aged. The particles of α (dark) in an α′ matrix have a vertical orientation, parallel to the applied field direction. As-polished. Original magnification 100,000×

Aging is usually a two-step process to produce the iron-cobalt-rich α′ particles in the aluminum-nickel-rich α matrix. To obtain strong shape anisotropy, the aspect ratio of the α′ particles must be high. Estimates of the size of the α′ precipitates vary from 40 to 150 nm (400 to 1500 Å) in length and 7.5 to 40 nm (75 to 400 Å) in diameter.

Addition of titanium, as in Alnico 5E or Alnico 6B, produces an α phase that is a modification of Fe_2Ti. This is an fcc precipitate (a = 0.572 nm, or 5.72 Å) coherent with the α′ precipitates that increases the coercivity while decreasing the remanence. The grain size of these alloys is finer due to the presence of titanium nitride. Some manufacturers add niobium rather than titanium, which produces a hexagonal ε phase, Fe_2Nb.

Alnico 8 contains 35% Co and 5% Ti and exhibits increased coercivity due to the α phase. Alnico 8 magnets have a finer, elongated precipitate with a higher aspect ratio, sharper delineation between the phases, and less interconnecting growth between the particles than Alnico 5. The particles are rich in iron and cobalt, and the matrix is rich in nickel, aluminum, and titanium. The structure consists of α′ precipitates in an α matrix. Both are metastable body-centered tetragonal phases (bct). Processing must be carefully controlled to obtain the optimal α′ shape without formation of α, which will impair magnetic properties. Columnar grains in as-cast Alnico 8 can be obtained by additions of sulfur, selenium, and tellurium.

References cited in this section

9. R. Skomski and J.M.D. Coey, *Permanent Magnetism,* Inst. of Physics Publ., 1999

59. F.E. Luborsky, Permanent Magnets in Use Today, *J. Appl. Phys.,* Vol 37, 1 March 1966, p 1091–1094

60. P. Thompson, O. Gutfleisch, J.N. Chapman, and I.R. Harris, A Comparison of the Micromagnetic and Microstructural Properties of Four NdFeB-Type Materials Processed by the HDDR Route, *J. Magn. Magn. Mater.,* Vol 202, 1999, p 53–61

61. I.R. Harris and A.J. Williams, The Character and Role of Grain Boundaries in NdFeB-type Alloys and Magnets, *Z. Metallkde.,* Vol 93, 2002, p 983–990

62. G.C. Hadjipanayis, Nanophase Hard Magnets, *J. Magn. Magn. Mater.,* Vol 200, 1999, p 373–391

63. J.M.D. Coey, Whither Magnetic Materials?, *J. Magn. Magn. Mater.,* Vol 196–197, 1999, p 1–7

64. L.R. Moskowitz, *Permanent Magnet Design and Application Handbook,* Kreiger Publishing Co., 2nd ed., 1995

65. K.J. Strnat, The Recent Development of Permanent Magnet Materials Containing Rare Earth Metals, *IEEE Trans. Magnetics,* MAG-6, 1970, p 182–190

66. J.D. Livingston and D.L. Martin, Microstructure of Aged $(Co, Cu, Fe)_7Sm$ Magnets, *J. Appl. Phys.,* Vol 48 (No. 3), 1977, p 1350–1354

67. K.J. DeVos, Alnico Permanent Magnet Alloys, in *Magnetism and Metallurgy,* Vol 1, Academic Press, 1969, p 473–512

M.A. Willard and G.F. Vander Voort, Microstructure and Domain Imaging of Magnetic Materials, *Metallography and Microstructures,* Vol 9, *ASM Handbook,* ASM International, 2004, p. 969–993

Microstructure and Domain Imaging of Magnetic Materials

Matthew A. Willard, Naval Research Laboratory; George F. Vander Voort, Buehler Ltd.

Magnetism and Magnetic Domains

Ferromagnetic materials, such as iron, are made up of atoms possessing magnetic moments. The atomic moments are aligned parallel to their near neighbors by a quantum mechanical exchange interaction. Iron, nickel, cobalt, and their alloys are typically ferromagnetic at room temperature, possessing a spontaneous magnetization even in the absence of an applied magnetic field. Heating to above the Curie temperature (770 °C, or 1418 °F, for iron; 360 °C, or 680 °F, for nickel; 1115 °C, or 2039 °F, for cobalt) eliminates the preferred alignment; cooling below this temperature restores the dominance of the exchange coupling forces, causing realignment. Reduction of fringing fields (i.e., magnetic fields leaving the sample due to the magnetic moment of the sample) during this process results in the formation of regions with large-scale alignment of atomic moments, known as domains. Alignment within the domain is produced by the exchange coupling forces; an external field is not required (i.e., spontaneous magnetization).

The alignment direction of the magnetic moments varies with the crystal lattice of the material. Body-centered cubic iron has the atomic moments aligned in the direction of the cube faces (e.g., [100] direction). For fcc nickel, the atomic moments are aligned in the direction of the body diagonals (e.g., [111] directions). These preferred alignment directions arise as a result of coupling between the magnetic moments and the crystalline lattice creating magnetic anisotropy forces, called magnetocrystalline anisotropy.

Boundaries between domains are referred to as domain walls (e.g., Bloch walls) and have approximate thickness of tens to many hundreds of atomic distances depending on the material. The atomic moment orientations change within the wall from the direction of one domain to that of its neighbor. The relative orientations of adjacent domains determine the character of the domain wall. Since the local atomic moment direction is determined by the magnetocrystalline anisotropy (i.e., preferred crystal axes), the walls are referred to by the rotation angle between the magnetization axes. Typically, 90° and 180° domain walls are observed for bcc iron, 180° domain walls for uniaxial materials (e.g., cobalt), and 70.53° and 109.47° walls for fcc nickel (the angle between adjacent ⟨111⟩ directions). Each grain in a typical polycrystalline ferromagnetic metal contains numerous domains and domain walls.

When a ferromagnetic core is placed within a magnetic field, the domain walls begin to move. Wall movement continues as the field strength is increased, with the growth of domains that have magnetic moments most aligned with the field at the expense of other domains. When a large enough field is applied, all the atomic moments become aligned preferentially along the applied field direction. This is known as the saturated state. This process can be observed using domain imaging microscopy. If the applied magnetic field is rapidly increased, the domain walls jump from their “rest” position and continue to move until they encounter an obstacle. Such jumps or abrupt changes are referred to as the Barkhausen effect. When only preferentially oriented domains are left, the magnetization of the remaining domains rotates away from the preferred crystalline axis and into the applied field direction. Temperature influences the magnitude of the saturation value, with a maximum at absolute zero and essentially none at the Curie temperature. For any given temperature, the magnitude of saturation depends on the composition of the material and its crystal structure.

Observation of Domains

Numerous techniques are commonly used to observe magnetic domain structures. The more prevalent methods (and therefore ones that are examined more closely in this section) include the Bitter technique, the magneto-optical Kerr and Faraday methods, scanning electron microscopy (magnetic contrast Types I and II), scanning electron microscopy with polarization analysis (SEMPA), Lorentz transmission electron microscopy, and magnetic force microscopy (MFM). X-ray topography, interferometry, electron holographic procedures,

photoemission electron microscopy, and polarized x-ray microscopies are also used for domain imaging, but are beyond the scope of this article (for more information see Ref 68, 69, 70, 71, 72, 73, 74, 75, 76).

Bitter Patterns. The oldest and easiest procedure for studying magnetic domains is the powder pattern technique, or Bitter method, developed in 1931 (Ref 77, 78). This method uses a colloidal magnetic nanoparticle solution spread on the surface of a metallography sample to create magnetic contrast. For optimal results, the specimen must first be carefully polished to minimize residual stresses and subsequent artifacts in the images (Ref 79, 80). For this reason, final preparation by electropolishing is recommended. After the surface has been prepared, a small drop of ferrofluid, approximately 5 μL, is placed on the surface, and a cover slip is placed over the drop to produce a very thin film against the sample. Observation is conducted under bright-field (BF) or dark-field (DF) illumination using a standard metallurgical microscope (Ref 81, 82). Applied stress or magnetic fields can manipulate the location of magnetic domains; therefore, a solenoid or tensile/compression stage may be desirable. As shown in Fig. 15, a thick film sample of Ni-Co is observed under an applied field and with DF illumination. The Bitter pattern clearly shows the domain walls (magnetization directions are indicated by the arrows). The 180° walls are much wider than the 90° walls; therefore, the field gradient is smaller. This manifests itself in the images by the faintness of the 180° walls brought about by the smaller amount of particle collection at those walls.

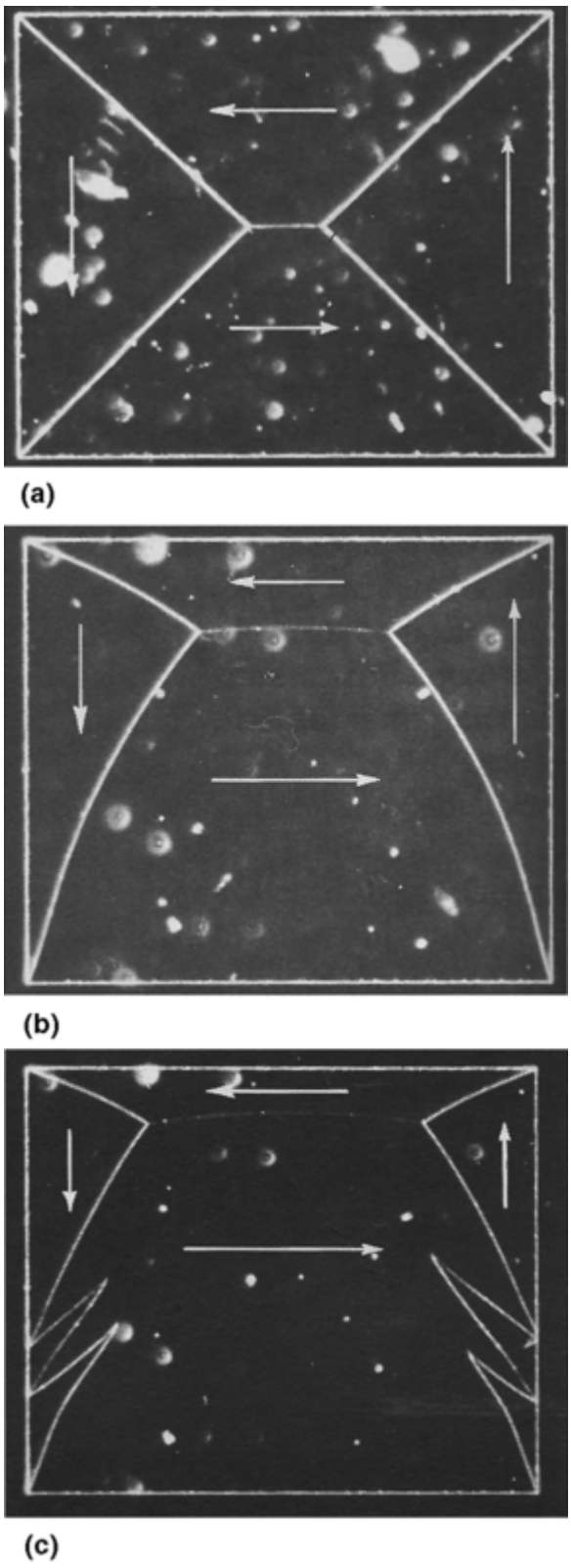

Fig. 15 Bitter domain images of a nickel-cobalt single crystal thick film using dark-field imaging and a microscope with attached field coils. (a) Demagnetized sample with no applied field showing the closure domains. (b) An applied field of 3.6 Oe to the right makes the domain walls reversibly move to increase the volume of the energetically favorable domain. (c) Further increase of the applied field to 4.1 Oe irreversibly moves the domain walls. Original width of rectangle, 165 μm. Reproduced with permission from Ref 4

A unique feature of this domain imaging technique is the use of ferromagnetic colloid solutions, also called ferrofluids. Chemical synthesis methods have been developed for the preparation of ferrofluids; therefore, homegrown and commercial products are potential sources of useful fluids (Ref 83, 84, 85, 86, 87). The

modified Elmore suspension contains small aggregates of Fe_3O_4 particles (Ref 86). The average diameter of the aggregates is typically 100 nm, with individual particles approximately 10 nm in diameter (Ref 88, 89). However, commercially available ferrofluids are frequently used due to their limited agglomeration and uniform mean size and size distribution (Ref 90). These commercial ferrofluids made up of particles smaller than 30 nm are available as organic or aqueous suspensions. The density is approximately 10^{18} particles per cubic centimeter. Regardless of the origin of the ferrofluids, the solution has a limited shelf life, with increased agglomeration as the solution ages beyond a few months.

The surface chosen for examination should contain at least one easy axis of magnetization when using the Bitter technique. This facilitates analysis of the domain patterns. When conditions are favorable, the colloid particles will be attracted to the domain walls that intersect the specimen surface and produce a well-defined pattern. As shown in Fig. 16(a), the magnetization rotates from the in-page domain to the out-of-page domain within the domain wall. At some point, the magnetization becomes perpendicular to the surface. The intersection of the magnetization with the surface creates the fringing field that attracts the colloid particles. Figure 16(b) and (c) illustrate the contrast that accompanies the accumulation of particles in the BF and DF, respectively.

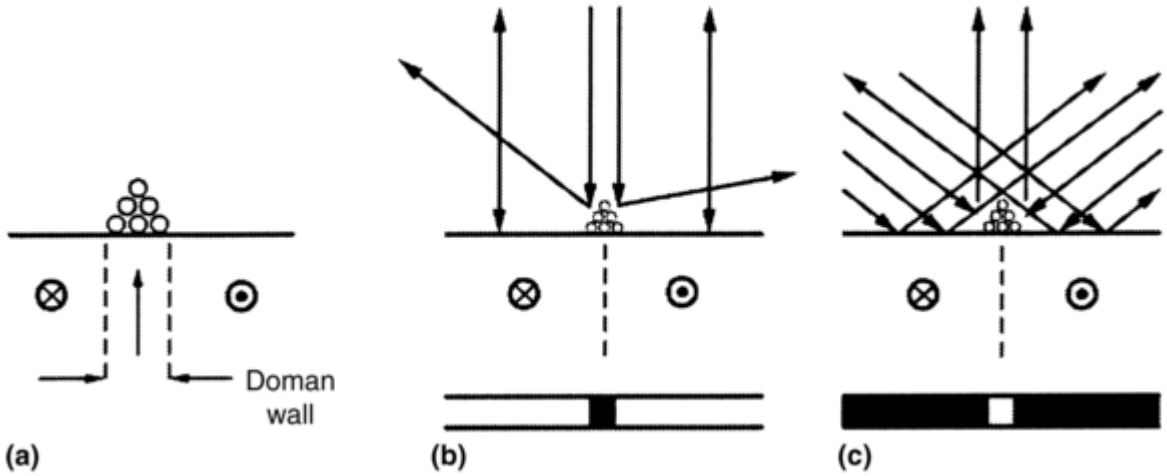

Fig. 16 Basic imaging of domain walls by the Bitter technique for samples with strain free surfaces is shown in this line drawing. (a) Ferrofluid particles collect at domain walls due to the fringe field associated with the magnetization rotation through the wall width and the particle accumulation at the fringe fields causes contrast under both bright field (b) and dark field (c) (after Ref 4)

Preparation of the sample surface, beyond polishing and electropolishing, can aid in image quality. The specimen surface may be coated with a thin layer of collodion before adding the colloidal suspension (Ref 89). The collodion layer thickness produces first-order interference colors and protects the specimen surface from staining by the colloidal suspension. Magnetic contrast can also be developed by intentionally scratching the surface of the sample, lightly running a quartz filament brush across the sample, for example. When the scratches are parallel to the magnetization direction, the scratches do not produce fringe fields (Fig. 17a). However, when the magnetization has a component perpendicular to the scratch direction, a fringe field is formed and particles may accumulate at the scratch (Fig. 17b). Additional magnetic contrast is found in many samples with strain-free surfaces, perpendicular to the magnetization direction. This may be brought about by surface imperfections and surface roughness, which cause fringe fields (see Fig. 17c).

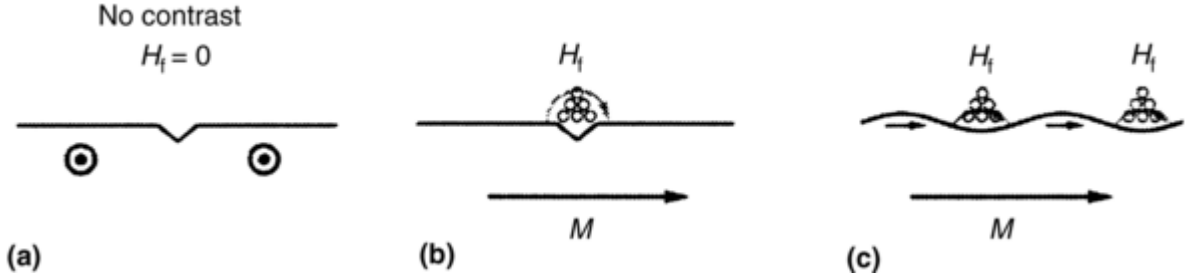

Fig. 17 Line drawings depicting some configurations of the magnetization that produce magnetic contrast for the Bitter technique. The intentional introduction of scratches oriented parallel (a) and perpendicular (b) to the magnetization direction provide different levels of contrast due to the fringing field variation. (c) In general, even materials without intentional scratches have variations in the surface roughness that can provide magnetic contrast occurring as streaks perpendicular to the magnetization direction.

If the magnetic anisotropy of the surface is dominated by polishing induced strains, the domain structure will not be representative of the underlying grain orientations. The strain-induced anisotropy term is proportional to both the stress and the magnetostrictive coefficient of the material, leading to an energy minimum that inverts the domain positions as the magnetic fields with opposite signs are applied. An example showing contrast from both strain-based domains and domain walls is found in Fig. 18. The metallic glass image was taken using a DF technique with significant residual stress from the rapid-solidification processing. The straight white lines indicate domain walls between relatively large domains with low residual stress, while the densely striped regions have significant stress (e.g., near the center of the micrograph).

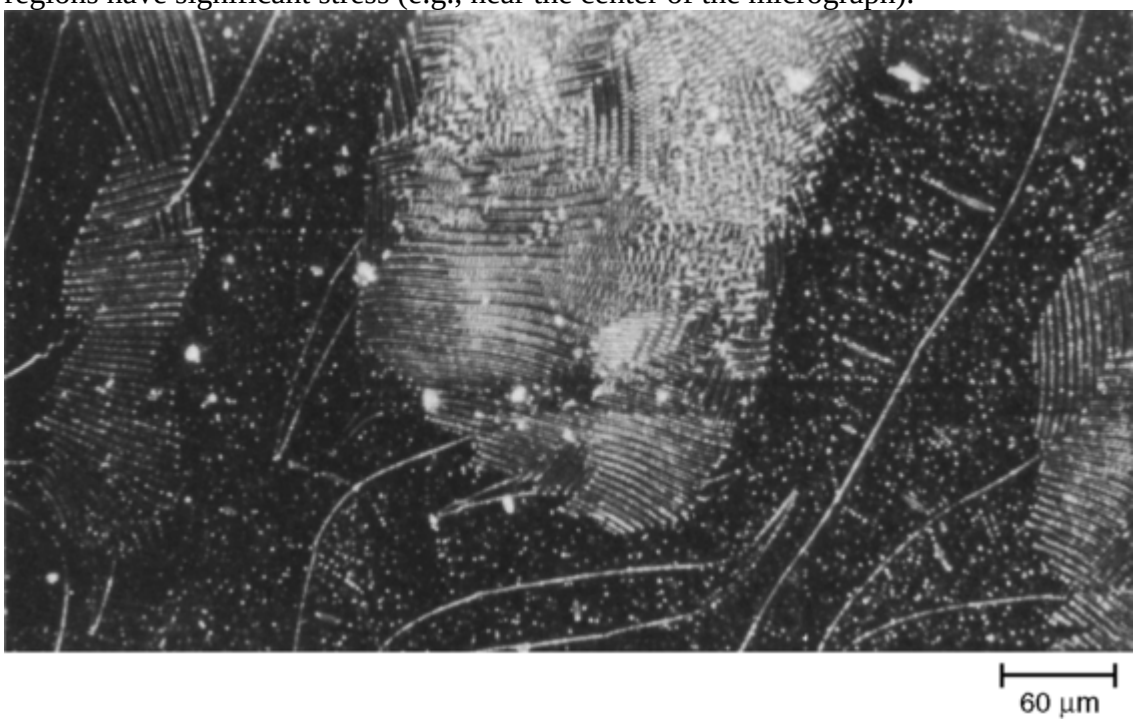

Fig. 18 As-cast $Fe_{80}B_{18.3}P_{1.7}$ metallic glass alloy. Complex magnetic domain structure resulting from the residual stress pattern due to rapid-solidification processing. Dark-field imaging and the Bitter powder pattern technique were used to produce this image. Reproduced with permission from Ref 91. Original magnification 165×

Domain walls have been found to pin on grain boundaries, planar defects, and inclusions for large-grained magnetic materials. When the grains are larger than the domain wall width, reversal of the domains becomes easier as the grain size is increased, thereby decreasing the surface area per unit volume of the grain boundaries. Grains with sizes near the domain wall width tend to pin the walls more strongly. Finally, grain sizes smaller than the domain wall width have reduced coercivity since the domain walls are no longer sufficiently pinned by the grain boundaries. Therefore, depending on application, a certain grain size will be optimal. For example, grain sizes near 100 nm to 1 μm are desirable for permanent magnets, while soft magnetic materials require either a coarse grain size (<100 μm) or very fine grain size (>50 nm); both cases call for low inclusion content. When the inclusion content is high, the most effective inclusions for pinning domain walls are those whose size is similar to the domain wall thickness and reside within the grains. All of these conditions may produce interesting domain images.

Polycrystalline ferromagnetic materials may have randomly oriented grains or may exhibit a well-defined crystallographic texture (see the article “Textured Structures” in this Volume). If the texture is high, the

domains in a polycrystalline specimen may exhibit characteristics much like those of a single crystal. In a few such cases, domains have been observed to be continuous over more than one grain.

The colloid technique is useful for many materials; however, it has some significant drawbacks. First, as with most domain imaging techniques, only surface domains are observed. Second, certain materials, including some nickel-iron alloys with low magnetocrystalline anisotropy, cannot be studied using this method, because the domain walls are wide with small field gradients at the walls that do not attract the colloid particles. Other limitations include a limited temperature range (experiments have been conducted from -90 to 380 °C, or -130 to 715 °F), poor pattern quality for high-coercivity materials using high fields, and examination of only static or slowly moving domain structures. The Bitter method cannot be applied to coated, highly oriented silicon-iron electrical steels. An alternate technique (Ref 92) has been developed and refined for these samples (Ref 93). Despite these problems, the method remains one of the best procedures for studying domain structures on a wide range of materials.

Improved resolution of Bitter patterns can be obtained with optical or electron microscopy through use of a dry Bitter method procedure (Ref 88, 94, 95). Improvements to image quality have been made by the use of digital image processing and the wet colloid method (Ref 96). This technique allows for higher image contrast, and sharpness, and makes possible the removal of background intensity. In recent years, the use of scanning tunneling microscopy in conjunction with Bitter pattern techniques has improved the possible spatial resolution (Ref 97).

Magneto-Optical Faraday Effect. When plane-polarized light is passed through a transparent ferromagnetic material, the direction of polarization is rotated by the magnetic component parallel to the direction of light transmittance. This phenomenon is called the Faraday effect. The degree of rotation varies with the magnitude of magnetization, and the sense of the rotation is influenced by the magnetization direction.

Three geometries for the Faraday effect are possible, each giving contrast for different magnetization directions with respect to the light propagation direction. Longitudinal and transverse Faraday contrast are found for in-plane magnetization, while polar Faraday rotations are observed for magnetization perpendicular to the plane of the sample. Figure 19(a) shows a diagram of the longitudinal Faraday effect, providing magnetic contrast for oblique incidence of the polarized light and magnetization parallel to the direction of the light propagation. The degree of the polarization rotation is proportional to the thickness of the film and the magnetization of the material. When the magnetization of the material is parallel to the plane of the surface, but perpendicular to the plane of incidence (Fig. 19b), the magnitude of the polarization is changed; however, there is no rotation of the polarization.

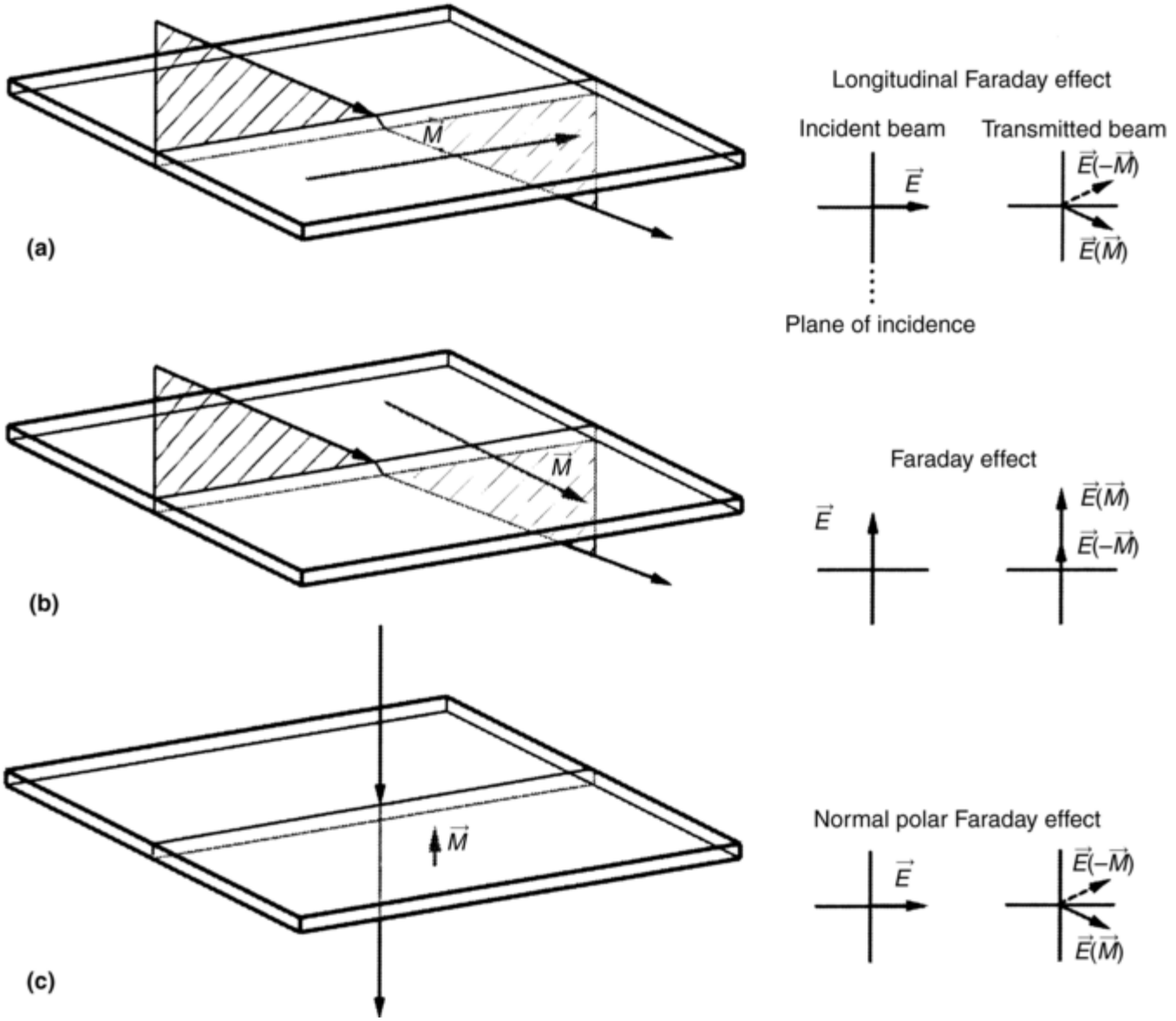

Fig. 19 An illustration of the three Faraday effect geometries identified by the relative orientation of the incident polarized light transmitted compared to the magnetization direction. (a) Longitudinal Faraday effect: oblique incidence of polarized light transmitted through a material with magnetization in the plane of the sample and the plane of incidence. (b) Transverse Faraday effect: oblique incidence of polarized light transmitted through a material with magnetization in the plane of the sample and perpendicular to the plane of incidence. (c) Normal polar Faraday effect: largest contrast effect for normal incidence or polarized light transmitted through a material with magnetization normal to the plane of the sample. The incoming and outgoing electric field vectors are indicated to the right of the corresponding diagram, where the vertical axis is parallel to the plane of incidence. The direction of light propagation is into the plane of the page.

The most commonly used Faraday effect technique is for samples with the magnetization perpendicular to the plane of the sample (Fig. 19c), called the polar Faraday effect. In this configuration the light is typically transmitted perpendicular to the film surface, creating the most contrast from any of the Faraday effects. An example of a convergent probe polar Faraday effect microscope is shown in Fig. 20. In this case, a laser is used as a light source to minimize the dispersion of Faraday rotations due to wavelength variation. Also, the beam is focused onto the surface, allowing it to be scanned across the sample. The direction of polarization of the laser light is set by the polarizer, with components of the electric field of the light perpendicular to the film surface. As shown in Fig. 20(a), the light is transmitted through the sample with a corresponding rotation, either clockwise or counterclockwise, depending on the relative direction of the magnetization. The light is selected by its polarization direction at the analyzer. Maximum contrast is produced by adjustment of the analyzer

generally to collect photons from one domain preferentially (the up magnetization domains in Fig. 20b, for example).

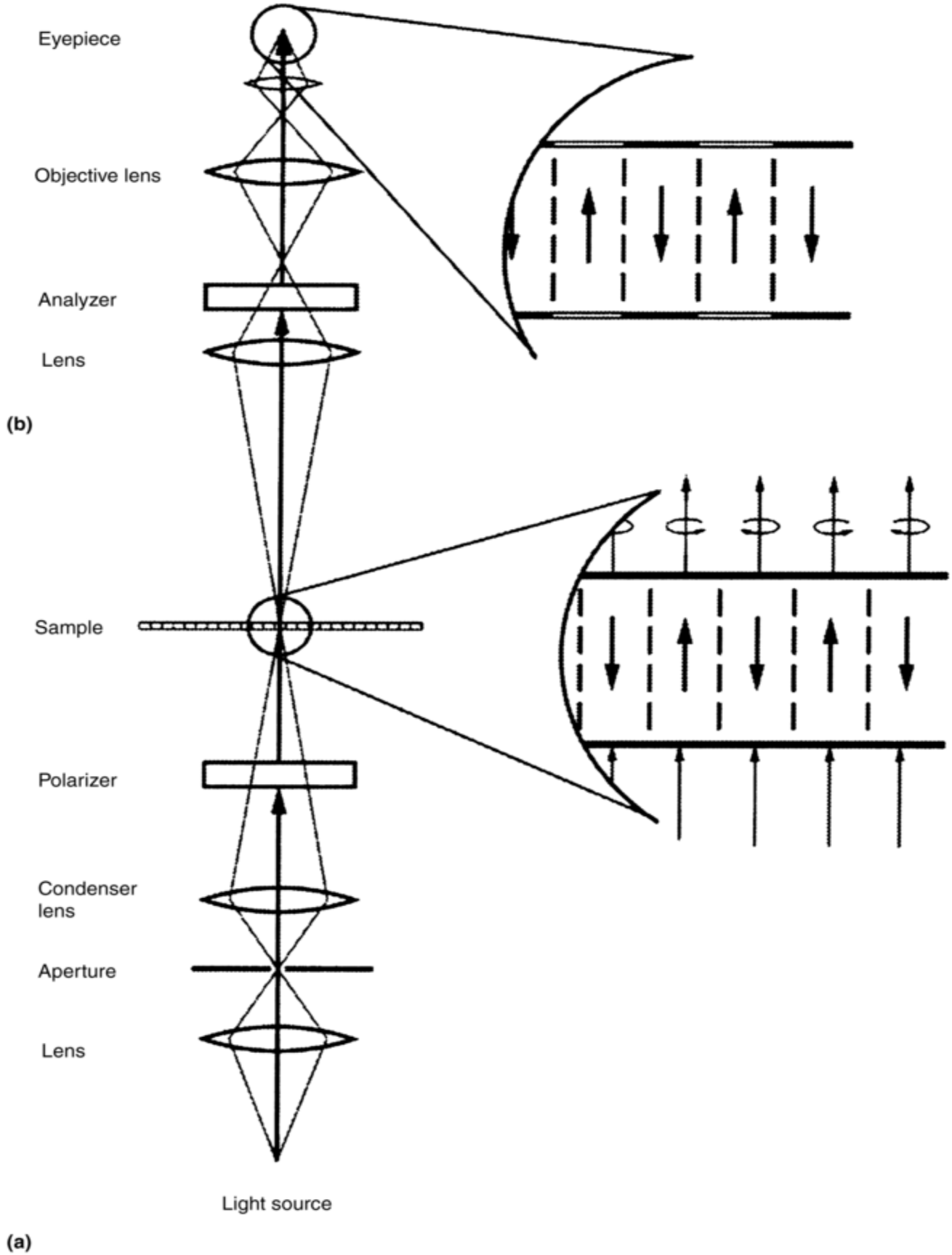

Fig. 20 Polar Faraday effect microscope using a monochromatic light source and convergent beam optics. A standard transmission optical microscope is used. The Faraday effect is typically observed in this geometry, where the light and sample magnetization are perpendicular to the sample surface. (a) The Faraday rotation of the polarized incident beam is reversed for magnetization in antiparallel

directions. (b) The corresponding domain structure shows the light/dark domains for magnetization in the up/down orientations by adjusting the analyzer for maximum contrast.

This effect has been employed for the study of domains in a 50 nm thick nickel-iron film (Ref 98). Because the magnetization directions are in the plane of the film, the film was inclined 45° to the light path. A telescope system with a rotatable analyzer adjusted for optimal contrast was used to observe the domains. To obtain transmittance through metal films, the specimen must be thinner than 200 nm. This restriction is a major disadvantage for metals, but it has been used to examine domains in hexagonal ferrites, which will transmit light with thicknesses to approximately 100 μm (Ref 99), and in ferrimagnetic garnets (Ref 100) and other transparent oxides (Ref 101). Typically, the normal polar geometry is used for measurements of samples with magnetization perpendicular to the sample surface, with the beam perpendicular to the film surface.

Preparation of specimens for observation by the Faraday effect is time consuming. The thin metal films discussed in the above study of domains were made by evaporation (Ref 98). Preparation of ferrimagnetic garnets begins by cutting a thin slice from a bulk sample after the crystal orientation is determined by x-ray procedures (Ref 100). Both sides are ground and polished flat and parallel in much the same way as for double-polished mineralogical thin sections. Final polishing is performed by extended lapping with 0.25 μm diamond abrasive. A hot stage has been used to observe the ferrimagnetic garnets up to the Curie temperature, at which magnetic contrast was lost (Ref 100). The domain image may also be manipulated using a magnetic field, as shown in Fig. 21.

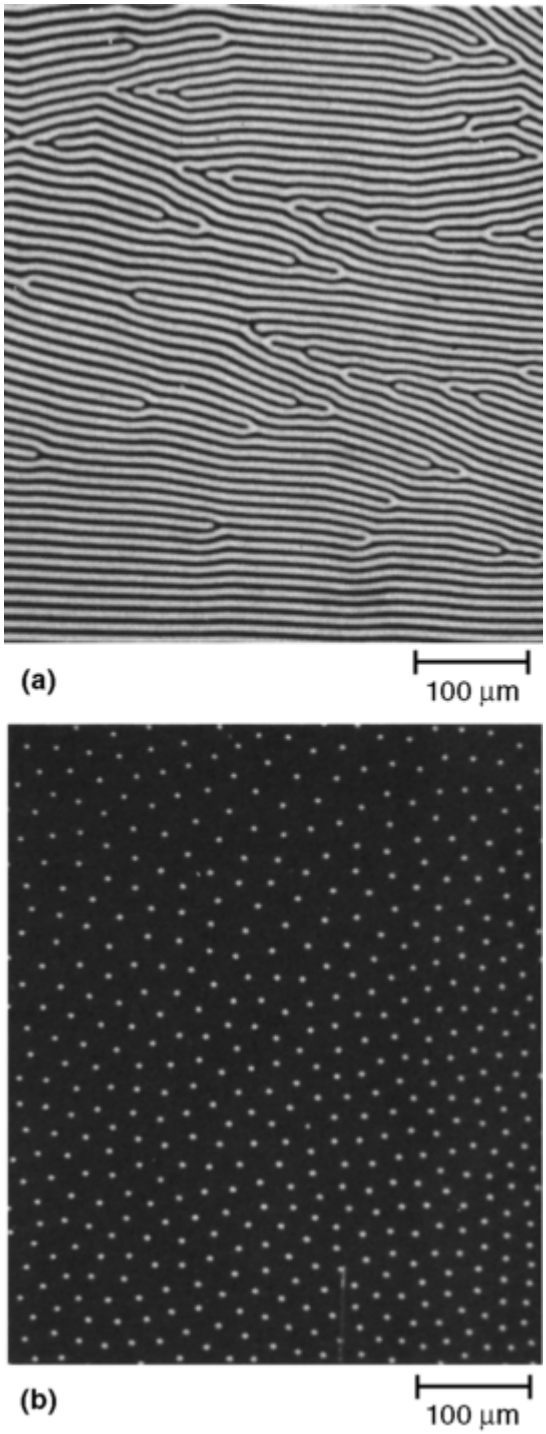

Fig. 21 Domain imaging using the Faraday effect for a $Gd_{0.94}Tb_{0.75}Er_{1.31}Al_{0.5}Fe_{4.5}O_{12}$ garnet crystal, grown in a PbO and B_2O_3 flux at 1300 °C (2370 °F). (a) Magnetic domain structure of 50 μm thick platelet cut parallel to the (111) plane. Black and white areas represent domains with opposing magnetic vectors normal to the surface. As-polished. (b) The same garnet as (a), but with an applied magnetic field of 150 Oe, which reduced white domains of (a) to cylinders (seen here as dots) 5 μm in diameter. As-polished. Both Original magnification 100×

In some cases, it is important to compare images taken by different techniques. Figure 22 is taken from the same region of a barium ferrite single crystal, using the Faraday imaging and Bitter imaging methods (Ref 102). Markedly different domain structures are found because the Faraday technique measures the light transmitted through the sample, yielding an image based on the domain structure throughout the specimen, while the Bitter method is a surface technique.

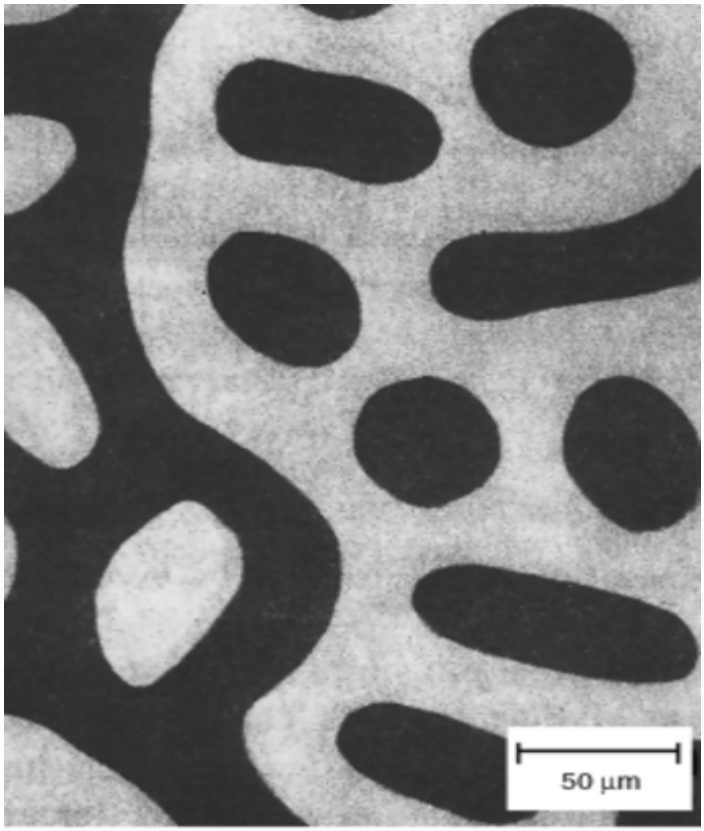

(a)

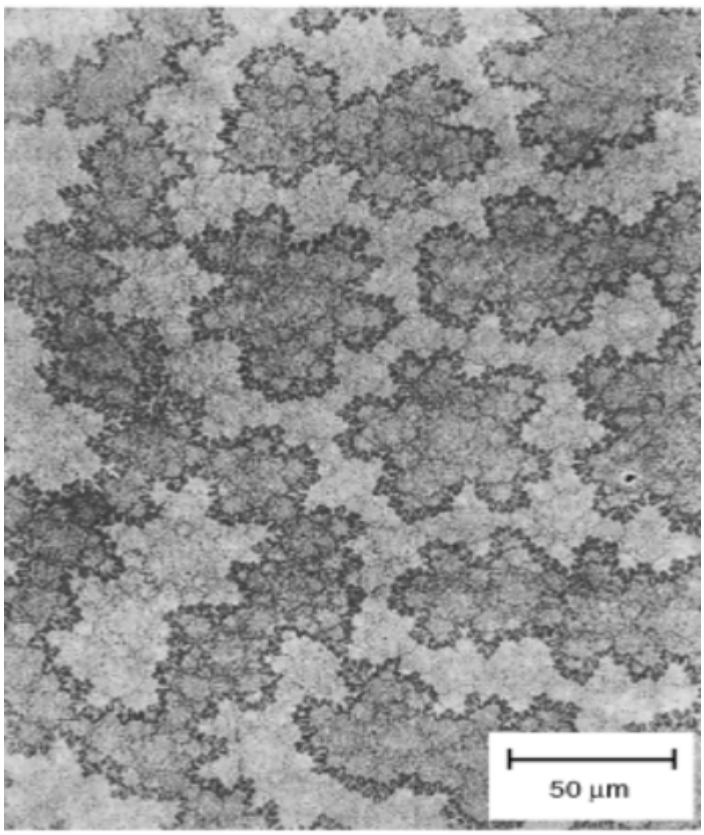

(b)

Fig. 22 Domain images of a barium ferrite single crystal (85 μm thick) with hexagonal plane normal to the plane of the sample. (a) Faraday effect image showing the characteristic domain structure throughout the thickness of the sample. (b) Bitter pattern of the same area as (a), indicating the surface has a different domain structure due to stress at the surface. Reproduced with permission from Ref 102

Use of a high-resolution microscope to examine thin specimens by the Faraday effect and the Kerr effect has been discussed (Ref 103). Modifications to this technique include an electromagnet to study the domains under the influence of strong fields approaching saturation (Ref 99). In addition, a photomultiplier has been incorporated into the system to measure intensity variations when the specimen is cycled (Ref 104).

Magneto-Optical Kerr Effect. When plane-polarized light is reflected from a metal surface, it is elliptically polarized, except when the incident plane is a symmetry plane, which results in plane-polarized reflected light. However, if the specimen is magnetized, the reflected light is always elliptically polarized, because the magnetic field produces the Kerr component, which removes any influence from crystal symmetry. The net result is a rotation of the plane of polarization of the reflected light rays. However, the degree of rotation is much smaller than that observed using transmitted light by the Faraday effect. The smaller contrast found in Fig. 23 (when compared to the Faraday effect images in Fig. 21) is due in part to the smaller rotation angles, characteristic of the Kerr effect.

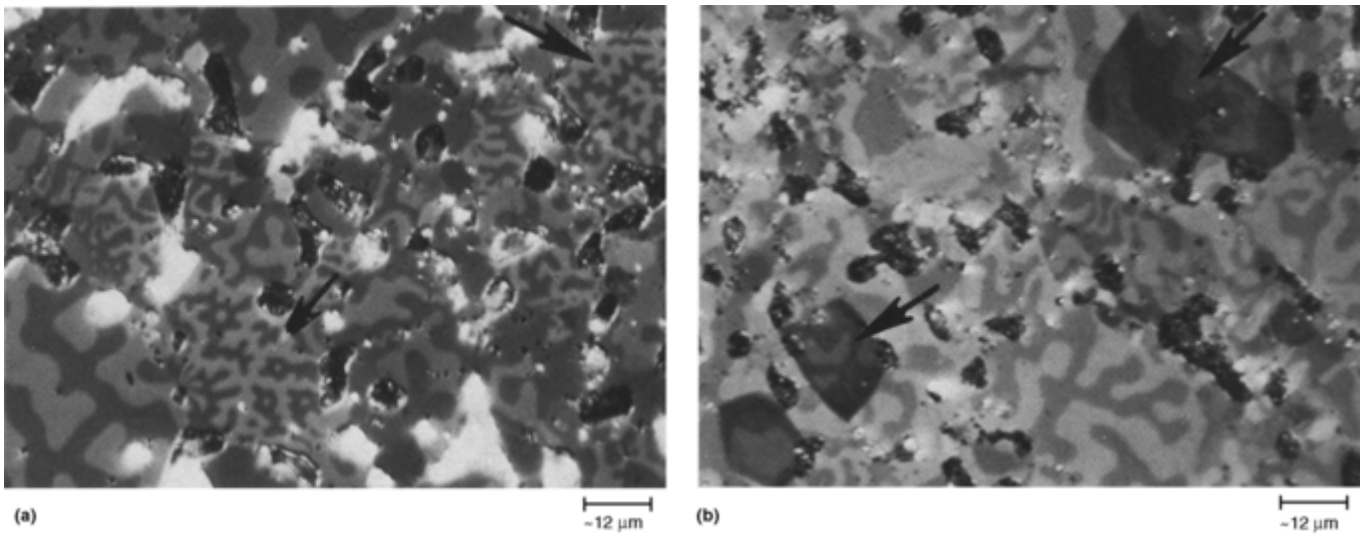

Fig. 23 Kerr effect micrographs (using polarized light) of $SmCo_5$ permanent magnet (adjacent domains). (a) Large Sm_2Co_{17} grains easily identified by the finer domain structure (arrows). (b) Dark Sm_2Co_7 grains continuous with the surrounding $SmCo_5$. As-polished. Reproduced with permission from Ref 105. Both Original magnification 850×

Three forms of the Kerr effect are possible with respect to the incident plane and reflecting surface plane (as shown in Fig. 24). The magnetic contrast is proportional to the component of magnetization along the direction of the incident beam. The polar Kerr effect provides the most rotation of the plane of polarization and arises when magnetization is perpendicular to the reflecting surface (Fig. 24c). The polar effect, however, is limited to materials with high uniaxial anisotropy perpendicular to the plane of the sample. The normal polar Kerr effect provides the strongest signal and occurs when the incident beam is perpendicular to the plane of the sample.

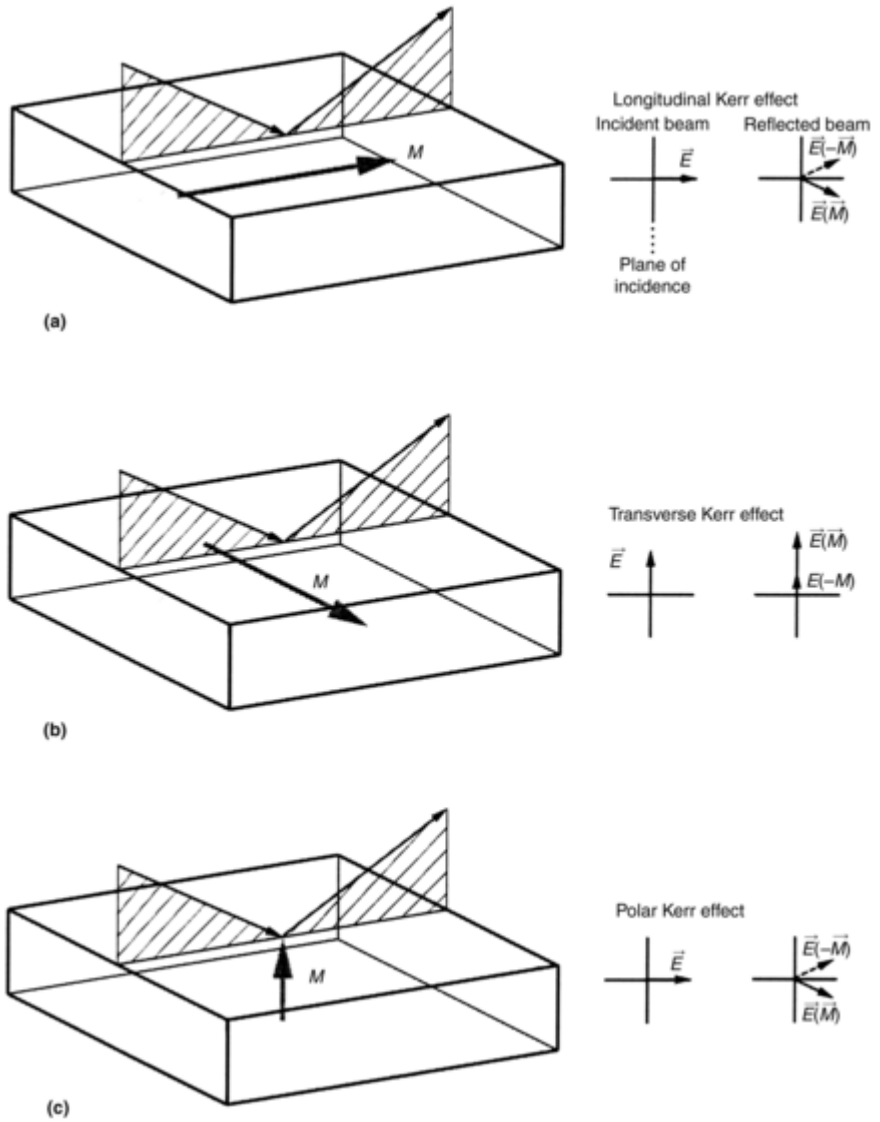

Fig. 24 The three forms of Kerr effect. (a) Longitudinal Kerr effect: magnetization direction is within the plane of incidence and plane of the sample (polarization rotation accompanies reflection). (b) Transverse Kerr effect: magnetization direction parallel to the plane of the sample but perpendicular to the plane of incidence. (c) Polar Kerr effect: magnetization perpendicular to the plane of the sample

The longitudinal Kerr effect produces approximately one-fifth the rotation of the polar effect and arises when magnetization is in the plane of incidence and in the plane of the sample. Rotation of the plane of polarization is zero when the specimen surface is perpendicular to the incident light and maximum when the specimen is 60° to the incident light (Fig. 24a). Both polar and longitudinal Kerr effects exhibit both a rotation of the polarization and change from linear to elliptical polarization after reflection.

The transverse Kerr effect has magnetization in the reflecting surface plane, but also in a plane perpendicular to the incident light (Fig. 24b). Rotation of the plane of polarization does not occur, but there are reflectivity differences in the light polarized in the incident plane when the magnetization has a component parallel to the beam direction. An additional constraint requires that the polarization of the incident beam is in the plane of incidence (this is not required for either polar or longitudinal). Contrast from the longitudinal and transverse Kerr effects is similar. Few studies of domains have been conducted using the transverse Kerr effect. The transverse Kerr effect has been used to study domains in vapor-deposited nickel-iron films using a phase-adjusting arrangement to improve image contrast substantially (Ref 106).

Specimen preparation is the most critical factor in producing good images by the Kerr effect (Ref 107). The specimen surface must be prepared strain-free, scratch-free, and flat. Strain, if excessive, alters the domain structure, and scratches and surface undulations reduce contrast. A preparation procedure has been outlined for grain-oriented (3% Si) steel (Ref 107). Samples are sheared to size, deburred, and flattened by heating for 2 h at 1150 °C (2100 °F) in dry hydrogen. The specimen is mounted on a flat polishing block and wet ground with

light pressure using a series of finer grade papers. Polishing is performed using simultaneous electrolytic and mechanical polishing (electromechanical polishing) or alternate electrolytic and mechanical polishing. Finally, the specimen is stress-relief annealed 2 h at 800 °C (1475 °F) in dry hydrogen, then coated with zinc sulfide. A similar preparation technique has been described for examination by the Kerr effect (Ref 108).

A normal polar Kerr effect microscope with parallel beam optics and a white light source is shown in Fig. 25. A green filter reduces the dispersion of the Kerr rotation (which is sensitive to the wavelength of the light). In the normal geometry, the magnetic domains must have components perpendicular to the sample surface; generally this technique must be used for uniaxial magnetic anisotropy samples for which the demagnetization fields are small compared to magnetocrystalline anisotropy. Alternatively, an applied magnetic field at the sample can provide the necessary magnetization direction. Figure 25(a) shows the Kerr rotation of the linearly polarized incident beam, with opposite sense of rotation for opposite direction of magnetization. The corresponding image contrast is attained by adjusting the analyzer until the contrast is maximized, as indicated in Fig. 25(b). In this case, the analyzer is set to give domains with magnetization up a bright intensity.

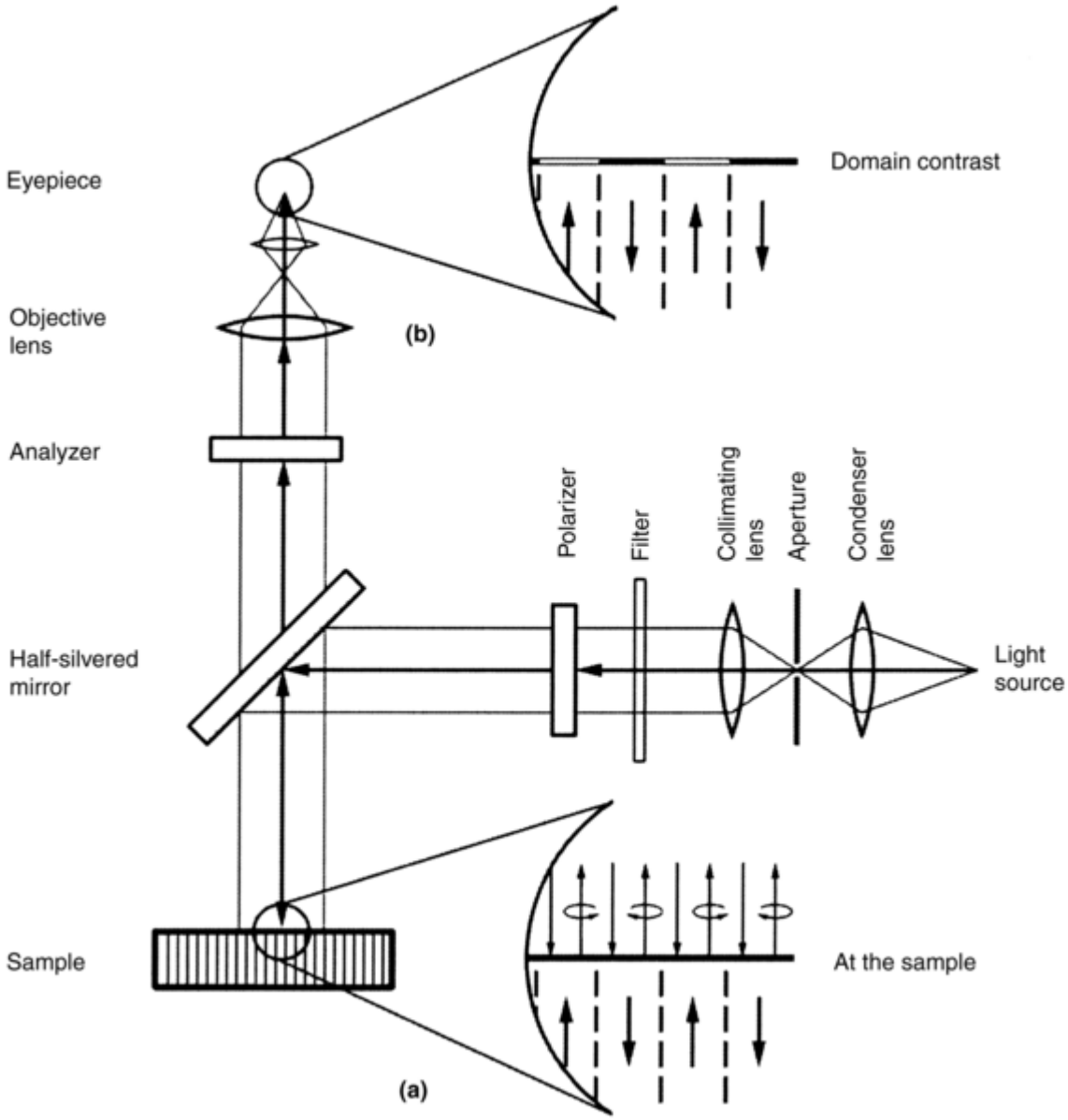

Fig. 25 Normal polar Kerr effect microscope using white light and parallel beam optics. (a) At the surface of the sample, incoming polarized light is reflected with an accompanying Kerr rotation. Domains with opposite direction of magnetization have corresponding opposite direction of polarization rotation upon reflection. (b) Adjusting the analyzer for maximum contrast provides a domain image with light/dark contrast for magnetization in the up/down orientations, respectively.

A similar set of optical components is necessary for longitudinal Kerr effect measurements; however, the configuration is quite different (Fig. 26). A component of the magnetization must lie in the direction of the beam to provide the magnetic contrast; therefore, magnetic moments parallel to the surface do not show contrast in the normal configuration. For samples with magnetization in the plane of the surface, the sample must be rotated away from normal incidence, with a maximum Kerr rotation at an angle of 60° to the sample normal.

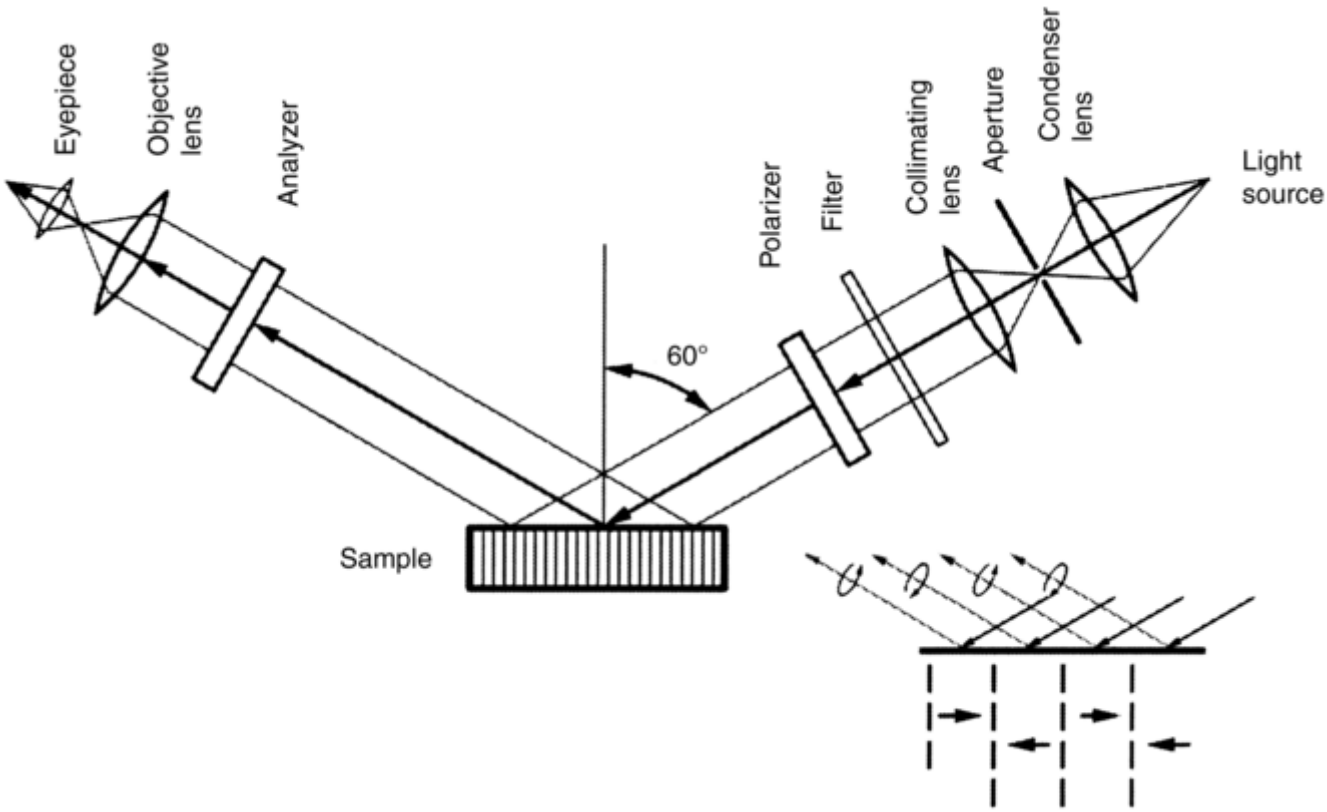

Fig. 26 Longitudinal Kerr effect microscope using a white light source. Similar to the polar Kerr effect microscope, the Kerr rotation is reversed for magnetization with opposite direction.

Of these methods, the polar Kerr effect was the first used to examine domain structures during study of the basal plane of a cobalt single crystal (Ref 109). The polar Kerr effect and the hot-stage microscope have been used to examine manganese-bismuth films (Ref 110). The polar Kerr effect has been implemented to inspect domain structures in several orthoferrites (Ref 111).

Use of the longitudinal Kerr effect to examine domains first took place in a study of 180° domain walls on a silicon-iron crystal (Ref 112). In this work, the specimen was inclined 60° to the incident light source, which produced a rotation of the plane of polarization of approximately 4 min of arc. Therefore, image brightness and contrast between domains was low. In addition, light scattered from surface imperfections was present and obscured detail.

Contrast can be improved to approximately 1° of rotation by vacuum deposition of a quarter-wavelength dielectric coating after specimen preparation (Ref 113). This procedure is similar to the Pepperhoff method for improving contrast differences between phases (see the article “Color Metallography” in this Volume). Zinc sulfide has been chiefly used for this purpose. The layer is deposited until reflectivity is decreased approximately 50% and a deep purple macroscopic color is produced. The influence of zinc sulfide coating thickness on the Kerr effect using nickel-iron films has been studied (Ref 114).

The limitations of the longitudinal Kerr magneto-optical effect have been examined in depth, reaching the conclusion that the major problem is the ellipticity produced by reflection from the metallic surface (Ref 115). It was determined that image contrast could be maximized by compromising between rotation and ellipticity, with maximum contrast occurring with a specimen inclination angle of approximately 20° and a beam divergence of approximately 10°. These ideas were used to design a new Kerr instrument (Ref 116). Further improvements led to a resolution of approximately 1.7 μm for the Kerr effect (Ref 103). A stroboscopic light source has been used to photograph magnetization reversals (Ref 107, 117).

Scanning Electron Microscopy (SEM). The scanning electron microscope has various operating modes that are useful for studying magnetic materials (see the article “Scanning Electron Microscopy” in this Volume). In contrast with the preceding sections on optical methods, electron optical methods reveal domain structures by the interaction of the Lorentz force with the electron beam. Although a number of such contrast mechanisms have been discovered using the scanning electron microscope, two procedures are most often used. These are referred to as type I and type II magnetic contrast. They arise from different effects, and each is useful for certain magnetic materials. A third type of magnetic contrast resulting from the spin polarization of the secondary electrons requires specialized spin-sensitive detectors. This technique, called SEMPA, is also discussed.

Type I magnetic contrast arises from the presence of a leakage field above the specimen surface and was first observed in studies of magnetic recording tape, recording heads, and cobalt metal (Ref 118, 119). The leakage field alters the initial direction of secondary electrons emitted from the surface. Depending on the magnetic orientation of the domains, the secondary electrons are deflected toward or away from the collector, producing magnetic contrast (see Fig. 27).

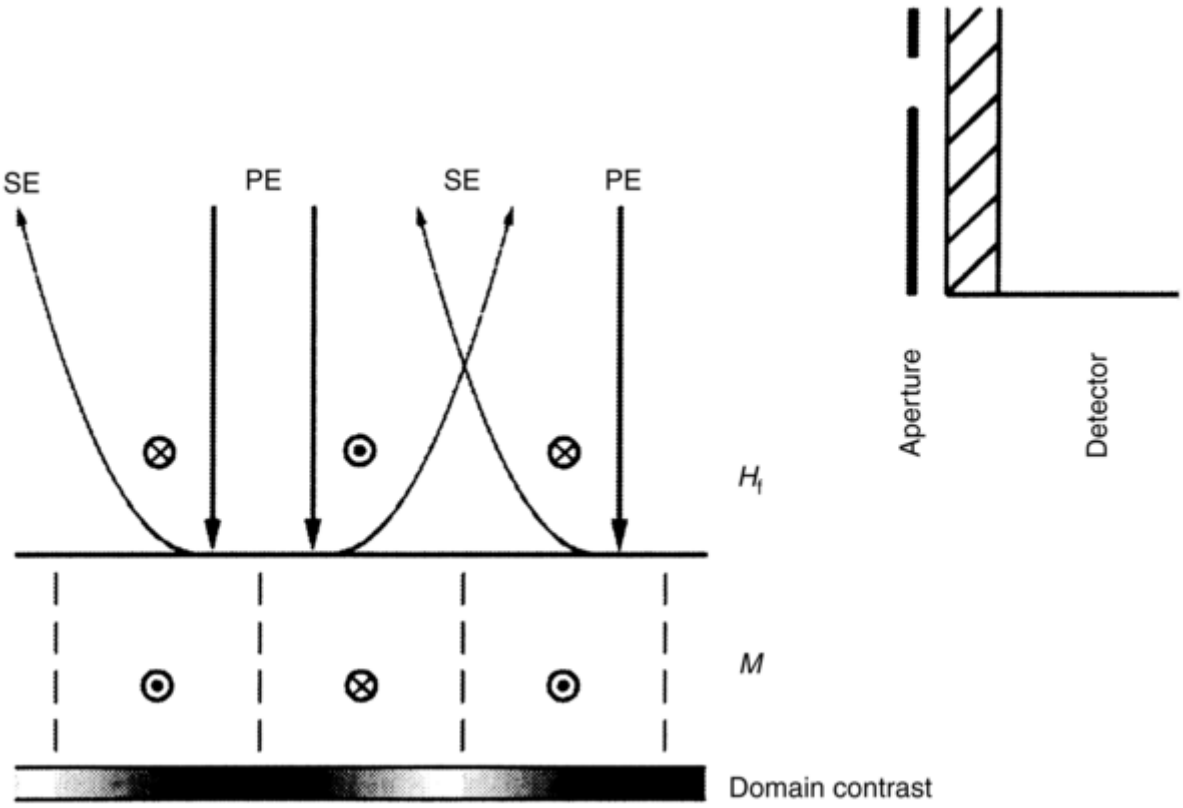

Fig. 27 Type I magnetic contrast from using a scanning electron microscope. The contrast arises from primary electrons (PE) impinging at normal incidence to the sample and the resulting secondary electrons (SE) changing trajectory due to the Lorentz force produced by the fringing field of the sample. The resulting SE image has contrast variation across the width of the domain with peak brightness and darkness at the domain walls.

Because type I magnetic contrast is produced above the specimen, contrast is not observed in the specimen current mode. In addition, the high-energy backscattered electrons are not significantly influenced by the leakage field, and contrast is not observed in the backscattered mode. Type I contrast is observed only with secondary electron images, obtaining reasonably good contrast, which can be improved by altering the detector orientation to reduce the collection efficiency of the Everhart-Thornley secondary electron detector. Varying the accelerating potential has little influence on the contrast, but low potentials, which produce a greater yield of secondary electrons, are preferred due to a better signal-to-noise ratio. Placing a diaphragm over the detector also enhances contrast (Ref 120). As shown in Fig. 27, the domain image intensity varies continuously across a single domain with peaks and valleys at domain walls.

Resolution of domain structures using type I magnetic contrast varies with the material studied from approximately 1 μm for cobalt to 45 μm for $YFeO_3$ (Ref 121). The contrast produced, however, is not as sharp

as that obtained using the Kerr effect. Despite this limitation, the technique has many advantages (Ref 121), such as simple specimen preparation, good depth of focus, performance of dynamic experiments, observation of surface and internal domain structure, reasonably good resolution for many materials, and ease in interpreting results. The scanning electron microscope can also be used to study general features of the microstructure. Chemical details of features can be obtained by energy-dispersive spectroscopy. An excellent example of the strengths of this technique are found in Ref 122, where L.H. Lewis et al. show the domain configuration of a $Nd_2Fe_{14}B$ single crystal (see Fig. 28).

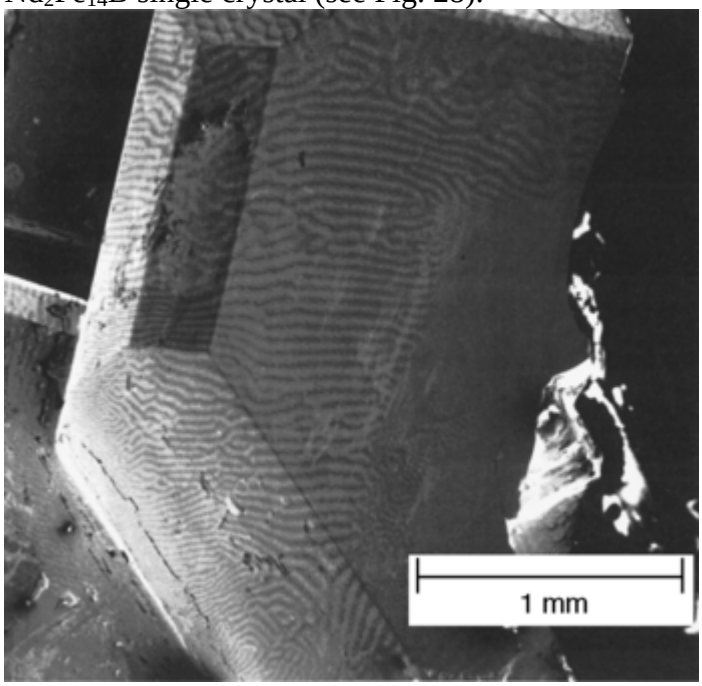

Fig. 28 Secondary electron image of a $Nd_2Fe_{14}B$ single crystal grown using flux growth synthesis. Type I magnetic contrast clearly shows the maze pattern domains, typical of these uniaxial materials. The large depth of field, characteristic of scanning electron imaging techniques is particularly evident in this image. Reproduced with permission from Ref 122

Type II magnetic contrast was first observed in a study of iron. Details of type II contrast have been discussed (Ref 123). Type II magnetic contrast arises from interaction of the internal magnetic field with the electrons from the beam that are deflected by the Lorentz force within the specimen creating differences in the backscattered electron yield. High beam potentials of 30 keV or greater are used. As shown in Fig. 29, the specimen must be tilted with respect to the beam (angles of 50 to 64° have been used) and rotated about its surface normal until maximum contrast is obtained (Ref 124, 125, 126, 127). The maximum contrast corresponds to magnetization parallel to the tilt axis, changing abruptly at domain boundaries. Because the contrast is weak, the beam current must exceed 100 nA. The contrast can be observed in the backscattered electron mode or in the specimen current mode; secondary electron images do not provide type II contrast. Signal processing must be used to enhance the weak contrast to a visible level. Beam probe size limits resolution.

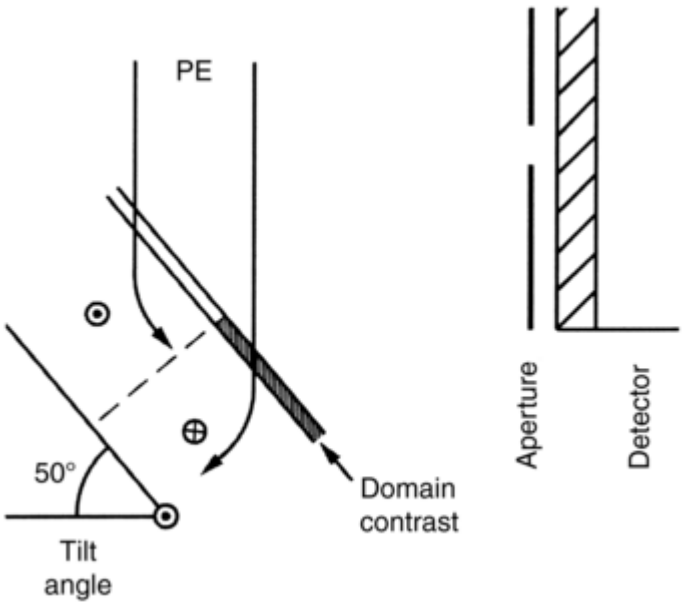

Fig. 29 Type II magnetic contrast using a scanning electron microscope originates from the Lorentz force deflection of primary electrons due to the magnetization within the specimen. The backscattered electrons are collected with contrast being proportional to the saturation magnetization and the accelerating voltage. The specimen must be tilted relative to the primary electrons (PE) with an optimum contrast at ~50°. Magnetic contrast results from magnetization aligned with the tilt axis.

Most of the SEM work with type II magnetic contrast has concerned domain structures in silicon irons, although other magnetic materials have been examined using high-voltage scanning electron microscopes. Type II magnetic contrast is one of few contrast modes that improve with increasing potential. For example, the domain structures of coated silicon iron can be observed directly and, by changing the accelerating potential, as a function of depth. Examples of high-voltage SEM domain studies are provided in Ref 128, 129, 130, 131. Reference 128 and 130 discuss the experimental procedure and optimization of image contrast.

Scanning Electron Microscopy with Polarization Analysis (SEMPA). The scanning electron microscopy with polarization analysis (SEMPA) technique measures spin polarization of secondary electrons excited by unpolarized primary electrons interacting with the magnetization of the specimen, as shown in Fig. 30 (Ref 132). The total secondary electron image is collected simultaneously, forming the conventional scanning electron micrograph, while the spin-polarized signal gives an image of the magnetic domain structure. Unlike most domain imaging techniques, both the magnitude and direction of the magnetization are measured directly. This technique provides a high spatial resolution of better than 40 nm and has high sensitivity to the surface of the sample (only ~1 nm of depth sampled) (Ref 133). SEMPA is useful for bulk samples and thin films; however, electrically conducting materials are necessary to reduce charging in the SEM and large fringing fields should be avoided (Ref 134).

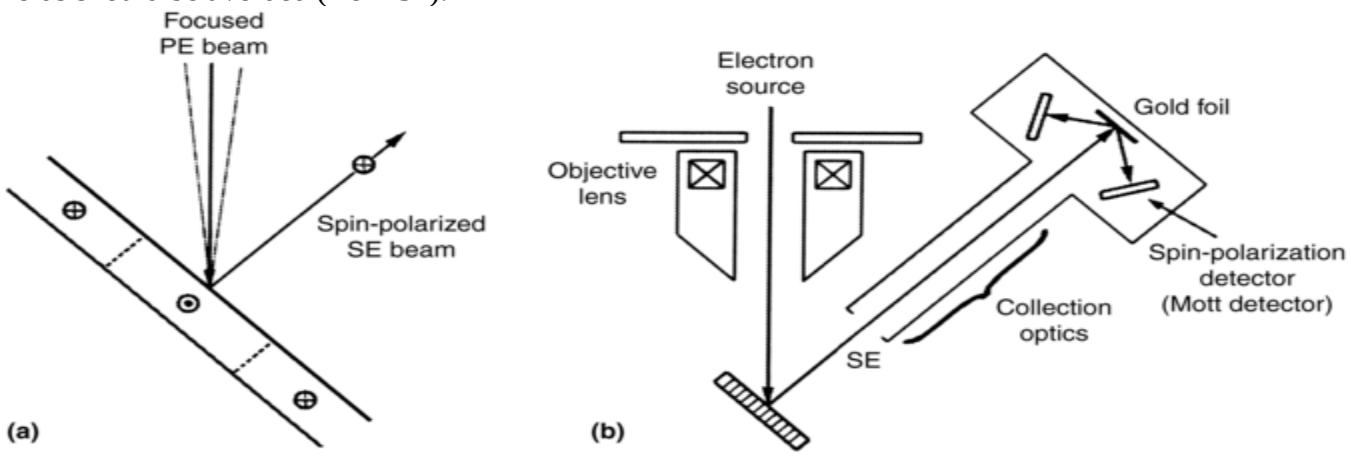

Fig. 30 Scanning electron microscope with polarization analysis (SEMPA). (a) The unpolarized primary electrons are rastered across the sample, emitting spin-polarized secondary electrons (SE). The spin-

polarization is proportional to the magnetization at the surface of the sample. (b) A standard scanning electron microscope source is used for SEMPA, with specialized collection optics and spin-sensitive detectors for determination of the domain configuration.

An example of the SEMPA imaging is illustrated in Fig. 31. The sample shown in these images is an Fe-Si crystal with (100) orientation. The secondary electron image without polarization analysis shows very little contrast (Fig. 31a). Spin-polarized electrons are collected to form the magnetic domain images in Fig. 31(b) and (c), with independent imaging for the *x*- and *y*-components of the magnetization, respectively. The total magnitude of the magnetization is given in Fig. 31(d), where due to an imaging artifact the domain boundaries show contrast. This does not imply that the magnetization is smaller at the domain wall, but is rather a manifestation of the probe diameter being larger than the domain wall (Ref 133).

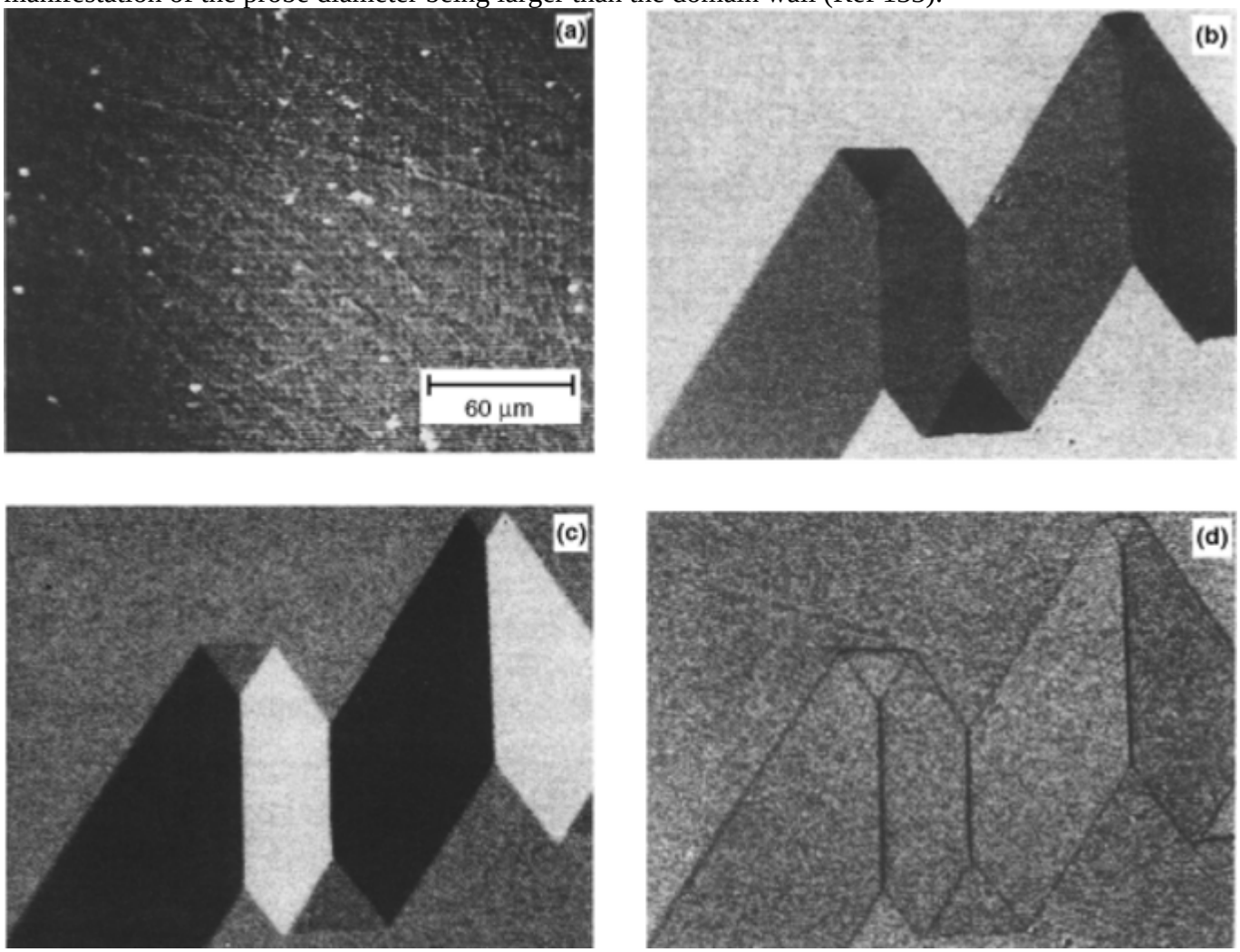

Fig. 31 Scanning electron microscope with polarization analysis (SEMPA) images of a (100) surface of an iron-silicon crystal. (a) Secondary electron intensity image, with little contrast. (b) Image of the x-component of the magnetization, with white coloring for magnetization pointing to the right and black to the left. (c) Image of the y-component of the magnetization (white contrast upward and black contrast downward). (d) Total in-plane magnetization intensity, with image contrast at the domain walls due to larger probe diameter than the domain wall width. Reproduced with permission from Ref 133

Lorentz Microscopy. Thin foils of ferromagnetic materials can be examined in the transmission electron microscope using a technique known as Lorentz microscopy. In such work, the electron beam of the microscope is deflected by the magnetic field of the specimen to permit examination of the domain structure at high magnification and high resolution. At the same time, the fine structure of the material can also be examined. The technique was developed using nickel-iron thin films (Ref 135, Ref 136).

Two Lorentz microscopy techniques have been developed. Due to the small amplitude of the electron beam deflection from the magnetization of the sample (being much smaller than Bragg reflections), the contrast in the

in-focus electron micrograph is only slightly affected by the magnetic domain image. For this reason, magnetic contrast must be obtained by either changing the degree of focus or using the objective apertures. In the first technique, called Fresnel imaging, the objective lens is not used, except as an applied field to produce movement of the domain walls. The condenser lens is overfocused, and the projector lens is adjusted to produce an out-of-focus shadow image of the specimen in the projector focal plane and a screen image at 300 to 400×. As shown in Fig. 32, the domain walls appear as alternate light and dark lines. In the second technique, Foucault imaging, the transmission electron microscope is operated in a more conventional manner that permits higher resolutions and magnifications. The placement of apertures to block electrons transmitted through some domains while allowing electrons to pass through regions with opposite magnetization creates the magnetic contrast. However, because of the high magnetic field of the objective lens at the sample, lower beam currents are used. A high degree of control for the aperture positioning is necessary due to the small deflection angles from the Lorentz force (see Fig. 33).

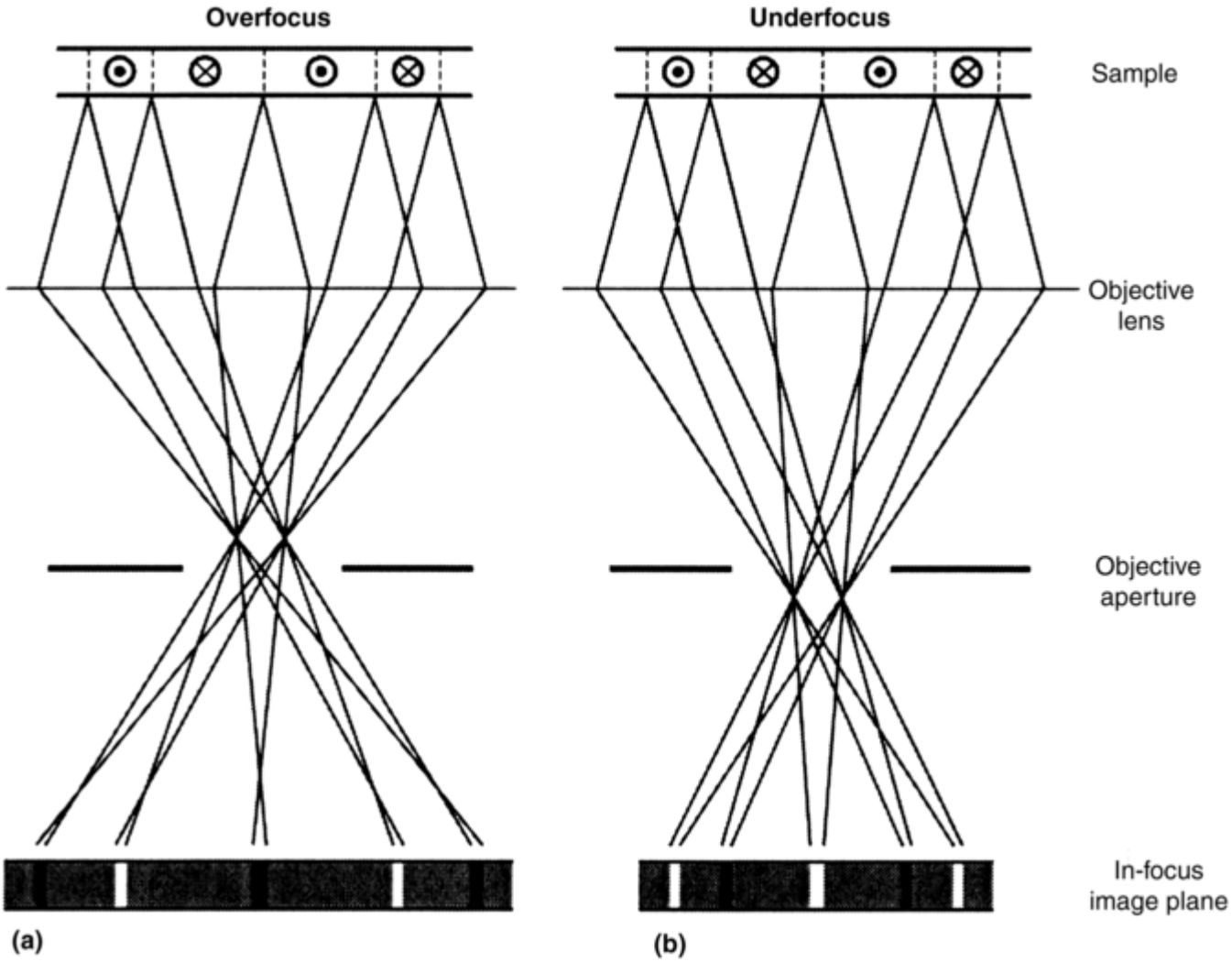

Fig. 32 A ray diagram for the Fresnel imaging of magnetic domains using a transmission electron microscope. (a) When the current to the objective lens is increased above the in-focus condition, the image becomes overfocused and the electrons are deflected toward and away from the domain walls depending on the orientation of the adjacent domains. (b) Opposite contrast is found when the lens current is lowered below the in-focus amount (underfocused).

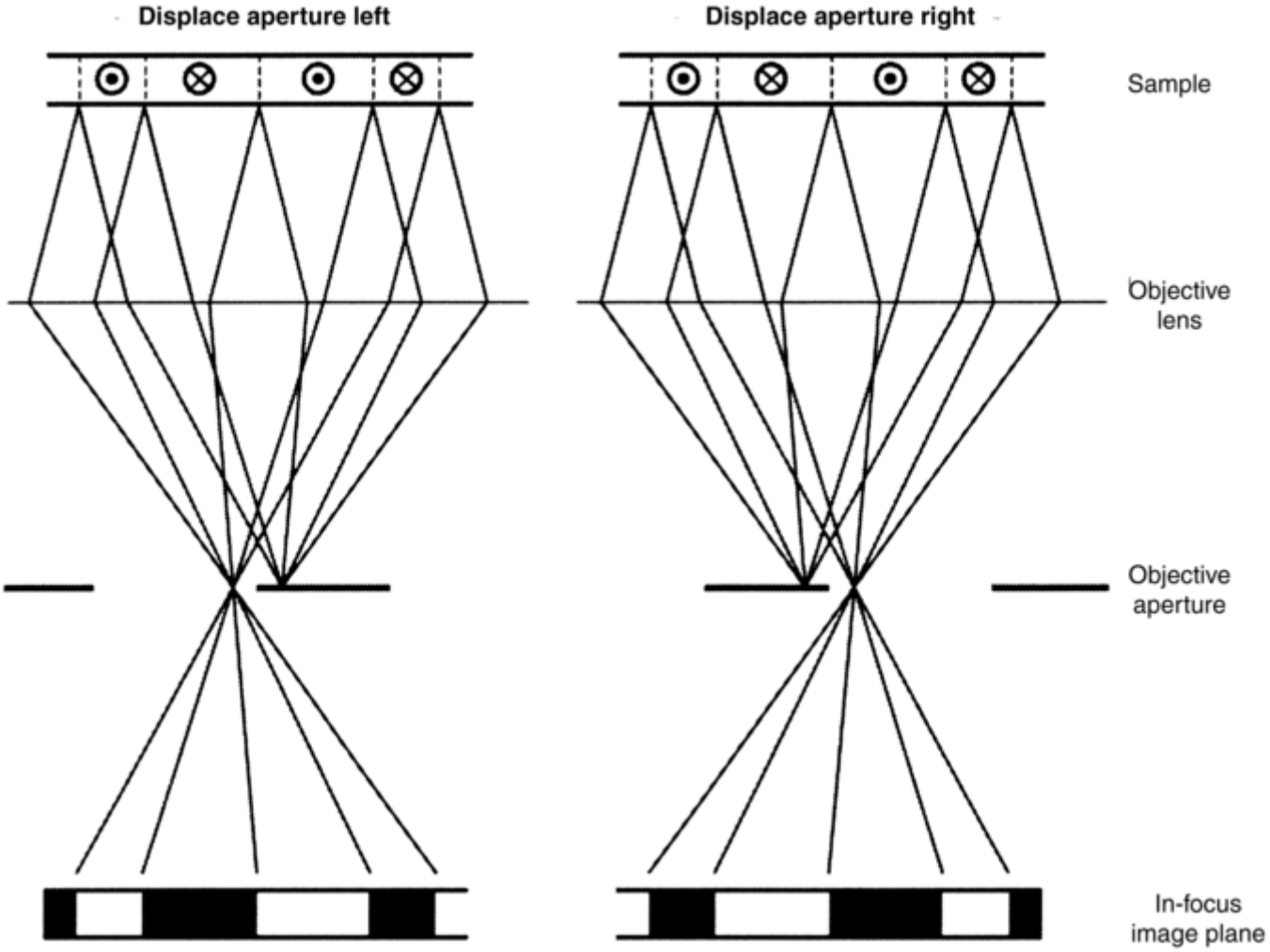

Fig. 33 A ray diagram illustrating the Foucault imaging of magnetic domains using a transmission electron microscope. The Lorentz force on the electrons passing through the magnetic material causes a deflection of their trajectory. A displacement of the objective aperture allows the electrons from a single domain orientation to be preferentially collected. Displacement in the opposite direction provides illumination of domains with opposite direction of magnetization.

The high magnetic field of the objective lens can be controlled in other ways. A specimen holder is available that raises the foil approximately 5 mm (0.2 in.) closer to the electron beam (Ref 137). Again, lower currents are required at the objective lens, but high magnification and resolution can be obtained. An electrostatic transmission electron microscope has been used to avoid the high magnetic field of the objective lens (Ref 138). In this work, a knife edge is inserted from one side at the back focal plane of the intermediate lens or objective lens. This blocks image detail from some of the domains, producing magnetic contrast referred to as Foucault contrast. Difficulty in positioning the knife edge makes the method inconvenient.

Reviews of the Lorentz TEM procedures and examples of its application can be found in Ref 139 and 140. Other related techniques, such as differential phase contrast electron microscopy (Ref 141), interference electron microscopy (Ref 142, 143, 144), and electron holography (Ref 144, 145), are currently being applied to the study of magnetic materials. Energy-filtered Lorentz microscopy in combination with simulated Foucault images has been used to elegantly describe the microstructure/domain structure relationship in Terfenol-D alloys ($Tb_{0.73}Dy_{0.27}Fe_{1.95}$) (Ref 146). Figure 34 illustrates the use of the Fresnel technique as applied to Fe-55Pd after annealing at 500 °C (930 °F) (Ref 147).

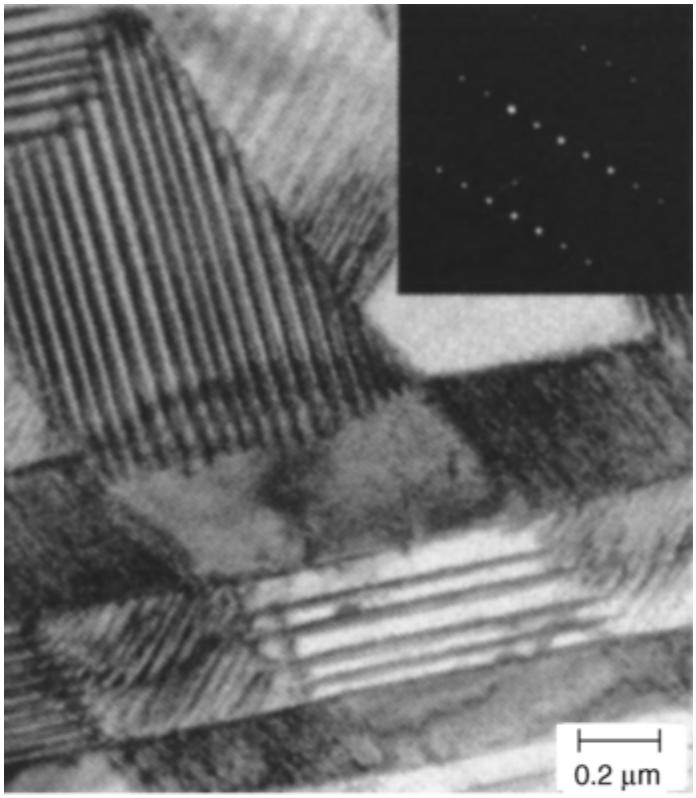

(a)

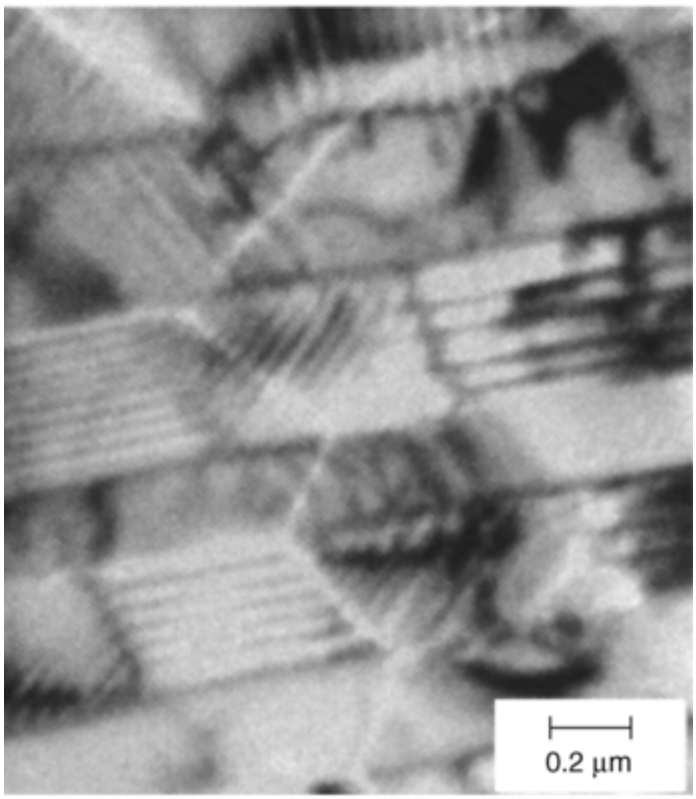

(b)

Fig. 34 Transmission electron micrographs of Fe-55Pd arc-melted alloy annealed at 500 °C (930 °F) for 36 h. (a) Bright-field image of the sample (with [130] zone axis) exhibiting a polytwinned microstructure. (b) Lorentz under-focus (Fresnel) image of the sample showing the immobile domain walls pinned on the polytwins and the mobile zigzag domain walls (at the edges of the polytwinned regions). Reproduced with permission from Ref 146

Magnetic Force Microscopy. First demonstrated in 1987, an atomic force microscope (AFM) outfitted with a magnetic tip (or a silicon tip coated with a ferromagnetic material) has been used for high resolution domain imaging (Ref 148). This technique, called magnetic force microscopy (MFM) uses a noncontact scanning probe to image stray fields above the surface of magnetic materials, with spatial resolution of about 100 nm. This is accomplished by measuring the deflection of the tip due to the magnetic stray field of the sample using lasers and a cantilever beam geometry standardized for AFM use (see Fig. 35). Magnetic force microscopy has become widely used for characterization of microstructures and their correlated magnetic domain structures over the past decade. Many reviews have been written describing the technique itself (Ref 149), as well as progress in the refinement of the technique for higher spatial resolution and quantitative analysis (Ref 150 and 151).

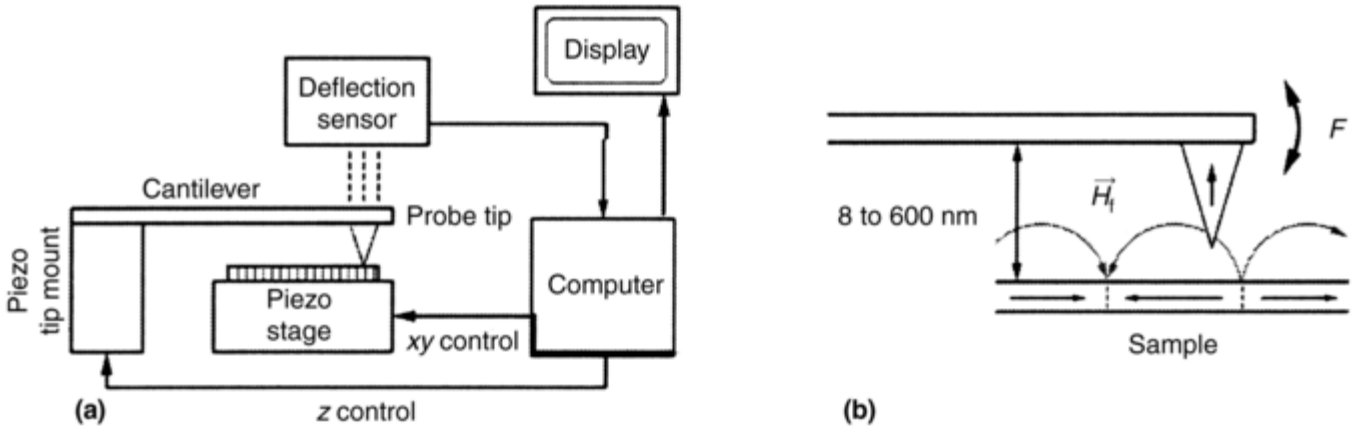

Fig. 35 (a) Block diagram indicating the essential components of a magnetic force microscope (MFM). The probe tip is scanned across the sample in contact mode (atomic force microscope imaging) to provide a topographical image of the sample surface. (b) The magnetic contrast is found by scanning the magnetic probe at a constant distance from the surface. A force due to the interaction of the magnetic tip with the magnetic field gradient from the sample provides the image.

Due to the close proximity of the scan probe tip to the sample, the magnetic stray fields are quite large at the sensing tip. Therefore, sample preparation is minimal, as contrasted by Lorentz microscopy, a technique with similar spatial resolution for domain imaging. Magnetic force microscopes can be modified for controlled magnetic field, temperature, and atmosphere (Ref 152). The flexibility of the technique and the minimal amount of sample preparation make this technique accessible to many nonexperts as a qualitative measure of microstructure and domain structure.

Magnetic force microscopy has been used by the magnetic recording industry, where examination of the domain structures with high resolution is paramount (Ref 151). However, this technique is equally applicable to bulk materials, including soft iron and amorphous ribbons (Ref 152, 153). Classic fir-tree pattern domains, imaged by MFM and Kerr microscopy, are shown in Fig. 36 for an αFe whisker with slight deviation from (100) normal (Ref 152).

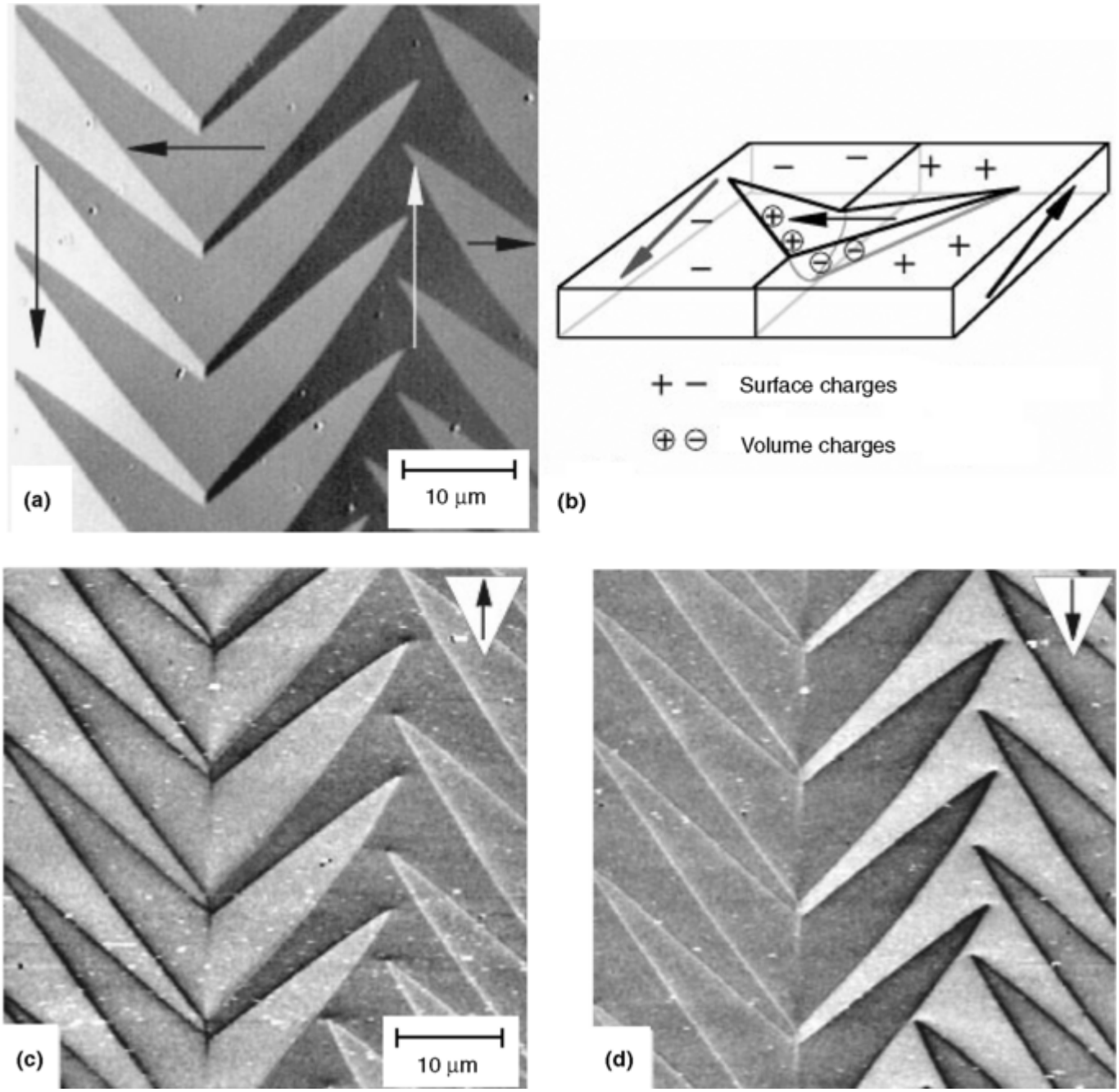

Fig. 36 Comparison of Kerr microscopy domain image (a) with magnetic force microscopy images (c) and (d) for a "fir-tree" domain structure, typical of slight misorientation from the (100) surface of an αFe whisker. (b) Indicates the direction of the magnetization for each of the chevrons. Reproduced with permission from Ref 152

References cited in this section

4. B.D. Cullity, *Introduction to Magnetic Materials,* Addison-Wesley, 1972

68. J. Kirschner, Studies of Surface Magnetism Using Electron and Ion Beam Probes (Invited), *J. Appl. Phys.,* Vol 64, 1988, p 5915–5920

69. M. De Graef and Y. Zhu, Ed., *Magnetic Imaging and Its Applications to Materials,* Vol 36, *Experimental Methods in the Physical Sciences,* Academic Press, 2001

70. A. Hubert and R. Schafer, *Magnetic Domains: The Analysis of Magnetic Microstructures,* Springer-Verlag, 1998

71. D.J. Craik and R.S. Tebble, *Ferromagnetism and Ferromagnetic Domains,* North-Holland/John Wiley & Sons, 1965

72. R. Carey and E.D. Isaac, *Magnetic Domains and Techniques for Their Observation,* Academic Press, 1966

73. K.H. Stewart, *Ferromagnetic Domains,* Cambridge University Press, 1954

74. F.U. Hillebrecht, Magnetic Imaging, *J. Phys.: Cond. Matt.,* Vol 13, 2001, p 11163–11180

75. P. Fischer et al., Study of In-Plane Magnetic Domains with Magnetic Transmission X-Ray Microscopy, *J. Appl. Phys.,* Vol 89, 2001, p 7159–7161

76. E.D. Dahlberg and R. Proksch, Magnetic Microscopies: The New Additions, *J. Magn. Magn. Mater.,* 200, 1999, p 720–728

77. F. Bitter, On Inhomogeneities in the Magnetization of Ferromagnetic Materials, *Phys. Rev.,* Vol 38, 15 Nov 1931, p 1903–1905

78. F. Bitter, Experiments on the Nature of Ferromagnetism, *Phys. Rev.,* Vol 41, 15 Aug 1932, p 507–515

79. W.C. Elmore, Properties of the Surface Magnetization in Ferromagnetic Crystals, *Phys. Rev.,* Vol 51, 1937, p 982–988

80. W.C. Elmore, Ferromagnetic Colloid for Studying Magnetic Structures, *Phys. Rev.,* Vol 54, 1938, p 309–310

81. R.J. Gray, Magnetics Etching with Ferrofluid, in *Metallographic Specimen Preparation,* Plenum Press, 1974, p 155–177

82. K.J. Kronenberg and D. Feldmann, The Use of Variable, High Magnetic Fields for the Investigation of Magnetic Domain Structures, *Pract. Metallogr.,* Vol 11, 1974, p 140–154

83. H.J. Williams, Direction of Domain Magnetization in Powder Patterns, *Phys. Rev.,* Vol 71, 1947, p 646–647

84. H.J. Williams and W. Shockley, A Simple Domain Structure in an Iron Crystal Showing a Direct Correlation with the Magnetization, *Phys. Rev.,* Vol 75, 1 Jan 1949, p 178–183

85. H.J. Williams et al., Magnetic Domain Patterns on Single Crystals of Silicon Iron, *Phys. Rev.,* Vol 75, 1 Jan 1949, p 155–178

86. C. Kittel and J.K. Galt, Ferromagnetic Domain Theory, *Solid State Physics,* Vol 3, Academic Press, 1956, p 437–564

87. H. Pfützner, A New Colloid Technique Enabling Domain Observations of Si-Fe Sheets with Coating at Zero Field, *IEEE Trans. Magnetics,* MAG-17, No. 2, March 1981, p 1245–1247

88. D.J. Craik, A Study of Bitter Figures Using the Electron Microscope, *Proc. Phys. Soc. (London),* Vol B69, 1956, p 647–650

89. J.R. Garrood, Methods of Improving the Sensitivity of the Bitter Technique, *Proc. Phys. Soc. (London),* Vol 79, 1962, p 1252–1262

90. www.ferrotec.com, Ferrotec Corp., 40 Simon St., Nashua, NH

91. J.D. Livingston, Stresses and Magnetic Domains in Amorphous Metal Ribbons, *Phys. Status Solidi (a),* Vol 56, 1979, p 637–645

92. K. Mohri et al., Domain and Grain Observations Using a Colloid Technique for Grain-Oriented Si-Fe with Coatings, *IEEE Trans. Magnetics,* MAG-15, Sept 1979, p 1346–1349

93. G.C. Rauch et al., Enhanced Domain Imaging Techniques, *J. Appl. Phys.,* Vol 55, 15 March 1984, p 2145–2147

94. D.J. Craik and P.M. Griffiths, A New Colloid for Use with the Bitter Figure Technique, *Proc. Phys. Soc.,* Vol B70, 1957, p 1000–1002

95. D.J. Craik and P.M. Griffiths, New Technique for the Study of Bitter Figures, *Br. J. Appl. Phys.,* Vol 9, July 1958, p 279–282, 276–277

96. W. Szmaja, Improvements in Domain Study with the Conventional Bitter Method by Digital Image Processing System, *Phys. Status Solidi (a),* Vol 194, 2002, p 315–330

97. P. Rice and J. Moreland, A New Look at the Bitter Method of Magnetic Imaging, *Rev. Sci. Instrum.,* Vol 62, 1991, p 844–845

98. C.A. Fowler and E.M. Fryer, Magnetic Domains in Thin Films of Nickel-Iron by the Faraday Effect, *Phys. Rev.,* Vol 104 (No. 2), 1956, p 552–553

99. C. Kooy and U. Enz, Experimental and Theoretical Study of the Domain Configuration in Thin Layers of $BaFe_{12}O_{19}$, *Philips Res. Rep.,* Vol 15, 1960, p 7–29

100. J.F. Dillon, Jr., The Observation of Domains in the Ferrimagnetic Garnets by Transmitted Light, *J. Appl. Phys.,* Vol 29, Sept 1958, p 1286–1291

101. R.C. Sherwood et al., Domain Behavior in Some Transparent Oxides, *J. Appl. Phys.,* Vol 30, 1959, p 217–225

102. R. Szymczak, Observation of Internal Domain Structure of Barium Ferrite in Infrared, *Acta Phys. Polon.,* Vol A43, 1973, p 571–578

103. A. Green et al., A Polarizing Microscope for Observation of Magnetic Domains, *J. Sci. Instrum.,* Vol 40 (No. 10), 1963, p 490–493

104. M.A. Jepperson and W.A. Sloan, Optical Observation of Ferrimagnetic Domains, *Am. J. Phys.,* Vol 29, 1961, p 789

105. J.D. Livingston, Domains in Sintered Co5Sm Magnets, *Phys. Status Solidi (a),* Vol 18, 1973, p 579–588

106. D.B. Dove, Photography of Magnetic Domains Using the Transverse Kerr Effect, *J. Appl. Phys.,* Vol 34, July 1963, p 2067–2070

107. G.L. Houze, Domain-Wall Motion in Grain-Oriented Silicon Steel in Cyclic Magnetic Fields, *J. Appl. Phys.,* Vol 38, 1 March 1967, p 1089–1096

108. J.A. Salsgiver, Magnetic Domain Observations on 0.014-inch 50-Percent Ni-Fe Strip, *IEEE Trans. Magnetics*, MAG-6, No. 3, Sept 1970, p 741–744

109. H.J. Williams et al., Observation of Magnetic Domains by the Kerr Effect, *Phys. Rev.*, Ser. 2, Vol 82, 1 April 1951, p 119–120

110. L. Mayer, Observations on MnBi Films During Heat Treatment, *J. Appl. Phys.*, Vol 31, Feb 1960, p 346–351

111. C.A. Fowler et al., Magnetic Domains in Orthoferrites by the Kerr Effect, *J. Appl. Phys.*, Vol 34, July 1963, p 2064–2067

112. C.A. Fowler and E.M. Fryer, Magnetic Domains on Silicon-Iron by the Longitudinal Kerr Effect *Phys. Rev.*, Vol 86, 1 May 1952, p 426

113. M. Prutton, The Observation of Domain Structure in Magnetic Thin Films by Means of the Kerr Magneto-Optic Effect, *Philos. Mag.*, Vol 4, Sept 1959, p 1063–1067

114. P.H. Lissberger, Kerr Magneto-Optic Effect in Nickel-Iron Films, *J. Opt. Soc. Am.*, Vol 51, 1961, p 948–966

115. D. Treves, Limitations of the Magneto-Optic Kerr Technique in the Study of Microscopic Magnetic Domain Structures, *J. Appl. Phys.*, Vol 32, March 1961, p 358–364

116. C.A. Fowler et al., Observation of Domains in Iron Whiskers Under High Fields, *J. Appl. Phys.*, Vol 31, Dec 1960, p 2267–2272

117. R.L. Conger and G.H. Moore, Direct Observation of High-Speed Magnetization Reversal in Films, *J. Appl. Phys.*, Vol 34, April 1963, p 1213–1214

118. J.R. Banbury and W.C. Nixon, The Direct Observation of Domain Structure and Magnetic Fields in the Scanning Electron Microscope, *J. Sci. Instrum.*, Vol 44, Nov 1967, p 889–892

119. D.C. Joy and J.P. Jakubovics, Direct Observation of Magnetic Domains [in Cobalt] by Scanning Electron Microscopy, *Philos. Mag.*, Vol 17, Jan 1968, p 61–69

120. D.C. Joy and J.P. Jakubovics, Direct Observation of Magnetic Domains by Scanning Electron Microscopy, *J. Phys. D*, Vol 2, 1969, p 1367–1375

121. G.A. Jones, Magnetic Contrast in the Scanning Electron Microscope: An Appraisal of Techniques and Their Applications, *J. Magn. Magn. Mater.*, Vol 8 (No. 4), 1978, p 263–285

122. L.H. Lewis, J.-Y. Wang, and P. Canfield, Magnetic Domains of Single-Crystal $Nd_2Fe_{14}B$ Imaged by Unmodified Scanning Electron Microscopy, *J. Appl. Phys.*, Vol 83, 1998, p 6843

123. D.J. Fathers et al., A New Method of Observing Magnetic Domains by Scanning Electron Microscopy, *Phys. Status Solidi*, Vol 20, 16 Dec 1973, p 535–554; Vol 22, 16 April 1974, p 609–619

124. D.J. Fathers et al., Magnetic Domain Contrast from Cubic Materials in the Scanning Electron Microscope, *Philos. Mag.*, Vol 27, March 1973, p 765–768

125. D.E. Newbury, H. Yakowitz, and R.L. Myklebust, Monte Carlo Calculations of Magnetic Contrast from Cubic Materials in the Scanning Electron Microscope, *Appl. Phys. Lett.*, Vol 23, 1973, p 488–490

126. H. Yakowitz and D.E. Newbury, Magnetic Domains Structures in Fe-3.2 Si Revealed by Scanning Electron Microscopy—A Photo Essay, *J. Test. Eval.,* Vol 3, Jan 1975, p 75–78

127. G. Zwilling, Observation of Magnetic Domains in the Scanning Electron Microscope, *Pract. Metallogr.,* Vol 11, 1974, p 716–727

128. T. Yamamoto et al., Observation of Domain Structure in Soft-Magnetic Materials by Means of High Voltage Scanning Electron Microscopy, in *Magnetism and Magnetic Materials 1975,* American Institute of Physics, 1976, p 572–573

129. J.W. Shilling, W.G. Morris, M.L. Osborn, and P. Rao, Orientation Dependence of Domain Wall Spacing and Losses in 3-Percent Si-Fe Single Crystals, *IEEE Trans. Magnetics,* Vol 14, 1978, p 104–111

130. T. Yamamoto et al., Magnetic Domain Contrast in Backscattered Electron Images Obtained with a Scanning Electron Microscope, *Philos. Mag.,* Vol 34 (No. 2), 1976, p 311–325

131. J.D. Livingston and W.G. Morris, SEM Studies of Magnetic Domains in Amorphous Ribbons, *IEEE Trans. Magnetics,* MAG-17, No. 6, Nov 1981, p 2624–2626

132. R.J. Celotta and D.T. Pierce, Polarized Electron Probes of Magnetic Surfaces, *Science,* Vol 234, 1986, p 333–340

133. R. Allenspach, Spin-Polarized Scanning Electron Microscopy, *IBM J. Res. Develop.,* Vol 44, 2000, p 553–570

134. M.R. Scheinfein, J. Unguris, M.H. Kelley, D.T. Pierce, and R.J. Celotta, Scanning Electron Microscopy with Polarization Analysis (SEMPA), *Rev. Sci. Instrum.,* Vol 61, 1990, p 2501–2527

135. M.E. Hale et al., Magnetic Domain Observations by Electron Microscopy, *J. Appl. Phys.,* Vol 30, May 1959, p 789–791

136. H.W. Fuller and M.E. Hale, Determination of Magnetization Distribution in Thin Films Using Electron Microscopy, *J. Appl. Phys.,* Vol 31, Feb 1960, p 238–248

137. J. Silcox, Magnetic Domain Walls in Thin Films of Nickel and Cobalt, *Philos. Mag.,* Vol 8 (No. 85), Jan 1963, p 7–28

138. H.W. Fuller and M.E. Hale, Domains in Thin Magnetic Films Observed by Electron Microscopy, *J. Appl. Phys.,* Vol 31, Oct 1960, p 1699–1705

139. D. Wohlleben, Magnetic Phase Contrast, in *Electron Microscopy in Materials Science,* Academic Press, 1971, p 712–757

140. R.H. Wade, Lorentz Microscopy or Electron Phase Microscopy of Magnetic Objects, in *Advances in Optical and Electron Microscopy,* Vol 5, Academic Press, 1973, p 239–296

141. J.N. Chapman et al., The Direct Determination of Magnetic Domain Wall Profiles by Differential Phase Contrast Electron Microscopy, *Ultramicroscopy,* Vol 3, 1978, p 203–214

142. G.F. Missiroli et al., Electron Interferometry and Interference Electron Microscopy, *J. Phys. E., Sci. Instrum.,* Vol 14, 1981, p 649–671

143. A. Tonomura, The Electron Interference Method for Magnetization Measurement of Thin Films, *Jpn. J. Appl. Phys.,* Vol 11, 1972, p 493–502

144. G. Matteucci et al., Interferometric and Holographic Techniques in Transmission Electron Microscopy for the Observation of Magnetic Domain Structures, *IEEE Trans. Magnetics,* MAG-20, Sept 1984, p 1870–1875

145. T. Matsuda et al., Observation of Microscopic Distribution of Magnetic Fields by Electron Holography, *J. Appl. Phys.,* Vol 53, 1982, p 5444–5446

146. J. Dooley and M. De Graef, Energy Filtered Lorentz Microscopy, *Ultramicroscopy,* Vol 67, 1997, p 113–131

147. L. Wang, D. E. Laughlin, Y. Wang, A. G. Khachaturyan, Magnetic Domain Structure of Fe-55at.%Pd Alloy at Different Stages of Atomic Ordering, *J. Appl. Phys.,* Vol 93, 2003, p 7984–7986

148. Y. Martin and H.K. Wickramasinghe, Magnetic Imaging by "Force Microscopy" with 1000 Å Resolution, *Appl. Phys. Lett.,* Vol 50, 1987, p 1455–1457

149. U. Hartmann, Magnetic Force Microscopy, *Ann. Rev. Mater. Sci.,* Vol 29, 1999, p 53–87

150. M.R. Koblischka and U. Hartmann, Recent Advances in Magnetic Force Microscopy, *Ultramicroscopy,* Vol 97, 2003, p 103–112

151. R. Proksch, Recent Advances in Magnetic Force Microscopy, *Curr. Opin. Sol. State Mat. Sci.,* Vol 4, 1999, p 231–236

152. E. Zueco, W. Rave, R. Schafer, M. Mertig, and L. Schultz, Observations of Fe Surfaces with Magnetic Force and Kerr Microscopy, *J. Magn. Magn. Mater.,* Vol 196–197, 1999, p 115–117

153. G.W. Brown, M.E. Hawley, D.J. Markiewicz, F. Spaepen, and E.P. Barth, Magnetic Structure of Deformation-Induced Shear Bands in Amorphous $Fe_{80}B_{16}Si_4$ Observed by Magnetic Force Microscopy, *J. Appl. Phys.,* Vol 85, 1999, p 4415–4417

M.A. Willard and G.F. Vander Voort, Microstructure and Domain Imaging of Magnetic Materials, *Metallography and Microstructures,* Vol 9, *ASM Handbook,* ASM International, 2004, p. 969–993

Microstructure and Domain Imaging of Magnetic Materials

Matthew A. Willard, Naval Research Laboratory; George F. Vander Voort, Buehler Ltd.

References

1. R.C. O'Handley, *Modern Magnetic Materials: Principles and Application,* John Wiley and Sons, 2000

2. S. Chikazumi, *Physics of Ferromagnetism,* 2nd ed., Clarendon Press, 1997

3. R.M. Bozorth, *Ferromagnetism,* IEEE Press, 1978

4. B.D. Cullity, *Introduction to Magnetic Materials,* Addison-Wesley, 1972

5. C. Heck, *Magnetic Materials and Their Applications,* Crane, Russak and Co., 1974

6. C.-W. Chen, *Magnetism and Metallurgy of Soft Magnetic Materials,* Dover Publications, 1986

7. R. Boll, Ed., *Soft Magnetic Materials,* Heyden & Son, Ltd., 1978

8. R.S. Tebble and D.J. Craik, *Magnetic Materials,* Wiley-Interscience, 1969

9. R. Skomski and J.M.D. Coey, *Permanent Magnetism,* Inst. of Physics Publ., 1999

10. W. Schatt, Control of Textured Sheet by Means of Line Etching, *Pract. Metallog.,* Vol 4, Dec 1967, p 620–627

11. I. Friede, A Modification of Line Etching According to Sved Using Alkaline Sodium Picrate on Transformer Sheet, *Pract. Metallog.,* Vol 5, June 1968, p 325–333

12. L. Kosec et al., Production of Etch Figures on Transformer Sheet, *Pract. Metallog.,* Vol 5, June 1968, p 333–337

13. H. Klemm, Uses of Sodium Thiosulphate (Klemm's Reagent) as an Etchant, *Pract. Metallog.,* Vol 5, April 1968, p 163–177

14. W. Schatt, New Investigations on Hatch-Etching, *Radex Runschau,* No. 3/4, 1967, p 657–667

15. L.J. Regitz, Simultaneous Observation of Grain Structure and Orientation in Oriented Silicon Steel, *IEEE Trans. Magnetics,* MAG-6, Sept 1970, p 576–579

16. G.F. Vander Voort, Grain Size Measurement, *Practical Applications of Quantitative Metallography,* STP 839, ASTM, 1984, p 85–131

17. G.F. Vander Voort, *Metallography: Principles and Practice,* McGraw-Hill, 1984

18. A. Scortecci and E. Stagno, New Metallographic Method for Revealing Magnetic Patterns in Ferrite, *Mem. Sci. Rev. Met.,* BISI No. 5569, Vol 62, 1965, p 741–746

19. S.J. Lillywhite, A.J. Williams, B.E. Davies, and I.R. Harris, A Preliminary Electron Backscattered Diffraction Study of Sintered NdFeB-type Magnets, *J. Microsc.,* Vol 205, 2002, p 270–277

20. M. De Graef, *Introduction to Conventional Transmission Electron Microscopy,* Cambridge University Press, 2004

21. L.E. Murr, *Electron and Ion Microscopy and Microanalysis: Principles and Applications,* (Optical Engineering, No. 29) Marcel Dekker, 2nd ed., 1991

22. P.J. Goodhew, *Practical Methods in Electron Microscopy,* Vol 11, *Thin Foil Preparation for Electron Microscopy,* Elsevier Science Ltd., 1986

23. G. Thomas and M.J. Goringe, *Transmission Electron Microscopy of Materials,* John Wiley & Sons, 1987

24. M. Von Heimendahl and A. Norwick, *Electron Microscopy of Materials: An Introduction,* Academic Press, 1980

25. K.C. Thompson-Russell and J.W. Edington, *Electron Microscope Preparation Techniques in Materials Science,* Macmillan, Philips Technical Library, 1977

26. E.T. Stephenson and M.R. Amann, Effects of Composition, Grain Size and Texture on the AC Core Loss of Magnetic Lamination Steel, in *Energy Efficient Electrical Steels,* American Institute of Mining, Metallurgical, and Petroleum Engineers, 1981, p 43–60

27. "Specification for Nonoriented Electrical Steel Fully Processed Types," A 677/A 677M, *Annual Book of ASTM Standards,* Vol 03.04, ASTM, 2003

28. "Specification for Nonoriented Electrical Steel, Semiprocessed Types," A 683/A 683M, *Annual Book of ASTM Standards,* Vol 03.04, ASTM, 2002

29. R.R. Judd and K.E. Blazek, Effect of High-Temperature Annealing on the Magnetic Properties of Fully Processed Nonoriented Silicon-Steel Sheets, in *Energy Efficient Electrical Steels,* American Institute of Mining, Metallurgical, and Petroleum Engineers, 1981, p 147–155

30. H. Shimanaka et al., Non-Oriented Si-Steels Useful for Energy Efficient Electrical Apparatus, in *Energy Efficient Electrical Steels,* American Institute of Mining, Metallurgical, and Petroleum Engineers, 1981, p 193–204.

31. Y. Shimoyama et al., Development of Non-Oriented Silicon Steel Sheet with Very Low Core Loss, *IEEE Trans. Magnetics,* MAG-19, Sept 1983, p 2013–2015

32. R.G. Aspden et al., Anisotropic and Heterogeneous Nucleation During the Gamma to Alpha Transformation in Iron, *Acta Metall.,* Vol 16, Aug 1968, p 1027–1035

33. R.F. Krause and B.A. Popovic, Magnetic Properties of Textured Annealed Commercial Black Plate, *J. Appl. Phys.,* Vol 52, March 1981, p 2419–2421

34. N.P. Goss, New Development in Electrical Strip Steels Characterized by Fine Grain Structure Approaching the Properties of a Single Crystal, *Trans. ASM,* Vol 23, June 1935, p 511–544

35. R.M. Bozorth, The Orientation of Crystals in Silicon Iron, *Trans. ASM,* Vol 23, Dec 1935, p 1107–1111

36. F. Assmus et al., Iron-Silicon Alloy With Cubic Structure, Parts I and II. *Z. Metallkde.,* Vol 48, June 1957, p 341–349

37. J.E. May and D. Turnbull, Secondary Recrystallization in Silicon Iron, *Trans. AIME,* Vol 212, Dec 1958, p 769–781

38. S. Taguchi and A. Sakakura, Characteristics of Magnetic Properties of Grain-Oriented Silicon Iron with High Permeability, *J. Appl. Phys.,* Vol 40, 1 March 1969, p 1539–1541

39. A. Sakakura et al., Recent Developments in Magnetic Properties of Grain-Oriented Silicon Steel with High Permeability, *Magnetism and Magnetic Materials—1974,* AIP Conference Proceedings No. 24, American Institute of Physics, 1975, p 714–715

40. S.M. Pegler, The Magnetic Properties of Japanese HI-B (110) [001] Grain-Oriented Silicon-Iron, *Magnetism and Magnetic Materials—1974,* AIP Conference Proceedings No. 24, American Institute of Physics, 1975, p 718–720

41. M. Barisoni and M. Candiotti, A New High Permeability Grain Oriented Fe-3% Si Steel, *IEEE Trans. Magnetics,* MAG-14, Sept 1978, p 345–349

42. M. Barisoni et al., Effect of Second Phase on the Primary and Secondary Recrystallization Texture of Grain Oriented Si-Fe Sheets, *IEEE Trans. Magnetics,* MAG-11, 1975, p 1361–1363

43. T. Matsuoka, Effect of Impurities on the Development of (110) [001] Secondary Recrystallization Texture in 3% Silicon Iron, *Trans. ISIJ,* Vol 7 (No. 1), 1967, p 19–28

44. L.J. Regitz, Origins of Streaks of Poorly Oriented Grains in Oriented Silicon Steel, *J. Met.,* Vol 23, Sept 1971, p 17–25

45. J.W. Shilling and G.L. Houze, Jr., Magnetic Properties and Domain Structure in Grain-Oriented 3% Si-Fe, *IEEE Trans. Magnetics,* MAG-10, No. 2, June 1974, p 195–223

46. G.C. Rauch et al., Development of (110) [001] Texture in Low-Alloy Iron by Primary Recrystallization and Normal Grain Growth, *Met. Trans.,* Vol 8A, Jan 1977, p 210–212, 510, 1835

47. D.R. Thornburg et al., The Effect of Manganese and Sulfur on the Development of Orientation (110) [001]-Oriented Low-Alloy Iron, *J. Appl. Phys.,* Vol 52, March 1981, p 2413–2415

48. C.W. Chen, Metallurgy and Magnetic Properties of an Fe-Co-V Alloy, *J. Appl. Phys.,* Vol 32, March 1961, p 348S–355S

49. D.R. Thornburg, High-Strength High-Ductility Cobalt-Iron Alloys, *J. Appl. Phys.,* Vol 40, 1 March 1969, p 1579–1580

50. M.R. Pinnel and J.E. Bennett, The Metallurgy of Remendur: Effects of Processing Variations, *Bell System Tech. J.,* Vol 52, Oct 1973, p 1325–1340

51. J.E. Bennett and M.R. Pinnel, Aspects of Phase Equilibria in Fe/Co/2.5 to 3.0% V. Alloys, *J. Mater. Sci.,* Vol 9, 1974, p 1083–1090

52. S. Mahajan, M.R. Permel, and J.E. Bennett, Influence of Heat Treatments on Microstructures in an Fe-Co-V Alloy, *Met. Trans.,* Vol 5, June 1974, p 1263–1272

53. M.R. Pinnel and J.E. Bennett, Correlation of Magnetic and Mechanical Properties with Microstructure in Fe/Co/2-3Pct V Alloys, *Met. Trans.,* Vol 5, June 1974, p 1273–1283

54. M.R. Pinnel, S. Mahajan, and J.E. Bennett, Influence of Thermal Treatments on the Mechanical Properties of an Fe-Co-V Alloy (Remendur), *Acta Metall.,* Vol 24, 1976, p 1095–1106

55. M.E. McHenry, M.A. Willard, and D.E. Laughlin, Amorphous and Nanocrystalline Materials for Applications as Soft Magnets, *Prog. Mater. Sci.,* Vol 44, 1999, p 291–434

56. G.C. Jain et al., On the Origin of Core Losses in a Manganese Zinc Ferrite with Appreciable Silica Content, *J. Appl. Phys.,* Vol 49, May 1978, p 2894–2897

57. G. Winkler, *Magnetic Garnets,* Vieweg, 1981

58. E.C. Snelling, *Soft Ferrites: Properties and Applications,* Iliffe, 1969

59. F.E. Luborsky, Permanent Magnets in Use Today, *J. Appl. Phys.,* Vol 37, 1 March 1966, p 1091–1094

60. P. Thompson, O. Gutfleisch, J.N. Chapman, and I.R. Harris, A Comparison of the Micromagnetic and Microstructural Properties of Four NdFeB-Type Materials Processed by the HDDR Route, *J. Magn. Magn. Mater.,* Vol 202, 1999, p 53–61

61. I.R. Harris and A.J. Williams, The Character and Role of Grain Boundaries in NdFeB-type Alloys and Magnets, *Z. Metallkde.,* Vol 93, 2002, p 983–990

62. G.C. Hadjipanayis, Nanophase Hard Magnets, *J. Magn. Magn. Mater.,* Vol 200, 1999, p 373–391

63. J.M.D. Coey, Whither Magnetic Materials?, *J. Magn. Magn. Mater.,* Vol 196–197, 1999, p 1–7

64. L.R. Moskowitz, *Permanent Magnet Design and Application Handbook,* Kreiger Publishing Co., 2nd ed., 1995

65. K.J. Strnat, The Recent Development of Permanent Magnet Materials Containing Rare Earth Metals, *IEEE Trans. Magnetics,* MAG-6, 1970, p 182–190

66. J.D. Livingston and D.L. Martin, Microstructure of Aged (Co, Cu, Fe)$_7$Sm Magnets, *J. Appl. Phys.,* Vol 48 (No. 3), 1977, p 1350–1354

67. K.J. DeVos, Alnico Permanent Magnet Alloys, in *Magnetism and Metallurgy,* Vol 1, Academic Press, 1969, p 473–512

68. J. Kirschner, Studies of Surface Magnetism Using Electron and Ion Beam Probes (Invited), *J. Appl. Phys.,* Vol 64, 1988, p 5915–5920

69. M. De Graef and Y. Zhu, Ed., *Magnetic Imaging and Its Applications to Materials,* Vol 36, *Experimental Methods in the Physical Sciences,* Academic Press, 2001

70. A. Hubert and R. Schafer, *Magnetic Domains: The Analysis of Magnetic Microstructures,* Springer-Verlag, 1998

71. D.J. Craik and R.S. Tebble, *Ferromagnetism and Ferromagnetic Domains,* North-Holland/John Wiley & Sons, 1965

72. R. Carey and E.D. Isaac, *Magnetic Domains and Techniques for Their Observation,* Academic Press, 1966

73. K.H. Stewart, *Ferromagnetic Domains,* Cambridge University Press, 1954

74. F.U. Hillebrecht, Magnetic Imaging, *J. Phys.: Cond. Matt.,* Vol 13, 2001, p 11163–11180

75. P. Fischer et al., Study of In-Plane Magnetic Domains with Magnetic Transmission X-Ray Microscopy, *J. Appl. Phys.,* Vol 89, 2001, p 7159–7161

76. E.D. Dahlberg and R. Proksch, Magnetic Microscopies: The New Additions, *J. Magn. Magn. Mater.,* 200, 1999, p 720–728

77. F. Bitter, On Inhomogeneities in the Magnetization of Ferromagnetic Materials, *Phys. Rev.,* Vol 38, 15 Nov 1931, p 1903–1905

78. F. Bitter, Experiments on the Nature of Ferromagnetism, *Phys. Rev.,* Vol 41, 15 Aug 1932, p 507–515

79. W.C. Elmore, Properties of the Surface Magnetization in Ferromagnetic Crystals, *Phys. Rev.,* Vol 51, 1937, p 982–988

80. W.C. Elmore, Ferromagnetic Colloid for Studying Magnetic Structures, *Phys. Rev.,* Vol 54, 1938, p 309–310

81. R.J. Gray, Magnetics Etching with Ferrofluid, in *Metallographic Specimen Preparation,* Plenum Press, 1974, p 155–177

82. K.J. Kronenberg and D. Feldmann, The Use of Variable, High Magnetic Fields for the Investigation of Magnetic Domain Structures, *Pract. Metallogr.,* Vol 11, 1974, p 140–154

83. H.J. Williams, Direction of Domain Magnetization in Powder Patterns, *Phys. Rev.,* Vol 71, 1947, p 646–647

84. H.J. Williams and W. Shockley, A Simple Domain Structure in an Iron Crystal Showing a Direct Correlation with the Magnetization, *Phys. Rev.,* Vol 75, 1 Jan 1949, p 178–183

85. H.J. Williams et al., Magnetic Domain Patterns on Single Crystals of Silicon Iron, *Phys. Rev.,* Vol 75, 1 Jan 1949, p 155–178

86. C. Kittel and J.K. Galt, Ferromagnetic Domain Theory, *Solid State Physics,* Vol 3, Academic Press, 1956, p 437–564

87. H. Pfützner, A New Colloid Technique Enabling Domain Observations of Si-Fe Sheets with Coating at Zero Field, *IEEE Trans. Magnetics,* MAG-17, No. 2, March 1981, p 1245–1247

88. D.J. Craik, A Study of Bitter Figures Using the Electron Microscope, *Proc. Phys. Soc. (London),* Vol B69, 1956, p 647–650

89. J.R. Garrood, Methods of Improving the Sensitivity of the Bitter Technique, *Proc. Phys. Soc. (London),* Vol 79, 1962, p 1252–1262

90. www.ferrotec.com, Ferrotec Corp., 40 Simon St., Nashua, NH

91. J.D. Livingston, Stresses and Magnetic Domains in Amorphous Metal Ribbons, *Phys. Status Solidi (a),* Vol 56, 1979, p 637–645

92. K. Mohri et al., Domain and Grain Observations Using a Colloid Technique for Grain-Oriented Si-Fe with Coatings, *IEEE Trans. Magnetics,* MAG-15, Sept 1979, p 1346–1349

93. G.C. Rauch et al., Enhanced Domain Imaging Techniques, *J. Appl. Phys.,* Vol 55, 15 March 1984, p 2145–2147

94. D.J. Craik and P.M. Griffiths, A New Colloid for Use with the Bitter Figure Technique, *Proc. Phys. Soc.,* Vol B70, 1957, p 1000–1002

95. D.J. Craik and P.M. Griffiths, New Technique for the Study of Bitter Figures, *Br. J. Appl. Phys.,* Vol 9, July 1958, p 279–282, 276–277

96. W. Szmaja, Improvements in Domain Study with the Conventional Bitter Method by Digital Image Processing System, *Phys. Status Solidi (a),* Vol 194, 2002, p 315–330

97. P. Rice and J. Moreland, A New Look at the Bitter Method of Magnetic Imaging, *Rev. Sci. Instrum.,* Vol 62, 1991, p 844–845

98. C.A. Fowler and E.M. Fryer, Magnetic Domains in Thin Films of Nickel-Iron by the Faraday Effect, *Phys. Rev.,* Vol 104 (No. 2), 1956, p 552–553

99. C. Kooy and U. Enz, Experimental and Theoretical Study of the Domain Configuration in Thin Layers of $BaFe_{12}O_{19}$, ***Philips Res. Rep.,*** Vol 15, 1960, p 7–29

100. J.F. Dillon, Jr., The Observation of Domains in the Ferrimagnetic Garnets by Transmitted Light, ***J. Appl. Phys.,*** Vol 29, Sept 1958, p 1286–1291

101. R.C. Sherwood et al., Domain Behavior in Some Transparent Oxides, ***J. Appl. Phys.,*** Vol 30, 1959, p 217–225

102. R. Szymczak, Observation of Internal Domain Structure of Barium Ferrite in Infrared, ***Acta Phys. Polon.,*** Vol A43, 1973, p 571–578

103. A. Green et al., A Polarizing Microscope for Observation of Magnetic Domains, ***J. Sci. Instrum.,*** Vol 40 (No. 10), 1963, p 490–493

104. M.A. Jepperson and W.A. Sloan, Optical Observation of Ferrimagnetic Domains, ***Am. J. Phys.,*** Vol 29, 1961, p 789

105. J.D. Livingston, Domains in Sintered Co5Sm Magnets, ***Phys. Status Solidi (a),*** Vol 18, 1973, p 579–588

106. D.B. Dove, Photography of Magnetic Domains Using the Transverse Kerr Effect, ***J. Appl. Phys.,*** Vol 34, July 1963, p 2067–2070

107. G.L. Houze, Domain-Wall Motion in Grain-Oriented Silicon Steel in Cyclic Magnetic Fields, ***J. Appl. Phys.,*** Vol 38, 1 March 1967, p 1089–1096

108. J.A. Salsgiver, Magnetic Domain Observations on 0.014-inch 50-Percent Ni-Fe Strip, ***IEEE Trans. Magnetics,*** MAG-6, No. 3, Sept 1970, p 741–744

109. H.J. Williams et al., Observation of Magnetic Domains by the Kerr Effect, ***Phys. Rev.,*** Ser. 2, Vol 82, 1 April 1951, p 119–120

110. L. Mayer, Observations on MnBi Films During Heat Treatment, ***J. Appl. Phys.,*** Vol 31, Feb 1960, p 346–351

111. C.A. Fowler et al., Magnetic Domains in Orthoferrites by the Kerr Effect, ***J. Appl. Phys.,*** Vol 34, July 1963, p 2064–2067

112. C.A. Fowler and E.M. Fryer, Magnetic Domains on Silicon-Iron by the Longitudinal Kerr Effect ***Phys. Rev.,*** Vol 86, 1 May 1952, p 426

113. M. Prutton, The Observation of Domain Structure in Magnetic Thin Films by Means of the Kerr Magneto-Optic Effect, ***Philos. Mag.,*** Vol 4, Sept 1959, p 1063–1067

114. P.H. Lissberger, Kerr Magneto-Optic Effect in Nickel-Iron Films, ***J. Opt. Soc. Am.,*** Vol 51, 1961, p 948–966

115. D. Treves, Limitations of the Magneto-Optic Kerr Technique in the Study of Microscopic Magnetic Domain Structures, ***J. Appl. Phys.,*** Vol 32, March 1961, p 358–364

116. C.A. Fowler et al., Observation of Domains in Iron Whiskers Under High Fields, ***J. Appl. Phys.,*** Vol 31, Dec 1960, p 2267–2272

117. R.L. Conger and G.H. Moore, Direct Observation of High-Speed Magnetization Reversal in Films, *J. Appl. Phys.,* Vol 34, April 1963, p 1213–1214

118. J.R. Banbury and W.C. Nixon, The Direct Observation of Domain Structure and Magnetic Fields in the Scanning Electron Microscope, *J. Sci. Instrum.,* Vol 44, Nov 1967, p 889–892

119. D.C. Joy and J.P. Jakubovics, Direct Observation of Magnetic Domains [in Cobalt] by Scanning Electron Microscopy, *Philos. Mag.,* Vol 17, Jan 1968, p 61–69

120. D.C. Joy and J.P. Jakubovics, Direct Observation of Magnetic Domains by Scanning Electron Microscopy, *J. Phys. D,* Vol 2, 1969, p 1367–1375

121. G.A. Jones, Magnetic Contrast in the Scanning Electron Microscope: An Appraisal of Techniques and Their Applications, *J. Magn. Magn. Mater.,* Vol 8 (No. 4), 1978, p 263–285

122. L.H. Lewis, J.-Y. Wang, and P. Canfield, Magnetic Domains of Single-Crystal $Nd_2Fe_{14}B$ Imaged by Unmodified Scanning Electron Microscopy, *J. Appl. Phys.,* Vol 83, 1998, p 6843

123. D.J. Fathers et al., A New Method of Observing Magnetic Domains by Scanning Electron Microscopy, *Phys. Status Solidi,* Vol 20, 16 Dec 1973, p 535–554; Vol 22, 16 April 1974, p 609–619

124. D.J. Fathers et al., Magnetic Domain Contrast from Cubic Materials in the Scanning Electron Microscope, *Philos. Mag.,* Vol 27, March 1973, p 765–768

125. D.E. Newbury, H. Yakowitz, and R.L. Myklebust, Monte Carlo Calculations of Magnetic Contrast from Cubic Materials in the Scanning Electron Microscope, *Appl. Phys. Lett.,* Vol 23, 1973, p 488–490

126. H. Yakowitz and D.E. Newbury, Magnetic Domains Structures in Fe-3.2 Si Revealed by Scanning Electron Microscopy—A Photo Essay, *J. Test. Eval.,* Vol 3, Jan 1975, p 75–78

127. G. Zwilling, Observation of Magnetic Domains in the Scanning Electron Microscope, *Pract. Metallogr.,* Vol 11, 1974, p 716–727

128. T. Yamamoto et al., Observation of Domain Structure in Soft-Magnetic Materials by Means of High Voltage Scanning Electron Microscopy, in *Magnetism and Magnetic Materials 1975,* American Institute of Physics, 1976, p 572–573

129. J.W. Shilling, W.G. Morris, M.L. Osborn, and P. Rao, Orientation Dependence of Domain Wall Spacing and Losses in 3-Percent Si-Fe Single Crystals, *IEEE Trans. Magnetics,* Vol 14, 1978, p 104–111

130. T. Yamamoto et al., Magnetic Domain Contrast in Backscattered Electron Images Obtained with a Scanning Electron Microscope, *Philos. Mag.,* Vol 34 (No. 2), 1976, p 311–325

131. J.D. Livingston and W.G. Morris, SEM Studies of Magnetic Domains in Amorphous Ribbons, *IEEE Trans. Magnetics,* MAG-17, No. 6, Nov 1981, p 2624–2626

132. R.J. Celotta and D.T. Pierce, Polarized Electron Probes of Magnetic Surfaces, *Science,* Vol 234, 1986, p 333–340

133. R. Allenspach, Spin-Polarized Scanning Electron Microscopy, *IBM J. Res. Develop.,* Vol 44, 2000, p 553–570

134. M.R. Scheinfein, J. Unguris, M.H. Kelley, D.T. Pierce, and R.J. Celotta, Scanning Electron Microscopy with Polarization Analysis (SEMPA), *Rev. Sci. Instrum.,* Vol 61, 1990, p 2501–2527

135. M.E. Hale et al., Magnetic Domain Observations by Electron Microscopy, *J. Appl. Phys.,* Vol 30, May 1959, p 789–791

136. H.W. Fuller and M.E. Hale, Determination of Magnetization Distribution in Thin Films Using Electron Microscopy, *J. Appl. Phys.,* Vol 31, Feb 1960, p 238–248

137. J. Silcox, Magnetic Domain Walls in Thin Films of Nickel and Cobalt, *Philos. Mag.*, Vol 8 (No. 85), Jan 1963, p 7–28

138. H.W. Fuller and M.E. Hale, Domains in Thin Magnetic Films Observed by Electron Microscopy, *J. Appl. Phys.,* Vol 31, Oct 1960, p 1699–1705

139. D. Wohlleben, Magnetic Phase Contrast, in *Electron Microscopy in Materials Science,* Academic Press, 1971, p 712–757

140. R.H. Wade, Lorentz Microscopy or Electron Phase Microscopy of Magnetic Objects, in *Advances in Optical and Electron Microscopy,* Vol 5, Academic Press, 1973, p 239–296

141. J.N. Chapman et al., The Direct Determination of Magnetic Domain Wall Profiles by Differential Phase Contrast Electron Microscopy, *Ultramicroscopy,* Vol 3, 1978, p 203–214

142. G.F. Missiroli et al., Electron Interferometry and Interference Electron Microscopy, *J. Phys. E., Sci. Instrum.,* Vol 14, 1981, p 649–671

143. A. Tonomura, The Electron Interference Method for Magnetization Measurement of Thin Films, *Jpn. J. Appl. Phys.,* Vol 11, 1972, p 493–502

144. G. Matteucci et al., Interferometric and Holographic Techniques in Transmission Electron Microscopy for the Observation of Magnetic Domain Structures, *IEEE Trans. Magnetics,* MAG-20, Sept 1984, p 1870–1875

145. T. Matsuda et al., Observation of Microscopic Distribution of Magnetic Fields by Electron Holography, *J. Appl. Phys.,* Vol 53, 1982, p 5444–5446

146. J. Dooley and M. De Graef, Energy Filtered Lorentz Microscopy, *Ultramicroscopy,* Vol 67, 1997, p 113–131

147. L. Wang, D. E. Laughlin, Y. Wang, A. G. Khachaturyan, Magnetic Domain Structure of Fe-55at.%Pd Alloy at Different Stages of Atomic Ordering, *J. Appl. Phys.,* Vol 93, 2003, p 7984–7986

148. Y. Martin and H.K. Wickramasinghe, Magnetic Imaging by "Force Microscopy" with 1000 Å Resolution, *Appl. Phys. Lett.,* Vol 50, 1987, p 1455–1457

149. U. Hartmann, Magnetic Force Microscopy, *Ann. Rev. Mater. Sci.,* Vol 29, 1999, p 53–87

150. M.R. Koblischka and U. Hartmann, Recent Advances in Magnetic Force Microscopy, *Ultramicroscopy,* Vol 97, 2003, p 103–112

151. R. Proksch, Recent Advances in Magnetic Force Microscopy, *Curr. Opin. Sol. State Mat. Sci.,* Vol 4, 1999, p 231–236

152. E. Zueco, W. Rave, R. Schafer, M. Mertig, and L. Schultz, Observations of Fe Surfaces with Magnetic Force and Kerr Microscopy, *J. Magn. Magn. Mater.*, Vol 196–197, 1999, p 115–117

153. G.W. Brown, M.E. Hawley, D.J. Markiewicz, F. Spaepen, and E.P. Barth, Magnetic Structure of Deformation-Induced Shear Bands in Amorphous $Fe_{80}B_{16}Si_4$ Observed by Magnetic Force Microscopy, *J. Appl. Phys.*, Vol 85, 1999, p 4415–4417

L.F. Pease III and D.L. Pease, Metallography and Microstructures of Powder Metallurgy Alloys, *Metallography and Microstructures*, Vol 9, *ASM Handbook*, ASM International, 2004, p. 994–1020

Metallography and Microstructures of Powder Metallurgy Alloys

Leander F. Pease III and Douglas L. Pease, Powder-Tech Associates, Inc.

Introduction

POWDER METALLURGY (P/M) MATERIALS encompass enough differences to necessitate specific specimen preparation procedures in addition to typical metallographic techniques described elsewhere in this Volume. The major difference between parts made of metal powders and those made of wrought metal is the amount of porosity. Sintered materials generally exhibit 0 to 50% porosity, which affects mechanical properties and strongly interferes with metallographic preparation and interpretation of the structure. When examining micrographs, it is important to understand how the specimens were prepared. Careful metallographic preparation is significant in the analysis of sintered structures because the shape of the porosity is as important as the amount in judging sintered strength and degree of sintering.

In the metallographic preparation of most sintered specimens, the pores are smeared during sectioning, grinding, and rough polishing. This occurs to some degree even in materials whose pores have been filled with plastic resins. Proper polishing should open the smeared pores, then reveal their true shapes and area fractions. Routine metallography of the type used on a medium-carbon, ingot-base steel will not suffice. Because test method ASTM B 328 (Ref 1) cannot be used to measure density differences over short distances such as 0.25 to 6.25 mm (0.01 to 0.25 in.), the true amount of porosity must be determined by image analysis to facilitate local density measurement. When the specimen is properly prepared, the area fraction of porosity will equal the volume fraction of porosity, and these must equal the porosity calculated from the actual measured density and pore-free density of a uniformly dense part:

$$V_p = (P_d - M_d)/P_d$$

where V_p is the volume fraction porosity, P_d is the pore-free density, and M_d is the measured density, for example, by ASTM B 328.

Assuming that a part is uniformly 80% dense, in a properly prepared specimen, 20% of the area should appear as porosity. The surface of cold-pressed-and-sintered parts will always be somewhat denser than the interior because of pressure losses caused by interparticle friction. However, parts that are P/M forged in tools at approximately 370 °C (700 °F) can have a chilled surface lower in density than the hotter, softer interior.

During sintering of cold-pressed compacts, the original particle boundaries disappear and result in a plane of fine pores that then grow into larger pores. In as-pressed parts, particle boundaries appear as thin gray lines in the metallographically mounted material. The progress of sintering can be judged by the disappearance of these boundaries. The original particle boundaries are similar to elongated, disk-shaped pores and have very sharp corners. These are extreme stress raisers. There is virtually no bonding across the original particle boundaries. Proper specimen preparation is required to distinguish residual original particle boundaries from the thin, gray

boundaries that often appear between the edges of a particle and pores that were smeared during grinding and polishing. Therefore, an improperly prepared specimen with smeared porosity is often erroneously judged to be undersintered. If microhardness testing is to be performed, proper presentation of the porosity will result in fewer Knoop diamond indentations falling into hidden pores and thus in fewer wasted or incorrect readings.

The open porosity in a mounted sintered part may trap water (moisture). During etching, this water may bleed out, resulting in staining. Water also corrodes some sintered materials. It may evaporate and then condense on the objective lens of the microscope, resulting in a foggy image. Etchants cause similar problems. Open porosity may trap abrasives and carry them onto subsequent cloths, which should hold only fine abrasives. The result is an increased tendency toward scratching of specimen surfaces. Filling the pores with epoxy resins alleviates these difficulties, but requires considerable technique.

Many of the interesting structures seen in P/M parts are caused by porosity and by the mixtures of elemental powders that constitute many alloys. These mixtures do not always result in homogeneous, well-diffused structures. Such heterogeneity is not necessarily detrimental and, in certain nickel steels and diffusion-alloyed steels, may be advantageous because the softer nickel-rich phases increase impact resistance and reduce the tendency toward ductility-limited tensile strength. It is therefore important to recognize when the observed heterogeneity is beneficial. The pores allow carburizing and nitriding gases to penetrate the interior of a sintered steel part, resulting in less-well-defined cases on carbon steel and the nitriding of 300 series stainless steels. The P/M steels are generally low in manganese. When the low alloys are prepared as elemental mixes with nickel and carbon, hardenability is lower than for fully dense, homogeneous low-alloy steels. Hardenability is not a problem in the fully dense prealloyed steels fabricated by forging or metal injection molding.

Reference cited in this section

1. "Standard Test Method for Density and Interconnected Porosity of Sintered Powder Metal Structural Parts and Oil-Impregnated Bearings," B 328, *Annual Book of ASTM Standards,* Vol 2.05, ASTM, 1998

L.F. Pease III and D.L. Pease, Metallography and Microstructures of Powder Metallurgy Alloys, *Metallography and Microstructures,* Vol 9, *ASM Handbook*, ASM International, 2004, p. 994–1020

Metallography and Microstructures of Powder Metallurgy Alloys

Leander F. Pease III and Douglas L. Pease, Powder-Tech Associates, Inc.

Sample Preparation

Sample Record. It is very useful to begin a metallographic investigation by making a photographic record of the sample prior to any sectioning. This may be conveniently done with a handheld Polaroid (Polaroid Corp., Cambridge, MA) camera such as the Macro 5 SLR, which captures images from 0.2 to 3× or with a digital handheld camera. In preparing a report on the sample, it is then a simple matter to mark the image with arrows to show the location of the sectioning. If the sample is then sectioned into several much smaller pieces, they may be similarly recorded for later identification.

Specimen Selection and Sectioning. It is usually necessary to examine a section that extends from the surface to the interior of the part and from top to bottom, in the pressing direction (a longitudinal section). The surface is susceptible to changes from (1) the sintering atmosphere, such as decarburization in a steel, (2) being sealed over with pure copper during infiltration, or sealed over by tumbling, or (3) shallow hardenability in elemental mixes of steels. Density can vary from point to point. During sintering, the protected bottom of the part "sees" a different atmosphere than the top, and the internal area may be more protected from the sintering atmosphere than an outer surface. Infiltrated parts have certain artifacts that appear where the infiltrant entered, for example, erosion or adhering copper alloy.

Improper tool design or press setup can cause cracks or laminations at different levels in a part, such as between a hub and flange; low-density regions normally occur just below flanges. If a part is overpressed in certain regions or if the tooling does not have the correct exit taper, microcracks can occur upon ejection. These are usually parallel to a punch face (normal to the direction of applied pressure) and are best seen in longitudinal sections that run parallel to the pressing direction. In a case-carburized gear, a section showing the plan view of the teeth would show the depth of case and whether or not the teeth were through-hardened. Therefore, likely potential defects in a P/M part influence selection of the planes of sectioning.

Because of the difficulty in opening all the smeared pores on a P/M part, the use of smaller sections is recommended. An easily polished specimen will measure less than 12 by 12 mm (0.5 by 0.5 in.). A soft abrasive wheel that breaks down easily will control overheating at cutoff and will not glaze easily. A composite wheel 0.4 mm (0.015 in.) thick is especially recommended for specimens less than 25 mm (1 in.) in section and when very precise cuts are needed. Composite wheels consist of rubber-bonded aluminum oxide. Because of their 0.4 mm (0.015 in.) width, they cut with low force and quite quickly. Low-speed diamond wheels are very precise and damage free, but require long sectioning times. If the conventional abrasive wheel glazes or cuts slowly because the workpiece is too large, four small notches (3 cm^2, or 0.5 $in.^2$) can be removed using pliers at 90° positions around the periphery of the wheel. Because this weakens the wheel somewhat, it should always be operated in a well-guarded enclosure. A substantial flow of water that correctly strikes the interface between the wheel and the part is also required. Rust inhibitor should be added to recirculated water.

Sectioning an annularly shaped part parallel to its axis with the wheel advancing from the outer diameter toward the inner diameter may result in the wheel being captured when it penetrates the inner diameter. This often occurs in heat treated parts containing residual stresses and may cause wheel breakage. This can be avoided if the part is sectioned with the wheel moving along the axis of the part so that material on both sides of the inner diameter is cut at the same time. In general, it is preferable to secure in a vise the section of the specimen to be mounted. This section rarely contains burrs and may be mounted without further hand grinding.

Fluid Removal and Washing. Entrapped oil from heat treating or machining as well as water and rust inhibitors from the cutoff wheel must be removed from the pores before the specimen is mounted. Other sources of contamination include the sizing lubricants used at re-pressing and rust inhibitors added during tumble deburring of the parts. Failure to remove these contaminants will obscure the specimen surface when viewed under the microscope, bringing new meaning to the term “interference fringes.” Entrapped oils also seem to interfere with polishing by slowing down the removal rate. If the specimen was not heat treated, contains no substantial amount of oil, and can tolerate heating to 260 to 370 °C (500 to 700 °F) for approximately 1 min, then the fluids can be removed on a hot plate under a hood. The specimens are easily heated until straw-colored or light blue. Water or small amounts of oil will evaporate or burn off quickly. At higher burnoff temperatures, a layer of oxide is created in the surface pores.

When the specimen cannot be heated as above, an extractor-condenser of the type shown in Fig. 1 or a Soxhlet apparatus may be used. The extractor-condenser consists of a flask, a siphon cup, and a condensing-coil unit that fits on the top of the flask. A solvent, such as toluene or petroleum ether, is placed in the flask, and the specimens to be cleaned are placed in the siphon cup. Multiple specimens must first be coded for subsequent identification. For small specimens, a group photograph provides handy identification.

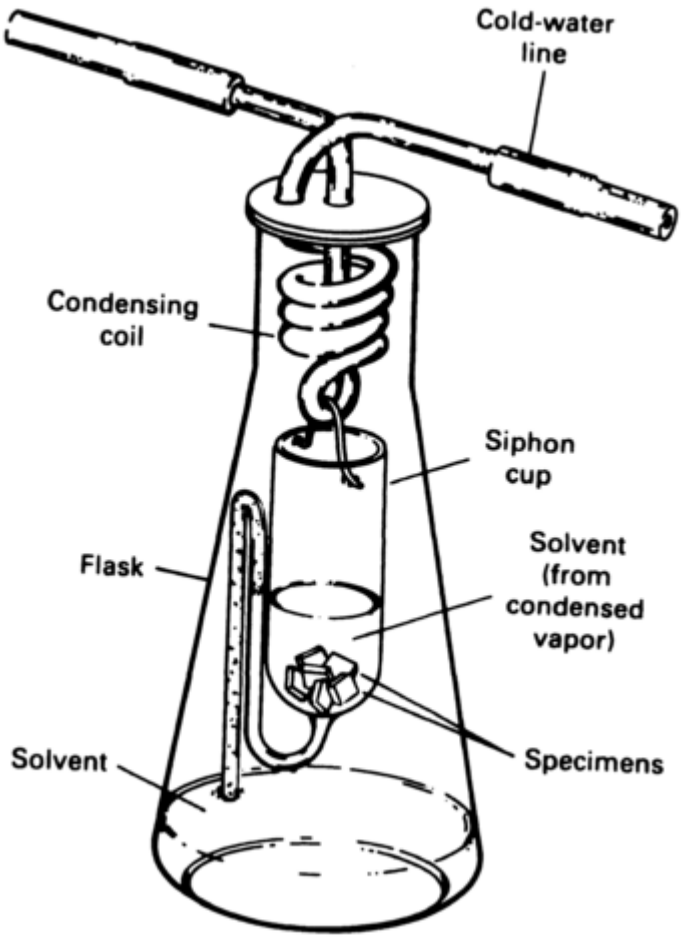

Fig. 1 Extractor-condenser used for washing P/M specimens to remove contaminants from pores

A cold-water line is connected to the condensing coil. The flask is heated to the boiling temperatures of the solvent. The solvent evaporates, and when the vapor contacts the cold condensing coil, the hot condensate drips into the siphon cup and onto the parts. When the siphon cup is filled to the level determined by the upper bend in the exit tube, it empties, returning solvent and dissolved oil to the boiling flask. Recycling allows a subsequent flow of clean solvent over the specimens. The oil and foreign matter remain in the flask and are periodically discarded along with the toluene.

Six cycles of siphoning, requiring a total of approximately 1 h, will usually ensure removal of the oil. This method is also described in ASTM B 328 (Ref 1) and ISO 2738 (Ref 2). The latter test method includes the technique for removing oil when testing for total carbon. Because laboratory investigations often involve testing for carbon along with metallography, it may be efficient to use the more rigorous ISO method. Following extraction with the solvents, it is necessary to dry the parts for approximately 1 h at 120 °C (250 °F) to remove the solvent. When carbon content is to be measured, several repetitions of extraction and drying are carried out until the weight change between consecutive dryings is less than 0.01 wt%.

Mounting of Compacted Specimens. Epoxy resins, rather than wax and Bakelite (Union Carbide Corp., Danbury, CT) are especially preferred for filling the pores and mounting the specimens because the pores can be sealed as the multiple specimens are mounted. A convenient container for mounting is a length of 25 mm (1 in.) copper or aluminum tubing with an inner diameter of 32 mm ($1\frac{1}{4}$ in.). This may be placed on a small, flat sheet of glass. To prevent resin from leaking under the edge of the tubing, a sheet of single-sided adhesive mounting paper may be placed under the tubing. The interior of the tube and the glass are coated with a mold-release agent. A convenient alternate two-piece cup could be machined from low-carbon steel (Fig. 2). The steel base can be ground flat in the lab as needed, and excess epoxy can be removed by sintering or heat treating the base. The bases of the plastic cups commercially available become concave after a few uses, but they are still very convenient to use for mounting specimens. The concave bases can be ground out by hand on a grinding lap. The plastic cups, when new, result in mounts with clear sides, which is a convenience when looking into the mount to check location or orientation.

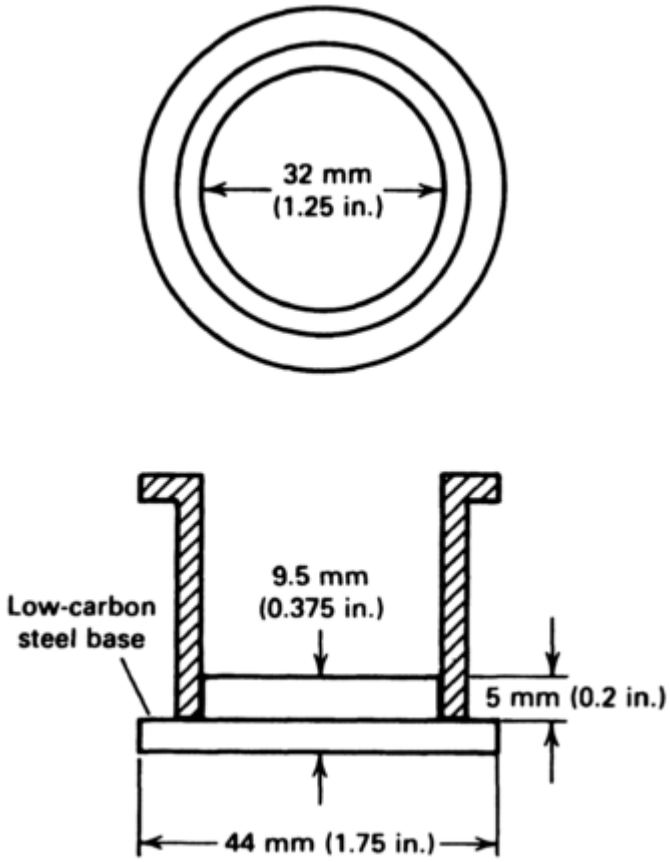

Fig. 2 Machined two-piece cup for mounting P/M specimens

When more than one specimen is to be inserted in the same mount, each specimen must be identified for future reference. The use of an asymmetric arrangement of specimens or the mounting of a distinctive object such as a small, twisted piece of a paper clip, will permit easy, accurate reference. The use of the epoxy resin makes it easy to mount several small pieces in one mount. It is recommended that a sketch or map be drawn for each mount, for future reference. It is usually easier if the sketch shows the view of the polished surface, and the samples are carefully placed in the mounting cup in mirror image to the sketch.

The epoxy resin should be selected for low vapor pressure of resin and hardener, and any new resin should be tested in the vacuum chamber to note the pressure at which it bubbles. For example, some epoxies should not be used below 150 torr (20 kPa). This limits the amount of air that can be removed and the volume of pores that can be filled. Epoxy resins should be placed in disposable cups for stirring and mixing of resin and hardener. Volumetric measurement of the components with plastic syringes works reasonably well, but weighing the liquids on an electronic balance is easier. Epoxy resins should be selected for low viscosity. Rapid hardening is convenient, but must not be allowed to interfere with pore filling. Many resins heat cure in 1.5 to 2.0 h at 50 °C (120 °F), for example, Caldofix (Struers, Westlake, OH). The Caldofix resin is crystal clear, which allows good viewing of the interior samples and ease of scribing the identification code on the back side.

Epoxy-Resin Impregnation. In one method, the resin is carefully poured over the specimens in their mounting cups to a depth of approximately 6 mm ($\frac{1}{4}$ in.) above the sample with the cup filled to a total depth of 14 to 18 mm ($\frac{5}{8}$ to $\frac{3}{4}$in.). The cups should be placed in a container that will catch any minor epoxy spills, and the container should be placed in a vacuum chamber. The air is then evacuated to the lowest pressure tolerated by the resin. The specimens should bubble for approximately 10 min. Air pressure is then restored and allowed to impregnate the specimens for 15 min. The specimens may then be cured overnight, or at an accelerated rate of 1.5 to 2.0 h at 50 °C (120 °F), or by following manufacturer's directions.

An alternate method for impregnation with epoxy resin involves suspending the specimen above the epoxy bath during air evacuation. This allows the air to exit the pores rapidly without causing air bubbling in the epoxy. It is similar to the technique used to fill the pores with oil in a sintered bearing. Another method is to hold the specimen above the oil magnetically or with a vacuum feedthrough manipulator. After 1 to 2 min at low pressure, no air will remain in the specimen, and it can be lowered into the epoxy bath, at which point the

pressure is readmitted into the chamber. This method is limited by the vapor pressure of the epoxy resin and hardener. Commercial equipment with vacuum feedthrough evacuates air from the specimens and directs a stream of epoxy from outside the chamber into the specimen cup located in the vacuum. Again, the vapor pressure of the resins determines the lowest usable pressure.

Most mounts show a case effect where resin mainly enters the specimen through unmachined surfaces. The surface against the bottom of the specimen cup is almost always machined. Therefore, most mounts show evidence of epoxy resin in the surface pores, but the interior pores are rarely full. This effect is apparent to the unaided eye during initial polishing, because the outer edges appear more porous (like an orange peel) and the interior more mirrorlike.

Edge retention is achieved by adding light or dark -60 mesh alumina (Al_2O_3) granules to the epoxy resin (Fig. 3). Some of the ceramic may be mixed with resin and poured around the specimens to form a 1.6 mm ($\frac{1}{16}$ in.) thick layer. The rest of the mount is formed from clear resin poured on top of the mixture.

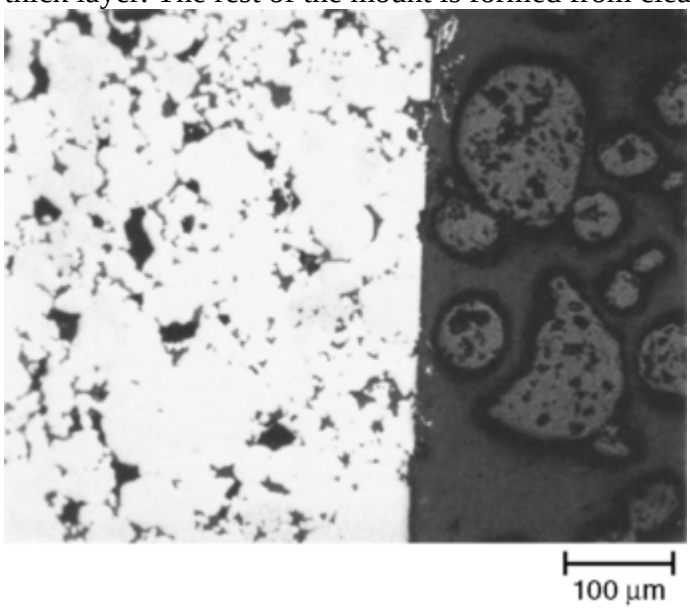

Fig. 3 Edge-retention technique in which dark Al_2O_3 granules (right) are added as a reinforcer to the epoxy resin. Not all of the pores are open, which indicates that Al_2O_3 additions necessitate extended polishing times. Fe-0.8C specimen (7.0 g/cm^3) pressed at 550 MPa (40 tsi) and sintered 30 min in dissociated ammonia at 1120 °C (2050 °F). 2% nital. 95×

Alternatively, loose Al_2O_3 may be poured into the specimen cup to a depth of 1.6 mm ($\frac{1}{16}$ in.), surrounding the specimens, and the clear resin carefully poured on top. During vacuum evacuation, the resin flows in among the Al_2O_3 particles. This ceramic reinforces the epoxy and results in very little rounding of the specimen edge during polishing. Because the oxide greatly slows the rate of grinding and polishing, the times recommended below must be adjusted. A third technique involves forming a thin oxide-reinforced layer around the specimen itself by applying a thick, pasty mixture of resin and oxide to the specimen surface. In this way, the entire surface of the mount is not hardened, just a layer approximately 0.5 mm (0.020 in.) adjacent to the specimen. Therefore, the polishing time is not unduly increased.

Specimen Identification. The use of some epoxy resins, particularly when air cured, produces a surface that is soft and cloudy and inconvenient for scribing the specimen identification. The back of the specimen mount should be ground through 600 grit, then polished for 1 min using 1 μm Al_2O_3 on a medium-nap cloth. This yields a flat surface that can be scribed for clear identification. If it is necessary to look through the side of the mount to see the specimen inside the epoxy, the round-side surfaces must be polished as described previously, or a new plastic mounting cup used. Specimens that have been filled with wax can also be mounted in thermosetting Bakelite resins, Lucite (Clorox Co., Oakland, CA), or clear-liquid cold-mounting resins.

Wax Impregnation, an Alternative to Epoxy Impregnation. After removal of fluid from the pores, subsequent abrasive, water, and etchants must be kept out of the pores. Wax impregnation may be used for specimens that are to be handheld or mounted in Bakelite. The specimens are soaked 2 to 4 h in a molten synthetic wax at 175

°C (350 °F). After cooling and removal of the surface wax, the specimens are ready to hand grind or to mount in Bakelite.

Ideally, wax impregnation should be carried out in a vacuum oven at the recommended temperature. The vacuum allows the air entrapped in the pores to bubble up through the molten wax. The atmospheric pressure is returned to the system with the specimens immersed in the molten wax. The air pressure then should be allowed to act on the molten wax for 30 min to force it into the pores. Subsequently, the specimens may be cooled and the excess wax removed.

References cited in this section

1. "Standard Test Method for Density and Interconnected Porosity of Sintered Powder Metal Structural Parts and Oil-Impregnated Bearings," B 328, *Annual Book of ASTM Standards,* Vol 2.05, ASTM, 1998

2. "Permeable Sintered Metal Materials, Determination of Density, Open Porosity and Oil Content," ISO 2738, International Organization for Standardization, American National Standards Institute

---

L.F. Pease III and D.L. Pease, Metallography and Microstructures of Powder Metallurgy Alloys, *Metallography and Microstructures,* Vol 9, *ASM Handbook*, ASM International, 2004, p. 994–1020

Metallography and Microstructures of Powder Metallurgy Alloys

Leander F. Pease III and Douglas L. Pease, Powder-Tech Associates, Inc.

Automatic Grinding and Polishing

An automatic grinder can produce flat specimens using wet SiC papers of 220, 500, and 1200 mesh, 30 N (6.7 lbf) force per specimen, 300 mm wheel, 125 rpm, counterrevolving the specimen. Grind no more than 60 s on a paper, for six 30 mm (1.25 in.) mounts done at the same time. Before polishing, ultrasonically clean for about 5 min. The ultrasonic cleaner used for washing P/M specimens consists of a power supply and a small tank, which holds a water bath containing a small amount of surfactant such as liquid soap. The surfactant provides the energy coupling needed between the water bath and a beaker of solvent, such as isopropyl alcohol, is suspended in the bath. The water bath and beaker together should fill the ultrasonic tank to within 25 mm (1 in.) of the top (to provide protection to heating elements that the ultrasonic cleaner may contain). The specimen is placed inside the beaker and rests face down on cotton wadding or a paper towel. The power source produces high-frequency waves in the room-temperature water bath. The waves strike the beaker and force the alcohol into the pores of the specimen, removing foreign substances. Because the specimen is placed in the alcohol bath, the washing takes place in what soon becomes a contaminated solution. Debris accumulates in the cotton or on the paper towel, and the solution must be changed periodically. In addition to removing polishing grit when changing to successively finer media, it has also been reported that the ultrasonic action may help to open pores that were smeared at grinding (Ref 3).

Rough polishing consists of 10 min on a very short-nap cloth (e.g., Struers DAC cloth) with a 3 μm diamond paste at 30 N (6.7 lbf) force on each specimen and 125 rpm on a 300 mm (11.8 in.) wheel. Final polishing for 1 to 2 min with 0.05 μm alumina on long-nap microcloth at 125 rpm, 1 N (0.25 lbf) force results in a mount free of scratches and flat to the edge. If the pores were well filled with epoxy resin, they will be seen in their true area fraction and shape. If the interior pores are not well filled, the above procedure must be supplemented by several repetitions of light etching (15 s immersion in 2% nital) and repolishing 1 to 2 min with the 0.05 μm alumina. To learn if the pores are still smeared, examine the mount at about 1000× and look for thin gray boundaries of the pore edges, for example, Fig. 4.

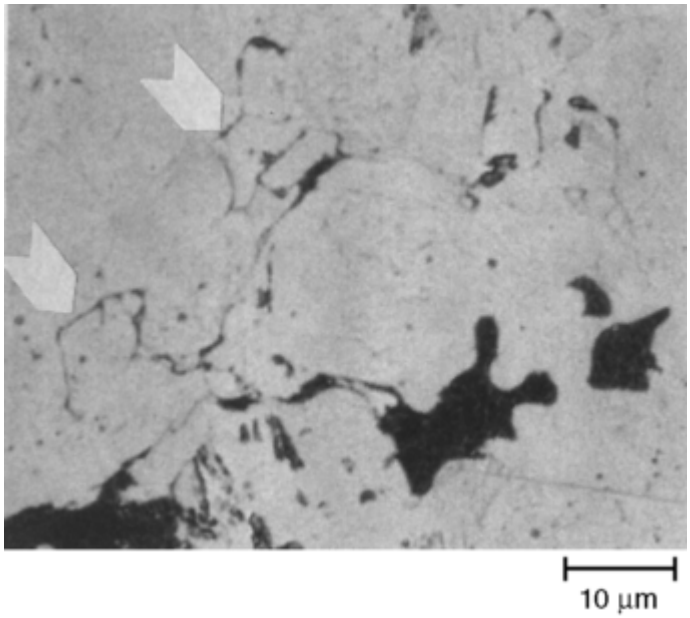

Fig. 4 Intermediate stage of polishing showing the edges of smeared pores (see arrows), which have not yet been opened by the polishing. The material is pressed-and-sintered Fe-2%Cu-0.8%C, 6.8 g/cm^3. Magnifications of 500 to 1000× are required to see these features. These smeared pore edges must be removed by polishing and etching so that the original particle boundaries characteristic of undersintering can be seen, in the unetched condition, e.g., Fig. 24 Unetched. 960×

Reference cited in this section

3. G.A. Blann et al., Principles and Practices for Metallographic Preparation for Powder Metallurgy, *Microstr. Sci.*, Vol 22, 1995, p 135

L.F. Pease III and D.L. Pease, Metallography and Microstructures of Powder Metallurgy Alloys, *Metallography and Microstructures,* Vol 9, *ASM Handbook,* ASM International, 2004, p. 994–1020

Metallography and Microstructures of Powder Metallurgy Alloys

Leander F. Pease III and Douglas L. Pease, Powder-Tech Associates, Inc.

Manual Grinding and Polishing

Grinding. Rough grinding of the mount must produce a planar surface for subsequent grinding and polishing. The preferred procedure involves using a water-cooled and lubricated wheel with 240, 400, and 600 mesh SiC papers. The paper is held to a rotating disk that makes use of the vacuum created by a thin layer of water under the sheet of abrasive paper. Alternatively, the paper can be held in place adhesively or by special flat magnets that grip a thin ferrous backing on the grinding paper. The same grinding may be carried out on wet papers placed on top of a sheet of glass. When using grinding wheels, the specimen is held in a fixed position on the wheel so that all scratches are in one direction, which requires even and moderate pressure. When changing papers, the specimen is rotated 90° to allow one to note the disappearance of the previous scratches. The use of one single sheet of SiC paper for more than two or three specimen mounts is not recommended because it leads to lack of flatness of the specimen surface. Grinding using 240 to 600 grit abrasives and moderate pressure at 125 to 250 rpm on 200 mm (8 in.) laps requires approximately 30 s for each paper. Using Al_2O_3 for edge retention (Fig. 3) gives a hard mount surface that requires longer grinding and polishing times.

It is important to grind a 30° bevel around the mount periphery. This allows the mount to pass smoothly over the subsequent polishing cloths and prevents the plowing aside of abrasives by a sharp edge. Failure to use a bevel slows polishing on long-nap cloths.

Polishing. Following grinding, the specimen is flat to the edges, and the pores are almost completely smeared (Fig. 5). Subsequent polishing generally rounds the specimen edges, because the mounting resin is much softer than the metal specimen. This rounding can be prevented by the use of embedded ceramic materials for edge retention, or such conventional techniques as plating of the specimen surface before mounting. Polishing must open all the pores, show true area fraction of porosity, remove scratches and disturbed metal, and minimize edge rounding. The presence of epoxy resin or wax in the pores facilitates opening the smeared pores, but does not eliminate the problem.

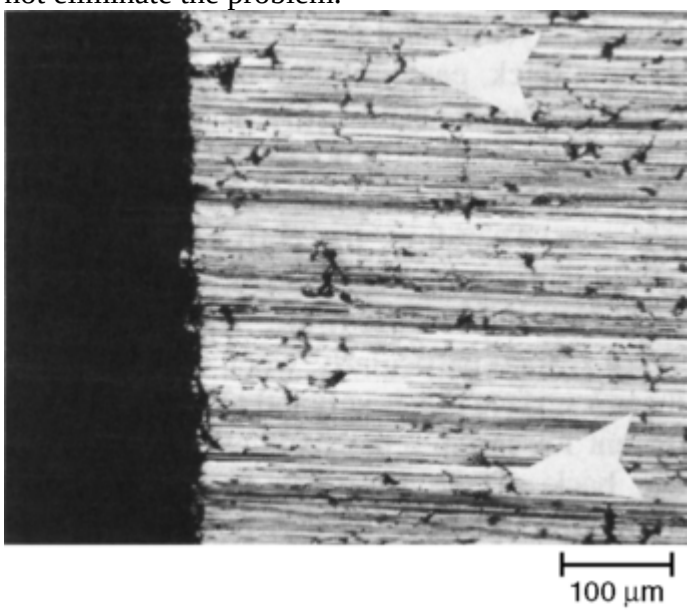

Fig. 5 Pressed-and-sintered Fe-0.8C alloy (6.8 g/cm^3), as-ground on 600 grit silicon carbide. Micrograph shows the closure of pores and flatness of specimen (the surface is shown at left). Arrows indicate closed pore edges. 95×

During polishing, the abrasives first open the pores closest to the specimen edges (Ref 4, 5), giving the impression that surfaces are less dense than interiors (Fig. 6, 7, 8). For ferrous materials, the fastest way to reveal the pores results in slight edge rounding but is adequate for routine work. These steps should be followed:

1. Etch 2 min in 2% nital by immersion. For materials other than low-alloy steels, use the customary agents. Etching before polishing initiates pore opening, but does not exaggerate pore size.
2. Rough polish 2 min using 1 μm Al_2O_3 moderate hand pressure on a long-nap felt cloth (Ref 6). Use 250 rpm on a 200 mm (8 in.) diam wheel rotating the specimen counter to the wheel to prevent comet tails. The long-nap cloth and the fairly coarse Al_2O_3 rapidly open the pores (see Ref 7 for an example of another technique that requires 300 min).
3. Repeat steps 1 and 2 once or twice. This procedure generally opens all the pores. To the unaided eye, the surface of the specimen should exhibit a uniform orange-peel appearance with no shiny specular (mirrorlike) regions. If necessary, repeat steps 1 and 2 until the surface is uniformly roughened. Even P/M forgings and metal-injection-molded parts at 98 to 99% of full density display porosity to the unaided eye. This aggressive rough polishing exaggerates the pore area fraction by eroding and rounding pore edges. That is, the specimen will appear erroneously low in density. Final polishing must restore the true area fraction of porosity.
4. Polish 2 min using 1 μm diamond on a short-nap cloth (e.g., Struers MOL cloth) at 250 rpm with moderate hand pressure. This sharpens pore edges and restores the pores to their true area fraction and eliminates most scratches, but leaves the edges of the specimen slightly rounded. A 19 mm (0.75 in.) long bead of diamond paste, weighing approximately 0.06 g (0.002 oz), is recommended for each 2 min

of polishing. Use an alcohol-base solvent or thinner for the diamond paste so that it will wash off in water. Oily thinners penetrate the residual pores and bleed out of the specimen.

5. Final polish 30 s using a long-nap microcloth and 0.05 μm deagglomerated Al_2O_3. Use light hand pressure or an automatic polisher with 100 g weight (1 N, or 0.25 lbf) on the specimen at 125 rpm. This removes the fine scratches on most ferrous materials. The true area fraction of porosity of the surface is now restored.

Reference 5 includes information on this method, and it also demonstrates that it is possible to open pores and show the correct porosity area fraction using a method that requires approximately 12 min and does not use diamond. It consists of 10 min of hand polishing using 1 μm Al_2O_3 on a synthetic suede, short-nap cloth at 250 rpm on a 200 mm (8 in.) lap and 2 min of light hand polishing using 0.05 μm Al_2O_3 at 125 rpm on the same type of cloth.

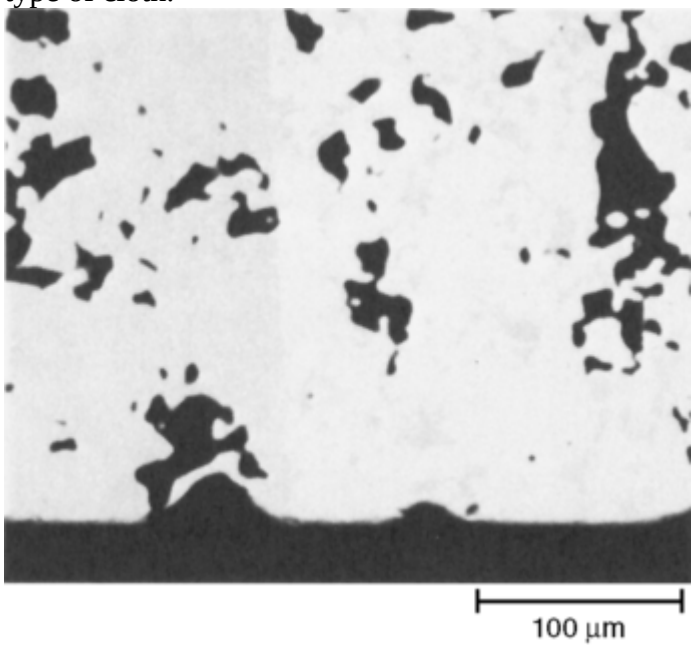

Fig. 6 Effect of polishing on pore opening in a pressed-and-sintered Fe-0.8C alloy: deliberately underpolished specimen. This region, which is adjacent to the specimen edge, shows all the pores open. Compare with Fig. 7 (center of specimen). 180×

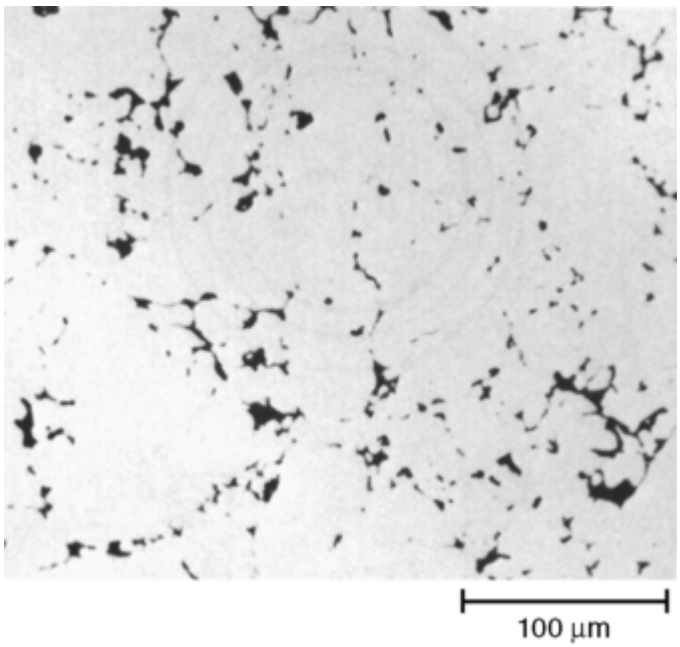

Fig. 7 Effect of polishing on pore opening in a pressed-and-sintered Fe-0.8C alloy: interior of same specimen as in Fig. 6 After 2 min of polishing, there are numerous smeared pores. Compare the amount

of porosity with Fig. 6 This micrograph shows how the inner part of a specimen polishes more slowly than the edge. 180×

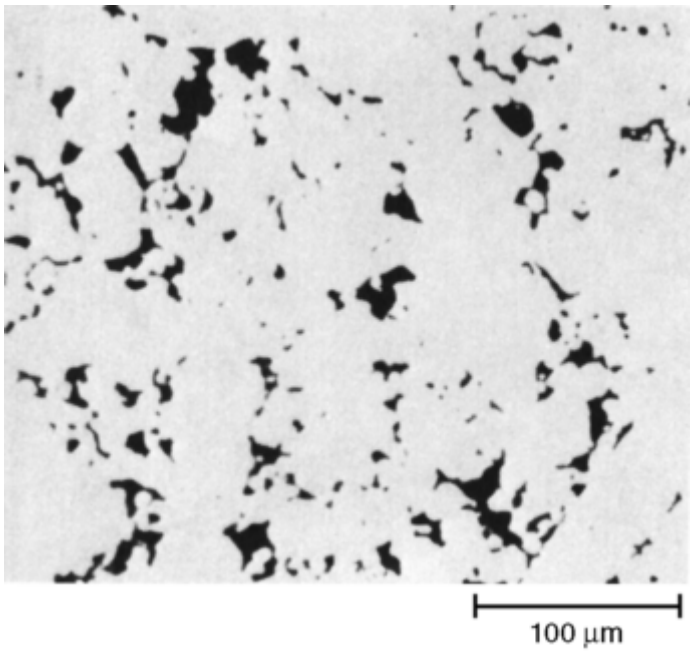

Fig. 8 Effect of polishing on pore opening in a pressed-and-sintered Fe-0.8C alloy: repolished version of Fig. 7 showing more pores in the center of the part (some remain smeared over). The density appears higher than the true density of 6.8 g/cm^3. 180×

To produce a surface with no edge rounding, it is necessary to eliminate the 1 μm Al_2O_3 and long-nap cloth polishing. Instead, after the 2 min etch in 2% nital, step 4 should be repeated several times. More than five repetitions may be required to open all the pores on a large specimen, particularly if it is soft and undersintered. The wheel should be recharged with diamond at each repetition. However, the 2 min etching should not be repeated, because the 1 μm diamond paste does not rapidly remove etching effects.

Newly developed P/M materials require modified polishing procedures to show the correct area fraction of porosity. Such methods could be developed using standards of known density. Other modern methods of automatic polishing may open all pores, but should first be tested by preparing a specimen of known density, then measuring the area fraction of pores. The measured area fraction should agree with calculations made from the known density.

A vibratory machine in which the specimens circulate around a bowl with the abrasive slurry may also be used. The use of a short-nap chemotextile cloth (Texmet) and 0.3 or 1 μm Al_2O_3 will yield a specimen that is virtually free of edge rounding. However, for specimens that have been ground through 600 grit, this procedure requires approximately 3 h because of the slow material removal rate and the need to open all the pores.

The rate of material removal may be measured using a Knoop indenter mark as a reference (Fig. 9). First, a mark approximately 100 μm long is made in a known location on the specimen. A simple reference point in the interior of the specimen can be made using a Rockwell superficial indenter with the 15 kgf load. The Knoop mark is then placed approximately 0.4 mm (0.015 in.) away from the superficial indenter mark and at a known orientation to it. The Knoop mark is measured from a photograph or with the measuring stage of the microhardness tester. After polishing for a fixed time, such as 1 to 2 min, the Knoop mark is relocated and remeasured. The material removed normal to the specimen surface is the change in length of the Knoop diagonal divided by 30.51 (for a standard indenter). For a 25 by 25 mm (1 by 1 in.) specimen, polishing using a 250 rpm, 200 mm (8 in.) diam lap, 1 μm Al_2O_3 on a synthetic suede, short-nap cloth, and moderate hand pressure will remove 0.4 μm/min. A smaller specimen, such as 12 by 6 mm (0.5 by 0.25 in.) will polish at 1.45 μm/min. Additional information on material removal rates can be found in Ref 4.

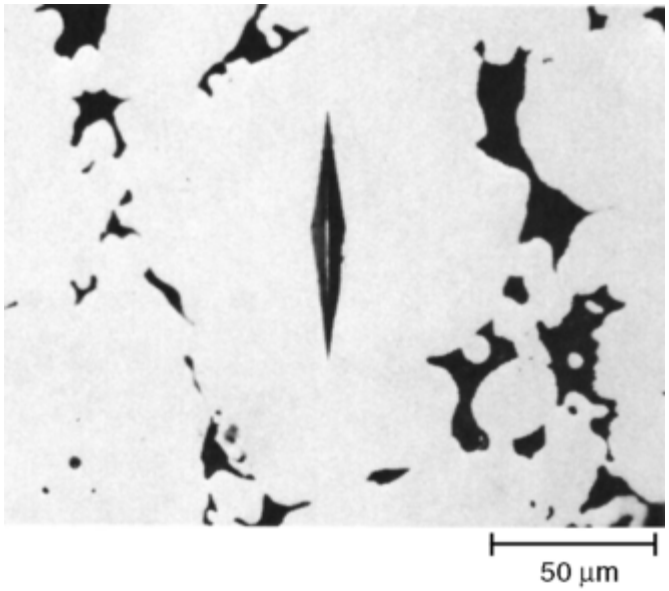

Fig. 9 Knoop indenter mark (100 gf) used as a reference to note the rate of material removal from the surface by measuring the change in length and depth of the indentation. Surrounding black pores in this unetched, pressed-and-sintered Fe-0.8C alloy (6.8 g/cm^3) are also revealed. 295×

Soft material, such as pure iron or copper, may still exhibit some fine scratches after the 0.05 μm Al_2O_3 polishing described previously in step 5. One solution is to use a new long-nap cloth (microcloth) with adhesive backing attached to a flat glass plate or to a flat bench top. With the deagglomerated 0.05 μm Al_2O_3, charged onto the cloth at a ratio of 1 part (by volume) powder to 4 parts distilled water, the specimen should be polished in the abrasive slurry using approximately 50 light hand strokes straight back and forth. This will eliminate the fine scratches from the prior polishing; remaining scratches will be aligned parallel to the direction of polishing, and their source identified. This light final polishing does not cause comet tails or pore beveling. Colloidal silica, for example, Mastermet (Buehler, Ltd., Lake Bluff, IL), is excellent for a final polish.

Titanium alloys require a 4 min rough polishing using 1 μm Al_2O_3 on felt cloth at 250 rpm on a 200 mm (8 in.) diam lap with moderate hand pressure. This opens and slightly enlarges the pores. The autopolisher with 3 μm diamond on DAC cloth for 10 min at 30 N can be used. Final polish is colloidal silica on microcloth, at 1 N (0.25 lbf), 125 rpm, and for 1 min.

References cited in this section

4. L.F. Pease III, Metallography of Powder Metallurgy Materials, *Powder Metal Technologies and Applications*, Vol 7, *ASM Handbook*, ASM International, 1998, p 722–723

5. L.F. Pease III, Metallography and Properties of Sintered Steels, *Progress in Powder Metallurgy*, Vol 33, Metal Powder Industries Federation, 1977

6. O. Struglics, Hoeganaes Corporation, Hoeganaes, Sweden, personal communication

7. S. Coleman and D. Tomkins, A Quantitative Assessment of the Mechanical Properties of Sintered Iron Micrographic Specimens, *Powder Metall.*, No. 2, 1976, p 53

L.F. Pease III and D.L. Pease, Metallography and Microstructures of Powder Metallurgy Alloys, *Metallography and Microstructures,* Vol 9, *ASM Handbook,* ASM International, 2004, p. 994–1020

Metallography and Microstructures of Powder Metallurgy Alloys

Leander F. Pease III and Douglas L. Pease, Powder-Tech Associates, Inc.

Uncompacted Powder

Manufacturers of sintered parts have occasion to examine raw materials (powders) metallographically. This is important because different production methods can result in powders with the same nominal chemistry, but with disparate powder characteristics in terms of flow rate, apparent density, compressibility, and sinterability. These behavioral differences of powders occur because of various powder characteristics such as surface area, residual alloying, internal porosity, particle size, and particle shape. Powder characteristics can be evaluated by microscopic examination of cross-sectional views (e.g., Fig. 10, 11, 12, 13) and/or by analysis of particle size and shapes with light or electron microscopes.

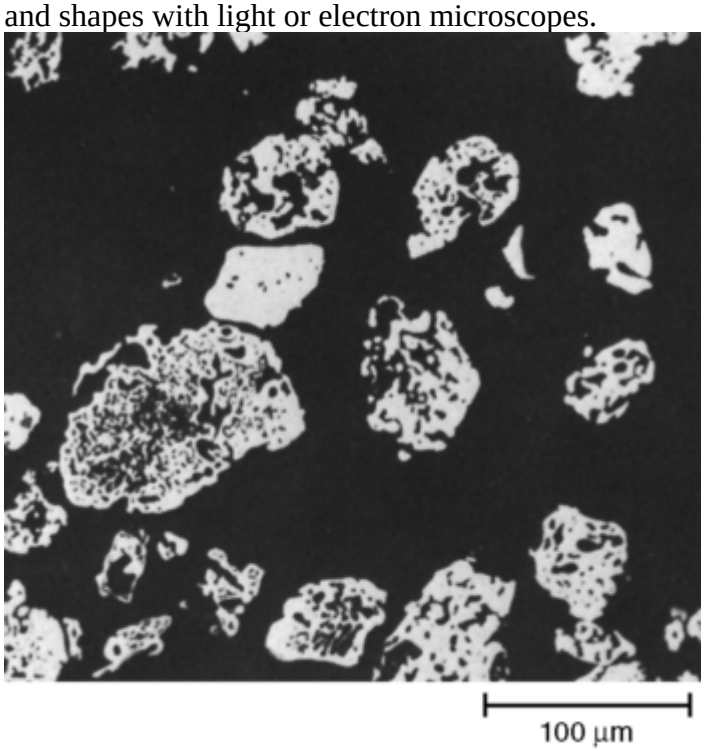

Fig. 10 Sponge iron powder (-100 mesh), hydrogen-reduced mill scale (Pyron D63) with particles containing fine, internal pores and some coarse pores. As-polished. 180×

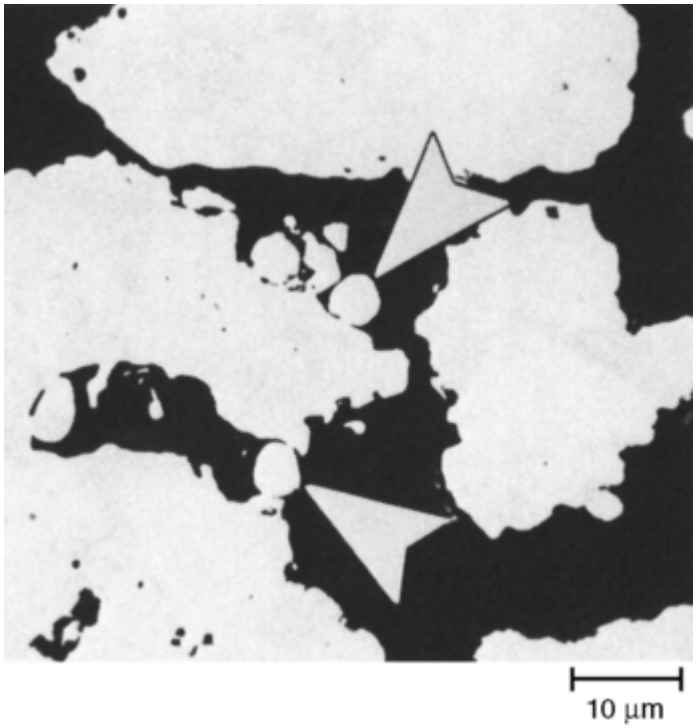

Fig. 11 Water-atomized iron (-80 mesh), Arrows indicate fine particles agglomerated to coarser ones during annealing. As-polished. 960×

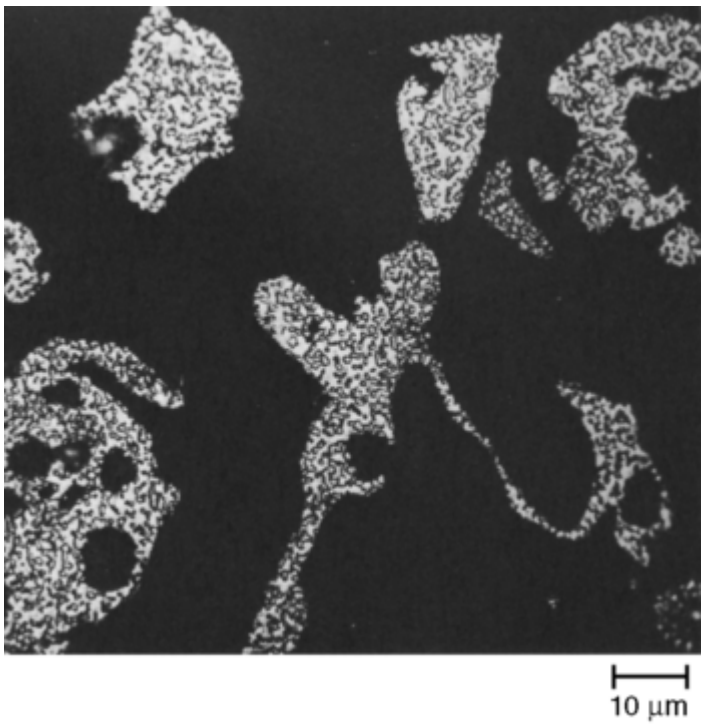

Fig. 12 Water-atomized, vacuum-annealed tool steel powder (M2), Irregular particles with a fine carbide phase. Equal parts 4% picral and 4% nital. 645×

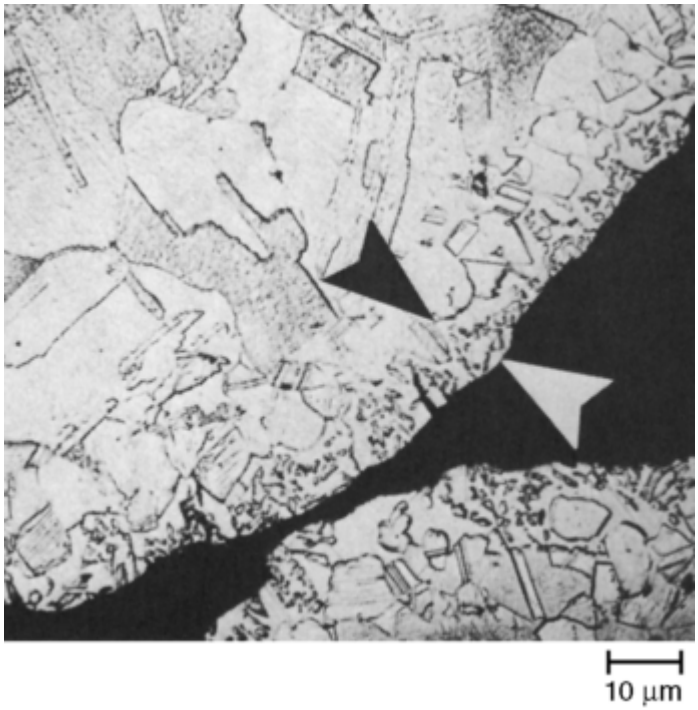

Fig. 13 Atomized bronze (92Cu-8Sn) filter powder (-40+60 mesh). Surface of copper is coated with tin, which is partly alloyed, forming intermetallics and some α-bronze. Arrows show depth of tin diffusion. As-polished. 645×

Powders are produced by various mechanical or chemical/electrochemical methods, as indicated in Fig. 14 and 15 (Ref 8). Some common metal powders and production methods are:

- *Iron:* sponge, atomized, electrolytic, and carbonyl powder
- *Steel:* atomization
- *Copper:* by reduction of oxides, atomization, electrolysis, and hydrometallurgical processing
- *Tin:* by atomization
- *Aluminum:* by atomization
- *Magnesium:* by mechanical comminution and atomization
- *Nickel:* by carbonyl vapormetallurgy, hydrometallurgy, and atomization
- *Cobalt:* by carbonyl vapor metallurgy, hydrometallurgy, reduction of oxides, and atomization
- *Silver:* by chemical precipitation, electrolysis, and reduction of oxides
- *Gold, platinum, and palladium:* by chemical precipitation
- *Tungsten and molybdenum:* by reduction of oxides
- *Metal carbides:* by carburization, Menstruum process, and exothermic thermite reactions
- *Tantalum:* by reduction of potassium tantalum fluoride and a sequence of electron beam melting, hydriding, comminution, and degassing (dehydriding)
- *Niobium:* by aluminothermic reduction of oxides
- *Titanium:* by reduction of oxides and atomization
- *Beryllium:* by reduction of vacuum-melted ingots by comminution
- *Composite powders:* by diffusion (alloy coating)

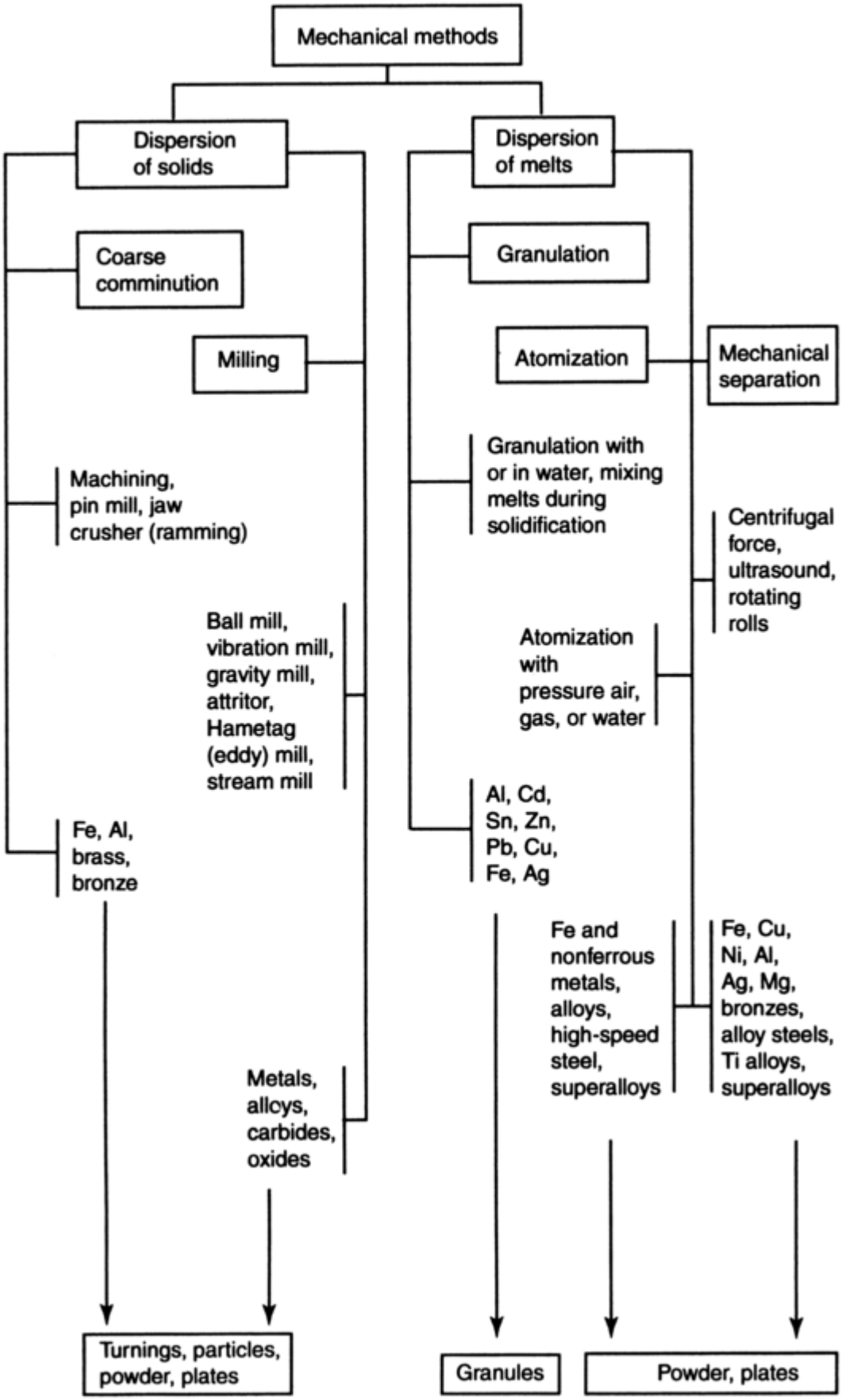

Fig. 14 Mechanical methods of powder production. Source: Ref 8

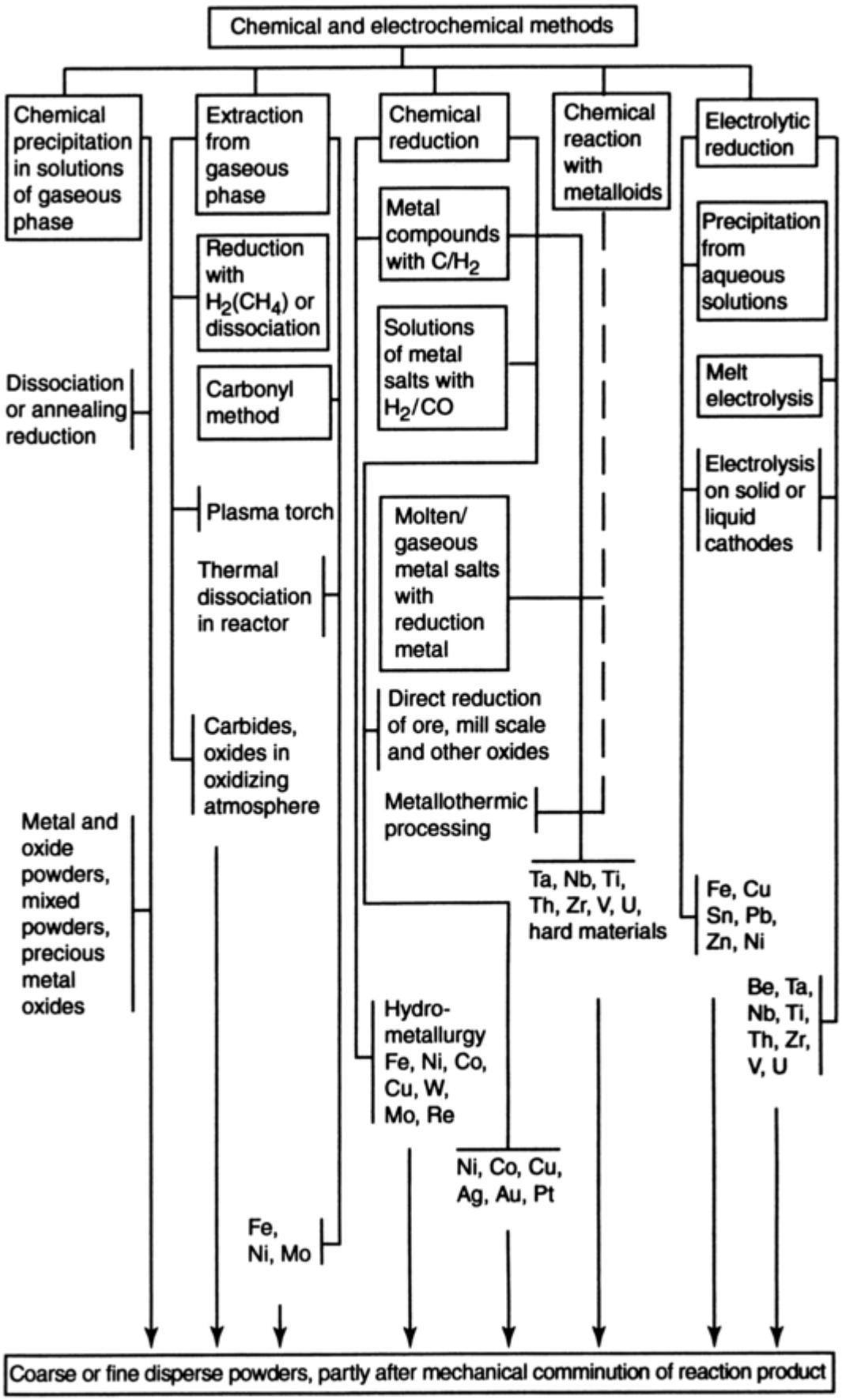

Fig. 15 Chemical and electrochemical methods of powder production. Source: Ref 8

In terms of tonnage, water atomization is the most common method with significant production of ferrous metal powders. The largest commercial application of water atomization is iron powder for pressed-and-sinter applications, and about 60 to 70% of the world's production of iron powder is produced by water atomization.

Water atomization is also used for the commercial production of copper, copper alloys, stainless steels, tool steels, and soft magnetic powders for pressing and sintering. Water-atomized precious metals are used in dental amalgams, sintered electrical contacts, and brazing pastes.

Water-atomized powders generally are quite irregular in shape (Fig. 16) compared to gas-atomized powders (Fig. 17) with relatively higher surface oxygen contents (depending on the alloy reactivity). Gas-atomized powders, on the other hand, generally are more spherical or rounded in shape and, if atomized by an inert gas, generally have lower oxygen (oxide) contents. There are, of course, exceptions in each type. For high-volume, low-cost production, water atomization generally is preferred over gas atomization, providing powder characteristics are compatible with the application. In general, water atomization is less expensive than the other methods of atomization because of the low cost of the medium (water), low energy use for pressurization compared with gas or air, and the very high productivity that can be achieved (up to 30 tons/h or about 500 kg/min in the case of iron powder). The primary limitations of water atomization are powder purity and particle shape, particularly with more reactive metals and alloys. These generally give irregular powders of (relatively) high oxygen content.

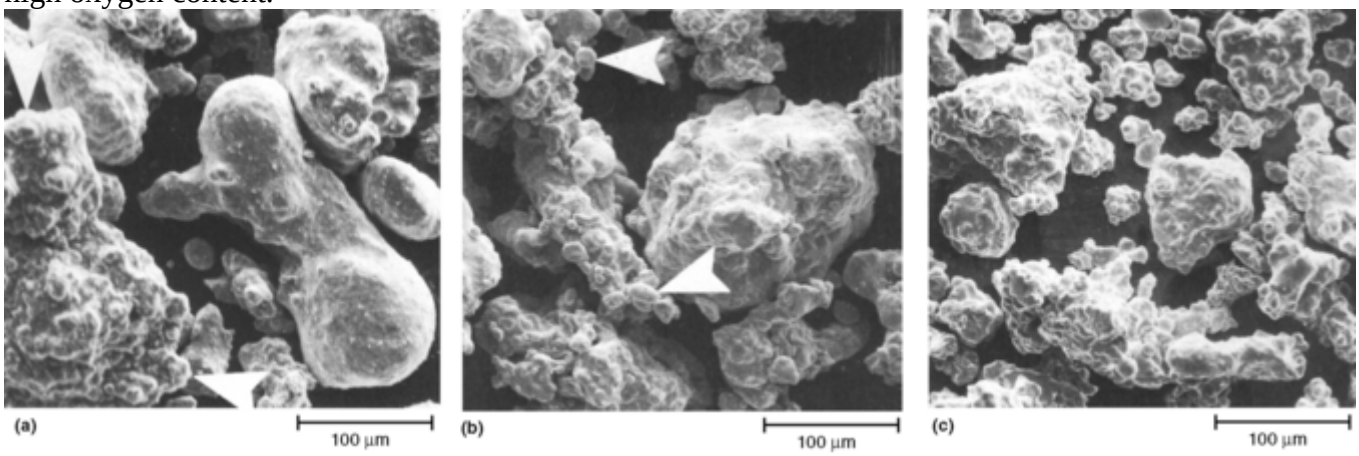

Fig. 16 Scanning electron microscope images of water-atomized iron powders (a) Arrows indicate a fair degree of irregularity or roughness on the surface. (b) Water-atomized and annealed iron powder. Arrows indicate small fines that were agglomerated onto the larger particles. (c) Water-atomized and double-annealed iron powder. Annealing improves the compressibility and green strength of a powder due to the softening of the metal. Frequently, annealing also produces slightly agglomerated powders with lower apparent densities and further increases in green strength. All at 190×

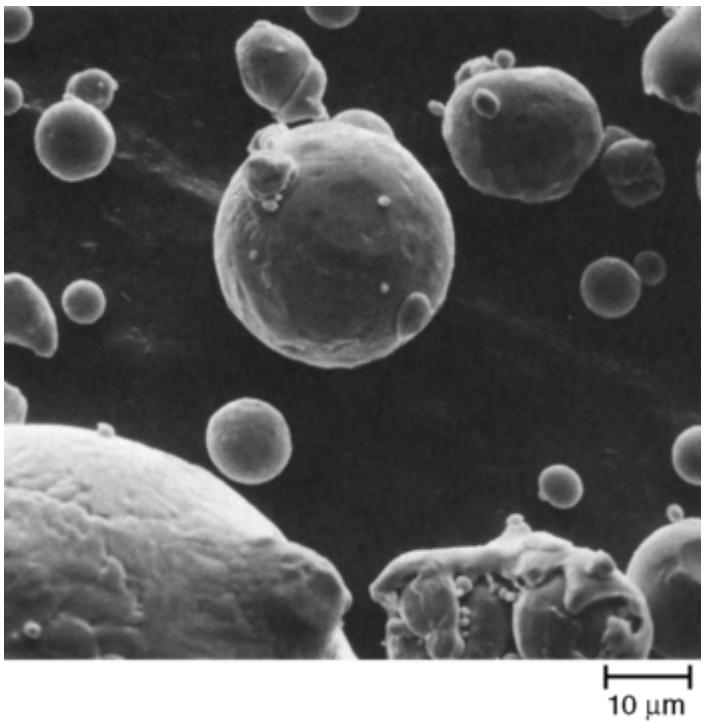

Fig. 17 Type 316, gas-atomized stainless steel powder. Note attached satellites. SEM. 750×

Preparation of Powder Specimens

Mounting of uncompacted metal powders requires special procedures that include the use of epoxy resin and vacuum impregnation. A small amount of properly sampled powder per ASTM B 215 (Ref 9) should be placed in the center of the specimen cup that will hold the epoxy resin. The pile should be approximately 13 mm ($\frac{1}{2}$ in) in diameter and approximately 3 mm ($\frac{1}{8}$ in.) deep at the center. The epoxy should be poured around the pile of powder without disturbing or segregating it. The cup should be filled with resin to a depth of 12 to 18 mm ($\frac{1}{2}$ to $\frac{3}{4}$ in.). The specimen is then evacuated at approximately 150 torr (20 kPa) for 10 min and returned to atmospheric pressure. Curing can take place at room temperature; higher temperatures hasten the process.

An alternate method is to mix the metal powder with a small amount of epoxy resin, then pour it into the bottom of the cup. This should be a thick, pasty mixture whose consistency will prevent the particles of metal from falling and segregating and will display several particles in a micrograph at 200×. If segregation is suspected, the specimen may be sectioned vertically after hardening. The sections can be remounted to note any segregation between top and bottom of the pile. This is important when attempting to measure the particle size distribution from a micrograph of the assembled powder particles.

Polishing and Etching. The powders, if mounted in epoxy resin as noted above, present a planar surface suitable for fine grinding. It is usually possible to begin using wet 600 grit SiC on revolving wheels or fixed sheets of paper. Approximately 30 s of grinding exposes enough particles to be viewed. The specimen is washed and then polished by hand for 2 min using 1 μm diamond on a short-nap cloth (MOL) at 250 rpm on a 200 mm (8 in.) diam lap. The use of an alcohol-base, water-soluble lubricant allows easy specimen cleaning in water.

The powders must not be overpolished, or the epoxy resin will be polished away between them and the particle edges will become rounded. Final polishing should be performed using deagglomerated 0.05 μm Al_2O_3 on a long-nap microcloth for 30 s with light hand pressure on a 200 mm (8 in.) diam, 125 rpm lap. Prolonged polishing or heavy hand pressure during final polishing rounds the particle edges.

Because some particles have internal pores that may have been smeared, it is important to examine some of the particles, unetched at 500 or 1000×, for the thin, gray lines that are the edges of smeared pores (Fig. 4). If such undisclosed pores are noted, 15 s etching and 1 μm diamond polish must be repeated. Etching the mounted powders removes enough surface material to lower the particles below the surface of the epoxy resin, which then provides an opportunity to repolish them. The repolishing should always be performed using 1 μm diamond followed by 0.05 μm Al_2O_3 for 30 s on a long-nap cloth.

Aluminum powders and alloys must be polished using 1 μm diamond, rather than Al_2O_3, which reacts with aluminum powders. Final polishing is best done with colloidal silica on microcloth for 30 to 60 s. Hard powders, such as tungsten, may be examined as-polished using 1 μm diamond. Final polishing of very soft materials, such as pure copper, may be carried out using a fixed, long-nap cloth, as described previously for full-size specimens. The colloidal silica noted previously also works well on pure copper. Pure iron powder may require two or three 30 s fine polishings and light 15 s etching in 2% nital to remove fine scratches. The procedure also opens porosity in fine-porosity sponge iron.

Particle Size and Shape Analysis

Microscopy is used in analysis of particle size and shape. Image analysis of particle size distribution is a very precise quantitative practice, while particle shape analysis is more qualitative in nature. Advancements in qualitative shape analysis are based on the use of the scanning electron microscope (SEM) for determination of particle shape. In addition to its high-magnification capability, the three-dimensional appearance of SEM images has largely replaced light microscopy in the shape and topographical analyses of metal powders. Interest in more quantitative analysis of particle shape also has increased with the advent of advanced computers and graphics systems for the analysis of images from light and scanning electron microscopes. For example, Fourier analysis and fractal geometry are two mathematical disciplines that are being applied to describe particle shape. Because of the computational intensity of these disciplines, most of the work has been confined to a two-dimensional space (e.g., see the section “Particle Shape Characterization” in “Particle Image Analysis” in

Powder Metal Technologies and Applications, Volume 7 of *ASM Handbook.* The current challenge is to develop three-dimensional modeling programs that can accurately describe the shape of irregularly shaped particles.

Various techniques are used to measure the size of irregularly shaped particles when viewed through a microscope. This has resulted in different measurements, which are used to classify these two-dimensional particle images in terms of an equivalent spherical particle. Accepted measurements (Fig. 18) include:

- Feret's diameter (*F*): the maximum length of the particle measured in a fixed direction
- Martin's diameter (*M*): the length of a line that bisects the area of the particle image; all particles measured in the same direction
- Project area diameter (d_a): the diameter of a circle with the same area as the two-dimensional image of the particle
- Longest dimension: the maximum Feret's diameter (F_{max}) for each particle: no set direction
- Perimeter diameter (d_p): the diameter of a circle having the same circumference as the perimeter of the particle
- Maximum horizontal intercept: the length of the longest line that can be drawn through the particle in a fixed direction

Feret's diameter is the easiest to measure manually. Generally, the first three of the above diameters are related to one another by the expression $M < d_a < F$. Their ratios remain fairly constant for a given material. The expression F/M has been used as a shape function, which is equal to 1 for spherical particles and increases in magnitude as particle shape becomes more acicular. Perimeter diameter and maximum horizontal intercept (or longest chord) are measured easily by some of the automatic particle sizing analyzers.

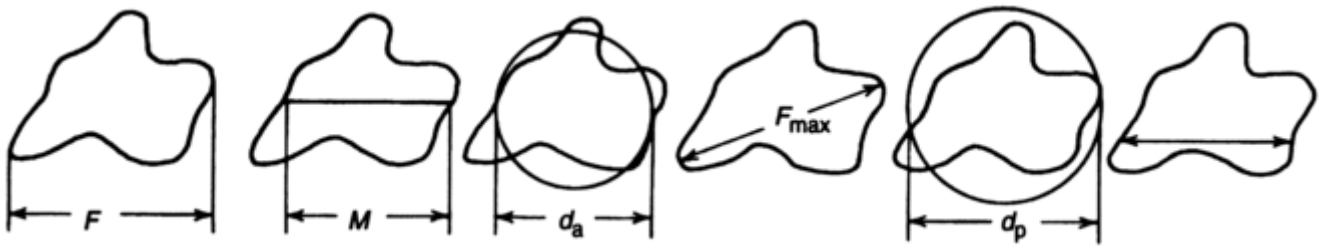

Fig. 18 Techniques for measuring sizes of irregularly shaped particles. See text for identification of variables.

The most important step in any particle size analysis, but especially by microscopic techniques, is sampling from the bulk. Because an extremely small quantity of material is used to determine the particulate size, an accurate analysis cannot be obtained if the bulk material is not properly sampled. Particles tend to segregate according to size. If handling has caused vibration of the sample, coarse material tends to collect near the surface. When free-flowing material is poured into a pile, the coarse portion collects near the outside of the pile, and the fines concentrate in the center. Sampling techniques are discussed in more detail in the article "Sampling and Classification of Powders" in *Powder Metal Technologies and Applications,* Volume 7 of *ASM Handbook.*

Optical microscopy is used to count and size particles ranging from 100 to 0.5 μm diameter. The resolution of an optical microscope is optimally about 0.25 μm, but diffraction effects at the edges of small particles result in significant errors in measurements within this size range. Resolution down to 0.1 μm can be improved by using ultraviolet light and quartz optics. Particle sizing usually is performed indirectly in the optical microscope, because the small depth of field frequently requires refocusing on individual particles. If the size range is narrow and the preparation is carefully made in a single plane, photographs or automatic particle counting devices can be used. Projection microscopes are also available that reduce operator fatigue for analyses that require numerous counts.

Particle diameters can be measured directly in an optical microscope with the use of a filar micrometer eyepiece. This eyepiece contains a scale and a movable crosshair that is operated by a calibrated knob on the side of the eyepiece. A particle is moved so that one side touches one of the fixed scale markings, and the crosshair is moved to touch the other side of the particle. The difference between the two readings is the Feret's

diameter of the particle. The eyepiece is calibrated with an optical stage micrometer. This technique is time consuming, and because absolute measurements are not required for accurate size analysis, eyepiece graticules are usually used for direct measurements. Many devices are available to shorten the time required to complete a particle size analysis by either semiautomatic or automatic techniques.

A severe limitation of the optical microscope is its small depth of field, which is about 10 μm at 100 and 0.5 μm at 1000×. This requires that the specimen powders be mounted carefully in one plane and eliminates the use of automatic counting devices on samples with wide particle size ranges. Another limitation is that due to the small number of particles usually counted, only the field of view can be characterized, not the entire lot from which the specimen was obtained.

Preparation of slides for light microscopy is an art, and the quality of a dispersion depends more on skillful preparation than on the particular technique used. Care must be taken to prevent segregation of particle sizes and to prevent the formation of agglomerates. Preparation techniques vary with the type of powder and depend on particle size, particle size range, and particle composition. Typical dispersion techniques are described below.

Dry Mounting. When a permanent slide is not required, and the powder exhibits good flow characteristics, slides can be prepared by “puffing” dry powder onto the slide or by applying it with a brush.

Dispersing Fluids. In applications that require shearing action to disperse the powder, a dispersing fluid such as cedar oil or glycerol can be used. The simplest technique involves placing a drop of dispersing fluid on a glass slide and placing a small amount of powder onto the drop. A cover slip is then placed carefully over the mounting fluid and pressed evenly with an eraser, while gently rotating the cover slip back and forth.

Another method involves placing some of the powder on a glass slide, adding a few drops of dispersing fluid, and working the mixture with a flexible spatula or soft brush. More fluid is added until the proper concentration is obtained. A drop of this mixture is then transferred to a new slide and covered with a cover slip.

Permanent Slides. A small amount of powder is placed in a beaker to which 2 or 3 mL (0.07 or 0.10 fluid oz) of a solution of 1 to 2% collodion in butyl acetate is added. The mixture is stirred vigorously, and a drop of the suspension is placed on the surface of distilled water. The drop spreads and forms a thin film as the solvent evaporates. The film is then picked up on a microscope slide and dried.

Other films can be produced by dissolving parlodion in amyl acetate, Canada balsam in xylene, and polystyrene in xylene. Films are formed by casting a 1% solution on water or a 0.5% solution directly on a glass slide. After the films dry, the powder is applied by spraying or by letting a drop of aqueous suspension dry on the surface. The particles sink into the medium, forming a permanent slide. Melted Canada balsam or glycerol jelly also can be used to form permanent samples.

Other Methods. Certain applications may require samples prepared by specialized techniques, such as heating magnetic particles above their Curie points for dispersion. These examples generally serve as guidelines for technique development.

Transmission electron microscopy (TEM) (TEM) is used for counting particles that range from 0.001 to 5 μm in diameter. This instrument has a large depth of field; consequently, all particles in the field of view are in focus regardless of size. Particles are usually not counted directly from the viewing screen of the transmission electron microscope. Photographs are normally taken, and counts are made from prints or projected images using the negatives.

The electron beam is easily absorbed, and films greater than 100 to 200 nm (1000 to 2000 Å) are completely opaque. It is therefore necessary to produce very thin support films on which powders can be dispersed for counting. These films usually are made of carbon. One of the best techniques for producing strong, flat carbon support films involves cleaving high-quality mica and placing it immediately in a vacuum evaporation unit. After a hard vacuum has been obtained, carbon is evaporated onto the mica surface to a thickness of about 10 nm (100 Å).

Film thickness can be calculated by including a white porcelain slide containing a drop of vacuum oil in the vacuum chamber. When the porcelain that is not covered by the oil appears as a light chocolate shade, the carbon film is about 10 nm (100 Å) thick. The mica is then removed from the vacuum and slowly lowered at an angle into a beaker of distilled water. The carbon film floats off the mica onto the water surface, where it can be picked up on an electron microscope grid.

Another technique involves casting a thin film of parlodion onto the surface of distilled water by depositing two or three drops of 1% parlodion dissolved in amyl acetate onto a clean glass slide. The slide is allowed to drain

and dry, and the film is floated from the slide onto distilled water. The plastic film is then picked up on TEM grids, placed in a vacuum evaporator, and coated with carbon.

The parlodion can be carefully dissolved in amyl acetate by placing the grids on a fine stainless steel mesh bridge suspended in the center of a petri dish. Amyl acetate is added to the petri dish until the level of the liquid reaches the bottom of the mesh. The dish is then covered and left for a few hours, after which the grids are carefully removed.

If the parlodion film is thin enough, it can be left on the grids. However, this requires fresh, water-free solutions and care in handling, or holes will form in the thin plastic film as the solvent evaporates. Prepared carbon substrates on grids are available.

Powders are dispersed on the surface of support films by puffing from an aspirator or by allowing a drop of aqueous suspension to dry. Carbon films are hydrophobic; use of an aqueous suspension requires that they be rendered hydrophilic by either treatment with a thin solution of albumen or exposure to reactive oxygen in a low-temperature oxygen asher. Exposure to reactive oxygen must be done at a very low setting (4 W) for several seconds, or the carbon film will be destroyed.

Powders that require additional dispersion can be prepared by placing a small amount of powder on a clean glass slide and adding several drops of 1% parlodion in amyl acetate. This mixture is sandwiched between a second glass slide. As the amyl acetate evaporates, the mixture becomes more viscous. Immediately before the parlodion dries, the slides are sheared apart. This preparation can be viewed in the optical microscope to find the area of best dispersion. This area is then scribed into 3.2 mm ($\frac{1}{8}$ in.) squares and floated from the glass slide onto distilled water. The squares are picked up on electron microscope grids and coated with carbon to add stability to the electron beam.

For some samples that are difficult to disperse, ethylene glycol may be a suitable dispersing agent. A small amount of powder is added to a few drops of this viscous liquid on a glass slide and mulled until a good dispersion is obtained. A carbon substrate grid is then touched to the thin liquid film, which sticks to the grid. The grid is placed in a vacuum chamber and pumped for a few minutes, during which time the ethylene glycol sublimates, leaving the particles on the carbon substrate.

Particle thicknesses can be measured in the transmission electron microscope by “shadowing” particle dispersions in which the particles sit on a substrate and are not embedded in a plastic film. This is done by evaporating a small amount of metal placed at an angle to the substrate surface in a vacuum chamber. The metal coats the surface and particles in a line-of-sight fashion, leaving a “shadow” cast behind the particles. Commercially available precision-sized latex spheres can be included with the powder sample so that the ratio of shadow length to particle height can be calculated.

Of the pure metals, platinum is best suited for shadowing because of its fine structure in an evaporated film. About 12 mm (0.5 in.) of 250 μm (10 mil) platinum wire, evaporated from a point source at an angle of 30° and a distance of 100 mm (4 in.), casts a good shadow. Many other preparation techniques are used to observe powders in TEM, and most analysis methods are modified to suit the application and the operator's ability.

Scanning Electron Microscopy. The scanning electron microscope has a resolution of about 10 nm (100 Å) and is capable of very low magnification (about 10×) up to about 50,000×. It therefore can be used to count particles ranging in size from 1 mm to 0.1 μm. Particles smaller than 0.1 μm usually have too low a contrast with the background to be counted efficiently. The scanning electron microscope has about 300× the depth of field of an optical microscope.

The image in the scanning electron microscope usually is obtained by using the secondary electron output of the sample as it is scanned by a very narrow electron beam. The contrast of the image depends more on the topography of the sample than on differences in atomic number. Therefore, prepared powders must not be embedded in films, but dispersed on a smooth substrate. Any smooth surface can be used as a substrate. However, if energy dispersive x-ray (EDX) analysis is to be performed for particle identification, a carbon or polystyrene surface is preferred.

An excellent substrate can be made by placing a polystyrene pellet on a glass slide and heating it on a hot plate until it softens. A second glass slide is then placed over this slide and pressed until the pellet forms a thin disk. The slides are removed from the hot plate and pressed together until the polystyrene sets. The disk thus formed is as smooth as the glass and contains no elements that may hinder EDX analysis. For sample preparations using aqueous suspensions, polystyrene surfaces can be rendered hydrophilic by a brief treatment in an oxygen asher at low power (5 to 10 W for 5 s).

While the substrates for SEM do not have to be as thin as those used for TEM, they must be conductive. Consequently, if glass or plastic surfaces are to be used, they must be coated with an evaporated metal (or carbon, for EDX analysis) film. This coating is usually applied after the particles have been dispersed on the surface.

Many of the dispersing techniques used for TEM can be applied to SEM. Particle dusting, drying from liquid suspensions, and mulling in liquids that can be sublimed in a vacuum are suitable dispersing methods, depending on the powder. If the technique of mulling in parlodion and amyl acetate is used, parlodion can be removed in an oxygen asher, thus leaving the particles on the substrate. Suitable substrates include glass or metal, because they are not affected by the ashing.

The prepared sample should always be placed in the scanning electron microscope with the surfaces normal to the electron beam so that the magnification, which changes with working distance, will be the same on all areas of the viewing screen. Particle counting can be done directly from the viewing screen, from photographs, or by using an automatic image analyzer. As noted, SEM images provide excellent displays of three-dimensional features, as shown in Fig. 16 and 17 of water- and gas-atomized powders.

References cited in this section

8. A. Ŝalak, *Ferrous Powder Metallurgy,* Cambridge International Science Publishing, 1995

9. "Standard Method of Sampling Finished Lots of Metal Powders," B 215, *Annual Book of ASTM Standards,* Vol 2.05, ASTM, 1998

L.F. Pease III and D.L. Pease, Metallography and Microstructures of Powder Metallurgy Alloys, *Metallography and Microstructures,* Vol 9, *ASM Handbook,* ASM International, 2004, p. 994–1020

Metallography and Microstructures of Powder Metallurgy Alloys

Leander F. Pease III and Douglas L. Pease, Powder-Tech Associates, Inc.

Compacted and Consolidated Powders

Powders are compacted and consolidated into parts by various methods, as briefly described in the next section, "Representative Microstructures of P/M Alloys." This section describes techniques used in the examination of compacted and consolidated (sintered) powders.

Macroexamination

Macroexamination of sintered materials is not commonly practiced. In wrought or ingot-base materials, forging flow lines, oxide segregation, and stringers are studied extensively. These features are not usually found in P/M materials, but there are certain other uses for macroexamination.

In sectioning a heat treated P/M steel, care must be taken not to overheat the specimen and temper or reharden it locally. The etching performed during grinding and polishing to help open the pores will indicate any macroscopic striated darkening from overheating, as shown in Fig. 19 and 20. By revealing a lighter or darker surface than the interior, this same intermediate etching using 2% nital on steels will show if a specimen ground through 600 grit SiC paper is likely to have a decarburized or carburized surface layer. This effect is apparent to the unaided eye.

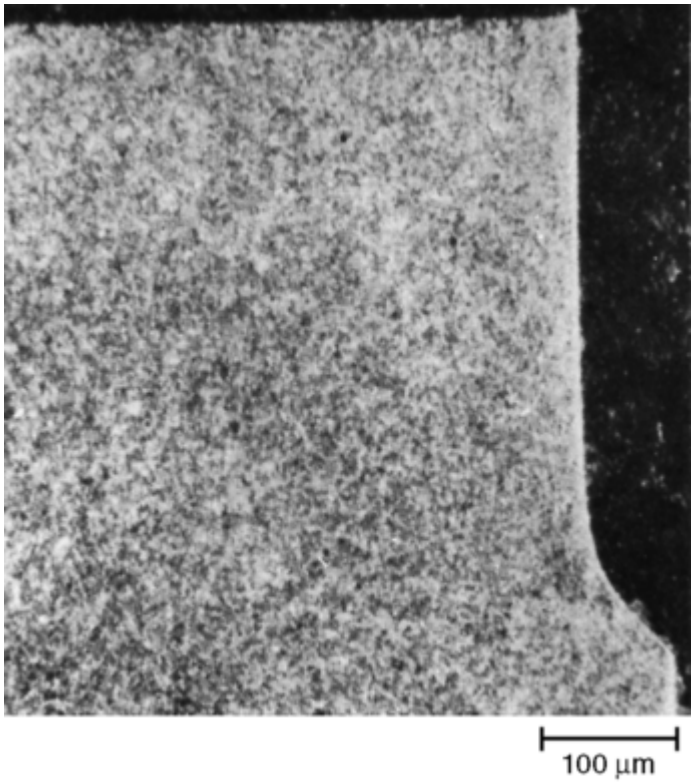

Fig. 19 Ferrous P/M specimen cut with the use of a coolant. No evidence of overheating. Nital. 12×

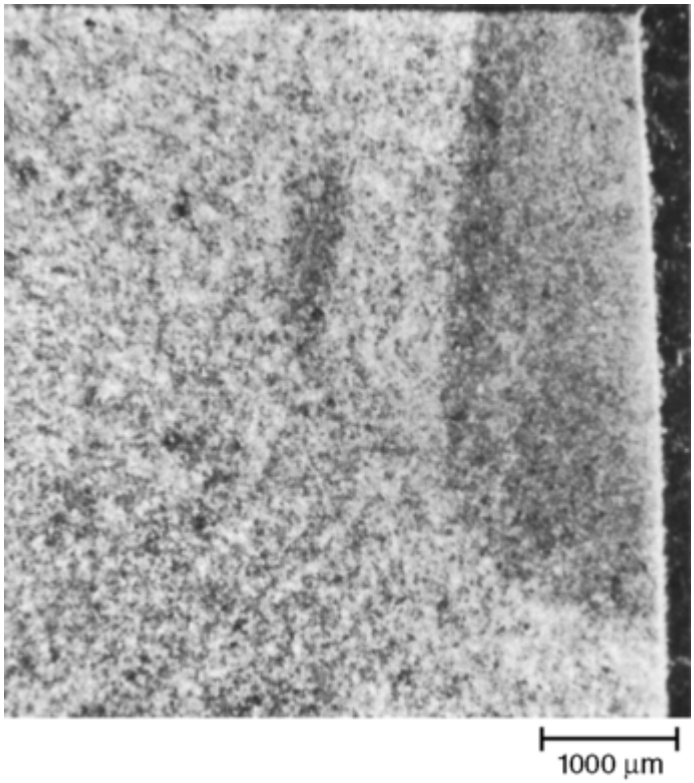

Fig. 20 Ferrous P/M specimen cut without the use of a coolant. Evidence of overheating (dark area at right edge of specimen). Nital. 12×

During manual polishing with 1 μm Al_2O_3, a porous-appearing layer similar to orange peel develops near the outer edges of the specimen adjacent to the mounting medium. This layer spreads inward during subsequent polishing until the entire cross section appears uniformly porous to the unaided eye. If the surface is shiny or specular in certain regions, it almost surely will be found to contain pores that polishing has failed to open (Fig. 4 and 7). The penetration depth of the epoxy resin through the side surfaces of the specimen can be seen during

polishing, because the regions where the epoxy is in the pores displays the orange peel appearance. The regions with unfilled pores are temporarily smeared over and shiny. After final polishing, the surface roughness from the pores is much diminished, but significant variations in density in a part are visible to the unaided eye.
Nital etching of elemental nickel steels reveals the nickel-rich areas as light-reflecting sparkles. Unsintered (green) or sintered, unprepared parts may be examined to 25× for cracks or the presence of added copper in iron. The fracture surface of a heat treated part shows varying degrees of discoloration in bands parallel to the outer surfaces. These dark bands are probably caused by oil impregnation during oil quenching, and the color is caused by in situ partial decomposition of the oil during quenching or tempering. The Metal Powder Industries Federation (MPIF) test method 37 for case depth (now obsolete) used the difference in the fracture appearance of the case region and the interior to measure case depth (Ref 10).

Scanning Electron Microscopy

In addition to the examination of uncompacted powders, the scanning electron microscope is also useful for examining fracture surfaces, as-pressed and sintered surfaces formed by dies and punches, and, potentially, the as-polished sections used for optical microscopy. For example, Fig. 21 and 22 show the smooth outer surfaces of parts that were contacted by punches or dies during consolidation. Figure 22 illustrates the unsintered view of the side of a part that contacted the die. The powders have been pressed into close contact, and the boundaries between particles are readily visible.

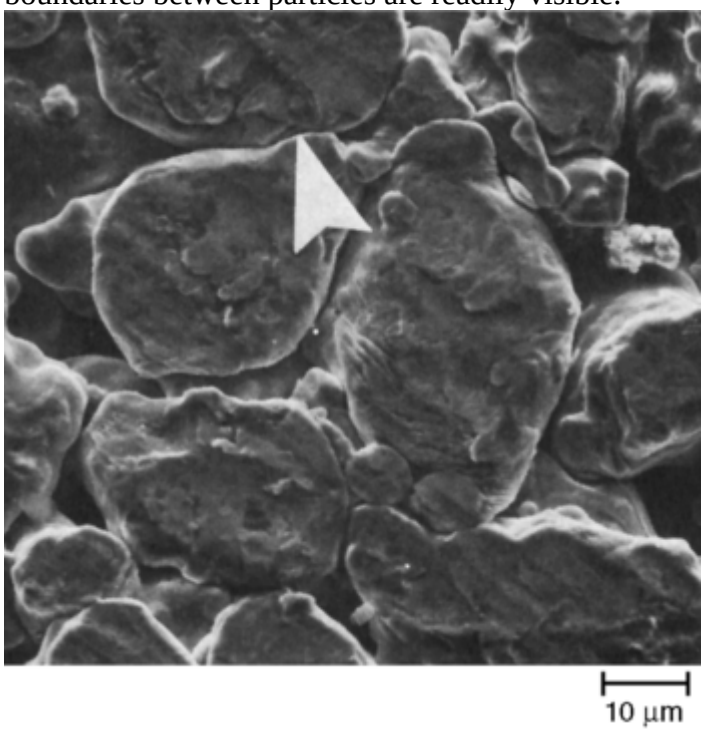

Fig. 21 Unsintered iron powder. Surface of part, which had been contacted by the upper punch at 275 MPa (20 tsi). Arrow shows the particle boundaries that will disappear during proper sintering. SEM. 750×

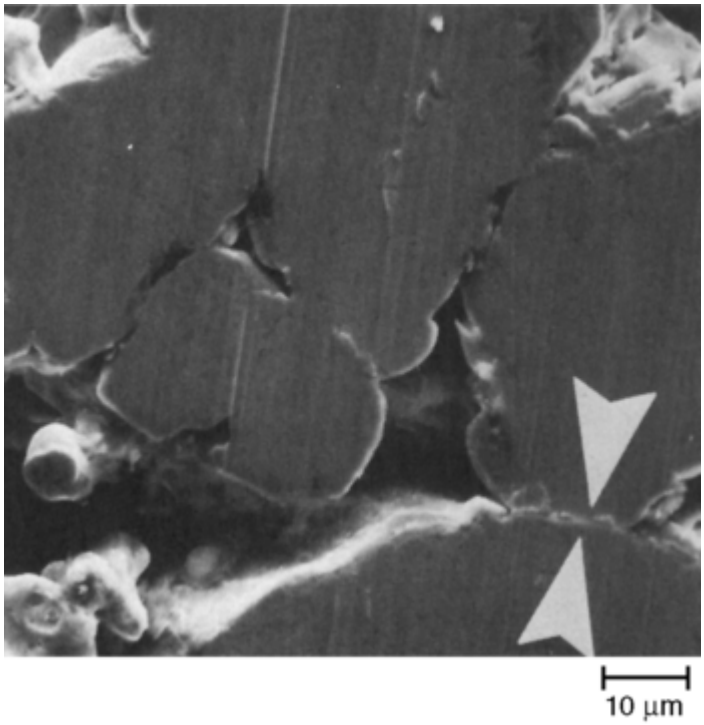

Fig. 22 Same as Fig. 21 but showing the view of the surface that was in contact with the die wall. Arrows show the boundary between particles that must be eliminated during sintering. SEM. 750×

The development of bonding between metal particles may also be followed by examining their fracture surfaces. As bonds develop, the fracture shows cup-and-cone or dimpled-fracture regions where the bonds have been torn apart. The regions between the ductile cups and cones are the smooth surfaces of the original particles, which were not bonded to the adjacent particles. The progress of sintering may be followed through the increasing number and area fraction of the ductile torn regions. This is well illustrated in Fig. 23 (Ref 11) (see also Fig. 32 through 38 in the article "Metallography of Powder Metallurgy Materials" in *Powder Metal Technologies and Applications,* Volume 7 of *ASM Handbook*). The energy spectra of the x-rays generated by the electron beam striking the atoms of the specimen can be analyzed to determine which elements are present at the fracture surface. The fracture surface may be scanned for the wavelength characteristic of a particular element and to record the intensity or concentration of the element as a function of location. This concentration appears on an x-ray map as a collection of dots. That display shows if the element is uniformly distributed or somewhat segregated, which is useful for monitoring the dissolution of copper or nickel in steel, or for checking for oxides of manganese or silicon.

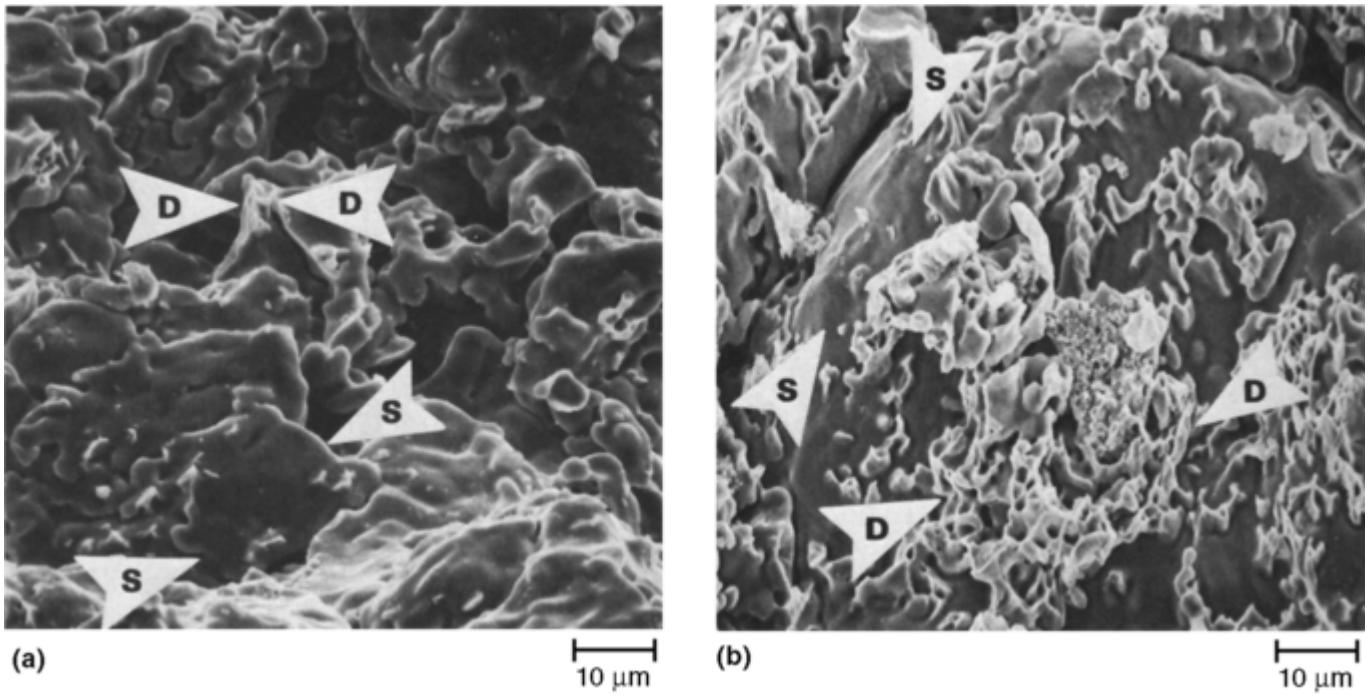

Fig. 23 Variation in fracture surface with sintering time for iron powder pressed to 6.6 g/cm^3 and sintered in hot zone at 1120 °C (2050 °F) with dissociated ammonia for (a) 3 min and (b) 10 min. Image (a) from 3 min sinter shows where a bond has broken (arrows D). Arrows S outline the smooth, rounded surface of a particle that did not bond to the adjacent particle above it. Image (b) shows more regions of ductile cup-and-cone fractures (arrows D) when the particle was torn from an adjacent particle. Arrows S shows the smooth surface of the particle that had not sintered to any adjacent particle. SEM. 750×. Source: Ref 11

Microexamination and Etchants

Etchants commonly used for the metallographic examination of sintered metals are listed in Table 1. The initial use of the etchant, as noted previously, is to open the smeared porosity before and during the coarse polishing with 1 μm Al_2O_3. However, once fine polishing is completed, it is very important to examine sintered parts in the unetched condition to display the number and distribution of original particle boundaries present (Fig. 24). Etching reveals grain boundaries, which would be easily confused with the particle boundaries that also appear as thin gray or black lines. Cracks, density variation, oxide films or particles, and pore shape or rounding are easier to view in the absence of distracting etched features.

Table 1 Etchants used for examination of P/M materials

Etchant	Procedures and applications
2% nital: methyl alcohol plus 2% concentrated HNO_3	For as-sintered irons and steels (best for ferrite and low-carbon steels); immersed for 10–15 s; heat treated steels: 6–7 s
Concentrated picral: picric acid in methyl alcohol; some undissolved crystals remain in the container bottom	For higher carbon-containing materials to develop good contrast with carbides, pearlite, other eutectoid products, martensite, and retained austenite; etch by immersion, 15–20 s
Glyceregia: 10 mL HNO_3 conc, 15 mL HCl, 35 mL glycerol[(a)]	Shows grain boundaries, twin boundaries, and carbides in austenitic and martensitic stainless steel; immerse for 1–2 min or swab lightly
4% $FeCl_3$ in H_2O	Develops red color in copper-rich regions in bronze; etch by swabbing, 10–20 s
2 g $K_2Cr_2O_7$, 4 mL NaCl, 8 mL H_2SO_4, 100 mL H_2O	Develops grain boundaries and small grain clusters in bronze; etch by swabbing, 10–20 s
Keller's reagent: 2.5 mL HNO_3, 1.5 mL	For aluminum and aluminum alloys; immerse 8–15 s, wash in

HCl, 1.0 mL HF, 95 mL H_2O	water; do not remove etchant products from surface
5% nital	For as-sintered tool steels; immerse 5 min
5 mL HNO_3 conc, 10 mL 48% HF, 85 mL H_2O	For titanium and titanium alloys; immerse 5 s
5 mL NH_4OH, 3 drops H_2O_2, 5 mL H_2O	For brasses; swab 20 s; make fresh solution every 20 min
450 mL H_2O, 25 mL H_2SO_4, 25 mL HNO_3, 25 g chromic oxide, 4 g NH_4Cl	For bronzes not etching clearly in the above $K_2Cr_2O_7$: Just before use, mix a few mL of this etchant with equal amount of 3% H_2O_2 and swab for 10 s

(a) Use hood for fumes and hand and eye protection when mixing this solution

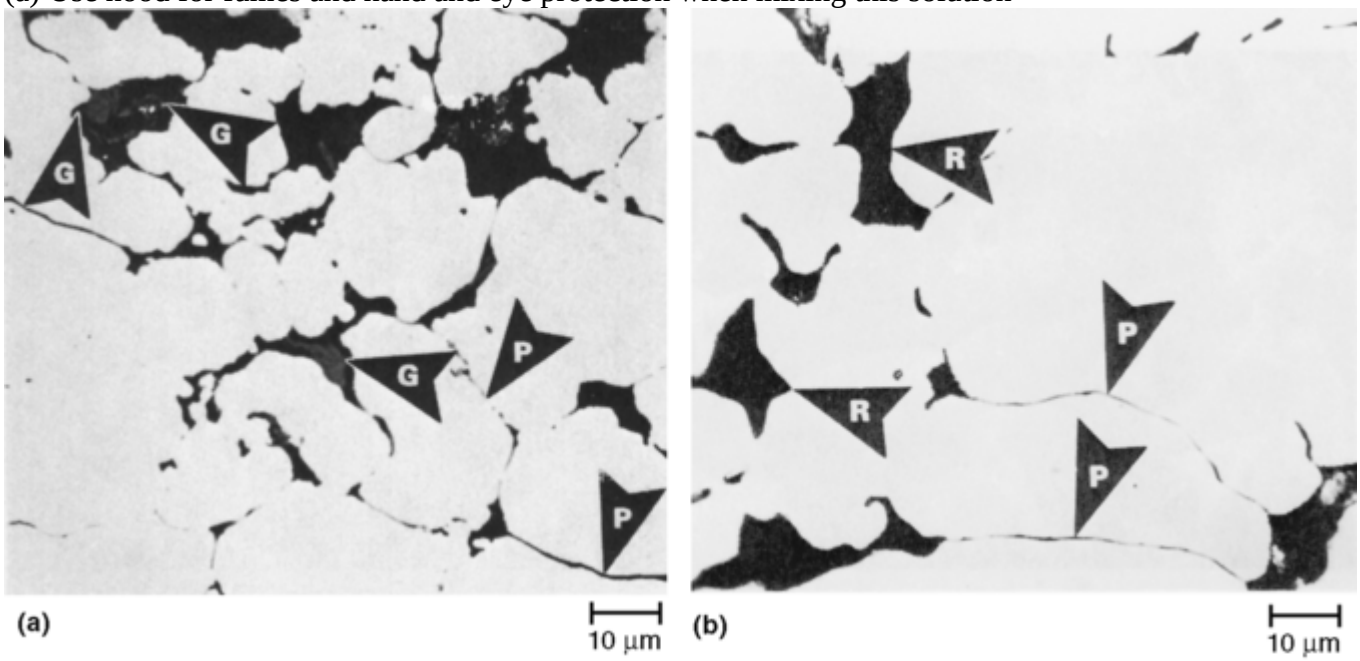

Fig. 24 Distribution of original particle boundaries in unetched specimens from a diffusion-alloyed steel (6.7 g/cm^3), pressed at 480 MPa and sintered in dissociated ammonia in hot zone at 1120 °C (2050 °F). Image (a) is from materials sintered for 5 min. Numerous particle boundaries (arrows P) are indicative of undersintering. Arrows G are undiffused, gray flakes of graphite in pores. Image (b) is from material sintered for 15 min. Pores are rounded (arrows R). Arrows P indicate persistence of original particle boundaries; as-polished. 645×

For etching iron and low-carbon sintered materials, 2% nital is preferred because it reveals the ferrite grain boundaries. It is applied by immersion for 10 to 15 s. The specimen is washed in running water, rinsed in methyl alcohol (optional), then dried in a cool air stream or wiped dry. (If any open porosity is present, the use of warm air may cause subsequent evaporation of entrapped water or alcohol onto the lens of the microscope.) For steels with medium to high carbon content or for heat treated structures, concentrated picral in methanol works well. It enhances the contrast of carbide platelets in the eutectoid in as-sintered structures.

Picral develops good contrast in the martensite needles and retained austenite of heat treated materials. The 2% nital also works well for these structures and does not stain hands and clothing. Heat treated specimens etched in nital should be immersed 3 to 8 s (swabbing causes streaks), rinsed in running water then alcohol, and then blown dry. This underetches the martensite, but enhances contrast between the fine pearlite (a dark, unresolved, nodular constituent) and the light-colored martensite. This is an optimal condition for checking microhardness, because the martensite is light, clearly seen, and forms a good background for measuring the length of the Knoop diamond indentation. The use of picral for 15 to 20 s or 2% nital for slightly longer enhances the contrast of martensite and retained austenite. For magnifications of 1000×, a lightly etched structure affords maximum clarity.

Sintered stainless steels are best etched in glyceregia using a protective hood and ventilation. Because this is a strong acid mixture, eye and hand protection are advised. The glyceregia is applied by immersion with the specimen surface upward; a fraction of a millimeter of the liquid is poured on top of the metal to be etched. When freshly prepared, the action is fairly slow and may require 1 to 2 min. The etchant may also be applied

using a very light swabbing action. Glyceregia decomposes with time; it may turn orange and emit nitrous oxide. As the etchant darkens toward orange or brown, it becomes more reactive and less predictable. Shelf life may be extended by cool storage. Nonetheless, glyceregia can rarely be used for more than 2 h before disposal. Additional etching should be preceded by repolishing using 1 μm diamond and 0.05 μm Al_2O_3 to avoid unwanted etching artifacts.

In well-sintered stainless steel, moderate grain size, annealing twins, and grain boundaries free of precipitated carbides are visible. When carbides are present, the grain boundaries are not clean and straight, but ragged, broader, and fast etching. Prolonged etching causes the formation of pits, which may be confused with pores. The stainless steels are judged by freedom from precipitated carbides and original particle boundaries. Some of the new classes of high-temperature sintered stainless steels exhibit very well-rounded pores, which may even be isolated from each other. Such high degrees of sintering are rare in low-alloy steels.

Copper and bronze materials are etched in a 4% ferric chloride ($FeCl_3$) solution or the potassium dichromate ($K_2Cr_2O_7$) solution in Table 1. The $K_2Cr_2O_7$ etchant is preferred for bronze. During sintering of bronzes, the elemental tin melts, forming a series of increasingly higher temperature intermetallic compounds, then completely dissolves in the copper at approximately 785 to 845 °C (1450 to 1550 °F). The result of good sintering is a bronze with a moderate grain size and no free tin or blue-gray copper-tin intermetallic compounds. Intermetallic compounds are present during the early stage of sintering and in a final undersintered condition.

As sintering proceeds, the copper recrystallizes and its grains grow as the tin diffuses to form α-bronze. The presence of many reddish copper areas or large area fractions of fine-grained copper-rich or α-bronze indicates undersintering. The undersintered materials are the most difficult to etch and to show clear structures. The $K_2Cr_2O_7$ etchant should be applied (always by swabbing) for 15 s. The specimen is then placed under running water, and swabbing is continued for a few seconds. It may be necessary to polish and etch several times to obtain a clear structure free of distortion from grinding.

Some bronzes are made from mixtures of copper and copper-tin compounds. During sintering, the gray copper-tin compounds should dissolve in the copper and form α-bronze. If the sintering is not complete, the rounded gray copper-tin particle will be seen in the unetched microstructure. Interestingly, upon etching, they are preferentially attacked by the ($K_2Cr_2O_7$) reagent and are not visible in the etched structure. They are, therefore, easily overlooked. Other bronzes are not uniformly etched by the ($K_2Cr_2O_7$) reagent, and the final etchant in Table 1 is recommended to reveal their grain structure.

Bronzes may contain up to 4% free graphite. The epoxy resin helps secure the graphite flakes for polishing and viewing. The use of 1 μm diamond and light final polishing with 0.05 μm Al_2O_3 on a long-nap cloth usually preserves the graphite.

Brasses and nickel silver are etched using a mixture of ammonium hydroxide (NH_4OH) diluted with 50% H_2O and a few drops of 10 to 30% hydrogen peroxide (H_2O_2) added at the time of etching. This is carried out by placing approximately 5 mL of the diluted ammonia solution in a watch glass and adding 3 to 4 drops H_2O_2. The mixture is swabbed on the brass with a cotton-tipped stick for 20 to 40 s (Ref 12). The nickel silver requires 1 to 2 min to etch. The etchant decomposes after 30 min, and a new mixture with the H_2O_2 should be prepared as required. The $K_2Cr_2O_7$ etchant noted previously for bronze also works well on the brass and nickel silver.

Etchants for other nonferrous P/M alloys:

- *Aluminum parts* are etched using Keller's reagent, which is applied by swabbing with cotton for 15 to 30 s.
- *Titanium parts* are etched by immersion for 15 s using 10% concentrated hydrofluoric acid (HF), 5 mL concentrated nitric acid (HNO_3), and 85 mL H_2O.
- *Tool steels* are etched using 5% nital (5% HNO_3 concentrated in methyl alcohol). As-sintered materials should be swabbed for 5 min. As-annealed materials may etch within 20 s.

References cited in this section

10. “Effective Case Depth of Powder Metallurgy Products, Determination of,” Standard 52, Metal Powder Industries Federation

11. S. Kaufmann, Ford Motor Company, Dearborn, MI, personal communication

12. P. Schmey, United States Bronze Powders, Inc., Flemington, NJ, personal communication

L.F. Pease III and D.L. Pease, Metallography and Microstructures of Powder Metallurgy Alloys, *Metallography and Microstructures,* Vol 9, *ASM Handbook,* ASM International, 2004, p. 994–1020

Metallography and Microstructures of Powder Metallurgy Alloys

Leander F. Pease III and Douglas L. Pease, Powder-Tech Associates, Inc.

Representative Microstructures of P/M Alloys

The two general methods of P/M alloying are:

- Cold pressing and sintering of powder admixtures (consisting of blended elemental powders along with master alloy or other desired additions)
- High-density consolidation of prealloyed powders

Consolidation of powder admixtures by pressing and sintering is the most common and economical production method, although other alternatives may be considered because of porosity and the heterogeneous mixing of elemental powders. Prealloyed powders are used when more uniform alloying is required. For example, admixed nickel requires economically prohibitive sintering times (even at high sintering temperatures) for complete alloying. The requirement of complete alloying in these alloy classes makes the elemental powder approach impractical. Most high-alloy P/M materials, such as stainless steels, tool steels, and superalloys, are consolidated from prealloyed powders. Many low-alloy steel (with nickel, molybdenum, and manganese as alloying elements) also use prealloyed steel powders for more uniform composition to ensure greater hardenability than is possible with admixed copper or nickel. However, prealloyed powders have lower compressibility, which results in lower green density and/or lower green strength. This problem is solved by high-temperature and liquid-phase sintering and through the use of special consolidation methods, such as hot isostatic pressing and extrusion.

This section describes and illustrates some typical microstructures of P/M alloys by various consolidation methods. Emphasis is placed on pressed-and-sintered steels from admixed powders. Other consolidation methods and nonferrous alloys (copper, aluminum, and titanium) are also briefly discussed. Also included are examples of unusual and/or defective structures, and parts subjected to other finishing and fabrication operations, such as steam blackening and joining, are also discussed. An extensive atlas of P/M microstructures for both ferrous and nonferrous is given on pages 730 to 748 (Fig. 12–173) of the article "Metallography of Powder Metallurgy Materials" in *Powder Metal Technologies and Applications,* Volume 7 of *ASM Handbook.*

Pressed-and-Sintered Steels

Pressed-and-sintered P/M alloys typically contain 12 to 18% pores, where most of the pores are interconnected. Reduction or elimination of porosity usually requires the application of other techniques. For example, a process known as warm compaction also can produce P/M steel parts having substantially reduced porosity (8 to 10%) while utilizing a modified, yet economical pressed-and-sinter technique (see the article "Warm Compaction" in *Powder Metal Technologies and Applications,* Volume 7 of *ASM Handbook*). More expensive double-press, double-sinter technique is also capable of producing these higher densities. High-density P/M alloys (less than 2% porosity) require the application of relatively expensive nonconventional processes, such as hot isostatic pressing, P/M forging, metal injection molding, or hot pressing. Other approaches to producing substantially pore-free materials include molten-metal infiltration and liquid-phase sintering (Ref 13).

This section briefly describes typical microstructures of conventional pressed-and-sintered P/M steels. As previously noted, many of the interesting structures seen in P/M parts are caused by porosity and heterogeneous

mixing of elemental powders that constitute many alloys. For example, pores allow carburizing and nitriding gases to penetrate the interior of a sintered steel part, resulting in less-well-defined cases on carbon steel and the nitriding of 300 series stainless steels. Most P/M materials do not form a definite shallow case because of penetration of the carburizing gases. At densities above approximately 7.2 g/cm^3, a definite case tends to form if the core contains less than 0.2% C, as shown in Fig. 25.

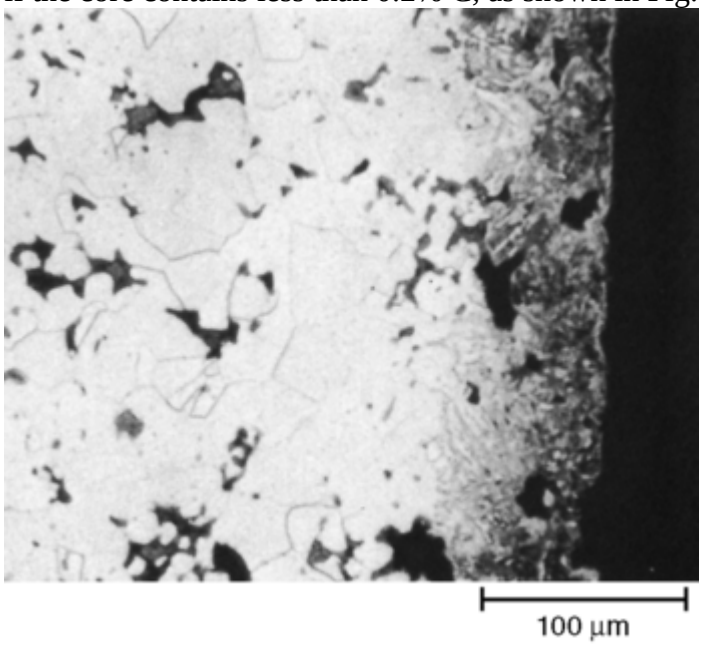

Fig. 25 Atomized iron powder, pressed to 6.8 g/cm^3, sintered in dissociated ammonia, austenitized 30 min in vacuum, gas carburized less than 5 min, and oil quenched. The 0.1 mm (0.004 in.) thick case is the dark martensite on right. Interior is all white ferrite. 2% nital. 180×. Courtesy of J. Hurst, C.I. Hayes, Inc.

When low-alloy steels are prepared as elemental mixes with nickel and carbon, hardenability is lower than for fully dense, homogeneous low-alloy steels. Hardenability is not a problem in the fully dense prealloyed steels fabricated by forging or metal injection molding. The heat treated structures may display retained austenite, carbides, and subsurface quench cracking. In the etched condition, sintered steels may exhibit carburization or decarburization. Microindentation hardness testing is usually limited to a particular phase when testing with the 100 gf Knoop indenter, for example, martensite.

If parts of nonuniform section are pressed, density may vary, which may be noted and measured metallographically. If parts are overpressed, the particles will separate vertically, showing microlaminations. Cracks may occur upon ejection, at the change in diameter between two sections of a part. Even in simple shapes, such as flat tensile bars, improper tool design can cause cracks.

Sintering completes the bonding of adjacent powder particles. During the sintering process a wide variety of physical, chemical, and metallurgical phenomena occur within the mass of metal powder particles. These effects are influenced by the sintering conditions (time, temperature, atmosphere), as well as by the chemical composition of the powder mass. Because most of these phenomena are directly related to time and temperature, they have been listed in two categories. The first group primarily is associated with the early stages of sintering (conventional sintering practices), and the second group is related to the more advanced stages of sintering, typical of high-temperature methods.

Early stages of sintering (conventional) include the following mechanisms:

- *Homogenization:* The as-cast, dendritic structure of the atomized particles is removed and microsegregation within the particles is eliminated; diffusion between powder particles begins to occur.
- *Alloying:* As the diffusion process continues, admixed additives begin to form alloyed structures with the base ferrous particles. For species such as carbon, this takes place early in the sintering process; for elements such as nickel or molybdenum, diffusion is much slower and takes longer times and higher temperatures to achieve a reasonable level of homogeneity.

- *Removal of gases/oxides:* Chemical reactions between the sintering atmosphere or admixed additives such as graphite and the surface oxides on the metal particles also begin early in the sintering cycle. This breakdown of oxides and removal of adsorbed gases cleanses the metal particle surfaces and promotes the diffusion process.
- *Particle bonding:* The formation of solid bridges or necks between individual or clusters of powder particles is the critical result of the early stages of sintering. These particle bonds give the powder mass integrity and mechanical strength.

Advanced stages of sintering (high temperature) influence several important characteristics, such as:

- *Densification:* As the sintering process continues at higher temperatures, the inherent porosity in the powder mass is reduced as pores are eliminated by bulk diffusion to grain boundaries. This reduction in the amount of porosity results in an increase in the density of the powder compact.
- *Porosity shape:* The remaining pores in the P/M structure lose their angular, irregular nature and become smooth, tending toward perfect spheres, as the sintering temperature increases.
- *Grain growth:* The individual powder particles lose their identity completely as grain boundaries move across prior particle boundaries. Larger grains replace the original fine grain structure.
- *Liquid phase:* Depending on the chemical constituents in the powder mass and the sintering temperature, a transient or permanent liquid phase may be formed. This liquid phase will accelerate particle rearrangement and diffusion, thereby aiding densification and pore elimination. For some additives, such as copper and phosphorus, liquid-phase sintering will occur at conventional temperatures, while for silicon iron and the tool steels, high-temperature sintering is required. The phenomena attributed to the early stages of sintering will continue during high-temperature sintering. Thus a greater number and more complete particle bonding, as well as more homogeneous alloying, will occur during the advanced stages of sintering than occur during the early stages.

The phenomenological changes that occur during sintering are shown in Fig. 26 for the microstructures of an austenitic stainless steel. Figure 26(a) shows the microstructure of the original compacted powder particles. The dendritic pattern in these particles is clearly seen. After sintering for 5 min at 1066 °C (1950 °F) (Fig. 26b), the cored dendritic structure is still visible, but the particles already show signs of homogenization. The structure after 30 min at 1121 °C (2050 °F), shown in Fig. 26(c), finds homogenization almost complete and particle-to particle bonding beginning to occur. Sintering for 2 h at 1316 °C (2400 °F) (Fig. 26d) produces a completely homogeneous structure, spheroidized porosity, and considerable grain growth. The original particle boundaries have completely disappeared with the formation of a single-phase austenitic structure, peppered with annealing twins.

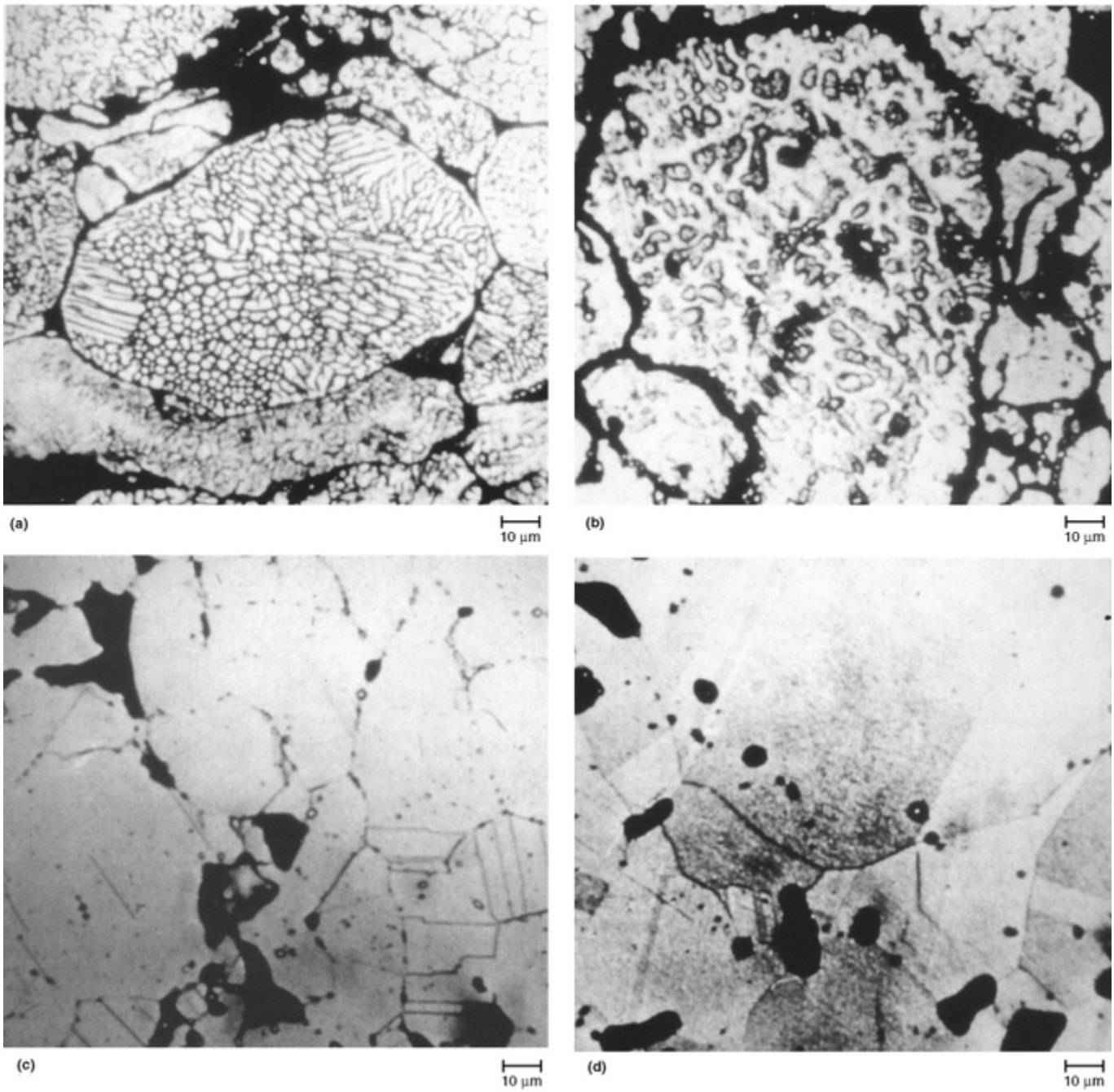

Fig. 26 Micrographs of pressed-and-sintered 316 stainless steel. (a) As-compacted powder particles. (b) Sintered at 1066 °C (1950 °F) for 30 min. (c) Sintered at 1121 °C (2050 °F) for 30 min. (d) Sintered at 1316 °C (2400 °F) for 2 h. ~650×. Courtesy of Howard Sanderow

Insufficient sintering, either for too short a time or at too low a temperature, will result in sintered parts showing insufficient bonding, original particle boundaries, and sharp, angular pores (e.g., Fig. 27). Undersintered parts are evidenced by the presence of excessive numbers of original particle boundaries. In general, for ferrous materials, a field of view at 200× would not be expected to show more than approximately five small segments of original particle boundaries. The presence of larger numbers of particle boundaries would necessitate verifying the sintering conditions and the strength of the part.

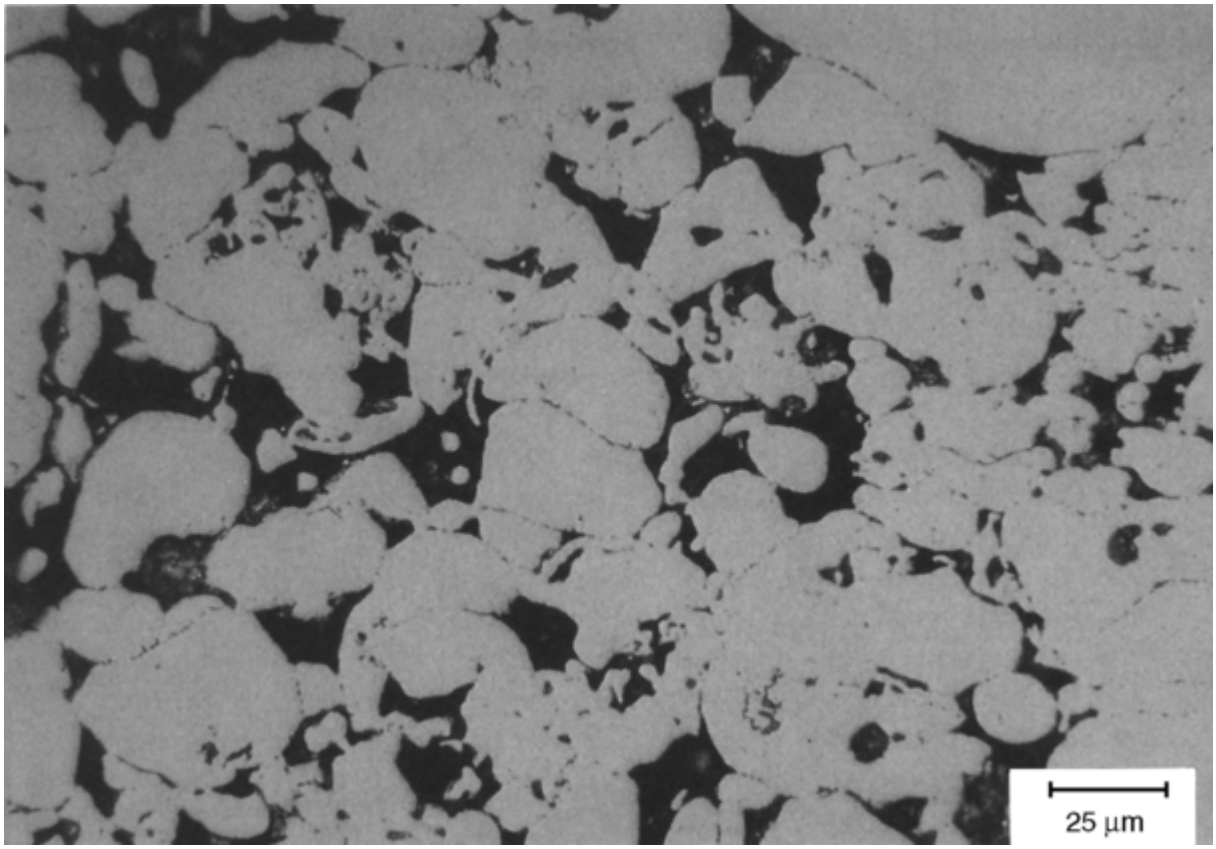

Fig. 27 Insufficiently sintered 316L stainless steel part showing original particle boundaries and sharp, angular pores. As-polished cross section. Part sintered for 30 min at 1093 °C (2000 °F) in H_2. Courtesy of OMG Americas

If a fracture occurs in the green state and the part is then sintered, the particles on the fracture surface will be rounded. If a fracture occurs after sintering, the surfaces of the particles show ductile cups, cones, and asperities, as in the SEM view (Fig. 23). If an SEM is not available, one can plate the fracture surface with 25 μm (0.001 in.) electroless nickel, Edgemet (Buehler Ltd., Lake Bluff, IL), in about 2 h. The plating is done on a specimen that was sectioned perpendicular to the fracture surface. The specimen is then mounted in epoxy resin, ground, and polished. The plating saves the details of the fracture surface, which is viewed at right angles to the fracture plane. In this way, any asperities and cones can be seen in profile view, at 1000×. It is best to create a deliberate fracture through a sintered region to serve as a comparison with the questioned fracture. Figure 28 shows the fracture that occurred in a green part, and it has rounded particle surfaces. Figure 29 shows a fracture that occurred in a sintered and heat treated part, and the asperities where sinter bonds were broken are shown by the arrows.

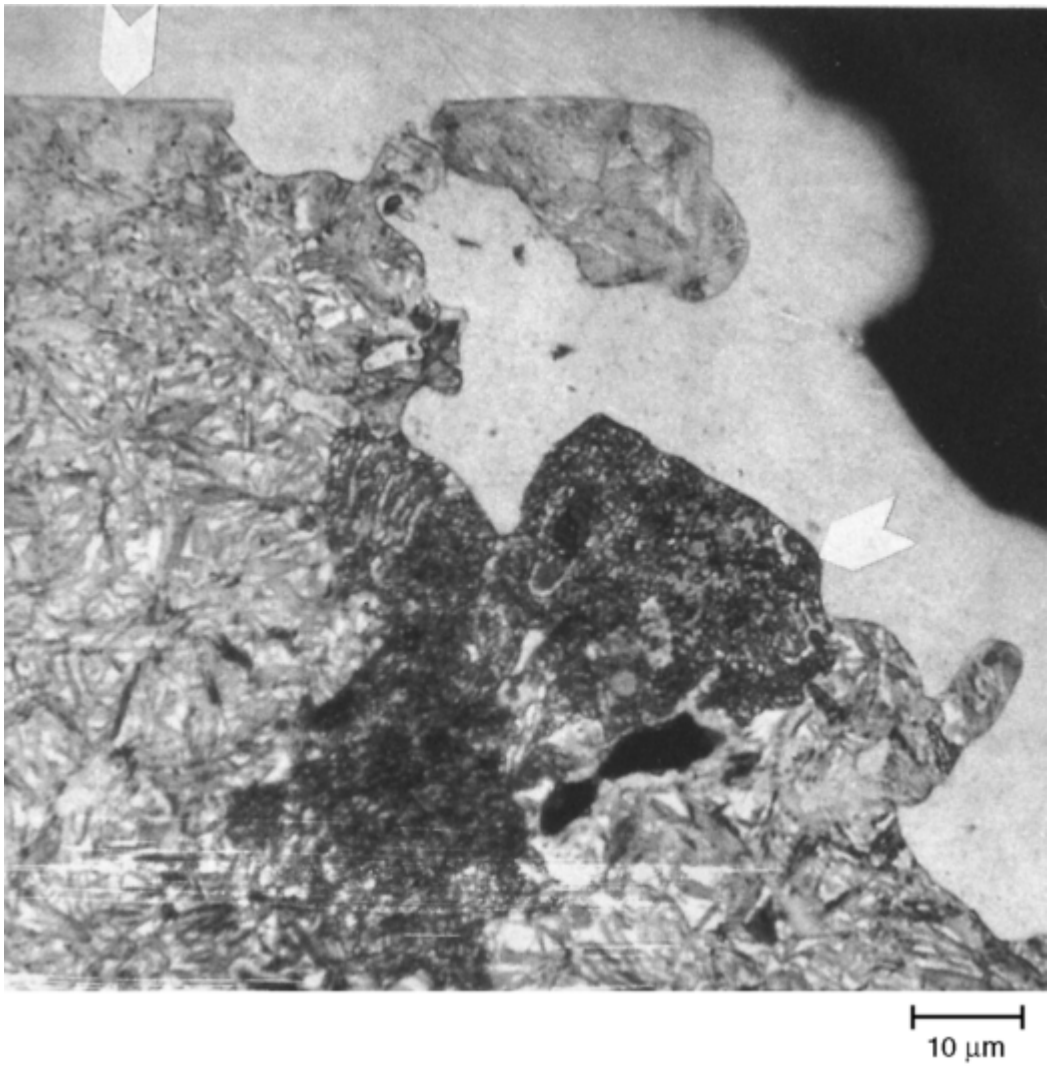

Fig. 28 Fracture surface of a heat treated P/M steel where the fracture occurred in the unsintered state. Top arrow shows the compacted surface. Right arrow points to rounded particle surfaces with no indication of ductile cups and cones that would be typical of a fracture in the sintered state. White layer is electroless nickel plating used to preserve the surface details during polishing. Etched. Compare with Fig. 29 960×

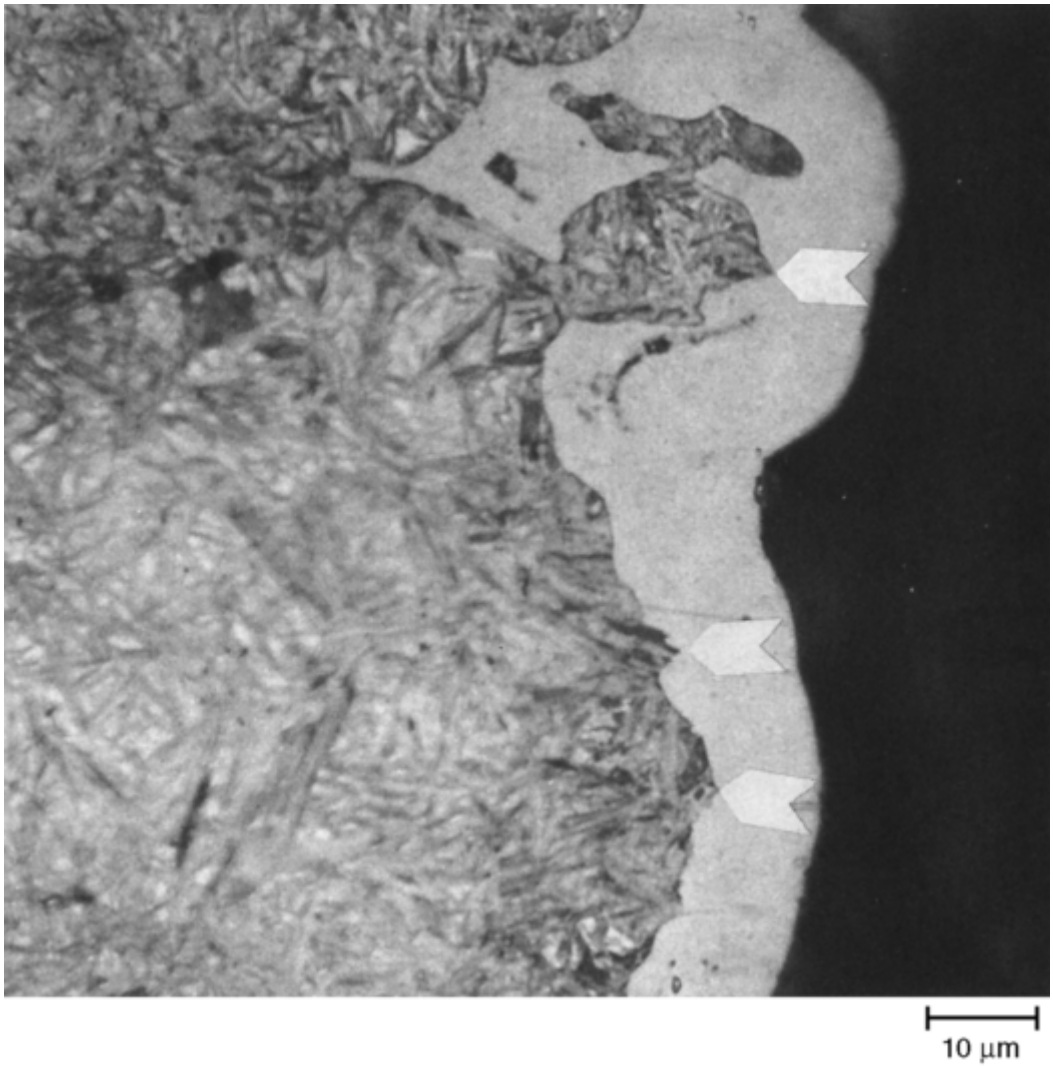

Fig. 29 Same material as Fig. 28 but a fracture surface deliberately created in the sintered and heat treated state. Arrow points to sharp asperities where the particles were torn away from the adjacent material on the opposite fracture surface. Such asperities are not created when a P/M part is fractured in the unsintered state. Even if they were so created, the asperities would become rounded during the usual sintering cycles. Etched. 960×

The plating keeps epoxy resin from filling pores during sample mounting. This creates some difficulty at polishing, in trying to open all the pores. This is best accomplished at final polishing with 0.05 μm alumina on microcloth with a succession of 15 second nital etchings and 2 to 3 min polishing with 1 N (0.25 lbf) force. Several iterations may be required. Smeared pores are most easily viewed at 1000× and are seen as thin gray lines in the unetched structure.

Iron Powders. Unalloyed iron materials (e.g., F-0000 in MPIF Standard 35) are used for lightly loaded structural applications and structural parts requiring self-lubrication where strength is not critical. The combined carbon content of these materials can be from 0 to 0.3 wt%. Iron parts that are essentially carbon free are often used, particularly at higher part densities, for their soft magnetic properties. Effects of sintering temperature on P/M iron are shown in Fig. 30 (see also Fig. 41–48 in the article “Metallography of Powder Metallurgy Materials” in *Powder Metal Technologies and Applications,* Volume 7 of *ASM Handbook*). Figure 30(a) is from the as-pressed condition with multigranular particles completely separated by voids. Figure 30(b) to (d) are micrographs that show progressively more particle bonding and pore spheroidization at higher temperatures.

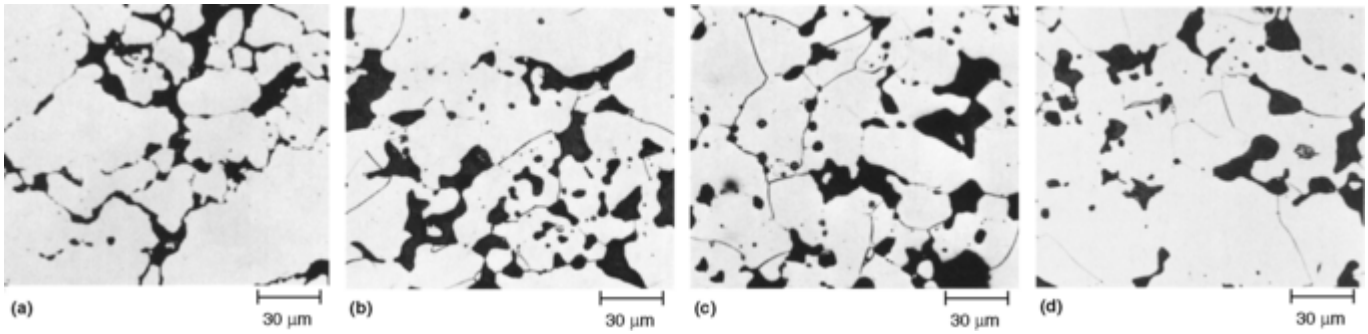

Fig. 30 Effect of sintering (in dissociated ammonia for 30 min) at different temperatures with pressed iron powder (mixed with 0.75% lubricant and pressed density of 6.5 g/cm^3). (a) As-pressed condition with multigranular particles completely separated by voids (black). (b) Sintering at 1065 °C (1950 °F) forms many bonds between particles, but with numerous particles boundaries and angular pores. (c) Sintering temperature at 1120 °C (2050 °F) results in more numerous and extensive bonds with some grain growth and spheroidization of pores. (d) Sintering at 1175 °C (2150 °F) results in only a few particle boundaries with considerable grain growth, grain boundary migration, and spheroidization of pores. All with 2% nital etch at 300×.

Direct reduced sponge iron or water-atomized iron powders are typically used as the base powder for admixed materials. The density required to achieve the desired mechanical properties generally dictates the type of powder. Sponge powders are selected typically for the density range of 6.4 g/cm^3 and lower, while atomized iron powders are used for parts with a density of 6.7 g/cm^3 and higher. Either type of powder can be used for the intermediate density range; the choice generally depends on the part geometry and the available compaction press tonnage.

Electrolytic Iron Powder. Because of its high production costs, use of electrolytic iron is limited. However, the high green strength, high compressibility, irregular particle shape (Fig. 31), and high purity of electrolytic iron make it suitable for a number of applications, such as soft magnetic parts and enrichment of food products.

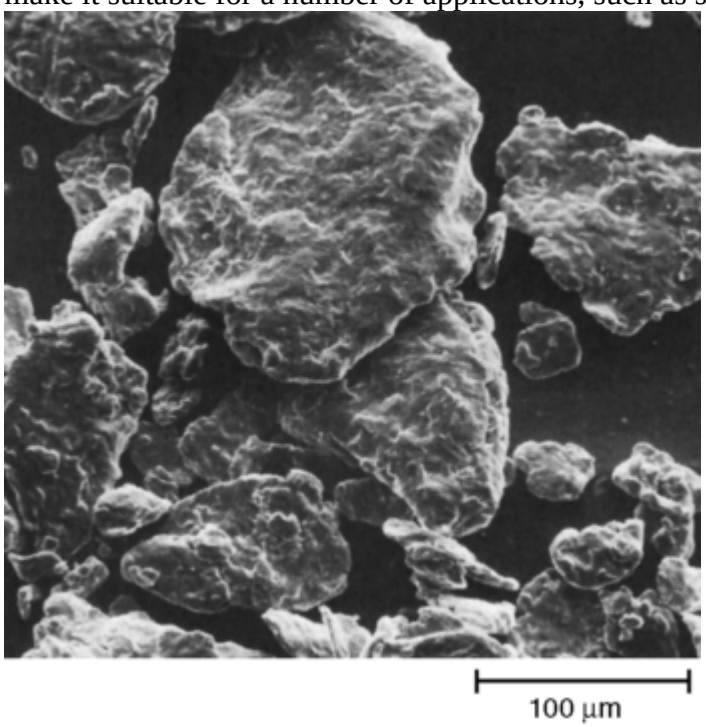

Fig. 31 Example of irregular and flaky shape of an electrolytic iron powder (SCM A283). SEM. 190×

Carbonyl iron powders may have a particle size of 2 to 5 μm and are often used in metal-injection-molded P/M parts. Their high surface area and fine particle size allow the material to sinter to near-full density with large associated shrinkages. The resulting structure will be ferrite, with small rounded and isolated pores.

P/M Steels from Admixed Powders. Admixed materials are in widespread use throughout the ferrous P/M industry. Alloying additions, in elemental form or as ferroalloys, such as Fe_3P, FeMn, or FeCr, can be mixed with an iron powder. Iron powders generally have low carbon contents because carbon forms an interstitial solid solution with iron and significantly reduces the compressibility of the powder. The P/M steels also are generally low in manganese.

Admixed powders for carbon and low-alloy P/M steels generally contain sufficient graphite to provide the desired carbon content after sintering. In addition to graphite, the mixes contain a lubricant that aids particle rearrangement during the initial stages of compaction and reduces adhesion to the die wall. When the mix is pressed, the additions are not yet alloyed with the iron powder; admixed materials therefore retain most of the compressibility of the base iron powder. The degree of alloying during sintering is limited by the diffusivity of the alloying elements in the iron at the sintering temperature. The resulting microstructures can be chemically and microstructurally heterogeneous. However, as previously noted, such heterogeneity is not necessarily detrimental, as in the case of some certain nickel steels and diffusion-alloyed steels, where the softer nickel-rich phases improve toughness.

Because the various powders that comprise the admixed alloys have differing particle size and density, admixed alloys are particularly susceptible to dusting and segregation during handling and transfer to the die cavity. Compositional variations, which result from these demixing phenomena, cause inconsistencies in the green and sintered properties of P/M parts. The tendency for mixes to dust and segregate can be reduced significantly through the use of binder-treated mixes. Binder-treated mixes also improve powder flow and die-filling characteristics during part manufacturing. This results in more consistent part sectional densities and improved control of part mass. Improved flow and die fill uniformity result in reduced press cycle times and more consistency throughout the entire part manufacturing process.

Iron-Graphite P/M Steels. These steels contain up to 0.8% C with increasing amounts of pearlite with higher carbon content. P/M carbon steels with 0.3 to 0.6 wt% combined carbon (grade F-0005 in MPIF Standard 35) possess moderate strength and apparent hardness. They are used where such properties combined with machinability are desired. Higher-carbon P/M steels (e.g., MPIF grade F-0008) have moderately higher strength compared with F-0005 materials, but are more difficult to machine. In the as-sintered condition carbon steels have a ferrite/pearlite microstructure (Fig. 32). Both F-0005 and F-0008 steels can be heat treated to increase tensile strength, improve apparent hardness, and enhance wear resistance. Heat treated carbon steels have a martensitic microstructure (Fig. 33).

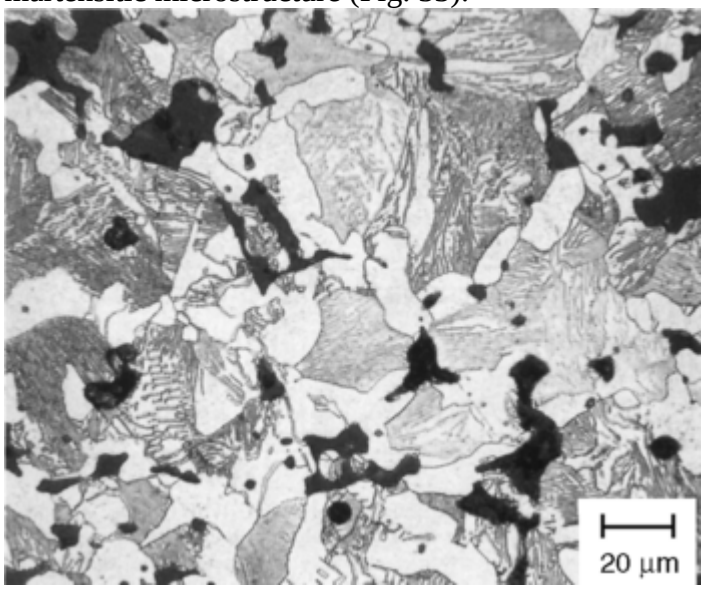

Fig. 32 Ferrite/pearlite microstructure of an as-sintered P/M carbon steel (F-0005)

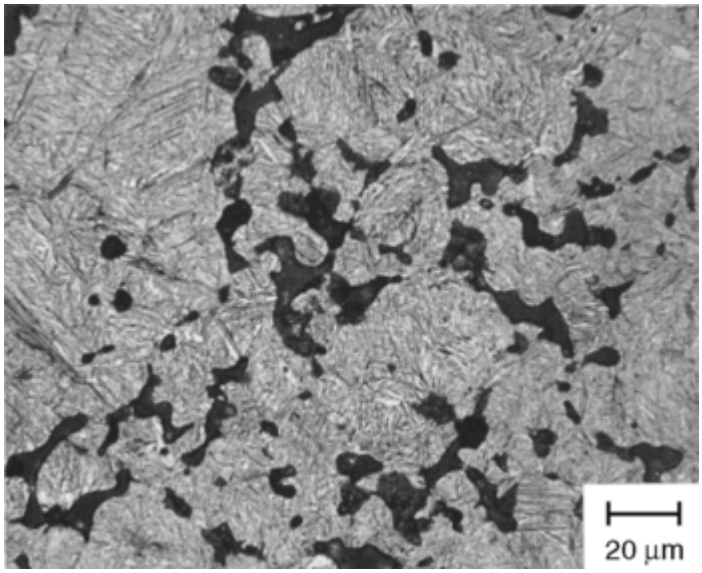

Fig. 33 Tempered martensitic microstructure of a quench-hardened and tempered P/M carbon steel (F-0008)

The main factor affecting the properties of a sintered steel, apart from density and proper sintering, is the amount of combined carbon in the steel. Overall expansion during sintering is directly proportional to the amount of combined carbon, and the strength of sintered steel increases rapidly with increasing combined carbon content. The combined carbon for these materials is approximately 0.8% times the area fraction of pearlite. That area fraction does not include the area associated with porosity. For materials with hypereutectoid carbon contents (typically >0.8%), iron carbide networks appear in the grain boundaries, and the impact, tensile strength, and elongation are reduced. This carbide network is not to be confused with the divorced eutectoid carbide platelets that will appear occasionally in a grain boundary in the hypoeutectoid steels with less than 0.3% C. This effect is seen in ingot-based steels as well. Sintered iron bearings are fabricated with graphite in solution as well as present as free graphite flakes. The combined carbon is judged by the aforementioned lever rule, which is important in quality control of iron-graphite bearing materials.

Typical sintering temperature of iron-graphite alloys is 1120 °C (2050 °F) (Table 2). Proper sintering ensures (a) establishment and growth of iron-to-iron bonds, (b) diffusion of carbon into and combination of carbon with iron, and (c) spheroidization of pores. An all-pearlite structure is obtained during the initial stages of sintering at 1120 °C (2050 °F), as shown in Fig. 34(a). Further sintering results in almost complete bonding and increased pore spheroidization (Fig. 34b) (see also Fig. 53–57 in the article "Metallography of Powder Metal Materials" in *Powder Metal Technologies and Applications,* Volume 7 of *ASM Handbook*). During sintering, the major portion of the oxide must be reduced by the graphite and the sintering atmosphere before the iron and graphite can combine. The oxide content of iron is therefore an important factor in determining the reactivity of iron with graphite. To ensure high reactivity with the iron for rapid reduction of oxide and fast carburization, fine graphite powder—free of silicon carbide and having low ash content—usually is used.

Table 2 Sintering temperatures for various iron-base alloys

Material	Sintering temperature[(a)], °C
Fe, Fe-Cu, Fe-Cu-Ni	1120–1280
Fe-C, Fe-Cu-C, Fe-Cu-Ni-C	1120–1150
Fe-Cu-Ni-Mo (Distaloy)-C	1120–1200
Fe-Mn, Fe-Mn-C	1120–1280
Fe-Cr, Fe-Cr-C	1150–1280
Fe-Mn-Cu	1120
Fe-Cr-Cu	1200–1280
Fe-Mo, Fe-Mo-C	1120–1280
Fe-Cr carbide	>1280

Fe-V carbide	>1280
Fe-Ti carbide	1200–1280
Fe-W carbide	1200–1280
Fe-Mn-Cr-Mo-C, Fe-Mn-V-Mo-C	>1280
Fe-Cr-Ni	>1280

(a) Temperatures represent the range of typical or possible sintering temperatures. Source Ref 8

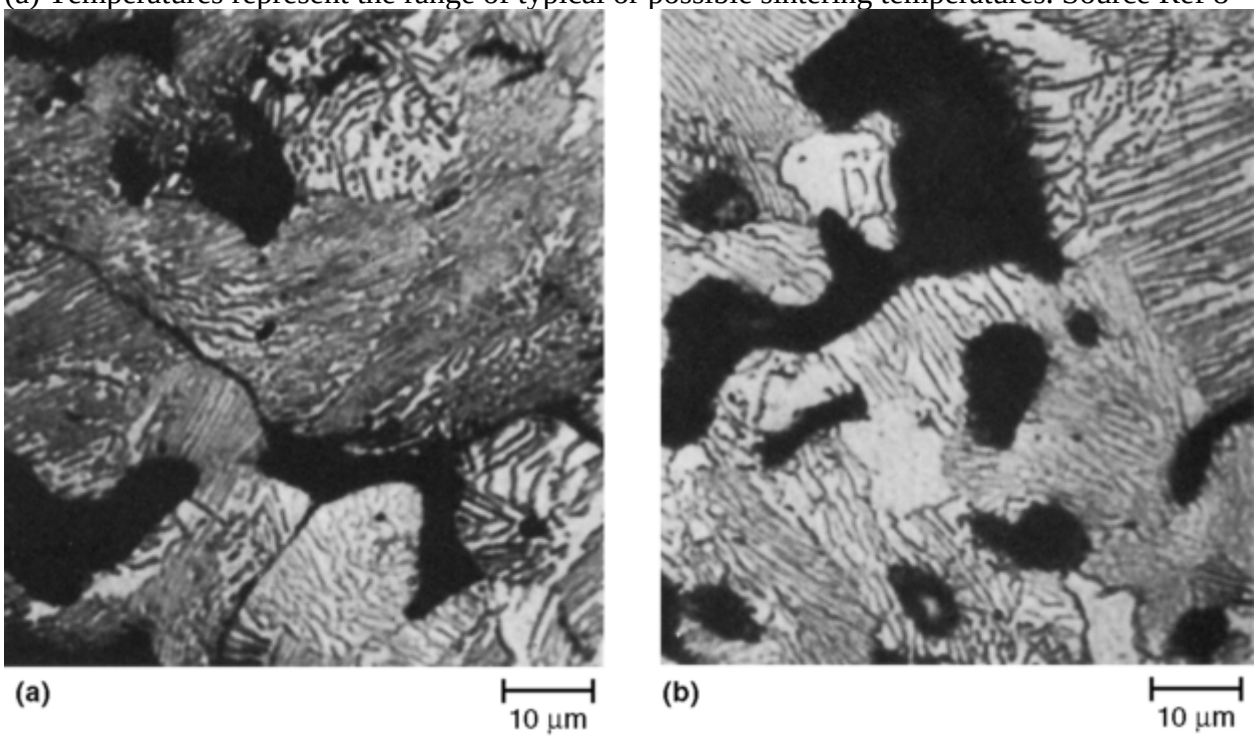

Fig. 34 Effect of sintering time on iron powder and graphite mix (pressed to 6.1 g/cm^3) with a sintering temperature of 1120 °C (2050 °F). (a) Sintered for 5 min, which resulted in all-pearlite structure (combined content at 0.70%) and some bonding of particles. (b) Sintered for 120 min, resulting in almost complete bonding and increased pore spheroidization. 4% picral plus 0.5% HNO_3 at 800×

Iron-Copper Alloys. Copper is frequently added to iron because it melts and rapidly dissolves, greatly increasing the strength of the iron. When copper melts, it is drawn by capillary action into the smallest available pores and capillaries. In an atomized iron powder, the copper flows between the particles that are pressed into close contact. It then dissolves in the iron at these points of contact. The copper activates the sintering of the particles that are in contact, resulting in rapid disappearance of particle boundaries and substantial neck growth. The copper may physically separate the iron particles as it flows among them, causing growth of the part in 1 to 2 min. The subsequent dissolution of the copper and local lattice expansion at points of contact cause later growth. In an undersintered part with 2% added Cu, some of the residual copper may still be visible as a thin copper-colored line between two iron particles. With sponge irons, the copper can flow into the fine pores inside the particles and thus not cause as much separation of particles. The high sponge iron surface area also contributes to rapid sintering. These two effects are thought to explain why the sponge iron and copper mixtures do not expand as much on sintering as the mixes based on atomized iron.

Copper melts at 1082 °C (1980 °F), leaving a pore at the site of the prior copper powder particle. In conventional sintering of iron-copper alloys (20 to 30 min at 1105 to 1120 °C, or 2025 to 2050 °F), at least 2% Cu disappear into solution in the iron. With 5% or more Cu, some free copper is always present as a copper-rich solid solution with the iron. Depending on the rate of cooling, copper-rich phases precipitate in the iron, and vice versa. The copper-rich phases precipitate in the iron, darkening the ferrite (Fig. 35); slow cooling increases darkening (Fig. 36). The coring effect is limited to the outside of the iron particles, because the melted copper does not readily diffuse to the particle centers under conventional sintering conditions. Picral etching will help to stain the copper precipitate areas for easier identification.

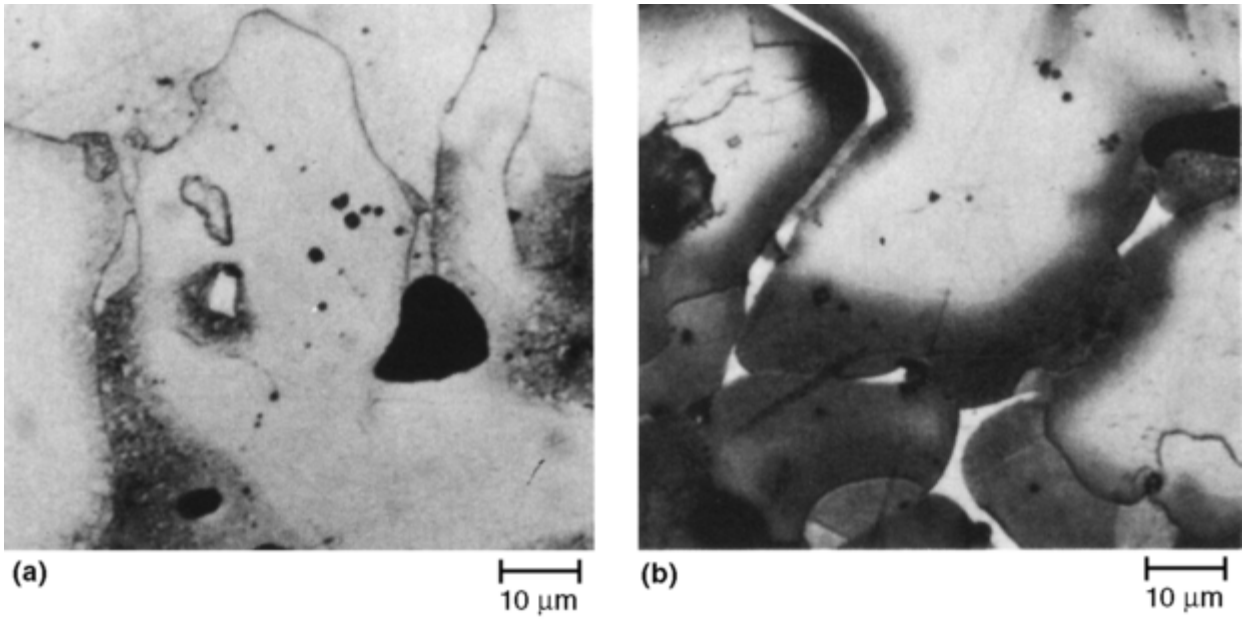

Fig. 35 Effect of copper content in iron-copper alloys sintered for 30 min at 1120 °C (2050 °F). (a) Some copper dissolves in the iron (gray areas) with a powder mix of 98% Fe and 2% Cu. (b) With 7.5% Cu, much more copper is dissolved in the iron. 2% nital. 700×

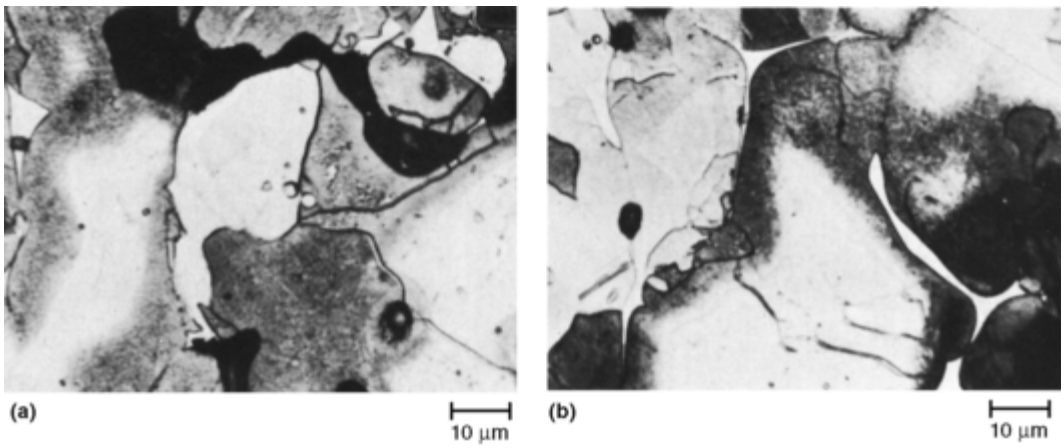

Fig. 36 Effect of cooling rate on pressed-and-sintered iron-copper alloys (92.5% Fe, 7.5% Cu) sintered at 1120 °C (2050 °F) for 30 min. (a) With a relatively fast cool normal for a small part, the dissolved copper in iron precipitates as a fine dispersion (gray areas). (b) With a slow normal for a large part, a coarser copper precipitates is indicated by a darker shade of gray than in (a). 2% nital. 700×

Iron-Copper-Carbon Alloys. The most common of the moderate-strength, as-sintered alloys is Fe-Cu-C with 0.5 to 0.8% C and 2 to 5% Cu. Copper steels such as FC-0205 and FC-0208 are used in medium-strength structural applications to increase strength, apparent hardness, and wear resistance. It combines the features described previously for iron-carbon and iron-copper alloys. The carbon goes rapidly into solution in the iron (perhaps in 5 min at 1040 °C, or 1900 °F) and tends to prevent the sintering expansion prevalent in zero- or low-carbon iron-copper alloys. The combined carbon can be estimated by the lever rule, although the eutectoid may be as low as 0.75% C in this ternary system.

Admixed copper powders are typically -270 mesh (-53 mm). This is considerably coarser than the size of admixed nickel powders (8 μm), and the pore structure of copper steels is considerably different from that of admixed nickel steels (Ref 14). In the as-sintered condition, copper steels have a ferrite/pearlite microstructure. The FC-0208 material shown in Fig. 37 is almost of the eutectoid composition and is mostly pearlitic. Copper steels can be heat treated to increase strength, apparent hardness, and wear resistance. Heat treated copper steels have martensitic microstructures (Fig. 38). Higher copper contents can be used for increased wear resistance when heat treatment is not practical.

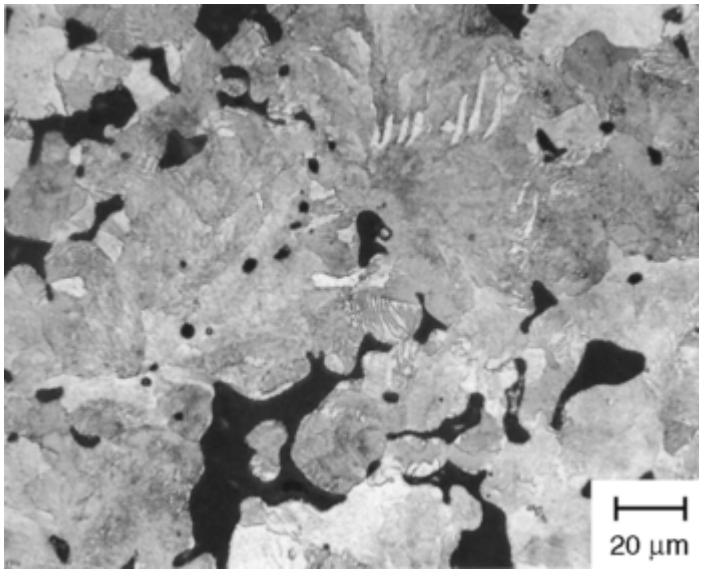

Fig. 37 Ferrite/pearlite microstructure of an as-sintered P/M copper steel (FC-0208)

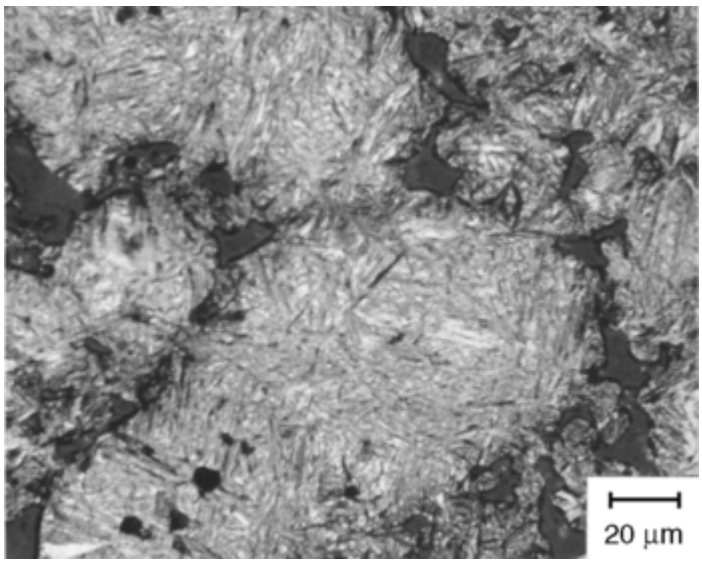

Fig. 38 Tempered martensitic microstructure of a quench-hardened and tempered P/M copper steel (FC-0208)

Similar to the iron-copper alloys, sintered copper steels with 2 wt% Cu generally show little or no undissolved copper. At higher percentages, the copper will be seen as a separate phase. The form of the copper phase indicates whether the material has been heated to a temperature in excess of 1082 °C (1980 °F) (Fig. 39). When copper has precipitated from solid solution, there is a considerable difference in the shape and distribution of the copper. The copper is no longer in the form of discrete particles; typically, it follows grain-boundary contours and fills small pores (Fig. 40). (See also Fig. 63–66 in the article "Metallography of Powder Metallurgy Materials" in *Powder Metal Technologies and Applications,* Volume 7 of *ASM Handbook.*)

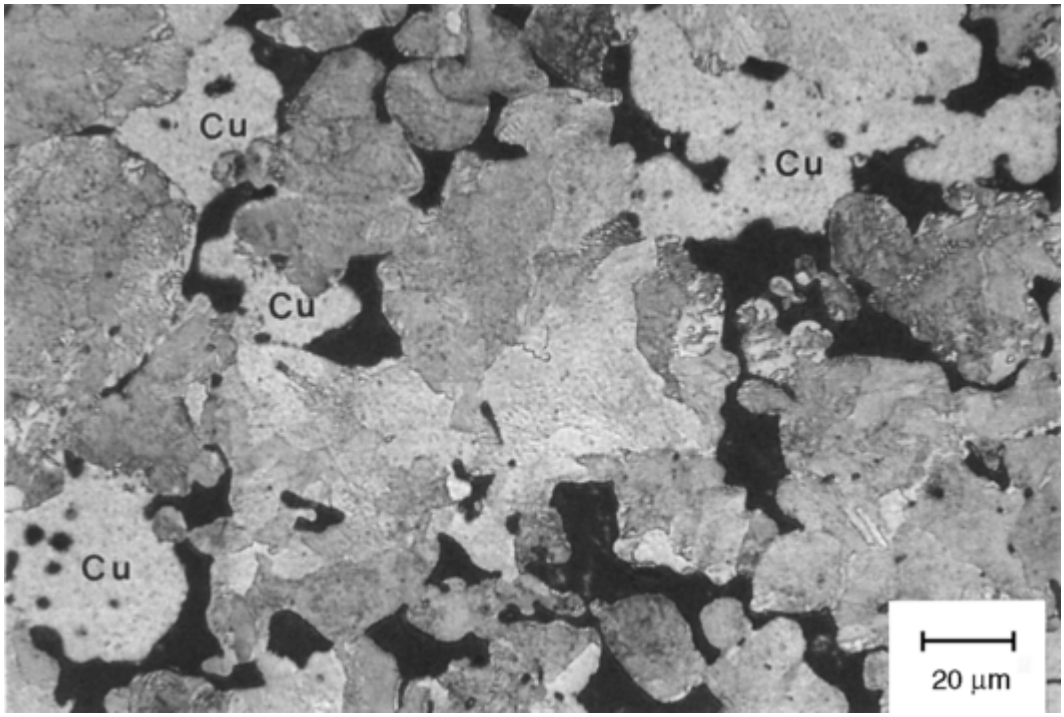

Fig. 39 Free copper in a P/M copper steel (FC-0508) that has not reached a temperature of 1082 °C (1980 °F) during sintering

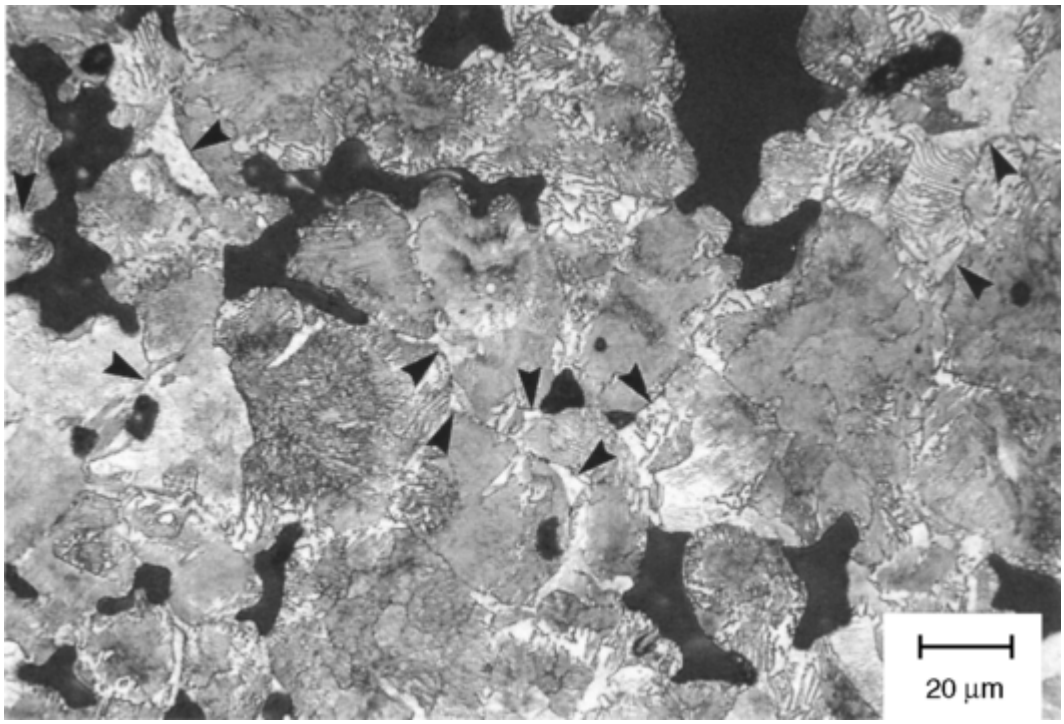

Fig. 40 Free copper that has precipitated from solution in a P/M copper steel (FC-0508)—see arrows

Iron-Phosphorus Alloys. Phosphorus irons are admixed alloys made by adding fine (<20 μm and preferably close to 10 μm) ferrophosphorus particles to high compressibility iron powders. These alloys exhibit a good combination of tensile strength, ductility, and impact absorption energy. Their primary use is for parts requiring superior soft electromagnetic performance, as phosphorus irons have higher resistivity, permeability, and induction and reduced coercive force. Typical applications for parts made from the phosphorus irons include antilock brake sensors, magnetic solenoids, and plungers.

The additions of iron phosphide (Fe_3P) to atomized iron results in the dissolution of phosphorus in amounts less than 1%. The phosphorus initiates a transient liquid-phase sintering reaction, then goes partly into solution in the iron, resulting in a material with excellent soft magnetic properties. Some of the phosphorus remains visible

as a second phase with the ferrite (Fig. 41). For magnetic properties, a low carbon content and freedom from pearlite are required. For optimal toughness and strength characteristics, a mixture of up to 1% P and up to 0.3% C is used. The phosphorus also causes pore rounding by virtue of the transient liquid phase, which gives the alloys their toughness and characteristic well-sintered appearance.

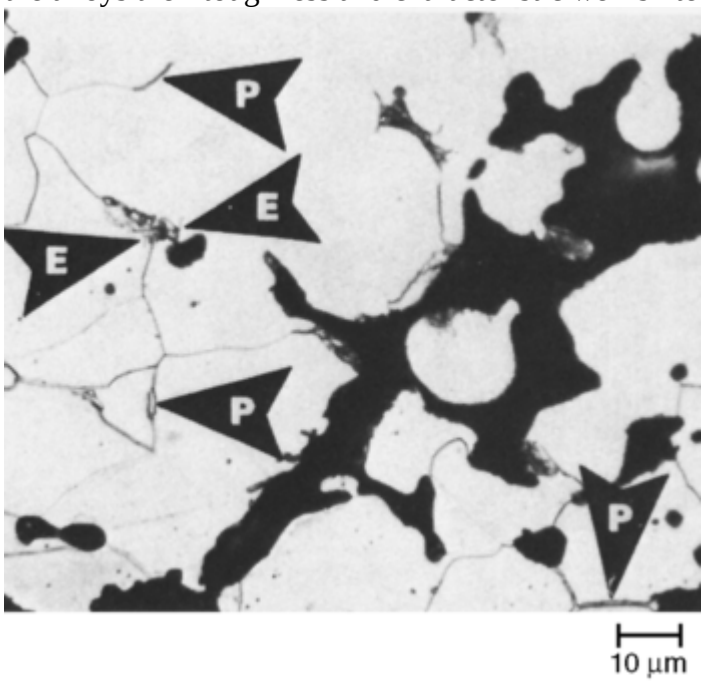

Fig. 41 Iron-phosphorus alloy (atomized iron mixed with Fe_3P to yield 0.45% P) for soft magnetic applications (6.7 g/cm^3). Pressed at 410 to 480 MPa (30 to 35 tsi) and sintered 30 min at 1120 °C (2050 °F) in dissociated ammonia. Phosphorus forms a liquid phase that causes pore rounding during sintering. Arrows E show fine two-phase eutectoid or eutectic of Fe-C-P. Arrows P indicate isolated phosphorus-rich phase in grain boundaries. Matrix is all white ferrite. 2% nital. 545×

Free-Machining Steels. The machinability of sintered irons and alloys is improved by adding sulfur. Historically, this has been accomplished by mixing fine sulfur powder (-325 mesh) into sponge iron. More recently, sulfur is dissolved in the liquid melt before atomizing (prealloyed sulfur) to form manganese sulfide (MnS) with carefully controlled amounts of manganese. Manganese sulfide particles have also been mixed with iron for a similar benefit. These additions result in particles of MnS in the pores as a gray phase (Fig. 42) or a MnS phase inside the iron particles (Fig. 43) if it was prealloyed. The use of high-hydrogen atmospheres at sintering desulfurizes a material to depths of 0.25 to 0.50 mm (0.01 to 0.02 in.), an effect whose analog in carbon is better known. Boron nitride powder is also mixed into iron in small amounts to improve machinability. Finally, the most effective enhancer of machinability is impregnation of the pores of the sintered material, using a plastic resin.

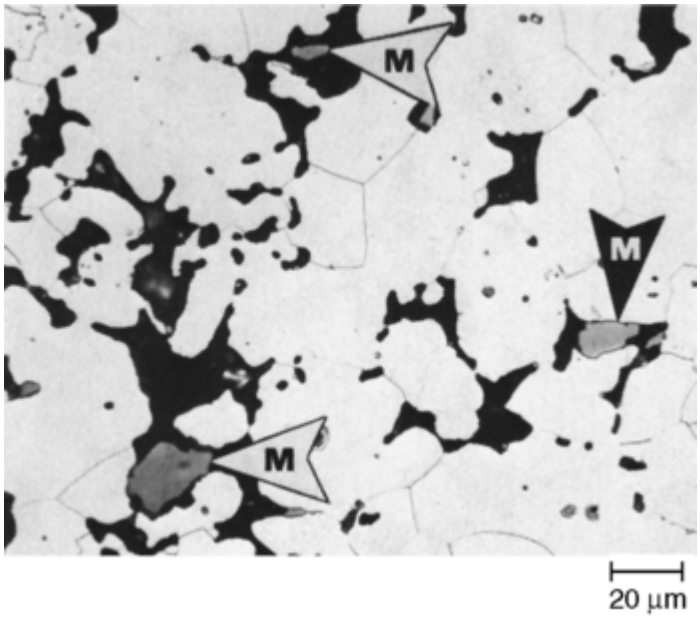

Fig. 42 Water-atomized iron powder with 0.5% MnS blended for increased machinability. The MnS is the gray material (see arrows M) inside the darker pores. 2% nital. 330×

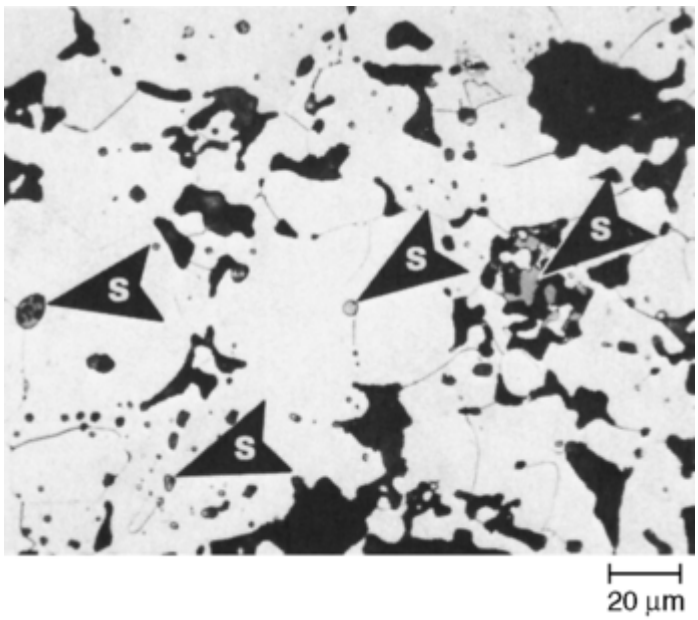

Fig. 43 Sponge iron powder with 0.27% S and 0.9% Mn added to the melt before particle formation. Arrows S show gray MnS inclusions within the iron particles and also in the spongy areas. 2% nital. 330×

Nickel Steels. The most common high-strength heat treated materials are the nickel steels. In these mixtures, 2 or 4% elemental Ni is added to iron, along with 0.4 to 0.8% C and up to 2% Cu (optional). The typical nickel is very finely divided and is often prepared by carbonyl decomposition. The copper is generally added for size control during sintering, because nickel induces shrinkage and copper causes expansion. The copper activates sintering and promotes the dissolution of nickel in the iron.

Nickel does not diffuse very rapidly in iron at the typical sintering temperature of 1120 °C (2050 °F), and the sintered microstructure of these materials contains nickel-rich regions (Fig. 44). As previously noted, heterogeneous regions of nickel improve toughness significantly, particularly in the heat treated condition. Nickel-rich regions comprise 20 to 50% of the area of these structures. The regions are extensive because the nickel content of their interiors has been diluted to 12% Ni by inward diffusion of iron.

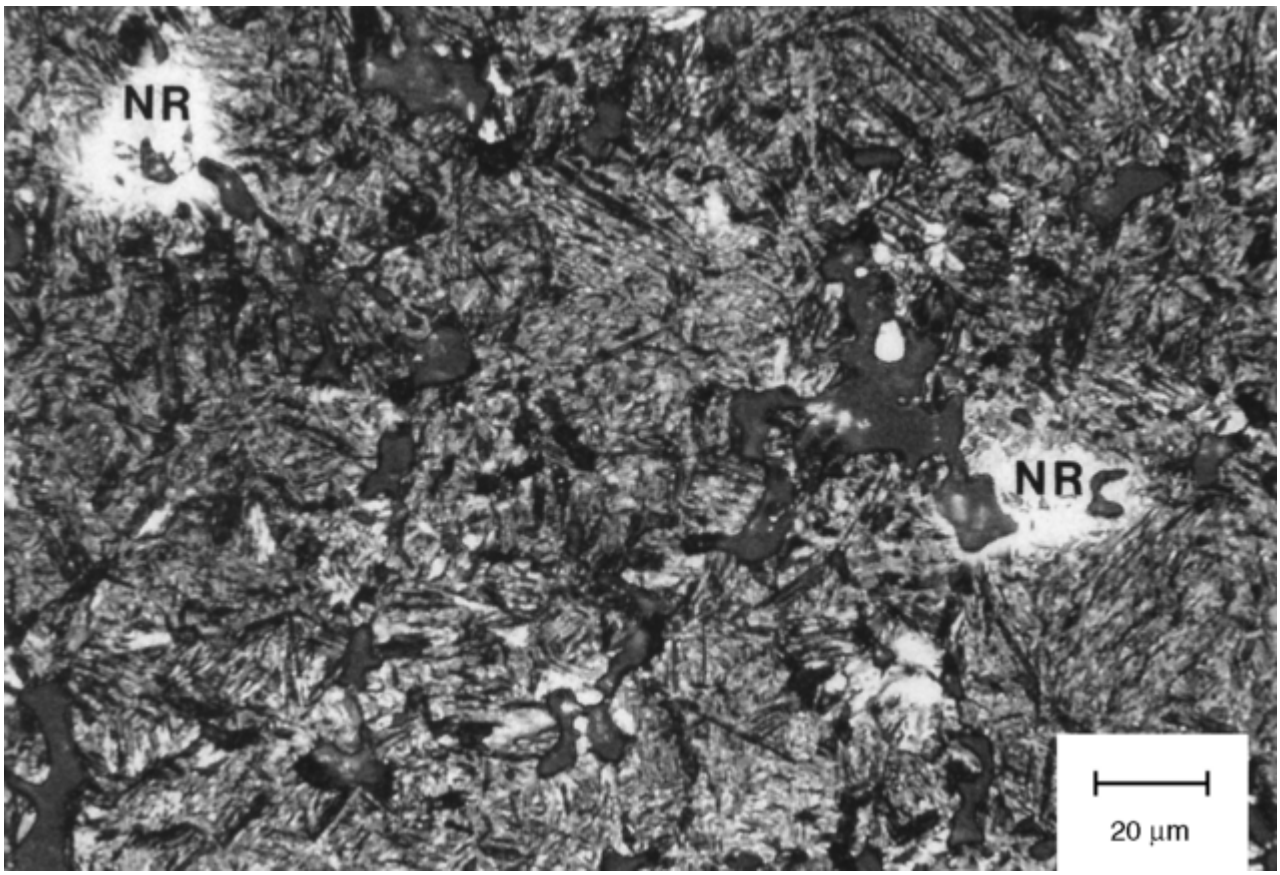

Fig. 44 Nickel-rich regions (NR) in a tempered martensitic structure of a quench-hardened and tempered P/M nickel steel (FN-0208)

The nickel-rich regions tend to etch lightly. Their interiors often are unetched austenite, and their peripheries contain martensite or bainite with microindentation hardnesses of 40 to 55 HRC, converted from 100 gf Knoop. The pearlite colonies are usually surrounded by a white band that appears similar to ferrite, but never contains eutectoid products. It is probably a higher-alloy diffusion zone. The austenitic cores of the nickel-rich regions increase toughness and strength in these alloys and tend to inhibit ductility. The undiffused nickel-rich regions figure significantly in the overall performances of the alloy. These islands with hard phases in the as-sintered condition contribute a high degree of wear resistance that would not normally be expected.

It is difficult to assess the degree of sintering by studying the nickel-rich areas because copper additions greatly affect their extent and appearance. Sintering is best judged by the disappearance of original particle boundaries and by pore rounding. It is difficult to discern the combined carbon level in the nickel steels because of the presence of the nickel-rich regions, the white diffusion layer, porosity, and the probable lowering of the eutectoid carbon level by the nickel.

Diffusion-alloyed ferrous powders, also known as partially alloyed powders, have other powder additions that are metallurgically bonded to either an elemental iron powder or to a prealloyed powder base. In diffusion-alloyed iron powders, alloying elements of molybdenum, nickel, and copper are added as finely divided elements or oxides to the iron powder. They are then coreduced with the iron powders at an annealing step, resulting in the firm attachment and partial diffusion of the elements to the iron. This partial alloying increases hardenability compared to elemental mixtures, yet these powders exhibit good compressibility. Bonding of the alloying elements also reduces the tendency toward powder segregation.

The sintered structures exhibit ferrite, pearlite, and nickel-rich regions such as those described previously for the elemental mixes. Figure 45 is an example of a complex as-sintered microstructure consisting of areas of martensite, bainite, fine unresolved pearlite, nickel-rich ferrite containing blocky carbides, as well as dispersed nickel-rich areas of retained austenite. The nickel-rich regions have the benefits noted previously. With added copper, additional partial hardening during sintering occurs. In Europe, this is used to advantage by producing medium-carbon alloys that are sold in the pressed, sintered, and sized conditions, but have good strength and impact resistance. This procedure avoids the distortions that can occur during normal heat treating. There is a wide range of diffusion alloyed powders available in Europe. Commercial grades in use in North America,

South America, and Canada are based on a highly compressible iron powder, contain nominally 1.5 wt% Cu and 0.5 wt% Mo, and differ with respect to their nickel contents. One powder contains 2 wt% Ni, while the other has a nickel content of 4 wt% (FD-0205 and FD-0405).

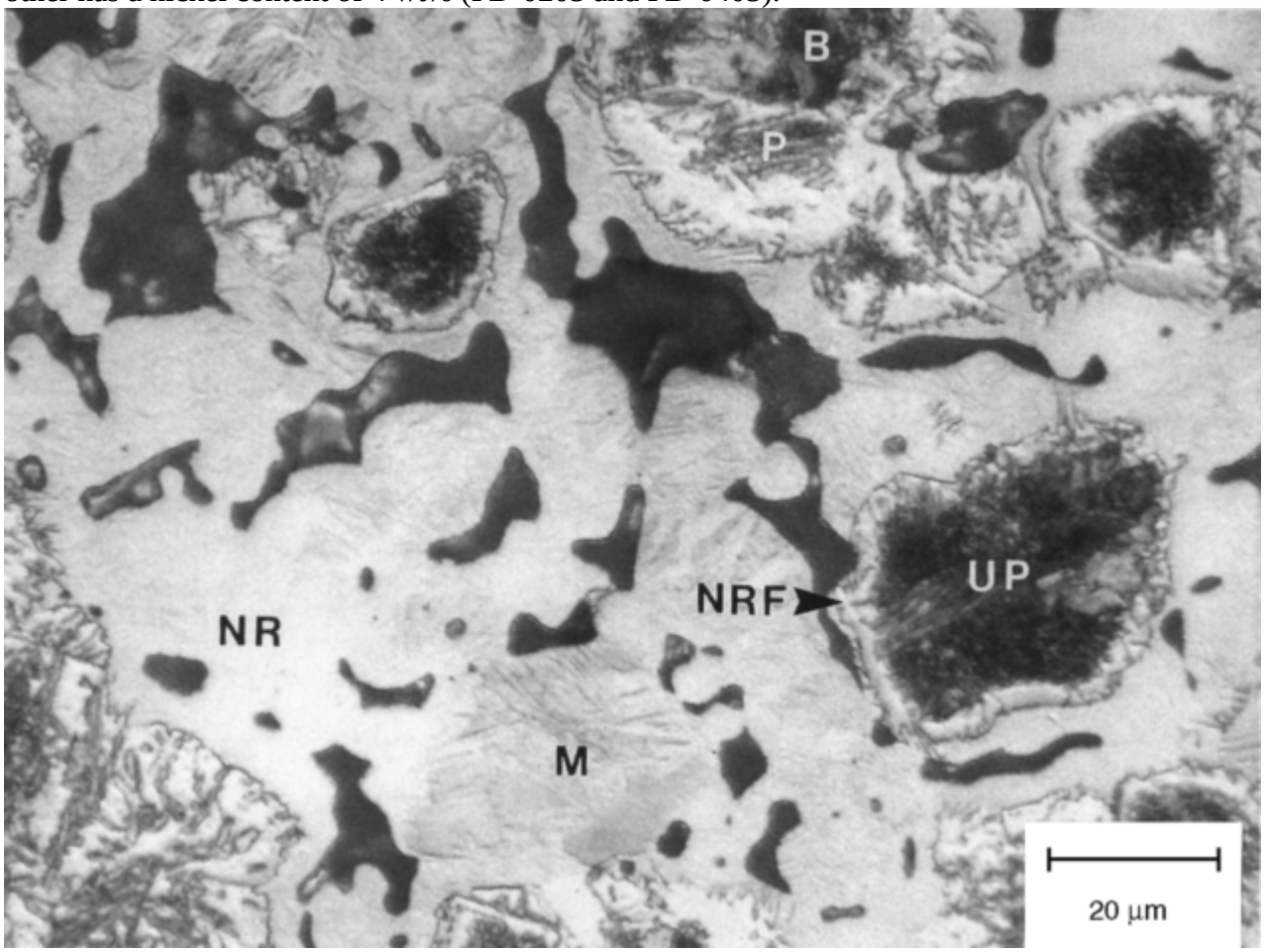

Fig. 45 As-sintered microstructure of a part made from a partially alloyed powder FD-0405: B, bainite; P, pearlite; UP, unresolved pearlite; NR, nickel rich region; NRF, nickel rich ferrite; M, martensite

Prealloyed low-alloy steel powders are particularly useful in the manufacture of P/M parts designed for high-performance applications. Combinations of molybdenum, manganese, and nickel are added to molten iron during the steelmaking process to produce a chemically uniform powder. Practices are followed during melting and atomization to ensure the production of powders with nonmetallic inclusion contents suitable for the most stringent requirements. The reactivity of carbon, in the form of graphite, with the prealloyed powders is excellent, enabling close control of the combined carbon content during sintering. In general, the compressibility of prealloyed powders is lower than that of admixed or partially alloyed powders. However, prealloyed powders in which molybdenum is the principal alloy addition have compressibilities that are comparable to those of iron powders (Ref 15).

Prealloyed powders generally are used for parts that require heat treatment. The hardenability of the prealloyed materials is controlled by the amount and type of alloying employed. Nickel-molybdenum prealloyed powders have lower compressibility than prealloyed powders that use molybdenum alone as the principal alloying agent. Parts made from prealloyed powders have a homogeneous microstructure and uniform apparent hardness. In the as-sintered condition, the carbides that form are not lamellar in nature (compare Fig. 46 with Fig. 32). In the as-sintered condition, prealloyed materials can be identified by this characteristic carbide morphology. In the heat treated condition, parts made from prealloyed powders exhibit a uniform tempered martensitic microstructure (Fig. 47).

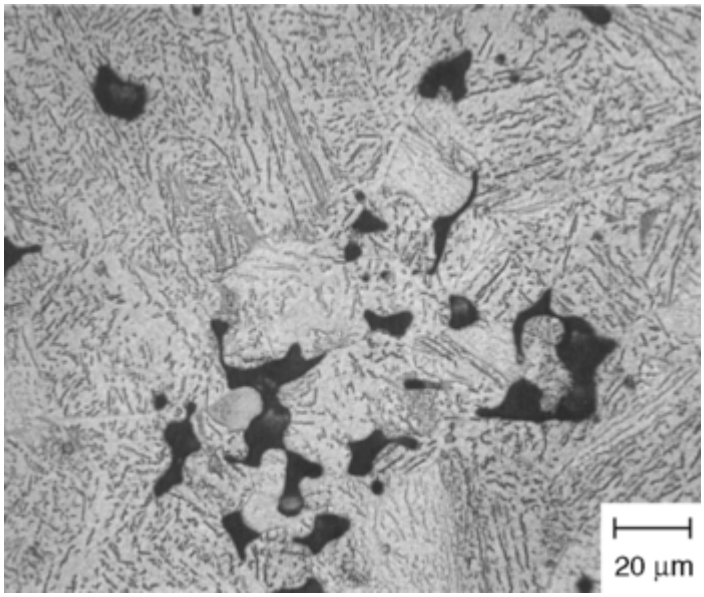

Fig. 46 As-sintered microstructure of a part made from a prealloyed steel material (FL-4405)

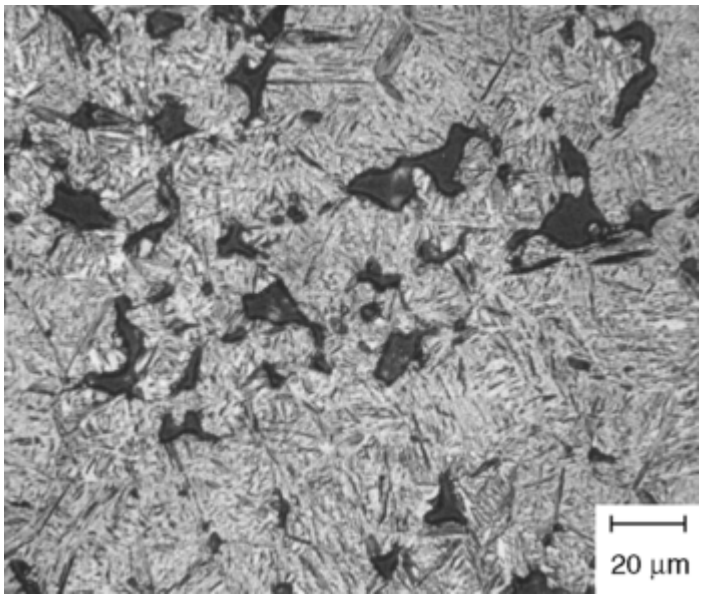

Fig. 47 Tempered martensitic microstructure of a quench-hardened and tempered part made from a prealloyed steel (FL-4605)

Hybrid alloys consist of either prealloyed or partially alloyed base powders to which elemental or ferroalloy additions are made to achieve the desired chemical composition. The practice of making nickel or copper additions to prealloyed powders has become widespread since the introduction of the highly compressible, prealloyed powders with molybdenum as the principal alloy addition.

Sintered Stainless Steels. Stainless steel P/M parts are produced from powders in both the 300 (austenitic) series and the 400 (ferritic) series. The 300 series austenitic alloys are typically used in applications that require good corrosion resistance, while ferritic grades are used in applications that require magnetic properties or good thermal conductivity and/or durability in applications that involve thermal cycling (such as automotive exhaust systems). Substantial quantities of stainless steel powders also are used to make porous materials possessing controlled interconnected porosity.

All commercial compacting-grade stainless steel powders are produced by atomization. Water-atomized powders (with irregular particle shapes) are typically used for conventional pressed-and-sintered parts, while gas-atomized powders (with spherical shapes) are used for high-density consolidation. Although stainless steels powders are virtually always prepared from prealloyed powders, some variants contain added tin or copper for improved corrosion resistance. The 410 materials are often fabricated with 0.15% graphite mixed with

prealloyed powders. This results in such high hardenability that the as-sintered structures are essentially all martensite and require tempering after sintering for optimal properties.

Compared with low-alloy ferrous powders, stainless steel powders require higher compacting pressures and have lower green strength. Stainless steel powders with lower carbon and nitrogen contents also improve compressibility and compactibility (green strength). Powder annealing also improves green strength at similar carbon + nitrogen levels. Medium-density stainless steels are typically sintered at ~1120 to 1150 °C (~2050 to 2100 °F), except when improved mechanical properties and corrosion resistance are required. Higher sintering temperatures up to 1315 °C (2400 °F) are used for improved mechanical properties and corrosion resistance. Because carbon lowers corrosion resistance, the lubricant must be completely removed to prevent carbon diffusion into the part.

In the early years of stainless steel parts production, much of the sintering was done in dissociated ammonia at 1120 to 1150 °C (2050 to 2100 °F). Under these conditions, lubricant removal in the preheat zone of the furnace occurs under partial decomposition such that residual carbon contents typically exceed 0.03%. As this residual carbon is not sufficiently removed during low-temperature (<1205 °C, or 2200 °F) sintering, the sintered parts have low corrosion resistance due to the formation of chromium-rich carbides upon cooling. Delubing was, therefore, often done separately in air, which resulted in lower carbon contents because of the more complete combustion of the lubricant. While air delubing reduced the carbon content to more acceptable levels, particularly for austenitic stainless steels, it also was at the expense of increased oxidation.

With higher sintering temperature (>1205 °C, or 2200 °F), the reaction between residual oxygen and carbon is more complete, and delubing is, therefore, preferably completed in a reducing atmosphere. It is partly because of these relationships that stainless steel parts sintered at high temperatures often exhibit better corrosion resistance than those sintered at lower temperatures. For high-temperature vacuum sintering, the reaction between residual carbon and oxygen is even greater so that carbon can even be added, in the form of graphite, to some stainless steels to achieve lower oxygen contents at acceptable carbon contents (Ref 16, 17, 18). Lower oxygen contents are beneficial to both corrosion resistance and dynamic mechanical properties.

The austenitic stainless steels display austenite grains and annealing twins (Fig. 48). A significant concern may be decoration of the grain boundaries with chromium carbides, indicating loss of chromium from solution and reduction in corrosion resistance. For a number of austenitic stainless steels, the maximum carbon content allowable to avoid sensitization is 0.03%. Higher carbon contents are tolerable only if the cooling rate after sintering is high enough to prevent sensitization and if the parts are not subjected to elevated temperatures again such as in welding. Critical cooling rates can be estimated from time-temperature-sensitization curves for wrought austenitic stainless steels. Carbide precipitates can be readily shown with optical microscopy. A properly sintered low-carbon austenitic structure (Fig. 48a) is free of carbide precipitates and has clean and thin grain boundaries with evidence of twinning. Higher-carbon structures show necklace-type (Fig. 48b) or continuous precipitates of chromium-rich carbides in the grain boundaries.

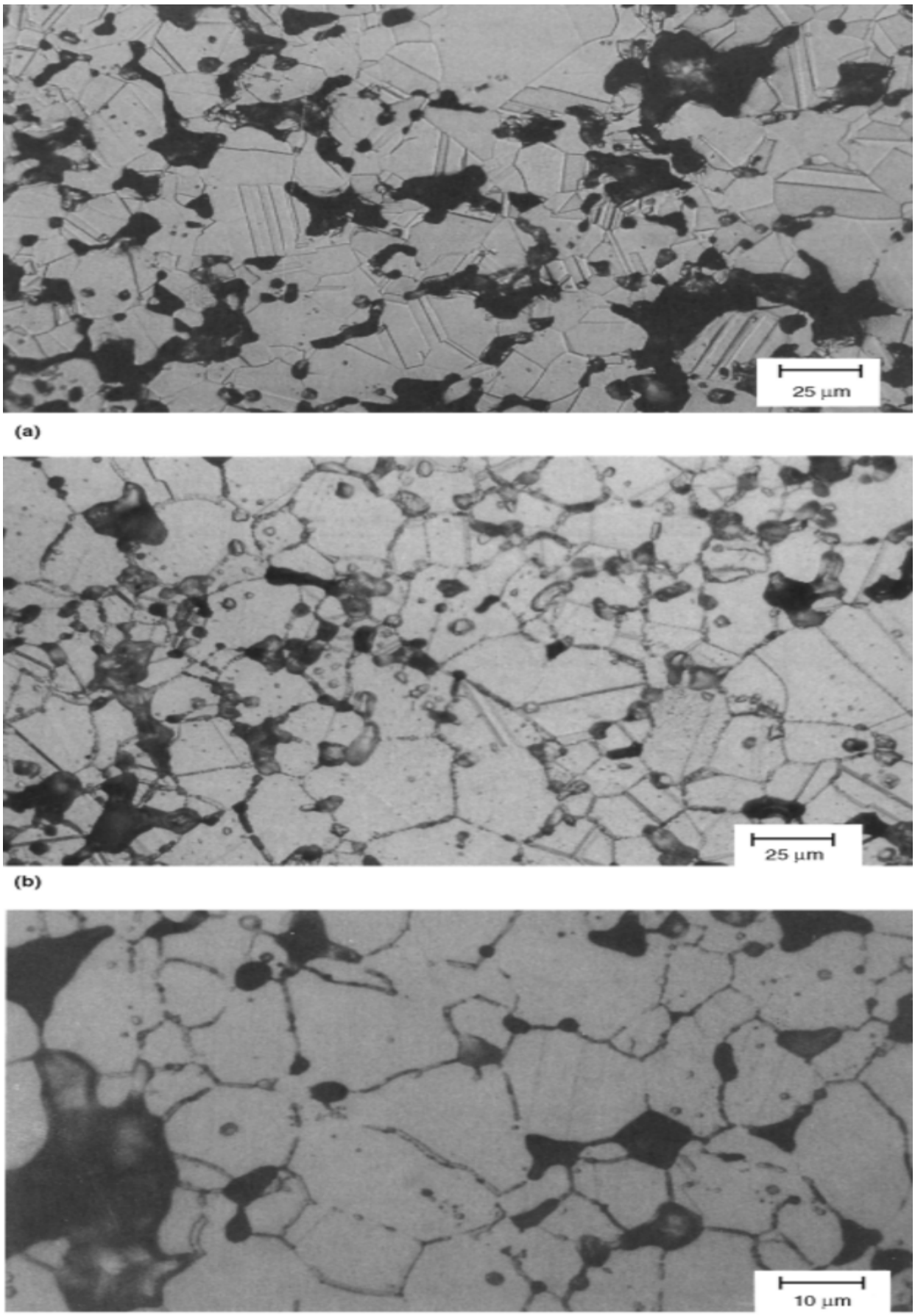

Fig. 48 Microstructures of type 316L stainless steel sintered in hydrogen at 1150 °C (2100 °F) (glyceregia). (a) 0.015% C, clean and thin grain boundaries. (b) 0.07% C, necklace-type chromium-rich carbide precipitates in grain boundaries. (c) 0.11% C, continuous chromium-rich carbide precipitates in grain boundaries

The degree of pore rounding is the most important indication of strength and ductility. High-temperature (1290 °C, or 2350 °F) sintered austenitic stainless steel does not exhibit particle boundaries, and the degree of rounding of the pores must be examined to compare sintering (see Fig. 102–111 in the article “Metallography of Powder Metallurgy Materials” in *Powder Metal Technologies and Applications,* Volume 7 of *ASM Handbook*). Injection-molded parts made of fine powders tend to sinter to a closed-pore state with no original particle boundaries. Powder metallurgy forgings and hot isostatically pressed parts would not display such boundaries.

Ferritic Stainless Steels. The maximum amounts of C + N allowable to avoid sensitization are much lower, namely ~100 to 150 ppm for ferritic stainless steels. Because such low contents of interstitials are difficult to obtain in practice, niobium and/or titanium are often used as stabilizers in wrought ferritics. For P/M versions of ferritic stainless steels, niobium is the stabilizer of choice as niobium becomes less oxidized during water atomization than titanium.

Liquid-Phase Sintering

Liquid-phase sintering (LPS) involves the formation of a liquid phase to promote higher densification rates and lower the sintering temperatures. Because of cost and productivity advantages, it is estimated that more than 70% of sintering products are processed using liquid-phase sintering. An example micrograph from a high-carbon wear-resistant steel (Ancorwear 500) after LPS consolidation is shown in Fig. 49. Common systems for liquid-phase sintering include Cu-Co, W-Cu, W-Ni-Fe, W-Ag, Cu-Sn, Fe-Cu, WC-Co, TiC-Ni, and Fe-Cu-P. Key factors in determining whether a liquid phase forms during sintering of a specific material system include surface energies, solubilities, and diffusivities.

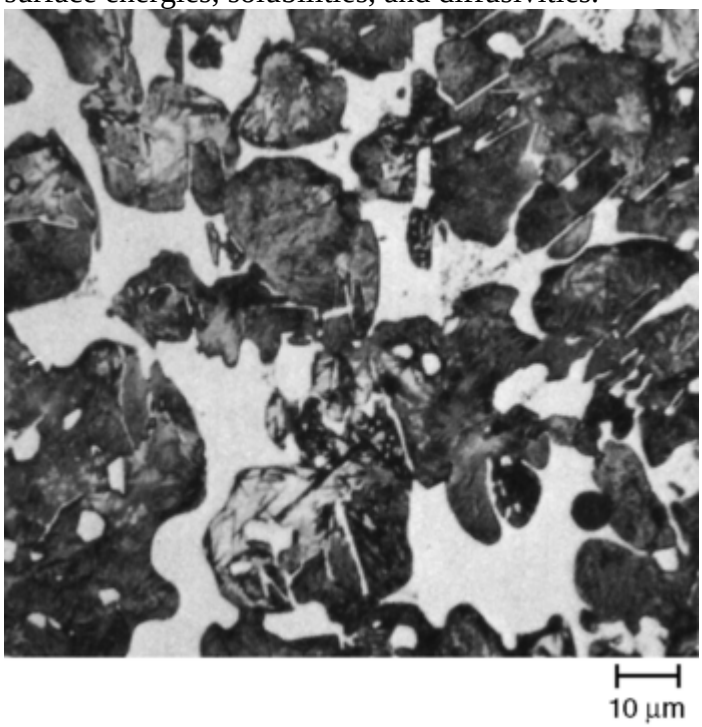

Fig. 49 P/M steel (Fe-5Cr-1Mo-2Cu-0.5P-2.5C) pressed at 550 MPa; liquid-phase sintered 30 min at 1110 °C (2030 °F) in dissociated ammonia to 7.6 g/cm^3. White areas are primary M_3C for wear resistance. 2% nital. 545×. Courtesy of F. Hanejko, Hoeganaes Corporation

There are two main forms of LPS. When a liquid phase is obtained by inducing melting in a mixture of powders and is persistent throughout the high-temperature portion of the sintering cycle, the process is known as persistent LPS. Classic LPS systems such as W-Ni-Fe and WC-Co are excellent examples of LPS with a persistent liquid. A persistent liquid can also be obtained by partially melting a prealloyed powder above its solidus temperature (termed supersolidus LPS, or SLPS) and is widely used for processing tool steels, stainless steels, and superalloys. In some systems (for example, W-Cu and Mo-Cu) with a low intersolubility even in the presence of a persistent liquid, an activator can be used to enhance sintering. This is known as activated liquid-phase sintering (ALPS). Alternatively, transient liquid-phase sintering (TLPS) involves liquid that disappears

due to dissolution into the solid or formation of a new phase/compound. Although each material system has its own set of fabrication concerns, many general LPS concepts can be used to guide their processing.

Phase diagrams are useful in identifying solubility parameters and other characteristics conducive to LPS (Ref 19, 20, 21). An ideal phase diagram for LPS is shown in Fig. 50. A deep eutectic is favorable due to the large reduction in sintering temperature with the formation of the liquid phase. The formation of intermediate compounds is generally unfavorable. High-temperature phases can lower diffusion rates, while brittle intermetallic phases that form during cooling can degrade mechanical properties. Phase diagrams also indicate the tendency of alloying elements and impurities to segregate to grain boundaries. The greater the separation of the solidus and the liquidus, the greater the solute segregation to interfaces. A downward sloping liquidus and solidus also indicate a tendency for solute segregation and lower surface energies (Ref 22). A sintering temperature just above the eutectic temperature is optimal for a composition in the L + β region. A classical LPS microstructure for such a case, as shown in Fig. 51, consists of relatively large, rounded grains suspended in a liquid matrix, with the degree of grain contact governed by the dihedral angle.

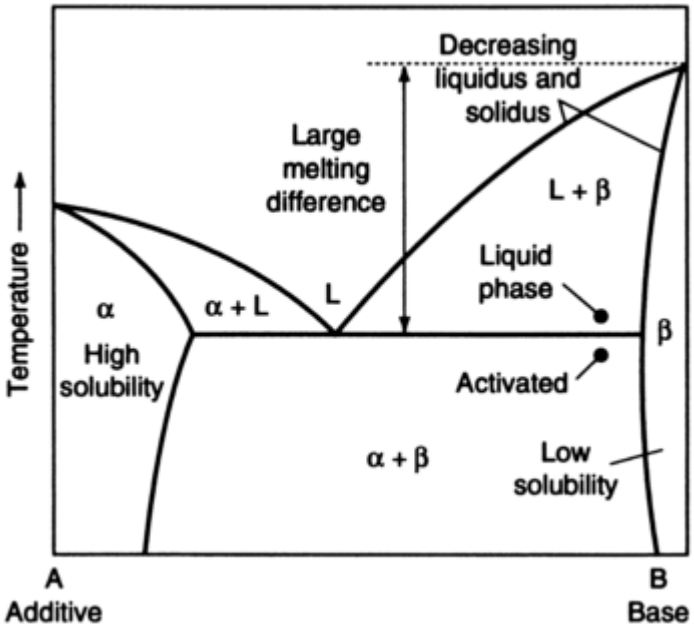

Fig. 50 Phase diagram of an ideal system for liquid-phase sintering

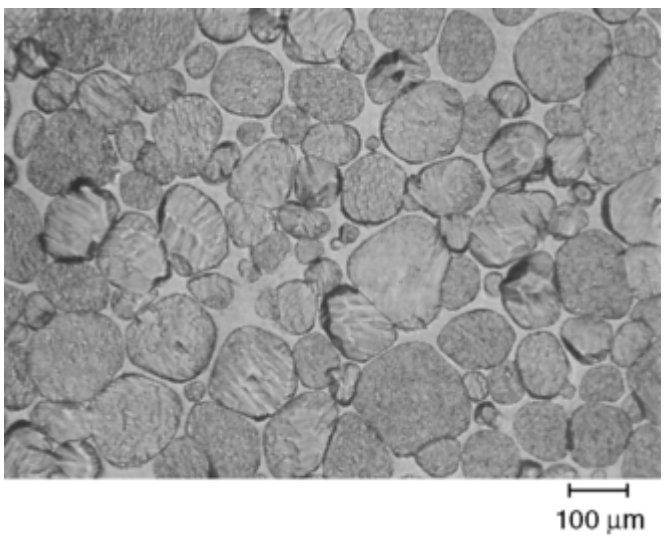

Fig. 51 Typical microstructure of a liquid-phase sintering system with the phase diagram characteristics shown in Fig. 51

For systems that lack solubility of the solid in the liquid phase, a rigid skeletal structure is expected with densification governed by solid-state diffusion. High sintered densities are possible with the use of extremely fine starting powders or by using segregating activators that enhance solid-state sintering in the presence of the

liquid phase. These techniques are covered in more detail in the section “Activated Liquid-Phase Sintering” in the article “Liquid-Phase Sintering” in *Powder Metal Technologies and Applications,* Volume 7 of *ASM Handbook.*

Infiltration

Infiltration is a method of producing substantially pore-free material by filling interconnected porosity (commonly known as the matrix) with another metal of lower melting point (commonly known as infiltrant). During infiltration, a liquid metal mass or front moves through or penetrates the pore system of a solid-phase powder compact. This process is similar to liquid-phase sintering, in which one of the constituent powders of a compact melts and disperses throughout the compact in situ. Voids are filled by shrinkage and particle rearrangement. During infiltration, liquid externally contacts the porous solid, and capillary forces draw it inward. Reduction of total surface-free energy of the system is a prerequisite during infiltration and determines whether a particular solid-liquid phase system is suitable for infiltration.

The two most important classes of materials that are manufactured via infiltration methods are copper- and silver-infiltrated refractory metals and refractory carbides, and copper-infiltrated steels. A variation of capillary-action infiltration at ambient pressure consists of penetration of pores by liquid assisted by external force. Impregnation treatment of this type is widely used to fill pores of sintered products with hydrocarbons, organics, and nonmetallic fillers.

Copper-Infiltrated Steels. High-density iron-carbon alloys with 10 or 20% Cu are prepared by infiltrating the copper alloy into the porous steel matrix. Infiltrants are generally alloys of copper with iron, zinc, and manganese (Ref 23). Upon sintering and infiltrating, the copper alloy melts and flows into the iron-carbon matrix with which it is in contact. The copper tends to fill the highest-density, smallest-capillary regions of the matrix first. The coarse-pored lowest-density regions are filled last with whatever liquid copper remains. The structure often appears as islands of ferrite and pearlite with a continuous copper-alloy phase. The alloy of copper may include such elements as manganese and cobalt, which dissolve in iron and alter the alloy content of the steel matrix. Manganese increases the hardenability of the matrix. Elemental nickel contained in the matrix goes into solution in iron and copper, greatly increasing hardenability. Such materials may exhibit regions of martensite, even as furnace cooled.

Infiltration can be either combined with the sintering step (one step) or can be carried out separately (two steps), where sintering of the matrix is carried out separately prior to infiltration. In the single-step process when the parts are infiltrated during sintering, it is extremely important for the green compact to be properly delubricated prior to reaching the high heat zone of the sintering furnace. Improper delubrication will lead to problems with infiltration. In double-step infiltration, parts are sintered and cooled to room temperature under a protective atmosphere. Infiltrant slugs are then positioned, and the parts are subjected to a second sintering operation during which infiltration of the interconnected porosity occurs. Some parts have selected areas infiltrated to enhance properties in critical areas, a process known as selective infiltration.

Conventional (partial) infiltration results in infiltrated density of about 93 to 94% pore-free. Areas of low green density, which usually contain large pores, remain uninfiltrated because of their weak capillarity. Fully infiltrated steels (with properties similar to those of the lower range of wrought steels) can be obtained if the infiltration process is conducted so that practically all pores are infiltrated. Full infiltration requires careful control of defects through:

- Selection of high-purity powders and erosion-free copper infiltrants
- Processing that controls maximum pore size
- Processing that ensures complete infiltration of the largest pores present
- Heat treatments which produce microstructures that give rise to ductile fracture (dimple rupture)

Residue adherence is minimized by selecting an infiltrant/matrix ratio that provides for full infiltration without an excess of copper. Figure 52 shows the microstructures of a conventionally and a fully infiltrated steel, respectively.

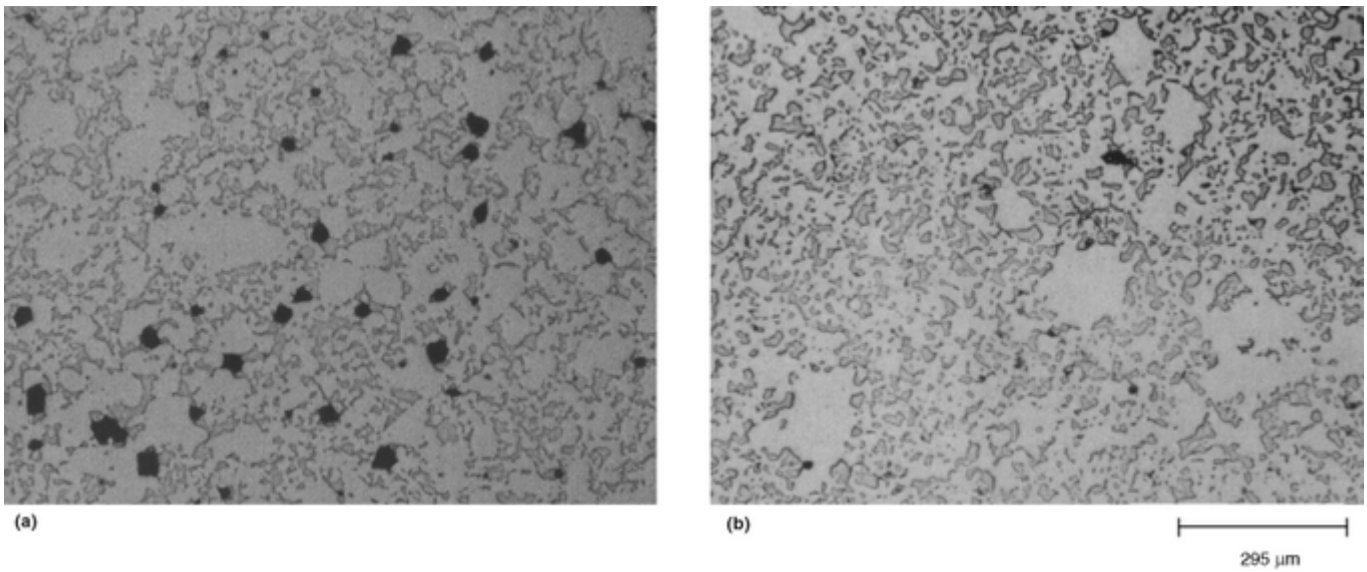

Fig. 52 Microstructures of (a) conventionally (partially) infiltrated steel showing the degree of pore filling and (b) fully infiltrated steel showing completeness of pore filling. Unetched. 75×

Tool steels

Powder metallurgy tool steels have long been used for tooling components such as punches and dies. These materials are produced by hot isostatic pressing of water-atomized tool steel powders, resulting in a fully dense product with fine grain size and very fine, uniform carbide size. The product displays grindability that is superior to ingot-base tool steels. Such alloys as M2 and T15 are also available in molding grade powders. In addition to hot isostatic pressing, P/M tool steels can be fabricated by pressing to approximately 80% density, followed by vacuum sintering to full density. Tool steel powders of the M2 and T15 compositions can be cold pressed at 550 to 825 MPa (40 to 60 tsi), then liquid-phase sintered to full density. For M2, sintering requires 1 h in vacuum at 1240 °C (2260 °F) at 100 to 1000 μm nitrogen or argon; T15 takes 1 h at 1260 °C (2300 °F) in the same vacuum. Temperature control within 5 °C (9 °F) may be required for product uniformity. The as-sintered T15 structures contain retained austenite, because of the high amount of carbon in solution, as well as primary M_6C and fine MC (vanadium carbide). The M_2 structures contain mainly M_6C of varying small sizes against a matrix of retained austenite. The martensite start, M_s, temperature for these materials with the high carbon in solution is below room temperature. Upon annealing, the carbon precipitates out of solution onto the M_6C phase, reducing the carbon in the matrix. This structure may then be heat treated at 1150 to 1205 °C (2100 to 2200 °F), but heating and cooling times must be minimized to avoid putting too much carbon back into solution. Upon furnace cooling or air cooling, the matrix then forms martensite with the proper distribution of fine carbides.

The distinguishing characteristic of wrought P/M high-alloy tool steels compared to conventionally ingot cast and wrought materials of similar compositions is the uniform distribution and small size of the primary carbides that form in the P/M tool steels during rapid solidification of the powder particles during atomization from the melt. The P/M microstructure shown would appear essentially the same for all product cross sections, while larger cross sections of high-alloy conventional tool steels exhibit inherently coarser carbides and a more pronounced carbide network due to slow ingot solidification and insufficient hot working to break up the as-cast structure. For similar reasons, sulfides in P/M tool steels are smaller and more uniformly distributed than in conventional wrought steels from ingot. The ability to resulfurize to very high levels without detrimentally affecting hot workability or transverse toughness properties is a distinct advantage for P/M processing, and it is done routinely for P/M tool steel applications requiring good machinability.

Porous P/M materials

Using similar manufacturing equipment and technology as structural P/M components, porous P/M materials are normally sintered to densities between 25 and 85% of the pore-free density. Structural P/M components are typically 85 to 99.9% pore free. These unique engineered materials provide specialized products for

applications such as filtration, fluid-flow control, self-lubricating bearings, spargers, and battery electrodes. The four most common porous P/M materials are bronze, stainless steel, nickel, and nickel-base alloys. Other materials such as titanium, aluminum, copper, platinum, gold, silver, iron, iron aluminide (Fe_3Al), niobium, tantalum, and zirconium are fabricated into porous materials from powder. Figure 53 and Figure 54 are micrographs of a gravity-sintered porous bronze.

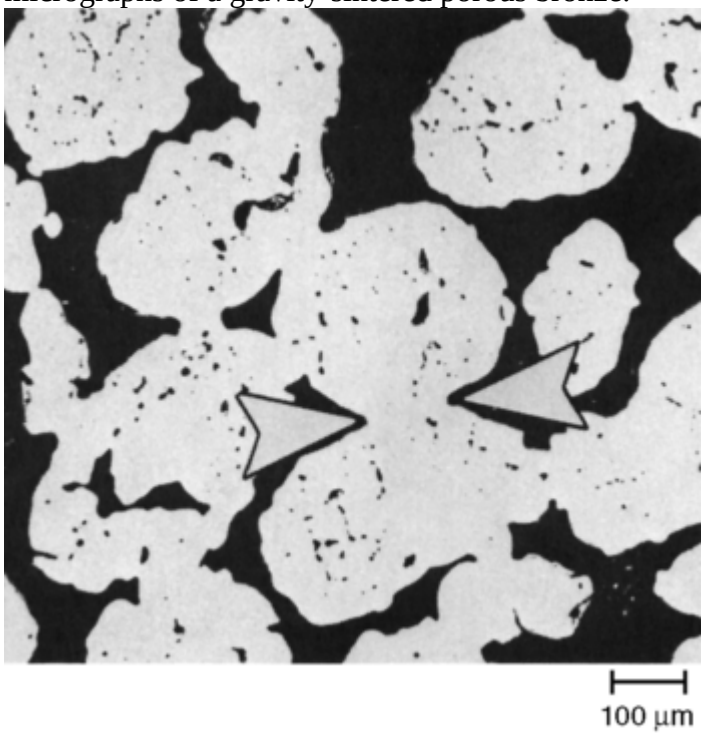

Fig. 53 Cu-8Sn filter powder, gravity sintered 30 min at 870 °C (1600 °F) in dissociated ammonia. Arrows N show bonding between particles. Dark areas are pores filled with epoxy. As-polished. 65×

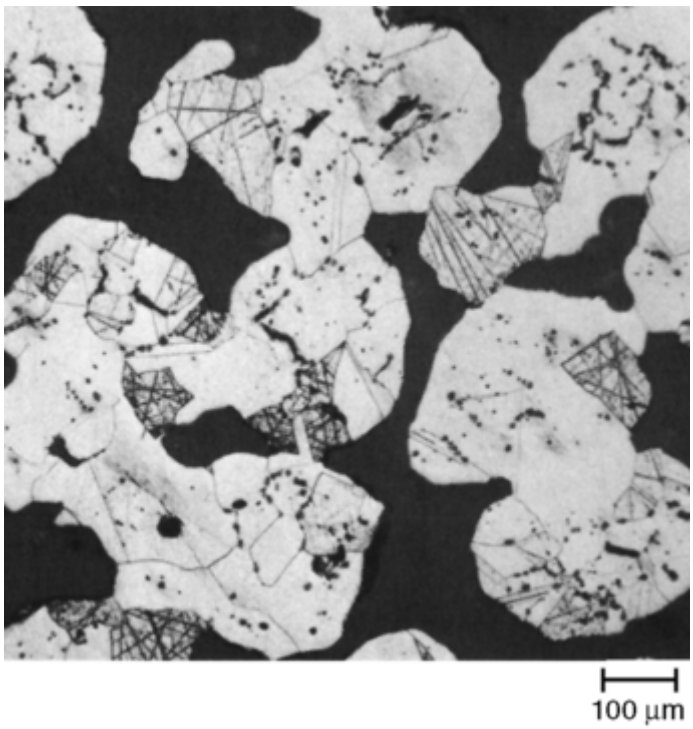

Fig. 54 Same as Fig. 53 but etched, showing well-sintered α-bronze grains. Cross-hatched grains result from residual scratches and etching. $K_2Cr_2O_7$. 65×

Nonferrous P/M Materials

Copper-base alloys include pure copper for high-density electrical applications: 90Cu-10Sn bronzes for bearings and structural parts; brasses with 10, 20, and 30% Zn; and nickel silver (Cu-18Zn-18Ni). The brasses and nickel silvers are used for structural parts that require ductility, moderate strength, corrosion resistance, and decorative value.

Copper exhibits a single-phase structure with some annealing twins. The most significant feature is the presence or absence of particle boundaries. There should be virtual freedom from particle boundaries from the surface to the center of the part.

Bronzes should display all α-bronze with no blue-gray copper-tin intermetallic compounds. Optimal mechanical properties and machinability dictate a minimum of reddish copper-rich areas and small grain clusters of bronze (Fig. 55). Mixes containing admixed graphite show the mottled gray flakes in the pores of the part (Fig. 56). Bearings exhibit varying degrees of sintering, depending on the final application. In general, however, a well-sintered bearing results in greater ease of oil impregnation.

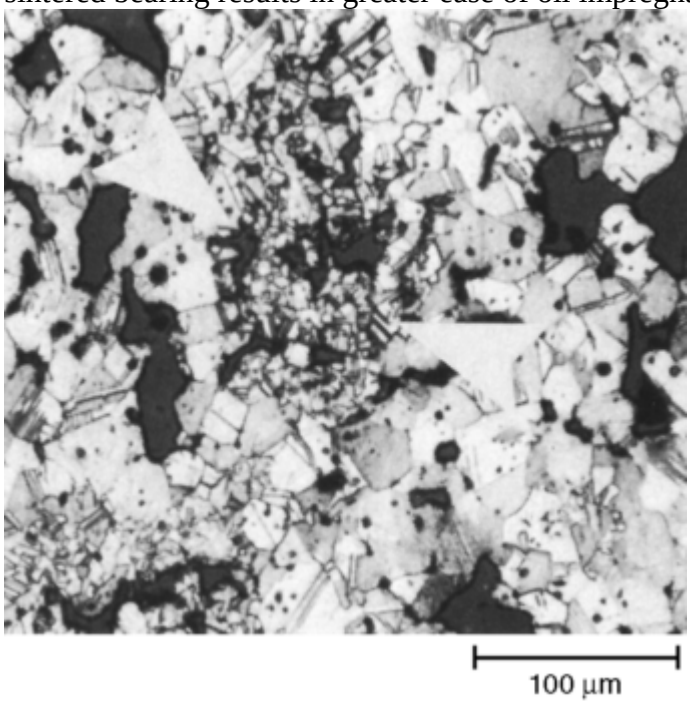

Fig. 55 Bronze (Cu-10Sn, 6.4 g/cm^3) pressed at 140 to 205 MPa (10 to 15 tsi), sintered (conditions not known), and sized for tolerances. Mostly all α-bronze grains. Gray areas are pores. Arrows indicate clusters of small grains that have not grown into larger α grains. $K_2Cr_2O_7$. 180×

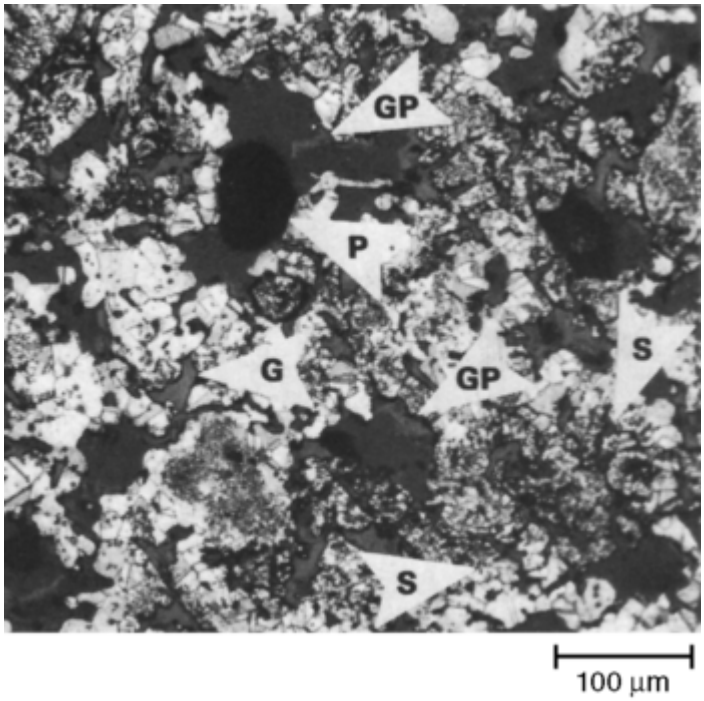

Fig. 56 Bronze (Cu-10Sn) with 4% graphite pressed at 165 to 205 MPa (12 to 15 tsi) to 6.4 g/cm^3, sintered 15 min at 845 °C (1550 °F), and sized. Arrows GP show graphite in pores surrounded by darker gray epoxy resin; arrow G, graphite flake in the matrix. Arrows S surround a small grain cluster; arrow P indicates a pore. $K_2Cr_2O_7$. 120×

Brasses and nickel silvers are generally single-phase structures. They should display good pore rounding and almost no original particle boundaries. Some of the materials may contain up to 2% Pb within the particles as an aid to machinability; this will appear as a fine, rounded gray phase.

Titanium and titanium alloys such as Ti-6Al-4V are produced from metal powders in several ways. The powders may be prealloyed or may be an admixture of blended elemental (BE) powders of titanium and a master alloy of vanadium and aluminum. The latter can be pressed and vacuum sintered to an impermeable state, which may then be hot isostatically pressed to full density without a can. The prealloyed materials may be vacuum hot pressed or preformed, canned, and hot isostatically pressed to full density. Titanium alloys can also be consolidated by metal injection molding.

Postcompaction treatment of titanium P/M alloys are used for microstructure refinement to improve tensile and fatigue strengths. In most cases, process economics do not allow subsequent working because it nullifies the objectives of a true net-shape technology. Therefore, postcompaction methods leading to microstructure refinement are typically of two types: heat treatment and thermochemical processing (TCP). In the case of BE Ti-6Al-4V, the only successfully used heat treatment has been the broken-up structure (BUS) treatment in which a β quench is followed by 850 °C (1560 °F) long-term annealing (Ref 24). After such treatment, the microstructure of the alloy is showing broken-up α phase in a matrix of β (Fig. 57).

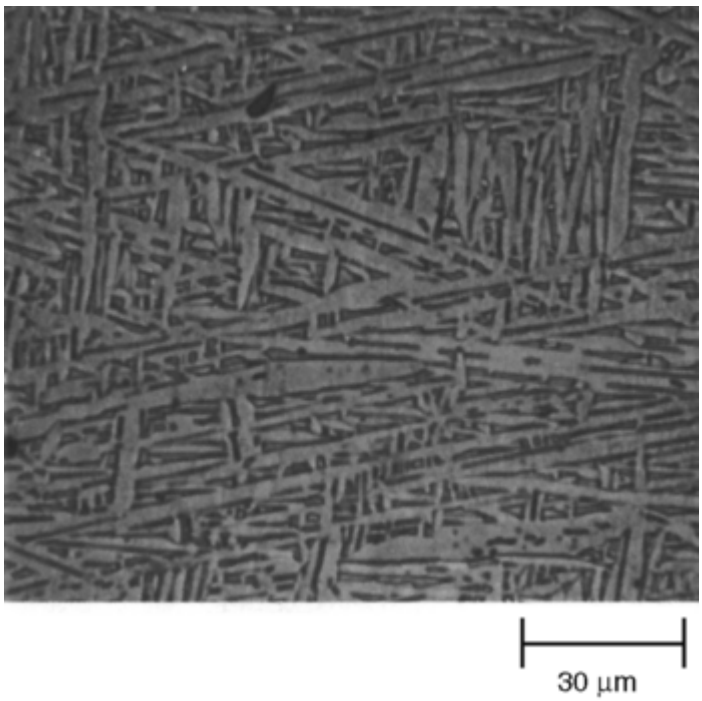

Fig. 57 Micrograph of Ti-6Al-4V BE compact treated to produce a broken-up structure

The TCP method (Ref 25) involves the use of hydrogen as a temporary alloying element to refine the microstructure of titanium alloys. This method is very suitable for net-shape products because no hot or cold work is needed to refine the microstructure. An example of the refinement obtained in Ti-6Al-4V P/M products can be seen in Fig. 58. This microstructural refinement provides slightly higher strength levels than those typically obtained in ingot metallurgy or conventional P/M materials.

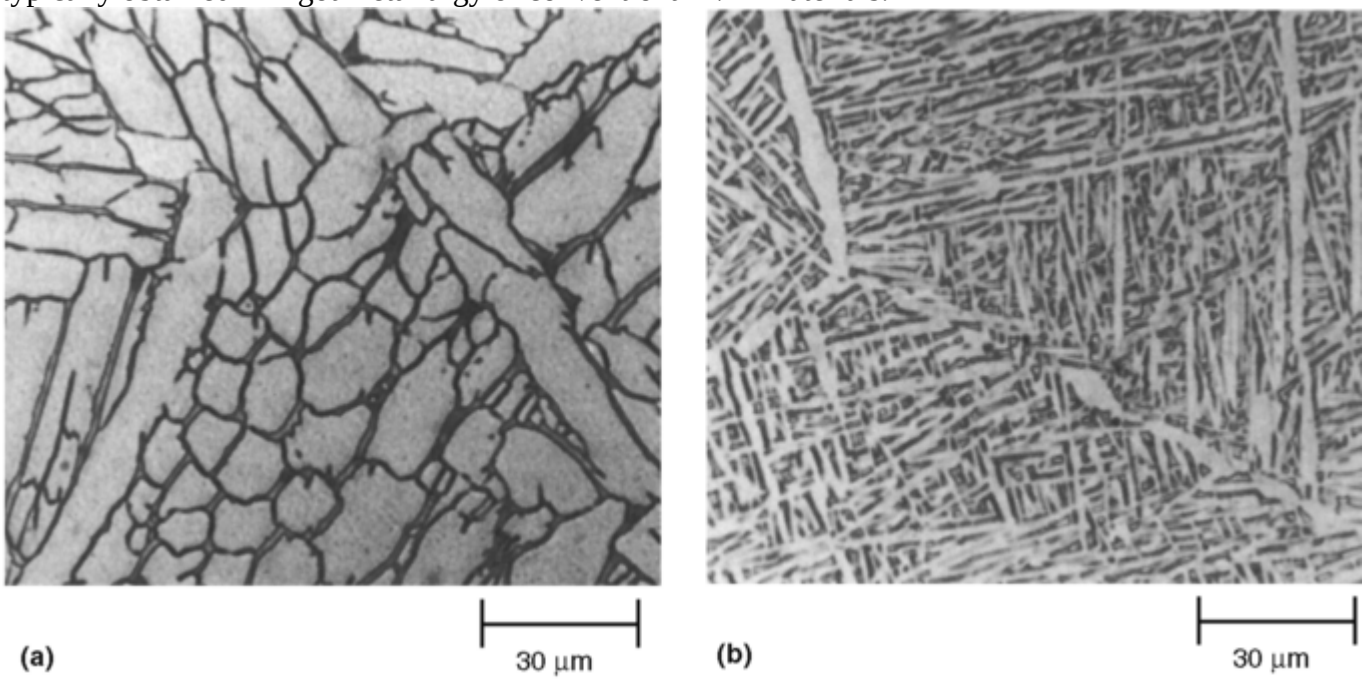

Fig. 58 Micrographs of Ti-6Al-4V BE compact. (a) Fully dense, pressed-and-sintered, and hot isostatically pressed compact. (b) Compact treated with thermochemical processing

Aluminum P/M alloys are pressed and sintered to 90 to 95% density. The common alloys are 201AB and 601AB. The alloys are prepared using low-alloy aluminum powder with additions of elemental or master alloy copper, magnesium, and silicon. During sintering, the additions cause a liquid phase to form that fluxes away the surface oxides and allows bonding between the aluminum particles. Sintering in nitrogen is performed at approximately 595 or 620 °C (1100 or 1150 °F) at a dewpoint of -50 °C (-60 °F) to prevent further oxidation of

the aluminum. After sintering, the alloys are often solutionized and quenched, then re-pressed before aging. The re-pressing densifies the material and establishes close dimensional tolerances. The materials may also be cold forged or rolled to varying reductions in thickness because of their favorable as-sintered ductility.

Secondary Processes

Steam Blackening of P/M Steels. Powder metallurgy parts can be finished by steam blackening. The degree of blackening, which should be controlled, generally lowers impact and tensile properties (Ref 26). The gray Fe_3O_4 layer (Fig. 59) penetrates the pores and increases compressive strength and abrasive wear resistance. The thickness of the oxide layer can be measured metallographically, 3–6 μm (0.0001–0.0002 in.).

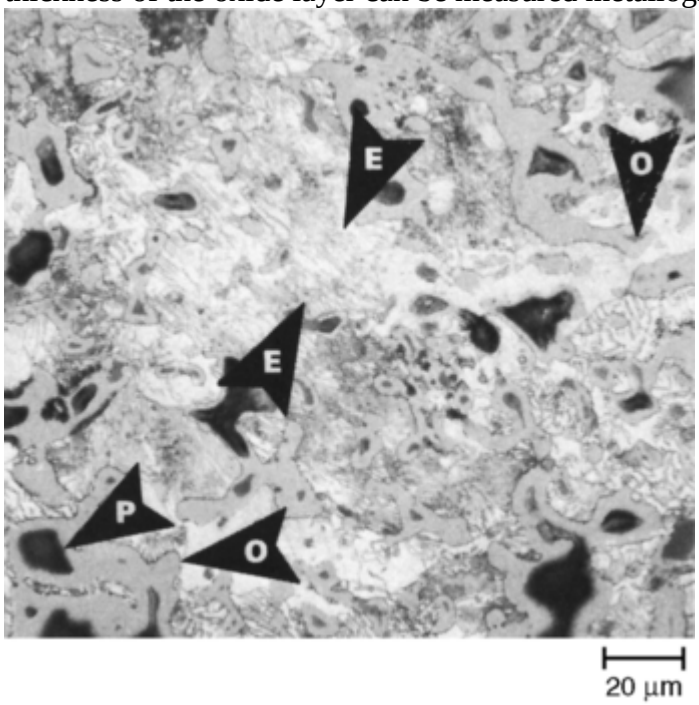

Fig. 59 Pressed-and-sintered Fe-0.8C steel (6.4 g/cm^3) that was steam blackened. The pores are nearly all filled with gray Fe_3O_4 (arrows O). Arrow P shows a pore not filled with oxide. Arrows E surround a eutectoid region. White areas are ferrite. 2% nital. 365×

Impregnation. Most P/M parts that are to be plated are first impregnated with a resin to prevent the corrosive plating solutions from entering and remaining in the pores. The resin is visible using optical metallography. The various plated layers are also visible, but polishing should be limited to 3 and 1 μm diamond on a short-nap (DAC) cloth to prevent rounding of the plated edge. To examine the original resin in the pores, the part should be mounted in an epoxy resin of contrasting color, for example, red. Also, impregnation with the red epoxy of a specimen that has no existing resin in the pores allows the epoxy resin to be easily seen. The gray epoxy resins are difficult to image in the light microscope. Often, unfilled pores look dark or filled with debris. An epoxy-filled pore allows one to look through the epoxy at 1000× and see a specular reflection off the bottom.

References cited in this section

8. A. Ŝalak, *Ferrous Powder Metallurgy,* Cambridge International Science Publishing, 1995

13. L.F. Pease III and W. West, Fundamentals of Powder Metallurgy, Metal Powder Industries Federation, 2002

14. W.B. James, G.T. West, Ferrous Powder Metallurgy Materials, *Powder Metal Technologies and Applications,* Vol 7, *ASM Handbook,* ASM International, 1998, p 756

15. W.B. James, Recent Developments in Ferrous Powder Metallurgy Alloys, *Int. J. Powder Metall.*, Vol 30 (No. 2), 1994, p 157–162

16. E. Klar and P.K. Samal, Optimization of Vacuum Sintering Parameters for Improved Corrosion Resistance of P/M Stainless Steels, *Advances in Powder Metallurgy and Particulate Materials*, Vol 7, Metal Powder Industries Federation, 1994, p 239–251

17. T. Tunberg, L. Nyborg, and C.X. Liu, Enhanced Vacuum Sintering of Water-Atomized Stainless Steel Powder by Carbon Addition, *Advances in Powder Metallurgy and Particulate Materials*, Vol 3, 1992, p 383–396

18. R.M. Larsen and K.A. Thorsen, Removal of Oxygen and Carbon During Sintering of Austenitic Stainless Steels, *Proc. of 1993 Powder Metallurgy World Congress Part 1* (Kyoto, Japan), p 377–380

19. R.M. German, The Identification of Enhanced Sintering Systems through Phase Diagrams, *Modern Developments in Powder Metallurgy*, Vol 15, E.N. Aqua and C.I. Whitman, Ed., Metal Powder Industries Federation, 1985, p 253–273

20. R.M. German and B.H. Rabin, Enhanced Sintering through Second Phase Additions, *Powder Met.*, Vol 28, 1985, p 7–12

21. C.M. Kipphut and R.M. German, Alloy Phase Stability in Liquid Phase Sintering, *Sci. Sintering*, Vol 20, 1988, p 31–41

22. J.J. Burton and E.S. Machlin, Prediction of Segregation to Alloy Surfaces from Bulk Phase Diagrams, *Phys. Rev. Lett.*, Vol 37, 1976, p 1433–1436

23. A.N. Ashurst, E. Klar, and H.R. McCurdy, Copper Infiltration of Steel—Part 1, Properties, *Met. Powder, Rep.*, June 1984, p 329; Copper Infiltration of Steel—Part 2, Applications, *Met. Powder Rep.*, Aug, 1984, p 438

24. D. Eylon, R.G. Vogt, and F.H. Froes, Property Improvement of Low Chlorine Titanium Alloy Blended Elemental Powder Compacts by Microstructure Modification, *Progress in Powder Metallurgy*, Vol 42, compiled by E.A. Carlson and G. Gaines, Metal Powder Industries Federation, 1986, p 625-634

25. F.H. Froes and D. Eylon, Thermochemical Processing (TCP) of Titanium Alloys by Temporary Alloying with Hydrogen, *Hydrogen Effects on Material Behavior*, A.W. Thompson and N.R. Moody, Ed., The Metallurgical Society, 1990

26. L.F. Pease III, J. Collette, and D.A. Pease, Mechanical Properties of Steam Blackened P/M Materials, *Modern Developments in Powder Metallurgy*, Vol 18–21, Metal Powder Industries Federation, 1988, p 275

L.F. Pease III and D.L. Pease, Metallography and Microstructures of Powder Metallurgy Alloys, *Metallography and Microstructures,* Vol 9, *ASM Handbook,* ASM International, 2004, p. 994–1020

Metallography and Microstructures of Powder Metallurgy Alloys

Leander F. Pease III and Douglas L. Pease, Powder-Tech Associates, Inc.

Acknowledgments

Portions of this article contain content adapted from the following articles in *Powder Metal Technologies and Applications,* Volume 7 of *ASM Handbook,* (1998):

- Metallography of Powder Metallurgy Materials, pages 719–748, by Leander F. Pease III and Douglas L. Pease
- Ferrous Powder Metallurgy Materials, pages 751–768 by W.B. James and G.T. West
- Copper-Infiltrated Steels, pages 769–773, by Prasan K. Samal and Erhard Klar
- High-Temperature Sintering of Ferrous Powder Metallurgy Components, pages 828–833, by Howard I. Sanderow
- Sintering of Stainless Steel, pages 476–482, by E. Klar and P.K. Samal
- Liquid-Phase Sintering, pages 565–573, by Rajiv Tandon and John Johnson
- Particle Image Analysis, page 259–273

L.F. Pease III and D.L. Pease, Metallography and Microstructures of Powder Metallurgy Alloys, *Metallography and Microstructures,* Vol 9, *ASM Handbook,* ASM International, 2004, p. 994–1020

Metallography and Microstructures of Powder Metallurgy Alloys

Leander F. Pease III and Douglas L. Pease, Powder-Tech Associates, Inc.

References

1. "Standard Test Method for Density and Interconnected Porosity of Sintered Powder Metal Structural Parts and Oil-Impregnated Bearings," B 328, *Annual Book of ASTM Standards,* Vol 2.05, ASTM, 1998

2. "Permeable Sintered Metal Materials, Determination of Density, Open Porosity and Oil Content," ISO 2738, International Organization for Standardization, American National Standards Institute

3. G.A. Blann et al., Principles and Practices for Metallographic Preparation for Powder Metallurgy, *Microstr. Sci.,* Vol 22, 1995, p 135

4. L.F. Pease III, Metallography of Powder Metallurgy Materials, *Powder Metal Technologies and Applications,* Vol 7, *ASM Handbook,* ASM International, 1998, p 722–723

5. L.F. Pease III, Metallography and Properties of Sintered Steels, *Progress in Powder Metallurgy,* Vol 33, Metal Powder Industries Federation, 1977

6. O. Struglics, Hoeganaes Corporation, Hoeganaes, Sweden, personal communication

7. S. Coleman and D. Tomkins, A Quantitative Assessment of the Mechanical Properties of Sintered Iron Micrographic Specimens, *Powder Metall.,* No. 2, 1976, p 53

8. A. Ŝalak, *Ferrous Powder Metallurgy,* Cambridge International Science Publishing, 1995

9. "Standard Method of Sampling Finished Lots of Metal Powders," B 215, *Annual Book of ASTM Standards,* Vol 2.05, ASTM, 1998

10. "Effective Case Depth of Powder Metallurgy Products, Determination of," Standard 52, Metal Powder Industries Federation

11. S. Kaufmann, Ford Motor Company, Dearborn, MI, personal communication

12. P. Schmey, United States Bronze Powders, Inc., Flemington, NJ, personal communication

13. L.F. Pease III and W. West, Fundamentals of Powder Metallurgy, Metal Powder Industries Federation, 2002

14. W.B. James, G.T. West, Ferrous Powder Metallurgy Materials, *Powder Metal Technologies and Applications,* Vol 7, *ASM Handbook,* ASM International, 1998, p 756

15. W.B. James, Recent Developments in Ferrous Powder Metallurgy Alloys, *Int. J. Powder Metall.,* Vol 30 (No. 2), 1994, p 157–162

16. E. Klar and P.K. Samal, Optimization of Vacuum Sintering Parameters for Improved Corrosion Resistance of P/M Stainless Steels, *Advances in Powder Metallurgy and Particulate Materials,* Vol 7, Metal Powder Industries Federation, 1994, p 239–251

17. T. Tunberg, L. Nyborg, and C.X. Liu, Enhanced Vacuum Sintering of Water-Atomized Stainless Steel Powder by Carbon Addition, *Advances in Powder Metallurgy and Particulate Materials,* Vol 3, 1992, p 383–396

18. R.M. Larsen and K.A. Thorsen, Removal of Oxygen and Carbon During Sintering of Austenitic Stainless Steels, *Proc. of 1993 Powder Metallurgy World Congress Part 1* (Kyoto, Japan), p 377–380

19. R.M. German, The Identification of Enhanced Sintering Systems through Phase Diagrams, *Modern Developments in Powder Metallurgy,* Vol 15, E.N. Aqua and C.I. Whitman, Ed., Metal Powder Industries Federation, 1985, p 253–273

20. R.M. German and B.H. Rabin, Enhanced Sintering through Second Phase Additions, *Powder Met.,* Vol 28, 1985, p 7–12

21. C.M. Kipphut and R.M. German, Alloy Phase Stability in Liquid Phase Sintering, *Sci. Sintering,* Vol 20, 1988, p 31–41

22. J.J. Burton and E.S. Machlin, Prediction of Segregation to Alloy Surfaces from Bulk Phase Diagrams, *Phys. Rev. Lett.,* Vol 37, 1976, p 1433–1436

23. A.N. Ashurst, E. Klar, and H.R. McCurdy, Copper Infiltration of Steel—Part 1, Properties, *Met. Powder, Rep.,* June 1984, p 329; Copper Infiltration of Steel—Part 2, Applications, *Met. Powder Rep.,* Aug, 1984, p 438

24. D. Eylon, R.G. Vogt, and F.H. Froes, Property Improvement of Low Chlorine Titanium Alloy Blended Elemental Powder Compacts by Microstructure Modification, *Progress in Powder Metallurgy*, Vol 42, compiled by E.A. Carlson and G. Gaines, Metal Powder Industries Federation, 1986, p 625-634

25. F.H. Froes and D. Eylon, Thermochemical Processing (TCP) of Titanium Alloys by Temporary Alloying with Hydrogen, *Hydrogen Effects on Material Behavior*, A.W. Thompson and N.R. Moody, Ed., The Metallurgical Society, 1990

26. L.F. Pease III, J. Collette, and D.A. Pease, Mechanical Properties of Steam Blackened P/M Materials, *Modern Developments in Powder Metallurgy*, Vol 18–21, Metal Powder Industries Federation, 1988, p 275

L.F. Pease III and D.L. Pease, Metallography and Microstructures of Powder Metallurgy Alloys, *Metallography and Microstructures*, Vol 9, *ASM Handbook*, ASM International, 2004, p. 994–1020

Metallography and Microstructures of Powder Metallurgy Alloys

Leander F. Pease III and Douglas L. Pease, Powder-Tech Associates, Inc.

Selected References

- P. Beiss, K. Dalal, and R. Peters, *International Atlas of Powder Metallurgical Microstructures*, Metal Powder Industries Federation, 2002
- W.J. Hupmann and K. Dalal, *Metallographic Atlas of Powder Metallurgy*, Verlag Schmid, GmbH, 1986
- *Metallographic Handbook, Ferrous Powder Metallurgy*, Hoeganaes Corporation, 1995
- G.F. Vander Voort, *Metallography: Principles and Practice*, McGraw Hill, 1984, reprinted by ASM International, 1999

E.J. Vinarcik, Metallography and Microstructures of Semisolid Formed Alloys, *Metallography and Microstructures,* Vol 9, *ASM Handbook*, ASM International, 2004, p. 1021–1037

Metallography and Microstructures of Semisolid Formed Alloys

Edward J. Vinarcik

Introduction

SEMISOLID METALWORKING is a forming process in which a partially liquid/partially solid metal mixture is injected into a die or mold and allowed to solidify. Although the origins of semisolid metalworking can be traced back to the 1970s, the process did not become commercialized for high-volume production until the early to mid-1990s. The process was developed at the Massachusetts Institute of Technology as an outgrowth from casting defect research (Ref 1, 2). When inducing hot tears in aluminum castings, researchers found that the partially solidified alloy exhibited thixotropic properties. Material that is heated to a semisolid state can be sheared and formed easily. Depending on the solid fraction of the mixture, a billet heated to the semisolid state can retain its structure, yet be cut with a dull knife (Fig. 1). A billet heated to a lower solid fraction will lose its rigidity and puddle with the consistency of a hot breakfast cereal.



Fig. 1 Aluminum billet cut using a knife while in a semisolid state. Courtesy of John Jorstad

With an understanding of semisolid metal behavior, several new net-shape manufacturing processes were developed based on closed-die forging, die casting, extrusions, rolling, and hybrids of these processes (Ref 1, 2, 3). Since its conception, semisolid metalworking has been applied to numerous metal alloy systems including aluminum, magnesium, zinc, titanium, and copper, as well as numerous ferrous alloys. In general, any alloy with a wide freezing range is suitable for use in semisolid metalworking. Most semisolid metalworking processes in use today parallel high-pressure die casting. As such, aluminum and magnesium are the dominant alloy systems processed using semisolid metalworking methods.

From an economic standpoint, semisolid metalworking processes can be more costly due to the equipment and energy costs associated with preparing semisolid metal. However, in certain applications this additional investment results in a total lower cost through reduced scrap rates and less wear on dies. The integrity of components manufactured with semisolid technology, however, is much improved in comparison to conventional die-casting components. Semisolid metalworking extends the capabilities of conventional die casting by:

- Reducing the amount of entrapped gases due to planar die filling
- Reducing the amount of solidification shrinkage due to a high solid fraction during forming
- Creating a nondendritic microstructure in the manufactured component

Unlike products manufactured using traditional casting methods, the microstructure of products manufactured using semisolid metalworking is not dendritic. During processing, the dendritic structure is broken up and evolves into a spheroidal structure. The mechanical properties of the spheroidal microstructure is superior to those found in castings with dendritic microstructures as reported in numerous case studies (Ref 1, 4, 5). In many cases, the strength of products produced using semisolid metalworking rivals that of forgings.

References cited in this section

1. M. Flemings, Behavior of Metal Alloys in the Semisolid State, *Metall. Trans. B,* 1991, p 269

2. M. Keeney et al., Semisolid Metal Casting and Forging, *Casting,* Vol 15, *ASM Handbook,* ASM International, 1988, p 327

3. A. Alexandrou and G. Burgos, Semisolid Metal Processing, *Proc. Materials Solution Conference,* ASM International, 1998, p 23

4. K. Young, Semi-Solid Metal Cast Automotive Components: New Markets for Die Casting, *Transactions,* North American Die Casting Association, 1993

5. R. Wolfe and R. Bailey, High Integrity Structural Aluminum Casting Process Selection, *Casting Solutions for the Automotive Industry,* Society of Automotive Engineers, 2000, p 129

E.J. Vinarcik, Metallography and Microstructures of Semisolid Formed Alloys, *Metallography and Microstructures,* Vol 9, *ASM Handbook*, ASM International, 2004, p. 1021–1037

Metallography and Microstructures of Semisolid Formed Alloys

Edward J. Vinarcik

Semisolid Processes

Numerous variants of the semisolid metalworking process exist. However, all of the processes can be grouped into one of two categories: indirect processing and direct processing (Ref 6).

Indirect semisolid metalworking does not immediately produce a component. Stock material, called billet, must first be manufactured with a nondendritic microstructure. This manufacturing method, using precast billet, has many names, including thixocasting, thixoforming, or thixoforging. (Note, although the term thixoforging may be used to describe this process, the microstructure of products produced does not exhibit a traditional forged structure.) The most common method of billet manufacture is by stirring solidifying metal mechanically or with magnetohydrodynamics (MHD). A second method is to extrude dendritic as-cast bar stock to refine the grain

structure. This stress-induced melt-activation method (SIMA) is especially well suited in the manufacture of small-diameter billet. A third method used to manufacture semisolid billet with a fine-grained structure relies on homogenizing or preheating cast bar stock in the semisolid processing temperature range for a sufficient time to transform the small dendritic grains into globules. Another method first continuously casts rectangular bar stock by the Properzi method followed by a forging operation. The strain introduced during forging causes rapid recrystallization and globulization when the billet is preheated for semisolid processing. Finally, appropriate stock can also be manufactured by spray forming, wherein the billet structure is created by building up layers of tiny frozen droplets that become globular upon reheating into the semisolid temperature regime.

Regardless of the way billets are manufactured, the stock material is heated to a semisolid state and injected into a die. A typical indirect semisolid metalworking manufacturing cell is pictured in Fig. 2. Such cells begin by sawing continuously cast semisolid stock material into billets of known volume. Billets are fed to an induction heating system, which raises the temperature of the billets to the semisolid state. They are loaded automatically into the shot sleeve of the casting machine, which injects the semisolid metal into the die. (Often a single robotic arm is used for loading both the induction heating system and the casting machine.) The solidified component is ejected and extracted from the die, then the gate and runner system is removed, followed by flash and overflow removal in a trim press.

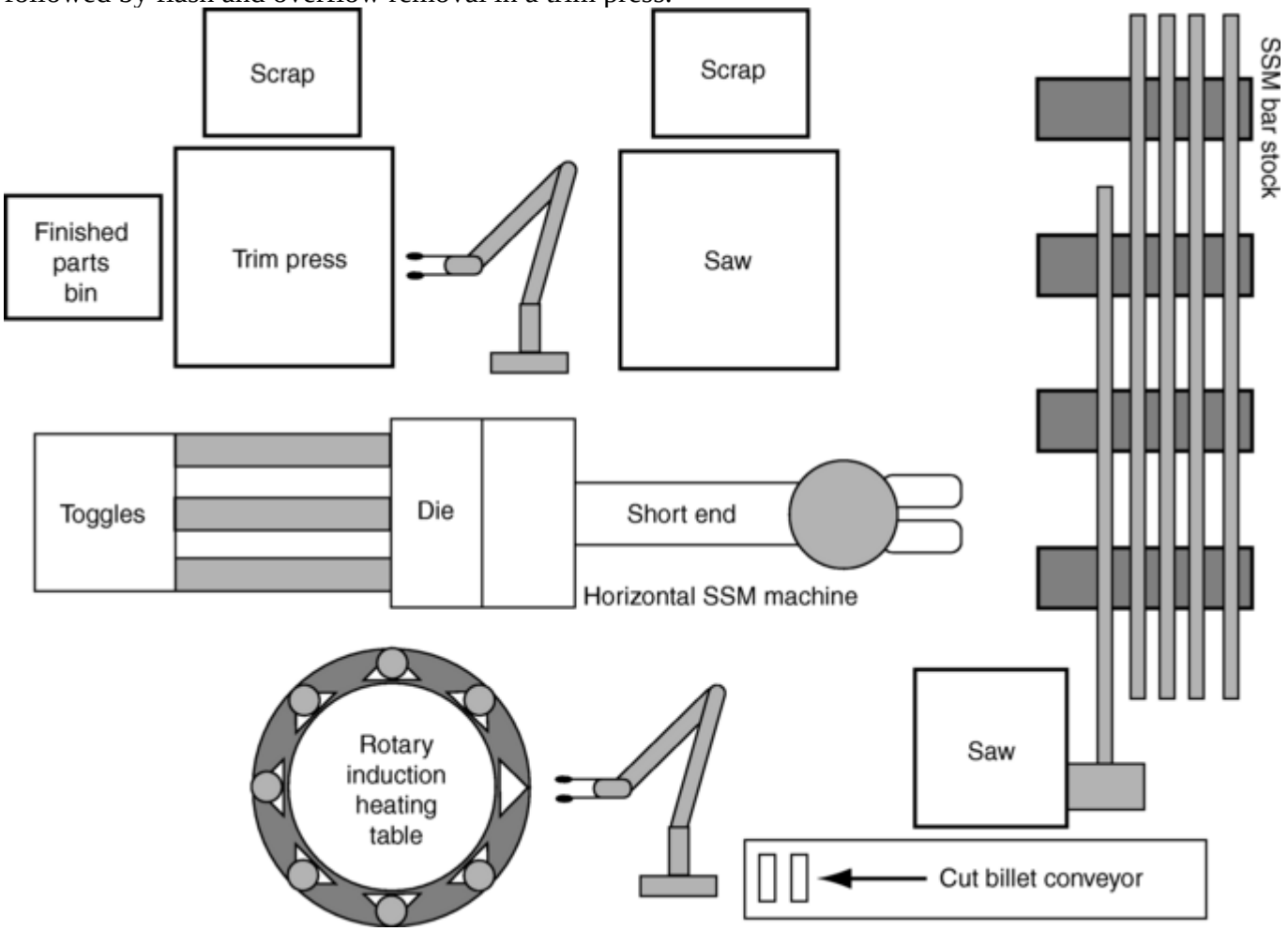

Fig. 2 Typical indirect semisolid metalworking manufacturing cell

Direct processes, usually termed rheocasting, avoid the production and reheating of billet stock material. The semisolid metal mixture is produced on demand and injected directly into the die. This greatly reduces the total cycle time. Numerous variants of this process exist. Some processes hold a large quantity of molten metal on hand and cool metered amounts of metal to the semisolid state. Other processes melt pelletized or chipped material on demand to produce a semisolid mixture without becoming fully liquid. An ideal manufacturing cell utilizing pelletized feedstock is shown in Fig. 3. The process begins by blowing feedstock into the feed bin mounted above the molding machine. The feedstock is metered into a screw where it is heated, sheared, and injected into the die cavity. The solidified component is ejected and extracted from the die and then loaded into

a trim press for removal of the runner system and flash. Scrap is conveyed to a grinder, which chips the off-fall into usable feedstock.

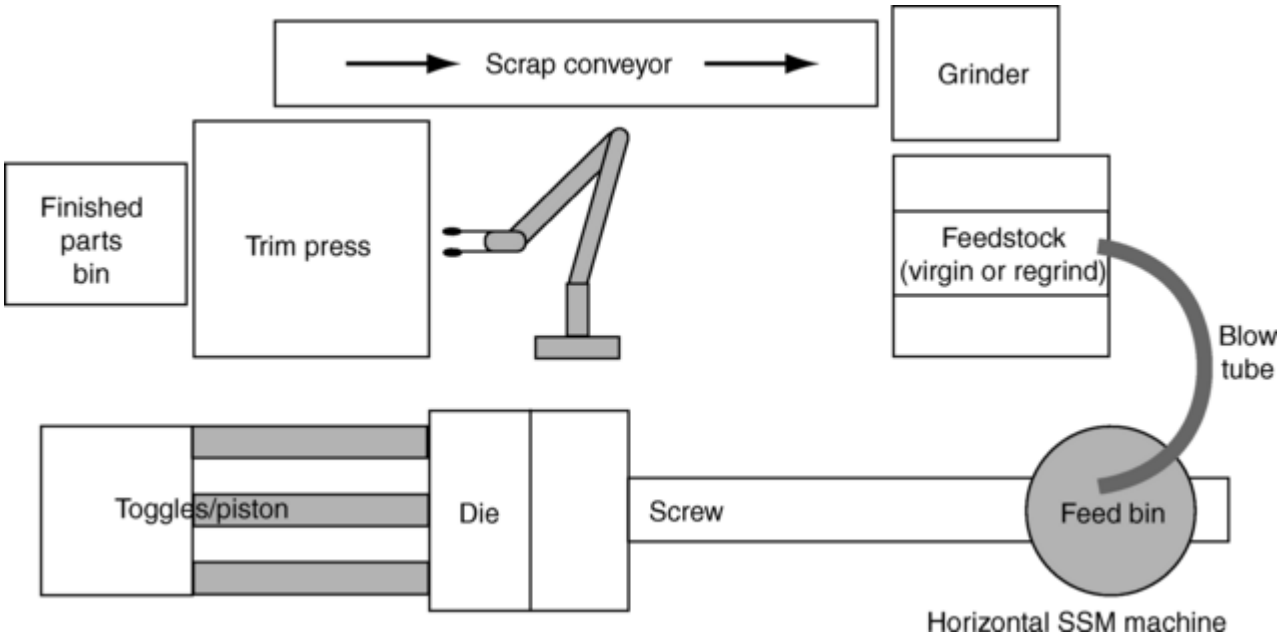

Fig. 3 Typical direct semisolid metalworking manufacturing cell

Processing cycles are compared in Fig. 4 among direct semisolid metalworking (Fig. 4a), indirect semisolid metalworking (Fig. 4b), and conventional casting processes (Fig. 4c). As the thermal history for each semisolid metalworking method is different, the microstructure for a given alloy can vary greatly depending on the process variant employed and the solid fraction of the semisolid metal mixture.

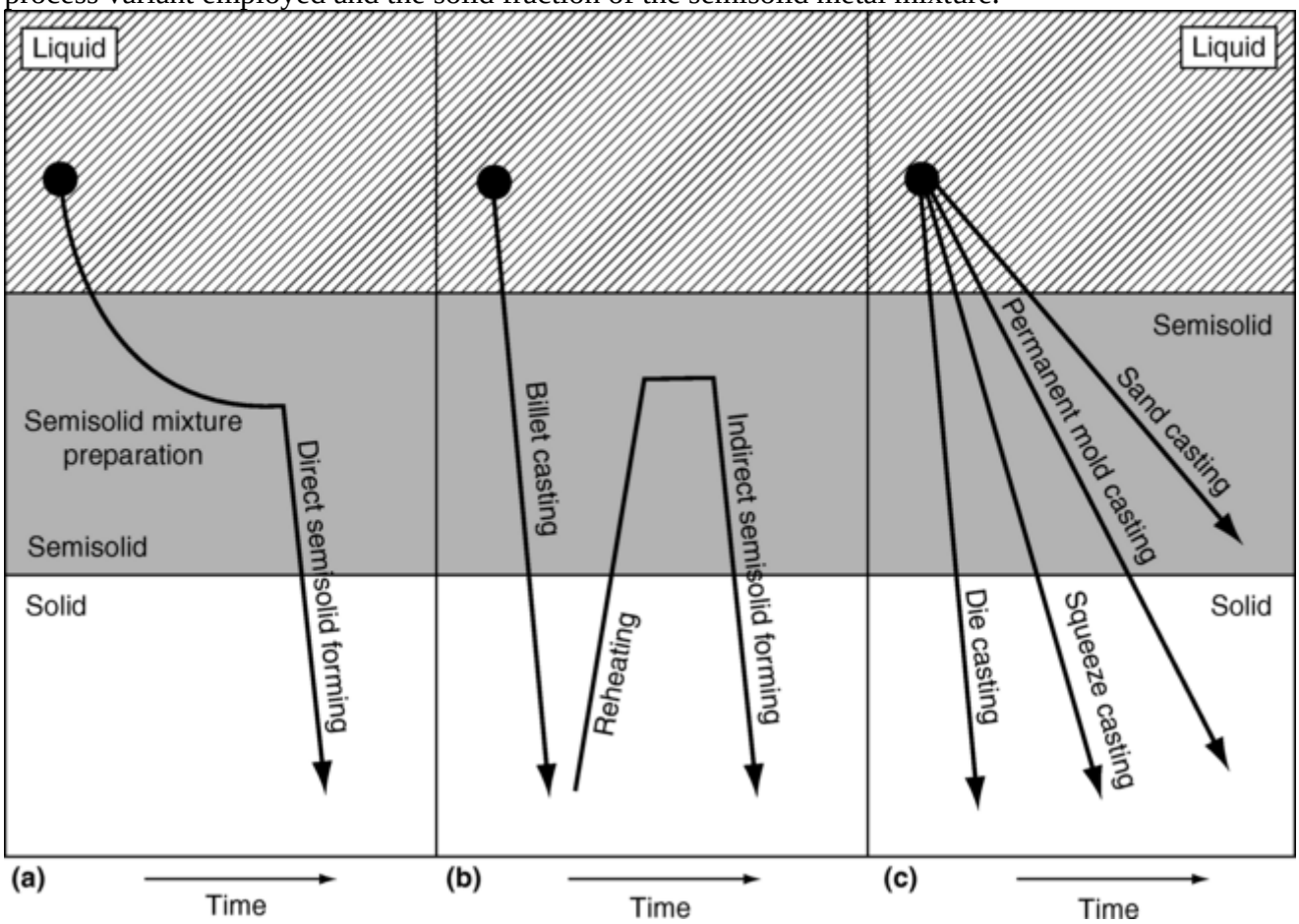

Fig. 4 Process time-temperature comparison between (a) direct semisolid metalworking, (b) indirect semisolid metalworking, and (c) conventional casting processes

Applications. Even though semisolid metalworking is perceived as an emerging process, millions of products are manufactured each year using this high-integrity process. The automotive industry has utilized aluminum components produced using semisolid metalworking in structural and pressure vessel parts (Fig. 5). Due to the reactivity of liquid magnesium with the atmosphere, casting methods for magnesium often require special safety precautions, which add to the cost. Direct semisolid metalworking of magnesium alloys allows a component producer to process net-shape magnesium parts with little or no atmospheric interaction, no greenhouse gases, and no hazardous scrap. The environmental friendliness and minimal secondary-machining operations are the most significant advantages of direct semisolid metalworking over conventional die casting. Numerous components are currently manufactured in magnesium using direct semisolid metalworking methods as shown in Fig. 6. Additional information is available in the article, "Semisolid Metal Casting and Forging," in *Casting,* Volume 15 of the *ASM Handbook* (1988).



Fig. 5 Aluminum components manufactured using semisolid metalworking processes. Courtesy of John Jorstad

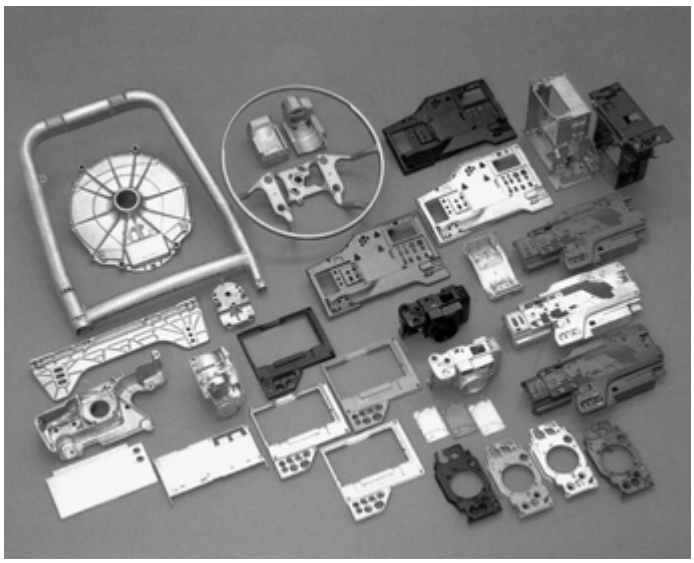

Fig. 6 Magnesium components manufactured using semisolid metalworking processes. Courtesy of Thixomat Inc.

Reference cited in this section

6. E.J. Vinarcik, *High Integrity Die Casting Processes,* John Wiley & Sons, 2002

E.J. Vinarcik, Metallography and Microstructures of Semisolid Formed Alloys, *Metallography and Microstructures,* Vol 9, *ASM Handbook*, ASM International, 2004, p. 1021–1037

Metallography and Microstructures of Semisolid Formed Alloys

Edward J. Vinarcik

Compositions of Common Alloys Produced Using Semisolid Metalworking

Semisolid metalworking may be applied to any alloy with a wide freezing range. Experimental studies have shown that aluminum, lead, tin, bismuth, magnesium, zinc, titanium, and copper as well as numerous ferrous alloys may be formed using semisolid metalworking technologies. (Ref 1, 2, 3). The most common commercial alloy systems used in semisolid applications are aluminum and magnesium.

Aluminum Alloys. The aluminum alloys most often used in semisolid metalworking are the aluminum-silicon 300 series alloys. The freezing ranges for some of these are shown in Table 1, and their corresponding chemical compositions are in Table 2. The alloys suitable for direct semisolid metalworking processes cover a much broader range and include both high-purity primary alloys such as those in Table 1 and less pure secondary alloys (Ref 7). Minor (tramp) elements and other additions are kept below 0.20%. The most common of these additions are strontium, used to modify the eutectic silicon structure, and titanium and boron, used as the primary aluminum grain refiner.

Table 1 Solidification ranges for common aluminum semisolid metalworking alloys

Alloy designation	Solidification range		Total range	
	°C	**°F**	**°C**	**°F**
319	604–516	1119–961	88	158
356	613–557	1135–1035	56	100
A356	613–557	1135–1035	56	100
357	613–557	1135–1035	56	100
A357	613–557	1135–1035	56	100

Source: Ref 7

Table 2 Alloy compositions of common aluminum semisolid metalworking alloys

Designation	Composition[(a)], %								
	Si	**Fe**	**Cu**	**Mn**	**Mg**	**Ni**	**Zn**	**Ti**	**Be**
319	5.5–6.5	1.0	3.0–4.0	0.5	0.1	0.35	1.0	0.25	…
356	6.5–7.5	0.6	0.25	0.35	0.20–0.45	…	0.35	0.25	…
A356	6.5–7.5	0.2	0.20	0.10	0.25–0.45	…	0.10	0.20	…
357	6.5–7.5	0.15	0.05	0.03	0.45–0.60	…	0.05	0.20	…
A357	6.5–7.5	0.2	0.20	0.10	0.40–0.70	…	0.10	0.04–0.20	0.04–0.07

(a) Values not given as ranges are maximum. Aluminum and normal impurities constitute the remainder.

Source: Ref 7

Magnesium Alloys. Although numerous magnesium casting alloys have wide freezing ranges, reported research related to magnesium semisolid metalworking focuses on either AZ91D or AM60B. The chemical compositions of additional magnesium die-casting alloys are presented in Table 3 as these may be used in semisolid metalworking in the future (Ref 8, 9).

Table 3 Alloy compositions of the primary die-cast magnesium alloys

Designation	Composition[(a)], %							
	Al	**Mn**	**Zn**	**Si**	**Cu**	**Ni**	**Fe**	**Rare earth**
AZ91D	8.5–9.5	0.17–0.40	0.45–0.90	0.05	0.025	0.001	0.004	…
AM60B	6.5–6.4	0.26–0.50	0.20	0.05	0.008	0.001	0.004	…
AM50A	4.5–5.3	0.28–0.50	0.20	0.05	0.008	0.001	0.004	…
AS41B	3.7–4.8	0.35–0.60	0.10	0.60–1.4	0.015	0.001	0.0035	…
AE42	3.6–4.4	0.10(b)	0.20	…	0.04	0.001	0.004	2.0–3.0

(a) Values not given as ranges are maximum. The remainder is magnesium and normal impurities. (b) Minimum.
Source: Ref 8, 9

References cited in this section

1. M. Flemings, Behavior of Metal Alloys in the Semisolid State, *Metall. Trans. B,* 1991, p 269

2. M. Keeney et al., Semisolid Metal Casting and Forging, *Casting,* Vol 15, *ASM Handbook,* ASM International, 1988, p 327

3. A. Alexandrou and G. Burgos, Semisolid Metal Processing, *Proc. Materials Solution Conference,* ASM International, 1998, p 23

7. J. Jorstad and W. Rasmussen, *Aluminum Casting Technologies,* 2nd ed., The American Foundry Society, 1993

8. "Magnesium Die Casting Alloys," Form 141-0636-6/95, Dow Magnesium, Midland, MI, 1995

9. *Magnesium Alloy Selector,* Hydro Magnesium, Livonia, MI, 1999

E.J. Vinarcik, Metallography and Microstructures of Semisolid Formed Alloys, *Metallography and Microstructures,* Vol 9, *ASM Handbook,* ASM International, 2004, p. 1021–1037

Metallography and Microstructures of Semisolid Formed Alloys

Edward J. Vinarcik

Macrostructural Examination

Due to the refined grain size and spheroidal structure of semisolid products, macrostructural examination alone can offer insight into the structure of some components and the study of defects. The examination of a cut and polished section can offer insight into the phase content and distribution of a component.

Examination of Defects

Many potential defects commonly found in conventional die casting can also occur in semisolid metalworking. These defects can be classified as external defects, internal defects, and dimensional defects.

External Defects. Macrostructural examination should begin by inspecting the exterior of the component. In some cases, an exterior defect does not render the component unfit for use. Discarding a component because it

“looks bad” if aesthetics are not a requirement creates unnecessary waste. Surface contamination commonly identified by discoloration may occur in die-casting processes and is often caused by manufacturing lubricants. Drags and scoring are the result of mechanical interference between the component and the die cavity during ejection due to improper die design and maintenance. Severe drags may cause distortion or cracking of the component. Sinks are surface defects, which are caused by localized solidification shrinkage beneath the surface of the casting. In semisolid metalworking, sinks suggest the presence of a low solid fraction during processing.

Cracks sometimes occur in semisolid formed components. In some cases, cracks may be caused by cold shuts or residual stresses that form within the component during solidification and cooling, caused by poor material handling techniques. To accomplish the high production rates associated with semisolid metalworking, components might be ejected from the die near their solidification temperature. While in this fragile state, care must be taken in handling the components. Cracks may occur due to uneven ejection from the die or due to an impact if they are dropped immediately after ejection. The condition that most often causes cracks during semisolid casting is local hot spots in the die. These cracks appear as hot tears and may be visible on the cast surface, or they may be internal and only revealed by x-ray or cross sectioning.

Cold shuts (also known as cold laps or knit lines) are imperfections visible on the surface of the casting due to unsatisfactory fusion of partially solidified metal. Although this defect can usually be seen on the surface of the casting, the defect may run deep into the structure. During filling of the die, the convergence of two nearly solidified fill fronts may not knit properly, resulting in a weak zone.

Laminations are a type of cold shut that occurs at the surface of the component. Due to the viscous, stable-front flow typical during semisolid casting, metal may not always lay up tightly against a die surface; when terminal pressure is reached upon the completion of cavity fill, any gap that might have been left between the die wall and casting might backfill with near-pure eutectic, the only fraction of the melt remaining sufficiently molten to flow. The result is a thin, partially attached lamination.

A short shot is the incomplete filling of the die cavity caused by an undersized billet or volume of slurry being metered into the metal-injection system or premature solidification of metal in the runner system inhibiting complete fill of the die cavity. Such defects are easy to detect by examining the ejected component(s) and the runner system. Without enough metal in the injection system, the biscuit at the start of the runner system may be too small, and the component is not fully formed.

Repetitive thermal cycling of dies from the injection of metal followed by the application of lubricants results in fine cracking of the die face. This phenomenon is referred to as heat checking. Once these cracks are present, metal will fill these fine cracks, creating veins or fins on the manufactured component.

During semisolid casting, the metal introduced to the die is at a much lower temperature and is already partially solidified, thus less sensible heat and heat of fusion is introduced to the tool. Because the metal is partially solidified, tools are also typically maintained at higher temperatures than for conventional die casting or squeeze casting. This combination results in a much smaller temperature change between shots and thus less stress on the tool surface. Heat checking may still occur; however, tools typically last three to five times longer than with conventional die-casting or squeeze-casting processes.

Lubricants are applied to the surface of a die to lessen interaction between the die surface and the metal injected into the die. Interactions may still occur, however, resulting in a metallurgical bond between the die and the injected metal. This phenomenon is known as soldering and occurs most often when injecting aluminum into ferrous dies at high velocity. When soldering occurs, pits are often left on the surface of the component with a corresponding mass adhering to the die surface. Soldering is less in alloys containing greater than 0.8% Fe (the ternary Al-Si-Fe eutectic), as these are less driven to attack and dissolve tool steel. To make high-integrity components using high-purity primary alloys that contain very little iron (present only as an impurity), lower metal velocities and effective die lubricants must be used.

Internal defects can occur below the surface of a semisolid formed component resulting in less-than-ideal mechanical properties. Macroscopic examination of these defects can be performed after cross sectioning. Although low-speed sawing is ideal for this type of analysis, the time required is often prohibitive in a high-volume manufacturing environment. Band saws and water-cooled abrasive cutting wheels may be used; however, the surface of the cross section may be distorted, masking a defect. Additional grinding using 320 and 400 grit papers may be required. Contamination is revealed by cross sectioning. Common sources of contamination include degrading refractories, lubricants, fractured equipment, and unclean remelted scrap that may become trapped in billet material when continuously cast or during the preparation of semisolid slurries.

Although many fluxes are restricted due to environmental regulations, fluxes are still commonly used to clean and control metal chemistries. The wrong flux, excessive amounts of flux, or failure to properly remove dross after flux cleaning may contaminate an alloy. Components manufactured with flux-contaminated metal have less-than-ideal mechanical properties and higher susceptibility to corrosion. In some cases, macrostructural examination can identify chunks of flux trapped within a component. Comparative corrosion testing with a cross-sectioned suspect component and a known clean component can verify the presence of flux contamination.

When heating metal billets to the semisolid state for injection into the die, surface oxidation will occur. Various "oxide skimmers" are employed to remove or turn away this oxide layer and prevent it from entering the die cavity. If not properly excluded from the metal entering the die, this oxide may become entrapped in the component during injection, forming inclusions visible only through microscopic examination. In some cases, however, the metal oxide inclusions may not disperse, so inclusions are visible through cross sectioning and macroscopic examination.

Porosity is a potential defect rarely seen on the surface. When injecting a liquid metal into a die, as during die or squeeze casting, extremely rapid solidification initially occurs on the surface of the component producing a thin, tenacious skin. Porosity subsequently formed by either solidification shrinkage or gas entrapment can only be viewed after cross sectioning. Porosity can also occur during semisolid processing. Due to the planar fill front associated with the process, entrapped gas porosity is easier to control with proper venting. Solidification shrinkage is minimized because the alpha phase, wherein much volumetric shrinkage occurs during solidification, is largely solid before being injected into the die.

Most alloys have a higher density in their solid state as compared to their density in the liquid state. This results in shrinkage during solidification. Centerline porosity can occur in alloys that freeze over a narrower temperature range, as in eutectic metalworking alloys. Interdendritic porosity can occur in alloys that freeze over wider temperatures. This form of solidification shrinkage porosity is best viewed using microscopic examination.

Porosity from entrapped gas can originate from several sources, sometimes making identification and elimination difficult. Air can become physically entrapped in the metal during injection if venting is not satisfactory. Gases soluble in the liquid alloy may exceed their solubility limit during solidification. However, the high-pressure nature of semisolid metalworking processes would increase solubility limits and would compress any precipitated gases to infinitesimally small size. The entrapped gases may go unnoticed or manifest as blisters if subsequent heat treating is required. Reactions can occur between the metal and slags producing gas. Decomposition of lubricants and chemicals used during manufacture can result in gas formation and entrapment in the metal, usually close to the cast surface.

Dimensional Defects. Numerous dimensional defects of the component can be evaluated macroscopically. Although more common to liquid metal processes, flash, the undesired formation of thin metal sections along the parting lines of die components, can occur in semisolid metalworking processes with its potential increasing as the solid fraction decreases.

Warpage is caused by asymmetric geometric features that contract at different rates during cooling. This defect is easily detected in a macroscopic examination by simply placing parts on a flat surface and looking for gaps. Warpage can be corrected by improving part or tooling design.

Repetitive flow of metal across the surface of the die results in erosion. Macrostructural examination of components often reveals the regions of die erosion. Depending on the metal alloy system, erosion can be both mechanical and chemical in nature. During semisolid processing, erosion is most prevalent near in-gates, so this area is often made as a separate insert to facilitate easy replacement.

Thermal cycling failures occur to cores and along die features with sharp corners. Thermal management within cores is difficult. Small cores cannot be cooled with water lines and must be cooled exclusively with die lubricant sprays. Excessive thermal cycling combined with soldering causes cores to fail. When this occurs, the core is retained in a finished component during ejection from the die. All subsequent components are produced without the cored feature. Such dimensional defects are easily identified.

Examination of Gating Systems

Macrostructural examination should not be limited solely to components. Much can be learned by examining the gating system and biscuit. If the biscuit on the runner system is absent or very small, the short shot was caused by too little metal in the injection system. If the biscuit is oversized, premature solidification occurred.
Short shots can also be induced on purpose by stopping the metal injection prematurely. Macroscopic examination of short shots can yield insight into metal fill patterns within a die. When qualifying a die for semisolid metalworking, it is common practice to produce short shots in known graduations, that is, with the die 25%, 50%, 75%, and 90% filled. This helps die makers and tooling engineers balance runner systems in multicavity dies, verify vent effectiveness, and map knit-line locations.

Examination of Feedstock

Semisolid bar feedstock, such as that shown in Fig. 7, is manufactured by two primary methods: extrusion and continuous casting. Semisolid feedstock manufactured by extruding grain-refined material has a fine equiaxed structure. Due to the microscopic homogenous structure of extruded billet materials, little can be learned from macrostructural examination.



Fig. 7 Continuously cast semisolid metalworking feedstock. Courtesy of John Jorstad

Typically, MHD stirring is used when continuously casting semisolid feedstock to fracture dendrites as they form in the liquid metal as it solidifies. This stirring action creates a fine, nondendritic structure within the core of the feedstock, but a dendritic structure forms on the outer surface (Ref 6). This dendritic case (Fig. 8), not present in extruded feedstock, forms as a result of the substantial temperature gradient present at the liquid metal/mold interface.

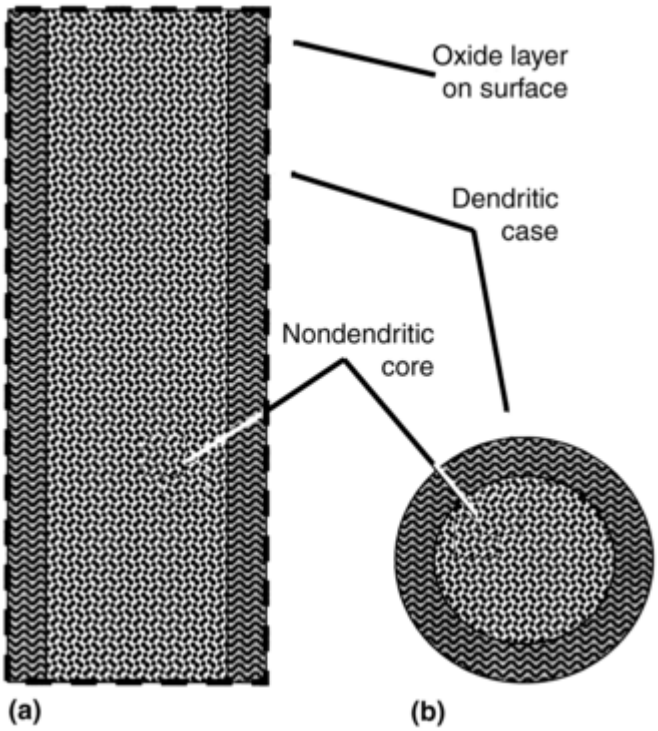

Fig. 8 Continuously cast semisolid metalworking billet before heating. (a) Longitudinal section. (b) Cross section

When heating feedstock to the semisolid state, the dendritic case plus a layer of oxide formed during heating aids material handling by holding the billet together. The dendritic and oxide case does not flow well within the die and are retained in the biscuit when forming a component. The thickness of the dendritic case of a billet can be determined using macrostructural examination by etching one end of a sawed billet. After etching, a distinctive ring will be visible, revealing the transitional region from the dendritic case to the bulk material in the core. A typical macroetching agent for aluminum and magnesium billet analysis is sodium hydroxide and acetic acid, respectfully. Other macroetchants can be used as described in the articles “Metallographic Techniques for Aluminum and Its Alloys” and “Metallographic Techniques for Magnesium and Its Alloys” in this Volume.

After a billet is heated to the semisolid state, the solid fraction alpha structure largely retains its shape, while the melted eutectic flows by gravity down through the alpha skeleton. In cases with low solid fraction, the alpha skeleton can break down with solid particles sinking to the lower regions of the billet (Fig. 9). This results in a bulge or barreling at the base of heated billets, termed elephant footing. Macrostructural examination of quenched heated billet may be cross sectioned along its axis and etched to reveal the variations in liquid and solid fractions. This form of analysis may also aid in the troubleshooting of the billet heating process by identifying nonspheroidized cold spots.

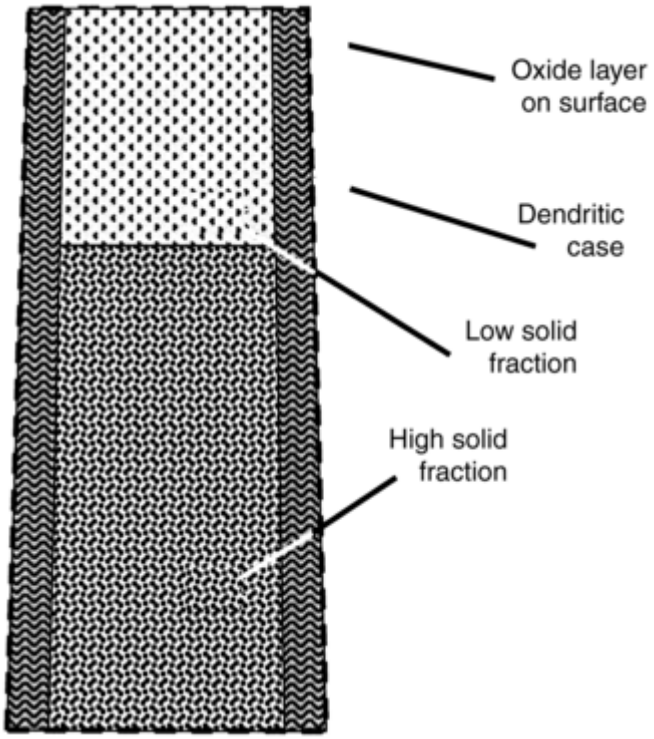

Fig. 9 Continuously cast semisolid metalworking billet after heating (longitudinal section)

In some cases, the origin of the porosity can be the billet feedstock. Air may become entrapped in the liquid metal when continuously casting billet material. This entrapped gas can be transferred directly into a component produced by semisolid metalworking. Macrostructural examination of raw cross-sectioned billet may reveal this form of porosity.

Porosity can also originate from gases soluble in the liquid alloy (typically hydrogen in aluminum alloys). Due to the high solidification rate experienced when continuously casting semisolid billet feedstock, dissolved gases do not have time to come out of solution. However, these gases may come out of solution when reheating billet material prior to forming a component. Macrostructural examination of the exterior of a billet may reveal blisters formed by hydrogen gas pockets forming in the softened material, and cross sections may reveal dissolved gas porosity.

In some cases, feedstock is not in billet form. Many magnesium direct semisolid metalworking processes use chipped feedstock, which can be examined at the macroscopic level. As shown in Fig. 10, morphologies of

particulate feedstock can vary greatly with respect to size and shape and method of manufacture (Ref 10). Chipped feedstock produced by mechanical fragmentation have a rough acicular geometry. Pelletized feedstock produced by the rapid solidification of liquid metal typically has a rounded shape.

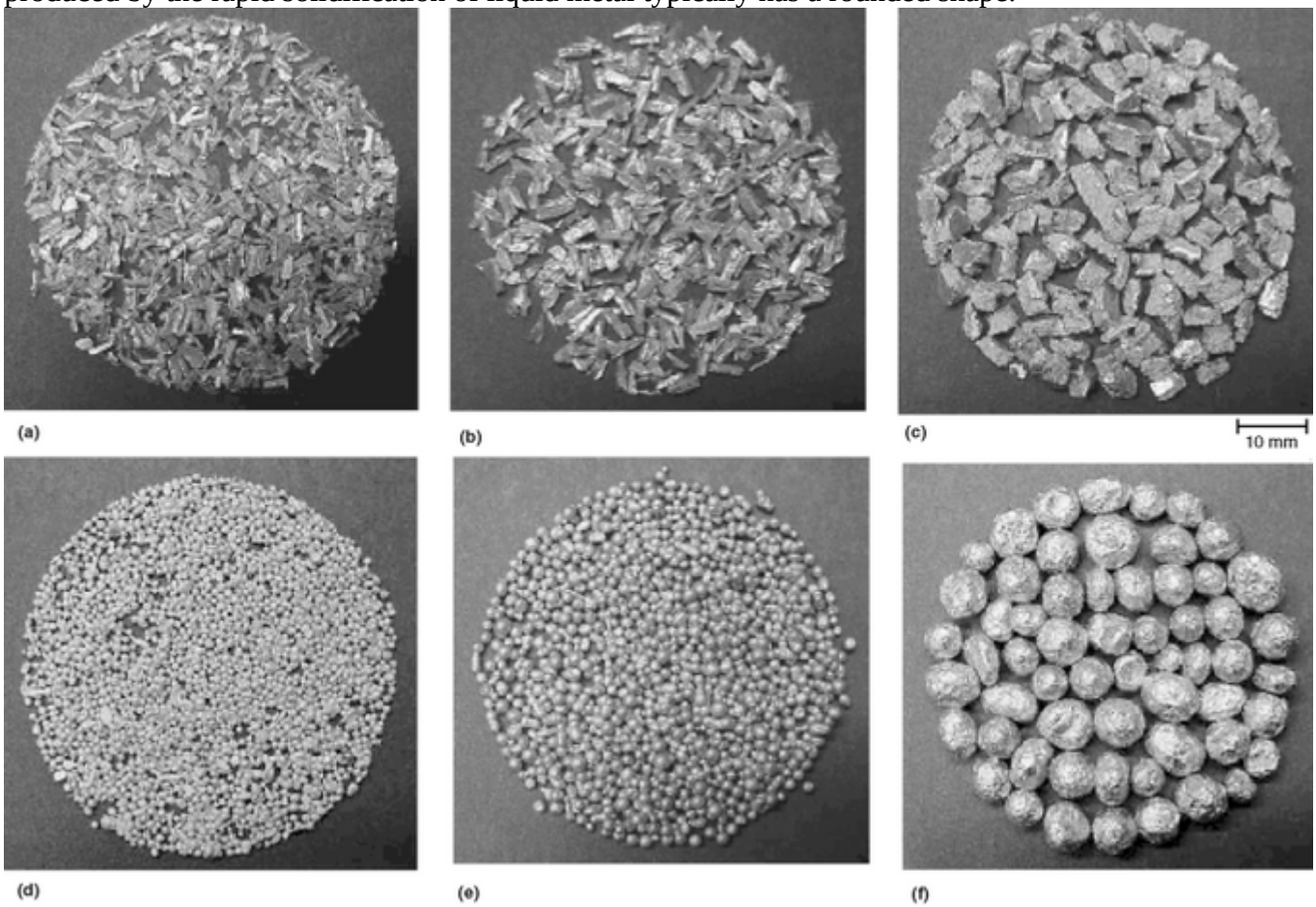

Fig. 10 Varying sizes of AZ91D magnesium particles produced by mechanical fragmentation (a), (b), and (c) or using rapid-solidification techniques (d), (e), and (f) for use as semisolid metalworking feedstock. Courtesy of Husky Injection Molding Systems

References cited in this section

6. E.J. Vinarcik, *High Integrity Die Casting Processes,* John Wiley & Sons, 2002

10. F. Czerwinski, On the Generation of Thixotropic Structures During Melting of Mg-9%Al-1%Zn Alloy, *Acta Mater.*, Vol 50, 2002, p 3265

E.J. Vinarcik, Metallography and Microstructures of Semisolid Formed Alloys, *Metallography and Microstructures,* Vol 9, *ASM Handbook*, ASM International, 2004, p. 1021–1037

Metallography and Microstructures of Semisolid Formed Alloys

Edward J. Vinarcik

Specimen Preparation, Bulk Extraction, and Etching

Specimen preparation and bulk extraction of semisolid metalworking components, billet feedstock, pelletized feedstock, and the like vary greatly depending on the alloy system. As such, the sample preparation guidelines are presented in this Volume for specific alloy systems for sectioning, mounting, grinding, polishing, and bulk extraction. Detailed tables of general, selective, and color etching are also presented in this Volume by alloy type.

Unique to components produced using semisolid metalworking is the creation of a spheroidal microstructure. This microstructure forms as broken and sheared dendrites ripen into a nodular or spheroidal structure. Selective etching techniques can be used to isolate primary particles by dissolving the eutectic matrix, allowing analysis of the spheroid morphology and size. Conversely, selective etching of the primary spheroidal particles will create a hollow eutectic matrix sponge in the areas treated. Such analyses however, are limited to etchants compatible with the alloy type under investigation. Comprehensive tables of selective etchants are presented in the alloy-specific sections of this Volume. Etching aids the identification of different constituents; color variation between constituents of the same type denote variations in orientation. This form of analysis allows one to determine if like constituents are conjoined below the surface under examination.

Anodizing is used extensively with aluminum (Ref 11). Anodized microstructures viewed with polarized light reveal the grain structure in color.

As with general sample preparation methods for microstructural analysis, thin-film preparation techniques for use with transmission electron microscopy (TEM) vary greatly with the alloy type.

Reference cited in this section

11. A. Kazakov, Alloy Compositions for Semi-solid Forming, *Adv. Mater. Process.*, March 2000, p 31

E.J. Vinarcik, Metallography and Microstructures of Semisolid Formed Alloys, *Metallography and Microstructures,* Vol 9, *ASM Handbook*, ASM International, 2004, p. 1021–1037

Metallography and Microstructures of Semisolid Formed Alloys

Edward J. Vinarcik

Microstructure of Semisolid- processed Metals and Alloys

Series 300 aluminum casting alloys and magnesium die-casting alloys are the dominant metal systems for commercial semisolid metalworking, and thus this section will focus on these alloy groups.

Aluminum Semisolid Microstructures

As aluminum alloy microstructures vary based on thermal history, unique microstructures are observed at different stages of the semisolid metalworking process. Similarly, each variant of semisolid metalworking yields unique microstructures. As such, this section is further divided by addressing feedstock microstructures and direct and indirect semisolid metalworking component microstructures.

Aluminum Feedstock Microstructures. In general, stirred billet material has a finer microstructure than grain-refined billets (Ref 12).

Presented in Fig. 11 is the typical bulk microstructure of a 357 aluminum alloy billet produced by continuous casting with MHD stirring. Although the microstructure clearly shows evidence of dendrite formation, the dendrites are broken and ripened. Subsequent billet preheating and processing under shear (as in semisolid metal forming) will further spheroidize and fragment the microstructure.

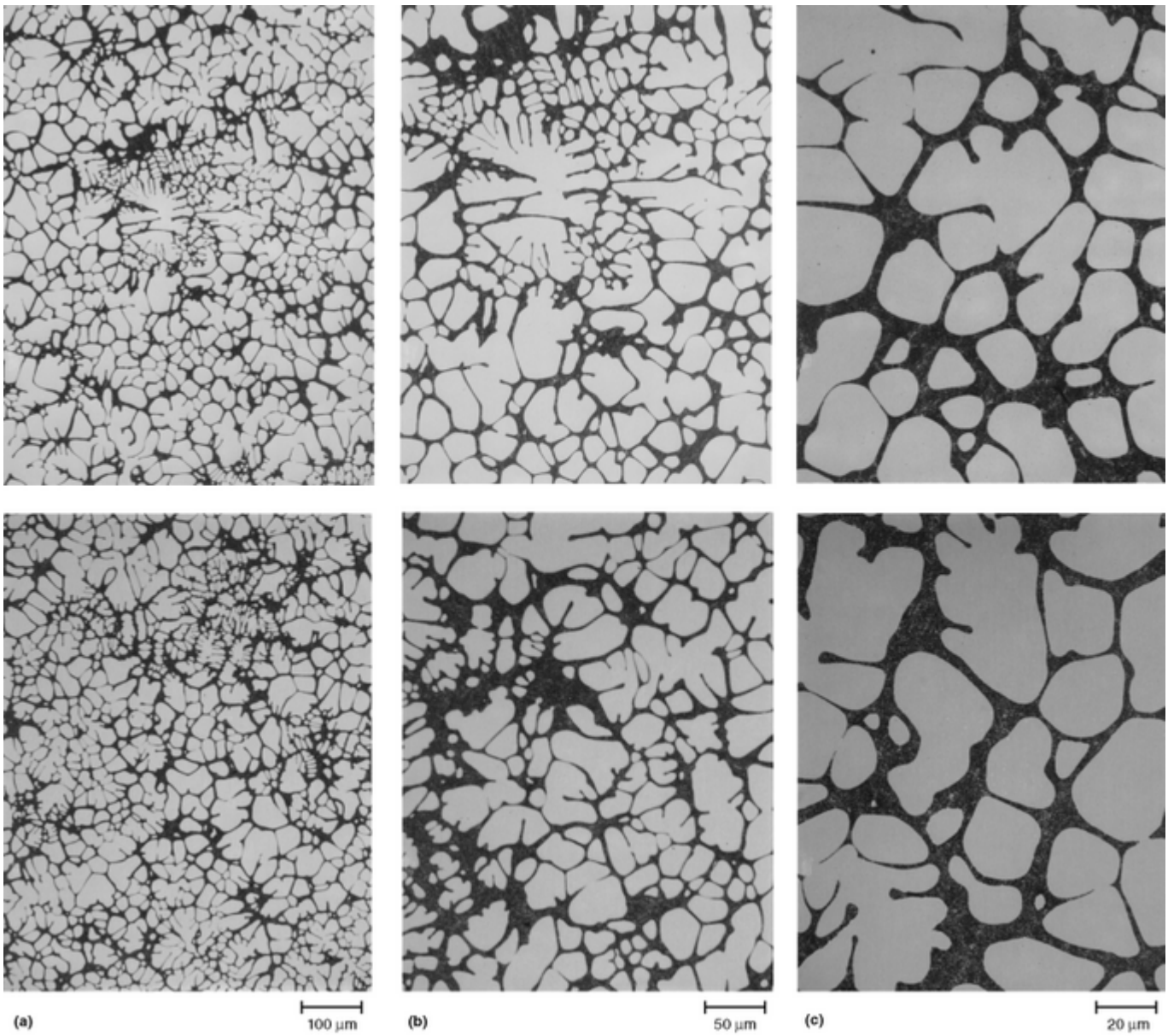

Fig. 11 Microstructures of an as-received electromagnetically stirred Al 357 billet at (a) 100×, (b) 200×, and (c) 500× prepared using Keller's etch (top) and 0.5% HF acid (bottom)

Aluminum Direct Semisolid Metalworking Component Microstructures. Many processes have been developed to produce semisolid aluminum metal mixture on demand. Often referred to as rheocasting, these processes produce components with spheroidal microstructures.

Presented in Fig. 12 and 13 are two A356 aluminum alloy samples. Both samples were prepared using standard grinding methods using 400, 600, and 800 grit papers followed by polishing with 3 and 1 μm alumina medium in suspension (Ref 13). A final polish was performed using 0.5 μm colloidal silica. No etchants were used. Figure 12 shows the spheroidal microstructure produced in a component manufactured using semisolid metalworking. The light gray spheroidal constituents are α-aluminum surrounded by a darker eutectic constituent. The sample shown in Fig. 13 was reheated to 585 °C (1085 °F) and held for 10 min before quenching in water. This reheating and quenching process further ripened the α-aluminum in the structure and refined the eutectic constituent, making it appear darker.

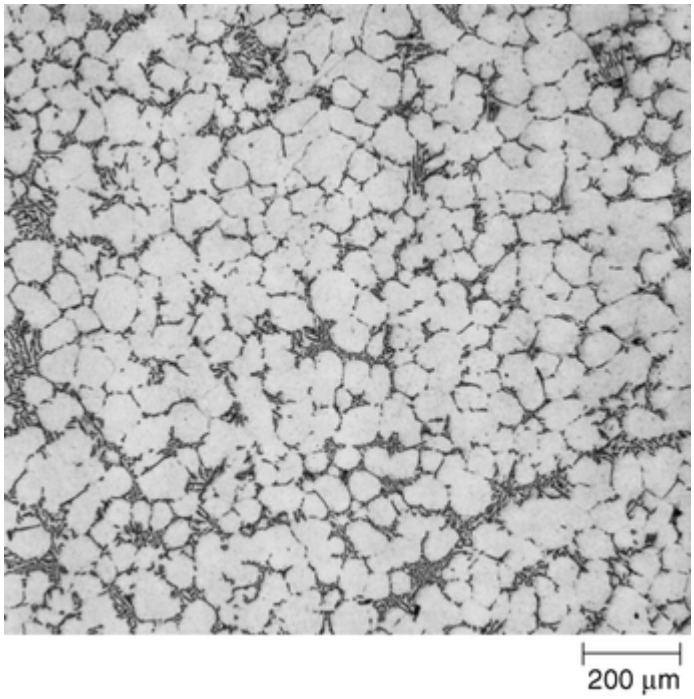

Fig. 12 As-formed microstructures of an A356 aluminum alloy component. Courtesy of IdraPrince Inc.

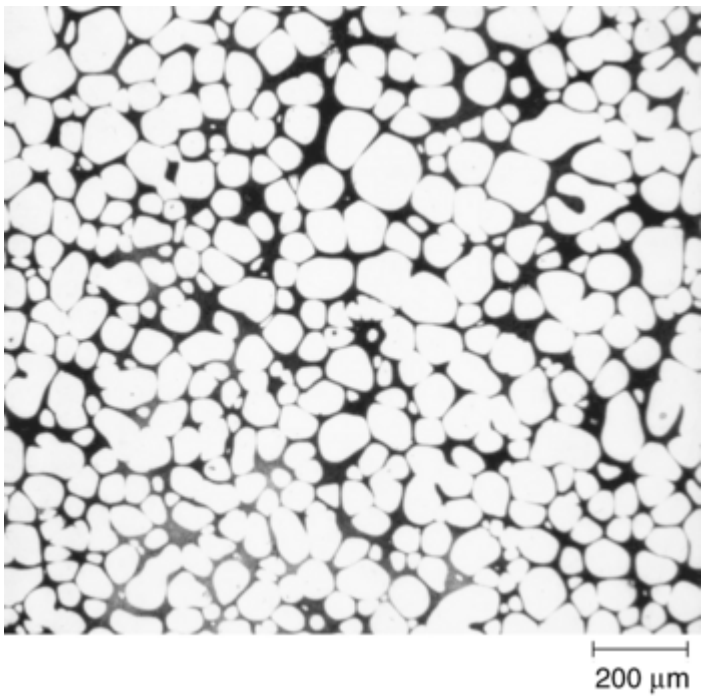

Fig. 13 Reheated microstructures of an A356 aluminum alloy component. Courtesy of IdraPrince Inc.

Aluminum Indirect Semisolid Metalworking Component Microstructures. When examining microstructures, the feedstock should be kept in mind; continuously cast bar stock and grain-refined extrusion billets will produce very different microstructures in the final component (Ref 12). When heating an aluminum billet to the semisolid state, the primary will ripen and become spheroidal. The extent of spheroidization of the α-aluminum phase is greatly influenced by the initial microstructure of the billet. Grain-refined billets having a starting grain size of 200 µm or more are known to undergo less spheroidization than continuously cast MHD stirred billets. This is shown in the microstructures of components cast in 319 aluminum alloy using continuously cast electromagnetically stirred billet and grain-refined extruded billet as shown in Fig. 14 and 15, respectively.

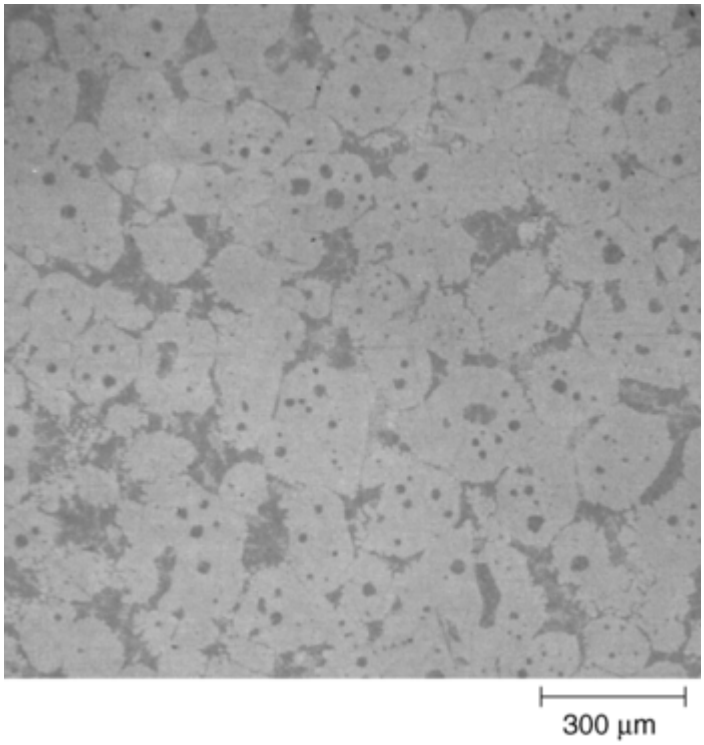

Fig. 14 Microstructure of an as-formed plate formed from an electromagnetically stirred 319 aluminum alloy billet at 100×. Courtesy of SPC Contech, Inc.

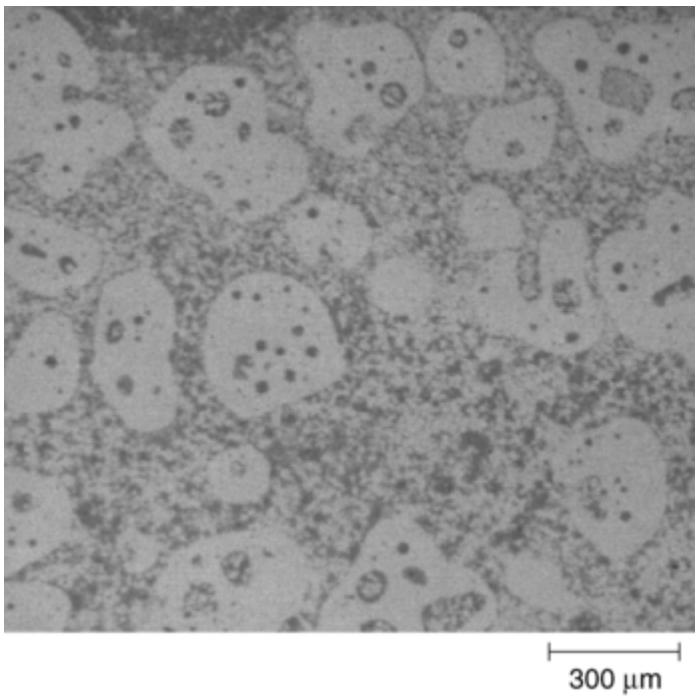

Fig. 15 Microstructure of an as-formed plate formed from a grain refined 319 aluminum alloy billet at 100×. Courtesy of SPC Contech, Inc.

Regardless of the initial billet microstructure, components manufactured using semisolid metalworking will have the characteristic spheroidal structure, but the microstructure of a component produced using an indirect process will have a characteristic rarely seen in direct metalworking. When forming the alloy, liquid eutectic is often entrapped within the primary solid phase. This phenomenon is clearly seen in Fig. 16 (Ref 14). This microstructure is typical of a 356 aluminum alloy formed using an indirect semisolid metalworking process. The structure consists of primary α-aluminum particles in an aluminum-silicon eutectic (dark) matrix. Within the primary α-aluminum particles, specks of the eutectic can be clearly distinguished.

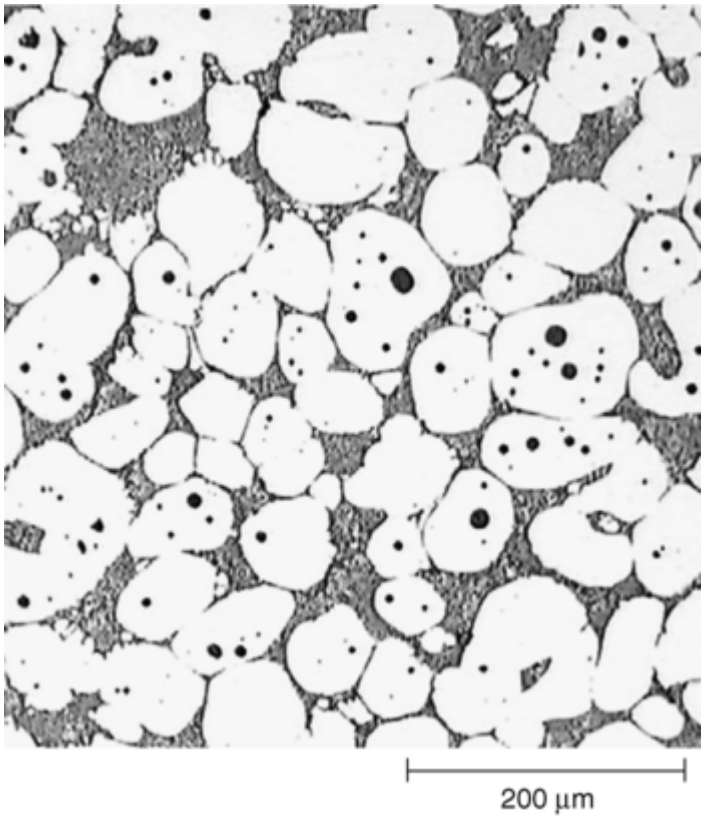

Fig. 16 Typical microstructure of a 356 aluminum alloy produced via indirect semisolid metalworking prepared by polishing to a 1 µm finish on a diamond wheel and etched with a 0.5% HF solution. Courtesy of the Industrial Materials Institute, National Research Council Canada

The microstructure of a component manufactured using semisolid metalworking is rarely homogeneous. Although the bulk material will exhibit a spheroidal structure as shown in Fig. 16, other regions of the component will exhibit other microstructures. In many cases, segregation of eutectic phase is observed on the surface of the component, forming the classical tenacious skin observed in die-cast components. In conjunction with the segregated eutectic are fine nodules of the primary solid phase. This phenomenon is illustrated in Fig. 17 with an as-formed 356 aluminum alloy component and is especially indicative of lower solid fractions (Ref 14). Along the surface of the component, the fine aluminum-silicon eutectic phase is dominant. Further from the edge, fine nodules of α-aluminum are observed mixed with the large α-aluminum spheroids.

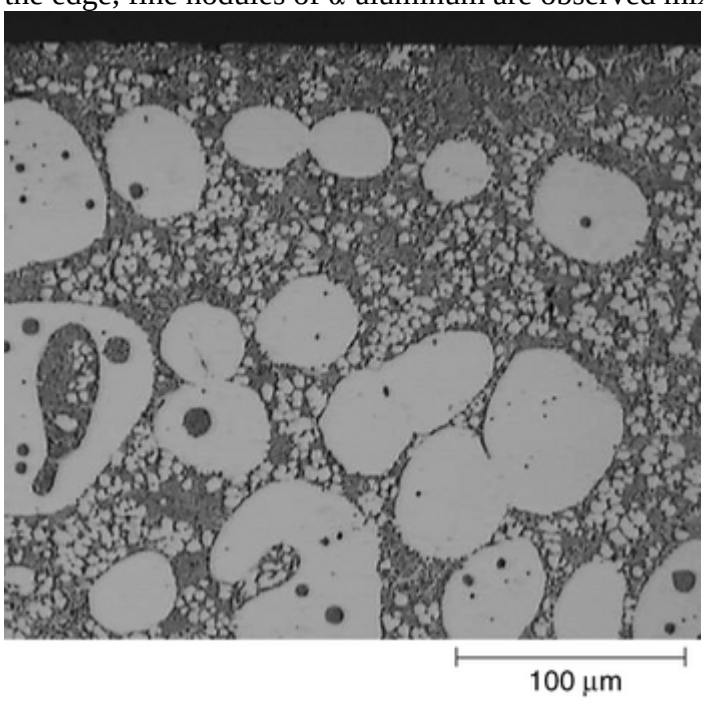

Fig. 17 Segregation of eutectic phase observed near the surface of a 356 aluminum alloy component. Sample prepared by polishing to a 1 μm finish on a diamond wheel and etched with a 0.5% HF solution. Courtesy of the Industrial Materials Institute, National Research Council Canada

When utilizing lower solid fractions, the primary solid phase will not form nodules in the segregated eutectic region near the surface of the component. The primary phase will form a dendritic structure as shown in Fig. 18. In this example, the fine aluminum-silicon eutectic phase is dominant along the surface of the component. Further from the edge, fine dendrites of α-aluminum formed between large α-aluminum spheroids. Uniform heating of billets to the semisolid state is difficult. Variations in temperature can result in localized low solid fractions or localized melting within the billet. The consequence of this variation is the formation a dendritic microstructure in some regions of the component, as shown in Fig. 19 (Ref 14).

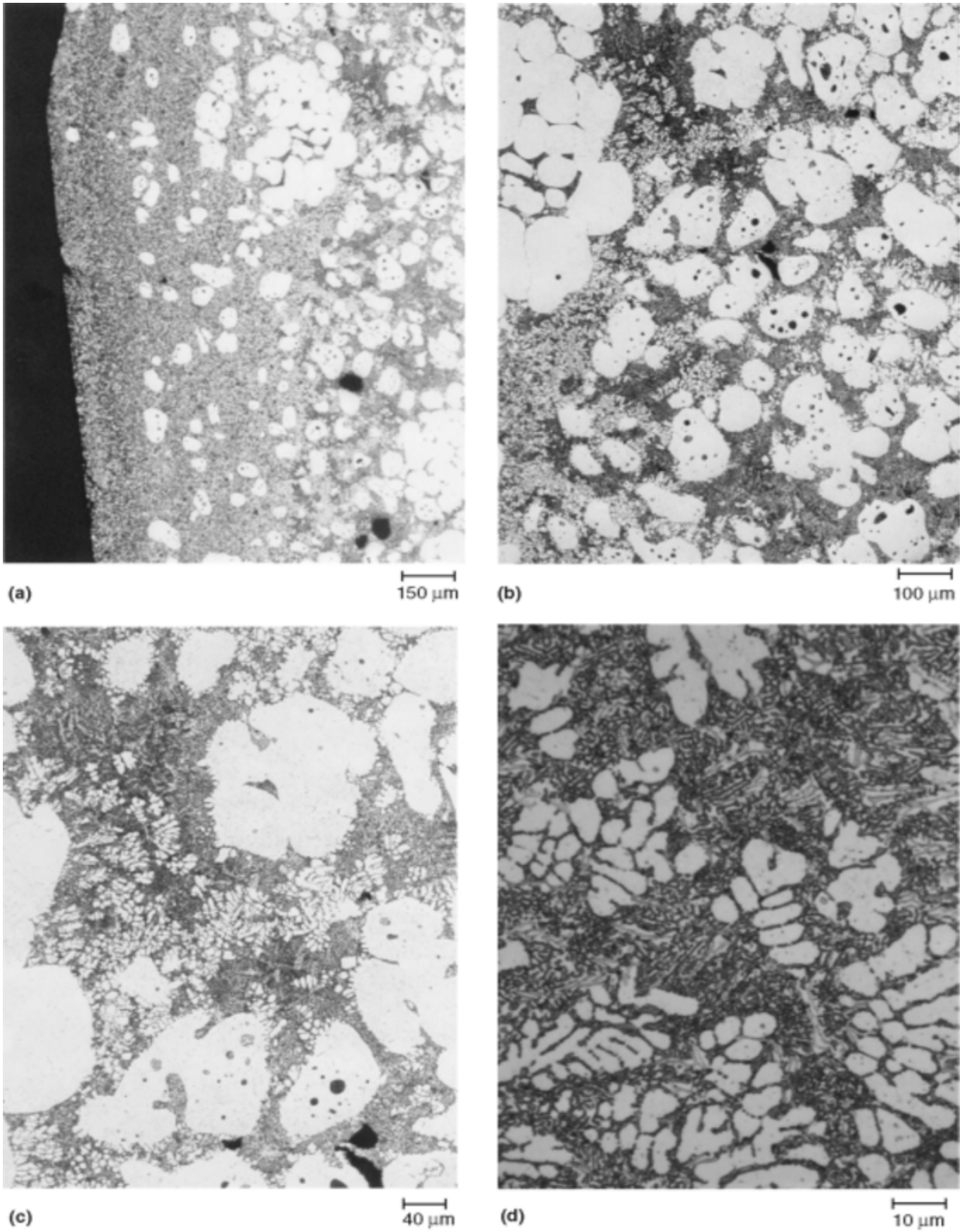

Fig. 18 Segregation of eutectic phase with α-aluminum dendrite formation observed near the surface of a 357 aluminum alloy component at (a) 50×, (b) 100×, (c) 200×, and (d) 1000×. Sample prepared using Keller's etch.

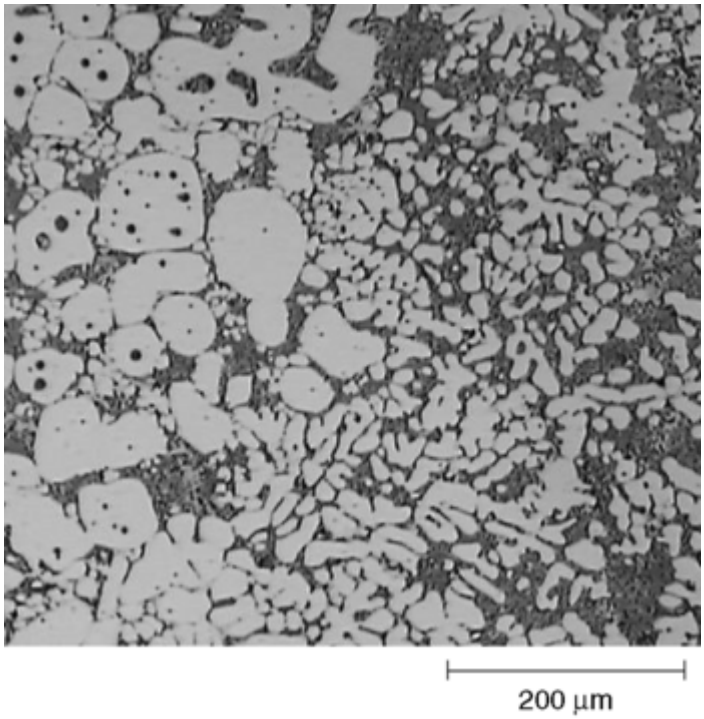

Fig. 19 Dendritic microstructure caused by billet overheating adjacent the typical spheroidal microstructure in an as-formed 356 aluminum alloy component. Sample prepared by polishing to a 1 μm finish on a diamond wheel and etched with a 0.5% HF solution. Courtesy of the Industrial Materials Institute, National Research Council Canada

Although the potential for shrinkage porosity in semisolid metalworking is greatly reduced compared to conventional die casting, shrinkage porosity can still form under specific conditions. This type of porosity can form if there is insufficient feeding of the liquid eutectic alloy during solidification. An example is presented in Fig. 20 with an as-formed 356 aluminum alloy component (Ref 14). Voids are clearly visible between α-aluminum spheroids where the eutectic fraction is expected.

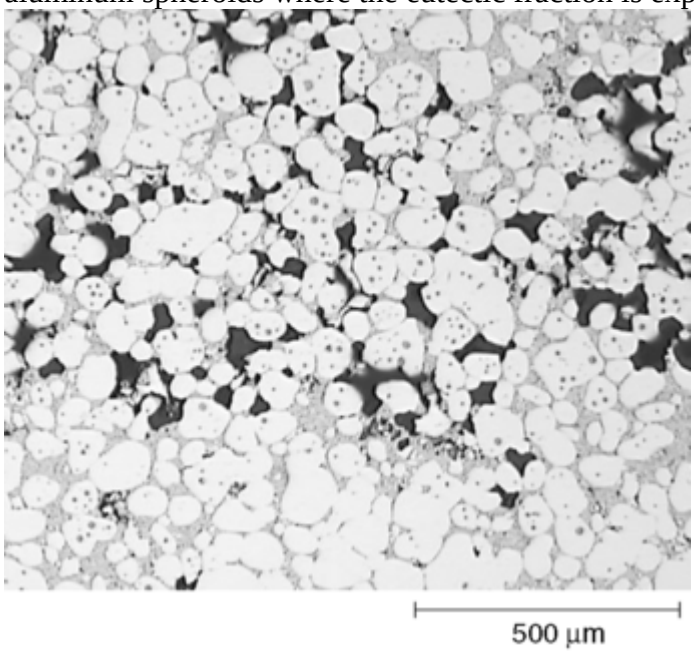

Fig. 20 Shrinkage voids between α-aluminum particles caused by insufficient feeding in an as-formed 356 component. Sample prepared by polishing to a 1μm finish on a diamond wheel and etched with a 0.5% HF solution. Courtesy of the Industrial Materials Institute, National Research Council Canada

An important semisolid metalworking process parameter is the solid fraction percentage. Depending on the process variant and the component being produced, significantly different microstructures can be created by varying the solid fraction of the semisolid mixture prior to injection into the die as shown in Fig. 21. The low-solid-fraction (LSF) and high-solid-fraction (HSF) samples illustrated were produced using A357 aluminum alloys from two different semisolid metalworking processes (Ref 15).

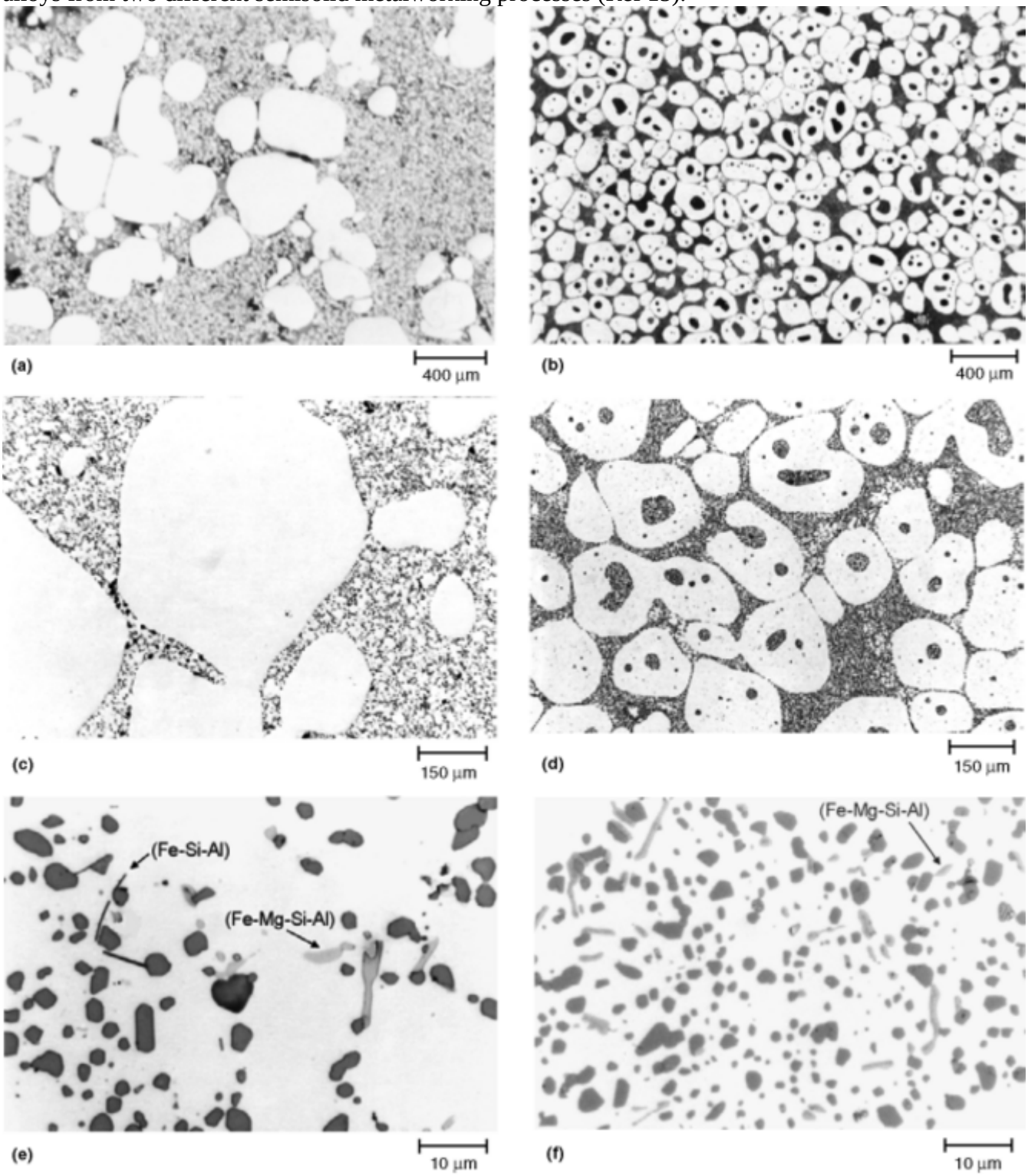

Fig. 21 Typical microstructures of low-solid-fraction (LSF) and high-solid-fraction (HSF) semisolid formed A357 aluminum alloy. (a) LSF as-formed. (b) HSF as-formed. (c) LSF-T6. (d) HSF-T6. (e) LSF-T6 eutectic. (f) HSF-T6 eutectic. Courtesy Delphi Automotive Systems

Typical as-formed and heat treated (T6 temper) microstructures of the LSF and HSF material are shown in Fig. 21. The round white objects in the as-formed microstructures (Fig. 21a and b) are primary α-aluminum spheroids, which are solid during metal injection. The surrounding matrix (the liquid portion during injection)

is composed of fine primary aluminum dendrites in white and a dark eutectic phase. The matrix of the as-formed HSF material is composed primarily of eutectic phase, as the material was injected into the die just above the eutectic temperature. The eutectic phase of the LSF-T6 material (Fig. 21e) consists of rounded primary silicon particles (dark gray), rounded Fe-Mg-Si-Al intermetallics (light gray), and needle-shaped Fe-Si-Al intermetallics. The eutectic phase of the HSF-T6 material (Fig. 21f) also has rounded silicon particles (dark gray) and rounded Fe-Mg-Si-Al intermetallics (light gray). The HSF-T6 microstructure, however, does not exhibit the needle-shaped Fe-Si-Al intermetallics. Basner et al. attributed this difference to a lower iron content in the HSF sample (Ref 15).

Methods have been developed to further quantity the microstructure of semisolid metalworking components. Basner et al. utilized an image analysis system in their studies to quantify key microstructural features including area fraction solid, spheroid size, spheroid shape factor, T6 eutectic particle size, and T6 eutectic particle aspect ratio (Ref 15). The solid fraction and spheroid features were measured from as-formed samples, while the eutectic particle features were measured in the T6 condition. Spheroid size is defined as the area equivalent diameter of the spheroid. The spheroid shape factor (SF) is a perimeter-sensitive measurement, which looks at the area of the spheroid relative to its perimeter:

$$SF = 4\pi A/p^2$$

where A is the spheroid cross-sectional area and p is the perimeter. The SF has a value of 1 or less, with a perfectly circular spheroid having a SF of 1. The T6 eutectic silicon and intermetallic particles were measured conjointly, with features in contact with each other measured as one feature.

Table 4 summarizes Basner (Ref 15) results for the components presented in Fig. 21. The size of the LSF spheroids is significantly larger than the HSF spheroids. The average spheroid shape factor for the HSF material is closer to the ideal value of 1 than the LSF material. The lower value for the LSF material can be attributed to the agglomeration of the spheroids, which increases the perimeter of the feature. Particles in the LSF eutectic are larger and have a higher aspect ratio than the particles in the HSF eutectic. Figure 21(e) shows several intermetallic particles in the LSF eutectic in contact with the eutectic silicon particles, while the intermetallic and silicon particles in the HSF material (Fig. 21f) appear to be more disassociated.

Table 4 Microstructural features in low solid fraction and high solid fraction A357 aluminum alloy

	Low solid fraction	High solid fraction
Spheroidal features		
Solid fraction	0.31–0.36	0.67
Area equivalent diameter, μm	235	130
Shape factor	0.60	0.71
T6 eutectic particle features		
Area equivalent diameter, μm	2.04	1.75
Aspect ratio	1.60	1.50
Density, particles/μm^2	29,908	65,323
Mean free path, mm	9.19	5.30
Longest dimension, average, μm	2.93	2.38
Longest dimension, maximum, μm	18.38	14.64

Source: Ref 15

To close this section, a comparison is presented of a 357 aluminum alloy sample prepared using Keller's etch and 0.5% HF at a range of equivalent magnification (Fig. 22). As discussed previously in this section, the round white objects in the microstructures are primary α-aluminum spheroids, which make up the solid fraction of the material during manufacture. The surrounding matrix in the microstructure is composed of fine primary aluminum dendrites and the eutectic phase, which was formerly the liquid fraction during manufacture. Dark specks within the primary α-aluminum spheroids are entrapped eutectic.

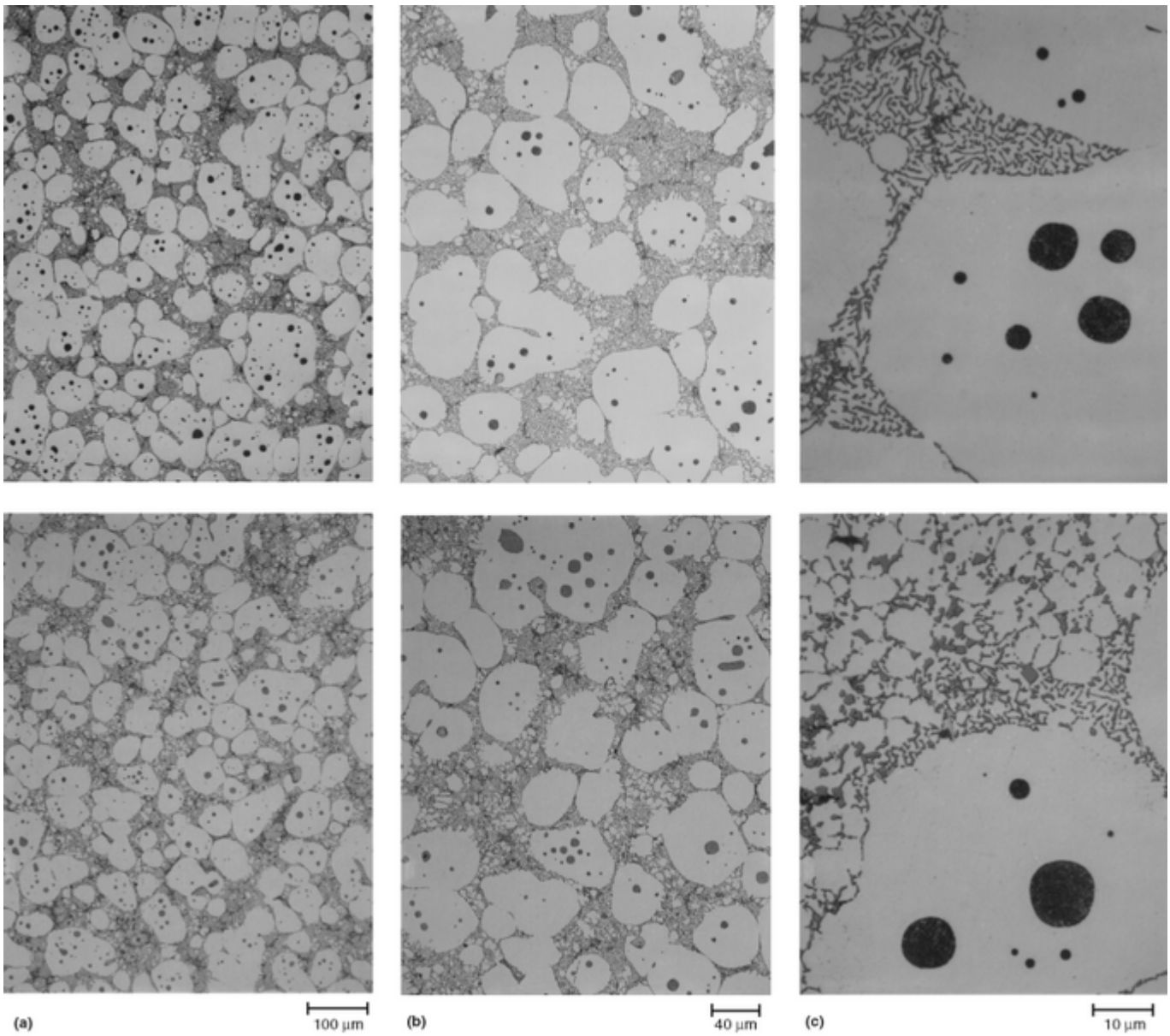

Fig. 22 Microstructures of a 357 aluminum alloy component with T5 artificial aging at (a) 100×, (b) 200×, and (c) 1000× prepared using Keller's etch (top) and 0.5% HF acid (bottom)

Magnesium Semisolid Microstructures

Feedstock microstructures, direct semisolid metalworking component microstructures, and indirect semisolid metalworking component microstructures are discussed separately for magnesium alloys.

Magnesium Billet Feedstock Microstructures. Methods similar to that used to produce aluminum continuously cast feedstock are used to produce magnesium billet material. Magnetohydrodynamic stirring is the most common method employed to break up dendrites during processing. When MHD stirring is not used, continuously cast magnesium bar stock exhibits a classical dendritic structure (Fig. 23). Dendrites are still present in the microstructure formed when stirring is employed, but the dendrites are broken up into smaller rosettes (Fig. 24) (Ref 16).



Fig. 23 Microstructure of AZ91D magnesium alloy feedstock produced without stirring. Samples prepared by polishing to a 1 µm finish on a diamond wheel then etched with acetic picral. Courtesy of CANMET

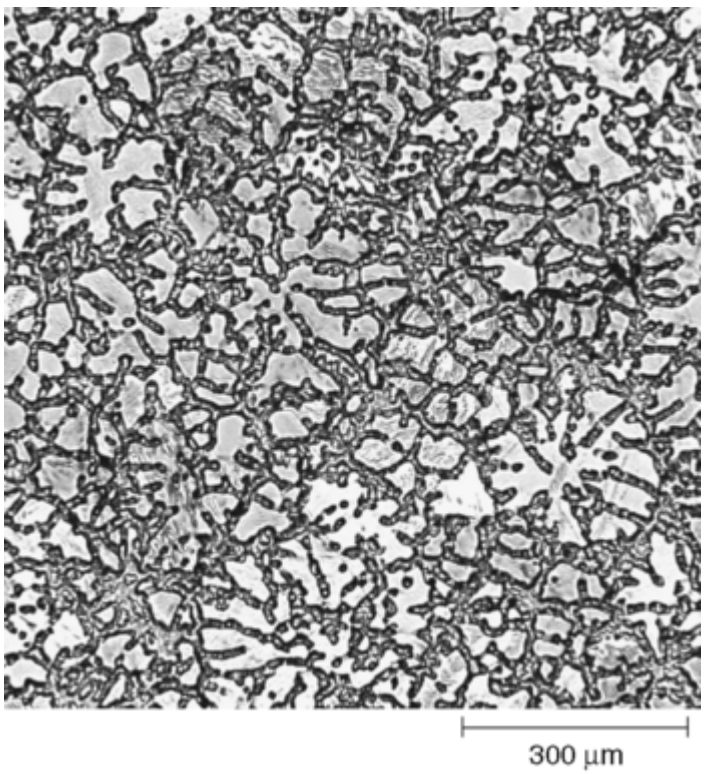

Fig. 24 Microstructure of AZ91D magnesium feedstock casting with electromagnetic stirring. Samples prepared by polishing to a 1 µm finish on a diamond then wheel etched with acetic picral. Courtesy of CANMET

Numerous direct semisolid metalworking processes have been developed for magnesium using pelletized feedstock. Unlike aluminum, magnesium does not aggressively attack tool steels. Screw-fed melting and

injection systems, much like those used in plastic injection molding, have been developed for use with magnesium alloys. The microstructure of the pelletized feedstock can vary greatly. Shown in Fig. 25 are typical microstructures for AZ91D chipped and rapidly solidified feedstock (Ref 10). Some typical microcracks are indicated in the chipped samples. Although chipped feedstock is typically ground from cast ingot, the microstructure is not entirely dendritic. Although portions of a chip may retain a dendritic structure (Fig. 25a), the mechanical work required to chip the material will cause localized severe deformation. These regions are frequently accompanied by cracks originating between γ-phase $Mg_{17}Al_{12}$ precipitates and the primary magnesium phase as shown in Fig. 25(b). In some cases, cracking of large $Mg_{17}Al_{12}$ intermetallic precipitates will extend into the α-magnesium matrix (Fig. 25c). The typical microstructure found in rapidly solidified AZ91D pellets is very different from that found in chipped feedstock (Fig. 25d). This is due to the high solidification rate in a very small volume of metal. The microstructure is composed of very fine dendritic grains with the γ-phase compound $Mg_{17}Al_{12}$ at the grain boundaries.

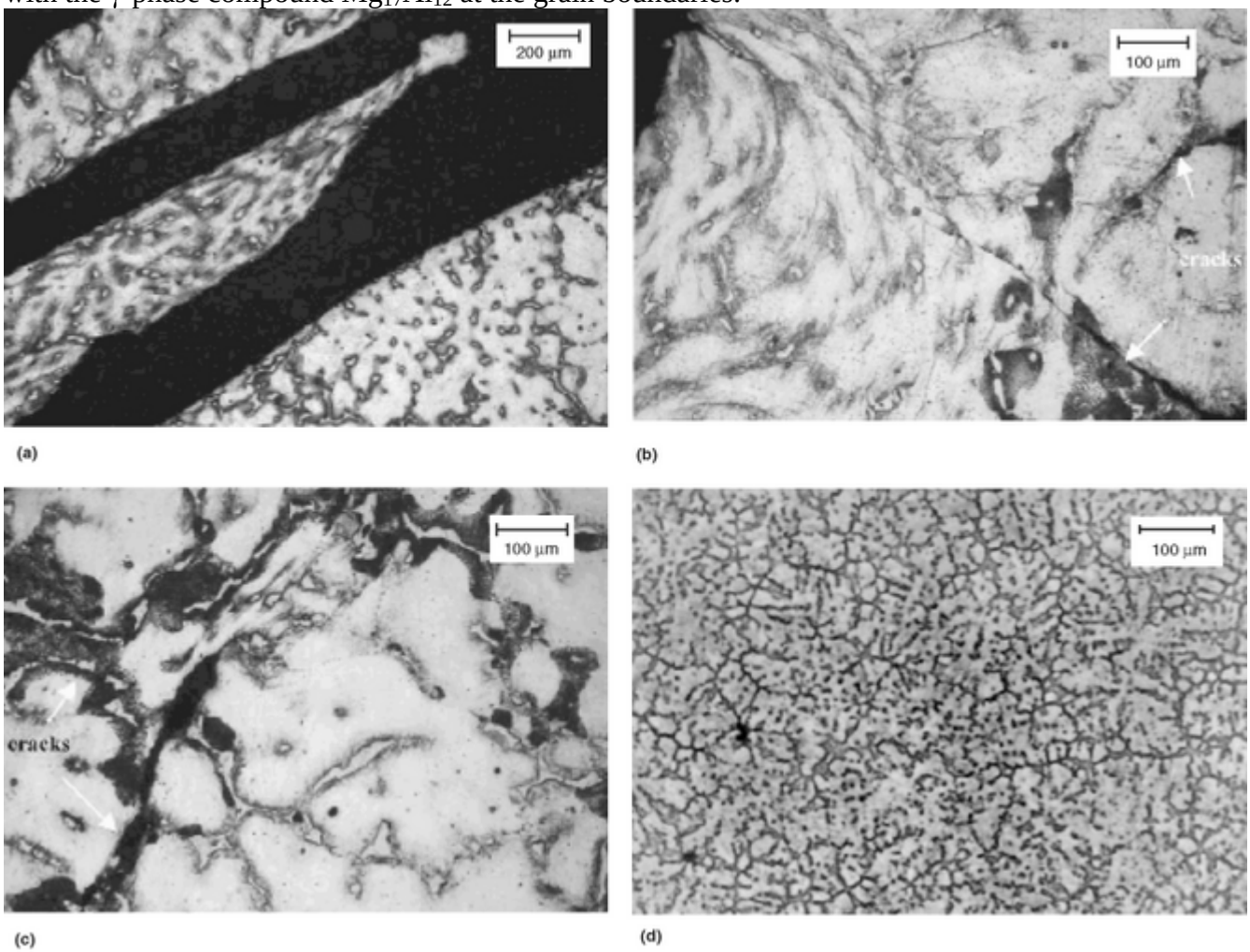

Fig. 25 The initial microstructures of pelletized AZ91D magnesium feedstock. (a) General view of chipped feedstock. (b) Heavy plastic deformation within a chip. (c) Minor deformation features within a chip. (d) Initial microstructure of rapidly solidified feedstock with a dendritic structure. Samples prepared by cold mounting, polishing, and etching with 1% nitric acid in ethanol. Courtesy of Husky Injection Molding Systems

Regardless of the differences between mechanically chipped and rapidly solidified feedstock, both types undergo a similar transformation when heated to a semisolid state. Figure 26 and Figure 27 show (a) partially bonded pellets removed from a crucible for metallographic examination, an evolving equiaxed grain structure within partially bonded pellets at low (b) and (c) high magnifications, and the spheroidal microstructure (c) formed with melting at approximately 25% solid fraction for chipped and rapidly solidified pellets, respectively. The amount of entrapped eutectic is typically lower in products produced using chipped feedstock.

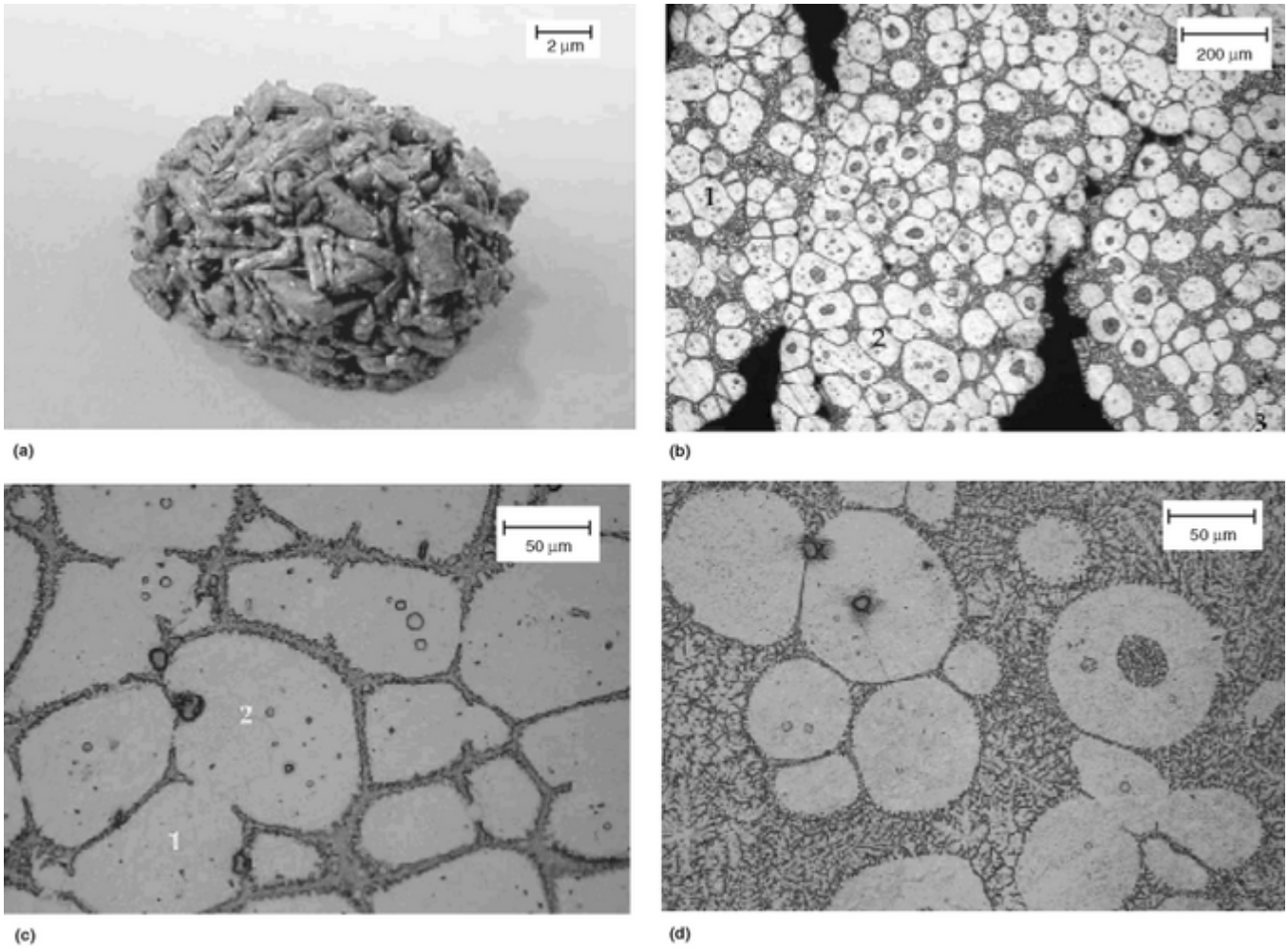

Fig. 26 Microstructural evolution of chipped AZ91D magnesium feedstock during melting. (a) Macroscopic view of chips removed from a crucible. (b) Equiaxed grain structure in bonded chips. (c) Initial chip melting with an equiaxed grain structure. (d) Spheroidal morphology containing 22% of solid fraction. Samples prepared by cold mounting, polishing, and etching with 1% nitric acid in ethanol. Courtesy of Husky Injection Molding Systems

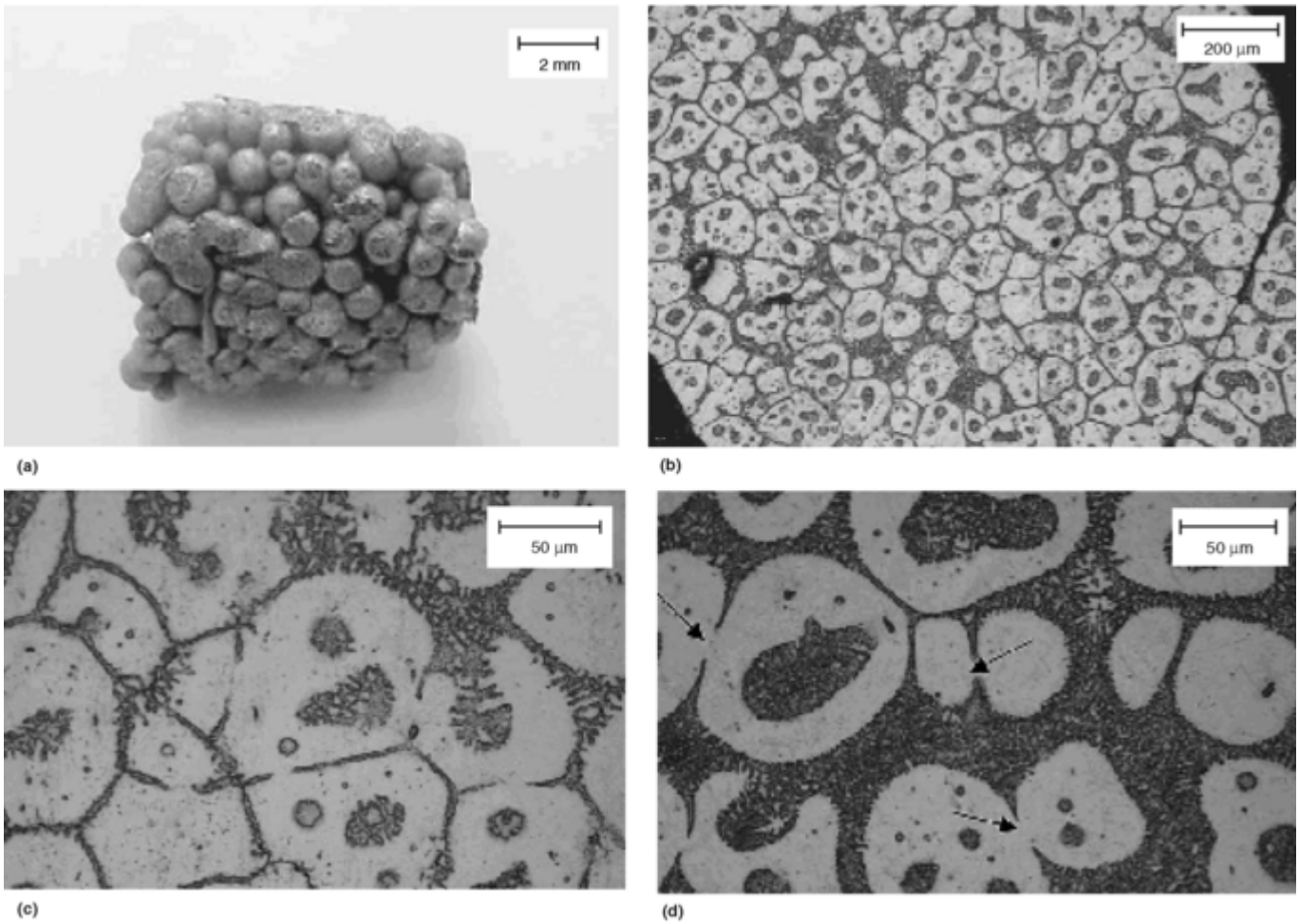

Fig. 27 Microstructural evolution of dendritic AZ91D magnesium feedstock during melting. (a) Macroscopic view of pellets removed from a crucible. (b) Equiaxed grain structure in bonded pellets. (c) Equiaxed grain structure during initial melting. (d) Spheroidal morphology containing 26% solid fraction. Samples prepared by cold mounting, polishing, and etching with 1% nitric acid in ethanol. Courtesy of Husky Injection Molding Systems

Magnesium Direct Semisolid Metalworking Component Microstructures. Direct semisolid metalworking of magnesium alloys can be a very efficient and safe method for manufacturing net-shape components. In some cases, such as that of thixomolding, the heated magnesium semisolid mixture alloy never comes in contact with the open atmosphere.

Since the semisolid metal mixture is completely contained within the screw, the liquid/solid fraction can be adjusted easily without creating any complications associated with billet-type indirect processes. As such, multiple microstructures may be obtained by varying the percent solid, as shown in Fig. 28 for an AM60B alloy. In extreme cases, the metal may be heated to a completely liquid state.

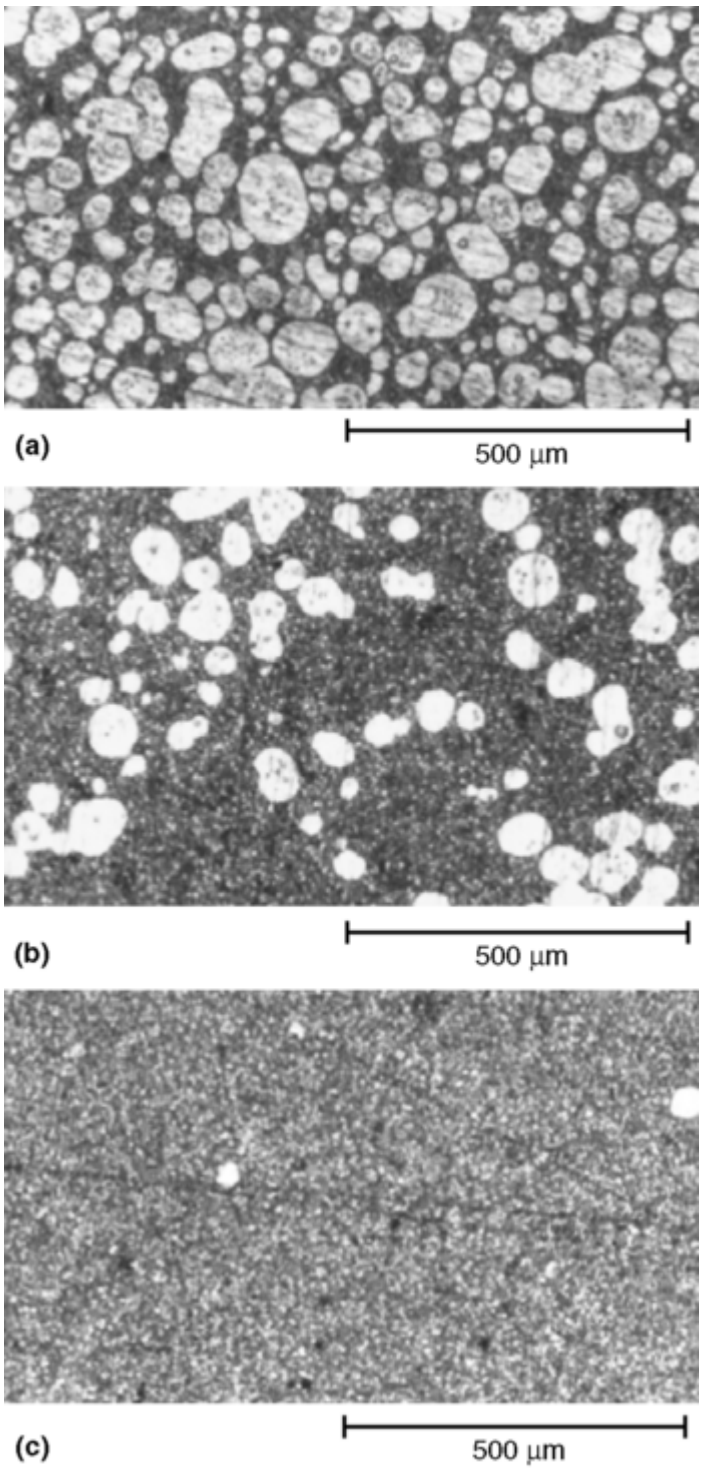

Fig. 28 Multiple microstructures of AM60B magnesium are obtained by varying the percent solid during metal injection when using the direct semisolid metalworking processes. (a) Semisolid molding at 565 °C (1050 °F). (b) Semisolid molding at 585 °C (1085 °F). (c) Die casting at 605 °C (1120 °F). Courtesy of Thixomat

Scanning electron microscopy (SEM) images (Fig. 29) show fine-grained components for varying degrees of solid fraction formed by the rapid solidification of the liquid portion of the semisolid slurry (Ref 17). Samples were polished and etched using an argon ion beam inclined at 4° to the sample surface and subsequently imaged with SEM. Due to differences in electrical conductivity between microstructural constituents, a distinct contrast is shown between phases. While the α-magnesium, having higher conductivity, is seen as a dark phase, the intermetallic component, with a lower conductivity, gathers electrons, creating a bright color. A simple visual assessment indicates that, in addition to variations in the content of the primary solid particles, there is also a difference in the morphology of the eutectic component.

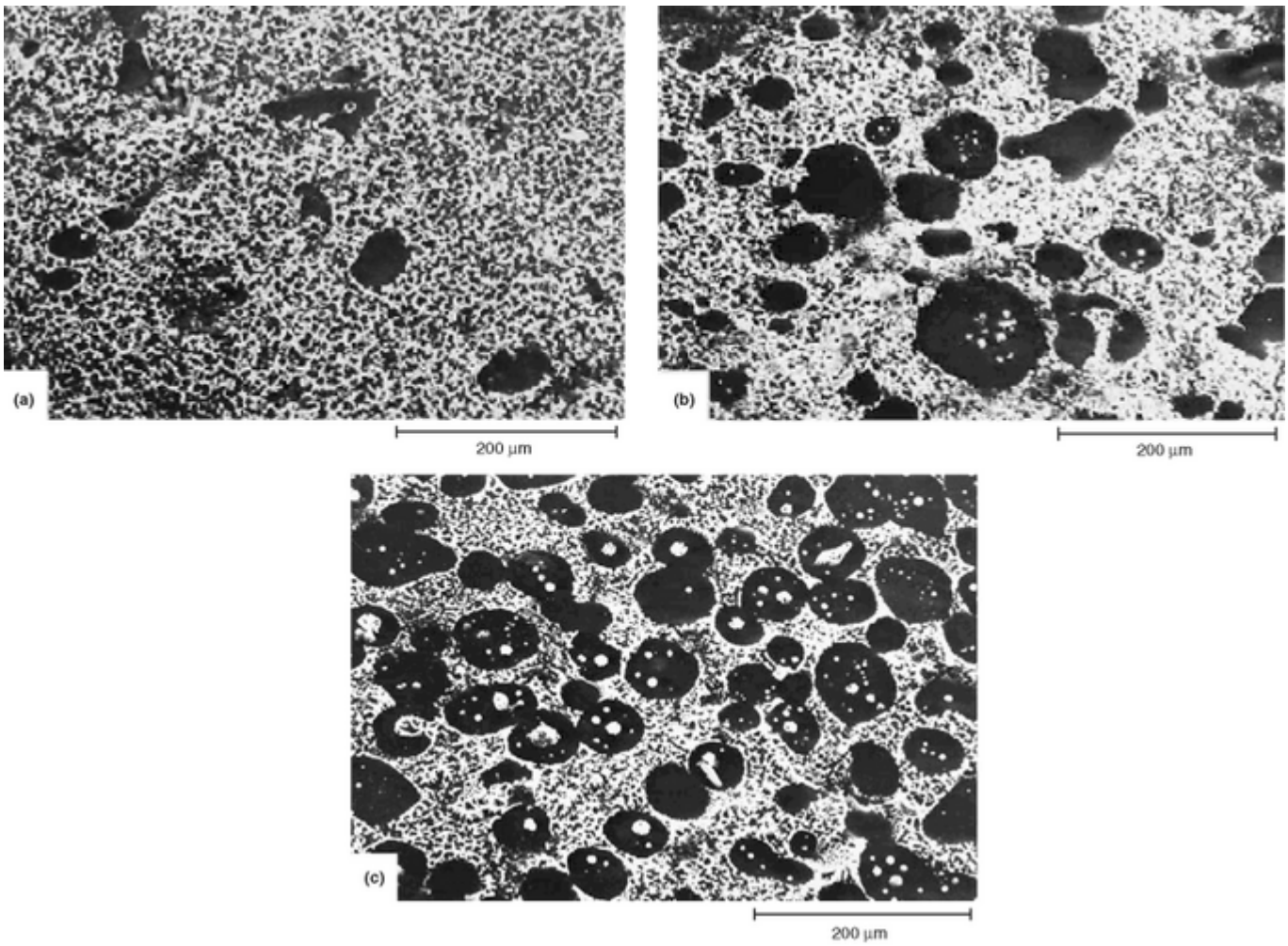

Fig. 29 SEM images of AZ91D magnesium microstructures showing the primary solid and eutectic components within alloys containing: (a) 5%; (b) 22%; and (c) 43%, solid fractions. Courtesy of Husky Injection Molding Systems

Transmission electron microscopy (TEM) is also an effective method for evaluating the microstructures of components produced using semisolid metalworking processes. Transmission electron microscopy is particularly useful in revealing the subtle details of the internal microstructure. For example, Fig. 30 is composed of TEM micrographs of an AZ91D component produced with a solid fraction of 43%. These TEM micrographs were prepared using an instrument with an accelerating voltage of 100 kV. Thin foils were prepared by electrolytic polishing in a solution composed of one part nitric acid and two parts ethanol, at a temperature of -10 °C (15 °F) and a voltage of 30 V. In some cases, argon-ion thinning was also applied. A selected area electron diffraction technique (SAD) in TEM was used for phase identification. The microstructure comprises 1 to 5 μm thick laths, with a varying density of dislocations (Fig. 30a). As indicated by the accompanying SAD pattern, the entire region imaged has one major crystallographic orientation expressed by the zone axis of $1\bar{2}1\bar{3}$. However, the oversized (double in some cases) diffraction spotas suggest a small misorientation existing between individual laths. The eutectic component in the alloy containing the 43% solid fraction is shown in Fig. 30(b). Some α-magnesium particles are as small as 1 μm. The intermetallic compound (Fig. 30c) was also verified as being $Mg_{17}Al_{12}$ per the attached diffraction pattern (Ref 17).

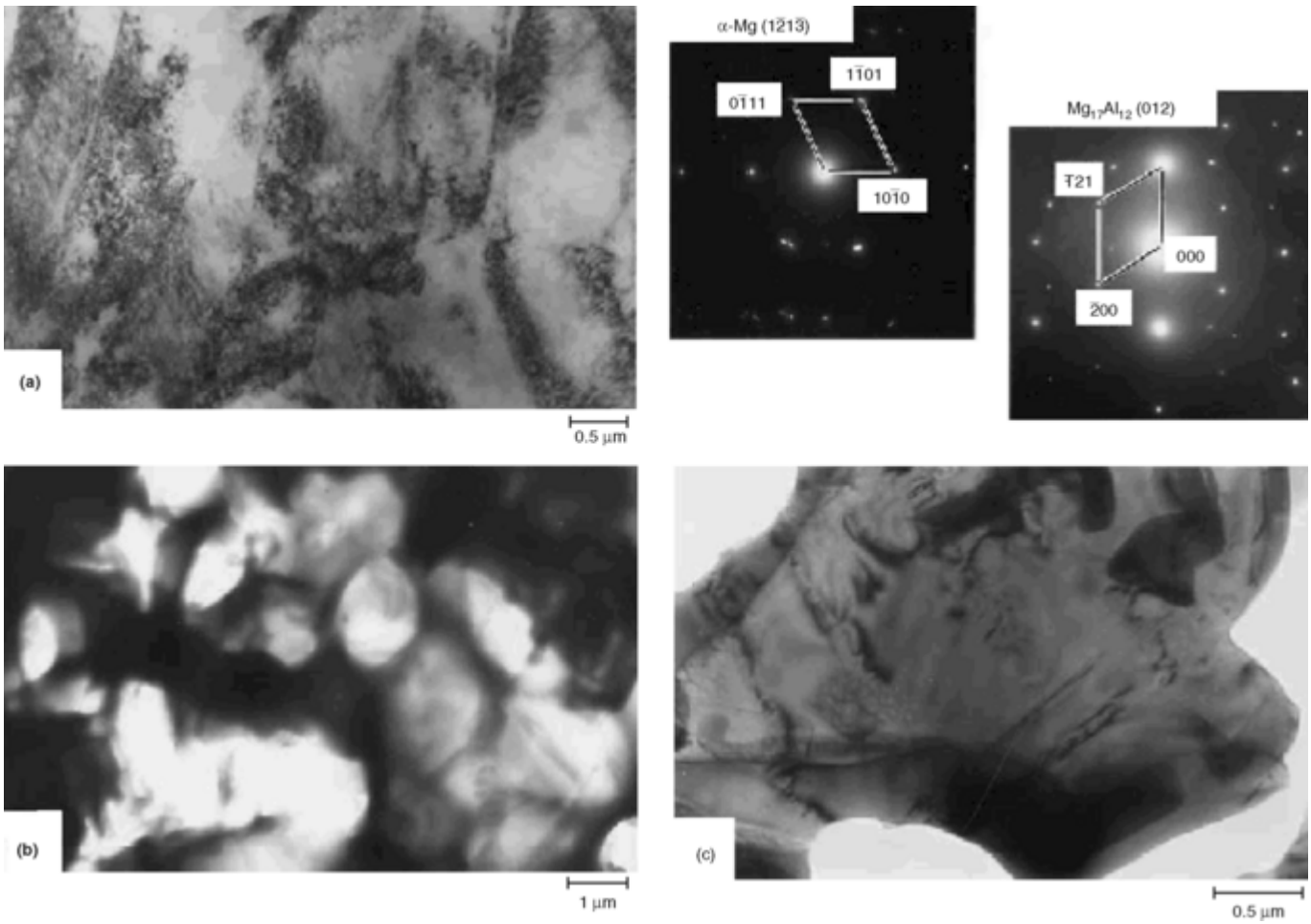

Fig. 30 TEM microstructure of an AZ91D magnesium sample containing 43% solid fraction. (a) Primary α-magnesium phase with laths having different dislocation densities and corresponding SAD pattern. (b) Fine-grained eutectic with α-magnesium particles on the order of 1 μm. (c) Thin section of $Mg_{17}Al_{12}$ intermetallics with corresponding SAD pattern. Courtesy of Husky Injection Molding Systems

Magnesium Indirect Semisolid Metalworking Component Microstructures. Components produced with magnesium alloys using indirect processes have very similar microstructures to components produced using aluminum alloys. Metallographically, many of the same basic preparation techniques can be followed. However, the typical etchants used to augment the grain structure are different. Magnesium alloys exhibit entrapped grains of eutectic within the primary phase. For the microstructure shown in Fig. 31 for a component produced using AZ91D alloy, the primary solid fraction phase is α-magnesium. The matrix and specks trapped within the α-magnesium is the Mg-$Mg_{17}Al_{12}$ eutectic (Ref 16).

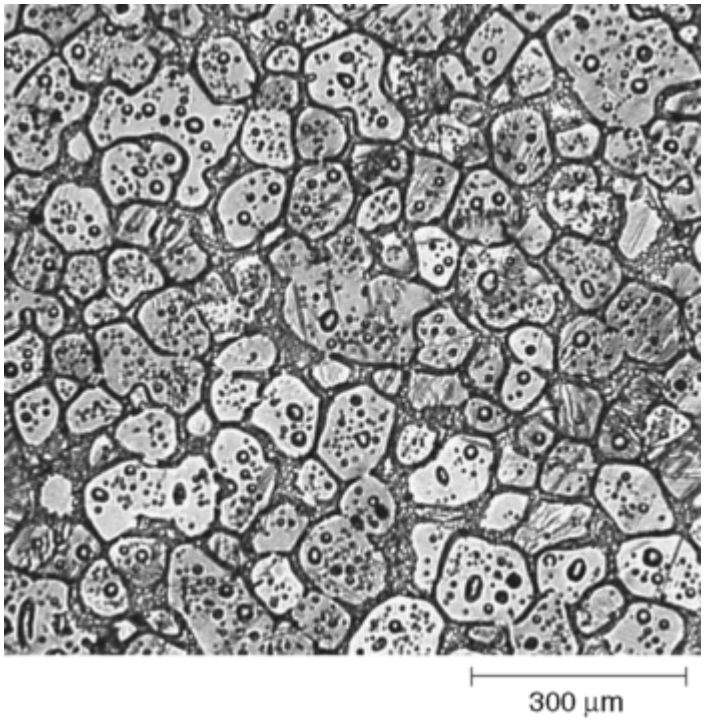

Fig. 31 Microstructure of an AZ91D magnesium component produced using indirect semisolid metalworking. Sample prepared by polishing to a 1 µm finish on a diamond wheel etched with acetic picral. Courtesy of CANMET

References cited in this section

10. F. Czerwinski, On the Generation of Thixotropic Structures During Melting of Mg-9%Al-1%Zn Alloy, *Acta Mater.,* Vol 50, 2002, p 3265

12. R. DasGupta and D. Killingsworth, Automotive Applications Using Advanced Aluminum Die Casting Processes, *Casting Solutions for the Automotive Industry,* Society of Automotive Engineers, 2000, p 39

13. R. Martinez et al., Efficient Formation of Structures Suitable for Semi-Solid Forming, *Transactions,* North American Die Casting Association, 2001

14. C. Loong et al., Semi-Solid Casting and Forging of A357 Aluminum Alloy Components, *Proc. Seventh S2P International Conference on Semi-Solid Processing of Alloys and Composites* (Tsukuba, Japan), 25–27 Sept, 2002, p 213

15. T. Basner, R. Pehlke, and A. Sachdev, Fatigue Behavior of Semi-solid Formed A357-T6 Aluminum, *Automotive Casting Processes and Materials,* Society of Automotive Engineers, 2001, p 81

16. M. Shehata et al., Production and Die Casting of Semi-Solid Magnesium Alloy AZ91D, *Light Metals for the Automotive Industry,* Society of Automotive Engineers, 2002, p 73

17. F. Czerwinski et al., Correlating the Microstructure and Tensile Properties of a Thixomolded AZ91D Magnesium Alloy, *Acta Mater.,* Vol 49, 2001, p 1225

E.J. Vinarcik, Metallography and Microstructures of Semisolid Formed Alloys, *Metallography and Microstructures,* Vol 9, *ASM Handbook*, ASM International, 2004, p. 1021–1037

Edward J. Vinarcik

Future Developments

Driven by economics, efforts are underway to further improve aspects of semisolid metalworking processes and materials.

Currently, the commercial magnesium alloys used in semisolid metalworking are limited to near room-temperature applications due to decreased creep resistance as the temperature is elevated. Some magnesium alloys containing rare-earth elements are available that can operate at temperatures as high as 150 °C (300 °F) with a significant cost penalty. Past research has shown that additions of aluminum and alkaline rare-earth elements (barium, strontium, and calcium) in magnesium form fine precipitates of $Al_{11}E_3$ at grain boundaries (Ref 18, Ref 19). These precipitates inhibit creep at elevated temperatures. Of the alkaline metals currently researched, calcium is the least costly as well as the least dense. Several magnesium alloys containing aluminum and calcium are under development.

Discontinuously reinforced metal-matrix composites are under development for commercial use with semisolid metalworking. Discontinuous reinforced casting alloys are a class of metal-matrix composites in which a metal alloy matrix is reinforced with ceramic particles or whiskers. Figure 32 is an illustration of a component produced using such a composite. Discontinuously reinforced composite materials exhibit improved characteristics when compared to traditional casting alloys, including reduced structural weight, increased tensile modulus, improved yield strength, increased ultimate tensile strength, improved fatigue limit, improved elevated temperature properties, improved dynamic response, and enhanced wear resistance.

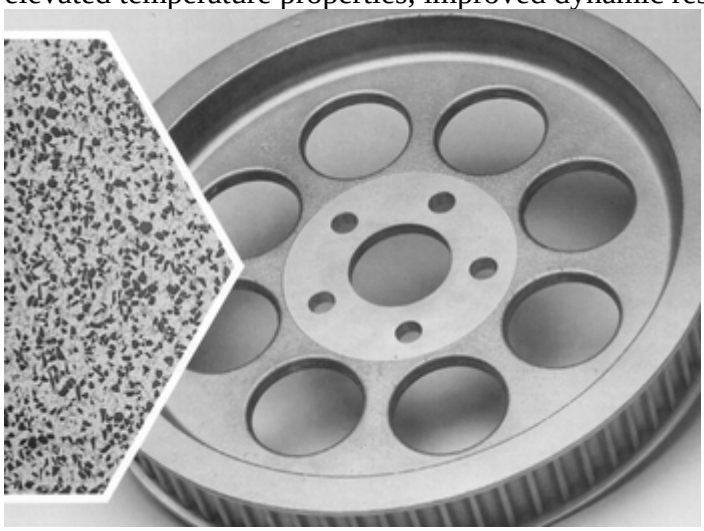

Fig. 32 Motor cycle sprocket die cast using a SiC particulate-reinforced aluminum-matrix composite. Courtesy of Alcan, Inc.

Several aluminum and magnesium metal-matrix composites are commercially available with several ceramic reinforcing materials. Reinforcing materials used with magnesium have been limited to SiC (Ref 20). However, reinforcing materials commonly used with aluminum alloys include SiC, Al_2O_3, B_4C, and fly ash (Ref 21, 22, 23). Of these reinforcing materials, fly ash is the most economically favorable filler as it is a waste product from coal-burning power plants. Fly ash has a raw material cost ranging from $16 to $33 USD/1000 kg ($15 to 30 USD/ton). Unlike most casting processes, semisolid metalworking is very well suited for use with metal-matrix composites. Maintaining homogeneity is difficult when the composite material is molten due to

differences in densities. The thixotropic properties of the semisolid metal mixture and the stirring inherent to semisolid metal preparation create ideal conditions for maintaining composite homogeneity.

References cited in this section

18. B. Powell, A. Luo, V. Rezhets, J. Bommarito, and B. Tiwari, Development of Creep-Resistant Magnesium Alloys for Powertrain Applications: Part 1, *Light Metal Applications for the Automotive Industry*, Society of Automotive Engineers, 2001, p 29

19. A. Luo, M. Balogh, and B. Powell. Development of Creep-Resistant Magnesium Alloys for Powertrain Applications: Part 2, *Light Metal Applications for the Automotive Industry*, Society of Automotive Engineers, 2001, p 37

20. T. Wilks, Cost-Effective Magnesium MMCs, *Adv. Mater. Process.*, Aug 1992, p 27

21. P. Rohatgi, Cast Aluminum-Matrix Composites for Automotive Applications, *J. Met.*, April 1991, p 10

22. P. Rohatgi, Aluminum-Flyash Composites, *Foundry Manage. Technol.*, Oct 1995, p 32

23. P. Rohatgi, Low Cost, Flyash Containing Aluminum-Matrix Composites, *J. Met.*, Nov 1994, p 55

E.J. Vinarcik, Metallography and Microstructures of Semisolid Formed Alloys, *Metallography and Microstructures*, Vol 9, *ASM Handbook*, ASM International, 2004, p. 1021–1037

Metallography and Microstructures of Semisolid Formed Alloys

Edward J. Vinarcik

Acknowledgment

The author wishes to express his gratitude to several colleagues who provided figures and supporting data for this article. Specifically, the author thanks George Vander Voort and Gabriel Lucas of Buehler Ltd., Mahmoud T. Shehata of CANMET Materials Technology Laboratory, Timothy Basner of Delphi Automotive Systems, Frank Czerwinski of Husky Injection Molding Systems, James Yurko of IdraPrince Inc., C.A. Loong of the Industrial Materials Institute for the National Research Council in Canada, John Jorstad of J.L.J. Technologies Inc., Rathindra DasGupta of SPX Contech, and Steve LeBeau of Thixomat Inc.

E.J. Vinarcik, Metallography and Microstructures of Semisolid Formed Alloys, *Metallography and Microstructures*, Vol 9, *ASM Handbook*, ASM International, 2004, p. 1021–1037

Metallography and Microstructures of Semisolid Formed Alloys

Edward J. Vinarcik

References

1. M. Flemings, Behavior of Metal Alloys in the Semisolid State, *Metall. Trans. B*, 1991, p 269

2. M. Keeney et al., Semisolid Metal Casting and Forging, *Casting,* Vol 15, *ASM Handbook,* ASM International, 1988, p 327

3. A. Alexandrou and G. Burgos, Semisolid Metal Processing, *Proc. Materials Solution Conference,* ASM International, 1998, p 23

4. K. Young, Semi-Solid Metal Cast Automotive Components: New Markets for Die Casting, *Transactions,* North American Die Casting Association, 1993

5. R. Wolfe and R. Bailey, High Integrity Structural Aluminum Casting Process Selection, *Casting Solutions for the Automotive Industry,* Society of Automotive Engineers, 2000, p 129

6. E.J. Vinarcik, *High Integrity Die Casting Processes,* John Wiley & Sons, 2002

7. J. Jorstad and W. Rasmussen, *Aluminum Casting Technologies,* 2nd ed., The American Foundry Society, 1993

8. "Magnesium Die Casting Alloys," Form 141-0636-6/95, Dow Magnesium, Midland, MI, 1995

9. *Magnesium Alloy Selector,* Hydro Magnesium, Livonia, MI, 1999

10. F. Czerwinski, On the Generation of Thixotropic Structures During Melting of Mg-9%Al-1%Zn Alloy, *Acta Mater.,* Vol 50, 2002, p 3265

11. A. Kazakov, Alloy Compositions for Semi-solid Forming, *Adv. Mater. Process.,* March 2000, p 31

12. R. DasGupta and D. Killingsworth, Automotive Applications Using Advanced Aluminum Die Casting Processes, *Casting Solutions for the Automotive Industry,* Society of Automotive Engineers, 2000, p 39

13. R. Martinez et al., Efficient Formation of Structures Suitable for Semi-Solid Forming, *Transactions,* North American Die Casting Association, 2001

14. C. Loong et al., Semi-Solid Casting and Forging of A357 Aluminum Alloy Components, *Proc. Seventh S2P International Conference on Semi-Solid Processing of Alloys and Composites* (Tsukuba, Japan), 25–27 Sept, 2002, p 213

15. T. Basner, R. Pehlke, and A. Sachdev, Fatigue Behavior of Semi-solid Formed A357-T6 Aluminum, *Automotive Casting Processes and Materials,* Society of Automotive Engineers, 2001, p 81

16. M. Shehata et al., Production and Die Casting of Semi-Solid Magnesium Alloy AZ91D, *Light Metals for the Automotive Industry,* Society of Automotive Engineers, 2002, p 73

17. F. Czerwinski et al., Correlating the Microstructure and Tensile Properties of a Thixomolded AZ91D Magnesium Alloy, *Acta Mater.,* Vol 49, 2001, p 1225

18. B. Powell, A. Luo, V. Rezhets, J. Bommarito, and B. Tiwari, Development of Creep-Resistant Magnesium Alloys for Powertrain Applications: Part 1, *Light Metal Applications for the Automotive Industry,* Society of Automotive Engineers, 2001, p 29

19. A. Luo, M. Balogh, and B. Powell. Development of Creep-Resistant Magnesium Alloys for Powertrain Applications: Part 2, *Light Metal Applications for the Automotive Industry,* Society of Automotive Engineers, 2001, p 37

20. T. Wilks, Cost-Effective Magnesium MMCs, *Adv. Mater. Process.,* Aug 1992, p 27

21. P. Rohatgi, Cast Aluminum-Matrix Composites for Automotive Applications, *J. Met.,* April 1991, p 10

22. P. Rohatgi, Aluminum-Flyash Composites, *Foundry Manage. Technol.,* Oct 1995, p 32

23. P. Rohatgi, Low Cost, Flyash Containing Aluminum-Matrix Composites, *J. Met.,* Nov 1994, p 55

J.R. Davis, Microstructural Characterization of Thermal Spray Coatings, *Metallography and Microstructures,* Vol 9, *ASM Handbook*, ASM International, 2004, p. 1038–1046

Microstructural Characterization of Thermal Spray Coatings

J.R. Davis, Davis & Associates

Introduction

THERMAL SPRAY is a generic term for a "family" of coating processes used to deposit metallic or nonmetallic coatings. During the process, powders, wires, or rods are injected into combustion-, electric arc-, or plasma arc-heated gas jets, where they are melted or softened, accelerated, and directed toward the surface or substrate being coated. On impact, the resultant particles or droplets rapidly solidify, cool, contract, and incrementally build up to form a lamellar deposit structure (Fig. 1, 2). The thin, individual globules deposited on the substrate, referred to as "splats," undergo very high cooling rates, typically in excess of 10^6 K/s for metals (Ref 1).

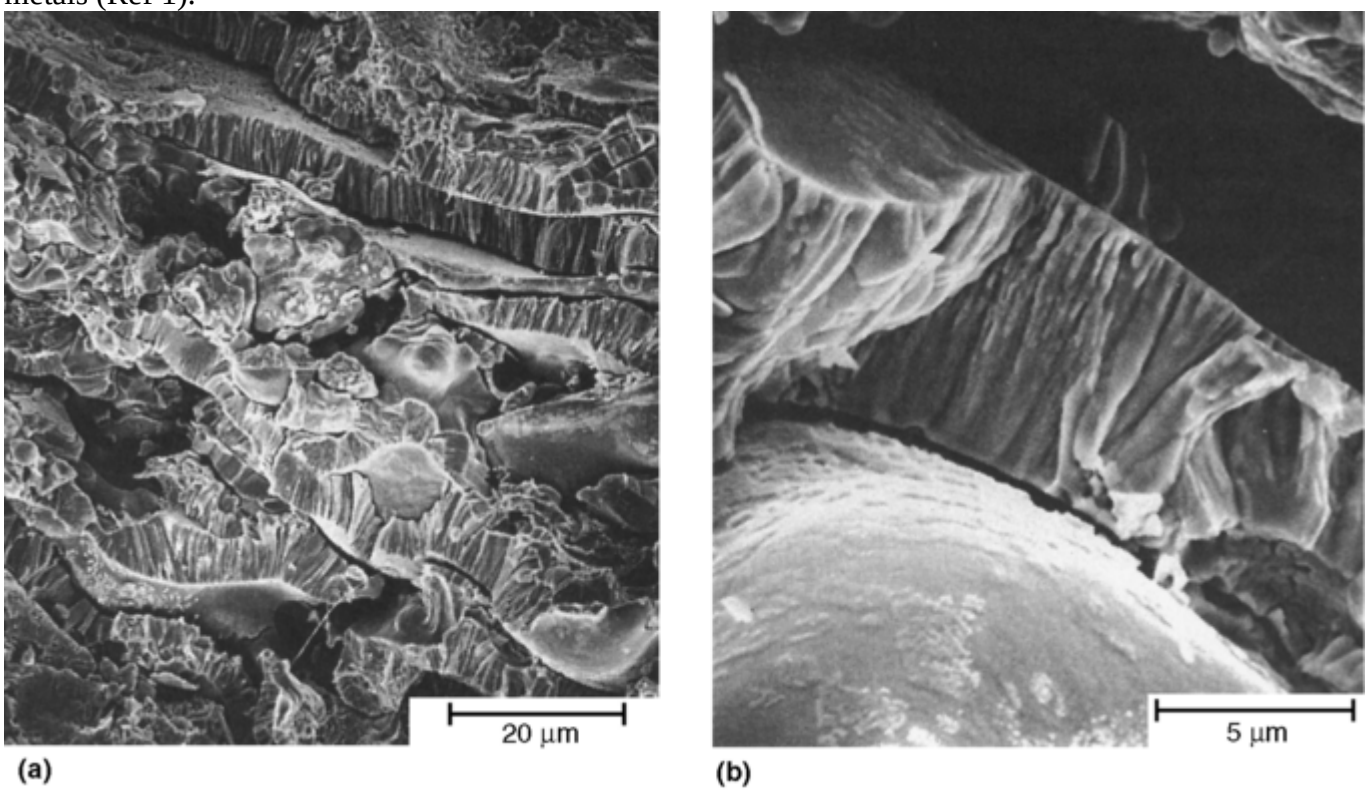

Fig. 1 Scanning electron micrographs of fracture cross sections of an air plasma sprayed tungsten coating. (a) Lamellar microstructure. (b) The presence of a columnar grain structure within the splats. Source: S.J. Bull, AEA Technology

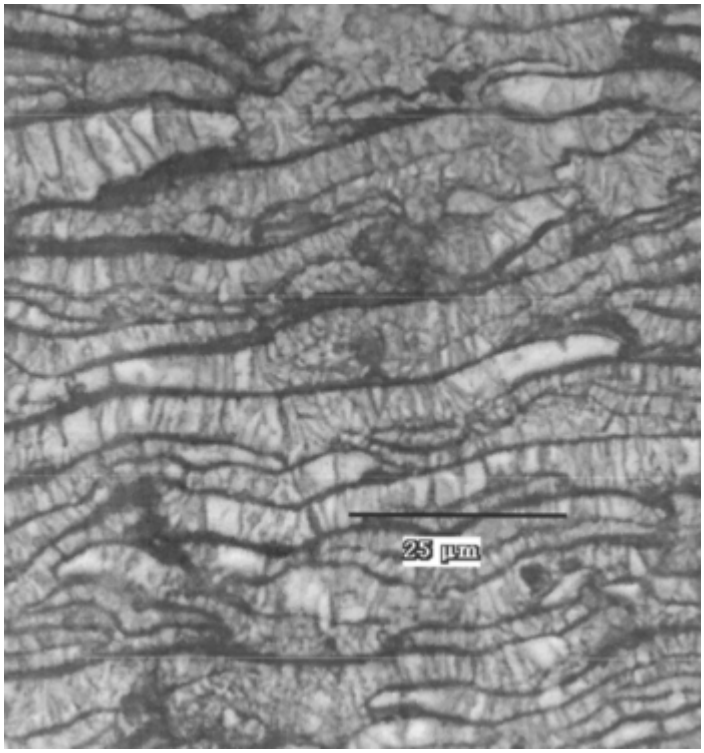

Fig. 2 Metallographic cross section of a pure tungsten coating revealing its lamellar microstructure and splat network. 500×. Source: W. Riggs, TubalCain Company Inc.

A major advantage of the thermal spray processes is the extremely wide variety of materials that can be used to produce a coating (Ref 2). Virtually any material that melts without decomposing can be used. A second major advantage is the ability of most of the thermal spray processes to apply coatings to substrates without significant heat input. Thus, materials with very high melting points, such as tungsten, can be applied to finely machined, fully heat treated parts without changing the properties of the part and without thermal distortion of the part. A third advantage is the ability, in most cases, to strip and recoat worn or damaged coatings without changing the properties or dimensions of the part. A disadvantage is the line-of-sight nature of these deposition processes. They can only coat what the torch or gun can "see." Of course, there are also size limitations prohibiting the coating of small, deep cavities, into which a torch or gun will not fit.

Thermal spray coatings are used to improve the resistance of substrate materials against corrosion and wear and to improve their heat resistance. The use of thermal spray coatings has moved from being extensively used in the aerospace industry to other applications, such as the processing industries (e.g., chemical and pulp and paper) and petroleum, infrastructure, and medical prosthesis applications (Ref 3). There has also been an increase in the use of thermal spray coatings in the automotive industry. These applications are performed on engine components, exhaust system components, and other large and small components, both mechanical and electrical.

References cited in this section

1. R. Knight and R.W. Smith, Thermal Spray Forming of Materials, *Powder Metal Technologies and Applications*, Vol 7, *ASM Handbook*, ASM International, 1998, p 408–419

2. R.C. Tucker, Jr., Thermal Spray Coatings, *Surface Engineering*, Vol 5, *ASM Handbook*, ASM International, 1994, p 497–509

3. G.A. Blann, Standardization of Metallographic Practices for Thermally Sprayed Coatings in the Automotive Industry, *Proceedings of the 15th International Thermal Spray Conference*, 25–29 May 1998 (Nice, France), ASM International, 1998, p 677–681

J.R. Davis, Microstructural Characterization of Thermal Spray Coatings, *Metallography and Microstructures,* Vol 9, *ASM Handbook,* ASM International, 2004, p. 1038–1046

Microstructural Characterization of Thermal Spray Coatings

J.R. Davis, Davis & Associates

Process Variations (Ref 4)

Before addressing the microstructural characteristics of thermal spray coatings, it is important to briefly review how process variations influence coating characteristics. The controllable parameters for each of the major thermal spray types are different, but all share some common fundamentals. Converting feedstock material (whether powders, wires, or rods) into a coating requires:

- Heat energy for melting
- A gas flow for atomization and/or particle acceleration to propel the particles toward the substrate

Input heat energy and gas flow, in turn, directly influence the following process variables:

- Flame/plasma/jet temperature
- Flame/plasma/jet velocity
- Particle temperature
- Particle speed
- Particle trajectory
- Deposit temperature

Each of these variables affects spray-pattern formation and particle heating differently. Table 1 shows a simple overview comparing heat energy and particle velocity for various thermal spray processes. In general, combustion-flame, combustion-wire, and twin-wire arc sprayed coatings are generated from high heat input plus low particle velocity. These coatings tend to exhibit high oxide contents, a large number of rounded particles, and relatively high porosity. As a result of higher particle velocity, the superheated particles present in plasma sprayed coatings are flattened more than in combustion sprayed coatings. The resulting coatings are also denser, with finer porosity. Very-high-velocity systems (such as detonation gun and high-velocity oxyfuel, or HVOF), combined with lower heat inputs, will typically produce very dense coatings not achievable by the other processes.

Table 1 Heat energy input and particle velocity for common thermal spray processes

Process	Input heat energy to particle		Output particle velocity[(a)]				
	High	**Low**	**Highest**	**High**	**Medium high**	**Medium**	**Low**
Combustion wire	X	X	X			X	
Combustion powder	X						X
Standard plasma	X				X		
High-velocity plasma	X			X			
Vacuum plasma	X			X			
Standard wire arc	X					X	
Vacuum arc	X				X		
High-velocity oxyfuel							
Detonation gun		X	X				

(a) Particle speed ranges from a high of approximately 1000 m/s (3000 ft/s) to a low of 25 m/s (80 ft/s). Further variations within each process depend on the particle size, material type, and gas velocity.
Source: Ref 4

Reference cited in this section

4. F.N. Longo, Coating Operations, *Handbook of Thermal Spray Technology,* ASM International, 2004, p 120–127

J.R. Davis, Microstructural Characterization of Thermal Spray Coatings, *Metallography and Microstructures,* Vol 9, *ASM Handbook*, ASM International, 2004, p. 1038–1046

Microstructural Characterization of Thermal Spray Coatings

J.R. Davis, Davis & Associates

Microstructural Characteristics (Ref 1)

As stated in the opening paragraph, the term *thermal spray* describes a family of processes that uses the heat energy generated by combustion or electrical (plasma or arc) methods to melt, or at least soften, and accelerate fine dispersions of droplets to velocities in the range of 50 to >1000 m/s (165 to >3300 ft/s). The high particle velocities and speeds achieved result in significant droplet deformation on impact at the surface, producing thin layers or lamellae (i.e., splats) that conform and adhere to the substrate surface. Solidified droplets build up rapidly, particle by particle, as a continuous stream of droplets impact to form continuous solidified layers. Individual splats are generally thin (~1 to 20 μm), and each droplet cools at very high rates (>10^6 K/s for metals) to form uniform, very fine-grained, polycrystalline coatings or deposits. Figure 3 shows a schematic of a generic thermal spray powder process, illustrating the key features and a typical deposit microstructure.

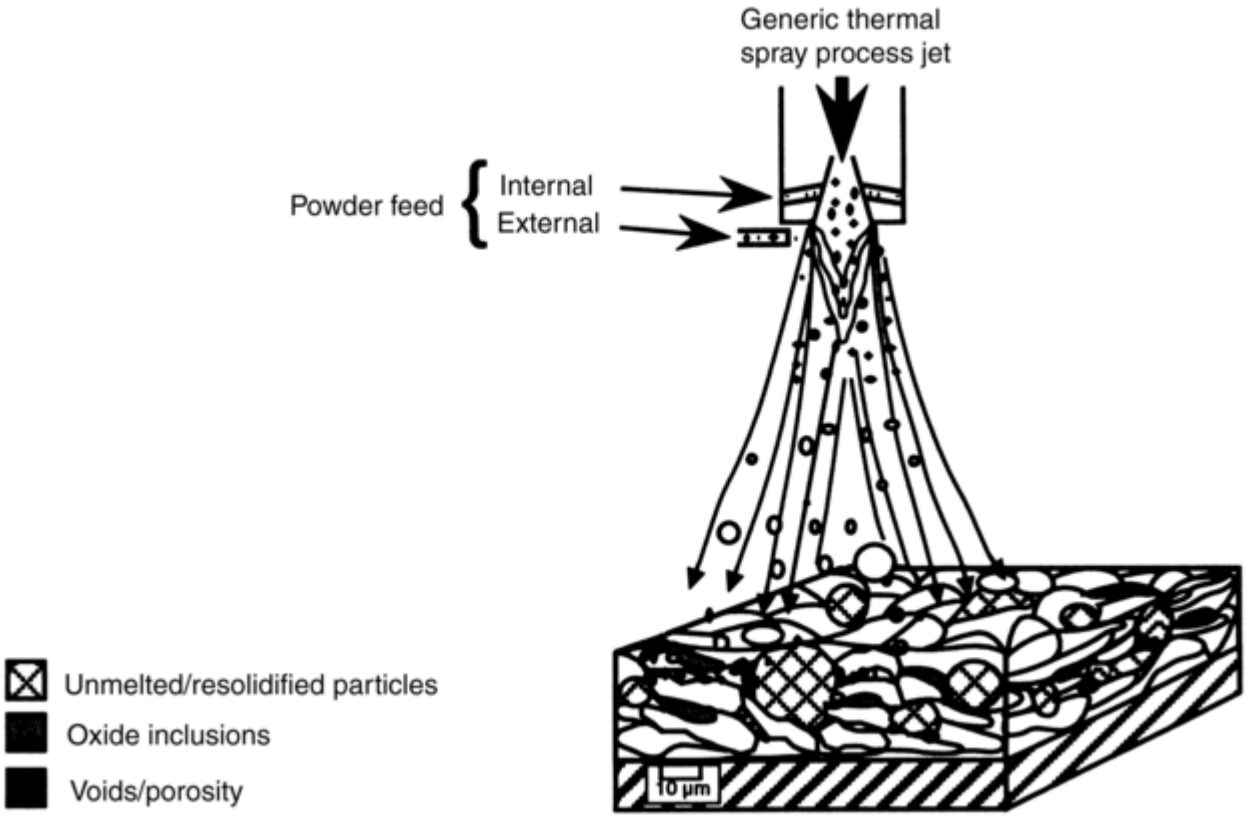

Fig. 3 Schematic of a typical thermal spray powder process. Source: Ref 1

Coating Microstructural Constituents. Sprayed deposits usually contain some level of porosity, some unmelted or partially melted particles, fully melted and deformed splats, metastable phases, and oxidation from entrained air. Thermal spray process jets or plumes are characterized by having large gradients of both temperature and velocity. Feedstock is usually in powdered form, having a distribution of particle sizes (see, for example, Fig. 4). When these powdered materials are fed into the plume, portions of the powder distribution take preferred paths according to their inertia. As a result, some particles may be completely unmelted and can create porosity or become trapped as “unmelts” in the coating. When wire and rod feedstock materials are used, distributions of particle sizes are produced because of nonuniform heating and unpredictable drag forces, which shear molten material from the parent wire or rod. The level of these coating defects varies depending on the particular thermal spray process used, the operating conditions selected, and the material being sprayed. Figure 5 is a micrograph of a thermal sprayed 80Ni-20Cr alloy coating applied with the HVOF process. The microstructure includes partially melted particles and dark oxide inclusions that are characteristic of many metallic coatings sprayed in air. Such coatings exhibit characteristic lamellar microstructures, with the long axis of the impacted splats oriented parallel to the substrate surface, together with a distribution of similarly oriented oxides. Oxide content of coatings varies with the process. The progressive increases in particle speed of thermal spray processes lead to differing levels of oxide and differing degrees of oxide breakup on impact at the surface. Oxides may increase coating hardness and wear resistance and may provide lubricity. Conversely, excessive and continuous oxide networks can lead to cohesive failure of a coating and contribute to excessive wear debris. Oxides can also reduce corrosion resistance. It is important to select materials, coating processes, and processing parameters so that oxide content and structure can be controlled to acceptable levels for a given application.

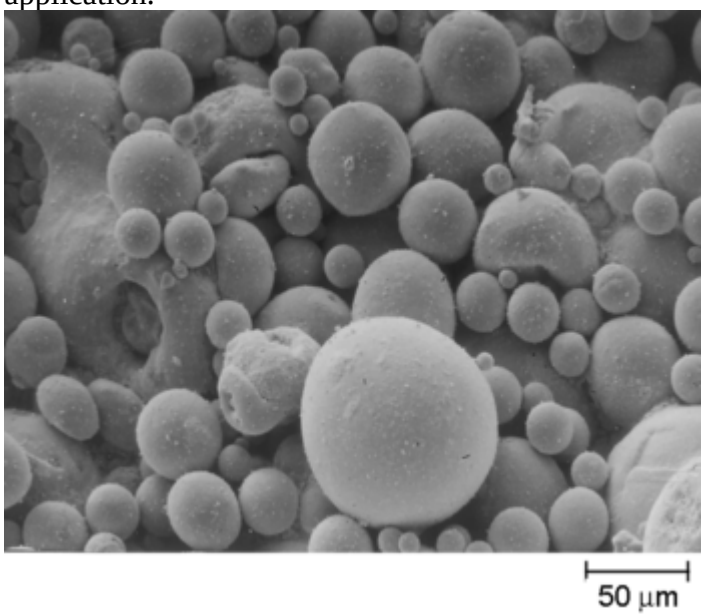

Fig. 4 Scanning electron micrograph showing the spherical shape and particle size distribution of yttria-stabilized zirconia powder feedstock. A wide range of particle sizes will result in irregular deposition due to inconsistent particle trajectories. Source: C.C. Berndt, State University of New York at Stony Brook

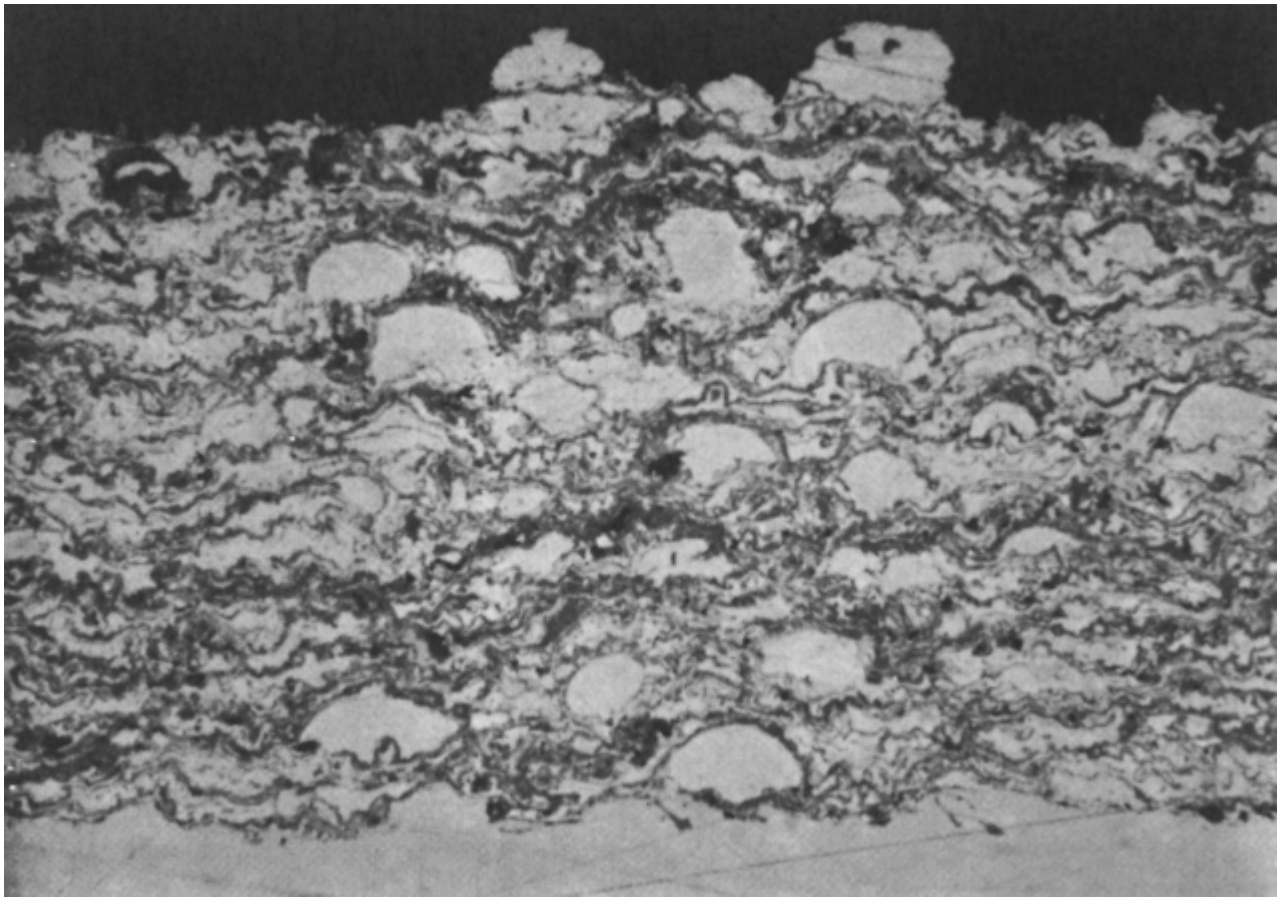

Fig. 5 Micrograph of an 80Ni-20Cr alloy deposited by the high-velocity oxyfuel process. Note the dark oxide inclusions and the rounded, partially melted particles. Source: Ref 1

Porosity. As discussed earlier, thermal spray coatings contain varying levels of porosity, depending on the spray process, the particle speed and size distribution, and the spray distance. As with oxide inclusions, porosity can either be beneficial or harmful. Oil/grease-impregnated or solid-lubricant bearings can be produced by creating 10 to 30% coating porosity into which lubricants can infiltrate. Porosity is also usually desirable in ceramic thermal barrier coatings, which are widely used in aircraft and land-based turbines and diesel engines. Thermal barrier coatings are generally composed of oxide ceramics, which by themselves are inherently good thermal insulators; the inclusion of 8 to 15% porosity further increases their insulating properties. Porosity also increases thermal shock and thermal cycling (fatigue) resistance. Medical implant prostheses are another useful application of porous coatings, where as much as 40% porosity is intentionally included. Porosity is used in implant coatings to allow bone matter to grow into the coating, which accelerates patient healing and shortens recovery time.

Excessive porosity in some applications is undesirable, and porosity levels are kept between 0 and ~10%. Porosity creates poor coating cohesion and allows for higher wear and corrosion rates. Porosity is generally associated with a high number of unmelted or resolidified particles that become trapped in the coating. Poor splat or particle cohesion resulting from excessive porosity leads to premature coating cracking, delamination, or spalling. Open porosity can interconnect to the coating surface, enabling corrosion or oxidizing elements to attack the base material. Porosity can thus “short circuit” the inherent corrosion resistance of a coating. For wear-resistant coatings, porosity lowers the hardness of the coating and contributes to poor surface finishes, thus decreasing the wear resistance of the coating. Porosity in wear coatings can also lead to the generation of coating fragments that break away and become abrasive cutting agents, increasing coating wear rates.

Grain Structure. Other key features of thermal sprayed deposits are their generally very fine grain structures and microcolumnar orientation (Fig. 1b). Thermal sprayed metals, for example, have reported grain sizes of <1 μm prior to postdeposition heat treatment (Ref 1). Grain structures across an individual splat normally range from 10 to 50 μm, with typical grain diameters of 0.25 to 0.5 μm, owing to the high cooling rates achieved.

Reference cited in this section

1. R. Knight and R.W. Smith, Thermal Spray Forming of Materials, *Powder Metal Technologies and Applications*, Vol 7, *ASM Handbook*, ASM International, 1998, p 408–419

J.R. Davis, Microstructural Characterization of Thermal Spray Coatings, *Metallography and Microstructures*, Vol 9, *ASM Handbook*, ASM International, 2004, p. 1038–1046

Microstructural Characterization of Thermal Spray Coatings

J.R. Davis, Davis & Associates

Microstructural Analysis by Light Microscopy

Successful development and application of reliable thermal spray coatings depends largely on strict process control, as well as coating microstructural analysis (metallography). However, accurate microstructural analysis of these coatings is possible only if specimen preparation produces a surface that clearly reveals the true microstructure. Yet, the heterogeneous or composite nature of the thermal spray deposit can make choosing the right metallographic preparation process very difficult. Comparison of similar specimens prepared by different laboratories, or different personnel in the same laboratory, often shows significant differences or variations in the microstructures, producing conflicting information that lowers the confidence level of microstructural analysis.

During the 1990s, considerable work was carried out on advanced specimen preparation techniques for thermal spray coatings (Ref 3, 5, 6). This work resulted in an ASTM standard being issued in 1997 (ASTM E 1920, "Standard Guide for Metallographic Preparation of Thermal Sprayed Coatings"). The methods described in this section are consistent with the ASTM recommendations as well as those of major manufacturers of metallographic consumables and equipment.

Problems Associated with Metallographic Preparation (Ref 7)

Thermal spray coatings have microstructural and physical properties, based on their chemical and thermal history, that differ dramatically from the substrate materials. For example, the extreme difference in the hardness of coatings and substrate leads to severe microstructural relief at the coating/substrate interface, which makes microscopic examination of this area very difficult.

As described in the section "Microstructural Characteristics," thermal spray coatings contain oxides that are brittle and easily fractured and lost, leaving voids that can be mistakenly interpreted as porosity. Coatings also contain hard constituents, such as carbides, that tend to be left in relief above the softer matrix. There also may be unmelted globules of the sprayed material that are not metallurgically bonded and can be pulled out if specimen preparation techniques are too abusive. In addition, the coating process itself may produce varying degrees of porosity. An accurate measure of porosity is important to the microstructural evaluation; thus, the pore edges must not be rounded during the specimen preparation process. If a large amount of edge rounding occurs, the percentage of apparent porosity will be higher than it actually is.

Traditional specimen preparation methods, in addition to being long and tedious, usually produce an excessive amount of microstructural relief and edge rounding, and hard, brittle constituents commonly present in thermal spray coatings are easily fractured and pulled out. Improper specimen preparation techniques also induce defects into the coating, leading to an inaccurate interpretation of the coating microstructure.

The objective of the more recently developed specimen preparation techniques discussed in the following section is to provide a specimen that will allow accurate microstructural analysis. Features necessary to achieve this include:

- Flatness across the entire specimen
- No edge rounding and microstructural relief

- No fracturing and pulling out of brittle constituents
- No removal of unmelted globules from the matrix
- No smearing of the softer matrix material

Recommended Metallographic Practices

Metallography is usually done on cross sections of small specimens coated under standard setup conditions, such as torch standoff distance, angle of deposition, traverse rate, and so on. These specimens, if appropriately sized, may be mounted for examination directly or, if too large, sectioned using abrasive cutoff blades. Following sectioning (if necessary) and mounting, a series of nonabusive grinding and polishing steps are carried out to reveal information concerning the following (Ref 8):

- Variations in structure from the surface to the substrate
- The distribution of unmelted particles throughout the coating
- The distribution of linear detachment throughout the coating. Linear detachment is defined in ASTM E 1920 as the region within a thermal spray coating in which two successively deposited splats of coating material have not metallurgically bonded.
- The distribution of porosity throughout the coating
- The presence of contamination within the coating
- The thickness of the coating (top coat and bond coat, where applicable)
- The presence of interfacial contamination
- The integrity of the interface between the coating and the substrate
- The integrity of the coating microstructure with respect to chemistry

It should be noted that a substantial amount of training and skill is necessary to be able to grind and polish thermal spray coatings properly and reproducibly by hand. It is therefore recommended that semiautomatic or automatic equipment be used, following procedures developed for each coating. Table 2, Table 3, Table 4 list guidelines established by ASTM that are suitable for a wide variety of thermal spray/substrate material combinations.

Table 2 ASTM E 1920 preparation method I for thermal spray coatings using silicon carbide (SiC) abrasive paper grinding

Surface	Coolant/lubricant	Abrasive size/type ANSI[a] (FEPA)[b]	Time, s	Force[c]		Surface speed, rpm	Relative rotation
				N	**lbf**		
Paper	Water	180- (P180-) grit SiC	Planar grinding, 15–25	20–30	4.5–6.7	200–300	Complementary[d]
Paper	Water	240- (P220-) grit SiC	Fine grinding, 15–25	20–25	4.5–5.6	200–300	Complementary
Paper	Water	320- (P500-) grit SiC	Fine grinding, 15–25	20–25	4.5–5.6	200–300	Complementary
Paper	Water	600- (P1200-) grit SiC	Fine grinding, 15–25	20–25	4.5–5.6	200–300	Complementary
Paper	Water	800- (P2400-) grit SiC	Fine grinding, 15–25	20–25	4.5–5.6	200–300	Complementary
No/low-nap cloth	Lapping oil or extending fluid	3–6 μm diamond	Rough polishing,	20–30	4.5–6.7	100–150	Complementary

			120–300				
Synthetic suede	None Water[e]	Colloidal silica 0.04–0.06 μm Al_2O_3	Final polishing, 60–120	10–20	2.2–4.5	100–150	Contrary[f]

(a) American National Standards Institute (ANSI) designation of grit size.
(b) Federation of European Producers of Abrasives (FEPA) designation of grit size.
(c) Force per 32 mm (1.25 in.) diameter specimen.
(d) Complementary rotation: surface and specimens spin in same direction (see Fig. 12)
(e) Water free of particulate is required; distilled water is recommended.
(f) Contrary rotation: surface and specimens spin in opposite directions (see Fig). 12)

Table 3 ASTM E 1920 preparation method II for thermal spray coatings using diamond grinding

Surface	Coolant/lubricant	Abrasive size/type ANSI[a] (FEPA)[b]	Time, min	Force[c]		Surface speed, rpm	Relative rotation
				N	**lbf**		
Paper	Water	240- (P220-) grit SiC	Planar grinding, 0.25–0.5	20–30	4.5–6.7	250–350	Complementary[d]
Hard woven cloth	Water-based suspension	6–9 μm diamond	Fine grinding, 4–7	20–25	4.5–5.6	100–150	Complementary
No/low-nap cloth	Lapping oil or extending fluid	3 μm diamond	Rough polishing, 1–3	20–30	4.5–6.7	100–150	Complementary
Synthetic suede	Water[e]	Colloidal silica	Final polishing, 1–3	23–35	5.2–7.9	100–150	Contrary[f]

(a) American National Standards Institute (ANSI) designation of grit size.
(b) Federation of European Producers of Abrasives (FEPA) designation of grit size.
(c) Force per 32 mm (1.25 in.) diameter specimen.
(d) Complementary rotation: surface and specimens spin in same direction (see Fig. 12)
(e) Water free of particulate is required; distilled water is recommended.
(f) Contrary rotation: surface and specimens spin in opposite directions (see Fig). 12)

Table 4 ASTM E 1920 preparation method III for thermal spray coatings using diamond grinding

Surface	Coolant/lubricant	Abrasive size/type	Time, min	Force[a]		Surface speed, rpm	Relative rotation
				N	**lbf**		
Fixed diamond disc	Water	40–60 μm diamond	Planar grinding, 2–4	20–25	4.5–5.6	250–350	Complementary[b]
Medium-hard composite disc	Water-based suspension	6–9 μm diamond	Fine grinding, 3–5	20–25	4.5–5.6	100–150	Complementary
No/low-nap cloth	Water-based suspension	3 μm diamond	Rough polishing, 1–3	20–30	4.5–6.7	100–150	Complementary
Synthetic	Water[c]	Colloidal	Final	20–	5.2–	100–150	Contrary[d]

suede	silica	polishing, 1–3	35	7.9

(a) Force per 32 mm (1.25 in.) diameter specimen.
(b) Complementary rotation: surface and specimens spin in same direction (see Fig. 12)
(c) Water free of particulate is required; distilled water is recommended.
(d) Contrary rotation: surface and specimens spin in opposite directions (see Fig). 12)

Sectioning. Thermal spray coating specimens should be sectioned perpendicular to their axis using a precision diamond saw with either a metal-bonded diamond wafering blade or an ultrathin aluminum oxide abrasive blade. Generally, an abrasive cutoff blade selected to cut the substrate effectively will be the best blade for the combination of thermal spray coating and substrate. The specimen should be rigidly clamped in the vise and positioned so that the cutting blade enters the coated side and exits the substrate side, thus substantially reducing fracturing of the coating. Figure 6 shows the suggested wheel rotation and specimen position/type. As shown in Fig. 6(b), friable, porous, or brittle coatings to be sectioned may be vacuum impregnated with epoxy mounting compound prior to sectioning to protect the specimen. Typical sectioning parameters are (Ref 9):

- Speed: 2500 to 3500 rpm
- Applied load: 300 to 500 gf
- Lubricant: water soluble solution

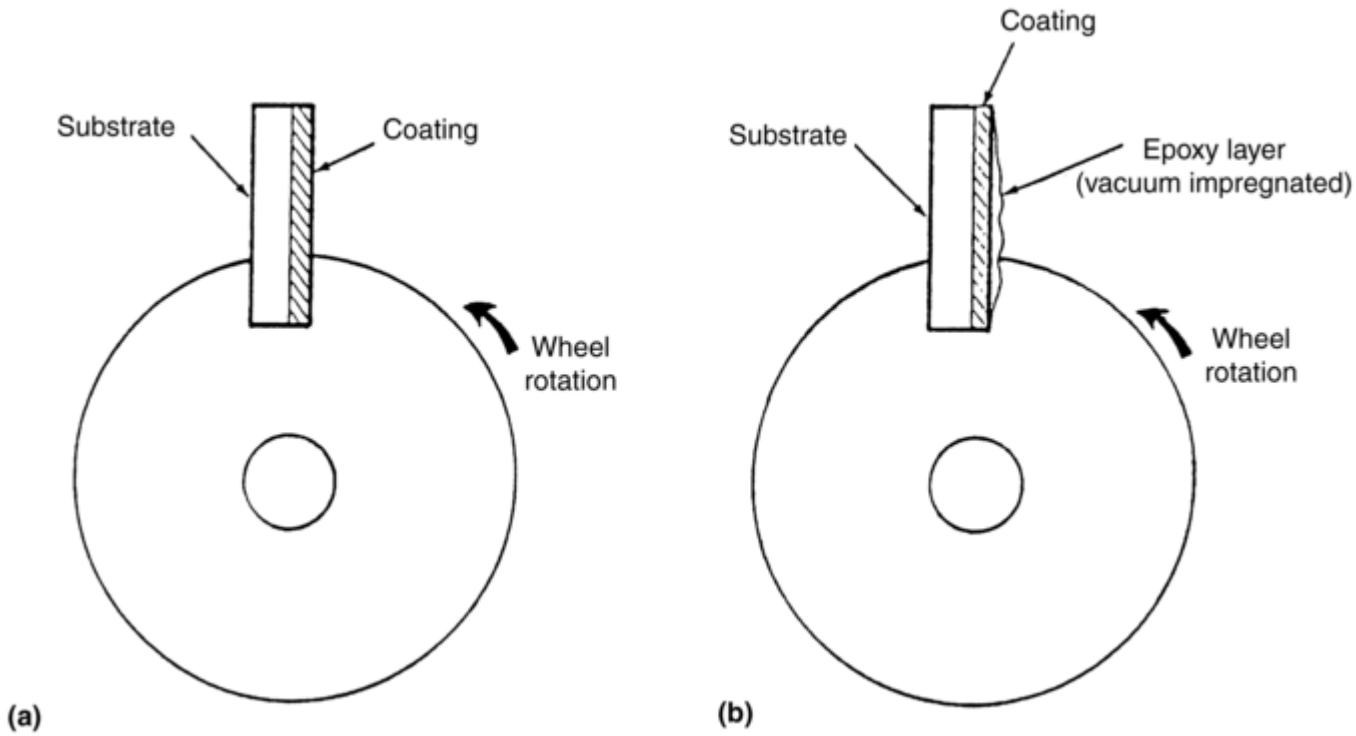

Fig. 6 Proper sectioning of thermal spray coatings. (a) Sectioning of dense, nonfriable coatings. (b) Sectioning of porous, friable coatings. Source: Ref 9

Cleaning. Thorough cleaning of each sectioned specimen is necessary prior to mounting. Specimens should be cleaned in an organic solvent (e.g., an acetone bath) and dried in an oven at 70 °C (160 °F). Ultrasonic cleaning of thermal spray specimens is not recommended, especially for fragile or brittle coatings, because coating particles may be lost during this type of “energetic” cleaning process (Ref 8). In addition, pore enlargement in prepared specimens is common with ultrasonic cleaning, as shown in Fig. 7.

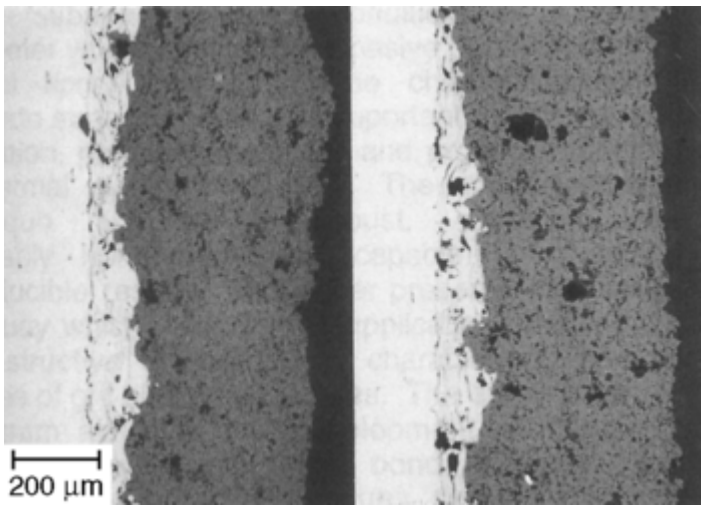

Fig. 7 Comparison of a yttria-stabilized zirconia microstructure in the as-polished (left) and ultrasonically cleaned (right) condition. The porosity increased by 450% after 16 min of ultrasonic cleaning. Due to the high density of the coating, the epoxy did not infiltrate the majority of pores. These pores enlarged during the ultrasonic cleaning due to the absence of epoxy and the friable nature of the coating. Source: Ref 10

Mounting. Thermal spray coating specimens must be mounted in order to maintain their original structure during grinding and polishing. Both compression mounting and castable mounting compounds can be used. Thermosetting or room-temperature-setting epoxy mounting compounds are the most commonly employed. Thermosetting compression mounting compounds require the use of heat (140 to 150 °C, or 285 to 300 °F) and pressure (20 to 29 MPa, or 3000 to 4200 psi) to cure the mount (Fig. 8a). Thermosetting compression mounting should only be used for dense, nonfriable coatings. Castable low-to-medium viscosity epoxy mounting compounds can be used for all thermal spray coatings and are particularly suited for porous or friable coatings. As shown in Fig. 8(b), the specimen is placed in a mold into which the epoxy is poured. In order to produce complete infiltration of the epoxy into the open pores of the coating, a vacuum of 85 to 100 kPa (25 to 30 in. Hg) is employed. The vacuum is maintained for approximately 2 to 10 min before allowing air into the chamber. Pressurizing the mount following the release of the vacuum significantly improves epoxy infiltration (Fig. 9, 10).

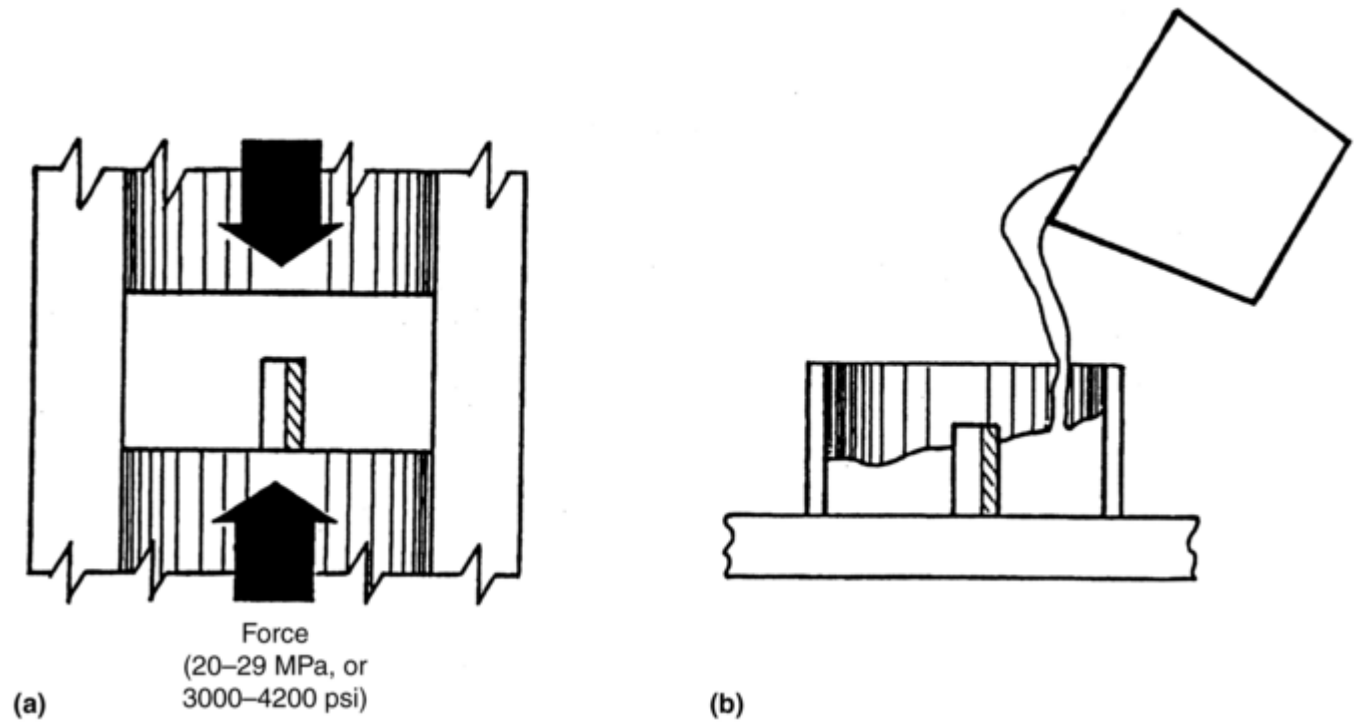

Fig. 8 Proper encapsulation of thermal spray coatings. (a) Thermosetting encapsulation for dense, nonfriable coatings. Temperature: 140 °C (285 °F). Heat time: 4 to 6 min. Cool time: 2 min. (b) Room-temperature epoxy encapsulation with vacuum impregnation (25 in. mercury) for porous, friable coatings. Source: Ref 9

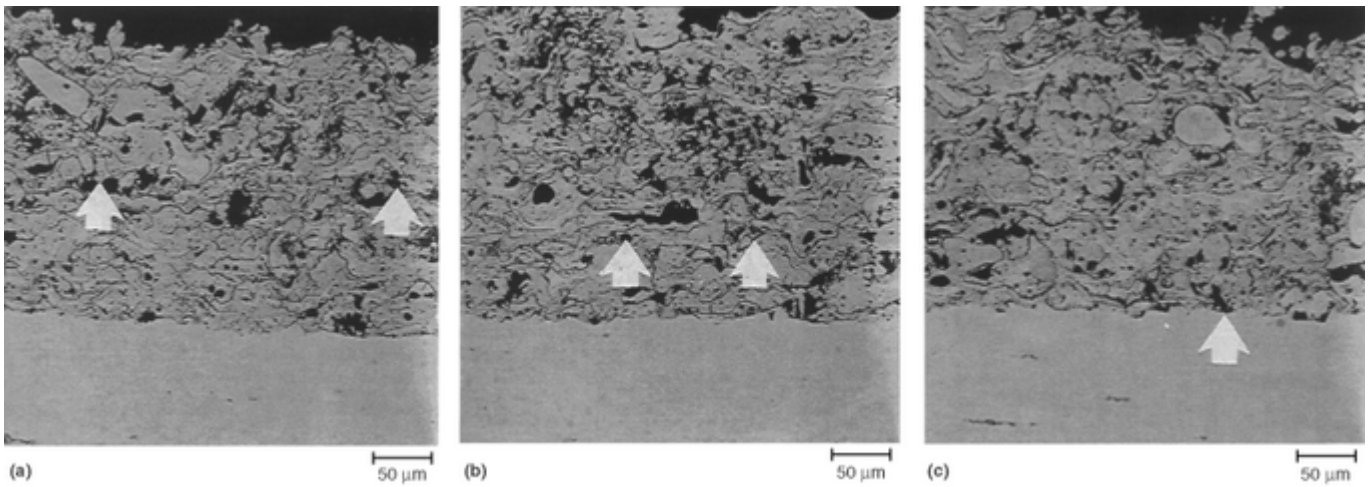

Fig. 9 Levels of epoxy impregnation in a chromium carbide coating using three different mounting methods. The arrows denote level of penetration. (a) Vaccum alone. (b) Vacuum and 1380 kPa (200 psi) pressurization. (c) Vacuum and 2760 kPa (400 psi) pressurization. All at 200×. See also Fig. 10) Source: Ref 11

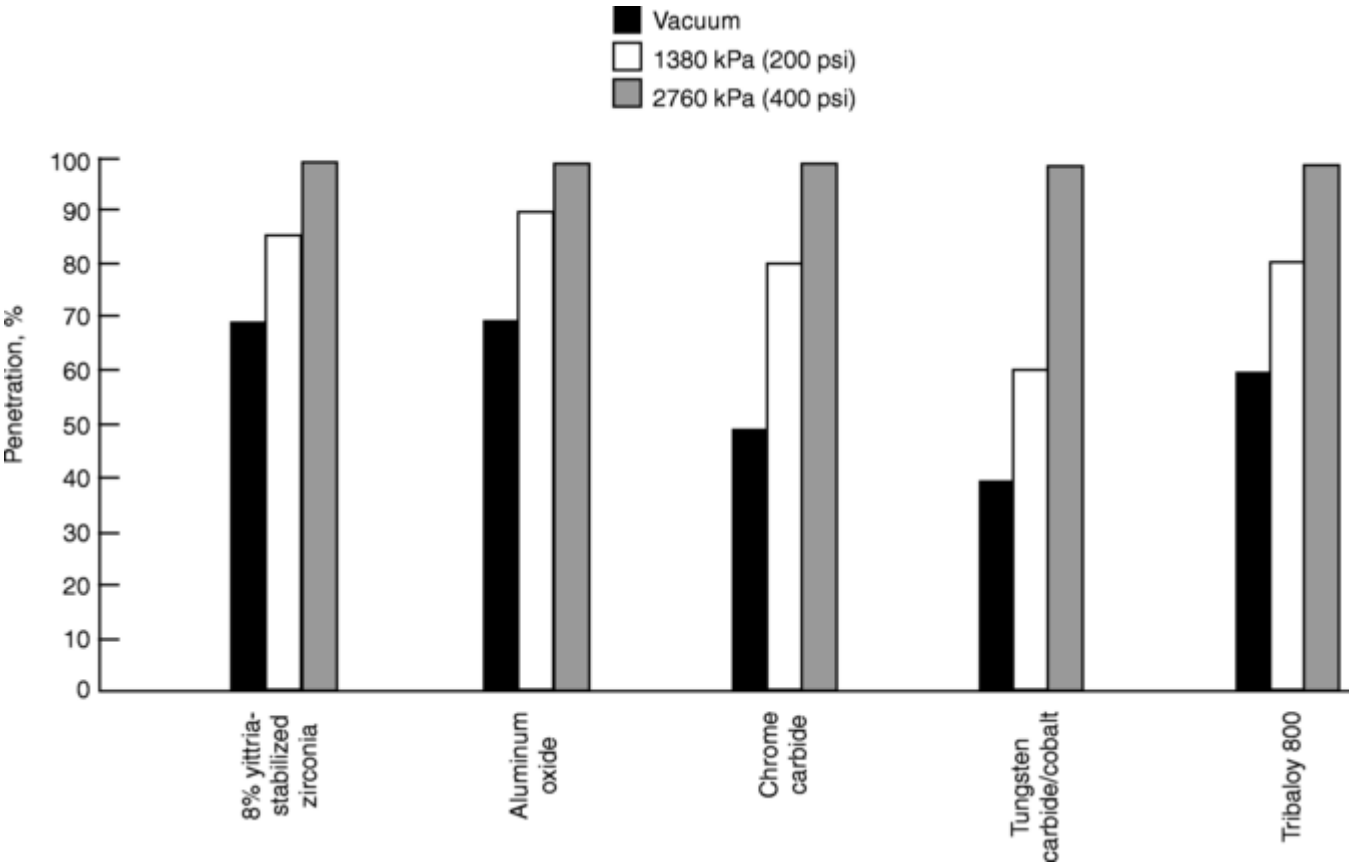

Fig. 10 Percent of epoxy penetration as a function of mounting method for various thermal spray coatings. See also Fig. 9) Source: Ref 11

Planar grinding is used to produce flat specimens in multiple-specimen racks, with all specimen surfaces being on one plane prior to subsequent grinding—hence the term *planar grinding.* This first stage prepares the specimen for the subsequent fine grinding and polishing stages. It has a significant influence on the success of

the entire specimen preparation process, because it establishes the initial depth of deformation in addition to producing a flat surface (Ref 9). When properly performed, it will lead to fewer subsequent steps, each of shorter duration. Although planar grinding can be carried out using silicon carbide abrasive papers (Table 2, 3), some laboratories prefer to accomplish planar grinding using a hard composite lap surface charged with a 40 to 60 μm diamond suspension (Table 4). The rolling diamond particles on the hard lap surface produce a flat specimen surface, which contains only a minimal amount of damage to the coating. There is an absence of any major pullout of brittle constituents, a condition that commonly results from the use of coarse bonded-abrasive papers during initial grinding when using traditional preparation methods (Ref 7). Figure 11 shows the results of planar grinding followed by subsequent fine grinding and rough polishing stages.

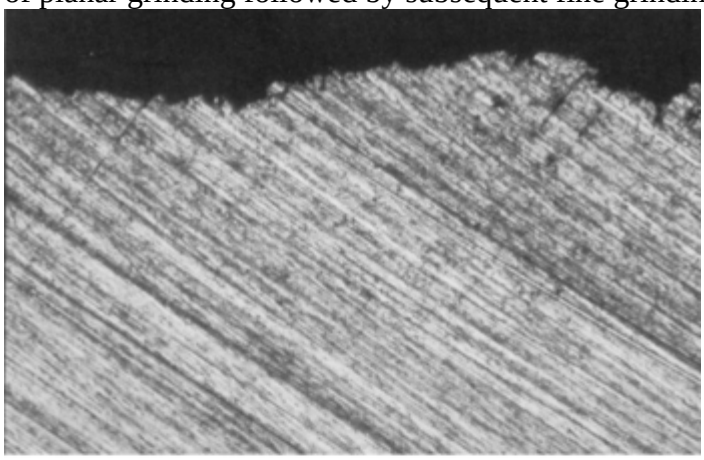

(a)

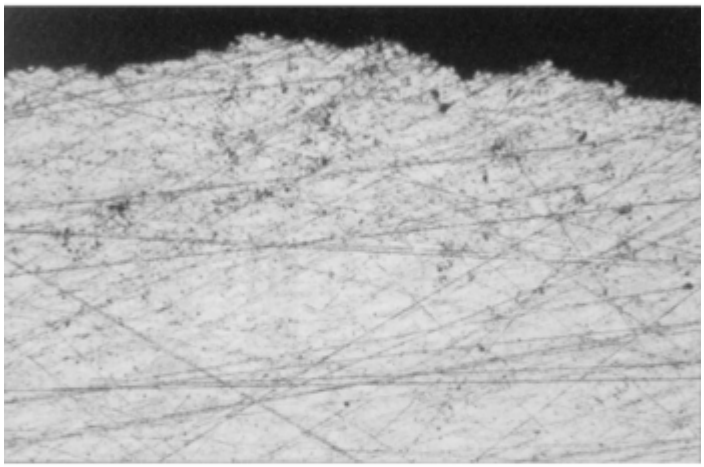

(b)

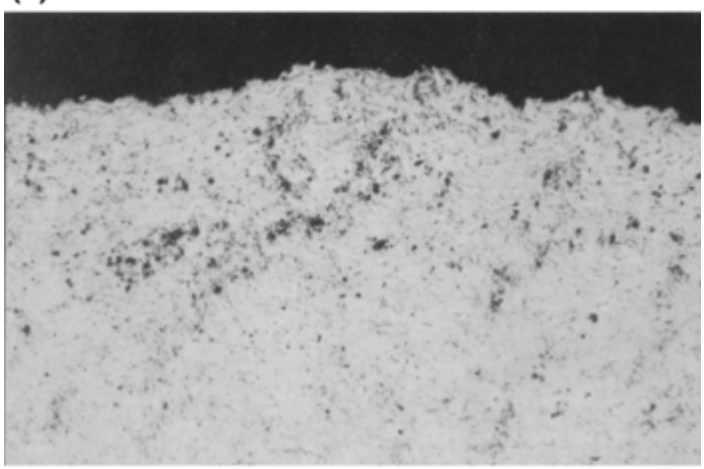

(c)

Fig. 11 Effects of various grinding and polishing stages on the specimen surface. (a) The rolling action of diamond particles on a hard lap surface during planar grinding produces a flat specimen with a minimal amount of damage to the coating. (b) During fine grinding, rotating the specimen in a direction

complementary to a medium-hard lap surface reduces specimen surface damage by minimizing pullout of oxides or unmelted particles from the coating. (c) A specimen surface with minimal deformation and pullout is obtained during the rough polishing step on a napless cloth charged with a 3 μm diamond suspension. Source: Ref 7

Fine Grinding and Rough Polishing. This two-step operation removes planar grinding scratches and deformation while maintaining flatness (Fig. 11), despite extreme differences in specimen hardness. Microstructural integrity as well as coating flatness are achieved by this operation. Key to the success of this operation is the use of power lapping to replace the traditional use of a series of successively finer bonded-abrasive papers (Ref 7). In the first step of this operation, the specimen is rotated in a direction complementary to the lap surface to reduce surface damage due to pullout of oxides or unmelted globules in the coating (Fig. 12). The second step is performed on a hard napless cloth charged with 3 μm diamond paste using an oil-based extender (Ref 7). See Table 2, 3, and 4 for details of this two-step operation.

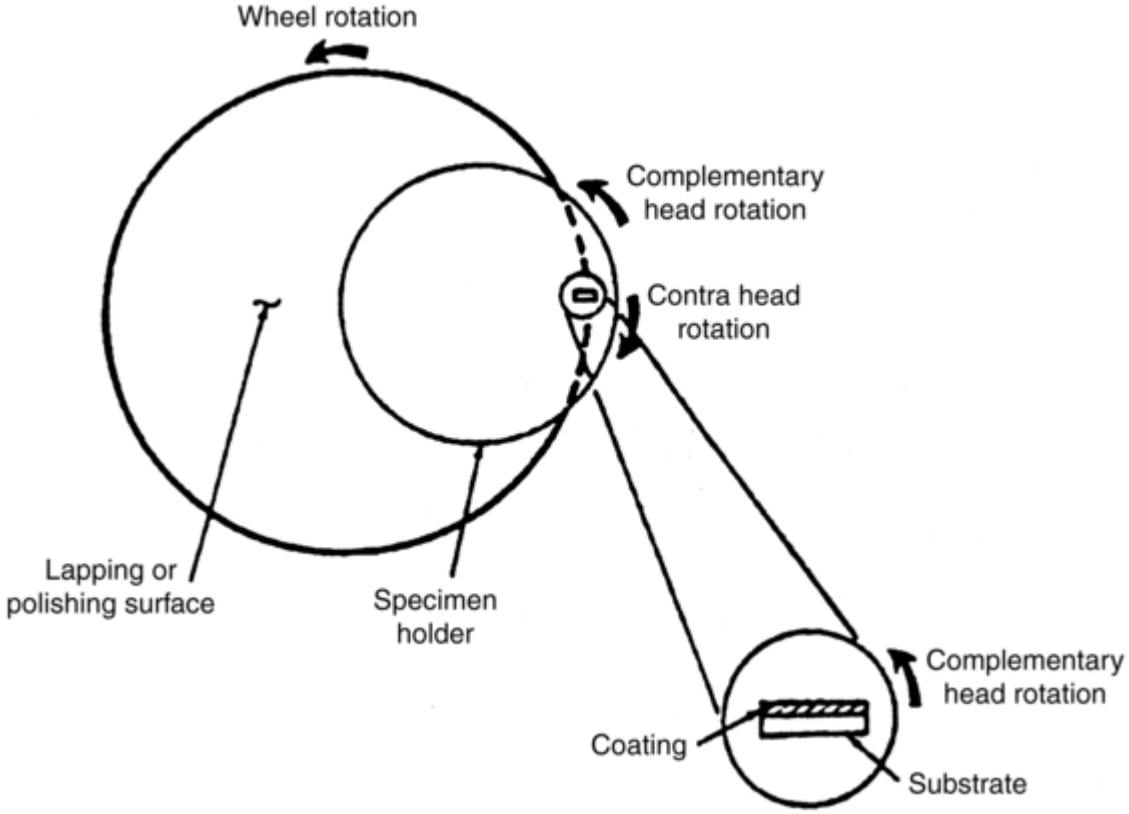

Fig. 12 Proper setup and relative rotation of equipment during specimen preparation of thermal spray coatings. Source: Ref 12

Final polishing is performed to remove fine scratches and to produce the high surface luster necessary for microscopic examination. With traditional specimen preparation, the metallographer is faced with the task of removing not only fine scratches but also specimen surface deformation that has not been removed during earlier preparation steps. Final polishing cannot correct the inadequacies of earlier steps, because the fine abrasives used with medium- to high-napped cloths remove only small amounts of material (Ref 7). Normally, the metallographer compensates to overcome this problem by continuing final polishing for a longer time, which results in excessive relief, rounding, and pullout. The use of napless cloths charged with diamond paste or suspension during the rough polishing step will brighten the surface while maintaining flatness; hence, final polishing time will be short. Table 2, 3, and 4 list the parameters for final polishing.

Etching. Selection of an etchant or etchants for a particular combination of coating and substrate materials is one of the most important and least understood steps in the microstructural analysis of thermal spray coatings (Ref 12). This is due to the complex chemistry within the coatings and the extreme chemistry differences between the coating and the substrate material. In some cases, a satisfactory analysis may be made if the coating alone is etched. This means that a single etchant, correctly applied, will suffice. However, the most complete analysis will result if both the coating and substrate material are etched. When multiple etchants are

used, there is a risk that one etchant may etch the coating satisfactorily but over- or underetch the substrate material.

Table 5 lists various etchants that have been used for the analysis of thermal spray coatings. The number (1 to 5) that follows each etchant is an index of the aggressiveness of that etchant. For example, “1” indicates a mild etchant, while “5” indicates a very aggressive one (Ref 12). This index number acts as a guide when determining which etchant should be applied first when multiple etchants are used. The etchant having the lowest number should be applied first. The proper use of etchants provides a clearer picture of the coating-to-substrate interface, unmelted particles, the splat microstructure, and the presence of foreign particles. Figure 13 compares as-polished and etched specimens.

Table 5 Suitable etchants for microstructural analysis of thermal spray coating/substrate combinations

Refer to text for a discussion of the response index.

Etchant name	Composition	Response index
2% nital	100 mL ethyl alcohol, 2 mL nitric acid	1
Vilella's	100 mL ethyl alcohol, 5 mL hydrochloric acid	2–3
Kalling's	33 mL ethyl alcohol, 33 mL distilled water, 33 mL hydrochloric acid, 1.5 mL cupric chloride	3–4
Keller's	190 mL distilled water, 3 mL hydrochloric acid, 5 mL nitric acid, 2 mL hydrofluoric acid	2
Kroll's	100 mL distilled water, 5 mL nitric acid, 2 mL hydrofluoric acid	4
Murikami's	100 mL distilled water, 10 g potassium ferricyanide, 10 g potassium hydroxide	4
Phosphoric electrolytic	60 mL distilled water, 40 mL phosphoric acid	5
Flat etch	25 mL water, 25 mL acetic acid, 50 mL nitric acid	4
Chromic electrolytic	100 mL water, 10 mL chromic trioxide	4
Oxalic	100 mL water	3
Alcoholic ferric chloride	33 mL ethyl alcohol, 30 mL hydrochloric acid, 6.5 g ferric chloride	3

Source: Ref 12

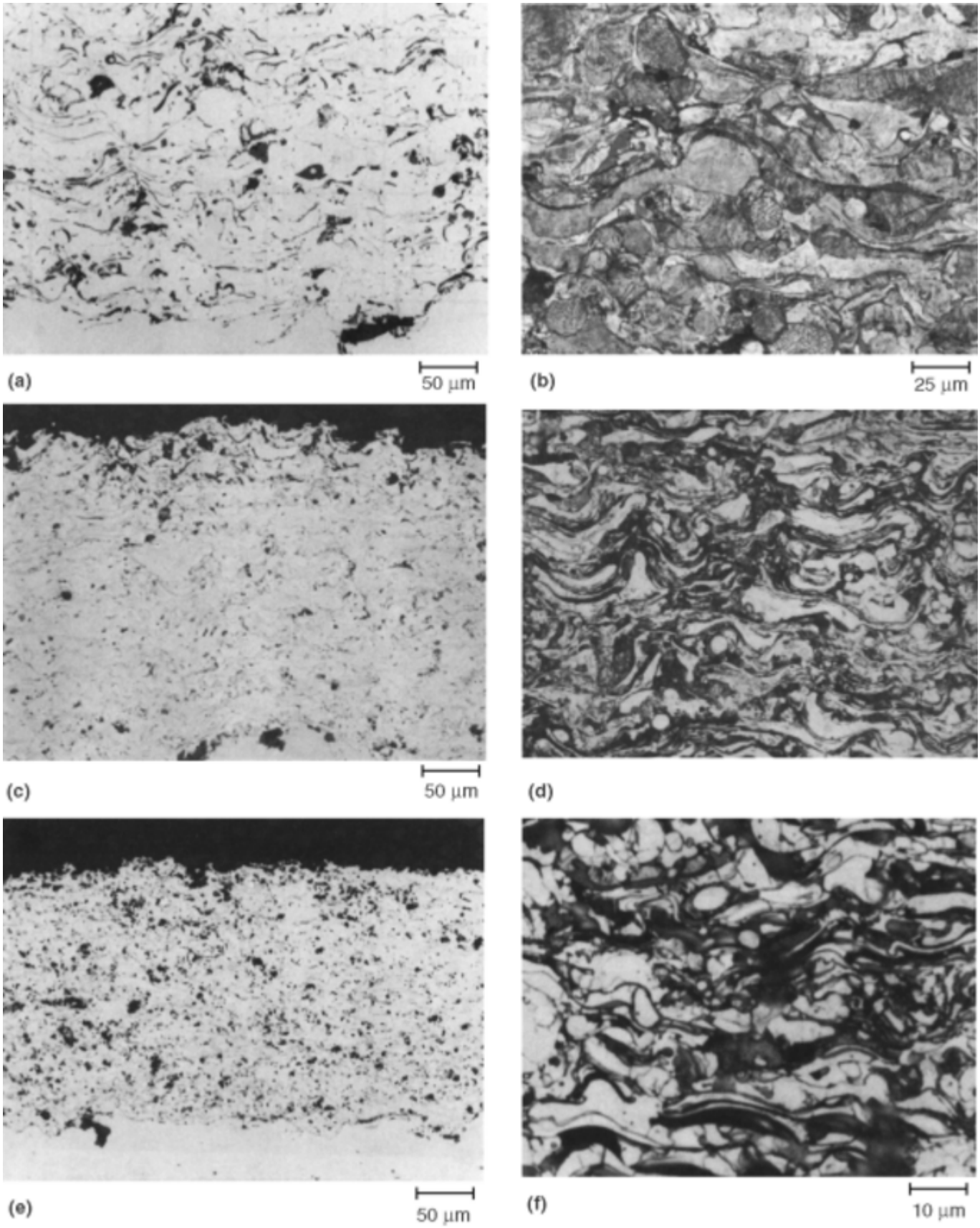

Fig. 13 Examples of as-polished and etched thermal spray coating specimens. (a) Ni-Cr/Al alloy, as-polished. 200×. (b) Ni-Cr/Al alloy, etched in 10% oxalic acid for 3 s. 400×. (c) Co-Mo-Cr-Si (Laves phase) alloy, as-polished. 200×. (d) Co-Mo-Cr-Si (Laves phase) alloy, etched in 10% oxalic acid for 3 s. (e) 75Cr_3C_2/25Ni-Cr, as-polished. 200×. (f) 75Cr_3C_2/25Ni-Cr, etched in oxalic acid for 3 s. 1000×. Source: Ref 12

References cited in this section

3. G.A. Blann, Standardization of Metallographic Practices for Thermally Sprayed Coatings in the Automotive Industry, *Proceedings of the 15th International Thermal Spray Conference,* 25–29 May 1998 (Nice, France), ASM International, 1998, p 677–681

5. G.A. Blann and D.J. Diaz, The Development of ASTM Standards for Metallographic Preparation Practices of Thermally Sprayed Coatings, *Proceedings of the Seventh National Thermal Spray Conference*, 20–24 June 1994 (Boston, MA), ASM International, 1994, p 721–725

6. "Practice of Preparation of Metallographic Specimens," E 3, ASTM International

7. G.A. Blann, D.J. Diaz, and J.A. Nelson, Raising the Standards for Coating Analysis, *Adv. Mater. Process.,* Vol 136 (No. 6), Dec 1989, p 31–36

8. "Standard Guide for Metallographic Preparation of Thermal Spray Coatings," E 1920, ASTM International

9. G.A. Blann, The Important Role of Microstructural Evaluation in Each Phase of Thermally Sprayed Coatings Application, *Proceedings of the 13th International Thermal Spray Conference,* 28 May–5 June 1992 (Orlando, FL), ASM International, 1992, p 959–966

10. G.A. Blann, The Effects of Ultrasonic Cleaning on the Microstructural Characteristics of Thermally Sprayed Coatings, *Proceedings of the Eighth National Thermal Spray Conference,* 11–15 Sept 1995 (Houston, TX), ASM International, 1995, p 499–503

11. D.M. Gagnon and G.A. Blann, Thermal Spray Coating Impregnation—Vacuum vs. High Pressure/Vacuum Technique, *Proceedings of the Seventh National Thermal Spray Conference,* 20–24 June 1994 (Boston, MA), ASM International, 1994, p 743–750

12. G.A. Blann, Microetching Techniques for Revealing Thermally Sprayed Coating Microstructures, *Proceedings of the Fourth National Thermal Spray Conference,* 4–10 May 1991 (Pittsburgh, PA), ASM International, 1991, p 175–186

J.R. Davis, Microstructural Characterization of Thermal Spray Coatings, *Metallography and Microstructures,* Vol 9, *ASM Handbook*, ASM International, 2004, p. 1038–1046

Microstructural Characterization of Thermal Spray Coatings

J.R. Davis, Davis & Associates

Other Methods of Analysis

Image Analysis. While conventional metallographic analysis leads to qualitative interpretation of the microstructural characteristics, automatic image analysis provides a means of quantitatively evaluating coating structures. This method is increasingly being used to detect and measure voids (porosity), oxides, unmelted spray particles, and interfacial contamination (Ref 13, 14, 15). Coated specimens for image analysis are prepared in the same manner described in the section "Recommended Metallographic Practices." Cross sections are observed using a light optical microscope, a charge-coupled device camera, and an image analysis system (see the article "Quantitative Image Analysis" in this Volume for more details on these systems). ASTM E 2109, "Test Methods for Determining Area Percentage in Thermal Spray Coatings," covers procedures to perform porosity ratings on thermal spray coatings by direct comparison to standard images and through the use

of automatic image analysis. Recommended procedures used to detect and measure thermal spray coating defects using image analysis are summarized in Table 6.

Table 6 Procedures used to detect and measure thermal spray coating features with image analysis

Void evaluation
Acquire image
Set illumination to give maximum brightness range
Perform image averaging
Correct shading
Stretch linear gray scale
Detach voids
Select brightness-threshold range (darkest pixels should include all apparent porosity)
Produce binary image
Measure processed binary image
Calculate detected pixels/total image pixels
Report result as area fraction (%)
Perform 1 dilation of binary image (including halo around void)
Store binary image of voids
Oxidation evaluation
Use gray image acquired for void detection
Detect oxides
Select brightness-threshold range (pixels should include all apparent oxides; may include halo pixels around voids)
Produce binary image of oxides
Subtract previously stored binary image of voids from binary image of oxides
Measure resultant binary image
Count oxides in field of view
Calculate detected pixels/total image pixels
Report results as area fraction (%)
Perform object count
Calculate total oxide area/total field area
Unmelted-particle evaluation
Acquire image
Set illumination level to give maximum brightness range
Perform image averaging
Correct shading
Stretch linear gray scale
Detect coating matrix material
Select brightness-threshold range (brightest pixels should include all apparent matrix material)
Produce binary image
Process binary image
Perform 5 cycles of open function to minimize detection of nonuniform (melted) matrix material
Delete binary objects having areas less than determined value
Perform fill-object function to remove holes in detected binary unmelts
Measure processed binary image
Count unmelted particles in field of view
Calculate detected pixels/total image pixels
Report results as area fraction (%)
Perform object count
Calculate total unmelt area/total field area
Evaluation of coating/base-material interface

Acquire image
Orient specimen so interface is horizontal and approximately in center of field of view
Set illumination to give maximum contrast between coating and base material
Perform image averaging
Correct shading
Transform input image-brightness values (using look-up table having a parabolic function) to enhance contrast between base material and coating
Detect base material
Select brightness-threshold range (brightness range should include maximum amount of base material while avoiding connectivity with white phase in coating: may not include some areas in base material, but may include some areas in coating)
Produce binary image
Process binary image
Perform fill-operation function to remove holes in binary image of base material
Perform 3 cycles of open function to break any connectivity in binary image between base material and coating and eliminate detected areas in coating (undetected areas may remain along edges of field of view)
Remove any remaining detected objects within coating by deletion of relatively small areas
Store binary image of base material
Perform 1 cycle of dilate function
Subtract stored binary image of base material from dilated image of base material (resultant binary image is one-pixel-wide tracing of coating/base-material interface)
Remove lines not associated with interface tracing by deleting objects with length less than width of field
Measure interface length
Store length measurement
Store binary image of interface tracing
Evaluation of interface contamination
Detect dark phases in coating
Select brightness-threshold range (darkest pixels should include all apparent voids, delamination, grit, etc.)
Produce binary image
Process binary image
Perform 1 cycle of dilate function
Combine stored binary image of interface tracing with binary image of voids using "And" Boolean operator (this image contains one-pixel-wide lines representing contact lengths of contamination features with interface)
Perform measurement of contamination-feature length
Calculate ratio of contamination length to total length of coating/base-material interface
Report result as percent of total interface length

Source: Ref 13

The scanning electron microscope (SEM) provides additional evaluation information because of its higher-magnification and depth-of-field capabilities when compared to the light optical microscope. The use of SEM for visual identification of voids and other microstructural features provides a way to qualitatively determine whether voids are part of the true microstructure or are artifacts produced during specimen preparation. Even at the same magnification, SEM provides more void detail (the entire inner void surface can be observed) than the light optical microscope.

In addition to void examination, SEM is also used to evaluate the characteristics of thermal spray powders, grit-blasted substrate surfaces, and the coating after spraying (Ref 9). Particle shapes and size distribution can be accurately determined, as shown in Fig. 4. Grit-blasted substrate surfaces can be evaluated for surface roughness and the presence of embedded grit particles prior to spraying. Grit spraying parameters can be altered, if necessary, in order to improve the surface roughness and reduce the amount of embedded particles. Evaluation of the coating surface after spraying provides information concerning the coating density of the

exposed surface and the surface topography. Coating density throughout the coating thickness can be determined by cryogenic fractography. The substrate is sectioned up to the coating and then immersed in liquid nitrogen for approximately 5 to 10 min. The specimen is removed quickly, secured in a vise, and impacted with a hammer on the substrate side. The fractured specimen is allowed to return to room temperature, sputter coated, and placed in the SEM for evaluation (Fig. 14).

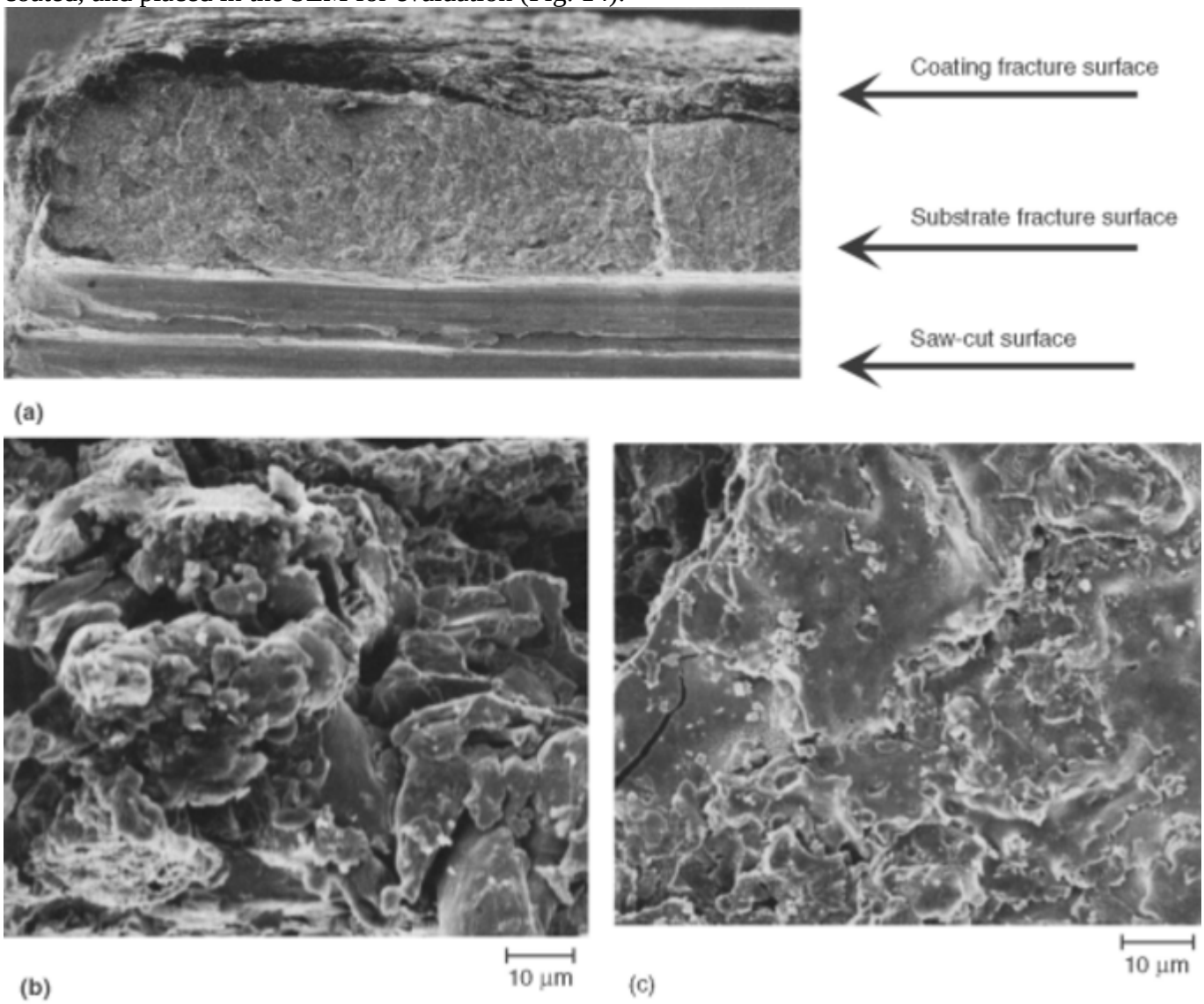

Fig. 14 Scanning electron microscope fractographs of a specimen that was cryogenically fractured for density evaluation. (a) Specimen cross section. (b) Coating fracture surface. 1000×. (c) Coating top surface. 1000×. Source: Ref 9

Energy dispersive spectroscopy (EDS) is used to provide quantitative chemical analysis and to confirm optical microscope and SEM analyses. For example, it is possible to determine positively whether a void is true porosity or the result of pullout by analyzing for encapsulating material in the void (Ref 7). A void free of encapsulating material is the result of pullout during specimen preparation. The EDS analysis of a true pore in the coating also shows the presence of oxides of the coating material, whereas a “clean” pore (containing no oxide) is representative of a void produced during specimen preparation.

The coating evaluation procedure combining the light optical microscope and SEM to determine the percentage of apparent porosity, and EDS to determine elemental composition provides a more extensive assessment of the specimen surface and indicates that proper metallographic practices have been carried out.

References cited in this section

7. G.A. Blann, D.J. Diaz, and J.A. Nelson, Raising the Standards for Coating Analysis, *Adv. Mater. Process.,* Vol 136 (No. 6), Dec 1989, p 31–36

9. G.A. Blann, The Important Role of Microstructural Evaluation in Each Phase of Thermally Sprayed Coatings Application, *Proceedings of the 13th International Thermal Spray Conference,* 28 May–5 June 1992 (Orlando, FL), ASM International, 1992, p 959–966

13. D.B. Fowler, W. Riggs, and J.C. Russ, Inspecting Thermally Sprayed Coatings, *Adv. Mater. Process.,* Vol 138 (No. 5), Nov 1990, p 41–52

14. G. Montavon, C. Coddet, C.C. Berndt, and S.-H. Leigh, Microstructural Index to Quantify Thermal Spray Deposit Microstructures Using Image Analysis, *J. Therm. Spray Technol.,* Vol 7 (No. 2), June 1998, p 229–241

15. D.B. Fowler, A Method for Evaluating Plasma Spray Coating Porosity Content Using Stereological Data Collected by Automatic Image Analysis, *Computer-Aided Microscopy and Metallography,* ASM International, 1990, p 13–21

J.R. Davis, Microstructural Characterization of Thermal Spray Coatings, *Metallography and Microstructures,* Vol 9, *ASM Handbook,* ASM International, 2004, p. 1038–1046

Microstructural Characterization of Thermal Spray Coatings

J.R. Davis, Davis & Associates

References

1. R. Knight and R.W. Smith, Thermal Spray Forming of Materials, *Powder Metal Technologies and Applications,* Vol 7, *ASM Handbook,* ASM International, 1998, p 408–419

2. R.C. Tucker, Jr., Thermal Spray Coatings, *Surface Engineering,* Vol 5, *ASM Handbook,* ASM International, 1994, p 497–509

3. G.A. Blann, Standardization of Metallographic Practices for Thermally Sprayed Coatings in the Automotive Industry, *Proceedings of the 15th International Thermal Spray Conference,* 25–29 May 1998 (Nice, France), ASM International, 1998, p 677–681

4. F.N. Longo, Coating Operations, *Handbook of Thermal Spray Technology,* ASM International, 2004, p 120–127

5. G.A. Blann and D.J. Diaz, The Development of ASTM Standards for Metallographic Preparation Practices of Thermally Sprayed Coatings, *Proceedings of the Seventh National Thermal Spray Conference,* 20–24 June 1994 (Boston, MA), ASM International, 1994, p 721–725

6. "Practice of Preparation of Metallographic Specimens," E 3, ASTM International

7. G.A. Blann, D.J. Diaz, and J.A. Nelson, Raising the Standards for Coating Analysis, *Adv. Mater. Process.,* Vol 136 (No. 6), Dec 1989, p 31–36

8. “Standard Guide for Metallographic Preparation of Thermal Spray Coatings,” E 1920, ASTM International

9. G.A. Blann, The Important Role of Microstructural Evaluation in Each Phase of Thermally Sprayed Coatings Application, *Proceedings of the 13th International Thermal Spray Conference,* 28 May–5 June 1992 (Orlando, FL), ASM International, 1992, p 959–966

10. G.A. Blann, The Effects of Ultrasonic Cleaning on the Microstructural Characteristics of Thermally Sprayed Coatings, *Proceedings of the Eighth National Thermal Spray Conference,* 11–15 Sept 1995 (Houston, TX), ASM International, 1995, p 499–503

11. D.M. Gagnon and G.A. Blann, Thermal Spray Coating Impregnation—Vacuum vs. High Pressure/Vacuum Technique, *Proceedings of the Seventh National Thermal Spray Conference,* 20–24 June 1994 (Boston, MA), ASM International, 1994, p 743–750

12. G.A. Blann, Microetching Techniques for Revealing Thermally Sprayed Coating Microstructures, *Proceedings of the Fourth National Thermal Spray Conference,* 4–10 May 1991 (Pittsburgh, PA), ASM International, 1991, p 175–186

13. D.B. Fowler, W. Riggs, and J.C. Russ, Inspecting Thermally Sprayed Coatings, *Adv. Mater. Process.,* Vol 138 (No. 5), Nov 1990, p 41–52

14. G. Montavon, C. Coddet, C.C. Berndt, and S.-H. Leigh, Microstructural Index to Quantify Thermal Spray Deposit Microstructures Using Image Analysis, *J. Therm. Spray Technol.,* Vol 7 (No. 2), June 1998, p 229–241

15. D.B. Fowler, A Method for Evaluating Plasma Spray Coating Porosity Content Using Stereological Data Collected by Automatic Image Analysis, *Computer-Aided Microscopy and Metallography,* ASM International, 1990, p 13–21

J.R. Davis, Microstructural Characterization of Thermal Spray Coatings, *Metallography and Microstructures,* Vol 9, *ASM Handbook,* ASM International, 2004, p. 1038–1046

Microstructural Characterization of Thermal Spray Coatings

J.R. Davis, Davis & Associates

Selected References

- G.A. Blann, The Effects of Manual vs. Semi-Automatic Metallographic Specimen Preparation of Thermally Sprayed Coatings, *Proceedings of the First United Thermal Spray Conference,* 15–18 Sept 1997 (Indianapolis, IN), ASM International, 1997, p 965–969
- D.B. Fowler, Metallographic Evaluation of Thermally Sprayed Coatings, *ASTM Stand. News,* May 1991, p 54–57
- W. Riggs, K. Larson, and K. Couch, Metallography and Image Analysis, *Handbook of Thermal Spray Technology,* ASM International, 2004, p 224–259

Metallography and Microstructures of Weldments, *Metallography and Microstructures,* Vol 9, *ASM Handbook,* ASM International, 2004, p. 1047–1056

Metallography and Microstructures of Weldments

Introduction

FUSION WELDING is the joining of two or more pieces of material by melting a portion of each and allowing the liquefied portions to solidify together. This can be accomplished with or without filler metal, and one or more passes can be made.

The term “weld” denotes the area of coalescence produced by welding (Ref 1). A welded joint is a composite of three regions: the fusion zone, heat-affected zone, and unaffected base metal. These zones are shown in Fig. 1, 2, and 3. The fusion zone is the material that was melted during welding. It is bordered by the fusion line. The fusion zone material usually has a chemical composition similar to that of the base metal(s). In the heat-affected zone, which is the area adjacent to the fusion zone, the material has undergone a thermal cycle that observably alters the microstructure of the base material. The base metal is the material that is not observably altered by welding. In multiple-pass welds, successive passes produce changes in the fusion and heat-affected zones of earlier passes. These regions, shown in Fig. 3, are called reheat zones. Additional terms used to refer to specific portions of welded joints are illustrated in Fig. 1.

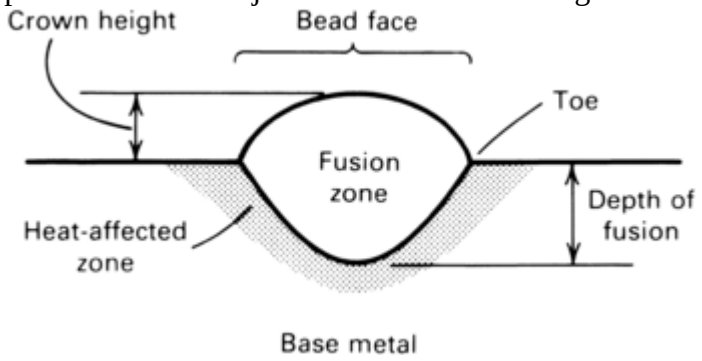

Fig. 1 Fusion weld bead defining terminology used in this article

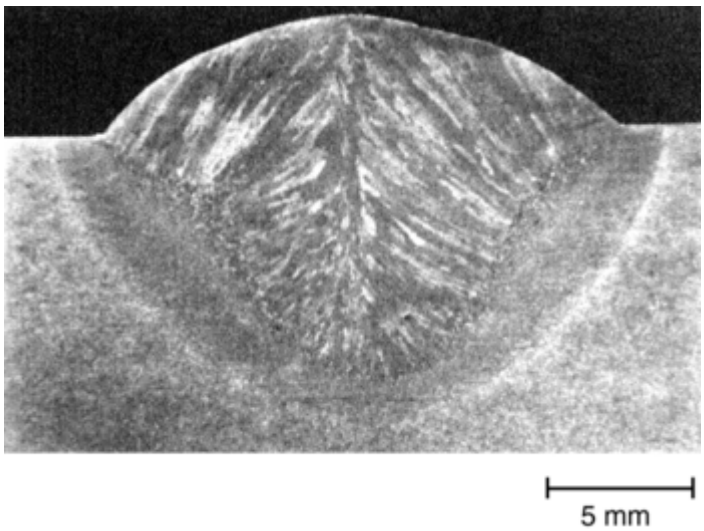

Fig. 2 19 mm (0.75 in.) A-710 steel plate, submerged arc weld. Heat input: 3.0 MJ/m. Macrostructure shows the fusion zone, heat-affected zone, and base metal in a single-pass, bead-on-plate weld. Etchant: 85 mL H_2O + 15 mL HNO_3 + 5 mL methanol. Magnification: 3.5×

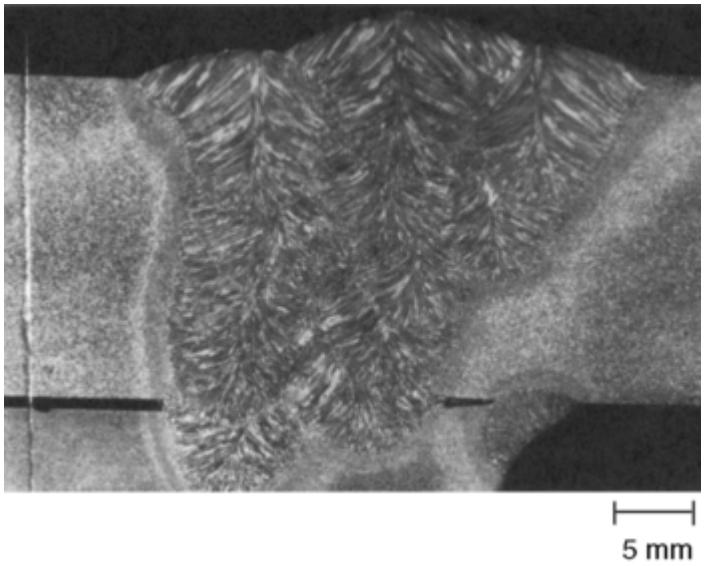

Fig. 3 Same as Fig. 2. Weld wire: 2.4 mm ($\frac{3}{32}$ in.). MIL Spec 100S-1, OP121TT flux. Heat input: 1.0 MJ/m. Macrostructure shows the fusion zone, heat-affected zone, reheat zones, and base metal in a multiple-pass butt weld. Etchant: 85 mL H_2O + 15 mL HNO_3 + 5 mL methanol. Magnification: 2×

This article considers joints produced by arc welding. The metallography and structure of welded joints and the problems and techniques associated with their study are discussed. When standard sample preparation and analytical techniques for a given material are used, they are covered briefly here, and the reader is referred to the article on that topic in this Volume. Similarly, the metallurgical aspects of welding and specific materials are discussed only to the extent necessary to explain the microstructures observed. Chemical compositions of base metal, filler metal (weld wires), and fusion zones for which micrographs are shown in this article are given in Table 1.

Table 1 Chemical composition of base metals, weld wires, and fusion zones

Fig.	Alloy	Composition, %											
		C	**Mn**	**S**	**P**	**Si**	**Cr**	**Ni**	**Mo**	**Nb**	**Al**	**Cu**	**Other**
Low-alloy steels													
Fig. 2	A-710	0.05	0.54	0.006	0.01	0.26	0.72	0.91	0.20	0.05	0.03	1.20	0.005 Ti
	Base metal												
	Fusion zone	0.06	0.85	0.005	0.01	0.22	0.53	0.62	0.24	0.03	0.025	0.90	0.001 B
Fig. 3	A-710												
	Base metal	0.05	0.54	0.006	0.01	0.26	0.72	0.91	0.20	0.05	0.03	…	…
	Weld wire	0.06	1.40	…	…	0.35	0.10	1.75	0.35	…	…	…	…
Fig. 5, 29	A-170[(a)]	0.04	0.55	0.01	0.01	0.25	0.70	0.90	…	0.05	0.03	1.20	…
Fig. 7	2.25Cr-1 Mo												
	Base metal	0.11	0.51	0.004	0.003	0.13	2.23	0.01	0.93	0.05	0.026	0.01	…
Fig. 8, 21	Lukens Frostline[(b)]												
	Fusion zone	0.14	1.4	…	…	0.4	…	0.14	0.05	…	…	0.18	…
Fig. 13, 27	AISI 4340												
	Base metal	0.41	0.65	0.04	0.01	0.20	0.76	1.65	0.21	…	…	…	…
	Weld wire	0.31	0.55	0.01	0.01	0.65	1.25	…	0.50	…	…	…	…
Fig. 16, 20, 22	A-36[(c)]												0.027 O
	Fusion zone	0.05	1.07	0.016	0.019	0.42	0.01	0.05	0.01	…	…	…	0.009

Fig. 19	A-710												N
	Fusion zone	0.06	1.4	0.01	0.01	0.31	0.15	1.8	0.35	…	…	0.15	…
Fig. 26	HY 80												
	Base metal	0.08	0.75	…	…	0.35	1.10	2.30	0.4	…	…	…	…
	Weld wire	0.04	1.0	…	…	0.60	…	1.50	0.5	…	…	…	…

Fig.	Alloy	Composition, %									
		Al	**V**	**Nb**	**Ta**	**Mo**	**C**	**N**	**Fe**	**O**	**H**
Titanium alloys											
Fig. 11, 15, 24, 25	Ti-6Al-2Nb-1Ta-1Mo	6.0	…	1.9	0.9	0.81	0.02	0.009	0.09	0.071	0.005
	Base metal										
	Weld wire[(d)]	5.7	…	2.1	1.0	0.68	0.03	0.01	0.04	0.07	0.004
Fig. 12, 23,	Ti-6Al-4V										
	Base metal	6.59	4.11	…	…	…	0.14	0.01	0.13	0.07	0.007
	Fusion zone[(e)]										

(a) Nominal composition.
(b) Welded using AWS E70S-3 wire.
(c) Welded using AWS E7018 wire.
(d) Weld wire chemistry for Fig. 15 and 25 only.
(e) Same as base metal for Fig. 12, except for addition of 0.01 wt% yttrium

The remainder of this article consists of six sections. The first describes the techniques used in the sectioning and sample preparation of welded joints. The next four sections each deal with a particular metallurgical aspect of welded joints: the overall bead morphology, the solidification structure, the solid-state transformation structure, and metallurgical defects produced by the welding process. The techniques required to study each particular metallurgical aspect in several common alloy systems are discussed. The last section is an overview of characteristics specific to several different welding processes.

Reference cited in this section

1. W.H. Kearns, Ed., *Welding Handbook,* American Welding Society, Miami, 1978–1984

Metallography and Microstructures of Weldments, *Metallography and Microstructures,* Vol 9, *ASM Handbook,* ASM International, 2004, p. 1047–1056

Sample Preparation

The transverse section, which is most often used to observe and document welded joint macrostructure and microstructure, may be supplemented by additional viewing and sectioning techniques, including the top-view photograph, the longitudinal section, and the normal section. For studies of solidification effects, a section normal to the solidification direction may be useful. These sections are illustrated in Fig. 4. Applications for sectioning techniques are summarized in Table 2.

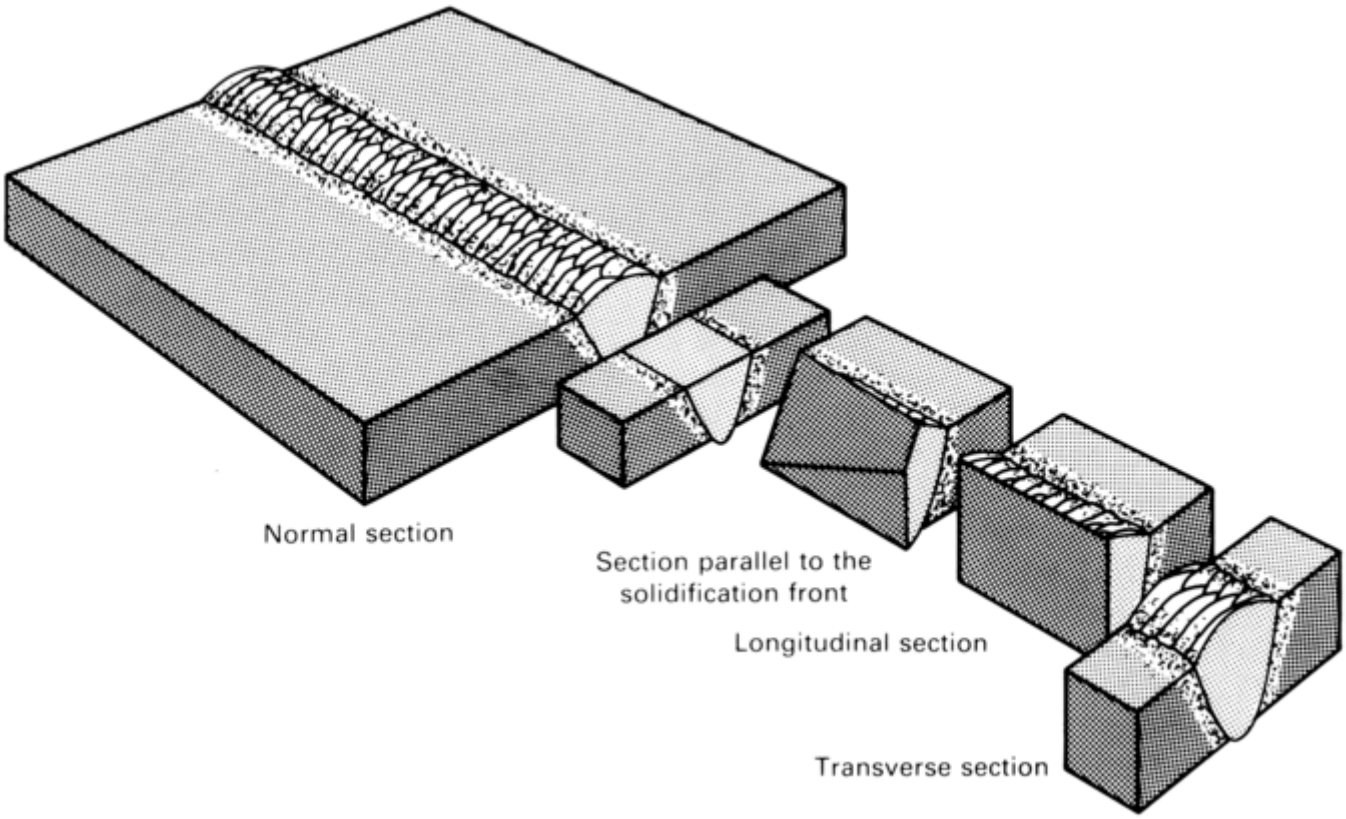

Fig. 4 Sections used in the metallographic examination of welded joints. See also Table 2.

Table 2 A summary of welded joint sections and their uses

See also Fig. 4.

Section	Uses
Transverse	Bead geometry
	Joint characterization
	Microstructural characterization
	Solidification structure
	Defect documentation
	Solidification shrinkage cracks
	Underbead cracks
	Toe cracks
	Hydrogen cracks
	Weld metal longitudinal cracks
	Weld metal root cracks
	Slag entrapment
	Incomplete fusion
	Inadequate joint penetration
	Pile-up
	Undercut
	Porosity
Longitudinal	Solidification structure
	Defect documentation
	Transverse heat-affected zone base metal cracks
	Transverse weld metal cracks
Normal to solidification direction	Solidification cell or dendrite characterization
Normal	Solidification structure

	Defect documentation
	Solidification shrinkage cracks
	Hydrogen cracks
Top surface[(a)]	Appearance of joint
	Defect documentation
	Arc strike
	Spatter
	Porosity (blow holes)
	Weld metal crater cracks
	Transverse heat-affected zone base metal cracks
	Transverse weld metal cracks
	Weld metal longitudinal cracks
	Toe cracks

(a) Not truly a section; does not require destructive sampling

Preparation of weld metal sections requires the same precautions as those for wrought and cast material. Sufficient material must be removed during grinding to eliminate the thermal and mechanical effects of rough cutting or sawing. Care must then be taken to maintain the proper plane of section, particularly when the section is used for such measurements as bead area, depth of fusion, or grain aspect ratio. Clear or translucent mounting materials are therefore recommended for small pieces when the joint is subject to quantitative measurement. Preservation of the proper plane of section may become a problem when materials of significantly different hardness are joined or when the weld deposit differs greatly in hardness from the substrate. In these cases, extra care and/or automatic grinding equipment are recommended. Final grinding and polishing should be performed as recommended for the alloy system(s) present in the joint.

Special precautions apply to welds made with a backing plate, The gap between the base and backup plates should be filled with epoxy or a similar material to prevent buildup of grinding debris. Heavy oxides on surfaces between the base and backup plates should be removed by pickling before the epoxy is applied to prevent dragout during polishing (Fig. 5).

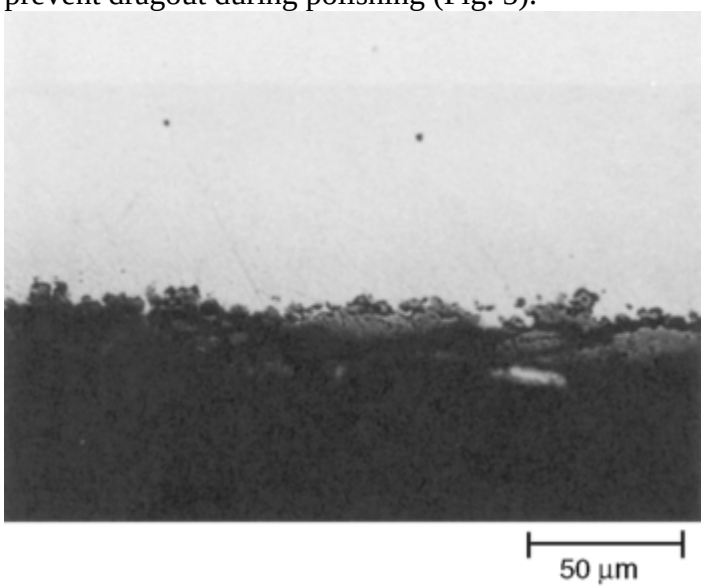

Fig. 5 19 mm (0.75 in.) A-710 steel plate, submerged arc weld. Microstructure shows dragout of base metal scale between the base metal and the epoxy filler used in the gap between the base plate and backup plate in a multiple-pass butt weld. As-polished. Magnification: 280×

Metallography and Microstructures of Weldments, *Metallography and Microstructures,* Vol 9, *ASM Handbook,* ASM International, 2004, p. 1047–1056

Weld Bead Morphology

The weld bead morphology for fusion welding can be described by the appearance of the bead face and the weld bead cross section. A top-view photograph will depict the general appearance of the weld, illustrating surface irregularities, spatter, or macroscopic defects such as hot cracking or porosity. The weld bead cross section can be described by measurement of toe-to-toe width, bead penetration or depth of fusion, crown height, and total area of the weld bead. All of these parameters are best determined from a transverse section. Incorrect sectioning will cause errors in depth of penetration and bead area measurement. These errors are summarized in Fig. 6. Except in the most severe cases, the sectioning error introduced on bead area and depth of fusion measurements will likely be lower than the sampling error due to variability along the length of the weld. The welding process, parameters, consumables, and base material are equally important in determining the final weld bead morphology. Various bead morphologies may be observed in Fig. 2, 3, 7, and 8.

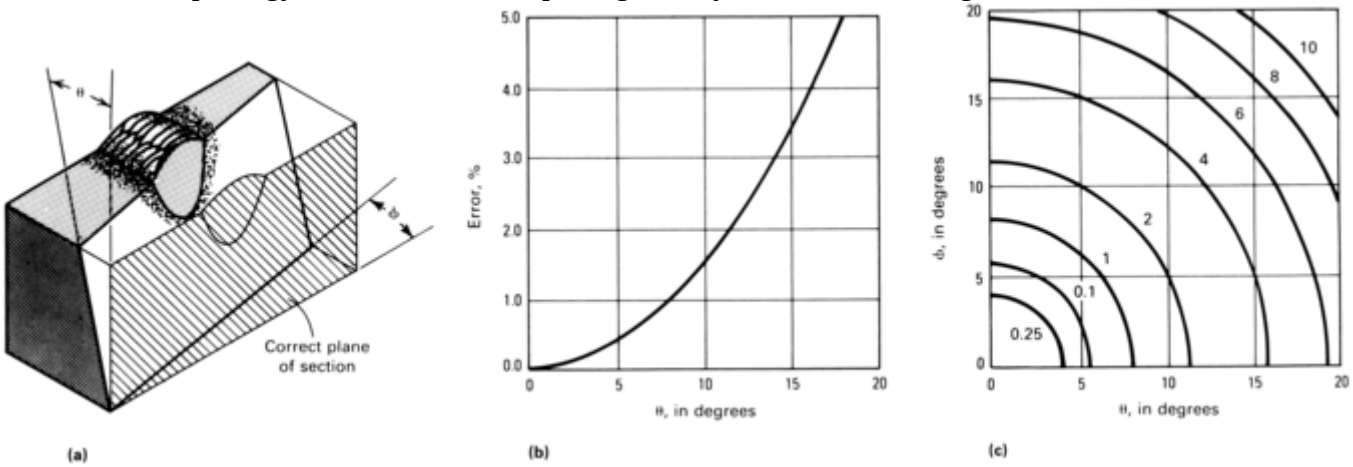

Fig. 6 Measurement errors introduced in the determination of joint penetration (or depth of fusion) and weld bead area as a function of θ and φ as shown in (a). (b) Joint penetration error. (c) Weld bead area error

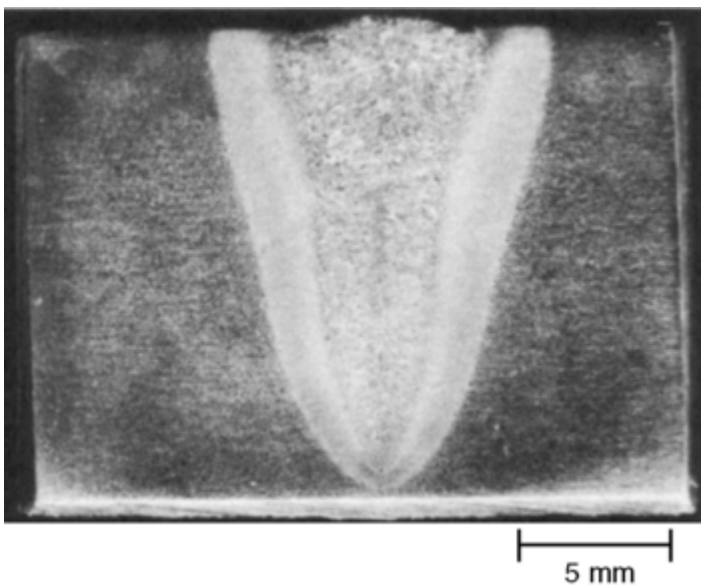

Fig. 7 2.25Cr-1Mo steel plate, single-pass electron beam weld. Heat input: 0.5 MJ/m. Macrostructure shows high depth-to-width ratio of the fusion zone, which is typical of high-energy density welding processes. Etchant: 85 mL H_2O + 15 mL HNO_3 + 5 mL methanol. Magnification: 2.8×

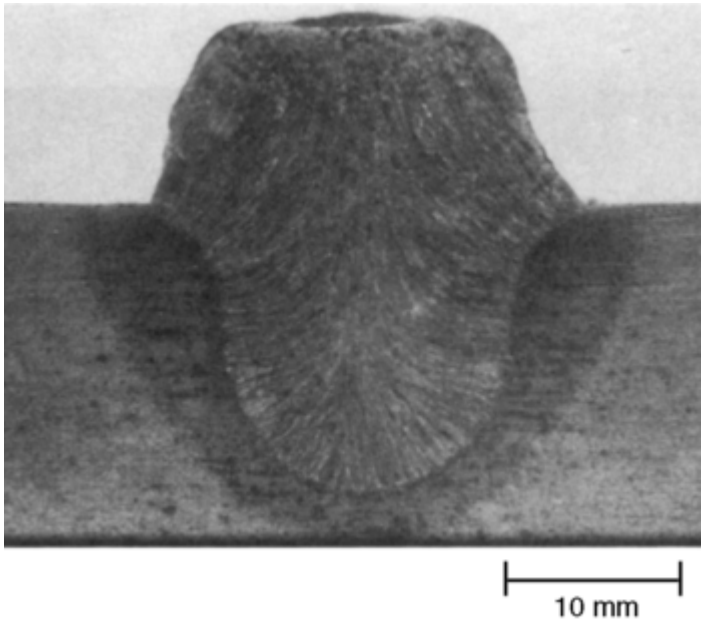

Fig. 8 13 mm (0.5 in.) Lukens Frostline steel plate, submerged arc weld. Heat input: 2.0 MJ/m. Weld wire: AWS E70S-3. Macrostructure shows unusual bead shape due to surface tension and viscosity abnormalities in a calcium-fluoride-base experimental fused flux. Etchant: 85 mL H_2O + 15 mL HNO_3 + 5 mL methanol. Magnification: 1.5×

Metallography and Microstructures of Weldments, *Metallography and Microstructures,* Vol 9, *ASM Handbook*, ASM International, 2004, p. 1047–1056

Solidification Structures in Welded Joints

Fusion metal in a welded joint solidifies by epitaxial growth from partially melted grains in the heat-affected zone. Cells or dendrites grow in packets from each heat-affected zone grain into the weld pool in a preferential crystallographic direction (Ref 2). A dendritic structure in a type 304 stainless steel weldment is shown in Fig. 9. One consequence of epitaxial growth is that a single, favorably oriented grain (packet) can traverse many successive beads in a multiple-pass weld (Fig. 10). As solidification progresses, grains bend to follow the maximum thermal gradient (Fig. 11). This phenomenon can be employed to map solidification isotherms through the use of longitudinal, transverse, and normal sections.

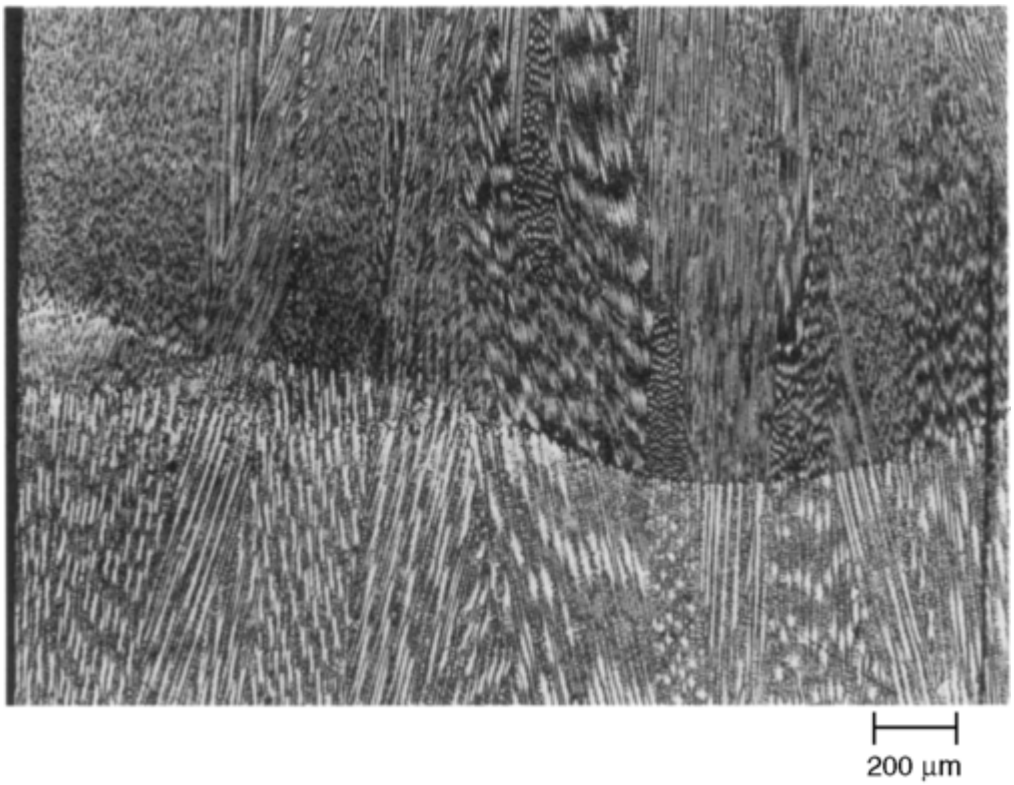

Fig. 9 25 mm (1.0 in.) type 304 stainless steel plate, shielded metal arc weld. Heat input: 1.0 MJ/m. Micrograph shows austenite-dendrite structure retained across successive weld passes in the fusion zone. Etchant: 10% oxalic acid electroetch. Magnification: 40×

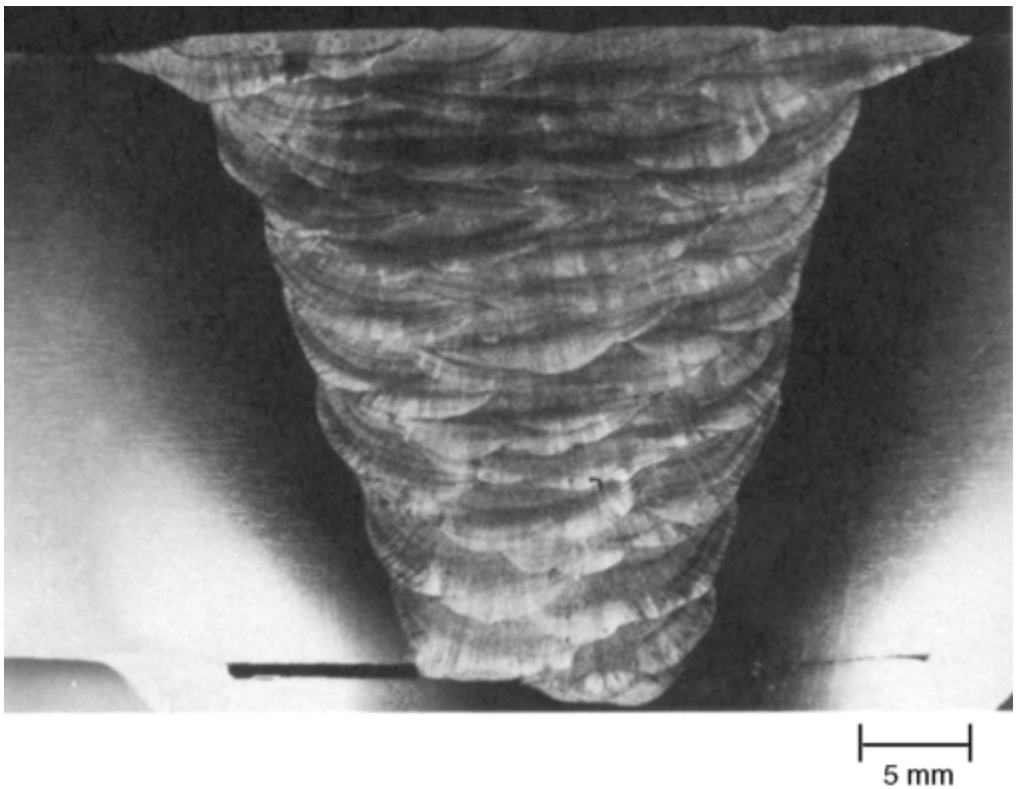

Fig. 10 25 mm (1.0 in.) type 304 stainless steel plate, shielded metal arc weld. Heat input: 1.0 MJ/m. Macrograph shows epitaxial grain growth resulting in continuous columnar grains occurring through successive passes in a multiple-pass weld. Etchant: 10% oxalic acid electroetch. Magnification: 2×

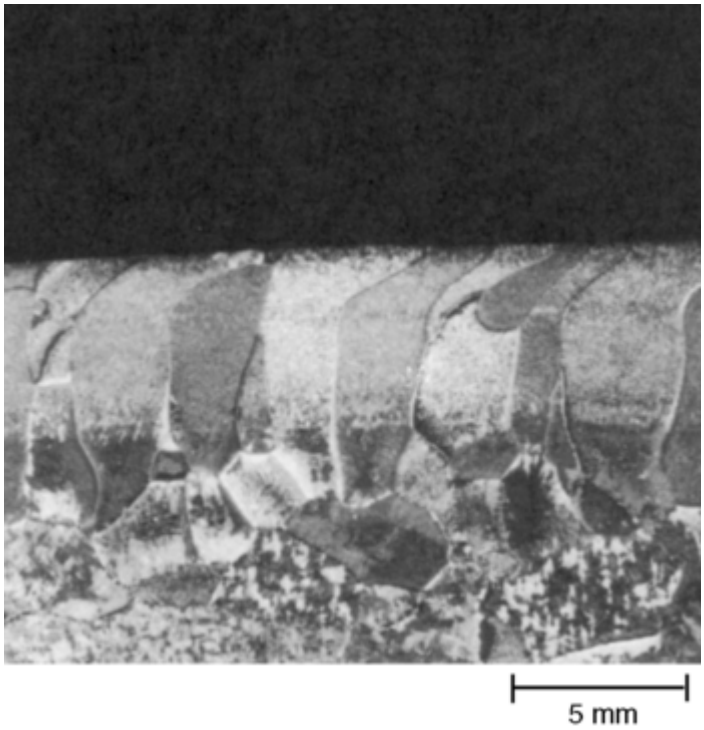

Fig. 11 13 mm (0.5 in.) Ti-6Al-2Nb-1Ta-1Mo alloy plate, autogenous single-pass gas tungsten arc weld. Heat input: 2.0 MJ/m. Longitudinal section showing curvature of the prior-β grains, which follow the maximum thermal gradient in the weld pool. Etchant: one-to-one solution, Kroll's reagent and distilled water. Magnification: 3×

During solidification, alloying elements may be rejected by the solid into the liquid regions between the dendrites, cells, and/or neighboring grains. With sufficient segregation, the solidification mode (cellular or dendritic) can be determined using appropriate etches. The pattern of oxides entrapped between cells or dendrites (Fig. 12) may also reveal how the weld metal solidified.

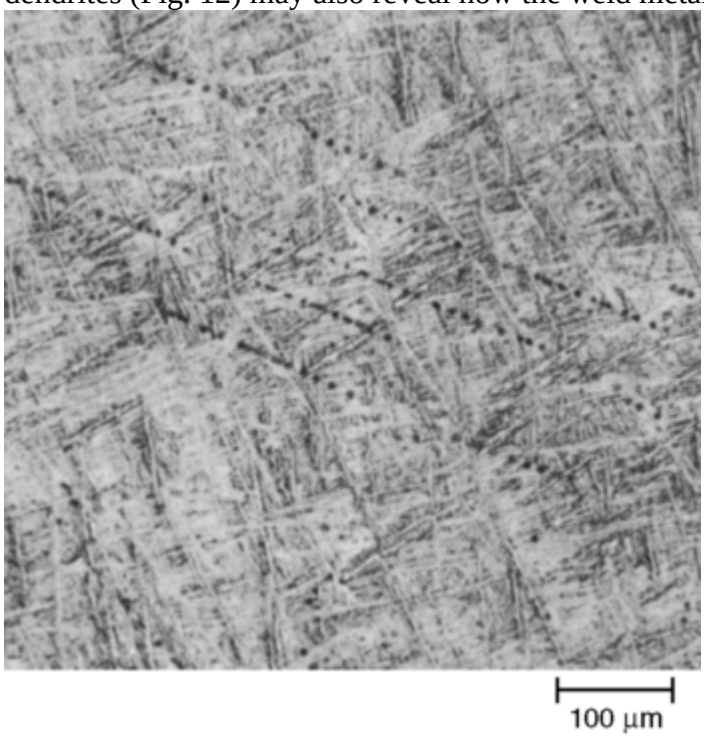

Fig. 12 13 mm (0.5 in.) Ti-6Al-4V alloy plate, autogenous two-pass gas tungsten arc weld. Heat input: 2.0 MJ/m. Weld was made over a groove in the base plate into which metallic yttrium had been pressed. Microstructure shows aligned yttrium oxide particles, indicating the segregation that occurred during solidification. Etchant: one-to-one solution, Kroll's reagent and distilled water. Magnification: 100×

It is often difficult to observe the as-solidified structure, because the microstructure is altered by one or more solid-state phase transformations during cooling. However, in some materials the solidification grain or packet boundaries act as preferential sites for the nucleation of solid-state transformation products. In these cases, the solidification grain structure is marked by discontinuities in the transformation structure.

Ferrous Alloys. In low-alloy steels, the solidification packet or austenite grain size may be marked by continuous veins of proeutectoid ferrite (Fig. 13). The solidification mode is often difficult to determine because of solid-state phase transformations that mask the solidification structure. However, in some low-alloy steels segregation is sufficient to allow observation. This is usually the case with alloys that contain slightly higher concentrations of chromium and nickel, such as AISI 4340. In these alloys, the solidification structure can be inferred from the distribution of the solid-state transformation products and is best shown by using a picral or nital etch (Fig. 13).

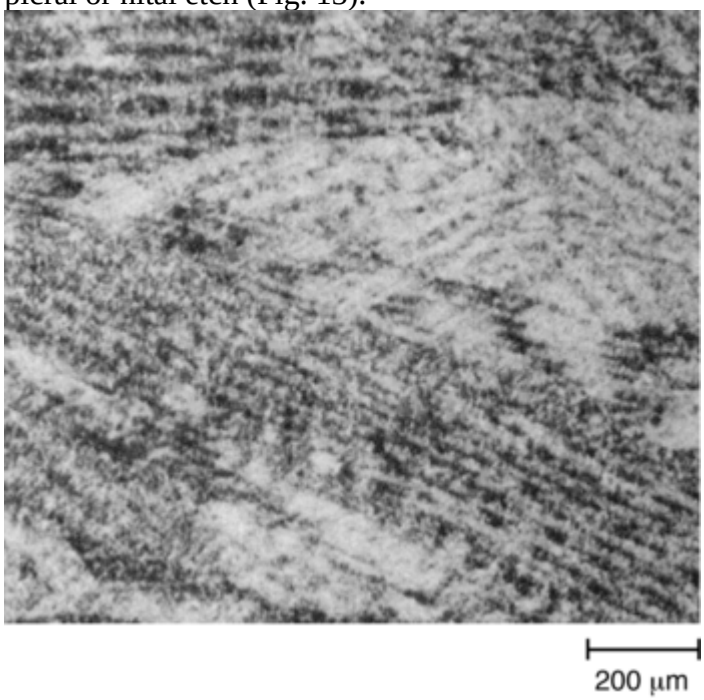

Fig. 13 13 mm (0.5 in.) AISI 4340 steel plate, submerged arc weld. Heat input: 1.9 MJ/m. Fusion-zone microstructure in which the dendrite solidification structure is revealed by the distribution of tempered martensite and upper bainite. Etchant: 2% nital. Magnification: 50×

Many austenitic steels are welded with filler metals that have a stable duplex δ-ferrite/austenite structure at room temperature. These filler metals solidify by epitaxial growth of the phase present (austenite) in the heat-affected zone (Ref 3, 4). In many commercial stainless steel alloys, this results in primary austenite dendrites with some δ-ferrite in the interdendritic regions. In these alloys, the solidification structure is observable due to segregation (Fig. 9). Delta-ferrite is highlighted by the use of Murakami's etch, allowing the volume fraction of δ-ferrite, an important parameter in the welding of these alloys, to be determined by point counting (Ref 5). However, the volume fraction of δ-ferrite retained at room temperature is usually indicated by the magnetic properties of the material rather than by point counting.

Aluminum Alloys. Commercial alloys of aluminum are usually based on eutectic systems with limited solid solubility. Weld metal in these alloys solidifies by epitaxial growth of proeutectic, aluminum-rich dendrites. Solute rejection during solidification results in a final structure of divorced eutectic between aluminum-rich dendrites (Fig. 14).

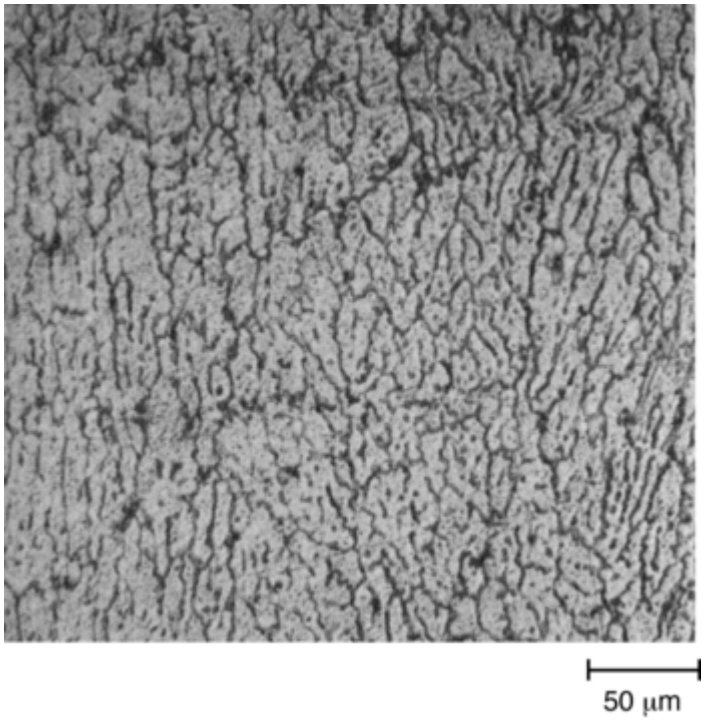

Fig. 14 2219 aluminum alloy, gas metal arc weld (parameters unknown). Fusion-zone microstructure in which the cellular solidification structure is revealed by the distribution of the divorced eutectic microconstituent between the cells. Etchant: Kroll's reagent. Magnification: 200×

Titanium Alloys. Metastable β-titanium alloys retain their solidification structure to room temperature. Evidence of the solidification type in β and heavily stabilized α-β alloys can be seen due to microsegregation. Solidification structures have been studied using a hydrofluoric acid plus nitric acid ($HF + HNO_3$) etch and oblique illumination or dendrite decoration techniques (Ref 6). The solidification grain structure of α alloys and "lean" α-β alloys, which contain much more α than β, remains observable (Fig. 15), although these alloys undergo extensive solid-state phase transformations. The large, columnar, prior-β grains in the fusion and grain-growth zones can be easily seen. Another aspect of welded joints in these alloys is the extensive epitaxial growth and the similarity of structures in the fusion and grain-growth zones, which causes difficulty in locating the fusion line (Fig. 15). Observation of solidification structures in titanium alloys may be accomplished with the use of a $HF + HNO_3$-based etchant. A detailed guide to the metallography of titanium alloys can be found in Ref 7.

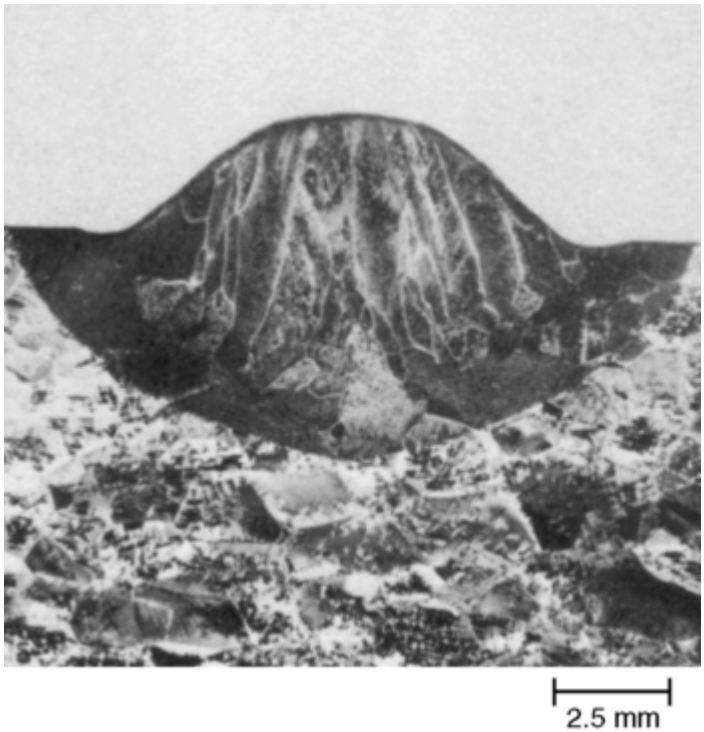

Fig. 15 13 mm (0.5 in.) Ti-6Al-2Nb-1Ta-1Mo alloy plate, single-pass gas metal arc weld. Heat input: 0.8 MJ/m. Macrograph showing the columnar prior-β grains resulting from epitaxial growth. Etchant: one-to-one solution, Kroll's reagent and distilled water. Magnification: 4×

Other Alloy Systems. Weld metal solidification structures in copper alloys based on eutectic systems are similar to commercial aluminum alloys with divorced eutectic outlining copper-rich dendrites. The dendritic solidification structures in the peritectic systems (brasses, beryllium coppers, and silicon bronzes) and continuous solid-solution systems, such as nickel-copper alloys, are frequently discernible due to microsegregation (Ref 8, 9). Etch-polish and electropolishing techniques are recommended to prevent smearing or embedding particles in the specimen surface. Etchants used for copper-base alloy weldments are similar to those used for wrought plate material of the same composition.

Solidification structures in the welds of highly alloyed nickel-, cobalt-, and iron-base superalloys are usually discernible due to the segregation of one or more solute elements during solidification. For example, in the iron-base A286 and JBK75 alloys, titanium, phosphorus, and sulfur strongly segregate to the interdendritic regions, allowing the solidification structure to be revealed by a phoschromic electroetch (Ref 5, 10). In aged welds, the solidification structure may be inferred from the inhomogeneous distribution of γ' precipitates. Nickel-base superalloys with low aluminum and titanium contents are considered to be readily weldable (Ref 11). In these alloys, the solidification structure can be revealed by electroetching with phoschromic or a solution of 10 mL phosphoric acid (H_3PO_4) plus 50 mL sulfuric acid (H_2SO_4) plus 40 mL HNO_3. A technique of etch polishing with a one-to-one solution of acetic acid and HNO_3 followed by etching with glyceregia also produces good results with many nickel-base superalloys (Ref 5). As in copper systems, special care must be taken to avoid smearing the sample.

In most alloy systems, the solidification type or grain structure can be observed. Etchants appropriate for the base plate often will be suitable for weld metal of the same composition. Etchants used for several alloy systems are listed in Table 3. For further information, see Ref 5.

Table 3 Room-temperature macroetches used for the characterization of welded joints

The steel etches are normally used only for welded joints.

Etching solution	Surface preparation[(a)]	Comments
Carbon and low-alloy steels		
10 g $(NH_3)_2S_2O_8$ (ammonium persulfate) + 100 mL H_2O	B	Swab; macroetch brings out fusion line, heat-affected zone, reheated zones, columnar zones
15 mL HNO_3 + 85 mL H_2O + 5 mL methanol or ethanol	A, B	Swab; macroetch brings out fusion line, heat-affected zone, reheated zones, columnar zones; scrub gently under running water to remove any black residue
8 mL HNO_3 + 2 g picric acid + 10 g $(NH_3)_2S_2O_8$ + 10 g citric acid + 10 drops (0.5 mL) benzalkonium chloride + 1500 mL H_2O	B	Immerse; highlights partially transformed regions in reheat and heat-affected zones (Ref 13)
Aluminum alloys		
Tucker's reagent, 45 mL HCl + 15 mL HNO_3 + 15 mL HF (48%) + 25 mL H_2O	A, B	Immerse or swab; use freshly mixed; general macroetch, all alloys
Poulton's reagent, 60 mL HCl + 30 mL HNO_3 + 5 mL HF (48%) + 5 mL H_2O	A, B	Immerse or swab; general macroetch, all alloys
Copper and copper alloys		
50 mL HNO_3 + 0.5 g $AgNO_3$ (silver nitrate) + 50 mL H_2O	A, B	Immerse; general macroetch, all alloys
Titanium alloys		
Kroll's reagent, 10–30 mL HNO_3 + 5–15 mL HF + 50 mL H_2O	B	Immerse; general macro- and microetch; increase HNO_3 and reduce HF to bring out the fine structures in weldments

(a) Surface preparation: A, finish grind; B, polish

References cited in this section

2. W.F. Savage and A. Aaronson, Preferred Orientation in the Weld Fusion Zone, *Weld. J.,* Vol 45 (No. 2), Feb 1966, p 855s–895s

3. K. Easterling, *Introduction to the Physical Metallurgy of Welding,* Butterworths, 1983

4. V.P. Kujanpaa, Weld Discontinuities in Austenitic Stainless Steel Sheets—Effects of Impurities and Solidification Mode, *Weld. J.,* Vol 63 (No. 12), Dec 1984, p 369s–375s

5. C.A. Johnson, "Metallography Principles and Procedures," Leco Corp., St. Joseph, MI, 1977

6. J.E. Gould and J.C. Williams, Solidification Structures and Phase Transformations in Welded Ti Alloys, *Titanium '80 Science and Technology,* Proc. Fourth International Conference on Titanium, H. Kimura and O. Izumi, Ed., TMS-AIME, 1980, p 2337–2346

7. "Facts About the Metallography of Titanium," RMI Co., Niles, OH, 1970

8. R.W. Heckel, J.H. Ricketts, Jr., and J. Buchwald, Measurement of the Degree of Segregation in Monel 404 Weld Metal by X-Ray Line Broadening, *Weld. J.,* Vol 44 (No. 7), July 1965, p 332s–340s

9. W.F. Savage, E.F. Nippes, and T.W. Miller, Microsegregation in 70Cu-30Ni Weld Metal, *Weld. J.,* Vol 55 (No. 7), July 1976, p 165s–173s

10. M.J. Strum, L.T. Summers, and J.W. Morris, Jr., The Aging Response of a Welded Iron-Base Superalloy, *Weld. J.*, Vol 62 (No. 9), Sept 1983, p 235s–242s

11. B. Jahnke, High-Temperature Electron Beam Welding of the Nickel-Base Super-alloy IN-738 LC, *Weld. J.*, Vol 61 (No. 11), Nov 1982, p 343s–347s

13. S.S. Strunk and R.D. Stout, Heat Treatment Effects in Multipass Weldments of a High Strength Steel, *Weld. J.*, Vol 51 (No. 10), Oct 1972, p 508s–520s

Metallography and Microstructures of Weldments, *Metallography and Microstructures,* Vol 9, *ASM Handbook*, ASM International, 2004, p. 1047–1056

Solid-State Transformation Structures in Welded Joints

The room-temperature microstructure of the fusion zone can consist of a combination of both solidification structures and the products of one or more solid-state transformations. For example, low-alloy steel weld metal solidifies as austenite, then upon cooling transforms to a mixture of ferrite and M_3C carbide (Fig. 16). The prior austenite grain size and the resulting ferrite plus carbide transformation structure are easily observed.

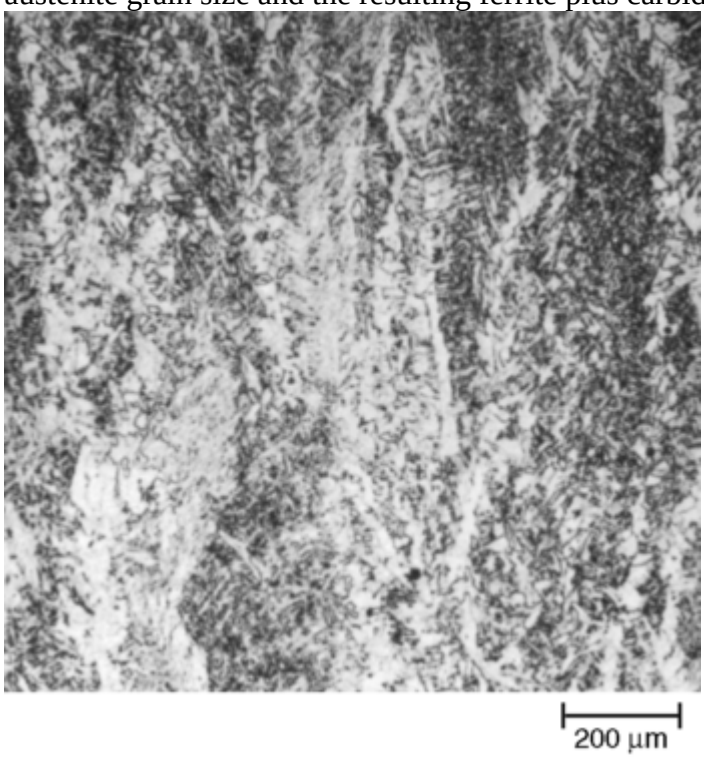

Fig. 16 16 mm ($\frac{5}{8}$ in.) A-36 steel plate, single-V butt multiple-pass shielded metal arc weld. Heat input: 1.3 MJ/m. Weld wire: AWS E7018. Low-carbon fusion-zone microstructure showing veins of grain-boundary ferrite on prior austenite grain boundaries. Etchant: 2% nital. Magnification: 50×

Solid-state phase transformations often create nonequilibrium phases or structures, which are usually characterized by continuous cooling transformation (CCT) diagrams (Fig. 17). If a welding process or parameter change can be described in terms of cooling rates, the resulting microstructural effects can be predicted by superimposing a particular cooling rate onto an applicable CCT diagram (Ref 12). However, any

predictions based on a CCT diagram are only approximate, because factors other than the bulk composition of a material affect solid-state transformations. Solid-state transformation structures in welded joints are usually examined using a transverse section, although other views can be used.

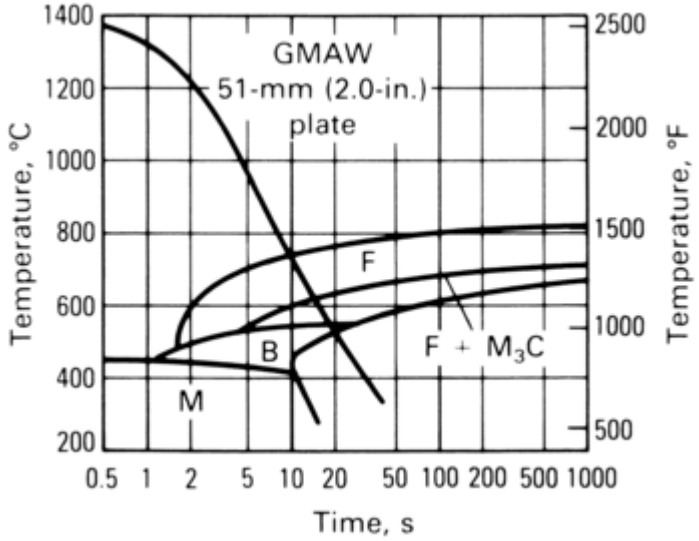

Fig. 17 Weld metal CCT curve for low carbon-manganese steel plate. Weld process: gas metal arc welding (GMAW). Heat input: 1.6 MJ/m. M, martensite; F, ferrite; B, bainite. Source: Ref 12

Ferrous Alloys. Most ferrous weld metal deposits consist of plain carbon and low-alloy plate as well as structural steel weldments. The microstructural classifications and weld zones specific to weldments in these materials are considered in this section. The fusion zone, heat-affected zone, and, in the case of multiple-pass welds, the reheated zones can be further classified.

The transformation behavior of the reheated zones and heat-affected zone are identical, resulting in microstructures that can be divided into four regions, traversing from the fusion zone outward: the grain-growth zone, the fine grain zone, the partially transformed zone, and the tempered zone. Examples of these zones in a carbon steel welded joint are shown in Fig. 18. The reaustenitized region, consisting of coarse and fine grain regions, is often referred to as the recrystallized zone. The unaffected weld metal as well as the partially transformed and tempered zones in the fusion zone are often collectively referred to as columnar zones. Etches that assist the delineation of the fusion line, reheated zone, or heat-affected zone in steel weldments are presented in Table 3 (Ref 5, 13).

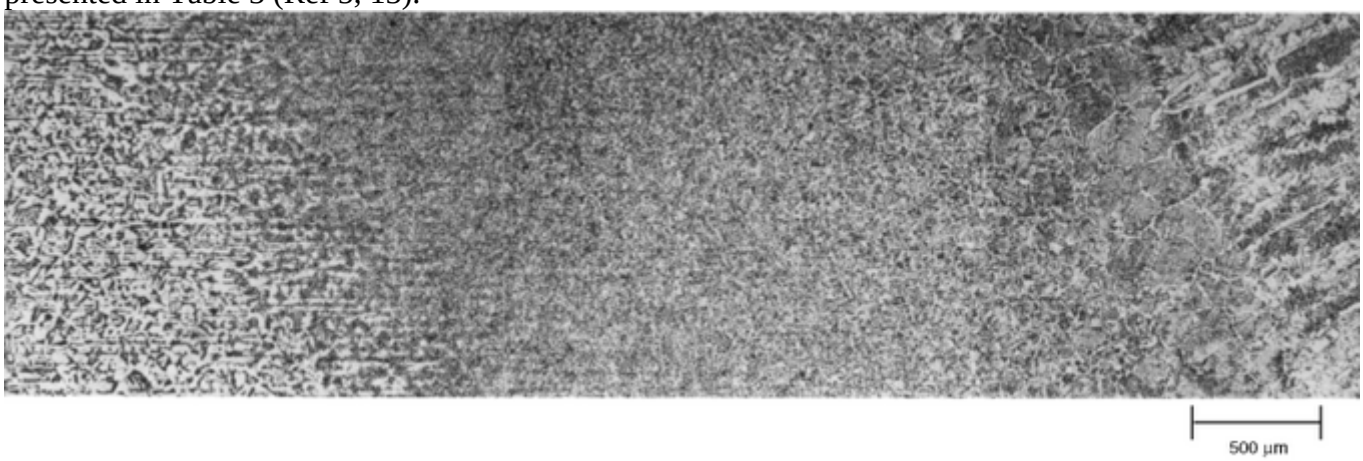

Fig. 18 16 mm ($\frac{5}{8}$ in.) A-36 steel plate, multiple-pass shielded metal arc weld. Heat input: 1.3 MJ/m. Composite micrograph of the heat-affected zone showing (from left to right) base plate, tempered zone, partially transformed zone, fine grain zone, coarse grain zone, fusion line, and fusion zone. Etchant: 2% nital. Magnification: 36×

The following microstructure constituent classifications for the fusion zone in ferritic weldments have been adopted by the International Institute for Welding (Ref 14, 15, 16). Proeutectoid ferrite that nucleates at

austenite grain boundaries and often results in a grain-boundary film is classified as grain-boundary ferrite (Fig. 19). Proeutectoid ferrite that nucleates intragranularly is classified as polygonal ferrite (Fig. 20). Upper bainite and Widmanstätten ferrite are classified as ferrite with aligned second phase (Fig. 21, 22). Pearlite and nonaligned ferrite-carbide eutectoid decomposition products are classified as ferrite carbide aggregate (Fig. 22). An interlocking aggregate of fine, randomly oriented, intragranular laths of ferrite with an aspect ratio of approximately four to one is classified as acicular ferrite (Fig. 19, 20). Martensite may also be present as a constituent in fusion-zone microstructures.

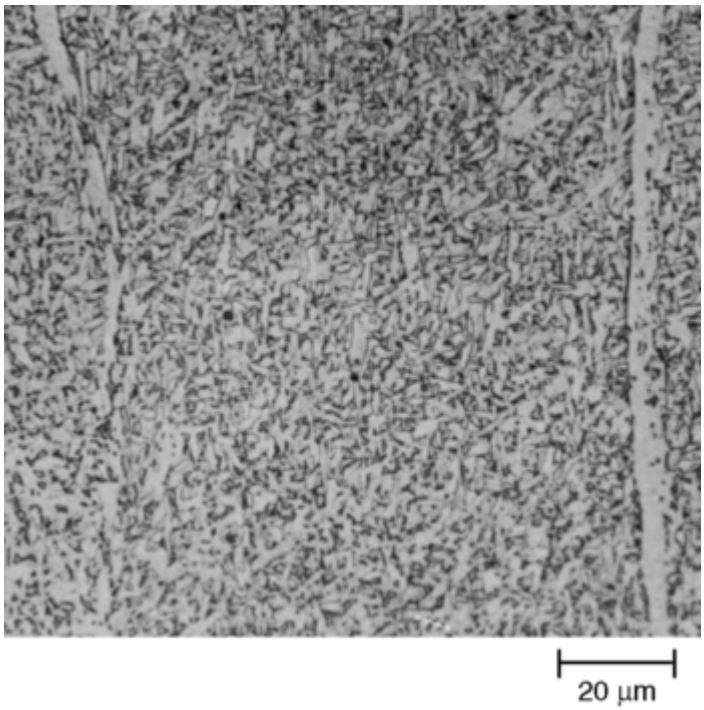

Fig. 19 19 mm (0.75 in.) A-710 steel plate, last pass (12th) of a submerged arc single-V butt weld. Heat input: 1.3 MJ/m. Grain-boundary ferrite on prior austenite grain boundaries in a microstructure of fine acicular ferrite. Etchant: 2% nital. Magnification: 500×

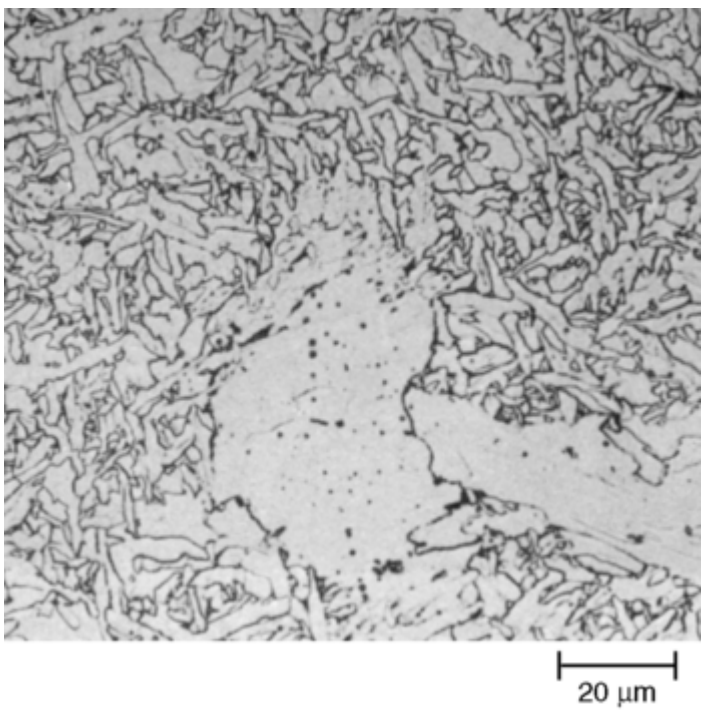

Fig. 20 16 mm ($\frac{5}{8}$ in.) A-36 steel plate, multiple-pass shielded metal arc single-V butt weld. Heat input: 1.3 MJ/m. Weld wire: AWS E7018. Fusion-zone microstructure containing polygonal ferrite in coarse acicular ferrite. Etchant: 2% nital. Magnification: 500×

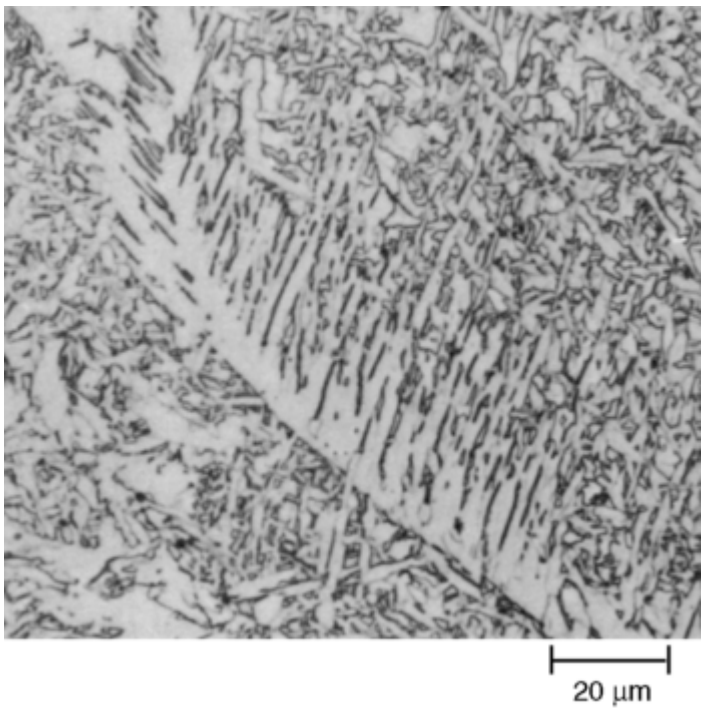

Fig. 21 13 mm (0.5 in.) Lukens Frostline steel plate, submerged arc bead-on-plate weld. Heat input: 1.9 MJ/m. Weld wire: AWS E70S-3. Fusion-zone microstructure with Widmanstätten ferrite growth from grain-boundary ferrite with coarse acicular ferrite. Etchant: 2% nital. Magnification: 500×

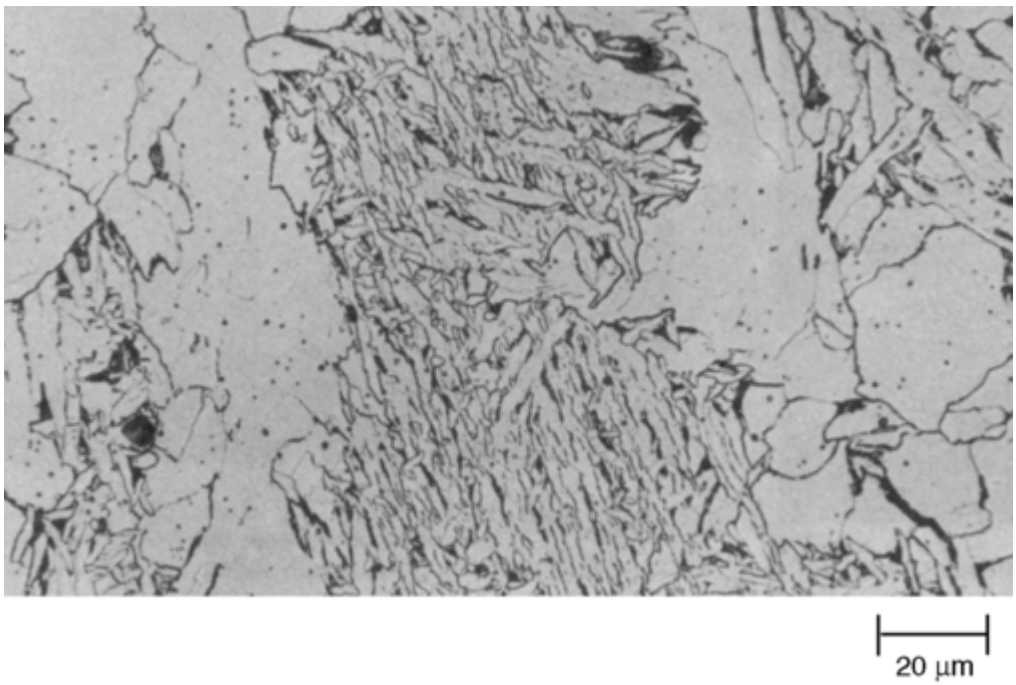

Fig. 22 16 mm ($\frac{5}{8}$ in.) A-36 steel plate, multiple-pass shielded metal arc single-V butt weld. Heat input: 1.3 MJ/m. Weld wire: AWS E7018. Fusion-zone microstructure containing bainite and ferrite-carbide aggregate in coarse grain-boundary ferrite. Etchant: 2% nital. Magnification: 500×

Aluminum alloys may undergo solid-state transformations that alter their microstructures. However, these transformations do not usually occur during welding processes due to the rapid thermal cycles in welding. Thus, the microstructures observed in aluminum weldments will usually be the solidification structure.

Titanium alloys are classified as α, α-β, or metastable β alloys based on the structure present at room temperature. Metastable β alloys, which are not significantly altered by solid-state transformations during welding, are not discussed here. The structures observed in α and α-β alloys are composed of retained β and one or more β decomposition products, including grain boundary and Widmanstätten α, massive α, and α′ or α″ martensites (Ref 17, 18, 19). These structures, essentially identical to those that occur in plate material exposed to similar cooling rates, are observed using standard sample preparation techniques and a one-to-one solution of Kroll's reagent in distilled water. Resolving the fine transformation products usually seen in weldments often requires reducing the HF and increasing the HNO_3 in the etching solution. This is especially true for low-energy welding processes and/or higher alloy contents. For additional information on the metallography and physical metallurgy of titanium, see Ref 6, 7, and 17, 18, 19, 20.

The most common microstructural constituent in the fusion and grain-growth zones of α alloy welded joints is acicular α (Ref 17). At high cooling rates, α′ hexagonal martensite may also be formed, but this constituent is difficult to distinguish from acicular α. In α-β titanium alloys, the structure most often observed in the fusion and grain-growth zones is a combination of grain-boundary α, massive α, Widmanstätten α + β, and α′, as shown in Fig. 23 and 24 and discussed in Ref 19. In more heavily β-stabilized alloys, α″ orthorhombic martensite may be formed rather than α′, but the two martensites are similar in appearance.



Fig. 23 13 mm (0.5 in.) Ti-6Al-4V alloy plate, autogenous single-pass gas tungsten arc weld. Heat input: 2.0 MJ/m. Fusion-zone microstructure consisting of fine Widmanstätten α + β and grain boundary α. Etchant: one-to-one solution, Kroll's reagent and distilled water. Magnification: 100×

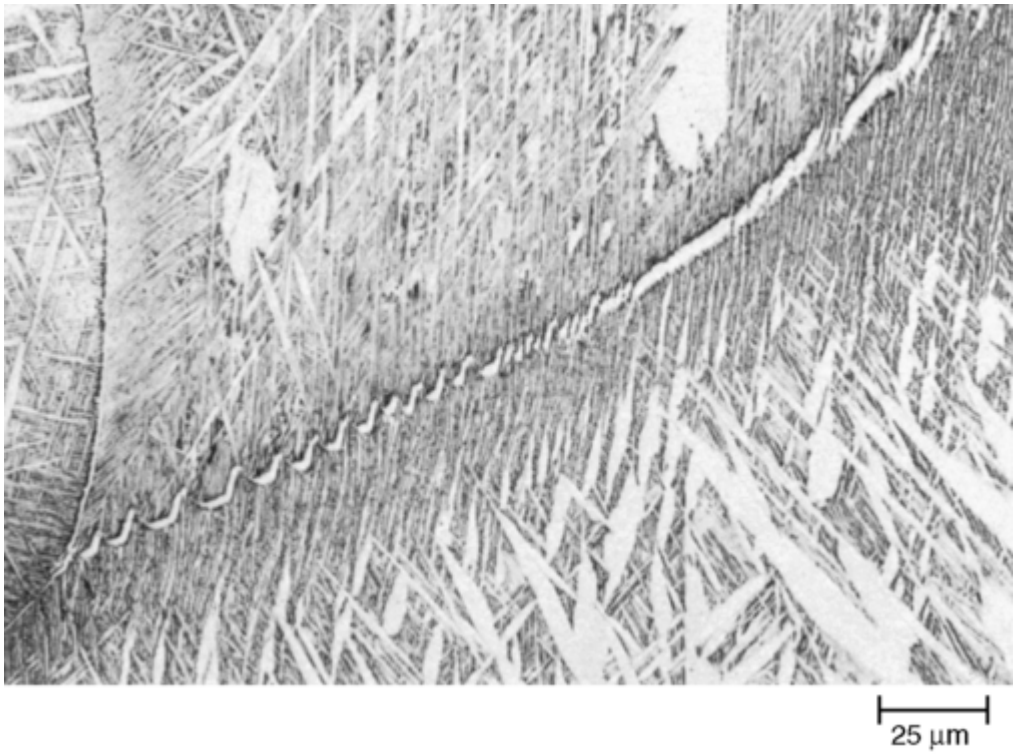

Fig. 24 13 mm (0.5 in.) Ti-6Al-2Nb-1Ta-1Mo alloy plate, autogenous single-pass gas tungsten arc weld. Heat input: 2.0 MJ/m. Fusion-zone microstructure containing grain-boundary α, α′, massive α, and Widmanstätten α + β. Etchant: one-to-one solution, Kroll's reagent and distilled water. Magnification: 400×

Reheat zones in α-β alloys consist of two regions. The grain-growth zone next to the weld appears identical to the grain-growth zone in the heat-affected zone. The partially transformed zone, rarely observed in the heat-affected zone, is easily detected in the reheat zones. This region contains equiaxed primary α as well as β and β decomposition products and retains a slightly larger amount of β at room temperature (Fig. 25). The area etches more heavily than the surrounding material with a HF + HNO_3-based etchant.



Fig. 25 13 mm (0.5 in.) Ti-6Al-2Nb-1Ta-1Mo alloy plate, three-pass gas metal arc weld. Heat input: 0.8 MJ/m. Reheat zone of the third pass showing α′, Widmanstätten α + β, equiaxed α, and slightly higher amount of retained β than the areas surrounding the reheat zone. Etchant: one-to-one solution, Kroll's reagent and distilled water. Magnification: 250×

Other alloy systems that undergo solid-state transformations during welding include cobalt, tin, uranium, and zirconium. Etchants appropriate for wrought and cast material of similar composition are usually adequate for examining weld metal microstructures. Etching techniques and appropriate etchants can be found in the articles on these specific alloy systems in this Volume.

References cited in this section

5. C.A. Johnson, “Metallography Principles and Procedures,” Leco Corp., St. Joseph, MI, 1977

6. J.E. Gould and J.C. Williams, Solidification Structures and Phase Transformations in Welded Ti Alloys, *Titanium '80 Science and Technology*, Proc. Fourth International Conference on Titanium, H. Kimura and O. Izumi, Ed., TMS-AIME, 1980, p 2337–2346

7. “Facts About the Metallography of Titanium,” RMI Co., Niles, OH, 1970

12. J.E. Lyttle, K.E. Dorschu, and W.A. Fraagetta, Some Metallurgical Characteristics of Tough High Strength Welds, *Weld. J.*, Vol 48 (No. 11), Nov 1969, p 493s–498s

13. S.S. Strunk and R.D. Stout, Heat Treatment Effects in Multipass Weldments of a High Strength Steel, *Weld. J.*, Vol 51 (No. 10), Oct 1972, p 508s–520s

14. D.J. Abson and R.E. Dolby, A Scheme for the Quantitative Description of Weld Metal Microstructures, *Weld. Inst. Res. Bull.*, Vol 21 (No. 4), 1980, p 100–103

15. “Classification of Microstructure in Low C Low Alloy Steel Weld Metal and Terminology,” IIW Report IX-1282-83, Committee on Welding Metallurgy, Japan Welding Society, Tokyo, Japan, 1983

16. R.W. Pargeter, “Quantification of Weld Metal Microstructure,” IIW Document No. 1XJ-78-83, International Institute of Welding, London, England, 1983

17. D.W. Becker, R.W. Messler, and W.A. Baeslack, Titanium Welding—A Critical Review, *Titanium '80 Science and Technology*, Proc. Fourth International Conference on Titanium, H. Kimura and O. Izumi, Ed., TMS-AIME, 1980, p 255–276

18. J.C. Williams, Critical Review Kinetics and Phase Transformations, *Titanium Science and Technology*, Proc. Second International Conference on Titanium, R.I. Jaffee and J.M. Burte, Ed., Plenum Press, 1973, p 1433–1487

19. R.E. Lewis, W.C. Koons, J.C. Williams, and G.K. Scarr, Continuous Cooling Transformation in Ti-6Al-2Cb-1Ta-0.8Mo, *Solid-Solid Phase Transformations*, Proc. International Conference, H.I. Aaronson, D.E. Laughlin, R.F, Sekerka, and C.M. Wayman, Ed., TMS-AIME, 1982, p 1499–1503

20. M. Kimchi, “Resistance Spot Welding,” paper presented at the Colorado School of Mines, Golden, CO, 19 April 1984

Metallography and Microstructures of Weldments, *Metallography and Microstructures,* Vol 9, *ASM Handbook,* ASM International, 2004, p. 1047–1056

Defects in Welded Joints

Visual inspection, with or without the aid of some other nondestructive testing technique, is usually used to evaluate production weldments (Ref 1). However, metallography is a valuable tool in the evaluation of weld quality if destructive sectioning techniques can be tolerated. The sectioning technique used must ensure that the type of defect expected is in the plane of section. Typical defects and the sections used for their documentation are listed in Table 2. A discussion of the defects commonly seen in the welding of most alloy systems is available in Ref 1.

A macrosection can be used for detecting large defects, such as porosity and slag entrapment (Fig. 26). Macrosections also allow the integrity of the welded joint to be evaluated, allowing detection of such defects as inadequate fusion or insufficient penetration. Small defects, such as micropores and inclusions, may be observed in as-polished sections. Locating cracks, porosity, or slag entrapment is sometimes further aided by etching, because residual etchant “bleeds out” of the defect and stains adjacent areas (Fig. 27).

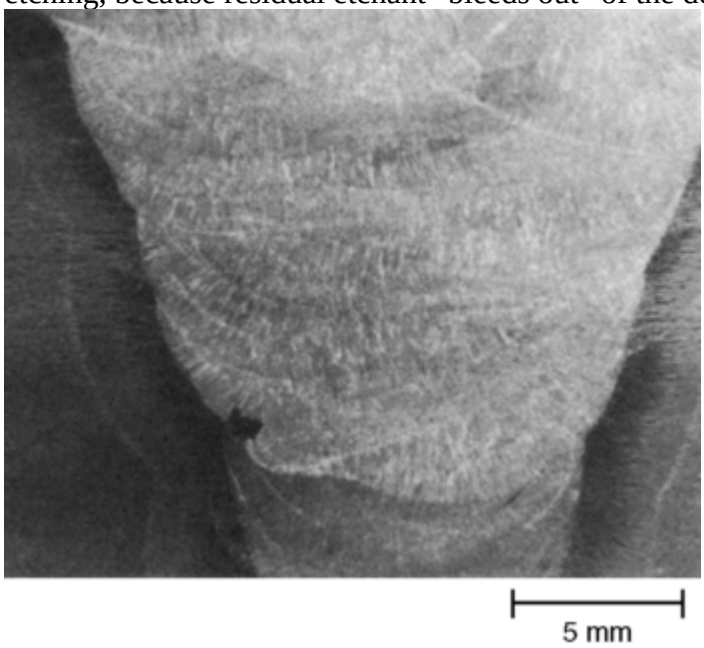

Fig. 26 38 mm (1.5 in.) HY 80 steel plate, gas-shielded flux core weld. Heat input: 2.0 MJ/m. Macrosection revealing slag entrapment in a double-V buff weld. Use of etchants is helpful in locating such defects because residual etchant “bleeds out” of defect and stains adjacent areas. Etchant: 2% nital. Magnification: 3×

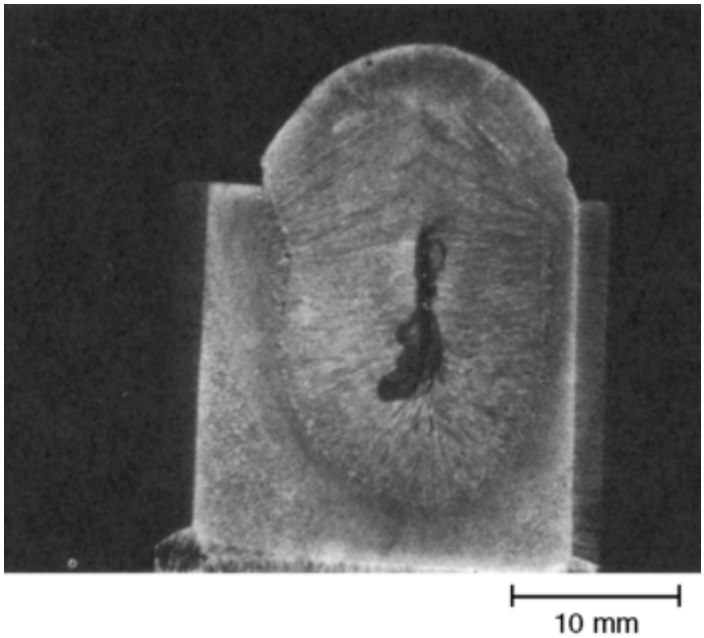

Fig. 27 13 mm (0.5 in.) AISI 4340 steel plate, submerged arc weld. Heat input: 1.9 MJ/m. Macrograph shows solidification (centerline) cracking. Crack position is highlighted by etchant "bleed out." Etchant: 85 mL H_2O + 15 mL HNO_3 + 5 mL methanol. Magnification: 1.5×

Reference cited in this section

1. W.H. Kearns, Ed., *Welding Handbook,* American Welding Society, Miami, 1978–1984

Metallography and Microstructures of Weldments, *Metallography and Microstructures,* Vol 9, *ASM Handbook,* ASM International, 2004, p. 1047–1056

Additional Welding Processes

Although arc welding is the most commonly used technique, many other processes are also employed. This section briefly discusses the metallographic considerations particular to three areas: laser and electron beam welding, resistance and spot welding, and dissimilar-metal welding. For additional information about specific welding processes, see *Welding, Brazing, and Soldering,* Volume 6 of the *ASM Handbook* and the AWS *Welding Handbook* (Ref 1).

Laser and Electron Beam Welding. Many alloy systems can be welded using laser and electron beam processes, including materials that cannot be easily welded by other methods, such as refractory or highly reactive metals. The high-energy densities of these processes allow welds to be made with low heat inputs. This results in a welded joint with a high depth-to-width ratio, a small heat-affected zone, and nonequilibrium microstructural components reflecting the high cooling rates (Fig. 7 and 28). Metallography is often used to evaluate weld bead integrity and workpiece alignment, which are critical because of the narrow width of the welded joint. If the high cooling rate of these welding processes can create deleterious phases in a particular system, the metallography of the welded joint should be directed toward the detection of these phases. Porosity can also be a problem in some systems due to the metal vaporization inherent in these processes. In most cases, metallographic techniques suitable for rapidly cooled plate material of the same composition will produce good results in laser and electron beam welded joints.

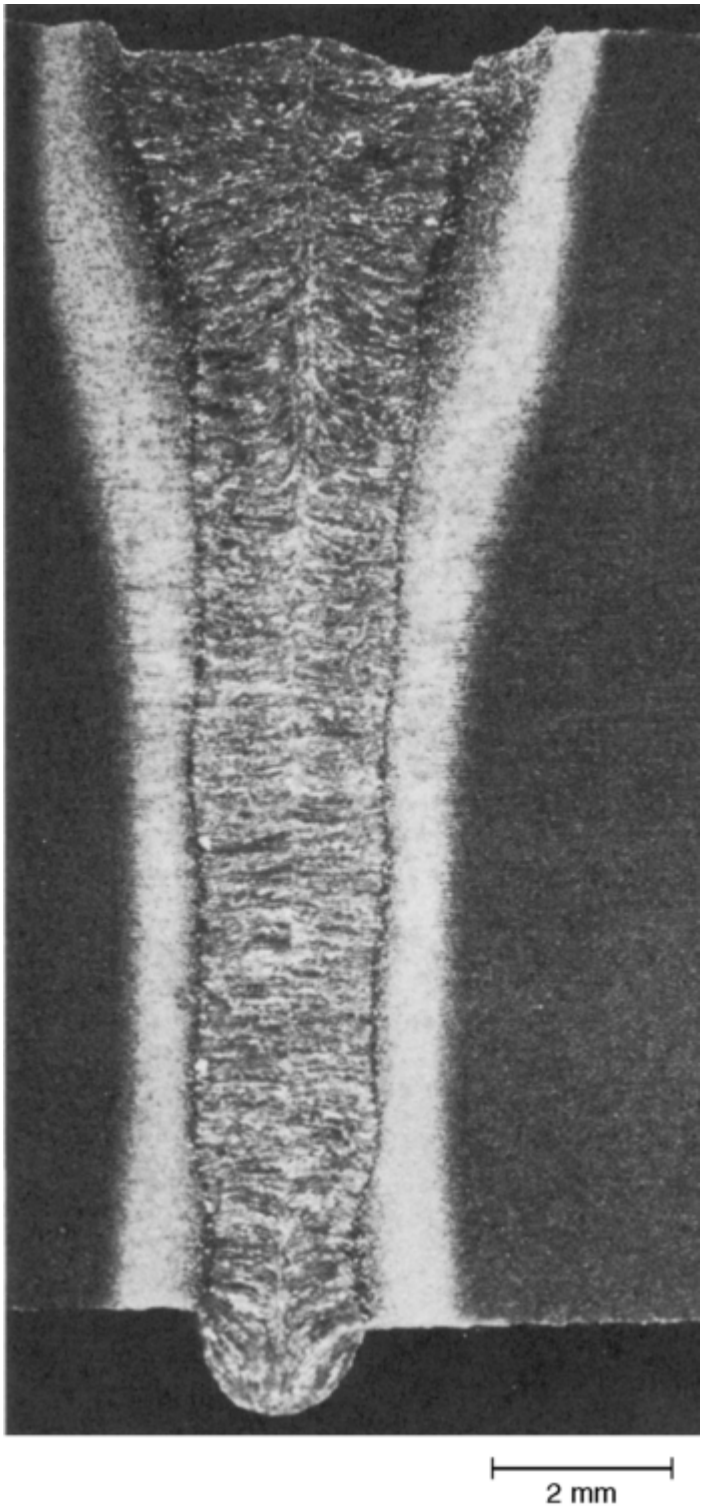

Fig. 28 14 mm ($\frac{9}{16}$ in.) A-710 steel plate, autogenous single-pass laser butt weld. Heat input: 0.014 MJ/m. Macrograph shows the high depth-to-width ratio of the weld bead and the limited size of the heat-affected zone. Etchant: 2% nital. Magnification: 8×

Resistance Spot and Seam Welding. Metal sheets and thin section shapes are often joined by resistance spot or seam welding. These processes result in a fusion zone, referred to as the "nugget," between the overlapping sheets (Fig. 29). Although the surface appearance of the welded joint is important for aesthetic reasons in the manufacture of consumer goods, it provides no indication of the size and soundness of spot welds. The soundness of spot welds may be estimated by measurements of penetration and nugget diameter (Ref 1, 20). In resistance spot welds, these measurements may be made with sections through the center of the nugget. The plane of section cannot deviate from the true plane of section by more than 16% of the nugget diameter if measurement errors of more than 5% are to be avoided. Clear mounting materials are recommended. The

sectioning considerations for arc welds apply to seam welds, which are best characterized with transverse sections.

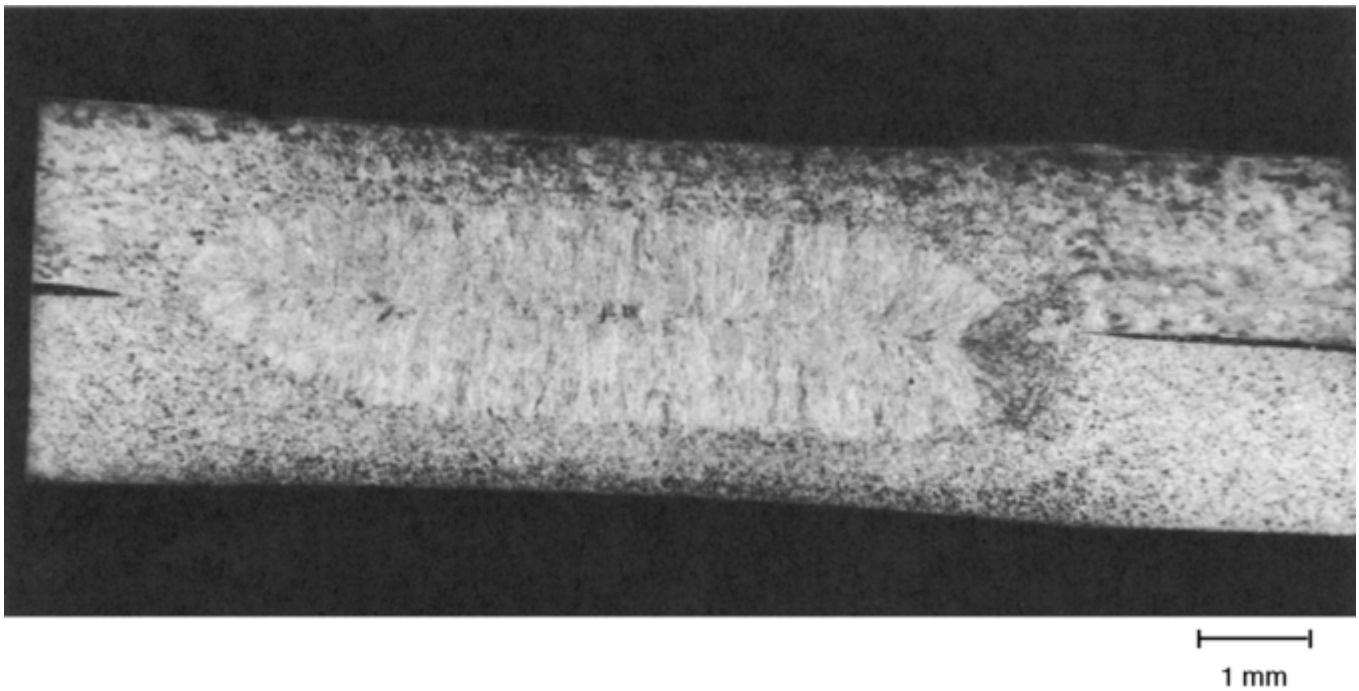

Fig. 29 Low-carbon hot-rolled sheet, resistance spot weld (composition and weld parameters unknown). Macrostructure shows 60% penetration of the weld and columnar growth pattern in the fusion zone. Etchant: 85 mL H_2O + 15 mL HNO_3 + 5 mL methanol. Magnification: 10×

Dissimilar-metal sheets or coated sheet steels are often resistance spot or seam welded and may require the special preparation techniques described below.

Dissimilar-metal welded joints are often made between materials of widely differing structures and properties, both with and without the addition of filler metal. Not only can this create microstructures uncommon to either base material and severe microstructural variations, but the welded joint and base material can have very different hardnesses. As a result, two specific considerations are involved in the metallography of dissimilar-metal joints: first, the preparation of a suitable specimen for metallographic examination and, second, the selection of the proper etching technique to allow identification of the phases present in the welded joint.

The hardness variations of many dissimilar-metal welded joints require that special care be taken during sample preparation to avoid preferential material removal of any part of the sample. Automatic grinding and polishing equipment is recommended for maximum flatness retention. Best polishing results are obtained with diamond polishing compounds and napless polishing cloths.

Different etchants are often required for different portions of the welded joint. If the sample geometry permits, parts of the specimen may be masked with glyptal or a similar product, and each portion of the sample etched individually. In joints with similar base metals, the sample can be mounted in copper-filled Bakelite to minimize the relative electrochemical difference between regions of the sample, then electroetched (Ref 6).

In most cases, the microstructures produced by dissimilar-metal welding cannot be accurately predicted, and metallography must be used to evaluate the weld structures to ensure that no deleterious phases are present. However, in welded joints of carbon or alloy steels and stainless steels, predictions can be made using a Schaeffler diagram (Ref 21) or one of its modified forms (Ref 22, 23). Examples of Schaeffler diagrams can be found in the articles “Welding of Stainless Steels” and “Hardfacing, Weld Cladding, and Dissimilar Metal Joining” in *Welding, Brazing, and Soldering,* Volume 6 of the *ASM Handbook.* Dissimilar-metal welding of several important alloy systems is discussed in Volume 4 of Ref 1.

References cited in this section

1. W.H. Kearns, Ed., *Welding Handbook,* American Welding Society, Miami, 1978–1984

6. J.E. Gould and J.C. Williams, Solidification Structures and Phase Transformations in Welded Ti Alloys, *Titanium '80 Science and Technology,* Proc. Fourth International Conference on Titanium, H. Kimura and O. Izumi, Ed., TMS-AIME, 1980, p 2337–2346

20. M. Kimchi, "Resistance Spot Welding," paper presented at the Colorado School of Mines, Golden, CO, 19 April 1984

21. A.L. Schaeffler, Constitutional Diagram for Stainless Steel Weld Metal, *Met. Prog.*, Vol 56, 1949, p 680–687

22. C.J. Long and W.T. DeLong, The Ferrite Content of Austenitic Stainless Steel Weld Metal, *Weld. J.*, Vol 52 (No. 7), July 1973, p 281s–297s

23. J.A. Self, D.K. Matlock, and D.L. Olson, An Evaluation of Austenitic Fe-Mn-Ni Weld Metal for Dissimilar Metal Welding, *Weld. J.*, Vol 63 (No. 9), Sept 1984, p 282s–288s

Metallography and Microstructures of Weldments, *Metallography and Microstructures,* Vol 9, *ASM Handbook,* ASM International, 2004, p. 1047–1056

Acknowledgment

This article is adapted from G.S. Huppi, B.K. Damkroger, and C.B. Dallam, Weldments, *Metallography and Microstructures,* Volume 9 of the *ASM Handbook* (1985), pages 577 to 586.

Metallography and Microstructures of Weldments, *Metallography and Microstructures,* Vol 9, *ASM Handbook,* ASM International, 2004, p. 1047–1056

Metallography and Microstructures of Weldments

References

1. W.H. Kearns, Ed., *Welding Handbook,* American Welding Society, Miami, 1978–1984

2. W.F. Savage and A. Aaronson, Preferred Orientation in the Weld Fusion Zone, *Weld. J.*, Vol 45 (No. 2), Feb 1966, p 855s–895s

3. K. Easterling, *Introduction to the Physical Metallurgy of Welding,* Butterworths, 1983

4. V.P. Kujanpaa, Weld Discontinuities in Austenitic Stainless Steel Sheets—Effects of Impurities and Solidification Mode, *Weld. J.*, Vol 63 (No. 12), Dec 1984, p 369s–375s

5. C.A. Johnson, "Metallography Principles and Procedures," Leco Corp., St. Joseph, MI, 1977

6. J.E. Gould and J.C. Williams, Solidification Structures and Phase Transformations in Welded Ti Alloys, *Titanium '80 Science and Technology*, Proc. Fourth International Conference on Titanium, H. Kimura and O. Izumi, Ed., TMS-AIME, 1980, p 2337–2346

7. "Facts About the Metallography of Titanium," RMI Co., Niles, OH, 1970

8. R.W. Heckel, J.H. Ricketts, Jr., and J. Buchwald, Measurement of the Degree of Segregation in Monel 404 Weld Metal by X-Ray Line Broadening, *Weld. J.*, Vol 44 (No. 7), July 1965, p 332s–340s

9. W.F. Savage, E.F. Nippes, and T.W. Miller, Microsegregation in 70Cu-30Ni Weld Metal, *Weld. J.*, Vol 55 (No. 7), July 1976, p 165s–173s

10. M.J. Strum, L.T. Summers, and J.W. Morris, Jr., The Aging Response of a Welded Iron-Base Superalloy, *Weld. J.*, Vol 62 (No. 9), Sept 1983, p 235s–242s

11. B. Jahnke, High-Temperature Electron Beam Welding of the Nickel-Base Super-alloy IN-738 LC, *Weld. J.*, Vol 61 (No. 11), Nov 1982, p 343s–347s

12. J.E. Lyttle, K.E. Dorschu, and W.A. Fraagetta, Some Metallurgical Characteristics of Tough High Strength Welds, *Weld. J.*, Vol 48 (No. 11), Nov 1969, p 493s–498s

13. S.S. Strunk and R.D. Stout, Heat Treatment Effects in Multipass Weldments of a High Strength Steel, *Weld. J.*, Vol 51 (No. 10), Oct 1972, p 508s–520s

14. D.J. Abson and R.E. Dolby, A Scheme for the Quantitative Description of Weld Metal Microstructures, *Weld. Inst. Res. Bull.*, Vol 21 (No. 4), 1980, p 100–103

15. "Classification of Microstructure in Low C Low Alloy Steel Weld Metal and Terminology," IIW Report IX-1282-83, Committee on Welding Metallurgy, Japan Welding Society, Tokyo, Japan, 1983

16. R.W. Pargeter, "Quantification of Weld Metal Microstructure," IIW Document No. 1XJ-78-83, International Institute of Welding, London, England, 1983

17. D.W. Becker, R.W. Messler, and W.A. Baeslack, Titanium Welding—A Critical Review, *Titanium '80 Science and Technology*, Proc. Fourth International Conference on Titanium, H. Kimura and O. Izumi, Ed., TMS-AIME, 1980, p 255–276

18. J.C. Williams, Critical Review Kinetics and Phase Transformations, *Titanium Science and Technology*, Proc. Second International Conference on Titanium, R.I. Jaffee and J.M. Burte, Ed., Plenum Press, 1973, p 1433–1487

19. R.E. Lewis, W.C. Koons, J.C. Williams, and G.K. Scarr, Continuous Cooling Transformation in Ti-6Al-2Cb-1Ta-0.8Mo, *Solid-Solid Phase Transformations*, Proc. International Conference, H.I. Aaronson, D.E. Laughlin, R.F, Sekerka, and C.M. Wayman, Ed., TMS-AIME, 1982, p 1499–1503

20. M. Kimchi, "Resistance Spot Welding," paper presented at the Colorado School of Mines, Golden, CO, 19 April 1984

21. A.L. Schaeffler, Constitutional Diagram for Stainless Steel Weld Metal, *Met. Prog.*, Vol 56, 1949, p 680–687

22. C.J. Long and W.T. DeLong, The Ferrite Content of Austenitic Stainless Steel Weld Metal, *Weld. J.*, Vol 52 (No. 7), July 1973, p 281s–297s

23. J.A. Self, D.K. Matlock, and D.L. Olson, An Evaluation of Austenitic Fe-Mn-Ni Weld Metal for Dissimilar Metal Welding, *Weld. J.*, Vol 63 (No. 9), Sept 1984, p 282s–288s

U. Täffner, V. Carle, U. Schäfer, and M.J. Hoffmann, Preparation and Microstructural Analysis of High-Performance Ceramics, *Metallography and Microstructures,* Vol 9, *ASM Handbook*, ASM International, 2004, p. 1057–1066

Preparation and Microstructural Analysis of High-Performance Ceramics

Ulrike Täffner, Veronika Carle, and Ute Schäfer, Max-Planck-Institut für Metallforschung, Stuttgart, Germany; Michael J. Hoffmann, Institut für Keramik im Maschinenbau, Universität Karlsruhe, Germany

Introduction

IN CONTRAST TO METALS, high-performance ceramics have higher hardness, lower ductility, and a basically brittle nature. Other general properties to note are: excellent high-temperature performance, good wear resistance and thermal insulation (low thermal conductivity), as well as high resistance to corrosion and oxidation. However, the full advantage that these materials can provide is strongly dependent on composition and microstructure.

Most high-performance ceramics are based on high-purity oxides, nitrides, carbides, and borides with carefully controlled compositions. Ceramic engineering components are usually produced by powder metallurgical methods. The required properties of a specific part are optimized by selecting parameters associated with the powder mixture and the pressing and sintering operations to obtain the desired microstructure.

High-performance ceramics can be divided into two main categories; structural and functional ceramics. While optimization of structural ceramics is directed toward improved mechanical properties, the performance of components produced from functional ceramics is controlled by electrical, magnetic, dielectric, or optical properties. Therefore, restrictions with respect to mechanical properties can be tolerated. Typical structural ceramics are aluminum oxide (Al_2O_3), zirconium dioxide (ZrO_2), silicon nitride (Si_3N_4), and silicon carbide (SiC). However, Al_2O_3-, ZrO_2- and SiC-based ceramics are also often used as functional ceramics. Other functional ceramics of technological interest are barium titanate ($BaTiO_3$) and lead zirconate titanate ($Pb(Ti,Zr)O_3$).

Due to the large variations in microstructure, different ceramographic preparation techniques are applied to achieve the surface quality desired so structural details are revealed under the microscope. For ceramographic preparation, it is not sufficient to know that a sample is Al_2O_3. The manufacturing conditions must also be known because they provide important information regarding expected porosity, grain size, and impurities. These microstructural variables have a strong influence on the method selected for preparation. An example for two different ZrO_2 ceramic materials is illustrated in Fig. 1 and 2. Figure 1 shows the microstructure of tetragonal ZrO_2 (TZP, or tetragonal zirconia polycrystals). This is a high-strength structural ceramic used for room-temperature applications (e.g., knives and scissors). Tetragonal zirconia polycrystals have a grain size less than 1 μm, an extremely high bending strength ranging from 800 to 2400 MPa (115 to 350 ksi), and fracture toughness (K_{Ic}) between 6 and 15 MPa$\sqrt{m}$ (5.5 and 15.5 ksi$\sqrt{in.}$), which renders this material resistant to pullout during preparation.

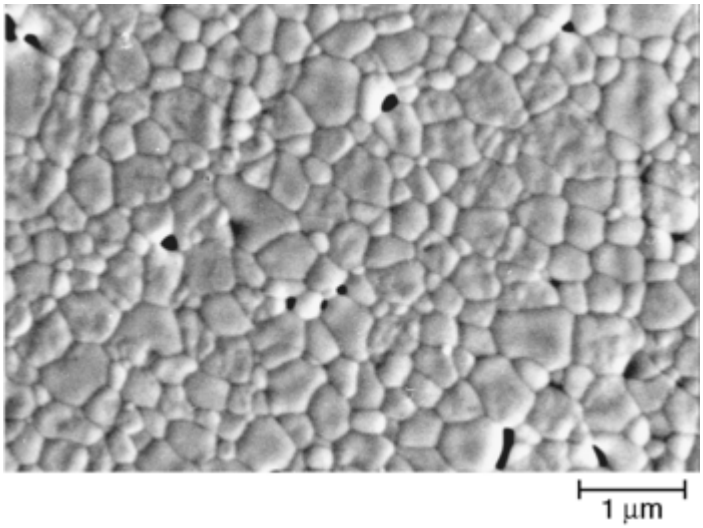

Fig. 1 Tetragonal zirconia polycrystals (TZP) with 2 mol% Y_2O_3, thermally etched in air at 1300 C (2730 °F). The scanning electron micrograph shows a fine-grained microstructure. Pores appear black.

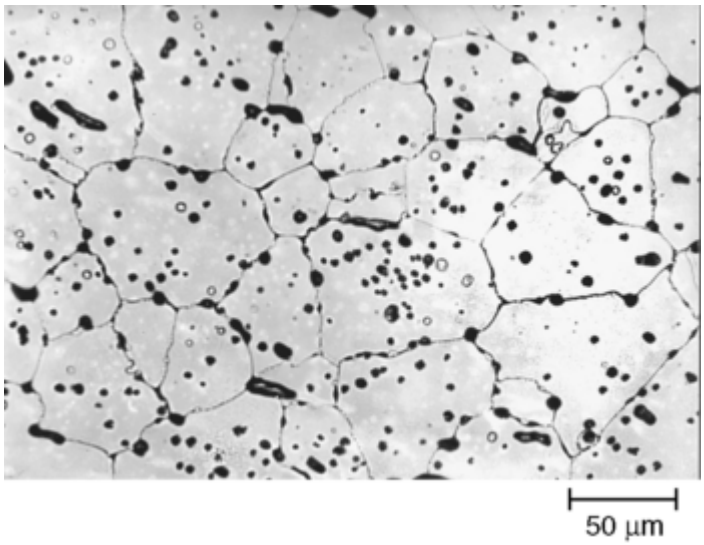

Fig. 2 Light micrograph of a cubic stabilized zirconia (CSZ) with 12 mol% Y_2O_3, thermally etched in air at 1300 °C (2730 °F). The large cubic grains show inter- and intragranular porosity.

The microstructure of cubic ZrO_2 (CSZ, or cubic stabilized zirconia) is shown in Fig. 2. The mechanical properties of this material are considerably poorer than TZP, with a bending strength of 200 MPa (29 ksi) and a fracture toughness of 2 to 3 MPa$\sqrt{m}$ (1.8 to 2.7 ksi$\sqrt{\text{in}}$). The microstructure is characterized by a high intragranular porosity and a grain size of approximately 30 to 50 µm. These materials are very sensitive to mechanical shock. Applications of TZP and CSZ are focused on their high ion conductivity (e.g., mobility of O_2 ions across the cubic ZrO_2 lattice). Cubic stabilized zirconia is also used in as λ-sensors for automobile catalytic converters and for $p(O_2)$ measurement in liquid metals.

Because of these differences in mechanical properties and microstructure, the ceramographic preparation of TZP and CSZ is quite different. The tough, fine-grained TZP requires longer polishing times for the fine-polishing step with 1 and 0.25 µm diamond, while CSZ needs longer polishing times for the coarser polishing with 6 and 3 µm diamond compounds.

Depending on the type of ceramic or ceramic component, the mechanical properties (e.g., fracture toughness and strength) may vary considerably, and therefore the ceramographic preparation procedures have to be adjusted accordingly.

U. Täffner, V. Carle, U. Schäfer, and M.J. Hoffmann, Preparation and Microstructural Analysis of High-Performance Ceramics, *Metallography and Microstructures*, Vol 9, *ASM Handbook*, ASM International, 2004, p. 1057–1066

Preparation and Microstructural Analysis of High-Performance Ceramics

Ulrike Täffner, Veronika Carle, and Ute Schäfer, Max-Planck-Institut für Metallforschung, Stuttgart, Germany; Michael J. Hoffmann, Institut für Keramik im Maschinenbau, Universität Karlsruhe, Germany

Specimen Preparation

Similarly to metallographic preparation, sequential steps have to be performed to prepare ceramics for microstructural investigations (Ref 1, 2, 3). Careful selection of sectioning, mounting, grinding, polishing, and etching procedures is required, and each step must be optimized for each type of ceramic. However, due to the brittleness, porosity, and chemical resistance of ceramics it is quite often difficult to polish them in the same way as metals. Automated sample preparation is recommended. The capability to adjust polishing pressure and the use of special grinding disks with diamond as the abrasive material is also preferred. With this equipment, a flat surface that displays an undistorted "true" microstructure may be prepared in a reasonable time.

Sectioning. Generally, ceramics are cut with a lubricated (water or a special cutting fluid), rotating diamond cutting wheel on a bench-type lab machine or on a precision cutting machine. The cutting speed (low-speed cutting machine: 25 to 500 rpm; high-speed cutting machine: 500 to 5000 rpm) and the cutting pressure should be optimized for the properties of a given material. A slow cutting speed and low pressure produce less cutting and surface damage for most ceramics, although some ceramic materials require the opposite (e.g., TZP-ZrO_2). Diamond cutting wheels are either metal bonded or resin bonded, and normally metal-bonded cutting wheels are selected. However, for very brittle and sensitive ceramics, resin-bonded cutting wheels are recommended. These wheels are softer and will generally produce a better cut-surface finish than a metal-bonded diamond wheel, but their weaker bond shortens service life. Additional criteria for selection of cutting wheels also include: the concentration of abrasive, the grain size of abrasive, and the wheel thickness. Generally, low abrasive concentration blades are used, because the lower the abrasive loading, the higher the contact stress on each abrasive particle and therefore the higher the cutting rate. The grain size of a diamond blade is usually 94 μm, but for delicate samples, it may be advisable to cut with a diamond blade of a finer grit to avoid unnecessary damage to the material. The thickness of the diamond cutting wheel is dependent on the thickness of the sample. For samples with limited dimensions it is advisable to use a thinner wheel.

Mounting. For automatic sample preparation, specimens can be mounted or may be glued directly onto a sample holder. The two possibilities for metallographic mounting are hot mounting, with compression and heat, and cold mounting. It should be noted that sensitive, small, and very brittle ceramics specimen are susceptible to damage and cracking when using hot mounting, because of the high pressure and temperature that is needed for this process. The mounting material should be either very hard or have good abrasion resistance. Additionally, before the sample is mounted consideration must be given to the etching technique that is to be used. This will guide the selection of a mounting material most suited to the complete sample preparation. For example, when using thermal etching techniques or molten-salt etching techniques the sample should be removed from the mount before etching. When etching in a boiling chemical solution, the mount should be of a material that will not be attacked by the acid mixture.

Mechanical Preparation (Grinding and Polishing). It is preferable to perform the grinding and polishing procedures with an automatic or semiautomatic machine. The structure of each and every ceramic product has been specifically adjusted to exhibit required properties, and thus each material will exhibit a unique behavior during preparation. Table 1 contains preparation standards for structural ceramics (e.g., Si_3N_4 and Al_2O_3) as well as AlN, and Table 2 provides the preparation standards for functional ceramics (e.g., $BaTiO_3$ and PZT). These tables should be used as a rough guide only; the parameters will need to be adjusted according to the preparation requirements of specific ceramics.

Table 1 Standard preparation conditions for structural ceramics (e.g., Si_3N_4, AlN, SiC and Al_2O_3), semiautomatic preparation

Process	Base	Diamond grade, μm	Lubricant	Speed, rpm	Pressure[(a)]		Time, min
					N	**lbf**	
Grinding	Diamond disk	65	Water	300	~180	~40	Until flat
	Diamond disk	20	Water	300	~180	~40	5–10
Fine grinding	Composite disk	6	Alcohol-based	300	~100	~23	5–15
Polishing	Pellon cloth	6	Alcohol-based	150	~150	~34	15–120
	Hard synthetic cloth	3	Alcohol-based	150	~120	~27	15–120
	Hard silk cloth	1	Alcohol-based	150	~90	~20	5–10
Fine polishing	Short napped, fiber cloth	Silicon dioxide suspension		150	~50	~11	0.5–5

This table should be used as a rough guide only, and parameters will need to be adjusted according to the preparation requirements of specific ceramic samples.
(a) Pressure specification for a sample holder with six 25 mm (1 in.) diam specimens

Table 2 Standard preparation conditions for functional ceramics (e.g., $BaTiO_3$, PZT, and ZnO), semiautomatic preparation

Process	Base	Diamond grade, μm	Lubricant	Speed, rpm	Pressure[(a)]		Time, min
					N	**lbf**	
Grinding	Silicon carbide paper	320	Water	300	~150	~34	Until flat
Lapping	Hard synthetic cloth	6	Lubricant	150	~100	~23	2–15
Polishing	Hard synthetic cloth	3	Lubricant	150	~120	~27	5–30
	Hard silk cloth	1	Lubricant	150	~90	~20	5–15
Fine polishing	Short napped, fiber cloth	Silicon dioxide suspension		150	~50	~11	0.5–1

This table should be used as a rough guide only, and parameters will need to be adjusted according to the preparation requirements of specific ceramic samples.
(a) Pressure specification for a sample holder with six 25 mm (1 in) diam specimens

In general, resin-bonded diamond disks are employed for grinding. In individual cases, silicon carbide paper is used. For example, this type of paper would be selected for the functional ceramics.

The surface damage generated during sectioning and grinding has to be removed during fine grinding, or lapping and polishing. Fine grinding and/or lapping retains the plane of the specimen surface, and no further damage is introduced. Complete removal of the damaged surface must therefore be achieved by subsequent polishing steps. Polishing should be performed on hard cloths. The highest removal rates will occur during steps with the application of 6 and 3 μm diamond grain size. Polishing with 1 μm diamond removes a minimal amount of material. All breakouts and scratches should be removed during these steps. In general, fine polishing with a SiO_2 suspension is only applied if small and fine scratches have to be removed. In some cases, this final step can also produce a slight relief on the sample surface, which may be beneficial for microscopy.

References cited in this section

1. G. Petzow, *Metallographic Etching*, 2nd ed., ASM International, 1999

2. G. Elssner, H. Hoven, G. Kiessler, and P. Wellner, *Ceramic and Ceramic Composites: Materialographic Preparation*, Elsevier, 1999

3. W.E. Lee and W.M. Rainforth, *Ceramic Microstructures: Property Control by Processing*, Chapman & Hall, London, 1994

U. Täffner, V. Carle, U. Schäfer, and M.J. Hoffmann, Preparation and Microstructural Analysis of High-Performance Ceramics, *Metallography and Microstructures*, Vol 9, *ASM Handbook*, ASM International, 2004, p. 1057–1066

Preparation and Microstructural Analysis of High-Performance Ceramics

Ulrike Täffner, Veronika Carle, and Ute Schäfer, Max-Planck-Institut für Metallforschung, Stuttgart, Germany; Michael J. Hoffmann, Institut für Keramik im Maschinenbau, Universität Karlsruhe, Germany

Microscopic Examination

For the investigation of ceramic microstructures and the identification of flaws and defects, the use of light optical microscopy (LOM) or scanning electron microscopy (SEM) are most common. Since most of the ceramics are electrical insulators, samples for SEM investigations have to be coated by an electrical conductive layer such as carbon, gold, or gold-palladium alloys. Metals are used for simple microstructural analysis, while carbon is used for simultaneous chemical analysis, for example, energy-dispersive x-ray (EDX) analysis. Standard scanning electron microscopes are normally equipped with different detectors. The backscatter detector is useful for multiphase materials, when the different phases reveal a strong mass contrast. In this case, no etching is required. Secondary electron detectors are sensitive to small differences in height of a polished and etched surface. The microscopic examination of ceramic specimens in the as-polished state has proved useful. An evaluation of the number of pores, their distribution, and possible pullouts can only be assessed in this state. Evaluation of inclusions, contamination, and cracks should also be made before etching.

In order to reveal grain boundaries, phases, and other microstructural details, ceramic specimens have to be etched. Ceramic microstructures, examined under the LOM (>200×) will show a low contrast and a milky image. Ceramics permit light rays to penetrate the surface where scattering and internal reflection occurs. To eliminate light scattering and to improve the reflectivity, coating the surface with a reflective layer is recommended. Such a layer should be between 5 and 10 nm thick and can be applied by sputter coating with either gold or aluminum.

Thin-Section Polarized Light Microscopy. In general, all nonmetallic materials are suitable for examination by transmission polarized light microscopy, including the high-performance ceramics (Ref 4). The only limitations are the grain size of the material and its mechanical behavior. Many ceramics have a very small grain size (<1 μm), which makes LOM examination impossible. Because resolution depends on the wavelength of light, the smallest particle size that can be observed is 1 μm. In order for a thin section to be mechanically stable it needs to be about 5 to 30 μm thick. At this thickness, however, the grains in fine-grained materials lie over one another, and this multioverlayering results in formation of a diffuse image. This can cause difficulty in differentiating between certain optical effects. It is for this reason that a grain size of at least 5 μm is preferred.

The preparation of thin sections requires the use of precision cutting, grinding, and polishing machines. It should be remembered that several square centimeters of specimen must be removed by cutting, grinding, and polishing to achieve a specimen of uniform 5 to 30 μm thickness with a smooth, polished surface on either side, free of surface breakouts.

In the first stage of preparation, the specimens are treated in the same way as polished sections for incident light microscopy. The ceramic is cut and mounted and then ground and polished using a semiautomatic grinding and polishing machine. A roughened glass slide is then bonded to the polished surface of the specimen with a drop of epoxy resin (Fig. 3). To prevent the formation of pores and air bubbles between the specimen and the glass slide, this operation should be carried out in a vacuum infiltration chamber. Once the specimen has fully hardened, which generally takes about two days, the specimen is sliced off to a thickness of about 500 μm. Thereafter, the specimen is ground down to a thickness of about 80 to 100 μm using a diamond grinding disk. Because there is always a danger of deep pullouts and cracking, which then have to be eliminated by the

following stages of preparation, the specimen should not be ground any thinner than 80 μm. Depending on the material being prepared, the specimen is either manually or semiautomatically fine ground and then polished. As the thin section nears the end of its preparation, it must be handled extremely carefully and must be repeatedly checked with the microscope under polarized light. When the target thickness is achieved—that is, when all the grains, depending on their double refraction, exhibit the colors gray, yellow-brown, or blue-green—a thin cover glass is bonded to the surface of the specimen for protection, using thinned epoxy resin.

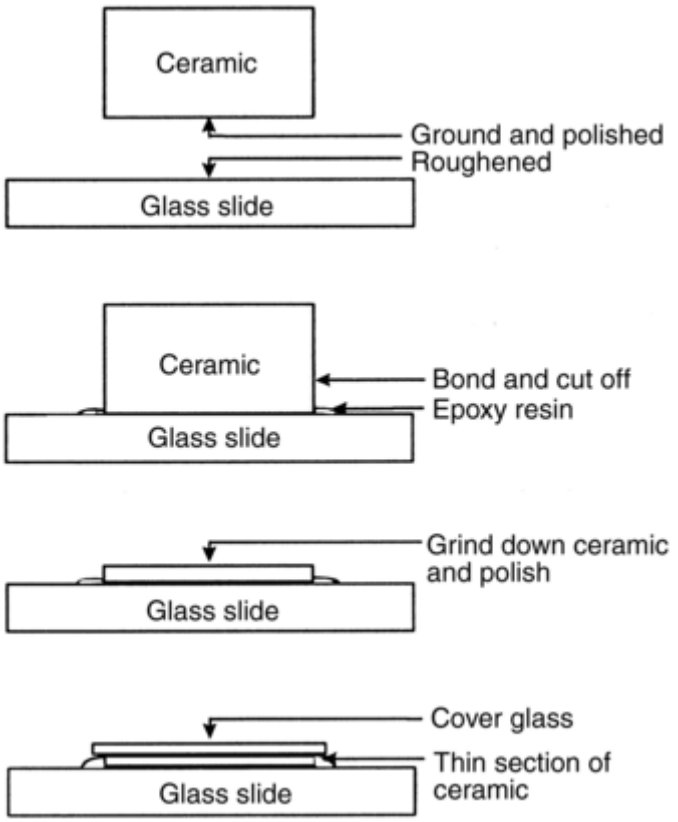

Fig. 3 Ceramographic specimen preparation sequence from top to bottom for a thin section

Reference cited in this section

4. U. Täffner, Transmission Polarised Light Microscopy of High Performance Ceramics, *Pract. Metallogr.*, Vol 38, 1990; p 385–390

U. Täffner, V. Carle, U. Schäfer, and M.J. Hoffmann, Preparation and Microstructural Analysis of High-Performance Ceramics, *Metallography and Microstructures*, Vol 9, *ASM Handbook*, ASM International, 2004, p. 1057–1066

Preparation and Microstructural Analysis of High-Performance Ceramics

Ulrike Täffner, Veronika Carle, and Ute Schäfer, Max-Planck-Institut für Metallforschung, Stuttgart, Germany; Michael J. Hoffmann, Institut für Keramik im Maschinenbau, Universität Karlsruhe, Germany

---

Ceramographic Etching

Figure 4 presents a review of ceramographic etching methods (Ref 1, 5). Three etching methods can be distinguished: optical, electrochemical, and physical contrasting. The most frequently used etching methods for high-performance ceramics are solution etching, thermal etching, and plasma etching. Plasma etching works

only in case of silicon-base ceramics (SiC, Si_3N_4). Details of the etching procedure are described below. Thermal etching is mostly used for oxide ceramics. Typical etching temperatures are 150 °C (270 °F) below sintering temperature in air. Etching time can vary between 15 min and some hours, depending on the structure and composition of the grain boundary that evaporates during the heat treatment. Thermal etching of nonoxide ceramics requires an inert atmosphere or an encapsulation of the sample in a quartz tube. Due to the chemical resistance of many ceramics, solution etching of polished specimens requires the application of very aggressive chemicals at elevated temperatures, or the application of molten-salt reagents. For the etchants given in Table 3, only general details can be given in regard to the concentration and etching time required for a given sample. The desired level of etching on a sample must be determined by trial and error.

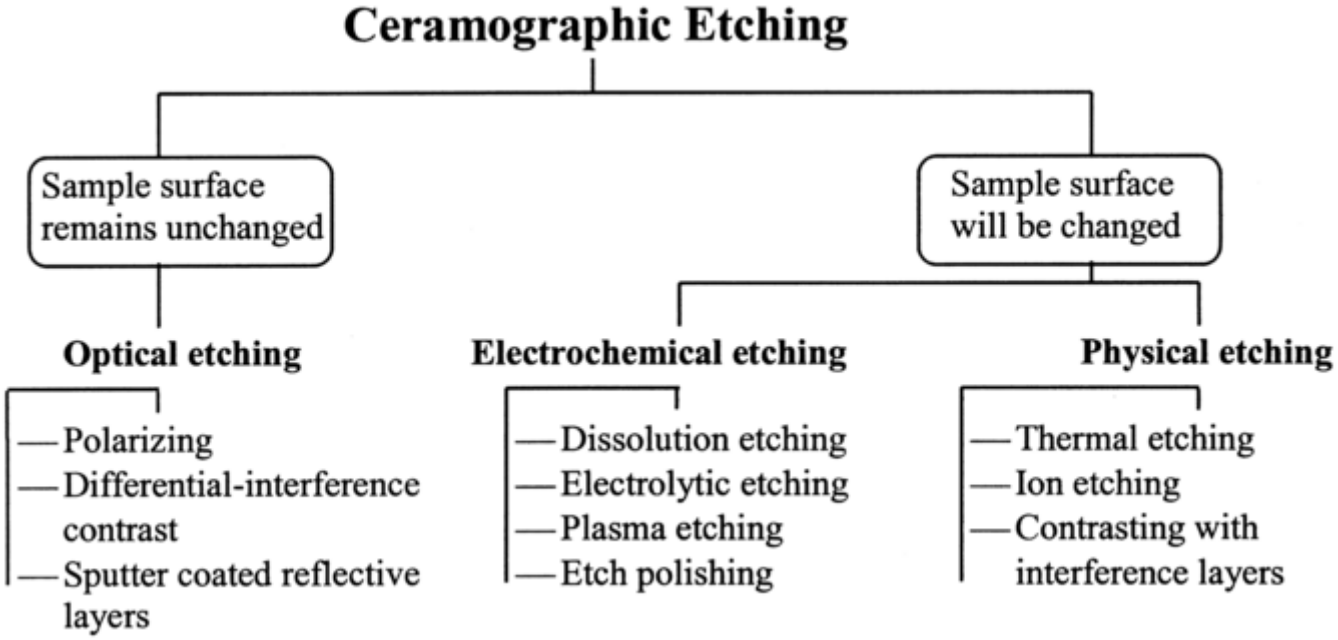

Fig. 4 Etching techniques used in ceramography

Table 3 Etchants for ceramics

Etchant composition	Conditions	Comments	Uses
Oxide Ceramics			
Thermal etch in air	15–20 min at 1300–1400 °C (2370–2550 °F) (Etch temperature is approximately 150 °C (300 °F) below sintering temperature.)	Grain-boundary etchant, also small grains	Al_2O_3, pure and with additives
H_3PO_4 (85%)	5 s to 3 min at 250 °C (480 °F)	Grain boundaries are not uniformly revealed Spinel and glass phases are dissolved.	Al_2O_3, pure and with additives
100 mL alumina **10 mL Murakami's solution**	10–15 min etch polishing on a hard fiber synthetic cloth	Identification of the spinal phase, glass phase and secondary phases	Al_2O_3 with additives
Thermal etch in air	10 min at 1460 °C (2660 °F)	Grain-boundary etchant	Na β-Al_2O_3
HBF_4 (35%)	1–2 min at 110 °C (230 °F)	Grain-boundary etchant	Na β-Al_2O_3
10 mL glycerol (87%) **10 mL HNO_3 (65%)** **10 mL HF (40%)**	1 min	Grain-boundary etchant	Al_2TiO_5
95 mL distilled	5 s to 2 min	Grain-boundary etchant	$BaTiO_3$

H_2O			
3 mL HCl (32)			
2 mL HF (40%)			
Thermal etch in air	30–60 min at 1200 °C (2190 °F)	Grain-boundary etchant	$BaTiO_3$
95 mL distilled H_2O	5 s to 2 min	Grain-boundary etchant	PZT (PbZrTiO)
4 mL HCl (32%)			
1 mL HF (40%)			
100 mL distilled H_2O	10 s to 5 min	Grain-boundary etchant	$SrTiO_3$
25 mL HF (40%)			
20 mL distilled H_2O	5 s to 5 min	Grain-boundary etchant	$SrTiO_3$, $MgTiO_3$
20 mL HNO_3 (65%)			
10 mL HF (40%)			
20 mL distilled H_2O	Seconds to minutes	Reveals twins	ZnO
1 mL glacial acetic acid			
100 mL distilled H_2O	Seconds to minutes	Grain-boundary etchant	ZnO
10 g NaOH			
10 g $K_3Fe(CN)_6$			
Thermal etch in air	Minutes to 1 h at 1300–1400 °C (2370–2550 °F) (according to sintering temperature)	Grain-boundary etchant	ZrO_2-TZP, -PSZ, -CSZ, -ZTC
H_3PO_4 (85%)	3 s to 2 min at 250 °C (480 °F)	Grain-boundary etchant	ZrO_2-TZP, -PSZ, -CSZ, -ZTC
Nitride Ceramics			
50 mL distilled H_2O	1–3 min at 100 °C (212 °F)	Secondary phase remain	AlN-La_2O_3
50 mL saturated aqueous NaOH			
50 mL cold saturated aqueous picric acid			
10 mL distilled H_2O	40–60 min at 100 °C (212 °F)	Grain-boundary etchant	AlN-Y_2O_3
10 mL glacial acetic acid			
10 mL HNO_3			
50 mL distilled H_2O	30 min at 100 °C (212 °F)	Grain-boundary etchant	AlN-Al_2O_3
10 mL 10% aqueous NaOH solution			
10 mL 10% aqueous potassium ferricyanide solution			
(Modified			

Murakami's etchant)			
Plasma etching **CF_4 gas and O_2 gas (2:1)**	1–5 min, 60–80 W	Secondary phase remain	Si_3N_4
H_3PO_4 (85%)	5–30 min at 250 °C (480 °F)	Grain-boundary etchant	Si_3N_4
Molten NaOH (free of water)	20 s to 3 min at 300–350 °C (570–660 °F), 2–3 samples per melt	Grain-boundary etchant	Si_3N_4
Carbide Ceramics			
Plasma etching **CF_4 gas and O_2 gas (1:1)**	3–5 min, 60–80 W	Secondary phase remain	SiC with 5–15% oxide Additions
60 mL distilled H_2O **30 g $K_3Fe(CN)_6$** **3 g NaOH**	5–30 min at 110 °C (230 °F)	Alpha/alpha (α/α) grain boundaries. Alpha/beta (α/β) phase boundaries	SSiC
20 mL distilled H_2O **10 g NaOH** **10 g $K_3Fe(CN)_6$**	5–10 min	Grain-boundary etchant	SSiC doped with B
80 mL distilled H_2O **10 g NaOH** **10 g $K_3Fe(CN)_6$**	10–20 min	Grain-boundary etchant	SSiC doped with Al
90 g KOH **10 g KNO_3 Melt**	5–10 min at 480°C Preheat the samples.	Beta/beta (β/β) grain boundaries	SSiC
100 mL distilled H_2O **10 mL HNO_3 (65%)** **10 g $K_3Fe(CN)_6$**	30–40 min at 60 °C	Grain-boundary etchant	SiC with B_4C
100 mL distilled H_2O **10 mL HNO_3 (65%)** **10 g $K_3Fe(CN)_6$**	Seconds to minutes, boiling	Grain-boundary etchant	B doped SiC
60 mL distilled H_2O **3 g NaOH** **30 g $K_3Fe(CN)_6$**	8–15 min Use boiling	Grain-boundary etchant	SiSiC

Oxide Ceramics. Apart from etching with very aggressive chemical solutions, thermal etching in air is also an important method for developing the microstructures of Al_2O_3 and ZrO_2 ceramics (Ref 6, 7). The polished and "de-mounted" samples are placed in an air furnace. Exposure temperature and time are selected so that the heat treatment does not alter the microstructure. The temperature should be approximately 100 to 150 °C (180 to 270 °F) below the sintering temperature. Temperatures that are too high or etching times that are too long may result in grain growth.

Generally, chemical solutions are used to develop microstructures, grain boundaries, and the domain structure of other oxide ceramics such as $BaTiO_3$ and PZT (see Table 3). Thermal etching in air can also be used to show the grain boundaries, but it will not develop the domain structure. If the grain size exceeds 5 μm, the microstructure of the ceramic material can also be revealed with a thin section under polarized light. An example is shown in Fig. 19 for $BaTiO_3$.

Nitride Ceramics. When Si_3N_4 is prepared with solutions containing concentrated phosphoric acid or molten NaOH, the intergranular grain-boundary phase between the Si_3N_4 grains is dissolved away by chemical attack

(Fig. 5, 6, 7) (Ref 8). One disadvantage of these two etchants is their poor reproducibility. This is because the optimal etching time is extremely dependent on both the microstructure and the composition of the glass phase, which changes with the composition of the additives used.

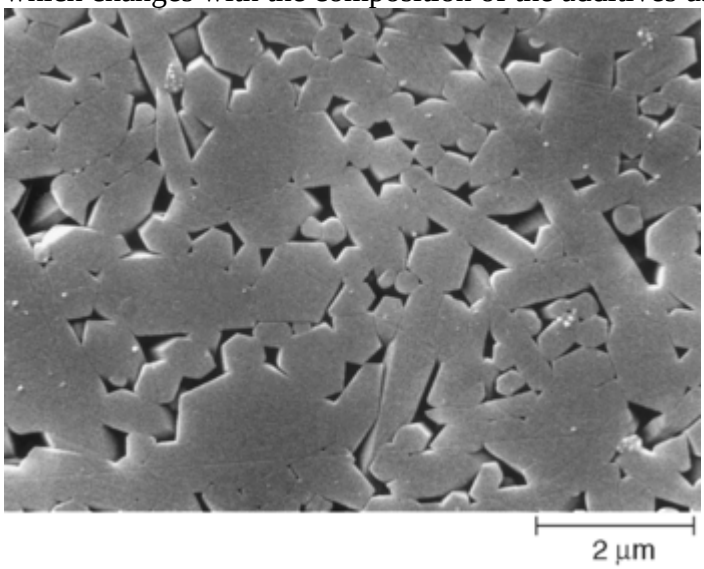

Fig. 5 Scanning electron micrograph of a sintered Si_3N_4 ceramic (SSN) after etching in phosphoric acid at 250 °C (480 °F) for 30 min. The intergranular glassy phase between the Si_3N_4 grains has been dissolved by the etchant.

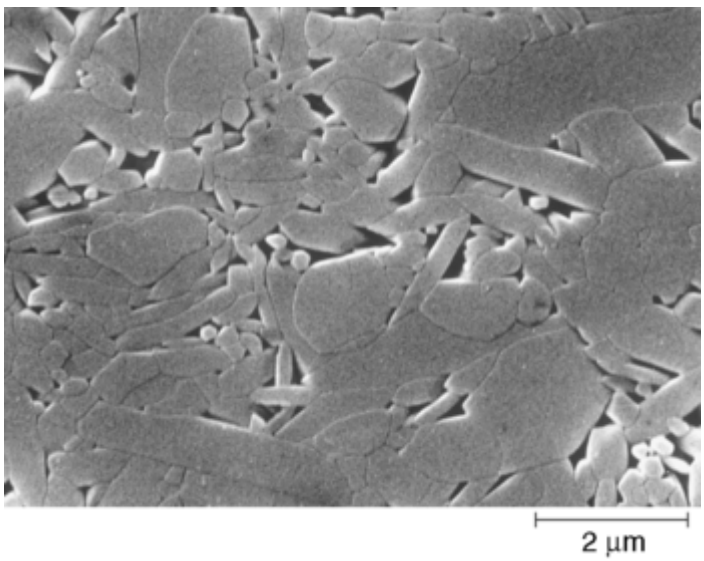

Fig. 6 Scanning electron micrograph of a hot-pressed Si_3N_4 ceramic (HPSN) etched for 30 min. in phosphoric acid at 250 °C (480 °F). The volume fraction of the intergranular grain boundary phase is lower in comparison to SSN (Fig). 5

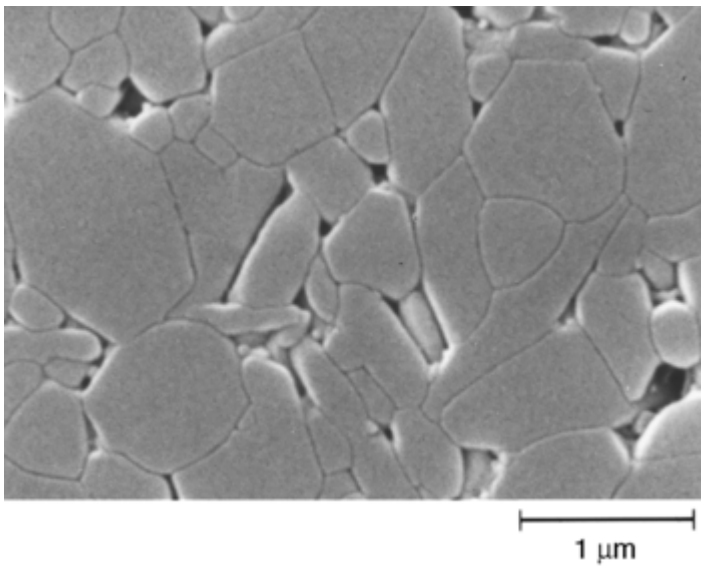

Fig. 7 Scanning electron micrograph of hot isostatically pressed Si_3N_4 (HIPSN) etched in molten NaOH at 320 °C (610 °F) for 2 min. The intergranular glassy phase between the Si_3N_4 grains has been attacked by the etchant. It is not possible to identify intergranular porosity using this etching technique.

In contrast to solution etching for Si_3N_4 materials, plasma etching attacks the ceramic-matrix grains and not the grain-boundary phase (Fig. 8 and 9) (Ref 9). Plasma etching is carried out inside a special chamber, which provides a gaseous mixture of CF_4 and O_2. A radio frequency generator emits high-frequency electromagnetic oscillations and thus produces fluorine radicals inside the reaction chamber. These radicals then react with the silicon contained in the matrix of the ceramic (Si_3N_4). The intergranular grain-boundary phase remains unattacked by the plasma etching process. The etchants for AlN, given in Table 3, are proven for chemical solution etching and give reproducible results (Ref 10).

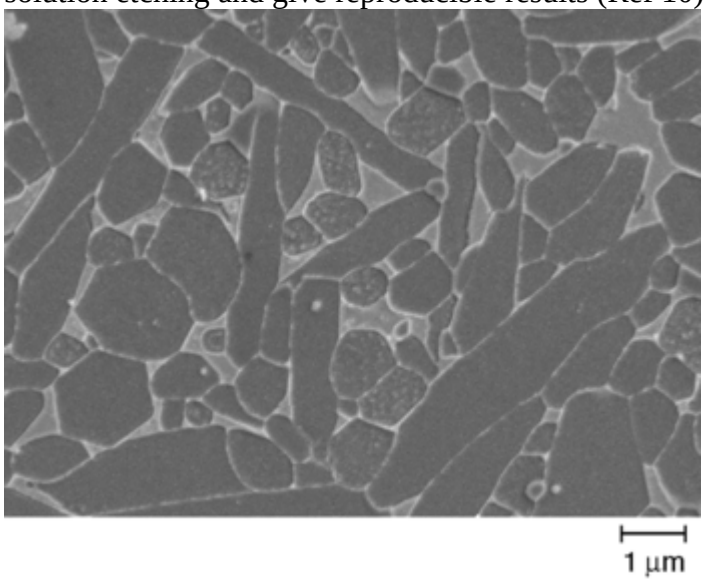

Fig. 8 Scanning electron micrograph of a plasma etched gas-pressure sintered Si_3N_4 (GPSN) ceramic with typical acicular Si_3N_4 crystallites. The microstructure shows gray Si_3N_4 matrix grains and a lighter grain-boundary phase.

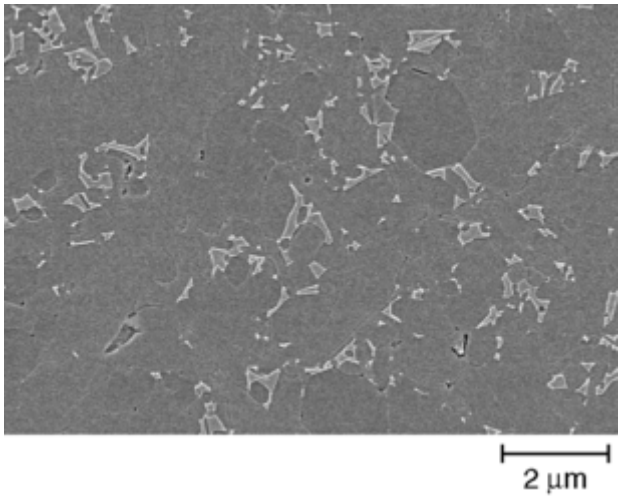

Fig. 9 Scanning electron micrograph of hot isostatically pressed Si_3N_4 (HIPSN) after plasma etching. HIPSN ceramics show more equiaxed grains and less grain-boundary phase compared to GPSN (see Fig). 8

Carbide Ceramics. Several suitable etchants for different SiC materials exist (Table 3). Molten salt, thermal etching, hot chemical etchants, and a number of Murakami solutions with different modifications reveal the microstructure by attacking the grain-boundary phases (Ref 11). For SiC with 5 to 15% oxide additions, the plasma etching technique (see above for Si_3N_4) can be successfully applied. In this case the SiC grains are attacked, leaving the grain-boundary phase untouched.

References cited in this section

1. G. Petzow, *Metallographic Etching*, 2nd ed., ASM International, 1999

5. V. Carle, U. Schäfer, U. Täffner, F. Predel, R. Telle, and G. Petzow, Ceramography of High Performance Ceramics: Description of the Materials, Preparation, Etching Techniques, and Description of the Microstructure—Part I, Ceramographic Etching, *Pract. Metallogr.*, Vol 28, 1991, p 359–377

6. V. Carle, B. Trippel, U. Täffner, U. Schäfer, F. Predel, R. Telle, and G. Petzow, Ceramography of High Performance Ceramics: Description of the Materials, Preparation, Etching Techniques, and Description of the Microstructure—Part VIII, Aluminum Oxide, *Pract. Metallogr.*, Vol 32, 1995, p 54–76

7. U. Schäfer, H. Schubert, V. Carle, U. Täffner, F. Predel, and G. Petzow, Ceramography of High Performance Ceramics: Description of the Materials, Preparation, Etching Techniques, and Description of the Microstructure—Part III, Zirconium Oxide, *Pract. Metallogr.*, Vol 28, 1991, p 468–483

8. U. Täffner, V. Carle, U. Schäfer, F. Predel, and G. Petzow, Ceramography of High Performance Ceramics: Description of the Materials, Preparation, Etching Techniques, and Description of the Microstructure—Part V, Silicon Nitride, *Pract. Metallogr.*, Vol 28, 1991, p 592–610

9. U. Täffner, M.J. Hoffmann, and M. Krämer, A Comparison of Different Physical-Chemical Methods of Etching for Silicon Nitride Ceramics, *Pract. Metallogr.*, Vol 27, 1990; p 385–390

10. F. Predel, J.P. Bazin, V. Carle, U. Schäfer, U. Täffner, R. Telle, and G. Petzow, Ceramography of High Performance Ceramics: Description of the Materials, Preparation, Etching Techniques, and Description of the Microstructure—Part IV, Aluminum Nitride, *Pract. Metallogr.*, Vol 28, 1991, p 542–552

11. V. Carle, U. Schäfer, U. Täffner, F. Predel, R. Telle, and G. Petzow, Ceramography of High Performance Ceramics: Description of the Materials, Preparation, Etching Techniques, and Description of the Microstructure—Part II, Silicon Carbide, *Pract. Metallogr.*, Vol 28, 1991, p 420–434

U. Täffner, V. Carle, U. Schäfer, and M.J. Hoffmann, Preparation and Microstructural Analysis of High-Performance Ceramics, *Metallography and Microstructures*, Vol 9, *ASM Handbook*, ASM International, 2004, p. 1057–1066

Preparation and Microstructural Analysis of High-Performance Ceramics

Ulrike Täffner, Veronika Carle, and Ute Schäfer, Max-Planck-Institut für Metallforschung, Stuttgart, Germany; Michael J. Hoffmann, Institut für Keramik im Maschinenbau, Universität Karlsruhe, Germany

Classification and Microstructure of Frequently Used Ceramics

Details of the microstructure of common structural and functional ceramics along with typical applications follows.

Aluminum oxide (Al_2O_3) is the most common ceramic and, depending on the adjusted properties, is either used as a structural or a functional ceramic material (Ref 12). Applications of high-temperature-resistant alumina are crucibles, tubes, and rods for furnaces. Sealing disks, pumps, thread guides, and other specialized items are made of alumina, due to its excellent wear and corrosion resistance. It is used as an electrical insulator in spark plugs and, taking advantage also of its high thermal conductivity, as substrate material for integrated circuits (Ref 13).

Fully dense and coarse-grained alumina becomes optically transparent and is used as the lamp tube for high-temperature sodium vapor street lamps. It is also biocompatible; therefore, many prosthetic devices are either made from alumina or contain alumina components.

The densification of alumina powder compacts is achieved by a sintering process, which controls density and grain size (Ref 12). These parameters determine the strength characteristics of the final product. Figure 10 shows a cross section of a fluorescent tube with isotropically grown grains with 15 μm average grain size and a porosity of less than 0.5%. Figure 11 illustrates a microstructure characterized by anisotropically grown grains with an average size of 2 to 4 μm. The resulting texture is caused by a preferred orientation of alumina seed crystals during injection molding. The microstructure of a ceramic sealing disk with a typical residual porosity of 3 to 4%, a bimodal grain size distribution, and a glassy phase at the grain boundaries (liquid-phase sintering) is given in Fig. 12. Figure 13 shows the microstructure of a spark plug with anisotropic grains, a glassy grain-boundary phase, and large pores. The effect of different etching techniques is demonstrated in Fig. 14 and 15. After thermal etching of the magnesium-doped sample at 1500 °C (2730 °F) in air, equiaxed grains with black gaps along the grain boundaries can be seen. The gaps are pores and voids formed by an evaporated spinel phase ($MgAl_2O_4$) (Fig. 14). The microstructure shown in Fig. 15 is from the same material, but chemically etched in phosphoric acid at 270 °C (520 °F). The spinel phase is dissolved, and the grain boundaries look broader.

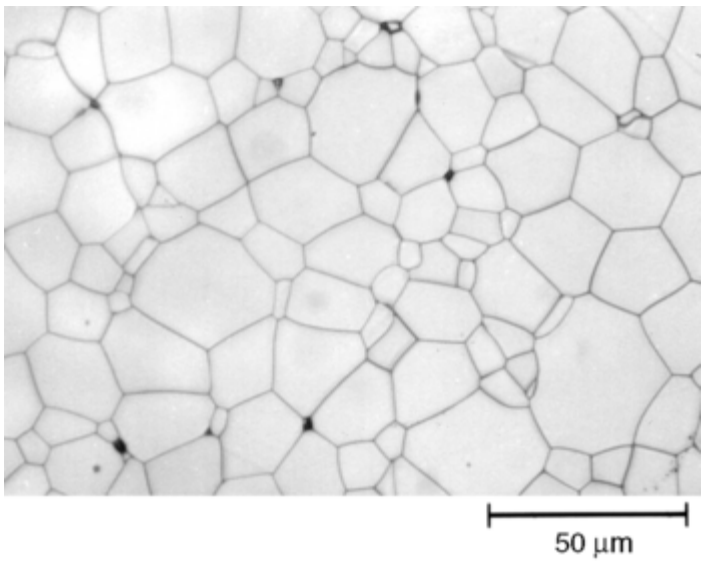

Fig. 10 Light micrograph of translucent alumina. Isotropically grown grains with 15 µm average grain size and a porosity of less than 0.5%. Thermally etched at 1500 °C (2730 °F)

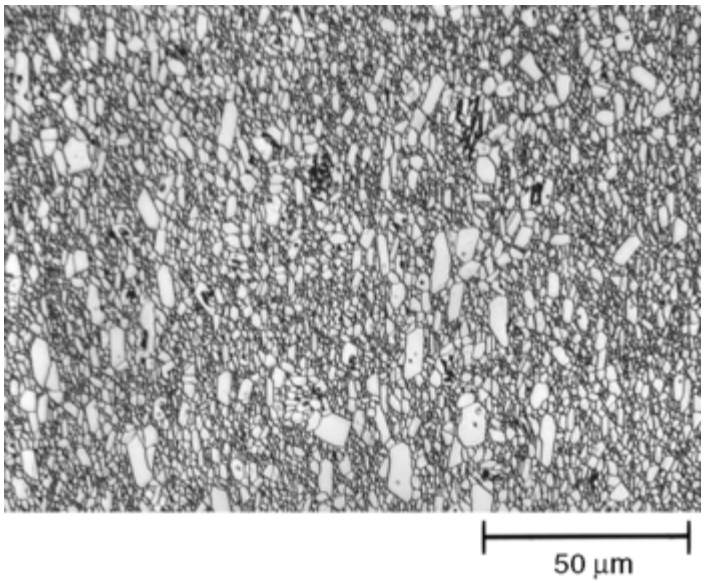

Fig. 11 Light micrograph of a dental prosthesis. Textured alumina with anisotropically grown grains, with an average size of 2–4 µm and a porosity of <0.5%. Thermally etched at 1500 °C (2730 °F)

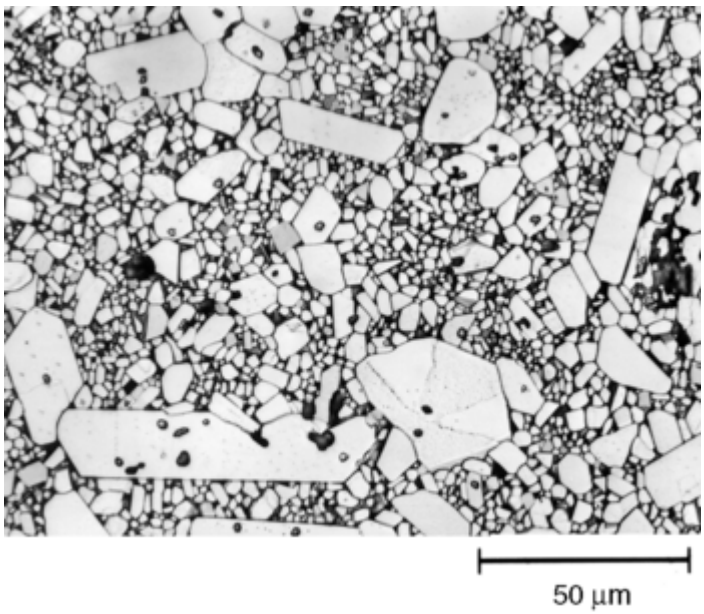

Fig. 12 Sealing disk of alumina. The light micrograph shows typical residual porosity of 3–4%, a bimodal grain size distribution, and a glassy phase at the grain boundaries (liquid-phase sintering). Thermally etched at 1400 °C (2550 °F)

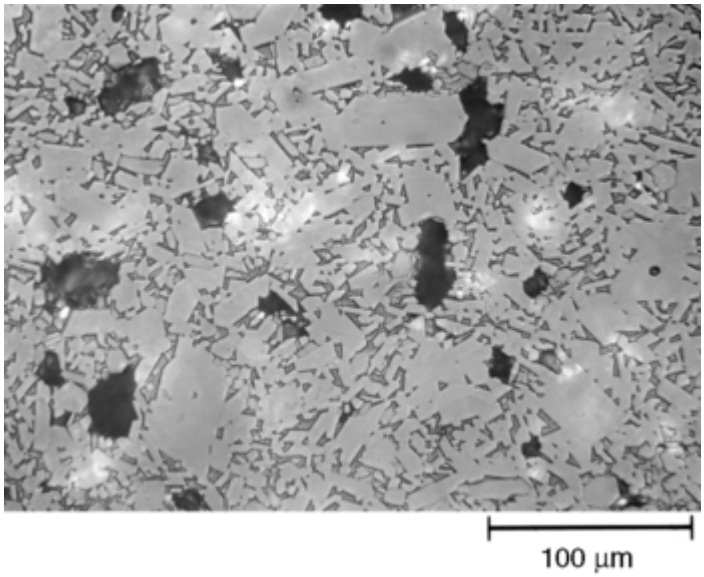

Fig. 13 Spark plug alumina insulator. The light micrograph shows the microstructure with anisotropic grains, a glassy grain-boundary phase, and large pores. Etch polished with alumina and Murakami's solution

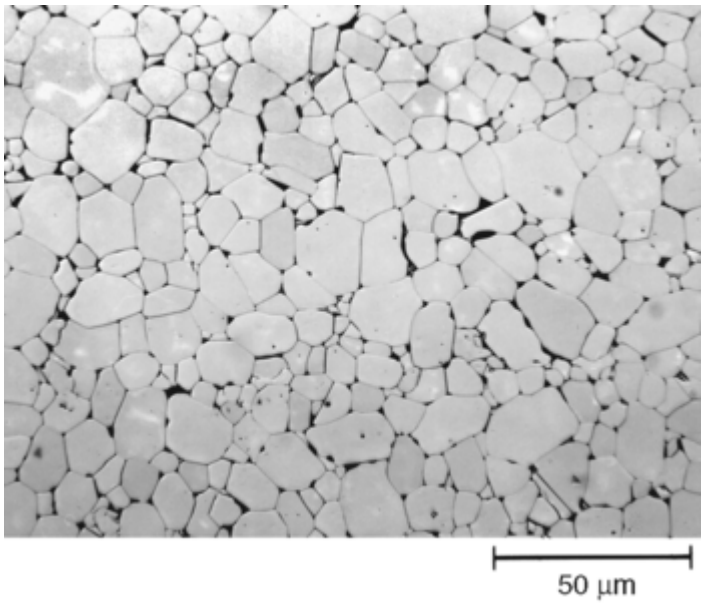

Fig. 14 Light micrograph of magnesium-doped alumina after thermal etching at 1500 °C (2730 °F) in air for 40 min. Equiaxed grains with black gaps along the grain boundaries can be seen. The gaps are pores and voids formed by an evaporated spinel phase ($MgAl_2O_4$).

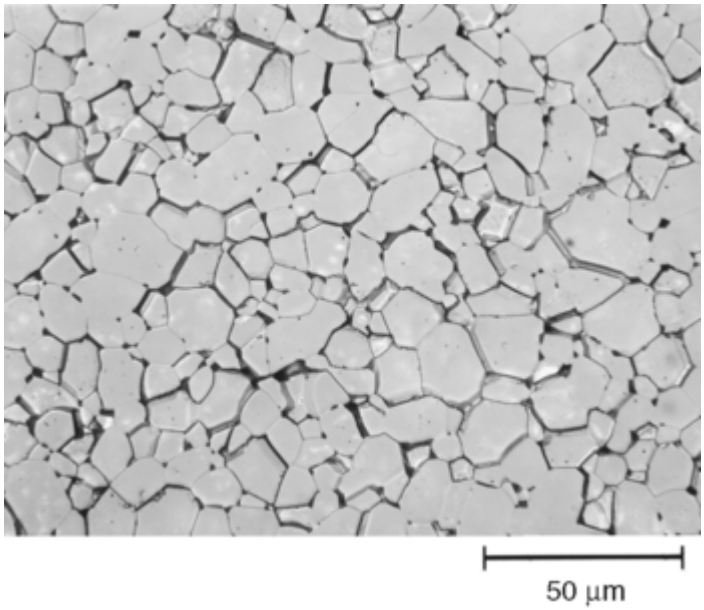

Fig. 15 Light micrograph of the same sample shown in Fig. 14 but chemically etched in phosphoric acid at 270 °C (520 °F) for 3 min. The spinel phase is dissolved, and grain boundaries look broader.

Zirconium dioxide (ZrO_2) based ceramics belong to those materials that are characterized by having both good mechanical properties and exceptional electrical properties (Ref 14, 15). The thermomechanical and electrical properties have led to a wide range of applications. Tough, wear-resistant, and refractory ZrO_2 is being developed for applications as extrusion dies, machinery wear parts, and piston heads. Zirconium dioxide is a good ion conductor and, as a solid electrolyte, is used in oxygen sensors and in solid oxide fuel cells (SOFC). Zirconium dioxide is also used for furnace elements. The low thermal conductivity of ZrO_2 makes it important as a thermal barrier coating in aerospace engine components and land-based gas turbines. The different kinds of application require different properties that are realized by four basic types of microstructure: cubic stabilized zirconia (CSZ), partially stabilized zirconia (PSZ), tetragonal zirconia polycrystals (TZP), and zirconia toughened ceramics (ZTC).

The CSZ microstructure is a solid solution of ZrO_2 and a stabilizing oxide such as Y_2O_3, MgO, or CaO. These additives maintain the cubic structure down to room temperature. Cubic stabilized zirconia is manufactured from powder mixtures or prealloyed powders and homogenized completely during sintering in the homogeneous cubic region at temperature between 1600 and 1800 °C (2910 and 3270 °F). The microstructure of stabilized ZrO_2 consists of cubic grains together with an intergranular glassy phase (Fig. 2). As a result of the high processing temperatures, a comparatively large grain size in the range 10 to 150 µm is formed. The intergranular glassy phase contains various impurities originating from the manufacturing process and the raw materials, but these are mainly SiO_2.

Partially stabilized zirconia is a ceramic with 5 to 15 mol% of stabilizer additives (Y_2O_3, MgO, CaO). It is sintered in the cubic homogeneity range. The PSZ microstructural development requires a special program of sintering. Initially, the ceramic is compacted at high temperatures (>1700 °C) in the cubic solid-solution region. A coarse microstructure with cubic grains and an intergranular glassy phase forms. By heat treating in the two-phase field (tetragonal and cubic), small lenticular particles of the tetragonal phase are precipitated. These particles are not resolved in the LOM. They are coherent with the cubic {100} planes. The precipitates are shown in the electron microscope image insert in Fig. 16.

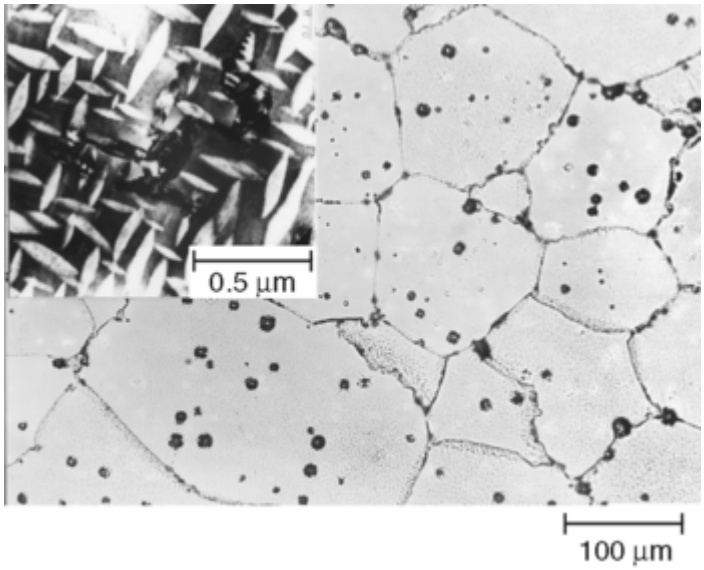

Fig. 16 Partially stabilized zirconia (PSZ) with 7 mol% Y_2O_3, thermally etched in air at 1300 °C (2730 °F). The light micrograph shows a coarse-grained microstructure with pores (black dots). The transmission electron microscope image insert shows tetragonal precipitates within the cubic grains.

Tetragonal zirconia polycrystals contains only 2 to 3 mol% Y_2O_3 (or 10 to 20 mol% CeO_2) as stabilizer and crystallizes in a metastable tetragonal form. However, due to the high activation energy of the transformation, the tetragonal structure is retained down to room temperature and can be activated for a strain-induced transformation to the stable monoclinic structure. The tetragonal and monoclinic crystallites (grains) both have the same morphology and cannot be distinguished by LOM or SEM, but require x-ray diffraction. An example of the TZP microstructure, taken in the SEM, is shown in Fig. 1.

Zirconia toughened ceramics consist of a ceramic matrix (e.g. Al_2O_3) in which 3 to 15 vol% of ZrO_2 particles are embedded (Fig. 17). The difference between the thermal expansion coefficients of the matrix and the ZrO_2 particles causes stresses during cooling, which is essential to the stability of the dispersoid. The increase in toughness results from the strain-induced transformation and microcrack formation (Ref 16).

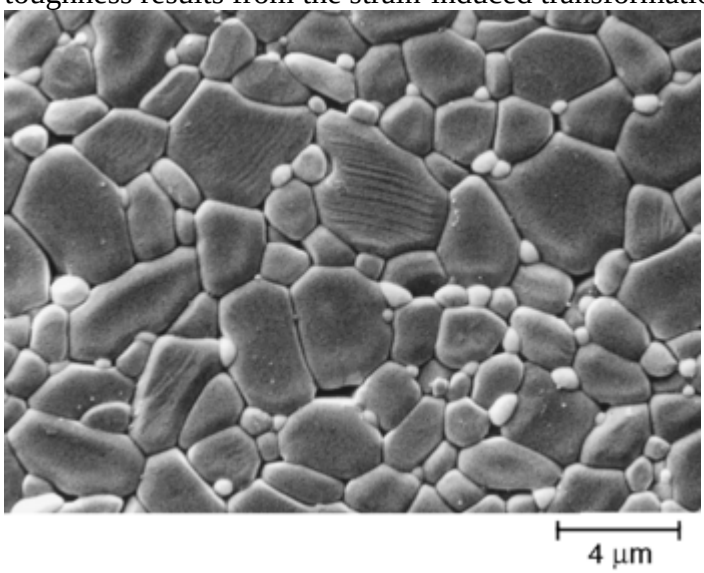

Fig. 17 Scanning electron micrograph of a zirconia toughened ceramic (ZTC), thermally etched in air at 1300 °C (2730 °F). Lighter, tetragonal ZrO_2 grains are dispersed in the Al_2O_3 matrix. The parallel arrays of facets within the grains are related to the ZTC crystallography.

Piezoelectric Ceramics. $BaTiO_3$ and PZT ($Pb(Ti,Zr)O_3$) are the most widely used piezoelectric materials, in electronic devices. The properties can be varied over a wide range by donor or acceptor dopants to achieve the required properties for a given application. $BaTiO_3$ is mainly used in capacitors because of its high dielectric strength as well as the ability to have a positive or negative temperature coefficient of the dielectric by dopant

addition and process procedures. $Pb(Ti,Zr)O_3$ exhibits a high piezoelectric constant and is used for sensors and actuators and for ultrasonic wave generation (Ref 17, 18).

The starting powders with the corresponding dopants are usually prepared by a mixed-oxide process. The required oxides and/or carbonates are first milled and subsequently calcined to obtain a single-phase powder. Consolidation of the prereacted powders is achieved by either pressing or tape casting. Sintering is performed in air or in an oxygen atmosphere at a temperature range of 1000 to 1350 °C (1830 to 2460 °F). Both $BaTiO_3$ and $Pb(Ti,Zr)O_3$ crystallize above the Curie temperature in the cubic perovskite structure and transform into a lower symmetry structure during cooling. The phase transformation is accompanied by lattice distortion, typically about 1% for $BaTiO_3$ and 1.0 to 2.5% for $Pb(Ti,Zr)O_3$, depending on the zirconium-to-titanium ratio. The lattice distortion generates internal stresses, which are reduced by the formation of domains.

The phase transformation from the paraelectric cubic phase to the tetragonal ferroelectric phase occurs for $BaTiO_3$ at 130 °C (265 °F). Below 0 °C (32 °F) other phase transformations occur, but they have no technological interest. The domain configuration consists of 90° and 180° domains based on the different possibilities for the orientation of the spontaneous polarization vector. The domain structures can be readily observed by chemical etching of polished $BaTiO_3$ ceramics samples (Fig. 18) or by using the thin-section technique (Fig. 19).

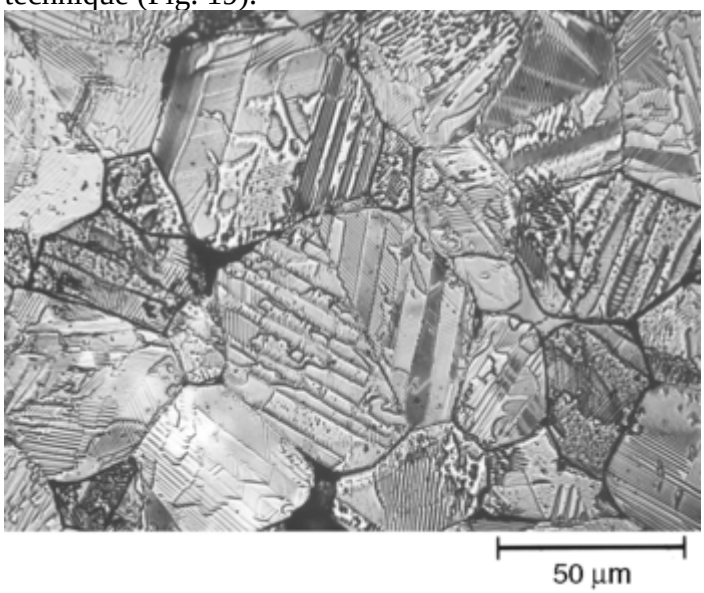

Fig. 18 Light micrograph of a chemically etched surface of a $BaTiO_3$ ceramic showing the grains and domain patterns within the grains

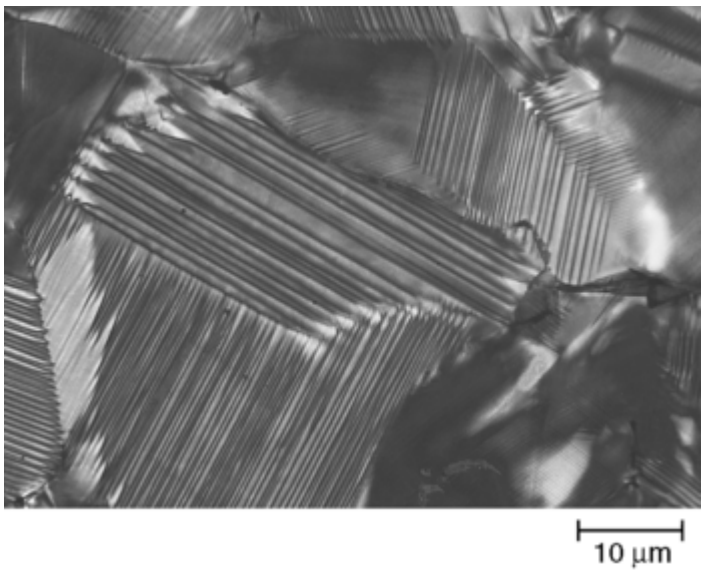

Fig. 19 Transmission optical micrograph of a thin section of a $BaTiO_3$ ceramic with crossed polars and a 530 nm filter. The parallel stripes represent 90° domain walls.

Paraelectric PZT is a solid solution between lead zirconate and lead titanate with a cubic crystal structure. Below the Curie temperature it transforms into a ferroelectric tetragonal phase for titanium-rich PZT and ferroelectric rhombohedral phase for zirconium-rich PZT. The Curie temperature is not well defined and depends on the zirconium-to-titanium ratio and the amount of additives. The maximum piezoelectric constants and coupling factors are achieved for compositions with approximately equal volume fractions of tetragonal and rhombohedral PZT (morphotropic PZT). The domain structures of these materials are more complex than in $BaTiO_3$ because both crystallographic modifications can coexist within one grain, and they have different possible directions for the spontaneous polarization vector. Tetragonal PZT forms have only 90° and 180° domains, but rhombohedral PZT also has 71° and 109° domains. A typical microstructure of a PZT ceramic is shown in Fig. 20. After chemical etching, the grain boundaries, as well as the domain structures within the grains, are revealed in this SEM image.

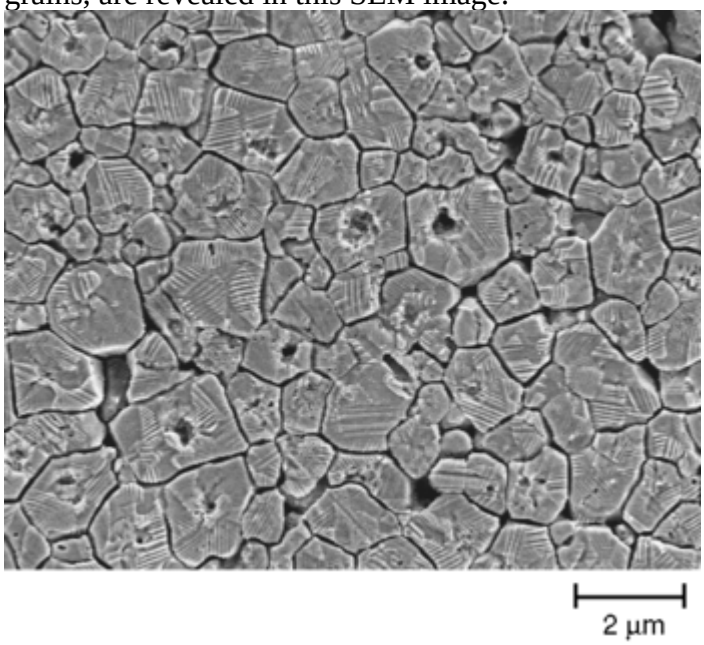

Fig. 20 Scanning electron micrograph of a lanthanum-doped PZT ceramic. The grain boundaries as well as the domain structure are visible after chemical etching.

Aluminum Nitride (AlN). High-purity AlN has a high thermal conductivity of more than 200 W/m · K together with a low thermal expansion coefficient. These, and other useful properties, make AlN a very suitable material for application as a substrate in the electronics industry. Aluminum nitride has an hexagonal crystal structure. Pressureless sintering is impossible for pure AlN powder, because of its covalent bonding. Densification is achieved by liquid-phase sintering with additives. Commonly used additives are Y_2O_3 (Fig. 21), rare earth oxides (Fig. 22), or fluorides such as CaF_2 and YF_3. The thermal conductivity of AlN is affected by the presence of both secondary phases and impurities at the grain boundaries.

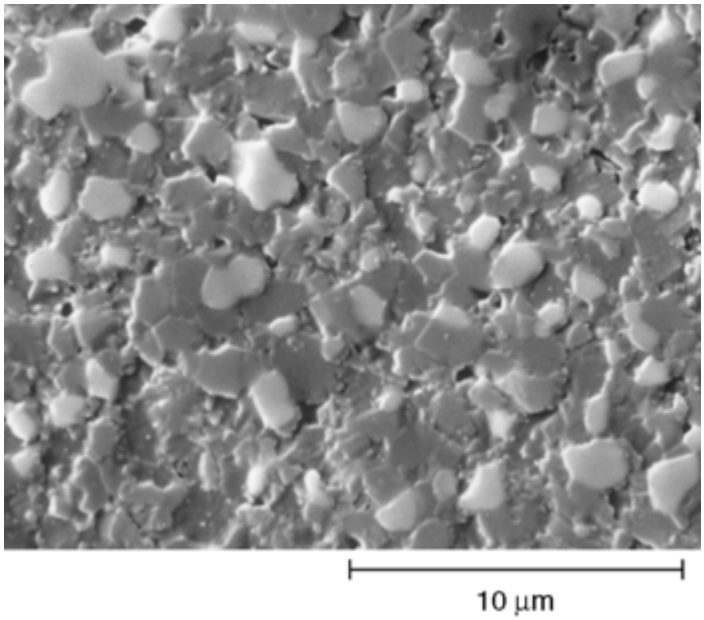

Fig. 21 Scanning electron micrograph of an AlN ceramic, densified with 10 wt% Y_2O_3. The AlN grains appear dark gray. Yttrium-aluminum-garnet particles, formed by reaction between Y_2O_3 and Al_2O_3 in the starting powder mixture, appear as the light gray phase.

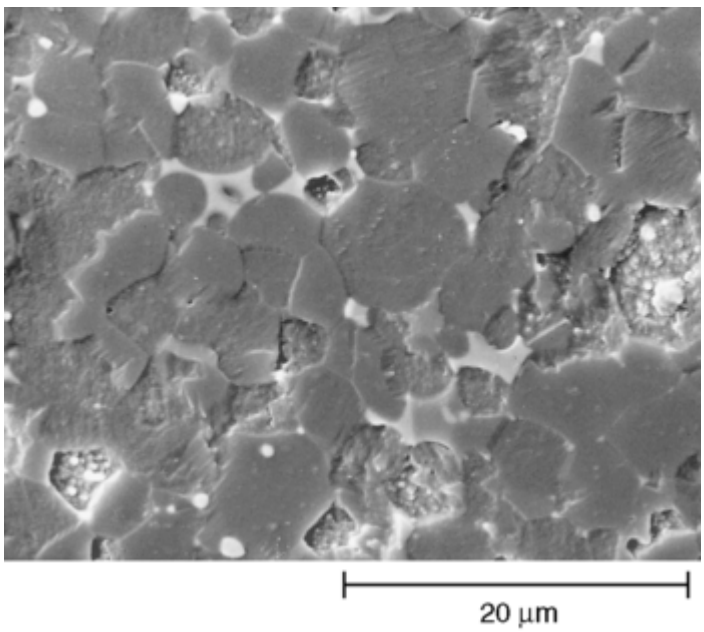

Fig. 22 Scanning electron micrograph of an AlN ceramic, densified with 2.5 wt% La_2O_3. Etching attack of AlN grains depends on crystallographic orientation. A secondary phase ($LaAlO_3$) is retained in the microstructure and appears bright.

Silicon nitride (Si_3N_4) is a structural ceramic with excellent mechanical properties, good oxidation resistance, and good thermal shock behavior at ambient and high temperatures (Ref 19, 20). Si_3N_4 ceramics can be processed by two different methods: reaction-bonded silicon nitride (RBSN) and (pressureless) sintered silicon nitride (SSN). Other variants of the latter are known by the following abbreviations, according to their method of manufacture: gas-pressure sintered, GPSN; hot-pressed, HPSN; and hot isostatically pressed silicon nitride, HIPSN.

Porous Si_3N_4 ceramics produced from inexpensive raw materials are used as refractories. Dense materials with high strength in combination with a high wear resistance are developed for cutting tools to machine cast iron. The high-temperature-resistant Si_3N_4-based ceramics are being studied for applications in gas turbines engines and for components in motor vehicles (e.g., valves).

RBSN ceramics are made from a silicon powder compact, which is converted into a Si_3N_4 ceramic by nitriding at temperatures between 1200 and 1400 °C (2190 and 2550 °F) in the presence of H_2/N_2 gas. Because iron is required as a catalyst, iron silicides can also be formed. They are visible in the LOM as metallic inclusions. Although the chemical reaction is combined with a volume expansion, fully dense ceramics are not obtained. The porosity can vary between 5 and 15%. Figure 23 shows a typical micrograph of a RBSN ceramic in the unetched condition.

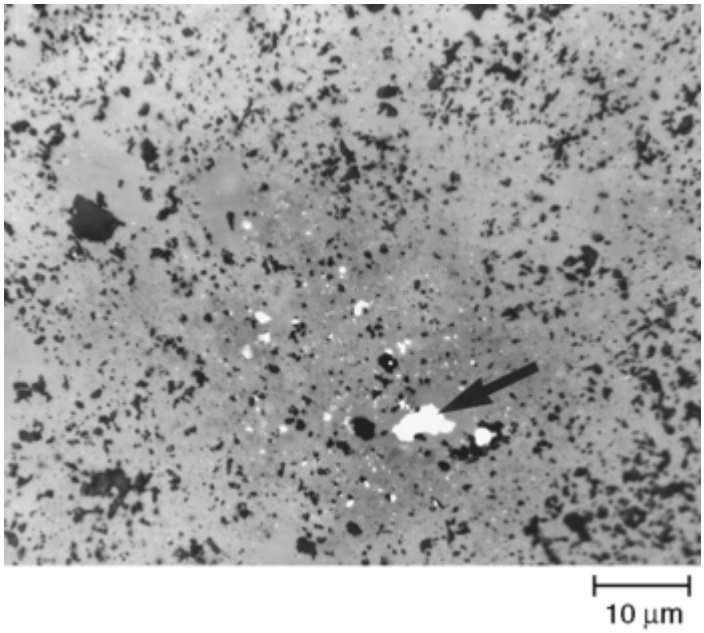

Fig. 23 Light micrograph of a reaction-bonded Si_3N_4 (RBSN). The unetched specimen contains iron silicides (arrow) and characteristic high porosity (black).

All high-performance silicon nitride ceramic components are densified by liquid-phase sintering. The most common sintering additives are MgO, Al_2O_3, Y_2O_3, and RE_2O_3 (rare earth oxides) or mixtures of these materials. A typical polished surface of a sintered silicon nitride with some residual porosity and a few silicide inclusions is shown in Fig. 24. The end use of the Si_3N_4 and the selected sintering conditions determine the amount and type of sintering additives. After densification, the sintering additives form an intergranular phase that significantly affects the properties of the material. Depending on the sintering parameters, the material produced is SSN, HPSN, GPSN, or HIPSN. Figure 5 and 6 compare the microstructure of an SSN material with that of an HPSN material after etching in phosphoric acid. The different amount of sintering additives in the SSN and HPSN materials becomes clearly visible when the grain boundaries are dissolved by chemical attack (large black areas between the grains). In contrast, Fig. 8 and 9 compare the microstructure of a GPSN material with that of an HIPSN material after plasma etching, where the Si_3N_4 matrix grains are attacked, not the grain-boundary phase. At higher magnification, the HIPSN microstructure (Fig. 25) shows that the etching attack is also sensitive to the crystallographic orientation. Some Si_3N_4 grains are deeper etched than others. The same sample etched in molten NaOH at 320 °C (610 °F) for 2 min is shown in Fig. 7. A comparison of both etching techniques reveals that molten NaOH attacks the grain boundary, whereas plasma etching attacks the matrix. After plasma etching, the grain boundaries remain intact and the evidence of residual porosity is not lost.

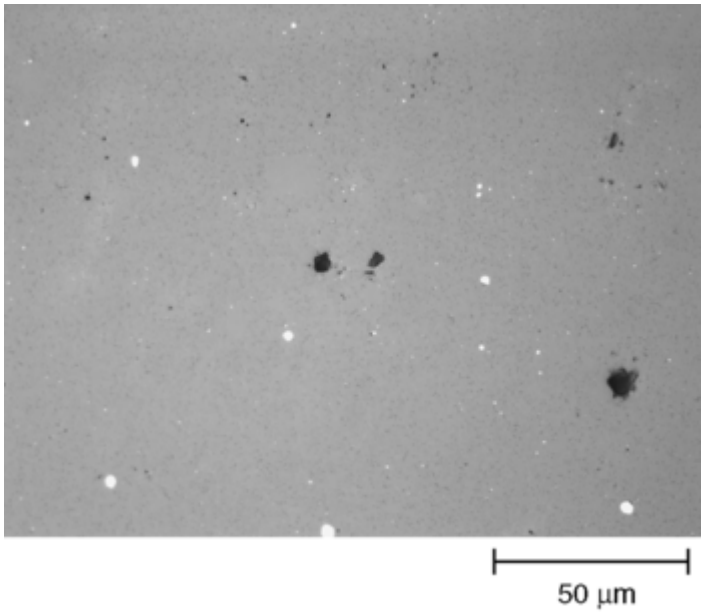

Fig. 24 Light micrograph of an unetched sintered Si_3N_4 (GPSN) specimen. The white inclusions are iron silicide, and porosity is black. The porosity is much lower compared to Fig. 23 (RBSN).

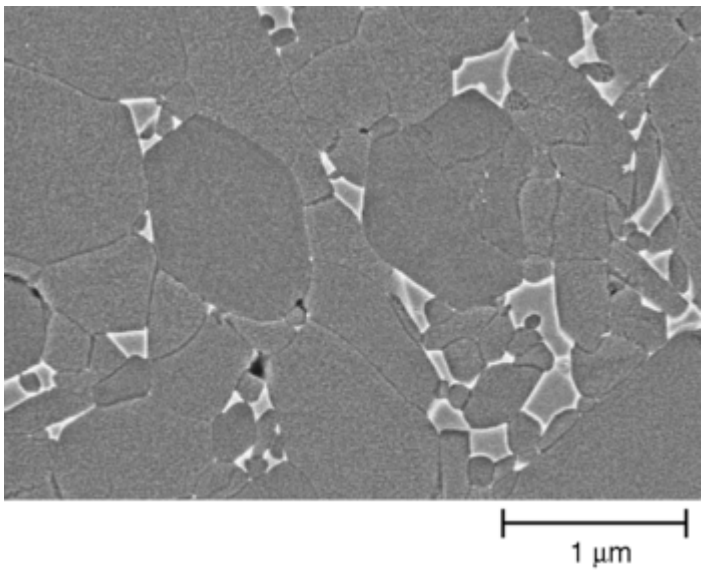

Fig. 25 Scanning electron micrograph of hot isostatically pressed Si_3N_4 (HIPSN) after plasma etching, shown at a magnification sufficient to reveal microporosity.

Silicon carbide (SiC) is the most widely used nonoxide ceramic material with superior high-temperature abrasion and corrosion resistance (Ref 21). Dense SiC ceramics exhibit a high thermal conductivity. This is due to its closely packed wurtzite structure. The electrical properties depend on the impurities and vary from the high electrical resistivity of pure silicon carbide to an electrically conductive material when the impurity content increases. Silicon carbide ceramics can be used under high mechanical and thermal stresses in corrosive atmospheres and in aggressive media. Important silicon carbide products in the area of chemical and mechanical engineering are wear parts, such as sealing disks, and components for pumps. Other types of application include kiln supports, heat exchangers, or burner nozzles. Electrically conductive SiC ceramics are used as heating elements for furnaces for operation up to 1400 °C (2550 °F) in air.

Four types of SiC ceramics can be produced: recrystallized SiC (RSiC), silicon-infiltrated SiC (SiSiC), sintered SiC (SSiC), and liquid-phase sintered SiC (LPS-SiC). They have significantly different manufacturing routes and therefore different microstructures and properties. Recrystallized SiC is produced by a powder compact with a bimodal grain size distribution. During heat treatment, the fine-grained powder evaporates and condenses at the points of contact with the large SiC particles. Because no densification occurs during heat

treatment, a higher volume fraction of porosity remains, and this results in a relatively low strength. Figure 26 shows a typical microstructure of an RSiC ceramic.

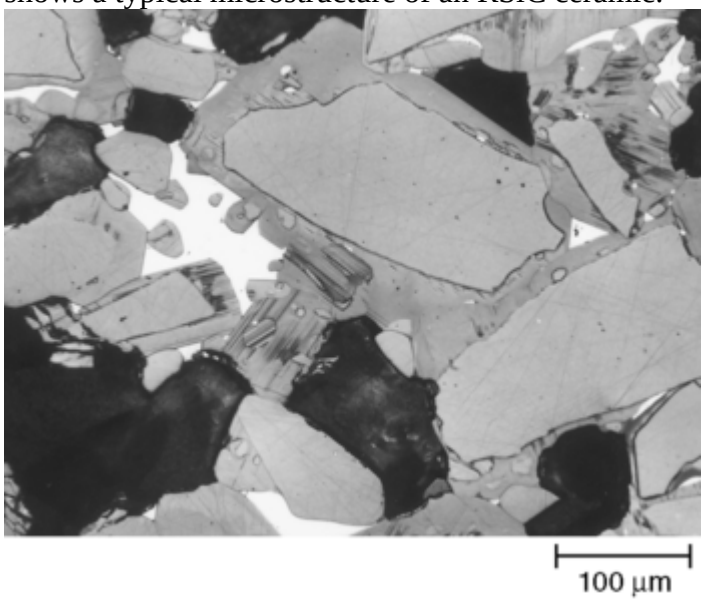

Fig. 26 Light micrograph of an RSiC ceramic. Gray areas are α-grains on which β-SiC has recrystallized, dark areas are pores, and white areas are silicon. Etchant: modified Murakami's solution

Silicon-infiltrated SiC is produced by an infiltration of a SiC/C powder compact with liquid silicon. Part of the silicon reacts with the carbon to form fine-grained secondary silicon carbide. A larger volume fraction of silicon remains unreacted and reduces the oxidation and corrosion resistance of SiSiC, but increases the strength in comparison to RSiC. A typical microstructure of the multiphase ceramic SiSiC with the primary and secondary SiC and the unreacted silicon is shown Fig. 27.

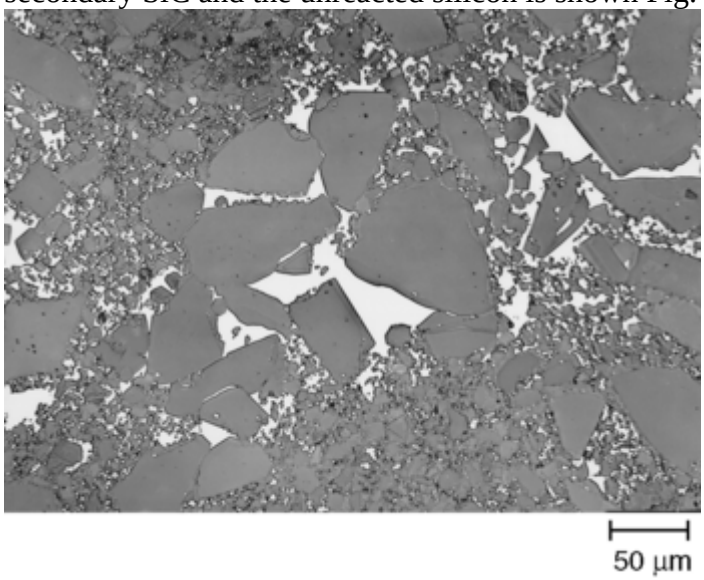

Fig. 27 Light micrograph of an SiSiC microstructure with large α-SiC grains and a fine-grained fraction of the β modification. The bright phases represent infiltrated silicon, which densifies the material but also impairs its corrosion resistance. Etchant: Murakami's solution

Densification of SiC ceramics can be achieved by solid-state sintering with boron, B_4C, or aluminum as sintering additives. The microstructures can be designed over a wide range, which enables components to withstand a variety of different conditions. This is demonstrated for highly loaded wear parts. The grain shape is influenced by sintering aids; equiaxed grains can be generated by the presence of boron (Fig. 28) or as plates in the presence of aluminum (Fig. 29). Anisotropic grain growth results in a strong interlocking of the grains and reduces the risk of breakout compared to a microstructure with globular grains. Small grains increase strength, but large grains have proportionally fewer grain boundaries and the material becomes less susceptible

to grain-boundary corrosion. Small grains can be pulled out and ground into the wear surface, which can lead to hydrodynamic grain-boundary corrosion. The presence of pores reduces the strength and reliability of the component. However, these pores can also serve as lubricant reservoirs under certain wear and sliding conditions and so improve the material properties under abnormal stress conditions. A predetermined porosity level can be introduced during sintering, as shown in Fig. 29. The material behavior under abnormal stress can be further improved by introducing graphite as a secondary phase (Fig. 30).

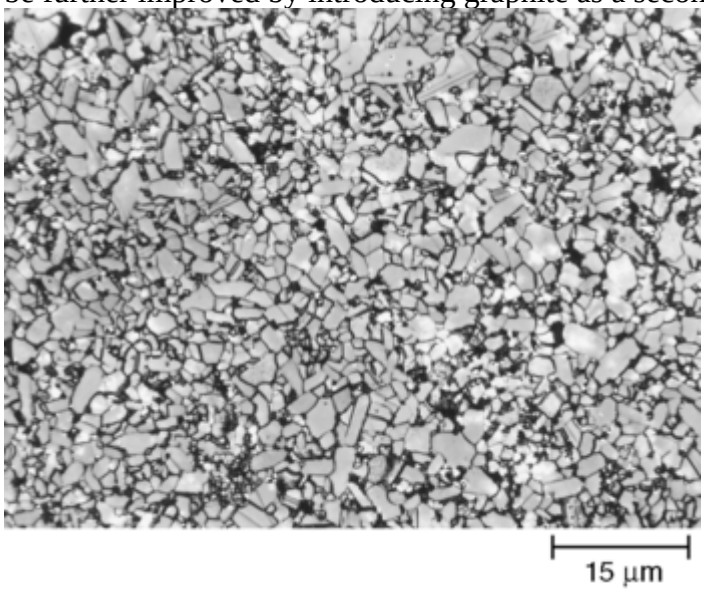

Fig. 28 Light micrograph of an SSiC ceramic, pressureless sintered with boron as additive. The microstructure shows fine equiaxed grains and pores (dark). Etchant: modified Murakami's solution

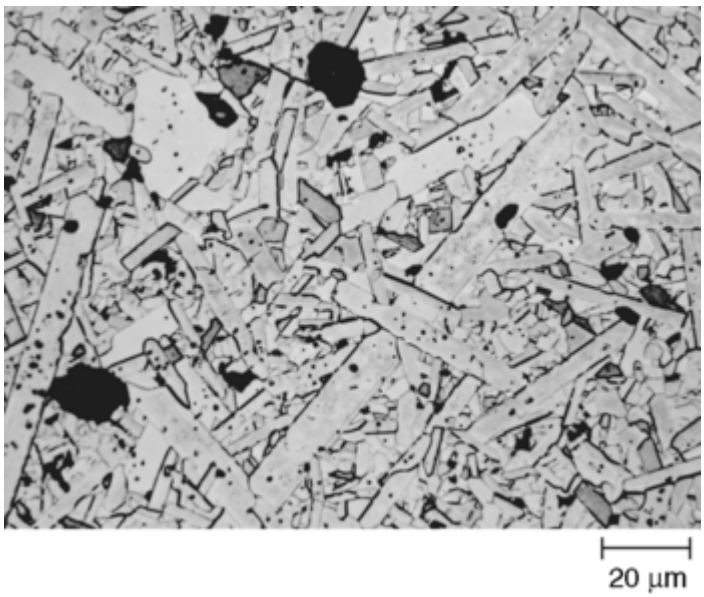

Fig. 29 Light micrograph of a pressureless-sintered SSiC ceramic with a bimodal grain size distribution and 3.5% porosity. Etchant: modified Murakami's solution

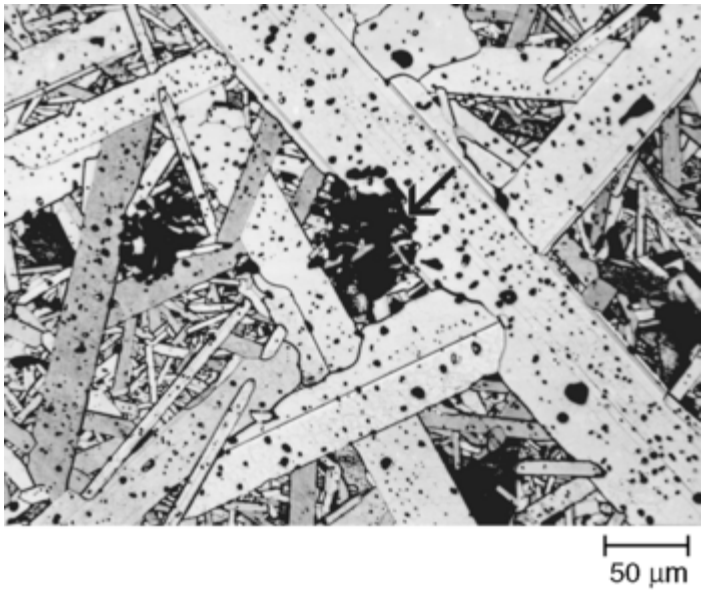

Fig. 30 Light micrograph of a pressureless-sintered SSiC ceramic with a pronounced bimodal platelet microstructure consisting of α-SiC grains. The large dark spherical particles, approximately 50 µm in diameter, are graphite (arrow). The smaller dark spots within the SiC grains are intragranular pores. Etchant: modified Murakami's solution

Silicon carbide powder compacts can also be densified by liquid-phase sintering (LPS) in the presence of oxides and nitrides (LPS-SiC). The most common additives are similar to the silicon nitride ceramics: Y_2O_3, rare earth oxides, Al_2O_3, and AlN. After complete densification, most of the liquid phase forms an oxide-rich grain-boundary phase, which may be either amorphous or crystalline. This grain-boundary phase leads to a weaker bonding between the grains compared to SSiC ceramics. The weaker interface results in an increase in fracture toughness as well as strength, but the strength at higher temperature as well as the creep resistance is reduced. Figure 31 shows a microstructure of LPS-SiC after plasma etching. Two phases are visible: the bright, unattacked grain-boundary phase and the SiC grains. Some of the SiC grains reveal a darker region within them. This is the remnant of the original SiC seed. The different etching attack between the seed material and the rest of the grain is attributed to a small difference in chemical composition (i.e., solid-solution differences between SiC and AlN).

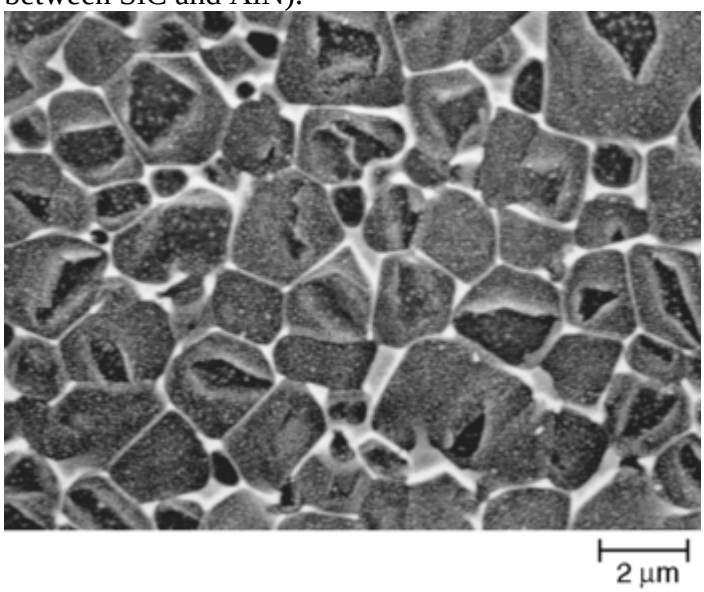

Fig. 31 Scanning electron micrograph of a liquid-phase sintered SiC ceramic (LPS-SiC) after plasma etching. The central and edge zones of the gray SiC matrix grains differ in their chemical composition, which causes a different etching attack. The light constituent is the grain-boundary phase, formed by the sintering additives.

References cited in this section

12. E. Dörre and H. Hübner, *Alumina,* Springer Verlag, 1984

13. A.J. Moulson and J.M. Herbert, *Electroceramics: Materials, Properties, Applications,* Chapman and Hall, London, 1990

14. A.H. Heuer and L.W. Hobbs, Ed., *Science and Technology of Zirconia,* Vol 3, *Advances in Ceramics,* American Ceramic Society, 1981

15. N. Claussen and M. Rühle, Ed., *Science and Technology of Zirconia II,* Vol 12, *Advances in Ceramics,* American Ceramic Society, 1983

16. N. Claussen, Strengthening Strategies for ZrO_2-Toughened Ceramics (ZTC) at High Temperatures, *Mater. Sci. Eng.,* Vol 71, 1995, p 23

17. B. Jaffe, W.R. Cooke, and H. Jaffe, *Piezoelectric Ceramics,* Academic Press, 1971

18. Y. Xu, *Ferroelectric Materials and Their Applications,* North Holland, 1991

19. M.J. Hoffmann, Si_3N_4 Ceramics, Structure and Properties of, *Encyclopedia of Materials Science and Technology,* Elsevier Science Ltd, 2001, p 8469–8471

20. F.L. Riley, Silicon Nitride and Related Materials, *J. Am. Ceram. Soc.,* Vol 83 (No. 2), 2000, p 245–265

21. S. Somiya and Y. Inomata, *Silicon Carbide Ceramics—1, Fundamental and Solid Reaction,* Elsevier Applied Science, 1991

U. Täffner, V. Carle, U. Schäfer, and M.J. Hoffmann, Preparation and Microstructural Analysis of High-Performance Ceramics, *Metallography and Microstructures,* Vol 9, *ASM Handbook,* ASM International, 2004, p. 1057–1066

Preparation and Microstructural Analysis of High-Performance Ceramics

Ulrike Täffner, Veronika Carle, and Ute Schäfer, Max-Planck-Institut für Metallforschung, Stuttgart, Germany; Michael J. Hoffmann, Institut für Keramik im Maschinenbau, Universität Karlsruhe, Germany

---

Acknowledgment

The authors would like to thank Chris Bagnall for the helpful discussions and the critical review of the manuscript.

U. Täffner, V. Carle, U. Schäfer, and M.J. Hoffmann, Preparation and Microstructural Analysis of High-Performance Ceramics, *Metallography and Microstructures*, Vol 9, *ASM Handbook*, ASM International, 2004, p. 1057–1066

Ulrike Täffner, Veronika Carle, and Ute Schäfer, Max-Planck-Institut für Metallforschung, Stuttgart, Germany; Michael J. Hoffmann, Institut für Keramik im Maschinenbau, Universität Karlsruhe, Germany

References

1. G. Petzow, *Metallographic Etching*, 2nd ed., ASM International, 1999

2. G. Elssner, H. Hoven, G. Kiessler, and P. Wellner, *Ceramic and Ceramic Composites: Materialographic Preparation*, Elsevier, 1999

3. W.E. Lee and W.M. Rainforth, *Ceramic Microstructures: Property Control by Processing*, Chapman & Hall, London, 1994

4. U. Täffner, Transmission Polarised Light Microscopy of High Performance Ceramics, *Pract. Metallogr.*, Vol 38, 1990; p 385–390

5. V. Carle, U. Schäfer, U. Täffner, F. Predel, R. Telle, and G. Petzow, Ceramography of High Performance Ceramics: Description of the Materials, Preparation, Etching Techniques, and Description of the Microstructure—Part I, Ceramographic Etching, *Pract. Metallogr.*, Vol 28, 1991, p 359–377

6. V. Carle, B. Trippel, U. Täffner, U. Schäfer, F. Predel, R. Telle, and G. Petzow, Ceramography of High Performance Ceramics: Description of the Materials, Preparation, Etching Techniques, and Description of the Microstructure—Part VIII, Aluminum Oxide, *Pract. Metallogr.*, Vol 32, 1995, p 54–76

7. U. Schäfer, H. Schubert, V. Carle, U. Täffner, F. Predel, and G. Petzow, Ceramography of High Performance Ceramics: Description of the Materials, Preparation, Etching Techniques, and Description of the Microstructure—Part III, Zirconium Oxide, *Pract. Metallogr.*, Vol 28, 1991, p 468–483

8. U. Täffner, V. Carle, U. Schäfer, F. Predel, and G. Petzow, Ceramography of High Performance Ceramics: Description of the Materials, Preparation, Etching Techniques, and Description of the Microstructure—Part V, Silicon Nitride, *Pract. Metallogr.*, Vol 28, 1991, p 592–610

9. U. Täffner, M.J. Hoffmann, and M. Krämer, A Comparison of Different Physical-Chemical Methods of Etching for Silicon Nitride Ceramics, *Pract. Metallogr.*, Vol 27, 1990; p 385–390

10. F. Predel, J.P. Bazin, V. Carle, U. Schäfer, U. Täffner, R. Telle, and G. Petzow, Ceramography of High Performance Ceramics: Description of the Materials, Preparation, Etching Techniques, and Description of the Microstructure—Part IV, Aluminum Nitride, *Pract. Metallogr.*, Vol 28, 1991, p 542–552

11. V. Carle, U. Schäfer, U. Täffner, F. Predel, R. Telle, and G. Petzow, Ceramography of High Performance Ceramics: Description of the Materials, Preparation, Etching Techniques, and Description of the Microstructure—Part II, Silicon Carbide, *Pract. Metallogr.*, Vol 28, 1991, p 420–434

12. E. Dörre and H. Hübner, *Alumina*, Springer Verlag, 1984

13. A.J. Moulson and J.M. Herbert, *Electroceramics: Materials, Properties, Applications*, Chapman and Hall, London, 1990

14. A.H. Heuer and L.W. Hobbs, Ed., *Science and Technology of Zirconia,* Vol 3, *Advances in Ceramics,* American Ceramic Society, 1981

15. N. Claussen and M. Rühle, Ed., *Science and Technology of Zirconia II,* Vol 12, *Advances in Ceramics,* American Ceramic Society, 1983

16. N. Claussen, Strengthening Strategies for ZrO_2-Toughened Ceramics (ZTC) at High Temperatures, *Mater. Sci. Eng.,* Vol 71, 1995, p 23

17. B. Jaffe, W.R. Cooke, and H. Jaffe, *Piezoelectric Ceramics,* Academic Press, 1971

18. Y. Xu, *Ferroelectric Materials and Their Applications,* North Holland, 1991

19. M.J. Hoffmann, Si_3N_4 Ceramics, Structure and Properties of, *Encyclopedia of Materials Science and Technology,* Elsevier Science Ltd, 2001, p 8469–8471

20. F.L. Riley, Silicon Nitride and Related Materials, *J. Am. Ceram. Soc.,* Vol 83 (No. 2), 2000, p 245–265

21. S. Somiya and Y. Inomata, *Silicon Carbide Ceramics—1, Fundamental and Solid Reaction,* Elsevier Applied Science, 1991

A.T. Santhanam, Metallography of Cemented Carbides, *Metallography and Microstructures,* Vol 9, *ASM Handbook,* ASM International, 2004, p. 1067–1078

Metallography of Cemented Carbides

A.T. Santhanam, Kennametal, Inc.

Introduction

CEMENTED CARBIDES belong to a class of hard, wear-resistant, refractory materials in which the hard carbides of Groups 4 to 6 (IVB to VIB) metals are bound together, or cemented, by a soft and ductile metal binder such as cobalt or nickel. Although the term “cemented carbides” is widely used in the United States, these materials are better known internationally as “hard metals.”

The first commercially available cemented carbides consisted of tungsten carbide (WC) particles bonded with cobalt. Over the years, the basic WC-Co material has been modified with additions of titanium carbide (TiC), tantalum carbide (TaC), niobium carbide (NbC), hafnium carbide (HfC), zirconium carbide (ZrC), vanadium carbide (VC), and chromium carbide (Cr_3C_2) as well as other binders such as nickel and iron to produce a variety of compositions. Another family of cemented carbides called “cermets” also evolved with titanium carbonitride (TiCN) as the major hard phase and nickel as the binder phase.

Cemented carbides are manufactured by a powder metallurgy process using liquid phase sintering. The sintered product is directly used or ground and coated by chemical vapor deposition (CVD) or physical vapor deposition (PVD) to suit different metalcutting applications.

Cemented carbides are endowed with a unique combination of properties such as high compressive strength, good abrasion resistance, high elastic modulus, good impact and shock resistance, corrosion resistance, and toughness. These properties make cemented carbides suitable for a wide range of wear applications including metalcutting, mining, construction, rock drilling, metal forming, structural and fluid-handling components, and wear parts.

A.T. Santhanam, Metallography of Cemented Carbides, *Metallography and Microstructures,* Vol 9, *ASM Handbook,* ASM International, 2004, p. 1067–1078

Metallography of Cemented Carbides

A.T. Santhanam, Kennametal, Inc.

Metallographic Considerations

The fine scale of cemented carbide microstructures necessitates the use of the highest practical magnifications in optical metallography, requiring high optical resolution at magnifications of 1500×. Scanning electron microscopy (SEM), transmission electron microscopy (TEM), and scanning Auger microscopy (SAM) are also employed depending on the need for more detailed microstructural characterization.

The very properties that make cemented carbides good tool materials severely restrict the techniques that can be used to prepare metallographic specimens. The high hardness of these materials requires the use of diamonds in grinding and polishing. Automatic machinery capable of exerting forces up to 200 N (45 lbf) normal to the sample is also necessary. Although it is possible to grind and polish manually, the effort and time required as well as requirements for reproducibility generally rule out these techniques (Ref 1). All the micrographs in this article are from specimens prepared using an automatic machine. A standard practice of metallographic sample preparation of cemented carbides is given in ASTM B 665 procedure (Ref 2).

References cited in this section

1. "Metallographic Procedures for Sintered Carbide," Report 01.84, Struers Inc., Cleveland, OH

2. "Standard Practice for Metallographic Sample Preparation of Cemented Tungsten Carbides," B 665, *Annual Book of ASTM Standards,* Vol 02.05, ASTM International, 2003, p 395–396

A.T. Santhanam, Metallography of Cemented Carbides, *Metallography and Microstructures,* Vol 9, *ASM Handbook,* ASM International, 2004, p. 1067–1078

Metallography of Cemented Carbides

A.T. Santhanam, Kennametal, Inc.

Specimen Preparation

Sectioning. Cemented carbides are cut into sizes suitable for metallography by high-speed cutoff machines. Cutting wheels should be metal-bonded diamond, and attention must be paid to the cutting forces or pressure, because these materials will fracture readily when heavily stressed. Wheel speeds of ~3000 rpm are recommended. Water is used as a coolant, and the pressure should be regulated to eliminate deflection or binding of the cutting wheel, which causes fracturing near the end of the cut. Despite all precautions, the last part of the sample being cut usually fractures, leaving a small burr. A short hand dressing on a 15 to 30 μm metal-bonded diamond lap at 150 to 300 rpm can easily remove this burr.

Mounting. The samples are mounted using thermosetting resins or epoxy resins containing a hard filler addition. Typical examples are diallylphthalate with fiberglass (thermosetting) or epoxy resins to which alumina (Al_2O_3) particles have been added. These are required due to the extreme edge rounding that occurs

during polishing when hard materials are mounted in soft embedding media. No embedding medium without hardener has been found to yield adequate edge retention and flatness for machine grinding and polishing.
Mounted specimens in 25 to 38 mm (1.0 to 1.5 in.) diam size are most frequently used. Unmounted specimens as large as 150 mm (6 in.) square may also be used on most automatic machines. However, the heavy weight of carbides may cause difficulties with optical microscope stages.
Preservation of the hard coatings requires that the specimens be mounted, which is readily accomplished with available mounting presses. Epoxy resins, depending on their chemical formulation, require 15 min to 8 h to harden, but the thermosetting resins will produce a mount ready for polishing in 15 min.
Grinding and Polishing. After mounting, the specimens are ground flat and polished in holders appropriate for the automatic machine being used. The holders typically accept 4 to 8 specimens. The initial grinding is done using a 220-grit resin-bonded diamond lap. Scratches and work-hardened regions must be removed with finer abrasives until the desired surface finish is obtained. Final grinding is done in a two-step process: first with a 600-grit diamond lap and next with a 6 μm diamond lap. All grindings are performed at 300 rpm, using copious amount of water for coarse grinding and an alcohol-based lubricant for fine grinding.
Coarse polishing is performed using a cloth with 6 μm diamond for 2 to 4 min. Polishing is continued with 3 μm diamond media for 2 to 3 min. Final polishing step involves 1 μm diamond lap for 1 min. The coarse and fine polishing is performed at 150 rpm using an alcohol-based lubricant. The surfaces should be cleaned between steps with an alcohol rinse, because the cobalt at the surface is chemically active during polishing and will be electrolytically attacked by tap water.
Automatic machine manufacturers can supply detailed information for grinding and polishing cemented carbides following the general procedures outlined previously. Details on grinding equipment, materials, and methodology for metallographic preparation are available in Ref 3.

Reference cited in this section

3. G. Vander Voort, *Metallography Principles and Practice,* McGraw-Hill, 1984, reprinted by ASM International, 1999

A.T. Santhanam, Metallography of Cemented Carbides, *Metallography and Microstructures,* Vol 9, *ASM Handbook,* ASM International, 2004, p. 1067–1078

Metallography of Cemented Carbides

A.T. Santhanam, Kennametal, Inc.

Macroexamination

Cemented carbides are macroscopically examined with a low-power microscope at 20× or 30× to detect pits, pressing flaws, contamination, segregation, free (excess) carbon, and carbon deficiency (eta, or η, phase: Co_3W_3C or Co_6W_6C). Examination of fracture surfaces at 20× reveals defects larger than ~0.02 mm. Fracture can initiate in and propagate through such defects as pits and pressing flaws.
Free carbon appears on an as-sintered or fracture surface as clustered dark spots (Fig. 1). A specimen with free carbon often has an as-sintered surface that is slippery to touch. Carbon deficiency or η phase can be detected by examining the fracture surface and, depending on the degree of deficiency, is often detectable on an as-sintered surface.

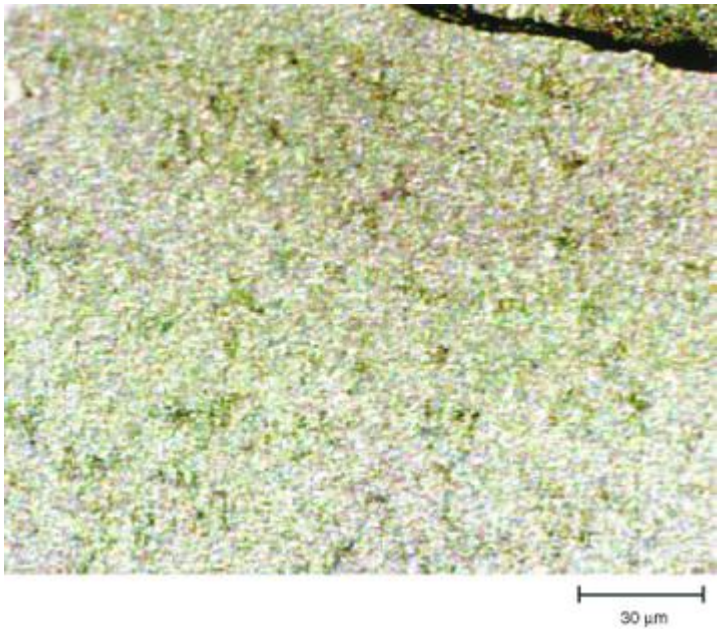

Fig. 1 Free (excess) carbon appears as clustered dark spots on the fracture surface of 86WC-8(Ta,Ti,Nb)C-6Co alloy. 500×.

A.T. Santhanam, Metallography of Cemented Carbides, *Metallography and Microstructures,* Vol 9, *ASM Handbook*, ASM International, 2004, p. 1067–1078

Metallography of Cemented Carbides

A.T. Santhanam, Kennametal, Inc.

Microexamination

Qualitative metallography in cemented carbides consists of evaluation of apparent porosity and carbide grain size. Apparent porosity is evaluated on the as-polished specimen using the ASTM B 276 procedure (Ref 4). The ASTM method rates vol% porosity in the specimen using standard comparison charts:

A-porosity	**Pore diameter: d_p < 10 µm**	**Rate at 200×**
B-porosity	Pore diameter: 10 µm ≤ d_p ≤ 25 µm	Rate at 100×
C-porosity	Rosette pattern: d_p > 25 µm	Rate at 100×

The degree of porosity is given by numbers ranging from 02 to 08. The number provides a measure of pore volume as a percentage of total volume of the sample. Acceptance criteria for porosity vary with application. An example of A-porosity in a WC-3wt%Co alloy is shown in Fig. 2.

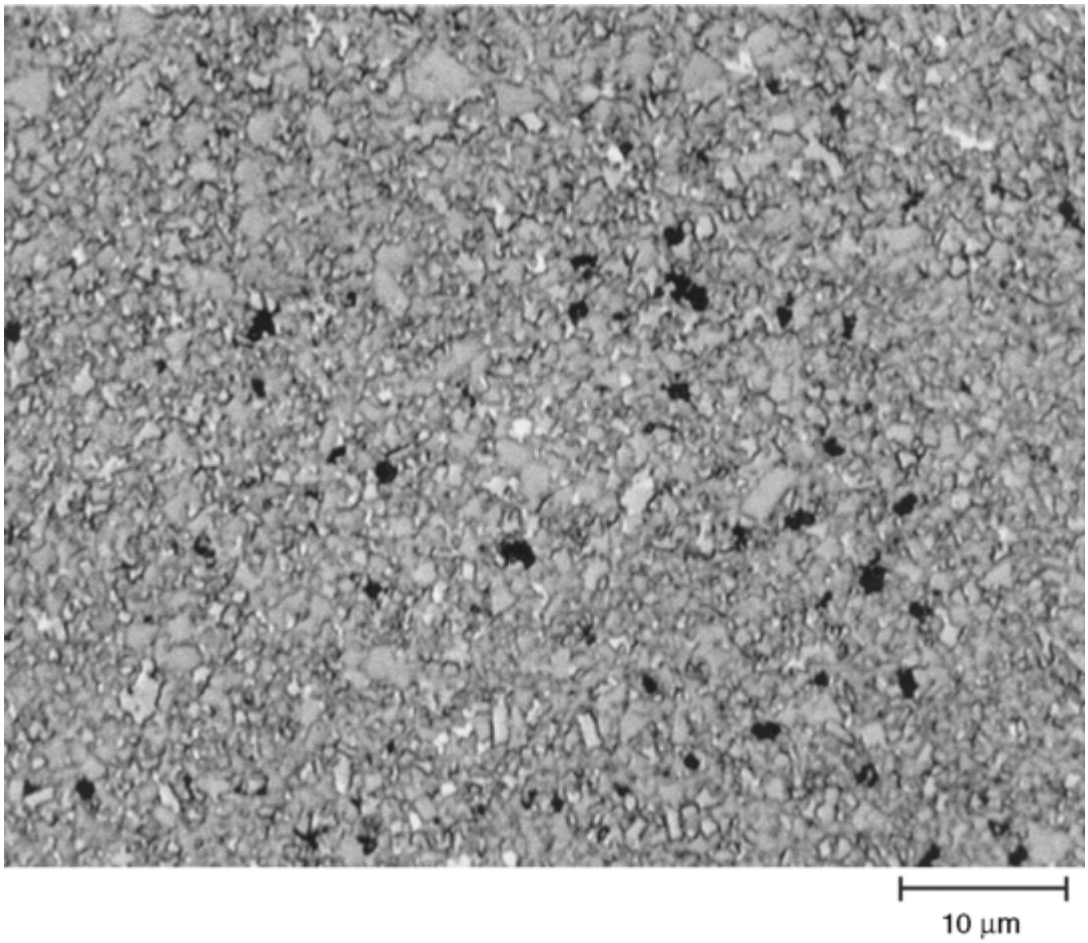

Fig. 2 97WC-3Co alloy, 93 HRA. An example of A08-porosity that appears as black areas. 1500×

Figure 3 shows an example of C-porosity that is due to the precipitation of free carbon in the form of graphite during the sintering process. The rigorous grinding and polishing required for these specimens usually result in almost complete removal of the graphite from the polished surface, leading to the concept of “porosity” for this phase.

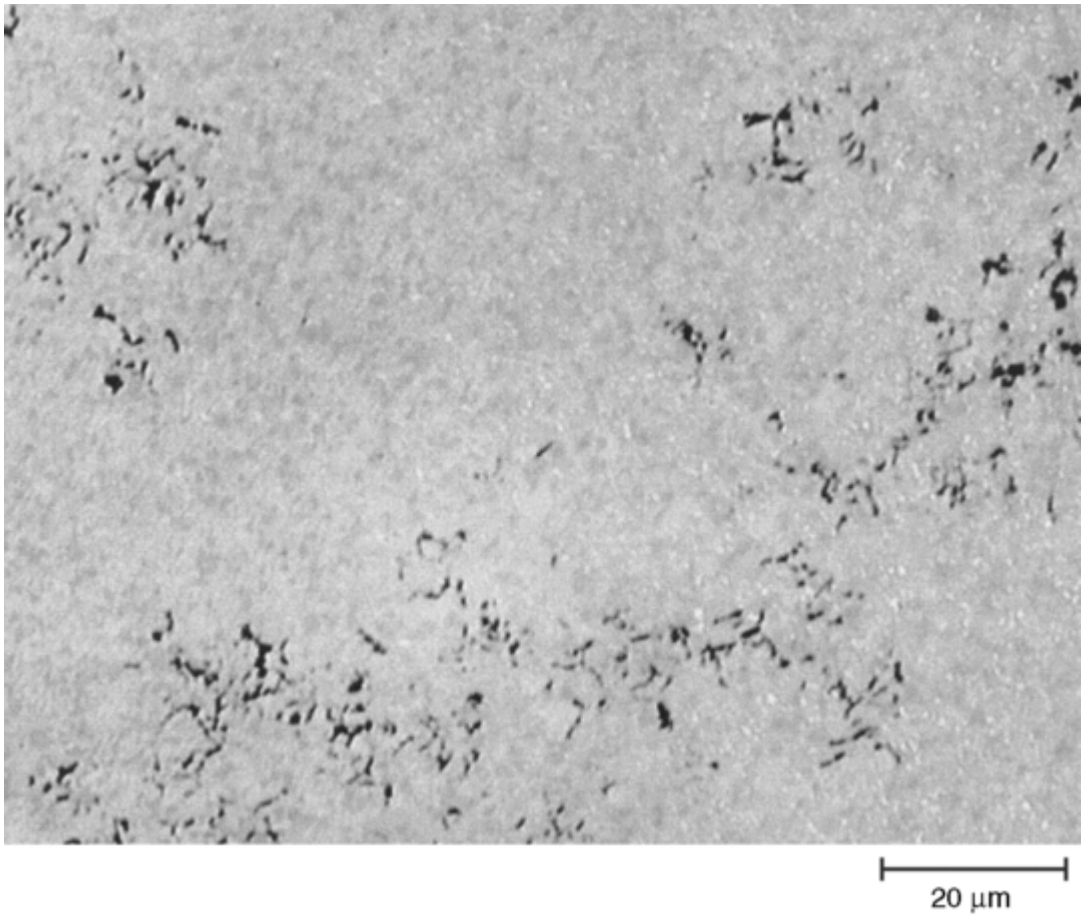

Fig. 3 86WC-8(Ta,Ti,Nb)C-6Co alloy, 91.6 HRA. An example of C-porosity (see Ref 5). Black areas are porosity, some of which may still contain graphite.

The carbide grain size is determined by comparing the structure of the specimen at 1500× with micrographs given in ASTM B 390 and B 657 procedures (Ref 5, 6). Structures are sometimes rated according to cobalt content (wt%) and grain size (fine, medium, or coarse).
Microstructural evaluation of cemented carbides is based on the different reaction rates of Murakami's reagent with the various phases of the microstructure, which include:

- Tungsten carbide (α-phase): WC
- Binder (β-phase): Co, Ni, Fe
- Mixed carbides (γ-phase): (Ti,Ta,Nb,W)C
- Eta (η-phase): Co_3W_3C (M_6C), Co_6W_6C ($M_{12}C$)
- Free carbon or graphite

The variable reaction rates of these phases is apparent in the backscattered scanning electron micrograph (SEM) in Fig. 4, which shows that the cobalt binder phase is not attacked and is therefore the highest feature in the micrograph (light areas). At mid-height, the structure consists of angular WC grains. The mixed carbides (solid solution of TaC, TiC, and NbC with WC) are etched deeper. Etching experiments have led to a classification of the reaction rates of the carbide constituents using Murakami's reagent, as shown in Table 1. Therefore, cemented carbides are usually etched in several stages to assess various constituents. Compositions of etchants used in the microexamination of cemented carbides are listed in Table 2.

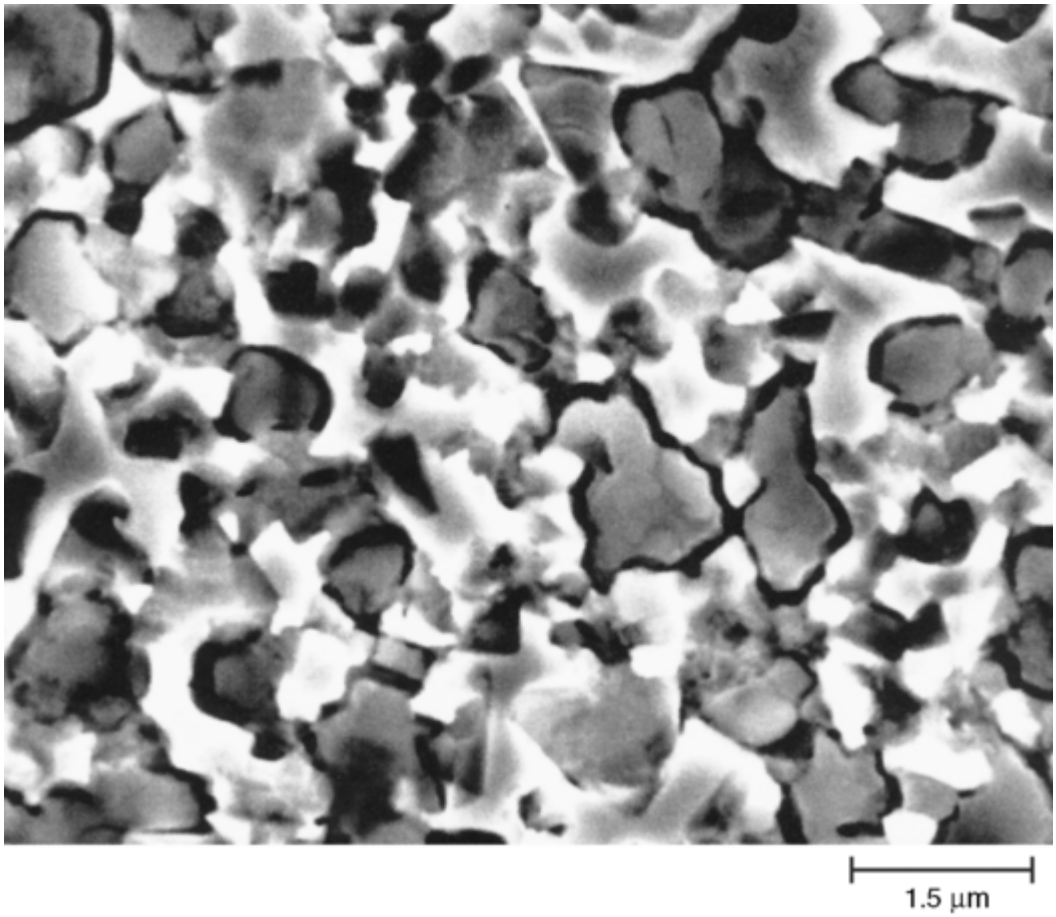

Fig. 4 Scanning electron micrograph (secondary electron image) of 72.5WC-17(Ta,Ti,Nb)C-10.5Co alloy, 91.4 HRA. Raised areas are cobalt binder; gray particles are tungsten carbide; rounded deeply etched particles are mixed carbides. Murakami's reagent (see Table 2), 2 min. 10,000×

Table 1 Relative reaction rates of cemented carbide phases to Murakami's reagent

Component	Reaction rate (WC = 1)	Etching duration, s
Co, Ni	0	…
WC	1	120
(Ta,Ti,Nb,W)C	4	60
η phase (Co_3W_3)C	20	3
η phase (Co_6W_6)C	40	3

Table 2 Chemical etchants for cemented carbides

Reagent	Composition	Procedure
Murakami's	10 g $K_3Fe(CN)_6$ (potassium ferricyanide), 10 g NaOH (sodium hydroxide), and 100 mL H_2O. Make fresh daily.	Swab specimen continuously for appropriate time (see Table 1).
Ferric chloride	3 g $FeCl_3$ and 100 mL H_2O. Make fresh daily.	Swab specimen continuously for 10 s (for nickel and cobalt binder removal).
Hydrogen peroxide (etchant for TiC-based cermets)[(a)]	20 vol% in water	Immerse specimen at 70–90 °C (160–195 °F) for 4 min, swabbing surface occasionally to remove reaction products.

(a) From Ref 7

A good general procedure to evaluate cemented carbide microstructures consists of three steps: (1) porosity assessment on the as-polished sample, (2) a 3 s etch using Murakami's reagent for η-phase, and (3) a final 1 to 2 min etch for the overall structure. An example of a cemented carbide specimen after a 2 min Murakami etch is shown in Fig. 5. The WC grains are gray and angular. The white intergranular areas represent the cobalt binder phase. An alternative method for locating the position of the cobalt phase in the microstructure is shown in Fig. 6, in which the cobalt has been completely removed by a 10 s etch with ferric chloride ($FeCl_3$). No other constituent is attacked by this etchant.

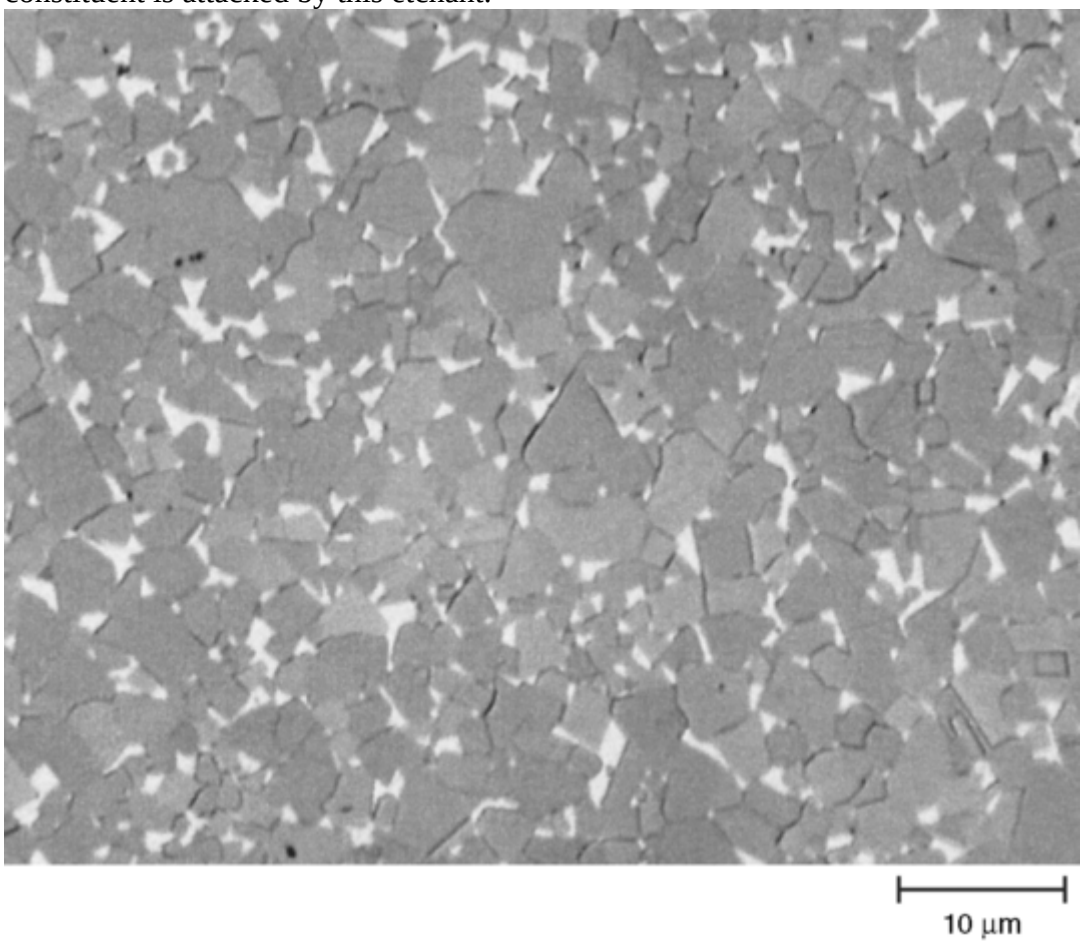

Fig. 5 94WC-6Co alloy, 90 HRA, etched with Murakami's reagent for 2 min. Light gray particles are tungsten carbide; white intergranular areas are cobalt binder. 1500×

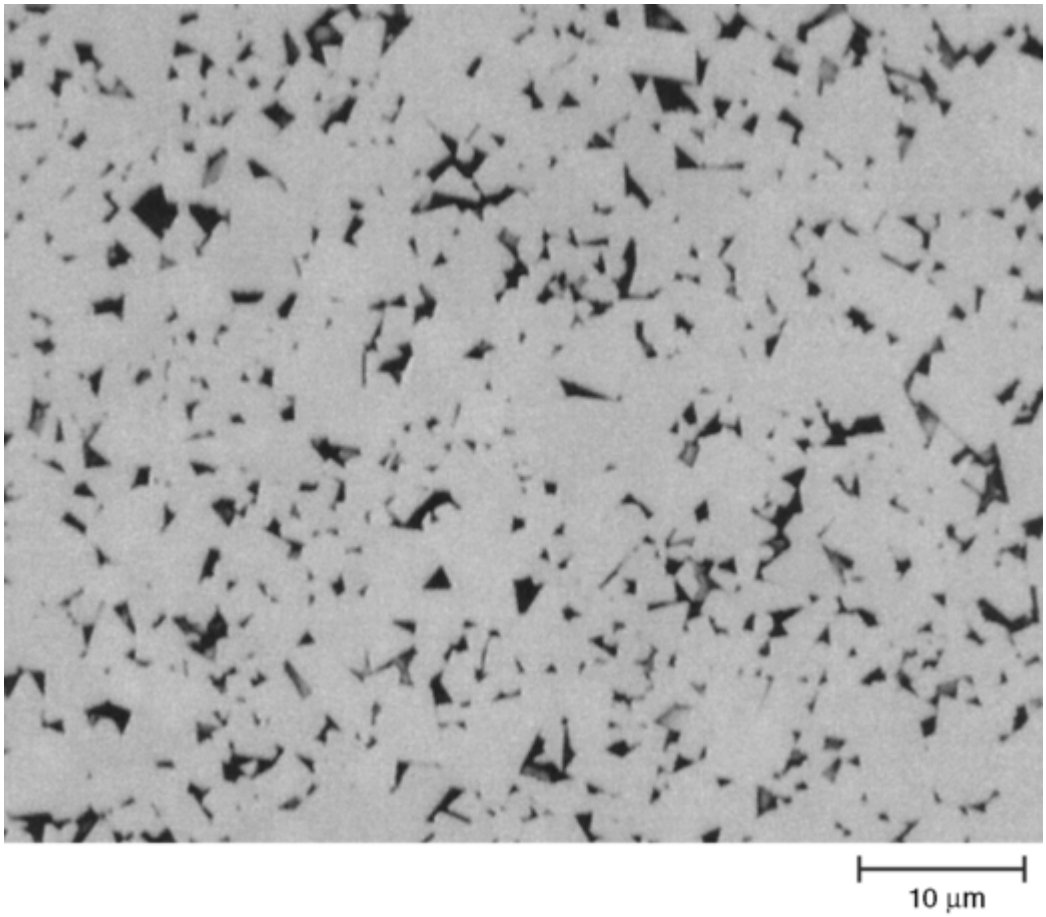

Fig. 6 Same specimen as Fig. 5 except etched with $FeCl_3$ (see Table 2) for 10 s to remove the cobalt binder phase (black areas). 1500×

The only exception to the use of Murakami's reagent is found in the evaluation of titanium carbonitride based cermets. These materials are rapidly attacked by Murakami's reagent, which leaves a reaction layer on the etched surface. A good general etchant for these materials is hydrogen peroxide (H_2O_2), which is listed in Table 2. However, because of their complex microstructures, the TiCN-based cermets are more easily evaluated by SEM examination. Figure 7 shows a backscattered SEM image of a cermet alloy used for general-purpose machining. The dark round grain cores are TiCN; the gray rims around the dark cores and the gray rounded grains are solid-solution carbonitride (Ta,Nb,Mo)CN; the white round phase is tungsten-rich phase, and the intergranular regions are nickel and cobalt binder.

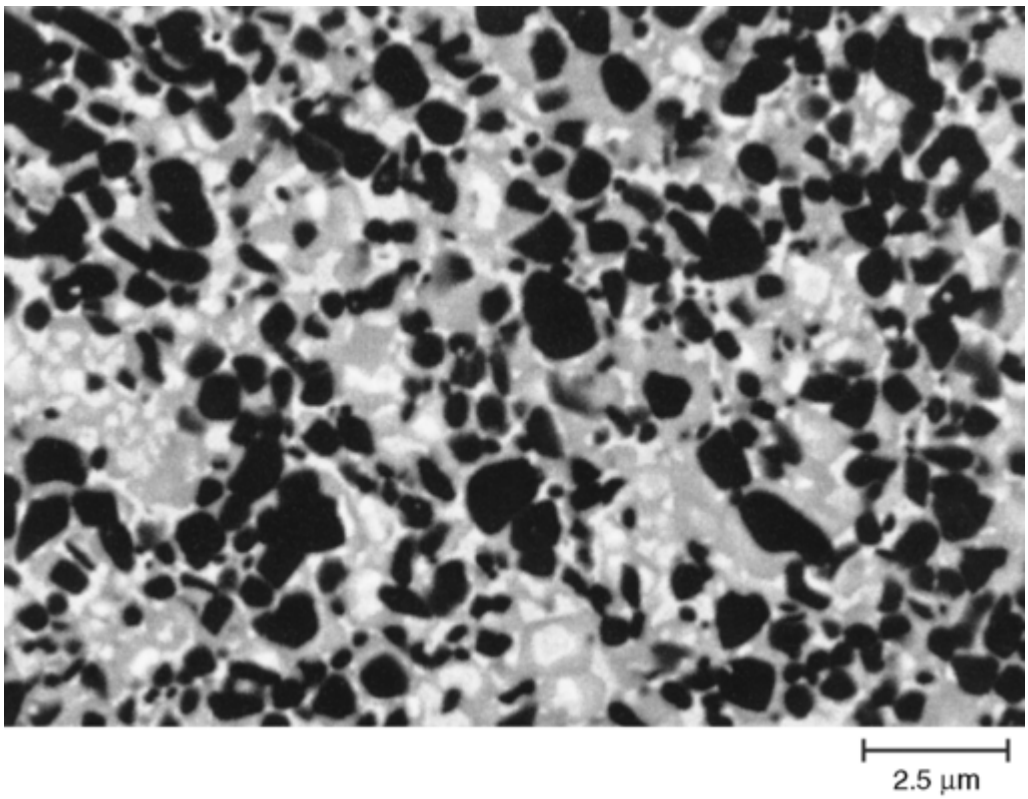

Fig. 7 Backscattered scanning electron micrograph of a cermet alloy [63TiCN-10(Ta,Nb,Mo)CN-15WC-8Co-4Ni], 92.6 HRA. The dark rounded grain cores are titanium carbonitride; gray rims of grains and gray grains are solid solution carbonitride (Ta,Nb,Mo)CN; the white round phase is tungsten-rich phase, and the intergranular regions are nickel and cobalt binder. As-polished. 5000×

Eta Phase. Two types of η phases exist in cemented carbides. The first consists of the approximate formula $(Co_3W_3)C$; the second is $(Co_6W_6)C$. Both types result from decarburizing reactions during sintering (Ref 8) or during high-temperature CVD of hard coatings onto cemented carbide substrates. The $(Co_3W_3)C$ type of η phase is shown in Fig. 8. This phase nucleates and grows due to the constant dissolution of tungsten carbide in the liquid cobalt. Its presence is controlled by the amount of carbon present in the cobalt. When properly etched, this phase develops a spectrum of colors (white, gold, green, blue, and red, but predominantly gold or brown), probably as a result of crystal orientation effects.

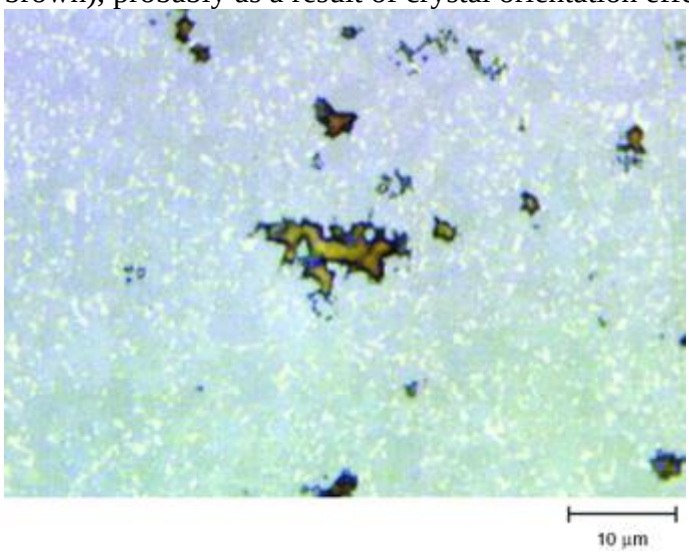

Fig. 8 86WC-4Cr_3C_2-10Co alloy, 92 HRA. The deeply etched brown regions are eta-phase $(Co_3W_3)C$. Background consists of gray tungsten carbide grains and white cobalt binder. Murakami's reagent, 3 s. 1500×.

The second stable form [$(Co_6W_6)C$] of η phase is shown in Fig. 9. It is seen only at the substrate/CVD TiC coating interface and is the result of titanium atoms selectively removing carbon from the cobalt in the substrate, a reaction thermodynamically favored even in the presence of atmospheric carbon during coating deposition. Because the CVD process occurs at temperatures below the liquidus of the Co-W-C binder, the reactions occur in the solid state. As a result, the η phase is discontinuous and occupies only that volume formerly occupied by the cobalt. Both forms of η phase are hard, brittle compounds that degrade the fracture toughness of the cemented carbide and must therefore be controlled or eliminated.

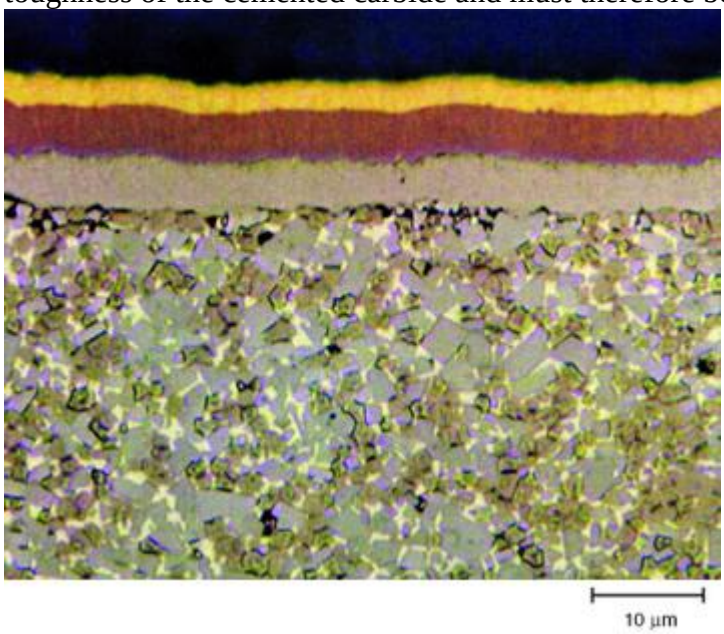

Fig. 9 75.5WC-16(Ta,Ti,Nb)C-8.5Co alloy substrate, 91.2 HRA, coated with multilayer hard coating. Microstructure shows (from bottom) cemented carbide substrate, $(Co_6W_6)C$ eta phase at the substrate/coating interface, TiC, TiCN, and TiN coating layers. Murakami's reagent, 1 min. 1500×.

References cited in this section

4. "Standard Test Method for Apparent Porosity in Cemented Carbides," B 276, *Annual Book of ASTM Standards,* Vol 02.05, ASTM International, 2003, p 70–75

5. "Standard Method for Metallographic Determination of Microstructure in Cemented Tungsten Carbides," B 657, *Annual Book of ASTM Standards,* Vol 02.05, ASTM International, 2003, p 386–391

6. "Standard Practice for Evaluating Apparent Grain Size and Distribution of Cemented Tungsten Carbides," B 290, *Annual Book of ASTM Standards,* Vol 02.05, ASTM International, 2003, p 147–150

7. G. Petzow, *Metallographic Etching*, 2nd ed., ASM International, 1999

8. L. Akesson, An Experimental and Thermodynamic Study of the Co-W-C System in the Temperature Range 1470–1700 K, *Science of Hard Materials,* R.K. Viswanadham, et al., Ed., Plenum Press, 1983, p 71–82

A.T. Santhanam, Metallography of Cemented Carbides, *Metallography and Microstructures,* Vol 9, *ASM Handbook,* ASM International, 2004, p. 1067–1078

Metallography of Cemented Carbides

A.T. Santhanam, Kennametal, Inc.

Microstructures of Cemented Carbides

The micrographs shown in this article represent the variety of cemented carbides now available. They cover the range of cobalt concentration from 3 to 25 wt% and mixed carbide contents from 0 to ~25 wt%. The carbide grain sizes range from <1 to ~10 μm. The Rockwell A scale hardness (HRA) is given for each of the included micrographs, as this is an important property of cemented carbides.

Classification. Cemented carbides are broadly classified into two groups: “straight carbides” and “mixed carbides.” Straight carbides have only two phases in the microstructure, a hard WC phase (gray particles) and a soft cobalt binder (white phase) (Fig. 10). Mixed carbides have three phases: two hard phases—gray WC particles and brown solid solution (Ti,Ta,Nb,W)C carbide particles—and a soft cobalt binder (Fig. 11). The atomic number contrast between WC and solid-solution carbide can be seen clearly in the backscattered SEM on a polished sample in Fig. 12. The bright gray angular grains are WC (high atomic number) and dark gray round grains are mixed carbide, (Ti,Ta,Nb,W)C, with lower atomic number.

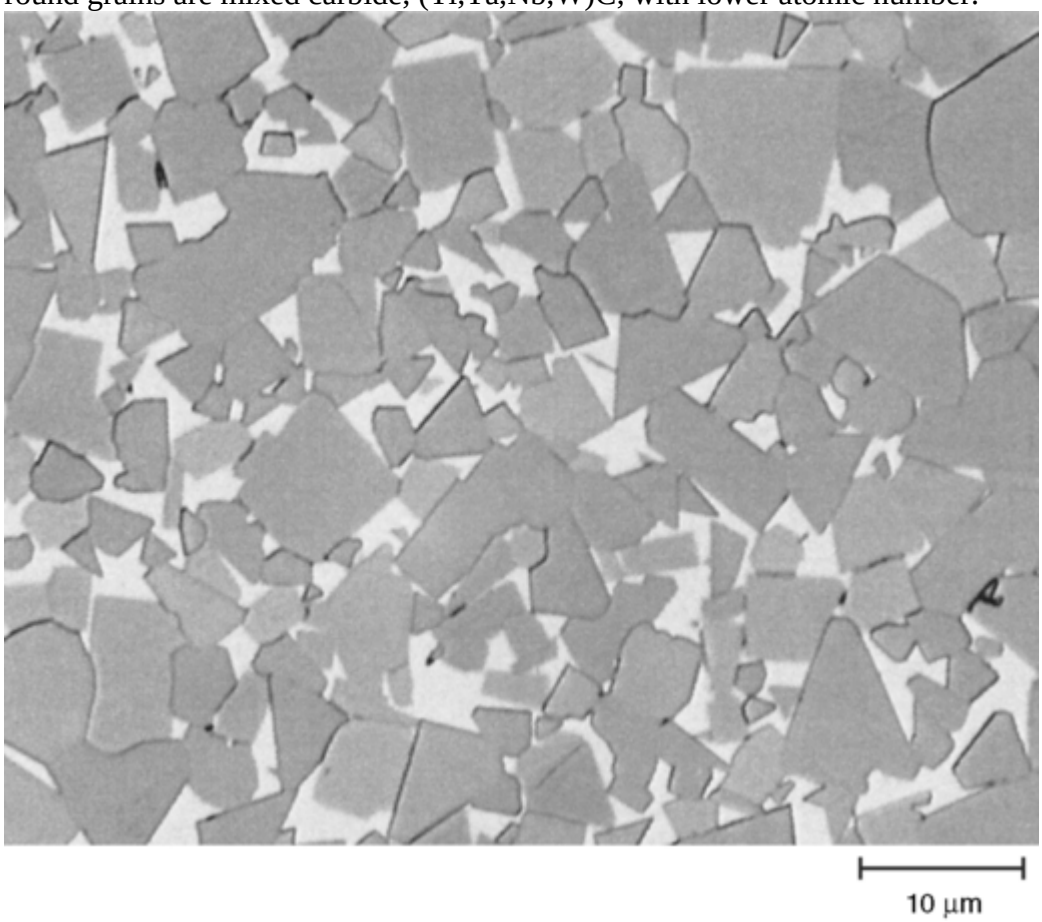

Fig. 10 90.5WC-9.5Co alloy, 86 HRA. An example of “straight carbide” with only two phases in the microstructure: gray tungsten carbide phase and white cobalt binder phase. Murakami's reagent, 2 min. 1500×

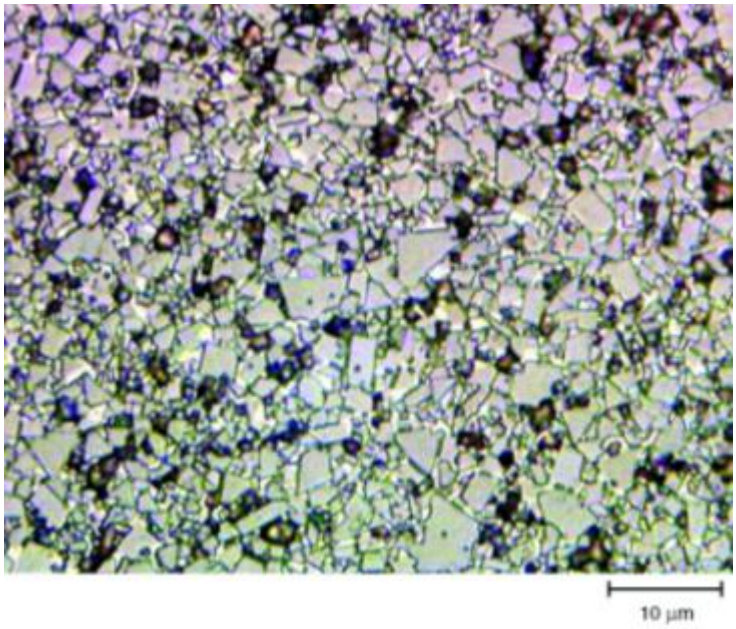

Fig. 11 85.5WC-8(Ta,Ti,Nb)C-6.5Co alloy, 91 HRA. An example of "mixed carbide" with three phases in the microstructure: deeply etched, brown, rounded, solid-solution carbide; gray, angular tungsten carbide grains; and white cobalt binder. Murakami's reagent, 2 min. 1500×.

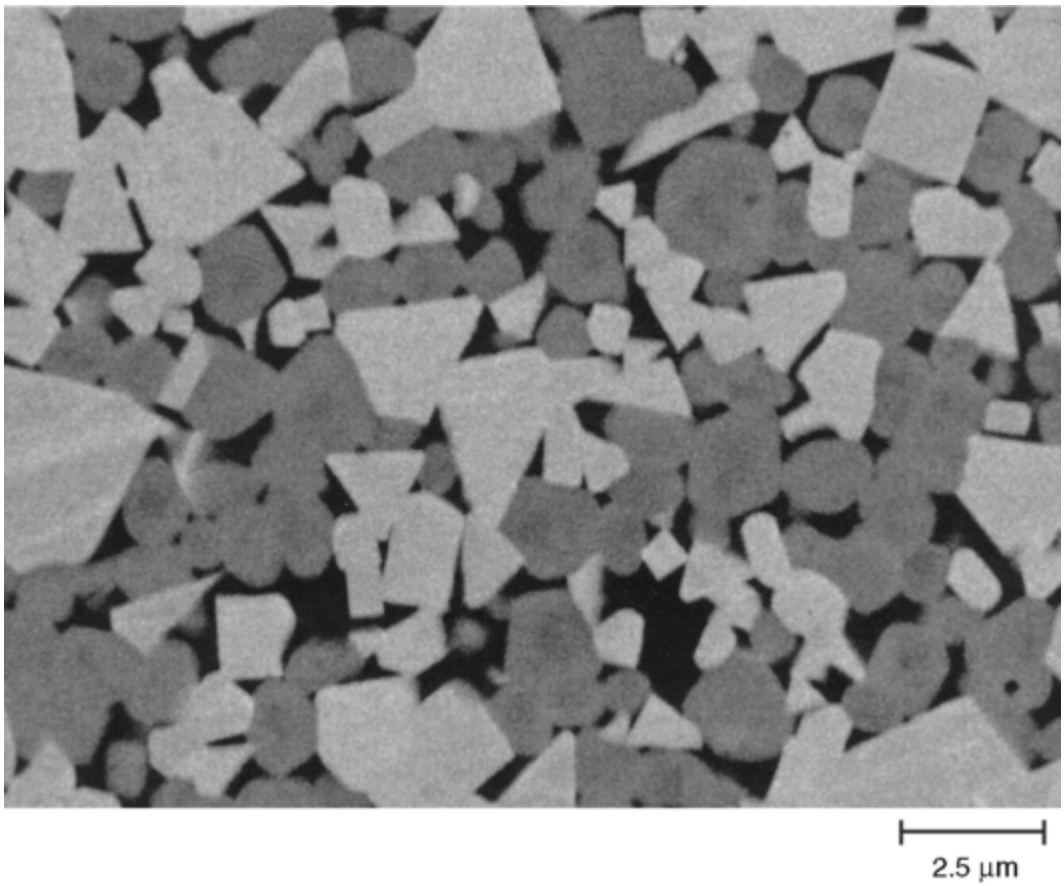

Fig. 12 Backscattered scanning electron micrograph of 75.5WC-16(Ta,Ti,Nb)C-8.5Co alloy, 91.2 HRA. Gray angular particles are tungsten carbide; dark gray, rounded particles are mixed carbide; and cobalt binder is black. As-polished, 5000×

The straight WC-Co alloys have excellent resistance to simple abrasive wear and are widely used for machining materials that produce short chips, for example, gray cast irons and nonferrous alloys, and in a broad spectrum of industrial applications, including metalworking, metal or coal mining, transportation, and construction

industries. Mixed carbides are mainly used for steel machining because of their ability to reduce crater wear from diffusion of WC into the steel chip.

The physical and mechanical properties of these materials are directly related to their composition (amount of hard carbide and soft binder phase) and microstructure (particle size and distribution of these phases). Increasing the cobalt content or WC grain size increases the toughness of the tool material at the expense of deformation resistance and abrasion resistance. The trade-off between toughness and deformation resistance enables the cemented carbide manufacturer to tailor these materials to a wide variety of metalcutting and nonmetalcutting applications. In general, the cobalt content can vary from 5 to 25 wt% and WC grain sizes range from ~0.2 to ~10 μm (Fig. 13, 14, 15, 16, 17, 18).

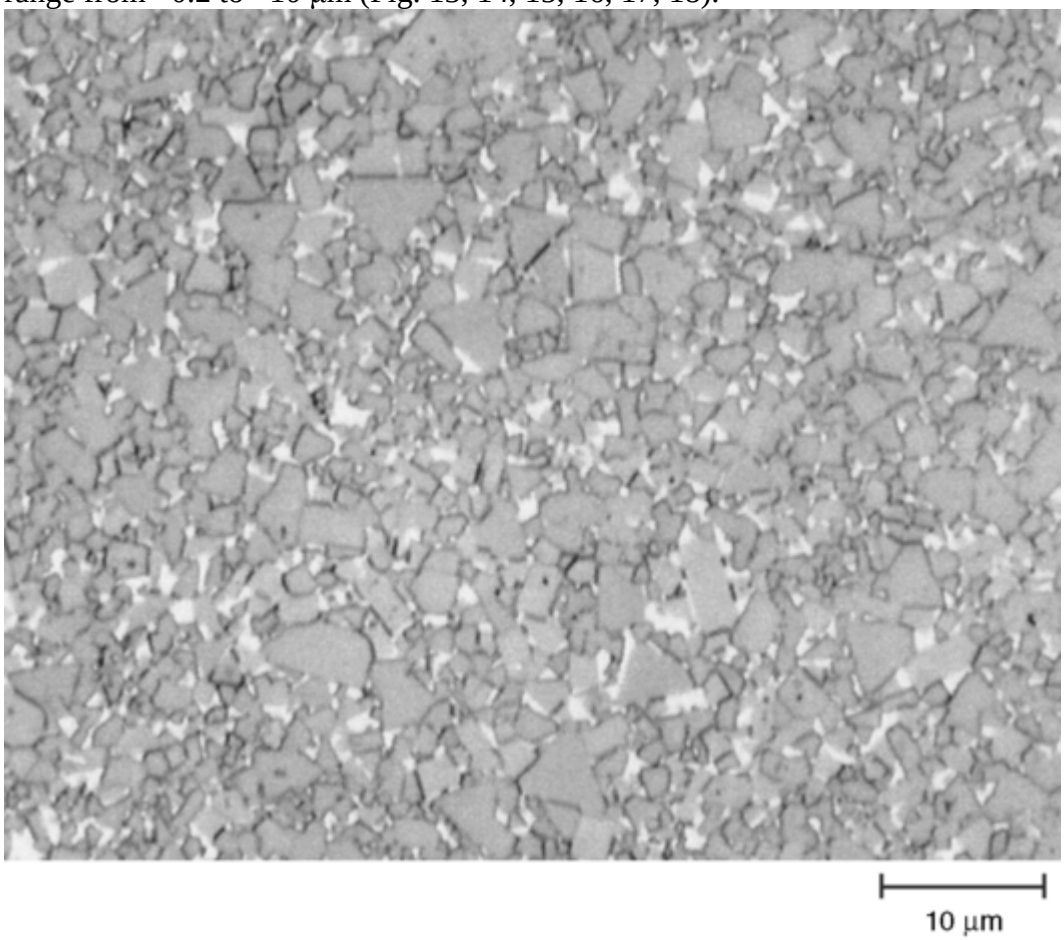

Fig. 13 94WC-6Co alloy, 91 HRA. Gray particles are tungsten carbide; white areas are cobalt binder in this medium-size grain structure. Murakami's reagent, 2 min. 1500×

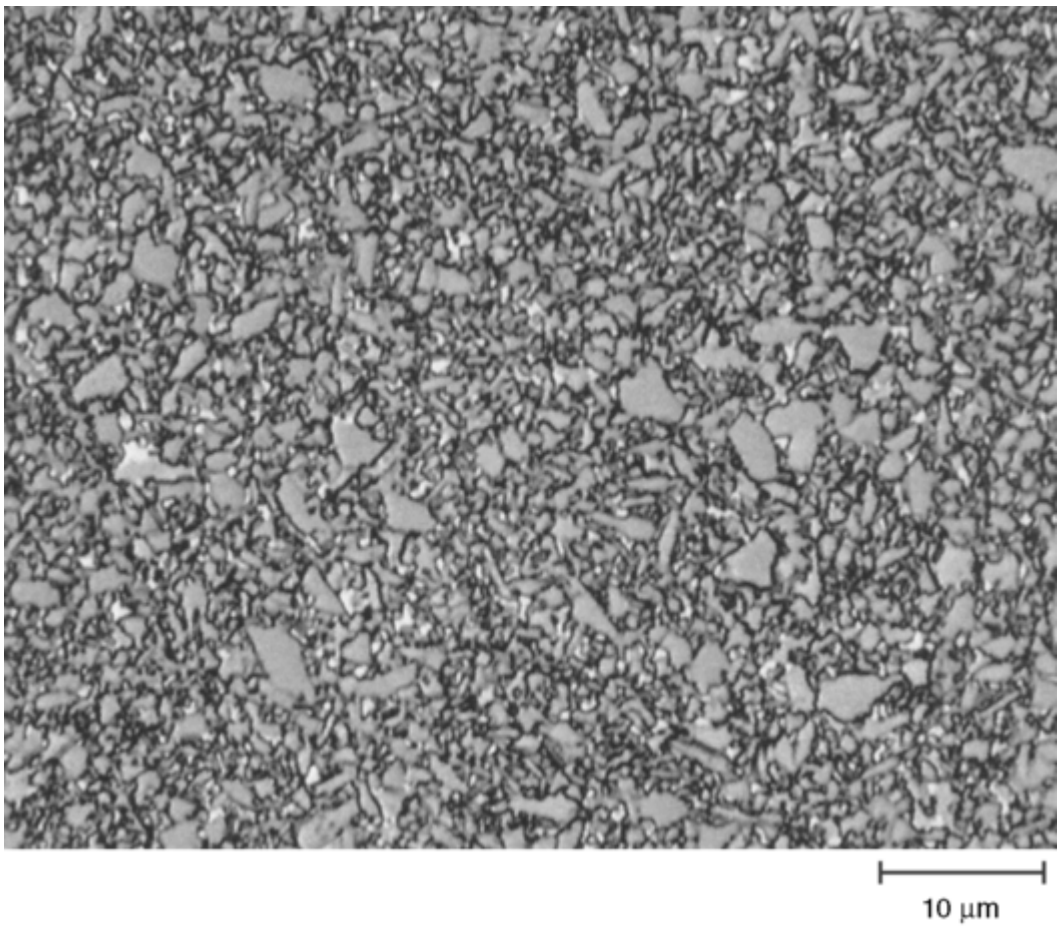

Fig. 14 94WC-6Ni alloy, 90.7 HRA. Gray particles are tungsten carbide (medium to fine grained); white areas are nickel binder. Murakami's reagent, 2 min. 1500×

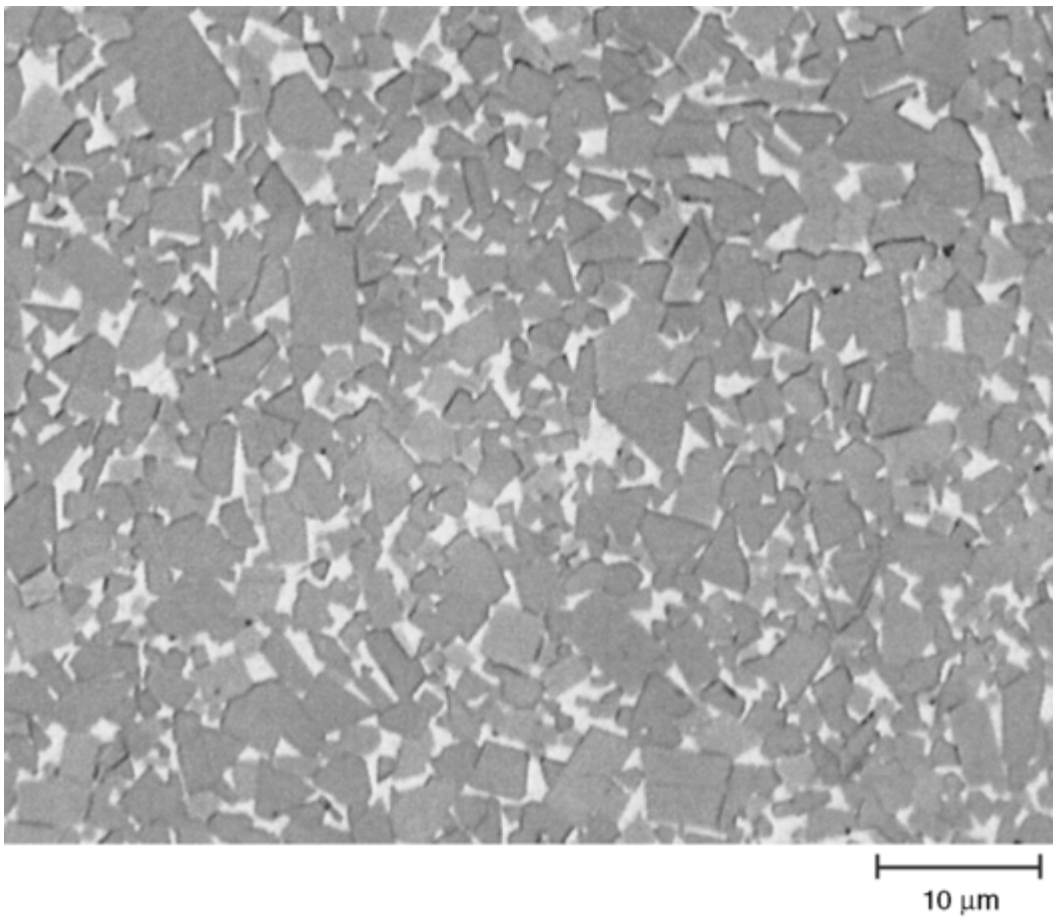

Fig. 15 90WC-10Co alloy, 88 HRA. Gray particles are tungsten carbide (coarse to medium grained); white areas are cobalt binder. Murakami's reagent, 2 min. 1500×

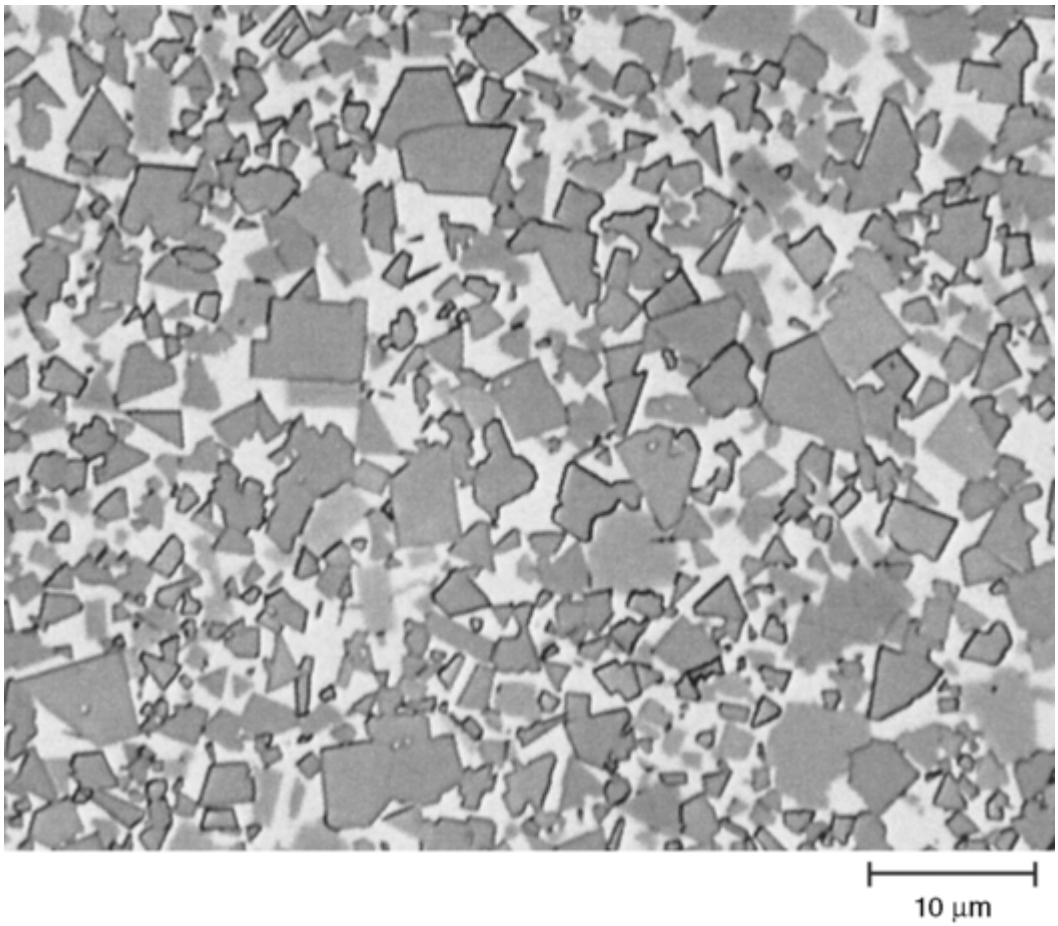

Fig. 16 80WC-20Co alloy, 84 HRA. Gray particles are tungsten carbide (coarse to medium grained); white areas are cobalt binder. Note that HRA decreases as binder content increases (compare with Fig. 14, 15.) Murakami's reagent, 2 min. 1500×

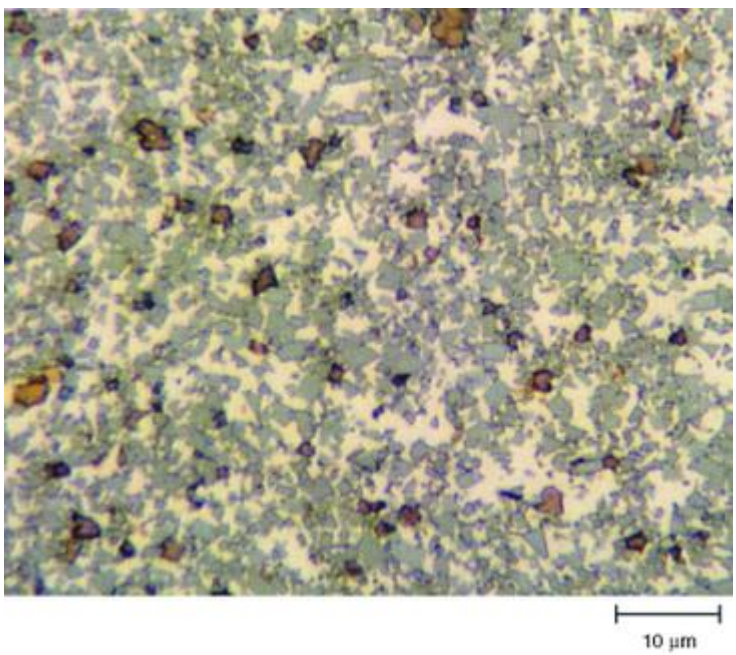

Fig. 17 70WC-5(Ta,Nb)C-25Co alloy, 85 HRA. The high-cobalt alloy is used for non-machining applications. Gray particles are tungsten carbide; white areas are cobalt binder. Murakami's reagent, 2 min. 1500×.



Fig. 18 71WC-23(Ta,Ti,Nb)C-6Co alloy, 92.9 HRA. This fine-grained microstructure consists of gray, angular tungsten carbide; rounded mixed carbides; and white cobalt binder phase. Murakami's reagent, 2 min. 1500×.

Straight WC-Co alloys with submicrometer carbide grain sizes (Fig. 19 and 20) are used for applications requiring more toughness or tool edge strength. Such applications include indexable metalcutting inserts, solid carbide drills (including circuit board drills), and milling tools. Grain refinement in these alloys is obtained by small additions (0.2 to 3.0 wt%) of VC, Cr_3C_2, TaC, or NbC.



Fig. 19 93.5WC-0.5Cr_3C_2-6Co alloy, 93 HRA. This straight carbide alloy has submicrometer-sized gray tungsten carbide grains. The cobalt binder is difficult to see because of the fine carbide grain size. Murakami's reagent, 2 min. 1500×

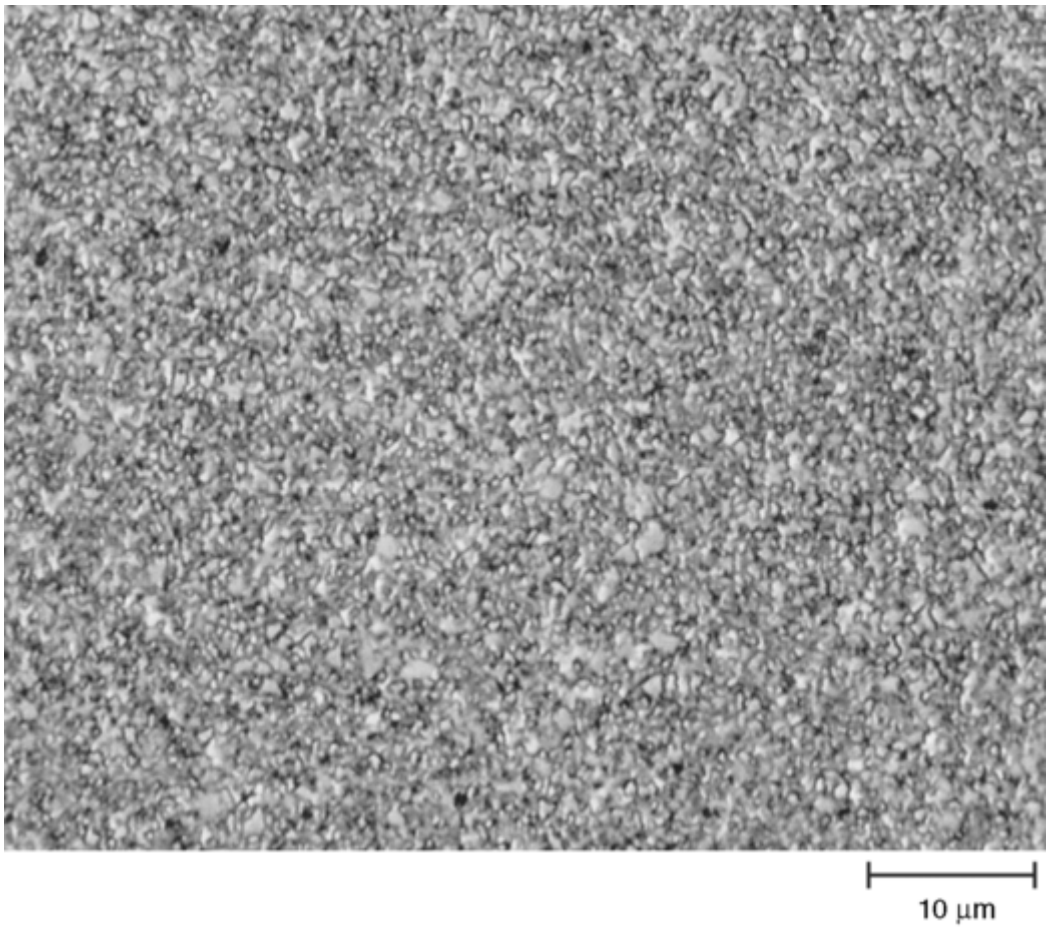

Fig. 20 89.8WC-0.2VC-10Co alloy, 92.2 HRA. Similar to Fig. 19 but with higher cobalt binder content. Murakami's reagent, 2 min. 1500×

Coated Carbide Tools. Most metalcutting carbide tool inserts are now coated either by CVD or PVD process to suppress various tool wear processes and enhance tool life. Coatings also permit the use of higher cutting speeds, boosting machining productivity. Modern CVD hard coatings feature multiple layers involving various combinations of TiC, TiCN, ZrCN, TiN, and Al_2O_3 (Fig. 21, 22, 23). Chemical vapor deposited coatings (4 to 30 μm thick) are applied at high temperatures (~1000 °C, or 1800 °F) or moderate temperatures (MT-CVD, ~850 °C, or 1560 °F) or lower temperatures (~600 °C, or 1100 °F) by plasma-assisted process (PA-CVD). Physical vapor deposited coatings (typically 2 to 6 μm thick) are processed at still lower temperatures (~550 °C, or 1020 °F). The PVD process offers unique advantages, including the ability to apply a fine-grained, smooth, low-friction, and thermal crack-free coating over sharp edges. Physical vapor deposited coatings also feature compressive residual stresses, which are beneficial in resisting crack propagation and preventing premature tool failure. Typical commercial PVD coatings include TiN, TiCN, TiAlN, TiB_2, CrN, and multilayers of TiN-TiAlN (Fig. 24, 25, 26, 27, 28, 29).

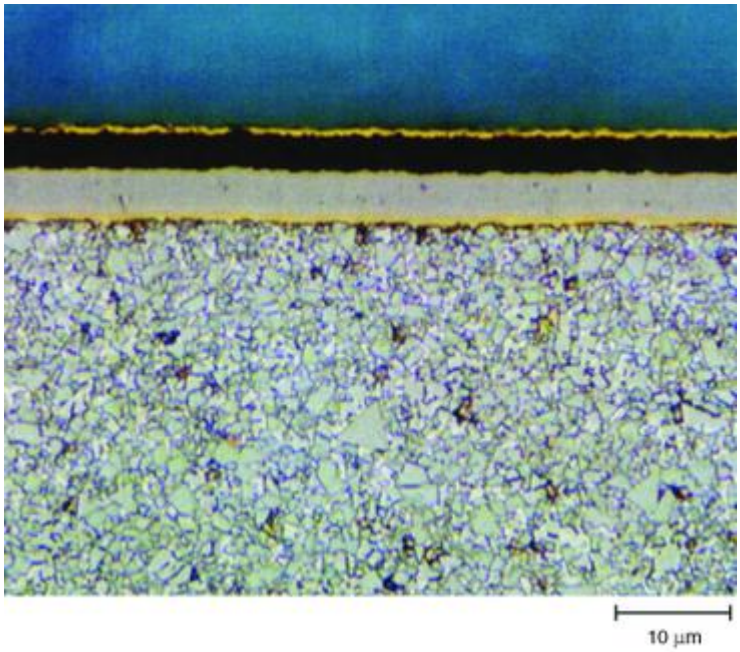

Fig. 21 90.5WC-3.5(Ta,Ti,Nb)C-6Co alloy, 92 HRA, coated with multilayer hard coating. Microstructure shows (from bottom) cemented carbide substrate, TiN, TiCN, Al_2O_3, and TiN layers coated by the chemical vapor deposition process. Murakami's reagent, 1 min. 1500×.

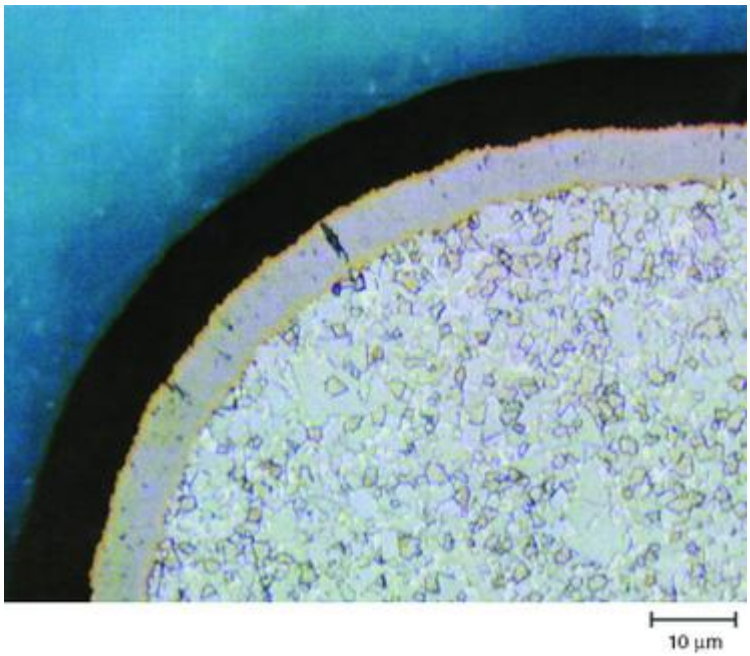

Fig. 22 86.5WC-7.5(Ta,Ti,Nb)C-6Co alloy, 91.3 HRA, with chemical-vapor-deposited titanium carbonitride (TiCN) and alumina (Al_2O_3) coating. Microstructure shows a honed edge of a metalcutting insert. Murakami's reagent, 1 min. 1500×.

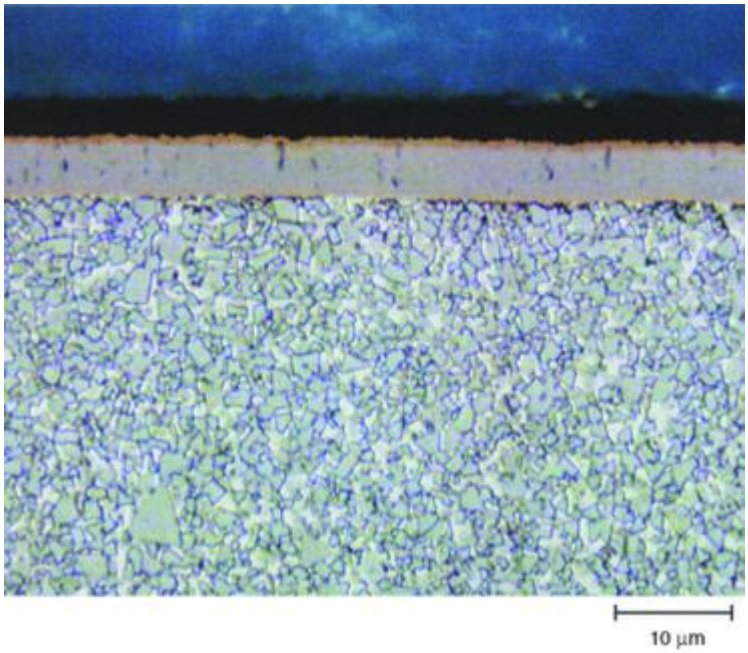

Fig. 23 88.5WC-11.5Co alloy, 89.8 HRA, with chemical-vapor-deposited TiCN and Al_2O_3 coating. Murakami's reagent, 1 min. 1500×.

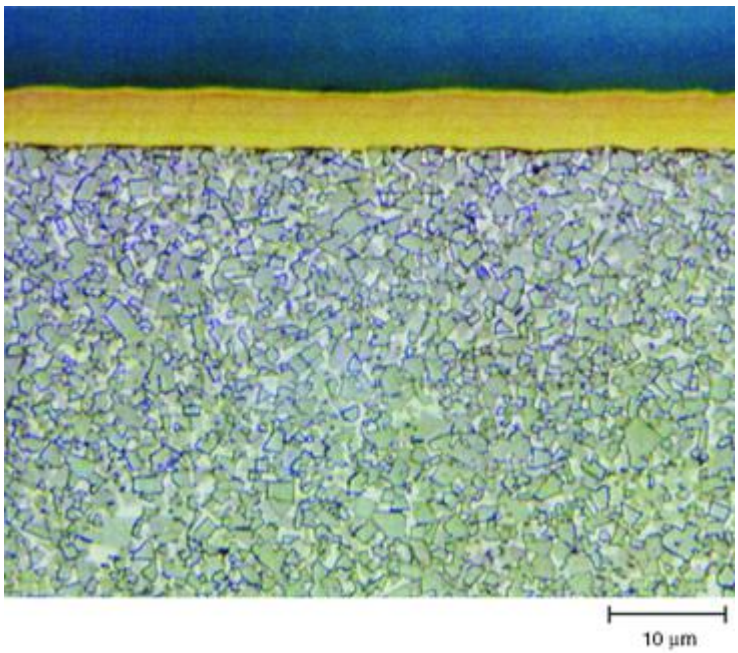

Fig. 24 88.5WC-11.5Co alloy, 89.8 HRA, with physical-vapor-deposited TiCN coating. Murakami's reagent, 1 min. 1500×.

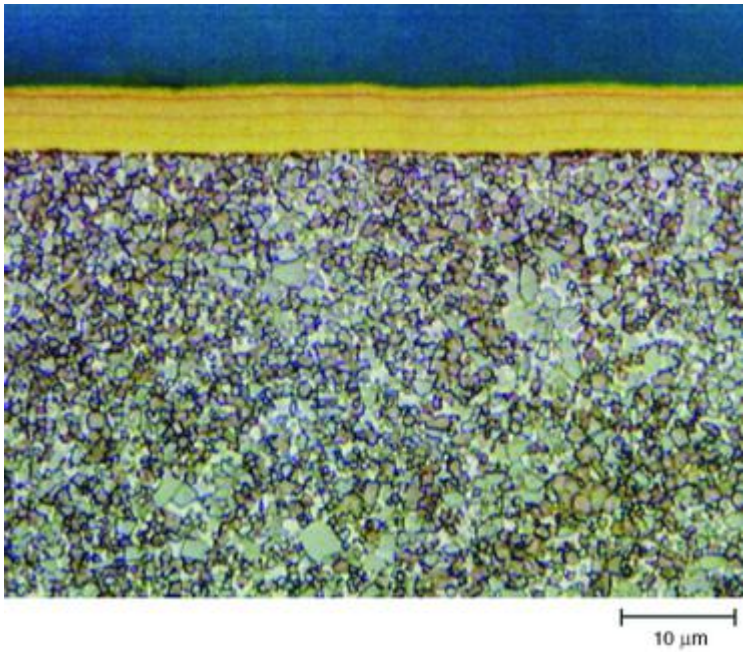

Fig. 25 72.5WC-17(Ta,Ti,Nb)C-10.5Co alloy, 91.4 HRA, with physical-vapor-deposited TiCN coating. Murakami's reagent, 1 min. 1500×.

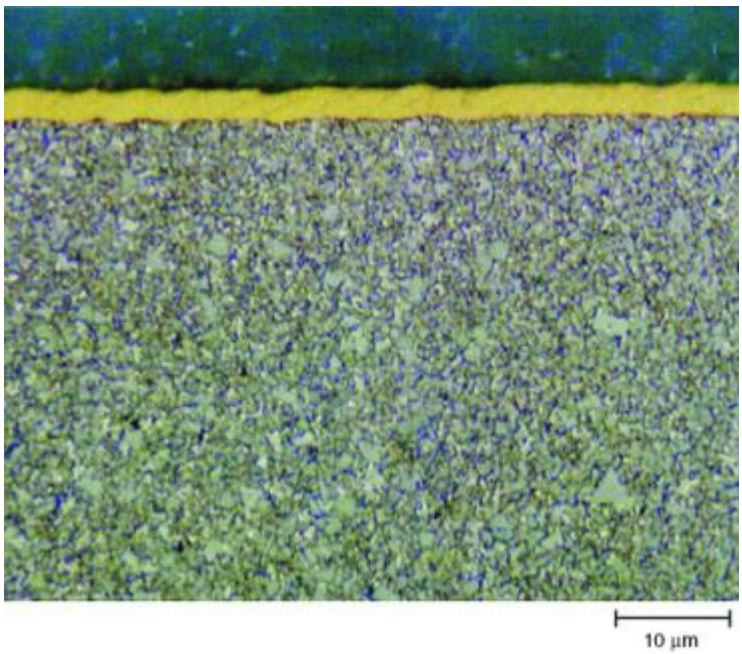

Fig. 26 93.5WC-0.5Cr_3C_2-6Co alloy, 93 HRA, with a thin layer (1 to 2 µm) of physical-vapor-deposited titanium nitride (TiN) coating. Murakami's reagent, 1 min. 1500×.

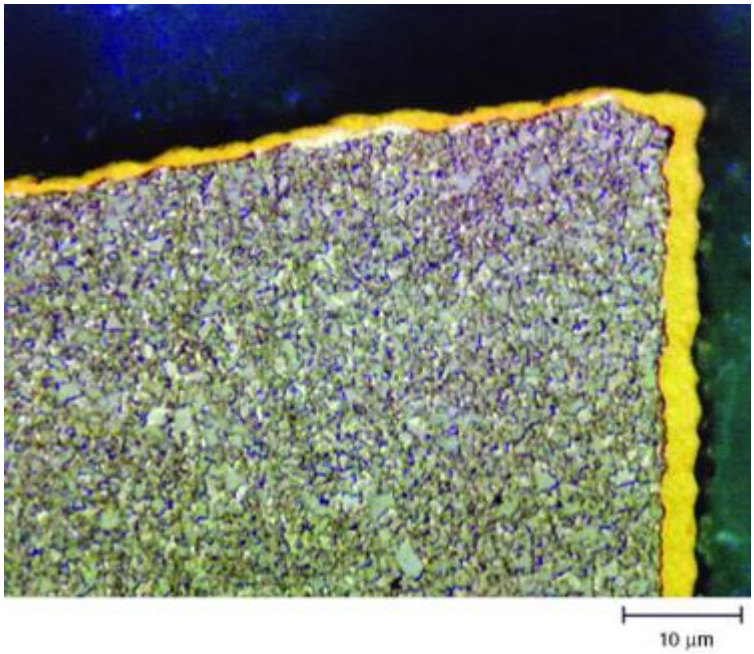

Fig. 27 Same physical-vapor-deposited TiN-coated insert as in Fig. 108, but the micrograph shows the coating over the sharp insert edge. Murakami's reagent, 1 min. 1500×.

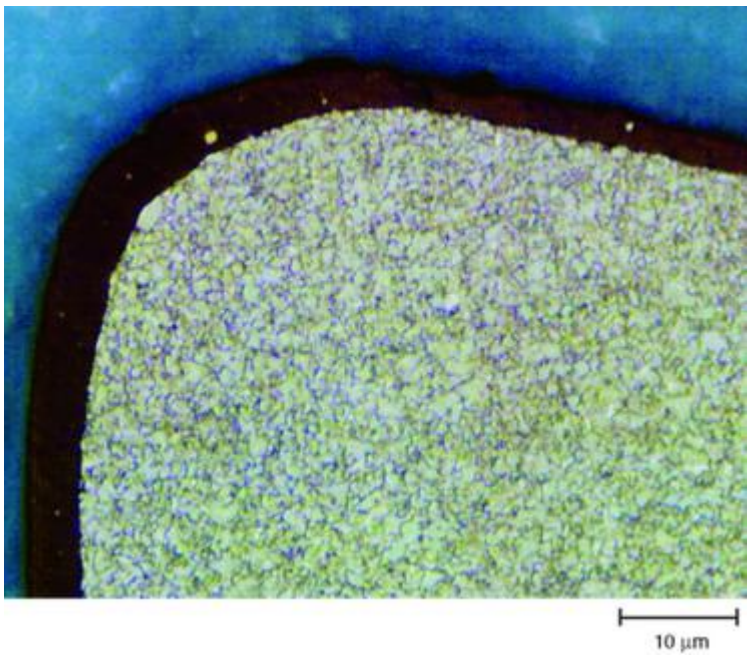

Fig. 28 93.5WC-0.5Cr_3C_2-6Co alloy, 93 HRA, with physical-vapor-deposited titanium-aluminum nitride (TiAlN) coating. Microstructure shows a small honed edge of a metalcutting insert. Murakami's reagent, 1 min. 1500×.

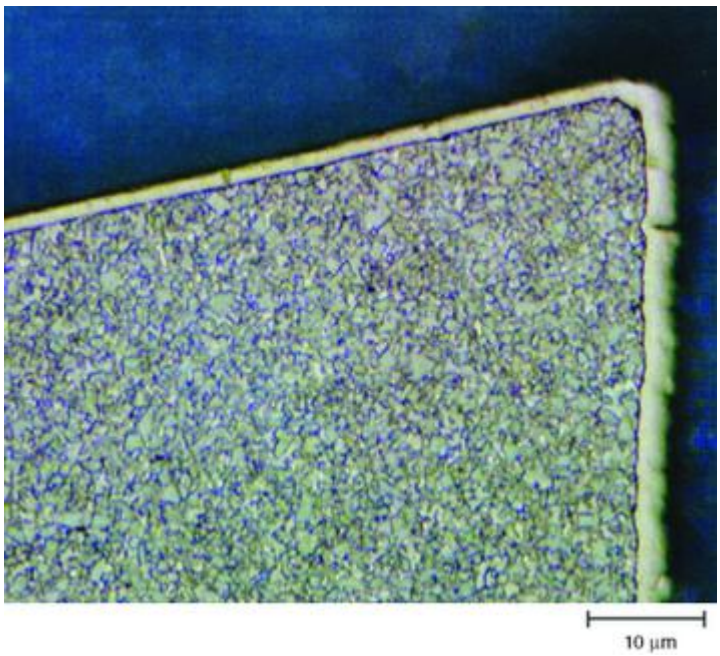

Fig. 29 93.5WC-0.5Cr_3C_2-6Co alloy, 93 HRA, with a thin layer (1 to 2 µm) of physical-vapor-deposited (PVD) titanium diboride (TiB_2) coating. Note again that the PVD coating has been applied over a sharp insert edge. Murakami's reagent, 1 min. 1500×.

Coated Carbides with Functionally Gradient Substrate Microstructures. In the late 1970s a TiC-TiCN-TiN coated tool was developed with a peripherally cobalt-enriched substrate (two to three times higher cobalt at the tool insert periphery than in the bulk). The cobalt-enriched periphery (~15 to 20 µm deep) was also slightly depleted in cubic carbides. The bulk of the tool insert had lower cobalt and higher level of cubic carbides (Fig. 30). The combination provided superior edge strength while maintaining the edge and crater wear resistance of the coating layers (Ref 9). This development permitted users to make heavy interrupted machining cuts such as those encountered in scaled forgings and castings at lower speeds. Refinements to the cobalt-enrichment concept (1.5 to 2 times higher cobalt and complete depletion of cubic carbides in the tool periphery compared to the bulk), in combination with Al_2O_3 coating (Fig. 31 and 32) expanded the application range of this type of tool to higher speeds (Ref 10).

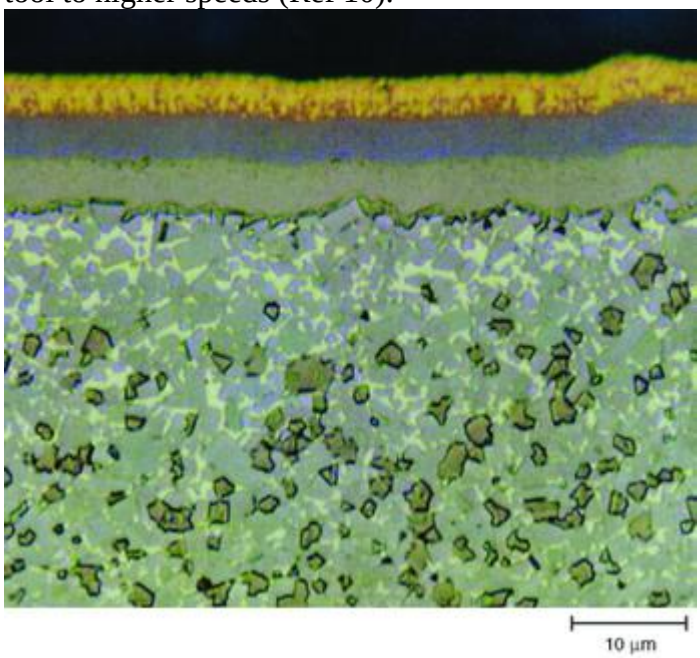

Fig. 30 86WC-8(Ta,Ti,Nb)C-6Co alloy, 91.6 HRA, coated with chemical-vapor-deposited multilayers of TiC, TiCN, and TiN. Note the gradient microstructure of the substrate (first-generation cobalt-enriched

alloy), with the insert periphery (below the coating layers) showing higher levels of cobalt binder (white, stratified phase) than the interior. Murakami's reagent, 1 min. 1500×.

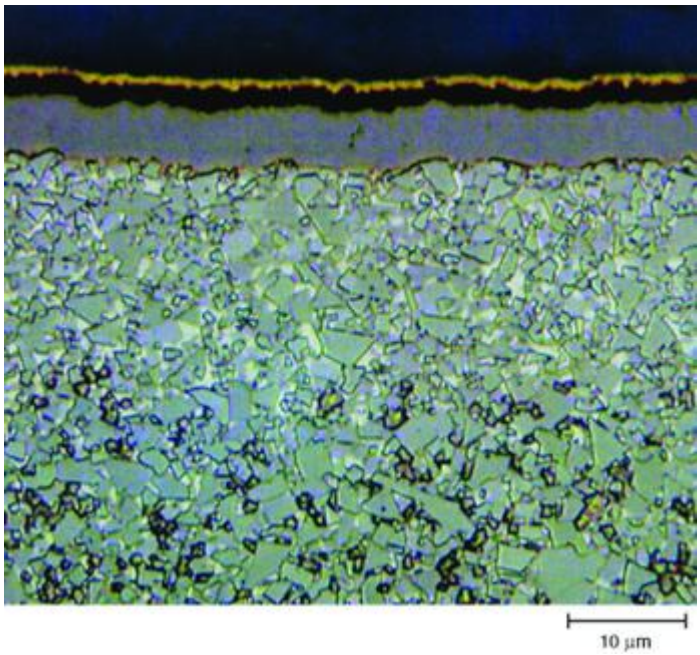

Fig. 31 87WC-7(Ta,Ti,Nb)C-6Co alloy, 91.6 HRA. This second-generation cobalt-enriched alloy is coated with chemical-vapor-deposited TiCN and Al_2O_3 coating. Note that the cobalt-enriched zone at the insert periphery is also devoid of mixed carbides. Murakami's reagent, 1 min. 1500×.

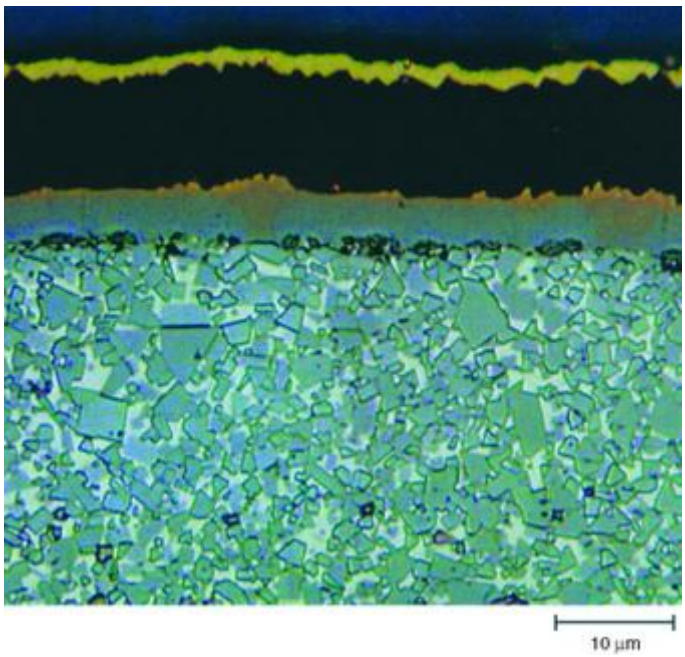

Fig. 32 86WC-7(Ta,Ti,Nb)C-7Co alloy, 90.6 HRA. Another example of a second-generation cobalt-enriched alloy coated with chemical-vapor-deposited TiCN and a thick Al_2O_3 coating (total coating thickness: 15 µm). Murakami's reagent, 1 min. 1500×.

CVD-PVD Combination Coatings. In the late 1980s, a new coating technology was developed in which an outer layer of PVD TiN was combined with CVD TiN/TiCN inner layers (Fig. 33). When combined with a cobalt-enriched substrate with good bulk deformation resistance, the CVD-PVD combination coating has been found to provide improved tool performance in milling of steel workpieces at relatively high speeds (Ref 11).

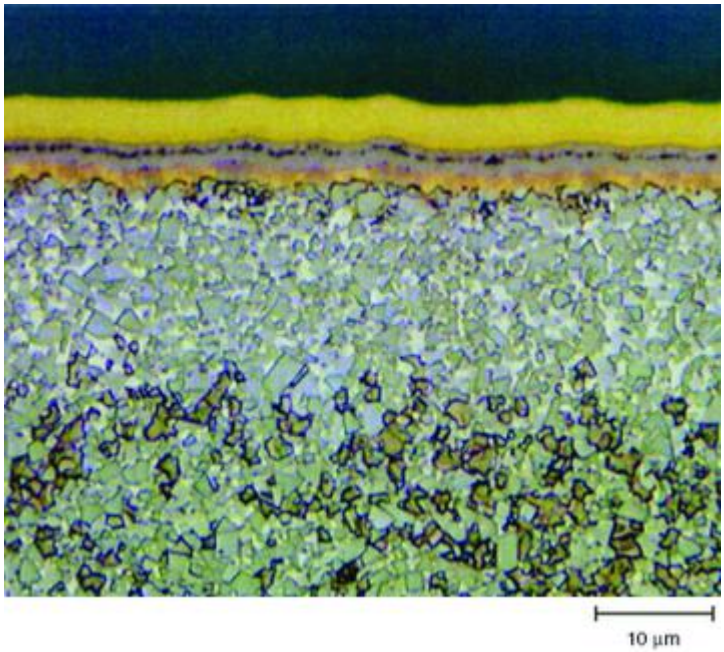

Fig. 33 83.5WC-10.5(Ta,Ti,Nb)C-6Co alloy, 92 HRA. This cobalt-enriched alloy is coated with chemical-vapor-deposited TiN/TiCN and physical-vapor-deposited TiN (gold coating on top) layers. Murakami's reagent, 1 min. 1500×.

Postcoat Surface Treatments. Modern coated tool inserts are given postcoat polishing treatments that polish either the insert edge or the entire tool surface to suppress the flaking of the multilayer coating in certain machining applications. The top TiN layer is removed, exposing the alumina layer underneath (Fig. 34).

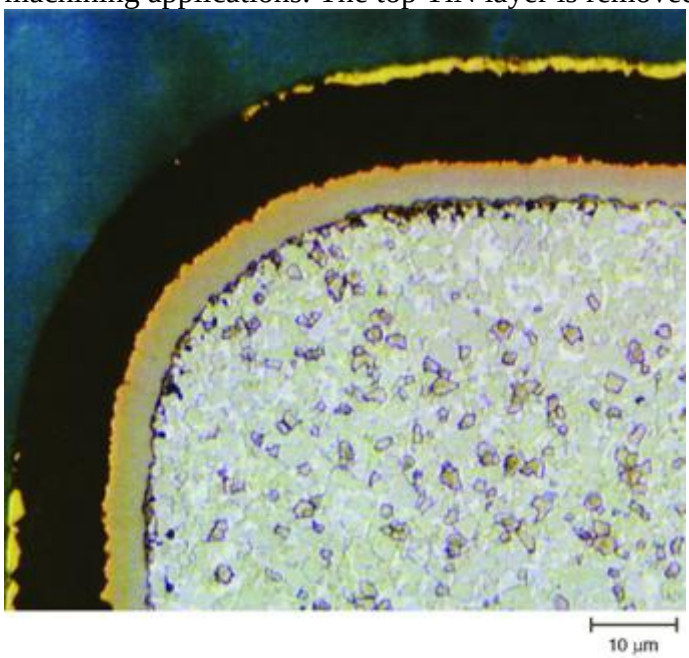

Fig. 34 86WC-7(Ta,Ti,Nb)C-7Co alloy, 90.6 HRA. An example of postcoat treatment on a chemical-vapor-deposited TiCN/Al_2O_3-coated insert. Note the smooth edge at the hone, with the top TiN layer removed by the post-coat treatment. Murakami's reagent, 1 min. 1500×.

References cited in this section

9. B.J. Nemeth, A.T. Santhanam, and G.P. Grab, *Proc. Tenth International Plansee Seminar,* Metallwerk Plansee GmbH, 1981, p 613–627

10. A.T. Santhanam, G.P. Grab, G.A. Rolka, and P. Tierney, An Advanced Cobalt-Enriched Grade Designed to Enhance Productivity, in *High Productivity Machining—Materials and Processes,* American Society for Metals, 1985, p 113–121

11. A.T. Santhanam, R.V. Godse, G.P. Grab, D.T. Quinto, K.E. Undercoffer, and P.C. Jindal, U.S. Patent 5,250,367, 5 Oct 1993

A.T. Santhanam, Metallography of Cemented Carbides, *Metallography and Microstructures,* Vol 9, *ASM Handbook,* ASM International, 2004, p. 1067–1078

Metallography of Cemented Carbides

A.T. Santhanam, Kennametal, Inc.

Quantitative Metallography

The current status of quantitative metallography of cemented carbides is presented in Ref 12, 13, 14, 15. The important parameters measured are pore volume, binder volume fraction, binder mean free path, carbide grain size and shape, and the contiguity, which is the particle-to-particle grain-boundary ratio to total surface area. Using well-established stereological techniques, microstructural parameters such as the volume fraction of binder, the WC mean linear intercept grain size, the carbide contiguity, and the binder mean linear intercept distance can be measured or calculated from appropriate micrographs (Ref 13.

The precision and accuracy with which this can be accomplished, however, depends on the particular carbide structure being investigated. This has led to the use of many imaging techniques and contrasting methods. Because the quantities to be measured vary in size from 20 μm particles to less than 0.1 μm thick binder layers, no single imaging technique is suitable. Research laboratories report the use of heat tinting (Ref 16), electrolytic etching (Ref 17), interference vapor-deposited films (Ref 18), and ion etching (Ref 19), as well as chemical etchants other than Murakami's. Each has particular advantages for certain grades and compositions of carbide or for particular imaging methods.

Imaging methods other than bright-field optical microscopy include differential interference microscopy, SEM, TEM, photoemission electron microscopy (Ref 20, 21, 22), and scanning Auger microscopy (Ref 23). Of these, SEM and photoemission electron microscopy are the most useful techniques, especially when used in conjunction with automatic image analyzers. The cited references provide good information on the evaluation of the techniques for specific applications.

References cited in this section

12. H.E. Exner, Qualitative and Quantitative Interpretation of Microstructures in Cemented Carbides, *Science of Hard Materials,* R. K. Viswanadham, et al., Ed., Plenum Press, 1983, p 233–259

13. J. Gurland, Application of Quantitative Microscopy to Cemented Carbides, *Practical Applications of Quantitative Metallography,* STP 839, J.L. McCall and J.H. Steele, Jr., Ed., ASTM, 1984, p 65–84

14. "Standard Test Methods for Determining Average Grain Size Using Semiautomatic and Automatic Image Analysis," E 1382-97, ASTM International, June 1997, p 866

15. B. Roebuck, et al., "Measurement of WC Grain Size," Report CMMT(A) 141, Issued by Natl. Phys. Lab (Teddington, U.K.), Jan 1999, p 2

16. H. Grewe, Structural Investigation on Hard Metals, *Prakt. Metallogr.,* Vol 5, 1969, p 411–419

17. W. Mader and K.F. Muller, Determination and Comparison of Structural Parameters of Hard Metal Alloys Using Electron and Optical Micrographs, *Prakt. Metallogr.,* Vol 5, 1968, p 616–625

18. W. Peter, E. Kohlhaas, and O. Jung, Revealing of Hard Metal Structures by Interference Vapor-Deposition, *Prakt. Metallogr.,* Vol 4, 1967, p 288–290

19. A. Doi, T. Nishikawa, and A. Hara, Ion-Etching Techniques for Microstructural Characterization of Cemented Carbides and Ceramics, *Science of Hard Materials,* R.K. Viswanadham, et al., Ed., Plenum Press, 1983, p 329–339

20. H. Gahm, S. Karagoz, and G. Kompek, Metallographic Methods for the Characterization of the Microstructure of Cemented Carbides, *Prakt. Metallogr.,* Vol 18, 1981, p 14–30

21. E.M. Vyger, Metallography and Microstructural Characterization of Some Hardmetal Grades by Optical and Electron Microscopy, *Prakt. Metallogr.,* Vol 19, 1982, p 592–604, 639–649

22. B. Egg, Experiences with Quantitative Automatic Scanning Electron Microscopy, *Prakt. Metallogr.,* Vol 22, 1985, p 78–87

23. D.T. Quinto, G.J. Wolfe, and M.N. Haller, Low-Z Element Analysis in Hard Materials, *Science of Hard Materials,* R.K. Viswanadham, et al., Ed., Plenum Press, 1983, p 947–971

A.T. Santhanam, Metallography of Cemented Carbides, *Metallography and Microstructures,* Vol 9, *ASM Handbook,* ASM International, 2004, p. 1067–1078

Metallography of Cemented Carbides

A.T. Santhanam, Kennametal, Inc.

Acknowledgment

The author wishes to express his appreciation to Kennametal Materials Analysis Department for their contributions to metallography used in this article. The author is also grateful to Doug Moore for assistance with the graphics.

A.T. Santhanam, Metallography of Cemented Carbides, *Metallography and Microstructures,* Vol 9, *ASM Handbook,* ASM International, 2004, p. 1067–1078

Metallography of Cemented Carbides

A.T. Santhanam, Kennametal, Inc.

References

1. “Metallographic Procedures for Sintered Carbide,” Report 01.84, Struers Inc., Cleveland, OH

2. “Standard Practice for Metallographic Sample Preparation of Cemented Tungsten Carbides,” B 665, *Annual Book of ASTM Standards,* Vol 02.05, ASTM International, 2003, p 395–396

3. G. Vander Voort, *Metallography Principles and Practice,* McGraw-Hill, 1984, reprinted by ASM International, 1999

4. “Standard Test Method for Apparent Porosity in Cemented Carbides,” B 276, *Annual Book of ASTM Standards,* Vol 02.05, ASTM International, 2003, p 70–75

5. “Standard Method for Metallographic Determination of Microstructure in Cemented Tungsten Carbides,” B 657, *Annual Book of ASTM Standards,* Vol 02.05, ASTM International, 2003, p 386–391

6. “Standard Practice for Evaluating Apparent Grain Size and Distribution of Cemented Tungsten Carbides,” B 290, *Annual Book of ASTM Standards,* Vol 02.05, ASTM International, 2003, p 147–150

7. G. Petzow, *Metallographic Etching,* 2nd ed., ASM International, 1999

8. L. Akesson, An Experimental and Thermodynamic Study of the Co-W-C System in the Temperature Range 1470–1700 K, *Science of Hard Materials,* R.K. Viswanadham, et al., Ed., Plenum Press, 1983, p 71–82

9. B.J. Nemeth, A.T. Santhanam, and G.P. Grab, *Proc. Tenth International Plansee Seminar,* Metallwerk Plansee GmbH, 1981, p 613–627

10. A.T. Santhanam, G.P. Grab, G.A. Rolka, and P. Tierney, An Advanced Cobalt-Enriched Grade Designed to Enhance Productivity, in *High Productivity Machining—Materials and Processes,* American Society for Metals, 1985, p 113–121

11. A.T. Santhanam, R.V. Godse, G.P. Grab, D.T. Quinto, K.E. Undercoffer, and P.C. Jindal, U.S. Patent 5,250,367, 5 Oct 1993

12. H.E. Exner, Qualitative and Quantitative Interpretation of Microstructures in Cemented Carbides, *Science of Hard Materials,* R. K. Viswanadham, et al., Ed., Plenum Press, 1983, p 233–259

13. J. Gurland, Application of Quantitative Microscopy to Cemented Carbides, *Practical Applications of Quantitative Metallography,* STP 839, J.L. McCall and J.H. Steele, Jr., Ed., ASTM, 1984, p 65–84

14. “Standard Test Methods for Determining Average Grain Size Using Semiautomatic and Automatic Image Analysis,” E 1382-97, ASTM International, June 1997, p 866

15. B. Roebuck, et al., “Measurement of WC Grain Size,” Report CMMT(A) 141, Issued by Natl. Phys. Lab (Teddington, U.K.), Jan 1999, p 2

16. H. Grewe, Structural Investigation on Hard Metals, *Prakt. Metallogr.,* Vol 5, 1969, p 411–419

17. W. Mader and K.F. Muller, Determination and Comparison of Structural Parameters of Hard Metal Alloys Using Electron and Optical Micrographs, *Prakt. Metallogr.,* Vol 5, 1968, p 616–625

18. W. Peter, E. Kohlhaas, and O. Jung, Revealing of Hard Metal Structures by Interference Vapor-Deposition, *Prakt. Metallogr.,* Vol 4, 1967, p 288–290

19. A. Doi, T. Nishikawa, and A. Hara, Ion-Etching Techniques for Microstructural Characterization of Cemented Carbides and Ceramics, *Science of Hard Materials,* R.K. Viswanadham, et al., Ed., Plenum Press, 1983, p 329–339

20. H. Gahm, S. Karagoz, and G. Kompek, Metallographic Methods for the Characterization of the Microstructure of Cemented Carbides, *Prakt. Metallogr.*, Vol 18, 1981, p 14–30

21. E.M. Vyger, Metallography and Microstructural Characterization of Some Hardmetal Grades by Optical and Electron Microscopy, *Prakt. Metallogr.*, Vol 19, 1982, p 592–604, 639–649

22. B. Egg, Experiences with Quantitative Automatic Scanning Electron Microscopy, *Prakt. Metallogr.*, Vol 22, 1985, p 78–87

23. D.T. Quinto, G.J. Wolfe, and M.N. Haller, Low-Z Element Analysis in Hard Materials, *Science of Hard Materials*, R.K. Viswanadham, et al., Ed., Plenum Press, 1983, p 947–971

A.T. Santhanam, Metallography of Cemented Carbides, *Metallography and Microstructures*, Vol 9, *ASM Handbook*, ASM International, 2004, p. 1067–1078

Metallography of Cemented Carbides

A.T. Santhanam, Kennametal, Inc.

Selected References

- Superhard Tool Materials, *Properties and Selection: Stainless Steels, Tool Materials, and Special-Purpose Metals*, Vol 3, *Metals Handbook*, 9th ed., American Society for Metals, 1980, p 448–465
- H.E. Exner, Physical and Chemical Nature of Cemented Carbides, *Int. Met. Rev.*, Vol 24 (No. 4), 1979, p 149–173
- A.T. Santhanam and D. T. Quinto, Surface Engineering of Carbide, Cermet, and Ceramic Cutting Tools, *Surface Engineering*, Vol 5, *ASM Handbook*, ASM International, 1994, p 900–908
- A.T. Santhanam, P. Tierney, and J.L. Hunt, Cemented Carbides, *Properties and Selection: Nonferrous Alloys and Special Purpose Materials*, Vol 2, *ASM Handbook*, ASM International, 1990, p 950–977

Laboratory Safety in Metallography, *Metallography and Microstructures*, Vol 9, *ASM Handbook*, ASM International, 2004, p. 1081–1090

Laboratory Safety in Metallography

George Vander Voort, Buehler Ltd.

Introduction

THE METALLOGRAPHIC LABORATORY is a relatively safe working environment; however, there are dangers inherent to the job. Included in these dangers is exposure to heat, acids, bases, oxidizers, and solvents. Specimen preparation devices, such as drill presses, shears, and cutoff saws, also present hazards. In general, these dangers can be minimized if the metallographer consults documents such as ASTM E 2014 (Standard Guide on Metallographic Laboratory Safety) and relevant Material Safety Data Sheets (MSDS) before working with unfamiliar chemicals. Common sense, caution, training in basic laboratory skills, a laboratory safety

program, access to safety reference books—these are some of the ingredients of a recipe for laboratory safety. Table 1 lists the main requirements for a comprehensive safety program.

Table 1 Elements of a comprehensive metallography laboratory safety plan

1. Emergency response **1. First responders** **2. Emergency phone numbers** **3. First aid** **4. Spills**
2. Chemical procurement, distribution, and storage **1. Material Safety Data Sheet management** **2. Labeling/storage**
3. Laboratory standard operating procedures **1. Handling chemicals** **2. Mixing chemicals** **3. Rules** **4. Hygiene**
4. Employee health and exposure **1. Personal protective equipment** **2. Monitoring of exposure levels** **3. Medical evaluations** **4. Additional protections for employees working with particularly hazardous substances (carcinogens, toxins)**
5. Disposal of hazardous materials **1. Etchants and chemicals** **2. Recirculating tanks** **3. Lubricants and abrasives**
6. Equipment use **1. Sectioning** **2. Mounting** **3. Grinding and polishing** **4. Electropolishing** **5. Etching**
7. Facility **1. Facility and equipment maintenance** **2. Housecleaning** **3. Fume hood air flow** **4. Fire extinguishers and fire protection** **5. Spill response** **6. Showers and eye washes**

7. **Air lines and filters**
8. **Plumbing**
9. **Electricals**

8. Employee training

1. **Safety**
2. **Indications and symptoms of exposure**
3. **Job functions**

9. Scheduled and documented safety inspections and meetings

Safe working habits begin with good housekeeping. A neat, orderly laboratory promotes safe working habits, while a sloppy, messy work area invites disaster. Good working habits include such obvious, common-sense items as washing the hands after handling chemicals or before eating. Simple carelessness can cause accidents. For example, failure to clean glassware after use can cause an accident for the next user. Another common problem is burns due to failure to properly clean acid spills or splatter.

Most reagents, chemical or electrolytic polishing electrolytes, and solvents should be used under a ventilation hood designed for use with chemicals. Many of these chemicals used in metallography can cause serious damage on contact. It is best to assume that all chemicals are toxic and that all vapors or fumes will be toxic if inhaled or will be damaging to the eyes. A hood will prevent the working area from being contaminated with these fumes. However, one will not be protected when one's head is inside the hood. In most cases, a protective plastic or shatterproof glass shield can be drawn across the front of the hood for further protection from splattering or any unexpected reactions.

All laboratories should be equipped with a shower and eyewash for emergency use. This equipment should be near the work area so that the injured can reach it quickly and easily. Fire alarms and fire extinguishers (CO_2 type) should be available and tested periodically. A good first aid kit and a chemical spill treatment kit should be readily available.

Laboratory Safety in Metallography, *Metallography and Microstructures,* Vol 9, *ASM Handbook,* ASM International, 2004, p. 1081–1090

Laboratory Safety in Metallography

George Vander Voort, Buehler Ltd.

Hazard Communication Standards

Material Safety Data Sheet. In order to satisfy the hazard communication standard of the Occupational Safety and Health Administration (OSHA), an MSDS is required to contain a certain minimum amount of information for compliance with the OSHA Regulation for Hazard Communication (Ref 1). OSHA form 174 has a suggested format that stipulates MSDS sections (Table 2). However, an MSDS can contain more information than that required by OSHA. For instance, the ANSI standard MSDS contains 16 sections, with more explicit headings:

- Chemical product and company identification
- Composition and information on ingredients
- Hazards identification
- First aid measures
- Firefighting measures
- Accidental release measures
- Handling and storage
- Exposure controls/personal protection
- Physical and chemical properties
- Stability and reactivity
- Toxicological information
- Ecological information
- Disposal considerations
- Transportion information
- Regulatory information
- Other information

Table 2 Essential Material Safety Data Sheet (MSDS) information and suggested format in accordance with Occupational Safety and Health Administration (OSHA) form 174

Identity
The chemical identity on the MSDS as it appears on the product label
Section I
This section includes the manufacturer's name, address, phone number, emergency number, date of preparation, and possibly the person who prepared the MSDS. It tells where to get more information, if necessary.
Section II Hazard ingredients/identity information
The hazardous components of the material are listed by specific chemical name. The recommended exposure limits, OSHA permissible exposure limit, and American Conference of Governmental Industrial Hygienists—Threshold Level Value are listed in this section.
Other common names may also appear, as well as the Chemical Abstracts Service (CAS) numbers and percentages of the component chemicals (optional). While the CAS registry number is not a requirement, it is recommended, because it is a unique identifier for chemicals that can be named using several nomenclatures.
OSHA defines a hazardous chemical as one that poses a physical hazard or a health hazard.
Chemicals that pose health hazards (either acute or chronic) include “carcinogens, toxic or highly toxic agents, reproductive toxins, irritants, corrosives, sensitizers, hepatotoxins, nephrotoxins, neurotoxins, agents which act on the hematopoietic system, and agents which damage the lungs, skin, eyes, or mucous membranes.”[(a)]

A chemical that poses a physical hazard can be "a combustible liquid, a compressed gas, explosive, flammable, an organic peroxide, an oxidizer, pyrophoric, unstable (reactive), or water-reactive"(a). Storage requirements will differ depending on the hazard presented by the material; for example, flammables are stored in a special grounded cabinet away from ignition sources. Other materials must be kept dry, some must be stored in the dark, and many chemicals must be separated from incompatibles.

Section III Physical/chemical characteristics

Where appropriate, the manufacturer will determine the substance boiling point, specific gravity, vapor pressure, melting point, vapor density, evaporation rate, solubility in water, and will list the physical appearance and odor of the substance. This information is important for storage, use, transport, and exposure considerations.

For example, if a low-boiling-point material is stored next to a heat source (or in sunlight), it might vaporize and pose a fire or explosion hazard.

Vapor pressure is an indicator of the volatility of the material, which is important with regard to flammability and explosivity. Volatile substances can generate significant amounts of vapor and exceed (health) exposure limits or pose a physical asphyxiation hazard. Respiratory protection is essential around volatiles.

Evaporation rates are reported as a ratio in relation to a given standard (usually *n*-butyl acetate).

Solubility in water (or a solvent) helps determine possible concentrations of solutions and levels of possible contamination.

Section IV Fire and explosion hazard data

The hazard data should include the flash point, flammable limits, extinguishing media, special fire-fighting procedures, and unusual fire and explosion hazards. Some manufacturers will include the National Fire Protection Association hazard classifications (health, fire, reactivity, and special measures) in this section.

The lower the flash point of a liquid material, the easier it is to ignite. Store such materials away from ignition sources. It is important to be aware of the flashpoint of a substance that will be used in or near a heat bath or heat source.

The flammable limits refer to the concentration of the chemical in air, above which is too oxygen deficient to burn and below which lacks sufficient fuel to burn. Concentrations of the chemical between these limits are flammable. It is not difficult to exceed the lower flammability limit of substances (i.e., solvents) when working in a confined or poorly ventilated space.

Firefighting measures and the appropriate fire extinguisher classification should be identified. The two most common types of extinguishers in a chemical laboratory are pressurized dry chemical type BC or ABC and carbon dioxide extinguishers. A specialized class D dry powder extinguisher is required for use on flammable metal fires. Water-filled extinguishers are not acceptable for use in chemical laboratories.

Section V Reactivity data

Reactivity data will contain information about the stability of the substance, the conditions to avoid that will make the substance unstable, the materials that are incompatible with the substance, any hazardous decomposition or byproducts, whether the substance can undergo hazardous polymerization, and the conditions that may cause polymerization.

It is obviously important to know incompatibilities when mixing chemicals and also when storing chemicals. Most accidents between incompatible materials occur when disposing or cleaning up chemicals. Mixtures of incompatible materials may present explosion hazards or toxic health hazards.

Unstable materials may decompose into other materials that are toxic, flammable, or explosive. Decomposition reactions can be highly exothermic (heat-generating), sometimes accelerating rapidly.

Hazardous polymerization is an undesirable exothermic reaction. Under the wrong circumstances, an exothermic reaction can ignite a fire or explosion.

Section VI Health hazard data

This section must contain the health hazards posed by the substance, the routes of entry for the hazard, carcinogeneity, signs and symptoms of exposure, medical conditions that can be aggravated by exposure, and emergency and first aid procedures. The Hazardous Material Information System ratings for health, fire, reactivity, and personal protection precautions are sometimes provided in this section.

Health hazards can be acute (adverse effects from one exposure) or chronic (cumulative effects) and can present danger to health in a number of ways:

The carcinogeneity of a substance (whether it is cancer-causing) is determined by the National Toxicology

Program and the International Agency for Research on Cancer.
An irritant is a substance that, on immediate, prolonged, or repeated contact with normal living tissue, will induce a local inflammatory reaction. Wear proper personal protection equipment (PPE) (such as gloves, goggles, aprons, or dust masks) that is effective for the kind of irritant being worked with.
Toxic materials (poisons) can cause serious injury or death. Avoid their use whenever possible. If they must be used, take process measures to limit their use and engineering controls to minimize hazards. Be aware of the signs of exposure and the appropriate first aid measures, and always wear appropriate PPE.
Teratogens are reproductive toxins and usually cause the most severe damage during the first three months of pregnancy.
OSHA defines *corrosive* as a chemical "that causes visible destruction of, or irreversible alterations in, living tissue by chemical action at the site of contact." Also referred to as caustics (acids and bases)
Sensitizers cause one to develop an allergic reaction in normal tissue after repeated exposure. Once sensitized to a particular chemical, even minimal exposure will cause symptoms, and the sensitization is usually a life-long effect.
Chronic exposure to hepatoxins can result in liver damage. Nephrotoxins damage the kidneys.
Neurotoxins affect the central nervous system and must be avoided due to the potential for long-lasting or permanent effects and death. Exposure can be acute or chronic. Institute proper engineering controls (such as fume hoods) to minimize the number of exposed workers, and wear appropriate PPE.
Section VII Precautions for safe handling and use
This section should contain the steps to be taken in case the material is released or spilled. It may also contain the waste disposal method and should contain any precautions relating to handling and storage, as well as any other precautions associated with the material. Typically, these recommendations are very general, because the disposal and spill response are very site-dependent. State regulations for disposal vary widely.
Section VIII Control measures
OSHA requires that PPE and engineering controls for protection against hazards be specified in this section, including respiratory protection, ventilation and/or exhaust, PPE, and hygienic practices.

Note: (Nonmandatory form) form approved Operations Manual Bulletin 1218-0072; OSHA form 174 complies with OSHA's Hazard Communication Standard, 29CFR 1910.1200 Z (Ref 1).

(a) Quotes are from (c) "Definitions" in 29CFR 1910 (Ref 1)

Hazard ratings of the National Fire Protection Association (NFPA) and the Hazardous Materials Identification System (HMIS) have three color-coded fields to indicate the flammability (red), health (blue), and reactivity (yellow) hazards associated with the material. The ratings range from 0 (least severe hazard) to 4 (most severe hazard).

The systems vary slightly in format; NFPA arranges the four rating fields in a diamond, and HMIS uses a stacked bar. The fourth (white) field addresses special handling precautions in the NFPA system and precautions for personal protection in the HMIS.

More important is that the hazard ratings may not agree between systems, even for the exact same chemicals. The NFPA ratings are intended for use in firefighting situations and are based on the assumption that fire is present. This assumption may alter the severity of the hazard ratings.

Reference cited in this section

1. "OSHA's Hazard Communication Standard," 29CFR 1910.1200, *Code of Federal Regulations*, Vol 29, Office of the Federal Register, National Archives and Records Administration

Laboratory Safety in Metallography, *Metallography and Microstructures,* Vol 9, *ASM Handbook,* ASM International, 2004, p. 1081–1090

Laboratory Safety in Metallography

George Vander Voort, Buehler Ltd.

Laboratory Equipment

Specimen preparation devices used in metallographic laboratories are generally quite safe to use. Information supplied by the manufacturer usually describes safe operating procedures. It is good laboratory practice to prepare a job safety analysis detailing potential hazards and describing the safe operating procedure for each piece of equipment. This information should be provided to all users, and it must be revised and reviewed periodically.

Band saws or abrasive cutoff saws are commonly used by metallographers. The cutting area of band saws is exposed and potentially dangerous. One's hands should never be used to guide the workpiece during cutting. A guiding device or block of wood should always be used between the workpiece and the hands. After cutting is completed, the saw should be turned off before pieces near the blade are removed. Samples should be handled carefully, because considerable heat can be generated. In addition, sharp burrs are often present, which should be carefully removed by filing or grinding. Abrasive cutoff saws are safer to use, because the cutting area is closed off during use. The chief danger is from flying pieces from a broken wheel. Fortunately, the closed cover contains these pieces within the cutting chamber. Wheel breakage usually occurs when the part is not firmly clamped in place or if excessive pressure is applied, a bad practice from the standpoint of specimen damage as well.

Dust produced during grinding of metals is always dangerous. For certain metals, such as beryllium, magnesium, lead, manganese, and silver, the dusts are extremely toxic. Wet grinding is preferred, both for dust control and for preventing thermal damage to the specimen. Bench grinders must be firmly mounted to prevent sudden movement. Care must be exercised to avoid grinding one's fingers or striking the edge of a grinding belt, which will cause painful lacerations. With nearly all materials, wet grinding is preferred and produces the best results. For routine handling of dangerous metals, grinding should be done wet under a ventilation hood. Waste must be handled carefully and disposed of properly. Radioactive materials require special remote-handling facilities and elaborate safety precautions.

A drill press is frequently used in the laboratory. Drilling holes in thin sections requires secure clamping; otherwise, the sample can be grabbed by the drill and spun around, inflicting serious lacerations. Hair, ties, and shirt cuffs can become tangled in a drill, inflicting serious injuries. Safety glasses should always be worn when using drill presses or when cutting or grinding. Mounting presses or laboratory heat treatment furnaces present potential burn hazards. Gloves should be worn when working with these devices. Modern mounting presses that cool the cured resin back to near room temperature dramatically reduce the potential for burns. It is a good practice to place a "*hot*" sign in front of a laboratory furnace when it is in use.

It is occasionally necessary to heat solutions during their preparation or use. Although Bunsen burners are commonly employed for this purpose, it is much safer to use a hot plate or water bath and thus avoid the use of an open flame. If a Bunsen burner is used, the flame should never be applied directly to a flask, beaker, or dish. Plain- or asbestos-centered wire gauze should always be placed between the flame and the container.

Laboratory Safety in Metallography, *Metallography and Microstructures,* Vol 9, *ASM Handbook,* ASM International, 2004, p. 1081–1090

Laboratory Safety in Metallography

George Vander Voort, Buehler Ltd.

Personal Protective Equipment

Metallographers must take certain precautions to ensure their personal safety. A laboratory coat is useful for protecting the operator's clothing and should be changed regularly and cleaned professionally. When handling caustics, a rubberized or plastic-coated apron provides better protection. Gloves should be worn when handling bulk samples, working with hot material, or using hazardous solutions. Lightweight surgeon's gloves are very popular, because the operator retains the ability to feel. Many metallographers wear these to protect their skin when mounting with epoxies and polishing with oxide suspensions. When using these gloves with chemicals, always inspect for holes, because they are easily punctured. Thick rubber gloves are often used for handling specimens during macroetching, chemical polishing, pickling, and so on. The gloves should always be checked first for small holes or cracks, because gloves can impart a false sense of security. The operator's hands generally perspire when using rubber gloves, and it is sometimes difficult to tell if the moisture is due solely to perspiration or to leakage. Safety glasses should be worn during processes that generate particulate matter. Goggles are appropriate for use with chemicals, and a chemical face shield is recommended when handling large quantities of hazardous liquids. The appropriate personal protective equipment will be specified on the MSDS for most laboratory chemicals and products.

Laboratory Safety in Metallography, *Metallography and Microstructures,* Vol 9, *ASM Handbook,* ASM International, 2004, p. 1081–1090

Laboratory Safety in Metallography

George Vander Voort, Buehler Ltd.

Chemicals, Storage, and Handling

Many of the chemicals used in metallography are toxic, corrosive, flammable, or potentially explosive. Therefore, purchase only small quantities that are likely to be used within a reasonably short time. Flammable solvents should be stored in fireproof steel cabinets. Acids and bases should be stored separately, again in fireproof steel cabinets. Strong oxidants must not be stored along with acids, bases, or flammable solvents.

Reagent-grade chemicals or solvents of highest purity are recommended. Although more expensive, the amounts used are small, and the gain in safety and reliability compensates for the cost difference. Chemicals may deteriorate during storage; only reasonably small quantities should be purchased. Exposure to light can accelerate deterioration of some chemicals. Hence, they should be stored in a closed metal cabinet.

Etchants. Most laboratories mix commonly used reagents in quantities of 250 to 1000 mL and then store them as stock reagents. Many reagents can be safely handled in this manner. It is best to store only those reagents that are used regularly. Glass-stoppered bottles are commonly used as stock reagent bottles. If these bottles are opened regularly, the stopper will not become “frozen.” However, if they are used infrequently, a frozen stopper often results. Holding the neck of the bottle under a stream of hot water will usually loosen the stopper. If thermal expansion does not free the stopper, it can be gently tapped with a piece of wood. Glass bottles with plastic screw-on tops can be used so long as the solution does not attack the plastic. These bottles are useful for holding solutions, such as nital, that can build up gas pressure within a tightly stoppered bottle. A small hole

can be drilled through the cap top to serve as a pressure relief vent. Tightly stoppered bottles of nital and some other solutions have exploded as the result of pressure buildup. Be certain that the reagent is safe to store, and store only small quantities. All bottles should be clearly labeled. Polyethylene bottles are required for etchants containing hydrofluoric acid, which attacks glass.

Most recipes for etchants or electrolytes list the ingredients by weight if they are solids and by volume if they are liquids. In a few cases, all amounts are given in weight percentages. In most cases, reagent compositions are not extremely critical. An ordinary laboratory balance provides adequate weighing accuracy, while graduated cylinders provide acceptable accuracy for volumetric measurements. These devices should be cleaned after use to prevent accidents to the next user. For weight measurements, a clean piece of filter paper or a cup should be placed on the balance pan to hold the chemical, to protect the pan surface, and to facilitate transfer to the mixing beaker. A large graduated beaker is usually employed for mixing solutions. When using hydrofluoric acid, all containers should be made of polyethylene.

With many etchants, the mixing order is important, especially when dangerous chemicals are used. When water is specified, distilled water should always be used, because most tap water contains minerals or may be chlorinated or fluorinated. Tap water can produce poor results or unexpected problems. Cold water should always be used, never warm or hot water, which can cause a reaction to become violent. In mixing, one should start with the solvents, such as water and alcohol, then dissolve the specified salts. A magnetic stirring device (Fig. 1) is of great value. Then, the dangerous chemicals, such as acids, should be added carefully and slowly while the solution is being stirred. Whenever sulfuric acid (H_2SO_4) is specified, it should be added last. It should be added slowly, while stirring, and it should be cooled, if necessary, to minimize heating. Never just pour one liquid into another (Fig. 2). If sulfuric acid is added to water without stirring, it can collect at the bottom of the beaker, and enough local heating can occur to throw the contents out of the beaker.



Fig. 1 Magnetic stirring plate with a magnetic bar for stirring, for use when mixing etchants. Slowly add the liquid ingredients to the solvent by dripping them down a glass stirring rod. If the solution is more dangerous than this one, wear protective gloves and use a face shield. If mixing generates substantial heat, it is a good practice to place a cooling jacket around the beaker.



Fig. 2 Illustration of a bad mixing practice. The acid ingredient was poured into an empty acid bottle, and the solvents were added without stirring or cooling. The solution may erupt in the metallographer's face at any moment. It is recommended to keep the hands clear of the area and to remove rings.

The literature contains references to a great many formulas for etchants, chemical polishes, and electrolytes that are potentially dangerous or extremely dangerous. Few of these references contain comments regarding safe handling procedures or potential hazards. Fortunately, metallographic applications involve small quantities of these solutions, and accidents do not usually produce catastrophic results. However, even with small solution volumes, considerable damage can be, and has been, done. Table 3 lists examples from the literature (Ref 2, 3, 4) of chemical polishing solutions, electrolytic polishing solutions, and etchants that have been involved in accidents. Table 4 lists a number of commonly used chemicals and incompatible chemicals.

Table 3 Chemical and electrolytic polishing solutions and etchants known to be dangerous

Solution	Use	Problems
5 parts lactic acid **5 parts HNO_3** **2 parts water** **1 part HF**	Chemical polishing solution for Zr	Lactic and nitric acids react autocatalytically. Explosion will occur if stored.
50 parts lactic acid **30 parts HNO_3** **2 parts HF**	Chemical polishing solution for Ta, Nb, and alloys	Same as above
3 parts perchloric acid	Electropolishing solution for Al	Mixture is unstable and can, and has, exploded with heating or in the presence of organic compounds, adding to the potential hazard.

1 part acetic anhydride		
60–90 parts perchloric acid **40–10 parts butyl cellosolve**	Electropolishing solution	Solution will explode at room temperature. Solutions with ≤30% $HClO_4$ will be safe if temperature is <20 °C (70 °F).
100 g CrO_3 **200 mL water** **700 mL acetic anhydride**	Electropolishing solution	CrO_3 was dissolved in water, cooled to approximately 20 °C (70 °F), and the acetic anhydride was added very slowing with stirring. The solution became warm to the touch. Approximately 20 s later, it erupted from the beaker.
1 part HNO_3 **2 parts methanol**	Electropolishing solution for Muntz (Cu-40%Zn) metal	Mixture is unstable and cannot be stored.
20 mL HF **10 mL HNO_3** **30 mL glycerol**	Etchant for Nb, Ta, Ti, V, Zr	This etchant is unstable. At 20 °C (70 °F), it reacted after 18 h. At 30–35 °C (85–95 °F), it reacted with violence after 8 h. At 100 °C (212 °F), it will react after 1 min.
20–30 mL HCl **10 mL HNO_3** **30 mL glycerol**	Etchant for Ni and stainless steels	Incidents occurred where a violent reaction resulted, producing NO_2 and a spray of acid after the etch was left standing for 2–3 h.
40 mL acetic acid **40 mL acetone** **40 mL HNO_3**	Etchant for Ni	A closed bottle exploded approximately 4 h after it was mixed. Solutions without the acetic acid also cannot be stored.
10 mL HNO_3 **10 mL acetic acid** **20 mL acetone**	Etchant	The solution reacted spontaneously approximately 2 min after mixing, with evolution of heat and fumes (nitrous and nitric oxides). The mixed acids were poured into the acetone. The beaker was externally cooled.
50 mL nitric acid **950 mL isopropyl alcohol**	Etchant	Mixtures have exploded violently after mixing or approximately 20 min after mixing.

Table 4 Some incompatible chemicals

Chemical	Use in metallography	Do not mix with the following
Acetic acid	Chemical polishing, electrolytic polishing	Chromic acid, glycol, hydroxol compounds, nitric acid, peroxides, permanganates
Acetone	Degreasing, cleaning, etchants	Concentrated solutions of nitric and sulfuric acids
Chromic acid	Electropolishing	Acetic acid, flammable liquids, glycerol
Hydrogen peroxide	Chemical polishing, etchants	Flammable liquids, organic materials
Nitric acid (conc.)	Chemical polishing, etchants	Acetic acid, chromic acid, flammable liquids, isopropyl alcohol
Perchloric acid	Electropolishing	Acetic anhydride, alcohol, some organics, oil, grease
Sulfuric acid	Etchants	Methyl alcohol, potassium chlorate, potassium perchlorate, and potassium permanganate

Solvents. Numerous organic solvents are used for cleaning or are ingredients in chemical or electrolytic polishing solutions or etchants, in which they are used to control ionization or the speed and mode of attack. Commonly employed solvents include water, acetone, ethyl ether, ethylene glycol, glycerol (glycerin), kerosene, petroleum ether, trichloroethylene, butyl cellosolve, and alcohols, such as amyl alcohol, ethanol, methanol, and isopropyl alcohol. Most are flammable, and their vapors can form explosive mixtures with air. They should be kept closed when not in use and should be stored in a cool place away from heat and open flames.

Acetone (CH_3COCH_3) is a colorless liquid with a fragrant, mintlike odor. It is volatile and highly flammable. It is an irritant to the eyes and the mucous membranes. Its vapor is denser than air, can travel along the ground, and can be ignited at a distance. Acetone can form explosive peroxides on contact with strong oxidizers, such as acetic acid, nitric acid, and hydrogen peroxide. It is an irritant to the eyes and respiratory tract and will cause the skin to dry and crack.

Butyl cellosolve ($HOCH_2CH_2OC_4H_9$), or ethylene glycol monobutyl ether, is a colorless liquid with a rancid odor that is used in electropolishing solutions. It is combustible and may form explosive peroxides. It is toxic in contact with the skin, can be absorbed through the skin, and can cause serious damage to the eyes and irritation to the skin and respiratory tract.

Carbitol ($C_2H_5OCH_2CH_2OCH_2CH_2OH$), or diethylene glycol monoethyl ether, is a colorless, viscous solvent that is compatible with water and is used in electropolishing solutions. It irritates the skin, eyes, mucous membranes, and upper respiratory tract and is harmful if inhaled or swallowed.

Ethylene glycol ($HOCH_2CH_2OH$) is a colorless, hygroscopic liquid with a sweet taste (but do not swallow, because it is poisonous) that reacts with strong oxidants and strong bases. It is slightly flammable. The substance irritates the eyes, skin, and respiratory tract.

Glycerol (glycerin) ($CH_2OHCHOHCH_2OH$) is a colorless or pale yellow, odorless, hygroscopic, syrupy liquid with a sweet, warm taste. It is relatively nontoxic and nonvolatile but can cause iritis (inflammation of the iris). It is combustible and a moderate fire hazard. Glycerol should never be used in anhydrous solutions containing nitric and sulfuric acids, because nitroglycerin can form. Glycerol should not be used with strong oxidizing agents, such as chromium trioxide and potassium permanganate, because an explosion may occur. Glycerol is often added to aqua regia (glyceregia). This mixture decomposes readily and should be discarded immediately after use. This etchant should not be allowed to stand for more than approximately 15 min after mixing.

Kerosene is occasionally employed in grinding samples and with diamond paste as a lubricant. Only the deodorized form should be used. It is flammable, but the vapors do not readily explode. Contact defattens the skin and can cause dermatitis, irritation, or infections.

Trichloroethylene ($CHCl:CCl_2$) is a stable, colorless liquid with a chloroform-like odor. Effective laboratory ventilation is necessary. At ambient temperatures, it is nonflammable and nonexplosive but becomes hazardous at higher temperatures. In the presence of strong alkalies, with which it can react, it can form explosive mixtures. In the presence of moisture, the substance can be decomposed by light to corrosive hydrochloric acid. It is probably carcinogenic to humans and is toxic when inhaled or ingested, which may cause acute poisoning.

Amyl alcohol ($CH_3(CH_2)_4OH$), or 1-pentanol, is a colorless liquid with a noxious odor. It is flammable, and the vapors may form explosive mixtures at elevated temperatures. The substance reacts violently with strong

oxidants and attacks alkaline metals. The fumes are irritating to the eyes, upper respiratory tract, and skin. The substance is toxic through ingestion, inhalation, or absorption through the skin.

Ethyl alcohol (CH_3CH_2OH), or ethanol, is a colorless, inoffensive solvent commonly used in metallography. Ethanol is miscible with water and rapidly absorbs up to 5% water from the air. The denatured version is less expensive, contains 5% absolute methanol, and is suitable for any recipe requiring ethyl alcohol. It is a dangerous fire hazard, and its vapors are irritating to the eyes and upper respiratory tract. High concentrations of its vapor can produce intoxication. Because ethanol is completely burned in the body, it is not a cumulative poison like methanol.

Methyl alcohol (CH_3OH) is an excellent, nonhygroscopic solvent, but it is a cumulative poison. Ingestion, inhalation, or absorption through the skin in toxic levels can damage the central nervous system, kidneys, liver, heart, and other organs. Blindness has resulted from severe poisoning. It is particularly dangerous because repeated low-level exposures can also cause acute poisoning as a result of accumulation. Thus, whenever possible, ethanol should be used. When using methanol, always work under a ventilation hood. Mixtures of methanol and sulfuric acid can form dimethyl sulfate, which is extremely toxic. Solutions of methanol and nitric acid are more stable than mixtures of nitric acid and higher alcohols.

Isopropyl alcohol [$CH_3CH(OH)CH_3$], also known as 2-propanol, is a clear, colorless liquid that, like ethanol, does not accumulate in the body, although it does have a strong narcotic effect. It is a flammable liquid and a dangerous fire hazard. Metallographers have used it as a substitute for ethanol, but isopropyl alcohol has quite different characteristics and should not be used. Fatal injuries and explosions have been reported due to its use.

Acids. Inorganic and organic acids are common constituents in chemical and electrolytic polishing solutions and in etchants. The inorganic or mineral acids, including the very familiar acids such as hydrochloric, nitric, perchloric, phosphoric, and sulfuric, are highly corrosive and poisonous. They should be stored in a cool, well-ventilated location away from potential fire hazards and, of course, away from open flames. They should not be stored in a location that receives direct sunlight. When the pure acids contact metals, most liberate hydrogen gas—a fire and explosion hazard. The organic acids are naturally occurring substances in sour milk, fruits, and plants and include the following acids: acetic, lactic, citric, oxalic, and tartaric.

Hydrochloric acid (HCl), commonly used in metallography, is a colorless gas or fuming liquid with a sharp, choking odor. It is very dangerous to the eyes and irritating to the nose and throat. It attacks the skin strongly, causing severe burns.

Nitric acid (HNO_3), also commonly used in metallography, is a colorless or yellowish fuming liquid, highly toxic, and dangerous to the eyes. If it contacts organic material or other easily oxidizable materials, it can cause fires and possibly explosions. When it reacts with other materials, toxic oxides of nitrogen are produced. The oxides, which vary with the conditions, include nitrous acid, nitrogen dioxide, nitric oxide, nitrous oxide, and hydroxylamine. A commonly encountered problem involves pouring nitric acid into a graduated cylinder that contains some methanol or ethanol from prior use. The brown fumes given off are quite harmful. Mixtures of nitric acid and alcohols higher than ethanol should not be stored. Mixtures of concentrated nitric and sulfuric acids are extremely dangerous, while strong mixtures of nitric acid and glycerin or glycols can be explosive. Aqua regia, a mixture of one part nitric acid and two to four parts hydrochloric acid, forms several products, including nitrosyl chloride, an exceptionally toxic gas. Aqua regia is a popular etchant but must be used with care under a hood.

Ethanol with additions of up to 3% nitric acid (nital) can be safely mixed and stored in small quantities. Higher concentrations result in pressure buildup in tightly stoppered bottles. Explosions of 5% nitric acid in ethanol have occurred as a result of failure to relieve the pressure. If higher concentrations are desired, they can be mixed daily, placed in an open dish, and used safely. Discard the etchant at the end of the day. Mixtures of methanol with up to 5% nitric acid are safe to use and store in small quantities. Mixtures of methanol with more than 5% nitric acid are subject to violent decomposition if heated. Mixtures of 33% nitric acid in methanol have decomposed suddenly and violently.

Never add nitric acid to isopropyl alcohol. Anderson (Ref 2) reported that a liter bottle of 5% nitric acid in isopropyl alcohol was mixed and placed in a cabinet. Although this had been done many times in the past without problems, 20 min later, the bottle exploded, destroying the cabinet, other stored bottles, and throwing debris up to 6 m (20 ft) away. Anderson (Ref 2) also reported that a metallographer was pouring a freshly mixed liter of 5% nitric acid in isopropyl alcohol into another bottle when it exploded. The person died within 3 h without being able to tell anyone what happened. As with the other explosion, this same procedure had been

performed many times previously without mishap. Anderson recommends avoiding the use of isopropyl alcohol completely.

Most metallographers consider nital to be very safe to use, and indeed it is. However, even with such an apparently safe solution, one can have accidents. One such accident occurred when an employee, not a skilled metallographer, was replenishing a stock of 5% nitric acid in ethanol using a procedure that he had claimed to have performed many times previously (he was not taught the safe way to mix nital, because it was a union chemist's job to mix nital, i.e., not his job). The worker began by adding the desired volume of concentrated nitric acid into the container that contained a small residual amount of stale 5% nital. To his surprise, the contents began boiling and spewing out of the container, along with dense, brown fumes. The acid splashed the worker, resulting in burns on his forehead, face, and eyes. The small amount of aged nitric acid solution (the concentration may have been increased due to evaporation of the alcohol), present in the container when the fresh acid was added, created a dangerous chemical reaction. An experiment also showed that a similar reaction can occur when nitric acid is poured into a graduated cylinder containing only remnants of ethanol or methanol. If the employee had added alcohol to the container first, the accident would have been avoided.

Sulfuric acid (H_2SO_4) is a colorless, oily liquid that is highly corrosive, a strong oxidizing agent, and dangerously reactive. It reacts violently with bases and is corrosive to most metals, forming flammable/explosive hydrogen gas. It reacts violently with water and organic materials, with the evolution of heat. Upon heating, toxic sulfur oxides are formed. One should add sulfuric acid very slowly to water, with constant stirring. If added without stirring, it will produce a pocket of steam in the bottom of the vessel, throwing the contents out of the vessel. Concentrated sulfuric acid can cause severe, deep burns on contact with the skin, and permanent vision loss on contact with the eyes. Tissue is destroyed by the dehydrating action of the acid. Lungs may be affected by long-term or chronic exposure to its aerosol. Skin lesions, tooth erosion, and conjunctivitis are other long-term effects.

Hydrofluoric acid (HF) is a clear, colorless, fuming liquid or gas with a sharp, penetrating odor. It is very dangerous to the eyes, skin, and upper respiratory tract. The substance can be absorbed into the body by inhalation, through the skin, and by ingestion. A harmful concentration of the gas in air can be reached quickly, making it very dangerous to handle. Exposure by ingestion, inhalation, or contact can be fatal. Undissociated HF poses a unique threat in that it can destroy soft tissues and result in decalcification of the bone. Moreover, the effects may be delayed. Laboratories where HF is used should stock an antidote kit to be used in case of exposure. Although it is a relatively weak mineral acid, HF will attack glass or silicon compounds and should be measured, mixed, and stored in polyethylene vessels (see the section “Safety Precautions for Concentrated HF” in this article). Hydrofluoric acid reacts with many compounds, including metals, and will liberate explosive hydrogen gas.

Orthophosphoric acid (H_3PO_4), a colorless, thick liquid or hygroscopic crystal, is a medium-strong acid. It is corrosive to the skin, eyes, and respiratory tract. Phosphoric acid decomposes on contact with alcohols, aldehydes, cyanides, sulfides, ketones, and can react with halogenated organic compounds, forming organophosphorus nerve-gas-type compounds that are extremely toxic. It reacts violently with bases and will generate hydrogen gas when it reacts with metals.

Perchloric acid ($HClO_4$) is a colorless, fuming, hygroscopic liquid. It is extremely unstable in concentrated form and may explode by shock or concussion when dry or drying, so commercially available perchloric acids come in concentrations of 65 to 72%. In this form, contact with perchloric acid will cause irritation and burns, while its fumes are highly irritating to the mucous membranes. Contact with organic or other easily oxidized material can form highly unstable perchlorates, which can ignite and cause explosions. Regular use of perchloric acid requires that the ventilation system must be specifically designed and maintained for perchloric acid. Special fume hoods with a waterfall-type fume washer will remove the perchlorate fumes before they can enter the exhaust system.

Perchloric acid is very useful in electropolishing solutions. However, never electropolish samples mounted in phenolic (Bakelite, Georgia-Pacific) or other plastics with perchloric acid solutions, because explosions can result. The mixture of perchloric acid and acetic anhydride, which was developed by P.A. Jacquet, is difficult to prepare and highly explosive. Jacquet has reviewed the accidents involving perchloric acid and has described safety procedures (Ref 5). The worst accident occurred on February 20, 1947, in an electroplating factory in Los Angeles. In this accident, 17 people were killed and 150 were injured (Ref 4). Médard, Jacquet, and Sartorius have prepared a ternary diagram showing safe compositions of perchloric acid, acetic anhydride, and water (Fig. 3). Anderson, however, states that accidents have still occurred with solutions in the “safe” region

of this diagram (Ref 2). Thus, electropolishing solutions composed of perchloric acid and acetic anhydride are not recommended. Indeed, many companies forbid the use of such mixtures, and some cities have banned their use. Electropolishing solutions of perchloric acid and alcohol, with or without organic additions, and mixtures of perchloric acid and glacial acetic acid are safe to use. Nevertheless, in using these "safe" mixtures, one should follow the formula instructions carefully, mix only small quantities, keep the temperature under control, and avoid evaporation. These solutions should not be stored.

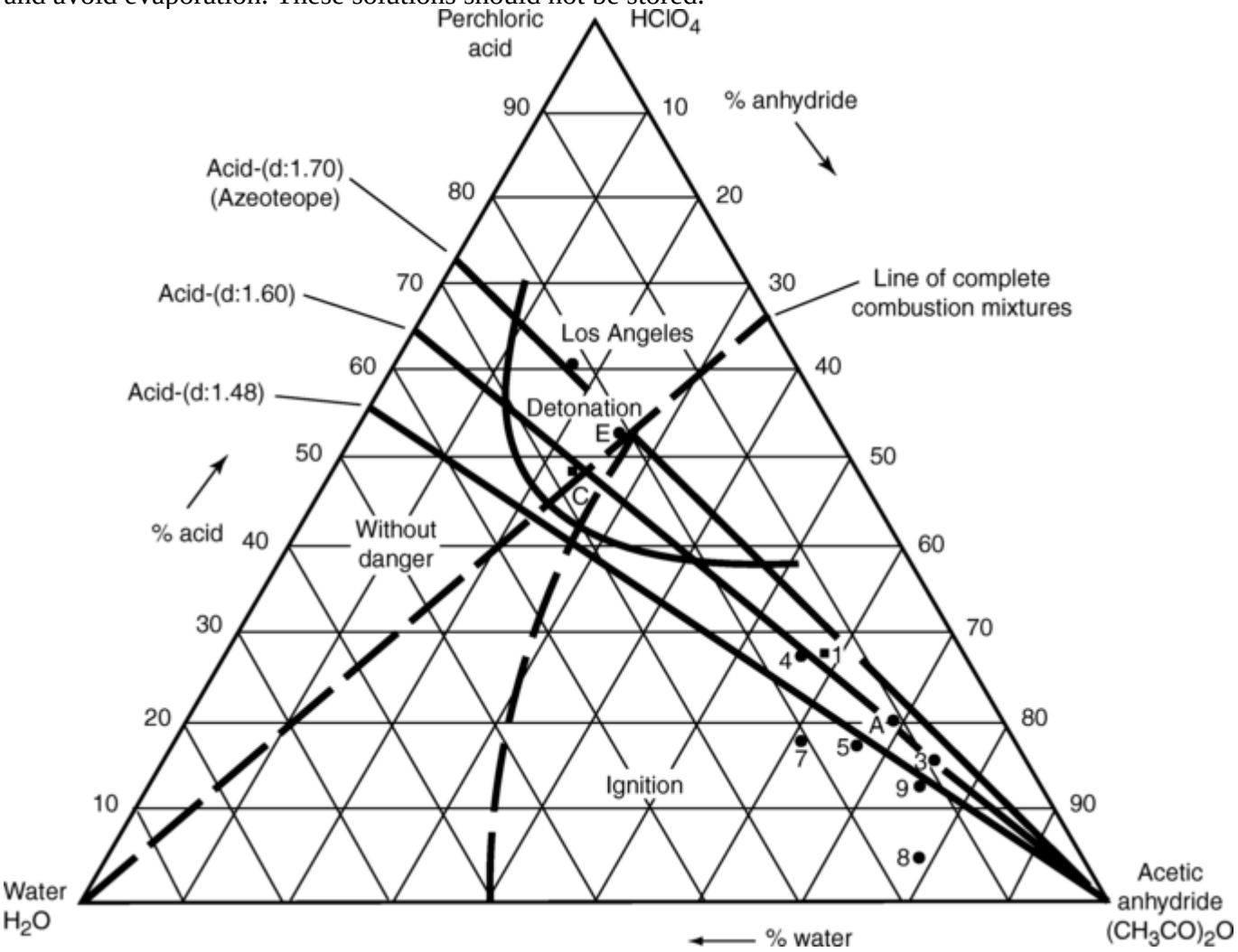

Fig. 3 Diagram developed by Médard, Jacquet, and Sartorius showing safe (A and 1 to 9) nonexplosive electropolishing solutions and explosive (C, E, and Los Angeles) compositions of perchloric acid, acetic anhydride, and water (brought in by the perchloric acid but not corrected for the effect of acetic anhydride). The Los Angeles accident occurred in an electroplating factory on February 20, 1947 (Ref 4).

Mixtures of acetic acid and 5 to 10% perchloric acid have been commonly used to electropolish iron-base alloys and are reasonably safe. Do not use these solutions to electropolish bismuth, arsenic, or tin, because explosions have occurred. Anderson suggests that arsenic, antimony, and tin may also be incompatible with perchloric electrolytes (Ref 2). Do not store these electrolytes for more than a few days. Discard them when they become colored by dissolved metallic ions (from electropolishing). Always keep these solutions cool; increasing the temperature increases the oxidizing power of perchloric acid.

Comas et al. have studied the hazards associated with mixtures consisting of butyl cellosolve and from 10 to 95% of 70% perchloric acid (Ref 6). Mixtures with 60 to 90% acid were explosive at room temperature. Acid concentrations of 30% or less were inflammable but were judged to be safe to use as long as the operating temperature does not exceed 20 °C (70 °F).

Acetic acid (CH_3COOH) is a clear, colorless liquid with a pungent odor. It is a weak acid that reacts with strong oxidizers, bases, and metals. It is flammable and not easily ignited, although when heated, it releases vapors that can be ignited and can travel some distance to an ignition source. Contact with the skin results in serious burns. Inhalation of the fumes irritates the mucous membranes. Anderson states that acetic acid is a good

solvent for nitric acid, and that a 50% solution can be prepared, but not stored, without danger (Ref 2). Lewis and Sax, however, state that mixtures of nitric and acetic acids are dangerous (Ref 7).

Acetic anhydride [$(CH_3CO)_2O$], or acetic oxide, is a colorless liquid with a very strong acetic odor. It can cause irritation and severe burns to the skin and eyes. Acetic anhydride decomposes on heating, producing toxic fumes. It reacts violently with boiling water, steam, strong oxidants (specifically, sulfuric acid), alcohols, amines, strong bases, and others. It attacks metals and is very corrosive, especially in the presence of water or moisture. It is extremely flammable and should be avoided. The electrolytic polishing mixtures of acetic anhydride and perchloric acid (4:1 to 2:1 mixtures) developed by Jacquet, as mentioned previously, are exceptionally dangerous and should never be used. Dawkins (Ref 8) reported an accident involving a mixture of chromium trioxide and acetic anhydride that had been used for electropolishing (Table 3).

Citric acid [$C_3H_4(OH)(COOH)_3 \cdot H_2O$] comes as colorless, odorless crystals that are water soluble. It is an irritant to the skin, eyes, and respiratory tract, and no unusual problems are encountered except for occasional allergic reactions.

Lactic acid ($CH_3CHOHCOOH$) is a yellow or colorless, thick liquid. It is damaging to the eyes.

Oxalic acid ($COOHCOOH \cdot 2H_2O$) comes as transparent, colorless crystals. It is poisonous if ingested and is irritating to the upper respiratory tract and digestive system if inhaled. Skin contact produces caustic action and will discolor and embrittle the fingernails. It is not compatible with nitric acid, because it reacts violently with strong oxidants. It can also form explosive compounds due to reactions with silver.

Picric acid [$(NO_2)_3C_6H_2OH$], or 2,4,6-trinitrophenol, comes as yellow crystals that are wet with 10 to 350% water. When picric acid is dry, it is a dangerous explosive. It is toxic and stains the skin. It is incompatible with all oxidizable substances. Picrates, which are metal salts of picric acid, are explosive. When picrates are dry, they can detonate readily, possibly spontaneously. Purchase in small quantities, keep it moist, and store it in a safe, cool place. If it starts to dry out, add a small amount of water to keep it moist. The maximum solubilities of picric acid in water and in ethanol are approximately 1.3 and 8 g/100 mL, respectively. Picral can be stored safely. During use, the solution should not be allowed to dry out. The etching residue should be discarded at the end of the day to avoid potential explosions.

Bases, such as ammonium hydroxide (NH_4OH), potassium hydroxide (KOH), and sodium hydroxide (NaOH), are commonly used in metallography, chiefly in etchants.

Ammonium hydroxide is a colorless liquid with a strong, obnoxious odor. Solutions are extremely corrosive and irritating to the skin, eyes, and mucous membranes. It reacts exothermically with sulfuric acid and other strong mineral acids, producing boiling solutions.

Sodium and potassium hydroxides are strong bases, available as white deliquescent pellets that are soluble in water. They can rapidly absorb carbon dioxide and water from the air. Solutions stored in flasks with ground stoppers may leak air and freeze the stoppers, making reopening difficult. Dissolving NaOH or KOH in water will generate considerable heat. Do not dissolve either in hot water. Never pour water onto these hydroxides; always add the pellets slowly to the water. Alkali metal hydroxides react violently with acid and are corrosive in moist air to metals such as zinc, aluminum, tin, and lead, forming flammable/explosive hydrogen gas. They are very corrosive to the skin, eyes, and respiratory tract. Long-term exposure may lead to dermatitis. Potassium hydroxide is somewhat more corrosive than sodium hydroxide.

Other Chemicals. Hydrogen peroxide (H_2O_2) is available as a liquid in concentrations of either 3 or 30%. The 3% solution is reasonably safe to use, while the 30% solution is a very powerful oxidant whose effect on the skin is approximately as harmful as that produced by contact with sulfuric acid. Hydrogen peroxide by itself is not combustible, but if brought in contact with combustible materials, it can produce violent combustion. Hydrogen peroxide is very damaging to the eyes. Because the release of oxygen can cause high pressures to develop within the container, the container caps are vented.

Bromine (Br_2), a fuming, reddish-brown liquid with a pungent, suffocating odor, is commonly used in deep-etching solutions. It is very corrosive, reacting violently with easily oxidized substances, including some metals. Bromine is a dangerous liquid that should only be handled by well-qualified personnel. Its vapors are extremely irritating to the eyes, skin, and mucous membranes. Skin contact produces deep, penetrating burns that are slow to heal. Contact with organic matter can cause fires.

Chromic acid (H_2CrO_4) is formed when chromium trioxide (CrO_3) is dissolved in water. Chromium trioxide is used in electropolishing solutions (see the previous comment and Table 3 about the explosive nature of mixtures with acetic anhydride). Dilute aqueous solutions are widely used for attack polishing. It is a powerful

oxidant; always wear gloves when using it for attack polishing, or use automatic devices and avoid contact potential. Chronic or long-term inhalation exposure may produce asthmalike reactions.

Potassium permanganate ($KMnO_4$), a black crystalline powder, is a powerful oxidant used in etchants. It is a dangerous fire and explosion hazard, especially when in contact with organic materials. Ingestion produces serious damage. Potassium permanganate and sulfuric acid should never be mixed together, because a violent explosion can result.

Potassium dichromate ($K_2Cr_2O_7$), a bright-orange crystalline powder, is another powerful oxidant that is also used in etchants. Contact can cause ulceration of the hands, severe damage to nasal tissue, or asthma and allergies with long-term exposure.

Cyanide compounds are occasionally used in metallographic applications. Potassium cyanide (KCN) and sodium cyanide (NaCN) are extremely dangerous and highly toxic. Exposure by eye or skin contact or by ingestion is fatal. The vapors of NaCN and KCN are intensely poisonous. They are particularly hazardous when brought in contact with acids or acid fumes because of liberation of hydrogen cyanide, which is extremely toxic and highly flammable. Potassium ferricyanide ($K_3Fe(CN)_6$), a ruby-red crystalline powder and an ingredient in Murakami-type reagents, is poisonous but stable and reasonably safe to use.

A number of nitrates, such as ferric nitrate [$Fe(NO_3)_3 \cdot 6H_2O$], lead nitrate [$Pb(NO_3)_6$], and silver nitrate ($AgNO_3$), are employed by metallographers. Because they are powerful oxidizers, they pose a dangerous fire hazard, especially when in contact with organic materials. They may evolve toxic fumes, such as oxides of nitrogen and lead, and are poisonous and corrosive to the eyes, skin, and respiratory tract.

References cited in this section

2. R.L. Anderson, “Safety in Metallographic Laboratory,” Westinghouse Research Laboratory Science Paper 65-1P30-METLL-P2, 29 March 1965

3. G.F. Vander Voort, *Metallography: Principles and Practice,* McGraw-Hill, 1984; reprinted by ASM International, 1999, p 148–159

4. R.C. Nester and G.F. Vander Voort, Safety in the Metallographic Laboratory, *Standard. News,* Vol 20, May 1992, p 34–39

5. P.A. Jacquet, The Safe Use of Perchloric-Acetic Electropolishing Baths, *Met. Finish.,* Vol 47, 1949, p 62–69

6. S.M. Comas, R. Gonzalez Palacin, and D. Vassallo, Hazards Associated with Perchloric Acid-Butylcellosolve Polishing Solutions, *Metallography,* Vol 7, 1974, p 47–57

7. R.J. Lewis and N.I. Sax, *Dangerous Properties of Industrial Materials,* 10th ed., Wiley-Interscience, 2000

8. A.E. Dawkins, Chromic Acid-Acetic Anhydride Explosion, *J. Iron Steel Inst.,* Vol 182, 1956, p 388

Conclusions

In general, the metallographic laboratory is a reasonably safe environment. However, depending on the materials being prepared, dangerous situations can arise. Some hazards, such as the preparation of radioactive or reactive metals, are quite obvious, while others are not. In the preceding discussion, some of the potential hazards that can be encountered are summarized; others undoubtedly exist that are not covered.

Most accidents can be prevented by simple common-sense rules. It is best to assume that all metal dust and all chemicals are hazardous. Inhalation of dust and fumes, ingestion, or bodily contact should be avoided. Personal protective equipment is very useful, but it should not be used as a substitute for good laboratory equipment. The use of such equipment does not guarantee freedom from injury.

The metallographic literature contains many references to the use of dangerous materials, often without any mention of the dangers involved or safe handling procedures. This is unfortunate, because the unwary may be injured. Many are tempted to experiment when a recommended procedure does not work as claimed. The development of electrolytes, chemical polishing agents, or etchants should be left to those who are fully versed in the potential dangers. Metallographic laboratories should have some of the referenced safety publications (see Selected References) readily available in the laboratory, and these safety publications should be consulted when working with new or infrequently used materials.

Laboratory Safety in Metallography, *Metallography and Microstructures,* Vol 9, *ASM Handbook,* ASM International, 2004, p. 1081–1090

Laboratory Safety in Metallography

George Vander Voort, Buehler Ltd.

Acknowledgment

The author thanks Paula A. Didier, Harley-Davidson, for the information regarding MSDS sheets and Timothy C. Eck, Alcoa, for the information on HF.

Laboratory Safety in Metallography, *Metallography and Microstructures,* Vol 9, *ASM Handbook,* ASM International, 2004, p. 1081–1090

Laboratory Safety in Metallography

George Vander Voort, Buehler Ltd.

References

1. "OSHA's Hazard Communication Standard," 29CFR 1910.1200, *Code of Federal Regulations,* Vol 29, Office of the Federal Register, National Archives and Records Administration

2. R.L. Anderson, "Safety in Metallographic Laboratory," Westinghouse Research Laboratory Science Paper 65-1P30-METLL-P2, 29 March 1965

3. G.F. Vander Voort, *Metallography: Principles and Practice,* McGraw-Hill, 1984; reprinted by ASM International, 1999, p 148–159

4. R.C. Nester and G.F. Vander Voort, Safety in the Metallographic Laboratory, *Standard. News,* Vol 20, May 1992, p 34–39

5. P.A. Jacquet, The Safe Use of Perchloric-Acetic Electropolishing Baths, *Met. Finish.,* Vol 47, 1949, p 62–69

6. S.M. Comas, R. Gonzalez Palacin, and D. Vassallo, Hazards Associated with Perchloric Acid-Butylcellosolve Polishing Solutions, *Metallography,* Vol 7, 1974, p 47–57

7. R.J. Lewis and N.I. Sax, *Dangerous Properties of Industrial Materials,* 10th ed., Wiley-Interscience, 2000

8. A.E. Dawkins, Chromic Acid-Acetic Anhydride Explosion, *J. Iron Steel Inst.,* Vol 182, 1956, p 388

Laboratory Safety in Metallography, *Metallography and Microstructures,* Vol 9, *ASM Handbook,* ASM International, 2004, p. 1081–1090

Laboratory Safety in Metallography

George Vander Voort, Buehler Ltd.

Selected References

Web sites

- "International Chemical Safety Cards," The National Institute for Occupational Safety and Health/Centers for Disease Control and Prevention, http://www.cdc.gov/niosh/ipcsneng/nengsyn.html
- "Laboratory Chemical Safety Summaries," HHMI Laboratory Safety Program, http://www.hhmi.org/research/labsafe/lcss/lcss.html
- "Right to Know Hazardous Substance Fact Sheets," New Jersey Department of Health and Senior Services, http://www.state.nj.us/health/eoh/rtkweb/rtkhsfs.htm

Books

- G.D. Clayton and F.E. Clayton, Ed., *Patty's Industrial Hygiene and Toxicology, Part D: Toxicology,* 4th ed., Wiley-Interscience, 1994
- L.J. DiBerardinis et al., *Guidelines for Laboratory Design: Health and Safety Considerations,* 3rd ed., Wiley-Interscience, 2001
- A.K. Furr, *CRC Handbook of Laboratory Safety,* 5th ed., CRC Press, 2000
- A. Fuscaldo et al., Ed., *Laboratory Safety: Theory and Practice,* Academic Press, 1980
- E. Gershey, A. Wilkerson, and E. Party, *Laboratory Safety in Practice,* Van Nostrand Reinhold, 1991

- C.A. Kelsey and A.F. Gardner, Ed., *Radiation Safety for Laboratory Technicians,* Warren H. Green, Inc., 1983
- R.J. Lewis, Sr., *Hawley's Condensed Chemical Dictionary,* 14th ed., Wiley, 2001
- R.J. Lewis and N.I. Sax, *Dangerous Properties of Industrial Materials,* 10th ed., Wiley-Interscience, 2000
- S.B. Pal, Ed., *Handbook of Laboratory Health and Safety Measures,* 2nd ed., Kluwer Academic, 1991
- *Prudent Practices in the Laboratory: Handling and Disposal of Chemicals,* National Academy Press, 1995.
- S.R. Rayburn, *The Foundations of Laboratory Safety,* Brock-Springer Series in Contemporary Bioscience, Springer-Verlag, 1989
- "Standard Guide on Metallographic Laboratory Safety," E 2014, ASTM International
- P. Urben and L. Bretherick, *Bretherick's Handbook of Reactive Chemical Hazards,* 6th ed., Butterworth-Heinemann, London, 1999
- N. Van Houten, *Laboratory Safety Standards for Industry, Research, Academe,* Sci. Tech. Pubs., 1990
- G. Wesenberg, N. Proctor, and J. Hughes, *Proctor and Hughes' Chemical Hazards in the Workplace,* 4th ed, Wiley, 1996

Grit Sizes and Grain Size Conversions, *Metallography and Microstructures,* Vol 9, *ASM Handbook,* ASM International, 2004, p. 1093–1093

Grit Sizes and Grain Size Conversions

Table 1 Conversion of average grain intercept length (microns) to ASTM number

ASTM No.	Average intercept	ASTM No.	Average intercept	ASTM No.	Average intercept	ASTM No.	Average intercept
14.0	2.5	10.8	7.6	7.6	22.9	4.3	72
13.9	2.6	10.7	7.8	7.5	23.7	4.2	74
13.8	2.7	10.6	8.1	7.4	24.4	4.1	77
13.7	2.8	10.5	8.4	7.3	25.4	4.0	80
13.6	2.9	10.4	8.7	7.2	26.3	3.9	83
13.5	3.0	10.3	9.0	7.1	27.2	3.8	86
13.4	3.1	10.2	9.3	7.0	28.2	3.7	89
13.3	3.2	10.1	9.6	6.9	29.2	3.6	92
13.2	3.3	10.0	10.0	6.8	30.3	3.5	95
13.1	3.4	9.9	10.3	6.7	31.3	3.4	98
13.0	3.5	9.8	10.7	6.6	32.4	3.3	102
12.9	3.7	9.7	11.1	6.5	33.6	3.2	105
12.8	3.8	9.6	11.5	6.4	34.7	3.1	109
12.7	3.9	9.5	11.9	6.3	35.9	3.0	113
12.6	4.1	9.4	12.3	6.2	37.2	2.9	117
12.5	4.2	9.3	12.7	6.1	38.5	2.8	121
12.4	4.3	9.2	13.2	6.0	39.9	2.7	125
12.3	4.5	9.1	13.6	5.9	41.3	2.6	130
12.2	4.7	9.0	14.1	5.8	42.8	2.5	134
12.1	4.8	8.9	14.6	5.7	44.3	2.4	139
12.0	5.0	8.8	15.1	5.6	45.8	2.3	144
11.9	5.2	8.7	15.6	5.5	47.4	2.2	149
11.8	5.4	8.6	16.2	5.4	49.1	2.1	154
11.7	5.5	8.5	16.8	5.2	53	2.0	160
11.6	5.7	8.4	17.3	5.1	55	1.8	171
11.5	5.9	8.3	18.0	5.0	56	1.6	183
11.4	6.1	8.2	18.6	4.9	58	1.4	196
11.3	6.4	8.1	19.3	4.8	60	1.2	210
11.2	6.6	8.0	20.0	4.7	63	1.0	225
11.1	6.8	7.9	20.6	4.6	65	0.5	268
11.0	7.1	7.8	21.4	4.5	67	0	313
10.9	7.3	7.7	22.1	4.4	69	00	453

Table 2 Grit sizes for metallographic grinding papers

European grit No. (FEPA)	U.S. grit No. (ANSI/CAMI)	Approximate particle size, μm
Standard sizes		
P-60	60	250
P-80	…	180
P-120	120	125
P-180	180	75
P-220	…	63
	240	59
P-320	…	46
	320	41
P-500	…	30
	400	26
P-800	…	22
P-1000	…	18
P-1200	600	15
Finer sizes		
P-2400	800	8
P-4000	1200	3

FEPA, Federation of European Producers of Abrasives; ANSI, American National Standards Institute; CAMI, Coated Abrasives Manufacturing Institute

Tables of Chemicals and Etchants, *Metallography and Microstructures*, Vol 9, *ASM Handbook*, ASM International, 2004, p. 1094–1114

Tables of Chemicals and Etchants

Table 1 List of chemicals

Before using any chemicals, Material Safety Data Sheets (MSDS) should be reviewed.

Description	Formula	Hazards	Remarks
Acetic acid ≤96%	CH_3COOH	Corrosive, slightly flammable	Liquid: colorless aqueous solution, pungent smell, reacts violently with alkaline solutions; very hygroscopic; density, 1.06 g/cm^3
Acetone	$CO-(CH_3)_2$	Highly flammable (<21 °C, or 70 °F), irritating	Liquid: colorless; density, 0.79 g/cm^3
Aluminum chloride	$AlCl_3$	Corrosive	Crystalline: colorless to pale yellow; very hygroscopic: fuming when exposed to humid air, forming HCl; density, 2.46 g/cm^3; violent to explosion-like reaction with water and

Description	Formula	Hazards	Remarks
			alcohol
Ammonia	NH_3	Poison, corrosive, irritating	Gaseous: becomes liquid in pressure vessels, pungent smell; density, 0.235 g/cm^3; explosive with oxidizing gases
Ammonium acetate	CH_3COONH_4	…	Crystalline: white; hygroscopic; density, 1.171 g/cm^3
Ammonium chloride (salmiac)	NH_4Cl	Light poison, irritating	Crystalline: white, stable in air, salty/bitter taste; density, 1.52 g/cm^3
Ammonium citrate	$C_6H_{14}N_2O_7$ $(NH_4)_2C_6H_6O_7$	…	Crystalline: white; density, 1.48 g/cm^3
Ammonium ferrous sulfate (Mohr's salt)	$(NH_4)_2Fe(SO_4)_2{\cdot}6H_2O$	…	Crystalline: slightly bluish-green, sensitive to light; density, 1.86 g/cm^3
Ammonium hydrogen fluoride	$(NH_4)HF_2$	Acute poison, corrosive	Crystalline: colorless; forms HF when in contact with acids; density, 1.21 g/cm^3
Ammonium hydroxide	NH_4OH	Corrosive (>35%), irritating	Liquid: aqueous solution; pungent smell; density, 0.882–0.96 g/cm^3
Ammonium molybdate	$(NH_4)_6Mo_7O_{24}{\cdot}4H_2O$	…	Crystalline: colorless; releases NH_3 when exposed to air
Ammonium persulfate	$(NH_4)_2S_2O_8$	Irritating, supports burning	Crystalline: white, store in dry area, dissociates into O_2 and ozone by contact with water; the same reaction occurs when heated; density, 1.98 g/cm^3; strong oxidizing reagent
Ammonium polysulfide	$(NH_4)_2S_x$	Corrosive (>5%)	Liquid: yellow
Ammonium tartrate	$(NH_4)_2C_4H_4O_6$	…	Crystalline: colorless; releases NH_3 when exposed to air
Ammonium tetrachlorocuprate II	$(NH_4)_2CuCl_4{\cdot}2H_2O$	…	Crystalline: yellow; hygroscopic; density, 2.0 g/cm^3
Ammonium thiocyanate	$(NH_4)SCN$	Light poison	Contact with acids will generate HSCN; crystalline: clear; density, 1.3 g/cm^3
Ammonium thiosulfate	$(NH_4)_2S_2O_3$	…	Crystalline
Antimony trioxide	Sb_2O_3	Poison, corrosive	White; density, 5.2–5.8 g/cm^3
Aqua regia (nitrohydrochloric acid, Kingswater)	3 vol% HCl 1 vol% HNO_3	Poison, corrosive	Generates chlor- and nitrosyl chloridents; liquid: yellow with pungent odor, do not store; extremely

Description	Formula	Hazards	Remarks
			corrosive
Argon	Ar	…	Gaseous (liquid below -189.2 °C, or -308.6 °F); density, 0.536 g/cm^3
Benzene	C_6H_6	Highly flammable, poison, irritating	Liquid: colorless, aromatic smell; density, 0.88 g/cm^3; is explosive with air and strong oxidizing agent
Benzoyl peroxide	$C_{14}H_{10}O_4$	Explosive, irritating	Crystalline: white; organic oxidizing agent
Bromine	Br_2	Acute poison, corrosive	Liquid: deep red-brown, fuming, pungent smell; density, 3.14 g/cm^3; strong oxidizing agent
Butanol	$CH_3(CH_2)_3OH$	Slightly flammable (21–55 °C, or 70–131 °F), light poison, irritating	Liquid: colorless; density, 0.81 g/cm^3
2-butoxyethanol	$C_6H_{14}O_2$	Light poison, irritating	Liquid (not volatile): difficult to ignite; forms peroxides when exposed to air; reacts violently with strong oxidizing agents; density, 0.9 g/cm^3
Cadmium chloride	$CdCl_2$	Poison	Crystalline: colorless; mother-of-pearl appearance; hygroscopic: decomposes by moisture absorption from air to a white powder; density, 4.05 g/cm^3
Carbon tetrachloride	CCl_4	Acute poison	Liquid: colorless, very volatile, sweetish aromatic to pungent odor; density, 1.59 g/cm^3
Cerium (IV) nitrate	$Ce(NO_3)_4$	…	Crystalline
Chromic acid	H_2CrO_4	Poison, corrosive	Liquid: aqueous solution of chromium trioxide, yellow-red; causes fire with organic substances; strong oxidizing agent; carcinogen
Chromium (III) oxide	Cr_2O_3	…	Crystalline: green; density, 5.22 g/cm^3
Chromium (VI) oxide	CrO_3	Poison, corrosive	Crystalline: dark red, strong sour taste; hygroscopic: becomes liquid in air; density, 2.7 g/cm^3; is ignitable with flammable substances; strong oxidizing agent
Chromosulfuric acid	$H_2SO_4 + CrO_3$	Acute poison,	Liquid: deep red-brown, oil-

Description	Formula	Hazards	Remarks
		corrosive, supports burning	like consistency; density, ~1.85 g/cm^3; flammable with ignitable materials; strong oxidizing agent
Citric acid	$C_6H_8O_7$	…	Crystalline: white; density, 1.542 g/cm^3
Copper ammonium persulfate	$\{Cu(NH_3)\}S_2O_8$	…	Crystalline
Copper (II) chloride	$CuCl_2 \cdot 2H_2O$	…	Crystalline: sky blue (green when contaminated); density, 2.51 g/cm^3
Copper (II) nitrate	$Cu(NO_3)_2 \cdot 3H_2O$	…	Crystalline: deep blue; stable in air; density, 2.32 g/cm^3; strong oxidizing agent
Copper (II) sulfate	$CuSO_4 \cdot 5H_2O$	…	Crystalline: glacier blue; density, 2.284 g/cm^3
Cryolite	Na_3AlF_6	Light poison, irritating	Crystalline: bright white or transparent; density, 2.95 g/cm^3
1.3-dimethyl, 2-thiourea	$C_3H_8N_2S(CH_3NHCSNHCH_3)$	…	Crystalline; hygroscopic
Ethanol	C_2H_5OH	Highly flammable (<21 °C, or 70 °F)	Produces violent reactions with strong oxidizing agents; can self-ignite; liquid: colorless, volatile; hygroscopic; density, 0.79–0.81 g/cm^3
Ethylenediamine tetraacetic acid (EDTA)	$C_{10}H_{16}N_2O_8$	…	Crystalline: colorless
Ethylene glycol, glycol	$OH\text{-}(CH_2)_2\text{-}OH$	Light poison, irritating	Liquid: colorless, not very volatile, sweetish taste; hygroscopic; density, 1.11 g/cm^3; produces violent reactions and may self-ignite with strong oxidizing agents
Fluoroboric acid	HBF_4	Corrosive	Liquid: aqueous solution, colorless; density, 1.23 g/cm^3
Formic acid	HCOOH	Corrosive	Liquid: aqueous solution, colorless and volatile, pungent smell; density, 1.19–1.22 g/cm^3
Glacial acetic acid ≥96%	CH_3COOH	Corrosive, slightly flammable (21–55 °C, or 70–131 °F)	Liquid: glacial acetic acid without water is clear, without color, and has a pungent smell; very hygroscopic; density, 1.05 g/cm^3; violent to explosive reactions with alkaline solutions and strong oxidizing agents

Description	Formula	Hazards	Remarks
Glycerol, glycerine	$C_3H_8O_3(HOCH_2CHOHCH_2OH)$	…	Liquid: viscous, colorless, clear, sweetish taste; hygroscopic; density, 1.26 g/cm^3; flammable at >100 °C (210 °F); reacts violently with oxidizing agents; may self-ignite
Gold (III) chloride	$AuCl_3$	…	Crystalline; density, 3.9 g/cm^3
Hexamethylenetetramine	$C_6H_{12}N_4$	Slightly flammable, irritating	Crystalline: white; hygroscopic
Hydrogen	H_2	Highly flammable	Gaseous (is liquid below -253 °C, or -423 °F); density, 0.03 g/cm^3; forms explosive mixtures with air and strong oxidizing agents
Hydrogen peroxide	H_2O_2	Corrosive, supports burning	Liquid: colorless; density, 1.12–1.13 g/cm^3
Hydrochloric acid	HCl	Corrosive (>25%), irritating	Liquid: clear to yellowish, fuming; density, 1.12–1.19 g/cm^3
Hydrofluoric acid	HF	Acute poison, corrosive	Liquid: waterlike solution; pungent smell; hygroscopic; density, 1.01–1.16 g/cm^3
Iodine	I_2	Light poison	Crystalline (also in alcoholic mixture): gray to black, volatile at room temperature; vapor (violet); density, 4.93 g/cm^3; ammonia solution and iodine form explosive iodine nitride
Iron (III) chloride	$FeCl_3 \cdot 6H_2O$	Corrosive, light poison	Crystalline: dirty yellow; hygroscopic: becomes liquid when exposed to humid air, smells slightly of HCl; density, 2.8 g/cm^3
Iron (III) nitrate	$Fe(NO_3)_3 \cdot 9H_2O$	…	Crystalline: nearly colorless
Iron (II) sulfate	$FeSO_4$	Light poison, irritating	Crystalline: with soluble water, light green; without soluble water, white; density, 1.9–2.97 g/cm^3
Lactic acid	$C_3H_6O_3$	…	Liquid: viscous, colorless; hygroscopic; density, 1.21 g/cm^3
Lead acetate	$Pb(CH_3COO)_2 \cdot 3H_2O$	Poison	Crystalline: white; density, 2.55 g/cm^3
Lithium hydroxide	LiOH	Corrosive, light poison	Crystalline: white; hygroscopic; density, 1.4 g/cm^3

Description	Formula	Hazards	Remarks
Magnesium oxide	MgO	…	Crystalline: white; density, 3.58 g/cm^3
Magnesium perchlorate	$Mg(ClO_4)_2$	…	Crystalline: colorless; hygroscopic; density, 2.21 g/cm^3
Mercury (II) nitrate	$Hg(NO_3)_2 \cdot H_2O$	Poison	Crystalline: colorless; hygroscopic; density, 4.3 g/cm^3
Methanol	CH_3OH	Poison, highly flammable (<21 °C, or 70 °F)	Liquid: volatile, colorless; density, 0.79 g/cm^3
Methyl methacrylate	$C_5H_8O_2$	Highly flammable (<21 °C, or 70 °F), irritating	Liquid: colorless, clear; density, 0.94 g/cm^3; explosive when exposed to air; reacts violently or ignites when exposed to strong oxidizing agents
Molybdic acid	MoO_3	…	Crystalline: white, contains ammonium molybdate; density, 4.696 g/cm^3
Nitric acid	HNO_3	Corrosive, supports burning	Liquid: colorless, fumes when exposed to humid air, pungent smell; density, 1.37–1.52 g/cm^3; develops nitrous gases when concentrated acid is in contact with metals and organic substances
Nitrogen	N_2	Light poison	Gaseous (is liquid below -210 °C, or -345 °F); density, 0.31 g/cm^3
Orthophosphoric acid	H_3PO_4	Corrosive	Liquid: aqueous solution, colorless, viscous; hygroscopic; density, 1.77–1.88 g/cm^3
Oxalic acid	$(COOH)_2$	Light poison, irritating	Crystalline: colorless; density, 1.9 g/cm^3; explosive when oxidizing agents are present
Perchloric acid	$HClO_4$	Corrosive, supports burning (>50%)	Liquid: colorless, fumes when exposed to air; very hygroscopic; density, 1.15–1.76 g/cm^3; explosive when in contact with oxidizing inorganic and organic substances; strong oxidizing agent
Picric acid	$C_6H_3N_3O_7$	Poison, explosive	Crystalline: yellow, bitter taste; density, 1.8 g/cm^3
Potassium carbonate	K_2CO_3	Irritating	Crystalline: white, CO_2 will form with acid;

Description	Formula	Hazards	Remarks
			hygroscopic; density, 2.43 g/cm^3
Potassium chlorate	$KClO_3$	Light poison, supports burning	Crystalline: white; density, 2.32 g/cm^3; explosive with organic materials; strong oxidizing agent
Potassium chloride	KCl	…	Crystalline: colorless, salty; density, 1.984 g/cm^3
Potassium chromate	K_2CrO_4	Irritating, supports burning	Crystalline: bright yellow; density, 2.73 g/cm^3; oxidizing agent; inflammable when in contact with flammable materials
Potassium cyanide	KCN	Poison	Crystalline: granular; hygroscopic; density, 1.52 g/cm^3; HCN will form when in contact with moist air, carbonized water, and acids
Potassium dichromate	$K_2Cr_2O_7$	Poison, irritating, supports burning when in contact with flammable materials	Crystalline: orange-red; density, 2.69 g/cm^3; strong oxidizing agent
Potassium disulfate	$K_2S_2O_5$	…	Crystalline: white; density, 2.34 g/cm^3
Potassium ferricyanide	$K_3\{Fe(CN)_6\}$	Light poison, irritating	Crystalline: intense dark red; density, 1.85 g/cm^3; with strong acids, HCN will be released; strong oxidizing agent
Potassium ferrocyanide	$K_4\{Fe(CN)_6\}\cdot 3H_2O$	Light poison, irritating	Crystalline: light yellow, stable in air but decomposes in light; density, 1.853 g/cm^3; when in contact with strong acids, HCN will be released
Potassium hydrogen carbonate	$KHCO_3$	Light poison	Crystalline: colorless, transparent, or white; density, 2.17 g/cm^3
Potassium hydrogen fluoride	KHF_2	Poison, corrosive	Crystalline: white; hygroscopic; density, 2.37 g/cm^3; will release HF when heated
Potassium hydrogen sulfate	$KHSO_4$	Corrosive, irritating	Crystalline: white, transparent; density, 2.322 g/cm^3
Potassium hydroxide	KOH	Corrosive	Crystalline: white pellets; hygroscopic: becomes liquid when exposed to air,

Description	Formula	Hazards	Remarks
			absorbing moisture and carbon dioxide; violent exothermic reaction with strong acids; density, 2.04 g/cm^3
Potassium hydroxide solution	KOH	Corrosive (>5%)	Liquid: aqueous solution, colorless, viscous-to-thin liquid; violent exothermic reaction with strong acids; density, 1.007–1.51 g/cm^3
Potassium iodide	KI	Corrosive, light poison	Crystalline: aqueous solution, colorless, decomposes slowly and turns yellow when exposed to air and light; density, 3.12 g/cm^3
Potassium nitrate	KNO_3	Supports burning	Crystalline: colorless or white, stable in air, will generate nitrous gases when heated; density, 2.09 g/cm^3; strong oxidizing agent
Potassium permanganate	$KMnO_4$	Light poison, supports burning	Crystalline: deep red, stable in air; density, 2.7 g/cm^3; explosive with organic materials and with reducing agents, may ignite; strong oxidizing agent
Potassium phthalate	$C_8H_4K_2O_4$	…	Crystalline
Potassium thiocyanate	KSCN	Light poison	Crystalline: colorless; hygroscopic: forms HSCN or HCN when exposed to acids; density, 1.886 g/cm^3
Selenic acid	H_2SeO_4	Poison	Liquid: colorless; hygroscopic; density, 3.0 g/cm^3; strong oxidizing agent
Silver cyanide	AgCN	Poison, irritating	Crystalline: white, can be exposed to air; density; 3.95 g/cm^3; generates cyanides when in contact with strong acids
Silver nitrate	$AgNO_3$	Corrosive, supports burning	Crystalline: colorless, transparent; very sensitive to light; density, 4.35 g/cm^3; generates nitrous gases when heated
Sodium carbonate	Na_2CO_3	Irritating	Crystalline: white granular; density, 2.53 g/cm^3
Sodium chlorate	$NaClO_3$	Light poison, supports burning	Crystalline: white; hygroscopic; density, 2.49 g/cm^3; explosive when mixed with organic materials; strong oxidizing

Description	Formula	Hazards	Remarks
			agent
Sodium chloride	NaCl	…	Crystalline: colorless, salty; density, 2.164 g/cm^3
Sodium chromate	$Na_2CrO_4 \cdot 10H_2O$	Poison, irritating	Crystalline: yellow; hygroscopic; density, 1.48 g/cm^3; ignites when in contact with flammable material; oxidizing agent
Sodium cyanide	NaCN	Light poison	Crystalline; density, 1.86 g/cm^3; generates extremely poisonous HCN when exposed to humid air, carbon dioxide containing water, and acids
Sodium dichromate	$Na_2Cr_2O_7$	Light poison, irritating	Crystalline: orange-red; hygroscopic; density, 2.52 g/cm^3; ignites when in contact with flammable material; oxidizing agent
Sodium fluoride	NaF	Poison	Crystalline: white or greenish; hygroscopic; density, 2.79 g/cm^3; generates HF when in contact with acids
Sodium hydrogen carbonate	$NaHCO_3$	…	Crystalline: white; stable in air; density, 2.159 g/cm^3
Sodium hydrogen phosphate	$Na_2HPO_4 \cdot 12H_2O$	Light poison	Crystalline; hygroscopic
Sodium hydroxide	NaOH	Corrosive	Crystalline: white; hygroscopic: becomes liquid in air by absorbing moisture and carbon dioxide; violent exothermic reaction with strong acids; density, 2.13 g/cm^3
Sodium hydroxide solution	NaOH	Corrosive (>5%), irritating	Liquid: aqueous solution, colorless, viscous-to-thin liquid; violent exothermic reactions when in contact with strong acids; density, 1.01–1.53 g/cm^3
Sodium hypochlorite	NAOCl	Corrosive (>10% chlor)	Liquid: aqueous solution with >10% active chlor, light yellow- greenish; density, 1.22 g/cm^3; generates poisonous chlor gas with acids; oxidizing agent
Sodium peroxide	Na_2O_2	Corrosive, supports burning, possible ignition by	Crystalline: white to yellow; hygroscopic; store in a dry and closed container, otherwise will decompose by generating

Description	Formula	Hazards	Remarks
		strong oxidizing effect	O_2, H_2O_2, and heat; density, 2.81 g/cm^3; fire hazard with flammable substances
Sodium sulfate	$Na_2SO_4 \cdot 10H_2O$	…	Crystalline: colorless, decomposes in air; density, 1.464 g/cm^3
Sodium sulfide	Na_2S	Corrosive	Crystalline: colorless or yellow to brownish-red, reacts with acid, generating H_2S; density, 1.86 g/cm^3
Sodium tetraborate	$Na_2B_4O_7 \cdot 10H_2O$	…	Crystalline: white; density, 1.72 g/cm^3
Sodium thiocyanate	NaSCN	Light poison	Crystalline: colorless; hygroscopic; generates HSCN in presence of acids
Sodium thiosulfate; photographic fixer	$Na_2S_2O_3 \cdot 5H_2O$	…	Crystalline: colorless, salty to bitter taste; density, 1.729 g/cm^3
Sulfuric acid	H_2SO_4	Corrosive (>15%), irritating	Liquid: clear, oily consistency; very hygroscopic; density, 1.18–1.84 g/cm^3
Tartaric acid	$C_4H_6O_6$	…	Crystalline: colorless; density, 1.7598–1.788 g/cm^3
Tetrafluoromethane	CF_4	…	Gaseous: thermal decomposition generates poisonous and corrosive gases; density, 0.63 g/cm^3
Thioglycolic acid	$HSCH_2COOH$	Poison, corrosive	Liquid: colorless; strong odor; oily consistency; density, 1.27–1.33 g/cm^3
Thiorurea	$CS(NH_2)_2$	Light poison	Crystalline: white, shiny, bitter taste; density, 1.405 g/cm^3; generates sulfur or SO_2 with strong oxidizing agents and when heated
Tin (II) chloride	$SnCl_2$	Corrosive	Crystalline: white; density, 3.95 g/cm^3
Toluene	$C_6H_5\text{-}CH_3$	Slightly flammable, light poison, irritating	Liquid: colorless, volatile, aromatic odor; density, 0.87 g/cm^3; explosive with air
Trichloroethylene	C_2HCl_3	Light poison, irritating	Liquid: colorless, volatile, sweetish etherlike odor; density, 1.462 g/cm^3; may be explosive with oxygen
Triethylamine	$C_6H_{51}N$	Highly flammable (<21 °C, or 70 °F), irritating	Liquid: colorless to yellowish, volatile, oily consistency, has ammonia odor; density, 0.73 g/cm^3; vapors form explosive

Description	Formula	Hazards	Remarks
			mixtures with air
Vanadium oxide	V_2O_5	Light poison, irritating	Crystalline: rusty-red to red; density, 3.36 g/cm^3; is a catalyst for many oxidizing reactions, also has an ignition effect; strong oxidizing agent
Xylene	$C_6H_4(CH_3)_2$	Highly flammable (21–55 °C, or 70–131 °F), light poison, irritating	Liquid: colorless to yellowish, volatile, aromatic odor, violent reactions or ignitions with strong oxidizing agents; vapors form explosive mixtures with air; density, 0.86–0.88 g/cm^3
Zinc chloride	$ZnCl_2$	Corrosive	Crystalline: white; very hygroscopic; density, 2.91 g/cm^3

Table 2 Dangerous reactions of chemicals

Chemical	Dangerous reaction with:
Acetone	Chloroform, chromium (VI) oxide, hydrogen peroxide
Alcohols	Perchloric acid, mercury nitrate, hydrogen peroxide, chromium (VI) oxide, aluminum chloride
Aluminum chloride	Water, alcohols
Ammonium hydroxide	Metal powders, acids, mercury, hydrofluoric acid
Bromine, iodine	Ammonium hydroxide, unsaturated reagents, metal powders, alkaline and rare earth metals, hydrocarbons, light (use dark-colored bottles)
Chlor	Aluminum and aluminum salts, acids, metal powders, sulfuric acid, cyanides, finely dispersed organic substances, inflammable materials; see also perchloric acid
Chromium (VI) oxide	Ammonium hydroxide, glacial acetic acid, glacial acetic acid anhydrous, glycerol, alcohol, organic materials, sodium, inflammable liquids
Cyanides	Acids, oxidizing agents, especially nitrites and mercury (II) nitrate
Formic acid	Aluminum, oxidizing agents
Glacial acetic acid	Chromium (VI) oxide, nitric acid, perchloric acid, hydrogen peroxide, permanganate, alcohol, ethylene glycol, potassium hydroxide
Halogen hydrocarbons	Alkaline and earth alkaline metals, concentrated bases, metal powders, perchloric acid, nitric acid, aluminum containers
Hydrofluoric acid	Ammonium hydroxide, alkali metals, glass
Hydrochloric acid	Aluminum, organic substances
Hydrogen peroxide	Copper, chromium, iron, metals and their salts, alcohol, acetone, organic substances or other flammable materials, formic acid, bronze, glycerol, potassium or sodium hydroxide, potassium permanganate
Nitric acid	Ammonium hydroxide, acetic acid anhydrous, chromium (VI) oxide, hydrocyanic acid, flammable liquids and gases, ethanol
Oxalic acid	Silver, mercury, oxidizing agents
Perchloric acid	Acetic acid, acetic acid anhydrous, bismuth and bismuth alloys, alcohol, concentrated sulfuric acid, concentrated phosphoric acid, substances that oxidize, paper, wood
Peroxide	Acetone, alkali hydroxide, alcohol, formic acid, glycerol, potassium or sodium

Chemical	Dangerous reaction with:
	hydroxide, potassium permanganate, heavy metals (including oxides and salts), dust, oxidizing materials, ammonium hydroxide
Picric acid and picrates	Heat, ammonium hydroxide, alkaline and earth alkaline metals, aluminum, nitric acid, peroxide, oxidizing media, sulfuric acid
Potassium hydroxide	Glacial acetic acid, aluminum, zinc, halogen hydrocarbons, water
Potassium permanganate	Oxidizing organic and inorganic materials, hydrochloric acid, concentrated mineral acids, sulfuric acid, hydrogen peroxide, glycerol, ethylene glycol
Silver nitrate	Ammonium hydroxide, ethanol, sodium hydroxide
Sodium hydroxide	Aluminum, concentrated acid, silver nitrate, trichloroethylene, chloroform, water, hydrogen peroxide
Sodium peroxide	Aluminum, aluminum persulfate, magnesium, organic materials, methanol, ethanol, glycerol, ethylene glycol, glacial acetic acid, acetic acid anhydrous
Sulfuric acid	Potassium (per)chlorate, potassium permanganate, flammable substances, sodium carbonate, sodium hydroxide, picrates, water

Table 3 Designation of Etchants

Name	Composition	Caution	Application
Adler **Macroetchant** **Microetchant**	25 mL distilled water 50 mL hydrochloric acid (32%) 15 g iron (III) chloride 3 g ammonium tetrachlorocuprate (II)	Hazardous	High-alloy, corrosion-resistant steels Cobalt and nickel alloys
Aluminum hydroxide/hydrogen peroxide	1 vol ammonium hydroxide 2 vol hydrogen peroxide (3%) 2 vol water		Apply by swabbing at room temperature Develops twin-line, twin-band, and shear-band etch markings in copper alloys The swabbing necessary for effective etching inevitably scratches the surface of the specimen.
Aqua regia	60 mL hydrochloric acid (32%) 20 mL nitric acid (65%)	Hazardous	Pure gold and noble metal alloys Use fresh!
Barker **Anodic etchant**	200 mL distilled water 5 g fluoboric acid (35%)	Hazardous	Pure aluminum and aluminum alloys Aluminum, lead, or stainless steel cathode 20–40 V dc
Baumann print **Sulfur print** **Macroetchant**	100 mL distilled water 5 mL sulfuric acid (95–97%)		Unalloyed steels. Sulfide inclusions Grind sample to 320-grit SiC paper. Soak photographic paper with the solution and press firmly onto the sample surface. After approximately 3 min, rinse, fix (photo fix), wash, and dry. Sulfur-rich regions will turn

Name	Composition	Caution	Application
			brown. Better contrast is obtained by etching the sample with Heyn's reagent prior to the Baumann print.
Beraha I **Color etchant**	100 mL Beraha I stock solution 1 g potassium disulfite **Beraha I stock solution:** 1000 mL distilled water 200 mL hydrochloric acid (32%) 24 g ammonium hydrogen fluoride	Hazardous	Unalloyed and low-alloy steels. Manganese hard steels Store the stock solution in a plastic bottle.
Beraha II **Color etchant**	100 mL Beraha II stock solution 1 g potassium disulfite **Beraha II stock solution:** 800 mL distilled water 400 mL hydrochloric acid (32%) 48 g ammonium hydrogen fluoride	Hazardous	High-alloy steels Store the stock solution in a plastic bottle.
Beraha III **Color etchant**	100 mL Beraha III stock solution 1 g potassium disulfite **Beraha III stock solution:** 600 mL distilled water 400 mL hydrochloric acid (32%) 50 g ammonium hydrogen fluoride	Hazardous	Nickel- and cobalt-base alloys Store stock solution in a plastic bottle.
Beraha III 1 **Color etchant**	50 mL distilled water 7 g ammonium hydrogen fluoride	Hazardous	Nickel-base alloys Hastelloy X Hastelloy

Name	Composition	Caution	Application
	50 mL hydrochloric acid (32%) 0.5 g potassium disulfite		
Bitter-technique	Solution A: 300 mL distilled water 2 g iron (II) chloride 5.4 g iron (III) chloride Heat solution A to 30–40 °C (85–105 °F). Solution B: 50 mL distilled water 5 g sodium hydroxide		Magnetic materials The samples should be electrolytically polished. In order to make a colloidal Fe_3O_4 suspension, solution A is added slowly but by stirring vigorously to solution B. Fe_3O_4 is filtered and washed several times. Mix 1 cm^3 Fe_3O_4 with 30 mL of a 0.3% soap solution. Add 1 drop of this suspension to the sample surface and cover with a cover glass for uniform distribution. Examine under the microscope with bright-field or dark-field illumination. The Fe_3O_4 particles will decorate the domain walls because of their nonuniform magnetic fields.
Carapella **Macroetchant**	20–100 mL distilled water or ethanol (96%) 2–25 mL hydrochloric acid (32%) 5–8 g iron (III) chloride		Nickel-iron, nickel-copper, and nickel-silver alloys Nickel-base superalloys Monel metal
Chromosulfuric acid	50 g sodium dichromate or potassium dichromate or 20 g chromium (VI) oxide 1000 mL sulfuric acid (95–97%)	Hazardous	Polypropylene
Crowell **Microetchant**	100 mL distilled water 3 mL sulfuric acid (95–97%) 2 g potassium dichromate 1 g sodium fluoride	Hazardous	Ag-Sn-Zn-Cu alloys Cu-Sn-Ag dental alloys
Cupric ammonium chloride	10 g cupric ammonium chloride 100 mL water Ammonium hydroxide (conc) added drop by drop until the solution		Immersion at room temperature develops twin-line, twin-band, and shear-band etch markings in copper alloys.

Name	Composition	Caution	Application
	is alkaline		
Czochralski **Microetchant**	30 mL distilled water 15 mL hydrochloric acid 50 mL aqueous sodium thiosulfate (16 %) 3 mL aqueous chromium (VI) oxide solution (10%)	Hazardous	Antimony alloys
Dix-Keller **Microetchant**	190 (190) mL distilled water 5 (10) mL nitric acid (65%) 3 (6) mL hydrochloric acid (32%) 2 (4) mL hydrofluoric acid (40%)	Hazardous	Pure aluminum and aluminum alloys
Ferric chloride	5 g ferric chloride 10 mL hydrochloric acid 100 mL water		Immersion at room temperature develops twin-band and shear-band etch markings in copper alloys.
Ferric nitrate **(common name: Prohaska's etch)**	5 g ferric nitrate 10 mL hydrochloric acid 70 mL water		Immerse at room temperature. Used as general etchant for copper and copper alloys. Develops twin-band and shear-band etch markings but not twin-line etch markings
Flick **Macroetchant**	90 mL distilled water 15 mL hydrochloric acid (32%) 10 mL hydrofluoric acid (40%)	Hazardous	Pure aluminum and aluminum alloys
Fry **Macroetchant**	100 mL distilled water 120–180 mL hydrochloric acid (32%) 45–90 g copper (II) chloride		Flow lines in low-carbon N_2 steels. Thomas steels
Microetchant	30 mL distilled water 40 mL hydrochloric		Anneal sample at 150–200 °C (300–390 °F) prior to etching. After etching, immerse into 32% hydrochloric acid, rinse with water, and

Name	Composition	Caution	Application
	acid (32%) 25 mL ethanol (96%) 5 g copper (II) chloride		neutralize with a 25% ammonium hydroxide solution.
Groesbeck **Color etchant**	100 mL distilled water 4 g sodium hydroxide 4 g potassium permanganate		High-alloy steels Cast materials
Hasson **Color etchant**	75 mL ethanol (96%) 40–60 mL aqueous iron (III) chloride solution (1300 g/L) 25 mL hydrochloric acid (32%)		Pure molybdenum
Heyn **Macroetchant**	100 mL distilled water 9 g ammonium tetrachlorocuprate II		Low-carbon steels
Kalling 1 **Microetchant**	33 mL distilled water 33 mL ethanol (96%) 33 mL hydrochloric acid (32%) 1.5 g copper (II) chloride		Martensitic stainless steels
Kalling 2 **Microetchant**	100 mL ethanol (96%) 100 mL hydrochloric acid (32%) 5 g copper (II) chloride		Stainless steels Nickel-copper alloys Nickel-base superalloys
Keller **Microetchant** **Macroetchant**	190 (20) mL distilled water 3 (20) mL hydrochloric acid (32%) 5 (20) mL nitric acid (65%) 1 (5) mL hydrofluoric acid (40%)	Hazardous	Pure aluminum and aluminum alloys Titanium alloys Rare earth/aluminum alloys
Klemm	Stock solution: 300 mL distilled water		Heat solution to 30–40 °C (85–105 °F). Let stand for 1 day; a part of the salt will crystallize at the bottom of the beaker. Use this stock solution and replenish the remaining

Name	Composition	Caution	Application
	1000 g sodium thiosulfate		solution with distilled water until all the crystals have been dissolved again. This stock solution can be stored indefinitely. The etchant itself can be used for 1–2 days.
Klemm I **Color etchant**	100 mL stock solution 2 g potassium disulfite		Unalloyed and low-alloy steels. Cast iron. Manganese steels. Pure zinc and low-alloy zinc
Klemm II **Color etchant**	100 mL stock solution 5 g potassium disulfite		Copper and copper alloys and soft solders. Solders and welds with brass
Klemm III **Color etchant**	100 mL distilled water 11 mL stock solution 40 g potassium disulfite		Pure copper and copper alloys
Kroll **Microetchant**	100 mL distilled water 2–6 mL nitric acid (65%) 1–3 mL hydrofluoric acid (40%)		Aluminum-copper alloys. Titanium alloys, mainly Ti-Al-V(-Sn) alloys
Lichtenegger and Bloech **Color etchant**	100 mL distilled water 20 g ammonium hydrogen fluoride 0.5 g potassium disulfite		Austenitic CrNi steels
Marble **Macroetchant** **Microetchant**	100 mL distilled water 100 mL hydrochloric acid (32%) 20 g copper (II) sulfate		Austenitic and high-temperature-resistant steels Cobalt superalloys
Murakami **Microetchant**	100 mL distilled water 5–10 g potassium or sodium hydroxide 5–10 g potassium ferricyanide		Pure tungsten and tungsten alloys and tungsten-nickel alloys. Cast iron. Alloyed chromium steels. Chromium, molybdenum, and molybdenum-chromium alloys. Molybdenum-iron and molybdenum-rhenium alloys. Tungsten and tungsten-base alloys. Rhenium and rhenium-base alloys. InP, SbTe, and BiTe. Uranium alloys. SiC. Use fresh!
Nital **Microetchant**	100 mL ethanol (96%) 1–10 mL nitric acid (65%)		Pure iron, carbon steels, low-alloy steels, and gray cast iron. Pure magnesium and most magnesium alloys. Pure tin. Tin-rich alloys with cadmium, copper, iron, and antimony. Pure titanium. Pure cadmium and cadmium alloys. Pure gadolinium. Rare earth/cobalt alloys. General etchant for steel, in particular,

Name	Composition	Caution	Application
			structures of ferritic phases
Oberhoffer **Macroetchant**	500 mL distilled water 500 mL ethanol (96%) 50 mL hydrochloric acid (32%) 30 g iron (III) chloride 1 g copper (II) chloride 0.5 g tin (II) chloride		Unalloyed and low-alloy steels
Oxalic acid	10 g oxalic acid 100 mL water		Etch electrolytically, using specimen as anode and using a cathode of stainless steel or platinum located at a distance of 2–3 cm (0.8–1.2 in.). Apply 1–6 V. General etchant for austenitic steels
Palmerton **Macroetchant**	100 mL distilled water 20 g chromium (VI) oxide 1.5 g sodium sulfate anhydrous	Hazardous	Copper-containing zinc alloys
Microetchant	200 mL distilled water 20 g chromium (VI) oxide 1.5 g sodium sulfate anhydrous	Hazardous	Pure zinc and zinc alloys Lead-containing zinc rolling alloys
Picral **Microetchant**	100 mL ethanol (96%) 4 g picric acid	Hazardous	Pure iron, carbon steels, low-alloy steels, and cast iron Tin-coated steels and cast irons General etch for steels, particularly to reveal carbides
Schramm **Macroetchant** **Microetchant**	900 mL distilled water 60 mL saturated aqueous copper (III) nitrate solution 122 g potassium hydroxide 75 g potassium cyanide 6.5 g citric acid	Hazardous	Zinc-copper, zinc-iron, zinc-magnesium, zinc-nickel, and zinc-lead alloys The mixing sequence must be followed, or cyanide acid may be generated; this may also occur during incorrect disposal practice!
Sodium bisulfite	20 g sodium bisulfite		To ensure even wetting of the specimen by the

Name	Composition	Caution	Application
(Beaujard's reagent)	100 mL water		primary etchant, it is often desirable first to etch briefly in nital. Immerse at room temperature for 10 to 25 s. Wash and dry, taking particular care not to disturb the surface film deposited by the etchant. Enhanced contrast in and between ferrite grains; produces good distinction between lightly tempered martensite and ferrite
Sodium thiosulfate **(Jacquet's etch)**	High sensitivity: 0.25 g sodium thiosulfate 100 mL water 15–25 ppm sodium chloride Low sensitivity: 0.50 g sodium thiosulfate 100 mL water 15–25 ppm sodium chloride		Etch electrolytically, using a copper anode and an applied potential of 6 V and the following current densities: high sensitivity, 3.5 A/dm^2; low sensitivity, 1.0 A/dm^2 Develops twin-line, twin-band, and shear-band etch markings in copper alloys If the specimen is electrolytically polished, the specimen must be removed from the bath with the potential still applied; otherwise, an interfering film of copper will deposit on the surface. Moreover, an electrolytically polished surface must first be etched for 20 s in a solution containing 100 g of phosphoric acid per liter, then immersed for 20 s in water, and then placed immediately in the etching solution. The purpose of this treatment is to remove an interfering film of a copper phosphate that forms during electrolytic polishing. This etching method was devised and developed by Jacquet[(a)], but the additional precautions included previously which were elucidated by Samuels[(b)] and by Manion and Mulhearn[(c)], must be followed if reliable results are to be obtained.
Tucker **Macroetchant**	25 mL distilled water 45 mL hydrochloric acid (32%) 15 mL nitric acid (65%) 15 mL hydrofluoric acid (40%)	Hazardous	Pure aluminum, manganese-aluminum, silicon-aluminum, magnesium-aluminum, magnesium-silicon-aluminum alloys Use fresh!
Vilella **Microetchant**	45 mL glycerol (87%) 30 mL hydrochloric acid (32%) 15 mL nitric acid (65%) (Variable concentration)	Hazardous	Ferritic chromium steels. Austenitic CrNi steels. Austenitic cast alloys. Palladium and its alloys Use fresh!

Name	Composition	Caution	Application
Vilella and Beregekoff **Macroetchant**	80 mL glycerol (87%) 10 mL glacial acetic acid 10 mL nitric acid (65%)	Hazardous	Lead-tin alloys
Wallner **Microetchant**	16 g iron chloride dissolved in 50 mL distilled water 9 g ammonium persulfate dissolved in 50 mL distilled water 60 mL hydrochloric acid (32%)		Corrosion-resistant CrNi steels
Weck **Color etchant**	100 mL distilled water 50 mL ethanol (96%) 2 g ammonium hydrogen fluoride	Hazardous	Pure titanium and titanium alloys

(a) P.A. Jacquet, *Compt. Rendus,* Vol 228, 1949, p 1027, and *Rev. Met.,* Vol 47, 1950, p 255.
(b) L.E. Samuels, *J. Inst. Met.,* Vol 83, 1954–1955, p 359.
(c) S.A. Manion and T.O. Mulhearn, *Metallography,* Vol 4, 1971, p 551

Table 4 Chemical-polishing solutions for irons and steels

Before using any chemicals, Material Safety Data Sheets (MSDS) should be reviewed.

Reagent	To polish	Composition	Remarks
Plichta	Carbon steels (pure iron to 0.8% C and up to 3% alloys)	100 mL H_2O 100 mL H_2O_2 (30%) 14 mL HF	Use fresh cold solution 15–20 °C (60–70 °F) (very important). Immerse sample for 3–30 s and shake vigorously or immerse up to 3 min. Prior to chemical polishing, the sample should be ground to a 600-grit finish. To prevent staining, rinse the sample in H_2O_2 (30%), followed by an ethyl alcohol rinse, and dry.
Anderson	Carbon steels	80 mL H_2O 28 g oxalic acid 4 mL H_2O_2 (30%)	Use at room temperature.
Anderson	Carbon steels	100 mL H_2O 50 g chromic acid 15 mL H_2SO_4	Use at room temperature.
Wiesinger	Iron, iron-silicon alloys	94 mL H_2O_2 (30%) 6 mL HF	Use at room temperature. Rinse in water, flush with ethyl alcohol, and dry.

Reagent	To polish	Composition	Remarks
de Magalhaes	Steels	Solution A: 3 parts H_2O_2 (30%) 10 parts H_2O 1 part HF Solution B: 1 part H_3PO_4 15 parts H_2O	Steels > 0.3% C: Grind to 150 grit, immerse in solution A for 15–25 s, wash with water, clean with solution B with cotton, wash in water, dry. Steels 0.15–0.30% C: Grind to 320 grit, immerse in solution A for 12–18 s, then same procedure as for steels > 0.3% C. Steels < 0.15% C: Grind to 600 grit, immerse in solution A for 3–5 s, then same procedure as for steels > 0.3% C. Extrasoft sheet steels: Grind to 200 grit, immerse in solution A for 3–5 s, mechanical polish with chromium oxide, then with alumina.
de Jong	Austenitic stainless steel	4 parts HNO_3 3 parts HCl 5 parts acetic acid	First, passivate surface by dipping in boiling 4% aqueous H_2SO_4. Then, chemical polish at 70 °C (160 °F) for 1 min.
Gramzow/Heim	Cast iron, low-alloy steels	70 mL H_2O_2 (30%) 5 mL HF 40 mL H_2O	Use at 15–25 °C (60–75 °F).
Graham	Carbon steel	7 parts oxalic acid (100 g/L) 1 part H_2O_2 (100%) 20 parts H_2O	Grind to 0-grade emery or equivalent. Immerse sample 15 min at 35 °C (95 °F).
Kawamura	Low-carbon steels	90 mL H_2O_2 (30%) 10 mL H_2O 15 mL H_2SO_4	Use at 25 °C (75 °F) for 2–5 min.
Hallett	Carbon steels	Solution A: 25 g oxalic acid 1000 mL H_2O	Use fresh for 30 min. Ratio of solution A to B varies with carbon content.

Reagent	To polish	Composition	Remarks
		Solution B: 100 vol H_2O_2	
Chia	Pure iron	5 mL HF 70 mL H_2O_2 (30%)	Grind through 600-grit SiC. Immerse in solution at 20 °C (70 °F) for 25–45 s.
Chia	Fe-3%Si alloy	100 mL H_3PO_4 115 mL H_2O_2 (30%)	Grind through 600-grit SiC. Immerse in solution at 25 °C (75 °F) for 8–10 min. Cool during use.
Uhlig	Stainless steel	Percent by weight: 30% HCl 40% H_2SO_4 5.5% titanium tetrachloride 24.5% H_2O	Use by immersion of sample at 70–80 °C (160–175 °F) for 2–5 min. Can add 0.5% HNO_3 to solution
Conn	Low-carbon steels	3 parts H_3PO_4 1 part H_2SO_4 1 part HNO_3	Use at 85 °C (185 °F).
Kawamura	Low-carbon steels	1 part H_2O_2 (30%) 2 parts 20% oxalic acid in H_2O	Use at 30–70 °C (85–160 °F).
Kawamura	Medium-carbon steels	10 parts H_2O_2 (30%) 10 parts H_2O 1 part HF	Use at room temperature.
Beaujard	Iron, low-carbon steels	30 mL HNO_3 70 mL HF 300 mL H_2O	Use at 60 °C (140 °F).
Marshall	Iron, low-carbon steels	25 g oxalic acid 10 mL H_2O_2 (13 g) 1 drop H_2SO_4 (0.1 g)	Grind through 600-grit SiC. Immerse sample for 5 min at 20 °C (70 °F).

Reagent	To polish	Composition	Remarks
		1000 mL H_2O	
Christ/Smith	Iron, low-carbon steels, Fe-20%Ni-5%Mn alloy	80 mL H_2O_2 (30%) 15 mL H_2O 5 mL HF	Prepolish sample through 6 μm diamond. Swab with fresh solution at 20–25 °C (70–75 °F) for 4–10 s. Flush immediately with cold water.
Rzepski	Iron, low-carbon steels, low-alloy steels	3 mL HF 97 mL H_2O_2 (30%)	Adjust HF concentration to obtain gas evolution. Good for thinning transmission electron microscopy samples

Sources: B. Bramfitt and A. Benscoter, *Metallographer's Guide: Practices and Procedures for Irons and Steels,* ASM International, 2002. G. Vander Voort, *Metallography Principles and Practices,* McGraw-Hill, 1984; reprinted by ASM International, 1999

Table 5 Chemical-polishing solutions for nonferrous materials

When water is specified, always use distilled water.

Reagent	To polish	Composition	Remarks
Alford/Stephens	Alumina	H_3PO_4	Use at 425 °C (795 °F); remove sample from mount before polishing, 2–3 min required.
King	Alumina	Borax glass	Use at 800–900 °C (1470–1650 °F); rotate sample periodically for approximately 5 min. Dissolve adherent glass with dilute acid.
Janowski/Conrad	Alumina-0.04% Cr	H_3PO_4	Heat sample slowly in gas flame to 425 °C (795 °F), then immerse in acid at 425 °C (795 °F) for 1–2 min.
Montgomery/Craig	Aluminum	60 mL H_2SO_4 30 mL H_3PO_4 10 mL HNO_3	Use at 100 °C (210 °F) for 2–5 min.
Herenguel/Segond	Aluminum	25 mL H_2SO_4 70 mL H_3PO_4 5 mL HNO_3	Use at 85 °C (185 °F) for 30 s–2 min. Good for alloys with intermetallic phases
Herenguel/Segond	Al-Mg, Al-Mg-Si, Al-Zn-Mg, and Al-Cu-Mg alloys	Solution A: 30–60 mL H_3PO_4 60–30 mL H_2SO_4 5–10 mL HNO_3 Solution B:	Use solution A at 95–120 °C (205–250 °F); good for preliminary polish. Use solution B at 85–110 °C (185–230 °F); good for final polish. Use solution C at 85 °C (185 °F); etches grain boundaries.

Reagent	To polish	Composition	Remarks
		70–90 mL H_3PO_4 25–5 mL H_2SO_4 3–8 mL HNO_3 Solution C: 90 mL H_3PO_4 10 mL HNO_3	
Meyer/Brown	Aluminum	70 mL H_3PO_4 15 mL acetic acid 15 mL H_2O	Use at 100–120 °C (210–250 °F) for 2–6 min.
Spahn	Aluminum	83 mL H_3PO_4 15 mL acetic acid 5 mL HNO_3	Use at 100–105 °C (210–220 °F) for a few minutes.
Meyer/Brown	Aluminum	70 mL H_3PO_4 3 mL HNO_3 12 mL acetic acid 15 mL H_2O	Use at 100–120 °C (210–250 °F) for 2–6 min. Good for many aluminum alloys
Chia	Aluminum	90 mL H_3PO_4 5 mL HNO_3 5 g sodium nitrate 0.2 g copper nitrate	Grind through 600-grit SiC, immerse in solution at 90 °C (195 °F) for 4 min.
Chia	Aluminum	80 mL H_3PO_4 15 mL H_2SO_4 5.5 mL HNO_3	Grind through 600-grit SiC, immerse in solution at 95 °C (205 °F) for 4 min.
Arrowsmith	Aluminum	77.5 mL H_3PO_4 16.5 mL H_2SO_4 6 mL HNO_3	Use for $1\frac{1}{2}$–2 min. Temperature not given, probably approximately 100 °C (210 °F)

Reagent	To polish	Composition	Remarks
		3.9 g $CuSO_4 \cdot 5H_2O$ 1000 mL H_2O	
de Jong	Aluminum	47.7 mL H_3PO_4 6.4 mL HNO_3 6.0 mL acetic acid 25.0 mL H_2SO_4 12.5 mL H_2O 0.3 g $Ni(NO_3)_2$	Use at 90–110 °C (195–230 °F) for 30–120 s. Good for aluminum alloys
de Jong	Pure aluminum and Al-1%Si-1% Fe-0.1% Cu alloy	15 mL HNO_3 4 mL HCl 46 mL H_3PO_4	Use at 100 °C (210 °F) for 8–10 min.
Black/Faust	Beryllium	44 mL H_3PO_4 3 mL H_2SO_4 13 mL H_2O 7 g CrO_3	Use at 49 °C (120 °F). Removes 1 mil (25 μm) in 20 min.
Gilman/De Carlo	Cadmium	2 parts H_2O_2 (30%) 2 parts ethanol 1 part HNO_3	Immerse sample in solution for 2 min—always add HNO_3 to ethanol when preparing solution.
Stoloff/Gensamer	Cd-1.5% Zn alloy	320 g CrO_3 20 g Na_2SO_4 1000 mL H_2O	If staining occurs, use above solution.
Dudrova/Copova	Cadmium and cadmium-silver alloys (up to 3% Ag)	Solution A: 1 part H_2O_2 (3%) 1 part NH_4OH Solution B: 2 mL HF 28 mL HCl 50 mL H_2O	Immerse or gently swab with solution A for 1 min to remove grinding scratches. Follow with very fine diamond on satin, 500 rev/min, for 15 min. Wipe with a solution of HCl and ethanol, swab with solution B for 50–60 s. Remove surface deposit by immersing in solution C for 30 s.

Reagent	To polish	Composition	Remarks
		Solution C: 25 mL H_2O 25 mL H_2O_2 25 mL NH_4OH	
de Gregorio	Cadmium	3–6 g $K_2Cr_2O_7$ 100 mL HNO_3	Prepolish through alumina. Use solution at 40–60 °C (105–140 °F); immerse sample for 8–10 s, wash with water. Repeat cycle 6–7 times until polished.
Morral	Cobalt	40 mL lactic acid 30 mL HCl 5 mL HNO_3	Good for cobalt alloys also
Morral	Cobalt	1 part acetic acid 1 part HNO_3	…
Pray	Copper and alpha brass	55 mL H_3PO_4 20 mL HNO_3 25 mL acetic acid	0.5 mL HCl can be added. Use at 55–80 °C (130–175 °F) for 2–4 min. Agitate solution.
Pisek	Copper	6 mL HNO_3 65 mL acetic acid 27 mL H_3PO_4	Grind samples through 600-grit SiC. Immerse in solution at 60 °C (140 °F) for 1 min.
Meyer/Dunleavey	Copper	80 mL H_2SO_4 20 mL HNO_3 1 mL HCl 55–60 g CrO_3 200 mL H_2O	Use at 20–40 °C (70–105 °F) for 1–3 min. Good for copper alloys also
De Jong	Cu-8%Al, Cu-0.5%Be, and Cu-5%Al-2%Si alloys	1 part HNO_3 1 part H_3PO_4 1 part acetic acid	Use at 60–70 °C (140–160 °F) for 1–2 min.
De Jong	Cu-4.85%Si alloy	30 mL HNO_3 10 mL HCl 10 mL H_3PO_4	Use at 70–80 °C (160–175 °F) for 1–2 min. Agitate sample.

Reagent	To polish	Composition	Remarks
		50 mL acetic acid	
Camenisch	Alpha brass	17 mL HNO_3 17 mL H_3PO_4 66 mL acetic acid	Use at 50 °C (120 °F) for 30–120 s.
Blau	Oxygen-free high conductivity copper, copper-zinc alloys (10–15% Zn), and Cu-7.5%Al alloy	57 mL H_3PO_4 20 mL HNO_3 16 mL acetic acid	Use at 50–60 °C (120–140 °F) for 20 s.
Packard	Gallium arsenide	5 mL HCl 5 mL HNO_3 40 mL glycerin	Suspend sample in solution, agitate lightly to dislodge bubbles. Polishing rate is 0.37 mg/(cm^2·min).
Fuller/Allison	Gallium phosphide	100 mL methanol Saturate with chlorine	Use under hood, 5–20 min.
Haynes/Shockley	Germanium	15 mL HF 25 mL HNO_3 15 mL acetic acid 3–4 drops bromine	Use at 20 °C (70 °F) for 5–10 s.
Kawamura	Magnesium	90 mL H_2O_2 (30%) 10 mL H_2O 15 mL H_2SO_4	Use at 25 °C (75 °F) for 2–5 min.
Gifkins/Corbitt	Pure lead	20 mL acetic acid 30 mL H_2O_2 50 mL methanol	…
Gifkins	Pure lead and lead alloys	75 mL acetic acid 25 mL H_2O_2	Pour solution rapidly over sample (50 mL in 3–4 s) in a random pattern. Quickly wash in running water, rinse with alcohol, and dry. Repeat until good polish is obtained.
Scott/Pask	Lithium fluoride	H_3PO_4	Use at 60–120 °C (140–250 °F) for 6–12 h; cool to ambient temperature, rinse in water, ethanol, and anhydrous ether.
Grall	Magnesium	10 mL HNO_3	Use at 20 °C (70 °F).

Reagent	To polish	Composition	Remarks
		90 mL methanol	
Haddrell	Magnesium	0.4 g potassium dichromate 6 g boric acid 140 mL H_2O 15 drops HNO_3	Use for 1–2 min. Good for polarized-light work
Chia	Magnesium and Mg-MgO alloys (0–5% MgO)	8 mL HNO_3 12 mL HCl 100 mL ethanol	Grind to 600-grit SiC. Use at 20 °C (70 °F) for 30 s.
De Jong	Pure nickel	3 parts HNO_3 1 part H_2SO_4 1 part H_3PO_4 5 parts acetic acid	Grind through 600-grit SiC. Use at 85–95 °C (185–205 °F) for less than 1 min. Wash immediately in water.
Fox	Pure nickel and nickel-cobalt alloys	65 mL acetic acid (ice-cooled) 35 mL HNO_3 0.5 mL HCl	Fine grinding not required for pure nickel. Use at 20 °C (70 °F) for 2–4 min. For nickel-cobalt alloys, grind through 600-grit SiC, use at 20 °C (70 °F) for 1–2 min. (U.S. Patent 2,680,678)
Eary/Johnston	Niobium, vanadium, and tantalum	6 g $FeCl_3$ 30 mL HCl 120 mL H_2O 16 mL HF	Use at room temperature, 1 min for vanadium, 2 min for niobium, 3 min for tantalum.
…	Niobium, vanadium, and tantalum	30 mL H_2O 30 mL HNO_3 30 mL HCl 15 mL HF	Use at room temperature.
…	Platinum	20 mL HF 5 mL HNO_3	Use hot (temperature not specified) under hood.
Roman	Rare earth metals; erbium, dysprosium, gadolinium, holmium, and lanthanum	Solution A: 20 mL lactic acid 5 mL H_3PO_4	Solution A: Polish through 3 μm diamond. Do not add water to solution. Swab sample gently for 10–15 s (good for samples with low amount of inclusions).

Reagent	To polish	Composition	Remarks
		10 mL acetic acid 15 mL HNO_3 1 mL H_2SO_4 Solution B: 10 mL H_3PO_4 10 mL lactic acid 30 mL HNO_3 20 mL acetic acid	Solution B: Etches with a slight chemical-polishing action. Use for samples with larger amounts of inclusions. Polish through $\frac{1}{2}$–1 μm diamond, then use solution A for 2–3 s.
Koch/Picklesimer	Cerium	20 parts of solution A above 10 parts dimethyl-formamide (inhibits oxidation)	Do not add water to solution. Use for 10–15 s.
Butlinelli	Silicon	93 mL HNO_3 70 mL HF 17 mL H_2O 30 mL acetic anhydride 30 mL acetic acid	Use at 20 °C (70 °F) for 10–15 min. Discard after use.
CP-4 reagent	Silicon	20 mL HNO_3 5 mL HF	Use at 20 °C (70 °F) for 5–10 s.
Balk	SiO_2	1 part HF 2 parts acetic acid 3 parts HNO_3	Stir solution.
Levinstein/Robinson	Silver	100 g CrO_3 65 mL H_2O 5 drops HCl	Polish to 6 μm diamond, swab with solution (rinse frequently with water) for approximately 5 min. If a film forms, swab with H_3PO_4.
Soderberg	Silver	21 g NaCN	Use at 32 °C (90 °F) for a few seconds. When gas evolution begins, remove and

Reagent	To polish	Composition	Remarks
		78 g H_2O_2 (30%) 1000 mL H_2O	wash with 37.5 g NaCN per liter of water. Immerse in chemical polish and repeat cycle until polished.
Chase etch	Ag-30% Zn alloy	4 g Cr_2O_3 7.5 g NH_4Cl 150 mL HNO_3 52 mL H_2SO_4 H_2O-to 1 L	Use at 60 °C (140 °F).
Isaacs/Singer	Sodium	5–50% methanol in acetone	Use at room temperature for less than 10 s. Dip in pure acetone, wash immediately in petroleum ether. Place in mineral oil for viewing.
Vermilyea	Tantalum	2 parts acetic acid 5 parts H_2SO_4 1 part HF	…
Noer	SnTe	0.35 g I_2 40 mL ethanol (or methanol) 10 mL H_2O 4 mL HF	To prepare solution, dissolve iodine in ethanol (or methanol). Add water, then add HF. Prepolish sample to Linde A abrasive. Saturate cloth with solution. Lightly rub sample over wet cloth in figure-eight motion for 15–20 min. Add solution periodically. Rinse in methanol, then water, and dry.
Cain	Iodide titanium	60 mL H_2O_2 (30%) 30 mL H_2O 8–10 mL HF	Swab for 30–60 s.
Cain	Titanium	1 part HF 1 part HNO_3	Immerse sample and agitate vigorously. When polishing action becomes violent, continue for approximately 10 s. Discard solution when it turns green.
Rice	Titanium	30 mL HF 70 mL HNO_3	Polish through gamma alumina. Chemical polish for 10 s.
Hirthe/Brittain	TiO_2	KOH	Heat to 650 °C (1200 °F); immerse sample (remove from mount) for 8 min.
Miller	Zinc	20 g CrO_3 95 mL H_2O 5 mL HNO_3 4 g zinc sulfate	Use at 20 °C (70 °F) for 2–5 min. Use fresh solution. Discard when done. Hold sample vertical to minimize pitting. Remove chromic acid film by dipping in 5–7% aqueous HCl.
Gilman/De Carlo	Zinc	1 part HNO_3	Immerse sample for approximately 2 min.

Reagent	To polish	Composition	Remarks
		1 part H_2O_2 (30%) 1 part ethanol	When preparing solution, always add HNO_3 to ethanol.
Soderberg	Zinc	43 mL H_2O_2 27 mL H_2SO_4 900 mL H_2O	Immerse for 30 s.
Soderberg	Zinc and cadmium	200 g $Na_2Cr_2O_7$ 6–9 mL H_2SO_4 1000 mL H_2O	Use at 20 °C (70 °F) for 5–10 min.
Soderberg	Zinc	200 g CrO_3 15 g Na_2SO_4 52.5 mL HNO_3 950 mL H_2O	Use at 20–30 °C (70–85 °F) for 10–30 s.
Soderberg	Zinc	25 wt% CrO_3 10 wt% HCl 65 wt% H_2O	Use at 20–30 °C (70–85 °F) for 10–30 s.
Cain	Zirconium, Zircaloys, and hafnium	45 mL HNO_3 45 mL glycerol 8–10 mL HF	Use under hood. Swab (preferred) or dip sample. A few seconds after contact, NO_2 is given off (do not inhale)—polishing has started. Continue 5–10 s.
Cain	Zirconium, Zr-2½% Nb alloy, Zircaloy-2, Zircaloy-4, and hafnium	45 mL NHO_3 45 mL H_2O 8–10 mL HF	Use as above.
Cain	Zirconium and hafnium	45 mL H_2O_2 (30%) 45 mL HNO_3 8–10 mL HF	Use as above.
Cain	Zircaloy-2 and hafnium	70 mL H_2O 30 mL HNO_3 2–5 mL HF	Use as above.
Rumball/Elder	Zr-Cr-O alloys, and zirconium alloys other than Zircaloys	45 mL lactic acid 45 mL HNO_3	Polish to 6 μm diamond.

Reagent	To polish	Composition	Remarks
		8 mL HF	
Aqua/Owens	Zircaloy-4	50 mL HNO_3 50 mL H_2O 10 mL HF	…
Mackay	Zirconium	15 mL HF 80 mL HNO_3 80 mL H_2O	Use for 2 min.

Table 6 Attack-polishing solutions

When water is specified, always use distilled water.

Reagent	To polish	Attack-polishing solution	Remarks
Samuels	Aluminum	0.5 wt% NaOH in H_2O	Add dropwise to the charged cloth.
Bonfield	Beryllium	Alumina in warm solution of 20% oxalic acid and H_2O	Use after 600 grit.
Udy	Beryllium	5% oxalic acid in H_2O Alumina on cloth	Use with 1750 rev/min wheel. Apply small amount of abrasive and solution. As polishing progresses, add solution only. Near end, add water, a few drops at a time, to moisten the cloth. Commercially pure Fe_2O_3 is better but slower than alumina.
Boyd	Beryllium	Solution A: 10% oxalic acid 0.3 μm alumina Solution B: 100 mL water 14 mL H_3PO_4 1 mL H_2SO_4 20 g CrO_3 0.05 μm alumina	Two-step procedure. Dilute 1 part solution B with 10 parts water before use. Use silk cloth with solution A, synthetic suede cloth with solution B. Use 1200 rev/min wheel with solution B. Add solution dropwise and polish 15–30 s.
Udy	Beryllium	Magnesia suspended in H_2O_2 (30%)	Mix fresh. Charge wheel heavily. Use when magnesium-rich particles are present. Slow; requires a few minutes
Calabra/Jackson	Beryllium	200 cm^3 0.05 μm alumina 600 mL H_2O	Use with vibratory polisher, short-nap cloth, 24 h polish.

Reagent	To polish	Attack-polishing solution	Remarks
		20 mL 10% CrO_3 in H_2O	
Woods	Beryllium	10 g oxalic acid 100 mL H_2O	Use with two grades of alumina on silk cloths.
Anderson	Bismuth	30% HNO_3 in glycerol Gamma alumina	Add gamma alumina to solution.
Haddrell	Bismuth	50 mL HNO_3 150 mL glycerol Rouge or alumina abrasives	Use with Terylene-covered laps. Polish for 3–5 min. Good for polarized-light work.
Haddrell	Chromium	15 g acetic acid 150 mL H_2O Rouge or alumina abrasive	Use with Terylene-covered laps. Polish for 5–10 min.
Ogleby	Chromium	1% oxalic acid in 1:1 solution of ethyl alcohol and H_2O Alumina abrasive	…
Anderson	Chromium and tungsten	75 mL H_2O 15 g 0.05 μm alumina 1 g CrO_3	Near end of polish, flush with water and finish without solution.
Chang	Chromium-silicon alloys (2–76 atomic wt% Si)	5% CrO_3 in H_2O Alumina abrasive	Grind through 600 grit; use with nylon cloth.
Samuels	Copper and brass (high zinc content)	Aqueous ammonium persulfate 10–15 g/L (for copper) 15–30 g/L (for brass) MgO abrasive	Insert plastic between cloth and wheel to prevent pitting. Use skid-polish technique. Good for aluminum or zinc also.
Buchheit	Copper	2–10% CrO_3 in H_2O Rouge or alumina abrasives	Use napped cloth.
…	Copper	1% ferric nitrate in H_2O	Use with medium-nap cloth.

Reagent	To polish	Attack-polishing solution	Remarks
		Alumina or colloidal silica abrasives	
Slepian/Prohaska	Copper	5 g $Fe(NO_3)_3$ 25 mL HCl 370 mL H_2O Gamma alumina	Attack polish for 3 min, wash off wheel, add solution only, and polish for 2–5 s.
Cocks/Taplin	Cu-30%Zn alloy	12 g/L aqueous ammonium persulfate MgO abrasive	Skid polish for 20 min with high-nap cloth.
Beland	Nickel	4 g cupric sulfate 20 mL HCl 20 mL H_2O	Marble's reagent. Dilute 1 part etch to 10 parts H_2O. Apply to napped cloth charged with gamma alumina. Use very light pressure, 500 rev/min wheel speed.
O'Mara	Nickel alloys and some alloy steels	2.5 g copper chloride 50 mL H_2O 50 mL HCl	Dilute 1 part etch to 10 parts H_2O. Charge billiard cloth with abrasive, add small amount of etch. Insulate cloth from wheel.
Buchheit	Niobium	15 g gamma alumina 35 mL H_2O 5 mL of 20% CrO_3 in H_2O	Use napped cloth, 1750 rev/min wheel. Finish polishing without etch on slow wheel, napped cloth.
Anderson	Niobium and tantalum	200 mL H_2O 10 mL H_2SO_4 3 mL HNO_3 2 mL HF	Use stainless steel wheel. Add etch, then alumina to cloth. As polishing progresses, flush with water and finish with alumina only.
Anderson	Niobium and tantalum	450 mL H_2O 15 mL HF 5 mL HNO_3 10 mL H_2SO_4	Use as above but works best with automatic devices.
Taylor/Doyle	Niobium-hafnium alloys	50 mL H_2O_2 (30%) 10 mL HNO_3 1 drop HF Gamma alumina	Use with hafnium-rich alloys. Use gamma-alumina abrasive.
Taylor/Doyle	Niobium-hafnium	50 mL lactic acid	Use with niobium-rich alloys. Use with

Reagent	To polish	Attack-polishing solution	Remarks
	alloys	30 mL HNO_3 5 mL HF Gamma alumina	gamma alumina.
Taylor	Nb-Mo-C alloys	5% CrO_3 in H_2O Gamma alumina	Add solution, amount not specified, to alumina-water suspension.
Buchheit	Platinum and palladium	10 g rouge abrasive 35 mL H_2O 5 mL of 20% CrO_3 in H_2O	Final polish with napped cloth on 250 rev/min wheel.
Buchheit	Rhenium	15 g fine alumina 35 mL H_2O 5 mL of 20% CrO_3 in H_2O	Rough polish with slurry on napped cloth, 1750 rev/min wheel. Final polish without etch, napped cloth, 250 rev/min wheel.
Taylor	Rhenium-hafnium alloys	50 mL H_2O_2 (30%) 50 mL HNO_3 5 mL HF	Add solution to gamma alumina/water suspension, concentration not given.
Buchheit	Ruthenium, rhodium, iridium, and osmium	15 g fine alumina 35 mL H_2O 5 mL of 20% CrO_3 in H_2O	Use napped cloth, 1750 rev/min wheel. Final polish with solution on napped cloth, 250 rev/min wheel.
Coons	Silicon	Alpha alumina in 3–5% solution of CrO_3 and H_2O	Use silk-covered bronze wheel at 1150 rev/min, firm pressure.
Gaylor	Ag-Sn-Hg alloys	Dilute aqueous solution of ammonium persulfate	Concentration and abrasive not given. Add a few drops of ammonia during polishing.
Buchheit	Tantalum	15 g fine alumina 35 mL H_2O 5 mL of 20% CrO_3 in H_2O	Use napped cloth, 1750 rev/min wheel, medium to heavy pressure. Recharge periodically.
Buchheit	Tantalum	Solution A: 2–5% aqueous CrO_3 Alumina abrasive	Use napped cloth, 1750 rev/min wheel with solution A. Follow with chemical polishing with solution B.

Reagent	To polish	Attack-polishing solution	Remarks
		Solution B: 50 mL lactic acid 30 mL HNO_3 2 mL HF	
Vaughan	Tantalum	Solution A: 2–5% aqueous CrO_3 Alumina abrasive Solution B: 30 mL lactic acid 10 mL HNO_3 10 mL HF	Use wax lap instead of cloth with solution A. Follow with chemical polishing with solution B.
Lott	Tantalum	100 mL acetic acid 60 mL HNO_3 3 mL HF Alpha alumina	Polish through 6 μm diamond. Add solution to napped cloth; add dry abrasive. Use 30 lb/in^2 pressure for 8 min, 10 lb/in^2 for 1 min.
Buchheit	Thorium	Solution A: 10% oxalic acid in H_2O Alumina abrasive Solution B: 10 mL HNO_3 1 mL HF 98 mL H_2O Rouge or alumina abrasive	Use solution A for rough-polishing step; add abrasive to etch. Use solution B for final-polishing step. Add etch to cloth charged with abrasive.
Buchheit	Titanium	15 g fine alumina 35 mL H_2O 5 mL of 20% CrO_3 in H_2O	Charge napped cloth with slurry; use 1750 rev/min wheel. Heavy pressure initially, decrease gradually. Etch with Kroll's reagent. Final polish without CrO_3 on 500 rev/min wheel, napped cloth, light, firm pressure.
Timet	Titanium	0.3 μm alumina	Use for 3 min.

Reagent	To polish	Attack-polishing solution	Remarks
		suspended in 5% aqueous oxalic acid	
Sylvania	Titanium	10 g gamma alumina 15 drops HF 15 drops HNO_3 100 mL H_2O	Use for 1 min, napped cloth.
…	Titanium	1% HF in H_2O Gamma alumina	Moisten napped cloth with solution; add gamma alumina.
…	Titanium	1% HF in H_2O Gamma alumina	Insulate wheel surface; use napped cloth. Moisten cloth with solution; add dry abrasive. If the surface is dull, add more abrasive. Followed by electropolish
Craver	Titanium	5% oxalic acid in H_2O Two grades of alumina	Alumina abrasives suspended in water plus small amount of liquid soap and a few drops of reagent. Polish, etch, repolish.
Yih/Wang	Tungsten	Solution A: 8–10 g alpha alumina 10 mL of 20% CrO_3 in H_2O 150 mL H_2O Solution B: 3.5 g $K_3Fe(CN)_6$ 0.2–0.3 g NaOH 150 mL H_2O	Two-step process. Rough polish with solution A on 1750 rev/min wheel covered with Metcloth (Buehler, Ltd.) and silk. Polish, etch, repolish. Final polish with solution B on 250–550 rev/min wheel covered with Metcloth. Add gamma alumina; moisten with solution B.
Woods	Tungsten	10 g gamma alumina 3.5 g $K_3Fe(CN)_6$ 1 g NaOH 150 mL H_2O	Pregrind to 600-grit SiC. Add solution to velvet cloth; polish for approximately 15 s.
Miller/Sass	Tungsten	1 g $CuSO_4 \cdot 5H_2O$ 20 mL NH_4OH 1000 mL H_2O	Add a few drops of solution to wheel charged with abrasive; polish for 15–20 min.
Lott	Tungsten	30 g rouge abrasive	Intermediate polish. Swab-etch with a solution of 70 mL lactic acid, 20 mL

Reagent	To polish	Attack-polishing solution	Remarks
		30 g CrO_3 100 mL H_2O	HNO_3, and 10 mL HF. If deformation is present, repeat polish with light pressure.
Newton/Olson	Tungsten	1 part H_2O 1 part NH_4OH 1 part H_2O_2 (30%) (add last) (Use under hood, with rubber gloves)	Two-step process. Pregrind to 600-grit SiC. Insulate wheel, add 1 μm alumina to Kitten Ear (Buehler, Ltd.) cloth. Pour solution onto abrasive, mix. Polish 4–5 min with heavy pressure. Final polish: Kitten Ear cloth with alpha alumina and solution, light pressure. Repeat, if necessary, with gamma alumina.
Ambler/Slattery	Uranium	5% suspension of H_2O_2 (30%) in fine alumina slurry	Use Terylene cloth.
Haddrell	Uranium	50 g CrO_3 100 mL H_2O 10 mL HNO_3 Alumina	Use Terylene-covered wheel, 20–30 min.
Metz/Woods	Uranium	30 mL HF 30 mL HNO_3 60 mL H_2O 5–8 g fine alumina	Swab surface with conc HNO_3 immediately after polishing.
Bauer	U-Mo-Ti alloys	100 g CrO_3 118 mL H_2O Gamma-alumina abrasive	Attack polish sample; follow by electropolishing.
Filer/Asaud	UO_2, carbide-coated graphite, and pyrolitic graphite	30 g gamma alumina 140 mL H_2O_2 (30%)	Polish with slurry on Texmet (Buehler, Ltd.) or Pellon for 4–5 min, 5–6 lb pressure on mount. Wet cloth with water before adding slurry. Follow with 30 s polish on Microcloth (Buehler, Ltd.), same load. Wash with water immediately to prevent staining.
Ambler	UO_2 and U_3Si	H_2O_2 (30%) Chromic oxide abrasive (Concentrations not given)	Use freshly prepared Cr_2O_3 abrasive. Grind UO_2 through 600-grit SiC before attack polishing. Polish U_3Si to 1 μm diamond before attack polishing.
Hunlich	UO_2 and UO_2CeO_2	50 g CrO_3 10 mL HNO_3	Grind through 600-grit SiC. Attack polish on coarse felt, 10 min maximum. Final polish with fine alumina on napped cloth.

Reagent	To polish	Attack-polishing solution	Remarks
		70 mL H_2O 30 cm^3 alumina or chromic oxide abrasive	
Buchheit	Vanadium	15 g fine alumina 35 mL H_2O 5 mL of 20% CrO_3 in H_2O	Charge 1750 rev/min wheel, napped cloth, with solution. Use medium to heavy pressure; recharge as needed. Polish for short time without CrO_3, medium pressure. Follow with electropolishing.
Lott	Vanadium	60 g rouge abrasive 60 g CrO_3 200 mL H_2O	Boil solution 20 min before use. If deformation is present after attack polishing, swab-etch with 1 part HF, 1 part HNO_3, and 2 parts H_2O; repeat polish and etch until deformation is removed.
Henry	Vanadium-oxygen alloys	15 g gamma alumina 35 mL H_2O 5 mL of 20% CrO_3 in H_2O	For alloys with more than 5% O. Use 8 in. wheel, 1150 rev/min.
Haddrell	Zirconium	50 mL HNO_3 150 mL glycerol Alumina abrasive	Use terylene cloth, 1–10 min.
Roth	Zirconium	4–30 drops HF added to 100 mL polishing solution	…
Roth	Zirconium	1% HF 0.5% HNO_3 in H_2O	…
Roth	Zirconium	3–10% oxalic acid in H_2O	…
Roth	Zirconium	50% HNO_3 in H_2O Few drops HF or fluosilicic acid	…
Ambler	Zirconium	Slurry of chromic oxide abrasive plus $\frac{1}{2}$ % aqueous HF	Use freshly prepared Cr_2O_3. Polish sample through 6 μm diamond before attack polishing. Near end of polish, dilute with water.
Westinghouse	Zircalloy-2 and hafnium	200 mL H_2O 200 mL HNO_3 72 drops HF	Add approximately 5–10 mL of solution to wheel charged with alumina abrasive.
Grange	Copper-lead alloys	Aqueous solution of CrO_3 and HCl	Concentrations and abrasive not given.

Reagent	To polish	Attack-polishing solution	Remarks
Buchheit	Gold	5–10% CrO_3 in H_2O Rouge or alumina abrasives	Use napped cloth.
Buchheit	Gold	12.5 g potassium iodide 100 mL H_2O Alumina abrasive	Add a few drops of etch to charged cloth.
Woods	Hafnium	4–30 drops HF to 100 mL of alumina-H_2O suspension	Use napped cloth.
Rudy/St. Windisch	Hafnium-vanadium and hafnium-chromium alloys	5% CrO_3 in H_2O Gamma alumina	…
Schmidt	Lead telluride	50% H_2O_2 (30%) 50% glacial acetic acid Alpha alumina	Use twill-jean cloth on glass plate. Saturate cloth with solution and abrasive. Polish 2–3 min. Wash cloth, apply etch only, polish 2–3 min. Wash with warm water, then acetone or alcohol, and dry.
Haddrell	Magnesium	20 mL of 2% potassium dichromate 150 mL saturated boric acid 15 drops HNO_3 Alumina	Other recipes for specific magnesium alloys [(a)]
Coons	Molybdenum	10 g NaOH 30 g $K_3Fe(CN)_6$ 100 mL H_2O	1 part etch to 5 parts C-RO[(a)] polishing compound. Use for 3–5 s. Another method is adding the chemicals of the attack agent (usually a dilute etchant) to either colloidal silica or alumina suspensions.
Buchheit	Molybdenum and tungsten	Solution A: 15 g fine alumina 5 mL of 20% CrO_3 in H_2O Solution B: 10 g rouge abrasive 35 mL H_2O 5 mL of 20% CrO_3	Rough polish with napped cloth on 1750 rev/min wheel with solution A. Use heavy pressure, recharge. Final polish with napped cloth on 250–500 rev/min wheel with solution B.

Reagent	To polish	Attack-polishing solution	Remarks
		in H_2O	
Miller/Sass	Molybdenum	2 g/L $CuSO_4 \cdot 5H_2O$ in H_2O 20 mL NH_4OH	Abrasive not specified. Polish 15–20 min.
Rudy	Molybdenum-carbon alloys	5% CrO_3 in H_2O Gamma-alumina abrasive	Use napped cloth.
Hodkin	Molybdenum, niobium, tantalum, and tungsten	5% KOH in H_2O Alumina abrasive	Prepolish to 1 μm diamond.
Ambler	Zr_3Al-base alloys	Slurry of chromic oxide abrasive in water plus a few drops of $\frac{1}{2}$% aqueous HF	Use freshly prepared Cr_2O_3. Dilute with water as polishing progresses.
Buchheit; Cameron/Van Rensburg	Minerals	10 g rouge abrasive 35 mL H_2O 5 mL of 20% CrO_3 in H_2O	Use with napped cloth. For galena, dilute with 10 parts H_2O.
Lott	Pyrolytic graphite	2% CrO_3 in H_2O Gamma alumina	Polish to 1 μm diamond. Attack polish with slurry on napped cloth, heavy pressure. Final polish with MgO on Rayvel (Buehler, Ltd.).
Coons	Pyrolytic graphite	5% CrO_3 in H_2O	Polish through 1 μm diamond. Add solution to automatic polishing device charged with C-RO[(b)] abrasive, 325 g weight, 10 min.
McBride	Cermets and sintered carbides	7–10% CrO_3 in water plus H_3PO_4 (<1%)	Attack polish with rouge on 1750 rev/min wheel. Add a few drops of solution periodically.
Robinson/Gardner	Silicon carbide	20% CrO_3 in H_2O Gamma alumina	Polish through 1 μm diamond. Attack polish on Texmet or Pellon cloth.
Rudy/St. Windisch	Borides of hafnium, niobium, titanium, vanadium, or zirconium	10–20 g abrasive 10 g $K_3Fe(CN)_6$ 10 g KOH 100 mL H_2O	…
Coons	Tungsten boride	10 g NaOH 35 g $K_3Fe(CN)_6$ 150 mL H_2O	Add solution to cloth charged with Cer-Cro abrasive.

(a) Source: V.J. Haddrell, "An Attack-Polishing Technique for the Metallographic Preparation of Magnesium and its Dilute Alloys," *J. Inst. Met.*, Vol. 92, 1963–1964, p. 121.
(b) C-RO is an old proprietary polishing compound of Leco Corp.
Source: G. Vander Voort, *Metallography Principles and Practice*, McGraw-Hill, 1984; reprinted by ASM International, 1999

Table 7 Macrostructure etchants for iron and steel

Before using any chemicals, Material Safety Data Sheets (MSDS) should be reviewed.

Etching reagent	To reveal	Composition	Remarks
Hydrochloric acid	Segregation, porosity, cracks, and depth of hardened zones in tool steels	50 mL H_2O 50 mL HCl	Use at 71–82 °C (160–180 °F) for 1–60 min, depending on type of steel and type of structure to be developed.
Mixed acids	Welds, segregation, cracks, and hardened zones	50 mL H_2O 38 mL HCl 12 mL H_2SO_4	Use at 93 °C (200 °F) for 15–45 s or 22 °C (72 °F) for 2–4 h.
Ammonium persulfate (Rawdon)	Welds	90 mL H_2O 10 mL $(NH_4)_2S_2O_8$	Surface should be rubbed with absorbent cotton during etching. Etch to desired contrast.
Nitric acid	Same as hydrochloric acid	75 mL H_2O 25 mL HNO_3	Use cold on large surfaces that cannot be conveniently heated.
Oberhoffer's reagent	Develops dendritic pattern in steel. Iron-enriched areas are darkened.	500 mL H_2O 30 g $FeCl_3$ 0.5 g $SnCl_3$ 1 g $CuCl_2$ 500 mL ethyl alcohol 50 mL HCl	Use at room temperature. Immerse approximately 20 s.
Kalling's reagent	Develops dendritic pattern in steel; attacks ferritic and martensitic stainless steels. Ferrite darkened; martensite darker; austenite light	33 mL H_2O 1.5 g $CuCl_2$ 33 mL methyl alcohol 33 mL HCl	Etch to desired contrast.
Humfrey's reagent	Develops dendritic segregation	500 mL H_2O 25 mL HCl 60 g $Cu(NH_3)_4Cl_2$	Slight abrasion of surface after etching is recommended.
Bell's reagent (electrolytic)	Welds in stainless steel	40 mL H_2O	Stainless steel cathode, 5 V. Etch to desired contrast.

Etching reagent	To reveal	Composition	Remarks
		60 mL H_2NO_3	
Watertown arsenal	For carbon and stainless steels, general structure	50 mL H_2O 12 mL H_2SO_4 38 mL HCl	Use at 71–82 °C (160–180 °F) for 10–60 min. Use with cut or ground surfaces.
Dilute aqua regia	For high-alloy steels and iron-cobalt high-temperature alloys	25 mL H_2O 25 ml HNO_3 50 mL HCl	Time: 10–15 min at room temperature
Piearcy and co-workers	Maraging steel macrostructure	60 mL lactic acid 20 mL HNO_3 10 mL HCl	Use at room temperature.
Burg and Weiss	Nitriding steels macrostructure	85 mL H_2O 15 mL ammonium persulfate	Use at 71 °C (160°F) for 10 min.
Marble's reagent	General etch for austenitic stainless steel	50 mL H_2O 10 g $CuSO_4$ 50 mL HCl	Solution can be heated.
Miller and Houston	Welds and general macrostructure of austenitic stainless steel	90 mL H_2O 10 g CrO_3	Use electrolytically with polished surface. Platinum or stainless steel cathode. Use at 16–38 °C (60–100 °F), 6 V, for 2–7 min.
Loria (nitrosulfuric acid etch)	As-cast structure and grain size in cast steels	20 mL H_2O 20 mL HNO_3 10 mL H_2SO_4	Use at room temperature.
Nielsen	Stress-corrosion cracks in austenitic stainless steel	95 mL methyl alcohol 5 mL bromine	Use at room temperature for approximately 1 h. Crack pattern vividly revealed

Table 8 Major microstructure etchants for common phases and constituents in ferrous materials

Etching reagent	Composition	Remarks
Ferrite grain boundaries		
Nital	1–5 mL HNO_3 (nitric acid) 99–95 mL ethyl alcohol	A 2% solution is recommended; usually samples are etched 10–20 s with a gentle agitation and the polished surface facing upward to reveal the ferrite grain boundaries. In order to reveal all the grain boundaries, the last polishing step should be with silicon dioxide for at least 60 s, and the sample should then be etched shortly after polishing, before a passive layer forms,

Etching reagent	Composition	Remarks
		thus preventing an even etch. If the sample is to be examined in the as-polished condition, it should be repolished for 10–15 s with silicon dioxide prior to etching. Note: A nital etch is not recommended for etching pearlite, because it does not etch evenly.
Marshall's reagent	Stock solution A: 100 mL H_2O 8 g oxalic acid 5 mL H_2SO_4 (sulfuric acid) Stock solution B: H_2O_2 (30%) (hydrogen peroxide)	Excellent etchant to show both equiaxed and cold-worked microstructures. Mix stock solution A to equal parts of solution B just prior to etching. Place the polished face of the sample on its side during immersing in the etchant to prevent or minimize pitting. If the sample does not react to the reagent, add 1 mL hydrofluoric acid to 100 mL of solution. If a haze covers the surface, remove by placing the sample in a 3% aqueous disodium ethylenediamine tetraacetate (EDTA) solution. Place the sample and solution in an ultrasonic cleaner for several minutes. Flush the sample with water, then alcohol, then dry.
Beraha's	100 mL H_2O 10 g $Na_2S_2O_3$ (potassium thiosulfate) 3 g $K_2S_2O_5$	Pre-etch for 3 s with 2% nital. Etch in Beraha's reagent with the polished side of the sample face up for 45 s; do not agitate. Rinse with water, flush with alcohol, and dry. If the sample is over- or underetched, remove etchant by polishing with 0.3 μm aluminum oxide for 15 s, followed by silicon dioxide for 45 s, and re-etch.
Pearlite structure		
4% picral	96 mL ethyl alcohol 4 g picric acid 5 drops 17% zephiran (benzalkonium chloride, Sanofi-Synthelabo Inc.) per 75 mL solution	Picral is one of few etchants that improves with use. A common practice is to age the etchant by placing a ground piece of steel into the solution until the etchant turns a dark green. This technique makes the etching time constant, usually 20 s for pearlite or Fe_3C carbides. The etchant can be saved for future use. For samples with more then 0.5% Cr, add 5 drops of hydrochloric acid per 100 mL of solution.
Marshall's reagent	Stock solution A: 100 mL H_2O 8 g oxalic acid 5 mL H_2SO_4 (sulfuric acid) Stock solution B: H_2O_2 (30%) (hydrogen peroxide)	Excellent etchant to outline pearlite colony boundaries.
Alkaline sodium picrate	100 mL H_2O 25 g NaOH 2 g picric acid	Bring the solution to a low boil; do not boil dry. Etching time: 5–10 min. The solution will attack Bakelite (Georgia-Pacific Corp.) mounts; thermosetting epoxy mounts are recommended. The solution will color cementite but will not color carbides with high (10%) chromium content. The solution will also attack sulfides and delineate grain boundaries in steels that

Etching reagent	Composition	Remarks
		have been cooled slowly.
Klemm's reagent	50 mL H_2O $Na_2S_2O_3$ (enough for saturation) 1 g $K_2S_2O_5$ (potassium metabisulfite)	Tint etches pearlite. Etching time: 40–120 s. Etch in Klemm's reagent with the polished side of the sample face up; do not agitate. Ferrite appears black-brown, but carbides, nitrides, and phosphides remain white. Phosphorus distribution can be detected more sensitively than with usual phosphorus reagents based on copper salts.
Fe_3C carbides		
4% picral	96 mL ethyl alcohol 4 g picric acid 5 drops 17% zephiran chloride per 75 mL solution	Carbides will be delineated from the ferrite by a black boundary.
Marshall's reagent	Stock solution A: 100 mL H_2O 8 g oxalic acid 5 mL H_2SO_4 (sulfuric acid) Stock solution B: H_2O_2 (30%) (hydrogen peroxide)	Excellent reagent that will color carbides a light tan. The color variation will assist in differentiating small carbides on ferrite grain boundaries.
Alkaline sodium picrate	100 mL H_2O 25 g NaOH 2 g picric acid	Bring the solution to a low boil; do not boil dry. Etching time: 5 to 10 min. The solution will attack Bakelite mounts. Thermosetting epoxy mounts are recommended. The solution will color cementite but will not color carbides with high (10%) chromium content. The solution will also attack sulfides and delineate grain boundaries in steels that have been cooled slowly.
Ferrite and pearlite		
2% nital/4% picral **4% picral followed by 2% nital**	Mix equal parts 2% nital and aged 4% picral 96 mL ethyl alcohol 4 g of picric acid 5 drops of 17% zephiran chloride per 75 mL solution 2 mL HNO_3 + 96 mL ethyl alcohol	Etchant will reveal both ferrite and pearlite boundaries. Etch the sample for 20 s in 4% picral. Rinse in an alcohol bath, flush with alcohol, and dry. Next, etch the sample for 10–15 s in 2% nital.
Bainite		
4% picral	96 mL ethyl alcohol 4 g picric acid	Etch to desired contrast. Sometimes, additional etching in 2% nital will reveal substructure. This etchant is excellent for upper and lower banite.

Etching reagent	Composition	Remarks
	5 drops 17% zephiran chloride per 75 mL solution	
Sodium metabisufite	100 mL H_2O 12 g $Na_2S_2O_5$	Pre-etch for 3 s in 2% nital. Rinse in water and immediately immerse in the sodium metabisulfite; do not agitate. Time may vary from 10–30 s. Rinse in water, flush with alcohol, and dry.
4% picral + HCl	96 mL ethyl alcohol 4 g of picric acid 5 drops 17% zephiran chloride per 75 mL solution plus a few drops to several millimeters of hydrochloric acid	…
Ferrite, pearlite, bainite, and martensite		
Sodium metabisulfite	100 mL H_2O 12 g $Na_2S_2O_5$	Pre-etch the sample for 3 s in 2% nital. Rinse the sample in water, then immediately immerse the sample in the sodium metabisulfite. Do not agitate. Etchant time is approximately 20 s.
4% picral followed by 2% nital	96 mL ethyl alcohol 4 g picric acid 5 drops 17% zephiran chloride per 75 mL solution 2 mL H_2NO_3 + 96 mL ethyl alcohol	…
Martensite		
2% nital	2 mL HNO_3 (nitric acid) 98 mL ethyl or methyl alcohol	Use this etchant for lath and plate martensite. Retained austenite in plate martensite structure appears white between the plates. For this etchant to be effective, it is necessary to slightly temper the martensite. A mounting temperature of 149 °C (300 °F) is sufficient.
Sodium metabisulfite	100 mL H_2O 12 g $Na_2S_2O_5$	Pre-etch for 3 s in 2% nital. Rinse in water and immediately immerse in the sodium metabisulfite. Do not agitate. Time may vary from 10–30 s. Rinse in water, flush with alcohol, and dry.
4% picral	96 mL ethyl alcohol 4 g picric acid 5 drops 17% zephiran chloride per 75 mL solution	This etchant works best on highly tempered martensite. To reveal residual laths in lath martensite, use 2% nital over the 4% picral etch.
Marshall's reagent	Stock solution A: 100 mL H_2O 8 g oxalic acid 5 mL H_2SO_4 (sulfuric	Works great on lath martensite, especially to reveal the prior-austenite grain boundaries

Etching reagent	Composition	Remarks
	acid) Stock solution B: H_2O_2 (30%) (hydrogen peroxide)	
4% picral followed by 2% nital	96 mL ethyl alcohol 4 g picric acid 5 drops 17% zephiran chloride per 75 mL solution 2 mL H_2NO_3 + 96 mL ethanol alcohol	Works well on martensite that has been tempered at high temperatures or for long periods of time
Prior-austenite grain boundaries		
Vilella's	100 mL ethyl alcohol 1 g picric acid 5 mL hydrochloric acid	…
Alkaline sodium picrate	100 mL H_2O 25 g NaOH 2 g picric acid	Bring the solution to a low boil. Do not boil dry. Etching time: 10 min followed by 10 s in 2% nital, then 20 s in 4% picral. The solution will attack Bakelite mounts. Thermosetting epoxy mounts are recommended.
Modified Winsteard's	Part A: 10 mL ethyl alcohol 2 g picric acid Part B: 200 mL H_2O 5 mL sodium tridecylbenzene sulfunate 5 drops hydrochloric acid	Mix part A with part B. Solution can be stored and reused many times. Sodium tridecylbenzene sulfunate can be substituted with All (Lever Brothers Co.) detergent or Calsoft 90 (Pilot Chemical Co.). Volume of hydrochloric acid can be increased after the following procedures are tried: (a) At room temperature up to 5 min; observe, first using bright-field illumination. If no results are obtained, try dark-field illumination. (b) If no results, heat the solution 15–21 °C (60–70 °F) and repeat the room-temperature procedure. (c) If no results, place the sample and solution in an ultrasonic cleaner, repeating the room-temperature procedure.
Saturated aqueous picric acid	10 g picric acid 100 mL H_2O 1 g sodium tridecylbenzene sulfanate (wetting agent)	Add picric acid crystals to water while stirring. Decant liquid from undissolved crystals. Add wetting agent to liquid. Immerse sample; rinse with water, followed by an alcohol rinse, and blow dry.
Internal oxidation		
4% picral	96 mL ethyl alcohol 4 g picric acid 5 drops 17% zephiran chloride per 75 mL solution	Etch no less than 20 s.

Etching reagent	Composition	Remarks
Stainless steel microstructures, austenite		
60/40	40 mL H_2O 60 mL HNO_3 (nitric acid)	Electrolytic etchant. Stainless steel cathode at 6 V for 10–20 s or until desired contrast; will outline austenite grain boundaries and annealing twins. A platinum cathode will produce austenite grain boundaries without revealing annealing twins.
HCl/methanol	95 mL methyl alcohol 5 mL HCl	Electrolytic etchant. Stainless steel cathode, 10 V. Suggested use for Invar
Oxalic acid	100 mL H_2O 10 g oxalic acid	Electrolytic etchant. Stainless steel cathode, 5–6 V for 10–20 s
Aqua regia	45 mL HCl (conc) 15 mL HNO_3 (conc)	Use at room temperature. For austenite grain structure. Outlines carbides
Chromic oxide	10 g CrO_3 100 mL H_2O	Electrolytic etchant. Stainless steel cathode, 6V for 10–20 s. For welds, outlines carbides
Stainless steel microstructures, ferrite		
Glyceregia	30 mL glycerol 20 mL HCl 10 mL HNO_3	Immerse until desired contrast is obtained.
Murakami's reagent	10 g $K_3Fe(CN)_6$ 10 g KOH 100 mL H_2O	Use hot (75 °C, or 165 °F) to darken sigma phase. Use at room temperature to darken carbides.
Stainless steel microstructures, martensite		
Kalling's No. 1	33 mL H_2O 1.5 g $CuCl_2$ 33 mL ethyl alcohol 33 mL HCl	Immerse until desired contrast is obtained. For maraging steel
Fry's	25 mL H_2O 5 g $CuCl_2$ 25 mL ethyl alcohol 40 mL HCl	Immerse until desired contrast is obtained. For Custom 630 (precipitation-hardening grade)
Vilella's	100 mL ethyl alcohol 1 g picric acid 5 mL HCl	Recommended for revealing martensitic structure in AISI 410 stainless steel
Stainless steel microstructures, delta ferrite		
60/40	40 mL H_2O	Electrolytic etchant. Stainless steel cathode, 10 V for several seconds

Etching reagent	Composition	Remarks
	60 mL HNO_3 nitric acid	
Sodium hydroxide	20 g NaOH 100 mL H_2O	Electrolytic etchant. Stainless steel cathode, 3V for 5–10 s. Colors delta ferrite tan to orange
Stainless steel microstructures, duplex		
Oxalic acid	100 mL H_2O 10 g oxalic acid	Electrolytic etchant. Stainless cathode, 5 V for 5–10 s
Kalling's reagent No. 2	100 mL ethyl alcohol 5 g $CuCl_2$ 100 mL HCl	Ferrite attacked most readily. Austenite slightly attacked, and carbides not attacked. Etch by immersion.
Potassium hydroxide	100 mL H_2O 10 g potassium hydroxide	Electrolytic etchant. Stainless steel cathode, 3 V for 5–20 s
Lichtenegger/Bloech reagent	100 mL H_2O 20 g ammonium bifluoride 0.5 g potassium bisulfide	Etchant can be stored in plastic bottle. Etching time: 1–5 min at 25–30 °C (75–85 °F)
Stainless steel microstructures, sensitized		
4% picral + HCl	96 mL ethyl alcohol 4 g picric acid 5 mL HCl	…
Vilella's reagent	100 mL ethyl alcohol 1 g picric acid 5 mL hydrochloric acid	…
50/50/50	Equal parts H_2O, nitric acid, and hydrochloric acid	To 50 mL of cold water, add 50 mL nitric acid. Cool to below room temperature, and slowly add 50 mL hydrochloric acid (solution should be clear).
Coated steels, zinc-base coatings		
Amyl nital	1 mL HNO_3 (conc) 99 mL amyl alcohol	For Galvalume coatings
Amyl picral/nital	Part A: 1 g picric acid 99 mL amyl alcohol	Mix parts A and B together in a beaker. Separate the solution into two beakers. Add 3–4 drops HF to first solution. Immerse specimen in first solution for 20 s.
	Part B: 1 mL HNO_3 (conc) 99 mL amyl alcohol	Rinse in ethyl alcohol. Immerse specimen in second solution for 10 s. Flush with ethyl alcohol and blow dry.
Rowland's reagent	Part A: 0.75 g picric acid	Dissolve picric acid crystals in ethyl alcohol. Add part A to Part B.

Etching reagent	Composition	Remarks
	Part B: 480 mL H_2O	
Coated steels, aluminum-base coatings		
Nital	2 mL HNO_3 (conc) 98 mL ethyl alcohol	For aluminized coatings

Source: B. Bramfitt and A. Benscoter, *Metallographer's Guide: Practices and Procedures for Irons and Steels,* ASM International, 2002. For additional etchants, see individual articles in this Volume, ASTM E 407, "Microetching Metals and Alloys;" and G. Vander Voort, *Metallography Principles and Practice,* McGraw-Hill, 1984; reprinted by ASM International, 1999.

Glossary of Terms, Vol 9, *ASM Handbook*, ASM International, 2004, p. 1115–1134

Glossary of Terms

1-butanol.
See n-butyl alcohol.

2-butoxyethanol.
See butyl cellosolve.

A

aberration.
Any error that causes image degradation. Such an error may be chromatic, spherical, astigmatic, or comatic and can result from design, execution, or both. See also astigmatism, chromatic aberration, coma, and spherical aberration.

abrasion.
The process of grinding or wearing away through the use of abrasives; a roughening or scratching of a surface due to abrasive wear.

abrasion artifact.
A false structure introduced during an abrasion stage of a surface-preparation sequence.

abrasion fluid.
A liquid added to an abrasion system. The liquid may act as a lubricant, as a coolant, or as a means of flushing abrasion debris from the abrasion track.

abrasion process.
An abrasive machining procedure in which the surface of the workpiece is rubbed against a two-dimensional array of abrasive particles under approximately constant load.

abrasion rate.
The rate at which material is removed from a surface during abrasion. It is usually expressed in terms of the thickness removed per unit of time or distance traversed.

abrasive.
A substance capable of removing material from another substance in machining, abrasion, or polishing that usually takes the form of several small, irregularly shaped particles of a hard material.

abrasive machining.
A machining process in which the points of abrasive particles are used as machining tools. Grinding is a typical abrasive machining process.

abrasive wear.
The removal of material from a surface when hard particles slide or roll across the surface under pressure. The particles may be loose or may be part of another surface in contact with the surface being abraded. Contrast with adhesive wear.

a-butyl alcohol.

Liquid; normal butyl alcohol; also called butyl alcohol and 1-butanol.

accelerating potential.

A relatively high voltage applied between the cathode and anode of an electron gun to accelerate electrons.

achromatic.

Free of color. A lens or objective is achromatic when corrected for longitudinal chromatic aberration for two colors. See also achromatic objective.

achromatic objective.

Objective are achromatic when corrected chromatically for two colors, generally red and green, and spherically for light of one color, usually in the yellow-green portion of the spectrum.

acicular alpha.

A product of nucleation and growth from β to the lower-temperature allotrope α phase. It may have a needlelike appearance in a photomicrograph and may have needle, lenticular, or flattened bar morphology in three dimensions. See also alpha.

acid extraction.

Removal of phases by dissolution of the matrix metal in an acid. See also extraction.

adhesive wear.

The removal of material from a surface by the welding together and subsequent shearing of a minute area of two surfaces that slide across each other under pressure. Contrast with abrasive wear.

age hardening.

Hardening by aging, usually after rapid cooling or cold working. See also aging.

aging.

A change in properties that occurs at ambient or moderately elevated temperatures after hot working, heat treating, or cold working (strain aging). The change in properties is often due to a phase change (precipitation) but does not alter chemical composition. See also age hardening, artificial aging, interrupted aging, natural aging, overaging, precipitation hardening, precipitation heat treatment, progressive aging, quench aging, step aging, and strain aging.

alignment.

A mechanical or electrical adjustment of the components of an optical device so that the path of the radiating beam coincides with the optical axis or other predetermined path in the system. See also magnetic alignment, mechanical alignment, and voltage alignment.

allotriomorphic crystal.

A crystal having a normal lattice structure but an outward shape that is imperfect, because it is determined to some extent by the surroundings. The grains in a metallic aggregate are allotriomorphic crystals. Compare with idiomorphic crystal.

allotropy.

The property by which certain elements may exist in more than one crystal structure. See also polymorphism.

alloying element.

An element added to and remaining in a metal that changes structure and properties.

alloy system.

A complete series of compositions produced by mixing in all proportions any group of two or more components, at least one of which is a metal.

alpha (α)

The low-temperature allotrope of titanium with a hexagonal close-packed crystal structure that occurs below the β transus.

alpha-beta structure.

A microstructure containing α and β as the principal phases at a specific temperature. See also beta.

alpha brass.

A solid-solution phase of one or more alloying elements in copper having the same crystal lattice as copper.

alpha case.

The oxygen-, nitrogen-, or carbon-enriched α-stabilized surface resulting from elevated-temperature exposure. See also alpha stabilizer.

alpha double prime (orthorhombic martensite).

A supersaturated, nonequilibrium orthorhombic phase formed by a diffusionless transformation of the β phase in certain alloys.

alpha iron.

Solid phase of pure iron that is stable below 910 °C (1670 °F), possesses the body-centered cubic lattice, and is ferromagnetic below 768 °C (1415 °F).

alpha prime (hexagonal martensite).

A supersaturated, nonequilibrium hexagonal α phase formed by a diffusionless transformation of the β phase. It is often difficult to distinguish from acicular α, although the latter is usually less well defined and frequently has curved, instead of straight, sides.

alpha stabilizer.

An alloying element that dissolves preferentially in the α phase and raises the α-β transformation temperature.

alpha transus.

The temperature that designates the phase boundary between the α and α + β fields.

aluminum chloride, anhydrous.

Solid; $AlCl_3$; reacts violently with water, evolving HCl gas; use of hydrated form, $AlCl_3 \cdot 6H_2O$, is preferred.

ammonium molybdate.

Crystals; also called ammonium paramolybdate or heptamolybdate; $(NH_4)_6Mo_7O_{42} \cdot 4H_2O$; can be used interchangeably with "molybdic acid, 85%."

amplifier.

A negative lens used instead of an eyepiece to project under magnification the image formed by an objective. The amplifier is designed for flatness of field and should be used with an apochromatic objective.

analyzer.

An optical device capable of producing plane-polarized light. It is used for detecting the effect of the object on plane-polarized light produced by the polarizer.

angle of reflection.

(1) Reflection: the angle between the reflected beam and the normal to the reflecting surfaces. See also normal. (2) Diffraction: the angle between the diffracted beam and the diffracting planes.

angstrom unit (Å).

A unit of linear measure equal to 10^{-10} m, or 0.1 nm. Although not an accepted SI unit, it is occasionally used for small distances, such as interatomic distances, and some wavelengths.

angular aperture.

In optical microscopy, the angle between the most divergent rays that can pass through a lens to form the image of an object. See also aperture (optical).

anisotropy.

Characterized by having different values of a property in different directions.

annealing.

A generic term denoting a treatment—heating to and holding at a suitable temperature, followed by cooling at a suitable rate—used primarily to soften metallic materials but also to produce desired changes simultaneously in other properties or in microstructure. When applied only for the relief of stress, the process is called stress relieving or stress-relief annealing. In ferrous alloys, annealing is carried out above the upper critical temperature, but the time-temperature cycles vary widely in maximum temperature attained and cooling rate used, depending on composition, material condition, and desired results. See also black annealing, blue annealing, box annealing, bright annealing, cycle annealing, flame annealing, graphitizing, isothermal annealing, malleabilizing, process annealing, quench annealing, spheroidizing, and subcritical annealing. In nonferrous alloys, annealing cycles are designed to remove part or all the effects of cold working (recrystallization may or may be involved), cause complete coalescence of precipitates from the solid solution in relatively coarse form, or both,

depending on composition and material condition. See also anneal to temper, final annealing, intermediate annealing, recrystallization annealing, and stress relieving.

annealing carbon.

See temper carbon.

annealing twin.

A twin formed in a crystal during recrystallization.

annealing twin bands.

See twin bands.

anneal to temper.

A final partial anneal that softens a cold-worked nonferrous alloy to a specified level of hardness or tensile strength.

anode aperture.

In electron microscopy, the opening in the accelerating voltage anode shield of an electron gun through which the electrons must pass to illuminate or irradiate the specimen.

anodic etching.

Reveals the microstructure by selective anodic dissolution of the polished surface using a direct current. Variation with layer formation: anodizing.

aperture (electron).

See anode aperture, condenser aperture, and physical objective aperture.

aperture (optical).

In optical microscopy, the working diameter of a lens or a mirror. See also angular aperture.

aplanatic.

Corrected for spherical aberration and coma.

apochromatic objective.

Objectives corrected chromatically for three colors and spherically for two colors are called apochromats. These corrections are superior to those of the achromatic series of lenses. Because apochromats are not well corrected for lateral color, special eyepieces are used to compensate. See also achromatic.

artifact.

A feature of artificial character, such as a scratch or a piece of dust on a metallographic specimen, that can be erroneously interpreted as a real feature. See also abrasion artifact, mounting artifact, and polishing artifact.

artificial aging.

Aging above room temperature. Compare with natural aging.

astigmatism.

A defect in a lens or optical system that causes rays in one plane parallel to the optical axis to focus at a distance different from those in the plane at right angles to it.

ASTM grain size number.

See grain size.

athermal.

Not isothermal. Changing rather than constant temperature conditions.

atomic replica.

A thin replica devoid of structure on the molecular level. It is prepared by the vacuum or hydrolytic deposition of metals or simple compounds of low molecular weight. See also replica.

atomic scattering factor, *f*.

The ratio of the amplitude of the wave scattered by an atom to that scattered by a single electron.

attack polishing.

Simultaneous etching and mechanical polishing.

austempering.

Cooling (quenching) an austenitized steel at a rate high enough to suppress formation of high-temperature transformation products, then holding the steel at a temperature below that for pearlite formation and above that for martensite formation until transformation to an essentially bainitic structure is complete.

austenite.

Generally, a solid solution of one or more alloying elements in a face-centered cubic polymorph of iron (γ-iron). Specifically, in carbon steels, the interstitial solid solution of carbon in γ-iron.

austenitic grain size.

The size attained by the grains in steel when heated to the austenitic region. This may be revealed by appropriate etching of cross sections after cooling to room temperature.

austenitizing.

Forming austenite by heating a ferrous alloy into the transformation range (partial austenitizing) or above the transformation range (complete austenitizing).

average grain diameter.

The mean diameter of an equiaxed grain section whose size represents all the grain sections in the aggregate being measured. See also grain size.

axial ratio.

The ratio of the length of one axis to that of another, for example, c/a, or the continued ratio of three axes, such as *a:b:c.*

axis (crystal).

The edge of the unit cell of a space lattice. Any one axis of any one lattice is defined in length and direction relative to other axes of that lattice.

B

backing film.

A film used as auxiliary support for the thin replica or specimen-supporting film.

back reflection.

The diffraction of x-rays at a Bragg angle approaching 90°.

bainite.

A eutectoid transformation product of ferrite and a fine dispersion of carbide generally formed below 450 to 500 °C (840 to 930 °F). Upper bainite is an aggregate that contains parallel lath-shaped units of ferrite, produces the so-called “feathery” appearance in optical microscopy, and is formed above approximately 350 °C (660 °F). Lower bainite, which has an acicular appearance similar to tempered martensite, is formed below approximately 350 °C (660 °F).

banding.

Inhomogeneous distribution of alloying elements or phases aligned in filaments or plates parallel to the direction of working. See also ferrite-pearlite banding and segregation banding.

barrel distortion.

See negative distortion.

basal plane.

That plane of a hexagonal or tetragonal crystal perpendicular to the axis of highest symmetry. Its Miller indices are (001).

basketweave.

Alpha platelets with or without interweaved β platelets that occur in colonies in a Widmanstätten structure.

benzalkonium chloride.

Crystals; essentially alkyl-dimethyl-benzyl-ammonium chloride. May not be readily available in this form; see zephiran chloride.

beta (β)

The high-temperature allotrope of titanium with a body-centered cubic crystal structure that occurs above the β transus.

beta eutectoid stabilizer.

An alloying element that dissolves preferentially in the β phase, lowers the α-β to β transformation temperature, and results in β decomposition to α plus a compound. This eutectoid reaction can be sluggish for some alloys.

beta fleck.

Alpha-lean region in the α-β microstructure significantly larger than the primary α width. This β-rich area has a β transus measurably below that of the matrix. Beta flecks have reduced amounts of primary α that may exhibit a morphology different from the primary α in the surrounding α-β matrix.

beta isomorphous stabilizer.

An alloying element that dissolves preferentially in the β phase, lowers the α-β to β transformation temperature without a eutectoid reaction, and forms a continuous series of solid solution with β-titanium.

beta structure.

Structurally analogous body-centered cubic phases (similar to β-brass) or electron compounds that have ratios of three valence electrons to two atoms.

beta transus.

The minimum temperature above which equilibrium α does not exist. For β eutectoid additions, the β transus ordinarily is applied to hypoeutectoid compositions or those that lie to the left of the eutectoid composition.

bifilar eyepiece.

A filar eyepiece with motion in two mutually perpendicular directions.

binary alloy.

Any specific composition in a binary system.

binary system.

The complete series of compositions produced by mixing a pair of components in all proportions.

binodal curve.

In a two-dimensional phase diagram, a continuous line consisting of both of the pair of conjugate boundaries of a two-phase equilibrium that join without inflection at a critical point. See also miscibility gap.

birefringence.

A double-refraction phenomenon in anisotropic materials in which an unpolarized beam of light is divided into two beams with different directions and relative velocities of propagation. The amount of energy transmitted along an optical path through a crystal that exhibits birefringence becomes a function of crystalline orientation.

bivariant equilibrium.

A stable state among several phases equal to the number of components in a system and in which any two of the external variables of temperature, pressure, or concentration may be varied without necessarily changing the number of phases. Sometimes termed divariant equilibrium.

black annealing.

Box annealing of ferrous alloy sheet, strip, or wire.

blackbody.

A hypothetical “body” that completely absorbs all incident radiant energy, independent of wavelength and direction, that is, neither reflects nor transmits any of the incident radiant energy.

blocky alpha.

Alpha phase that is considerably larger and more polygonal in appearance than the primary α in the sample. It may arise from extended exposure high in the α-β phase field or by slow cooling through the β transus during forging or heat treating. It may be removed by β recrystallization, or all-β working, followed by further α-β work, and may accompany grain-boundary α.

blowholes.

A hole produced in a casting or weld by gas trapped during solidification.

blue annealing.

Heating hot-rolled ferrous sheet in an open furnace to a temperature within the transformation range, then cooling in air to soften the metal. A bluish oxide surface layer forms.

body-centered.

Having an atom or group of atoms separated by a translation of $\frac{1}{2}, \frac{1}{2}, \frac{1}{2}$ from a similar atom or group of atoms. The number of atoms in a body-centered cell must be a multiple of 2.

boundary grain.

In the Jeffries' method for grain size measurement, a grain that is intersected by the boundary of the standard area and is therefore counted only as one-half of a grain.

box annealing.

Annealing of a metal or alloy in a sealed container under conditions that minimize oxidation. See also black annealing.

Bragg angle.

The angle between the incident beam and the lattice planes considered.

Bragg equation.

$n\lambda = 2d \sin \theta$, where n is the order of reflection, λ is the wavelength of x-rays, d is the distance between lattice planes, and θ is the Bragg angle. See also order (in x-ray reflection).

Bragg method.

A method of x-ray diffraction in which a single crystal is mounted on a spectrometer with a crystal face parallel to the axis of the instrument.

bright annealing.

Annealing in a protective medium to prevent discoloration of the bright surface.

bright-field illumination.

For reflected light, the form of illumination that causes specularly reflected surfaces normal to the axis of the microscope to appear bright. For transmission electron microscopy, the illumination of an object so that it appears on a bright background.

brittle fracture.

Rapid fracture preceded by little or no plastic deformation.

brittleness.

The tendency of a material to fracture without first undergoing significant plastic deformation.

buffer.

A substance added to aqueous solutions to maintain a constant hydrogen-ion concentration even in the presence of acids or alkalis.

burning.

(1) During austenitizing, permanent damage of a metal or alloy by heating to cause incipient melting or intergranular oxidation. See also overheating. (2) During subcritical annealing, particularly in continuous annealing, production of a severely decarburized and grain-coarsened surface layer that results from excessively prolonged heating to an excessively high temperature. (3) In grinding, sufficient heating of the workpiece to cause discoloration or to change the microstructure by tempering or hardening.

burnishing.

Smoothing surfaces through frictional contact between the workpiece and some hard pieces of material, such as hardened steel balls.

butyl carbitol.

Liquid; diethylene glycol monobutyl ether.

butyl cellosolve.

Liquid; ethylene glycol monobutyl ether; also called 2-butoxyethanol.

C

capping (of abrasive particles).

A mechanism of deterioration of abrasive points in which the points become covered by caps of adherent abrasion debris.

carbide.

A compound of carbon with one or more metallic elements.

carbitol.

Liquid; diethylene glycol monoethyl ether.

carbonitriding.

A case-hardening process in which a suitable ferrous material is heated above the lower transformation temperature in a gaseous atmosphere having a composition that results in simultaneous absorption of carbon and nitrogen by the surface and, by diffusion, creates a concentration gradient. The process is completed by cooling at a rate that produces the desired properties in the workpiece.

carbon potential.

A measure of the capacity of an environment containing active carbon to alter or maintain, under prescribed conditions, the carbon concentration in a steel.

carbon restoration.

Replacing the carbon lost in the surface layer during previous processing by carburizing this layer to the original carbon level.

carburizing.

A case-hardening process in which an austenitized ferrous material contacts a carbonaceous atmosphere having sufficient carbon potential to cause absorption of carbon at the surface and, by diffusion, to create a concentration gradient.

case.

That portion of a ferrous alloy, extending inward from the surface, whose composition has been altered during case hardening. Typically considered to be the portion of an alloy (a) whose composition has been measurably altered from the original composition, (b) that appears dark when etched, or (c) that has a higher hardness value than the core. Contrast with core.

case hardening.

A generic term covering several processes applicable to steel that change the chemical composition of the surface layer by absorption of carbon, nitrogen, or both and, by diffusion, create a concentration gradient. See also carbonitriding, carburizing, cyaniding, nitriding, nitrocarburizing, and quench hardening.

cast replica.

A reproduction of a surface in plastic made by the evaporation of the solvent from a solution of the plastic or by polymerization of a monomer on the surface. See also replica.

cast structure.

The metallographic structure of a casting evidenced by shape and orientation of grains as well as segregation of impurities.

cathodic etching.

See ion etching.

cell block (CB).

A contiguous group of cells in which the same set of glide systems operates.

cell boundaries.

Low-angle dislocation boundaries that surround the cells and are classified as incidental dislocation boundary.

cellosolve.

Liquid; ethylene glycol monoethyl ether.

cementite.

A very hard and brittle iron-carbon compound, Fe_3C, also known as iron carbide. It is characterized by its orthorhombic crystal structure. Its occurrence as a phase in steels alters chemical composition by the presence of manganese and other carbide-forming elements.

chemical polishing.

A process that produces a polished surface by the action of a chemical etching solution. The etching solution is compounded so that peaks in the topography of the surface are dissolved preferentially.

Chinese-script eutectic.

A configuration of eutectic constituents, found particularly in some cast alloys of aluminum containing iron and silicon and in magnesium alloys containing silicon, that resembles the characters in Chinese script.

chlorine extraction.

Removal of phases by formation of a volatile chloride. See also extraction.

chromatic aberration.

A defect in a lens or lens system that results in different focal lengths of the lens for radiation of diverse wavelengths. The dispersive power of a simple positive lens focuses light from the blue end of the spectrum at a shorter distance than light from the red end. An image produced by such a lens will exhibit color fringes around the border of the image. The difference in position along the axis for the focal points of light is called longitudinal chromatic aberration. The difference in magnification due to variations in position of the principal points for light of different wavelengths, also a difference in focal length, is known as lateral chromatic aberration.

chromic acid.

Dark-red crystals or flakes; CrO_3; also called chromic anhydride, chromic acid anhydride, and chromium trioxide. See chromic oxide.

chromic anhydride.

See chromic acid.

chromic oxide.

Fine green powder; Cr_2O_3; a polishing abrasive; do not confuse with CrO_3, which is a strong acid and a component of many etchants.

cleavage.

Transgranular brittle fracture of crystal by crack propagation across a crystallographic plane of low index.

cleavage crack.

A crack that extends along a plane of easy cleavage in a crystalline material.

cleavage fracture.

A fracture, usually of a polycrystalline metal, in which most of the grains have failed by cleavage, resulting in bright reflecting facets. See also crystalline fracture.

cleavage plane.

A characteristic crystallographic plane or set of planes in a crystal on which cleavage fracture occurs easily.

close-packed.

A geometric arrangement in which a collection of equally sized spheres (atoms) may be packed together in a minimum total volume.

coalescence.

Growth of grains at the expense of the remainder by absorption or the growth of a phase or particle at the expense of the remainder by absorption or reprecipitation.

coarse grains.

Grains larger than normal for the particular wrought metal or alloy or of a size that produces a surface roughening known as orange peel or alligator skin.

coated abrasive product.

A two-body abrasion device in which a backing paper or cloth is coated with a layer of abrasive grits, that are cemented to the backing.

coherent precipitate.

A precipitated particle of a second phase whose lattice maintains registry with the matrix lattice. Because the lattice spacings are usually different, strains often exist at the interface.

coherent scattering.

A type of x-ray or electron scattering in which the phase of the scattered beam has a definite (not random) relationship to the phase of the incident beam. Also termed unmodified scattering. See also incoherent scattering.

cold etching.

Development of microstructure at room temperature and below.

cold-worked structure.

A microstructure resulting from plastic deformation of a metal or alloy below its recrystallization temperature.

collimation.

The operation of controlling a beam of radiation so that its rays are as nearly parallel as possible.

collodian replica.

A replica of a surface cast in nitrocellulose.

colonies.

Regions within prior-β grains with α platelets having nearly identical orientations. In commercially pure titanium, colonies often have serrated boundaries. Colonies arise as transformation products during cooling from the β field at cooling rates that induce platelet nucleation and growth.

color filter.

A device that transmits principally a predetermined range of wavelengths. See also contrast filter and filter.

color temperature.

The temperature in degrees Kelvin at which a blackbody must be operated to provide a color equivalent to that of the source in question. See also blackbody.

columnar structure.

A coarse structure of parallel, elongated grains formed by unidirectional growth that is most often observed in castings but sometimes seen in structures. This results from diffusional growth accompanied by a solid-state transformation.

coma.

A lens aberration occurring in the part of the image field that is some distance from the principal axis of the system. It results from different magnification in the various lens zones. Extra-axial object points appear as short, cometlike images, with the brighter small head toward the center of the field (positive coma) or away from the center (negative coma).

combined carbon.

That part of the total carbon in steel or cast iron present as other than free carbon.

comet tails (on a polished surface).

A group of comparatively deep unidirectional scratches that form adjacent to a microstructural discontinuity during mechanical polishing. They have the general shape of a comet tail. Comet tails form only when a unidirectional motion is maintained between the surface being polished and the polishing cloth.

comparison standard.

A standard micrograph or a series of micrographs, usually taken at 75 to 100×, used to determine grain size by direct comparison with the image.

compensating eyepiece.

An eyepiece designed for use with apochromatic objectives. They are also used to advantage with high-power (oil-immersion) achromatic objectives. Because apochromatic objectives are undercorrected chromatically, these eyepieces are overcorrected. See also apochromatic objective.

complex silicate inclusions.

A general term describing silicate inclusions containing visible constituents in addition to the silicate matrix. An example is corundum or spinel crystals occurring in a silicate matrix in steel.

condenser.

A system of lenses or mirrors designed to collect, control, and concentrate light.

condenser aperture.

In electron microscopy, an opening in the condenser lens controlling the number of electrons entering the lens and the angular aperture of the illuminating beam.

condenser lens.

A device used to focus radiation in or near the plane of the object.

conjugate phases.

Those states of matter of unique composition that coexist at equilibrium at a single point in temperature and pressure. For example, the two coexisting phases of a two-phase equilibrium.

conjugate planes.

Two planes of an optical system such that one is the image of the other.

constituent.

A phase or combination of phases that occurs in a characteristic configuration in a microstructure.

constitutional diagram.

See phase diagram.

continuous phase.

The phase that forms the background or matrix in which the other phase or phases may be dispersed.

continuous precipitation.

Precipitation from a supersaturated solid solution in which the precipitate particles grow by long-range diffusion without recrystallization of the matrix. Continuous precipitates grow from nuclei distributed more or less uniformly throughout the matrix. They usually are randomly oriented but may form a Widmanstätten structure. Also called general precipitation. Compare with discontinuous precipitation, and localized precipitation.

continuous spectrum (x-rays).

The polychromatic radiation emitted by the target of an x-ray tube. It contains all wavelengths above a certain minimum value, known as the short wavelength limit.

contrast enhancement (electron optics).

An improvement in electron image contrast by the use of an objective aperture diaphragm, shadow casting, or other means. See also shadowing.

contrast filter.

A color filter, usually with strong absorption, that uses the special absorption bands of the objective to control the contrast of the image by exaggerating or diminishing the brightness difference between differently colored areas.

contrast perception.

The ability to differentiate various components of the object structure by various intensity levels in the image.

controlled etching.

Electrolytic etching with selection of suitable etchant and voltage resulting in a balance between current and dissolved metal ions.

controlled rolling.

A hot-rolling process in which the temperature of the steel is closely controlled, particularly during the final rolling passes, to produce a fine-grain microstructure.

cooling curve.

A graph showing the relationship between time and temperature during the cooling of a material. It is used to find the temperatures at which phase changes occur. A property or function other than time may occasionally be used—for example, thermal expansion.

cooling rate.

The average slope of the time-temperature curve taken over a specified time and temperature interval.

core.

(1) In a ferrous alloy that has undergone case hardening, that portion of the alloy structure not part of the case. Typically considered to be the portion that (a) appears light when etched, (b) has an unaltered chemical composition, or (c) has a hardness value lower than that of the case. (2) A specially formed material inserted in a mold to shape the interior or other part of a casting that cannot be shaped as easily by the pattern.

coring.

A variation in composition between the center and surface of a unit of structure, such as a dendrite, a grain, or a carbide particle, that results from nonequilibrium growth over a temperature range.

corundum.

A naturally occurring, impure α-aluminum oxide. A purer form of the oxide than emery.

critical cooling rate.

The minimum rate of continuous cooling for preventing undesirable transformations. For steel, unless otherwise specified, it is the slowest rate at which austenite can be cooled from above critical temperature to prevent its transformation above the martensite start temperature.

critical curve.

In a binary or higher-order phase diagram, a line along which the phases of a heterogeneous equilibrium become identical.

critical illumination.

The formation of an image of the light source in the object field.

critical point.

(1) The temperature or pressure at which a change in crystal structure, phase, or physical properties occurs. Also termed transformation temperature. (2) In an equilibrium diagram, that combination of composition, temperature, and pressure at which the phases of an inhomogeneous system are in equilibrium.

critical pressure.

That pressure above which the liquid and vapor states are no longer distinguishable.

critical rake angle.

The rake angle at which the action of a V-point tool changes from cutting to plowing.

critical strain.

That strain resulting in the formation of very large grains during recrystallization.

critical surface.

In a ternary or higher-order phase diagram, the area on which the phases in equilibrium become identical.

critical temperature.

That temperature above which the vapor phase cannot be condensed to liquid by an increase in pressure. Synonymous with critical point if pressure is constant.

cross direction.

See transverse direction.

cross rolling.

A hot-rolling process in which rolling reduction proceeds perpendicular to and parallel to the length of the original slab.

crystal.

A solid composed of atoms, ions, or molecules arranged in a pattern that is periodic in three dimensions.

crystal analysis.

A method for determining crystal structure, for example, the size and shape of the unit cell and the location of all atoms within the unit cell.

crystal-figure etching.

Discontinuity in etching depending on crystal orientation. Distinctive sectional figures form at polished surfaces. Closely related to dislocation etching.

crystalline fracture.

A pattern of brightly reflecting crystal facets on the fracture surface of a polycrystalline metal resulting from cleavage fracture of many individual crystals. Contrast with fibrous fracture.

crystallite.

A crystalline grain not bounded by habit planes.

crystal system.

One of seven groups into which all crystals may be divided: triclinic, monoclinic, orthorhombic, hexagonal, rhombohedral, tetragonal, and cubic.

cube texture.

A texture found in wrought metals in the cubic system in which nearly all the crystal grains have a plane of the type (100) parallel or nearly parallel of the plane of working and a direction of the type [001] parallel or nearly parallel to the direction of elongation.

cubic.

Having three mutually perpendicular axes of equal length.

cupping.

The condition sometimes occurring in heavily cold-worked rods and wires in which the outside fibers remain intact and the central zone has failed in a series of cup-and-cone fractures.

cupric ammonium chloride.

Crystals; a double salt, $CuCl_2 \cdot 2NH_4Cl \cdot 2H_2O$; if not available, substitute 0.6 g $CuCl_2 \cdot 2H_2O$ plus 0.4 g NH_4Cl for each gram of the double salt.

curvature of field.

A property of a lens that causes the image of a plane to be focused into a curved surface instead of a plane.

cyaniding.

A case-hardening process in which a ferrous material is heated above the lower transformation temperature range in a molten salt containing cyanide to cause simultaneous absorption of carbon and nitrogen at the surface and, by diffusion, create a concentration gradient. Quench hardening completes the process.

cycle annealing.

An annealing process that uses a predetermined and closely controlled time-temperature cycle to produce specific properties or microstructures.

D

dark-field illumination.

The illumination of an object such that it appears bright and the surrounding field dark. This results from illuminating the object with rays of sufficient obliquity so that none can enter the objective directly. In electron microscopy, the image is formed using only electrons scattered by the object.

Debye ring.

A continuous circle, concentric about the undeviated beam, produced by monochromatic x-ray diffraction from a randomly oriented crystalline powder. An analogous effect is obtained using electron diffraction.

Debye-Scherrer method.

A method of x-ray diffraction using monochromatic radiation and a polycrystalline specimen mounted on the axis of a cylindrical strip of film. See also powder method.

decarburization.

Loss of carbon from the surface of a ferrous alloy as a result of heating in a medium that reacts with carbon.

decoration (of dislocations).

Segregation of solute atoms to the line of a dislocation in a crystal. In ferrite, the dislocations may be decorated with carbon or nitrogen atoms.

deep etching.

Macroetching, especially for steels, to determine the overall character of the material (presence of imperfections such as seam defects, rolling defects, forging bursts, remnant shrinkage voids, cracks, and coring).

define (x-rays).

To limit a beam of x-rays by passage through apertures to obtain a parallel, divergent, or convergent beam.

definition.

The clarity or sharpness of a microscopic image.

deformation bands.

Parts of a crystal that have rotated differently during deformation to produce bands of varied orientation within individual grains.

deformation lines.

Thin bands or lines produced by cold working in grains of some metals, particularly those of face-centered cubic structure. They are not removed by repolishing and re-etching.

degrees of freedom.

The number of independent variables, such as temperature, pressure, or concentration, within the phases present that may be adjusted independently without causing a phase change in an alloy system at equilibrium.

delta ferrite.

Designation commonly assigned to δ-iron that indicates inclusion of elements in solid solution. Small amounts of carbon and large amounts of other alloying elements markedly affect the high- and low-temperature limit of equilibrium.

delta iron.

Solid phase of pure iron that is stable from 1400 to 1539 °C (2550 to 2800 °F) and possesses the body-centered cubic lattice.

dendrite.

A crystal with a treelike branching pattern. It is most evident in cast metals slowly cooled through the solidification range.

dendritic segregation.

Inhomogeneous distribution of alloying elements through the arms of dendrites.

dense dislocation wall.

A single, nearly planar, deformation-induced boundary, classified as a geometrically necessary boundary, enclosing a cell block at small-to-intermediate strains.

deoxidation products.

Those nonmetallic inclusions that form as a result of adding deoxidizing agents to molten metal.

depletion.

Selective removal of one component of an alloy, usually from the surface or preferentially from grain-boundary regions.

depth of field.

The depth in the subject over which features can be seen to be acceptably in focus in the final image produced by a microscope.

deviation (x-ray).

The angle between the diffracted beam and the transmitted incident beam. It is equal to twice the Bragg angle θ.

devitrification.

Crystallization of an amorphous substance.

dezincification.

A type of corrosion in which zinc is selectively leached from zinc-containing alloys. This occurs most commonly in copper-zinc alloys.

diethylene glycol.

Syrupy liquid; also called 2,2′-oxydiethanol and dihydroxydiethyl ether; $(HOCH_2CH_2)_2O$; more viscous than ethylene glycol—otherwise similar in behavior.

diethylene glycol monobutyl ether.

See butyl carbitol.

diethylene glycol monoethyl ether.

See carbitol.

diethyl ether.

See ether.

differential interference contrast illumination.

A microscopic technique using a beam-splitting double-quartz prism, that is, a modified Wollaston prism placed ahead of the objective together with a polarizer and analyzer in the 90° crossed positions. The two light beams are made to coincide at the focal plane of the objective, revealing height differences as variations in color. The prism can be moved, shifting the interference image through the range of Newtonian colors.

diffraction.

(1) A modification that radiation undergoes, for example, in passing by the edge of opaque bodies or through narrow slits, in which the rays appear to be deflected. (2) Coherent scattering of x-rays by the atoms of a crystal that necessarily results in beams in characteristic directions. Sometimes termed reflection. (3) The scattering of electrons by any crystalline material through discrete angles depending only on the lattice spacings of the material and the velocity of the electrons.

diffraction grating.

An artificially produced periodic array of scattering centers capable of producing a pattern of diffracted energy, such as accurately ruled lines on a plane surface.

diffraction pattern (x-rays).

The spatial arrangement and relative intensities of diffracted beams.

diffraction ring.

The diffraction pattern produced by a given set of planes from randomly oriented crystalline material. See also Debye ring.

diffusion.

(1) Spreading of a constituent in a gas, liquid, or solid that tends to make the composition of all parts uniform. (2) The spontaneous movement of atoms or molecules to new sites within a material.

diffusion zone.

The zone of variable composition at the junction between two different materials, such as in welds or between the surface layer and the core of clad materials or sleeve bearings, in which interdiffusion between the various components has taken place.

discontinuous precipitation.

Precipitation from a supersaturated solid solution in which the precipitate particles grow by short-range diffusion, accompanied by recrystallization of the matrix in the region of precipitation. Discontinuous precipitates grow into the matrix from nuclei near grain boundaries, forming cells of alternate lamellae of precipitate and depleted (and recrystallized) matrix. Often referred to as cellular or nodular precipitation. Compare with continuous precipitation and localized precipitation.

dislocation.

A linear imperfection in a crystalline array of atoms. The two basic types recognized are (a) an edge dislocation that corresponds to the row of mismatched atoms along the edge formed by an extra, partial plane of atoms within the body of a crystal and (b) a screw dislocation that corresponds to the axis of a spiral structure in a crystal and is characterized by a distortion joining normally parallel lines together to form a continuous helical ramp (with a pitch of one interplanar distance) winding about the dislocation. A mixed dislocation, which is any combination of a screw dislocation and an edge dislocation, is prevalent.

dislocation etching.

Etching of exit points of dislocations on a surface. Depends on the strain field ranging over a distance of several atoms. Etching of dislocations is caused by their strain field ranging over a distance of several atoms. Crystal figures (etch pits) are formed at the exiting points. For example, etch pits for cubic materials are cube faced.

disordered structure.

The crystal structure of a solid solution in which the atoms of different elements are randomly distributed relative to the available lattice sites. Contrast with ordered structure.

dispersoid.

Finely divided particles of relatively insoluble constituents visible in the microstructure of certain alloys.

dissociation.

As applied to heterogeneous equilibria, the transformation of one phase into two or more new phases of different composition.

dissociation pressure.

At a designated temperature, the pressure at which a phase will transform into two or more new phases of different composition.

dissolution etching.

Development of microstructure by surface removal.

divariant equilibrium.

See bivariant equilibrium.

divorced eutectic.

A structure in which the components of a eutectic appear to be entirely separate.

double etching.

Use of two etching solutions in sequence. The second etchant emphasizes a particular microstructural feature.

drift.

In electron optics, motion of the electron beam or image due to current, voltage, or specimen instabilities or to charging of a projection, such as dirt in or near the electron beam.

drop etching.

Placing a drop of an etchant on a selected area of the sample surface to develop the alloying microconstituents (drip reaction).

dry etching.

Development of microstructure under the influence of gases.

dry objective.

Any microscope objective designed for use without liquid between the cover glass and the objective or, in the case of metallurgical objectives, in the space between objective and specimen.

duplex grain size.

The simultaneous presence of two grain sizes in substantial amounts, with one grain size appreciably larger than the others. Also termed mixed grain size.

duplex microstructure.

A two-phase structure.

E

edge-trailing technique.

A unidirectional motion perpendicular to and toward one edge of the specimen during abrasion or polishing used to improve edge retention.

elastic electron scatter.

The scatter of electrons by an object without loss of energy, usually an interaction between electrons and atoms.

electrical discharge machining.

Removal of stock from an electrically conductive material by rapid, repetitive spark discharge through a dielectric fluid flowing between the workpiece and a shaped electrode.

electrochemical (chemical) etching.

General expression for all developments of microstructure through reduction and oxidation (redox reactions).

electrolytic etching.

See anodic etching.

electrolytic extraction.

Removal of phases by using an electrolytic cell containing an electrolyte that preferentially dissolves the metal matrix. See also extraction.

electrolytic polishing.

An electrochemical polishing process in which the metal to be polished is made the anode in an electrolytic cell where preferential dissolution at high points in the surface topography produces a specularly reflective surface.

electromagnetic focusing device.

See focusing device.

electromagnetic lens.

An electromagnet designed to produce a suitably shaped magnetic field for the focusing and deflection of electrons or other charged particles in electron-optical instrumentation.

electromechanical polishing.

An attack-polishing method in which the chemical action of the polishing fluid is enhanced or controlled by the application of an electric current between the specimen and polishing wheel.

electron.

An elementary particle that is the negatively charged constituent of ordinary matter. The electron is the lightest known particle possessing an electric charge. Its rest mass is $m_e \approx 9.1 \times 10^{-28}$ g, approximately $\frac{1}{1836}$ of the mass of the proton or neutron, which are, respectively, the positively charged and neutral constituents of ordinary matter. The charge of the electron is $-e \approx -4.8 \times 10^{-10}$ esu $= -1.6 \times 10^{-19}$ C.

electron beam.

A stream of electrons in an electron-optical system.

electron diffraction.

The phenomenon, or the technique, of producing diffraction patterns through the incidence of electrons on matter.

electron gun.

A device for producing and accelerating a beam of electrons.

electron image.

A representation of an object formed by a beam of electrons focused by an electron-optical system. See also image.

electron lens.

A device for focusing an electron beam to produce an image of an object.

electron micrograph.

A reproduction of an image formed by the action of an electron beam on a photographic emulsion.

electron microscope.

An electron-optical device that produces a magnified image of an object. Detail may be revealed by selective transmission, reflection, or emission of electrons by the object. See also scanning electron microscope and transmission electron microscope.

electron microscope column.

The assembly of gun, lenses, specimen, and viewing and plate chambers.

electron microscopy.

The study of materials by means of an electron microscope.

electron microscopy impression.

See impression.

electron-optical axis.

The path of an electron through an electron-optical system, along which it suffers no deflection due to lens fields. This axis does not necessarily coincide with the mechanical axis of the system.

electron-optical system.

A combination of parts capable of producing and controlling a beam of electrons to yield an image of an object.

electron probe.

A narrow beam of electrons used to scan or illuminate an object or screen.

electron trajectory.

The path of an electron.

electron velocity.

The rate of motion of an electron.

electron wavelength.

The wavelength necessary to account for the deviation of electron rays in crystals by wave-diffraction theory. It is numerically equal to the quotient of Planck's constant divided by the electron momentum.

electropolishing.

See electrolytic polishing.

electrostatic focusing device.

See focusing device.

electrostatic immersion lens.

See immersion objective.

electrostatic lens.

A lens producing a potential field capable of deflecting electron rays to form an image of an object.

elongated alpha.

A fibrous structure brought about by unidirectional metalworking. It may be enhanced by the prior presence of blocky and/or grain-boundary α.

elongated grain.

A grain with one principal axis significantly longer than either of the other two.

embedded abrasive.

Fragments of abrasive particles forced into the surface of a workpiece during grinding, abrasion, or polishing.

emery.

A naturally occurring, impure α-aluminum oxide. A less pure form of the oxide than corundum.

enantiotropy.

The relation of crystal forms of the same substance in which one form is stable above a certain temperature and the other form is stable below that temperature. For example, ferrite and austenite are enantiotropic in ferrous alloys.

end-centered.

Having an atom or group of atoms separated by a translation of the type $\frac{1}{2}, \frac{1}{2}, 0$ from a similar atom or group of atoms. The number of atoms in an end-centered cell must be a multiple of 2.

epitaxy.

Oriented growth of a crystalline substance on a substrate with the same crystal orientation.

epsilon (ε).

Designation generally assigned to intermetallic, metal-metalloid, and metal-nonmetallic compounds found in ferrous alloy systems, for example, Fe_3Mo_2, FeSi, and Fe_3P.

epsilon carbide.

Carbide with hexagonal close-packed lattice that precipitates during the first stage of tempering of primary martensite. Its composition corresponds to the empirical formula $Fe_{2.4}C$.

epsilon structure.

Structurally analogous close-packed phases or electron compounds that have ratios of seven valence electrons to four atoms.

equiaxed grain structure.

A structure in which the grains have approximately the same dimensions in all directions.

equilibrium.

A state of dynamic balance between the opposing actions, reactions, or velocities of a reversible process.

equilibrium diagram.

A graph of the temperature, pressure, and composition limits of phase fields in an alloy system as they exist under conditions of thermodynamical equilibrium. In metal systems, pressure is usually considered constant. Compare with phase diagram.

etchant.

A chemical solution used to etch a metal to reveal structural details.

etch cracks.

Shallow cracks in hardened steel containing high residual surface stresses, produced by etching in an embrittling acid.

etch figures.

Characteristic markings produced on crystal surfaces by chemical attack, usually having facets parallel to low-index crystallographic planes.

etching.

Subjecting the surface of a metal to preferential chemical or electrolytic attack to reveal structural details for metallographic examination.

etch rinsing.

Pouring the etchant over a tilted sample surface until the structure is revealed. Used for etching with severe gas evolution.

ether.

Liquid; also called ethyl ether and diethyl ether; very low flash point; highly explosive; boiling point is 34.4 °C (94 °F).

ethylene glycol.

Syrupy liquid; also called 1,2-ethanediol and dihydroxyethane; $(CH_2)_2/(OH)_2$. Less viscous than diethylene glycol; otherwise similar in behavior.

ethylene glycol monobutyl ether.

Liquid; also called 2-butoxyethanol or butyl cellosolve.

ethylene glycol monoethyl ether.

See cellosolve.

ethyl ether.

See ether.

eutectic.

(1) An isothermal reversible reaction in which a liquid solution is converted into two or more intimately mixed solids on cooling; the number of solids formed equals the number of components in the system. (2) An alloy having the composition indicated by the eutectic point on an equilibrium diagram. (3) An alloy structure of intermixed solid constituents formed by a eutectic reaction.

eutectic arrest.

In a cooling or heating curve, an approximately isothermal segment corresponding to the time interval during which the heat of transformation from the liquid phase to two or more solid phases is evolving.

eutectic carbides.

Carbide formed during freezing as one of the mutually insoluble phases participating in the eutectic reaction of a hypereutectic tool steel. See also hypereutectic alloy.

eutectic-cell etching.

Development of eutectic cells (grains).

eutectic point.

The composition of a liquid phase in univariant equilibrium with two or more solid phases; the lowest melting alloy of a composition series.

eutectoid.

(1) An isothermal, reversible transformation in which a solid solution is converted into two or more intimately mixed solids. The number of solids formed equals the number of components in the system. (2) An alloy having the composition indicated by the eutectoid point on an equilibrium diagram. (3) An alloy structure of intermixed solid constituents formed by a eutectoid transformation.

evaporation.

The vaporization of a material by heating, usually in a vacuum. In electron microscopy, this process is used for shadowing or to produce thin support films by condensation of the vapors of metals or salts.

Ewald sphere.

A geometric construction, of radius equal to the reciprocal of the wavelength of the incident radiation, with its surface at the origin of the reciprocal lattice. Any crystal plane will reflect if the corresponding reciprocal lattice point lies on the surface of this sphere.

exogenous inclusions.

Nonmetallic inclusions generally large in size and representing accidental contamination from materials, such as fireclay refractories.

extinction.

A decrease in the intensity of the diffracted beam caused by perfection or near perfection of crystal structure. See also primary extinction and secondary extinction.

extinction coefficient.

The ratio of the diffracted beam intensity when extinction is present to the diffracted beam intensity when extinction is absent. It applies to primary or secondary extinction.

extraction.

A general term denoting chemical methods of isolating phases from the metal matrix.

eyepiece.

A lens or system of lenses for increasing magnification in a microscope by magnifying the image formed by the objective.

F

face (crystal).

An idiomorphic plane surface on a crystal.

face-centered.

Having atoms or groups of atoms separated by translations of $\frac{1}{2}, \frac{1}{2}, 0$; $\frac{1}{2}, 0, \frac{1}{2}$ and $0, \frac{1}{2}, \frac{1}{2}$ from a similar atom or group of atoms. The number of atoms in a face-centered cell must be a multiple of 4.

ferric nitrate.

Crystals; $Fe(NO_3)_3 \cdot 9H_2O$; there is no anhydrous form of this salt.

ferrite.

Generally, a solid solution of one or more elements in body-centered cubic iron. In plain carbon steels, the interstitial solid solution of carbon in α-iron.

ferrite-pearlite banding.

Inhomogeneous distribution of ferrite and pearlite aligned in filaments or plates parallel to the direction of working.

ferritic grain size.

The grain size of the ferritic matrix of a steel.

ferritizing anneal.

The process of producing a predominantly ferritic matrix in a ferrous alloy through an appropriate heat treatment.

fiber.

(1) The characteristic of wrought metal that indicates directional properties. It is revealed by etching a longitudinal section or manifested by the fibrous appearance of a fracture. It is caused chiefly by extension of the metallic and nonmetallic constituents of the metal in the direction of working. (2) The pattern of preferred orientation of metal crystals after a given deformation process.

fiber texture.

A texture characterized by having only one preferred crystallographic direction.

fibrous fracture.

A fracture whose surface is characterized by a dull gray or silky appearance. Contrast with crystalline fracture.

fibrous structure.

(1) In forgings, a structure revealed as laminations, not necessarily detrimental, on an etched section or as a ropy appearance on a fracture. (2) In wrought iron, a structure consisting of slag fibers embedded in ferrite. (3) In rolled steel plate stock, a uniform, lamination-free, fine-grained structure on a fractured surface.

filar eyepiece.

An eyepiece having in its focal plane a fiducial line that can be moved using a calibrated micrometer screw. Useful for accurate determination of linear dimensions. Also termed filar micrometer.

filter.

A device that modifies the light from the light source.

final annealing.

The last anneal given a nonferrous alloy before shipment.

final polishing.

A polishing process in which the primary objective is to produce a final surface suitable for microscopic examination.

flake graphite.

An irregularly shaped body, usually appearing as long, curved plates of graphitic carbon, such as that found in gray cast irons.

flakes.

Short, discontinuous internal cracks in ferrous metals attributed to stresses produced by localized transformation and hydrogen-solubility effects during cooling after hot working. In fracture surfaces, flakes appear as bright, silvery areas with a coarse texture. In deep acid-etched transverse sections, they appear as discontinuities that are usually in the midway to center location of the section. Also termed hairline cracks and shatter cracks.

flame annealing.

Annealing in which the heat is applied directly by a flame.

flow lines.

Texture showing the direction of metal flow during hot or cold working. Flow lines often can be revealed by etching the surface or a section of a metal part.

focal length.

The distance from the second principal point to the point on the axis at which parallel rays entering the lens will converge or focus.

focal spot.

That area on the target of an x-ray tube that is bombarded by electrons.

focus.

A point at which rays originating from a point in the object converge or from which they diverge or appear to diverge under the influence of a lens or diffracting system.

focusing device (electrons).

A device that effectively increases the angular aperture of the electron beam illuminating the object, rendering the focusing more critical.

focusing (x-rays).

The operation of producing a convergent beam in which all rays meet in a point or line.

forged structure.

The macrostructure through a suitable section of a forging that reveals direction of working.

Formvar.

A plastic material used for the preparation of replicas or for specimen-supporting membranes.

Formvar replica.

A reproduction of a surface in a plastic Formvar film. See also replica.

fractography.

Descriptive treatment of fracture, especially in metals, with specific reference to photography of the fracture surface.

fracture grain size.

Grain size determined by comparing a fracture of a specimen with a set of standard fractures. For steel, a fully martensitic specimen is generally used, and the depth of hardening and the prior-austenitic grain size are determined.

fragmentation.

The subdivision of a grain into small, discrete crystallite outlined by a heavily deformed network of intersecting slip bands as a result of cold working. These small crystals or fragments differ in orientation and tend to rotate to a stable orientation determined by the systems.

freckling.

A type of segregation revealed as dark spots on a macroetched specimen of a consumable-electrode vacuum-arc-remelted alloy.

free carbon.

The part of the total carbon content in steel or cast iron present in elemental form as graphite.

free-energy diagram.

A graph of the variation with concentration of the Gibbs free energy at constant pressure and temperature.

free-energy surface.

In a ternary or higher-order free-energy diagram, the locus of points representing the Gibbs free energy as a function of concentration, with pressure and temperature constant.

free ferrite.

See proeutectoid ferrite.

freezing point.

See melting point.

frequency (x-ray).

The number of alternations per second of the electric vector of the x-ray beam. It is equal to the velocity divided by the wavelength.

Fresnel fringes.

A class of diffraction fringes formed when the source of illumination and the viewing screen are at a finite distance from a diffracting edge. In the electron microscope, these fringes are best seen when the object is slightly out of focus.

G

gamma iron.

Solid nonmagnetic phase of pure iron that is stable from 910 to 1400 °C (1670 to 2550 °F) and possesses the face-centered cubic lattice.

gamma structure.

Structurally analogous phases or electron compounds having ratios of 21 valence electrons to 13 atoms. This is generally a large, complex cubic structure.

gelatin replica.

A reproduction of a surface prepared in a film composed of gelatin. See also replica.

general precipitate.

A precipitate that is dispersed throughout the matrix. See also continuous precipitation.

geometrically necessary boundary.

Boundaries whose angular misorientations are controlled by the difference in glide-induced lattice rotations in the adjoining volumes.

Gibbs free energy.

The maximum useful work obtainable from a chemical system without net change in temperature or pressure.

Gibbs triangle.

An equilateral triangle used for plotting composition in a ternary system.

glancing angle.

The angle (usually small) between an incident x-ray beam and the surface of the specimen.

glide.

See slip.

glycerol.

Syrupy liquid; also called glycerin or glycerine; $C_3H_5(OH)_3$; contains up to 5% (by weight) H_2O.

graded abrasive.

An abrasive powder in which the sizes of the individual particles are confined to certain specified limits.

grain.

An individual crystal in a polycrystalline metal or alloy, including twinned regions or subgrains if present.

grain boundary.

An interface separating two grains at which the orientation of the lattice changes from that of one grain to that of the other. When the orientation change is very small, the boundary is sometimes referred to as a subboundary structure.

grain-boundary etching.

Development of intersections of grain faces with the polished surface. Because of severe, localized crystal deformation, grain boundaries have higher dissolution potential than grains themselves. Accumulation of impurities in grain boundaries increases this effect.

grain-boundary liquation.

An advanced stage of overheating in which material in the region of austenitic grain boundaries melts. Also termed burning.

grain-boundary sulfide precipitation.

An intermediate stage of overheating in which sulfide inclusions are redistributed to the austenitic grain boundaries by partial solution at the overheating temperature and reprecipitation during subsequent cooling.

grain coarsening.

A heat treatment that produces excessively large austenitic grains.

grain-contrast etching.

Etching the surface of the grains according to their crystal orientation. They become distinct by the different reflectivity caused by reaction layers or surface roughness.

grain fineness number.

A weighted average grain size of a granular material. The American Foundrymen's Society grain fineness number is calculated with prescribed weighting factors from the standard screen analysis.

grain flow.

Fiberlike lines on polished and etched sections of forgings caused by orientation of the constituents of the metal in the direction of working during forging. Grain flow produced by proper die design can improve required mechanical properties of forgings.

grain growth.

An increase in the grain size of a metal, usually as a result of heating at an elevated temperature.

grain size.

(1) A measure of the areas or volumes of grains in a polycrystalline metal or alloy, usually expressed as an average when the individual sizes are fairly uniform. In metals containing two or more phases, the grain size refers to that of the matrix unless otherwise specified. Grain size is reported in terms of number of grains per unit area or volume, average diameter, or as a number derived from area measurements. (2) For grinding wheels, see the preferred term grit size.

granular fracture.

An irregular surface produced when metal fractures. This fracture is characterized by a rough, grainlike appearance. It can be subclassified into transgranular and intergranular forms. This fracture is frequently called crystalline fracture, but the implication that the metal failed because it crystallized is misleading, because all metals are crystalline in the solid state.

graphite.

The polymorph of carbon with a hexagonal crystal structure. See also flake graphite, nodular graphite, rosette graphite, and spheroidal graphite.

graphitization.

Formation of graphite in iron or steel. Primary graphitization refers to formation of graphite during solidification; secondary graphitization, later formation during heat treatment.

graphitizing.

Annealing a ferrous alloy such that some or all the carbon precipitates as graphite.

grinding.

Removing material from a workpiece using a grinding wheel or abrasive belt.

grit size.

Nominal size of abrasive particles in a grinding wheel, corresponding to the number of openings per linear inch in a screen through which the particles can pass.

Guinier-Preston (G-P) zone.

A small precipitation domain in a supersaturated metallic solid solution. A G-P zone has no well-defined crystalline structure of its own and contains an abnormally high concentration of solute atoms. The formation of G-P zones constitutes the first stage of precipitation and is usually accompanied by a change in properties of the solid solution in which they occur.

H

habit plane.

The plane or system of planes of a crystalline phase along which some phenomenon, such as twinning or transformation, occurs.

hairline cracks.

See flakes.

hardenability.

The relative ability of a ferrous alloy to form martensite when quenched from a temperature above the upper critical temperature. Hardenability is commonly measured as the distance below a quenched surface at which the metal exhibits a specific hardness—50 HRC, for example—or a specific percentage of martensite in the microstructure.

hardening.

Increasing hardness by suitable treatment, usually involving heating and cooling. See also age hardening, case hardening, induction hardening, precipitation hardening, and quench hardening.

heat-affected zone.

That portion of the base metal that was not melted during brazing, cutting, or welding but whose microstructure and mechanical properties were altered by the heat.

heat tinting.

Formation of interference film on a metal surface through thermal oxidation in air or other gases, usually at elevated temperature.

herringbone pattern.

The term chevron pattern is sometimes used interchangeably with the term herringbone pattern. However, there are differences in appearance. First, a chevron pattern is a macroscale pattern, while a herringbone pattern is a microscale pattern. Secondly, a herringbone pattern, although it is a series of nested Vs, is created by the different mechanism of a central spine created by cleavage on a {100} plane and continued intermittent lateral crack expansion of the crack on {1,1,2} twinning planes.

heterogeneous equilibrium.

In a chemical system, a state of dynamic balance among two or more homogeneous phases capable of stable coexistence in mutual or sequential contact.

hexagonal (lattices for crystals).

Having two equal coplanar axes, $\underline{a}_1$ and $\underline{a}_2$, at 120° to each other and a third axis, $\underline{c}$, at right angles to the other two; $\underline{c}$ may or may not equal $\underline{a}_1$ and $\underline{a}_2$.

hexagonal close-packed.

(1) A structure containing two atoms per unit cell located at (0, 0, 0) and $(\frac{1}{3}, \frac{2}{3}, \frac{1}{2})$ or $(\frac{2}{3}, \frac{1}{3}, \frac{1}{2})$. (2) One of the two ways in which spherical objects can be most closely packed together so that the close-packed planes are alternately staggered in the order A-B-A-B-A-B.

high aluminum defect.

An α-stabilized region in titanium containing an abnormally large amount of aluminum that may span a large number of β grains. It contains an inordinate fraction of primary α but has a microhardness only slightly higher than the adjacent matrix. Also termed type II defects.

high interstitial defect.

Interstitially stabilized α-phase region in titanium of substantially higher hardness than surrounding material. It arises from very high local nitrogen or oxygen concentrations that increase the β transus and produce the high-hardness, often brittle α phase. Such a defect is often accompanied by a void resulting from thermomechanical working. Also termed type I or low-density interstitial defects, although they are not necessarily low density.

homogenizing.

Holding at high temperature to eliminate or decrease chemical segregation by diffusion.

hot cathode gun.

See thermionic cathode gun.

hot crack.
See solidification shrinkage crack.
hot etching.
Development and stabilization of the microstructure at elevated temperature in etchants or gases.
hot quenching.
An imprecise term for various quenching procedures in which a quenching medium is maintained at a prescribed temperature above 70 °C (160 °F).
hot-worked structure.
The structure of a material worked at a temperature higher than the recrystallization temperature.
hot working.
Deformation under conditions that result in crystallization.
hydride phase.
The phase TiH_x formed in titanium when the hydrogen content exceeds the solubility limit, generally locally due to some special circumstance.
hypereutectic alloy.
In an alloy system exhibiting a eutectic, any alloy whose composition has an excess of alloying element compared with the eutectic composition and whose equilibrium microstructure contains some eutectic structure.
hypereutectoid alloy.
In an alloy system exhibiting a eutectoid, any alloy whose composition has an excess of alloying element compared with the eutectoid composition and whose equilibrium microstructure contains some eutectoid structure.
hypoeutectic alloy.
In an alloy system exhibiting a eutectic, any alloy whose composition has an excess of base metal compared with the eutectic composition and whose equilibrium microstructure contains some eutectic structure.
hypoeutectoid alloy.
In an alloy system exhibiting a eutectoid, any alloy whose composition has an excess of base metal compared with the eutectoid composition and whose equilibrium microstructure contains some eutectoid structure.

I

identification (selective) etching.
Etching for the identification of particular microconstituents without attacking any others.
idiomorphic crystal.
Single crystals that have grown without restraint so that the habit planes are clearly developed.
illumination.
See bright-field illumination, dark-field illumination, differential interference contrast illumination, and polarized light illumination.
image.
A representation of an object produced by radiation, usually with a lens or mirror system.
image rotation.
In electron optics, the angular shift of the electron image of an object about the optic axis induced by the tangential component of force exerted on the electrons perpendicular to the direction of motion in the field of a magnetic lens.
immersion etching.
The sample is immersed in the etchant with the polished surface up and is agitated. This is the most common etching method.
immersion etching (cyclic).
Alternate immersion into two etchants: 1, the actual etchant; 2, solution to dissolve the layer formed during the etching process of 1.
immersion lens.
See immersion objective.
immersion objective.

An objective in which a medium of high refractive index is used in the object space to increase the numerical aperture and therefore the resolving power of the lens.

immersion objective (electron optics).

A lens system in which the object space is at a potential or in a medium of index of refraction different from that of the image space.

imperfection.

In crystallography, any deviation from an ideal space lattice.

impression.

(1) In electron microscopy, the reproduction of the surface contours of a specimen formed in a plastic material after the application of pressure, heat, or both. (2) In hardness testing, the imprint or dent made in the specimen by the indenter of a hardness-measuring device.

impression replica.

A surface replica made by impression. See also impression and replica.

impurities.

Undesirable elements or compounds in a material.

incidental dislocation boundary.

A dislocation boundary formed by the mutual and statistical trapping of glide dislocations and supplemented by forest dislocations.

inclusion count.

Determination of the number, kind, size, and distribution of nonmetallic inclusions.

inclusions.

Particles of foreign material in a metallic matrix. The particles are usually compounds, such as oxides, sulfides, or silicates, but may be any substance foreign to and essentially insoluble in the matrix.

incoherent scattering.

The deflection of electrons by electrons or atoms that results in a loss of kinetic energy by the incident electron. See also coherent scattering.

indentation.

See impression.

indices.

See Miller indices.

indigenous inclusions.

See deoxidation products.

induction hardening.

A surface-hardening process in which only the surface layer of a suitable ferrous workpiece is heated by electrical induction to above the upper transformation temperature and immediately quenched.

induction heating.

Heating by electrical induction.

inelastic electron scatter.

See incoherent scattering.

inflection point.

Position on a curved line, such as a phase boundary, at which the direction of curvature is reversed.

intensity (x-rays).

The energy per unit of time of a beam per unit area perpendicular to the direction of propagation.

intensity of scattering.

The energy per unit time per unit area of the general radiation diffracted by matter. Its value depends on the scattering power of the individual atoms of the material, the scattering angle, and the wavelength of the radiation.

intercept method.

A quantitative metallographic technique in which the desired quantity, such as grain size or amount of precipitate, is expressed as the number of times per unit length a straight line on a metallographic image crosses particles of the feature being measured.

intercrystalline.

Between crystals or between grains. Also termed intergranular.

intercrystalline cracks.

Cracks or fractures that occur between the grains or crystals in a polycrystalline aggregate.

interdendritic.

Located within the branches of a dendrite or between the boundaries of two or more dendrites.

interdendritic porosity.

Voids occurring between the dendrites in cast metal.

interference.

The effect of a combination of wave trains of various phases and amplitudes.

interference filter.

A combination of several thin optical films to form a layered coating for transmitting or reflecting a narrow band of wavelengths by interference effects.

intergranular.

See intercrystalline.

intergranular beta.

Beta phase situated between α grains. It may be at grain corners, as in the case of equiaxed α-type microstructures in alloys having low β-stabilizer contents.

intermediate annealing.

Annealing wrought metal at one or more stages during manufacture and before final thermal treatment.

intermediate phase.

In a chemical system, a distinguishable homogeneous substance whose composition range of existence does not extend to any of the pure components of the system.

intermetallic compound.

An intermediate phase in an alloy system having a narrow range of homogeneity and relatively simple stoichiometric proportions. Nearly all are brittle and of stoichiometric composition.

intermetallic phases.

Compounds, or intermediate solid solutions, containing two or more metals that usually have compositions, characteristic properties, and crystal structures different from those of the pure components of the system.

internal oxidation.

Preferential in situ oxidation of certain components of phases within the bulk of a solid alloy accomplished by diffusion of oxygen into the body. This is commonly used to prepare electrical contact materials.

interplanar distance.

The perpendicular distance between adjacent parallel lattice planes.

interrupted aging.

Aging at two or more temperatures by steps and cooling to room temperature after each step. Compare with progressive aging and step aging.

interrupted quenching.

Quenching in which the metal object being quenched is removed from the quenching medium while the object is at a temperature substantially higher than that of the quenching medium.

interstitial solid solution.

A type of solid solution that sometimes forms in alloy systems having two elements of widely different atomic sizes. Elements of small atomic size, such as carbon, hydrogen, and nitrogen, often dissolve in solid metals to form this solid solution. The space lattice is similar to that of the pure metal, and the atoms of carbon, hydrogen, and nitrogen occupy the spaces or interstices between the metal atoms.

intracrystalline.

Within or across crystals or grains. Same as transcrystalline and transgranular.

intracrystalline cracking.

See transcrystalline cracking.

inverse segregation.

A concentration of low-melting constituents in those regions in which solidification first occurs.

inverted microscope.

A microscope arranged so that the line of sight is directed upward through the objective to the object.

ion etching.

Surface removal by bombarding with accelerated ions in vacuum (1 to 10 kV).

isometric.

A crystal form in which the unit dimension on all three axes is the same.

isomorphous.

Having the same crystal structure. This usually refers to intermediate phases that form a continuous series of solid solutions.

isomorphous system.

A complete series of mixtures in all proportions of two or more components in which unlimited mutual solubility exists in the liquid and solid states.

isothermal annealing.

Austenitizing a ferrous alloy, then cooling to and holding at a temperature at which austenite transforms to a relatively soft ferrite-carbide aggregate. See also austenitizing.

isothermal transformation.

A change in phase at any constant temperature.

isothermal transformation (IT) diagram.

A diagram that shows the isothermal time required for transformation of austenite to begin and to finish as a function of temperature. Same as time-temperature-transformation (TTT) diagram or S-curve.

isotropic.

Having equal values of properties in all directions. Quasi-isotropic refers to material in which statistical uniformity exists, such as polycrystalline metals.

isotropy.

The condition of having the same values of properties in all directions.

J

Jeffries' method.

A method for determining grain size based on counting grains in a prescribed area.

K

Kikuchi lines.

Light and dark lines superimposed on the background of a single-crystal electron-diffraction pattern caused by diffraction of diffusely scattered electrons within the crystal; the pattern provides information on the structure of the crystal.

kink band (deformation).

In polycrystalline materials, a volume of crystal that has rotated physically to accommodate differential deformation between adjoining parts of a grain while the band itself has deformed homogeneously. This occurs by regular bending of the slip lamellae along the boundaries of the band.

K radiation.

Characteristic x-rays produced by an atom when a vacancy in the K shell is filled by one of the outer electrons.

K series.

The set of x-ray wavelengths comprising K radiation.

L

lamellar boundaries.

A single, nearly planar boundary, classified as a geometrically necessary boundary, enclosing a narrow cell block at large strains.

lamellar tear.

A system of cracks or discontinuities aligned generally parallel to the worked surface of a plate. This is usually associated with a fusion weld in thick plate.

lamination.

An abnormal structure resulting in a separation or weakness aligned generally parallel to the worked surface of the metal.

lap.

(1) A flat surface that holds an abrasive for polishing operations. (2) A surface imperfection on worked metal caused by folding over a fin overfill or similar surface condition, then impressing this into the surface by subsequent working without welding it.

lath martensite.

Martensite formed partly in steels containing less than approximately 1.0% C and solely in steels containing less than approximately 0.5% C as parallel arrays of packets of lath-shaped units 0.1 to 0.3 μm thick.

lattice.

(1) A space lattice is a set of equal and adjoining parallellopipeds formed by dividing space by three sets of parallel planes, the planes in any one set being equally spaced. There are seven ways of so dividing space, corresponding to the seven crystal systems. The unit parallelopiped is usually chosen as the unit cell of the system. See also crystal system. (2) A point lattice is a set of points in space located so that each point has identical surroundings. There are 14 ways of so arranging points in space, corresponding to the 14 Bravais lattices. See the article "Crystal Structure" in this Volume.

lattice constants.

See lattice parameter.

lattice parameter.

The length of any side of a unit cell of a given crystal structure. The term is also used for the fractional coordinates x, *y*, and z of lattice points when these are variable.

Laue equations.

The three simultaneous equations that state the conditions to be met for diffraction from a three-dimensional network of diffraction centers.

Laue method (for crystal analysis).

A method of x-ray diffraction using a beam of white radiation, a fixed single-crystal specimen, and a flat photographic film usually normal to the incident beam. If the film is located on the same side of the specimen as the x-ray source, the method is known as the back reflection Laue method; if on the other side, as the transmission Laue method.

ledeburite.

A eutectic structure formed below 1148 °C (2098 °F) consisting of austenite and cementite in metastable equilibrium in alloys of iron and carbon containing greater than 2% but less than 6.67% C. Further slow cooling causes decomposition of the austenite into ferrite and cementite (pearlite) as a result of the eutectoid reaction.

lever rule.

A method that can be applied to any two-phase field of a binary phase diagram to determine the amounts of the different phases present at a given temperature in a given alloy. A horizontal line, referred to as a tie line, represents the lever, and the alloy composition its fulcrum. The intersection of the tie line with the boundaries of the two-phase field fixes the compositions of the coexisting phases, and the amounts of the phases are proportional to the segments of the tie line between the alloy and the phase compositions.

levigation.

A process by which a powder is separated into a fraction with a restricted range of particle sizes.

light-field illumination.

See bright-field illumination.

light filter.

See color filter.

limited solid solution.

A crystalline miscibility series whose composition range does not extend all the way between the components of the system; that is, the system is not isomorphous.

line (in x-ray diffraction patterns).

An array of small diffraction spots arranged so that they appear to form a continuous line on the film.

lineage structure.

(1) Deviations from perfect alignment of parallel arms of a columnar dendrite as a result of interdendritic shrinkage during solidification from liquid. This type of deviation may vary in orientation from a few minutes to as much as two degrees of arc. (2) A type of substructure consisting of elongated subgrains.

line indices.

The Miller indices of the set of planes producing a diffraction line.

liquation.

Partial melting of an alloy, usually as a result of coring or other compositional heterogeneities.

liquidus.

In a phase diagram, the locus of points representing the temperatures at which various components begin to freeze during cooling or finish melting during heating. See also solidus.

localized precipitation.

Precipitation from a supersaturated solid solution similar to continuous precipitation, except that the precipitate particles form at preferred locations, such as along slip planes, grain boundaries, or incoherent twin boundaries.

longitudinal direction.

That direction parallel to the direction of maximum elongation in a worked material. See also normal direction and transverse direction.

long-term etching.

Etching times of a few minutes to hours.

Lüders lines or bands.

Elongated surface markings or depressions caused by localized plastic deformation that results from discontinuous (inhomogeneous) yielding.

M

macroetching.

Etching a metal surface to accentuate or reveal macroscopic structural details (such as grain flow, segregation, porosity, or cracks) with the unaided eye or at a magnification of 50× or less.

macrograph.

A graphic reproduction of a prepared surface of a specimen at a magnification not exceeding 25×.

macroscopic.

Visible at magnifications to 25×.

macrostructure.

The structure of metals as revealed by macroscopic examination of the etched surface of a polished specimen.

magnetic alignment.

An alignment of the electron-optical axis of the electron microscope so that the image rotates about a point in the center of the viewing screen when the current flowing through a lens is varied. See also alignment.

magnetic lens.

A device for focusing an electron beam using a magnetic field.

magnetic shielding.

In electron microscopy, shielding for the purpose of preventing extraneous magnetic fields from affecting the electron beam in the microscope.

magnetite.

The oxide of iron of intermediate valence that has a composition close to the stoichiometric composition Fe_3O_4.

magnification.

The ratio of the length of a line in the image plane, for example, ground glass or photographic plate, to the length of the same line in the object. Magnifications are usually expressed in linear terms and in units called diameters.

malleabilizing.

Annealing white cast iron so that some or all of the combined carbon is transformed into graphite or, in some instances, so that part of the carbon is removed completely.

martempering.

(1) A hardening procedure in which an austenitized ferrous material is quenched into an appropriate medium at a temperature just above the martensite start temperature of the material, held in the medium until the temperature is uniform throughout, although not long enough for bainite to form, then cooled in air. The treatment is frequently followed by tempering. (2) When the process is applied to carburized material, the controlling martensite start temperature is that of the case. This variation of the process is frequently called marquenching.

martensite.

A generic term for microstructures formed by diffusionless phase transformation in which the parent and product phases have a specific crystallographic relationship. Martensite is characterized by an acicular pattern in the microstructure in ferrous and nonferrous alloys. In alloys in which the solute atoms occupy interstitial positions in the martensitic lattice, such as carbon in iron, the structure is hard and highly strained; however, if the solute atoms occupy substitutional positions, such as nickel in iron, the martensite is soft and ductile. The amount of high-temperature phase that transforms to martensite on cooling depends to a large extent on the lowest temperature attained, there being a distinct starting temperature (M_s) and a temperature at which the transformation is essentially complete (M_f), which is the martensite finish temperature. See also transformation temperature.

martensite range.

The interval between the martensite start (M_s) and martensite finish (M_f) temperatures.

martensitic.

A platelike constituent having an appearance and a mechanism of formation similar to that of martensite.

matrix.

The continuous or principal phase in which another constituent is dispersed.

McQuaid-Ehn grain size.

The austenitic grain size developed in steels by carburizing at 927 °C (1700 °F), followed by slow cooling. Eight standard McQuaid-Ehn grain sizes rate the structure, from No. 8, the finest, to No. 1, the coarsest.

mechanical alignment.

A method of aligning the geometrical axis of the electron microscope by relative physical movement of the components, usually as a step preceding magnetic or voltage alignment. See also alignment.

mechanical polishing.

A process that yields a specularly reflecting surface entirely by the action of machining tools, which are usually the points of abrasive particles.

mechanical stage.

A device provided for adjusting the position of a specimen, usually by translation in two directions at right angles to each other.

mechanical twin.

A twin formed in a metal during plastic deformation by simple shear of the structure.

melting point.

The temperature at which a pure metal, compound, or eutectic changes from solid to liquid; the temperature at which the liquid and the solid are in equilibrium.

melting pressure.

At a stated temperature, the pressure at which the solid phases of an element or congruently melting compound may coexist at equilibrium with liquid of the same composition.

melting temperature.

See melting point.

membrane.

Any thin sheet or layer.

metallograph.

An optical instrument designed for visual observation and photomicrography of prepared surfaces of opaque materials at magnifications of 25 to approximately 2000×. The instrument consists of a high-intensity illuminating source, a microscope, and a camera bellows. On some instruments, provisions are made for examination of specimen surfaces using polarized light, phase contrast, oblique illumination, dark-field illumination, and bright-field illumination.

metallography.

The science dealing with the constitution and structure of metals and alloys as revealed to the unaided eye or by using such tools as low-power magnification, optical microscopy, electron microscopy, and diffraction or x-ray techniques.

metal shadowing.

The enhancement of contrast in a microscope by vacuum depositing a dense metal onto the specimen at an angle generally not perpendicular to the surface of the specimen. See also shadowing.

metastable.

Possessing a state of pseudoequilibrium that has a free energy higher than that of the true equilibrium state.

metastable beta.

A β-phase composition that can be partially or completely transformed to martensite, α, or eutectoid decomposition products with thermal or strain-energy activation during subsequent processing or service exposure.

microbands.

Thin, sheetlike volumes of constant thickness in which cooperative slip occurs on a fine scale. They are an instability that carry exclusively the deformation at medium strains when normal homogeneous slip is precluded. The sheets are aligned at ±55° to the compression direction and are confined to individual grains, which usually contain two sets of bands. Compare with shear bands. Platelike region formed by two closely spaced *dense dislocation walls* and defining the edge of a cell block.

microcrack.

A crack of microscopic proportions.

microetching.

Development of microstructure for microscopic examination. The usual magnification exceeds 25× (50× in Europe).

microfissure.

See microcrack.

micrograph.

A graphic reproduction of the prepared surface of a specimen at a magnification greater than 25×.

microporosity.

Extremely fine porosity in castings.

microscope.

An instrument capable of producing a magnified image of a small object.

microscopic.

Visible at magnifications above 25×.

microsegregation.

Segregation within a grain, crystal, or small particle. See also coring.

microstructure.

The structure of a prepared surface of a metal revealed by a microscope at a magnification exceeding 25×.

Miller-Bravais indices.

Indices used for the hexagonal system. They involve the use of a fourth axis, a_3, coplanar with and at 120° to a_1 and a_2.

Miller indices (for lattice planes).

The reciprocals of the fractional intercepts a plane makes on the three axes. The symbols are (*hkl*).

mirror illuminator.

A thin, half-round opaque mirror interposed in a microscope for directing an intense oblique beam of light to the object. The light incident on the object passes through one half of the aperture of the objective, and the light reflected from the object passes through the other half aperture of the objective.

miscibility gap.

A region of multiphase equilibrium. It is commonly applied to the specific case in which an otherwise continuous series of liquid or solid solutions is interrupted over a limited temperature range by a two-phase field terminating at a critical point. See also binodal curve.

mixed grain size.

See duplex grain size.

molybdic acid, 85%.

Crystals or powder containing the equivalent of 85% MoO_3. This misnamed chemical consists mostly of ammonium molybdate, or paramolybdate, which is $(NH_4)_6Mo_7O_{24}\cdot 4H_2O$; the two chemicals can be used interchangeably. See ammonium molybdate.

monochromatic (homogeneous).

Of the same wavelength.

monochromatic objective.
An objective, usually of fused quartz, that has been corrected for use with monochromatic light only.

monoclinic.
Having three axes of any length, with two included angles equal to 90° and one included angle not equal to 90°.

monotropism.
The ability of a solid to exist in two or more forms (crystal structures) but in which one form is the stable modification at all temperatures and pressures. Ferrite and martensite are a monotropic pair below the temperature at which austenite begins to form, for example, in steels. Alternate spelling is monotrophism.

mosaic crystal.
An imperfect single crystal composed of regions that are slightly disoriented relative to each other.

mosaic structure.
In crystals, a substructure in which adjoining regions have only slightly different orientations.

mounting.
A means by which a specimen may be held during preparation of a section surface. The specimen can be embedded in plastic or secured mechanically in clamps.

mounting artifact.
A false structure introduced during the mounting stages of a surface-preparation sequence.

multiple etching.
Sequential etching of a microsection, with specific reagents attacking distinct microconstituents.

muriatic acid.
Liquid; technical-grade HCl.

N

napped cloth.
A woven cloth in which some fibers are aligned approximately normal to one of its surfaces.

natural aging.
Spontaneous aging of supersaturated solid solution at room temperature. See also aging.

n-butyl alcohol.
Liquid; normal butyl alcohol; also called butyl alcohol and 1-butanol.

negative distortion.
The distortion in the image that occurs when the magnification in the center of the field exceeds that in the edge of the field. Also termed barrel distortion. Contrast with positive distortion.

negative eyepiece.
An eyepiece in which the real image of the object forms between the lens elements of the eyepiece.

negative replica.
A method of reproducing a surface obtained by the direct contact of the replicating material with the specimen. Using this technique, contour of the replica surface is reversed with respect to that of the original. See also replica.

network etching.
Formation of networks, especially in mild steels, after etching in nitric acid. These networks relate to subgrain boundaries.

network structure.
A structure in which one constituent occurs primarily at the grain boundaries, partially or completely enveloping the grains of the other constituents.

Neumann band.
A mechanical twin in ferrite.

neutral filter.
(1) A color filter that reduces the intensity of the transmitted illumination without affecting its hue. (2) A color filter having identical transmission at all wavelengths throughout the spectrum. Such an ideal filter does not exist in practice.

Nicol prism.
A prism used for polarizing or analyzing light made by cementing together two pieces of calcite using Canada balsam so that the extraordinary ray from the first piece passes through the second piece, while

the ordinary ray is reflected to the side into an absorbing layer of black paint. No light passes through when two Nicol prisms are crossed.

nitride-carbide inclusion types.

A compound with the general formula $M_x(C,N)_y$ observed generally as colored idiomorphic cubic crystals, where M includes titanium, niobium, tantalum, and zirconium.

nitriding.

A case-hardening process that introduces nitrogen into the surface layer of a ferrous material by holding it at a suitable temperature in a nitrogenous atmosphere, usually ammonia or molten cyanide of appropriate composition. Quenching is not required to produce a hard case.

nitrocarburizing.

Any of several case-hardening processes in which nitrogen and carbon are absorbed into the surface layers of a ferrous material at temperatures below the lower critical temperature and, by diffusion, create a concentration gradient. Compare with carbonitriding.

nodular graphite.

Rounded clusters of tempered carbon, such as that obtained in malleable cast iron as a result of the thermal decomposition of cementite.

nodular pearlite.

Pearlite that has grown as a colony with an approximately spherical morphology.

nonmetallic inclusions.

See inclusions.

normal.

An imaginary line forming right angles with a surface or other lines sometimes called the perpendicular. It is used as a basis for determining angles of incidence reflection and refraction. See also angle of reflection.

normal direction.

That direction perpendicular to the plane of working in a worked material. See also longitudinal direction and transverse direction.

normalizing.

Heating a ferrous alloy to suitable temperature above the transformation range, then cooling in air to a temperature substantially below the transformation range. See also transformation temperature.

normal segregation.

A concentration of alloying components or constituents having lower melting points in those regions that are the last to solidify.

nucleation.

Initiation of a phase transformation at discrete sites, with the new phase growing from the nuclei. See also nucleus.

nucleus.

(1) The first structurally stable particle capable of initiating recrystallization of a phase or the growth of a new phase. It is separated from the matrix by an interface. (2) The heavy central core of an atom in which most of the mass and the total positive electrical charge are concentrated.

numerical aperture.

The product of the lowest index of refraction in the object space multiplied by the sine of half the angular aperture of the objective.

O

objective.

The primary magnifying system of a microscope. A system, generally of lenses and less frequently of mirrors, that forms a real, inverted, and magnified image of the object.

objective aperture.

See aperture (electron) and aperture (optical).

oblique evaporation shadowing.

The condensation of evaporated material onto a substrate that is inclined to the direct line of the vapor stream to produce shadows. See also shadowing.

oblique illumination.

Illumination from light inclined at an oblique angle to the optical axis.

ocular.

See eyepiece.

omega phase.

A nonequilibrium, submicroscopic phase that forms as a nucleation growth product; often thought to be a transition phase during the formation of α from β. It occurs in metastable β alloys and can lead to severe embrittlement. It typically occurs during aging at low temperature but can also be induced by high hydrostatic pressures.

optical etching.

Development of microstructure under application of special illumination techniques, such as dark-field illumination, differential interference contrast illumination, phase contrast illumination, and polarized light illumination.

order (in x-ray reflection).

The factor n in the Bragg equation. In x-ray reflection from a crystal, the order is an integral number that is the path difference measured in wavelengths between reflections from adjacent planes.

order-disorder transformation.

A phase change among two solid solutions having the same crystal structure but in which the atoms of one phase (disordered) are randomly distributed; in the other, the different kinds of atoms occur in a regular sequence on the crystal lattice, that is, in an ordered arrangement.

ordered structure.

That crystal structure of a solid solution in which the atoms of different elements seek preferred lattice positions. Contrast with disordered structure.

orientation (crystal).

Arrangements in space of the axes of the lattice of a crystal with respect to a chosen reference or coordinate system. See also preferred orientation.

orthochromatic filter.

A color filter that modifies the illumination quality reaching the film so that the brightness of colored objects will be relatively the same in the resultant black-and-white positive.

orthorhombic.

Having three mutually perpendicular axes of unequal lengths.

overaging.

Aging under conditions of time and temperature greater than those required to obtain maximum change in a certain property. See also aging.

overheating.

(1) In ferrous alloys, heating to an excessively high temperature so that the properties/structure undergo modification. The resulting structure is very coarse grained. Unlike burning, it may be possible to restore the original properties/structure by further heat treatment, mechanical working, or both. (2) In aluminum alloys, overheating produces structures that show areas of resolidified eutectic or other evidence indicating the metal has been heated within the melting range.

oxidation grain size.

(1) Grain size determined by holding a specimen at a suitably elevated temperature in a mildly oxidizing atmosphere. The specimen is polished before oxidation and etched afterwards. (2) Refers to the method involving heating a polished steel specimen to a specified temperature, followed by quenching and repolishing. The grain boundaries are sharply defined by the presence of iron oxide.

oxide film replica.

A thin film of an oxide of the specimen to be examined. The replica is prepared by air, oxygen, chemical, or electrochemical oxidation of the parent metal and is subsequently freed mechanically or chemically for examination. See also replica.

oxide-type inclusions.

Oxide compounds occurring as nonmetallic inclusions in metals, usually as a result of deoxidizing additions. In wrought steel products, they may occur as a stringer formation composed of distinct granular or crystalline-appearing particles.

P

pancake grain structure.

A structure in which the lengths and widths of individual grains are large compared to their thicknesses.

parameter (in crystals).
See lattice parameter.
parfocal eyepiece.
Eyepieces, with common focal planes, that are interchangeable without refocusing.
pattern.
See diffraction pattern.
pearlite.
A metastable eutectoid-transformation product consisting of alternating lamellae of ferrite and cementite resulting from the transformation of austenite at temperatures above the bainite range.
pearlitic structure.
A microstructure resembling that of the pearlite constituent in steel. Therefore, it is a lamellar structure of varying degrees of coarseness.
peritectic.
An isothermal reversible reaction in which a liquid phase reacts with a solid phase to produce another solid phase.
peritectic equilibrium.
A reversible univariant transformation in which a solid phase stable only at lower temperature decomposes into a liquid and a solid phase that are conjugate at higher temperature, or conversely.
peritectoid equilibrium.
A reversible univariant transformation in which a solid phase stable only at low temperature decomposes with rising temperature into two or more conjugate solid phases.
perpendicular section.
A section cut perpendicular to a surface of interest in a specimen. Compare with taper section.
petrography.
The study of nonmetallic matter under suitable microscopes to determine structural relationships and to identify the phases or minerals present. With transparent materials, the determination of the optical properties, such as the indices of refraction and the behavior in transmitted polarized light, are means of identification. With opaque materials, the color, hardness, reflectivity, shape, and etching behavior in polished sections are means of identification.
phase.
A physically homogeneous and distinct portion of a material system.
phase contrast illumination.
A special method of controlled illumination ideally suited to observing thin, transparent objects whose structural details vary only slightly in thickness or refractive index. This can also be applied to the examination of opaque materials to determine surface elevation changes.
phase diagram.
A graph of the temperature and composition limits of phase fields in an alloy system as they actually exist under the specific conditions of heating or cooling (synonymous with constitutional diagram). A phase diagram may be an equilibrium diagram, an approximation to an equilibrium diagram, or a representation of metastable conditions of phases. Compare with equilibrium diagram.
phase rule.
The maximum number of phases (P) that may coexist at equilibrium is two, plus the number of components (C) in the mixture, minus the number of degrees of freedom (F): $P + F = C + 2$.
photomicrograph.
A micrograph made by photographic means.
physical etching.
Development of microstructure through removal of atoms from the surface or lowering the grain-surface potential.
physical objective aperture.
In electron microscopy, a metal diaphragm centrally pierced with a small hole used to limit the cone of electrons accepted by the objective lens. This improves image contrast, because highly scattered electrons are prevented from arriving at the Gaussian image plane and therefore cannot contribute to background fog.
picric acid.

Crystals; 2,4,6-trinitrophenol; crystals of the laboratory chemical contain 10 to 15% H_2O; explosive; its crystalline metallic salts are even more explosive; do not use grades that do not have the 10 to 15% H_2O content.

pincushion distortion.

See positive distortion.

pinhole eyepiece.

An eyepiece, or a cap to place over an eyepiece, that has a small central aperture instead of an eye lens. It is used in adjusting or aligning microscopes.

pinhole ocular.

See pinhole eyepiece.

pinholes.

(1) Very small holes that are sometimes found as a type of porosity in a casting because of the microshrinkage or gas evolution during solidification. In wrought products, due to removal of inclusions or microconstituents during macroetching of transverse sections. (2) In photography, a very small circular aperture.

pinhole system.

A group of two or more pinholes arranged to define a beam.

plane (crystal).

An idiomorphic face of a crystal. Any atom-containing plane in a crystal.

plane glass illuminator.

A thin, transparent, flat glass disk interposed in a microscope or a lens imaging system to direct light to the object without reducing the useful aperture of the lens system.

plane of working.

The plane of maximum area extension.

planimetric method.

See Jeffries' method.

plasma etching.

High-frequency electromagnetic vibrations produce radicals in a gas mixture that react with the sample surface and cause its removal.

plastic deformation.

Deformation that remains or will remain permanent after release of the stress that caused it.

plasticity.

The capacity of a metal to deform nonelastically without rupturing.

plastic replica.

A reproduction in plastic of the surface to be studied. It is prepared by evaporation of the solvent from a solution of plastic, polymerization of a monomer, or solidification of a plastic on the surface. See also replica.

platelet alpha structure.

Acicular alpha of a coarser variety, usually with low aspect ratios. This microstructures arises from cooling α or α-β alloys from temperatures at which a significant fraction of β phase exists.

plate martensite.

Martensite formed partly in steel containing more than approximately 0.5% C and solely in steel containing more than approximately 1.0% C that appear as lenticular-shaped plates on irrational habit planes near $\{225\}_A$, or $\{259\}_A$ in high-carbon steels (>0.9% C).

polarized light illumination.

A method of illumination in which the incident light is plane polarized before it impinges on the specimen.

polarizer.

A Nicol prism, polarizing film, or similar device into which normal light passes and from which polarized light emerges.

pole figure (crystalline aggregates).

A graph of the crystal orientations present in an aggregate.

polished surface.

A surface that reflects a large proportion of the incident light in a specular manner.

polishing.

A mechanical, chemical, or electrolytic process or combination thereof used to prepare a smooth, reflective surface suitable for microstructural examination that is free of artifacts or damage introduced during prior sectioning or grinding.

polishing artifact.

A false structure introduced during a polishing stage of a surface-preparation sequence.

polishing rate.

The rate at which material is removed from a surface during polishing. It is usually expressed in terms of the thickness removed per unit of time or distance traversed.

polycrystalline.

Comprising an aggregate of more than one crystal and usually a large number of crystals.

polymorphism.

A general term for the ability of a solid to exist in more than one form. In metals, alloys, and similar substances, this usually means the ability to exist in two or more crystal structures, or in an amorphous state and at least one crystal structure. See also allotropy, enantiotropy, and monotropism.

porosity.

Holes in a solid, not necessarily connected.

positive distortion.

The distortion in the image that results when the magnification in the center of the field is less than that at the edge of the field. Also termed pincushion distortion. Contrast with negative distortion.

positive eyepiece.

An eyepiece in which the real image of the object is formed below the lower lens elements of the eyepiece.

positive replica.

A replica whose contours correspond directly to the surface being replicated. Contrast with negative replica.

potentiometer.

An instrument that measures electromotive force by balancing against it an equal and opposite electromotive force across a calibrated resistance carrying a definite current.

potentiostat.

An instrument that automatically maintains an electrode in an electrolyte at a constant potential or controlled potentials relative to a suitable reference electrode.

potentiostatic etching.

Anodic development of microstructure at a constant potential. Adjusting the potential makes possible a defined etching of singular phases.

powder method.

Any method of x-ray diffraction involving a polycrystalline and preferably randomly oriented powder specimen and a narrow beam of the monochromatic radiation.

precipitation.

Separation of a new phase from solid or liquid solution, usually with changing conditions of temperature, pressure, or both.

precipitation etching.

Development of microstructure through formation of reaction products at the surface of the microsection. See also staining.

precipitation hardening.

Hardening caused by precipitation of a constituent from a supersaturated solid solution. See also age hardening and aging.

precipitation heat treatment.

Artificial aging in which a constituent precipitates from a supersaturated solid solution.

preferred orientation.

A condition of a polycrystalline aggregate in which the crystal orientations are not random but tend to align in a specific direction in the bulk material that is completely related to the direction of working. See also texture.

preshadowed replica.

A replica formed by the application of shadowing material to the surface to be replicated. It is formed before the thin replica film is cast or otherwise deposited on the surface. See also shadowing.

primary (x-ray).

The beam incident on the specimen.

primary alpha.

Alpha phase in a crystallographic structure that is retained from the last high-temperature α-β working or heat treatment. The morphology of α is influenced by the prior thermomechanical history.

primary crystals.

The first type of crystals that separate from a melt during solidification.

primary etching.

Develops the cast microstructures, including coring.

primary extinction.

A decrease in intensity of a diffracted x-ray beam caused by perfection of crystal structure extending over such a distance (approximately 1 μm or greater) that interference between multiply reflected beams inside the crystal decreases the intensity of the externally diffracted beam.

print etching (printing).

A carrier material is soaked with an etching solution and pressed onto the sample surface. The etchant reacts with one of the microstructural constituents, forming substances that affect the carrier material. The result is a direct imprint as a life-size image. It is used for the identification of specific elements, for example, sulfur (sulfur prints).

prior-beta grain size.

Size of β grains established during the most recent β-field excursion. Grains may be distorted by subsequent subtransus deformation. Beta grain boundaries may be obscured by a superimposed α-β microstructure and detectable only by special techniques.

process annealing.

A heat treatment used to soften metal for further cold working. In ferrous sheet and wire industries, heating to a temperature close to but below the lower limit of the transformation range and subsequently cooling for working. In the nonferrous industries, heating above the recrystallization temperatures at a time and temperature sufficient to permit the desired subsequent cold working.

proeutectoid (phase).

Particles of a phase that precipitate during cooling after austenitizing but before the eutectoid transformation takes place.

proeutectoid carbide.

Primary crystals of cementite formed directly from the decomposition of austenite exclusive of that cementite resulting from the eutectoid reaction.

proeutectoid ferrite.

Primary crystals of ferrite formed directly from the decomposition of austenite exclusive of that ferrite resulting from the eutectoid reaction.

progressive aging.

Aging by increasing the temperature in steps or continuously during the aging cycle. Compare with interrupted aging and step aging.

projection distance.

Distance from the eyepiece to the image screen.

projection lens.

The final lens in the electron microscope corresponding to an ocular or projector in a compound optical microscope. This lens forms a real image on the viewing screen or photographic film.

P-T diagram.

A two-dimensional graph of phase relationships in a system of any order by means of the pressure and temperature variables.

P-T-X diagram.

A three-dimensional graph of the phase relationships in a binary system by means of the pressure, temperature, and concentration variables.

P-X diagram.

A two-dimensional graph of the isothermal phase relationships in a binary system; the coordinates of the graph are pressure and concentration.

P-X projection.

A two-dimensional graph of the phase relationships in a binary system produced by making an orthographic projection of the phase boundaries of a P-T-X diagram on a pressure-concentration plane.

pyrophosphoric acid.

Crystals of viscous liquid; $H_4P_2O_7$, anhydrous; hydrolyzes to H_3PO_4 slowly in cold H_2O and rapidly in hot H_2O.

Q

quadrivariant equilibrium.

A stable state among several conjugate phases equal to two less than the number of components, that is, having four degrees of freedom.

quantitative metallography.

Determination of specific characteristics of a microstructure by quantitative measurements of micrographs or metallographic images. Quantities so measured include volume concentration of phases, grain size, particle size, mean free path between like particles or secondary phases, and surface-area-to-volume ratio of microconstituents, particles, or grains.

quasi-isotropic.

See isotropic.

quaternary system.

The complete series of compositions produced by mixing four components in all proportions.

quench aging.

Aging induced from rapid cooling after solution heat treatment.

quench annealing.

Annealing an austenitic ferrous alloy by solution heat treatment followed by rapid quenching.

quench hardening.

(1) Hardening suitable α-β alloys—most often certain copper or titanium alloys—by solution treating and quenching to develop a martensite-like structure. (2) In ferrous alloys, hardening by austenitizing, then cooling at a rate so that a substantial amount of austenite transforms to martensite.

quenching crack.

Cracks formed as a result of thermal stresses produced by rapid cooling from a high temperature.

R

random orientation.

A condition of a polycrystalline aggregate in which the orientations of the constituent crystals are completely random relative to each other. Contrast with preferred orientation.

recalescence.

The increase in temperature that occurs after undercooling, because the rate of liberation of heat during transformation of a material exceeds the rate of dissipation of heat.

recarburizing.

(1) Increasing the carbon content of molten cast iron or steel by adding carbonaceous material, high-carbon pig iron, or a high-carbon alloy. (2) Carburizing a metal part to return surface carbon lost in processing.

reciprocal lattice.

A lattice of points, each representing a set of planes in the crystal lattice, so that a vector from the origin of the reciprocal lattice to any point is normal to the crystal planes represented by that point and has a length that is the reciprocal of the plane spacing.

recovery.

Reduction or removal of strain-hardening effects, without motion of large-angle grain boundaries.

recrystallization.

(1) A change from one crystal structure to another, such as that occurring on heating or cooling through a critical temperature. (2) Formation of a new, strain-free grain structure from the structure existing in cold-worked metal.

recrystallization annealing.

Annealing cold-worked metal to produce a new grain structure without a phase change.

recrystallization temperature.

The approximate minimum temperature at which recrystallization of a cold-worked metal occurs within a specified time.

recrystallized grain size.

(1) The grain size developed by heating cold-worked metal. The time and temperature are selected so that, although recrystallization is complete, essentially no grain growth occurs. (2) In aluminum and magnesium alloys, the grain size after recrystallization, without regard to grain growth or the recrystallization conditions.

reflection (x-ray).

See diffraction.

reflection method.

The technique of producing a diffraction pattern by x-rays or electrons that have been reflected from a specimen surface.

refractive index (electrons).

The ratio of electron wavelength in free space to its wavelength in a material medium.

regular reflection.

See specular reflection.

replica.

A reproduction of a surface in a material. It is usually accomplished by depositing a thin film of suitable material, such as plastic, onto the specimen surface. This film is subsequently extracted and examined by transmission electron microscopy. See also atomic replica, cast replica, collodian replica, Formvar replica, gelatin replica, impression replica, negative replica, oxide film replica, plastic replica, positive replica, preshadowed replica, tape replica method (faxfilm), and vapor-deposited replica.

replicate.

In electron microscopy, to reproduce using a replica.

residual elements.

Small quantities of elements unintentionally present in an alloy.

resolution.

The capacity of an optical or radiation system to separate closely spaced forms or entities; in addition, the degree to which such forms or entities can be discriminated. Resolution is usually specified as the minimum distance by which two lines or points in the object must be separated before they can be revealed as separate lines or points in the image. See also resolving power and shape resolution.

resolving power.

The ability of a given lens system to reveal fine detail in an object. See also resolution.

retardation plate.

A plate placed in the path of a beam of polarized light for the purpose of introducing a difference in phase. Usually quarter-wave or half-wave plates are used, but if the light passes through them twice, the phase difference is doubled.

rhombohedral.

Having three equal axes, with the included angles equal to each other but not equal to 90°.

rolling direction (in rolled metals).

See longitudinal direction.

rosette.

(1) Rounded configuration of microconstituents arranged in whorls or radiating from a center. (2) Strain gages arranged to indicate at a single position strains in three different directions.

rosette graphite.

Arrangement of graphite flakes in which the flakes extend radially from the center of crystallized areas in gray cast iron.

rough-polishing process.

A polishing process having the primary objective of removing the layer of significant damage produced during earlier machining and abrasion stages of a metallographic preparation sequence. A secondary objective is to produce a finish of such quality that a final polish can be produced easily.

S

saturated gun.

A self-biased electron gun in which electron emission is limited by space charge rather than filament temperature.

S bands.

A coarse slip band that intersects parallel groups of *dense dislocation walls* or lamellar boundaries. A string of S-shaped perturbations in lamellar boundaries. The length of an S-band is generally shorter than a grain diameter.

scale.

A layer of oxidation products formed on a metal at high temperature.

scanning electron microscope.

An electron microscope in which the image is formed by a beam operating in synchronism with an electron probe scanning the object. The intensity of the image-forming beam is proportional to the scattering or secondary emission of the specimen where the probe strikes it.

scattering (x-ray).

A general term including coherent scattering and incoherent scattering.

scoring.

Marring or scratching of a smooth surface. It is most often caused by sliding contact with a mating member having a hard projection or embedded particle on its surface.

scratch.

A groove produced in a surface by an abrasive point.

scratch trace.

A line of etch markings produced on a surface at the site of a pre-existing scratch, the physical groove of the scratch having been removed. The scratch trace develops when the deformed material extending beneath the scratch has not been removed with the scratch groove and when the residual deformed material is attacked preferentially during etching.

seam.

An unwelded fold or lap on the surface of a metal that appears as a crack. This is usually the result of defects in casting or working that have not welded shut.

secondary etching.

Development of microstructures deviating from the primary structure through transformation and heat treatment in the solid state.

secondary extinction.

A decrease in the intensity of a diffracted x-ray beam caused by parallelism or near-parallelism of mosaic blocks in a mosaic crystal; the lower blocks are partially screened from the incident radiation by the upper blocks, which have reflected some of it.

secondary x-rays.

The x-rays emitted by a specimen irradiated by a primary beam.

segregation.

Nonuniform distribution of alloying elements, impurities, or phases.

segregation banding.

Inhomogeneous distribution of alloying elements aligned in filaments or plates parallel to the direction of working.

segregation (coring) etching.

Development of segregation (coring) mainly in macrostructures and microstructures of castings.

selective etching.

See identification (selective) etching.

sensitive tint plate.

A gypsum plate used in conjunction with polarizing filters to provide very sensitive detection of birefringence and double refraction.

serial sectioning.

A technique in which an identified area on a section surface is observed repeatedly after successive layers of known thickness have been removed from the surface. It is used to construct a three-dimensional morphology of structural features.

shadow angle.

The angle between the line of motion of the evaporated atoms and the surface being shadowed. The angle analogous to the angle of incidence in optics. It may be specified as arc tangent a so that a is in the ratio between the height of the object casting the shadow over the length of the shadow. See also shadowing.

shadow cast replica.

A replica that has been shadowed. See also shadowing.

shadowing.

A process by which a metal or salt is deposited on a specimen at an angle from a heated filament in a vacuum to enhance image contrast by inhibiting the deposition of the shadowing material behind projections. See also metal shadowing, oblique evaporation shadowing, and shadow angle.

shadow microscope.

An electron microscope that forms a shadow image of an object using electrons emanating from a point source located close to the object.

shales.

Abrasive particles of platelike shape. The term is applied particularly to diamond abrasives.

shape resolution.

An electron image exhibits shape resolution when a polygon can be recognized as such in the image. Roughly, the particle diameter—defined as the diameter of a circle of the same area as the particle—must exceed the resolution by a factor equal to the number of sides on the polygon.

shatter cracks.

See flakes.

shear bands.

Bands in which deformation has been concentrated inhomogeneously in sheets that extend across regional groups of grains. Only one system is usually present in each regional group of grains, different systems being present in adjoining groups. The bands are noncrystallographic and form on planes of maximum shear stress (55° to the compression direction). They carry most of the deformation at large strains. Compare with microbands. A region of intense local shear that spans several grains.

shelling.

A mechanism of deterioration of coated abrasive products in which entire abrasive grains are removed from the cement coating that held the abrasive to the backing layer of the product.

shielding.

In an electron-optical instrument, the protection of the electron beam from distortion due to extraneous electric and magnetic fields. Because the metallic column of the microscope is at ground potential, it provides electrostatic shielding. Magnetic shields may be made of a high-permeability material.

shortness.

A form of brittleness in metal. It is designated as “cold,” “hot,” and “red” to indicate the temperature range in which the brittleness occurs.

short-term etching.

Etching times of seconds to a few minutes.

shrink etching.

Precipitation on grain surfaces. Shrinkage takes place during drying, which cracks the layer formed during etching. Crack orientation depends on the underlying structure.

sigma (σ).

Solid phase found originally in binary iron-chromium alloys that is in stable equilibrium below 820 °C (1510 °F). It is now used to identify any structure having the same complex body-centered crystal structure.

silicate-type inclusions.

Inclusions composed essentially of silicate glass, normally plastic at forging and hot-rolling temperatures, that appear in steel in the wrought condition as small elongated inclusions usually dark in color under reflected light as normally observed.

simple (lattices).

Having similar atoms or groups of atoms separated by integral translations only.

skid-polishing process.

A mechanical polishing process in which the surface to be polished is made to skid across a layer of paste, consisting of the abrasive and the polishing fluid, without contacting the fibers of the polishing cloth.

slag.

A nonmetallic product resulting from mutual dissolution of flux and nonmetallic impurities in smelting and refining operations.

slip.

Plastic deformation by the irreversible shear displacement (translation) of one part of a crystal relative to another in a definite crystallographic direction and usually on a specific crystallographic plane. Sometimes termed glide.

slip band.

A group of parallel slip lines so closely spaced as to appear as a single line when observed under an optical microscope. See also slip line.

slip direction.

The crystallographic direction in which the translation of slip takes place.

slip line.

The trace of the slip plane on the viewing surface; the trace is usually observable only if the surface has been polished before deformation. The usual observation on metal crystals (under an optical microscope) is of a cluster of slip lines known as a slip band.

slip plane.

The crystallographic plane in which slip occurs in a crystal.

slivers.

Abrasive particles of rodlike shape with an aspect ratio greater that 3. The term is applied particularly to diamond abrasives.

solidification range.

The temperature range between the liquidus and the solidus.

solidification shrinkage crack.

A crack that forms, usually at elevated temperature, because of the shrinkage stresses accumulating during solidification of a metal casting. Also termed hot crack.

solid solution.

A solid crystalline phase containing two or more chemical species in concentrations that may vary between limits imposed by the phase equilibrium.

solidus.

In a phase diagram, the locus of points representing the temperatures at which various components finish freezing on cooling or begin to melt on heating.

solute.

The component of a liquid or solid solution that is present to the lesser or minor extent; the component that is dissolved in the solvent.

solution.

In a chemical system, a phase existing over a range of composition.

solution heat treatment.

A heat treatment in which an alloy is heated to a suitable temperature, held at that temperature long enough to cause one or more constituents to enter into solid solution, then cooled rapidly enough to hold these constituents in solution.

solvent.

The component of a liquid or solid solution that is present to the greater or major extent; the component that dissolves the solute.

solvus.

In a phase or equilibrium diagram, the locus of points representing the temperature at which solid phases with various compositions coexist with other solid phases, that is, the limits of solid solubility.

sorbite (obsolete).

A fine mixture of ferrite and cementite produced by regulating the rate of cooling of steel or by tempering steel after hardening. The former is very fine pearlite that is difficult to resolve under the microscope; the latter is tempered martensite.

source (x-rays).

The area emitting primary x-rays in a diffraction experiment. The actual source is always the focal spot of the x-ray tube, but the virtual source may be a slit or pinhole, depending on the conditions of the experiment.

space-charge aberration.

An aberration resulting from the mutual repulsion of the electrons in a beam. This aberration is most noticeable in low-voltage, high-current beams. This repulsion acts as a negative lens, causing rays, which were originally parallel, to diverge.

space lattice.

See lattice.

spacing (lattice planes).

See interplanar distance.

spatial grain size.

The average size of the three-dimensional grains, as opposed to the more conventional grain size determined by a simple average of observations made on a cross section of the material.

specimen chamber (electron optics).

The compartment located in the column of the electron microscope in which the specimen is placed for observation.

specimen charge (electron optics).

The electrical charge resulting from the impingement of electrons on a nonconducting specimen.

specimen contamination (electron optics).

The contamination of the specimen caused by the condensation on it of residual vapors in the microscope under the influence of electron bombardment.

specimen distortion (electron optics).

A physical change in the specimen caused by desiccation or heating by the electron beam.

specimen grid.

See specimen screen.

specimen holder (electron optics).

A device that supports the specimen and specimen screen in the correct position in the specimen chamber of the microscope.

specimen screen (electron optics).

A disk of fine screen, usually 200-mesh stainless steel, copper, or nickel, that supports the replica or specimen support film for observation in the microscope.

specimen stage.

The part of the microscope that supports the specimen holder and specimen in the microscope and can be moved in a plane perpendicular to the optic axis from outside the column.

specimen strain.

A distortion of the specimen resulting from stresses occurring during preparation or observation. In electron metallography, strain may be caused by stretching during removal of a replica or during subsequent washing or drying.

specular reflection.

The condition in which all the incident light is reflected at the same angle as the angle of the incident light relative to the normal at the point of incidence. The reflection surface then appears bright, or mirrorlike, when viewed with the naked eye. Sometimes termed regular reflection.

spherical aberration.

The zonal aberrations of a lens referred to an axial point. When rays from a point on the axis passing through the outer lens zones are focused closer to the lens than rays passing the central zones, the lens suffers positive spherical aberration. If the condition is reversed, that is, the outer zones have a longer focal length than the inner zones, the lens has negative spherical aberration. In the first instance, the lens is uncorrected or undercorrected; in the second, overcorrected.

spherical projection.

A projection in which the orientation of a crystal plane is represented by the point at which the plane normal intersects a sphere drawn with the crystal as the center.

spheroidal graphite.

Graphite of spheroidal shape with a polycrystalline radial structure. This structure can be obtained, for example, by adding cerium or magnesium to the melt.

spheroidite.

An aggregate of iron or alloy carbides of essentially spherical shape dispersed throughout a matrix of ferrite.

spheroidized structure.

A microstructure consisting of a matrix containing spheroidal particles of another constituent.

spheroidizing.

Heating and cooling to produce a spheroidal or globular form of carbide in steel.

spinodal curve.

A graph of the realizable limit of the supersaturation of a solution.

spinodal structure.

A fine, homogeneous mixture of two phases that form by the growth of composition waves in a solid solution during suitable heat treatment. The phases of a spinodal structure differ in composition from each other and from the parent phase but have the same crystal structure as the parent phase.

sputtering.

The production of specimens in the form of thin films by deposition from a cathode subjected to positive-ion bombardment.

stage.

A device for holding a specimen in the desired position in the optical path.

staining.

Precipitation etching that causes contrast by distinctive staining of microconstituents; different interference colors originate from surface layers of varying thickness. Identifies inhomogeneities.

standard grain-size micrograph.

A micrograph taken of a known grain size at a known magnification that is used to determine grain size by direct comparison with another micrograph or with the image of a specimen.

steadite.

A hard structural constituent of cast iron that consists of a binary eutectic of ferrite, containing some phosphorus in solution, and iron phosphide (Fe_3P). The eutectic consists of 10.2% P and 89.8% Fe. The melting temperature is 1050 °C (1920 °F).

step aging.

Aging at two or more temperatures by steps, without cooling to room temperature after each step. Compare with interrupted aging and progressive aging.

stepdown test.

A test involving the preparation of a series of machined steps progressing inward from the surface of a bar for the purpose of detecting by visual inspection the internal laminations caused by inclusion segregates.

stereo angle.

One half of the angle through which the specimen is tilted when taking a pair of stereoscopic micrographs. The axis of rotation lies in the plane of the specimen.

stereoscopic micrographs.

A pair of micrographs of the same area but taken from different angles so that the two micrographs, when properly mounted and viewed, reveal the structures of the objects in their three-dimensional relationships.

stereoscopic specimen holder.

A specimen holder designed for the purpose of making stereoscopic micrographs. It makes possible the tilting of the specimen through the stereo angle.

strain aging.

Aging induced by cold work.

strain etching.

Etching that provides information on deformed and undeformed areas if present side by side. Strained areas show increased segregation of precipitates.

strain hardening.

An increase in hardness and strength caused by plastic deformation at temperatures below the recrystallization range.

strain markings.

Manifestations of prior plastic deformation visible after etching of a metallographic section. These markings may be referred to as slip strain markings, twin strain markings, and so on, to indicate the specific deformation mechanism of which they are a manifestation.

stress relieving.

Heating to a suitable temperature, holding long enough to reduce residual stresses, then cooling slowly enough to minimize the development of new residual stresses.

stretcher strains.

Elongated markings that appear on the surfaces of some materials when they are deformed just past the yield point. These markings lie approximately parallel to the direction of maximum shear stress and are the result of localized yielding. See also Lüders lines.

stringer.

A microstructural configuration of alloy constituents or foreign nonmetallic material lined up in the direction of working.

structure.

As applied to a crystal, the shape and size of the unit cell and the location of all atoms within the unit cell. As applied to microstructure, the size, shape, and arrangement of phases.

structure factor, *F*.

The ratio of the amplitude of the wave scattered by all the atoms of a unit cell to the amplitude of the wave scattered by a single electron.

subboundary structure (subgrain structure).

A network of low-angle boundaries, usually with misorientations less than 1° within the main grains of a microstructure.

subcritical annealing.

An annealing treatment in which a steel is heated to a temperature below the A_1 temperature, then cooled slowly to room temperature. See also transformation temperature.

subgrain.

A portion of a crystal or grain slightly different in orientation from adjoining portions of the same crystal. Generally, adjoining subgrains are separated by low-angle boundaries. Nearly empty volumes surrounded by higher-angle boundaries that fill spaces external to the cell blocks.

submicroscopic.

Below the resolution of the microscope.

substitutional element.

An alloying element with an atomic size and other features similar to the solvent that can replace or substitute for the solvent atoms in the lattice and form a significant region of solid solution in the phase diagram.

substitutional solid solution.

A solid solution in which the solvent and solute atoms are located randomly at the atom sites in the crystal structure of the solution.

substrate.

The layer of metal underlying a coating, regardless of whether the layer is base metal.

sulfide spheroidization.

A stage of overheating in which sulfide inclusions are partly or completely spheroidized.

sulfide-type inclusions.

In steels, nonmetallic inclusions composed essentially of manganese iron sulfide solid solutions (Fe,Mn)S. They are characterized by plasticity at hot-rolling and forging temperatures and, in the hot-worked product, appear as dove-gray elongated inclusions varying from a threadlike to oval outline.

sulfur print.

A macrographic method of examining distribution of sulfide inclusions. See also print etching.

supercooling.

Cooling to a temperature below that of an equilibrium phase transformation without the transformation taking place. Also termed undercooling.

superheating.

(1) Heating a phase to a temperature above that of a phase transformation without the transformation taking place. (2) Heating molten metal to a temperature above the normal casting temperature to obtain more complete refining or greater fluidity.

superlattice.

See ordered structure.

swabbing.

Wiping the sample surface with cotton saturated with the etchant; this will simultaneously remove undesired reaction products.

syntectic equilibrium.

A reversible univariant transformation in which a solid phase that is stable only at lower temperature decomposes into two conjugate liquid phases that remain stable at higher temperature.

system (crystal).

See crystal system.

T

tape replica method (faxfilm).

A method of producing a replica by pressing the softened surface of tape or plastic sheet material onto the surface to be replicated.

taper section.

A section made at an acute angle to a surface of interest, achieving a geometrical magnification of depth. A sectioning angle of 5° 43′ achieves a depth magnification of 10:1.

target (x-ray).

That part of an x-ray tube that the electrons strike and from which x-rays are emitted.

temper carbon.

Clusters of finely divided graphite, such as that found in malleable iron, that are formed as a result of decomposition of cementite, for example, by heating white cast iron above the ferrite-austenite transformation temperature and holding at these temperatures for a considerable period of time. Also termed annealing carbon. See also nodular graphite.

tempered layer.

A surface or subsurface layer in a steel specimen that has been tempered by heating during some stage of the preparation sequence. When observed in a section after etching, the layer appears darker than the base material.

tempered martensite.

The decomposition products that result from heating martensite below the ferrite-austenite transformation temperature. Under the optical microscope, darkening of the martensite needles is observed in the initial stages of tempering. Prolonged tempering at high temperatures produces spheroidized carbides in a matrix of ferrite. At the higher resolution of the electron microscope, the initial stage of tempering is observed to result in a structure containing a precipitate of fine ε iron carbide particles. At approximately 260 °C (500 °F), a transition occurs to a structure of larger and elongated cementite particles in a ferrite matrix. With further tempering at higher temperatures, the cementite particles become spheroidal, decreased in number, and increased in size.

tempering.

In heat treatment, reheating hardened steel to some temperature below the eutectoid temperature to decrease hardness and/or increase toughness.

temper rolling.

Light cold rolling of sheet steel to improve flatness, to minimize the formation of stretcher strains, and to obtain a specified hardness or temper.

terminal solid solution.

In a multicomponent system, any solid phase of limited composition range that includes the composition of one of the components of the system.

ternary system.

The complete series of compositions produced by mixing three components in all proportions.

tetragonal.

Having three mutually perpendicular axes, two equal in length and unequal to the third.

texture.

In a polycrystalline aggregate, the state of distribution of crystal orientations. In the usual sense, it is synonymous with preferred orientation, in which the distribution is not random.

thermal etching.

Annealing the specimen in a vacuum or inert atmosphere. This is a preferred technique for high-temperature microscopy and for ceramics.

thermionic cathode gun.

An electron gun that derives its electrons from a heated filament, which may also serve as the cathode. Also termed hot cathode gun.

thermionic emission.

The ejection of a stream of electrons from a hot cathode, usually under the influence of an electrostatic field.

thermocouple.

Two dissimilar electrical conductors so joined as to produce a thermal electromotive force when the junctions are at different temperatures.

time-temperature curve.

A curve produced by plotting time against temperature.

time-temperature-transformation (TTT) diagram.

See isothermal transformation (IT) diagram.

tinting.

See heat tinting.

transcrystalline.

See intracrystalline.

transcrystalline cracking.

Cracking or fracturing that occurs through or across a crystal. Also termed intracrystalline cracking.

transformation ranges.

Those ranges of temperature within which austenite forms during heating and transforms during cooling. The two ranges are distinct, sometimes overlapping but never coinciding. The limiting temperatures of the ranges depend on the composition of the alloy and on the rate of change of temperature, particularly during cooling. See also transformation temperature.

transformation temperature.

The temperature at which a change in phase occurs. The term is sometimes used to denote the limiting temperature of a transformation range. The following symbols are used for iron and steels:

Ac_{cm}.

In hypereutectoid steel, the temperature at which the solution of cementite in austenite is complete during heating.

Ac_1.

The temperature at which austenite begins to form during heating.

Ac_3.

The temperature at which transformation of ferrite to austenite is complete during heating.

Ac_4.

The temperature at which austenite transforms to δ-ferrite during heating.

Ae_1, Ae_3, Ae_{cm}, Ae_4.

The temperatures of phase changes at equilibrium.

Ar_{cm}.

In hypereutectoid steel, the temperature at which precipitation of cementite begins during cooling.

Ar_1.

The temperature at which transformation of austenite to ferrite or to ferrite plus cementite is complete during cooling.

Ar_3.

The temperature at which austenite begins to transform to ferrite during cooling.

Ar_4.

The temperature at which δ-ferrite transforms to austenite during cooling.

M_s.

The temperature at which transformation of austenite to martensite begins during cooling.

M_f.

The temperature, during cooling, at which transformation of austenite to martensite is substantially complete.

transformed beta.

A local or continuous structure consisting of decomposition products arising by nucleation and growth processes during cooling from above the local or overall β transus. Primary and regrowth α may be present. Transformed β typically consists of α platelets that may or may not be separated by β phase.

transgranular.

See intracrystalline.

transition phase.

A nonequilibrium state that appears in a chemical system in the course of transformation between two equilibrium states.

transition structure.

In precipitation from solid solution, a metastable precipitate that is coherent with the matrix.

transmission electron microscope.

A microscope in which the image-forming rays pass through (are transmitted by) the specimen being observed.

transmission method.

A method of x-ray or electron diffraction in which the recorded diffracted beams emerge on the same side of the specimen as the transmitted primary beam.

transverse direction.

Literally, "across," usually signifying a direction or plane perpendicular to the direction of working. In rolled plate or sheet, the direction across the width is often called long transverse, and the direction through the thickness, short transverse. See also longitudinal direction and normal direction.

triclinic.

Having three axes of any length, none of the included angles being equal to one another or equal to 90°.

triple curve.

In a P-T diagram, a line representing the sequence of pressure and temperature values along which two conjugate phases occur in univariant equilibrium.

triple point.

The intersection of the boundaries of three adjoining grains, as observed in a section.

troostite.

A previously unresolvable, rapidly etching, fine aggregate of carbide and ferrite produced by tempering martensite at approximately 400 °C (750 °F). The term is variously and erroneously applied to bainite and nodular fine pearlite. Confusion arose because of the similarity in appearance among the three structures before the advent of high-power microscopy. With reference to tool steels, synonymous with upper bainite.

twin.

Two portions of a crystal with a definite orientation relationship; one may be regarded as the parent, the other as the twin. The orientation of the twin is a mirror image of the orientation of the parent across a twinning plane or an orientation that can be derived by rotating the twin portion about a twinning axis. See also annealing twin and mechanical twin.

twin bands.

Bands across the crystal grain, observed on a polished and etched section, where crystallographic orientations have a mirror-image relationship to the orientation of the matrix grain across a composition plane that is usually parallel to the sides of the band.

T-X diagram.

A two-dimensional graph of the isobaric phase relationship in a binary system; the coordinates of the graph are temperature and concentration.

U

ultramicroscopic.

See submicroscopic.

unary system.

Composed of one component.

undercooling.

See supercooling.

unit cell.

A parallelepiped element of crystal structure, containing a certain number of atoms, the repetition of which through space will build up the complete crystal. See also lattice.

univariant equilibrium.

A stable state among several phases equal to one more than the number of components, that is, having one degree of freedom.

V

vacancy.

A structural imperfection in which an individual atom site is temporarily unoccupied.

vapor-deposited replica.

A replica formed of a metal or a salt by the condensation of the vapors of the material onto the surface to be replicated.

variability.

The number of degrees of freedom of a heterogeneous phase equilibrium. Also termed variance.

variance.

See variability.

veining.

A subboundary structure that can be delineated because of the presence of a greater-than-average concentration of precipitate or solute atoms.

vertical illumination.

Light incident on an object from the objective side so that smooth planes perpendicular to the optical axis of the objective appear bright.

vibratory polishing.

A mechanical polishing process in which the specimen is made to move around the polishing cloth by imparting a suitable vibratory motion to the polishing system.

voltage alignment.

A condition of alignment of an electron microscope so that the image expands or contracts symmetrically about the center of the viewing screen when the accelerating voltage is changed. See also alignment.

V-X diagram.

A graph of the isothermal or isobaric phase relationships in a binary system, the coordinates of the graph being specific volume and concentration.

W

wavelength (x-rays).

The minimum distance between points at which the electric vector of an electromagnetic wave has the same value. It is measured along the direction of propagation of the wave, and it is equal to the velocity divided by the frequency. See also electron wavelength.

weld structure.

The microstructure of a weld deposit and heat-affected base metal. See also heat-affected zone.

wet etching.

Development of microstructure with liquids, such as acids, bases, neutral solutions, or mixtures of solutions.

white-etching layer.

A surface layer in a steel that, as viewed in a section after etching, appears whiter than the base metal. The presence of the layer may be due to a number of causes, including plastic deformation induced by machining or surface rubbing, heating during a preparation stage to such an extent that the layer is austenitized and then hardened during cooling, and diffusion of extraneous elements into the surface.

Widmanstätten structure.

A structure characterized by a geometrical pattern resulting from the formation of a new phase along certain crystallographic planes of the parent solid solution. The orientation of the lattice in the new phase is related crystallographically to the orientation of the lattice in the parent phase. The structure

was originally observed in meteorites but is readily produced in many alloys, such as titanium, by appropriate heat treatment.

wipe etching.

See swabbing.

work hardening.

See strain hardening.

working distance.

The distance between the surface of the specimen being examined and the front surface of the objective lens.

X

x-radiation.

Electromagnetic radiation of the same nature as visible light but having a wavelength approximately $\frac{1}{1000}$ that of visible light. Commonly referred to as x-rays.

x-rays.

See x-radiation.

x-ray tube.

A device for the production of x-rays by the impact of high-speed electrons on a metal target.

Z

zephiran chloride.

Aqueous solution; a proprietary material produced in grades containing approximately 12 and 17% (by weight) benzalkonium chloride (alkyl-dimethyl-benzyl-ammonium chloride) as the active constituent, plus some ammonium acetate; also called sephiran chloride; available from pharmacies or pharmaceutical distributors. See benzalkonium chloride.

zone.

Any group of crystal planes that are all parallel to one line, which is called the zone axis.

Copyright © 2005 ASM International®. All Rights Reserved.

Next section in this article >

< Previous section in this article

Glossary of Terms, Vol 9, *ASM Handbook*, ASM International, 2004, p. 1115–1134

Glossary of Terms

Selected References

- B. Bramfitt and A. Benscoter, Glossary, *Metallographer's Guide: Practices and Procedures for Irons and Steels*, ASM International, 2002
- J.R. Davis, Ed., *ASM Materials Engineering Dictionary*, ASM International, 1992
- G. Petzow, *Metallographic Etching*, 2nd ed., ASM International, 1999
- L.E. Samuels, *Metallographic Polishing by Mechanical Methods*, 4th ed., ASM International, 2003
- L.E. Samuels, *Optical Microscopy of Carbon Steels*, ASM International, 1999
- "Standard Definitions of Terms Relating to Heat Treatment of Metals," E 44, *Annual Book of ASTM Standards*, Vol 03.03, ASTM International
- "Standard Definitions of Terms Relating to Metallography," E 7, *Annual Book of ASTM Standards*, Vol 03.03, ASTM International

Abbreviations and Symbols, *Metallography and Microstructures,* Vol 9, *ASM Handbook,* ASM International, 2004, p. 1138–1139

Abbreviations and Symbols

a crystal lattice length along the *a* axis
A ampere
Å angstrom
AA Aluminum Association
ac alternating current
Ac_{cm} in hypereutectoid steel, the temperature at which solution of cementite in austenite is completed during heating
A_1 eutectoid isothermal of austenite in steel (same as Ae;i1)
Ac_1 the temperature at which austenite begins to form during heating
Ac_3 the temperature at which the transformation of ferrite to austenite is completed during heating
Ac_4 the temperature at which austenite transforms to δ-ferrite during heating
ACI Alloy Casting Institute
Ae_{cm}, Ae_1, Ae_3, Ae_4 the temperatures of phase transformations at equilibrium
AFS American Foundrymen's Society
AIME American Institute of Mining, Metallurgical and Petroleum Engineers
AIP American Institute of Physics
AISI American Iron and Steel Institute
AMS Aerospace Material Specification
ANSI American National Standards Institute
APB antiphase boundary
API American Petroleum Institute
Ar_{cm} in hypereutectoid steel, the temperature at which precipitation of cementite starts during cooling
Ar_1 the temperature at which transformation of austenite to ferrite or to ferrite plus cementite is completed during cooling
Ar_3 the temperature at which austenite begins to transform to ferrite during cooling
Ar_4 the temperature at which δ-ferrite transforms to austenite during cooling
ASM American Society for Metals
ASME American Society of Mechanical Engineers
ASTM American Society for Testing and Materials
at.% atomic percent
atm atmosphere
AWS American Welding Society
b crystal lattice length along the *b* axis
b barn (unit of nuclear cross section); Burgers vector
bal balance or remainder
bcc body-centered cubic
bct body-centered tetragonal
BE backscattered electron
BF bright-field (illumination)
BSE backscattered electron
Btu British thermal unit
***BI*c** crystal lattice length along the *c* axis
C coulomb
cal calorie
CCT continuous cooling transformation (diagram)
CDA Copper Development Association
cm centimeter

COE cube-on-edge
conc concentrated
CRT cathode ray tube
dc direct current
DF dark-field (illumination)
diam diameter
DIC differential interference contrast (illumination)
DPH diamond pyramid hardness (Vickers hardness)
e natural log base, 2.71828…
ECM electrochemical machining
EDM electrical discharge machining
EDS energy-dispersive spectroscopy
EDXA energy-dispersive x-ray analysis
EMC electromagnetic casting
EMPA electron microprobe analysis
Eq equation
et al. and others
ETP electrolytic tough pitch (copper)
eV electron volt
F farad
fcc face-centered cubic
Fig. figure
FRTP fire-refined tough pitch (copper)
ft foot
g gram; diffraction vector
G gauss
gcp geometrically close-packed
GdIG gadolinium-iron garnet
GIF graphics interchange format
GP Guinier-Preston (zone)
Gy gray
h hour
HAD high aluminum defect
HAZ heat-affected zone
HB Brinell hardness
hcp hexagonal close-packed
HID high interstitial defect
HK Knoop hardness
HR Rockwell hardness (requires scale designation, such as HRC for Rockwell C hardness)
HSLA high-strength, low-alloy
HV Vickers hardness (diamond pyramid hardness)
Hz hertz
ID inside diameter
in. inch
INCRA International Copper Research Association
ISO International Organization for Standardization
J joule
JPEG Joint Photographic Experts Group
JPG file extension for JPEG files
k wave vector
K Kelvin
kbar kilobar (pressure)
kg kilogram
kPa kilopascal

ksi kips per square inch (1000 pounds per square inch)
kV kilovolt
L liter
lb pound
log common logarithm (base 10)
ln natural logarithm (base *e*)
m meter
mA milliampere
max maximum
$\mathbf{M_f}$ the temperature at which martensite formation finishes during cooling
min minimum; minute
MJ megajoule
mL milliliter
mm millimeter
MPa megapascal
MPIF Metal Powder Industries Federation
ms millisecond
$\mathbf{M_s}$ the temperature at which martensite starts to form from austenite on cooling
n refractive index
N Newton
N normal (solution)
NA numerical aperture
NACE National Association of Corrosion Engineers
NASA National Aeronautics and Space Administration
NBS National Bureau of Standards
nm nanometer
No. number
NRC Nuclear Regulatory Commission
ns nanosecond
OD outside diameter
OFE oxygen-free electronic (copper)
OFHC oxygen-free high-conductivity (copper)
ORNL Oak Ridge National Laboratory
OSHA Occupational Safety and Health Administration
oz ounce
p page
Pa pascal
pH negative logarithm of hydrogen-ion activity
PH precipitation-hardenable
pixel picture element
P/M powder metallurgy
ppm parts per million
psi pounds per square inch
PVC polyvinyl chloride
R roentgen
RE rare earth (elements)
Ref reference
REG rare-earth garnet
rem roentgen equivalent man; remainder or balance
rpm revolutions per minute
s second
SAE Society of Automotive Engineers
SCE saturated calomel electrode
SE secondary electrons

SEM scanning electron microscopy
SHE standard hydrogen electrode
SI Système International d' Unités
SME Society of Manufacturing Engineers
STEM scanning transmission electron microscopy
t time; thickness
T tesla
tcp topologically close-packed
TEM transmission electron microscopy
TIFF tagged image file format
TTT time-temperature transformation (diagram)
UNS Unified Numbering System (ASTM-SAE)
V volt
vol volume
vol;pc volume percent
W watt
wt;pc weight percent
YIG yttrium-iron garnet
yr year
° degree; angular measure
°C degree Celsius (centigrade)
°F degree Fahrenheit
↔ direction of reaction
÷ divided by
= equals
≈ approximately equals
≠ not equal to
≡ identical with
> greater than
» much greater than
≥ greater than or equal to
∫ integral of
∞ infinity
α varies as; is proportional to
< less than
« much less than
≤ less than or equal to
± maximum deviation
- minus; negative ion charge
× multiplied by; diameters (magnification)
· multiplied by
/ per
% percent
+ plus; in addition to; positive ion charge
√ square root of
~ similar to; approximately
µF microfarad
µin. microinch
µm micron (micrometer)
µs microsecond

Greek Alphabet

A, α alpha
B, β beta
Γ, γ gamma

Δ, δ delta
E, ε epsilon
Z, ζ zeta
H, η eta
Θ, θ theta
I, ι iota
K, κ kappa
Λ, λ lambda
M, μ mu
N, ν nu
Ξ, ξ xi
O, o omicron
Π, π pi
P, ρ rho
Σ, σ sigma
T, τ tau
Y, υ upsilon
Φ, φ phi
X, χ chi
Ψ, ψ psi
Ω, ω omega